FORTY-FOURTH ANNUAL REPORT

OF THE

NATIONAL ADVISORY COMMITTEE FOR AERONAUTICS

1958

ADMINISTRATIVE REPORT
INCLUDING TECHNICAL REPORTS

Nos. 1342 to 1392

(Final Report)

UNITED STATES
GOVERNMENT PRINTING OFFICE
WASHINGTON : 1959

For sale by the Superintendent of Documents, U.S. Government Printing Office, Washington 25 D.C. — Price $10.50 (Buckram)

CONTENTS

	Page
Letter of Transmittal	v
Letter of Submittal	vii
Forty-fourth Annual Report	ix
Part I. Technical Activities	1
The NACA—What It Is and How It Operates	1
Forty Years of Aeronautical Research	3
The Following Years, 1955–58	29
Aerodynamic Research	31
Power Plants for Aircraft	45
Aircraft, Missile, and Spacecraft Construction	55
Operating Problems	61
Research Publications	67
Part II. Committee Organization and Membership	83
Part III. Financial Report	94
Part IV. Final Meeting of NACA	95
Appendix	
National Aeronautics and Space Act of 1958, approved July 29, 1958	105
Proclamation Making Said Act Effective at Close of Business September 30, 1958	115
Technical Reports	117

TECHNICAL REPORTS

No.		Page
1342.	A Variational Theorem for Creep with Applications to Plates and Columns. By J. Lyell Sanders, Jr., Harvey G. McComb, Jr., and Floyd R. Schlechte, NACA	117
1343.	A Phenomenological Relation Between Stress, Strain Rate, and Temperature for Metals at Elevated Temperatures. By Elbridge Z. Stowell, NACA	125
1344.	A Simplified Method for Approximating the Transient Motion in Angles of Attack and Sideslip During a Constant Rolling Maneuver. By Leonard Sternfield, NACA	131
1345.	The Response of an Airplane to Random Atmospheric Disturbances. By Franklin W. Diederich, NACA	142
1346.	Differential Equations of Motion for Combined Flapwise Bending, Chordwise Bending, and Torsion of Twisted Nonuniform Rotor Blades. By John C. Houbolt and George W. Brooks, NACA	179
1347.	Ditching Investigations of Dynamic Models and Effects of Design Parameters on Ditching Characteristics. By Lloyd J. Fisher and Edward L. Hoffman, NACA	197
1348.	Ground Simulator Studies of the Effects of Valve Friction, Stick Friction, Flexibility, and Backlash on Power Control System Quality. By B. Porter Brown, NACA	225
1349.	A Low-Speed Experimental Investigation of the Effect of a Sandpaper Type of Roughness on Boundary-Layer Transition. By Albert E. von Doenhoff and Elmer A. Horton, NACA	239
1350.	Methods for Obtaining Desired Helicopter Stability Characteristics and Procedures for Stability Predictions. By F. B. Gustafson and Robert J. Tapscott, NACA	255
1351.	Theory of Self-Excited Mechanical Oscillations of Helicopter Rotors with Hinged Blades. By Robert P. Coleman and Arnold M. Feingold, NACA	267
1352.	Effect of Fuel Variables on Carbon Formation in Turbojet-Engine Combustors. By Edmund R. Jonash, Jerrold D. Wear, and William P. Cook, NACA	309
1353.	An Experimental Investigation of Sting-Support Effects on Drag and a Comparison with Jet Effects at Transonic Speeds. By Maurice S. Cahn, NACA	327
1354.	Effect of Chord Size on Weight and Cooling Characteristics of Air-Cooled Turbine Blades. By Jack B. Esgar, Eugene F. Schum, and Arthur N. Curren, NACA	359
1355.	A Theoretical and Experimental Study of Planing Surfaces Including Effects of Cross Section and Plan Form. By Charles L. Shuford, Jr., NACA	373
1356.	Investigation of Separated Flows in Supersonic and Subsonic Streams with Emphasis on the Effect of Transition. By Dean R. Chapman, Donald M. Kuehn, and Howard K. Larson, NACA	419
1357.	Experimental Determination of Effects of Frequency and Amplitude on the Lateral Stability Derivatives for a Delta, a Swept, and an Unswept Wing Oscillating in Yaw. By Lewis R. Fisher, NACA	461
1358.	On Flow of Electrically Conducting Fluids Over a Flat Plate in the Presence of a Transverse Magnetic Field. By Vernon J. Rossow, NACA	489
1359.	Thin Airfoil Theory Based on Approximate Solution of the Transonic Flow Equation. By John R. Spreiter and Alberta Y. Alksne, NACA	509
1360.	Growth of Disturbances in a Flame-Generated Shear Region. By Perry L. Blackshear, Jr., NACA	546
1361.	Approximate Analysis of Effects of Large Deflections and Initial Twist on Torsional Stiffness of a Cantilever Plate Subjected to Thermal Stresses. By Richard R. Heldenfels and Louis F. Vosteen, NACA	593
1362.	Theoretical Combustion Performance of Several High-Energy Fuels for Ramjet Engines. By Leonard K. Tower, Roland Breitwieser, and Benson E. Gammon, NACA	605
1363.	Origin and Prevention of Crash Fires in Turbojet Aircraft. By I. Irving Pinkel, Solomon Weiss, G. Merritt Preston, and Gerard J. Pesman, NACA	623
1364.	Measurement of Static Pressure on Aircraft. By William Gracey, NACA	643
1365.	A Correlation of Results of a Flight Investigation With Results of an Analytical Study of Effects of Wing Flexibility on Wing Strains Due to Gusts. By C. C. Shufflebarger, Chester B. Payne, and George L. Cahen, NACA	669
1366.	The Mechanism of Thermal-Gradient Mass Transfer in the Sodium Hydroxide—Nickel System. By Charles E. May, NACA	683
1367.	Calculated and Measured Stresses in Simple Panels Subject to Intense Random Acoustic Loading Including the Near Noise Field of a Turbojet Engine. By Leslie W. Lassiter and Robert W. Hess, NACA	703
1368.	Systematic Two-Dimensional Cascade Tests of NACA 65-Series Compressor Blades at Low Speeds. By James C. Emery, L. Joseph Herrig, John R. Erwin, and A. Richard Felix, NACA	713
1369.	Blowing-Type Boundary-Layer Control as Applied to the Trailing-Edge Flaps of a 35° Swept-Wing Airplane. By Mark W. Kelly, Seth B. Anderson, and Robert C. Innis, NACA	799
1370.	Area-Suction Boundary-Layer Control as Applied to the Trailing-Edge Flaps of a 35° Swept-Wing Airplane. By Woodrow L. Cook, Seth B. Anderson, and George E. Cooper, NACA	823
1371.	Investigation of Some Wake Vortex Characteristics of an Inclined Ogive-Cylinder Body at Mach Number 2. By Leland H. Jorgensen and Edward W. Perkins, NACA	857

No.		Page
1372.	A Method of Computing the Transient Temperature of Thick Walls From Arbitrary Variation of Adiabatic-Wall Temperature and Heat-Transfer Coefficient. By P. R. Hill, NACA	877
1373.	Theoretical Analysis of Total-Pressure Loss and Airflow Distribution for Tubular Turbojet Combustors with Constant Annulus and Liner Cross-Sectional Areas. By Charles C. Graves and Jack S. Grobman, NACA	899
1374.	The Similarity Rules for Second-Order Subsonic and Supersonic Flow. By Milton D. Van Dyke, NACA	925
1375.	A Wind-Tunnel Investigation of the Aerodynamic Characteristics of a Full-Scale Supersonic-Type Three-Blade Propeller at Mach Numbers to 0.96. By Albert J. Evans and George Liner, NACA	933
1376.	Elliptic Cones Alone and With Wings at Supersonic Speeds. By Leland H. Jorgensen, NACA	975
1377.	Measurements of Free-Space Oscillating Pressures Near Propellers at Flight Mach Numbers to 0.72. By Max C. Kurbjun and Arthur W. Vogeley, NACA	999
1378.	A Method for Simulating the Atmospheric Entry of Long-Range Ballistic Missiles. By A. J. Eggers, Jr., NACA	1009
1379.	Compressible Laminar Boundary Layer Over a Yawed Infinite Cylinder With Heat Transfer and Arbitrary Prandtl Number. By Eli Reshotko and Ivan E. Beckwith, NACA	1016
1380.	An Analysis of Pressure Studies and Experimental and Theoretical Downwash and Sidewash Behind Five Pointed-Tip Wings at Supersonic Speeds. By William B. Boatright, NACA	1067
1381.	A Study of the Motion and Aerodynamic Heating of Ballistic Missiles Entering the Earth's Atmosphere at High Supersonic Speeds. By H. Julian Allen and A. J. Eggers, Jr., NACA	1125
1382.	A Comparative Analysis of the Performance of Long-Range Hypervelocity Vehicles. By Alfred J. Eggers, Jr., H. Julian Allen, and Stanford E. Neice, NACA	1141
1383.	Survey of Hydrogen Combustion Properties. By Isadore L. Drell and Frank E. Belles, NACA	1161
1384.	A Summary of Preliminary Investigations Into the Characteristics of Combustion Screech in Ducted Burners. By Lewis Laboratory Staff, NACA	1195
1385.	Drag Minimization for Wings and Bodies in Supersonic Flow. By Max. A. Heaslet and Franklyn B. Fuller, NACA	1213
1386.	Investigation of the Drag of Various Axially Symmetric Nose Shapes of Fineness Ratio 3 for Mach Numbers from 1.24 to 7.4. By Edward W. Perkins, Leland H. Jorgensen, and Simon C. Sommer, NACA	1231
1387.	Full-Scale Investigation of Several Jet-Engine Noise-Reduction Nozzles. By Willard D. Coles and Edmund E. Callaghan, NACA	1249
1388.	NACA Research on Slurry Fuels. By M. L. Pinns, W. T. Olson, H. C. Barnett, and R. Breitwieser, NACA	1273
1389.	Characteristics of the Langley 8-Foot Transonic Tunnel With Slotted Test Section. By Ray H. Wright, Virgil S. Ritchie, and Albin O. Pearson, NACA	1297
1390.	Incompressible Flutter Characteristics of Representative Aircraft Wings. By C. H. Wilts, California Institute of Technology	1385
1391.	Investigation of a Nonlinear Control System. By I. Flügge-Lotz, C. F. Taylor, and H. E. Lindberg, Stanford University	1423
1392.	Boron and Zirconium From Crucible Refractories in a Complex Heat-Resistant Alloy. By R. F. Decker, John P. Rowe, and J. W. Freeman, University of Michigan	1457

Letter of Transmittal

To the Congress of the United States:

In compliance with the provisions of the Act of March 3, 1915, as amended, which established the National Advisory Committee for Aeronautics, I transmit herewith the Forty-fourth and Final Annual Report of the Committee for the Fiscal Year 1958. This report covers the activities of the Committee through the close of business September 30, 1958, when it was superseded by the National Aeronautics and Space Administration.

The National Advisory Committee for Aeronautics is to be commended for its many contributions to the progress of aeronautical science in the United States and for the spirit of teamwork in aeronautics it has inspired among leaders in science, the military and industry. I wish also to acknowledge at this time the excellent work and dedication of the Committee's research staff who, over the years, have given unstintingly of their talents in a manner which reflects credit upon them and all other civil service personnel of the United States.

DWIGHT D. EISENHOWER.

THE WHITE HOUSE,
APRIL 27, 1959.

Letter of Submittal

NATIONAL ADVISORY COMMITTEE FOR AERONAUTICS,
WASHINGTON, D.C., *September 30, 1958.*

DEAR MR. PRESIDENT:

In compliance with the act of Congress approved March 3, 1915, as amended (U.S.C. title 50, sec. 151), I submit herewith the Forty-fourth Annual Report of the National Advisory Committee for Aeronautics for 1958.

At the close of business on this date the National Advisory Committee for Aeronautics goes out of existence. Under the terms of the National Aeronautics and Space Act of 1958, the property, facilities, and personnel (other than the members of the Committee) are absorbed in the establishment of the new National Aeronautics and Space Administration. This is, therefore, the concluding Annual Report of the National Advisory Committee for Aeronautics.

Respectfully submitted.

JAMES H. DOOLITTLE,
Chairman.

THE PRESIDENT,
The White House, Washington, D.C.

Preceding Page Blank

National Advisory Committee for Aeronautics

Headquarters, 1512 H Street NW., Washington 25, D.C.

Created by Act of Congress approved March 3, 1915, for the supervision and direction of the scientific study of the problems of flight (U.S. Code, title 50, sec. 151). Its membership was increased from 12 to 15 by act approved March 2, 1929, and to 17 by act approved May 25, 1948. The members have been appointed by the President and serve as such without compensation.

JAMES H. DOOLITTLE, Sc. D., Vice President, Shell Oil Co., Chairman
LEONARD CARMICHAEL, Ph. D., Secretary, Smithsonian Institution, Vice Chairman

ALLEN V. ASTIN, Ph. D., Director, National Bureau of Standards.
PRESTON R. BASSETT, D. Sc.
DETLEV W. BRONK, Ph. D., President, Rockefeller Institute for Medical Research.
FREDERICK C. CRAWFORD, Sc. D., Chairman of the Board, Thompson Products, Inc.
WILLIAM V. DAVIS, Jr., Vice Admiral, U.S. Navy (detached May 22, 1958, as Deputy Chief of Naval Operations (Air) and NACA membership terminated).
PAUL D. FOOTE, Ph. D., Assistant Secretary of Defense (Research and Engineering).
WELLINGTON T. HINES, Rear Admiral, U.S. Navy, Deputy and Assistant Chief of the Bureau of Aeronautics.
JEROME C. HUNSAKER, Sc. D., Massachusetts Institute of Technology.
CHARLES J. MCCARTHY, S.B., Chairman of the Board, Chance Vought Aircraft, Inc.
DONALD L. PUTT, Lieutenant General (retired from U.S. Air Force June 30, 1958, from service as Deputy Chief of Staff, Development, and NACA membership terminated).
JAMES T. PYLE, A.B., Administrator of Civil Aeronautics.
FRANCIS W. REICHELDERFER, Sc. D., Chief, U.S. Weather Bureau.
EDWARD V. RICKENBACKER, Sc. D., Chairman of the Board, Eastern Air Lines, Inc.
LOUIS S. ROTHSCHILD, Ph. B., Under Secretary of Commerce for Transportation.
THOMAS D. WHITE, General, U.S. Air Force, Chief of Staff.

HUGH L. DRYDEN, Ph. D., *Director*
JOHN W. CROWLEY, Jr., B.S., *Associate Director for Research*

JOHN F. VICTORY, LL.D., *Executive Secretary*
EDWARD H. CHAMBERLIN, *Executive Officer*

HENRY J. E. REID, D. Eng., Director, Langley Aeronautical Laboratory, Langley Field, Va.
SMITH J. DEFRANCE, D. Eng., Director, Ames Aeronautical Laboratory, Moffett Field, Calif.
EDWARD R. SHARP, Sc. D., Director, Lewis Flight Propulsion Laboratory, Cleveland, Ohio
WALTER C. WILLIAMS, B.S., Chief, High-Speed Flight Station, Edwards, Calif.

FORTY-FOURTH ANNUAL REPORT
National Advisory Committee for Aeronautics

WASHINGTON, D.C., *September 30, 1958.*

To the Congress of the United States:

In accordance with act of Congress, approved March 3, 1915, as amended (U.S.C., title 50, sec. 151), which established the National Advisory Committee for Aeronautics, the Committee submits its Forty-fourth Annual Report for the fiscal year 1958. This is the Committee's final report to the Congress.

The National Aeronautics and Space Act of 1958 (Public Law 85–568) provides in section 301 that the NACA "shall cease to exist" and "all functions, powers, duties, and obligations, and all real and personal property, personnel (other than members of the Committee), funds, and records" of the NACA shall be transferred to the National Aeronautics and Space Administration. The aforesaid act provides that "this section shall take effect 90 days after the date of the enactment of this act, or on any earlier date on which the Administrator shall determine, and announce by proclamation published in the Federal Register, that the Administration has been organized and is prepared to discharge the duties and exercise the powers conferred upon it by this act." The Administrator, Hon. T. Keith Glennan, has advised the Committee of his intention to issue such proclamation, effective October 1, 1958.

During the 43 years that the NACA was charged with responsibility to "supervise and direct the scientific study of the problems of flight, with a view to their practical solution," its great strength, as reflected in the advances in aeronautics resulting from its researches, has been the high caliber of its scientists, engineers, and supporting personnel. The gratitude of the entire Nation is due these public servants.

There is another reason—subordinate only to that cited above—why the NACA was so successful in accomplishing the technological progress in aeronautics that enabled the United States to achieve and maintain superiority in the air. This was the support the Congress gave over the years, appropriating funds for construction of highly specialized laboratory facilities. These were provided for the study of new problems posed by the steady increases in aircraft performance that earlier work had made possible.

On following pages, there appear brief accounts of the history of the NACA, covering the first 40 years by Dr. J. C. Hunsaker, my predecessor as Chairman, and summarizing activities of the past 3 years, by the undersigned.

The extent of our penetration into space in the next few years will depend in large measure upon how effectively we use knowledge in hand, and upon how hard we work to reach the distant performance goals set for instrumented and man-carrying spacecraft. I know I can speak with confidence and without reservation on behalf of the 8,000 dedicated people of the NACA, who will serve as the nucleus of the National Aeronautics and Space Administration. They will continue to merit the confidence, and the support, of the President, the Congress, and the people of the United States as they perform their new and tremendously important work.

J. H. DOOLITTLE,
Chairman.

526597—60——2

Part I—TECHNICAL ACTIVITIES

THE NACA—WHAT IT IS AND HOW IT OPERATES

During the 43 years since the Congress founded it as an independent Federal agency, the National Advisory Committee for Aeronautics has sought to assess the current stage of development of aircraft, both civil and military; to anticipate the research needs of aeronautics; to build the scientific staff and unique research facilities required for these research needs; and to acquire the needed new knowledge as rapidly as the national interest requires.

By discharging its primary responsibility—scientific laboratory research in aeronautics—the NACA serves the needs of all departments of the Government. The President appoints the 17 unpaid members of the Committee, who report directly to him. They establish policy and plan the research to be carried out by the 7,900 scientists, engineers, and other persons who make up the staff of the agency.

The NACA research programs have both the all-inclusive, long-range objective of acquiring new scientific knowledge essential to assure United States leadership in aeronautics and space and the immediate goal of solving, as quickly as possible, the most pressing problems. In this way, they effectively support the Nation's current aircraft and missile construction program.

Most of the problems to be studied are assigned to the NACA's research centers. The Langley Aeronautical Laboratory in Virginia works on structural, general aerodynamic, and hydrodynamic problems. The Ames Aeronautical Laboratory in California concentrates on high-speed aerodynamics. The Lewis Flight Propulsion Laboratory in Ohio is a center for powerplant studies. At the High-Speed Flight Station in California special fully instrumented research aircraft probe transonic and supersonic problems in flight. The Pilotless Aircraft Research Station at Wallops Island, Va., is a branch of the Langley Laboratory where rocket-powered free-flight models are used to attack aerodynamic problems in the transonic, supersonic, and hypersonic speed ranges.

A major task of the NACA since its beginning in 1915 has been coordinating aeronautical research in the United States. Through the members of the Committee and its 27 technical subcommittees, the NACA links the military and civil government agencies concerned with flight. The aviation industry, allied industries, and scientific institutions are also represented.

Assisting the Committee in determining and coordinating research programs are 4 major and 23 subordinate technical committees with a total membership of nearly 500. Members are chosen because of technical ability, experience, and recognized leadership in a special field. They also serve without pay, in a personal and professional capacity. They furnish valuable assistance in considering problems related to their technological fields, review research in progress at NACA laboratories and in other establishments, recommend new research to be undertaken, and assist in coordinating research programs.

Members of the technical committees and subcommittees and of the Industry Consulting Committee are listed in Part II of this report, beginning on page 83.

Research coordination is also accomplished through frequent discussions by NACA scientists with the staffs of research organizations of the aircraft industry, educational and scientific institutions, and other aeronautical and space agencies. Through a west coast office the NACA maintains close liaison with aeronautical research and engineering staffs in that important aviation area.

The first report of aeronautical research published by the NACA covered a study conducted at the Massachusetts Institute of Technology under a research contract. Throughout its existence, NACA has utilized this means of obtaining the benefits of the special talents, unique facilities, and fresh points-of-view of scientists outside its own laboratories. The resulting independent thought and novel attacks upon research problems are a continuing stimulus to NACA scientists. They produce valuable data and theoretical analyses to complement internal NACA research. Fifty-two reports of sponsored research were published during the fiscal year 1958. During this period the following institutions participated in the program:

Polytechnic Institute of Brooklyn
California Institute of Technology
University of California
Georgia Institute of Technology
University of Illinois
Iowa State College
Johns Hopkins University
Lightning & Transients Research Institute
University of Maryland

Massachusetts Institute of Technology
University of Michigan
University of Minnesota
New York University
Ohio State University
Rensselaer Polytechnic Institute
Southwest Research Institute
Stanford University
Syracuse University
University of Washington

Proposals from such institutions are carefully weighed to assure best use of the limited funds available to the NACA for sponsoring research outside its own facilities. Published research reports of the useful results of this part of the NACA program are distributed as widely as other NACA publications.

Most of NACA's research information is distributed by means of its publications. Technical Notes and Reports are not classified for military security reasons and are available to the public in general. Translations of important foreign research reports appear as Technical Memorandums. The NACA also prepares research reports containing classified information. For reasons of national security, these receive carefully controlled circulation. When such information can be declassified, the research reports may be given wider distribution. Current NACA publications are announced in the NACA Research Abstracts.

Every year the NACA holds a number of technical conferences with representatives of the aviation industry, the universities, and the military services present. Attendance at these conferences is restricted because classified material is presented and the subject matter discussed at each conference is focused on a specific field of interest.

Forty Years of Aeronautical Research

By J. C. HUNSAKER
*Chairman, National Advisory Committee for Aeronautics**
Regent, Smithsonian Institution

FROM THE SMITHSONIAN REPORT
FOR 1955

Before the Wrights' airplane flew, all the elements of the airplane were known: wings, rudders, engine, and propeller. The Wrights showed how to combine a man's senses and reflexes with the controls of a flying machine to make the machine both controllable about its attitude of equilibrium and steerable as desired. The secret of flight was manual control, in a three-dimensional fluid medium, in accordance with visual signals (the pilot's view of the ground and observation of his attitude relative to it—fixed axes of references), and monitored by visual observation of the response to his control actions (feedback). The Wrights' airplane was, however, like the Wrights' bicycles, inherently unstable and was controllable only when it had sufficient forward speed. Controlled by the sight, brain, nerves, and muscles of man, the Wrights' unstable vehicle was the first practical flying machine in the history of the world!

The Wright airplane was quick to respond to control action because it had no righting tendency if disturbed. The pilot was expected to act at once to recover from any disturbance of equilibrium. There was no fixed tail to push it into a safe glide if the engine stopped.

The early pioneers of flight worked with gliders and with self-propelled models. They strove for inherent stability and conceived the ideal to be an inherently stable flying platform on which the pilot need do no more than steer. Pénaud's model gliders of the 1870's, with long tails, were stable; Lanchester developed prior to 1908 a theory of dynamical stability for his model "aerodromes"; Langley flew stable steam-powered models in 1896, and Bryan in 1903 published the dynamical equations of motion for a glider, and criteria for inherent stability. In all cases, stability was found to require a tail and slightly elevated wingtips.

As might be expected from complete and constant dependence on one man's sometimes defective judgments and reactions, the Wright airplane could be tricky and even dangerous, especially in rough air. Furthermore, the gasoline engines of the day were notoriously unreliable. As a result of what later came to be known as the stall, Wright airplanes too often dived into the ground out of control. The press blamed it on an "air pocket" or "hole in the air."

European airplane builders were prompt to copy the Wright's system of control but soon discovered the dangers of instability. They abandoned the Wright's form of structure but retained their system of controls on airplanes shaped more like successful gliders.

The world was astonished in 1909 when Louis Bleriot flew across the English Channel in his little monoplane. It had a long tail, tractor propeller, and wheel landing gear. It was, in fact, the prototype of the airplanes of the next 20 years.

After 1910, with the mounting tension of approaching war, aeronautical development in Britain, France, Germany, Austria, Russia, and Italy was intensively pushed. Scientists, engineers, and industrialists were encouraged by their governments to devote their skills and resources to the new art. European progress was rapid, and at times spectacular.

While development of the airplane in the United States was dependent largely upon the efforts of a host of amateur inventors, there was in Europe a quick recognition of the gains to be had from aeronautical laboratories staffed by competent engineers.

The French were among the first to utilize scientific techniques in aeronuatics. The army's aeronautical laboratory at Chalais-Meudon and Gustav Eiffel's private wind tunnel clarified some of the principles of powered flight. As early as 1904 Riabouchinski had an aeronautical laboratory in Koutchino, Russia, and the same year Ludwig Prandtl began his classic aerody-

*Elected annually and served as chairman, 1941–56.

namic research at Göttingen University, Germany. After 1908, German aeronautical work was rapidly expanded, first at Göttingen and later at the government establishment at Adlershof, near Berlin. Italy provided an aerodynamics laboratory for her Specialist Brigade of Engineers.

Great Britain was relatively late in undertaking a national program of aeronautical research. However, Great Britain could record a full century of experiment. In the first half of the nineteenth century, Sir George Cayley had made important contributions, and Stringfellow and Henson had succeeded, as early as 1848, in flying a steam-powered monoplane model a distance of 120 feet. In 1866 the Aeronautical Society of Great Britain was formed; it served to stimulate research and experiment by individuals, and to provide a forum for interchange of information. Wenham (the Society's first president) and Phillips were the first to devise and use wind tunnels.

After the public demonstration of practical human flight by Wilbur Wright on his 1908 visit to France and Bleriot's 1909 cross-channel flight, the British Prime Minister was moved to appoint an Advisory Committee for Aeronautics with the great physicist Lord Rayleigh as chairman.

During the same period the United States made no special effort. The Army Signal Corps bought a few airplanes to train pilots and the Navy set up a flying school equipped with Glenn Curtiss seaplanes. When World War I erupted in 1914 it was reported that France had 1,400 airplanes, Germany 1,000, Russia 800, Great Britain, 400, and the United States 23!

DRIVE FOR A NATIONAL LABORATORY

The backward position of the United States in the application of applied science to this new art was realized by a growing list of prominent Americans who believed the situation was not only a national disgrace, but a possible danger to our security. More Americans, including the leaders in Congress, were strong for neutrality, and felt that any special government concern with aeronautical development might imply belligerent intentions.

Capt. W. I. Chambers, USN, officer-in-charge of naval-aviation experiments, proposed in 1911 that a national aeronautical research laboratory be set up under the Smithsonian Institution. Along with objections by both the War and Navy Departments, the plan was referred to President Taft's Committee on Economy and Efficiency, from which it was never returned.

Two men who were more influential in the drive for a national aeronautical laboratory were Alexander Graham Bell and Charles Doolittle Walcott. The former, as a regent of the Smithsonian Institution, had been a supporter of Langley and had experimented with the lifting capabilities of kites. With Mrs. Bell he formed the Aerial Experiment Association in 1907 to support the airplane experiments of Glenn Curtiss, Lt. T. E. Selfridge, F. W. ("Casey") Baldwin, and J. A. D. McCurdy. Their efforts resulted in the development of the Curtiss biplanes and the use of ailerons to replace the Wright's wing warping for lateral control.

Dr. Walcott was no aeronautical scientist; his field was geology. But Dr. Walcott, as successor to Professor Langley as Secretary of the Smithsonian, was determined that the Institution should resume its position as a leader of aeronautical science in America. How better than to have the new aeronautical laboratory attached to the Smithsonian!

The establishment of a national aeronautical laboratory was pressed by members of the National Academy of Sciences, notably by Bell and Walcott. The Academy had been created by Congress during the Civil War and had the duty of giving advice to the Government, when asked. The Academy, as a body, was not asked for advice on this matter, but its members appear to have been influential in persuading President Taft to appoint on December 19, 1912, a 19-man commission to consider such a national laboratory and its scope, organization, and cost, and to make a recommendation to the Congress.

The President's Commission was headed by Dr. R. S. Woodward of the National Academy of Sciences and the Carnegie Institution of Washington and included Dr. Walcott. The Army, Navy, Weather Bureau, and Bureau of Standards were represented, as well as interested civilians. The Commission recommended that the laboratory be established in Washington and administered by the regents of the Smithsonian Institution. President Maclaurin of the Massachusetts Institute of Technology objected to the location at Washington, which the majority report favored as "conveniently accessible to statesmen of the National Government who may wish to witness aeroplane demonstrations."

Unfortunately, the President had appointed the Commission without "the advice and consent of the Senate." Authorizing legislation failed to get unanimous consent and the Commission's report was buried in the archives.

Probably as a result of his service with the President's Commission, President Maclaurin in May 1913 persuaded the Corporation of M.I.T. to authorize a graduate course in aeronautical engineering and a wind tunnel for aerodynamic research in the Department of Naval Architecture. He requested the Secretary of the Navy to detail an officer of the Construction Corps to take charge. The writer was so detailed for 3 years.

At about the same time, the Smithsonian regents decided to reopen Langley's old laboratory, with Dr. Al-

bert F. Zahm in charge. It was arranged by Walcott and Maclaurin to send Zahm and Hunsaker abroad, armed with personal introductions to scientific friends. Their objective was to visit the principal aeronautical research laboratories and, as far as possible, to learn how to operate the special facilities and equipment in use there with a view to duplicating them in this country.

Visits were made to the Royal Aircraft Factory, the National Physical Laboratory, and Cambridge University in England; to the St. Cyr, Chalais-Meudon, and Eiffel Laboratories in France; and to the Deutsche Versuchsanstalt für Luftfahrt and Göttingen University in Germany. In 1913, security restrictions did not apply to scientific and engineering work and the visitors were cordially received. In fact, the Massachusetts Institute of Technology later built its wind tunnel from drawings supplied by Sr. Richard Glazebrook of the NPL and the NPL aerodynamic balances duplicated by Sir Horace Darwin's Cambridge scientific instrument shops.

Dr. Zahm's report, published by the Smithsonian in 1914, made clear the width of the gap between European and American positions in aeronautical science. This report had an important influence on the decision of the Smithsonian regents in 1915 to memorialize the Congress once again on the subject of a national aeronautical laboratory.

Woodrow Wilson approved the Smithsonian plan of reopening Langley's laboratory with representatives of the War, Navy, Agriculture, and Commerce Departments serving on an Advisory Committee. However, the Comptroller ruled that, under an act of 1909, such an Advisory Committee could not serve without the authority of the Congress.

On December 10, 1914, the Chancellor of the Smithsonian, Chief Justice White, appointed Dr. Alexander Graham Bell; Senator William J. Stone of Missouri; Representative Ernest W. Roberts of Massachusetts, and John B. Henderson, Jr., regents; and Dr. Walcott, Secretary, to consider once again "questions relative to the Langley Aerodynamical Laboratory." On February 1, 1915, a "memorial on the need for a National Advisory Committee for Aeronautics" was delivered to the Speaker of the House. Pertinent sentences from the memorial follow:

> This country led in the early development of heavier-than-air machines. Today it is far behind. . . . A National Advisory Committee for Aeronautics cannot fail to be of inestimable service in the development of the art of aviation in America. Such a committee, to be effective, should be permanent and attract to its membership the most highly trained men in the art of aviation. . . . Through the agency of subcommittees, the main advisory committee could avail itself of the advice and suggestions of a large number of technical and practical men. . . . The aeronautical committee should advise in relation to the work of the Government in aeronautics and the coordination of the activities of governmental and private laboratories, in which questions concerned with the study of the problems of aeronautics can be experimentally investigated.

The Navy heartily endorsed the idea in a letter dated February 12 and signed by Franklin D. Roosevelt as Acting Secretary.

ESTABLISHMENT OF NACA

The joint resolution establishing the Advisory Committee and authorizing the President to appoint its 12 members was given final form in February. The people of the United States were at the time generally anxious to avoid involvement in what was then called the War in Europe. President Wilson is said to have felt that the establishment of a new aeronautical enterprise might reflect on American neutrality. Such reasoning may explain why the resolution was attached to the naval appropriation bill; perhaps a more likely reason was that in the rush to clear the legislative "logjam" by March 4, the date for adjournment of the Congress, Representative Roberts, Smithsonian regent, had found it simpler to effect its adoption by introducing the measure, as a rider to the naval appropriation bill, in the Committee on Naval Affairs, of which he was a member.

Following is the provision in the Naval Appropriations Act, approved March 3, 1915:

> An Advisory Committee for Aeronautics is hereby established, and the President is authorized to appoint not to exceed twelve members, to consist of two members from the War Department, from the office in charge of military aeronautics; two members from the Navy Department, from the office in charge of naval aeronautics; a representative each of the Smithsonian Institution, of the United States Weather Bureau, and of the United States Bureau of Standards; together with not more than five additional persons who shall be acquainted with the needs of aeronautical science, either civil or military, or skilled in aeronautical engineering or its allied sciences: *Provided*, That the members of the Advisory Committee for Aeronautics, as such, shall serve without compensation: *Provided further*, That it shall be the duty of the Advisory Committee for Aeronautics to supervise and direct *the scientific study of the problems of flight, with a view to their practical solution, and to determine the problems*[1] which should be experimentally attacked, *and to discuss their solution and their application to practical questions.* In the event of a laboratory or laboratories, either in whole or in part, being placed under the direction of the committee, the committee may direct and conduct research and experiment in aeronautics in such laboratory or laboratories: *And provided further*, That rules and regulations for the conduct of the work of the committee shall be formulated by the committee and approved by the President.
>
> That the sum of $5,000 a year, or so much thereof as may be necessary, for five years is hereby appropriated, out of any money in the Treasury not otherwise appropriated, to be immediately available, for experimental work and investigations undertaken by the committee, clerical expenses and supplies, and necessary expenses of members of the committee in going to, returning from, and while attending meetings of the committee:

[1] Italics in this and the following quotation supplied by the author for emphasis.

Provided, That an annual report to the Congress shall be submitted through the President, including an itemized statement of expenditures.

This language establishing the NACA closely followed that used by the British Prime Minister when he announced the formation of a similar committee to the House of Commons on May 5, 1909, in the following words:

It is no part of the general duty of the Advisory Committee for Aeronautics either to construct or to invent. Its function is not to initiate but to consider what is initiated elsewhere, and is referred to it by the executive offices of the Navy and Army construction departments. The problems which are likely to arise in this way for solution are numerous, and it will be the work of the committee to advise on these problems and to seek their solution by the application of both theoretical and experimental methods of research.

The work desired thus falls into three sections: (1) *The scientific study of the problems of flight, with a view to their practical solution.* (2) Research and experiment into these subjects in a properly equipped laboratory with a trained staff. (3) The construction and use of dirigibles and aeroplanes, having regard mainly to their employment in war.

The Advisory Committee are to deal with the first section, and also *to determine the problems* which the experimental branch should attack, *and discuss their solutions and their application to practical questions.* The second section represents the work referred to the laboratory (the National Physical Laboratory), while the duties concerned with the third section remain with the Admiralty and the War Office.

On April 2, 1915, President Woodrow Wilson appointed to the new Committee: Prof. Joseph S. Ames, of the Physics Department of Johns Hopkins University; Capt. Mark L. Bristol, USN, Director of Naval Aeronautics, Navy Department; Prof. William F. Durand, of the Engineering Department of Leland Stanford University; Prof. John F. Hayford of the Engineering Department of Northwestern University; Dr. Charles F. Marvin, Chief of the U.S. Weather Bureau; Hon. Byron R. Newton, Assistant Secretary of the Treasury; Prof. Michael I. Pupin of the Physics Department of Columbia University; Lt. Col. Samuel Reber, USA, Officer-in-Charge, Aviation Section of the Signal Corps, War Department; Naval Constructor Holden C. Richardson, USN, Department of Construction and Repair, Washington Navy Yard; Brig. Gen. George P. Scriven, USA, Chief Signal Officer, War Department; Dr. Samuel W. Stratton, Director, National Bureau of Standards; and Dr. Charles D. Walcott, Secretary, Smithsonian Institution.

Of the initial 12 members, 6 were members of the National Academy of Sciences (within the period of their NACA membership). It is of interest to note that for 40 years all chairmen of the NACA except the first, General Scriven, have been members of the National Academy. In 1955, there are 5 Academy members out of 17 members of the NACA. This statistic is of significance in view of the increasing impact on aeronautics of advances in many fields of science: for example, physiology and psychology of pilots, chemistry of combustion, physics of metals, physics of the atmosphere, acoustics, communications, electronics. The Committee is strengthened by the special knowledge of its individual members.

By direction of the President, the Secretary of War called the first meeting. The date was April 23, 1915; the place, his office. Conforming with the designation in the call for the first meeting, the word "National" was prefixed to the title "Advisory Committee for Aeronautics." General Scriven was elected temporary chairman, and Naval Constructor Richardson temporary secretary. With formulation of rules and regulations, subsequently approved by the President, the temporary chairman and secretary were elected for one year.

Perhaps the most important regulation adopted was for an executive committee, composed of 7 of the 12 members of the Advisory Committee. The full Committee was to meet only semiannually. The executive committee was set up to meet regularly throughout the year and was charged with the administration of the affairs of the Committee and "general supervision of all arrangements for research."

Dr. Walcott was the first chairman of the executive committee. The other members were Dr. Ames, Captain Bristol, Dr. Marvin, Dr. Pupin, Colonel Reber, and Dr. Stratton, with Naval Constructor Richardson, ex officio, as secretary. Improvised quarters in the Army's Aviation Section were used the first year.

In the beginning the executive committee was a working group; the NACA had no paid personnel. It was not until June 23 that the first employee was hired. He was John F. Victory; 41 years later he is continuing his faithful, effective service to the Committee. In 1917 he was named assistant secretary of the Committee; 10 years later he became secretary, and in 1945, executive secretary.

One of the first problems was to examine what aeronautical research was then in progress in the United States—both under Government auspices and by private organizations—and then to effect rational coordination to assure maximum value from the total effort. Congressman Roberts, reporting on the need for the NACA on February 19, 1915, had well stated the situation:

Besides these governmental agencies [he named the Bureau of Standards, the Weather Bureau and the War and Navy Departments] for the development of aviation, individuals in civil life have devoted time and expense in the scientific study and practical development of aeronautics. At the present time all of these agencies, both governmental and private, work independently without any coordination of activities.

Ten years later Dr. Ames gave a prime reason for "the great success of the Committee, because the Committee is a success," the coordination, on a rational scale,

of American aeronautical research. His comments were made before hearings of the President's Aircraft Board (often called the Morrow Board). He spoke as chairman of the executive committee, to which position he had been elected when Dr. Walcott became Committee chairman in 1919.

In part, Dr. Ames said:

> The organization has an Executive Committee which appoints a number of technical subcommittees whose function it is to coordinate the research work throughout the country. . . . The various problems which all the services of the Government and the people engaged in industry, so far as we know, have in mind are brought before these subcommittees. The importance of each problem is discussed, and a program is laid out. . . .
>
> Around our table meet . . . representatives from all the Government services involved. . . . We work for all the departments of the Government.
>
> Furthermore, there are discussions going on at our table between the Army and the Navy and all other people interested which otherwise would not take place. We are really a coordinating body and that function would be impossible if our organization were to be transferred to any executive department as such, because if our Committee were to be a part of any department it would necessarily follow that the aeronautical needs of that department would be primarily served. . . .
>
> We think, therefore, that in our independent existence we offer a wonderful opportunity for serving all the departments.

In 1915 one of the first projects undertaken by the executive committee was a survey of facilities available "for the carrying on of aeronautic investigations." It was determined that "a number of institutions have available mechanical laboratories and engineering courses capable of application to aeronautics, but only the Massachusetts Institute of Technology and the University of Michigan so far offer regular courses of instruction and experimentation." Note was made of the experiments with full-scale propellers mounted on a whirling table, being conducted at Worcester Polytechnic Institute.

"It appears that the interest of colleges is more one of curiosity than that of considering the problem as a true engineering one, requiring development of engineering resources and, therefore, as not yet of sufficient importance to engage their serious attention," the NACA commented in its first annual report. "Manufacturers are principally interested in the development of types which will meet Government requirements or popular demand, but which will not involve too radical or sudden changes from their assumed standard types."

The Committee recognized that "considerable work had already been accomplished with which the general public is not acquainted." The annual report said of this point: "This covers lines of development and investigation which if published would save money and effort on the part of individual investigators and inventors who are now duplicating investigations already made by others. . . . Some of this information is already embodied in reports which are only accessible to a few interested parties who know of its existence."

The Smithsonian Institution had published a bibliography of aeronautics, covering the period through the middle of 1909. Now the NACA undertook publication of later bibliographies compiled by Paul Brockett of the Smithsonian. The first such volume covered the period 1909–16; as soon as past years had been "caught up," the bibliography was published annually into the early thirties.

The Committee was fully aware that to fulfill its obligations would require not only a well-equipped, suitably staffed laboratory, but also a flight test center where engineers could determine "the forces acting on full-sized machines." It was felt, however, that "since the equipment of such a laboratory as could be laid down at this time might well prove unsuited to the needs of the early future, it is believed that such provision should be the result of gradual development."

In October 1916 the Committee recommended that the War Department (which alone had funds available) purchase land about 4 miles north of Hampton, Va., for use by the Army and Navy as an aircraft proving ground. Named Langley Field, this site became the home of NACA's first research center. The War Department used it for pilot training during World War I. Aircraft development work of both the Army and Navy was centered elsewhere.

Lacking its own facilities, the NACA took prompt steps to contract for research to be performed for it by others. The first annual report included seven reports, as follows:

No. 1. Report on behavior of aeroplanes in gusts, by the Massachusetts Institute of Technology.
- Part 1. Experimental analysis of inherent longitudinal stability for a typical biplane, by J. C. Hunsaker.
- Part 2. Theory of an aeroplane encountering gusts, by E. B. Wilson.

No. 2. Investigation of pitot tubes, by the United States Bureau of Standards.
- Part 1. The pitot tube and other anemometers for aeroplanes, by W. H. Herschel.
- Part 2. The theory of the pitot and venturi tubes, by E. Buckingham.

No. 3. Report on investigations of aviation wires and cables, their fastenings and terminal connections, by John A. Roebling's Sons Co.

No. 4. Preliminary report on the problem of the atmosphere in relation to aeronautics, by Prof. Charles F. Marvin.

No. 5. Relative worth of improvements on fabrics, by the Goodyear Tire & Rubber Co.

No. 6. Investigations of balloon and aeroplane fabrics, by the United States Rubber Co.
- Part 1. Balloon and aeroplane fabrics, by Willis A. Gibbons and Omar H. Smith.
- Part 2. Skin friction of various surfaces in air, by Willis A. Gibbons.

No. 7. Thermodynamic efficiency of present types of internal-combustion engines for aircraft, by Columbia University.
- Part 1. Review of the development of engines suitable for aeronautic service, by Charles E. Lucke.
- Part 2. Aero engines analyzed with reference to elements of process or function, by Charles E. Lucke.

"What has already been accomplished by the Committee has shown that although its members have devoted as much personal attention as practicable to its operations, yet in order to do all that should be done technical assistance should be provided which can be continuously employed," the Committee said in its first Annual Report.

For the fiscal year 1917 the NACA asked for and received $85,000. Of the funds available, $68,957.35 (all that was not spent otherwise) went toward construction of the new laboratory at Langley Field. Its total cost was estimated at $80,000, a figure that later was revised upward.

The war was over before the "Committee's field station" at Langley Field could be said to be in useful operation. The annual report for 1919 noted that the Committee's first wind tunnel, with a 5-foot test section, was completed but inoperative for lack of power. The Army's power plant at Langley Field was incomplete, with construction stopped for lack of money.

With the Army planning to keep its experimental work in aeronautics at McCook Field, Dayton, and with the Navy's experimental aviation work centered at Norfolk, the NACA in 1919 felt it had good reasons for moving its field station activities to Bolling Field, just across the Anacostia River from the Capital. It asked Congress to authorize the move:

> The Committee believes it uneconomical and unsatisfactory to remain at Langley Field. The same work can be carried on more efficiently, more promptly, and more economically at Bolling Field, where the work can be closely watched by all members of the Committee, and where the members of the engineering staff in charge of work can have ready access to the Committee, to large libraries, and other sources of information, constant communication with the Bureau of Standards, a more satisfactory market for labor and supplies and adequate power supply, and relief from the perplexing question of securing quarters at Langley Field or in Hampton or other nearby towns.

Congressional approval for the move to Bolling Field did not come. In April 1920, the Committee, perhaps with a collective sigh, took action that accepted as permanent the Langley Field site for the "field station." It sought Presidential approval of the name, "Langley Memorial Aeronautical Laboratory." President Wilson concurred, and dedicatory exercises were conducted on June 11. Attendance included guests, it was later reported, "of whom a number had flown to the field."

This date, June 11, 1920, may be considered the real beginning of NACA's own program of aeronautical research, conducted by its own staff in its own facilities. The previous year a start had been made in obtaining full-scale performance data from flight tests, but now the availability of a wind tunnel made possible systematic investigations of critical aerodynamic problems, such as: (1) Comparison between the stability of airplanes as determined from full-flight test and as determined from calculations based on wind-tunnel measurements; (2) comparison between the performance of full-scale airplanes and the calculations based on wind-tunnel experiments, and (3) airfoils, including control surfaces, with special attention to thick sections, plus combinations and modification of such sections.

THE COMMITTEE'S ADVISORY FUNCTIONS

This has been essentially a chronological account, first, of events preceding establishment of the NACA, and then its early steps to undertake its responsibilities as the nation's aeronautical research establishment. At this point it is in order to glance briefly at some early activities of the Committee which were consonant with the "Advisory" in its name.

In 1916 the executive committee invited engine manufacturers to attend a meeting on June 8 in Dr. Walcott's office at the Smithsonian Institution to discuss the problem of obtaining more powerful and more reliable engines and to bring about a better understanding between builders and users. Representatives of the military services were in attendance, and although it is to be doubted that many problems were solved, unquestionable good was done by bringing them into sharp focus. Another benefit from the meeting was an arrangement whereby the Society of Automotive Engineers became active in providing assistance in the solution of aircraft powerplant problems.

Also in 1916 the Committee examined the problem of the carriage of mail by air. The Post Office Department had failed in efforts to establish a contract airmail service in Alaska and from New Bedford to Nantucket Island. Airmail was then considered to be justified only over almost impossible terrain. "Conditions of both these routes were so severe as to deter responsible bidders from undertaking this service," the Committee decided. It felt, nonetheless, that because of the great progress made in aviation, the Post Office should set up one or more experimental routes, "with a view to determining the accuracy, frequency, and rapidity of transportation which may reasonably be expected under normal and favorable conditions, and therefrom to determine the desirability of extending this service wherever the conditions are such as to warrant its employment."

The above-stated opinion was transmitted to Congress in 1916 as a recommendation. In 1918, when $100,000 was appropriated for creation of an experimental airmail service, the NACA invited the attention of the Secretary of War to the following facts: "Practically all aircraft manufacturing facilities in the United States were being utilized by the War and Navy Departments, and all capable aviators were in the military or naval air services . . . [and] it was exceedingly desirable that Army aviators be regularly

and systematically trained in long-distance flying . . . [and that] it would appear to be to the advantage of the War Department and of the Government generally that military airplanes be used to render practical and effective service" in carrying mail between Washington, Philadelphia, and New York. In its 1918 annual report the NACA viewed with satisfaction the manner in which the experimental airmail service had been established along the lines recommended, and expressed the opinion it had already "been sufficiently well demonstrated since its inauguration to justify its extension generally."

In 1921, the Committee noted in a special report to the President that—

> There are several causes which are delaying the development of civil aviation, such as the lack of airways, landing fields, aerological service, and aircraft properly designed for commercial uses. The Air Mail Service stands out as a pioneer agency, overcoming these handicaps and blazing the way, so to speak, for the practical development of commercial aviation. As a permanent proposition, however, the Post Office Department, as its functions are now conceived, should no more operate directly a special airmail service than it should operate a special railroad mail service; but until such time as the necessary aids to commercial aviation have been established it will be next to impossible for any private corporation to operate under contract an airmail service in competition with the railroads.

In January 1917, the War and Navy Departments complained to the NACA about prohibitive prices for aircraft, said to be due to "the extra item of royalty added by each firm in anticipation of infringement suits by owners of alleged basic aeronautic patents who were then threatening all other airplane and seaplane manufacturers with such suits, and causing thereby a general demoralization of the entire industry."

The Committee held meetings with Government officials, owners of patents, and aircraft manufacturers. It then recommended organization of a Manufacturers Aircraft Association to effect the cross licensing of aeronautic patents and to make the use of all such patents available to any member firm at the relatively small cost of $200 per airplane. This happy solution was adopted, and resulted, in the Committee's opinion, in "the prevention of the virtual deadlock with danger of monopoly existing under the patent situation."

In many other ways the Committee gave advisory service on such varied matters as provision of insurance for aviators, naming of flying fields "in commemoration of individuals who had rendered conspicuous service," aerial mapping techniques, and selection of a site near Washington for a "landing field" to provide "accommodation of transient aviators."

A special subcommittee during World War I examined some 7,000 inventions and suggestions in the field of aeronautics. Of this work the NACA later said, "The great majority of the suggestions received are obviously of an impractical nature. Several, however, have seemed worthy of further consideration and have been referred to military or naval experts." In addition to this arduous task, the Committee served as arbitrator in the settlement of disputes involving technical questions between private parties and the military services.

Perhaps the most important of NACA's advisory services was the leadership which the Committee gave to the efforts for legislation necessary to the orderly development of civil aviation. With cessation of hostilities in 1918, the Committee promptly took up the basic question of what should be done about the civil use of aircraft. Although it would be nearly 8 years before the required Federal legislation was adopted (the Air Commerce Act of 1926), the recommendations made by the Committee in 1918 encompassed what was needed: "Federal legislation . . . governing the navigation of aircraft in the United States and including the licensing of pilots, inspection of machines, uses of landing fields, etc. . . . designed to . . . encourage the development of aviation . . . and at the same time to guide the development . . . along such lines as will render immediate and effective military service to the Nation in time of war."

On April 1, 1921, President Harding directed the Committee to meet with representatives of interested Government departments to determine what could be done to achieve Federal regulation of air navigation without legislative action, and what new legislation was needed. April 9, the recommendations were formulated. The Committee was brief: "Federal regulation of air navigation cannot be accomplished under existing laws. . . . It is recommended that a Bureau of Aeronautics be established in the Department of Commerce."

There were other NACA proposals in 1921: That the Post Office be authorized to extend its airmail routes across the continent, and that naval aviation activities be centered in a Bureau of Aeronautics within the Navy Department.

In its Annual Report for 1921, the NACA noted the principal reason for delay in passing the recommended legislation:

> The Committee is not unmindful of the legal sentiment that a constitutional amendment should first be adopted before such legislation is enacted, on the ground that effective regulation of air navigation as proposed would otherwise be unconstitutional as violating the rights of property and encroaching upon the rights of States. To postpone such legislation until a constitutional amendment can be proposed and ratified would have the effect of greatly retarding the development of commercial aviation, with no assurance that sufficient popular interest would ever be aroused to accomplish such an amendment. The Committee is of the opinion that the most effective course to be

followed for the development of aviation would be first to enact the legislation deemed necessary for the Federal regulation of air navigation and the encouragement of the development of civil aviation, and let the question of the constitutionality of such legislation be tested in due course. In the meantime, there would be development in civil and commercial aviation, and if eventually the legislation which made possible such development should be definitely determined to be unconstitutional there would then, in all probability, be sufficient public interest in the subject and popular demand to adopt an amendment to the Constitution.

Years of perseverance culminated, in April 1926, in a careful analysis by the Committee of fundamental differences of opinion respecting certain aspects of the basic legislation then before the Congress. The solutions then proposed by the NACA were accepted by the joint Senate-House conferees, and the Air Commerce Act became law on May 20, 1926.

"This act provides the legislative cornerstone for the development of commercial aviation in America," the Committee said. It "gives an important measure of stability to commercial aviation as a business proposition and in its direct effects will go far toward encouraging the development of civil and commercial aviation."

AERONAUTICAL RESEARCH

The Air Commerce Act made the Secretary of Commerce responsible for the regulation of civil aviation, and for its encouragement. At the same time, this action freed the NACA from an "advisory" burden it had carried during its first 10 years. From now on, the Committee could concentrate upon its chief responsibility—the conduct of aeronautical research.

During the first 10 years of the Committee's existence demands upon the time of NACA members were very heavy. From 1915 to 1919 the Committee had three chairmen: General Scriven, 1915; Dr. Durand, 1916–18, and Dr. John R. Freeman, 1919. Dr. Freeman was sent on a mission to China and was succeeded as chairman in 1919 by Dr. Walcott, who had served as chairman of the executive committee since its formation in 1915.

Dr. Walcott was succeeded as chairman of the executive committee by Dr. Ames, who effectively supported Dr. Walcott until the latter's death in 1927. At that time Dr. Ames became chairman to serve until his retirement in 1939. The fact that he was located in Baltimore, where he headed the physics department of Johns Hopkins University until he became president of the University in 1929, proved no handicap. Dr. Ames was in Washington as often and as long as Committee business required.

With the development of laboratory facilities at Langley, the NACA began building a competent engineering staff. The Langley Laboratory attracted young men with good training, who could grow to do work of increasing importance. The independence of the NACA was one of the attractions, as was also the opportunity for the young engineer to sign the published report of his own research. So was the availability of superior research and test equipment.

In 1919 the Committee invited Dr. George W. Lewis, professor of mechanical engineering at Swarthmore College, to become its executive officer. In this capacity, he was called upon to guide the research programs and to plan and build the research tools needed. In 1924 Dr. Lewis' title was changed to one that more closely described his responsibilities, director of aeronautical research. From then until 1945, when his health failed under the tremendous burdens he insisted upon carrying during World War II, George Lewis gave devoted and effective leadership to the staff of the Committee.

While the Committee was acquiring the equipment at Langley necessary for the research programs envisioned, use was made of facilities available elsewhere for certain investigations. Before the end of World War I, Dr. Durand was conducting most valuable research on air propellers at Leland Stanford University, and at MIT the availability of a wind tunnel and staff made possible fundamental aerodynamic research on stability and control and on the characteristics of wing sections.

The National Bureau of Standards worked on aeronautical problems at the request of the NACA and with its financial support. The Bureau developed apparatus for the study of combustion problems under simulated conditions of high altitude and later equipped itself with wind tunnels for fundamental research on turbulence and boundary-layer problems.

The aeronautical experimentation carried on at the Navy Yard in Washington and at McCook Field in Dayton was correlated with a comprehensive plan which the NACA formulated and which was kept up to date as military and industry needs changed. The pioneering work by Naval Constructor Richardson on seaplane hulls, and the later researches directed by Chief Constructor David W. Taylor, contributed significantly to the advancement of naval aviation. At McCook Field (later moved and enlarged to become Wright Field) the availability of a wind tunnel caused the NACA to detail one of its first technical employees, Dr. George de Bothezat (best known, perhaps, for his later work with helicopters) to Dayton to assist with aeronautical research there.

In 1920 the NACA's first wind tunnel was put to work. With relatively minor exceptions, this first major piece of equipment was patterned after one at the British National Physical Laboratory. The work that could be done with this tunnel was essentially no different from that which could be accomplished at the Navy Yard, McCook Field, MIT, or other locations where conventional wind tunnels were located.

In June 1921, the executive committee decided to build a new kind of wind tunnel. Utilizing compressed air,

it would allow for "scale effects" in aerodynamic model experiments. This tunnel represented the first bold step by the NACA to provide its research personnel with the novel, often complicated, and usually expensive equipment necessary to press forward the frontiers of aeronautical science. It was designed by Dr. Max Munk, formerly of Göttingen.

The value of the new tunnel was explained in 1922 by Dr. Ames:

> When a new design of airplane . . . is made, it is customary to construct a model of it, one-twentieth the size or less, and to experiment upon this. The method now in universal use is to suspend the model from suitable balances in a stream of air . . . at a velocity of 60 mph. . . . The balances register the forces and moments acting on the model. From the results of such measurements one decides whether the original design is good or not. But is one justified in making such a decision? Why should the same laws apply to a little model inside the wind tunnel, as it is called, and to the actual airplane flying freely through the air? Evidently there is ground for grave uncertainty. The Committee has perfected a method for obviating this. It has been known from aerodynamic theory for some time that the change in scale, from airplane to its model, could be compensated by compressing the air from ordinary pressure to 20 or 25 atmospheres: as the structure moving through the air is reduced in size from 50 feet to 2 feet, the molecules of the air are brought, by comparison, closer and closer together until their distance apart is one twenty-fifth of what it was originally. The effect of scale is thus fully compensated and experiments upon a model in this compressed air have a real meaning. The Committee has constructed a large steel tank, 34 feet long and 15 feet in diameter, inside which is placed a wind tunnel with its balances, etc., and in which the air may be kept in a state of high compression. The information to be obtained from the apparatus will be the most important ever given airplane designers.

Experience with simple airplane models without propellers in the variable-density tunnel encouraged the NACA, in June 1925, to construct a wind tunnel large enough to test full-scale airplane propellers under conditions of flight. This was a costly decision, but the cost was repaid manyfold by improved airplane performance.

The propeller research tunnel was put into operation in 1927. It had a circular test section 20 feet in diameter and was powered by two Diesel engines rated at 1,000 hp. each. Its air speed was 110 mph. and, at the time, it was the largest wind tunnel in the world. Almost from the beginning of its use, the PRT provided information leading to design changes which resulted in dramatic improvements in airplane performance.

The first and most spectacular of these productive researches brought about the development of what became known as the NACA cowling for air-cooled radial engines. In its 1928 report, the Committee said that "by the application of the results of this study to a Curtiss AT-5A Army pursuit training plane, the maximum speed was increased from 118 to 137 mph. This is equivalent to providing approximately 83 additional horsepower without additional weight or cost of engine, fuel consumption, or weight of structure. This single contribution will repay the cost of the Propeller Research Tunnel many times."

The Collier Trophy, awarded annually "for the greatest achievement in aviation in America, the value of which has been thoroughly demonstrated by actual use during the preceding year," went to the NACA for the development of this form of cowling. President Hoover made the presentation on January 3, 1930 (for the year 1928), and after the reading of the citation Dr. Ames responded that "a scientist receives his reward from his own work in believing that he has added to human knowledge; but he is always gratified when his work is recognized as good by those competent to judge."

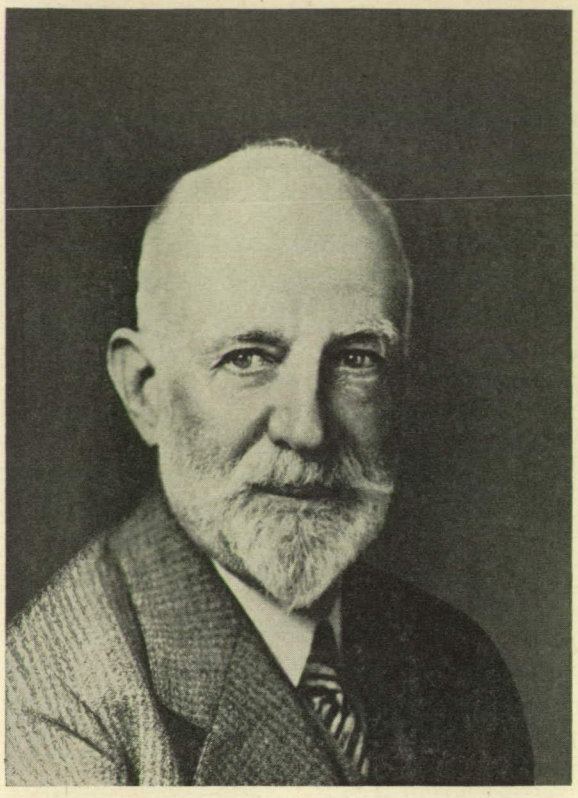
A second important benefit accruing from work in the PRT was more positive information about the best location of engine nacelles. The engines of the Ford Tri-motor, and similar aircraft of the twenties, were hung below the wing. As a consequence of research reported confidentially in 1930, multiengine aircraft designed thereafter had their engines faired into the leading edge of the wing with an important gain in speed.

The systematic work accomplished in the PRT led to other practical design changes. For example, it was possible to obtain an accurate estimate of the drag caused by such apparently insignificant details as the location of a gasoline filler cap. Similarly, engineers studied the aerodynamic interference of wings and fuselage, and the use of fillets to reduce the interference was proposed. (In 1928 the NACA published its first Technical Note on this subject, by Melvin N. Gough.)

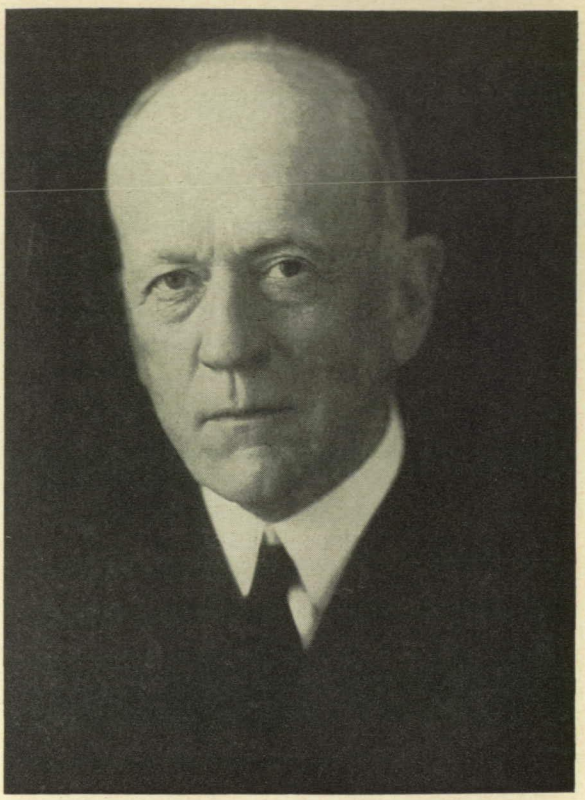
That the fixed landing gear represented a large amount of drag had long been appreciated, but it was not until the PRT became operative that the drag penalties of fixed landing gear could be determined precisely. The higher speeds made possible by use of the NACA cowling, the wing positioning of the engine nacelles, the filleting of wing-fuselage junctures, and other aerodynamic refinements now made attractive the investment of added cost and weight implicit in retractable landing gear.

In 1933, looking at the gains from the research at its Langley Laboratory, the Committee said: "No money estimate can be placed on the value of superior performance of aircraft in warfare . . . nor can a money estimate be placed on . . . improved safety. . . . The value in dollars and cents of improved efficiency in aircraft resulting from the Committee's work can, however, be fairly estimated. For example, the results of . . . researches completed by the Committee within the last few years, show that savings in money alone will be made possible in excess annually of the total appropriations for the Committee since its establishment in 1915."

The economic depression that began with the stock-market crash of 1929 was not an unmixed evil for the NACA. Although there were strong pressures to re-



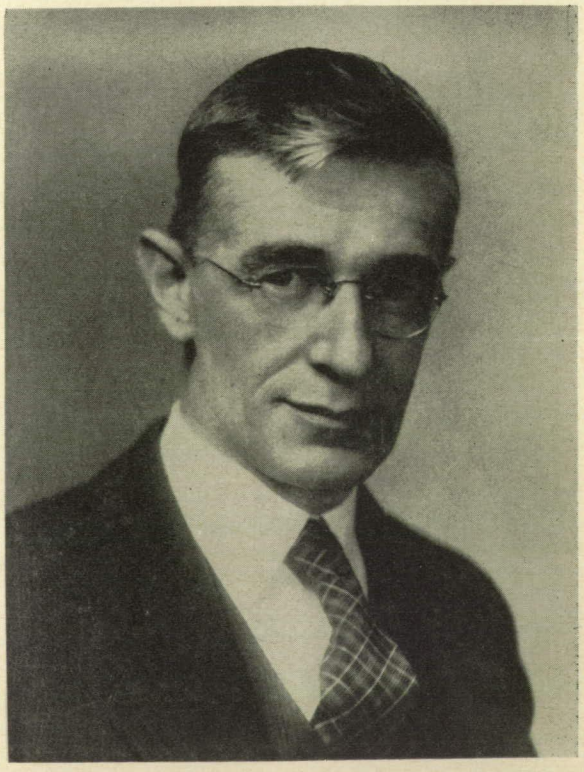
Dr. William F. Durand, member National Advisory Committee for Aeronautics 1915–33, 1941–45; Chairman, 1916–18.



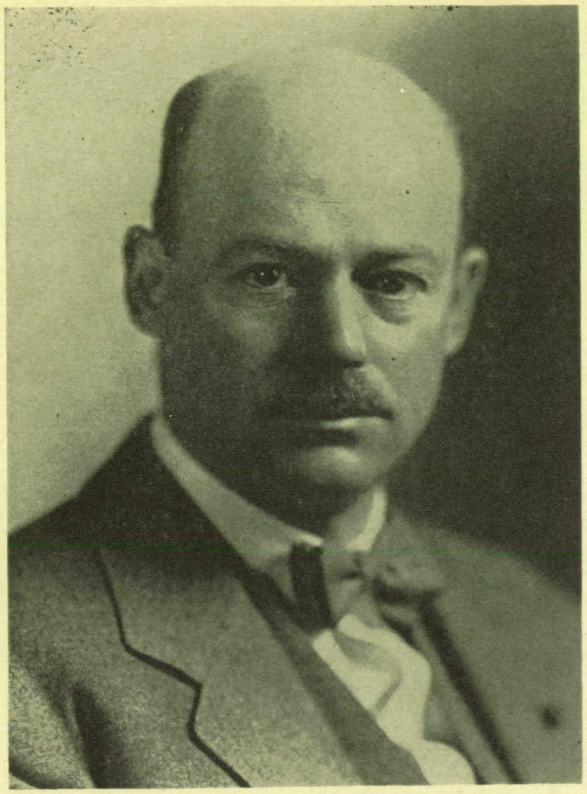
Dr. Charles Doolittle Walcott, Secretary Smithsonian Institution 1907–27; member National Advisory Committee for Aeronautics 1915–27; Chairman, Executive Committee, 1915–19; Chairman, 1919–27.



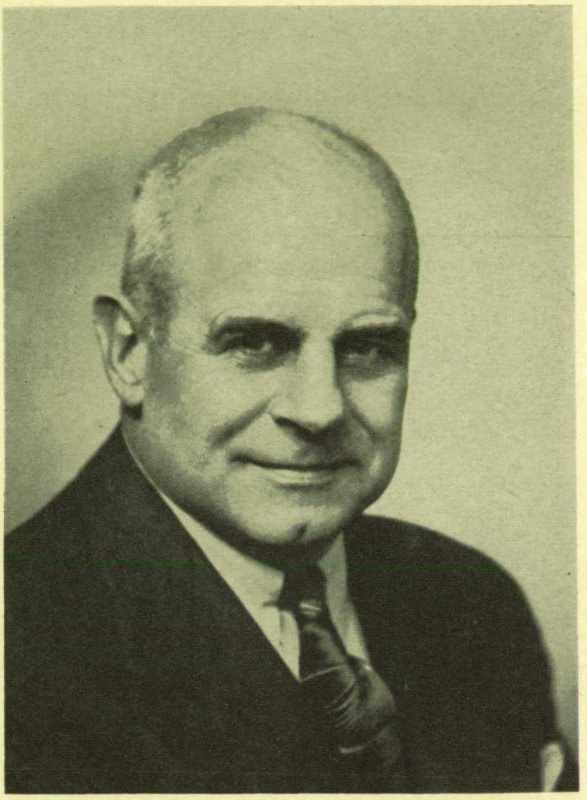
Dr. Joseph S. Ames, member National Advisory Committee for Aeronautics 1915–39; Executive Committee, 1919–37; Chairman, 1927–39.



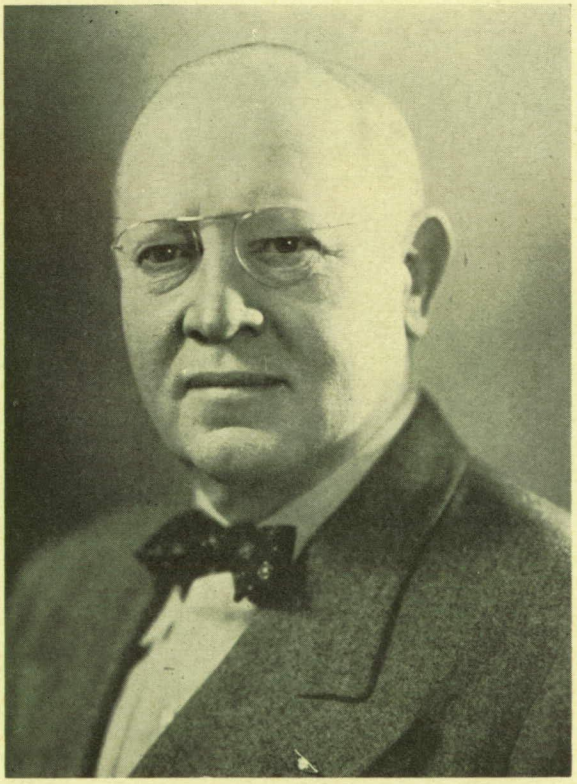
Dr. Vannevar Bush, member National Advisory Committee for Aeronautics 1938–48; Vice Chairman, 1938–39; Chairman, Executive Committee, 1938–41; Chairman, 1939–41.



Jerome C. Hunsaker, member National Advisory Committee for Aeronautics 1922–23, 1938–58; Chairman, 1941–56; Chairman, Executive Committee, 1941–56.



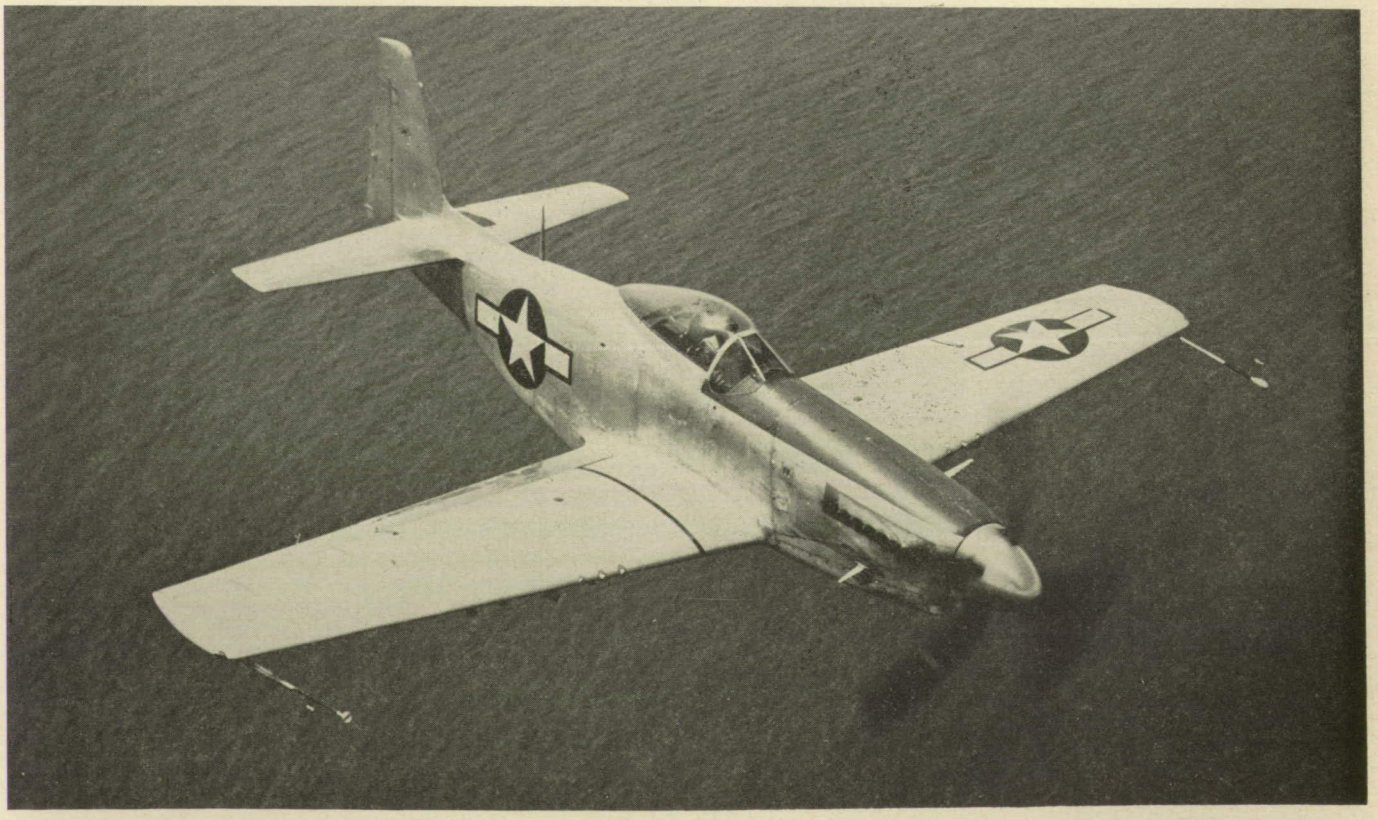
James H. Doolittle, member National Advisory Committee for Aeronautics 1948–58; Chairman, 1956–58; Chairman, Executive Committee, 1956–58.



Dr. George W. Lewis, Director of Aeronautical Research, National Advisory Committee for Aeronautics, 1919–47.



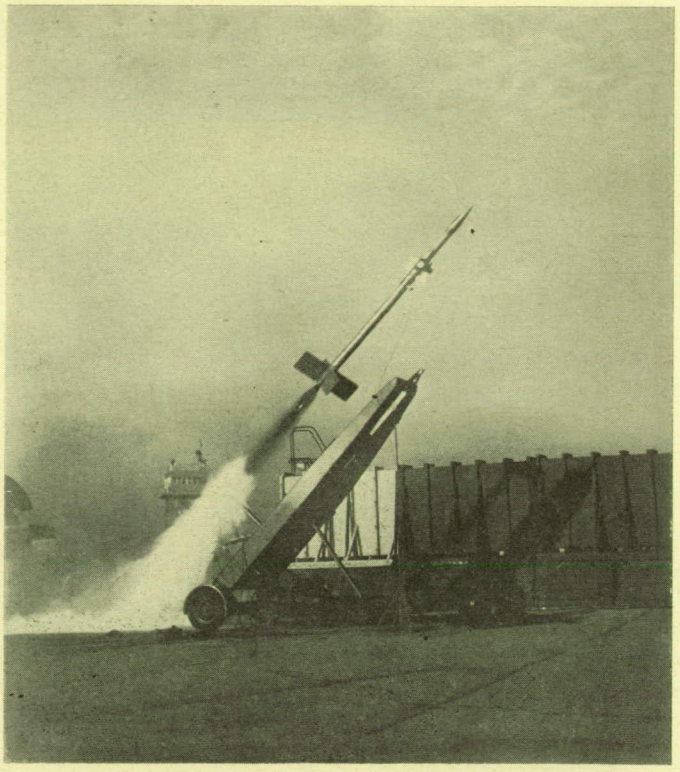
Application of NACA cowling on AT–5A Army pursuit training plane increased its speed from 118 to 137 m.p.h. This was equivalent to providing 83 additional horsepower.



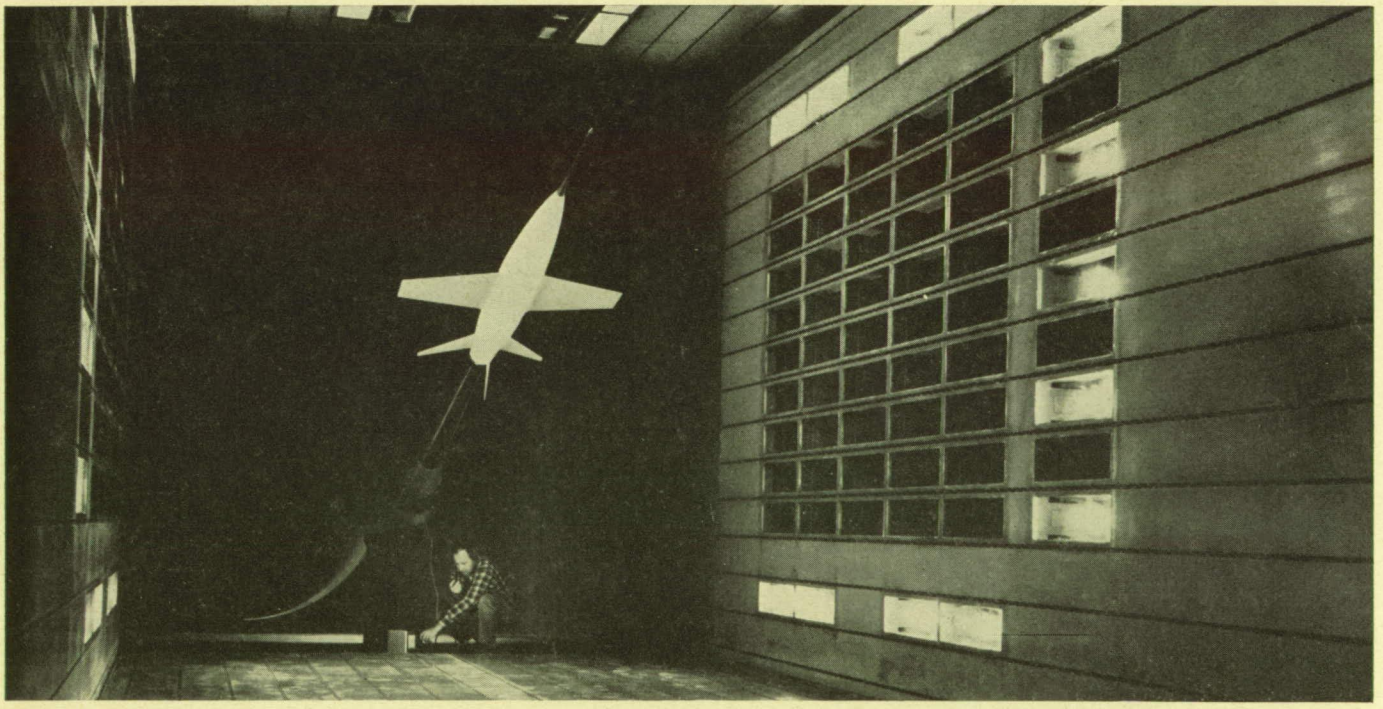
The NACA Langley Laboratory's low-drag wing was first used on the P–51 Mustang fighter, making it the fastest propeller-driven airplane of World War II.



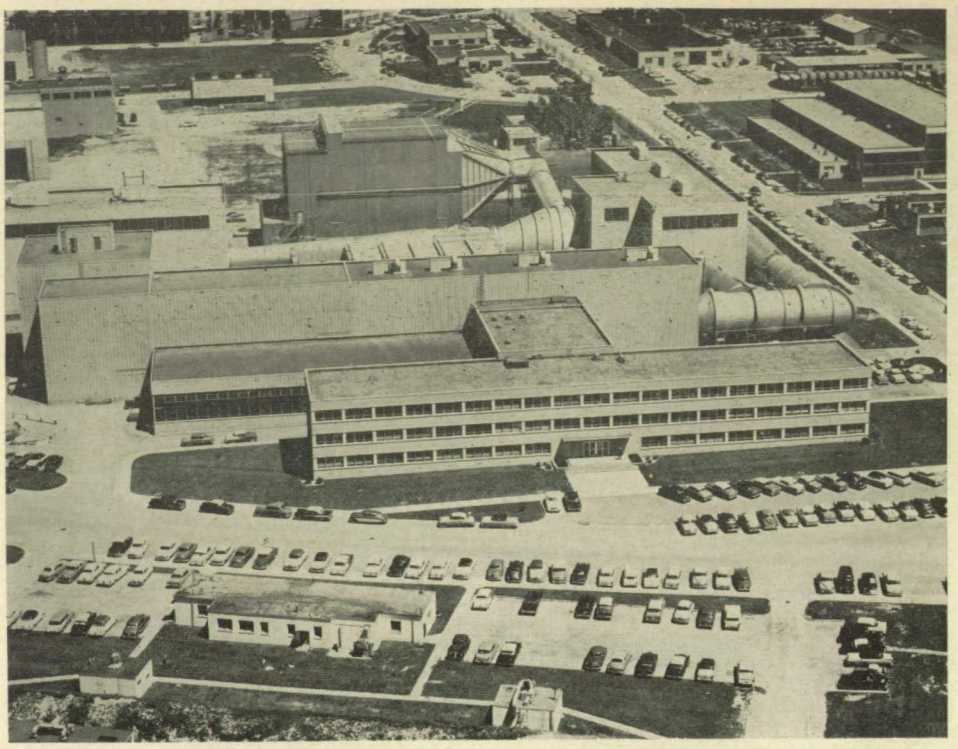
An engineer in NACA's towing tank at Langley Aeronautical Laboratory prepares a dynamic model equipped with hydro-skis for a test run.



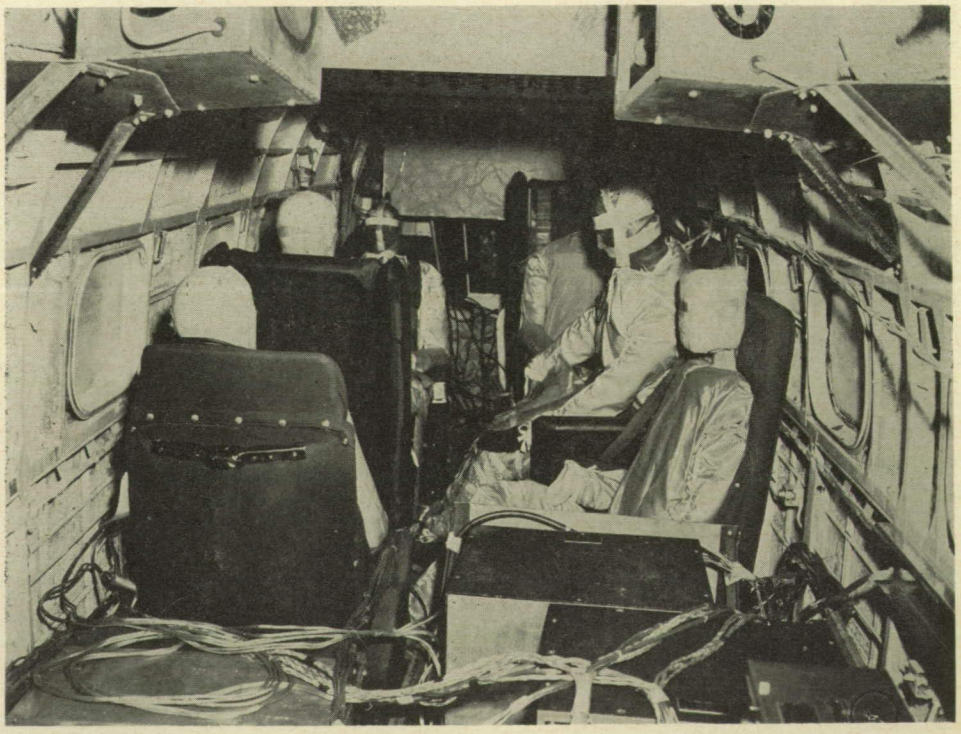
This rocket-powered model, one of a series tested by the NACA to investigate the flutter characteristics of low aspect ratio wings, shoots skyward toward the Atlantic Ocean from its launching ramp at the NACA Pilotless Aircraft Research Station, Wallops Island, Va.



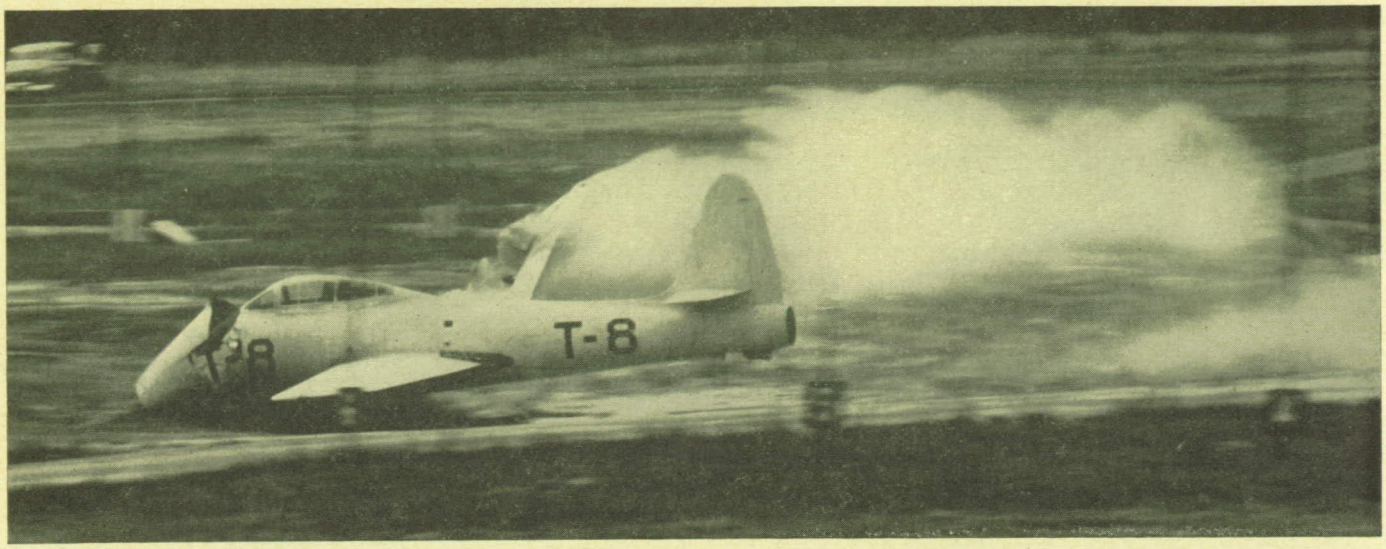
The 14-foot test section of the Ames Unitary Plan wind tunnel. It is capable of operating smoothly from subsonic speeds through the speed of sound to low supersonic values, a region where conventional wind tunnels are not usable, owing to choking. The perforated or slotted walls of the tunnel permit flow disturbances to pass through the open parts while retaining sufficient solid area to guide the air uniformly past the model. Two other test sections operate at speeds up to Mach No. 3.5.



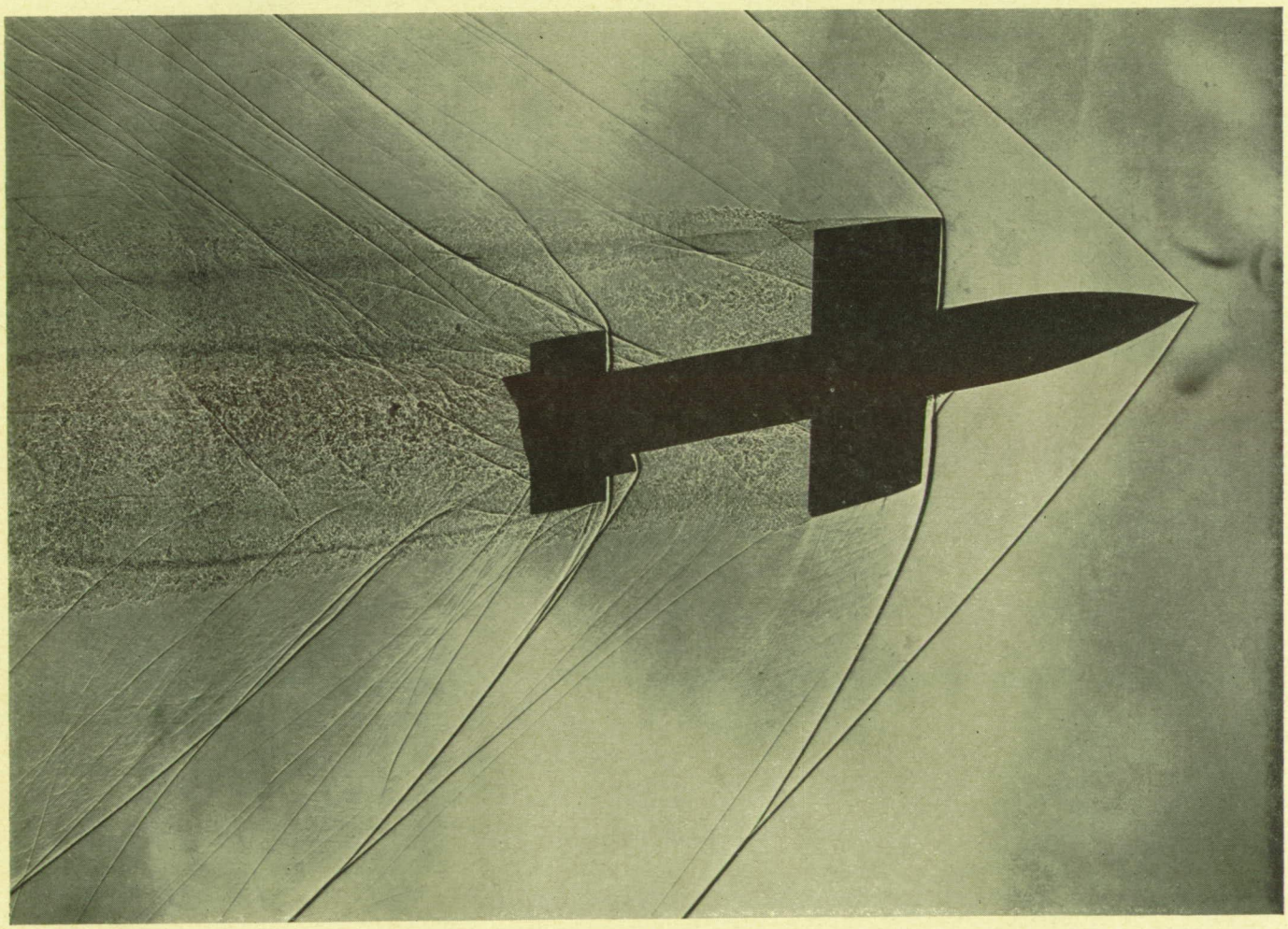
The NACA Lewis Laboratory's new 10-by-10-foot supersonic wind tunnel is used for research on aircraft power plants. This tunnel is designed for speeds of Mach Nos. 2 to 3.5.



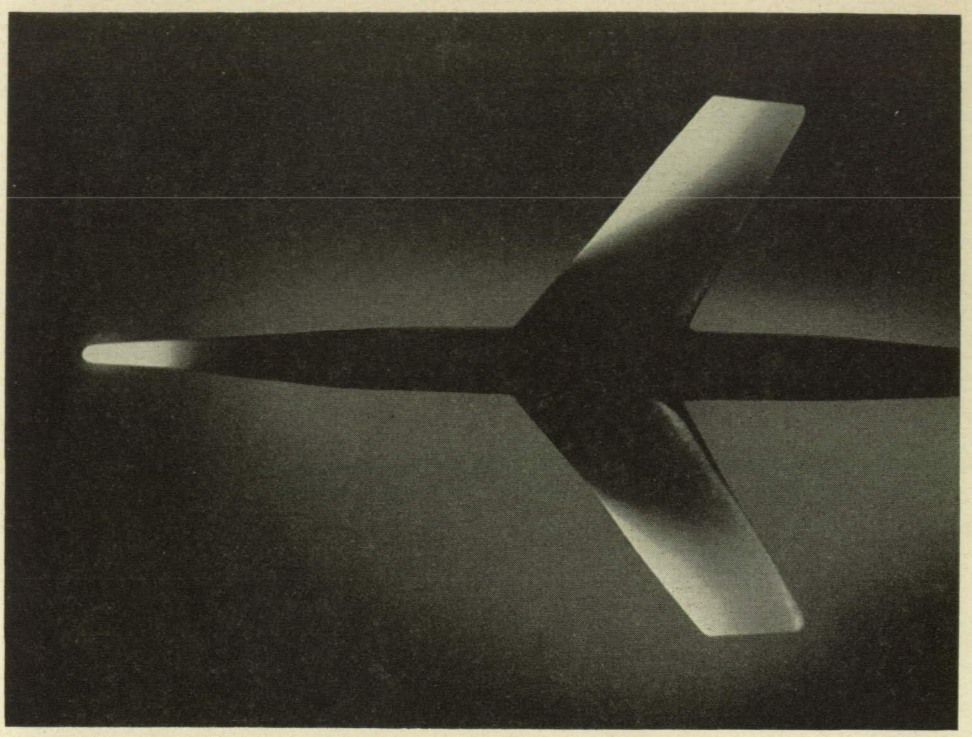
Six dummies, seated in various positions and in several types of seats, rode a service-weary Lodestar transport plane through a severe crash, one of a series staged by a research group of the NACA Lewis Flight Propulsion Laboratory. Objective of the crash program is to gather data on passenger and pilot survival problems in aircraft accidents.



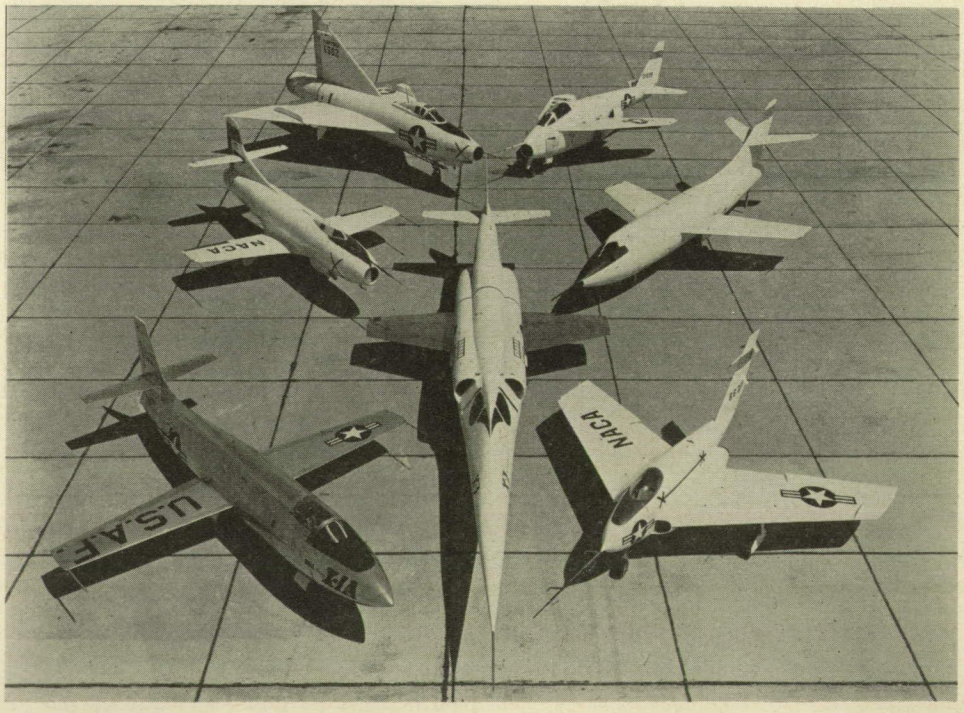
Damage was heavy but fire was prevented in this experimental crash because of a fire-inerting system devised by the NACA Lewis Flight Propulsion Laboratory. A series of crashes was staged with worn-out turbojet- and piston-powered aircraft to study problems of fire and human survival in crash accidents. The white cloud in the picture is jet fuel issuing from the ripped tank in the right wing.



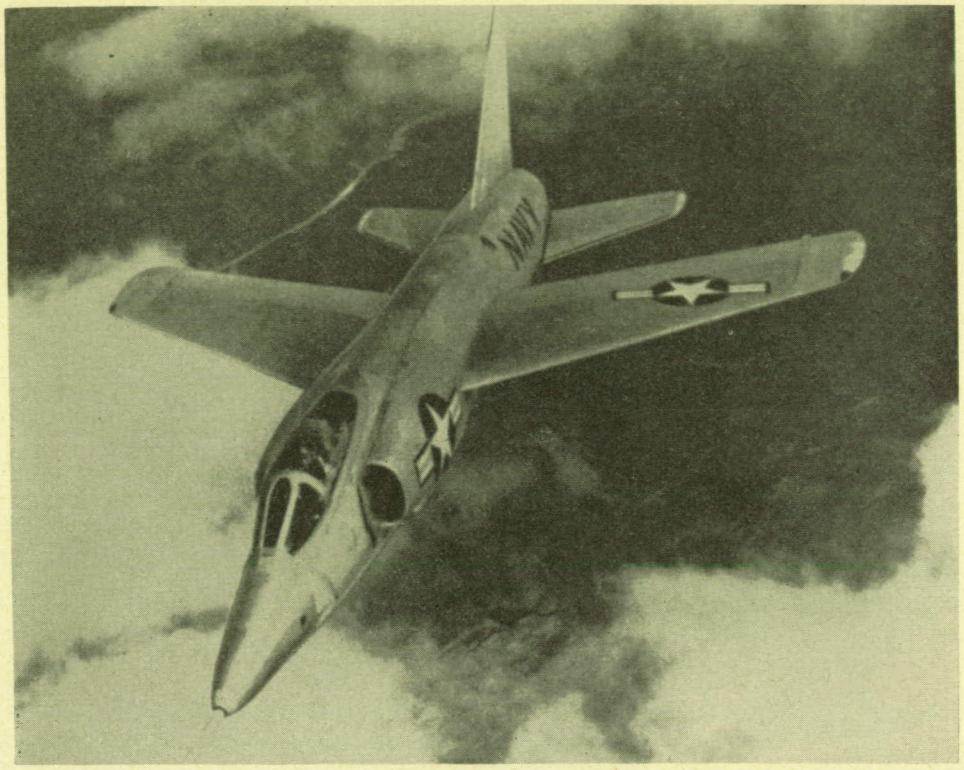
Caught in flight by shadowgraph technique, this free-flight research model shows the complicated pattern of shock waves and vortexes associated with high-speed flight. Vortexes are left in the wake of the model. The unsymmetrical shock-wave pattern shows that the model is turning. The model is 7 inches long and has just been fired from a 3-inch smooth-bore Naval gun into still air. Mach number at the instant of this photograph is 1.6.



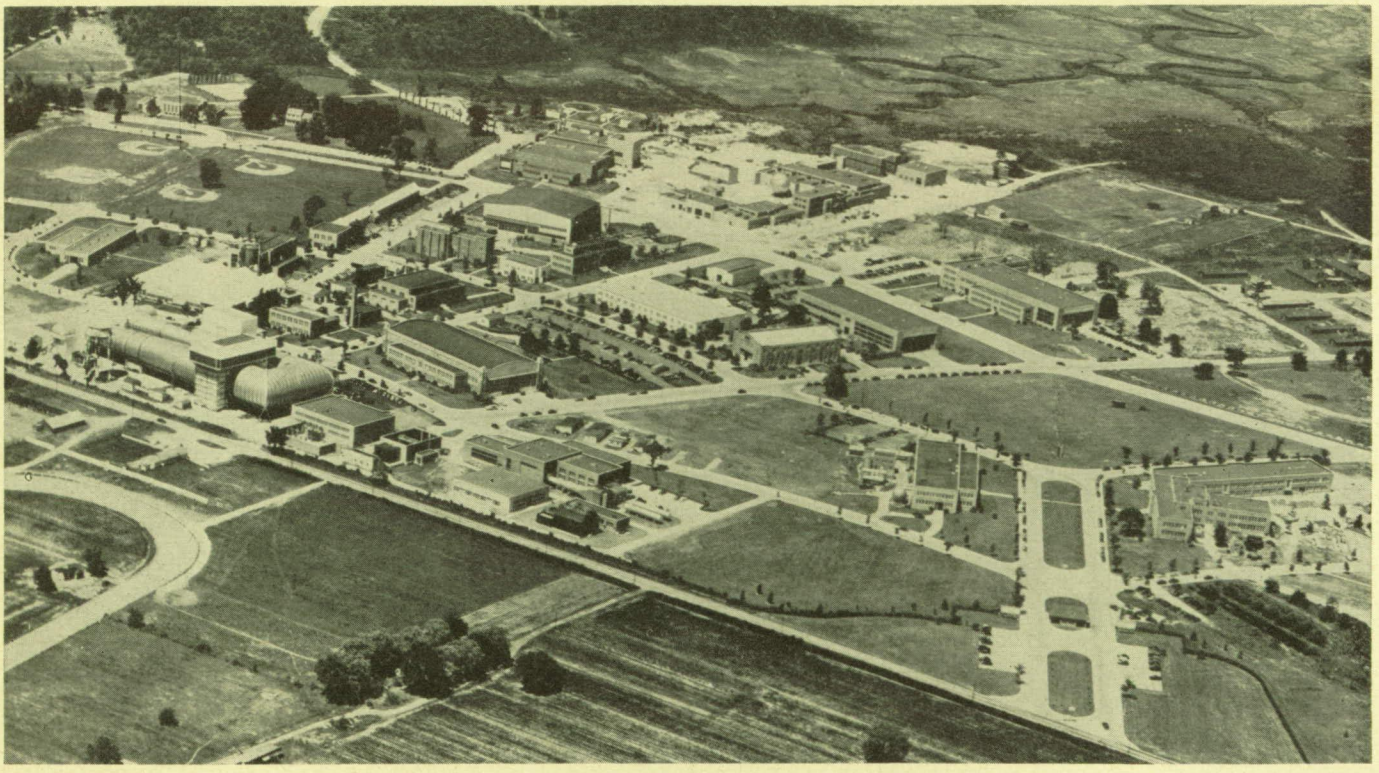
Infrared photograph of a laboratory experiment simulating aerodynamic heating. At 2,000 miles per hour, sustained flight could produce temperatures up to 1,200° F. Much additional research is required to permit successful operation under such conditions.



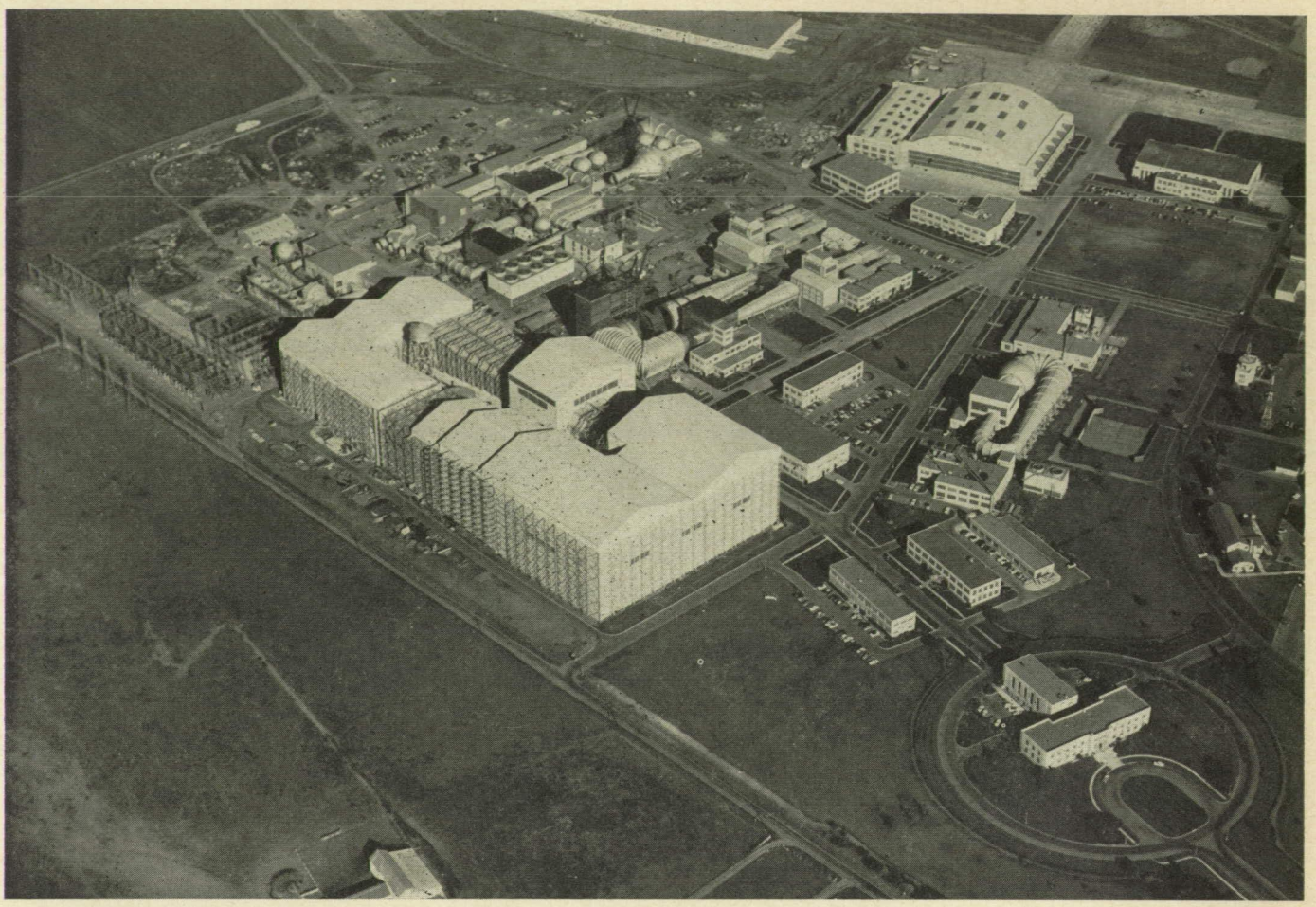
Flying regularly at transonic and supersonic speeds, these research airplanes are exploring new fields for data needed to design the military and civil airplanes of the future. In the center is the Douglas X–3; at lower left, the Bell X–1A flown late in 1953 at a record 1,650 m.p.h. or 2.5 times the speed of sound. Continuing clockwise from the X–1A are the Douglas D–558–I "Skystreak"; Convair XF–92A; Bell X–5 with variable sweepback wings; Douglas D–558–II "Skyrocket," first piloted airplane to fly at twice the speed of sound; and the Northrop X–4. The National Advisory Committee for Aeronautics, the Air Force, the Navy, and the aircraft manufacturing industry are joined to design, build, and fly these and other advanced airplanes in a high-speed flight research program.



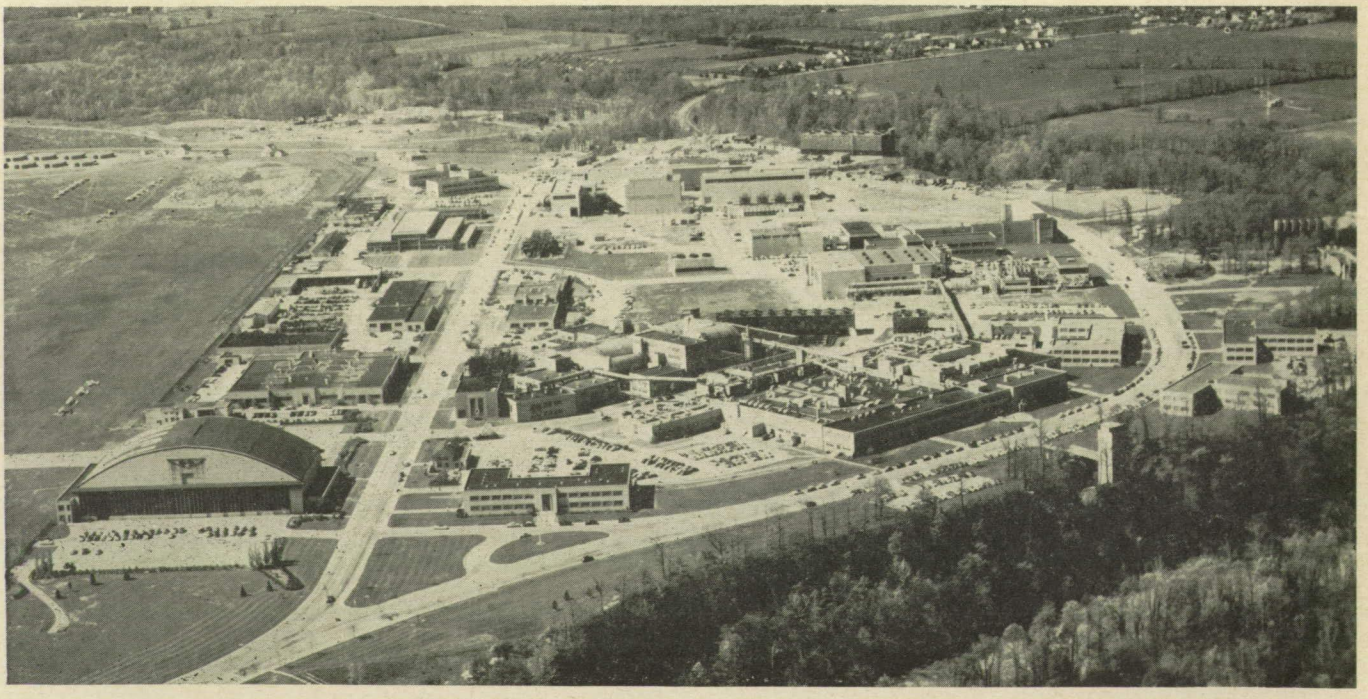
Grumman F11F–1. Use of the NACA-developed "area rule" concept for decreasing drag rise at transonic speeds gave this "Tiger" fighter plane supersonic performance. The "wasp-waisted" Navy carrier plane uses one-third less thrust than other airplanes of equivalent performance.



West Area, Langley Aeronautical Laboratory, Langley Field, Va.



Ames Aeronautical Laboratory, Moffett Field, Calif.



Lewis Flight Propulsion Laboratory, Cleveland, Ohio.

duce operating expenditures, these were successfully resisted, in the main, by such impressive evidence of the money value of the Committee's work as that just cited. On the favorable side was the opportunity for the NACA to construct at depression costs new research equipment with funds already appropriated, and the availability of engineers, from whom many of its future leaders have developed.

The 30- by 60-foot, "full-scale" wind tunnel and the 2,000-foot towing tank (for study of hydrodynamic characteristics of water-based aircraft) were completed in 1931. The designer of the $900,000 "full-scale" wind tunnel (then the world's largest) was Smith J. DeFrance, who became director of the Committee's second research center, at Moffett Field, Calif., when it was established in 1941.

A somewhat later "depression baby" was the 500-mph., 8-foot wind tunnel. For some time after its completion in 1936, it was known, somewhat optimistically, as the "full-speed wind tunnel." Other novel research equipment constructed at Langley in these years included a free-spinning wind tunnel and a refrigerated wind tunnel (for study of icing problems).

In this depression period NACA engineers first disclosed the ability to use air more than once. Soon after the variable-density tunnel was rebuilt following a fire in 1927, it was suggested that some use should be made of the air released each time the tunnel was returned to atmospheric pressure. Why not discharge the pressurized air through an appropriate nozzle and thus obtain a really high-speed airstream? The result was a blowdown device, with a 12-inch test section in which aerodynamic phenomena could be studied at speeds almost that of sound (about 760 mph. at 60° F.).

Thus far, the discussion of research by the NACA has been largely concerned with aerodynamics where the greatest effort was made. Nevertheless there was fruitful work on powerplants, loads, and structures, which will be noted later. In retrospect, one marvels that so much could be accomplished. At the beginning of 1930, for example, the total employment at the Langley Laboratory was only 181.

By the mid-thirties, the work of the NACA had become internationally known and respected. Somewhat earlier the British journal Aircraft Engineering had commented about the Committee: "They were the first to establish, and indeed to visualize, a variable-density tunnel; they have led again with the construction of the 20-foot propeller research tunnel; and . . . [with] a 'full-scale' tunnel in which complete aeroplanes up to 35-foot span can be tested. The present-day American position in all branches of aeronautical knowledge can, without doubt, be attributed mainly to this far-seeing policy and expenditure on up-to-date laboratory equipment."

Somewhat wryly, A. J. Sutton Pippard of the University of London observed in 1953 "that many of our most capable design staffs prefer to base their technical work upon the results of the American NACA."

An important effort of the NACA was to make its research findings fully available for use. First, there were Reports, comprehensive presentations expected to have lasting value. Then there were Technical Notes, preliminary or narrower in scope. Technical Memorandums were reprints, or translations, from the aeronautical literature of other nations. Aircraft Circulars reported information about foreign aircraft and engines. In later years Research Memorandums were added; these were limited in distribution for reasons of military security or because they contained proprietary information.

Recognizing the importance of knowing what was available in the aeronautical literature of the world, Dr. Ames had been instrumental in the formation of an Office of Aeronautical Intelligence as an integral part of the Committee's program, and for years he served both as its director and as chairman of the NACA's subcommittee on publications and intelligence. Beginning soon after World War I and continuing (except for a break in World War II) until 1950, the Committee maintained a technical assistant in Europe. From 1921 the post was held by John Jay Ide, who faithfully and intelligently served the NACA both as European reporter and in a liaison capacity with foreign aeronautical research organizations. It was decided in 1950 to close the NACA's European office because the art and science of aeronautics had become too complex for reportage by a one-man bureau. International exchange of information is now handled by other means.

Beginning in 1926, the Committee sponsored an annual conference at the Langley Laboratory with representatives of the military services and the industry. In addition to the opportunity to see what the NACA was doing, guests had an occasion to criticize and to suggest new research on problems they felt were especially pressing. In the first years of the conference, "everyone" from the industry and the military services attended; even so, the guest list numbered little more than 200, and the journey to and from Langley, via Potomac River steamer, resulted in many unofficial but profitable sessions. After World War II, it became necessary to provide two types of meetings: (1) Technical conferences concerned with a specific subject, usually classified for security reasons, e.g., supersonic aerodynamics. (2) Inspections. Held annually, on a rotating basis at each laboratory, the NACA inspections seek to give the industry and military services a comprehensive view of technical progress. As many as 1,500 attend these meetings, which are not classified.

Also of importance from the standpoint of communication is a steady traffic of industry and military visitors

to NACA research centers. Much is accomplished by discussion of matters of specific concern to those involved. No less important are the visits by NACA technical personnel to specific industry plants.

Beginning in the mid-thirties, the NACA reported annually to the Congress and to the President that certain European nations were making a determined effort to achieve technical and quantitative supremacy in aeronautics. Each year the Committee's comments on this subject were stronger. In 1937, for example, Dr. Ames reported: "The greatly increased interest of the major powers in fostering aeronautical research and their determined efforts to excel in this rapidly expanding engineering science constitute a scientific challenge to America's present leadership." He explained:

> Up to 1932 the Committee had constructed at its laboratories at Langley Field . . . special equipment such as the variable-density tunnel, the propeller-research tunnel, the full-scale tunnel, and . . . a seaplane towing basin. They were at the time of construction the only such pieces of equipment in the world. The possession of such equipment was one of the chief factors in enabling the United States to become the recognized leader in the technical development of aircraft. Since 1932 this research equipment has been reproduced by foreign countries and in some cases special research equipment . . . abroad . . . is superior to the equipment existing at Langley Field.
>
> This condition has impressed the Committee with the advisability of providing additional facilities promptly as needed for the study of problems that are necessary to be solved, in order that American aircraft development, both military and commercial, will not fall behind.

EXPANSION OF FACILITIES

In 1938, the Committee reported that its laboratory employees at Langley Field were "working under high pressure." It warned that "the recent great expansion of research facilities by other nations will bring to an end the period of American leadership in the technical development of aircraft unless the United States also constructs additional research facilities." Dr. Ames, in October 1938, appointed a Special Committee on Future Research Facilities to make recommendations.

But even before the Special Committee met, the NACA was making a strong recommendation for special facilities for research on aircraft structures. "With the advance in size and speed of aircraft . . . the problems involved require the conduct of laboratory research on structures on an increasing scale," the Committee wrote Congress. "This is the greatest single need for additional research equipment and . . . in the interests of safety and of further progress in aeronautics, it should be provided at the earliest possible date."

On December 30, 1938, the Special Committee recommended immediate establishment of a second NACA research center, in California, to relieve what the late Maj. Gen. Oscar Westover (then Chief of the Army Air Corps and a member of the NACA) called "the congested bottleneck of Langley Field." Although the recommendations had been presented as emergency in character, it was not until midsummer—August 9, 1939—just before the start of World War II, that the second laboratory was authorized by Congress. Hardly a month later, September 14, ground was broken at Moffett Field, some 40 miles south of San Francisco, for what became the Ames Aeronautical Laboratory.

Earlier that year an expansion of Langley facilities was authorized by Congress. S. Paul Johnston (now managing head of the Institute of the Aeronautical Sciences) was named Coordinator of Research to assist Dr. Lewis. Further intensification of research effort obviously was needed in the face of war in Europe, and a second Special Committee, headed by Charles A. Lindbergh, was appointed. This group recommended, October 19, 1939, that a powerplant research center be established at once.

"There is a serious lack of engine research facilities in the United States," Lindbergh's committee stated. "The reason for foreign leadership in certain important types of military aircraft is due in part to the superiority of foreign liquid-cooled engines. At the present time, American facilities for research on aircraft powerplants are inadequate and cannot be compared with the facilities for research in other fields of aviation." It was June 26, 1940—after Belgium and Holland had been overrun—that congressional authorization for the new flight-propulsion laboratory was forthcoming.

A site was made available by the city of Cleveland adjacent to its municipal airport. Immediate steps were taken by Dr. Lewis to plan and construct a complex of laboratories equipped with facilities for the investigation of airplane engines, their parts and materials, fuels and lubricants, ignition and combustion, heat transfer and cooling, intake and exhaust aerodynamics, as well as for the fundamental physics, chemistry, and metallurgy of power generation. In addition, facilities were provided for flight testing in laboratory-instrumented airplanes—practical flying laboratories for propulsion research.

There is no doubt that this flight-propulsion center was a large step in advance of any comparable facility in the world. It has cost up to date about $110 million and now employs about 2,800 people.

After the death of Dr. Lewis in 1948, the Committee decided on the name "Lewis Flight Propulsion Laboratory," as a memorial to that great engineer's crowning achievement.

Here it may be proper to explain why the research effort on powerplants and on structures had been so much less than that devoted to aerodynamics. In the first place, it must be remembered that between World Wars I and II, the United States was an intensely peace-minded nation. In addition, the thousands of

miles of ocean to our east and west gave a feeling of safety from attack, a complacent sense of detachment. The Congress was unwilling to expend really large sums for national defense or on research to improve it.

Until the eve of Pearl Harbor, the annual expenditure by the United States to support aeronautical research was indeed modest. Even as late as the summer of 1939, the NACA's total complement was 523, including only 278 technical people.

The major effort by the NACA over the years had been deliberately concentrated on aerodynamic problems. Here, for a given expenditure, the possible gains to be achieved were very large, particularly in view of the relatively few engineers who could be assigned to the work.

Powerplant research and structural research are expensive, and require extensive facilities for full-scale investigations. Small models are of limited utility in powerplant research. Furthermore, powerplants and structures are the immediate concern of strong and highly competitive industrial firms. The Committee evidently felt that under its fiscal restrictions, it would do better to concentrate on basic aerodynamic problems and might, hopefully, leave research and development of powerplants and structures to the industry and the military services.

However, the Lindbergh committee in 1939 said that this past policy was wrong, and the NACA agreed. It appeared that leaving fundamental research to the industry meant, in effect, that such research would be indefinitely postponed.

A competitive engine firm must concentrate on what its customers want. The firm improves its engine with small changes based on experience. It seeks the minimum risk of interruption of production. The military services, its principal customers, conduct competitive trials based on standard performance specifications. After quantity orders are placed, no major changes are possible. The services, of course, welcome small changes based on experience, if the risk of trouble be slight. As a result, engine development tends to adhere to a definite pattern and progresses slowly.

An engine manufacturer must make a relatively heavy investment in plant and tooling for production of a particular engine. The manufacturer is naturally inclined to concentrate on improvements in this engine to prolong its commercial life. These improvements are essentially proprietary in character.

Similar remarks apply to the airplane industry. Every effort is made to improve a particular airplane to prolong its vogue in production. This development effort is restricted to conservative changes in a basic design acceptable to the customer.

In this country, the Navy standardized on air-cooled radial engines that met Navy requirements, while the Army insisted on 12-cylinder, liquid-cooled engines to power the fighters in their program.

However, there were important fundamental applications of science to engine design that needed investigation in 1940.

From the beginning, one of the principal technical committees of the NACA was concerned with powerplants. During World War I, a few research projects in the powerplant field were carried on under its auspices, notably in the altitude facility at the Bureau of Standards, where engines could be operated under conditions simulating those experienced by high-flying aircraft. A program of systematic tests was conducted there for the NACA, including supercharging with a Roots-type blower.

At Langley the small but expert powerplant staff made some important contributions, in addition to their cooperation with the wind-tunnel people in developing the remarkable NACA cowling for air-cooled engines. One recalls improved finning for air-cooled engine cylinders, methods to decrease the octane requirements of high-compression engines, and work on such fundamental matters as the behavior of fuels—how they ignite, how they burn, and how this burning corrodes critical parts of the engine. A principal tool in the study of these latter questions was high-speed photography, and cameras capable of taking pictures at the rate of 400,000 per second were developed by the NACA.

In the field of jet propulsion the NACA exhibited an early awareness of its possible advent but did little about it. In 1923, in Report No. 159, "Jet Propulsion for Airplanes," Edgar Buckingham of the Bureau of Standards, reported that: "The relative fuel consumption and weight of machinery for the jet decrease as the flying speed increases; but at 250 mph. the jet would still take about four times as much fuel per thrust horsepower-hour as the air screw, and the powerplant would be heavier and much more complicated. Propulsion by the reaction of a simple jet cannot compete, in any respect, with air screw propulsion at such flying speeds as are now in prospect." This conclusion was entirely rational on the basis of the technology at that time.

In the early thirties, the NACA was asked by a representative of the airframe industry to resurvey jet-propulsion prospects and, although airplane speeds by then had passed the 250-mph. mark which Buckingham considered a goal, the story was much the same. The inefficiency of the jet engine at the speeds contemplated ruled it out of consideration.

Near the end of the 1930's, some preliminary experimental work on jet propulsion was undertaken at the Langley Laboratory. These experiments indicated that jet engines would be so fuel thirsty as to limit their useful application to very high-speed, very

526597—60——3

short-range aircraft. American thinking, perhaps because of geography, was focused on long-range performance where fuel economy was paramount. This idea served to discourage any real jet-development effort in the United States until intelligence of British and German experiments reached us.

In March 1941, Dr. Durand was recalled from retirement to head a special NACA Committee on Jet Propulsion. The fact that he was in his 82d year was only a matter of calendar counting. The vigor with which he and his committee launched a belated development effort would have done credit to a man less than half his age. Later in 1941, Gen. H. H. Arnold secured from the British one of the earliest of the Whittle jet engines to aid the development program initiated by Dr. Durand. In this program, the Durand committee was handicapped by the fact that the country had just been plunged into a war for which it was ill prepared and the principal airplane-engine firms were overloaded. The decision came "from the summit" that we would fight with the weapons in hand. First priority was given their production in immense quantity. Consequently, the Durand committee had to arrange with nonaeronautical firms to undertake the development of turbojet engines for possible later use to power fighter airplanes.

Over some 20 years, aerodynamic and powerplant improvement, much of it based on application of research results, permitted the top speed of military airplanes and the cruising speed of commercial airplanes to be doubled; the air loads imposed on the faster airplanes were severely increased, especially in rough air and when maneuvering.

The loads research group at the Langley Laboratory consisted of but 20 men in 1939, but their contribution was considerable, notably the V–G recorder (V for velocity, G for gravity) by R. V. Rhode and H. J. E. Reid. It was devised to measure continuously the loads experienced by an airplane flying in rough air. This was but one of many novel instruments which NACA engineers have devised for precise measurements in flight.

The research problem directly related to loads deals with structures to carry the loads. Here again the manpower available at Langley prior to World War II was small; as late as October 1940, only 10 men were working on airplane structures. Their work was concerned, principally, with fundamental knowledge about structures from which a trustworthy theory could be developed for design application. Delicate experiments and mathematical analyses dealing with the behavior of thin-walled cylinders, stiffened panels, and other structural units produced useful conclusions that were used on our World War II aircraft.

On October 7, 1939, Dr. Ames resigned from the Committee because of failing health. His responsibilities as chairman of the Committee were given to Dr. Vannevar Bush, who had been serving both as vice chairman and as chairman of the executive committee.

Note has been made already of the manner in which Dr. Ames had provided leadership of the highest quality to the Committee for nearly a quarter-century. The letter President Roosevelt wrote upon the occasion of his retirement contained this statement:

> Our Republic would not be worthy of the devoted service you have rendered for over 24 years without compensation if it could not on this occasion pause to pay tribute where it is so justly due. . . . That the people generally have not known of your brilliant and patriotic service is because it has been overshadowed by your passion for accomplishment without publicity. But the fact remains, and I am happy to give you credit, that the remarkable progress for many years in the improvement of the performance, efficiency, and safety of American aircraft, both military and commercial, has been due largely to your own inspiring leadership in the development of new research facilities and in the orderly prosecution of comprehensive research programs.

The Committee resolution, tendered to Dr. Ames in Baltimore by a special delegation, said:

> When aeronautical science was struggling to discover its fundamentals, his was the vision that saw the need for novel research facilities and for organized and sustained prosecution of scientific laboratory research. His was the professional courage that led the Committee along scientific paths to important discoveries and contributions to progress that have placed the United States in the forefront of progressive nations in the development of aeronautics. His was the executive ability and far-sighted policy of public service that, without seeking credit for himself or for the Committee, developed a research organization that holds the confidence of the governmental and industrial agencies concerned, and commands the respect of the aeronautical world. Withal, Dr. Ames was an inspiring leader of men and a man beloved by all his colleagues because of his rare qualities.

In July 1941, the President appointed Dr. Bush director of the newly established Office of Scientific Research and Development, and he resigned as chairman of the NACA. The writer was elected chairman, an honor he has been privileged since to hold.

WORLD WAR II AND AFTER

The war years for the NACA were plagued by the necessity for rapid expansion of the civil service staff from hardly 500 in 1939 to more than 6,800. Trained engineering personnel were unavailable. Consequently, it was mandatory that professionals be spread ever thinner, while loom fixers, toymakers, mechanics, blacksmiths, and women schoolteachers were recruited for jobs they could do or for which quick instruction could be given.

Especially in the matter of skilled management of research programs, the NACA might have been expected to be sorely weak. And yet, somehow, with each expansion of effort, new leaders were found from within the permanent NACA staff. No sooner did Henry

J. E. Reid, director of the Langley Laboratory, see some of his best men on their way to build the new laboratory at Moffet Field—named in 1944 in honor of Dr. Ames—than the process of designating the leaders of the new engine laboratory—named in honor of Dr. Lewis in 1948—was begun. Smith J. DeFrance was named director of the Ames Aeronautical Laboratory, and later Edward R. Sharp became director of the Lewis Flight Propulsion Laboratory. Both of these men were senior members of the permanent staff at Langley.

NACA's war effort was of necessity devoted very largely to applied research, the business of finding "quick fixes" to make existing aircraft better performers, and production engines more powerful. Fortunately, a considerable backlog of design data was available for application to such subjects as low-drag wings, high-speed propellers, stability and control, and improved systems for cowling and cooling engines. Between December 1941 and December 1944, the Committee's research centers worked on 115 different airplane types. In July 1944, 78 different models were under simultaneous investigation.

Perhaps the best comment on the value of NACA's World War II work is to quote from a statement by the late Frank Knox, made in 1943 when he was Secretary of the Navy:

> New ideas are weapons of immense significance. The United States Navy was the first to develop aircraft capable of vertical dive bombing; this was made possible by the prosecution of a program of scientific research by the NACA. The Navy's famous fighters—the Corsair, Wildcat, and Hellcat—are possible only because they were based on fundamentals developed by the NACA. All of them use NACA wing sections, NACA cooling methods, NACA high-lift devices. The great sea victories that have broken Japan's expanding grip in the Pacific would not have been possible without the contributions of the NACA.

The end of World War II marked the end of the development of the airplane as conceived by Wilbur and Orville Wright. The power available in the newly developed turbojet and rocket engines for the first time brought within man's reach flight through and beyond the speed of sound.

In the years following World War II there were changes, too, in the membership of the Committee. In 1948, the death of Orville Wright closed 28 years of his membership on the NACA. Though he was but one among many strong men who had given of time and talent to the work of the Committee, his passing sharpened the realization that in the working years of one man's life—between December 17, 1903, and January 30, 1948—the speed of the airplane had been increased from hardly 30 mph. to almost 1,000 mph.

In 1948 the membership of the Committee was increased to 17. This permitted the inclusion of a representative from the Department of Defense, presently the Assistant Secretary (Research and Development). Since the war the Committee has included one Presidentially appointed member from the airframe, the engine, and the air-transport industries, thus insuring awareness of the needs of those major segments of American airpower.

In 1948 Dr. Lewis died. In 1945, his health broken by the war effort, he had been forced to withdraw from active participation in the work of the Committee. For almost 2 years, John W. Crowley, Jr., served as acting director of aeronautical research. With the Committee since 1921, Crowley had been chief of research at Langley for a number of years. He provided vitally needed leadership during a critical period.

To succeed Dr. Lewis, the Committee in 1947 chose the Associate Director of the National Bureau of Standards, Dr. Hugh L. Dryden. He was no stranger to the NACA. Trained in physics and mathematics by Dr. Ames at Johns Hopkins University, he had gone to the Bureau of Standards in 1917, where he soon earned an international reputation by his aerodynamic researches in turbulence and boundary layer. His new task at the NACA was extremely difficult, yet it was vital to the Nation that a "new look" at the postwar situation be taken, and new objectives defined in terms of supersonic jet-propelled vehicles potentially available for the worldwide exercise of air power and, eventually, for civil air transportation.

At the end of World War II, the most urgently sought goal was attainment of practical flight at supersonic speed. It was realized that success in this effort required new knowledge which could be obtained only with new tools and new techniques. Even before the end of the war efforts were made to acquire needed data. Efforts to develop useful transonic aerodynamic theory had failed and it was necessary to resort to direct experimentation at velocities passing through the speed of sound. The fact that the principal tool of aerodynamic research, the wind tunnel, was subject to "choking" phenomena near the speed of sound forbade its use for the critical experimentation. Entirely new techniques had to be devised. The NACA's attack was broadened to include all approaches which offered promise.

The earliest attempt used especially instrumented aerodynamic bodies dropped from a high altitude, but it was not until late in 1943 that advances in radar and radiotelemetering equipment made it possible to obtain reliable data by this method. Even then, the velocity of a free-falling body seldom went much beyond a Mach number of 1 ($M=1$ equals the speed of sound).

Other attempts sought to use the acceleration of airflow above a curved surface. Small model wings were mounted near the leading edge of the wing of an airplane. In this way, lift, drag, and other aerodynamic characteristics of the model were measured. The meth-

od was employed also to study stability and trim of airplane shapes in the transonic speed range. The same principle of accelerating airflow was tried with small models positioned over a "hump" in the test section of a subsonic wind tunnel, but scale effects complicated the interpretation of test results for use in design.

Use of rocket-propelled models fired from the ground followed the first work with free-falling bodies by about a year. As instrumentation has been improved, this technique has become a valuable tool for transonic research. By the addition of powerful booster rockets, models of this kind are being used to study aerodynamic problems at speeds ranging up to a Mach number of 10 and higher. The fact that very high speeds are reached at low altitude, where the air is dense, makes the aerodynamic data readily usable for plane and missile design. In 1945, the NACA established a Pilotless Aircraft Research Station at Wallops Island off the Virginia coast, to carry on this work. It is attached to the Langley Laboratory.

In 1943, the idea was advanced of using specially designed piloted airplanes to explore the transonic speed range. Propelled by powerful rocket engines and provided with elaborate data-recording equipment, the research airplane could be safely flown at high altitudes where the density of the air, and hence the loads imposed on the structure, would be low.

The spectacular accomplishments of the research airplanes—the supersonic flight of the Bell X–1, October 14, 1947; the twice-the-speed-of-sound flight of the Douglas D–558–II, November 20, 1953, and the even faster flights of the Bell X–1–A which followed soon after—have sometimes obscured the fact that these airplanes were tools for research. These flights are historic; all agreed as to the rightness of the Collier Trophy award to three men for the year 1947: John Stack, Langley Laboratory, for conception of the research airplane program; Lawrence D. Bell, for design and construction of the X–1; and Capt. Charles E. Yeager, USAF, for making the first supersonic flight.

But even more valuable than the dispelling of the myth about the sound barrier was the accumulation of information about the transonic speed region. The shape and the performance of tactical military aircraft which have been designed since reflect the use of data obtained by the research airplane program centered at the NACA's High-Speed Flight Station at Edwards Air Force Base, Calif.

Despite the success of this flight program, there remained the need for a technique whereby transonic experimentation could be carried on under the closely controlled conditions possible only in the laboratory. Actually, the data coming from the research airplanes accented this need, because they pointed up the fundamental problems of fluid mechanics that would have to be studied in great detail for the design of useful supersonic aircraft.

By late 1950, following intensive theoretical work, there was put into operation at the Langley Laboratory a new type of wind tunnel. Incorporating a "slotted throat" at the test section, it was free from choking near the speed of sound and truly could be described as a transonic wind tunnel. Again, the Collier Trophy was awarded to John Stack and his Langley associates for the conception, design, and construction of this most useful research tool.

One must appreciate the very great difference between airplane design in the past and today. In the past, the difference between the best design and the second best, assuming the same power, might be at most only a few miles an hour. Now the difference may be measured in hundreds of miles an hour. The art is being extended so rapidly that no longer is there a comfortable time margin between the acquisition of research data and its application.

Hardly had the first of the NACA's transonic wind tunnels gone into full operation, in 1951, when Richard T. Whitcomb, a young engineer at the Langley Laboratory, began the experimental verification of what has since become known as the "area rule." In essence, Whitcomb worked out a rational way to balance the lengthwise distribution of volume of fuselage and wings to produce an airplane form with minimum drag at high speeds. Seemingly slight modifications to the shape of the airplane fuselage greatly improved performance.

As soon as the new design principle was verified in preliminary form, it was made available in confidence to the designers of military airplanes and the new information was promptly applied.

In one instance, the prototype of a new fighter aircraft was unable on test to attain supersonic speeds. With the deceptively subtle modifications dictated by the "area rule," the airplane enjoyed a performance gain in speed of as much as 25 percent.

At the velocities contemplated for our future missiles and airplanes, temperatures measured in thousands of degrees Fahrenheit will be encountered owing to aerodynamic heating—friction. The consequent structural problems are little short of fantastic and, with presently available materials of construction, the solution is not in sight. More research is needed.

The performance possible from the harnessing of nuclear energy for airplane propulsion would be nonstop flight over virtually unlimited range. Again, one is faced with problems of enormous complexity and difficulty, but national security requires that research and development be carried forward with imagination and vigor.

Millions of passengers are now carried by air. Air transportation also expedites the delivery of great volumes of mail and goods. Airliners regularly span oceans and continents, and smaller utility planes serve remote regions in the Arctic and tropical jungles. There is promise of helicopter service between nearby cities, with no need for large outlying airports.

The safety record of civil aeronautics is remarkably good, but it is never good enough. We still read, from time to time, of disasters from collision, fire, storm, human error, and, rarely, from structural or mechanical failure of the airplane itself. The human pilot is aided by wonderful instruments and by radio, radar, gyros, etc., but we still depend on his judgment and skill. He must be better protected against noise and fatigue—subjects for research.

Air transportation is fast and can be faster. But greater flight speed is illusory if it requires too long a climb to reach the high altitude necessary for economy. Furthermore, higher speed airplanes tend to require longer runways and bigger airports. This could mean a new program of airport building at colossal expense, with the new airports even farther from the passengers' ultimate destination. Getting to and from the airport could consume more time than is saved by faster flight. Research continues on improving landing and takeoff characteristics of airliners.

It may be that airliners of the future will be designed to the limitations of the airports they are to serve, just as transatlantic steamers are designed to enter only a few major seaports, where the channel and piers have adequate depth of water.

Civil aeronautics can make its greatest contribution to trade and commerce under a favorable international climate of free interchange of people, goods, and ideas. Greater economy, efficiency, and safety are prerequisites for its full utilization. Research can show the way to advance toward these goals.

Through the years the NACA has been provided by Congress with the most modern research equipment at a total cost of approximately $300 million, and the present operating staff numbers about 7,600 persons, of whom over 2,000 have professional degrees. These resources, in the present hostile and threatening international climate, are directed for the most part toward research helpful to national security. Research to improve military aircraft is ultimately applied to civil aviation, when proved to be thoroughly practical by experience, but there are differences in emphasis, because safety, comfort, and economy are relatively more important in civil airplanes. The Committee has numerous investigations in progress which are directed toward the immediate problems of civil aviation, as for example the work on noise, icing, fire prevention, atmospheric turbulence, and reduction of landing speed.

A more favorable international climate would permit greater emphasis on civil aviation, but it is likely that for some time to come the national security will require a great effort to penetrate more rapidly into the vast region of the unexplored and unknown. The Committee feels its responsibility for guidance of the overall research effort in aeronautics, and it is hoped that through its work aeronautics may make the maximum possible contribution to human welfare.

The Following Years

1955–58

By James H. Doolittle
Chairman NACA, 1956–58

The latter years of the NACA were among its most productive. It was almost as if the talented scientists and engineers of the organization during the years of World War II when they were so intensively engaged in efforts to improve current airplanes, had been saving up bold, big ideas about how to accomplish dramatic improvements in aircraft performance. Once peace was restored, even though it was soon to prove an ephemeral thing, there was a steady flow from the people at the Langley, Ames, and Lewis Laboratories, of new information about the laws governing flight that the designers of the industry could incorporate quickly into their new aircraft. Much of what I shall describe in this brief summary belongs, really, to the 40-year period covered by Dr. J. C. Hunsaker's preceding account of the NACA. The principal reason he could not include this information was security. There is much more I should like to say about current work, but again, some of the story must await a future occasion.

One of the most important aspects of NACA research during the postwar years was the systematic study of such problems as aircraft and rocket fuels. Any high school or college chemistry student can look at the charts and determine that hydrogen has the highest energy content per pound and therefore should be a principal element in the ideal fuel, the one that will produce the most thrust per pound. The goal is to devise such an ideal fuel and methods of practical use in the face of such obstacles as toxicity, availability, cost, etc. Here, there is no easy quick path to accomplishment; hard work, sustained research over long periods, is the only sure way to success.

At the Lewis Laboratory, beginning with the closing days of the war, a program to develop "super fuels" was begun that, even in mid-1958, is still producing useful information. Progress, long-range progress, has been and continues to be made, despite a succession of inevitable disappointments. One promising lead after another had to be studied and discharged until it became known that the answers were to be found elsewhere. Finally, of course, this systematic effort pointed toward the "best answers."

For example, one way to obtain more powerful, more useful fuels was to burn such materials as aluminum or magnesium. The problems of compounding slurries of these metals had to be solved, but when solutions to these problems were found, the realization followed that this approach was not useful, for reasons that need not be dealt with here. Other solutions to the problem had to be sought. In passing, I should like to emphasize that in the business of learning how to fly faster, higher, and farther, it is sometimes very important to *learn what won't work*. With this essentially negative information in hand, it then becomes possible to work rapidly and surely toward goals that will pay off.

Even today, the subject of "exotic fuels" remains heavily classified. I may state, however, that basic produce the most thrust per pound. The goal is to dework by scientists and engineers at the Lewis Flight Propulsion Laboratory on fuels incorporating boron compounds has been so successful that large industrial plants have been built to produce these new fuels. They will be used to send our new bombers and interceptors to speeds approaching or exceeding 3 times that of sound (2,000 mph) over very long ranges.

Before turning to other aspects of NACA research, it is appropriate to mention the work being done to find ways and means of providing rocket motors having the greater thrust needed by the ballistic missiles of today and the spacecraft of tomorrow. These efforts include studies of such basic fuel components as hydrogen and fluorine. Slightly farther away on the time scale is the development of engines utilizing nuclear energy. Here, the NACA people have been in closest cooperation with their opposite numbers in the Atomic Energy Commission. Again it is too early to describe in detail the progress that has been made; we must be content to observe that substantial progress is being made. Also some time in the future will come exploitation of "electric propulsion," including such devices as ion jets and plasma jets. We must succeed in learning how to design and build these completely new engines by the

Preceding Page Blank

day, not too distant, when we shall be ready to launch voyages of discovery to Venus and Mars, and beyond. A good start has been made; there is much more to do.

In the area of aerodynamic loads and structures, the goal remains much the same as in the earliest days of NACA, to learn how to make our airplane structure, and more recently, our missile and spacecraft structures, strong enough to withstand the greater loads imposed by the greater speeds we are attaining, with, of course, the continuing stipulation that our structures contain not 1 ounce of unnecessary weight. The total structures problem is made the more difficult because our airplanes have attained speeds where aerodynamic heating—air friction—imposes new and more difficult requirements. We have to think in terms of materials that will maintain their high-strength characteristics at temperatures beyond the 1,000° F mark. We have to take into account problems of thermal stress that, by themselves, are complicated and hard to solve. And, all the time, we have to remember that weight must be kept to the absolute minimum. All this has made necessary the calculation, to the closest numbers possible, of the structural requirements that will just satisfy our needs.

Difficult as is this problem with respect to airplanes and guided missiles, it becomes even more challenging in the cases of ballistic missiles and space vehicles. The ballistic missile arches high into space on its way to the target. Most of its flight is at speeds measured in thousands of miles per hour. During reentry into the atmosphere it is subjected to heating problems many times more severe than those affecting the high-speed airplanes mentioned earlier. Spacecraft, as they return to earth, will experience not only very serious heating problems but difficult deceleration problems. The decelerational loads imposed on structure, instrumentation, and passengers must all be within tolerable limits. Spacecraft requirements also are so weight sensitive as to be enormously more difficult to meet than is the case with the airplane.

Research in this area has made necessary the design and construction of novel facilities in which the complex problem can be broken down into solvable parts, and studied under the precisely controlled conditions of the laboratory. The NACA has been a leader in this area, and its new facilities are already producing research information that is immediately useful.

One result of such research that has been especially valuable was development of the "waffle grid" concept of construction. Systematic studies demonstrated the value, both structurally and as a weight saver, of plates that were strengthened and lightened by cutting away metal, either mechanically or by chemical etching, on the inner surface. Today the design of virtually all ballistic missiles and spacecraft makes extensive use of the "waffle grid" concept, and its use is hardly less extensive in the newest airplane designs.

Not unrelated to the structural heating problem is the successful development of H. Julian Allen's "blunt nose" concept. Although Allen's concept, worked out at the Ames Aeronautical Laboratory, was essentially completed in 1952, it was not until 1957 that public disclosure became possible.

In essence, Allen's concept called for a complete reversal of the existing practice of designing ballistic missile warheads with a finely pointed, low drag shape. Instead, he proposed a blunt-nose shape which would create a very high-pressure drag during the reentry phase of flight, where aerodynamic heating was so critical. In this way, he reasoned, most of the heat would be dissipated in the region of the shock wave. To reduce this dramatic story to its barest essentials, Allen's work was verified in special, new laboratory apparatus, and today, every U.S. ballistic missile warhead is designed in accordance with his once radical precepts.

The X–15 is the most recent of research airplanes. It is a direct result of research studies by the NACA that were begun in 1952. The Air Force and Navy agreed on the need for such a project and on a plan of joint financing by contracting with North American Aviation for complete design and construction. The X–15 is intended to be used to provide for full-scale scientific investigations in flight of such space flight problems as weightlessness, reentry heating, and control at altitudes approaching 100 miles, where aerodynamic forces are no longer effective, and at speeds exceeding 3,600 miles per hour. The X–15, however, is definitely not a spacecraft. Rather, it is a vehicle that will permit studying problems that must be solved to enable space flight. It is a successor to the earlier research airplanes of the "X series," and, like them, is a joint venture, with the military services, the aircraft industry, and the NACA working smoothly as a team.

Here it may be pertinent to note that for the past dozen years the research programs of the NACA have been undergoing a gradual change in emphasis, away from airplane problems toward missile and space problems. To be sure, many of the problem areas were of interest and concern to designers of airplanes as well as of missiles and spacecraft. Nonetheless, the reorientation process has been positive and, in fact, accelerating. By the end of the fiscal year, June 30, 1958, approximately 50 percent of the NACA research effort was being devoted to problems affecting missiles and space vehicles.

But, as has been said so often and so forcefully, the military airplane is not yet facing extinction, and NACA research in recent years has contributed importantly to the continued worth of manned aircraft. The Convair B–58, America's first supersonic bomber, makes use of Whitcomb's area-rule principle, described

in Dr. Hunsaker's account, and of the conical camber concept developed at the Ames Laboratory. The North American B–70, often described in the newspapers as the "Mach 3 chemical bomber," has yet to fly. When it does, it will incorporate much in the way of NACA research information that still has high security classification and cannot be mentioned. In the lower speed ranges, Whitcomb's work is being applied to commercial turbojet transport design, in the case of the Convair 600.

Despite the seemingly insatiable demand for more speed, in both military and commercial categories, the NACA has been aware of the need for continued research in the areas of the "low and the slow." Aircraft with the capability to take off and land, either vertically or with short runs, continue to be of interest, and progress has been made in solving problems peculiar to this type. Similarly, the Nation's flight research agency has done important work on such special matters as aircraft noise and operating problems.

Perhaps the most accurate assessment of the effectiveness of the NACA organization—its 8,000 technical and supporting personnel, its $300 million of laboratories, and its comprehensive research programs—came on July 29, 1958, when President Eisenhower signed the National Aeronautics and Space Act of 1958 that created the National Aeronautics and Space Administration. That act provided that the new agency be built upon the NACA as its nucleus. In this way, the lawmakers made sure that the country gained a running start on its bold, exciting ventures in space exploration for "peaceful purposes for the benefit of all mankind."

AERODYNAMIC RESEARCH

With the rapid advent of satellite, ballistic missile, and other hypervelocity vehicle operation, the NACA has intensified its aerodynamic research of both a basic and applied nature on problems of hypervelocity flight. All such vehicles have severe aerodynamic problems during operation within the atmosphere. Studies bearing on advanced flight concepts, aerodynamic heating and stability of reentry and hypersonic boost-glide vehicles, automatic guidance and stability and control of antiballistic missiles have all been pursued vigorously. Likewise emphasis has been placed on equally important basic gas dynamics research dealing with such subjects as high-temperature gas flows, dissociation and ionization phenomena, air properties at high speeds and temperatures, and magnetogasdynamics principles. Experimental investigations have encompassed temperatures up to 15,000° F. in arc jets, 25,000° F. in shock tubes, and speeds of more than 16,000 miles per hour. Such studies are providing new knowledge imperative for the success of launching man into space, with his safe return to earth assured.

The need for improvements in the efficiency as well as the speed, stability, control, and flying qualities of aircraft and conventional missiles has continued to merit a major part of the NACA research effort. The information obtained is being applied rapidly in new aircraft and missile designs. Unfortunately, aircraft for more efficient operation at the higher speeds have aggravated landing and takeoff problems. An important part of the NACA's research effort is being directed toward improving the low-speed characteristics and establishing low-speed piloting techniques of both high-speed and VTOL/STOL-type aircraft.

As may be seen from the following pages, aerodynamic research encompasses a speed range from takeoff to satellite velocity.

FLUID MECHANICS

Many problems in fluid mechanics, still very incompletely understood, are generated by ballistic missiles, hypersonic gliders, and satellites or space vehicles. Aerodynamic heating is a major factor in determining weight and propulsion requirements of these vehicles, and reduction in heating rates and heating loads pays large dividends. Thus, it is of the utmost urgency that methods of minimizing heat transfer and optimizing vehicle configurations be found. Progress has been made both along the lines of practical solutions to these problems and increased fundamental understanding of the underlying basic fluid flow and gas dynamic phenomena. In spite of the fact that at the high gas temperatures encountered in the flow about hypersonic vehicles, real-gas effects such as dissociation and ionization play an important role, much knowledge has been gained by considering air as a perfect gas. However, an important fact is that the ionized gas in the flow about a hypersonic vehicle permits electrical and magnetic fields to exert forces on the charged particles themselves, thus introducing the whole field of magnetogasdynamics. Activity has increased in this field of research having potential application to the reduction of heat transfer to the surfaces of hypersonic and space vehicles and in the generation of magnetohydrodynamic forces for vehicle lift, control, and propulsion. A brief description of some investigations in these and other areas follows.

526597—60——4

Boundary-Layer Transition and Skin Friction

Basic to the aerodynamic heating problem is an understanding of the boundary layer flow conditions inasmuch as turbulent flow produces significantly higher heating rates than laminar flow. Skin friction drag, especially important in airplane design, is likewise considerably lower for laminar than turbulent flow. Consequently, several important investigations of transition have been undertaken.

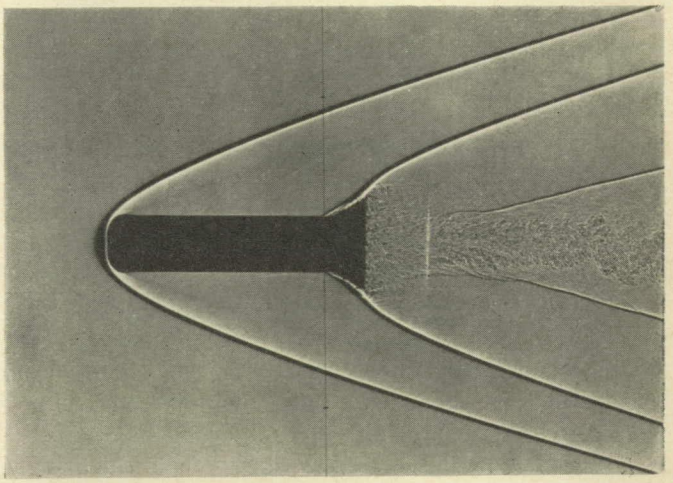
A study has been concluded concerned with the fundamental features of the transition process. Turbulence frequently begins in an unsteady fashion with an isolated burst of turbulence. Studies using a Mach-Zehnder interferometer were made of the shape, growth rates, and velocities of movement of such turbulent bursts at Mach numbers up to 7. Much progress has been made recently in wind-tunnel, flight and free-flight model tests in obtaining a better understanding of the effects of roughness on transition. Exploratory results first indicated that transition in most cases was caused by small roughnesses rather than inherent instability of the boundary layer. The limits, or conditions, in terms of basic boundary layer and roughness parameters, under which individual grains and bits of roughness will induce transition, have been clearly established for several basic shapes over an extended range of Reynolds and Mach numbers. Some of the roughness tests were made on blunt bodies. Both two-dimensional and three-dimensional roughness elements have been tested. If the roughness is below a certain critical height, it does not affect the skin friction drag perceptibly. Several investigations have been made for fully turbulent flow to study skin friction over a wide range of Mach and Reynolds numbers, boundary layer noise, and effects of high accelerations of a body on the flow.

It has been well established by tests in a number of facilities, including rocket model tests, that the effect of blunting the otherwise sharp leading edges of cones and flat plates is generally to move transition downstream. This effect has been explored up to Mach numbers of 10 and to very high Reynolds numbers. It has also been shown in recent years that moderate amounts of cooling tend to delay transition, although extreme cooling reverses this effect. Several research programs have yielded additional information on the phenomenon of "transition reversal due to overcooling" as may result when a body is heated rapidly on reentering the dense atmosphere. Perhaps the most important new result is that bluntness on some bodies may aggravate the reversal process, thus creating an interplay in the amount of nose or leading-edge bluntness to be incorporated from the opposing effects of reversal and theoretical transition delay due to bluntness.

Wing leading-edge sweep and shock interactions are known to promote early transition. Wind-tunnel and free-flight tests at Mach numbers up to 10 are continuing, including configurations appropriate for hypersonic boost-glide vehicles. One study has been directed at obtaining a better understanding of the flow mechanism at a sweptwing leading edge using an X-ray densitometer. Various flow visualization techniques have been developed for general transition experiments in both flight and wind-tunnel research.

Heat Transfer

Experimental studies of the aerodynamic heating of various shapes of blunt bodies applicable to reentering vehicles such as ballistic missile noses, hypersonic gliders, and satellites have been extended to higher temperatures, Reynolds numbers and to Mach numbers above 16 in some cases in flight, heated jets, wind tunnels, and shock tubes. Parallel theoretical work has firmy established analytical methods for calculating laminar heat transfer to basic blunt bodies, and both theory and experiments have shown the large reductions in heat transfer that can be obtained by making noses



Shadowgraph indicating heat-protecting shock wave generated at hypersonic speeds around gun-launched model of a blunt-nosed, flare-stabilized body.

flatter or less convex. One series of tests indicated a slightly curved surface to have the lowest maximum heat rates as well as the lowest total heating rates of a number of bodies tested. Extension of the nose-flattening concept to concave bodies has been shown to have further promise if the flow can be kept steady. Some aerodynamic heating investigations have also been made in a high temperature jet and in flight at Mach numbers up to 14 to determine the effects of erosion, roughness, and depressions as might be inflicted on body noses by meteorites and flak. Exploratory studies have been made of erosion by ion bombardment using an ion beam apparatus.

Afterbody heating can also be a serious problem on reentering bodies. A principal controlling variable is the local air pressure. At low supersonic speeds the air pressure on a boattail afterbody is lower than free-stream pressure. However, tests at Mach numbers up to 14 have revealed that the afterbody pressure increased systematically with increasing Mach number and was several times the free-stream pressure at the highest speed. Base heat transfer measurements have been made on flared cone cylinder models and on surfaces submerged in the wake of forebodies.

Although much of the above basic body heat transfer research is pertinent to supersonic aircraft, hypersonic boost-glide, and other hypervelocity winged vehicles, considerable additional research has been accomplished on other heating problems of such vehicles. The wings of such vehicles are critical from a heating standpoint and most configurations have regions of flow interaction aggravating heating. Investigations have been made of the beneficial effect of wing leading-edge sweep in alleviating the heating. Some of the investigations have been of a fundamental nature using yawed cylinders at speeds up to 6,500 feet per second to assist in developing new compressibility theories. In other tests, complete model configurations with different amounts of leading-edge sweep have been investigated in hot jets, hypersonic wind tunnels, and flight at Mach numbers up to 14.5. In one basic investigation of the heat transfer at the body-wing juncture of hypersonic aircraft, a small heating increase was shown as compared to a flat plate reference value; in other cases large effects have been noted. Intensive studies of heat transfer to basic configurations are now underway in a number of facilities where juncture effects, together with leading-edge blunting, transition, and shock impingement effects are simultaneously assessed. New "thin skinned" model construction techniques have been developed to permit thermocouple installation for heat transfer measurements on more complicated configurations.

In many heat transfer investigations considerably more emphasis is now being placed on studying the important effects of angle of attack or yaw and pressure gradient. In one rocket model experiment rolling, the model was observed to have only a secondary effect on heat transfer. Analyses have been made of the heat transfer to a high Mach number ramjet engine and to subsonic and supersonic diffusers. It has been observed in wind-tunnel tests that a protuberance increases local heat transfer rates on the side of a model by large amounts.

Some research has been concerned with the flow of heat through separated boundary layers. Theory has predicted that the heat transfer through a separated laminar boundary layer is roughly half of that through an attached layer. On the other hand, theory suggested a greater heat transfer through a separated turbulent boundary layer than through an attached layer. Preliminary experiments have indicated that the theoretical prediction is correct for the laminar case but incorrect for the turbulent case, so that flow separation may have promise for reducing heat transfer in both laminar and turbulent flow.

Cooling

Many types of advanced reentry vehicles will more than likely utilize some form of reenforced cooling in critical areas to overcome the heating problem. A number of investigations are presently underway dealing with transpiration, film, internal and ablation cooling. The transpiration cooling process has been generally investigated in hot jets and wind tunnels with flat-plate models and with conical and flat-faced nose shapes as well as a porous cylindrical leading edge using helium primarily as a coolant. The effectiveness of helium transpiration cooling for body noses is also being investigated in flight. Film cooling by upstream injection of gaseous and liquid coolants is likewise being investigated in the same manner with various shaped bodies having conical, hemispherical, flat faced, inverse hemispherical, and other blunt noses.

One cooling technique for reentry vehicles receiving attention is underskin cooling by natural convection of liquids. Both theoretical and experimental programs are underway to determine the feasibility of such heat sinks. Models of double-walled structures are being used to investigate the effectiveness of convection cooling derived from the circulation of gases and liquids within the walls. The effects of vehicle rotation on the internal flow is also being evaluated.

Considerable effort has recently been expended in investigating the basic theoretical principles of ablation cooling. As a part of this work exploratory measurements have been made of the effective heats of ablation of a large number of materials and combinations of new materials in air jets at moderate to high heating rates. The ablation program includes flight tests of several models at Mach numbers above 14. Considerable effort has been expended in the development of suitable ablation rate sensors for flight application.

Air Properties at Elevated Temperatures

Flight at extreme hypersonic velocities and the accompanying high temperatures make it necessary ultimately to consider air as a real gas and not a perfect one. Thermodynamic and transport properties of air in the disturbed flow fields about hypervelocity vehicles can deviate widely from ideal gas values due to dissociation and ionization. As temperature increases, air becomes subject first to molecular vibration, then to dissociation of the oxygen molecules to form atomic

oxygen and then to a similar dissociation of nitrogen molecules. An analytical study has been completed of the effect of oxygen vibration and dissociation in one-dimensional channel flow. The effects of the rates of the chemical and physical reactions were found to be appreciable. Theories for rates of reaction were found to be in serious disagreement indicating the need for experiments. A study has been made of the influence of the equilibrium chemical reaction in the air on expansion flows past corners termed Prandtl-Meyer flows. This type of flow has wide application in analyzing pressures on wings and bodies. The influence of the gas reactions was found to be subject to an exact analysis and the changes in flow properties were considerable.

Theoretical studies of air at extremely high temperatures have yielded approximate analytical expressions having considerable value in engineering applications in giving thermodynamic and transport properties of air that agree closely with those obtained by lengthy iteration methods.

Magnetogasdynamics

Ionization of air at high temperatures offers the possibility that airflow and hence heat transfer can be altered by application of magnetic fields about a body. The electrical conductivity of the high temperature gas at the nose of blunt bodies is appreciable during critical reentry conditions. Also, the conductivity may be increased by seeding the flow with easily ionizable materials such as the alkali metals. Such ideas have been theoretically explored and methods have been developed for permitting estimates of magnetohydrodynamic effects on heat transfer and skin friction to be made for cases hitherto unsolved.

Magnetogasdynamics opens a vitally important possibility of the generation and acceleration in the laboratory of high-velocity plasma flows that truly simulate hypersonic flight conditions. Considerable theoretical and experimental work is being accomplished on key problems, including electron diffusion, stability of plasma flows, boundary-layer flows in magnetic fields, rates of recombination of ions, and methods of ionization and electron emission. Arc jets and low-pressure seeded flows have been developed as ion sources.

There are indications that the conducting gas layer about a hypersonic vehicle may create a serious problem with regard to radio or telemeter transmission. Theoretical work has been carried out suggesting the use of magnetic fields to improve transmission. Radio transmission experiments are in progress using a cyanogen-oxygen flame seeded with potassium to simulate an ionized sheath about a body.

Body and Airfoil Flow Fields

An understanding of the basic flow fields around bodies and wings is fundamental to many design aspects of aircraft, missiles, and spacecraft. Several investigations of such nature have been completed or are in progress at all NACA laboratories throughout the speed spectrum. These include airfoil pressure distribution measurements, refinements in means of determining and reducing wave drag through area and moment-of-area rule principles, generalized theoretical studies of drag due to lift, generalized theoretical and experimental studies of body and wing-body flow fields at Mach numbers up to 10, and improvement of nose probe devices for measuring flow field characteristics.

Research Facilities and Techniques

An important part of the NACA's effort in basic fluid mechanics is continually devoted to exploring new techniques and apparatus in order that advanced facilities can be provided for research in the expanding frontiers of flight. Along these lines considerable progress has been made in the use of helium for high Mach number flows in wind tunnels. Advances have been made in tunnel-wall correction techniques. Work has continued in improving shock tubes to provide higher Mach numbers and stronger shocks. New shock tube and ultraviolet absorption techniques are being employed for studying air dissociation and recombination rates. Arc-powered wind tunnels and jets are likewise being developed to push the limits of their potentialities. Continued effort is being expended in improving the performance and utility of rocket free-flight test vehicles.

The combustion of cyanogen and oxygen yields CO and N_2 at a very high temperature suggesting a number of possible test uses which are being explored, for example, (1) heat transfer and ablation without chemical reaction, (2) chemical reaction effects and ablation by addition of contaminants to the hot flow, and (3) magnetohydrodynamics tests by seeding the flow with an alkali metal to obtain higher electrical conductivity. A low-velocity burner has been seeded with potassium and a supersonic jet is under construction.

A free-piston compressor has been put into operation in conjunction with a M=11.2 nozzle. The feasibility of using the thermal decomposition of nitrous oxide in the compressor has been demonstrated successfully. Nitrous oxide decomposes with the release of heat into nitrogen and oxygen in proportions closely simulating air. Whereas for air the theoretical final temperature for a typical case is 6,000° F., the nitrous oxide decomposition products raise the temperature to about 13,500° F. The compressor walls considerably lower these temperatures; nevertheless, indirect measurements have in-

dicated temperatures greater than 5,000° F. using nitrous oxide.

HIGH-SPEED PERFORMANCE

All flight vehicles, whether an airplane, a missile, or a space vehicle that is to be recovered, must fly through the earth's atmosphere. Many aerodynamic problems must be overcome to accomplish this flight objective whether the vehicle is controlled by a human pilot or artificially. The aerodynamic characteristics of reentry vehicles are of such importance that the penalty for improper aerodynamic design is destruction. The NACA has conducted analytical and experimental studies to supply the information required for the solution of problems of atmospheric reentry. At the same time, work has continued on other problems of flight within the atmosphere. A very brief description of some of this work is contained in the following paragraphs.

Ballistic Missile, Satellite, and Spacecraft Configurations

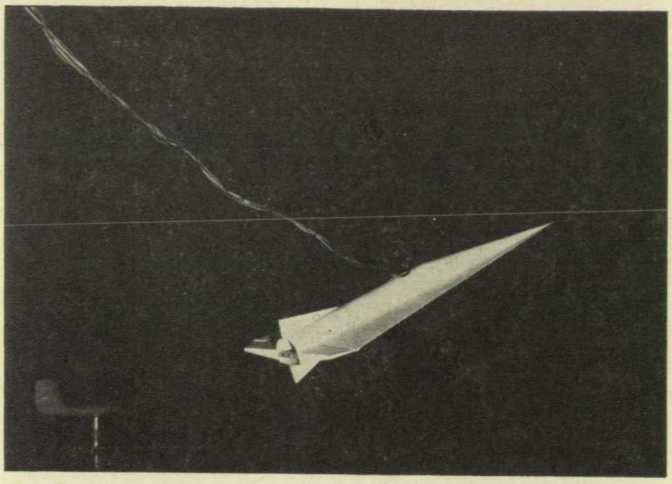
Broad analyses have been made of the heat transfer, atmosphere entry deceleration, and propulsion problems of vehicles for satellite, lunar, and interplanetary missions. Simplified equations have been developed by which a wide range of flight trajectories can be studied and important parameters varied so that designers can readily visualize trends, such as the effect of entry angle, speed, drag, and lift. The analyses included numerical calculation of the trajectories for round trips to the moon and the near planets using ranges of thrust-to-weight ratio and specific impulse typical of chemical rockets, nuclear rockets, and electric propulsion systems.

Proposals for manned satellites have been based on several design concepts such as high-drag blunt ballistic configurations, low-drag winged configurations, and combinations of the two utilizing small wings or body shaping to produce lift with high drag. The blunt wingless vehicles depend on a concept developed at the Ames Laboratory for the dissipation of heat due to aerodynamic heating. This is the concept that is used for the nose cones of present ballistic missiles. The winged vehicle utilizes lift to hold itself in the upper regions of the atmosphere while its speed is gradually reduced by drag forces; its heat is dissipated largely by radiation. The winged vehicle, being a glider after it enters the atmosphere, possesses the potential for some degree of control, thus providing a pilot with a choice of landing area. Ballistic high-drag vehicles would land by parachute, and a pilot would have virtually no control over the landing point once the vehicle entered the atmosphere. The low-lift, high-drag vehicle with small wings would also land by parachute, although some aerodynamic control can be provided to permit a pilot to make limited correction for errors in reentry angle or speed.

Studies of the many problems associated with these three types of vehicles are continuing. Research on reentry vehicles has been devoted to both blunt, nonlifting bodies of revolution applicable to ballistic missiles as well as reentering satellites and to body shapes which utilize lift in attempts to alleviate deceleration and aerodynamic heating problems. The high decelerations that are imposed on an occupant during reentry create a serious problem. Basic studies on methods of controlling decelerations and heat transfer of satellite vehicles and of predicting with reasonable accuracy the range covered during the return of the vehicle into the earth's atmosphere have been initiated. In one analytical study of the entry of a general class of high-drag vehicles having low-aspect-ratio wings, the deceleration, heating, and range were controlled by programing the angle of attack as a function of several measurable quantities such as initial flight-path angle and wing loading. Another theoretical and experimental study has been made of the stability and heat transfer to basic bodies of revolution shaped for minimum heat-transfer rates and suitable for ballistic missile or satellite use. The aerodynamic and heat-transfer characteristics of bodies employing lift during atmospheric entry are being studied, and a shape has been found which appears promising for manned satellites from the standpoint of aerodynamic heating, reentry deceleration, stability, and control. Some experimental investigations of the longitudinal characteristics of blunt, wingless reentry configurations at a Mach number of 7 have indicated that simple fins or flaps can provide satisfactory trim characteristics.

Another advanced flight concept that possesses aerodynamic problems akin to those of the winged satellite vehicle is the boost-glide vehicle, so named because of its mode of operation, which consists of rocket boost to its cruising speed and altitude and a powerless glide to its destination. Experimental and analytical studies have indicated the feasibility of the boost-glide flight concept and work has been conducted in the NACA Laboratories to provide solutions for many of the design problems.

Three main problems are the achievement of required lift-drag ratios, alleviation of the severe aerodynamic heating, and provision of satisfactory stability. Experimental and theoretical work is being conducted at all NACA Laboratories on the performance and stability of a number of boost-glide configurations. Wind-tunnel and rocket-model tests are being conducted to study the effects of body and wing planform geometry on the lift-drag characteristics at supersonic and hypersonic speeds. Aerodynamic heating, stability, and con-



Model of a hypersonic boost glide vehicle being flight tested in a wind tunnel to determine low speed dynamic stability characteristics during landing approach. Controls of the hydrogen-peroxide powered model are electrically activated by "pilots" outside tunnel through slack wires shown.

trol are also being studied over the anticipated operational Mach number and angle-of-attack range.

In addition to the reentry and glide phase of flight for these advanced flight concepts, there is the problem of launching the vehicles to the required speeds and altitudes. Some studies have been completed and others are continuing to provide information on booster vehicle staging, separation, aerodynamic loads, and stability.

Airplane Configurations

Although the program of research into space has been intensified, effort also has continued to improve the efficiency of flight within the atmosphere to the point where supersonic flight of fighter and research airplanes has become routine. Aerodynamic efficiency is improved by shaping the airframe to generate the required lift with the least possible drag. Propulsive efficiency requires that the air-breathing engine together with its intake and exhaust systems yield the greatest possible thrust for the lowest consumption of fuel. Structural efficiency seeks the lightest weight at greatest strength.

High-speed wind tunnels have been used advantageously to exploit the potential drag reductions suggested by supersonic wing theory. The benefits of sweepback have been systematically analyzed and new studies have revealed methods of accomplishing an elliptical distribution of lift over the wing surface which, in theory, would result in minimum drag due to lift. The advantages of cambering and twisting wings have been well established, and several supersonic airplanes now in operational use or in development incorporate these principles. However, the full potential of this approach as predicted by theory has not been realized in experiments and work is continuing on this problem. Friction drag is a major portion of the drag of supersonic and hypersonic aircraft as well as the source of aerodynamic heating. Research in this area has been pursued actively at all NACA research facilities.

New studies of interference pressure fields show promise in supersonic design application. By properly shaping an airplane the pressure fields resulting from interference between various airplane components can be made to react favorably to improve flight efficiency and stability. The study of the basic components of a vehicle and how these components can be combined is essential to understanding the problems and providing design information. Through the study of wings, bodies, and wing-body combinations, the feasibility of the advanced concepts and aircraft configurations described above has been established. Many of these fundamental studies have been conducted and are continuing. Considerable work has also been conducted on cockpit canopies with regard to shape and location on the fuselage. Improper design of the cockpit canopy can be a source of severe drag penalties.

Inlet problems, too, are of great importance in supersonic aircraft. Aside from the requirement of efficient inlets, it is necessary that the inlets be located so as to produce the lowest overall airplane drag. Research results have indicated that inlets can be located to alleviate interference adversely affecting flight efficiency.

In addition to the aerodynamic interference between the major components of aircraft, the interference of such elements as external stores, missiles, and nacelles can be important and have been studied. With regard to missile interference effects, the aircraft flow field can affect the missile-launching characteristics to the extent in some severe cases that the missile could collide with and destroy the parent aircraft. Considerable work has been done on the launching problem for both externally and internally carried stores and missiles.

INTERNAL FLOW

The performance characteristics of supersonic airplanes and missiles with air-breathing engines are strongly influenced by the overall efficiency of the engine induction and exhaust systems. The pressure recovery of these systems must be high to obtain both a maximum thrust for a given weight and a low rate of fuel consumption. The components must be shortened wherever possible to reduce weight. The overall drag must be kept small and the propulsion system must be capable of satisfactory operation at off-design conditions. During the past year considerable research has been conducted to determine methods for improving the performance of aircraft and missile internal flow systems. At Mach numbers up to 3, the research has been of a detailed nature, whereas at higher speeds the research is of a more exploratory nature to determine the problems which must be solved.

Inlets

Considerable research effort has been expended during the past year on inlet designs suitable for operation at high supersonic speeds. These tests have included all-internal contraction, external-internal contraction, and all-external contraction inlets. Methods investigated for improving performance over the operating range have consisted of boundary-layer control, variable geometry, airflow bypass, and location of the inlet in favorable airplane pressure fields. In addition, methods have been developed for maintaining high performance during angle-of-attack operation.

Several programs have been conducted in the area of inlet dynamics and the experimental results of an inlet-engine configuration have been correlated with a simple theory. Two inlet control systems were also evaluated and found to be effective in maintaining high inlet performance with varying flight and engine operating conditions.

A theoretical study has been concerned with the calculation of the external pressures on inlet cowls and the internal pressures in internal compression inlets designed to have isentropic compression. Comparison of a number of theories for computing the external pressure on inlet cowls has been made to assess their accuracy. Analytical studies have also been made to determine the effect of surface temperature on the properties of the boundary layer handled by an inlet scoop system. These results permit a prediction of boundary-layer-removal-system performance at high speeds.

Exploratory studies have been conducted on a variety of inlets designed for flight at hypersonic Mach numbers. These investigations permit a comparison of the performance of the basic types of inlets operating in this flight regime and indicate many of the design parameters which must be considered before efficient hypersonic flight can be obtained. Since flight at hypersonic speeds will require blunted inlet leading edges to reduce heat transfer and to facilitate cooling, an investigation was conducted at Mach 3 to determine the effects of such blunting on off-design performance.

Inlet designs for a number of specific engines and airplanes have been investigated and methods for obtaining improved performance from these designs have been found. Flight measurements with several military aircraft have also been made and the actual inlet operating characteristics determined.

Ducts and Diffusers

During the past year subsonic diffuser research has been concentrated on a study of the effects on pressure recovery and flow distortion of a diffuser operating with or without a normal shock near the throat. Boundary-layer shock interaction effects have been studied and the effects of boundary-layer control in a short diffuser are being determined.

A basic investigation of the characteristics of a turbulent boundary layer in a continuous adverse pressure gradient is also in progress to determine a method for minimizing boundary-layer effects in supersonic inlets.

Jet Exits

Several studies at transonic speeds have been made of the effects of jet exits on base and afterbody drag characteristics. A comprehensive investigation of clustered, multiple exits was included in this program, and the performance of several jet-exit configurations was determined. In addition, a family of divergent ejector nozzles was investigated to determine the off-design thrust levels that could be maintained, and a series of convergent-divergent exhaust nozzles were investigated to determine the separation characteristics at low-pressure ratios.

The interaction of the rocket nozzle flow and the external airstream in the base region of several ballistic missile configurations has received continued attention. Conditions for base burning and the general level of base temperature to be expected were determined for a number of configuration variables as well as for the basic prototypes.

Investigation of a method of varying the effective flow area of a convergent exhaust nozzle by aerodynamic means was conducted on an unheated-flow duct rig. Effective control was obtained and analytical expressions relating the performance with significant design and operating variables were developed.

Several model jet deflectors were investigated to determine the effects of design variables on their performance and operating characteristics. Transonic tests of the effects of a target-type thrust reverser have been conducted, while swiveled nozzles, auxiliary nozzles, and mechanical and aerodynamic deflectors which were designed to be adaptable to a wide variety of turbojet exhaust systems have been investigated in quiescent air. Analytical expressions relating the performance of each type deflector with significant design variables were also determined.

AERODYNAMIC STABILITY AND CONTROL

Stability

During the past year continued study has been made of factors affecting airplane pitchup—a longitudinal instability discomforting to the pilot and often dangerous. Detailed experimental studies were made to investigate methods for eliminating or alleviating the pitchup tendency; information was obtained on the effects of such modifications as changing the location of the horizontal tail and wing, of modifying the wing shape, and of adding auxiliary horizontal tails.

The problem of providing adequate but not excessive longitudinal stability over the complete speed range for high-performance airplanes has also received additional attention; this problem is of concern inasmuch as a very stable airplane will not only be difficult to maneuver but the large control deflections required for trim and maneuvering will result, especially at high speeds, in large loads, and high trim drag. Extensive wind-tunnel studies have been made to determine the static aerodynamic characteristics of canard configurations which have been found to have some advantages over conventional, tail-rearward designs. Analytical studies have been made to study the flight characteristics of a canard airplane having various amounts of longitudinal stability, and to investigate the need for automatic pitch-damping devices.

The loss of directional stability with increasing speed and angle of attack, characteristic of most supersonic airplanes, continues to be a design problem. Experimental model studies have been conducted which indicate the important influence of such factors as vertical tail and ventral fin size; wing planform, dihedral, and location; and fuselage nose length and cross-sectional shape. Guided by the results of such tests, theoretical methods have been developed which enable accurate design estimates of the directional stability characteristics of airplane configurations.

Accurate prediction of the dynamic stability characteristics of high-performance airplanes has also become of increasing importance to designers. Inasmuch as questions concerning dynamic stability can usually be resolved from a study of the rotary derivatives of a particular aircraft, increased attention has been given to obtaining information on these derivatives for a variety of configurations over a large angle-of-attack range. With these and other stability derivatives used as inputs into ground simulators, studies have been made of the ability of a pilot to control various airplane configurations under different flight conditions. Particular emphasis has been given to approximating the flight characteristics of the X–15 research airplane as fully as possible before its actual high-speed, high-altitude flights are initiated.

Although much of the information obtained in studies of conventional aircraft provide stability and control information applicable to very high-speed airplane and recoverable-satellite vehicles now being considered, additional and higher speed studies are required to determine the effect of the basic differences in such configurations on the aerodynamic characteristics. Extensive studies have been made on several hypersonic boost-glide designs to determine their stability and control characteristics over large speed ranges. Some of the models have been studies in free flight, simulating their characteristics in the low-speed, approach-to-landing flight condition, and providing information on the adequacy of the controls as well as on the possible need for artificial damping devices at these speeds. Analytical studies of the flight characteristics of such vehicles have also been made.

Experimental and analytical investigations to determine the stability and motion characteristics of configurations having lower lift-drag ratios considered more suitable for manned satellite or spacecraft during flight back into the earth's atmosphere have been initiated; the effects of fuselage nose blunting, stabilizing fins and flares, afterbody shape, and various types of controls have been studied experimentally. In addition to high-speed wind-tunnel studies to determine the basic stability and control characteristics of these configurations, low-speed information required to predict landing characteristics have been obtained. Analytical studies have been carried out with specific reference to the dynamic stability of a hypothetical manned vehicle which enters the atmosphere on a "skip-type" braking trajectory, executing an upward turn to eject itself from the atmosphere or to a less dense atmosphere to reenter at reduced speed. A general solution describing the dynamic stability and oscillatory characteristics of such vehicles following any trajectory has been developed.

The current importance of producing an effective long-range ballistic missile and of developing methods for combating them has resulted in an expansion of stability and control research in these areas. Experimental static and rotary derivative data have been obtained on a variety of configurations suitable for the warhead stage of the ballistic missile as well as for the previously mentioned studies of spacecraft entering the atmosphere. The effects of configuration changes, such as body-nose bluntness and afterbody shape, have been extensively investigated. These data, together with other calculated information, have been used in analytical studies to estimate the trajectory, stability, and aerodynamic heating during terminal descent.

Considerable effort has been devoted to the investigation of the supersonic aerodynamic characteristics of a series of missile models having configurations suitable for the interception of ballistic missile warheads. Various means of providing stability and control on tail-aft, canard, and flared-body models have been studied. Studies have also continued of the characteristics of more conventional, lower performance air-to-air, ground-to-air, ground-to-ground, and air-to-ground missiles.

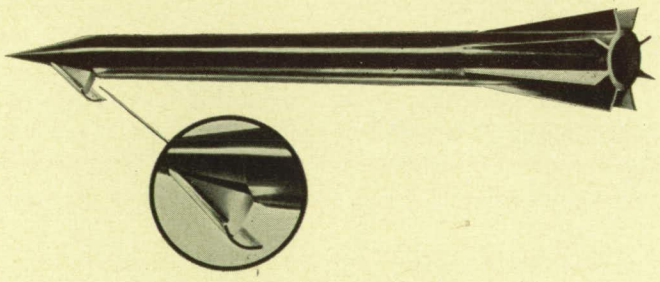
Controls

The increasing variety of airplane and missile configurations being designed has necessitated a broader knowledge of the characteristics of conventional controls and consideration of new concepts of control.

Wind-tunnel investigations have been made of such controls as flap and spoiler-slot deflectors, differentially deflected (rolling) tails, jet spoilers, and lateral blowing jets to determine the effects of various wing geometric parameters on the control characteristics. The effectiveness of the canard control surface, previously mentioned as being an attractive means of providing longitudinal trim for high-performance aircraft, has also been extensively studied.

Research has increased on jet-reaction controls having application to flight at very low speeds or high altitudes where aerodynamic controls have reduced effectiveness. One investigation has been made of the performance of a number of reaction control devices having possible application to the landing of VTOL aircraft and space vehicles. Analog studies have also been conducted to determine the effectiveness of reaction-jet controls similar to those to be used in flight tests of the X–15 research airplane.

Aerodynamic control systems intended for low aspect-ratio winged missiles have been studied over a range of supersonic Mach numbers; the relative effectiveness of tail, canard, swivel nose, and all-moving wing controls was determined. Other studies have been completed of the effectiveness of body-flap controls for air-launched, wingless missile configurations; such missiles require a minimum of stowage space and hence a minimum compromise of the drag characteristics of the missile-carrying aircraft. Body-flap controls have also been studied on missile configurations considered suitable for hypersonic antimissile use. In addition, basic studies have been made of vehicle control requirements for programing decelerations and heat transfer of vehicles reentering the atmosphere.



Model of a wingless air-to-air missile utilizing a retractable body flap as a lift-producing control device.

Flying Qualities

The flying qualities of airplanes designed to have very low or even negative static longitudinal stability at supersonic speed (in order to provide low trim drag and therefore increased range) have been studied recently. The limit of negative stability that can be tolerated, the effect of artificial pitch damping, and other factors affecting controllability were investigated from the standpoint of pilot opinion and measured performance using a pilot-controlled analog simulator.

Several projects to determine the acceptability of a side-located controller that requires an up-and-down hand motion pivoting at the wrist for longitudinal control and a lateral hand or forearm motion for lateral control have been undertaken. With this type of controller it is easier to restrain the pilot's arm so that high-acceleration levels will not introduce unwanted controller motions. Use of this type of controller also clears the center cockpit area which may then be used to good advantage for navigational instrument displays. Another fundamental flight research project was undertaken to determine the nature of such factors as pilot reaction time delay and response time in correcting airplane motions. Results of this research will aid in designing control systems to take best advantage of pilot capabilities. The results are also of value in determining the validity of other human-response tests conducted with ground simulators.

Investigation of the spin characteristics of models of many specific current and proposed military airplanes has continued utilizing the free-spinning tunnel. In some cases force data on the complete model or the fuselage nose alone have been required before proper interpretation of model spin-tunnel data could be made in terms of recovery characteristics for the corresponding airplane. The results show that recovery from the spin of some of the current-type fighters is so difficult that it would be very desirable to avoid entering fully developed spins. This can best be accomplished by determining the most expeditious way of recovery from the incipient phase of the spin. Preliminary tests have therefore been made to study methods of effecting such recovery on a scale model representing a current fighter airplane. A recently developed helicopter-launched, radio-controlled model technique has been utilized.

Flying quality research studies during the last year have also given additional consideration to the factors affecting pilot selection of landing-approach speed, Dutch-roll damping, and lateral-control requirements of several current fighter-type airplanes.

AUTOMATIC CONTROL

Missiles

Studies of missile stabilization and control have considered improved means of simplifying and analyzing complex automatic control and guidance devices. Although this program was initiated with reference to air-to-air attack missiles, the results have application to other classes of missiles, including ballistic and antiballistic, as well as to automatically controlled and guided airplanes. Some of these studies are discussed now.

Changes that occur in missile response characteristics to control deflections for varying flight conditions have led to complicated methods of adjusting automatic con-

trol parameters. In studying a number of simplifying techniques, consideration has been given to a control actuator whose torque output is proportional to the input of the control system. Results indicate that such actuators can simplify the control system and result in acceptable target-miss distances.

A study has been made to determine the relative importance of factors that place limitations on the minimum obtainable miss distance for a missile navigation system in which the missile follows a radar beam that is tracking the target. The factors considered were the natural motions, and steady-state acceleration capabilities of the missile, target evasive maneuvers, and radar angular scintillation noise. Simple correlation equations expressing minimum miss distance in terms of these factors were obtained. Possibilities for system improvements were indicated. Also studied were the effects on the average target-miss distance of limiting the allowable acceleration of a beam-rider missile. Contrary to intuitive thinking, the study showed that miss distance decreased as the ratio of the limiting to the design acceleration increased when the guidance system was designed for best performance at a given acceleration.

The determination of optimum radar-noise filtering characteristics to be used in weapon system design is generally a long and tedious process. Studies of these complex equations have been successful in determining simplifications and approximations to enable sufficiently accurate explicit solutions. From these results it has been possible to answer in a quantitative manner important questions regarding the effect of the target maneuver on the effectiveness of the guidance system.

Other work on improving missile systems indicated the need for enlarging the scope of filter theory to include nonlinear considerations. This is due to the trend of potential targets to fly at higher speeds and altitudes where the maneuverability advantage of the defensive missile is lost. Under these circumstances present theory is inadequate because the problem becomes a nonlinear one. A study was undertaken to generalize previous theory by exploiting the intentional use of nonlinearities as a means of minimizing miss distances.

Present theory dealing with noise contamination is restricted to systems whose design constants do not vary with time of flight. However, many systems have time-varying constants. Studies have been carried out to enlarge the scope of the theory so as to be applicable to these systems. Factors considered were target evasive maneuver, radar glint noise, missile maneuverability, and the inherent time-varying character of the missile maneuvers. The results of this and the preceding filter studies are applicable to many aircraft interception systems.

The problem of storing air-to-air missiles on parent airplanes has led to the consideration of wingless or very low aspect ratio missiles. These missiles rely on body-lift capabilities for maneuvering which require large pitch and yaw angles. The effects of these large angles on the performance of a navigation system was investigated analytically. It was shown that a problem requiring careful attention is space stabilization of the radar antenna against body motions.

Guidance and control requirements for antiballistic missiles have been investigated, considering both aerodynamic and reaction controls. Two types of interception were considered; one in which the relative-approach speed is small compared with the target speed, and the other where the relative-approach speeds are extremely large as would be associated with head-on interception. As part of this study, roll stabilization of hypersonic vehicles was investigated. Considered were the effects of large fuel expenditures and large dynamic pressure variations.

Aircraft and Spacecraft

Flight control studies of current high-performance airplanes and advanced airplane-design concepts have included ways and means of providing automatically stability and control characteristics acceptable to the human pilot for specific tasks such as landing and target tracking, and completely automatic flight-control where improved mission performance dictates.

Slow airplane response to various control commands such as roll, yaw, and throttle adversely affects the pilot's ability to control an airplane in landing approaches. Flight studies conducted in smooth and rough air with an airplane modified to provide artificial variation of roll and yaw damping have provided boundaries defining acceptable levels of damping and control response. Flight studies have also shown automatic throttle control to be a promising way of allowing reduced speeds in landing-approach maneuvers.

In many high-performance airplanes it is possible for the pilot to exceed inadvertently the design loads in accelerated and/or high angle-of-attack maneuvers. Analytical and ground simulator studies of an elevator-motion braking device actuated by normal acceleration, pitching acceleration, and pitching velocity signals were extended to flight. The flight studies indicate that inadvertent accelerations will be limited to tolerable levels.

Other studies have resulted in the development of a method of predicting the relative severity of pitchup and the effects of aerodynamic modifications and stability augmentation devices on several supersonic airplanes with pitchup problems. An automatic pitchup control system incorporating an angle-of-attack sensing device to retrim the horizontal stabilizer as the "pitchup region" is approached and entered has alleviated the pitchup considerably on a test airplane.

To increase the utilization of computer systems carried on aircraft, it has been thought that some functions need not be carried as continuous processes but could be handled intermittently on a time-sharing basis. Studies of yaw and pitch stabilization have led to the belief that discontinuous control systems could reduce complexity and system power requirements of airplane automatic control systems. A study has been made of the application of sampled-data theory to an airplane with an altitude control system. A better understanding of switching criteria has been obtained and should lead to useful design techniques.

On future airplane designs it may be necessary to tolerate marginal levels of static and/or dynamic stability for reasons of performance improvement and to obtain desired characteristics by stability augmentation. The problem of marginal flight control characteristics when the primary stability augmentation system fails has been studied to determine whether the pilot can cope with the emergency or whether secondary systems must be provided.

An airplane which can have its longitudinal dynamic response and control system characteristics varied has been utilized in a study of control system dynamics. Similar studies have been made on a ground-based simulator. Insight has been gained regarding the desired dynamics of longitudinal control systems for airplanes varying from transport types to those proposed for atmospheric entry vehicles.

Studies of airplane control systems where the pilot controls the airplane through commands to an automatic pilot were extended to take into consideration flight in rough air and flight at negative static stability margins as may be encountered at subsonic speeds by hypersonic designs. The systems involving angular-rate command and normal-acceleration command appear to be able to cope with small degrees of longitudinal instability.

The use of information derived from airborne radar equipment tracking a target at the end of a runway to assist in making an automatically controlled approach has been studied analytically. Such systems would eliminate the need for auxiliary ground equipment as employed in present landing control systems and make use of radar equipment already carried on many airplanes for other purposes. A usable airplane control scheme has been devised.

Flight and analytical research has continued on tracking control problems of current and projected interceptor airplanes. Studies included consideration of computer and radar display parameters for manual-mode tracking and study of factors that affect flight path stability and aiming accuracy in attacks with an automatically controlled interceptor, including consideration of system changes to improve performance against maneuvering targets. Studies were also made of the effects of high closing rates with consideration of the effects of interceptor maneuverability on guidance systems designed for interception in collision course attacks, and of an automatically controlled interceptor using bank-angle-error for lateral-control commands.

Piloting problems in exit and entry of manned flight from the atmosphere of the earth expose the pilot to an acceleration environment beyond his past experience. A joint NACA-contractor-military service program in support of the X–15 airplane program was conducted in a centrifuge to determine the effects of typical exit and entry acceleration time histories on pilots' ability to control the airplane. Specific factors considered were airplane stability augmentation and flight data presentation to the pilot. Other studies with hypersonic airplane type configurations have involved the use of a ground-based flight simulator to investigate damping requirements with regard to longitudinal, lateral-directional, and roll modes of motion.

Prediction of the dynamic behavior of large vehicles representative of ballistic missiles, hypersonic aircraft, or spacecraft during boost is complicated by the characteristic lightweight, flexible structure, and the large variable internal mass. In order to understand the stability and control problems of this class of vehicle, studies were undertaken considering autopilot and thrust control response, aerodynamic forces, fuel sloshing, and structural elasticity. These studies have given some insight to the problem of automatically stabilizing complete high-performance vehicle systems. Also the effects of reaction controls on the automatic stability control and orientation of these types of vehicles have been studied in the flight regimes where low air density makes conventional aerodynamic controls ineffective.

The flight dynamics of vehicles reentering the earth's atmosphere must be such that the vehicle does not exceed limiting attitude angles associated with aerodynamic heating and/or other structural considerations. Studies have been conducted to determine the degree of inherent aerodynamic or artificial stability required for typical bodies. Studies have also been made of the possible utilization of a man aboard a satellite for piloting purposes. Considered were flight-data instrumentation as well as vehicle stabilization and control requirements.

Preliminary considerations indicate that certain types of satellites will require accurate placement in orbit and accurate control of attitude. In a generalized investigation of satellite stabilization and control, consideration was given to such matters as the earth's force fields, internal power requirements and sources, control and sensing devices, and initial placement of the



Electronic Simulator Explores Piloting Problems

Cockpit in left background which is free to rotate in pitch and roll, coupled with electronic equipment in foreground, constitutes one of a number of flight simulators which enable study of piloting and control problems of high speed flight. In view of the safety and economy of simulators their use is becoming widespread.

satellite in the design orbit. The matter of attitude control was given special consideration. Control systems considered include hydrogen peroxide jets, inertia wheels, and permanent magnets that react with the magnetic field of the earth.

LOW-SPEED AERODYNAMICS

VTOL and STOL Aircraft

Emphasis in the field of VTOL and STOL aircraft has shifted somewhat from basic configuration studies to the broader problem of performance and stability of complete configurations. Dynamic models of two propeller-driven, tilt-wing experimental aircraft have been tested to determine the behavior of the aircraft during the transition from hovering to forward flight. Jet-powered models of the tilting-engine and tilting-wing-and-engine types have also been flown. Full-scale wind-tunnel tests of an unloaded rotor-type convertiplane have been made to investigate the vibration characteristics of the wing-pylon-rotor combination. In addition to free-flight model and wind-tunnel tests of VTOL and STOL aircraft, the NACA is becoming engaged in flight tests of test-bed VTOL/STOL aircraft to investigate handling qualities as well as stability and control characteristics.

Interest continues in a wide variety of VTOL/STOL applications involving both propellers and jet power plants. Recent investigations of a deflected slip-stream model showed that improved hovering efficiency is obtained when the number of propellers along the wing-span is increased, even when some overlapping of the propellers becomes necessary. The large amount of information now available on deflected slipstreams has been used as the basis for a semiempirical procedure for predicting lift and drag in transition of this type of vehicle.

Shrouded-propeller applications in the form of a stand-on aircraft and multiple-fan "flying jeeps" are also being investigated in model flight tests. These include investigation of the stability and control characteristics of two- and four-propeller arrangements in both shrouded and unshrouded configurations. A supporting program involves force tests of the same models. Initial flight tests with the two-propeller model showed that it required roll stabilization in hovering flight. As forward speed increased, increasing amounts of roll stabilization were required. The flight tests also showed that a greater angle of inclination was required to achieve a given forward speed than was anticipated.

Jet Flaps

Research on providing greater lift in order to improve the landing and takeoff performance of airplanes is continuing, with a significant portion of the effort directed toward the augmentation of lift by means of the jet-flap principle. Although some attention is still being given to refinement of methods of providing lift by suitable location of the jet exhaust on the wing profile and to the effect of flap span, increased emphasis is being placed on studies of the stability and control characteristics of complete configurations and on noise suppression possibilities of the various arrangements. In addition to low-speed wind-tunnel studies, free-flying models are being used to study the dynamic stability and control characteristics of jet-flap arrangements flying at high-lift coefficients. In these studies various methods of providing longitudinal trim and control are being used including downward-directed fuselage nose jets, jet-augmented flaps on canard surfaces, and various tail sizes and locations. Models of conventional jet-transport-type configurations with jet flaps have been flown at lift coefficients up to 12, using a nose jet for trimming.

Two other jet-flap areas receiving attention are cruise performance and the large loss of lift in ground effect. Research on the ground proximity problem is continuing in static wind-tunnel studies and is being extended to include takeoffs and landings with flying models. High-speed cruise performance studies have shown that the lift can be increased by blowing downward through closely spaced holes along and near the trailing edge.

Propellers

Among the several means of achieving VTOL operation of airplanes is the tilting propeller concept. Propeller data (performance and stress) are rather lim-

ited at high angles of attack. To attack the problem of obtaining full-scale propeller data under conditions typical of VTOL operation, a 3,000-horsepower tilting dynamometer has been put in operation, enabling the determination of isolated propeller characteristics under full-scale VTOL conditions in a wind tunnel. This includes operation at angles of attack up to 90°, corresponding to hovering and low-speed forward flight, and also at 180° corresponding to descending flight. The characteristics measured include not only conventional propeller coefficients but also levels of blade stresses encountered during the unconventional operating conditions. The first propeller type studied had flapping blades designed with the intention of alleviating the 1–P stresses encountered during high angle-of-attack operation and to permit a lighter propeller, although at the expense of a more complicated hub. In descent conditions the propeller had flapping instability introducing unacceptably large stresses.

Increasing interest in shrouded propellers for VTOL aircraft has prompted questions concerning their operation at zero forward speed and low forward speeds at high angles of attack. Performance, efficiency, and general design information is being gathered on a series of shrouded propellers from zero forward speed to high subsonic forward speeds, and from angles of attack from 0° to 90°. In addition, a systematic investigation has been started to determine the low-speed and hovering characteristics of shrouded propellers operating in the presence of wings and in the chord plane of wings.

An investigation of the aerodynamic characteristics of propellers designed for transonic forward speeds is essentially complete, utilizing a propeller research airplane. Three propellers were tested in conjunction with several spinners. Two propellers were designed for a forward Mach number of 0.95 and the third for a Mach number of 0.82. The first was a true supersonic propeller; the second a modified supersonic propeller; and the third, a transonic propeller. Efficiencies as high as 80 percent were measured at a forward Mach number 0.95 with the supersonic propellers. Minimum thickness-ratio distribution was determined to be the most important parameter in the design of propellers for transonic forward speed. Although all the propellers were noisy, the investigation indicated that supersonic propellers provide an attractive means of propulsion for long-range airplanes in which economy of operation, flexibility, and high static thrust are important.

SEAPLANES

Hydrodynamic research of both a basic and applied nature is progressing toward improving hydroski and hydrofoil development as well as seaplane configuration development having improved supersonic performance. At the same time a substantial amount of research has been initiated on underwater-launched missiles and on the water recovery or landing of manned spacecraft and hypersonic boost-glide vehicles.

Hydroskis

Fundamental research on hydroskis in the submerged and planing regimes has continued with the derivation of a unified method for calculating the lift of a rectangular flat plate in both regimes. Experimental investigations are likewise continuing on the effects of upper surface camber on a submerged surface and of longitudinal convexity on the bottom of a planing surface. Studies have been made of the characteristics of a submerged hydroski having a shape easily adaptable to practical construction methods, suitable means of reducing the spray of such elements during emergence and planing, and the influence of mutual wakes in multiple hydroski installations. Applications of the ski concept have been investigated on models of fighter aircraft, guided missiles as a recovery device, and hull-type seaplanes as a load-alleviating device.

Superactivating Hydrofoils

The new concept of using supercavitating hydrofoil sections on water-based aircraft elements to combat the adverse effects of high water speeds has been vigorously pursued both theoretically and experimentally. Analytical methods for dealing with ventilated as well as supercavitated flows, effects of aspect ratio, depth of submersion, and development of optimum sections have been derived and verified by model tests. Design charts to facilitate routine use of the theory have been devised. The physical process of ventilation is becoming better understood by the use of new methods to visualize the complex flows associated with this phenomenon. Attention is being given to practical application by investigation of structurally sound, surface-piercing arrangements such as highly tapered monoplanes, biplanes, and cascades with end plates. A specific application of two supercavitating hydrofoil systems is being investigated with a model of a full-scale test-bed airplane. The ability to accept highly cavitated flows at high water speeds gained in the research on hydrofoils has also led to investigation of supercavitating principles applied to underwater missiles.

Hull-Type Seaplanes

Research on hydrodynamic configurations and evaluations of advanced water-based aircraft concepts or preliminary design configurations has remained a substantial part of the hydrodynamic effort. With increasing interest in hydro-ski and hydrofoil solutions, the continued usefulness and versatility of the flying-boat hull have not been neglected. Experimental investigations have been continued in this area over a wide range

of requirements from the very low landing speeds associated with antisubmarine warfare seaplanes to the very high landing speeds associated with supersonic attack aircraft. The configurations of interest have included those of large transonic transport aircraft, bomber aircraft, and small supersonic interceptor aircraft. In one series of tests of supersonic attack bomber-type configurations, attention has centered on means of obtaining spray clearance for air-breathing engine intakes and various hydrodynamic features for water takeoffs and landings. An investigation to determine the comparative rough-water capabilities of hulls, skis, and hydrofoils for such aircraft is also in progress.

Recovery of Spacecraft and Hypersonic Glide Vehicles

New horizons in the evolution of water-based aircraft have appeared in the form of manned hypersonic boost-glide vehicles and spacecraft which must be safely "ditched" or recovered after flight outside the atmosphere. Hydrodynamic investigations have accordingly been initiated of the water landing characteristics of typical satellite vehicles, including both high-drag winged and wingless reentry types. It is anticipated that through further research, the decelerations associated with water entry in favorable areas on the earth can be kept within reasonable human and structural tolerances.

Hydrodynamic Facilities

Investigation of the use of a small high-speed water jet to obtain fundamental hydrodynamic data has been completed. It was concluded that the use of a simple slotted boundary for such a jet reduced the boundary corrections on planing lift to a point where direct agreement with towing tank data could be obtained at high speeds for a wide range of test conditions. An improved towing carriage for the Langley high-speed hydrodynamic facility is being provided to increase the range of water speeds available by conventional tank procedures.

ROTARY WING AIRCRAFT

Performance

The extension of basic rotor theory in accordance with anticipated state-of-the-art changes has been a continuing process. Current efforts relate primarily to clarification of rotor force and blade-flapping phenomena for the severe flight conditions brought about by the considerable increases in installed power which are evident in new designs. This work utilizes published numerical procedures, in conjunction with electronic computers and full-scale experimental setups.

Limitations of helicopter speed due to retreating blade stall have been largely based on pilot reactions to roughness caused by the blade stall. A technique has been developed whereby the beginning of this blade stall can be detected readily under high forward-speed conditions. This is accomplished by monitoring blade-pitching moments and power input so that blade stall can occur to a measurable but not catastrophic degree. As a consequence, it has been possible to establish the allowable increase in forward speed for a rotor of a tandem helicopter resulting from a change in blade section from a symmetrical to a cambered section. A 20- to 25-percent increase in forward speed at the same weight or a 15-percent increase in gross weight appears possible.

Investigations are in progress to determine the static aerodynamic characteristics of helicopter rotors operating at tip speeds up to 900 fps. The effects of centrifugal forces on the rotor-blade boundary layer, tip flow field, and varying stall or compressibility areas over the rotor in forward flight are also being studied. Rotors having a wide range of blade-thickness ratios, thickness form, and leading-edge radius have been tested. These investigations have resulted in successful attempts to "synthesize" airfoil data from rotating rotor tests. Such data are expected to provide greater accuracy in the calculation of the forward flight characteristics of rotors operating at high tip speeds.

Vibration

As helicopters have become larger and more flexible, the magnitude of the vibrations associated with them has increased. The use of the helicopter for longer military missions and the increasing use of helicopters in civil applications have made the present vibration levels an increasingly serious matter. The designer is frequently unable to predict vibration sources and to provide methods of alleviation.

As a result of the increasing importance of this problem, a flight investigation was made to measure the vibration encountered by a specially equipped tandem helicopter. The first phase of the project involved the development of a method for measuring rotor blade, fuselage-coupled frequencies in flight. The technique involved the use of a mechanical shaker mounted in the helicopter. The results indicated that the method developed would provide a satisfactory means for flight testing of prototype helicopters for coupled frequency effects.

The project was extended to include the measurement of relative aerodynamic inputs for several flight conditions, of vibration effects due to blade out-of-track, and flight vibration mode shapes, through use of magnetic tape data recording. Vibration was only slightly increased when the blade out-of-track was less than 1 inch. However, as the out-of-track increased to slightly over 2 inches, the vibration became nearly intolerable. These efforts have not resulted in a state of knowledge

which will permit satisfactory prediction and reduction of helicopter vibrations; however, use of the research technique holds promise for the attainment of this goal.

Stability and Control

Stability and control studies utilizing a variable-stability helicopter have succeeded in determining the degree of improvement attainable by increased damping and control power during instrument-flight landing approaches.

Low airspeed flights, including efforts to hover over a ground reference, have been conducted under simulated instrument conditions with a single-rotor helicopter having electronic autopilot-type components which permit alteration of the apparent (to the pilot) stability and control characteristics of the helicopter. By means of these components, systematic variations in such parameters as control power, damping in roll, yaw and pitch, stick force gradient and stabilization about each axis can be evaluated singly or in combination. The results confirm earlier work showing that improvements in handling qualities result with increases in damping. Also there is a large range of damping values within which desirable control powers are independent of the damping. However, as the damping is increased, the allowable maximum control power tends to increase.

A device that supplies signals to the pilot's instruments to indicate helicopter position and rate of change of position with respect to a ground reference, as well as helicopter altitude over the ground, has been constructed. The purpose of the device is to permit hovering on instruments so that handling qualities in hovering may be investigated. An additional device is also being constructed which will provide position and rate signals to the pilot in the form of stick forces.

Current efforts to assist in modernization of military flying qualities specifications for helicopters serve to emphasize both the value of the damping and control-power work completed and the need for more information; for example, how to apply the results established for helicopters of typical size to size extremes which can range from 250 to 100,000 pounds gross weight. As one step in learning possible effects of size, and also the effects of gross changes in the ratio of rotor inertia to aircraft inertia, brief tests have recently been completed with a tip-jet-driven helicopter of far smaller size but of higher relative rotor inertia than any previously tested. Certain beneficial effects related to high rotor inertia were readily apparent and led to additional comparative tests with more typical designs. Correlation of these results with those obtained with other larger helicopters is continuing.

POWERPLANTS

During the past year, the NACA increased its effort on studies of those powerplants believed to have potential as space propulsion systems and secondary power sources. The first results were presented at the NACA 1957 Flight Propulsion Conference, given at Cleveland in November 1957, 1 month after Sputnik I. This classified conference encompassed analyses of space missions, chemical propulsion systems, nuclear propulsion systems, electrical propulsion systems, auxiliary power systems, and propellants.

The conference also presented an NACA survey and assessment of air-breathing engines required for a "next generation" of airborne vehicles. Data, technology, research requirements and potential, with reference to turbojet and ramjet engines for flight from Mach 4 to Mach 18 were discussed.

SPACE PROPULSION

Analyses of satellite space vehicle problems and interplanetary space missions have been made. These analyses, while based on present knowledge and therefore very preliminary, have led to certain broad conclusions concerning the relative merits of various propulsion and auxiliary power systems and have helped to delineate the many areas of propulsion research that will be of increasing importance for space applications.

Auxiliary Electric Power

Systems using solar energy (solar batteries and solar turboelectric systems) involve the least weight for power requirements up to a few kilowatts, provided almost-continuous operation in the sun is possible. If only half time is spent in the sun, a number of systems are competitive, including radioisotope hydrogen-oxygen cells and radioisotope turboelectric systems. The nuclear turboelectric system without shielding is also competitive in this range of power, but shielding requirements, particularly for manned vehicles, may rule it out. Chemical batteries are competitive weightwise only for durations of operations of the order of a few days. The required voltage must also be considered in selecting auxiliary power systems. (Figs. 1 and 2.)

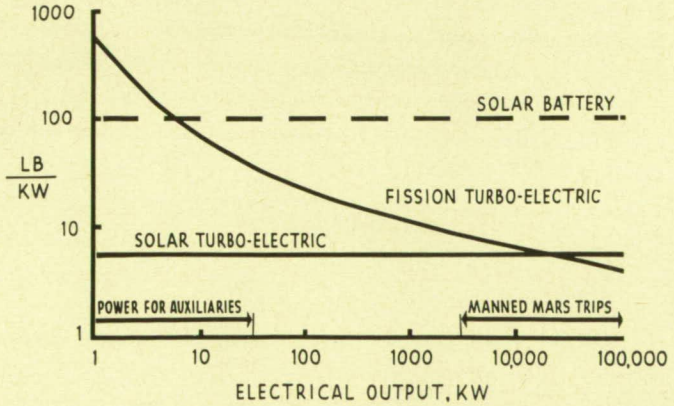


Figure 1.—Weights for kilowatts of electrical power.

Satellite Sustainers and Orbit Control

For periods of operation of the order of 100 to 200 days or less, a low-thrust chemical rocket can provide the required propulsive energy without excessive weight penalty relative to electric systems. Particularly, if rapid orbit changes are required, the chemical rocket seems to be the only feasible propulsion system. For very long durations, or for permanent satellites, electric propulsion systems using solar energy or nuclear energy require less initial weight or resupply weight than chemical rockets.

Lunar and Mars Journeys

Many missions involving trips to the Moon and Mars can be accomplished without excessive weight penalty with high performance chemical rockets. These missions include one-way instrumented journeys to the Moon and Mars, and manned trips to the Moon. Electric propulsion systems seem undesirable for the Moon trip because of the long times required for the journey compared with those required for high-thrust rockets. For manned trips to Mars, however, electric propulsion

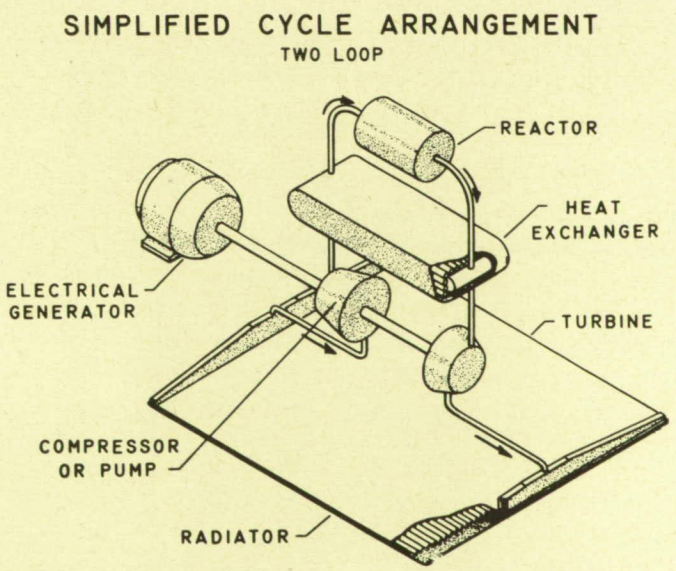
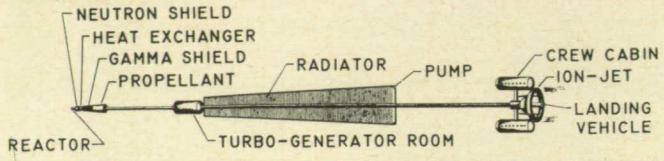


Figure 2.—Auxiliary power from nuclear turbo-electric system.

Preceding Page Blank

systems require only moderately more time for the complete journey than the chemical rocket, and their advantage in initial weight becomes greater and greater as the size of the expedition increases. Of the electric systems considered, the nuclear turboelectric, the solar turboelectric, and possibly the fusion-powered systems are capable of supplying the required electric power with sufficiently low weight. Of the thrust generators considered, the ion-electric accelerator appears to be most promising on the basis of current technology. (Fig. 3.)



PAYLOAD FOR 8 MAN CREW	LB	LENGTH	600 FT
		GROSS WT	322,000 LB
10 LB/DAY/MAN	88,000	POWERPLANT WT	60,400 LB
CABINS	50,000	PROPELLANT	60,400 LB
LANDING VEHICLE	40,000	THRUST	32.2 LB
TOTAL	178,000	POWER	11 MW

EXPLORATION TIME AT MARS, 329 DAYS
TOTAL ROUND TRIP TIME, 1100 DAYS

Figure 3.—**Electric spacecraft for round trip to Mars.**

The low-pressure, high-specific-impulse nuclear rocket is competitive with electric systems for large-scale Mars expeditions and has the advantage of higher thrust-weight ratio. It has the disadvantages that much higher temperatures are required than in the electric systems and that hydrogen must be used to attain the required high specific impulse. The latter requirement may impose severe storage difficulties for long-duration journeys.

Another advantage of the electric system over both the nuclear and chemical rockets is the resupply advantage. Since the electric system has the higher specific impulse, its propellant replacement weight is much less than that of the chemical and nuclear rockets.

PROPELLANTS

A continuing need exists for accurate and up-to-date theoretical performance data for a large number of rocket propellant combinations. A program for automatic computing equipment to permit calculation of the theoretical performance of any rocket or ramjet propellant has been set up. Calculations of the theoretical performance of many propellant combinations are kept up to date by a continual revision of the thermodynamic data necessary as various research organizations determine that data. (Fig. 4.)

Although the emphasis on rockets has grown considerably, work has continued on fuels for air-breathing engines, especially on the problems of applying the boron-hydride fuels.

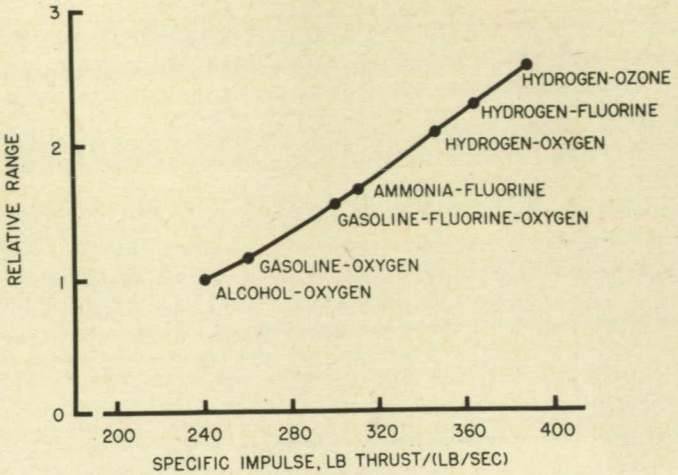


Figure 4.—**High energy fuels increase range.**

COMBUSTION

Combustion research has been directed toward studies of the vigorous combustion of high-energy fuel systems and rocket propellant combinations.

The value of gas analysis as a diagnostic tool for turbojet combustor research was demonstrated. It appears that the technique may also be of advantage in rocket research. In the turbojet combustor, estimates were made of local, rather than overall, fuel-air ratios, efficiencies, and heat release rates.

With the trend toward higher combustion temperatures that are associated with high-flight Mach numbers in air-breathing systems and with the use of rocket engines, studies of the physical chemistry of the burned gases are becoming more important. The rates of reaction and recombination in the burned gases are of special importance and are being studied. The effects of chemical reaction on heat transfer from combustion and other high-temperature gases are also under investigation.

Rocket combustion is a complex phenomenon involving many simultaneous physical and chemical processes. The rates of individual processes have been studied in order to predict overall performance in terms of the slowest rates. Detailed calculations of the evaporation rates of various rocket propellants have shown great promise for computing rocket performance, and a method relating the performance to the quantity of liquid propellant vaporized has been devised. The relation indicates that incomplete vaporization is responsible for combustor inefficiency.

COMPRESSORS

Over the past 15 years the results of research on compressors for turbojet engines have been reported in numerous publications. In the majority of instances, each of these reports presents only an incremental bit of information which taken by itself may appear to

have only limited value. Taken altogether and properly correlated, however, this information represents significant advances in the design of axial flow compressors. The NACA, therefore, has compiled and assimilated into one report, virtually all of the advanced axial flow compressor technology.

During the past year, primary emphasis in compressor research has been on high-performance transonic and supersonic compressors for supersonic aircraft gas turbine engines.

A method was developed for the prediction of the off-design performance of axial-flow compressors. This method is consistent with a framework of equations and blade-element performance correlations commonly used in compressor design, and represents an attempt to provide a more general off-design performance prediction procedure than "stage-stacking" techniques which use assumed stage performance data. The performance of a rotating blade row was predicted, using this method, and compared with the experimental performance characteristics. At rotor-tip speeds that resulted in low relative inlet Mach numbers, computed performance was in good agreement with the experimental data. For high speeds, where the basic cascade data are not so applicable, a narrower satisfactory operating range was predicted than was obtained experimentally. It is believed that the discrepancies can be reduced by improvement of the estimation of high Mach number effects on blade-element performance.

PUMPS

A major part of the turbomachinery research effort has been directed at the problems of liquid pumps for rocket engine application. The objectives of this research are to increase operating limits of pumps, to reduce size and weight, and to provide pumps capable of operating with high-energy propellants. Initial research in this area involved the application of compressor design techniques to rocket pumps. The major problems were considered to fall into two categories: (1) cavitation, and (2) allowable loading (or velocity gradients) on pump blading. Fundamental research on the phenomenon of cavitation has been started, with emphasis on cryogenic fluids. In the category of blade-loading research, programs have been started on both centrifugal and axial-flow pumps, to establish blade-loading limits.

A study of flow-starting transients in a rocket was completed. A configuration consisting of a tank, suction line, constant speed pump (with bypass), variable flow-control valve, injector, and rocket chamber was analyzed theoretically. From this study, it was found that the time history of the main flow control has a decisive effect on the inlet pump head.

As part of the research program on pumping of cryogenics, a study was made of the conditions existing in a closed cryogenic container that typified a rocket propellant tank. This study showed that surface temperature controlled the pressure in a closed cryogenic container and verified the existence of temperature gradients in the liquid.

TURBINES

One phase of the turbine research program considered fundamental aspects of turbine design and performance. These studies are applicable to turbines for air-breathing engines as well as to turbodrives for rocket engines. As the culmination of some of this basic turbine research, an analysis (with substantiating experimental data) was made to establish turbine efficiency in terms of basic turbine design parameters for a range of turbine work and speed requirements and for various types of turbines.

A large part of the turbine research effort was directed at problems of turbodrives for rocket applications. These applications are characterized by very high work per pound of working fluid. The basic objectives of the research are to obtain high turbine efficiency, to reduce turbine size and weight, and to evolve turbines capable of operating in the working gases of rocket engines using advanced high-energy propellants. The initial phases of this turbodrive research included certain basic studies intended to establish research needs in the field. Analyses are being made to establish the effects of turbine-inlet temperature and turbine exhaust-gas thrust recovery on missile performance. A method was developed for determining turbine design characteristics for rocket turbodrive applications. A facility is being built to determine the effect on turbine performance of using cryogenic gases as the working fluid.

TURBINE COOLING

Turbine-coooling research was directed toward the study of air-cooled turbine blades that will be capable of operating at gas-temperature levels of 500° F. or more above those temperatures currently being employed in aircraft gas-turbine engines.

Research, using full-scale turbojet engines as test vehicles, was continued on shell-supported blades and strut-supported blades. The shell-supported blades offer very good heat-transfer characteristics and a relatively lightweight blade. Strut-supported blades offer very good heat-transfer characteristics but are heavier than shell-supported blades. Blades with porous shells for transpiration cooling were also investigated; such blades will theoretically cool more efficiently than other types of blades, but control of porosity and the obtaining of sufficient strength in the porous material are major problems. (Fig. 5.)

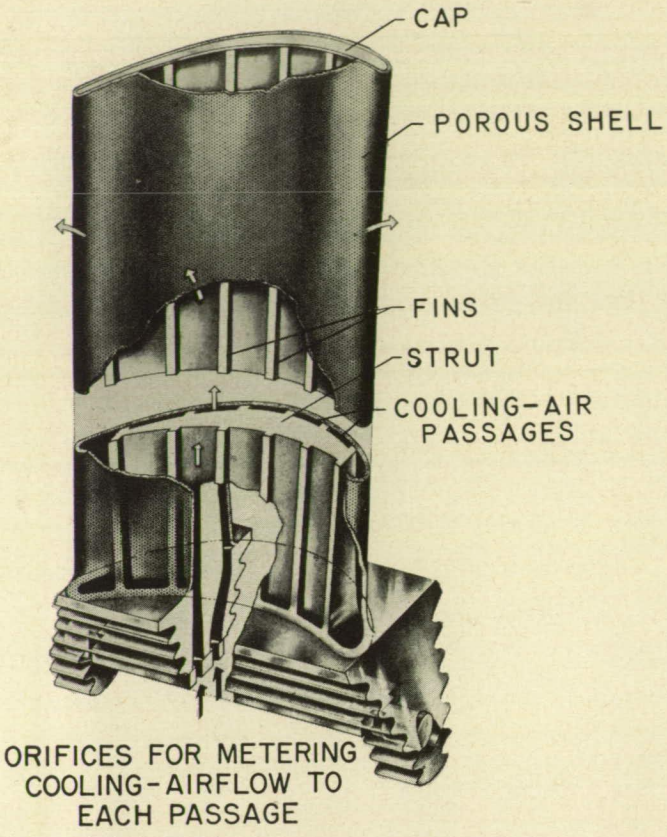


Figure 5.—**Transpiration cooled blade.**

Special studies of the cooling problems in the leading-edge regions of cooled turbine blades were inaugurated by investigating the cooling of small airfoils in a tunnel capable of operating at gas temperatures up to 3,000° F.

A special engine incorporating an air-cooled turbine stator and rotor for making full-scale engine investigations under actual high-temperature operating conditions is being prepared for operation. In order to provide turbine blades for this engine, it was necessary first to investigate a number of problems such as brazing techniques, effect of brazing on material strength, attachment of blade shell to blade base, and heat treatment, that are associated with air-cooled turbine blades. These problems have now been resolved, and a set of cooled blades for the engine has been fabricated and is now being instrumented prior to installation in the engine for research purposes.

An analysis of heat transfer and flow in boundary layers with variable fluid properties in the entrance region of smooth tubes and flat plates was completed. Also completed was an analysis on the effect of variable fluid properties on free convection, and an analytical and experimental study of laminar heat transfer in a vertical circular tube under combined forced and free convection. A new method for measuring residual stresses in disks was devised and analytically confirmed.

ENGINE CONTROLS

Emphasis on control research has been directed toward rocket engines, together with initial explorations of nuclear rocket and other space propulsion systems. Research is underway on rocket fuel systems with respect to such items as the dynamic characteristics of long hydraulic lines, dynamics of centrifugal pumps, combustion chamber pressure control, and propellant mixture ratio control. A study of the requirements of rocket engines and reaction devices for control of the trajectory of missiles has been initiated.

A major effort is being expended in an attempt to correlate analytical expressions for the dynamics of rocket components and for rates of propellant vaporization with experimentally observed liquid propellant rocket motor instability. The ultimate goal in this work is to permit accurate prediction of rocket instability and to determine design criteria for rocket scaling and for development of variable thrust rocket motors.

An analysis of control requirements for nuclear turbojet propulsion systems was initiated. System components were analyzed, reactor kinetics were simulated on an analog computer, and nuclear reactivity was determined.

The dynamic response of supersonic diffusers to disturbances in downstream conditions was analyzed. The analysis included the shock motion in the diffuser as a function of downstream pressure disturbances, and the response of subsonic diffuser pressures to disturbances in fuel flow for ramjet engines. The analysis relates the various dynamics to the particular operating conditions and to the physical dimensions of the system considered, and thereby makes possible control design prior to physical testing of the system.

Turbojet engine performance was investigated experimentally with several configurations of interacting multiple loop controls to determine the mode of control required for obtaining optimum rotor speed and turbine discharge temperature transient response characteristics during (1) thrust increase and (2) afterburner ignition, with manipulation of engine fuel flow and exhaust nozzle area. Good engine transient performance, near the design point, was obtained with a control system in which engine speed was controlled by exhaust nozzle area and the turbine-discharge temperature was controlled by manipulation of the engine fuel flow.

POWERPLANT MATERIALS

High Temperature Alloys

Despite the extensive test work done in the past which has established good correlations between stress-rupture data in the laboratory and service life in engines, several questions have remained unanswered. One concerns the

effect of "overtemperature" operation on the life of turbine blades. Since the stress-rupture life of the material may be shortened by overtemperature in a stress-rupture test, does it follow that engine life is affected by overtemperature operation? Does reheat treating the blades help?

To answer these questions, a recent study was made of S–816 (a cobalt-base alloy) blades overtemperatured in J–47 engines. An example of one of the conditions of overtemperature encountered was engine overspeed by 4 percent, with tailpipe temperature about 200° F. over normal, for an unknown period of time. These blades were removed from service and tested in a laboratory J–47 engine under repeated cycles of 15 minutes rated and 5 minutes idle speeds. Stress-rupture tests and metallographic examinations were made in an attempt to correlate properties and microstructure with engine results.

It was found that overtemperatured buckets did not fracture in service in abnormally short operating times. Cracking, particularly on the leading edge, was the principle mode of failure of buckets. Although cracks developed after short operating times, they did not propagate to fracture during several hundred hours of operation. The overtemperatured buckets failed in stress-rupture tests in shorter periods of time than buckets directly from stock and also failed in shorter periods of time than the overtemperatured buckets which had been subsequently heat treated. In fact, full reheat treatment of overtemperatured buckets, using the standard heat treatment, increased the resistance of the blades to leading edge cracking and also improved the stress-rupture life of the material. Such buckets performed both in the engine and in stress-rupture tests equivalently to new standard buckets.

A laboratory investigation of overheating indicates the complexity of the high-temperature alloy studies. In this investigation, periodic overheats were conducted at temperatures to 2,000° F. both with no stress and with stress present. (No engine tests were performed.) The alloy studied was a nickel-base alloy, M–252. It was found that periodic 2-minute overheats to 1,900° or 2,000° F. very substantially increased the rupture time of M–252 alloy at 1,500° F., provided no stress was present during overheat. Such overheating was damaging only if a sufficient high stress were present to use up a significant proportion of total rupture life. However, when M–252 alloy is repeatedly overheated to 1,650° and 1,800° F. in the absence of stress, the rupture life at 1,500° F. is reduced. In the presence of stress, however, the damage is less than anticipated. Consequently, if stress is present it must be quite high to do any significant damage.

Physics of Solids

The aim of the physics of solids research is to provide basic knowledge to aid in the development of materials for use at very high temperatures and in chemically active atmospheres. Among the problems under study are the chemical reaction of materials in certain environments which may be affected by nuclear reactor design, aerodynamic heating, and flight in the upper atmosphere.

Platinum has long been known as an inert metal; in fact, it has been the standard crucible material used in chemical analysis because of its resistance to oxidation and direct flames and its resistance to attack by rather active chemicals. Previous studies of the rates of oxidation of platinum at temperatures to 1,400° C. in molecular oxygen have indicated a very low oxidation rate. However, recent studies conducted at these temperatures and at pressures below 0.1 millimeter of mercury have indicated a very marked increase in oxidation rate at low pressures. These results appear contradictory when one considers the pressure of a gas is a measure of the concentration of the gas. However, the studies have been conclusive and indicate that previously observed rates under relatively static conditions may be in error when dynamic conditions, namely free motion of the gases, is present. At pressures above 0.1 millimeter of mercury, oxidation is strongly inhibited by back reflection from the gas.

LUBRICATION AND WEAR

Bearing Research

In recent years the statistical design of experiments has found favor as a device for planning experimental research. Many factors which affect the course and results of an experiment can be varied simultaneously and their effects separately and concurrently analyzed. However, with phenomena such as the fatigue failure of bearings, which are so complex and have so many factors contributing to or alleviating failure, statistical design has not been successful. Therefore, it has been necessary to return to the classical experimental method of studying one variable at a time in order to make any progress in the study of bearing failure.

Tests are performed on a rolling contact fatigue spin rig where balls are rolled around the inside of a cylinder by the action of compressed-air jets. Previous studies of the rig had indicated similar patterns of failure and fatigue lives on the balls in comparison with those obtained in actual bearings. In addition, the number of test variables is reduced.

One research area which appears very promising is the study of the metallographic structure of balls and races as a clue to variable bearing life. Balls and races

are made of steel which has been forged or rolled so that it has a definite crystal orientation. This orientation shows up on etching a cross section and is usually referred to as fiber. It has been found recently that if the fibers are not oriented parallel to the axis of the cylinder (which corresponds to the outer race of a bearing), the fatigue life of the cylinder is drastically reduced.

In this investigation, cylinders were prepared in three groups from forged stock. In the first group, the cylinders had their axes parallel to the fibers of the steel stock. In another group the fiber was arranged so that it was from 0° to 45° to the axis of the cylinder, and in a third group the axis of the cylinder was at 0° to 90° from the fiber of the material. When comparing the data obtained on these cylinders, it was evident that by using material whose fiber was parallel to the surface of the cylinder, a large increase in life of the cylinders was obtained. For example, in this series of tests only 10 percent of the cylinders with surfaces parallel to the fiber of the material had failed by 5 million cycles. By 60 million stress cycles, 80 percent of the cylinders had failed. However, with cylinders oriented from 81° to 90° to the fiber, 10 percent of the failures has been obtained by 1¼ million stress cycles and 80 percent by 3 million stress cycles. We thus see a profound effect of fiber orientation both on the first failures and on all failures. The study of the relation of failure to fiber orientation in balls is considerably more complex since fiber orientation can be determined only after the balls have been tested. However, the striking relationship of fiber orientation to ball failure is also illustrated by a polar projection of failure incidences versus fiber orientation. (Fig. 6.)

NUCLEAR PROPULSION

The NACA nuclear research program has been directed toward solving the problems associated with the application of nuclear power to the propulsion of aircraft and rockets. Analytical studies have been and are being carried out on nuclear aircraft propulsion systems, nuclear booster-rocket systems, nuclear heat-transfer, interplanetary propulsion systems, and nuclear electric-generating systems for space-travel application. These studies have been specifically directed toward defining the research problems that must be solved in order to achieve the potential indicated for these various systems.

The construction of reactor facilities to be used in conducting experimental nuclear research studies is continuing. The construction of the low-power, solution-type research reactor located at Lewis has been completed. Work is continuing on the Plum Brook

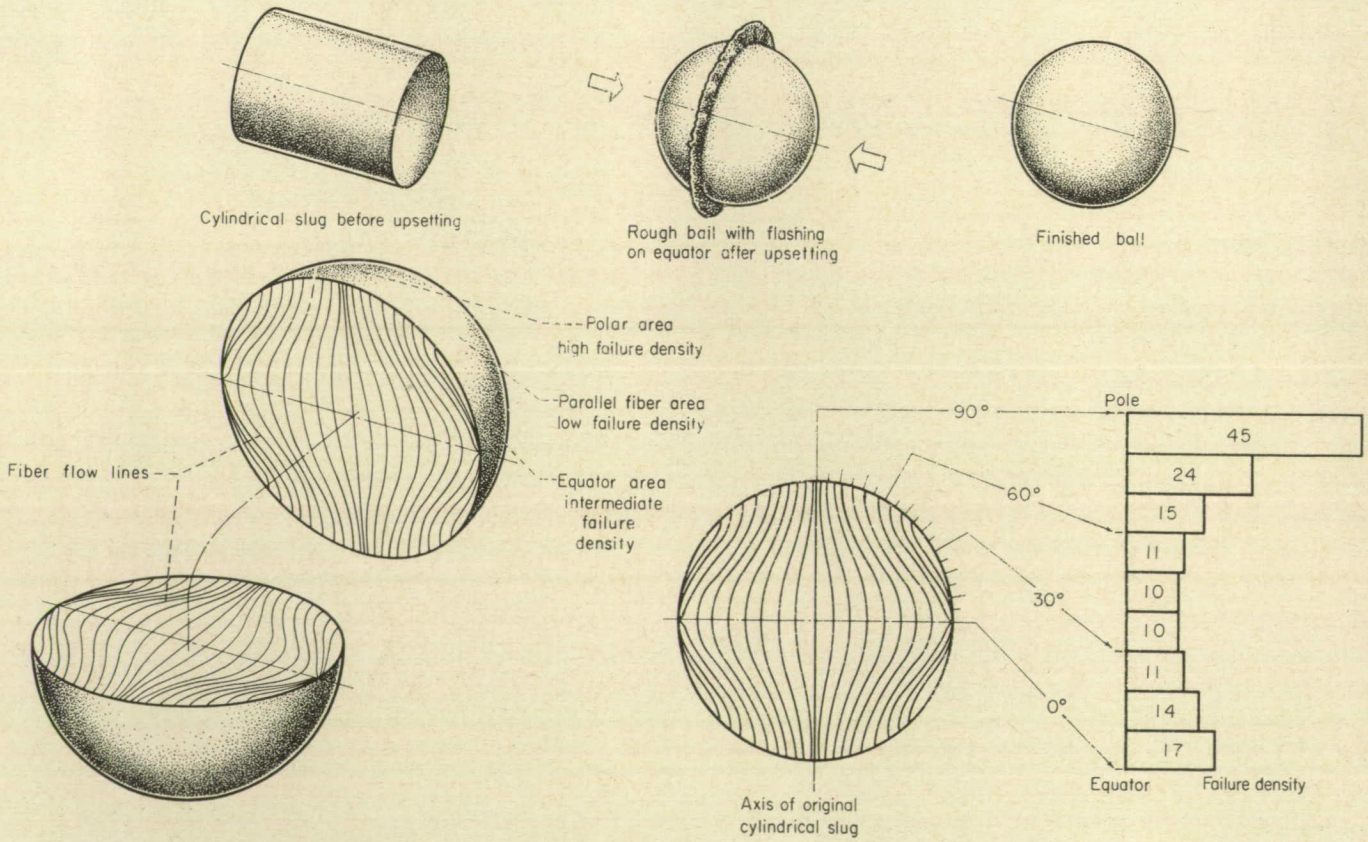


Figure 6.—**Susceptibility to fatigue failure in bearing balls as influenced by forging fiber orientation.**

Reactor Facility. Experiments applicable to space-flight systems are being planned and designed for both of these facilities.

Methods have been devised for evaluating weights of shields for aircraft and rocket systems. Studies of various methods of shield design, including the statistical methods, are continuing. Equipment is being fabricated to study the attenuation of gamma photons in various shield materials and also to study the gamma ray streaming through ducts in shields.

The effort on reactor analysis has been devoted to studies of reactors for jet engine propulsion systems and various rocket systems in order to determine effects of core size, composition, reflector thickness and material, moderator material, and fuel-element material on uranium requirements, and flux and power distributions. Analyses and experiments are being conducted to develop methods of predicting nuclear characteristics of reactors of unusual or complex geometry for space-flight systems.

A number of heat-transfer and flow problems associated with nuclear powerplants are being studied. This work is intended to provide pertinent information of a fundamental nature that will be of general usefulness in the development of various types of nuclear propulsion systems.

Sodium hydroxide is in many ways an attractive choice as a high-temperature, heat-transfer fluid. Unfortunately, only a few materials are suitable for containing it in the molten condition at temperatures of 1,500° to 1,700° F. Among these are nickel, copper, silver, gold, and some nickel-base alloys. Even these materials exhibit a form of corrosion termed "thermal-gradient mass transfer." Thermal-gradient mass transfer is the phenomenon by which the container metal is removed (either chemically or physically) from the hotter regions of a system and deposited in colder regions by the heat transfer fluid. With the previously listed metals the deposit is in the form of needlelike crystals, the size of which depend upon the experimental conditions. (Fig. 7.)

In order to find ways of inhibiting this type of corrosion, an investigation was conducted concerning the possible mechanisms. The mechanisms were found to depend on chemical reactions between hot and cold zones and molecular diffusion within each zone.

The diffusion of the molecular species in the melt will allow the process to continue indefinitely. In dynamic tests, the rate of transfer is controlled by the rate of the zone reactions and thus is constant with time. In static tests, the rate of transfer is controlled by the rate of diffusion and increases with time.

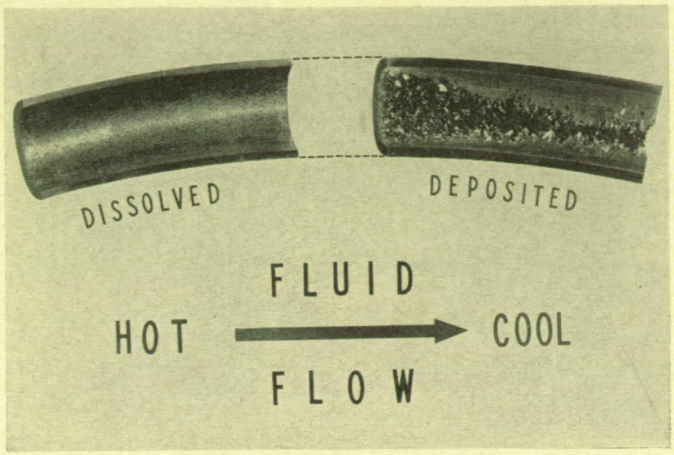


Figure 7.—**Mass transfer of structural materials by a coolant.**

The effects of additives upon the rate of transfer were also explained. Additives which effectively increased the sodium oxide concentration increase the rate of transfer; those which decrease this concentration decrease the rate of transfer. Reducing agents decrease the rate of transfer in static tests and have no effect in dynamic tests. Oxidizing agents have the opposite effect in static tests.

Experiments are being set up on the 60-inch cyclotron to study the heat-transfer characteristics of ionized gases and also to study the range of fission fragments in ionized gases. Such studies are directly applicable to the space nuclear-propulsion systems now being evaluated.

A two-dimensional diffusion theory has been developed for determination of reactivity effects of a fuel-plate-removal experiment. This and other diffusion theory analyses are being checked experimentally by duplicating the essential neutron-diffusion phenomena with a point source of fast neutrons.

Heat-transfer characteristics of liquid metals flowing over a flat plate were analyzed using laminar boundary-layer equations. Numerical solutions of the appropriate differential equations were carried for the situation of uniform wall temperature and uniform wall heat flux.

Laminar free convection from a vertical flat plate with nonuniform surface temperature was analyzed. Analyses of transient forced-convection flow and heat transfer, and of effects of internal heat sources on forced convection in ducts were completed.

AIRCRAFT, MISSILE, AND SPACECRAFT CONSTRUCTION

It is in the field of construction that the designers' ideas are translated into structure or "hardware" which will possess the serviceability and structural integrity necessary to attain the desired vehicle mission.

The operation of hypersonic aircraft and missiles and the venturing into space raise many new problems with regard to structural design, materials, and influences of environment for which solutions are actively being sought. A great deal of attention has been required in the way of defining new problems and developing new facilities.

STRUCTURES

Structures research during the past year has been directed primarily to the problems of aerodynamic heating, with particular attention being focused upon the problems associated with hypersonic gliders and various types of reentry vehicles. Consideration was also given to the structural problems of space vehicles, and some fundamental structural studies were reoriented in this direction.

The types of structural configurations suitable for hypersonic boost-glide aircraft and orbital reentry vehicles were investigated. Comparisons were made of the various structural approaches such as the use of unprotected structures, heat sink structures, insulation, cooling, and ablation. The successful use of unprotected structures is dependent on development and improvement of refractory metals, whereas insulated and cooled structures may be developed using existing materials. Research on insulation and cooling has included experimental and theoretical studies of the effectiveness of gas coolants in the passages of corrugated core sandwiches, investigations of the feasibility of using built-up ceramic coatings as thermal shields, and simple methods of providing coolant as an integral, noncirculating part of sandwich construction. The optimum combination of insulation with various types of structural elements has been studied theoretically, and structural integrity tests have been made on several types of thermal shields and insulating panels.

The thermal stresses induced in structures by transient aerodynamic heating can have adverse effects on their strength and stiffness. Theoretical and experimental studies of these effects have been conducted for various structural configurations. Experimental studies of the effect of thermal stress on the buckling and ultimate strength of ring stiffened cylinders and multiweb beams have continued. Additional data have been obtained on the combination of compressive, shear, and thermal stresses that cause permanent buckling of plates. An analytical determination of the minimum weight of a multiweb beam subjected to combined bending and thermal stress is nearing completion.

A reasonably accurate knowledge of the temperature distribution in a structure is a prerequisite to all elevated-temperature structural analyses. The relative importance of heat transfer by conduction, convection, and radiation in sandwich panels was studied and an approximate procedure for estimating radiation effects was devised.

A program for the development of several basic type insulating structures is currently in progress. The structures as conceived are applicable to hypersonic vehicles and manned satellites, and are capable of extended operation with wall temperatures in the range from 1,500° to 2,500° F. Conventional metals as well as materials such as graphite have been used for the outer walls, and fibrous materials have been employed as insulators. Tests of some specimens have been conducted in radiant heater and hot-jet facilities with promising results.

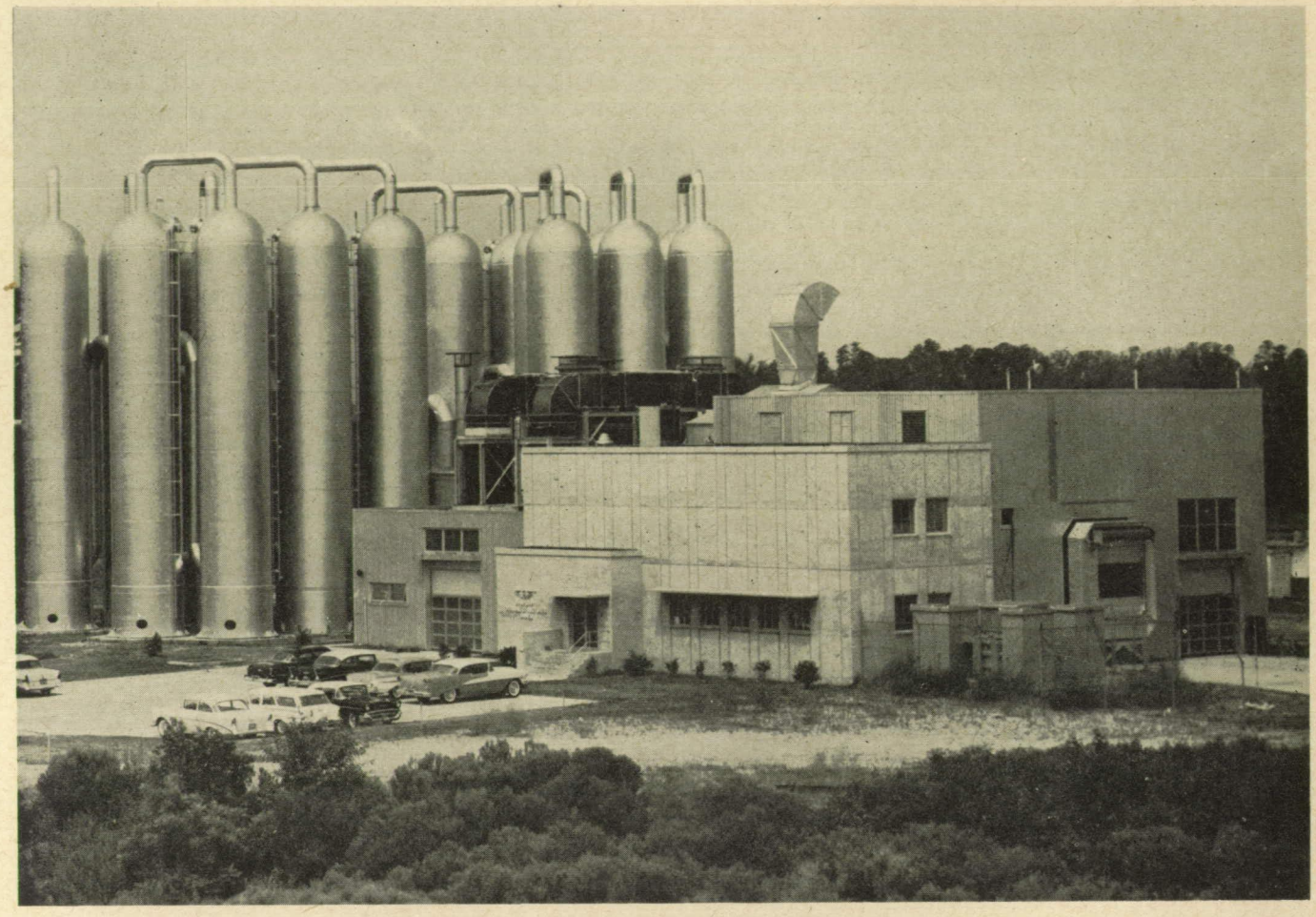
Creep of structures at high temperatures can lead to large deformations and premature failures. Data have been obtained on the creep behavior of stainless-steel plates at temperatures from 700° to 1,000° F., and on the creep behavior of built-up structures such as box beams and unstiffened cylinders.

If all of the complex interactions between aerodynamic heating and loading are to be studied, it is essential that some structural testing be done in an aerodynamic environment. Work of this type was initiated several years ago, using small facilities and has continued during the past year. A new facility, the 9- by 6-foot Thermal Structures Tunnel, was put into operation during the past year. This facility can produce a Mach 3 airstream with a stagnation pressure of 200 psi and a stagnation temperature of 660° F. This facility affords testing of structures under realistic aerodynamic and thermal conditions.

Accurate methods of deflection analysis are essential to the determination of the response of structures to dynamic loads. Studies of structural dynamics included the vibration characteristics of an integrally stiffened 60° delta wing, secondary effects in the vibration of monocoque beams, and a comparative analysis of the accuracy of several methods for calculating transient

526597—60——5

Preceding Page Blank



The 9- by 6-foot thermal structures tunnel.

response. A blast simulator apparatus is being used to study the failure of multiweb beams subjected to very short time, high-intensity loadings.

The problem of designing a structure of minimum weight and of the desired strength at room and elevated temperatures is basic to all aircraft and missile designs, and requires continued research if the performance goals of future vehicles are to be achieved. Sandwich construction is the most probable configuration for efficient utilization of high density and refractory metals in high-speed vehicles; consequently, research on sandwich construction is continuing and has included analytical studies of the local instability of the elements of truss-core sandwiches, tests of sandwich elements, plates and beams at room temperatures, and crippling tests of shell sandwich construction at temperatures up to 1,200° F. with temperature gradients through the thickness. Investigations of sandwich materials suitable for use in the 2,000° to 2,500° F. range have been initiated.

Cylindrical and conical shell structures find extensive use in long-range missiles and space vehicles, but many configurations are in a range where theory is inadequate and data are scarce. The work in this area has been intensified to determine the cause of the deficiencies of present theoretical methods and to formulate new shell theories. Experimental work is also in progress to determine the strength of longitudinally stiffened curved sheet and of ring-stiffened cylinders.

Fatigue problems continue to be a major factor in the operation of many civilian and military aircraft. Recent investigation of the fatigue of structures has been principally concerned with the fail-safe design approach. Structures designed under this approach can tolerate appreciable damage by fatigue cracks without suffering catastrophic failure. During the past year tests have been continued on panels and box beams to better understand the factors affecting fatigue crack growth and the reduction in static strength resulting from cracks. Tests of full-scale airplane wings have been continued to provide information on their resistance to fatigue.

LOADS

The effort devoted to various phases of loads research continues to change because parameters important to structural design such as airspeed, range, structural flexibility, ratio of payload to total weight, heat transfer into the structure, and control inputs continue to vary over wide limits. Accordingly, increasing em-

phasis is being placed on the theoretical and analytical methods for predicting effects of these variables and on methods for analyzing experimental data so as to permit generalization of results.

Because of the high rate of fuel consumption and the wide range in altitude that is rapidly traversed in some aircraft operations, it is becoming increasingly important to account for fuel consumption, air density, etc., as function of time rather than handling these quantities as constant for short time periods. Studies have shown that it is practicable to extend existing analytical procedures to account for these additional complexities.

The manner in which the newer types of aircraft and spacecraft will be operated is expected to change so radically from present-day operation that philosophies of structural design which are based on past experience in the low-speed range will be outmoded; as a result, various types of craft having differing missions are being studied to determine how present structural load requirements must be modified to place the design of such craft on a more rational basis.

The problems concerned with the effects of flexibility on the loads and structural strains experienced by an airplane in rough air are becoming increasingly important because of the higher flight speeds and the use of thin sweptback wings. A flight investigation of structural response showed large amplifications in the structural strains and wing deformations. The strain amplification factor measured during rough air flights varied from 10 to 20 percent at the wing root to values in excess of 100 percent at the midspan station. The major source of aerodynamic forces that are developed in rough air are due to wing structural deflection and twisting, particularly at frequencies corresponding to the first wing-bending mode.

In order to obtain turbulence data which may be used in synthesizing the gust histories for a wide variety of operations, the airline gust data collection programs have been supplemented with projects aimed at establishing the turbulence characteristics for particular flight conditions. Among these conditions are the very low altitudes (below 1,000 feet), high-speed flight, and the more severe weather disturbances represented by hurricanes or tornadoes. The very low altitude data have been derived primarily from tower measurements, while results for other weather conditions are being obtained from cooperative flight tests with the Air Force, Weather Bureau, and Navy. In addition to determining the intensity of the turbulence for direct application to airplane and missile operations, effort is also being made to establish the significant meteorological parameters associated with the turbulence.

Rocket-propelled, free-flight models are used to obtain data on the effect of high Mach number flight on the airplane response to gusts. Because autopilots and yaw dampers add artificial damping to the airplane motions, the effect of these devices on wing and tail loads in rough air has been investigated experimentally and analytically, and for one airplane showed that increased damping of the lateral mode was effective in reducing the gust loads on the vertical tail by about 50 percent. These and other available gust data and studies have been applied to both airplane and missile operations to developing gust-load design criteria.

For several years landing impact loads have been studied intensively; consequently, methods have been developed for calculating these loads for a given landing gear with a good degree of accuracy if the initial conditions at touchdown are known. Vertical velocity at contact is the most important single parameter connected with impact loads, and an accurate statistical determination of this quantity for routine operations will make it possible to specify more precisely the value of this important design quantity. A method for obtaining statistical data on airplane vertical velocity at ground contact from measurements of center-of-gravity acceleration has been utilized to interpret acceleration peaks from VGH recorders obtained during routine operational landings. Measurements of vertical velocity for over 600 separate landings representing 6 different airlines' operations were also obtained at mile-high Denver and sea-level San Francisco airports. This new information, together with that previously available, provides a statistical sample of sufficient size for reliable analysis.

Other primary problems associated with landing aircraft result from the high speed of landings, characteristics of tires, and the friction coefficient between the tire and runway. Landing requirements for future high-speed aircraft have increased the desirability of using skid-type landing gear; consequently, a model with skid landing gear and nose wheel was investigated on a treadmill-type runway and it was found that changes which reduced the side loads on the wheel or moving the skid aft reduced the tendency toward a divergent notion. A comprehensive summary of research on the elastic and mechanical properties of tires has been prepared. For each tire characteristic semi-empirical equations which account for the major factors pertinent to the characteristic were developed. A significant contribution to the complete understanding of friction coefficient and drag loads for which a landing gear must be designed was obtained from realistic, closely controlled impact tests of a modern heavily loaded aircraft tire conducted on the Landing Loads Track for many conditions, such as vertical velocities up to 9.3 fps, forward speeds up to 110 knots, tire pressure ranging from 35 to 210 psi, wet and dry concrete surface, and wheels partially and completely locked.

The landing-impact phenomena is now well understood, although the complete determination of landing

conditions remains to be made; in fact, may never be completed because of changing designs and operational procedures. Not so well understood, however, is the subject of airplane structural response to taxiing and ground handling. It has been known that taxiing and ground handling over runways and taxiways, which are more or less rough, impose loads which are critical for structural design, notably in the attachment of wing-mounted, large-mass items. As a step toward solving the taxiing and ground-handling problems, a comprehensive collection of airport profiles for the United States, Canada, and European NATO countries has been assembled through a cooperative program initiated by the Advisory Group for Aeronautical Research and Development of the North Atlantic Treaty Organization. High-speed analog or digital computers that permit simulation of all the nonlinear landing-gear and tire characteristics are being used to investigate the response of the landing gear, its associated structure, and supported load to accelerations and motions induced by taxiing over representative runway profiles.

Experimental studies of fundamentals of hydrodynamic impact loads have been completed at the Langley Impact Basin. These studies have considered the relation of airplane design and construction parameters and of airplane operating parameters to impact loads. Among the design and construction parameters studied are hull or hydro-ski configuration, airplane weight, and structural elasticity and mass distribution of the airplane. The operational-parameter studies include landing approach conditions such as trim angle, flight-path angle, velocity and aerodynamic lift, and seaway conditions. The hull and hydro-ski configurations studied were limited to basic shapes which could be incorporated in specific designs.

VIBRATION AND FLUTTER

Flutter

Flutter is a self-induced vibration of an aircraft or missile produced by the interaction of the air forces and structural stiffness and inertia. The flag or leaf fluttering in the breeze, the venetian blind vibrating in an open window, are more common examples of flutter. Flutter of an aircraft differs from these examples in that it is relatively more violent and destructive; consequently, aircraft are designed to be free from flutter, not to withstand it.

A major part of flutter research involves the determination of the speed at which flutter occurs and the mode of vibration of wind-tunnel models. One aspect of this research is the establishment of the effects of various parameters by tests of models which represent a systematic variation of particular parameters. Another aspect is to furnish experimental verification of the accuracy of theoretical prediction methods. A third aspect, and one which has become increasingly important, is the determination of the flutter characteristics of models which simulate dynamically a particular aircraft design. This affords a more accurate answer than a theoretical analysis. This is particularly true for aircraft whose structure and weight distribution are such as to produce complicated vibrational patterns and for the transonic speed range in which separated flow aerodynamics may prevail.

One of the more troublesome types of flutter has been that involving control surfaces. Control-surface flutter, including flutter of all-movable tail surfaces as well as flap-type controls, has been studied. The kernel-function method is being used to predict theoretical flutter boundaries for a series of all-movable horizontal stabilizers and these theoretical results are being compared with the experimental flutter boundaries. The widespread use of hydraulic boost servos to operate controls has introduced another factor which has an important effect on the dynamics of the control system. Experimental wind-tunnel flutter studies have been carried out, using models with miniature hydraulic components which simulate full-scale actuators.

Emphasis is being shifted to aeroelastic problems of very high speed aircraft and missiles. Considerable experimental effort has been directed toward aeroelastic studies of components of the X–15 and other hypersonic configurations. Programs to study fuel sloshing, panel flutter, aeroelastic characteristics of ICBM configurations, structural feedback instabilities, boost-glide aeroelastic characteristics, and other dynamic and static aeroelastic problems induced by hypersonic flight capabilities are receiving a larger proportion of research effort.

It has been established that aerodynamic heating increases the tendency of structures to flutter by reducing the effective stiffness. In a continuing study of this problem, a series of multiweb-wing structural models have been designed for tests in the 9- by 6-foot Thermal Structures Tunnel, where flutter data can be obtained under aerodynamic heating conditions.

Aerodynamic Aspects of Flutter

Improvements in theoretical approaches have been aimed at providing oscillatory aerodynamic forces and moments with greater accuracy. As noted in the 1957 annual report, considerable effort has gone into development of methods of flutter analysis using the kernel-function method to obtain the aerodynamic forces. Considerable success has been encountered in developing procedures for programing the kernel-function method for high-speed computing machines.

As noted previously, flutter of flap-type control surfaces has been an increasingly important problem. Particular emphasis has been placed on the measurement at transonic speeds of aerodynamic control surface de-

rivatives pertinent to flutter. This study has included a variation of control surface contours. Similar measurement of the oscillatory derivations have been made on all movable controls and on T-tail configurations.

Panel Flutter

Panel flutter is a term used to describe a type of vibration of individual panels on sections of skin that can occur at supersonic speeds. Susceptibility of panels to this type of flutter is greater for thinner skins, larger panels, and for panels having buckles. Thus on hypersonic vehicles or thin-skinned rockets in which buckling of the skin has occurred because of loadings or heating, panel flutter is a serious problem.

Previous theoretical work has produced methods of analyses for flat, rectangular, buckled and unbuckled panels, and for infinitely long, thin cylinders. This work is being extended to include nonlinear flutter analysis of buckled rectangular panels for both large-deflection and small-deflection flutter. Another extension is concerned with the flutter of thin-walled cylinders of finite length.

Panel-flutter tests were conducted in a supersonic jet to determine if heat shields proposed for a hypersonic aircraft would be flutter free. Other experimental programs were initiated to obtain data in the 9- by 6-foot Thermal Structures Tunnel on the flutter of thin-wall cylinders typical of ICBM boosters and of blunt conical shells such as would be used for a manned satellite capsule.

STRUCTURAL MATERIALS

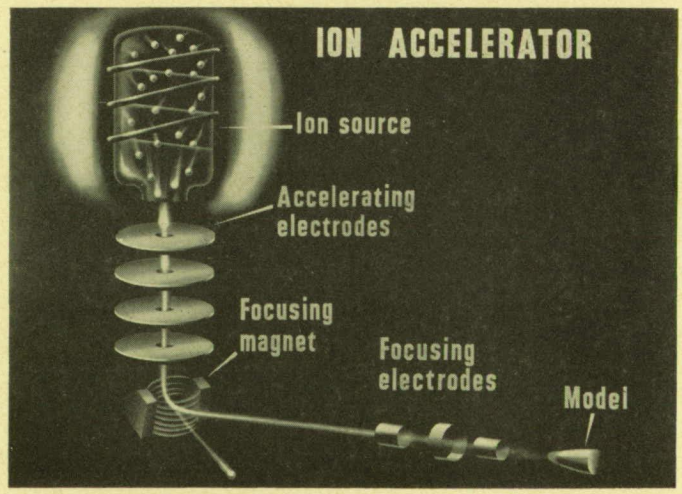
Research on structural materials has continued to be concerned primarily with materials for high-speed aircraft and missiles, although considerable work was also done on problems of fundamental importance to all materials. Consideration was also given to the materials problems created by the environment of space, such as impact on spacecraft of cosmic particles, ranging from ions to micrometeors. It is to be expected that surface pitting by ions striking spacecraft and satellites may constitute operational problems in these environments.

Not enough is known about the properties of our constructional materials at high temperatures to permit the designers to arrive at the most rational and efficient design of high-speed aircraft. The accumulation of data on the mechanical properties of materials at temperatures up to 1,800° F. has continued, and apparatus is being developed to extend the temperature range to 5,000° F. In the past year, tensile and compression creep data were obtained for 2024–T3 and 7075–T6 aluminum alloys, and generalized master curves for predicting rupture, minimum creep rate, and creep strain were derived. Studies of the effects of rapid heating on tensile properties were continued, with special consideration being given to materials of interest for structures of high-speed aircraft. Studies of the dynamic and static modulus of materials have been extended to include the determination of frequency dependence and temperature dependence of the shear and elastic moduli.

As has always been the case in the past, fatigue is still one of the major causes of failure in aircraft. Investigation of fatigue phenomena in materials included: A fundamental study of the role of dislocation and vacancies on fatigue; experimental investigation of effects of cumulative damage, based on gust-frequency spectrum; and the determination of crack propagation rates in sheet material of conventional alloys. The first series of tests to determine the effect of atmospheric corrosion on fatigue of aluminum alloys was completed, and showed that fatigue life of specimens tested out of doors can be lower by a factor of 3, as compared with fatigue life as determined by indoor tests.

Entry into the earth's atmosphere by ballistic missiles or satellites impress conditions of extreme severity. Research work on the most promising method of protecting reentry bodies that will experience the highest heat flux was continued and accelerated. Ablation tests of various promising materials were carried out at heating rates up to 2,000 Btu/ft ^{2}/sec and at stagnation temperatures to 10,000° F. A program for investigating the behavior of other materials for use at lower heating rates was continued, and a large number of conventional metals, as well as refractory metals and ceramics and cermets, were tested in the high-temperature Ceramic Heated Jet. Determination of the emissivity of structural materials, at temperatures up to 2,000° F., was continued, and apparatus is being constructed that will allow emissivity measurements up to 6,000° F.

One of the unknown factors in the operation of space vehicles is the effect of strikes by micrometeoric and larger particles. An investigation is under way of the



Magnets focus beam of ions.

effects of various projectiles striking targets which simulate full-scale structures. Spheres of various materials were fired into targets of various materials at speeds up to 10,000 ft/sec. A theoretical correlation between properties of the projectile and target materials and the results of impact was established.



The apparatus shown is being used to explore the erosion that occurs when ionized particles strike metal surfaces at speeds of 15,000 m.p.h. or faster.

OPERATING PROBLEMS

The daily operations of aircraft and missiles present problems which require solution or alleviation for purposes of safety, efficiency, and economy. Research information is also needed by the designers and manufacturers as well as the operators. For many years, therefore, the NACA has studied various aspects of aircraft operating problems such as atmospheric turbulence, icing, ditching, aircraft and missile noise, crash fire and survival, flight instrumentation, landing and takeoff operations, and aircraft braking.

The NACA has been aided in its research activities in the above areas by the deliberations of the Committee on Operating Problems, the Subcommittee on Meteorological Problems, the Subcommittee on Aircraft Noise, the Subcommittee on Flight Safety, and, until this year, the Subcommittee on Icing Problems. During this year NACA icing research has been limited to writing reports on previous investigations and to supervising the use of NACA icing research facilities by non-NACA personnel who were testing aircraft components under simulated icing conditions.

FLIGHT SAFETY

Flight safety research encompasses many problem areas associated with the operation of aircraft. Hazardous conditions may arise at any time from sources such as the runway, the weather, the engines, the instruments, the controls, and the landing gear. NACA investigations are thus aimed at specific problems to obtain information useful to the manufacturer and the aircraft crew in the industrywide effort to improve safety.

Aircraft Instrumentation

The angle between the relative wind in the plane of symmetry and the longitudinal axis of the airplane is the angle of attack, and its measurement is an important requirement for stall warning, cruise control, and armament considerations. Three types of angle-of-attack sensing devices have been tested in a wind tunnel and in flight to determine calibration and position error data. One result showed that the best sensor location for operation throughout the subsonic, transonic, and supersonic speed ranges is a position ahead of the fuselage nose.

Accurate measurement of airspeed is necessary for safe and efficient flight operations. An investigation has been made to determine the external interference effects of flow through the orifices of an airspeed head such as would occur due to instrument volume at high rates of ascent or descent in flight. The results indicated that the static-pressure error increased almost linearly with increase in mass flow through the orifices.

A study has also been made on the accuracy with which pressure altitude can be measured with current systems. The analysis showed that the accuracy depends on errors in the measuring systems, errors arising from operation of the system, and variation in atmospheric pressure. In another study a survey was made of the errors associated with the measurement of static pressure on aircraft. The errors considered were associated with the static-pressure tube or fuselage vent and the location of the sensor in the flow field of the airplane.

Engine Reliability

Turbojet engines must either be repaired or replaced after specified number of hours of operation. For reasons of safety and economy, it is necessary to know as accurately as possible when engine changes are to be accomplished. An investigation has been made to obtain information on the effect of overtemperature and heat treatment on the life of turbine buckets. Results indicated that overtemperatured buckets did not fracture in abnormally short operating times. Cracking was the principal mode of failure of buckets.

In another study a method was developed to help decide whether jet-engine compressor blades that have been nicked in service are safe from fatigue failure with continued engine operation. These nicks are the result of foreign objects being drawn into the air inlet. A procedure has been worked out for making limit charts that indicate whether a blade showing damage should be accepted or rejected.

Aircraft Ditching

For years the NACA has conducted scale-model ditching investigations of aircraft configurations to furnish designers and operators with information on ditching characteristics and behavior. Models of fighters, bombers, and various types of transports have been tested by utilizing a catapult and water tank system. With the advent of turbojet aircraft, the need for additional ditching data on new configurations has been met by recent tests. In addition, ditching aids such as hydro-skis and hydrofoils attached to the aircraft fuselage bottom have been under study to determine their effectiveness in helping to make a water landing more successful.

In recent studies, an investigation of a 0.043-scale dynamic model of a jet transport was undertaken to study its ditching behavior in rough water. Test results have indicated that hydro-skis or hydrofoils may be made to improve the ditching performance and reduce the damage to the fuselage bottom. Twin hydro-skis with a loading of about 2,500 lbs/square foot resulted in smooth runs with very little damage to the fuselage bottom. Smaller hydro-skis with a loading of 4,400 psf, or twin hydrofoils with a loading of 7,500 psf, or a single hydrofoil with a loading of about 8,300 psf, all resulted in ditching runs which caused moderate damage to the aft fuselage of the model.

In tests with the landing gear extended, the results indicated that the nose gear will fail and that the main gear may or may not fail. When the main gear failed, a deep run resulted causing moderate damage throughout the length of the fuselage bottom. When the main gear did not fail, a dive resulted and the front portion of the fuselage bottom was demolished, causing severe flooding of the entire fuselage.

Flight Operations

Several investigations have been continued in an effort to determine more accurately pilot and aircraft characteristics in different flight areas. Under certain conditions, a pilot's capability to control his airplane may be compromised. The effects of airplane acceleration on the pilot's arm as a result of maneuvers or power changes have been studied with a small side-located controller to allow arm support and hand motions. Several pilots participated in ground tests to obtain measurements of their force capabilities with such a device. (See photo.)

Further tests have been made to determine the suitability of a takeoff indicator to detect abnormal airplane acceleration during takeoff such as occasioned by loss of engine power. The instrument performed satisfactorily in a jet bomber and other tests are being continued in a large, jet-transport-type airplane.

A general flight study of jet transport aircraft has been conducted to obtain operational information in the approach, landing, and cruise regions. Using an airplane similar to the commercial jet transport, preliminary data were obtained on sinking speed prior to touchdown, lift and drag characteristics, high-speed characteristics, lateral control combinations, and yaw damping augmentation.

As a first step in a general investigation of the use in flight of thrust reversers on turbojet-powered airplanes, the effect of a target-type thrust reverser on the aerodynamic characteristics of a full-scale jet airplane has been measured in a wind tunnel. Changes in the aerodynamic characteristics of the airplane, particularly with regard to the pitching moment, were determined for various amounts of thrust reversal.



Pilot's seat with control stick.

In another study, a fully modulating target-type thrust reverser has been installed and tested on a jet-fighter airplane to evaluate the effect of more powerful incremental thrust control devices on the landing-approach characteristics of aircraft. The thrust reverser was also studied to determine its usefulness for inflight deceleration from high speeds and as a braking device to reduce the ground-roll distance in landings.

Runway and Landing-Gear Research

There are several problems associated with airport runways which can lead to hazardous aircraft operating conditions. For example, tire behavior during landing on wet runways has been found to contribute to a number of aircraft accidents. As part of a general program, the NACA has investigated the effects of water depth, tire speed, pressure and tread, braking friction forces, and cornering forces by use of an instrumented tire treadmill. The results indicate that the maximum and the full-skid braking friction coefficients decrease rapidly with increasing velocity until all braking effectiveness is lost and a tire-planing condition is reached.

Runway lights which project above the runway surface are a potential hazard to aircraft operations. Accordingly, an investigation was made to obtain data on

the landing-gear loads developed during landing and taxiing tests over various types of runway lights. The test results indicated that vertical loads on the nose landing gear were larger for landings on the lights than on plain concrete, and that the nose gear loads developed while taxiing over the lights were relatively more severe than those developed on the main gear.

A study was also made of ground-reaction forces measured during landing impacts of a large airplane. Results of the analysis of the data showed the effect of vertical velocity at contact on the vertical force and the variations of coefficients of friction with slip ratio during spinup on wet and dry concrete surfaces.

Crash Survival Research

Several fighter airplanes were crashed under circumstances approximating those observed in the military service; unflared landings at various angles, a ground cartwheel, and a ground loop. The magnitude, duration, and direction of the crash accelerations were measured on the airplane structure and on an anthropomorphic dummy installed in the cockpit. The accelerations measured were compared with existing data on human tolerance to the sudden loads that occur in crashes to see whether the human tolerances had been exceeded.

AERONAUTICAL METEOROLOGY

To achieve the goal of safe and efficient all-weather flight, aircraft and missile designers and operators must take into account the changes in weather conditions and the effects of the meteorological elements on the vehicle. Two of the environmental problems, atmospheric turbulence and icing, have been under study by the NACA for several years, while other factors have only been under investigation from time to time.

Atmospheric Turbulence

Rough air flight of aircraft brings discomfort to passengers and crew, may cause structural damage, may decrease the fatigue life of the airframe, and can present control problems to the pilot. In addition, turbulent air poses problems for missile takeoff and reentry operations. As one approach to the gust-loads problem, the NACA has been active for years in obtaining information on the extent, frequency, and severity of atmospheric turbulence in clouds and free air at altitudes up to 60,000 feet. Data have been obtained by specially instrumented aircraft, parachute assemblies, and rockets over several areas of the world.

The severest turbulence is generally found in the clouds associated with storm areas, but the available gust data are not sufficient for study. Accordingly, a fighter-type airplane has been specially instrumented for probing cumulus-type clouds to obtain gust measurements useful to designers, operators, and meteorologists.

The characteristics of turbulent air below 1,000 feet are not too well known; however, such information is required for landing and takeoff operations as well as low-level military missions. A study of gust data derived primarily from wind-tower measurements indicates that turbulence intensity is affected by windspeed, altitude, temperature lapse rate, and the ground roughness.

At the higher altitudes, investigations of cloud and clear-air turbulence have continued in order to shed more light on these phenomena. The NACA has cooperated with the Navy, Air Force, and Weather Bureau by furnishing VGH (velocity, acceleration, altitude) recorders and by analyzing gust data for several programs. Instrumented aircraft have probed the jetstream and have flown in and near hurricanes to obtain the needed data.

As part of the NACA analytical investigation of the aircraft-gust problem, a method has been developed to calculate the statistical forces and moments exerted on an airplane due to random distributions of gusts. A previous report covered the development of the rolling and yawing moments on a wing in random turbulence. Recent calculations have been made of the complete lateral response of an airplane while flying in continuous isotropic turbulence.

Environmental Data

Besides turbulence, other meteorological elements in and beyond our atmosphere affect the design and operation of aircraft and missiles. From time to time in answer to requests for specific information, the NACA has been able to obtain and analyze data useful to manufacturers, operators, and meteorologists.

Knowledge of atmospheric temperatures is of importance to designers and operators of aircraft and missiles. To provide this information, a study has been made of radiosonde temperature measurements taken over a 5-year period for several locations in the Northern Hemisphere. Probability distributions of temperature up to 100,000 feet have been determined from data provided, sorted, and tabulated by the U.S. Weather Bureau.

In cooperation with the Air Weather Service, an NACA flight program with instrumented U–2 aircraft is continuing to collect data up to 55,000 feet on such variables as water vapor, wind shear, clouds, temperature, the jetstream, clear-air turbulence, ozone, and cosmic rays. Recent data on atmospheric turbulence over the western part of the United States have been published.

526597—60——6

The Icing Cloud

For efficient design of icing protection systems for aircraft and missiles, detailed and statistical knowledge is required of worldwide icing conditions in which these vehicles may operate. The NACA has sought to obtain information on the extent, frequency, and severity of icing conditions by installation of suitable instruments in research, commercial, and military aircraft. Currently, icing-rate meters are on loan to several aircraft companies and Government organizations.

The icing problem for high-altitude, intercepter aircraft has been evaluated and the results published. At two Air Defense Command airbases, fighter-interceptors equipped with NACA icing-rate meters collected data during climb and descent operations, and information was obtained on the frequency and severity of icing clouds over the north-central and northwestern United States.

AIRCRAFT ICING

Because of the state of the art, active NACA icing research on aircraft and engine components has been diminishing since 1956 and was terminated in the fiscal year 1957. NACA icing research activities conducted during the fiscal year 1958 have been concerned primarily with completing the analyses and publication of the results of icing programs conducted over the preceding 24 months.

The Lewis Flight Propulsion Laboratory icing tunnel, because of its unique features, is continually made available to the aircraft industry and Government organizations under a plan whereby industry representatives conduct icing tests on their specific models with guidance by NACA personnel. The raw data obtained from such development studies are available upon request to interested personnel. Analysis and reporting of the data are being made by each company or organization. Thus, NACA reports on these projects are usually not prepared for formal publication.

Water-Droplet Impingement and Icing Protection

In order to design efficient icing protection systems for an aircraft engine component or airframe surface, detailed information is required as to the area and weight of ice accumulation under various icing and operating conditions. To determine droplet impingement characteristics, the NACA has tested both models and full-scale components in the Lewis Laboratory icing research tunnel. In addition, analytical studies have been made to obtain similar data.

An experimental investigation has been conducted to measure the amount and areas of cloud-droplet impingement on a ¼-scale model of a fighter airplane engine inlet. Angles of attack from 2° to 8°, droplet diameters from 7 to 23 microns, and ratios of inlet to free-stream velocity from 0.4 to 1.5 were studied. Significant impingement rates and areas were found on the curved outboard wall of the inlet duct and on regions within a few inches of the cowl lips and leading edges of the duct splitter vanes.

Icing tests were conducted in the 6- by 9-foot icing research tunnel to evaluate the effectiveness of ice protection systems for a jet transport. The proposed systems utilized hot gas to anti-ice the leading edge regions of the wing and cyclic-electric deicing for the tail surfaces. The manufacturer's personnel conducted the tests and the raw data are available for study.

As part of a general study of icing and icing protection for bodies of revolution, an investigation was conducted to determine the impingement characteristics, heat transfer, and icing-protection requirements for simple bodies of revolution. The bodies investigated included spheres, elliptical forebodies, and a conical forebody of 30° included angle. The investigation covered a wide range of conditions both in clear air and in icing, and included studies at angles of attack both with and without rotation.

The rate and the area of cloud-droplet impingement has been obtained for the above types of bodies. Results are presented in the form of dimensionless parameters, which enable the icing characteristics of bodies of revolution to be determined over a wide range of flight and atmospheric conditions.

Data on the heat transfer in clear air from the elliptical body of fineness ratio 3.0 and the conical forebody have also been obtained. Information required in the use of conventional wet-air analysis for the design of anti-icing systems for bodies of revolution was determined from these data.

Penalties Due to Icing

Aerodynamic effects caused by ice formations on an unheated NACA 65A004 airfoil were determined over a wide range of icing conditions and the results published. The drag changes due to these ice formations were correlated with the various icing conditions, as well as with the physical dimensions of the ice accumulated and with the measured droplet-impingement rates. The correlation resulted in an empirical equation that may be used to predict changes in drag coefficients for this airfoil based on meteorological, impingement, and flight conditions. The correlation was also extended to include aerodynamic data for four other airfoils.

Noise Research

The noise produced by current jet engines is of sufficient intensity to cause damage to nearby personnel and aircraft structures and serious discomfort or an-

noyance to personnel over a considerable distance from the engine. Noise annoyance alone is a major problem in the introduction of jet transports and may be an important factor influencing the operation of such transports.

The NACA has been conducting at its Lewis and Langley Research Centers a broad research program to determine the mechanisms by which jet noise is produced and to find means for reducing jet noise. Conclusive evidence from this research program shows that the major source of noise from a turbojet or rocket engine is the exhaust and that the noise from this source dominates all other noise during full power operations. The jet exhaust noise is caused by the intense turbulence produced by the mixing of the high speed exhaust stream with the surrounding air as well as by oscillating shock waves within the jet exhaust and interaction of these shock waves and turbulence. The major NACA research effort has been directed toward reduction of noise created by turbulence since this is the dominant factor in the production of noise during take-off and climb of jet aircraft which are the operating conditions producing the noise nuisance in communities near airports. Reducing the velocity of the jet exhaust will reduce the noise; however, this imposes a penalty on the efficiency of the engine. Since most of the jet noise is produced within ten nozzle diameters downstream of a conventional circular nozzle, it has been determined that less noise would be produced if the jet exhaust stream could be slowed down as rapidly as possible after leaving the nozzle; that is in less distance than the ten diameters. This has been accomplished by the development of special jet exit nozzles which rapidly mix low energy surrounding air into the jet exhaust stream and thereby decrease the overall jet velocity and noise. Scores of nozzle configurations have been investigated to determine the basic design parameters required to produce the best nozzles for given conditions. The corrugated multiple-tube and shrouded nozzles now being produced for jet transports are examples of nozzles developed from this program. Some nozzles are designed to produce significant reductions in overall noise output, others are designed to alter the mixing process in such a way as to change the amount of noise in certain frequencies, and still others are designed to reduce the width of the pattern of noise distribution beneath an aircraft so as to minimize the number of people annoyed by take-offs. More research is underway to increase the noise suppression effectiveness of these nozzles.

Although suppressors do reduce the noise level, they also add weight to the aircraft, slightly decrease engine performance, and increase the drag of the airplane. The amount of noise suppression desired must be balanced against the economic and performance penalties imposed by the use of these suppressors. As a result of extensive NACA wind tunnel tests of suppressor configurations, the aerodynamic performance of suppressors has been evaluated to help assess a reasonable balance. Much additional work is required before a satisfactory solution can be attained.

With the advent of supersonic aircraft a new problem has entered into flight operations—the sonic boom. This boom is the shock wave produced by an object traveling through the air at supersonic speeds and is similar to the bow wave from a boat. This boom or wave can easily be of sufficient intensity to crack plaster and break windows in buildings beneath the path of the supersonic aircraft. The NACA has investigated the parameters which affect the strength of this wave when it hits the ground and has found that primary factors are the altitude of the aircraft, the climatic conditions, and the size of the aircraft. The speed of the aircraft is not important after the aircraft is well into the supersonic regime. Data are being obtained which will allow the estimation of the strength of sonic booms for various flight conditions, and more work is being done to establish flight procedures to minimize the boom intensity. Some research has been accomplished on aircraft design concepts for the future which may reduce the magnitude of the boom problem, and more work is underway along such lines.

The effects of sonic boom from one aircraft on other nearby aircraft also have been investigated, and it appears that if the aircraft are not flying at the same speed so that one aircraft remains in the shock wave from the other aircraft, or if the aircraft are separated by distances of approximately 500 feet or more, the sonic boom problem appears to be of negligible importance to aircraft in flight.

RESEARCH PUBLICATIONS

REPORTS

1296. A Theoretical Study of the Aerodynamics of Slender Cruciform-Wing Arrangements and Their Wakes. By John R. Spreiter and Alvin H. Sacks.

1297. Nonlifting Wing-Body Combinations with Certain Geometric Restraints Having Minimum Wave Drag at Low Supersonic Speeds. By Harvard Lomax.

1298. An Analysis of the Effects of Aeroelasticity on Static Longitudinal Stability and Control of a Swept-Wing Airplane. By Richard B. Skoog.

1299. Correlation, Evaluation, and Extension of Linearized Theories for Tire Motion and Wheel Shimmy. By Robert F. Smiley.

1300. Basic Considerations in the Combustion of Hydrocarbon Fuels With Air. By Propulsion Chemistry Division, Lewis Flight Propulsion Laboratory.

1301. Linearized Lifting-Surface and Lifting-Line Evaluations of Sidewash Behind Rolling Triangular Wings at Supersonic Speeds. By Percy J. Bobbitt.

1302. On Panel Flutter and Divergence of Infinitely Long Unstiffened and Ring-Stiffened Thin-Walled Circular Cylinders. By Robert W. Leonard and John M. Hedgepeth.

1303. Wind-Tunnel Investigation of a Number of Total-Pressure Tubes at High Angles of Attack—Subsonic, Transonic, and Supersonic Speeds. By William Gracey.

1304. Flight Investigation of the Effectiveness of an Automatic Aileron Trim Control Device for Personal Airplanes. By William H. Phillips, Helmut A. Kuehnel, and James B. Whitten.

1305. Measurement of Aerodynamic Forces for Various Mean Angles of Attack on an Airfoil Oscillating in Pitch and on Two Finite-Span Wings Oscillating in Bending With Emphasis on Damping in the Stall. By A. Gerald Rainey.

1306. Bodies of Revolution Having Minimum Drag at High Supersonic Airspeeds. By A. J. Eggers, Jr., Meyer M. Resnikoff, and David H. Dennis.

1307. Lift and Center of Pressure of Wing-Body-Tail Combinations at Subsonic, Transonic, and Supersonic Speeds. By William C. Pitts, Jack N. Nielsen, and George E. Kaattari.

1308. Investigation of the Compressive Strength and Creep Lifetime of 2024–T3 Aluminum-Alloy Plates at Elevated Temperatures. By Eldon E. Mathauser and William D. Deveikis.

1309. Aerodynamic Characteristics at High Speeds of Related Full-Scale Propellers Having Different Blade-Section Cambers. By Julian D. Maynard and Leland B. Salters, Jr.

1310. An Investigation of Four Wings of Square Plan Form at a Mach Number of 6.9 in the Langley 11-Inch Hypersonic Tunnel. By Charles M. McLellan, Mitchel H. Bertram, and John A. Moore.

1311. Determination of Vortex Paths by Series Expansion Technique With Application to Cruciform Wings. By Alberta Y. Alksne.

1312. Some Effects of Bluntness on Boundary-Layer Transition and Heat Transfer at Supersonic Speeds. By W. E. Moeckel.

1313. Exploratory Investigation of Boundary-Layer Transition on a Hollow Cylinder at a Mach Number of 6.9. By Mitchel H. Bertram.

1314. Summary of Scale-Model Thrust-Reverser Investigation. By John H. Povolny, Fred W. Steffen, and Jack G. McArdle.

1315. On Slender-Body Theory at Transonic Speeds. By Keith C. Harder and E. B. Klunker.

1316. Torsional Stiffness of Thin-Walled Shells Having Reinforcing Cores and Rectangular, Triangular, or Diamond Cross Section. By Harvey G. McComb, Jr.

1317. Cloud-Droplet Ingestion in Engine Inlets With Inlet Velocity Ratios of 1.0 and 0.7. By Rinaldo J. Brun.

1318. Three-Dimensional Transonic Flow Theory Applied to Slender Wings and Bodies. By Max. A. Heaslet and John R. Spreiter.

1319. Induced Velocities Near a Lifting Rotor With Nonuniform Disk Loading. By Harry H. Heyson and S. Katzoff.

1320. An Evaluation of Four Experimental Methods for Measuring Mean Properties of a Supersonic Turbulent Boundary Layer. By George J. Nothwang.

1321. Theoretical Calculation of the Power Spectra of the Rolling and Yawing Moments on a Wing in Random Turbulence. By John M. Eggleston and Franklin W. Diederich.

1322. Method for Calculating the Aerodynamic Loading on an Oscillating Finite Wing in Subsonic and Sonic Flow. By Harry L. Runyan and Donald S. Woolston.

1323. Investigation of the Laminar Aerodynamic Heat-Transfer Characteristics of a Hemisphere-Cylinder in the Langley 11-Inch Hypersonic Tunnel at a Mach Number of 6.8 By Davis H. Crawford and William D. McCauley.

1324. Comparison of Several Methods for Obtaining the Time Response of Linear Systems to Either a Unit Impulse or Arbitrary Input From Frequency-Response Data. By James J. Donegan and Carl R. Huss.

1325. Average Properties of Compressible Laminar Boundary Layer on Flat Plate With Unsteady Flight Velocity. By Franklin K. Moore and Simon Ostrach.

1326. Flight and Analytical Methods for Determining the Coupled Vibration Response of Tandem Helicopters. By John E. Yeates, Jr., George W. Brooks, and John C. Houbolt.

1327. Theoretical and Experimental Investigation of the Subsonic-Flow Fields Beneath Swept and Unswept Wings With Tables of Vortex-Induced Velocities. By William J. Alford, Jr.

1328. A Second-Order Shock-Expansion Method Applicable to Bodies of Revolution Near Zero Lift. By Clarence A. Syvertson and David H. Dennis.

1329. Far Noise Field of Air Jets and Jet Engines. By Edmund E. Callaghan and Willard D. Coles.

1330. Experimental and Predicted Longitudinal and Lateral-Directional Response Characteristics of a Large Flexible 35° Swept-Wing Airplane at an Altitude of 35,000 Feet. By Henry A. Cole, Jr., Stuart C. Brown, and Euclid C. Holleman.

1331. Influence of Alloying Upon Grain-Boundary Creep. By F. N. Rhines, W. E. Bond, and M. A. Kissel.

Preceding Page Blank

1332. Seat Design for Crash Worthiness. By I. Irving Pinkel and Edmund G. Rosenberg.
1333. Attenuation in a Shock Tube Due to Unsteady-Boundary-Layer Action. By Harold Mirels.
1334. Relation of Turbojet and Ramjet Combustion Efficiency to Second-Order Reaction Kinetics and Fundamental Flame Speed. By J. Howard Childs, Thaine W. Reynolds, and Charles C. Graves.
1335. Minimum Wave Drag for Arbitrary Arrangements of Wings and Bodies. By Robert T. Jones.
1336. An Investigation of Single- and Dual-Rotation Propellers at Positive and Negative Thrust, and in Combination With an NACA 1-Series D-Type Cowling at Mach Numbers up to 0.84. By Robert M. Reynolds, Robert I. Sammonds, and John H. Walker.
1337. Determination of Longitudinal Stability and Control Characteristics From Free-Flight Model Tests With Results at Transonic Speeds for Three Airplane Configurations. By Clarence L. Gillis and Jesse L. Mitchell.
1338. Near Noise Field of a Jet-Engine Exhaust. By Walton L. Howes, Edmund E. Callaghan, Willard D. Coles, and Harold R. Mull.
1339. A Summary and Analysis of the Low-Speed Longitudinal Characteristics of Swept Wings at High Reynolds Number. By G. Chester Furlong and James G. McHugh.
1340. Investigation of Downwash, Sidewash, and Mach Number Distribution Behind a Rectangular Wing at a Mach Number of 2.41. By David Adamson and William B. Boatright.
1341. Influence of Hot-Working Conditions on High-Temperature Properties of a Heat-Resistant Alloy. By John F. Ewing and J. W. Freeman.

TECHNICAL NOTES [1]

3289. The Minimization of Wave Drag for Wings and Bodies With Given Base Area or Volume. By Max A. Heaslet.
3290. On the Minimization of Airplane Responses to Random Gusts. By Murray Tobak.
3585. Determination of Surge and Stall Limits of an Axial-Flow Turbojet Engine for Control Applications. By Ross D. Schmidt, George Vasu, and Edward W. McGraw.
3781. Handbook of Structural Stability. Part I—Buckling of Flat Plates. By George Gerard and Herbert Becker.
3782. Handbook of Structural Stability. Part II—Buckling of Composite Elements. By Herbert Becker.
3783. Handbook of Structural Stability. Part III—Buckling of Curved Plates and Shells. By George Gerard and Herbert Becker.
3784. Handbook of Structural Stability. Part IV—Failure of Plates and Composite Elements. By George Gerard.
3785. Handbook of Structural Stability. Part V—Compressive Strength of Flat Stiffened Panels. By George Gerard.
3786. Handbook of Structural Stability. Part VI—Strength of Stiffened Curved Plates and Shells. By Herbert Becker.
3883. Propellant Vaporization as a Criterion for Rocket-Engine Design; Calculations of a Chamber Length To Vaporize Various Propellants. By Richard J. Priem.
3924. Discharge Coefficients for Combustor-Liner Air-Entry Holes. II—Flush Rectangular Holes, Step Louvers, and Scoops. By Ralph T. Dittrich.
3985. Propellant Vaporization as a Criterion for Rocket Engine Design; Calculations of Chamber Length To Vaporize a single n-Heptane Drop. By Richard J. Priem.
3987. Effect of Environments of Sodium Hydroxide, Air, and Argon on the Stress-Rupture Properties of Nickel at 1,500° F. By Howard T. McHenry and H. B. Probst.
3988. Experimental and Calculated Histories of Vaporizing Fuel Drops. By R. J. Priem, G. L. Borman, M. M. El Wakil, O. A. Uyehara, and P. S. Myers.
3989. Strength and Ductility of Bainitic Steels. By Donald H. Desy, J. O. Brittain, and M. Gensamer.
3990. Effect of Crystal Orientation on Fatigue-Crack Initiation in Polycrystalline Aluminum Alloys. By J. G. Weinberg and J. A. Bennett.
3991. Interface Thermal Conductance of Twenty-Seven Riveted Aircraft Joints. By Martin E. Barzelay and George F. Holloway.
3995. An Investigation of Flow in Circular and Annular 90° Bends With a Transition in Cross Section. By Stafford W. Wilbur.
4005. An Experimental Investigation of the Effect of Various Parameters Including Tip Mach Number on the Flutter of Some Model Helicopter Rotor Blades. By George W. Brooks and John E. Baker.
4007. An Investigation of Discharge and Thrust Characteristics of Flapped Outlets for Stream Mach Numbers From 0.40 to 1.30. By Allen R. Vick.
4013. Low-Speed Experimental Investigation of the Magnus Effect on Various Sections of a Body of Revolution With and Without A Propeller. By M. J. Queijo and Herman S. Fletcher.
4014. Recent Research on the Creep of Airframe Components. By Eldon E. Mathauser, Avraham Berkovits, and Bland A. Stein.
4016. Some Factors Affecting the Variation of Pitching Moment With Sideslip of Aircraft Configurations. By Edward C. Polhamus.
4017. Momentum Transfer for Flow Over a Flat Plate With Blowing. By H. S. Mickley and R. S. Davis.
4018. Influence of Turbulence on Transfer of Heat From Cylinders. By J. Kestin and P. F. Maeder.
4019. Some Observations on Stress-Corrosion Cracking of Single Crystals of AZ61X Magnesium Alloy. By F. Meller and M. Metzger.
4020. Investigation of Minimum Drag and Maximum Lift-Drag Ratios of Several Wing-Body Combinations Including a Cambered Triangular Wing at Low Reynolds Numbers and at Supersonic Speeds. By Clinton E. Brown and L. K. Hargrave.
4026. Effects of Thermal Relaxation and Specific-Heat Changes on Measurements With a Pneumatic-Probe Pyrometer. By P. W. Kuhns.
4027. Application of Obliquely Mounted Strain Gage to Measurement of Residual Stresses in Disks. By M. H. Hirschberg, R. H. Kemp, and S. S. Manson.
4028. Preliminary Investigation of Propane Combustion in a 3-Inch-Diameter Duct at Inlet-Air Temperatures of 1,400° to 1,600° F. By Erwin A. Lezberg.
4029. Turbulence Measurements in Multiple Interfering Air Jets. By James C. Laurence and Jean M. Benninghoff.
4030. Experimental Investigation of Cermet Turbine Blades in an Axial-Flow Turbojet Engine. By William C. Morgan and George C. Deutsch.
4031. Stability Limits and Burning Velocities for Some Laminar and Turbulent Propane and Hydrogen Flames at Reduced Pressure. By Burton Fine.

[1] The missing numbers in the series of Technical Notes were released before or after the period covered by this report.

4032. Reduction of Oxidized Nichrome V Powders and Sintering of Nichrome V Bodies. By Paul Sikora and Philip Clarkin.

4033. Screen-Type Noise Reduction Devices for Ground Running of Turbojet Engines. By Willard D. Coles and Warren J. North.

4034. Effect of Fluid-System Parameters on Starting Flow in a Liquid Rocket. By Richard P. Krebs.

4035. Impingement of Cloud Droplets on 36.5-Percent-Thick Joukowski Airfoil at Zero Angle of Attack and Discussion of Use as Cloud Measuring Instrument in Dye-Tracer Technique. By R. J. Brun and Dorothea E. Vogt.

4036. Creep of Aluminum-Copper Alloys During Age Hardening. By E. E. Underwood, L. L. Marsh, and G. K. Manning.

4037. Stability of Laminar Boundary Layer Near a Stagnation Point Over an Impermeable Wall and a Wall Cooled by Normal Fluid Injection. By Morris Morduchow, Richard G. Grape, and Richard P. Shaw.

4039. Investigation of the Effects of Profile Shape on the Aerodynamic and Structural Characteristics of Thin, Two-Dimensional Airfoils at Supersonic Speeds. By Elliott D. Katzen, Donald M. Kuehn, and William A. Hill, Jr.

4040. Estimation of Incremental Pitching Moments Due to Trailing-Edge Flaps on Swept and Triangular Wings. By Harry A. James and Lynn W. Hunton.

4041. The Subsonic Static Aerodynamic Characteristics of an Airplane Model Having a Triangular Wing of Aspect Ratio 3. I—Effects of Horizontal-Tail Location and Size on the Longitudinal Characteristics. By Bruce E. Tinling and Armando E. Lopez.

4042. The Subsonic Static Aerodynamic Characteristics of an Airplane Model Having a Triangular Wing of Aspect Ratio 3. II—Lateral and Directional Characteristics. By Howard F. Savage and Bruce E. Tinling.

4043. The Subsonic Static Aerodynamic Characteristics of an Airplane Model Having a Triangular Wing of Aspect Ratio 3. III—Effects of Trailing-Edge Flaps. By Bruce E. Tinling and A. V. Karpen.

4044. Ground Effects on the Longitudinal Characteristics of Two Models With Wings Having Low Aspect Ratio and Pointed Tips. By Donald A. Buell and Bruce E. Tinling.

4045. Elliptic Cones Alone and With Wings at Supersonic Speeds. By Leland H. Jorgensen.

4046. A Comparative Analysis of the Performance of Long-Range Hypervelocity Vehicles. By Alfred J. Eggers, Jr., H. Julian Allen, and Stanford E. Neice.

4047. A Study of the Motion and Aerodynamic Heating of Missiles Entering the Earth's Atmosphere at High Supersonic Speeds. By H. Julian Allen and A. J. Eggers, Jr.

4048. Motion of a Ballistic Missile Angularly Misalined With the Flight Path Upon Entering the Atmosphere and Its Effect Upon Aerodynamic Heating, Aerodynamic Loads, and Miss Distance. By H. Julian Allen.

4050. Studies of Structural Failure Due to Acoustic Loading. By Robert W. Hess, Robert W. Fralich, and Harvey H. Hubbard.

4055. Effects of Airplane Flexibility on Wing Bending Strains in Rough Air. By Thomas L. Coleman, Harry Press, and C. C. Shufflebarger.

4058. Calculated Effect of Some Airplane Handling Techniques on the Ground-Run Distance in Landing on Slippery Runways. By John A. Zalovcik.

4059. Noise Survey of a Full-Scale Supersonic Turbine-Driven Propeller Under Static Conditions. By Max C. Kurbjun.

4061. Flight Measurements of Boundary-Layer Temperature Profiles on a Body of Revolution (NACA RM-10) at Mach Numbers From 1.2 to 3.5. By Andrew G. Swanson, James J. Buglia, and Leo T. Chauvin.

4062. Effect of Sweep on Performance of Compressor Blade Sections as Indicated by Swept-Blade Rotor, Unswept-Blade Rotor, and Cascade Tests. By William R. Godwin.

4063. Equations, Tables, and Figures for Use in the Analysis of Helium Flow at Supersonic and Hypersonic Speeds. By James N. Mueller.

4064. Review and Investigation of Unsatisfactory Control Characteristics Involving Instability of Pilot-Airplane Combination and Methods for Predicting These Difficulties From Ground Tests. By William H. Phillips, B. Porter Brown, and James T. Matthews, Jr.

4065. Tensile Properties of Inconel X Sheet Under Rapid-Heating and Constant-Temperature Conditions. By Ivo M. Kurg.

4066. A Method Utilizing Data on the Spiral, Roll-Subsidence, and Dutch Roll Modes for Determining Lateral Stability Derivatives From Flight Measurements. By Bernard B. Klawans and Jack A. White.

4068. Effects of Blade Plan Form on Free-Space Oscillating Pressures Near Propellers at Flight Mach Numbers to 0.72. By Max C. Kurbjun.

4069. Effect of Angle of Attack and Thickness on Aerodynamic Coefficients of a Rigid Wing Oscillating at Very Low Frequencies in Two-Dimensional Supersonic Flow. By Frank S. Malvestuto, Jr., and Julia M. Goodwin.

4070. Flight-Test Investigation on the Langley Control-Line Facility of a Model of a Propeller-Driven Tail-Sitter-Type Vertical-Take-Off Airplane With Delta Wing During Rapid Transitions. By Robert O. Schade.

4071. A Correlation of Results of a Flight Investigation With Results of an Analytical Study of Effects of Wing Flexibility on Wing Strains Due to Gusts. By C. C. Shufflebarger, Chester B. Payne, and George L. Cahen.

4072. Experimental Investigation of Attenuation of Strong Shock Waves in a Shock Tube With Hydrogen and Helium as Driver Gases. By Jim J. Jones.

4073. Tables for the Numerical Determination of the Fourier Transform of a Function of Time and the Inverse Fourier Transform of a Function of Frequency, With Some Applications to Operational Calculus Methods. By Carl R. Huss and James J. Donegan.

4074. Compressive Stress-Strain Properties of 17-7 PH and AM 350 Stainless-Steel Sheet at Elevated Temperatures. By Bland A. Stein.

4075. Tensile Stress-Strain Properties of 17-7 PH and AM 350 Stainless-Steel Sheet at Elevated Temperatures. By Ivo M. Kurg.

4076. Calculated and Measured Stresses in Simple Panels Subject to Intense Random Acoustic Loading Including the Near Noise Field of a Turbojet Engine. By Leslie W. Lassiter and Robert W. Hess.

4077. Static Longitudinal and Lateral Stability Characteristics at Low Speed of 45° Sweptback-Midwing Models Having Wings With an Aspect Ratio of 2, 4, or 6. By David F. Thomas, Jr., and Walter D. Wolhart.

4078. A Discussion of Cone and Flat-Plate Reynolds Numbers for Equal Ratios of the Laminar Shear to the Shear Caused by Small Velocity Fluctuations in a Laminar Boundary Layer. By Neal Tetervin.

4079. Wind-Tunnel Investigation of External-Flow Jet-Augmented Double Slotted Flaps on a Rectangular Wing at an Angle of Attack of 0° to High Momentum Coefficients. By Edwin E. Davenport.

4080. Some Effects of Vanes and of Turbulence in Two-Dimensional Wide-Angle Subsonic Diffusers. By Carl A. Moore, Jr., and Stephen J. Kline.

4081. Effect of Overheating on Creep-Rupture Properties of S–816 Alloy at 1,500° F. By John P. Rowe and J. W. Freeman.

4082. Abnormal Grain Growth in Nickel-Base Heat-Resistant Alloys. By R. F. Decker, A. I. Rush, A. G. Dano, and J. W. Freeman.

4083. Effect of Overheating on Creep-Rupture Properties of HS–31 Alloy at 1,500° F. By John P. Rowe and J. W. Freeman.

4084. Abnormal Grain Growth in M–252 and S–816 Alloys. By R. F. Decker, A. I. Rush, A. G. Dano, and J. W. Freeman.

4085. Method of Split Rigidities and Its Application to Various Buckling Problems. By P. P. Bijlaard.

4086. Discrete Potential Theory for Two-Dimensional Laplace and Poisson Difference Equations. By Charles Saltzer.

4087. Drop-Size Distribution for Crosscurrent Breakup of Liquid Jets in Airstreams. By Robert D. Ingebo and Hampton H. Foster.

4088. Practical Solution of Plastic Deformation Problems in Elastic-Plastic Range. By A. Mendelson and S. S. Manson.

4089. The Mechanism of Thermal-Gradient Mass Transfer in the Sodium Hydroxide-Nickel System. By Charles E. May.

4090. Analysis of Shock Motion in Ducts During Disturbances in Downstream Pressure. By Herbert G. Hurrell.

4091. Experimental Investigation of Transpiration Cooling for a Turbulent Boundary Layer in Subsonic Flow Using Air as a Coolant. By William E. Brunk.

4092. Experimental Droplet Impingement on Four Bodies of Revolution. By James P. Lewis and Robert S. Ruggeri.

4093. Investigation of Heat Transfer From a Stationary and Rotating Conical Forebody. By Robert S. Ruggeri and James P. Lewis.

4094. Effects of Extreme Surface Cooling on Boundary-Layer Transition. By John R. Jack, Richard J. Wisniewski, and N. S. Diaconis.

4095. An Analysis of the Effect of Several Parameters on the Stability of an Air-Lubricated Hydrostatic Thrust Bearing. By William H. Roudebush.

4096. Flow-Turning Losses Associated With Zero-Drag External-Compression Supersonic Inlets. By Rudolph C. Meyer.

4097. Investigation of Some Mechanical Properties of Thermenol Compressor Blades. By Donald F. Johnson.

4098. Propellant Vaporization as a Criterion for Rocket-Engine Design; Calculations Using Various Log-Probability Distributions of Heptane Drops. By Richard J. Priem.

4099. Heat Transfer and Boundary-Layer Transition on Two Blunt Bodies at Mach Number 3.12. By N. S. Diaconis, Richard J. Wisniewski, and John R. Jack.

4100. Vibration Survey of Four Representative Types of Air-Cooled Turbine Blades. By Howard F. Calvert and Gordon T. Smith.

4101. Effect of Lubricant Viscosity on Rolling-Contact Fatigue Life. By Thomas L. Carter.

4102. Velocity and Friction Characteristics of Laminar Viscous Boundary-Layer and Channel Flow Over Surfaces With Ejection or Suction. By E. R. G. Eckert, Patrick L. Donoughe, and Betty Jo Moore.

4103. Impact-Loads Investigation of Chine-Immersed Model Having a Circular-Arc Transverse Shape. By Philip M. Edge, Jr.

4104. The Use of Pure Twist for Drag Reduction on Arrow Wings With Subsonic Leading Edges. By Frederick C. Grant.

4105. A Method of Computing the Transient Temperature of Thick Walls From Arbitrary Variation of Adiabatic-Wall Temperature and Heat-Transfer Coefficient. By P. R. Hill.

4106. Impact-Loads Investigation of a Chine-Immersed Model Having a Longitudinally Curved Bow and a V-Bottom With a Dead-Rise Angle of 30°. By Philip M. Edge, Jr., and John S. Mixon.

4107. Effects of Airplane Flexibility on Wing Strains in Rough Air at 5,000 Feet as Determined by Flight Tests of a Large Swept-Wing Airplane. By Richard H. Rhyne and Harold N. Murrow.

4108. A Thermal System for Continuous Monitoring of Laminar and Turbulent Boundary-Layer Flows During Routine Flight. By Norman R. Richardson and Elmer A. Horton.

4109. Low-Speed Yawed-Rolling Characteristics and Other Elastic Properties of a Pair of 40-Inch-Diameter, 14-Ply-Rating, Type VII Aircraft Tires. By Walter B. Horne and Robert F. Smiley.

4110. Mechanical Properties of Pneumatic Tires With Special Reference to Modern Aircraft Tires. By Robert F. Smiley and Walter B. Horne.

4111. Investigation of the Compressive Strength and Creep of 7075–T6 Aluminum-Alloy Plates at Elevated Temperatures. By William D. Deveikis.

4112. Generalized Master Curves for Creep and Rupture. By George J. Heimerl and Arthur J. McEvily, Jr.

4113. Study of Pressure Distributions on Simple Sharp-Nosed Models at Mach Numbers From 16 to 18 in Helium Flow. By Wayne D. Erickson.

4114. Weight-Strength Studies of Structures Representative of Fuselage Construction. By James P. Peterson.

4115. Theory of Aircraft Structural Models Subject to Aerodynamic Heating and External Loads. By William J. O'Sullivan, Jr.

4116. Wind-Tunnel Investigation at Low Speeds To Determine Flow-Field Characteristics and Ground Influence on a Model With Jet-Augmented Flaps. By Raymond D. Vogler and Thomas R. Turner.

4117. Experimental Investigation of Lift, Drag, and Pitching Moment of Five Annular Airfoils. By Herman S. Fletcher.

4118. Low-Temperature, Vapor-Phase Oxidation of Fuel-Rich Hydrocarbon Mixtures. By William T. House and Milton Orchin.

4119. Wind-Tunnel Investigation of Effects of Ground Proximity and of Split Flaps on the Lateral Stability Derivatives of a 60° Delta-Wing Model Oscillating in Yaw. By Byron M. Jaquet.

4120. Theoretical Calculations of Supersonic Wave Drag at Zero Lift for a Particular Store Arrangement. By Kenneth Margolis, Frank S. Malvestuto, Jr., and Peter J. Maxie, Jr.

4121. Theory and Apparatus for Measurement of Emissivity for Radioactive Cooling of Hypersonic Aircraft With Data for Inconel and Inconel X. By William J. O'Sullivan, Jr., and William R. Wade.

4122. External Interference Effects of Flow Through Static-Pressure Orifices of an NACA Airspeed Head at a Mach Number of 3. By Norman S. Silsby.

4123. Rough-Water Impact-Load Investigation of a Chine-Immersed V-Bottom Model Having a Dead-Rise Angle of 10°. By Melvin F. Markey and Thomas D. Carpini.

4124. Effect of Ground Proximity on the Aerodynamic Characteristics of a Four-Engine Vertical-Take-Off-and-Landing Transport-Airplane Model With Tilting Wing and Propellers. By William A. Newsom, Jr.

4125. Heat Transfer and Recovery Temperatures on a Sphere With Laminar, Transitional, and Turbulent Boundary Layers at Mach Numbers of 2.00 and 4.15. By Ivan E. Beckwith and James J. Gallagher.

4126. Experimental Investigation of the Effects of Some Shroud Design Variables on the Static Thrust Characteristics of a Small-Scale Shrouded Propeller Submerged in a Wing. By Robert T. Taylor.

4127. The Measurement of Pressure Altitude on Aircraft. By William Gracey.

4128. A Thermocouple Subcarrier Oscillator for Telemetering Temperatures From Pilotless Aircraft. By Clifford L. Fricke.

4129. Analysis of Operational Airline Data To Show the Effects of Airborne Weather Radar on the Gust Loads and Operating Practices of Twin-Engine Short-Haul Transport Airplanes. By Martin R. Copp and Walter G. Walker.

4130. NACA 65-Series Compressor Rotor Performance With Varying Annulus-Area Ratio, Solidity, Blade Angle, and Reynolds Number and Comparison With Cascade Results. By Wallace M. Schulze, John R. Erwin, and George C. Ashby, Jr.

4131. Transition-Flight Investigation of a Four-Engine-Transport Vertical-Take-Off Airplane Model Utilizing a Large Flap and Extensible Vanes for Redirecting the Propeller Slipstream. By Louis P. Tosti.

4132. Fatigue Investigation of Full-Scale Transport-Airplane Wings. Variable-Amplitude Tests With a Gust-Loads Spectrum. By Richard E. Whaley.

4133. Boundary-Layer Displacement Effects in Air at Mach Numbers of 6.8 and 9.6. By Mitchel H. Bertram.

4134. Stall Propagation in a Cascade of Airfoils. By Anthony R. Kriebel, Barry S. Seidel, and Richard G. Schwind.

4135. Influence of Solid-Body Rotation on Screen-Produced Turbulence. By Stephen C. Traugott and Hsuan Yeh.

4136. Theoretical Investigation of Subsonic Oscillatory Blade-Row Aerodynamics. By Frank Land and Manfred Friedman.

4137. Fatigue Behavior of Aircraft Structural Beams. By W. S. Hyler, H. G. Popp, D. N. Gideon, S. A. Gordon, and H. J. Grover.

4138. Creep Deformation Patterns of Joints Under Bearing and Tensile Loads. By E. G. Bodine, R. L. Carlson, and G. K. Manning.

4139. Wall Pressure Fluctuations in a Turbulent Boundary Layer. By William W. Willmarth.

4140. Turbulent Shearing Stress in the Boundary Layer of Yawed Flat Plates. By Harry Ashkenas.

4141. The Useful Heat Capacity of Several Materials for Ballistic Nose-Cone Construction. By Jackson R. Stalder.

4142. Effects of Leading-Edge Blunting on the Local Heat Transfer and Pressure Distributions Over Flat Plates in Supersonic Flow. By Marcus O. Creager.

4143. Development of a Piston-Compressor Type Light-Gas Gun for the Launching of Free-Flight Models at High Velocity. By A. C. Charters, B. Pat Denardo, and Vernon J. Rossow.

4144. Effect of Oxygen Recombination on One-Dimensional Flow at High Mach Numbers. By Steve P. Heims.

4145. An Analysis of the Optimization of a Beam Rider Missile System. By Marvin Shinbrot and Grace C. Carpenter.

4146. Contribution of the Wing Panels to the Forces and Moments of Supersonic Wing-Body Combinations at Combined Angles. By J. Richard Spahr.

4147. Measured and Predicted Dynamic Response Characteristics of a Flexible Airplane to Elevator Control Over a Frequency Range Including Three Structural Modes. By Henry A. Cole, Jr., and Euclid C. Holleman.

4148. Theoretical Pressure Distributions for Several Related Nonlifting Airfoils at High Subsonic Speeds. By John R. Spreiter, Alberta Y. Alksne, and B. Jeanne Hyett.

4149. An Analysis of the Turbulent Boundary-Layer Characteristics on a Flat Plate With Distributed Light-Gas Injection. By Morris W. Rubesin and Constantine C. Pappas.

4150. Approximations for the Thermodynamic and Transport Properties of High-Temperature Air. By C. Frederick Hansen.

4151. Correlations Among Ice Measurements, Impingement Rates, Icing Conditions, and Drag Coefficients for Unswept NACA 65A004 Airfoil. By Vernon H. Gray.

4152. Laminar Boundary Layer With Heat Transfer on a Cone at Angle of Attack in a Supersonic Stream. By Eli Reshotko.

4153. Effect of Wall Cooling on Inlet Parameters of a Scoop Operating in a Turbulent Boundary Layer on a Flat or Conical Surface for Mach Numbers 2 to 10. By Andrew Beke.

4154. Approximate Calculation of the Compressible Turbulent Boundary Layer With Heat Transfer and Arbitrary Pressure Gradient. By Eli Reshotko and Maurice Tucker.

4155. Aerodynamic Effects Caused by Icing of an Unswept NACA 65A004 Airfoil. By Vernon H. Gray and Uwe H. von Glahn.

4156. Effect of Initial Mixture-Temperature on Burning Velocity of Hydrogen-Air-Mixtures With Preheating and Simulated Preburning. By Sheldon Heimel.

4157. Corrosion Resistance of Nickel Alloys in Molten Sodium Hydroxide. By H. B. Probst, C. E. May, and Howard T. McHenry.

4158. Accelerations in Transport-Airplane Crashes. By G. Merritt Preston and Gerard J. Pesman.

4159. Experimental Investigation of Turbojet-Engine Multiple-Loop Controls for Non Afterburning and Afterburning Modes of Engine Operation. By Donald B. Kirsch, Leon M. Wenzel, and Clint E. Hart.

4160. Thermal Fatigue of Ductile Materials. I—Effect of Variations in the Temperature Cycle on the Thermal-Fatigue Life of S–816 and Inconel 550. By Francis J. Clauss and James W. Freeman.

4161. Effect of Lubricant Base Stock on Rolling-Contact Fatigue Life. By Thomas L. Carter.

4162. Study of Some Burner Cross-Section Changes That Increase Space-Heating Rates. By Donald R. Boldman and Perry L. Blackshear, Jr.

4163. Effect of Temperature on Rolling-Contact Fatigue Life With Liquid and Dry Powder Lubricants. By Thomas L. Carter.

4164. Two-Dimensional Diffusion Theory Analysis of Reactivity Effects of a Fuel-Plate-Removal Experiment. By Edward R. Gotsky, James P. Cusick, and Donald Bogart.

4165. Thermal Fatigue of Ductile Materials. II—Effect of Cyclic Thermal Stressing on the Stress-Rupture Life and Ductility of S–816 and Inconel 550. By Francis J. Clauss and James W. Freeman.

4166. An Experimental and Theoretical Study of the Effect of Fuel on Pitching-Translation Flutter. By John L. Sewall.

4167. A Rapid Method for Predicting Attached-Shock Shape. By Eugene S. Love and Ronald H. Long.

4168. A Method for Calculation of Hydrodynamic Lift for Submerged and Planing Rectangular Lifting Surfaces. By Kenneth L. Wadlin and Kenneth W. Christopher.

4169. Atmospheric Temperature Observations to 100,000 Feet for Several Climatological Regions of the Northern Hemisphere. By H. B. Tolefson.

4170. A Reexamination of the Use of Simple Concepts for Predicting the Shape and Location of Detached Shock Waves. By Eugene S. Love.

4171. Some Ground Measurements of the Forces Applied by Pilots to a Side-Located Aircraft Controller. By Roy F. Brissenden.

4172. Noise Survey Under Static Conditions of a Turbine-Driven Full-Scale Modified Supersonic Propeller With an Advance Ratio of 3.2. By Max C. Kurbjun.

4173. An Analytical Investigation of the Gust-Alleviating Properties of a Simple Pitch Damper. By Norman L. Crabill.

4174. Wind-Tunnel Investigation of the Static Lateral Stability Characteristics of Wing-Fuselage Combinations at High Subsonic Speeds. Taper-Ratio Series. By James W. Wiggins and Paul G. Fournier.

4175. Investigation of Deflectors as Gust Alleviators on a 0.09-Scale Model of the Bell X–5 Airplane With Various Wing Sweep Angles From 20° to 60° at Mach Numbers From 0.40 to 0.90. By Delwin R. Croom and Jarrett K. Huffman.

4176. Effect of Flow Incidence and Reynolds Number on Low-Speed Aerodynamic Characteristics of Several Noncircular Cylinders With Applications to Directional Stability and Spinning. By Edward C. Polhamus.

4177. Wind-Tunnel Investigation of the Static Longitudinal Stability and Trim Characteristics of a Sweptback-Wing Jet-Transport Model Equipped With an External-Flow Jet-Augmented Flap. By Joseph L. Johnson, Jr.

4178. Low-Speed Cascade Investigation of Compressor Blades Having Loaded Leading Edges. By James C. Emery.

4179. Analytical Investigation of Acceleration Restriction in a Fighter Airplane With an Automatic Control System. By James T. Matthews, Jr.

4180. Investigation of Spoilers at a Mach Number of 1.93 to Determine the Effects of Height and Chordwise Location on the Section Aerodynamic Characteristics of a Two-Dimensional Wing. By James N. Mueller.

4181. Investigation of the Effects of Propeller Diameter on the Ability of a Flapped Wing, With and Without Boundary-Layer Control, To Deflect a Propeller Slipstream Downward for Vertical Take-Off. By Kenneth P. Spreemann.

4182. Physical Characteristics and Test Conditions of an Ethylene-Heated High-Temperature Jet. By Roland D. English, Abraham Spinak, and Eldred H. Helton.

4183. Investigation of Effects of Distributed Surface Roughness on a Turbulent Boundary Layer Over a Body of Revolution at a Mach Number of 2.01. By John R. Sevier, Jr., and K. R. Czarnecki.

4184. Measurement of Static Pressure on Aircraft. By William H. Gracey.

4185. Wind-Tunnel Investigation of Effect of Sweep on Rolling Derivatives at Angles of Attack up to 13° and at High Subsonic Mach Numbers, Including a Semiempirical Method of Estimating the Rolling Derivatives. By James W. Wiggins.

4186. Heat Transfer in Isotropic Turbulence During the Final Period of Decay. By D. W. Dunn and W. H. Reid.

4187. High-Speed Hydrodynamic Characteristics of a Flat Plate and 20° Dead-Rise Surface in Unsymmetrical Planing Conditions. By Daniel Savitsky, R. E. Prowse, and D. H. Lueders.

4188. Charts Relating the Compressive and Shear Buckling Stresses of Longitudinally Supported Plates to the Effective Deflectional Stiffness of the Supports. By Aldie E. Johnson, Jr.

4189. Lift and Moment on Thin Arrowhead Wings With Supersonic Edges Oscillating in Symmetric Flapping and Roll and Application to the Flutter of an All-Movable Control Surface. By H. J. Cunningham.

4190. Experimental Investigation of the Lateral Trim of a Wing-Propeller Combination at Angles of Attack up to 90° With All Propellers Turning in the Same Direction. By William A. Newsom, Jr.

4191. Analysis of Horizontal-Tail Loads in Pitching Maneuvers on a Flexible Swept-Wing Jet Bomber. By William S. Aiken, Jr.

4192. Three-Degree-of-Freedom Evaluation of the Longitudinal Transfer Functions of a Supersonic Canard Missile Configuration Including Changes in Forward Speed. By Ernest C. Seaberg.

4193. Subsonic Flight Investigation of Methods To Improve the Damping of Lateral Oscillations by Means of a Viscous Damper in the Rudder System in Conjunction With Adjusted Hinge-Moment Parameters. By Harold L. Crane, George J. Hurt, Jr., and John M. Elliott.

4194. Comparison of Hydrodynamic-Impact Acceleration and Response for Systems With Single and With Multiple Elastic Modes. By Robert W. Miller.

4195. Shape of Initial Portion of Boundary of Supersonic Axisymmetric Free Jets at Large Jet Pressure Ratios. By Eugene S. Love and Louise P. Lee.

4196. A Method for the Calculation of the Lateral Response of Airplanes to Random Turbulence. By John M. Eggleston and William H. Phillips.

4197. Summary of Flutter Experiences as a Guide to the Preliminary Design of Lifting Surfaces on Missiles. By Dennis J. Martin.

4198. Effects of Airplane Flexibility on Wing Strains in Rough Air at 35,000 Feet as Determined by a Flight Investigation of a Large Swept-Wing Airplane. By Richard H. Rhyne.

4199. A Flight Investigation of the Effects of Varied Lateral Damping on the Effectiveness of a Fighter Airplane as a Gun Platform. By Helmut A. Kuehnel, Arnold R. Beckhardt, and Robert A. Champine.

4200. Effectiveness of Boundary-Layer Control, Obtained by Blowing Over a Plain Rear Flap in Combination With a Forward Slotted Flap, in Deflecting A Slipstream Downward for Vertical Take-Off. By Kenneth P. Spreemann.

4201. Collection of Zero-Lift Drag Data on Bodies of Revolution From Free-Flight Investigations. By William E. Stoney, Jr.

4202. Qualitative Simulator Study of Longitudinal Stick Forces and Displacements Desirable During Tracking. By Stanley Faber.

4203. Flight Investigation of Effects of Atmospheric Turbulence and Moderate Maneuvers on Bending and Torsional Moments Encountered by a Helicopter Rotor Blade. By LeRoy H. Ludi.

4204. Compilation of Information on the Transonic Attachment of Flows at the Leading Edges of Airfoils. By Walter F. Lindsey and Emma Jean Landrum.

4205. Transient Heating Effects on the Bending Strength of Integral Aluminum-Alloy Box Beams. By Richard A. Pride and John B. Hall, Jr.

4206. Measurements of Total Hemispherical Emissivity of Various Oxidized Metals at High Temperature. By William R. Wade.

4207. Effect of a Stringer on the Stress Concentration Due to a Crack in a Thin Sheet. By J. Lyell Sanders, Jr.

4208. Turbulent Boundary Layer on a Yawed Cone in a Supersonic Stream. By Willis H. Braun.

4209. Experimental Thermal Conductivities of the $N_2O_4 \rightleftarrows 2NO_2$ System. By Kenneth P. Coffin and Cleveland O'Neal, Jr.

4210. Stability of Propane-Air Flames in Vortex Flow. By A. E. Potter, Jr., E. L. Wong, and A. L. Berlad.

4211. Friction Studies of Various Materials in Liquid Nitrogen. By D. W. Wisander, W. F. Hady, and R. L. Johnson.

4212. Central Automatic Data Processing System. By the Staff of the Lewis Laboratory.

4213. Recovery Temperatures and Heat Transfer Near Two-Dimensional Roughness Elements at Mach 3.1. By Paul F. Brinich.

4214. Boundary-Layer Transition on an Open-Nose Cone at Mach 3.1. By Paul F. Brinich.

4215. Application of a High-Temperature Static Strain Gage to the Measurement of Thermal Stresses in a Turbine Stator Vane. By R. H. Kemp, C. R. Morse, and M. H. Hirschberg.

4216. Effect of Fiber Orientation in Races and Balls Under Rolling-Contact Fatigue Conditions. By Thomas L. Carter.

4217. Effect of Jet Temperature on Jet-Noise Generation. By Vern G. Rollin.

4218. Analysis of Stresses and Deflections in a Disk Subjected to Gyroscopic Forces. By M. H. Hirschberg and A. Mendelson.

4219. Propellant Vaporization as a Criterion for Rocket Engine Design; Relation Between Percentage of Propellant Vaporized and Engine Performance. By Marcus F. Heidman and Richard J. Priem.

4220. A Flight Evaluation and Analysis of the Effect of Icing Conditions on the ZPG–2 Airship. By William Lewis and Porter J. Perkins, Jr.

4221. Turbulent Flow Through Porous Resistances Slightly Inclined to the Flow Direction. By Albert L. Loeffler, Jr., and Morris Perlmutter.

4222. Drop-Size Distributions for Impinging-Jet Breakup in Airstream Simulating the Velocity Conditions in Rocket Combustors. By Robert D. Ingebo.

4223. Relation of Journal Bearing Performance to Minimum Oil-Film Thickness. By F. W. Ocvirk and G. B. DuBois.

4224. Effect of Overheating on Creep-Rupture Properties of M–252 Alloy. By John P. Rowe and J. W. Freeman.

4225. Internal-Friction Study of Aluminum Alloy Containing 4 Weight Percent Copper. By B. S. Berry and A. S. Nowick.

4226. Analysis of Harmonic Forces Produced at Hub by Imbalance in Helicopter Rotor Blades. By M. Morduchow and A. Muzyka.

4227. Drag Minimization for Wings in Supersonic Flow, With Various Constraints. By Max A. Heaslet and Franklyn B. Fuller.

4228. Effects of Fixing Boundary-Layer Transition for an Unswept-Wing Model and an Evaluation of Porous Tunnel-Wall Interference for Mach Numbers From 0.60 to 1.40. By Louis S. Stivers, Jr., and Garth W. Lippmann.

4229. Stagnation-Point Heat Transfer to Blunt Shapes in Hypersonic Flight, Including Effects of Yaw. By A. J. Eggers, Jr., C. Frederick Hansen, and Bernard E. Cunningham.

4230. Prandtl-Meyer Expansion of Chemically Reacting Gases in Local Chemical and Thermodynamic Equilibrium By Steve P. Heims.

4231. Skin-Friction Measurements in Incompressible Flow. By Donald W. Smith and John H. Walker.

4232. A Method for the Calculation of Wave Drag on Supersonic-Edged Wings and Biplanes. By Harvard Lomax and Loma Sluder.

4233. Experimental Study of the Equivalence of Transonic Flow About Slender Cone-Cylinders of Circular And Elliptic Cross Section. By William A. Page.

4234. Pressure Distributions at Transonic Speeds for Parabolic-Arc Bodies of Revolution Having Fineness Ratios of 10, 12, and 14. By Robert A. Taylor and John B. McDevitt.

4235. Observations of Turbulent-Burst Geometry and Growth in Supersonic Flow. By Carlton S. James.

4236. Effects of Mach Number and Wall-Temperature Ratio on Turbulent Heat Transfer at Mach Numbers From 3 to 5. By Thorval Tendeland.

4237. General Instability of Stiffened Cylinders. By Herbert Becker.

4238. Normal Component of Induced Velocity for Entire Field of a Uniformly Loaded Lifting Rotor With Highly Swept Wake as Determined by Electromagnetic Analog. By Walter Castles, Jr., Howard L. Durham, Jr., and Jirair Kevorkian.

4239. Experimental Investigation of the Drag of Flat Plates and Cylinders in the Slipstream of a Hovering Rotor. By John W. McKee and Rodger L. Naeseth.

4240. Some Measurements of Aerodynamic Forces and Moments at Subsonic Speeds on a Rectangular Wing of Aspect Ratio 2 Oscillating About the Midchord. By Edward Widmayer, Jr., Sherman A. Clevenson, and Sumner A. Leadbetter.

4241. An Approximate Method for Design or Analysis of Two-Dimensional Subsonic-Flow Passages. By E. Floyd Valentine.

4242. General Solutions for Flow Past Slender Cambered Wings With Swept Trailing Edges and Calculation of Additional Loading Due to Control Surfaces. By E. B. Klunker and Keith C. Harder.

4243. An Experimental Study of the Turbulent Boundary Layer on a Shock-Tube Wall. By Paul B. Gooderum.

4244. On Solutions for the Transient Response of Beams. By Robert W. Leonard.

4245. Flutter Analysis of Rectangular Wings of Very Low Aspect Ratio. By Robert W. Fralich and John M. Hedgepeth.

4246. Further Investigation of Fatigue-Crack Propagation in Aluminum-Alloy Box Beams. By Herbert F. Hardrath and Herbert A. Leybold.

4247. Study of Ground-Reaction Forces Measured During Landing Impacts of a Large Airplane. By Albert W. Hall, Richard H. Sawyer, and James M. McKay.

4248. Summary of Experimental Heat-Transfer Measurements in Turbulent Flow for a Mach Number Range From 0.87 to 5.05. By Maurice J. Brevoort and Barbara D. Arabian.

4249. A Theoretical Analysis of the Effect of Engine Angular Momentum on Longitudinal and Directional Stability in Steady Rolling Maneuvers. By Ordway B. Gates, Jr., and C. H. Woodling.

4250. Effect of the Proximity of the Wing First-Bending Frequency and the Short-Period Frequency on the Airplane Dynamic-Response Factor. By Carl R. Huss and James J. Donegan.

4251. An Experimental Investigation of Wake Effects on Hydro-Skis. By Ellis E. McBride and Lloyd J. Fisher.

4252. Experimental Investigation of an Impulse-Type Supersonic Compressor Rotor Having a Turning of 73° at the Mean Radius. By James R. Sterrett.

4253. Design and Tests of a Six-Stage Axial-Flow Compressor Having a Tip Speed of 550 Feet per Second and a Flat Operating Characteristic at Constant Speed. By Willard R. Westphal and John W. Maynard, Jr.

4254. Flight Investigation of Effects of Retreating-Blade Stall on Bending and Torsional Moments Encountered by a Helicopter Rotor Blade. By LeRoy H. Ludi.

4255. Wind-Tunnel Investigation at Low Speeds of Flight Characteristics of a Sweptback-Wing Jet-Transport Airplane Model Equipped With an External-Flow Jet-Augmented Slotted Flap. By Joseph L. Johnson, Jr.

4256. Water-Impact Theory for Aircraft Equipped With Nontrimming Hydro-Skis Mounted on Shock Struts. By Emanuel Schnitzer.

4257. Results of an Experimental Investigation of Small Viscous Dampers. By Milton A. Silveira, Domenic J. Maglieri, and George W. Brooks.

4258. A Numerical Method for Evaluating Wave Drag. By Maurice S. Cahn and Walter B. Olstad.

4259. Temperature-Pressure-Time Relations in a Closed Cryogenic Container. By Sidney C. Huntley.

4260. Ground Reflection of Jet Noise. By Walton L. Howes.

4261. Acoustic, Thrust, and Drag Characteristics of Several Full-Scale Noise Suppressors for Turbojet Engines. By Carl C. Ciepluch, Warren J. North, Willard D. Coles, and Robert J. Antl.

4262. Analysis of Turbulent Flow and Heat Transfer on a Flat Plate at High Mach Numbers With Variable Fluid Properties. By R. G. Deissler and A. L. Loeffler, Jr.

4263. Effect of Prior Air Force Overtemperature Operation on Life of J47 Buckets Evaluated in a Sea-Level Cyclic Engine Test. By Robert A. Signorelli, James R. Johnston, and Floyd B. Garrett.

4264. Internal Characteristics and Performance of Several Jet Deflectors at Primary-Nozzle Pressure Ratios up to 3.0. By Jack G. McArdle.

4265. Composition and Thermodynamic Properties of Air in Chemical Equilibrium. By W. E. Moeckel and Kenneth C. Weston.

4266. Studies of OH, CO, CH, and C_2 Radiation From Laminar and Turbulent Propane-Air and Ethylene-Air Flames. By Thomas P. Clark.

4267. Preliminary Survey of Propulsion Using Chemical Energy Stored in the Upper Atmosphere. By Lionel V. Baldwin and Perry L. Blackshear.

4268. Droplet Impingement and Ingestion by Supersonic Nose Inlet in Subsonic Tunnel Conditions. By Thomas F. Gelder.

4269. Transonic Drag of Several Jet-Noise Suppressors. By Warren J. North.

4270. A Performance Analysis of Methods for Handling Excess Inlet Flow at Supersonic Speeds. By Donald P. Hearth and James F. Connors.

4271. Maximum Theoretical Tangential Velocity Component Possible From Straight-Back Converging and Converging-Diverging Stators at Supercritical Pressure Ratios. By Thomas P. Moffitt.

4272. Use of the Coanda Effect for Obtaining Jet Deflection and Lift With a Single Flat-Plate Deflection Surface. By Uwe H. von Glahn.

4273. On Pairs of Solutions of a Class of Internal Viscous Flow Problems With Body Forces. By Simon Ostrach and Lynn U. Albers.

4274. Measurement of the Effect of an Axial Magnetic Field on the Reynolds Number of Transition in Mercury Flowing Through a Glass Tube. By Michel Bader and William C. A. Carlson.

4275. Dynamic Stability of Vehicles Traversing Ascending or Descending Paths Through the Atmosphere. By Murray Tobak and H. Julian Allen.

4276. An Approximate Analytical Method for Studying Entry Into Planetary Atmospheres. By Dean R. Chapman.

4277. A Body Modification To Reduce Drag Due to Wedge Angle of Wing With Unswept Trailing Edge. By William C. Pitts and Jack N. Nielsen.

4278. Application of Statistical Theory to Beam-Rider Guidance in the Presence of Noise. II—Modified Wiener Filter Theory. By Elwood C. Stewart.

4279. Effects of Fixing Transition on the Transonic Aerodynamic Characteristics of a Wing-Body Configuration at Reynolds Numbers From 2.4 to 12 Million. By Lynn W. Hunton.

4280. Pressure Distributions at Transonic Speeds for Slender Bodies Having Various Axial Locations of Maximum Diameter. By John B. McDevitt and Robert A. Taylor.

4281. Second-Order Slender-Body Theory-Axisymmetric Flow. By Milton D. Van Dyke.

4282. Boundary-Layer Stability Diagrams for Electrically Conducting Fluids in the Presence of a Magnetic Field. By Vernon J. Rossow.

4283. Full-Scale Wind-Tunnel Tests of a 35° Sweptback-Wing Airplane With Blowing From the Shroud Ahead of the Trailing-Edge Flaps. By William H. Tolhurst, Jr.

4284. Cumulative Fatigue Damage at Elevated Temperature. By William K. Rey.

4285. Transgranular and Intergranular Fracture of Ingot Iron During Creep. By L. A. Shepard and W. H. Giedt.

4286. Mechanism of Beneficial Effects of Boron and Zirconium on Creep-Rupture Properties of a Complex Heat-Resistant Alloy. By R. F. Decker and J. W. Freeman.

4287. Relationship of Metal Surfaces to Heat-Aging Properties of Adhesive Bonds. By J. M. Black and R. F. Blomquist.

4288. Turbulence and Temperature Fluctuations Behind a Heated Grid. By R. R. Mills, Jr., A. L. Kistler, V. O'Brien, and S. Corrsin.

4289. Boundary-Induced Downwash Due to Lift in a Two-Dimensional Slotted Wind Tunnel. By S. Katzoff and Raymond L. Barger.

4290. A Fuselage Addition to Increase Drag-Rise Mach Number of Subsonic Airplanes at Lifting Conditions. By Richard T. Whitcomb.

4291. An Evaluation of Effects of Flexibility on Wing Strains in Rough Air for a Large Swept-Wing Airplane by Means of Experimentally Determined Frequency-Response Functions With an Assessment of Random-Process Techniques Employed. By Thomas L. Coleman, Harry Press, and May T. Meadows.

4292. Local Instability of the Elements of a Truss-Core Sandwich Plate. By Melvin S. Anderson.

4293. Special Bodies Added on a Wing To Reduce Shock-Induced Boundary-Layer Separation at High Subsonic Speeds. By Richard T. Whitcomb.

4294. Effects of Nose Shape and Spray Control Strips on Emergence and Planing Spray of Hydro-Ski Models. By John R. McGehee.

4295. Reflection and Transmission of Sound by a Slotted Wall Separating Two Moving Fluid Streams. By Raymond L. Barger.

4296. Compressive Strength and Creep of 17–7 PH Stainless-Steel Plates at Elevated Temperatures. By Bland A. Stein.

4297. Flight Investigation of the Acceptability of a Small Side-Located Controller Used With an Irreversible Hydraulic Control System. By Helmut A. Kuehnel and Robert W. Sommer.

4298. Exploratory Wind-Tunnel Investigation To Determine the Lift Effects of Blowing Over Flaps From Nacelles Mounted Above the Wing. By John M. Riebe and Edwin E. Davenport.

4299. Effects of Fabrication-Type Roughness on Turbulent Skin Friction at Supersonic Speeds. By K. R. Czarnecki, John R. Sevier, Jr., and Melvin M. Carmel.

4300. Heat-Transfer and Pressure Measurements on Flat-Faced Cylinders at a Mach Number of 2. By William E. Stoney, Jr., and J. Thomas Markley.

4301. Effects of Boundary-Layer Displacement and Leading-Edge Bluntness on Pressure Distribution, Skin Friction, and Heat Transfer of Bodies at Hypersonic Speeds. By Mitchel H. Bertram and Arthur Henderson, Jr.

4302. Analytical and Experimental Investigation of Aerodynamic Forces and Moments on Low-Aspect-Ratio Wings Undergoing Flapping Oscillations. By Donald S. Woolston, Sherman A. Clevenson, and Sumner A. Leadbetter.

4303. Measurements and Power Spectra of Runway Roughness at Airports in Countries of the North Atlantic Treaty Organization. By Wilbur E. Thompson.

4304. Matrix Method for Obtaining Spanwise Moments and Deflections of Torsionally Rigid Rotor Blades With Arbitrary Loadings. By Alton P. Mayo.

4305. Wind-Tunnel Investigation of Effects of Spoiler Location, Spoiler Size, and Fuselage Nose Shape on Directional Characteristics of a Model of a Tandem-Rotor Helicopter Fuselage. By James L. Williams.

4306. Temperature and Thermal-Stress Distributions in Some Structural Elements Heated at a Constant Rate. By William A. Brooks, Jr.

4307. Experimental Measurements of the Effects of Airplane Motions on Wing and Tail Angles of Attack of a Swept-Wing Bomber in Rough Air. By Jerome N. Engel.

4308. Transient Temperature Distribution in a Two-Component Semi-Infinite Composite Slab of Arbitrary Materials Subjected to Aerodynamic Heating With a Discontinuous Change in Equilibrium Temperature or Heat-Transfer Coefficient. By Robert L. Trimpi and Robert A. Jones.

4309. Use of Short Flat Vanes for Producing Efficient Wide-Angle Two-Dimensional Subsonic Diffusers. By D. L. Cochran and S. J. Kline.

4310. Measurements of the Motions of a Large Swept-Wing Airplane in Rough Air. By Richard H. Rhyne.

4311. Prandtl Number Effects on Unsteady Forced-Convection Heat Transfer. By E. M. Sparrow and J. L. Gregg.

4312. Internal Characteristics and Performance of an Aerodynamically Controlled, Variable-Discharge Convergent Nozzle. By Jack G. McArdle.

4313. Effect of Favorable Pressure Gradients on Transition for Several Bodies of Revolution at Mach 3.12. By John R. Jack.

4314. Icing Frequencies Experienced During Climb and Descent by Fighter-Interceptor Aircraft. By Porter J. Perkins.

4315. An Estimate of the Fluctuating Surface Pressures Encountered in the Reentry of a Ballistic Missile. By Edmund E. Callaghan.

4316. Friction and Wear With Reactive Gases at Temperatures up to 1200° F. By Gordon P. Allen, Donald H. Buckley, and Robert L. Johnson.

4317. Turbojet Engine Noise Reduction With Mixing Nozzle-Ejector Combinations. By Willard D. Coles, John A. Mihaloew, and Edmund E. Callaghan.

4318. Analytical Relation for Wake Momentum-Thickness and Diffusion Ratio for Low-Speed Compressor Cascade Blades. By Seymour Lieblein.

4319. On Fully Developed Channel Flows: Some Solutions and Limitations, and Effects of Compressibility, Variable Properties, and Body Forces. By Stephen H. Maslen.

4320. Compressible Laminar Flow and Heat Transfer About a Rotating Isothermal Disk. By Simon Ostrach and Philip R. Thornton.

4321. An Analytical Study of Turbulent and Molecular Mixing in Rocket Combustion. By David A. Bittker.

4322. Ordinates and Theoretical Pressure-Distribution Data for NACA 6- and 6A-Series Airfoil Sections With Thicknesses From 2 to 21 and 2 to 15 Percent Chord, Respectively. By Elizabeth W. Patterson and Albert L. Braslow.

4323. Natural Convection Inside a Flat Rotating Container. By Simon Ostrach and Willis H. Braun.

4324. Method for Determining the Need To Rework or Replace Compressor Rotor Blades Damaged by Foreign Objects. By Albert Kaufman.

4325. A Mach 4 Rocket-Powered Supersonic Tunnel Using Ammonia-Oxygen as Working Fluid. By Robert W. Graham, Eleanor Costilow Guentert, and Vearl N. Huff.

4326. Lightning Hazards to Aircraft Fuel Tanks. By J. D. Robb, E. L. Hill, M. M. Newman, and J. R. Stahmann.

4327. Hypersonic Viscous Flow Over Slender Cones. By Lawrence Talbot, Toyoki Koga, and Pauline M. Sherman.

4328. Study of Hydrogen Embrittlement of Iron by Internal-Friction Methods. By R. E. Maringer, E. B. Swetnam, L. L. Marsh, and G. K. Manning.

4329. Influence of Heat Treatment on Microstructure and High-Temperature Properties of a Nickel-Base Precipitation-Hardening Alloy. By R. F. Decker, John P. Rowe, W. C. Bigelow, and J. W. Freeman.

4330. Flow Induced by a Rotor in Power-on Vertical Descent. By Walter Castles, Jr.

4331. An Investigation of the Effects of Atmospheric Corrosion on the Fatigue Life of Aluminum Alloys. By Herbert A. Leybold, Herbert F. Hardrath, and Robert L. Moore.

4332. An Approach to the Problem of Estimating Severe and Repeated Gust Loads for Missile Operations. By Harry Press and Roy Steiner.

4333. Effect of Some External Crosswise Stiffeners on the Heat Transfer and Pressure Distribution on a Flat Plate at Mach Numbers of 0.77, 1.39, and 1.98. By Howard S. Carter.

4334. Lag in Pressure Systems at Extremely Low Pressures. By William T. Davis.

4335. Procedure for Calculating Flutter at High Supersonic Speed Including Camber Deflections, and Comparison With Experimental Results. By Homer G. Morgan, Vera Huckel, and Harry L. Runyan.

4336. Experimental Investigation of Axial and Normal Force Characteristics of Skewed Nozzles. By David J. Carter, Jr., and Allen R. Vick.

4337. An Investigation of Some Phenomena Relating to Aural Detection of Airplanes. By Harvey H. Hubbard and Domenic J. Maglieri.

4338. Graphs of Reduced Variables for Computing Histories of Vaporizing Fuel Drops, and Drop Histories Under Pressure. By G. L. Borman, M. M. El Wakil, O. A. Uyehara, and P. S. Myers.

4339. Hydrodynamic Impact Loads of a —20° Dead-Rise Inverted —V Model and Comparisons With Loads of a Flat-Bottom Model. By Philip M. Edge, Jr.

4340. Wind-Tunnel Investigation of the High-Subsonic Static Longitudinal Stability Characteristics of Several Wing-Body Configurations Designed for High Lift-Drag Ratios at a Mach Number of 1.4. By Paul G. Fournier.

4341. Low-Speed Experimental Determination of the Effects of Leading-Edge Radius and Profile Thickness on Static and Oscillatory Lateral Stability Derivatives for a Delta Wing with 60° of Leading-Edge Sweep. By Herman S. Fletcher.

4342. Flight Measurements of the Vibratory Bending and Torsional Stresses on a Modified Supersonic Propeller for Forward Mach Numbers up to 0.95. By Thomas C. O'Bryan.

4343. A Comparison of Two Methods for Calculating Transient Temperatures for Thick Walls. By James J. Buglia and Helen Brinkworth.

4344. Performance at Low Speeds of Compressor Rotors Having Low-Cambered NACA 65-Series Blades With High Inlet Angles and Low Solidities. By James C. Emery and Paul W. Howard.

4345. Similar Solutions for the Compressible Boundary Layer on a Yawed Cylinder With Transpiration Cooling. By Ivan E. Beckwith.

4346. Approximate Method for Calculating Motions in Angles of Attack and Sideslip Due to Step Pitching- and Yawing-Moment Inputs During Steady Roll. By Martin T. Moul and Teresa R. Brennan.

4347. A Nonlinear Theory for Predicting the Effects of Unsteady Laminar, Turbulent, or Transitional Boundary Layers on the Attenuation of Shock Waves in a Shock Tube With Experimental Comparison. By Robert L. Trimpi and Nathaniel B. Cohen.

4348. Effect of Temperature on Dynamic Modulus of Elasticity of Some Structural Alloys. By Louis F. Vosteen.

4349. Heat Transfer and Thermal Stresses in Sandwich Panels. By Robert T. Swann.

4350. Theoretical Distribution of Laminar-Boundary-Layer Thickness, Boundary-Layer Reynolds Number and Stability Limit, and Roughness Reynolds Number for a Sphere and Disk in Incompressible Flow. By Neal Tetervin.

4351. Summary of Methods of Measuring Angle of Attack on Aircraft. By William Gracey.

4352. Tables and Graphs of Normal-Shock Parameters at Hypersonic Mach Numbers and Selected Altitudes. By Paul W. Huber.

4353. Exploratory Wind-Tunnel Investigation at High Subsonic and Transonic Speeds of Jet Flaps on Unswept Rectangular Wings. By Vernard E. Lockwood and Raymond D. Vogler.

4354. Measurements in a Shock Tube of Heat Transfer Rates at the Stagnation Point of a 1.0-Inch-Diameter Sphere for Real-Gas Temperatures up to 7,900° R. By Alexander P. Sabol.

4355. Low Tip Mach Number Stall Characteristics and High Tip Mach Number Compressibility Effects on a Helicopter Rotor Having an NACA 0009 Tip Airfoil Section. By Robert D. Powell, Jr., and Paul J. Carpenter.

4356. Effects of Compressibility on Rotor Hovering Performance and Synthesized Blade-Section Characteristics Derived From Measured Rotor Performance of Blades Having NACA 0015 Airfoil Tip Sections. By James P. Shivers and Paul J. Carpenter.

4357. Lift and Profile-Drag Characteristics of an NACA 0012 Airfoil Section as Derived From Measured Helicopter-Rotor Hovering Performance. By Paul J. Carpenter.

4358. Supersonic Wave Interference Affecting Stability. By Eugene S. Love.

4359. A Review of the Thermodynamic, Transport, and Chemical Reaction Rate Properties of High-Temperature Air. By C. Frederick Hansen and Steve P. Heims.

4360. Measurements of the Effects of Wall Outflow and Porosity on Wave Attenuation in a Transonic Wind Tunnel With Perforated Walls. By Joseph M. Spiegel, Phillips J. Tunnell, and Warren S. Wilson.

4361. Idealized Wings and Wing-Bodies at a Mach Number of 3. By Elliott D. Katzen.

4362. Force and Pressure Measurements at Transonic Speeds for Several Bodies Having Elliptical Cross Sections. By John B. McDevitt and Robert A. Taylor.

4363. Simplified Method for Determination of Critical Height of Distributed Roughness Particles for Boundary-Layer Transition at Mach Numbers From 0 to 5. By Albert L. Braslow and Eugene C. Knox.

4364. An Investigation of Supersonic Turbulent Boundary Layers on Slender Bodies of Revolution in Free Flight by Use of a Mach-Zehnder Interferometer and Shadowgraphs. By Alvin Seiff and Barbara J. Short.

4365. Large-Scale Wind-Tunnel Tests of an Airplane Model With an Unswept, Aspect-Ratio-10 Wing, Two Propellers, and Area-Suction Flaps. By James A. Weiberg, Roy N. Griffin, Jr., and George L. Florman.

4366. The Effects of an Inverse-Taper Leading-Edge Flap on the Aerodynamic Characteristics in Pitch of a Wing-Body Combination Having an Aspect Ratio of 3 and 45° of Sweepback at Mach Numbers to 0.92. By Fred A. Demele and K. Harmon Powell.

4367. Wind-Tunnel Tests of a Full-Scale Helicopter Rotor With Symmetrical and With Cambered Blade Sections at Advance Ratios From 0.3 to 0.4. By John L. McCloud III and George B. McCullough.

4368. A Study of Several Theoretical Methods for Computing the Zero-Lift Wave Drag of a Family of Open-Nosed Bodies of Revolution in the Mach Number Range of 2.0 to 4.0. By Leroy L. Presley and Emmet A. Mossman.

4369. Slip-Flow Heat Transfer From Cylinders in Subsonic Airstreams. By Lionel V. Baldwin.

4370. Some Numerical Solutions of Similarity Equations for Three-Dimensional Laminar Incompressible Boundary-Layer Flows. By Peggy L. Yohner and Arthur G. Hansen.

4371. Some Observations Relating to Recovery of Internal Friction During Fatigue of Aluminum. By S. R. Valluri.

4372. Effect of Precipitate Particles on Creep of Aluminum-Copper Alloys During Age Hardening. By E. E. Underwood, L. L. Marsh, and G. K. Manning.

4373. Theoretical and Experimental Analysis of the Reduction of Rotor Blade Vibration in Turbomachinery Through the Use of Modified Stator Vane Spacing. By Richard

H. Kemp, Marvin H. Hirschberg, and William C. Morgan.

4374. Rate of Reaction of Gaseous Fluorine With Water Vapor at 35° C. By Vernon A. Slabey and Edward A. Fletcher.

4375. Approximate Solutions of a Class of Similarity Equations for Three-Dimensional, Laminar, Incompressible Boundary-Layer Flows. By Arthur G. Hansen and Howard Z. Herzig.

4376. Analytical and Experimental Investigation of Temperature Recovery Factors for Fully Developed Flow of Air in a Tube. By R. G. Deissler, W. F. Weiland, and W. H. Lowdermilk.

4377. Use of the Coanda Effect for Jet Deflection and Vertical Lift With Multiple-Flat-Plate and Curved-Plate Deflection Surfaces. By Uwe H. von Glahn and Thomas F. Gelder.

4378. Preliminary Heat-Transfer Studies on Two Bodies of Revolution at Angle of Attack at a Mach Number of 3.12. By Norman Sands and John R. Jack.

4379. Torque-Speed Characteristics for High-Specific-Work Turbines. By Warner L. Stewart.

4380. Approximate Method for Calculation of Laminar Boundary Layer With Heat Transfer on a Cone at Large Angle of Attack in Supersonic Flow. By William E. Brunk.

4381. Effect of Pressure and Duct Geometry on Bluff-Body Flame Stabilization. By Andrew E. Potter, Jr., and Edgar L. Wong.

4382. Investigation of Boiling Burnout and Flow Stability for Water Flowing in Tubes. By Warren H. Lowdermilk, Chester D. Lanzo, and Byron L. Siegel.

4383. A Cooled-Gas Pyrometer for Use in High-Temperature Gas Streams. By Lloyd N. Krause, Robert C. Johnson, and George E. Glawe.

4384. Analysis of Turbulent Flow and Heat Transfer in Noncircular Passages. By Robert G. Deissler and Maynard F. Taylor.

4385. Comparison of Shock-Expansion Theory With Experiment for the Lift, Drag, and Pitching-Moment Characteristics of Two Wing-Body Combinations at M=5.0. By Raymond C. Savin.

4386. An Analysis of Ramjet Engines Using Supersonic Combustion. By Richard J. Weber and John S. MacKay.

4387. Experimental Evaluation of Low-Band-Pass Landing-Gear Shock Absorber for Pulse Loadings. By Emanuel Schnitzer.

4388. Effects of Nose Angle and Mach Number on Transition on Cones at Supersonic Speeds. By K. R. Czarnecki and Mary W. Jackson.

4389. Effect of Advance Ratio on Flight Performance of a Modified Supersonic Propeller. By Jerome B. Hammack and Thomas C. O'Bryan.

4390. Effects of Frequency and Amplitude on the Yawing Derivatives of Triangular, Swept, and Unswept Wings and of a Triangular-Wing-Fuselage Combination With and Without a Triangular Tail Performing Sinusoidal Yawing Oscillations. By William Letko and Herman S. Fletcher.

4391. Mass Transfer Cooling Near the Stagnation Point. By Leonard Roberts.

4392. A Theoretical Study of Stagnation-Point Ablation. By Leonard Roberts.

4393. Some Static Longitudinal Stability Characteristics of an Overlapped-Type Tandem-Rotor Helicopter at Low Airspeeds. By Robert J. Tapscott.

4394. The Rate of Fatigue-Crack Propagation in Two Aluminum Alloys. By Arthur J. McEvily, Jr., and Walter Illg.

4395. Use of the Kernel Function in a Three-Dimensional Flutter Analysis With Application to a Flutter-Tested Delta-Wing Model. By Donald S. Woolston and John L. Sewell.

4396. A Phenomenological Theory for the Transient Creep of Metals at Elevated Temperatures. By Elbridge Z. Stowell.

4397. Static Longitudinal and Lateral Stability Characteristics at Low Speed of 60° Sweptback-Midwing Models Having Wings With an Aspect Ratio of 2, 4, or 6. By Walter D. Wolhart and David F. Thomas, Jr.

4398. Analysis of the Creep Behavior of a Square Plate Loaded in Edge Compression. By Harvey G. McComb, Jr.

4399. Relative Motion in the Terminal Phase of Interception of a Satellite or a Ballistic Missile. By Richard A. Hord.

4400. Measurements of Ground-Reaction Forces and Vertical Center-of-Gravity Accelerations of a Bomber Airplane Taxiing Over Obstacles. By James M. McKay, Richard H. Sawyer, and Albert W. Hall.

4401. Hydrodynamic Impact Loads on 30° and 60° V-Step Plan-Form Models With and Without Dead Rise. By Philip M. Edge, Jr., and Jean P. Mason.

4402. Measurements of Aerodynamic Forces and Moments at Subsonic Speeds on a Simplified T-Tail Oscillating in Yaw About the Fin Midchord. By Sherman A. Clevenson and Sumner A. Leadbetter.

4403. Tests of Ring-Stiffened Circular Cylinders Subjected to a Transverse Shear Load. By James P. Peterson and Richard G. Updegraff.

4404. Effects of Propeller Position and Overlap on the Slipstream Deflection Characteristics of a Wing-Propeller Configuration Equipped With a Sliding and Fowler Flap. By William C. Hayes, Jr., Richard E. Kuhn, and Irving R. Sherman.

4405. Free-Flight Investigation To Determine the Drag of Flat- and Vee-Windshield Canopies on a Parabolic Fuselage With and Without Transonic Indentation Between Mach Numbers of 0.75 and 1.35. By Walter L. Kouyoumjian and Sherwood Hoffman.

4406. Low Tire Friction and Cornering Forces on a Wet Surface. By Eziaslav N. Harrin.

4407. Effects of Ground Proximity on the Thrust of a Simple Downward-Directed Jet Beneath a Flat Surface. By Kenneth P. Spreemann and Irving R. Sherman.

4408. The Theory of Diffusion in Strained Systems. By Louis A. Girifalco and Hubert H. Grimes.

4409. Flight Measurements of the Vibration Experienced by a Tandem Helicopter in Transition, Vortex-Ring State, Landing Approach, and Yawed Flight. By John E. Yeates.

4410. Flight Measurements of the Vibratory Stresses on a Propeller Designed for an Advance Ratio of 4.0 and a Mach Number of 0.82. By Thomas C. O'Bryan.

TECHNICAL MEMORANDUMS [1]

1404. Investigation of Aperiodic Time Processes With Autocorrelation and Fourier Analysis. By Marie Luise Exner. From Acustica, v. 4, no. 3, 1954, p. 365–379.

[1] The missing numbers in the series of Technical Memorandums were released before or after the period covered by this report.

1407. Free Convection Under the Conditions of the Internal Problem. By G. A. Ostroumov. From Russian Book, 1952.

1408. The Principles of Turbulent Heat Transfer. By H. Reichardt. Translation from Archiv fur die gesamte Wärmetechnik, no. 6/7, 1951, p. 129–142.

1409. Reflection and Refraction of Acoustic Waves by a Shock Wave. By J. Brillouin. From Acustica, v. 5., no. 3, 1955, p. 149–163.

1410. Theory and Experiments on Supersonic Air-to-Air Ejectors. By J. Fabri and J. Paulon. From Office National d'Etudes et de Recherches Aéronautiques. Note Technique no. 36, 1956.

1411. Study of the Micro-Nonuniformity of the Plastic Deformation of Steel. By B. B. Chechulin. From Fizika Metallov i Metallovedenie, v. 1, no. 2, 1955, p. 251–260.

1412. Aerodynamic Forces on a Vibrating Unstaggered Cascade. By H. Söhngen. From Zeitschrift für angewandte Mathematik und Mechanik, v. 35, no. 3, March 1955, p. 81–88.

1413. Impact on a Compressible Fluid. By I. T. Egorov. From Prikladnaia Matematika i Mekhanika, v. 20, no. 1, 1956, p. 67–72.

1414. Aerodynamic Research on Fuselages With Rectangular Cross Section. By K. Maruhn. From Jahrbuch 1942 der deutschen Luftfahrtforschung, p. 263–279.

1417. On the Spectrum of Natural Oscillations of Two-Dimensional Laminar Flows. By D. Grohne. From Zeitschrift für angewandte Mathematik und Mechanik, v. 34, no. 8–9, Aug.–Sept. 1954, p. 344–357.

1418. The Interaction of a Reflected Shock Wave With the Boundary Layer in a Shock Tube. By Herman Mark.

1431. On the Statistical Theory of Turbulence. By W. Heisenberg. From Zeitschrift für Physik, v. 124, 1948, p. 628–657.

1432. Evaporation, Heat Transfer, and Velocity Distribution in Two-Dimensional and Rotationally Symmetrical Laminar Boundary-Layer Flow. By Nils Frössling. From Lunds Universitets Arsskrift, v. 36, no. 4. Kungl. Fysiografiska Sallskapets Handlingar, v. 51, no. 4, 1940.

1433. Stability of Cylindrical and Conical Shells of Circular Cross Section, With Simultaneous Action of Axial Compression and External Normal Pressure. By Kh. M. Mushtari and A. V. Sachenkov. From Prikladnaia Matematika i Mekhanika, v. 18, no. 6, Nov.–Dec. 1954, p. 667–674.

1434. Extreme Speeds and Thermodynamic States in Supersonic Flight. By Klaus Oswatitsch. From Zeitschrift für Flugwissenschaften, v. 4, no. 3/4, 1956, p. 95–108.

1435. Elliptic Functions and Integrals With Real Modulus in Fluid Mechanics. By Robert Legendre. From Office National d'Etudes et de Recherches Aéronautiques, Publication 71, 1954.

1436. Statistical Study of Turbulence—Spectral Functions and Correlation Coefficients. By Francois N. Frenkiel. From Office National d'Etudes et de Recherches Aéronautiques. Rapport Technique no. 34, 1948.

1437. On Possible Similarity Solutions for Three-Dimensional Incompressible Laminar Boundary-Layer Flows Over Developable Surfaces and With Proportional Mainstream Velocity Components. By Arthur G. Hansen, Case Institute of Technology.

1438. On the Flutter of Cylindrical Shells and Panels Moving in a Flow of Gas. By R. D. Stepanov. From Prikladnaia Matematika i Mekhanika, v. 21, no. 5, 1957, p. 644–657.

1439. Application of the Method of Coordinate Perturbation to Unsteady Duct Flow. By Seymour C. Himmel, Case Institute of Technology.

1440. The Turbulent Boundary Layer on a Rough Curvilinear Surface. By V. F. Droblenkov. From Akademiia Nauk SSSR, Izvestiia, Otdelenie Tekhnicheskikh Nauk, no. 8, 1955, p. 17–21.

1441. The Effect of Free-Stream Turbulence on Heat Transfer From a Flat Plate. By Sugao Sugawara, Takashi Sato, Hiroyasu Komatsu, and Hiroichi Osaka. From Journal of Japan Society of Mechanical Engineering, v. 19, no. 18, 1953, p. 18–25.

OTHER TECHNICAL PAPERS BY STAFF MEMBERS

Allen, Harry Julian: Hypersonic Flight and the Re-Entry Problem. Jour. Aero. Sci., vol. 25, no. 4, Apr. 1958, pp. 217–230.

Anderson, Roger A.: Weight-Efficiency Analysis of Thin-Wing Construction. Trans. A.S.M.E., vol. 79, no. 5, July 1957, pp. 974–979.

Beeler, De Elroy: Flight Loads Measurements on NACA Research Airplanes. Presented at the Fifth Meeting of the Structures and Materials Panel (Copenhagen, Denmark, Apr. 29–May 3, 1957), Advisory Group for Aeronautical Research and Development Report 109.

Beeler, De Elroy, Bellman, Donald R., and Saltzman, Edwin J.: Flight Techniques for Determining Airplane Drag at High Mach Numbers. Presented at the Ninth Meeting of the Flight Test Panel (Brussels, Belgium, Aug. 27–31, 1956). Advisory Group for Aeronautical Research and Development Report 84.

Belles, Frank, and O'Neal, Cleveland, Jr.: Effects of Halogenated Extinguishing Agents on Flame Quenching and a Chemical Interpretation of Their Action. Sixth Symposium (International) on Combustion (Yale Univ., New Haven, Conn., Aug. 19–24, 1956). Reinhold Pub. Corp., N.Y., 1957, pp. 806–813.

Belles, Frank: Flame Propagation in Premixed Gases. Advances in Chemistry Series, no. 20, Am. Chem. Soc., 1958, pp. 166–186.

Benser, William A., and Finger, Harold B.: Compressor-Stall Problems in Gas-Turbine Type Aircraft Engines. Trans. SAE, vol. 65, 1957, pp. 187–199; Discussion, pp. 199–200.

Bisson, Edmond E., Johnson, Robert L., and Anderson, William J.: Friction and Lubrication With Solid Lubricants at Temperatures to 1,000° F. with Particular Reference to Graphite. Presented at Conference on Lubrication and Wear (London, Oct. 1–2, 1957), Inst. Mech. Eng'rs. (Gt. Brit.), Paper 23, 1957.

Bisson, Edmond E., Johnson, Robert L., and Swikert, Max A.: Friction, Wear, and Surface Damage of Metals as Affected by Surface Films: A Review of NACA Research. Presented at Conference on Lubrication and Wear (London, Oct. 1–3, 1957), Inst. Mech. Eng'rs. (Gt. Brit.), Paper 31, 1957.

Blackshear, Perry L., Jr.: The Growth and Disturbances in a Flame-Generated Shear Region. Sixth Symposium (International) on Combustion (Yale Univ., New Haven, Conn., Aug. 19–24, 1956). Reinhold Pub. Corp., N.Y., 1957, pp. 512–522.

Brokaw, Richard S., and Gerstein, Melvin: Correlations of Burning Velocity, Quenching Distances, and Minimum Ignition Energies for Hydrocarbon-Oxygen-Nitrogen Systems. Sixth Symposium (International) on Combustion (Yale Univ.,

New Haven, Conn., Aug. 19–24, 1956). Reinhold Pub. Corp., N.Y., 1957, pp. 66–74.

Brown, William F., Jr., Meyer, Andre J., and Jones, Melvin H.: Application of Laboratory Test Data to Design of Aircraft Gas Turbine Blade Fastening Models. Proceedings of the Third Sagamore Ordnance Materials Research Conference, Materials Evaluation in Relation to Component Behavior (Duke Univ., Durham, N.C., Dec. 5–7, 1956), Syracuse Univ. Research Inst. Met365–574, pp. 302–336.

Childs, J. Howard, and Graves, Charles C.: Correlation of Turbine-Engine Combustion Efficiency With Theoretical Equations. Sixth Symposium (International) on Combustion (Yale Univ., New Haven, Conn., Aug. 19–24, 1956). Reinhold Pub. Corp., N.Y., 1957, pp. 869–878.

Clauss, Francis J.: Thermal Fatigue of Ductile Materials. Proceedings of the Fourth Sagamore Ordnance Materials Research Conference, High Temperature Materials, Their Strength Potentials and Limitations (Sagamore Conference Center, Raquette Lake, N.Y., Aug. 21–23, 1957), Syracuse Univ. Research Inst. Met497–582, pp. 174–192.

Coleman, Thomas L., Murrow, Harold N., and Press, Harry: Some Structural Response Characteristics of a Large Flexible Swept-Wing Airplane in Rough Air. Preprint 785, Inst. Aero. Sci., 1958.

Deissler, Robert G., and Taylor, Maynard F.: Analysis of Axial Turbulent Flow and Heat Transfer Through Banks of Rods or Tubes. Collected Papers and Reports of 1956 Reactor Heat Transfer Conference (New York, Nov. 1–2, 1956), Book 2, AEC Rept. TID–7529, pt. 1, Nov. 1957, pp. 416–461.

Deissler, Robert G., and Perlmutter, Morris: An Analysis of the Energy Separation in Laminar and Turbulent Compressible Vortex Flows. 1958 Heat Transfer and Fluid Mechanics Institute (Univ. Calif., Berkeley, Calif., June 19–21, 1958), Preprints of Papers, Stanford Univ. Press, Stanford, Calif., 1958, pp. 40–53.

Deissler, Robert G.: On the Decay of Homogeneous Turbulence Before the Final Period. Physics of Fluids, vol. 1, no. 2, Mar.–Apr. 1958, pp. 111–121.

Diederich, Franklin W.: Divergence of Delta and Swept Surfaces in the Transonic and Supersonic Speed Ranges. Presented at the Third Meeting of the Structures and Materials Panel (Washington, D.C., Apr. 10–17, 1956), Advisory Group for Aeronautical Research Development Report 42.

Dryden, Hugh L.: Combined Effects of Turbulence and Roughness on Transition. Festschrift Jakob Ackeret, Zeit, fur. Angew. Math. Phys., vol. 9b, no. 5/6, Sonderband, Mar. 25, 1958, pp. 249–258.

Duberg, John E.: Some NACA Research on Effect of Transient Heating on Aircraft Structures. Trans. A.I.M.E., vol. 79, no. 5, July 1957, pp. 1014–1018.

Eggers, Alfred J., Jr.: Performance of Long Range Hypervelocity Vehicles. Jet Propulsion, vol. 27, no. 11, Nov. 1957, pp. 1147–1151.

Gabriel, David S., Wallner, Lewis E., Lubick, Robert J., and Vasu, George: Some Effects on Inlet Pressure and Temperature Transients on Turbojet Engines. Aero. Eng. Rev., vol. 16, no. 9, Sept. 1957, pp. 54–59, 68.

Garrick, Isadore E.: Aerodynamic Theory and its Application to Flutter. Presented at the Third Structures and Materials Panel (Washington, D.C., Apr. 10–17, 1956), Advisory Group for Aeronautical Research and Development Report 34.

Garrick, Isadore E.: Some Concepts and Problem Areas in Aircraft Flutter. (The 1957 Minta Martin Aeronautical Lecture.) Sherman M. Fairchild Fund Paper FF–15, Inst. Aero. Sci., 1957.

Gerstein, Melvin, and Potter, Andrew E., Jr.: Considerations Related to the Quenching of Flames With Simple Kinetics. 1958 Heat Transfer and Fluid Mechanics Institute (Univ. Calif., Berkeley, Calif., June 19–21, 1958), Preprints of Papers, Stanford Univ. Press, Stanford, Calif., 1958, pp. 69–79.

Girifalco, Louis A., and Streetman, J. R.: A Theoretical Calculation of the Relaxation of Atoms Surrounding a Vacancy in the Body-Centered Cubic Lattice. Phys. and Chem. of Solids, vol. 4, no. 3, 1958, pp. 182–189.

Glahn, Uwe, H. von, and Povonly, John H.: Considerations of Some Jet-Deflection Principles for Directional Control and for Lift. Preprint 219, SAE, 1957.

Gough, Melvin N., Sawyer, Richard H., and Trant, James P., Jr.: Tire-Runway Braking Friction Coefficients. Reports Presented at the Fifth Annual Air Safety Forum of the Air Line Pilots Association (Chicago, Ill., Mar. 5–7, 1957), Sec. 1, 7th Paper, 22 pp.

Gray, Vernon H.: Correlation of Airfoil Ice Formations and Their Aerodynamic Effects With Impingement and Flight Conditions. Preprint SAE, 225, 1957.

Grobman, Jack S., Dittrich, Ralph T., and Graves, Charles C. (Nuclear Development Corp.): Pressure Drop and Air-Flow Distribution in Gas-Turbine Combustors. Trans. A.I.M.E., vol. 79, no. 7, Oct. 1957, pp. 1601–1607.

Hansen, C. Frederick: Some Characteristics of the Upper Atmosphere Pertaining to Hypervelocity Flight. Jet Propulsion, vol. 27, no. 11, Nov. 1957, pp. 1151–1156.

Hedgepeth, John M.: Flutter of Rectangular Simply Supported Panels at High Supersonic Speeds. Jour. Aero. Sci., vol. 24, no. 8, Aug. 1957, pp. 563–573, 586.

Heimel, Sheldon, and Weast, Robert C.: Effect of Initial Mixture Temperature on the Burning Velocity of Benzene-Air, n-Heptane-Air, and Isooctane-Air Mixtures. Sixth Symposium (International) on Combustion (Yale Univ., New Haven, Conn., Aug. 19–24, 1956). Reinhold Pub. Corp., N.Y., 1957, pp. 296–302.

Heimerl, George J.: Tensile Properties of Some Structural Sheet Materials Under Rapid-Heating Conditions. Proceedings of the Fourth Sagamore Ordnance Materials Research Conference, High Temperature Materials, Their Strength Potentials and Limitations (Sagamore Conference Center, Raquette Lake, N.Y., Aug. 21–23, 1957), Syracuse Univ. Research Inst. Met497–582, pp. 115–145.

Hoffman, Charles A.: Strengths and Failure Characteristics of AMS 5765A (S–816) Alloy in Direct Tensile Fatigue at Elevated Temperatures. Proc. A.S.T.M., vol. 56, 1956, pp. 1063–1080.

Huston, Wilber B.: A Study of the Correlation Between Flight and Wind-Tunnel Buffet Loads. Presented at Fifth Meeting of Structures and Materials Panel (Copenhagen, Denmark, Apr. 29–May 3, 1957), Advisory Group for Aeronautical Research and Development Report 111.

Ingebo, Robert D.: Atomization, Acceleration, and Vaporization of Liquid Fuels. Sixth Symposium (International) on Combustion (Yale Univ., New Haven, Conn., Aug. 19–24, 1956). Reinhold Pub. Corp., N.Y., 1957, pp. 684–687.

James, Edward W. (E. I. du Pont de Nemours), and Boksenbom, Aaron S.: How to Establish the Control Problem for an On-Line Computer. Control Eng., vol. 4, no. 9, Sept. 1957, pp. 148–159.

Johnson, Robert L.: Possibilities in the Field of Dry Lubricants. Preprint, SAE 18B, 1958.

Jones, Melvin H., Shannon, John L., Jr., and Brown, William F., Jr.: Influence of Notch Preparation and Eccentricity of Loading on the Notch Rupture Life. Proc. A.S.T.M., vol. 57, 1957, pp. 833–853.

Jones, Robert T., and Van Dyke, Milton D.: The Compressibility Rule for Drag of Airfoil Noses. Jour. Aero. Sci., vol. 25, no. 3, Mar. 1958, pp. 171–172, 180.

Kemp, Richard H.: Advances in Static and Dynamic High Temperature Strain Gage Research. Electronic Ind., vol. 17, no. 5, May 1958, pp. 52–57, 88, 90.

Kotanchik, Joseph N.: The Use of High-Intensity Arcs in Arc-Image Furnaces and Electric Arc-Powered Jets. Papers Presented at the High Intensity Arc Symposium, Jointly Sponsored by the Dept. of the AF and the Carborundum Co. (Niagara Falls, N.Y., June 13–14, 1957), Stanley D. Mark, Jr., ed., Carborundum Co., Niagara Falls, N.Y., May 1958, pp. 14–28.

Kramer, James J.: Analysis of Incompressible, Nonviscous Blade-to-Blade Flow in Rotating Blade Rows. Trans. A.S.M.E., vol. 80, no. 2, Feb. 1958, pp. 263–275.

Kuhn, Richard E.: Take-Off and Landing Distances and Power Requirements of Propeller-Driven STOL Airplanes. Aero. Eng. Rev., vol. 16, no. 11, Nov. 1957, pp. 38–42.

Lovell, Powell M., Jr.: NACA Flight Tests a VTOL Model. Ryan Reporter, vol. 18, no. 4, Oct. 15, 1957, pp. 12–14, 32–33.

McCafferty, Richard J., and Hibbard, Robert R.: Combustion in Aircraft Gas Turbine Engines. Advances in Chemistry Series, No. 20, Am. Chem. Soc., 1958, pp. 120–123.

McComber, John: Cam-Actuated Servo Valves Control Wind Tunnel Area. Appl. Hydraulics, vol. 11, no. 3, Mar. 1958, pp. 120–123.

McFarland, Keith H., and Dimeff, John: Problems Involved in Precision Measurements With Resistance Strain Gages. Presented at the Eighth Meeting of the Wind Tunnel and Model Testing Panel (Rome, Italy, Feb. 20–25, 1956), Advisory Group for Aeronautical Research and Development Report 12.

McKee, John W.: Pitch-Lag Instability as Encountered During Tests of a Model Rotor. Preprint 807, Inst. Aero. Sci., 1958.

McNulty, James F.: Problems Involved in Revitalizing a Wind Tunnel. (Presented at Annual Meeting, Virginia Section, Am. Soc. Civil Eng., Richmond, Dec. 7, 1956). Virginia Engineer, Summer 1957.

Manson, Samuel S., and Brown, William F., Jr.: A Survey of the Effects of Nonsteady Load and Temperature Conditions on the Creep of Metals. Proceedings of the Fourth Sagamore Ordnance Materials Research Conference, High Temperature Materials, Their Strength Potentials and Limitations (Sagamore Conference Center, Raquette Lake, N.Y., Aug. 21–23, 1957), Syracuse Univ. Research Inst. Met497–582, pp. 281–338.

Maslen, Stephen H., and Moeckel, Wolfgang E.: Inviscid Hypersonic Flow Past Blunt Bodies. Jour. Aero. Sci., vol. 24, no. 9, Sept. 1957, pp. 683–693.

Meyer, Rudolph C.: On Reducing Aerodynamic Heat Transfer Rates by Magnetohydrodynamic Techniques. Preprint 816, Inst. Aero. Sci., 1958.

Mickelsen, William R.: An Analysis of Fuel-Oxidant Mixing in Screaming Combustors. Jet Propulsion, vol. 28, no. 3, Mar. 1958, pp. 172–177.

Mickelsen, William R., and Ernstein, Norman E.: Growth Rates of Turbulent Free Flames. Sixth Symposium (International) on Combustion (Yale Univ., New Haven, Conn., Aug. 19–24, 1956). Reinhold Pub. Corp., N.Y., 1957, pp. 325–333.

Morgan, Homer G., Runyan, Harry L., Huckel, Vera: Theoretical Considerations of Flutter at High Mach Numbers. Jour. Aero. Sci., vol. 25, no. 6, June 1958, pp. 371–381.

Morris, Garland J., and Lina, Lindsay John: Description and Preliminary Flight Investigation of an Instrument for Detecting Subnormal Acceleration During Take-Off (NACA TN–3252). Reports Presented at the Fifth Annual Air Safety Forum of the Air Line Pilots Association (Chicago, Ill., Mar. 5–7, 1957), Sec. 1, Sixth Paper, 19 pp.

Olson, Walter T.: Possibilities and Problems of Some High Energy Fuels for Aircraft. Preprint 41B, SAE, 1958.

Ostrach, Simon, and Thornton, Philip R.: On the Stagnation of Natural-Convection Flows in Closed-End Tubes. Trans. A.S.M.E., vol. 80, no. 2, Feb. 1958, pp. 363–366.

Pearson, Ernest O.: Introductory Remarks Concerning Some Aspects of Hypersonic Research and Research Facility Requirements. Presented at the 11th Meeting of the Wind Tunnel and Model Testing Panel (Scheveningen, Holland, July 8–12, 1957), Advisory Group for Aeronautical Research and Development Report 132.

Potter, Andrew E., Jr., and Berlad, Abraham L.: The Effect of Fuel Type and Pressure on Flame Quenching. Sixth Symposium (International) on Combustion (Yale Univ., New Haven, Conn., Aug. 19–24, 1956). Reinhold Pub. Corp., N.Y., 1957, pp. 27–36.

Press, Harry: Atmospheric Turbulence Environment With Special Reference to Continuous Turbulence. Presented at Fifth Meeting of Structures and Materials Panel (Copenhagen, Denmark, Apr. 29–May 3, 1957), Advisory Group for Aeronautical Research and Development Report 115.

Preston, George M., and Pesman, Gerard J.: Transport Airplane Crash Loads. Preprint 772, Inst. Aero. Sci., 1958.

Priem, Richard J.: Breakup of Water Drops and Sprays With a Shock Wave. Jet Propulsion, vol. 27, no. 10, Oct. 1957, pp. 1084–1087, 1093.

Purser, Paul E., and Bond, Aleck C.: NACA Hypersonic Rocket and High-Temperature Jet Facilities. Presented at the 11th Meeting of the Wind Tunnel and Model Testing Panel, Scheveningen, Holland, July 8–12, 1957), Advisory Group for Aeronautical Research and Development Report 140.

Reed, Wilmer, H., III: Effects of a Time-Varying Test Environment on the Evaluation of Dynamic Stability With Application to Flutter Testing. Preprint 822, Inst. Aero. Sci., 1958.

Reshotko, Eli: Heat Transfer to a General Three-Dimensional Stagnation Point. Jet Propulsion, vol. 28, no. 1, Jan. 1958, pp. 58–60.

Robbins, William H. and Plohr, Henry W.: Recent Advances in the Aerodynamic Design of Axial Turbomachinery. Can. Aero. Jour., vol. 4, no. 2, Feb. 1958, pp. 63–68.

Rossow, Vernon J.: On Magnete-Aerodynamic Boundary Layers. Festschrift Jakob Ackeret, Zeit. fur Angew. Math. Phys., vol. 9b, no. 5/6, Sonderband, Mar. 25, 1958, pp. 519–527.

Saari, Martin J.: More Accurate Measure of Jet Thrust Described. (Abridgment of "Thrust Measurement for Jet Transport Operation", Preprint, SAE 94, 1957), SAE Jour., Aug. 1957, pp. 109, 112.

Sanders, John C., Novik, David, and Hart, Clint E.: Effect of Dynamic Characteristics of Rocket Control (Revised and Condensed Version of IAS Preprint 710, 1957), Aero. Eng. Rev., vol. 16, no. 10, Oct. 1957, pp. 73–77.

Sanders, Newell D., and Laurence, James C.: Fundamental Investigation of Noise Generation by Turbulent Jets. Trans. SAE, vol. 65, 1957, pp. 244–249.

Sanders, Newell D.: Turbulence Noise Created by Jet Engines. Presented to General Electric Co. Industrial Acoustics Course V, Session 3 (General Electric Co., Schenectady, N.Y., July 1, 1957). Included in Appendix I "Aerodynamic Noise: Its Generation and Suppression", by Peter J. Westervelt, General Electric Co. Report R57GL222.

Schalla, Rose L., and Fletcher, Edward A.: The Behavior of the System Triethylamine-White Fuming Nitric Acid Under Conditions of Rapid Mixing. Sixth Symposium (International) on Combustion (Yale Univ., New Haven, Conn., Aug. 19–24, 1956). Reinhold Pub. Corp., N.Y., 1957, pp. 911–917.

Seiff, Alvin: The Use of Gun-Launched Models for Experimental Research at Hypersonic Speeds. Presented at the 11th Meeting of the Wind Tunnel and Model Testing Panel (Scheveningen, Holland, July 8–12, 1957), Advisory Group for Aeronautical Research and Development Report 138.

Sessler, John G., and Brown, William F., Jr.: Notch and Smooth Bar Stress-Rupture Characteristics of Several Heat-Resistant Alloys in the Temperature Range Between 600 and 1,000° F. Proc. A.S.T.M., vol. 56, 1956, pp. 738–752.

Sharp, Elmer M.: An Automatic Data Recording System for Aeronautical Research. Trans. Inst. Radio Eng., vol. I–6, no. 3, Sept. 1957, pp. 186–191.

Shinbrot, Marvin: A Generalization of a Method for the Solution of the Integral Equation Arising in Optimization of Time-Varying Linear Systems With Nonstationary Inputs. Trans. Inst. Radio Eng., vol. IT–3, no. 4, Dec. 1957, pp. 220–224.

Shinbrot, Marvin: On the Integral Equation Occurring in Optimization Theory With Nonstationary Inputs. Jour. Math. and Phys., vol. 36, no. 2, July 1957, pp. 121–129.

Shinbrot, Marvin: Optimization of Time-Varying Linear Systems with Nonstationary Inputs. Trans. A.S.M.E., vol. 80, no. 2, Feb. 1958, pp. 457–462.

Siegel, Robert, and Perlmutter, Morris: Heat Transfer in a Swirling Laminar Pipe Flow. Jour. Appl. Mech., vol. 25, no. 2, June 1958, pp. 295–297.

Siegel, Robert, Sparrow, Ephraim M., and Hallman, Theodore M.: Steady Laminar Heat Transfer in a Circular Tube With Prescribed Wall Heat Flux. Appl. Sci. Res., Sec. A, vol. 7, no. 5, 1958, pp. 386–392.

Siegel, Robert: Transient Free Convection From a Vertical Flat Plate. Trans. A.S.M.E., vol. 80, no. 2, Feb. 1958, pp. 347–359.

Sparrow, Ephraim, M.: Combined Effects of Unsteady Flight Velocity and Surface Temperature on Heat Transfer. Jet Propulsion, vol. 28, no. 6, June 1958, pp. 403–405.

Sparrow, Ephraim M., and Gregg, John L.: Similar Solutions for Free Convection From a Nonisothermal Vertical Plate. Trans. A.S.M.E., vol. 80, no. 2, Feb. 1958, pp. 379–386.

Sparrow, Ephraim M., Hallman, Theodore M., and Siegel, Robert: Turbulent Heat Transfer in the Thermal Entrance Region of a Pipe With Uniform Heat Flux. Appl. Sci. Res., Sec. A, vol. 7, no. 1, 1957, pp. 37–52.

Sparrow, Ephraim M., and Gregg, John L.: The Variable Fluid Property Problem in Free Convection. Trans. A.S.M.E., vol. 80, no. 4, May 1958, pp. 879–886.

Stalder, Jackson R.: A Survey of Heat Transfer Problems Encountered by Hypersonic Aircraft. Jet Propulsion, vol. 27, no. 11, Nov. 1957, pp. 1178–1184.

Stone, Ralph W., Jr., and Polhamus, Edward C.: Some Effects of Shed Vortices on the Flow Fields Around Stabilizing Tail Surfaces. Presented at the Fifth Meeting of the Structures and Materials Panel (Copenhagen, Denmark, Apr. 29–May 3, 1957), Advisory Group for Aeronautical Research and Development Report 108.

Swett, Clyde C., Jr.: Spark Ignition of Flowing Gases Using Long-Duration Discharges. Sixth Symposium (International) on Combustion (Yale Univ., New Haven, Conn., Aug. 19–24, 1956). Reinhold Pub. Corp., N.Y., 1957, pp. 523–531,

Swikert, Max A., and Johnson, Robert L.: Wear of Carbon-Type Seal Materials With Varied Graphite Content. Trans. Am. Soc. Lubrication Eng., vol. 1, no. 1, Apr. 1958, pp. 115–120.

Vaglio-Laurin, Roberto (Polytechnic Inst. Brooklyn), and Van Dyke, Milton D.: A Discussion of Higher-Order Approximations for the Flow Field About a Slender Elliptic Cone. Jour. Fluid Mech., vol. 3, no. 6, Mar. 1958, pp. 638–644.

Van Dyke, Milton D.: A Model of Supersonic Flow Past Blunt Axisymmetric Bodies, With Application to Chester's Solution. Jour. Fluid Mech., vol. 3, no. 5, Feb. 1958, pp. 515–522.

Van Dyke, Milton D.: The Paraboloid of Revolution in Subsonic Flow. Jour. Math. and Phys., vol. 37, Apr. 1958, pp. 38–51.

Van Dyke, Milton D.: The Supersonic Blunt-Body Problem—A Review and Extension. Preprint 801, Inst. Aero. Sci., 1958.

Warshawsky, Isidore: Pyrometry of High Velocity Gases. Sixth Symposium (International) on Combustion (Yale Univ., New Haven, Conn., Aug. 19–24, 1956). Reinhold Pub. Corp., N.Y., 1957.

Weeton, John W., Ault, G. Mervin, and Garrett, Floyd B.: Bucket Failure Mechanisms and Problems in Correlation of Laboratory Data with Gas-Turbine Bucket Performance. Proceedings of the Third Sagamore Ordnance Materials Research Conference, Materials Evaluation in Relation to Component Behavior (Duke Univ., Durham, N.C., Dec. 5–7, 1956), Syracuse Univ. Research Inst. Met365–574, pp. 235–263.

Welber, Benjamin, and Quimby, Shirley L. (Columbia Univ.): Adiabatic Young's Modulus and Internal Friction of Superconducting Lead and Tin. Acta Metallurgica, vol. 6, no. 5, 1958, pp. 351–359.

Welber, Benjamin, and Quimby, Shirley L.: Measurement of the Product of Viscosity and Density of Liquid Helium With a Torsional Crystal. Phys. Rev., vol 107, no. 3, Aug. 1, 1957, pp. 645–646.

White, James A.: Electronics in Aeronautical Research. Inst. Radio Eng., Wescon Convention, pt. 8, 1957, pp. 10–16.

Williams, Walter C., and Drake, Hubert M.: The Research Airplane—Past, Present, and Future. Aero. Eng. Rev., vol. 17, no. 1, Jan. 1958, pp. 36–41.

Zimmerman, Charles H.: NACA Research in the Field of VTOL and STOL Aircraft. Preprint 814, Inst. Aero. Sci., 1958.

Zimmerman, Charles H.: Some General Considerations Concerning VTOL Aircraft. Trans. SAE, vol. 65, 1957, pp. 159–171; Discussion, pp. 171–174.

Part II—COMMITTEE ORGANIZATION AND MEMBERSHIP

The National Advisory Committee for Aeronautics was established by act of Congress approved March 3, 1915 (U.S. Code, title 50, sec. 151). The organic act as amended provided that the Committee be composed of 17 members appointed by the President, including two representatives each of the Department of the Air Force, the Department of the Navy, and the Civil Aeronautics Authority; one representative each of the Smithsonian Institution, the U.S. Weather Bureau, and the National Bureau of Standards; and "one Department of Defense representative who is acquainted with the needs of aeronautical research and development." The law further provided that the membership include seven members appointed for five-year terms from persons "acquainted with the needs of aeronautical science, either civil or military, or skilled in aeronautical engineering or its allied sciences." The representatives of the Government organizations were appointed without definite terms, and all members served as such without compensation.

In accordance with the regulations of the Committee as approved by the President, the chairman and vice chairman and the chairman and vice chairman of the Executive Committee were elected annually. The officers now serving, reelected at the annual meeting of the Committee October 10, 1957, are: Dr. James H. Doolittle, Chairman of the NACA and Chairman of the Executive Committee; Dr. Leonard Carmichael, Vice Chairman of the NACA; and Dr. Detlev W. Bronk, Vice Chairman of the Executive Committee.

The following changes in membership have taken place during the past year:

On October 22, 1957, President Eisenhower appointed Hon. Paul D. Foote, Assistant Secretary of Defense (Research and Engineering), as the Department of Defense representative on the Committee authorized in the law. He succeeded Hon. Clifford C. Furnas, whose membership on NACA was terminated February 15, 1957, as a result of his resignation as Assistant Secretary of Defense (Research and Development).

The NACA membership of Lt. Gen. Donald L. Putt, who had been serving as Deputy Chief of Staff, Development, of the Air Force, was automatically terminated June 30, 1958, on his retirement from the Air Force. He had been a member of NACA more than nine years, having been appointed March 22, 1949. Because of the legislation then pending in the Congress which would result in the termination of the existence of the NACA, the President did not appoint a successor to General Putt on the Committee. In the interim, Lt. Gen. Roscoe C. Wilson, USAF, General Putt's successor as Deputy Chief of Staff, Development, served as acting member of NACA.

Because of his detachment as Deputy Chief of Naval Operations (Air) and transfer to duty with the Atlantic Fleet, the membership of Vice Adm. William V. Davis, USN, on the NACA was terminated May 22, 1958. As in the case of General Putt, the President did not appoint a successor on the Committee, and in the meantime Vice Adm. Robert B. Pirie, USN, Admiral Davis' successor in his Navy post, served as acting NACA member.

Reference was made in the opening statement of this report to the National Aeronautics and Space Act of 1958 (Public Law 85–568), approved July 29, 1958. In accordance with that act, and by proclamation of the Administrator of the National Aeronautics and Space Administration which he has indicated he will publish in the Federal Register of September 30, 1958, the National Advisory Committee for Aeronautics will cease to exist at the close of business September 30, 1958. At that time all its functions, powers, duties, and obligations, and all real and personal property, personnel (other than members of the Committee), funds, and records will be transferred to the National Aeronautics and Space Administration. All memberships on the NACA will then be terminated.

The members of the National Advisory Committee for Aeronautics at the end of its existence, September 30, 1958, are as follows:

James H. Doolittle, Sc. D., Vice President, Shell Oil Co., Chairman.

Leonard Carmichael, Ph. D., Secretary, Smithsonian Institution, Vice Chairman.

Allen V. Astin, Ph. D., Director, National Bureau of Standards.

Preston R. Bassett, D. Sc.

Detlev W. Bronk, Ph. D., President, Rockefeller Institute for Medical Research.

Frederick C. Crawford, Sc. D., Chairman of the Board, Thompson Products, Inc.

Paul D. Foote, Ph. D., Assistant Secretary of Defense (Research and Engineering).

Wellington T. Hines, Rear Admiral, U.S. Navy, Deputy and Assistant Chief of the Bureau of Aeronautics.

Jerome C. Hunsaker, Sc. D., Massachusetts Institute of Technology.

Charles J. McCarthy, S.B., Chairman of the Board, Chance Vought Aircraft, Inc.

James T. Pyle, A.B., Administrator of Civil Aeronautics.

Francis W. Reichelderfer, Sc. D., Chief, U.S. Weather Bureau.

Edward V. Rickenbacker, Sc. D., Chairman of the Board, Eastern Air Lines, Inc.

Preceding Page Blank

Louis S. Rothschild, Ph. B., Under Secretary of Commerce for Transportation.
Thomas D. White, General, U.S. Air Force, Chief of Staff.

In its coordination of aeronautical research and the formulation of its research programs, the NACA has been assisted for a number of years by four main technical committees. Under each of these committees, subcommittees have been organized varying in number from three to eight, the total number in 1958 being 23. On February 26, 1958, the names of the four main technical committees, as well as those of certain subcommittees, were changed to indicate more definitely their cognizance of problems applicable to missiles and spacecraft as well as aircraft. The four main technical committees now are: Committee on Aircraft, Missile, and Spacecraft Aerodynamics (formerly Committee on Aerodynamics); Committee on Aircraft, Missile, and Spacecraft Propulsion (formerly Committee on Power Plants for Aircraft); Committee on Aircraft, Missile, and Spacecraft Construction (formerly Committee on Aircraft Construction); and Committee on Aircraft Operating Problems (formerly Committee on Operating Problems). Effective January 1, 1958, the Subcommittee on Icing Problems, formerly organized under the Committee on Operating Problems, was discontinued, since it was the opinion of the NACA that the demands for research in this field had decreased to such an extent that the maintenance of a separate subcommittee was not justified, and such research as was needed in this field could be conducted under the cognizance of the Subcommittee on Flight Safety and the Subcommittee on Meteorological Problems.

The NACA at its meeting on November 21, 1957, authorized the establishment of a Special Committee on Space Technology, to be composed of experts especially qualified in the field, to survey the whole problem of space technology from the point of view of needed research and development, and to make recommendations to the NACA. It was pointed out that, while the NACA already had a substantial effort on problems of flight beyond the earth's atmosphere, as exemplified by the X–15 research airplane being constructed by North American Aviation, Inc., as a joint Air Force-Navy-NACA project, and by its research program on ballistic missile problems, there was need for a review of the whole problem of space technology. The Special Committee on Space Technology was organized in January 1958 under the chairmanship of Dr. H. Guyford Stever, Associate Dean of Engineering of the Massachusetts Institute of Technology, and has been engaged in a survey of the entire field, with the aid of seven working groups established for study of the following areas: Space Research Objectives; Vehicular Program; Reentry; Range, Launch, and Tracking Facilities; Instrumentation; Space Surveillance; and Human Factors and Training. The report of the Special Committee on Space Technology will be completed in the near future.

The NACA has also been assisted since 1945 by an Industry Consulting Committee, whose function has been to advise the NACA as to general research policy and programs, especially with regard to the needs of industry.

At the final meeting of the National Advisory Committee for Aeronautics on August 21, 1958, the members of the Committee expressed the firm opinion that the advice and cooperation of NACA committees and subcommittees have been a highly significant factor in the effective discharge of the duties of NACA.

The Administrator of the National Aeronautics and Space Administration, Hon. T. Keith Glennan, has indicated that the proclamation which he will issue for publication in the Federal Register of September 30 will include a provision that the committees and subcommittees of the NACA are being reconstituted advisory committees to the NASA for the purpose of bringing their current work to orderly completion.

The membership of the committees and their subcommittees and working groups is as follows:

COMMITTEE ON AIRCRAFT, MISSILE, AND SPACECRAFT AERODYNAMICS

Mr. Preston R. Bassett, Chairman.
Dr. Theodore P. Wright, Vice President for Research, Cornell University, Vice Chairman.
Maj. Gen. Ralph P. Swofford, Jr., USAF, Assistant Deputy Chief of Staff, Development, U.S. Air Force.
Col. Randall D. Keator, USAF, Chief, Aircraft Laboratory, Wright Air Development Center.
Rear Adm. L. D. Coates, USN, Assistant Chief of the Bureau of Aeronautics for Research and Development, Department of the Navy.
Mr. Abraham Hyatt, Bureau of Aeronautics, Department of the Navy.
Capt. Robert L. Townsend, USN, Assistant Director, Research and Development Division, Bureau of Ordnance, Department of the Navy.
Maj. Gen. H. N. Toftoy, USA, Commanding General, Aberdeen Proving Ground.
Col. George P. Seneff, Jr., USA, Office of the Chief of Research and Development, Department of the Army.
Mr. Harold D. Hoekstra, Civil Aeronautics Administration.
Dr. Hugh L. Dryden (ex officio).
Mr. Floyd L. Thompson, NACA Langley Aeronautical Laboratory.
Mr. Russell G. Robinson, NACA Ames Aeronautical Laboratory.
Dr. Milton U. Clauser, Director, Aeronautical Research Laboratory, The Ramo-Wooldridge Corp.
Capt. W. S. Diehl, USN (Ret.).
Mr. Clarence L. Johnson, Vice President, Research and Development, Lockheed Aircraft Corp.
Dr. A. Kartveli, Vice President, Research and Development, Republic Aviation Corp.
Mr. Schuyler Kleinhans, Assistant Chief Engineer, Santa Monica Division, Douglas Aircraft Co., Inc.
Dr. Clark B. Millikan, Director, Daniel Guggenheim Aeronautical Laboratory, California Institute of Technology.

Mr. Kendall Perkins, Vice President, Engineering, McDonnell Aircraft Corp.
Mr. George S. Schairer, Director of Research, Seattle Division, Boeing Airplane Co.
Prof. William R. Sears, Cornell University.
Mr. R. C. Sebold, Vice President, Engineering, Convair, Division of General Dynamics Corp.
Mr. H. A. Storms, Jr., Chief Engineer, Los Angeles Division, North American Aviation, Inc.
Mr. George S. Trimble Jr., Vice President-Chief Engineer, The Martin Co.

Mr. Milton B. Ames, Jr., Secretary

Subcommittee on Fluid Mechanics

Prof. William R. Sears, Cornell University, Chairman.
Lt. Col. B. W. Marschner, USAF, Air Force Missile Development Center.
Mr. E. Haynes, Air Force Office of Scientific Research.
Dr. Frederick S. Sherman, Office of Naval Research, Department of the Navy.
Mr. John D. Nicolaides, Bureau of Ordnance, Department of the Navy.
Dr. Joseph Sternberg, Ballistic Research Laboratories, Aberdeen Proving Ground.
Dr. G. B. Schubauer, Chief, Fluid Mechanics Section, National Bureau of Standards.
Dr. Adolf Busemann, NACA Langley Aeronautical Laboratory.
Mr. Clinton E. Brown, NACA Langley Aeronautical Laboratory.
Dr. D. R. Chapman, NACA Ames Aeronautical Laboratory.
Mr. Robert T. Jones, NACA Ames Aeronautical Laboratory.
Dr. John C. Evvard, NACA Lewis Flight Propulsion Laboratory.
Dr. J. V. Charyk, Aeronutronic Systems, Inc.
Prof. Wallace D. Hayes, Princeton University.
Prof. Otto Laporte, University of Michigan.
Prof. Lester Lees, California Institute of Technology.
Prof. Hans W. Liepmann, California Institute of Technology.
Prof. C. C. Lin, Massachusetts Institute of Technology.
Prof. E. L. Resler, Jr., Cornell University.

Mr. Ernest O. Pearson, Jr., Secretary

Subcommittee on High-Speed Aerodynamics

Dr. Clark B. Millikan, Director, Daniel Guggenheim Aeronautical Laboratory, California Institute of Technology, Chairman.
Mr. Robert F. Robinson, Air Research and Development Command.
Mr. Oscar Seidman, Bureau of Aeronautics, Department of the Navy.
Dr. H. H. Kurzweg, Associate Technical Director for Aeroballistic Research, Naval Ordnance Laboratory.
Mr. C. L. Poor, Chief, Exterior Ballistics Laboratory, Ballistic Research Laboratories, Aberdeen Proving Ground.
Mr. John Stack, NACA Langley Aeronautical Laboratory.
Mr. H. Julian Allen, NACA Ames Aeronautical Laboratory.
Dr. Abe Silverstein, NACA Lewis Flight Propulsion Laboratory.
Mr. Walter C. Williams, NACA High-Speed Flight Station.
Mr. John R. Clark, Assistant Chief Engineer, Chance Vought Aircraft, Inc.
Mr. Alexander H. Flax, Vice President and Assistant Director, Technical, Cornell Aeronautical Laboratory, Inc.
Mr. L. P. Greene, Chief Aerodynamicist, North American Aviation, Inc.
Mr. R. P. Jackson, General Manager, Tactical Weapon Systems Division, Aeronutronic Systems, Inc.
Mr. C. J. Koch, Chief of Staff, Advanced Design, The Martin Co.
Mr. John G. Lee, Director of Research, United Aircraft Corp.
Dr. Albert E. Lombard, Jr., Director of Research, McDonnell Aircraft Corp.
Mr. Harlowe J. Longfelder, Systems Engineering Director, Boeing Airplane Co.
Prof. John R. Markham, Professor of Aeronautical Engineering, Massachusetts Institute of Technology.
Mr. W. F. Radcliffe, Chief of Aerophysics, Convair, Division of General Dynamics Corp.
Mr. Ronald Smelt, Director, New Design Office, Missile Systems Division, Lockheed Aircraft Corp.

Mr. Albert J. Evans, Secretary

Subcommittee on Aerodynamic Stability and Control

Capt. W. S. Diehl, USN (Ret.), Chairman.
Mr. Melvin Shorr, Wright Air Development Center.
Mr. Jerome Teplitz, Bureau of Aeronautics, Department of the Navy.
Mr. Joseph E. Long, Bureau of Ordnance, Department of the Navy.
Mr. J. G. McHugh, Transportation Research and Engineering Command.
Mr. D. L. Baker, Civil Aeronautics Administration.
Mr. Charles J. Donlan, NACA Langley Aeronautical Laboratory.
Mr. Charles F. Hall, NACA Ames Aeronautical Laboratory.
Mr. Hubert M. Drake, NACA High-Speed Flight Station.
Mr. E. A. Bonney, Applied Physics Laboratory, The Johns Hopkins University.
Mr. W. O. Breuhaus, Cornell Aeronautical Laboratory, Inc.
Mr. Paul C. Emmons, Manager, Development Analysis, Bell Aircraft Corp.
Mr. J. E. Goode, Jr., Convair, Division of General Dynamics Corp., Fort Worth.
Mr. William T. Hamilton, Chief Aerodynamics Engineer, Boeing Airplane Co.
Mr. Maxwell W. Hunter, Chief Missiles Design Engineer, Douglas Aircraft Co., Inc.
Mr. R. B. Katkov, Northrop Aircraft, Inc.
Prof. E. E. Larrabee, Massachusetts Institute of Technology.
Mr. Conrad A. Lau, Chance Vought Aircraft, Inc.

Mr. Jack D. Brewer, Secretary

Subcommittee on Automatic Stabilization and Control

Mr. Warren E. Swanson, North American Aviation, Inc., Chairman.
Mr. George L. Yingling, Wright Air Development Center.
Dr. Gerhard W. Braun, Air Force Missile Development Center.
Mr. William Koven, Bureau of Aeronautics, Department of the Navy.
Mr. J. M. Lee, Bureau of Ordnance, Department of the Navy.
Mr. Karl L. Kocmanek, Signal Corps Engineering Laboratories.
Mr. Charles W. Mathews, NACA Langley Aeronautical Laboratory.
Mr. Harry J. Goett, NACA Ames Aeronautical Laboratory.
Mr. A. S. Boksenbom, NACA Lewis Flight Propulsion Laboratory.
Mr. Joseph Weil, NACA High-Speed Flight Station.
Mr. Frank Andrix, Director of Engineering, Avionics Division, Bell Aircraft Corp.
Mr. Frank A. Gaynor, Aeronautical and Ordnance Systems Division, General Electric Co.
Dr. William J. Jacobi, The Ramo-Wooldridge Corp.

Mr. Floyd E. Nixon, Manager, Systems Analysis Department, The Martin Co.
Mr. Louis A. Payne, Convair, Division of General Dynamics Corp.
Mr. Duncan Pitman, Missiles Division, Douglas Aircraft Co., Inc.
Dr. Allen E. Puckett, Associate Director, Systems Development Laboratories, Hughes Aircraft Co.
Mr. O. H. Schuck, Minneapolis-Honeywell Regulator Co.
Dr. Robert C. Seamans, Jr., RCA Airborne Systems Laboratory.
Mr. Bernard Maggin, Secretary

Subcommittee on Internal Flow

Dr. William J. O'Donnell, Chief, Engineering and Aircraft Missiles Division, Republic Aviation Corp., Chairman.
Mr. Frederick T. Rall, Jr., Wright Air Development Center.
Mr. Robert E. Roy, Wright Air Development Center.
Mr. R. T. Miller, Bureau of Aeronautics, Department of the Navy.
Dr. Thomas W. Williams, Office of Naval Research, Department of the Navy.
Mr. V. S. Kupelian, U.S. Naval Ordnance Experimental Unit.
Mr. John V. Becker, NACA Langley Aeronautical Laboratory.
Mr. Richard Scherrer, NACA Ames Aeronautical Laboratory.
Mr. DeMarquis D. Wyatt, NACA Lewis Flight Propulsion Laboratory.
Mr. Donald R. Bellman, NACA High-Speed Flight Station.
Mr. J. S. Alford, Aircraft Gas Turbine Division, General Electric Co.
Mr. Bernard F. Beckelman, Boeing Airplane Co.
Mr. John A. Drake, Director of Long-Range Planning and Research Programs, Marquardt Aircraft Co.
Mr. Harry Drell, Propulsion Department Manager, Lockheed Aircraft Corp.
Dr. Antonio Ferri, Head, Department of Aeronautical Engineering, Polytechnic Institute of Brooklyn.
Mr. Donald J. Jordan, Pratt & Whitney Aircraft, United Aircraft Corp.
Mr. Darrel B. Parke, McDonnell Aircraft Corp.
Mr. M. A. Sulkin, Chief Thermodynamicist, North American Aviation, Inc.
Mr. Stafford W. Wilbur, Secretary

Subcommittee on Low-Speed Aerodynamics

Mr. R. Richard Heppe, Manager, Advanced Aerodynamics Research, Lockheed Aircraft Corp., Chairman.
Maj. E. B. Owens, USAF, Air Research and Development Command.
Mr. Harvey L. Anderson, Wright Air Development Center.
Mr. Gerald L. Desmond, Bureau of Aeronautics, Department of the Navy.
Maj. Darrell L. Ritter, USMC, Office of Naval Research, Department of the Navy.
Lt. Col. T. E. Haynes, USA, Office of the Chief of Research and Development, Department of the Army.
Mr. John Beebe, Office of the Chief of Transportation, Department of the Army.
Mr. C. W. Von Rosenberg, Chief, Flight Test Branch, Civil Aeronautics Administration.
Mr. Charles H. Zimmerman, NACA Langley Aeronautical Laboratory.
Mr. Charles W. Harper, NACA Ames Aeronautical Laboratory.
Mr. Jack Fischel, NACA High-Speed Flight Station.
Mr. M. M. Blair, North American Aviation, Inc., Columbus, Ohio.
Mr. James B. Edwards, Douglas Aircraft Co., Inc.
Mr. Robert A. Fuhrman, Missile Systems Division, Lockheed Aircraft Corp.
Mr. Robert L. Gustafson, Chief of Aerodynamics, Grumman Aircraft Engineering Corp.
Mr. D. H. Jacobson, Aeroproducts Operations, Allison Division, General Motors Corp.
Mr. Frank W. Kolk, American Airlines, Inc.
Mr. J. M. Mergen, Director of Engineering, Propeller Division, Curtiss-Wright Corp.
Mr. James A. O'Malley, Jr., Chief, Aerodynamic and Propulsion Design Department, Bell Aircraft Corp.
Dean Kenneth Razak, Dean, School of Engineering, University of Wichita.
Mr. W. Z. Stepniewski, Chief, Research and Development, Vertol Aircraft Corp.
Mr. Ralph W. May, Secretary

Subcommittee on Seaplanes

Rear Adm. R. S. Hatcher, USN (Ret.), Aerojet-General Corp., Chairman.
Capt. J. G. Ironmonger, USAF, Air Research and Development Command.
Mr. Eugene H. Handler, Bureau of Aeronautics, Department of the Navy.
Mr. F. W. S. Locke, Jr., Bureau of Aeronautics, Department of the Navy.
Mr. Phillip Eisenberg, Office of Naval Research, Department of the Navy.
Mr. M. St. Denis, David W. Taylor Model Basin.
Comdr. T. E. Maurer, USN, Naval Air Test Center, Patuxent.
Capt. R. R. Johnson, USCG, Western Area, U.S. Coast Guard.
Mr. William J. Husic, Civil Aeronautics Administration.
Mr. John B. Parkinson, NACA Langley Aeronautical Laboratory.
Mr. H. E. Brooke, Chief of Hydrodynamics, Convair, Division of General Dynamics Corp.
Mr. C. L. Fenn, Chief Engineer, Edo Corp.
Mr. Grover Loening.
Mr. J. D. Pierson, The Martin Co.
Mr. Daniel Savitsky, Stevens Institute of Technology.
Mr. Henry B. Suydam, Grumman Aircraft Engineering Corp.
Mr. Ralph W. May, Secretary

Subcommittee on Helicopters

Mr. L. L. Douglas, Vice President, Engineering, Vertol Aircraft Corp., Chairman.
Mr. Bernard Lindenbaum, Wright Air Development Center.
Mr. Paul A. Simmons, Jr., Wright Air Development Center.
Comdr. J. D. Kuser, USN, Bureau of Aeronautics, Department of the Navy.
Mr. T. L. Wilson, Office of Naval Research, Department of the Navy.
Lt. Col. Harry L. Bush, USA, Office of the Chief of Research and Development, Department of the Army.
Mr. L. J. Borges, Office of the Chief of Transportation, Department of the Army.
Capt. W. W. Vennel, USCG, Headquarters, U.S. Coast Guard.
Mr. Herbert M. Toomey, Civil Aeronautics Administration.
Mr. Richard C. Dingeldein, NACA Langley Aeronautical Labortary.
Mr. F. B. Gustafson, NACA Langley Aeronautical Laboratory.
Mr. Donald H. Wood, NACA Ames Aeronautical Laboratory.
Mr. Friedrich L. V. Doblhoff, Chief Engineer, Helicopter Engineering Division, McDonnell Aircraft Corp.

Mr. J. O. Emmerson, Vice President and Chief Engineer, The Kaman Aircraft Corp.
Mr. Jack E. Gallagher, Vice President, Operations, New York Airways, Inc.
Mr. Bartram Kelley, Vice President, Engineering, Bell Helicopter Corp.
Mr. Ralph B. Lightfoot, Chief Engineer, Sikorsky Aircraft, United Aircraft Corp.
Prof. R. H. Miller, Massachusetts Institute of Technology.
Mr. Charles M. Seibel, Chief Engineer, Helicopter Division, Cessna Aircraft Co.
Mr. Robert Wagner, Chief Engineer, Hiller Helicopters.
Mr. P. M. Lovell, Jr., Secretary

COMMITTEE ON AIRCRAFT, MISSILE, AND SPACECRAFT PROPULSION

Dr. Frederick C. Crawford, Chairman of the Board, Thompson Products, Inc., Chairman.
Dean C. R. Soderberg, Dean of Engineering, Massachusetts Institute of Technology, Vice Chairman.
Col. Donald H. Heaton, USAF, Directorate of Research and Development.
Col. John J. B. Calderbank, USAF, Wright Air Development Center.
Capt. Willoughby Mercer, USN, Bureau of Aeronautics, Department of the Navy.
Mr. W. R. Slivka, Aeronautical Turbine Laboratory, Naval Air Turbine Test Station.
Col. Chester W. Clark, USA, Office of the Chief of Ordnance, Department of the Army.
Mr. Donald D. Weidhuner, Office of the Chief of Transportation, Department of the Army.
Mr. Stephen H. Rolle, Chief, Power Plant Branch, Aircraft Engineering Division, Civil Aeronautics Administration.
Dr. Hugh L. Dryden (ex officio).
Dr. Abe Silverstein, NACA Lewis Flight Propulsion Laboratory.
Mr. J. P. Butterfield, Chief Engineer, Missile Operations Division, Chrysler Corp.
Dr. Alfred G. Cattaneo, Shell Development Co.
Mr. Allan Chilton, Director, Weapon Systems Planning Group, Westinghouse Electric Corp.
Mr. D. Cochran, General Manager, Flight Propulsion Laboratory Department, General Electric Co.
Dr. C. Stark Draper, Head, Department of Aeronautical Engineering, Massachusetts Institute of Technology.
Mr. Dimitrius Gerdan, Director of Engineering, Allison Division, General Motors Corp.
Mr. S. K. Hoffman, General Manager, Rocketdyne Division, North American Aviation, Inc.
Mr. Wright A. Parkins, Vice President, Engineering, United Aircraft Corp.
Mr. James A. Reid, Executive Vice President and General Manager, Astrodyne, Inc.
Mr. C. C. Ross, Vice President, Engineering, Aerojet-General Corp.
Mr. Rudolf H. Thielemann, Senior Metallurgist, Stanford Research Institute.
Mr. Don L. Walter, Vice President, Engineering, Marquardt Aircraft Co.
Mr. William H. Woodward, Secretary

Subcommittee on Fuels

Mr. James A. Reid, Executive Vice President and General Manager, Rocketdyne, Inc., Chairman.
Mr. Ben F. Wilkes, Directorate of Research and Development, U.S. Air Force,
Mr. Marc P. Dunnam, Wright Air Development Center.
Comdr. John C. Bangert, USN, Bureau of Aeronautics, Department of the Navy.
Mr. N. L. Klein, Office of the Chief of Ordnance, Department of the Army.
Mr. Ralph S. White, Civil Aeronautics Administration.
Mr. Henry C. Barnett, NACA Lewis Flight Propulsion Laboratory.
Mr. A. J. Blackwood, Esso Research & Engineering Co.
Mr. C. S. Brandt, Convair, Division of General Dynamics Corp.
Mr. J. L. Cooley, Vice President, California Research Corp.
Dr. Allen R. Deschere, Rohm & Haas Co.
Mr. F. G. Dougherty, Allison Division, General Motors Corp.
Mr. E. A. Droegemueller, Pratt & Whitney Aircraft, United Aircraft Corp.
Mr. John B. Duckworth, Research Coordinator, Standard Oil Co. (Indiana).
Mr. D. N. Harris, Shell Oil Co.
Mr. W. M. Holaday, Director of Guided Missiles, Department of Defense.
Dr. Bernard M. Sturgis, Director, Petroleum Laboratory, E. I. du Pont de Nemours & Co.
Dr. R. J. Thompson, Rocketdyne Division, North American Aviation, Inc.
Mr. Harold F. Hipsher, Secretary

Subcommittee on Combustion

Dr. Alfred G. Cattaneo, Shell Development Co., Chairman.
Mr. Howard P. Barfield, Wright Air Development Center.
Mr. Karl Scheller, Wright Air Development Center.
Mr. Nelson F. Rekos, Bureau of Aeronautics, Department of the Navy.
Mr. Alfred G. Lundquist, Office of Naval Research, Department of the Navy.
Dr. Martin Schilling, Redstone Arsenal.
Mr. F. R. Caldwell, National Bureau of Standards.
Dr. Walter T. Olson, NACA Lewis Flight Propulsion Laboratory.
Dr. W. H. Avery, Applied Physics Laboratory, The Johns Hopkins University.
Mr. William J. Bennet, Marquardt Aircraft Co.
Mr. Charles H. King, Jr., United Aircraft Corp.
Mr. Yuan C. Lee, Director of Research, Aerojet-General Corp.
Dr. Robert S. Levine, Rocketdyne Division, North American Aviation, Inc.
Dr. Bernard Lewis, Combustion & Explosives Research, Inc.
Dr. John P. Longwell, Esso Research & Engineering Co.
Dr. S. S. Penner, California Institute of Technology.
Prof. Glenn C. Williams, Massachusetts Institute of Technology.
Mr. L. M. Zubko, General Electric Co.
Mr. Harold F. Hipsher, Secretary

Subcommittee on Lubrication and Wear

Mr. Frank W. Wellons, Assistant Chief Engineer, SKF Industries, Inc., Chairman.
Mr. Bernard Rubin, Wright Air Development Center.
Mr. R. C. Sheard, Wright Air Development Center.
Mr. Sidney M. Collegeman, Bureau of Aeronautics, Department of the Navy.
Mr. R. E. Streets, Office of the Chief of Ordnance, Department of the Army.
Mr. Edmond E. Bisson, NACA Lewis Flight Propulsion Laboratory.

526597—60——7

Mr. G. J. Andreini, Pratt & Whitney Aircraft, United Aircraft Corp.
Dr. Merrell R. Fenske, Director, Petroleum Refining Laboratory, School of Chemistry and Physics, The Pennsylvania State University.
Mr. A. S. Irwin, Director of Research, Marlin-Rockwell Corp.
Dr. E. G. Jackson, Small Aircraft Engine Department, General Electric Co.
Dr. Robert G. Larsen, Research Director, Martinez Refinery, Shell Oil Co.
Dr. M. Eugene Merchant, Cincinnati Milling Machine Co.
Dr. W. H. Millett, Carbide & Carbon Chemicals Co.
Mr. D. H. Moreton, Douglas Aircraft Co.
Mr. Earle A. Ryder.
Mr. J. M. Stokely, California Research Corp.
Mr. George P. Townsend, Jr., Manager of Engineering, Sundstrand Turbo.
Mr. E. J. Zeilberger, Rocketdyne Division, North American Aviation, Inc.
Mr. Harold Hessing, Secretary

Subcommittee on Compressors and Turbines

Dr. George F. Wislicenus, Ordnance Research Laboratory, The Pennsylvania State University, Chairman.
Mr. Ernest C. Simpson, Wright Air Development Center.
Mr. H. D. Rochen, Bureau of Aeronautics, Department of the Navy.
Lt. Comdr. Frank T. Hemler, USN, Office of Naval Research, Department of the Navy.
Mr. Ambrose Ginsburg, NACA Lewis Flight Propulsion Laboratory.
Mr. Gordon Banerian, Manager, Turbo-Machinery Division, Aerojet-General Corp.
Mr. William G. Cornell, General Electric Co.
Prof. Howard W. Emmons, Harvard University.
Mr. John R. Foley, Pratt & Whitney Aircraft, United Aircraft Corp.
Mr. John E. Sanders, Curtiss-Wright Corp.
Dr. Alan H. Stenning, Assistant Professor of Mechanical Engineering, Massachusetts Institute of Technology.
Mr. M. A. Sulkin, Chief Thermodynamicist, North American Aviation, Inc.
Mr. Paul R. Vogt, Assistant Director of Engineering, Rocketdyne Division, North American Aviation, Inc.
Mr. David Novik, Secretary

Subcommittee on Engine Performance and Operation

Mr. Don L. Walter, Vice President, Engineering, Marquardt Aircraft Co., Chairman.
Lt. Col. H. W. Robbins, USAF, Air Research and Development Command.
Mr. Ewell C. Phillips, Wright Air Development Center.
Mr. A. S. Atkinson, Bureau of Aeronautics, Department of the Navy.
Col. William A. Tesch, Division of Reactor Development, Atomic Energy Commission.
Mr. E. J. Briggs, Civil Aeronautics Administration.
Mr. Bruce T. Lundin, NACA Lewis Flight Propulsion Laboratory.
Mr. Rudolph Bodemuller, Bendix Products Division, Bendix Aviation Corp.
Mr. Russell S. Hall, Allison Division, General Motors Corp.
Dr. Krafft A. Ehricke, Convair, Astronautics, Division of General Dynamics Corp.
Mr. R. D. Geckler, Vice President, Solid Rocket Plant, Aerojet-General Corp.
Mr. Elliott V. Mock, Boeing Airplane Co.
Mr. Perry W. Pratt, Vice President and Chief Scientist, United Aircraft Corp.
Mr. John F. Tormey, Director of Development, Astrodyne, Inc.
Mr. George S. Trimble, Jr., Vice President, Engineering, The Martin Co.
Mr. R. H. Widmer, Assistant Chief Engineer, Convair, Division of General Dynamics Corp., Fort Worth.
Mr. E. Woll, Manager, Engineering, Small Aircraft Engine Department, General Electric Co.
Mr. Lee R. Woodworth, Propulsion Research Corp.
Mr. James Lazar, Secretary

Subcommittee on Power Plant Controls

Dr. C. Stark Draper, Head, Department of Aeronautical Engineering, Massachusetts Institute of Technology, Chairman.
Mr. J. G. Barrett, Wright Air Development Center.
Mr. Robert R. Brown, Bureau of Aeronautics, Department of the Navy.
Dr. C. F. Bjork, Redstone Arsenal.
Mr. John C. Sanders, NACA Lewis Flight Propulsion Laboratory.
Dr. John L. Barnes, President, Systems Corp. of America.
Mr. Rudolph Bodemuller, Bendix Products Division, Bendix Aviation Corp.
Mr. R. T. Dungan, Marquardt Aircraft Co.
Mr. Harold E. Francis, Chief Project Engineer, Chandler-Evans Division, Pratt & Whitney Co., Inc.
Dr. Hans R. Friedrich, Convair, Astronautics, Division of General Dynamics Corp.
Dr. E. H. Gamble, General Electric Co.
Mr. William H. Hand, North American Aviation, Inc.
Mr. George F. Kinghorn, Missile Systems Division, Lockheed Aircraft Corp.
Mr. Bruce N. Torell, Pratt & Whitney Aircraft, United Aircraft Corp.
Dr. James W. Wheeler, Director, Instrument Engineering, Sperry Gyroscope Co., Division of Sperry Rand Corp.
Mr. David Novik, Secretary

Subcommittee on Power Plant Materials

Mr. Rudolf H. Thielemann, Senior Metallurgist, Stanford Research Institute, Chairman.
Lt. Col. R. W. Conners, USAF, Air Research and Development Command.
Mr. J. B. Johnson, Wright Air Development Center.
Mr. Nathan E. Promisel, Bureau of Aeronautics, Department of the Navy.
Mr. J. J. Harwood, Office of Naval Research, Department of the Navy.
Mr. Norman L. Reed, Watertown Arsenal.
Mr. S. S. Manson, NACA Lewis Flight Propulsion Laboratory.
Mr. W. L. Badger, Manager, Thomson Laboratory, Small Aircraft Engine Department, General Electric Co.
Mr. Lee S. Busch, Mallory-Sharon Titanium Corp.
Dr. F. N. Darmara, Utica Metals Division, Kelsey-Hayes Co.
Mr. Glenn A. Fritzlen, Technical Director, Development and Technical Services, Haynes Stellite Co.
Mr. L. L. Gilbert, Head, Materials Department, Azusa Operations, Aerojet-General Corp.
Prof. Nicholas J. Grant, Massachusetts Institute of Technology.

Mr. William D. Manly, Associate Director, Metallurgy Division, Oak Ridge National Laboratory, Union Carbide Corp.
Dr. Edward E. Reynolds, Assistant Director of Research, Allegheny Ludlum Steel Corp.
Mr. Francis M. Richmond, Manager of Materials Research, Universal Cyclops Steel Corp.
Mr. W. H. Sharp, Pratt & Whitney Aircraft, United Aircraft Corp.
Dr. E. N. Skinner, International Nickel Co.
Mr. Andrew G. Slachta, Wright Aeronautical Division, Curtiss-Wright Corp.

Mr. Harold Hessing, Secretary

Subcommittee on Rocket Engines

Mr. C. C. Ross, Vice President, Engineering, Aerojet-General Corp., Chairman.
Maj. William J. Henderson, USAF, Air Research and Development Command.
Lt. Col. L. F. Ayres, USAF, Ballistic Missile Division, Air Research and Development Command.
Mr. Oscar Bessio, Bureau of Aeronautics, Department of the Navy.
Mr. Frank I. Tanczos, Bureau of Ordnance, Department of the Navy.
Mr. James R. Patton, Office of Naval Research, Department of the Navy.
Mr. James E. Norman, Redstone Arsenal.
Col. J. L. Armstrong, Division of Reactor Development, Atomic Energy Commission.
Mr. John L. Sloop, NACA Lewis Flight Propulsion Laboratory.
Mr. John D. Alexander, Advanced Projects Engineer Manager, Pilotless Aircraft Division, Boeing Airplane Co.
Mr. Richard B. Canright, Advanced Research Projects Agency, Department of Defense.
Mr. Allen F. Donovan, The Ramo-Wooldridge Corp.
Dr. H. F. Dunholter, Chief Development Engineer, Convair, Astronautics, Division of General Dynamics Corp.
Mr. W. M. Hawkins, Missile Systems Division, Lockheed Aircraft Corp.
Dr. P. L. Nichols, Jr., Jet Propulsion Laboratory, California Institute of Technology.
Dr. H. W. Ritchey, Technical Director, Rocket Divisions, Thiokol Chemical Corp.
Mr. H. L. Thackwell, Jr., Vice President, Grand Central Rocket Co., Inc.
Mr. John F. Tormey, Director of Development, Astrodyne, Inc.
Mr. John R. Youngquist, Denver Division, The Martin Co.
Dr. Maurice J. Zucrow, Professor of Jet Propulsion, School of Mechanical Engineering, Purdue University.

Mr. Benson E. Gammon, Secretary

COMMITTEE ON AIRCRAFT, MISSILE, AND SPACECRAFT CONSTRUCTION

Mr. Charles J. McCarthy, Chairman of the Board, Chance Vought Aircraft, Inc., Chairman.
Mr. George Snyder, Engineering Manager, Pilotless Aircraft Division, Boeing Airplane Co., Vice Chairman.
Mr. Carl E. Reichert, Wright Air Development Center.
Comdr. G. S. Parrett, USN, Bureau of Aeronautics, Department of the Navy.
Mr. D. M. Thompson, Office of the Chief of Transportation, Department of the Army.
Mr. Albert A. Vollmecke, Civil Aeronautics Administration.
Dr. Hugh L. Dryden (ex officio).
Mr. Robert R. Gilruth, NACA Langley Aeronautical Laboratory.
Mr. John F. Parsons, NACA Ames Aeronautical Laboratory.
Prof. Raymond L. Bisplinghoff, Professor of Aeronautical Engineering, Massachusetts Institute of Technology.
Mr. Ralph B. Davidson, Director, Technical Support Division, Radioplane, Division of Northrop Aircraft, Inc.
Mr. Martin Goland, Director, Southwest Research Institute.
Dr. Nicholas J. Hoff, Head, Division of Aeronautical Engineering, Stanford University.
Mr. D. R. Kirk, Convair, Division of General Dynamics Corp., Fort Worth.
Mr. Jerome F. McBrearty, Assistant General Manager, California Division, Lockheed Aircraft Corp.
Dr. J. C. McDonald, Missile Systems Division, Lockheed Aircraft Corp.
Mr. Herman Pusin, Director of Engineering, Engineering Division, The Martin Co.
Mr. George D. Ray, Chief Engineer, Aircraft Division, Bell Aircraft Corp.
Mr. Richard L. Schleicher, Chief Structures Engineer, North American Aviation, Inc.
Mr. C. H. Stevenson, Douglas Aircraft Co., Inc.

Mr. Franklyn W. Phillips, Secretary

Subcommittee on Structures

Mr. C. H. Stevenson, Douglas Aircraft Co., Inc., Chairman.
Capt. W. T. McGinness, USAF, Air Research and Development Command.
Mr. William B. Miller, Wright Air Development Center.
Mr. Ralph L. Creel, Bureau of Aeronautics, Department of the Navy.
Mr. Emil A. H. Hellebrand, Army Ballistic Missile Agency.
Lt. Col. Richard L. Long, USA, Transportation Supply and Maintenance Command.
Mr. James E. Dougherty, Jr., Civil Aeronautics Administration.
Mr. Richard R. Heldenfels, NACA Langley Aeronautical Laboratory.
Mr. Glen Goodwin, NACA Ames Aeronautical Laboratory.
Mr. Lewis H. Abraham, Missiles Division, Douglas Aircraft Co., Inc.
Mr. George N. Mangurian, Chief Analytical Engineer, Northrop Aircraft, Inc.
Mr. William R. Micks, The Rand Corp.
Prof. Paul E. Sandorff, Massachusetts Institute of Technology.
Prof. E. E. Sechler, Professor of Aeronautics, California Institute of Technology.
Mr. Robert S. Shorey, Convair, Astronautics, Division of General Dynamics Corp.
Mr. Arne Sorensen, Boeing Airplane Co.
Mr. E. H. Spaulding, Chief Structures Engineer, Structural Engineering, Lockheed Aircraft Corp.
Mr. John E. Stevens, Chance Vought Aircraft, Inc.

Mr. Melvin G. Rosché, Secretary

Subcommittee on Loads

Mr. Ralph B. Davidson, Director, Technical Support Division, Radioplane, Division of Northrop Aircraft, Inc., Chairman.
Capt. Roy E. Hale, Jr., USAF, Air Research and Development Command.
Mr. Howard E. Kugel, Wright Air Development Center.
Mr. Clinton T. Newby, Bureau of Aeronautics, Department of the Navy.
Mr. John Beebe, Office of the Chief of Transportation, Department of the Army.

Mr. Charles R. Foster, Waterways Experiment Station, Corps of Engineers, U.S. Army.
Mr. Robert Rosenbaum, Civil Aeronautics Administration.
Mr. Philip Donely, NACA Langley Aeronautical Laboratory.
Mr. Manley J. Hood, NACA Ames Aeronautical Laboratory.
Mr. D. E. Beeler, NACA High-Speed Flight Station.
Mr. Albert Epstein, Republic Aviation Corp.
Mr. Robert Goldin, Chief Structural Design Engineer, Bell Aircraft Corp.
Mr. E. Z. Gray, Boeing Airplane Co.
Mr. H. J. Hoge, North American Aviation, Inc.
Mr. H. W. Huntley, Jr., North American Aviation, Inc., Downey.
Mr. Albert J. Kullas, Manager, Flight Vehicle Design Department, The Martin Co.
Mr. W. A. Stauffer, Lockheed Aircraft Corp.
Dr. Leo Stoolman, Head, Aerodynamics Department, Hughes Aircraft Co.
Mr. Yale Weisman, Convair, Division of General Dynamics Corp.

Mr. R. Fabian Goranson, Secretary

Subcommittee on Vibration and Flutter

Mr. Martin Goland, Director, Southwest Research Institute, Chairman.
Mr. Fred L. Daum, Wright Air Development Center.
Mr. W. J. Mykytow, Wright Air Development Center.
Mr. Douglas Michel, Bureau of Aeronautics, Department of the Navy.
Mr. Philipp W. Zettler-Seidel, Army Ballistic Missile Agency.
Maj. Walter B. Schlotterbeck, USA Transportation Research and Engineering Command.
Mr. Robert Rosenbaum, Civil Aeronautics Administration.
Mr. I. E. Garrick, NACA Langley Aeronautical Laboratory.
Mr. Albert Erickson, NACA Ames Aeronautical Laboratory.
Mr. André J. Meyer, Jr., NACA Lewis Flight Propulsion Laboratory.
Mr. Thomas F. Baker, NACA High-Speed Flight Station.
Mr. Walter E. Arnoldi, Hamilton Standard Div., United Aircraft Corp.
Prof. Holt Ashley, Massachusetts Institute of Technology.
Mr. Eugene F. Baird, Chief Flutter and Vibration Engineer, Grumman Aircraft Engineering Corp.
Mr. Michael Dublin, Chief of Dynamics, Convair, Division of General Dynamics Corp.
Mr. Warren T. Hunter, Chief, Automatic Control Section, Missile Engineering, Douglas Aircraft Co., Inc.
Mr. H. Clay Johnson, Jr., Configuration Manager, The Martin Co., Orlando.
Mr. William R. Laidlaw, North American Aviation, Inc., Columbus.
Mr. L. I. Mirowitz, McDonnell Aircraft Corp.
Mr. M. J. Turner, Unit Chief, Structural Dynamics, Seattle Division, Boeing Airplane Co.

Mr. Harvey H. Brown, Secretary

Subcommitee on Structural Materials

Dr. J. C. McDonald, Missile Systems Division, Lockheed Aircraft Corp., Chairman.
Maj. F. C. Krug, USAF, Air Research and Development Command.
Mr. J. B. Johnson, Wright Air Development Center.
Mr. Nathan E. Promisel, Bureau of Aeronautics, Department of the Navy.
Mr. Jerome Persh, Bureau of Ordnance, Department of the Navy.
Dr. W. H. Steurer, Redstone Arsenal.
Mr. George I. Schuck, Transportation Research and Engineering Command.
Dr. Gordon M. Kline, Chief, Organic and Fibrous Materials Division, National Bureau of Standards.
Mr. James E. Dougherty, Jr., Civil Aeronautics Administration.
Mr. Paul Kuhn, NACA Langley Aeronautical Laboratory.
Mr. G. Mervin Ault, NACA Lewis Flight Propulsion Laboratory.
Mr. Robert S. Ames, Goodyear Aircraft Corp.
Mr. Paul W. Boone, The Martin Co.
Mr. Harry A. Campbell, Bell Aircraft Corp.
Mr. Edgar H. Dix, Jr., Assistant Director of Research, Aluminum Co. of America.
Prof. Pol Duwez, California Institute of Technology.
Dr. Walter L. Finlay, Director of Research, Crucible Steel Co. of America.
Mr. L. R. Jackson, Assistant Director, Battelle Memorial Institute.
Mr. Peter Payson, Assistant Director of Research, Crucible Steel Co. of America.
Mr. M. J. Rudick, Chance Vought Aircraft, Inc.
Dr. George V. Smith, Professor of Metallurgical Engineering, Cornell University.
Mr. J. W. Sweet, Boeing Airplane Co.

Mr. R. H. Raring, Secretary

Committee on Aircraft Operating Problems

Capt. E. V. Rickenbacker, Chairman of the Board, Eastern Air Lines, Inc., Chairman.
Hon. James T. Pyle, Administrator of Civil Aeronautics, Vice Chairman.
Col. Joseph Davis, Jr., USAF, Wright Air Development Center.
Capt. J. R. Brown, USN, Bureau of Aeronautics, Department of the Navy.
Col. Hallett D. Edson, USA, Office of the Deputy Chief of Staff for Military Operations, Department of the Army.
Col. J. L. Marinelli, USA, President, U.S. Army Aviation Board.
Mr. William B. Davis, Deputy Administrator, Civil Aeronautics Administration.
Mr. Donald M. Stuart, Director, Technical Development Center, Civil Aeronautics Administration.
Dr. F. W. Reichelderfer (ex officio), Chief, U.S. Weather Bureau.
Dr. Hugh L. Dryden (ex officio).
Mr. Melvin N. Gough, NACA Langley Aeronautical Laboratory.
Mr. Lawrence A. Clousing, NACA Ames Aeronautical Laboratory.
Mr. Eugene J. Manganiello, NACA Lewis Flight Propulsion Laboratory.
Mr. Ralph L. Bayless, Chief Engineer, San Diego Division, Convair, Division of General Dynamics Corp.
Mr. M. G. Beard, Assistant Vice President, Equipment Research, American Airlines, Inc.
Mr. John G. Borger, Pan American World Airways System.
Mr. Warren T. Dickinson, Executive Engineer, Douglas Aircraft Co., Inc.
Mr. Charles Froesch, Vice President, Engineering, Eastern Air Lines, Inc.
Mr. M. Carl Haddon, Director, Marketing, California Division, Lockheed Aircraft Corp.
Mr. Raymond D. Kelly, Superintendent of Technical Development, United Air Lines, Inc.
Mr. Jerome Lederer, Managing Director, Flight Safety Foundation.
Mr. William Littlewood, Vice President, Equipment Research, American Airlines, Inc.

Mr. Maynard L. Pennell, Chief Engineer, Transport Division, Boeing Airplane Co.
Mr. Robert W. Rummel, Vice President, Engineering, Trans World Airlines, Inc.
Mr. Clarence N. Sayen, President, Air Line Pilots Association.
Mr. Arthur E. Smith, Assistant General Manager, Pratt & Whitney Aircraft, United Aircraft Corp.
Dr. T. L. K. Smull, Secretary

Subcommittee on Meteorological Problems

Dr. F. W. Reichelderfer, Chief, U.S. Weather Bureau, Chairman.
Mr. Edmund Bromley, Air Research and Development Command.
Capt. John F. Tatom, USN, Director, Naval Weather Service Division, Office of the Chief of Naval Operations.
Mrs. Frances L. Whedon, Office of the Chief Signal Officer, Department of the Army.
Dr. Harry Wexler, Director of Meteorological Research, U.S. Weather Bureau.
Mr. William R. Krieger, Civil Aeronautics Administration.
Mr. William L. Halnon, Civil Aeronautics Board.
Mr. Harry Press, NACA Langley Aeronautical Laboratory.
Mr. William Lewis, NACA Lewis Flight Propulsion Laboratory.
Dr. Horace R. Byers, Professor of Meteorology, The University of Chicago.
Mr. Carl F. Eck, Air Line Pilots Association.
Mr. Joseph J. George, Eastern Air Lines, Inc.
Dr. Ross Gunn.
Mr. Henry T. Harrison, Jr., Director, Meteorology, United Air Lines, Inc.
Prof. H. G. Houghton, Massachusetts Institute of Technology.
Mr. D. S. Little, Superintendent, Airway Aids and Electronics, American Airlines, Inc.
Mr. H. J. Reid, Manager, Flight Operations, Capital Airlines, Inc.
Dr. George F. Taylor, Missile Systems Division, Lockheed Aircraft Corp.
Mr. Frank C. White, Air Transport Association of America.
Mr. Mason T. Charak, Secretary

Subcommittee on Flight Safety

Mr. Charles Froesch, Vice President, Engineering, Eastern Air Lines, Inc., Chairman.
Dr. Albert W. Hetherington, Jr., Air Research and Development Command.
Col. John P. Stapp, USAF, Chief, Aero Medical Laboratory, Wright Air Development Center.
Mr. Sydney D. Berman, Office of the Inspector General, U.S. Air Force.
Capt. Elwin L. Farrington, USN, Director, Aviation Safety Division, Office of the Chief of Naval Operations.
Col. James F. Wells, USA, Director, U.S. Army Board for Aviation Accident Research.
Mr. W. H. Weeks, Chief, Aircraft Engineering Division, Civil Aeronautics Administration.
Hon. James T. Pyle (ex officio), Administrator of Civil Aeronautics.
Mr. Melvin N. Gough, NACA Langley Aeronautical Laboratory.
Mr. George E. Cooper, NACA Ames Aeronautical Laboratory.
Mr. I. Irving Pinkel, NACA Lewis Flight Propulsion Laboratory.
Mr. Joseph A. Walker, NACA High-Speed Flight Station.
Hon. Joseph P. Adams, Association of Local and Territorial Airlines.
Mr. Robert N. Buck, Trans World Airlines, Inc.
Mr. Carl M. Christenson, United Air Lines, Inc.
Mr. Allen W. Dallas, Director, Engineering Division, Air Transport Association of America.
Dr. Paul M. Fitts, Jr., Department of Psychology, University of Michigan.
Mr. Scott Flower, Pan American World Airways, Inc.
Mr. Dunstan Graham, Lear, Inc.
Mr. A. Howard Hasbrook, Director, Aviation Crash Injury Research of Cornell University.
Mr. Otto E. Kirchner, Sr., Operational Consultant, Transport Division, Boeing Airplane Co.
Mr. Jerome Lederer, Managing Director, Flight Safety Foundation.
Dr. Ross A. McFarland, Harvard School of Public Health.
Mr. William I. Stieglitz, Design Safety Engineer, Republic Aviation Corp.
Mr. R. L. Thoren, Chief Engineer, Flight Test, California Division, Lockheed Aircraft Corp.
Mr. H. H. Young, Flight Safety Engineer, Douglas Aircraft Co., Inc.
Mr. Boyd C. Myers II, Secretary

Subcommittee on Aircraft Noise

Mr. William Littlewood, Vice President, Equipment Research, American Airlines, Inc., Chairman.
Dr. H. O. Parrack, Wright Air Development Center.
Dr. H. E. von Gierke, Wright Air Development Center.
Comdr. B. K. Weaver, USN, Bureau of Aeronautics, Department of the Navy.
Mr. Joseph Matulaitis, Office of the Chief of Transportation, Department of the Army.
Mr. Stephen H. Rolle, Chief, Power Plant Branch, Aircraft Engineering Division, Civil Aeronautics Administration.
Mr. B. S. Spano, Civil Aeronautics Administration.
Mr. Arthur A. Regier, NACA Langley Aeronautical Laboratory.
Mr. Newell D. Sanders, NACA Lewis Flight Propulsion Laboratory.
Dr. Leo L. Beranek, President and Bolt, Beranek & Newman, Inc.
Mr. A. W. Cobb, Aerojet-General Corp.
Mr. Allen W. Dallas, Director, Engineering Division, Air Transport Association of America.
Mr. Harry H. Howell, Transport Division, Boeing Airplane Co.
Mr. E. J. Kirchman, The Martin Co.
Dr. Robert B. Lawhead, Rocketdyne Division, North American Aviation, Inc.
Prof. R. W. Leonard, University of California.
Mr. M. M. Miller, Chief, Acoustics Section, Douglas Aircraft Co., Inc.
Dr. Charles T. Molloy, Lockheed Aircraft Corp.
Mr. John M. Tyler, Pratt & Whitney Aircraft, United Aircraft Corp.
Dr. P. J. Westervelt, Assistant Professor, Department of Physics, Brown University.
Mr. J. F. Woodall, Convair, Division of General Dynamics Corp.
Mr. George P. Bates, Jr., Secretary

INDUSTRY CONSULTING COMMITTEE

Mr. J. L. Atwood, President, North American Aviation, Inc., Chairman.
Mr. M. P. Ferguson, President, Bendix Aviation Corp., Vice Chairman.
Mr. Harvey Gaylord, President, Bell Helicopter Corp.
Mr. William Littlewood, Vice President, Equipment Research, American Airlines, Inc.

Mr. J. S. McDonnell, President, McDonnell Aircraft Corp.
Mr. E. B. Newill, General Manager, Allison Division, General Motors Corp.
Dr. Arthur E. Raymond, Vice President, Engineering, Douglas Aircraft Co., Inc.
Mr. C. J. Reese, President, Continental Motors Corp.
Mr. Juan T. Trippe, President, Pan American World Airways, Inc.

Dr. T. L. K. Smull, Secretary

SPECIAL COMMITTEE ON SPACE TECHNOLOGY

Dr. H. Guyford Stever, Associate Dean of Engineering, Massachusetts Institute of Technology, Chairman.
Col. Norman C. Appold, USAF, Air Research and Development Command.
Mr. Abraham Hyatt, Bureau of Aeronautics, Department of the Navy.
Dr. Wernher von Braun, Army Ballistic Missile Agency.
Dr. Hugh L. Dryden (ex officio).
Mr. Robert R. Gilruth, NACA Langley Aeronautical Laboratory.
Mr. H. Julian Allen, NACA Ames Aeronautical Laboratory.
Dr. Abe Silverstein, NACA Lewis Flight Propulsion Laboratory.
Dr. Hendrik W. Bode, Vice President, Bell Telephone Laboratories, Inc.
Dr. Milton U. Clauser, Director, Aeronautical Research Laboratory, The Ramo-Wooldridge Corp.
Prof. Dale R. Corson, Cornell University.
Mr. J. R. Dempsey, Manager, Convair, Astronautics, Division of General Dynamics Corp.
Mr. S. K. Hoffman, General Manager, Rocketdyne Division, North American Aviation, Inc.
Dr. W. Randolph Lovelace II, Lovelace Foundation for Medical Education and Research.
Dr. W. H. Pickering, Director, Jet Propulsion Laboratory, California Institute of Technology.
Dr. Louis N. Ridenour, Assistant General Manager, Research and Development, Missile Systems Division, Lockheed Aircraft Corp.
Dr. J. A. Van Allen, State University of Iowa.

Mr. Carl B. Palmer, Secretary

Working Group on Space Research Objectives

Dr. J. A. Van Allen, State University of Iowa, Chairman.
Prof. Dale R. Corson, Cornell University, Vice Chairman.
Col. Norman C. Appold, USAF, Air Research and Development Command.
Mr. Robert Cornog, The Ramo-Wooldridge Corp.
Mr. Robert P. Haviland, Systems Planning Engineer, General Electric Co.
Dr. J. R. Pierce, Director of Research, Electrical Communications, Murray Hill Laboratory, Bell Telephone Laboratories, Inc.
Prof. Lyman Spitzer, Jr., Princeton University Observatory.

Mr. E. O. Pearson, Secretary

Working Group on Vehicular Program

Dr. Wernher von Braun, Director, Development Operations Division, Army Ballistic Missile Agency, Chairman.
Mr. S. K. Hoffman, General Manager, Rocketdyne Division, North American Aviation, Inc., Vice Chairman.
Col. Norman C. Appold, USAF, Air Research and Development Command.
Mr. Abraham Hyatt, Bureau of Aeronautics, Department of the Navy.
Dr. Louis N. Ridenour, Assistant General Manager, Research and Development, Missile Systems Division, Lockheed Aircraft Corp.
Dr. Abe Silverstein, NACA Lewis Flight Propulsion Laboratory.
Dr. Krafft A. Ehricke, Convair, Astronautics, Division of General Dynamics Corp.
Mr. M. W. Hunter, Chief Missiles Design Engineer, Douglas Aircraft Co., Inc.
Mr. C. C. Ross, Vice President, Engineering, Aerojet-General Corp.
Dr. Homer J. Stewart, Jet Propulsion Laboratory, California Institute of Technology.
Mr. George S. Trimble, Jr., Vice President, Engineering, The Martin Co.

Mr. William H. Woodward, Secretary

Working Group on Reentry

Dr. Milton U. Clauser, Director, Aeronautical Research Laboratory, The Ramo-Wooldridge Corp., Chairman.
Mr. H. Julian Allen, NACA Ames Aeronautical Laboratory, Vice Chairman.
Dr. Mac C. Adams, Deputy Director, Avco Research Laboratory, Avco Manufacturing Corp.
Dr. Alfred J. Eggers, Jr., NACA Ames Aeronautical Laboratory.
Mr. Maxime A. Faget, NACA Langley Aeronautical Laboratory.
Dr. A. H. Flax, Vice President and Assistant Director, Technical, Cornell Aeronautical Laboratory, Inc.
Prof. Lester Lees, Guggenheim Aeronautical Laboratory, California Institute of Technology.
Mr. Harlowe J. Longfelder, Systems Engineering Director, Boeing Airplane Co.
Dr. J. C. McDonald, Missile Systems Division, Lockheed Aircraft Corp.
Prof. S. A. Schaaf, University of California.
Col. John P. Stapp, USAF, Chief, Aero Medical Laboratory, Wright Air Development Center.

Mr. R. Fabian Goranson, Secretary

Working Group on Range, Launch, and Tracking Facilities

Mr. J. R. Dempsey, Manager, Convair, Astronautics, Division of General Dynamics Corp., Chairman.
Mr. Robert R. Gilruth, NACA Langley Aeronautical Laboratory, Vice Chairman.
Col. Paul T. Cooper, USAF, Deputy Commander, Range, Air Force Missile Test Center.
Mr. L. G. deBey, Chief, Electronic Measurements Branch, Ballistic Research Laboratories, Aberdeen Proving Ground.
Mr. Carl Ernest Duckett, Army Ballistic Missile Agency.
Comdr. Robert F. Freitag, USN, Naval Air Missile Test Center.
Prof. J. Allen Hynek, Astrophysical Observatory, Smithsonian Institution.
Mr. John T. Mengel, Naval Research Laboratory.
Mr. Grayson Merrill, General Manager, Fairchild Guided Missiles Division, Fairchild Engine & Airplane Corp.

Mr. Carl B. Palmer, Secretary

Working Group on Instrumentation

Dr. W. H. Pickering, Director, Jet Propulsion Laboratory, California Institute of Technology, Chairman.
Dr. Louis N. Ridenour, Assistant General Manager, Research and Development, Missile Systems Division, Lockheed Aircraft Corp., Vice Chairman.
Dr. Henrik W. Bode, Vice President, Bell Telephone Laboratories, Inc.

Mr. Robert W. Buchheim, The Rand Corp.
Mr. Harry J. Goett, NACA Ames Aeronautical Laboratory.
Dr. Albert C. Hall, Director of Engineering, Denver Division, The Martin Co.
Mr. Eberhardt Rechtin, Jet Propulsion Laboratory, California Institute of Technology.
Dr. William T. Russell, Space Technology Laboratories, Inc.
Dr. Robert C. Seamans, Jr., RCA Airborne Systems Laboratory.
Mr. Bernard Maggin, Secretary

Working Group on Space Surveillance

Dr. Hendrik W. Bode, Vice President, Bell Telephone Laboratories, Inc., Chairman.
Dr. W. H. Pickering, Director, Jet Propulsion Laboratory, California Institute of Technology, Vice Chairman.
Mr. Wilbur B. Davenport, Jr., Head, Communications and Components Division, Lincoln Laboratory, Massachusetts Institute of Technology.
Mr. W. B. Hebenstreit, Director, Special Programs, Space Technology Laboratories, Inc.
Mr. Richard S. Leghorn, ITEK Corp.
Mr. K. G. Macleish, Assistant Director, Research and Development Department, Apparatus and Optical Division, Eastman Kodak Co.
Dr. William B. McLean, Technical Director, U.S. Naval Ordnance Test Station.
Mr. A. H. Shapley, Boulder Laboratories, National Bureau of Standards.
Dr. Fred L. Whipple, Director, Astrophysical Observatory, Smithsonian Institution.
Mr. Carl B. Palmer, Secretary

Working Group on Human Factors and Training

Dr. W. Randolph Lovelace II, Lovelace Foundation for Medical Education and Research, Chairman.
Mr. A. Scott Crossfield, North American Aviation, Inc.
Mr. Hubert M. Drake, NACA High-Speed Flight Station.
Brig. Gen. Donald D. Flickinger, USAF (MC), Director of Human Factors and Staff Surgeon, Air Research and Development Command.
Col. Edward B. Giller, USAF, Deputy Commander for Special Projects, Air Force Special Weapons Center.
Dr. James D. Hardy, Medical Laboratory, U.S. Naval Air Development Center.
Mr. Wright Haskell Langham, Los Alamos Scientific Laboratory, University of California.
Dr. Ulrich C. Luft, Head, Physiology Department, Lovelace Foundation for Medical Education and Research.
Mr. Boyd C. Myers II, Secretary

Part III—FINANCIAL REPORT

Funds appropriated for the Committee for the fiscal years 1958 and 1959 and obligations against the fiscal year 1958 appropriations are as follows:

	Fiscal year 1958		Fiscal year 1959
	Allotments	Obligations	Allotments
SALARIES AND EXPENSES APPROPRIATION			
NACA Headquarters	$1, 971, 000	$1, 958, 201	$2, 083, 650
Langley Aeronautical Laboratory	28, 947, 150	28, 897, 306	30, 368, 000
Ames Aeronautical Laboratory	15, 194, 498	15, 149, 417	16, 380, 350
Lewis Flight Propulsion Laboratory	25, 221, 525	25, 192, 055	27, 538, 000
High-Speed Flight Station	2, 584, 527	2, 565, 353	2, 833, 100
Pilotless Aircraft Station	1, 750, 310	1, 743, 025	1, 179, 920
Western Coordination Office	40, 797	39, 170	49, 605
Wright-Patterson Liaison Office	19, 000	18, 782	21, 375
Research contracts with educational institutions	410, 000	410, 000	850, 000
Research contracts with Government agencies	90, 000	90, 000	150, 000
Cost of Federal Employees Salary Increase Act of 1958 included above	(1, 508, 807)	(1, 488, 719)	(3, 354, 000)
Unobligated balance	−152, 598	12, 900	
Total	[1] 76, 076, 209	76, 076, 209	[2] 81, 454, 000
CONSTRUCTION AND EQUIPMENT APPROPRIATION			
Langley Aeronautical Laboratory	11, 879, 000	3, 877, 606	11, 350, 000
Ames Aeronautical Laboratory	11, 355, 000	5, 162, 672	3, 720, 000
Lewis Flight Propulsion Laboratory	16, 406, 000	5, 269, 793	7, 800, 000
Pilotless Aircraft Station	1, 560, 000	580, 440	130, 000
Unobligated balance		[4] 26, 309, 489	
Total	[3] 41, 200, 000	41, 200, 000	[5] 23, 000, 000

[1] Appropriated in the Independent Offices Appropriation Act, 1958, approved June 29, 1957; the Second Supplemental Appropriation Act, 1958, approved Mar. 28, 1958; and Public Law 85-472, approved June 30, 1958.

[2] $78,100,000 appropriated in the Independent Offices Appropriation Act, 1959, approved Aug. 28, 1958; includes $3,454,000 to be submitted in a supplemental appropriation request to cover the fiscal year 1959 cost of the Federal Employees Salary Increase Act, 1958.

[3] Appropriated in the Independent Offices Appropriation Act, 1958, approved June 29, 1957; and the Second Supplemental Appropriation Act, 1958, approved Mar. 28, 1958.

[4] This balance remains available until expended.

[5] Appropriated in the Independent Offices Appropriation Act, 1959, approved Aug. 28, 1958.

Funds appropriated in the Supplemental Appropriation Act, 1959, approved August 27, 1958, for the National Aeronautics and Space Administration for the fiscal year 1959 are set forth below. Under authority of the National Aeronautics and Space Act of 1958, approved July 29, 1958, all balances of National Advisory Committee for Aeronautics funds were transferred to National Aeronautics and Space Administration accounts at the close of business September 30, 1958.

	Fiscal year 1959
Salaries and Expenses appropriation	$5, 000, 000
Research and Development appropriation	[1] 167, 000, 000
Construction and Equipment appropriation	25, 000, 000

[1] Includes funds in the amount of $117 million transferred from the Department of Defense.

Part IV—FINAL MEETING OF NACA

The final meeting of the National Advisory Committee for Aeronautics was held at 2 p.m., August 21, 1958, at its headquarters, 1512 H Street NW., Washington, D.C. Present at this meeting were:

James H. Doolittle, Sc. D., Vice President, Shell Oil Co., Chairman.
Leonard Carmichael, Ph. D., Secretary, Smithsonian Institution, Vice Chairman.
Allen V. Astin, Ph. D., Director, National Bureau of Standards.
Preston R. Bassett, Sc. D., retired.
Frederick C. Crawford, Sc. D., Chairman of the Board, Thompson Products Co., Inc.
Paul D. Foote, Ph. D., Assistant Secretary of Defense, Research and Engineering.
Wellington T. Hines, Rear Admiral, USN, Assistant Chief for Procurement, Bureau of Aeronautics, Navy.
Charles J. McCarthy, B.S., Chairman of the Board, Chance Vought Aircraft, Inc.
James T. Pyle, A.B., Administrator of Civil Aeronautics.
Francis W. Reichelderfer, Sc. D., Chief, U.S. Weather Bureau.
Louis S. Rothschild, Ph. B., Undersecretary of Commerce for Transportation.
Thomas D. White, General, U.S. Air Force, Chief of Staff.

And on invitation:

Vice Adm. Robert B. Pirie, USN, acting member.
Maj. Gen. Marvin C. Demler, USAF, representing Lt. Gen. Roscoe C. Wilson, acting member.

And:

Hugh L. Dryden, Director.
John F. Victory, Executive Secretary.
John W. Crowley, Jr., Associate Director for Research.

Also present on invitation of Chairman Doolittle was Dr. T. Keith Glennan, newly appointed Administrator of the National Aeronautics and Space Administration (NASA). The Chairman announced that Dr. Glennan and Dr. Hugh Dryden, Director of NACA, had been confirmed by the Senate and had taken their respective oaths of office as Administrator and Deputy Administrator of NASA at the White House in the presence of President Eisenhower on August 19.

The Chairman welcomed Dr. Glennan and expressed the best wishes of the NACA for complete success in his new duties.

Dr. Glennan said he recognized in some degree the kind of task he was undertaking, and that he thought it quite wonderful to have the NACA staff and organization as a base on which to build. He then exhibited and explained a draft chart of proposed organization based on plans developed by the NACA Headquarters staff, with some modifications. Especially important, he said, would be an Office of Program Planning and Evaluation, reporting to the Administrator and the Deputy Administrator, and cooperating with the National Aeronautics and Space Council in the development of national programs of aeronautical and space activities. Dr. Glennan said he would welcome the advice of members of NACA at any time.

Chairman Doolittle extended to Dr. Glennan the thanks, congratulations, and best wishes of the members of NACA. Dr. Glennan expressed his appreciation of the privilege of appearing before the Committee, and, with the applause of the members, withdrew.

National Aeronautics and Space Act of 1958

The Chairman reported that the National Aeronautics and Space Act of 1958 (Public Law 85–568), approved by the President July 29, 1958, established the National Aeronautics and Space Administration, headed by an Administrator appointed from civilian life by the President by and with the advice and consent of the Senate, with a Deputy Administrator appointed in the same manner.

The functions of the Administration provided by the act are—

1. To plan, direct, and conduct aeronautical and space activities, except activities peculiar to or primarily associated with the development of weapons systems, military operations, or the defense of the United States, which will be the responsibility of the Department of Defense.
2. To arrange for participation by the scientific community in planning scientific measurements and observations to be made through use of aeronautical and space vehicles, and conduct or arrange for the conduct of such measurements and observations.
3. To provide for the widest practicable and appropriate dissemination of information concerning its activities and the results thereof.

In Section 301 of the act, it is provided:

> The National Advisory Committee for Aeronautics, on the effective date of this section, shall cease to exist. On such date all functions, powers, duties, and obligations, and all real and personal property, personnel (other than members of the Committee), funds, and records of that organization, shall be transferred to the Administration.
>
> This section shall take effect 90 days after the date of the enactment of this act, or on any earlier date on which the Administrator shall determine, and announce by proclamation



Final meeting of National Advisory Committee for Aeronautics, August 21, 1958. Around table clockwise: Hon. James T. Pyle, Administrator of Civil Aeronautics Dr. Hugh L. Dryden, Director, NACA; Mr. Preston R. Bassett; Hon. Louis S. Rothschild, Under Secretary of Commerce for Transportation; Dr. Leonard Carmichael, Secretary, Smithsonian Institution; Dr. James H. Doolittle, Chairman, NACA; Dr. John F. Victory, Executive Secretary, NACA; Dr. Francis W. Reichelderfer, Chief, U.S. Weather Bureau; Dr. Frederick C. Crawford, Chairman of the Board, Thompson Products, Inc.; Maj. Gen. Marvin C. Demler, USAF (attended in place of Lt. Gen. Roscoe C. Wilson, USAF, Deputy Chief of Staff, Development); General Thomas D. White, USAF, Chief of Staff, U.S. Air Force; Hon. Paul D. Foote, Assistant Secretary of Defense (Research and Engineering); Vice Admiral Robert B. Pirie, USN, Deputy Chief of Naval Operations (Air); Rear Admiral Wellington T. Hines, USN, Deputy and Assistant Chief, Bureau of Aeronautics; Mr. Charles J. McCarthy, Chairman of the Board, Chance Vought Aircraft, Inc.; and J. W. Crowley, Associate Director for Research, NACA.

published in the Federal Register, that the Administration has been organized and is prepared to discharge the duties and exercise the powers conferred upon it by this act.

(In accordance with the proclamation issued in accordance with the foregoing authority, the National Aeronautics and Space Administration became the legal successor to the National Advisory Committee for Aeronautics, effective as at the close of business September 30, 1958.)

Further provisions of the act include—

A declaration that it is the policy of the United States that activities in space should be devoted to peaceful purposes for the benefit of all mankind.

The establishment of a nine-member National Aeronautics and Space Council, to include the President, the Secretary of State, the Secretary of Defense, the Administrator of NASA, the Chairman of the Atomic Energy Commission, one additional member to be appointed by the President from Federal Agencies, and three other members to be appointed by the President from among individuals in private life who are eminent in science, engineering, technology, education, administration, or public affairs; the functions of the Council being to advise the President regarding policies, plans, programs, and accomplishments of United States agencies engaged in aeronautical and space activities, and the development of a comprehensive program.

NOTE.—The President on September 4 appointed as members of the Council: James H. Doolittle, Detlev W. Bronk, W. A. M. Burden, and Alan T. Waterman.

Provision for a Civilian-Military Liaison Committee, headed by a chairman to be appointed by the President, and including representatives of the Department of Defense and the Departments of the Army, Navy, and Air Force, and of the NASA.

STATEMENT BY THE PRESIDENT, JULY 29, 1958

I have today signed H.R. 12575, the National Aeronautics and Space Act of 1958.

The enactment of this legislation is a historic step, further equipping the United States for leadership in the space age. I wish to commend the Congress for the promptness with which it has created the organization and provided the authority needed for an effective national effort in the fields of aeronautics and space exploration.

The new act contains one provision that requires comment. Section 205 authorizes cooperation with other nations and groups of nations in work done pursuant to the act and in the peaceful application of the results of such work, pursuant to international agreements entered into by the President with the advice and consent of the Senate. I regard this section merely as recognizing that international treaties may be made in this field, and as not precluding, in appropriate cases, less formal arrangements for cooperation. To construe the section otherwise would raise substantial constitutional questions.

The present National Advisory Committee for Aeronautics (NACA), with its large and competent staff and well-equipped laboratories, will provide the nucleus for the NASA. The NACA has an established record of research performance and of cooperation with the armed services. The combination of space exploration responsibilities with the NACA's traditional aeronautical research functions is a natural evolution.

The enactment of the law establishing the NACA in 1915 proved a decisive step in the advancement of our civil and military aviation. The Aeronautics and Space Act of 1958 should have an even greater impact on our future.

After the Committee disposed of all business before it, including approval of its final statement to the Congress of the United States, submitting its 44th annual report, the following statements were made:

Undersecretary of Commerce Rothschild said that his 4 years of service as a member of the NACA had been a wonderful and illuminating experience and that it had been a great pleasure to serve with men of the caliber of NACA.

Gen. Thomas D. White, Chief of Staff, USAF, said that he would write a letter to the Chairman thanking the NACA for its support, cooperation, and assistance, virtually since the beginning of military aviation.

Vice Adm. Robert B. Pirie, DCNO (Air), expressed the same sentiments regarding the services rendered by the NACA to the Navy throughout the past 43 years.

Dr. Leonard Carmichael, Secretary, Smithsonian Institution, said that he was proud of the fact that the Smithsonian Institution, through its former Secretary, Dr. Charles D. Walcott, had been instrumental in the establishment of NACA and that all Secretaries of the Smithsonian since that time have served as members of NACA.

NOTE.—Dr. Walcott was the father of NACA, the first Chairman of its Executive Committee, 1915–19, and from 1919 until his death in 1927, chairman of the main committee.

Dr. Doolittle said it had been a great pleasure for him to serve with the other members for the past 10 years and thanked them for their cooperation and assistance during his chairmanship.

Dr. Victory said that the nameplate now on the back of each member's chair would be removed, suitably mounted, and transmitted to each member as a souvenir of his service with NACA.

At the conclusion of the brief meeting of the Committee held at the Ames Aeronautical Laboratory, Moffett Field, Calif., in connection with the triennial inspection of that Laboratory, July 14, 1958, the Executive Secretary, Dr. Victory, made a statement on behalf of the NACA staff, expressing appreciation of the leadership

of the members of NACA throughout its history. He was instructed to record that statement. It follows:

This may be the last meeting of the National Advisory Committee for Aeronautics which was established by law in 1915 to supervise and direct the scientific study of the problems of flight with a view to their practical solution. The great record of outstanding contributions to the progress of aeronautics made by the Committee, the members can always remember with pride and satisfaction.

On behalf of the entire staff of the organization, numbering about 7,800, I wish to express to the members of the Committee our profound sense of gratitude for the privilege and the honor that has been ours in working under the inspiring leadership of the members of the Committee and their illustrious chairmen throughout the life of the Committee. From their fine example and patriotic devotion to the cause of American supremacy in the air, from their vision and success in providing novel research facilities and ideal working conditions, we have drawn the inspiration and determination to do our best for the utmost advancement of aeronautical science in America.

We share the pride that is justly yours in the accomplishments of the era that is closing, and whatever the future may hold, it will ever be our high resolve to continue to render to our country loyal and devoted service."

Following are the letters to the Chairman, NACA, which General White, Admiral Pirie, and Secretary Rothschild offered to prepare on behalf of the Air Force, Navy, and Department of Commerce.

DEPARTMENT OF THE AIR FORCE
OFFICE OF THE CHIEF OF STAFF
UNITED STATES AIR FORCE
WASHINGTON, D. C.

26 August 1958

Dr. James H. Doolittle
Chairman
National Advisory Committee
for Aeronautics
1512 H Street, Northwest
Washington 25, D. C.

Dear Dr. Doolittle:

It was with mixed feelings that I attended the last meeting of the National Advisory Committee for Aeronautics on 21 August 1958.

There was regret at the passing of an agency that for 43 years has set the world's standard in aeronautical research. The United States as a nation, and the Air Force in particular, are deeply indebted to the NACA. In war and peace NACA has led the way; and there has always been, for us in the Air Force, the knowledge that NACA was ready to help in any aerodynamic trouble.

I hope that the new National Aeronautics and Space Agency, which will encompass many of the people of the old NACA, will go forward with the same competence and spirit of cooperation to reach new levels of accomplishment in the enlarged field.

Let me, on behalf of the Air Force, express sincerest thanks for all that the NACA has done for us over the years, and ask that you transmit my thanks to all the people of NACA who have served so long and so well.

Sincerely,



THOMAS D. WHITE
Chief of Staff

NATIONAL ADVISORY COMMITTEE FOR AERONAUTICS
1512 H STREET NORTHWEST
WASHINGTON 25, D. C.

TELEPHONE: LIBERTY 5-6700
TWX: WA 755

JAMES H. DOOLITTLE, SC. D., CHAIRMAN
LEONARD CARMICHAEL, PH. D., VICE CHAIRMAN

ALLEN V. ASTIN, PH. D.
PRESTON R. BASSETT, D. SC.
DETLEV W. BRONK, PH. D.
FREDERICK C. CRAWFORD, SC. D.
VICE ADM. WILLIAM V. DAVIS, JR., U. S. N.
PAUL D. FOOTE, PH. D.
REAR ADM. WELLINGTON T. HINES, U. S. N.
JEROME C. HUNSAKER, SC. D.
CHARLES J. McCARTHY, S. B.
LT. GEN. DONALD L. PUTT, U. S. A. F.
JAMES T. PYLE, A. B.
FRANCIS W. REICHELDERFER, SC. D.
EDWARD V. RICKENBACKER, SC. D.
LOUIS S. ROTHSCHILD, PH. B.
GEN. THOMAS D. WHITE, U. S. A. F.

LANGLEY AERONAUTICAL LABORATORY
LANGLEY FIELD, VA.

AMES AERONAUTICAL LABORATORY
MOFFETT FIELD, CALIF.

LEWIS FLIGHT PROPULSION LABORATORY
21000 BROOKPARK ROAD, CLEVELAND 11, OHIO

September 10, 1958

General Thomas D. White, USAF
Chief of Staff
Department of the Air Force
Washington 25, D. C.

Dear General White:

Your letter of August 26 is deeply appreciated by me personally. I am taking the liberty of bringing it to the attention of the nearly 8,000 employes of the National Advisory Committee for Aeronautics.

The great skill with which these devoted people have performed their researches over the years has been the prime reason for the contributions made by the NACA as a partner, together with the Military Services and the industry, on the air power team.

I know I can assure you, on behalf of these dedicated workers, that they will continue to merit the confidence, and the support, of the American people as they take up new and tremendously important work as the nucleus of the National Aeronautics and Space Administration.

Sincerely,

J. H. Doolittle
Chairman

THE ASSISTANT SECRETARY OF THE NAVY FOR AIR
WASHINGTON

17 SEP 1958

Dear Jimmy:

Upon the occasion of the disestablishment of the National Advisory Committee for Aeronautics, I would like to express the sincere appreciation of the United States Navy for the many achievements made by the NACA in the advancement of American aviation. Through the years, from the birth of the National Advisory Committee for Aeronautics by Congressional Act in 1915, when aircraft speeds of 100 knots were the marvel of the day, research by the NACA has been responsible for world leadership in aviation by the United States. During World War II, when American aviation manufacturing reached fantastic proportions, the superiority of design of American aircraft was in no small measure a compliment to the vision of the laboratories of the NACA in probing the unknown.

The well known fighters of the Navy, the Corsair, the Wildcat, and the Hellcat, which maintained control of the air in the Pacific and did so much to make the eventual naval victories possible, were all products of the application of research done by the NACA. Development in NACA laboratories of high lift devices, low drag wings, high speed propellers, improved engine cooling systems, and improved aircraft structural systems allowed the Navy's carrier task forces to strike the enemy where and when we chose.

Korea found the Navy operating jet aircraft from carriers in combat for the first time, and the distinct success of these operations was in no small measure proof of the validity of basic research conducted by the NACA.

Today, as speeds of manned aircraft near the hypersonic range, and with missile velocities transiting the hypersonic areas, the Free World owes a debt of gratitude to the comprehensive fundamental research in the problems of flight conducted by the NACA. The wealth of knowledge acquired by the NACA in its thirty-three years is a broad foundation upon which the Nation can build as the Jet Age gives way to the Age of Space.

Again, Jimmy, I would like to express the sincere appreciation of the Navy for the outstanding contributions to naval aviation made by the National Advisory Committee for Aeronautics. The National Aeronautics and Space Administration has a rich heritage indeed, and we of the Navy rejoice in the good news of your appointment as a member of the Board.

Sincerely,

GARRISON NORTON

James H. Doolittle, Sc.D.,
Chairman
National Advisory Committee for Aeronautics
1512 H Street NW
Washington 25, D.C.

THE SECRETARY OF COMMERCE
WASHINGTON 25

September 15 1958

Dear General Doolittle:

On behalf of the Department of Commerce and its representatives who serve as members of the National Advisory Committee for Aeronautics, it is a pleasure to express appreciation for the outstanding achievements of the NACA during its 43 years of activity. American leadership in aeronautics is due in no small measure to the research carried forward in NACA laboratories and to developments fostered by the Committee over the years in cooperation with industry and government agencies concerned with aviation. Many studies and discoveries that have led to revolutionary advancements in aeronautics have come directly from the laboratories of the organization. Forthcoming expansion of operations to explore outer space and develop the possibilities of interplanetary vehicles will bring an important transition which the United States will accomplish by building on experience and knowledge to which the NACA has contributed very materially.

From the beginning of the NACA in 1915, the Department of Commerce has always had one or more representatives in the membership of the Committee. The Director of the National Bureau of Standards was ex officio one of the original members. After passage of the Air Commerce Act of 1926 the Assistant Secretary of Commerce for Air also was a member, succeeded later on the Committee by the Administrator of Civil Aeronautics. In 1940 when the Weather Bureau was transferred to the Department of Commerce, the Chief of that Bureau, whose office had been among the original ex officio members, became another from this Department to serve on the Committee. In recent years the Under Secretary of Commerce for Transportation, Mr. Louis S. Rothschild, has made a fourth member from the Department of Commerce.

I express the feelings of these representatives as well as my own when I say that it has been a real privilege to have had an active part in the work of the Committee. It is indeed gratifying to see how successfully this unique group has functioned as an advisory and executive body. Although the organization and its advisory group will change with inauguration of the National

Aeronautics and Space Agency, the interest of the Department of Commerce in future progress in these highly important fields will continue undiminished, and I look forward to continued cooperation and participation by the Department and its representatives in the advancement of aeronautics and space exploration.

Sincerely,

Secretary of Commerce

General James H. Doolittle
Chairman, National Advisory
Committee for Aeronautics
1512 H Street, N.W.
Washington 25, D.C.

APPENDIX

Public Law 85-568
85th Congress, H.R. 12575
July 29, 1958

AN ACT To provide for research into problems of flight within and outside the earth's atmosphere, and for other purposes.

Be it enacted by the Senate and House of Representatives of the United States of America in Congress assembled,

National Aeronautics and Space Act of 1958

TITLE I—SHORT TITLE, DECLARATION OF POLICY AND DEFINITIONS

SHORT TITLE

SEC. 101. This Act may be cited as the "National Aeronautics and Space Act of 1958".

DECLARATION OF POLICY AND PURPOSE

SEC. 102. (a) The Congress hereby declares that it is the policy of the United States that activities in space should be devoted to peaceful purposes for the benefit of all mankind.

(b) The Congress declares that the general welfare and security of the United States require that adequate provision be made for aeronautical and space activities. The Congress further declares that such activities shall be the responsibility of, and shall be directed by, a civilian agency exercising control over aeronautical and space activities sponsored by the United States, except that activities peculiar to or primarily associated with the development of weapons systems, military operations, or the defense of the United States (including the research and development necessary to make effective provision for the defense of the United States) shall be the responsibility of, and shall be directed by, the Department of Defense; and that determination as to which such agency has responsibility for and direction of any such activity shall be made by the President in conformity with section 201(e).

72 Stat. 426.

(c) The aeronautical and space activities of the United States shall be conducted so as to contribute materially to one or more of the following objectives:

72 Stat. 427.

(1) The expansion of human knowledge of phenomena in the atmosphere and space;

(2) The improvement of the usefulness, performance, speed, safety, and efficiency of aeronautical and space vehicles;

(3) The development and operation of vehicles capable of carrying instruments, equipment, supplies, and living organisms through space;

(4) The establishment of long-range studies of the potential benefits to be gained from, the opportunities for, and the problems involved in the utilization of aeronautical and space activities for peaceful and scientific purposes;

(5) The preservation of the role of the United States as a leader in aeronautical and space science and technology and in the application thereof to the conduct of peaceful activities within and outside the atmosphere;

(6) The making available to agencies directly concerned with national defense of discoveries that have military value or significance, and the furnishing by such agencies, to the civilian agency established to direct and control nonmilitary aeronautical and space activities, of information as to discoveries which have value or significance to that agency;

(7) Cooperation by the United States with other nations and groups of nations in work done pursuant to this Act and in the peaceful application of the results thereof; and

(8) The most effective utilization of the scientific and engineering resources of the United States, with close cooperation among all interested agencies of the United States in order to avoid unnecessary duplication of effort, facilities, and equipment.

(d) It is the purpose of this Act to carry out and effectuate the policies declared in subsections (a), (b), and (c).

DEFINITIONS

SEC. 103. As used in this Act—

(1) the term "aeronautical and space activities" means (A) research into, and the solution of, problems of flight within and outside the earth's atmosphere, (B) the development, construction, testing, and operation for research purposes of aeronautical and space vehicles, and (C) such other activities as may be required for the exploration of space; and

(2) the term "aeronautical and space vehicles" means aircraft, missiles, satellites, and other space vehicles, manned and unmanned, together with related equipment, devices, components, and parts.

TITLE II—COORDINATION OF AERONAUTICAL AND SPACE ACTIVITIES

NATIONAL AERONAUTICS AND SPACE COUNCIL

Establishment.

SEC. 201. (a) There is hereby established the National Aeronautics and Space Council (hereinafter called the "Council") which shall be composed of—

(1) the President (who shall preside over the meetings of the Council);

72 Stat. 427.
72 Stat. 428.

(2) the Secretary of State;

(3) the Secretary of Defense;

(4) the Administrator of the National Aeronautics and Space Administration;

(5) the Chairman of the Atomic Energy Commission;

(6) not more than one additional member appointed by the President from the departments and agencies of the Federal Government; and

(7) not more than three other members appointed by the President, solely on the basis of established records of distinguished achievement, from among individuals in private life who are eminent in science, engineering, technology, education, administration, or public affairs.

Alternate.

(b) Each member of the Council from a department or agency of the Federal Government may designate another officer of his department or agency to serve on the Council as his alternate in his unavoidable absence.

(c) Each member of the Council appointed or designated under paragraphs (6) and (7) of subsection (a), and each alternate member designated under subsection (b), shall be appointed or designated to serve as such by and with the advice and consent of the Senate, unless at the time of such appointment or designation he holds an office in the Federal Government to which he was appointed by and with the advice and consent of the Senate.

(d) It shall be the function of the Council to advise the President with respect to the performance of the duties prescribed in subsection (e) of this section.

Duties of President.

(e) In conformity with the provisions of section 102 of this Act, it shall be the duty of the President to—

(1) survey all significant aeronautical and space activities, including the policies, plans, programs, and accomplishments of all agencies of the United States engaged in such activities;

(2) develop a comprehensive program of aeronautical and space activities to be conducted by agencies of the United States;

(3) designate and fix responsibility for the direction of major aeronautical and space activities;

(4) provide for effective cooperation between the National Aeronautics and Space Administration and the Department of Defense in all such activities, and specify which of such activities may be carried on concurrently by both such agencies notwithstanding the assignment of primary responsibility therefor to one or the other of such agencies; and

(5) resolve differences arising among departments and agencies of the United States with respect to aeronautical and space activities under this Act, including differences as to whether a particular project is an aeronautical and space activity.

Employees. Compensation.

(f) The Council may employ a staff to be headed by a civilian executive secretary who shall be appointed by the President by and with the advice and consent of the Senate and shall receive compensation at the rate of

$20,000 a year. The executive secretary, subject to the direction of the Council, is authorized to appoint and fix the compensation of such personnel, including not more than three persons who may be appointed without regard to the civil service laws or the Classification Act of 1949 and compensated at the rate of not more than $19,000 a year, as may be necessary to perform such duties as may be prescribed by the Council in connection with the performance of its functions. Each appointment under this subsection shall be subject to the same security requirements as those established for personnel of the National Aeronautics and Space Administration appointed under section 203(b)(2) of this Act.

63 Stat. 954. 5 USC 1071 note.

Security check.

(g) Members of the Council appointed from private life under subsection (a)(7) may be compensated at a rate not to exceed $100 per diem, and may be paid travel expenses and per diem in lieu of subsistence in accordance with the provisions of section 5 of the Administrative Expenses Act of 1946 (5 U.S.C. 73b–2) relating to persons serving without compensation.

Per diem. 72 Stat. 428. 72 Stat. 429. 69 Stat. 394.

NATIONAL AERONAUTICS AND SPACE ADMINISTRATION

SEC. 202. (a) There is hereby established the National Aeronautics and Space Administration (hereinafter called the "Administration"). The Administration shall be headed by an Administrator, who shall be appointed from civilian life by the President by and with the advice and consent of the Senate, and shall receive compensation at the rate of $22,500 per annum. Under the supervision and direction of the President, the Administrator shall be responsible for the exercise of all powers and the discharge of all duties of the Administration, and shall have authority and control over all personnel and activities thereof.

Administrator.

(b) There shall be in the Administration a Deputy Administrator, who shall be appointed from civilian life by the President by and with the advice and consent of the Senate, shall receive compensation at the rate of $21,500 per annum, and shall perform such duties and exercise such powers as the Administrator may prescribe. The Deputy Administrator shall act for, and exercise the powers of, the Administrator during his absence or disability.

Deputy Administrator.

(c) The Administrator and the Deputy Administrator shall not engage in any other business, vocation, or employment while serving as such.

Restriction.

FUNCTIONS OF THE ADMINISTRATION

SEC. 203. (a) The Administration, in order to carry out the purpose of this Act, shall—

(1) plan, direct, and conduct aeronautical and space activities;

(2) arrange for participation by the scientific community in planning scientific measurements and observations to be made through use of aeronautical and space vehicles, and conduct or arrange for the conduct of such measurements and observations; and

(3) provide for the widest practicable and appropriate dissemination of information concerning its activities and the results thereof.

(b) In the performance of its functions the Administration is authorized—

(1) to make, promulgate, issue, rescind, and amend rules and regulations governing the manner of its operations and the exercise of the powers vested in it by law;

Rules and regulations.

(2) to appoint and fix the compensation of such officers and employees as may be necessary to carry out such functions. Such officers and employees shall be appointed in accordance with the civil-service laws and their compensation fixed in accordance with the Classification Act of 1949, except that (A) to the extent the Administrator deems such action necessary to the discharge of his responsibilities, he may appoint and fix the compensation (up to a limit of $19,000 a year, or up to a limit of $21,000 a year for a maximum of ten positions) of not more than two hundred and sixty of the scientific, engineering, and administrative personnel of the Administration without regard to such laws, and (B) to the extent the Administrator deems such action necessary to recruit specially qualified scientific and engineering talent, he may establish the entrance grade for scientific and engineering personnel without previous service in the Federal Government at a level up to two grades higher than the grade provided for such personnel under the General Schedule established by the Classification Act of 1949, and fix their compensation accordingly;

Employees. 63 Stat. 954. 5 USC 1071 note. 72 Stat. 429. 72 Stat. 430.

Acquisition of property.

(3) to acquire (by purchase, lease, condemnation, or otherwise), construct, improve, repair, operate, and maintain laboratories, research and testing sites and facilities, aeronautical and space vehicles, quarters and related accommodations for employees and dependents of employees of the Administration, and such other real and personal property (including patents), or any interest therein, as the Administration deems necessary within and outside the continental United States; to lease to others such real and personal property; to sell and otherwise dispose of real and personal property (including patents and rights thereunder) in accordance with the provisions of the Federal Property and Administrative Services Act of 1949, as amended (40 U.S.C. 471 et seq.); and to provide by contract or otherwise for cafeterias and other necessary facilities for the welfare of employees of the Administration at its installations and purchase and maintain equipment therefor;

63 Stat. 377.

Gifts.

(4) to accept unconditional gifts or donations of services, money, or property, real, personal, or mixed, tangible or intangible;

Contracts, etc.
60 Stat. 809.

(5) without regard to section 3648 of the Revised Statutes, as amended (31 U.S.C. 529), to enter into and perform such contracts, leases, cooperative agreements, or other transactions as may be necessary in the conduct of its work and on such terms as it may deem appropriate, with any agency or instrumentality of the United States, or with any State, Territory, or possession, or with any political subdivision thereof, or with any person, firm, association, corporation, or educational institution. To the maximum extent practicable and consistent with the accomplishment of the purpose of this Act, such contracts, leases, agreements, and other transactions shall be allocated by the Administrator in a manner which will enable small-business concerns to participate equitably and proportionately in the conduct of the work of the Administration;

Agency cooperation.

(6) to use, with their consent, the services, equipment, personnel, and facilities of Federal and other agencies with or without reimbursement, and on a similar basis to cooperate with other public and private agencies and instrumentalities in the use of services, equipment, and facilities. Each department and agency of the Federal Government shall cooperate fully with the Administration in making its services, equipment, personnel, and facilities available to the Administration, and any such department or agency is authorized notwithstanding any other provision of law, to transfer to or receive from the Administration, without reimbursement, aeronautical and space vehicles, and supplies and equipment other than administrative supplies or equipment;

Advisory committees.

(7) to appoint such advisory committees as may be appropriate for purposes of consultation and advice to the Administration in the performance of its functions;

Coordination.

(8) to establish within the Administration such offices and procedures as may be appropriate to provide for the greatest possible coordination of its activities under this Act with related scientific and other activities being carried on by other public and private agencies and organizations;

72 Stat. 430.
72 Stat. 431.
60 Stat. 810.

(9) to obtain services as authorized by section 15 of the Act of August 2, 1946 (5 U.S.C. 55a), at rates not to exceed $100 per diem for individuals;

Employment Aliens.

(10) when determined by the Administrator to be necessary, and subject to such security investigations as he may determine to be appropriate, to employ aliens without regard to statutory provisions prohibiting payment of compensation to aliens;

Retired officers.

(11) to employ retired commissioned officers of the armed forces of the United States and compensate them at the rate established for the positions occupied by them within the Administration, subject only to the limitations in pay set forth in section 212 of the Act of June 30, 1932, as amended (5 U.S.C. 59a);

68 Stat. 18.
Agreements.

(12) with the approval of the President, to enter into cooperative agreements under which members of the Army, Navy, Air Force, and Marine Corps may be detailed by the appropriate Secretary for services in the performance of functions under this Act to the same extent as that to which they might be lawfully assigned in the Department of Defense; and

(13) (A) to consider, ascertain, adjust, determine, settle, and pay, on behalf of the United States, in full satisfaction thereof, any claim for $5,000 or less against the United States for bodily injury, death, or damage to or loss of real or personal property resulting from the conduct of the Administration's functions as specified in subsection (a) of this section, where such claim is presented to the Administration in writing within two years after the accident or incident out of which the claim arises; and Claims.

(B) if the Administration considers that a claim in excess of $5,000 is meritorious and would otherwise be covered by this paragraph, to report the facts and circumstances thereof to the Congress for its consideration. Report to Congress.

CIVILIAN-MILITARY LIAISON COMMITTEE

SEC. 204. (a) There shall be a Civilian-Military Liaison Committee consisting of—

(1) a Chairman, who shall be the head thereof and who shall be appointed by the President, shall serve at the pleasure of the President, and shall receive compensation (in the manner provided in subsection (d)) at the rate of $20,000 per annum;

(2) one or more representatives from the Department of Defense, and one or more representatives from each of the Departments of the Army, Navy, and Air Force, to be assigned by the Secretary of Defense to serve on the Committee without additional compensation; and

(3) representatives from the Administration, to be assigned by the Administrator to serve on the Committee without additional compensation, equal in number to the number of representatives assigned to serve on the Committee under paragraph (2).

(b) The Administration and the Department of Defense, through the Liaison Committee, shall advise and consult with each other on all matters within their respective jurisdictions relating to aeronautical and space activities and shall keep each other fully and currently informed with respect to such activities.

(c) If the Secretary of Defense concludes that any request, action, proposed action, or failure to act on the part of the Administrator is adverse to the responsibilities of the Department of Defense, or the Administrator concludes that any request, action, proposed action, or failure to act on the part of the Department of Defense is adverse to the responsibilities of the Administration, and the Administrator and the Secretary of Defense are unable to reach an agreement with respect thereto, either the Administrator or the Secretary of Defense may refer the matter to the President for his decision (which shall be final) as provided in section 201(e). 72 Stat. 431. 72 Stat. 432.

(d) Notwithstanding the provisions of any other law, any active or retired officer of the Army, Navy, or Air Force may serve as Chairman of the Liaison Committee without prejudice to his active or retired status as such officer. The compensation received by any such officer for his service as Chairman of the Liaison Committee shall be equal to the amount (if any) by which the compensation fixed by subsection (a)(1) for such Chairman exceeds his pay and allowances (including special and incentive pays) as an active officer, or his retired pay. Chairman.

INTERNATIONAL COOPERATION

SEC. 205. The Administration, under the foreign policy guidance of the President, may engage in a program of international cooperation in work done pursuant to this Act, and in the peaceful application of the results thereof, pursuant to agreements made by the President with the advice and consent of the Senate.

REPORTS TO THE CONGRESS

SEC. 206. (a) The Administration shall submit to the President for transmittal to the Congress, semiannually and at such other times as it deems desirable, a report of its activities and accomplishments.

(b) The President shall transmit to the Congress in January of each year a report, which shall include (1) a comprehensive description of the programed activities and the acomplishments of all agencies of the United States in the field of aeronautics and space activities during the preceding calendar year, and (2) an evaluation of such activities and acomplishments

in terms of the attainment of or the failure to attain, the objectives described in section 102(c) of this Act.

(c) Any report made under this section shall contain such recommendations for additional legislation as the Administrator or the President may consider necessary or desirable for the attainment of the objectives described in section 102(c) of this Act.

(d) No information which has been classified for reasons of national security shall be included in any report made under this section, unless such information has been declassified by, or pursuant to authorization given by, the President.

TITLE III—MISCELLANEOUS

NATIONAL ADVISORY COMMITTEE FOR AERONAUTICS

Termination. Transfer of functions.

SEC. 301. (a) The National Advisory Committee for Aeronautics, on the effective date of this section, shall cease to exist. On such date all functions, powers, duties, and obligations, and all real and personal property, personnel (other than members of the Committee), funds, and records of that organization, shall be transferred to the Administration.

Definitions. 70A Stat. 127.

(b) Section 2302 of title 10 of the United States Code is amended by striking out "or the Executive Secretary of the National Advisory Committee for Aeronautics." and inserting in lieu thereof "or the Administrator of the National Aeronautics and Space Administration."; and section 2303 of such title 10 is amended by striking out "The National Advisory Committee for Aeronautics." and inserting in lieu thereof "The National Aeronautics and Space Administration."

64 Stat. 476. 72 Stat. 432. 72 Stat. 433.

(c) The first section of the Act of August 26, 1950 (5 U.S.C. 22–1), is amended by striking out "the Director, National Advisory Committee for Aeronautics" and inserting in lieu thereof "the Administrator of the National Aeronautics and Space Administration", and by striking out "or National Advisory Committee for Aeronautics" and inserting in lieu thereof "or National Aeronautics and Space Administration".

63 Stat. 936.

(d) The Unitary Wind Tunnel Plan Act of 1949 (50 U.S.C. 511–515) is amended (1) by striking out "The National Advisory Committee for Aeronautics (hereinafter referred to as the 'Committee')" and inserting in lieu thereof "The Administrator of the National Aeronautics and Space Administration (hereinafter referred to as the 'Administrator')"; (2) by striking out "Committee" or "Committee's" wherever they appear and inserting in lieu thereof "Administrator" and "Administrator's", respectively; and (3) by striking out "its" wherever it appears and inserting in lieu thereof "his".

Effective date.

(e) This section shall take effect ninety days after the date of the enactment of this Act, or on any earlier date on which the Administrator shall

Publication in F.R.

determine, and announce by proclamation published in the Federal Register, that the Administration has been organized and is prepared to discharge the duties and exercise the powers conferred upon it by this Act.

TRANSFER OF RELATED FUNCTIONS

SEC. 302. (a) Subject to the provisions of this section, the President, for a period of four years after the date of enactment of this Act, may transfer to the Administration any functions (including powers, duties, activities, facilities, and parts of functions) of any other department or agency of the United States, or of any officer or organizational entity thereof, which relate primarily to the functions, powers, and duties of the Administration as prescribed by section 203 of this Act. In connection with any such transfer, the President may, under this section or other applicable authority, provide for appropriate transfers of records, property, civilian personnel, and funds.

Reports to Congress.

(b) Whenever any such transfer is made before January 1, 1959, the President shall transmit to the Speaker of the House of Representatives and the President pro tempore of the Senate a full and complete report concerning the nature and effect of such transfer.

(c) After December 31, 1958, no transfer shall be made under this section until (1) a full and complete report concerning the nature and effect of such proposed transfer has been transmitted by the President to the Congress, and (2) the first period of sixty calendar days of regular session of the Congress following the date of receipt of such report by the Congress

has expired without the adoption by the Congress of a concurrent resolution stating that the Congress does not favor such transfer.

ACCESS TO INFORMATION

SEC. 303. Information obtained or developed by the Administrator in the performance of his functions under this Act shall be made available for public inspection, except (A) information authorized or required by Federal statute to be withheld, and (B) information classified to protect the national security: *Provided*, That nothing in this Act shall authorize the withholding of information by the Administrator from the duly authorized committees of the Congress.

SECURITY

SEC. 304. (a) The Administrator shall establish such security requirements, restrictions, and safeguards as he deems necessary in the interest of the national security. The Administrator may arrange with the Civil Service Commission for the conduct of such security or other personnel investigations of the Administration's officers, employees, and consultants, and its contractors and subcontractors and their officers and employees, actual or prospective, as he deems appropriate; and if any such investigation develops any data reflecting that the individual who is the subject thereof is of questionable loyalty the matter shall be referred to the Federal Bureau of Investigation for the conduct of a full field investigation, the results of which shall be furnished to the Administrator.

Requirements.

72 Stat. 433.
72 Stat. 434.

Referral to F.B.I.

(b) The Atomic Energy Commission may authorize any of its employees, or employees of any contractor, prospective contractor, licensee, or prospective licensee of the Atomic Energy Commission or any other person authorized to have access to Restricted Data by the Atomic Energy Commission under subsection 145 b. of the Atomic Energy Act of 1954 (42 U.S.C. 2165(b)), to permit any member, officer, or employee of the Council, or the Administrator, or any officer, employee, member of an advisory committee, contractor, subcontractor, or officer or employee of a contractor or subcontractor of the Administration, to have access to Restricted Data relating to aeronautical and space activities which is required in the performance of his duties and so certified by the Council or the Administrator, as the case may be, but only if (1) the Council or Administrator or designee thereof has determined, in accordance with the established personnel security procedures and standards of the Council or Administration, that permitting such individual to have access to such Restricted Data will not endanger the common defense and security, and (2) the Council or Administrator or designee thereof finds that the established personnel and other security procedures and standards of the Council or Administration are adequate and in reasonable conformity to the standards established by the Atomic Energy Commission under section 145 of the Atomic Energy Act of 1954 (42 U.S.C. 2165). Any individual granted access to such Restricted Data pursuant to this subsection may exchange such Data with any individual who (A) is an officer or employee of the Department of Defense, or any department or agency thereof, or a member of the armed forces, or a contractor or subcontractor of any such department, agency, or armed force, or an officer or employee of any such contractor or subcontractor, and (B) has been authorized to have access to Restricted Data under the provisions of section 143 of the Atomic Energy Act of 1954 (42 U.S.C. 2163).

Access to AEC restricted data.

68 Stat. 942.

68 Stat. 942.

(c) Chapter 37 of title 18 of the United States Code (entitled Espionage and Censorship) is amended by—

(1) adding at the end thereof the following new section:

Espionage and Censorship.
62 Stat. 736–738:
65 Stat. 719.
18 USC 791–798.

"§ 799. Violation of regulations of National Aeronautics and Space Administration

Violation.

"Whoever willfully shall violate, attempt to violate, or conspire to violate any regulation or order promulgated by the Administrator of the National Aeronautics and Space Administration for the protection or security of any laboratory, station, base or other facility, or part thereof, or any aircraft, missile, spacecraft, or similar vehicle, or part thereof, or other property or equipment in the custody of the Administration, or any real or personal property or equipment in the custody of any contractor under any contract with the Administration or any subcontractor of any such contractor, shall be fined not more than $5,000, or imprisoned not more than one year, or both."

Penalty.

(2) adding at the end of the sectional analysis thereof the following new item:

72 Stat. 434.
72 Stat. 435.

"799. Violation of regulations of National Aeronautics and Space Administration."

(d) Section 1114 of title 18 of the United States Code is amended by inserting immediately before "while engaged in the performance of his official duties" the following: "or any officer or employee of the National Aeronautics and Space Administration directed to guard and protect property of the United States under the administration and control of the National Aeronautics and Space Administration,".

Protection of U.S. officers and employees.
62 Stat. 756.

Permission to use firearms.

(e) The Administrator may direct such of the officers and employees of the Administration as he deems necessary in the public interest to carry firearms while in the conduct of their official duties. The Administrator may also authorize such of those employees of the contractors and subcontractors of the Administration engaged in the protection of property owned by the United States and located at facilities owned by or contracted to the United States as he deems necessary in the public interest, to carry firearms while in the conduct of their official duties.

PROPERTY RIGHTS IN INVENTIONS

SEC. 305. (a) Whenever any invention is made in the performance of any work under any contract of the Administration, and the Administrator determines that—

(1) the person who made the invention was employed or assigned to perform research, development, or exploration work and the invention is related to the work he was employed or assigned to perform, or that it was within the scope of his employment duties, whether or not it was made during working hours, or with a contribution by the Government of the use of Government facilities, equipment, materials, allocated funds, information proprietary to the Government, or services of Government employees during working hours; or

(2) the person who made the invention was not employed or assigned to perform research, development, or exploration work, but the invention is nevertheless related to the contract, or to the work or duties he was employed or assigned to perform, and was made during working hours, or with a contribution from the Government of the sort referred to in clause (1),

such invention shall be the exclusive property of the United States, and if such invention is patentable a patent therefor shall be issued to the United States upon application made by the Administrator, unless the Administrator waives all or any part of the rights of the United States to such invention in conformity with the provisions of subsection (f) of this section.

Contract provision.

(b) Each contract entered into by the Administrator with any party for the performance of any work shall contain effective provisions under which such party shall furnish promptly to the Administrator a written report containing full and complete technical information concerning any invention, discovery, improvement, or innovation which may be made in the performance of any such work.

Patent application.

(c) No patent may be issued to any applicant other than the Administrator for any invention which appears to the Commissioner of Patents to have significant utility in the conduct of aeronautical and space activities unless the applicant files with the Commissioner, with the application or within thirty days after request therefor by the Commissioner, a written statement executed under oath setting forth the full facts concerning the circumstances under which such invention was made and stating the relationship (if any) of such invention to the performance of any work under any contract of the Administration. Copies of each such statement and the application to which it relates shall be transmitted forthwith by the Commissioner to the Administrator.

(d) Upon any application as to which any such statement has been transmitted to the Administrator, the Commissioner may, if the invention is patentable, issue a patent to the applicant unless the Administrator, within ninety days after receipt of such application and statement, requests that such patent be issued to him on behalf of the United States. If, within such time, the Administrator files such a request with the Commissioner, the Commissioner shall transmit notice thereof to the applicant, and shall issue

72 Stat. 435.
72 Stat. 436.

Board of Patent Interferences.

such patent to the Administrator unless the applicant within thirty days after receipt of such notice requests a hearing before a Board of Patent Interferences on the question whether the Administrator is entitled under this section to receive such patent. The Board may hear and determine, in accordance with rules and procedures established for interference cases, the question so presented, and its determination shall be subject to appeal by the applicant or by the Administrator to the Court of Customs and Patent Appeals in accordance with procedures governing appeals from decisions of the Board of Patent Interferences in other proceedings.

(e) Whenever any patent has been issued to any applicant in conformity with subsection (d), and the Administrator thereafter has reason to believe that the statement filed by the applicant in connection therewith contained any false representation of any material fact, the Administrator within five years after the date or issuance of such patent may file with the Commissioner a request for the transfer to the Administrator of title to such patent on the records of the Commission. Notice of any such request shall be transmitted by the Commissioner to the owner of record of such patent, and title to such patent shall be so transferred to the Administrator unless within thirty days after receipt of such notice such owner of record requests a hearing before a Board of Patent Interferences on the question whether any such false representation was contained in such statement. Such question shall be heard and determined, and determination thereof shall be subject to review, in the manner prescribed by subsection (d) for questions arising thereunder. No request made by the Administrator under this subsection for the transfer of title to any patent, and no prosecution for the violation of any criminal statute, shall be barred by any failure of the Administrator to make a request under subsection (d) for the issuance of such patent to him, or by any notice previously given by the Administrator stating that he had no objection to the issuance of such patent to the applicant therefor.

Waiver.

(f) Under such regulations in conformity with this subsection as the Administrator shall prescribe, he may waive all or any part of the rights of the United States under this section with respect to any invention or class of inventions made or which may be made by any person or class of persons in the performance of any work required by any contract of the Administration if the Administrator determines that the interests of the United States will be served thereby. Any such waiver may be made upon such terms and under such conditions as the Administrator shall determine to be required for the protection of the interests of the United States. Each such waiver made with respect to any invention shall be subject to the reservation by the Administrator of an irrevocable, nonexclusive, nontransferrable, royalty-free license for the practice of such invention throughout the world by or on behalf of the United States or any foreign government pursuant to any treaty or agreement with the United States. Each proposal for any waiver under this subsection shall be referred to an Inventions and Contributions Board which shall be established by the Administrator within the Administration. Such Board shall accord to each interested party an opportunity for hearing, and shall transmit to the Administrator its findings of fact with respect to such proposal and its recommendations for action to be taken with respect thereto.

Inventions and Contributions Board.

License regulations.

(g) The Administrator shall determine, and promulgate regulations specifying, the terms and conditions upon which licenses will be granted by the Administration for the practice by any person (other than an agency of the United States) of any invention for which the Administrator holds a patent on behalf of the United States.

72 Stat. 436.
72 Stat. 437.

Protection of title.

(h) The Administrator is authorized to take all suitable and necessary steps to protect any invention or discovery to which he has title, and to require that contractors or persons who retain title to inventions or discoveries under this section protect the inventions or discoveries to which the Administration has or may acquire a license of use.

Defense agency.
66 Stat. 805–808.

(i) The Administration shall be considered a defense agency of the United States for the purpose of chapter 17 of title 35 of the United States Code.

Definitions.

(j) As used in this section—

(1) the term "person" means any individual, partnership, corporation, association, institution, or other entity;

(2) the term "contract" means any actual or proposed contract, agreement, understanding, or other arrangement, and includes any assignment, substitution of parties, or subcontract executed or entered into thereunder; and

(3) the term "made", when used in relation to any invention, means the conception or first actual reduction to practice of such invention.

CONTRIBUTIONS AWARDS

SEC. 306. (a) Subject to the provisions of this section, the Administrator is authorized, upon his own initiative or upon application of any person, to make a monetary award, in such amount and upon such terms as he shall determine to be warranted, to any person (as defined by section 305) for any scientific or technical contribution to the Administration which is determined by the Administrator to have significant value in the conduct of aeronautical and space activities. Each application made for any such award shall be referred to the Inventions and Contributions Board established under section 305 of this Act. Such Board shall accord to each such applicant an opportunity for hearing upon such application, and shall transmit to the Administrator its recommendation as to the terms of the award, if any, to be made to such applicant for such contribution. In determining the terms and conditions of any award the Administrator shall take into account—

(1) the value of the contribution to the United States;

(2) the aggregate amount of any sums which have been expended by the applicant for the development of such contribution;

(3) the amount of any compensation (other than salary received for services rendered as an officer or employee of the Government) previously received by the applicant for or on account of the use of such contribution by the United States; and

(4) such other factors as the Administrator shall determine to be material.

(b) If more than one applicant under subsection (a) claims an interest in the same contribution, the Administrator shall ascertain and determine the respective interests of such applicants, and shall apportion any award to be made with respect to such contribution among such applicants in such proportions as he shall determine to be equitable. No award may be made under subsection (a) with respect to any contribution—

(1) unless the applicant surrenders, by such means as the Administrator shall determine to be effective, all claims which such applicant may have to receive any compensation (other than the award made under this section) for the use of such contribution or any element thereof at any time by or on behalf of the United States, or by or on behalf of any foreign government pursuant to any treaty or agreement with the United States, within the United States or at any other place;

72 Stat. 437.
72 Stat. 438.

(2) in any amount exceeding $100,000, unless the Administrator has transmitted to the appropriate committees of the Congress a full and complete report concerning the amount and terms of, and the basis for, such proposed award, and thirty calendar days of regular session of the Congress have expired after receipt of such report by such committees.

72 Stat. 438.

APPROPRIATIONS

SEC. 307. (a) There are hereby authorized to be appropriated such sums as may be necessary to carry out this Act, except that nothing in this Act shall authorize the appropriation of any amount for (1) the acquisition or condemnation of any real property, or (2) any other item of a capital nature (such as plant or facility acquisition, construction, or expansion) which exceeds $250,000. Sums appropriated pursuant to this subsection for the construction of facilities, or for research and development activities, shall remain available until expended.

(b) Any funds appropriated for the construction of facilities may be used for emergency repairs of existing facilities when such existing facilities are made inoperative by major breakdown, accident, or other circumstances and such repairs are deemed by the Administrator to be of greater urgency than the construction of new facilities.

Approved July 29, 1958.

NATIONAL AERONAUTICS AND SPACE ADMINISTRATION

Washington, D. C.

A PROCLAMATION

1. By virtue of the authority vested in me by the National Aeronautics and Space Act of 1958 (Public Law 85-568, approved July 29, 1958, 72 Stat. 426, 433) I hereby proclaim that as of the close of business September 30, 1958, the National Aeronautics and Space Administration has been organized and is prepared to discharge the duties and exercise the powers conferred upon it by said law

2. In accordance with the provisions of the Act, all functions, powers, duties, and obligations, and all real and personal property, personnel (other than members of the Committee), funds, and records of the National Advisory Committee for Aeronautics are hereby transferred to the National Aeronautics and Space Administration.

3. The existing National Advisory Committee for Aeronautics Committees on Aircraft, Missile and Spacecraft Aerodynamics; Aircraft, Missile and Spacecraft Propulsion; Aircraft, Missile and Spacecraft Construction; Aircraft Operating Problems; the Industry Consulting Committee; and the Special Committee on Space Technology and their subcommittees are hereby reconstituted advisory committees to the Administration through December 31, 1958, for the purpose of bringing their current work to an orderly completion.

4. Existing policies, regulations, authorities, and procedural instructions governing the activities of the National Advisory Committee for Aeronautics, not inconsistent with law, and which are applicable to the activities of the National Aeronautics and Space Administration, shall be continued in effect until superseded or revoked.

5. The Langley Aeronautical Laboratory, the Ames Aeronautical Laboratory, and the Lewis Flight Propulsion Laboratory are hereby renamed the Langley Research Center, the Ames Research Center, and the Lewis Research Center, respectively.

DONE at the City of Washington, District of Columbia this 25th day of September in the year Nineteen Hundred and Fifty-Eight.

T. Keith Glennan
Administrator

REPORT 1342

A VARIATIONAL THEOREM FOR CREEP WITH APPLICATIONS TO PLATES AND COLUMNS [1]

By J. Lyell Sanders, Jr., Harvey G. McComb, Jr., and Floyd R. Schlechte

SUMMARY

A variational theorem is presented for a body undergoing creep. Solutions to problems of the creep behavior of plates, columns, beams, and shells can be obtained by means of the direct methods of the calculus of variations in conjunction with the stated theorem. The application of the theorem is illustrated for plates and columns by the solution of two sample problems.

INTRODUCTION

Interest in the various effects of creep in metals has intensified in recent years in the aeronautical field because of actual or envisaged operation of aircraft in an elevated-temperature environment. Much experimental work has been done to determine the creep stress-strain relations of various metals at elevated temperatures, and much data have been accumulated on the creep collapse of columns and plates. Analytically, creep problems for beams, columns, and plates are more difficult than the corresponding elastic problems, because the creep stress-strain relations (which generally include the possibility of elastic and plastic strains) are nonlinear. One consequence of this nonlinearity is that the distribution of the stresses through the thickness of the beam, plate, or column is not nearly so simple as in the elastic case. Mathematical analyses of these structural components have often been restricted to simplified models (**H**-section columns, for example) to avoid this difficulty.

No known systematic procedures have been devised for reducing a given creep problem to a set of differential equations, although some efforts have been made to develop variational methods for use in attacking these problems mathematically. Hoff (refs. 1 and 2) has suggested the use of a minimum-complementary-energy principle based on an analog between the creep-strain rates and the elastic strains in a nonlinearly elastic body; however, elastic and plastic strains are neglected and the method does not apply readily to plate and column problems. Wang and Prager (ref. 3) have given two general extremum principles (for a body with elastic, plastic, thermal, and creep strains) analogous to the minimum-complementary-energy and minimum-potential-energy principles in elasticity. In the present report, an analog of Reissner's variational theorem in elasticity (refs. 4 and 5) is formulated (for a body with elastic, plastic, and creep strains), and special forms of it are found to be convenient for handling creep problems of plates, columns, beams, and shells. The use of the variational theorem presented herein is illustrated by applications to two creep problems: creep collapse of columns and plate bending.

SYMBOLS

E	Young's modulus
I	integral to be varied (see eq. (7))
I_1,I_2,I_3	integrals defined by equations (46)
J_2	second invariant of stress-deviator tensor
M_r,M_t	radial and tangential bending moments, respectively, per unit length
$M_{r,0},M_{t,0},M_{t,1}$	radial and tangential bending-moment coefficients defined by equations (44)
P	compressive load
P_c	buckling load for column
S	surface of a body
S_s	part of surface where stresses are prescribed
S_d	part of surface where displacements are prescribed
T_i	surface traction
$\overline{T}_i$	prescribed surface traction on S_s
U	displacement of neutral surface in x-direction
U_0	displacement coefficient in x-direction (see eqs. (28))
V	displacement of neutral surface in y-direction; also used as volume integral
W	deflection of neutral surface in z-direction
W_0,W_1	deflection coefficients (see eqs. (28) or (44))
R	radius of circular plate
b	width of column
h	thickness of column or plate
l	length of column
m	empirical constant in creep law
n_j	unit external normal to surface of undeformed body
p	empirical constant in creep law
q	lateral load intensity on circular plate
r	radial coordinate

[1] Supersedes NACA Technical Note 4003 by J. Lyell Sanders, Jr., Harvey G. McComb, Jr., and Floyd R. Schlechte, 1957.

Preceding Page Blank

s_{ij}	stress-deviator tensor
t	time
u	displacement in x-direction
u_i	displacement vector
$\bar{u}_i$	prescribed displacement vector on S_d
v	displacement in y-direction
w	displacement in z-direction
x,y,z	coordinates
$\gamma_{xz},\gamma_{yz},\gamma_{xy}$	shear strains in xz-, yz-, and xy-directions, respectively
Δ	amplitude of initial bow of column divided by column thickness
δ_{ij}	Kronecker delta
ϵ	strain, positive in tension
ϵ_{ij}	strain tensor
ϵ'_{ij}	noncreep portion of strain tensor
ϵ''_{ij}	creep strain tensor
ϵ_r,ϵ_t	radial and tangential strains, respectively
$\epsilon_x,\epsilon_y,\epsilon_z$	strain in x-, y-, and z-directions, respectively
θ	angular coordinate
λ	empirical constant in creep law
μ	Poisson's ratio
$\rho=r/R$	
σ	stress, positive in tension
σ_{ij}	stress tensor
σ_0^*,σ_1^*	stresses defined in equation (27)
σ_0,σ_1	stress coefficients in equations (28)
σ_r,σ_t	radial and tangential stresses, respectively

Dots over quantities denote differentiation with respect to time, a single prime denotes the elastic-plastic part of the strain, and a double prime denotes the creep part of the strain.

FORMULATION OF GENERAL VARIATIONAL THEOREM

For a body subject to creep, the equilibrium equations and strain-displacement relations are the same as those for an elastic body; the only difference in the mathematical formulation of a creep problem is in the stress-strain relation. In the present development, the nonlinear strain-displacement relations and equilibrium equations are used because of the intended application of the variational theorem to collapse problems of columns and plates. However, the strains are still assumed to be small, and the stress-strain relations are written as for infinitesimal strains. The total strain rate is separated into a creep part and a part which includes elastic and plastic effects. The creep part of the strain rate is allowed to depend on time and on the stress deviator but not on the stress rate or the first invariant of stress. In this report, the temperature of the body is assumed to be uniform and constant in time.

In tensor notation, a simple example of the creep law assumed is

$$\dot{\epsilon}''_{ij}=f(J_2,t)s_{ij} \tag{1}$$

where s_{ij} is the stress deviator and J_2 is the second invariant $\frac{1}{2}s_{ij}s_{ij}$. For purposes of the present report, the only restriction on the stress-strain relation for the elastic-plastic part of the strain is that the following relation hold (see ref. 6):

$$\dot{\sigma}_{ij}d\dot{\epsilon}'_{ij}\equiv\dot{\epsilon}'_{ij}d\dot{\sigma}_{ij} \tag{2}$$

The equation for the components of finite strain is

$$\epsilon_{ij}=\frac{1}{2}(u_{i,j}+u_{j,i}+u_{k,i}u_{k,j}) \tag{3}$$

or, in differentiated form,

$$\dot{\epsilon}_{ij}=\frac{1}{2}(\dot{u}_{i,j}+\dot{u}_{j,i}+\dot{u}_{k,i}u_{k,j}+u_{k,i}\dot{u}_{k,j}) \tag{4}$$

The equilibrium equation is

$$[(\delta_{ik}+u_{i,k})\sigma_{jk}]_{,j}=0 \tag{5}$$

The equation giving the surface traction T_i in terms of stresses and displacements on the boundary is

$$T_i=\sigma_{jk}n_j(\delta_{ik}+u_{i,k}) \tag{6}$$

where n_j is the unit external normal to the surface of the undeformed body.

The components of the tensor ϵ_{ij} are not true strains, and neither are the components of the tensor σ_{ij} true stresses. However, the specific virtual work due to a virtual displacement δu_i is given by

$$\delta W=\sigma_{ij}\delta\epsilon_{ij}$$

Therefore, the tensor σ_{ij} may be considered to be the generalized force conjugate to the generalized displacement ϵ_{ij}. In reference 7, this tensor is called k_{ij} and in reference 8 it is called σ^*_{ij}.

As in many of the variational theorems of the mathematical theory of plasticity (see ref. 6), the variational theorem to be stated here is for stress rates and strain rates; that is, if the states of stress and strain throughout the body are known at a given instant, then application of the variational theorem singles out the stress rates or strain rates that actually occur from those rates of stress or strain considered in the enunciation of the theorem. Thus, the operator δ in the formal process of taking the variations is applied only to time derivatives of quantities and not to the quantities themselves. Because of this, for example, $\delta\dot{\epsilon}''_{ij}=0$ because $\dot{\epsilon}''_{ij}$ depends upon the state of stress but not upon the stress rate. (See eq. (1).)

The quantity to be varied was constructed by an inverse process guided by the form of Reissner's theorem and the first theorem of Wang and Prager. By trial and error, the terms necessary to obtain the desired result were found for the integral to be varied. Let $\dot{T}_i=\dot{\bar{T}}_i$ be prescribed on the part S_s of the bounding surface S of a body and let $\dot{u}_i=\dot{\bar{u}}$ be prescribed on the remaining part S_d of the boundary. The variational theorem to be proved is $\delta I=0$ where

$$I=\int_V\left[\dot{\epsilon}_{ij}\dot{\sigma}_{ij}+\frac{1}{2}\dot{u}_{k,i}\dot{u}_{k,j}\sigma_{ij}-\frac{1}{2}(\dot{\epsilon}'_{ij}+2\dot{\epsilon}''_{ij})\dot{\sigma}_{ij}\right]dV-\int_{S_s}\dot{\bar{T}}_i\dot{u}_i\,dS-\int_{S_d}(\dot{u}_i-\dot{\bar{u}}_i)\dot{T}_i\,dS \tag{7}$$

In the first term of the volume integral, $\dot{\epsilon}_{ij}$ is understood to

be written in terms of displacements and velocities (eq. (4)). In the third term of the volume integral, $\dot{\epsilon}'_{ij}$ is understood to be written in terms of stresses and stress rates, whereas $\dot{\epsilon}''_{ij}$ is written in terms of stresses.

The variation of I is given by

$$\delta I=\int_V\left[\dot{\epsilon}_{ij}\delta\dot{\sigma}_{ij}+\dot{\sigma}_{ij}\delta\dot{\epsilon}_{ij}+\sigma_{ij}\dot{u}_{k,i}\,\delta\dot{u}_{k,j}-\frac{1}{2}\,\dot{\sigma}_{ij}\delta\dot{\epsilon}'_{ij}-\frac{1}{2}\,(\dot{\epsilon}'_{ij}+2\dot{\epsilon}''_{ij})\delta\dot{\sigma}_{ij}\right]dV-\int_{S_\sigma}\dot{\bar{T}}_i\delta\dot{u}_i dS-\int_{S_d}[(\dot{u}_i-\dot{\bar{u}}_i)\delta\dot{T}_i+\dot{T}_i\delta\dot{u}_i]\,dS \quad (8)$$

where $\delta\dot{\epsilon}''_{ij}=0$ as previously noted. The second term in the volume integral may be transformed by an integration by parts. The following formula applies:

$$\int_V\dot{\sigma}_{ij}\delta\dot{\epsilon}_{ij}dV=\int_S\dot{\sigma}_{ij}n_j(\delta_{ik}+u_{k,i})\delta\dot{u}_k dS-\int_V[(\delta_{ik}+u_{k,i})\dot{\sigma}_{ij}]_{,j}\,\delta\dot{u}_k dV \quad (9)$$

The third term may also be integrated by parts; thus,

$$\int_V\sigma_{ij}\dot{u}_{k,i}\,\delta\dot{u}_{k,j}\,dV=\int_S\sigma_{ij}n_j\dot{u}_{k,i}\,\delta\dot{u}_k dS-\int_V(\sigma_{ij}\dot{u}_{k,i})_{,j}\,\delta\dot{u}_k dV \quad (10)$$

By using equations (9), (10), and (2), equation (8) becomes

$$\delta I=\int_V\{\dot{\epsilon}_{ij}\delta\dot{\sigma}_{ij}-[(\delta_{ik}+u_{k,i})\dot{\sigma}_{ij}]_{,j}\,\delta\dot{u}_k-(\sigma_{ij}\dot{u}_{k,i})_{,j}\,\delta\dot{u}_k-(\dot{\epsilon}'_{ij}+\dot{\epsilon}''_{ij})\delta\dot{\sigma}_{ij}\}dV+\int_S[\dot{\sigma}_{ij}n_j(\delta_{ik}+u_{k,i})+\sigma_{ij}n_j\dot{u}_{k,i}]\delta\dot{u}_k dS-\int_{S_\sigma}\dot{\bar{T}}_i\delta\dot{u}_i dS-\int_{S_d}[(\dot{u}_i-\dot{\bar{u}}_i)\delta\dot{T}_i+\dot{T}_i\,\delta\dot{u}_i]dS \quad (11)$$

or

$$\delta I=\int_V\left\{(\dot{\epsilon}_{ij}-\dot{\epsilon}'_{ij}-\dot{\epsilon}''_{ij})\,\delta\dot{\sigma}_{ij}-\delta\dot{u}_k\frac{d}{dt}[(\delta_{ik}+u_{k,i})\sigma_{ij}]_{,j}\right\}dV+\int_{S_\sigma}(\dot{T}_i-\dot{\bar{T}}_i)\delta\dot{u}_i dS-\int_{S_d}(\dot{u}_i-\dot{\bar{u}}_i)\delta\dot{T}_i dS \quad (12)$$

The coefficient of each of the variations vanishes by virtue of the stress-strain relations, equilibrium equations, stress boundary conditions, and displacement boundary conditions, respectively. Thus, it is proved that $\delta I=0$ for the stress rates and strain rates that actually occur.

A term may be added to the volume integral to include the effects of body forces if necessary. In some special cases, the boundary integrals should be modified if boundary conditions other than those on T_i or u_i are imposed.

In the next section, a form for I appropriate for application to thin-plate and column problems is developed.

THEORETICAL APPLICATION OF VARIATIONAL THEOREM TO PLATE AND COLUMN PROBLEMS

The variational theorem proved in the preceding section provides a powerful means for deriving an appropriate two-dimensional theory for thin plates subject to creep (or one-dimensional theory for beams and columns) analogous to the two-dimensional theory for thin elastic plates. If certain simplifying assumptions are made about the dependence of the various displacements and stresses on the z-coordinate (measured normal to the middle surface), the integrations with respect to z in the integral I may then be carried out. The equations resulting from $\delta I=0$ then involve only x, y, and t as independent variables.

In this report, the same simplifying assumptions with regard to displacements are made that were made in the elastic case. In particular, the Bernoulli-Euler hypothesis is retained. This hypothesis can be regarded as a consequence of the equilibrium equations and the strain-displacement equations as applied to a thin plate. The transverse shear stresses vanish on the surface of the plate and are thus expected to be negligible (compared with inplane stresses) throughout the thickness. By any of the common stress-strain relations (elastic, plastic, or creep), it follows that the transverse shear strains are negligible. If w is assumed to be approximately independent of z, then from

$$\gamma_{xz}=\frac{\partial w}{\partial x}+\frac{\partial u}{\partial z}=0 \quad (13)$$

$$\gamma_{yz}=\frac{\partial w}{\partial y}+\frac{\partial v}{\partial z}=0 \quad (14)$$

it follows that

$$u=U-z\,\frac{\partial W}{\partial x} \quad (15)$$

$$v=V-z\,\frac{\partial W}{\partial y} \quad (16)$$

$$w=W \quad (17)$$

where U, V, and W can now be identified as the displacements of the middle surface. Equations (15), (16), and (17) express the Bernoulli-Euler hypothesis.

A more rigorous treatment, in which the dependence of the various quantities on the z-coordinate is deduced by expanding them in powers of a thickness parameter, might be possible. In some derivations of plate equations, U, V, and W are interpreted as weighted averages of u, v, and w. (See refs. 4 and 9, for example.) However, the consequences of assuming equations (15), (16), and (17) to be true are expected to lead to accurate results for thin plates.

Equation (3) for the finite strains in terms of displacements is simplified by dropping all nonlinear terms except those containing powers or products of slopes. This simplification leads to the Von Kármán equations for an elastic plate. The resulting equations for the strains are

$$\epsilon_x=\frac{\partial U}{\partial x}-z\,\frac{\partial^2 W}{\partial x^2}+\frac{1}{2}\left(\frac{\partial W}{\partial x}\right)^2 \quad (18)$$

$$\epsilon_y=\frac{\partial V}{\partial y}-z\,\frac{\partial^2 W}{\partial y^2}+\frac{1}{2}\left(\frac{\partial W}{\partial y}\right)^2 \quad (19)$$

$$2\epsilon_{xy}=\gamma_{xy}=\frac{\partial U}{\partial y}+\frac{\partial V}{\partial x}-2z\,\frac{\partial^2 W}{\partial x\partial y}+\frac{\partial W}{\partial x}\,\frac{\partial W}{\partial y} \quad (20)$$

$$\epsilon_z=\gamma_{xz}=\gamma_{yz}=0 \tag{21}$$

In order to be consistent with these approximations, only terms containing powers or products of rates of slope are retained in the second term of the volume integral in I. (See eq. (7).)

Before the integration with respect to z can be carried out in the expression for I, the dependence of the stresses upon z must be assumed. Unlike the elastic case, the stresses do not vary linearly through the thickness, even though the strains do vary linearly. The particular advantage of the generalized form of Reissner's variational theorem for use in the present problem is that approximations for the stresses and strains can be made independently. Thus, there is no necessity to invert the stress-strain relations in order to determine appropriate approximations for the stresses; in fact, to invert the stress-strain relations would generally be impossible.

Many possibilities exist for assuming the form of the stresses as functions of z, and each possibility leads to a different set of plate equations; thus, no particular system of equations can be set up which can be called the creep equations for a plate, column, or beam. Generally, it is advantageous to assume the form of the stresses and displacements as functions of x and y also, in which case all the integrations in I may be performed. Setting the variation of the resulting expression equal to zero leads to a set of ordinary differential equations in which the independent variable is the time. Further details of the application of the variational theorem to creep-collapse and creep-bending problems of columns and plates can best be communicated by means of examples, two of which are given in the following sections.

EXAMPLE OF APPLICATION OF VARIATIONAL THEOREM TO CREEP COLLAPSE OF COLUMNS

A simplified treatment of the problem of creep collapse of the uniform, pin-ended, rectangular-section column shown in figure 1 is given as the first example. The plastic part of the strain is omitted, and the stress-strain relation is assumed to be

$$\dot{\epsilon}=\frac{\dot{\sigma}}{E}+\lambda p t^{p-1}\sigma^m \tag{22}$$

where the second term on the right includes the effects of primary and secondary creep. The axial displacement u is assumed to be given by

$$u=U-z\frac{\partial W}{\partial x} \tag{23}$$

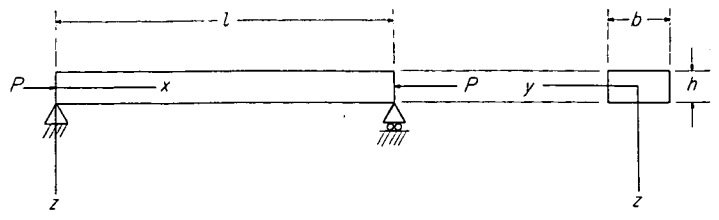


FIGURE 1.—Pin-ended rectangular-section column.

and the axial strain ϵ by

$$\epsilon=\frac{\partial U}{\partial x}-z\frac{\partial^2 W}{\partial x^2}+\frac{1}{2}\left(\frac{\partial W}{\partial x}\right)^2 \tag{24}$$

In the present case, the following terms enter into the expression for I:

$$\left.\begin{aligned}
&\dot{\sigma}_{ij}\dot{\epsilon}_{ij}=\dot{\sigma}\left(\frac{\partial\dot{U}}{\partial x}+\frac{\partial W}{\partial x}\frac{\partial\dot{W}}{\partial x}-z\frac{\partial^2\dot{W}}{\partial x^2}\right)\\
&\frac{1}{2}\sigma_{ij}\dot{u}_{k,i}\dot{u}_{k,j}=\frac{1}{2}\sigma\left(\frac{\partial\dot{W}}{\partial x}\right)^2\\
&\frac{1}{2}(\dot{\epsilon}'_{ij}+2\dot{\epsilon}''_{ij})\dot{\sigma}_{ij}=\frac{\dot{\sigma}^2}{2E}+\lambda p t^{p-1}\dot{\sigma}\sigma^m\\
&\int_{S_\sigma}\dot{\bar{T}}_i\dot{u}_i\,dS=-P\dot{U}(l,t)=0 \qquad (P \text{ is constant})
\end{aligned}\right\} \tag{25}$$

where $U(0, t)=0$. The special form of I for the column is then

$$I=\int_V\left[\dot{\sigma}\left(\frac{\partial\dot{U}}{\partial x}+\frac{\partial W}{\partial x}\frac{\partial\dot{W}}{\partial x}-z\frac{\partial^2\dot{W}}{\partial x^2}\right)+\frac{1}{2}\sigma\left(\frac{\partial\dot{W}}{\partial x}\right)^2-\frac{\dot{\sigma}^2}{2E}-\lambda p t^{p-1}\dot{\sigma}\sigma^m\right]dV \tag{26}$$

For simplicity, the variation of σ in the z-direction is assumed to be linear; thus,

$$\sigma=\sigma_0^*+\frac{z}{h}\sigma_1^* \tag{27}$$

The variation of displacements and stresses in the x-direction is assumed as follows:

$$\left.\begin{aligned}
&W=hW_0\sin\frac{\pi x}{l}\\
&U=U_0 x\\
&\sigma_0^*=\frac{P}{bh}\sigma_0\\
&\sigma_1^*=\frac{P}{bh}\sigma_1\sin\frac{\pi x}{l}
\end{aligned}\right\} \tag{28}$$

where h is the thickness of the column, b is the width, and l is the length. The dimensionless quantities on the right-hand sides of equations (28) are functions of time alone. The integrations in I may be carried out, and the result is (for $m=3$)

$$I=\frac{P^2 l}{bhE}\left[\frac{P_c}{P}\left(6\dot{\sigma}_0W_0\dot{W}_0+\frac{1}{2}\dot{\sigma}_1\dot{W}_0+3\sigma_0\dot{W}_0^2\right)-\frac{1}{2}\left(\dot{\sigma}_0^2+\frac{1}{24}\dot{\sigma}_1^2\right)+\frac{bhE}{P}\dot{\sigma}_0\dot{U}_0-\lambda p t^{p-1}E\left(\frac{P}{bh}\right)^2\left(\sigma_0^3\dot{\sigma}_0+\frac{1}{8}\sigma_0\sigma_1^2\dot{\sigma}_0+\frac{1}{8}\sigma_0^2\sigma_1\dot{\sigma}_1+\frac{3}{640}\sigma_1^3\dot{\sigma}_1\right)\right] \tag{29}$$

where P_c is the buckling load of the column. The system of

differential equations to which the present approximate analysis leads is obtained by equating to zero the partial derivatives of I with respect to each of the dotted quantities; thus, the result is

$$\left.\begin{aligned}
&\dot{\sigma}_0=0\\
&6\dot{\sigma}_0W_0+\frac{1}{2}\dot{\sigma}_1+6\sigma_0\dot{W}_0=0\\
&6\frac{P_c}{P}W_0\dot{W}_0-\dot{\sigma}_0+\frac{bhE}{P}\dot{U}_0-\lambda pt^{p-1}E\left(\frac{P}{bh}\right)^2\left(\sigma_0^3+\frac{1}{8}\sigma_0\sigma_1^2\right)=0\\
&\frac{1}{2}\frac{P_c}{P}\dot{W}_0-\frac{1}{24}\dot{\sigma}_1-\lambda pt^{p-1}E\left(\frac{P}{bh}\right)^2\left(\frac{1}{8}\sigma_0^2\sigma_1+\frac{3}{640}\sigma_1^3\right)=0
\end{aligned}\right\}\quad(30)$$

The solution of this set of equations depends on the initial conditions assigned. Suppose that the column has an initial bow in the form of a half sine wave before the load P is applied. If the load is assumed to be applied rapidly, but not rapidly enough to introduce inertia effects, then the initial conditions for the creep problem are those existing immediately after the load is applied. If the initial bow is given by

$$h\Delta\sin\frac{\pi x}{l}$$

the initial conditions for the dimensionless quantities are

$$\left.\begin{aligned}
W_0(0)&=\frac{\Delta}{1-\frac{P}{P_c}}\\
\sigma_0(0)&=-1\\
\sigma_1(0)&=\frac{12\Delta}{1-\frac{P}{P_c}}
\end{aligned}\right\}\quad(31)$$

The problem can now be reduced to solving the following equation for W_0:

$$\left(\frac{P_c}{P}-1\right)\dot{W}_0-3\lambda pt^{p-1}E\left(\frac{P}{bh}\right)^2\left(W_0+\frac{27}{5}W_0^3\right)=0\quad(32)$$

Except for differences in notation, this equation is similar to one given by Kempner (eq. (27) of ref. 10) for an idealized two-element column problem solved by a collocation method, except that the constant $^{27}/_{5}$ is replaced by $^{3}/_{5}$ and p is replaced by 1. Equation (32) is easily integrated to give

$$t^p=\frac{\frac{P_c}{P}-1}{6\lambda E\left(\frac{P}{bh}\right)^2}\log\left[\frac{W_0^2}{1+\frac{27}{5}W_0^2}\,\frac{1+\frac{27}{5}W_0^2(0)}{W_0^2(0)}\right]\quad(33)$$

The collapse time t_c is found by taking the limit as $W_0\to\infty$; thus,

$$t_c=\left\{\frac{\frac{P_c}{P}-1}{6\lambda E\left(\frac{P}{bh}\right)^2}\log\left[1+\frac{5\left(1-\frac{P}{P_c}\right)^2}{27\Delta^2}\right]\right\}^{1/p}\quad(34)$$

The foregoing analysis is intended merely as an example; more elaborate assumptions as to the stress variation through the thickness and the variation of the several unknowns along the length of the column lead to systems of nonlinear differential equations which may be solved by some numerical method.

EXAMPLE OF APPLICATION OF VARIATIONAL THEOREM TO CREEP BENDING OF PLATES

For a second example, the bending of a simply supported circular plate under a constant uniform load is considered. (See fig. 2.) For simplicity, the analysis is restricted to the time during which the deflections are small so that the linear strain-displacement relations can apply. The general form for I in this case is

$$I=\int_V\left[\dot{\epsilon}_{ij}\dot{\sigma}_{ij}-\frac{1}{2}(\dot{\epsilon}'_{ij}+2\dot{\epsilon}''_{ij})\dot{\sigma}_{ij}\right]dV\quad(35)$$

Here, again, the effects of plasticity are neglected. The creep law is that given by equation (1). The various terms in the integrand must be specialized to apply to the present plate problem. In polar coordinates the shear stress and shear strain are zero from symmetry, and the remaining stresses

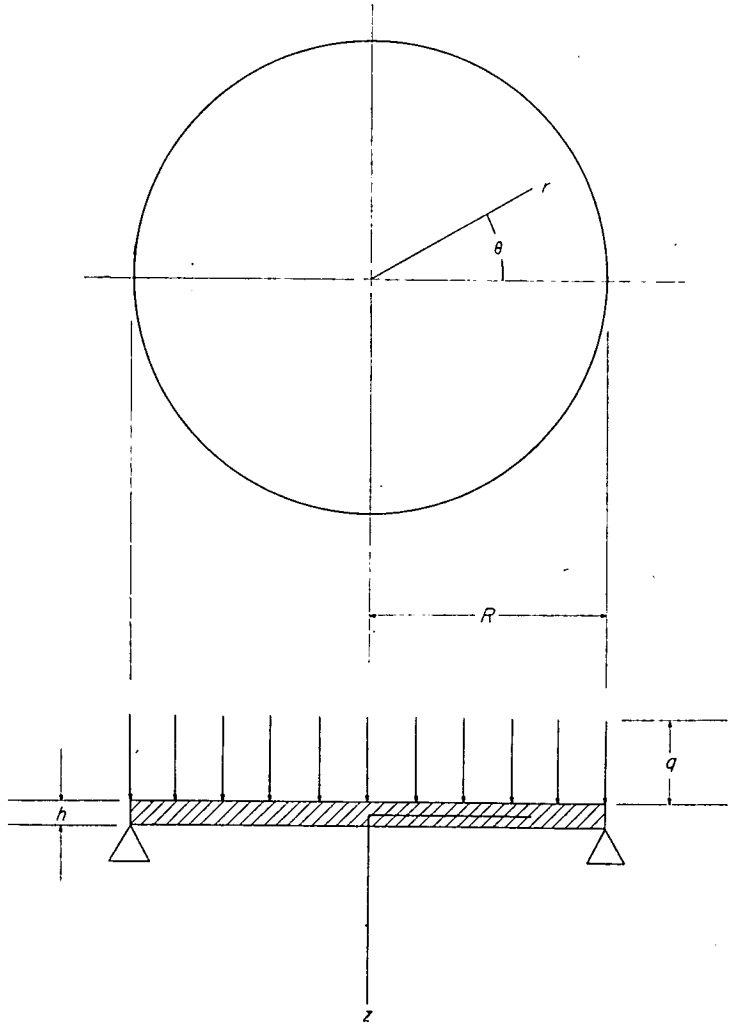


FIGURE 2.—Simply supported circular plate with lateral load.

and strains give

$$\dot{\epsilon}_{ij}\dot{\sigma}_{ij}=\dot{\epsilon}_r\dot{\sigma}_r+\dot{\epsilon}_t\dot{\sigma}_t \tag{36}$$

If a linear strain distribution through the thickness is assumed,

$$\dot{\epsilon}_{ij}\dot{\sigma}_{ij}=-z\frac{\partial^2\dot{W}}{\partial r^2}\dot{\sigma}_r-\frac{z}{r}\frac{\partial\dot{W}}{\partial r}\dot{\sigma}_t \tag{37}$$

For the elastic part of the second term in equation (35)

$$\frac{1}{2}\dot{\epsilon}'_{ij}\dot{\sigma}_{ij}=\frac{1}{2E}(\dot{\sigma}_r^2+\dot{\sigma}_t^2-2\mu\dot{\sigma}_r\dot{\sigma}_t) \tag{38}$$

For the creep part of the second term,

$$\dot{\epsilon}''_{ij}\dot{\sigma}_{ij}=f(J_2)s_{ij}\dot{\sigma}_{ij}=f(J_2)\dot{J}_2 \tag{39}$$

Further, it is assumed that the form of f is such that

$$\dot{\epsilon}''_{ij}\dot{\sigma}_{ij}=\lambda J_2^m\dot{J}_2 \tag{40}$$

In this example, the exponent m is taken to be unity; this assumption corresponds to the cubic law in the uniaxial stress case. Then,

$$\dot{\epsilon}''_{ij}\dot{\sigma}_{ij}=\frac{1}{9}\lambda(\sigma_r^2+\sigma_t^2-\sigma_r\sigma_t)[\dot{\sigma}_r(2\sigma_r-\sigma_t)+\dot{\sigma}_t(2\sigma_t-\sigma_r)] \tag{41}$$

The variation of the stresses through the thickness is assumed to be linear; thus,

$$\left.\begin{aligned}\sigma_r&=\frac{12M_rz}{h^3}\\ \sigma_t&=\frac{12M_tz}{h^3}\end{aligned}\right\} \tag{42}$$

Doubtless, after creep is well established, the stress distribution cannot actually be linear in the thickness direction, but, for purposes of this example, such an approximation is sufficient. When integration in the z-direction is carried out,

$$I=-\int_0^{2\pi}\int_0^1\left\{\rho M_r\dot{W}''+\dot{M}_t\dot{W}'+\frac{6R^2\rho}{Eh^3}(\dot{M}_r^2+\dot{M}_t^2-2\mu\dot{M}_r\dot{M}_t)+\frac{144}{5}\frac{\lambda R^2\rho}{h^7}(M_r^2+M_t^2-M_rM_t)[\dot{M}_r(2M_r-M_t)+\dot{M}_t(2M_t-M_r)]\right\}d\rho\,d\theta \tag{43}$$

where R is the radius of the plate, $\rho=r/R$, and the primes denote differentiation with respect to ρ. The following expressions, based on the elastic solution for this problem, are assumed for the displacements and moments:

$$\left.\begin{aligned}W&=h(1-\rho^2)(W_0+\rho^2W_1)\\ M_r&=Eh^2M_{r,0}(1-\rho^2)\\ M_t&=Eh^2(M_{t,0}+\rho^2M_{t,1})\end{aligned}\right\} \tag{44}$$

Equations (44) are substituted into equation (43) and the integrations carried out. Then, on equating to zero the partial derivatives with respect to the dotted quantities, the following equations are obtained:

$$\left.\begin{aligned}&\dot{M}_{r,0}+2\dot{M}_{t,0}+\dot{M}_{t,1}=0\\ &3\dot{M}_{r,0}+\dot{M}_{t,1}=0\\ &\dot{W}_0+\dot{W}_1-2\left(\frac{R}{h}\right)^2[2\dot{M}_{r,0}-\mu(3\dot{M}_{t,0}+\dot{M}_{t,1})]=2\frac{144\lambda E^3}{5}\left(\frac{R}{h}\right)^2I_1\\ &\dot{W}_0-3\left(\frac{R}{h}\right)^2(2\dot{M}_{t,0}+\dot{M}_{t,1}-\mu\dot{M}_{r,0})=\frac{144\lambda E^3}{5}\left(\frac{R}{h}\right)^2I_2\\ &3\dot{W}_0+\dot{W}_1-6\left(\frac{R}{h}\right)^2(3\dot{M}_{t,0}+2\dot{M}_{t,1}-\mu\dot{M}_{r,0})=6\frac{144\lambda E^3}{5}\left(\frac{R}{h}\right)^2I_3\end{aligned}\right\} \tag{45}$$

where

$$\left.\begin{aligned}(Eh^2)^3I_1&=\int_0^1\rho(1-\rho^2)(2M_r-M_t)(M_r^2-M_rM_t+M_t^2)d\rho\\ (Eh^2)^3I_2&=\int_0^1\rho(2M_t-M_r)(M_r^2-M_rM_t+M_t^2)d\rho\\ (Eh^2)^3I_3&=\int_0^1\rho^3(2M_t-M_r)(M_r^2-M_rM_t+M_t^2)d\rho\end{aligned}\right\} \tag{46}$$

Equations (45) can be solved for the five dotted quantities to give

$$\left.\begin{aligned}\dot{W}_0&=\frac{144\lambda E^3}{5}\left(\frac{R}{h}\right)^2\left[I_2-\frac{3(1+\mu)}{8}(3I_3-I_1-I_2)\right]\\ \dot{W}_1&=\frac{144\lambda E^3}{5}\left(\frac{R}{h}\right)^2\left[\frac{3}{2}(I_1-I_2+I_3)+\frac{3(1+\mu)}{8}(3I_3-I_1-I_2)\right]\\ \dot{M}_{r,0}&=\dot{M}_{t,0}=-\frac{1}{3}\dot{M}_{t,1}=\frac{18\lambda E^3}{5}(3I_3-I_1-I_2)\end{aligned}\right\} \tag{47}$$

where the expressions for I_1, I_2, and I_3 are

$$\left.\begin{aligned}I_1&=\frac{1}{40}(3M_{t,0}^3-3M_{t,0}^2M_{t,1}-3M_{t,0}M_{t,1}^2-M_{t,1}^3)\\ I_2&=\frac{5}{40}(5M_{t,0}^3+9M_{t,0}^2M_{t,1}+7M_{t,0}M_{t,1}^2+2M_{t,1}^3)\\ I_3&=\frac{1}{40}(14M_{t,0}^3+32M_{t,0}^2M_{t,1}+27M_{t,0}M_{t,1}^2+8M_{t,1}^3)\end{aligned}\right\} \tag{48}$$

Equations (47) are a system of first-order nonlinear differential equations with time as the independent variable. The initial conditions required to determine the solution are given by the elastic solution to the loaded plate. (See ref. 11.)

Thus,

$$\left.\begin{aligned} W_0(0)&=\frac{q}{E}\left(\frac{R}{h}\right)^4\frac{3(5+\mu)(1-\mu)}{16}\\ W_1(0)&=-\frac{q}{E}\left(\frac{R}{h}\right)^4\frac{3(1-\mu^2)}{16}\\ M_{r,0}(0)&=M_{t,0}(0)=\frac{q}{E}\left(\frac{R}{h}\right)^2\frac{3+\mu}{16}\\ M_{t,1}(0)&=-\frac{q}{E}\left(\frac{R}{h}\right)^2\frac{1+3\mu}{16} \end{aligned}\right\} \tag{49}$$

Since $\dot{M}_{r,0}=\dot{M}_{t,0}$ and $M_{r,0}(0)=M_{t,0}(0)$, it follows that $M_{r,0}=M_{t,0}$. Equations (47) with initial conditions of equations (49) can be integrated numerically by the modified Euler method (ref. 12). Numerical calculations were made for a plate having a ratio of radius to thickness of 50. The value of E used was 7.4×10^6 psi and the value of λE^3 used was 2.72×10^6 per hour. These values together with the cubic uniaxial creep law correspond approximately to characteristics of 2024–T3 aluminum alloy at a temperature of 600° F. (See ref. 2.) Results showing the time history of the maximum deflection of a circular plate under lateral load are presented in figure 3.

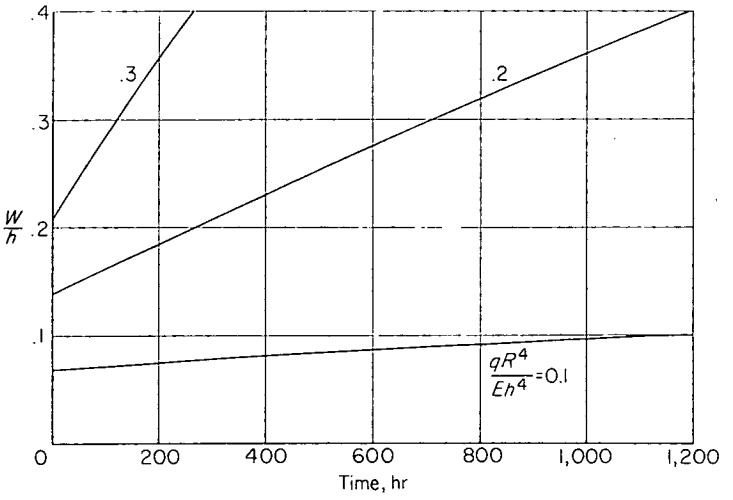


FIGURE 3.—Time history of maximum deflection of simply supported circular plate under lateral load. $\frac{R}{h}=50$; material, 2024–T3 aluminum alloy at 600° F.

CONCLUDING REMARKS

A variational theorem for creep has been formulated which is an extension of a variational theorem developed by Reissner. Various systems of equations leading to approximate solutions to problems of the creep behavior of plates, columns, beams, and shells may be obtained by using direct methods of the calculus of variations in conjunction with the stated theorem. The application of the theorem is illustrated for plates and columns by the solution of two sample problems.

LANGLEY AERONAUTICAL LABORATORY,
NATIONAL ADVISORY COMMITTEE FOR AERONAUTICS,
LANGLEY FIELD, VA., *March 5, 1957.*

REFERENCES

1. Hoff, N. J.: Approximate Analysis of Structures in the Presence of Moderately Large Creep Deformations. Quarterly Appl. Math., vol. XII, no. 1, Apr. 1954, pp. 49–55.
2. Hoff, N. J.: Rapid Creep in Structures. Jour. Aero. Sci., vol. 22, no. 10, Oct. 1955, pp. 661–672, 700.
3. Wang, Alexander, J., and Prager, William: Thermal and Creep Effects in Work-Hardening Elastic-Plastic Solids. Jour. Aero. Sci., vol. 21, no. 5, May 1954, pp. 343–344, 360.
4. Reissner, Eric: On a Variational Theorem in Elasticity. Jour. Math. and Phys., vol. XXIX, no. 2, July 1950, pp. 90–95.
5. Reissner, Eric: On a Variational Theorem for Finite Elastic Deformations. Jour. Math. and Phys., vol. XXXII, nos. 2–3, July–Oct. 1953, pp. 129–135.
6. Hill, R.: The Mathematical Theory of Plasticity. The Clarendon Press (Oxford), 1950, p. 61.
7. Trefftz, E.: Über die Ableitung der Stabilitätskriterien des Elastischen Gleichgewichtes aus der Elastizitätstheorie Endlicher Deformationen. Proc. Third Int. Cong. Appl. Mech. (Stockholm, Sweden, Aug. 24–29, 1930), vol. III, P. A. Norstedt & Söner (Stockholm), 1931, pp. 44–50.
8. Novozhilov, V. V.: Foundations of the Nonlinear Theory of Elasticity. Graylock Press (Rochester, N. Y.), 1953, pp. 61–93.
9. Reissner, Eric: On Bending of Elastic Plates. Quarterly Appl. Math., vol. V, no. 1, Apr. 1947, pp. 55–68.
10. Kempner, Joseph: Creep Bending and Buckling of Nonlinearly Viscoelastic Columns. NACA TN 3137, 1954.
11. Timoshenko, S.: Theory of Plates and Shells. McGraw-Hill Book Co., Inc., 1940, p. 62.
12. Scarborough, James B.: Numerical Mathematical Analysis. Second ed., The Johns Hopkins Press (Baltimore), 1950, pp. 235–240.

REPORT 1343

A PHENOMENOLOGICAL RELATION BETWEEN STRESS, STRAIN RATE, AND TEMPERATURE FOR METALS AT ELEVATED TEMPERATURES [1]

By Elbridge Z. Stowell

SUMMARY

A phenomenological relation between stress, strain rate, and temperature is suggested to account for the behavior of polycrystalline metals above the equicohesive temperature. The properties of the metal included in the relation are elasticity, linear thermal expansion, and viscosity. The relation may be integrated under various conditions to provide information on creep rates, creep rupture, stress-strain curves, and rapid-heating curves. It is shown that for one material—7075–T6 aluminum-alloy sheet—the information yielded by the relation for these four applications agrees reasonably well with test data.

INTRODUCTION

The behavior of metals at elevated temperatures is constantly becoming a more important problem. Not only must information be at hand concerning creep at these temperatures, but information must also be available concerning when rupture might be expected if the creep were allowed to continue, what the stress-strain curve is likely to be at some particular temperature and strain rate, and how the material will behave when rapidly heated to a high temperature. It would be a useful achievement if some fundamental law characteristic of the material could be found, such that these and other apparently distinct problems could be shown to be simply different aspects of the application of one law.

In studies of the creep of metals, it has become apparent that the creep behavior at elevated temperatures is different from that at low temperatures. For relatively pure metals, the line of demarcation for temperature occurs at about one-half the melting point and may be tentatively identified with the equicohesive temperature. In the high-temperature region, certain laws have been found and explicitly stated (ref. 1). These laws appear to give some promise that the behavior of metals in this region may be predicted for effects other than creep.

Creep is characterized by an initial transient or primary region which is followed by a steady or secondary region in which viscous flow occurs and finally by an accelerating or tertiary region which leads to rupture. A theory based on rate-process considerations is already available and accounts in a qualitative manner for the main effects shown by the steady creep in the high-temperature region (ref. 2). For stable metals, this theory requires a knowledge of only three constants to specify the creep behavior: one constant is roughly predictable from the melting point, and the other two must be determined from tests.

In this report, a phenomenological relation between stress, strain rate, and temperature is suggested for this region, and this relation utilizes the existing rate-process theory for steady creep. The relation is not an equation of state of the type proposed by Hollomon (ref. 3) but is an equation of "rate of change of state." Since different integrals of this relation exist under different conditions, there is no single "equation of state" in this case. These integrals are applied to creep, creep rupture, stress-strain curves, and rapid-heating curves, and comparisons of these numerical results are made with experimental results for 7075–T6 aluminum-alloy sheet.

SYMBOLS

ϵ	strain
t	time, hr
$\dot{\epsilon}$	strain rate, per hr
$\dot{\epsilon}_o$	strain rate used in obtaining stress-strain curves, per hr
σ	stress, ksi
σ_o	constant, ksi
σ_{lim}	limiting stress, ksi
E	Young's modulus, ksi
α	linear expansion coefficient, per °K
T	temperature, °K unless otherwise indicated
$\dot{T}_o$	rate of temperature change, °K per hr unless otherwise indicated
$\Delta T=\dot{T}_o t$	
ΔH	activation energy, cal per mole
R	gas constant, taken as 2 cal per mole per °K
s	constant, per hr per °K
$\beta=\frac{\dot{\epsilon}_o}{2sT}e^{\frac{\Delta H}{RT}}$	
$M=\frac{\sqrt{1+\beta^2}}{2\beta}\frac{E\epsilon}{\sigma_o}$	
Subscript:	
r	conditions at rupture

[1] Supersedes NACA Technical Note 4000 by Elbridge Z. Stowell, 1957. (Subsequent to publication of TN 4000, a new and simpler solution for the rapid-heating case has been derived by the author and published as follows: "The Properties of Metals Under Rapid Heating Conditions," Jour. Aero. Sci. (Readers' Forum), vol. 24, no. 12, Dec. 1957, pp. 922-923.)

Preceding Page Blank

STATEMENT OF PHENOMENOLOGICAL RELATION

A metal undoubtedly retains a certain elasticity at elevated temperatures, even though the elastic range is reduced from that prevailing at lower temperatures. The elasticity resides in the crystalline grains and is a measure of the resistance of the crystal lattice to distortion by stress. In addition to the elasticity, a polycrystalline metal also possesses a quasi-viscosity in the high-temperature region; in this region the application of a constant stress will result in a constant strain rate. Also, thermal expansion (or contraction) due to temperature change will create an apparent strain which can contribute to the total strain.

The suggested phenomenological relation which includes all these properties and which takes into account possible temperature changes may be stated as follows:

$$\frac{d\epsilon}{dt}=\dot{\epsilon}=\frac{d}{dt}\left(\frac{\sigma}{E}\right)+\alpha\frac{dT}{dt}+2sTe^{-\frac{\Delta H}{RT}}\sinh\frac{\sigma}{\sigma_o} \tag{1}$$

In this relation the first term on the right supplies the contribution to the strain rate due to elasticity; the middle term, the contribution due to possible thermal expansion; and the final term, the contribution due to viscosity. A relation somewhat similar to this but without the middle term has been proposed for plastics. (See ref. 4.)

The form of the viscous term is taken from reference 2 and is now well established. The exponential term describes the principal effect of temperature. The hyperbolic sine term describes the effect of stress. Kauzmann in reference 2 gave this term as $\sinh\left(m\frac{\sigma}{T}\right)$ where m is a constant, but it has been demonstrated repeatedly by tests that the argument of the term is independent of temperature and is of the form $\frac{\sigma}{\sigma_o}$, where σ_o is a constant. The remainder of the expression, which consists of a number of individual constants multiplied by the temperature T as given in reference 2, is replaced here by $2sT$; the factor 2 is retained for convenience.

The quantities E and α are values which are usually known as functions of the temperature. The quantities s, $\Delta H/R$, and σ_o are found from measurements of the steady creep of the metal under constant stress and temperature. A range of temperature in the high-temperature region and also a range of stress are required to establish $\Delta H/R$ and σ_o, respectively.

APPLICATIONS

With different conditions imposed upon the metal, the suggested relation should generate in turn the laws governing such phenomena as steady creep, creep rupture, stress-strain characteristics, and behavior under rapid-heating conditions. These laws are derived from equation (1).

STEADY CREEP

If stress σ and temperature T are constant, equation (1) reduces to

$$\dot{\epsilon}=2sTe^{-\frac{\Delta H}{RT}}\sinh\frac{\sigma}{\sigma_o} \tag{2}$$

or

$$\dot{\epsilon}=sTe^{-\frac{\Delta H}{RT}}e^{\frac{\sigma}{\sigma_o}} \qquad (\sigma\gg\sigma_o) \tag{2a}$$

which indicates steady creep. Equation (2a) may also be written as

$$\frac{\sigma}{\sigma_o}=\frac{\Delta H}{RT}+\log_e\dot{\epsilon}-\log_e sT \tag{3}$$

in which $\log_e sT$ is substantially constant over a limited temperature range. Stress plotted against $\log_e\dot{\epsilon}$ should, therefore, yield straight lines with slope σ_o which are displaced from one another at different temperatures by amounts depending mainly on the value of $\frac{\Delta H}{RT}$. Stress is sometimes plotted against the parameter $\frac{\Delta H}{RT}+\log_e\dot{\epsilon}$ (ref. 5) to demonstrate that data taken at different temperatures will fall on a single curve.

CREEP RUPTURE

At constant stress and temperature, the strain at a time t after the application of stress is

$$\epsilon=\dot{\epsilon}t$$

since the creep is steady under these conditions.

Reference 6 discloses as an experimental fact that if t_r is the time to rupture under conditions of creep, then

$$\dot{\epsilon}t_r\approx\text{Constant}=\epsilon_r$$

Thus,

$$\dot{\epsilon}=\frac{\epsilon_r}{t_r}$$

and equation (3) may be rewritten as

$$\frac{\sigma_r}{\sigma_o}=\frac{\Delta H}{RT}-\log_e t_r+\log_e\frac{\epsilon_r}{sT} \tag{3a}$$

Since the last term is substantially constant, the rupture stress σ_r plotted against the parameter $\frac{\Delta H}{RT}-\log_e t_r$ should yield a single straight line with slope σ_o. Such a parameter has been employed in the correlation of creep-rupture tests (ref. 7).

STRESS-STRAIN CURVES

At constant temperature, equation (1) becomes

$$\dot{\epsilon}=\frac{1}{E}\frac{d\sigma}{dt}+2sTe^{-\frac{\Delta H}{RT}}\sinh\frac{\sigma}{\sigma_o} \tag{4}$$

Obviously, if the stress is applied very rapidly, the effect of the final viscous term may be negligible compared with the term $\frac{1}{E}\frac{d\sigma}{dt}$; thus, the material may appear to be elastic.

If an attempt is made to hold the strain rate constant, as is sometimes done with conventional testing machines, by setting the strain rate equal to the testing rate $\dot{\epsilon}_o$, a differential equation in σ results, and the solution which is a

family of theoretical stress-strain curves is given as follows:

$$\frac{\sigma}{\sigma_o}=\log_e \frac{\sqrt{1+\beta^2}+(1+\beta)\tanh M}{\sqrt{1+\beta^2}+(1-\beta)\tanh M} \tag{5}$$

where

$$\beta=\frac{\dot{\epsilon}_o}{2sT}e^{\frac{\Delta H}{RT}}$$

$$M=\frac{\sqrt{1+\beta^2}}{2\beta}\frac{E\epsilon}{\sigma_o}$$

$$\epsilon=\dot{\epsilon}_o t$$

Replacement of tanh M by exponentials gives

$$\frac{\sigma}{\sigma_o}=\log_e \frac{(\sqrt{1+\beta^2}+1+\beta)e^{2M}+\sqrt{1+\beta^2}-1-\beta}{(\sqrt{1+\beta^2}+1-\beta)e^{2M}+\sqrt{1+\beta^2}-1+\beta}$$

and since ordinarily $\beta \gg 1$, the expression for the stress-strain curves becomes

$$\frac{\sigma}{\sigma_o}=\log_e \frac{(2\beta+1)e^{2M}-1}{e^{2M}+2\beta-1} \tag{6}$$

At the lower end of the curves where the strain is small, M is small, $e^{2M}\approx 1+2M$, and

$$\frac{\sigma}{\sigma_o}=\log_e \frac{2\beta+2M+4M\beta}{2\beta+2M}=\log_e\left(1+\frac{2M\beta}{M+\beta}\right)\approx\frac{2M\beta}{M+\beta}\approx 2M=\frac{E\epsilon}{\sigma_o}$$

which shows that the initial portion of the curves is elastic. At the upper end of the curves where the strains are large, M is large, and from equation (6),

$$\frac{\sigma_{lim}}{\sigma_o}=\log_e(2\beta+1)\approx\log_e 2\beta \tag{7}$$

where σ_{lim} is the limiting stress which can be developed at that temperature and strain rate.

As a corollary, note that the following equation results when the value of 2β is substituted into equation (7):

$$\dot{\epsilon}_o=sTe^{-\frac{\Delta H}{RT}e^{\frac{\sigma_{lim}}{\sigma_o}}}$$

which is of the same form as equation (2a) for steady creep. Thus, the limiting stress σ_{lim} obtainable bears the same relation to the testing rate $\dot{\epsilon}_o$ that any creep stress σ bears to its corresponding creep rate $\dot{\epsilon}$. This correlation has been noted experimentally by Sherby and Dorn in reference 5 where the ultimate strength in tension is used for σ_{lim}.

RAPID-HEATING CURVES

The material composing the skin of a high-speed airplane or missile may be subjected to rapid increases in temperature as a result of aerodynamic heating during flight. It is important to know what to expect from the material under such conditions.

In equation (1), let $\frac{dT}{dt}=\dot{T}_o$ in which $\dot{T}_o$ is a constant. Then, for a constant stress $\sigma \gg \sigma_o$,

$$\epsilon=\int \dot{\epsilon}\,dt=\sigma\int d\left(\frac{1}{E}\right)+\alpha\dot{T}_o t+se^{\frac{\sigma}{\sigma_o}}\int Te^{-\frac{\Delta H}{RT}}dt \tag{8}$$

in which allowance should be made for the variation of E and α with temperature. Equation (8) may be written in terms of finite increments as follows:

$$\epsilon=\frac{\sigma}{E}+\alpha\,\Delta T+se^{\frac{\sigma}{\sigma_o}}\sum Te^{-\frac{\Delta H}{RT}}\Delta t \tag{9}$$

where

$$\Delta T=\dot{T}_o t$$

The initial term $\frac{\sigma}{E}$ gives the contribution to the total strain of the application of stress, the second term gives the contribution due to thermal expansion, and the last term gives the contribution due to viscosity.

COMPARISON OF THEORY AND EXPERIMENT

A comparison of the laws generated by the assumed relation of equation (1) with experiments performed on one material, 7075–T6 aluminum-alloy sheet, is given in this section.

The alloy is in the solution heat treated and aged condition. Further exposure to elevated temperature results in overaging. The material becomes unstable and suffers a marked reduction in strength with time when subsequently heated in the range from 300° to 600° F. In addition, different batches of the material may vary somewhat among themselves in properties. In view of this variability in the material, the constants in the viscous term were adjusted in each case to give a reasonable fit to the data. Table I shows the constants used in the calculations.

The temperature which separates the high and the low regions is about 300° F for this alloy. Tests performed at temperatures below 300° F should not be expected to show any agreement with calculations. In most cases, the results of such tests have been included to show the extent of the disagreement.

TABLE I

VALUES OF THE CONSTANTS USED IN THE APPLICATIONS

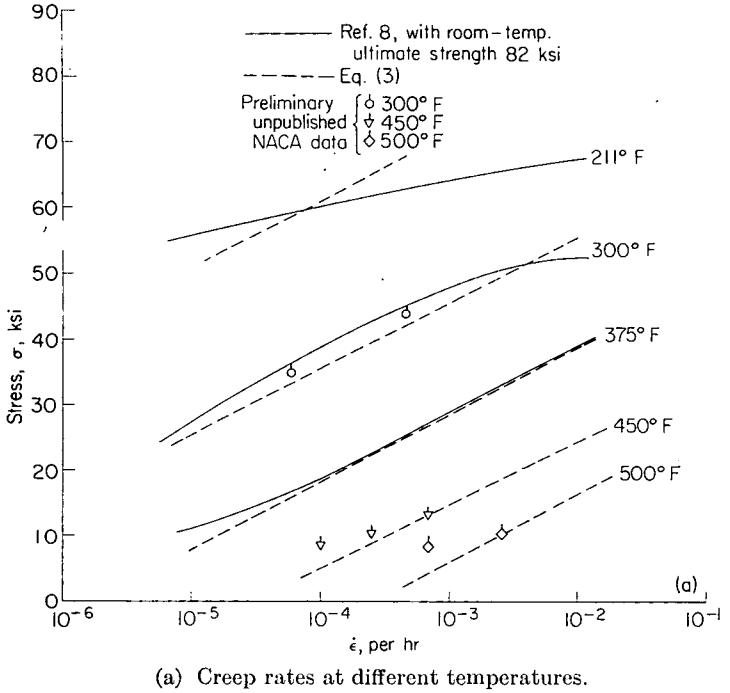
Figure	Application	Reference for experimental data	Equations used in calculations	Constants used in viscous term		
				ΔH, cal per mole	σ_o, ksi	s, per hr per °K
1(a)	Steady creep	8	(3)	35,800	4.3	1.62×10^5
1(b)	Steady creep	8	(3)	35,800	4.3	1.62
2	Creep rupture	8	(3a)	35,800	4.3	1.62
3	Stress-strain curves	9	(6)	34,700	4.3	1.50
4	Rapid-heating curves	9	(9)	34,700	4.3	3.60

526597—60——10

STEADY CREEP

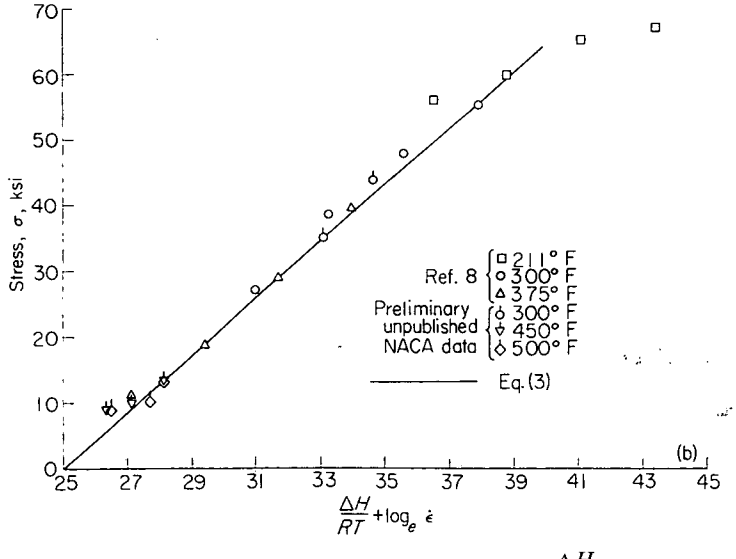
Figure 1 (a) shows steady-creep data for 7075–T6 aluminum-alloy sheet. These data are obtained from reference 8 (solid curves) and from preliminary unpublished NACA data (points). The dashed lines were computed from equation (3) by using the appropriate constants in table I. The dashed lines show a good fit to the data from reference 8 at 300° F and 375° F; the disagreement at 211° F is plainly evident. The dashed lines computed for 450° F and 500° F go through the points obtained at the higher stresses in each case; whereas, the lower stresses give somewhat less creep than would be expected from equation (3). This peculiarity at low stresses has been observed previously by Dorn and Shepard (ref. 1).

Figure 1 (b) shows the same data plotted against the parameter $\frac{\Delta H}{RT}+\log_e \dot{\epsilon}$. All the data fit reasonably well with the calculated curve (eq. (3)) with the exception of the points obtained at 211° F.



(a) Creep rates at different temperatures.

FIGURE 1.—Steady creep rates for 7075–T6 aluminum-alloy sheet.



(b) Correlation of creep rates with parameter $\frac{\Delta H}{RT}+\log_e \dot{\epsilon}$.

FIGURE 1.—Concluded.

CREEP RUPTURE

Figure 2 shows the creep-rupture data, taken from reference 8 and from preliminary unpublished NACA data, plotted against the parameter $\frac{\Delta H}{RT}-\log_e t_r$, where t_r is the rupture time at the stress σ_r and the temperature T. Data show that a reasonable value for the constant ϵ_r is 0.0077; the straight line computed from equation (3a), which uses this value and the values given in table I, goes through the line of points, with the exception as noted before of the very lowest stresses and of the points at 212° F.

STRESS-STRAIN CURVES

Several investigators in the past have pointed out relations between creep and stress-strain data; for example, Hollomon (ref. 3) suggested a graphical procedure for passing from one to the other. In the present report, the passage is accomplished analytically through equation (6).

Figure 3 shows stress-strain curves for the 7075–T6 aluminum-alloy sheet, as given in reference 9, for three temperatures. The strain rate was 0.12 per hr. The theoretical curves obtained by computation from equation (6) (see table I) fit the data well at the higher temperatures but overshoot the 200° F curve by a considerable amount.

RAPID-HEATING CURVES

Figure 4 shows the rapid-heating curves for the 7075–T6 aluminum alloy, taken from reference 9, for three stresses and for widely different temperature rates. The calculated curves represent a severe test of the assumed relation given in equation (1) not only because the cooperation of all four terms is required in equation (9), which is used for computation, but also because the temperatures reached may be considerably higher and the strain rates considerably larger than those encountered in other types of tests. Near the

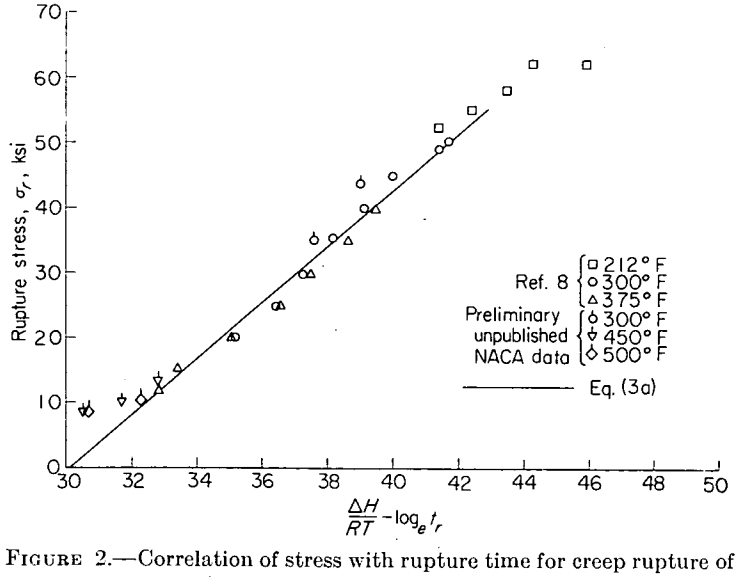


FIGURE 2.—Correlation of stress with rupture time for creep rupture of 7075–T6 aluminum-alloy sheet.

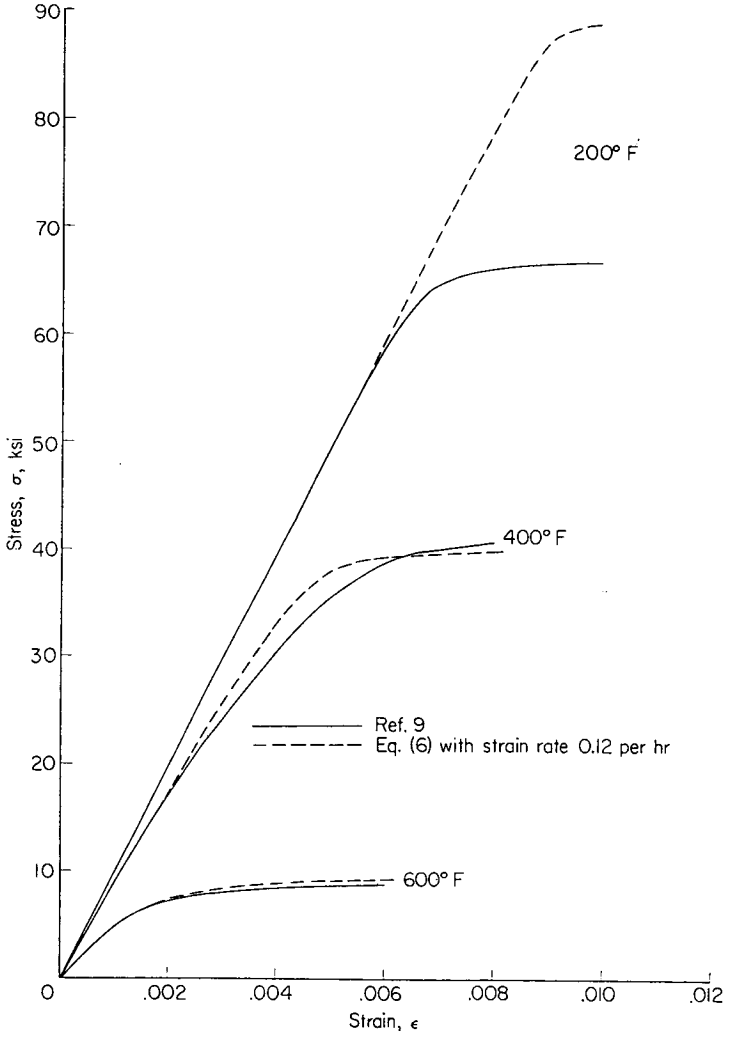


FIGURE 3.—Tensile stress-strain curves for 7075–T6 aluminum-alloy sheet.

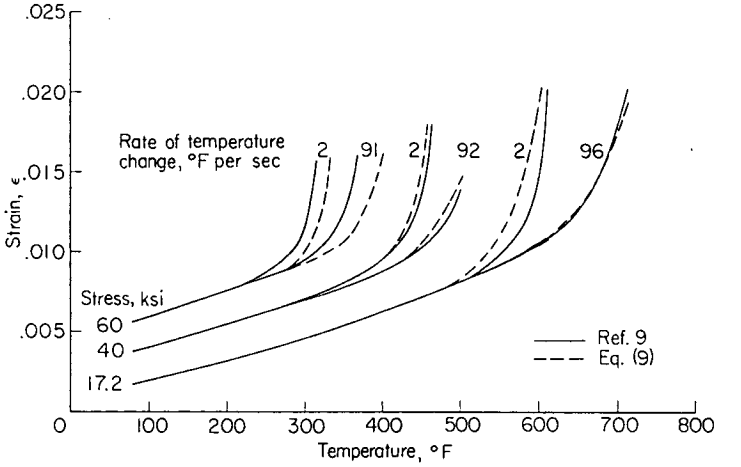


FIGURE 4.—Rapid-heating curves for 7075–T6 aluminum-alloy sheet for three stresses.

upper ends of the curves, calculations were made at sufficiently close intervals of temperature, usually 5° to 10° K, to establish better the points. The shape and the separation of the curves with heating rate are given reasonably well by the theoretical curves except near 300° F, and then the predicted final rapid increases in strain occur at a somewhat higher temperature than that actually observed. The agreement at the lower temperature rate on the curve for 17.2 ksi is not as good as the others.

DISCUSSION

It would appear from the tests reported here that the validity of the relation suggested in equation (1) is borne out for the 7075–T6 aluminum alloy. The relation has shown itself capable of accounting for the steady creep, the creep-rupture data, the stress-strain curves, and the rapid-heating curves for this alloy.

A more satisfactory test of the validity of the relation would be with a more stable material such as pure aluminum. The alloy selected in this report is not such a material but was used because of the existence of the different types of data available. The elevated-temperature phenomena are reasonably well accounted for, however, in spite of this handicap.

The constants in the viscous term vary to different degrees. The activation energy ΔH of the three constants is most nearly constant and is structurally insensitive, being independent of stress, temperature, grain size, and minor alloy additions, and has been tentatively identified with the activation energy for self-diffusion (ref. 1). The magnitude of ΔH is roughly proportional to the melting point of the metal. The quantity σ_o, on the other hand, is structurally sensitive; for pure aluminum, it has a magnitude of about 0.2 ksi, whereas for the 7075–T6 alloy it has a magnitude of 4.3 ksi. For stable materials, it is independent of stress, temperature, and grain size. The quantity s was found to be a constant that is independent of stress and temperature and is subject to the same degree of uncertainty as the strain rate. Repeated steady-creep tests on the same material under identical conditions will yield creep rates within a range of perhaps 2:1. This uncertainty in the creep rate is reflected in a similar uncertainty in the quantity s. It is, therefore, not surprising to find a similar variation in s in the different applications. (See table I.)

For materials which are unstable in the sense that the constants in the viscous term are mainly functions of the temperature, one might expect equation (1) to be still usable if such variations in the constants are allowed for in the computations. If the materials are unstable in the sense that the constants in the viscous term are mainly functions of the time, however, then equation (1) is probably not usable.

Equation (1) is evidently valid for values of stress and temperature which are changing smoothly in one direction, even though these changes may be fairly rapid. For sudden or discontinuous changes in stress or temperature, transients are known to occur which will not be given by equation (1). Some modification of this relation, perhaps by an additional term, will be required to account properly for such transients. Such a modification would have to account for transient creep as well as for other conditions; the nature of the modification is obscure at the present time.

Certain parameters have appeared as a result of this relation and may prove useful in comparing data at different temperatures above the equicohesive temperature. For example, if steady-creep data are available at different stresses and temperatures, stress plotted against the parameter

$\frac{\Delta H}{RT}+\log_e \dot{\epsilon}$ should yield a straight line with slope equal to σ_o. For the stress-strain curves, the parameter which determines the separation of the curves with temperature is $2\beta=\frac{\dot{\epsilon}_o}{sT}e^{\frac{\Delta H}{RT}}$, since the maximum height of the curves is $\sigma_o \log_e 2\beta$. For rupture resulting from creep, rupture stress plotted against $\frac{\Delta H}{RT}-\log_e t_r$ should yield a single straight line with slope equal to σ_o. If the rupture stress were plotted against the parameter $\frac{\Delta H}{RT}+\log_e \frac{\epsilon_r}{sT}-\log_e t_r$, the straight line should pass through the origin.

CONCLUDING REMARKS

The application of the suggested phenomenological rate relation to the determination of steady creep rates, creep-rupture time, stress-strain curves, and rapid-heating curves for 7075–T6 aluminum-alloy sheet has shown that such a relation can be used to cover a wide variety of applications. The possibility of predicting the behavior of materials under widely different load and temperature conditions is indicated for temperatures above the equicohesive temperature for the material. Additional verification of the validity of the relation would be desirable as suitable data over a sufficiently wide range of test conditions become available.

LANGLEY AERONAUTICAL LABORATORY,
NATIONAL ADVISORY COMMITTEE FOR AERONAUTICS,
LANGLEY FIELD, VA., *February 18, 1957.*

REFERENCES

1. Dorn, John E., and Shepard, Lawrence A.: What We Need To Know About Creep. Symposium on Effect of Cyclic Heating and Stressing on Metals at Elevated Temperatures. ASTM Special Tech. Pub. No. 165, ASTM, 1954, pp. 3–30.
2. Kauzmann, Walter: Flow of Solid Metals From the Standpoint of the Chemical-Rate Theory. Tech. Pub. No. 1301, Am. Inst. Mining and Metallurgical Eng., Feb. 1941.
3. Hollomon, John H.: The Mechanical Equation of State. Trans. Am. Inst. Mining and Metallurgical Eng., vol. 171, 1947, pp. 535–545.
4. Freudenthal, Alfred M.: The Inelastic Behavior of Engineering Materials and Structures. John Wiley & Sons, Inc., 1950, pp. 246–247.
5. Sherby, Oleg D., and Dorn, John E.: On the Correlation Between Creep and Tensile Properties of Dilute Alpha Solid Solutions of Aluminum. Sixteenth Tech. Rep. (Ser. 22, Issue 16, N7–onr–295, Task Order II, NR–031–048), Univ. Calif. Inst. Eng. Res., Nov. 15, 1951.
6. Monkman, Forest C., and Grant, Nicholas J.: An Empirical Relationship Between Rupture Life and Minimum Creep Rate in Creep-Rupture Tests. Paper No. 72, A.S.T.M. (Presented at Fifty-Ninth Annual Meeting of A.S.T.M., June 17–22, 1956.)
7. Orr, Raymond L., Sherby, Oleg D., and Dorn, John E.: Correlations of Rupture Data for Metals at Elevated Temperatures. Twenty-Seventh Tech. Rep. (Ser. 22, Issue 27, N7–onr–295, Task Order II, NR–031–048), Univ. Calif. Inst. Eng. Res., July 1, 1953.
8. Anon.: Strength of Metal Aircraft Elements. ANC–5 Bull., Rev. ed., Depts. of Air Force, Navy, and Commerce, Mar. 1955.
9. Heimerl, George J., and Inge, John E.: Tensile Properties of 7075–T6 and 2024–T3 Aluminum-Alloy Sheet Heated at Uniform Temperature Rates Under Constant Load. NACA TN 3462, 1955.

REPORT 1344

A SIMPLIFIED METHOD FOR APPROXIMATING THE TRANSIENT MOTION IN ANGLES OF ATTACK AND SIDESLIP DURING A CONSTANT ROLLING MANEUVER[1]

By Leonard Sternfield

SUMMARY

The transient motion in angles of attack and sideslip during a constant rolling maneuver has been analyzed. Simplified expressions are presented for the determination of the pertinent modes of motion as well as the modal coefficient corresponding to each mode.

Calculations made with and without the derivatives C_{Y_β} (side force due to sideslip) and C_{L_α} (lift-curve slope) indicate that although these derivatives increase the total damping of the system they do not markedly affect the transient motion.

INTRODUCTION

Recent flight tests of airplanes designed with their mass concentrated primarily in the fuselage have indicated that during a rolling maneuver the airplane experiences large uncontrollable motions in angles of attack and sideslip. A fundamental analysis of this pitch-yaw divergence problem, in which the rolling velocity of the airplane is assumed constant, is presented in reference 1. This analysis, concerned primarily with the stability of the system, makes possible the calculation of the divergence boundaries and the prediction of the range of rolling velocities for which the airplane motions will diverge. Analog studies made at the National Advisory Committee for Aeronautics for several research airplanes have indicated that reference 1 is a helpful guide in a roll-coupling investigation, but detailed-motion studies based on five degrees of freedom and with pilot inputs taken into account are essential to the analysis. Also, calculated time histories of the airplane motion indicate that large angles of attack and sideslip which are objectionable to a pilot and which may induce severe loads on the airplane may be encountered for constant rolling velocities outside the critical range.

The purpose of this paper is to extend the analysis of reference 1 by analyzing the transient motion in angles of attack and sideslip. Simplified expressions are presented which permit an accurate and rapid estimate of the maximum angles of attack and sideslip for an airplane rolling at a constant velocity which should apply to the case of an airplane entering a rolling maneuver up to the point of recovery from the maneuver. The airplane is assumed to be initially disturbed by an input in the side-force equation equal to the product of the rolling velocity and trim angle of attack. A comparison is made of the time histories obtained by using the simplified and exact expressions (obtained from the four degrees of freedom assuming constant rolling velocity) for a currently designed swept-wing fighter flying at a Mach number of 0.7 at an altitude of 32,000 feet.

SYMBOLS

b	wing span, ft
$\bar{c}$	wing mean aerodynamic chord, ft
C_L	lift coefficient, $\frac{\text{Lift}}{qS}$
C_l	rolling-moment coefficient, $\frac{\text{Rolling moment}}{qSb}$
C_m	pitching-moment coefficient, $\frac{\text{Pitching moment}}{qS\bar{c}}$
C_n	yawing-moment coefficient, $\frac{\text{Yawing moment}}{qSb}$
C_Y	side-force coefficient, $\frac{\text{Side force}}{qS}$
I_X	moment of inertia of airplane about principal X-axis, slug-ft^2
I_Y	moment of inertia of airplane about principal Y-axis, slug-ft^2
I_Z	moment of inertia of airplane about principal Z-axis, slug-ft^2
M_X	rolling moment, ft-lb
m	airplane mass, slugs
P	period, sec
p	rolling velocity, radians/sec
p_0	steady rolling velocity, radians/sec
q	pitching velocity, radians/sec; dynamic pressure, lb/sq ft
r	yawing velocity, radians/sec
S	wing area, sq ft
t	time, sec
$T_{1/2}$	time to damp to one-half amplitude, sec
T_2	time to double amplitude, sec
V	airplane velocity, ft/sec
α_0	initial angle of attack of airplane principal axis, radians
$\Delta\alpha$	incremental change in angle of attack, radians
$\alpha=\alpha_0+\Delta\alpha$	
β	angle of sideslip, radians
λ	root of characteristic equation
$a\pm i\omega$	complex roots of characteristic equation
λ_1,λ_2	real roots of characteristic equation

[1] Supersedes recently declassified NACA Research Memorandum L56F04 by Leonard Sternfield, 1956

$$\omega_\psi^2=\frac{C_{n_\beta}qSb}{I_Zp_0^2}$$

$$\omega_\theta^2=\frac{-C_{m_\alpha}qS\bar{c}}{I_Yp_0^2}$$

$$C_{m_\alpha}=\frac{\partial C_m}{\partial\alpha}$$

$$C_{n_\beta}=\frac{\partial C_n}{\partial\beta}$$

$$C_{L_\alpha}=\frac{\partial C_L}{\partial\alpha}$$

$$C_{l_p}=\frac{\partial C_l}{\partial\frac{pb}{2V}}$$

$$C_{m_q}=\frac{\partial C_m}{\partial\frac{q\bar{c}}{2V}}$$

$$C_{n_r}=\frac{\partial C_n}{\partial\frac{rb}{2V}}$$

$$C_{Y_\beta}=\frac{\partial C_Y}{\partial\beta}$$

$$L_\alpha=qSC_{L_\alpha}$$

$$M_\alpha=qS\bar{c}C_{m_\alpha}$$

$$M_q=\frac{qS\bar{c}^2}{2V}C_{m_q}$$

$$N_\beta=qSbC_{n_\beta}$$

$$N_r=\frac{qSb^2}{2V}C_{n_r}$$

$$Y_\beta=qSC_{Y_\beta}$$

EQUATIONS OF MOTION

In this analysis, on the assumption of constant forward velocity and constant rolling velocity, the following linearized equations of motion of an airplane referred to the principal axes were used:

Pitching:

$$\dot{q}-\left(\frac{I_Z-I_X}{I_Y}\right)p_0r=\frac{M_qq}{I_Y}+\frac{M_\alpha}{I_Y}\Delta\alpha \tag{1a}$$

Yawing:

$$\dot{r}-\left(\frac{I_X-I_Y}{I_Z}\right)p_0q=\frac{N_r}{I_Z}r+\frac{N_\beta}{I_Z}\beta \tag{1b}$$

Side force:

$$\dot{\beta}+r-p_0\Delta\alpha=\frac{Y_\beta}{mV}\beta+p_0\alpha_0 \tag{1c}$$

Normal force:

$$\dot{\alpha}-q+p_0\beta=-\frac{L_\alpha}{mV}\Delta\alpha \tag{1d}$$

When the substitutions $q=q_0e^{\lambda t}$, $r=r_0e^{\lambda t}$, $\beta=\beta_0e^{\lambda t}$, and $\Delta\alpha=(\Delta\alpha)_0e^{\lambda t}$ are used in the equations written in determinant form, λ must be a root of the stability equation

$$A\lambda^4+B\lambda^3+C\lambda^2+D\lambda+E=0 \tag{2}$$

where

$$A=1$$

$$B=-\frac{N_r}{I_Z}-\frac{M_q}{I_Y}-\frac{Y_\beta}{mV}+\frac{L_\alpha}{mV}$$

$$C=-\left(\frac{I_X-I_Y}{I_Z}\right)\left(\frac{I_Z-I_X}{I_Y}\right)p_0^2-\frac{M_\alpha}{I_Y}+\frac{N_\beta}{I_Z}+\frac{M_q}{I_Y}\frac{N_r}{I_Z}+p_0^2+\frac{Y_\beta}{mV}\frac{N_r}{I_Z}+\frac{Y_\beta}{mV}\frac{M_q}{I_Y}-\frac{L_\alpha}{mV}\frac{N_r}{I_Z}-\frac{L_\alpha}{mV}\frac{M_q}{I_Y}-\frac{L_\alpha}{mV}\frac{Y_\beta}{mV}$$

$$D=-\left(\frac{N_r}{I_Z}+\frac{M_q}{I_Y}\right)p_0^2-\frac{M_q}{I_Y}\frac{N_\beta}{I_Z}+\frac{M_\alpha}{I_Y}\frac{N_r}{I_Z}-\frac{M_q}{I_Y}\frac{N_r}{I_Z}\frac{Y_\beta}{mV}+\frac{M_q}{I_Y}\frac{N_r}{I_Z}\frac{L_\alpha}{mV}+\frac{N_\beta}{I_Z}\frac{L_\alpha}{mV}+\frac{M_\alpha}{I_Y}\frac{Y_\beta}{mV}+\frac{L_\alpha}{mV}\frac{Y_\beta}{mV}\frac{N_r}{I_Z}+\frac{L_\alpha}{mV}\frac{Y_\beta}{mV}\frac{M_q}{I_Y}+\frac{Y_\beta}{mV}\left(\frac{I_X-I_Y}{I_Z}\right)\left(\frac{I_Z-I_X}{I_Y}\right)p_0^2-\frac{L_\alpha}{mV}\left(\frac{I_X-I_Y}{I_Z}\right)\left(\frac{I_Z-I_X}{I_Y}\right)p_0^2$$

and

$$E=-\left(\frac{I_X-I_Y}{I_Z}\right)\left(\frac{I_Z-I_X}{I_Y}\right)p_0^4-\frac{M_\alpha}{I_Y}\left(\frac{I_X-I_Y}{I_Z}\right)p_0^2-\frac{N_\beta}{I_Z}\left(\frac{I_Z-I_X}{I_Y}\right)p_0^2+\frac{M_q}{I_Y}\frac{N_r}{I_Z}p_0^2-\frac{M_\alpha}{I_Y}\frac{N_\beta}{I_Z}-\frac{M_q}{I_Y}\frac{N_\beta}{I_Z}\frac{L_\alpha}{mV}-\frac{M_\alpha}{I_Y}\frac{N_r}{I_Z}\frac{Y_\beta}{mV}-\frac{M_q}{I_Y}\frac{N_r}{I_Z}\frac{L_\alpha}{mV}\frac{Y_\beta}{mV}+\frac{L_\alpha}{mV}\frac{Y_\beta}{mV}\left(\frac{I_X-I_Y}{I_Z}\right)\left(\frac{I_Z-I_X}{I_Y}\right)p_0^2$$

In reference 1, C_{L_α} and C_{Y_β} were assumed to be equal to zero; this assumption is representative of the condition in which the center of gravity is moving in a straight line. In this analysis the case where $C_{L_\alpha}=C_{Y_\beta}=0$ (referred to as case (a)) is considered, as well as the case where the values of C_{L_α} and C_{Y_β} are finite (referred to as case (b)).

ANALYSIS AND DISCUSSION

DIVERGENCE BOUNDARIES

The conditions necessary for the system described by equations (1) to be stable are that the coefficients of the characteristic equation (eq. (2)) must be positive and that Routh's discriminant, $BCD-AD^2-B^2E$, must be greater than zero. From an examination of the characteristic equation of this system, it can be shown that, for aircraft designed with positive static stability and for conditions where each of the damping derivatives C_{n_r}, C_{m_q}, C_{L_α}, and C_{Y_β} adds damping to the system, the oscillatory modes will be stable for all values of the steady rolling velocity. Thus, the only type of instability that could be encountered is an aperiodic mode which occurs when the constant term of the characteristic equation, the E coefficient, is negative. As shown in reference 1, divergence boundaries, obtained by setting $E=0$,

can be plotted as a function of the squares of the natural frequencies in pitch and yaw nondimensionalized to the square of the rolling velocity, ω_θ^2 and ω_ψ^2, respectively. These divergence boundaries are shown in figure 1 for cases (a) and (b) for an airplane whose mass and aerodynamic characteristics are presented in table I. The nondimensional pitch and yaw frequencies of the airplane described in table I fall along the straight line, with the slope equal to $\frac{-C_{m_\alpha}}{C_{n_\beta}} \frac{I_Z}{I_Y} \frac{\bar{c}}{b}$, shown in figure 1. Each point on this line corresponds to a particular value of p_0 and, as p_0 increases, the point moves along the line toward the origin. For case (a), the airplane line intersects the divergence boundaries at two points and thus defines the critical range of rolling velocities where a divergent mode exists, namely, $1.86 < |p_0| < 2.33$. For case (b) the airplane line lies in the stable region and the motion is therefore stable for all values of p_0.

TABLE I

MASS AND AERODYNAMIC CHARACTERISTICS OF AIRPLANE

m, slugs	745
I_X, slug-ft^2	10, 976
I_Y, slug-ft^2	57, 100
I_Z, slug-ft^2	64, 975
C_{n_r}, per radian	−0. 095
C_{m_q}, per radian	−3. 5
C_{m_α}, per radian	−0. 36
C_{n_β}, per radian	0. 057
C_{Y_β}, per radian	−0. 28
C_{L_α}, per radian	3. 85
C_{l_p}, per radian	−0. 255
V, ft/sec	691
S, sq ft	377
$\bar{c}$, ft	11. 3
b, ft	36. 6
q, lb/sq ft	197

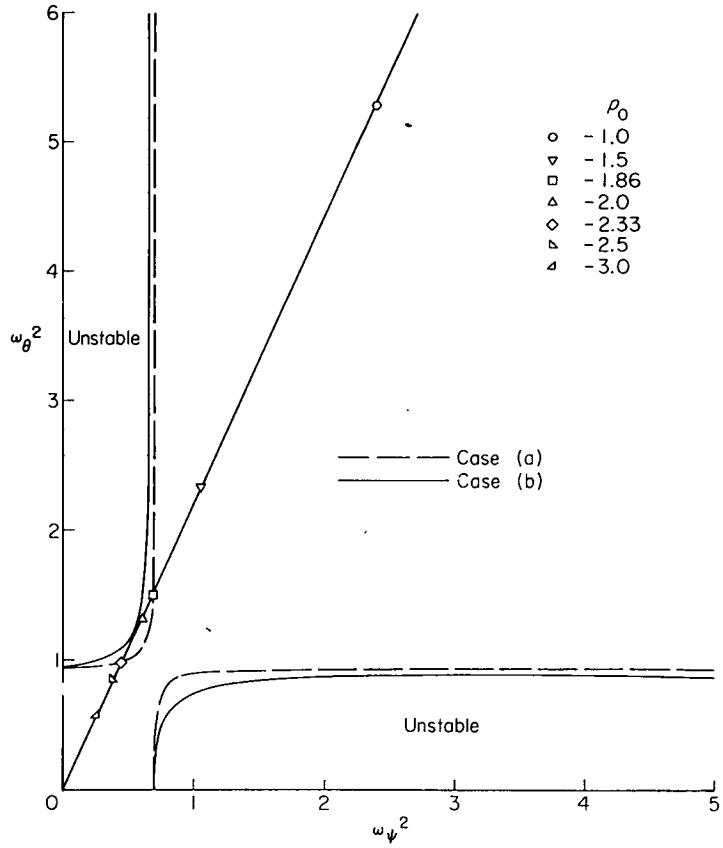


FIGURE 1.—Boundaries in the ω_θ^2, ω_ψ^2 plane which define regions of aperiodic divergence for example airplane.

CHARACTERISTIC MODES

The roots of the characteristic stability equation corresponding to the absolute values of p_0 shown in figure 1 are presented in tables II (a) and II (b) for cases (a) and (b),

TABLE II

ROOTS OF THE CHARACTERISTIC EQUATION FOR VALUES OF p_0 SHOWN IN FIGURE 1

(a) Roots for case (a)

p_0	Exact		Approximate	
0	−0. 210 ± 2. 29i	−0. 0526 ± 1. 54i		
−1. 0	−0. 156 ± 2. 90i	−0. 107 ± 0. 922i	−0. 152 ± 3. 06i	−0. 111 ± 0. 874i
−1. 5	−0. 143 ± 3. 34i	−0. 12 ± 0. 464i	−0. 144 ± 3. 39i	−0. 119 ± 0. 457i
−1. 86	−0. 137 ± 3. 66i	−0. 251 0	−0. 133 ± 3. 67i	−0. 25 0
−2. 0	−0. 135 ± 3. 79i	−0. 355 + 0. 0996	−0. 136 ± 3. 79	−0. 354 + 0. 0997
−2. 33	−0. 131 ± 4. 09i	−0. 256 0	−0. 132 ± 4. 10i	−0. 252 0
−2. 5	−0. 129 ± 4. 24i	−0. 134 ± 0. 267i	−0. 130 ± 4. 26i	−0. 133 ± 0. 294i
−3. 0	−0. 124 ± 4. 70i	−0. 139 ± 0. 768i	−0. 125 ± 4. 77i	−0. 138 ± 0. 756i

(b) Roots for case (b)

p_0	Exact		Approximate	
0	−0. 488 ± 2. 30i	−0. 0729 ± 1. 54i		
−1. 0	−0. 362 ± 2. 89i	−0. 199 ± 0. 942i	−0. 352 ± 3. 10i	−0. 209 ± 0. 876i
−1. 5	−0. 337 ± 3. 33i	−0. 224 ± 0. 483i	−0. 340 ± 3. 42i	−0. 221 ± 0. 469i
−1. 86	−0. 327 ± 3. 66i	−0. 322 −0. 145	−0. 332 ± 3. 71i	−0. 311 −0. 146
−2. 0	−0. 324 ± 3. 79i	−0. 453 −0. 020	−0. 329 ± 3. 83i	−0. 444 −0. 020
−2. 33	−0. 318 ± 4. 08i	−0. 374 −0. 111	−0. 322 ± 4. 13i	−0. 363 −0. 113
−2. 5	−0. 316 ± 4. 24i	−0. 245 ± 0. 258i	−0. 320 ± 4. 29i	−0. 241 ± 0. 255i
−3. 0	−0. 311 ± 4. 70i	−0. 250 ± 0. 760i	−0. 312 ± 4. 80i	−0. 248 ± 0. 743i

respectively. A method of approximating the roots of the characteristic equation is presented in the appendix. The roots for $p_0=0$ which correspond to the condition where no coupling exists between the lateral and longitudinal modes are also given in the table. If the roots are complex, $\lambda=a\pm i\omega$, $P=\frac{2\pi}{\omega}$, and $T_{1/2}=\frac{-0.693}{a}$; whereas, for a real root λ_1, $T_{1/2}=\frac{-0.693}{\lambda_1}$ or $T_2=\frac{0.693}{\lambda_1}$.

The roots for $p_0=0$, for both cases (a) and (b), indicate that the motion consists of two independent oscillatory modes, a longitudinal and lateral oscillation with periods of 2.74 seconds and 4.08 seconds, respectively. The damping of the oscillation for case (b) is greater than that for case (a) because the damping derivatives C_{Y_β} and C_{L_α} were assumed equal to zero in case (a). The values of $T_{1/2}$ in seconds are given in the following table:

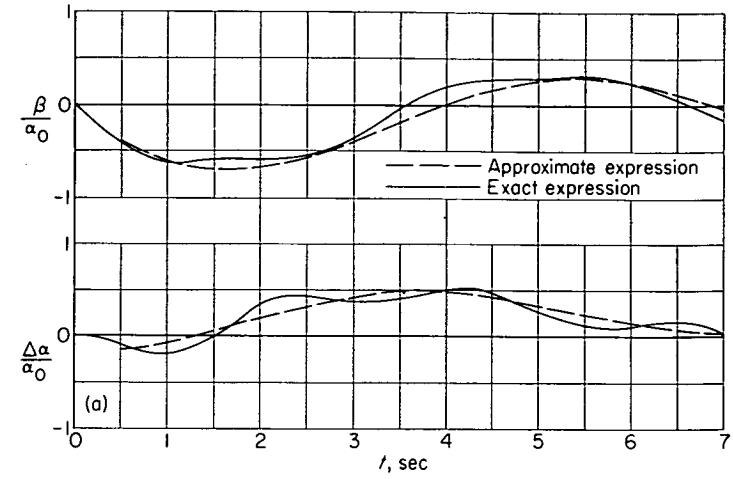
Case	$T_{1/2}$	
	Longitudinal oscillation	Lateral oscillation
(a)	3.3	13.2
(b)	1.4	9.5

For values of $|p_0|$ other than zero, the lateral variables β and r are coupled with the longitudinal variables α and q and the system now has the characteristic modes shown in table II for each of the variables β, r, α, and q. It should be noted that as $|p_0|$ increases, the frequency of the high frequency mode continues to increase and the damping decreases. However, the frequency of the other oscillation decreases until $|p_0|$ reaches approximately 1.86 when the oscillation breaks down into two aperiodic modes. In case (a) at this value of $|p_0|$, a zero root is obtained and the unstable region begins. The system remains unstable, with one aperiodic divergent mode, until $|p_0|$ becomes equal to 2.33. In case (b), the system is stable although two aperiodic modes occur for $1.86<|p_0|<2.33$. For $|p_0|>2.33$, the oscillation reappears in cases (a) and (b) and the frequency and damping increase as $|p_0|$ increases.

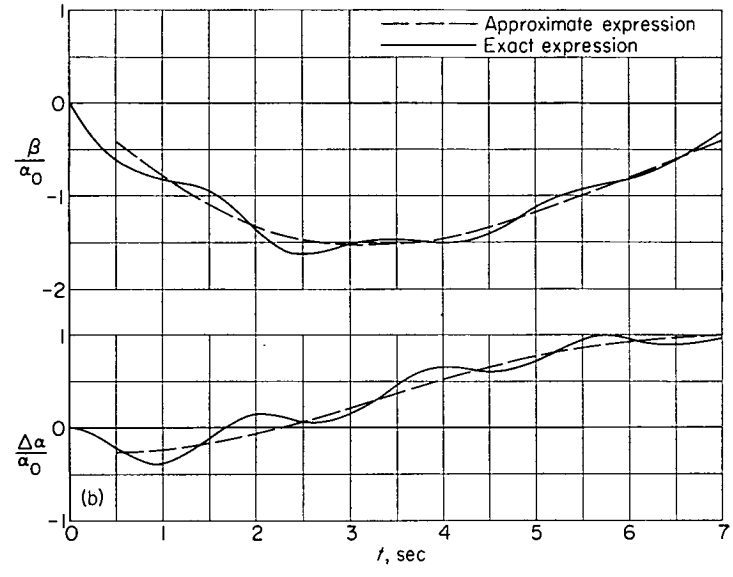
From the contour lines of constant oscillation frequencies presented in reference 1, it appears that, in general, the frequency of one of the oscillatory modes will always decrease and probably break down into two aperiodic modes as $|p_0|$ increases.

MOTIONS IN $\beta(t)$ AND $\Delta\alpha(t)$

Time histories were calculated by the method of Laplace transform (ref. 2) of the motions in β and $\Delta\alpha$ for the several values of p_0 shown in figure 1. The disturbance acting on the airplane is represented by the term $p_0\alpha_0$ in the side-force equation while the airplane is rolling in a negative direction. The motions in $\frac{\beta(t)}{\alpha_0}$ and $\frac{\Delta\alpha(t)}{\alpha_0}$ are presented in figures 2 and 3 for cases (a) and (b), respectively. A comparison of figures 2 and 3 shows that the inclusion of C_{L_α} and C_{Y_β} modifies



(a) $p_0=-1.0$.



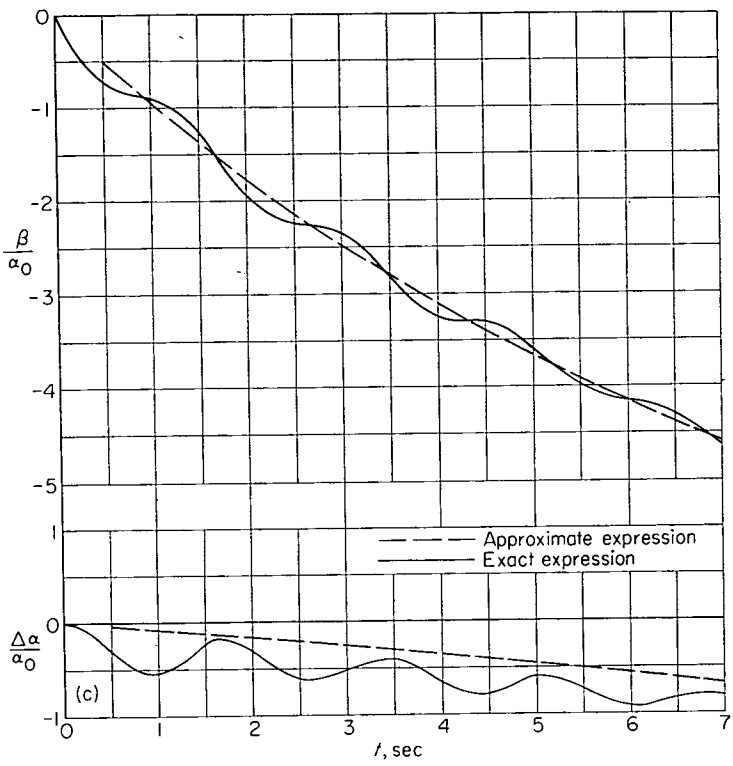
(b) $p_0=-1.5$.

FIGURE 2.—Time histories of β/α_0 and $\Delta\alpha/\alpha_0$ for case (a).

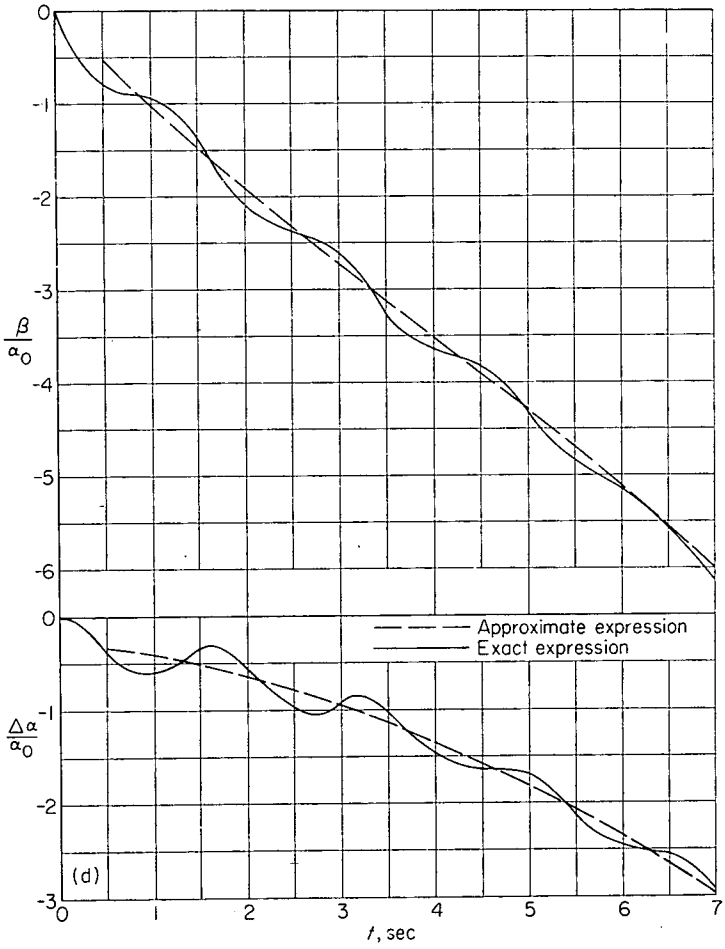
the motions slightly. Additional time histories were made and are presented in figure 4 for the same airplane but with the following assumed values of the derivatives: $C_{m_\alpha}=-0.09$, $C_{n_\beta}=0.114$, and $C_{Y_\beta}=C_{L_\alpha}=0$. For $p_0=-1.0$, the airplane would be located in figure 1 at the point $\omega_\theta^2=1.32$ and $\omega_\psi^2=4.77$.

Although the modes of motion involved in the transient behavior of the airplane will be stable for points along the airplane line located in the stable region, that is, $2.33<|p_0|<1.86$ in case (a) and for all values of $|p_0|$ in case (b), the magnitudes of $\Delta\alpha$ and β developed during the transient motion may be large enough to cause severe loads on the airplane. For example, in the particular flight condition for which the motions were calculated, where $\alpha_0=5°$, the airplane develops a sideslip angle of about $-8°$ at $p_0=-1.5$ and $\Delta\alpha$ is about $-20°$ at $p_0=-3.0$. These values are reached in about 3 seconds.

In all the motions the high-frequency mode is clearly evident, although the amplitude of this mode is relatively small. Hence, the high-frequency mode modifies the shape of the motion only slightly. Thus, for $p_0=-1.0$, -1.5, -2.5,

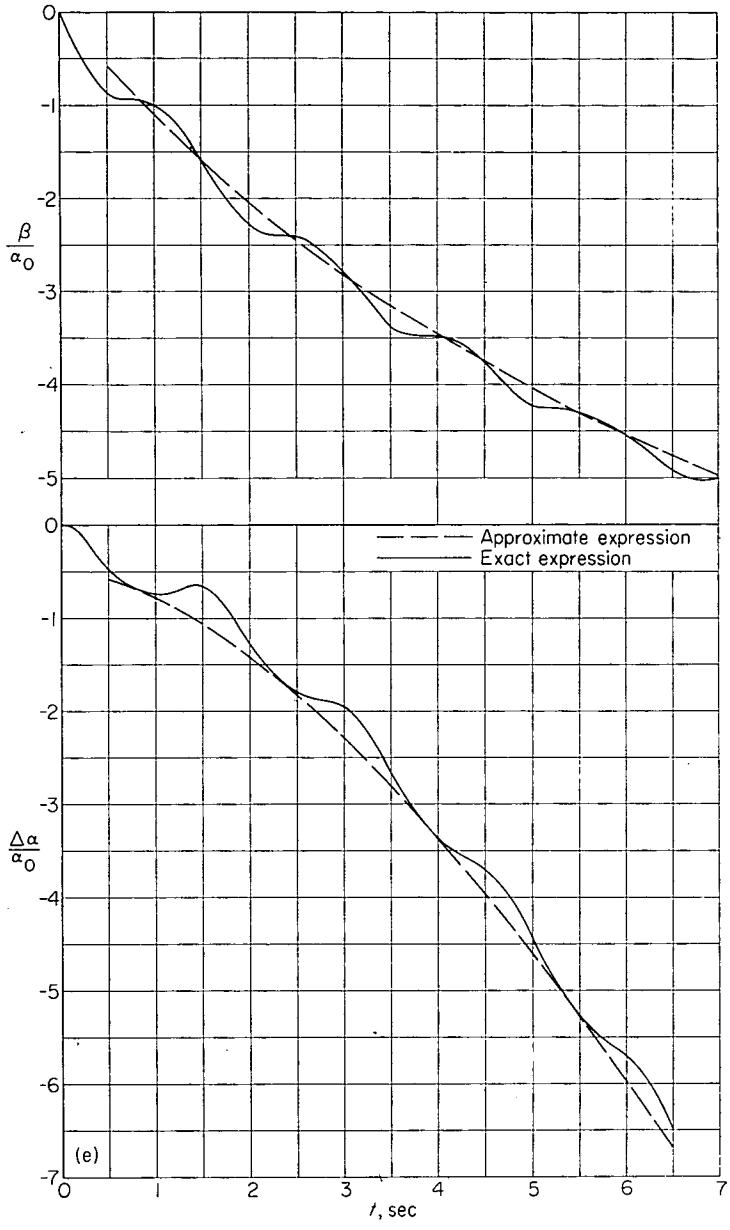


(c) $p_0=-1.86$.



(d) $p_0=-2.0$.

FIGURE 2.—Continued.



(e) $p_0=-2.33$.

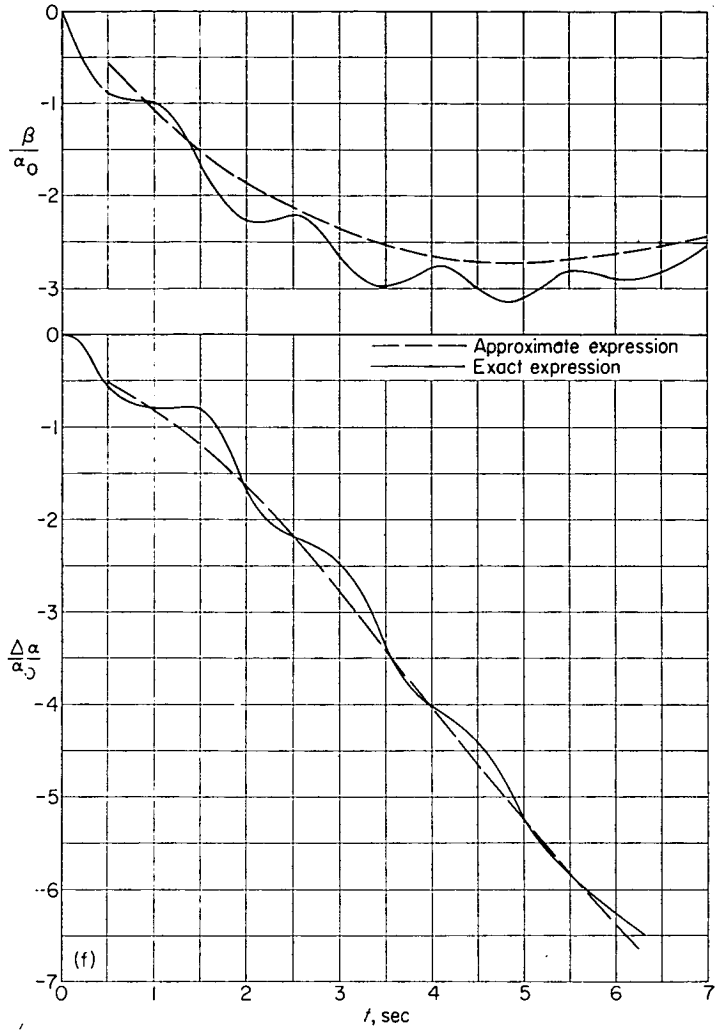
FIGURE 2.—Continued.

and -3.0, the low-frequency mode is of primary importance in the motions, whereas for $p_0=-1.86$, -2.0, and -2.33, the aperiodic modes are of primary importance. In addition, the analytical expressions for the motions would also contain a constant term which represents the steady-state value of β and $\Delta\alpha$ if the system is stable. A good approximation to the time history could therefore be expressed in general form for $p_0=-1.0$, -1.5, -2.5, and -3.0 as

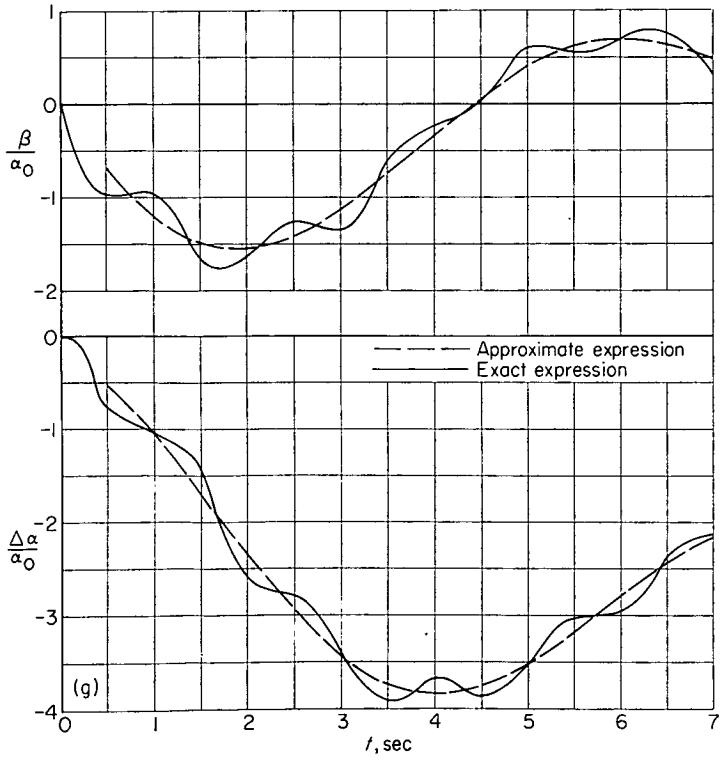
$$\frac{\beta(t)}{\alpha_0} \text{ or } \frac{\Delta\alpha(t)}{\alpha_0}=K_0+K_1e^{at}\sin(\omega t+\epsilon) \tag{3}$$

For case (b) when $p_0=-1.86$, -2.0, and -2.33 and for case (a) when $p_0=-2.0$, the following equation is obtained:

$$\frac{\beta(t)}{\alpha_0} \text{ or } \frac{\Delta\alpha(t)}{\alpha_0}=K_0+K_2e^{\lambda_1 t}+K_3e^{\lambda_2 t} \tag{4}$$

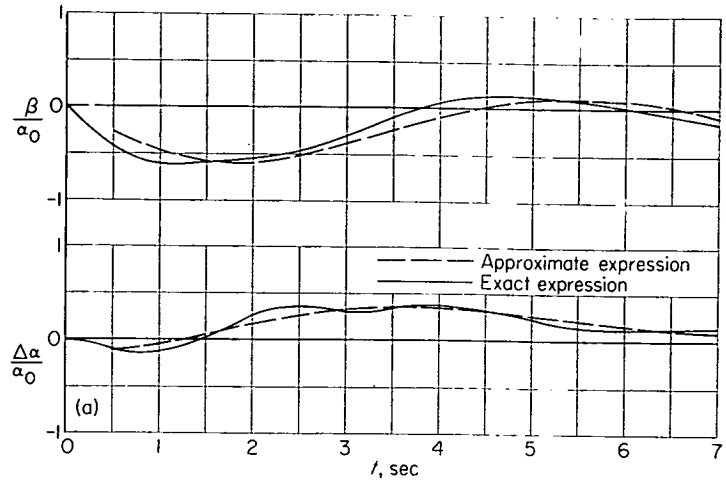


(f) $p_0 = -2.5$.

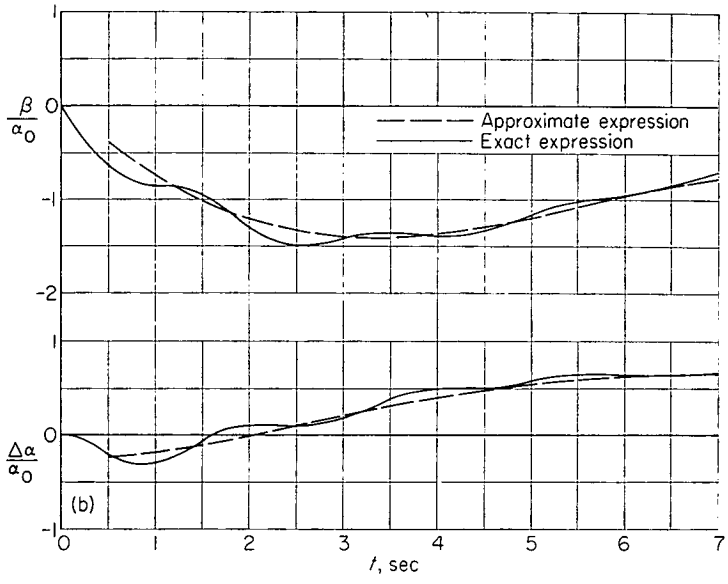


(g) $p_0 = -3.0$.

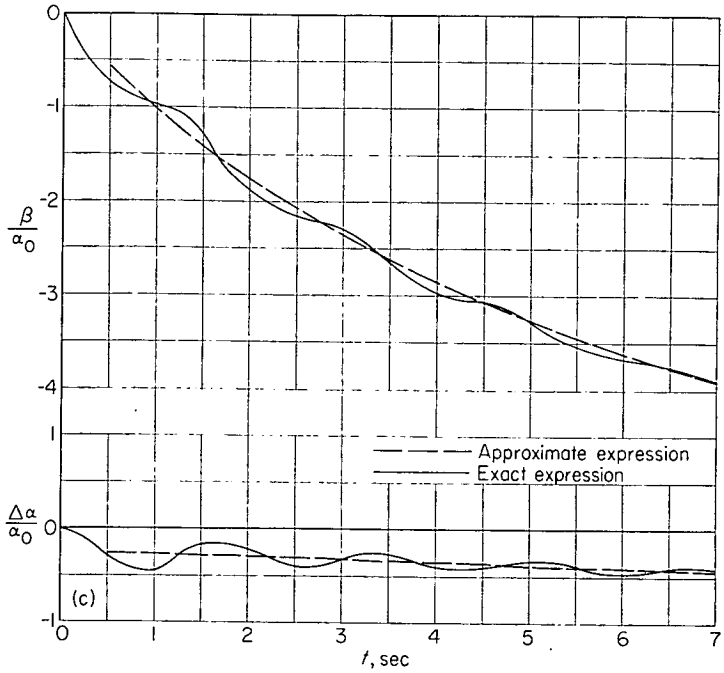
FIGURE 2.—Concluded.



(a) $p_0 = -1.0$.

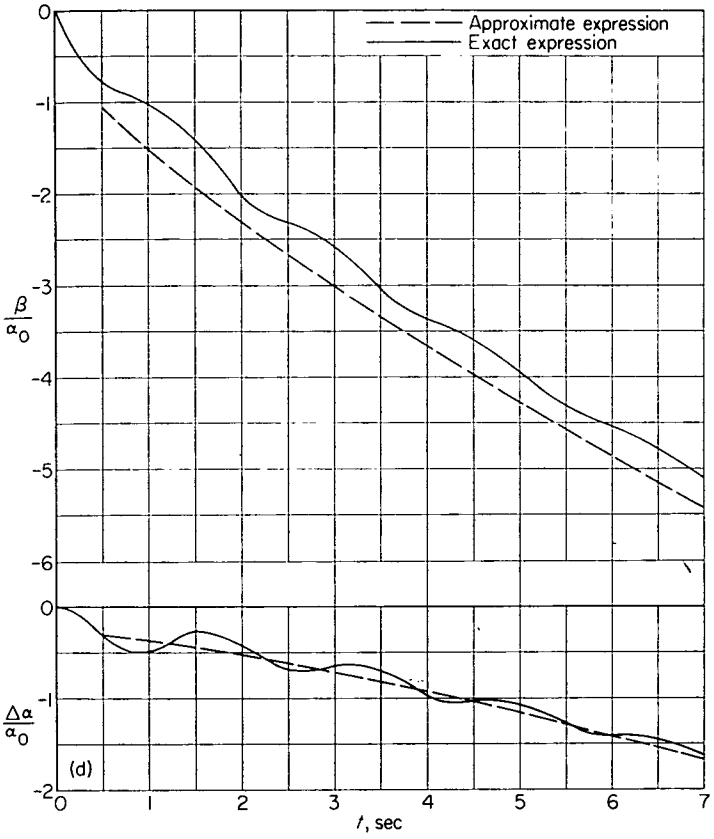


(b) $p_0 = -1.5$.



(c) $p_0 = -1.86$.

FIGURE 3.—Time histories of β/α_0 and $\Delta\alpha/\alpha_0$ for case (b).



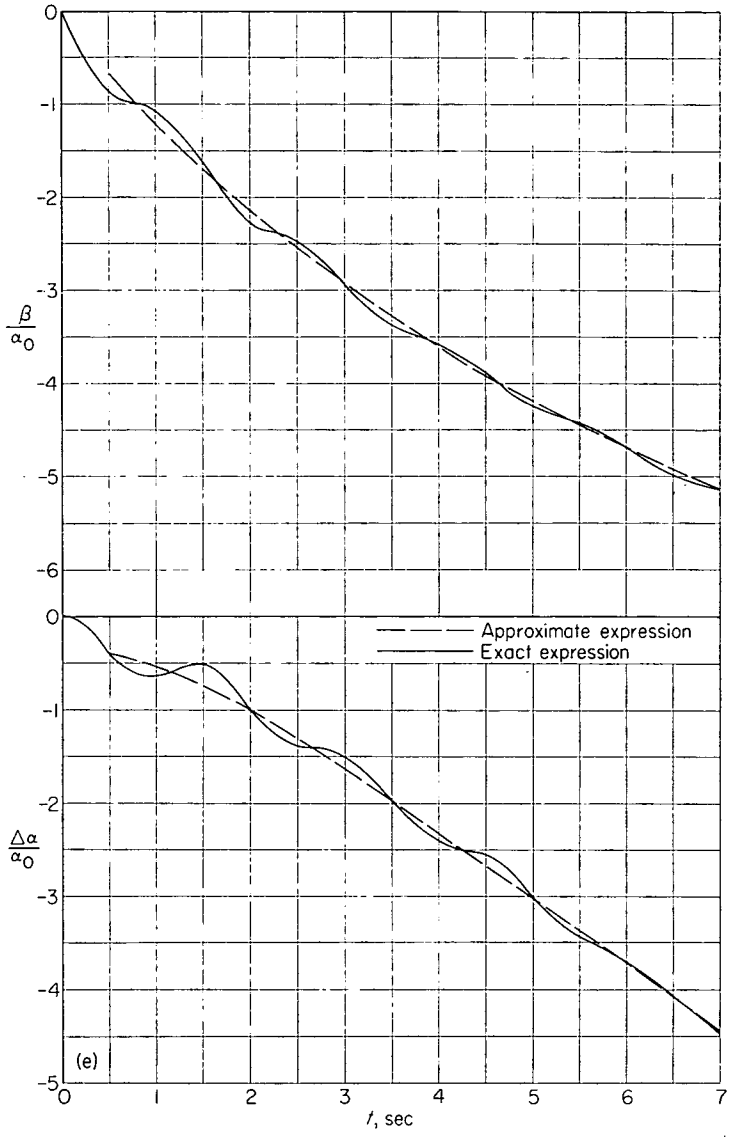
(d) $p_0=-2.0$.

FIGURE 3.—Continued.

and for case (a) when $p_0=-1.86$ and -2.33,

$$\frac{\beta(t)}{\alpha_0} \text{ or } \frac{\Delta\alpha(t)}{\alpha_0}=K_4t+K_5(e^{\lambda t}-1) \tag{5}$$

Since the high-frequency mode is omitted from expressions (3), (4), and (5), the values of $\frac{\beta(t)}{\alpha_0}$ and $\frac{\Delta\alpha(t)}{\alpha_0}$ will not satisfy the initial condition of being zero at $t=0$.



(e) $p_0=-2.33$.

FIGURE 3.—Continued.

By differentiating expressions (3), (4), and (5) and setting them equal to zero, the maximum values of β and $\Delta\alpha$ and the time at which they occur could be easily determined. In these calculations, β and $\Delta\alpha$ occurred at about ¼ and ½ of the period, respectively.

APPROXIMATION OF THE AMPLITUDE COEFFICIENTS AND PHASE ANGLE

The amplitude coefficients K_0, K_1, K_2, K_3, K_4, and K_5 and the phase angle ϵ in expressions (3), (4), and (5) can be calculated directly by using the Heaviside expansion formula given on page 45 of reference 2. A detailed examination of the exact expressions for the amplitude coefficients and phase angle indicated that many of the terms appearing in the expressions had a negligible effect on the resultant magnitudes. Thus the following simplified expressions were derived which result in good agreement with the exact values.

In the expressions for $\frac{\beta(t)}{\alpha_0}$,

$$K_0=\frac{p_0}{E}\left\{\frac{M_\alpha}{I_Y}\frac{N_r}{I_Z}+\frac{L_\alpha}{mV}\left[\frac{M_q}{I_Y}\frac{N_r}{I_Z}+p_0^2\left(\frac{I_Y-I_X}{I_Z}\right)\left(\frac{I_Z-I_X}{I_Y}\right)\right]\right\}$$

$$K_1=\frac{p_0}{(a^2+\omega^2)(C-2\omega^2)}\sqrt{\omega^2\left[-\omega^2-\frac{M_\alpha}{I_Y}+p_0^2\left(\frac{I_Y-I_X}{I_Z}\right)\left(\frac{I_Z-I_X}{I_Y}\right)\right]^2+\left[\frac{M_\alpha}{I_Y}\frac{N_r}{I_Z}+\omega^2\left(-2a+\frac{N_r}{I_Z}+\frac{M_q}{I_Y}\right)+\frac{L_\alpha}{mV}\left(\frac{I_Y-I_X}{I_Z}\right)\left(\frac{I_Z-I_X}{I_Y}\right)p_0^2\right]^2}$$

$$\epsilon=\tan^{-1}\frac{1}{\omega}\frac{-\frac{M_\alpha}{I_Y}\frac{N_r}{I_Z}-\omega^2\left(-2a+\frac{N_r}{I_Z}+\frac{M_q}{I_Y}\right)-\frac{L_\alpha}{mV}\left(\frac{I_Y-I_X}{I_Z}\right)\left(\frac{I_Z-I_X}{I_Y}\right)p_0^2}{\left[-\omega^2-\frac{M_\alpha}{I_Y}+p_0^2\left(\frac{I_Y-I_X}{I_Z}\right)\left(\frac{I_Z-I_X}{I_Y}\right)\right]}$$

$$K_2, K_3, \text{ and } K_5=\frac{p_0\left[\frac{M_\alpha}{I_Y}\left(\frac{N_r}{I_Z}\frac{1}{\lambda}-1\right)+p_0^2\left(\frac{I_Y-I_X}{I_Z}\right)\left(\frac{I_Z-I_X}{I_Y}\right)\left(1+\frac{L_\alpha}{mV}\frac{1}{\lambda}\right)\right]}{2C\lambda+D}$$

$$K_4=\frac{p_0}{D}\left\{\frac{M_\alpha}{I_Y}\frac{N_r}{I_Z}+\frac{L_\alpha}{mV}\left[\frac{M_q}{I_Y}\frac{N_r}{I_Z}+p_0^2\left(\frac{I_Y-I_X}{I_Z}\right)\left(\frac{I_Z-I_X}{I_Y}\right)\right]\right\}$$

In the expressions for $\frac{\Delta\alpha(t)}{\alpha_0}$,

$$K_0=-\frac{p_0^2}{E}\left[\left(\frac{I_Y-I_X}{I_Z}\right)\left(\frac{I_Z-I_X}{I_Y}\right)p_0^2-\frac{N_\beta}{I_Z}\left(\frac{I_Z-I_X}{I_Y}\right)+\frac{M_q}{I_Y}\frac{N_r}{I_Z}\right]$$

$$K_1=\sqrt{C_2^2+C_1^2}$$

$$K_2, K_3, \text{ and } K_5=-\frac{p_0^2\left[\lambda^2-\left(\frac{M_q}{I_Y}+\frac{N_r}{I_Z}\right)\lambda+p_0^2\left(\frac{I_Y-I_X}{I_Z}\right)\left(\frac{I_Z-I_X}{I_Y}\right)-\frac{N_\beta}{I_Z}\left(\frac{I_Z-I_X}{I_Y}\right)+\frac{M_q}{I_Y}\frac{N_r}{I_Z}\right]}{\lambda\,(2C\lambda+D)}$$

$$K_4=-\frac{p_0^2}{D}\left[\left(\frac{I_Y-I_X}{I_Z}\right)\left(\frac{I_Z-I_X}{I_Y}\right)p_0^2-\frac{N_\beta}{I_Z}\left(\frac{I_Z-I_X}{I_Y}\right)+\frac{M_q}{I_Y}\frac{N_r}{I_Z}\right]$$

$$\epsilon=\tan^{-1}\frac{C_2}{C_1}$$

where

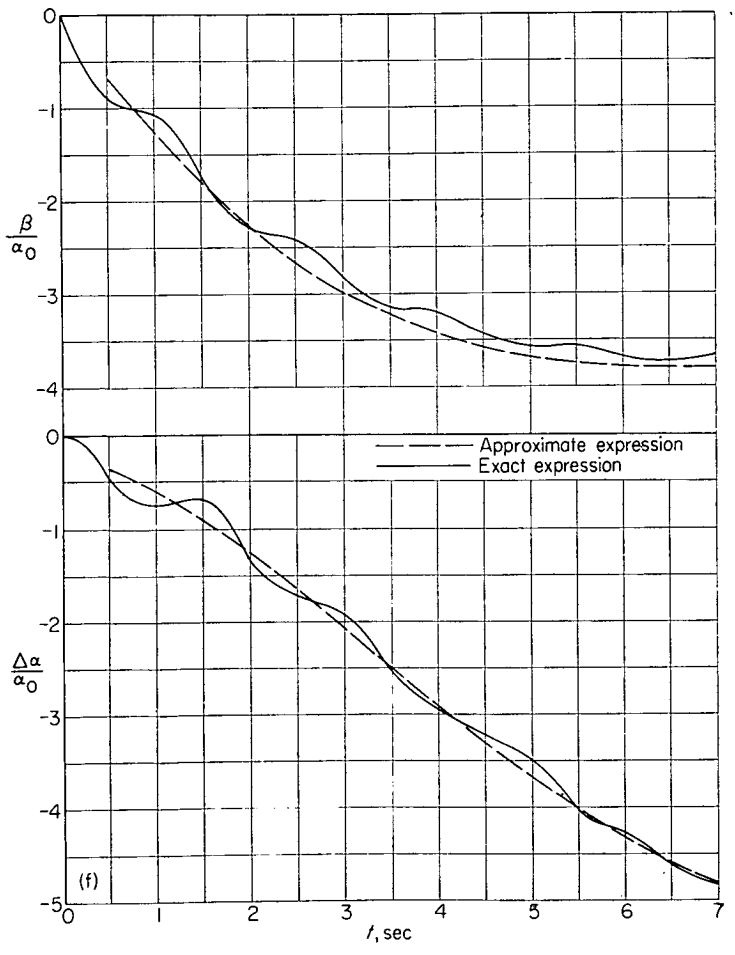
$$C_2=-\frac{p_0^2}{\omega^2\,(C-2\omega^2)}\left[\omega^2+\left(\frac{I_Z-I_X}{I_Y}\right)\frac{N_\beta}{I_Z}-p_0^2\left(\frac{I_Z-I_X}{I_Y}\right)\left(\frac{I_Y-I_X}{I_Z}\right)\right]$$

$$C_1=-C_2\left(\frac{a}{\omega}\right)-\frac{2a-p_0^2\left(\frac{M_q}{I_Y}+\frac{N_r}{I_Z}\right)}{\omega\,(C-2\omega^2)}$$

The C, D, and E appearing in the preceding expressions are the coefficients of the characteristic equation. A comparison of the motions obtained by using the exact and approximate coefficients is shown in figures 2 to 4 to be very good.

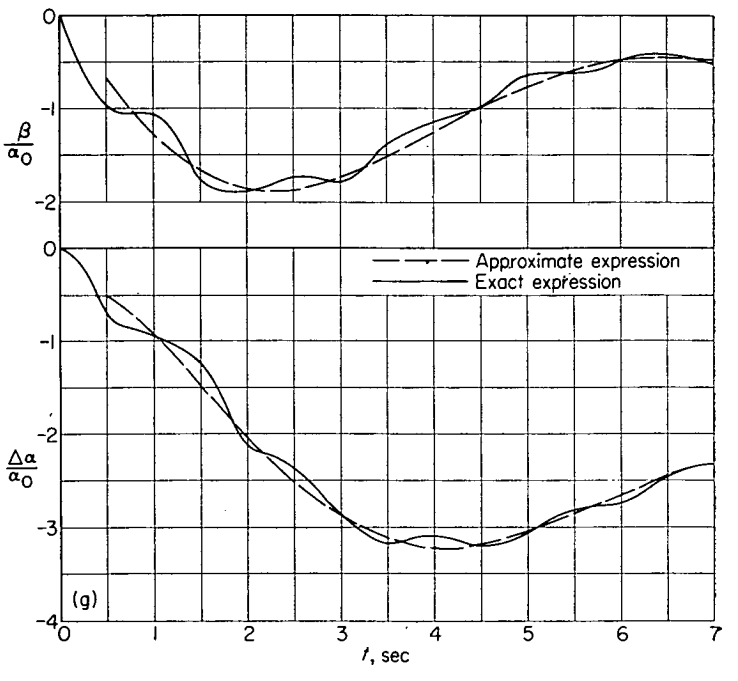
EFFECT OF ASSUMING p_0 CONSTANT AT $t=0$

In general, the rolling velocity builds up exponentially in response to an aileron input instead of being constant at $t=0$ as assumed in this analysis. In order to determine the effect of the assumption on the motions in β and $\Delta\alpha$, an analog study was conducted with the assumption that the rolling velocity reaches its steady-state value exponentially. The resultant motions in β and $\Delta\alpha$ were compared with the



(f) $p_0=-2.5$.

FIGURE 3.—Continued.



(g) $p_0=-3.0$.

FIGURE 3.—Concluded.

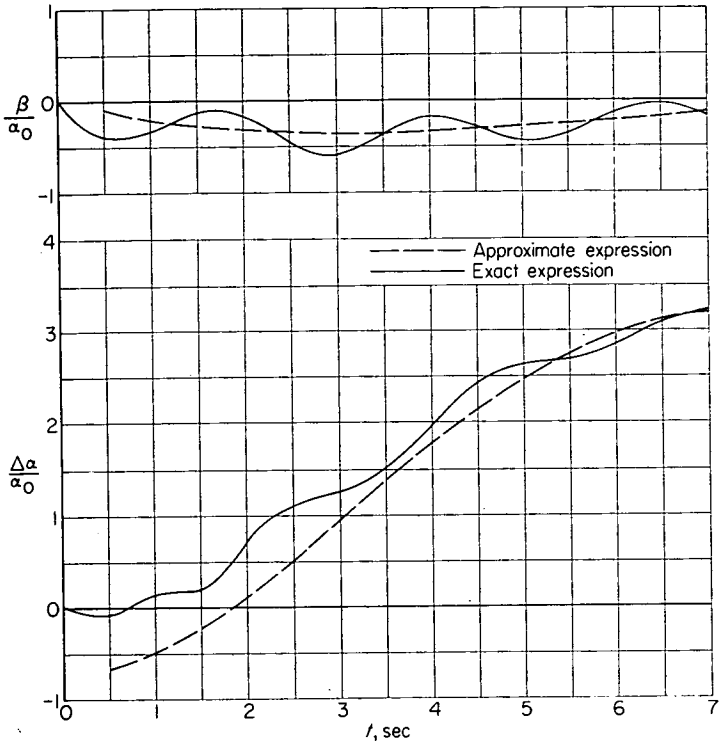


FIGURE 4.—Time histories of β/α_0 and $\Delta\alpha/\alpha_0$ for $C_{m_\alpha}=-0.09$, $C_{n_\beta}=0.114$, $p_0=-1.0$, and $C_{Y_\beta}=C_{L_\alpha}=0$.

motions in β and $\Delta\alpha$ obtained on the assumption that p_0 is constant at $t=0$. Equations (1) were used in the analog study and, in addition, a simplified roll equation $\dot{p}-\frac{qSb^2}{2VI_X}C_{l_p}p=\frac{M_X}{I_X}$ was introduced. This equation states that p reaches its steady-state value, p_0, according to the expression $p=p_0(e^{\lambda t}-1)$. In general, the resultant motions obtained in the analog study were very similar to the motions shown in figures 2 and 3. The only significant difference noted was that different peak values of $\frac{\Delta\alpha}{\alpha_0}$ and $\frac{\beta}{\alpha_0}$ were encountered. Table III presents a comparison between the maximum values of $\frac{\Delta\alpha}{\alpha_0}$ and $\frac{\beta}{\alpha_0}$ obtained from the analog study and from figures 2 and 3 for $p_0=-1.0$, -1.5, and -3.0. It is seen from the values presented in table III that higher maximum values occur for $p_0=-1.0$ and -1.5 for the condition of constant p_0 at $t=0$ whereas the opposite is true for $p_0=-3.0$. These results can be explained by the fact that, during the first several seconds of the transient motion, the average value of p_0 in the analog study is smaller than under the assumption of constant p_0. Hence in the analog study for $p_0=-1.0$ and -1.5 the airplane may be considered to be located farther away from the stability boundary, but for $p_0=-3.0$ the airplane is located closer to the stability boundary.

CALCULATIONS OF MOTIONS FOR AN AIRPLANE PERFORMING A 360° ROLL

The analysis presented thus far is applicable to the condition of the airplane performing a continuous rolling motion. Of particular interest are the motions of the airplane when the pilot performs a 360° roll. These motions can be approximated by first determining the values of β, r, α, and q at the time the airplane has rolled through 360°, that is, at $t=\frac{2\pi}{p_0}$. At this value of t, the constant rolling velocity is returned to $p_0=0$ and the motion originally described by four degrees of freedom is now separable into its lateral and longitudinal values, the former represented by the yawing and sideslipping equations and the latter represented by the pitching-moment and normal-force equations. Thus, the values of β, r, α, and q at $t=\frac{2\pi}{p_0}$ are the initial conditions required to calculate the motions subsequent to $t=\frac{2\pi}{p_0}$. The values of β and α can be determined from equation (3), (4), or (5). From equations (1c) and (1d), the following equations are obtained:

$$r=\frac{Y_\beta}{mV}\beta+p_0\alpha_0+p_0\,\Delta\alpha-\dot{\beta} \tag{6}$$

and

$$q=\frac{L_\alpha}{mV}\Delta\alpha+p_0\beta+\dot{\alpha} \tag{7}$$

A good approximation of r and q at $t=\frac{2\pi}{p_0}$ is obtained by neglecting the terms $\dot{\beta}$ and $\dot{\alpha}$ in equations (6) and (7). The following table compares the values of r and q at $t=\frac{2\pi}{p_0}$ for $p_0=-1.5$, -1.7, and -3.0 when $\dot{\beta}$ and $\dot{\alpha}$ are included in

TABLE III
COMPARISON OF MAXIMUM VALUES OF $\frac{\beta}{\alpha_0}$ AND $\frac{\Delta\alpha}{\alpha_0}$

p_0	C_{L_α}, C_{Y_β}	$\left(\frac{\beta}{\alpha_0}\right)_{max}$		$\left(\frac{\Delta\alpha}{\alpha_0}\right)_{max}$	
		p_0 constant at $t=0$	$p=p_0\,(e^{\lambda t}-1)$	p_0 constant at $t=0$	$p=p_0\,(e^{\lambda t}-1)$
−1.0	0	−0.64	−0.48	0.5	0.4
−1.0	Finite	−.6	−.48	.4	.3
−1.5	0	−1.64	−1.27	1.0	.9
−1.5	Finite	−1.48	−1.12	.68	.6
−3.0	0	−1.75	−1.91	−3.92	−4.15
−3.0	Finite	−1.90	−2.1	−3.25	−3.3

equations (6) and (7) and then deleted from equations (6) and (7):

p_0	$\dot{\beta}$ and $\dot{\alpha}$ included		$\dot{\beta}$ and $\dot{\alpha}$ deleted	
	r	q	r	q
−1.5	−0.20	0.20	−0.19	0.19
−1.7	−.12	.33	−.14	.32
−3.0	.25	.30	.29	.40

EFFECT OF GRAVITY TERMS ON THE β AND $\Delta\alpha$ MOTIONS

The effect of the gravity components which would appear in the side force (eq. (1c)) and normal force (eq. (1d)) equations have been neglected in this analysis. In order to determine the effect of the gravity terms on the β and $\Delta\alpha$ motions, an analog study was conducted using equations (1c) and (1d) with the gravity terms included and then deleted from the equations. The airplane was assumed to be performing a 360° roll for rolling velocities of $p_0=-1.5$, -1.7, and -3.0. A comparison of the maximum values of $\frac{\beta}{\alpha_0}$ and $\frac{\Delta\alpha}{\alpha_0}$ obtained with and without the gravity terms is presented in table IV. The two values given for $\frac{\Delta\alpha}{\alpha_0}$, that is, $\frac{\Delta\alpha_1}{\alpha_0}$ and $\frac{\Delta\alpha_2}{\alpha_0}$, correspond to the maximum values of $\frac{\Delta\alpha}{\alpha_0}$ obtained during the initial part of the transient motion (p_0=constant) and during the recovery part of the motion ($p_0=0$), respectively. The comparison shows that with the gravity terms included the maximum values of β are about 2° greater and the maximum values of $\Delta\alpha$ increase by about 1° for an initial α_0 of 5°.

TABLE IV

COMPARISON OF MAXIMUM VALUES OF $\frac{\beta}{\alpha_0}$ AND $\frac{\Delta\alpha}{\alpha_0}$

p_0	Gravity terms included			Gravity terms deleted		
	$\left(\frac{\beta}{\alpha_0}\right)_{max}$	$\left(\frac{\Delta\alpha_1}{\alpha_0}\right)_{max}$	$\left(\frac{\Delta\alpha_2}{\alpha_0}\right)_{max}$	$\left(\frac{\beta}{\alpha_0}\right)_{max}$	$\left(\frac{\Delta\alpha_1}{\alpha_0}\right)_{max}$	$\left(\frac{\Delta\alpha_2}{\alpha_0}\right)_{max}$
−1.5	−1.8	−0.50	0.90	−1.4	−0.30	0.90
−1.7	−2.5	−.60	1.3	−2.1	−.40	1.2
−3.0	−3.0	−2.4	1.5	−2.7	−2.2	1.6

CONCLUDING REMARKS

From the analysis presented in this paper it appears that the transient motion in angles of attack and sideslip during a constant rolling maneuver consists chiefly of either an oscillatory mode or two aperiodic modes. Approximate expressions are derived for the determination of these modes as well as the modal coefficient corresponding to each mode. Inclusion of the derivatives C_{Y_β} (side force due to sideslip) and C_{L_α} (lift-curve slope) increases the total damping of the system but does not markedly affect the transient motions.

The sole input considered in this paper is the term $p_0\alpha_0$ (the product of rolling velocity and trim angle of attack) in the side-force equation.

LANGLEY AERONAUTICAL LABORATORY,
NATIONAL ADVISORY COMMITTEE FOR AERONAUTICS,
LANGLEY FIELD, VA., *May 22, 1956.*

APPENDIX

METHOD OF APPROXIMATING THE ROOTS OF THE CHARACTERISTIC EQUATION

The fourth-degree characteristic equation

$$A\lambda^4+B\lambda^3+C\lambda^2+D\lambda+E=0$$

may be factored as follows:

$$(\lambda^2+a_1\lambda+b_1)(\lambda^2+a_2\lambda+b_2)=0$$

where

$$A=1$$

$$B=a_1+a_2$$

$$C=b_1+b_2+a_1a_2$$

$$D=a_2b_1+a_1b_2$$

$$E=b_1b_2$$

An examination of the quadratic equations from which the exact roots presented in tables II (a) and II (b) were obtained indicated that $b_1 \gg b_2$ and that a_1 and a_2 are of the same order of magnitude and much smaller than b_1. Thus, one may write

$$A=1$$

$$B=a_1+a_2$$

$$C=b_1$$

$$D=a_2b_1$$

$$E=b_1b_2$$

The solution of these equations yields

$$a_1=\frac{BC-D}{C}$$

$$b_1=C$$

$$a_2=\frac{D}{C}$$

$$b_2=\frac{E}{C}$$

The roots of $\lambda^2+a_1\lambda+b_1=0$ approximate the high-frequency mode whereas the roots of $\lambda^2+a_2\lambda+b_2=0$ approximate the remaining two roots of primary importance in the motion calculations presented herein. A comparison between the exact roots and the approximate roots presented in tables II (a) and II (b) indicates that the agreement is excellent.

REFERENCES

1. Phillips, William H.: Effect of Steady Rolling on Longitudinal and Directional Stability. NACA TN 1627, 1948.
2. Churchill, Ruel V.: Modern Operational Mathematics in Engineering. McGraw-Hill Book Co., Inc., 1944.

REPORT 1345

CONTENTS

	Page
SUMMARY	143
INTRODUCTION	143
SYMBOLS	144
AERODYNAMIC FORCES RESULTING DIRECTLY FROM ATMOSPHERIC TURBULENCE	145
Definitions of Statistical Parameters	146
Lift-Influence Functions in Unsteady Flow	147
Mean-Square Lift and Its Spectral Resolution for the Unswept Wing	147
Basic equations	147
Two alternative approaches	148
Results of calculations	149
Mean-Square Lift of the Swept Wing	151
Mean-Square Rolling Moment	152
Generalized Aerodynamic Influence Functions in Unsteady Flow	153
Mean-Square Bending and Pitching Moments	155
Wing-Tail Correlation Effects	157
DYNAMICS OF THE RIGID AIRPLANE	158
Equations of Longitudinal Motion	158
Solution of the Equations of Longitudinal Motion	160
Transfer functions	160
Normal-acceleration spectrum and mean-square value	160
Bending-moment spectrum and mean-square value	161
Special Problems Related to the Longitudinal Motion of Large Airplanes	162
Single-degree-of-freedom case	162
Two-degree-of-freedom case	163
Special Problems Related to the Lateral Motion of Large Airplanes	163
Combination of the Results Obtained From Analyses of the Longitudinal and Lateral Degrees of Freedom	164
DYNAMICS OF THE SMALL FLEXIBLE AIRPLANE	165
Loads Applied to the Wing	165
Loads Applied to the Tail	167
Wing and Tail Deformations	168
Equations of Motion	169
Solution of the Equations of Motion	170
DYNAMICS OF THE LARGE FLEXIBLE AIRPLANE	171
Extension of the Statistical Approach	171
Calculation of the Required Transfer Functions	174
DISCUSSION	176
Some Implications of the Assumptions Concerning the Nature of Atmospheric Turbulence	176
Considerations Pertinent to the Application of Stationary-Random-Process Techniques to Gust-Load Problems	177
CONCLUDING REMARKS	177
REFERENCES	178

REPORT 1345

THE RESPONSE OF AN AIRPLANE TO RANDOM ATMOSPHERIC DISTURBANCES[1]

By Franklin W. Diederich

SUMMARY

The statistical approach to the gust-load problem which consists in considering flight through turbulent air to be a stationary random process is extended by including the effect of lateral variation of the instantaneous gust intensity on the aerodynamic forces. The forces obtained in this manner are used in dynamic analyses of rigid and flexible airplanes free to move vertically, in pitch, and in roll. The effect of the interaction of longitudinal, normal, and lateral gusts on the wing stresses is also considered.

The method of analyzing the rigid-body motions is similar to that used for analyses of the dynamic stability of airplanes, in that the equations of motion are referred to stability axes and expressed in terms of conventional stability derivatives. The method of analyzing the dynamic effects of structural flexibility consists in an extension of a numerical-integration approach to the static aeroelastic problem and is in a form which offers the possibility of calculating divergence and flutter speeds with relatively little additional effort.

The mean-square values, correlation functions, and power spectra of some of the aerodynamic forces required in this type of analysis are calculated for one special correlation function of the atmospheric turbulence. It is shown, for instance, that if the span is relatively large compared with the integral scale of turbulence, the mean-square lift and root bending moment directly due to the gust are substantially reduced when the differences in instantaneous intensity of the turbulence along the span are taken into account. However, if the motions of the airplane are taken into account the mean-square root bending moment may be increased as a result of these differences. Also, the mean-square pitching moment is shown to be substantially increased if the tail length is relatively large compared with the scale of turbulence. Finally, the wing stresses due to longitudinal, normal, and lateral gusts are shown to be statistically independent under certain conditions.

INTRODUCTION

The local velocity fluctuations acting on an airplane flying through atmospheric turbulence are functions of time defined only in a statistical sense and, hence, constitute a stochastic or random process. Consequently, the responses of the airplane, whether they are motions (linear or angular displacement, velocities, or accelerations), forces (lift, pitching moment, bending moment, and so on), stresses, or any other phenomena determined by the turbulence, can also be known as functions of time in only a statistical sense.

This report is concerned with the statistical characteristics of those responses which have a bearing on the loads and stresses experienced by the airplane; although other problems such as those relating to passenger comfort or to the stability of the airplane as a gun platform can be treated in the same manner, they will not be considered here.

The first approaches to the gust-load problem which use the statistical techniques developed for stationary random processes appear to be those of references 1, 2, and 3. (An earlier investigation concerned with the motions of an airplane in turbulent air is reported in ref. 4.) The fundamentals of these approaches are discussed in some detail in reference 1, and mention is made therein of investigations in other fields of engineering and physics that have dealt with the problem of deducing the statistical characteristics of the output or response of a dynamic system from those of its input. The mean-square normal acceleration of a rigid airplane free to move in one degree of freedom, namely, vertical motion, is calculated in reference 2. In addition to being rigid, the airplane is implicitly assumed to be small enough for all its components to experience the same gust velocity at any instant of time. This means that the span of the airplane must be small compared with the integral scale of atmospheric turbulence, which on the basis of the available knowledge concerning the properties of the atmosphere (ref. 4, for instance) appears to be in the order of several hundred to 1,000 or 2,000 feet; that is, the span of the airplane must be less than about 100 feet.

The purpose of the present report is to extend this approach to large flexible airplanes free to move in all directions. As used herein, the terms "small" and "large" airplane refer to airplanes which are very small and not very small, respectively, compared with the integral scale of turbulence; thus, an airplane flying in a wide variety of atmospheric conditions may be "small" under certain conditions and "large" under others. Similarly, the terms "rigid" airplane and "flexible" airplane are used to designate airplanes flying, respectively, at speeds far below those at which dynamic and aeroelastic effects become important, and at speeds at which these effects have to be taken into account; the same airplane can thus be "rigid" under some conditions and "flexible" under others.

[1] Supersedes NACA Technical Note 3910 by Franklin W. Diederich, 1957. This report represents, except for some minor changes, a thesis submitted in May 1954 in partial fulfillment of the requirements for the degree of Doctor of Philosophy at the California Institute of Technology, Pasadena, Calif.

Several fundamental assumptions are inherent in the analysis contained in this report. In the first place, all atmospheric disturbances, motions, and structural deformations are assumed to be small enough to produce forces that are linear and, hence, superposable. Also, the turbulent "input" to the airplane is assumed to be stationary in a statistical sense; that is, the turbulence in the plane of the flight path is homogeneous. For the large airplane, the additional assumption is made that the turbulence is axisymmetric with respect to vertical axes, a condition less severe than complete isotropy. The statistical characteristics of the turbulence are thus assumed to be invariant under a translation of the space origin within the horizontal plane and under a rotation of the coordinates about the vertical axis. Finally, Taylor's hypothesis to the effect that time displacements are equivalent to longitudinal space displacements is assumed to be valid.

The aerodynamic forces directly due to atmospheric turbulence, which constitute the input forces for the dynamic system represented by the airplane, are calculated in the first part of this report for the large airplane, that is, for the case where the spanwise distribution of the intensity of turbulence has to be taken into account. (The effect of spanwise variation of gust intensity on the lift has been treated by a slightly different method in ref. 5.)

The dynamics of the rigid airplane are considered in the second part. The dynamic system is now represented by a set of three simultaneous ordinary differential equations, rather than one as in reference 2; nonetheless, the problem of calculating the required transfer functions is still one of simple algebra.

The next part is concerned with the small flexible airplane and thus has direct application to fighter-type airplanes and guided missiles operating at relatively high speeds, in addition to serving as a preliminary to the last part of the report. The dynamic system is now represented by a partial differential equation, and the calculation of the transfer functions requires the solution of ordinary differential equations. Once these functions are calculated, however, the statistical techniques are the same as before, as a result of the fact that the lateral variation in gust intensity is ignored. Either modal or numerical-integration approaches may be used to analyze the dynamics of a swept-wing airplane with arbitrary stiffness and mass distribution. Although modal approaches have usually been preferred in the past for similar problems, it was believed that, in view of the highly complex nature of modern aircraft structures and the advanced type of computing machinery required and generally available for their analysis, the numerical-integration approach would be preferable and it has, therefore, been used.

The last part contains the analysis of the large flexible airplane. The statistical problem is now that of a system which is characterized by a partial differential equation with time and a space coordinate as independent variables and which is subjected to a random input that varies in time and space, so that more is required than the transfer functions from the gust intensity at one point on the wing to the stresses at another. The particular statistical problem presented by this case is considered in some detail, and the appropriate transfer functions are then obtained by using the numerical-integration approach presented in the preceding part to solve, in effect, the ordinary differential equations which describe the wing deformations at any given frequency.

SYMBOLS

A	aspect ratio
b	span
$C(k)$	Theodorsen function
C_L	lift coefficient, L/qS
C_{L_α}	lift-curve slope
C_l	rolling-moment coefficient, L'/qSb
C_{l_p}	coefficient of damping in roll, defined as positive for positive damping
C_{m_q}	damping-in-pitch derivative
C_{m_α}	static pitching derivative
c	chord, parallel to plane of symmetry
$\bar{c}$	average chord, S/b
c_l	section lift coefficient at station y, l/qc
EI	bending stiffness
e_1	distance from section aerodynamic center to shear center, fraction of chord
e_2	distance from shear center to section center of gravity, fraction of chord
e_3	distance from shear center to the midchord point, fraction of chord
e_4	distance from shear center to the ¾-chord point, fraction of chord
$G(y, \eta)$	dimensionless lift-influence function (Green's function for the spanwise lift distribution)
GJ	torsional stiffness
g	acceleration due to gravity
$H(\omega)$	response to sinusoidal oscillation, Fourier transform of $h(t)$
$h(t)$	indicial-response function
I_x	mass moment of inertia about X-axis
I_y	mass moment of inertia about Y-axis
J_0,J_1	Bessel functions of the first kind, order 0 and 1
K_0,K_1	modified Bessel functions of the second kind, order 0 and 1
Ki_0	integral of K_0
k	reduced frequency, $\omega\bar{c}/2U$
k'	dimensionless frequency, $\omega L^*/U$
L	lift
L'	rolling moment
L^*	integral scale of turbulence
l	distributed lift per unit distance along the span
M	pitching moment
M_B	bending moment
M_T	twisting moment
m	mass (of airplane, unless designated otherwise by subscripts)
$\tilde{m}$	distributed mass per unit distance along the span
m_T	distributed twisting moment (about axes perpendicular to the plane of symmetry) per unit distance along the span
q	dynamic pressure

r radius of gyration about center of gravity; longitudinal displacement corresponding to time displacement τ
S wing area
s scale parameter, $\frac{L^*}{\overline{c}/2}$
t time
U mean flying speed
u longitudinal component of gust velocity
u_p horizontal component of disturbed motion
v lateral component of gust velocity
W weight of airplane
w vertical component of gust velocity
w_p vertical component of disturbed motion
x coordinate along mean flight path
Δx distance from intersection of elastic axis and root chord to airplane center of gravity
x_t tail length, distance from airplane center of gravity to aerodynamic center of tail
x_t' modified tail length, distance from intersection of elastic axis and root chord to aerodynamic center of tail
y coordinate perpendicular to plane of symmetry
z coordinate in plane of symmetry perpendicular to mean flight path; vertical deflection
α inclination of chord to X-axis
β span ratio, b/L^*
$\Gamma(\eta)$ autoconvolution function for $\gamma(y)$
$\gamma(y)$ dimensionless lift distribution, $cc_l/\overline{c}C_L$
$\gamma'(y)$ dimensionless lift distribution in roll, $cc_l/\overline{c}C_{l_p}$
η variable of integration corresponding to y
θ angle of pitch
Λ angle of sweepback
ρ mass density of the air
τ time displacement, argument of time-correlation function
Φ the power spectrum $\tilde{\Phi}$ in the case of axisymmetry
$\tilde{\Phi}$ two-dimensional power spectrum (double Fourier transform of $\tilde{\psi}$)
$\phi(k)$ Sears function (unsteady-lift function for gust penetration)
φ one-dimensional or point power spectrum
$\tilde{\varphi}$ two-dimensional power spectrum (single Fourier transform of $\tilde{\psi}$)
ψ one-dimensional or point correlation function
$\tilde{\psi}$ two-dimensional correlation function
ω frequency of oscillation

Subscripts:

e, ϵ effective
f fuselage
r wing root
t tail
u horizontal component of turbulence
w wing; vertical component of turbulence

Matrix notation:

$[\ ]$ square or rectangular matrix
$\lfloor\ \rfloor$ diagonal matrix
$[\ ]$ row matrix
$\{\ \}$ column matrix

Dots over symbols indicate derivatives with respect to time.

AERODYNAMIC FORCES RESULTING DIRECTLY FROM ATMOSPHERIC TURBULENCE

The motions of a rigid airplane depend on the overall forces and moments, whereas the stresses of a rigid airplane and the motions and stresses of a flexible airplane depend on the distribution of these forces, as well. This part of the report is concerned with the calculation of the integrated and distributed forces and moments directly due to atmospheric turbulence when the spanwise variation of gust intensity has to be taken into account. (The forces and moments caused by the motions which result from the forces treated in this part can be calculated by conventional methods and will not be considered here, although the combined forces will be considered in the following parts.) Thus, this part serves as a basis for all the material presented in the later parts pertaining to the large airplane, and, hence, the fundamental notions required for an analysis of the large airplane are introduced here and discussed in some detail.

The basic approach is as follows: First, the instantaneous value of the quantity of interest, such as the lift, is expressed in terms of the instantaneous gust intensity at a point and a suitable influence function. For the lift this influence function can and will be identified with a certain lift distribution on the given wing in reverse flow; the same procedure may and, in the case of the rolling moment, will be followed for other integrated forces. On the other hand, for the local lift the influence function is the Green's function for the three-dimensional unsteady-lift problem and cannot be identified with an easily calculated lift distribution on the wing in reverse flow. Inasmuch as no knowledge concerning this function appears to be available, a method of calculating an approximate Green's function for this problem is outlined herein. The required influence functions for integrated effects can be synthesized from this function, and if the associated lift distribution in reverse flow cannot be calculated conveniently this approach may be preferable. This technique is illustrated here by means of the bending moment.

The next step consists in using the expression for the instantaneous value of the given quantity to calculate a correlation function for this quantity in terms of a correlation function of the normal component of the atmospheric turbulence. The power spectrum for the given quantity can then be obtained by taking the Fourier transform of its correlation function. This power spectrum is considered herein to be the desired end result, because the mean-square values of the quantity and its derivatives can be obtained from it, and other statistical parameters of interest can be obtained from these mean-square values. Several alternative approaches for calculating the aforementioned spectrum, either from the correlation function or directly from the spectrum of atmospheric turbulence, are given in connection with the lift and are directly applicable to other quantities as well.

In this part of the report the assumption is made that the influence functions of concern can be written as products of a function of time alone and a function of distance along

the span alone, and advantage is taken of this simplification in calculating the desired spectra. This restriction is removed in the last part of the report, where the influence functions considered cannot be separated into space-dependent and time-dependent constituents, and so the approaches outlined there are generalizations of those presented in this part; they may also be used for the calculation of the spectra of the quantities considered in this part if the assumption concerning the influence functions is not valid.

DEFINITIONS OF STATISTICAL PARAMETERS

As pointed out in the introduction, the intensity of the vertical component of turbulence $w(t)$ is a random process, so that the resulting forces can also be known only in a statistical sense. The purpose of this part is to calculate certain statistical properties of these forces, namely, their mean-square values, their correlation functions, and their power spectra. The fundamental principles involved in statistical analyses of the type considered herein are expounded in some detail, and citations of the literature on the subject are given in references 1 and 2. These fundamentals will therefore not be repeated here. However, both for the sake of ready reference and inasmuch as the statistical terms are not always defined in the same manner, the forms that are used herein are indicated in the succeeding paragraphs.

The time average of a time-dependent quantity is designated by a bar placed over the symbol,[2] and is defined as follows:

$$\bar{\xi} \equiv \lim_{T\to\infty} \frac{1}{2T}\int_{-T}^{T} \xi(t)dt$$

The assumption will always be made that this limit exists and is invariant under a translation of the origin of time. This assumption implies that the processes considered here are stationary in a statistical sense.

The mean of a random process $f(t)$ is defined as its time average, and is always assumed to be zero. In dealing with processes with nonzero mean this analysis is thus pertinent only to the process which consists of the difference between the original process and its mean value. Similarly, the mean-square value of a random process $f(t)$ is defined as the time average of the square of the process, so that

$$\overline{f^2} \equiv \lim_{T\to\infty} \frac{1}{2T}\int_{-T}^{T} f^2(t)\,dt$$

The time-correlation function of $f(t)$ is defined as

$$\psi_f(\tau) \equiv \overline{f(t)f(t+\tau)}$$

so that

$$\overline{f^2} = \psi_f(0)$$

and the power spectrum of $f(t)$ is defined as the Fourier transform of the correlation function:

$$\varphi_f(\omega) = \frac{1}{\pi}\int_{-\infty}^{\infty} e^{-i\omega\tau}\psi_f(\tau)\,d\tau$$

$$= \frac{1}{\pi U}\int_{-\infty}^{\infty} e^{-i\frac{\omega}{U}r}\psi_f\left(\frac{r}{U}\right)dr$$

The second form is the more convenient one when ψ_f represents more nearly a space correlation than a time correlation, so that it depends directly on a space displacement $r \equiv U\tau$ rather than on a time displacement τ. For the purposes of the analysis presented herein, the gust or input correlation functions have this property, so that, for instance, ψ_w may be defined as

$$\psi_w(r) = \overline{w(t)w\left(t+\frac{r}{U}\right)}$$

By virtue of the reciprocal properties of Fourier transforms and the symmetry of $\psi_f(\tau)$, which is a direct consequence of the assumed stationarity of $f(t)$, $\overline{f^2}$ may be expressed in terms of the spectrum of f as

$$\overline{f^2} = \int_0^{\infty} \varphi_f(\omega)\,d\omega \tag{1}$$

If $f(t)$ is the input of a linear system, the power spectrum of the response $x(t)$ of the system is related to the power spectrum of $f(t)$ by

$$\varphi_x(\omega) = |H(\omega)|^2\varphi_f(\omega) \tag{2}$$

where $H(\omega)$ is the transfer function of the system, that is, the complex amplitude of the response of the system to unit sinusoidal input. Hence, $H(\omega)$ is also the Fourier transform of the indicial response $h(t)$ of the system, which is defined herein as the response of the system to a unit impulsive input:

$$H(\omega) = \int_{-\infty}^{\infty} e^{-i\omega t}h(t)dt \tag{3}$$

where the lower limit could be taken as zero, since $h(t)$ is zero for $t<0$. Conversely, $h(t)$ can be obtained from $H(\omega)$ by means of the inverse of equation (3):

$$h(t) = \frac{1}{2\pi}\int_{-\infty}^{\infty} e^{i\omega t}H(\omega)\,d\omega \tag{3a}$$

The mean-square value of the response can then be obtained by integrating its spectrum. Similarly, the mean-square values of the nth time derivative of the response can be obtained from the $(2n)$th moment of the output spectrum. For instance,

$$\overline{\left(\frac{dx}{dt}\right)^2} = \int_0^{\infty} \varphi_x(\omega)\,\omega^2\,d\omega$$

From the mean-square values of these derivatives other statistical quantities of interest, such as the expected number of peaks of the response per unit time, can then be calculated.

[2] When no possibility of confusion exists, a bar is also used to designate a space average, as in the case of $\bar{c}$ and $\bar{y}$. Also, for the components of turbulence the correlation functions depend primarily on space displacements and can be defined by space averages. For the sake of consistency, however, they are considered to be defined by time averages.

LIFT-INFLUENCE FUNCTIONS IN UNSTEADY FLOW

At any time the lift on a wing which results directly from atmospheric disturbances can be expressed for an unswept wing as

$$L(t)=\int_{-\infty}^{\infty} dt_1 \int_{-b/2}^{b/2} h(t_1,y)w(U(t-t_1),y)\,dy \qquad (4)$$

where $h(t,y)dy$ is a lift-influence function which represents the lift caused by an impulsive vertical gust of width dy which at time $t=0$ impinges on the wing at station y.

The influence functions required in equation (4) are difficult to calculate directly; methods for obtaining lift distributions on wings of finite span in unsteady flow usually require numerical solutions which do not lend themselves readily to the analysis of angle-of-attack distributions represented by delta functions. However, by virtue of the reciprocity theorems of linearized lifting-surface theory (ref. 6, for instance) the lift influence function for a twisted wing in indicial motion is equal to the lift distribution on that wing during indicial motion in the reverse direction with uniform unit angle of attack. The lift distribution in indicial motion with uniform angle of attack can be calculated relatively easily.

For the few cases for which calculations have been made (namely, some unswept wings), this lift distribution tends to be substantially invariant in time, except for overall magnitude. For instance, the calculations of reference 7 indicate that the lift distribution of an oscillating rectangular or elliptic wing in incompressible flow is substantially independent of frequency, so that in indicial motion it is substantially independent of time. This simplification may not be valid for swept wings.

The lift influence function can then be written as

$$h(t,y)=\frac{1}{b}h_L(t)\,\gamma(y) \qquad (5)$$

where $\gamma(y)$ defines the steady-state lift distribution for uniform unit angle of attack:

$$\gamma(y)\equiv\frac{cc_l}{\bar{c}C_L}$$

and where $h_L(t)$ describes the variation of the overall magnitude of the lift as a function of time after entry into a sharp-edge gust and may be written as

$$h_L(t)=\frac{C_{L_\alpha}qS}{U}\frac{d}{dt}k_2\left(\frac{Ut}{\bar{c}/2}\right)$$

In turn, k_2 is the lift response to a unit sharp-edge gust normalized to a steady-state value of unity and is, as in the preceding equation, usually expressed in terms of semichord lengths traveled $\frac{Ut}{\bar{c}/2}$. The time derivative is taken here because the response wanted is the one to a unit impulsive gust rather than a sharp-edge gust.

The Fourier transform $H_L(\omega)$ of this function $h_L(t)$ is proportional to a function $\phi(k)$, which may be termed the generalized Sears function because for two-dimensional incompressible flow it is the Sears function:

$$H_L(\omega)=\frac{C_{L_\alpha}qS}{U}\phi(k) \qquad (6)$$

where

$$k\equiv\frac{\omega\bar{c}}{2U}$$

The function $H_L(\omega)$ represents the complex amplitude of the lift due to sinusoidal gusts of unit amplitude and is thus the transfer function from the gust to the lift.

Actually, only the absolute square of $\phi(k)$ will be required. For two-dimensional incompressible flow the following approximation is given in reference 1:

$$|\phi(k)|^2\approx\frac{1}{1+2\pi k} \qquad (7)$$

This expression has the advantage of simplicity, although it is somewhat in error compared with the absolute square of the Sears function at very low frequencies, a fact which could be remedied by using the approximation

$$|\phi(k)|^2\approx\frac{1+ak}{1+ak(1+2\pi k)}$$

where a is about 15 for a good overall fit to the exact expression. However, the behavior of the Sears function itself at very high frequencies is unrealistic, because its absolute square goes to zero as $1/k$, whereas for any nonzero Mach number and any finite span the absolute square of the generalized Sears function can be shown to tend to zero at least as rapidly as $1/k^2$. As a result of these discrepancies, the approximation given by equation (7) and, for the same reason, the absolute square of the exact Sears function, cannot be used to obtain moments of the lift spectrum, that is, values of the mean-square derivatives of the lift, although they may be adequate for calculating the mean-square value of the lift itself in many cases, particularly when absolute accuracy is not required. Whenever possible the values of $|\phi(k)|^2$ given in reference 8 for the plan form and Mach number of interest should be used.

MEAN-SQUARE LIFT AND ITS SPECTRAL RESOLUTION FOR THE UNSWEPT WING

Basic equations.—The correlation function of the lift can be expressed, by virtue of equation (4), as

$$\psi_L(\tau)=\int_{-\infty}^{\infty}\int_{-\infty}^{\infty}\int_{-b/2}^{b/2}\int_{-b/2}^{b/2} h(t_1,y_1)h(t_2,y_2)\,\overline{w(U(t-t_1),y_1)w(U(t+\tau-t_2),y_2)}\,dy_1dy_2dt_1dt_2 \qquad (8)$$

where the averaged product on the right side represents a velocity correlation function. This function depends in general on both space and time displacements. However, if Taylor's hypothesis is made, the time displacements are equivalent to

longitudinal space displacements. The velocity correlation functions are then functions only of longitudinal and lateral space displacements. Thus, for homogeneous turbulence,

$$\overline{w(x+Ut,y)w(x+\xi+U(t+\tau),y+\eta)}=\tilde{\psi}_w(\xi+U\tau,\eta) \tag{9}$$

In addition to Taylor's hypothesis and the assumption of homogeneity, the turbulence is assumed to be axisymmetric with respect to vertical axes, so that $\tilde{\psi}_w(\xi,\eta)$ is a function only of $\sqrt{\xi^2+\eta^2}$. This function is the ordinary space-correlation function ψ_w, so that

$$\tilde{\psi}_w(U\tau+\xi,\eta)=\psi_w\left(\sqrt{(U\tau+\xi)^2+\eta^2}\right)$$

and, hence,

$$\psi_L(\tau)=\int_{-\infty}^{\infty}\int_{-\infty}^{\infty}\int_{-b/2}^{b/2}\int_{-b/2}^{b/2}h(t_1,y_1)h(t_2,y_2)\psi_w\left(\sqrt{U^2(\tau+t_1-t_2)^2+(y_2-y_1)^2}\right)dy_1dy_2dt_1dt_2$$

If the assumption implicit in equation (5) is now made, the preceding equation can be written as

$$\psi_L(\tau)=\int_{-\infty}^{\infty}\int_{-\infty}^{\infty}h_L(t_1)\,h_L(t_2)\,\psi_{w_e}(U(\tau+t_1-t_2))\,dt_1\,dt_2 \tag{10}$$

where

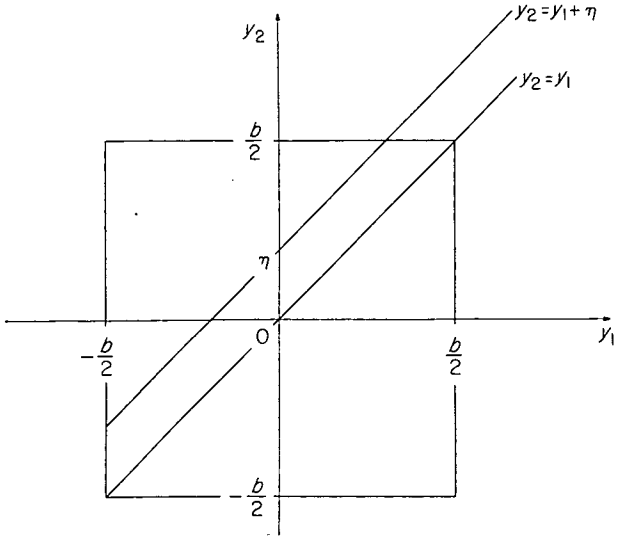
$$\psi_{w_e}(U\tau)=\frac{1}{b^2}\int_{-b/2}^{b/2}\int_{-b/2}^{b/2}\psi_w\left(\sqrt{U^2\tau^2+(y_2-y_1)^2}\right)\gamma(y_1)\,\gamma(y_2)\,dy_1\,dy_2$$

$$=\frac{1}{b}\int_0^b\Gamma(\eta)\,\psi_w\left(\sqrt{U^2\tau^2+\eta^2}\right)d\eta \tag{11}$$

where, in turn, $\Gamma(\eta)$ is an autoconvolution of $\gamma(y)$ defined by

$$\Gamma(\eta)=\frac{2}{b}\int_{-b/2}^{\frac{b}{2}-\eta}\gamma(y)\,\gamma(y+\eta)\,dy \tag{12}$$

The validity of equation (11) can be demonstrated by performing the integration in the y_1,y_2 plane as indicated in the following sketch:



That is, integration is performed first over y_1, with a variable $\eta\equiv y_2-y_1$ held constant. For this integration ψ_w is constant, so that only $\gamma(y_1)$ and $\gamma(y_1+\eta)$ are involved, and the result is a function of η which is one-half of the function $\Gamma(\eta)$ defined by equation (12). The second integration is then performed over η, yielding equation (11) except for a factor of ½. In this process, only the part of the square above the line $y_2=y_1$ is covered. However, by a similar process, the part of the integral corresponding to the part of the plane below this line can be evaluated and shown to be equal to the first part, so that by defining Γ as in equation (12), both parts are taken into account simultaneously in equation (11).

The quantity

$$w_e^2\equiv\psi_{w_e}(0)$$

$$=\frac{1}{b}\int_0^b\Gamma(\eta)\,\psi_w(\eta)\,d\eta$$

may be considered an averaged mean-square vertical component of turbulence; $\psi_{w_e}(U\tau)$ is then the corresponding correlation function, and the Fourier transform of the latter,

$$\varphi_{w_e}(\omega)=\frac{1}{\pi U}\int_{-\infty}^{\infty}e^{-i\frac{\omega}{U}(U\tau)}\psi_{w_e}(U\tau)\,d(U\tau) \tag{13}$$

is the corresponding power spectrum.

Once $\varphi_{w_e}(\omega)$ has been obtained, the power spectrum of the lift can be obtained by taking the Fourier transforms of both sides of equation (10). The result is

$$\varphi_L(\omega)=|H_L(\omega)|^2\varphi_{w_e}(\omega) \tag{14}$$

where $H_L(\omega)$ is the transfer function defined in the preceding section. The mean square of the lift can then be obtained by integrating its spectrum, as indicated in equation (1).

Equation (14) has the same form as the corresponding equation for the case where spanwise averaging of the effects of turbulence is not taken into account (see eq. (2) and ref. 1), except that $\varphi_w(\omega)$ is now replaced by $\varphi_{w_e}(\omega)$. Thus, the spectrum of the averaged turbulence must approach that of the unaveraged turbulence when the span approaches zero, as may be seen to be the case from equation (11) and the definitions of $\gamma(y)$ and $\Gamma(\eta)$.

Two alternative approaches.—The defining relations for $\varphi_{w_e}(\omega)$, equations (11) and (13), do not necessarily represent the best method of calculating it in any given case. A slightly different expression appears to be more convenient in general. It consists in substituting equation (11) into equation (13) and inverting the order of integration to yield

$$\varphi_{w_e}(\omega)=\frac{1}{b}\int_0^b\Gamma(\eta)\tilde{\varphi}_w(\omega,\eta)\,d\eta \tag{15}$$

where

$$\tilde{\varphi}_w(\omega,\eta)=\frac{1}{\pi U}\int_{-\infty}^{\infty} e^{-i\frac{\omega}{U}(U\tau)}\psi_w\left(\sqrt{U^2\tau^2+\eta^2}\right)d(U\tau) \tag{16}$$

so that

$$\tilde{\varphi}_w(\omega,0)=\varphi_w(\omega)$$

A third approach, which has certain advantages over the others, is similar to the one that has been used in reference 5. In this approach the assumption of axisymmetry is not made initially, and use is made of the spectrum

$$\tilde{\Phi}_w(\lambda_1,\lambda_2)=\frac{1}{\pi^2}\int_{-\infty}^{\infty}\int_{-\infty}^{\infty} e^{-i(\lambda_1\xi+\lambda_2\eta)}\tilde{\psi}_w(\xi,\eta)\,d\xi\,d\eta \tag{17a}$$

The correlation function $\psi_{w_e}(U\tau)$ can then be written as

$$\psi_{w_e}(U\tau)=\frac{1}{b^2}\int_{-b/2}^{b/2}\int_{-b/2}^{b/2}\gamma(y_1)\,\gamma(y_2)\,dy_1\,dy_2\,\frac{1}{4}\int_{-\infty}^{\infty}\int_{-\infty}^{\infty} e^{i[\lambda_1 U\tau+\lambda_2(y_2-y_1)]}\,\tilde{\Phi}_w(\lambda_1,\lambda_2)\,d\lambda_1\,d\lambda_2$$

Substitution of this expression into equation (13) and then interchanging the order of integration yields:

$$\varphi_{w_e}(\omega)=\frac{1}{2U}\int_{-\infty}^{\infty}\tilde{\Phi}_w\left(\frac{\omega}{U},\lambda_2\right)\left|\tilde{\Gamma}(\lambda_2)\right|^2 d\lambda_2$$

where

$$\tilde{\Gamma}(\lambda)=\frac{1}{b}\int_{-b/2}^{b/2}\gamma(y)\,e^{-i\lambda y}\,dy$$

and is, as a result of the symmetry of $\gamma(y)$, real and symmetric in λ.

Now, if the turbulence is axisymmetric, $\tilde{\Phi}_w$ depends only on $\lambda\equiv\sqrt{\lambda_1^2+\lambda_2^2}$, that is,

$$\tilde{\Phi}_w(\lambda_1,\lambda_2)=\Phi_w\left(\sqrt{\lambda_1^2+\lambda_2^2}\right) \tag{17b}$$

so that the expression for $\varphi_{w_e}(\omega)$ becomes

$$\varphi_{w_e}(\omega)=\frac{1}{U}\int_0^{\infty}\Phi_w\left(\sqrt{\left(\frac{\omega}{U}\right)^2+\lambda^2}\right)\tilde{\Gamma}^2(\lambda)\,d\lambda \tag{18}$$

where $\Phi_w(\lambda)$ is related to $\psi_w(r)$ by

$$\Phi_w(\lambda)=\frac{2}{\pi}\int_0^{\infty} r\,J_0(\lambda r)\,\psi_w(r)\,dr$$

Although the spectra used in the last two approaches have been defined by expressions involving the point correlation function $\psi_w(r)$, they can be expressed equally well in terms of the point spectrum $\varphi_w(\omega)$, so that if, say, an experimentally obtained point spectrum is to be used, it need not be transformed into a correlation function before it can be used in these calculations. The required relations are

$$\tilde{\varphi}_w(\omega,\eta)=\varphi_w(\omega)-\frac{|\eta|}{U}\int_{|\omega|}^{\infty}\varphi_w(\omega_1)\,\frac{\omega_1}{\sqrt{\omega_1^2-\omega^2}}\,J_1\left(\frac{|\eta|\sqrt{\omega_1^2-\omega^2}}{U}\right)d\omega_1 \tag{19}$$

and

$$\Phi_w(\lambda)=-\frac{2U^2}{\pi}\left[\int_{\lambda U}^{\infty}\varphi(\omega)\,\frac{\omega}{(\omega^2-\lambda^2U^2)^{3/2}}\,d\omega \right. \tag{20}$$

where the notation $\lceil\ \rceil$ is used to specify that the finite part of the integral is to be taken, an operation which may be performed by integrating by parts and ignoring the infinite part, so that, in terms of a proper integral,

$$\Phi_w(\lambda)=-\frac{2U^2}{\pi}\int_{\lambda U}^{\infty}\frac{d\varphi_w(\omega)}{d\omega}\,\frac{d\omega}{\sqrt{\omega^2-\lambda^2U^2}}$$

Also, the function $\Phi_w(\lambda)$ can be obtained from $\tilde{\varphi}_w(\omega,\eta)$ by means of either of the relations

$$\Phi_w(\lambda)=\frac{1}{\pi U}\int_{-\infty}^{\infty}e^{-i\lambda\eta}\tilde{\varphi}_w(0,\eta)\,d\eta$$

$$=\frac{2}{\pi U}\int_0^{\infty}\tilde{\varphi}_w(\lambda U,\eta)\,d\eta$$

Results of calculations.—In order to illustrate the magnitude of the effects under consideration, calculations have been made for a uniform loading $\gamma(y)=1$ and a point correlation function which has been used in references 1 and 2 and appears to fit experimental data (ref. 4) fairly well over a large portion of the significant frequency range, namely,

$$\psi_w(r)=\overline{w^2}\left(1-\frac{|r|}{2L^*}\right)e^{-|r|/L^*}$$

so that

$$\varphi_w(\omega)=\frac{\overline{w^2}L^*}{\pi U}\,\frac{1+3k'^2}{(1+k'^2)^2}$$

where L^* is the integral scale of turbulence, which is here defined as

$$L^*=\frac{2}{\overline{w^2}}\int_0^{\infty}\psi_w(r)\,dr$$

and where

$$k'\equiv\frac{\omega L^*}{U}$$

This correlation function has the drawback that the moments of the spectrum associated with it are infinite, so that

it implies a process with infinite mean-square derivatives, but it is quite useful if only the mean-square value of the process itself is of interest.

For uniform loading,

$$\Gamma(\eta)=2\left(1-\frac{\eta}{b}\right)$$

and

$$\tilde{\Gamma}(\lambda)=\frac{\sin\frac{\lambda b}{2}}{\frac{\lambda b}{2}}$$

and for the given correlation function,

$$\tilde{\varphi}_w(\omega,y)=\frac{\overline{w^2}L^*}{\pi U}\left[\frac{y}{L^*}\frac{1+3k'^2}{(1+k'^2)^{3/2}}K_1\left(\frac{y}{L^*}\sqrt{1+k'^2}\right)-\left(\frac{y}{L^*}\right)^2\frac{1}{1+k'^2}K_0\left(\frac{y}{L^*}\sqrt{1+k'^2}\right)\right]$$

where K_0 and K_1 are modified Bessel functions of the second kind, and

$$\Phi_w(\lambda)=\frac{3\overline{w^2}L^{*2}}{\pi U^2}\frac{k'^2}{(1+k'^2)^{5/2}}$$

The mean-square average gust intensity for this case is given by

$$\overline{w_e^2}=\overline{w^2}\,\frac{1-e^{-\beta}}{\beta}$$

where $\beta\equiv b/L^*$, and is shown in figure 1 (a). The correlation function ψ_{w_e} is given by

$$\psi_{w_e}(r)=\frac{\overline{w^2}}{\beta}\left[\sigma\tilde{K}_1\left(\sigma;\ \sinh^{-1}\frac{\beta}{\sigma}\right)-\sigma^2\tilde{K}_0\left(\sigma;\ \sinh^{-1}\frac{\beta}{\sigma}\right)+\frac{\sigma^2}{\beta}\left(e^{-\sigma}-e^{-\sqrt{\sigma^2+\beta^2}}\right)\right]$$

where $\sigma\equiv r/L^*$, and where $\tilde{K}_0(\sigma;\vartheta)$ and $\tilde{K}_1(\sigma;\vartheta)$ are incomplete modified Bessel functions of the second kind defined by

$$\tilde{K}_n(\sigma;\vartheta)\equiv\int_0^{\vartheta}\cosh n\vartheta\ e^{-\sigma\cosh\vartheta}\,d\vartheta$$

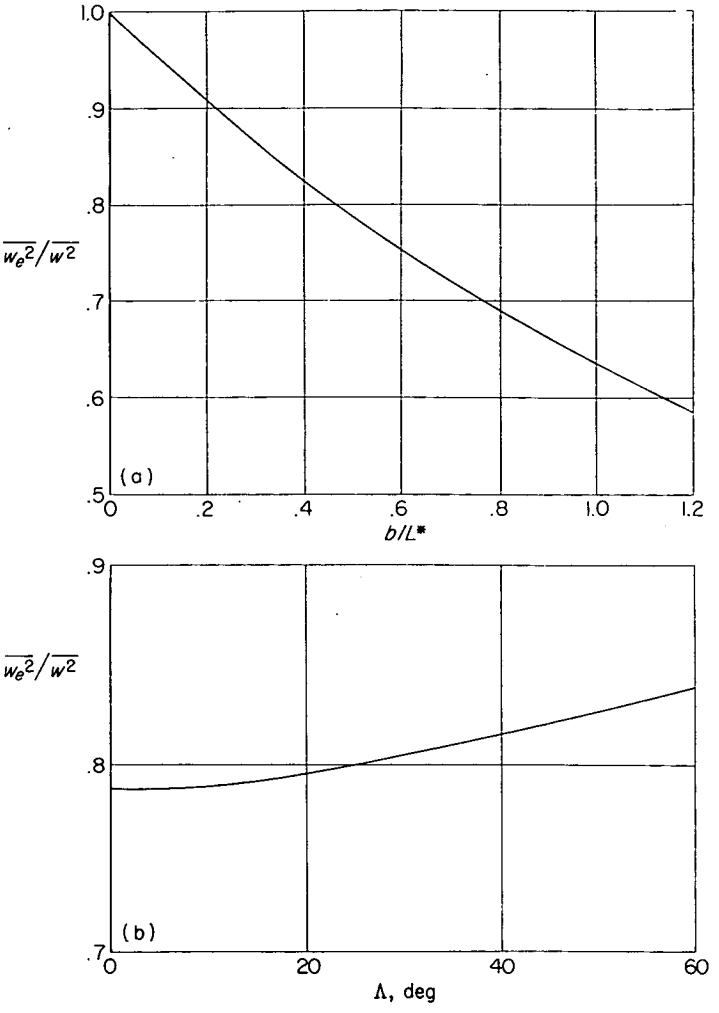
The spectrum $\varphi_{w_e}(\omega)$ is given by

$$\varphi_{w_e}(\omega)=\frac{\overline{w^2}}{\beta^2}\frac{2L^*}{\pi U}\frac{1}{(1+k'^2)^3}\{3k'^2\beta\sqrt{1+k'^2}\,[Ki_0(\beta\sqrt{1+k'^2})-\beta\sqrt{1+k'^2}K_0(\beta\sqrt{1+k'^2})]+(1-3k'^2)[2-2\beta\sqrt{1+k'^2}K_1(\beta\sqrt{1+k'^2})-\beta^2(1+k'^2)K_0(\beta\sqrt{1+k'^2})]\}$$

where $Ki_0(x)$ is the integral of $K_0(x)$:

$$Ki_0(x)=\int_0^x K_0(x_1)dx_1$$

The functions ψ_{w_e} and φ_{w_e} (normalized with the averaged mean-square turbulent velocity) are shown in figures 2 and 3, respectively. The effect of the span ratio on the normalized correlation function of the averaged turbulence may be seen to be relatively small, so that the effect on the unnormalized correlation function is primarily the decrease in overall level given by the ratio of $\overline{w_e^2}$ to $\overline{w^2}$. A similar statement may be made for the power spectrum. If the power spectrum were not normalized the averaging effect of the span would tend to reduce the intensity of the spectrum at all frequencies, but the high frequencies would be attenuated much more than the low ones, as might be expected. In fact, although the unaveraged spectrum decreases as ω^{-2} at high frequencies, the averaged spectrum decreases as ω^{-3}.



(a) Unswept wings.

(b) Swept wings, $\frac{b}{L^*\cos\Lambda}=0.5$.

FIGURE 1.—The mean-square averaged vertical component of turbulence.

The asymptotic values for $b/L^*\to\infty$ are shown in figures 2 and 3 in order to indicate the nature of the functions considered here when the scale of turbulence is small compared with the span, as may be the case for a wind-tunnel model responding to natural or artificial tunnel turbulence, or for a buffeting wing or tail surface, although this condition is not of practical concern for the gust-load problem.

The power spectrum of the lift is equal to the product of the power spectrum $\varphi_{w_e}(\omega)$ and the absolute square of the transfer function $H_L(\omega)$, as indicated in equation (14).

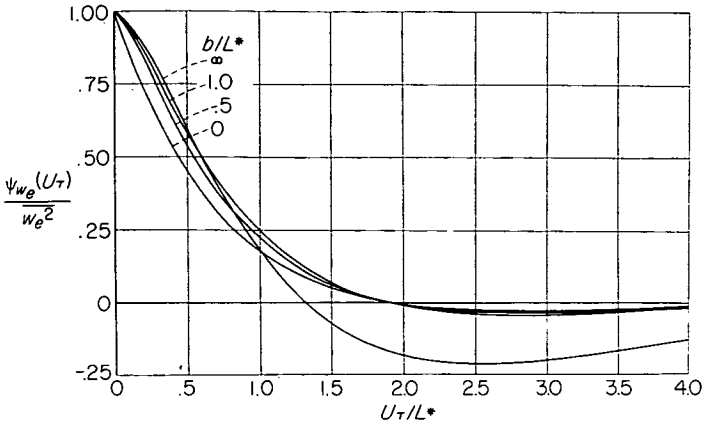


FIGURE 2.—The correlation function of the averaged vertical component of turbulence.

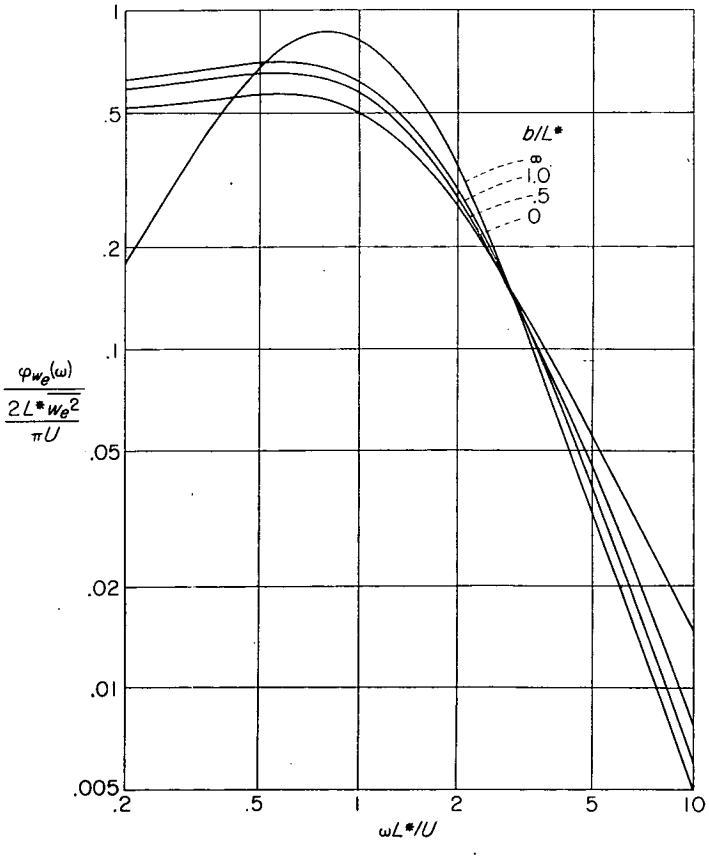


FIGURE 3.—The power spectrum of the averaged vertical component of turbulence.

Inasmuch as this lift is not an end in itself but only one of the parameters that enter into the calculations of the motion of the airplane, its mean-square intensity is of little practical significance; its spectrum is the quantity needed in further calculations. However, if the mean-square intensity is wanted for any reason it can be obtained by integrating the spectrum. Thus, for instance, the approximate expression for $|\phi(k)|^2$ given by equation (7) and the spectrum $\varphi_w(\omega)$ used for the preceding calculation yields the mean-square lift:

$$(\overline{L^2})_{\beta\to 0}=\left(\frac{C_{L_\alpha}qS}{U}\right)^2\overline{w^2}\,\frac{s}{2\pi^2}\left\{\frac{1+3\left(\frac{s}{2\pi}\right)^2}{\left[1+\left(\frac{s}{2\pi}\right)^2\right]^2}\left(\frac{s}{4}-\log\frac{s}{2\pi}\right)-\frac{\frac{s}{4}-1}{1+\left(\frac{s}{2\pi}\right)^2}\right\}$$

where

$$s\equiv\frac{L^*}{\overline{c}/2}$$

and, in view of the observation that much of the turbulent energy is contained in a region for which the span has a very small effect on the (normalized) spectrum, this equation should serve to furnish an approximation to the mean-square lift for nonvanishing span, provided $\overline{w_e^2}$ is used instead of $\overline{w^2}$. However, the mean-square values of the derivatives of the lift cannot be calculated in this simple manner, because the deviation of the normalized averaged spectrum from the point spectrum at high frequencies cannot be ignored in calculating the moments of the lift spectrum.

MEAN-SQUARE LIFT OF THE SWEPT WING

For the yawed or sideslipping unswept wing, equations (10) and (14) for the lift-correlation function and spectrum are still valid if an appropriate lift-influence function is used, and if the correlation function for the averaged turbulence is defined by

$$\psi_{w_e}(U\tau)=\frac{1}{b\cos\Lambda}\int_0^{b\cos\Lambda}\Gamma(\eta)\,\psi_w\left(\sqrt{(U\tau+\eta\tan\Lambda)^2+\eta^2}\right)d\eta$$

where $\Gamma(\eta)$ now pertains to a lift-distribution function $\gamma(y)$ which is appropriate for yawed motion and is defined for $-\frac{b}{2}\cos\Lambda\leqq y\leqq\frac{b}{2}\cos\Lambda$. The mean-square averaged intensity of the vertical component of turbulence is then

$$\overline{w_e^2}=\frac{1}{b\cos\Lambda}\int_0^{b\cos\Lambda}\Gamma(\eta)\,\psi_w\left(\frac{\eta}{\cos\Lambda}\right)d\eta$$

$$=\frac{1}{b}\int_0^b\Gamma(\eta'\cos\Lambda)\,\psi_w(\eta')\,d\eta'$$

where $\eta'\equiv\frac{\eta}{\cos\Lambda}$. Thus, this mean-square intensity is unaffected by the yawing process, except for the slight change which results from the change in $\Gamma(\eta)$, although the spectral resolution of the averaged intensity changes in the process.

For the swept wing both y_2-y_1 and $|y_2|-|y_1|$ occur in the integral, so that the reduction of the double integral for $\psi_{w_e}(U\tau)$ to a single integral (see eq. (11)) cannot be affected so simply. The double integral for the swept wing is

$$\psi_{w_e}(U\tau)=\frac{1}{b^2}\int_{-b/2}^{b/2}\int_{-b/2}^{b/2}\gamma(y_1)\,\gamma(y_2)\,\psi_w\left(\sqrt{[U\tau+(|y_2|-|y_1|)\tan\Lambda]^2+(y_2-y_1)^2}\right)dy_1\,dy_2 \qquad (21)$$

From this integral, by using rectangular lift distributions and the aforementioned point correlation function, the mean square of the averaged turbulence as well as the corresponding correlation function and power spectrum have been calculated by numerical integration for various sweep angles Λ, the ratio $\frac{\beta}{\cos\Lambda}$ being maintained at 0.5. (The decision to hold $\frac{\beta}{\cos\Lambda}$ rather than β constant was reached as a result of the foregoing analysis of the yawed unswept wing, which indicated that the effects of sweep should be minimized in this manner.) The results for $\overline{w_e^2}$ are shown in figure 1, and the effect of sweep on $\overline{w_e^2}$ is seen to be small for this comparison. The calculated correlation functions and spectra (normalized with respect to $\overline{w_e^2}$) are not shown because they agreed with those for $\Lambda=0$ within less than 1 percent for most values of $U\tau$ and k', respectively.

MEAN-SQUARE ROLLING MOMENT

In the preceding sections the averaging effect of the span has been shown to consist, essentially, in reducing the effective intensity of the turbulence sensed by the wing; thus, it only modifies the forces present on a wing of small span. If the analysis is extended to the rolling moment, however, a new phenomenon appears. When a wing is so small relative to the scale of turbulence that at any instant all of its points experience the same turbulent velocity, the wing experiences no rolling moment as the result of the direct action of turbulence (although it may experience a rolling moment indirectly as a result of the rolling and yawing motion caused by the lateral component of the turbulence). On the other hand, on a large wing the different intensities of the turbulence at different points on the span give rise directly to a net rolling moment, which then results in rolling motion. In this section the mean-square value of this moment is calculated.

At any instant t the rolling moment $L'(t)$ can be written in the same form as the lift $L(t)$ in equation (4); however, according to the previously mentioned reciprocity theorem, the lift-influence function $h(t,y)$ is now the lift distribution for an indicial roll with unit helix angle at the wing tip. If the assumption of invariance of this distribution with time is made, as for the symmetric case (see eq. (5)), then the required lift-influence function can be written as

$$h(t,y)=\frac{1}{b}h'(t)\gamma'(y)$$

where $h'(t)=\frac{C_{l_p}(t)qSb}{2U}$, and where the steady-state lift distribution $\gamma'(y)\equiv\frac{cc_l}{\bar{c}C_l}$ now pertains to a unit linear antisymmetric angle of attack.

The correlation function for the moment can then be written as

$$\psi_{L'}(\tau)=\int_{-\infty}^{\infty}\int_{-\infty}^{\infty}h'(t_1)h'(t_2)\psi_{w_e'}(U(\tau+t_1-t_2))dt_1dt_2 \quad (22)$$

where

$$\psi_{w_e'}(U\tau)=\frac{1}{b^2}\int_{-b/2}^{b/2}\int_{-b/2}^{b/2}\gamma'(y_1)\gamma'(y_2)\psi_w(\sqrt{U^2\tau^2+(y_2-y_1)^2})dy_1dy_2$$

$$=\frac{1}{b}\int_0^b\Gamma'(\eta)\psi_w(\sqrt{U^2\tau^2+\eta^2})d\eta \quad (23)$$

where, in turn, in analogy with equation (12),

$$\Gamma'(\eta)=\frac{2}{b}\int_{-b/2}^{(b/2)-\eta}\gamma'(y)\gamma'(y+\eta)dy$$

Hence, the second and third approaches indicated in the section concerned with the mean-square lift (see eqs. (15) and (16)) can be used to obtain

$$\varphi_{w_e'}(\omega)=\frac{1}{b}\int_0^b\Gamma'(\eta)\tilde{\varphi}_w(\omega,\eta)d\eta \quad (24)$$

and

$$\varphi_{w_e'}(\omega)=\frac{1}{U}\int_0^\infty\Phi_w\left(\sqrt{\left(\frac{\omega}{U}\right)^2+\lambda^2}\right)|\tilde{\Gamma}'(\lambda)|^2d\lambda$$

where

$$\tilde{\Gamma}'(\lambda)=\frac{1}{b}\int_{-b/2}^{b/2}\gamma'(y)e^{-i\lambda y}dy$$

and

$$\varphi_{L'}(\omega)=\left(\frac{C_{l_p}qSb}{2U}\right)^2|\phi(k)|^2\varphi_{w_e'}(\omega) \quad (25)$$

so that the mean-square rolling moment can be obtained by integrating this spectrum.

A qualitative indication of the effect of span on the mean-square rolling moment sensed by an airplane may be obtained from the quantity $\psi_{w_e'}(0)$, which represents the integral of the spectrum $\varphi_{w_e'}$. For a linear loading, $\gamma'=6\frac{y}{b/2}$ and

$$\Gamma'(\eta)=6\left[4-6\frac{\eta}{b/2}+\left(\frac{\eta}{b/2}\right)^3\right]$$

$$\tilde{\Gamma}'(\lambda)=6i\frac{\frac{\lambda b}{2}\cos\frac{\lambda b}{2}-\sin\frac{\lambda b}{2}}{\left(\frac{\lambda b}{2}\right)^2}$$

Hence, using the aforementioned expression for the point correlation function yields

$$\varphi_{w_e'}(\omega)=\frac{L^*\overline{w^2}}{\pi U}\frac{18}{\beta'^4(1+k'^2)^4}\{[-32+2\beta'^2+(16\beta'^2+\beta'^4)K_0(\beta')+$$
$$(32\beta'+6\beta'^3)K_1(\beta')]+k'^2[32-6\beta'^2-16\beta'^2K_0(\beta')-$$
$$(32\beta'+2\beta'^3)K_1(\beta')+\beta'^3Ki_0(\beta')]\}$$

where

$$\beta'\equiv\beta\sqrt{1+k'^2}$$

and

$$\psi_{w_e'}(0)=\frac{12\overline{w^2}}{\beta^4}\left[\frac{\beta^3}{4}-6+e^{-\beta}\left(6+6\beta+3\beta^2+\frac{3}{4}\beta^3\right)\right]$$

This spectrum and its integral approach zero linearly as β tends to zero.

GENERALIZED AERODYNAMIC INFLUENCE FUNCTIONS IN UNSTEADY FLOW

The aerodynamic influence functions used in the preceding sections define the contribution of a given station of a wing to the total lift and rolling moment. In the analysis of a flexible wing, and even in the calculation of certain properties of a rigid wing, generalized aerodynamic influence functions are required, which define the contribution of one station on the wing to the lift at another station and thus represent a Green's function for the unsteady spanwise lift distribution. No work appears to have been done on such functions. For steady flow, apart from some calculations for supersonic speeds which are based on the subdivision of a given wing into a number of squares, the only available results appear to be those given in references 9 and 10.

The analysis in this section is based on reference 8 and consists in a generalization of the method presented therein to unsteady flow. This method constitutes an attempt to predict the lift distribution for any given twist on the basis of knowledge concerning a few definite angle-of-attack distributions, and may therefore be termed a function-interpolation method. For the present purpose, the presumably known lift distributions are the ones for uniform angle of attack in direct and reverse flow in a dimensionless form, namely, $cc_l/\overline{c}C_L$; they will be referred to as $\gamma_D(y)$ and $\gamma_R(y)$, respectively. (The function $\gamma(y)$ used previously is the one now designated by $\gamma_R(y)$.) Also required is the coefficient of damping in roll C_{l_p}. (The lift-curve slope and the coefficient of damping in roll are the same in direct and reverse flow by virtue of the reciprocity theorem, so that no distinction will be made.)

The approach of reference 9 then yields the following approximate expression for the lift distribution due to any angle-of-attack distribution:

$$\frac{cc_l}{\overline{c}}=C_{L_\alpha}\{\overline{\alpha}\,\gamma_D(y)+K[\alpha(y)-\overline{\alpha}]\,\gamma_R(y)\} \tag{26}$$

where

$$\overline{\alpha}=\frac{1}{b}\int_{-b/2}^{b/2}\gamma_R(y)\,\alpha(y)\,dy$$

$$K=\frac{C_{l_p}}{C_{L_\alpha}}\frac{b^3}{4\int_0^{b/2}\gamma_R(y)\,y^2dy} \tag{27}$$

Values of K may be obtained from the information given in references 9 and 10. As the aspect ratio tends to zero, K approaches ½, whereas for aspect ratios approaching infinity, K tends to 1. The following relations can be obtained from elementary definitions and from the aforementioned reciprocity theorem:

$$C_L=\frac{1}{b}\int_{-b/2}^{b/2}\frac{cc_l}{\overline{c}}\,dy$$

$$=\frac{C_{L_\alpha}}{b}\int_{-b/2}^{b/2}\gamma_R(y)\,\alpha(y)\,dy$$

$$\frac{1}{b}\int_{-b/2}^{b/2}\gamma_D(y)\,dy=\frac{1}{b}\int_{-b/2}^{b/2}\gamma_R(y)\,dy=1$$

$$C_l=\frac{1}{b^2}\int_{-b/2}^{b/2}\frac{cc_l}{\overline{c}}\,y\,dy$$

$$C_{l_p}=\frac{1}{b^2}\int_{-b/2}^{b/2}\left(\frac{cc_l}{\overline{c}}\right)_{\alpha=\frac{y}{b/2}}y\,dy$$

With the aid of these relations the lift distributions given by equation (26) may readily be seen to have the correct lift and rolling moment for all angle-of-attack distributions, and to reduce to the exact lift distributions for angle-of-attack distributions which vary linearly along the span. A lift distribution which possesses these properties could readily be obtained by approximating any given angle-of-attack distribution by a suitably chosen linear one. However, this procedure would yield poorer approximations than the ones furnished by equation (26); for a parabolic angle-of-attack distribution on a wing of very small aspect ratio, for instance, this procedure would yield the lift distribution

$$\frac{cc_l}{\overline{c}}=\frac{A}{2}\sqrt{1-\left(\frac{y}{b/2}\right)^2}$$

with a bending moment too low by 17 percent compared with the one of the exact lift distribution,

$$\frac{cc_l}{\overline{c}}=\frac{A}{3}\sqrt{1-\left(\frac{y}{b/2}\right)^2}\left[1+2\left(\frac{y}{b/2}\right)^2\right]$$

whereas equation (26) yields

$$\frac{cc_l}{\overline{c}}=\frac{A}{4}\sqrt{1-\left(\frac{y}{b/2}\right)^2}\left[1+4\left(\frac{y}{b/2}\right)^2\right]$$

with a bending moment 8 percent too high. For very large aspect ratios, γ_D and γ_R both tend to the chord distribution $c/\overline{c}$, so that the lift distributions given by equation (26) tend to the correct limiting value,

$$\left(\frac{cc_l}{\overline{c}}\right)_{A\to\infty}=C_{l_\alpha}\frac{c}{\overline{c}}\alpha \tag{28}$$

Therefore the accuracy of the results furnished by equation (26) may be expected to increase as the aspect ratio increases, whereas the accuracy of the other approximation is independent of aspect ratio.

In this connection, it may be mentioned that "strip theory" consists in using equation (28) for all aspect ratios and, hence, is not very satisfactory for wings with medium and low aspect ratios. For instance, for the case discussed in the preceding paragraph, it furnishes a bending moment which is too low by 25 percent for a delta wing, and too high by 25 to 100

percent for tapered wings. (The two figures pertain to taper ratios of ¼ and 1, respectively.)

Substituting the value for $\bar{\alpha}$ from equation (27) into equation (26) gives the following expression for $cc_l/\bar{c}$:

$$\frac{cc_l}{\bar{c}}=\frac{C_{L_\alpha}}{b}\int_{-b/2}^{b/2}\{[\gamma_D(y)-K\gamma_R(y)+bK\,\delta(y-\eta)]\,\gamma_R(\eta)\}\alpha(\eta)\,d\eta$$

The expression in braces in the integrand is the desired generalized aerodynamic influence function and will be designated by $G(y,\eta)$, so that

$$G(y,\eta)=[\gamma_D(y)-K\gamma_R(y)+bK\,\delta(y-\eta)]\,\gamma_R(\eta) \tag{29}$$

and

$$\frac{cc_l}{\bar{c}}=\frac{C_{L_\alpha}}{b}\int_{-b/2}^{b/2}G(y,\eta)\,\alpha(\eta)\,d\eta \tag{30}$$

In the limiting cases of wings of very low or very high aspect ratio, γ_D and γ_R approach a common value, say γ. Thus, for wings of very low aspect ratio,

$$G(y,\eta)=\frac{1}{2}[\gamma(y)+b\,\delta(y-\eta)]\,\gamma(\eta) \tag{31a}$$

where δ is the Dirac delta (unit-impulse) function, and for wings of very high aspect ratio,

$$G(y,\eta)=b\,\delta(y-\eta)\,\gamma(\eta) \tag{31b}$$

which is the Green's function associated with strip theory. Thus, on wings of very high aspect ratio all the lift produced by the local angle of attack at a given station is carried in the immediate vicinity of that station, whereas on wings of very low aspect ratio much of the lift is carried elsewhere. This tendency for a given station to affect a greater portion of the wing as the span decreases is, of course, to be expected.

The preceding analysis can be applied to the oscillatory case at a given reduced frequency k, as well as to the steady case. If the assumption of invariance of normalized distributions with time or frequency is made, as before, then $\gamma_D(y)$, $\gamma_R(y)$, and K are independent of frequency, so that equation (30) can be written as

$$l(y;k)=\frac{C_{L_\alpha}(k)qS}{b^2}\int_{-b/2}^{b/2}G(y,\eta)\alpha(\eta)d\eta \tag{32a}$$

where $G(y,\eta)$, defined as before, is independent of k. By applying a Fourier transformation to both sides of this equation the following relation is then obtained for flight through continuously varying turbulence (cf. eq. (4)), as modified by the assumption stated in equation (5):

$$l(y,t)=\frac{1}{b}\int_{-\infty}^{\infty}h_L(t_1)dt_1\frac{1}{b}\int_{-b/2}^{b/2}G(y,\eta)w(U(t-t_1),\eta)d\eta \tag{32b}$$

where $l(y,t)$ is the lift per unit span at station y and time t, and where the function $h_L(t)$ is the one used previously.

The correlation function for this lift can then be written as

$$\psi_{l(y)}(\tau)=\frac{1}{b^2}\int_{-\infty}^{\infty}\int_{-\infty}^{\infty}h_L(t_1)h_L(t_2)\,dt_1dt_2\,\frac{1}{b^2}\int_{-b/2}^{b/2}\int_{-b/2}^{b/2}G(y,\eta_1)G(y,\eta_2)\psi_w\left(\sqrt{U^2(\tau+t_1-t_2)^2+(\eta_2-\eta_1)^2}\right)d\eta_1d\eta_2$$

$$=\frac{1}{b^2}\int_{-\infty}^{\infty}\int_{-\infty}^{\infty}h_L(t_1)h_L(t_2)dt_1dt_2\psi_{w_\epsilon}(U(\tau+t_1-t_2),y) \tag{33a}$$

where the function

$$\psi_{w_\epsilon}(U\tau,y)\equiv\frac{1}{b^2}\int_{-\infty}^{\infty}\int_{-\infty}^{\infty}G(y,\eta_1)\,G(y,\eta_2)\,\psi_w\left(\sqrt{U^2\tau^2+(\eta_2-\eta_1)^2}\right)d\eta_1d\eta_2$$

represents an effective correlation function, which when transformed into the equivalent power spectrum $\varphi_{w_\epsilon}(\omega,y)$ can be used to obtain the power spectrum for $l(y,t)$ and hence its mean-square value. Thus

$$\varphi_{l(y)}(\omega)=\frac{1}{b^2}\left(\frac{C_{L_\alpha}qS}{U}\right)^2|\phi(k)|^2\varphi_{w_\epsilon}(\omega,y) \tag{33b}$$

Before the calculation of $\varphi_{w_\epsilon}(\omega,y)$ is discussed, the function $\psi_{w_\epsilon}(U\tau,y)$ will be defined in a somewhat more general form than in the preceding paragraph in order to anticipate future needs, namely

$$\psi_{w_\epsilon}(U\tau,y_1,y_2)$$

$$\equiv\frac{1}{b^2}\int_{-b/2}^{b/2}\int_{-b/2}^{b/2}G(y_1,\eta_1)\;G(y_2,\eta_2)\;\psi_w\left(\sqrt{U^2\tau^2+(\eta_2-\eta_1)^2}\right)d\eta_1\,d\eta_2$$

If the assumption is now made that $\gamma_R(y)$ and $\gamma_D(y)$ are the same, as is the case for all unswept wings and for wings of very low or very high aspect ratio, they can both be identified with the function $\gamma(y)$ used previously, so that

$$G(y,\eta)=[(1-K)\,\gamma(y)+bK\,\delta(y-\eta)]\,\gamma(\eta) \tag{34}$$

and

$$\psi_{w_\epsilon}(U\tau,y_1,y_2)=\{(1-K)^2\psi_{w_e}(U\tau)+K(1-K)[\psi_{w_e}{}^*(U\tau,y_1)+$$

$$\psi_{w_e}{}^*(U\tau,y_2)]+K^2\psi_w\left(\sqrt{U^2\tau^2+(y_2-y_1)^2}\right)\}\,\gamma(y_1)\;\gamma(y_2)$$

where $\psi_{w_e}(U\tau)$ is the correlation function calculated previously for the averaged vertical component of turbulence, and where

$$\psi_{w_e}{}^*(U\tau,y)=\frac{1}{b}\int_{-b/2}^{b/2}\gamma(\eta)\;\psi_w\left(\sqrt{U^2\tau^2+(y-\eta)^2}\right)d\eta$$

Similarly, then,

$$\varphi_{w_\epsilon}(\omega,y_1,y_2)=\{(1-K)^2\varphi_{w_e}(\omega)+K(1-K)[\varphi_{w_e}{}^*(\omega,y_1)+\varphi_{w_e}{}^*(\omega,y_2)]+K^2\tilde{\varphi}_w(\omega,y_2-y_1)\}\gamma(y_1)\gamma(y_2) \quad (35)$$

where $\varphi_{w_e}{}^*(\omega,y)$ is the Fourier transform of $\psi_{w_e}{}^*(U\tau,y)$, so that

$$\varphi_{w_e}{}^*(\omega,y)=\frac{1}{b}\int_{-b/2}^{b/2}\gamma(\eta)\tilde{\varphi}_w(\omega,|y-\eta|)d\eta \quad (36)$$

and thus represents an averaged form of the spectrum $\tilde{\varphi}_w$ introduced previously. (See eqs. (16) and (19).) For uniform spanwise loading and the point correlation function used previously, this function is

$$\varphi_{w_e}{}^*(\omega,y)=\frac{L^*\overline{w^2}}{\pi U}\frac{1}{\beta}\frac{1}{(1+k'^2)^{5/2}}\{3k'^2[Ki_0(a_1)+Ki_0(a_2)-a_1K_0(a_1)-a_2K_0(a_2)]+[a_1{}^2K_1(a_1)+a_2{}^2K_1(a_2)]\}$$

where

$$a_1,a_2\equiv\frac{\frac{b}{2}\pm y}{L^*}\sqrt{1+k'^2}$$

and is shown in figure 4 for several values of $\frac{|y|}{b/2}$.

The more restricted form of φ_{w_ϵ} required in equation (33b) can now be obtained from the more general form given in

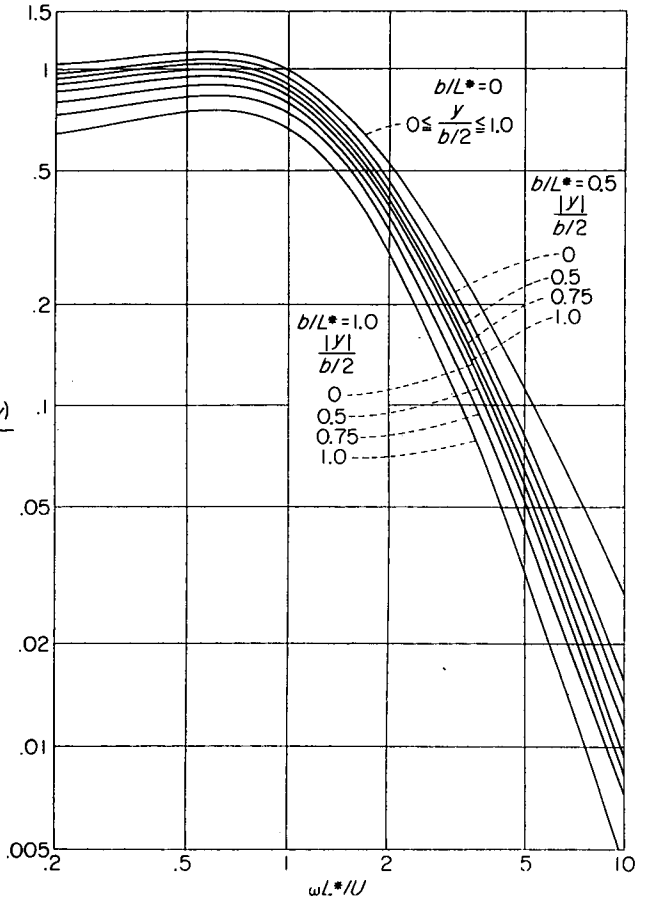


FIGURE 4.—The power spectrum $\varphi_{w_e}{}^*(\omega, y)$.

equation (35) by setting $y_2=y_1=y$ in the latter, to yield

$$\varphi_{w_\epsilon}(\omega)=[(1-K)^2\varphi_{w_e}(\omega)+2K(1-K)\varphi_{w_e}{}^*(\omega,y)+K^2\varphi_w(\omega)]\gamma^2(y) \quad (37)$$

MEAN-SQUARE BENDING AND PITCHING MOMENTS

When the variation of the gust intensity along the span is taken into account, the mean-square lift $\overline{L^2}$ is not an adequate index of the stresses in the wing, nor can the stresses be obtained from the mean-square lift distribution $\overline{l^2(y)}$. Instead, the mean-square bending and twisting moments, as well as the mean-square vertical shear, must be calculated directly.

In a manner analogous to that employed for the lift and rolling moment, each of these quantities can be expressed in terms of a certain influence function which, by means of the reciprocity theorem, can be related to a lift distribution on the wing in reverse flow. For instance, for the root bending moment the desired lift distribution is the one for an angle of attack which is zero on one wing and proportional to y on the other, as may be seen from the fact that the bending moment can be expressed as

$$M_B=\int_{-b/2}^{b/2}[l(y)]_{\alpha(y)}f(y)dy$$

where

$$f(y)\equiv 0 \qquad (y<0)$$

$$f(y)\equiv y \qquad (y\geq 0)$$

so that, according to the reciprocity theory for unswept wings in steady or indicial flow,

$$M_B=\int_{-b/2}^{b/2}[l(y)]_{f(y)\alpha(y)}dy$$

Similarly, for the root shear the required lift distribution corresponds to an angle of attack which is zero on one wing and uniform on the other.

Such lift distributions can be calculated readily. For instance, for subsonic flow and unswept wings they can be obtained from those given in reference 10; the lift distribution for the root bending moment is one-half the sum of a linear symmetric and linear antisymmetric lift distribution, and the lift distribution for the root shear is one-half the sum of a lift distribution due to a uniform angle of attack and a lift distribution due to deflection of a full-span aileron.

However, in some cases such calculations may be time-consuming, and an alternative approach may be desirable. One such approach consists in synthesizing the desired influence function from the generalized lift-influence (Green's) function discussed in the preceding section. In order to illustrate the use of this approach, it is adopted in this section.

The bending moment at any station $y\left(0\leq y\leq\frac{b}{2}\right)$ and at

any time t can be obtained from the lift distribution considered in the preceding section as

$$M_B(y,t)=\int_y^{b/2}(y'-y)l(y',t)\,dy'$$

$$=\frac{1}{b}\int_y^{b/2}(y'-y)\,dy'\int_{-\infty}^{\infty}h_L(t_1)\,dt_1\,\frac{1}{b}\int_{-b/2}^{b/2}G(y',\eta)w(U(t-t_1),\eta)\,d\eta$$

$$=\frac{1}{b}\int_{-\infty}^{\infty}h_L(t_1)\,dt_1\int_{-b/2}^{b/2}\tilde{M}(y,\eta)w(U(t-t_1),\eta)d\eta \tag{38}$$

where the influence function for the bending moment is

$$\tilde{M}(y,\eta)=\frac{1}{b}\int_y^{b/2}(y'-y)G(y',\eta)\,dy' \tag{39a}$$

so that, upon introducing the previously used function for $G(y,\eta)$

$$\tilde{M}(y,\eta)=[(1-K)M_1(y)+KM_2(y,\eta)]\gamma(\eta) \tag{39b}$$

where

$$M_1(y)=\frac{1}{b}\int_y^{b/2}(y'-y)\gamma(y')\,dy'$$

$$M_2(y,\eta)=\eta-y \quad (\eta>y)$$

$$M_2(y,\eta)=0 \quad (\eta\leqq y)$$

and, hence, for the root bending moment,

$$M_1(0)=\frac{1}{b}\int_0^{b/2}y'\gamma(y')\,dy'$$

$$M_2(0,\eta)=\eta \quad (\eta>0)$$

$$M_2(0,\eta)=0 \quad (\eta\leqq 0)$$

Hence, the correlation function for the root bending moment is

$$\psi_{M_B}(\tau)=\int_{-\infty}^{\infty}\int_{-\infty}^{\infty}h_L(t_1)h_L(t_2)dt_1dt_2\frac{1}{b^2}\int_{-b/2}^{b/2}\int_{-b/2}^{b/2}\{(1-K)^2M_1^2(y)+K(1-K)M_1(0)[M_2(0,\eta_1)+$$

$$M_2(0,\eta_2)]+K^2M_2(0,\eta_1)M_2(0,\eta_2)\}\gamma(\eta_1)\gamma(\eta_2)\psi_w(\sqrt{U^2(\tau+t_1-t_2)^2+(\eta_2-\eta_1)^2})d\eta_1d\eta_2 \tag{40}$$

The approach used in the preceding sections can now be used to obtain the power spectrum of the root bending moment by evaluating the inner pair of integrals of equation (40), taking the Fourier transform of the result with respect to τ, and multiplying the power spectrum obtained in this manner by $\left(\frac{C_{L_\alpha}qS}{U}\right)^2|\phi(k)|^2$ or by using one of the alternative approaches indicated for the lift.

The spectrum corresponding to the inner pair of integrals is, for $K=1$ and uniform loading,

$$\varphi_{w_e''}(\omega)=\frac{L^*\overline{w^2}}{\pi U\beta^4(1+k'^2)^4}\left\{\left[(-64+2\beta'^2)+8\beta'^2K_0\left(\frac{\beta'}{2}\right)+\right.\right.$$

$$(32\beta'+\beta'^3)K_1\left(\frac{\beta'}{2}\right)\Big]+k'^2\Big[\beta'^3Ki_0\left(\frac{\beta'}{2}\right)+(64-6\beta'^2)-$$

$$\left.\left.8\beta'^2K_0\left(\frac{\beta'}{2}\right)-(32\beta'-\beta'^3)K_t\left(\frac{\beta'}{2}\right)\Big]\right]\right\}$$

where $\beta'\equiv\beta\sqrt{1+k'^2}$, as before.

The integral of this spectrum is

$$\psi_{w_e''}(0)=\frac{\overline{w^2}}{3\beta^4}\left[\left(-24+\frac{\beta^3}{2}\right)+e^{-\beta/2}(24+12\beta+3\beta^2)\right]$$

Examination of $\psi_{w_e''}(0)$ indicates that, although the mean-square bending moment tends to decrease as the span increases, it decreases less rapidly than the mean-square lift, with the result that the effective lateral center of pressure moves outboard. Quantitatively, the distance from the plane of symmetry to the effective lateral center of pressure can be defined as the square root of the ratio of the mean-square root bending moment to the mean square of the lift on one wing, that is, of the root shear. Although these mean squares have not been calculated, the square root of the ratio of $\psi_{w_e''}(0)$ to the corresponding value for the root shear increases by 15.5 percent as β increases from 0 to infinity, with much of the increase realized at fairly small values of β.

For a swept wing the variation of the gust intensity along the span results in a pitching moment which must be taken

into account in calculations of the dynamic response of the airplane to continuous turbulence. This pitching moment can be obtained in substantially the same manner as the bending moment. Thus, if $\bar{y}$ is the station of the mean aerodynamic chord,

$$M(t)=\tan\Lambda\int_{-b/2}^{b/2}(\bar{y}-|y|)\,l\,(y,t)\,dy$$

$$=\tan\Lambda\,\frac{1}{b}\int_{-\infty}^{\infty}h_L(t_1)\,dt_1\int_{-b/2}^{b/2}M_3(\eta)w(U(t-t_1),\eta)\,d\eta \qquad (41)$$

where

$$M_3(\eta)=\frac{1}{b}\int_{-b/2}^{b/2}(\bar{y}-|y|)\,G(y,\eta)\,dy$$

so that, with the previously used approximation to the Green's function,

$$M_3(\eta)=\{(1-K)[\bar{y}-2M_1(0)]+K(\bar{y}-|\eta|)\}\gamma(\eta)$$

The correlation function, spectrum, and mean-square value of the pitching moment can then be obtained in the manner used in the preceding sections.

WING-TAIL CORRELATION EFFECTS

The tail strikes a given gust some time after the wing does; as a result, a pitching moment arises which does not exist in steady or quasi-steady motion, nor if the airplane is very small, because then the time lag is insignificant. This pitching moment can, for the purpose of the present paper, be analyzed either in terms of the correlation between the gusts at the wing and those at the tail or, if a time-lag term is included in the indicial-response function of the tail, in terms of the correlation between the wing and tail response functions. The first point of view serves to exhibit the effect under consideration more clearly and is adopted first; the second is more convenient and is adopted in the subsequent parts of this report.

In the somewhat artificial case of a small wing and tail separated by a relatively large distance, only the distribution of turbulence along a line (the flight path) rather than in a portion of a plane is needed. The pitching moment due to the vertical component of atmospheric turbulence can then be written as

$$M(t)=\int_{-\infty}^{\infty}h_w(t_1)w(U(t-t_1))dt_1+\int_{-\infty}^{\infty}h_t(t_1)w(x_t+U(t-t_1))dt_1$$

where x_t is the tail length, and where $h_w(t)$ and $h_t(t)$ are the pitching-moment responses to indicial gusts hitting the wing and tail, respectively, at $t=0$; both may include unsteady-lift effects, and, if downwash effects are to be considered, $h_w(t)$ should include the contribution to the pitching moment of the tail lift caused by the downwash at the tail associated with the lift on the wing which results from the indicial gust.

The spectrum of this moment can then be written as

$$\varphi_M(\omega)=\left[|H_w(\omega)+H_t(\omega)|^2-2\mathrm{R}\left\{\left(1-e^{i\frac{\omega}{U}x_t}\right)H_w^*(\omega)H_t(\omega)\right\}\right]\varphi_w(\omega)$$

where the symbols R{ } and * designate, respectively, the real part and the complex conjugate of a complex number. Obviously, when x_t approaches 0 the second term in the bracket in this equation vanishes, so that the first term represents the perfect-correlation effect, and the second represents the correction for imperfect correlation.

In order to furnish an estimate of the magnitude of the effects under consideration, some calculations have been made on the basis of the assumption that a real coefficient μ exists such that

$$H_w(\omega)=\mu H_t(\omega)$$

which implies that the attenuation with frequency of the contributions of the wing lift and tail lift, respectively, to the pitching moment is the same. The ratio μ is -1 for neutral stability, and $\mu>-1$ for stable flight; it is positive when the aerodynamic-center location (tail off) is behind the center of gravity, so that positive values of μ are not likely to be incurred with normal configurations and flight conditions.

For this case,

$$\varphi_M(\omega)=|H_t(\omega)|^2\left[(1+\mu)^2-2\mu\left(1-\cos\frac{\omega x_t}{U}\right)\right]\varphi_w(\omega)$$

and

$$\frac{\overline{M^2}}{(\overline{M^2})_{(tail\ alone)}}=(1+\mu)^2-2\mu\Psi\left(\frac{x_t}{L^*},\frac{x_t}{\bar{c}/2}\right)$$

where

$$\Psi\left(\frac{x_t}{L^*},\frac{x_t}{\bar{c}/2}\right)\equiv\frac{\int_0^{\infty}|H_t(\omega)|^2\varphi_w(\omega)\left(1-\cos\frac{\omega x_t}{U}\right)d\omega}{\int_0^{\infty}|H_t(\omega)|^2\varphi_w(\omega)d\omega}$$

The function Ψ has been calculated for several values of its arguments by means of the lift-attenuation function given in equation (7) and the point spectrum used in the preceding sections, and is shown in figure 5. Also shown is the ratio of the mean-square moments as a function of the factor μ which in figure 5 is referred to as M_w/M_t. The effect of imperfect correlation is seen to be very large as the condition of neutral stability is approached; the entire pitching moment is then the result of instantaneous differences in gust intensities at the wing and tail.

In general, however, the tail length and the span are of the same order of magnitude, so that an analysis of the effect of imperfect correlation between the wing and tail must take into account the averaging effect of the wing span. The pitching moment at any instant is then

$$M(t)=\frac{1}{b}\int_{-\infty}^{\infty}h_w(t_1)dt_1\int_{-b/2}^{b/2}\gamma(y)\,w(U(t-t_1),y)dy+$$

$$\int_{-\infty}^{\infty}h_t(t_1)w(x_t+U(t-t_1),0)\,dt_1 \qquad (42a)$$

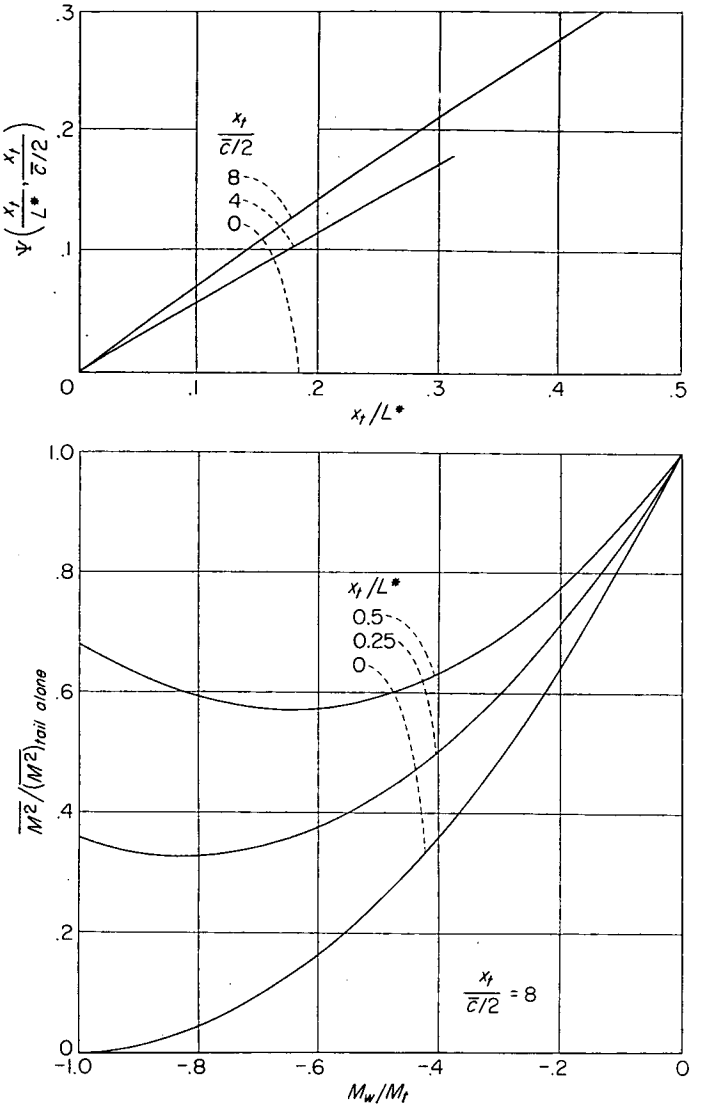


FIGURE 5.—Effect of tail length x_t on the mean-square pitching moment.

Hence, the power spectrum of this moment is

$$\varphi_M(\omega)=|H_w(\omega)|^2\varphi_{w_e}(\omega)+|H_t(\omega)|^2\varphi_w(\omega)+2\mathrm{R}\left\{e^{i\frac{\omega}{U}x_t}H_t(\omega)H_w{}^*(\omega)\right\}\varphi_{w_e{}^*}(\omega,0) \qquad (42b)$$

where $\varphi_{w_e}(\omega)$ is the averaged spectrum of equations (11) and (13), and $\varphi_{w_e{}^*}(\omega,0)$ is the spectrum of equation (36) for $y=0$. (It should be noted that $h_t(t)$ is the response to an indicial response which strikes the tail at $t=0$; if it were the indicial response to a gust which strikes the wing at $t=0$, the factor $e^{i\frac{\omega}{U}x_t}$ in the preceding equation would not be required.)

DYNAMICS OF THE RIGID AIRPLANE

In this part of the report the motions of a rigid airplane subjected to atmospheric disturbances are considered. This part thus applies directly to those airplanes which fly at relatively low speeds and do not experience any significant structural deformations, and also serves as a preliminary to the treatment of the flexible airplane in the later parts.

The assumption is made that the motions are small enough to permit the use of linear approximations to the resulting aerodynamic forces and to permit the linear superposition of these forces. The longitudinal degrees of freedom (pitching, vertical, and horizontal motion) and the lateral degrees of freedom (yaw, sideslip, and roll) can therefore be considered separately. The first two sections of this part are concerned with the longitudinal motions of a small airplane. The material presented here is thus a generalization of the single-degree-of-freedom analysis presented in reference 2. Mathematically, the dynamic system is now described by a set of simultaneous ordinary differential equations rather than a single one, but the problem of calculating the pertinent transfer functions is still one of simple algebra. The extension of these results to the large airplane is effected in the third section, using the techniques developed in the first part of this report. The lateral motions of a large airplane are considered briefly in the fourth section, and the combination of the stresses due to longitudinal and lateral motion of a large airplane is discussed in the fifth section.

EQUATIONS OF LONGITUDINAL MOTION

The equations of motion of an airplane can be expressed in several coordinate systems. The system which is generally the most convenient one for analyses of airplane stability and is generally referred to as stability axes, consists of body-centered axes which are normal and parallel to the relative air velocity and rotate with the airplane as it pitches or yaws. (See ref. 11, for instance.) The aerodynamic forces related to this axis system can be measured more readily in wind tunnels than those related to other axis systems. In view of the very close relation of a stability analysis to the problem considered here, these axes will be used in this part of the paper, but in the analysis of the flexible airplane in the subsequent parts of the report space-centered axes will be used, because they are slightly more convenient for that purpose.

The airplane will be considered to be in steady level flight prior to disturbance. The motions studied will be the deviations from their mean values; for instance, the angle θ considered here will be the difference between the disturbed and the initial value of the angle of pitch. Hence, the motions and forces calculated by the method indicated here must be added to their mean values to obtain the total motions and forces.

Inasmuch as, for the purpose of a statistical analysis, the dynamic characteristics of the airplane are represented most conveniently by its transfer functions, attention will be confined in this section to sinusoidal gusts and motions.

For this case the linearized equations of longitudinal motion can be written as follows (see eqs. II–193 of ref. 11, for instance):

$$\begin{bmatrix} i\omega-Z_w & -Z_u & -i\omega U \\ -X_w & i\omega-X_u & g \\ -i\omega M_{\dot{w}}-M_w & -M_u & -\omega^2-i\omega M_q \end{bmatrix}\begin{Bmatrix} w_p \\ u_p \\ \theta \end{Bmatrix} = \phi(k)\begin{bmatrix} Z_w & Z_u \\ X_w & X_u \\ M_w & M_u \end{bmatrix}\begin{Bmatrix} w \\ u \end{Bmatrix} \qquad (43)$$

The stability derivatives which appear in these equations are defined in table 1 in terms of conventional aerodynamic coefficients, and the numerical values are given for the example used in reference 11. (The value of the mean chord is not given in ref. 11 but it is assumed herein to be 10 feet on the basis of other information given in ref. 11.)

In analyses of the stability of a rigid airplane the quasi-steady approximation to unsteady-lift effects is usually made, in which, in effect, the forces corresponding to a steady attitude, to constant disturbance velocities, and to constant accelerations are considered. This approximation is justified because the motions of concern are generally sufficiently slow. For the same reason this approximation can also be made in analyzing the response of an airplane to atmospheric turbulence.

However, in this problem another type of unsteady-lift effect occurs, namely, that related to the forces directly attributable to the turbulence. This effect is here taken into account by multiplying the quasi-steady values of the forces due to gusts on the right side of equation (43) by the attenuation function $\phi(k)$. This procedure implies the assumption that the airplane is small relative to the scale of turbulence, inasmuch as no averaging effects have been taken into account; these effects will be discussed presently. Also, this attenuation function is strictly applicable only to the normal forces.

The unsteady effects on the drag are not known because of the relatively complicated nature of the mechanism which gives rise to drag. If, however, the assumption is made that upon entry into a sharp-edge gust the drag rises linearly and attains its steady-state value in the time required to travel

TABLE 1.—DEFINITIONS AND NUMERICAL VALUES OF STABILITY DERIVATIVES

Derivative	Definition	Numerical value for the example
Z_w	$-\frac{qS}{mU}(C_{L_\alpha}+C_D)$	−1. 430
Z_u	$-\frac{2qS}{mU}(C_{L_u}+C_L)$	−0. 0955
X_w	$\frac{qS}{mU}(C_L-C_{D_\alpha})$	0. 0016
X_u	$-\frac{2qS}{mU}(C_{D_u}+C_D)$	−0. 0097
M_w	$\frac{qS\bar{c}}{I_{yy}U}C_{m_\alpha}$	−0. 0235
$M_{\dot{w}}$	$\frac{qS\bar{c}^2}{2I_{yy}U^2}C_{m_{\dot{\alpha}}}$	−0. 0013
M_u	$\frac{2qS\bar{c}}{I_{yy}U}(C_{m_u}+C_m)$	0
M_q	$\frac{qS\bar{c}^2}{2I_{yy}U}C_{m_q}$	−1. 920

W, lb	30, 500
U, fps	660
$\bar{c}$, ft	10
Altitude, ft	20, 000

526597—60——12

N chord lengths, the drag equivalent of $|\phi(k)|^2$ is the function

$$\frac{1-\cos 2Nk}{2N^2k^2}$$

which, for N equal to about 5 or 6, agrees fairly well with $|\phi(k)|^2$ in the region of main interest ($k>1$).

The unsteady moment is also difficult to predict because of the paucity of knowledge concerning unsteady downwash effects for wings of finite span. However, inasmuch as the wing lift contributes part of the moment and, through the mechanism of downwash, determines to a large extent the moment contributed by the tail, the use of the lift attenuation function for the moment appears reasonable for a first approximation, and the use of the same function for the lift, drag, and moment facilitates the analysis.

For a more refined analysis, the time lag between the instants at which the gust hits the wing and the tail must be taken into account, not only for large airplanes, but even for small airplanes if phugoid motions are important. (See ref. 12.) Also, the lag in downwash should be taken into account for large airplanes and possibly also for small airplanes in some cases. One way of achieving this result is indicated in the next part of the present paper; another is discussed in reference 12.

In equation (43) the unknown quantities w_p and u_p are the normal and axial components of the disturbance velocities of the airplane relative to the free stream. Inasmuch as the coordinate axes rotate during the motion, the time derivatives of these quantities do not represent the actual airplane accelerations, which are required in analyses of the loads experienced by the airplane and the degree of passenger discomfort. If the deviations from a mean flight path are assumed to be small, the accelerations normal and parallel to the chord or longitudinal axis of the airplane are substantially the same as the absolute vertical and horizontal accelerations $\ddot{z}$ and $\ddot{x}$, which can be obtained from the relations

$$\ddot{z}=-\dot{w}_p+U\dot{\theta}$$

$$x=-\dot{u}_p-g\theta$$

The transfer functions for these quantities can then be obtained by introducing these relations into equation (43).

In studies of the longitudinal stability of airplanes, equation (43) is rarely solved in the form given here. It is usually reduced to two equations with two unknowns, either u_p and θ (the phugoid case) or w_p and θ (the short-period case), the short-period case being usually the one of primary interest. The part of the turbulent energy contained in the frequency range near the phugoid frequency is relatively small, so that the phugoid case has no significance for the analysis of loads and accelerations resulting from atmospheric turbulence. Hence, the short-period case, which ignores the phugoid oscillations, furnishes an excellent approximation to the loads and accelerations associated with the longitudinal motions of an airplane in turbulent air. However, another two-degree-of-freedom case, the one involving w_p and u_p, is useful in certain studies of the effects related to the interaction of horizontal and vertical components of turbulence.

Both of these two-degree cases can be reduced to the single-degree-of-freedom case involving only z (or w_p). For airplanes which have a large moment of inertia in pitch this simple case furnishes a good approximation. It has been studied in reference 2, where substantially the same approximations to the unsteady-lift effects were made as are made here, except that in reference 2 apparent-mass effects were included. (These effects are not included in the stability derivatives used in equation (43) because they are usually small—less than 1 percent of the mass of the airplane—and are different for each degree of freedom. However, if desired, the apparent mass pertaining to a given degree of freedom can easily be added to the airplane mass in calculating the stability derivatives.) However, this approximation is more nearly valid for calculating peak loads pursuant to an entry into a sharp-edge gust than for calculating the response due to random turbulence. Consequently, in the following sections, attention will be confined to the short-period case, although the analysis is equally applicable to the other case and easily extended to the case of three degrees of freedom.

SOLUTION OF THE EQUATIONS OF LONGITUDINAL MOTION

Transfer functions.—If the degree of freedom pertaining to x (or u_p) is ignored, the solution of equation (43) can be written as

$$\begin{Bmatrix} \ddot{z} \\ \ddot{\theta} \end{Bmatrix} = \begin{bmatrix} H_{\ddot{z}}^{w}(\omega) & H_{\ddot{z}}^{u}(\omega) \\ H_{\ddot{\theta}}^{w}(\omega) & H_{\ddot{\theta}}^{u}(\omega) \end{bmatrix} \begin{Bmatrix} w \\ u \end{Bmatrix} \tag{44}$$

where the transfer function $H_{\ddot{z}}^{w}(\omega)$ is defined by

$$H_{\ddot{z}}^{w}(\omega) = \phi(k)\frac{-A_{\ddot{z}}^{w}\omega^2 + B_{\ddot{z}}^{w} i\omega + C_{\ddot{z}}^{w}}{-A_0\omega^2 + B_0 i\omega + C_0} \tag{45}$$

where, in turn, the coefficients are defined in terms of the stability derivatives (see table 1) by

$$A_0 = 1 \qquad A_{\ddot{z}}^{w} = -Z_{w'}$$

$$B_0 = -(Z_w + M_q + UM_{\dot{w}}) \qquad B_{\ddot{z}}^{w} = Z_{w'}(UM_{\dot{w}} + M_q)$$

$$C_0 = M_q Z_w - UM_w \qquad C_{\ddot{z}}^{w} = -U(M_{w'}Z_w - M_w Z_{w'})$$

The transfer function $H_{\ddot{\theta}}^{w}(\omega)$ can be defined similarly in terms of the coefficients

$$A_{\ddot{\theta}}^{w} = M_{w'} + Z_{w'}M_{\dot{w}}$$

$$B_{\ddot{\theta}}^{w} = -(M_{w'}Z_w - M_w Z_{w'})$$

$$C_{\ddot{\theta}}^{w} = 0$$

In these equations a distinction has been made between the values of Z_w and M_w which occur on the right side of equation (43) and are here designated by a prime mark, and those on the left side of that equation. The primed derivatives pertain to the lift and moment directly due to gusts, whereas the unprimed derivatives pertain to the lift and moment due to airplane motion; the reason for this distinction is discussed in a later section. Furthermore, the coefficients $A_{\ddot{z}}^{u}$, $B_{\ddot{z}}^{u}$, $C_{\ddot{z}}^{u}$, $A_{\ddot{\theta}}^{u}$, $B_{\ddot{\theta}}^{u}$, and $C_{\ddot{\theta}}^{u}$ are the same as the coefficients $A_{\ddot{z}}^{w}$, $B_{\ddot{z}}^{w}$, . . . except that Z_w, $Z_{w'}$, M_w, and $M_{w'}$ are replaced by Z_u, $Z_{u'}$, M_u, and $M_{u'}$.

With these transfer functions the mean-square values of $\ddot{z}$ and $\ddot{\theta}$ can be calculated from the spectra of w and u by using equation (1), provided that the simultaneous action of w and u is taken into account. In order to analyze this effect the vertical acceleration $\ddot{z}$ will be considered, but the analysis will be applicable to $\ddot{\theta}$ or any other characteristic of the airplane which responds to w and u. Furthermore, the transfer functions need not be those considered in equation (44), but can be those calculated for the three-degree-of-freedom system or for a flexible airplane.

Normal-acceleration spectrum and mean-square value.—For the present purpose the indicial-response functions $h_{\ddot{z}}^{w}(t)$ and $h_{\ddot{z}}^{u}(t)$, which are the Fourier transforms of the transfer functions (see eq. (3a)), are more convenient. In terms of these indicial-response functions,

$$\ddot{z}(t) = \int_{-\infty}^{\infty} h_{\ddot{z}}^{w}(t_1) w(U(t-t_1))\, dt_1 + \int_{-\infty}^{\infty} h_{\ddot{z}}^{u}(t_1)\, u(U(t-t_1))\, dt_1$$

Then, if $w(t)$ and $u(t)$ are stationary in a statistical sense, the correlation function for $\ddot{z}(t)$ can be written as

$$\begin{aligned}\psi_{\ddot{z}}(\tau) = \int_{-\infty}^{\infty}\int_{-\infty}^{\infty} [&h_{\ddot{z}}^{w}(t_1)\, h_{\ddot{z}}^{w}(t_2)\, \psi_w(U(\tau + t_1 - t_2)) + \\ &h_{\ddot{z}}^{u}(t_1)\, h_{\ddot{z}}^{u}(t_2)\, \psi_u(U(\tau + t_1 - t_2)) + \\ &h_{\ddot{z}}^{w}(t_1)\, h_{\ddot{z}}^{u}(t_2)\, \psi_{wu}(U(\tau + t_1 - t_2)) + \\ &h_{\ddot{z}}^{u}(t_1)\, h_{\ddot{z}}^{w}(t_2)\, \psi_{wu}(U(-\tau + t_1 - t_2))]\, dt_1\, dt_2\end{aligned} \tag{46}$$

where $\psi_{wu}(U\tau)$ is a cross correlation of w and u defined by

$$\psi_{wu}(U\tau) = \overline{w(x + Ut)\, u(x + U(t+\tau))}$$

Now, if the turbulence is isotropic, the mutually perpendicular velocity components u and w at points in the XY-plane are statistically independent, and their cross correlation is zero. Therefore, the two terms in equation (46) involving $\psi_{wu}(U\tau)$ vanish, and the power spectrum of $\ddot{z}$ is

$$\varphi_{\ddot{z}}(\omega) = |H_{\ddot{z}}^{w}(\omega)|^2 \varphi_w(\omega) + |H_{\ddot{z}}^{u}(\omega)|^2 \varphi_u(\omega) \tag{47}$$

so that, generally speaking, the power spectrum of a response which depends on both the horizontal and the vertical component of turbulence is simply the sum of the power spectra of the two contributions, provided the turbulence is isotropic. (This statement can be shown to be true even if the distribution of the gusts over the span is taken into account.)

For the short-period two-degree-of-freedom case, then, the contribution due to w is

$$\overline{\ddot{z}^2} = \int_0^{\infty} |\phi(k)|^2 \frac{(A_{\ddot{z}}^{w})^2\omega^4 - [2A_{\ddot{z}}^{w}C_{\ddot{z}}^{w} - (B_{\ddot{z}}^{w})^2]\omega^2 + (C_{\ddot{z}}^{w})^2}{\omega^4 - (2C_0 - B_0^2)\omega^2 + C_0^2} \varphi_w(\omega)\, d\omega$$

and the contribution due to u can be obtained from the same expression, but with the subscript and superscript w replaced by u. However, the ratio of the two contributions is in the

order of $4\alpha^2$, where α is the trim angle of attack in radians, measured from the zero-lift conditions. Consequently, except at very high lift coefficients, such as those used in landing, the contribution due to u is usually negligible compared with the one due to w and is disregarded in subsequent sections.

By means of the lift-attenuation function given in equation (7) and the point spectrum used in the first part of the report, the integral for $\overline{\ddot{z}^2}$ has been evaluated (by using the technique of partial fractions for the integrand) for the example of reference 11. (The lift-attenuation function of equation (7) has been used despite its shortcomings in order to facilitate the analytic integration of the spectra.) The results are shown in figure 6, as are the results calculated similarly for the three-degree-of-freedom case, the other two-degree-of-freedom case (horizontal and vertical motion; referred to in the figure as the zero-pitch approximation), and the single-degree-of-freedom case (vertical motion). An examination of this figure indicates that, at least for this airplane, inclusion of horizontal motions does not affect the mean-square normal-acceleration response to any significant extent. These calculations pertain to a "small" airplane, and no distinction has been made between the primed and unprimed values of Z_w and M_w.

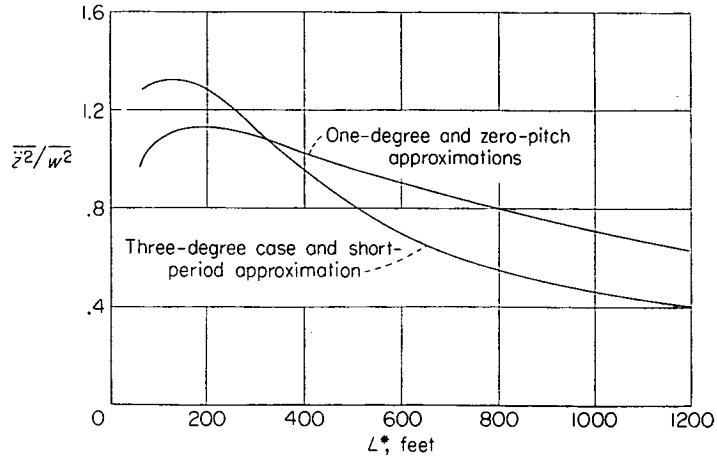


FIGURE 6.—Effect of scale of turbulence on the mean-square acceleration of the example airplane.

The preceding treatment of the short-period case has the advantage of using readily available information concerning the characteristics of any given airplane. For the purpose of trend studies a dimensionless form of the transfer functions is preferable. The preceding equation for $\overline{\ddot{z}^2}$ can be written in dimensionless form (the contribution of horizontal gusts again being neglected) as

$$\frac{\overline{\ddot{z}^2}}{g^2}=\left(\frac{U^2}{g\bar{c}/2}\right)^2\frac{\overline{w^2}}{U^2}\frac{4}{\kappa^2}\int_0^\infty|\phi(k)|^2\frac{k^4+4\left(\nu-\frac{1}{\kappa}\right)^2k^2}{k^4-2(k_o^2-\nu^2)k^2+(k_o^2+\nu^2)^2}\frac{U\varphi_w(\omega)}{L^*\overline{w^2}}dk' \tag{48a}$$

and, similarly,

$$\frac{\overline{\ddot{\theta}^2}}{(2g/\bar{c})^2}=\left(\frac{U^2}{g\bar{c}/2}\right)^2\frac{\overline{w^2}}{U^2}\left[\left(\nu-\frac{2}{\kappa}\right)^2+k_o^2\right]^2\int_0^\infty|\phi(k)|^2\frac{k^4}{k^4-2(k_o^2-\nu^2)k^2+(k_o^2+\nu^2)^2}\frac{U\varphi_w(\omega)}{L^*\overline{w^2}}dk' \tag{48b}$$

where κ is the mass parameter

$$\kappa\equiv\frac{8m}{C_{L_\alpha}\rho S\bar{c}}$$

ν is the dimensionless damping coefficient

$$\nu\equiv\frac{c}{2U}\frac{\log_e 2}{T_{1/2}}$$

$T_{1/2}$ is the time to damp to one-half amplitude, which is given by

$$\frac{\log_e 2}{T_{1/2}}=-\frac{1}{2}(Z_w+M_q+UM_{\dot{w}})$$

so that

$$\nu=\frac{1}{\kappa}\left(1-\frac{1}{2}\frac{m\bar{c}^2}{I_y}\frac{C_{m_q}+C_{m_{\dot{\alpha}}}}{C_{L_\alpha}}\right)$$

and k_o is the dimensionless frequency of the short-period oscillations,

$$k_o\equiv\frac{\omega_o\bar{c}}{2U}$$

with

$$\omega_o=\sqrt{M_qZ_w-UM_w-\frac{1}{4}\left(Z_w+M_q+UM_{\dot{w}}\right)^2}$$

so that

$$k_o=\frac{1}{\kappa}\sqrt{-\frac{m\bar{c}^2}{I_y}\left(\kappa\frac{C_{m_\alpha}}{C_{L_\alpha}}+2\frac{C_{m_q}}{C_{L_\alpha}}\right)-\left(1-\frac{1}{2}\frac{m\bar{c}^2C_{m_q}+C_{m_{\dot{\alpha}}}}{I_y}\frac{}{C_{L_\alpha}}\right)^2}$$

Thus, for this two-degree-of-freedom case the dimensionless mean-square responses are functions of only two additional parameters, which are dimensionless forms of the main characteristics of the short-period case (the short-period frequency and the time to damp to one-half amplitude), beyond those encountered in the single-degree-of-freedom case, namely, the mass parameter κ and the scale parameter $s\equiv\frac{L^*}{\bar{c}/2}$.

Bending-moment spectrum and mean-square value.—For a small airplane the instantaneous bending moments at various points on the span are proportional to the instantaneous normal acceleration. For instance, the root bending moment can be written as

$$M_B=\frac{L_w}{2}\bar{y}-\frac{m_w}{2}\bar{\bar{y}}\ddot{z} \tag{49a}$$

where L_w and m_w are, respectively, the lift on and the mass of the wing, and where $\overline{y}$ and $\overline{\overline{y}}$ are the lateral distances to the center of pressure of the lift on one wing and the center of gravity of the mass of one wing. However, L_w is proportional to the lift L on the entire airplane, which in turn is proportional to the normal acceleration, so that

$$L_w=\frac{L_w}{L}m\ddot{z}$$

and

$$M_B=\left[\frac{m}{2}\left(\frac{L_w}{L}\overline{y}-\frac{m_w}{m}\overline{\overline{y}}\right)\right]\ddot{z} \tag{49b}$$

Hence, the spectrum and mean-square value of M_B are proportional to the spectrum and mean-square value of $\ddot{z}$, respectively, the constant of proportionality being the square of the quantity in the brackets of equation (49b).

SPECIAL PROBLEMS RELATED TO THE LONGITUDINAL MOTION OF LARGE AIRPLANES

Single-degree-of-freedom case.—In the preceding sections the airplane has been assumed to be small in the sense of this report, and neither the instantaneous lateral variation of the intensity of turbulence nor the difference between instantaneous intensities at the wing and the tail has been taken into account. In this section this restriction is removed by introducing the aerodynamic forces calculated in the first part of this report into the dynamic analysis of the preceding sections. The arguments advanced in the preceding section for ignoring horizontal gusts and horizontal motions are equally valid for the large airplane; therefore these gusts and motions will not be considered here.

For the single-degree-of-freedom case involving only vertical motion the required modification for the normal acceleration is very simple. For this case the transfer function is

$$H_{\ddot{z}}^{w}(\omega)=-\phi(k)\frac{Z_w'}{i\omega-Z_w} \tag{50}$$

where Z_w', attenuated by $\phi(k)$, is the stability derivative for vertical gusts and, hence, represents the lift per unit gust intensity. Therefore, if the result for the lift calculated in the first part of this report is used, the mean-square normal acceleration becomes

$$\overline{\ddot{z}^2}=\int_0^\infty |\phi(k)|^2\frac{Z_w{}^2\omega^2}{\omega^2+Z_w{}^2}\varphi_{w_e}(\omega)\,d\omega$$

(The function $\varphi_{w_e}(\omega)$ is defined in the first part of this report.) This expression differs from the result obtained in reference 2 only in that $\varphi_w(\omega)$ is here replaced by $\varphi_{w_e}(\omega)$.

However, even for the single-degree case the calculation of the bending moment now becomes a considerably more complicated problem, because the lateral centers of pressure of the lifts due to the motion of the airplane and directly due to turbulence no longer coincide. Equation (49a) now becomes

$$M_B=-\frac{\overline{y}}{2}\frac{L_w}{L}\frac{C_{L_\alpha}qS}{U}\frac{\dot{z}}{U}-\frac{m_w}{2}\overline{\overline{y}}\,\ddot{z}+\frac{1}{b}\int_{-\infty}^{\infty}h_L(t_1)\,dt_1\int_{-b/2}^{b/2}\gamma_M(y)\,w(U(t-t_1),y)\,dy \tag{51}$$

where C_{L_α} is the lift-curve slope for the entire airplane, $h_L(t)$ is the response function used in equation (38), and $\gamma_M(y)$ is the function $\tilde{M}(y,\eta)$ used in equation (38), with $y=0$. In the first two terms on the right side of equation (51), $\dot{z}$ and $\ddot{z}$ can be related to w by means of $h_{\dot{z}}^{w}$ (the Fourier transform of the function $H_{\dot{z}}^{w}$ presented in eq. (50)) and the lift directly due to turbulence obtained in the first part of this report, so that these two terms can be written in the form

$$\frac{1}{b}\int_{-\infty}^{\infty}h_M(t_1)\,dt_1\int_{-b/2}^{b/2}\gamma(y)\,w(U(t-t_1),y)\,dy$$

and, hence, equation (51) becomes

$$M_B(t)=\frac{1}{b}\int_{-\infty}^{\infty}dt_1\int_{-b/2}^{b/2}[h_L(t_1)\gamma_M(y)+h_M(t_1)\gamma(y)]\,w(U(t-t_1),y)\,dy \tag{52}$$

The required influence function for the bending moment is, thus,

$$h_{M_B}(y,t)=\frac{1}{b}[h_L(t)\gamma_M(y)+h_M(t)\gamma(y)] \tag{53}$$

Although the two terms of this function are products of a time-dependent and a space-dependent constituent, as in equation (5), their sum cannot be split up in this manner. Hence, the techniques used in the first part of this paper are not directly applicable. The general treatment of problems involving influence functions for which the assumption of equation (5) is not valid will be considered in the last part of this paper. However, in this section a special technique will be used that applies to cases for which the influence function can be expressed as a sum of several terms (two in this case), each of which can be expressed as a product of two functions, which depend, respectively, on time alone and distance along the span alone. (See also ref. 13.) This approach is more convenient than the general approach of the last part of this report when the number of terms is two or, possibly, three. (Although in this section only two terms will be considered, the generalization to three or more terms is straightforward.) When the number of terms is greater than three, the general approach becomes more covenient.

If the value of M_B given by equation (52) for $t+\tau$ is multiplied by the value for t and the result is averaged, and if the Fourier transform of the resultant correlation function is then taken, the following expression is obtained for the spectrum of the bending moment:

$$\varphi_{M_B}(\omega)=|H_L(\omega)|^2\varphi_{w_{e_2}}(\omega)+|H_M(\omega)|^2\varphi_{w_e}(\omega)+2\mathrm{R}\{H_L(\omega)H_M{}^*(\omega)\}\varphi_{w_{e_1}}(\omega) \tag{54}$$

where the symbols R{ } and * designate, respectively, the real part and the complex conjugate of a complex number. In this equation $H_M(\omega)$ and $H_L(\omega)$ are the Fourier transforms of $h_M(t)$ and $h_L(t)$, $\varphi_{w_e}(\omega)$ is the previously defined averaged spectrum for the lift, and $\varphi_{w_{e_1}}$ and $\varphi_{w_{e_2}}$ are averaged

spectra obtained in a similar manner but with the value of Γ given by equation (12) replaced by

$$\left.\begin{aligned}\Gamma_1(\eta)&=\frac{2}{b}\int_{-b/2}^{(b/2)-\eta}\gamma(y)\,\gamma_{M_s}(y+\eta)\,dy\\ \Gamma_2(\eta)&=\frac{2}{b}\int_{-b/2}^{(b/2)-\eta}[\gamma_{M_s}(y)\,\gamma_{M_s}(y+\eta)+\gamma_{M_a}(y)\,\gamma_{M_a}(y+\eta)]\,dy\end{aligned}\right\}\quad(55)$$

where the subscripts s and a refer to the symmetric and antisymmetric parts of γ_M, respectively.

The contribution of the antisymmetric part of γ_M to Γ_2 and, hence, to the spectrum for the bending moment stems basically from the asymmetry of the instantaneous distribution of gust intensity over the span. This asymmetry gives rise to a rolling moment (which was considered in the first part of this report) and, hence, to rolling motions, which contribute additional bending moments due to the aerodynamic and inertia loads associated with these motions. If, for the purpose of calculating the bending moment due to symmetric flight through turbulent air alone, these motions are disregarded, then the contribution of γ_M to Γ_2 should be disregarded as well. The problem of combined symmetric and antisymmetric motion will be considered presently.

As pointed out in reference 13, the mean-square bending moment calculated in this manner may be smaller or greater than the value calculated by ignoring spanwise variations in gust intensity. If the mass of the airplane is almost entirely contained in the fuselage, the decrease in the lift which results from taking these variations into account causes a decrease in bending moment. However, if most of the mass is in the wing, the net bending moments (aerodynamic less inertia) for a uniform spanwise gust are very small, and the effect of taking spanwise variations of gust intensity into account is to increase the mean-square bending moments.

Two-degree-of-freedom case.—For the two-degree-of-freedom (short-period) case the analysis given for the normal acceleration in the preceding section can be extended as follows: As indicated in equation (44) the transfer function for $\ddot{z}$ is now

$$H_{\ddot{z}}^{w}(\omega)=\left[-\frac{1}{m}\frac{\omega^2+(UM_{\dot{w}}+M_q)i\omega+UM_w}{-\omega^2+B_0 i\omega+C_0}\right]m(-Z_{w'})\,\phi(k)+\left[\frac{1}{I_y}\frac{U(-Z_w)}{-\omega^2+B_0 i\omega+C_0}\right]I_y M_{w'}\,\phi(k)\quad(56)$$

(The following analysis can be applied equally well to $\ddot{\theta}$ by using $H_{\ddot{\theta}}^{w}(\omega)$ instead of $H_{\ddot{z}}^{w}(\omega)$.)

If the expressions inside the brackets of equation (56) are designated, respectively, by $H_1(\omega)$ and $H_2(\omega)$, and their Fourier transforms by $h_1(t)$ and $h_2(t)$, then, as a result of the definitions of $Z_{w'}$ and $M_{w'}$,

$$\ddot{z}(t)=\int_{-\infty}^{\infty}h_1(t_1)\,L(t-t_1)\,dt_1+\int_{-\infty}^{\infty}h_2(t_1)\,M(t-t_1)\,dt_1\quad(57)$$

where $L(t)$ and $M(t)$ are the instantaneous lift and pitching moment due to the vertical component of atmospheric turbulence, which have been obtained in the first part of this report. The calculation of $\varphi_{\ddot{z}}(\omega)$ or of $\overline{\ddot{z}^2}$ thus requires not only the spectra of L and M, the calculation of which has been discussed, but also the cross spectrum of L and M, which has to be calculated directly from equations (4) and (42a). The result is

$$\varphi_{\ddot{z}}(\omega)=|H_1(\omega)|^2\,|H(\omega)|^2\,\varphi_{w_e}(\omega)+|H_2(\omega)|^2\Big[|H_w(\omega)|^2\,\varphi_{w_e}(\omega)+|H_t(\omega)|^2\,\varphi_w(\omega)+2\mathrm{R}\left\{e^{i\frac{\omega}{U}x_t}H_t(\omega)\,H_w^*(\omega)\right\}\varphi_{w_e^*}(\omega,0)\Big]+2\left[\mathrm{R}\{H_1(\omega)\,H_2^*(\omega)\,H(\omega)\,H_w^*(\omega)\}\varphi_{w_e}(\omega)+\mathrm{R}\{H_1(\omega)\,H_2^*(\omega)\,H(\omega)\,H_t^*(\omega)\}\varphi_{w_e^*}(\omega,0)\right]\quad(58)$$

where the first two terms represent the contributions of the spectra of L and M, respectively (see eqs. (14) and (42b)), and the third represents the contribution of the cross spectrum of L and M. For the present purpose the functions $H(\omega)$, $H_w(\omega)$, and $H_t(\omega)$ can be expressed as

$$H(\omega)=m(-Z_w)\,\phi(k)$$
$$H_w(\omega)=m\,\Delta x_a\,(-Z_w)\,\phi(k)$$
$$H_t(\omega)=[I_{yy}M_w-m\,\Delta x_a\,(-Z_w)]\,\phi(k)$$

where Δx_a is the distance from the aerodynamic center (tail off) to the airplane center of gravity. This definition of the contributions of the wing and tail to the pitching moment is based on the considerations that the direct contribution of the wing can be estimated with good accuracy and the total pitching moment is likely to be known from experiments, so that the contribution of the tail (which includes the effect of the wing lift on the downwash at the tail) can be determined as the difference of the two. The functions $\varphi_{w_e}(\omega)$ and $\varphi_{w_e^*}(\omega,0)$ have been defined in the first part of this report. In view of the fact that the function $\phi(k)$ contained in some of the terms of equation (58) always appears in terms multiplied by others which contain $\phi^*(k)$, only the absolute square of this function is required, as before.

SPECIAL PROBLEMS RELATED TO THE LATERAL MOTION OF LARGE AIRPLANES

The equations of motion in the lateral degrees of freedom (roll, yaw, sideslip) have the same form and can be solved in the same way as the equations for the longitudinal motion. (See pp. III–53 to III–67 of ref. 11.) Again it is convenient to cast the problem in the form used in a stability analysis in order to take advantage of the results of such an analysis. For a small airplane it is necessary only to replace the terms due to rudder deflection by corresponding terms involving side gusts, namely,

$$Y_{\dot{\delta}_R}\dot{\delta}_R \text{ by } Y_v\frac{v}{U}\phi'(k)$$

$$L_{\dot{\delta}_R}\dot{\delta}_R \text{ by } L_\beta\frac{v}{U}\phi'(k)$$

$$N_{\dot{\delta}_R}\dot{\delta}_R \text{ by } N_\beta\frac{v}{U}\phi'(k)$$

where $\phi'(k)$ is a suitable side-force attenuation function for side gusts and the notation of reference 11 is used for the other terms. The terms corresponding to aileron deflection can be disregarded for the small airplane. In the lateral degrees of freedom the small airplane thus reacts only to side gusts. On the other hand, the large airplane also reacts in the lateral degrees of freedom to vertical gusts through the rolling moment calculated in the first part of the present report. If this rolling moment is to be included, it replaces the term $L_{\delta_A}\,\delta_A$ used in reference 11.

Instead of treating all three degrees of freedom simultaneously, in stability analyses two one-degree-of-freedom cases are often considered, namely, the one of sideslip alone, with angle of yaw equal and opposite to angle of sideslip (the Dutch roll case), and the one of rolling alone.

The Dutch roll case may be used for gust-load purposes in connection with yawing and sideslipping motion due to lateral gusts, provided the phase of the motion is not important. (As may be noted from the preceding sections, the phase of a transfer function is important only in terms involving cross spectra.) Also, the Dutch roll case may prove useful in calculating the vertical-tail loads resulting from flight through turbulent air, particularly if the human or automatic pilot holds the wings substantially level by means of the ailerons. However, in general it does not appear to be as satisfactory an approximation as the one- and two-degree-of-freedom approximations for longitudinal motion.

For rolling motions due to rolling moments, the single-degree case of rolling alone appears to furnish a very good approximation. Although the rolling motion causes yawing and sideslipping motions, these motions do not appear to reflect on the rolling motion. Thus, the rolling motion which results from the rolling moment can probably be calculated fairly accurately without regard to the other lateral degrees of freedom. Furthermore, within the assumption of small motions, the stresses associated with these other lateral degrees of freedom do not generally contribute appreciably to those associated with the longitudinal degrees of freedom in the parts of the structure for which the latter are critical, such as the wing (although they may be critical for other parts of the structure, such as the vertical tail). Therefore these degrees of freedom (yaw and sideslip) will be ignored in the treatment of the large flexible airplane in the last part of this paper. However, if chordwise bending effects (deformations parallel to the chord) are important, as they may be in some cases at speeds close to the flutter speed, these other lateral degrees of freedom may have to be included in the analysis.

For the large airplane, which responds in the lateral degrees of freedom both to vertical gusts and to side gusts, the superposition of the resulting responses, such as stresses, may be effected in the way indicated for the interaction of horizontal and vertical gusts. If the turbulence is isotropic, the vertical and lateral gusts are statistically independent for points in the XY-plane, so that the spectrum of a given response is equal to the sum of the spectrum of that part of the given response which is due to vertical gusts and the spectrum of that part of the response which is due to lateral gusts.

COMBINATION OF THE RESULTS OBTAINED FROM ANALYSES OF THE LONGITUDINAL AND LATERAL DEGREES OF FREEDOM

The instantaneous wing stresses depend both on the motions in the longitudinal degrees of freedom (primarily vertical motion and pitching) and on those in the lateral degrees of freedom (primarily rolling). The purpose of this section is to indicate how the stresses associated with vertical motion and pitching can be combined with those associated with rolling due to vertical gusts, particularly in the case of a large rigid airplane. (A small airplane, flexible or rigid, does not roll as a result of the action of vertical gusts, and for the large flexible airplane it is more convenient to consider rolling motion simultaneously with the other motions, so that the superposition is effected automatically in the process of obtaining the required transfer functions.) For all airplanes the effect of side gusts can then be taken into account, if isotropy is assumed, by adding the stress spectra directly.

In this section the instantaneous stress at a given part of the wing will be assumed to be proportional to the instantaneous bending moment at that section of the wing, so that consideration can be confined to this bending moment; also, the airplane will be considered to be free to move in only two degrees of freedom, namely, vertical motion and rolling. The extension of the following arguments to stresses which depend on the vertical shear and the torque as well, and the inclusion of pitching as an additional degree of freedom, can be effected readily and will not alter the conclusion reached here.

When rolling motions of the airplane are taken into account, the bending moment due to the aerodynamic forces associated with rate of roll and to the inertia load associated with rolling acceleration can be expressed in terms of the rolling moment by a superposition integral. In turn, the rolling moment can be expressed in terms of a superposition integral involving the instantaneous gust intensities along the span, the influence function $\gamma'(y)$ used in the first part of the report, and an associated response function $h'_M(t)$. Hence, equation (52) is modified by the inclusion of a third term and becomes

$$M_B(t)=\int_{-\infty}^{\infty} dt_1 \int_{-b/2}^{b/2} [h_L(t_1)\gamma_M(y)+h_M(t_1)\gamma(y)+ h'_M(t_1)\gamma'(y)]w(U(t-t_1),y)\,dy$$

If the spectrum for M_B is now calculated in the manner used previously, the following result is obtained:

$$\varphi_{M_B}(\omega)=|H_L(\omega)|^2\varphi_{w_{e_2}}(\omega)+|H_M(\omega)|^2\varphi_{w_e}(\omega)+ 2\mathrm{R}\{H_L(\omega)H_M^*(\omega)\}\varphi_{w_{e_1}}(\omega)+|H'_M(\omega)|^2\varphi_{w_{e_3}}(\omega)+ 2\mathrm{R}\{H_L(\omega)H'^*_M(\omega)\}\varphi_{w_{e_4}}(\omega) \quad (59)$$

where $H'_M(\omega)$ is the Fourier transform of $h'_M(t)$, and where

$\varphi_{w_{e_3}}(\omega)$ and $\varphi_{w_{e_4}}(\omega)$ can be obtained from equation (12) with the following values of Γ_3 and Γ_4, respectively:

$$\Gamma_3(\eta)=\frac{2}{b}\int_{-b/2}^{(b/2)-\eta}\gamma'(y)\gamma'(y+\eta)\,dy$$

$$\Gamma_4(\eta)=\frac{2}{b}\int_{-b/2}^{(b/2)-\eta}\gamma'(y)\gamma_{M_a}(y+\eta)\,dy$$

(The function $\Gamma_3(\eta)$ is four times the function $\Gamma'(\eta)$ considered previously in connection with the rolling moment. This factor of four must be taken into account in $h'_M(t)$.)

The spectrum φ_{M_B} may be considered to consist of two parts: The first three terms listed in equation (59), but excluding the contribution of γ_{M_a} to $\varphi_{w_{e_2}}$ (see eq. (55)), represent the contribution of the symmetric parts of the instantaneous gust distributions or the contribution associated with symmetric motion; the last two terms and the contribution of γ_{M_a} to $\varphi_{w_{e_2}}$ represent the contribution of the antisymmetric parts of the instantaneous gust distributions or the contribution associated with rolling motion. Therefore, the power spectrum of the stress due to gusts and combined symmetric and rolling motion resulting from the gusts is the sum of the two power spectra (that for the gusts and symmetric motion alone and that for the gusts and rolling motion alone), provided the direct contribution of the gusts is split up into a symmetric and antisymmetric part and each is taken into account only once, in connection with the appropriate type of motion. The cross-correlation terms between the symmetric and antisymmetric contributions to the stress can be shown to involve integrals which contain products of symmetric and antisymmetric influence functions and, hence, vanish, so that the cross correlations are zero; hence, the two parts of the combined spectrum are statistically independent and, therefore, directly additive.

DYNAMICS OF THE SMALL FLEXIBLE AIRPLANE

The purpose of this part of the report is to consider the transfer functions relating the stresses at various points of a small flexible airplane to the vertical gusts which cause them. The longitudinal and lateral degrees of freedom are still separable, and only the longitudinal degrees will be considered; the lateral degrees, which are involved in analysis of the response to side gusts acting on the vertical tail, can be analyzed in the same way. Therefore, for this case only one-half of the wing need be considered as a result of the symmetry (or antisymmetry, in the case of the lateral degrees of freedom) of the problem.

The method which is outlined in this part consists in an extension of the numerical-integration method of aeroelastic analysis described in reference 14 to sinusoidal motions of the airplane. This extension takes into account the facts that the aerodynamic forces now have out-of-phase as well as in-phase parts and that vertical deflections must now be calculated separately because the structural deformations can no longer be characterized by angle-of-attack changes. Also, the "rigid-body" degrees of freedom (vertical and pitching motion of the airplane as a whole and structural deformations of the tail) are now taken into account.

The result is a set of linear algebraic equations (which serve as an approximation to the ordinary differential equations that characterize the problem) for the airplane motions and deformations in terms of the applied aerodynamic forces directly due to gusts. The desired transfer functions can then be obtained from solutions of these equations at various frequencies, and the power spectra of the stresses are given by the product of the absolute square of these transfer functions and the point power spectrum of the vertical component of turbulence. The same equations may be used to calculate with little additional effort certain aeroelastic effects, such as the static aeroelastic deformations and the flutter speed, which are usually obtained in separate analyses.

LOADS APPLIED TO THE WING

The loads applied to the wing stem from three sources: The aerodynamic loads directly due to the action of the gusts, the aerodynamic loads due to the motions of the airplane, and the inertia loads.

The lift and pitching moment (about the elastic axis) per unit span on a two-dimensional airfoil undergoing sinusoidal angle-of-attack changes and vertical motions in incompressible flow are (see ref. 15)

$$\left.\begin{aligned} l_a=2\pi qc\Bigg\{C(k)\left[(1+2e_4ik)\alpha-ik\frac{z}{c/2}\right]+\\ \left(\frac{ik}{2}-e_3k^2\right)\alpha+\frac{k^2}{2}\frac{z}{c/2}\Bigg\}\\ m_a=2\pi qc^2\Bigg\{C(k)e_1\left[(1+2e_4ik)\alpha-ik\frac{z}{c/2}\right]-\\ \left[\frac{e_4}{2}ik-\left(\frac{1}{32}+e_3^2\right)k^2\right]\alpha-\frac{e_3}{2}k^2\frac{z}{c/2}\Bigg\}\end{aligned}\right\} \tag{60}$$

The terms multiplied by $C(k)$ are referred to as the circulatory terms because they are calculated from the bound and shed vorticity, and the others are referred to as the potential terms. The potential terms are in the nature of additional-apparent-mass effects, and all those that involve k^2 are usually treated together with the inertia forces rather than with the aerodynamic forces. For compressible flow, however, the forces are calculated in a different manner, and the division of the forces into circulatory and potential parts then has little meaning. Consequently, in order to facilitate the extension of this analysis to compressible flow, this distinction will not be made herein.

The aerodynamic forces are therefore written as

$$\left.\begin{aligned} l_a=2\pi qc\left[\tilde{C}_1(k)\alpha+\tilde{C}_2(k)\frac{z}{c/2}\right]\\ m_a=2\pi qc^2\left[\tilde{C}_3(k)\alpha+\tilde{C}_4(k)\frac{z}{c/2}\right]\end{aligned}\right\} \tag{61}$$

so that for incompressible flow

$$\tilde{C}_1(k)=(1+2e_4ik)C(k)+\frac{ik}{2}-e_3k^2$$

$$\tilde{C}_2(k)=-ikC(k)+\frac{k^2}{2}$$

$$\tilde{C}_3(k)=(1+2e_4ik)e_1C(k)-\frac{e_4}{2}ik+\left(\frac{1}{32}+e_3^2\right)k^2$$

$$\tilde{C}_4(k)=-ike_1C(k)-\frac{e_3}{2}k^2$$

In order to calculate the lift at a given point of a wing of finite span an appropriate Green's function is required. An approximation to this function based on a reciprocity theorem of linearized lifting-surface theory, is given in the first part of this report; as used for the computations of that part, this function implies the assumptions that the spanwise distribution of the lift for oscillations of the wing as a whole is substantially invariant with frequency and that this distribution is the same in direct as in reverse flow. Neither of these assumptions is essential to the analysis but both, and particularly the first, simplify it considerably. With these assumptions, the desired lift distribution is then given by expressions of the form of equations (32a) and (34).

For the present purpose, however, a set of aerodynamic influence coefficients is required, rather than influence functions. Such a set of coefficients, based on the same ideas, can be obtained readily by the techniques used in references 9 and 10. The result may be expressed as follows:

$$\{l\}_a=C_{L_\alpha}\bar{c}q\left\{\tilde{C}_1(k)\,[Q]\{\alpha\}+\tilde{C}_2(k)\,[Q]\left\{\frac{z}{\bar{c}/2}\right\}\right\} \quad (62a)$$

where the aerodynamic-influence-coefficient matrix $[Q]$ is defined by

$$[Q]=(1-K)\lfloor\gamma\rfloor\{1\}\lfloor I\rfloor\lfloor\gamma\rfloor+K\lfloor\gamma\rfloor$$

where, in turn, $\{1\}$ is a unit column matrix, and $\lfloor I\rfloor$ is a row of integrating coefficients suitable for integrating a continuous function for a range of its argument from 0 to 1. Thus, for instance, if n equidistant points on the semispan are considered, and n is odd, then according to Simpson's rule

$$\lfloor I\rfloor=\frac{1}{n-1}\left\lfloor\frac{1}{3},\frac{4}{3},\frac{2}{3},\frac{4}{3},\cdots\frac{4}{3},\frac{1}{3}\right\rfloor$$

Very little information is available concerning the spanwise distributions of the pitching moment on wings of finite span in unsteady flow. By means of the reciprocity theorems an appropriate Green's function could be estimated if the lift distribution for wings with parabolic camber were known; however, such lift distributions do not appear to have been calculated for wings of finite span in unsteady flow. In fact, relatively little is known about moment distributions even in steady flow. However, the available information indicates that the local center of pressure does not appear to be very sensitive to the lift distribution. (See ref. 9, for instance.) It will be assumed that this is also true in unsteady flow at a given frequency, and that, furthermore, these centers of pressure are given by two-dimensional theory. With this assumption the moment can be written as

$$\{m_T\}_a=C_{L_\alpha}\bar{c}q\left\{\tilde{C}_3(k)\lfloor c\rfloor[Q]\{\alpha\}+\tilde{C}_4(k)\lfloor c\rfloor[Q]\left\{\frac{z}{\bar{c}/2}\right\}\right\} \quad (62b)$$

The lift and moment distribution due to the gust can be calculated in a similar manner. In the following analysis, the magnitude of the gust intensity is considered to be unity, and the longitudinal reference point is the intersection of the elastic axis and the wing root, so that the instantaneous gust intensity at any station y is

$$w=e^{-ik\frac{|y|}{\bar{c}/2}\tan\Lambda} \quad (63)$$

With this function w,

$$\left.\begin{aligned}\{l\}_g&=\frac{C_{L_\alpha}\bar{c}q\phi(k)}{U}[Q]\{w\}\\ \{m_T\}_g&=\frac{C_{L_\alpha}\bar{c}q\phi(k)}{U}\lfloor e_1c\rfloor[Q]\{w\}\end{aligned}\right\} \quad (64)$$

where $\phi(k)$ is the Sears function, as before.

Finally, the inertia loads are

$$l_i=-\tilde{m}\ddot{z}+\tilde{m}e_2c\ddot{\alpha}$$

$$m_{T_i}=-(r^2+(e_2c)^2)\tilde{m}\ddot{\alpha}+\tilde{m}e_2c\ddot{z}$$

or

$$\left.\begin{aligned}\{l\}_i&=-\frac{q}{\frac{\rho}{2}\left(\frac{\bar{c}}{2}\right)^2}k^2\lfloor\tilde{m}e_2c\rfloor\{\alpha\}+\frac{q}{\frac{\rho}{2}\left(\frac{\bar{c}}{2}\right)^2}k^2\lfloor\tilde{m}\rfloor\{z\}\\ \{m_T\}_i&=\frac{q}{\frac{\rho}{2}\left(\frac{\bar{c}}{2}\right)^2}k^2\lfloor r^2+(e_2c)^2\rfloor\lfloor\tilde{m}\rfloor\{\alpha\}-\frac{q}{\frac{\rho}{2}\left(\frac{\bar{c}}{2}\right)^2}k^2\lfloor\tilde{m}e_2c\rfloor\{z\}\end{aligned}\right\} \quad (65)$$

The loads applied to the wing can thus be written, in summary, as

$$\begin{Bmatrix} l \\ m_T \end{Bmatrix} = q \left[\begin{array}{c|c} 2C_{L_\alpha}\tilde{C}_2(k)\,[Q] + \dfrac{k^2}{\frac{\rho}{2}\left(\frac{\bar{c}}{2}\right)^2}[\tilde{m}] & C_{L_\alpha}\bar{c}\tilde{C}_1(k)\,[Q] - \dfrac{k^2}{\frac{\rho}{2}\left(\frac{\bar{c}}{2}\right)^2}[me_2c] \\ \hline 2C_{L_\alpha}\tilde{C}_4(k)[c]\,[Q] - \dfrac{k^2}{\frac{\rho}{2}\left(\frac{\bar{c}}{2}\right)^2}[\tilde{m}e_2c] & C_{L_\alpha}\bar{c}\tilde{C}_3(k)[c]\,[Q] + \dfrac{k^2}{\frac{\rho}{2}\left(\frac{\bar{c}}{2}\right)^2}[r^2+(e_2c)^2][m] \end{array}\right] \begin{Bmatrix} z \\ \alpha \end{Bmatrix} + q \left[\begin{array}{c} \dfrac{C_{L_\alpha}\bar{c}\phi(k)}{U}[Q] \\ \hline \dfrac{C_{L_\alpha}\bar{c}\phi(k)}{U}[e_1c][Q] \end{array}\right] \begin{Bmatrix} w \end{Bmatrix} \tag{66}$$

LOADS APPLIED TO THE TAIL

The loads applied to the tail are similar in nature to those applied to the wing, but the tail experiences additional loads as a result of the downwash produced by the lift on the wing. Again, little is known about the downwash in unsteady flow, and even in steady flow the downwash cannot be predicted accurately because of boundary-layer effects on the fuselage and the wing root. Consequently, even in steady-flow analyses experimental results are usually relied upon.

In the following analysis, the assumption is therefore made that experimental results are available for steady flow, in the form of the downwash derivative $\partial\epsilon/\partial\alpha$. In order to determine the attenuation of this value with frequency, the results of the analysis of reference 16 will be used. These results indicate that the time variation of the tail lift due to the downwash caused by the wing lift which results from a unit jump in the wing angle of attack can be approximated by an immediate jump in the tail lift of —0.16 of the steady-state value and another jump to the steady-state value after the time required to travel the distance from the 45-percent-chord point of the wing to the quarter-chord point of the tail plus another eighth of the chord length. Hence, for sinusoidal angle-of-attack changes the tail lift due to downwash is

$$(L_{t_\epsilon})_{\alpha,z} = -C_{L_{\alpha_t}} q_t S_t \frac{\partial\epsilon}{\partial\alpha}\left[-0.16+1.16e^{-ik\left(\frac{x_t'}{\bar{c}/2}+\frac{1}{4}\frac{c_r}{\bar{c}}\right)}\right]\left[(1+2e_4ik)\alpha_r - ik\frac{z_r}{\bar{c}/2}\right] \tag{67}$$

where x_t' is the distance from the intersection of the elastic axis and the wing root (assumed for this purpose to be at the 45 percent point on the root chord) to the aerodynamic center of the tail. As pointed out in reference 16, this approximation is valid only for $k<0.35$; however, this range is adequate for the present purpose.

Similarly, the downwash associated with the wing lift due to sinusoidal gusts gives rise to a tail lift which, within this approximation, is

$$(L_{t_\epsilon})_g = -C_{L_{\alpha_t}} q_t \frac{S_t}{U}\frac{\partial\epsilon}{\partial\alpha}\left[-0.16+1.16e^{-ik\left(\frac{x_t'}{\bar{c}/2}+\frac{1}{4}\frac{c_r}{\bar{c}}\right)}\right] e^{-0.6ik\frac{c_r}{\bar{c}}} w_r \tag{68}$$

(The additional lag represents the time required to travel the 0.6 root semichords from the 45-percent-chord point of the root, which is the reference point for the gusts, to the 75-percent-chord point of the wing root, which is assumed to be the point governing the lift at the wing root, inasmuch as it is the centroid of the influence function for the chordwise pressure distribution.)

The other aerodynamic forces are those due to the motions of the airplane, those due to the tail deformations, and those directly due to the gusts. On the basis of the assumptions made in the preceding section, these forces are

$$L_{t_a} = C_{L_{\alpha_t}} q_t S_t\left[\tilde{C}_5(k)\alpha_r + \tilde{C}_6(k)\frac{z_r}{\bar{c}/2} + \tilde{C}_7(k)\Delta\alpha + \tilde{C}_6(k)\frac{\Delta z}{\bar{c}/2}\right] \tag{69}$$

$$L_{t_g} = \frac{C_{L_{\alpha_t}} q_t S_t}{U}\phi\left(\frac{c_t}{\bar{c}}k\right) e^{-ik\frac{x_t'-\frac{c_t}{4}}{\bar{c}/2}} \tag{70}$$

where

$$\tilde{C}_5(k) = \left(1+2ik\frac{x_t'+\frac{c_t}{2}}{\bar{c}}\right) C\left(\frac{c_t}{\bar{c}}k\right) + \frac{i}{2}\frac{c_t}{\bar{c}}k - \frac{c_t}{\bar{c}}\frac{x_t'+\frac{c_t}{4}}{\bar{c}}k^2$$

$$\tilde{C}_6(k) = -ikC\left(\frac{c_t}{\bar{c}}k\right) + \frac{1}{2}\frac{c_t}{\bar{c}}k^2$$

$$\tilde{C}_7(k) = \left(1+2ik\frac{e_{4_t}c_t}{\bar{c}}\right) C\left(\frac{c_t}{\bar{c}}k\right) + \frac{i}{2}\frac{c_t}{\bar{c}}k - e_{3_t}\left(\frac{c_t}{\bar{c}}\right)^2 k^2$$

and α_r and z_r are the angle of attack and vertical displacement of the airplane at the wing root.

The inertia load on the tail is

$$L_{t_i} = -m_t(\ddot{z}_r + \Delta\ddot{z} - x_t'\ddot{\alpha}_r)$$

or

$$L_{t_i} = \frac{m_t q k^2}{\frac{\rho}{2}\left(\frac{\bar{c}}{2}\right)^2}(z_r + \Delta z - x_t'\alpha_r) \tag{71}$$

Here the center of gravity of the tail has been assumed to coincide with its aerodynamic center; in order to remove this assumption it is necessary only to add (or subtract) the distance between the two to x_t' in equation (71).

The normal forces on the tail can then be summarized as follows:

$$L_t=q[F_1(k)z_r+F_2(k)\alpha_r+F_3(k)\Delta\alpha+F_4(k)\Delta z+F_5(k)w_t] \quad (72)$$

where

$$F_1(k)=2C_{L_{\alpha_t}}\frac{q_t}{q}\frac{S_t}{\bar{c}}\left\{\tilde{C}_6(k)+ik\frac{\partial\epsilon}{\partial\alpha}\left[-0.16+1.16e^{-ik\left(\frac{x_t'}{\bar{c}/2}+\frac{1}{4}\frac{c_t}{\bar{c}}\right)}\right]\right\}+\frac{m_t}{\frac{\rho}{2}\left(\frac{\bar{c}}{2}\right)^2}k^2$$

$$F_2(k)=C_{L_{\alpha_t}}\frac{q_t}{q}S_t\left\{\tilde{C}_5(k)-(1+2e_4ik)\frac{\partial\epsilon}{\partial\alpha}\left[-0.16+1.16e^{-ik\left(\frac{x_t'}{\bar{c}/2}+\frac{1}{4}\frac{c_t}{\bar{c}}\right)}\right]\right\}-\frac{m_t x_t'}{\frac{\rho}{2}\left(\frac{\bar{c}}{2}\right)^2}k^2$$

$$F_3(k)=C_{L_{\alpha_t}}\frac{q_t}{q}S_t\tilde{C}_7(k)$$

$$F_4(k)=2C_{L_{\alpha_t}}\frac{q_t}{q}\frac{S_t}{\bar{c}}\tilde{C}_6(k)+\frac{m_t}{\frac{\rho}{2}\left(\frac{\bar{c}}{2}\right)^2}k^2$$

$$F_5(k)=\frac{C_{L_{\alpha_t}}q_tS_t}{U}\left\{\phi\left(\frac{c_t}{\bar{c}}k\right)e^{ik\frac{c_t}{2\bar{c}}}-\frac{\partial\epsilon}{\partial\alpha}\left[-0.16+1.16e^{-ik\left(\frac{x_t'}{\bar{c}/2}+\frac{1}{4}\frac{c_r}{\bar{c}}\right)}\right]e^{ik\left(\frac{x_t'}{\bar{c}/2}-0.6\frac{c_r}{\bar{c}}\right)}\right\}$$

and

$$w_t=e^{-ik\frac{x_t}{\bar{c}/2}}$$

The pitching moments corresponding to these normal forces can be obtained in the manner employed for the wing. However, inasmuch as the tail chord is usually small compared with the fuselage length, the travel of the center of pressure of the tail is small compared with the length x_t'. Hence, the center of pressure will be assumed to remain at the aerodynamic center of the tail, and the pitching moments are then $-x_t'$ times the corresponding forces, so that

$$M_t=-qx_t'[F_1(k)z_r+F_2(k)\alpha_r+F_3(k)\Delta\alpha+F_4(k)\Delta z+F_5(k)w_t] \quad (73)$$

WING AND TAIL DEFORMATIONS

The wing deformations may be calculated either from structural influence coefficients or from the bending and torsion stiffnesses of the wing used in conjunction with simple beam theory. The latter approach will be followed here, based on the method of reference 12.

The bending and torsion moments on the wing structure may be obtained by integrating the applied loads. If numerical methods are employed to perform these integrations the results may be written as follows:

$$\begin{Bmatrix}M_B\\M_T\end{Bmatrix}=\left[\begin{array}{c|c}\frac{(b/2)^2}{\cos\Lambda}[\mathrm{II}] & -\sin\Lambda\frac{b}{2}[\mathrm{I}]\\ \hline [0] & \cos\Lambda\frac{b}{2}[\mathrm{I}]\end{array}\right]\begin{Bmatrix}l\\m_T\end{Bmatrix} \quad (74)$$

Similarly, the deformations are

$$\begin{Bmatrix}z-z_r\\ \alpha-\alpha_r\end{Bmatrix}=\left[\begin{array}{c|c}\left(\frac{b}{2\cos\Lambda}\right)^2[\mathrm{II}'']\left[\frac{1}{EI}\right] & [0]\\ \hline \frac{b}{2}[\mathrm{I}'']\left[\frac{1}{GJ}\right] & -\frac{b}{2}\tan\Lambda[\mathrm{I}'']\left[\frac{1}{EI}\right]\end{array}\right]\begin{Bmatrix}M_B\\M_T\end{Bmatrix}$$

$$=\left[\begin{array}{c|c}\left(\frac{b}{2}\right)^4\frac{1}{\cos^2\Lambda}[\mathrm{II}'']\left[\frac{1}{EI}\right][\mathrm{II}] & -\left(\frac{b}{2}\right)^3\frac{\sin\Lambda}{\cos^2\Lambda}[\mathrm{II}'']\left[\frac{1}{EI}\right][\mathrm{I}]\\ \hline \left(\frac{b}{2}\right)^3\frac{1}{\cos\Lambda}[\mathrm{I}'']\left[\frac{1}{GJ}\right][\mathrm{II}] & -\sin\Lambda\left(\frac{b}{2}\right)^2[\mathrm{I}'']\left[\frac{1}{EI}+\frac{1}{GJ}\right][\mathrm{I}]\end{array}\right]\begin{Bmatrix}l\\m_T\end{Bmatrix} \quad (75)$$

where the integrating matrices (see ref. 12) perform the following operations:

$$[\mathrm{I}]\{f\}\backsim\int_\xi^1 f(\xi')d\xi'$$

$$[\mathrm{II}]\{f\}\backsim\int_\xi^1\int_{\xi'}^1 f(\xi'')d\xi''d\xi'$$

$$[\mathrm{I}'']\{f\}\backsim\int_0^\xi f(\xi')d\xi'$$

$$[\mathrm{II}'']\{f\}\backsim\int_0^\xi\int_0^{\xi'} f(\xi'')d\xi''d\xi'$$

These integrating matrices may be based on the trapezoidal rule, Simpson's rule, or any other numerical method; the intervals chosen for ξ ($0 \leqq \xi \leqq 1$) need not be of constant width unless a specific rule demands a uniform spacing.

The structural deformations of the wing may then be written in terms of the applied loads as

$$\begin{Bmatrix} z-z_r \\ \alpha-\alpha_r \end{Bmatrix} = q \left[\begin{array}{c|c} ① & ② \\ \hline ③ & ④ \end{array}\right] \begin{Bmatrix} z \\ \alpha \end{Bmatrix} + q \left[\begin{array}{c} ⑤ \\ \hline ⑥ \end{array}\right] \{w\} \tag{76}$$

where the submatrices [①], [②], [③], [④], [⑤], and [⑥] designate, respectively, the four quadrants and two halves of the matrices, obtained by postmultiplying the square matrix of equation (75) by the square and the rectangular matrix of equation (66), respectively.

For the purpose of the present analysis, which is concerned primarily with the wing stresses, the tail deformations are treated by including only the vertical displacement and angle-of-attack change of the tail as a whole due to the tail load. These quantities may be obtained from a static test which consists in applying a concentrated normal load at the aerodynamic center of the tail and measuring these deformations. They may also be obtained from a vibration test in which the deflection curve of the rear part of the fuselage in the lowest vertical-bending mode is measured; in this case the desired spring constants can be deduced from the frequency relation of a simple mass oscillator in terms of the measured frequency and of the mass of the empennage (including the part of the fuselage which may be considered to move with the empennage). In the absence of such tests these constants may be calculated in an analogous manner.

The tail deformations may then be written as

$$\left.\begin{aligned} \Delta\alpha &= -K_1 L_t \\ \Delta z &= K_2 L_t \end{aligned}\right\} \tag{77}$$

so that, also,

$$\Delta z = -\frac{K_2}{K_1} \Delta\alpha \tag{78}$$

Inasmuch as these deformations are not independent of each other, only one need be retained in the analysis. Therefore, if Δz is eliminated by means of equation (78), $\Delta\alpha$ can then be obtained in a form similar to that used for the wing deformations in equation (76):

$$\Delta\alpha = -qK_1 \left\{ F_1(k) z_r + F_2(k)\alpha_r + \left[F_3(k) - \frac{K_2}{K_1} F_4(k) \right] \Delta\alpha \right\} - qK_1 F_5(k) w_t \tag{79}$$

EQUATIONS OF MOTION

Equations (76) and (79) are equations of motion inasmuch as they describe balances of aerodynamic, structural, and inertia forces. In fact, if the airplane fuselage were immobile ($\alpha_r = z_r = 0$), they would be sufficient to calculate all unknown quantities. However, if the fuselage is free to move, two additional equations are required to obtain the two additional unknown quantities α_r and z_r. These additional equations are those expressing the dynamic equilibrium of the forces on the fuselage, namely,

$$\left.\begin{aligned} &L_w + L_t - m_f (\ddot{z}_r - \Delta x\, \ddot{\alpha}_r) = 0 \\ &M_w - x_t L_t - (r_f^2 + (\Delta x)^2)\, m_f \ddot{\alpha}_r + \Delta x\, m_f \ddot{z}_r = 0 \end{aligned}\right\} \tag{80}$$

where the wing lift and pitching moment can be expressed in terms of the lift and moment distributions l and m as

$$\left.\begin{aligned} L_w &= \left\lfloor 2\frac{b}{2}[\mathrm{I}], [0] \right\rfloor \begin{Bmatrix} l \\ m_T \end{Bmatrix} \\ M_w &= \left\lfloor -2\left(\frac{b}{2}\right)^2 \tan\Lambda\,[\mathrm{II}],\ 2\frac{b}{2}[\mathrm{I}] \right\rfloor \begin{Bmatrix} l \\ m_T \end{Bmatrix} \end{aligned}\right\} \tag{81}$$

or

$$\left.\begin{aligned} L_w &= q\lfloor ⑪ \rfloor \begin{Bmatrix} z \\ \alpha \end{Bmatrix} + q\lfloor ⑬ \rfloor \{w\} \\ M_w &= q\lfloor ⑫ \rfloor \begin{Bmatrix} z \\ \alpha \end{Bmatrix} + q\lfloor ⑭ \rfloor \{w\} \end{aligned}\right\} \tag{82}$$

where [⑪], [⑫], [⑬], and [⑭] are the rows obtained by postmultiplying the rows of equation (81) by the square and rectangular matrices of equation (66). In equation (80) the fuselage lift and moment have been neglected; they can easily be expressed in terms of α_r and z_r and included, if desired.

The equations for the tail deformation $\Delta\alpha$ and those for the overall normal force and pitching moment can be combined with equation (76) as follows: For the sake of definiteness it will be assumed that n stations on the wing are considered, including the one at the root, so that there are $2n+1$ unknown quantities, and that in the column matrices defining applied loads, deformations, and so on, the values at the root of the wing are written at the top:

$$\begin{Bmatrix} z \\ \alpha \\ \Delta\alpha \end{Bmatrix} \equiv \begin{Bmatrix} z_{root} \\ \cdot \\ \cdot \\ \cdot \\ z_{tip} \\ \alpha_{root} \\ \cdot \\ \cdot \\ \cdot \\ \alpha_{tip} \\ \Delta\alpha \end{Bmatrix}$$

The first and $(n+1)$th equations of the system defined by equation (76) express only the trivial fact that the structural deformation at the wing root is zero. They are replaced by

equations (82) and (79), which are adjoined to the system, to yield the combined equation of motion

$$\begin{bmatrix} 0 & & & \\ -1 & 1 & & \\ -1 & 0 & 1 & \\ -1 & 0 & 0 & 1 \\ \cdots & \cdots & \cdots & \cdots \\ & & 0 & \\ & 0 & & \\ & & & \\ 0 & & 0 & 1 \end{bmatrix} \begin{Bmatrix} z \\ \\ \alpha \\ \\ \Delta\alpha \end{Bmatrix} = q \begin{bmatrix} \textcircled{1'} & \textcircled{2'} & \\ & & \\ \textcircled{3'} & \textcircled{4'} & \\ & & \\ & & 0 \end{bmatrix} \begin{Bmatrix} z \\ \\ \alpha \\ \\ \Delta\alpha \end{Bmatrix} + q \begin{bmatrix} \textcircled{5'} & \\ & \\ \textcircled{6'} & \\ & \\ 0 & \end{bmatrix} \begin{Bmatrix} w \\ \\ w_t \end{Bmatrix} \tag{83a}$$

If the square matrix on the right side of this equation is designated by $[A]$, the rectangular matrix by $[B]$, and the quasi-unit matrix on the left side of the equation by $[1']$, the equation can also be written as

$$\Big[[1']-q[A]\Big]\begin{Bmatrix} z \\ \alpha \\ \Delta\alpha \end{Bmatrix} = q[B]\begin{Bmatrix} w \\ w_t \end{Bmatrix} \tag{83b}$$

The matrices $[\textcircled{1'}]$ to $[\textcircled{6'}]$ are the same as the matrices $[\textcircled{1}]$ to $[\textcircled{6}]$ of equation (76), except that the first rows of the latter, which are all zero, are replaced as follows:

First row of—	Replacement	Quantity added to the leading element
①	First half of [⑪]	$F_1(k)+\dfrac{m_f}{\frac{\rho}{2}\left(\frac{\bar{c}}{2}\right)^2}k^2$
②	Second half of [⑪]	$F_2(k)-\dfrac{m_f\Delta x}{\frac{\rho}{2}\left(\frac{\bar{c}}{2}\right)^2}k^2$
③	First half of [⑫]	$-x_tF_1(k)-\dfrac{m_fx_t}{\frac{\rho}{2}\left(\frac{\bar{c}}{2}\right)^2}k^2$
④	Second half of [⑫]	$-x_tF_2(k)+\dfrac{m_f[r_f^2+(\Delta x)^2]}{\frac{\rho}{2}\left(\frac{\bar{c}}{2}\right)^2}k^2$
⑤	[⑬]	0
⑥	[⑭]	0

Also, the elements of the last rows and columns of the matrices $[A]$ and $[B]$ are zero, except for the following:

$$A_{1,2n+1}=F_3(k)-\frac{K_2}{K_1}F_4(k)$$

$$A_{n+1,2n+1}=-x_t\left[F_3(k)-\frac{K_2}{K_1}F_4(k)\right]$$

$$A_{2n+1,1}=-K_1F_1(k)$$

$$A_{2n+1,n+1}=-K_1F_2(k)$$

$$A_{2n+1,2n+1}=-K_1\left[F_3(k)-\frac{K_2}{K_1}F_4(k)\right]$$

$$B_{1,n+1}=F_5(k)$$

$$B_{n+1,n+1}=-x_tF_5(k)$$

$$B_{2n+1,n+1}=-K_1F_5(k)$$

SOLUTION OF THE EQUATIONS OF MOTION

For the purpose of calculating the desired transfer functions, equation (83b) may be solved directly for a given value of q as a set of linear algebraic equations with coefficients given by the matrix $[1']-q[A]$ and with "knowns" given by the column matrix $q[B]\begin{Bmatrix} w \\ w_t \end{Bmatrix}$ (where $[A]$, $[B]$, and $\begin{Bmatrix} w \\ w_t \end{Bmatrix}$ are functions of k). The result is a column matrix of the unknown amplitudes of the motions of the airplane. If this column is calculated for several values of k in the range of interest, these amplitudes, considered as functions of k, are transfer functions from the gust to the motions.

This column matrix can be substituted into equation (66) and the resulting column matrix $\begin{Bmatrix} l \\ m_T \end{Bmatrix}$ substituted into equation (74), to yield a column matrix of bending and twisting moments which again, considered as a function of k, represents transfer functions from the gust to these moments. A set of transfer functions for the vertical shear could be calculated similarly from the relation

$$\{V\}=\left[\frac{b}{2}[\mathrm{I}] \;\vdots\; [0]\right]\begin{Bmatrix} l \\ m_t \end{Bmatrix}$$

The stress at any point of the structure can be assumed to be given by a linear superposition of the bending moment, twisting moment, and vertical shear at the given station, if elementary beam theory is used. If elementary beam theory cannot be used because of the interaction of bending and torsion stresses or because of shear lag, the stress at a given point can be expressed as a linear superposition of moments and shears at other stations as well as the given station. In either case, the transfer function for the given stress is then

produced by the same linear superposition of the transfer functions for the corresponding moments and shears.

It may be noted that, at zero frequency, solution of equation (83b) yields the static aeroelastic deformations and thus permits the calculation of the changes in the lift distribution and the shift of the aerodynamic center that result from static aeroelastic action. Also, inasmuch as this equation completely describes the dynamic behavior of the airplane, the speeds at which aeroelastic instability phenomena occur can be calculated from it, although such calculations are beyond the scope of this report. Suffice it to point out that for such a calculation the degrees of freedom of the body must be eliminated first, as a result of the way in which the problem has been set up. This elimination can be effected readily by considering the first and $(n+1)$th rows of $[A]$, but with A_{11}, $A_{1,n+1}$, $A_{n+1,1}$, and $A_{n+1,n+1}$ replaced by 0. If these rows are premultiplied by

$$-\begin{bmatrix} A_{11} & A_{1,n+1} \\ A_{n+1,1} & A_{n+1,n+1} \end{bmatrix}^{-1}$$

and used as the first and $(n+1)$th rows of a matrix which is otherwise a unit matrix, and if this resulting matrix is referred to as $[1'']$, then equation (83b) can be written for this homogeneous case as

$$[[1'][1'']-q[A][1'']]\begin{Bmatrix} z \\ \alpha \\ \Delta\alpha \end{Bmatrix}=\{0\}$$

The products $[1'][1'']$ and $[A][1'']$ will now have two null rows and columns each, which correspond to z_r and α_r. If these rows and columns are deleted and z_r and α_r are deleted in $\begin{Bmatrix} z \\ \alpha \\ \Delta\alpha \end{Bmatrix}$, yielding a column $\begin{Bmatrix} z \\ \alpha \\ \Delta\alpha \end{Bmatrix}'$, the remaining matrices are nonsingular, so that they can be inverted and the preceding equation can be written as

$$[[E]-q[D(k)]]\begin{Bmatrix} z \\ \alpha \\ \Delta\alpha \end{Bmatrix}'=\{0\} \tag{84}$$

where $[E]$ is the identity matrix, and

$$[D(k)]\equiv\left[\widehat{[1'][1'']}\right]^{-1}\left[\widehat{[A][1'']}\right]$$

The horizontal braces designate the fact that the null rows and columns have been deleted.

Equation (84) is in the canonical form for the calculation of eigenvalues. If k is set equal to zero and the eigenvalues of $[D(0)]$ are calculated by iteration, expansion of the determinant, or any other suitable method, the lowest real and positive one represents the value of the dynamic pressure at divergence. For swept wings the value lowest in absolute magnitude is usually negative and is therefore of no practical significance, although it is often used as an index of the aeroelastic behavior of the airplane.

This calculation can be repeated for various positive values of k, the first few eigenvalues being obtained for each. The results, which will generally be complex, can be plotted against k. When any of the eigenvalues becomes purely real, it represents a dynamic pressure at flutter, and the corresponding value of k represents the reduced frequency at flutter. (This statement is true only if the structural damping is zero; such damping effects can easily be included, but the details of the process are beyond the scope of this report.)

DYNAMICS OF THE LARGE FLEXIBLE AIRPLANE

For the large flexible airplane the fundamental proposition of power spectral analysis, that the output power spectrum of a system is the product of the absolute square of the transfer function and the input power spectrum, is no longer valid if the input is considered to be the gust intensity at a point. Nor can the output power spectrum be expressed directly in terms of an effective input spectrum, as in the case of the rigid airplane, where this simplification resulted from the assumption that the indicial-response function was expressible as the product of a function of time alone and a function of distance along the span alone.

In the first section of this part of the report the statistical problems involved in an analysis of the response of a large flexible airplane are considered. The nature of the generalized transfer functions required for this purpose is described, and the means whereby they are combined with the input spectrum are indicated.

The second section is concerned with an extension of the method outlined in the preceding part to the case of the large airplane. Although fundamentally the dynamic aspects of the problem are unchanged, and although the longitudinal and lateral degrees of freedom can still be separated, a direct application of the approaches outlined in the preceding parts of the report to the large airplane requires consideration of the entire wing, rather than only one half of the wing. Little additional computing time is then required to treat the lateral and longitudinal degrees of freedom simultaneously, and the necessity of combining the results of two separate analyses is obviated. However, attention can still be confined to one half of the wing by using the technique outlined in the discussion following equation (55) and in the section headed "Combination of the Results Obtained From Analyses of the Longitudinal and Lateral Degrees of Freedom." Basically this technique consists in splitting the influence functions of concern into symmetric and antisymmetric parts and using one part for an analysis involving the longitudinal degrees, and the other in an analysis involving the lateral degrees. If this approach is adopted, separate analysis of longitudinal and lateral degrees of freedom is still preferable.

EXTENSION OF THE STATISTICAL APPROACH

The power spectrum and, hence, the mean-square values of the responses such as the stress at a given point on the wing of a large flexible airplane due to flight through turbulent air can be calculated in several ways. Perhaps the most direct of these consists in using the basic approach outlined in the first part of this paper and starting with an expression

for the instantaneous value of the stress in terms of a suitable indicial-response influence function, namely,

$$\sigma(t)=\int_{-\infty}^{\infty}\int_{-b/2}^{b/2} h_\sigma^w(t_1,y)\,w(U(t-t_1),y)\,dy\,dt_1 \qquad (85)$$

The function $h_\sigma^w(t,y)$ is, as before, an indicial-response influence function or Green's function for the partial differential equation. It relates the stress as a function of space and time coordinates to the applied loads, which are also functions of space and time coordinates. The essential difference between the problem considered in this section and those treated in the first two parts of the report is that this function can no longer be expressed as a product of a function of t alone and y alone. In some cases—in a modal approach, for instance—it may be expressible as a sum of several such functions, and then the approach used previously for the bending moment of a large rigid airplane free to move vertically may be adopted, as has been done in reference 13. However, in this section the case is considered in which even this simplification cannot be made.

The correlation function for σ can be calculated directly from equation (85), and for the case of axisymmetric turbulence it is

$$\psi_\sigma(\tau)=\int_{-\infty}^{\infty}\int_{-\infty}^{\infty}\int_{-b/2}^{b/2}\int_{-b/2}^{b/2} h_\sigma^w(t_1,y_1)h_\sigma^w(t_2,y_2)\,\psi_w\left(\sqrt{U^2(\tau+t_1-t_2)^2+(y_2-y_1)^2}\right)dy_1\,dy_2\,dt_1\,dt_2 \qquad (86)$$

Hence, the power spectrum of σ can be obtained by calculating the Fourier transform of this function and is

$$\varphi_\sigma(\omega)=\int_{-b/2}^{b/2}\int_{-b/2}^{b/2} H_\sigma^{w*}(\omega,y_1)H_\sigma^w(\omega,y_2)\,\tilde{\varphi}_w(\omega,|y_2-y_1|)\,dy_1\,dy_2 \qquad (87)$$

where $\tilde{\varphi}_w(\omega,\eta)$ is the two-dimensional spectrum considered previously, $H_\sigma^w(\omega,y)$ is the Fourier transform of $h_\sigma^w(t,y)$ with respect to time, and the asterisk designates a complex conjugate, as before. Thus, the function $H_\sigma^w(\omega,y)$ is a transfer function from sinusoidal vertical gusts (of width dy) impinging on the wing at a given station y on the wing to the stress σ, or a Green's function for the ordinary differential equation (with the quantity ω as a parameter) that relates the stress amplitude as a function of the space coordinate y to the amplitude of the applied sinusoidal gusts.

The term $H_\sigma^{w*}(\omega,y_1)\,H_\sigma^w(\omega,y_2)$ in equation (87) is complex; however, the imaginary part can be ignored because it contributes nothing to the integral as a result of the fact that $\tilde{\varphi}_w$ depends only on $|y_2-y_1|$.

In a manner analogous to the one employed in the first part of this report, the double integral in equation (87) can be evaluated by introducing the function $\tilde{H}_\sigma^w(\omega,\eta)$ which takes the place of the function $\Gamma(\eta)$ used previously and is defined by an autoconvolution of $H_\sigma^w(\omega,\eta)$:

$$\tilde{H}_\sigma^w(\omega,\eta)=2\int_{-b/2}^{b/2}\mathrm{R}\{H_\sigma^{w*}(\omega,y)\,H_\sigma^w(\omega,y+\eta)\}\,dy$$

where R{ } designates the real part. Hence,

$$\varphi_\sigma(\omega)=\int_0^b \tilde{H}_\sigma^w(\omega,\eta)\,\tilde{\varphi}_w(\omega,\eta)\,d\eta \qquad (88)$$

Another approach consists in using the double Fourier transform $\Phi_w(\lambda)$ of the axisymmetric input correlation defined in the first part of this report. In terms of this function the correlation function $\psi_\sigma(\tau)$ can be written as

$$\begin{aligned}\psi_\sigma(\tau)&=\frac{1}{4}\int_{-\infty}^{\infty}\int_{-\infty}^{\infty}\int_{-b/2}^{b/2}\int_{-b/2}^{b/2}\int_{-\infty}^{\infty}\int_{-\infty}^{\infty} h_\sigma^w(t_1,y_1)h_\sigma^w(t_2,y_2)\,e^{i[\lambda_1U(\tau+t_1-t_2)+\lambda_2(y_2-y_1)]}\Phi_w\left(\sqrt{\lambda_1^2+\lambda_2^2}\right)d\lambda_1 d\lambda_2 dy_1 dy_2 dt_1 dt_2\\&=\frac{1}{4}\int_{-\infty}^{\infty}\int_{-\infty}^{\infty} e^{i\lambda_1U\tau}\left|\hat{H}_\sigma^w(\lambda_1,\lambda_2)\right|^2\Phi_w\left(\sqrt{\lambda_1^2+\lambda_2^2}\right)d\lambda_1 d\lambda_2\end{aligned}$$

where the function

$$\hat{H}_\sigma^w(\lambda_1,\lambda_2)=\int_{-\infty}^{\infty}\int_{-b/2}^{b/2} h_\sigma^w(t,y)\,e^{-i(\lambda_1Ut+\lambda_2y)}\,dy\,dt$$

represents the Fourier transform (with respect to y) of the function $H_\sigma^w(\omega,y)$, that is,

$$\hat{H}_\sigma^w(\lambda_1,\lambda_2)=\int_{-b/2}^{b/2} e^{-i\lambda_2y}H_\sigma^w(\lambda_1U,y)\,dy \qquad (89)$$

Hence,

$$\varphi_\sigma(\omega)=\frac{1}{4\pi}\int_{-\infty}^{\infty}\int_{-\infty}^{\infty}\int_{-\infty}^{\infty}e^{i\lambda_1 U\tau}e^{-i\omega\tau}\left|\hat{H}_\sigma^w(\lambda_1,\lambda_2)\right|^2\Phi_w\left(\sqrt{\lambda_1^2+\lambda_2^2}\right)d\lambda_1 d\lambda_2\, d\tau$$

$$=\frac{1}{2U}\int_{-\infty}^{\infty}\left|\hat{H}_\sigma^w\left(\frac{\omega}{U},\lambda\right)\right|^2\Phi_w\left(\sqrt{\left(\frac{\omega}{U}\right)^2+\lambda^2}\right)d\lambda \tag{90}$$

With the approach outlined in the next section, the function $H_\sigma^w(\omega,y)$ can be calculated either directly or indirectly, by first calculating the transfer function from the gust to the lift distribution and then the transfer function from the lift distribution to the stress. For the indirect method,

$$H_\sigma^w(\omega,y)=\int_{-b/2}^{b/2}H_\sigma^l(\omega,y)H_l^w(\omega)\,G(\eta,y)d\eta$$

where the function $H_l^w(\omega)\ G(\eta,y)$ is the influence function for the local lift or the Green's function for the aerodynamic problem involving sinusoidal gusts considered in the first part of this report; the symbols η and y in $G(\eta,y)$ are interchanged, however, so that the function now defines the contribution of a gust at station y to the lift at station η. The transfer function $H_\sigma^l(\omega,\eta)$ relates the (sinusoidal) stress at the given point to a unit concentrated (sinusoidal) normal force acting at station η.

With this indirect method, the power spectrum for the stress at a given point can be calculated by starting with the power spectrum for the lift distribution calculated in the first part of the report. For this approach $\sigma(t)$ may be written as

$$\sigma(t)=\int_{-\infty}^{\infty}\int_{-b/2}^{b/2}h_\sigma^l(t_1,y)\,l(t-t_1,y)dy\,dt_1$$

so that

$$\psi_\sigma(\tau)=\int_{-\infty}^{\infty}\int_{-\infty}^{\infty}\int_{-b/2}^{b/2}\int_{-b/2}^{b/2}h_\sigma^l(t_1,y_1)h_\sigma^l(t_2,y_2)\psi_l(\tau+t_1-t_2,y_1,y_2)dy_1dy_2dt_1dt_2$$

and

$$\varphi_\sigma(\omega)=\int_{-b/2}^{b/2}\int_{-b/2}^{b/2}H_\sigma^{l*}(\omega,y_1)H_\sigma^l(\omega,y_2)\varphi_l(\omega,y_1,y_2)dy_1\,dy_2 \tag{91}$$

where

$$\psi_l(\tau,y_1,y_2)\equiv\overline{l(t,y_1)l(\tau+t,y_2)}$$

The Fourier transform of this correlation function is, then,

$$\varphi_l(\omega,y_1,y_2)=|H_l^w(\omega)|^2\varphi_{w_\epsilon}(\omega) \tag{92}$$

(See the section headed "Generalized Aerodynamic Influence Functions in Unsteady Flow.") Hence,

$$\varphi_\sigma(\omega)=|H_l(\omega)|^2\int_{-b/2}^{b/2}\int_{-b/2}^{b/2}H_\sigma^{l*}(\omega,y_1)H_\sigma^l(\omega,y_2)\varphi_{w_\epsilon}(\omega)dy_1dy_2 \tag{93}$$

If $\varphi_{w_\epsilon}(\omega)$ is given by equation (35), the double integral can be expressed in terms of single integrals as follows:

$$\varphi_\sigma(\omega)=|H_l^w(\omega)|^2\left[(1-K)^2|G(\omega)|^2\varphi_{w_\epsilon}(\omega)+2K(1-K)\mathrm{R}\{G(\omega)G'^*(\omega)\}+K^2\int_0^b G''(\omega,\eta)\varphi_w(\omega,\eta)\,d\eta\right] \tag{94}$$

where

$$G(\omega)\equiv\int_{-b/2}^{b/2}H_\sigma^l(\omega,y)\gamma(y)\,dy$$

$$G'(\omega)\equiv\int_{-b/2}^{b/2}H_\sigma^l(\omega,y)\varphi_{w_\epsilon}{}^*(\omega,y)\gamma(y)dy$$

$$G''(\omega,\eta)\equiv 2\int_{-b/2}^{(b/2)-\eta}[\mathrm{R}\{H_\sigma^l(\omega,y)\}\mathrm{R}\{H_\sigma^l(\omega,y+\eta)\}+\mathrm{I}\{H_\sigma^l(\omega,y)\}\mathrm{I}\{H_\sigma^l(\omega,y+\eta)\}]\gamma(y)\gamma(y+\eta)dy$$

as before, R{ } designates the real part, and I{ } designates the imaginary part.

Equations (88), (90), and (93) thus represent three methods of obtaining the power spectrum of the given stress. One requires a transfer function from the local gust intensities directly to the stress, an autoconvolution of this transfer function, and the spectrum of turbulence defined by equation (16); the second requires a two-dimensional spectrum of the turbulence defined by equations (17a) and (17b) and a Fourier transform of the aforementioned transfer function with respect to y; the third utilizes an autoconvolution of the transfer functions from local concentrated loads to the stress and the spectrum for local lifts due to vertical gusts calculated in the first part of the report. The choice of approach depends to some extent on the information available, but is largely a matter of individual preference.

The analysis in this section has been based on the premise that both halves of the wing would be treated simultaneously. Attention can be confined to one wing by using only the symmetric parts of the influence functions in an analysis involving the longitudinal degrees of freedom, and only the antisymmetric parts in an analysis involving the lateral degrees of freedom. The symmetric part of an influence function for a unit concentrated load or gust acting at station y is the response function for two loads or gusts of ½ unit intensity acting at stations y and $-y$, respectively. Similarly, the antisymmetric part is the response for a load or gust of ½ unit intensity acting at station y and an equal and opposite load or gust acting at station $-y$. If this approach is chosen, some of the integral expressions given in this section assume slightly simpler forms. For instance, equation (89) can then be written for the symmetric part as

$$\hat{H}_\sigma^w(\lambda_1,\lambda_2)=2\int_0^{b/2}\cos\lambda_2 y H_\sigma^w(\lambda_1 U,y)dy$$

and for the antisymmetric part as

$$\hat{H}_\sigma^w(\lambda_1,\lambda_2)=-2i\int_0^{b/2}\sin\lambda_2 y H_\sigma^w(\lambda_1 U,y)dy$$

CALCULATION OF THE REQUIRED TRANSFER FUNCTIONS

Depending on which of the methods outlined in the preceding section is used, one of two types of transfer functions is required—either the one from local gusts to the stress of interest, or the one from the local lift to that stress. Both of these functions differ in several respects from those considered in the preceding part of this report.

For either type of transfer function the structural deformations of the wing under concentrated loads as well as under distributed loads will be required, so that the numerical-integration schemes used in the preceding part have to be modified to some extent. Also, it may now be preferable to consider the entire wing (rather than the one semispan considered in the case of the small flexible airplane), so that the various transfer functions are asymmetric. With the degrees of freedom considered in the analysis thus doubled, it becomes preferable to include one additional degree of freedom, roll, rather than to perform two separate analyses for symmetric and antisymmetric motions with, respectively, one and two less degrees of freedom, and then to combine the results. However, if the alternative approach of splitting up the influence functions into symmetric and antisymmetric parts for use in two separate analyses is adopted, only one semispan need be considered, and the results presented in this section can then be simplified to a large extent.

Before discussing the modifications required to extend the dynamic analysis outlined in the preceding part of the report to the large airplane, it might be pointed out that chordwise deformations (deformations parallel to the chord) will again be ignored. Again, they can readily be included by a straightforward extension of the approach used here if it is felt that they may be significant in any given case. If they are included, however, yawing and possibly also sideslipping motions can probably no longer be ignored, because they may give rise to large forces in the chordwise direction. If the entire wing is treated, these two additional degrees of freedom can readily be included, and all longitudinal and lateral degrees of freedom are then treated simultaneously; if two separate analyses are performed for the longitudinal and lateral degrees of freedom, the symmetric and antisymmetric parts of the influence functions being used and only one semispan being treated, these additional degrees of freedom enter only into the lateral analysis.

The structural deformation due to local (concentrated) loads can be obtained in several ways. If measured influence coefficients are used, they pertain precisely to such loads and, in fact, must be modified before they can be used for distributed loads (see ref. 12) so that it is necessary only to use the unmodified coefficients.

If the deformations are to be calculated in a manner similar to that employed in the preceding part, the integrating matrices must be replaced as follows:

$$\frac{b}{2}[\mathrm{I}] \text{ by } \frac{b}{2}[\mathrm{I}']$$

where

$$\mathrm{I}_{pq}'=1 \qquad (q>p)$$

$$\mathrm{I}_{pq}'=\frac{1}{2} \qquad (q=p)$$

$$\mathrm{I}_{pq}'=0 \qquad (q<p)$$

and

$$\left(\frac{b}{2}\right)^2[\mathrm{II}] \text{ by } \frac{b}{2}[\mathrm{II}']$$

where

$$\mathrm{II}_{pq}'=y_q-y_p \qquad (q\geqq p)$$

$$\mathrm{II}_{pq}'=0 \qquad (q<p)$$

The factor of ½ for $I_{pp'}$ constitutes an approximation which implies fairing through a discontinuity. If this approximation is to be avoided, the deflections due to unit concentrated loads (the structural influence coefficients) can be calculated directly from simple beam theory, in which case the limits of integration take care of the discontinuities. Thus, for instance, for an unswept wing, the normal deflection and twist at y_p due to a unit concentrated load and torque, respectively, at y_q are

$$z_{pq}=\int_0^{y_p}\int_0^{y'}\frac{y_q-y}{EI(y)}\,dy\,dy' \qquad (y_p \leqq y_q)$$

$$z_{pq}=\int_0^{y_q}\int_0^{y'}\frac{y_q-y}{EI(y)}\,dy\,dy'+(y_p-y_q)\int_0^{y_q}\frac{y_q-y}{EI(y)}\,dy \qquad (y_p > y_q)$$

$$\alpha_{pq}=\int_0^{y_p}\frac{1}{GJ(y)}\,dy \qquad (y_p \leqq y_q)$$

$$\alpha_{pq}=\int_0^{y_q}\frac{1}{GJ(y)}\,dy \qquad (y_q < y_p)$$

The concentrated loads under consideration arise as follows: For the transfer functions relating local lifts to the desired stress, the local lifts may be considered to be concentrated loads of unit magnitude, associated with concentrated torques of magnitude e_1c. Equation (83b) can then be written as (see also eq. (76))

$$\left[[1']-q[A]\right]\begin{bmatrix}z\\ \alpha\\ \Delta\alpha\end{bmatrix}=[R']\begin{bmatrix}[w]\\ \hline [e_1c]\,[w]\end{bmatrix} \qquad (95)$$

where $[w]$ is a diagonal matrix of the values of w defined by equation (63), and where the matrix $[R']$ represents either the four influence-coefficient matrices for z and α due to concentrated loads and torques, or the square matrix of equation (75) with modified integrating matrices, as discussed in the preceding paragraphs.

It may be noted that equation (95) now represents not one set of simultaneous equations but several, all having the same coefficients but different sets of knowns (as defined by the columns of the matrix on the right side) and, hence, different sets of unknowns (the columns of the matrix $\begin{bmatrix}z\\ \alpha\\ \Delta\alpha\end{bmatrix}$). This situation is due to the fact that the functions under consideration are, in effect, the responses of the airplane as a whole to sinusoidally varying concentrated loads and are different for each location of the applied load.

Once this equation has been modified to take into account the overall body motions and tail deflections (as explained in the preceding part) as well as the rolling motions (as explained in the following paragraphs), it can be solved to yield the unknown values of $\begin{bmatrix}z\\ \alpha\\ \Delta\alpha\end{bmatrix}$. From these values the bending and twisting moments, as well as the vertical shears, can be calculated and added to those due to the concentrated loads. When combined linearly as required for the desired stress, these moments and shears yield the desired transfer functions $H_\sigma^l(\omega, y)$.

If the transfer function directly from the local gusts to the desired stress is to be determined, the response of the airplane to the lift distribution induced by a sinusoidal gust of width dy acting at station y must be calculated. This lift distribution is the Green's function considered previously. If it is represented by the relation $H_l^w(\omega)\ G(y,\eta)$, with $G(y,\eta)$ defined by the approximation given in equation (34), the concentrated loads arise from the delta function in that expression. The right side of equation (95) becomes, in that case,

$$q(1-K)\,H_l^w(\omega)\,[R]\begin{bmatrix}[\gamma(y)\,\gamma(\eta)]\\ \hline [e_1c]\,[\gamma(y)\,\gamma(\eta)]\end{bmatrix}[w]+ qbK\,H_l^w(\omega)\,[R']\begin{bmatrix}[\gamma(y)]\,[w]\\ \hline [e_1c]\,[\gamma(y)]\,[w]\end{bmatrix}$$

where $[R]$ represents the square matrix of equation (75), and $[R']$ the one discussed in connection with equation (95). Again, several sets of simultaneous equations are implied. Their solution (after modification for overall motions and tail deflections) yields values of z and α from which the transfer functions $H_\sigma^w(\omega,y)$ can be calculated.

The extension of the method of the preceding part to the calculation of the deformations on both wings is straightforward. Essentially, distributed lifts and torques now have to be calculated for both wings and integrated with matrices which can be assembled from those used for one wing alone. No new problems arise in this process, so that it need not be discussed further.

The inclusion of rolling motion, however, is not so straightforward. One method consists in replacing all values of z in equation (83a) or its equivalent by $z+\Theta y$ and then reducing the columns involving this quantity by the following relation (which assumes that the new unknown quantity, the roll angle Θ, is listed at the end of the column):

$$\begin{Bmatrix}z+\Theta y\\ \hline \alpha\\ \hline \Delta\alpha\\ \Theta\end{Bmatrix}=\left[\begin{array}{ccc:c:c}1 & & & & \\ & 1 & & & \\ & & 1 & & \\ & & & 1 & \\ & & & & \ddots \\ & & & & \ddots \\ \hdashline & & & 1 & \\ & & & & 1 \\ & & & & & \ddots \\ \hdashline & & & & \\ & & & & \end{array}\right.\begin{array}{c}0\\ \hline 0\\ \hline 0\\ 0\end{array}\left.\begin{array}{c}\left\{\begin{matrix}y\\ \\ \\ \\ \\ \end{matrix}\right\}\\ \hline \\ \hline \\ \end{array}\right]\begin{Bmatrix}z\\ \hline \alpha\\ \hline \Delta\alpha\\ \Theta\end{Bmatrix}$$

An additional equation must then be joined to the set, namely, the equation of equilibrium in roll

$$\int_{-b/2}^{b/2} l(y)\, y\, dy - I_x\ddot{\Theta} - M_{D_t}\dot{\Theta} = 0 \qquad (96)$$

where I_x is the inertia in roll of the fuselage and empennage alone inasmuch as the inertia effects of the wing are included in $l(y)$, and M_{D_t} is the coefficient of damping in roll for the empennage. For most cases both of these contributions are negligible. If they are ignored, equation (96) can be written in matrix notation as

$$[\mathrm{II}]\{l\} = 0$$

where [II] is now a matrix which serves to perform the integration required in equation (96). This condition can then be adjoined to the other equations of the set in the same manner as equations (82) were adjoined to the set in the preceding part.

The result, again, is a set of simultaneous equations for z, α, $\Delta\alpha$, and Θ from the solution of which the desired transfer functions can be obtained as outlined in the preceding paragraphs. Also, as before, once the unknowns z_r, α_r, and Θ are eliminated from the set, the divergence and flutter speeds can be calculated by conventional matrix operations; these speeds will then pertain to an airplane free to move vertically as well as in pitch and roll and, hence, will include divergence and flutter speeds in antisymmetric as well as symmetric modes.

DISCUSSION

SOME IMPLICATIONS OF THE ASSUMPTIONS CONCERNING THE NATURE OF ATMOSPHERIC TURBULENCE

The turbulence was assumed to be homogeneous in order to make the problem stationary in the statistical sense and thus permit the use of the mathematical techniques developed for such problems. In a practical sense, turbulence can be homogeneous only in a limited body of air. The assumption thus implies that the dimension of this body of air along the flight path is large compared with the distance traversed in the reaction time of the airplane, which in the case of load studies is of the order of the time to damp to one-half amplitude, but in the case of motion studies may be much larger. Obviously, the greater the body of air, the greater the reliability with which the loads and motions can be predicted (in a statistical sense) for one run through it. In general, turbulence at very low altitudes, which may be influenced significantly by the configuration of the ground, and turbulence in thunderstorms may not be sufficiently homogeneous for the purpose of this type of analysis, but other types of turbulence are likely to be substantially homogeneous over sufficiently large distances.

Isotropy was assumed in order to permit the required two-dimensional correlation functions to be expressed simply in terms of the one-dimensional correlation functions. For sufficiently short wave lengths all turbulence is isotropic, but for long wave lengths it can be isotropic only if it is homogeneous (both in the plane of the flight path and perpendicular to it). The condition of axisymmetry, which is sufficient for most of the results presented herein, is less restrictive than isotropy inasmuch as it does not specify the variation of the characteristics of the turbulence in the vertical direction. In practical problems, if the turbulence may be assumed to be homogeneous, the conditions of axisymmetry and isotropy are likely to be satisfied to a sufficient extent to permit the use of the approach presented herein for all but very long wave lengths. The wave length at which it ceases to be valid depends on the size of the body of air under consideration, being larger for a large body.

Taylor's hypothesis (to the effect that a space displacement Δx along the flight path may be identified with a time displacement $\tau = \Delta x/U$ in the gust correlation functions) implies that the variation in gust intensity that prevails along the flight path at any instant will remain substantially the same until the airplane has traversed the given body of air. The required correlation functions for atmospheric turbulence are thus in the nature of space correlation functions (rather than time correlation functions) and have been considered as such. The statistical characteristics of the turbulence are then independent of the speed at which it is traversed. Clearly, whether or not this hypothesis is valid depends on the flying speed of the airplane. On the basis of present knowledge no definite lower limiting speed can be quoted. However, indications are that the hypothesis is valid for flying speeds greater than about 100 or 200 feet per second. The effect of finite flying speed on the gust correlation function can be expected to be most pronounced for large distances, where the correlation is weak, so that the effect on the various spectra is likely to be small and to occur at the longest wave lengths, where, as previously mentioned, the spectrum is somewhat uncertain for other reasons as well; this effect is thus more likely to be significant for large than for small airplanes.

The particular correlation function used herein for the calculations of the "averaged" correlation functions and spectra has certain theoretical shortcomings—primarily that the associated spectrum does not decrease rapidly enough for very short wave lengths. However, it does appear to be adequate to represent the available information concerning the spectra of atmospheric turbulence (see ref. 17, for instance) because the behavior at very short wave lengths is relatively unimportant, inasmuch as airplanes cannot respond to them, and the behavior at very long wave lengths is usually in doubt by reason of the nonhomogeneity of actual turbulence. In the intermediate range of wave lengths, this correlation function appears to be quite satisfactory.

The parameter L^* (the integral scale of turbulence) used herein is, for practical purposes, a largely fictitious quantity, inasmuch as it is proportional to the values of the gust spectrum for infinite wave lengths, which, in view of the uncertainties in the values of the spectra at large wave lengths, have little physical significance. Therefore, at present, insufficient information is available to give a value for L^* to be used in connection with the numerical results calculated herein, although a value of 1,000 to 2,000 feet appears to be appropriate. As more information concerning the spectrum of atmospheric turbulence becomes avail-

able, more definite values can be deduced by fitting an analytical expression of the type used here to measured results in the range of frequencies of primary interest, and then using this expression as a means of obtaining a value of L^* by extrapolation of the measured results to infinite wave lengths (zero frequency).

CONSIDERATIONS PERTINENT TO THE APPLICATION OF STATIONARY-RANDOM-PROCESS TECHNIQUES TO GUST-LOAD PROBLEMS

The purpose of this section is to point out how, in principle, the results of analyses of the type outlined herein may be used in overall load analysis and, hence, in the design of an airplane.

Consideration is confined in this paper primarily to the power spectra of the motions and stresses of interest. As pointed out in references 1, 2, 3, and 11, for instance, a great deal of statistical information of direct interest can be obtained from the power spectrum. For instance, if the random process of concern (say, the given stress as a function of time) has a Gaussian probability distribution, the expected number of peaks at or beyond a given level in a given period of time can be calculated very simply from the integral of the spectrum and its second and fourth moments.

The results obtained in this manner pertain to continued flight in a given body of turbulent air. They have to be generalized by determining the likelihood of flying through turbulence of the given characteristics. (See ref. 18.) The probability of exceeding a given stress level during the expected life of the airplane while flying through atmospheric turbulence can thus be calculated in straightforward fashion. To this probability must then be added the probability of exceeding this level in maneuvers, landings, and, possibly, also in turbulence due to thunderstorms, because in view of the possibly nonhomogeneous character of turbulence in thunderstorms and the possibly nonlinear nature of the aerodynamic forces incurred while flying through them, the techniques used herein may not be applicable to flight through thunderstorms, and a separate analysis may have to be performed.

Although the available information concerning atmospheric turbulence is inadequate to permit of any definite conclusion, the results obtainable with the approach outlined herein may turn out to be most significant for the prediction of the low- and medium-amplitude stress cycles which are important to fatigue studies; their validity for or contribution to the prediction of very severe loads remains to be seen.

CONCLUDING REMARKS

The statistical approach to the problem of calculating the dynamic responses and the stresses of an airplane subjected to continuous random atmospheric turbulence has been extended in several respects; basically, only the assumptions of linearity, that is, of small motions and deformations, as well as homogeneity and axisymmetry of the turbulence are retained.

The first problem considered was the effect of spanwise variations of the instantaneous turbulent velocities on the lift and moments due to turbulence. The mean-square lift has been shown to be reduced considerably if the span of the airplane is relatively large compared with the integral scale of turbulence. The shape of the spectrum of this lift is affected relatively little by spanwise variations of gust intensity, except at very high frequencies, if the decrease in the effective mean-square intensity is taken into account. The effect of sweep on the mean-square lift and its spectrum has been shown to be small for wings with a given distance from root to tip.

If the variation of the instantaneous velocities is taken into account, the rolling moment to which the airplane is subjected can be calculated. The mean-square rolling moment has been shown to be proportional to the ratio of the wing span to the integral scale of turbulence for small values of that ratio. Similarly, expressions for the mean-square values and the power spectra of the local lift, the bending moments, and the pitching moment have been given. For some of these forces the required aerodynamic information cannot be calculated by existing methods. Therefore, certain approximations, based on experience with steady aerodynamic forces and available knowledge concerning unsteady forces, had to be made for the aerodynamic influence functions in unsteady flow.

The next problem considered was the dynamic response of a rigid airplane to random turbulence. This problem had previously been treated for the case of an airplane free to move only in the vertical direction and small enough so that variation of the turbulent velocities along the span could be neglected. In the present report the response of an airplane in three longitudinal degrees of freedom was considered; calculations were made which suggest that the inclusion of deviations from the mean horizontal motion is superfluous in gust-load calculations. For the remaining two longitudinal degrees of freedom, the mean-square normal and angular acceleration have been shown to be functions of only two parameters other than the mass ratio and scale parameter of the single-degree-of-freedom case, namely, dimensionless forms of the short-period frequency and of the time to damp to one-half amplitude. An indication is given of the manner in which the results obtained in connection with the first problem can be used to extend this dynamic analysis to the case in which variations of the turbulent velocity along the span have to be taken into account.

The last problem treated was the dynamic response of a flexible airplane, including vertical motion, pitch, and, when necessary (as when spanwise variations in gust intensity are taken into account), roll. Horizontal and lateral (yawing and sideslipping) motions were disregarded because they do not generally affect the wing stresses due to vertical gusts. A method which represents an extension to the dynamic case of a numerical-integration approach to the static aeroelastic problem has been outlined for the analysis of the problem at hand. The modifications required in the basic statistical approach and in this method of dynamic analysis in order to treat the case in which spanwise variations of the gust intensity are important have been discussed.

Although most of this analysis has been confined to the vertical component of turbulence, it has been shown that the simultaneous action of longitudinal, vertical, and lateral

gusts on the wing stresses (with due allowance for the fact that vertical gusts affect both the longitudinal and the lateral motions of the airplane) can be taken into account by simply adding the power spectra of the various contributions, provided the turbulence is isotropic; the cross correlations or spectra have been shown to vanish either by the symmetry or antisymmetry of the influence functions involved or as a result of the statistical independence of mutually perpendicular velocity components.

The approach presented herein thus furnishes a foundation for the prediction of the statistical properties of the stress experience of a given airplane once the appropriate statistical characteristics of the atmosphere have been determined.

LANGLEY AERONAUTICAL LABORATORY,
NATIONAL ADVISORY COMMITTEE FOR AERONAUTICS,
LANGLEY FIELD, VA., *November 5, 1956.*

REFERENCES

1. Liepmann, H. W.: An Approach to the Buffeting Problem From Turbulence Considerations. Rep. No. SM-13940, Douglas Aircraft Co., Inc., Mar. 13, 1951.
2. Fung, Y. C.: Statistical Aspects of Dynamic Loads. Jour. Aero. Sci., vol. 20, no. 5, May 1953, pp. 317–330.
3. Press, Harry, and Mazelsky, Bernard: A Study of the Application of Power-Spectral Methods of Generalized Harmonic Analysis to Gust Loads on Airplanes. NACA Rep. 1172, 1954. (Supersedes NACA TN 2853.)
4. Clementson, Gerhardt C.: An Investigation of the Power Spectral Density of Atmospheric Turbulence. Ph. D. Thesis, M.I.T., 1950.
5. Liepmann, H. W.: Extension of the Statistical Approach to Buffeting and Gust Response of Wings of Finite Span. Jour. Aero. Sci., vol. 22, no. 3, Mar. 1955, pp. 197–200.
6. Heaslet, Max A., and Spreiter, John R.: Reciprocity Relations in Aerodynamics. NACA Rep. 1119, 1953. (Supersedes NACA TN 2700.)
7. Reissner, Eric, and Stevens, John E.: Effect of Finite Span on the Airload Distributions for Oscillating Wings. II—Methods of Calculation and Examples of Application. NACA TN 1195, 1947.
8. Drischler, Joseph A.: Calculation and Compilation of the Unsteady-Lift Functions for a Rigid Wing Subjected to Sinusoidal Gusts and to Sinusoidal Sinking Oscillations. NACA TN 3748, 1956.
9. Diederich, Franklin W.: A Simple Approximate Method for Calculating Spanwise Lift Distributions and Aerodynamic Influence Coefficients at Subsonic Speeds. NACA TN 2751, 1952.
10. Diederich, Franklin W., and Zlotnick, Martin: Calculated Spanwise Lift Distributions, Influence Functions, and Influence Coefficients for Unswept Wings in Subsonic Flow. NACA Rep. 1228, 1955. (Supersedes NACA TN 3014.)
11. Anon.: Fundamentals of Design of Piloted Aircraft Flight Control Systems. Vol. II—Dynamics of the Airframe. Rep. AE-61-4, Bur. Aero., Feb. 1953.
12. Phillips, William H., and Kraft, Christopher C., Jr.: Theoretical Study of Some Methods for Increasing the Smoothness of Flight Through Rough Air. NACA TN 2416, 1951.
13. Diederich, Franklin W.: The Dynamic Response of a Large Airplane to Continuous Random Atmospheric Disturbances. Jour. Aero. Sci., vol. 23, no. 10, Oct. 1956, pp. 917–930.
14. Diederich, Franklin W.: Calculations of the Aerodynamic Loading of Swept and Unswept Flexible Wings of Arbitrary Stiffness. NACA Rep. 1000, 1950.
15. Theodorsen, Theodore: General Theory of Aerodynamic Instability and the Mechanism of Flutter. NACA Rep. 496, 1935.
16. Jones, Robert T., and Fehlner, Leo F.: Transient Effects of the Wing Wake on the Horizontal Tail. NACA TN 771, 1940.
17. Crane, Harold L., and Chilton, Robert G.: Measurements of Atmospheric Turbulence Over a Wide Range of Wavelength for One Meteorological Condition. NACA TN 3702, 1956.
18. Press, Harry, Meadows, May T., and Hadlock, Ivan: Estimates of Probability Distribution of Root-Mean-Square Gust Velocity of Atmospheric Turbulence From Operational Gust-Load Data by Random-Process Theory. NACA TN 3362, 1955.

REPORT 1346

DIFFERENTIAL EQUATIONS OF MOTION FOR COMBINED FLAPWISE BENDING, CHORDWISE BENDING, AND TORSION OF TWISTED NONUNIFORM ROTOR BLADES [1]

By JOHN C. HOUBOLT and GEORGE W. BROOKS

SUMMARY

The differential equations of motion for the lateral and torsional deformations of twisted rotating beams are developed for application to helicopter rotor and propeller blades. No assumption is made regarding the coincidence of the neutral, elastic, and mass axes, and the generality is such that previous theories involving various simplifications are contained as subcases to the theory presented in this paper.

Special attention is given the terms which are not included in previous theories. These terms are largely coupling-type terms associated with the centrifugal forces. Methods of solution of the equations of motion are indicated by selected examples.

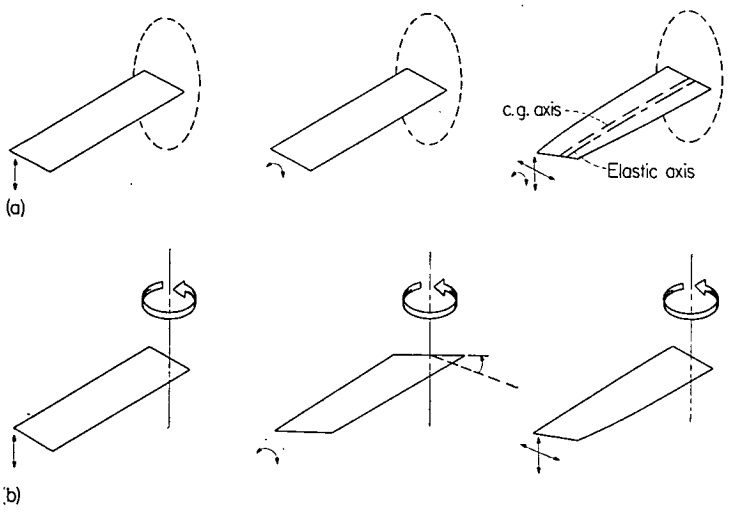
INTRODUCTION

This paper deals with the deformation theory of rotating blades. The structural problems of these blades have become more acute in almost every phase of aeronautical-engineering application: For example, propellers have become larger and thinner, particularly in connection with aircraft designed for vertical take-off and landing and short take-off and landing, and as a consequence are more susceptible to vibration and flutter troubles; helicopter blades are subject to numerous vibration, divergence, and flutter problems; and turbine and compressor blades fail frequently because of some vibration phenomena. There is therefore much interest in the development of a more general deformation theory which is fundamental in the structural and dynamic analysis of these problems.

Although many theories on blade deformation exist, these theories either neglect some of the factors of concern or treat them only approximately. The factors are many and include variable stiffness and mass distributions, noncoincidence of the elastic and mass axes, built-in twist, coupling brought about by inertia and centrifugal forces, and so forth. In order to give a rough perspective of the scope of available theory, figure 1 has been prepared. The nonrotating-beam cases have also been included in figure 1 (a). The first two cases refer to uncoupled bending and uncoupled torsion of beams without twist, and much work on these cases has been done; their treatment is in fact classical. The third case is that of coupled bending in two directions and torsion of a twisted beam, wherein the elastic and mass axes are noncoincident (see ref. 1); the subcase where no twist is present has also been given extensive treatment. Additional treatments on general theory of pretwisted beams are also given in references 2 to 4.

The rotating-beam cases which have been treated with the inclusion of centrifugal forces are shown in figure 1 (b). The first case, that of pure flapwise bending of an untwisted beam, has been considered by several investigators; reference 5 is a notable example in which beams of variable cross section and different root-end suspensions are analyzed from a design-application standpoint in considerable detail. References 6 to 8 also give substantial treatments to this case. Pure torsion of untwisted rotating beams is treated in references 9 and 10, and combined bending in two directions is treated by various means which include both vector and matrix methods in references 11 to 16.

The case treated in the present paper is shown in figure 2; this case represents the coupled bending in two directions and torsion of a twisted rotating beam where the elastic axis, mass axis, and tension axis are not necessarily coincident. The tension axis is defined as the spanwise locus of the centroids of the cross-sectional area effective in carrying tension. The specific purpose of the paper is to develop the differential equation of deformation of the blade under



(a) Nonrotating beams.
(b) Rotating beams.
FIGURE 1.—Cases treated in previous theory.

[1] Supersedes NACA Technical Note 3905 by John C. Houbolt and George W. Brooks, 1957.

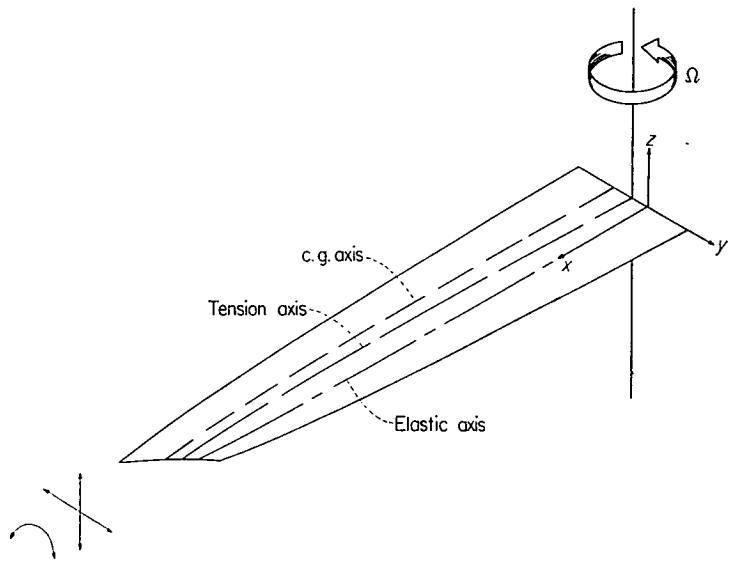


FIGURE 2.—Present theory. Case of coupled bending-torsion of twisted rotating beam.

the action of various applied loads. The development is made along the principles of "engineering" beam theory, and secondary effects, such as deformation due to shear, are not included. The theory is therefore intended primarily for blades of moderate to high aspect ratios, for which plate bending effects are probably not significant. Special subcases which involve simplifications that appear justified in the treatment of certain problems (for example, helicopter blade deformation) are then deduced. Finally, methods of solving the equations are discussed, and examples are given.

SYMBOLS

A cross-sectional area of blade effective in carrying axial tension

B_1, B_2 section constants, see equations (9)

ds incremental distance measured along beam fiber in undeformed state

ds_1 incremental distance measured along beam fiber in deformed state

E Young's modulus of elasticity

e distance between mass and elastic axis, positive when mass axis lies ahead of elastic center

e_A distance between area centroid of tensile member and elastic axis, positive for centroid forward

e_o distance at root between elastic axis and axis about which blade is rotating, positive when elastic axis lies ahead

G shear modulus of elasticity

I_1, I_2 bending moments of inertia about major and minor neutral axes, respectively (both pass through centroid of cross-sectional area effective in carrying tensions)

J torsional stiffness constant

k_A polar radius of gyration of cross-sectional area effective in carrying tensile stresses about elastic axis

k_m polar radius of gyration of cross-sectional mass about elastic axis ($k_m^2=k_{m1}^2+k_{m2}^2$)

k_{m1}, k_{m2} mass radii of gyration about major neutral axis and about an axis perpendicular to chord through the elastic axis, respectively

L_y intensity per unit length of laterally applied aerodynamic load in plane of rotation

L_z intensity per unit length of applied aerodynamic loading perpendicular to plane of rotation

M intensity per unit length of applied aerodynamic torque loading

M_1 resultant cross-sectional moment about major principal axis

M_2 resultant cross-sectional moment about axis perpendicular to major principal axis and passing through elastic axis

M_x, M_y, M_z resultant moments in x-, y-, and z-directions, respectively, of M_1, M_2, and Q moments

m mass of beam per unit length

$\bar{p}_x$, $\bar{p}_y$, $\bar{p}_z$ resultant or total loadings per unit length in x-, y-, and z-directions

Q resultant cross-sectional torque about elastic axis

q torque loading per unit length

$\bar{q}_x$, $\bar{q}_y$, $\bar{q}_z$ resultant torque loadings per unit length in x-, y-, and z-directions

R blade radius

T tension in beam, $T\cong\int_x^R \Omega^2 mx\,dx$

t thickness of cross section at any chordwise position

V_y, V_z cross-sectional shears in y- and z-directions

v, w lateral displacements of beam, in plane of rotation and normal to plane, respectively

x, y, z coordinate system which rotates with blade such that x-axis falls along initial or undeformed position of elastic axis (see figs. 2 and 3)

β blade angle of station x prior to any deformation, positive when leading edge is upward

ϵ strain

ϵ_T strain due to tension, $\frac{T}{EA}$

ζ,η cross-sectional coordinates; η-axis lies along major axis, ζ-axis is perpendicular to major axis and passes through elastic axis (see fig. 3)

η_{te}, η_{le} values of η for trailing edge and leading edge of cross section

ρ mass density

σ stress

ϕ angle of twisting deformation, positive when leading edge is upward

Ω angular velocity of rotation

ω frequency of vibration, radians/sec

Primes denote derivatives with respect to x; dots denote derivatives with respect to time.

ANALYSIS

GENERAL PROCEDURE

As noted from figure 2, the beam is considered as though it were a rotating helicopter blade with rotation counterclockwise when viewed from above. The x-axis of the x, y, z coordinate axes system shown lies outward along the blade and is coincident with the undeformed position of the elastic axis. This set of axes moves with the blade around the axis of rotation at the given rotational velocity Ω, and all deformations of the blade are referred to this coordinate system. The blade is considered under the action of distributed aerodynamic loadings in the y- and z-directions and under a distributed torque loading about the elastic axis, where the intensities per unit length are denoted by L_y, L_z, and M, respectively. The tension in the beam is denoted by T.

Figures 3 (a) and (b) show the coordinate system used for the blade cross section and the chosen displacements of this analysis. The η- and ζ-axes, with the origin at the elastic axis and the η-axis along the major axis of the cross section, move with the cross section. The blade deformations are denoted by a displacement v of the elastic axis in the plane of rotation, positive when in the direction of rotation, a displacement w out of the plane of rotation, positive upward, and a rotation ϕ about the elastic axis. The built-in twist β and also ϕ are positive when the blade leading edge is up.

The aim of this analysis is to derive the differential equation of motion in terms of v, w, and ϕ. The derivation proceeds along the following steps:

(1) The equation for longitudinal strain at any point on the cross section is derived in terms of the displacements.

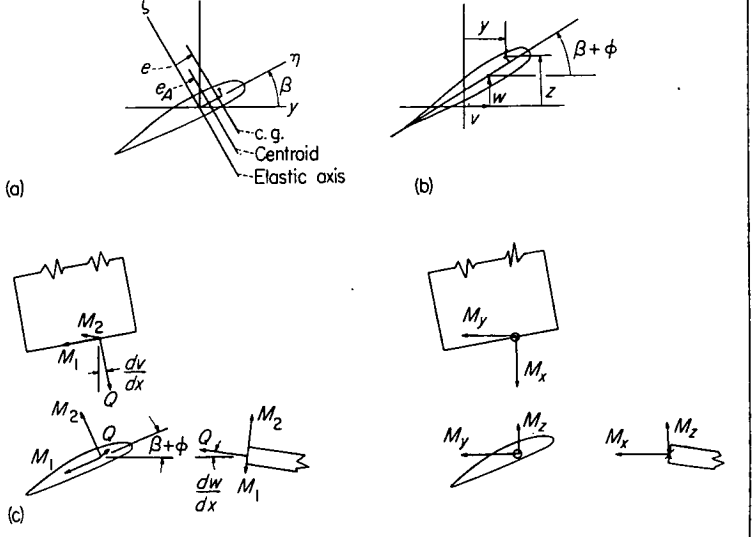
(2) With the aid of this strain equation the internal elastic moments are derived; these are the resultant moments taken about the η- and ζ-axes and are shown in figure 3 (c).

(3) The transformation is then made of these elastic moments to the more easily handled moments which have vectors parallel to the x, y, z axes system. (See fig. 3 (c).)

(4) The equilibrium expressions for these latter moments are derived, and this consideration involves the introduction of the total loading on the beam.

(5) The total loadings, composed of the body forces and applied loadings, are derived.

(6) Steps 3, 4, and 5 are combined to give the final differential equations.



(a) Coordinates. (b) Displacements. (c) Moments.

FIGURE 3.—Nomenclature.

DERIVATION OF STRAIN EQUATION

Both longitudinal and shearing strains are, of course, produced during bending and torsion of the beam. In general, both types of strains must be considered in determining the resultant forces and moments that act on a given cross section. In the treatment given in the present paper, however, an approach is used which requires that only the longitudinal strains have to be considered explicitly. In appendix A a derivation akin to an engineering beam theory is given for the strain that develops in any longitudinal fiber of a twisted beam which undergoes translational displacements v and w and a torsional displacement ϕ. The derivation is mainly formal, but a physical insight of how strain is developed may be gained by considering the possible motions of the imaginary cutting planes shown in figure 4 and which are assumed to remain plane during deformation. In general, strain may arise from four types of motion: pure displacement of the planes toward or away from each other, rotation of the planes associated with chordwise bending, rotation of the planes associated with flapwise bending, and rotation of the planes relative to one another about the elastic axis to cause beam twisting. With the assumption that the cross section is symmetrical about the major principal axis, the resulting longitudinal strain is found to be

$$\epsilon=\epsilon_T+(e_A-\eta)\ (v''\cos\beta+w''\sin\beta)+\zeta\ (v''\sin\beta-w''\cos\beta)+(\zeta^2+\eta^2-k_A^2)\beta'\phi' \tag{1}$$

The longitudinal stresses follow directly from this equation and are

$$\sigma=E[\epsilon_T+(e_A-\eta)\ (v''\cos\beta+w''\sin\beta)+\zeta(v''\sin\beta-w''\cos\beta)+(\zeta^2+\eta^2-k_A^2)\beta'\phi'] \tag{2}$$

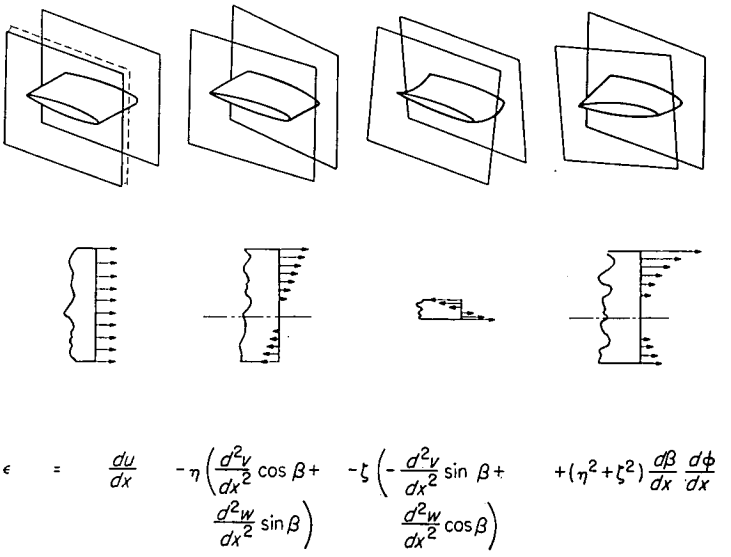


FIGURE 4.—Strains.

No further development of cross-sectional stresses or strains is necessary. The consideration of shearing stresses which are associated with longitudinal stresses, that is, the shearing stresses which are necessary to satisfy equilibrium of an elemental tube, is avoided by choosing the elastic axis (defined here as the locus of shear centers) as a reference axis; the consideration of shearing stresses due to twisting deformation is obviated through use of the assumption that the resisting torque includes a St. Venant type torsional term which is the same as would develop if the beam were initially untwisted. Both of these items will be introduced in the next section.

DERIVATION OF INTERNAL ELASTIC MOMENTS

The stress distributions over the cross section may now be resolved into effective internal resisting moments at the elastic-axis position, as shown in figures 3 and 5. In order to determine these moments, the inclination relative to the elastic axis of the general beam fiber due to initial twist and twisting deformation must be considered. The stress along this fiber is resolved into two components, one parallel to the elastic axis and one in a plane perpendicular to the elastic axis. (See fig. 5.) From the longitudinal component, the flapwise bending moment M_1 and the chordwise bending moment M_2 are given as follows:

$$M_1=-\int_{\eta_{te}}^{\eta_{le}}\int_{-t/2}^{t/2}\sigma\zeta\,d\zeta\,d\eta \tag{3}$$

$$M_2=-\int_{\eta_{te}}^{\eta_{le}}\int_{-t/2}^{t/2}\sigma\eta\,d\zeta\,d\eta \tag{4}$$

where the minus signs have been introduced to make the moments positive when they produce compression in the upper and nose fibers, respectively.

The component in the plane normal to the elastic axis leads to an effective torsional resisting moment. The consideration of this component and the addition of the torque associated with St. Venant twisting mentioned previously leads to the following equation for total resisting torque:

$$Q=GJ\phi'+\int_{\eta_{te}}^{\eta_{le}}\int_{-t/2}^{t/2}\sigma(\beta+\phi)'\,(\eta^2+\zeta^2)d\zeta\,d\eta \tag{5}$$

where a positive torque is associated with a positive ϕ'. In equation (5), the choice of the elastic axis as a reference axis is significant. The elastic axis does not necessarily coincide with the centroidal axis, and if the centroidal axis, or for that matter any other axis, were used as a reference, then the shearing stresses associated with longitudinal stresses would contribute to the total resisting torque.

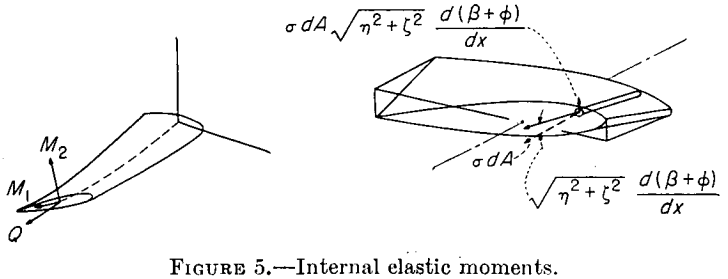


FIGURE 5.—Internal elastic moments.

Such a term would have to be included in equation (5) and would thus lead to considerable complication in the analysis. With the choice of the elastic axis, however, no such term appears, because the elastic axis is defined herein as the axis about which the resultant torque of the shearing stresses due to longitudinal stresses is zero.

Since the elastic axis is important, the establishment of this axis position will be discussed now. Consider differential longitudinal stresses to arise which have a cross-sectional distribution the same as that given by equation (2). The differential longitudinal stresses associated with the expression $E[\epsilon_T+e_A(v''\cos\beta+w''\sin\beta)-k_A^2\beta'\phi']$ are uniform across the cross section and hence do not produce any shearing stresses. For the expression

$$E[-\eta(v''\cos\beta+w''\sin\beta)+(\zeta^2+\eta^2)\beta'\phi']$$

the differential stresses would be symmetrical about the major axis (η-axis) and, since the cross section is assumed symmetrical, would lead to a resultant shear directed along the major axis. Only the remaining term $E\zeta(v''\sin\beta-w''\cos\beta)$ can lead to shearing stresses which produce torque. Thus in order to locate the position of the elastic axis, it is sufficient to consider the beam in bending about the major axis only, with a linear stress distribution in the ζ-direction, and then to determine the shearing stresses over the cross section (in the η- and ζ-directions) and the position along the major axis for which these shearing stresses produce no resultant torque. (See treatments on elastic axis and shear center in ref. 17.)

The substitution of equation (2) into equations (3), (4), and (5) gives the following equations for total elastic moments in terms of the displacements:

$$M_1=EI_1(-v''\sin\beta+w''\cos\beta) \tag{6}$$

$$M_2=EI_2(v''\cos\beta+w''\sin\beta)-Te_A-EB_2\beta'\phi' \tag{7}$$

$$Q=[GJ+Tk_A^2+EB_1(\beta')^2]\phi'+Tk_A^2\beta'-EB_2\beta'(v''\cos\beta+w''\sin\beta) \tag{8}$$

where I_1 and I_2 are the principal moments of inertia of the tensile carrying area (I_2 is the moment of inertia about the mean principal axis, not about the ζ-axis) and where B_1 and B_2 are section constants defined by

$$\left.\begin{aligned}B_1&=\int_{\eta_{te}}^{\eta_{le}}t\eta^2\left(\eta^2+\frac{t^2}{6}-k_A^2\right)d\eta\\ B_2&=\int_{\eta_{te}}^{\eta_{le}}t\eta\left(\eta^2+\frac{t^2}{12}-k_A^2\right)d\eta\end{aligned}\right\} \tag{9}$$

In equations (9) it is interesting to note that if displacements parallel and perpendicular to the blade chord had been used instead of v and w the results obtained would differ from those used by other investigations. (See appendix A for the results obtained.) Also of interest is the form that equation (8) would take if large deflections in ϕ were considered, but with $v=w=0$. This point, which is connected with the possibility of a torsional instability, is discussed also in appendix A.

MOMENT TRANSFORMATION

In the consideration of the equilibrium between moments, shears, and tension, it is more convenient to deal with moments that are orientated parallel to the x-, y-, and z-axes, that is, the moments M_x, M_y, and M_z shown in figure 3. A simple transformation of the moments M_1, M_2, and Q to these newer moments is thus desired. When the M_1, M_2, and Q moments are resolved into components in the x-, y-, and z-directions, respectively, and use is made of the relations that when ϕ is small

$$\left.\begin{aligned}\sin(\beta+\phi)&=\sin\ \beta+\phi\ \cos\ \beta\\ \cos(\beta+\phi)&=\cos\ \beta-\phi\ \sin\ \beta\end{aligned}\right\} \tag{10}$$

the following relations are obtained:

$$\left.\begin{aligned}M_x=&Q+M_1(\cos\ \beta-\phi\ \sin\ \beta)v'+\\ &M_1(\sin\ \beta+\phi\ \cos\ \beta)w'+M_2(\sin\ \beta+\\ &\phi\ \cos\ \beta)v'-M_2(\cos\ \beta-\phi\ \sin\ \beta)w'\\ M_y=&M_1(\cos\ \beta-\phi\ \sin\ \beta)+M_2(\sin\ \beta+\phi\ \cos\ \beta)-Qv'\\ M_z=&-M_1(\sin\ \beta+\phi\ \cos\ \beta)+M_2(\cos\ \beta-\phi\ \sin\ \beta)+Qw'\end{aligned}\right\} \tag{11}$$

Now when equations (6), (7), and (8) are substituted into equations (11), and all the second-order terms are dropped, the following desired equations for M_x, M_y, and M_z in terms of the displacements are found:

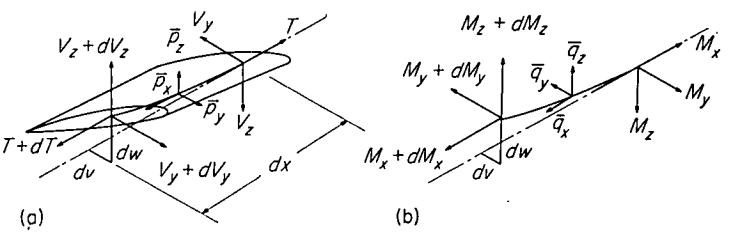
$$M_x=[GJ+Tk_A^2+EB_1(\beta')^2]\phi'+Tk_A^2\beta'-EB_2\beta'(v''\cos\ \beta+w''\sin\ \beta)-Te_Av'\sin\ \beta+Te_Aw'\cos\ \beta \tag{12}$$

$$M_y=(EI_1\cos^2\beta+EI_2\sin^2\beta)w''+(EI_2-EI_1)\sin\ \beta\cos\ \beta v''-(Te_A+EB_2\beta'\phi')\sin\ \beta-Te_A\phi\cos\ \beta \tag{13}$$

$$M_z=(EI_2-EI_1)\sin\ \beta\cos\ \beta\ w''+(EI_1\sin^2\beta+EI_2\cos^2\beta)v''-(Te_A+EB_2\beta'\phi')\cos\ \beta+Te_A\phi\sin\ \beta \tag{14}$$

EQUILIBRIUM CONDITIONS

The equilibrium of the forces and moments that act on a differential beam element is now considered. In this consideration the element is formed by slices parallel to the yz-plane, because this choice leads to rather simple results. The forces that act on such an element are shown in figure 6(a); the moments, in figure 6(b). The quantities $\bar{p}_x$, $\bar{p}_y$, $\bar{p}_z$, $\bar{q}_x$, $\bar{q}_y$, and $\bar{q}_z$ are resultant force and moment loadings, which involve both the acceleration body forces and the applied aerodynamic loading. The acceleration body forces,



(a) Forces. (b) Moments.

FIGURE 6.—Equilibrium of forces and moments.

due to both centrifugal and transverse accelerations, are derived in appendix B.

Summation of the forces in the x-, y-, and z-directions and summation of the moments about the x-, y-, and z-axes lead to the following equilibrium conditions for shear and moment:

$$\left.\begin{aligned}T'+\bar{p}_x&=0\\ V_y'+\bar{p}_y&=0\\ V_z'+\bar{p}_z&=0\end{aligned}\right\} \tag{15}$$

$$M_x'-V_yw'+V_zv'+\bar{q}_x=0 \tag{16a}$$

$$M_y'-Tw'+V_z+\bar{q}_y=0 \tag{16b}$$

$$M_z'-Tv'+V_y+\bar{q}_z=0 \tag{16c}$$

By substitution the shears in these equations may be eliminated to give the following basic equilibrium conditions:

$$\left.\begin{aligned}&M_x'-M_y'v'+M_z'w'-\bar{q}_yv'+\bar{q}_zw'+\bar{q}_x=0\\ &M_y''-(Tw')'+\bar{q}_y'-\bar{p}_z=0\\ &M_z''-(Tv')'+\bar{q}_z'-\bar{p}_y=0\end{aligned}\right\} \tag{17}$$

Substitution of equations (12), (13), and (14) into equations (17) gives

$$-\{[GJ+Tk_A^2+EB_1(\beta')^2]\phi'+Tk_A^2\beta'-EB_2\beta'(v''\cos\ \beta+w''\sin\ \beta)\}'+Te_Av''\sin\ \beta-Te_Aw''\cos\ \beta+\bar{q}_yv'-\bar{q}_zw'-\bar{q}_x=0 \tag{18}$$

$$[(EI_1\cos^2\beta+EI_2\sin^2\beta)w''+(EI_2-EI_1)\sin\ \beta\cos\ \beta\ v''-(Te_A+EB_2\beta'\phi')\sin\ \beta-Te_A\phi\cos\ \beta]''-(Tw')'+\bar{q}_y'-\bar{p}_z=0 \tag{19}$$

$$[(EI_2-EI_1)\sin\ \beta\cos\ \beta\ w''+(EI_1\sin^2\beta+EI_2\cos^2\beta)v''-(Te_A+EB_2\beta'\phi')\cos\ \beta+Te_A\phi\sin\ \beta]''-(Tv')'+\bar{q}_z'-\bar{p}_y=0 \tag{20}$$

where second-order terms have been dropped. Only the loadings now remain to be considered.

RESULTANT LOADINGS

As mentioned previously, the resultant or total loadings are composed of both the inertia loading due to centrifugal and vibratory accelerations and the applied aerodynamic loading. The inertia loadings, which consist of the forces and moments which oppose accelerations of the blade elements, are derived in appendix B whereas the aerodynamic loadings L_y, L_z, and M are left in this symbolic form, since they are in the nature of externally applied loadings.

The procedure that follows is employed in the derivation of the total loadings which is given in appendix B. The acceleration of any mass particle on the vibrating, rotating blade is derived and the components in the x-, y-, and z-directions are obtained. These component accelerations include terms for the Coriolis force and transverse and centrifugal accelerations along with higher order terms. The inertia force and moment loadings are then obtained by integrating over the cross section; these are simplified by

dropping second-order terms and are then added with the aerodynamic or applied loadings to yield the following desired resultant loadings $\bar{p}_x$, $\bar{p}_y$, $\bar{p}_z$, $\bar{q}_x$, $\bar{q}_y$, and $\bar{q}_z$:

$$\left.\begin{aligned}
&\bar{p}_x = -T' = \Omega^2 m x \\
&\bar{p}_y = L_y - m[\ddot{v} - \Omega^2(v+e_o)] + me[\ddot{\phi}\sin\beta + \Omega^2(\cos\beta - \phi\sin\beta)] \\
&\bar{p}_z = L_z - m(\ddot{w} + e\ddot{\phi}\cos\beta) \\
&\bar{q}_x = M - \Omega^2 me[(v+e_o)\sin\beta + e_o\phi\cos\beta] + me(\ddot{v}\sin\beta - \ddot{w}\cos\beta) - \Omega^2 m(k_{m2}^2 - k_{m1}^2)(\sin\beta\cos\beta + \phi\cos 2\beta) - mk_A^2\ddot{\phi} \\
&\bar{q}_y = -\Omega^2 mex(\sin\beta + \phi\cos\beta) \\
&\bar{q}_z = -\Omega^2 mex(\cos\beta - \phi\sin\beta)
\end{aligned}\right\} \quad (21)$$

FINAL DIFFERENTIAL EQUATIONS

The substitution of equations (21) into equations (18), (19), and (20) gives now the desired final differential equations of equilibrium

$$-\{[GJ + Tk_A^2 + EB_1(\beta')^2]\phi' - EB_2\beta'(v''\cos\beta + w''\sin\beta)\}' + \underline{Te_A(v''\sin\beta - w''\cos\beta)} + \underline{\Omega^2 mxe(-v'\sin\beta + w'\cos\beta)} + \underline{\Omega^2 me\sin\beta}v + \Omega^2 m[(k_{m2}^2 - k_{m1}^2)\cos 2\beta + \underline{ee_o\cos\beta}]\phi + mk_m^2\ddot{\phi} - me(\ddot{v}\sin\beta - \ddot{w}\cos\beta) = M + (Tk_A^2\beta')' - \Omega^2 m[(k_{m2}^2 - k_{m1}^2)\sin\beta\cos\beta + \underline{ee_o\sin\beta}] \quad (22)$$

$$[(EI_1\cos^2\beta + EI_2\sin^2\beta)w'' + (EI_2 - EI_1)\sin\beta\cos\beta v'' - \underline{Te_A\phi\cos\beta - EB_2\beta'\phi'\sin\beta}]'' - (Tw')' - \underline{(\Omega^2 mxe\phi\cos\beta)'} + m(\ddot{w} + e\ddot{\phi}\cos\beta) = L_z + \underline{(Te_A\sin\beta)''} + \underline{(\Omega^2 mxe\sin\beta)'} \quad (23)$$

$$[(EI_2 - EI_1)\sin\beta\cos\beta w'' + (EI_1\sin^2\beta + EI_2\cos^2\beta)v'' + \underline{Te_A\phi\sin\beta - EB_2\beta'\phi'\cos\beta}]'' - (Tv')' + \underline{(\Omega^2 mxe\phi\sin\beta)'} + \underline{\Omega^2 me\phi\sin\beta} + m(\ddot{v} - e\ddot{\phi}\sin\beta) - \Omega^2 mv = L_y + \underline{(Te_A\cos\beta)''} + \underline{(\Omega^2 mxe\cos\beta)'} + \underline{\Omega^2 m(e_o + e\cos\beta)} \quad (24)$$

In these equations, the terms that are not included in previous theories have been underlined. (It should be noted that ref. 18 suggests the existence of the centrifugal coupling terms $\Omega^2 mxew'$ and $(\Omega^2 mxe\phi)'$ for the case of a blade with $\beta=0$.) Many of these new terms are coupling-type terms which are associated with the centrifugal forces. A number of the new terms take the forms of lateral and twisting loadings which tend to deflect the blade even in the absence of externally applied loads; because of this fact they have been written on the right-hand sides along with the applied loads L_y, L_z, and M.

Importance of coupling forms.—It is beyond the scope of this paper to make a complete evaluation of the magnitude of each of the coupling terms and their influence on such phenomena as, say, blade vibration. A rough idea of their importance can be gathered by analyzing each term in detail and comparing them to other terms of known importance. As an example, consider $(Te_A\phi\cos\beta)''$ in equation (23). If, for simplicity in the consideration, e_A and m are considered independent of x, and if $\beta=0$, then this term would become on expansion

$$-\Omega^2 me_A\phi + 2T'(e_A\phi)' + T(e_A\phi)''$$

These terms may now be compared with other terms of known importance. Thus, if $e_A\phi$ is interpreted as a deflection, then the last two terms of this expansion are seen to be exactly comparable to the expansion of the well-known and important term $(Tw')' = T'w' + Tw''$. Also the first term $-\Omega^2 me_A\phi$ is directly comparable with the coupling term of established importance in the consideration of coupled bending-torsion of vibrating beams, namely, $\omega^2 me\phi$. A similar consideration may be given each of the other new terms in the final equations. The examples to be presented later will also give an indication of the importance of some of the terms.

Boundary conditions.—Since the problem is, of course, a boundary-value problem, some mention of the associated boundary conditions should be made. The most general case involves ten boundary conditions—two conditions associated with equation (22), and four each for equations (23) and (24). These conditions all evolve from the type of constraint that is imposed on the ends of the beam on the displacements v, w, and ϕ, the moments M_y and M_z (eqs. (13) and (14)), the torque Q (eq. (8)), and the shears V_y and V_z which are defined by equations (16b) and (16c). For a completely fixed end, the boundary conditions would be

$$v = w = \phi = v' = w' = 0$$

For a free end, the conditions would be

$$Q = M_y = M_z = V_y = V_z = 0$$

In this case, the alternate choice of $M_1 = M_2 = 0$ (see eqs. (6) and (7)) may be used instead of $M_y = M_z = 0$.

For the present system, an end cannot be referred to simply as pin-ended; care must be taken to specify the number and directions of pins present. For example, an end may have a pin which runs parallel to the y-axis but may be fixed as regards displacements v and ϕ. In this example, the moment M_y has been relaxed and the boundary conditions become

$$v = w = v' = \phi = M_y = 0$$

Other pin-ended conditions follow in a similar fashion.

Elastically restrained ends may be handled in a manner similar to that used in the usual treatment of beams, except that the direction of the restraint must be properly taken into account.

Subcases of the general theory.—In actual applications, several special subcases of the present theory are frequently

encountered. Three of these subcases are described as follows:

Case I: The built-in twist is zero, $\beta=0$.

Case II: Bending in two directions without torsion, $\phi=0$.

Case III: Torsion only, $v=w=0$.

The equations of motion which result when the theory is reduced to these special cases are as follows:

For case I, $\beta=0$,

$$-[(GJ+Tk_A^2)\phi']'-\underline{Te_Aw''}+\Omega^2mxew'+\Omega^2m(k_{m2}^2-k_{m1}^2+\underline{ee_o})\phi+mk_m^2\ddot{\phi}+me\ddot{w}=M \quad (25)$$

$$(EI_1w''-Te_A\phi)''-(Tw')'-(\Omega^2mxe\phi)'+m(\ddot{w}+e\ddot{\phi})=L_z \quad (26)$$

$$(EI_2v'')''-(Tv')'-\Omega^2mv+m\ddot{v}=L_y-\underline{(Te_A)''}+(\Omega^2mxe)'+\Omega^2\underline{m(e_o}+e) \quad (27)$$

For case II, $\phi=0$,

$$[(EI_1\cos^2\beta+EI_2\sin^2\beta)w''+(EI_2-EI_1)\sin\beta\cos\beta\,v'']''-(Tw')'+m\ddot{w}=L_z+(Te_A\sin\beta)''+(\Omega^2mxe\sin\beta)' \quad (28)$$

$$[(EI_2-EI_1)\sin\beta\cos\beta\,w''+(EI_1\sin^2\beta+EI_2\cos^2\beta)v'']''-(Tv')'-\Omega^2mv+m\ddot{v}=L_y+(Te_A\cos\beta)''+(\Omega^2mxe\cos\beta)'+\Omega^2m(e_o+e\cos\beta) \quad (29)$$

For case III, $v=w=0$,

$$-\{[GJ+Tk_A^2+EB_1(\beta')^2]\phi'\}'+\Omega^2m[(k_{m2}^2-k_{m1}^2)\cos2\beta+ee_o\cos\beta]\phi+mk_m^2\ddot{\phi}=M+(Tk_A^2\beta')'-\Omega^2m[(k_{m2}^2-k_{m1}^2)\sin\beta\cos\beta+ee_o\sin\beta] \quad (30)$$

ASSOCIATED ENERGY EQUATION

As a check on the derivation presented herein, the differential equations of equilibrium were derived by a completely different approach that involves energy principles. In this energy approach the strain energy of deformation, in which the longitudinal strains were arrived at in a different manner than that presented herein, and the work performed by all the forces present were considered. The equation for total potential energy of the system is, of course, closely allied to the differential equations and is of intrinsic value in the treatment of the problem of the present paper from an energy standpoint. For completeness, the equation is presented here without derivation. If U denotes the total strain energy and V represents the work performed by the centrifugal body forces and the applied loading, then

$$U-V=\frac{1}{2}\int_0^R\{EI_1(v''\sin\beta-w''\cos\beta)^2+EI_2(v''\cos\beta+w''\sin\beta)^2+[GJ+EB_1(\beta')^2](\phi')^2-2EB_2(v''\cos\beta+w''\sin\beta)\beta'\phi'\}dx-\int_0^R\Bigg(T\Big\{-\frac{1}{2}[(v')^2+(w')^2]+e_A(v''\cos\beta+w''\sin\beta)-e_A\phi(v''\sin\beta-w''\cos\beta)-k_A^2\Big[\frac{1}{2}(\phi')^2+\beta'\phi'\Big]\Big\}+\Omega^2m\Big\{xe[-(v'\cos\beta+w'\sin\beta)+\phi(v'\sin\beta-w'\cos\beta)]+\frac{1}{2}v^2+(e\cos\beta+e_o-e\phi\sin\beta)v+[-(k_{m2}^2-k_{m1}^2)\sin\beta\cos\beta-ee_o\sin\beta]\phi-\frac{1}{2}[(k_{m2}^2-k_{m1}^2)\cos2\beta+ee_o\cos\beta]\phi^2\Big\}+p_yv+p_zw+q\phi\Bigg)dx \quad (31)$$

where p_y, p_z, and q are the applied loadings considered in a static sense. Application of the minimum variational principles to this expression yields differential equations which are the same as those given by equations (22), (23), and (24) when ϕ, v, and w are not time dependent. The variation also gives the boundary conditions on moments, shears, and torques that are for stipulated geometrical conditions at the ends of the beam and are given in the section entitled "Boundary Conditions". The differential equations applicable when time dependent motion is considered may now be obtained by writing the loadings p_y, p_z, and q as the sum of the applied loadings and vibratory inertia loads (as obtained by D'Alembert's principle); specifically,

$$\left.\begin{aligned}p_y&=L_y-m(\ddot{v}-e\ddot{\phi}\sin\beta)\\p_z&=L_z-m(\ddot{w}+e\ddot{\phi}\cos\beta)\\q&=M+me(\ddot{v}\sin\beta-\ddot{w}\cos\beta)-mk_m^2\ddot{\phi}\end{aligned}\right\} \quad (32)$$

The substitution of these loadings into the differential equations obtained by the variational process then gives equations identical to equations (22), (23), and (24).

METHOD OF SOLUTION AND EXAMPLES

The general differential equations of this paper cannot be solved exactly, and it is therefore necessary to resort to some approximate means. Two means, which differ in manipulations but which yield equivalent results, will be considered here—one is a modified Galerkin type procedure, the other a Rayleigh-Ritz procedure.

In the modified Galerkin procedure, the displacements are assumed to be expressed in finite series of known functions as follows:

$$\left.\begin{aligned}\phi&=a_1\phi_1+a_2\phi_2+\ \ldots\ a_p\phi_p\\w&=b_1w_1+b_2w_2+\ \ldots\ b_qw_q\\v&=c_1v_1+c_2v_2+\ \ldots\ c_rv_r\end{aligned}\right\} \quad (33)$$

where a_n, b_n, and c_n are unknown coefficients, which may be time dependent, and ϕ_n, w_n, and v_n are chosen modal functions which satisfy the geometrical boundary conditions of the problem. A set of linear simultaneous equations which allow the evaluation of the unknown coefficients is now

formed through application of the following equations:

$$\int_0^R \phi_n D_1(\phi,w,v)\,dx+Q\phi_n\Big]_0^R=0 \qquad (n=1,2,3,\ldots p) \tag{34a}$$

$$\int_0^R w_n D_2(\phi,w,v)\,dx+M_y w_n'\Big]_0^R+V_z w_n\Big]_0^R=0 \qquad (n=1,2,3,\ldots q) \tag{34b}$$

$$\int_0^R v_n D_3(\phi,w,v)\,dx+M_z v_n'\Big]_0^R+V_y v_n\Big]_0^R=0 \qquad (n=1,2,3,\ldots r) \tag{34c}$$

where $D_1(\phi,w,v)$, $D_2(\phi,w,v)$, and $D_3(\phi,w,v)$ denote, respectively, equations (22), (23), and (24) with all the right-hand terms transferred to the left-hand side; Q, M_y, and M_z are given by equations (8), (13), and (14); and V_z and V_y are found from equations (16b) and (16c). For static or other externally imposed loading conditions, the set of equations formed by equations (34) will be nonhomogeneous; the solution for the unknown coefficients and, hence, the displacements then proceeds by ordinary means. For a characteristic-value problem, such as free vibrations, the set of equations will be homogeneous, and the vanishing determinant will yield the characteristic frequencies.

This procedure is called a modified Galerkin procedure because of the presence of the boundary terms in equations (34). In general, it would be very difficult to choose modal functions in equations (33) so that both the geometric and "force" (shear, moment, torque) boundary conditions are satisfied, which is necessary in the usual Galerkin approach. Therefore, the force boundary terms are added in equations (34), and, thus, the stipulations on the chosen modal functions are relaxed so that only the geometric conditions need be satisfied. It should be mentioned that in actual applications these force boundary conditions do not have to be evaluated, since they can always be cancelled by integrating certain of the terms of the integrals by parts. A justification of this procedure can be obtained from the Rayleigh-Ritz procedure.

In this Rayleigh-Ritz approach the displacements are expanded in series as before (see eqs. (33)), with the same requirement on the geometric boundary conditions. These expansions are substituted into the energy equation (31), and a minimization is then made with respect to the unknown coefficients; that is,

$$\left.\begin{aligned} \frac{\partial(U-V)}{\partial a_n}&=0 \qquad (n=1,2,\ldots p)\\ \frac{\partial(U-V)}{\partial b_n}&=0 \qquad (n=1,2,\ldots q)\\ \frac{\partial(U-V)}{\partial c_n}&=0 \qquad (n=1,2,\ldots r) \end{aligned}\right\} \tag{35}$$

The resulting equations will be identical with those of equations (34). As a matter of fact, equations (35) may be used to prove the validity of equations (34) (through appropriate integration by parts) and thus to show that the two procedures outlined here are really equivalent. Because of the confusion that often arises about boundary conditions when the Galerkin process is applied, the safest procedure is to use the Rayleigh-Ritz approach.

Two examples are now given to show the application of the two procedures discussed and to show further the importance of some of the coupling terms.

EXAMPLE 1

In example 1, it is desired to determine the natural frequencies of a rotating cantilever blade having zero initial twist or blade angle of attack ($\beta=0$) and with $v=0$. The Rayleigh-Ritz procedure will be used. Assume that the displacements ϕ and w are given as follows:

$$\left.\begin{aligned} \phi&=a_1\phi_1+a_2\phi_2+a_3\phi_3\\ w&=b_1w_1+b_2w_2+b_3w_3 \end{aligned}\right\} \tag{36}$$

where ϕ_n and w_n are the natural uncoupled modes of the nonrotating beam in torsion and bending, respectively, and are expressed in terms of a unit tip displacement. Equations (36) are substituted into equation (31) with $v=\beta=0$, and a minimization is made with respect to a_n and b_n, and then use is made of equations (32), with the applied loadings $L_y=L_z=M=0$. The resulting equations are then reduced as follows. First, the relations which apply to uncoupled vibrations are used, namely

$$\left.\begin{aligned} \int_0^R mw_m w_n\,dx&=0 && (m\neq n)\\ &=M_n && (m=n)\\ \int_0^R EI_1 w_m''w_n''\,dx&=0 && (m\neq n)\\ &=\omega_n^2\int_0^R mw_n^2\,dx && (m=n)\\ &=\omega_n^2M_n\\ \int_0^R mk_A^2\phi_m\phi_n\,dx&=0 && (m\neq n)\\ &=N_n && (m=n)\\ \int_0^R GJ\phi_m'\phi_n'\,dx&=0 && (m\neq n)\\ &=\mu_n^2\int_0^R mk_m^2\phi_n^2 && (m=n)\\ &=\mu_n^2N_n \end{aligned}\right\} \tag{37}$$

where ω_n and μ_n are the natural circular frequencies of the uncoupled bending and torsion modes, respectively. Second, the constant terms are dropped, since they apply to static deformation of the blade. And third, motion representative of simple harmonic motion is considered by setting

$$a_n=\bar{a}_n \sin \omega t$$

$$b_n=\bar{b}_n \sin \omega t$$

The final equations will be homogeneous, and the vanishing of the determinant of the $\bar{a}_n$ and $\bar{b}_n$ coefficients will define the natural coupled rotating frequencies. This determinant is

$$\begin{bmatrix}
(\omega_1^2-\omega^2)M_1+A_{11} & A_{12} & A_{13} & -B_{11}-\omega^2C_{11}+\Omega^2D_{11} & -B_{21}-\omega^2C_{21}+\Omega^2D_{21} & -B_{31}-\omega^2C_{31}+\Omega^2D_{31} \\
A_{12} & (\omega_2^2-\omega^2)M_2+A_{22} & A_{23} & -B_{12}-\omega^2C_{12}+\Omega^2D_{12} & -B_{22}-\omega^2C_{22}+\Omega^2D_{22} & -B_{32}-\omega^2C_{32}+\Omega^2D_{32} \\
A_{13} & A_{23} & (\omega_3^2-\omega^2)M_3+A_{33} & -B_{13}-\omega^2C_{13}+\Omega^2D_{13} & -B_{23}-\omega^2C_{23}+\Omega^2D_{23} & -B_{33}-\omega^2C_{33}+\Omega^2D_{33} \\
-B_{11}-\omega^2C_{11}+\Omega^2D_{11} & -B_{12}-\omega^2C_{12}+\Omega^2D_{12} & -B_{13}-\omega^2C_{13}+\Omega^2D_{13} & (\mu_1^2-\omega^2)N_1+E_{11}+\Omega^2F_{11} & E_{12}+\Omega^2F_{12} & E_{13}+\Omega^2F_{13} \\
-B_{21}-\omega^2C_{21}+\Omega^2D_{21} & -B_{22}-\omega^2C_{22}+\Omega^2D_{22} & -B_{23}-\omega^2C_{23}+\Omega^2D_{23} & E_{12}+\Omega^2F_{12} & (\mu_2^2-\omega^2)N_2+E_{22}+\Omega^2F_{22} & E_{23}+\Omega^2F_{23} \\
-B_{31}-\omega^2C_{31}+\Omega^2D_{31} & -B_{32}-\omega^2C_{32}+\Omega^2D_{32} & -B_{33}-\omega^2C_{33}+\Omega^2D_{33} & E_{13}+\Omega^2F_{13} & E_{23}+\Omega^2F_{23} & (\mu_3^2-\omega^2)N_3+E_{33}+\Omega^2F_{33}
\end{bmatrix}=0$$

where the coefficients are

$$\left.\begin{aligned}
M_n &= \int_0^R m w_n^2 dx \\
N_n &= \int_0^R m k_m^2 \phi_n^2 dx \\
A_{mn} &= \int_0^R T w_m' w_n' dx \\
B_{mn} &= \int_0^R T e_A \phi_m w_n'' dx \\
C_{mn} &= \int_0^R m e \phi_m w_n dx \\
D_{mn} &= \int_0^R m x e \phi_m w_n' dx \\
E_{mn} &= \int_0^R T k_A^2 \phi_m \phi_n dx \\
F_{mn} &= \int_0^R m (k_{m2}^2 - k_{m1}^2 + e e_o) \phi_m \phi_n dx
\end{aligned}\right\} \qquad (38)$$

No numerical evaluation of this example is made, but the importance of some of the new coupling terms of the present theory is realized by comparing the associated coupling terms which appear in the determinant. For example, $\Omega^2 D_{11}$, which is new, may be compared with $\omega^2 C_{11}$, a conventional term of established importance. The frequencies Ω^2 and ω^2 may be of the same order of magnitude; the factors under the integral are the same except for w_1 and xw_1'. These may be shown to be of the same order of magnitude, however, and so both coupling terms are comparable in magnitude. This is another indication, therefore, that the new coupling terms are of significance in the treatment of rotating blades.

EXAMPLE 2

The case treated for example 2 is a uniform blade with an offset mass at the tip and with β, v, e_A, and e_o equal 0. (See top sketch in fig. 7.) This system may be regarded as having a behavior similar to an actual helicopter blade which is heavily loaded along the leading edges, as depicted in the lower sketch of figure 7. An approximation to the first two natural frequencies will be found by the modified Galerkin procedure. The differential

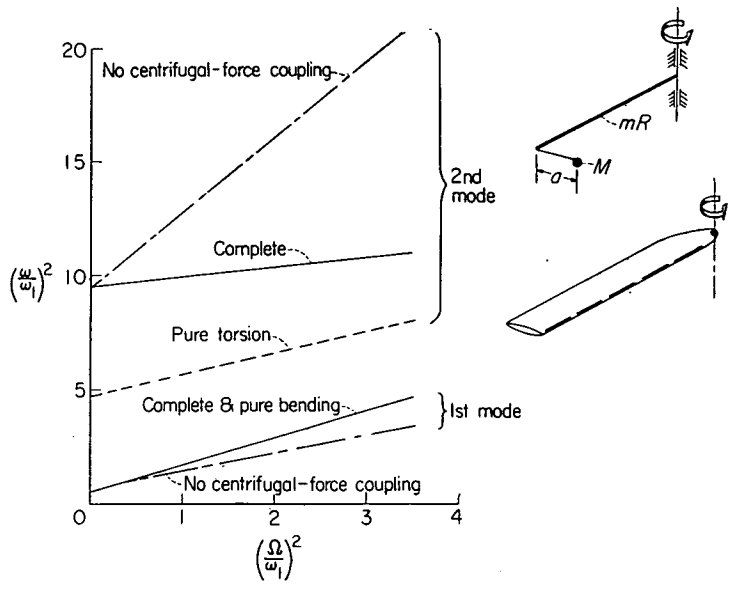


FIGURE 7.—Natural frequencies of example 2 showing the importance of centrifugal-force coupling.

equations for shear, moment, torque, and tension (eqs. (25), 26), (16), (13), and (8) with $\beta=v=e_A=e_o=0$) applicable here are

$$\left.\begin{aligned}-[(GJ+Tk_A^2)\phi']'+\Omega^2 mxew'+\Omega^2 m(k_{m2}^2-k_{m1}^2)\phi-\omega^2(mew+mk_m^2\phi)=0\\ (EI_1w'')''-(Tw')'-(\Omega^2 mxe\phi)'-\omega^2(mw+me\phi)=0\end{aligned}\right\} \quad (39)$$

$$\left.\begin{aligned}M_y&=EI_1w''\\ V_z&=-(EI_1w'')'+Tw'+\Omega^2 mex\phi\\ Q&=(GJ+Tk_A^2)\phi'\\ T&=\int_x^R \Omega^2 mx\,dx+\Omega^2 MR\end{aligned}\right\} \quad (40)$$

In these equations the mass per unit length m should be interpreted to apply to both the distributed mass of the beam and to the concentrated offset mass. This concentrated mass can be handled, for example, by imagining the mass to be distributed over an infinitesimal length, say λ, with intensity M/λ, then to perform the integrations of the Galerkin process as though all quantities involved in the integrations are uniform in this interval, and finally to squeeze the interval down to zero length. An equivalent procedure is to take the concentrated mass into account through means of the Dirac delta function.

With this in mind, equations (39) and (40) are substituted into equations (34a) and (34b); the terms $\phi_n(GJ+Tk_A^2)\phi'$ and $w_n[-(Tw')'-(\Omega^2 mxe\phi)']$ are integrated once by parts, the term $w_n(EI_1w'')''$ is integrated twice by parts, the boundary terms cancel, and the results are the following two equations:

$$\int_0^R (GJ+Tk_A^2)\phi'\phi_n'dx+\int_0^R [\underline{\Omega^2 mxew'}+\Omega^2 m(k_{m2}^2-k_{m1}^2)\phi-\omega^2(mew+mk_m^2\phi)]\phi_n dx=0 \quad (41)$$

$$\int_0^R EI_1w''w_n''dx+\int_0^R (Tw'+\underline{\Omega^2 mxe\phi})w_n'dx-\omega^2\int_0^R (mw+me\phi)w_n dx=0 \quad (42)$$

Approximations to the displacements are now chosen as

$$\left.\begin{aligned}\phi&=\bar{a}_1\phi_1\\ w&=\bar{b}_1w_1\end{aligned}\right\} \quad (43)$$

where ϕ_1 and w_1 are the fundamental uncoupled vibration modes of the beam without the tip mass, in torsion and bending, respectively, and each is given in terms of a unit tip displacement; these functions satisfy the equations

$$\left.\begin{aligned}\int_0^R GJ(\phi_1')^2dx&=\mu_1^2\int_0^R mk_m^2\phi_1^2dx\\ &=\mu_1^2 mk_m^2\frac{R}{2}\qquad\left(\mu_1=\frac{\pi}{2}\sqrt{\frac{GJ}{mk_m^2R^2}}\right)\\ \int_0^R EI_1(w_1'')^2dx&=\omega_1^2\int_0^R mw_1^2dx\\ &=\omega_1^2\frac{mR}{4}\qquad\left(\omega_1=3.46\sqrt{\frac{EI_1}{mR^4}}\right)\end{aligned}\right\} \quad (44)$$

where m refers only to the mass per unit length of the beam. Equations (43) are now substituted into equations (41) and (42), use is made of equations (44) and the equation for tension (applicable here) $T=\frac{1}{2}\Omega^2 m(R^2-x^2)+\Omega^2 MR$, and the integrations are performed with due cognizance being given the offset tip mass; the values found for the integrals are as follows:

$$\left.\begin{aligned}&\int_0^R GJ\phi_1^2dx=\mu_1^2 mk_m^2\frac{R}{2}\\ &\int_0^R \Omega^2 mxew_1'\phi_1dx=1.38\Omega^2 Ma\\ &\int_0^R \Omega^2 m(k_{m2}^2-k_{m1}^2)\phi_1^2dx=\Omega^2 Ma^2\\ &\int_0^R mew_1\phi_1dx=Ma\\ &\int_0^R mk_m^2\phi_1^2dx=mk_m^2\frac{R}{2}+Ma^2\\ &\int_0^R EI_1(w_1'')^2dx=\omega_1^2\frac{mR}{4}\\ &\int_0^R T(w_1')^2dx\approx\Omega^2\frac{4}{15}\left(mR+\frac{4}{3}M\right)\\ &\int_0^R mw_1^2dx=\frac{mR}{4}+M\end{aligned}\right\} \quad (45)$$

(The contribution of Tk_A^2 is found negligible in the first integral.) The final equations are given now in nondimensional form

$$\left[\frac{\mu_1^2}{\omega_1^2}\frac{mRk_m^2}{2Ma^2}+\frac{\Omega^2}{\omega_1^2}-\frac{\omega^2}{\omega_1^2}\left(\frac{mRk_m^2}{2Ma^2}+1\right)\right]\bar{a}_1+\left(\underline{1.38\frac{\Omega^2}{\omega_1^2}}-\frac{\omega^2}{\omega_1^2}\right)\frac{\bar{b}_1}{a}=0$$

$$\left(\underline{1.38\frac{\Omega^2}{\omega_1^2}}-\frac{\omega^2}{\omega_1^2}\right)\bar{a}_1+\left[\frac{mR}{4M}+\frac{\Omega^2}{\omega_1^2}\left(\frac{4}{3}+\frac{4mR}{15M}\right)-\frac{\omega^2}{\omega_1^2}\left(1+\frac{mR}{4M}\right)\right]\frac{\bar{b}_1}{a}=0$$

The vanishing of the determinant of these equations will yield the natural frequencies. Specific evaluation has been made for the following values:

$$M=\frac{mR}{4}$$

$$\frac{R}{a}=4$$

$$\frac{k_m}{a}=\sqrt{0.02}$$

$$\frac{\mu_1^2}{\omega_1^2}=0.152\frac{R^2}{k_m^2}$$

and the results are shown in figure 7. Results are shown for three conditions: (a) for vibration of the beam with offset mass in pure bending or pure torsion, (b) for vibration in the conventional coupled sense but with no centrifugal-force coupling (that is, the underlined terms of the equations of this example are omitted), and (c) for vibration with all coupling terms considered (the curves labeled complete in fig. 7). It may be seen that the inclusion of centrifugal-force coupling, which is new in this paper, has a very pronounced influence on the vibration characteristics. In fact, this centrifugal-force coupling seems to be of the same general strength as the conventional offset mass coupling normally considered.

CONCLUDING REMARKS

The differential equations of deformation of a twisted rotating blade under arbitrary loading have been derived. A special feature of the analysis is the consideration of the noncoincidence of the tension, mass, and elastic axes, whereby coupling is allowed to occur in a more general form than heretofore considered. This theory can therefore be used to solve problems in which these effects are significant and to evaluate the less complete theories which perhaps are more easily applied.

The aerodynamic loading considered was left in general form. It can be replaced, however, by whatever terms are appropriate for the case being treated. If these aerodynamic forces are taken as zero, then the loadings for free vibration result.

Because of its usefulness, the energy equation for blade deformation is also presented. Two methods of solution are discussed: one is a modified Galerkin process which makes use of the differential equations; the other is a Rayleigh-Ritz procedure which makes use of the energy expression. Two examples are presented which illustrate the application of both of these procedures.

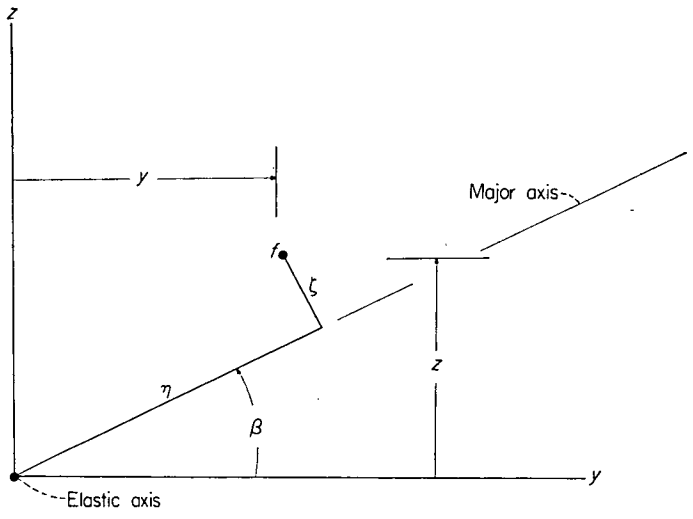
A discussion of the importance of the new coupling terms that arise is made and their significance is further brought out by the examples. The indications are that the centrifugal-force coupling may be as important as the mass coupling that is normally considered in beam analysis and therefore should be included as a regular part in the treatment of rotating blades.

LANGLEY AERONAUTICAL LABORATORY,
NATIONAL ADVISORY COMITTEE FOR AERONAUTICS,
LANGLEY FIELD, VA., *October 5, 1956.*

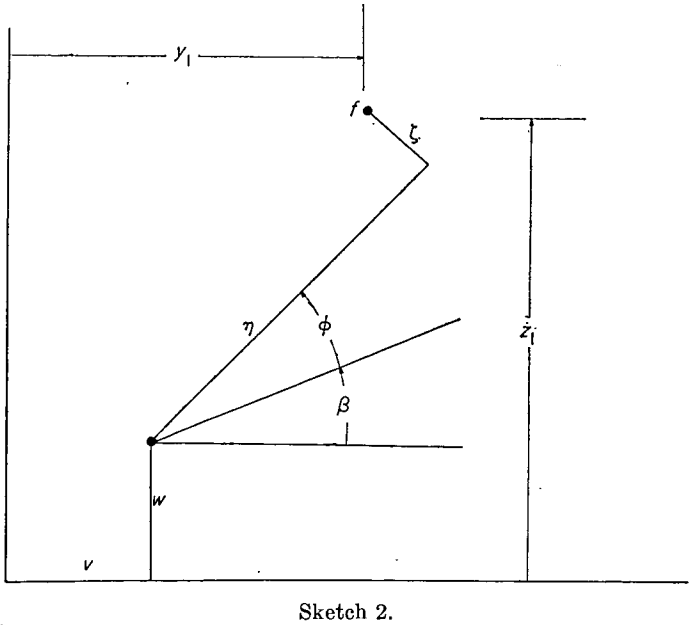
APPENDIX A

DERIVATION OF LONGITUDINAL STRAINS

In this appendix the equation is derived for the longitudinal strain that is developed when a twisted beam undergoes both lateral and twisting deformations. Consider an imaginary plane to cut through the beam perpendicular to the elastic axis; the location of a fiber f of the cross section, both before and after the deformation, may then be given according to sketches 1 and 2. The x-axis is normal to the paper and is made coincident with the undeformed position of the elastic axis. In terms of the distance η along the major axis, the distance ζ perpendicular to this axis, and the built-in twist β, the initial y- and z-positions of the fiber



Sketch 1.



Sketch 2.

and the rate of change of these positions with respect to the x are

$$\left.\begin{aligned} y &= \eta \cos\beta - \zeta \sin\beta \\ z &= \eta \sin\beta + \zeta \cos\beta \end{aligned}\right\} \tag{A1}$$

$$\left.\begin{aligned} y' &= -\eta\beta' \sin\beta - \zeta\beta' \cos\beta = -\beta' z \\ z' &= \eta\beta' \cos\beta - \zeta\beta' \sin\beta = \beta' y \end{aligned}\right\} \tag{A2}$$

Now consider beam displacements to occur so that the point of intersection of the elastic axis and the cutting plane moves the distances u, v, and w in the directions of x, y, and z, respectively, and so that the cutting plane remains perpendicular to the elastic axis and rotates around it by an angle ϕ. Then if the usual small-angle assumptions that $\cos(\beta+\phi) = \cos\beta - \phi\sin\beta$ and $\sin(\beta+\phi) = \sin\beta + \phi\cos\beta$ are made, the new position of the fiber is defined by the following equations:

$$\left.\begin{aligned} x_1 &= x + u - v'(y_1 - v) - w'(z_1 - w) \\ &= x + \mu - v'y - w'z \\ y_1 &= v + \eta(\cos\beta - \phi\sin\beta) - \zeta(\sin\beta + \phi\cos\beta) = v + y - z\phi \\ z_1 &= w + \eta(\sin\beta + \phi\cos\beta) + \zeta(\cos\beta - \phi\sin\beta) = w + z + y\phi \end{aligned}\right\} \tag{A3}$$

and the derivatives of x_1, y_1, and z_1 with respect to x are given as follows:

$$\left.\begin{aligned} x_1' &= 1 + u' - v''y + v'\beta' z - w''z - w'\beta' y \\ &= 1 + u' - y(v'' + \beta' w') - z(w'' - \beta' v') \\ y_1' &= v' - \beta' z - \beta' y\phi - z\phi' = v' - y\beta'\phi - z(\beta' + \phi') \\ z_1' &= w' + \beta' y - \beta' z\phi + y\phi' = w' + y(\beta' + \phi') - z\beta'\phi \end{aligned}\right\} \tag{A4}$$

The longitudinal strain that is developed in a fiber may be found from these equations by considering the amount an elemental fiber of length ds changes in length as a result of deformation. In terms of the differential components of length in the x-, y-, and z-directions, the final length ds_1 of a fiber is given by the following equation:

$$ds_1^2 = dx_1^2 + dy_1^2 + dz_1^2 \tag{A5}$$

Thus

$$\left(\frac{ds_1}{dx}\right)^2 = (x_1')^2 + (y_1')^2 + (z_1')^2 \tag{A6}$$

which becomes with the use of equations (A4)

$$\left(\frac{ds_1}{dx}\right)^2=1+2\,[u'-y(v''+\beta'w')-z(w''-\beta'v')]+z^2\beta'^2-2z\beta'(v'-y\beta'\phi-z\phi')+y^2\beta'^2+2y\beta'(w'+y\phi'-z\beta'\phi) \quad (A7)$$

or

$$\frac{ds_1}{dx}=\{1+(y^2+z^2)(\beta')^2+2\,[u'-yv''-zw''+(y^2+z^2)\beta'\phi']\}^{1/2} \quad (A8)$$

Now the analogous equation for the original length ds may be determined directly from equation (A8) by letting $u=v=w=\phi=0$. Thus

$$\frac{ds}{dx}=[1+(y^2+z^2)(\beta')^2]^{1/2} \quad (A9)$$

The tensile strain in the fiber can now be written

$$\epsilon=\frac{ds_1-ds}{ds}$$

$$=\frac{ds_1}{ds}-1$$

$$=\left\{1+\left[\frac{2}{1+(y^2+z^2)(\beta')^2}\right][u'-yv''-zw''+(y^2+z^2)\beta'\phi']\right\}^{1/2}-1$$

$$=\left[\frac{1}{1+(y^2+z^2)\beta'^2}\right][u'-yv''-zw''+(y^2+z^2)\beta'\phi'] \quad (A10)$$

Now with $(y^2+z^2)(\beta')^2\ll 1$ (say less than 0.03 to 0.04, which is generally the case), then

$$\epsilon=u'-yv''-zw''+(y^2+z^2)\beta'\phi' \quad (A11)$$

Use is now made of equations (A1) in order to express the strain in terms of the cross-sectional coordinates η and ζ as follows:

$$\epsilon=u'-\eta(v''\cos\beta+w''\sin\beta)-\zeta(-v''\sin\beta+w''\cos\beta)+(\eta^2+\zeta^2)\beta'\phi' \quad (A12)$$

It is convenient now to eliminate the strain component u'; this is done by making use of the equilibrium condition that the integral of the longitudinal stress over the cross section must be equal to the total tension. Thus, with the assumption that the cross section is symmetrical about the major principle axis, the following equation applies:

$$T=E\int_{\eta_{le}}^{\eta_{te}}\int_{-t/2}^{t/2}\epsilon\,d\zeta\,d\eta$$

$$=E\int_{\eta_{le}}^{\eta_{te}}\int_{-t/2}^{t/2}[u'-\eta(v''\cos\beta+w''\sin\beta)-\zeta(-v''\sin\beta+w''\cos\beta)+(\eta^2+\zeta^2)\beta'\phi']d\zeta\,d\eta \quad (A13)$$

526597—60——14

or

$$T=E[Au'-Ae_A(v''\cos\beta+w''\sin\beta)+Ak_A^2\beta'\phi'] \quad (A14)$$

This equation yields

$$u'=\frac{T}{EA}+e_A(v''\cos\beta+w''\sin\beta)+k_A^2\beta'\phi' \quad (A15)$$

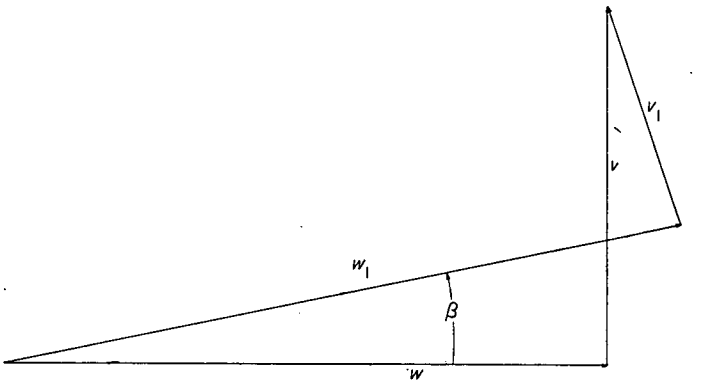
If T/EA is denoted by the tensile strain ϵ_T, then equation (A15) combined with equation (A12) yields

$$\epsilon=\epsilon_T+(e_A-\eta)(v''\cos\beta+w''\sin\beta)+\zeta(v''\sin\beta-w''\cos\beta)+(\eta^2+\zeta^2-k_A^2)\beta'\phi' \quad (A16)$$

which is the complete expression for the strain of any fiber in the cross section.

EXPRESSION FOR STRAIN IN TERMS OF DISPLACEMENTS IN AND NORMAL TO THE BLADE CHORD

Because of apparent anomalies that have arisen in the past, it is of interest to show the development of the strain in terms of displacements in and normal to the blade chord. These displacements have been used by some investigators and are shown in relation to the displacements of this paper in sketch 3.



Sketch 3.

These displacements are related according to the equations

$$\left.\begin{aligned}v&=v_1\cos\beta-w_1\sin\beta\\ w&=v_1\sin\beta+w_1\cos\beta\end{aligned}\right\} \quad (A17)$$

If two derivatives of these equations are taken, and due care is given the fact that β may vary with x, then the following combination of these derivatives may be found:

$$\left.\begin{aligned}v''\cos\beta+w''\sin\beta&=v_1''-2\beta'w_1'-\beta''w_1-(\beta')^2v_1\\ -v''\sin\beta+w''\cos\beta&=w_1''+2\beta'v_1'+\beta''v_1-(\beta')^2w_1\end{aligned}\right\} \quad (A18)$$

If these expressions are now substituted in equation (A16),

then the equation for strain becomes

$$\epsilon=\epsilon_T+(e_A-\eta)[v_1''-2\beta' w_1'-\beta'' w_1-(\beta')^2 v_1]-$$
$$\zeta[w_1''+2\beta' v_1'+\beta'' v_1-(\beta')^2 w_1]+(\eta^2+\zeta^2-k_A^2)\beta'\phi' \tag{A19}$$

The interesting fact to be noted here with respect to v_1 and w_1 is that the strain is not proportional only to the derivatives v_1'' and w_1'', as might first be supposed, but rather to additional terms which involve the rate of change of initial twist.

This observation has some significance. If the analysis of this paper had been carried through in terms of displacements v_1 and w_1, then the moments and all the results would be in terms of the group of terms appearing on the right-hand side of equations (A18), and the final result would be in agreement with the results presented in reference 11. This consideration indicates that the treatment in reference 1 may be subject to correction, since the assumption is made in this reference that the moments are proportional to v_1'' and w_1''. Evidently this assumption is not valid when the beam has a finite rate of change of initial twist.

STRAIN WHEN ϕ IS NOT SMALL

The preceding derivation was made on the assumption that the displacements u, v, w, and ϕ were small, and a linear equation for strain results. An interesting observation may be made, however, for the case of $v=w=0$, but with large displacements in ϕ, such that nonlinear effects are present. Thus, if the derivation is repeated with ϕ considered large, and with $v=w=0$, then equation (A11) would take the form

$$\epsilon=u'+(y^2+z^2)\left[\beta'\phi'+\frac{1}{2}(\phi')^2\right]$$
$$=u'+(\eta^2+\zeta^2)\left[\beta'\phi'+\frac{1}{2}(\phi')^2\right] \tag{A20}$$

The strain component u' is now handled as before, and the equation for strain becomes

$$\epsilon=\epsilon_T+(\eta^2+\zeta^2-k_A^2)\left[\beta'\phi'+\frac{1}{2}(\phi')^2\right] \tag{A21}$$

This equation may be used to demonstrate the fact pointed out in reference 19 that pretwisted blades may possess a torsional instability. Thus if use is made of equation (5), and the stress is based on equation (A21), then the following equation for internal elastic resisting torque results:

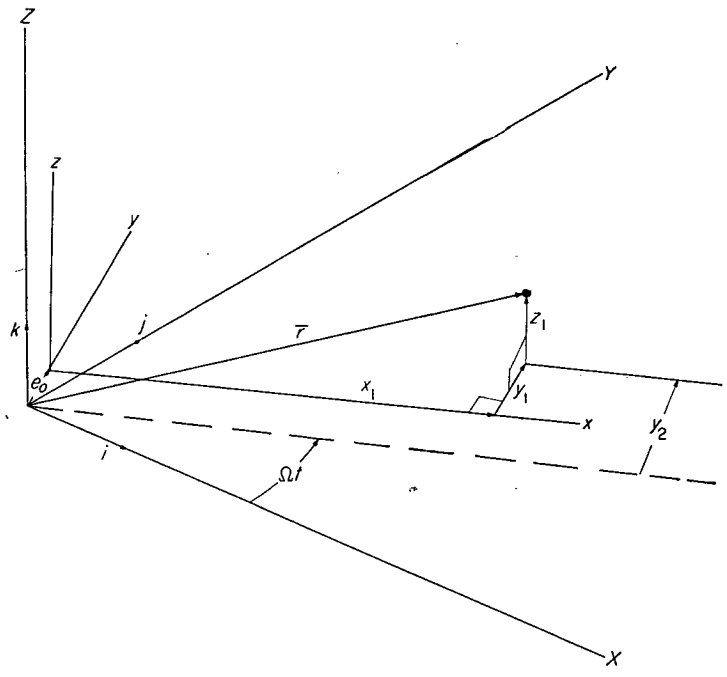
$$Q=GJ\phi'+Tk_A^2(\beta'+\phi')+EB_1\left[\beta'\phi'+\frac{1}{2}(\phi')^2\right](\beta'+\phi')$$
$$=GJ\phi'+Tk_A^2(\beta'+\phi')+\frac{EB_1}{2}[(\beta'+\phi')^3-(\beta')^2(\beta'+\phi')] \tag{A22}$$

Observations similar to those made in reference 19 may be made about equation (A22) with respect to the possibility of torsional instability; as a matter of fact, if the net tension over the cross section is zero, the equation becomes similar to equation (2) presented and discussed in reference 19.

APPENDIX B

DERIVATION OF ACCELERATIONS AND INERTIA LOADINGS

The purpose of this appendix is to derive the acceleration of a mass particle of the twisted rotating blade and to derive the inertia loadings from this acceleration. In order to do this it is convenient to introduce the fixed X, Y, Z coordinate axes system shown in sketch 4. This sketch



Sketch 4.

also shows the rotating x, y, z axes system (used in the body of the report and in appendix A) and the deformed positions x_1, y_1, and z_1 of the mass particle (see eqs. (A3)). The azimuth position of the rotating system relative to the fixed-axes system is denoted by Ωt.

In terms of the unit vectors i, j, and k, the vector $\bar{r}$ may be written

$$\bar{r}=(x_1\cos\Omega t-y_2\sin\Omega t)i+(x_1\sin\Omega t+y_2\cos\Omega t)j+z_1k \quad \text{(B1)}$$

Differentiating with respect to time gives the velocity vector of the mass particle

$$\dot{\bar{r}}=(\dot{x}_1\cos\Omega t-\Omega x_1\sin\Omega t-\dot{y}_2\sin\Omega t-\Omega y_2\cos\Omega t)i+$$
$$(\dot{x}_1\sin\Omega t+\Omega x_1\cos\Omega t+\dot{y}_2\cos\Omega t-\Omega y_2\sin\Omega t)j+\dot{z}_1k \quad \text{(B2)}$$

and differentiating once again gives the acceleration

$$\ddot{\bar{r}}=[(\ddot{x}_1-\Omega\dot{y}_2)\cos\Omega t-\Omega(\dot{x}_1-\Omega y_2)\sin\Omega t-(\ddot{y}_2+\Omega\dot{x}_1)\sin\Omega t-$$
$$\Omega(\dot{y}_2+\Omega x_1)\cos\Omega t]i+[(\ddot{x}_1-\Omega\dot{y}_2)\sin\Omega t+\Omega(\dot{x}_1-\Omega y_2)\cos\Omega t+$$
$$(\ddot{y}_2+\Omega\dot{x}_1)\cos\Omega t-\Omega(\dot{y}_2+\Omega x_1)\sin\Omega t]j+\ddot{z}_1k \quad \text{(B3)}$$

The components a_x, a_y, and a_z of the acceleration vector in the x–, y–, and z–directions may be found from this equation by letting $t=0$, thus

$$\ddot{\bar{r}}=(\ddot{x}_1-\Omega^2x_1-2\Omega\dot{y}_2)i+(\ddot{y}_2-\Omega^2y_2+2\Omega\dot{x}_1)j+\ddot{z}_1k$$
$$=a_xi+a_yj+a_zk \quad \text{(B4)}$$

Use is now made of equations (A3) and the fact that $y_2=y_1+e_o$. Thus,

$$x_1=x+u-v'y-w'z$$
$$y_2=v+y-z\phi+e_o$$
$$z_1=w+z+y\phi$$

The first two derivatives with respect to time are given as follows:

$$\left.\begin{aligned}\dot{x}_1&=\dot{u}-\dot{v}'y-\dot{w}'z\\ \dot{y}_2&=\dot{v}-z\dot{\phi}\\ \dot{z}_1&=\dot{w}+y\dot{\phi}\end{aligned}\right\} \quad \text{(B5)}$$

$$\left.\begin{aligned}\ddot{x}_1&=\ddot{u}-\ddot{v}'y-\ddot{w}'z\\ \ddot{y}_2&=\ddot{v}-z\ddot{\phi}\\ \ddot{z}_1&=\ddot{w}+y\ddot{\phi}\end{aligned}\right\} \quad \text{(B6)}$$

Substitution of these equations into equation (B4) yields the desired acceleration vector, with the following components in the x–, y–, and z–directions:

$$\left.\begin{aligned}a_x&=\ddot{u}-\ddot{v}'y-\ddot{w}'z-\Omega^2(x+u-v'y-w'z)-2\Omega(\dot{v}-z\dot{\phi})\\ a_y&=\ddot{v}-z\ddot{\phi}-\Omega^2(v+y-z\phi+e_o)+2\Omega(\dot{u}-\dot{v}'y-\dot{w}'z)\\ a_z&=\ddot{w}+y\ddot{\phi}\end{aligned}\right\} \quad \text{(B7)}$$

By substitution of the expressions (A1) for y and z, the accelerations of the particle are obtained as follows in terms of the coordinates of the cross-section ζ and η:

$$\left.\begin{aligned}a_x&=\ddot{u}-\Omega^2(x+u)-2\Omega v+\eta[-\ddot{v}'\cos\beta-\ddot{w}'\sin\beta+\\ &\quad\Omega^2(v'\cos\beta+w'\sin\beta)+2\Omega\dot{\phi}\sin\beta]+\zeta[\ddot{v}'\sin\beta-\\ &\quad\ddot{w}'\cos\beta+\Omega^2(-v'\sin\beta+w'\cos\beta)+2\Omega\dot{\phi}\cos\beta]\\ a_y&=\ddot{v}-\Omega^2(v+e_o)+2\Omega\dot{u}+\eta[-\ddot{\phi}\sin\beta-\Omega^2(\cos\beta-\\ &\quad\phi\sin\beta)+\\ &\quad2\Omega(-\dot{v}'\cos\beta-\dot{w}'\sin\beta)]+\zeta[-\ddot{\phi}\cos\beta-\\ &\quad\Omega^2(-\sin\beta-\phi\cos\beta)+2\Omega(\dot{v}'\sin\beta-\dot{w}'\cos\beta)]\\ a_z&=\ddot{w}+\eta\ddot{\phi}\cos\beta-\zeta\ddot{\phi}\sin\beta\end{aligned}\right\} \quad \text{(B8)}$$

The inertia loadings on the beam may now be derived from these acceleration equations by appropriate integrations over the cross section. The total or resultant loadings desired in the analysis given in the body of this paper are the sum of the inertia loadings and the applied loadings, and are given by the following equations, when the assumption is made that the cross section is symmetrical about the major principal axis:

$$\left.\begin{aligned}
\bar{p}_x &= -\int_{\eta_{te}}^{\eta_{le}}\int_{-t/2}^{t/2} a_x\rho\, d\zeta\, d\eta \\
\bar{p}_y &= L_y - \int_{\eta_{te}}^{\eta_{le}}\int_{-t/2}^{t/2} a_y\rho\, d\zeta\, d\eta \\
\bar{p}_z &= L_z - \int_{\eta_{te}}^{\eta_{le}}\int_{-t/2}^{t/2} a_z\rho\, d\zeta\, d\eta \\
\bar{q}_x &= M - \int_{\eta_{te}}^{\eta_{le}}\int_{-t/2}^{t/2} [-a_y(z_1-w)+a_z(y_1-v)]\rho\, d\zeta\, d\eta \\
\bar{q}_y &= -\int_{\eta_{te}}^{\eta_{le}}\int_{-t/2}^{t/2} [-a_x(z_1-w)]\rho\, d\zeta\, d\eta \\
\bar{q}_z &= -\int_{\eta_{te}}^{\eta_{le}}\int_{-t/2}^{t/2} [-a_x(y_1-v)]\rho\, d\zeta\, d\eta
\end{aligned}\right\} \quad \text{(B9)}$$

where ρ is the density of the structural material and may be a function of ζ and η. If the integrations are performed with the use of equations (B8), the following loadings are found:

$$\bar{p}_x = -m[\ddot{u}-\Omega^2(x+u)-2\Omega\dot{v}] - me[-\ddot{v}'\cos\beta - \ddot{w}'\sin\beta + \Omega^2(v'\cos\beta + w'\sin\beta) + 2\Omega\dot{\phi}\sin\beta] \quad \text{(B10)}$$

$$\bar{p}_y = L_y - m[\ddot{v}-\Omega^2(v+e_o)+2\Omega\dot{u}] - me[-\ddot{\phi}\sin\beta - \Omega^2(\cos\beta-\phi\sin\beta) + 2\Omega(-\dot{v}'\cos\beta - \dot{w}'\sin\beta)] \quad \text{(B11)}$$

$$\bar{p}_z = L_z - m(\ddot{w}) - me\ddot{\phi}\cos\beta \quad \text{(B12)}$$

$$\bar{q}_x = M - \Omega^2 me[(v+e_o)\sin\beta + e_o\phi\cos\beta] + me(\ddot{v}\sin\beta - \ddot{w}\cos\beta + 2\Omega\dot{u}\sin\beta) - \Omega^2 m[(k_{m2}^2-k_{m1}^2)\sin\beta\cos\beta + (k_{m2}^2-k_{m1}^2)\phi\cos 2\beta] - \ddot{\phi}mk_m^2 - 2\Omega m(k_{m2}^2-k_{m1}^2)\dot{v}'\cos\beta\sin\beta - 2\Omega m(k_{m2}^2\sin^2\beta + k_{m1}^2\cos^2\beta)\dot{w}' \quad \text{(B13)}$$

$$\bar{q}_y = -\Omega^2 me[(x+u)\sin\beta + x\phi\cos\beta] + me(\ddot{u}\sin\beta - 2\Omega\dot{v}\sin\beta) + \Omega^2 m[(k_{m2}^2-k_{m1}^2)v'\sin\beta\cos\beta + (k_{m2}^2\sin^2\beta + k_{m1}^2\cos^2\beta)w'] - m(k_{m2}^2-k_{m1}^2)\ddot{v}'\sin\beta\cos\beta + m(k_{m2}^2\sin^2\beta + k_{m1}^2\cos^2\beta)(2\Omega\dot{\phi}-\ddot{w}') \quad \text{(B14)}$$

$$\bar{q}_z = -\Omega^2 me[(x+u)\cos\beta - x\phi\sin\beta] + me(\ddot{u}\cos\beta - 2\Omega\dot{v}\cos\beta) + \Omega^2 m[(k_{m2}^2-k_{m1}^2)w'\sin\beta\cos\beta + (k_{m2}^2\cos^2\beta + k_{m1}^2\sin^2\beta)v'] - m(k_{m2}^2-k_{m1}^2)\ddot{w}'\sin\beta\cos\beta - m(k_{m2}^2\cos^2\beta + k_{m1}^2\sin^2\beta)\ddot{v}' + 2\Omega m(k_{m2}^2-k_{m1}^2)\dot{\phi}\sin\beta\cos\beta \quad \text{(B15)}$$

Equations (B10) to (B15) give the general expressions for the loadings and contain many terms of second order which for most engineering purposes can be neglected. In equation (B10), for example, all other terms are small in comparison to $m\Omega^2x$, which is the conventional expression for $\bar{p}_x$ (note that $\bar{p}_x=-T'$); for most practical purposes these small terms may therefore be neglected. For any specific application, however, particularly in the case of unusual configurations, the relative magnitude and importance of the terms should be determined. In the case of conventional helicopter or propeller blades, it is believed that the following first-order reductions of equations (B10) to (B15) are suitable for most engineering applications:

$$\left.\begin{aligned}
\bar{p}_x &= -T' = m\Omega^2 x \\
\bar{p}_y &= L_y - m[\ddot{v}-\Omega^2(v+e_o)] + me[\ddot{\phi}\sin\beta + \Omega^2(\cos\beta-\phi\sin\beta)] \\
\bar{p}_z &= L_z - m(\ddot{w}+e\ddot{\phi}\cos\beta) \\
\bar{q}_x &= M - \Omega^2 me[(v+e_o)\sin\beta + e_o\phi\cos\beta] + me(\ddot{v}\sin\beta - \ddot{w}\cos\beta) - \Omega^2 m(k_{m2}^2-k_{m1}^2)(\sin\beta\cos\beta+\phi\cos 2\beta) - mk_m^2\ddot{\phi} \\
\bar{q}_y &= -\Omega^2 mex(\sin\beta+\phi\cos\beta) \\
\bar{q}_z &= -\Omega^2 mex(\cos\beta-\phi\sin\beta)
\end{aligned}\right\} \quad \text{(B16)}$$

where

$$k_m^2 = k_{m2}^2 + k_{m1}^2$$

REFERENCES

1. Mendelson, Alexander, and Gendler, Selwyn: Analytical and Experimental Investigation of Effect of Twist on Vibrations of Cantilever Beams. NACA TN 2300, 1951.
2. Zickel, J.: General Theory of Pretwisted Beams and Columns. Tech. Rep. No. 73 (Contract N7onr–35801, Column Res. Council, and R. I. Dept. Public Works), Brown Univ., Graduate Div. Appl. Math., June 1952.
3. Zickel, J.: Buckling of Pretwisted Columns. Tech. Rep. No. 74 (Contract N7onr–35801), Brown Univ., Graduate Div. Appl. Math., June 1952.
4. Zickel, J.: Bending of Pretwisted Beams. Tech. Rep. No. 77 (Contract N7onr–35801), Brown Univ., Graduate Div. Appl. Math., Aug. 1952.
5. Yntema, Robert T.: Simplified Procedures and Charts for the Rapid Estimation of Bending Frequencies of Rotating Beams. NACA TN 3459, 1955. (Supersedes NACA RM L54G02.)
6. Flax, Alexander H.: The Bending of Rotor Blades. Jour. Aero. Sci., vol. 14, no. 1, Jan. 1947, pp. 42–50.
7. Daughaday, H., and Kline, J.: An Approach to the Determination of Higher Harmonic Rotor Blade Stresses. Proc. Ninth Annual Forum, Am. Helicopter Soc., Inc., May 14–17, 1953, pp. 90–126.
8. Flax, A. H., and Goland, L.: Dynamic Effect in Rotor Blade Bending. Jour. Aero. Sci., vol. 18, no. 12, Dec. 1951, pp. 813–829.
9. Wood, R. McKinnon, and Perring, W. G. A.: Stresses and Strains in Airscrews With Particular Reference to Twist. R. & M. No. 1274, British A.R.C., 1929.
10. Sterne, L. H. G.: The Structural Aspects of Propeller Design. Report No. Structures 5, British R.A.E., July 1947.
11. DiPrima, R. C., and Handelman, G. H.: Vibrations of Twisted Beams. Quarterly Appl. Math., vol. XII, no. 3, Oct. 1954, pp. 241–259.
12. Mendelson, Alexander: Effect of Centrifugal Force on Flutter of Uniform Cantilever Beam at Subsonic Speeds With Application to Compressor and Turbine Blades. NACA TN 1893, 1949.
13. Arnoldi, Walter E.: Response of a Rotating Propeller to Aerodynamic Excitation. NACA RM 8I07, 1949.
14. DeVries, J. A., and Stulen, F. B.: A Complete Matrix Solution for the Vibratory Bending Moments of a Propeller Blade Subjected to a Pure First Order Aerodynamic Excitation. Rep. No. C–2152, Curtiss-Wright Corp., Propeller Div. (Caldwell, N. J.), May 16, 1950.
15. Turner, M. J., and Duke, James B.: Propeller Flutter. Jour. Aero. Sci., vol. 16, no. 6, June 1949, pp. 323–336.
16. Love, E. R., and Silberstein, J. P. O. (Assisted by J. R. M. Radok): Vibration of Stationary and Rotating Propellers. Rep. ACA–36, Australian Council for Aeronautics, June 1947.
17. Timoshenko, S., and Goodier, J. N.: Theory of Elasticity. Second ed., McGraw-Hill Book Co., Inc., 1951, pp. 333–336.
18. Rosenberg, Reinhardt: Aero-Elastic Instability in Unbalanced Lifting Rotor Blades. Jour. Aero. Sci., vol. 11, no. 4, Oct. 1944, pp. 361–368.
19. Niedenfuhr, F. W.: On the Possibility of Aeroelastic Reversal of Propeller Blades. Jour. Aero. Sci. (Readers' Forum), vol. 22, no. 6, June 1955, pp. 438–440.

REPORT 1347

DITCHING INVESTIGATIONS OF DYNAMIC MODELS AND EFFECTS OF DESIGN PARAMETERS ON DITCHING CHARACTERISTICS [1]

By Lloyd J. Fisher and Edward L. Hoffman

SUMMARY

Data from ditching investigations conducted at the Langley Aeronautical Laboratory with dynamic scale models of various airplanes are presented in the form of tables. The effects of design parameters on the ditching characteristics of airplanes, based on scale-model investigations and on reports of full-scale ditchings, are discussed. Various ditching aids are also discussed as a means of improving ditching behavior.

INTRODUCTION

The designers of an airplane have control over many factors that will affect the chances of survival of the occupants of the airplane in a ditching. Since a considerable variation in ditching behavior is found in airplane designs that have similar performance in the air, it is evidently possible to choose values of design parameters that will give some measure of ditching safety without appreciable sacrifice of aerodynamic properties. Therefore, available ditching data are presented and evaluated herein in order to assist the designer and the operator in making preliminary ditching evaluations of airplanes by comparison with similar configurations or by the study of various design parameters. This information is based on data from scale-model investigations conducted at the Langley Aeronautical Laboratory and from actual full-scale ditchings. The data from ditching investigations with scale models are presented in the form of tables.

Scale-model investigations can give information regarding the motions of an airplane when ditched but data regarding the ability of personnel to withstand the motions, and subsequently to escape from the sinking airplane, must be obtained from other sources.

APPARATUS AND PROCEDURE

The investigations of the ditching characteristics of airplanes were conducted in Langley tank no. 2 with dynamic scale models. Damage which was likely to occur in a full-scale ditching was simulated in the models either by the removal of parts, by the installation of simulated crumpled sections, by the installation of scale-strength sections or aluminum-foil coverings which failed during the test, or by a combination of these methods. The models were launched either from the towing carriage or from the monorail so that they were free to glide onto the water at the desired landing attitude and speed. The control surfaces were set in such a manner that the model did not yaw or change attitude appreciably in flight. Landing attitude was measured between the longitudinal axis of the airplane and the smooth-water surface.

The behavior of the models was recorded from visual observations and from motion pictures of the tests. Average decelerations were derived from the landing speeds and lengths of run. Maximum longitudinal decelerations were measured with an accelerometer installed near the cockpit. Various accelerometers were used that had natural frequencies of about 20 to 70 cycles per second and all were damped to about 65 percent of the critical damping value. The reading accuracy of the least accurate instrument was about $\pm \frac{1}{2}g$.

RESULTS AND DISCUSSION

The results of the model-ditching investigations are shown in tables 1 to 37. The information in these tables is based on calm-water landing tests. In rough-water landings made parallel to waves or swells, the same general type of performance should be obtained. In landings made perpendicular to waves, however, more damage and more violent motions may occur, depending on the choice of ditching site and the size and portion of the wave contacted.

EFFECTS OF DESIGN PARAMETERS

Wing.—From a ditching standpoint, the vertical location of the wing with respect to the fuselage is a compromise between having the wing low enough to provide buoyancy to help keep the airplane afloat after ditching and having the wing high enough so that the landing flaps and engine installations (discussed further under "Flaps" and under "Engine installation") do not seriously impair ditching behavior. It is generally considered that the most favorable position of the wing is slightly above the bottom of the fuselage or in a low midwing position.

The thickness and size of the wings had little effect on ditching behavior other than the obvious effect on buoyancy. Sweptback and delta wings had little hydrodynamic influence on ditching but they did have aerodynamic influence

[1] Supersedes NACA Technical Note 3946 by Lloyd J. Fisher and Edward L. Hoffman, 1957.

Preceding Page Blank

on handling and landing characteristics. The flying wing appeared to have reasonably good ditching characteristics but it was very susceptible to damage although no violent motions occurred.

Flaps.—The landing flaps had a noticeable hydrodynamic effect on about 25 percent of the models investigated. For most of the models there was only a slight nose-down moment observed, and in no test was a flaps-up condition preferable. For certain models (as example, table 16), a flaps-down condition caused diving, but with the flaps retracted and with the corresponding increase in speed the damage and deceleration were even more severe than in the dives. It is therefore preferable to have flaps down in a ditching in order to obtain a low forward speed and thus to decrease fuselage damage; however, the flaps should be weak enough to fail before producing an undesirable diving moment. For airplanes having very low wings, the manner in which the flaps failed, that is, whether they were completely torn from the wing or whether the linkage failed and left the flaps free to rotate toward a neutral position, had an effect on the results. In table 28 it is noted that a flap which merely rotated toward a neutral position was occasionally detrimental.

Engine installation.—Reciprocating engines have caused differences in airplane ditching behavior because of the location of the nacelle. When placed low on an airplane, the engine nacelle acts as a "water brake" and increases decelerations; therefore, it is generally desirable to place the engine well above the level of the bottom of the fuselage.

Jet engines mounted on the wing (table 11) or turbopropeller engines mounted similarly will have about the same effect as a reciprocating-engine nacelle except that they may be smaller and have less water resistance. Pusher-propeller engines installed on the wing (table 10) also may have low water resistance.

Jet engines have brought about a design freedom in engine location because propeller clearance is no longer a factor. Jet engines installed at the wing root, on struts, under the fuselage, and on the side of the fuselage have been investigated in model-ditching tests. In general, the wing-root nacelles have very little effect on dynamic behavior and will have little influence on structural damage. The strut-mounted nacelles (tables 12 and 26) will probably be torn off in a ditching but will have little effect on dynamic behavior. With engine nacelles mounted under the fuselage, various effects can be expected, depending on the rigidity and the fore and aft location of the installation. If the engines are too far aft, a dive may be produced. A forward location may cause porpoising, but generally an intermediate position can be found that will produce a smooth run. Side-mounted engine nacelles will probably require the horizontal tail to be mounted high on the vertical tail. Generally, with a high tail the rear part of the fuselage runs deeply in the water and the nacelles cause considerable spray and drag as they enter the water. If the nacelles tear away during a ditching, extensive structural damage may result and possibly the aft portion of the fuselage will be torn away. Fighter airplanes usually have jet engines located within the fuselage; therefore, the location of the air intake is the most important feature of such installations. The inlets may cause detrimental behavior when a ditching is made at a low enough attitude to get them into the water at high speeds (see table 23). Usually, however, an airplane can be landed so that the inlets are held clear of the water until a fairly slow speed is reached. Tests were made of one fighter airplane model that had jet engines mounted on the underside of the fuselage (table 20); diving did not occur with this particular installation, but some very high decelerations resulted.

Tail surfaces.—The location of the tail surfaces has not previously been considered to have hydrodynamic influence on ditching behavior. However, data obtained in scale-model investigations indicate that the horizontal-tail location can affect the attitude at which the airplane will run on the water. When the horizontal tail is located very high on the vertical tail the model will, when there is a tendency to trim up, trim higher than when the horizontal tail is in a low position. Occasionally a horizontal tail was partially torn away in the scale-model tests but no appreciable change in behavior due to this damage was noted.

Landing gear.—It is considered advisable that ditchings be made with the landing gear retracted because an extended gear usually causes diving. (For example, see table 32.) There have been some full-scale ditchings with wheels down in which diving did not occur, but apparently these were exceptional.

The arrangement of the landing gear when retracted has not shown an appreciable effect on ditching behavior, but it can affect the amount of damage and the safety of personnel during a ditching. Tricycle-gear arrangements have nose-wheel doors that are likely to fail in a ditching. In no case have scale-model investigations shown that such a failure will cause diving, but secondary failures that ensue as a result of the water pouring into this opening may be extensive enough to endanger nearby personnel. In general, the landing-gear installation that has a tail wheel tends to give a better arrangement for ditching than the tricycle gear, provided that all wheels are retracted. However, if a ditching aid attached under the nose of the airplane were considered, the tricycle landing gear would provide structural members advantageously located to carry the concentrated load of the ditching aid. The bicycle-landing-gear installation requires doors in the fuselage bottom which are undesirable in ditching unless they are much stronger than doors generally are. In investigations of one airplane model employing the bicycle landing gear, the simulated main-wheel doors failed (table 12). In this test no detrimental behavior occurred but the fuselage was flooded. The outrigger wheels required with a bicycle main gear offer no difficulties in ditching. A contribution of the bicycle-landing-gear design favorable to ditching is a very strong fuselage structure. The fuselage of some airplanes has broken apart near the wing in ditching but it is unlikely that a fuselage strong enough to support a bicycle landing gear would separate in this manner. In an investigation of a model with the main landing gear located in nacelles on the sides of the fuselage (table 33), the nacelles crumpled considerably but the damage did not affect the ditching behavior. Damage is likely to occur when the

nacelle type of wheel fairing is used, and the damage could have undesirable effects on flotation unless precautions are taken to prevent entry of water into the main part of the fuselage.

Fuselage strength.—Most airplanes could be ditched with relative safety if extensive damage to the fuselage could be avoided; therefore, the strength of the fuselage bottom is probably the most important parameter influencing ditching behavior. It is impractical to consider designing fuselages which will not fail in ditching, but damage may be reduced by using ditching aids (discussed further under "Ditching Aids"), and the danger to personnel may be minimized by providing safe ditching stations (discussed under "Safe Location of Personnel"). The middle third of the fuselage bottom is considered the critical region because of its susceptibility to damage and the consequent effects on ditching behavior. The investigations with models by the use of scale-strength bottoms to determine the location and amount of probable damage have substantiated this conclusion.

Bombers are particularly susceptible to damage and undesirable ditching behavior because the bomb-bay doors are usually located in the critical region. Manufacturers estimate that the bomb-bay doors have an ultimate strength in resistance to water loads of approximately ½ to 2 pounds per square inch and that the remainder of the lower fuselage is also comparatively weak. Bomb-bay-door failure generally occurs and sometimes causes violent behavior; however, whether or not violent behavior occurred, safe ditching stations in the rear part of the fuselage are generally unobtainable because of the rush of water through the airplane when damage occurs.

There is a wide variation in the bottom strength of fighter airplanes; some have strength as low as 2 pounds per square inch, but others can withstand a pressure of 40 pounds per square inch on some parts of the fuselage bottom. Fighters frequently sustain extensive damage to the bottom skin, but the structure usually remains more or less intact. If damage does not occur, fighters will make smooth runs or at worst they might skip. If damage occurs, almost any behavior from a smooth run to a violent dive or flipover might result according to the amount of damage and the particular airplane configuration.

Transport airplanes have marginal-strength fuselages—the lower part of the fuselages sustains some damage when ditching but usually is not demolished. The average resistance to water loads is estimated by manufacturers to be from 8 to 12 pounds per square inch. The fuselage strength of a transport is greater than that of a bomber because the requirements for cargo floors and pressurized cabins in the transport contribute to a stronger fuselage and because the bomber fuselage is considerably weakened by the presence of the bomb-bay doors. Damage usually does not cause the behavior in transports to be violent, but water flooding into the fuselage through damaged sections is a hazard.

Fuselage shape.—Some current airplanes have large amounts of curvature at the rear of the fuselage. A high degree of longitudinal curvature results in a suction which causes the models to trim up in the water (tables 30, 31, and 37). A high degree of lateral curvature at the rear of the fuselage results in suctions and motions similar to those produced by high longitudinal curvature (ref. 1). Trimming up is not necessarily detrimental but could contribute to undesirable results such as skipping and subsequent diving. A fuselage bottom with little longitudinal and lateral curvature tends to decrease trimming up but is undesirable because of the accompanying high water loads. There are indications that flattened cross sections in combination with high longitudinal curvature tend to cause skipping (tables 19 and 30). Moderately curved sections rearward of the center of gravity are desirable with respect to stability and water loads.

From early scale-model tests, it was concluded that the small differences in the ratio of fuselage length forward of the center of gravity to the total fuselage length indicated no consistent differences in the hydrodynamic performance. Recent trends in fighter design have led to increases in this ratio from approximately ¼ to ½. There is evidence that the increase in nose length has been advantageous to fighter airplanes because it has resulted in a decrease in diving or nosing-in tendency. For bombers, the increase in this ratio has been small and there has been little noticeable effect on ditching behavior.

Curvature at the nose also has an influence on ditching behavior. A fuselage that is more or less straight on the bottom but curves up abruptly at the nose offers less nose-up moment and thus is more likely to dive than one that curves up gradually. The desirability of gradual curvature of the forward part of the fuselage has been substantiated by limited tests.

The effect of cross-sectional curvature of the forward part of the fuselage has not been investigated but it appears that a moderately curved cross section would probably be most desirable.

Size.—The physical magnitude of airplanes appears to affect the degree of violence of ditching behavior. Small differences are not noticeable but in the overall range from fighters to large bombers and transports the effect of size and pitching moment of inertia is apparent. As the size of airplanes increases, the ditching behavior becomes less violent.

Interior arrangement.—Probably the item of interior arrangement that has the greatest effect on ditching behavior is the bulkhead just aft of the bomb bay. Bomb-bay doors usually fail; therefore, this bulkhead is immediately subjected to water loads. For the configurations shown in tables 11 and 13, diving was prevented by removing the bulkhead and the part of the fuselage bottom that might be torn away if the bulkhead failed. In table 4, removing the bulkhead or part of the bulkhead reduced the severity of diving. There have been cases in which bomb-bay doors failed but diving was not produced; in such cases the bulkhead caused no detrimental behavior and offered some protection to the interior of the rearward part of the fuselage.

Protuberances.—Protuberances under the wing or the fuselage of an airplane may cause undesirable ditching behavior and high longitudinal decelerations. Protuberances located rearward of the center of gravity are the most undesirable and may cause diving. Radiators projecting below the fuselage rearward of the center of gravity have

caused dives. Radiators under the nose have caused violent ditching behavior and high decelerations. Belly-gun turrets and radar housings placed forward of the center of gravity generally have caused no diving or other violent motions when tested on models (tables 8 and 14). However, such protuberances located rearward of the center of gravity have caused diving (table 3).

Scale-model investigations with cargo containers located under the fuselage (table 27 (b)) indicated that no detrimental effect was due to the presence of the cargo container; in fact, it was beneficial because it afforded protection to the bottom of the airplane. The construction of the container was such that it caved in on contact with the water and thus acted as a shock absorber.

The need for greater fuel storage in jet-propelled airplanes has resulted in the use of external fuel tanks, usually located under the wing or at the wing tip. Streamlined auxiliary fuel tanks under the wing (table 23) should be jettisoned before ditching because they increase hydrodynamic resistance and because their shape is such that they produce a suction force detrimental to successful ditching. Tanks that were modified in shape by the addition of either chine strips or dead rise with chines (ref. 2) would improve the ditching behavior if they were strong enough to withstand the water loads. Wing-tip tanks probably will not be detrimental since they do not enter the water until a low speed is reached and, if empty, they offer additional buoyancy (tables 21 and 24).

SAFE LOCATION OF PERSONNEL

The availability of good ditching stations for personnel will in some measure compensate for unavoidable deficiencies in hydrodynamic characteristics. Scale-model investigations indicate that decelerations in severe ditchings may exceed $10g$, but apparently personnel can withstand such decelerations if they are braced against or strapped to a unit of the airplane that will not fail. The danger that parts of the airplane will be broken off and thrown against occupants cannot be completely eliminated, but adequate strength can be provided to prevent obvious hazards, such as overhead turrets, from being torn off.

Available records of ditchings indicate that the survival rate for fighter pilots is higher now than in the past. Although the behavior of current fighter airplanes is sometimes violent, a more important factor may be the increase in use of the safety harness. The fuselage of a fighter is strong and the pilot can usually be braced well enough to withstand the decelerations. The bottom skin of the fuselage may be damaged but there is little water flow through the pilot's compartment.

In bomber and transport airplanes, the pilot's compartment is usually high enough to avoid quick flooding except in a dive, damage is not severe, and escape hatches are available. The most dangerous ditching stations in a bomber airplane are rearward of the bomb bay because of the likelihood of an inrush of water through the low-strength bomb-bay doors and the probable failure of the bulkhead just rearward of the bomb bay. The survival rate for bombers as a whole is very low, and as a class the bomber is considered to have unacceptable ditching characteristics.

In a transport airplane, the fuselage generally has no predominantly weak part, such as bomb-bay doors, and the floor of the passenger compartment is more substantial than the floor of a bomber. Consequently, the rearward part of the fuselage is possibly less hazardous in a transport than in a bomber; however, because of the chance that the rear fuselage might sustain extensive damage, ditching stations should be as far forward as possible. In transports that have double decks (tables 36 and 37), the upper deck offers relatively safe ditching stations. The most hazardous type of transport, as far as ditching stations are concerned, is the "flying boxcar" (tables 29, 30, 32, and 33). This type of airplane has large doors and a wide flat bottom that are subject to high water pressures; therefore, some damage is very probable. The high wing of the flying boxcar affords no buoyancy until the airplane sinks deeply; consequently, the cargo or passenger compartment is likely to be flooded to a hazardous extent.

It would seem that the ditching requirements for transports should be more severe than for other types of airplanes because of the large number of passengers involved and the general lack of training in ditching procedures.

DITCHING AIDS

When the use of an airplane is such that a high degree of ditching safety is required, a ditching aid may be the best method of insuring such safety. If a ditching aid were included as an integral part of the airplane in the early stages of design, it possibly could be incorporated with little or no penalty in performance.

Hydroflap.—One method which can be used to prevent diving or "nosing in" during the high-speed part of a ditching run is to provide a device under the fuselage forward of the center of gravity that will have sufficient hydrodynamic lift to furnish the necessary positive pitching moment. Scale-model investigations have been made with planing surfaces, called hydroflaps, installed on models for this purpose. The hydroflaps, which usually have an incidence angle of about 30°, have been tested in various forms. In some investigations, existing rectangular doors in the fuselage were braced open to form hydroflaps (tables 2 (b) and 15 (b)). In other investigations where the hydroflap had a trapezoidal or triangular plan form (tables 4 (b), 11 (b), and 33 (b)), smoother runs were obtained than with rectangular plan forms. In addition to eliminating the diving, hydroflaps reduced the amount of damage sustained by scale-strength sections.

Certain types of airplanes require speed brakes or dive brakes. These devices have various forms, one of which is an approximately flat plate hinged at its leading edge to the bottom of the fuselage and opening outward. A few airplanes have had this type of brake located forward of the center of gravity. Such a device possibly could be located so that it could serve as a hydroflap as well as a speed brake. Speed brakes have not yet been located far enough forward of the center of gravity to serve advantageously as hydroflaps and have not been made strong enough for such use. Scale-model investigations (table 24 (b)) indicate that such

a brake could be used as a ditching aid if these requirements were met.

Hydrofoil.—Two general methods for using hydrofoils to improve hydrodynamic ditching characteristics of airplanes have been investigated with scale models: in one method, the hydrofoil was placed below the nose of the model with a positive incidence, and in the other it was placed aft of the center of gravity with a negative incidence in order to hold the tail down. Both schemes were effective in improving the performance of the models, but the hydrofoil below the nose of the model was a more positive and practical installation. In addition to improving ditching behavior, the hydrofoil forward of the center of gravity offered the possibility of reducing fuselage damage.

Hydro-ski.—Another possible ditching aid is a planing surface that can be extended on struts so that in a landing the airplane rides on the planing surface and the main body of the airplane is not subjected to large water loads at high water speeds. Such a device has been called a hydro-ski (tables 14 (c), 27 (c), and 34 (b)). With a hydro-ski ditching aid, the hazardous motions and structural damage associated with ditching can be eliminated. For a bomber airplane, twin skis retracting into the side of the fuselage or into the wings could be used. For a transport airplane, either a single ski or twin skis retracting into the bottom of the fuselage would be practical.

CONCLUDING REMARKS

Performance requirements and the relatively low frequency of emergency landings even in wartime make it unlikely that airplanes will ever be designed specifically for "safe" ditchings. It appears possible, however, to reduce the hazards by some attention to the effects of the design parameters. It may also in certain cases be possible to incorporate ditching aids to protect the structure from peak water loads without significant performance penalties. These possibilities together with the establishment of proper approach procedures, provision of adequate means of escape, and early rescue remain the most effective means of increasing survival rates in future ditchings.

LANGLEY AERONAUTICAL LABORATORY,
NATIONAL ADVISORY COMMITTEE FOR AERONAUTICS,
LANGLEY FIELD, VA., *November 16, 1956.*

REFERENCES

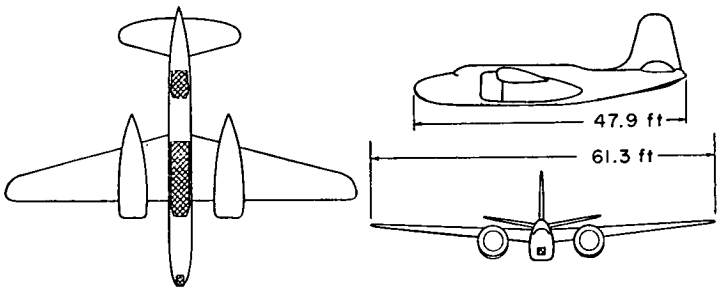
1. McBride, Ellis E., and Fisher, Lloyd J.: Experimental Investigation of the Effect of Rear-Fuselage Shape on Ditching Behavior. NACA TN 2929, 1953.
2. McBride, Ellis E.: Preliminary Investigation of the Effects of External Wing Fuel Tanks on Ditching Behavior of a Sweptback-Wing Airplane. NACA TN 3710, 1956.

TABLE 1

SUMMARY OF MODEL-DITCHING INVESTIGATION OF BOMBER A

Model scale, $\frac{1}{10}$; gross weight, 21,500 lb; center-of-gravity location, 28 percent M.A.C.; all values full scale]

Damage simulated by removal of parts (crosshatched areas).



Landing attitude, deg	Flap setting, deg	Landing speed, knots	Length of run, ft	Maximum longitudinal deceleration, g units	Average longitudinal deceleration, g units	Motions of model (*)
Undamaged model						
2	0	104	200	------	2½	u h
2	40	104	200	------	2½	u h
6	0	104	400	------	1	u h
6	40	87	200	------	1½	u h
10	0	87	350	------	1	u h
10	40	69	200	1½	1	u h
Damaged model						
2	40	104	150	5½	3	b
†10	40	69	100	3	2	b

*In this column, the letters indicate the following motions:

b ran deeply—the model settled deeply in the water with little change in attitude
h ran smoothly—the model made a very stable run
u trimmed up—the attitude of the model increased while running in the water

† Recommended ditching attitude and flap setting.

Remarks: Simulation of damage on this model stopped the trimming-up tendency and caused the model to run deeper in the water. The large nacelles caused violent turns when the model was ditched with one wing low.

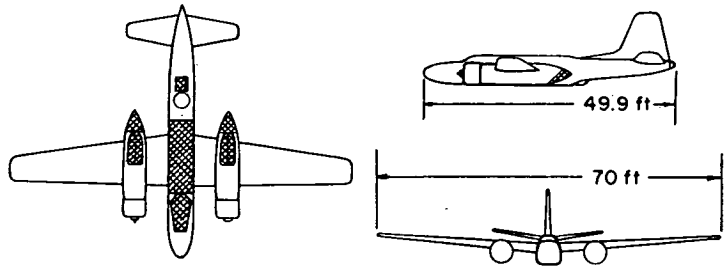
TABLE 2

SUMMARY OF MODEL-DITCHING INVESTIGATION OF BOMBER B

[Model scale, $\frac{1}{12}$; gross weight, 25,730 lb; center-of-gravity location, 28 percent M.A.C.; all values full scale]

(a) Without hydroflap.

Damage simulated by removal of parts (crosshatched areas).



Landing attitude, deg	Flap setting, deg	Landing speed, knots	Length of run, ft	Maximum longitudinal deceleration, g units	Average longitudinal deceleration, g units	Motions of model (*)
Undamaged model						
3	55	102	400	2	1	s d_1
3	55	102	400	3	1	s t
8	0	115	600	4½	1	s t
8	55	96	500	------	1	h
13	0	102	250	8	2	d_1
13	55	90	150	5	2½	d_1
Damaged model						
3	55	101	100	------	4½	d_1
8	0	115	250	6½	2½	d_1
†8	55	86	100	------	3½	d_1
13	0	102	250	------	2	d_1
13	55	86	150	------	2	d_1

*In this column, the letters indicate the following motions:

d_1 dived violently—the model stopped abruptly in a nose-down attitude with most of the model submerged
h ran smoothly—the model made a very stable run
s skipped—the model rebounded from the water
t turned sharply—the model pivoted quickly about a vertical axis
†Recommended ditching attitude and flap setting.

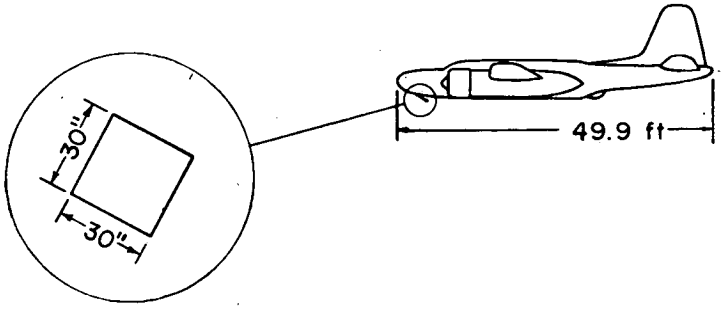
Remarks: The behavior of the model was exceptionally violent. Violent dives occurred with the undamaged model. In general, the dives at the attitude of 8° were less violent than those at the attitude of 13°. When the model was ditched with one wing slightly low, the large nacelles dug into the water and caused sharp turns.

TABLE 2—Concluded

SUMMARY OF MODEL-DITCHING INVESTIGATION OF BOMBER B

(b) With hydroflap.

Damage as shown in three-view sketch. All-purpose nose door (open at an angle of 30° to thrust line) used as hydroflap.



Landing attitude, deg	Flap setting, deg	Landing speed, knots	Length of run, ft	Maximum longitudinal deceleration, g units	Average longitudinal deceleration, g units	Motions of model (*)
3	55	101	300	------	2	p
†8	55	86	250	3½	1½	p
13	55	86	200	------	1½	p

*In this column, the letters indicate the following motions:
p porpoised—the model undulated about the transverse axis with some part of the model always in contact with the water
†Recommended ditching attitude and flap setting

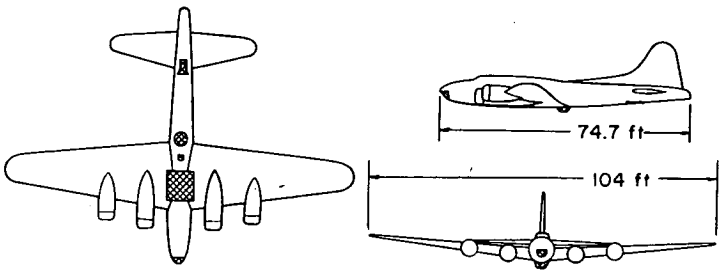
Remarks: Rather violent porpoising runs occurred with the hydroflap, but these runs were considerably better than the violent dives that occurred without the hydroflap.

TABLE 3

SUMMARY OF MODEL-DITCHING INVESTIGATION OF BOMBER C

[Model scale, $\frac{1}{16}$; gross weight, 57,000 lb; center-of-gravity location, 30 percent M.A.C.; all values full scale]

Damage simulated by removal of parts (crosshatched areas).



Landing attitude, deg	Flap setting, deg	Landing speed, knots	Length of run, ft	Maximum longitudinal deceleration, g units	Average longitudinal deceleration, g units	Motions of model (*)
Undamaged model						
0	45	122	---	7	------	d_1
3½	45	104	---	------	------	d_1
7	0	104	---	8	------	d_1
7	45	87	---	6½	------	t d_1
10	0	87	---	------	------	d_1
10	45	87	---	------	------	d_1
Damaged model						
0	45	122	---	7½	------	t
3½	45	104	---	------	------	t s
†7	45	87	---	------	------	s
10	45	87	---	------	------	p

*In this column, the letters indicate the following motions:
d_1 dived violently—the model stopped abruptly in a nose-down attitude with most of the model submerged
p porpoised—the model undulated about the transverse axis with some part of the model always in contact with the water
s skipped—the model rebounded from the water
t turned sharply—the model pivoted quickly about a vertical axis
†Recommended ditching attitude and flap setting.

Remarks: The tests indicated that the lower turret was the principal cause of diving. It was recommended that this turret be made easily jettisonable.

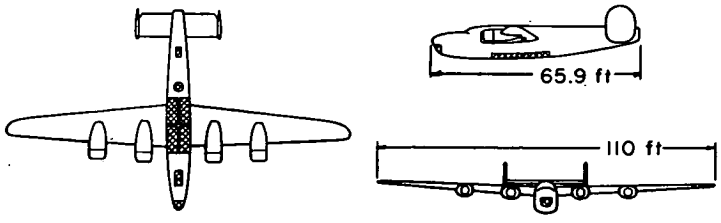
TABLE 4

SUMMARY OF MODEL-DITCHING INVESTIGATION OF BOMBER D

[Model scale, $\frac{1}{16}$; gross weight, 48,500 lb; center-of-gravity location, 30 percent M.A.C.; all values full scale]

(a) Without hydroflap.

Damage simulated by removal of parts (crosshatched areas).



Landing attitude, deg	Flap setting, deg	Landing speed, knots	Length of run, ft	Maximum longitudinal deceleration, g units	Average longitudinal deceleration, g units	Motions of model (*)
Undamaged model						
1	40	104	550	1½	1	h
			900	2½	½	s
5	0	104	950	1	½	s
			800	1	½	p
5	40	87	600	1½	½	h
			550	1½	½	p
9	0	87	300	3	1	h
9	40	87	250	3½	1½	h
			550	--	½	p
Damaged model						
1	40	104	200	------	2½	d_1
			300	------	1½	s
†5	40	87	250	------	1½	p d_1
9	40	87	150	------	2	d_1

*In this column, the letters indicate the following motions:
d_1 dived violently—the model stopped abruptly in a nose-down attitude with most of the model submerged
h ran smoothly—the model made a very stable run
p porpoised—the model undulated about the transverse axis with some part of the model always in contact with water
s skipped—the model rebounded from the water
†Recommended ditching attitude and flap setting.

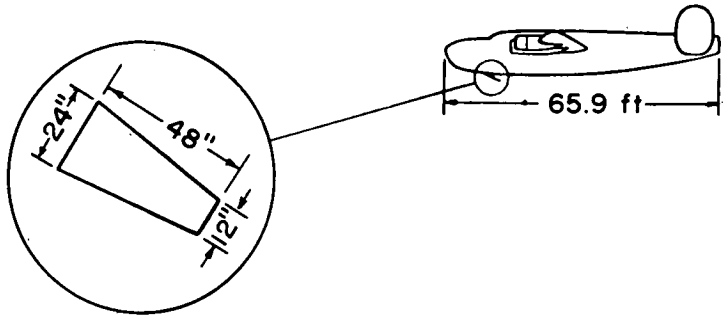
Remarks: The bomb-bay doors on this airplane are exceptionally weak and will probably fail in a ditching. The tests of models indicated that failure of the bomb-bay doors caused a diving moment. The amount of damage to the bulkhead aft of the bomb bay determined the severity of the behavior of the airplane.

TABLE 4—Concluded

SUMMARY OF MODEL-DITCHING INVESTIGATION OF BOMBER D

(b) With hydroflap.

Damage same as shown in three-view sketch. Hydroflap as indicated.



Landing attitude, deg	Flap setting, deg	Landing speed, knots	Length of run, ft	Maximum longitudinal deceleration, g units	Average longitudinal deceleration, g units	Motions of model (*)
1	40	104	450	------	1	p
†6	40	87	300	------	1	p
9	40	87	350	------	1	p

*In this column, the letters indicate the following motions:
p porpoised—the model undulated about the transverse axis with some part of the model always in contact with water
†Recommended ditching attitude and flap setting.

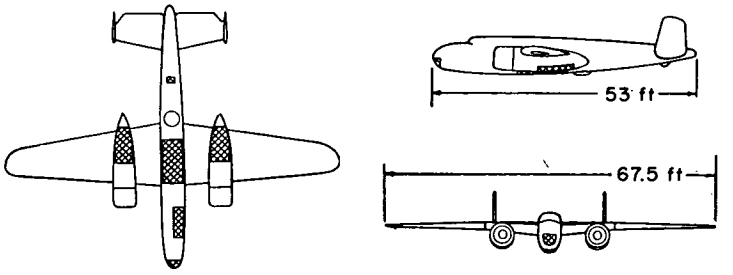
Remarks: The hydroflap was considered the most practical of several ditching aids which were tested on this model.

TABLE 5

SUMMARY OF MODEL-DITCHING INVESTIGATION OF BOMBER E

[Model scale, $\frac{1}{11}$; gross weight, 26,000 lb; center-of-gravity location, 25 percent M.A.C.; all values full scale]

Damage simulated by removal of parts (crosshatched areas).



Landing attitude, deg	Flap setting, deg	Landing speed, knots	Length of run, ft	Maximum longitudinal deceleration, g units	Average longitudinal deceleration, g units	Motions of model (*)
Undamaged model						
0	0	104	200	3½	2½	h
0	45	104	250	4	2	t
6	0	104	250	3	2	h
6	45	87	150	3	2	h
12	0	104	300	3	1½	h
12	45	87	200	3½	1½	h
Damaged model						
0	45	104	350	2½	1½	s
6	45	87	250	3	1½	b
†12	45	87	150	3½	2	b

*In this column, the letters indicate the following motions:
b ran deeply—the model settled deeply into the water with little change in attitude
h ran smoothly—the model made a very stable run
s skipped—the model rebounded from the water
t turned sharply—the model pivoted quickly about a vertical axis
†Recommended ditching attitude and flap setting.

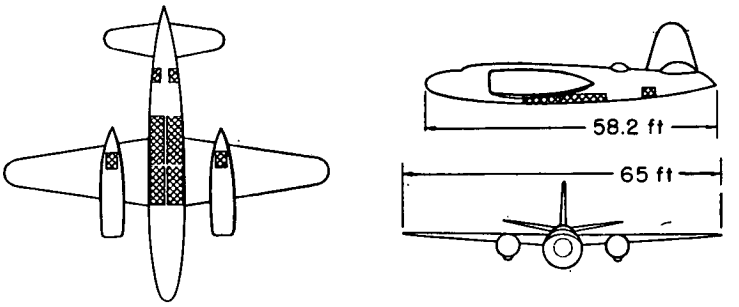
Remarks: The performance of the model was not appreciably changed by simulation of damage. The model ran deeper in the water with the parts removed, but the behavior in general was similar. The large nacelles tended to cause violent turns when one wing was low.

TABLE 6

SUMMARY OF MODEL-DITCHING INVESTIGATION OF BOMBER F

[Model scale, $\frac{1}{12}$; gross weight, 31,000 lb; center-of-gravity location, 14 percent M.A.C.; all values full scale]

Damage simulated by removal of parts (crosshatched areas).



Landing attitude, deg	Flap setting, deg	Landing speed, knots	Length of run, ft	Maximum longitudinal deceleration, g units	Average longitudinal deceleration, g units	Motions of model (*)
Undamaged model						
−1	0	122	400	------	1½	u h
−1	55	104	400	2	1	u h
6	0	104	350	------	1½	u h
6	55	104	350	------	1½	u s
13	0	104	300	------	1½	h
13	55	104	350	2	1½	h
Damaged model						
−1	55	104	400	3	1	s
†6	55	104	350	4	1½	s
13	55	104	300	6	1½	s

*In this column, the letters indicate the following motions:
h ran smoothly—the model made a very stable run
s skipped—the model rebounded from the water
u trimmed up—the attitude of the model increased while running in the water
†Recommended ditching attitude and flap setting.

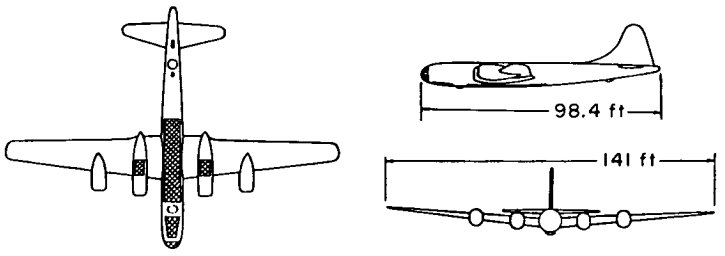
Remarks: The model had a trimming-up tendency in the undamaged condition. The large nacelles caused sharp turns when the model was ditched with one wing low.

TABLE 7

SUMMARY OF MODEL-DITCHING INVESTIGATION OF BOMBER G

[Model scale, $\frac{1}{20}$; gross weight, 105,000 lb; center-of-gravity location, 25 percent M.A.C.; all values full scale]

Damage simulated by removal of parts (crosshatched areas).



Landing attitude, deg	Flap setting, deg	Landing speed, knots	Length of run, ft	Maximum longitudinal deceleration, g units	Average longitudinal deceleration, g units	Motions of model (*)
Undamaged model						
1	45	122	250	8	2½	d_1
5	45	104	650	1	½	h
9	0	122	850	2	1	h
9	45	87	450	1	½	h
13	0	104	700	2	½	h
13	45	87	200	1½	1½	d_2
Damaged model						
1	45	122	600	------	1	p
			200	------	3½	d_1
5	45	104	350	------	1½	p
†9	45	87	300	------	1	h
13	45	87	250	------	1½	h

*In this column, the letters indicate the following motions:
d_1 dived violently—the model stopped abruptly in a nose-down attitude with most of the model submerged
d_2 dived slightly—the model stopped abruptly in a nose-down attitude with nose of the model submerged
h ran smoothly—the model made a very stable run
p porpoised—the model undulated about the transverse axis with some part of the model always in contact with the water
†Recommended ditching attitude and flap setting.

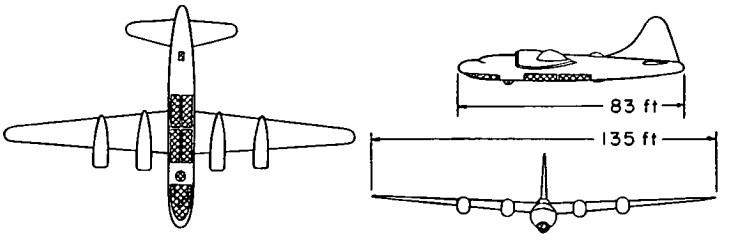
Remarks: The scale-strength landing flaps on the model did not fail consistently. When the flaps did not fail, the model usually dived.

TABLE 8

SUMMARY OF MODEL-DITCHING INVESTIGATION OF BOMBER H

[Model scale, $\frac{1}{20}$; gross weight, 100,000 lb; center-of-gravity location, 30 percent M.A.C.; all values full scale]

Damage simulated by removal of parts (crosshatched areas).



Landing attitude, deg	Flap setting, deg	Landing speed, knots	Length of run, ft	Maximum longitudinal deceleration, g units	Average longitudinal deceleration, g units	Motions of model (*)
Undamaged model						
0	40	122	550	1½	1	u h b
6	40	102	500	2	1	u h b
13	0	115	600	2	1	h b
13	40	88	450	1½	1	h b
Damaged model						
0	40	122	450	4	1½	p b
†6	40	102	350	4½	1½	h b
13	40	88	400	3½	1	h b

*In this column, the letters indicate the following motions:
b ran deeply—the model settled deeply into the water with little change in attitude
h ran smoothly—the model made a very stable run
p porpoised—the model undulated about the transverse axis with some part of the model always in contact with the water
u trimmed up—the attitude of the model increased while running in the water
†Recommended ditching attitude and flap setting.

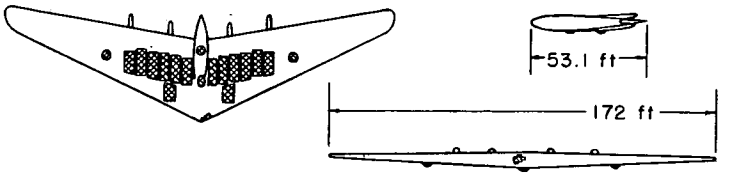
Remarks: Decelerations were increased when damage was simulated, but the behavior of the model was not appreciably changed.

TABLE 9

SUMMARY OF MODEL-DITCHING INVESTIGATION OF BOMBER I

Model scale, $\frac{1}{20}$; gross weight, 150,000 lb; center-of-gravity location, 25 percent M.A.C.; all values full scale]

Damage simulated by removal of parts (crosshatched areas).



Landing attitude, deg	Flap setting, deg	Landing speed, knots	Length of run, ft	Maximum longitudinal deceleration, g units	Average longitudinal deceleration, g units	Motions of model (*)
Undamaged model						
9	50	111	400	--------	1½	h t p t
Damaged model						
4	50	124	500	5	1½	u p t
†9	50	111	300	5	2	u p
9	50	111	300	6	2	u p t
14	50	98	250	6	1½	b
14	50	98	250	7	1½	b t

*In this column, the letters indicate the following motions:
b ran deeply—the model settled deeply into the water with little change in attitude
h ran smoothly—the model made a very stable run
p porpoised—the model undulated about the transverse axis with some part of the model always in contact with the water
t turned sharply—the model pivoted quickly about a vertical axis
u trimmed up—the attitude of the model increased while running in the water
†Recommended ditching attitude and flap setting.

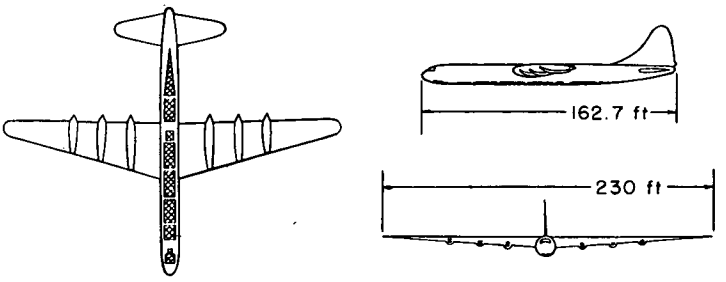
Remarks: The most pronounced ditching characteristic of this bomber model was its tendency to turn or yaw. Construction of the airplane is such that extensive damage is to be expected and it probably will be difficult to find ditching stations where crew members can adequately brace themselves and be reasonably sure of avoiding an inrush of water.

TABLE 10

SUMMARY OF MODEL-DITCHING INVESTIGATION OF BOMBER J

[Model scale, $\frac{1}{20}$ and $\frac{1}{30}$; gross weight, 255,000 lb; center-of-gravity location, 29 percent M.A.C.; all values full scale]

Damage simulated by removal of parts (crosshatched area).



Landing attitude, deg	Flap setting, deg	Landing speed, knots	Length of run, ft	Maximum longitudinal deceleration, g units	Average longitudinal deceleration, g units	Motions of model (*)
Undamaged 1/30-scale model						
1	40	124	1,000	--------	½	u h
1	40	124	1,000	--------	½	u s
5	40	106	650	--------	1	h
9	0	119	650	--------	1	h
9	40	95	1,000	--------	½	h
13	0	108	1,000	--------	½	p
13	40	87	650	--------	½	h
Damaged 1/20-scale model						
1	40	124	-----	4	--------	b
†9	40	95	-----	2	--------	h

*In this column, the letters indicate the following motions:
b ran deeply—the model settled deeply into the water with little change in attitude
h ran smoothly—the model made a very stable run
p porpoised—the model undulated about the transverse axis with some part of the model always in contact with the water
s skipped—the model rebounded from the water
u trimmed up—the attitude of the model increased while running in the water
†Recommended ditching attitude and flap setting.

Remarks: The behavior of the model was generally good. No violent motions such as diving occurred, and the maximum longitudinal deceleration recorded was about 4g.

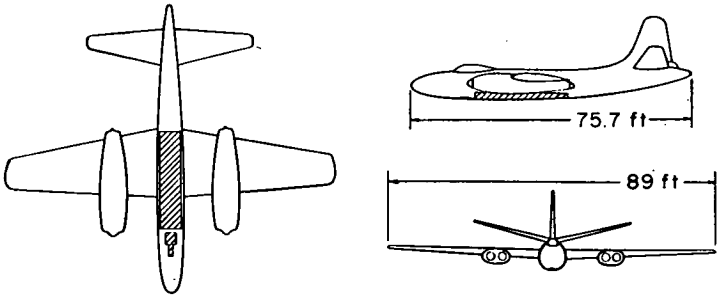
TABLE 11

SUMMARY OF MODEL-DITCHING INVESTIGATION OF BOMBER K

[Model scale, $\frac{1}{18}$; gross weight, 82,600 lb; center-of-gravity location, 29 percent M.A.C.; all values full scale]

(a) Without hydroflap.

Damage simulated by removal of parts and covering of openings with aluminum foil (hatched areas).



Landing attitude, deg	Flap setting, deg	Landing speed, knots	Length of run, ft	Maximum longitudinal deceleration, g units	Average longitudinal deceleration, g units	Motions of model (*)
Undamaged model						
2	40	131	950	1½	1	u h
6	40	119	850	1	½	u h
Damaged model						
2	40	131	200	9½	4	d_1
†6	40	119	300	5	2	d_1

*In this column, the letters indicate the following motions:
d_1 dived violently—the model stopped abruptly in a nose-down attitude with most of the model submerged
h ran smoothly—the model made a very stable run
u trimmed up—the attitude of the model increased while running in the water
†Recommended ditching attitude and flap setting.

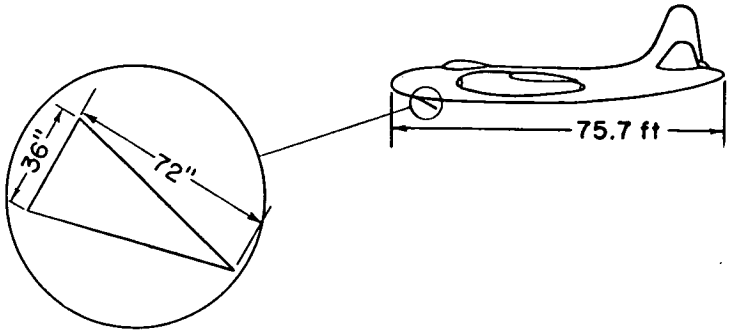
Remarks: The scale-strength bomb-bay doors and nose-wheel doors consistently failed on the model. The dives that occurred were very violent. Additional data have indicated that if the bulkhead and part of the fuselage bottom aft of the bomb bay fail in a ditching, diving may not occur.

TABLE 11—Concluded

SUMMARY OF MODEL-DITCHING INVESTIGATION OF BOMBER K

(b) With hydroflap.

Damage same as shown in three-view sketch. Hydroflap as indicated.



Landing attitude, deg	Flap setting, deg	Landing speed, knots	Length of run, ft	Maximum longitudinal deceleration, g units	Average longitudinal deceleration, g units	Motions of model (*)
2	40	131	720	3½	1	s p
†6	40	119	540	3½	1	s p

*In this column, the letters indicate the following motions:
p porpoised—the model undulated about the transverse axis with some part of the model always in contact with the water
s skipped—the model rebounded from the water
†Recommended ditching attitude and flap setting.

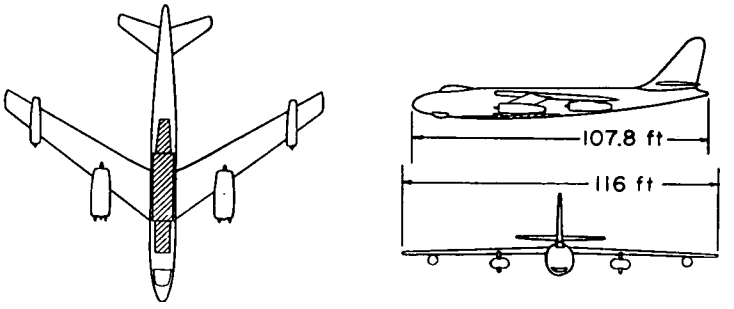
Remarks: The hydroflap stopped the diving and reduced the deceleration. It also kept the nose-wheel doors from failing.

TABLE 12

SUMMARY OF MODEL-DITCHING INVESTIGATION OF BOMBER L

[Model scale, $\frac{1}{24}$; gross weight, 125,000 lb; center-of-gravity location, 20 percent M.A.C.; all values full scale]

Damage simulated by removal of parts and covering of openings with aluminum foil (hatched areas).



Landing attitude, deg	Flap setting, deg	Landing speed, knots	Length of run, ft	Maximum longitudinal deceleration, g units	Average longitudinal deceleration, g units	Motions of model (*)
Undamaged model						
5	35	134	650	2	1	u s p
10	0	155	700	3	1½	h
10	35	120	650	2	1	h
15	35	115	550	1½	1	h
Damaged model						
5	35	134	650	3	1	b
†10	35	120	550	2½	1	h
15	35	115	450	3	1½	b

*In this column, the letters indicate the following motions:
b ran deeply—the model settled deeply into the water with little change in attitude
h ran smoothly—the model made a very stable run
p porpoised—the model undulated about the transverse axis with some part of the model always in contact with the water
s skipped—the model rebounded from the water
u trimmed up—the attitude of the model increased while running in the water
†Recommended ditching attitude and flap setting.

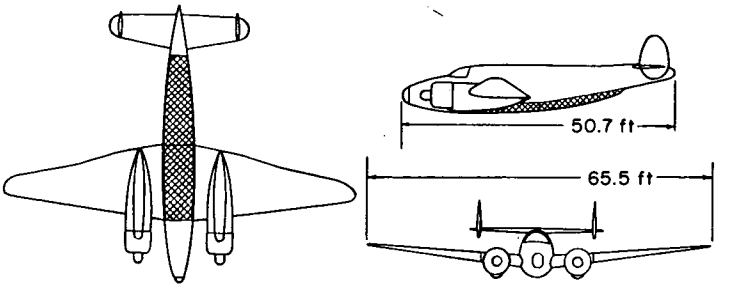
Remarks: Additional tests with the nacelles attached at scale strength indicated that the nacelles will probably be torn off in a ditching but will have little or no effect on behavior. The simulated main-wheel doors failed.

TABLE 13

SUMMARY OF MODEL-DITCHING INVESTIGATION OF BOMBER M

[Model scale, $\frac{1}{11}$; gross weight, 26,500 lb; center-of-gravity location, 30 percent M.A.C.; all values full scale]

Damage simulated by removal of part (crosshatched area).



Landing attitude, deg	Flap setting, deg	Landing speed, knots	Length of run, ft	Maximum longitudinal deceleration, g units	Average longitudinal deceleration, g units	Motions of model (*)
Undamaged model						
2	38	113	450	4	1	s p
7	0	122	650	------	1	s t
7	38	87	450	1½	1	p
12	0	104	700	1	1	h
12	38	87	350	2	1	h
Damaged model						
2	38	122	400	------	1½	s p
7	38	87	300	------	1	p
†12	38	87	300	------	1	p

*In this column, the letters indicate the following motions:
h ran smoothly—the model made a very stable run
p porpoised—the model undulated about the transverse axis with some part of the model always in contact with the water
s skipped—the model rebounded from the water
t turned sharply—the model pivoted quickly about a vertical axis
†Recommended ditching attitude and flap setting.

Remarks: From examination of full-scale ditching reports on this airplane, it is believed that the fuselage bottom section aft of the bomb bay will be torn away in a ditching with the results indicated above. If this section does not fail, violent dives occur.

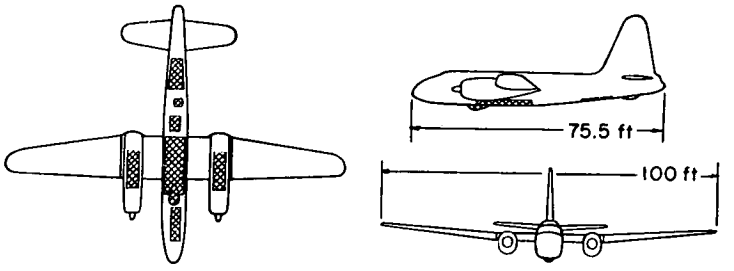
TABLE 14

SUMMARY OF MODEL-DITCHING INVESTIGATION OF BOMBER N

[Model scale, $\frac{1}{16}$; gross weight, 45,000 lb; center-of-gravity location, 29 percent M.A.C.; all values full scale]

(a) Without hydroflap or hydro-skis.

Damage simulated by removal of parts (crosshatched areas).



Landing attitude, deg	Flap setting, deg	Landing speed, knots	Length of run, ft	Maximum longitudinal deceleration, g units	Average longitudinal deceleration, g units	Motions of model (*)
Undamaged model						
2	32	89	400	2	1	u h
6	0	121	700	2	1	h
6	32	78	300	2	1	h
10	0	102	550	1½	1	h
10	32	71	300	2	1	h
Damaged model						
2	32	89	150	6	2½	d_1
†6	32	78	150	4	2	d_1
10	32	71	100	3½	2½	d_1

*In this column, the letters indicate the following motions:
d_1 dived violently—the model stopped abruptly in a nose-down attitude with most of the model submerged
h ran smoothly—the model made a very stable run
u trimmed up—the attitude of the model increased while running in the water
†Recommended ditching attitude and flap setting.

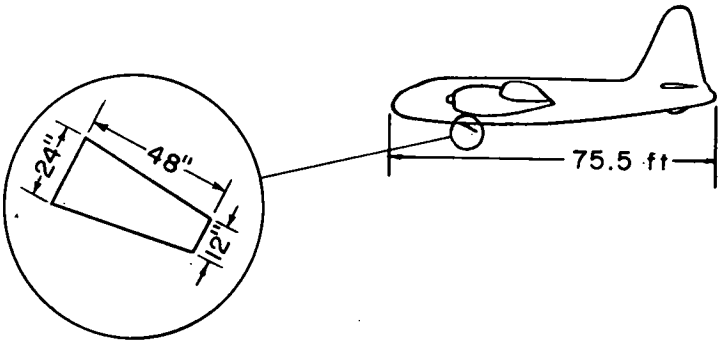
Remarks: Data obtained from the manufacturer indicates that the fuselage bottom is extremely weak so that considerable damage with this airplane could be expected. The diving caused by simulated damage was very violent.

TABLE 14—Concluded

SUMMARY OF MODEL-DITCHING INVESTIGATION OF BOMBER N

(b) With hydroflap.

Damage same as shown in three-view sketch except nose-wheel doors not removed. Hydroflap as indicated.



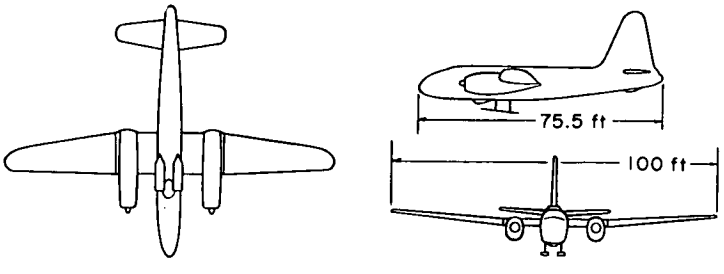
Landing attitude, deg	Flap setting, deg	Landing speed, knots	Length of run, ft	Maximum longitudinal deceleration, g units	Average longitudinal deceleration, g units	Motions of model (*)
2	32	89	450	3	1	p h
†6	32	78	300	3½	1	p h
10	32	71	250	4	1	p h

*In this column, the letters indicate the following motions:
h ran smoothly—the model made a very stable run
p porpoised—the model undulated about the transverse axis with some part of the model always in contact with water
†Recommended ditching attitude and flap setting.

Remarks: The location of the hydroflap on this airplane was critical. When located forward of the nose-wheel doors, it did not stop the diving.

(c) With hydro-skis.

No damage simulated. Skis as indicated.



Landing attitude, deg	Flap setting, deg	Landing speed, knots	Length of run, ft	Maximum longitudinal deceleration, g units	Average longitudinal deceleration, g units	Motions of model (*)
2	32	89	1, 350	1	½	h
6	32	78	950	--	½	h
10	32	71	500	½	½	h

*In this column, the letters indicate the following motions:
h ran smoothly—the model made a very stable run

Remarks: The ditching behavior with the hydro-skis was very good. It is possible that critical damage can be eliminated from ditchings by using a hydro-ski ditching gear, and thus the chances of survival and rescue would be greatly increased.

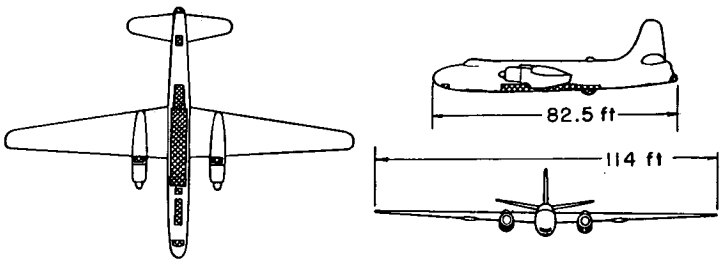
TABLE 15

SUMMARY OF MODEL-DITCHING INVESTIGATION OF BOMBER O

[Model scale, $\frac{1}{18}$; gross weight, 55,000 lb; center-of-gravity location, 22 percent M.A.C.; all values full scale]

(a) Without hydroflap.

Damage simulated by removal of parts (crosshatched areas).



Landing attitude, deg	Flap setting, deg	Landing speed, knots	Length of run, ft	Maximum longitudinal deceleration, g units	Average longitudinal deceleration, g units	Motions of model (*)
Undamaged model						
1	40	98	300	------	1½	h
7	0	108	400	------	1½	p
7	40	88	300	------	1	p
13	0	98	300	------	1½	h
13	40	82	300	------	1	h
Damaged model						
1	40	95	100	4½	4	d_2
†7	40	89	200	3	2	p
†7	40	89	100	4½	3½	d_2
13	40	82	150	3½	2	d_2
13	40	82	150	3½	2	t

*In this column, the letters indicate the following motions:
d_2 dived slightly—the model stopped abruptly in a nose-down attitude with the nose of the model submerged
h ran smoothly—the model made a very stable run
p porpoised—the model undulated about the transverse axis with some part of the model always in contact with the water
t turned sharply—the model pivoted quickly about a vertical axis
†Recommended ditching attitude and flap setting.

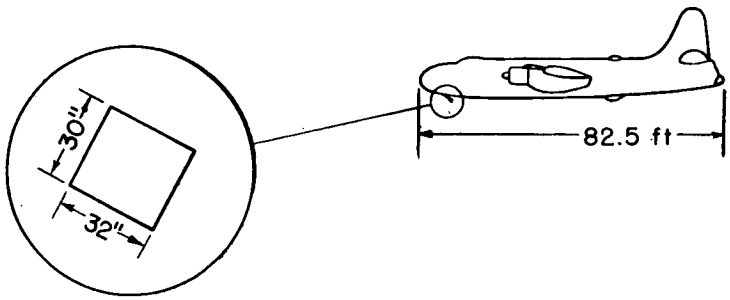
Remarks: The behavior of the damaged model varied inconsistently.

TABLE 15—Concluded

SUMMARY OF MODEL-DITCHING INVESTIGATION OF BOMBER O

(b) With hydroflap.

Damage same as shown in three-view sketch. Navigator's escape hatch (open at an angle of 30° to the thrust line) used as hydroflap.



Landing attitude, deg	Flap setting, deg	Landing speed, knots	Length of run, ft	Maximum longitudinal deceleration, g units	Average longitudinal deceleration, g units	Motions of model (*)
1	40	95	150	3	2½	p
†7	40	85	150	2½	2	p
13	40	82	150	3	2	p

*In this column, the letters indicate the following motions:
p porpoised—the model undulated about the transverse axis with some part of the model always in contact with water
†Recommended ditching attitude and flap setting.

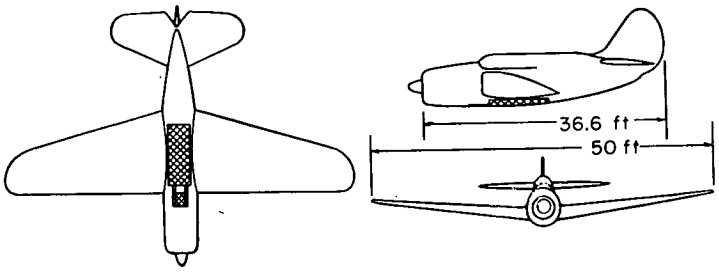
Remarks: The hydroflap is recommended as a ditching aid on this airplane to stop the diving that sometimes occurred. It also reduced the decelerations slightly.

TABLE 16

SUMMARY OF MODEL-DITCHING INVESTIGATION OF BOMBER P

[Model scale, $\frac{1}{8}$; gross weight, 13,060 lb; center-of-gravity location, 30 percent M.A.C.; all values full scale]

Damaged simulated by removal of parts (crosshatched areas).



Landing attitude, deg	Flap setting, deg	Landing speed, knots	Length of run, ft	Maximum longitudinal deceleration, g units	Average longitudinal deceleration, g units	Motions of model (*)
Damaged model						
2	30	113	150	8	4	d_1
2	60	104	100	5½	5	d_1
2	60	104	---	------	------	s
8	0	113	400	6½	1½	s
8	0	113	---	------	------	p
8	30	95	200	5	2	d_1
8	60	87	150	7	2	d_1
8	60	87	---	------	------	s
15	0	87	200	4½	1½	d_1
15	0	87	---	------	------	b
15	30	78	150	5	2	d_1
15	60	69	200	4	1	d_1
15	60	69	---	------	------	s b

*In this column, the letters indicate the following motions:
b ran deeply—the model settled deeply into the water with little change in attitude
d_1 dived violently—the model stopped abruptly in a nose-down attitude with most of the model submerged
p porpoised—the model undulated about the transverse axis with some part of the model always in contact with the water
s skipped—the model rebounded from the water

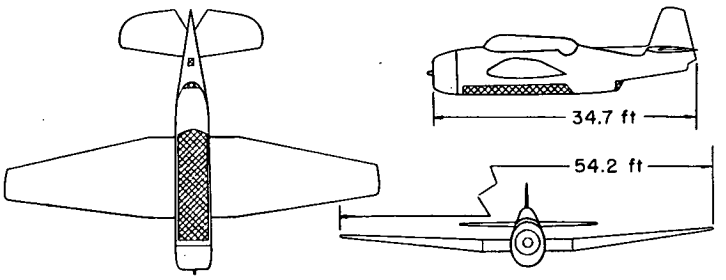
Remarks: The landing flaps were very strong on this scout bomber. When they failed, the model skipped or made a deep run; when they did not fail, the model dived.

TABLE 17

SUMMARY OF MODEL-DITCHING INVESTIGATION OF BOMBER Q

[Model scale, $\frac{1}{9}$; gross weight, 13,795 lb; center-of-gravity location, 26 percent M.A.C.; all values full scale]

Damage simulated by removal of parts (crosshatched areas).



Landing attitude, deg	Flap setting, deg	Landing speed, knots	Length of run, ft	Maximum longitudinal deceleration, g units	Average longitudinal deceleration, g units	Motions of model (*)
Undamaged model						
3	45	80	500	------	½	p h
7	0	86	550	------	½	s h
7	45	76	400	2	½	p h
11	0	85	500	1½	½	p h
11	45	68	450	1	½	p h
Damaged model						
3	45	77	100	4½	2½	d_1
†7	45	76	150	3½	1½	d_1
11	45	66	100	------	2	d_1

*In this column, the letters indicate the following motions:
d_1 dived violently—the model stopped abruptly in a nose-down attitude with most of the model submerged
h ran smoothly—the model made a very stable run
p porpoised—the model undulated about the transverse axis with some part of the model always in contact with the water
s skipped—the model rebounded from the water
†Recommended ditching attitude and flap setting.

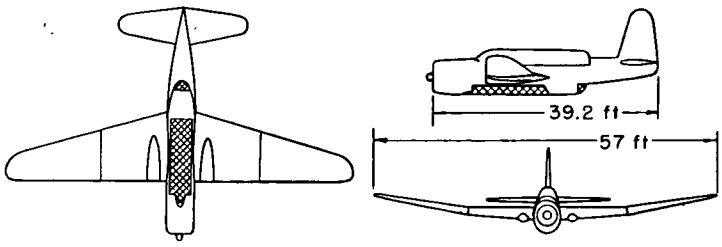
Remarks: Full-scale reports have indicated that all personnel aboard this airplane have a good chance to survive a ditching, and if the radioman moves to the upper part of the fuselage, his chances will be improved.

TABLE 18

SUMMARY OF MODEL-DITCHING INVESTIGATION OF BOMBER R

[Model scale, $\frac{1}{9}$; gross weight, 16,925 lb; center-of-gravity location, 32 percent M.A.C.; all values full scale]

Damage simulated by removal of parts (crosshatched areas).



Landing attitude, deg	Flap setting, deg	Landing speed, knots	Length of run, ft	Maximum longitudinal deceleration, g units	Average longitudinal deceleration, g units	Motions of model (*)
Undamaged model						
2	50	96	600	------	½	s
7	0	108	800	------	½	s
7	50	85	500	------	½	s
12	0	89	550	------	½	p
12	50	78	550	------	½	p
18	0	85	500	------	½	s p
18	50	71	450	------	½	p h
Damaged model						
2	50	100	80	------	5½	d_1
7	50	87	100	------	3½	d_1
†12	50	78	100	------	2½	d_1
18	50	71	100	------	2	d_1

*In this column, the letters indicate the following motions:
d_1 dived violently—the model stopped abruptly in a nose-down attitude with most of the model submerged
h ran smoothly—the model made a very stable run
p porpoised—the model undulated about the transverse axis with some part of the model always in contact with the water
s skipped—the model rebounded from the water.
†Recommended ditching attitude and flap setting.

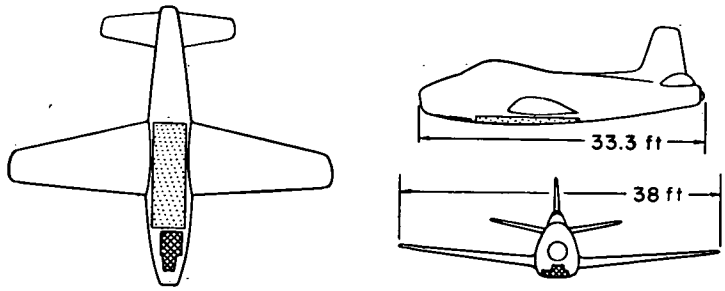
Remarks: This airplane closely resembles bomber Q. The ditching behavior of the models was similar, but the higher landing speeds of bomber R gave higher average decelerations.

TABLE 19

SUMMARY OF MODEL-DITCHING INVESTIGATION OF FIGHTER A

[Model scale, $\frac{1}{10}$; gross weight, 12,151 lb; center-of-gravity location, 23 percent M.A.C.; all values full scale]

Damage simulated by removal of parts (crosshatched areas) and installation of crumpled parts (dotted areas).



Landing attitude, deg	Flap setting, deg	Landing speed, knots	Length of run, ft	Maximum longitudinal deceleration, g units	Average longitudinal deceleration, g units	Motions of model (*)
Undamaged model						
2	40	128	650	9½	1	u s d_1
8	40	104	1, 000	4	½	u s h
12	0	118	900	6	½	u s p
12	40	94	700	2½	½	u s p h
Damaged model						
2	40	128	900	5	1	u s h
8	40	104	700	3	½	u s p h
†12	40	94	600	2½	½	h u p h

*In this column, the letters indicate the following motions:
d_1 dived violently—the model stopped abruptly in a nose-down attitude with most of the model submerged
h ran smoothly—the model made a very stable run
p porpoised—the model undulated about the transverse axis with some part of the model always in contact with the water
s skipped—the model rebounded from the water
u trimmed up—the attitude of the model increased while running in the water
†Recommended ditching attitude and flap setting.

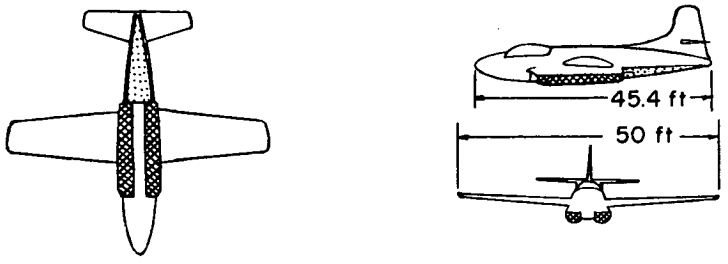
Remarks: The undamaged model trimmed up and skipped violently when it contacted the water. Simulation of damage improved the ditching behavior by reducing the trimming up and skipping.

TABLE 20

SUMMARY OF MODEL-DITCHING INVESTIGATION OF FIGHTER B

[Model scale, $\frac{1}{12}$; gross weight, 25,000 lb; center-of-gravity location, 22 percent M.A.C.; all values full scale]

Damage simulated by removal of parts (crosshatched areas) and installation of crumpled parts (dotted areas).



Landing attitude, deg	Flap setting, deg	Landing speed, knots	Length of run, ft	Maximum longitudinal deceleration, g units	Average longitudinal deceleration, g units	Motions of model (*)
Undamaged model						
4	40	127	550	------	1½	s t
8	0	139	1, 150	5	½	s p
8	40	111	600	2	1	u h
12	0	122	1, 200	4½	½	s p
12	40	101	650	2	½	u o
Damaged model						
4	40	127	650	------	1	s p
8	0	139	600	11	1½	h
†8	40	111	550	2	1	h
12	0	122	550	5	1	h
12	40	101	500	3	1	h

*In this column, the letters indicate the following motions:
h ran smoothly—the model made a very stable run
o oscillated—the model oscillated about the longitudinal or vertical axis
p porpoised—the model undulated about the transverse axis with some part of the model always in contact with the water
s skipped—the model rebounded from the water
t turned sharply—the model pivoted quickly about a vertical axis
u trimmed up—the attitude of the model increased while running in the water
†Recommended ditching attitude and flap setting.

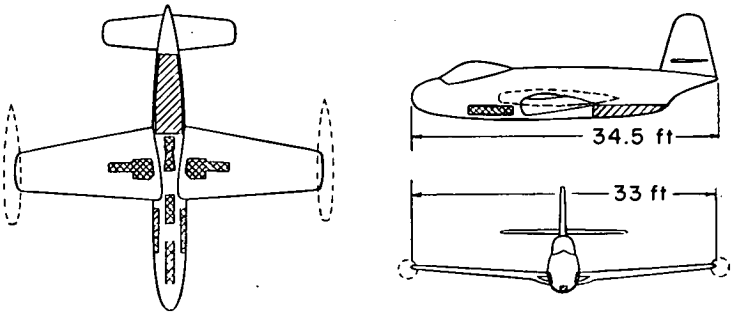
Remarks: The jet engines located below the fuselage did not cause diving in this installation, but a very high maximum longitudinal deceleration was obtained at one condition. Simulation of damage stopped the model from trimming up.

TABLE 21

SUMMARY OF MODEL-DITCHING INVESTIGATION OF FIGHTER C

[Model scale, $\frac{1}{8}$; gross weight, 9,706 lb; center-of-gravity location, 31 percent M.A.C.; all values full scale]

Damage simulated by use of scale-strength parts (hatched areas) and removal of other parts (crosshatched areas).



Landing attitude, deg	Flap setting, deg	Landing speed, knots	Length of run, ft	Maximum longitudinal deceleration, g units	Average longitudinal deceleration, g units	Motions of model (*)
Undamaged model						
4	27	124	500	2	1½	u s p
8	27	107	550	1	1	u s p
12	27	97	400	2	1	u p
Damaged model						
4	27	124	200	9	3½	p d_2
8	27	107	150	10	3½	d_1
†12	27	97	100	7	4	d_1

*In this column, the letters indicate the following motions:
d_1 dived violently—the model stopped abruptly in a nose-down attitude with most of the model submerged
d_2 dived slightly—the model stopped abruptly in a nose-down attitude with the nose of the model submerged
p porpoised—the model undulated about the transverse axis with some part of the model always in contact with the water
s skipped—the model rebounded from the water
u trimmed up—the attitude of the model increased while running in the water
†Recommended ditching attitude and flap setting.

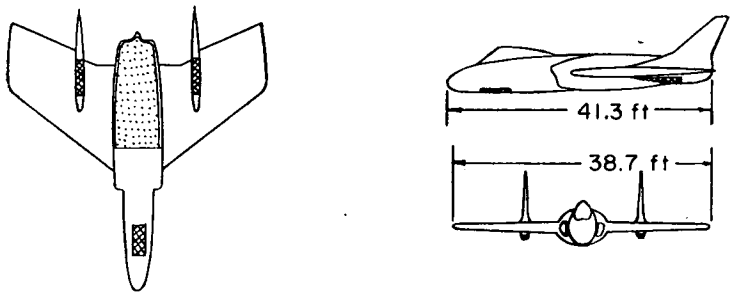
Remarks: The trimming up and diving of this model was extremely severe. The pilot should make sure that the safety harness is securely fastened in order to withstand the decelerations.

TABLE 22

SUMMARY OF MODEL-DITCHING INVESTIGATION OF FIGHTER D

[Model scale, $\frac{1}{11}$; gross weight, 22,800 lb; center-of-gravity location, 12 percent M.A.C.; all values full scale]

Damage simulated by removal of parts (crosshatched areas) and installation of crumpled parts (dotted areas).



Landing attitude, deg	Ailavator setting, deg	Landing speed, knots	Length of run, ft	Maximum longitudinal deceleration, g units	Average longitudinal deceleration, g units	Motions of model (*)
Undamaged model						
18	−20	131	940	------	1	u s
23	−30	117	870	2	½	s p
28	−40	106	720	1½	½	s p
Damaged model						
18	−20	131	600	------	1½	u s
23	−30	117	540	3½	1	s p
28	−40	106	500	3½	1	p

*In this column, the letters indicate the following motions:
p porpoised—the model undulated about the transverse axis with some part of the model always in contact with the water
s skipped—the model rebounded from the water
u trimmed up—the attitude of the model increased while running in the water

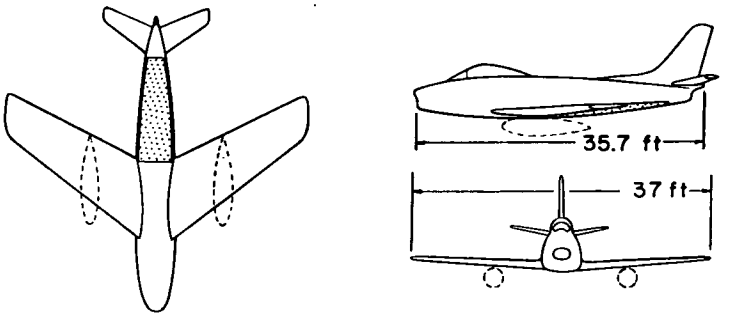
Remarks: The airplane can land at extremely high attitudes and should be ditched at the lowest speed and highest attitude consistent with adequate control.

TABLE 23

SUMMARY OF MODEL-DITCHING INVESTIGATION OF FIGHTER E

[Model scale, $\frac{1}{10}$; gross weight, 13,311 lb; center-of-gravity location, 22 percent M.A.C.; all values full scale]

Damage simulated by installation of crumpled part (dotted area).



Landing attitude, deg	Flap setting, deg	Landing speed, knots	Length of run, ft	Maximum longitudinal deceleration, g units	Average longitudinal deceleration, g units	Motions of model (*)
Undamaged model						
4	38	132	300	8	2½	d_1
9	38	109	800	1	½	h
14	0	113	700	2½	1	p s
14	38	98	650	1½	½	h
Damaged model						
4	38	132	200	7½	4	d_1
9	38	109	600	3	1	h
†14	38	98	600	3	½	h

*In this column, the letters indicate the following motions:
d_1 dived violently—the model stopped abruptly in a nose-down attitude with most of the model submerged
h ran smoothly—the model made a very stable run
p porpoised—the model undulated about the transverse axis with some part of the model always in contact with the water
s skipped—the model rebounded from the water
†Recommended ditching attitude and flap setting.

Remarks: Extreme care should be taken to avoid the violent dive at the low attitude. The tanks under the wing should be jettisoned before ditching.

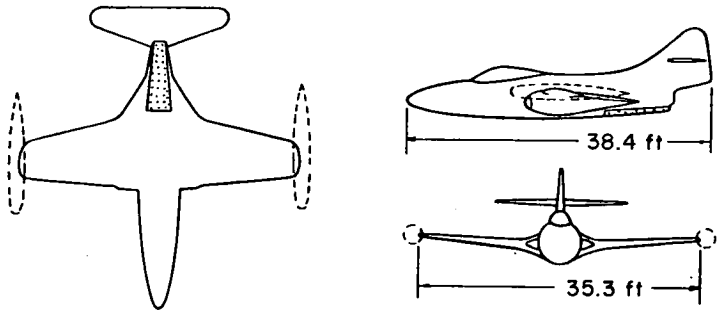
TABLE 24

SUMMARY OF MODEL-DITCHING INVESTIGATION OF FIGHTER F

[Model scale, $\frac{1}{10}$; gross weight, 12,100 lb; center-of-gravity location, 27 percent M.A.C.; all values full scale]

(a) Without hydroflap.

Damage simulated by installation of crumpled part (dotted area).



Landing attitude, deg	Flap setting, deg	Landing speed, knots	Length of run, ft	Maximum longitudinal deceleration, g units	Average longitudinal deceleration, g units	Motions of model (*)
Undamaged model						
4	Inboard 20 Outboard 55	133	740	5	1	s p
8	Inboard 20 Outboard 55	115	760	3	1	s p
12	Inboard 20 Outboard 55	102	590	2	1	s p
Damaged model						
4	Inboard 20 Outboard 55	133	760	5	1	s p
8	Inboard 20 Outboard 55	115	685	3	1	s p
†12	Inboard 20 Outboard 55	102	700	2	½	s p

*In this column, the letters indicate the following motions:
p porpoised—the model undulated about the transverse axis with some part of the model always in contact with the water
s skipped—the model rebounded from the water
†Recommended ditching attitude and flap setting.

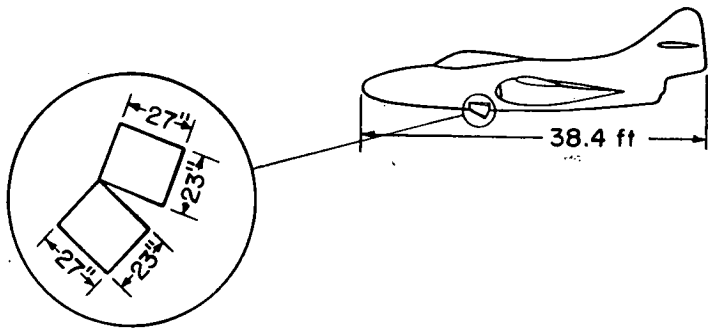
Remarks: This model made rather long runs with severe skipping.

TABLE 24—Concluded

SUMMARY OF MODEL-DITCHING INVESTIGATION OF FIGHTER F

(b) With hydroflap.

Damage same as shown on three-view sketch. Speed brake (open at angle of 30° to thrust line) used as hydroflap.



Landing attitude, deg	Flap setting, deg	Landing speed, knots	Length of run, ft	Maximum longitudinal deceleration, g units	Average longitudinal deceleration, g units	Motions of model (*)
8	Inboard 20 Outboard 55	115	765	2	1	s p
†12	Inboard 20 Outbaord 55	102	595	2	1	p s p

*In this column, the letters indicate the following motions:
p porpoised—the model undulated about the transverse axis with some part of the model always in contact with the water
s skipped—the model rebounded from the water
†Recommended ditching attitude and flap setting.

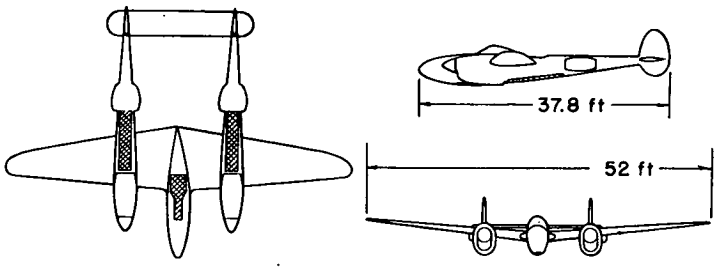
Remarks: The severity of the skipping was reduced by using the hydroflap.

TABLE 25

SUMMARY OF MODEL-DITCHING INVESTIGATION OF FIGHTER G

[Model scale, $\frac{1}{9}$; gross weight, 14,900 lb; center-of-gravity location, 28 percent M.A.C.; all values full scale]

Damage simulated by removal of parts (crosshatched areas).



Landing attitude, deg	Flap setting, deg	Landing speed, knots	Length of run, ft	Maximum longitudinal deceleration, g units	Average longitudinal deceleration, g units	Motions of model (*)
Undamaged model						
5	37	100	250	6	2	s
9	0	115	250	------	2½	b
9	37	88	200	4	1½	s o
13	0	100	250	8	2	b
13	37	79	200	------	1½	s
Damaged model						
2	37	113	100	------	5½	s d_2
5	37	100	200	------	2	s
†9	37	88	200	------	1½	s
†13	37	79	250	------	1	s

*In this column, the letters indicate the following motions:
b ran deeply—the model settled deeply into the water with little change in attitude
d_2 dived slightly—the model stopped abruptly in a nose-down attitude with the nose of the model submerged
o oscillated—the model oscillated about the longitudinal or vertical axis
s skipped—the model rebounded from the water
†Recommended ditching attitude and flap setting.

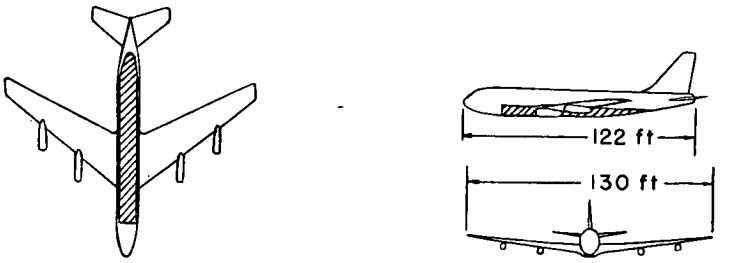
Remarks: The landing speed was the most important variable affecting performance of this airplane. At high speeds, the highest deceleration and the most violent behaviors were encountered. A tail-down attitude (from 9° to 13°) is recommended.

TABLE 26

SUMMARY OF MODEL-DITCHING INVESTIGATION OF TRANSPORT A

[Model scale, 0.043; gross weight, 130,000 lb; center-of-gravity location, 26 percent M.A.C.; all values full scale]

Damage simulated by scale-strength parts (hatched area) and scale-strength nacelle struts.



Landing attitude, deg	Flap setting, deg	Landing speed, knots	Length of run, ft	Maximum longitudinal deceleration, g units	Average longitudinal deceleration, g units	Motions of model (*)
Undamaged model with scale-strength nacelle struts						
6	0	146	1,100	2½	1	s b
6	50	113	1,040	2½	½	h
9	0	127	1,090	2½	½	h
9	50	104	850	1½	½	h
12	0	119	890	1½	½	h
12	50	100	640	2	½	h
Damaged model with scale-strength nacelle struts						
6	0	146	700	6½	1½	b
6	50	113	450	6	1½	h
9	0	127	500	5½	1½	h
9	50	104	420	5	1	h
12	0	119	480	6½	1½	h
†12	50	100	470	5	1	h

*In this column, the letters indicate the following motions:
b ran deeply—the model settled deeply into the water with little change in attitude
h ran smoothly—the model made a very stable run
s skipped—the model rebounded from the water
†Recommended ditching attitude and flap setting.

Remarks: One or more of the nacelles were frequently torn off in a ditching but had little or no effect on behavior.

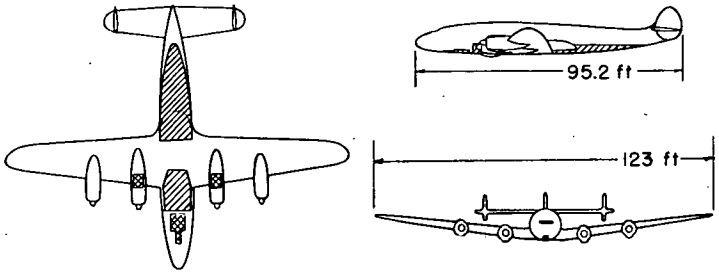
TABLE 27

SUMMARY OF MODEL-DITCHING INVESTIGATION OF TRANSPORT B

[Model scale, $\frac{1}{18}$; gross weight, 83,000 lb; center-of-gravity location, 25 percent M.A.C.; all values full scale]

(a) Without cargo container or hydro-ski.

Damage simulated by use of scale-strength parts (hatched areas) and removal of other parts (crosshatched areas).



Landing attitude, deg	Flap setting, deg	Landing speed, knots	Length of run, ft	Maximum longitudinal deceleration, g units	Average longitudinal deceleration, g units	Motions of model (*)
Undamaged model						
4	0	148	900	6	1	s h
4	40	91	250	4	1½	d_2
9	0	115	600	2	1	u h
9	40	79	400	4	½	b
12	0	102	600	1	1	h
12	40	74	250	3	1	b
Damaged model						
4	40	91	200	4	2	b d_2
†9	40	79	350	3	1	b d_2
12	40	74	200	4	1	h b

*In this column, the letters indicate the following motions:
b ran deeply—the model settled deeply into the water with little change in attitude
d_2 dived slightly—the model stopped abruptly in a nose-down attitude with the nose of the model submerged
h ran smoothly—the model made a very stable run
s skipped—the model rebounded from the water
u trimmed up—the attitude of the model increased while running in the water
†Recommended ditching attitude and flap setting.

Remarks: The fuselage will probably be damaged and leak substantially.

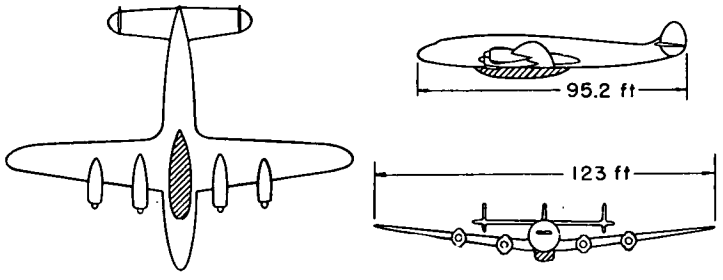
TABLE 27—Concluded

SUMMARY OF MODEL-DITCHING INVESTIGATION OF TRANSPORT B

[Gross weight of airplane plus cargo container, 93,000 lb; all values full scale]

(b) With cargo container

Model undamaged. Scale-strength cargo container (hatched area) attached as indicated.



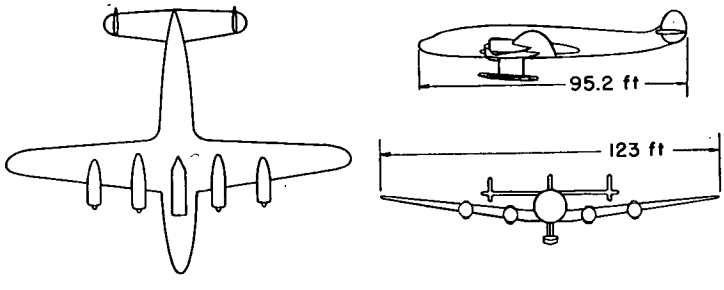
Landing attitude, deg	Flap setting, deg	Landing speed, knots	Length of run, ft	Maximum longitudinal deceleration, g units	Average longitudinal deceleration, g units	Motions of model (*)
4	40	95	650	--	½	h d_2
†9	40	85	500	1½	½	h b
12	40	78	250	2	1	h b

*In this column, the letters indicate the following motions:
b ran deeply—the model settled deeply into the water with little change in attitude
d_2 dived slightly—the model stopped abruptly in a nose-down attitude with the nose of the model submerged
h ran smoothly—the model made a very stable run
†Recommended ditching attitude and flap setting.

Remarks: The bottom of the cargo container was damaged considerably and evidently absorbed some of the landing loads. The decelerations were less and the behavior of the model was more favorable. The cargo container also protected the fuselage bottom.

(c) With hydro-ski.

No damage simulated. Ski as shown.



Landing attitude, deg	Flap setting, deg	Landing speed, knots	Length of run, ft	Maximum longitudinal deceleration, g units	Average longitudinal deceleration, g units	Motions of model (*)
4	40	91	1,220	½	½	h
9	40	79	720	--	½	h p

*In this column, the letters indicate the following motions:
h ran smoothly—the model made a very stable run
p porpoised—the model undulated about the transverse axis with some part of the model always in contact with the water

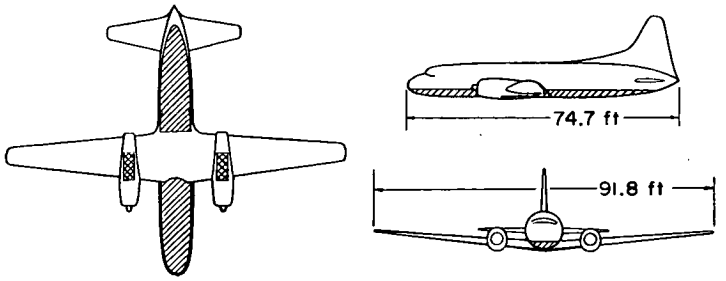
Remarks: The ditching behavior with the hydro-ski was very good. It is possible that critical damage can be eliminated from ditchings by using a hydro-ski ditching gear, thus greatly increasing the chances of survival and rescue.

TABLE 28

SUMMARY OF MODEL-DITCHING INVESTIGATION OF TRANSPORT C

[Model scale, $\frac{1}{15}$; gross weight, 43,500 lb; center-of-gravity location, 22 percent M.A.C.; all values full scale]

Damage simulated by use of scale-strength parts (hatched areas) and removal of other parts (crosshatched areas).



Landing attitude, deg	Flap setting, deg	Landing speed, knots	Length of run, ft	Maximum longitudinal deceleration, g units	Average longitudinal deceleration, g units	Motions of model (*)
Undamaged model						
1	0	164	850	4	1½	u h
1	39	100	350	5	1½	u h
5	0	122	650	3	1	u h
5	39	88	400	1½	1	h
9	0	105	600	3½	1	h
9	39	82	400	1	½	h
Damaged model						
5	0	122	250	8	2½	h b
5	39	88	300	3½	1	h
9	0	105	300	6	1½	h
†9	39	82	300	3	1	h

*In this column, the letters indicate the following motions:
b ran deeply—the model settled deeply into the water with little change in attitude
h ran smoothly—the model made a very stable run
u trimmed up—the attitude of the model increased while running in the water
†Recommended ditching attitude and flap setting.

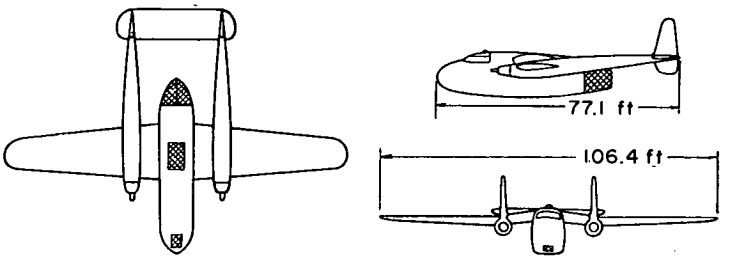
Remarks: The landing flaps were an important factor in the ditching behavior of this model. Failure of the scale-strength flaps was simulated by the flaps rotating up or being torn from the model. When the flaps rotated up, the model dived; but when the flaps were torn away, the model performed as indicated above.

TABLE 29

SUMMARY OF MODEL-DITCHING INVESTIGATION OF TRANSPORT D

[Model scale, $\frac{1}{15}$; gross weight, 50,000 lb; center-of-gravity location, 25 percent M.A.C.; all values full scale]

Damage simulated by removal of parts (crosshatched areas).



Landing attitude, deg	Flap setting, deg	Landing speed, knots	Length of run, ft	Maximum longitudinal deceleration, g units	Average longitudinal deceleration, g units	Motions of model (*)
Undamaged model						
2	40	109	700	1	1	u s p
7	40	90	300	2	1	u b
12	40	78	350	1	1	u b
Damaged model						
2	40	109	450	2½	1	u b
7	40	90	350	2	1	b
†12	40	78	300	1	1	b

*In this column, the letters indicate the following motions:
b ran deeply—the model settled deeply into the water with little change in attitude
p porpoised—the model undulated about the transverse axis with some part of the model always in contact with the water
s skipped—the model rebounded from the water
u trimmed up—the attitude of the model increased while running in the water
†Recommended ditching attitude and flap setting.

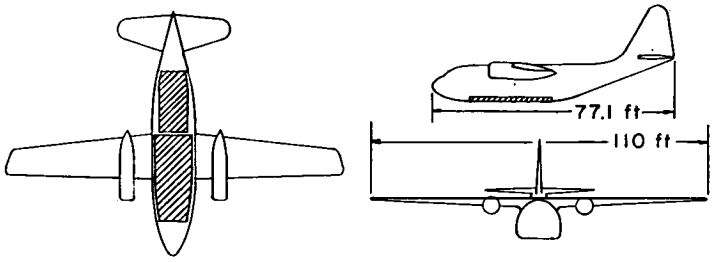
Remarks: The undamaged model trimmed up considerably when it contacted the water. Damage to the fuselage bottom greatly reduced the trimming up and caused the cargo compartment to flood rapidly, and thus to become a very hazardous ditching station.

TABLE 30

SUMMARY OF MODEL-DITCHING INVESTIGATION OF TRANSPORT E

[Model scale, $\frac{1}{14}$; gross weight, 44,000 lb; center-of-gravity location, 22 percent M.A.C.; all values full scale]

Damage simulated by scale-strength parts (hatched areas).



Landing attitude, deg	Flap setting, deg	Landing speed, knots	Length of run, ft	Maximum longitudinal deceleration, g units	Average longitudinal deceleration, g units	Motions of model (*)
Undamaged model						
4	45	80	385	------	½	u s
9	45	71	350	------	½	u h
14	45	65	350	------	½	u h
Damaged model						
4	45	80	450	2	½	s p
9	45	71	450	1½	½	h
†14	45	65	415	1	½	p

*In this column, the letters indicate the following motions:
h ran smoothly—the model made a very stable run
p porpoised—the model undulated about the transverse axis with some part of the model always in contact with the water
s skipped—the model rebounded from the water
u trimmed up—the attitude of the model increased while running in the water
†Recommended ditching attitude and flap setting.

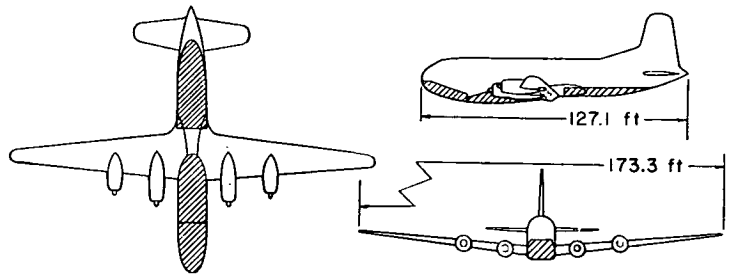
Remarks: The fuselage bottom will probably be damaged and the fuselage will fill with water and sink to the wing level.

TABLE 31

SUMMARY OF MODEL-DITCHING INVESTIGATION OF TRANSPORT F

[Model scale, $\frac{1}{24}$; gross weight, 175,000 lb; center-of-gravity location, 27 percent M.A.C.; all values full scale]

Damage simulated by use of scale-strength parts (hatched areas).



Landing attitude, deg	Flap setting, deg	Landing speed, knots	Length of run, ft	Maximum longitudinal deceleration, g units	Average longitudinal deceleration, g units	Motions of model (*)
Undamaged model						
2	40	109	750	2	½	u h
7	0	157	1, 150	2	1	u h
7	40	96	800	1	½	u h
12	0	123	900	2	½	h
12	40	91	700	2½	½	h
Damaged model						
2	40	109	550	4	1	h
†7	40	96	500	2½	1	h
12	40	91	500	4½	1	p

*In this column, the letters indicate the following motions:
h ran smoothly—the model made a very stable run
p porpoised—the model undulated about the transverse axis with some part of the model always in contact with the water
u trimmed up—the attitude of the model increased while running in the water
†Recommended ditching attitude and flap setting.

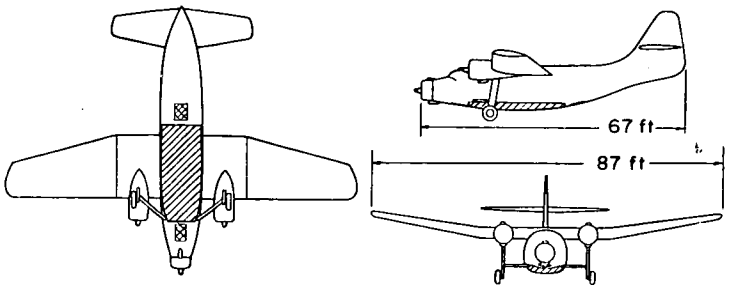
Remarks: The large clamshell doors in the nose of this airplane and the unusual shape of the fuselage bottom forward of the wing were of particular interest. With the scale-strength parts installed, only slight damage occurred to the clamshell doors and aft fuselage bottom, but considerable damage was sustained by the region just forward of the wing. However, the high location of the main floor should provide adequate ditching stations.

TABLE 32

SUMMARY OF MODEL-DITCHING INVESTIGATION OF TRANSPORT G

[Model scale, $\frac{1}{14}$; gross weight, 35,123 lb; center-of-gravity location, 31 percent M.A.C.; all values full scale]

Damage simulated by use of scale-strength parts (hatched areas) and removal of other parts (crosshatched areas).



Landing attitude, deg	Flap setting, deg	Landing speed, knots	Length of run, ft	Maximum longitudinal deceleration, g units	Average longitudinal deceleration, g units	Motions of model (*)
Undamaged model						
0	55	64	150	2½	1	d_1
4	0	102	200	5	2½	f
4	55	60	200	2	1	d_2
8	0	87	150	4	2	d_1
8	55	56	150	2	1	d_2
Damaged model						
0	55	64	150	4	1	d_1
4	55	60	150	2	1	d_2
†8	55	56	150	2	1	d_2

*In this column, the letters indicate the following motions:
d_1 dived violently—the model stopped abruptly in a nose-down attitude with most of the model submerged
d_2 dived slightly—the model stopped abruptly in a nose-down attitude with the nose of the model submerged
f flipped over—the model rotated about the transverse axis and stopped in an inverted position
†Recommended ditching attitude and flap setting.

Remarks: The fixed landing gear on this model caused diving and flipping over. When the gear was removed the model either ran smoothly or skipped and porpoised.

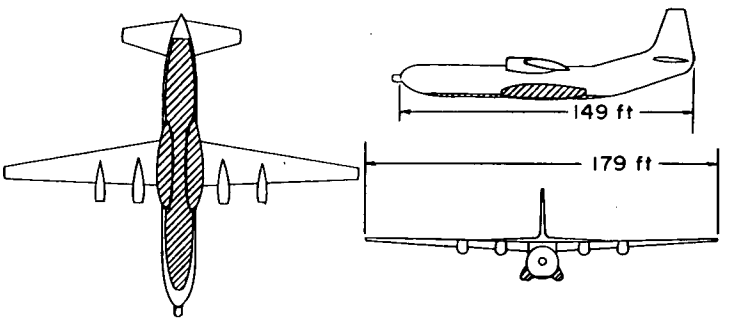
TABLE 33

SUMMARY OF MODEL-DITCHING INVESTIGATION OF TRANSPORT H

[Model scale, $\frac{1}{25}$; gross weight, 255,000 lb; center-of-gravity location, 25 percent M.A..C.; all values full scale]

(a) Without hydroflap.

Damage simulated by use of scale-strength parts (hatched areas).



Landing attitude, deg	Flap setting, deg	Landing speed, knots	Length of run, ft	Maximum longitudinal deceleration, g units	Average longitudinal deceleration, g units	Motions of model (*)
Undamaged model						
1	45	120	1, 270	2	½	u s h
5	0	155	1, 400	2½	1	s o
5	45	110	690	1½	1	u h
10	0	137	1, 490	2½	½	s
10	45	102	980	1½	½	u h
Damaged model						
1	45	120	570	2	1	b u h
5	0	155	810	5	1½	d_2 u h
5	45	110	580	3	1	b u h
10	0	137	740	5½	1	d_2 u h
†10	45	102	550	3	1	b u h

*In this column, the letters indicate the following motions:
b ran deeply—the model settled deeply into the water with little change in attitude
d_2 dived slightly—the model stopped abruptly in a nose-down attitude with the nose of the model submerged
h ran smoothly—the model made a very stable run
o oscillated—the model oscillated about the longitudinal or vertical axis
s skipped—the model rebounded from the water
u trimmed up—the attitude of the model increased while running in the water
†Recommended ditching attitude and flap setting.

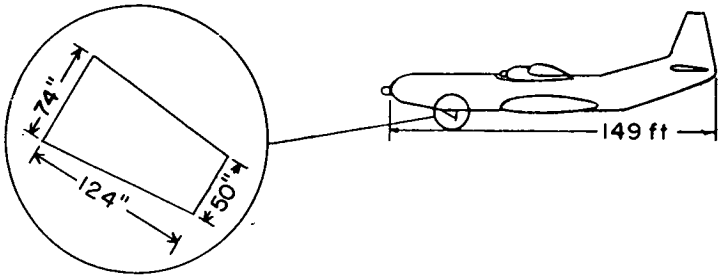
Remarks: With scale-strength fuselage bottoms installed, the model had a tendency to dive during the first part of the ditiching run, but recovered and ran smoothly. The landing-gear nacelles did not affect the ditching behavior. The fuselage is likely to flood rapidly and sink to the level of the wing.

TABLE 33—Concluded

SUMMARY OF MODEL-DITCHING INVESTIGATION OF TRANSPORT H

(b) With hydroflap.

Damage same as shown in three-view sketch. Hydroflap as indicated.



Landing attitude, deg	Flap setting, deg	Landing speed, knots	Length of run, ft	Maximum longitudinal deceleration, g units	Average longitudinal deceleration, g units	Motions of model (*)
5	45	110	690	2	1	h
†10	45	102	610	2½	1	p

*In this column, the letters indicate the following motions:
h ran smoothly—the model made a very stable run
p porpoised—the model undulated about the transverse axis with some part of the model always in contact with the water
†Recommended ditching attitude and flap setting.

Remarks: The hydroflap stopped the tendency to dive and decreased the amount of damage to the scale-strength sections.

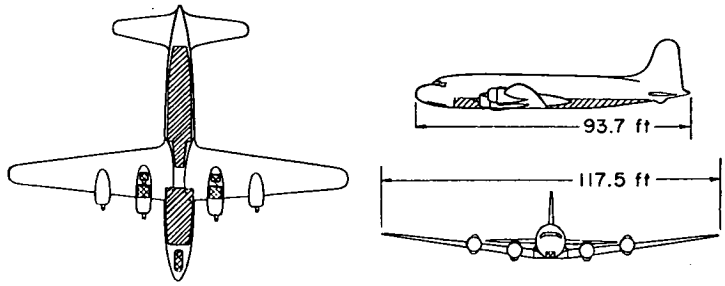
TABLE 34

SUMMARY OF MODEL-DITCHING INVESTIGATION OF TRANSPORT I

[Model scale, $\frac{1}{16}$; gross weight, 72,000 lb; center-of-gravity location, 28 percent M.A.C.; all values full scale]

(a) Without hydro-skis.

Damage simulated by use of scale-strength parts (hatched areas) and removal of other parts (crosshatched areas).



Landing attitude, deg	Flap setting, deg	Landing speed, knots	Length of run, ft	Maximum longitudinal deceleration, g units	Average longitudinal deceleration, g units	Motions of model (*)
Undamaged model						
2	50	98	650	2	½	h
7	50	87	600	1	½	h
12	50	79	450	1½	½	h
Damaged model						
7	50	87	200	6	1½	b
†12	50	79	250	4½	1	b

*In this column, the letters indicate the following motions:
b ran deeply—the model settled deeply into the water with little change in attitude
h ran smoothly—the model made a very stable run
†Recommended ditching attitude and flap setting.

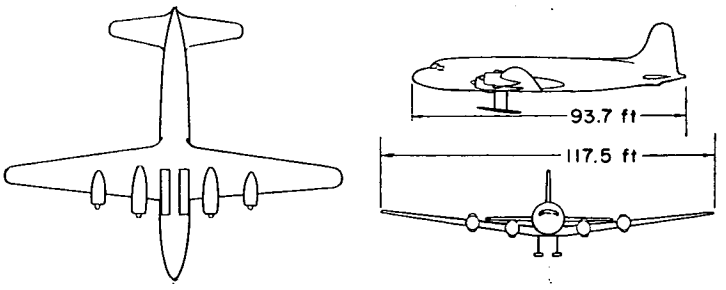
Remarks: The damage sustained by the scale-strength sections was not severe in calm water ditchings.

TABLE 34—Concluded

SUMMARY OF MODEL-DITCHING INVESTIGATION OF TRANSPORT I

(b) With hydro-skis.

No damage simulated. Hydro-skis as indicated.



Landing attitude, deg	Flap setting, deg	Landing speed, knots	Length of run, ft	Maximum longitudinal deceleration, g units	Average longitudinal deceleration, g units	Motions of model (*)
2	50	95	1,300	------	½	h
7	50	88	750	------	½	h

*In this column, the letters indicate the following motions:
h ran smoothly—the model made a very stable run

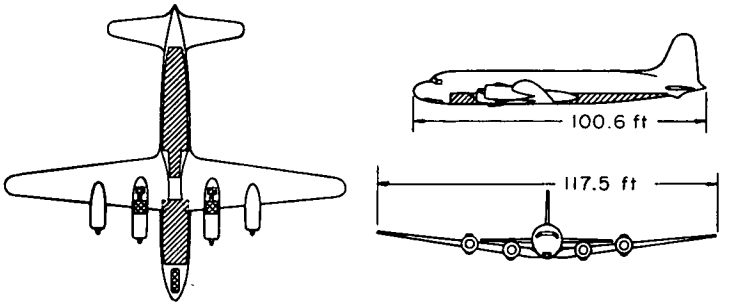
Remarks: The ditching behavior with the hydro-skis was very good. It is possible that critical damage can be eliminated from ditchings by using a hydro-ski ditching gear, and thus the chances of survival and rescue would be increased.

TABLE 35

SUMMARY OF MODEL-DITCHING INVESTIGATION OF TRANSPORT J

[Model scale, $\frac{1}{16}$; gross weight, 84,000 lb; center-of-gravity location, 28 percent M.A.C.; all values full scale]

Damage simulated by use of scale-strength parts (hatched areas) and removal of other parts (crosshatched areas).



Landing attitude, deg	Flap setting, deg	Landing speed, knots	Length of run, ft	Maximum longitudinal deceleration, g units	Average longitudinal deceleration, g units	Motions of model (*)
Undamaged model						
2	50	106	700	3	½	h
7	50	94	600	1	½	h
12	0	109	550	2	1	h
12	50	85	450	1½	½	h
Damaged model						
7	50	94	250	5	1½	b
†12	50	85	250	3½	1½	b

*In this column, the letters indicate the following motions:
b ran deeply—the model settled deeply into the water with little change in attitude
h ran smoothly—the model made a very stable run
†Recommended ditching attitude and flap setting.

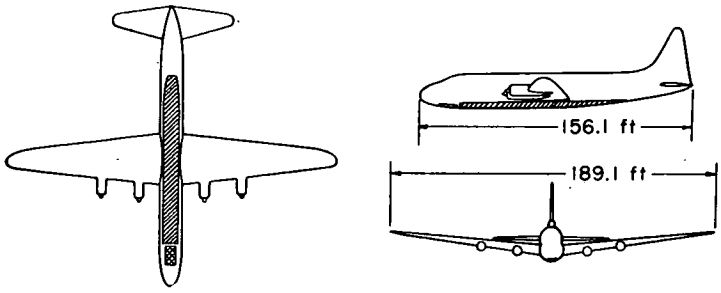
Remarks: The damage sustained by the scale-strength sections was not severe in calm water ditchings.

TABLE 36

SUMMARY OF MODEL-DITCHING INVESTIGATION OF TRANSPORT K

[Model scale, $\frac{1}{24}$; gross weight, 160,000 lb; center-of-gravity location, 40 percent M.A.C.; all values full scale]

Damage simulated by use of scale-strength parts (hatched areas) and removal of other parts (crosshatched areas).



Landing attitude, deg	Flap setting, deg	Landing speed, knots	Length of run, ft	Maximum longitudinal deceleration, g units	Average longitudinal deceleration, g units	Motions of model (*)
Undamaged model						
1	45	90	450	1	1	u h
5	0	115	800	2	½	h
5	45	79	450	½	½	u h
9	0	96	600	1	½	h
9	45	72	450	1	½	h
Damaged model						
1	45	90	300	2½	1	b
†5	45	79	300	2	1	b h
9	45	72	300	2	1	b

*In this column, the letters indicate the following motions:
b ran deeply—the model settled deeply into the water with little change in attitude
h ran smoothly—the model made a very stable run
u trimmed up—the attitude of the model increased while running in the water
†Recommended ditching attitude and flap setting.

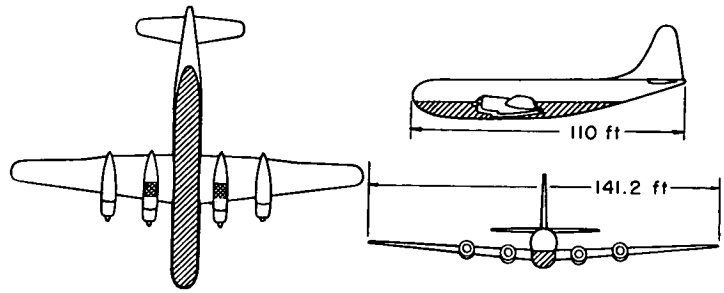
Remarks: The scale-strength sections did not sustain severe damage. Most damage usually occurred near the part of the fuselage that contacted the water first. It is likely that the cargo floor will not fail and that the interior of the airplane will be relatively safe in a ditching.

TABLE 37

SUMMARY OF MODEL DITCHING INVESTIGATION OF TRANSPORT L

[Model scale, $\frac{1}{20}$; gross weight, 130,000 lb; center-of-gravity location, 25 percent M.A.C.; all values full scale]

Damage simulated by use of scale-strength parts (hatched areas) and removal of other parts (crosshatched areas).



Landing attitude, deg	Flap setting, deg	Landing speed, knots	Length of run, ft	Maximum longitudinal deceleration, g units	Average longitudinal deceleration, g units	Motions of model (*)
Undamaged model						
3	45	109	650	2	1	u h
6	45	102	500	2	1	u h
9	0	129	800	3	1	u p
9	45	97	450	2	1	u o h
Damaged model						
3	45	109	400	3	1½	h
†6	45	102	400	4	1	p h
9	45	97	350	4	1	b h

*In this column, the letters indicate the following motions:
b ran deeply—the model settled deeply into the water with little change in attitude
h ran smoothly—the model made a very stable run
o oscillated—the model oscillated about the longitudinal or vertical axis
p porpoised—the model undulated about the transverse axis with some part of the model always in contact with the water
u trimmed up—the attitude of the model increased while running in the water
†Recommended ditching attitude and flap setting.

Remarks: The scale-strength sections sustained damage. The lower compartment of this airplane will probably fill with water. However, the strong cargo floor should provide protection for the upper deck and the low wing should provide enough buoyancy to give personnel time to escape.

REPORT 1348

GROUND SIMULATOR STUDIES OF THE EFFECTS OF VALVE FRICTION, STICK FRICTION, FLEXIBILITY, AND BACKLASH ON POWER CONTROL SYSTEM QUALITY[1]

By B. Porter Brown

SUMMARY

Tests have been made on a power control system by means of a ground simulator to determine the effects of various combinations of valve friction and stick friction on the ability of the pilot to control the system. Various friction conditions were simulated with a rigid control system, a flexible system, and a rigid system having some backlash. For the tests, the period and damping of the simulated airplane were held constant.

The results show that, when valve friction was present in a rigid system, the introduction of stick friction was beneficial in that it restored some of the quality lost because of the valve friction. When flexibility was introduced between the pilot and the source of stick friction, stick friction was still beneficial but, with flexibility between the source of stick friction and the valve, no benefits were obtained from stick friction. When backlash was introduced between the pilot and the source of stick friction, the valve-friction effect was not so objectionable as in the rigid system; stick friction improved this system still further. With backlash between the stick and the valve (± 0.025 inch at the valve), even the frictionless system was undesirable, and the addition of any combination of the frictions reduced the control quality still further.

INTRODUCTION

The ability of the pilot to control an airplane is dependent on a great number of control-system variables such as friction, backlash, and flexibility. Insofar as is known, no systematic study has been made to determine the effects of these variables. The National Advisory Committee for Aeronautics therefore has built a dynamic ground simulator for the purpose of such a study. In view of the large number of variables involved, it is doubtful that a precise definition of the optimum combination of these variables can be established; however, it is believed that the results will lead to a better understanding of each effect and may suggest some general design rules.

Previous investigations (for example, ref. 1) have shown that servocontrol-valve friction can reduce the quality of a power control system to such an extent that sensitivity problems and, in some cases, pilot-induced oscillations will result. It was suspected that the valve-friction effect is greatly dependent upon the mechanical characteristics of the linkages between the pilot and the valve such as static friction, flexibility, and backlash. Therefore, tests were made to study the effects of various ratios of valve friction to stick friction. The term "stick friction" is used hereinafter to denote the static friction in the mechanical parts of the system between the pilot and the valve. Various friction ratios were tested with a rigid control system, a flexible control system, and a rigid control system with backlash. For these tests the period and damping of the simulated airplane, the power-control time constant, the stick-force gradient, and the control-surface sensitivity were held constant. The results in this report are therefore limited to the fixed values of these parameters.

SYMBOLS

t	time, sec
α	angle of attack, deg
δ	control-surface deflection, deg
$\dot{\gamma}$	rate of change of flight-path angle, deg/sec
θ	attitude angle, deg
ζ	damping ratio
ω_n	natural frequency, radians/sec
D	differential operator, d/dt
$\left(\frac{\alpha}{\delta}\right)_0$	steady-state ratio of α to δ

APPARATUS

Figure 1 shows a photograph of the simulator used in the tests and figure 2 presents a schematic drawing of the simulator. The simulator consisted of a chair that was designed

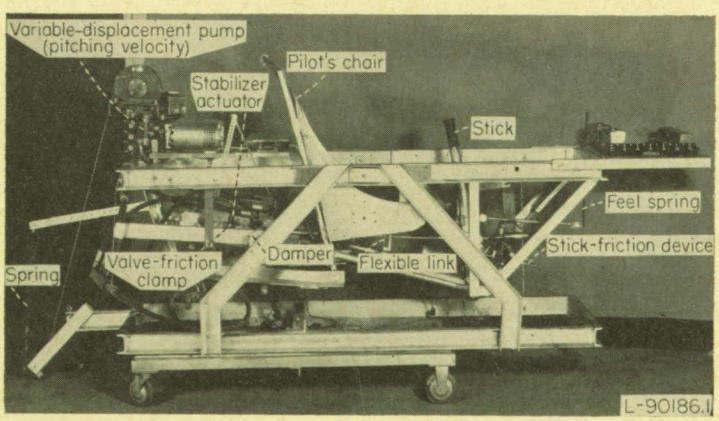


FIGURE 1.—Longitudinal power control simulator (Pitch chair).

[1] Supersedes NACA Technical Note 3998 by B. Porter Brown, 1957.

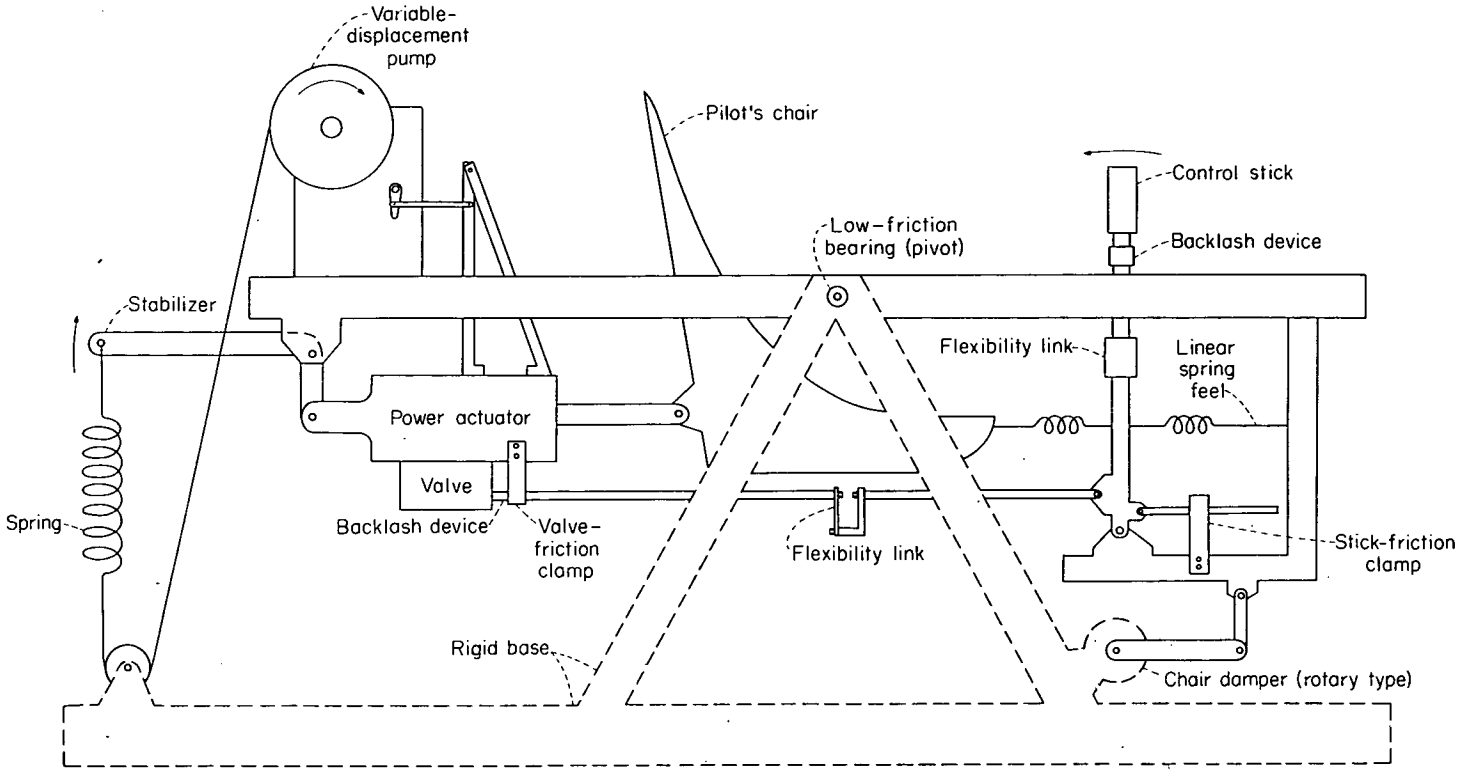


FIGURE 2.—Schematic drawing of simulator. Solid lines indicate movable parts. Arrows indicate direction of motion of stick, stabilizer, and pump drum associated with pull-up.

to pitch in response to control deflection. The pitching motion, which is closely associated with the short-period mode of an airplane, is expressed by the following equation:

$$\text{Chair angle}=\theta=\frac{\alpha}{\delta}\delta+\frac{\alpha}{\delta}\frac{\dot{\gamma}}{\alpha}\int_0^t \delta\, dt \qquad (1)$$

The term α/δ is the transfer function of a single-degree-of-freedom system with spring restraint and viscous damping. This transfer function may be written as follows:

$$\frac{\alpha}{\delta}=\left(\frac{\alpha}{\delta}\right)_0 \frac{{\omega_n}^2}{D^2+2\zeta\omega_n D+{\omega_n}^2} \qquad (2)$$

This expression neglects the effects of tail lift on the acceleration at the center of gravity. The term $\dot{\gamma}/\alpha$ is the transfer function relating rate of change of flight-path angle to angle of attack. If the tail lift and unsteady lift effects are neglected, this term is a constant for any given flight condition.

A slide-valve-type power control unit typical of those used in present-day fighter airplanes was installed to act as the driving unit to pitch the chair. The piston rod of the actuator was attached to the chair and the end of the cylinder body was attached to a spring through a bellcrank. As can be seen from figure 2, extension or retraction of the actuator moved the bellcrank. This bellcrank can be considered to be representative of an airplane's longitudinal control surface. Motion of this bellcrank δ, when multiplied by the transfer function α/δ, supplies the first term in equation (1).

A cable was attached to the other end of the spring and passed around a pulley connected to the rigid support. This cable was geared to a hydraulic motor which was driven by a variable-displacement pump. The input arm of the variable-displacement pump was mechanically linked to the output of the power control actuator. This linkage determines the steady-state value of the product $\frac{\alpha}{\delta}\frac{\dot{\gamma}}{\alpha}$ in equation (1). Since no followup system was attached to the variable-displacement pump, motion of the power control actuator not only moved the "tail surface" and caused an initial change in angle of attack but signaled the variable-displacement pump to rotate the drum at a rate proportional to the displacement of the power control actuator. Thus, the variable-displacement pump produces the integration of δ shown in equation (1). Since the variable-displacement pump also moves the chair through the same spring to which the power actuator is connected, the transfer function α/δ also appears in the second term of equation (1). The overall effect of the variable-displacement pump can be considered to represent the pitching motion associated with curvature of the flight path resulting from lift on the wing. As shown in figure 2, a rotary-type damper was used to provide damping to the chair. The short-period dynamic characteristics are adjustable so that any flight condition of any airplane can be simulated. For these tests, the airplane dynamics were held constant. A time history of the response characteristics of the chair and also the simulated response of angle of attack following a step stick deflection are shown in figure 3.

A control stick was mounted to the movable frame through a ball bearing and was connected directly to the control valve of the power control unit by a push-pull rod. The mechanical advantage between the stick and the valve (that

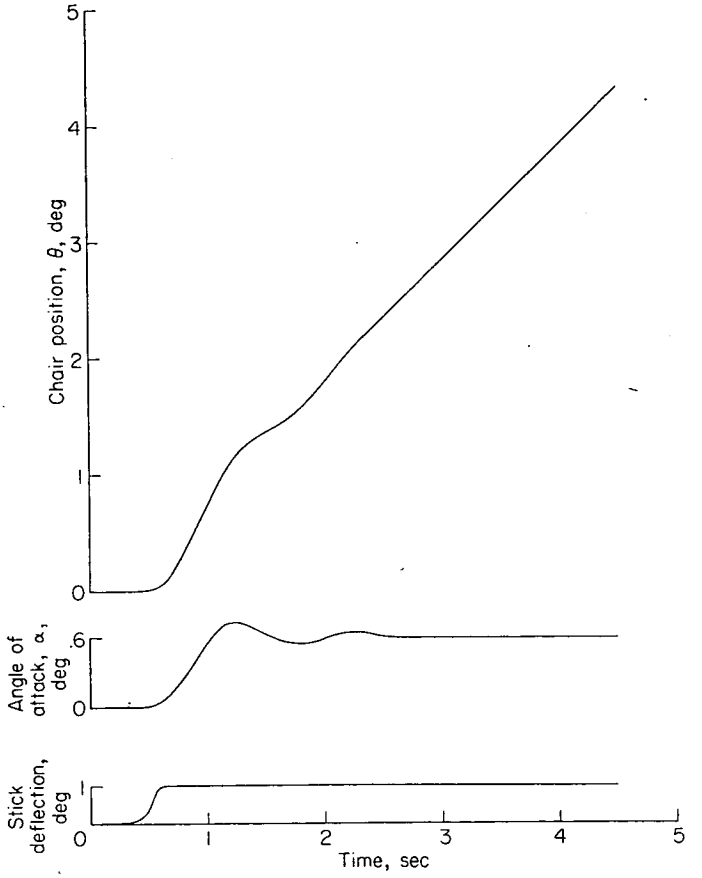


FIGURE 3.—Time history showing response of chair to step stick deflection.

is, the ratio between linear motion of the stick grip and the valve motion, the output being fixed) was about 4:1. The inertia of the stick and the push-pull rod was about 0.22 slug-feet^2 and the stick length was about 24 inches. The ratio between stick rotation and rotation of the output bellcrank δ was 1:5. Here again all attachment points were made as frictionless as possible. As indicated in figure 2, an adjustable friction clamp was used to vary the stick friction. A similar arrangement was installed on the control-valve stem so that valve friction could be varied.

For these tests a simple cantilever spring attached to the stick was used to provide the pilot with feel forces. This spring supplied linear forces with stick deflection; these forces resulted in a feel gradient of approximately 4 pounds per inch of stick displacement. No preload was provided in the feel device. The chair when disturbed would return to within 0.1 degree of its trim position. This condition was caused by the summation of the small amounts of friction in the main support bearings, the pulley, and the chair damper. The stick grip could be moved approximately ± 0.02 inch without causing any motion of the power control actuator. This dead spot in the stick motion was caused primarily by the dead spot in the control valve. The lost motion between the stick and the valve was not perceptible to the pilot. The flow-stroke characteristics of the valve were nonlinear, small deflections providing relatively slower control-surface rates. However, the time constant of the servo response was very short compared with the response time of the simulator and was not considered to be a significant factor in these tests. The control valve itself had some inherent friction which amounted to about 4 ounces in terms of stick force. This valve friction was eliminated for the zero-valve-friction tests by means of a small vibrator mounted on the valve stem as described in reference 2.

It should also be pointed out that the power control unit used incorporated a viscous damper on the valve for the purpose of eliminating valve chatter. This damper was not changed throughout the tests.

The light bulb, lens, and mirror were attached to the chair and arranged so that a spot of light was projected on a screen located in front of the pilot. Motions of the light spot indicated to the pilot the attitude angle of the chair. A second spot of light was also projected on the screen and was controlled by a cam. The cam-driven light spot moved from one vertical position to another on the screen, and the pilot attempted to make the light spot for the chair coincide with the cam-driven light spot.

Strain gages were mounted on the control stick to measure control forces, and slide-wire transmitters were used to measure stick position, chair angle, and cam position. These four quantities and time were continuously recorded on standard NACA recording instruments during the tests.

TESTS AND PROCEDURE

For these tests the dynamics of the simulator were adjusted to correspond approximately to those of a fighter airplane flying at an altitude of 10,000 feet and Mach number of 0.80. The period was set to be 1.0 second and the damping ratio, 0.45. The simulator was adjusted so that the stick deflection per degree of stabilizer deflection was made larger than its normal value to represent the gearing that would be provided by use of a mechanical-advantage changer in the airplane. With this arrangement, the steady-state ratio of angle of attack to stick deflection was approximately 0.60. The variable-displacement pump was adjusted to provide a steady-state value of about 1 degree per second per degree for the ratio of pitching velocity to stick deflection.

The pilots' task during the tests involved keeping the light spot for the chair lined up horizontally with the cam-driven light spot. The ease and precision with which the pilots could follow the cam-driven light spot provided the basis for the judging of the quality of the control system. In addition to the recorded data, the pilots' opinions were weighted heavily when the various configurations were evaluated.

The friction conditions tested are shown in figure 4. All values of friction quoted in this report are given in terms of stick force. These conditions were tested with a rigid control system, a flexible control system, and a rigid control system having some backlash.

For each test configuration, at least two NACA test pilots obtained data.

RESULTS AND DISCUSSION

RIGID CONTROL SYSTEM

Examples of the data obtained are shown as time histories in figure 5 for various representative friction conditions.

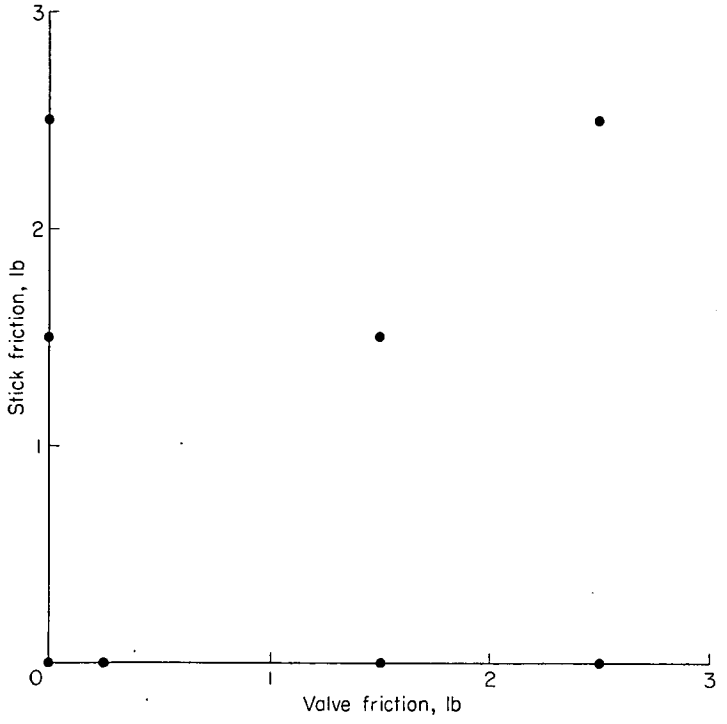
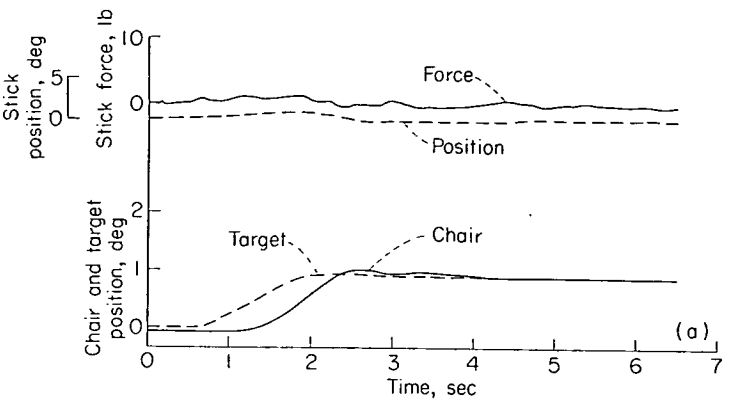


FIGURE 4.—Friction conditions tested.

The quality of each configuration is indicated by the overshoots and oscillations in the chair record and also by the length of time required to make the chair record coincident with the target record. Coincidence of the two records indicates that the pilot was "on target."

Figure 5 (a) shows representative results obtained when the control system was essentially free of all friction. The absence of large overshoots and oscillations in addition to the relatively short length of time required to get on the target indicated that the pilot had little difficulty in performing the task. The pilots commented favorably on this system although they believed that the ½-pound limit of stick friction quoted in reference 1 would be necessary in flight. The small stick friction would be helpful in alleviating the small unintentional control inputs that may result from such things as the many duties of the pilot which momentarily divert his attention from the control of the airplane or rough-air conditions.



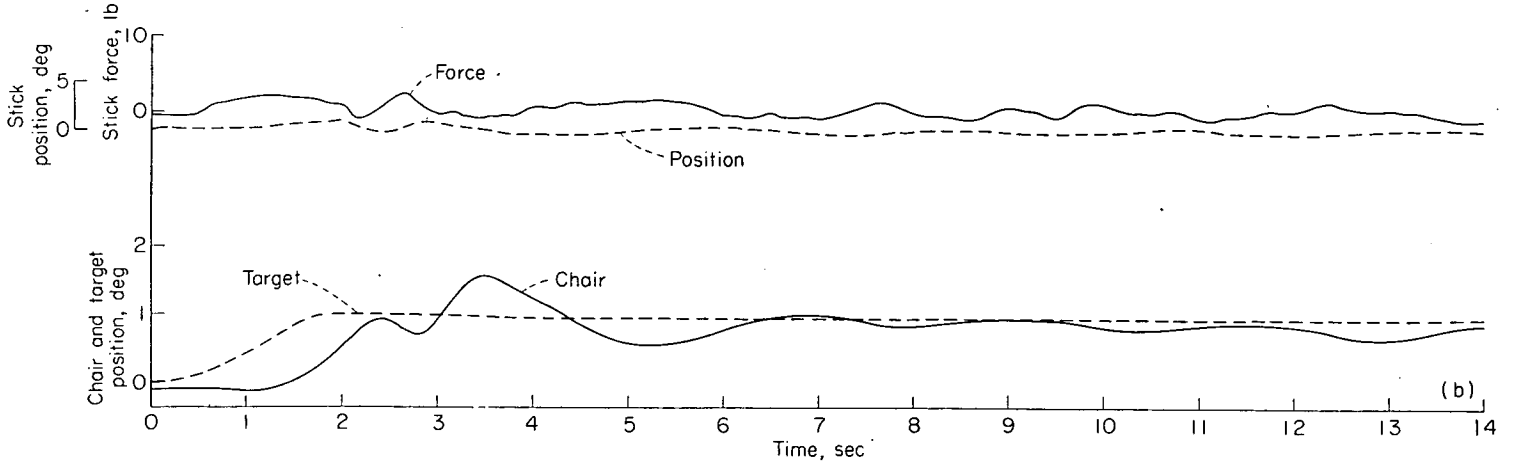
(a) No friction.

FIGURE 5.—Rigid control system.

Some tests were made with the vibrator removed from the valve stem. Without the vibrator the valve friction was about 4 ounces in terms of stick force. The pilots could not detect any effect of this small amount of friction and the records were very nearly identical to those shown in figure 5 (a). For this reason the tests with 4-ounce valve friction are not shown.

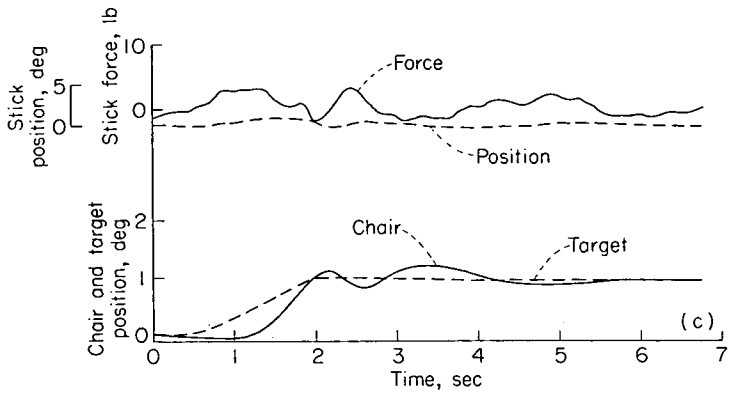
Figure 5 (b) shows the effects of 1½ pounds of friction in the control valve. The overshoots, oscillations, and the relatively long time required to get on the target are good indications of the amount of control system quality lost through the introduction of the valve friction. The latter portion of the record shows the extreme difficulties encountered in positioning the chair precisely on a given point. This effect has been measured in flight and is discussed in reference 1. During the simulator tests the pilots believed that 1½ pounds of valve friction were objectionable. They did not object on the grounds of the resulting increase in forces nor did they believe the system to be subject to violent pilot-induced oscillations. The objections were based simply on their inability to make fine corrections precisely and their feeling that the machine was flying the pilot.

Figure 5 (c) shows the results obtained when the 1½ pounds of stick friction were used in conjunction with the 1½ pounds of valve friction. Although the total breakout force at the stick due to friction was increased, the overall performance

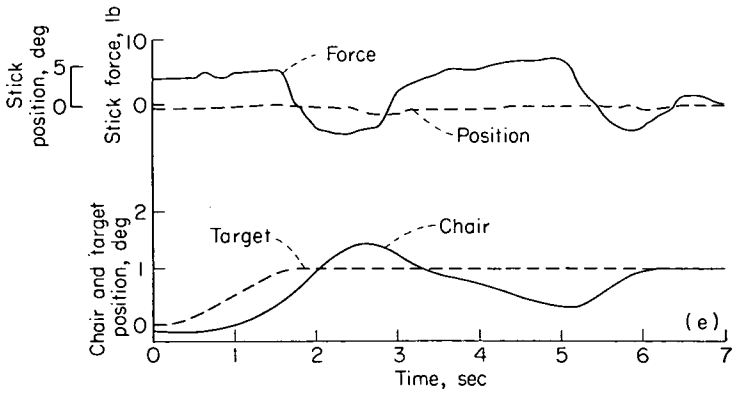


(b) 1½ pounds valve friction.

FIGURE 5.—Continued.



(c) 1½ pounds valve friction and 1½ pounds stick friction.
FIGURE 5. —Continued.



(e) 2½ pounds valve friction and 2½ pounds stick friction.
FIGURE 5.—Concluded.

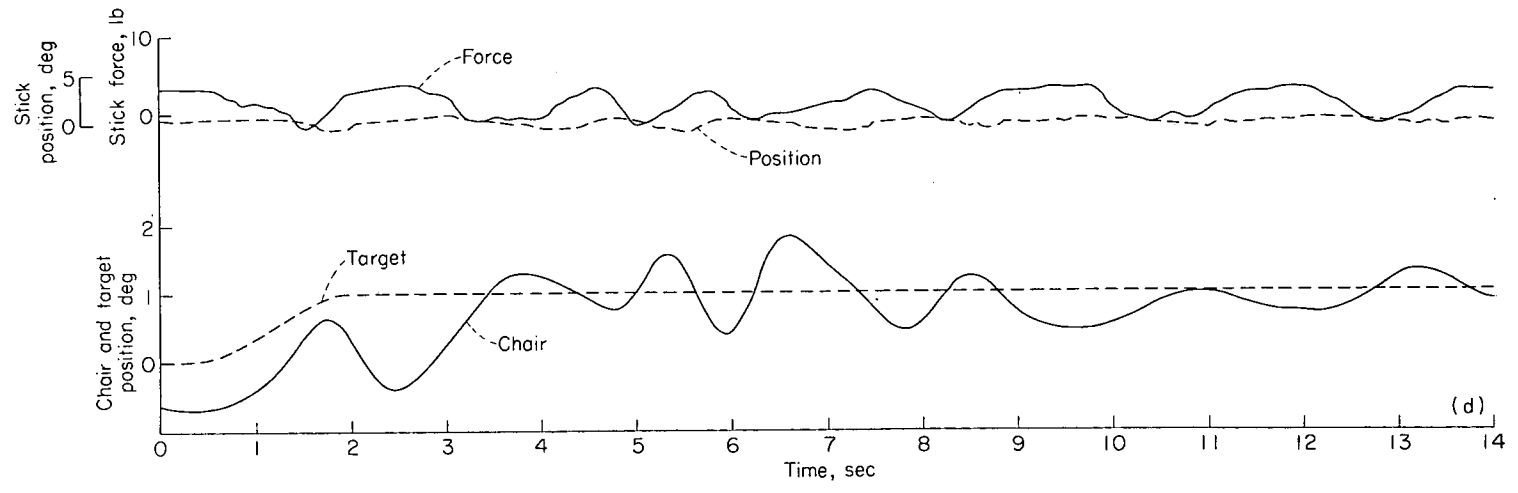
was improved; the stick friction also restored the pilot's feeling that he had control of the machine. The stick friction locked the valve push-pull rod and thereby allowed the followup to return the valve to neutral.

Figure 5 (d) presents the results obtained with about 2½ pounds of valve friction. The records show that control through such a system is rather hopeless. The tendency for the chair amplitude to increase is a good indication of the actual danger associated with this amount of valve friction. It should be remembered that the simulator does not include the effects of rough air or the acceleration effects on the pilot or parts of the system. These factors which are present in flight will aggravate the oscillatory nature of the system and therefore will magnify the danger involved. The pilots noted that, even though these aggravating factors were absent in the simulator, the slightest distraction could very easily lead to violent pilot-induced oscillations. It seems safe to say that violent oscillations could be caused in flight by valve-friction values less than the 2½ pounds for the same flight conditions and stability parameters set up in the simulator.

Figure 5 (e) shows the results when 2½ pounds of stick friction were introduced in addition to the 2½ pounds of valve friction. Even though the figure shows that the pilot could get on the target, the large overshoots suggest difficulties that make precise control somewhat uncertain. The stick friction, however, was noticeably beneficial since the violent oscillatory tendencies were eliminated. The pilots verified these observations but objected to the system not only on the basis of precise control but also because of the amount of work involved. All pilots agreed that a total breakout force due to friction of about 3 pounds or less would be more desirable in flight for airplanes of the type being simulated.

Some tests were also made in which the valve friction was reduced to zero by means of a small vibrator and various amounts of stick friction were evaluated. The pilots could do a much better job with the highest stick friction tested (3 pounds) than they could with only 1½ pounds of valve friction. Actually, the best performance was achieved when the stick friction was in the range between ½ and 2 pounds and the pilots believed on the basis of these tests and on the basis of their previous experience that they would prefer such systems for actual flight.

Tests were also made in which the valve friction was held constant and the stick friction was varied. From these tests it was learned that, when valve friction was present, the best control quality was achieved when the stick friction was equal to or very slightly greater than the valve friction. An excess or deficiency in stick friction, however, resulted in some quality reduction; the system with more stick friction than valve friction was considered to be desirable provided



(d) 2½ pounds valve friction.
FIGURE 5.—Continued.

that the total breakout force due to friction did not exceed 3 pounds.

The results thus far discussed have been condensed into a plot of stick friction against valve friction (fig. 6) which shows the good, tolerable, and unsatisfactory combinations of these two types of friction. It should be pointed out that the conditions rated unsatisfactory were, in general, flyable but would be very objectionable from a precision control standpoint and would be very tiring to the pilot over long periods of time. Even though the figure shows that good performance can be obtained with as much as 1 pound of valve friction and 1 pound of stick friction, the designer should strive to decrease the valve friction as much as possible. This decrease would result in a smaller total friction force and a better performing control system. This point is extremely difficult to show graphically and no attempt was made to do so in figure 6; however, it is worth mentioning because the tests indicated that, as the system approached the condition of pure stick friction, performance and pilot impression improved.

Another point that should be brought out is that figure 6 applies only to the conditions of the tests and would not be expected to apply if other devices such as valve centering springs were used to attempt to compensate for the valve friction.

FLEXIBLE CONTROL SYSTEM

Since this report is concerned primarily with the effects of friction, the complete effects of flexibility are not treated here. Subsequent tests should be made to determine the effects of various combinations of flexibility and valve friction on control quality. Limited tests on flexibility are included in this report to illustrate the effect that it produces when introduced in the presence of stick friction and valve friction.

The rigid push-pull rod connecting the stick to the control valve was modified to include a flexible link to simulate a flexible control system. This modification also placed the flexibility between the feel device and the valve. The spring constant of the flexible link was set to a low value (4 pounds of stick force per degree of stick angle) so that the effect would be easily recognized. The same type of tests and friction conditions as described in the previous section were evaluated and representative records of these tests are presented in figure 7.

Figure 7 (a) shows the results with a frictionless system, and the similarity between figure 7(a) and figure 5 (a) shows that the flexibility had little or no effect. The pilots agreed that the flexibility was not detectable in this condition and therefore they rated this system the same as the rigid system. Here again the system was tried with 4 ounces of valve friction. The pilots believed that the friction effect was a little more noticeable in the flexible system than in the rigid system but they still considered the configuration to be tolerable. The flexibility magnifies the undesirable valve friction effect by allowing the valve to "motor" the control surface through a certain range, dependent on the amount of valve friction, by deflecting the flexible link. Also, the forces which the pilot applies in attempting to compensate for the motoring must be transmitted to the valve through the flexible link. When valve friction is present, therefore, the valve will not move until the pilot's force has deflected the flexible link to the point at which the spring force in the link overcomes the valve friction.

Figure 7 (b) shows the difficulties introduced by 1½ pounds of valve friction in conjunction with the flexibility. Even though figure 7 (b) does not differ much from figure 5 (b), an overall comparison of all the records obtained showed that the flexibility caused a very definite reduction in control quality. The pilots remarked that pilot-induced oscillations were possible with this system; however, they felt that such oscillations could be controlled somewhat by intense concentration. The skill and experience of the pilots involved in these tests were believed to be important factors in the prevention of violent oscillations with this system.

Figure 7 (c), which shows the results for 1½ pounds of stick friction and 1½ pounds of valve friction, proves that stick friction is not beneficial when flexibility exists between

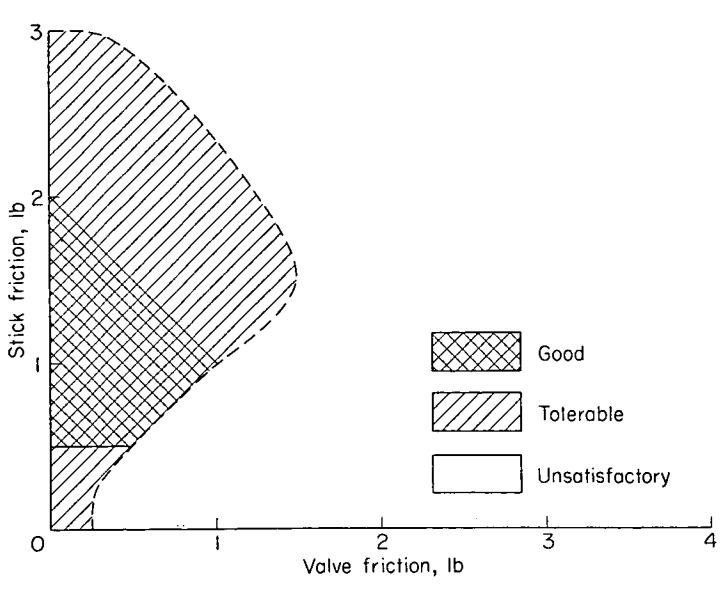
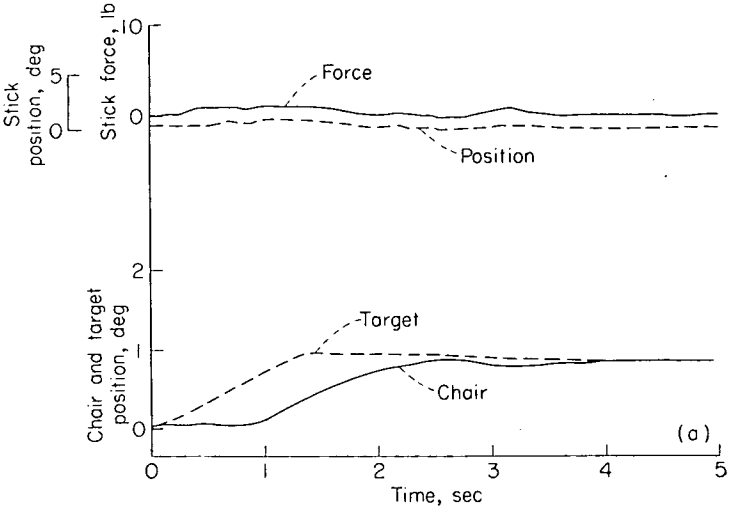
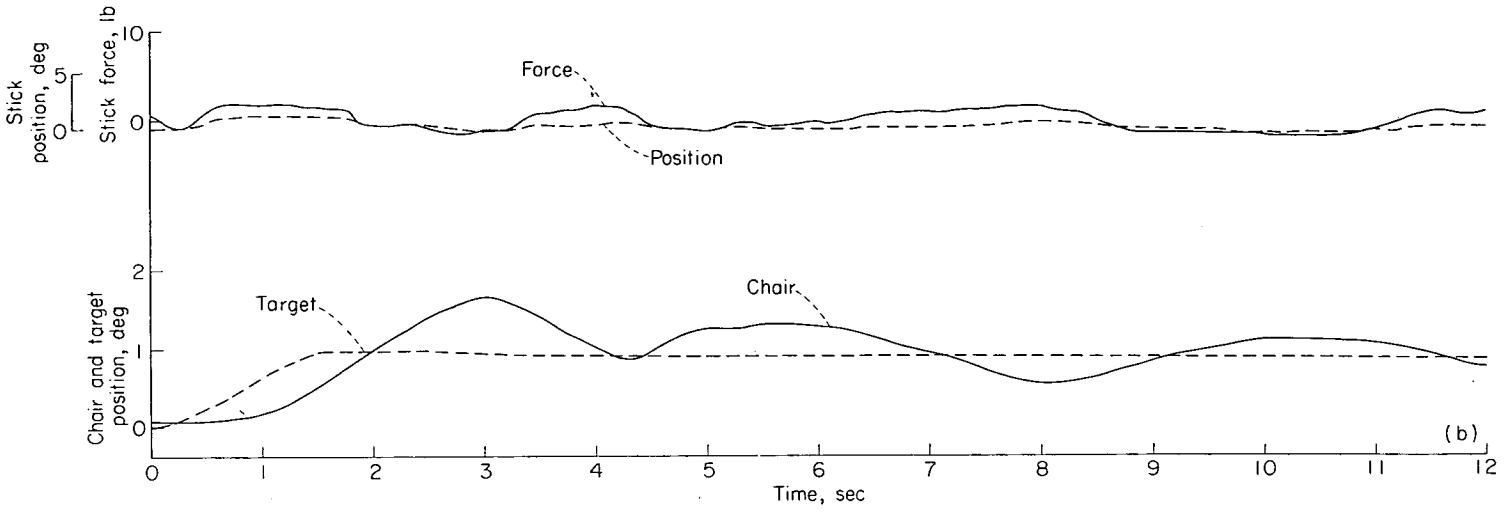


FIGURE 6.—Combinations of valve friction and stick friction for rigid control system.

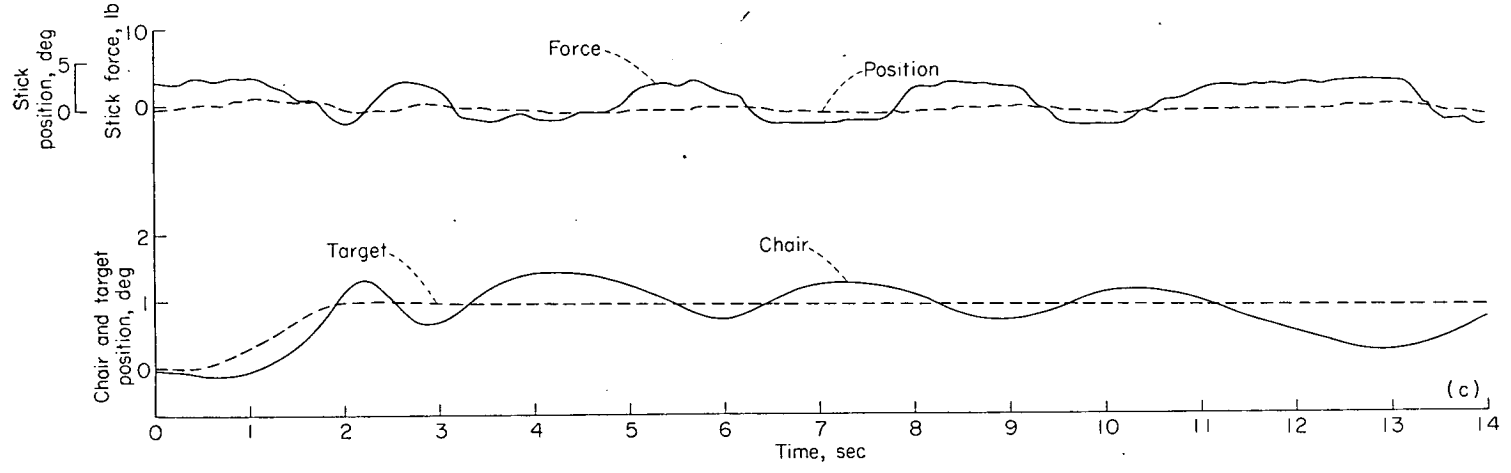


(a) No friction.

FIGURE 7.—Flexibility between stick friction and valve friction.



(b) 1½ pounds valve friction.
FIGURE 7.—Continued.

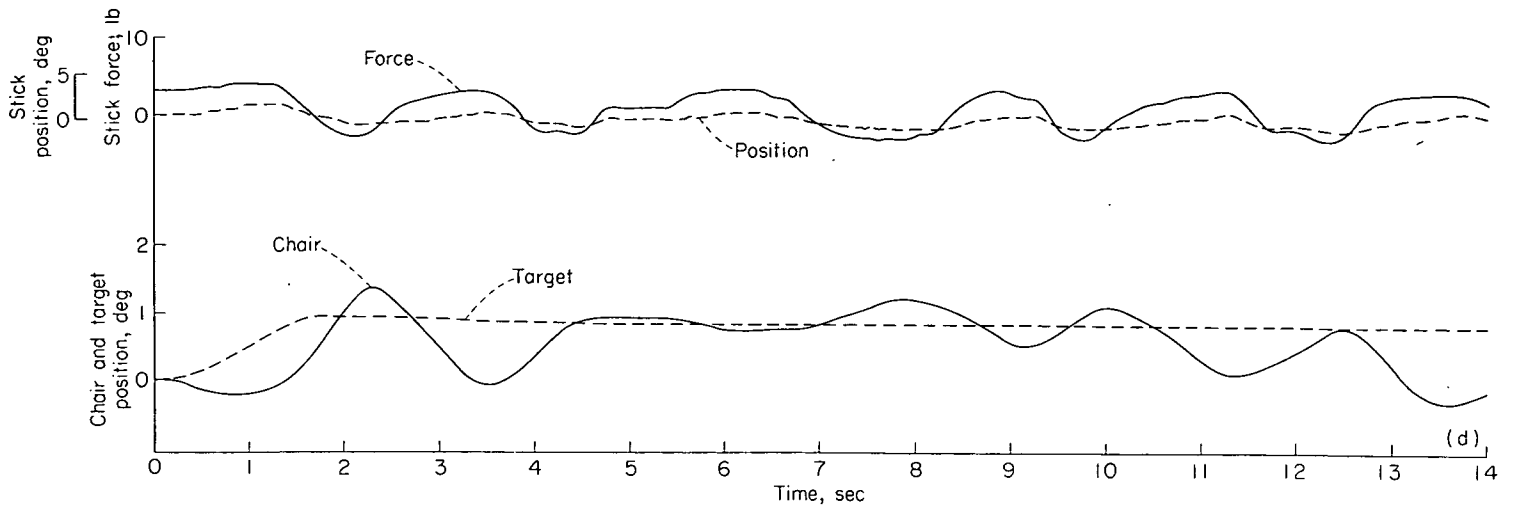


(c) 1½ pounds valve friction and 1½ pounds stick friction.
FIGURE 7.—Continued.

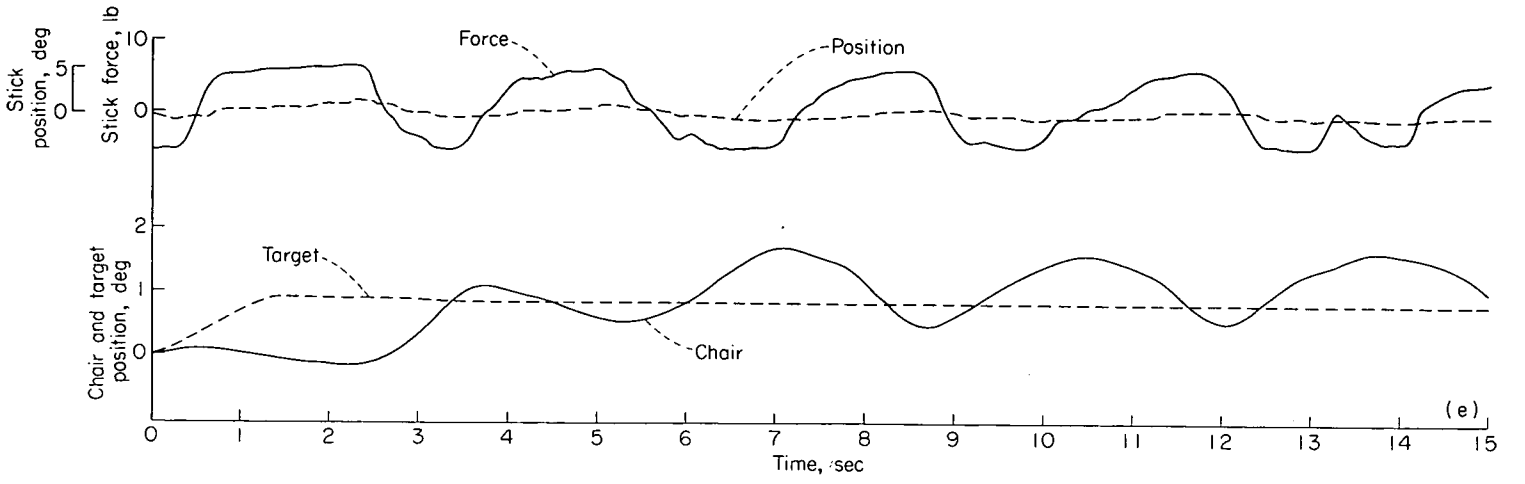
the stick and the control valve. In fact, the overall performance with this system seemed to be worse than that obtained with valve friction alone, and the pilots noted that the stick friction removed the small amount of control confidence that was present in the system with valve friction only. This result is understandable since the stick is no longer rigidly connected to the valve because of the flexible link; thus, the stick friction is prevented from "locking" the control push-pull rod and the valve is allowed to center itself. Stick friction in such a system only reduces the quality still further by causing a nonlinear relation between the stick force and stick motion. It is interesting to note that pilots having considerable experience in controlling systems involving valve friction alone can more or less cope with the difficulties and produce surprisingly good performance although they invariably comment that such systems are unsatisfactory. It is believed that these pilots are successful because they change their technique of flying, as explained in reference 1, from force consciousness to position consciousness because valve friction destroys the relationship between force application and control-surface position. This method of changing techniques is not successful, however, when flexibility is introduced in the presence of valve friction because the flexibility destroys the relationship between the stick position and the control-surface position.

Figure 7 (d) presents the results obtained with 2½ pounds of valve friction and figure 7 (e) shows the results obtained with 2½ pounds of stick friction and 2½ pounds of valve friction. The performance of both systems appears to be similar in that precise control is impossible; the pilots remarked that both systems were extremely susceptible to violent oscillations and they could not detect any benefits from the stick friction.

Figure 8 shows the ranges of good, tolerable, and unsatisfactory combinations of stick friction and valve friction when flexibility exists between the stick and the valve. This figure applies only to cases in which the flexibility is the same as that quoted previously. No doubt the limits will change depending upon the amount of flexibility present; however, the figure shows the detrimental effect on control quality since with this amount of flexibility only 4 ounces of valve friction could be tolerated.



(d) 2½ pounds valve friction.
FIGURE 7.—Continued.



(e) 2½ pounds valve friction and 2½ pounds stick friction.
FIGURE 7.—Concluded.

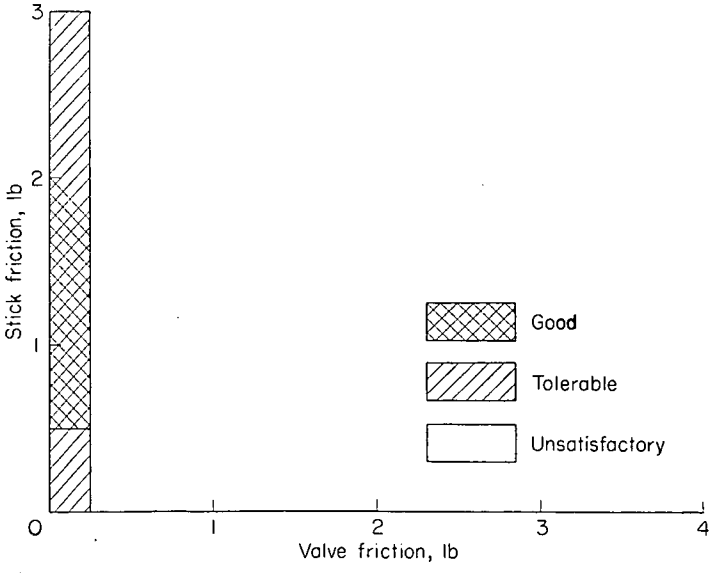


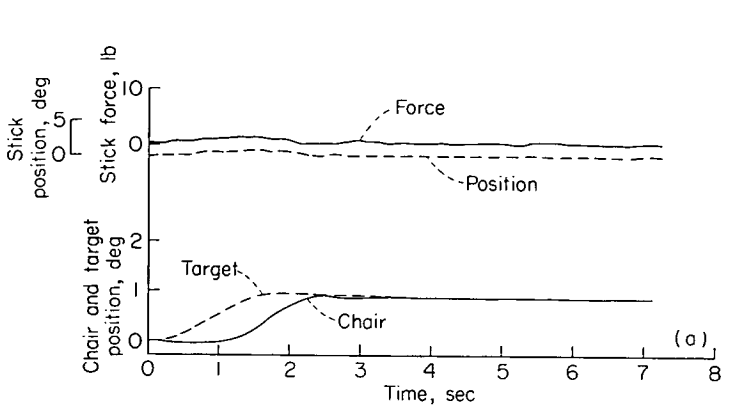
FIGURE 8.—Combinations of valve friction and stick friction with flexibility between the stick and the valve.

The control stick was modified to include a flexible link to simulate flexibility between the pilot and the point at which stick friction was applied. This modification also placed the flexibility between the pilot and the feel spring. The amount of flexibility in this system was the same as was introduced between the stick and valve. The stick was again connected to the control valve by means of a rigid push-pull rod.

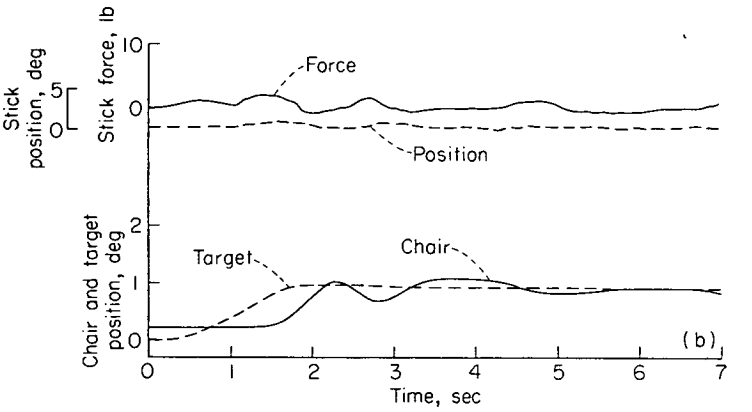
Figure 9 (a), which represents a frictionless system, shows no large differences from the rigid system of figure 5 (a) and the pilots could not feel any effects of the flexibility.

Figure 9 (b) presents the results with 1½ pounds of valve friction. Comparison with figure 5 (b) shows that a little less difficulty was encountered with this system than was experienced with the rigid system. The pilots' complaints, however, were very similar to those regarding the rigid system with 1½ pounds of valve friction in that precise control was difficult but violent oscillations were not probable.

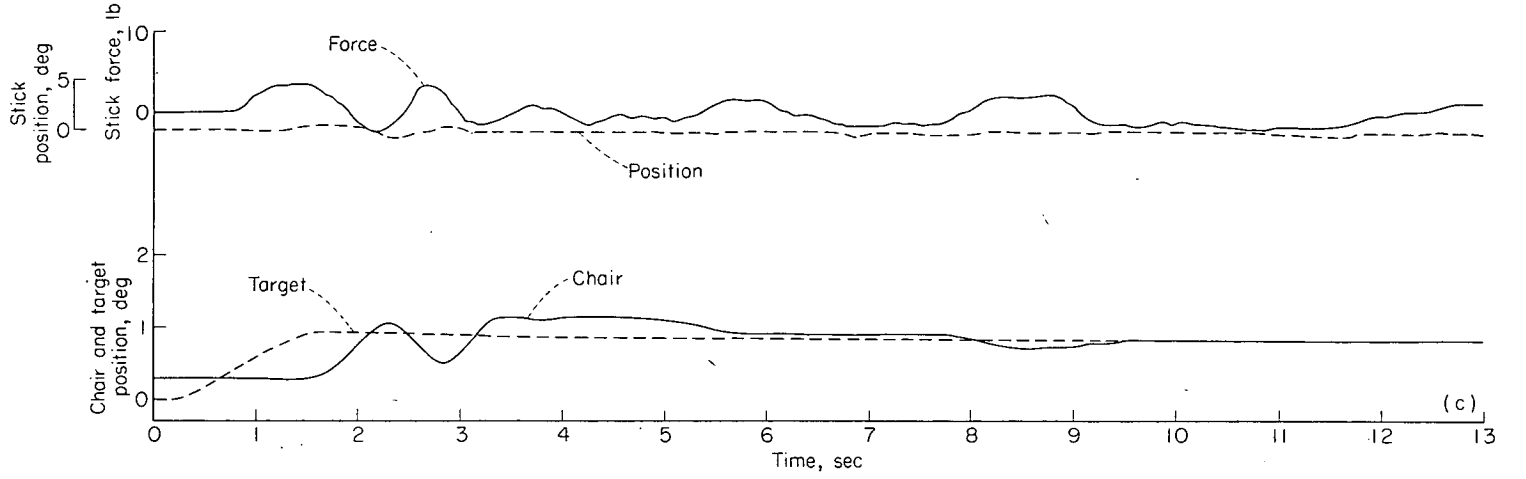
Figure 9 (c) shows the results of 1½ pounds of stick friction



(a) No friction.



(b) 1½ pounds valve friction.



(c) 1½ pounds valve friction and 1½ pounds stick friction.

FIGURE 9.—Flexibility between the pilot and the stick friction.

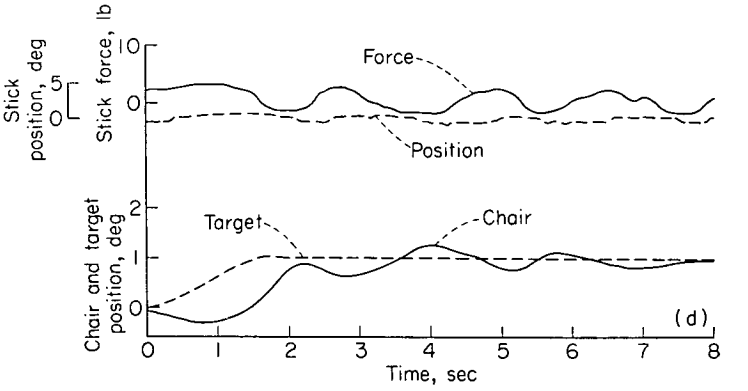
and 1½ pounds of valve friction. This figure shows that, in spite of the increase in breakout force, the performance is very similar to that shown in figure 9 (b). The pilots, however, stated that the stick friction was helpful in restoring their feeling of control and therefore they rated this system above the system represented by figure 9 (b).

The effect of 2½ pounds of valve friction, which is shown in figure 9 (d), was to cause the system to be subject to violent oscillations and to make precise control impossible. Comparison of figure 9 (d) with figure 5 (d) shows that the valve-friction effect was, however, not so severe as that obtained with the original rigid control system. The addition of 2½ pounds of stick friction, shown in figure 9 (e), did not improve the precise control of the system. It did, however, restore the pilots' feelings of being able to prevent any violent oscillations.

No attempt was made to establish limits, as was done in figures 6 and 8, because, as mentioned previously, more detailed tests are needed to do so. Comparison of figures 7 and 9 does show, however, the importance of the location of the flexibility when valve friction is present. The pilots commented that flexibility between the pilot and the source of stick friction is far more tolerable from the pilots' standpoint than flexibility between the source of stick friction and the valve. In practice, this result means that stick friction can be beneficial even in a flexible system if the equivalent stick friction (friction between the valve stem and airplane structure) is introduced very close to the power control unit. Also, the feel device should be located between the source of flexibility and the valve.

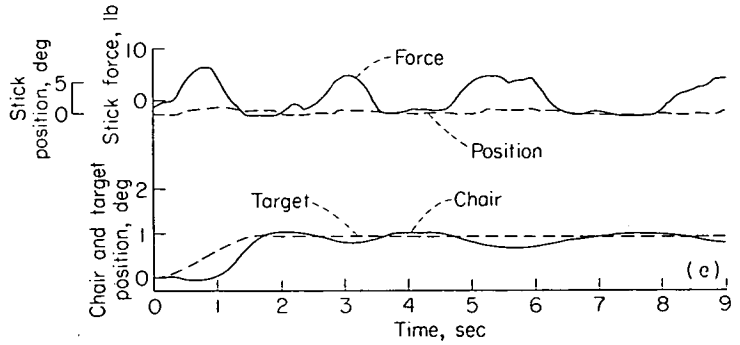
CONTROL SYSTEM WITH BACKLASH

As in the case of the flexibility tests, the limited results regarding backlash are included in this report to show the general effects of backlash when introduced between the

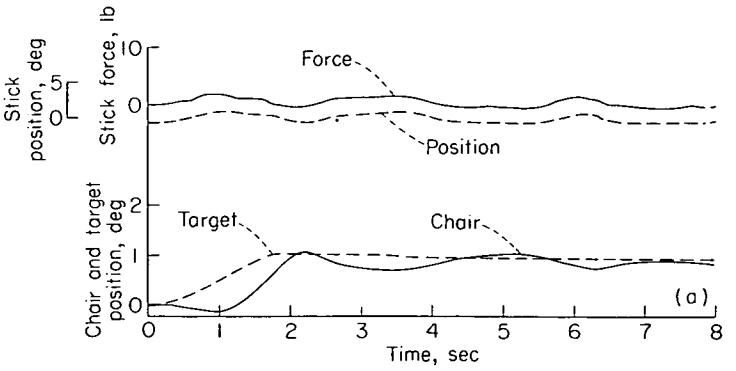


(d) 2½ pounds valve friction.

FIGURE 9.—Continued.



(e) 2½ pounds valve friction and 2½ pounds stick friction.
FIGURE 9.—Concluded.



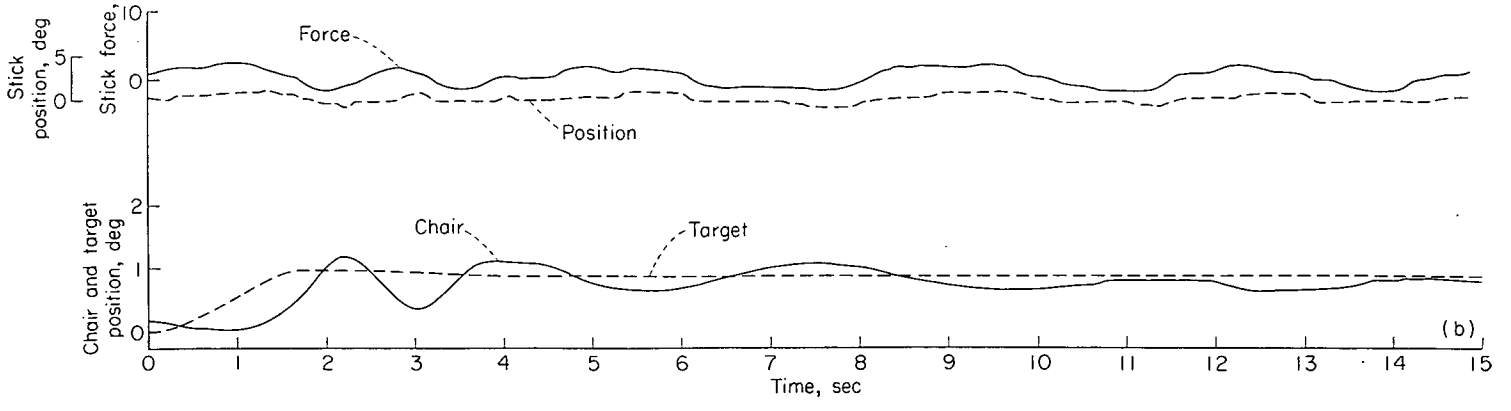
(a) No friction.
FIGURE 10.—Backlash between the stick and valve.

control stick and the valve and also between the pilot and the source of stick friction. The points at which the backlash was introduced are shown in figure 2.

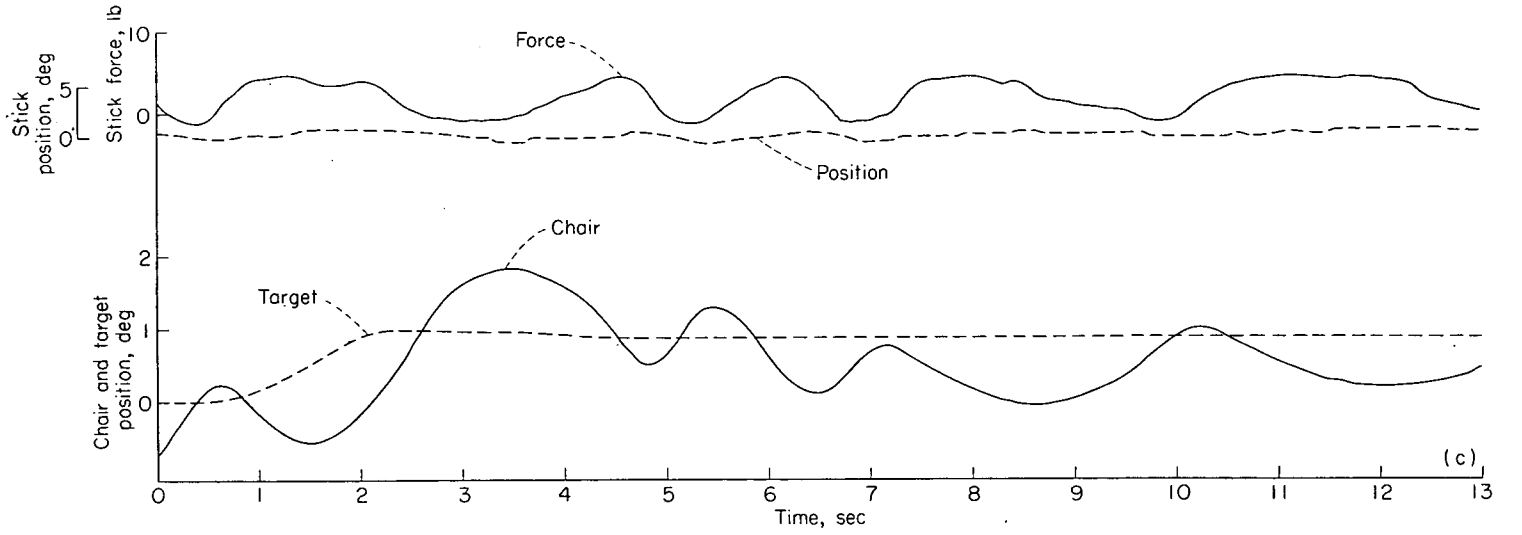
The push-pull rod connecting the stick to the valve was modified so that there was about ±0.025 inch of backlash, in terms of valve motion, between the stick and the valve. This modification also placed the backlash between the feel device and the valve. This backlash amounted to about ±0.10 inch of motion at the stick grip.

Figure 10 shows time histories of the effect of backlash between the stick and the valve for various friction conditions. These figures show that, even with a frictionless system, the pilots could not position the chair precisely and, as the breakout force was increased, the control quality deteriorated. The pilots noted that, even with the frictionless system, precise control was difficult and, as the valve friction was increased, the danger of oscillating became more pronounced. Stick friction also produced the same results but the pilots believed that the stick-friction effect was not so objectionable as the valve-friction effect. The important point is that none of the conditions were even tolerable with this amount of backlash at the valve.

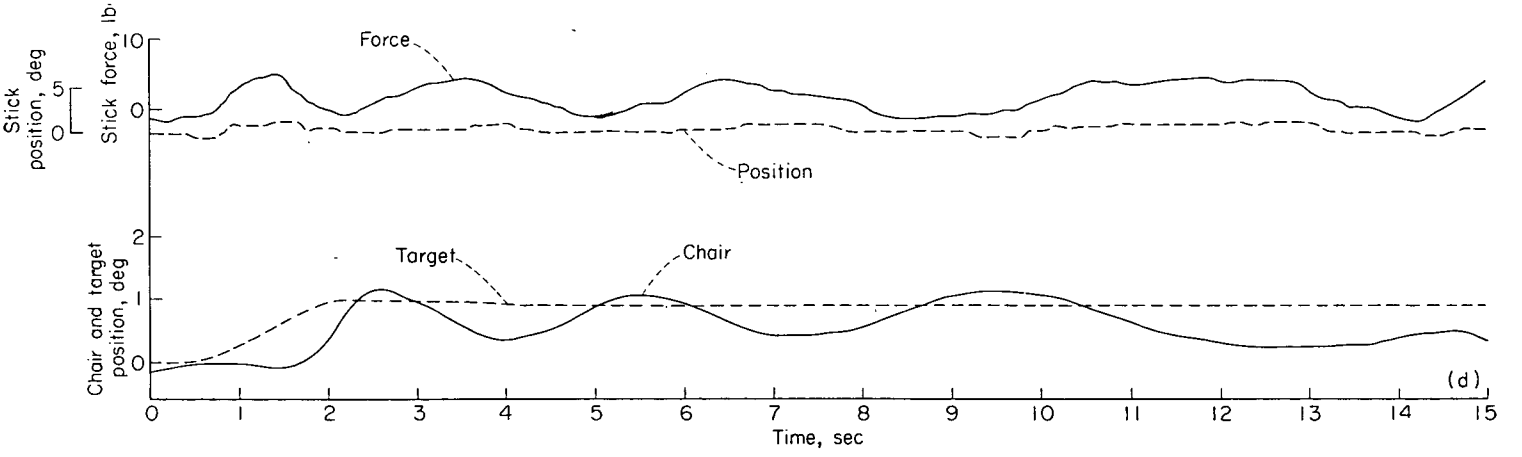
The backlash between the stick and the valve was then removed and the same amount of backlash was introduced between the pilot and the point at which the stick friction was applied. This modification also placed the backlash between the pilot and the feel spring. The results from these tests are presented in figure 11. The frictionless system, as shown in figure 11 (a), was not too difficult to control even though the pilots could feel the backlash in the stick. With 1½ pounds of valve friction (fig. 11 (b)), the system performance was very similar to, but possibly a little better than, the original rigid control system with the same friction condition. Precise control was difficult but the system showed no tendency to produce violent oscillations. It should be remembered that this same friction condition when coupled with backlash between the stick and the valve produced a very dangerous system that was susceptible to severe oscillations. With backlash between the pilot and the source of stick friction, the stick friction improved the system. (See fig. 11 (c).) Even though the initial overshoot tended to be larger, the pilot could position the chair on the target. This improvement is in direct contrast to the detrimental effects of stick friction when the backlash was between the stick and valve. Figure 11 (d) shows the results of 2½ pounds of valve friction and figure 11 (e) shows 2½ pounds of valve friction and 2½ pounds of stick friction.



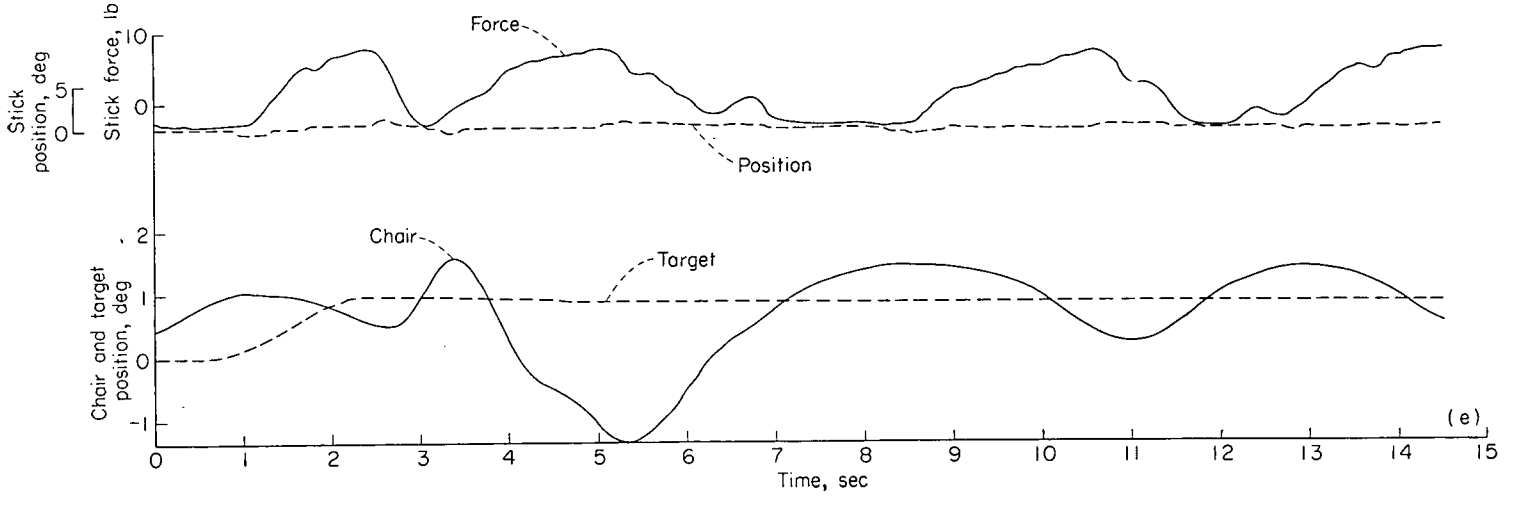
(b) 1½ pounds valve friction.
FIGURE 10.—Continued.



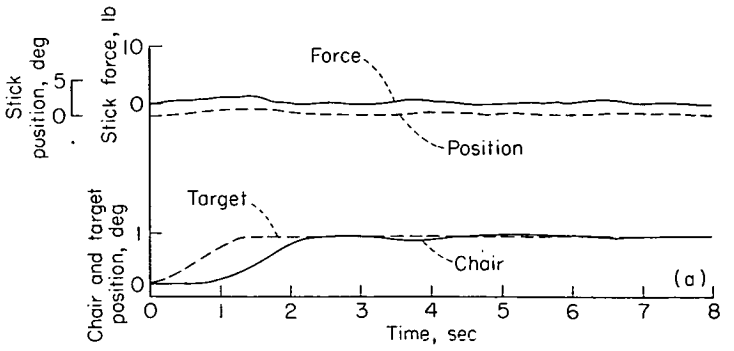
(c) 1½ pounds valve friction and 1½ pounds stick friction.
FIGURE 10.—Continued.



(d) 2½ pounds valve friction.
FIGURE 10.—Continued.

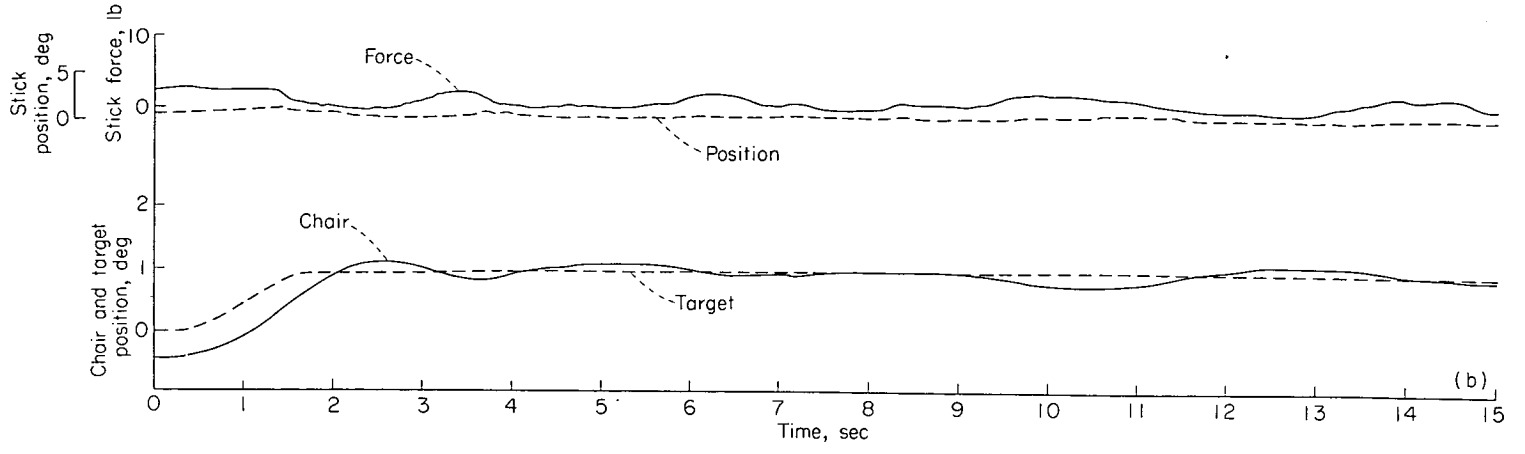


(e) 2½ pounds valve friction and 2½ pounds stick friction.
FIGURE 10.—Concluded.



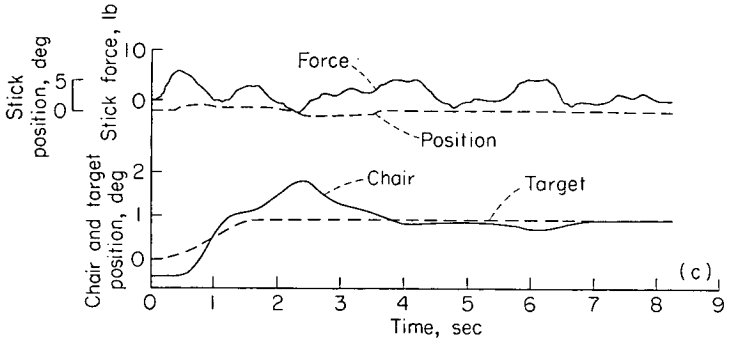
(a) No friction.

FIGURE 11.—Backlash between the pilot and the stick friction.



(b) 1½ pounds valve friction.

FIGURE 11.—Continued.



(c) 1½ pounds valve friction and 1½ pounds stick friction.

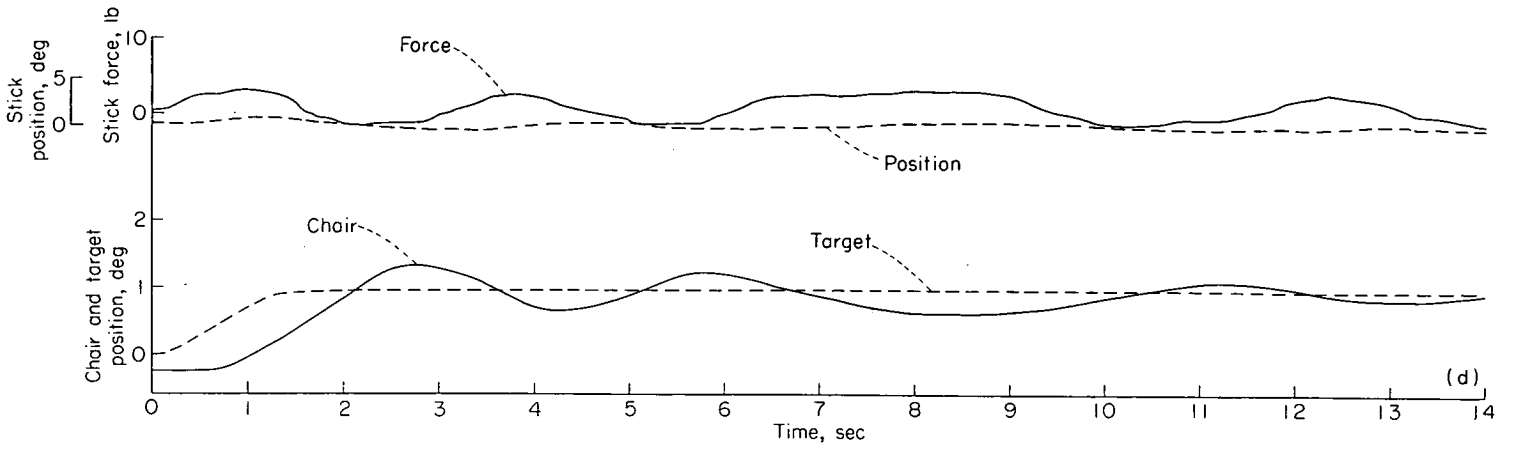
FIGURE 11.—Continued.

In each case the performance shows that no violent oscillations were ever encountered although precise control was extremely difficult. The pilots commented that with valve friction the system was subject only to mild oscillations and this tendency was completely removed by the addition of stick friction. These observations lead to the conclusion that the backlash between the pilot and source of stick friction is not nearly so dangerous as the backlash between the stick and the valve. In fact, the records and comments regarding the backlash between the pilot and stick friction indicate that valve friction was not so detrimental to this system as it was to the rigid control system with comparable friction conditions. It was noticed during the tests of the rigid system with valve friction alone that the pilots, when they wished to stop the chair motion, applied the necessary opposite force in a jerking manner that resulted in an instantaneous "kick" on the push-pull rod which centered the valve. It is possible that, with the backlash between the pilot and the source of stick friction, the stick acted as a convenient "hammer," within the backlash range, with which the pilots tapped the control rod to break the valve friction. More detailed tests are required, however, to establish a more definite explanation for the behavior of backlash in this particular location.

CONCLUSIONS

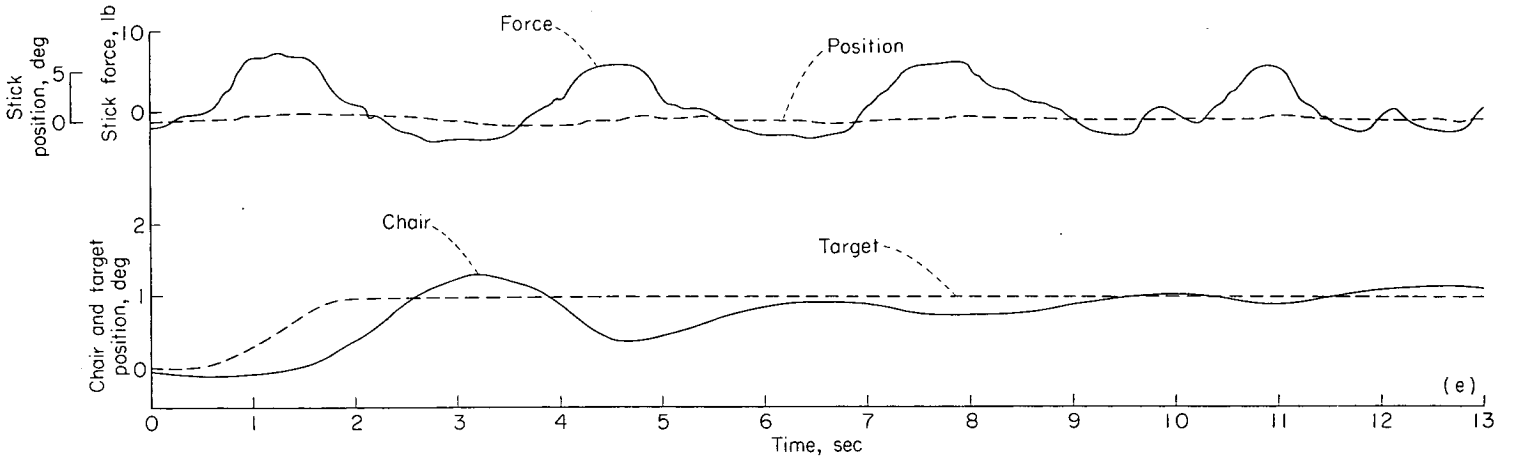
Tests have been made with a ground simulator incorporating a power control system. The purpose of the tests was to determine the effects of various combinations of valve friction and stick friction on the ability of the pilot to control the system. Various friction conditions were simulated with a rigid control system, a flexible system, and a rigid system having some backlash. From these tests the following conclusions can be drawn:

1. When valve friction is present in a rigid control system, stick friction is beneficial in restoring some of the quality lost because of the valve friction. The optimum quality is achieved when the stick friction is equal to or slightly greater than the valve friction measured at the stick.



(d) 2½ pounds valve friction.

FIGURE 11.—Continued.



(e) 2½ pounds valve friction and 2½ pounds stick friction.

FIGURE 11.—Concluded.

2. The total breakout force due to friction should not exceed 3 pounds in terms of stick force. Control-system quality improves as the valve friction is reduced; however, reducing the valve friction below 4 ounces did not yield any significant improvement.

3. When flexibility existed between the valve and the source of stick friction, the undesirable effects of valve friction were magnified by the flexibility, and the introduction of stick friction reduced the quality still further.

4. When flexibility was introduced between the pilot and the source of stick friction, stick friction was again beneficial in restoring some quality lost because of the valve friction.

5. With backlash between the stick and valve (±0.025 inch at the valve), precise control was difficult even with the frictionless system, and the quality deteriorated as valve friction or stick friction was increased.

6. With backlash between the pilot and the source of stick friction, the valve-friction effect was not as objectionable as it was in the rigid system, and the introduction of stick friction improved the system still further.

LANGLEY AERONAUTICAL LABORATORY,
NATIONAL ADVISORY COMMITTEE FOR AERONAUTICS,
LANGLEY FIELD, VA., *February 8, 1957.*

REFERENCES

1. Phillips, William H., Brown, B. Porter, and Matthews, James T., Jr.: Review and Investigation of Unsatisfactory Control Characteristics Involving Instability of Pilot-Airplane Combination and Methods for Predicting These Difficulties From Ground Tests. NACA TN 4064, 1957. (Supersedes NACA RM L53F17a.)
2. Phillips, William H.: Investigation of Effect of Reduction of Valve Friction in a Power Control System by Use of a Vibrator. NACA RM L55E18a, 1955.

REPORT 1349

A LOW-SPEED EXPERIMENTAL INVESTIGATION OF THE EFFECT OF A SANDPAPER TYPE OF ROUGHNESS ON BOUNDARY-LAYER TRANSITION [1]

By Albert E. von Doenhoff and Elmer A. Horton

SUMMARY

An investigation was made in the Langley low-turbulence pressure tunnel to determine the effect of size and location of a sandpaper type of roughness on the Reynolds number for transition. Transition was observed by means of a hot-wire anemometer located at various chordwise stations for each position of the roughness. These observations indicated that when the roughness is sufficiently submerged in the boundary layer to provide a substantially linear variation of boundary-layer velocity with distance from the surface up to the top of the roughness, turbulent "spots" begin to appear immediately behind the roughness when the Reynolds number based on the velocity at the top of the roughness and the roughness height exceeds a value of approximately 600.

At Reynolds numbers even slightly below the critical value (value for transition), the sandpaper type of roughness introduced no measurable disturbances into the laminar layer downstream of the roughness. The extent of the roughened area does not appear to have an important effect on the critical value of the roughness Reynolds number.

INTRODUCTION

An extensive correlation of transition data for individual three-dimensional roughness particles was made by Loftin in reference 1. This correlation was made in terms of a local roughness Reynolds number based on the roughness height and the velocity at the top of the roughness, a form suggested by Schiller in reference 2 and employed by Tani in reference 3. Reasonably consistent values of the critical roughness Reynolds number were obtained by Loftin in reference 1, so long as the roughness was sufficiently submerged in the boundary layer to provide a velocity variation that was substantially linear with distance from the surface up to a height equal to the height of the roughness. Schwartzberg and Braslow in reference 4 showed that this critical value of the roughness Reynolds number was not greatly increased, even when the boundary layer was stabilized to small two-dimensional disturbances by the application of area suction. Similar correlations were obtained by Klebanoff, Schubauer, and Tidstrom (ref. 5).

The difference in character for transition as caused by three-dimensional roughness (spheres cemented to the surface) from that caused by two-dimensional roughness (full-span cylindrical wire laid on the surface parallel to the leading edge) is clearly shown by Klebanoff, Schubauer, and Tidstrom in reference 5. Most of the recent data dealing with the effects of two-dimensional roughness on boundary-layer transition have been summarized by Dryden (ref. 6) for the case of zero pressure gradient in the form of curves of the ratio of the transition Reynolds number in the presence of roughness to the transition Reynolds number for the model smooth plotted against the ratio of the height of the roughness to the boundary-layer thickness. In this type of plot, the assumption is made that transition will occur some distance downstream of the roughness and will gradually approach the roughness position as the Reynolds number is increased.

The data of reference 1 suggested, and those of reference 5 confirmed, the conclusion that three-dimensional roughness elements either had no effect on the boundary layer (subcritical condition) or, within a very narrow range of either speed or height of roughness, caused transition to move substantially up to the element itself.

A remaining problem is the question of the proper criterion for the effects of roughness when interaction between the elements is a possibility, as, for example, in the case of randomly distributed roughness. Such randomly distributed roughness corresponds to the practical case where the leading edge of the wing may in effect become sand blasted or covered with a sandpaper type of roughness. In this connection, it may be noted that the results of tests of airfoils with roughened leading edges (refs. 7 and 8) appeared to indicate the possibility that such roughness would have an effect on the airfoil characteristics only when the Reynolds number based on the roughness height and the free-stream velocity exceeded a critical value which seemed to be independent of the roughness size and the size and shape of the airfoil. It is not apparent that such a criterion is consistent with the concept of a constant critical value of the local roughness Reynolds number based on the velocity at the top of the roughness.

The present experiments were carried out for the purpose of determining the transition-triggering characteristics of such three-dimensional roughness particles when the roughness particles are randomly distributed in a close pattern such as in a sandpaper type of roughness, as well as of examining the relation between the two previously mentioned three-dimensional roughness criteria. It was also desired to obtain the necessary experimental information in such a way

[1] Supersedes NACA Technical Note 3858 by Albert E. von Doenhoff and Elmer A. Horton, 1956.

Preceding Page Blank

as to show the details of the transition phenomenon more clearly than would be indicated by time averaged velocity or total-pressure boundary-layer measurements.

The investigation was made in the Langley low-turbulence pressure tunnel at Mach numbers ranging from 0.15 to 0.25 by use of an 85-inch-chord NACA $65_{(215)}$–114 airfoil section that completely spanned the 36-inch-wide test section. This airfoil is the same model on which extensive laminar flow studies were reported in reference 9. The occurrence of transition at various chordwise positions for each roughness position was determined by means of a hot-wire anemometer. A great many qualitative indications of the nature of the flow in the boundary layer, as well as a few quantitative measurements of the level of the velocity fluctuations in the boundary layer, were obtained by this method.

SYMBOLS

y	distance normal to surface of airfoil
δ	total boundary-layer thickness where $\frac{u}{U}=1.0$ in the Kármán-Pohlhausen method
k	height of projection
c	chord of airfoil
x	distance from airfoil leading edge measured along the chord
s	distance from airfoil forward stagnation point measured along the airfoil surface
U_∞	free-stream velocity
U	local velocity just outside boundary layer
u	local streamwise component of velocity inside boundary layer
u_k	value of u at top of roughness projection
u'	root-mean-square value of the streamwise component of fluctuating velocity
q_∞	free-stream dynamic pressure
ν	coefficient of kinematic viscosity
R_c	airfoil Reynolds number based on chord and free-stream velocity, $U_\infty c/\nu$
R_k	projection Reynolds number based on roughness height and velocity at the top of the roughness, $u_k k/\nu$
$R_{k,\infty}$	projection Reynolds number based on roughness height and free-stream velocity, $U_\infty k/\nu$
R'	Reynolds number per foot of chord based on free-stream velocity, U_∞/ν
R_θ	Reynolds number based on momentum thickness θ and local velocity, $U\theta/\nu$
θ	momentum thickness of the boundary layer, $\int_0^\infty \frac{u}{U}\left(1-\frac{u}{U}\right)dy$

Subscripts:

t	Reynolds number at which transition takes place
min	minimum value

APPARATUS AND TESTS

The tests were made in the Langley low-turbulence pressure tunnel on an 85-inch-chord NACA $65_{(215)}$–114 airfoil section (fig. 1), which completely spanned the 36-inch width of the test section. The turbulence level of the tunnel at the speeds involved in this investigation is only a few hundredths of 1 percent. A description of the tunnel is given in reference 10 and a detailed description of the model is given in reference 11. The surface finish of the model was such that laminar flow could be maintained to the 50-percent-chord point up to a Reynolds number of 14×10^6, a value substantially the same as that obtained previously in references 9 and 11 with the same model.

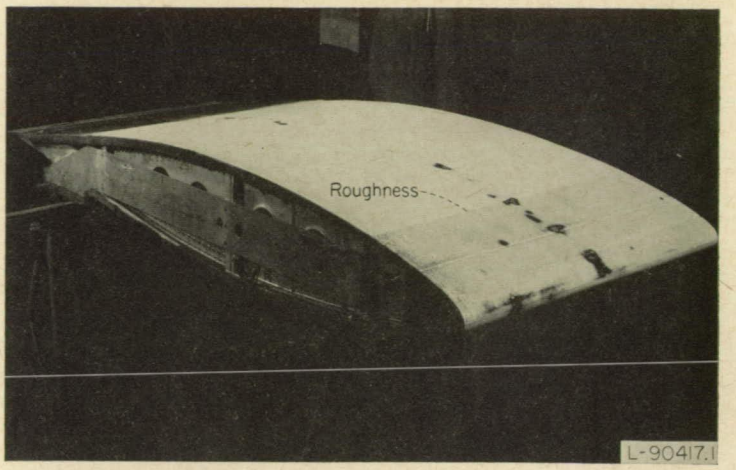


FIGURE 1.—Three-quarter view of 85-inch-chord NACA $65_{(215)}$–114 airfoil section with No. 60 carborundum grains from forward stagnation point to 12-inch station.

The pressure distribution of the model was measured from the leading-edge region back to approximately 65 percent of the chord by means of 0.008-inch-diameter pressure orifices drilled into the surface. Particular care was taken to provide numerous orifices near the leading edge so that the location of the forward stagnation point could be accurately determined. The nondimensional velocity distribution calculated from the measured pressure distribution along the upper surface is presented in figure 2.

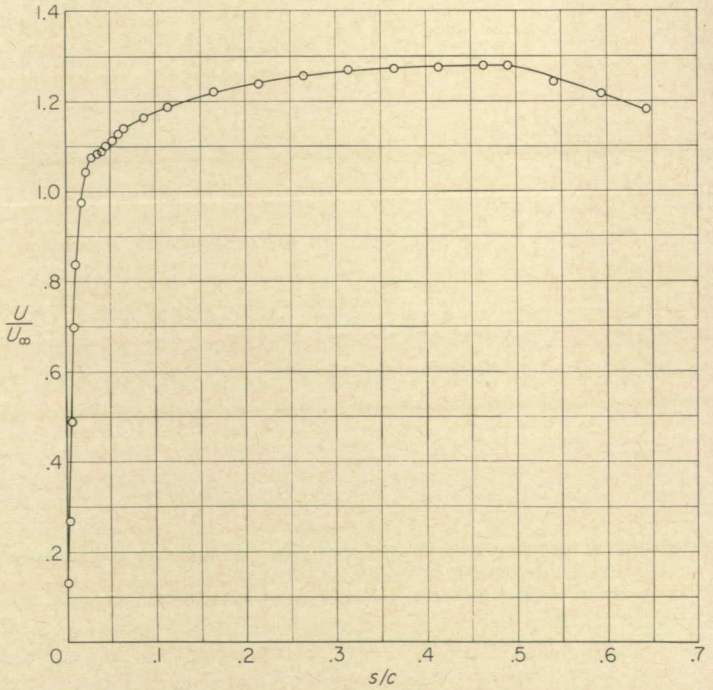


FIGURE 2.—Nondimensional velocity distribution outside of the boundary layer for NACA $65_{(215)}$–114 airfoil section at angle of attack of 0°.

The appearance of transition was determined by use of a hot-wire anemometer using a platinum iridium wire of 0.0003-inch diameter and of $\frac{3}{32}$-inch length. Figures 3 and 4 are photographs of the hot-wire holder. The output from the hot-wire anemometer was fed into an oscilloscope and the traces on the cathode-ray tube were recorded on 35 millimeter film by a special camera setup. The traces thus recorded were correlated with the tunnel velocity, wire position, and roughness location. The type of wire used in this investigation was one which was sensitive only to variations in the u-component of velocity. The wire was compensated for heat-capacity lag at one test condition, and this compensation setting was used for all observations. The cutoff frequency of the amplifier was about 12,000 cycles per second.

The tests were made with the leading edge of ¼-inch roughness strips 1 inch in span (fig. 4) located along the center line of the model at various positions from ¼ inch to 6¼ inches from the forward stagnation point measured along the surface and for full-span area-distributed roughness (fig. 1) from the forward stagnation point to 6 inches and to 12 inches back of the forward stagnation point. The roughness in all cases was provided by an application of either No. 60 or No. 120 carborundum grains, of grit sizes that met the specifications of reference 12. The grains were thinly spread over the surface to cover 5 to 10 percent of the surface area and were cemented by a thin coating of shellac applied before the roughness grains were spread. A closeup of the roughness as applied to the model is presented as figure 5.

In general, the No. 60 and No. 120 carborundum particles projected above the surface about 0.011 inch and 0.005 inch, respectively; however, the maximum particle height in each

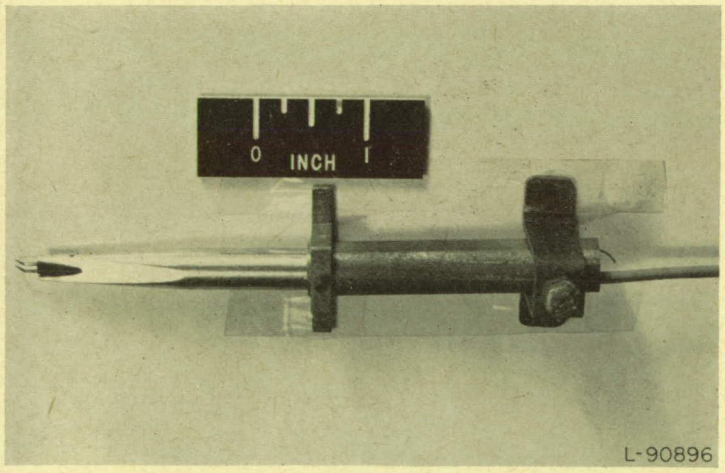


FIGURE 3.—Hot-wire holder used in investigation.

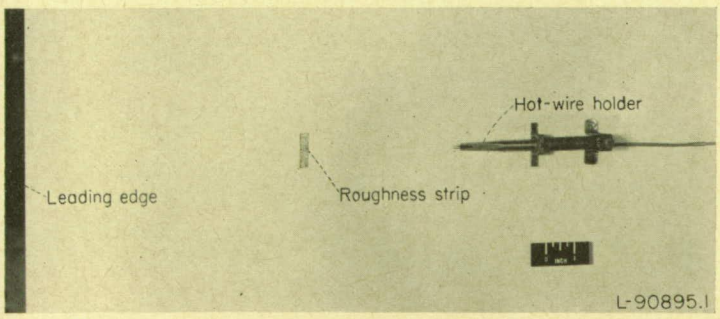


FIGURE 4.—View of hot-wire holder mounted on the airfoil surface relative to a typical ¼-inch by 1-inch roughness strip.

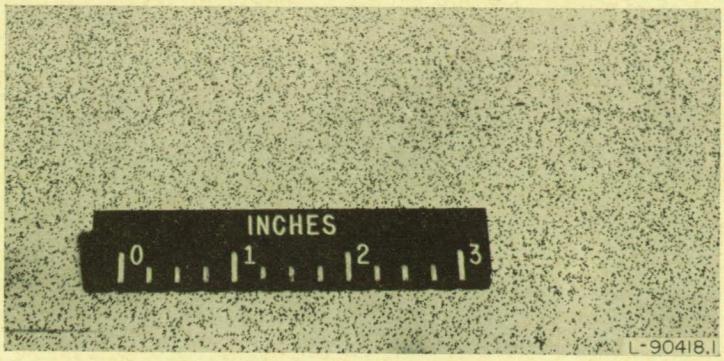


FIGURE 5.—Closeup of distributed No. 60 carborundum grains.

patch is also of interest. During the course of the investigation, although each roughness patch was examined carefully with the unaided eye, the height of the particles was not measured. Following completion of the tests, a series of ten patches ¼ inch by 1 inch of both sizes of grain were applied to a surface in the same manner used in applying the grains to the airfoil surface, and each of these patches was examined with a 15-power shop microscope to determine the actual particle height. The results of this examination are shown in figure 6, which shows the probability of finding at least one roughness particle of a given height in one patch of roughness. The curves of figure 6 show that, for No. 120 carborundum grain of 0.005-inch nominal size, it is virtually certain that each patch would have at least one particle projecting 0.008 inch above the surface, and about 50 percent of the patches would have at least one particle 0.009 inch high, whereas the chances of finding a particle 0.012 inch high would be very small. Similarly, for the No. 60 carborundum of 0.011-inch nominal size, it is virtually certain that every patch will contain at least one particle 0.016 inch high and approximately 50 percent of the patches will have at least one particle 0.018 inch high, whereas the chances of finding a particle 0.021 inch high in any patch is very small. The probable maximum height of a particle for No. 120 carborundum is

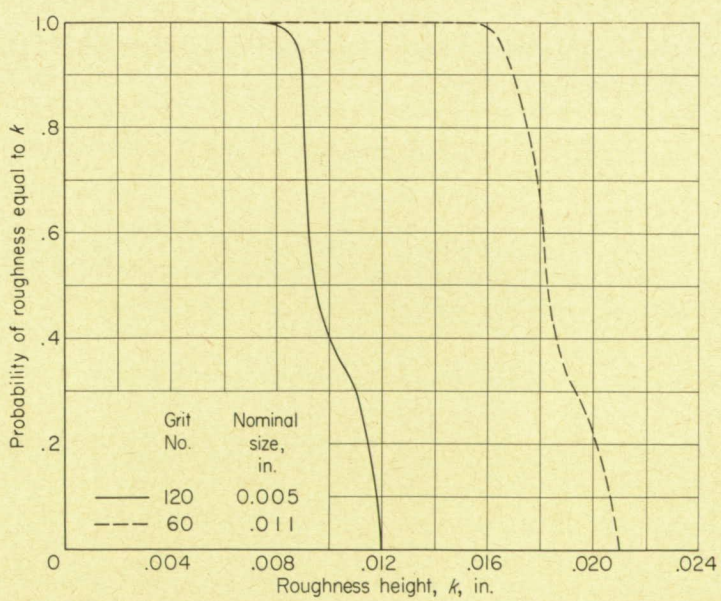


FIGURE 6.—Curves showing the probability of finding at least one grain of a given size of roughness in any ¼-inch by 1-inch roughness area when nominal size of carborundum grains is 0.005 or 0.011 inch.

therefore taken as 0.009 inch, and the probable maximum height of a particle for No. 60 carborundum is taken as 0.018 inch.

For each position of roughness, the hot-wire measurements were made at a sufficient number of chordwise positions back of the roughness to make possible determination of a curve of Reynolds number for transition as a function of chordwise position of the wire.

Some of the preliminary measurements were made with full-span strips of roughness ¼-inch wide. The relatively narrow width of the strip was chosen in order to permit correlation of transition with local boundary-layer conditions. When these measurements were made, it was found that, occasionally, the first indications of transition were obtained at a substantially lower tunnel speed for a downstream position than for more forward positions. In each such case, reexamination of the strip of roughness showed one or more particles in an off-center location projecting above the general level of the roughness. Because of the manner in which turbulent flow spreads, such unusually high projections affected the downstream observations but not the upstream ones. In order to facilitate inspection of the strip of roughness, its spanwise extent was reduced to 1 inch. Such small roughness strips were removed and reapplied two or more times, and the initial appearance of turbulence in each case occurred at very nearly the same Reynolds number; these results indicated that such roughness strips could be satisfactorily duplicated.

BOUNDARY-LAYER CALCULATIONS

In order to correlate the occurrence of transition with local boundary-layer conditions, it is of course necessary to know the velocity distribution in the boundary layer for all locations at which the roughness is placed. These laminar boundary-layer characteristics were calculated according to the method outlined in reference 13, that is, essentially by the Kármán-Pohlhausen method as modified by Walz (ref. 13, ch. 12, sec. B). This method is summarized in this section.

The momentum thickness θ of the boundary layer may be computed from the following equation:

$$\left(\frac{\theta}{c}\sqrt{R_c}\right)^2 \equiv \Theta^2 = \frac{0.470}{\left(\frac{U}{U_\infty}\right)^6}\int_0^{s/c}\left(\frac{U}{U_\infty}\right)^5 d\left(\frac{s}{c}\right) \tag{1}$$

The velocity distribution in the boundary layer may be obtained as follows: The form parameter K is defined as $\frac{\theta^2}{\nu}\frac{dU}{dx}$ or as

$$K \equiv \Theta^2 \frac{d\left(\frac{U}{U_\infty}\right)}{d\left(\frac{x}{c}\right)} \tag{2}$$

The form parameter K is related to the Pohlhausen shape parameter $\lambda = \frac{\delta^2}{\nu}\frac{dU}{dx}$ as follows

$$K = \left(\frac{37}{315} - \frac{\lambda}{945} - \frac{\lambda^2}{9072}\right)^2 \lambda \tag{3}$$

The parameter λ may also be written as

$$\lambda \equiv \Delta^2 \frac{d\left(\frac{U}{U_\infty}\right)}{d\left(\frac{x}{c}\right)} \tag{4}$$

where

$$\Delta \equiv \frac{\delta}{c}\sqrt{R_c}$$

Equation (3) is then solved for λ, and the velocity distribution in the boundary layer may be obtained by using the following expression

$$\frac{u}{U} = F(\eta) + \lambda G(\eta) \tag{5}$$

where

$$\eta \equiv \frac{y}{\delta}$$

$$F(\eta) \equiv 2\eta - 2\eta^3 + \eta^4$$

$$G(\eta) \equiv \frac{1}{6}\eta(1-\eta)^3$$

The measured velocity distribution over the airfoil used in these calculations is presented in figure 2. The boundary-layer parameters λ and Δ were calculated by the use of the aforementioned relations and the measured velocity distribution. The shape parameter λ is plotted against s/c in figure 7, and the nondimensional boundary-layer thickness

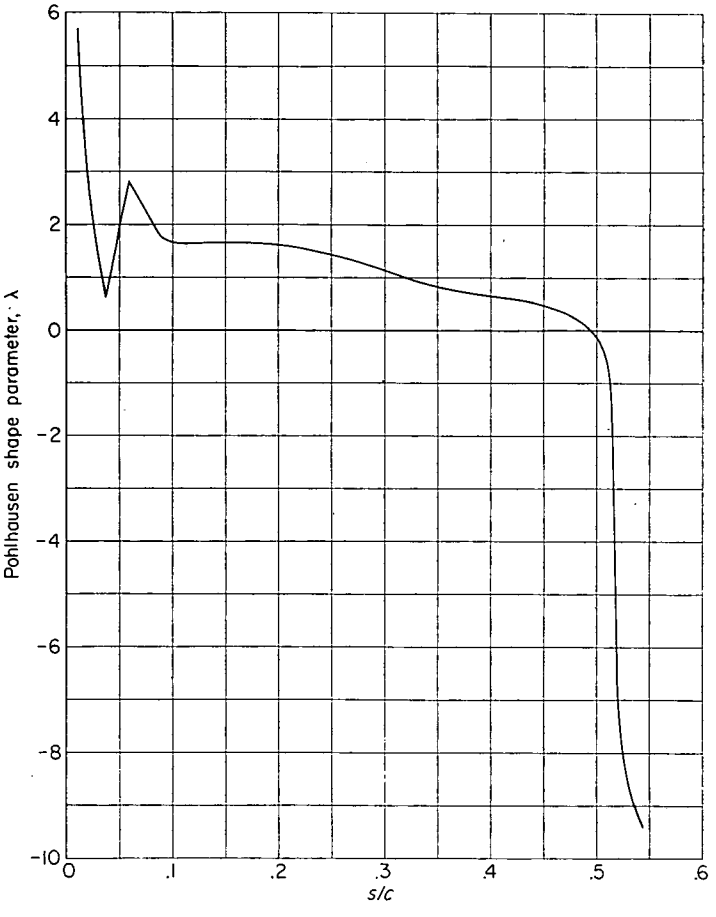


FIGURE 7.—Pohlhausen shape parameter λ for a laminar boundary layer on NACA $65_{(215)}$-114 airfoil section at angle of attack of 0°.

Δ or $\frac{\delta}{c}\sqrt{R_c}$ as a function of s/c is given in figure 8. In order to facilitate the calculations involved in the analysis of the data, the nondimensional velocity distribution u/U_∞ is also presented in figure 9 as a function of $\frac{y}{c}\sqrt{R_c}$ for various chordwise positions.

RESULTS AND DISCUSSION

Hot-wire traces of the time variation of velocity in the boundary layer as observed for various locations of the roughness are shown in figure 10. For each location of roughness, observations were made at various positions downstream throughout the range of speed necessary to include the transition phenomena at the point of observation. To the left of each hot-wire trace is a short tick which indicates the corresponding value of the Reynolds number per foot of chord as read on the vertical scale of the figure. The chordwise location of the point of observation of each group of hot-wire traces is indicated at the bottom of the figure, as is the height of the wire above the surface in thousandths of an inch. Also shown in the figure is the time scale for the traces. Time increases from left to right. It should be noted that the amplifier gain setting for the traces shown in figure 10 (a) was the same for all traces. This procedure resulted in substantially a straight line for the laminar traces. In parts (b), (c), (d), (e), and (f) of figure 10, however, the amplifier gain was increased for the conditions corresponding to completely laminar flow, and the traces for this condition, therefore, show some velocity fluctuations. These fluctuations, however, are of a completely different character from those corresponding to turbulent flow.

In general, transition appears to start as disturbances of very short duration that occur comparatively infrequently at a position just behind the roughness. As the position of observation moves downstream and the speed is kept constant, the frequency of the turbulent bursts does not appear to change, but the duration of each burst becomes longer. This phenomenon is shown very clearly in figure 10 (b) at

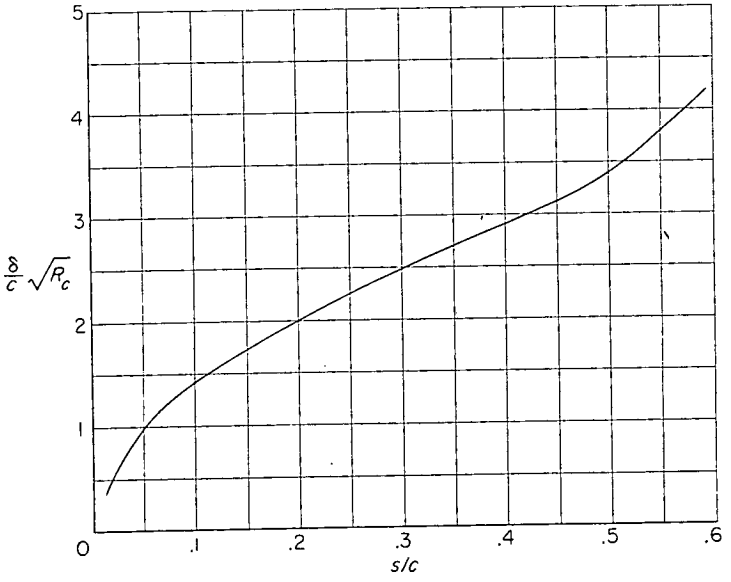


FIGURE 8.—Nondimensional laminar-boundary-layer thickness distribution for NACA $65_{(215)}$-114 airfoil section.

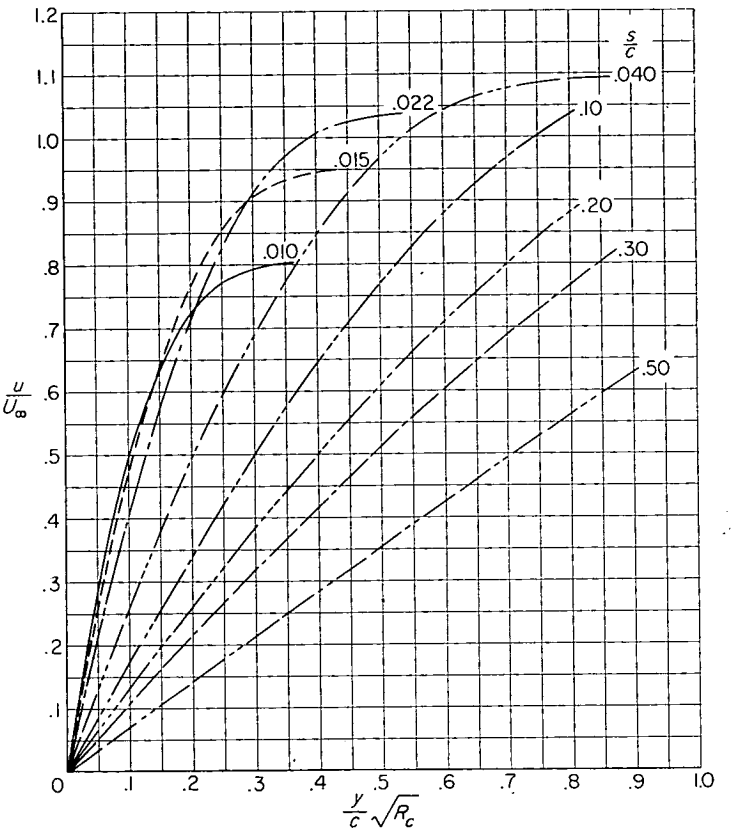
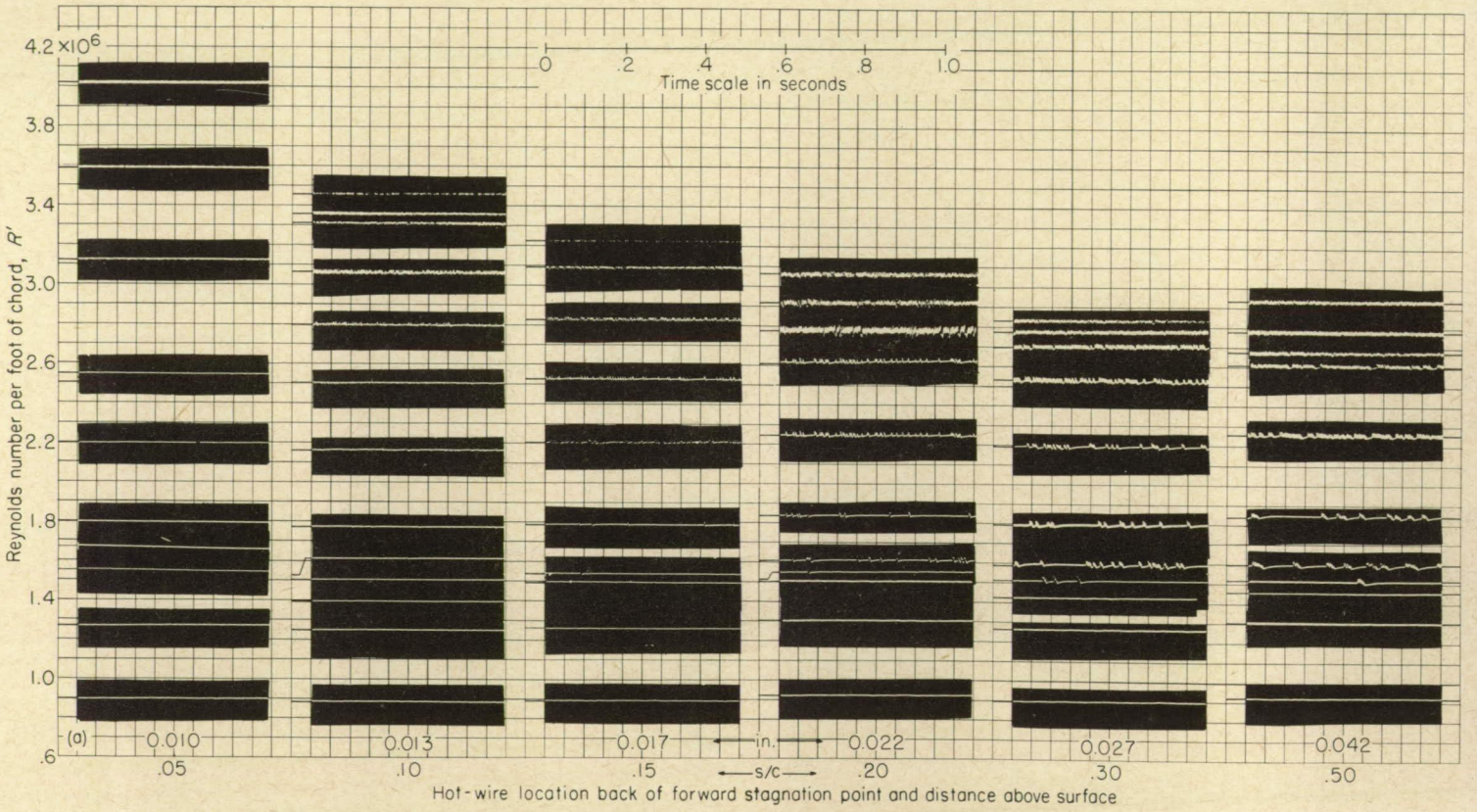


FIGURE 9.—Nondimensional velocity distribution within laminar boundary layer of NACA $65_{(215)}$-114 airfoil section for various positions along surface.

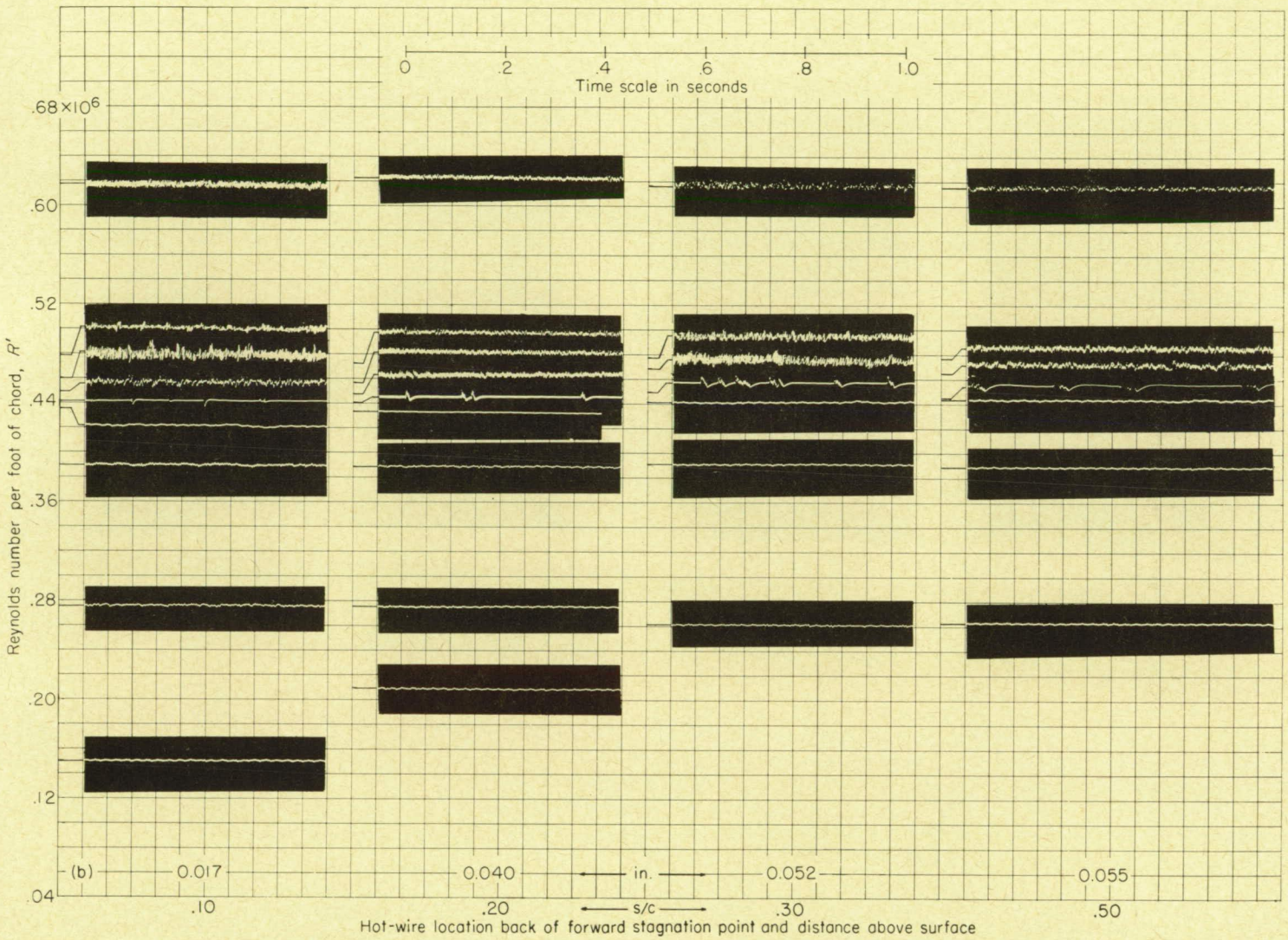
a Reynolds number of 0.44×10^6. Figure 10 also shows that each burst of turbulence is followed by a condition termed by Schubauer and Klebanoff (ref. 14) as a "logarithmic decrement" type of velocity variation. The increase in duration of individual bursts with distance downstream from the roughness is consistent with the description of the origin of transition given in reference 14; that is, it is consistent with the concept of transition beginning as turbulent spots that start in the vicinity of the roughness and grow as they move downstream.

A quantitative summary of the data of figure 10 is given by the data presented in figure 11. Each part of figure 11 consists essentially of a pair of curves. The lower curve of each pair gives approximately the lowest value of the Reynolds number per foot at which any turbulent bursts were observed for a given location of the roughness plotted against the observation position. The upper curve gives the maximum value of the Reynolds number per foot at which any traces of laminar flow could be detected. In other words, for conditions corresponding to the lower curve, the flow was nearly always laminar, and for those corresponding to the upper curve, the flow was nearly always turbulent. Examination of the various parts of figure 11 indicates that the lowest speed at which any turbulent flow could be found was substantially independent of the position of observation. This is generally true except for the most forward observation positions where, because of the extremely short duration of the bursts, they were difficult to observe and, as a result, these points may be plotted at too high a value of the unit Reynolds number.



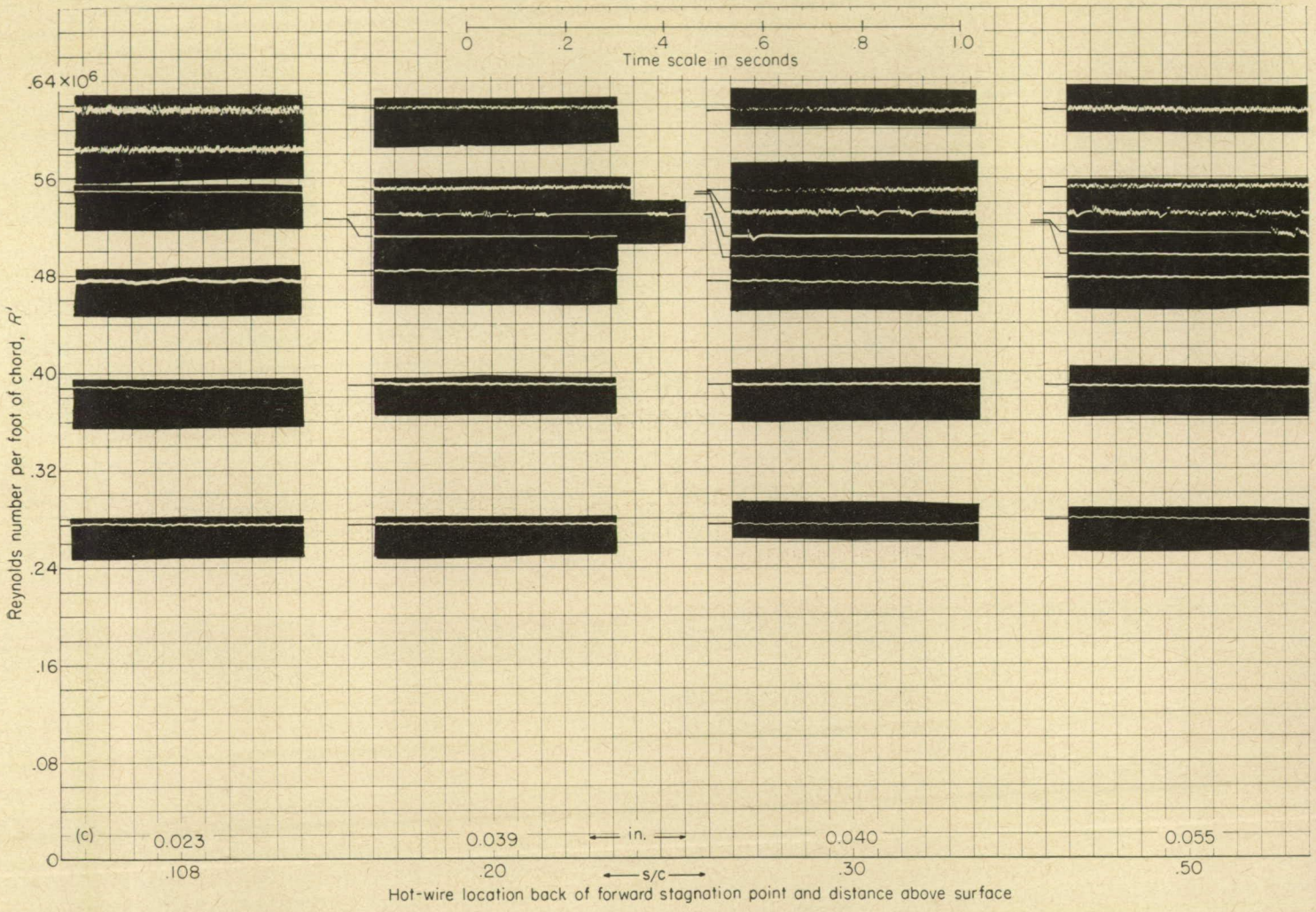
(a) No. 60 carborundum from 0.25 to 0.50 inch back of forward stagnation point.

FIGURE 10.—Typical oscillograph records at various chordwise positions through transition-speed range for 85-inch-chord NACA $65_{(215)}$–114 airfoil section with various locations and sizes of roughness.



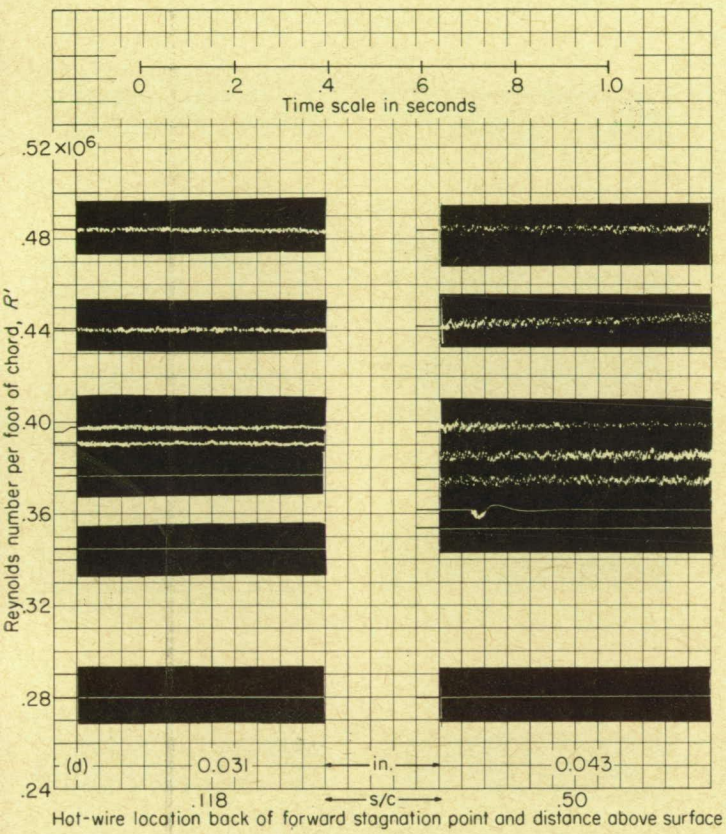
(b) No. 60 carborundum from 2.0 to 2.25 inches back of forward stagnation point.

FIGURE 10.—Continued.



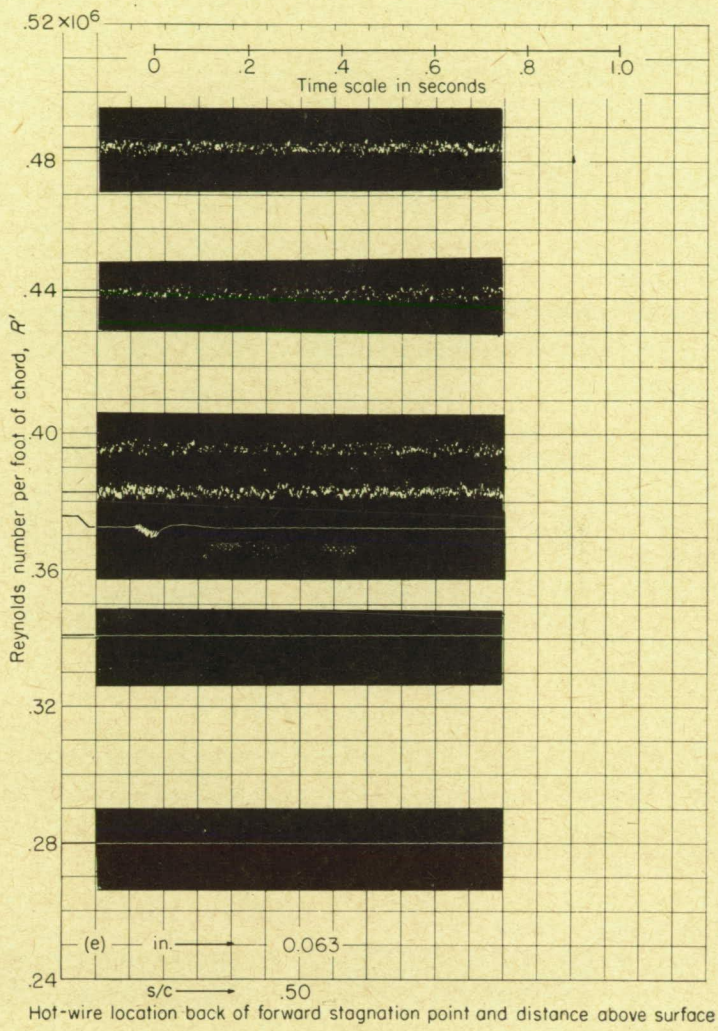
(c) No. 60 carborundum from 6.5 to 6.75 inches back of forward stagnation point.

FIGURE 10.—Continued.



(d) No. 60 carborundum from 0 to 6 inches back of forward stagnation point

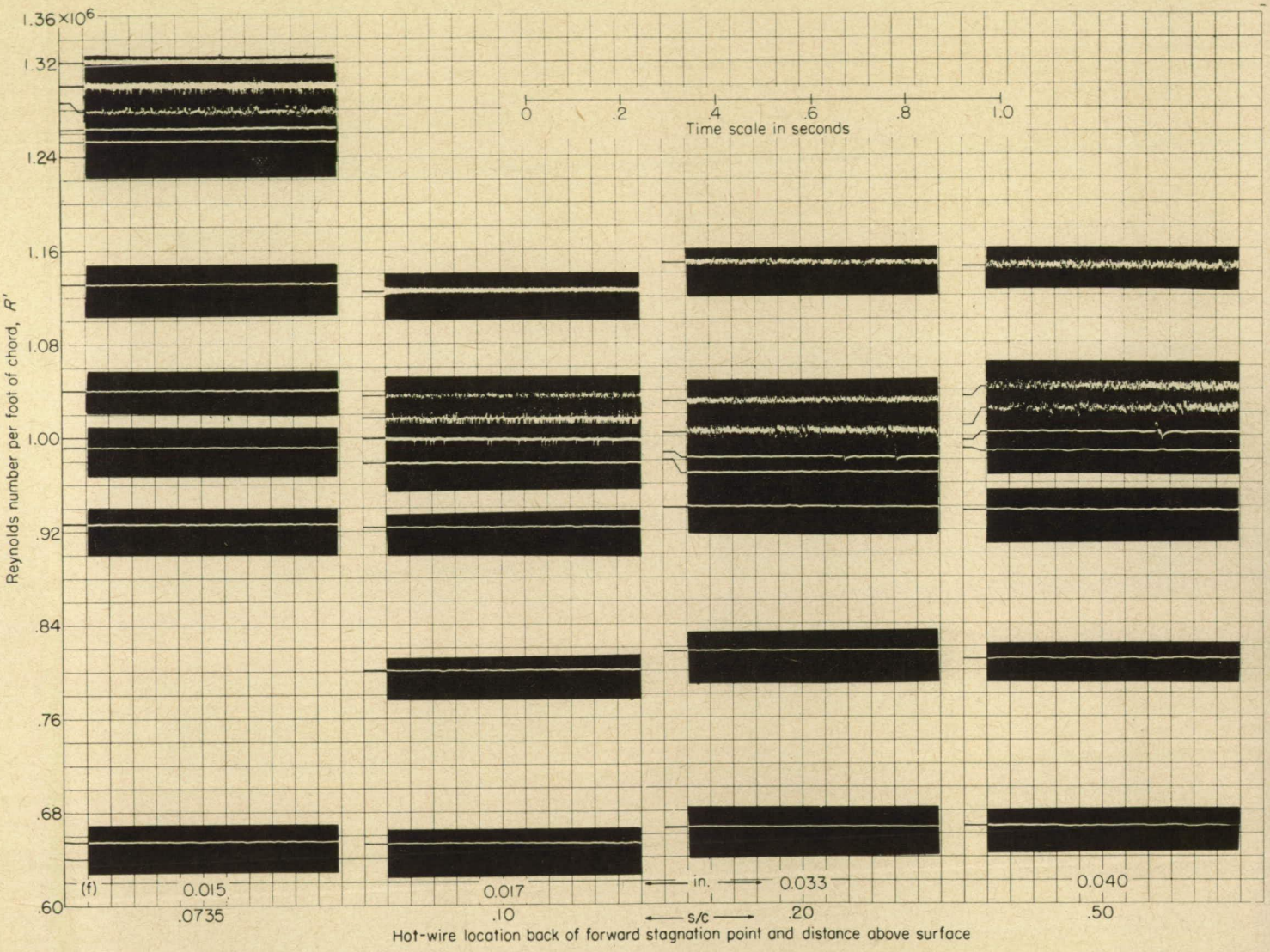
FIGURE 10.—Continued.



(e) No. 60 carborundum from 0 to 12 inches back of forward stagnation point.

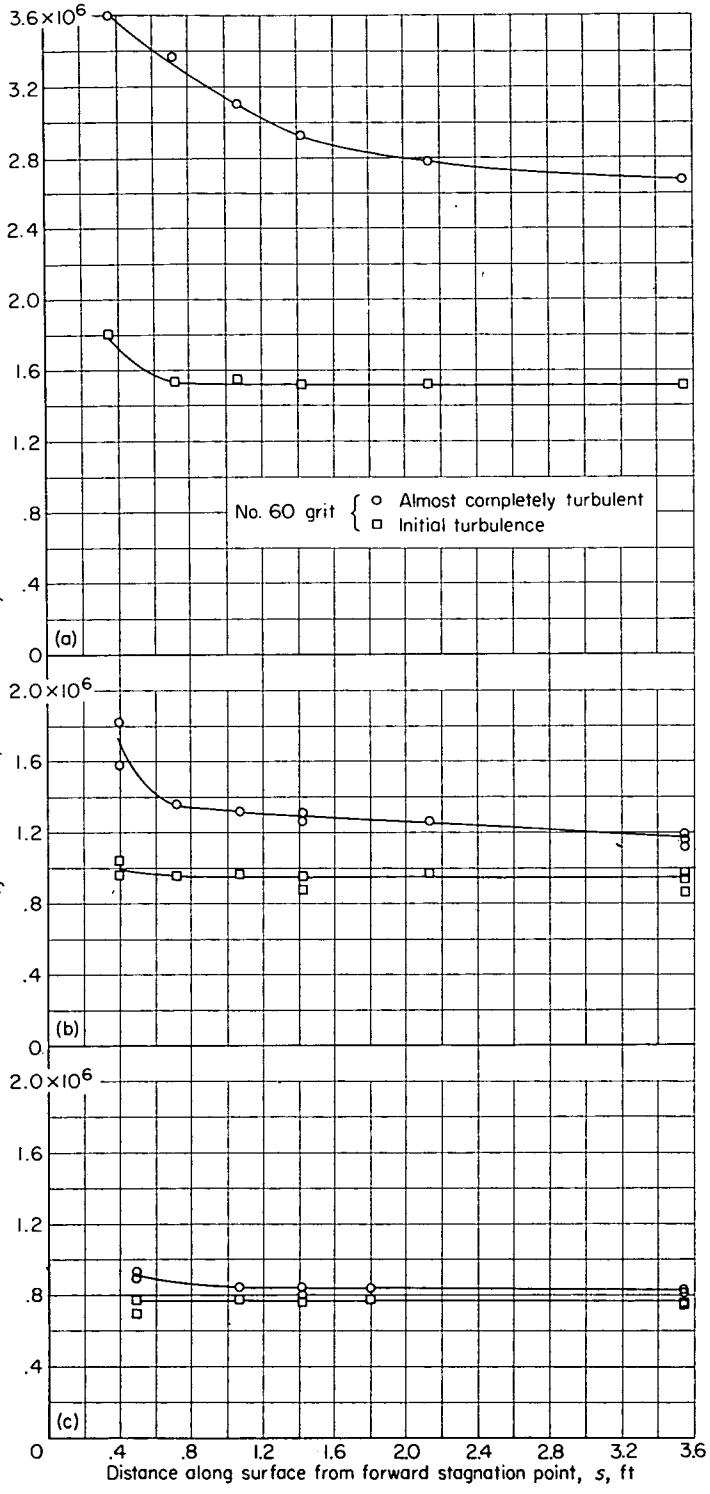
FIGURE 10.—Continued.

526597—60——17



(f) No. 120 carborundum from 2.00 to 2.25 inches back of forward stagnation point.

FIGURE 10.—Concluded.

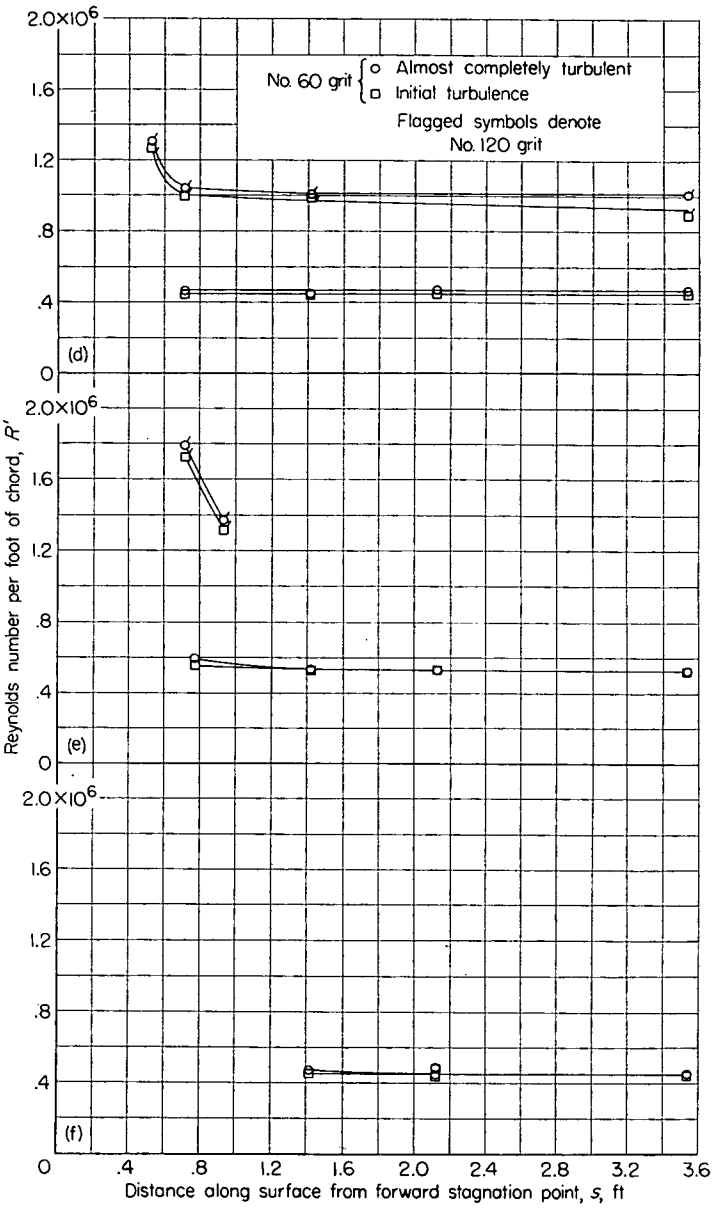


(a) Roughness located from 0.25 to 0.50 inch from forward stagnation point.

(b) Roughness located from 0.50 to 0.75 inch from forward stagnation point.

(c) Roughness located from 0.75 to 1.00 inch from forward stagnation point.

FIGURE 11.—Reynolds number per foot at which transition occurs at various chordwise positions for an NACA $65_{(215)}$–114 airfoil section with No. 60 and No. 120 carborundum at various chordwise positions.



(d) Roughness located from 2.00 to 2.25 inches from forward stagnation point.

(e) Roughness located from 6.5 to 6.75 inches from forward stagnation point.

(f) Roughness located from 12.00 to 12.25 inches from forward stagnation point.

FIGURE 11.—Concluded.

The value of the speed at which the flow is nearly completely turbulent decreases appreciably as the point of observation moves downstream for the more forward roughness locations (figs. 11 (a) and (b)). This trend is as would be expected if turbulence began as a series of turbulent bursts originating at or near the roughness and increasing in size as they moved downstream. For the more downstream positions of the roughness (figs. 11 (c) to 11 (f)), the upper and lower curves almost coalesce; that is, the speed range between fully laminar and fully turbulent flow almost vanishes. The data on which figure 11 is based include many more observations than those presented in figure 10,

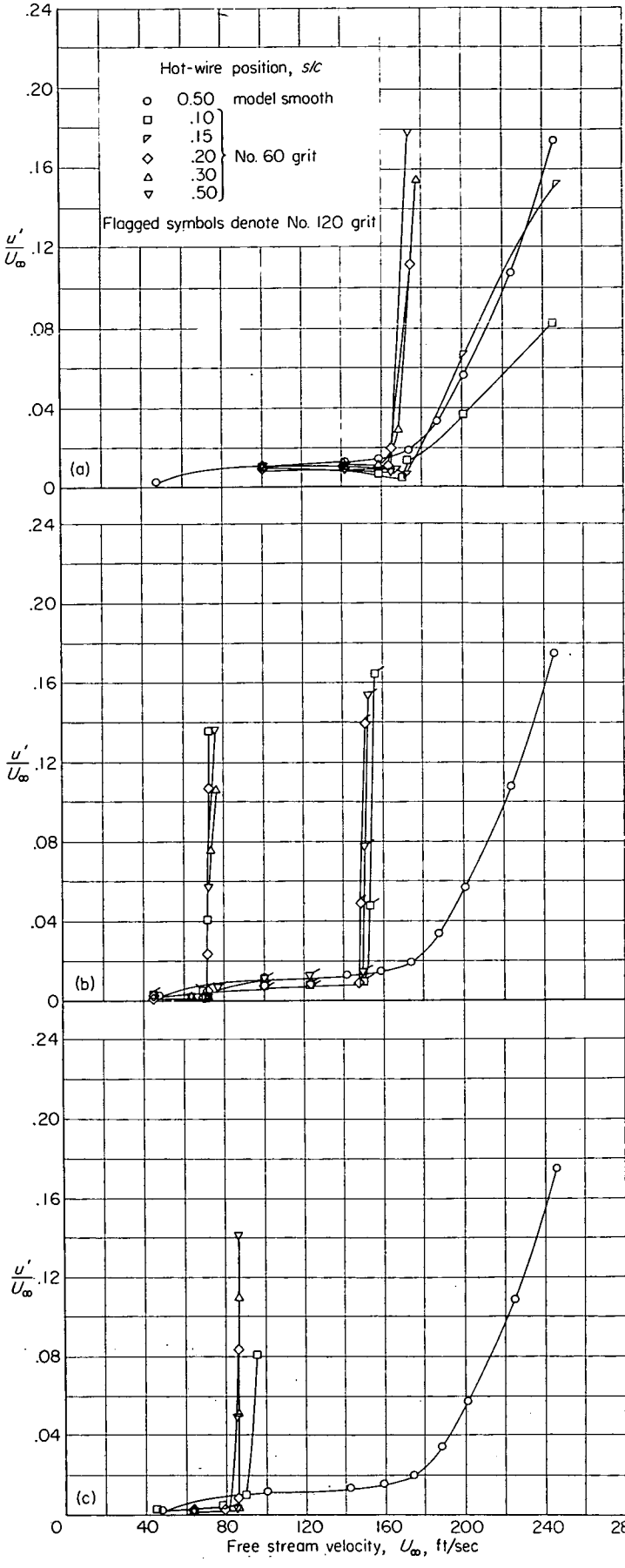
which are merely representative samples of the oscilloscope records.

Quantitative observations of the root-mean-square values of the fluctuations were made both with and without roughness through the speed range corresponding to that for which turbulence occurred when roughness was present. Typical examples of these measurements are presented in figure 12 as functions of the free-stream velocity. From figure 12, it is seen that the root-mean-square level of fluctuations in the laminar boundary layer, even at positions as far downstream as 50 percent of the chord, is as low on the airfoil with roughness present as on the smooth airfoil. It thus appears that, at speeds below those at which turbulent bursts occur, the presence of the roughness does not result in any measurable disturbance in the boundary layer that would hasten transition. It is therefore to be presumed that, at speeds below the critical speed for the roughness, no upstream movement of the transition region would occur even if the model were sufficiently long for transition to occur naturally in the region of favorable pressure gradient.

This type of phenomenon, therefore, appears to be strongly contrasted to the manner in which transition occurs when it is caused by two-dimensional disturbances. The data for the two-dimensional type of disturbance have been summarized in reference 6. This summary indicates that, for the case of two-dimensional disturbances, the roughness introduces into the boundary layer a measurable disturbance which grows until transition occurs.

If, as seems likely from an examination of the oscillograph records (see fig. 10), transition associated with the type of roughness of the present investigation results from the formation of discrete eddies or disturbances originating at the roughness particles, it should be possible to relate the occurrence of such disturbances to the characteristics of local flow about the roughness. That is, if all the roughness particles are regarded as being geometrically similar, and if the roughness is regarded as being sufficiently submerged in the boundary layer to provide substantially linear velocity variation from the surface to the top of the roughness, discrete eddies should form when the Reynolds number of the flow about the roughness reaches a critical value. This concept is not new; it was proposed by Schiller (ref. 2) and used by Loftin in analyzing the data presented in reference 1.

This view is supported by the data presented in figure 13, which is a plot of the critical Reynolds number $R_{k,t}$ based on the height of the roughness and the velocity at the top of the roughness as a function of the chordwise position of the roughness. The velocity at the top of the roughness was found either from the theoretical boundary-layer calculations previously described or, if the roughness projected completely through the boundary layer, from the measured pressure distribution. For all roughness positions more than $0.025c$ from the forward stagnation point, the critical roughness Reynolds number $R_{k,t}$ was substantially constant within rather close limits. For positions nearer the forward stagnation point than $0.025c$, the critical roughness Reynolds number $R_{k,t}$ increased markedly. It is to be noted that, for positions nearer the forward stagnation point than $0.025c$, the roughness protruded nearly through the boundary layer, and, for the three positions closest to the forward stagnation point, the roughness protruded completely through the boundary



(a) Roughness from 0.25 to 0.50 inch back of forward stagnation poin
(b) Roughness from 2.00 to 2.25 inches back of forward stagnation poin
(c) Roughness from 6.50 to 6.75 inches back of forward stagnation poin

FIGURE 12.—Turbulence-level measurements u'/U_∞ on NAC $65_{(215)}$–114 airfoil section as a function of free-stream velocity U for model smooth and three representative locations of the roughnes

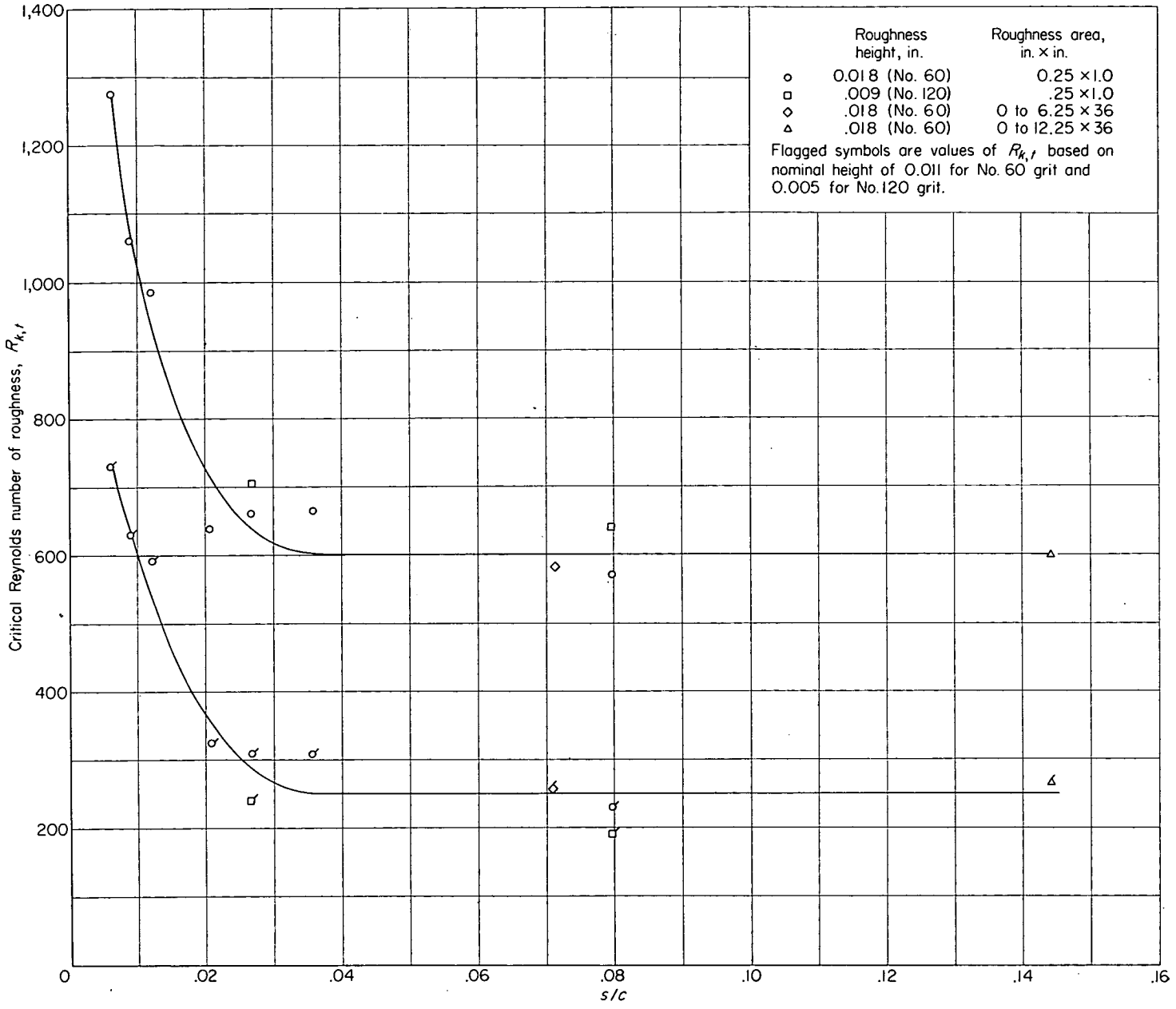


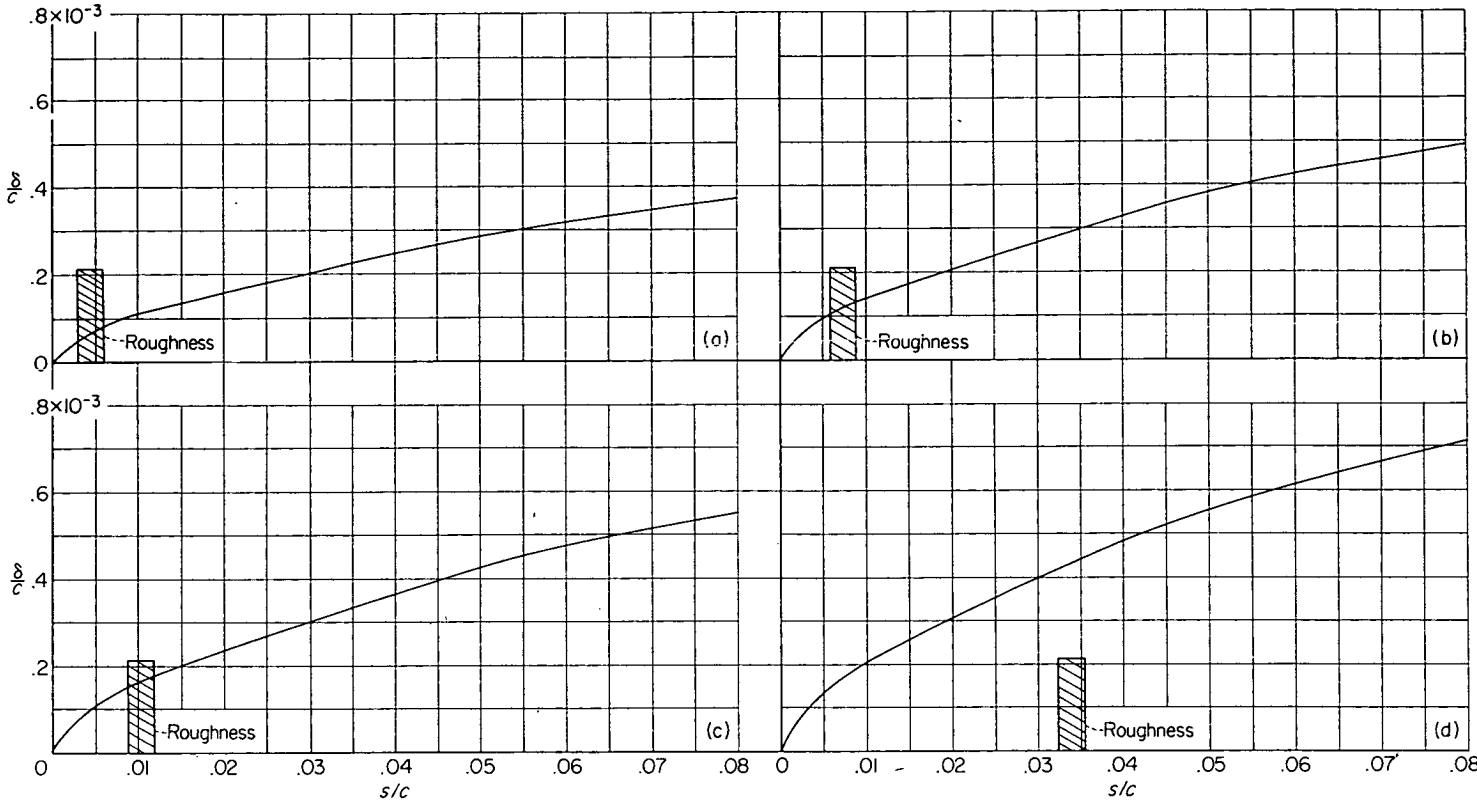
FIGURE 13.—Roughness Reynolds number for transition on NACA $65_{(215)}$-114 airfoil section as a function of roughness location.

yer. (See fig. 14.) It is entirely possible that for the range conditions of the present tests, the boundary layer over ie region of the airfoil in the vicinity of the forward stagnaon point was sufficiently stable to cause small eddies origating at the roughness to be damped out before they avelled downstream far enough to affect the less stable minar boundary layer farther downstream. At any rate, iese results indicate that if the height of the roughness article is so small that the roughness Reynolds number is ss than 600 based on maximum particle size or less than 50 based on nominal particle size, the roughness is not large nough to cause transition. This statement appears to be alid even for roughness heights several times the boundaryyer thickness. The order of magnitude of the critical roughess Reynolds number is within the range of those found by oftin (ref. 1) and is not much different from the value found y Schwartzberg and Braslow (ref. 4).

The extent of the roughened area does not appear to have n important effect on the height of roughness necessary to ause transition. When the grains of roughness were spread from the leading edge to 6 inches or 12 inches back of the leading edge (fig. 1), the airfoil Reynolds number at which transition occurred was substantially the same as for a spot of roughness 1 inch in span and ¼ inch in chord located from 2 to 2¼ inches from the forward stagnation point. This location (that is, the position at which, for given free-stream conditions, the value of the roughness Reynolds number R_k was a maximum) was approximately the most critical location for the height of roughness used.

APPLICATION OF RESULTS

An examination of the consequences of the inference drawn from the preceding discussion, namely, that transition occurs when the local roughness Reynolds number R_k exceeds a value of 600, is of interest. The nature of these consequences will be examined with particular reference to the airfoil studied in the present investigation by calculating the critical conditions for various heights of roughness. Figure 15 shows the variation of the roughness Reynolds number R_k for 0.018-inch roughness particles with position along the surface



(a) $R_{c,t}=11.8\times10^6$.
(b) $R_{c,t}=6.7\times10^6$.
(c) $R_{c,t}=5.4\times10^6$.
(d) $R_{c,t}=3.2\times10^6$.

FIGURE 14.—Illustration of height of roughness relative to laminar-boundary thickness for airfoil Reynolds number at which transition occurs for various positions of the roughness.

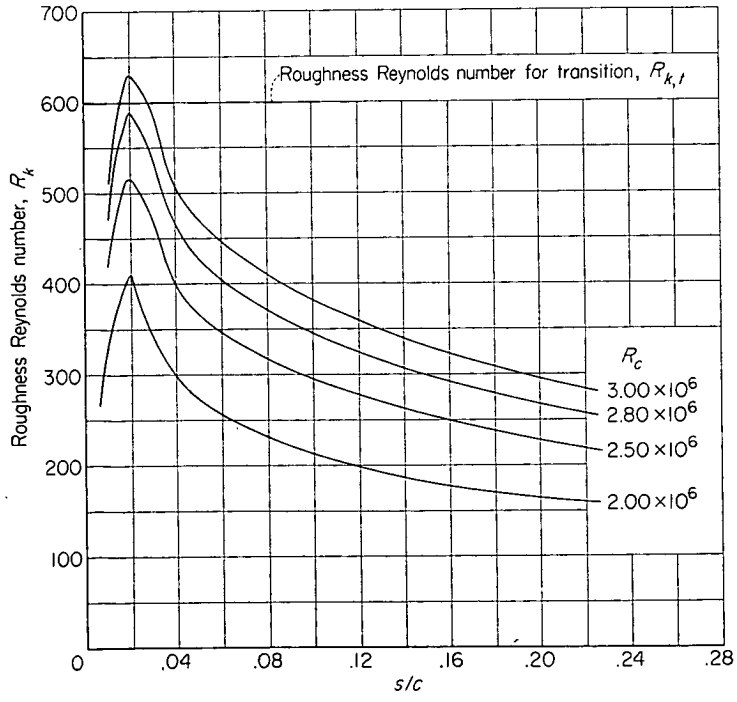


FIGURE 15.—The roughness Reynolds number R_k for roughness height of 0.018 inch as a function of roughness location for various airfoil Reynolds numbers R_c as calculated for an 85-inch-chord NACA $65_{(215)}$-114 airfoil section.

for several values of the airfoil Reynolds number. Th roughness position for maximum R_k does not vary rapidl with airfoil Reynolds number and occurs when the heigh of the roughness is slightly less than the total boundary-laye thickness. For far forward roughness positions, R_k is lo because of the low value of the potential flow velocity nea the forward stagnation point. For far rearward roughnes positions, R_k is low because the roughness is deeply buried in the boundary layer.

Several sets of calculations of this nature were made fo different heights of roughness. The results are summarize in figures 16 and 17. For each height of roughness, th position along the surface corresponding to a maximu value of R_k was found, and the value of R_c corresponding t a value of R_k of 600 at this location was then calculated This value of R_c is the smallest value at which a value of R of 600 can be obtained with the roughness of a given heigh situated at any position along the surface. Figure 16 give the relation between the minimum critical airfoil Reynold number and the most sensitive location of the roughnes with the height of the roughness as a parameter for a fixe value of the critical roughness Reynolds number of 60 Figure 17 plots the same information in a slightly differen manner. Here the minimum value of the critical airfo Reynolds number for a roughness Reynolds number $R_{k,t}$ 600 for roughness situated at the most sensitive location plotted against the ratio of the roughness height to airfo chord. From figure 17, it is seen that the curve of $R_{c,min}$ fo $R_{k,t}=600$, when plotted as a function of k/c on log log pape

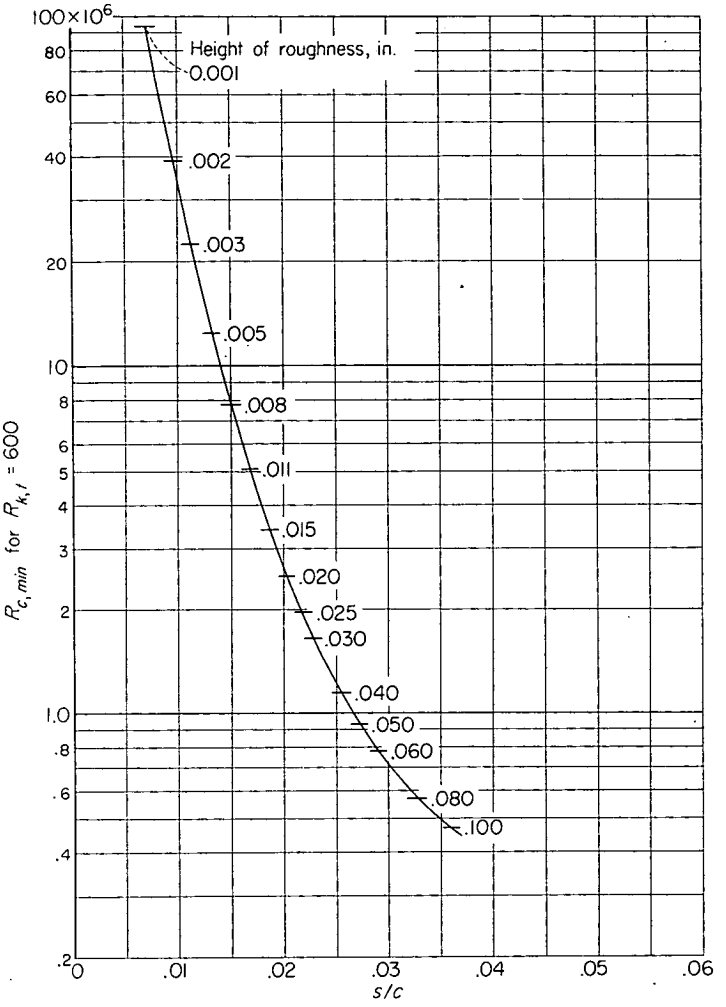


FIGURE 16.—The theoretical location, for various heights of roughness on an 85-inch-chord NACA $65_{(215)}$-114 airfoil section, at which, for a value of $R_{k,t}$ of 600, the airfoil Reynolds number R_c will be a minimum.

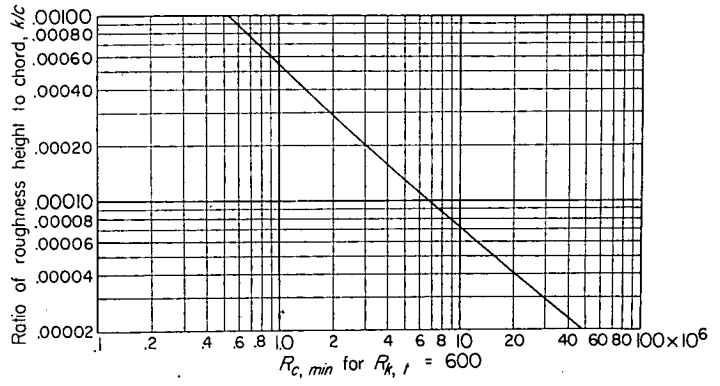


FIGURE 17.—Variation of the minimum airfoil Reynolds number $R_{c,min}$, for critical roughness Reynolds number $R_{k,t}$ of 600, with roughness height as calculated for an 85-inch-chord NACA $65_{(215)}$-114 airfoil section.

is nearly a straight line with a slope of −1. This result, of course, indicates that $R_{k,\infty}$, which is the product of k/c and $R_{c,min}$, is approximately constant and equal to about 680. If this value of $R_{k,\infty}=680$ is used as a criterion for transition, it becomes a simple matter to determine whether a given height of distributed roughness will cause transition for a given airfoil Reynolds number. If this criterion is expressed in terms of the nominal size of the roughness grain, the corresponding critical value of $R_{k,\infty}$ is 415. This criterion agrees very well with the data presented in references 7 and 8.

Although a particular pressure distribution was involved in the determination of the simple criterion $R_{k,\infty}=680$, it seems reasonable that the critical value should not be very sensitive to the particular type of pressure distribution. In general, if it is assumed that the value of $R_{k,t}$ is 600 for the case where the height of the roughness is less than the total boundary-layer thickness and is at least as large or larger for roughness that projects through the boundary layer, this condition will correspond to a value of $R_{k,\infty}$ of about 680 if the airfoil has a reasonably extensive region of low pressure gradient with a velocity outside the boundary layer approximately equal to the free-stream velocity. Consider, for example, the case of a flat plate with uniform pressure. If the roughness is so far forward that it projects through the boundary layer, the value of R_k will not change with further forward movement of the roughness. The data of figure 13 seem to indicate, however, that the value of $R_{k,t}$ has its lowest value when the roughness is just completely immersed in the boundary layer. For this case, the value of $R_{k,t}$ is 600 and the corresponding value of $R_{k,\infty}$ for a flat plate would be only slightly greater than this value and thus would not differ greatly from the value of 680 found for the present airfoil.

The minimum size of roughness that can be easily detected or the size of the splattered remains of insects are relatively fixed values completely independent of wing size. In view of these conditions, the significance of the unit Reynolds number $\left(R'=\frac{U_\infty}{\nu}\right)$ immediately becomes clear. For example, if k is the height of the splattered remains of insects, then if R' is so small that $R_{k,\infty}$ is less than about 680, the remains of the insects should not cause premature transition. If, for the sake of discussion, it is assumed that the height of the insect remains or the minimum size of roughness that can be easily detected is about 0.001 inch, the critical value of R' will be about 8.2×10^6. This value of the unit Reynolds number R' for transition is in general agreement with values considered acceptable on the basis of wind-tunnel experience in the Langley variable-density and low-turbulence pressure tunnels. In the variable-density-tunnel tests, in which R' was usually about 7×10^6, a fair amount of difficulty was experienced in maintaining the leading edge of the airfoils smooth enough to obtain consistent results for the maximum lift coefficients. In the low-turbulence-pressure tunnel, essentially no difficulty was experienced in obtaining the design laminar flow for a unit Reynolds number $R'=1.5\times10^6$ and only occasional difficulties for $R'=3\times10^6$; however, for R' above these values, the difficulty of obtaining extensive laminar flows increased markedly.

Figure 18 translates this criterion into more easily appreciated terms. The critical size of roughness for an assumed free-stream Mach number of 1.0 has been computed as a function of altitude by using NACA standard atmosphere (ref. 15). At sea level, the critical size is about 0.001 inch. This increases to about 0.002 inch at 20,000 feet and 0.010 inch at 60,000 feet. For altitudes above 30,000 or

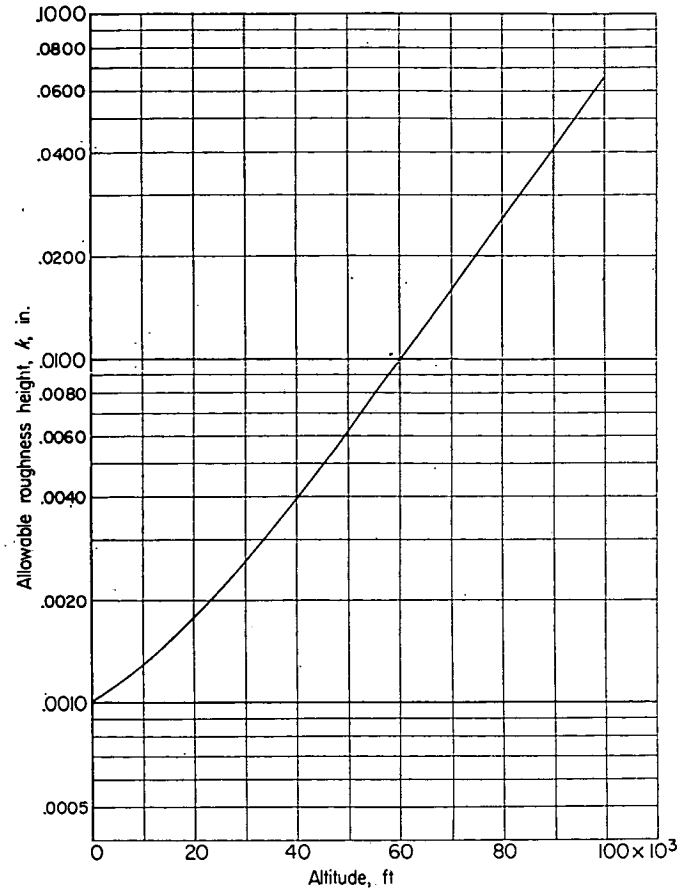


FIGURE 18.—Allowable roughness height for critical roughness Reynolds number, $R_{k,t}$ of 600, as function of altitude for Mach number of 1.0.

40,000 feet, it does not seem likely that accidental surface roughness should make it difficult to obtain extensive laminar flows. Of course, built-in roughness such as lap or butt joints, surface waviness, or rivet heads might still be sufficiently large to cause transition.

CONCLUSIONS

A low-speed investigation in the Langley low-turbulence pressure tunnel to determine the effect of grain height and location on the transition characteristics of sandpaper type of roughness on an NACA 65-series airfoil section indicates the following conclusions:

1. If the roughness is sufficiently submerged in the boundary layer to give substantially linear variation of the boundary-layer velocity with distance from the surface up to the height of the roughness, turbulent spots begin to appear immediately behind the roughness when the Reynolds number R_k, based on the velocity at the top of the roughness and the roughness height, exceeds a critical value $R_{k,t}$ of approximately 600.

2. At Reynolds numbers even slightly below the critical value, the sandpaper type of roughness introduced no measurable disturbances into the laminar layer downstream of the roughness.

3. The most sensitive position for roughness grains of a given size, that is, the roughness position for which the critical value of the model Reynolds number is least, is that at which the roughness height is slightly less than the total laminar boundary-layer thickness.

4. The chordwise extent of the roughened area does not appear to have an important effect on the critical value of the roughness Reynolds number $R_{k,t}$.

5. If the airfoil has a reasonably extensive region of low pressure gradient with a velocity outside the boundary layer approximately equal to the free-stream velocity and roughness so distributed over the leading-edge region as to include the most sensitive position, the condition $R_{k,t}=600$ may be approximately replaced by the more easily calculated condition $R_{k,\infty}=680$, where $R_{k,\infty}$ is the Reynolds number based on the size of the roughness and the free-stream velocity.

LANGLEY AERONAUTICAL LABORATORY,
NATIONAL ADVISORY COMMITTEE FOR AERONAUTICS,
LANGLEY FIELD, VA., *August 15, 1956.*

REFERENCES

1. Loftin, Laurence K., Jr.: Effects of Specific Types of Surface Roughness on Boundary-Layer Transition. NACA WR L–46, 1946. (Formerly NACA ACR L5J29a.)
2. Schiller, L.: Strömung in Rohren. Handbuch der Experimentalphysik; Bd. IV, 4. Teil, Hydro- und Aerodynamik; Ludwig Schiller, Hrsg.; Akad. Verlagsgesellschaft m.b.H. (Leipzig), 1932, p. 191.
3. Tani, Itiro, Hama, Ryosuke, and Mituisi, Satosi: On the Permissible Roughness in the Laminar Boundary Layer. Rep. No. 199 (vol. XV, 13), Aero. Res. Inst., Tokyo Imperial Univ., Oct. 1940.
4. Schwartzberg, Milton A., and Braslow, Albert L.: Experimental Study of the Effects of Finite Surface Disturbances and Angle of Attack on the Laminar Boundary Layer of an NACA 64A010 Airfoil With Area Suction. NACA TN 2796, 1952.
5. Klebanoff, P. S., Schubauer, G. B., and Tidstrom, K. D.: Measurements of the Effect of Two-Dimensional and Three-Dimensional Roughness Elements on Boundary-Layer Transition. Jour. Aero. Sci., vol. 22, no. 11, Nov. 1955, pp. 803–804.
6. Dryden, Hugh L.: Review of Published Data on the Effect of Roughness on Transition From Laminar to Turbulent Flow. Jour. Aero. Sci., vol. 20, no. 7, July 1953, pp. 477–482.
7. Quinn, John H., Jr.: Effects of Reynolds Number and Leading-Edge Roughness on Lift and Drag Characteristics of the NACA 65_3–418, a=1.0 Airfoil Section. NACA WR L–82, 1945. (Formerly NACA CB L5J04.)
8. Loftin, Laurence K., Jr., and Smith, Hamilton A.: Aerodynamic Characteristics of 15 NACA Airfoil Sections at Seven Reynolds Numbers From 0.7×10^6 to 9.0×10^6. NACA TN 1945, 1949.
9. Braslow, Albert L., and Visconti, Fioravante: Investigation of Boundary-Layer Reynolds Number for Transition on an NACA $65_{(215)}$–114 Airfoil in the Langley Two-Dimensional Low-Turbulence Pressure Tunnel. NACA TN 1704, 1948.
10. Von Doenhoff, Albert E., and Abbott, Frank T., Jr.: The Langley Two-Dimensional Low-Turbulence Pressure Tunnel. NACA TN 1283, 1947.
11. Quinn, John H., Jr.: Drag Tests of an NACA $65_{(215)}$–114, a=1.0 Practical-Construction Airfoil Section Equipped With a 0.295-Airfoil-Chord Slotted Flap. NACA TN 1236, 1947.
12. Anon: Abrasive Grain Sizes. Simplified Practice Recommendation 118–50, U. S. Dept. Commerce, June 1, 1950.
13. Schlichting, Hermann (J. Kestin, trans.): Boundary Layer Theory. McGraw-Hill Book Co., Inc., 1955, ch. 12, pt. B.
14. Schubauer, G. B., and Klebanoff, P. S.: Contributions on the Mechanics of Boundary-Layer Transition. NACA Rep. 1289, 1956. (Supersedes NACA TN 3489.)
15. Anon: Standard Atmosphere—Tables and Data for Altitudes to 65,800 Feet. NACA Rep. 1235, 1955. (Supersedes NACA TN 3182.)

REPORT 1350

METHODS FOR OBTAINING DESIRED HELICOPTER STABILITY CHARACTERISTICS AND PROCEDURES FOR STABILITY PREDICTIONS [1]

By F. B. GUSTAFSON and ROBERT J. TAPSCOTT

SUMMARY

In the first part of this report a brief review is presented of methods available to the helicopter designer for obtaining desired stability characteristics by modifications to the airframe design. The discussion is based on modifications made during the establishment of flying-qualities criteria and includes sample results of theoretical studies of additional methods.

The conclusion is reached that it is now feasible to utilize combinations of methods whereby stability-parameter values are realized which in turn provide the desired stability characteristics.

Part II reviews some of the methods of predicting rotor stability derivatives. The procedures by which these rotor derivatives are employed to estimate helicopter stability characteristics have been summarized. Although these methods are not always adequate for predicting absolute values of the stability of the helicopter, the effects on stability of changes in individua derivatives can generally be estimated satisfactorily.

INTRODUCTION

The problems relating to stability of helicopters have been the subject of numerous published works. Requirements established by the military services for satisfactory helicopter stability are specified in reference 1. Some of the pertinent work on this subject by the National Advisory Committee for Aeronautics is described in references 2 to 21. The purpose of part I of this report is to summarize some of the physical methods available to the designer for obtaining desired stability values by changing the airframe design. Although the direct application considered is that of meeting flying-qualities criteria, it may be worth pointing out that other reasons often arise for designing a configuration so that specific amounts of stability are provided; for example, the most efficient combination of autopilot and airframe design may be desired.

In order to predict helicopter stability, as for example to estimate theoretically whether a proposed helicopter will meet the flying-qualities requirements, both the applicable equations of motion and the necessary stability derivatives must be determined.

Processes for applying the equations of motion have been well established as a result of the extensive stability analysis made for airplanes, and the modification of these procedures for use with helicopters has been found a secondary problem in comparison with the provision of values of stability derivatives. In the past few years, sufficient information has been provided to permit the most pertinent rotor derivatives to be predicted with fairly good accuracy in applications where no stall is present. A summary of this work is presented in part II of this report.

I—METHODS FOR OBTAINING DESIRED HELICOPTER STABILITY CHARACTERISTICS

The scope of the discussion in part I is outlined in the following table:

Characteristic	Rotor type investigated
Damping in roll	Single and tandem
Maneuver stability	Single and tandem
Speed stability	Single and tandem
Lateral oscillation and turn characteristics	Tandem

Available results on static directional (weathercock) stability of tandem helicopters are not included in this discussion because of thorough coverage in reference 2. For helicopter types other than single-rotor or tandem-rotor configurations, no direct information is provided herein but much can be inferred from the more appropriate of the two types covered.

For each of the stability characteristics covered, modifications made to the design in the process of exploring a range of characteristics during the establishment of criteria for desirable flying qualities are discussed. The value of these examples lies in the fact that they are demonstrated cases for which stability parameters have been measured. Optimum design generally requires the choice of a method or combination of methods; therefore, sample results of theoretical studies of additional methods are included in each case.

SYMBOLS

L_δ rolling moment due to control deflection

L_p rolling moment due to rolling angular velocity

ΔW_b change in weight of blade

[1] Supersedes NACA Technical Note 3945 by F. B. Gustafson and Robert J. Tapscott, 1957.

526597—60——18

R blade radius
I_1 blade moment of inertia about flapping hinge
γ blade mass constant
M_α pitching moment per unit angle-of-attack change
M_q pitching moment due to unit pitching angular velocity
L rolling moment
v sideslip velocity
Ω rotor rotational speed
σ rotor solidity
B_1 longitudinal cyclic pitch
V forward velocity
c_m blade section pitching-moment coefficient
$\Delta\theta$ difference between collective-pitch angles of front and rear rotors
$\Delta\alpha_d$ difference between angles of attack of front and rear rotors due to longitudinal swashplate tilt

DAMPING AND CONTROL POWER IN ROLL

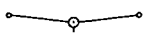
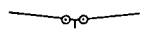
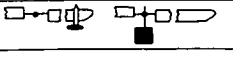
The ratio of control power to damping, which frequently tends to reach values that lead to a major problem in the hovering characteristics of small low-inertia helicopters, is treated in table I. The test vehicle was a two-place single-rotor helicopter. As used herein, "control power" is the rolling moment per unit stick deflection and "damping" is the resisting moment per unit angular velocity of the helicopter. Since changes in control power are restricted by trim requirements, this discussion is concerned solely with changes in damping.

The requirement of the current military specification (ref. 1) is that the rate of roll per inch of stick displacement (often referred to as "sensitivity") be less than 20° per second. The test helicopter provided the opportunity to explore a fair-sized range of values, always on the satisfactory side, by adjusting a mechanical gyroscopic device. The value of 14 for L_δ/L_p is obtained with the device locked out, and the value of 5.2 is obtained with the device as far beyond the production setting as feasible. Both from theory and from flight measurements on other helicopters, it is known that, with lighter blades and no special device, the requirements of reference 1 would not have been met.

TABLE I

RATIO OF CONTROL POWER TO DAMPING
[Single rotor; 2,200-lb gross wt]

Parameter	Value to meet MIL-H-8501	Range tested	Method used
$\frac{\text{Control power}}{\text{Damping}}$, $\frac{L_\delta, \text{deg/sec}}{L_p, \text{in.}}$	<20	14 to 5.2	Available gyro device; L_δ fixed

Additional methods (L_δ fixed)	Amount for range tested
Increase in I_1 via tip wt. 	$\Delta W_b = 0.6$
Hinge offset with $\gamma = 4.7$ 	2 % R
Aero servos 	----------

In addition, and of perhaps even greater importance, studies made subsequent to the establishment of the existing specifications have demonstrated the direct value of increased damping irrespective of L_δ/L_p. (For example, see ref. 20.) Therefore, examination of several additional methods for changing the damping is advisable.

Increasing the blade inertia is one method of changing the damping. If use of a tip weight is considered, calculations indicate that 60 percent of the blade weight is needed to duplicate the full change in L_δ/L_p from 14 to 5.2.

Offsetting the flapping hinge will increase damping, but if this method is used the control linkage has to be changed to prevent increase in control power, or else little change in L_δ/L_p will result. With the heavy blades of the test helicopter, an offset of only 2-percent radius would be needed to change L_δ/L_p from 14 to 5.2; with light blades, an offset of 5-percent radius would be enough.

A third design approach which makes possible increased damping is the use of aerodynamic servocontrols. Sketches of two types, as viewed from above the rotor, are shown in table I. One type uses a surface behind the outer part of the blade and the other uses a surface attached at right angles at the blade root. Such devices apparently can be designed to provide increases in damping sufficient to cover the test range. Some methods permit increase in both control power and damping, a combination which is sometimes desirable; examples are flapping-hinge offset and aerodynamic servocontrols as just discussed.

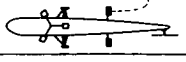
Damping and control power in roll for the tandem helicopter require no separate discussion since, in roll, it is possible simply to consider two single rotors instead of one.

MANEUVER STABILITY OF SINGLE-ROTOR HELICOPTERS

Two separate maneuver-stability (or divergence) problems with single-rotor helicopters at cruising speed are treated in table II. With one helicopter, the variations were made by way of angle-of-attack stability, and with the other, by way of damping in pitch. For the first case, a change to a value of angle-of-attack stability of 300 pound-feet per radian was enough to cause the requirement to be met. The range covered went from the unstable value of 7,000 pound-feet

TABLE II

MANEUVER STABILITY
[Single rotor; gross wts.: (1) 5,000 lb and (2) 2,200 lb; cruise speed]

Major parameter varied	Value to meet MIL-H-8501	Range tested	Method used
(1) M_α, $\frac{\text{lb-ft}}{\text{radian}}$	<300	7,000 to −2,100	Tail surface 
(2) M_q, $\frac{\text{lb-ft}}{\text{radian/sec}}$	<−1,200 (rotor)	−710 to −1,930	Available gyro device

Parameter	Additional methods	Amount for 1/2 range tested
M_α	Increased rpm	33 %
	Forward c.g. with offset hinges	Δc.g. = 2.5% R with 5% offset
M_q	Similar to roll sensitivity	

er radian to the stable value of −2,100 pound-feet per adian. (Minus is stable in accepted stability theory.) he test conditions actually extended somewhat farther an the value of −2,100 pound-feet per radian on the stable de but the M_α values were not recorded.

The tail assembly used has been discussed in published apers, particularly reference 3. It may bear repeating, owever, that a total tail area of 0.5 percent of the rotor area ould make the difference between the helicopter's diverging xcessively in a few seconds and being able to fly through ough air without the longitudinal control being moved. his result was obtained after linking the tail to the cyclic ontrols, which so reduced the design compromises as to ermit use of a somewhat more effective tail.

Tests were made with a different helicopter (labeled (2) table II), wherein the damping in pitch was varied in such way as to bracket the condition for which the requirement as met. The value of −1,200 pound-feet per radian eeded to cause the specification to be met falls about mid-ay in the range of −700 to −1,900 pound-feet per radian overed. Damping is another quantity where the minus gn is indicative of a stable condition. As to the method sed, the investigation was the same as that which provided ne damping-in-roll values given in table I.

As to alternate methods, for large changes in angle-of-ttack stability M_α, there do not seem to be many which will over the range singlehanded. Increase in rotor speed is sted because the effect of such an increase is calculated to be ufficient to warrant thought of some compromise with esign for optimum power. It will be understood that otational speed is appropriate because in all other respects ne design is fixed; more fundamentally, what is implied is ower values of pitch and tip-speed ratio. A 33-percent ncrease in rotor rotational speed is estimated to give half ne range covered and would not have been enough, in itself, o meet the specification. The effects are not linear and uch greater increase in stability by this method would ause extreme compromise with performance.

If offset flapping hinges are used, then the aircraft center-f-gravity position affects angle-of-attack stability. An esti-nate for this helicopter is that, with the hinges at 5 percent lade radius, moving the center of gravity 7 inches (2.5 per-ent of the rotor radius) forward from the rotor shaft would roduce as much change as the 33-percent increase in rotor otational speed. With the same offset, a center-of-gravity ift of 14 inches, if such is tolerable, would produce the hange to the −2,100 value and thus would permit the re-uirements to be exceeded.

For alternate methods of varying the rotor damping in itch M_q, the methods given in the roll-sensitivity discussion gain apply.

The discussion of this section is in terms of existing criteria hich in turn relate most specifically to normal-acceleration haracteristics in maneuvers. It might be remarked that in ertain instances, when the normal-acceleration criteria for naneuver stability are just met, the pitching velocity still ows appreciable divergent tendencies. Consideration of the problem suggests that when such situations arise, by carrying somewhat farther the methods that have just been described, logical development with time should be achieved for pitching velocity as well as normal acceleration, so that no fundamentally new problems seem to be represented.

MANEUVER STABILITY OF TANDEM-ROTOR HELICOPTERS

Maneuver stability of the tandem helicopter, again at cruising speed, is treated in table III. The parameter considered is again pitching moment per unit angle-of-attack change, and with the test helicopter the unstable value of 57,000 pound-feet per radian corresponded to a value that would just barely meet the requirements set forth in the specification. While a change of only 15,000 pound-feet per radian would have sufficed to just reach the marginal value of 57,000, a change of 88,000 in the direction of increased stability was explored. It is desirable to be able to make these larger changes. The test method used was not altogether appropriate for this discussion because so much of the range was obtained by choice of power setting. The available center-of-gravity range produced a useful but subordinate change, a forward center of gravity being the more stable.

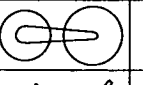
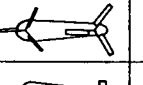
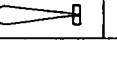
Because the test method was not altogether appropriate for large changes, calculations are again used to illustrate other methods. Changes which affect the relative lift-curve slopes of the front and rear rotors seem especially effective. It is estimated that, if the front-rotor radius is decreased and the rear-rotor radius is increased to provide a total difference of 10 percent of the mean radius, the test value of stability increase would be realized. If, instead, a differential in rotor solidities were effected by putting wider blades on the rear rotor and narrower ones on the front rotor, this same stability increase could be obtained with a solidity differential of 45 percent of the mean value.

The size of horizontal-tail surface necessary to contribute the same range was computed, in order to illustrate the indication in reference 9 that a horizontal tail is relatively less effective for tandems than for single rotors. A value of 4 percent of rotor area is indicated in distinction to the 0.5

TABLE III

MANEUVER STABILITY
[Tandem rotor; 7,000−lb gross wt.; cruise speed]

Major parameter	Value to meet MIL-H-8501	Range tested	Method used
M_α, $\frac{\text{lb-ft}}{\text{radian}}$	<57,000	72,000 to −16,000	c.g. and power setting

Additional methods	Amount for range tested
ΔR (same Ω) 	10%
$\Delta\sigma$ 	45%
Tail surface 	100 sq ft or 4% of total rotor area

percent indicated for the single-rotor helicopters. Although the two cases are not strictly comparable, the relative order of magnitude is considered to be reasonable.

SPEED STABILITY OF SINGLE-ROTOR HELICOPTERS

Table IV treats the speed stability of a single-rotor helicopter. For a helicopter to be stable with speed, it is required that, with fixed pitch and throttle, the stick be moved farther forward for trim with increase in speed. The parameter used to measure this change is the longitudinal cyclic pitch B_1 per unit velocity V (in knots). The range tested (B_1/V from 0 to 0.06 degrees per knot) was obtained by changes in horizontal-tail setting. When sufficient upload was provided on the tail surface, the stable contribution of the rotor could be cancelled; when download was provided, it could be increased. Incidentally, most of this exploration of near-zero speed stability was carried out with the tail linked to the cyclic stick, the reason being that a high, fixed, nose-up tail setting can be dangerous in the event of inadvertent speed increase.

The rotor tends to be stable, but counteracting factors must still be considered. Some fuselage shapes can be as destabilizing as a nose-up tail setting, although a range of 30 foot-pounds per knot would be rather unusual. A large rotor-blade-section diving moment could more than cancel the stable tendency of the rotor. The increment Δc_m of 0.06 actually was suggested by the dangerous characteristics which arose with autogiros having $c_m = -0.06$. A rough estimate indicated the value of 0.06 to be the right order of magnitude to produce the change under discussion as well.

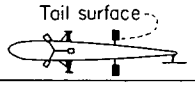
SPEED STABILITY OF TANDEM-ROTOR HELICOPTERS

Table V relates to speed stability of the tandem-rotor type of helicopter. The longitudinal control of this configuration is obtained primarily by changing the pitch-setting difference between front and rear rotors, and the parameter is written as $\Delta\theta/V$ to correspond. This quantity was varied from -0.01 to 0.003; thus, the requirement of at least zero is bracketed. This change was accomplished by changing the tilt angle between the front and rear rotor systems. The unstable setting was 0°; the stable one, 1.8° "toe-in."

TABLE IV

SPEED STABILITY

[Single rotor; 5,000-lb gross wt.; cruise speed]

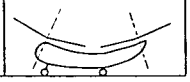
Parameter	Value to meet MIL-H-8501	Range tested	Method used
$\frac{B_1}{V}$, $\frac{\text{deg}}{\text{knot}}$	>0	0 to 0.06	Tail surface 

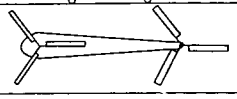
Additional factors	Amount for range tested
Moments, fuselage less tail	$\Delta\frac{\text{ft-lb}}{\text{knot}} = 30$
Blade section pitching-moment coefficient	$\Delta c_m \approx 0.06$

TABLE V

SPEED STABILITY

[Tandem rotor; 7,000-lb gross wt.; cruise speed]

Parameter	Value to meet MIL-H-8501	Range tested	Method used
$\frac{\Delta\theta}{V}$, $\frac{\text{deg}}{\text{knot}}$	>0	−0.01 to 0.003	$-1.8° \Delta a_g$ 

Additional factors	Amount for range tested
c.g. shift 	22%
$\Delta\sigma$ 	34%

Calculations indicate that a center-of-gravity shift from midway between the shafts to 22 percent ahead of the mid point should produce the equivalent range. The 22-percen value is based on total distance between shafts. Similarly giving the rear rotor higher solidity and the front less, with a total difference $\Delta\sigma$ of 34 percent of the mean, should achiev this same result. These values are for cruising speed; a low speeds the effect of center of gravity can even reverse whereas the solidity change becomes more effective. Th use of these methods in combination thus holds specia interest. It is also worth noting that these effects act i the same direction for speed stability as they do for maneuve stability.

LATERAL-OSCILLATION AND TURN CHARACTERISTICS OF TANDEM-ROTOR HELICOPTERS

Tandem-rotor lateral-oscillation and turn characteristic at cruise speed are treated in table VI. One of the mos effective parameters for both is rolling moment per uni sideslip velocity, or L/v, measured as foot-pounds of rollin moment per foot per second of sideslip velocity. Fortunately this quantity, which is the effective dihedral, is not critica in its own right, provided it stays on the stable side. (B convention, stable values are negative.) Most of the require change was obtained by attaching small wings (surface area

TABLE VI

LATERAL OSCILLATION AND TURN CHARACTERISTICS

[Tandem rotor; 7,000-lb gross wt.; cruise speed]

Major parameter	Value to meet MIL-H-8501	Range tested	Method used
Roll due to sideslip, $\frac{L}{V}$, $\frac{\text{ft-lb}}{\text{ft/sec}}$	>−26	−75 to −37	 Two wings 7 sq ft each

Additional method	Amount for range tested
Vertical c.g. − c.p. relationship	9 in.

square feet) to the landing gear. The front view and side ew are shown. It was most convenient in these flying-ualities trials to extend the test conditions further by chang-g the flight conditions; but with so many designs beginning appear with moderate-sized wings (much bigger than the anels used in these tests), making the full change needed ay often require only the determination of the correct eometric dihedral.

One additional method is to change the vertical location the center of gravity relative to the side-view area. Only major change in power-plant location, such as a shift to verhead turbines, seems likely to make a change of the ecessary magnitude (9-inch shift in center of gravity). ontributing changes, though, including some ventral-fin rea, may often prove feasible.

Increasing the damping in roll is another effective approach hat can be considered. This method is discussed, along ith still other approaches, in reference 4.

CONCLUDING REMARKS FOR PART I

Examples have been presented to illustrate methods for nproving helicopter stability. It will be realized that any of the numerical values which have been given apply nly for the case studied. For example, a tandem helicopter ight already have lower effective dihedral or might some-ow be designed with less nose-down inclination of the rincipal inertia axis and, in either event, might meet the teral requirements without reduction in effective dihedral.

The cases presented are believed to illustrate that it is ow feasible to choose one or more important stability arameters from theoretical studies and, in turn, to find a ombination of methods whereby values of the parameters re realized which provide the desired stability character-tics.

The obtainment of desired stability characteristics with a inimum of design compromise requires first of all a high egree of fundamental understanding. To achieve this end workable theory must be available. It is believed that the xistence of such theory has been demonstrated. In addition such use of theory, the outstanding key to the obtainment desired characteristics with minimum design compromise eems to be the availability and use of a variety of physical ethods in combination with one another. It is hoped that he sample methods presented may be helpful in suggesting ill more approaches to the helicopter designer.

—PROCEDURES FOR PREDICTING HELICOPTER STABILITY

The prediction of stability derivatives requires a knowledge the contributions of both the rotor and the fuselage. uselage characteristics are not open to as specific an analysis s rotor characteristics, and preliminary estimates can be andled on the basis of data from previous designs and from ind-tunnel model tests. The fuselage seems to be subject greater modification up to the time production starts; onsequently, this discussion is confined primarily to the otor contributions to the derivatives.

SYMBOLS

W	gross weight of helicopter, lb
m	mass of helicopter, slugs
g	acceleration due to gravity, 32.2 ft/sec^2
R	blade radius, ft
c	blade-section chord, ft
c_e	equivalent blade chord (on thrust basis), $\frac{\int_0^R cr^2dr}{\int_0^R r^2dr}$, ft
b	number of blades per rotor
σ	rotor solidity, $bc_e/\pi R$
Θ	instantaneous blade-section pitch angle (angle between line of zero lift of blade section and plane perpendicular to rotor shaft), $\theta - A_1 \cos\psi - B_1 \sin\psi$, radians
θ	collective-pitch angle (average value of Θ around azimuth), radians
ρ	mass density of air, slugs/cu ft
γ	mass constant of rotor blade (ratio of air forces to mass forces), $\rho caR^4/I_1$; also, flight-path angle, radians
I_X	helicopter rolling moment of inertia about center of gravity, slug-ft^2
I_Y	helicopter pitching moment of inertia about center of gravity, slug-ft^2
I_Z	helicopter yawing moment of inertia about center of gravity, slug-ft^2
$\Delta\theta$	difference between collective-pitch angles of front and rear rotors, positive when collective-pitch angle of rear rotor is greater, radians; also, increment of θ
I_1	mass moment of inertia of blade about flapping hinge, slug-ft^2
ΔT	difference between thrusts of front and rear rotors, positive when thrust of rear rotor is greater, lb
$\Delta R, \Delta(\Omega R), \Delta\sigma$	definitions analogous to that for ΔT
$\Delta\alpha_d$	difference between angles of attack of front and rear rotors due to longitudinal swashplate tilt, positive when rear-rotor angle of attack is greater
A_1, B_1	coefficients of $-\cos\psi$ and $-\sin\psi$, respectively, in expression for Θ; therefore, lateral and longitudinal cyclic pitch, respectively, radians
δ	control motion, inches from trim
t	time, sec
V	true airspeed of helicopter along flight path, ft/sec
v	sideslip velocity of helicopter in Y-direction, ft/sec
α	rotor angle of attack (angle between flight path and plane perpendicular to axis of no feathering), positive when axis is inclined rearward, radians
Ω	rotor angular velocity, radians/sec
μ	tip-speed ratio, $\frac{V\cos\alpha}{\Omega R}\left(\text{assumed equal to } \frac{V}{\Omega R}\right)$
U_T	component at blade element of resultant velocity perpendicular to blade-span axis and to axis of no feathering, ft/sec

$u_T = U_T/\Omega R$

ψ blade azimuth angle (measured in direction of rotation from downwind position of blade if wind axes are used; measured in direction of rotation from position of blade when it is pointing rearward along longitudinal axis of helicopter if body axes are used), radians

a slope of curve of blade section lift coefficient plotted against section angle of attack, per radian

L rotor lift, lb; also, rolling moment, lb-ft

T rotor thrust (component of rotor resultant force parallel to axis of no feathering), lb

Q rotor-shaft torque, lb-ft

C_T rotor thrust coefficient, $\frac{T}{\pi R^2 \rho (\Omega R)^2}$

C_Q rotor-shaft torque coefficient, $\frac{Q}{\pi R^2 \rho (\Omega R)^2 R}$

β blade flapping angle at particular azimuth position, $a_0 - a_1 \cos \psi - b_1 \sin \psi$ . . ., radians; also, sideslip angle, radians

a_0 constant term in Fourier series that expresses β; therefore, rotor coning angle

a_1 coefficient of $-\cos \psi$ in expression for β; therefore, longitudinal tilt of rotor cone

b_1 coefficient of $-\sin \psi$ in expression for β; therefore, lateral tilt of rotor cone

a' projection of angle between rotor resultant force vector and axis of no feathering in plane containing flight path and axis of no feathering

b' projection of angle between rotor resultant force vector and axis of no feathering in plane containing axis of no feathering and perpendicular to plane containing flight path and axis of no feathering

p helicopter rolling velocity, radians/sec

q helicopter pitching velocity, radians/sec

r helicopter yawing velocity, radians/sec; also, radial distance to blade element, ft

ϕ angle of roll, radians

N yawing moment, lb-ft

M pitching moment, lb-ft

h height of rotor hub above helicopter center of gravity, ft

η angle between principal longitudinal axis of inertia of helicopter and flight path, positive when nose is up, radians

X, Y, Z stability axes

Subscript:

AV average

Dots over symbols indicate derivatives with respect to time.

ROTOR STABILITY DERIVATIVES

In general, calculation of the stability derivatives needed for a study of helicopter characteristics depends on the knowledge of the individual rotor derivatives shown in th following table:

$\frac{\partial(C_T/\sigma)}{\partial\alpha}$	$\frac{\partial(C_T/\sigma)}{\partial V}$	$\frac{\partial(C_T/\sigma)}{\partial\Omega}$	$\frac{\partial(C_T/\sigma)}{\partial\theta}$	$\frac{\partial(C_T/\sigma)}{\partial q}$
$\frac{\partial a'}{\partial\alpha}$	$\frac{\partial a'}{\partial V}$	$\frac{\partial a'}{\partial\Omega}$	$\frac{\partial a'}{\partial\theta}$	$\frac{\partial a'}{\partial q} = \frac{\partial b'}{\partial p}$
$\frac{\partial(C_Q/\sigma)}{\partial\alpha}$	$\frac{\partial(C_Q/\sigma)}{\partial V}$	$\frac{\partial(C_Q/\sigma)}{\partial\Omega}$	$\frac{\partial(C_Q/\sigma)}{\partial\theta}$	$\frac{\partial(C_Q/\sigma)}{\partial q}$
$\frac{\partial a_0}{\partial\alpha}$	$\frac{\partial a_0}{\partial V}$	$\frac{\partial a_0}{\partial\Omega}$	$\frac{\partial a_0}{\partial\theta}$	$\frac{\partial a_0}{\partial q}$
$\frac{\partial a_1}{\partial\alpha}$	$\frac{\partial a_1}{\partial V}$	$\frac{\partial a_1}{\partial\Omega}$	$\frac{\partial a_1}{\partial\theta}$	$\frac{\partial a_1}{\partial q}$
$\frac{\partial b_1}{\partial\alpha}$	$\frac{\partial b_1}{\partial V}$	$\frac{\partial b_1}{\partial\Omega}$	$\frac{\partial b_1}{\partial\theta}$	$\frac{\partial b_1}{\partial q}$

As shown, the rotor parameters considered are C_T/σ and a' the magnitude and angle of the thrust vector, respectively rotor torque C_Q/σ; blade coning angle a_0; and b_1 and a_1, th lateral and longitudinal flapping, respectively. These roto parameters are functions of five independent variables: roto angle of attack α, forward speed V, rotational speed Ω, col lective pitch θ, and pitching velocity q. The values of th derivatives are determined by the variations from trim o the rotor parameters with changes in each of the five vari ables. The total number of derivatives shown here is large however, for most applications it is generally possible to re duce the number considerably. For instance, if the roto under consideration has no flapping-hinge offset, the flappin coefficients are not significant; thus, the number of deriva tives to be considered is immediately reduced by abou one-half. If necessary, however, these derivatives can b determined from the equations of references 10 and 14.

Of the remaining derivatives, the lift due to pitching an torque due to pitching generally can be neglected. Fo most cases, then, the derivatives needed have been reduce to those enclosed within the lines in the preceding table All the C_T/σ, C_Q/σ, and a' derivatives can be obtained fron the figures or equations of references 8 and 10, as is show in the following discussion.

The thrust due to angle of attack and that due to collec tive pitch are presented as functions of tip-speed ratio i figure 1. If the solidity and tip-speed ratio for a given cas are known, these quantities can be read directly from th curves. The equations on which this figure is based and th processes by which they were derived are discussed i reference 8.

The change in thrust coefficient with tip-speed ratio i presented in reference 8 in the form of an equation fron which, when the flight condition is known, the rate of chang

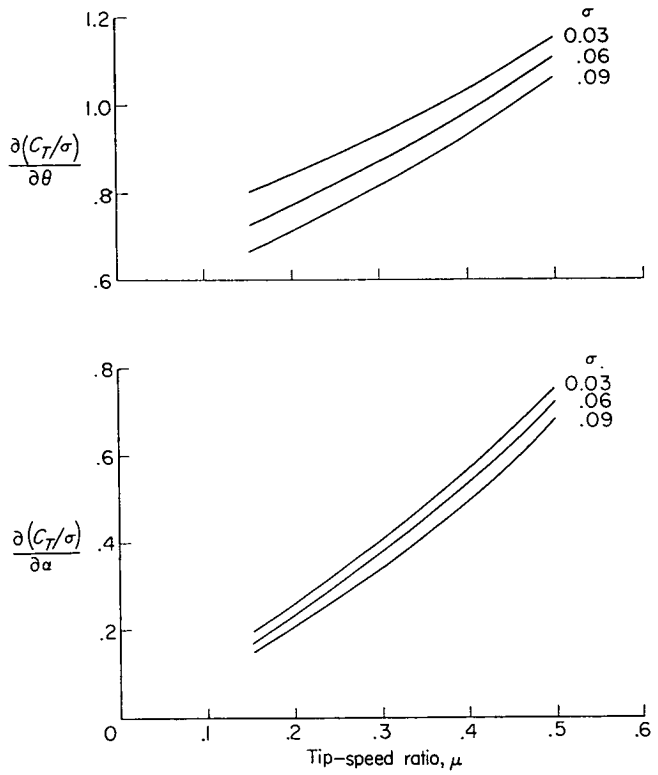


FIGURE 1.—Variation of C_T/σ derivatives with respect to μ.

of thrust coefficient with forward speed and rotational speed can be computed.

The change in inclination of the rotor force vector due to steady pitching or rolling velocity has been derived in reference 10. This derivative is shown in figure 2 as a function of the parameter $\frac{\theta}{C_T/\sigma}$. As the effect of tip-speed ratio μ is small, the formula shown in figure 2 is fairly accurate below a tip-speed ratio of 0.5 for both roll and pitch. The rotor damping moment is determined simply by multiplying the quantity obtained from the figure by $18/\gamma\Omega$ and by the rotor thrust and rotor height above the helicopter center of gravity; that is,

$$\frac{\partial M}{\partial q}=\frac{\partial a'/\partial q}{18/\gamma\Omega}\left(Th\,\frac{18}{\gamma\Omega}\right)$$

For the rotor-vector angle and rotor torque derivatives, charts such as those shown in figure 3 have been derived and are published in reference 8. These charts are given for a range of collective-pitch angles from 0° to 14° at 2° increments; the sample shown herein is for a collective pitch of 8°. In these charts, the longitudinal rotor-vector angle a' is plotted against the ratio of thrust coefficient to solidity for specified values of tip-speed ratio. Lines of constant power parameter $C_Q/C_T\mu$ are also plotted on the charts. Combinations of these parameters which result in angles of attack of 12° and 16° on the retreating blade are indicated by dashed lines; these lines, in effect, serve as limit lines above which account must be taken of stall. By using slopes or differences from these charts in conjunction with

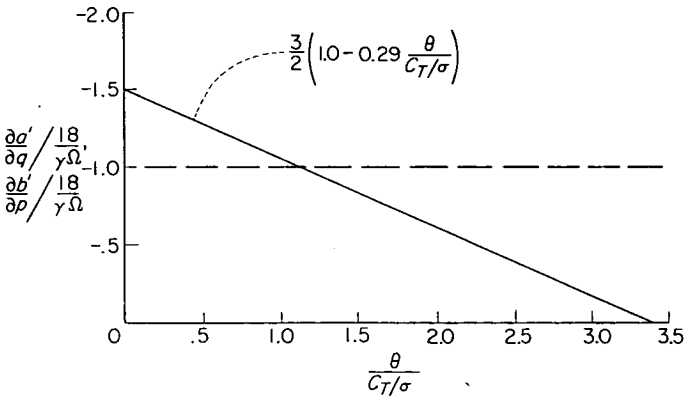


FIGURE 2.—Chart for determining rotor damping in pitch and roll.

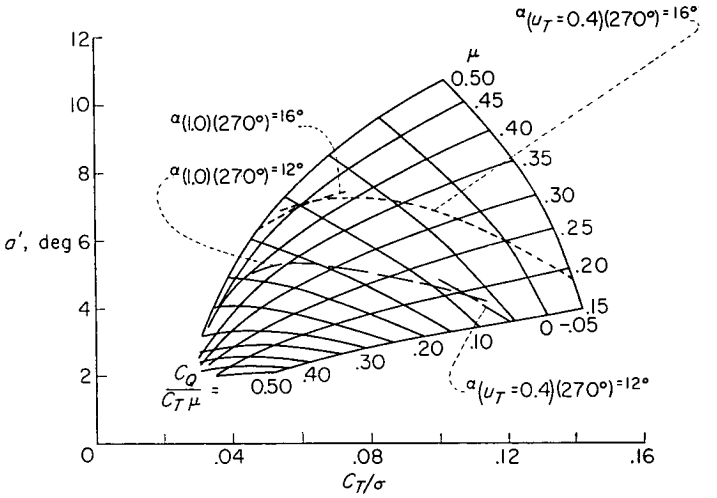


FIGURE 3.—Sample chart for determining derivatives of a' and C_Q/σ. $\theta=8°$.

other derivatives and some simple equations, the remaining derivatives of a' and of the torque coefficient can be obtained. As an example, consider the derivative of a' with respect to angle of attack. From charts such as figure 3, the rate of change of a' with thrust coefficient can be obtained at a given tip-speed ratio and thrust coefficient by scaling off the slope of the tip-speed-ratio line at the desired thrust coefficient. When this quantity is multiplied by the change in thrust coefficient with angle of attack, which has already been discussed, the result is the change in a' with angle of attack. The other a' and the torque coefficient derivatives can be obtained by similar procedures. These procedures are discussed in reference 8.

PREDICTION OF HELICOPTER STABILITY CHARACTERISTICS

It is believed that the rotor contribution to the essential helicopter derivatives can be predicted by using the rotor derivatives that have been discussed. These rotor derivatives are applicable, in most cases, to a study of the stability characteristics of either a single-rotor or a tandem-rotor configuration. Differences arise in using the rotor derivatives to determine the helicopter derivatives for use in the equations of motion and in accounting for the effects of flow

interference for a specific configuration. For most purposes, the lateral and longitudinal characteristics of the helicopter can be studied separately. Generally, equations of motion derived on the basis of constant forward speed are sufficient and are applicable to both single- and tandem-rotor configurations.

Longitudinal characteristics.—In a study of the longitudinal characteristics of the helicopter (refs. 5 and 11), an important criterion is that the time history of the normal acceleration shall be concave downward within 2 seconds after a step input to the longitudinal control; that is, the slope of the normal acceleration curve shall reach its maximum value and begin to decrease within 2 seconds. In order to assist in estimating theoretically whether a prospective helicopter will meet this criterion, the following equations of motion were devised:

$$\frac{\partial L}{\partial q}q+\frac{\partial L}{\partial \theta}\Delta\theta+\frac{\partial L}{\partial \alpha}\Delta\alpha-\frac{WV}{g}\dot{\gamma}=0$$

$$\frac{\partial M}{\partial q}q+\frac{\partial M}{\partial \theta}\Delta\theta+\frac{\partial M}{\partial \alpha}\Delta\alpha+\frac{\partial M}{\partial B_1}\Delta B_1-I_Y\dot{q}=0$$

$$\Delta\alpha=\int_0^t q\,dt-\Delta\gamma-\Delta B_1$$

These equations are based on stability axes and derived on the assumptions of constant forward speed, constant rotor speed, and constant stability derivatives. The assumption is also made that the dynamic maneuver can be represented by a series of static conditions; hence, the rotor parameters are always at their equilibrium values as determined by the instantaneous values of angle of attack, pitch angle, tip-speed ratio, and pitching velocity. The first and second equations shown represent, respectively, equilibrium normal to the flight path and equilibrium in pitch. The third equation simply relates the variables of the first two equations to permit a solution.

The form of these equations applies specifically to the single-rotor configuration. For the tandem configuration, the pitching moment due to control motion results primarily from differential collective pitch of the two rotors rather than from cyclic pitch; thus, the term in the equations expressing pitching moment due to control motion must be modified to account for this difference.

In reference 5, these equations of motion have been solved for the flight-path angle γ, which, in turn, permits an expression to be written for the time history of the normal acceleration. Values of combinations of derivatives have been determined which, when substituted into the expression for the time history of normal acceleration, will result in a time history that is concave downward at 2 seconds. These values have been presented in the form of a chart. (See fig. 4.) Thus the curve in figure 4 is a boundary line that separates combinations of significant longitudinal stability derivatives which result in satisfactory characteristics from those which result in unsatisfactory characteristics according to the criterion previously mentioned. Shown along

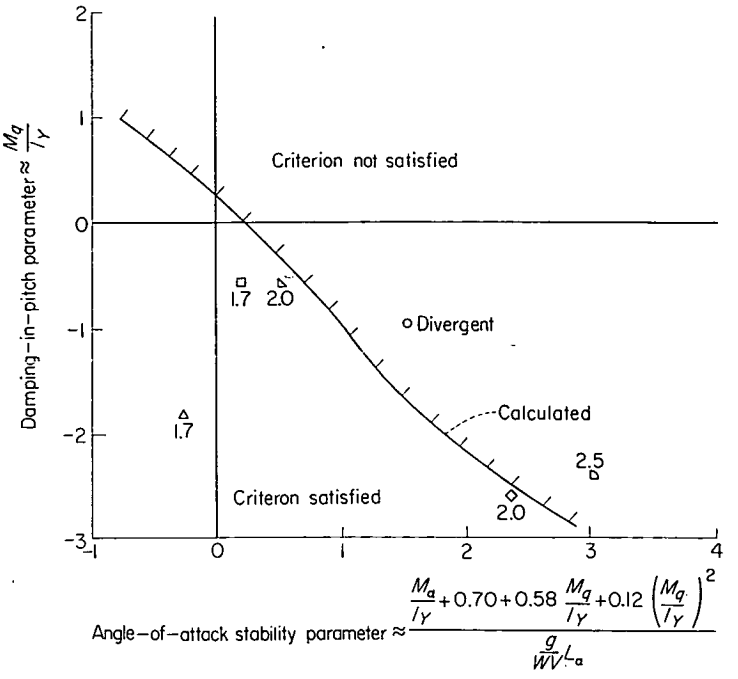


FIGURE 4.—Maneuver-stability chart for 2-second criterion.

with the theoretical curve are data points corresponding to five helicopter configurations. The derivatives for the configurations corresponding to the points shown were measured in flight and the adjacent number is the approximate time for the corresponding normal-acceleration time history to become concave downward. For both single- and tandem-rotor helicopters, the theoretical curve is indicated to be qualitatively correct for separating configurations which have satisfactory maneuver stability from those which have unsatisfactory maneuver stability according to the criterion; that is, the experimental points for which the normal-acceleration time history becomes concave downward in less than 2 seconds fall in the satisfactory region whereas, for times of more than 2 seconds, the points fall in the unsatisfactory region.

Figure 4 shows that an increase in the angle-of-attack stability or damping in pitch (that is, more negative M_α or M_q) or increases in the rotor lift-curve slope L_α are stabilizing. Also, it can be determined from this plot that an increase in the pitching moment of inertia I_Y can be destabilizing. Since the change in lift slope cannot be large and the lift slope is not expected to change sign, the primary changes in stability must be brought about by changes in the damping-in-pitch or angle-of-attack stability.

In the discussion of longitudinal stability so far, the forward speed has been assumed to be constant. For the tandem configuration, however, the downwash effects of the front rotor acting on the rear rotor cause an unstable variation in pitching moment with speed. A study of the speed stability of the tandem helicopter was made in reference 6. In that study, on the basis of the available derivatives discussed previously, an expression for the change of stick position with speed was derived. The equation, along with a plot of constants based on the rotor derivatives, is shown in

figure 5. These constants are presented for several values of rotor solidity over a range of tip-speed ratios. After a flight condition is selected and the tip-speed ratio and thrust coefficient are thereby established, the slope of the variation of stick position with speed can be determined. This equation takes into account the effects on speed stability of center-of-gravity position, differential rotor speed, differential rotor radius and solidity, and "longitudinal dihedral." Effects of these parameters can be studied either together or separately.

This analysis of tandem-helicopter speed stability is of particular value in studies, such as the study of the relative effects of changes in the various parameters, wherein it is not necessary to know accurately the value of downwash or the fuselage contribution. In order to predict the absolute value of speed stability, the downwash must be estimated for the configuration and flight condition under consideration, and the variation of the fuselage moments must be known. The results of flow-field measurements

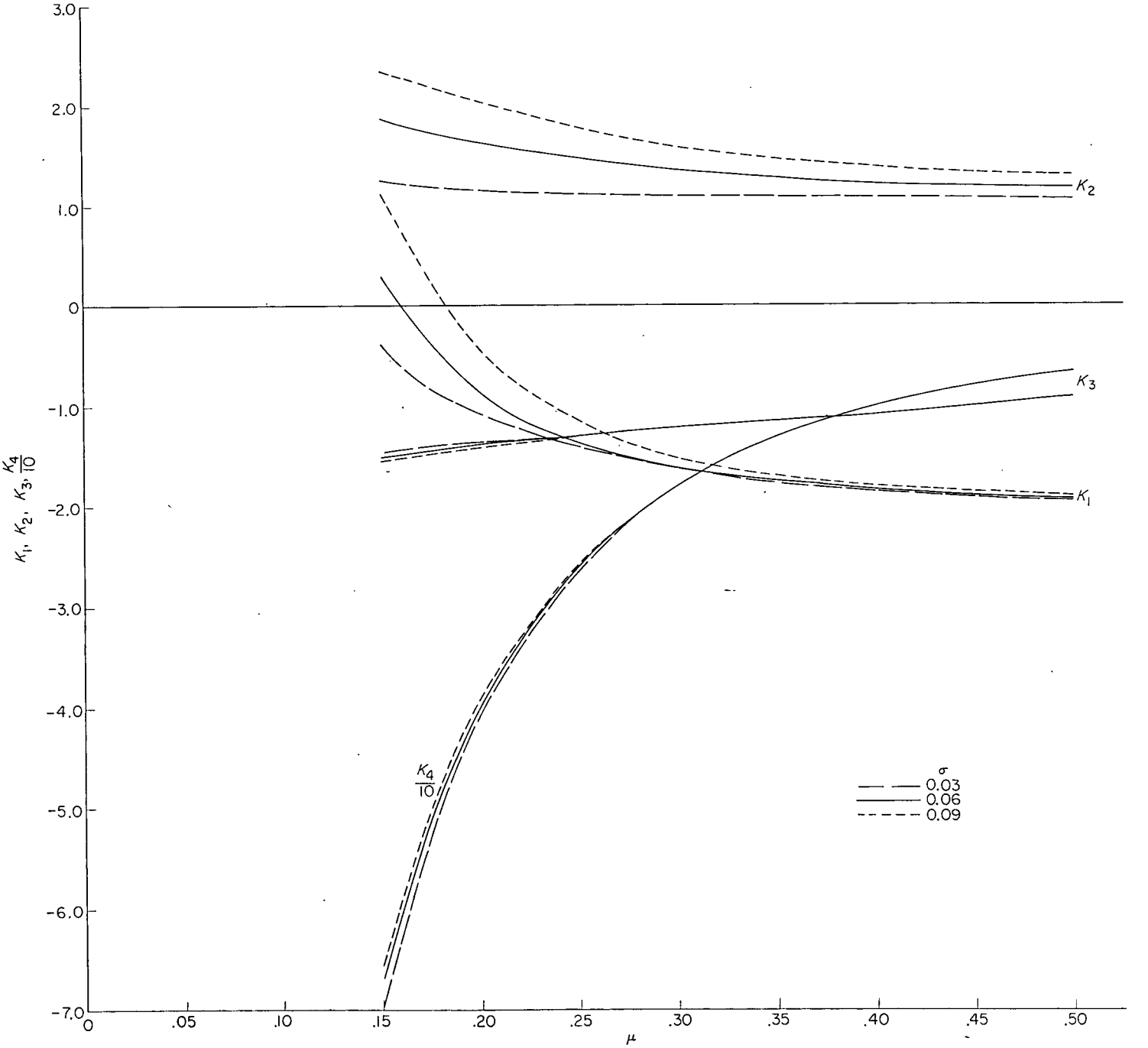


FIGURE 5.—Equation for speed stability of tandem-rotor helicopters.

$$\frac{d(\Delta\theta)}{d\mu}=K_1\left(\frac{C_T}{\sigma}\right)_{AV}\left(\frac{\Delta T}{W}-\frac{\Delta R}{R_{AV}}\right)+K_2\left(\frac{C_T}{\sigma}\right)_{AV}\left[\frac{\Delta\sigma}{\sigma_{AV}}+2\,\frac{\Delta(\Omega R)}{(\Omega R)_{AV}}\right]+K_3\Delta\alpha_d+K_4C_T$$

presented in references 15 to 18 should be useful in estimating the magnitude of the downwash applicable to a specific condition.

Lateral-directional characteristics.—The next important item in helicopter stability is the lateral-directional characteristics. If roll, yaw, and sideslip are considered as degrees of freedom, the equations of motion are as follows:

$$I_{x'}\ddot{\phi}+\frac{\partial L}{\partial p}\dot{\phi}+\frac{\partial L}{\partial v}v-\frac{\partial L}{\partial \delta}\delta=0$$

$$I_{z'}\ddot{\psi}+\frac{\partial N}{\partial r}\dot{\psi}+\frac{\partial N}{\partial v}v-\frac{\partial N}{\partial \delta}\delta=0$$

$$\left(mV-\frac{\partial Y}{\partial r}\right)\dot{\psi}-\left(mV\sin\eta+\frac{\partial Y}{\partial p}\right)\dot{\phi}-T\phi-T\psi\tan\gamma+m\dot{v}-\frac{\partial Y}{\partial v}v-\frac{\partial Y}{\partial \delta}\delta=0$$

For convenience in determining the derivatives, these equations are based on principal axes of inertia (primed symbols) rather than on the relative wind. In general, the rotor contribution to the derivatives needed in these equations can also be determined from rotor theory. Fuselage contributions can be predicted from wind-tunnel data and previous experience or from flight data where available.

These equations have been found useful particularly in estimating the effects on helicopter characteristics of changes in the individual stability derivatives. As an example, figure 6 shows the theoretically predicted time histories of rolling velocity and sideslip angle of a tandem-rotor helicopter. The curves on the left-hand side of figure 6 represent the predicted time histories for the original helicopter. On the right-hand side of figure 6 are time histories of the same quantities when the effective-dihedral derivative is reduced 50 percent. This figure indicates that a 50-percent reduction in the effective dihedral would substantially improve the oscillatory characteristics of the helicopter. In an attempt to improve the characteristics, this means was tried experimentally. The results are shown in figure 7, wherein the experimentally measured time histories of rolling velocity and sideslip angle before and after the derivative change are compared. The comparison shows that, as predicted by the theory, a reduction in the effective dihedral improved the

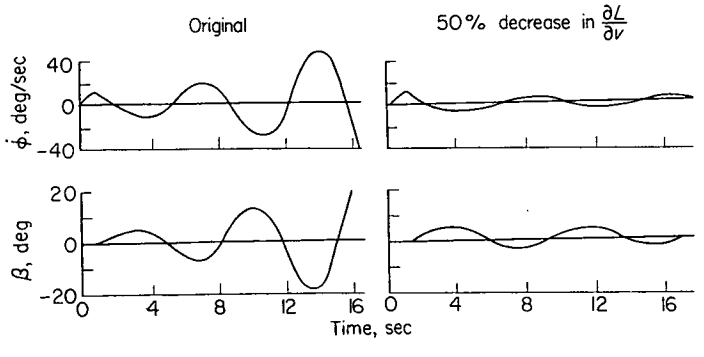


FIGURE 6.—Predicted effect of reduction in effective dihedral on lateral oscillation.

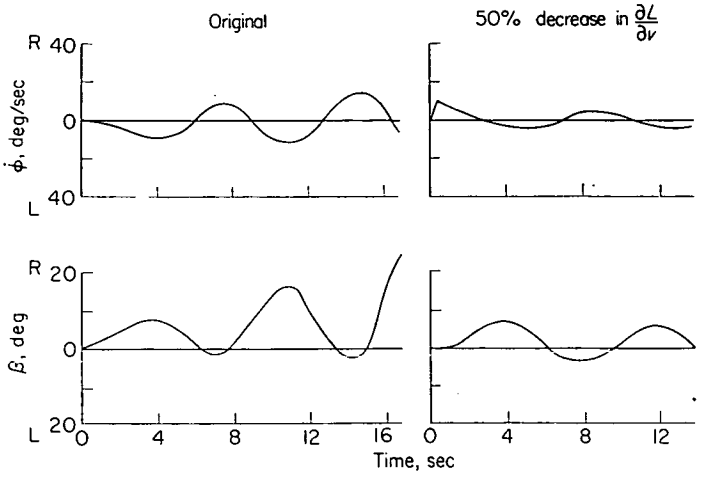


FIGURE 7.—Measured effect of reduction in effective dihedral on lateral oscillation.

oscillation. Thus, in this case, the theory was employed successfully to indicate the course to be followed in making an improvement.

CONCLUDING REMARKS FOR PART II

It will frequently not be feasible to predict accurately absolute magnitudes for the stability of the complete helicopter, particularly because of the difficulty of predetermining final, full-scale fuselage characteristics. However, on the basis of the studies discussed herein, a first approximation can be made, and by making some comparatively straightforward flight measurements of stability derivatives and reemploying the theory to show what modifications are needed, it appears feasible to handle at least those problems with which direct experience has been had. It appears likely that, in most cases, changes in several derivatives simultaneously would be necessary to achieve most efficiently the desirable stability characteristics, and the equations discussed herein should prove very useful in this type of study.

LANGLEY AERONAUTICAL LABORATORY,
NATIONAL ADVISORY COMMITTEE FOR AERONAUTICS,
LANGLEY FIELD, VA., *November 20, 1956.*

REFERENCES

1. Anon.: Military Specification; Helicopter Flying Qualities, Requirements for. Military Specification, MIL–H–8501, Nov. 5, 1952.
2. Williams, James L.: Directional Stability Characteristics of Two Types of Tandem Helicopter Fuselage Models. NACA TN 3201, 1954.
3. Gustafson, F. B.: Desirable Longitudinal Flying Qualities for Helicopters and Means To Achieve Them. Aero. Eng. Rev., vol. 10, no. 6, June 1951, pp. 27–33.
4. Amer, Kenneth B., and Tapscott, Robert J.: Studies of the Lateral-Directional Flying Qualities of a Tandem Helicopter in Forward Flight. NACA Rep. 1207, 1954. (Supersedes NACA TN 2984.)
5. Amer, Kenneth B.: Method for Studying Helicopter Longitudinal Maneuver Stability. NACA Rep. 1200, 1954. (Supersedes NACA TN 3022.)
6. Tapscott, Robert J., and Amer, Kenneth B.: Studies of the Speed Stability of a Tandem Helicopter in Forward Flight. NACA Rep. 1260, 1956. (Supersedes NACA RM L53F15a.)

7. Reeder, John P., and Whitten, James B.: Some Effects of Varying the Damping in Pitch and Roll on the Flying Qualities of a Small Single-Rotor Helicopter. NACA TN 2459, 1952.
8. Amer, Kenneth B., and Gustafson, F. B.: Charts for Estimation of Longitudinal-Stability Derivatives for a Helicopter Rotor in Forward Flight. NACA TN 2309, 1951.
9. Amer, Kenneth B.: Some Flying-Qualities Studies of a Tandem Helicopter. NACA RM L51H20a, 1951.
10. Amer, Kenneth B.: Theory of Helicopter Damping in Pitch or Roll and a Comparison With Flight Measurements. NACA TN 2136, 1950.
11. Gustafson, F. B., Amer, Kenneth B., Haig, C. R., and Reeder, J. P.: Longitudinal Flying Qualities of Several Single-Rotor Helicopters in Forward Flight. NACA TN 1983, 1949.
12. Reeder, John P., and Gustafson, F. B.: On the Flying Qualities of Helicopters. NACA TN 1799, 1949.
13. Gustafson, F. B., and Reeder, J. P.: Helicopter Stability. NACA RM L7K04, 1948.
14. Bailey, F. J., Jr.: A Simplified Theoretical Method of Determining the Characteristics of a Lifting Rotor in Forward Flight. NACA Rep. 716, 1941.
15. Gessow, Alfred: Review of Information on Induced Flow of a Lifting Rotor. NACA TN 3238, 1954.
16. Heyson, Harry H.: Preliminary Results From Flow-Field Measurements Around Single and Tandem Rotors in the Langley Full-Scale Tunnel. NACA TN 3242, 1954.
17. Heyson, Harry H.: Analysis and Comparison With Theory of Flow-Field Measurements Near a Lifting Rotor in the Langley Full-Scale Tunnel. NACA TN 3691, 1956.
18. Heyson, Harry H., and Katzoff, S.: Normal Component of Induced Velocity in the Vicinity of a Lifting Rotor With a Nonuniform Disk Loading. NACA TN 3690, 1956.
19. Amer, Kenneth B., and Gessow, Alfred: Charts for Estimating Tail-Rotor Contribution to Helicopter Directional Stability and Control in Low-Speed Flight. NACA Rep. 1216, 1955. (Supersedes NACA TN 3156.)
20. Whitten, James B., Reeder, John P., and Crim, Almer D.: Helicopter Instrument Flight and Precision Maneuvers as Affected by Changes in Damping in Roll, Pitch, and Yaw. NACA TN 3537, 1955.
21. Reeder, John P., and Tapscott, Robert J.: Note on Hovering Turns With Tandem Helicopters. NACA RM L55G21, 1955.

REPORT 1351

FOREWORD

During the early part of World War II, some of the helicopters designed for military use were observed during ground tests to exhibit a violent oscillatory rotor instability which endangered the safety of the aircraft. This instability was at first attributed to rotor-blade flutter, but a careful analysis indicated it to be caused by a hitherto unknown phenomenon in which the rotational energy of the rotor was converted into oscillatory energy of the blades. This phenomenon was usually critical when the helicopter was operating on or near the ground and, hence, was called ground resonance. An oscillatory instability of such magnitude as resulted from this phenomenon would generate forces that could quickly destroy a helicopter. The research efforts of the National Advisory Committee for Aeronautics were therefore enlisted to investigate the difficulties introduced by this phenomenon. During the interval between 1942 and 1947, a theory of the self-excited instability of hinged rotor blades was worked out by Robert P. Coleman and Arnold M. Feingold at the Langley Aeronautical Laboratory. This theory defined the important parameters and provided design information which made it possible to eliminate this type of instability. These results were originally released by the NACA in three separate papers, as follows:

(1) NACA Advance Restricted Report 3G29, 1943 (Wartime Report L–308) entitled "Theory of Self-Excited Mechanical Oscillations of Hinged Rotor Blades," by Robert P. Coleman.

(2) NACA Advance Restricted Report 3I13, 1943 (Wartime Report L–312) entitled "Theory of Mechanical Oscillations of Rotors With Two Hinged Blades," by Arnold M. Feingold.

(3) NACA Technical Note 1184, 1947, entitled "Theory of Ground Vibrations of a Two-Blade Helicopter Rotor on Anisotropic Flexible Supports," by Robert P. Coleman and Arnold M. Feingold.

These three reports have been recognized to contain the fundamental reference material on the subject of rotor mechanical instability but were for some time out of print. As a result of demands for this type of information, they were combined into a single volume and reissued with appropriate corrections as NACA Technical Note 3844. The combined volume (reissued here as an NACA Report) consists of three chapters representing the three aforementioned papers in consecutive order.

Inasmuch as the authors of these papers are no longer with the NACA, the task of checking these papers and incorporating such corrections as seemed proper was undertaken by George W. Brooks, Vibration and Flutter Branch, Dynamic Loads Division, of the Langley Aeronautical Laboratory. Mr. Brooks also prepared an appendix to chapter III, which deals with the general equations of motion for a two-blade rotor and includes the effects of damping.

Preceding Page Blank

CONTENTS

Chapter — Page

I. THEORY OF SELF-EXCITED MECHANICAL OSCILLATIONS OF HINGED ROTOR BLADES, by Robert P. Coleman — 269
SUMMARY — 269
INTRODUCTION — 269
SYMBOLS — 270
APPROACH TO THE VIBRATION PROBLEM — 271
Stability and Instability — 271
Choice of Degrees of Freedom — 271
Physical Parameters — 271
MATHEMATICAL DEVELOPMENTS — 272
Method of Analysis — 272
Example of Rotor With Locked Hinges — 272
Hinged Rotor — 273
Deviation of Equations of Motion — 274
The Characteristic Equation — 276
METHOD OF APPLYING THEORY — 277
Application Neglecting Damping — 277
Possibility of Avoiding Occurrence of Vibration — 278
Effect of Damping — 278
LIMITATIONS AND FURTHER DEVELOPMENTS OF THE THEORY — 281
Polar Symmetry — 281
Two Blades — 281
REFERENCES — 281

II. THEORY OF MECHANICAL OSCILLATIONS OF ROTORS WITH TWO HINGED BLADES, by Arnold M. Feingold — 282
SUMMARY — 282
INTRODUCTION — 282
SYMBOLS — 282
MATHEMATICAL ANALYSIS — 283
DISCUSSION OF FREQUENCY EQUATION — 285
Case of Zero Damping — 285
Effect of Damping — 286
Brief Description of Vibration Modes — 288
CONCLUSIONS — 288
REFERENCES — 288

III. THEORY OF GROUND VIBRATIONS OF A TWO-BLADE HELICOPTER ROTOR ON ANISOTROPIC FLEXIBLE SUPPORTS (REVISED), by Robert P. Coleman and Arnold M. Feingold — 289
SUMMARY — 289
INTRODUCTION — 289
DERIVATION OF THE EQUATIONS OF MOTION — 289
FORM OF SOLUTION OF EQUATIONS OF MOTION — 291
SOLUTION OF EQUATIONS OF MOTION — 291
Determinantal Equation — 291
Auxiliary Determinants and Recurrence Relations for Calculating $\Delta(\omega_a)$ — 293
The Behavior of $\Delta_n(\omega_a)$ for Large Values of n — 294
Evaluation of Roots of Equation (25) — 294
Conditions for Stability — 296
SPECIAL CASES OF GENERAL THEORY — 296
Case of $K_y=K_x$ — 296
Case of $K_y=0$ — 296
Case of $K_y=\infty$ — 297
DISCUSSION OF RESULTS — 298
Types of Instability — 298
General Behavior of Rotor System as a Function of Rotor Speed — 298
Comparison of Results for Different Values of K_y/K_x — 299
Effect of Damping — 300
APPLICATION TO DUAL ROTORS — 300
CONCLUSIONS — 301
APPENDIX A. SYMBOLS — 302
APPENDIX B. THE GENERAL EQUATIONS OF MOTION FOR TWO-BLADE ROTORS, by George W. Brooks — 303
General Case — 303
Special Case—Zero Damping — 303
Special Case of Isotropic Supports — 303
APPENDIX C. DERIVATION OF THE CONVERGENCE FACTOR FOR $K(0)$ — 304
APPENDIX D. MATHEMATICAL ANALYSIS FOR THE CASE OF $K_y=\infty$ — 305
REFERENCES — 307

REPORT 1351

THEORY OF SELF-EXCITED MECHANICAL OSCILLATIONS OF HELICOPTER ROTORS WITH HINGED BLADES [1]

By Robert P. Coleman and Arnold M. Feingold

CHAPTER I

THEORY OF SELF-EXCITED MECHANICAL OSCILLATIONS OF HINGED ROTOR BLADES

By Robert P. Coleman

SUMMARY

Vibrations of rotary-wing aircraft may derive their energy from the rotation of the rotor rather than from the air forces. A theoretical analysis of these vibrations is described and methods for its application are explained herein.

The theory includes the effects of unequal stiffness of the pylon for deflections in different directions and the effect of damping in the hinges and in the pylon. Both the derivation of the characteristics equation and the methods of application of the theory are given. In particular, the theory predicts the so-called "odd frequency" self-excited speed range as well as the shaft critical speed. Charts are presented from which the shaft critical and the self-excited instabilities can be predicted for a great variety of cases. The influence of each physical parameter upon the instabilities has been obtained. The comprehensive treatment applies to a rotor that has any number of blades greater than two. Only a brief discussion and the formula for shaft critical speed are given for the one- or two-blade rotor.

The use of complex variables in conjunction with Lagrange's equations has been found very convenient for the treatment of vibrations of rotating systems.

INTRODUCTION

A rotary-wing aircraft that has hinged blades will, under certain conditions, be subject to vibrations which derive their energy from the rotation of the rotor instead of from the air forces. The term "ground resonance" usually refers to vibrations of this type. Although such vibrations have apparently caused accidents in some rotary-wing aircraft and have impaired the flying qualities of others, very little attention has been given this problem in the literature. A theoretical analysis has therefore been undertaken, and the purpose of the present chapter is to present the theory and to describe the application of the theory to rotary-wing aircraft.

General vibration theory and its application to allied problems as well as to the particular problem of rotor vibration are discussed in references 1 to 4. A good general background for the present problem is provided in the chapters on rotating machinery and on self-excited vibrations in reference 1. References 2 and 3 treat in more abstract fashion the topics of rotation and damping. A discussion of the variety of modes of vibration that exist in rotors and a number of frequency formulas obtained by considering separately each degree of freedom are given in reference 4. This discussion does not, however, lead to a prediction of self-excited modes of vibration.

Experience has shown that two types of mechanical vibration may occur in rotors. The vibration frequency of the pylon is equal to the rotational speed in one type and is unequal in the other. The first type is sometimes called the even-frequency vibration or the one-to-one frequency, and the second type, the odd frequency. The one-to-one frequency vibration resembles the phenomenon occurring at a critical speed of the shaft of rotating machinery and will consequently be referred to in this chapter as a shaft critical vibration. The odd-frequency vibration is properly called a self-excited vibration.

A derivation of the characteristic equation for the whirling speeds of a three-blade rotor has been given by Wagner of the Kellett Autogiro Corporation. By considering only the case of a pylon having equal stiffness in all directions of deflection, Wagner has shortened the analysis by considering directly the equilibrium of forces and moments under conditions of steady circular whirling. Some examples of the dependence of whirling speed upon rotational speed are given, and the formula for the shaft critical speed is obtained.

In the present chapter, the theory also includes the effects of damping in the hinges and in the hub and the effects of different stiffnesses of pylon deflection in different directions. The method of analysis, particularly the use of complex

[1] Supersedes NACA Technical Note 3844 by Robert P. Coleman and Arnold M. Feingold, 1957.

variables in the equations of motion, is explained in some detail and all the previous results are shown to be a special case of the more general problem treated here.

SYMBOLS

a	radial position of vertical hinge
A_{11}, $\overline{A}_{11}$, $\Delta A_{11}=\Delta\overline{A}_{11}$, $A_{12}=\overline{A}_{12}$, $A_{21}=\overline{A}_{21}$, A_{22}, $\overline{A}_{22}$	elements of the characteristic determinant (see eq. (31))
b	distance from vertical hinge to center of mass of blade
B	damping force per unit velocity of pylon displacement $\left(B_f=\frac{B_x+B_y}{2}\right)$
$\Delta B_f=\frac{B_x-B_y}{2}$	
B_I	coefficient defined in equation (35)
B_R	coefficient defined in equation (34)
$c, C_1, \ldots C_4$	arbitrary constants
C_I	coefficient defined in equation (35)
C_R	coefficient defined in equation (34)
D	time-derivative operator, d/dt
F	dissipation function
I	moment of inertia of blade about hinge, $m_b b^2\left(1+\frac{r^2}{b^2}\right)$
$I_1, \ldots I_5$	coefficients defined in expressions (37)
j, k	indices and subscripts used with hinge coordinates (eq. (14))
K	spring constant $\left(K_f=\frac{K_x+K_y}{2}\right)$
$\Delta K_f=\frac{K_x-K_y}{2}$	
m	effective mass of pylon $\left(m_f=\frac{m_x+m_y}{2}\right)$
m_b	blade mass
$\Delta m_f=\frac{m_x-m_y}{2}$	
M	total effective mass of blades and pylon, m_f+nm_b
ΔM	mass added at hub for vibration test
n	total number of blades
r	radius of gyration of blade about its center of mass
$R_1, \ldots R_5$	coefficients defined in expressions (37)
s	stiffness ratio, K_y/K_x
t	time
T	kinetic energy
T_r	kinetic energy of rotation of blade about its center of mass
T_k	kinetic energy of translational motion of kth blade
T_s	kinetic energy of pylon
V	potential energy
x, y	displacements
x_o, y_o	values of x and y when $t=0$
z	complex displacement, $x+iy$
$\bar{z}$	complex conjugate of z, $x-iy$
α	angle between blades, $2\pi/n$
$\beta_0, \beta_1, \ldots \beta_k$	angular displacements of blades
β_{k_o}	value of β_k when $t=0$
$\zeta_0, \zeta_1, \ldots \zeta_k$	variables representing hinge deflections when equations are expressed in fixed coordinate system
$\theta_0, \theta_1, \ldots \theta_k$	variables representing hinge deflections when equations are expressed in rotating coordinate system
$\lambda_x=\frac{B_x}{M_x}\left(\frac{B_x}{M_x\omega_r}\text{ in applications}\right)$	
$\lambda_y=\frac{B_y}{M_y}\left(\frac{B_y}{M_y\omega_r}\text{ in applications}\right)$	
$\lambda_\beta=\frac{B_\beta}{I}\left(\frac{B_\beta}{I\omega_r}\text{ in applications}\right)$	
$\lambda_f=\frac{B_f}{M}$	
$\lambda_a=\frac{B_a}{M}$	
$\Delta\lambda_f=\frac{\Delta B_f}{M}$	
$\Lambda_1=\frac{a}{b\left(1+\frac{r^2}{b^2}\right)}$	
$\Lambda_2=\frac{K_\beta}{I}\left(\frac{K_\beta}{I\omega_r^2}\text{ in applications}\right)$	
$\Lambda_3=\frac{\mu}{2\left(1+\frac{r^2}{b^2}\right)}$	
μ	mass ratio, $\frac{nm_b}{m_f+nm_b}$
ν_1, ν_2	expressions defined in equation (3)
ω	angular velocity of rotor (the dimensionless ratio ω/ω_r is called ω in applications)
ω_a	angular whirling velocity measured in rotating coordinate system (used in nondimensional form in applications)
ω_f	angular whirling velocity measured in fixed coordinate system (used in nondimensional form in applications)
ω_r	reference frequency, $\sqrt{K_x/M_x}$
Subscripts:	
f	fixed coordinate system
a	rotating coordinate system
β	hinge deflection
x, y	component directions in fixed coordinate system

APPROACH TO THE VIBRATION PROBLEM

STABILITY AND INSTABILITY

If a vibrator were attached to a rotorcraft, several modes of vibration could be excited at any rotor speed. Only the modes that are likely to be excited during operation of the aircraft, however, are important.

In the present discussion, it is convenient to classify the modes of vibration according to the circumstances required for their excitation. The different types of vibration are identified analytically by the nature of the roots of the characteristic equation. A hinged rotor may encounter three types of vibration which, for convenience, are herein designated ordinary, self excited, and shaft critical. At zero or slow rotational speeds, an external force is required to excite vibration. The friction always present in such systems causes the vibration to be damped out when the force is removed. Modes of vibration requiring an external applied force to maintain them will be called ordinary vibrations. The mathematically idealized case of zero damping will also be considered an ordinary vibration when it is understood to be an approximation to a system actually damped. Self-excited modes of vibration are those with negative damping and are recognized analytically by the fact that a root of the characteristic equation is a complex number which has a negative imaginary part. A slight disturbance will tend to increase with time instead of damping out.

When a rotating system is not perfectly balanced, the centrifugal force of the unbalanced mass may excite vibrations that have peak amplitudes at certain rotational speeds. Vibration excited by unbalance and in resonance with the rotation will be called shaft critical vibration. This type occurs at the rotational speed at which the spring stiffness of the pylon is neutralized by the centrifugal force. In the analysis, the shaft critical vibration is recognized in rotating coordinates as a zero frequency and in fixed coordinates as a frequency equal to the rotational speed. The critical speeds of a rotating shaft are a common example of this class.

The purpose of a theory of rotor vibration is mainly to predict the occurrence of and, if possible, to show how to avoid self-excited and shaft critical vibrations.

CHOICE OF DEGREES OF FREEDOM

Of the large number of degrees of freedom of a hinged rotor, the important ones for the present problem have been found to be hinge deflection of the blades in the plane of rotation and horizontal deflections of the pylon. Other degrees of freedom, such as the flapping hinge motion of the blades, the bending or torsion of the blades, and the torsion of the drive shaft, are considered unimportant in the problem of self-excited oscillations. Some motions, such as landing-gear deflection, that produce lateral deflection at the top of the pylon may, however, be important.

PHYSICAL PARAMETERS

The theoretical results given later provide a means of predicting the natural frequencies and, in particular, the critical speeds and unstable speed ranges in terms of certain physical parameters, such as mass, stiffness, and length. The successful application of the theory depends upon the determination of the proper values of these physical parameters for the aircraft or model being studied.

The important parameters to be determined are:

a radial position of vertical hinge

b distance from vertical hinge to center of mass of blade

m_b mass of blade (Flexibility of the blade structure may have to be taken into account by the use of an effective value of m_b different from the actual blade mass. The effective blade mass can be taken as the value required to make the theory predict the correct pylon natural frequency when the rotor has a zero or very slow rotational speed.)

I moment of inertia of blade about hinge,

$$m_b b^2 \left(1+\frac{r^2}{b^2}\right)$$

K_β spring constant of self-centering springs, which can be determined by a force test or from the hinge frequency with the hub rigidly supported

m_x, m_y effective mass of pylon for deflections in x- and y-directions

K_x, K_y effective stiffness of pylon

The effective mass of the pylon is the value of a concentrated mass that would have the same kinetic energy expressed in terms of the deflections at the hub as the actual pylon and hub if it were placed at the rotor hub in the plane of rotation. The effective stiffness of the pylon is the stiffness of a spring that, if placed at the hub in the plane of rotation, would have the same potential energy in terms of deflections at the hub as the actual pylon. Equivalent definitions are that, if a simple spring and mass were imagined to be substituted at the hub in the plane of rotation for the pylon and hub, the natural frequency and the change of natural frequency with added mass would be the same as for the actual pylon.

An experimental method of measuring the effective mass m_x and stiffness K_x of the pylon is to replace the rotor by an approximately equal, rigid, concentrated mass ΔM at the hub and to measure the natural frequency for two or more values of this added mass. The quantities are then related by the equation

$$\omega_x=\sqrt{\frac{K_x}{m_x+\Delta M}}$$

or

$$\frac{1}{\omega_x^2}=\frac{1}{K_x}(m_x+\Delta M)$$

If measured values of $1/\omega_x^2$ are plotted against added mass ΔM and a straight line is drawn through the points, the intercept and the slope of the line will determine the effective values of K_x and m_x.

For the parameters a and b, the actual geometric lengths should be used unless the flexibility of the hinge offset arm a is comparable in magnitude with the hinge spring stiffness. In this case, it is recommended that an effective value of a be guessed and that b be determined by subtraction from the

correct geometric value of $a+b$.

The damping parameters may be defined by the form of a dissipation function F. The function

$$2F=B_x\dot{x}_f^2+B_y\dot{y}_f^2+\sum_{k=0}^{n-1}B_\beta\dot{\beta}_k^2$$

is equal to the rate of dissipation of energy by damping. The parameters B_x and B_y thus measure the damping force per unit velocity referred to linear displacements of the top of the pylon and B_β is the damping torque per unit angular velocity at a blade hinge. If the damping force per unit velocity is not a constant, effective values should be used that will represent the same dissipation of energy per cycle as actually occurs with a reasonable amplitude of vibration. The amplitude of free vibration in a single degree of freedom is given in terms of B_x, B_y, and B_β by

$$x_f=x_oe^{-\frac{B_x}{2M}}$$

$$y_f=y_oe^{-\frac{B_y}{2M}}$$

$$\beta_k=\beta_{k_o}e^{-\frac{B_\beta}{2I}t}$$

The damping parameters are probably the most difficult ones to measure accurately. In practice, it is advisable to make calculations for a given case, first on the basis of no damping and then with the use of the estimated values of the damping parameters.

MATHEMATICAL DEVELOPMENTS

METHOD OF ANALYSIS

The derivation of the characteristic equation that is used as the basis for predicting the unstable oscillations of a rotor is presented in this section. Readers interested solely in applications can omit this section and proceed immediately to the section entitled "Method of Applying Theory."

The method of analysis treats the equations of motion for small displacements from the equilibrium condition with steady rotation. A proper choice of coordinates leads to equations with constant coefficients. The solutions are exponential or trigonometric functions.

The mathematical manipulations involved in treating the motions of a mass in a plane of rotation are facilitated by the use of a complex variable. The typical disturbed motion obtained by solving the equations of motion is an elliptic whirling motion, which is represented in terms of a complex variable $z=x+iy$. At any instant, z represents the displacement of the pylon from its equilibrium position. An expression such as

$$z=ce^{i\omega_f t}$$

represents whirling of the pylon in a circle of radius c with angular velocity ω_f. The sign of ω_f determines the sense of the rotation. Two rotations in opposite sense with the same radius are equivalent to a vibratory motion in a straight line and are given as follows:

$$z=c(e^{i\omega_f t}+e^{-i\omega_f t})$$

$$=2c\cos\omega_f t$$

Two opposite rotations of different radii are equivalent to whirling in an ellipse. A complex value of ω_f represents whirling in a spiral, which may be either a damped or a self-excited motion depending upon the sign of the imaginary part. A self-excited motion exists when the imaginary part of ω_f is negative, and the magnitude of z increases with time.

The displacements may be referred to a fixed or to a rotating coordinate system. If z_f and z_a are the displacements with respect to a fixed and to a rotating reference system, respectively,

$$z_f=z_ae^{i\omega t}$$

$$z_a=ce^{i\omega_a t}$$

then

$$z_f=ce^{i(\omega_a+\omega)t}$$

A whirling speed ω_a with respect to the rotating coordinates thus corresponds to a whirling speed $\omega_f=\omega_a+\omega$ with respect to the fixed coordinates. A shaft critical vibration corresponds to $\omega_a=0$ in the rotating coordinate system or to $\omega_f=\omega$ in the fixed coordinate system.

EXAMPLE OF ROTOR WITH LOCKED HINGES

An example that involves a partial use of complex variables is given on page 253 of reference 2. The problem given there of a mass particle moving on the inner surface of a rotating spherical bowl is mathematically equivalent to the disturbed motion of a flywheel and shaft or of a rotor with locked hinges. The equations of motion obtained in real form in rotating coordinates

$$\left.\begin{aligned}\ddot{x}_a-2\omega\dot{y}_a-\omega^2x_a&=-\frac{B_a\dot{x}_a}{M}-\frac{K}{M}x_a\\ \ddot{y}_a+2\omega\dot{x}_a-\omega^2y_a&=-\frac{B_a\dot{y}_a}{M}-\frac{K}{M}y_a\end{aligned}\right\}\quad(1)$$

are combined in the single equation

$$\ddot{z}_a+\left(2i\omega+\frac{B_a}{M}\right)\dot{z}_a+\left(\frac{K}{M}-\omega^2\right)z_a=0\quad(2)$$

where

$$z_a=x_a+iy_a$$

is the complex position vector in the rotating coordinate system. The complete solution, if small damping is assumed, is

$$z_ae^{i\omega t}=C_1e^{-\nu_1 t+i\omega_r t}+C_2e^{-\nu_2 t-i\omega_r t}\quad(3)$$

where

$$\nu_1=\frac{1}{2}\frac{B_a}{M}\left(1-\frac{\omega}{\omega_r}\right)$$

$$\nu_2=\frac{1}{2}\frac{B_a}{M}\left(1+\frac{\omega}{\omega_r}\right)$$

The path of the motion is represented by rotations of a complex vector in a plane.

The use of a complex variable has thus cut in half the number of equations to be handled and has yielded a solution from which the geometric path of the motion may easily be reconstructed. The advantage of the z-notation is not fully

realized, however, unless it is used from the very beginning of the problem. The close similarity of this problem to the rotor-vibration problem makes it worthwhile to show the full application of the z-notation to the preceding example. The complex variable z_a at any instant determines the position of the mass particle relative to the rotating coordinate system. If the position in a fixed coordinate system is denoted by z_f,

$$z_f=z_a e^{i\omega t} \tag{4}$$

and z_a can be treated as a generalized coordinate in the Lagrangian equations of motion. The kinetic- and potential-energy expressions can be immediately written as

$$T=\frac{1}{2}M\dot{z}_f\dot{\bar{z}}_f$$

$$=\frac{1}{2}M(\dot{z}_a+i\omega z_a)(\dot{\bar{z}}_a-i\omega\bar{z}_a)$$

$$V=\frac{1}{2}Kz_a\bar{z}_a$$

A dissipation function for damping that depends upon motion relative to the rotating system can be written

$$F=\frac{1}{2}B_a\dot{z}_a\dot{\bar{z}}_a$$

The equations of motion are now obtained by considering z_a and $\bar{z}_a$ as generalized coordinates in the Lagrangian equations. Substitution in the equation

$$\frac{d}{dt}\left(\frac{\partial T}{\partial\dot{\bar{z}}_a}\right)-\frac{\partial T}{\partial\bar{z}_a}+\frac{\partial F}{\partial\dot{\bar{z}}_a}+\frac{\partial V}{\partial\bar{z}_a}=0$$

thus yields the equation previously given

$$\ddot{z}_a+\left(2i\omega+\frac{B_a}{M}\right)\dot{z}_a+\left(\frac{K}{M}-\omega^2\right)z_a=0$$

The same method can be used to obtain the equations of motion in the fixed coordinate system. In this case,

$$\left.\begin{aligned}T&=\frac{1}{2}M\dot{z}_f\dot{\bar{z}}_f\\ V&=\frac{1}{2}Kz_f\bar{z}_f\\ F&=\frac{1}{2}B_a\,(\dot{z}_f-i\omega z_f)\,(\dot{\bar{z}}_f+i\omega\bar{z}_f)\end{aligned}\right\} \tag{5}$$

The equation of motion in terms of z_f becomes

$$\ddot{z}_f+\frac{B_a}{M}\,(\dot{z}_f-i\omega z_f)+\frac{K}{M}\,z_f=0 \tag{6}$$

and the solution for small values of damping is

$$z_f=C_1e^{-\frac{B_a}{2M}\left(1-\frac{\omega}{\sqrt{K/M}}\right)t+i\sqrt{K/M}t}+C_2e^{-\frac{B_a}{2M}\left(1+\frac{\omega}{\sqrt{K/M}}\right)t-i\sqrt{K/M}t} \tag{7}$$

This solution shows that the motion consists of two circular vibrations in opposite directions and, moreover, that for $\omega>\sqrt{K/M}$ the first term represents unstable motion; that is, the vibration has negative damping.

This example illustrates a shaft critical speed for $\omega=\sqrt{K/M}$ and a self-excited instability for $\omega>\sqrt{K/M}$. A discussion of the physical picture of this instability due to damping is given on page 293 of reference 1.

The effect of damping in a nonrotating part of the system can be included in the analysis merely by adding to the previous dissipation function the term

$$\frac{1}{2}B_f\dot{z}_f\dot{\bar{z}}_f$$

The equation of motion then becomes

$$M\ddot{z}_f+B_f\dot{z}_f+B_a(\dot{z}_f-i\omega z_f)+Kz_f=0 \tag{8}$$

The solution for small values of damping becomes

$$Z_f=C_1e^{\left[-\frac{B_f}{2M}-\frac{B_a}{2M}\left(1-\frac{\omega}{\sqrt{K/M}}\right)+i\sqrt{K/M}\right]t}+$$

$$C_2e^{\left[-\frac{B_f}{2M}-\frac{B_a}{2M}\left(1+\frac{\omega}{\sqrt{K/M}}\right)-i\sqrt{K/M}\right]t} \tag{9}$$

The motion is now unstable above the speed

$$\omega=\sqrt{\frac{K}{M}}\left(1+\frac{B_f}{B_a}\right) \tag{10}$$

HINGED ROTOR

Inclusion of the effect of hinge motion in the plane of rotation increases the number of degrees of freedom and the number of equations of motion. For example, three hinged blades and two directions of pylon deflection give five degrees of freedom to be considered. If special linear combinations of the hinge deflections β_k are used as generalized coordinates, no more than four degrees of freedom need be considered simultaneously. The use of complex variables reduces these four equations to two equations.

Appropriate variables in the rotating system for a three-blade rotor are

$$\left.\begin{aligned}\theta_0&=\frac{bi}{3}\,(\beta_0+\beta_1+\beta_2)\\ \theta_1&=\frac{bi}{3}\left(\beta_0+\beta_1e^{\frac{2\pi i}{3}}+\beta_2e^{\frac{4\pi i}{3}}\right)\\ \theta_2&=\frac{bi}{3}\left(\beta_0+\beta_1e^{\frac{4\pi i}{3}}+\beta_2e^{\frac{8\pi i}{3}}\right)\end{aligned}\right\} \tag{11}$$

These variables and their complex conjugates satisfy the relations

$$\bar{\theta}_1=-\theta_2$$

$$\bar{\theta}_2=-\theta_1$$

and also

$$\theta_0\bar{\theta}_0+\theta_1\bar{\theta}_1+\theta_2\bar{\theta}_2=-\theta_0^2+2\theta_1\bar{\theta}_1$$

$$=\frac{b^2}{3}\left(\beta_0^2+\beta_1^2+\beta_2^2\right)$$

The variables β_k, by virtue of their meaning, are referred to a rotating coordinate system. The special linear combinations of the β_k denoted by θ_k are also referred to a rotating

coordinate system. The appropriate variables to represent the hinge deflections when fixed coordinates are used are defined by

$$\zeta_k=\theta_k e^{i\omega t} \tag{12}$$

and $\bar{\zeta}_k$ is the complex conjugate of ζ_k.

Geometrically, θ_1 or ζ_1 is the complex vector representing the displacement due to hinge deflection of the center of mass of all the blades, just as z represents the position of the shaft due to pylon deflection. It will be shown later that in equations of motion, θ_1 is coupled with z and θ_0 is an independent principal coordinate. Equations (11) when solved for β_0, β_1, and β_2 become

$$\theta_0+\theta_1+\theta_2=bi\beta_0$$

$$\theta_0+\theta_1 e^{-i\alpha}+\theta_2 e^{i\alpha}=bi\beta_1$$

$$\theta_0+\theta_1 e^{i\alpha}+\theta_2 e^{-i\alpha}=bi\beta_2$$

Then, in a mode involving θ_1,

$$\left.\begin{aligned}\theta_0&=0\\ \theta_1&=\frac{b}{2}e^{i\omega_a t}\\ \theta_2&=-\bar{\theta}_1\\ \beta_0&=\sin\omega_a t\\ \beta_1&=\sin(\omega_a t-\alpha)\\ \beta_2&=\sin(\omega_a t+\alpha)\end{aligned}\right\} \tag{13}$$

Equations (13) show that in the θ_1-mode, the blades are undergoing sinusoidal vibrations 120° out of phase with one another in a manner analogous to three-phase electrical currents.

General formulas for any number of blades are

$$\left.\begin{aligned}\theta_j&=\frac{bi}{n}\sum_{k=0}^{n-1}\beta_k e^{ijak}\\ \alpha&=\frac{2\pi}{n}\\ \bar{\theta}_j&=-\theta_{n-j}\\ \theta_n&=\theta_0\\ \sum_{k=0}^{n-1}\theta_k\bar{\theta}_k&=\frac{b^2}{n}=\sum_{k=0}^{n-1}\beta_k{}^2\end{aligned}\right\} \tag{14}$$

DERIVATION OF EQUATIONS OF MOTION

The equations of motion and the characteristic equation of whirling speeds are herein derived for the general case of three or more equal blades on a pylon that may have different stiffness properties in different directions of deflection. The effects of damping in the blade hinges and in the pylon are included. The equations are first formulated in a nonrotating reference system. The required modifications are then given for the case of isotropic support stiffness. The corresponding equations referred to the rotating coordinates are then obtained.

Let the position of the center of mass of the kth blade be represented by the complex quantity z_k in the plane of rotation. (See fig. I–1.) Let the bending deflection of the pylon be represented by z_f in a nonrotating coordinate system and let β_k be the hinge deflection of the kth blade. Then

$$z_k=z_f+(a+be^{i\beta_k})e^{i(\alpha k+\omega t)} \tag{15}$$

The complex velocity is

$$\dot{z}_k=\dot{z}_f+[bi\dot{\beta}_k e^{i\beta_k}+i\omega(a+be^{i\beta_k})]e^{i(\alpha k+\omega t)} \tag{16}$$

Because only small displacements are being considered, the exponential factors containing β_k can be expanded and only the terms that lead to quadratic terms for the kinetic-energy expression need be considered.

Some terms can be ignored either because they cancel after summation for all the blades or because the corresponding derivative expressions in the Lagrangian equations vanish. The substitution

$$e^{i\beta_k}=1+i\beta_k-\frac{\beta_k{}^2}{2}$$

leads to the following expression for the kinetic energy of translational motion of the kth blade:

$$T_k=\frac{1}{2}m_b\dot{z}_k\dot{\bar{z}}_k \tag{17}$$

where

$$\dot{z}_k\dot{\bar{z}}_k=\dot{z}_f\dot{\bar{z}}_f+\dot{\bar{z}}_f bi(\dot{\beta}_k+i\omega\beta_k)e^{i(\alpha k+\omega t)}+$$
$$\dot{z}_f(-bi)(\dot{\beta}_k-i\omega\beta_k)e^{-i(\alpha k+\omega t)}+b^2\dot{\beta}_k{}^2-\omega^2 ab\beta_k{}^2$$

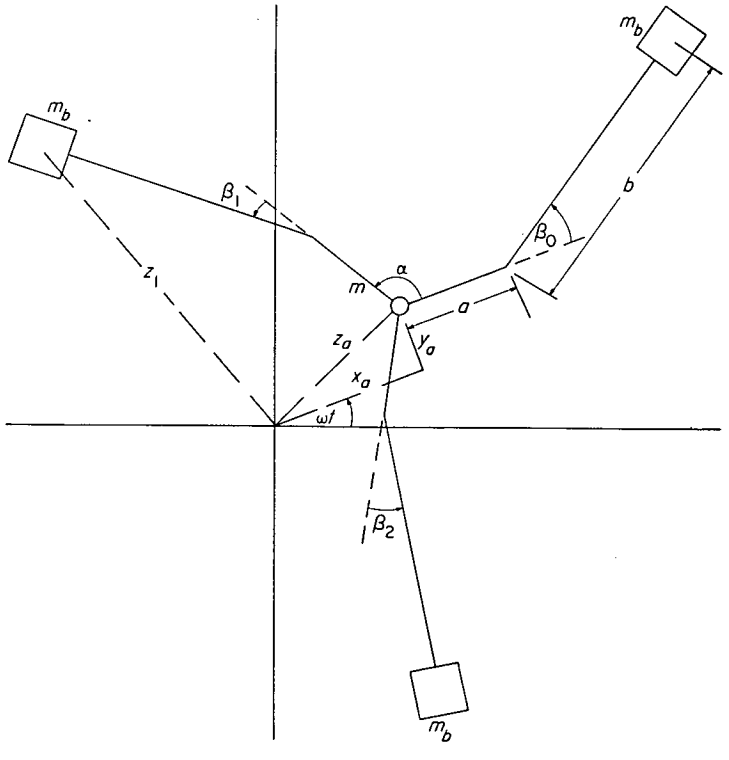


FIGURE I–1.—Simplified mechanical system representing rotor.

The kinetic energy of rotation about the center of mass of the blade is

$$T_r=\frac{1}{2}m_b r^2\dot{\beta}_k^2 \tag{18}$$

The effective mass of the pylon may be different in the x_f- and in the y_f-directions. Allowance for this possibility is made by writing the kinetic energy of the pylon as

$$T_s=\frac{1}{2}(m_x\dot{x}_f^2+m_y\dot{y}_f^2)$$

$$=\frac{1}{2}\left[m_f\dot{z}_f\dot{\bar{z}}_f+\Delta m_f\left(\frac{\dot{z}_f^2+\dot{\bar{z}}_f^2}{2}\right)\right] \tag{19}$$

where

$$m_f=\frac{m_x+m_y}{2}$$

$$\Delta m_f=\frac{m_x-m_y}{2}$$

The total kinetic energy is the sum of the expressions for the separate kinetic energies.

The pylon spring constant may differ in the x_f- and in the y_f-directions and, consequently, the potential energy can be expressed as

$$V=\frac{1}{2}\left(K_f z_f\bar{z}_f+\Delta K_f\frac{z_f^2+\bar{z}_f^2}{2}+\sum_{k=0}^{n-1}K_\beta\beta_k^2\right. \tag{20}$$

The effect of damping will be expressed with the aid of a dissipation function. If damping exists in the pylon, in the rotating shaft, and in the hinges, this function becomes

$$F=\frac{1}{2}\left(B_f\dot{z}_f\dot{\bar{z}}_f+\Delta B_f\frac{\dot{z}_f^2+\dot{\bar{z}}_f^2}{2}+B_a\dot{z}_a\dot{\bar{z}}_a+\sum_{k=0}^{n-1}B_\beta\dot{\beta}_k^2\right) \tag{21}$$

The sum of the various energy expressions for all the blades, expressed in terms of the variables z_f and ζ_k in the nonrotating coordinates, becomes

$$\left.\begin{aligned}
T=&\frac{1}{2}\left\{\Delta m_f\frac{\dot{z}_f^2+\dot{\bar{z}}_f^2}{2}+(m_f+nm_b)\,\dot{z}_f\dot{\bar{z}}_f+nm_b\left[(\dot{\bar{z}}_f\dot{\zeta}_1+\right.\right.\\
&\dot{z}_f\dot{\bar{\zeta}}_1)+\left(1+\frac{r^2}{b^2}\right)\sum_{k=0}^{n-1}(\dot{\zeta}_k-i\omega\zeta_k)(\dot{\bar{\zeta}}_k+i\omega\bar{\zeta}_k)-\\
&\left.\left.\omega^2\frac{a}{b}\sum_{k=0}^{n-1}\zeta_k\bar{\zeta}_k\right]\right\}\\
V=&\frac{1}{2}\left(\Delta K_f\frac{z_f^2+\bar{z}_f^2}{2}+K_f z_f\bar{z}_f+\frac{nK_\beta}{b^2}\sum_{k=0}^{n-1}\zeta_k\bar{\zeta}_k\right)\\
F=&\frac{1}{2}\left[\Delta B_f\frac{\dot{z}_f^2+\dot{\bar{z}}_f^2}{2}+B_f\dot{z}_f\dot{\bar{z}}_f+B_a(\dot{z}_f-i\omega z_f)\,(\dot{\bar{z}}_f+i\omega\bar{z}_f)+\right.\\
&\left.\frac{nB_\beta}{b^2}\sum_{k=0}^{n-1}(\zeta_k-i\omega\zeta_k)(\dot{\bar{\zeta}}_k+i\omega\bar{\zeta}_k)\right]
\end{aligned}\right\} \tag{22}$$

The Lagrangian equations of motion are

$$\left.\begin{aligned}
&\frac{d}{dt}\left(\frac{\partial T}{\partial\dot{\bar{z}}_f}\right)-\frac{\partial T}{\partial\bar{z}_f}+\frac{\partial F}{\partial\dot{\bar{z}}_f}+\frac{\partial V}{\partial\bar{z}_f}=0\\
&\frac{d}{dt}\left(\frac{\partial T}{\partial\dot{\bar{\zeta}}_1}\right)-\frac{\partial T}{\partial\bar{\zeta}_1}+\frac{\partial F}{\partial\dot{\bar{\zeta}}_1}+\frac{\partial V}{\partial\bar{\zeta}_1}=0
\end{aligned}\right\} \tag{23}$$

and similar expressions for the other variables. The equations of motion in fixed coordinates then become

$$\left.\begin{aligned}
&(n+nm_b)\ddot{z}_f+B\dot{z}_f+B_a(\dot{z}_f-i\omega z_f)+Kz_f+\Delta m\ddot{\bar{z}}_f+\Delta B\dot{\bar{z}}_f+\\
&\Delta K\bar{z}_f+nm_b\ddot{\zeta}_1=0\\
&nm_b\ddot{z}_f+2nm_b\left[\left(1+\frac{r^2}{b^2}\right)(\ddot{\zeta}_1-2i\omega\dot{\zeta}_1-\omega^2\zeta_1)+\right.\\
&\left.\frac{B_\beta}{m_b b^2}(\dot{\zeta}_1-i\omega\zeta_1)+\omega^2\frac{a}{b}\zeta_1+\frac{K_\beta}{m_b b^2}\zeta_1\right]=0\\
&nm_b\left[\left(1+\frac{r^2}{b^2}\right)(\ddot{\zeta}_k-2i\omega\dot{\zeta}_k-\omega^2\zeta_k)+\frac{B_\beta}{m_b b^2}(\dot{\zeta}_k-i\omega\zeta_k)+\right.\\
&\left.\omega^2\frac{a}{b}\zeta_k+\frac{K_\beta}{m_b b^2}\zeta_k\right]=0
\end{aligned}\right\} \tag{24}$$

where ζ_k refers to the ζ-variables other than ζ_1 and ζ_{n-1}. The complex conjugates of these equations are also obtained but give no additional information. Each complex equation is, of course, equivalent to two real equations. It is noticed that the first two equations contain only the variables z_f, $\bar{z}_f$, and ζ_1 and that the third equation represents n–2 equations, each containing one independent principal coordinate ζ_k. The physical meaning of this partial separation of variables is that a blade motion represented by ζ_1 involves a motion of the common center of mass of the blades and, thus, a coupling effect with the pylon. Blade motions in which the common center of mass does not move are represented by $\zeta_0, \ldots \zeta_n$. For three blades, the only such mode is the one corresponding to ζ_0. In this mode, all the blades move in phase; the motion is always damped and does not lead to instability.

The equations of motion of a one- or two-blade rotor are somewhat different from equations (24). The difference is connected with the circumstance that a rotor of three or more equal blades has no preferred direction in its plane; whereas, a one- or two-blade rotor has different dynamic properties in directions along and normal to the blades. Only a brief statement and the final equation for shaft critical speed will be given for the one- or two-blade rotor.

The equations of motion involving z_f and ζ_1 can be written more compactly by use of the notation

$$D=\frac{d}{dt}\qquad D^2=\frac{d^2}{dt^2}$$

and the substitutions

$$\frac{B_f}{M}=\lambda_f\qquad\frac{B_\beta}{m_b b^2\left(1+\frac{r^2}{b^2}\right)}=\lambda_\beta$$

$$\frac{B_a}{M}=\lambda_a \qquad \frac{a}{b\left(1+\frac{r^2}{b^2}\right)}=\Lambda_1$$

$$\frac{\Delta B_f}{M}=\Delta\lambda_f \qquad \frac{K_\beta}{m_b b^2\left(1+\frac{r^2}{b^2}\right)}=\Lambda_2$$

$$\frac{nm_b}{m_f+nm_b}=\mu$$

Then

$$\left.\begin{aligned}\left[D^2+\lambda_f D+\lambda_a(D-i\omega)+\frac{K_f}{M}\right]z_f+\left(\frac{\Delta m_f}{M}D^2+\Delta\lambda_f D+\frac{\Delta K_f}{M}\right)\bar{z}_f+\mu D^2\zeta_1=0\\ \frac{1}{2\left(1+\frac{r^2}{b^2}\right)}D^2 z_f+[(D-i\omega)^2+\lambda_\beta(D-i\omega)+\omega^2\Lambda_1+\Lambda_2]\zeta_1=0\end{aligned}\right\} \tag{25}$$

or, briefly,

$$\left.\begin{aligned}A_{11}(D)z_f+\Delta A_{11}(D)\bar{z}_f+A_{12}(D)\zeta_1=0\\ A_{21}(D)z_f\qquad\qquad\quad+A_{22}(D)\zeta_1=0\end{aligned}\right\} \tag{26}$$

THE CHARACTERISTIC EQUATION

The general form of solution of equations (26) is an elliptic whirling motion that can be represented by

$$\left.\begin{aligned}z_f&=C_1e^{i\omega_f t}+C_2e^{-i\bar{\omega}_f t}\\ \bar{z}_f&=\bar{C}_1e^{-i\bar{\omega}_f t}+\bar{C}_2e^{i\omega_f t}\\ \zeta_1&=C_3e^{i\omega_f t}+C_4e^{-i\bar{\omega}_f t}\end{aligned}\right\} \tag{27}$$

Special cases of this motion include whirling in a circle ($C_2=C_4=0$) and linear vibration ($C_1=C_2$, $C_3=C_4$). Substitution of equations (27) in equation (26) gives

$$\left.\begin{aligned}&[A_{11}(i\omega_f)C_1+\Delta A_{11}(i\omega_f)\bar{C}_2+A_{12}(i\omega_f)C_3]e^{i\omega_f t}+[A_{11}(-i\bar{\omega}_f)C_2+\Delta A_{11}(-i\bar{\omega}_f)\bar{C}_1+A_{12}(-i\bar{\omega}_f)C_4]e^{-i\bar{\omega}_f t}=0\\ &[A_{21}(i\omega_f)C_1+A_{22}(i\omega_f)C_3]e^{i\omega_f t}+[A_{21}(-i\bar{\omega}_f)C_2+A_{22}(-i\bar{\omega}_f)C_4]e^{-i\bar{\omega}_f t}=0\end{aligned}\right\} \tag{28}$$

In order for equations (27) to be a solution of equations (26), equations (28) must be satisfied for each value of t. The coefficient of each time factor $e^{i\omega_f t}$ or $e^{-i\bar{\omega}_f t}$ must therefore separately vanish. Because each bracketed expression represents a complex quantity that vanishes, its complex conjugate also must vanish. The condition for a solution can therefore be expressed by the vanishing of the first bracketed terms and the complex conjugates of the second bracketed terms. Hence,

$$\left.\begin{aligned}A_{11}(i\omega_f)C_1+\Delta A_{11}(i\omega_f)\bar{C}_2+A_{12}(i\omega_f)C_3&=0\\ A_{21}(i\omega_f)C_1+A_{22}(i\omega_f)C_3&=0\\ \Delta\bar{A}_{11}(i\omega_f)C_1+\bar{A}_{11}(i\omega_f)\bar{C}_2+\bar{A}_{12}(i\omega_f)\bar{C}_4&=0\\ \bar{A}_{21}(i\omega_f)\bar{C}_2+\bar{A}_{22}(i\omega_f)\bar{C}_4&=0\end{aligned}\right\} \tag{29}$$

where $\bar{A}_{11}(i\omega_f)$ is the complex conjugate of $A_{11}(-i\bar{\omega}_f)$ and is obtained from $A_{11}(i\omega_f)$ by changing $i\omega$ to $-i\omega$ without changing $i\omega_f$. The characteristic equation giving the rotational speeds is the determinant of the coefficients of C_1, $\bar{C}_2$, C_3, and $\bar{C}_4$ equated to zero. With the second and third columns interchanged for symmetry, the determinant becomes

$$\begin{vmatrix}A_{11} & A_{12} & \Delta A_{11} & 0\\ A_{21} & A_{22} & 0 & 0\\ \Delta\bar{A}_{11} & 0 & \bar{A}_{11} & \bar{A}_{12}\\ 0 & 0 & \bar{A}_{21} & \bar{A}_{22}\end{vmatrix}=0 \tag{30}$$

The expanded form of this determinant is

$$(A_{11}A_{22}-A_{12}A_{21})(\bar{A}_{11}\bar{A}_{22}-\bar{A}_{12}\bar{A}_{21})-\Delta A_{11}\Delta\bar{A}_{11}A_{22}\bar{A}_{22}=0 \tag{31}$$

where

$$A_{11}=-\omega_f^2+i\omega_f\lambda_f+i\lambda_a(\omega_f-\omega)+\frac{K_f}{M}$$

$$\bar{A}_{11}=-\omega_f^2+i\omega_f\lambda_f+i\lambda_a(\omega_f+\omega)+\frac{K_f}{M}$$

$$\Delta A_{11}=\Delta\bar{A}_{11}=-\frac{\Delta m_f}{M}\omega_f^2+i\omega_f\Delta\lambda_f+\frac{\Delta K_f}{M}$$

$$A_{12}A_{21}=\overline{A}_{12}\overline{A}_{21}=\frac{\mu}{2\left(1+\frac{r^2}{b^2}\right)}\omega_f{}^4=\Lambda_3\omega_f{}^4$$

$$A_{22}=-(\omega_f-\omega)^2+i\lambda_\beta(\omega_f-\omega)+\omega^2\Lambda_1+\Lambda_2$$

$$\overline{A}_{22}=-(\omega_f+\omega)^2+i\lambda_\beta(\omega_f+\omega)+\omega^2\Lambda_1+\Lambda_2$$

The roots ω_f of this equation are the characteristic whirling speeds of the rotor.

For the case of isotropic supports,

$$\Delta A_{11}=0$$

and the equations of motion are satisfied by equations (27) with $C_2=C_4=0$.

The characteristic equation is then simply

$$A_{11}A_{22}-A_{12}A_{21}=0 \tag{32}$$

In a rotating coordinate system, the complex coordinates are z_a and θ_1, where

$$z_f=z_ae^{i\omega t}$$

$$\zeta_1=\theta_1e^{i\omega t}$$

Then

$$Dz_f=(Dz_a+i\omega z_a)e^{i\omega t}$$

$$D\zeta_1=(D\theta_1+i\omega\theta_1)e^{i\omega t}$$

If the whirling speed in rotating coordinates is represented by ω_a,

$$z_a=C_1e^{i\omega_a t}$$

$$\theta_1=C_2e^{i\omega_a t}$$

The characteristic equation is then obtained by substituting $\omega_a+\omega$ for ω_f:

$$A_{11}(\omega_a+\omega)A_{22}(\omega_a+\omega)-A_{12}(\omega_a+\omega)A_{21}(\omega_a+\omega)=0 \tag{33}$$

The characteristic equation can thus be stated in terms of a whirling speed in either the fixed or the rotating coordinate system.

METHOD OF APPLYING THEORY

APPLICATION NEGLECTING DAMPING

In plotting curves for use in applications of the theory, it is convenient to consider one of the pylon bending frequencies $\omega_r=\sqrt{K_x/M_x}$ as a reference frequency and to refer all other frequencies as well as the rotational speed ω to the reference frequency as unit. The number of independent parameters is thus reduced by 1. All quantities in equations (31) to (33) are then expressed nondimensionally.

The natural whirling speeds and the three types of vibration—ordinary, self excited, and shaft critical—can now be predicted from a study of the roots of equation (31) in which ω_f is considered a function of ω for fixed values of the other parameters.

The case of no damping will be considered first. Because equation (31) with damping terms omitted is of the fourth degree in $\omega_f{}^2$ and of only the second degree in ω^2, it may be solved conveniently by first choosing values of ω_f and then solving the equation for ω^2. Similar indirect methods can be used with equations (32) and (33). Special methods to be used when damping is included will be discussed later.

The meaning of equations (31) to (33) will be illustrated by examples. The real part of ω_f will be plotted against ω for selected values of the parameters Λ_1, Λ_2, Λ_3, and s. The simplest case is that in which the mass of the blades is so small that any force on the pylon due to blade motions is negligible. The pylon motions are then independent of the blade motions. This case is obtained by putting $\Lambda_3=0$. The characteristic equation (31), (32), or (33) then factors into expressions yielding straight lines and hyperbolas.

An example of a rotor with particular values of the parameters is plotted as long-dash lines in figure I–2. The horizontal straight lines correspond to pylon bending and the slanting hyperbolas correspond to hinge deflection. Each curve represents the trend of one of the real roots ω_f. As Λ_3 increases slightly from zero, the greatest changes in the curves occur in the vicinity of the intersections of the straight lines with the hyperbolas. Here each branch breaks away from the intersection and rejoins the other branch. At a gap, such as C in figure I–2, the number of real roots of the frequency equation is reduced by I–2. The missing roots are complex conjugate numbers, and one of them must have a negative imaginary part, which implies a self-excited vibration.

Consider the interpretation of figure I–2 as ω is gradually increased from zero. At zero rotational speed, the values of ω_f are the natural frequencies that could be excited as ordinary vibration by applied vibrating force. Positive and negative values occur in pairs of equal magnitude and correspond to linear vibration modes represented in complex notation as

$$z_f=c(e^{i\omega_f t}+e^{-i\omega_f t})$$

As ω increases from zero, the positive and negative values of ω_f no longer are equal in magnitude. The normal modes are therefore whirling motions with angular velocities equal to the plotted values of ω_f.

The shaft critical speed is the rotational speed at which $\omega_f=\omega$ and hence is given by the point A where a 45° line

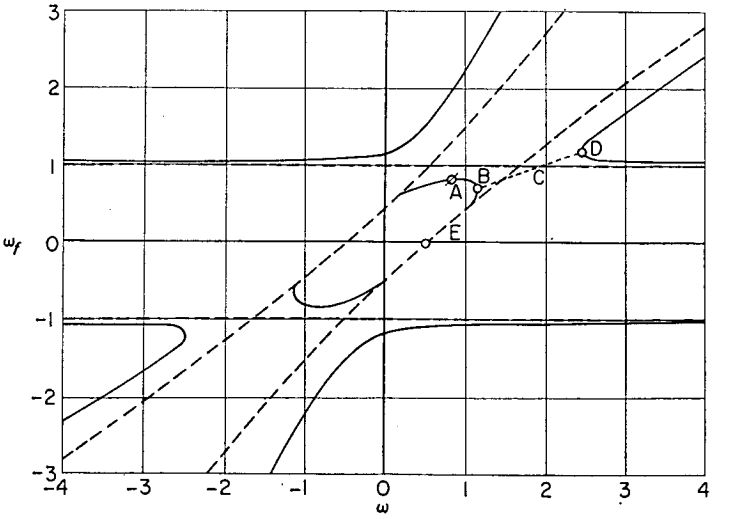


FIGURE I–2.—The effect of coupling between pylon and hinge motions.

through the origin intersects the ω_f-curve. This speed corresponds to the peak for vibrations excited by unbalance in the rotating system. As ω increases above the shaft critical speed, the modes of whirling are stable until, for the case of no damping, the value of ω_f becomes complex at the value of ω at which a vertical line is tangent to the plotted curve. This point B is the beginning of the self-excited range. At the point D, the motion again becomes stable. The real part of ω_f is plotted in the region C as a short-dash line. The complex roots in the region C have been calculated and plotted in figure I–3.

The point E, at which $\omega_f=0$, is of some interest. At this speed, a vibration of the blades could be excited by a steady force ($\omega_f=0$, $\omega_a=-\omega$), such as the force of gravity if the plane of the rotor is not horizontal.

Because the most important information to be obtained from the frequency equation is the critical value of ω for the shaft critical and self-excited vibrations, a set of charts that gives this information for a large variety of values of the physical parameters has been prepared. These charts are given in figures I–4 to I–6, which correspond to values of stiffness ratio $K_y/K_x=s$ of 1, ∞, and 0, respectively. The use of the charts is illustrated by a numerical example. Suppose the values of the parameters for a certain rotor are $\Lambda_1=0.07$, $\Lambda_2=0.22$, $\Lambda_3=0.1$, $s=1$, and $\omega_r=155$ cycles per minute. A straight line, such as AB in figure I–4, is first drawn to represent the function $\omega^2\Lambda_1+\Lambda_2$. This line intersects contours $\Lambda_3=0.1$ at $\omega^2=0.77$ for the shaft critical point and $\omega^2=1.6$ and 4.85 for the beginning and for the end of the self-excited range, respectively. With a reference frequency of 155 cycles per minute, these values correspond to actual rotational speeds of 136, 196, and 342 rpm.

All possible values of Λ_1, Λ_2, and Λ_3 are thus covered by suitably changing the straight line AB. The general effect of the stiffness ratio s is not large; any case can therefore be estimated with a fair degree of accuracy by use of figures I–4 to I–6.

POSSIBILITY OF AVOIDING OCCURRENCE OF VIBRATION

Figures I–4 to I–6 can also be used for the inverse problem of finding the values of the parameters that are required to obtain given values of critical rotational speed. These figures show that to eliminate entirely the self-excited instability requires that Λ_1 be equal to or greater than 1.

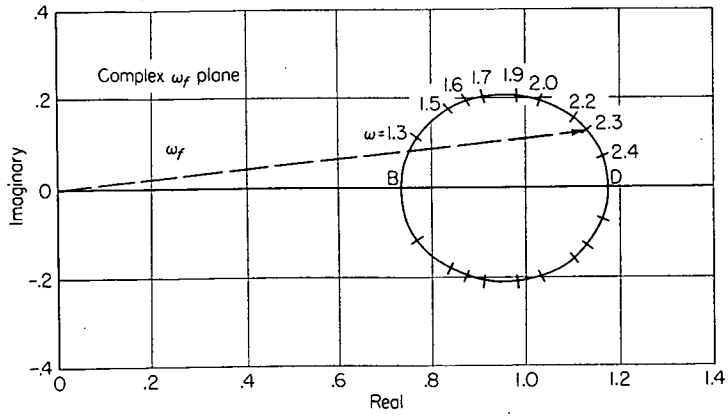


FIGURE I–3.—The complex frequency in the unstable range for $\Lambda_1=0.07$, $\Lambda_2=0.22$, $\Lambda_3=0.1$, and $s=1$.

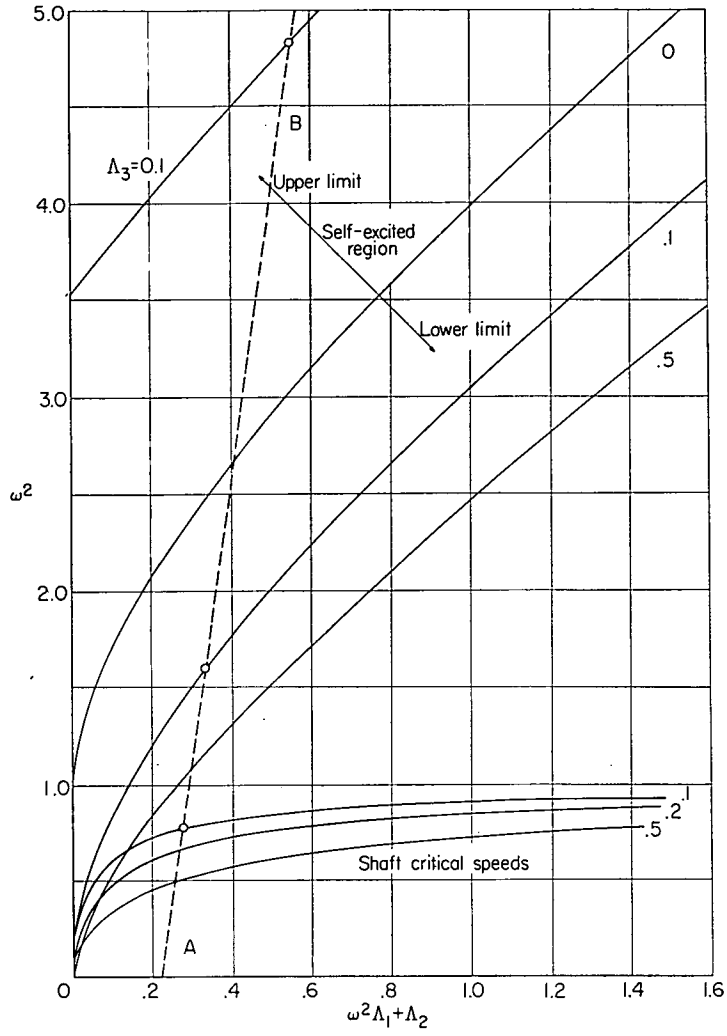


FIGURE I–4.—Stability chart for $s=1$.

The shaft critical instability can be entirely eliminated only with a value of Λ_1 in a small range near 4 and with $s=\infty$ or $s=0$. These values of Λ_1 differ radically from present designs in which a typical value is 0.07.

The satisfactory requirement of keeping the instabilities outside the operating range of rotational speed is found by first picking a reasonable value of the pylon frequency $\sqrt{K_x/M_x}$ to fix the scale unit for ω and by then observing the combinations of Λ_1 and Λ_2 that can be used to avoid the critical Λ_3-contours.

EFFECT OF DAMPING

The effect of damping has been included in equation (31) through the parameters λ_f, $\Delta\lambda_f$, λ_a, and λ_β. A method of computation similar to that used in flutter theory appears preferable to attempting to solve the equation directly for ω_f. The beginning and the end of an unstable range can be found by the following method: At a limit point between a stable and an unstable speed range, the value of ω_f is real. Equation (31) is first separated into real and imaginary parts with ω_f considered real. Each part is considered a functional relation between ω_f and ω and is plotted for a given set of values of the parameters. The intersections of the real and the imaginary equations give the rotor speeds and frequencies corresponding to the beginning and the end of the unstable

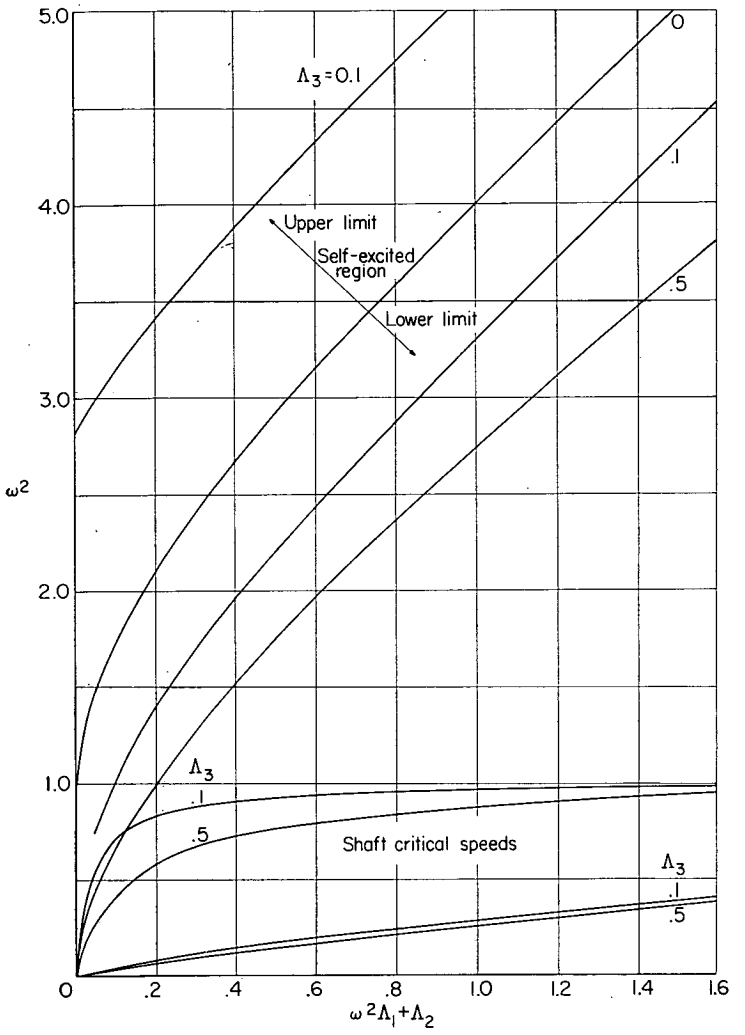


FIGURE I–5.—Stability chart for $s=\infty$.

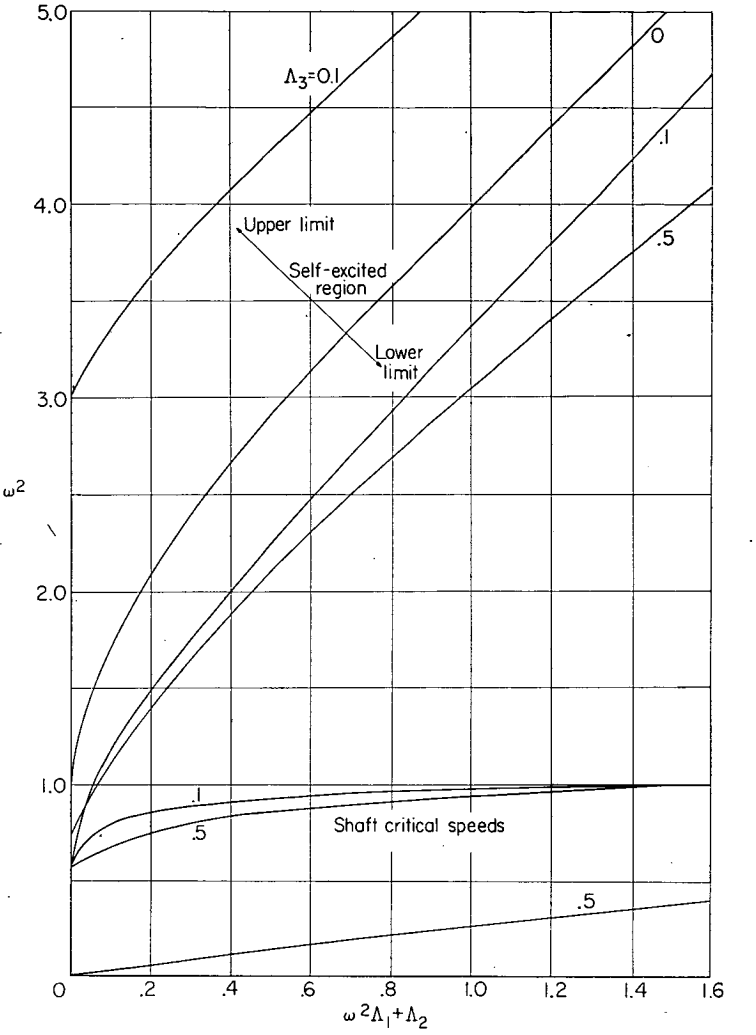


FIGURE I–6.—Stability chart for $s=0$.

ranges. In the computations, it is preferable to choose values of ω_f and to solve the equations for the corresponding values of ω.

The explicit form for computation in the simplest case of isotropic supports, with damping in the pylon and in the hinges but not in the rotating shaft ($\lambda_a=0$), is obtained from equation (32) rearranged as follows:

For the real equation

$$\omega^2-2B_R\omega+C_R=0 \qquad (34)$$

$$\omega=B_R\pm\sqrt{B_R^2-C_R}$$

where

$$B_R=\frac{\omega_f}{1-\Lambda_1}\left[1+\frac{\lambda_f\lambda_\beta}{2\left(-\omega_f^2+\frac{K_f}{M}\right)}\right]$$

and

$$C_R=-\frac{\omega_f^2}{1-\Lambda_1}\left(-1+\frac{\Lambda_2}{\omega_f^2}-\frac{\Lambda_3\omega_f^2+\lambda_f\lambda_\beta}{-\omega_f^2+\frac{K_f}{M}}\right)$$

For the imaginary equation

$$\omega^2-2B_I\omega+C_I=0 \qquad (35)$$

where

$$B_I=\frac{1}{1-\Lambda_1}\left[\omega_f-\frac{\lambda_\beta}{2\lambda_f\omega_f}\left(-\omega_f^2+\frac{K_f}{M}\right)\right]$$

and

$$C_I=-\frac{1}{1-\Lambda_1}\left[\frac{\lambda_\beta}{\lambda_f}\left(-\omega_f^2+\frac{K_f}{M}\right)+(-\omega_f^2+\Lambda_2)\right]$$

The real and imaginary equations for the most general case of equation (31) can be written, respectively, as follows:

$$\lambda_a^2(1-\Lambda_1)^2\omega^6+[R_1(1-\Lambda_1)^2+\lambda_a^2R_3]\omega^4+(R_1R_3-I_1I_3+\lambda_a^2R_2-R_5)\omega^2+R_1R_2-I_1I_2-R_4+\Lambda_3^2\omega_f^8=0 \qquad (36)$$

$$[I_1(1-\Lambda_1)^2+\lambda_a^2I_3]\omega^4+(R_1I_3+R_3I_1+\lambda_a^2I_2-I_5)\omega^2+R_1I_2+R_2I_1-I_4=0 \qquad (37)$$

where

$$R_1=\frac{M_xM_y}{M^2}\left(-\omega_f^2+\frac{K_x}{M_x}\right)\left(-\omega_f^2+\frac{K_y}{M_y}\right)-\omega_f^2\left(\lambda_x\frac{M_x}{M}+\lambda_a\right)\left(\lambda_y\frac{M_y}{M}+\lambda_a\right)$$

$$I_1=\frac{M_x}{M}\left(-\omega_f^2+\frac{K_x}{M_x}\right)\omega_f\left(\lambda_y\frac{M_y}{M}+\lambda_a\right)+\frac{M_y}{M}\left(-\omega_f^2+\frac{K_y}{M_y}\right)\omega_f\left(\lambda_x\frac{M_x}{M}+\lambda_a\right)$$

$$R_2=(-\omega_f^2+\Lambda_2)^2-\omega_f^2\lambda_\beta^2$$

$$I_2=2(-\omega_f^2+\Lambda_2)\omega_f\lambda_\beta$$

$$R_3=-2(1-\Lambda_1)(-\omega_f^2+\Lambda_2)-4\omega_f^2+\lambda_\beta^2$$

$$I_3=-2(1-\Lambda_1)\omega_f\lambda_\beta+4\omega_f\lambda_\beta$$

$$R_4=2\omega_f^4\Lambda_3\left[\left(-\omega_f^2+\frac{K_f}{M}\right)(-\omega_f^2+\Lambda_2)-\omega_f^2(\lambda_f+\lambda_a)\lambda_\beta\right]$$

$$I_4=2\omega_f^4\Lambda_3\left[\left(-\omega_f^2+\frac{K_f}{M}\right)\omega_f\lambda_\beta+\omega_f(\lambda_f+\lambda_a)(-\omega_f^2+\Lambda_2)\right]$$

$$R_5=2\omega_f^4\Lambda_3\left[-(1-\Lambda_1)\left(-\omega_f^2+\frac{K_f}{M}\right)-\lambda_a\lambda_\beta\right]$$

$$I_5=2\omega_f^4\Lambda_3[-(1-\Lambda_1)\omega_f(\lambda_f+\lambda_a)-2\lambda_a\omega_f]$$

Examples of calculated cases with damping are shown in figures I–7 to I–9. The presence of small amounts of damping in both the pylon and the hinge degrees of freedom does not greatly change the predictions that would be made from the equations with no damping. The plot of the real equation is practically the same as the plot obtained when damping is neglected. The intersections of the curves of the imaginary and the real equations with any reasonable value of λ_f/λ_β are near the points that would be considered the limits of the unstable range if damping were neglected. Increasing the amount of damping decreases the gap between the limits of stability until the unstable range is finally eliminated. An approximate solution for the amount of damping required to eliminate the self-excited instability is obtained by requiring that the damping be at least large enough to make the curve of the real equation pass through the point where $\omega_f=1$ and ω is the value given by the equation

$$1=\omega-\sqrt{\omega^2\Lambda_1+\Lambda_2}$$

The values required in the case of $s=\infty$ have been computed and plotted in figure I–10. The elimination of self-excited vibration by damping thus looks promising and merits further study with reference to specific application.

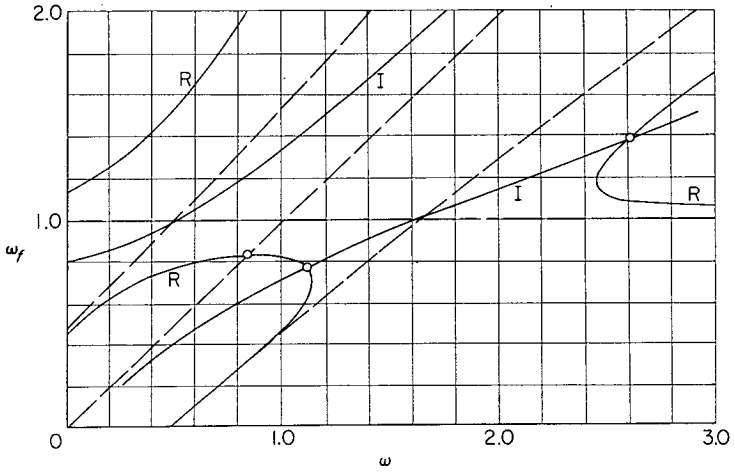


FIGURE I–7.—Plot of real and imaginary equations for a typical case. $s=1$; $\Lambda_1=0.07$; $\Lambda_2=0.22$; and $\Lambda_3=0.198$.

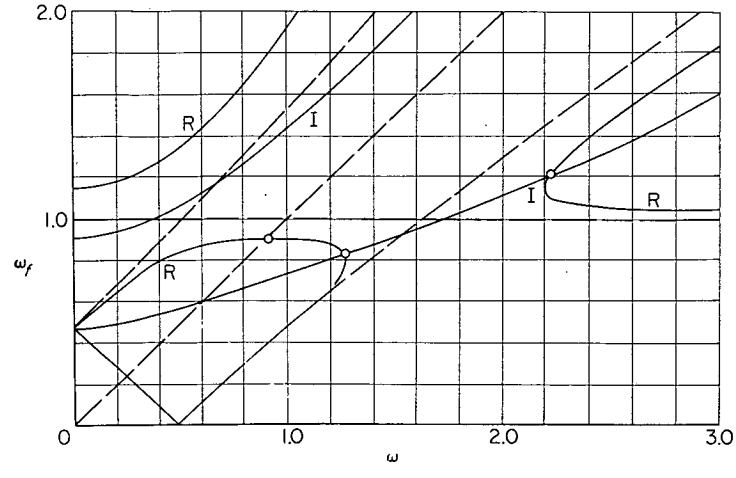


FIGURE I–8.—Plot of real and imaginary equations for case of $s=\infty$, $\Lambda_1=0.07$, $\Lambda_2=0.22$, and $\Lambda=0.198$.

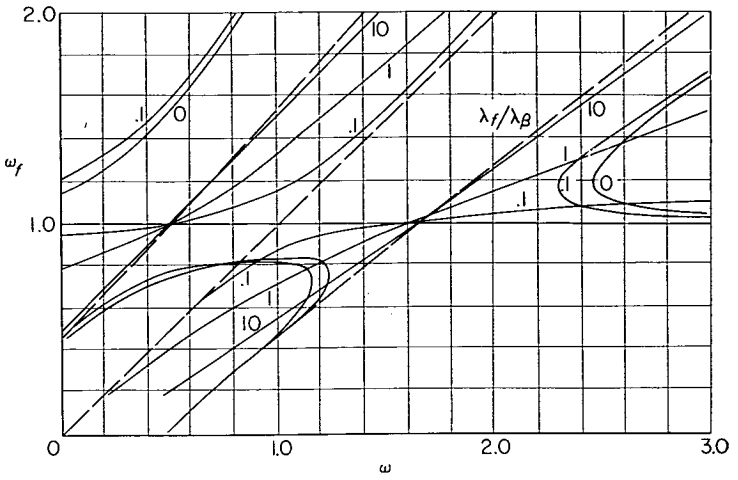


FIGURE I–9.—Effect of damping for case of $s=1$, $\Lambda_1=0.07$, $\Lambda_2=0.22$, and $\Lambda_3=0.198$.

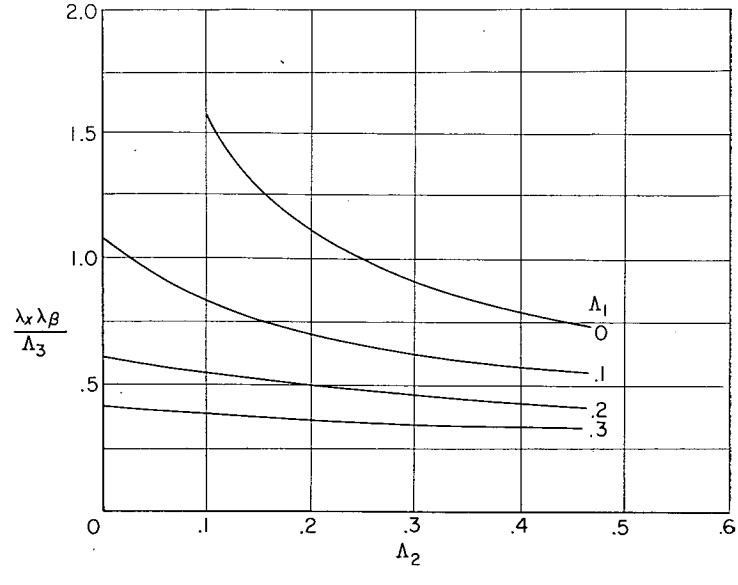


FIGURE I–10.—Damping required to eliminate self-excited oscillation for $s=\infty$.

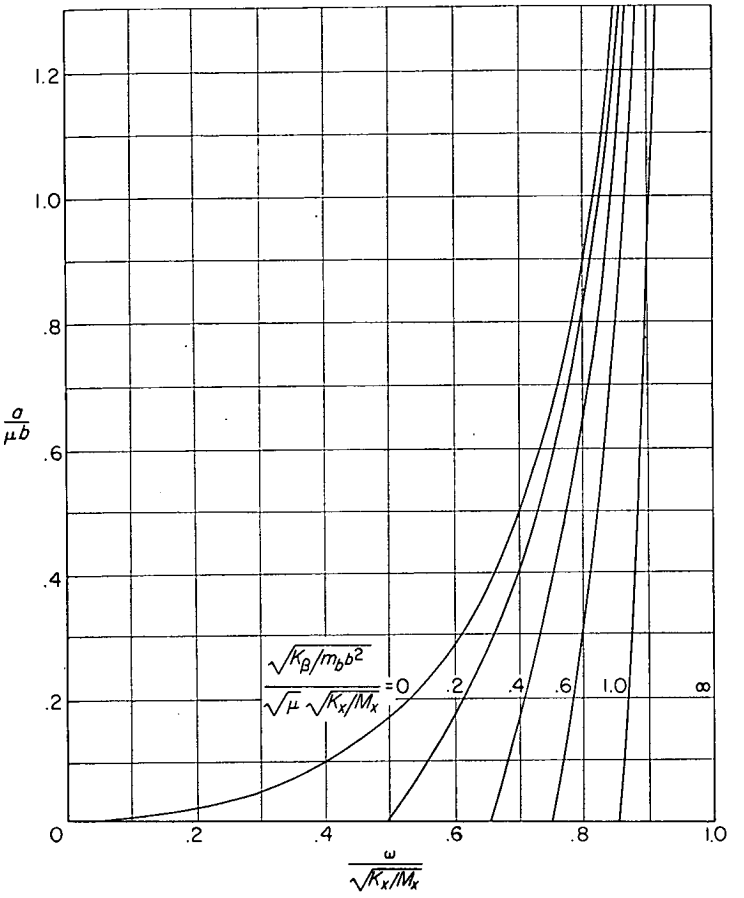


FIGURE I–11.—Shaft critical speeds for $s=1$.

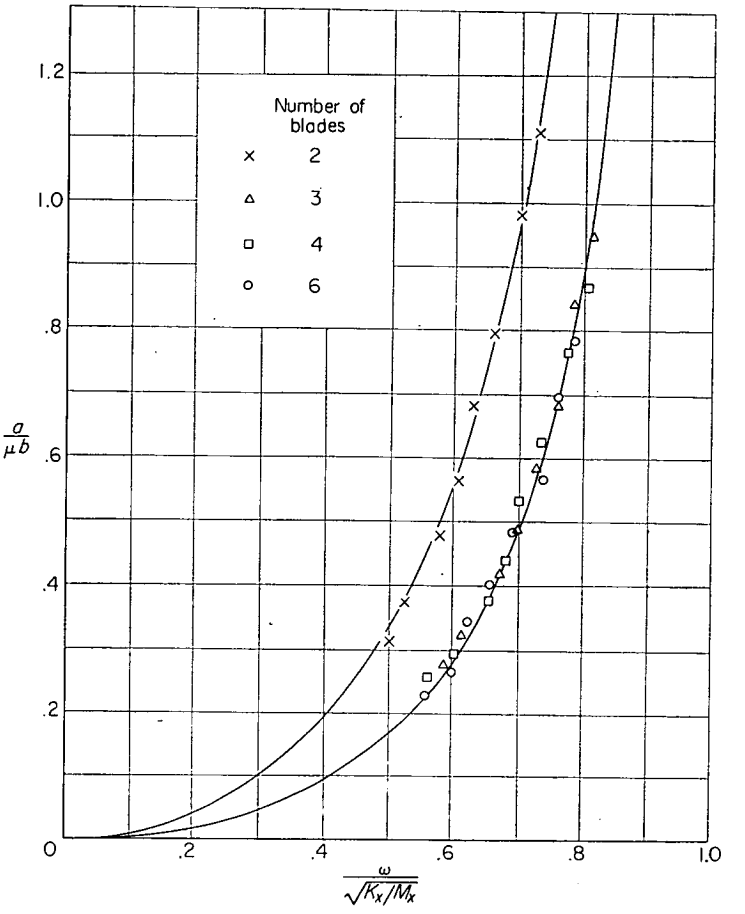


FIGURE I–12.—Experimental critical speeds on small models.

LIMITATIONS AND FURTHER DEVELOPMENTS OF THE THEORY

POLAR SYMMETRY

An important idea in the rotor vibration theory is the concept of polar symmetry. This concept implies the absence of a preferred direction in the plane of the rotor. A rotor of three or more equal blades has polar symmetry. A rotor of two blades or one with unequal centering springs does not have polar symmetry. A pylon for which $K_x=K_y$, $B_x=B_y$, and $m_x=m_y$ has polar symmetry. The possibility of solving the rotor vibration problem in terms of exponential or trigonometric functions depends upon the existence of polar symmetry in the rotating parts or in the nonrotating parts or in both. The general case of no polar symmetry would lead to Mathieu functions or something similar.

TWO BLADES

A brief comparison between the two-blade and the general case is presented herein. Polar symmetry of the pylon is assumed. The shaft critical speed is obtained by substituting $\omega_a=0$ in the characteristic equation as expressed in a rotating coordinate system. For one or two blades, the equation obtained is

$$\left[\left(-\omega^2+\frac{K_f}{M}\right)\left(\omega^2\frac{a}{b}+\frac{K_\beta}{m_b b^2}\right)-\mu\omega^4\right]\left(-\omega^2+\frac{K_f}{M}\right)=0 \qquad (38)$$

The first bracketed factor gives the beginning of a self-excited range and the second factor gives the end of the range.

Equation (38) can be compared with the following equation for the shaft critical speed of a rotor with three or more equal blades and polar symmetry:

$$\left(-\omega^2+\frac{K_f}{M}\right)\left(\omega^2\frac{a}{b}+\frac{K_\beta}{m_b b^2}\right)-\frac{\mu}{2}\omega^4=0 \qquad (39)$$

A useful chart based on equation (39) is given in figure I–11; some experimental results of tests of a simple model are given in figure I–12. These tests demonstrate the essential difference between the two-blade and the general case.

LANGLEY AERONAUTICAL LABORATORY,
NATIONAL ADVISORY COMMITTEE FOR AERONAUTICS,
LANGLEY FIELD, VA., *August 24, 1956.*

REFERENCES

1. Den Hartog, J. P.: Mechanical Vibrations. McGraw-Hill Book Co., Inc., 1934, pp. 237–328.
2. Lamb, Horace: Higher Mechanics. Second ed., Cambridge Univ. Press, 1929, pp. 200–201, 241–255.
3. Lamb, Horace: Hydrodynamics. Sixth ed., Cambridge Univ. Press, 1932, pp. 307–319, 562–571.
4. Prewitt, R. H., and Wagner, R. A.: Frequency and Vibration Problems of Rotors. Jour. Aero. Sci., vol. 7, no. 10, Aug. 1940, pp. 444–450.

CHAPTER II

THEORY OF MECHANICAL OSCILLATIONS OF ROTORS WITH TWO HINGED BLADES

By ARNOLD M. FEINGOLD

SUMMARY

The mechanical stability of a rotor having two vertically hinged blades mounted upon symmetrical supports, that is, of equal stiffness and mass in all horizontal directions, is investigated and reported herein. The frequency equation is derived and shows the existence, in general, of two ranges of rotational speeds at which instability occurs. The lower region of instability is bounded by two shaft critical speeds. At rotor speeds within this region, self-excited divergence of the rotor takes place analogous to the instability exhibited by a rotating shaft that is elliptical in cross section. Within the second instability range, the rotor system undergoes self-excited oscillations. Charts are presented giving the boundary points of both instability regions for a large variety of values of the physical parameters. The effect of damping is also included in the analysis.

INTRODUCTION

In chapter I, Coleman gives an analytical study of the mechanical stability of a rotor having three or more vertically hinged blades, mounted on flexible supports. It was shown that, in addition to the usual shaft critical speeds, self-excited vibrations occurred over a range of rotational speeds. Experiments with rotary-wing aircraft have confirmed the soundness of the analysis.

The present chapter is an investigation of the stability of the two-blade rotor mounted on symmetrical supports. As will be shown later, the results differ from those for a three-blade rotor. The reason for the different behavior lies in the inherent asymmetry of a rotor with only two blades. Motion of the center of mass of the blades of a two-blade rotor with respect to the rotor hub, due to small hinge deflections of the blades, must be normal to the line of the blades. This restraint, which does not appear in a rotor of three or more blades, results in the rotor system having different dynamic properties along and normal to the line of the blades. Therefore, with supports that have equal stiffness and mass in all directions attached to a two-blade rotor, two principal vibration axes of the rotor hub can still be distinguished. No preferred vibration axes can be distinguished for a three-blade rotor mounted on symmetrical supports. This distinction shows up physically in the shape of the vibration modes. Whereas a three-blade rotor whirls in a circle, a two blade rotor whirls in an ellipse, of which the principal axes are along and normal to the line of the rotor blades.

A two-blade rotor can be expected to show, in addition to some features of a three-blade rotor, some of the characteristics of a rotating shaft that is elliptical in cross section. Such a shaft, mounted on symmetrical bearings, is known to have two critical speeds, which correspond to each of the two principal stiffnesses. (See, for example, ref. 1.) For all rotational speeds between the critical speeds, the shaft is unstable and diverges. It will be shown that an exactly similar phenomenon exists for a two-blade rotor. The existence of this region of instability for a two-blade rotor is predicted in chapter I, in which the formula for the shaft critical speeds bounding this instability range is given. In addition to this region of instability, a second range of instability analogous to that exhibited by a three-blade rotor is also present.

Only the case of symmetrical supports is analyzed in the present report. In the case of asymmetric supports, the equations of motion are linear differential equations that are difficult to solve because the coefficients vary periodically with the time (Mathieu type). Similar equations are obtained in the problem of a rotating elliptical shaft mounted on asymmetric bearings. (See ref. 1.)

SYMBOLS

a	radial position of vertical hinge
b	distance from vertical hinge to center of mass of blade
B	damping force per unit velocity of rotor-hub displacement
B_β	damping force per unit angular velocity of blade displacement about hinge
D	time-derivative operator, d/dt
F	dissipation function
I	moment of inertia of blade about hinge, $m_b b^2\left(1+\frac{r^2}{b^2}\right)$
K	spring constant of rotor-hub displacement
K_β	spring constant of blade self-centering spring
m	effective mass of pylon
m_b	effective mass of rotor blade
M	total effective mass of blades and pylon, $m+2m_b$
r	radius of gyration of blade about its center of mass
s	arbitrary parameter
t	time
T	kinetic energy
T_1, T_2	kinetic energies of rotor blades
T_s	kinetic energy of rotor hub
V	potential energy
x, y	displacements of rotor hub in rotating coordinate system

X_a, Y_a rotating coordinate axes
X_f, Y_f fixed coordinate axes
x_o, y_o values of x and y when $t=0$
x_1, y_1 displacement of first rotor blade in fixed coordinate system
x_2, y_2 displacement of second rotor blade in fixed coordinate system
β_1, β_2 angular displacements of blades about their hinges

$$\theta_0=\frac{b(\beta_1+\beta_2)}{2}$$

$$\theta_1=\frac{b(\beta_1-\beta_2)}{2}$$

θ_{1_o} value of θ_1 when $t=0$

$$\lambda=\frac{B}{M\omega_r}$$

$$\lambda_\beta=\frac{B_\beta}{I\omega_r}$$

$$\Lambda_1=\frac{a}{b\left(1+\frac{r^2}{b^2}\right)}$$

$$\Lambda_2=\frac{K_\beta}{I\omega_r{}^2}$$

$$\Lambda_3=\frac{m_b}{M\left(1+\frac{r^2}{b^2}\right)}$$

ω angular velocity of rotor (the dimensionless ratio ω/ω_r is called ω in applications)
ω_a natural frequency of rotor system observed in rotating coordinate system (used in nondimensional form in applications)
ω_f natural frequency of rotor system in fixed coordinate system (nondimensional in applications)
ω_r reference frequency, $\sqrt{K/M}$

MATHEMATICAL ANALYSIS

Four degrees of freedom of the system are considered—horizontal deflection of the rotor hub in the x- and y-directions, and hinge deflections β_1 and β_2 of the blades in the horizontal plane of the rotor hub. The rotor is assumed to rotate at a constant velocity ω.

Deflection of the rotor hub may be due either to the bending of a flexible pylon or to a rocking of the rotor craft upon its landing gear. Ground-resonance vibrations usually involve landing-gear flexibility. The mathematical treatment is the same in both cases, but the values of several of the physical parameters will depend upon which mode is being investigated. In this chapter, the terms "rotor supports" and "pylon" will be used interchangeably to denote the nonrotating structure coupled with the rotor blades.

The mathematical treatment herein differs from that in chapter I, in which are used the complex notation and the notion of "whirling speeds," that is, directional frequencies resulting from the use of complex numbers. Although the method of chapter I is valuable for systems, such as the three-blade rotor on symmetrical supports, which have circular modes of vibration, it offers little advantage for the present problem, in which the rotor performs elliptical motion. Rectangular coordinates accordingly are used in the present report and frequencies are used instead of whirling speeds. In comparing the results of the present report with those of chapter I, care should be taken to distinguish between frequencies and whirling speeds. Whirling speeds have directional significance; whereas frequencies are essentially positive quantities and do not give any immediate information concerning the direction of whirl of the vibration.

The equations of motion are set up in a coordinate system rotating at the velocity ω. Let the deflection of the rotor hub be represented by x and y in rotating coordinates. (See fig. II–1 in which the intersection of the coordinate axes represents the undisturbed position of the rotor hub.) The disturbed positions of the two blades in fixed coordinates are

$$x_1=(x+a+b\cos\beta_1)\cos\omega t-(y+b\sin\beta_1)\sin\omega t$$

$$y_1=(y+b\sin\beta_1)\cos\omega t+(x+a+b\cos\beta_1)\sin\omega t$$

and

$$x_2=(x-a-b\cos\beta_2)\cos\omega t-(y-b\sin\beta_2)\sin\omega t$$

$$y_2=(y-b\sin\beta_2)\cos\omega t+(x-a-b\cos\beta_2)\sin\omega t$$

The kinetic energies of the two rotor blades are

$$T_1=\frac{1}{2}m_b\left[\dot{x}_1{}^2+\dot{y}_1{}^2+r^2(\omega+\dot{\beta}_1)^2\right]$$

and

$$T_2=\frac{1}{2}m_b\left[\dot{x}_2{}^2+\dot{y}_2{}^2+r^2(\omega+\dot{\beta}_2)^2\right]$$

The kinetic energy of the pylon is

$$T_s=\frac{1}{2}m\left[\dot{x}^2+\dot{y}^2+\omega^2(x^2+y^2)-2\omega(\dot{x}y-x\dot{y})\right]$$

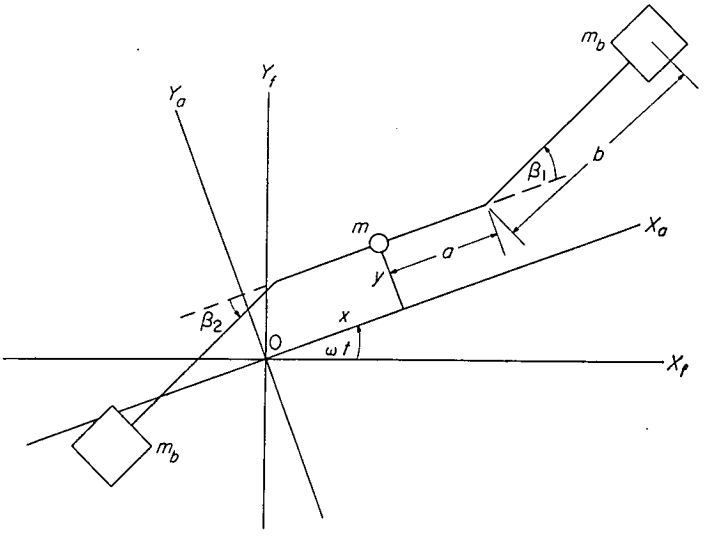


FIGURE II–1.—Simplified mechanical system representing rotor.

Because only small displacements from the equilibrium position are considered, the trigonometric expressions containing β_1 and β_2 may be expanded as power series and only the terms that lead to quadratic terms in the energy expressions need be retained. Thus

$$\sin \beta_1=\beta_1$$

$$\cos \beta_1=1-\frac{\beta_1^2}{2}$$

and

$$\sin \beta_2=\beta_2$$

$$\cos \beta_2=1-\frac{\beta_2^2}{2}$$

New variables introduced to replace β_1 and β_2 are

$$\theta_0=\frac{b}{2}(\beta_1+\beta_2)$$

$$\theta_1=\frac{b}{2}(\beta_1-\beta_2)$$

where θ_1 represents the shift, due to hinge motion, of the center of mass of the two blades with respect to the rotor hub. The introduction of θ_0 and θ_1 results in a partial decoupling of the equations of motion.

The total kinetic energy of the system is

$$T=T_1+T_2+T_s$$

Only the quadratic terms will be retained in the kinetic-energy expression, because the terms of lower degree vanish in the Lagrange equations of motion. Then

$$T=\frac{1}{2}M[\dot{x}^2+\dot{y}^2+\omega^2(x^2+y^2)-2\omega(\dot{x}y-x\dot{y})]+m_b\left[2\dot{y}\dot{\theta}_1+2\omega^2 y\theta_1+2\omega x\dot{\theta}_1-2\omega\dot{x}\theta_1+\left(1+\frac{r^2}{b^2}\right)(\dot{\theta}_0^2+\dot{\theta}_1^2)-\omega^2\frac{a}{b}(\theta_0^2+\theta_1^2)\right]$$

The potential energy of the system is

$$V=\frac{1}{2}K(x^2+y^2)+\frac{K_\beta}{2}(\beta_1^2+\beta_2^2)$$

$$=\frac{1}{2}K(x^2+y^2)+\frac{K_\beta}{b^2}(\theta_0^2+\theta_1^2)$$

Two types of damping of the rotor system are assumed to exist: (1) damping in the rotor supports, which is proportional to velocity displacements of the rotor hub in a fixed coordinate system, and (2) damping in the blade hinges. The dissipation function F then becomes

$$F=\frac{1}{2}B[\dot{x}^2+\dot{y}^2+\omega^2(x^2+y^2)-2\omega(\dot{x}y-x\dot{y})]+\frac{B_\beta}{b^2}(\dot{\theta}_0^2+\dot{\theta}_1^2)$$

where B is the damping force per unit velocity of rotor-hub displacement and B_β is the damping force per unit velocity of a rotor-blade displacement about the blade hinge.

The Lagrange equation of motion for the variable x is

$$\frac{d}{dt}\left(\frac{\partial T}{\partial \dot{x}}\right)-\frac{\partial T}{\partial x}+\frac{\partial V}{\partial x}+\frac{\partial F}{\partial \dot{x}}=0$$

The use of similar expressions for y, θ_0, and θ_1 lead to the following equations of motion:

$$\left(D^2-\omega^2+\frac{B}{M}D+\frac{K}{M}\right)x-\frac{4m_b}{M}\omega D\theta_1-\left(2\omega D+\frac{B}{M}\omega\right)y=0 \quad (1)$$

$$2\omega Dx+\left[\left(1+\frac{r^2}{b^2}\right)D^2+\frac{B_\beta}{m_b b^2}D+\frac{K_\beta}{m_b b^2}+\frac{a}{b}\omega^2\right]\theta_1+(D^2-\omega^2)y=0 \quad (2)$$

$$\left(2\omega D+\frac{B}{M}\omega\right)x+\frac{2m_b}{M}(D^2-\omega^2)\theta_1+\left(D^2-\omega^2+\frac{B}{M}D+\frac{K}{M}\right)y=0 \quad (3)$$

$$\left[\left(1+\frac{r^2}{b^2}\right)D^2+\frac{B_\beta}{m_b b^2}D+\omega^2\frac{a}{b}+\frac{K_\beta}{m_b b^2}\right]\theta_0=0 \quad (4)$$

where

$$D=\frac{d}{dt} \qquad D^2=\frac{d^2}{dt^2}$$

Equation (4) can be solved independently of the others because it is an equation in only one variable θ_0. Equation (4), which also was obtained in the study of the three-blade rotor (chapter I), represents blade motion with the blades moving in phase, uncoupled with pylon motion. Motion in this mode is damped and does not lead to instability.

Assuming solutions of the form

$$\left.\begin{aligned} x&=x_o e^{i\omega_a t}\\ y&=y_o e^{i\omega_a t}\\ \theta_1&=\theta_{1_o} e^{i\omega_a t}\end{aligned}\right\} \quad (5)$$

and substituting these solutions in equations (1) to (3) gives the characteristic or frequency equation

$$\begin{vmatrix} -\omega_a^2-\omega^2+i\lambda\omega_a+1 & 4\Lambda_3\omega\omega_a & 2\omega\omega_a-i\lambda\omega \\ 2\omega\omega_a & -\omega_a^2+i\lambda_\beta\omega_a+\Lambda_2+\Lambda_1\omega^2 & -\omega_a^2-\omega^2 \\ 2\omega\omega_a-i\lambda\omega & -2\Lambda_3(\omega_a^2+\omega^2) & -\omega_a^2-\omega^2+i\lambda\omega_a+1 \end{vmatrix}=0 \quad (6)$$

where the nondimensional parameters

$$\Lambda_1=\frac{a}{b\left(1+\frac{r^2}{b^2}\right)}$$

$$\Lambda_2=\frac{K_\beta}{I\omega_r^2}$$

$$\Lambda_3=\frac{m_b}{M\left(1+\frac{r^2}{b^2}\right)}$$

$$\lambda=\frac{B}{M\omega_r}$$

$$\lambda_\beta=\frac{B_\beta}{I\omega_r}$$

have been introduced, and the rotational velocity ω and the frequency ω_a have also been made nondimensional by using $\omega_r=\sqrt{K/M}$ as reference frequency.

The frequency ω_a generally is a complex number, of which the real part is the frequency of the vibration and the imaginary part determines the rate of damping of the vibration. If the imaginary part of ω_a is negative, the vibration increases in amplitude with time and the rotor is unstable.

DISCUSSION OF FREQUENCY EQUATION

CASE OF ZERO DAMPING

If the damping parameters λ and λ_β are neglected, the frequency equation (6) may be expanded to

$$2\Lambda_3(\omega^2+\omega_a{}^2-1)+[4\omega^2\omega_a{}^2-(\omega^2+\omega_a{}^2-1)^2][-2\Lambda_3(\omega^2+\omega_a{}^2+1)+\omega_a{}^2-\Lambda_2-\Lambda_1\omega^2]=0 \qquad (7)$$

where ω_a is the natural frequency of the rotor system in a coordinate system rotating with the rotor. (Although equation (7) is a cubic equation in both ω^2 and $\omega_a{}^2$, rectangular hyperbolas of the form $\omega_a{}^2=\omega^2+s$, where s is an arbitrary parameter, intersect equation (7) at only two values of ω^2. For purposes of computation, therefore, equation (7) can be reduced to a quadratic equation in ω^2 by replacing $\omega_a{}^2$ with ω^2+s.)

The solutions for zero damping (eq. (5)) represent motion of the pylon in an ellipse expressed relative to the rotating coordinate axes. In fixed coordinates, the pylon would move in an ellipse precessing at the velocity ω. This motion can be resolved into simultaneous circular motion at the two frequencies $|\omega+\omega_a|$ and $|\omega-\omega_a|$, in which the vertical lines indicate that the quantity inside is to be considered positive. If the pylon is subjected to a harmonic force in the fixed coordinate system of frequency ω_f, resonance will occur at each of the frequencies

$$\omega_f=|\omega\pm\omega_a|$$

The frequency ω_f will be referred to as the natural frequency of the rotor system in fixed coordinates.

The graph of the frequency equation (7) for a typical set of values of the parameters is given in figure II–2 in rotating coordinates and in figure II–3 in fixed coordinates. For zero coupling between the blades and rotor hub—that is, when Λ_3 equals zero—equation (7) factors into straight lines and a hyperbola, which are shown as long-dash lines in figures II–2 and II–3. The straight lines represent hub motion and the hyperbola represents blade motion. A small increase in Λ_3 results in a breaking away of the curves at their intersections to form two self-excited regions. It is interesting to compare figure II–3 with figure II–4, which is the graph of the natural frequencies of a three-blade rotor having the same values of Λ_1, Λ_2, and Λ_3.

The shaft critical speeds, or natural frequencies that would be in resonance with an unbalance in the rotor system, are found by putting $\omega_a=0$ in equation (7). Figure II–2 shows two such speeds, at points A and B (shown also in fig. II–3), that bound a region in which ω_a is a pure imaginary number. If ω_a is a complex root of the characteristic

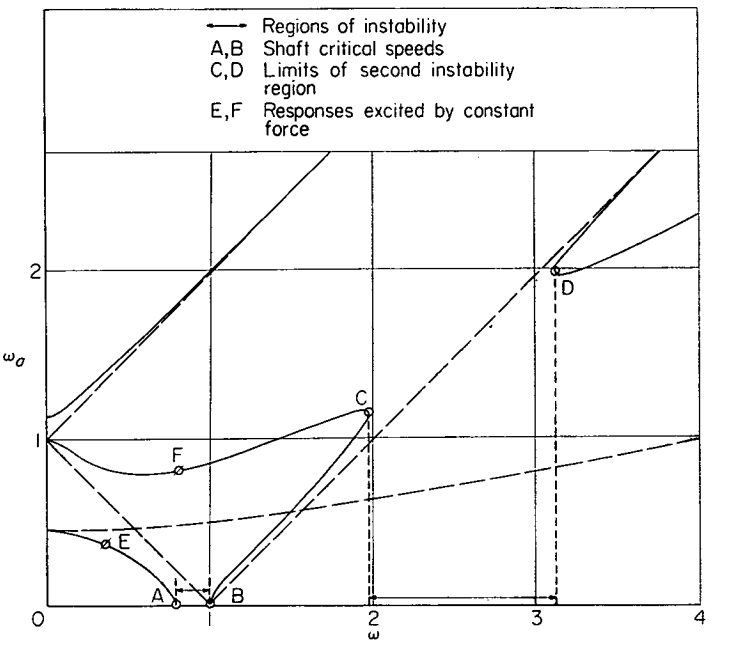


FIGURE II–2.—Natural frequencies of a two-blade rotor in rotating coordinates for case of $\Lambda_1=0.05$, $\Lambda_2=0.20$, and $\Lambda_3=0.10$.

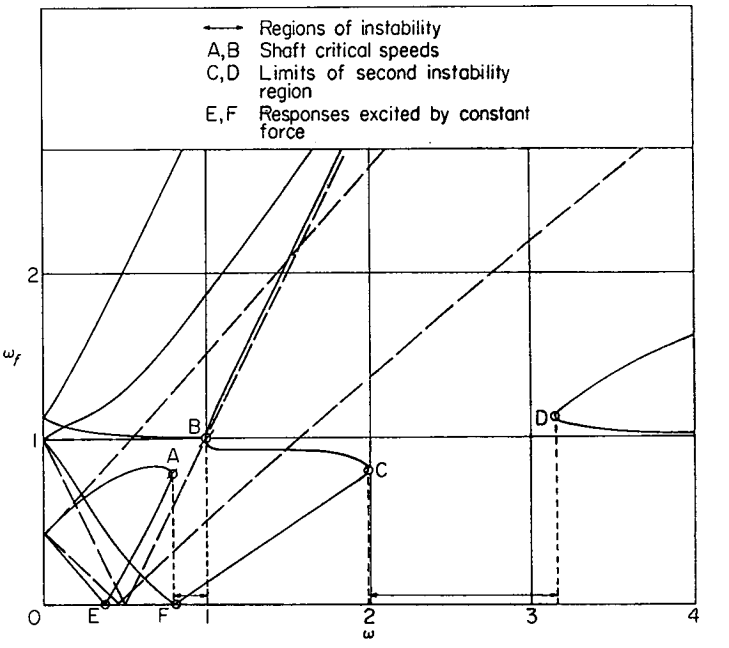


FIGURE II–3.—Natural frequencies of a two-blade rotor in fixed coordinates for case of $\Lambda_1=0.05$, $\Lambda_2=0.20$, and $\Lambda_3=0.10$.

equation, the complex conjugate of ω_a will also be a root and one of the two roots will have a negative imaginary part implying instability. The rotor system will thus be unstable for all rotational speeds between the two shaft critical speeds. Because ω_a is a pure imaginary number in this region, the frequency of the resultant self-excited vibration is zero in a rotating coordinate system—similar to the shaft critical speeds—and will appear as a self-excited divergence of the rotor.

The equation of the shaft critical speeds is

$$[(1-\omega^2)(\Lambda_2+\Lambda_1\omega^2)-2\Lambda_3\omega^4](1-\omega^2)=0 \qquad (8)$$

The first factor gives the lower shaft critical speed. The

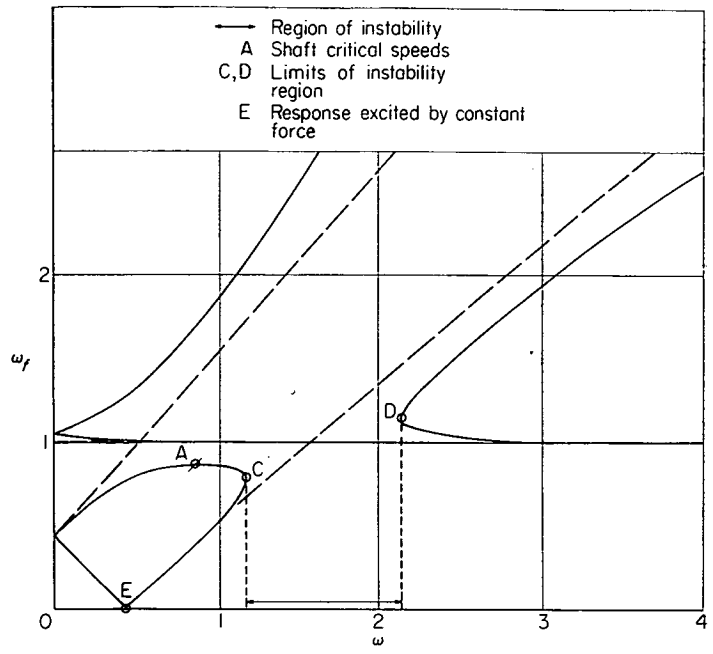


FIGURE II–4.—Natural frequencies of a three-blade rotor in fixed coordinates for case of $\Lambda_1=0.05$, $\Lambda_2=0.20$, and $\Lambda_3=0.10$.

second factor, which depends on only the reference frequency, marks the end of the range of instability and is the second shaft critical speed. Formula (8) and an experimental verification of it are given in chapter I. A convenient graph of equation (8) is given in figure II–5. It will be noticed that it is impossible to remove the two shaft critical speeds or the instability region between them by any possible change of the parameters Λ_1, Λ_2, or Λ_3; that is, without the introduction of damping, self-excited vibrations will always occur below the rotational speed ω_r.

Instability also occurs in a range of rotational speeds greater than ω_r. This range is shown in figures II–2 and II–3 as the region bounded by the points C and D and is similar in origin to the self-excited region exhibited by the three-blade rotor. In this region, the roots of the frequency equation are complex and self-excited vibrations will take place. Unlike the three-blade rotor, however, the rotor hub will be seen from a stationary position to be simultaneously executing self-excited vibrations at two different frequencies. Physically, of course, the rotor is moving in an ellipse at the frequency ω_a while precessing at the velocity ω.

A chart showing the lower and upper limits of this instability region for a wide choice of values for the parameters, Λ_1, Λ_2, and Λ_3 is given in figure II–6. The chart is used by drawing a straight line that represents the function $(1-4\Lambda_3)\omega^2$ plotted against $\Lambda_1\omega^2+\Lambda_2$. The intersections of this straight line with the proper Λ_3-curves give the desired values of ω. The short-dash line on the chart illustrates the method for the parameters of figure II–2.

The position of the instability region is very sensitive to the values of Λ_3. (See fig. II–7.) As Λ_3 increases, the region of instability occurs at greater rotational speeds and moves to infinity for $\Lambda_3=\frac{1}{4}(1-\Lambda_1)$. For values of Λ_3 greater than $\frac{1}{4}(1-\Lambda_1)$—that is, when the total effective mass of the rotor blades is greater than the effective mass of the rotor supports—the self-excited region does not appear.

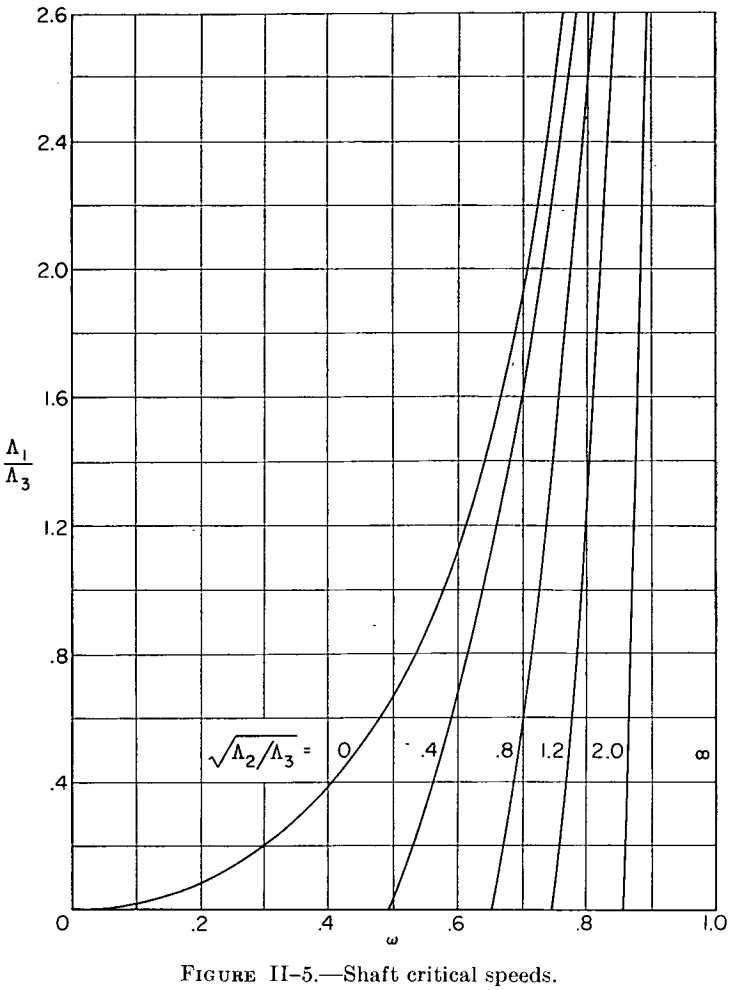


FIGURE II–5.—Shaft critical speeds.

At certain rotational speeds, $\omega_f=0$. At such speeds resonance may be excited by a steady force, constant in direction, acting on the pylon or blades—for example, gravity acting on a tilted rotor. The two-blade rotor has two such speeds, shown as points E and F in figures II–2 and II–3. The mathematical condition for such points is that $\omega_f=0$ or $\omega_a^2=\omega^2$ in equation (7). The equation giving the rotational speeds at which this condition may occur is

$$(\Lambda_1\omega^2+\Lambda_2)(4\omega^2-1)-\omega^2[\omega^2(4-16\Lambda_3)-1]=0 \qquad (9)$$

Equation (9) is plotted in figure II–8, which is used similarly to figure II–6. If $\Lambda_2=0$, then point E occurs at $\omega=0$. If $\Lambda_3\geqq\frac{1}{4}(1-\Lambda_1)$, as pointed out in reference 2, then point F occurs at $\omega=\infty$.

EFFECT OF DAMPING

The effect of damping will be determined in the same manner as for the three-blade rotor in chapter I. When the damping parameters λ and λ_β are retained, equation (6) in expanded form can be separated into powers of ω_a having real and imaginary coefficients. The terms of equation (6) with

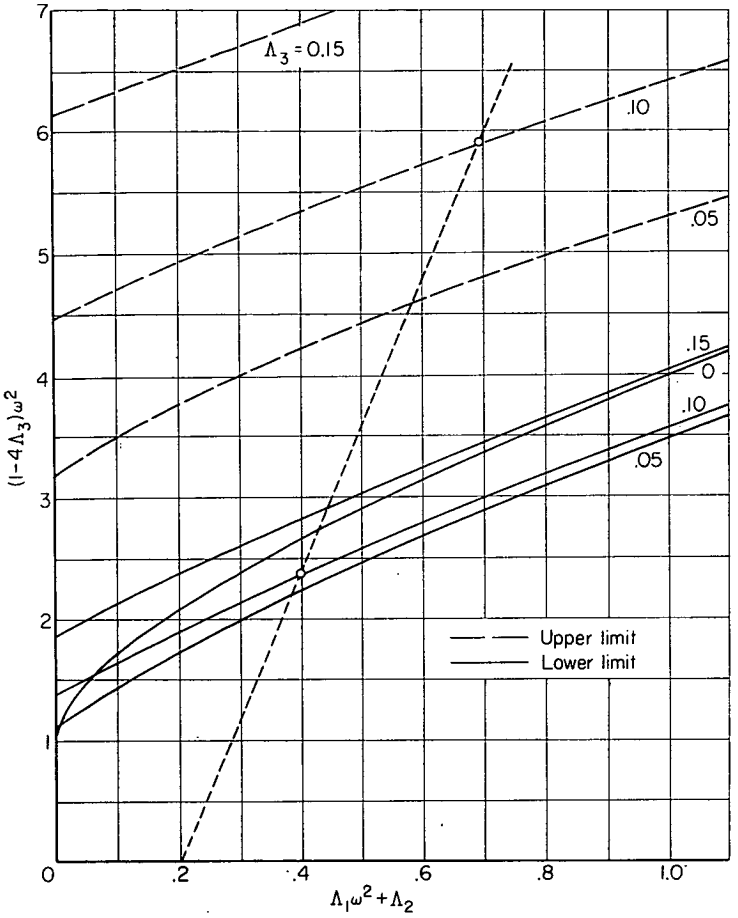


FIGURE II–6.—Stability chart for second instability region.

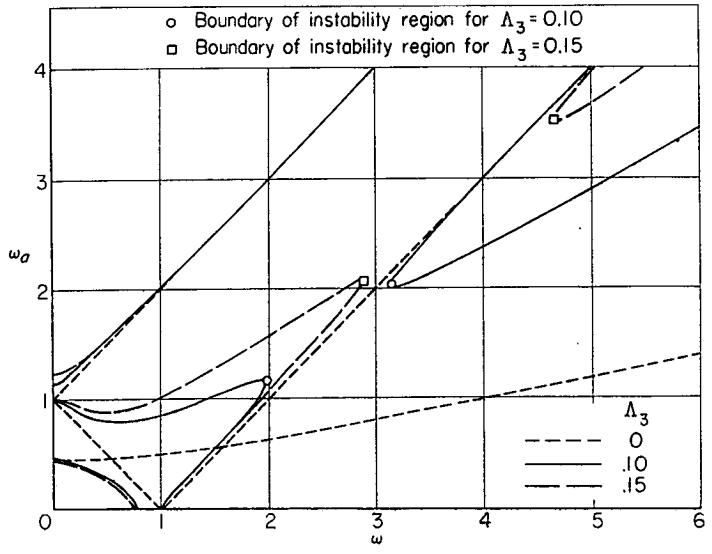


FIGURE II–7.—Effect of coupling parameter Λ_3 for case of $\Lambda_1=0.05$ and $\Lambda_2=0.20$.

real coefficients are

$$2\Lambda_3(\omega^2+\omega_a{}^2-1)+[4\omega^2\omega_a{}^2-(\omega^2+\omega_a{}^2-1)^2][-2\Lambda_3(\omega^2+\omega_a{}^2+1)+\omega_a{}^2-\Lambda_2-\Lambda_1\omega^2]+\lambda^2(-\omega_a{}^2+\Lambda_2+\Lambda_1\omega^2)(\omega^2-\omega_a{}^2)-2\lambda\lambda_\beta\omega_a{}^2(\omega^2-\omega_a{}^2+1) \quad (10)$$

526597—60——20

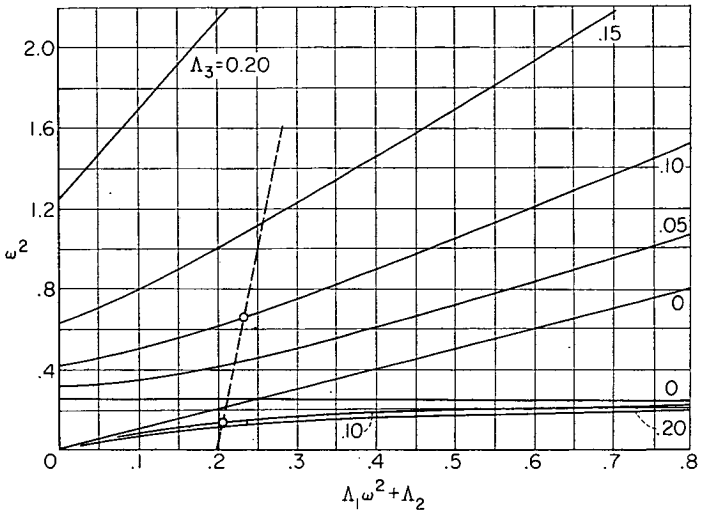


FIGURE II–8.—Rotational speeds at which vibration could be excited by steady force.

The terms with imaginary coefficients are

$$i\lambda_\beta\omega_a\left\{2\frac{\lambda}{\lambda_\beta}[(\omega^2-\omega_a{}^2+1)(\Lambda_1\omega^2+\Lambda_2-\omega_a{}^2)+\Lambda_3(3\omega^4-2\omega^2\omega_a{}^2-\omega_a{}^4)]+\omega^4+\omega_a{}^4+1-2\omega^2\omega_a{}^2-2\omega_a{}^2-2\omega^2-\lambda^2(\omega_a{}^2-\omega^2)\right\} \quad (11)$$

At a boundary between stability and instability, ω_a is real. Such points are the intersections of the equations formed by setting expressions (10) and (11) separately equal to zero and plotting them on the same coordinate axes. Figure II–9 shows a calculated case of damping. The imaginary equation is plotted for several values of the ratio of the damping parameters λ/λ_β, with λ^2 assumed to be negligible. It is seen that, for large values of λ/λ_β, the boundaries of the higher range of instability are not far different from the boundaries found by neglecting damping. Small values of λ/λ_β—that is, when most of the damping is concentrated in the blade

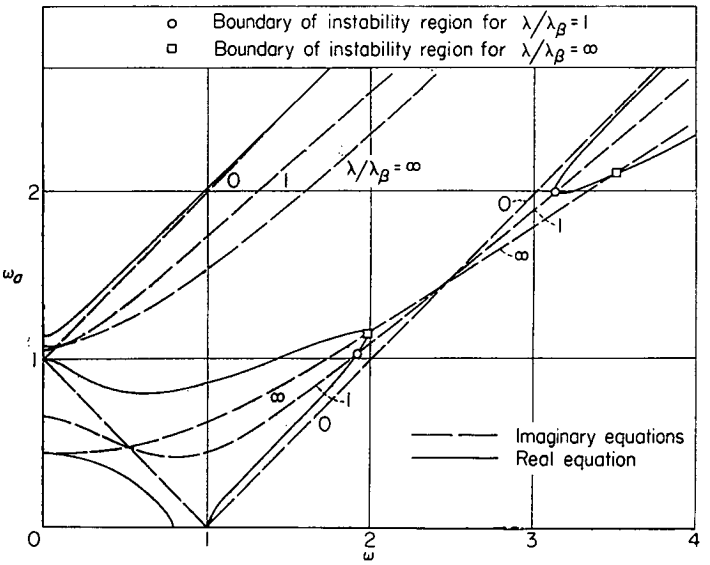


FIGURE II–9.—Plot of real and imaginary equations for case of $\Lambda_1=0.05$, $\Lambda_2=0.20$, $\Lambda_3=0.10$, and $\lambda\lambda_\beta\approx 0$.

hinges—lead to a beginning of the instability at lower rotational speeds.

For small amounts of damping, the plot of the real equation is practically the same as when damping is neglected. By introducing sufficient damping, however, the higher instability region may be eliminated. (See fig. II–10.) The two shaft critical speeds and the instability region between them can also be removed by putting enough damping into the rotor supports, although a large amount of damping is required.

BRIEF DESCRIPTION OF VIBRATION MODES

If damping is neglected, the shape of the free vibration modes can be found from the equations of motion (eqs. (1) to (4)) and the form of the solution (eq. (5)). The rotor hub generally moves in an elliptical path in rotating coordinates although, at certain speeds, the motion may become circular or linear. At zero rotational speed, two of the three modes involve hub motion normal to the line of the blades, with concomitant blade motion. In the third mode, the blades do not move about their hinges and the rotor hub moves in a straight line parallel to the line of the blades at a frequency equal to ω_r.

At the first shaft critical speed, the rotor hub diverges in a direction normal to the line of the blades; whereas, at the second shaft critical speed, the hub diverges parallel to the blades.

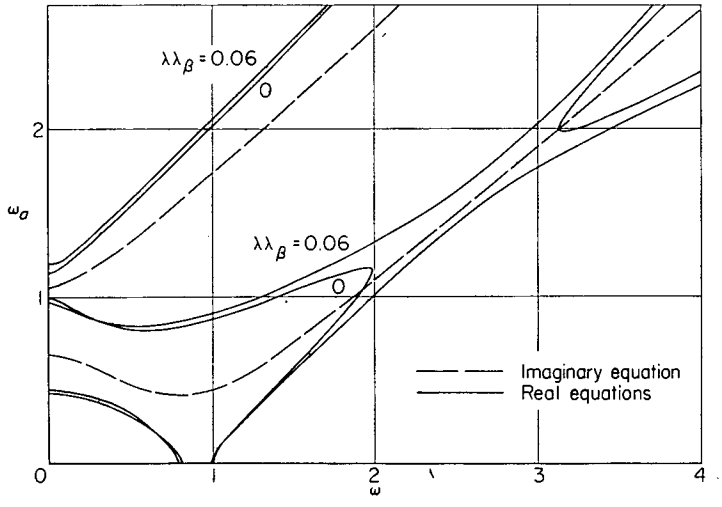


FIGURE II–10.—Plot of real and imaginary equations for case of $\Lambda_1=0.05$, $\Lambda_2=0.20$, $\Lambda_3=0.10$, and $\lambda=\lambda_\beta$.

The forced responses of the system to a vibrator attached to the pylon can also easily be determined and show that those responses lying closest to the lines $\omega_f^2=1$ are the strongest. When the coupling parameter Λ_3 is zero, no response occurs along the lines $\omega_f=|2\omega\pm1|$. This last conclusion is, of course, necessary if the theory is to give the correct results for the degenerate case of massless rotor blades.

CONCLUSIONS

The mechanical stability of a rotor having two vertically hinged blades mounted upon symmetrical supports has been investigated and reported in this chapter. This investigation indicated that the main features of such a rotor system may be summarized as follows:

1. The vibration modes are generally elliptical, as opposed to circular for the three-blade rotor. The ellipse precesses at a speed ω as observed from a fixed position; the result is six resonant or natural frequencies in a fixed coordinate system for a given rotor speed as against four natural frequencies for the three-blade rotor.

2. The asymmetry of the two-blade-rotor system gives rise to a range of rotor speeds in which self-excited divergence of the rotor occurs. This instability region is bounded by two shaft critical speeds. A three-blade rotor, in contrast, has only one shaft critical speed with no associated instability region.

3. The two-blade rotor has a second region of rotational speeds at which self-excited vibrations occur.

LANGLEY AERONAUTICAL LABORATORY,
NATIONAL ADVISORY COMMITTEE FOR AERONAUTICS,
LANGLEY FIELD, VA., *July 27, 1956.*

REFERENCES

1. Foote, W. R., Poritsky, H., and Slade, J. J., Jr.: Critical Speeds of a Rotor With Unequal Shaft Flexibilities, Mounted in Bearings of Unequal Flexibility—I. Jour. Appl. Mech., vol. 10, no. 2, June 1943, pp. A–77—A–84.
2. Leone, Peter F.: Mechanical Stability of a Two-Bladed Cantilever Helicopter Rotor. Jour. Aero. Sci., vol. 23, no. 7, July 1956, pp. 633–638.

CHAPTER III

THEORY OF GROUND VIBRATIONS OF A TWO-BLADE HELICOPTER ROTOR ON ANISOTROPIC FLEXIBLE SUPPORTS (REVISED)

By Robert P. Coleman and Arnold M. Feingold

SUMMARY

An extension of previous work on the theory of self-excited mechanical oscillations of hinged rotor blades has been made. Previously published papers cover the cases of three or more rotor blades on elastic supports (such as landing gear) having either equal or unequal support stiffness in different directions and the case of one- or two-blade rotors on supports having equal stiffness in all horizontal directions. The missing case of one or two blades on unequal supports has been treated.

The mathematical treatment of this case is considerably more complicated than the other cases because of the occurrence of differential equations with periodic coefficients. The characteristic frequencies are obtained from an infinite-order determinant. Recurrence relations and convergence factors are used in finding the roots of the infinite determinant.

The results show the existence of ranges of rotational speed at which instability occurs (changed somewhat in position and extent) similar to those possessed by the two-blade rotor on equal supports. In addition, the existence of an infinite number of instability ranges which occurred at low rotor speeds and which did not occur in the cases previously treated is shown.

Simplifications occur in the analysis for the special cases of infinite and zero stiffness in one of the axes. The case of infinite stiffness in one axis is also of special interest because it is mathematically equivalent to a counterrotating rotor system A design chart for finding the position of the principal self-excited-instability range for the case of infinite support stiffness in one direction is included for the convenience of designers. It is expected that designers will be able to obtain sufficiently accurate information by considering only the cases of infinite and zero support stiffness along one direction together with the cases treated previously.

INTRODUCTION

It is known that rotating-wing aircraft may experience violent vibrations while the rotor is turning and the aircraft is on the ground. It has been found that these vibrations can be explained without considering aerodynamic effects and that they are due to mechanical coupling between horizontal hub displacements and blade oscillations in the plane of rotation. A theoretical analysis of this vibration problem is given in chapters I and II. Chapter I deals with rotors having three or more equal blades on general supports and chapter II deals with two-blade rotors on supports having the same stiffness in all directions.

Although in actual two-blade rotary-wing aircraft, the stiffness of the supports along the longitudinal direction is certainly different from the lateral stiffness, the equality of the stiffnesses was assumed in chapter II because it permitted the mathematical simplification of dealing with differential equations having constant coefficients and it was believed that a theory employing such an assumption would be sufficient to indicate the nature of the most violent types of ground instability.

The present chapter gives a theoretical investigation of the general case of a two-blade rotor mounted upon supports of unequal stiffness along the two stationary principal axes. It thus generalizes the problem of chapter II, and rounds out the studies of ground resonance begun in chapter I. As was shown in chapter II, a two-blade rotor possesses different dynamic properties along and normal to the line of the blades. Equations of motion with constant coefficients for the problem treated in chapter II could be obtained by using a coordinate system rotating with the rotor. This procedure succeeded because the supports were assumed isotropic (equal stiffness in all directions). When the supports are anisotropic, however, it is impossible to avoid the appearance of periodic coefficients in the equations of motion.

The present method of solving the differential equations of motion follows closely the process employed in reference 1 for a vibration problem in two degrees of freedom. The form of solution is expressed by an exponential factor times a complex Fourier series. Substitution of the formal solution into the equations of motion yields an infinite set of algebraic equations and an infinite-order determinant for the determination of the Fourier coefficients and the characteristic frequencies. The subsequent analysis is concerned with methods of finding the roots of the infinite determinant.

Although the present chapter did not originally include the effects of damping on rotor instability, Mr. George W. Brooks has prepared appendix B to indicate how effects of damping may be included in the analyses.

It is expected that designers will be able to obtain sufficiently accurate information by considering only the cases of infinite or zero support stiffness along one direction together with the cases of chapters I and II. In order to avoid the necessity for extensive calculations, a design chart is included giving the location of the principal self-excited-instability range for the case of infinite support stiffness in one direction.

DERIVATION OF THE EQUATIONS OF MOTION

The symbols used in this chapter are defined in appendix A.

The equations of motion are obtained from Lagrange's equations and from the expressions for kinetic and potential

energy. Four degrees of freedom of the rotor system are considered: components of deflection of the rotor hub in the plane of rotation, and hinge deflections of the two rotor blades about their vertical hinges. All motions are thus assumed to occur in the plane of the rotor. The rotor is assumed to rotate at a constant angular velocity ω. The analysis can be applied to rotors without hinges by assuming an effective spring stiffness and hinge position to represent the elastic deflection of the blade.

The pertinent physical parameters are:

a	radial position of vertical hinge
b	distance from vertical hinge to center of mass of blade
m_b	mass of rotor blade
m	effective mass of rotor supports
r	radius of gyration of blade about center of mass
K_x, K_y	spring constants of the rotor supports along the X- and Y-directions, respectively
K_β	spring constant of hinge self-centering spring

Let the origin of the X, Y-coordinate system be placed at the undisturbed position of the rotor hub. At time t equal to 0, the line through the blade hinges and rotor hub is assumed parallel to the X-axis. After a time interval t, let the rotor hub deflection be z and hinge deflections be β_1 and β_2, respectively, where z is the complex position coordinate measured in a coordinate system rotating with the rotor. (See fig. III–1.) Then the positions of the centers of mass of the two blades, as measured in fixed coordinates, will be, respectively,

$$\left.\begin{aligned} z_1&=(z+a+be^{i\beta_1})e^{i\omega t}\\ z_2&=(z-a-be^{i\beta_2})e^{i\omega t}\end{aligned}\right\} \tag{1}$$

The kinetic energy of the rotor system T can be written as

$$T=\frac{1}{2}\,m_b\left\{\dot{z}_1\dot{\bar{z}}_1+\dot{z}_2\dot{\bar{z}}_2+r^2\left[(\omega+\dot{\beta}_1)^2+(\omega+\dot{\beta}_2)^2\right]\right\}+\frac{1}{2}\,m(\dot{z}+i\omega z)(\dot{\bar{z}}-i\omega\bar{z}) \tag{2}$$

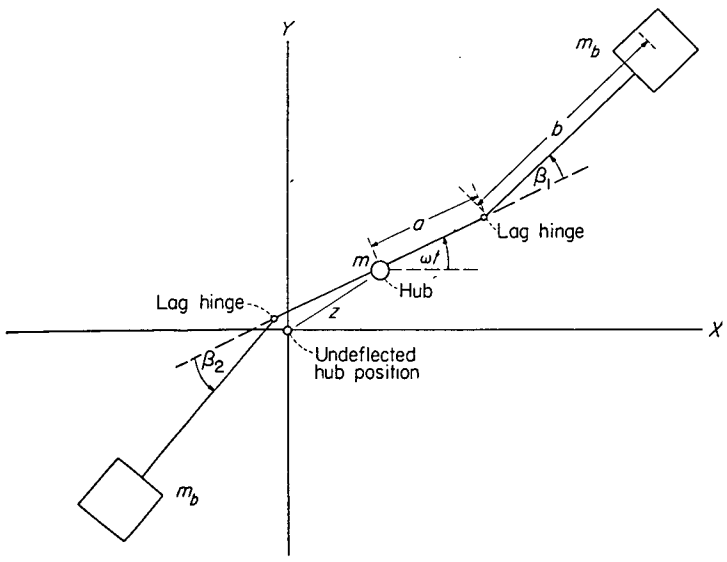


FIGURE III–1.—Simplified mechanical system representing rotor.

The first term in equation (2) represents the kinetic energy of the rotor blades, including the energy due to rotation, and the second term is the contribution of the rotor hub.

Upon expanding equation (1) into power series in β_1 and β_2 (only small deflections from equilibrium being considered) and substituting into equation (2), there is obtained

$$T=\frac{1}{2}\,M(\dot{z}+i\omega z)(\dot{\bar{z}}-i\omega\bar{z})+\frac{1}{2}\,m_b\Big[-(\beta_1-\beta_2)(i\omega^2 bz-i\omega^2 b\bar{z}+\omega b\dot{z}+\omega b\dot{\bar{z}})+(\dot{\beta}_1-\dot{\beta}_2)(bi\dot{\bar{z}}+\omega bz+\omega b\bar{z}-bi\dot{z})+(b^2+r^2)(\dot{\beta}_1^2+\dot{\beta}_2^2)-ab\omega^2(\beta_1^2+\beta_2^2)\Big] \tag{3}$$

where only the terms that are quadratic in the variables have been retained, and M represents the total mass of the rotor system.

The potential energy of the system V is given by

$$V=\frac{K_\beta}{2}\,(\beta_1^2+\beta_2^2)+\frac{K}{2}\,z\bar{z}-\frac{\Delta K}{4}\,(z^2e^{2i\omega t}+\bar{z}^2e^{-2i\omega t}) \tag{4}$$

where K is the average stiffness and ΔK is a measure of the difference of the two principal stiffnesses; that is,

$$K=\frac{K_y+K_x}{2}$$

$$\Delta K=\frac{K_y-K_x}{2}$$

As in chapters I and II, simplifications in the analysis are introduced by replacing the hinge variables β_1 and β_2 by the following new variables:

$$\theta_0=\frac{b}{2}\,(\beta_1+\beta_2)$$

$$\theta_1=\frac{b}{2}\,(\beta_1-\beta_2)$$

In terms of these new variables the expressions (3) and (4) become, respectively,

$$T=\frac{M}{2}\,(\dot{z}+i\omega z)\,(\dot{\bar{z}}-i\omega\bar{z})+m_b\Big[(\dot{\bar{z}}-i\omega\bar{z})\,(i\dot{\theta}_1-\omega\theta_1)-(\dot{z}+i\omega z)\,(i\dot{\theta}_1+\omega\theta_1)+\left(1+\frac{r^2}{b^2}\right)(\dot{\theta}_0^2+\dot{\theta}_1^2)-\frac{a}{b}\,\omega^2\,(\theta_0^2+\theta_1^2)\Big] \tag{5}$$

and

$$V=\frac{K}{2}\,z\bar{z}+\frac{K_\beta}{b^2}\,(\theta_0^2+\theta_1^2)-\frac{\Delta K}{4}\,(z^2e^{2i\omega t}+\bar{z}^2e^{-2i\omega t}) \tag{6}$$

By use of the Lagrangian form of the equations of motion

$$\frac{d}{dt}\left(\frac{\partial T}{\partial\dot{x}}\right)-\frac{\partial T}{\partial x}+\frac{\partial V}{\partial x}=0$$

the following equations of motion for the rotor system are finally obtained:

$$\ddot{\theta}_0+(\omega^2\Lambda_1+\Lambda_2)\theta_0=0 \tag{7}$$

$$(D+i\omega)^2z+i\mu(D+i\omega)^2\theta_1+\frac{K}{M}\,z-\frac{\Delta K}{M}\,\bar{z}e^{-2i\omega t}=0 \tag{8}$$

$$(D-i\omega)^2\bar{z}-i\mu(D-i\omega)^2\theta_1+\frac{K}{M}\bar{z}-\frac{\Delta K}{M}ze^{2i\omega t}=0 \tag{9}$$

$$(D+i\omega)^2z-(D-i\omega)^2\bar{z}+2i\left(1+\frac{r^2}{b^2}\right)(D^2+\Lambda_1\omega^2+\Lambda_2)\theta_1=0 \tag{10}$$

where the notation

$$D=\frac{d}{dt}$$

has been used, and the following combinations of the original parameters have been introduced:

$$\mu=\frac{2m_b}{M}$$

$$\Lambda_1=\frac{a}{b\left(1+\frac{r^2}{b^2}\right)}$$

$$\Lambda_2=\frac{K_\beta}{m_b b^2\left(1+\frac{r^2}{b^2}\right)}$$

Equations (7) to (10) do not include damping terms. The general equations for the damped case are derived in appendix B and it is shown that both the case for no damping and anisotropic supports, which is treated in the present chapter, and the case for damping and isotropic supports, which was treated in chapter II, are readily obtained as special cases of the generalized equations by neglecting appropriate terms.

Equation (7) can be solved independently of the others since it is an equation in θ_0 alone. The equivalent equation appeared also in chapters I and II, and its solution represents in-phase motion of the blades with no resultant reaction (except torsion) at the rotor hub. This motion will not be further considered in this chapter.

The problem is thus resolved into the solution of the three simultaneous equations (8) to (10). It will be noted that the terms with periodic coefficients in equations (8) and (9) disappear if $\frac{\Delta K}{M}=0$, that is, if $K_y=K_x$. Equations (8) and (9) are thus reduced to the problem treated in chapter II.

FORM OF SOLUTION OF EQUATIONS OF MOTION

The equations of motion (eqs. (8) to (10)) are similar in mathematical properties to Mathieu's equation, which occurs in the analysis of vibrating systems of one degree of freedom with variable elasticity. (See ref. 2.) A generalized form of Mathieu's equation was solved analytically by Hill. (See ref. 3, pp. 413–417.) An extension of Hill's method has been applied in reference 1 to a problem involving two degrees of freedom, and a further development of the method of reference 1 is followed in the present paper.

Equations (8) to (10) constitute a system of linear differential equations with periodic coefficients. Three second-order equations possess six linearly independent solutions that, according to the Floquet theory (ref. 3, p. 412), are of the form of an exponential factor times a periodic function of time. Particular solutions are of the form

$$\left.\begin{aligned} z&=e^{i\omega_a t}P(t)+e^{-i\bar{\omega}_a t}\bar{Q}(t)\\ \bar{z}&=e^{i\omega_a t}Q(t)+e^{-i\bar{\omega}_a t}\bar{P}(t)\\ \theta_1&=e^{-i\omega_a t}R(t)+e^{-i\bar{\omega}_a t}\bar{R}(t)\end{aligned}\right\} \tag{11}$$

where ω_a is known as the characteristic exponent, and $P(t)$, $Q(t)$, and $R(t)$ are periodic functions of period π/ω.

Since $P(t)$, $Q(t)$, and $R(t)$ are periodic functions of t, they can be represented by complex Fourier series, and equations (11) become

$$\left.\begin{aligned} z&=\sum_{-\infty}^{\infty}A_l e^{(2l\omega+\omega_a)it}+\sum_{-\infty}^{\infty}\bar{B}_l e^{-(2l\omega+\bar{\omega}_a)it}\\ \bar{z}&=\sum_{-\infty}^{\infty}B_l e^{(2l\omega+\omega_a)it}+\sum_{-\infty}^{\infty}\bar{A}_l e^{-(2l\omega+\bar{\omega}_a)it}\\ \theta_1&=\sum_{-\infty}^{\infty}C_l e^{(2l\omega+\omega_a)it}+\sum_{-\infty}^{\infty}\bar{C}_l e^{-(2l\omega+\bar{\omega}_a)it}\end{aligned}\right\} \tag{12}$$

where A_l, B_l, and C_l are complex constants.

Equations (11) and (12) show that, when the rotor system is stable and ω_a is real, the motion not only is not simple harmonic as was the case in chapters I and II, but, in general, is not even periodic. The motion can be said to consist of a fundamental frequency ω_a plus "harmonics" of frequency $\omega_a+2l\omega$ where l is any integer. From equations (12) it is seen that the value of ω_a is not uniquely determinate, since $\omega_a+2l\omega$ also satisfies equations (12). (The imaginary part of ω_a is definite, however.) It can be shown furthermore that, corresponding to each value of ω_a, $-\omega_a$ is also a solution. Only those three values of ω_a for which the real parts lie between 0 and ω need therefore be considered. These values will be referred to hereinafter as the three "principal" values of ω_a. These values of ω_a differing from the principal value by $2l\omega$, or having opposite sign, will be referred to as "harmonics" of the corresponding principal value.

Since z has been defined as a position coordinate in a rotating frame of reference, the values of ω_a can be interpreted as the natural frequencies of the rotor system in rotating coordinates.

SOLUTION OF EQUATIONS OF MOTION

DETERMINANTAL EQUATION

If the formal solution (eqs. (12)) is combined with the equations of motion (eqs. (8) to (10)), and the coefficients of each exponential time factor is separately equated to zero, an infinite set of homogeneous equations is obtained. These equations can be separated into two independent sets. Each equation of one set is the conjugate of an equation of the other set, and only one set need be considered. Thus

$$\left\{\frac{K}{M}-[\omega_a+(2l+1)\omega]^2\right\}A_l-\frac{\Delta K}{M}B_{l+1}-\mu i[\omega_a+(2l+1)\omega]^2C_l=0 \tag{13}$$

$$\left\{\frac{K}{M}-[\omega_a+(2l-1)\omega]^2\right\}B_l-\frac{\Delta K}{M}A_{l-1}+\mu i[\omega_a+(2l-1)\omega]^2C_l=0 \tag{14}$$

$$-[\omega_a+(2l+1)\omega]^2A_l+[\omega_a+(2l-1)\omega]^2B_l+2i\left(1+\frac{r^2}{b^2}\right)[-(\omega_a+2l\omega)^2+\Lambda_1\omega^2+\Lambda_2]C_l=0 \tag{15}$$

where l takes on all integral values from $-\infty$ to ∞.

In order that the values of A_l, B_l, and C_l not equal zero, the determinant of the coefficients of A_l, B_l, and C_l must be zero. This determinantal equation is

$$\begin{vmatrix}
\cdot & \cdot & \cdot & \cdot & \cdot & \cdot & \cdot & \cdot & \cdot & \cdot & \\
\cdot & \cdot & \cdot & \cdot & \cdot & \cdot & \cdot & \cdot & \cdot & \cdot & \\
\cdot & \cdot & \cdot & \cdot & \cdot & \cdot & \cdot & \cdot & \cdot & \cdot & \\
a_{-4,-4} & a_{-4,-3} & 0 & 0 & 0 & 0 & 0 & 0 & 0 & \cdots & \\
a_{-3,-4} & a_{-3,-3} & a_{-3,-2} & 0 & 0 & 0 & 0 & 0 & 0 & \cdots & \\
0 & a_{-2,-3} & a_{-2,-2} & a_{-2,-1} & 0 & 0 & 0 & 0 & 0 & \cdots & \\
0 & 0 & a_{-1,-2} & a_{-1,-1} & a_{-1,0} & 0 & 0 & 0 & 0 & \cdots & \\
0 & 0 & 0 & a_{0,-1} & a_{0,0} & a_{0,1} & 0 & 0 & 0 & \cdots & =\Delta(\omega_a)=0 \\
0 & 0 & 0 & 0 & a_{1,0} & a_{1,1} & a_{1,2} & 0 & 0 & \cdots & \\
0 & 0 & 0 & 0 & 0 & a_{2,1} & a_{2,2} & a_{2,3} & 0 & \cdots & \\
0 & 0 & 0 & 0 & 0 & 0 & a_{3,2} & a_{3,3} & a_{3,4} & \cdots & \\
0 & 0 & 0 & 0 & 0 & 0 & 0 & a_{4,3} & a_{4,4} & \cdots & \\
\cdot & \cdot & \cdot & \cdot & \cdot & \cdot & \cdot & \cdot & \cdot & & \\
\cdot & \cdot & \cdot & \cdot & \cdot & \cdot & \cdot & \cdot & \cdot & & \\
\cdot & \cdot & \cdot & \cdot & \cdot & \cdot & \cdot & \cdot & \cdot & &
\end{vmatrix} \tag{16}$$

where

$$a_{-4,-4}=-1+\frac{K/M}{(\omega_a-3\omega)^2} \qquad a_{-1,-2}=\frac{\Delta K/M}{(\omega_a-\omega)^2}$$

$$a_{-4,-3}=\Lambda_3 \qquad a_{-1,-1}=-1+\frac{K/M}{(\omega_a-\omega)^2}$$

$$a_{-3,-4}=\left(\frac{\omega_a-3\omega}{\omega_a-2\omega}\right)^2 \qquad a_{-1,0}=\Lambda_3$$

$$a_{-3,-3}=-1+\frac{\Lambda_1\omega^2+\Lambda_2}{(\omega_a-2\omega)^2} \qquad a_{0,-1}=\left(\frac{\omega_a-\omega}{\omega_a}\right)^2$$

$$a_{-3,-2}=\left(\frac{\omega_a-\omega}{\omega_a-2\omega}\right)^2 \qquad a_{0,0}=-1+\frac{\Lambda_1\omega^2+\Lambda_2}{\omega_a^2}$$

$$a_{-2,-3}=\Lambda_3 \qquad a_{0,1}=\left(\frac{\omega_a+\omega}{\omega_a}\right)^2$$

$$a_{-2,-2}=-1+\frac{K/M}{(\omega_a-\omega)^2} \qquad a_{1,0}=\Lambda_3$$

$$a_{-2,-1}=\frac{\Delta K/M}{(\omega_a-\omega)^2} \qquad a_{1,1}=-1+\frac{K/M}{(\omega_a+\omega)^2}$$

$$a_{1,2}=\frac{\Delta K/M}{(\omega_a+\omega)^2} \qquad a_{3,2}=\left(\frac{\omega_a+\omega}{\omega_a+2\omega}\right)^2$$

$$a_{2,1}=\frac{\Delta K/M}{(\omega_a+\omega)^2} \qquad a_{3,3}=-1+\frac{\Lambda_1\omega^2+\Lambda_2}{(\omega_a+2\omega)^2}$$

$$a_{2,2}=-1+\frac{K/M}{(\omega_a+\omega)^2} \qquad a_{3,4}=\left(\frac{\omega_a+3\omega}{\omega_a+2\omega}\right)^2$$

$$a_{2,3}=\Lambda_3 \qquad a_{4,3}=\Lambda_3$$

$$a_{4,4}=-1+\frac{K/M}{(\omega_a+3\omega)^2}$$

The determinant has been somewhat simplified by multiplying and dividing the rows and columns by various quantities, and the parameter Λ_3 has been substituted for its equivalent $\frac{\mu/2}{1+(r/b)^2}$.

Let this infinite determinant be $\Delta(\omega_a)$. The problem consists in solving the equation $\Delta(\omega_a)=0$ for its roots ω_a. These roots will be infinite in number, consisting of the three principal values of ω_a plus all their harmonics. The values

of $\omega_a/\sqrt{K/M}$, as a function of $\omega/\sqrt{K/M}$, are seen to depend only on the values of the three nondimensional parameters, Λ_1, $\frac{\Lambda_2}{K/M}$, and Λ_3 and the stiffness-ratio parameter $\Delta K/K$.

A determinant of infinite order has meaning only insofar as it is defined as the limit of a determinant of finite order. Define $\Delta_n(\omega_a)$ as the determinant of order $6n-3$ formed from a square array of $\Delta(\omega_a)$ centered on the term $-1+\frac{\Lambda_1\omega^2+\Lambda_2}{\omega_a^2}$. This term, which originally was associated with C_0 in equation (15), will be referred to hereinafter as the "origin" of the infinite determinant $\Delta(\omega_a)$. The choice of this term as center of $\Delta(\omega_a)$ is purely arbitrary, and it was selected solely for reasons of symmetry.

Thus

$$\Delta(\omega_a)=\lim_{n\to\infty}\Delta_n(\omega_a) \tag{17}$$

The limiting values of the roots of the equation

$$\Delta_n(\omega_a)=0$$

as n becomes infinite will be the values of the roots of the equation

$$\Delta(\omega_a)=0$$

The method of calculating the roots of $\Delta(\omega_a)=0$, by successively calculating the roots of $\Delta_n(\omega_a)=0$ for larger values of n, is entirely too tedious. Instead, the method reference 1 will be followed. This method involves the calculation of the value of $\Delta(\omega_a)$ for several specified values of ω_a. The roots of $\Delta(\omega_a)=0$ can then be obtained from a trigonometric equation involving the roots and the calculated values of $\Delta(\omega_a)$.

AUXILIARY DETERMINANTS AND RECURRENCE RELATIONS FOR CALCULATING $\Delta(\omega_a)$

Before the trigonometric equation is derived, it is convenient to have a systematic numerical procedure for determining the value of $\Delta(\omega_a)$. As n becomes infinite, the terms of $\Delta_n(\omega_a)$ extend to infinity both above and below the origin. By expanding $\Delta_n(\omega_a)$ in terms of the elements of the column containing the origin, it can be expressed in terms of auxiliary determinants that extend to infinity in only one direction. Recurrence relations can then be obtained that give the value of these auxiliary determinants.

The auxiliary determinants are minors of $\Delta_n(\omega_a)$ and are defined as follows:

$C_n(\omega_a)$ determinant of order $3n-2$ consisting of the terms below and to the right of the origin; that is, determinant having first row and column beginning with term $-1+\frac{K/M}{(\omega_a+\omega)^2}$

$D_n(\omega_a)$ determinant of order $3n-3$ formed from $C_n(\omega_a)$ by omitting last row and column

$E_n(\omega_a)$ determinant of order $3n-4$ formed from $D_n(\omega_a)$ by omitting last row and column

$L_n(\omega_a)$ determinant of order $3n-3$ formed from $C_n(\omega_a)$ by omitting first row and column

$M_n(\omega_a)$ determinant of order $3n-4$ formed from $L_n(\omega_a)$ by omitting last row and column

$N_n(\omega_a)$ determinant of order $3n-5$ formed from $M_n(\omega_a)$ by omitting last row and column

The following three determinants will also be needed:

$G_n(\omega_a)$ determinant of order $3n-4$ formed from $L_n(\omega_a)$ by omitting first row and column

$H_n(\omega_a)$ determinant of order $3n-5$ formed from $G_n(\omega_a)$ by omitting last row and column

$I_n(\omega_a)$ determinant of order $3n-6$ formed from $H_n(\omega_a)$ by omitting last row and column

Determinants similar to the foregoing can be formed in the same manner from the upper half of $\Delta_n(\omega_a)$. Denote these determinants by the subscript $-n$ instead of n. It is seen, however, that their values can be obtained from the values of the determinants already defined from the lower half of $\Delta_n(\omega_a)$, by merely replacing ω_a with $-\omega_a$ (for example, $C_{-n}(\omega_a)=C_n(-\omega_a)$).

Expanding $\Delta_n(\omega_a)$ in terms of the elements of the column containing the origin gives

$$\Delta_n(\omega_a)=\left(-1+\frac{\Lambda_1\omega^2+\Lambda_2}{\omega_a^2}\right)C_n(\omega_a)C_n(-\omega_a)-$$
$$\Lambda_3\left[\left(\frac{\omega_a-\omega}{\omega_a}\right)^2L_n(-\omega_a)C_n(\omega_a)+\left(\frac{\omega_a+\omega}{\omega_a}\right)^2L_n(\omega_a)C_n(-\omega_a)\right] \tag{18}$$

The auxiliary determinants $C_n(\omega_a)$, $D_n(\omega_a)$, and $E_n(\omega_a)$ satisfy the following recurrence relations (obtained by expanding each in terms of the elements of its last row):

$$\left.\begin{aligned}
C_n(\omega_a)&=\left\{-1+\frac{K/M}{[\omega_a+(2n-1)\omega]^2}\right\}D_n(\omega_a)-\Lambda_3\left[\frac{\omega_a+(2n-1)\omega}{\omega_a+(2n-2)\omega}\right]^2E_n(\omega_a)\\
D_n(\omega_a)&=\left\{-1+\frac{\Lambda_1\omega^2+\Lambda_2}{[\omega_a+(2n-2)\omega]^2}\right\}E_n(\omega_a)-\Lambda_3\left[\frac{\omega_a+(2n-3)\omega}{\omega_a+(2n-2)\omega}\right]^2C_{n-1}(\omega_a)\\
E_n(\omega_a)&=\left\{-1+\frac{K/M}{[\omega_a+(2n-3)\omega]^2}\right\}C_{n-1}(\omega_a)-\frac{(\Delta K/M)^2}{[\omega_a+(2n-3)\omega]^4}D_{n-1}(\omega_a)
\end{aligned}\right\} \tag{19}$$

The determinants $L_n(\omega_a)$, $M_n(\omega_a)$, and $N_n(\omega_a)$ and also the system $G_n(\omega_a)$, $H_n(\omega_a)$, and $I_n(\omega_a)$ satisfy the same recurrence relations as $C_n(\omega_a)$, $D_n(\omega_a)$, and $E_n(\omega_a)$, respectively.

The values of these nine determinants can be found from the recurrence relations (eqs. (19)) and the following

initial values, obtained directly from equation (16):

$$\left.\begin{aligned} C_1(\omega_a)&=-1+\frac{K/M}{(\omega_a+\omega)^2} \\ E_2(\omega_a)&=\left[-1+\frac{K/M}{(\omega_a+\omega)^2}\right]^2-\frac{(\Delta K/M)^2}{(\omega_a+\omega)^4} \\ N_2(\omega_a)&=-1+\frac{K/M}{(\omega_a+\omega)^2} \\ M_2(\omega_a)&=\left[1-\frac{K/M}{(\omega_a+\omega)^2}\right]\left[1-\frac{\Lambda_1\omega^2+\Lambda_2}{(\omega_a+2\omega)^2}\right]-\Lambda_3\left(\frac{\omega_a+\omega}{\omega_a+2\omega}\right)^2 \\ H_2(\omega_a)&=-1+\frac{\Lambda_1\omega^2+\Lambda_2}{(\omega_a+2\omega)^2} \\ G_2(\omega_a)&=\left[1-\frac{\Lambda_1\omega^2+\Lambda_2}{(\omega_a+2\omega)^2}\right]\left[1-\frac{K/M}{(\omega_a+3\omega)^2}\right]-\Lambda_3\left(\frac{\omega_a+3\omega}{\omega_a+2\omega}\right)^2 \end{aligned}\right\} \quad (20)$$

By use of the initial conditions (eqs. (20)), the recurrence relations (eqs. (19)), and equation (18), the value of $\Delta_n(\omega_a)$ can be calculated. The value of $\Delta(\omega_a)$ will then be the limiting value of $\Delta_n(\omega_a)$ as n becomes infinite.

THE BEHAVIOR OF $\Delta_n(\omega_a)$ FOR LARGE VALUES OF n

So far it has been tacitly assumed that the determinant $\Delta(\omega_a)$, as defined in equations (16) and (17), is convergent, and further, that it remains a function of ω_a in the limit as n becomes infinite; that is, it is not identically equal to zero, independent of the value of ω_a. It will now be shown that the function $\Delta_n(\omega_a)$ does become zero in the limit, independent of ω_a, but that when $\Delta_n(\omega_a)$ is divided by an appropriate function of n, a new function $F_n(\omega_a)$ will be obtained which will be convergent and remain an unambiguous function of ω_a in the limit.

The derivation of the appropriate function by which to divide $\Delta_n(\omega_a)$ evidently depends upon the behavior of $\Delta_n(\omega_a)$ as n becomes very large. As n becomes infinite, the recurrence relations (eqs. (19)) become

$$C_n=-D_n-\Lambda_3E_n \quad (21a)$$

$$D_n=-E_n-\Lambda_3C_{n-1} \quad (21b)$$

$$E_n=-C_{n-1} \quad (21c)$$

with identical equations for L_n, M_n, and N_n and for G_n, H_n, and I_n. Equations (21) are readily solvable since they constitute a system of difference equations with constant coefficients. They are satisfied by solutions of the form

$$C_n=C_0k^n \quad (22a)$$

where C_0 is some arbitrary constant and k is a constant to be determined. From equations (21c) and (21b), respectively,

$$E_n=-C_0k^{n-1} \quad (22b)$$

and

$$D_n=C_0k^{n-1}-\Lambda_3C_0k^{n-1}$$

$$=C_0(1-\Lambda_3)k^{n-1} \quad (22c)$$

Combining equations (22a), (22b), and (22c) with equation (21a) and dividing through by C_0k^{n-1} gives

$$k=2\Lambda_3-1 \quad (23)$$

Thus, by use of equation (18), it is seen that for large values of n, $\Delta_n(\omega_a)$ varies as k^{2n}. Since by definition Λ_3 must have a value between 0 and 1/2, k^2 must lie between 0 and 1. Thus, in the limit,

$$\lim_{n\to\infty}\Delta_n(\omega_a)=0$$

independent of ω_a.

Consider the function

$$F_n(\omega_a)=\frac{\Delta_n(\omega_a)}{k^{2n}}$$

The equation $F_n(\omega_a)=0$ will obviously have the same roots for ω_a as does $\Delta_n(\omega_a)=0$. The function $F_n(\omega_a)$ has the advantage, however, as is seen from the preceding discussion, of remaining an unambiguous function of ω_a in the limit as n becomes infinite. Define this limit as

$$F(\omega_a)=\lim_{n\to\infty}F_n(\omega_a)$$

$$=\lim_{n\to\infty}\frac{\Delta_n(\omega_a)}{k^{2n}} \quad (24)$$

The primary problem can now be redefined as the problem of determining the roots, infinite in number and consisting of ω_{a_1}, ω_{a_2}, and ω_{a_3} and all their harmonics, of the equation

$$F(\omega_a)=0 \quad (25)$$

EVALUATION OF ROOTS OF EQUATION (25)

The following trigonometric expression for $F(\omega_a)$ will now be derived:

$$F(\omega_a)\equiv\lim_{n\to\infty}\frac{\Delta_n(\omega_a)}{k^{2n}}$$

$$=\frac{1}{k}\frac{\prod_{j=1}^{3}\left[\sin^2\left(\frac{\pi\omega_a}{2\omega}\right)-\sin^2\left(\frac{\pi\omega_{a_j}}{2\omega}\right)\right]}{\sin^2\left(\frac{\pi\omega_a}{2\omega}\right)\cos^4\left(\frac{\pi\omega_a}{2\omega}\right)} \quad (26)$$

The function $F(\omega_a)$ is seen from equation (24) and equation (16) to be periodic of period 2ω, to have roots $\pm(\omega_{a_1}\pm2s\omega)$, $\pm(\omega_{a_2}\pm2s\omega)$, and $\pm(\omega_{a_3}\pm2s\omega)$ where s is any integer, to have second-order poles at $\omega_a=\pm2s\omega$, and to have fourth-order poles at $\omega_a=\pm(s+1)\omega$. Liouville's function theorem states that a function of a complex variable (in this case, ω_a) that is analytic everywhere in the complex plane, including the region at infinity, must be a constant. It will be shown that $F(\omega_a)$ is finite at infinity (except if ω_a proceeds to infinity along the real axis). If the poles along the real axis could be eliminated by forming a suitable function of $F(\omega_a)$, without at the same time introducing new poles, then that function, by Liouville's theorem, must be a constant.

Such a function of $F(\omega_a)$, which is analytic everywhere in

the complex plane, is

$$J(\omega_a)=\frac{F(\omega_a)\sin^2\left(\frac{\pi\omega_a}{2\omega}\right)\cos^4\left(\frac{\pi\omega_a}{2\omega}\right)}{\prod_{j=1}^{3}\left[\sin^2\left(\frac{\pi\omega_a}{2\omega}\right)-\sin^2\left(\frac{\pi\omega_{a_j}}{2\omega}\right)\right]} \tag{27}$$

where ω_{a_1}, ω_{a_2}, and ω_{a_3} are the three principal values of ω_a. The function $J(\omega_a)$ is therefore a constant. The value of $J(\omega_a)$ found by making ω_a approach infinity along the imaginary axis is

$$J(\omega_a)=F(\infty)$$

where $F(\infty)$ is the value of $F(\omega_a)$, as ω_a becomes infinite.

The value of $F(\infty)$ can be found by letting $\omega_a\to\infty$ in $\Delta_n(\omega_a)$ and then letting $n\to\infty$. From the form of $\Delta_n(\infty)$ it follows that

$$\Delta_n(\infty)=N_{2n}(\infty)=-C_{2n}(\infty)$$

The recurrence relations defining $C_n(\infty)$ are the same as equations (21). The expressions D_n and E_n may be eliminated from equations (21), and, therefore, C_n may be given as follows:

$$C_n=-(1-2\Lambda_3)C_{n-1}$$

The initial conditions (eqs. (20)) reduce to $C_1=-1$, from which it follows immediately that

$$\Delta_n(\infty)=-(1-2\Lambda_3)^{2n-1}$$
$$=k^{2n-1}$$

from equation (23). Therefore

$$F(\infty)\equiv\lim_{n\to\infty}\frac{\Delta_n(\infty)}{k^{2n}}=\lim_{n\to\infty}\frac{k^{2n-1}}{k^{2n}}=\frac{1}{k} \tag{28}$$

Thus equations (27) and (28) lead to the evaluation of equation (26).

After equation (26) has been obtained, the problem of determining ω_{a_1} ω_{a_2}, and ω_{a_3} may be considered theoretically complete inasmuch as equation (26) is really an identity in ω_a. Suppose that ω_a is assigned any specific value in equation (26) and $F(\omega_a)$ is computed to a certain degree of accuracy. If these computations are made for two more values of ω_a, all different, equation (26) will have yielded three equations in the three unknowns ω_{a_1}, ω_{a_2}, and ω_{a_3}. These equations can then be solved for the principal values of ω_a. Any degree of accuracy may be achieved by carrying out the computations for $F(\omega_a)$ to a sufficiently large value of n.

The foregoing procedure can be systematized by rewriting equation (26) as

$$K\left(\frac{\omega_a}{\omega}\right)\equiv\prod_{j=1}^{3}\left[\sin^2\left(\frac{\pi\omega_a}{2\omega}\right)-\sin^2\left(\frac{\pi\omega_{a_j}}{2\omega}\right)\right]$$
$$=kF(\omega_a)\sin^2\left(\frac{\pi\omega_a}{2\omega}\right)\cos^4\left(\frac{\pi\omega_a}{2\omega}\right) \tag{29}$$

A convenient choice for the three arbitrary values of ω_a is $\omega_a=0$, ω, and $\omega/2$. The explicit definitions of $K(0)$, $K(1)$, and $K(1/2)$ then become

$$\left.\begin{aligned}
K(0)&=-\sin^2\left(\frac{\pi\omega_{a_1}}{2\omega}\right)\sin^2\left(\frac{\pi\omega_{a_2}}{2\omega}\right)\sin^2\left(\frac{\pi\omega_{a_3}}{2\omega}\right)\\
K(1)&=\left[1-\sin^2\left(\frac{\pi\omega_{a_1}}{2\omega}\right)\right]\left[1-\sin^2\left(\frac{\pi\omega_{a_2}}{2\omega}\right)\right]\left[1-\sin^2\left(\frac{\pi\omega_{a_3}}{2\omega}\right)\right]\\
K(1/2)&=\left[\frac{1}{2}-\sin^2\left(\frac{\pi\omega_{a_1}}{2\omega}\right)\right]\left[\frac{1}{2}-\sin^2\left(\frac{\pi\omega_{a_2}}{2\omega}\right)\right]\left[\frac{1}{2}-\sin^2\left(\frac{\pi\omega_{a_3}}{2\omega}\right)\right]
\end{aligned}\right\} \tag{30}$$

The equations for evaluating $K(0)$, $K(1)$, and $K(1/2)$ are

$$\left.\begin{aligned}
K(0)&=\lim_{\omega_a\to 0}\left[kF(\omega_a)\sin^2\left(\frac{\pi\omega_a}{2\omega}\right)\cos^4\left(\frac{\pi\omega_a}{2\omega}\right)\right]\\
K(1)&=\lim_{\omega_a\to\omega}\left[kF(\omega_a)\sin^2\left(\frac{\pi\omega_a}{2\omega}\right)\cos^4\left(\frac{\pi\omega_a}{2\omega}\right)\right]\\
K(1/2)&=\lim_{\omega_a\to\omega/2}\left[kF(\omega_a)\sin^2\left(\frac{\pi\omega_a}{2\omega}\right)\cos^4\left(\frac{\pi\omega_a}{2\omega}\right)\right]
\end{aligned}\right\} \tag{31}$$

Carrying out the limiting operations indicated in equations (31) and using the auxiliary determinants $C_n(\omega_a)$, $D_n(\omega_a)$, and so forth, give

$$\left.\begin{aligned}
K(0)&=\lim_{n\to\infty}\left\{\frac{\pi^2[(\Lambda_1\omega^2+\Lambda_2)C_n^2(0)-2\Lambda_3\omega^2L_n(0)C_n(0)]}{-4\omega^2(1-2\Lambda_3)^{2n-1}}\right\}\\
K(1)&=\lim_{n\to\infty}\left[\frac{\pi^4\frac{K_x}{M}\frac{K_y}{M}G_n^2(-\omega)}{16(1-2\Lambda_3)^{2n-2}}\right]\\
K(1/2)&=\lim_{n\to\infty}\left\{\frac{\left[-1+\frac{4(\Lambda_1\omega^2+\Lambda_2)}{\omega^2}\right]C_n\left(\frac{\omega}{2}\right)C_n\left(\frac{-\omega}{2}\right)-\Lambda_3\left[L_n\left(\frac{-\omega}{2}\right)C_n\left(\frac{\omega}{2}\right)+9L_n\left(\frac{\omega}{2}\right)C_n\left(\frac{-\omega}{2}\right)\right]}{-8(1-2\Lambda_3)^{2n-1}}\right\}
\end{aligned}\right\} \tag{32}$$

where the quantities in brackets are conveniently represented by $K(0)_n$, $K(1)_n$, and $K(1/2)_n$, respectively. The quantities $K(\ )_n$ are used in numerical computations as approximations to the functions $K(\ )$.

The formulas (32) for $K(0)$, $K(1)$, and $K(1/2)$ converge slowly with increasing n. The convergence can be speeded up greatly by making use of the concept of convergence factors used in reference 1. A convergence factor for $K(\ )_n$ is a function of n approaching the limit 1 as n becomes infinite, which, when multiplied by $K(\ )_n$, gives an expression which converges rapidly with increasing values of n to the values of $K(\ )$. The details of the derivation of an appropriate convergence factor for $K(0)_n$ will be found in appendix C. Convergence factors for $K(1)_n$ and $K(1/2)_n$ are derived in a similar fashion. The resultant expressions are

$$\left.\begin{aligned} K(0)&=\lim_{n\to\infty}\left[\frac{K(0)_n \sin^2\frac{\pi\sqrt{Q}}{2}}{\frac{\pi^2 Q}{4}\prod_{j=1}^{n-1}\left(1-\frac{Q}{4j^2}\right)^2}\right] \\ K(1)&=\lim_{n\to\infty}\left[\frac{K(1)_n \cos^2\frac{\pi\sqrt{Q}}{2}}{\prod_{j=1}^{n-1}\left(1-\frac{Q}{(2j-1)^2}\right)^2}\right] \\ K(1/2)&=\lim_{n\to\infty}\left[\frac{K(1/2)_n \cos\frac{\pi\sqrt{Q}}{2}}{\prod_{j=1}^{2n-1}\left(1-\frac{4Q}{(2j-1)^2}\right)}\right] \end{aligned}\right\} \quad (33)$$

where

$$Q=\frac{2\frac{K}{M}(1-\Lambda_3)+\Lambda_1\omega^2+\Lambda_2+2\Lambda_3\omega^2}{\omega^2(1-2\Lambda_3)}$$

For a given value of n, the quantities in brackets are found to be better approximations to the respective values of $K(\ )$ than $K(\ )_n$ alone.

The method of obtaining the values of ω_a may be summarized as follows. By use of the initial conditions (eqs. (20)) and the recurrence relations (eqs. (19)), the values of the determinants $C_n(0)$, $L_n(0)$, $G_n(-\omega)$, $C_n(\omega/2)$, $C_n(-\omega/2)$, $L_n(\omega/2)$, and $L_n(-\omega/2)$ can be computed for increasing values of n. With the substitution of these values into equations (33) and with the use of equations (32), approximate values of $K(0)$, $K(1)$, and $K(1/2)$ can be computed. The process appears to be rapidly convergent with n, especially for large values of $\omega/\sqrt{K/M}$. The values of ω_{a_1}, ω_{a_2}, and ω_{a_3} can then be found from equations (31), the definitions of $K(0)$, $K(1)$, and $K(1/2)$.

CONDITIONS FOR STABILITY

From equation (13) the condition for stability of the system is seen to be that all three values of ω_a must be real numbers. If any one of them is complex or pure imaginary, then one of the terms in the solution (eqs. (11)) will increase indefinitely with the time, the motion therefore being unstable. This condition implies that the expressions $\sin^2\left(\frac{\pi\omega_{a_1}}{2\omega}\right)$, $\sin^2\left(\frac{\pi\omega_{a_2}}{2\omega}\right)$, and $\sin^2\left(\frac{\pi\omega_{a_3}}{2\omega}\right)$ all are real positive numbers less than or equal to 1. The conditions for stability can be expressed directly in terms of $K(0)$, $K(1)$, and $K(1/2)$ by means of their definitions (eqs. (30)). The three equations (30) are formally equivalent to a single cubic equation

$$x^3+bx^2+cx+d=0$$

the roots x_1, x_2, and x_3 of which are $\sin^2\left(\frac{\pi\omega_{a_1}}{2\omega}\right)$, $\sin^2\left(\frac{\pi\omega_{a_2}}{2\omega}\right)$, and so forth, and the coefficients b, c, and d of which are functions of $K(0)$, $K(1)$, and $K(1/2)$ where

$$2b=4K(0)+4K(1)-8K\left(\frac{1}{2}\right)-3$$

$$2c=-6K(0)-2K(1)+8K\left(\frac{1}{2}\right)+1$$

$$d=K(0)$$

After some manipulations involving the Descartes rule of signs, the necessary and sufficient conditions for stability are found to be

$$\left.\begin{aligned} &0\leqq -K(0)\leqq 1 \\ &0\leqq K(1)\leqq 1 \\ &-1\leqq 8K(1/2)\leqq 1 \\ &\Delta=18bcd-4b^3d+b^2c^2-4c^3-27d^3\geqq 0 \end{aligned}\right\} \quad (34)$$

The quantity Δ is the discriminant of the cubic equation.

SPECIAL CASES OF GENERAL THEORY

Three special cases of the general theory are of interest. These cases are the cases for which one of the principal stiffnesses K_y is respectively zero, equal, or infinite in magnitude in comparison with the second principal stiffness K_x.

CASE OF $K_y=K_x$

The case of $K_y=K_x$ has been treated in chapter II. If $K_y=K_x$, equations (8) to (10) reduce to the equations of chapter II. In this special case, the motion of the rotor system becomes simple harmonic, since all the coefficients A_l, B_l, and C_l in equations (12) are identically zero except A_0, B_0, and C_0.

CASE OF $K_y=0$

The special limiting case of $K_y=0$ is of interest in the case of a pylon of which the stiffness is negligible along one principal direction with interest centered on the frequencies involving the other principal stiffness. In the case of $K_y=0$, the function $K(1)$ as given by equations (32) becomes identically zero. This result is also evident from the original definition of $K(1)$ as given in equation (28), because one of the values of ω_a, say ω_{a_3}, is of necessity equal to $\pm\omega$. (It will be recalled that ω_a is the frequency as measured in rotating coordinates. In fixed coordinates it would be zero.)

It is possible to give much simpler stability criterions for this case because there are only two K-functions, $K(0)$ and $K(1/2)$, and two values of ω_a, ω_{a_1} and ω_{a_2}, to be determined. The new K-functions may be defined as follows:

$$\left.\begin{aligned} K_1&=\sin^2\left(\frac{\pi\omega_{a_1}}{2\omega}\right)\sin^2\left(\frac{\pi\omega_{a_2}}{2\omega}\right)=-K(0)\\ K_2&=\cos^2\left(\frac{\pi\omega_{a_1}}{2\omega}\right)\cos^2\left(\frac{\pi\omega_{a_2}}{2\omega}\right)=\frac{1+2K(0)-8K\left(\frac{1}{2}\right)}{2}\end{aligned}\right\}\quad(35)$$

In terms of K_1 and K_2, the criterions for stability become

$$0\leqq K_1\leqq 1 \qquad (36a)$$

$$0\leqq K_2\leqq 1 \qquad (36b)$$

$$\sqrt{K_1}+\sqrt{K_2}\leqq 1 \qquad (36c)$$

Given the values of K_1 and K_2, the values of ω_{a_1} and ω_{a_2} can be determined from equations (35). A graph of the relation in equations (35) is given in figure III–2 by means of which the real values of ω_{a_1} and ω_{a_2} can be read off directly once K_1 and K_2 are known.

A graph showing the variation of K_1 and K_2 with $\frac{\omega^2}{K_x/M}$, for the typical parameters $\Lambda_1=0.1$, $\Lambda_2=0$, $\Lambda_3=0.1$, and $K_y=0$, is shown in figure III–3. By use of figure III–2 the values of ω_{a_1} and ω_{a_2} can be obtained. These values are shown in figure III–4 plotted against $\omega/\sqrt{K_x/M}$. Calculations are carried down to $\frac{\omega}{\sqrt{K_x/M}}=0.5$. The general behavior below this speed is discussed in the section entitled "General Behavior of Rotor System as a Function of Rotor Speed."

CASE OF $K_y=\infty$

The formulas for the limiting case of $K_y=\infty$ cannot be obtained conveniently from the general theory. Instead of carrying out the limiting process, it appears preferable to begin by treating the problem as one of only three degrees of freedom (two hinge-deflection coordinates and one hub-position coordinate x) and by developing the theory along lines similar to those used for the general treatment. In this way a system of two simultaneous equations with periodic coefficients is obtained, with the variables θ_1 and x. These equations are solved in a manner similar to that for the general case, the treatment being simpler, however, since the solution has only two principal values of ω_a.

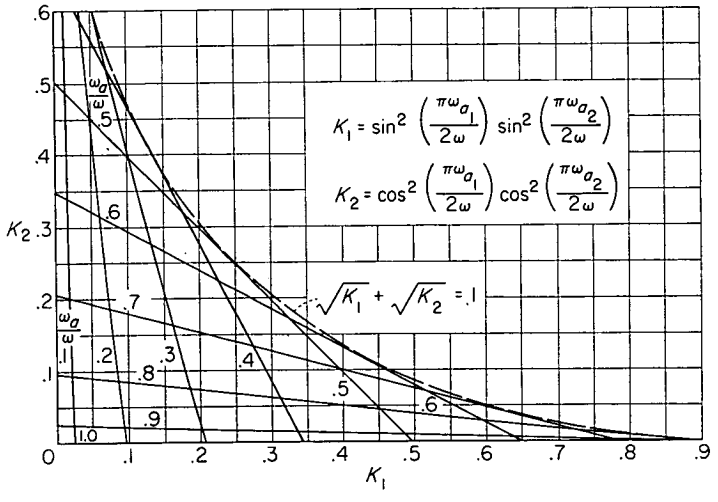


FIGURE III–2.—Chart for obtaining principal value of ω_a from values of K_1 and K_2. $K_y=0$ or $K_y=\infty$.

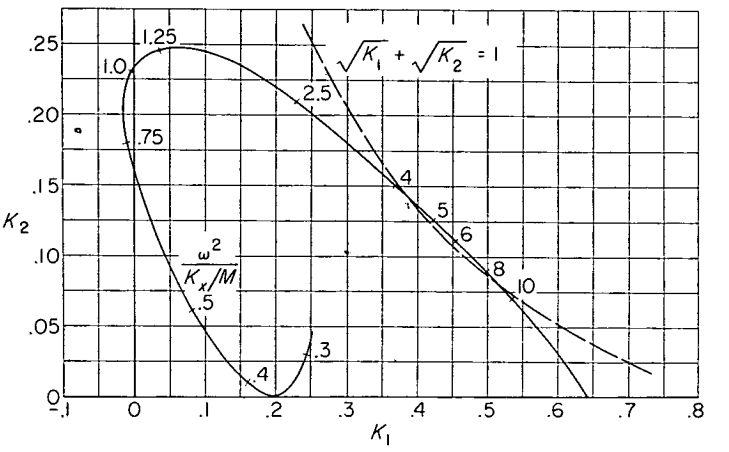


FIGURE III–3.—Graph of K_1 and K_2 as functions of rotor speed ω for $\Lambda_1=0.1$, $\Lambda_2=0$, $\Lambda_3=0.1$, and $K_y=0$.

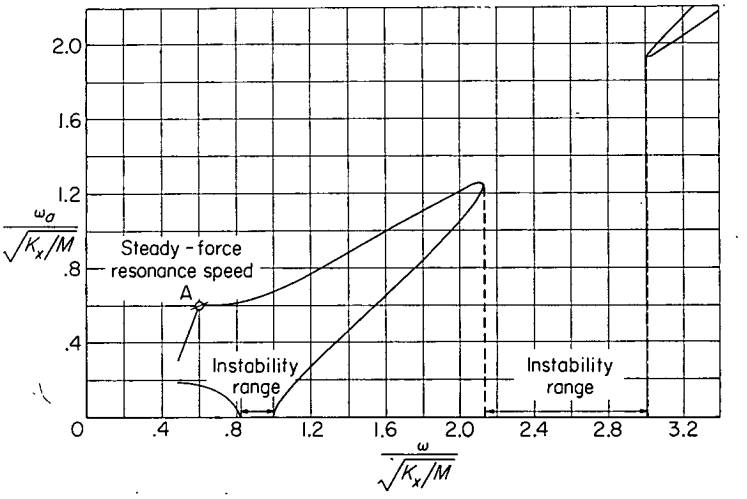


FIGURE III–4.—Principal values of ω_a plotted against rotor speed ω for case of $\Lambda_1=0.1$, $\Lambda_2=0$, $\Lambda_3=0.1$, and $K_y=0$.

The details of the solution of the equations of motion, together with the final formulas for the K-functions, including convergence factors, are given in appendix D. It is found that the same K_1 and K_2 occur as for $K_y=0$. The criterions for stability are exactly the same as those for $K_y=0$, the conditions of equations (36). Figure III–2 can also be used to determine the values of ω_a from the values of K_1 and K_2.

A graph giving the variation of K_1 and K_2 with $\frac{\omega^2}{K_x/M}$ for the parameters $\Lambda_1=0.1$, $\Lambda_2=0$, $\Lambda_3=0.1$, and $K_y=\infty$ is shown in figure III–5. In figure III–6 the values of $\omega_{a_1}/\sqrt{K_x/M}$ and $\omega_{a_2}/\sqrt{K_x/M}$ are shown plotted against $\omega/\sqrt{K_x/M}$.

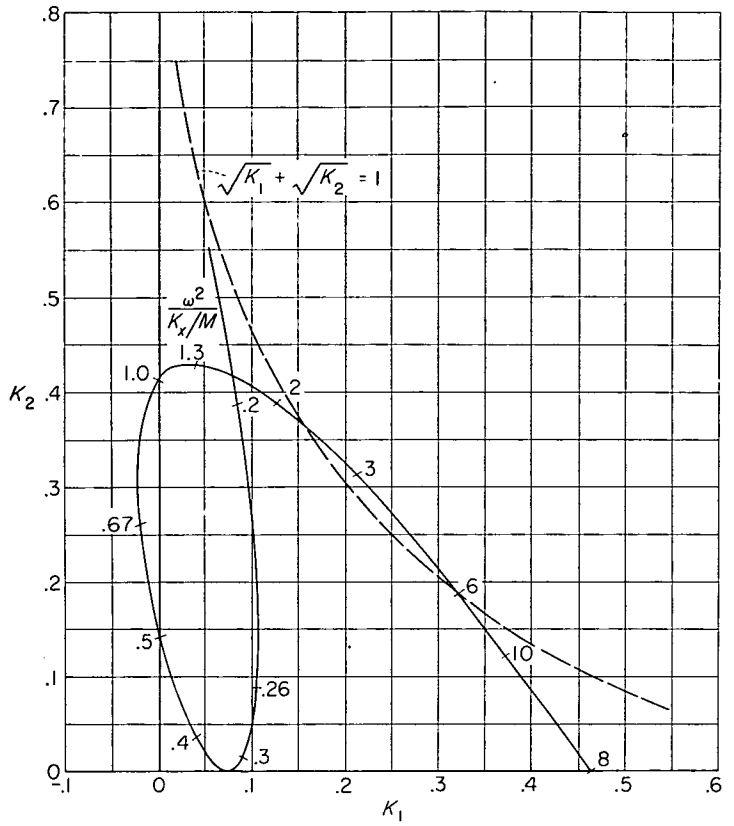


FIGURE III-5.—Graph of K_1 and K_2 as functions of the rotor speed ω for $\Lambda_1=0.1$, $\Lambda_2=0$, $\Lambda_3=0.1$, and $K_y=\infty$.

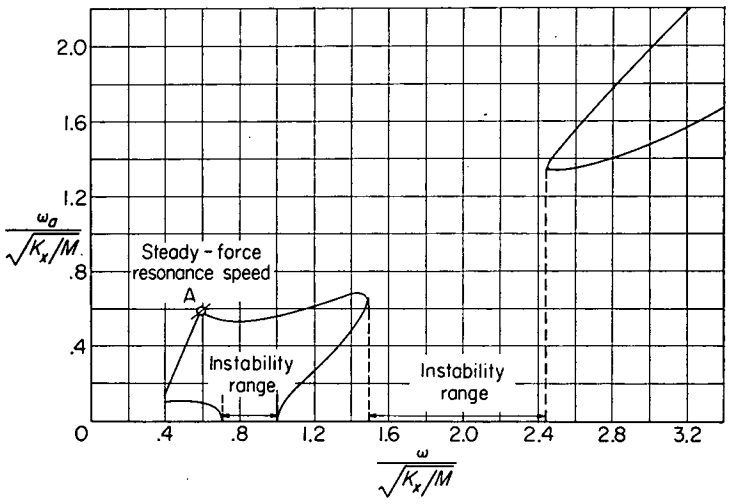


FIGURE III-6.—Principal values of ω_a plotted against rotor speed ω for case of $\Lambda_1=0.1$, $\Lambda_2=0$, $\Lambda_3=0.1$, and $K_y=\infty$.

DISCUSSION OF RESULTS

TYPES OF INSTABILITY

Instability may occur as a result of the violation of any one of the stability criterions of equations (34). Violation of each condition is associated with a different type of instability, which would show up differently in the motion of the rotor system. Experience with computations indicates, however, that the criterions of most practical importance for helicopters are

$$\Delta \geqq 0$$
$$-K(0) \geqq 0$$
$$K(1) \geqq 0$$

Similarly, the important criterions in the limiting cases of $K_y=0$ and $K_y=\infty$ are

$$\sqrt{K_1}+\sqrt{K_2} \leqq 1$$
$$K_1 \geqq 0$$
$$K_2 \geqq 0$$

If the condition $\Delta \geqq 0$ or $(\sqrt{K_1}+\sqrt{K_2} \leqq 1)$ is violated, the other conditions being satisfied, then ω_{a_1} and ω_{a_2} will be complex conjugates, and the rotor system will execute self-excited vibrations at frequencies, in general, incommensurate with the rotor speed. (Higher harmonics will also be present.) This type of instability will be referred to hereinafter as a "self-excited vibration."

If the stability condition $-K(0) \geqq 0$ (or $K_1 \geqq 0$) alone is violated, then one of the values of ω_a will be a pure imaginary number. Physically, the rotor system will execute self-excited vibrations having a basic frequency, as seen in rotating coordinates, of zero. This behavior is similar to the ordinary critical-speed behavior of a shaft. Frequencies at higher harmonics $2n\omega$ will also be present. This type of instability will be referred to as a "self-excited whirling."

The third stability condition $K(1) \geqq 0$ cannot be violated since $K(1)$ as given by equation (32) cannot be negative. However, $K(1)$ can be exactly equal to zero. (A similar statement applies to K_2.) At such a point, where the rotor system is on the border line between stability and instability, one of the values of ω_a will be equal to $\pm\omega$. In fixed coordinates this result means that the rotor system will have a natural frequency equal to zero. The rotor system will, therefore, be in resonance with a steady force—a force of zero frequency. The amplitude of the zero-frequency term for the hub motion in such a situation can be shown to be zero, but the blades will oscillate. Also, higher harmonic terms, notably the term of frequency 2ω (in nonrotating coordinates), will show up in the hub motion. This type vibration, which is a resonance phenomenon and not a self-excited vibration, will be called a "steady-force resonance" vibration.

Each of the vibrations described—self-excited vibrations, self-excited whirling, and a steady-force resonance vibration—appeared in the discussion of the two-blade rotor on equal supports (chapter II); however, there the motions were simple harmonic, no higher harmonics being present.

GENERAL BEHAVIOR OF ROTOR SYSTEM AS A FUNCTION OF ROTOR SPEED

The approximate location of the instability regions can easily be found by examining the limiting case of $\Lambda_3=0$, that is, the case of zero coupling between the blade and hub

motions. For simplicity, the discussion is also restricted to the case of free hinges ($\Lambda_2=0$) and $K_y=\infty$. The K_1 and K_2 functions become

$$\left.\begin{aligned} K_1&=\sin^2\left(\frac{\pi}{2}\sqrt{\Lambda_1}\right)\cos^2\left(\frac{\pi}{2\omega}\sqrt{\frac{K_x}{M}}\right)\\ K_2&=\cos^2\left(\frac{\pi}{2}\sqrt{\Lambda_1}\right)\sin^2\left(\frac{\pi}{2\omega}\sqrt{\frac{K_x}{M}}\right)\end{aligned}\right\} \tag{37}$$

Eliminating the rotor speed ω from equations (37) gives

$$\frac{K_1}{\sin^2\left(\frac{\pi}{2}\sqrt{\Lambda_1}\right)}+\frac{K_2}{\cos^2\left(\frac{\pi}{2}\sqrt{\Lambda_1}\right)}=1$$

which considered as an equation in the variables K_1 and K_2 represents a straight-line segment (one of the lines in fig. III–2) terminated by the K_1 and K_2 axes. The segment can be shown to be tangent to the curve $\sqrt{K_1}+\sqrt{K_2}=1$. As ω decreases, the representative point moves up and down the line segment, performing an infinite number of such oscillations as ω approaches zero. Whenever $K_1=0$, the point is at a self-excited-whirling speed. The corresponding speed is

$$\omega=\frac{\sqrt{K_x/M}}{2s+1}$$

where s represents any positive integer. Thus a self-excited whirling will occur when the rotor speed is approximately equal to 1, ⅓, ⅕, ⅐, and so forth of the natural frequency of the hub $\sqrt{K_x/M}$. Similarly it can be shown that there will be a steady-force resonance vibration whenever the rotor speed is approximately equal to ½, ¼, ⅙, and so forth of the hub natural frequency $\sqrt{K_x/M}$. Finally self-excited vibrations will occur at rotor speeds approximately equal to

$$\omega=\frac{\sqrt{K_x/M}}{2s+1-\sqrt{\Lambda_1}}$$

Figure III–7 shows the general pattern of response frequency plotted against rotor speed for a small value of the mass-ratio parameter Λ_3. Along the horizontal parts of the curves, blade motion predominates over pylon motion. Pylon motion predominates along the slanting parts.

Although the foregoing discussion was developed for the case of $K_y=\infty$, it is believed to apply equally well to the case of $K_y=0$ and also to the general case of $K_y\neq K_x$ if the rotor hub is considered to have two natural frequencies $\sqrt{K_x/M}$ and $\sqrt{K_y/M}$, each frequency having associated with it an infinite set of instability ranges located at approximately the speeds given.

COMPARISON OF RESULTS FOR DIFFERENT VALUES OF K_y/K_x

Figures III–4 and III–6 give the principal values of $\omega_a/\sqrt{K_x/M}$ plotted against the rotor speed $\omega/\sqrt{K_x/M}$ for $K_y=0$ and $K_y=\infty$, respectively, both calculated for the same set of parameters Λ_1, Λ_2, and Λ_3. The calculations have been carried down to $\frac{\omega}{\sqrt{K_x/M}}=0.4$. The similarity between the two curves is striking. So far as the calculations have been carried, each system shows the presence of one self-excited-vibration instability range, one self-excited-whirling instability range, and one steady-force resonance speed A. If the calculations were carried to lower values of ω, further instability ranges and steady-force resonance speeds would appear.

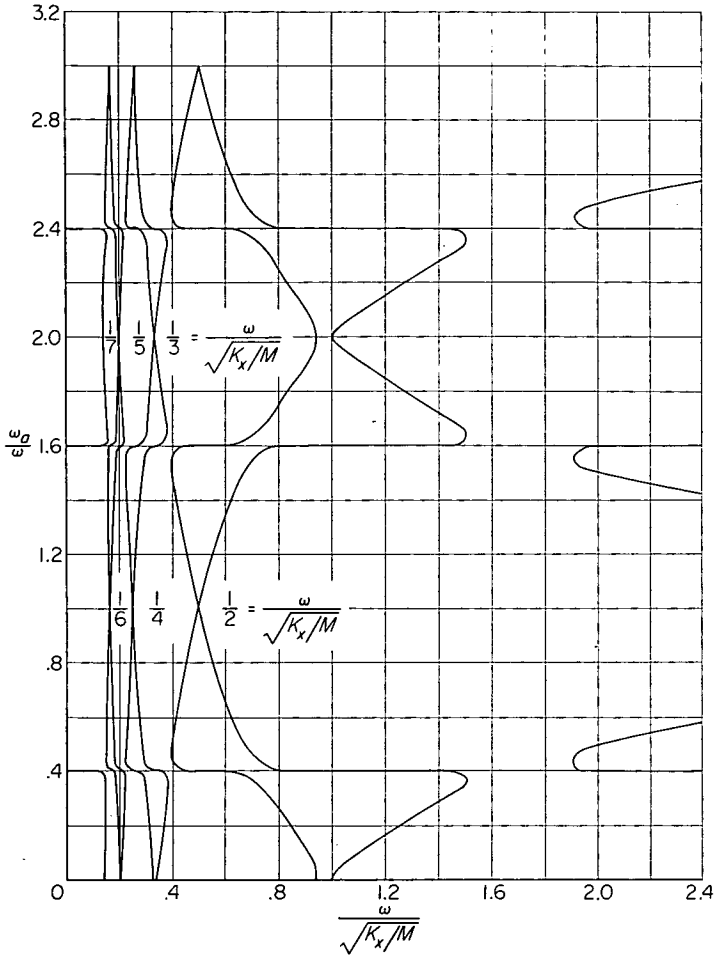


FIGURE III–7.—Typical pattern of response frequencies against rotor speed ω for a small value of the mass-ratio parameter Λ_3.

For comparison, the response frequencies of a two-blade rotor on equal supports ($K_y=K_x$) for the same set of parameters is shown in figure III–8. The frequencies were calculated from the formula in chapter II. Down to $\frac{\omega}{\sqrt{K_x/M}}=0.5$, this chart is very similar to figures III–4 and III–6. In addition it shows one range of rotational speed at which self-excited-vibration instability occurs, one range of rotational speed at which self-excited-whirling instability occurs, and one range of rotational speed at which a steady-force resonance speed occurs. Figure III–8 differs principally from the figures for $K_y\neq K_x$ in that it shows no further instability ranges at low values of ω.

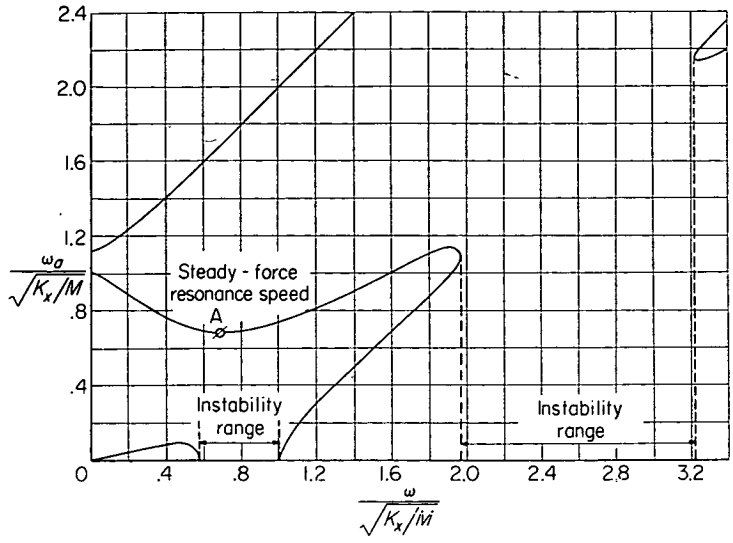


FIGURE III–8.—Response frequencies of a two-blade rotor on symmetric supports for $\Lambda_1=0.1$, $\Lambda_2=0$, $\Lambda_3=0.1$, and $K_y=K_x$.

In chapters I and II charts are presented giving the location of the self-excited-vibration instability range for various values of the parameters Λ_1, Λ_2, and Λ_3. A similar chart for the case of a two-blade rotor with $K_y=\infty$ is given in figure III–9. In using the chart, a straight line is drawn representing the variation of $\frac{\omega^2}{K_x/M}$ with the function $\frac{\Lambda_1\omega^2+\Lambda_2}{K_x/M}$. The intersections of this line with the appropriate Λ_3 curves give the beginning and end points of the instability range. The dashed line in figure III–9 indicates the stability ranges for the parameters of figure III–6.

Some observations concerning the relative location and extent of the various instability ranges in figures III–4, III–6, and III–8 appear to be applicable to a wide range of values of the parameters Λ_1, Λ_2, and Λ_3. Thus the self-excited-vibration instability range in the case of $K_y=K_x$ (fig. III–8) is wider (and hence the vibration probably more severe) than the corresponding ranges in the cases of $K_y=0$ and $K_y=\infty$. (See figs. III–4 and III–6.) Also, this instability range occurs at lower rotor speeds in the case of $K_y=\infty$ than it does in the cases of $K_y=K_x$ and $K_y=0$. The self-excited-whirling instability range is considerably narrower for $K_y=\infty$ than it is for the $K_y=K_x$ case, and it is still narrower in the $K_y=0$ case.

In the general case of $K_y\neq K_x$ the location and extent of the instability ranges can be found fairly accurately by considering the problem as the superposition of two problems, one of finding the significant rotor speeds referred to $\sqrt{K_x/M}$ as reference frequency with K_y assumed infinite and the other of finding the significant rotor speeds referred to $\sqrt{K_y/M}$ as reference frequency with K_x assumed zero. With the foregoing discussion as a guide, sufficiently accurate design information can be obtained without extensive calculations for each value of K_y/K_x encountered in practice.

EFFECT OF DAMPING

Although the effect of damping has not been examined mathematically, because complications would be introduced

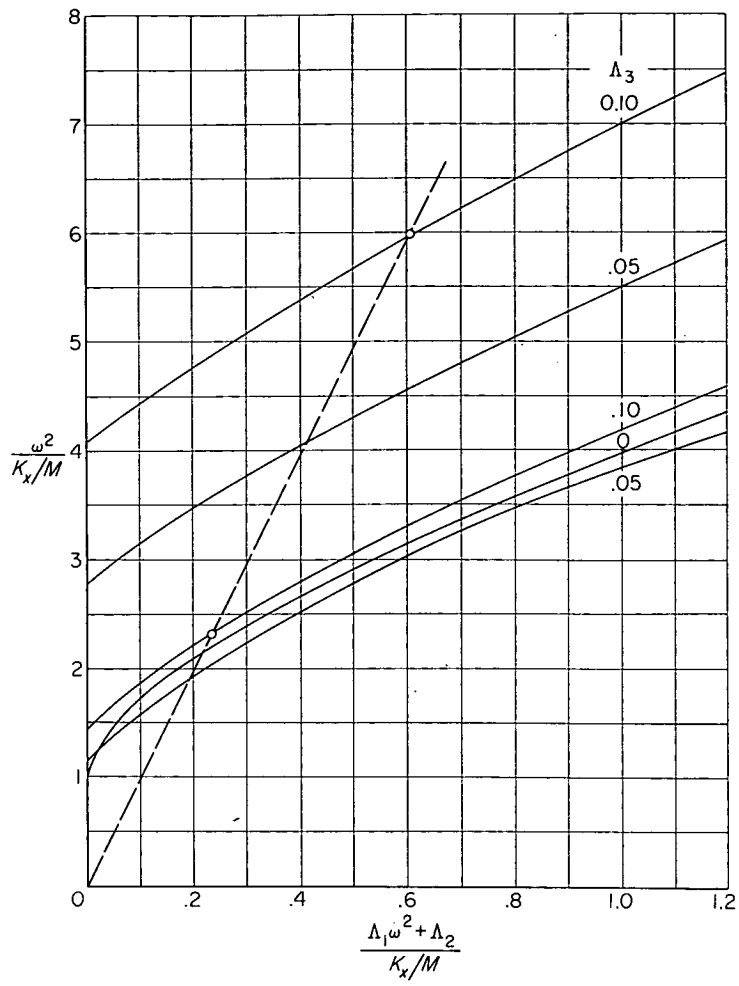


FIGURE III–9.—Chart giving position of the main instability range for $K_y=\infty$.

in the analysis, several inferences from the damping investigations in chapters I and II can probably be safely applied to the rotor-system studies in the present report. The numerous instability ranges occurring at low rotor speeds, which are very narrow and represent a mild type of instability, are probably completely eliminated by the presence of a slight amount of damping in the rotor system. The primary self-excited-vibration instability range can probably be narrowed and eliminated by introducing sufficient damping into both the rotor supports and the blade hinges.

APPLICATION TO DUAL ROTORS

It is easily shown that the analysis for the case of $K_y=\infty$ applies also to the case of a counterrotating rotor system consisting of two equal two-blade rotors revolving at equal speeds and acting equally upon the same flexible member. The rotors may be on the same shaft or on different shafts so long as the nonrotating flexible member is the same for both rotors. The supports, moreover, may have unequal stiffness in the X- and in the Y-directions, provided that the undeflected blade positions make equal angles with a principal stiffness axis.

The proof consists in showing that the energy expressions for the dual-rotating system can be separated into two independent sets of terms, each of which is of the same form as

for a single rotor with $K_y=\infty$. The resulting equations of motion will thus also be the same.

The separation is accomplished by introducing new variables

$$\xi_1=\frac{1}{2}(\theta_{1_{pos}}-\theta_{1_{neg}})$$

$$\xi_0=\frac{1}{2}(\theta_{0_{pos}}-\theta_{0_{neg}})$$

and

$$\eta_1=\frac{1}{2}(\theta_{1_{pos}}+\theta_{1_{neg}})$$

$$\eta_0=\frac{1}{2}(\theta_{0_{pos}}+\theta_{0_{neg}})$$

where the subscripts *pos* and *neg* refer to the θ's defined for the rotor turning in the positive direction and for the rotor turning in the opposite direction, respectively. The energy expressions become

$$\left.\begin{aligned} T=&\frac{1}{2}M\dot{x}^2+2m_b\left[-2\dot{x}(\dot{\xi}_1\sin\omega t+\omega\xi_1\cos\omega t)+\right.\\ &\left.\left(1+\frac{r^2}{b^2}\right)(\dot{\xi}_1^2+\dot{\xi}_0^2)-\frac{a}{b}\omega^2(\xi_1^2+\xi_0^2)\right]+\\ &\frac{1}{2}M\dot{y}^2+2m_b\left[2\dot{y}(\dot{\eta}_1\cos\omega t-\omega\eta_1\sin\omega t)+\right.\\ &\left.\left(1+\frac{r^2}{b^2}\right)(\dot{\eta}_1^2+\dot{\eta}_0^2)-\frac{a}{b}\omega^2(\eta_1^2+\eta_0^2)\right]\\ V=&\frac{2K_\beta}{b^2}(\xi_1^2+\xi_0^2+\eta_1^2+\eta_0^2)+\frac{1}{2}K_xx^2+\frac{1}{2}K_yy^2 \end{aligned}\right\} \quad (38)$$

where M is the total mass of the system ($M=m+4m_b$).

From equations (38) it is seen that ξ is coupled only with x and η is coupled only with y. Equations (38) yield equations of motion of the same form as equations (D2) and (D3).

The stability properties for the dual-rotating case are thus exactly the same as in the case of $K_y=\infty$ for the single-rotating two-blade rotor. In particular, figure III–9 can be used to find the location of the primary self-excited-vibration instability range. The value of Λ_3 for the dual-rotating rotor is defined as $\Lambda_3=\dfrac{2m_b}{(m+4m_b)\left(1+\dfrac{r^2}{b^2}\right)}$ rather than $\Lambda_3=\dfrac{m_b}{(m+2m_b)\left(1+\dfrac{r^2}{b^2}\right)}$ as for the single-rotating rotor. All other parameters are the same for both cases.

The quantity $\xi_1\sin\omega t$ can be interpreted physically as the x-component of the displacement of the center of gravity of the blades due to hinge deflections. The quantity $\eta_1\cos\omega t$ is the corresponding y-component. The separation of the variables means, physically, that the motion of the system can be separated into two independent modes, each of which involves linear motion of the supports along one of the principal stiffness axes.

Similarly, the stability of counterrotating rotor systems of six or more equal blades can be determined from the results of chapter I with $K_y=\infty$.

CONCLUSIONS

The following conclusions are indicated by the results of an investigation of the problem of vibration of a two-blade helicopter rotor on supports that have different stiffnesses along the two principal stiffness axes:

1. Many speed ranges are found in which self-excited oscillations can occur. These oscillations are of two types—self-excited vibration and self-excited whirling. There are also many speeds at which steady-force-resonance vibration may occur.

2. A stability chart which shows the self-excited vibration, self-excited whirling, and steady-force resonance speeds of the highest rotor speed for each support natural frequency for a two-blade rotor on anisotropic supports is similar in appearance to a stability chart for a two-blade rotor on isotropic supports. However, for the same rotor parameters, the instability regions are changed somewhat in position and extent.

3. Mild self-excited-whirling speed ranges exist at rotor speeds approximately ⅓, ⅕, ⅐, and so forth of each support natural frequency. Steady-force resonance speeds exist at approximately ½, ¼, ⅙, and so forth of each support frequency. Self-excited vibrations also occur at certain low rotor speeds. All these mild instability ranges are probably eliminated by the presence of moderate amounts of damping in the system.

4. A familiarity with typical results of limiting cases of the support-spring constants $K_y=\infty$, $K_y=K_x$, and $K_y=0$ should enable a designer to avoid extensive calculations of cases of unequal support stiffness. In the general case of unequal support stiffness, the location and extent of the instability ranges can be found fairly accurately by considering the problem as the superposition of two problems, one of finding significant rotor speeds referred to one support frequency $\sqrt{K_x/M}$ as reference frequency with K_y assumed infinite and the other of finding the significant rotor speeds referred to the other support frequency $\sqrt{K_y/M}$ as reference frequency with K_x assumed zero.

5. The analysis of a four-blade counterrotating rotor system in which the rotors cross along the principal stiffness axes of the rotor supports leads to the same equations as those considered for the special case of $K_y=\infty$, and the stability properties are given by the investigation of that special case.

LANGLEY AERONAUTICAL LABORATORY,
NATIONAL ADVISORY COMMITTEE FOR AERONAUTICS,
LANGLEY FIELD, VA., *August 24, 1956.*

APPENDIX A

SYMBOLS

a	radial position of vertical hinge
$a_{0,0}$, $a_{0,1}$, and so forth	elements of determinant defined in equation (16)
A_l, B_l, C_l	Fourier coefficients in equations (12)
$\overline{A}_l$, $\overline{B}_l$, $\overline{C}_l$	complex conjugates of A_l, B_l, and C_l, respectively
b	distance from vertical hinge to center of mass of blade
$C_n(\omega_a)$, $D_n(\omega_a)$, and so forth	minors of the determinate $\Delta_n(\omega_a)$
D	time-derivative operator, $\frac{d}{dt}$
$F(\omega_a)=\lim_{n\to\infty} F_n(\omega_a)$	
$F_n(\omega_a)=\frac{\Delta_n(\omega_a)}{k^{2n}}$	
j, n, s	integers
$J(\omega_a)$	function of $F(\omega_a)$ defined by equation (27)
$k=2\Lambda_3-1$	
$K(\omega_a/\omega)$	function of ω_a/ω defined in equation (29)
$K(0)$, $K(1)$, $K(1/2)$	functions defined by equations (30)
K_1, K_2	functions defined by equations (35)
K_x, K_y	spring constants of the rotor supports along the X- and Y-directions, respectively
K	average stiffness of rotor supports, $\frac{K_y+K_x}{2}$
$\Delta K=\frac{K_y-K_x}{2}$	
K_β	spring constant of blade self-centering spring
m	effective mass of rotor supports
m_b	mass of rotor blade
M	total mass of two-blade rotor system, $m+2m_b$
$P(t)$, $Q(t)$, $R(t)$	periodic functions defined in equations (11)
$\overline{P}(t)$, $\overline{Q}(t)$, $\overline{R}(t)$	complex conjugates of $P(t)$, $Q(t)$, and $R(t)$, respectively
Q	constant defined in equations (33)
r	radius of gyration of blade about center of mass
t	time
T	kinetic energy
V	potential energy
x, y	deflection of rotor hub measured in fixed X,Y-coordinate system
x_r,y_r	deflection of rotor hub measured in rotating X,Y-coordinate system
X, Y	fixed rectangular coordinate axes taken parallel to the principal stiffness directions of the rotor hub
z	complex position coordinate of the rotor hub in rectangular coordinate system rotating with angular velocity, x_r+iy_r
$\overline{z}$	complex conjugate of z, x_r-iy_r
β_1, β_2	angular hinge deflections of rotor blades, respectively
Δ	discriminant of cubic equation $x^3+bx^2+cx+d=0$
$\Delta(\omega_a)$	determinant of infinite order defined by equation (16)
$\Delta_n(\omega_a)$	determinant of order $6n-3$ formed from $\Delta(\omega_a)$
$\theta_0=\frac{b}{2}(\beta_1+\beta_2)$	
$\theta_1=\frac{b}{2}(\beta_1-\beta_2)$	
$\Lambda_1=\frac{a}{b\left(1+\frac{r^2}{b^2}\right)}$	
$\Lambda_2=\frac{K_\beta}{m_b b^2\left(1+\frac{r^2}{b^2}\right)}$	
$\Lambda_3=\frac{\mu}{2\left(1+\frac{r^2}{b^2}\right)}$	
ξ_1, ξ_0, η_1, η_0	blade variables for counterrotating rotor
μ	mass ratio, $\frac{2m_b}{M}$
ω	constant angular velocity of rotor
ω_a	characteristic exponent or natural frequency of rotor system as viewed in coordinates rotating at angular velocity ω
ω_{a_1}, ω_{a_2}, ω_{a_3}	principle values of ω_a

APPENDIX B

THE GENERAL EQUATIONS OF MOTION FOR TWO-BLADE ROTORS

By George W. Brooks

GENERAL CASE

The present chapter, although it generalizes the theory of ground vibrations of two-blade rotors by treating the case of anisotropic supports, does not consider the effects of damping. Chapter II treated the case of isotropic supports or equal pylon stiffness in all horizontal directions and included damping. The more general case is one which involves the treatment of the two-blade rotor with anisotropic supports and damping. The equations of motion for this case, derived in the complex coordinate notation of the present report, are given in this appendix.

The equations for the kinetic and potential energies of the rotor system are given by equations (5) and (6) of chapter III as follows:

$$T=\frac{M}{2}(\dot{z}+i\omega z)(\dot{\bar{z}}-i\omega\bar{z})+m_b\Big[(\dot{\bar{z}}-i\omega\bar{z})(i\dot{\theta}_1-\omega\theta_1)-(\dot{z}+i\omega z)(i\dot{\theta}_1+\omega\theta_1)+\Big(1+\frac{r^2}{b^2}\Big)(\dot{\theta}_0^2+\dot{\theta}_1^2)-\frac{a}{b}\omega^2(\theta_0^2+\theta_1^2)\Big] \tag{B1}$$

$$V=\frac{K}{2}z\bar{z}+\frac{K_\beta}{b^2}(\theta_0^2+\theta_1^2)-\frac{\Delta K}{4}(z^2e^{2i\omega t}+\bar{z}^2e^{-2i\omega t}) \tag{B2}$$

Two types of damping of the rotor system are assumed to exist: (1) damping in the rotor supports which is proportional to the translational velocity of the rotor hub and (2) damping of the rotation of the blades about the drag hinges. The damping dissipation function is then

$$F=\frac{B}{2}[\dot{z}\dot{\bar{z}}+\omega^2z\bar{z}+i\omega(z\dot{\bar{z}}-\bar{z}\dot{z})]+\frac{B_\beta}{b^2}(\dot{\theta}_0^2+\dot{\theta}_1^2) \tag{B3}$$

where B is the damping force per unit velocity of rotor-hub displacements and B_β is the damping torque per unit angular velocity of blade motion about the drag hinge.

By using the Lagrangian form of the equations of motion

$$\frac{d}{dt}\Big(\frac{\partial T}{\partial\dot{x}}\Big)-\frac{\partial T}{\partial x}+\frac{\partial F}{\partial\dot{x}}+\frac{\partial V}{\partial x}=0 \tag{B4}$$

and using as variables θ_0, $\bar{z}$, z, and θ_1, respectively, the following equations of motion for the rotor system are obtained:

$$(D^2+D\lambda_\beta+\omega^2\Lambda_1+\Lambda_2)\theta_0=0 \tag{B5}$$

$$\Big[(D+i\omega)^2+\lambda(D+i\omega)+\frac{K}{M}\Big]z-\frac{\Delta K}{M}\bar{z}e^{-2i\omega t}+i\mu(D+i\omega)^2\theta_1=0 \tag{B6}$$

$$-\frac{\Delta K}{M}ze^{2i\omega t}+\Big[(D-i\omega)^2+\lambda(D-i\omega)+\frac{K}{M}\Big]\bar{z}-i\mu(D-i\omega)^2\theta_1=0 \tag{B7}$$

$$(D+i\omega)^2z-(D-i\omega)^2\bar{z}+2i\Big(1+\frac{r^2}{b^2}\Big)(D^2+D\lambda_\beta+\Lambda_1\omega^2+\Lambda_2)\theta_1=0 \tag{B8}$$

where two additional combinations of parameters have been introduced, namely,

$$\lambda_\beta=\frac{B_\beta}{m_bb^2\Big(1+\frac{r^2}{b^2}\Big)}$$

and

$$\lambda=\frac{B}{M}$$

SPECIAL CASE—ZERO DAMPING

If damping is neglected, $\lambda_\beta=\lambda=0$ and the equations of motion, (B5) to (B8), reduce to

$$(D^2+\omega^2\Lambda_1+\Lambda_2)\theta_0=0 \tag{B9}$$

$$\Big[(D+i\omega)^2+\frac{K}{M}\Big]z-\frac{\Delta K}{M}\bar{z}e^{-2i\omega t}+i\mu(D+i\omega)^2\theta_1=0 \tag{B10}$$

$$-\frac{\Delta K}{M}ze^{2i\omega t}+\Big[(D-i\omega)^2+\frac{K}{M}\Big]\bar{z}-i\mu(D-i\omega)^2\theta_1=0 \tag{B11}$$

$$(D+i\omega)^2z-(D-i\omega)^2\bar{z}+2i\Big(1+\frac{r^2}{b^2}\Big)(D^2+\Lambda_1\omega^2+\Lambda_2)\theta_1=0 \tag{B12}$$

which are the equations of motion (eqs. (7) to (10)) for the case treated in the present chapter.

SPECIAL CASE OF ISOTROPIC SUPPORTS

If $K_x=K_y$, then $\Delta K=0$ and equations (B5) to (B8) reduce to

$$(D^2+D\lambda_\beta+\omega^2\Lambda_1+\Lambda_2)\theta_0=0 \tag{B13}$$

$$\Big[(D+i\omega)^2+\lambda(D+i\omega)+\frac{K}{M}\Big]z+i\mu(D+i\omega)^2\theta_1=0 \tag{B14}$$

$$\Big[(D-i\omega)^2+\lambda(D-i\omega)+\frac{K}{M}\Big]\bar{z}-i\mu(D-i\omega)^2\theta_1=0 \tag{B15}$$

$$(D+i\omega)^2z-(D-i\omega)^2\bar{z}+2i\Big(1+\frac{r^2}{b^2}\Big)(D^2+D\lambda_\beta+\Lambda_1\omega^2+\Lambda_2)\theta_1=0 \tag{B16}$$

Equation (B13) involves only the in-phase motion of the blades, can be solved separately, and will not be further considered here. If z and $\bar{z}$ are expressed in the equivalent notations $x+iy$ and $x-iy$, respectively, and equations (B14) and (B15) are added together, equation (1) of chapter II is obtained. Equation (2) of chapter II is obtained by direct substitution and equation (3) is obtained by subtraction of equation (B15) from equation (B14). Thus the equations of motion for the case treated in chapter II as well as for the case treated in the present report are shown to be special cases of the general equations of motion, equations (B5) to (B8), for a rotor mounted on anisotropic supports with hub and blade-hinge damping.

APPENDIX C

DERIVATION OF THE CONVERGENCE FACTOR FOR $K(0)$

A convergence factor for $K(0)$ is found by finding a simpler function G_n that changes with n in nearly the same way as $K(0)_n$. Then, if G denotes $\lim_{n\to\infty} G_n$, the expression

$$\frac{K(0)_n G}{G_n}$$

for a given value of n is a better approximation to $K(0)$ than is $K(0)_n$ alone. A suitable form for G_n is found from a study of the behavior of $K(0)_n$ for large values of n.

The behavior of $K(0)_n$ is studied by first observing the behavior of $C_n(0)$ and $L_n(0)$ for large values of n and then inferring the behavior of $K(0)_n$ from the appropriate relation of equations (32). In the discussion of equations (22) it was shown that, as n becomes infinite, the ratio C_{n+1}/C_n approaches the value k (eq. (22a)). A closer approximation to the value of this ratio can be written as

$$\frac{C_{n+1}(0)}{C_n(0)} = k\left(1 - \frac{P}{n} - \frac{Q}{4n^2}\right) \tag{C1}$$

where P and Q are constants to be determined.

Equations (19) become, for $\omega_a = 0$,

$$\left.\begin{aligned} C_{n+1}(0) &= \left[-1 + \frac{K/M}{(2n+1)^2\omega^2}\right] D_n(0) - \Lambda_3\left(\frac{2n+1}{2n}\right)^2 E_n(0) \\ D_{n+1}(0) &= \left[-1 + \frac{\Lambda_1\omega^2 + \Lambda_2}{(2n)^2\omega^2}\right] E_n(0) - \Lambda_3\left(\frac{2n-1}{2n}\right)^2 C_n(0) \\ E_{n+1}(0) &= \left[-1 + \frac{K/M}{(2n-1)^2\omega^2}\right] C_n(0) \end{aligned}\right\} \tag{C2}$$

where the second term in the equation for $E_n(\omega_a)$ in equations (19) has been neglected as being of higher order in powers of $1/n$ than the terms retained. Eliminating $E(0)$ and $D(0)$ from the equations (C2) results in

$$\frac{C_{n+1}(0)}{C_n(0)} = \left[-1 + \frac{K/M}{(2n+1)^2\omega^2}\right]\left[-1 + \frac{\Lambda_1\omega^2 + \Lambda_2}{(2n)^2\omega^2}\right]\left[-1 + \frac{K/M}{(2n-1)^2\omega^2}\right] - \Lambda_3\left\{\left(\frac{2n-1}{2n}\right)^2\left[-1 + \frac{K/M}{(2n+1)^2\omega^2}\right] + \left(\frac{2n+1}{2n}\right)^2\left[-1 + \frac{K/M}{(2n-1)^2\omega^2}\right]\right\}$$

Upon expanding this expression into powers of $1/n$ and retaining terms up to and including those in $1/n^2$

$$\frac{C_{n+1}(0)}{C_n(0)} = -1 + 2\Lambda_3 - \frac{1}{(2n)^2}\left[-\frac{2\frac{K}{M} + \Lambda_1\omega^2 + \Lambda_2}{\omega^2} + 2\Lambda_3\left(\frac{K/M}{\omega^2} - 1\right)\right] \tag{C3}$$

Comparing equation (C3) with equation (C1) results in

$$P = 0$$

$$Q = \frac{2\frac{K}{M}(1-\Lambda_3) + \Lambda_1\omega^2 + \Lambda_2 + 2\Lambda_3\omega^2}{\omega^2(1-2\Lambda_3)}$$

Similarly

$$\frac{L_{n+1}(0)}{L_n(0)} = k\left[1 - \frac{Q}{(2n)^2}\right]$$

Therefore, from equations (32)

$$\frac{K(0)_{n+1}}{K(0)_n} = \left(1 - \frac{Q}{4n^2}\right)^2$$

Hence, an approximate value of $K(0)$ can be obtained from

$$\frac{K(0)}{K(0)_n} \equiv \frac{K(0)_{n+1}}{K(0)_n}\frac{K(0)_{n+2}}{K(0)_{n+1}}\frac{K(0)_{n+3}}{K(0)_{n+2}}\cdots$$

$$\approx \prod_{j=n}^{\infty}\left(1 - \frac{Q}{4j^2}\right)^2 = \frac{\sin^2\left(\frac{\pi\sqrt{Q}}{2}\right)}{\frac{\pi^2 Q}{4}\prod_{j=1}^{n-1}\left(1 - \frac{Q}{4j^2}\right)^2} \tag{C4}$$

The right-hand side of equation (C4), which is seen to be of the form G/G_n, is a convergence factor. This convergence factor is the one used in equations (33).

APPENDIX D

MATHEMATICAL ANALYSIS FOR THE CASE OF $K_y = \infty$

In terms of the variables θ_0, θ_1, and x, the expressions for the kinetic and potential energy are

$$T=\frac{M}{2}\dot{x}^2+m_b\left[\left(1+\frac{r^2}{b^2}\right)(\dot{\theta}_0^2+\dot{\theta}_1^2)-\omega^2\frac{a}{b}(\theta_0^2+\theta_1^2)-2\dot{x}(\theta_1\sin\omega t+\omega\theta_1\cos\omega t)\right]$$

$$V=\frac{K_x}{2}x^2+\frac{K_\beta}{b^2}(\theta_0^2+\theta_1^2)$$

The three equations of motion are

$$\ddot{\theta}_0+(\omega^2\Lambda_1+\Lambda_2)\theta_0=0 \tag{D1}$$

$$\ddot{x}+\frac{K_x}{M}x-\mu\frac{d^2}{dt^2}(\theta_1\sin\omega t)=0 \tag{D2}$$

$$-\frac{1}{1+\frac{r^2}{b^2}}\ddot{x}\sin\omega t+\ddot{\theta}_1+(\omega^2\Lambda_1+\Lambda_2)\theta_1=0 \tag{D3}$$

Equation (D1) is identical with equation (7). Equations (D2) and (D3) constitute a system of two linear second-order differential equations with periodic coefficients.

Equations (D2) and (D3) are satisfied by solutions of the form

$$\left.\begin{aligned} x&=\sum_{l=-\infty}^{\infty}A_l e^{i(\omega_a+l\omega)t}\\ \theta_1&=\sum_{l=-\infty}^{\infty}B_{l+1}e^{i[\omega_a+(l+1)\omega]t}\end{aligned}\right\} \tag{D4}$$

where l takes on all odd integral values and A_l and B_{l+1} are constants to be determined along with the two principal values of ω_a (ω_{a_1} and ω_{a_2}). The constants A_l and B_{l+1} in equations (D4) are, of course, different from those in equations (12).

Combining equations (D4) with equations (D2) and (D3) and setting the coefficients of the various exponential time factors equal to zero give

$$\left[-1+\frac{K_x/M}{(\omega_a+l\omega)^2}\right]A_l-\frac{\mu}{2i}(-B_{l-1}+B_{l+1})=0$$

$$-\frac{1}{2i\left(1+\frac{r^2}{b^2}\right)}\left\{-\left[\frac{\omega_a+(l-2)\omega}{\omega_a+(l-1)\omega}\right]A_{l-2}+\left[\frac{\omega_a+l\omega}{\omega_a+(l-1)\omega}\right]^2A_l\right\}+\left\{-1+\frac{\omega^2\Lambda_1+\Lambda_2}{[\omega_a+(l-1)\omega]^2}\right\}B_{l-1}=0$$

The determinantal equation is then equal to

$$\begin{vmatrix}
\cdot & \cdot & \cdot & \cdot & \cdot & \cdot & \cdot & \\
\cdot & \cdot & \cdot & \cdot & \cdot & \cdot & \cdot & \\
\cdot & \cdot & \cdot & \cdot & \cdot & \cdot & \cdot & \\
\cdots & a_{-3,-3} & a_{-3,-2} & 0 & 0 & 0 & 0 & 0 & \cdots \\
\cdots & a_{-2,-3} & a_{-2,-2} & a_{-2,-1} & 0 & 0 & 0 & 0 & \cdots \\
\cdots & 0 & a_{-1,-2} & a_{-1,-1} & a_{-1,0} & 0 & 0 & 0 & \cdots \\
\cdots & 0 & 0 & a_{0,-1} & a_{0,0} & a_{0,1} & 0 & 0 & \cdots \\
\cdots & 0 & 0 & 0 & a_{1,0} & a_{1,1} & a_{1,2} & 0 & \cdots \\
\cdots & 0 & 0 & 0 & 0 & a_{2,1} & a_{2,2} & a_{2,3} & \cdots \\
\cdots & 0 & 0 & 0 & 0 & 0 & a_{3,2} & a_{3,3} & \cdots \\
 & \cdot & \cdot & \cdot & \cdot & \cdot & \cdot & \cdot & \\
 & \cdot & \cdot & \cdot & \cdot & \cdot & \cdot & \cdot & \\
 & \cdot & \cdot & \cdot & \cdot & \cdot & \cdot & \cdot &
\end{vmatrix} = \Delta(\omega_a)=0$$

where

$$a_{-3,-3}=-1+\frac{K_x/M}{(\omega_a-3\omega)^2} \qquad a_{0,0}=-1+\frac{\Lambda_1\omega^2+\Lambda_2}{\omega_a^2}$$

$$a_{-3,-2}=\frac{\Lambda_3}{2} \qquad a_{0,1}=\left(\frac{\omega_a+\omega}{\omega_a}\right)^2$$

$$a_{-2,-3}=\left(\frac{\omega_a-3\omega}{\omega_a-2\omega}\right)^2 \qquad a_{1,0}=\frac{\Lambda_3}{2}$$

$$a_{-2,-2}=-1+\frac{\omega^2\Lambda_1+\Lambda_2}{(\omega_a-2\omega)^2} \qquad a_{1,1}=-1+\frac{K_x/M}{(\omega_a+\omega)^2}$$

$$a_{-2,-1}=\left(\frac{\omega_a-\omega}{\omega_a-2\omega}\right)^2 \qquad a_{1,2}=\frac{\Lambda_3}{2}$$

$$a_{-1,-2}=\frac{\Lambda_3}{2} \qquad a_{2,1}=\left(\frac{\omega_a+\omega}{\omega_a+2\omega}\right)^2$$

$$a_{-1,-1}=-1+\frac{K_x/M}{(\omega_a-\omega)^2} \qquad a_{2,2}=-1+\frac{\omega^2\Lambda_1+\Lambda_2}{(\omega_a+2\omega)^2}$$

$$a_{-1,0}=\frac{\Lambda_3}{2} \qquad a_{2,3}=\frac{\omega_a+3\omega}{(\omega_a+2\omega)^2}$$

$$a_{0,-1}=\left(\frac{\omega_a-\omega}{\omega_a}\right)^2 \qquad a_{3,2}=\frac{\Lambda_3}{2}$$

$$a_{3,3}=-1+\frac{K_x/M}{(\omega_a+3\omega)^2}$$

The term $-1+\frac{\omega^2\Lambda_1+\Lambda_2}{\omega_a^2}$ will be taken as the origin of the determinant.

Define $\Delta_n(\omega_a)$ as the determinant of order $4n-1$ formed by taking a square array from $\Delta(\omega_a)$ centered on the origin. Then

$$\Delta(\omega_a)=\lim_{n\to\infty}\Delta_n(\omega_a)$$

Define auxiliary determinants from $\Delta_n(\omega_a)$ as follows:

$C_n(\omega_a)$ determinant of order $2n-1$ consisting of the terms to the right of and below the origin term

$D_n(\omega_a)$ determinant of order $2n-2$ obtained from $C_n(\omega_a)$ by omitting its last row and column

$M_n(\omega_a)$ determinant of order $2n-2$ obtained from $C_n(\omega_a)$ by omitting its first row and column

$N_n(\omega_a)$ determinant of order $2n-3$ obtained from $D_n(\omega_a)$ by omitting its first row and column

The determinants $C_n(\omega_a)$ and $D_n(\omega_a)$ satisfy the following recurrence relations:

$$\left.\begin{aligned} C_n(\omega_a)&=\left\{-1+\frac{K_x/M}{[\omega_a+(2n-1)\omega]^2}\right\}D_n(\omega_a)-\\ &\quad\frac{\Lambda_3}{2}\left[\frac{\omega_a+(2n-1)\omega}{\omega_a+(2n-2)\omega}\right]^2 C_{n-1}(\omega_a)\\ D_n(\omega_a)&=\left\{-1+\frac{\omega^2\Lambda_1+\Lambda_2}{[\omega_a+(2n-2)\omega]^2}\right\}C_{n-1}(\omega_a)-\\ &\quad\frac{\Lambda_3}{2}\left[\frac{\omega_a+(2n-3)\omega}{\omega_a+(2n-2)\omega}\right]^2 D_{n-1}(\omega_1) \end{aligned}\right\} \quad (D5)$$

The recurrence relations (eqs. (D5)) are also satisfied by $M_n(\omega_a)$ and $N_n(\omega_a)$, with M and N replacing C and D respectively. The initial values are

$$C_1(\omega_a)=-1+\frac{K_x/M}{(\omega_a+\omega)^2}$$

$$D_2(\omega_a)=\left[1-\frac{K_x/M}{(\omega_a+\omega)^2}\right]\left[1-\frac{\omega^2\Lambda_1+\Lambda_2}{(\omega_a+2\omega)^2}\right]-\frac{\Lambda_3}{2}\left(\frac{\omega_a+\omega}{\omega_a+2\omega}\right)^2$$

$$N_2(\omega_a)=-1+\frac{\omega^2\Lambda_1+\Lambda_2}{(\omega_a+2\omega)^2}$$

$$M_2(\omega_a)=\left[1-\frac{\omega^2\Lambda_1+\Lambda_2}{(\omega_a+2\omega)^2}\right]\left[1-\frac{K_x/M}{(\omega_a+3\omega)^2}\right]-\frac{\Lambda_3}{2}\left(\frac{\omega_a+3\omega}{\omega_a+2\omega}\right)^2$$

Expanding $\Delta_n(\omega_a)$ in terms of the elements of the column containing the origin gives

$$\Delta_n(\omega_a)=\left(-1+\frac{\omega^2\Lambda_1+\Lambda_2}{\omega_a^2}\right)C_n(-\omega_a)C_n(\omega_a)-$$
$$\frac{\Lambda_3}{2}\left[\left(\frac{\omega_a-\omega}{\omega_a}\right)^2 C_n(\omega_a)M_n(-\omega_a)-\left(\frac{\omega_a+\omega}{\omega_a}\right)^2 C_n(-\omega_a)M_n(\omega_a)\right]$$

As n becomes infinite, or as ω_a becomes infinite, the recurrence relations (eqs. (D5)) approach

$$\left.\begin{aligned} C_n&=-D_n-\frac{\Lambda_3}{2}C_{n-1}\\ D_n&=-C_{n-1}-\frac{\Lambda_3}{2}D_{n-1} \end{aligned}\right\} \quad (D6)$$

Equations (D6) are satisfied by a solution of the form

$$\left.\begin{aligned} C_n&=Ck^n\\ D_n&=-C\left(k+\frac{\Lambda_3}{2}\right)k^{n-1} \end{aligned}\right\} \quad (D7)$$

where k satisfies the equation

$$k^2-(1-\Lambda_3)k+\frac{\Lambda_3^2}{4}=0 \quad (D8)$$

The larger root of equation (D8) will be denoted by k and the smaller root by k_1. Although the complete solution of equation (D6) is of the form

$$C_n=Ck^n+C'k_1^n$$

for large values of n the term in k_1 becomes negligible compared with the term in k.

With the same values for k, M_n and N_n will have solutions similar to those of equations (D7). Thus as n becomes infinite $\Delta_n(\omega_a)$ will vary as the quantity k^{2n}.

Define the function

$$F(\omega_a)=\lim_{n\to\infty}F_n(\omega_a)=\lim_{n\to\infty}\frac{\Delta_n(\omega_a)}{k^{2n}}$$

The function $F(\omega_a)$ is periodic in ω_a of period 2ω, has roots

$\pm(\omega_{a_1}\pm 2s\omega)$, $\pm(\omega_{a_2}\pm 2s\omega)$, and second-order poles at $(\omega_a\pm s\omega)$ for all integral values of s. Furthermore, $F(\omega_a)$ approaches the limit

$$E=\lim_{\omega_a\to\infty} F(\omega_a)=\lim_{n\to\infty} F_n(\infty)$$

$$=\lim_{n\to\infty}\frac{C_{2n}(\infty)}{k^{2n}}=\frac{k^2}{k_1^2-k^2}$$

as ω_a becomes infinite in a direction other than along the real axis.

Form the function

$$J(\omega_a)=F(\omega_a)\frac{\sin^2\left(\frac{\pi\omega_a}{\omega}\right)}{\left[\sin^2\left(\frac{\pi\omega_a}{2\omega}\right)-\sin^2\left(\frac{\pi\omega_{a_1}}{2\omega}\right)\right]\left[\sin^2\left(\frac{\pi\omega_a}{2\omega}\right)-\sin^2\left(\frac{\pi\omega_{a_2}}{2\omega}\right)\right]} \tag{D9}$$

The function $J(\omega_a)$ is an analytic function of ω_a everywhere. Hence, by Liouville's theorem, $J(\omega_a)$ is a constant. By letting $\omega_a\to+\infty$ along the imaginary axis, it is seen that $J(\omega_a)=-4E$.

Substituting $-4E$ for $J(\omega_a)$ into equation (D9) results in

$$\lim_{n\to\infty}\frac{\Delta_n(\omega_a)}{k^{2n}}=F(\omega_a)$$

$$=-4E\frac{\left[\sin^2\left(\frac{\pi\omega_a}{2\omega}\right)-\sin^2\left(\frac{\pi\omega_{a_1}}{2\omega}\right)\right]\left[\sin^2\left(\frac{\pi\omega_a}{2\omega}\right)-\sin^2\left(\frac{\pi\omega_{a_2}}{2\omega}\right)\right]}{\sin^2\left(\frac{\pi\omega_a}{\omega}\right)}$$

Introducing K functions defined similarly to those used for the case $K_y=0$ gives

$$\left.\begin{aligned} K_1&\doteq\sin^2\left(\frac{\pi\omega_{a_1}}{2\omega}\right)\sin^2\left(\frac{\pi\omega_{a_2}}{2\omega}\right)\\ &=\lim_{\omega_a\to 0}\left[\frac{\sin^2\left(\frac{\pi\omega_a}{\omega}\right)F(\omega_a)}{-4E}\right]\\ K_2&=\cos^2\left(\frac{\pi\omega_{a_1}}{2\omega}\right)\cos^2\left(\frac{\pi\omega_{a_2}}{2\omega}\right)\\ &=\lim_{\omega_a\to\omega}\left[\frac{\sin^2\left(\frac{\pi\omega_a}{2\omega}\right)F(\omega_a)}{-4E}\right] \end{aligned}\right\} \tag{D10}$$

Carrying out the limit processes indicated in equations (D10) gives

$$K_1=\lim_{n\to\infty}K_{1_n}$$

$$=\lim_{n\to\infty}\left[\frac{\pi^2(\omega^2\Lambda_1+\Lambda_2)C_n^2(0)-\Lambda_3\pi^2\omega^2C_n(0)N_n(0)}{-4\omega^2C_{2n}(\infty)}\right]$$

$$K_2=\lim_{n\to\infty}K_{2_n}$$

$$=\lim_{n\to\infty}\left[\frac{\pi^2\frac{K_z}{M}kN_n^2(-\omega)}{-4\omega^2C_{2n}(\infty)}\right]$$

Finally, upon introducing appropriate convergence factors, the following quantities needed in equations (36) are obtained:

$$K_1=\lim_{n\to\infty}\left[\frac{K_{1_n}\sin^2\left(\frac{\pi R}{2}\right)}{\frac{\pi^2R^2}{4}\prod_{j=1}^{n}\left(1-\frac{R^2}{4j^2}\right)^2}\right]$$

$$K_2=\lim_{n\to\infty}\left\{\frac{K_{2_n}\cos^2\left(\frac{\pi R}{2}\right)}{\prod_{j=1}^{n}\left[1-\frac{R^2}{(2j-1)^2}\right]^2}\right\}$$

where

$$R^2=\frac{\frac{K_z}{M}+\omega^2\Lambda_1+\Lambda_2+\omega^2(1+k_1-k)}{\omega^2(k-k_1)}$$

REFERENCES

1. Foote, W. R., Poritsky, H., and Slade, J. J., Jr.: Critical Speeds of a Rotor With Unequal Shaft Flexibilities, Mounted in Bearings of Unequal Flexibility—I. Jour. Appl. Mech., vol. 10, no. 2, June 1943, pp. A-77—A-84.
2. Den Hartog, J. P.: Mechanical Vibrations. Second ed., McGraw-Hill Book Co., Inc., 1940, pp. 380-396.
3. Whittaker, E. T., and Watson, G. N.: A Course of Modern Analysis. Fourth ed., Cambridge Univ. Press (London), 1927. (Reprinted 1940.)

REPORT 1352

EFFECT OF FUEL VARIABLES ON CARBON FORMATION IN TURBOJET-ENGINE COMBUSTORS[1]

By Edmund R. Jonash, Jerrold D. Wear, and William P. Cook

SUMMARY

The effects of fuel properties and of a number of fuel additives on combustion-chamber carbon deposition and exhaust-gas smoke formation were investigated in a single tubular turbojet-engine combustor. Limited tests were conducted with a number of the fuels in several full-scale turbojet engines to verify single-combustor data.

At operating conditions simulating an engine with a compressor pressure ratio of 4 at an altitude of 20,000 feet and zero flight speed (condition A), carbon deposits and exhaust-gas smoke densities in the single combustor correlated with three empirical fuel factors: smoke-volatility index, smoke point, and NACA K factor (function of distillation characteristics and hydrogen-carbon ratio). The best correlations of deposits were obtained with smoke point and NACA K factor. At a condition of higher inlet air pressure and temperature simulating an engine with a compressor pressure ratio of 7 at sea level and a flight Mach number of 0.87 (condition B), the deposits and smoke densities did not satisfactorily correlate with any of the fuel factors considered. Further, only the data obtained at condition A correlated with limited full-scale-engine deposit data obtained with the same fuels. Deposits obtained at the higher pressure and temperature were considerably less uniform, and it is likely that large formations broke off the combustor walls during the test runs.

Carbon deposits in the single combustor were significantly reduced at condition A by the addition of organo-metallic compounds, commercial fuel additives that usually contained organo-metallic compounds, and oxygen-bearing compounds. Organo-metallic compounds, particularly those containing lead or iron, were most effective: dicyclopentadienyliron reduced deposits of a base fuel as much as 80 percent. The relative effectiveness of the additives depended on the properties of the base fuel. None of the additives significantly affected exhaust-gas smoke concentration.

INTRODUCTION

Carbon deposition in the combustors of turbojet engines constitutes an important operational problem, since such deposition can impair (1) combustion performance by affecting air and fuel distribution, (2) starting performance by fouling ignition electrodes, and (3) liner durability by causing liner cracking and warping. The presence of carbon as smoke in the exhaust gases of turbojet engines is less important; it does not, in general, impair engine performance, but it may be objectionable from a tactical or a nuisance standpoint. Deposits and smoke may be minimized by proper combustor design and by selection of fuel properties. However, presently known remedies are not completely compatible with other combustor performance requirements and with fuel availability. Experiments aimed toward developing means of controlling carbon formation by limiting fuel characteristics and by using fuel additives are reported herein.

Many investigations have been conducted in both small-scale and full-scale combustors in an effort to develop a satisfactory means of predicting the carbon-forming propensity of turbojet fuels from results of simple laboratory fuels tests. Much of this work is summarized in reference 1. Approximate relations were found between deposits and several empirical factors derived from fuel properties. Smoke point, measured with a simple laboratory wick lamp, and NACA K factor, an empirical function of distillation characteristics and hydrogen-carbon ratio, gave the most accurate predictions of deposits for the data presented in reference 1. A "smoke-volatility index" (*SVI*) is currently included in military procurement specifications to limit carbon-deposition tendencies of jet fuels. This index, which is a function of the distillation characteristics and smoke point of the fuel, is easily determined and also has shown a satisfactory degree of correlation with deposits. The relation between smoke-volatility index and carbon formation in turbojet combustors with jet fuels varying widely in physical and chemical properties is examined herein. Also the relations obtained with the smoke-volatility index are compared with those obtained with smoke point and the NACA K factor.

Twenty fuels were tested in a single tubular turbojet combustor operated at conditions simulating an engine with a compressor pressure ratio of 4 at zero flight speed and an altitude of 20,000 feet. The fuels included a number of production JP–3 and JP–4 fuel samples and a number of fuels specially blended to provide wide variations in "fuel quality." In order to examine the effect of operating conditions on deposition, and hence on the general applicability of the fuel factors, six fuels were tested in the same combustor at conditions simulating operation in an engine with a compressor pressure ratio of 7 at a flight Mach number of 0.87 at sea level. The data obtained are generally limited to carbon deposition in the combustion chamber; however, some information is included on exhaust-gas smoke concentration with several of the fuels. Limited data obtained with some of the fuels in several full-scale engines are presented and compared with the single-combustor results.

[1] Supersedes recently declassified NACA Research Memorandums E52G11 by Edmund R. Jonash, Jerrold D. Wear, and William P. Cook; E52H21 by Edmund R. Jonash, Jerrold D Wear, and William P. Cook; E53D15 by Jerrold D. Wear; E54H23 by Vincent F. Hlavjn and William P. Cook; E55D28 by Edmund R. Jonash, Helmut F. Butze, and William P. Cook; E55F30a by Edmund R. Jonash and William P. Cook; and E55J31 by Edmund R. Jonash, William P. Cook, and Jerrold D. Wear.

Preceding Page Blank

The use of a fuel additive capable of markedly reducing carbon deposition in combustion chambers would allow wider variations in jet fuel properties and hence greater fuel availability. A large variety of fuel additives has been suggested for preventing and removing carbon deposits in commercial furnaces and diesel engines. Several investigations in turbojet combustors have indicated at least moderate success with materials such as amyl nitrate, thiophene, and organo-metallic compounds (refs. 2 to 8). Carbon-deposition studies with some of the more promising fuel additives were conducted at the NACA Lewis laboratory, and the results of these studies are presented herein. The additives included four organo-metallic compounds, ten commercial fuel additives (most of which contained organo-metallic compounds), and nine oxygen-bearing compounds. The additives were blended, in most cases, with a No. 2 furnace oil. Limited data were also obtained with some of the additives blended with JP–3 and JP–4 fuels. Several additives were examined in more than one concentration to determine the effect of concentration. All experiments were conducted at the conditions simulating an engine with a pressure ratio of 4. The exhaust-gas smoke concentration was also measured.

FUELS AND ADDITIVES

The fuels used in this investigation are described in table I. They are designated by NACA-assigned numbers. Engine operating experience with fuels containing small concentrations of high-boiling aromatic hydrocarbons has shown that these components contribute markedly to carbon deposition.

TABLE I.—FUELS USED IN INVESTIGATION

Fuel (a)	Fuel type (b)	Description
50–264	JP–3	"Low quality"
51–353	JP–3	90 Weight-percent 50–264 plus 10 weight-percent triisopropylbenzene; high-boiling single-ring aromatic blend
52–50	JP–3	90 Weight-percent 50–264 plus 10 weight-percent of mixture of α- and β-monomethylnaphthalene; high-boiling dycyclic aromatic blend
52–32	JP–4	60 Weight-percent 50–264 plus 40 weight-percent triisopropylbenzene; high-boiling single-ring aromatic blend with H–C ratio very similar to 52–50
52–53	JP–4	"High-quality"
52–105	JP–4	90 Weight-percent 52–53 plus 10 weight-percent of mixture of α- and β-monomethylnaphthalene; high-boiling dicyclic aromatic blend; base fuel for additive tests
52–117	JP–4	"High quality"; blended from high-purity isoparaffinic hydrocarbons
52–118	JP–4	52–117 With low-boiling aromatic substituted for 15 percent isoparaffins of corresponding boiling range
52–119	JP–4	52–118 With polyethylbenzene substituted for isoparaffins of corresponding boiling range
52–120	JP–4	52–118 With methylnaphthalene substituted for isoparaffins of corresponding boiling range
52–166	JP–3	"Low quality"
52–28	JP–4	Used in single-combustor and full-scale-engine tests
52–30	JP–3	
52–76	JP–4	
54–108	JP–4	
54–109	JP–4	
54–110	JP–4	
54–111	JP–4	
52–288	JP–4	"High quality"
53–49	JP–4	
54–41	JP–4	"Low quality"; base fuel for additive tests
49–162	JP–3	Base fuels for additive tests
49–224	High-boiling aromatic	
53–193	Furnace oils	
55–89		

[a] NACA designation.
[b] "Fuel type" refers only to volatility characteristics. Many of these fuels do not fall within MIL–F–5624B specifications in all respects.

The effects of high-boiling single-ring and dicyclic aromatic hydrocarbons on deposition were investigated with fuels 50–264, 51–353, 52–32, 52–50, 52–53, and 52–105 prepared at the NACA Lewis laboratory. The effects of low- and high-boiling single-ring aromatics and high-boiling dicyclic aromatics on deposition were investigated with fuels 52–117, 52–118, 52–119, and 52–120, which were distributed by the Coordinating Research Council as a part of a cooperative research program on carbon deposition. Fuels 54–108, 54–109, 54–110, and 54–111 were similarly distributed by the Coordinating Research Council to study the reliability of the smoke-volatility index as a measure of the carbon-forming propensity of JP–4 fuels. Most of the remaining fuels were JP–3 and JP–4 fuels of both high and low quality with respect to carbon-forming tendencies; many were obtained from refinery production batches. Fuels 49–162, 49–224, 53–193, and 55–89 were base fuels for most of the additive tests; 52–105 and 54–41 were also used as base fuels in some of these tests.

Fuel 52–30 (JP–3) is indicated herein as a fuel tested in both the single combustor and in a full-scale engine. Actually, the full-scale test was conducted with two different batches of JP–3 fuel. Fuel 52–30 was blended from these two batches, in the same proportions as used in the full-scale engine. The components of the blend had similar physical and chemical properties.

Analyses of the fuels examined are presented in table II. Smoke-volatility index (*SVI*) is defined as

$$SVI = \text{Smoke point} + 0.42(\text{vol.-percent fuel boiling under } 400^\circ \text{ F})$$

Military fuel procurement specification MIL–F–5624B, which contains an *SVI* limitation, requires that smoke point be determined by method 2107 of specification VV–L–791. Most of the fuels listed in table II were tested before the acceptance of this method. The smoke points reported for these fuels were measured with the modified Davis factor lamp described in reference 9. The two test methods agree reasonably well, and no distinction is made between them in this report.

The NACA *K* factor (table II) is a function of the volatility and hydrogen-carbon ratio of the fuel:

$$K = (t+600)(0.7)\,\frac{(\text{H/C})-0.207}{(\text{H/C})-0.259}$$

where t is the volumetric average boiling temperature (°F), and H/C is the hydrogen-carbon ratio. Values of the *K* factor were estimated from an enlargement of figure 3 of reference 1.

Although the mechanism by which additives might reduce carbon formation is not understood, it has been suggested that the presence of an oxygen-bearing compound in the area where carbon is formed may result in oxidation of the carbon. Some success has been obtained in experiments with alkyl nitrates, particularly amyl nitrate (ref. 5). Other means of providing an oxygen-bearing compound would be fuel-soluble organo-metallic compounds, which, when burned, will produce a metallic oxide. The additives listed in table

526507—60——21

TABLE II.—FUEL PROPERTIES

	MIL-F-5624B		NACA fuel																								
	Grade JP-3	Grade JP-4	49-162	49-224	50-264	51-353	52-28	52-30	52-32	52-50	52-53	52-76	52-105	52-117	52-118	52-119	52-120	52-166	52-288	53-49	53-193	54-41	54-108	54-109	54-110	54-111	55-89
ASTM distillation D86-52, °F:																											
Percent evaporated:																											
Initial point	------	------	109	327	100	124	137	119	128	114	136	142	134	135	144	143	139	105	139	130	356	146	130	136	170	146	378
5	------	------	135	352	120	170	178	167	189	167	183	201	183	200	207	208	202	142	224	205	406	198	171	176	220	192	408
10	------	------	158	357	152	205	194	199	234	205	200	220	204	233	229	233	226	175	253	247	430	235	210	217	240	224	426
20	240 (max.)	270 (max.)	210	364	224	260	217	244	304	263	225	244	231	278	257	266	261	243	291	310	460	278	273	267	268	267	448
30	------	------	270	372	268	295	236	272	350	293	244	263	253	322	284	295	291	289	311	348	482	312	324	304	288	295	468
40	------	------	323	383	301	322	256	295	397	322	263	283	272	366	318	328	338	320	324	376	500	339	356	329	312	321	485
50	350 (max.)	370 (max.)	358	393	330	358	275	316	422	356	278	304	291	390	358	354	379	351	333	395	516	359	372	348	334	341	500
60	------	------	398	406	368	401	299	337	434	401	301	324	314	409	393	382	404	389	347	418	530	393	386	367	352	361	516
70	------	------	432	421	413	428	317	362	442	425	321	348	343	430	418	405	426	419	363	435	548	434	399	385	378	381	532
80	------	------	462	444	444	445	347	401	449	451	347	381	381	455	446	437	445	416	382	452	564	477	410	403	406	407	554
90	470 (max.)	470 (max.)	500	482	477	469	400	460	458	474	400	438	431	485	479	473	467	470	413	474	590	521	426	423	438	445	580
End point	------	------	584	583	512	512	486	517	500	516	498	494	488	536	533	533	532	515	486	510	622	572	475	476	499	514	613
Residue, %	1.5	1.5	1.0	1.4	1.2	1.3	1.2	1.4	1.1	1.2	1.2	1.2	0.9	1.7	1.7	1.5	1.1	1.3	-----	-----	1.5	1.2	1.0	1.2	1.5	1.5	2.0
Loss, %	1.5	1.5	1.0	.3	1.8	.3	.6	1.1	.4	.8	.7	.8	.3	.3	.4	.3	.4	.8	-----	-----	0	.8	1.0	.8	0	.5	0
Freezing point, °F	−76 (max.)	−76 (max.)	<−76	<−76	<−76	-----	-----	-----	-----	-----	-----	<−76	-----	<−76	<−76	<−76	<−76	<−76	<−76	<−76	−15	<−76	<−76	<−76	<−76	<−76	2
Reid vapor pressure, lb/sq in.	5.0–7.0	2.0–3.0	4.5	-----	6.0	-----	2.8	5.4	2.6	----	2.9	2.3	-----	2.1	1.9	1.9	2.0	6.1	2.7	2.3	-----	2.3	2.0	2.4	1.7	2.4	-----
Aromatics, % by volume	25.0 (max.)	25.0 (max.)	31	96	26	-----	10	-----	-----	-----	10.7	24	17	3	19	27	26	24	10	14	30	26.5	26.9	28.1	16.3	22.1	22.4
Bromine number	------	------	12	-----	8.0	-----	-----	-----	-----	-----	-----	-----	-----	2.5	2.9	2.4	4.9	10.6	-----	2.0	6	7.0	-----	-----	-----	-----	5.4
Accelerated gum, mg/100 ml	14 (max.)	14 (max.)	16	-----	12	-----	-----	-----	-----	-----	-----	3	-----	21	12	22	23	51	-----	12	61	80	85.7	34.7	5.1	15.3	37
Existent gum, mg/100 ml	7 (max.)	7 (max.)	8	-----	9	-----	-----	-----	-----	-----	-----	1	-----	4	5	5	11	18	-----	3	25	51	4.1	1.9	2.3	5.6	3
Hydrogen-carbon ratio [a]	------	------	0.150	0.111	0.153	0.152	0.171	0.168	0.149	0.148	0.170	0.156	0.160	0.181	0.168	0.163	0.156	0.152	0.168	[b]0.161	0.147	0.149	0.152	0.154	0.164	0.158	0.152
Heat of combustion, [c] Btu/lb	18,400 (min.)	18,400 (min.)	18,500	18,475	18,460	18,400	18,725	18,675	18,275	18,350	18,700	18,475	18,575	19,050	18,825	18,700	18,650	18,425	18,675	18,525	18,400	18,300	18,400	18,450	18,600	18,475	18,475
Aniline-gravity product	5250 (min.)	5250 (min.)	-----	-----	5119	4441	7460	6945	3138	3942	7335	5133	6059	10,518	8353	7212	6844	4703	6950	5547	4415	4160	4355	4888	6383	5455	5054
Specific gravity, 60°/60° F	------	------	0.801	0.907	0.791	0.804	0.756	0.771	0.822	0.816	0.757	0.787	0.779	0.752	0.768	0.778	0.791	0.800	0.776	0.811	0.861	0.825	0.803	0.793	0.785	0.794	0.849
Gravity, °API	50–60	45–55	-----	-----	47.3	44.5	55.8	52.1	40.6	41.8	55.4	48.2	50.2	56.7	52.7	50.4	47.3	45.4	50.8	43.0	32.9	40.0	44.8	47.0	48.8	46.7	35.1
Aniline point, °F	------	------	-----	-----	108.8	99.8	133.7	133.3	77.3	94.3	132.4	106.5	120.7	185.5	158.5	143.1	144.7	103.6	136.8	129.0	134.2	104.0	97.2	104.0	130.8	116.8	144.0
Smoke-volatility index	54.0 (min.)	54.0 (min.)	-----	-----	45.5	38.9	78	66	28.2	36.9	72.3	51	59.3	68.2	54.4	49.5	42.6	42.3	68.3	43	13.5	40.1	43.8	49.5	55.9	49.4	15.1
Smoke point, mm	------	------	-----	-----	[d]17.2	[d]13.9	[d]40.0	[d]32.3	[d]11.0	[d]11.9	[d]34.5	[d]16.5	[d]24.0	[d]45.1	[d]28.1	[d]21.0	[d]18.0	[d]15.6	[d]32.0	[e]21.0	11.8	[e]13.7	[e]14.2	[e]17.0	[e]23.6	[e]17.1	13.8
NACA K factor [f]	------	------	345	455	331	341	252	277	363	353	258	316	300	227	285	304	332	338	278	321	415	357	341	330	295	318	393

[a] Determined by combustion furnace.
[b] Method not listed.
[c] Estimated from aniline-gravity constant.
[d] Determined by modified Davis factor lamp (ref. 9).
[e] Determined by method 2107 of specification VV-L-791.
[f] Ref. 1.

TABLE III.—COMPOSITIONS OF ADDITIVE BLENDS

Additive	Composition	Additive concentrations: By volume, Gal additive / 1000 Gal fuel	Additive concentrations: By weight, percent by weight of blend	NACA base fuel
Materials of known composition				
n-Propyl nitrate		4.12, 8.27	0.5, 1.0	53–193
Amyl nitrate		4.32, 8.68	0.5, 1.0	53–193
Isooctyl nitrate		4.52, 9.08	0.5, 1.0	53–193
n-Butyl nitrate	Technical grade	30.9	3.7	55–89
Amyl nitrite	29.4 Weight-percent isoamyl nitrite, 70.6 weight-percent *n*-amyl nitrite.	28.1	2.76	55–89
2-Nitropropane	Technical grade	30.9	3.5	55–89
Nitrobenzol	Technical grade	30.9	4.2	55–89
tert-Butyl hydroperoxide.	60 Weight-percent solution in *tert*-butyl alcohol.	30.9	3.1	55–89
Diethyl ether	Pure grade	30.9	2.5	55–89
Dicyclopentadienyliron.	30 Weight-percent iron.		0.005, 0.01, 0.03, 0.04, 0.05	53–193
Cadmium naphthenate.	10 Weight-percent cadmium.		0.2	53–193
Lead naphthenate.	37 Weight-percent lead.		0.0025, 0.005 0.01, 0.10	52–105
			0.0025, 0.005	49–224
Tetraethyl lead	64 Weight-percent lead.		0.00145, 0.00292	49–224
Commercial additives [1]				
A	Lead, copper	1.0	0.106	53–193
		0.50, 1.0	0.0531, 0.1062	53–193
		1.0	0.1062	54–41
B	Copper, calcium	1.0	0.0982	53–193
C	Chromium	0.91	0.1000	53–193
D	Calcium, sodium	0.25	0.0299	53–193
		.25	.0299	54–41
E	Cobalt	1.06	0.1096	53–193
F	Lead, cobalt	1.0	0.0970	53–193
			0.05, 0.10, 0.21	49–162
G	Calcium	0.50, 1.0	0.0488, 0.0975	53–193
H	Lead	2.50	0.283	53–193
I	Lead	2.50	0.266	53–193
J	Lead	2.50	0.259	53–193

[1] Composition is result of qualitative spectroscopic analyses.

III that are of known composition were chosen to represent a variety of oxygen-bearing organic materials, including four alkyl nitrates, an alkyl nitrite, two nitro-compounds, a peroxide, an ether, and a variety of organo-metallic compounds of iron, cadmium, or lead. Two different compounds of lead were tested, lead naphthenate and tetraethyl lead. The commercial additives listed in table III varied in their intended application. They included diesel fuel additives, gasoline additives, and oil furnace cleaners. None were developed specifically for turbojet combustor application, but all were intended to remove or retard carbon and soot formation resulting from the combustion of low-grade fuels. In most cases these additives contained only a small concentration of an active ingredient in a fuel-soluble carrier. They were examined spectroscopically to determine their principal elemental constituents.

The additive concentrations investigated (table III) were based on published and unpublished test data obtained from other laboratories and on recommendations by the manufacturers of the additives. In several cases a number of

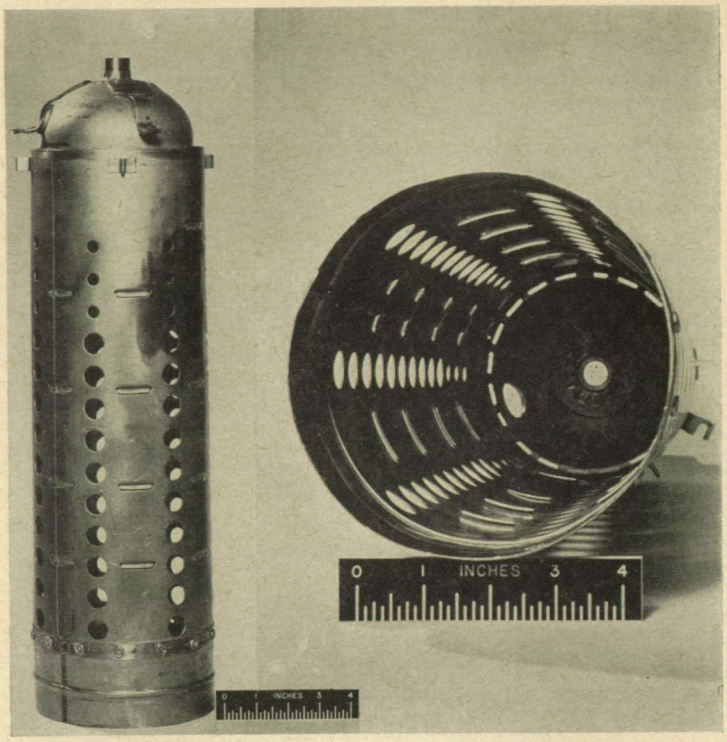


FIGURE 1.—Liner and dome of J33 single combustor used in carbon-deposition investigation.

additive concentrations were investigated; in many cases the quantity of additive available limited the number of tests conducted. Since the experiments were made over a period of years, several different base fuels were employed. The base fuels were chosen for their high carbon-forming propensity.

APPARATUS AND PROCEDURE

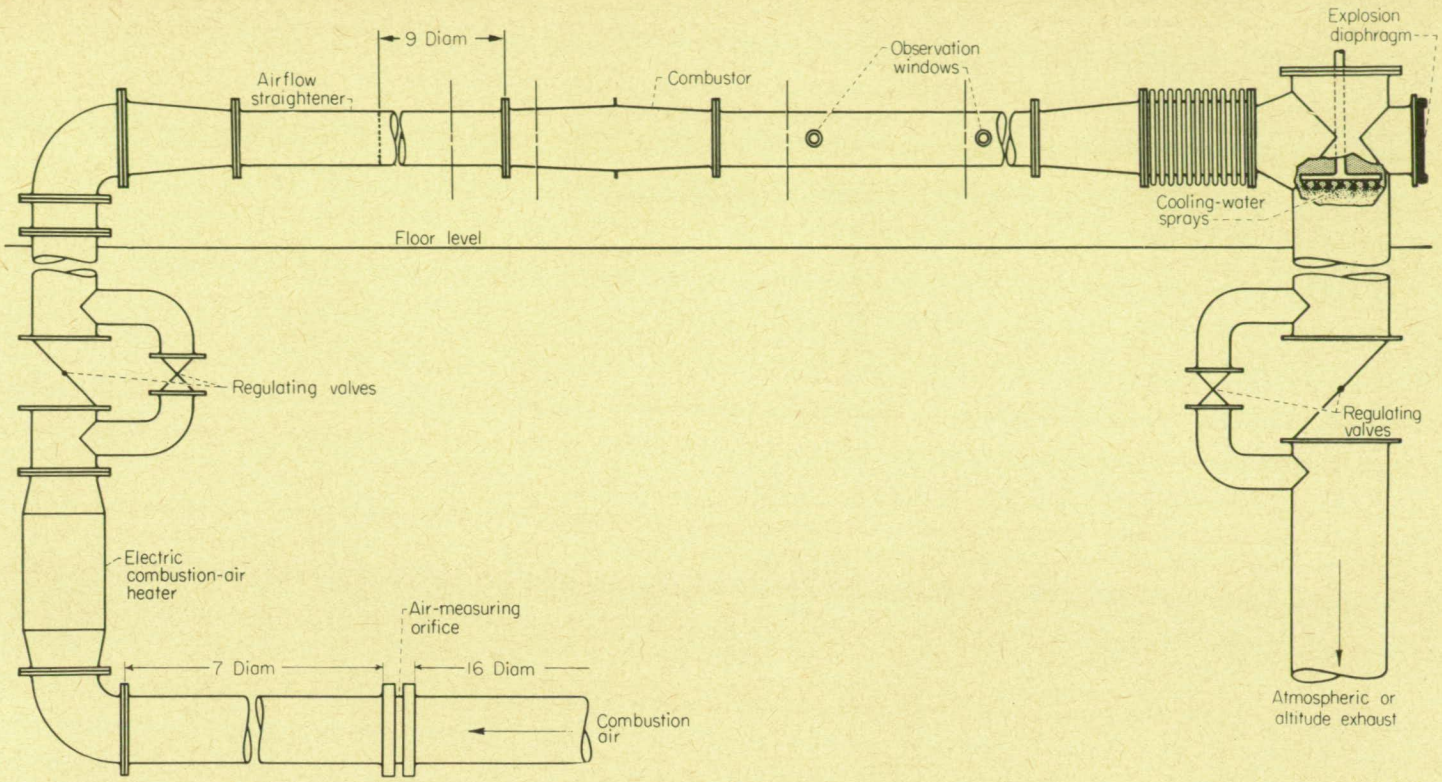
SINGLE COMBUSTORS

Installation.—The single-combustor tests were conducted with the J33 liner and dome assembly shown in figure 1. The liner and dome from a production engine were welded together to assure consistent alinement of parts in each test. The facility in figure 2(a) was used for tests at low inlet air pressure and temperature, and that in figure 2(b) for the higher inlet air pressure and temperature. The combustor liner and dome were installed in a housing similar to the J33 combustor housing, except that circular inlet and exhaust transition sections were used. Airflow rate and air pressure in the combustor were controlled by remotely operated valves in the combustor inlet and outlet ducting. Water-spray nozzles in the exhaust ducts cooled the gases prior to their passage through the exhaust control valves.

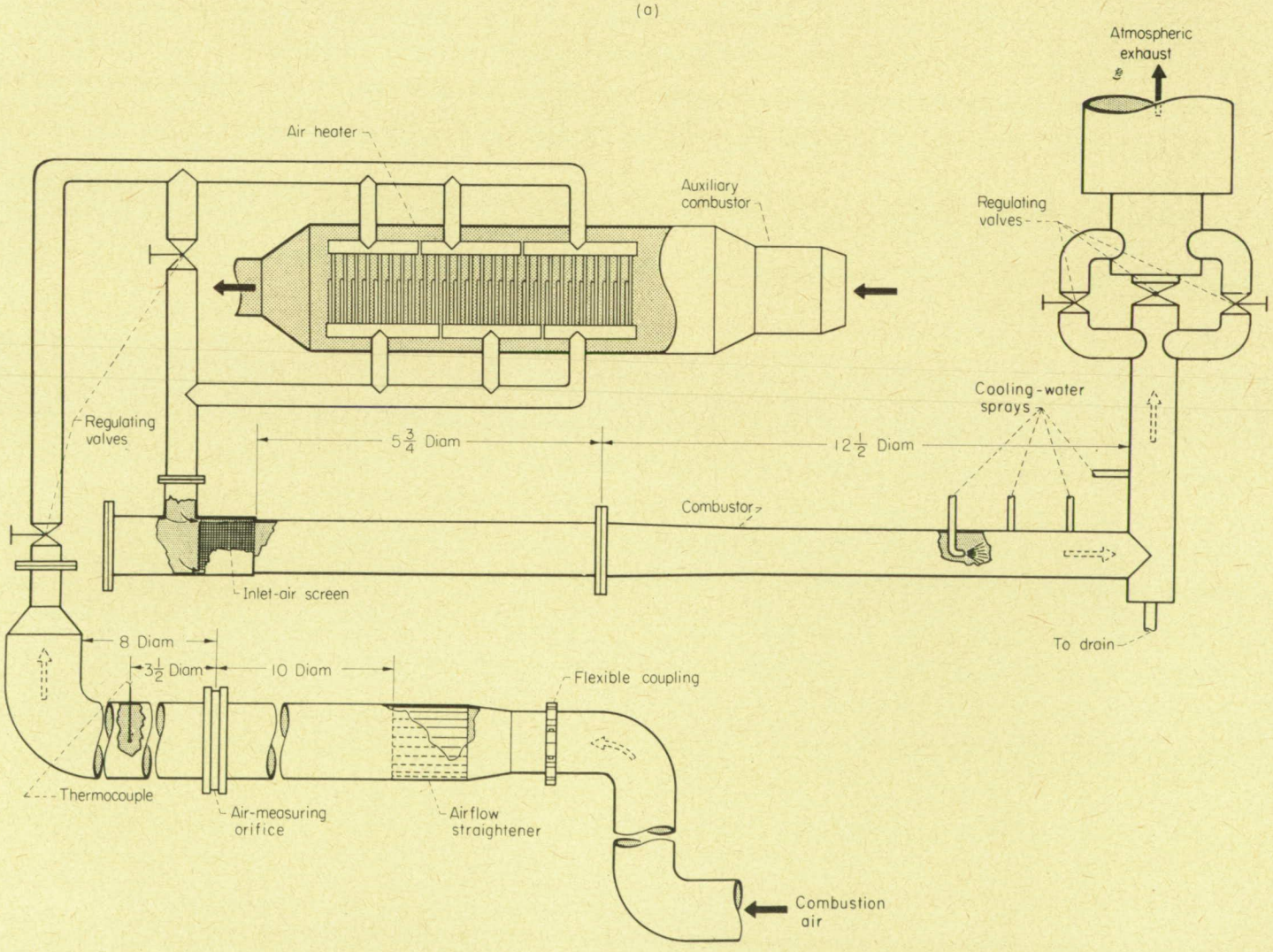
The desired combustor-inlet air temperature was obtained by using either electric preheaters (fig. 2(a)) or a gasoline-fired heat exchanger (fig. 2(b)). The gasoline-fired heat exchanger consisted of a series of coiled Inconel tubes, connected in parallel, through which the high-pressure air flowed. The tubes were heated externally, in crossflow, by combustion gases from an auxiliary turbojet combustor. Airflow and fuel-flow rates to the combustor were measured by means of square-edged orifice plates (installed according to ASME specifications) and calibrated rotameters, respectively.

(a) Low-pressure facility. (b) High-pressure facility. →

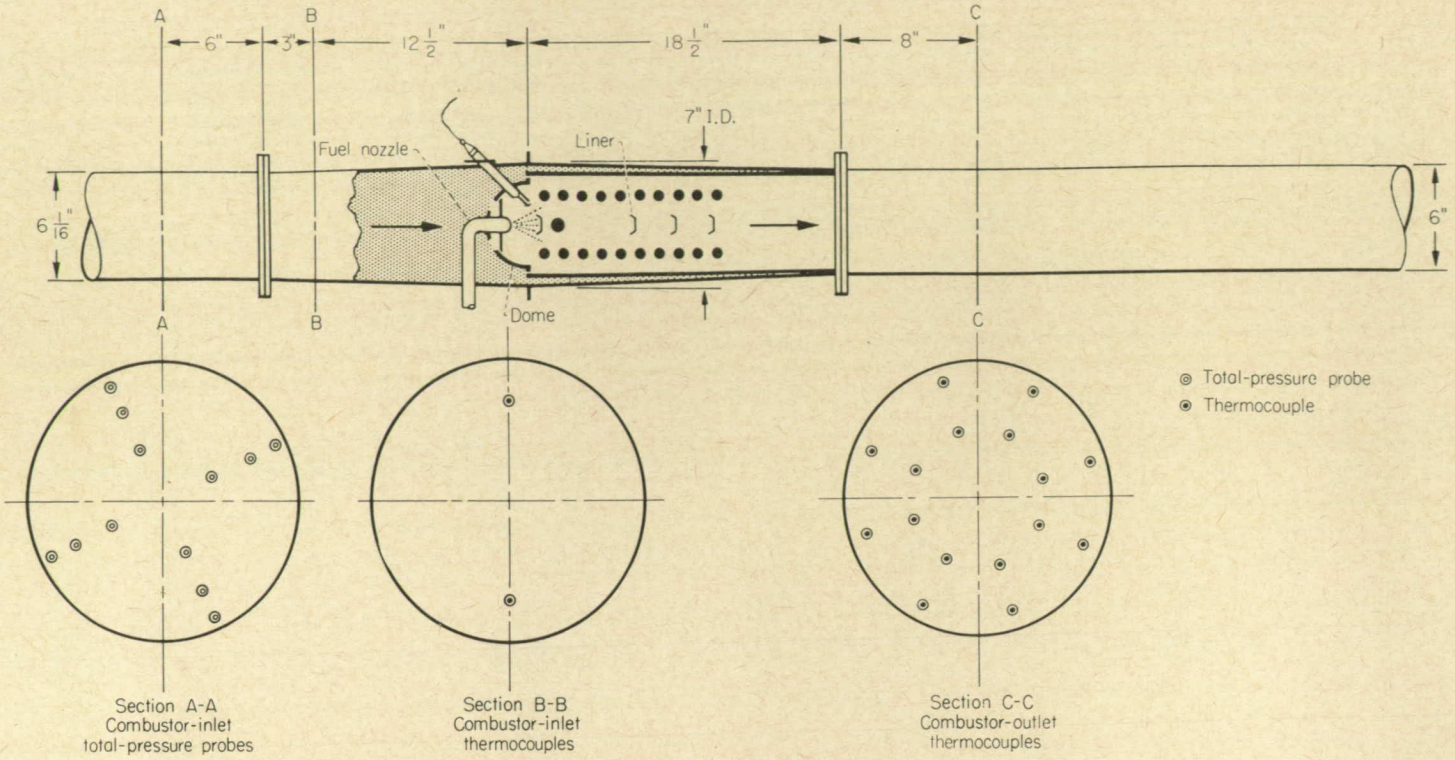
FIGURE 2.—Single-combustor installation and auxiliary equipment.


9 Diam
Airflow straightener
Combustor
Observation windows
Explosion diaphragm
Cooling-water sprays
Floor level
Regulating valves
Regulating valves
Electric combustion-air heater
Air-measuring orifice
7 Diam
16 Diam
Combustion air
Atmospheric or altitude exhaust

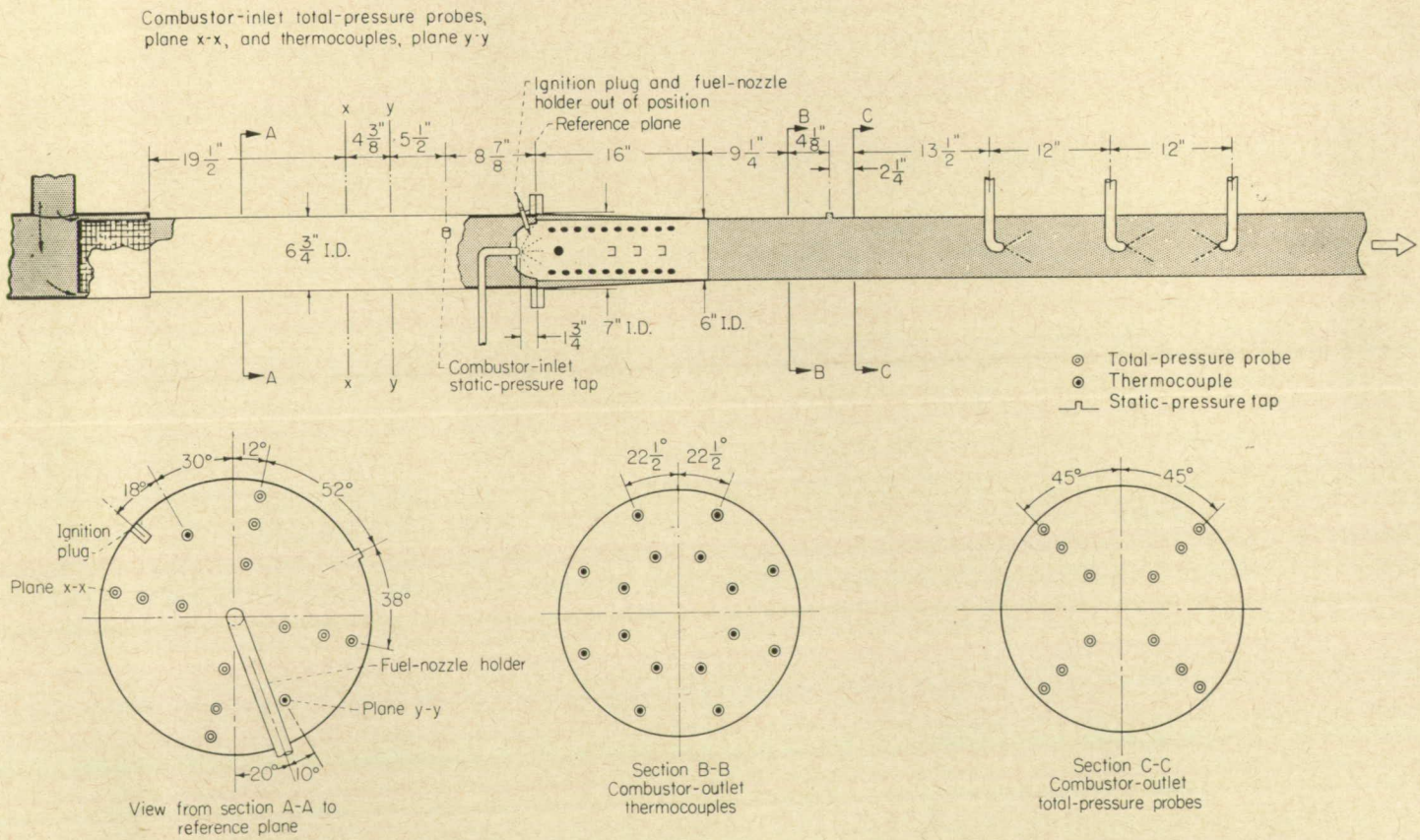
(a)


Atmospheric exhaust
Air heater
Auxiliary combustor
Regulating valves
Regulating valves
Cooling-water sprays
5 3/4 Diam
12 1/2 Diam
Combustor
Inlet-air screen
To drain
8 Diam
3 1/2 Diam
10 Diam
Flexible coupling
Thermocouple
Air-measuring orifice
Airflow straightener
Combustion air

(b)



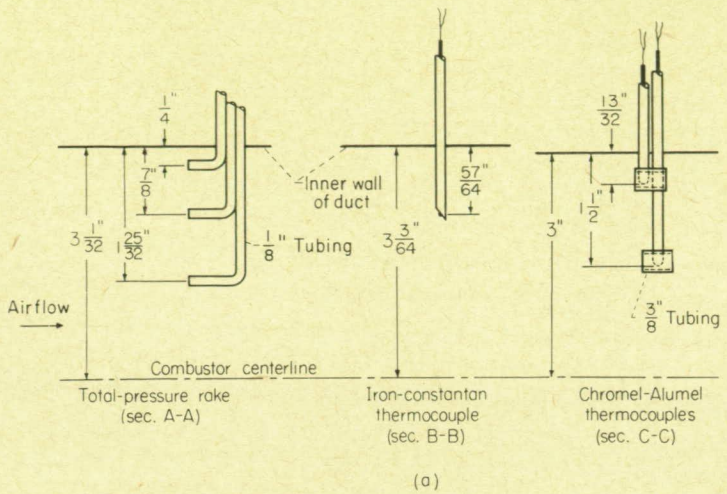
(a) Low-pressure facility.



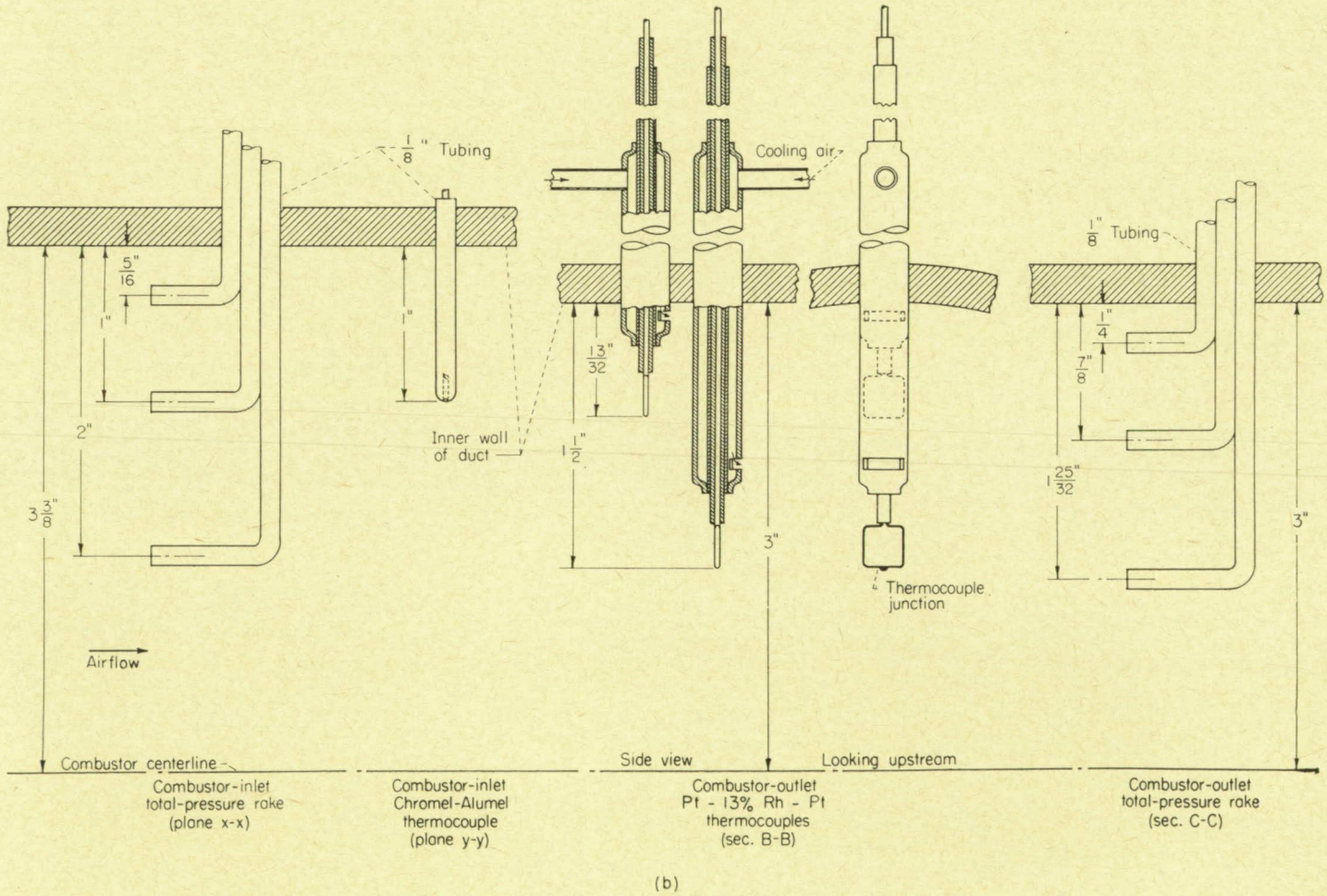
(b) High-pressure facility.

FIGURE 3.—Cross section of single-combustor installation showing auxiliary ducting and location of temperature- and pressure-measuring instruments in instrumentation planes.

Combustor temperature and pressure instrumentation.— Diagrammatic cross sections of the combustor and its auxiliary ducting and the position of instrumentation planes in the test installation are shown in figure 3. Thermocouples and total-pressure tubes in each instrumentation plane were located at centers of equal areas. Construction details of the temperature- and pressure-measuring instruments are shown in figure 4. In the low-pressure installation iron-constantan thermocouples were used to measure combustor-inlet air temperature (sec. B–B, fig. 3(a)), and Chromel-Alumel thermocouples to measure combustor-outlet gas temperature (sec. C–C, fig. 3(a)). The pressure and temperature data were obtained by means of manometers and automatic-balancing potentiometers, respectively. In the high-pressure facility the inlet air and exhaust gas temperatures were measured by Chromel-Alumel thermocouples (plane y–y, fig. 3(b)), and by platinum-13-percent-rhodium–platinum thermocouples (sec. B–B, fig. 3(b)), respectively. The supports for the platinum-rhodium–platinum thermocouples were made of brass and were cooled by a stream of high-pressure air bled from the combustion-air supply upstream of the orifice. Inlet air and exhaust gas total pressures were measured by the probes shown in figure 4(b) connected to strain-gage pressure transducers. All combustor pressures and temperatures were indicated on automatic-balancing potentiometers.



(a) Low-pressure facility.



(b) High-pressure facility.

FIGURE 4.—Construction details of temperature- and pressure-measuring instruments.

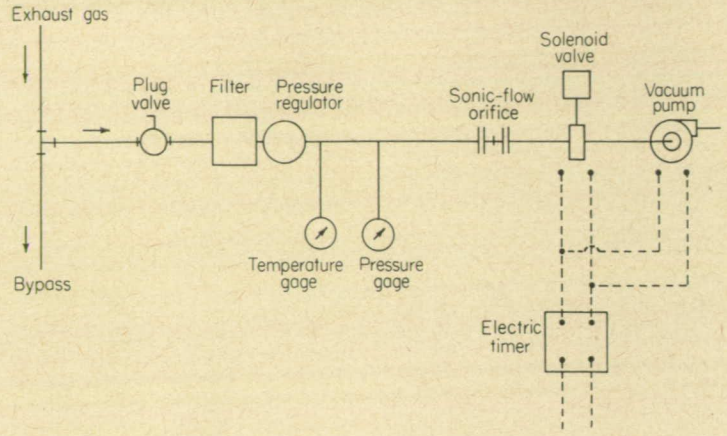


FIGURE 5.—Diagram of smoke meter.

Smoke measurements.—In the low-pressure facility, exhaust gas samples were withdrawn through a single total-head probe centrally located in the exhaust duct. In the high-pressure facility the samples were obtained from a three-point total-head probe located in the exhaust duct. The apparatus used to determine the relative quantity of smoke in the exhaust gases was a modification of a commercially available smoke tester (shown diagrammatically in fig. 5). The meter consisted essentially of an air-cooled filter press containing a paper filter disk, and an automatic metering system. The gas sample was metered through a sonic-flow orifice; the flow duration was controlled by a solenoid valve actuated by an electric timer. A pressure-regulating valve maintained constant upstream orifice pressure. Location of the filter upstream of the control equipment eliminated the possibility of depositing soot on the control valves and orifice. The relative amounts of exhaust-gas smoke, reported as "smoke density," were measured by a transmission densitometer. The values reported represent the difference in optical density between the smoke-covered and the clean filters.

Experimental procedure.—The single-combustor tests were conducted at the following combustor operating conditions:

	Condition	
	A	B
Inlet air total pressure, lb/sq in. abs	26.5	141.0
Inlet air temperature, °F	271	640
Airflow rate, lb/sec	2.87	12.0
Exhaust gas temperature, °F	1100	1800
Combustor reference velocity, ft/sec	110	130
Approximate fuel-air ratio	0.012	0.018
Run time, hr	4	1.5
Approximate simulated full-scale-engine conditions:		
Compressor pressure ratio	4	7
Engine rpm, percent rated	90	100
Altitude, ft	20,000	0
Flight Mach number	0	0.87

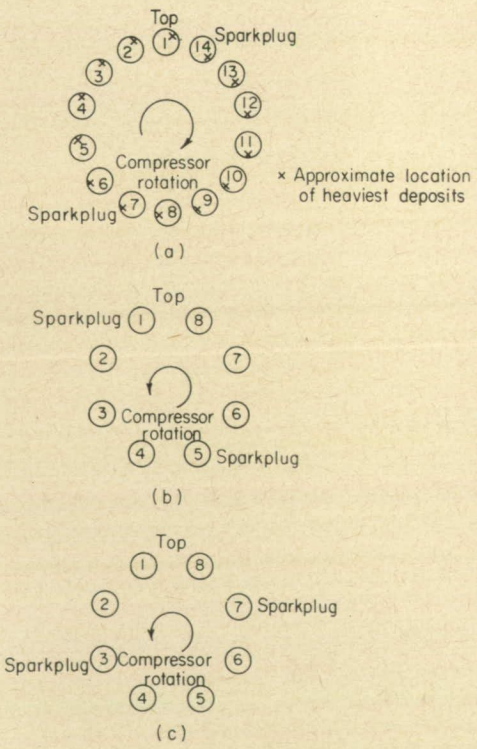
Combustor reference velocity is based on the maximum cross-sectional area of the combustor, the weight flow of air, and the density of the air at combustor-inlet conditions. The conditions were chosen to represent two widely different test conditions; no attempt was made to investigate the effect of any individual operating parameter. Twenty fuels were tested at condition A, and six JP–4 fuels were tested at condition B. The run time was decreased to 1.5 hours at condition B because of limited supplies of several of the fuels and because of the limited life of the combustor liner at the higher pressure and temperature. All additive tests were conducted at condition A.

For carbon-deposition measurements, the combustor liner and dome assembly, including the ignition plug, was cleaned with mechanical rotating brushes and weighed on a torsion-type balance before the test run. After the prescribed period of operation the assembly was reweighed; the difference in weight represented the amount of carbon deposition reported herein. Generally, at least one check test was conducted. The exhaust-gas smoke density was measured at intervals during each run. The values of smoke density reported herein are averages of the several individual measurements made during each test run.

After each test with a fuel-additive blend, the fuel system was drained and purged with the base fuel to remove any residual additive. One or more check runs with the base fuel were made between tests with each of the additives to determine the effectiveness of the purge and the reproducibility of the base-fuel deposits.

FULL-SCALE ENGINES

Three full-scale turbojet engines were run at various engine conditions in the carbon-deposition investigation.



(a) Engine I.
(b) Engine II.
(c) Engine III.

FIGURE 6.—Diagrams showing relative locations of combustors in full-scale engines (looking downstream).

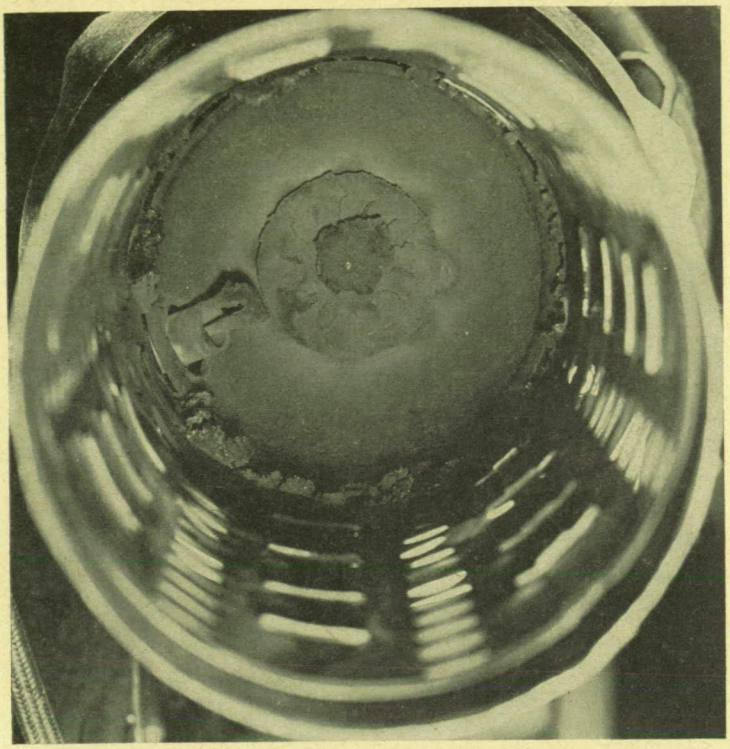


FIGURE 7.—Carbon deposits in J33 single-combustor liner after 4-hour run with fuel 49–224.

Engine I.—Engine I had a centrifugal-flow compressor with a pressure ratio of 4 and 14 individual tubular combustors. The combustor numbers, sparkplug locations, and direction of compressor rotation are shown schematically in figure 6(a). The engine was operated at sea level at zero flight speed on a cyclic operating schedule. The operating cycle consisted in approximately 5 minutes at idle engine speed (4000 rpm) followed by 15 minutes at takeoff speed (11,500 rpm). The idle time included the time for acceleration and deceleration. There was no regularly scheduled shutdown period. The performance of the engine was investigated at 6000 rpm before each day of operation to ascertain constancy of performance. The intended run time for each test was 50 hours. Both new and used combustor liners and used domes were cleaned, if necessary, but not weighed before any one test. After the completion of the test, the liners and domes were weighed, cleaned with wire brushes, and reweighed. The difference in weight was considered the weight of the carbon deposited.

Engine II.—Engine II had an axial-flow compressor with a pressure ratio of 5 and eight individual tubular combustors (fig. 6(b)). The engine was operated at sea-level static conditions for a total time of 25 hours. This time was divided into seven 3-hour periods followed by a 4-hour period. At the beginning and end of each period, the engine was operated for 5 minutes at rated conditions (7600 rpm); during the rest of each period, it was operated at 90-percent rated speed. Following each period of operation, the engine was shut down for approximately 2 hours. The new combustor liners used for the investigation were weighed before and after 25 hours of operation, and the increase in weight was considered as the weight of the carbon deposited.

Engine III.—Engine III had an axial-flow compressor with a pressure ratio of 5.2 and eight individual tubular combustors (fig. 6(c)). This engine was operated at sea-level static conditions for a total time of 37 hours and 47 minutes. The maximum running time for any one day was about 1½ hours, which included running at engine speeds from 3000 to 7950 rpm. About 75 percent of the total operating time was at 7950 (rated) rpm, and the other 25 percent at engine speeds varying between 3000 and 7950 rpm. The complete test covered a time period of about 1½ months. Combustor liners, which had been previously used, were cleaned with wire brushes and then weighed before and after the complete test. The increase in weight was considered as the weight of the carbon deposited.

RESULTS

EFFECT OF FUEL PROPERTIES ON CARBON DEPOSITS IN SINGLE COMBUSTORS

A photograph of carbon deposits obtained in the J33 combustor during a 4-hour test run with fuel 49–224 is presented in figure 7. The deposits, which were concentrated in the upstream end of the liner around the fuel-injection nozzle and the sparkplug, weighed about 34 grams. Carbon-deposition data obtained in this type combustor with 21 fuels are presented in table IV. At the lower inlet air pressure and temperature (condition A), average deviations in individual test results from average test results varied from 1 to 16 percent. At condition B the average deviations were greater, varying from 8 to 30 percent.

TABLE IV.—SINGLE-COMBUSTOR DEPOSITS WITH FUELS VARYING IN PHYSICAL AND CHEMICAL PROPERTIES

NACA fuel	Carbon deposit, g						Average variation, % [a]
	Run					Average	
	1	2	3	4	5		
Condition A							
50–264	9.2	12.8	11.6	10.4	------	11.0	11
51–353	13.5	15.4	14.3	------	------	14.4	5
52–28	------	------	------	------	------	[b,c] 2.5	------
52–30	------	------	------	------	------	[c] 3.7	------
52–32	16.1	17.9	17.5	------	------	17.2	4
52–50	14.4	13.9	14.0	------	------	14.1	1
52–53	2.2	2.4	------	------	------	2.3	4
52–76	------	------	------	------	------	[c] 7.4	------
52–105	6.4	6.8	------	------	------	6.6	3
52–117	1.1	1.2	1.3	------	------	1.2	5
52–118	4.8	5.4	4.9	------	------	5.0	5
52–119	6.8	6.8	6.1	------	------	6.6	5
52–120	11.4	12.0	13.1	------	------	12.2	5
52–166	[b] 7.2	[b] 7.7	[b] 7.1	------	------	[b] 7.3	3
53–49	------	------	------	------	------	[b,c] 6.9	------
54–41	21.4	23.3	24.0	28.0	26.8	24.7	9
54–108	16.2	17.0	16.3	------	------	16.5	2
54–109	13.9	15.3	15.5	------	------	14.9	5
54–110	8.1	6.4	6.4	------	------	7.0	11
54–111	[b] 8.9	[b] 6.0	[b] 9.0	------	------	[b] 8.0	16
Condition B							
52–288	3.3	2.4	------	------	------	2.9	16
54–41	7.0	9.2	6.3	------	------	7.5	15
54–108	5.2	2.8	------	------	------	4.0	30
54–109	11.0	9.0	------	------	------	10.0	10
54–110	6.3	5.4	------	------	------	5.9	8
54–111	2.3	3.5	------	------	------	2.9	21

[a] Arithmetical average percent variation of individual carbon-deposition value from arithmetical average deposition.
[b] Gray deposits.
[c] Average of two or more tests.

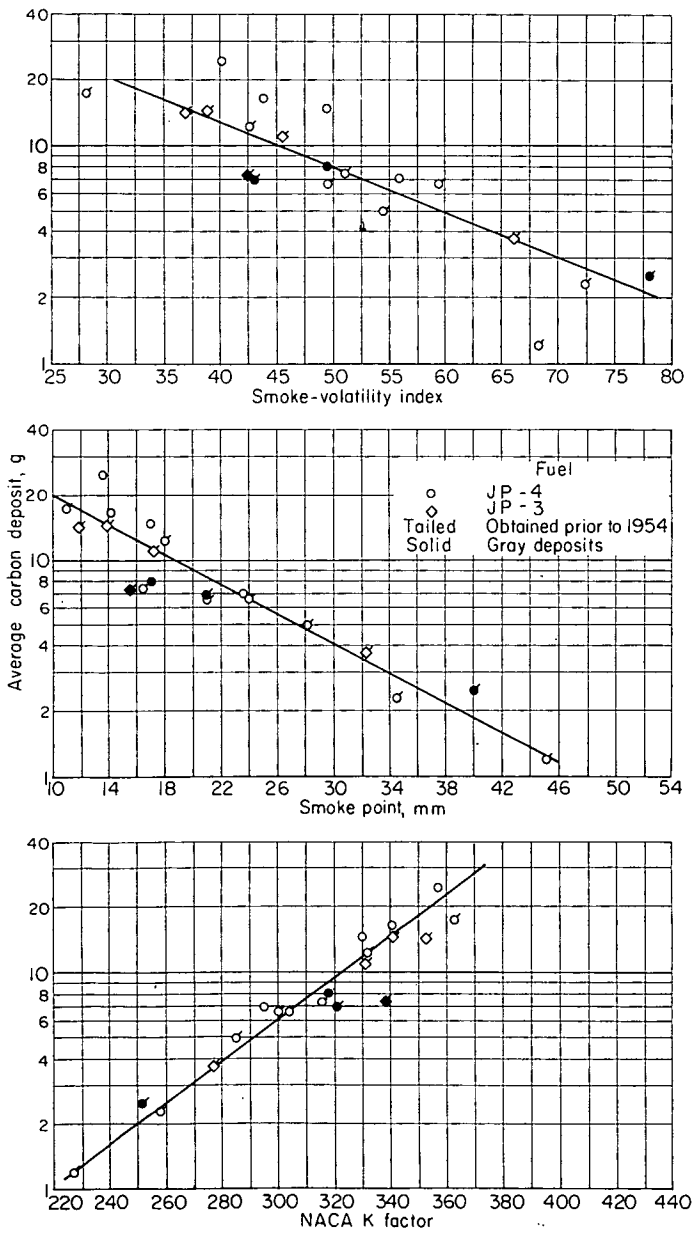
Gray deposits were obtained with fuels 52–28, 52–166, 53–49, and 54–111. As will be noted in a later section of this report, similar-colored deposits were observed in tests with fuels containing small amounts of lead or cadmium. Spectrographic analysis of the deposits with fuel 54–111 at condition A indicated lead, which is assumed to have been present in the fuel as a contaminant. The deposits with this fuel at condition B showed no evidence of lead. It is very possible that the lead was present in the fuel as tetraethyl lead, the antiknock additive used in aviation gasoline. The high inlet air temperature at condition B may have vaporized this volatile compound so rapidly that no significant quantity reached the carbon-forming areas of the liner walls. Another possible explanation for the inconsistency is that the fuel was received in fourteen 55-gallon drums, only a part of which may have been contaminated.

Average deposits obtained at conditions A and B are plotted against smoke-volatility index, smoke point, and NACA K factor in figure 8. At condition A the deposits generally increased with decreasing smoke-volatility index or smoke point and with increasing K factor. The solid symbols of figure 8 denote deposits that showed evidence of metal contamination. These data points were not considered in the fairing of the correlation curves. Tailed symbols in figure 8 denote deposit data obtained in earlier phases of the investigation. At condition B the general trends are the same as those at condition A; however, the deviations from a mean correlation curve are much greater.

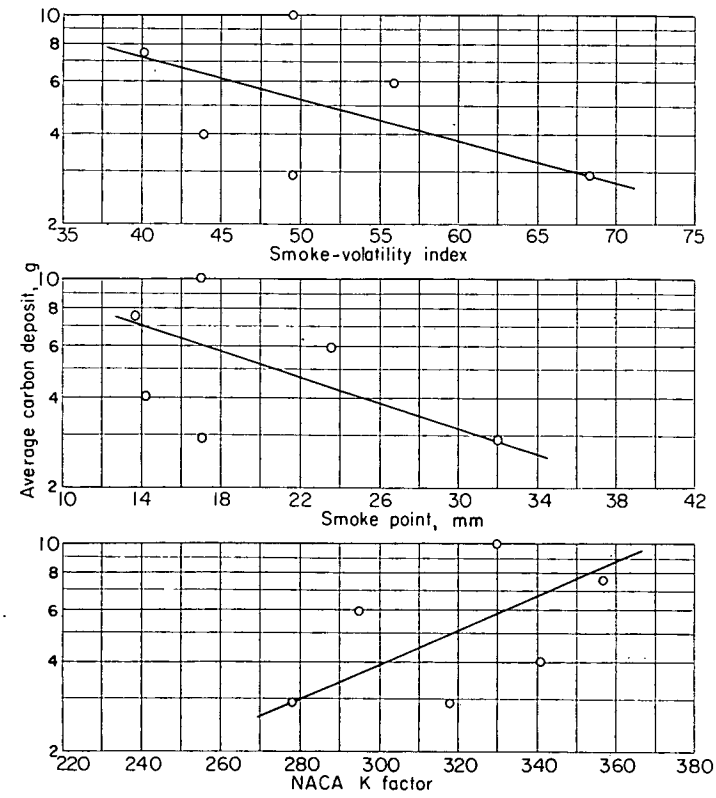
EFFECT OF FUEL PROPERTIES ON CARBON DEPOSITS IN FULL-SCALE ENGINES

Engine I.—The carbon deposits obtained with three test fuels in engine I are presented in table V(a). The values represent results of a single test with each fuel. Locations of the heaviest deposits are as shown in figure 6(a). No relation between the relative quantities of carbon and the circumferential position of the combustor is evident. Emission spectra of gray powder deposits obtained from the downstream end of liners after the test with fuel 52–28 indicated that these deposits contained a large amount of lead. Similar deposits were noted with this fuel in the single-combustor tests (table IV).

Fuel-nozzle filter plugging during the first test with fuel 52–76 limited the fuel flow to the engine to such an extent that the desired engine speed could not be maintained; the test was terminated after 37 hours and 54 minutes. This



(a) Condition A: Inlet air pressure, 26.5 pounds per square inch absolute; inlet air temperature, 271° F; reference velocity, 110 feet per second; outlet temperature, 1100° F.



(b) Condition B: Inlet air pressure, 141.0 pounds per square inch absolute; inlet air temperature, 640° F; reference velocity, 130 feet per second; outlet temperature, 1800° F.

FIGURE 8.—Relation between average carbon deposits in single tubular combustor and empirical fuel factors.

run is not included in the analysis of data but is shown in table V(a) only to indicate, approximately, the effect of time and the reproducibility of the amount of carbon obtained from a single fuel. In a second test with fuel 52–76 the desired number of running hours was obtained, although some filter plugging did occur. A considerable amount of carbon remained on the ignition plugs after fuel 52–76 was used.

Engine II.—The carbon deposits obtained in engine II with a minimum-quality JP–3 fuel (50–264) are presented in table V(b). The values represent results of a single test. Carbon deposits were found in the dome end of the combustor and on the fuel nozzle. There was some evidence of greater

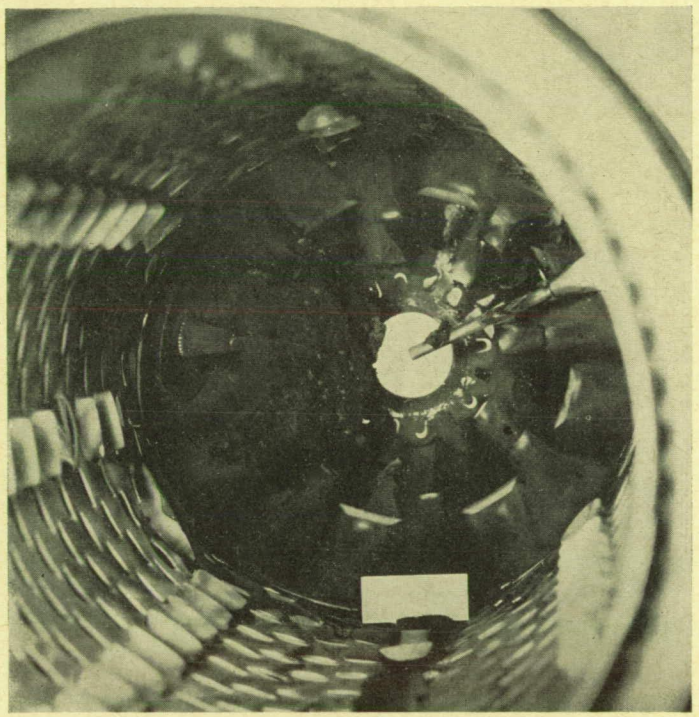


FIGURE 9.—Carbon deposits obtained in combustor 7 of full-scale engine III with fuel 52–76.

deposition in combustion chambers located at the bottom of the engine. A much larger amount of soot was found in the exhaust muffler than had been obtained from previous tests of this duration with a production JP–3 fuel.

Engine III.—Carbon deposits obtained in engine III with a minimum-quality JP–4 fuel (52–76) are shown in table V(c). The values represent results of a single test. The large deposit weight obtained in combustor 7 (fig. 6(c)) was caused by a large deposit on one of the sparkplugs, as shown in figure 9. Abnormally large deposits in combustors using the type of sparkplug shown in figure 9 have been obtained previously. Several of the liners were severely warped after the test and had to be replaced.

During the test with this fuel, the exhaust cooling water draining from the exhaust muffler was black. Inspection of the inside of the muffler showed large quantities of soot; one total-pressure rake was plugged with soot. This amount of exhaust soot was much greater than that normally encountered with production JP–4 fuel.

526597—60——22

TABLE V.—FULL-SCALE-ENGINE DEPOSITS WITH VARIOUS FUELS

(a) Three fuels in engine I.

Combustor	Fuel 52–30		Fuel 52–28		Fuel 52–76			
	Run time							
	49 hr 20 min				37 hr 54 min		50 hr 30 min	
	Carbon deposition, g							
	Liner	Dome	Liner [a]	Dome	Liner	Dome	Liner [a]	Dome
1	4.2	22.7	4.8	13.3	8.9	19.3	7.9	19.2
2	6.2	16.1	4.6	7.8	7.7	12.7	.6	1.5
3	7.7	10.0	5.9	7.9	4.9	11.2	9.8	19.1
4	7.4	12.9	4.8	5.1	.7	1.8	5.8	13.4
5	7.3	20.5	7.2	14.1	8.6	13.0	7.8	15.3
6	7.0	13.7	3.4	8.2	14.1	15.3	18.0	22.3
7	8.0	17.8	4.8	13.1	7.4	17.6	7.7	12.4
8	3.7	25.3	6.0	6.3	8.4	21.0	9.1	11.9
9	6.3	15.4	4.4	11.9	7.2	10.5	10.1	15.2
10	5.7	25.0	5.6	7.7	8.0	11.9	7.3	12.3
11	3.9	10.4	4.0	9.4	7.3	16.2	11.5	15.6
12	4.4	13.1	5.0	6.8	6.3	15.1	14.0	24.3
13	5.4	17.1	5.7	7.5	9.3	16.0	10.2	11.0
14	5.8	11.4	7.0	16.5	9.0	21.7	12.4	14.0
Total	83.0	231.4	73.2	135.6	107.8	203.3	132.2	207.5
Average per liner or dome	5.9	16.5	5.2	9.7	[b] 8.2	[b] 15.5	[c] 10.1	[c] 15.9
Average per combustor	22.4		14.9		[b] 23.7		[c] 26.0	

[a] New liners.
[b] Values of combustor 4 not used in averages, because partly plugged fuel-nozzle filter resulted in a lean mixture and consequently a decrease in carbon deposits.
[c] Values of combustor 2 not used in averages.

(b) Fuel 50–264 in engine II. Run time, 25 hours.

Combustor	Carbon, g
1	9.4
2	7.9
3	8.5
4	12.6
5	10.7
6	9.1
7	5.0
8	9.2
Total	72.4
Average	9.1

(c) Fuel 52–76 in engine III. Run time, 37 hours 47 minutes.

Combustor	Carbon, g
1	5.2
2	5.7
3	10.0
4	8.6
5	4.6
6	3.8
7	42.1
8	2.2
Total	82.2
Average	10.3

TABLE VI.—SINGLE-COMBUSTOR EXHAUST-GAS SMOKE DATA

NACA fuel	54–108		54–109		54–110		54–111	
Condition	A	B	A	B	A	B	A	B
Smoke density	0.14	0.28	0.18	0.31	0.07	0.13	0.13	0.12
	.10	.37	.14	.28	.06	.18	.13	.10
	.14	.29	.12	.41	.09	----	.13	.15
	.18	----	.13	.46	.05	----	.11	.16
	.21	----	.19	----	.03	----	.09	----
	.16	----	.20	----	.03	----	.11	----
	.18	----	.20	----	.04	----	.13	----
	.13	----	.14	----	.05	----	.07	----
	.10	----	----	----	----	----	----	----
Average smoke density	0.15	0.31	0.16	0.37	0.05	0.16	0.11	0.13
Average deviation, %	20	12	19	19	30	16	16	17

EFFECT OF FUEL PROPERTIES ON SMOKE FORMATION

Exhaust-gas smoke data were obtained only in the single combustor with fuels 54–108, 54–109, 54–110, and 54–111 (table VI). In most cases two or three determinations were made during each carbon-deposit test run. Average percentage deviations varied from 12 to 30 percent. Because of inaccuracies in the smoke measurement technique, the

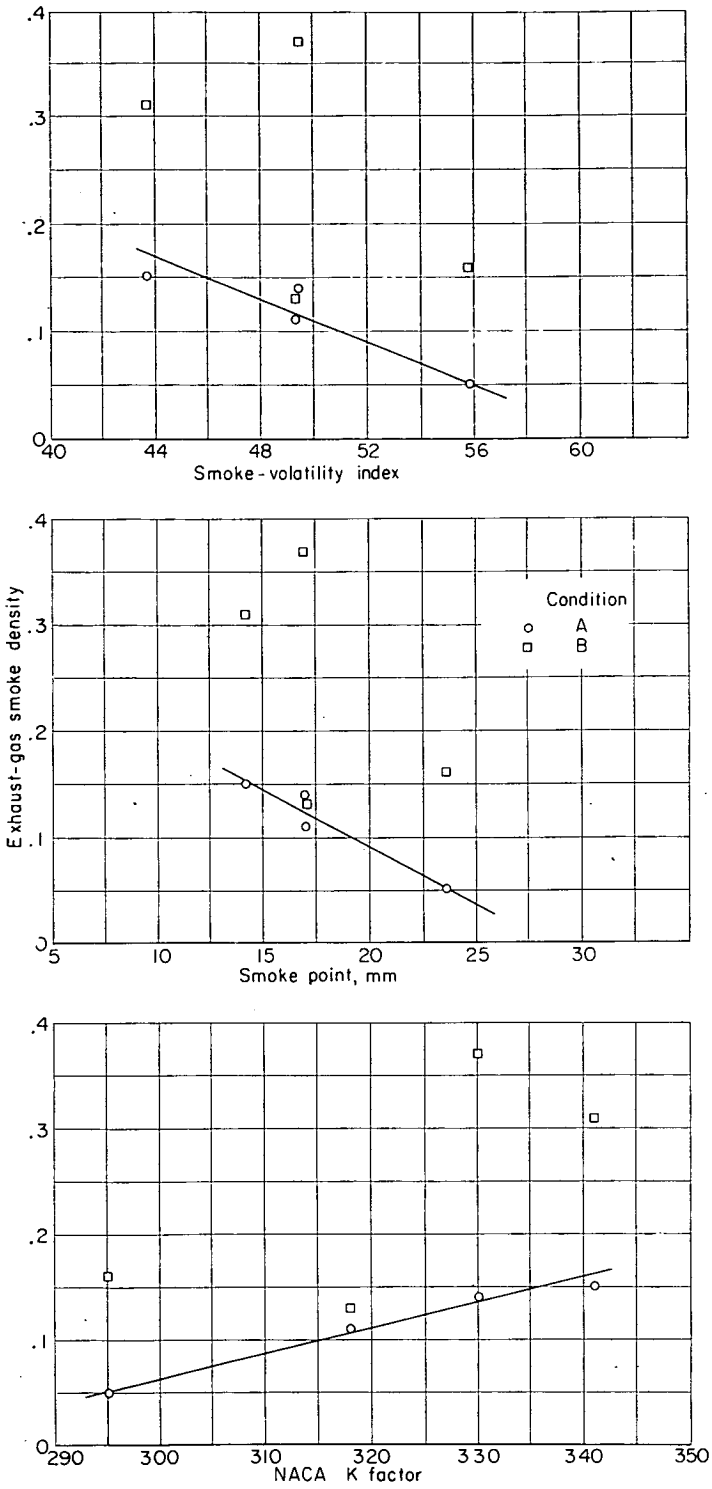


FIGURE 10.—Relation between exhaust-gas smoke density obtained with JP–4 fuels and empirical fuel factors.

larger percentage deviations generally occurred at lower values of smoke density. Average smoke densities are plotted in figure 10 against smoke-volatility index, smoke point, and NACA K factor. At both conditions exhaust-gas smoke density decreased with increasing smoke-volatility index or smoke point and with decreasing K factor. A reasonable correlation was obtained only at condition A, however; and only the data for this test condition were used to fair the curves in figure 10.

EFFECT OF ADDITIVES ON CARBON DEPOSITION AND EXHAUST-GAS SMOKE

The effect of a number of fuel additives on carbon deposition and exhaust-gas smoke concentration was investigated in the single turbojet combustor at condition A. The tests were conducted over a considerable period of time with a number of different base fuels. In some cases the base fuel was changed to determine the effect of some additives on the carbon-forming properties of different fuel compositions. In other cases, the supply of base fuel was depleted and new supplies varied in composition.

The results obtained in tests with 23 different additives are presented in table VII. With base fuels 49–162, 49–224, 52–105, 54–41, and 55–89, representing a wide variety of fuel properties, reproducibility was considered satisfactory; the average deviations in individual test runs from the average deposit obtained in all runs with the particular base fuel ranged from 2 to 21 percent. Base fuel 53–193 was used during several periods of the investigation. During any one period, reproducibility with this fuel was also satisfactory, with average deviations from 1 percent (run series 15) to 14 percent (run series 28 through 43). However, the average base-fuel deposit obtained in each of the several periods of operation differed considerably: The average deposit in run series 15 was 20.5 grams; in run series 28 through 43 it was 28.3 grams; and in run series 44 through 53, 35.6 grams. The large difference may be partly attributed to aging, which would increase the gum content of the fuel and may affect deposits (ref. 10).

Multiple additive test runs were conducted where sufficient quantities of the additive were available. For the multiple

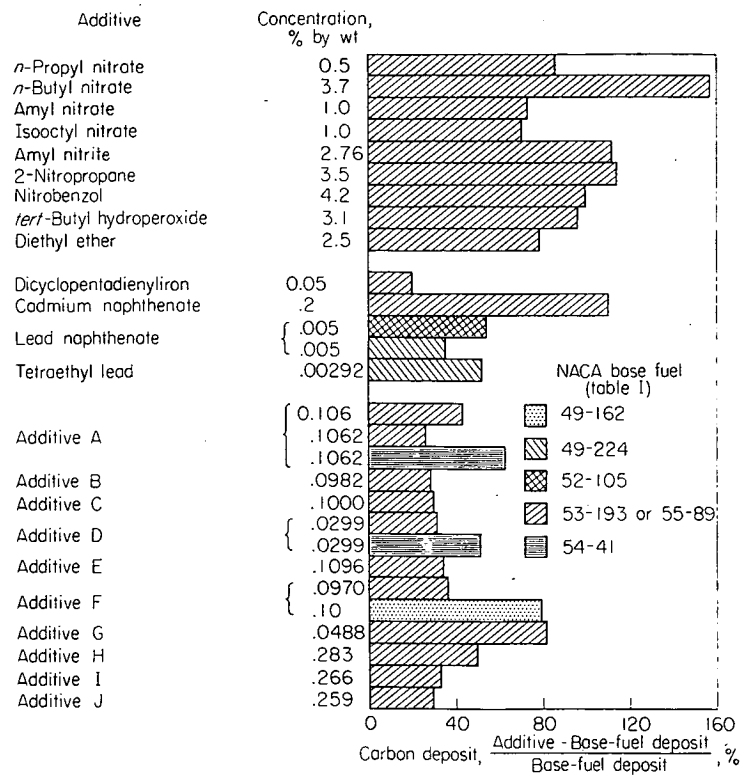


FIGURE 11.—Relative effectiveness of 23 additives in reducing turbojet combustion-chamber carbon deposits.

TABLE VII.—CARBON-DEPOSIT AND EXHAUST-GAS SMOKE DATA WITH FUEL ADDITIVES

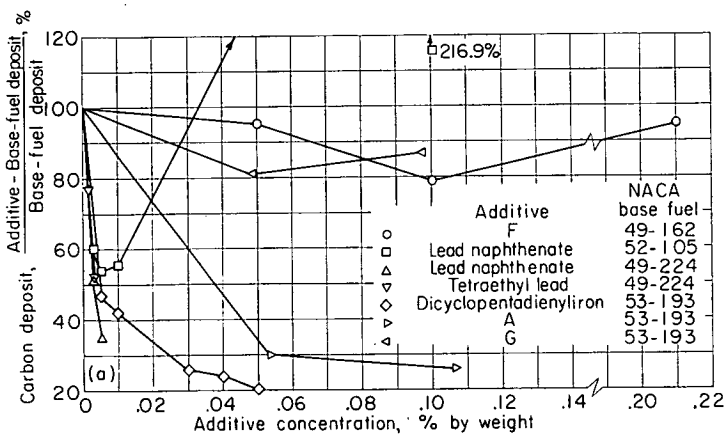
Run series	Base fuel	Additive (table III)	Additive concentration, % by weight	Carbon deposit, g							Av. variation, %	Change from base-fuel deposit, %	Exhaust-gas smoke rating					
				Run						Av.								
				1	2	3	4	5	6		(a)	(b)						
1	49–162	None	.....	13.9	15.0	13.5	13.8	....	....	14.1	3.6	.....	....	....	....	....	....	....
2		F	0.05	13.4	....	....	....	....	....	13.4	.....	−5.0	....	....	....	....	....	....
3			.10	10.7	11.8	10.9	....	....	....	11.1	3.9	−21.3	....	....	....	....	....	....
4			.21	13.3	....	....	....	....	....	13.3	.....	−5.7	....	....	....	....	....	....
5	52–105	None	.....	6.4	6.8	6.5	6.4	....	....	6.5	1.9	.....	....	....	....	....	....	....
6		Lead naphthenate	0.0025	3.9	....	....	....	....	....	3.9	.....	−40.0	....	....	....	....	....	....
7			.005	3.5	3.5	....	....	....	....	3.5	0	−46.2	....	....	....	....	....	....
8			.01	3.6	....	....	....	....	....	3.6	.....	−44.6	....	....	....	....	....	....
9			.10	14.9	13.2	....	....	....	....	14.1	6.1	116.9	....	....	....	....	....	....
10	49-224	None	.....	17.9	22.4	31.1	30.6	....	....	25.5	21.0	.....	....	....	....	....	....	....
11		Lead naphthenate	0.0025	13.0	....	....	....	....	....	13.0	.....	−49.0	....	....	....	....	....	....
12			.005	8.8	....	....	....	....	....	8.8	.....	−65.5	....	....	....	....	....	....
13		Tetraethyl lead	0.00145	19.6	....	....	....	....	....	19.6	.....	−23.1	....	....	....	....	....	....
14			.00292	13.3	....	....	....	....	....	13.3	.....	−47.8	....	....	....	....	....	....
15	53–193	None	.....	20.7	20.6	20.1	....	....	....	20.5	1.2	.....	0.40	0.38	0.45	....	....	....
16		A	0.1062	4.9	5.6	....	....	....	....	5.3	6.6	−74.1	0.37	0.47	....	....	....	....
17			.0531	5.9	6.2	....	....	....	....	6.1	2.6	−70.2	.41	....	....	....	....	....
18		B	0.0982	5.8	....	....	....	....	....	5.8	.....	−71.7	0.40	....	....	....	....	....
19		C	.1000	6.5	5.9	....	....	....	....	6.2	4.8	−69.8	.48	0.41	....	....	....	....
20		D	.0299	6.5	6.3	....	....	....	....	6.4	1.6	−68.8	.42	.49	....	....	....	....
21		E	.1096	7.3	6.5	....	....	....	....	6.9	5.8	−66.3	.36	.42	....	....	....	....
22		F	.0970	8.2	6.5	....	....	....	....	7.4	11.5	−63.9	.43	.38	....	....	....	....
23		G	0.0975	15.6	18.0	19.8	....	....	....	17.8	8.2	−13.2	0.42	0.38	0.32	....	....	....
24			.0488	16.6	....	....	....	....	....	16.6	.....	−19.0	.49	....	....	....	....	....
25	54–41	None	.....	21.4	23.3	24.0	....	....	....	22.9	4.2	.....	0.21	0.14	0.24	....	....	....
26		A	0.1062	13.1	15.1	....	....	....	....	14.1	7.1	−38.4	0.18	0.20	....	....	....	....
27		D	.0299	12.2	11.0	....	....	....	....	11.6	5.2	−49.3	.15	.24	....	....	....	....
28	53–193	None	.....	28.7	31.7	32.4	....	....	....	30.9	4.9	.....	0.18	0.22	0.24	....	....	....
29		Cadmium naphthenate	0.2	33.0	29.0	....	....	....	....	31.0	6.5	9.5	0.24	0.20	....	....	....	....
30		None	.....	33.4	....	....	....	....	....	33.4	.....	.....	0.15	....	....	....	....	....
31		A	0.106	12.1	....	....	....	....	....	12.1	.....	−57.2	0.26	....	....	....	....	....
32		H	.283	14.6	13.3	....	....	....	....	14.0	4.7	−50.5	.17	0.14	....	....	....	....
33		None	.....	23.2	18.0	....	....	....	....	20.6	12.6	.....	0.24	0.27	....	....	....	....
34		I	0.266	8.9	9.1	....	....	....	....	9.0	1.1	−68.2	0.17	0.26	....	....	....	....
35		J	.259	9.8	6.8	....	....	....	....	8.3	18.1	−70.7	.20	.23	....	....	....	....
36		None	.....	24.9	34.6	23.7	....	....	....	27.7	16.5	.....	0.27	0.17	0.22	....	....	....
37			.....	29.0	28.8	....	....	....	....	28.9	.3	.....	.36	.48	....	....	....	....
38		Dicyclopentadienyliron	0.005	14.0	12.3	....	....	....	....	13.2	6.5	−53.4	0.52	0.46	....	....	....	....
39			.03	8.1	6.4	....	....	....	....	7.3	11.7	−74.2	.54	.57	....	....	....	....
40			.01	12.1	11.6	....	....	....	....	11.9	2.1	−58.0	.45	.50	....	....	....	....
41			.04	6.8	....	....	....	....	....	6.8	.....	−76.0	.46	....	....	....	....	....
42			.05	5.7	....	....	....	....	....	5.7	.....	−79.9	.41	....	....	....	....	....
43		None	.....	31.4	....	....	....	....	....	31.4	.....	.....	0.34	....	....	....	....	....
44	53-193	*n*-Propyl nitrate	0.5	25.9	32.4	29.4	33.5	....	....	30.3	8.8	−14.9	0.26	0.19	0.23	0.21	....	....
45			1.0	34.4	35.3	....	....	....	....	34.9	1.3	−2.0	.23	.19	....	....	....	....
46		None	.....	32.4	28.8	32.1	33.7	....	....	31.8	4.6	.....	0.22	0.20	0.27	0.24	....	....
47		Isooctyl nitrate	0.5	30.7	37.3	28.5	....	....	....	32.2	10.7	−9.6	0.26	0.24	0.28	....	....	....
48			1.0	30.8	21.2	25.2	22.1	....	....	24.8	12.8	−30.3	.21	.17	.25	0.20	....	....
49		None	.....	36.3	37.7	41.1	31.4	35.5	36.5	36.4	5.6	.....	0.22	0.30	0.26	0.34	0.34	0.33
50		Amyl nitrate	0.5	24.3	25.7	29.9	....	....	....	26.6	8.1	−25.3	0.24	0.18	0.26	....	....	....
51		None	.....	43.0	29.8	42.7	35.6	....	....	37.8	13.5	.....	0.19	0.27	0.21	0.24	....	....
52		Amyl nitrate	1.0	26.8	30.0	21.1	....	....	....	26.0	12.4	−27.0	0.25	0.27	0.21	....	....	....
53		None	.....	38.1	....	....	....	....	....	38.1	.....	.....	0.16	....	....	....	....	....
54	55–89	None	.....	20.6	20.4	21.0	....	....	....	20.7	1.1	.....	0.23	0.36	0.41	....	....	....
55		2-Nitropropane	3.5	22.5	....	....	....	....	....	22.5	.....	13.6	0.38	....	....	....	....	....
56		None	.....	21.1	....	....	....	....	....	21.1	.....	.....	0.37	....	....	....	....	....
57		*n*-Butyl nitrate	3.7	31.0	....	....	....	....	....	31.0	.....	56.6	0.36	....	....	....	....	....
58		None	.....	18.3	....	....	....	....	....	18.3	.....	.....	0.34	....	....	....	....	....
59		*tert*-Butyl hydroperoxide	3.1	19.0	....	....	....	....	....	19.0	.....	−4.0	0.46	....	....	....	....	....
60		None	.....	18.6	16.1	17.5	....	....	....	17.4	5.0	.....	0.41	0.35	0.41	....	....	....
61		Nitrobenzol	4.2	19.7	....	....	....	....	....	19.7	.....	−0.5	0.50	....	....	....	....	....
62		None	.....	23.2	19.1	....	....	....	....	21.2	9.7	.....	0.41	0.50	....	....	....	....
63		Amyl nitrite	2.76	22.1	....	....	....	....	....	22.1	.....	11.6	0.40	....	....	....	....	....
64		None	.....	21.4	20.4	....	....	....	....	20.9	2.4	.....	0.47	0.36	....	....	....	....
65		Diethyl ether	2.5	15.5	....	....	....	....	....	15.5	.....	−21.7	0.45	....	....	....	....	....
66		None	.....	19.3	....	....	....	....	....	19.3	.....	.....	0.43	....	....	....	....	....

[a] Average variation of individual carbon-deposit values from average deposit value.

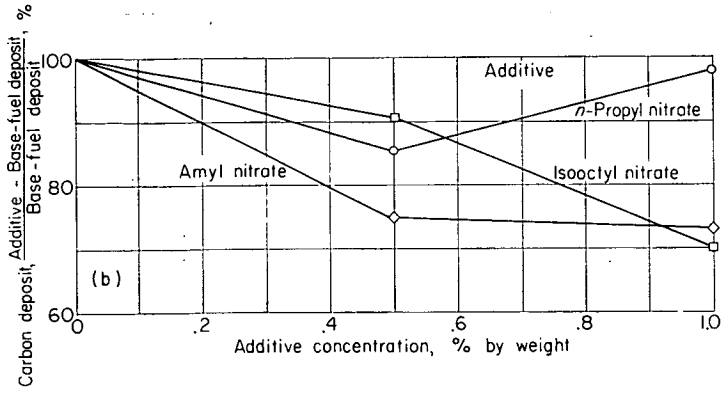
[b] $\frac{\text{Average deposit minus over-all average base-fuel deposit}}{\text{Over-all average base-fuel deposit}}$

tests the mean deviation of deposits in individual test runs from the average deposit values varied from 0 to 18 percent. The percent changes in deposit from the base-fuel deposit are based upon average deposit values obtained with the base fuel during the period of testing with the particular additive. For test run series 28 through 43 the average base-fuel deposit value of 28.3 (obtained from runs 28, 30, 33, 36, 37, and 43) was used for additive data obtained in intervening test runs. Similarly, for runs 44 through 53 an average base-fuel deposit value of 35.6, obtained from run series 46, 49, 51, and 53, was used.

The relative effectiveness of the additives in reducing carbon deposits is compared in figure 11. Average carbon deposits, in percentage of base-fuel deposits, are shown only for the additive concentrations that gave the largest reductions in deposit. In general, the oxygenated compounds (alkylated nitrates, amyl nitrite, nitropropane, nitrobenzol, *tert*-butyl hydroperoxide, and diethyl ether) were considerably less effective than the organo-metallic compounds and the commercial additives, which were also primarily organo-metallic. The most effective oxygenated compound, isooctyl nitrate, reduced base-fuel deposits almost 30 percent, while the most effective organo-metallic compound, dicyclopentadienyliron, reduced base-fuel deposits about 80 percent. Additive A, the most effective of the commercial additives, reduced base-fuel deposits 74 percent. A qualitative spectroscopic analysis of additive A showed that it contained lead and copper (table III).



(a) Organo-metallic and commercial compounds.



(b) Oxygenated compounds. Base fuel, 53–193.

FIGURE 12.—Effect of additive concentration on carbon deposit in single J33 combustor.

A comparison of results obtained with a number of additives (A, D, and lead naphthenate) that were tested in more than one base fuel indicates that the relative effectiveness of an additive varied markedly with the base fuel. For example, additive A in No. 2 furnace oil (53–193) reduced deposits 74 percent; the same concentration of additive A in the same furnace oil at a much later date (aged fuel) reduced deposits 57 percent; and the same additive in a high-carbon-forming JP–4 fuel (54–41) reduced deposits 38 percent.

The effect of additive concentration on carbon deposits was determined with nine of the additives. Figure 12 shows that the effect of additive concentration on deposits was not consistent. For some additives (dicyclopentadienyliron and lead naphthenate), small concentrations produced the large reductions in deposits. A high concentration of lead naphthenate in fuel 52–105 produced deposits greater than those obtained with the base fuel alone.

Deposits obtained with additive blends containing lead or cadmium were colored gray or yellow-gray in some areas of the combustor liner. The deposits obtained with dicyclopentadienyliron were reddish. These colorations indicate the presence of metal and metal oxides. The deposits were not chemically analyzed.

Exhaust-gas smoke data were obtained with many of the base fuels and additive–base-fuel blends; these data are presented in table VII. Large variations in smoke ratings were observed with the base fuels, and the smoke ratings of the additive blends were generally within the ranges obtained with the base fuels. Hence, no effect of the additives on smoke concentration is apparent.

DISCUSSION

EMPIRICAL RELATIONS BETWEEN CARBON DEPOSITS AND FUEL PROPERTIES

Single-combustor carbon deposits obtained at inlet air temperature and pressure simulating operation of an engine with a compressor pressure ratio of 4 at a 20,000-foot altitude (condition A) correlated reasonably well with any of three empirical fuel factors—smoke-volatility index, smoke point, and NACA *K* factor. The data included in the correlations were obtained over a considerable period of time, and there is some indication that the more recent data (plain symbols, fig. 8(a)) define a correlation curve at a slightly higher level of deposit. The correlations applied equally well to JP–3 and JP–4 fuels.

The relative accuracy of the three fuel-factor correlations can be judged by examining deviations of the deposit data from the correlation curve. The deviations for condition A are as follows:

Fuel factor	Av. deviation, %	Max. deviation, %
Smoke-volatility index	27	95
Smoke point	17	67
NACA *K* factor	12	30

The average deviations were calculated from the equation

$$\text{Average deviation} = \frac{\sum \frac{y-y_c}{y_c}}{n} \times 100$$

where $y-y_c$ is the absolute difference between the determined and predicted values of carbon deposit, y_c is the predicted value, and n is the number of determinations.

Data for fuels suspected of being contaminated were not included in these calculations. Based on average deviation or maximum deviation, both the smoke point and the K factor gave more accurate deposit correlations than the smoke-volatility index; the smallest deviations were obtained with the K factor. Smoke point and K factor were also the most accurate of about ten factors examined in reference 1. It should be pointed out that simplicity, as well as accuracy, is an important criterion for a satisfactory fuel procurement specification. The determination of an accurate value of hydrogen-carbon ratio, required to compute the K factor, is considerably more difficult than the measurement of smoke point.

The range of fuel properties included in the correlations of figure 8(a) is much greater than that normally considered for jet-engine fuels. For example, fuel 54–41 had accelerated and existent gum contents about 6 times those allowed by current procurement specifications. This particular fuel produced the high values of maximum deviation noted in the smoke-point and smoke-volatility-index correlations. Data of reference 10 show that high values of gum content can cause increased deposits that may not be predicted by empirical fuel factors. Restricting the range of fuel properties, in order to maintain other desirable fuel characteristics, would be expected to reduce deviations considerably.

At a higher inlet air temperature and pressure simulating an engine with a compressor pressure ratio of 7 operating at sea level (condition B), deposits did not satisfactorily correlate with any of the fuel factors. Preliminary examination of other fuel characteristics that could affect carbon deposition (ref. 1) did not yield any better correlation of the data. The mean straight lines drawn through the data in figure 8(b) are, however, approximately parallel to the corresponding correlation lines for condition A (fig. 8(a)). In reference 11 deposit data obtained at several different operating conditions in an annular combustor also gave approximately parallel correlation lines with K factor. The poor correlation obtained with the condition B data may be the result of more erratic carbon-deposition patterns that were observed at high inlet air temperature. At this condition carbon was deposited in isolated areas around the upstream end of the combustion chamber, and some of the heavier deposits may have broken away from the walls. In comparison, at low inlet air temperature conditions carbon was generally found uniformly deposited in a sizable area around the fuel nozzle of this combustor.

The full-scale-engine data obtained in this investigation are too limited to ascertain the applicability of the correlations to full-scale engines. Additional unpublished carbon-deposit data for three full-scale engines are presented in table VIII. Two of the engines (types I and III) were of the same type as used in the present investigation. Engine IV had an axial-flow compressor of 6.8 pressure ratio and an annular prevaporizing combustor. The engines were operated 10 hours at static sea-level conditions on cyclic operating schedules. The deposits listed are average values for each combustion chamber of engine types I and III or each vaporizer tube of the annular vaporizing combustor (type IV). Comparison of the data of tables VIII and IV shows that deposit deviations in the full-scale engines are considerably greater than those in the single combustor.

TABLE VIII.—FULL-SCALE-ENGINE CARBON DEPOSITS

NACA fuel	Average carbon deposit, g (a)	Average variation, percent (b)
Engine I		
54-108	45.9	16
54-109	45.3	12
54-110	39.0	11
54-111	43.0	15
Engine III		
54-108	10.4	74
54-109	3.2	74
54-110	1.9	65
54-111	6.0	33
Engine IV		
54-108	2.28	18
54-109	2.15	28
54-110	1.57	26
54-111	1.69	32

[a] Arithmetical average deposits in each combustor or fuel vaporizer.
[b] Arithmetical average percent variation of deposits in individual combustion chambers, or fuel vaporizers, from arithmetical average deposit values.

The carbon-deposit data obtained with three fuels in the type I full-scale engine at the NACA Lewis laboratory (table V(a)) and the full-scale-engine data of table VIII are plotted against smoke-volatility index, smoke point, and NACA K factor in figure 13. Data for the two type I engines would not be expected to fall on a single curve, since different operating conditions were used. The three fuel factors correlated the limited full-scale-engine (types I, III, and IV) deposit data with about equal accuracy. Percentage deviations for the full-scale-engine correlations were not computed because of the limited number of fuels tested. Carbon deposition in the full-scale engines was affected to a varying degree by changes in fuel properties. For example, deposits in engine IV increased only about 46 percent and those in engine III about 450 percent when the smoke-volatility index was decreased from 56 to 44.

Although less quantitative in nature, the results obtained in full-scale engines II and III tested at the NACA Lewis laboratory exhibited similar trends. In engine II (table V(b)), much more soot was observed in the exhaust muffler with fuel 50–264 (SVI=45.5, smoke point=17.2, K=331) than with a number of production batches of JP–3 having

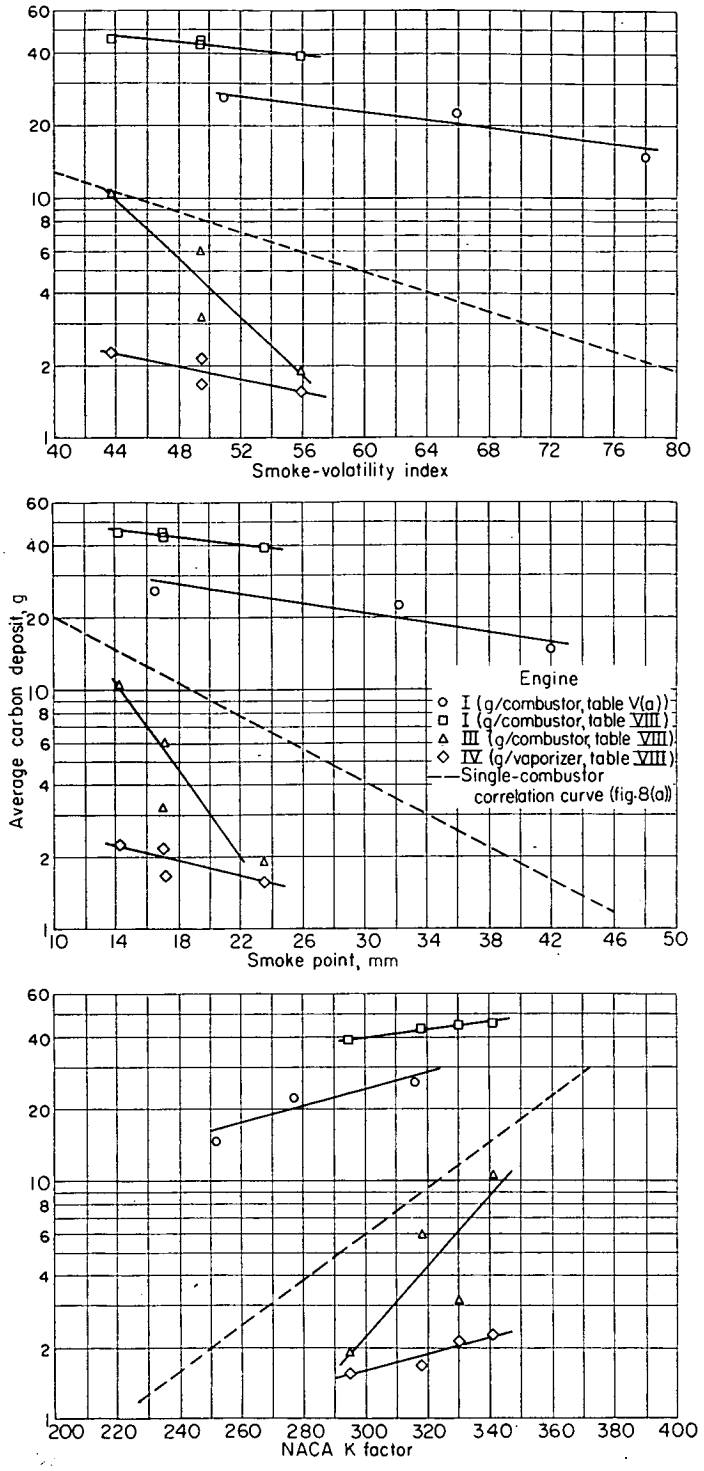


FIGURE 13.—Relation between carbon deposits in full-scale turbojet engines and empirical fuel factors.

properties very similar to those of fuel 52–30 (SVI=66, smoke point=32.3, K=277). In the type III full-scale engine (table V(c)) much more soot was observed in the exhaust muffler, along with a greater tendency toward spark-plug fouling, with fuel 52–76 (SVI=51, smoke point=16.5, K=316) than with production fuels similar to 52–28 (SVI=78, smoke point=40.0, K=252).

The order of carbon deposition among the fuels in the single combustor at condition A was the same as in the full-scale engines; however, figure 13 shows that percentage changes in the deposit values between the fuels were not the same. Except for engine III, deposits in the single combustor increased at a more rapid rate as "fuel quality" decreased. The variation in sensitivity between the single combustor and the full-scale engine is at least partly attributable to differences in operating conditions. The full-scale engines were operated on cyclic test schedules, whereas the single combustor was operated at constant test conditions. Also, the combustor inlet and outlet passage configurations were different in the single combustor and in the full-scale engines. At the higher pressure and temperature single-combustor condition B, no relation between single-combustor and full-scale-engine data is apparent. The reasons for this inconsistency are probably related to the erratic deposition in the single combustor at condition B.

Neither the absolute level of deposition nor the relative effects of fuel factors on these deposits should be used to distinguish between good and bad combustor design in the full-scale engines tested. In addition to carbon deposition, a number of other performance requirements (e.g., combustion efficiency and stability, structural durability, and ease of manufacture) enter into final combustor designs for turbojet engines.

The empirical fuel factors examined in this investigation represent the volatility characteristics, the hydrogen-carbon ratio, and the smoke point of the fuel. In reference 1, which summarizes early carbon-deposit research in laboratory combustors, many additional fuel properties were observed to affect deposits. Approximate relations between deposits and fuel properties such as aromatic content, aniline point, and specific gravity are reported. Many of these other properties are, for petroleum fuels, interrelated with distillation characteristics, hydrogen-carbon ratio, or smoke point. For example, aromatic content of a fuel directly influences the hydrogen-carbon ratio. Tests to determine the effects of adding specific single-ring and dicyclic aromatic hydrocarbons to jet-type fuels (fuel blends 51–353, 52–32, 52–50, 52–105, 52–118, 52–119, and 52–120) revealed that the smoke-volatility index, smoke point, and K factor satisfactorily predicted changes in carbon deposition.

Other properties of jet fuels (e.g., sulfur content and gum content) are not related to the fuel factors. The effects of sulfur and gum on deposits were investigated in studies reported in reference 10. Limited data indicated that moderate amounts of gum did not influence deposits; very high gum contents, well above those permitted in current

jet fuels, will cause increased deposits. Although the data were not conclusive, it appeared that one form of sulfur (mercaptan) significantly increased deposits while another form (disulfide) had no effect.

EMPIRICAL RELATIONS BETWEEN EXHAUST-GAS SMOKE AND FUEL PROPERTIES

The measured values of smoke density were generally very low and may be of questionable significance. Nevertheless, they did vary with fuel properties in much the same way as did carbon deposition; that is, smoke formation generally decreased with an increase in smoke-volatility index or smoke point and with a decrease in K factor. Satisfactory relations were obtained only at condition A. While these results indicate that smoke formation and carbon deposition are affected by the same factors, experience has shown that design features tending to alleviate the carbon-deposition problem frequently aggravate the smoke problem, and vice versa. Also, data presented in reference 12 show that, while fuel volatility affected smoke density in a single combustor, the effects were very different at different operating fuel-air ratios. This might explain the fact that correlations with fuel factors were obtained at one condition and not at another in the present investigation. It should also be pointed out that the empirical fuel factors considered were developed for carbon deposition and not for exhaust-gas smoke.

EFFECT OF ADDITIVES ON CARBON FORMATION

The fuel additives investigated represent a fairly wide variety of organo-metallic compounds, oxygen-bearing compounds, and commercial compounds recommended for use in reciprocating engines and furnaces to reduce carbonaceous deposits and smoke. Spectroscopic analyses of the commercial compounds showed that most of them contained some organo-metallic materials. Most of the additives tested significantly reduced carbon deposits of the base fuel. None of them produced effects on exhaust-gas smoke concentration that could be considered significant in view of the variations in smoke concentrations observed with the base fuel.

Among the additives tested, the oxygenated compounds were generally the least effective in reducing deposits in the single combustor. The most effective oxygenated compound, isooctyl nitrate, reduced base-fuel deposits almost 30 percent in a 1-percent-by-weight blend. Most of the organo-metallic compounds and the commercial additives reduced deposits 50 percent or more. Additives A, B, and J, which reduced base-fuel deposits around 70 percent, were the most effective of the commercial additives. Tests with tetraethyl lead and with lead naphthenate showed smaller but still very significant reductions. The most effective compound tested was dicyclopentadienyliron, known commercially as "Ferrocene." This material reduced deposits in all concentrations tested; the largest reduction was 80 percent, obtained with the highest additive concentration tested (0.05 percent by weight) in a No. 2 furnace oil (fuel 53–193).

The weights of deposits reported include any metallic deposits; therefore, actual reductions in carbon deposits obtained with additives containing organo-metallic compounds may have been somewhat greater than reported. Furthermore, since the density of metallic deposits would be expected to exceed the density of carbon deposits, the volume of deposits may be reduced. The volume, rather than the weight, of deposits probably determines the effects on combustor performance.

The results showed that the relative effectiveness of additives varied when they were used with different base fuels. However, the experimental data do not indicate a relation between the effectiveness of an additive and the carbon-forming propensity of the fuel. Thus, the choice of the best additive for use in jet fuels must result from tests with as many widely different fuels as are obtainable under the existing fuel procurement specifications.

The effectiveness of an additive may also be expected to vary with combustor design, since the environment in which the carbon is formed may vary considerably. For example, in a vaporizing-type combustor carbon forms inside the vaporizing tubes as well as in the flame zone. The deposits have been found to be of different composition, indicating differences in mode of formation. Unpublished data have in fact shown different effects of additives on deposits in the flame zone and in the vaporizing tubes of prevaporizing combustors.

Effectiveness in reducing deposits is not the only factor to be considered in choosing an additive. Other factors include possible effects on fuel- and combustion-system components, ease of handling, solubility in jet fuel, storage and high-temperature stability, availability, and cost. There is no information available to indicate whether the additives would be affected by a water-displacement storage system. Very limited data obtained with fuel 52–105 and the blend of 0.005-percent lead naphthenate in 52–105 indicated that the addition of the lead naphthenate caused small increases in both preformed gum (3 to 6 mg/100 ml) and accelerated gum (10 to 14 mg/100 ml). These data indicate the need to investigate this factor.

Limited field experience has indicated marked corrosion difficulties in the exhaust section of turbojet engines operating with fuels containing tetraethyl lead, such as high-octane aviation gasoline. Effects of other metallic additives, such as the dicyclopentadienyliron, on engine operation have not been examined.

All the additives tested are relatively easy to handle and sufficiently soluble in jet fuel, but the relative availability and cost of the additives are unknown.

SUMMARY OF RESULTS

An investigation of the effects of fuel properties and fuel additives on carbon deposition of JP–3 and JP–4 type fuels in turbojet-engine combustors gave the following results:

1. At operating conditions simulating an engine with a compressor pressure ratio of 4 at a 20,000-foot altitude and zero flight speed, carbon deposits and exhaust-gas smoke density correlated with three empirical fuel factors: smoke-volatility index, smoke point, and NACA K factor. More accurate correlations of deposits were obtained with smoke point and NACA K factor.

2. Single-combustor deposit data at the preceding conditions also correlated reasonably well with limited full-scale-engine deposit data. Deposition in different engines and in the single combustor was not, however, equally sensitive to changes in fuel properties.

3. At higher pressure and temperature operating conditions simulating an engine with a compressor pressure ratio of 7 at sea level and Mach 0.87, neither deposits nor smoke density satisfactorily correlated with any of the fuel factors considered. Also, the deposit data obtained at these conditions did not correlate with full-scale-engine data.

4. A number of fuel additives, including organo-metallic compounds, commercial additives, and oxygenated compounds, significantly reduced combustion-chamber carbon deposits. The most effective additives were those containing organo-metallic compounds, particularly lead and iron compounds. The most effective additive, dicyclopentadienyliron, reduced deposits of the base fuel by approximately 80 percent.

5. Limited tests showed that the relative effectiveness of the additives may vary markedly with properties of the base fuel.

6. None of the additives tested produced significant effects on the exhaust-gas smoke concentration.

LEWIS FLIGHT PROPULSION LABORATORY
NATIONAL ADVISORY COMMITTEE FOR AERONAUTICS
CLEVELAND, OHIO, *October 23, 1957*

REFERENCES

1. Jonash, Edmund R., Wear, Jerrold D., and Hibbard, Robert R.: Relations Between Fuel Properties and Combustion Carbon Deposition. NACA RM E52B14, 1952.

2. Starkman, E. S., Whitney, L. M., and Bollo, F. G.: Development of a Laboratory Method for Evaluation of Fuels for Gas Turbine Engines. Rep. No. S–13186, Final Rep. for period Feb. 9, 1949 to Apr. 15, 1950, Shell Dev. Co., Emeryville (Calif.). (AF Contract 33(038)–688.)

3. Bert, J. A.: Combustion Characteristics of Gas Turbine Fuels. Prog. Rep. No. 35, California Res. Corp., May 1951. (AF Contract W–33–038–ac–9083, AMC Proj. MX–587.)

4. Horstman, W. W., and Schramm, M. E.: G. E. 1–16 Jet Propulsion Burner Tests. Summary Rep. No. 1266, Wood River Res. Labs., Shell Oil Co., Apr. 28, 1946. (Army Contract W–33–038–ac–9813 (14169), Proj. MX–587.)

5. Moore, R. A., and Donnelly, J. J.: Summary Rep. No. 2, Rep. No. 48–1–DX, Res. and Dev. Div., Socony-Vacuum Labs., Jan. 9, 1948. (U. S. Govt. Contract W–33–038–ac–8527, AMC Proj. MX–587.)

6. Rogers, J. D.: G. E. J33 Jet Propulsion Burner Tests. Prog. Rep. No. 22, California Res. Corp., Feb. 28, 1949. (Army Contract W–33–038–ac–9083, AMC Proj. MX–587.)

7. Lenhart, A. F., and Moore, R. A.: Progress Rep. No. 20, Rep. No. 48.22–DX, Socony-Vacuum Labs., Dec. 22, 1948. (U. S. Govt. Contract NOa(s) 6583.)

8. Rickles, N. H., and Thwaites, H. L.: Summary Rep. on Fuels for Jet-Turbine Power Plants. Rep. No. FL–11M–46(21), Esso Labs., Res. Div. (Standard Oil Dev. Co.), Mar. 28, 1946. (AAF Contract W–33–038–ac–11119 (14660).)

9. Busch, Arthur M.: Correlation of Laboratory Smoke Test with Carbon Deposition in Turbojet Combustors. NACA RM E9K04, 1950.

10. Wear, Jerrold D., and Cook, William P.: Effect of Fuel Properties on Carbon Deposition in Atomizing and Prevaporizing Turbojet Combustors. NACA RM E52C24, 1952.

11. Wear, Jerrold D., and Jonash, Edmund R.: Carbon Deposition of 19 Fuels in an Annular Turbojet Combustor. NACA RM E8K22, 1949.

12. Butze, Helmut F.: Effect of Inlet-Air and Fuel Parameters on Smoking Characteristics of a Single Tubular Turbojet-Engine Combustor. NACA RM E52A18, 1952.

REPORT 1353

AN EXPERIMENTAL INVESTIGATION OF STING-SUPPORT EFFECTS ON DRAG AND A COMPARISON WITH JET EFFECTS AT TRANSONIC SPEEDS [1]

By Maurice S. Cahn

SUMMARY

Results are presented of an investigation of sting-support interference on afterbody drag at transonic speeds. Stings with varying diameter, cone angle, and cylindrical length were tested at the rear of a model with various afterbody shapes. The data were obtained at an angle of attack of 0° and at Mach numbers from 0.80 to 1.10. In general, the addition of a sting was found to cause a drag reduction. A method is presented whereby approximate sting-interference corrections may be made to models with afterbodies and sting supports of size and scale similar to those of this investigation, provided the boundary layer is turbulent at the model base and the Reynolds numbers are of the same order of magnitude. Reynolds number of the tests presented varied from 15.0×10⁶ to 17.4×10⁶ based on body length.

Sting effects are compared with data of jet effects on the same afterbodies. The results of this comparison indicate that, for the more gradually contoured afterbodies, a sting shape can be found which will duplicate the jet effects, but that for blunt afterbodies no solid sting shape will duplicate the jet effects.

INTRODUCTION

A large part of wind-tunnel testing involves the use of rear sting-supported models. Experimental data for sting-support effects on model characteristics are needed in order to estimate more exactly free-flight conditions. A recent summary of information on sting-support interference (ref. 1) presents a comprehensive study of sting effects at supersonic speeds; however, as noted in reference 1, the acute problem at transonic speeds requires more experimental data. An investigation has been conducted in the Langley 8-foot transonic tunnel to evaluate some of the effects of sting-support configuration on the drag characteristics of a systematic series of afterbodies. The tests were conducted at an angle of attack of 0° through the Mach number range from 0.80 to 1.10 for stings with varying cone-angle, length, and diameter. The sting effects determined are compared with data of jet effects on the same afterbodies.

SYMBOLS

A	cross-sectional area
C_1, C_2, C_3	representative constant values of D_b/l
C_D	pressure drag coefficient, $\sum \frac{p_l A_l}{A_{max}}$
ΔC_D	increment between total afterbody pressure drag coefficient at any given D_b/l and at $D_b/l=0$
$\Delta C_{D,max}$	increment between total afterbody pressure drag coefficient at $D_b/l=\infty$ and at $D_b/l=0$
C_p	pressure coefficient, $\frac{p_l-p_\infty}{q_\infty}$
D	diameter
L	body length
l	sting length between model base and sting cone
M	free-stream Mach number
p	static pressure
$p_{t,j}/p_\infty$	ratio of jet total pressure to free-stream static pressure
q	dynamic pressure
R	Reynolds number based on body length
T_j	jet total temperature, °F
x	station along longitudinal axis
β	afterbody boattail angle, deg
θ	sting cone half-angle, deg

SUBSCRIPTS:

A	afterbody
b	base
s	sting
∞	free stream
β	boattail
l	local
max	model maximum

APPARATUS AND METHODS

WIND TUNNEL

This investigation was conducted in the Langley 8-foot transonic tunnel, which has a dodecagonal slotted test section. Continuous testing up to a Mach number of 1.10 was possible for these models. Details of the test section are presented in reference 2. Characteristics of the airstream are given in reference 3, wherein the maximum deviation from the indicated free-stream Mach number is shown to be ±0.003.

[1] Supersedes recently declassified NACA Research Memorandum L56F18a by Maurice S. Cahn, 1956.

MODELS

The models used in the investigation were bodies of revolution that consisted of a single forebody with interchangeable afterbodies. These bodies had fineness ratios of 10 or 10.6, depending on the choice of afterbody. They were supported in the tunnel as shown in figure 1 by two 45° swept struts. These struts had chords of 11.25 inches and NACA 65-010 airfoil sections measured parallel to the airstream. Their leading edges intersected the bodies 21.7 inches from the nose.

Eight afterbody configurations (identified herein as afterbodies A to H) were designed, with the exception of afterbody E, on the basis of the following equation (see fig. 2):

$$r=r_{max}-(r_{max}-r_b)\left(\frac{x_a-x_0}{x_1-x_0}\right)^{\left(\frac{x_1-x_0}{r_{max}-r_b}\right)\tan\beta} \quad (1)$$

where

r radius at any station
r_{max} maximum radius
r_b radius at base
x_a distance from afterbody origin to any station
x_0 distance from afterbody origin to end of cylindrical section
x_1 distance from afterbody origin to body base
β boattail angle

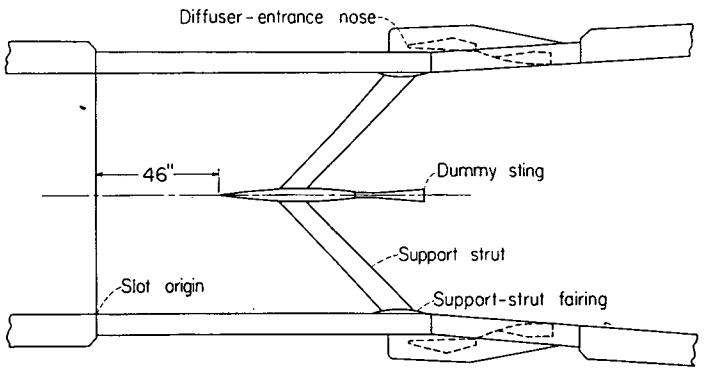


FIGURE 1.—Sting-interference model in Langley 8-foot transonic tunnel.

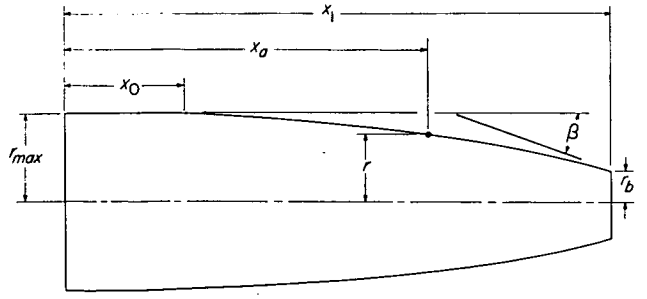


FIGURE 2.—Afterbody shape.

The design values of the afterbody variables are given in table I. Drawings of the afterbody shapes are shown in figure 3. Afterbody E, while not of this afterbody family, is included since it provides a low boattail angle otherwise not available for the bodies having a fineness ratio of 10.0. Tabulated in table II are the ordinates from which the body shapes were constructed. A sketch of the body shapes appears as figure 4.

The models were instrumented with 26 static-pressure orifices in each of three rows located 0°, 45°, and 72° from the plane of symmetry. Orifice distribution was the same in each row. Also, two diametrically opposite base-pressure orifices were located a short distance inside the model base annulus.

STINGS

The stings were constructed of wood and were attached to the rear of the models by means of an adapter contained within the sting and the afterbody. The models were tested with no sting and with the stings shown in figure 5. These stings included configurations having conical half-angles from 0° to 10° and no cylindrical sections ahead of the cone, stings with conical half-angles of 5° and cylindrical sections ahead of the cone varying from 0 to 13.40 inches, and cy-

TABLE I.—AFTERBODY DESIGN

Afterbody	r_{max}, in.	x_1, in.	β, deg	r_b, in.	x_0
A	2.5	15.70	8	0.836	2.81
B	2.5	15.70	16	.836	2.81
C	2.5	15.70	24	.836	2.81
D	2.5	15.70	45	.836	2.81
E	2.5	19.55	7.7	1.256	Not defined by eq. (1)
F	2.5	12.72	16	1.182	2.51
G	2.5	12.72	24	1.182	2.51
H	2.5	12.72	45	1.182	2.51

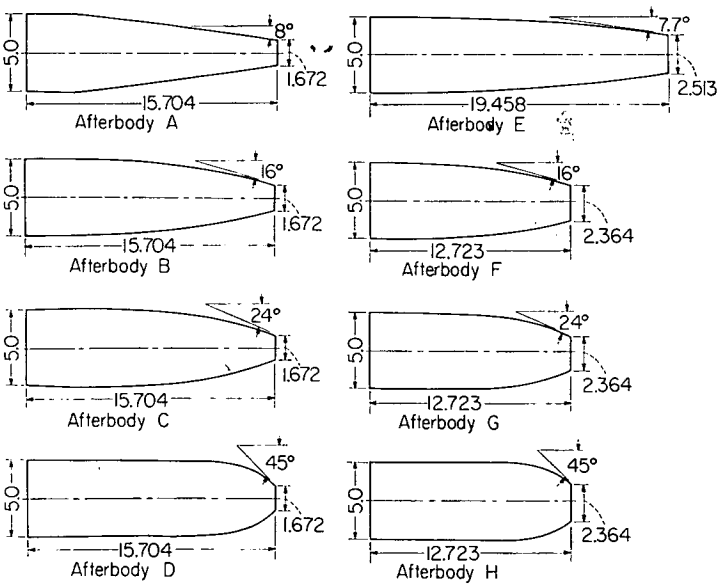


FIGURE 3.—Afterbody shapes investigated. All dimensions are in inches.

TABLE II.—BODY ORDINATES

(a) Forebody Ordinates

Station x, in.	Radius, r, in.	Station x, in.	Radius, r, in.
0.300	0.139	12.000	1.854
.450	.179	15.000	2.079
.750	.257	18.000	2.245
1.500	.433	21.000	2.360
3.000	.723	24.000	2.438
4.500	.968	27.000	2.486
6.000	1.183	30.000	2.500
9.000	1.556	30.480	2.500

(b) Afterbody Ordinates

Station x, in.	Radius, r, in.							
	Afterbody A	Afterbody B	Afterbody C	Afterbody D	Afterbody E	Afterbody F	Afterbody G	Afterbody H
30.48	2.500	2.500	2.500	2.500	2.500	2.500	2.500	2.500
33.12					2.478			
36.12					2.414			
37.31	2.500	2.500	2.500	2.500		2.500	2.500	2.500
39.12					2.305			
40.12	2.500	2.500	2.500	2.500		2.499	2.500	2.500
42.12	2.278	2.469	2.495	2.500	2.137	2.446	2.488	2.500
44.12	2.030	2.364	2.458	2.500		2.293	2.414	2.498
45.12					1.877			
46.12	1.772	2.176	2.350	2.496		2.031	2.211	2.469
48.12	1.506	1.901	2.130	2.459	1.516	1.654	1.814	2.235
50.03					1.257	1.182	1.182	1.182
50.12	1.235	1.534	1.752	2.268				
51.12	1.098	1.315	1.490	2.013				
52.12	.960	1.073	1.172	1.545				
53.01	.836	.836	.836	.836				

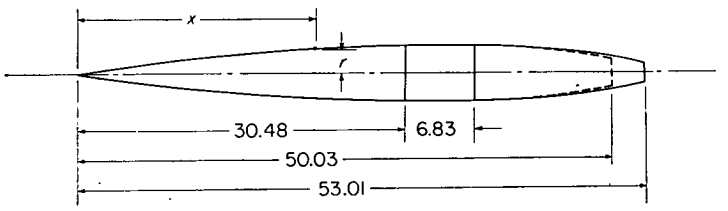


FIGURE 4.—Body shapes.

lindrical stings with diameters varying from 0.84 to 2.36 inches. The overall length of all stings was 26 inches.

TESTS AND MEASUREMENTS

Various stings were tested with each afterbody at an angle of attack of 0°. For each configuration, the Mach number was varied in 0.05 increments from 0.80 to 1.10. In order to compare sting effects with jet effects, an ethylene-air burner was exhausted through the base of the model with no sting in place. The total temperature of the jet exhaust gas was 1,200° F. Data were taken for ratios of the jet total pressure to free-stream static pressure varying from 2 to approximately 10 at free-stream Mach numbers of 0.80, 0.90, 1.00, and 1.10. Reynolds number based on body length varied from 15.0×10^6 to 17.4×10^6. (See fig. 6.) All pressures were photographically recorded from multiple tube manometers.

REDUCTION OF DATA

The pressure coefficients of these tests were numerically integrated to obtain values of afterbody pressure drag coefficient which are based on body frontal area. The stings used in this investigation had no effect on the forebody pressure drag as will be shown in the section entitled "Results and Discussion." Base drags were obtained by assuming that measured base pressures acted over the entire model base.

PRECISION

Total-drag-coefficient errors due to possible inaccuracies in measurement and to tunnel-empty stream nonuniformities are estimated generally to be less than 0.005 at subsonic speeds and not more than 0.010 at supersonic speeds.

The magnitude of the sting effects may be somewhat affected by tunnel-wall disturbances above $M=1.0$. A detailed analysis of shock reflections of this type may be found in reference 3.

RESULTS AND DISCUSSION

DESCRIPTION OF FLOW PHENOMENA

Prior to presentation of these results, a brief discussion of the flow mechanism occurring at the model base is considered to be desirable. Inasmuch as the flow separates from the body at the model base, a region of low-energy air is created immediately behind the base. As a consequence, the streamline adjacent to the wake has essentially a constant pressure. The way in which the pressure at the base arrives at its steady value can be illustrated by considering a cylindrical afterbody. If in some way an external stream is immediately imposed on this afterbody, the base pressure

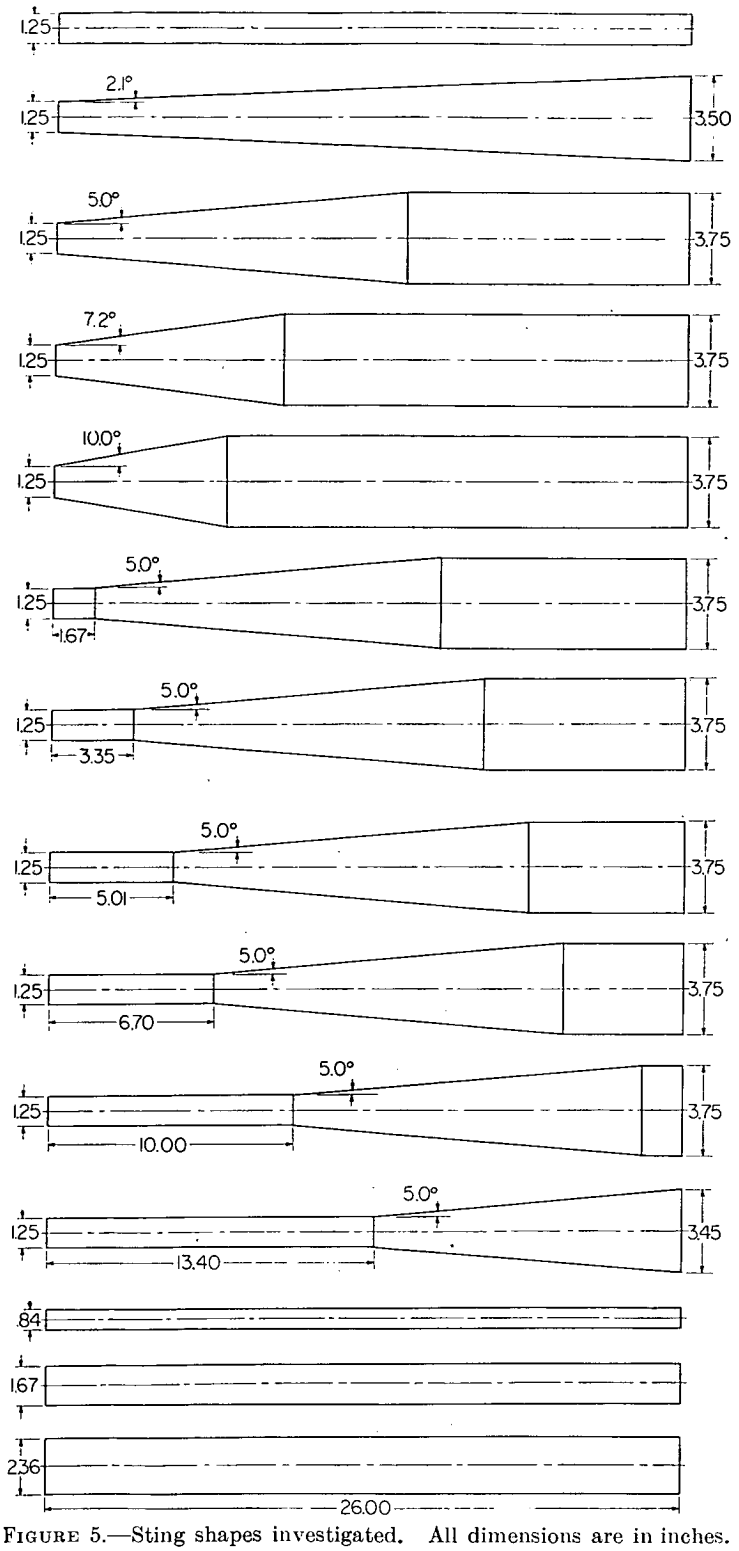


FIGURE 5.—Sting shapes investigated. All dimensions are in inches.

will in the first instant be equal to the free-stream static pressure. (See fig. 7 (a).) After some time, because of viscous mixing, the external stream aspirates the base region and lowers its pressure. The free stream is turned inward with an accompanying increase in velocity. Viscous mixing, now being strengthened, causes more aspiration of the base region with further turning inward of the free stream. Opposing this effect is the increase in pressure in the wake where the external stream must be turned to become horizontal again. Since the base region is also affected by this wake pressure rise, a base pressure is established when the two opposing effects are in equilibrium. (See fig. 7 (b).)

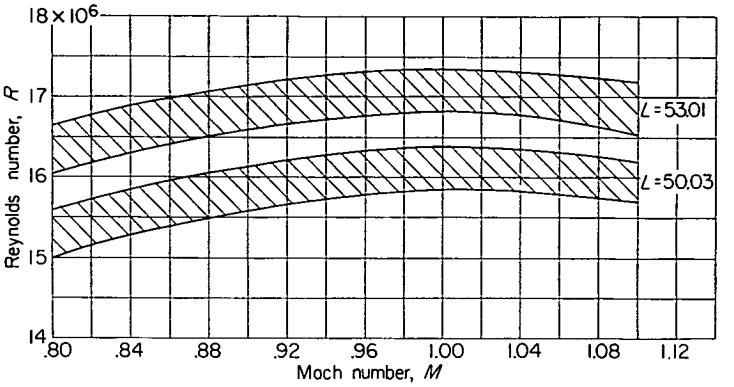


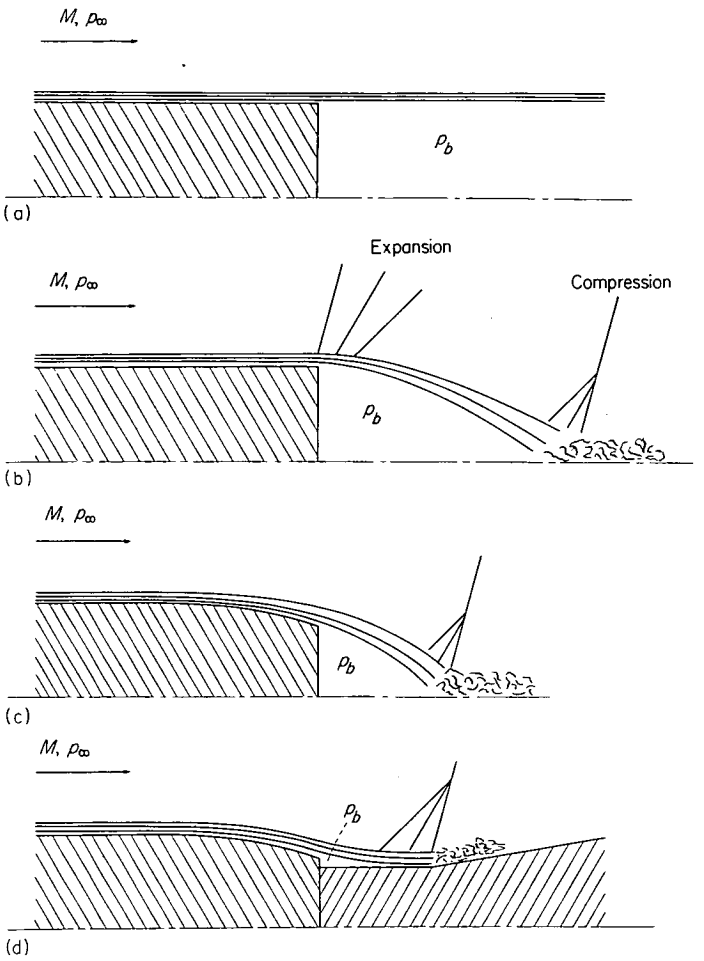
FIGURE 6.—Variation of Reynolds number, based on body length, with Mach number.

Boattailing, if not so great as to cause separation ahead of the base, will cause an increase in base pressure. (See fig. 7 (c).) This increase in base pressure results from an increase in compression over the body as well as from the fact that less wake region is exposed to the aspiration effects of the external stream. Placing a sting in the rear of a model, in addition to causing less wake exposure, requires the external stream to be turned outward more rapidly. (See fig. 7 (d).) These effects result in a base-pressure increase. Increasing the sting cone angle or moving the sting cone closer to the base thus causes a further increase in the turning rate of the external stream near the base and results in a further base-pressure increase.

A sting also has effects on the body pressures ahead of the model base that are similar to the sting effects on base pressure. These effects, which are transmitted through the body boundary layer, become smaller with increasing distance upstream of the base, as is shown in figure 8. In figure 8 are typical pressure distributions over the body with and without a sting. The pressure coefficients for the orifice row along the plane of symmetry are shown for afterbodies B and D at four Mach numbers. The two afterbodies represent a blunt and a gradually contoured rear end configuration, and the sting is the one which had the largest effect. These results indicate that the sting did not affect the body pressures forward of the 60-percent station.

EFFECT OF STING CONFIGURATION ON BASE PRESSURE

In figure 9, base pressure coefficients are presented as a function of sting half-angle, length, and cross-sectional-area parameters. As previously stated, the presence of a sting



(a) Cylindrical afterbody immediately after starting of external stream.
(b) Cylindrical afterbody fully developed flow.
(c) Boattailed afterbody.
(d) Boattailed afterbody with sting.

FIGURE 7.—Sketch of flow mechanism at base.

results in changes in base pressure as well as similar changes in body pressures upstream of the base. Consequently, as would be expected, the variations in afterbody drag, which will be discussed in the following sections, are similar to changes in base pressure.

EFFECT OF STING CONFIGURATION ON DRAG

Sting cone-angle effect.—Figure 10 shows the effect of sting half-angle on afterbody pressure drag. Presented at Mach numbers from 0.80 to 1.10 are curves of base, boattail, and total afterbody pressure drag coefficients as a function of sting half-angle for each body tested. The length l of the cylindrical section ahead of the sting cone is zero. These data show that in spite of the large differences in absolute drag values, the curves are similar for all afterbodies in that the drag became lower with increasing sting cone angle. This trend occurred primarily because of the more rapid rate of turning of the external stream with increasing sting cone angle. It should be pointed out that the downstream end of the sting cones was limited to a diameter of 3.75 inches.

Since the curves of figure 10 tended to be linear, slopes of the total afterbody drag curves were taken. These slopes are plotted in figure 11 and can be used to summarize the sting cone angle effect. For the cases where the variation of drag with sting cone angle was not linear, the slopes were taken so as to favor the low-angle portion of the curves. For afterbodies B, C, and D, the curves indicate that the sting cone angle effect near the speed of sound can be double the effect noted at higher and lower speeds. The subsonic and supersonic levels of the angle effect, $\partial C_{D,A}/\partial\theta$, for all bodies were of the order of -0.006 with the exception of afterbody H. Afterbody H was effectively the most blunt afterbody tested. It can be seen that increasing boattail angle in general caused an increase in sting-angle effect. This result was attributed to the increased turning rate required by the external stream at the model base.

Sting-cone-position effect.—Figure 12 shows the effect of varying sting-cone position along the sting on base, boattail, and afterbody pressure drag coefficients. These data were obtained with cones of 5° half-angle behind varying lengths of constant-diameter cylindrical sting sections. A drag reduction always occurred as the sting cone was moved toward the base (increasing D_b/l) and caused an increased rate of turning of the external flow. Similar trends, although of different magnitude, were noted in reference 4 for a somewhat different configuration. It should again be pointed out that the downstream end of the sting cones was limited to a diameter of 3.75 inches.

The effect of sting-cone position has been determined only for stings with a 5° cone half-angle. However, it is believed that reasonable approximations of the effect of varying cone position for stings with other cone angles can be obtained by proper interpolation of the results presented herein. A simple method of achieving this can be illustrated by use of a typical plot of drag coefficient against sting angle. (See fig. 13.) The entire range of angles and lengths is bounded by the two linear curves for $D_b/l=0$ and $D_b/l=\infty$. The curves for the intermediate values of D_b/l cannot cross over each other since the variation of drag with sting length is a monotonic function. Therefore, it would appear that the drag for intermediate values of D_b/l could be reasonably approximated with linear curves. Having the drag values for the intermediate D_b/l values for $\theta=5°$ will allow these approximation lines to be determined.

Let ΔC_D be defined as the difference between total afterbody drag coefficient at any given D_b/l and at $D_b/l=0$, and let $\Delta C_{D,max}$ be the difference between total afterbody drag coefficient at $D_b/l=\infty$ and $D_b/l=0$. Then, on the basis of the foregoing discussion $\Delta C_D/\Delta C_{D,max}$ for any D_b/l may be considered to be approximately a constant for all values of θ.

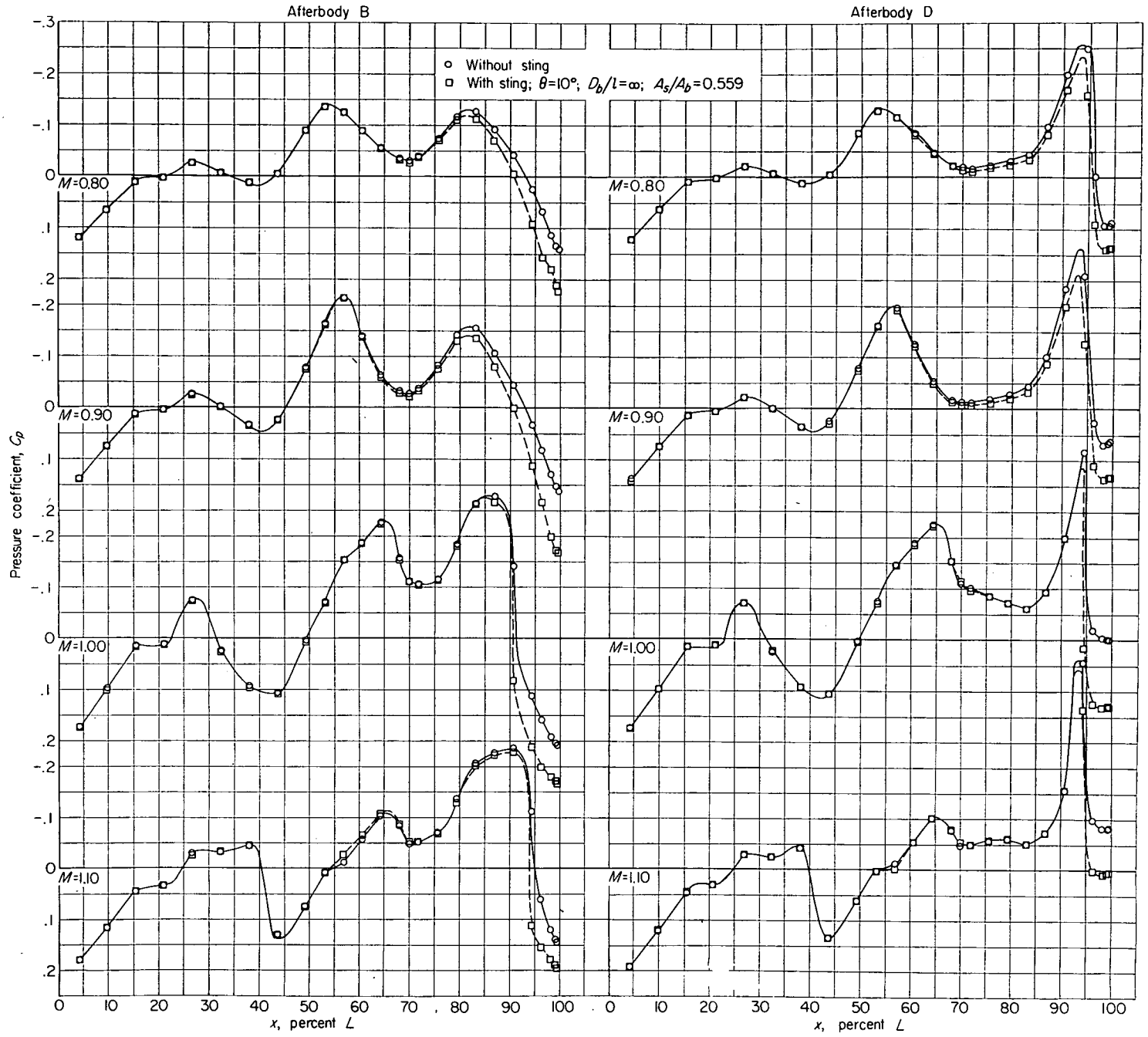
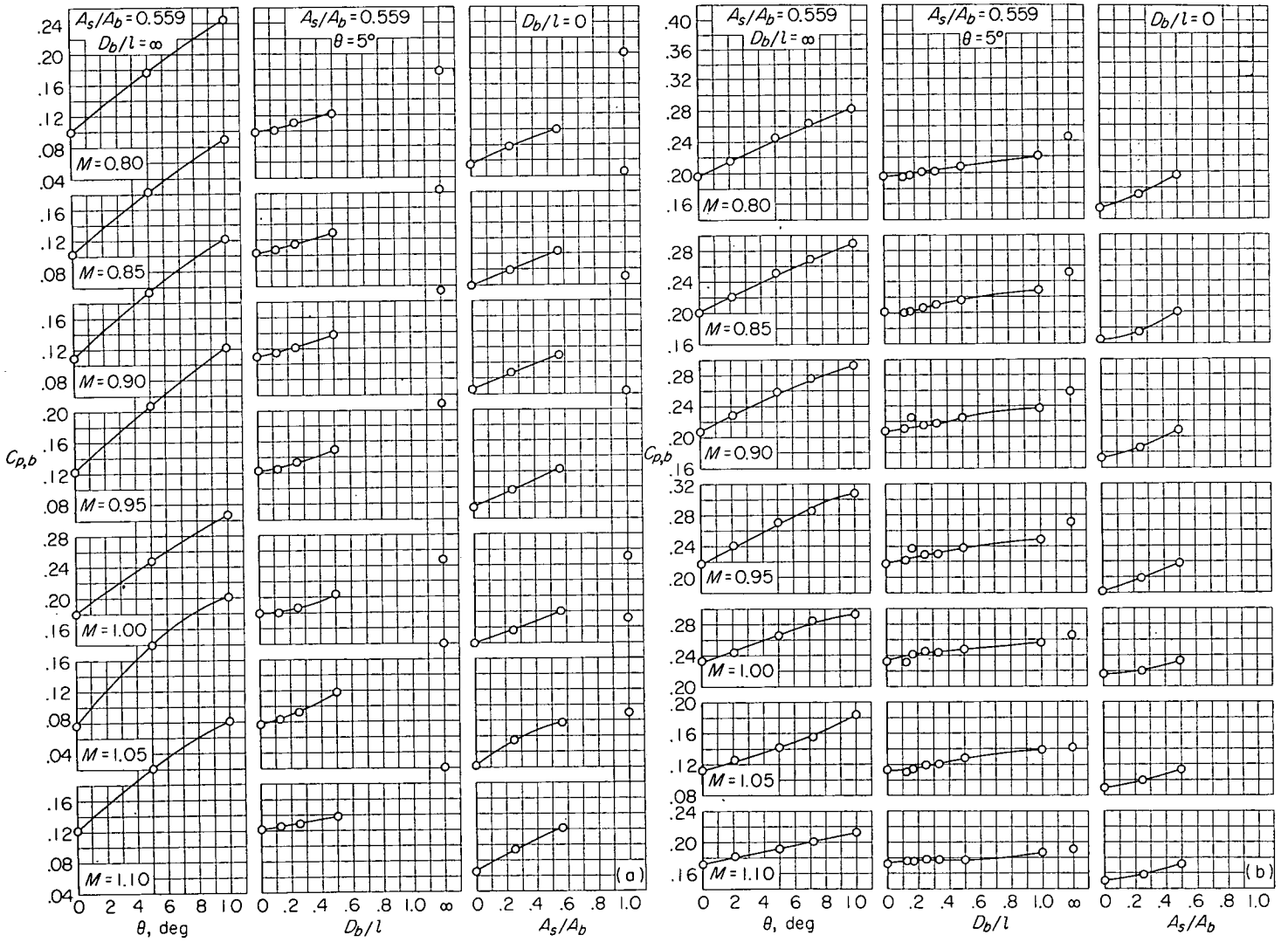


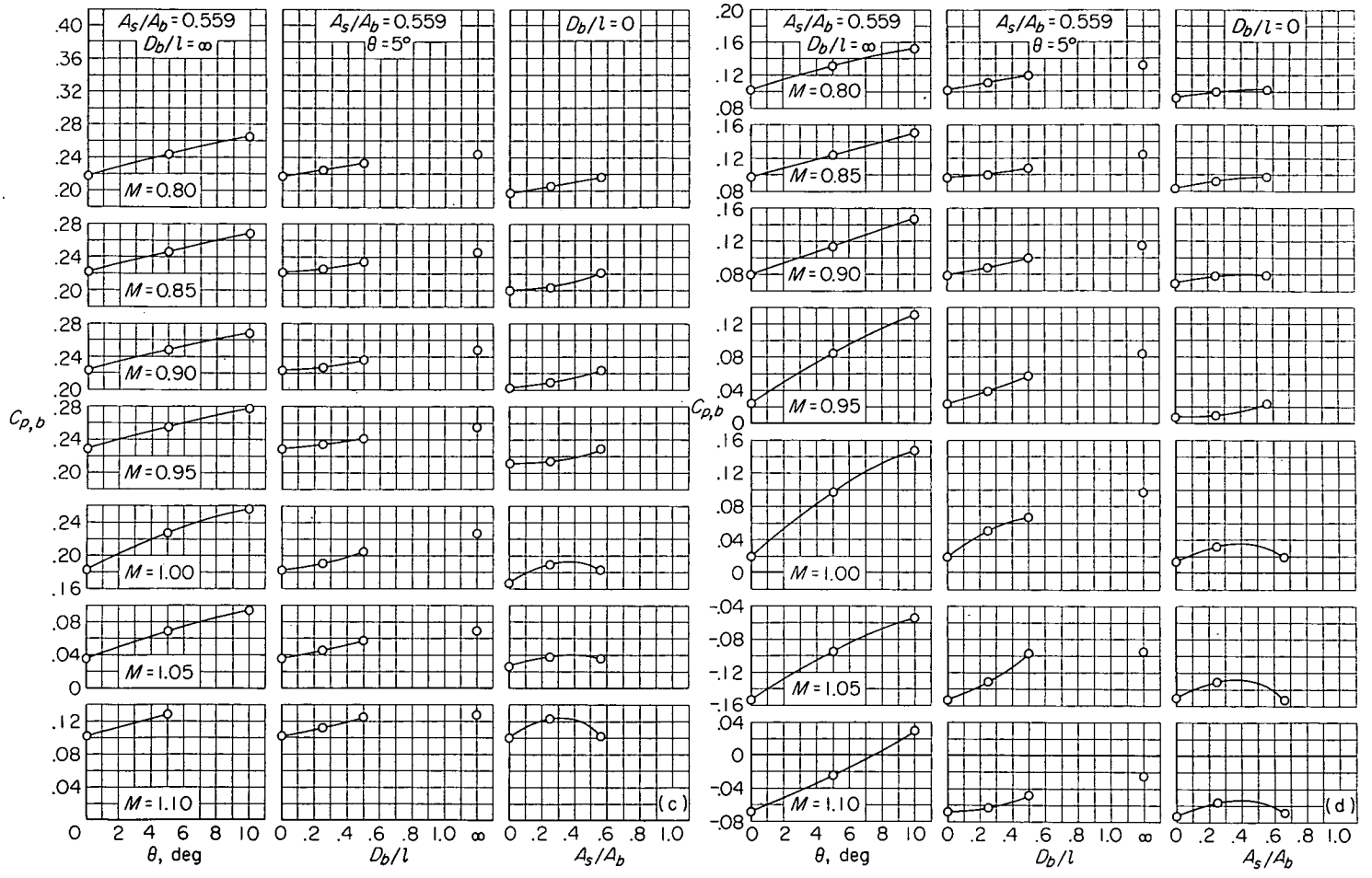
FIGURE 8.—Typical pressure distributions for orifice row along the plane of symmetry. Afterbodies B and D.



(a) Afterbody A. $\beta = 8°$; $\frac{D_b}{D_{max}} = 0.334$.

(b) Afterbody B. $\beta = 16°$; $\frac{D_b}{D_{max}} = 0.334$.

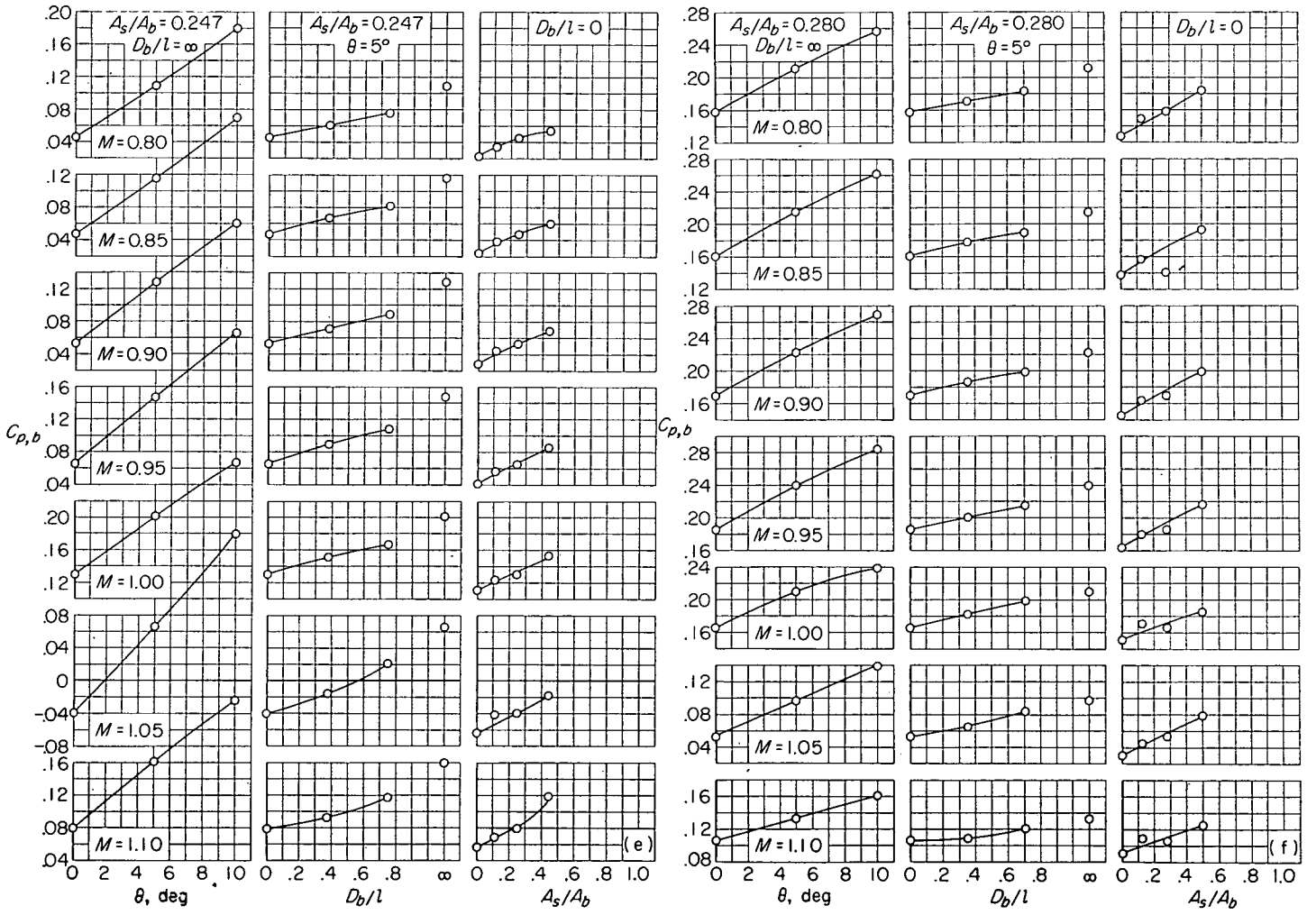
FIGURE 9.—Variation of base pressure coefficient with sting parameters.



(c) Afterbody C. $\beta = 24°$; $\frac{D_b}{D_{max}} = 0.334$.

(d) Afterbody D. $\beta = 45°$; $\frac{D_b}{D_{max}} = 0.334$.

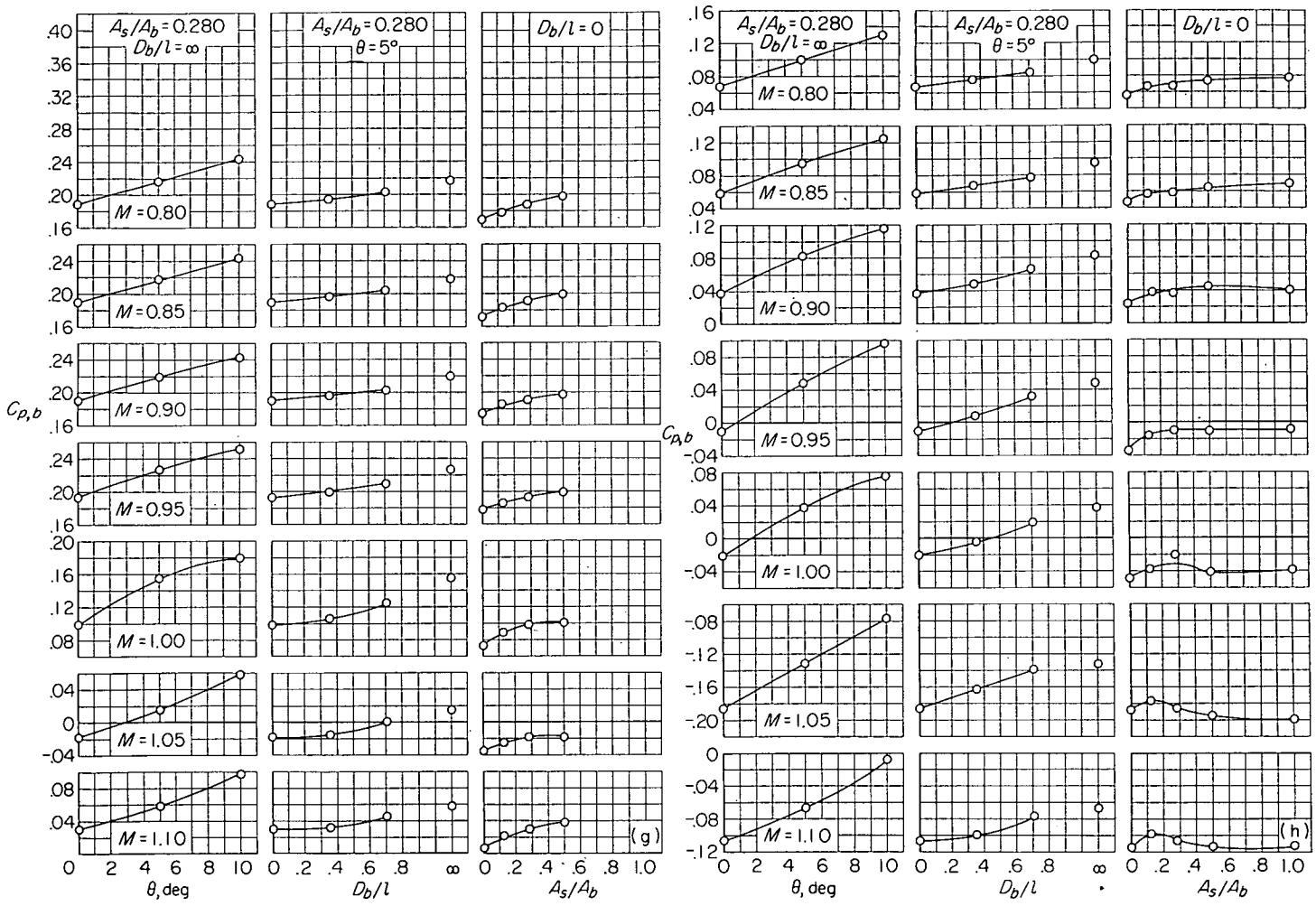
FIGURE 9.—Continued.



(e) Afterbody E. $\beta = 7.7°$; $\frac{D_b}{D_{max}} = 0.503$.

(f) Afterbody F. $\beta = 16°$; $\frac{D_b}{D_{max}} = 0.473$.

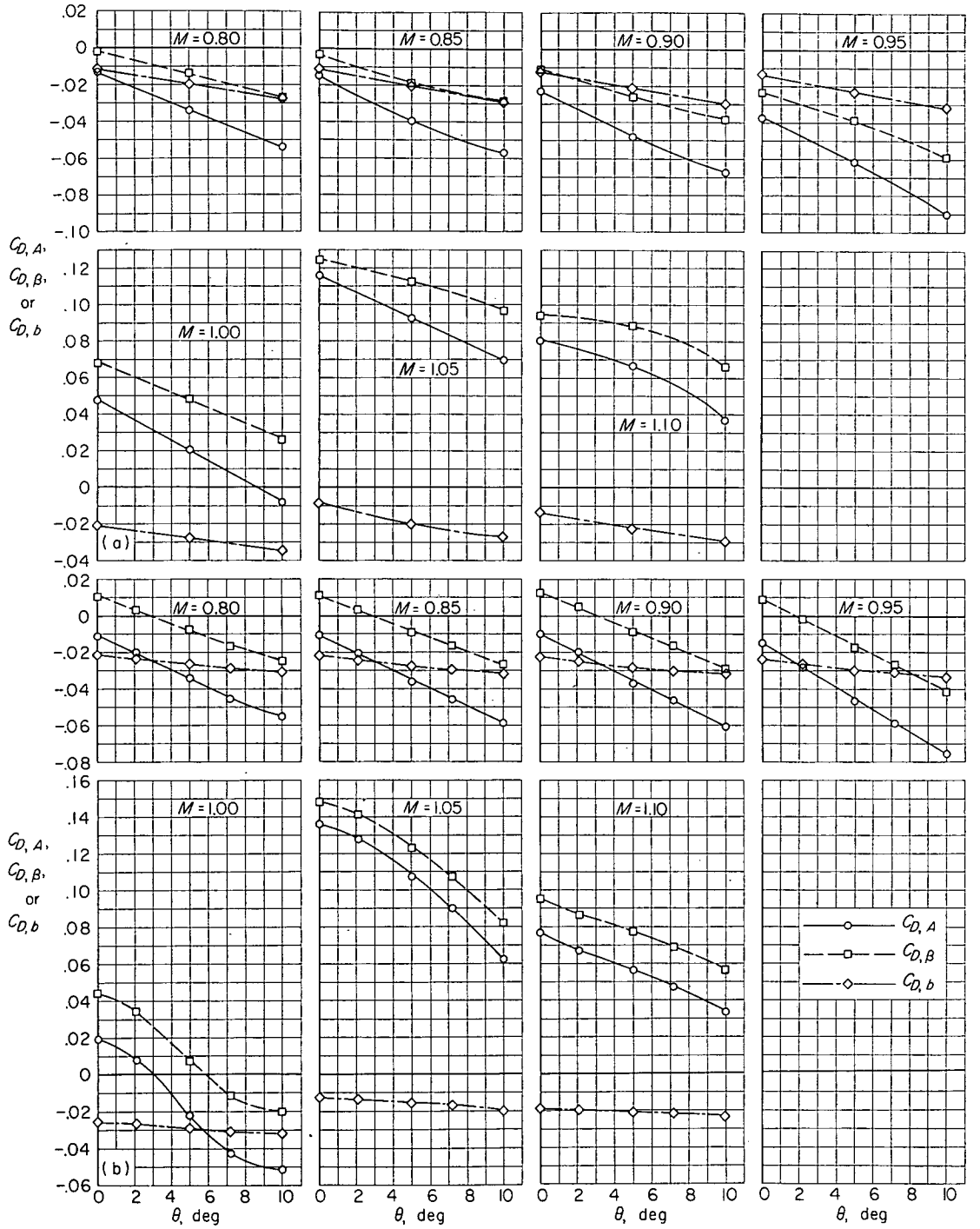
FIGURE 9.—Continued.



(g) Afterbody G. $\beta = 24°$; $\frac{D_b}{D_{max}} = 0.473$.

(h) Afterbody H. $\beta = 45°$; $\frac{D_b}{D_{max}} = 0.473$.

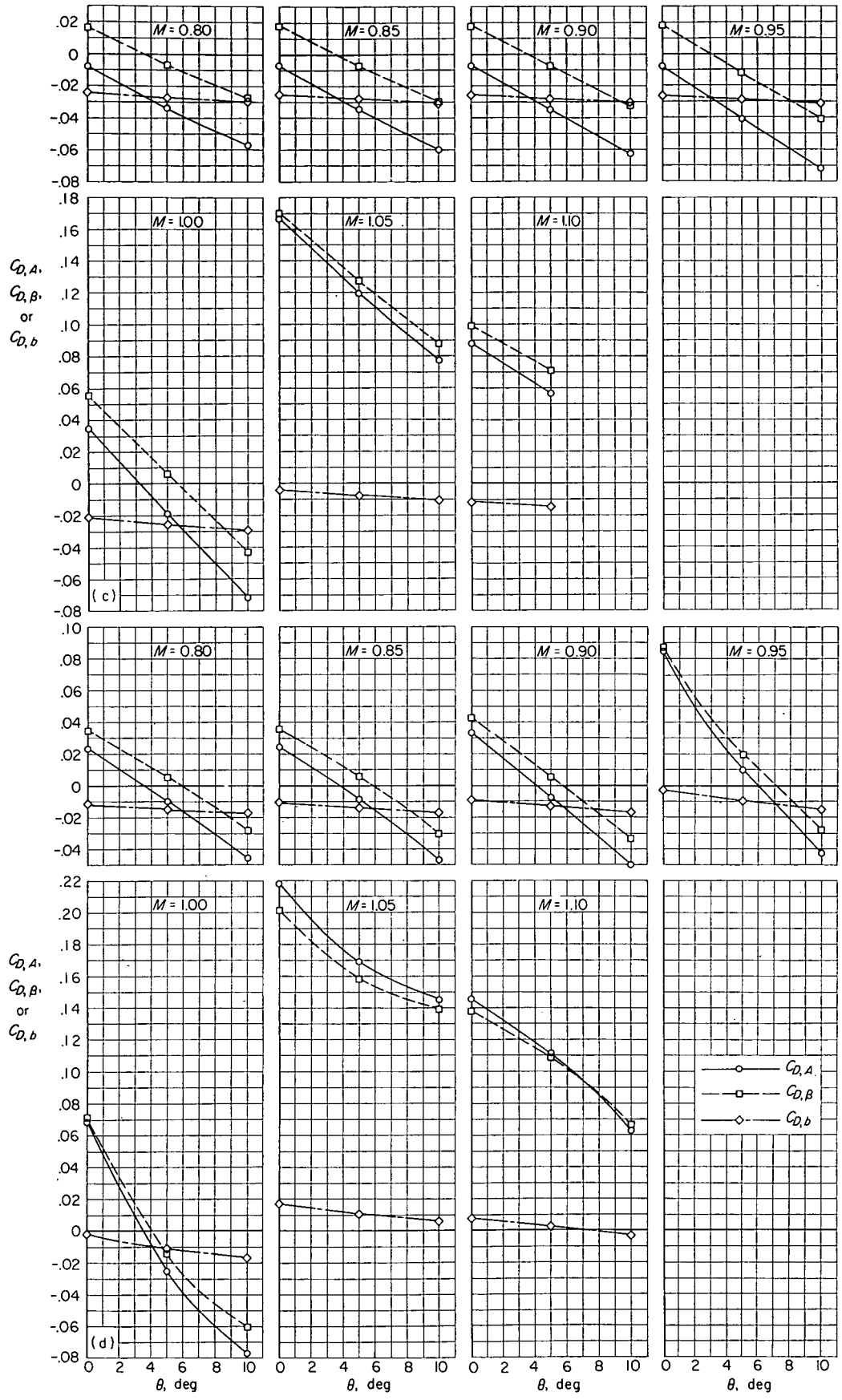
FIGURE 9.—Concluded.



(a) Afterbody A. $\beta=8°$; $\frac{A_s}{A_b}=0.559$; $\frac{D_b}{D_{max}}=0.334$.

(b) Afterbody B. $\beta=16°$; $\frac{A_s}{A_b}=0.559$; $\frac{D_b}{D_{max}}=0.334$.

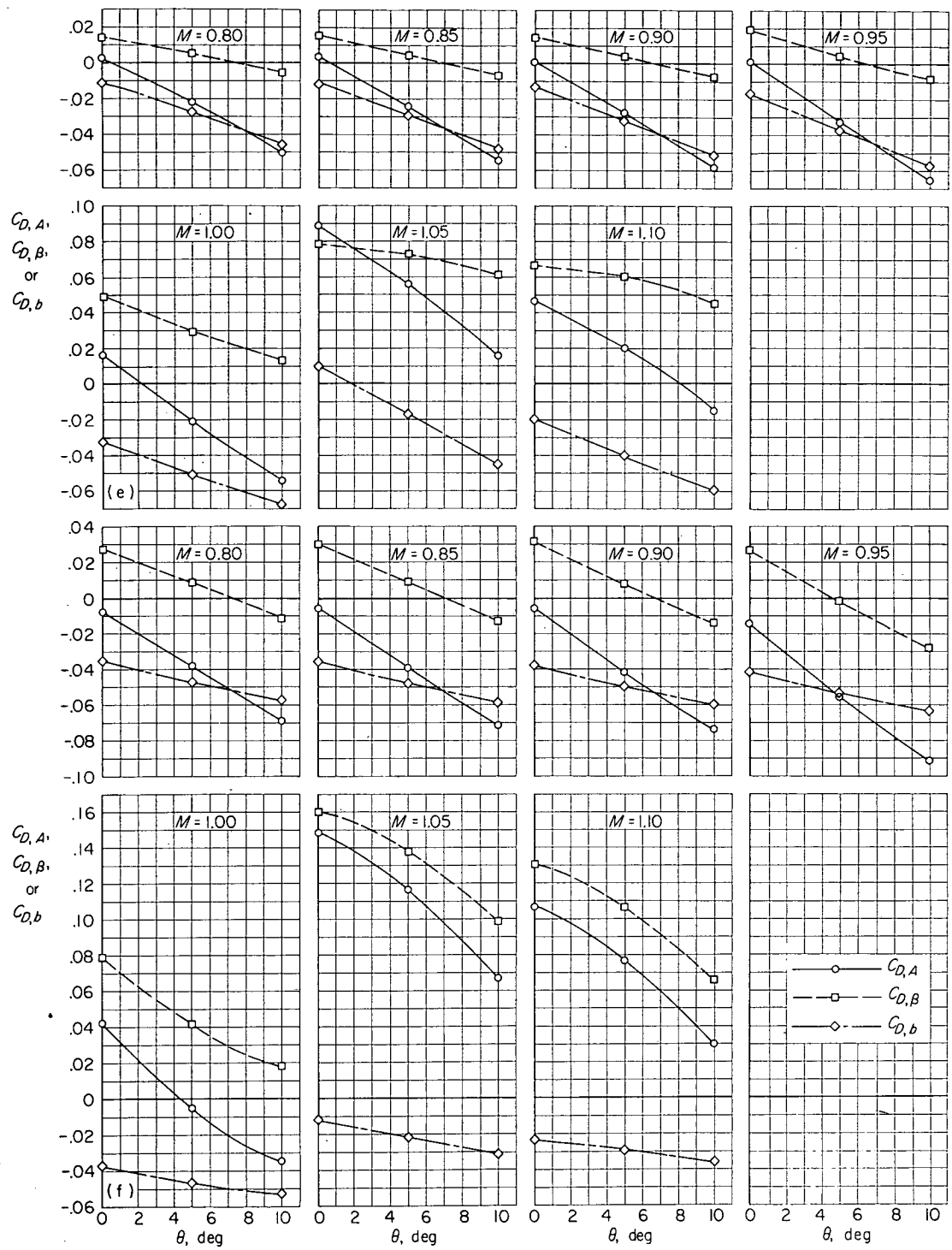
FIGURE 10.—Variation of base, boattail, and total afterbody pressure-drag coefficient with sting half-angle with $\frac{D_b}{l}=\infty$.



(c) Afterbody C. $\beta=24°$; $\frac{A_s}{A_b}=0.559$; $\frac{D_b}{D_{max}}=0.334$.

(d) Afterbody D. $\beta=24°$; $\frac{A_s}{A_b}=0.559$; $\frac{D_b}{D_{max}}=0.334$.

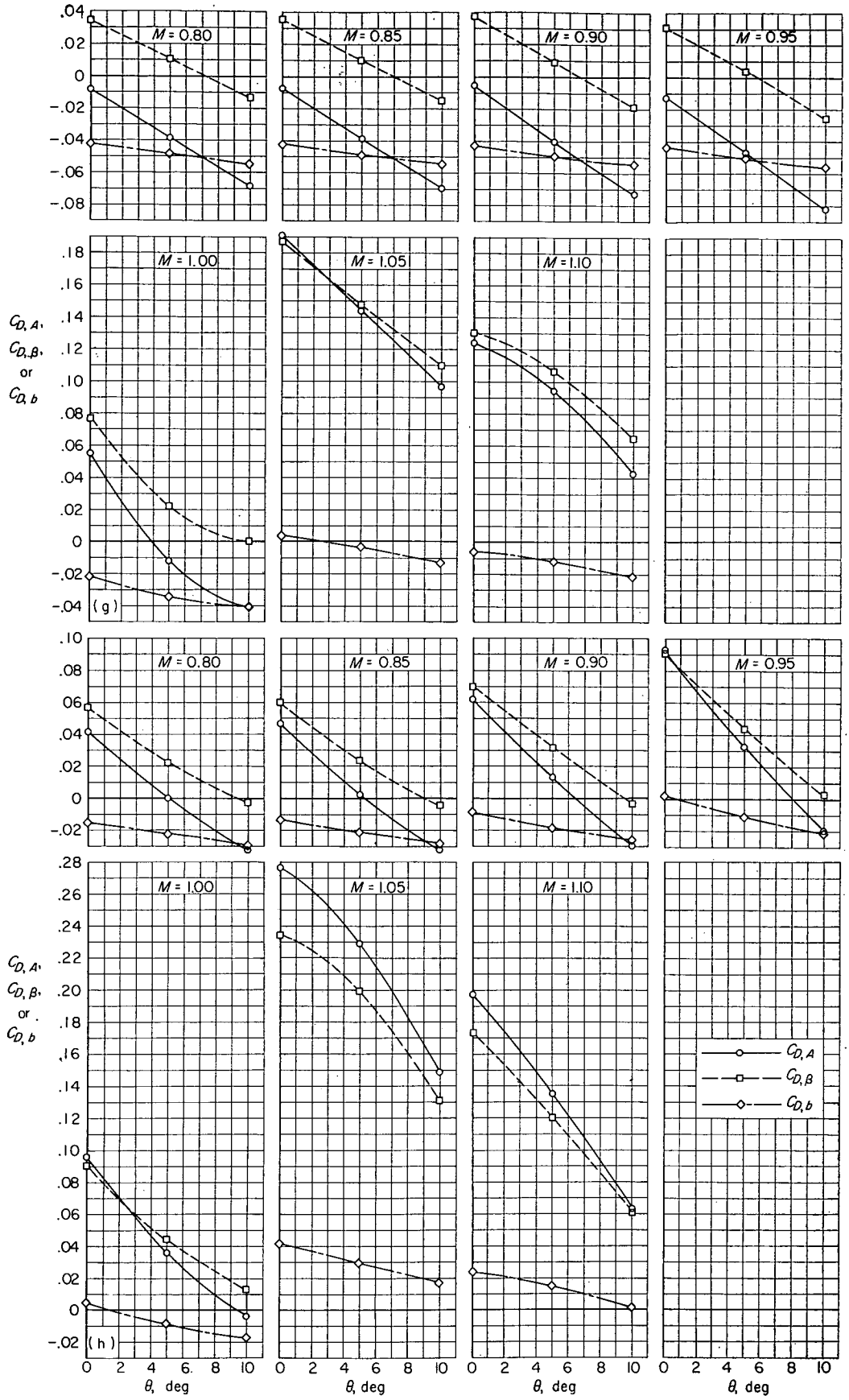
FIGURE 10.—Continued.



(e) Afterbody E. $\beta=7.7°$; $\frac{A_s}{A_b}=0.247$; $\frac{D_b}{D_{max}}=0.503$.

(f) Afterbody F. $\beta=16°$; $\frac{A_s}{A_b}=0.280$; $\frac{D_b}{D_{max}}=0.473$.

FIGURE 10.—Continued.



(g) Afterbody G. $\beta=24°$; $\frac{A_s}{A_b}=0.280$; $\frac{D_b}{D_{max}}=0.473$.

(h) Afterbody H. $\beta=45°$; $\frac{A_s}{A_b}=0.280$; $\frac{D_b}{D_{max}}=0.473$.

FIGURE 10.—Concluded.

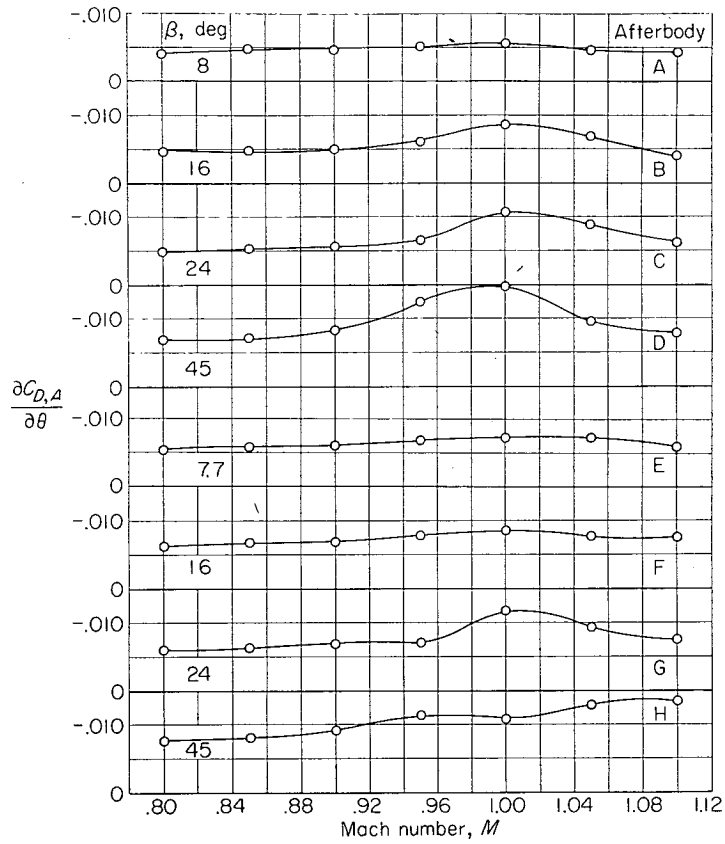
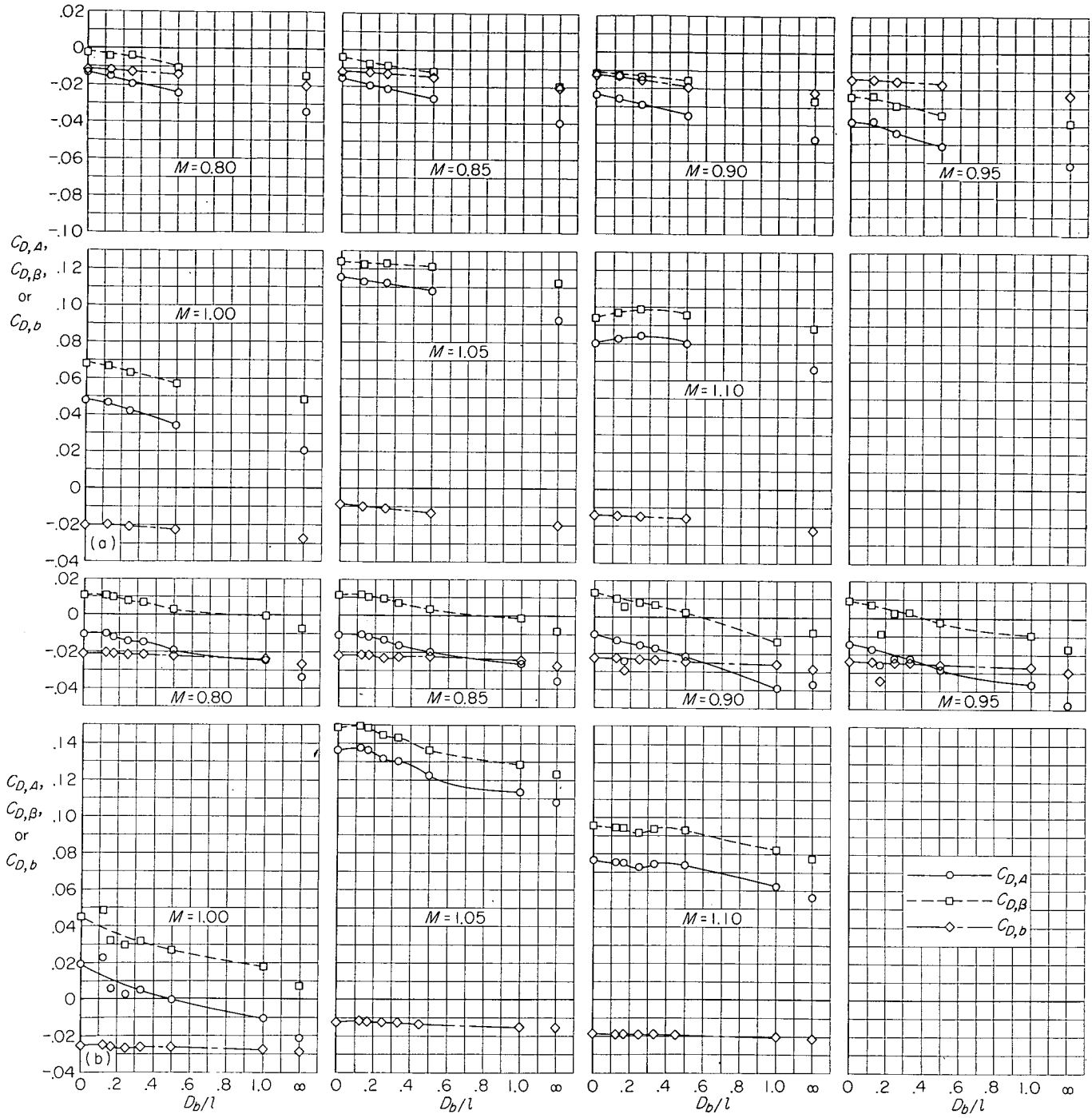


FIGURE 11.—Variation of sting-half-angle effect with Mach number.

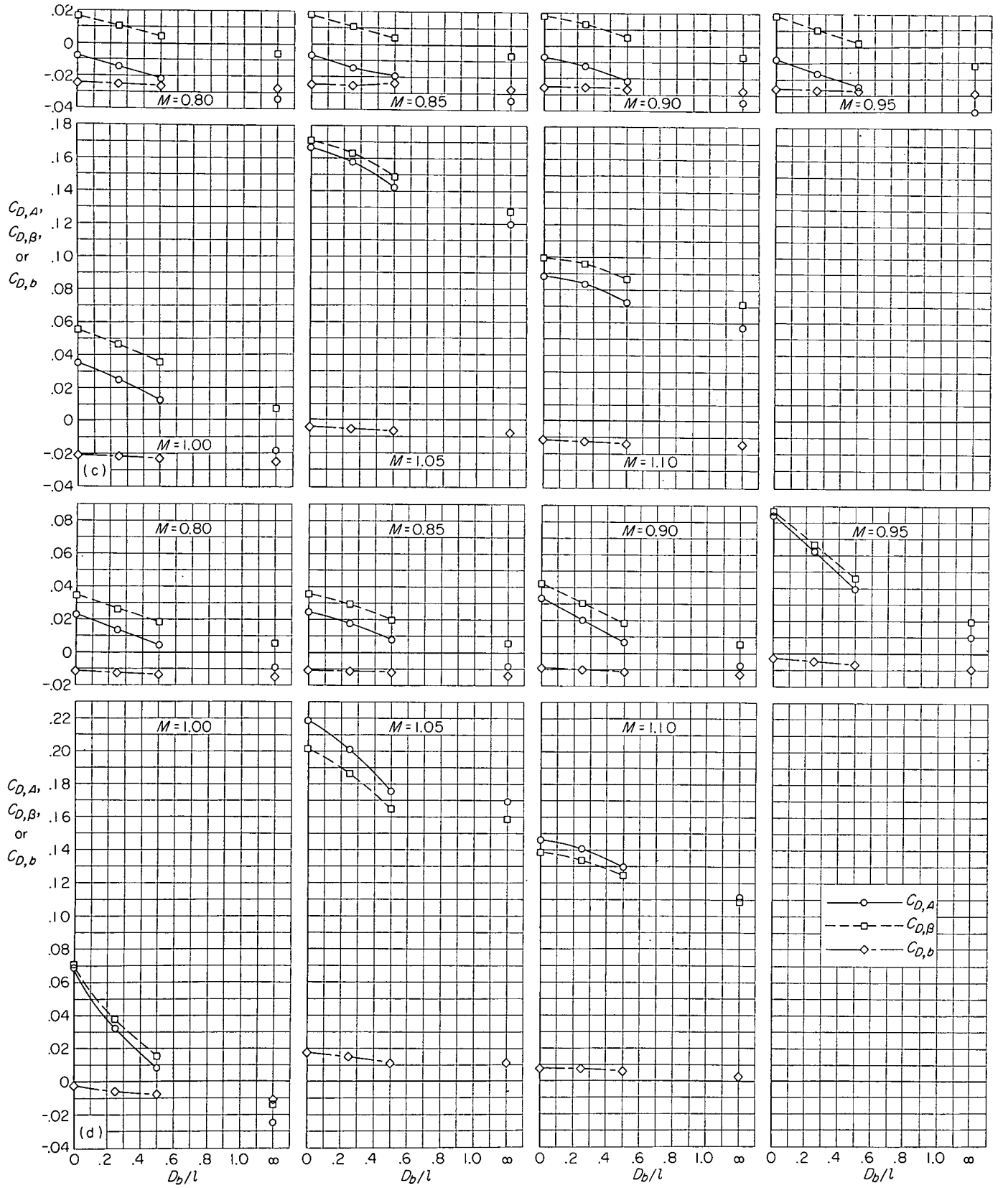
$\frac{D_b}{l} = \infty$.



(a) Afterbody A. $\beta=8°$; $\frac{A_s}{A_b}=0.559$; $\frac{D_b}{D_{max}}=0.334$.

(b) Afterbody B. $\beta=16°$; $\frac{A_s}{A_b}=0.559$; $\frac{D_b}{D_{max}}=0.334$.

FIGURE 12.—Variation of base, boattail, and total afterbody pressure-drag coefficient with ratio of base diameter to sting length with $\theta=5°$.

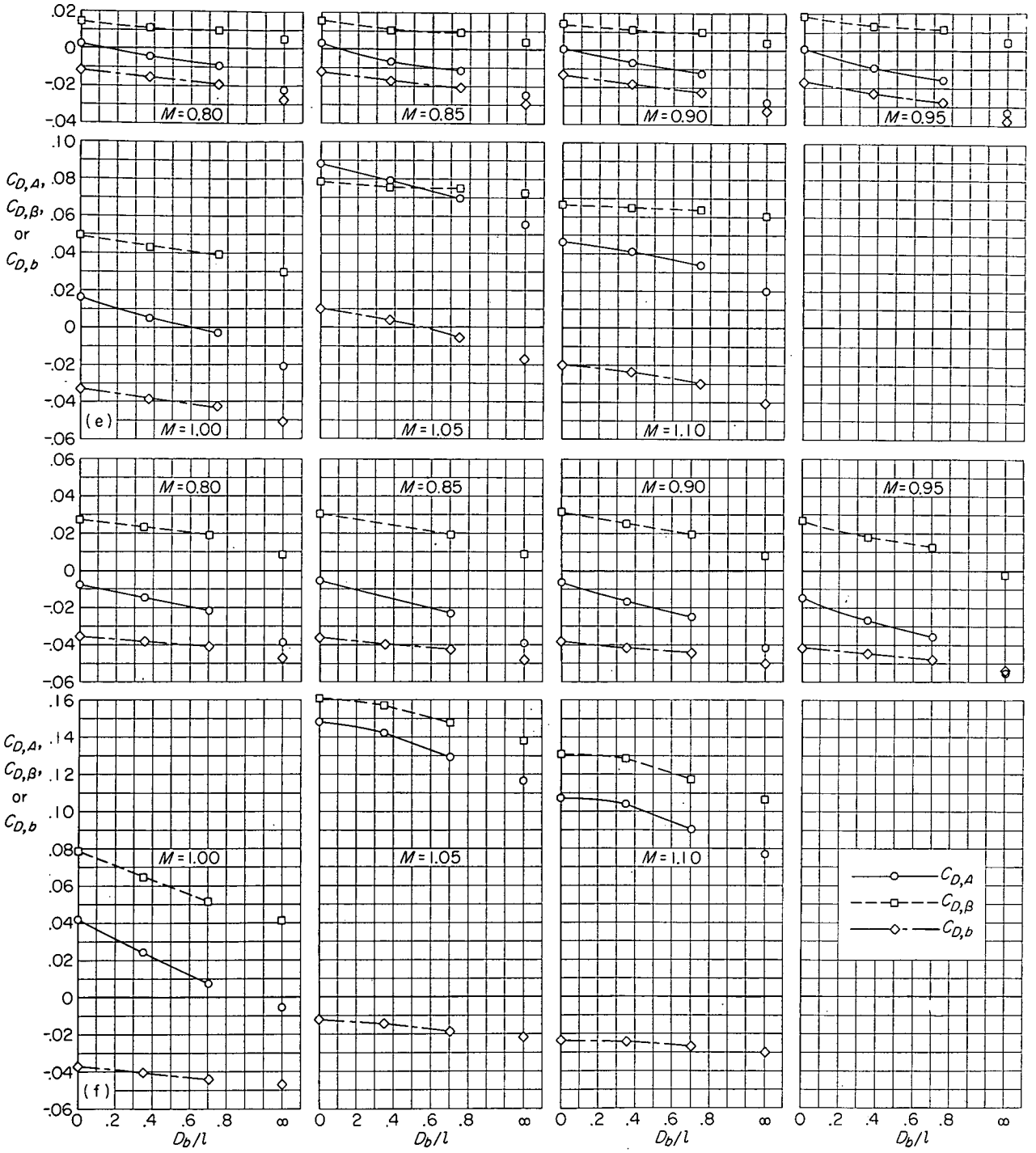


(c) Afterbody C. $\beta=24°$; $\frac{A_s}{A_b}=0.559$; $\frac{D_b}{D_{max}}=0.334$.

(d) Afterbody D. $\beta=45°$; $\frac{A_s}{A_b}=0.559$; $\frac{D_b}{D_{max}}=0.334$.

FIGURE 12.—Continued.

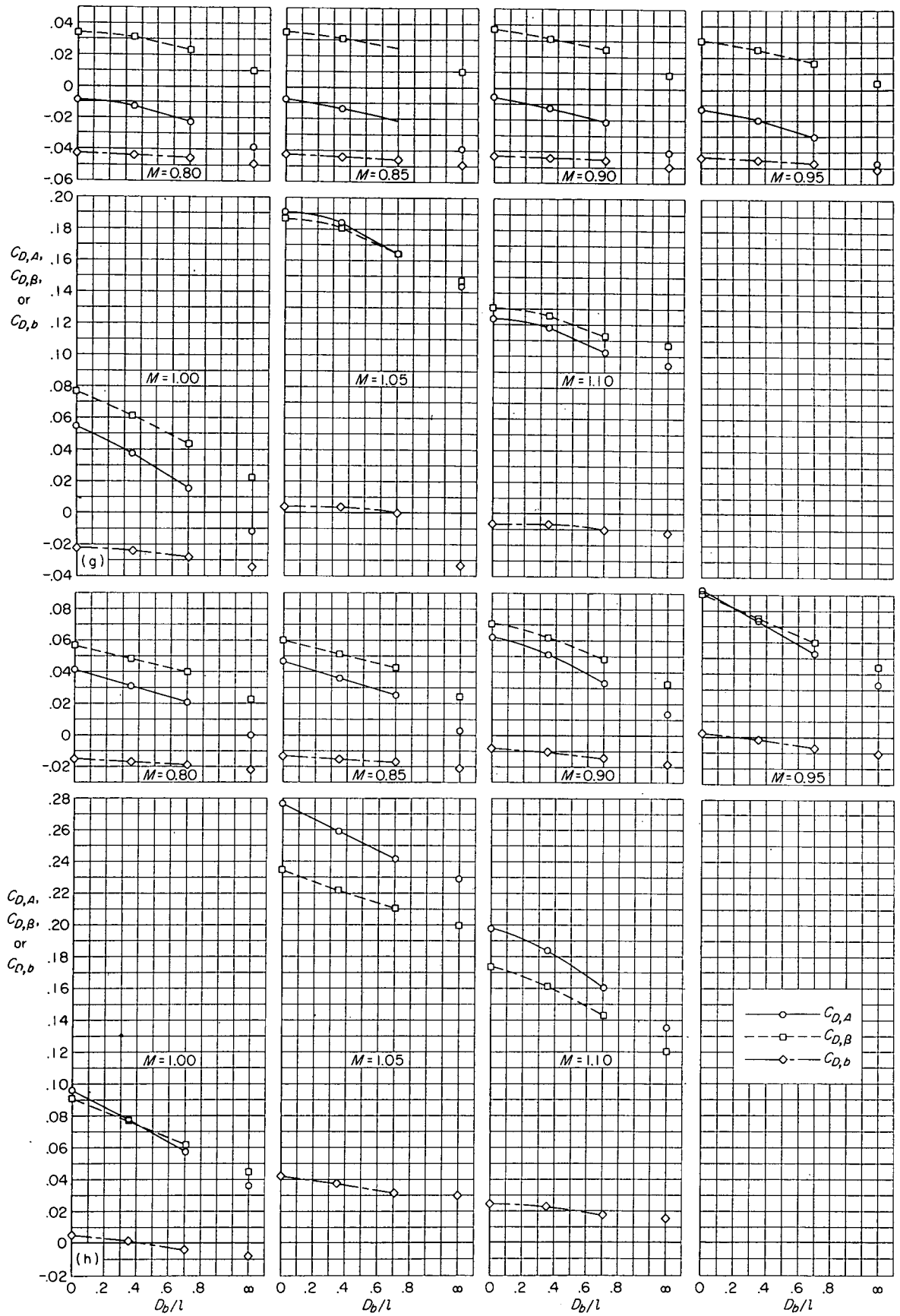
526597—60——23



(e) Afterbody E. $\beta=7.7°$; $\frac{A_s}{A_b}=0.247$; $\frac{D_b}{D_{max}}=0.503$.

(f) Afterbody F. $\beta=16°$; $\frac{A_s}{A_b}=0.280$; $\frac{D_b}{D_{max}}=0.473$.

FIGURE 12.—Continued.



(g) Afterbody G. $\beta=24°$; $\frac{A_s}{A_b}=0.280$; $\frac{D_b}{D_{max}}=0.473$.

(h) Afterbody H. $\beta=45°$; $\frac{A_s}{A_b}=0.280$; $\frac{D_b}{D_{max}}=0.473$.

FIGURE 12.—Concluded.

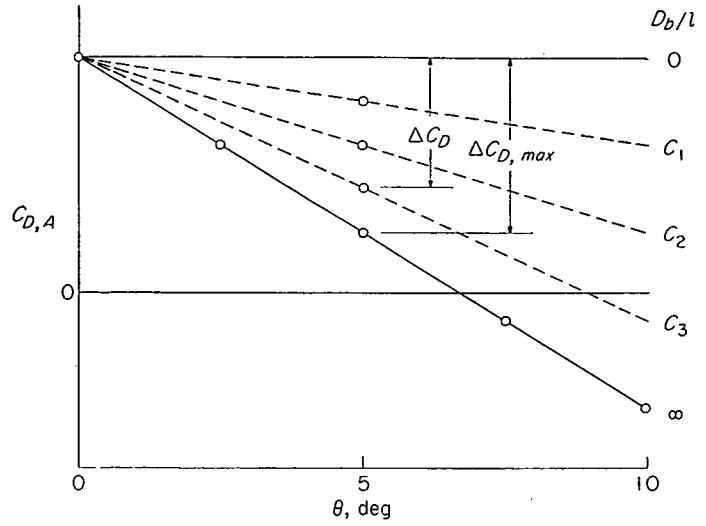


FIGURE 13.—Illustrative plot of $C_{D,A}$ against θ for various values of D_b/l.

The parameter $\Delta C_D/\Delta C_{D,max}$ represents the ratio of sting-cone effect on drag for a given sting length (D_b/l) to the maximum sting-cone effect on drag. The maximum effect is obtained when the sting length is zero ($D_b/l=\infty$). Values of $\Delta C_D/\Delta C_{D,max}$ obtained from the data of figure 12 are presented in figure 14 (a). Their variation with D_b/l is shown for each afterbody configuration through the Mach number range. Values of $\Delta C_D/\Delta C_{D,max}$ for configurations having larger values of D_b/l than those shown in figure 14 (a) may be obtained in figure 14 (b). These values are plotted against the reciprocal of D_b/l for each afterbody configuration through the Mach number range. Figure 15 presents the slopes of the linear portion of the curves shown in figure 14 (a). The magnitude of these slopes is about 1.0 for all configurations tested.

Sting-size effect.—The effect on the base, boattail, and afterbody pressure drag coefficients of varying the cross-sectional area of a cylindrical sting is presented in figure 16 for each afterbody. No sting cone was present on the sting for these data and the effect of limiting the sting length to 26 inches is believed to be negligible. In general, the effect of increasing the sting size was to decrease the drag. Average slopes of total afterbody pressure drag with the sting size parameter are plotted against Mach number in figure 17. The slopes are seen to vary from approximately zero to −0.05.

STING-INTERFERENCE CORRECTIONS

Inasmuch as a large number of afterbodies and stings were tested in combination, a general equation has been derived from the results to provide corrections to wind-tunnel drag measurements for sting-interference effects. Although the scope of the present investigation was rather large, it was necessarily limited. Therefore, any corrections obtained empirically from these results should be restricted to stings and afterbodies similar in scale and shape to those investigated. It is also recommended that the results be used only for models having Reynolds number and boundary-layer conditions that comply with those of the present tests. (See ref. 1.) The boundary layer was turbulent ahead of the model base for the present tests.

Provided the previously mentioned limitations apply, it is suggested that the derived general equation be used for obtaining sting interference corrections in the following manner. An afterbody shape should be selected from this report similar to the one for which corrections are desired. The correction due to the presence of the sting cone is

$$\Delta C_D=\left(\frac{\Delta C_D}{\Delta C_{D,max}}\right)\Delta C_{D,max} \tag{2}$$

where $\Delta C_D/\Delta C_{D,max}$ can be read from figure 14 for the proper values of D_b/l and M; or for D_b/l less than 0.5, $\Delta C_D/\Delta C_{D,max}$ can be approximated by using figure 15.

Inasmuch as the variation of C_D with sting angle is linear,

$$\Delta C_{D,max}=\theta\left(\frac{\partial C_{D,A}}{\partial\theta}\right) \tag{3}$$

where $\partial C_{D,A}/\partial\theta$ can be read from figure 11 for the correct value of M.

Substitution from equation (3) into equation (2) gives the drag correction

$$\Delta C_D=\theta\left(\frac{\Delta C_D}{\Delta C_{D,max}}\right)\left(\frac{\partial C_{D,A}}{\partial\theta}\right) \tag{4}$$

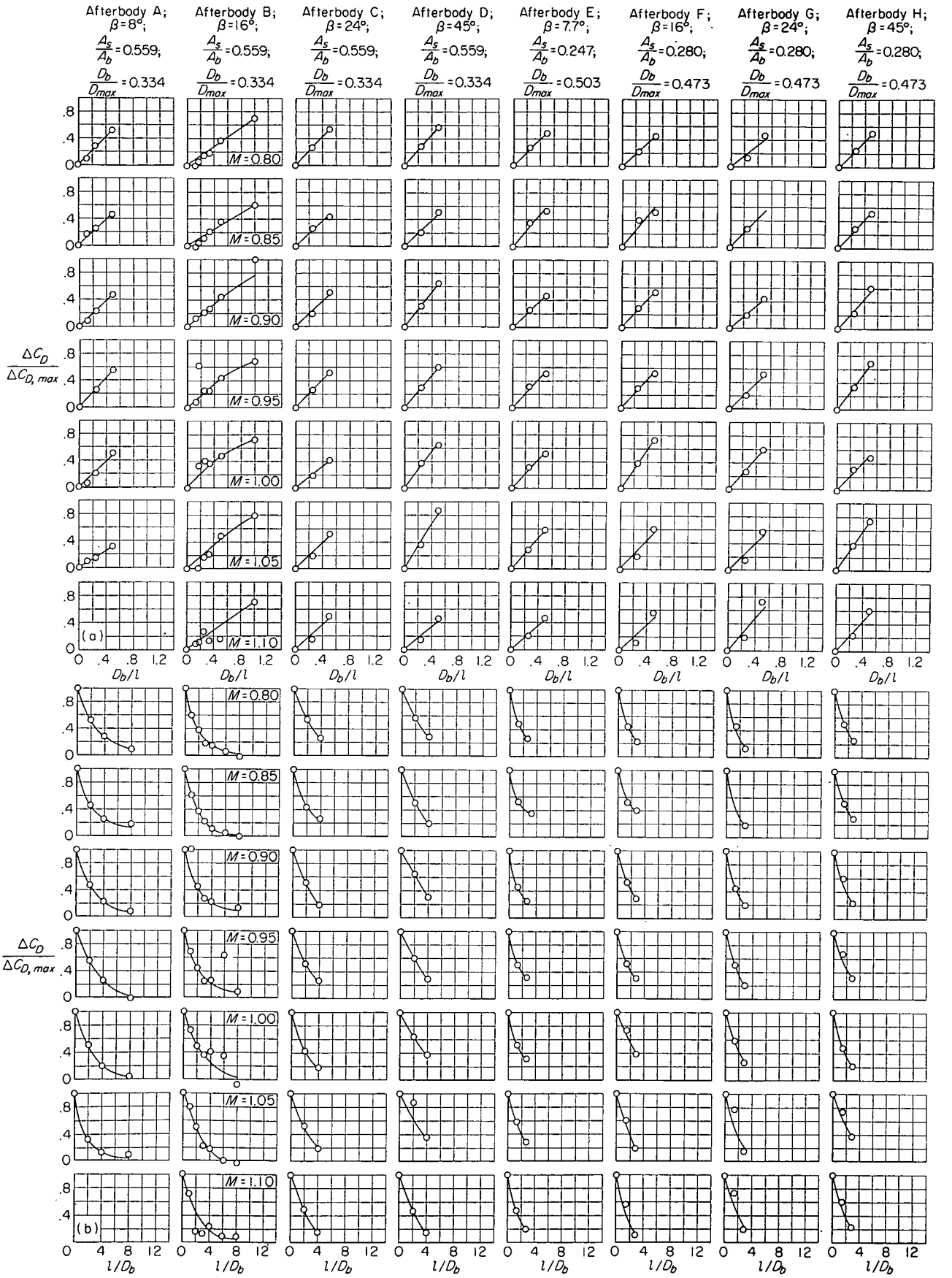
This relation will correct data for a sting with a conical section to data for a sting with only a cylindrical section.

In order to correct for the cylindrical-section diameter

$$\Delta C_D=\left(\frac{A_s}{A_b}\right)\left[\frac{\partial C_{D,A}}{\partial(A_s/A_b)}\right] \tag{5}$$

where $\frac{\partial C_{D,A}}{\partial(A_s/A_b)}$ can be read from figure 17. The complete sting correction then becomes

$$\Delta C_D=\theta\left(\frac{\Delta C_D}{\Delta C_{D,max}}\right)\left(\frac{\partial C_{D,A}}{\partial\theta}\right)+\left(\frac{A_s}{A_b}\right)\left[\frac{\partial C_{D,A}}{\partial(A_s/A_b)}\right] \tag{6}$$



(a) Variation of $\Delta C_D/\Delta C_{D,max}$ with ratio of base diameter to sting length.

(b) Variation of $\Delta C_D/\Delta C_{D,max}$ with ratio of sting length to base diameter.

FIGURE 14.—Sting-length effect with $\theta=5°$.

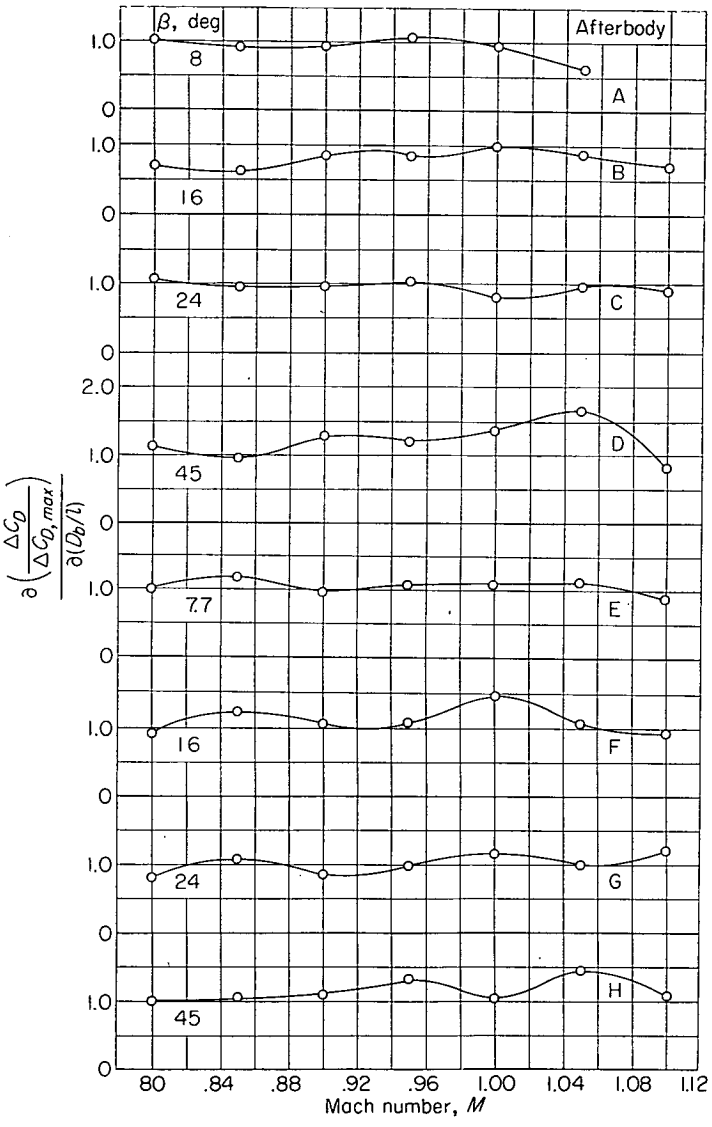
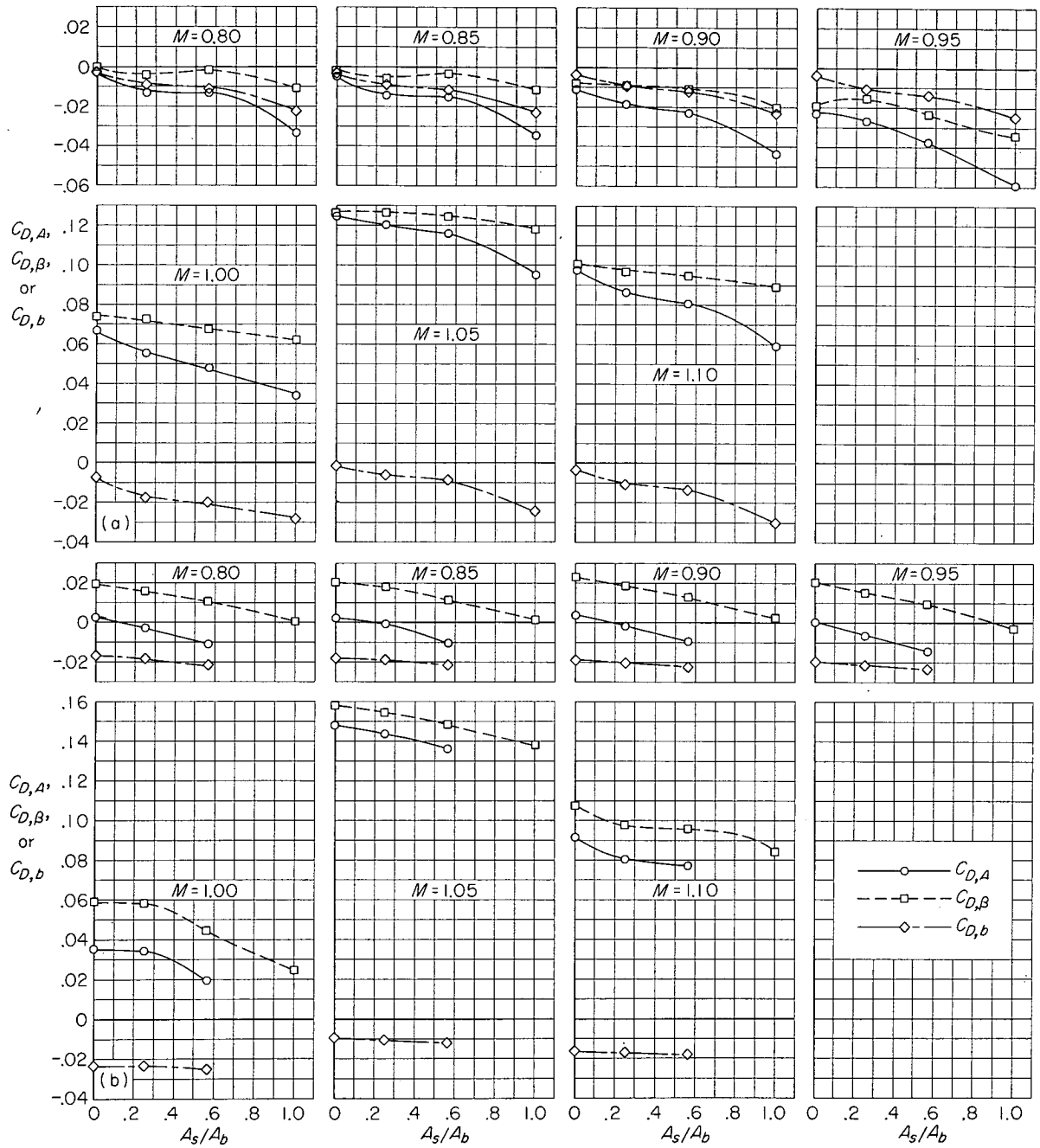


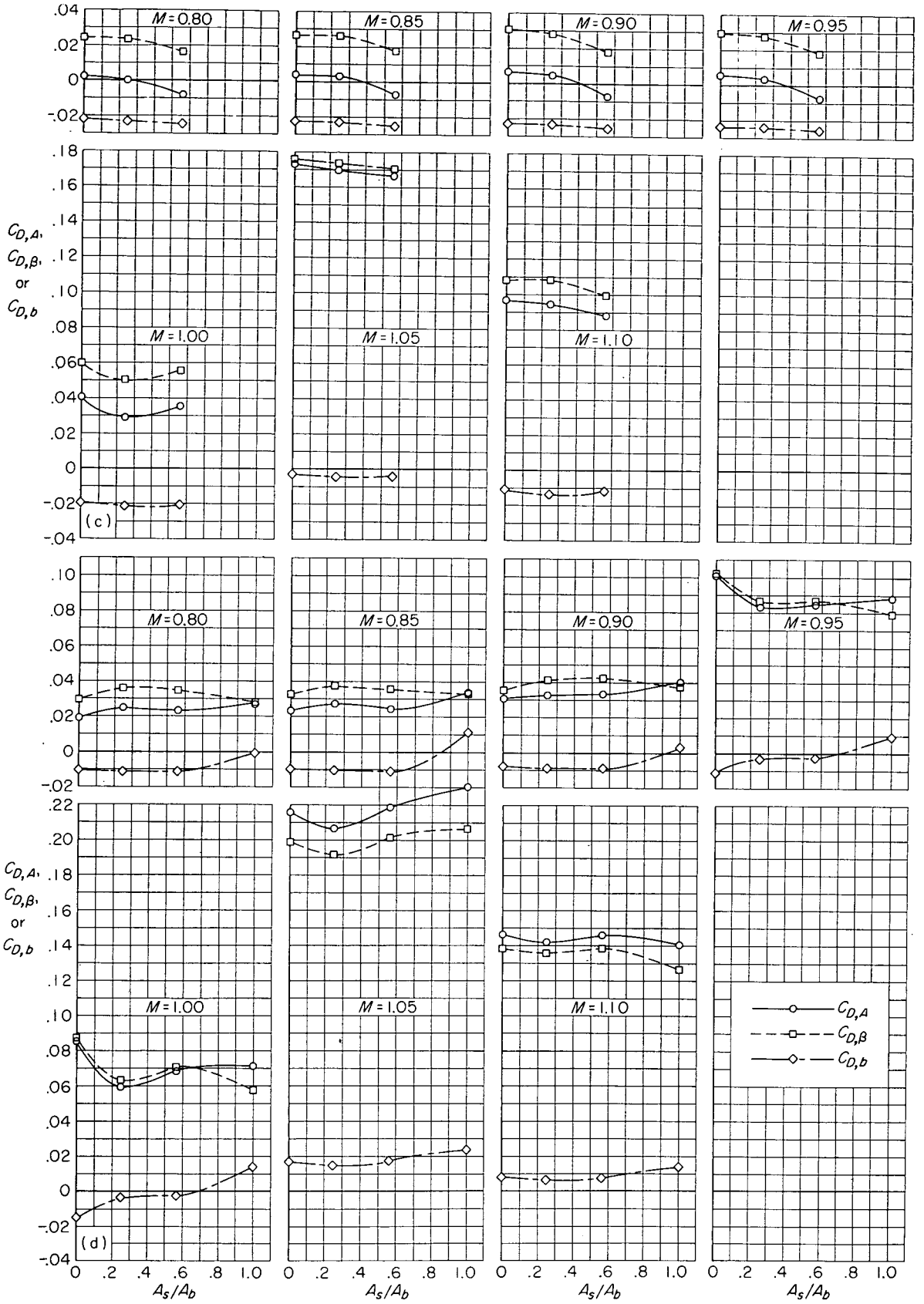
FIGURE 15.—Variation of sting-length effect with Mach number. $\theta=5°$.



(a) Afterbody A. $\beta = 8°$; $\frac{D_b}{D_{max}} = 0.334$.

(b) Afterbody B. $\beta = 16°$; $\frac{D_b}{D_{max}} = 0.334$.

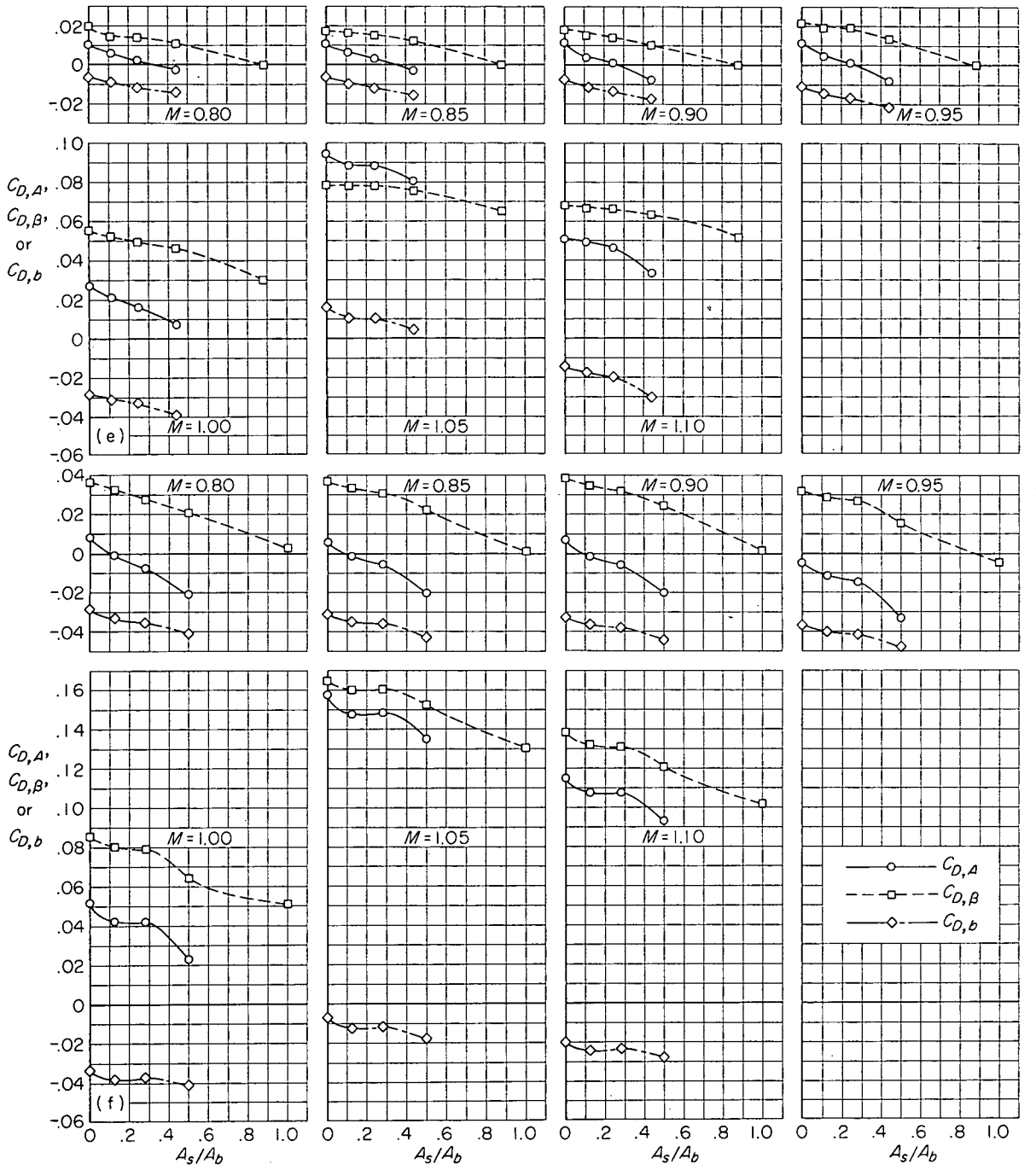
FIGURE 16.—Variation of base, boattail, and total afterbody pressure-drag coefficient with ratio of sting to base area with $\frac{D_b}{l} = 0$.



(c) Afterbody C. $\beta=24°$; $\frac{D_b}{D_{max}}=0.334$.

(d) Afterbody D. $\beta=45°$; $\frac{D_b}{D_{max}}=0.334$.

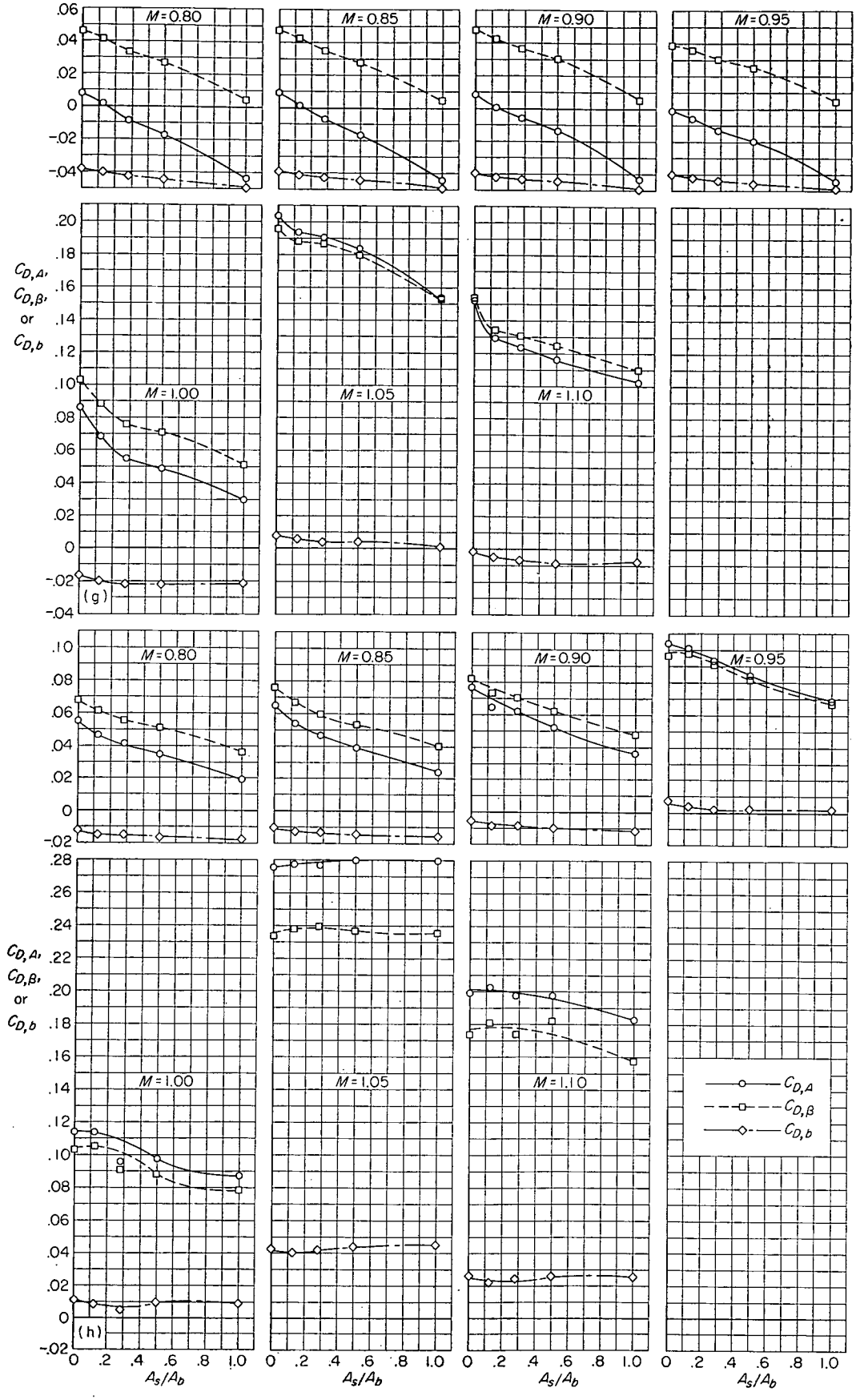
FIGURE 16.—Continued.



(e) Afterbody E. $\beta=7.7°$; $\frac{D_b}{D_{max}}=0.503$.

(f) Afterbody F. $\beta=16°$; $\frac{D_b}{D_{max}}=0.473$.

FIGURE 16.—Continued.



(g) Afterbody G. $\beta=24°$; $\frac{D_b}{D_{max}}=0.473$.

(h) Afterbody H. $\beta=45°$; $\frac{D_b}{D_{max}}=0.473$.

FIGURE 16.—Concluded.

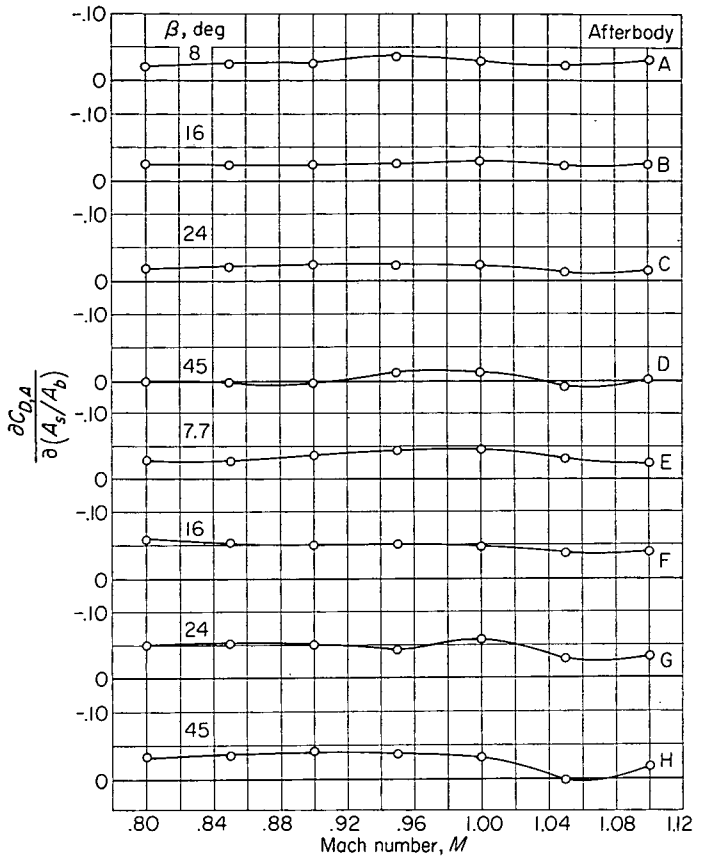


FIGURE 17.—Variation of sting-size effect with Mach number. $\frac{D_b}{l}=0$.

The correction thus obtained must be subtracted from the total-drag coefficient based on model frontal area. It should be noted that the value of ΔC_D will in all cases be negative and will result in a drag increase when data are corrected to the sting-off condition. It is estimated that the above method of obtaining sting corrections will give drag-coefficient increments generally within 0.03 of the values obtained by using the actual data points.

Corrections determined from the present results have been calculated for a model discussed in reference 5. In figure 18, the resulting corrections are compared with the corrections determined by the method described in reference 5. The model of reference 5 had $\beta=5.6°$, $D_b/D_{max}=0.416$, $\theta=4.2°$, $D_b/l=\infty$, and $A_s/A_b=0.85$. Afterbody E was chosen as most closely approximating the model. The model was tested in a closed-throat tunnel. The sting corrections in reference 5 were determined by using decreasing sting sizes and extrapolating the zero sting size. Figure 18 indicates good agreement between the present results and reference 5 for all configurations below a Mach number of 0.9. Above this speed, indications are that sting corrections are more sensitive to changes in tail configurations.

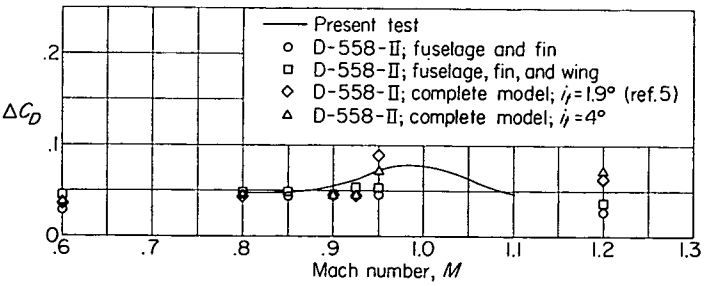


FIGURE 18.—Comparison of sting corrections from present test with corrections obtained in reference 5.

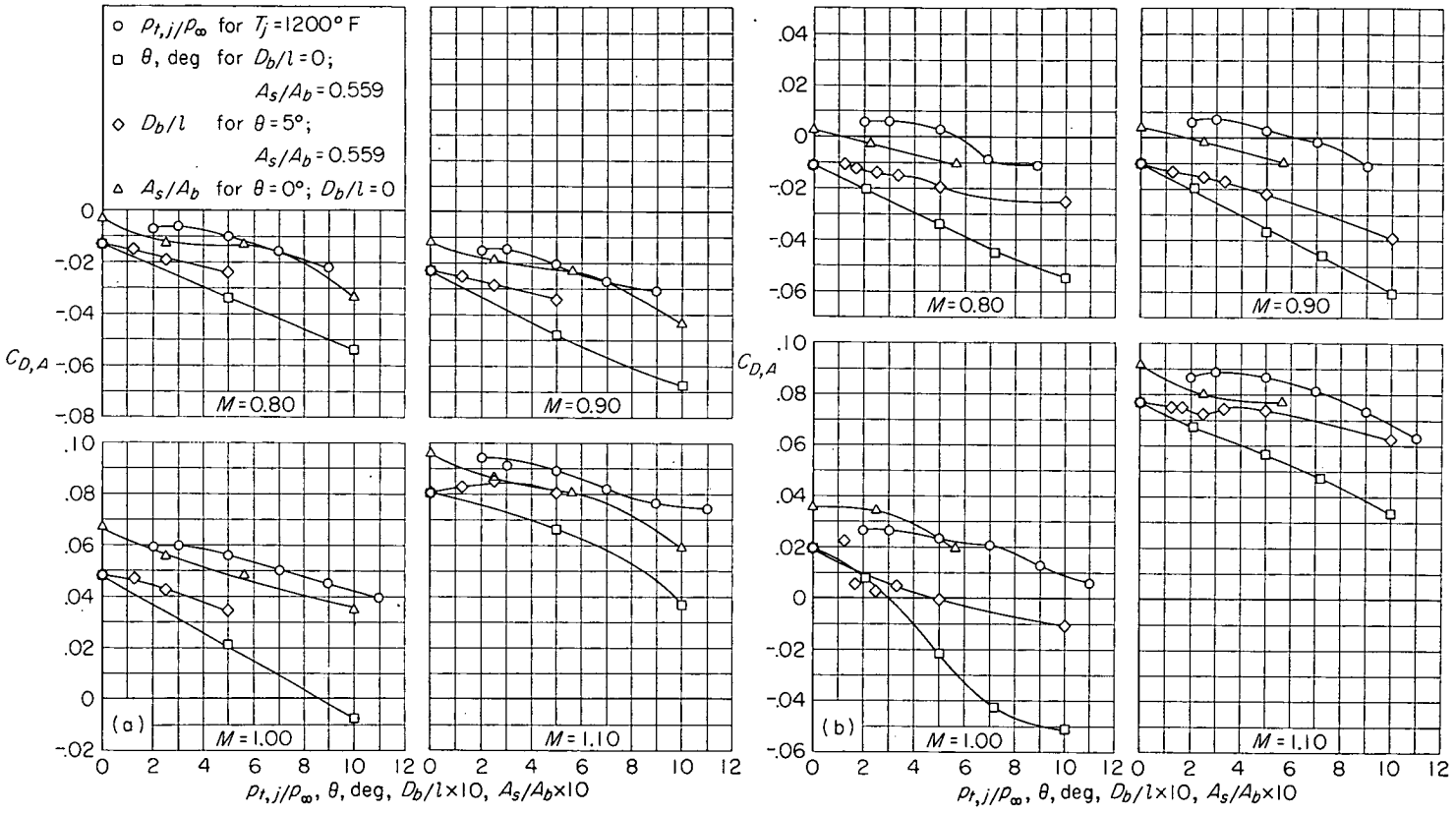
A direct comparison with the sting effects of references 4 and 6 could not be made since none of the afterbodies of this report approximate the configurations of references 4 and 6. However, it is worthy of note that the sting effects in references 4 and 6 are considerably larger than any of this test. This difference is a result of the configurations of references 4 and 6 having larger values of D_b/D_{max} (0.737 and 1.00, respectively).

SIMULATION OF JET EFFECTS WITH A STING

Jet effects studies were made on each afterbody including tests on a sting which had the shape of a free sonic jet expanding from the rear of the bodies. The sting shape was determined by measurements of a schlieren photograph of a jet at a total-pressure ratio of 5 and a temperature of 1,200° F. This sting having the same size and shape as the free jet always produced higher afterbody pressures than the jet. This result was as might be expected, since the sting could produce the solid-body effect but not the aspirating effect of the jet.

There is, however, a possibility of simulating jet effects with a sting of a different shape than that of the free jet. In figure 19 is shown the variation of afterbody pressure drag coefficient with the sting parameters of this investigation and with jet total-pressure ratio for a sonic free jet exhausting at 1,200° F.

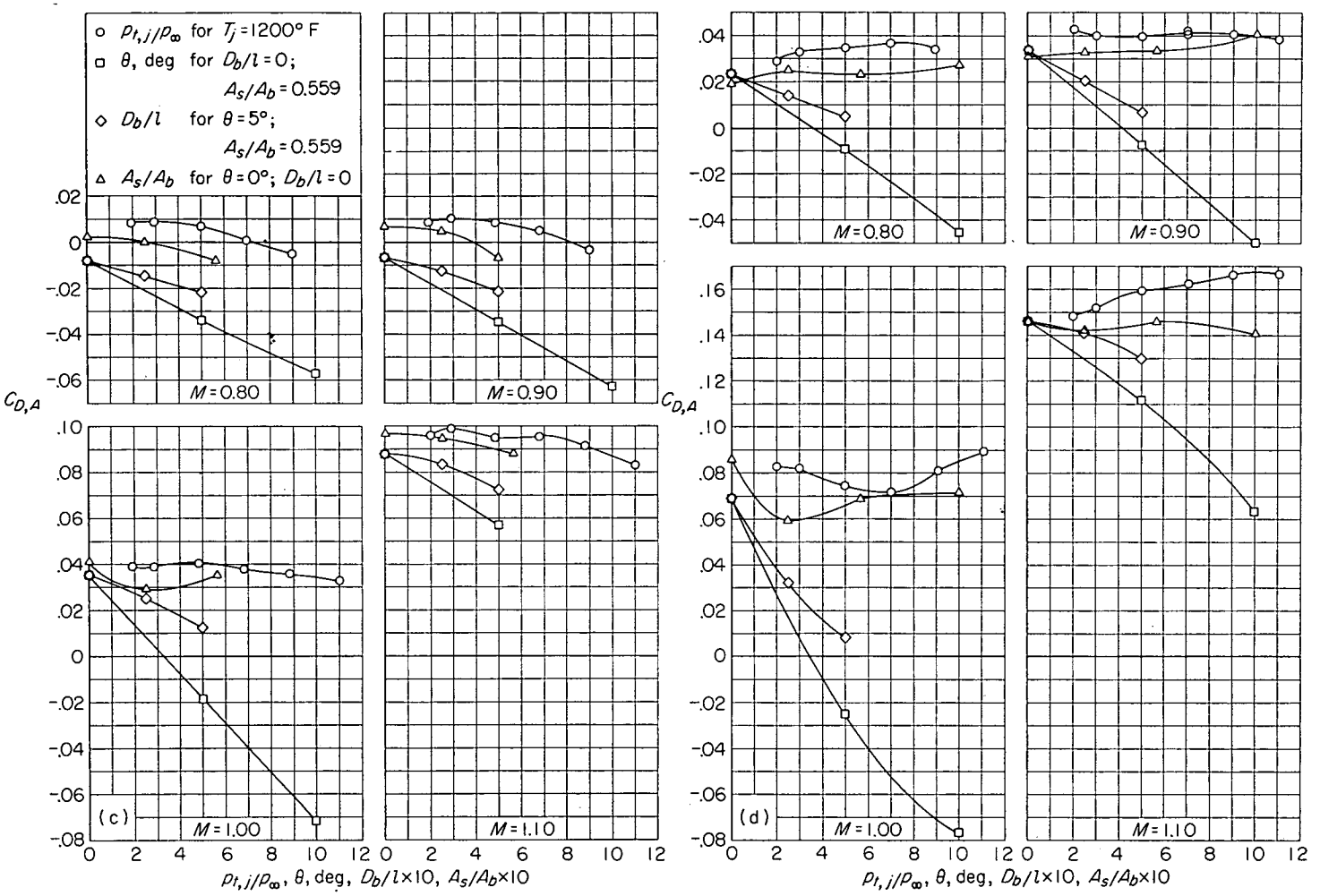
Figure 19 indicates that for the gradually contoured afterbodies a practical sting shape can be made which will produce the same drag as the jet at a given pressure ratio. As the afterbody shape becomes more blunt, the aspiration effect of the jet becomes increasingly predominant on the larger wake behind the blunt rear end, and it becomes increasingly more difficult to simulate the jet effect with solid sting shapes. This simulation is impossible for afterbodies D and H for reasonable jet-pressure ratios. Because of the small-diameter sting required, jet simulation is impractical for afterbody G. Afterbodies F and E would probably show agreement between sting and jet data at pressure ratios above those presented since for the higher jet pressure ratios, the free jet size would increase and cause higher pressures rearward of the base.



(a) Afterbody A. $\beta=8°$; $\frac{D_b}{D_{max}}=0.334$; $\frac{D_i}{D_b}=0.742$.

(b) Afterbody B. $\beta=16°$; $\frac{D_b}{D_{max}}=0.334$; $\frac{D_i}{D_b}=0.742$.

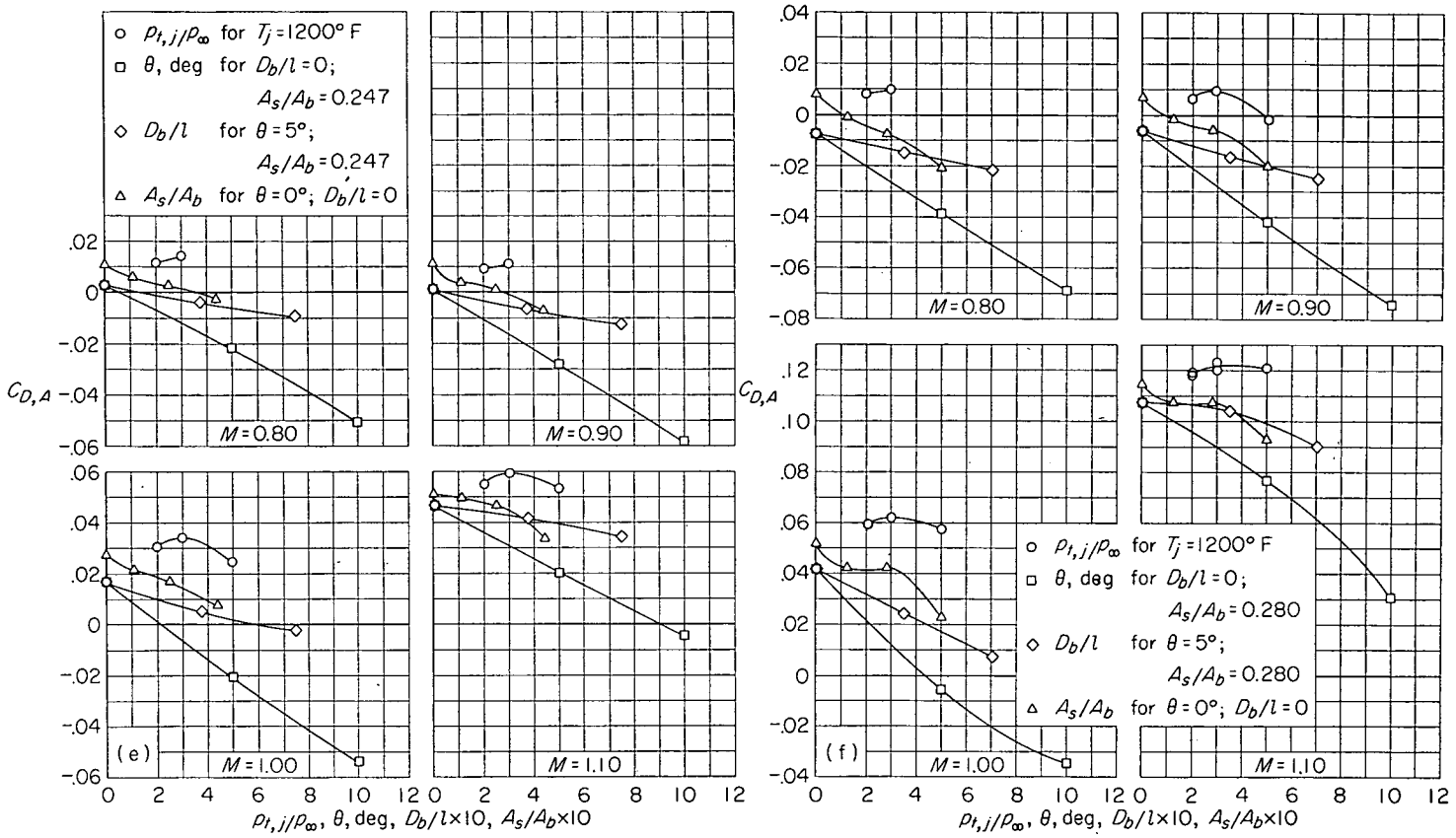
FIGURE 19.—Comparison of sting and jet effects.



(c) Afterbody C. $\beta = 24°$; $\frac{D_b}{D_{max}} = 0.334$; $\frac{D_j}{D_b} = 0.742$.

(d) Afterbody D. $\beta = 45°$; $\frac{D_b}{D_{max}} = 0.334$; $\frac{D_j}{D_b} = 0.742$.

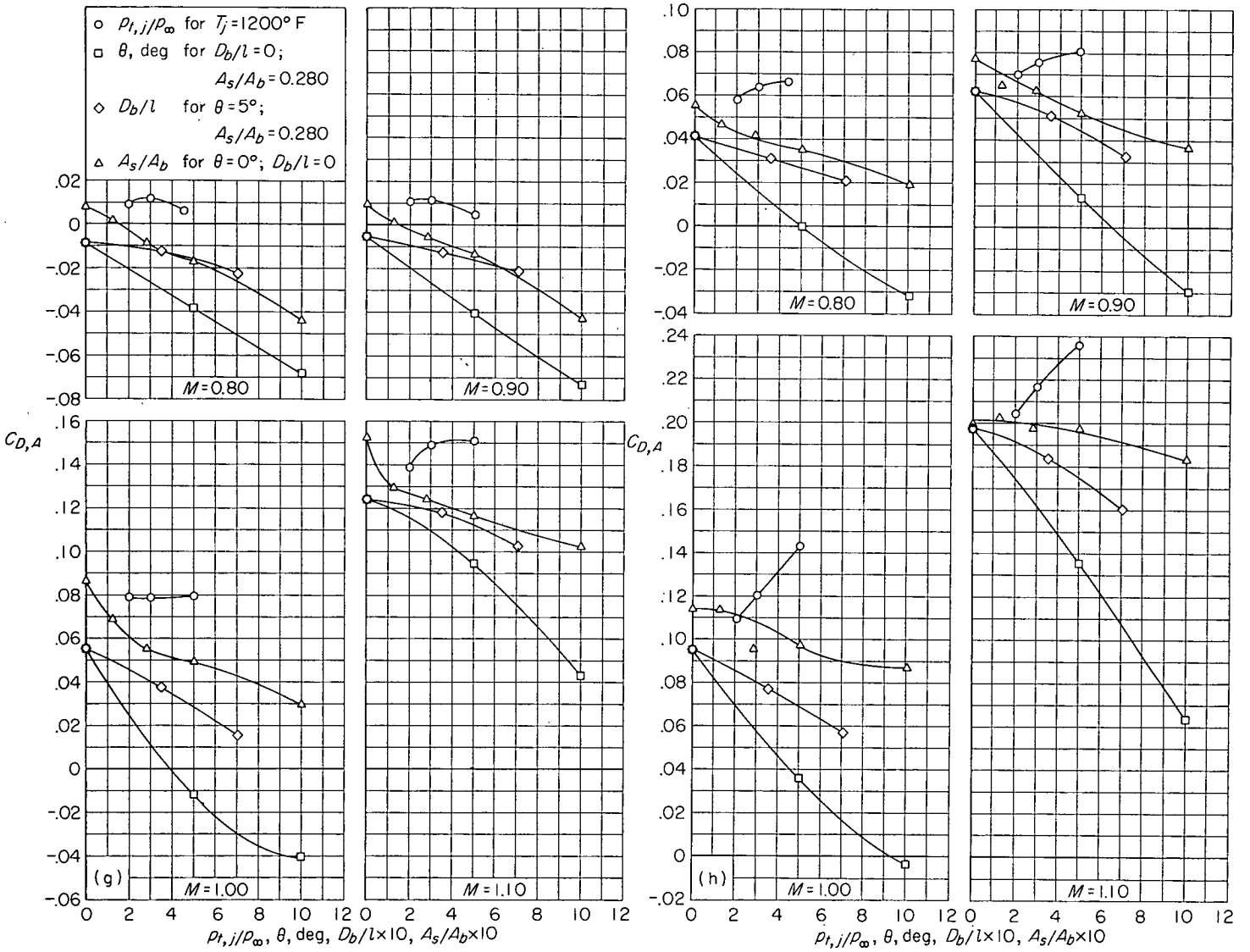
FIGURE 19.—Continued.



(e) Afterbody E. $\beta = 7.7°$; $\frac{D_b}{D_{max}} = 0.503$; $\frac{D_i}{D_b} = 0.698$.

(f) Afterbody F. $\beta = 16°$; $\frac{D_b}{D_{max}} = 0.473$; $\frac{D_i}{D_b} = 0.742$.

FIGURE 19.—Continued.



(g) Afterbody G. $\beta = 24°$; $\frac{D_b}{D_{max}} = 0.473$; $\frac{D_i}{D_b} = 0.742$.

(h) Afterbody H. $\beta = 45°$; $\frac{D_b}{D_{max}} = 0.473$; $\frac{D_i}{D_b} = 0.742$.

FIGURE 19.—Concluded.

CONCLUSIONS

From an investigation to determine the effects of sting-support on several body shapes, the following conclusions have been drawn:

1. The presence of a sting in general causes a drag reduction.

2. Increasing sting cone angle, decreasing sting cylindrical length ahead of the sting cone, and in general increasing sting diameter causes a drag reduction.

3. Sting-cone-angle effect increases with increasing boattail angle.

4. Approximate sting interference corrections can be made on models with afterbodies and sting supports similar in scale and geometry to those reported, provided the Reynolds number is of the same order of magnitude and the boundary layer ahead of the model base is turbulent.

5. For gradually contoured afterbodies, a sting can be made which will duplicate jet effects, but for blunt afterbodies no solid sting shape will produce the same effect as the jet.

LANGLEY AERONAUTICAL LABORATORY,
NATIONAL ADVISORY COMMITTEE FOR AERONAUTICS,
LANGLEY FIELD, VA., *June 4, 1956.*

REFERENCES

1. Love, Eugene S.: A Summary of Information on Support Interference at Transonic and Supersonic Speeds. NACA RM L53K12, 1954.
2. Wright, Ray H., and Ritchie, Virgil S.: Characteristics of a Transonic Test Section With Various Slot Shapes in the Langley 8-Foot High-Speed Tunnel. NACA RM L51H10, 1951.
3. Ritchie, Virgil S., and Pearson, Albin O.: Calibration of the Slotted Test Section of the Langley 8-Foot Transonic Tunnel and Preliminary Experimental Investigation of Boundary-Reflected Disturbances. NACA RM L51K14, 1952.
4. Tunnell, Phillips J.: An Investigation of Sting-Support Interference on Base Pressure and Forebody Chord Force at Mach Numbers From 0.60 to 1.30. NACA RM A54K16a, 1955.
5. Osborne, Robert S.: High-Speed Wind-Tunnel Investigation of the Longitudinal Stability and Control Characteristics of a 1/16-Scale Model of the D–558–2 Research Airplane at High Subsonic Mach Numbers and at a Mach Number of 1.2. NACA RM L9C04, 1949.
6. Hart, Roger G.: Effects of Stabilizing Fins and a Rear-Support Sting on the Base Pressures of a Body of Revolution in Free Flight at Mach Numbers From 0.7 to 1.3. NACA RM L52E06, 1952.

REPORT 1354

EFFECT OF CHORD SIZE ON WEIGHT AND COOLING CHARACTERISTICS OF AIR-COOLED TURBINE BLADES[1]

By Jack B. Esgar, Eugene F. Schum, and Arthur N. Curren

SUMMARY

An analysis has been made to determine the effect of chord size on the weight and cooling characteristics of shell-supported, air-cooled gas-turbine blades. In uncooled turbines with solid blades, the general practice has been to design turbines with high aspect ratio (small blade chord) to achieve substantial turbine weight reduction. With air-cooled blades, this study shows that turbine blade weight is affected to a much smaller degree by the size of the blade chord.

The heat-transfer analysis shows that considerable saving in coolant flow is possible by utilizing a smaller number of large-chord blades rather than a larger number of small-chord blades with constant blade solidity. Generally, turbines with a blade chord of only 1 inch require about twice as much coolant as turbines with 3-inch-chord blades for a turbine-inlet temperature of 2500° R. As the blade chord is reduced below 1 inch, as it might be in small-diameter engines, the coolant-flow requirements increase very rapidly. The coolant flow required for a blade with ½-inch chord may be more than twice that required for a 1-inch-chord blade. In addition to the high coolant flows necessary, the small-chord blades are often unable to pass the required coolant flow at the pressure levels encountered in engine operation. Although this investigation was conducted specifically on corrugated-insert blades, the trends of the results are believed to be general. The study shows that, in air-cooled-turbine design, efforts should be made to use blades with as large a chord as appears feasible with regard to disk stress and aerodynamics.

INTRODUCTION

Turbine blade chord is an important consideration in the design of uncooled turbines, primarily because of its effect on turbine weight. This investigation was conducted to determine how blade chord affects the weight and cooling characteristics of air-cooled turbines. In general, the number of blades in a turbine can vary considerably without significantly affecting the turbine performance as long as the blade solidity (ratio of chord to pitch) is maintained constant. For solid uncooled turbine blades, the total airfoil weight is inversely proportional to the number of blades in the turbine (directly proportional to chord) for constant solidity. Since aerodynamic performance is only slightly affected but weight is significantly affected by the number of blades, it has been common practice among manufacturers of uncooled turbines to use a large number of short-chord high-aspect-ratio blades in their turbines. With the introduction of cooling into the turbine, some of the old rules are no longer valid, and a new look is required to determine optimum blade sizes.

In order to permit increases in turbine-inlet temperature on the order of 500° to 1000° R, it is necessary to extend coolant passages well into the blade leading and trailing edges. The trailing-edge coolant passages usually cause a thickening of the trailing edge and increased gas-passage blockage for each blade. This gas-passage blockage results in an aerodynamic performance loss. The required trailing-edge thickness for air-cooled blades is almost independent of blade size. A method of reducing the total gas blockage for the turbine is to reduce the number of blades and increase the chord to maintain solidity. As a result, the optimum number of blades with respect to aerodynamic performance may therefore decrease as trailing-edge thickness is increased.

Other factors may also suggest the use of a smaller number of larger-chord blades in air-cooled turbines. It is easier to build the required internal surface area into larger blades, and the total coolant-passage flow area for the turbine is almost directly proportional to chord size (same as weight being proportional to chord for solid uncooled blades), so that, for a given flow rate, pressure losses should be smaller when the chord is increased. In addition, total airfoil weight for blades with a portion of the interior hollowed out is no longer directly proportional to the chord for constant solidity. If the airfoils were thin hollow shells, the total airfoil weight for constant-solidity turbines would almost be independent of chord size.

In order to obtain a better understanding of the effects of chord size on air-cooled turbine blade weight, cooling effectiveness, and cooling-air pressure losses, an analytical study was made of these effects for corrugated-insert blades with chords varying from ½ to 3½ inches. In these studies two-stage turbine engines were considered, with turbine diameters varying from 15 to 35 inches, so that the turbine blade aspect ratios varied from approximately 1 to 4 for the range of chords considered. Required coolant flow and pressure losses were calculated for an engine with a sea-level compressor pressure ratio of 10 flying at a Mach number of 2.0 at 50,000 feet. While these results may not be completely general, the trends should be indicative of the effect of turbine blade chord size for a wide range of application.

[1] Supersedes NACA Technical Note 3923 by Jack B. Esgar, Eugene F. Schum, and Arthur N. Curren, 1957.

SYMBOLS

A	cross-sectional metal area, sq in.
A_{fl}	flow area, sq ft
$\mathscr{A}$	turbine blade aspect ratio
C_{fr}	friction coefficient
c	turbine blade chord, ft
c_p	specific heat at constant pressure, Btu/(lb) (°R)
D	diameter, ft
E	pumping work, Btu/lb
$\overline{F}$	constant, function of blade transition ratio and Euler number
$\mathscr{F}$	centrifugal force, lb
g	acceleration due to gravity, ft/sec^2
h_f	effective inside heat-transfer coefficient, Btu/(sec) (sq ft) (°R)
h_i	blade-to-coolant heat-transfer coefficient, Btu/(sec) (sq ft) (°R)
h_o	gas-to-blade heat-transfer coefficient, Btu/(sec) (sq ft) (°R)
J	mechanical equivalent of heat, ft-lb/Btu
$K_1, K_2, \ldots K_5$	constants
k	thermal conductivity, Btu/(sec) (ft) (°R)
L	effective fin length, ft
l	blade perimeter, ft
M	mass, (lb) (sec^2)/ft
m	distance between fins, ft
Nu	Nusselt number
P'	relative total pressure, lb/sq ft abs
Pr	Prandtl number
p	static pressure, lb/sq ft abs
q	heat flow, Btu/sec
Re	Reynolds number
r	radius from center of rotation, ft
S	surface area, sq ft
T'	relative total temperature, °R
t	static temperature, °R
U_t	tip speed, ft/sec
w	flow rate, lb/sec
x	distance from blade root, ft
Y	corrugation amplitude, in.
z	exponent, function of blade transition ratio and Euler number
α	coolant-passage aspect ratio, ratio of corrugation amplitude to half corrugation pitch
Γ	metal density, lb/cu in.
μ	viscosity, (lb) (sec)/(sq ft)
σ	stress, psi
τ	fin thickness, ft
ϕ	$\sqrt{2h_i/k_b\tau}$
ω	angular velocity, radians/sec

Subscripts:

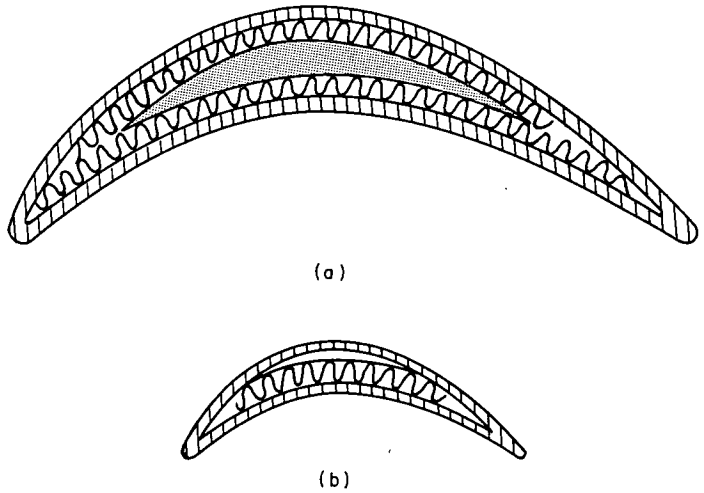
a	cooling air
b	blade, or based on blade temperature
c	corrugations
e	effective
g	gas
h	hub
i	inside
o	outside
T	turbine
t	tip
x	local condition at x feet above blade root

ANALYSIS AND PROCEDURE

AIRFOIL WEIGHT AND SURFACE AREAS

The internal surface area per unit length of span of air-cooled turbine blades depends upon the aerodynamic profile of the blade, the blade chord, and the shell thickness, as well as the type of internal configuration. As the blade chord is varied, it generally is not possible to scale the blade directly to make the ratio of internal to external surface area remain constant. There are several reasons for this. First, there are minimum practical dimensions with regard to strength and fabrication. It is possible to vary shell thickness somewhat, but there are minimum thicknesses that depend on impact loads that the shell must withstand from foreign objects in the gas stream such as sand and carbon flakes. Minimum thicknesses of both the shell and internal configuration are determined by structural rigidity and by the effect of braze penetration for configurations that rely on brazing. In addition, the individual coolant-passage size can be reduced only so far and then the cooling-air pressure losses may become exorbitant or the passages may become plugged by brazing during fabrication or by small particles of foreign matter in the cooling air. For these reasons, both large and small blades may have an internal configuration where each passage has the same dimensions.

A type of air-cooled turbine blade that offers considerable potentiality for permitting substantial increases in turbine-inlet temperature with moderate cooling-airflow requirements is the corrugated-insert blade such as shown in figure 1(a). In this type of blade, corrugations of uniform amplitude are brazed to the inside surfaces of the blade shell. The best corrugation geometry is generally one that provides a maximum of surface area within pressure-drop limitations. This best corrugation is usually independent of blade chord as long as it can be placed inside the blade cavity, but the relative chordwise length of this corrugation is very much dependent upon the blade chord, as illustrated in figure 1



(a) Typical corrugated-insert blade.
(b) Effect of placing corrugation in small-chord blade.

FIGURE 1.—Effect of blade chord on air-cooled blade inside heat-transfer surface area.

for two blades of the same profile but with different chord lengths.

The ratio of internal to external surface area gives an indication of blade-cooling effectiveness. A practical method of determining how chord size affects the internal surface area is to make layouts of each blade to be investigated. This method was used in this report by using an assumed outside blade profile at the mean section shown in figure 1, where the maximum blade thickness is approximately 15 percent of the chord. The coolant passage was assumed to be uniform from root to tip. The outside profile changed slightly to permit taper in the blade shell. These assumptions result in a slight approximation, because in actual practice the blade profile will change along the blade span more than considered herein, but it is possible with proper design to maintain internal surface area approximately constant from root to tip. In all cases it was assumed that metal corrugations and the sheet-metal island in the center of the blade were of uniform thickness along the span. The corrugations were assumed to be 0.005 inch thick, and the island sheet metal 0.010 inch thick. The pitch of the corrugations was assumed to be 0.050 inch, and the amplitude was varied from 0.030 to 0.070 inch. This range of internal geometries has been found to have effective heat-transfer characteristics from a study of corrugations by the method of reference 1. The chordwise length of the corrugations in each blade size being known from layouts, the surface area and the cross-sectional area were calculated from relations given in reference 1. The blade shell, including leading- and trailing-edge portions where there were no corrugations, was also included in these calculations. The blade weight was calculated from the cross-sectional area using a metal density of 0.3 pound per cubic inch.

For a linear variation in metal cross-sectional area from root to tip of turbine blades, an expression for the centrifugal-stress distribution in the blades can be derived in the following manner. The cross-sectional-area distribution along the span can be expressed by

$$\frac{A-A_x}{A_t-A_x}=\frac{r-r_x}{r_t-r_x} \tag{1}$$

or

$$A=A_x\left[1-\frac{r-r_x}{r_t-r_x}\left(1-\frac{A_t}{A_x}\right)\right] \tag{2}$$

where r and A are variables. The stress is obtained from

$$\sigma_x=\frac{\mathscr{F}_x}{A_x}=\int_{r_x}^{r_t}\frac{r\omega^2}{A_x}\,dM \tag{3}$$

where

$$dM=\frac{12\Gamma A\,dr}{g} \tag{4}$$

and the constant 12 is a conversion from feet to inches. Combining equations (2) to (4) and integrating give the following expression:

$$\sigma_x=\frac{12\omega^2r_t^2\Gamma}{g}\left\{\frac{1}{2}\left[1-\left(\frac{r_x}{r_t}\right)^2\right]-\frac{1}{3}\frac{1-\left(\frac{r_x}{r_t}\right)^3}{1-\frac{r_x}{r_t}}\left(1-\frac{A_t}{A_x}\right)+\frac{1}{2}\left[\frac{r_x}{r_t}+\left(\frac{r_x}{r_t}\right)^2\right]\left(1-\frac{A_t}{A_x}\right)\right\} \tag{5}$$

If it is noted that $U_t=\omega r$ and if terms are collected, equation (5) can be written

$$\sigma_x=\frac{12U_t^2\Gamma}{g}\left\{\frac{1}{2}\left[1-\left(\frac{r_x}{r_t}\right)^2\right]-\frac{1}{6}\left[2-\frac{r_x}{r_t}-\left(\frac{r_x}{r_t}\right)^2\right]\left(1-\frac{A_t}{A_x}\right)\right\} \tag{5a}$$

By letting $r_x=r_h$ and $A_x=A_h$ in equation (5a), the centrifugal stress at the blade root can be calculated; and by multiplying both sides of equation (5a) by $(1200/U_t)^2$ an equivalent root stress can be obtained. The resulting values of equivalent root stress $\sigma(1200/U_t)^2$ are then, of course, the actual stresses for a tip speed of 1200 feet per second, which is a representative turbine speed. The stress values are presented in this manner so that they can be quickly converted to the stress that would result for any other tip speed of interest.

TABLE I.—TEMPERATURES, PRESSURES, AND OTHER CONDITIONS USED IN ANALYSIS

Assigned conditions:	
Engine compressor pressure ratio	10 at sea-level-static conditions; 6.3 at flight conditions
Flight altitude, ft	50, 000
Flight Mach number	2. 0
Turbine-inlet temp., °R	2500
Ram recovery pressure ratio	0. 87
Compressor adiabatic efficiency	0. 85
Turbine adiabatic efficiency	0. 85
Relative Mach number of gas entering turbine	0. 6
Mach number of gas at turbine exit	0. 5
Max. centrifugal turbine blade root stress for taper factor of 0.7, psi	30, 000
Second-turbine-stage hub-tip radius ratio	0. 6
Turbine blade stress-ratio factor	1.0 (except fig. 11)
Turbine blade solidity at mean section (both stages)	1. 5
Calculated conditions:	
First-turbine-stage hub-tip radius ratio	0. 73
Turbine tip speed (same for both stages), ft/sec	1095
Compressor-discharge temp. (blade root cooling-air temp. for most calculations), °R	1247
Compressor-discharge total pressure, lb/sq ft	10, 420
Static gas pressure at blade tip, lb/sq ft	7340 (first-stage rotor); 4000 (second-stage rotor)
Effective gas temperature, °R	2390 (first-stage rotor); 2048 (second-stage rotor)
Constant K_4 in gas-to-blade heat-transfer coefficient, eq. (13)	0.721 (first-stage rotor); 0.467 (second-stage rotor)

TURBINE DESIGN

In order to make this analysis representative of conditions that might be encountered in cooled turbojet engines, a two-stage turbine was designed for an engine with a sea-level-static compressor pressure ratio of 10. The engine design point was taken for a flight Mach number of 2.0 at 50,000 feet. Heat-transfer calculations were also made for these conditions. The turbine was designed according to the methods in reference 2, and temperature and pressure conditions at various stations through the engine were calculated by means of reference 3. The assigned conditions and the resulting calculated conditions are listed in table I. The compressor pressure ratio of 6.3 at a flight Mach number of 2.0 would result from constant-mechanical-speed operation for an arbitrarily assumed compressor.

The assigned turbine conditions result in a conservative turbine design. In a conservative turbine there is considerable freedom in the choice of a blade profile. An assumed profile was used in this investigation that is believed to be typical of profiles that may be encountered in air-cooled engines. For the sake of simplicity, the same profile was used for both the first and second stages and for all chord lengths. The profile is shown in figure 1.

In order to investigate a representative range of engines, turbine diameters of 15, 25, and 35 inches were considered, with a corresponding size change in the rest of the engine. The turbine design was the same for all diameters, but of course the blade size varied with the diameter.

BLADE COOLANT-FLOW REQUIREMENTS

The coolant-flow requirements for air-cooled turbine blades depend on the gas-to-blade heat-transfer coefficients, the blade temperature, the gas temperature, the coolant temperature at the blade base, and the coolant-passage geometry. In this analysis all these factors except the gas temperature vary for one reason or another. The calculation methods include each of these effects.

Gas-to-blade heat-transfer coefficient.—The average Nusselt number Nu, from which the average gas-to-blade heat-transfer coefficient h_o is obtained, can be found from the following correlation equation (ref. 4):

$$Nu=\overline{F}(Re)^{z}(Pr)^{1/3} \tag{6}$$

The reference length in the Nusselt and Reynolds numbers is l_o/π, and $\overline{F}$ and z are functions of transition ratio and Euler number of the blade.

The Reynolds number in equation (6) may be written as

$$Re=\left(\frac{w_g\sqrt{T'_g}}{A_{fl,g}P'_g}\right)_T\left(\frac{P'_g}{\sqrt{T'_g}}\right)_T\left(\frac{t_g}{t_b}\right)\left(\frac{l_o/\pi}{\mu_{g,b}g}\right) \tag{7}$$

By combining equations (6) and (7), the gas-to-blade heat-transfer coefficient can be expressed by

$$h_o=\frac{\overline{F}k_{g,b}}{\left(\frac{l_o}{\pi}\right)^{1-z}}\left[\left(\frac{w_g\sqrt{T'_g}}{A_{fl,g}P'_g}\right)_T\left(\frac{P'_g}{\sqrt{T'_g}}\right)_T\left(\frac{t_g}{t_b}\right)\left(\frac{1}{\mu_{g,b}g}\right)\right]^{z}Pr^{1/3} \tag{8}$$

The term $w_g\sqrt{T'_g}/A_{fl,g}P'_g$ is a function of gas Mach number and is essentially constant for Mach numbers between 0.7 and 1.0 (max. variation is about 9 percent). A Mach number of 0.7 is probably representative for most turbine designs; consequently, $w_g\sqrt{T'_g}/A_{fl,g}P'_g$ was evaluated from reference 5 for that Mach number. For this investigation variations in gas pressure (due to altitude) and gas temperature were not considered. The gas fluid properties $\mu_{g,b}$, $k_{g,b}$, and Pr can be written as a function of the blade temperature:

$$k_{g,b}=K_1t_b^{0.85} \tag{9}$$

$$\mu_{g,b}=K_2t_b^{0.7} \tag{10}$$

$$Pr\approx K_3 \tag{11}$$

The perimeter of the blade used in this analysis is $2.34(c)$. The perimeter can then be expressed in terms of the turbine tip diameter and the blade aspect ratio and hub-tip radius ratio as follows:

$$l_o=2.34\left(\frac{D_T}{2\mathscr{A}}\right)\left(1-\frac{r_h}{r_t}\right)_T \tag{12}$$

Substitution of equations (9) to (12) into equation (8) results in

$$h_o=\frac{K_4}{t_b^{1.7z-0.85}}\left(\frac{\mathscr{A}}{D_T}\right)^{1-z} \tag{13}$$

where K_4 is a grouping of all the constant terms in equations (8) to (12).

In reference 6, ten blade profiles were analyzed, including both impulse and reaction blades. An average value of z for these ten blades is 0.70. Using the value of z for rotor blades, equation (13) becomes

$$h_o=\frac{K_4}{t_b^{0.34}}\left(\frac{\mathscr{A}}{D_T}\right)^{0.3} \tag{14}$$

Equations (13) and (14) can also be written

$$h_o=\frac{K_5}{t_b^{1.7z-0.85}c^{1-z}}=\frac{K_5}{t_b^{0.34}c^{0.3}} \tag{15}$$

In this investigation K_4 was evaluated for each turbine stage; and then the variations in h_o with turbine diameter, blade aspect ratio, and blade temperature were calculated by use of equation (14). The turbine blade temperature t_b varies along the span because of heating of the cooling air.

Blade-to-coolant heat-transfer coefficient.—The boundary-layer flow inside air-cooled blades may be laminar, turbulent, or in transition. In laminar flow the heat-transfer correlation equation depends on the coolant-passage aspect ratio α (ref. 7). For turbulent flow the Nusselt number can be written

$$\frac{Nu}{Re}=\frac{0.0199}{Re^{0.2}} \tag{16}$$

for a constant Prandtl number of 0.7 (ref. 8). In the transition region there is considerable uncertainty as to what the heat-transfer rates may be. In this analysis it was assumed that Nu/Re was a constant in this transition region and at the same value that results from turbulent flow for a Reynolds number of 8000. This transition region was assumed to extend down to a Reynolds number that would also result in the same Nu/Re in laminar flow. These heat-transfer correlations are represented graphically in figure 2 and mathematically in table II(a). In this manner the Reynolds number at which the flow changes from laminar to transition varies slightly with coolant-passage aspect ratio. The fluid properties of the coolant were based on the film temperature.

For finned coolant passages an effective heat-transfer coefficient h_f is required. The equation for evaluating h_f is given in reference 9 as

$$h_f=\frac{h_i}{m+\tau}\left(\frac{2\tanh\phi L}{\phi}+m\right) \tag{17}$$

The effective coefficient is related to the inside coefficient by a function of the metal thermal conductivity and the ratio of the inside wetted perimeter to the outside perimeter. For the limiting case with infinite thermal conductivity, equation (17) becomes

$$\begin{aligned} h_f&=\frac{h_i}{m+\tau}(2L+m) \\ &=h_i\frac{l_i}{l_o} \end{aligned} \tag{18}$$

Equation (17) is evaluated for corrugated surfaces in reference 1 for corrugations having the same chordwise length as the outside surface that is exposed to the gas stream. In corrugated-insert blades it generally is not possible to extend the corrugations around the entire inside periphery of the blade. At the leading and trailing edges there are usually areas where there is not room to place the corrugations. For this reason, an evaluation of an entire turbine blade using the value of h_f for a corrugated surface gives an optimistic answer. In this analysis it was assumed that the ratio of the effective coefficient for the entire blade to that for a corrugated surface was the same as the ratio of the inside and outside wetted perimeters for the entire blade to that for the corrugated surface, which is expressed in equation form as

$$\frac{(h_f)_b}{(h_f)_c}=\frac{\left(\frac{l_i}{l_o}\right)_b}{\left(\frac{l_i}{l_o}\right)_c} \tag{19}$$

where $(h_f)_c$ is evaluated from reference 1 for the geometry used in the blade. This relation assumes that conduction effects are the same for the entire blade as they are for the corrugations.

Spanwise blade temperature distribution.—The local blade temperature $t_{b,x}$ can be obtained from the following heat balance:

$$\frac{q}{S}=h_o(t_{g,e}-t_{b,x})=(h_f)_b(t_{b,x}-T'_{a,x}) \tag{20}$$

where $T'_{a,x}$ is the total cooling-air temperature relative to the blade at distance x from the blade root. This temperature is approximately equal to the effective air temperature at this

TABLE II.—EXPRESSIONS FOR BLADE COOLANT-PASSAGE NUSSELT NUMBER AND FRICTION COEFFICIENT

(a) Nusselt number

Corrugation amplitude, Y, in.	Coolant-passage aspect ratio, α	Reynolds number, Re	Nusselt number, Nu	Flow region
0. 03–0. 07	1. 25–3. 25	$\geq$8000	0. 0199$Re^{0.8}$	Turbulent
0. 07	3. 25	1470–8000	0. 0033Re	Transition
		$\leq$1470	4. 85	Laminar
0. 05	2. 25	1280–8000	0. 0033Re	Transition
		$\leq$1280	4. 22	Laminar
0. 03	1. 25	1125–8000	0. 0033Re	Transition
		$\leq$1125	3. 72	Laminar

(b) Friction coefficient

Corrugation amplitude, Y, in.	Coolant-passage aspect ratio, α	Reynolds number, Re	Friction coefficient, $4C_{fr}$	Flow region
0. 03–0. 07	1. 25–3. 25	$\geq$8000	$\frac{0.2935}{Re^{0.245}}$	Turbulent
0. 07	3. 25	2130–8000	0. 03255	Transition
		$\leq$2130	$\frac{69.2}{Re}$	Laminar
0. 05	2. 25	1970–8000	0. 03255	Transition
		$\leq$1970	$\frac{64.16}{Re}$	Laminar
0. 03	1. 25	1800–8000	0. 03255	Transition
		$\leq$1800	$\frac{58.65}{Re}$	Laminar

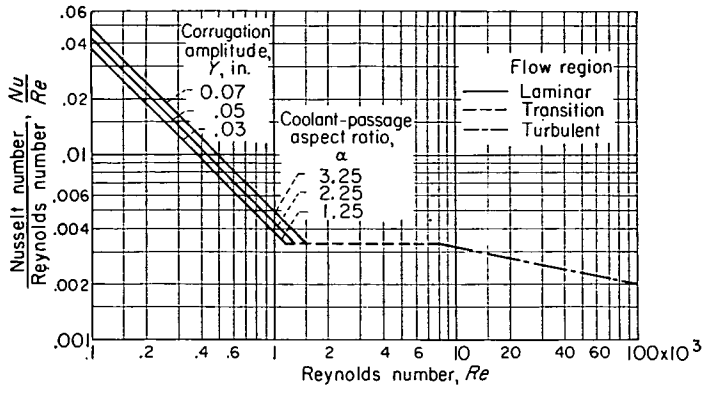


FIGURE 2.—Heat-transfer correlations for air-cooled-blade coolant passages.

point for subsonic Mach numbers. In this analysis the blade span was divided into ten equal increments, and a stepwise calculation procedure was used to calculate the temperature at each increment. To obtain the coolant-air temperature rise in each increment, the following heat balance was written:

$$q+w_aE=h_o l_o \Delta x(t_{g,e}-t_{b,x})+w_aE=w_a c_{p,a}\Delta T'_a \tag{21}$$

where the pumping work E done on the cooling air over the increment Δx is

$$E=\frac{\omega^2 r_x \Delta x}{gJ} \tag{22}$$

Combining equations (21) and (22) results in

$$\Delta T'_a=\frac{h_o l_o \Delta x}{w_a c_{p,a}}(t_{g,e}-t_{b,x})+\frac{\omega^2 r_x \Delta x}{gJc_{p,a}} \tag{23}$$

The blade temperature used to evaluate film temperature and fluid properties and to calculate T'_a at each increment was that temperature calculated in the previous increment. The spanwise temperature variations in the blade are generally small enough that this approximation has little or no effect on the final results.

Required cooling airflow.—The allowable blade temperature distribution for turbine blades depends on the spanwise blade stress distribution, the stress-rupture properties of the blade material, and the stress-ratio factor, as discussed in reference 10. The required cooling airflow is that which results in a curve of calculated blade temperature against blade span that is tangent to a curve of allowable blade temperature. This cooling airflow was found by an iterative procedure. A maximum difference of 2° between the calculated and allowable blade temperature was permitted at the blade critical section (spanwise position where difference in calculated and allowable temperature is smallest) in determining the required cooling airflow.

BLADE PRESSURE LOSSES

The cooling-air pressure change through the turbine blades was calculated by the method of reference 5 by using the required cooling airflow from the calculations described previously. The blade was divided into five equal increments for these calculations. The friction coefficients used were the same as those that can be read from figure 3 of reference 1, using the same values of coolant-passage aspect ratio α as shown in figure 2 of this report, except that in the transition region the friction coefficient was assumed to be independent of Reynolds number in exactly the same manner as Nu/Re was assumed to be independent of transition Reynolds number in figure 2. Equations for the friction coefficient are given in table II(b) in terms of $4C_{fr}$ for convenience in the use of the calculation procedure of reference 5.

The cooling-air pressure at the blade base was assumed to be 90 percent of the compressor-discharge pressure, which allowed for duct losses and some losses in velocity head. It was assumed that, if the calculated coolant static pressure at the blade tip was equal to or greater than the static gas pressure at the blade tip and if the Mach number at the tip was subsonic, then the blade was satisfactory with respect to loss. The static gas pressure at the blade tip was calculated from the turbine velocity diagram that was required to drive the compressor at the assumed flight conditions.

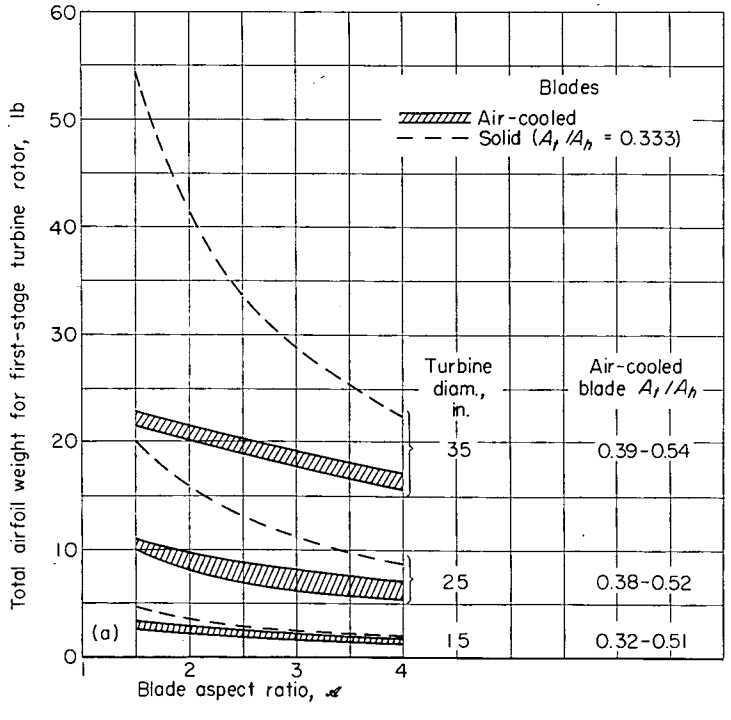
CALCULATION PROCEDURE

The entire calculation procedure for this analysis was set up in equation form, including the pressure-loss calculations and the relation between temperature and the 100-hour stress-rupture properties of A–286 alloy, the turbine blade material assumed for this analysis. The calculations were then made by an IBM 650 Magnetic Drum Data Processing Machine. Temperatures, pressures, and other conditions used in this analysis are listed in table I.

RESULTS AND DISCUSSION

AIRFOIL WEIGHT, STRESS, AND AREAS

Weight.—The total airfoil weights of all the rotor blades in a turbine stage are plotted against blade aspect ratio in figure 3 for both the first and second stages of the turbines for turbine diameters of 15, 25, and 35 inches. Although the



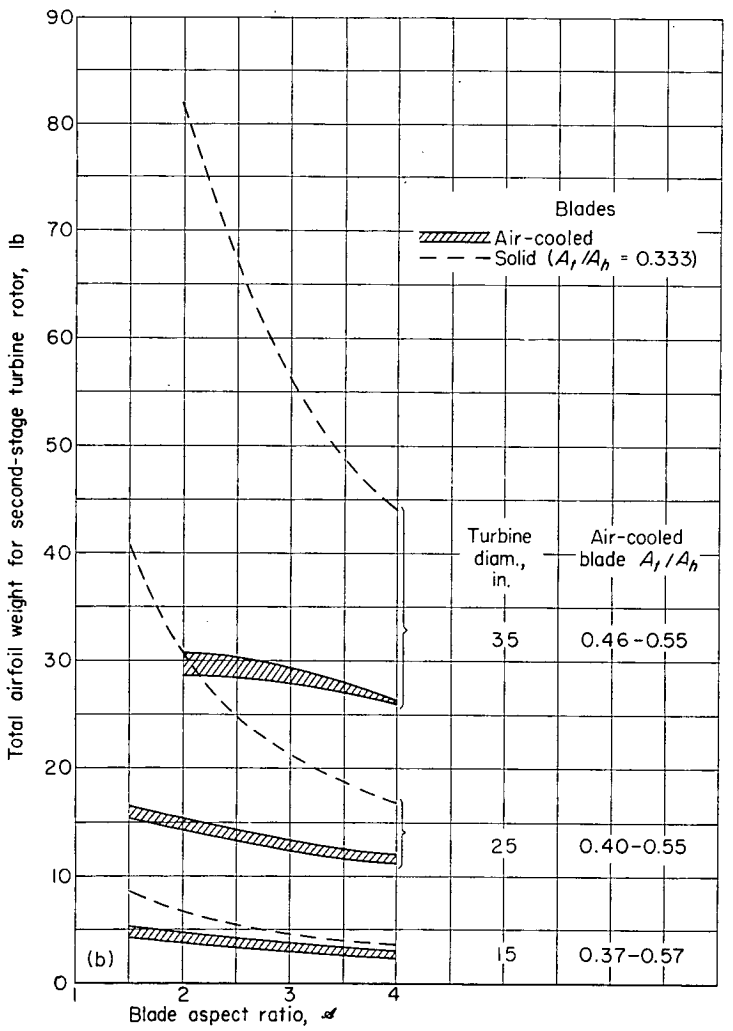
(a) First stage. Hub-tip radius ratio, 0.73.

FIGURE 3.—Variation of turbine blade airfoil weight with turbine diameter and blade aspect ratio.

analysis presented in this report is a study of the effects of blade chord on weight and cooling characteristics of air-cooled blades, it is more convenient to plot most of the results of the analysis against blade aspect ratio, because the range of aspect ratio is common to turbines of different diameters, while the range of chord size varies considerably for different diameter turbines.

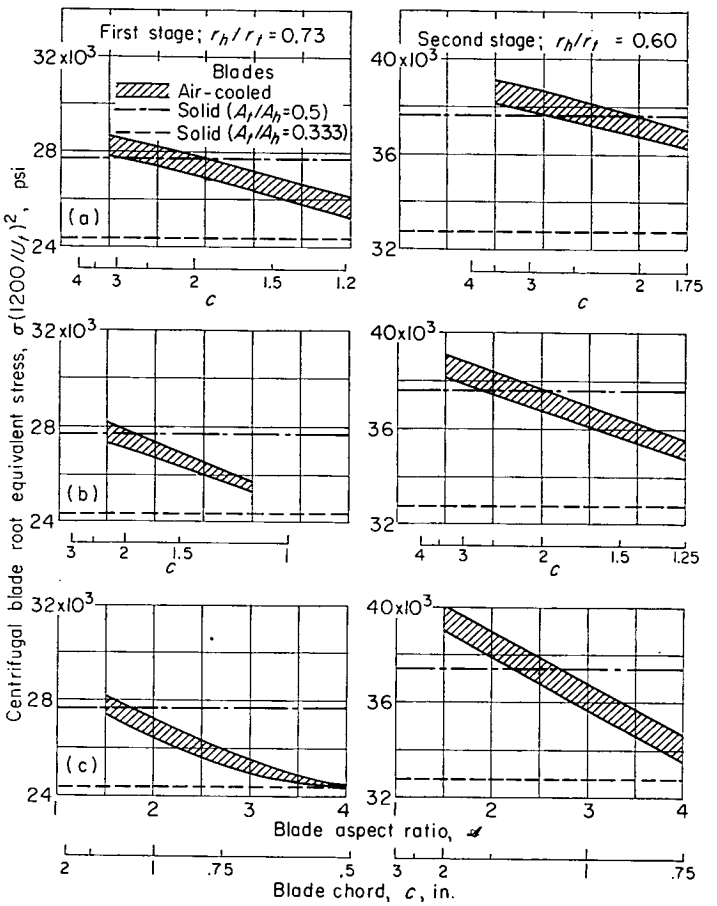
The weight of the air-cooled blades is represented by a shaded band. This band covers the range of weight values for the corrugation configurations considered herein. For turbine diameters of 25 and 35 inches, corrugation amplitudes of 0.03, 0.05, and 0.07 inch were considered, with an outside-shell thickness tapering from 0.045 inch at the root to 0.015 inch at the tip. For the 15-inch-diameter turbine, corrugation amplitudes of 0.03 and 0.05 inch were considered, with an outside-shell thickness tapering from 0.030 to 0.010 inch. Also shown in the figure are weights of solid uncooled blades having the same cross-sectional area at the root section of the blade and an aerodynamic taper of 3 to 1 from root to tip.

Two important conclusions may be drawn from figure 3. First, air-cooled blades are considerably lighter than solid blades having the same root profile, particularly for large



(b) Second stage. Hub-tip radius ratio, 0.60.

FIGURE 3.—Concluded. Variation of turbine blade airfoil weight with turbine diameter and blade aspect ratio.



(a) Turbine diameter, 35 inches.
(b) Turbine diameter, 25 inches.
(c) Turbine diameter, 15 inches.

FIGURE 4.—Air-cooled-turbine blade root stresses.

turbine diameters; and second, as aspect ratio (or chord) is varied, the total blade weight for the turbine is affected to a much smaller degree for air-cooled blades than for solid blades. Air-cooled blades of very low aspect ratio can be used, and the total turbine blade weight will still be lighter than with solid blades of high aspect ratio.

Airfoil weight does not show the entire picture with regard to turbine weight, however. The use of low-aspect-ratio blades requires alterations in the turbine disk design to support the longer chords. Generally, the longer chords will probably result in an increase in disk weight, so that the total turbine weight will increase with chord more than indicated in figure 3. Some types of disk structure, such as multiple disk wheels, may make it possible to increase chord with little or no increase in disk weight. An evaluation of disk weight, however, is beyond the scope of this report. A rather complete design study is required before representative variations in disk weight with blade chord can be made.

For constant-solidity turbines the total airfoil weight of solid blades varies inversely as the blade aspect ratio to the first power. (The individual blade weight varies inversely as the square of the aspect ratio.) In the study of air-cooled blades included herein, it was found that the total blade airfoil weight for the turbine varied inversely as the aspect ratio to a power varying between 0.1 and 0.65, depending on the turbine diameter. In general, the lower exponents ac-

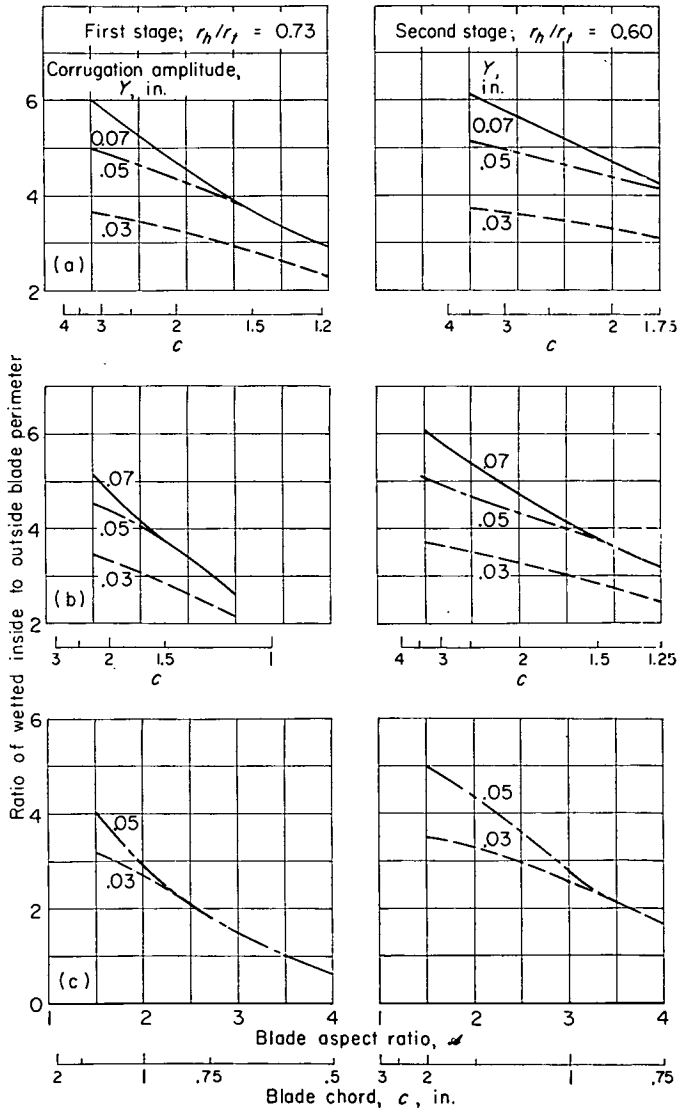
company the large turbines (larger physical size of blades). For the 35-inch turbine the exponent was found to be about 0.1 for the second stage and about 0.3 for the first stage. For the 15-inch turbine the exponent was about 0.5 for the second stage and 0.65 for the first stage. The reason for this is obvious: With the smaller blades the shell and corrugations occupy a much larger portion of the cross-sectional area (the proportion of flow area decreases) than with the larger blades, so that the small blades more nearly approach the weight variation that occurs with solid blades.

Stress.—From the root and tip cross-sectional areas that were determined for each blade configuration, the centrifugal root equivalent stress was calculated. The results are plotted against both blade aspect ratio and chord in figure 4. Subsequent figures are plotted in a similar manner. The stress values are presented as shaded bands, and they cover the same range of variables as discussed in connection with figure 3. For reference, root stresses are also shown for solid blades with tip-to-root area ratios of 0.5 and 0.333. The area ratios for the air-cooled blades vary with blade size. The shells of all the blades have an area ratio of 0.333, but the sheet metal making up the corrugations and islands in the blades is untapered. More corrugations can be installed in the larger-chord blades (low aspect ratio), which will help the heat-transfer characteristics; but the addition of this untapered sheet metal results in higher area ratios and thus higher root stresses.

Figure 4 shows that, generally, the centrifugal root stresses of corrugated-insert air-cooled blades will be of the same order of magnitude as those for solid blades with tip-to-root area ratios varying from 0.5 to 0.333. With low hub-tip radius ratios (on the order of 0.60 shown for the second stage) and for blade aspect ratios below 2.5 or 3, the air-cooled-blade stresses are likely to be higher than those for solid blades with an area ratio of 0.5. Figure 4 also compares tip-to-root cross-sectional-area ratios for air-cooled blades for various coolant-passage configurations, blade aspect ratios, and hub-tip radius ratios; however, a comparison based on root stress is probably of more general interest.

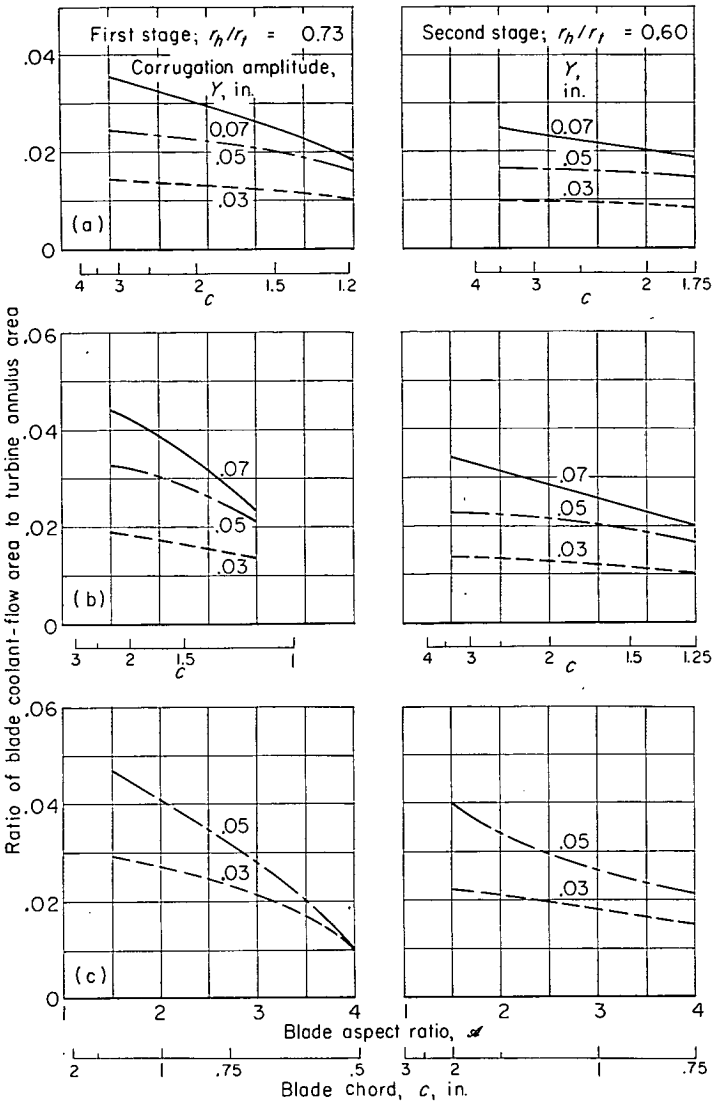
Inside heat-transfer surface area.—The amount of surface area that can be placed inside air-cooled turbine blades relative to the blade outside surface area affects the efficiency of blade-cooling. The ratio of the wetted perimeter on the inside of the blade to the outside perimeter is plotted in figure 5 as a function of blade chord and aspect ratio, turbine diameter, and corrugation amplitude Y. The ratio of perimeters can vary by as much as 7 to 1 as the blade chord is varied from about 1.5 to 0.5 inch (aspect ratio varying from 1.5 to 4) for the 15-inch-diameter turbine. For the larger turbine engines and the corresponding larger chords, the ratio of perimeters varies about 2 to 1 for the same range of aspect ratio. If it were possible to scale blade coolant passages geometrically, the ratio of inside to outside surface area would remain constant as chord is varied. As mentioned previously, this is not practical for turbine blades. The two sketches in figure 1 illustrate the problem involved when the blade chord is shortened and the same corrugation geometry is used for both blade sizes. The smaller sketch shows that it may not even be possible to attach separate corrugations to the portions of the shell on both the suction and pressure surfaces of the blade. It is obvious that the small blade is impractical as shown. A different internal configuration is required, possibly one in which the corrugation amplitude changes along the chord so that the corrugations will contact both shell surfaces. The sketch is shown here only to illustrate some of the problems involved in trying to obtain large internal surface areas in short-chord blades.

Figure 5 shows that in all cases the ratio of heat-transfer surface on the inside of blades to that on the outside can be increased substantially by increasing blade chord (reducing aspect ratio). For very small turbine blades with chords on the order of 0.5 inch, the inside surface area becomes less than the outside surface area. This condition makes cooling the turbine blades extremely difficult.



(a) Turbine diameter, 35 inches.
(b) Turbine diameter, 25 inches.
(c) Turbine diameter, 15 inches.

FIGURE 5.—Effect of turbine blade size on inside heat-transfer surface area.



(a) Turbine diameter, 35 inches.
(b) Turbine diameter, 25 inches.
(c) Turbine diameter, 15 inches.

FIGURE 6.—Effect of turbine blade size on coolant-passage flow area.

The corrugation amplitude also affects the amount of surface on the inside of the blade for a fixed corrugation pitch. It should be noted, however, that, with respect to area, frequently a corrugation of 0.07-inch amplitude is little or no better than one of 0.05-inch amplitude. The conduction path is longer with the larger amplitude, and the inside heat-transfer coefficients will be lower for a given mass velocity for the large corrugations, so that the extra heat-transfer surface area with the 0.07-inch-amplitude corrugations does not necessarily result in a blade that requires the smallest quantity of coolant flow. The large amplitude may be advantageous, however, because of large flow area and consequent smaller pressure losses, as is discussed subsequently.

Coolant-flow area.—The ratio of the total coolant-flow area in the blades to the gas-flow area in the turbine annulus gives an indication of the quantity of compressor air that can be bled for turbine cooling for a reasonable pressure drop through the blades; or, conversely, it gives an indication of the pressure losses that will be encountered in the blades for a given coolant-flow ratio. The ratio of blade coolant-flow area to turbine annulus area is plotted in figure 6 as a function of blade chord and aspect ratio, turbine diameter, and corrugation amplitude. The trends here are similar to those for heat-transfer surface area. As the chord is decreased, the coolant-flow area is reduced, which may result in pressure-loss difficulties. It will be noted, however, that large-amplitude corrugations are almost always an advantage as far as coolant-flow area is concerned.

BLADE COOLANT-FLOW REQUIREMENTS

Heat-flow rates.—The quantity of heat that must be removed from a turbine blade by the cooling air is a function of the gas-to-blade heat-transfer coefficient, the temperature difference between the gas and the blade, and the surface area. The temperature difference between gas and blade is essentially independent of blade chord, since allowable blade temperature is determined by blade stress level (affected only slightly by blade chord) and the stress-rupture properties of the blade material. Also, for constant-solidity turbines the total blade surface area is constant. Consequently, the heat-flow rate into the blade is almost solely a function of the gas-to-blade heat-transfer coefficient h_o. Equation (15) shows that h_o varies inversely as the blade chord to the $1-z$ power.

It is evident, then, that increasing blade chord (or reducing blade aspect ratio) will reduce the cooling loads in blades. This effect is shown on a relative basis in figure 7. As stated previously, it appears that a representative value of z for rotor blades is 0.70. In reference 11 a value of z of 0.52 is given for a reaction-type blade that might be suitable for stators. The curves in figure 7 were obtained with these values of z. The figure shows that doubling the blade chord will reduce the heat-flow rate about 19 percent for rotor blades and about 28 percent for stator blades.

Required coolant-flow rates.—The combined effects of the areas shown in figures 5 and 6 and the variations in heat flow illustrated in figure 7 on the coolant flow required to cool blades for the turbines considered in this analysis are

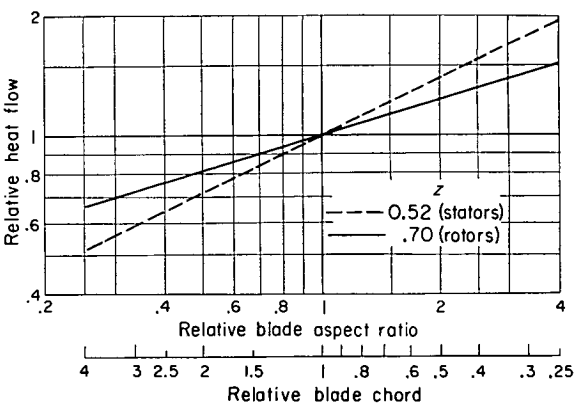
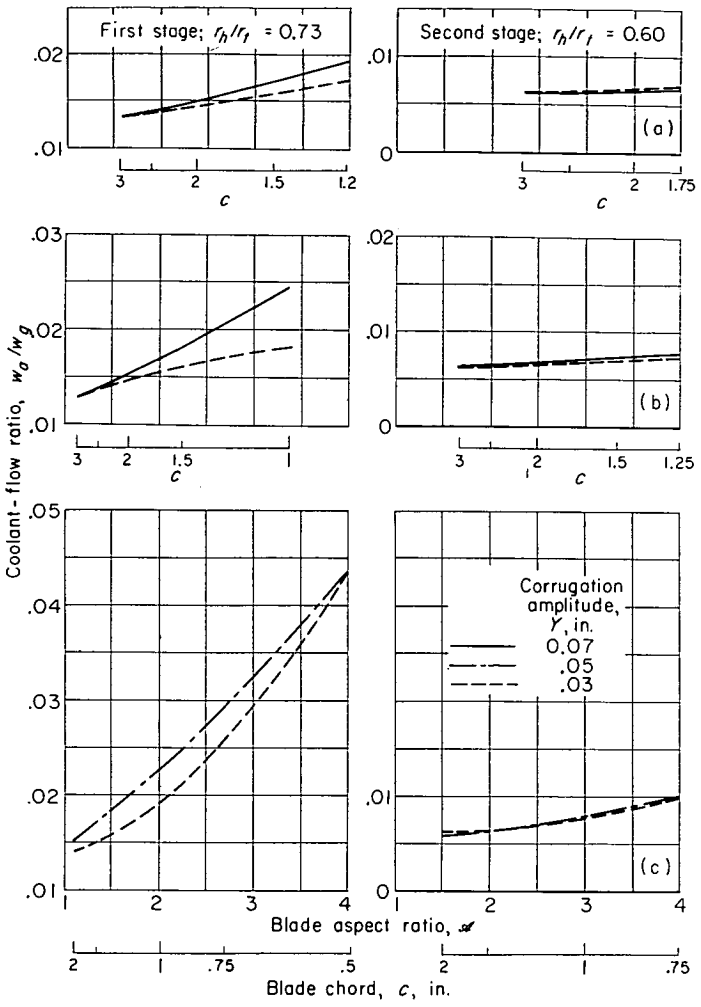


FIGURE 7.—Effect of turbine blade size on heat flow to blade.



(a) Turbine diameter, 35 inches.
(b) Turbine diameter, 25 inches.
(c) Turbine diameter, 15 inches.

FIGURE 8.—Effect of turbine blade size on coolant-flow requirements.

shown in figure 8, where the ratio of coolant flow to turbine gas flow is plotted against blade chord and aspect ratio. The figure shows that, invariably, as the blade chord is decreased (increased aspect ratio) the total quantity of air required for turbine cooling increases for a given corrugation configuration in the coolant passage. The reasons for this are, of course, obvious from the discussion of previous figures. However, in some cases the variations in required flow rate with blade chord and aspect ratio are quite large, particularly for small turbines, where the chord may become quite small. The analysis shows that the flow required for blades with 1-inch chord is generally about twice that required for blades with 3-inch chord. By further reducing the chord to 0.5 inch, the required coolant flow may become over twice that for blades with a 1-inch chord.

Figure 8 also shows the effect of corrugation amplitude on required cooling-airflow rate. Generally, the effect of amplitude is much smaller than the effect of blade chord on required coolant flow, particularly for the second stage of the turbines. In the second stage the gas temperature is reduced relative to that of the first stage, so that the cooling load is less severe and smaller variations due to either chord size or corrugation amplitude would be expected. Because of the small effect of corrugation amplitude on cooling-airflow requirements, the required flow for 0.05-inch corrugations is not shown for the 25- and 35-inch-diameter turbines. A few calculations were made, which showed that the flow required for a corrugation of 0.05 inch was intermediate between that required for the 0.07- and 0.03-inch corrugations.

The inside heat-transfer surface area can usually be increased by increasing the amplitude of the corrugations (fig. 5). Large surface area is usually desirable to improve cooling effectiveness, but it will be noted in figure 8 that slightly less cooling air is required with the smaller corrugation amplitude. The larger surface area of the large corrugations is more than offset by the reduced hydraulic diameter (which increases the heat-transfer coefficient) of the small corrugations.

The effect of corrugation geometry on required cooling airflow appears to have a different trend for the 15-inch-diameter turbine than for the other two diameters. For the larger-diameter turbines the difference in required cooling airflows for the 0.07- and 0.03-inch-amplitude corrugations increases with increasing aspect ratio (decreasing chord); but for the 15-inch turbine the required flows are the same for different amplitudes for an aspect ratio of 4. This effect can be explained by the fact that, for a turbine blade with 0.5-inch chord, it was not possible to place any corrugations inside the coolant cavity. For this reason the blade with 0.5-inch chord has the same flow area and same heat-transfer area for the blades represented by both the dashed and the dash-dot lines. The blade was actually a plain hollow blade.

With respect to heat transfer, figure 8 shows that there is generally considerably freedom in the choice of the corrugation amplitude, but pressure losses within the turbine blades should also be considered. Figure 8 gives no indication of the supply pressure required to force the cooling air through the blades. It is possible that under some conditions the pressure available from the engine compressor may be insufficient.

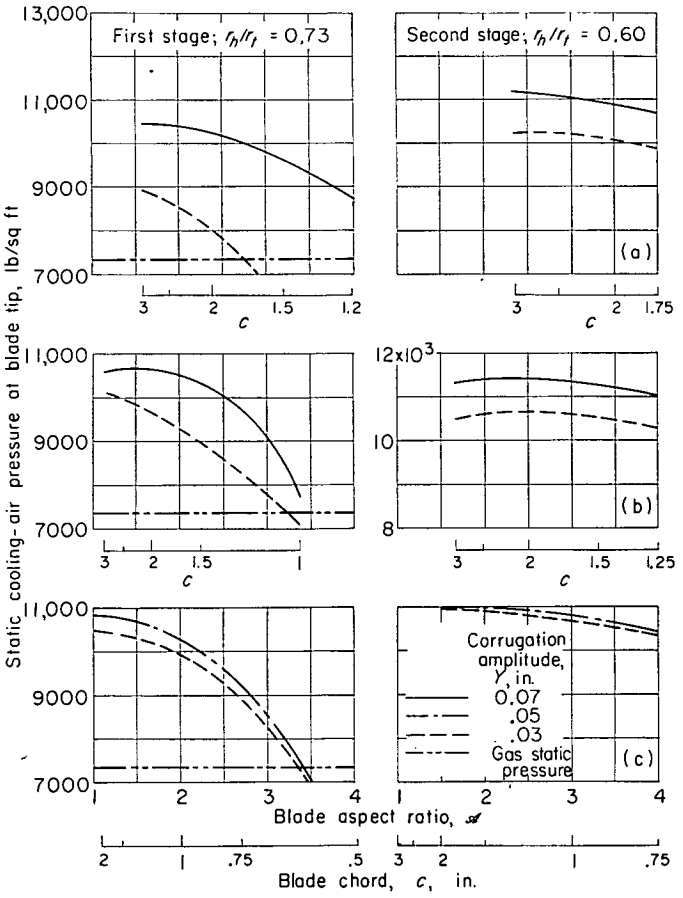
BLADE PRESSURE LOSSES

Coolant pressure at blade tip.—In order to force coolant through air-cooled turbine blades that discharge the cooling air at the blade tip, it is necessary that the static pressure of the coolant at the tip be at least as high as the static pressure of the gas at the tip. In this analysis coolant pressure losses were calculated for an inlet supply pressure that was as high as is considered feasible with the use of compressor bleed, in order to determine whether it would be possible to force the required flow through the blade. This supply pressure was 90 percent of compressor-discharge total pressure, since it seems likely that at least a 10-percent loss in pressure will result from loss of velocity head and duct losses. The cooling-

air temperature was assumed to be at compressor-discharge temperature. The static pressure of the cooling air at the blade tip is shown in figure 9 for these conditions of inlet pressure and temperature and for the flow rates shown in figure 8. The static gas pressure at the blade tip is also shown for the first stage of the turbine. For the second stage the static gas pressure is not shown, because it is much below the scale on the curves (4000 lb/sq ft, table I).

For all cases shown except one, the static cooling-air pressure at the blade tip in the first stage can become less than the static gas pressure as the blade chord is decreased. This pressure limitation very definitely limits the minimum blade chord that can be tolerated. There appear to be no pressure limitations in the second stage of the turbine.

Figure 9 shows that it may be advantageous to use large-amplitude corrugations in turbine blades to reduce pressure losses, even though the cooling-airflow requirements are somewhat higher (fig. 8). It can be observed from figure 9 that under some conditions it is possible to have a coolant pressure rise through the blades. The supply total pressure to the blades was approximately 9400 pounds per square foot; yet for many cases the tip static pressure is considerably higher than the supply total pressure. This pressure rise is a result of the pumping due to rotation.



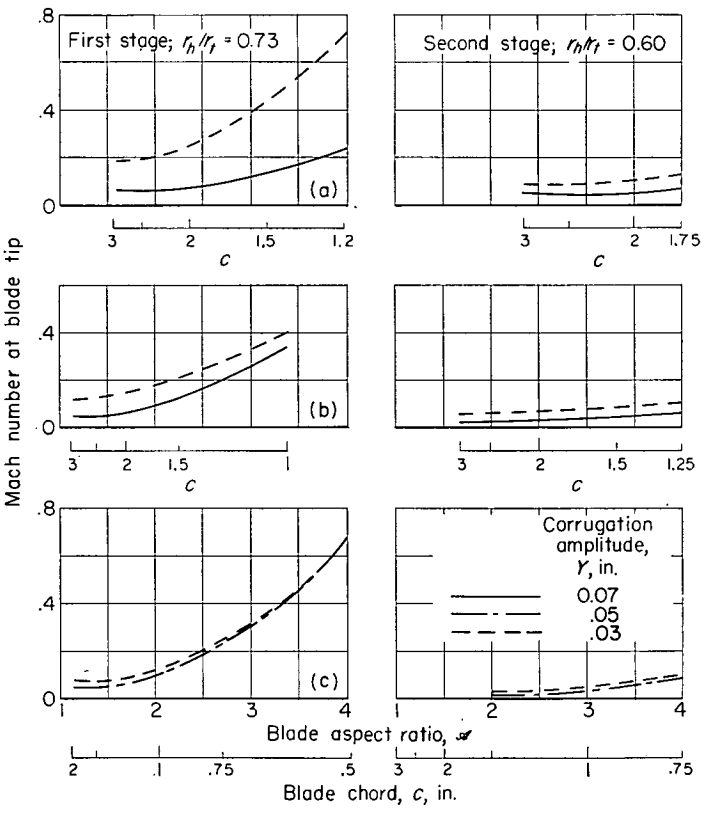
(a) Turbine diameter, 35 inches.
(b) Turbine diameter, 25 inches.
(c) Turbine diameter, 15 inches.

FIGURE 9.—Effect of turbine blade size on static cooling-air pressure at blade tip.

Coolant Mach number at blade tip.—Relatively low coolant-passage Mach numbers are generally desirable. High Mach numbers in themselves are not necessarily a disadvantage; but they cause static-pressure losses, and the blades may choke and make it impossible to increase the coolant-flow rate without increasing the coolant density. A high coolant-passage Mach number gives little margin for error in the design. For instance, if the Mach number is 0.7, the flow rate can only be increased about 9 percent for a constant total pressure and temperature before choking will occur. The coolant Mach numbers at the blade tip are shown in figure 10 for the same pressures and flows obtained from figures 8 and 9. Comparison of figures 9 and 10 shows that, when the tip Mach number approaches a value of about 0.4, the static-pressure losses in the blade may become excessive. Figure 10 gives further indication of flow difficulties that can be encountered with small-chord blades.

GENERALITY OF RESULTS

The results of this analysis are presented for specific engine conditions. Therefore, the values of blade aspect ratio or blade chord at which cooling may become difficult cannot be considered to be general. By changing the turbine blade material, the coolant temperature, the turbine-inlet temperature, the turbine stress level, the blade stress-ratio factor, or other design conditions, cooling limitations may



(a) Turbine diameter, 35 inches.
(b) Turbine diameter, 25 inches.
(c) Turbine diameter, 15 inches.

FIGURE 10.—Effect of turbine blade size on cooling-air Mach number at blade tip.

be met at entirely different conditions from those encountered in this analysis. For example, the cooling-airflow requirements were calculated for the 35-inch-diameter turbine for a chord of 2 inches and a coolant-passage amplitude for three different stress-ratio factors (ratio of design stress to average centrifugal stress). As the stress-ratio factor is increased, the blade is designed for a higher stress level; and consequently it must operate at a lower temperature. As a result, the coolant-flow requirements increase with increasing stress-ratio factor. Figure 11 shows the effect of stress-ratio factor on cooling airflow, tip Mach number, and coolant pressure at the tip. A similar effect would result from varying the blade material. A material capable of withstanding high temperatures might have the trend exhibited for a stress-ratio factor of 1, while a material that could not withstand such high temperatures would exhibit the trends shown for a higher stress-ratio factor. As would be expected, the required coolant flow and tip Mach number increase and tip static pressure decreases with an increase in stress-ratio factor; but there are no great changes that would indicate that the trends of figures previously presented would vary greatly if a different set of conditions were chosen for the calculations. Stress-ratio factor would, of course, have a much larger effect for a blade chord that resulted in higher tip Mach numbers and lower tip static pressures.

Figure 12 shows how coolant-flow requirements, Mach number, and tip pressure can be affected by the coolant temperature. Most of the calculations for this analysis were made with a coolant temperature of 1247° R, which corresponds to the temperature at the discharge of the compressor. By use of an aftercooling device, it may be possible to reduce the cooling-air temperature. In figure 12 curves are shown for cooling-air supply temperatures of 1247° and 1000° R for the first stage of the 35-inch-diameter turbine. A reduction in cooling-air temperature naturally reduces the quantity of air required for blade-cooling. The cooling-airflow reduction shown in figure 12 varies between about 20 and 25 percent over the range of blade chords investigated. At low coolant Mach numbers the Mach number reduction due to reducing cooling-air temperature is about the same order of magnitude as the reduction in cooling airflow. This effect on static pressure at the blade tip is quite small. For a blade chord of 1 inch, however, there is a large difference in tip Mach numbers owing to the cooling-air temperature effect; but, as can be seen from the shape of the curves, reducing the cooling-air temperature does not allow a significant reduction in permissible blade chord. The results shown in figure 12 are similar to those shown in figure 11, in that the conclusions that can be drawn from this study do not appear to be affected significantly by the value of cooling-air temperature used in the analysis.

It is not within the scope of this report to investigate the effects of turbine blade chord for all combinations of engine conditions. It is believed, however, that enough conditions were investigated to point out trends and to indicate that the use of small-chord blades can become a problem in air-cooled engines. Other blade configurations may possibly create less of a problem than corrugated blades for small chords, but even with those configurations similar trends would be expected. As turbine-inlet temperature is increased above 2500° R, the problems will become more severe than presented herein because of the higher coolant flows that will be required. It can be concluded from this study that in the design of air-cooled turbines it is generally

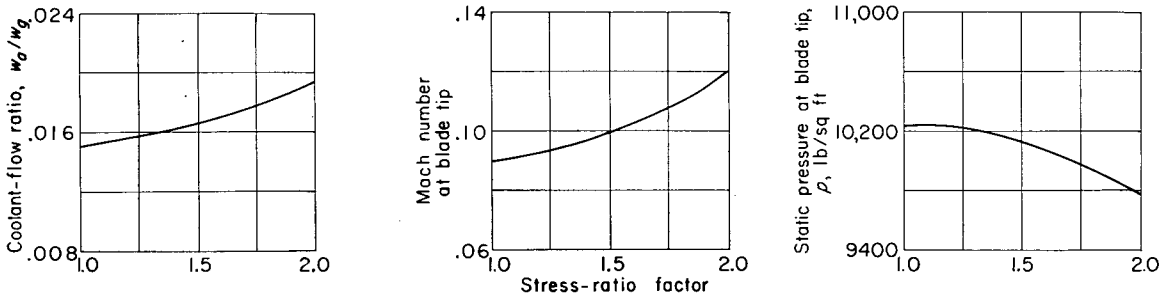


FIGURE 11.—Effect of stress-ratio factor on cooling and pressure-drop characteristics of turbine blades. First stage of 35-inch-diameter turbine; chord, 2 inches; corrugation amplitude, 0.07 inch.

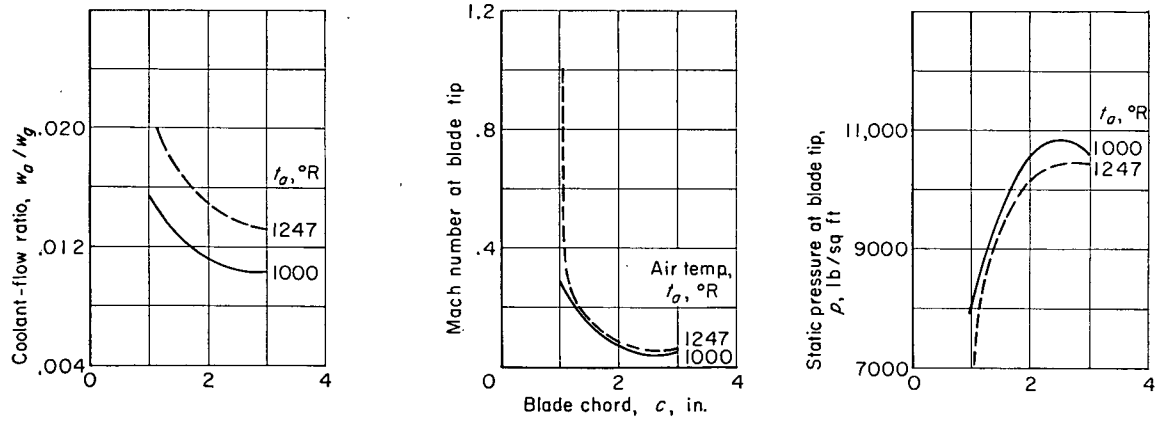


FIGURE 12.—Effect of cooling-air temperature on cooling and pressure-drop characteristics of turbine blades. First stage of 35-inch-diameter turbine; corrugation amplitude, 0.07 inch.

desirable to utilize blades with as large a chord as appears feasible from considerations of disk stress and aerodynamics.

SUMMARY OF RESULTS

The results of this investigation of the effects of chord size on weight and cooling characteristics of air-cooled turbine blades can be summarized as follows:

1. Air-cooled-turbine blade weight is affected to a much smaller degree by the size of the blade chord than is the weight of solid uncooled blades.

2. When solidity is maintained constant, the heat-transfer surface and the flow area in the coolant passage of air-cooled blades are considerably larger relative to the surface and flow area on the gas side of the blades with large-chord blades than with small-chord blades. As a result, cooling large-chord blades should be easier.

3. Heat-transfer and pressure-drop analyses show that small-chord blades require a larger total amount of cooling air for the turbine and have higher pressure losses than larger-chord blades. Cooling airflow for turbines with 1-inch-chord blades is generally about twice that required for turbines with 3-inch-chord blades. By further reducing the chord to 0.5 inch, the required cooling airflow may become more than twice that for blades with 1-inch chord.

4. Cooling-air pressure losses increase as blade chord is reduced, and it may often be impossible to pass the cooling airflow required at the pressure levels available from compressor bleed to cool blades with small chords.

5. The exact blade chords at which it may no longer be feasible to cool air-cooled blades depend upon the assumptions and conditions of the analysis, but the trends indicated in this report are probably general for other engines, other blade configurations, and other engine conditions.

LEWIS FLIGHT PROPULSION LABORATORY
NATIONAL ADVISORY COMMITTEE FOR AERONAUTICS
CLEVELAND, OHIO, *November 13, 1956*

REFERENCES

1. Slone, Henry O., Hubbartt, James E., and Arne, Vernon L.: Method of Designing Corrugated Surfaces Having Maximum Cooling Effectiveness Within Pressure-Drop Limitations for Application to Cooled Turbine Blades. NACA RM E54H20, 1954.
2. Cavicchi, Richard H., and English, Robert E.: A Rapid Method for Use in Design of Turbines Within Specified Aerodynamic Limits. NACA TN 2905, 1953.
3. Esgar, Jack B., and Ziemer, Robert R.: Methods for Rapid Graphical Evaluation of Cooled or Uncooled Turbojet and Turboprop Engine or Component Performance (Effects of Variable Specific Heat Included). NACA TN 3335, 1955.
4. Brown, W. Byron, and Donoughe, Patrick L.: Extension of Boundary-Layer Heat-Transfer Theory to Cooled Turbine Blades. NACA RM E50F02, 1950.
5. Hubbartt, James E., Slone, Henry O., and Arne, Vernon L.: Method for Rapid Determination of Pressure Change for One-Dimensional Flow with Heat Transfer, Friction, Rotation, and Area Change. NACA TN 3150, 1954.
6. Donoughe, Patrick L.: Outside Heat Transfer of Bodies in Flow—A Comparison of Theory and Experiment. M. S. Thesis, Case Inst. Tech., 1951.
7. Kays, W. M., and Clark, S. H.: A Summary of Basic Heat Transfer and Flow Friction Design Data for Plain Plate-Fin Heat Exchanger Surfaces. Tech. Rep. No. 17, Dept. Mech. Eng., Stanford Univ., Aug. 15, 1953. (Contract N6-ONR-251, Task Order 6 (NR-090-104) for Office Naval Res.)
8. McAdams, William H.: Heat Transmission. Second ed., McGraw-Hill Book Co., Inc., 1942.
9. Livingood, John N. B., and Brown, W. Byron: Analysis of Spanwise Temperature Distribution in Three Types of Air-Cooled Turbine Blades. NACA Rep. 994, 1950. (Supersedes NACA RM's E7B11e and E7G30.)
10. Ziemer, Robert R., and Slone, Henry O.: Analytical Procedures for Rapid Selection of Coolant Passage Configurations for Air-Cooled Turbine Rotor Blades and for Evaluation of Heat-Transfer, Strength, and Pressure-Loss Characteristics. NACA RM E52G18, 1952.
11. Hubbartt, James E.: Comparison of Outside-Surface Heat-Transfer Coefficients for Cascades of Turbine Blades. NACA RM E50C28, 1950.

REPORT 1355

A THEORETICAL AND EXPERIMENTAL STUDY OF PLANING SURFACES INCLUDING EFFECTS OF CROSS SECTION AND PLAN FORM [1]

By CHARLES L. SHUFORD, Jr.

SUMMARY

A summary is given of the background and present status of the pure-planing theory for rectangular flat plates and V-bottom surfaces. The equations reviewed are compared with experiment. In order to extend the range of available planing data, the principal planing characteristics for models having sharp chines have been obtained for a rectangular flat and two V-bottom surfaces having constant angles of dead rise of 20° and 40°. Planing data were also obtained for flat-plate surfaces with very slightly rounded chines for which decreased lift and drag coefficients are obtained.

A revision of the theory presented in NACA Technical Note 3233 is presented for the rectangular flat plate. The revised theory bases the aerodynamic suction effects on the total lift rather than solely on the linear component. Also a crossflow drag coefficient which is dependent on the shape of the chines was found from experiment to be constant for a given immersed cross section; however, for surfaces, such as those having horizontal chine flare or vertical chine strips, the crossflow drag coefficient is constant only for the chine-immersed condition. The theory is extended to include triangular flat plates planing with base forward and V-shaped prismatic surfaces having a constant angle of dead rise, horizontal chine flare, or vertical chine strips. A method is also presented for estimating the center of pressure for surfaces having either rectangular or triangular plan form. The results calculated by the proposed theory have been correlated only with the data considered to be pure planing; however, for conditions not considered pure planing, a method is given for estimating the effects of buoyancy. The agreement between the results calculated by the proposed theory and the experimental data is, in general, good for calculations of pure-planing lift and center-of-pressure location for flat plate, V-bottom, and related planing surfaces.

INTRODUCTION

Recent developments in water-based aircraft have resulted in configurations utilizing planing surfaces operating at angles of trim, length-beam ratio, and Froude number beyond those for which most of the available planing theories were correlated with experimental data. In reference 1 a preliminary review of these theories for a pure-planing rectangular flat plate was made to determine whether available planing theories were adequate in estimating the planing lift in these extended ranges. In addition to this review, a modification and addition to existing theory which is useful in predicting the lift and center of pressure for pure-planing rectangular flat plates was presented.

The review in reference 1 indicated there were no data available in the extended ranges of combined high trim and high length-beam ratios; consequently, the principal planing characteristics for models having sharp chines have been obtained in these extended ranges for a rectangular flat and two V-bottom surfaces. It was also noted in reference 1 that there was a difference in the lift coefficients obtained from various experimental investigations; therefore, data have been obtained for rectangular flat-plate surfaces having very slightly rounded chines to determine the influence of slight differences in construction at the point of flow separation on the lift coefficient.

The review of existing theories and data has been extended to include those applicable to V-bottom surfaces. The theory presented in reference 1 for estimating the lift and center-of-pressure location of a pure-planing rectangular flat plate has been revised and extended to include triangular flat plates planing with base forward and V-shaped prismatic surfaces having a constant angle of dead rise, horizontal chine flare, or vertical chine strips. Since water-based aircraft operate at low Froude numbers as well as high Froude numbers, an approximate method has also been presented for estimating the effect of buoyancy on lift coefficient.

SYMBOLS

A	aspect ratio, $\frac{b}{l_m}$
A_t	ratio of maximum beam to overall length (see fig. 40)
b	beam of planing surface, ft
$C_{D,b}$	drag coefficient based on square of beam, $\frac{D}{qb^2}$
$C_{D,c}$	crossflow drag coefficient
$(C_{D,c})_{\beta=0}$	crossflow drag coefficient for a cross section having an effective angle of dead rise of 0°
$C_{D,S}$	drag coefficient based on principal wetted area, $\frac{D}{qS}$
$C_{D,i}$	induced drag coefficient, $C_{L,S} \tan \tau$
C_f	skin-friction coefficient, $C_{D,S}-C_{L,S} \tan \tau$

[1] Supersedes NACA Technical Note 3939 by Charles L. Shuford, Jr., 1957.

Preceding Page Blank

C_L lift coefficient

$C_{L,B}$ lift coefficient due to buoyancy, $\frac{L_B}{qS}$ (see eq. (31))

$C_{L,b}$ lift coefficient based on square of beam, $\frac{L}{qb^2}$

$C_{L,S}$ lift coefficient based on principal wetted area, $\frac{L}{qS}$

$C_{L,Vol}$ lift coefficient due to buoyancy based on total wedge-shaped volumetric displacement of the planing surface, $\frac{L_{Vol}}{qS}$ (see eqs. (28) to (30))

C_V speed coefficient or Froude number, $\frac{V}{\sqrt{gb}}$

D drag of planing surface, lb

$G(\beta_e)$ dead-rise function (applied only to crossflow term, see fig. 2)

g acceleration due to gravity, 32.2 ft/sec^2

$K(\beta_e)$ dead-rise function (applied only to linear term, see fig. 1)

L lift of planing surface, lb

L_B lift due to buoyancy, lb

L_{Vol} lift due to buoyancy based on total wedge-shaped volumetric displacement of the planing surface, lb

l length of planing surface, ft

l_c chine wetted length, ft

l_k keel wetted length, ft

l_m mean wetted length (distance from aft end of planing surface to the mean of the heavy spray line), ft

l_{cp} center-of-pressure location (measured forward of trailing edge), ft

$\frac{l_{cp}}{l_m}$ nondimensional center-of-pressure location

N normal force, lb

q free-stream dynamic pressure, $\frac{1}{2}\rho V^2$, lb/sq ft

R Reynolds number, $\frac{Vl_m}{\nu}$

S principal wetted area (bounded by trailing edge, chines, and heavy spray line), sq ft

V horizontal velocity, ft/sec

β angle of dead rise, radians unless otherwise stated

β_e effective angle of dead rise (angle between a straight line drawn from keel to the chines and the horizontal), radians unless otherwise stated

β_{basic} basic angle of dead rise (angle between V-shaped portion of model and a horizontal line perpendicular to keel), radians unless otherwise stated

ρ mass density of water, slugs/cu ft

τ trim (angle between planing bottom and horizontal), radians unless otherwise stated

ν kinematic viscosity, sq ft/sec

Subscript:

1,2,3,. . . 9 used to indicate various terms in equations for lift coefficient

REVIEW OF EXISTING PLANING-LIFT THEORY

In reference 1 the pure-planing lift equations for rectangular flat plates presented in references 2 to 11 were reviewed and compared with experiment. In addition to lift theories for rectangular flat plates, the present review considers V-shaped surfaces having a constant angle of dead rise and V-shaped surfaces having horizontal chine flare.

Since publication of reference 1, Farshing (ref. 12) presented a cubic equation for the lift on rectangular flat plates derived from a consideration of deflected mass and based on an effective angle of attack. The equation has the form

$$C_L^3+[(2.292-1.571A)\tau-2.379-A]C_L^2+$$
$$[2A+4+(6.283A-4.584)\tau]C_L-6.283A\tau=0 \quad (1)$$

However, the lift coefficient obtained from equation (1) was multiplied by an empirical factor to get better agreement with experimental data; thus,

$$C_{L,S}=C_L\xi \quad (2)$$

where

$$\xi=1.359-\tanh\left(\frac{1+A}{8A}\right) \qquad (2^\circ \leqq \tau \leqq 18^\circ) \quad (3)$$

$$\xi=1.359-\tanh\left(\frac{1+A}{8A}\right)+\left(\frac{\tau-18^\circ}{90.53}\right)\tanh\frac{1}{A^2} \qquad (18^\circ \leqq \tau \leqq 30^\circ) \quad (4)$$

and τ is measured in degrees.

P. R. Crewe of Sanders-Roe Ltd. (British) in correspondence with the Langley Laboratory proposed an equation for rectangular flat plates and a V-shaped surface having a basic angle of dead rise of 20° and horizontal chine flare that had a linear term with a form analogous to airfoil lifting-surface theory. This equation, based on the data of Kapryan and Weinstein (ref. 13), is

$$C_{L,S}=\sin\tau\cos\tau\left[\frac{8}{\pi}\frac{1}{1+\sqrt{1+\left(\frac{2}{A}\right)^2}}\left(1-\frac{\beta_{basic}}{\pi}\right)+2\sin\tau-B\sin^2\tau\right] \quad (5)$$

where

$B=2.67$ $(A<2.0)$

$B=3.0$ $(A>2.0)$

and β_{basic} is the basic angle of dead rise in radians for a model having horizontal chine flare.

In reference 14, Korvin-Kroukovsky, Savitsky, and Lehman proposed an equation for rectangular flat plates and V-shaped surfaces having a constant angle of dead rise that was derived primarily on the basis of the data of Sottorf (ref. 15) and Sambraus (ref. 16). This formula can be written as

$$C_{L,S}=0.012(57.3\tau)^{1.1}A^{0.5}-0.0065(57.3\beta)A\left[\frac{0.012(57.3\tau)^{1.1}}{A^{0.5}}\right]^{0.6} \quad (6)$$

Locke (ref. 17) proposed that the lift characteristics of rectangular flat plates and V-shaped surfaces having a constant angle of dead rise can be presented by a power function of the form

$$C_{L,S}=0.5\left(1-\frac{2\beta}{\pi}\right)K\tau^{\eta} \tag{7}$$

where K and η depend only on aspect ratio and are obtained from curves given in reference 17.

Schnitzer (ref. 18) presented an equation for rectangular flat plates and V-shaped surfaces which was derived from a consideration of two-dimensional deflected mass and was modified for three-dimensional flow by Pabst's empirical aspect-ratio correction factor (ref. 19) and Bobyleff's flow coefficients presented in reference 20. The equation can be written in the form:

$$C_{L,S}=A\phi\cos^2\tau\sin\tau\left\{\frac{\pi}{4}\left[\left(\frac{\pi}{2\beta}-1\right)\tan\beta\right]^2+B\left(\frac{l_k}{b}\tan\tau-\frac{\tan\beta}{2}\right)\right\} \tag{8}$$

The term ϕ, which is dependent on aspect ratio, and the term B, which is dependent on angle of dead rise, are given in references 19 and 20, respectively. For the case of a flat-plate planing surface, equation (8) reduces to

$$C_{L,S}=\phi\left(\frac{\pi^3 A}{16}\sin\tau\cos^2\tau+0.88\sin^2\tau\cos\tau\right) \tag{9}$$

In reference 21, Brown presented empirical equations based on deflected-mass considerations for rectangular flat plates and V-shaped surfaces having a constant angle of dead rise. The equations for a flat plate can be written in the form:

$$C_{L,S}=\frac{2\pi}{\cot\frac{\tau}{2}+\pi+\left(2\cot\frac{\tau}{2}-\pi\right)\frac{l_m}{b}} \qquad (l_m\leqq b) \tag{10}$$

and

$$C_{L,S}=(1.67\sin\tau+0.09)\sin\tau\cos\tau\left(1-\frac{b}{l_m}\right)+\frac{2\pi}{3\cot\frac{\tau}{2}}\frac{b}{l_m} \qquad (l_m\geqq b) \tag{11}$$

For a surface having a constant angle of dead rise,

$$C_{L,S}=3.6\frac{l_k}{b}\cot^2\beta\sin^3\tau(1-\sin\tau)\cos\tau \qquad (l_k\leqq l_{k,cr}) \tag{12}$$

and

$$C_{L,S}=\left[1.67\left(1-\frac{2\beta}{\pi}\right)\sin\tau+0.09\right]\sin\tau\cos\tau\left(1-\frac{l_{k,cr}}{l_k}\right)+0.9\frac{b}{l_k}\sin\tau(1-\sin\tau)\cos^3\tau \qquad (l_k\geqq l_{k,cr}) \tag{13}$$

where

$$l_{k,cr}=\frac{b}{2}\cot\tau\tan\beta \tag{14}$$

which is defined as the critical keel wetted length. For surfaces having a constant angle of dead rise and a transverse step, the critical keel wetted length is defined as the keel wetted length at which the stillwater line passes through the rearmost point of the chine. For the flat plate the value of the critical keel wetted length was assumed, after analysis of experimental data, to be equal to the beam.

PROPOSED THEORY

LIFT

In reference 1 an equation for the lift on a rectangular flat plate was developed from a consideration of linear and nonlinear components of lift (an approach generally used in low-aspect-ratio and slender-body airfoil theory). In the present report this equation is revised and extended to include V-bottom surfaces. The equation is divided into three parts: (1) a reasonably accurate approximation to the linear components of lift is made; (2) a method for calculating the crossflow effects is presented; and (3) an estimation of the aerodynamic leading-edge suction is made.

Linear term.—The linear term is determined in reference 1 from a consideration of the lifting-line theory and is given by

$$C_{L,1}=\frac{0.5\pi A\tau}{1+A} \tag{15}$$

This relation gives the linear component of lift on a pure-planing flat plate.

In references 3 and 18, a dead-rise function was determined from a consideration of an iterative solution made by Wagner (ref. 2) for the impact force on a V-bottom surface immersing with a constant vertical velocity. The dead-rise function can be written

$$K(\beta)=\left(1-\frac{2\beta}{\pi}\right)^2\left(\frac{\tan\beta}{\beta}\right)^2$$

This dead-rise function (developed for application to equations derived from virtual mass concepts) does not correlate well with experiment when applied to equation (15) for angles of dead rise above approximately 25°. Therefore, another dead-rise function $1-\sin\beta_e$ which correlates well with experiment up to angles of dead rise of 50° is used; thus,

$$C_{L,2}=\frac{0.5\pi A\tau}{1+A}(1-\sin\beta_e) \tag{16}$$

This expression is for the linear component of lift on rectangular flat and V-bottom planing surfaces. A comparison of the dead-rise function $1-\sin\beta_e$ with the dead-rise function based on Wagner's solution is given in figure 1.

Crossflow effects.—For a simple theoretical consideration of the crossflow effects, the velocity component perpendicular to the surface of a flat plate is assumed to be of the magnitude $V\sin\tau$. The flow is projected into components

526597—60——25

perpendicular to and parallel to the planing surface, and the drag force associated with the flow perpendicular to the planing surface is calculated. The normal force on a flat plate, therefore, is

$$N=C_{D,c}\frac{\rho}{2}S(V\sin\tau)^2$$

Then

$$C_{L,3}=C_{D,c}\sin^2\tau\cos\tau \tag{17}$$

is a lift coefficient due to crossflow effects, and is proportional to $\sin^2\tau$. This relation is the concept presented for airfoils by Betz in reference 22. The crossflow drag coefficient $C_{D,c}$ used in this elementary derivation of the crossflow term was assumed in reference 1 to be one-half the value $C_{D,c}=2$ generally used for aerodynamic surfaces. The value of $C_{D,c}$ is known to vary with the shape of the cross section and to be sensitive to local shape at the edges. Since the theoretical determination of these effects is very difficult and the simple cases which have been solved have not correlated with experiment, the analysis of suitable experiments will generally provide the easiest and most accurate method of determining $C_{D,c}$.

For the case of the V-bottom the theoretical effect of dead rise is given by Bobyleff in reference 20 for a bent lamina, the section of which consists of two equal straight lines forming an angle. Bobyleff's flow coefficient, which can be approximated by $\cos\beta_e$ (see fig. 2), represents the ratio of the resultant pressure on a V-bottom to that experienced by a flat plate of the same beam in normal flow; thus,

$$C_{L,4}=(C_{D,c})_{\beta_e=0}\sin^2\tau\cos\tau\cos\beta_e \tag{18}$$

which is the crossflow component of lift.

Suction component of lift.—An airfoil has a suction component of lift due to the large negative pressures produced by the flow around the leading edge of the airfoil; however, for a planing surface where there is no flow around the leading edge, this suction does not appear. In the strictest sense the suction component of lift should be based only on the linear term (see ref. 1); however, comparison of experiment with theory indicates that better agreement is obtained if the suction component of lift is based on $C_{L,2}+C_{L,4}$. Therefore, the lift is less than that predicted by equations (16) and (18) by an amount

$$C_{L,5}=(C_{L,2}+C_{L,4})\sin^2\tau \tag{19}$$

Total lift.—The total lift on pure-planing surfaces can be obtained from the sum of the linear component of lift (eq. (16)) and the crossflow effects (eq. (18)) minus the suction component of lift (eq. (19)); thus, by combining terms

$$\left.\begin{aligned} C_{L,S}&=\left[\frac{0.5\pi A\tau}{1+A}\cos^2\tau\,(1-\sin\beta_e)\right]+\\ &\quad[(C_{D,c})_{\beta_e=0}\cos^3\tau\sin^2\tau\cos\beta_e]\\ C_{L,S}&=C_{L,6}+C_{L,7}\end{aligned}\right\} \tag{20}$$

where

$$C_{L,6}=\frac{0.5\pi A\tau}{1+A}\cos^2\tau\,(1-\sin\beta_e) \tag{21}$$

and

$$C_{L,7}=(C_{D,c})_{\beta_e=0}\cos^3\tau\sin^2\tau\cos\beta_e \tag{22}$$

For equation (20) to predict adequately the lift on triangular surfaces planing with base forward, it has been necessary to define the aspect ratio as the ratio of maximum beam to overall length; that is, $A_t=b/l$.

APPLICATION OF LIFT THEORY

In order to use equation (20) to predict the lift of planing surfaces, only the determination of the proper value of $C_{D,c}$ is required. Values of $C_{D,c}$ for various chine configurations for which experimental data are available are presented in figure 3. For a given model $C_{D,c}$ did not vary with trim or length-beam ratio. Also it can be seen that, as long as the angle of dead rise was constant for the entire beam, $C_{D,c}$ did not vary with the angle of dead rise.

Rectangular flat and V-bottom surfaces having a constant angle of dead rise.—The crossflow drag coefficient for the sharp-chine models was determined from tests (from ref. 23 and data presented in the present report) to be 4/3. This value is two-thirds the value given for a two-dimensional flat-plate airfoil; thus, from equation (20)

$$C_{L,S}=\frac{0.5\pi A\tau}{1+A}\cos^2\tau(1-\sin\beta_e)+\frac{4}{3}\sin^2\tau\cos^3\tau\cos\beta_e \tag{23}$$

The relative magnitudes of the total lift (eq. (23)), the total lift before removal of lift due to leading-edge suction $\left(\text{eq. (16) plus eq. (18) with } C_{D,c}=\frac{4}{3}\right)$, and the crossflow term $\left(\text{eq. (22) with } C_{D,c}=\frac{4}{3}\right)$ is shown in figure 4 for surfaces having angles of dead rise of 0°, 20°, and 40°.

Horizontal chine flare.—The total lift on a pure-planing V-shaped prismatic surface with horizontal chine flare similar to the models shown in figure 5 can be determined from equation (20). The crossflow drag coefficients $C_{D,c}$ determined from data presented in references 13, 24, and 25 are given in figure 3.

Vertical chine strips.—The total lift on a pure-planing V-shaped prismatic surface with vertical chine strips similar to the models shown in figure 6 can be determined from equation (20). The crossflow drag coefficients determined from the data presented in references 25 and 26 are given in figure 3.

Triangular flat plate.—The total lift on a pure-planing triangular flat plate planing with base forward can be estimated from equation (23) if the aspect ratio is defined as the ratio of the maximum beam to the overall length or $A_t=b/l$; thus,

$$C_{L,S}=\frac{0.5\pi A_t\tau}{1+A_t}\cos^2\tau+\frac{4}{3}\cos^3\tau\sin^2\tau \tag{24}$$

CENTER OF PRESSURE

The center of pressure on a planing surface may be determined from the lift coefficients given by equations (21) and (22) and by estimating the location of the center of pressure of these two components of the total lift coefficient for a given planing-surface plan form.

Rectangular plan form.—The center of pressure of the component of lift given by equation (21) is assumed to be located at seven-eighths of the mean wetted length from the trailing edge of the planing surface. This location is between the three-quarter-chord position generally assumed in lifting-line theory and the position obtained from the prediction of no lift behind the section maximum width for low-aspect-ratio airfoils (ref. 27).

The center of pressure for the lift due to crossflow effects is generally assumed to be located at the center of the area in airfoil theory. Therefore, the center of pressure for the component of lift given by equation (22) is assumed to be located at the center of the mean wetted length; thus,

$$\left(\frac{l_{cp}}{l_m}\right)_{calc}=\frac{\frac{7}{8}C_{L,6}+\frac{1}{2}C_{L,7}}{C_{L,S}} \tag{25}$$

where $C_{L,6}$ is given by equation (21), $C_{L,7}$ is given by equation (22), and $C_{L,S}$ is given by equation (20).

Triangular plan form.—The center of pressure of the component of lift given by the first term on the right-hand side of equation (24) is assumed to be located at the mean of the heavy spray line which is approximately the section of maximum wetted width.

The center of pressure for the component of lift given by the second term on the right-hand side of equation (24) (that is, the crossflow term) is assumed to be at approximately the center of the wetted area; thus,

$$\left(\frac{l_{cp}}{l_m}\right)_{calc}=\frac{C_{L,8}+\frac{2}{3}C_{L,9}}{C_{L,S}} \tag{26}$$

and is the center-of-pressure location for triangular flat plates planing with base forward. The value of $C_{L,S}$ is determined from equation (24) where $C_{L,8}$ and $C_{L,9}$ are given by the first and second terms on the right-hand side of equation (24), respectively.

COMPARISON OF PROPOSED AND PREVIOUS PLANING FORMULAS

A comparison of the values of lift coefficient (plotted against trim for constant length-beam ratio) calculated from the proposed theory (eq. (20)) and from previous summarized planing formulas is given in figures 7 to 10 and an index to the comparison is given in the following table:

Configuration	Equation (20)* compared with planing formulas presented in—		Lift coefficient values presented in figure—
	Reference	Equation	
Rectangular flat plate	4, 5, 6, and 7	----------	7(a)
	8, 9, and 10	----------	7(b)
	----------	(7), (9), (10), and (11)	7(c)
	----------	(2), (5), and (6)	7(d)
	1	----------	7(e)
	11	----------	**
V-shaped surface having a constant angle of dead rise of 20°	----------	(6) and (7)	8(a)
	----------	(8), (12), and (13)	8(b)
V-shaped surface having a constant angle of dead rise of 40°	----------	(6) and (7)	9(a)
	----------	(8), (12), and (13)	9(b)
V-shaped surface having an angle of dead rise of 20° and horizontal chine flare (β_s=16°)	----------	(5)***	10

*Value of $C_{D,c}$ of $\frac{4}{3}$ (see eq. (23)) used unless otherwise noted.

**Lift coefficients were not plotted since the results depended on the airfoil data used.

***Value of $C_{D,c}$ of 1.59 used in equation (20).

In figure 11 the values of lift coefficient (plotted against mean-wetted-length—beam ratio for constant trim) calculated from the proposed theory (eq. (23)) and planing formulas as presented in references 14, 17, 18, and 21 are compared with the data of the present report (see tables I(a), II, and III) and references 23 and 28 for models having angles of dead rise of 0° (fig. 11(a)), 20° (fig. 11(b)), and 40° (fig. 11(c)). Only the theories that apply to both flat-plate and V-shaped surfaces have been compared in figure 11.

It can be seen from figures 11 (a) to 11(c) that none of the planing formulas presented in references 14, 17, 18, and 21 are adequate for estimating the lift coefficients for either flat-plate or V-bottom planing surfaces, whereas the lift coefficients calculated from the equation proposed in the present report (eq. (23)) agree very well with experiment. The equation presented in reference 12 (eq. (2)), however, gives a good approximation of the lift coefficient for a flat plate. (See fig. 7(d).)

EXPERIMENTAL INVESTIGATION

DESCRIPTION OF MODELS

The models used for this investigation had a beam of 4 inches and a length of 36 inches. The models shown in figure 12 for a flat plate and surfaces having angles of dead rise of 20° and 40° were constructed of brass and are the same models investigated in references 23 and 28. Additional flat-plate models that had sharp chines, 1/64-inch-radius chines, and 1/16-inch-radius chines were constructed of plastic. (See fig. 13.) The model with the 1/64-inch-radius chines was made by rounding the chines on the sharp-chine model after the tests with the sharp-chine model had been completed. The plastic models were backed with a 1/2-inch reinforcing steel plate.

APPARATUS AND PROCEDURES

The experimental investigation was made with the main towing carriage in Langley tank no. 2 and existing strain-gage balances which independently measured the lift, drag, and moment. The lift and drag were measured with the balances capable of measuring: (1) 600 pounds of lift and 250 pounds of drag, and (2) 1,000 pounds of lift and 600 pounds of drag. The moment was measured about an arbitrary point above the model. The tests were made with the wind and spray shield installed, as shown in figure 14, unless otherwise indicated.

The wetted areas were determined from underwater photographs made with a 70-millimeter camera mounted in a waterproof box located at the bottom of the tank. The camera and high-speed flash lamps were set off by the action of the carriage interrupting a photoelectric beam. The wetted length was obtained from markings on the bottom of the models. In order to assure a very smooth bottom, the markings on the brass models were erased except in the region of the heavy spray line. (See fig. 15.) The plastic models had markings each 1/2 inch for the full length of the models.

The force measurements were made at constant speeds for fixed angles of trim. The change in trim due to structural deflection caused by the lift and drag forces on the model was obtained during the calibration of the balances and the trim of the model was adjusted accordingly before each run. Slight adjustments to lift and resistance to correct the data

to the desired trim were made after completion of tests for the cases where the forces or center-of-pressure location were different from the values used to estimate the trim due to structural deflection. The change in trim due to structural deflection did not exceed 0.2° for most conditions although in a few cases changes up to 0.6° occurred.

The aerodynamic forces on the model and towing gear were found to be negligible when the wind screen was used. The aerodynamic tares were subtracted from the data when the wind screen was not used.

The accuracy of the quantities measured are believed to be within the following limits:

Lift, lb	±5.0
Resistance, lb	±3.0
Trimming moment, ft-lb	±3.0
Wetted length, ft	±0.01
Trim, deg	±0.15
Speed, ft/sec	±0.20

The forces were converted to coefficient form by using a measured value of density of 1.942 slugs/cu ft. The kinematic viscosity measured during the tests varied from 1.53×10^{-5} sq ft/sec to 1.80×10^{-5} sq ft/sec.

RESULTS AND DISCUSSION

GENERAL

The lift coefficient, resistance coefficient, ratio of wetted length to beam, ratio of center-of-pressure location to mean wetted length, speed coefficient, and kinematic viscosity are presented at given trims in tables I to III for all models. The lift and drag coefficients are expressed both in terms of the square of the beam and in terms of principal wetted area.

Sharp chines.—The lift coefficients and center-of-pressure location for the sharp-chine models are considered in the section "Comparison of Theory and Experiment for Lift."

The resistance data for the sharp-chine brass models having constant angles of dead rise of 0°, 20°, and 40° are presented in figure 16 as plots of the variation of drag coefficient $C_{D,S}$ and induced drag coefficient $C_{D,i}$ (which is equal to $C_{L,S}\tan\tau$) with mean-wetted-length—beam ratios for given trims. The difference between the solid and dashed lines represents the friction drag. (Since the data were obtained for speeds above the critical speed of wave propagation for the 6-foot-deep tank, there is no wave drag due to transverse waves included; however, there may be some drag due to spray or other causes included in this difference.) At high trims and low length-beam ratios the induced drag exceeds the total drag and indicates an apparent negative friction force. (This result was previously reported in ref. 23.) The volume of forward spray is large at high trims and appears to have a high forward velocity with respect to the model. The relative velocity of the model in the region of forward spray therefore is effectively reversed (see fig. 17) so that the friction drag due to this spray acts in a direction opposite to that of the drag in the principal wetted area and thereby reduces the total drag. Therefore, at low length-beam ratios where the friction drag is small, this negative friction drag due to forward spray may cause a negative friction force at high trims.

The variation of $\frac{l_k-l_c}{b}$ with trim for the models having sharp chines and constant angles of dead rise of 0°, 20°, and 40° is given in figure 18. At a trim of 12°, the value of $\frac{l_k-l_c}{b}$ is approximately constant for all length-beam ratios for the models having constant angles of dead rise of 0°, 20°, or 40°. At high trims, however, the values of $\frac{l_k-l_c}{b}$ for the flat-plate model increase with increase in length-beam ratio, are approximately constant for a given trim for a model having a constant angle of dead rise of 20°, and decrease with an increase in length-beam ratio for a model having a constant angle of dead rise of 40°. The value of $\frac{l_k-l_c}{b}$ for the flat-plate model decreases with increase in trim at low length-beam ratios and increases with increase in trim at high length-beam ratios; however, the value of $\frac{l_k-l_c}{b}$ decreases with increase in trim for all length-beam ratios for the models having constant angles of dead rise of 20° and 40°.

Wind screen and spray shield.—The lift coefficient for the flat-plate model with wind screen and spray shield removed (aerodynamic tares subtracted) was approximately the same as the lift coefficient obtained when the wind screen and spray shield were used. (See fig. 19.) At a trim of 12° the drag coefficient for the flat-plate model with the wind screen removed was approximately the same as the drag coefficient obtained with the wind screen installed (see fig. 20); however, for a trim of 18° the drag coefficient of the flat plate with the wind screen removed was less than that obtained when the wind screen was used even before the aerodynamic tares were subtracted. The value of the difference is in the wrong direction to be explained by the aerodynamic tares. (The aerodynamic tares subtracted were less than the difference in fig. 20.) The variation of the center-of-pressure location with mean length-beam ratio on the flat-plate model was approximately the same for data taken with and without the wind screen and spray shield installed. (See fig. 21.)

Speed.—The effect of speed at high trims (24°) is shown in figures 22 to 24. The variation of lift coefficient, drag coefficient, and center-of-pressure location is approximately the same for speeds of 30 and 60 feet per second for 4-inch-beam prismatic models having constant angles of dead rise of 0°, 20°, and 40°; therefore, there was apparently no speed effect for this range of speeds.

Rounded chines.—The effect of $\frac{1}{64}$-inch-radius and $\frac{1}{16}$-inch-radius chines on the lift coefficient, drag coefficient, center-of-pressure location, skin-friction coefficient, and lift-drag ratio of a 4-inch-beam rectangular flat plate is shown in figures 25 to 29. Rounding the sharp chines of the flat-plate model to radii of $\frac{1}{64}$ inch and $\frac{1}{16}$ inch resulted in a decrease in lift and drag coefficients; however, the center-of-pressure location, skin-friction coefficients, and lift-drag ratios remained approximately the same. A decrease in lift of approximately 5 and 9 percent resulted from rounding the sharp chines to a radii of $\frac{1}{64}$ inch and $\frac{1}{16}$ inch, respectively. (See fig. 25.) A decrease in lift for a small rounding of the chines was also observed by Perry (ref. 29).

The variation of skin-friction coefficient with Reynolds

number for a trim of 8° is presented in figure 28 for a flat-plate model having sharp chines and 1/16-inch-radius chines. The agreement between the data and the Schoenherr turbulent-flow line indicates that, at low trims and high Reynolds numbers, the drag can be calculated with reasonable accuracy from

$$C_{D,S}=C_f+C_{L,S}\tan\tau \tag{27}$$

where C_f is determined from the Schoenherr turbulent flow line. (See ref. 30.) The lift-drag ratios at high trims are influenced little by the chine condition; however, at low trims (8°) the lift-drag ratios for the sharp-chine models are slightly higher than those for models having rounded chines. (See fig. 29.)

Pure planing.—The experimental data were considered as pure planing if the lift coefficient due to buoyancy based on the total wedge-shaped volumetric displacement of the planing surface $C_{L,Vol}$ did not exceed a given value. The lift coefficient due to buoyancy was calculated from the wedge-shaped volumetric displacement of the planing surface below the level water surface given by

$$C_{L,Vol}=\frac{l_m}{b}\frac{1}{2C_V{}^2}\sin 2\tau \tag{28}$$

for rectangular flat plates and

$$C_{L,Vol}=\frac{1}{(l_k+l_c)\,C_V{}^2}\left[\frac{l_c{}^2}{b}\sin 2\tau+\frac{1}{3}(2l_c+l_k)\tan\beta\right] \tag{29}$$

for rectangular surfaces having dead rise and

$$C_{L,Vol}=\frac{l}{b}\frac{1}{3C_V{}^2}\sin 2\tau \tag{30}$$

for triangular flat plates with straight leading edge and pointed trailing edge.

The allowable lift coefficient due to buoyancy $C_{L,Vol}$, as determined from equations (28) to (30), was arbitrarily selected as 0.01 at a trim of 16°. The maximum allowable lift coefficient due to buoyancy $C_{L,Vol}$ for other trims was determined by drawing a straight line from zero trim (and zero lift coefficient due to buoyancy $C_{L,Vol}$) through the value 0.01 at a trim of 16° on a curve of the variation of lift coefficient with trim. For the flat-plate data the maximum allowable lift coefficient due to buoyancy $C_{L,Vol}$ selected by this method at a trim of 2° varied from 16 percent of the predicted lift coefficient at a length-beam ratio of 8 to 3.3 percent of predicted lift coefficient (eq. (23)) at a length-beam ratio of ½. These values decreased with increasing trim so that at 30° they would vary from 6.6 percent at a length-beam ratio of 8 to 3.0 percent at a length-beam ratio of ½. The permissible lift coefficient for surfaces having dead rise is, in general, a slightly greater percentage of the predicted lift coefficient than the values given for the rectangular flat plate.

Buoyancy.—The experimental lift coefficients given in reference 31 less the lift coefficients calculated from equation (20) with $C_{D,c}=1.15$ plotted against the lift coefficient due to buoyancy $C_{L,Vol}$ calculated from equation (28) are plotted in figure 30. Since equation (20) with $C_{D,c}=1.15$ is approximately the pure-planing lift for the model investigated in reference 31 (see fig. 32 (c)), the subtraction of this value from the experimental lift coefficients should indicate the amount of lift due to buoyancy present in the data. Only values of the difference between the experimental lift coefficient and the calculated lift coefficient greater than 0.01 are considered since, for small differences between experimental and calculated values, this method is not considered to be sufficiently accurate to determine the lift coefficient due to buoyancy present in the experimental data; however, this method should give reasonably accurate indications of the lift coefficient due to buoyancy present in the experimental data for the cases where the lift coefficient due to buoyancy is large. Figure 30 shows that the magnitude of the lift coefficient due to buoyancy for different speeds is approximately one-half the lift due to buoyancy based on the total wedge-shaped volumetric displacement computed by equation (28); therefore, a rough empirical approximation of the increase in lift coefficient due to buoyancy can be calculated with reasonable accuracy from

$$C_{L,B}\approx\frac{1}{2}C_{L,Vol}\qquad(\tau\geqq 8°;\ C_V\geqq 3) \tag{31}$$

where $C_{L,Vol}$ is given in equations (28) to (30). For low trims (4°) a lift coefficient due to buoyancy greater than that given by equation (31) is required to account for the additional lift coefficient due to buoyancy as indicated by the flagged symbols in figure 30.

COMPARISON OF THEORY AND EXPERIMENT

Lift.—Only the experimental data indicated as pure planing by the method discussed in the preceding section are considered for the comparison with theory. Also, the data considered are only for the chine-immersed condition. The theory is applicable to the non-chine-immersed condition; however, for surfaces having other than a constant angle of dead rise such as those having horizontal chine flare or vertical chine strips, the shape of the cross section varies, and, therefore, the crossflow drag coefficient would not be the same value as that determined for the chine-immersed condition. The values were calculated from the proposed theory as if there were no non-chine-immersed conditions. For the non-chine-immersed condition, the lift coefficient for a surface having a constant angle of dead rise is approximately the value determined at the instant of chine immersion and is a constant for a given trim and angle of dead rise. (The length-beam ratio is approximately a constant value for all non-chine-immersed conditions for a given trim and angle of dead rise.)

In order to simplify the comparison, the data are summarized in the following table:

Configuration	Description of model used	Data to be compared— Equation of present paper—	Data to be compared— Experimental data of reference—	Data presented in figure—	Remarks
Rectangular flat plate	4-inch-beam brass model	(23)	----------	31 (a)	Agreement good except at trims above approximately 30° at large length-beam ratios
	Sharp chine plastic model		----------	31 (b)	
	4-inch-beam brass model		23	31 (c)	Agreement good
	Various models		12, 32, 31, 33, 34, 16, 15, and 25	31 (d) to 31 (k)	Agreement good; some differences with wooden models
	4-inch-beam plastic model with 1/16-inch-radius chines and 1/64-inch-radius chines	(20)	Present paper	32 (a) and 32 (b)	$C_{D,c}$ reduced to 1.15 and 1.20
	Wooden model (same model used in both ref. 31 and 35)		31, 32, and 35	32 (c) to 32 (e)	Models used in reference data had either slightly rounded or roughened chines and reduced values of $C_{D,c}$ resulted. In case of reference 35 the chines had greater chine radius or roughness as a result of wear in use; further reduction in $C_{D,c}$ resulted.
Basic V-surface	With angle of dead rise of 20°	(23)	28 and 25	33	Agreement good except for trims above approximately 30°
	With angle of dead rise of 40°		28 and 25	34	
	With angle of dead rise of 50°		36	35	Agreement good for length-beam ratios above 3.0; below this value the experimental data failed to show the usual increase in C_L as l_m/b decreased. Similar effect slightly evident in fig. 34 (b) for $\beta=40°$.
V-surface with horizontal chine flare	With an effective angle of dead rise of 16°	(20) ($C_{D,c}$ value from fig. 3)	13 and 25	36	Agreement good
	With an effective angle of dead rise of 32°47′		24 and 25	37	Agreement good
V-surface with vertical chine strip	With an effective angle of dead rise of 15°33′	(20) ($C_{D,c}$ value from fig. 3)	26	38	Agreement good
	With an effective angle of dead rise of 31°59′		26	39	Agreement good
Triangular flat plate (base forward)	Wooden surfaces (see fig. 40)	(24)	31 and unpublished tank no. 2 data	41	Agreement good up to trims of 16°. Values lower than those at trim of 20°; chines may be slightly rounded since they are made of wood.

Some of the experimental data that were obtained with wooden models (for example, see ref. 31) were lower than the values predicted by the proposed theory; this difference is thought to be due to the influence of the local shape at the edges (slightly rounded or roughened chines).

The effects of Reynolds number, scale, and nonuniform chine radii on $C_{D,c}$ have not been determined because of the limited data available.

The lift on various pure-planing surfaces with rectangular or triangular plan forms similar to those considered can be estimated by changing the value of the crossflow drag coefficient $C_{D,c}$ for a given configuration. Values of the crossflow drag coefficient should be determined from tests; however, reasonably accurate approximations that are satisfactory for engineering calculations can probably be made (see fig. 3) that will approximate the pure-planing lift for surfaces similar to those considered herein.

For planing surfaces that vary considerably from those considered herein, only data for a given angle of trim and aspect ratio (for a given effective angle of dead rise) are required to determine the value of $C_{D,c}$ from equation (20). (The experimental values of lift coefficient, trim, aspect ratio, and effective angle of dead rise are substituted into equation (20), which is then solved for the value of $C_{D,c}$.) Since the value of $C_{D,c}$ is a constant for a given planing-surface cross section, the lift coefficient for wide ranges of trim and aspect ratio can then be estimated. If values of $C_{D,c}$ are obtained for two or more effective angles of dead rise for a given type of planing surface, the value of $C_{D,c}$ for similar surfaces having a different effective angle of dead rise can be estimated by interpolation. Therefore, in order to calculate the lift coefficient from equation (20) for wide ranges of trim, length-beam ratio, and effective angle of dead rise for a given family of planing surfaces, only a very few test points are required.

Center-of-pressure location.—A comparison of theory and experiment for the center of pressure is given in the following table:

Configuration	Description of model used	Data to be compared— Equation of present paper [a]	Data to be compared— Experimental data of reference—	Data presented in figure—	Remarks
Rectangular flat plate	4-inch-beam brass model	(25)	23, 31, and 25	42	Good agreement
Basic V-surface	With angle of dead rise of 20°	(25)	25 and 28	43	Good agreement
	With angle of dead rise of 40°	(25)	25 and 28	44	Good agreement
	With angle of dead rise of 50°	(25)	36	45	Good agreement
V-surface with horizontal chine flare	With an effective angle of dead rise of 16°	(25)	13 and 25	46	Good agreement
	With an effective angle of dead rise of 32°47′	(25)	24 and 25	47	Good agreement
V-surface with vertical chine strips	With an effective angle of dead rise of 15°33′	(25)	26	48	Good agreement
	With an effective angle of dead rise of 31°59′	(25)	26	49	Good agreement
Triangular plan form	Wooden surfaces (see fig. 40)	(26)	31 and unpublished tank no. 2 data	50	Good agreement

[a] The values of $C_{D,c}$ for equation (25) were determined from figure 3.

CONCLUDING REMARKS

The principal planing characteristics for models have been obtained in extended ranges of trim and length-beam ratio for a rectangular flat plate and two V-bottom surfaces; therefore, force approximations for water-based aircraft can be made in these extended ranges with more confidence. The data obtained for rectangular-flat-plate surfaces having very slightly rounded chines indicated that slight differences in construction at the point of flow separation can result in decreased lift and drag coefficients obtained for a given flat-plate configuration; however, the center-of-pressure location, skin-friction coefficients, and lift-drag ratios remained approximately the same for the trims tested (8° to 18°). These data showed that slight differences in construction at the point of flow separation were probably the reason for the differences in experimental data obtained for a given configuration by various experimenters.

The proposed theory appears to predict with engineering accuracy the lift and center-of-pressure location of rectangular flat plates, triangular flat plates planing with base forward, and V-shaped surfaces having a constant angle of dead rise, horizontal chine flare, or vertical chine strips. A reasonably accurate approximation can probably be made for the crossflow drag coefficient of a given model that will result in satisfactory engineering calculations of lift and center of pressure for pure-planing surfaces similar to those considered in the present report. Also, the proposed theory (which can be applied to both the chine-immersed and the non-chine-immersed condition) together with the method for approximating the lift coefficient due to buoyancy gives a reasonably accurate method for estimating the lift characteristics of planing surfaces for a wide range of conditions.

LANGLEY AERONAUTICAL LABORATORY,
NATIONAL ADVISORY COMMITTEE FOR AERONAUTICS,
LANGLEY FIELD, VA., *November 23, 1956.*

REFERENCES

1. Shuford, Charles L., Jr.: A Review of Planing Theory and Experiment With a Theoretical Study of Pure-Planing Lift of Rectangular Flat Plates. NACA TN 3233, 1954.
2. Wagner, Herbert: Phenomena Associated With Impacts and Sliding on Liquid Surfaces. S–302, British A.R.C., July 14, 1936.
3. Mayo, Wilbur L.: Analysis and Modification of Theory for Impact of Seaplanes on Water. NACA Rep. 810, 1945. (Supersedes NACA TN 1008.)
4. Sokolov, N. A.: Hydrodynamic Properties of Planing Surfaces and Flying Boats. NACA TM 1246, 1950.
5. Sedov, L.: Scale Effect and Optimum Relations for Sea Surface Planing. NACA TM 1097, 1947.
6. Perelmuter, A.: On the Determination of the Take-Off Characteristics of a Seaplane. NACA TM 863, 1938.
7. Sottorf, W.: Analysis of Experimental Investigations of the Planing Process on the Surface of Water. NACA TM 1061, 1944.
8. Perring, W. G. A., and Johnston, L.: Hydrodynamic Forces and Moments on a Simple Planing Surface and on a Flying Boat Hull. R. & M. No. 1646, British A.R.C., 1935.
9. Korvin-Kroukovsky, B. V.: Lift of Planing Surfaces. Jour. Aero. Sci. (Readers' Forum), vol. 17, no. 9, Sept. 1950, pp. 597–599.
10. Siler, William: Lift and Moment of Flat Rectangular Low Aspect Ratio Lifting Surfaces. Tech. Memo. No. 96, Exp. Towing Tank, Stevens Inst. Tech., 1949.
11. Perry, Byrne: The Effect of Aspect Ratio on the Lift of Flat Planing Surfaces. Rep. No. E–24.5 (Contract N6onr–24424, Project NR 234–001), Hydrod. Lab., C.I.T., Sept. 1952.
12. Farshing, Donald David, Jr.: The Lift Coefficient of Flat Planing Surfaces. M. S. Thesis, Stevens Inst. Tech., 1955.
13. Kapryan, Walter J., and Weinstein, Irving: The Planing Characteristics of a Surface Having a Basic Angle of Dead Rise of 20° and Horizontal Chine Flare. NACA TN 2804, 1952.
14. Korvin-Kroukovsky, B. V., Savitsky, Daniel, and Lehman, William F.: Wetted Area and Center of Pressure of Planing Surfaces. Preprint No. 244, S.M.F. Fund Paper, Inst. Aero. Sci. (Rep. No. 360, Project No. NRO62–012, Office Naval Res., Exp. Towing Tank, Stevens Inst. Tech., Aug. 1949.)
15. Sottorf, W.: Experiments With Planing Surfaces. NACA TM 661, 1932.
16. Sambraus, A.: Planing-Surface Tests at Large Froude Numbers—Airfoil Comparison. NACA TM 848, 1938.
17. Locke, F. W. S., Jr.: An Empirical Study of Low Aspect Ratio Lifting Surfaces With Particular Regard to Planing Craft. Jour. Aero. Sci., vol. 16, no. 3, Mar. 1949, pp. 184–188.
18. Schnitzer, Emanuel: Theory and Procedure for Determining Loads and Motions in Chine-Immersed Hydrodynamic Impacts of Prismatic Bodies. NACA Rep. 1152, 1953. (Supersedes NACA TN 2813.)
19. Pabst, Wilhelm: Landing Impact of Seaplanes. NACA TM 624, 1931.
20. Lamb, Horace: Hydrodynamics. Sixth ed., Cambridge Univ. Press, 1932.
21. Brown, P. Ward: An Empirical Analysis of the Planing Characteristics of Rectangular Flat-Plates and Wedges. Hydrod. Note No. 47, Short Bros. & Harland Ltd. (Belfast), Sept. 1954.
22. Betz, A.: Applied Airfoil Theory. Airfoils or Wings of Finite Span. Vol. IV of Aerodynamic Theory, div. J, Ch. III, sec. 7, W. F. Durand, ed., Julius Springer (Berlin), 1935 (reprinted by Durand Reprinting Committee, 1943), pp. 69–72.
23. Weinstein, Irving, and Kapryan, Walter J.: The High-Speed Planing Characteristics of a Rectangular Flat Plate Over a Wide Range of Trim and Wetted Length. NACA TN 2981, 1953.
24. Blanchard, Ulysse J.: The Planing Characteristics of a Surface Having a Basic Angle of Dead Rise of 40° and Horizontal Chine Flare. NACA TN 2842, 1952.
25. Kapryan, Walter J., and Boyd, George M., Jr.: Hydrodynamic Pressure Distributions Obtained During a Planing Investigation of Five Related Prismatic Surfaces. NACA TN 3477, 1955.
26. Kapryan, Walter J., and Boyd, George M., Jr.: The Effect of Vertical Chine Strips on the Planing Characteristics of V-Shaped Prismatic Surfaces Having Angles of Dead Rise of 20° and 40°. NACA TN 3052, 1953.
27. Jones, Robert T.: Properties of Low-Aspect-Ratio Pointed Wings at Speeds Below and Above the Speed of Sound. NACA Rep. 835, 1946. (Supersedes NACA TN 1032.)
28. Chambliss, Derrill B., and Boyd, George M., Jr.: The Planing Characteristics of Two V-Shaped Prismatic Surfaces Having Angles of Dead Rise of 20° and 40°. NACA TN 2876, 1953.
29. Perry, Byrne: Lift Measurements on Small-Scale Flat Planing Surfaces. Rep. No. E–24.10 (Contract N6onr–24424, Project NR 234–001), Hydrod. Lab., C.I.T., Apr. 1954.
30. Davidson, Kenneth S. M.: Resistance and Powering. Detailed Considerations—Skin Friction. Vol. II of Principles of Naval Architecture, ch. II, pt. 2, sec. 7, Henry E. Rossell and Lawrence B. Chapman, eds., Soc. Naval Arch. and Marine Eng., 1939, pp. 76–83.

31. Wadlin, Kenneth L., and McGehee, John R.: Planing Characteristics of Three Surfaces Representative of Hydro-Ski Forms. NACA RM L9C03, 1949.
32. McBride, Ellis E.: An Experimental Investigation of the Scale Relations for the Impinging Water Spray Generated by a Planing Surface. NACA TN 3615, 1956.
33. Shoemaker, James M.: Tank Tests of Flat and V-Bottom Planing Surfaces. NACA TN 509, 1934.
34. Locke, F. W. S., Jr.: Tests of a Flat Bottom Planing Surface To Determine the Inception of Planing. NAVAER DR. Rep. 1096, Bur. Aero., Dec. 1948.
35. Christopher, Kenneth W.: Effect of Shallow Water on the Hydrodynamic Characteristics of a Flat-Bottom Planing Surface. NACA TN 3642, 1956.
36. Springston, George B., Jr., and Sayre, Clifford L., Jr.: The Planing Characteristics of a V-Shaped Prismatic Surface With 50 Degrees Dead Rise. Rep. 920, David W. Taylor Model Basin, Navy Dept., Feb. 1955.

TABLE I

EXPERIMENTAL PLANING DATA OBTAINED FOR A RECTANGULAR FLAT PLATE

(a) Brass model having sharp chines

Trim, τ, deg	C_V	$\frac{l_c}{b}$	$\frac{l_m}{b}$	$\frac{l_k}{b}$	$\frac{l_{cp}}{l_m}$	ν, sq ft/sec	$C_{D,b}$	$C_{L,b}$	$C_{D,S}$	$C_{L,S}$
12	18.22	1.59	1.64	1.66	0.705	1.80×10^{-5}	0.061	0.285	0.037	0.174
	18.13	2.66	2.72	2.74	.744	1.80	.087	.375	.032	.138
	18.19	3.68	3.74	3.77	.714	1.78	.108	.453	.029	.121
	18.19	4.82	4.85	4.87	.687	1.78	.126	.524	.026	.108
	18.19	5.60	5.65	5.68	.694	1.78	.141	.582	.025	.103
	18.17	6.74	6.80	6.82	.652	1.67	.156	.646	.023	.095
	18.38	7.70	7.76	7.78	.663	1.76	.171	.698	.022	.090
15	18.13	1.76	1.82	1.84	.706	1.80	.104	.389	.057	.214
	18.16	2.91	2.97	3.00	.698	1.80	.146	.517	.049	.174
	18.19	3.82	3.89	3.92	.700	1.78	.175	.615	.045	.158
	18.19	4.98	5.06	5.10	.673	1.78	.213	.739	.042	.146
	18.22	5.79	5.84	5.86	.669	1.67	.234	.806	.040	.138
	18.10	7.00	7.05	7.07	.659	1.78	.261	.902	.037	.128
	18.32	7.74	7.80	7.84	.660	1.76	.281	.959	.036	.123
18	18.13	1.82	1.88	1.92	.701	1.80	.160	.485	.085	.258
	18.16	3.01	3.05	3.07	.681	1.80	.220	.656	.072	.215
	18.16	3.88	3.93	3.95	.678	1.78	.263	.786	.067	.200
	18.19	4.45	4.49	4.51	.665	1.78	.287	.853	.064	.190
	18.13	5.92	5.96	5.98	.655	1.78	.352	1.025	.059	.172
	18.19	6.88	6.92	6.94	.646	1.67	.388	1.135	.056	.164
	18.53	6.91	7.00	7.04	.639	1.56	.385	1.141	.055	.163
	18.53	7.93	7.99	8.02	.640	1.56	.431	1.270	.054	.159
	18.19	8.02	8.07	8.10	.641	1.67	.444	1.283	.055	.159
21	18.13	1.95	2.00	2.02	.676	1.80	.226	.582	.113	.291
	18.13	2.75	2.80	2.82	.695	1.80	.300	.764	.107	.273
	18.16	2.88	2.92	2.95	.685	1.63	.307	.780	.105	.267
	18.13	4.08	4.12	4.14	.660	1.78	.379	.964	.092	.234
	18.19	5.14	5.19	5.22	.645	1.78	.441	1.111	.085	.214
	18.04	5.98	6.04	6.07	.629	1.78	.495	1.244	.082	.206
	18.38	7.10	7.16	7.20	.632	1.56	.566	1.425	.079	.199
	18.22	7.13	7.18	7.22	.638	1.67	.582	1.429	.081	.199
	18.44	7.99	8.03	8.05	.620	1.76	.610	1.510	.076	.188
24	18.13	.79	.82	.84	.745	1.63	.171	.387	.209	.472
	18.19	1.99	2.04	2.07	.673	1.80	.304	.685	.149	.336
	18.16	3.12	3.16	3.19	.678	1.80	.427	.942	.135	.298
	18.13	4.06	4.12	4.14	.644	1.78	.511	1.121	.124	.272
	18.19	5.16	5.22	5.24	.633	1.78	.606	1.315	.116	.252
	18.59	5.94	6.01	6.04	.642	1.56	.686	1.480	.114	.246
	18.19	6.12	6.17	6.20	.635	1.67	.697	1.512	.113	.245
	18.59	7.02	7.09	7.12	.636	1.56	.787	1.680	.111	.237
	18.50	8.10	8.15	8.18	.610	1.56	.864	1.866	.107	.229
	9.13	3.00	3.04	3.07	.660	1.63	.413	.912	.136	.300
	9.15	4.06	4.11	4.14	.635	1.63	.514	1.122	.125	.273
	9.16	5.13	5.21	5.24	.628	1.63	.604	1.318	.116	.253
30	18.25	.95	1.00	1.02	.757	1.63	.296	.520	.296	.520
	18.25	2.03	2.09	2.12	.662	1.63	.493	.851	.236	.407
	18.22	3.02	3.08	3.11	.687	1.63	.662	1.127	.215	.366
	18.33	4.24	4.57	4.36	.582	1.56	.850	1.474	.186	.323
	18.32	5.37	5.44	5.51	.620	1.56	1.035	1.744	.190	.320
	18.47	6.21	6.31	6.36	.607	1.56	1.148	1.986	.182	.315
	18.50	7.03	7.12	7.16	------	1.56	------	2.177	------	.306
	9.19	5.26	5.33	5.36	.645	1.63	1.002	1.748	.188	.328
	9.16	4.25	4.32	4.36	.649	1.63	.829	1.417	.192	.328
	9.16	3.03	3.10	3.16	.685	1.63	.639	1.111	.206	.358
34	18.25	.97	1.03	1.06	.742	1.63	.381	.582	.371	.566
	18.13	2.00	2.06	2.09	.674	1.63	.623	.914	.303	.444
	18.13	3.25	3.32	3.36	.615	1.56	.871	1.256	.262	.378
	18.32	4.25	4.37	4.42	.632	1.56	1.124	1.600	.257	.366
	18.28	5.38	5.49	5.54	.598	1.56	1.351	1.928	.246	.351
	18.65	6.47	6.57	6.62	------	1.56	------	2.227	------	.339

TABLE I.—Continued

EXPERIMENTAL PLANING DATA OBTAINED FOR A RECTANGULAR FLAT PLATE

(b) Brass model having sharp chines; no wind screen

Trim, τ, deg	C_V	$\frac{l_c}{b}$	$\frac{l_m}{b}$	$\frac{l_k}{b}$	$\frac{l_{cp}}{l_m}$	ν, sq ft/sec	$C_{D,b}$	$C_{L,b}$	$C_{D,S}$	$C_{L,S}$
12	18.28	1.64	1.69	1.72	0.761	1.80×10^{-5}	0.061	0.291	0.036	0.172
	18.13	2.40	2.44	2.47	.754	1.80	.081	.361	.033	.148
	18.16	3.54	3.59	3.62	.716	1.80	.101	.445	.028	.124
	18.12	4.67	4.72	4.75	.689	1.80	.118	.519	.025	.110
	18.13	5.66	5.72	5.74	.676	1.80	.132	.578	.023	.101
	18.19	7.80	7.86	7.88	.637	1.80	.165	.692	.021	.088
	18.18	6.87	6.92	6.95	.663	1.80	.152	.644	.022	.093
18	18.13	1.87	1.92	1.94	.719	1.80	.151	.493	.078	.257
	18.19	2.88	2.94	2.96	.705	1.80	.206	.653	.070	.222
	18.13	4.00	4.05	4.07	.666	1.80	.259	.798	.064	.197
	18.15	5.92	5.97	6.00	.651	1.80	.346	1.027	.058	.172
	18.13	7.10	7.25	7.18	.641	1.80	.399	1.189	.055	.164
	18.18	7.97	8.03	8.06	.628	1.80	.426	1.253	.053	.156

(c) Brass model having sharp chines; no wind screen or spray shield

Trim, τ, deg	C_V	$\frac{l_c}{b}$	$\frac{l_m}{b}$	$\frac{l_k}{b}$	$\frac{l_{cp}}{l_m}$	ν, sq ft/sec	$C_{D,b}$	$C_{L,b}$	$C_{D,S}$	$C_{L,S}$
12	18.28	1.54	1.59	1.62	0.744	1.64×10^{-5}	0.060	0.286	0.038	0.180
	18.19	2.70	2.75	2.78	.709	1.64	.089	.388	.032	.141
	18.13	3.83	3.88	3.91	.688	1.64	.105	.462	.027	.119
	18.22	4.74	4.80	4.82	.671	1.64	.120	.528	.025	.110
	18.19	5.84	5.89	5.92	.664	1.64	.135	.595	.023	.101

(d) Plastic model having sharp chines

Trim, τ, deg	C_V	$\frac{l_c}{b}$	$\frac{l_m}{b}$	$\frac{l_k}{b}$	$\frac{l_{cp}}{l_m}$	ν, sq ft/sec	$C_{D,b}$	$C_{L,b}$	$C_{D,S}$	$C_{L,S}$
8	18.00	1.24	1.29	1.31	0.725	1.78×10^{-5}	0.0255	0.1542	0.0198	0.1195
	18.00	2.48	2.52	2.54	.725	1.78	.0373	.2109	.0148	.0837
	18.00	3.58	3.62	3.64	.718	1.78	.0463	.2534	.0128	.0700
	18.00	4.47	4.52	4.54	.712	1.78	.0529	.2811	.0117	.0622
	18.00	5.30	5.34	5.36	.708	1.78	.0582	.3087	.0109	.0578
	18.00	6.40	6.45	6.48	.692	1.78	.0671	.3406	.0104	.0528
	18.00	7.53	7.57	7.59	.701	1.78	.0749	.3740	.0099	.0494
12	17.93	1.58	1.62	1.65	.709	1.78	.0611	.2885	.0377	.1781
	17.93	4.01	4.06	4.08	.686	1.78	.1092	.4669	.0269	.1150
	17.93	5.70	5.75	5.77	.675	1.78	.1374	.5773	.0239	.1004
	18.10	7.77	7.82	7.85	.666	1.80	.1713	.6889	.0219	.0881
18	17.86	1.94	1.91	1.86	.674	1.78	.1606	.4897	.0841	.2564
	17.93	2.92	2.96	2.98	.679	1.78	.2196	.6515	.0742	.2201
	17.93	5.14	5.19	5.21	.639	1.78	.3166	.9363	.0610	.1804
	18.19	6.94	6.99	7.02	.643	1.80	.3893	1.1310	.0557	.1618

TABLE I.—Concluded

EXPERIMENTAL PLANING DATA OBTAINED FOR A RECTANGULAR FLAT PLATE

(e) Plastic model having 1/64-inch-radius chines

Trim, τ, deg	C_V	$\frac{l_c}{b}$	$\frac{l_m}{b}$	$\frac{l_k}{b}$	$\frac{l_{cp}}{l_m}$	v, sq ft/sec	$C_{D,b}$	$C_{L,b}$	$C_{D,s}$	$C_{L,s}$
12	18.35	1.79	1.84	1.86	0.711	1.67×10^{-5}	0.0638	0.2950	0.0347	0.1603
	18.13	2.54	2.59	2.62	.705	1.67	.0761	.3445	.0294	.1330
	18.19	3.59	3.64	3.66	.708	1.67	.0972	.4222	.0267	.1160
	18.19	4.79	4.84	4.87	.685	1.67	.1181	.4995	.0244	.1032
	18.16	5.52	5.56	5.59	.663	1.67	.1290	.5399	.0232	.0971
	18.07	6.87	6.92	6.95	.663	1.67	.1550	.6297	.0224	.0910
	18.07	7.60	7.66	7.69	.651	1.67	.1662	.6764	.0217	.0883
18	18.28	2.00	2.05	2.08	.708	1.67	.1615	.4869	.0788	.2375
	18.19	2.84	2.90	2.93	.684	1.67	.2068	.6200	.0713	.2138
	18.19	3.79	3.84	3.86	.672	1.67	.2508	.7438	.0653	.1937
	18.19	4.92	4.98	5.00	.646	1.67	.2948	.8620	.0592	.1731
	18.13	5.89	5.94	5.97	.645	1.67	.3380	.9789	.0569	.1648
	18.19	7.02	7.06	7.08	.644	1.67	.3911	1.1261	.0554	.1595
	18.22	7.76	7.82	7.84	.637	1.67	.4197	1.2055	.0537	.1542

(f) Plastic model having 1/16-inch-radius chines

Trim, τ, deg	C_V	$\frac{l_c}{b}$	$\frac{l_m}{b}$	$\frac{l_k}{b}$	$\frac{l_{cp}}{l_m}$	v, sq ft/sec	$C_{D,b}$	$C_{L,b}$	$C_{D,s}$	$C_{L,s}$
8	18.13	1.64	1.68	1.58	0.712	1.78×10^{-5}	0.0272	0.1605	0.0162	0.0957
	18.13	2.13	2.18	2.20	.751	1.78	.0320	.1820	.0147	.0835
	18.00	3.50	3.55	3.58	.730	1.78	.0437	.2318	.0123	.0653
	18.00	4.50	4.54	4.56	.720	1.78	.0504	.2624	.0111	.0578
	17.86	5.38	5.43	5.45	.716	1.78	.0586	.2948	.0108	.0543
	17.93	6.49	6.54	6.56	.706	1.78	.0654	.3257	.0100	.0498
	18.00	7.53	7.58	7.61	.694	1.78	.0713	.3487	.0094	.0460
12	18.27	1.64	1.69	1.71	.707	1.80	.0558	.2630	.0330	.1556
	18.27	2.62	2.68	2.70	.704	1.80	.0748	.3371	.0279	.1258
	18.27	3.75	3.80	3.83	.692	1.80	.0931	.4081	.0245	.1074
	18.33	4.64	4.69	4.71	.689	1.78	.1116	.4728	.0238	.1008
	18.20	5.71	5.75	5.78	.678	1.78	.1288	.5365	.0224	.0933
	18.13	6.76	6.82	6.84	.674	1.78	.1453	.5981	.0213	.0877
	18.13	7.81	7.86	7.89	.665	1.78	.1651	.6626	.0210	.0843
18	18.13	1.75	1.80	1.83	.686	1.78	.1463	.4466	.0813	.2481
	18.13	2.74	2.79	2.81	.683	1.63	.1987	.5903	.0713	.2118
	18.13	4.01	4.06	4.08	.660	1.78	.2498	.7429	.0616	.1832
	18.13	5.02	5.09	5.09	.649	1.78	.2917	.8566	.0573	.1683
	18.26	6.22	6.26	6.29	.641	1.78	.3389	.9786	.0541	.1562
	18.13	6.90	6.95	6.99	.642	1.78	.3670	1.0627	.0528	.1529
	18.13	7.91	7.96	7.99	.641	1.78	.4068	1.1677	.0511	.1467

TABLE II

EXPERIMENTAL DATA OBTAINED FOR A PLANING SURFACE HAVING A 20° ANGLE OF DEAD RISE

Trim, τ, deg	C_V	$\frac{l_c}{b}$	$\frac{l_m}{b}$	$\frac{l_k}{b}$	$\frac{l_{cp}}{l_m}$	v, sq ft/sec	$C_{D,b}$	$C_{L,b}$	$C_{D,s}$	$C_{L,s}$
12	18.31	1.68	1.90	2.12	0.708	1.76×10^{-5}	0.051	0.236	0.027	0.124
	18.13	2.16	2.39	2.62	.721	1.73	.065	.275	.027	.115
	18.19	2.29	2.52	2.74	.725	1.73	.068	.277	.027	.110
	18.19	3.45	3.68	3.91	.696	1.73	.085	.353	.023	.096
	18.19	4.27	4.48	4.68	.680	1.71	.099	.403	.022	.090
	18.19	5.49	5.70	5.91	.665	1.71	.114	.467	.020	.082
	18.13	6.29	6.38	6.73	.684	1.71	.128	.485	.020	.076
	18.29	7.09	7.29	7.49	.663	1.71	.146	.554	.020	.076
18	18.47	1.80	1.93	2.06	.709	1.76	.129	.396	.067	.205
	18.31	2.78	2.90	3.03	.681	1.73	.174	.513	.060	.177
	18.28	3.80	3.93	4.06	.663	1.73	.212	.629	.054	.160
	18.13	4.72	4.85	4.98	.665	1.71	.252	.742	.052	.153
	18.13	5.70	5.83	5.95	.643	1.71	.286	.840	.049	.144
	18.22	6.66	6.79	6.92	.634	1.71	.326	.944	.048	.139
	18.16	7.81	7.94	8.06	.620	1.71	.373	1.064	.047	.134
24	18.31	2.02	2.12	2.21	.680	1.76	.257	.568	.121	.268
	18.25	3.04	3.14	3.20	.665	1.67	.349	.772	.111	.246
	18.16	3.94	4.03	4.12	.649	1.72	.423	.931	.105	.231
	18.13	4.90	4.99	5.08	.625	1.72	.509	1.103	.102	.221
	18.13	6.26	6.35	6.44	.620	1.67	.610	1.314	.096	.207
	18.19	7.06	7.14	7.24	.628	1.70	.671	1.442	.094	.202
	18.31	7.86	7.93	8.00	.616	1.54	.730	1.586	.092	.200
	9.10	3.11	3.19	3.28	.655	1.67	.348	.778	.109	.244
	9.11	4.12	4.19	4.27	.635	1.67	.436	.968	.104	.231
	9.07	5.17	5.24	5.33	.614	1.67	.529	1.148	.101	.219
30	18.28	1.40	1.45	1.51	.660	1.63	.302	.523	.208	.361
	18.19	2.32	2.38	2.43	.624	1.63	.445	.771	.187	.324
	18.19	3.38	3.44	3.50	.630	1.63	.605	1.020	.176	.297
	18.37	3.26	3.32	3.39	.637	1.56	.588	.993	.177	.299
	18.31	4.27	4.32	4.38	.620	1.56	.721	1.205	.167	.279
	18.31	5.38	5.43	5.49	.614	1.54	.885	1.472	.163	.271
	18.25	6.51	6.55	6.62	.604	1.54	1.035	1.703	.158	.260
	18.25	7.21	7.27	7.32	.609	1.54	1.156	1.876	.159	.258
34	18.13	1.54	1.61	1.68	.622	1.63	.406	.610	.252	.379
	18.16	2.42	2.46	2.49	.632	1.63	.590	.868	.240	.353
	18.31	3.66	3.70	3.75	.616	1.56	.821	1.184	.222	.320
	18.25	4.68	4.71	4.74	.605	1.56	.994	1.432	.211	.304
	18.31	5.61	5.66	5.69	.600	1.56	1.194	1.692	.211	.299
	18.41	6.42	6.46	6.50	.602	1.54	1.337	1.867	.207	.289
	18.32	7.52	7.56	7.60	-------	1.54	-------	2.192	-------	.290

TABLE III

EXPERIMENTAL DATA OBTAINED FOR A PLANING SURFACE HAVING 40° ANGLE OF DEAD RISE

Trim, τ, deg	C_V	$\frac{l_c}{b}$	$\frac{l_m}{b}$	$\frac{l_k}{b}$	$\frac{l_{cp}}{l_m}$	v, sq ft/sec	$C_{D,b}$	$C_{L,b}$	$C_{D,s}$	$C_{L,s}$
12	18.07	0.58	1.14	1.69	0.756	1.72×10^{-5}	0.025	0.100	0.022	0.088
	18.07	1.60	2.14	2.68	.688	1.72	.041	.167	.019	.078
	18.13	2.82	3.36	3.91	.655	1.72	.060	.228	.018	.068
	18.13	3.85	4.40	4.95	.639	1.72	.072	.273	.016	.062
	18.16	4.96	5.51	6.06	.634	1.72	.094	.331	.017	.060
	18.16	5.82	6.36	6.95	.627	1.69	.102	.350	.016	.055
	18.22	6.99	7.52	8.06	.622	1.69	.120	.414	.016	.055
18	18.13	1.14	1.48	1.81	.704	1.72	.074	.219	.050	.148
	18.13	2.28	2.59	2.90	.661	1.63	.119	.339	.046	.131
	18.19	3.40	3.71	4.01	.649	1.72	.156	.456	.042	.123
	18.19	4.32	4.65	4.98	.631	1.67	.195	.539	.042	.116
	18.13	5.42	5.74	6.04	.617	1.72	.224	.626	.039	.109
	18.25	6.36	6.67	6.99	-----	1.69	.253	.700	.038	.105
	18.16	7.46	7.77	8.07	.605	1.69	.280	.761	.036	.098
24	18.13	1.71	1.91	2.10	.633	1.63	.170	.371	.089	.194
	18.13	2.60	2.80	2.99	.630	1.72	.235	.515	.084	.184
	18.16	3.82	4.03	4.24	.618	1.72	.314	.673	.078	.167
	18.16	4.57	4.75	4.93	.611	1.72	.356	.760	.075	.160
	18.19	5.74	5.92	6.11	.611	1.67	.456	.953	.077	.161
	18.13	5.84	6.01	6.19	.616	1.72	.463	.962	.077	.160
	18.16	6.85	7.04	7.24	.596	1.69	.500	1.056	.071	.150
	18.16	7.61	7.79	7.96	.602	1.69	.553	1.151	.071	.148
	9.14	2.63	2.80	2.99	.622	1.67	.235	.512	.084	.183
	9.13	3.78	3.98	4.17	.611	1.67	.318	.689	.080	.173
	9.08	4.81	5.02	5.20	.601	1.67	.402	.828	.080	.165
30	18.13	1.15	1.27	1.39	.627	1.63	.185	.318	.146	.250
	18.16	2.04	2.14	2.25	.623	1.63	.295	.505	.138	.236
	18.13	3.05	3.14	3.24	.610	1.63	.424	.722	.135	.230
	18.13	4.05	4.13	4.23	.615	1.63	.545	.909	.132	.220
	18.31	4.95	5.01	5.12	.597	1.58	.626	1.032	.125	.206
	18.25	6.01	6.07	6.12	.587	1.58	.753	1.238	.124	.204
	18.19	7.47	7.53	7.58	.579	1.58	.911	1.483	.121	.197
34	18.07	1.29	1.37	1.48	.617	1.63	.255	.377	.186	.275
	18.25	2.38	2.46	2.55	.628	1.63	.445	.649	.181	.264
	18.13	3.10	3.16	3.22	.612	1.63	.547	.790	.173	.250
	18.19	4.20	4.22	4.25	.617	1.58	.692	.995	.164	.236
	18.33	5.32	5.35	5.38	.585	1.58	.883	1.263	.165	.236
	18.33	6.35	6.12	6.40	.583	1.58	.991	1.401	.162	.229
	18.30	7.16	7.20	7.25	.584	1.58	1.181	1.656	.164	.230

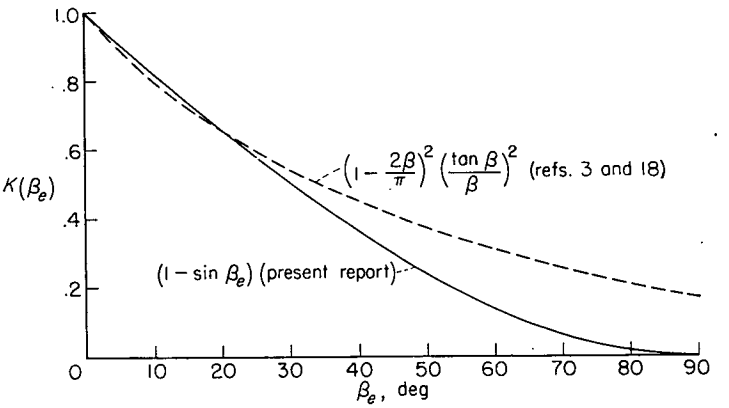


FIGURE 1.—Comparison of dead-rise function applied to linear term with dead-rise function based on Wagner's work.

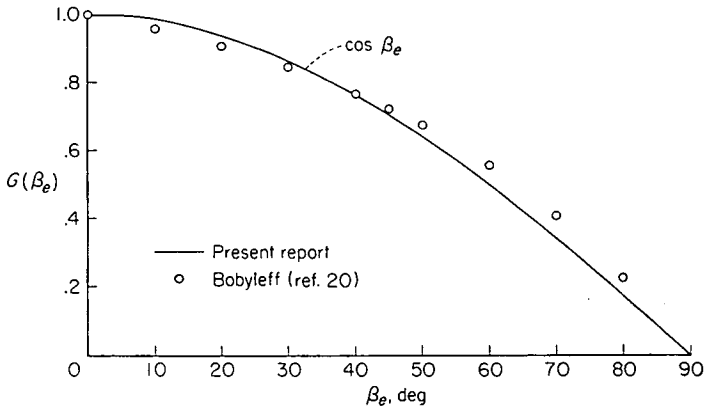


FIGURE 2.—Comparison of dead-rise function applied to crossflow term with Bobyleff's flow coefficient.

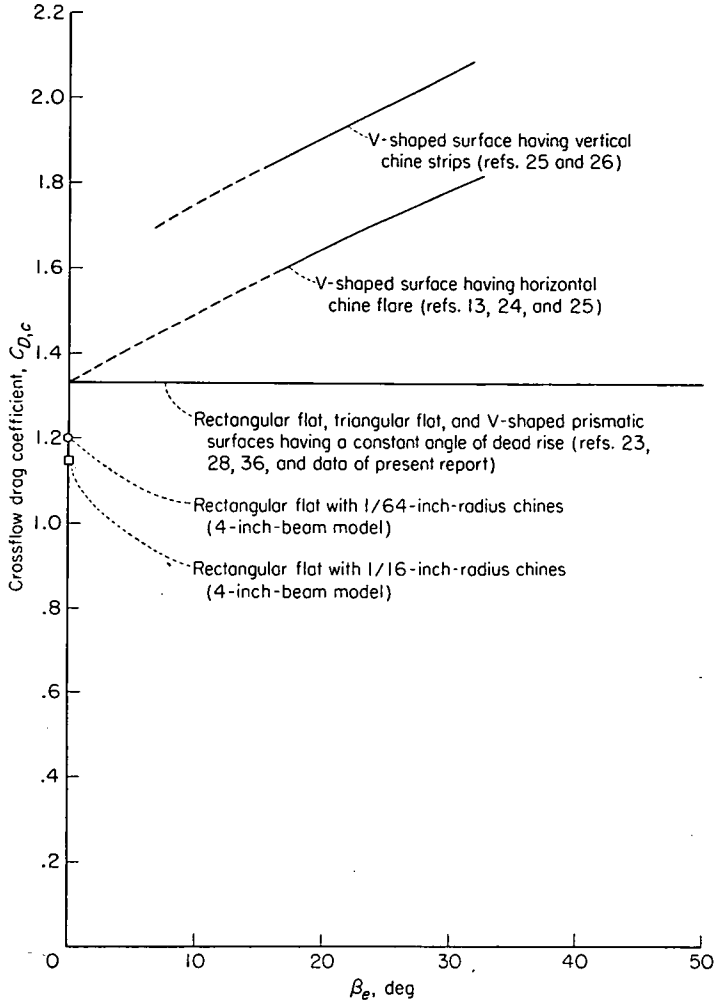
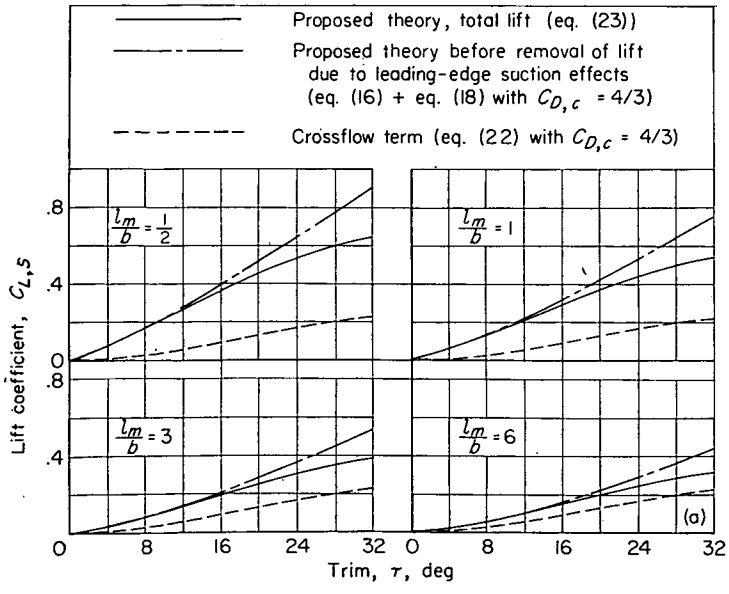
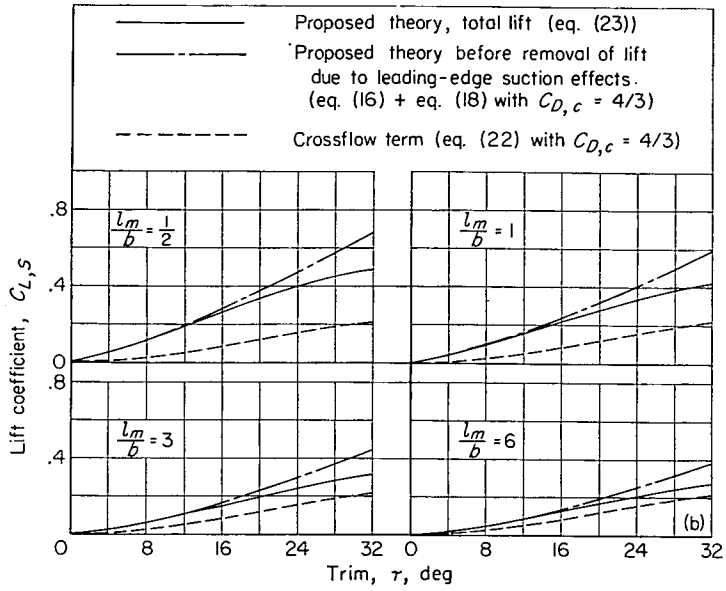


FIGURE 3.—Variation of crossflow drag coefficient for various types of planing surfaces.



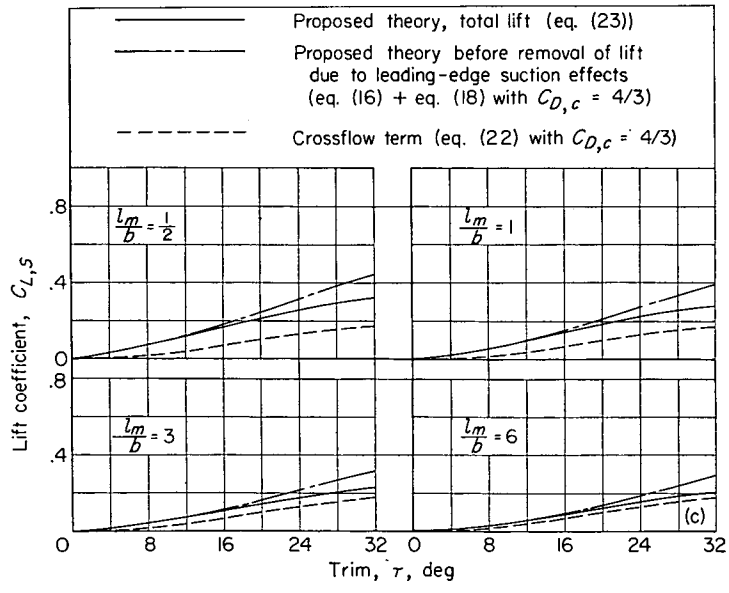
(a) Flat plate.

FIGURE 4.—Relative magnitude of components of proposed theory.



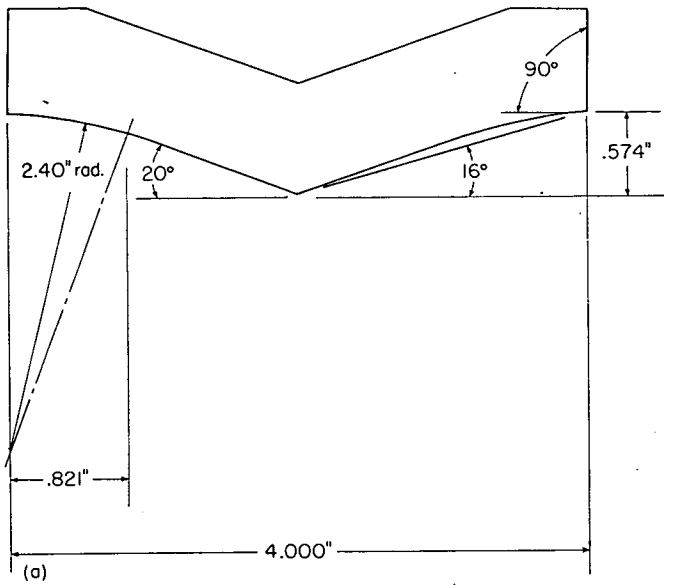
(b) Dead rise, 20°.

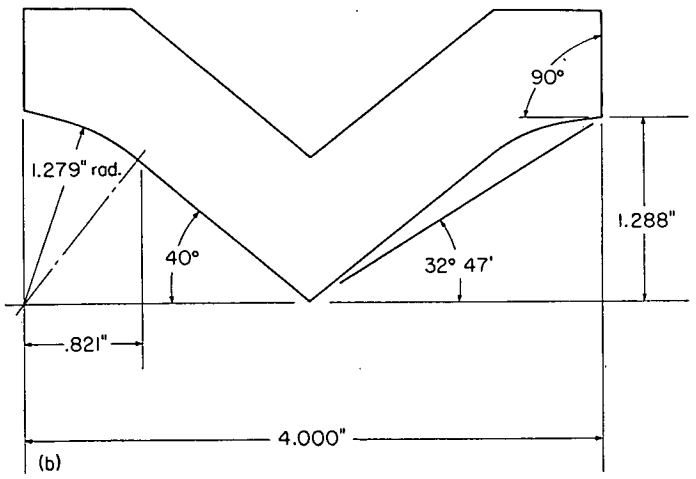
FIGURE 4.—Continued.



(c) Dead rise, 40°.

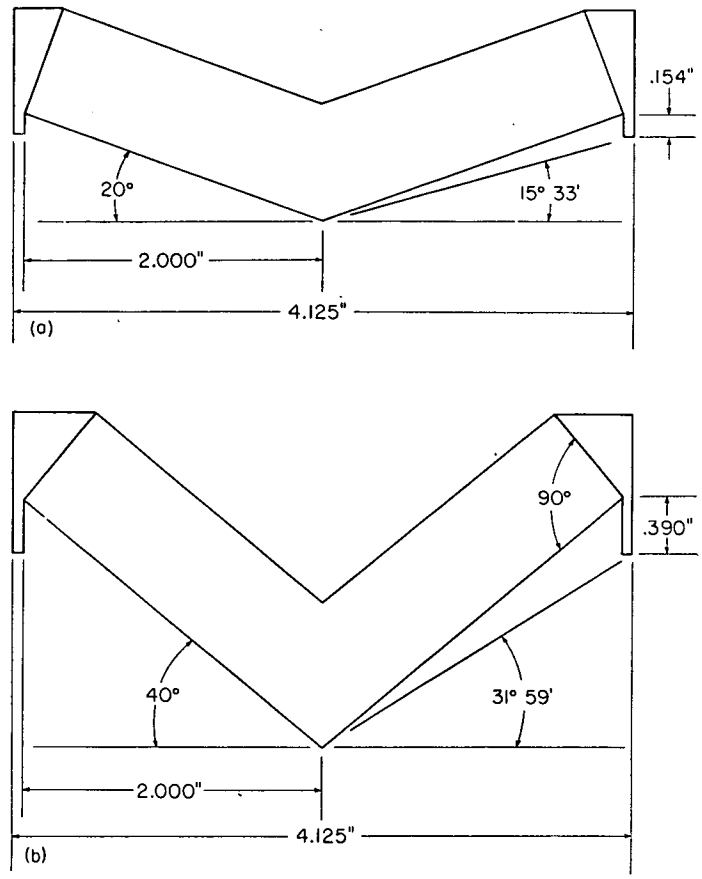
FIGURE 4.—Concluded.





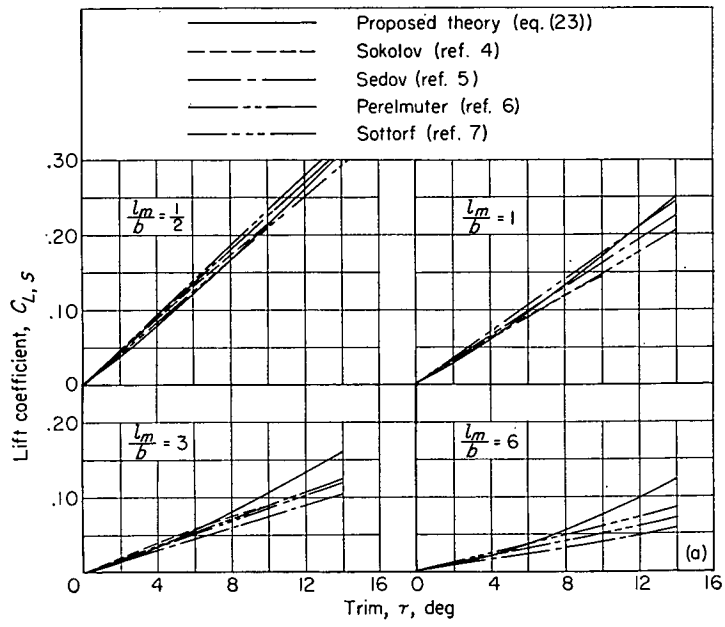
(a) Effective angle of dead rise, 16°. (See ref. 13.)
(b) Effective angle of dead rise, 32°47′. (See ref. 24.)

FIGURE 5.—Cross section of surfaces having horizontal chine flare.



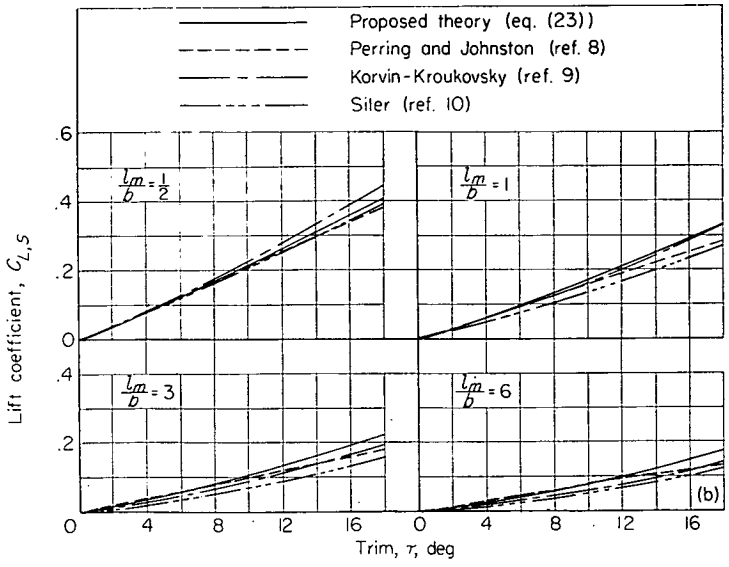
(a) Effective angle of dead rise, 15°33′. (See ref. 26.)
(b) Effective angle of dead rise, 31°59′. (See ref. 26.)

FIGURE 6.—Cross section of surfaces having vertical chine strips.

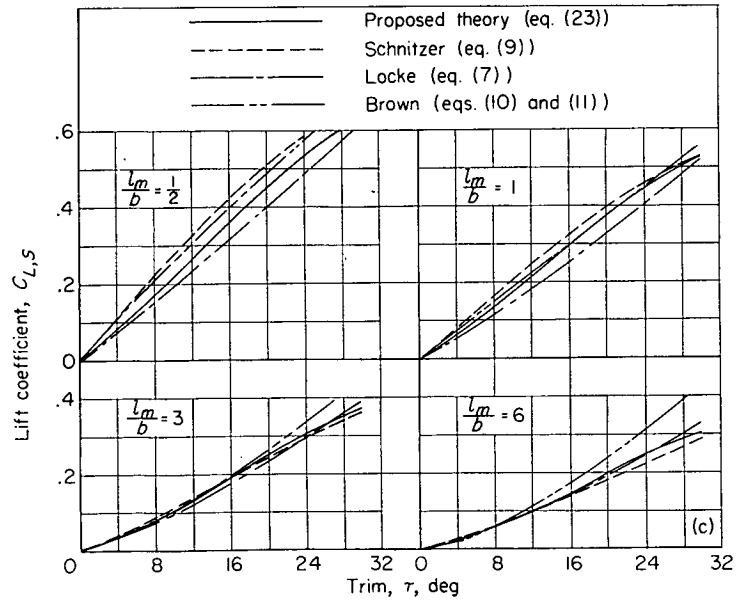


(a) Proposed theory and references 4 to 7.

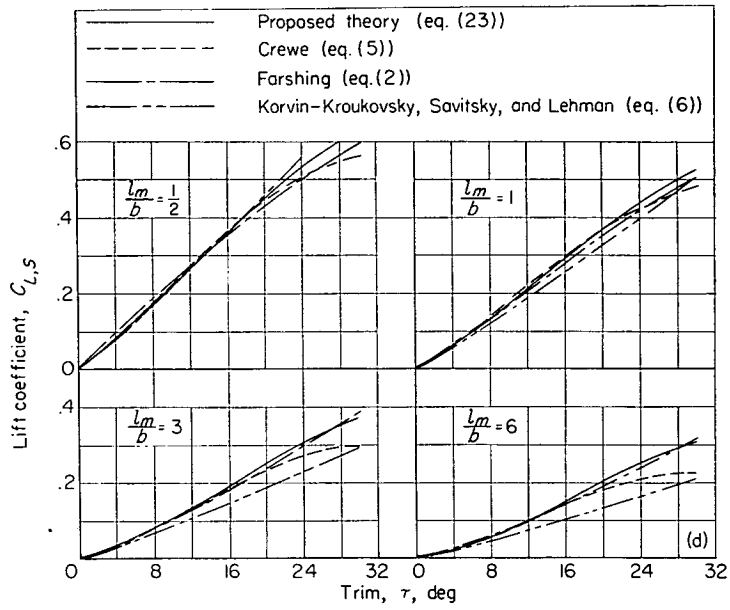
FIGURE 7.—Variation of lift coefficient with trim for rectangular flat-plate lift formulas.



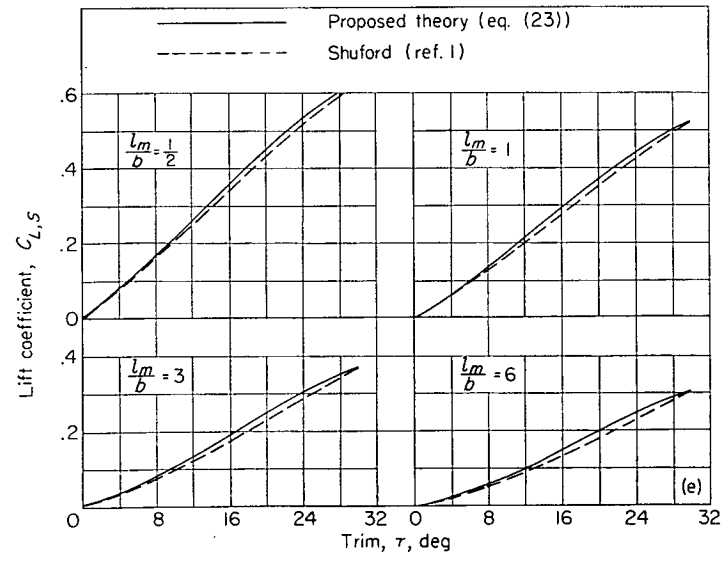
(b) Proposed theory and references 8 to 10.
FIGURE 7.—Continued.



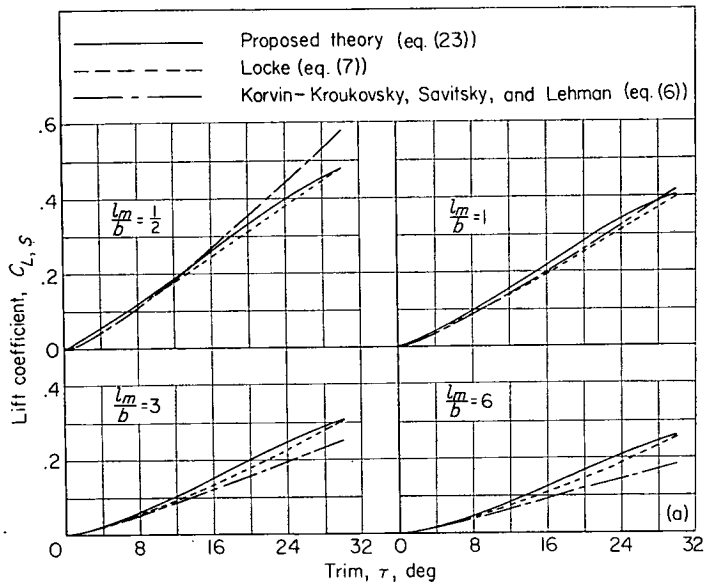
(c) Proposed theory and references 17, 18, and 21.
FIGURE 7.—Continued.



(d) Proposed theory and references 12, 14, and Crewe's equation (eq. (5)).
FIGURE 7.—Continued.

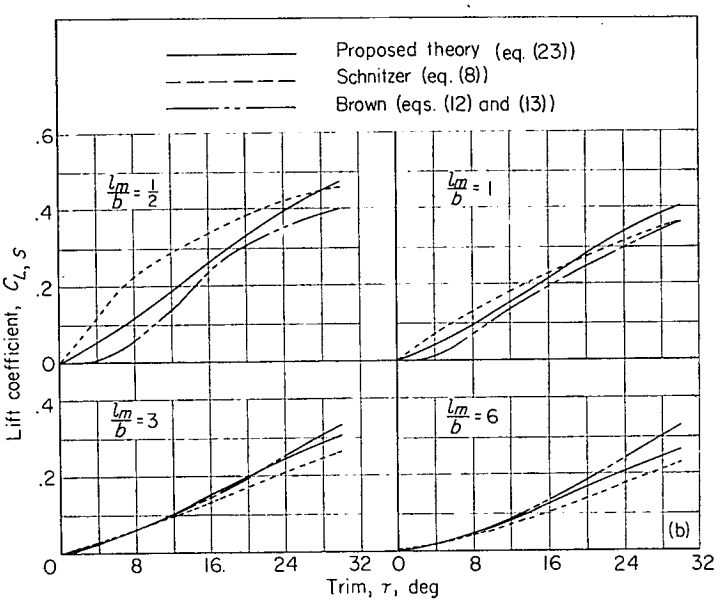


(e) Proposed theory and reference 1.
FIGURE 7.—Concluded.



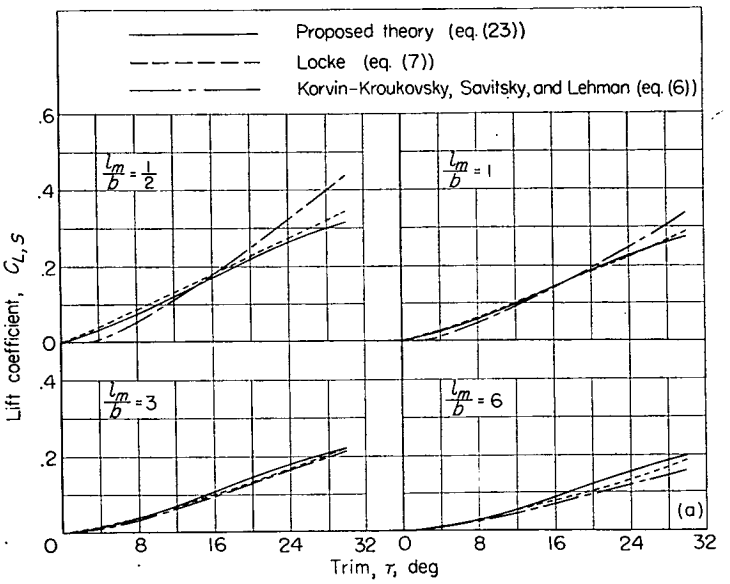
(a) Proposed theory and references 14 and 17.

FIGURE 8.—Variation of lift coefficient with trim for a surface having an angle of dead rise of 20°.



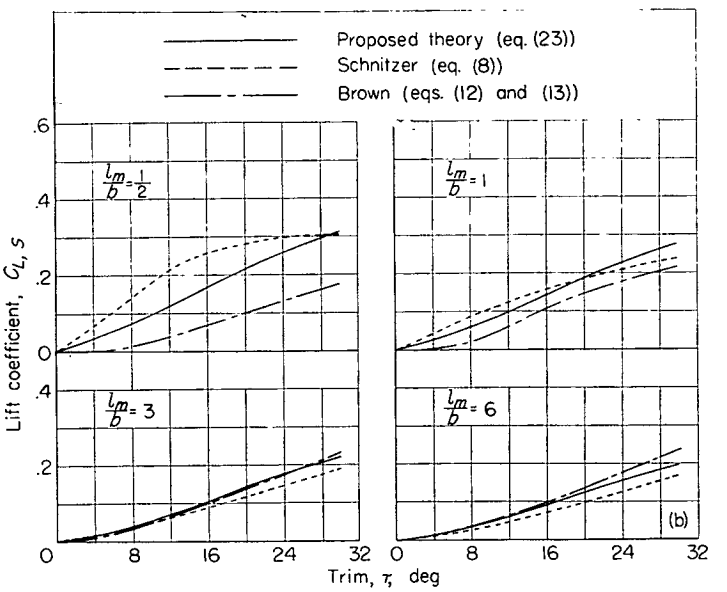
(b) Proposed theory and references 18 and 21.

FIGURE 8.—Concluded.



(a) Proposed theory and references 14 and 17.

FIGURE 9.—Variation of lift coefficient with trim for a surface having an angle of dead rise of 40°.



(b) Proposed theory and references 18 and 21.

FIGURE 9.—Concluded.

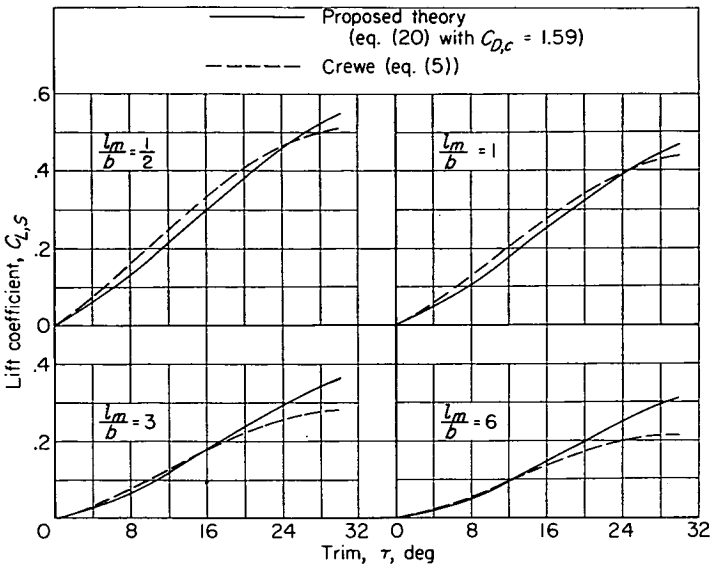
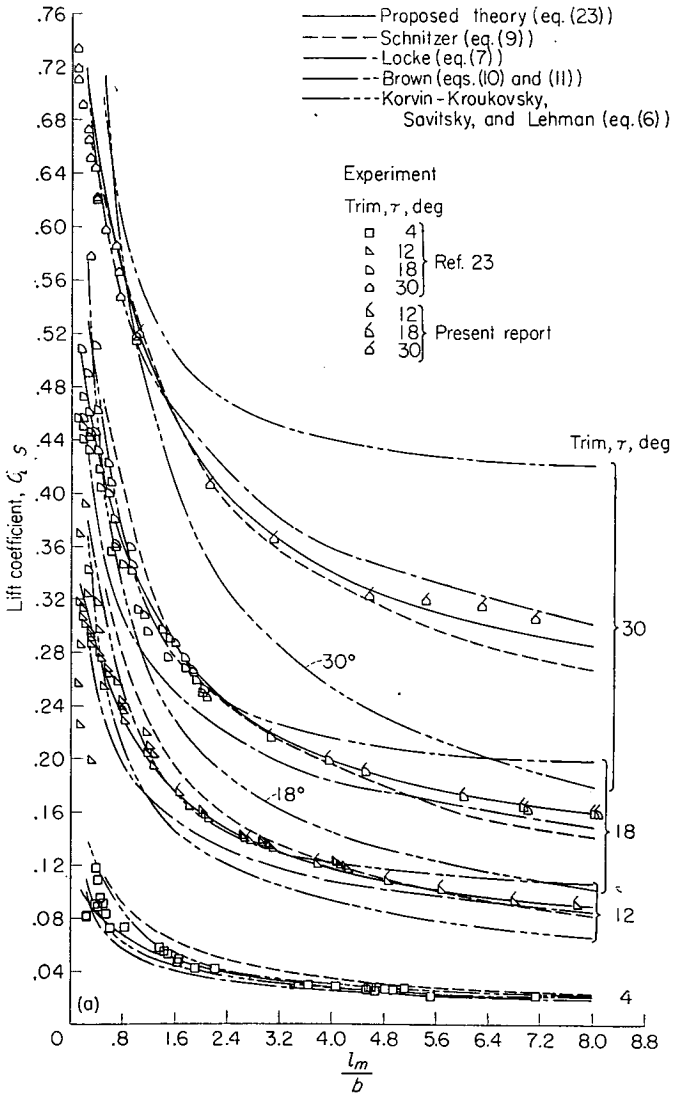
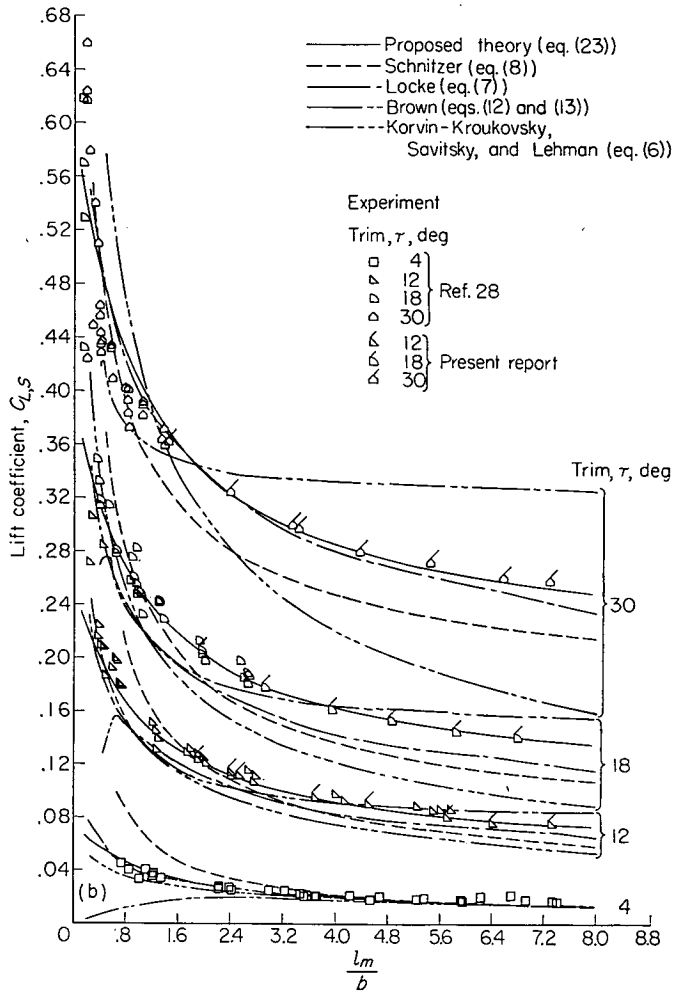


FIGURE 10.—Variation of lift coefficient with trim for a surface having a basic angle of dead rise of 20° and horizontal chine flare.



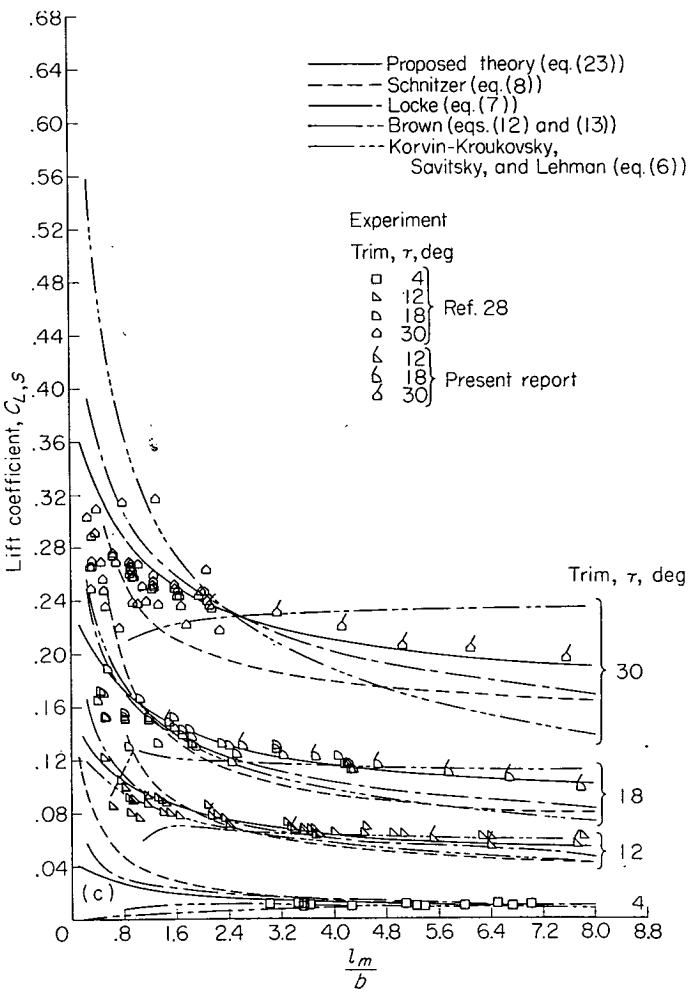
(a) Flat plate.

FIGURE 11.—Comparison of the results calculated from the proposed theory and references 14, 17, 18, and 21 with experiment.



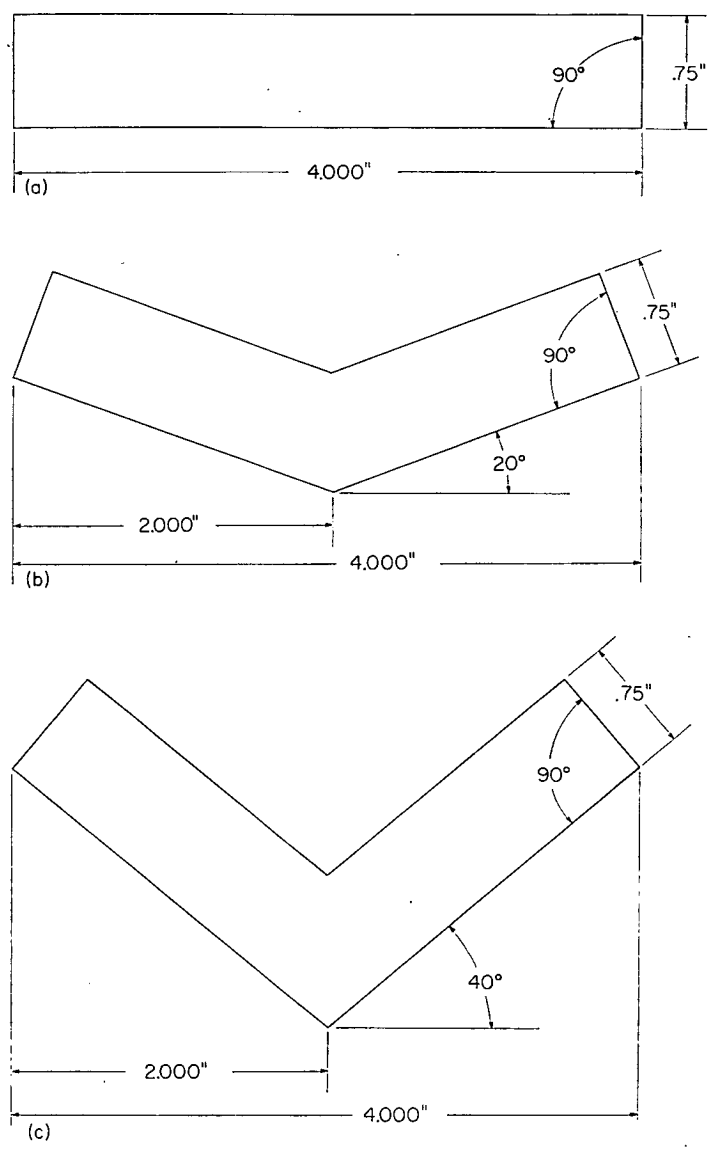
(b) Dead rise, 20°.

FIGURE 11.—Continued.



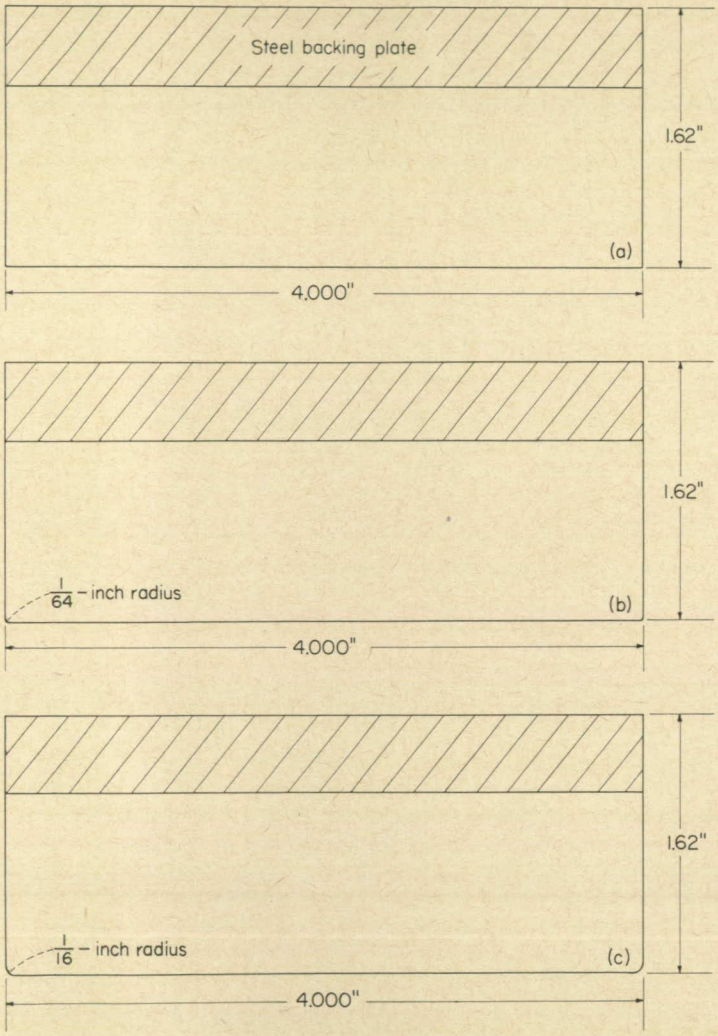
(c) Dead rise, 40°.

FIGURE 11.—Concluded.



(a) Flat plate.
(b) Dead rise, 20°.
(c) Dead rise, 40°.

FIGURE 12.—Cross sections of brass models



(a) Sharp chines.
(b) 1/64-inch-radius chines.
(c) 1/16-inch-radius chines.

FIGURE 13.—Cross sections of plastic models.

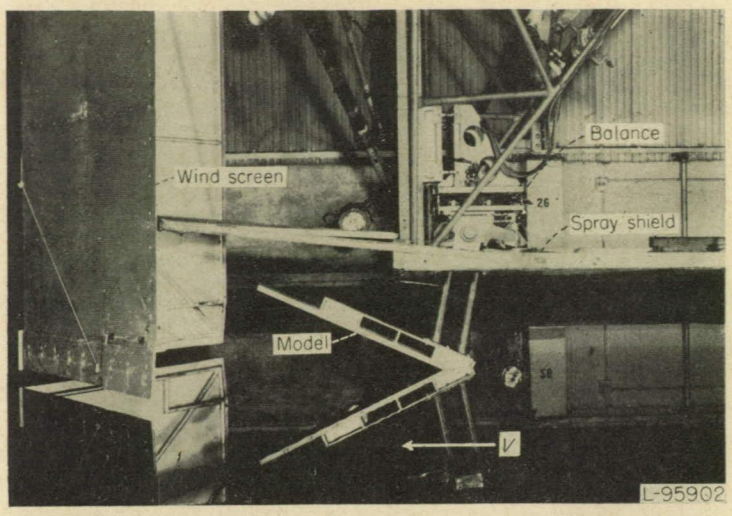
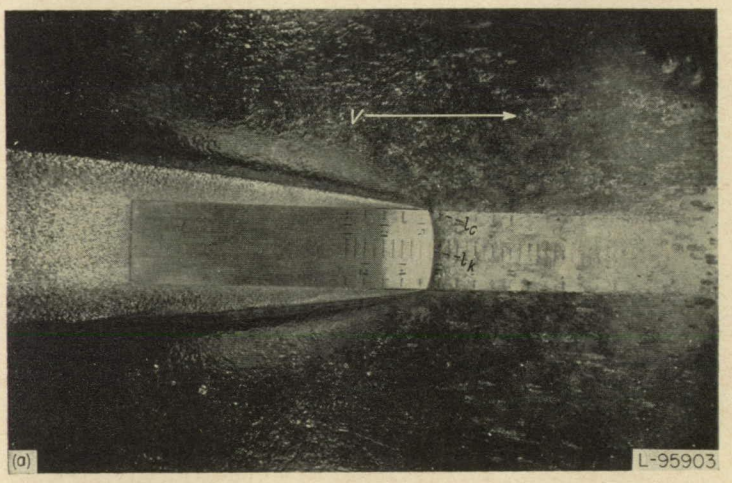
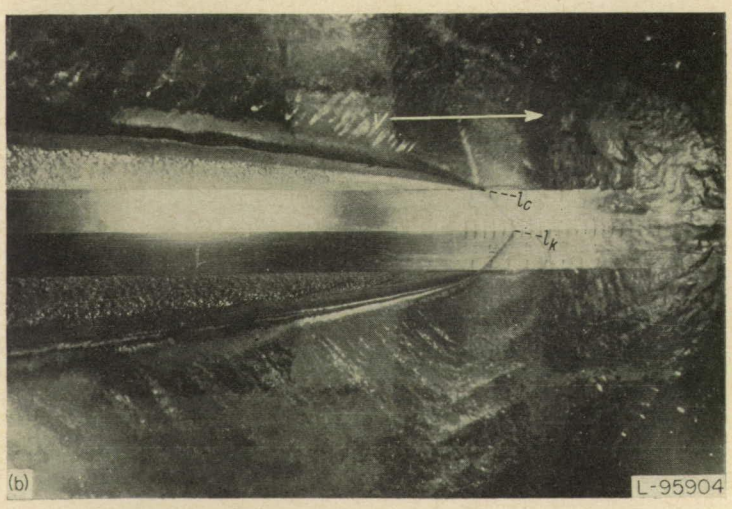


FIGURE 14.—Photograph of flat-plate model attached to towing carriage.



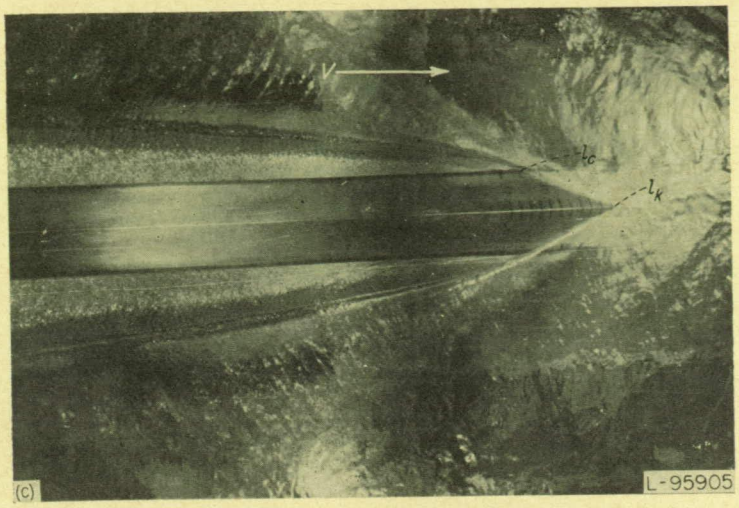
(a) Flat plate.

FIGURE 15.—Underwater photographs.

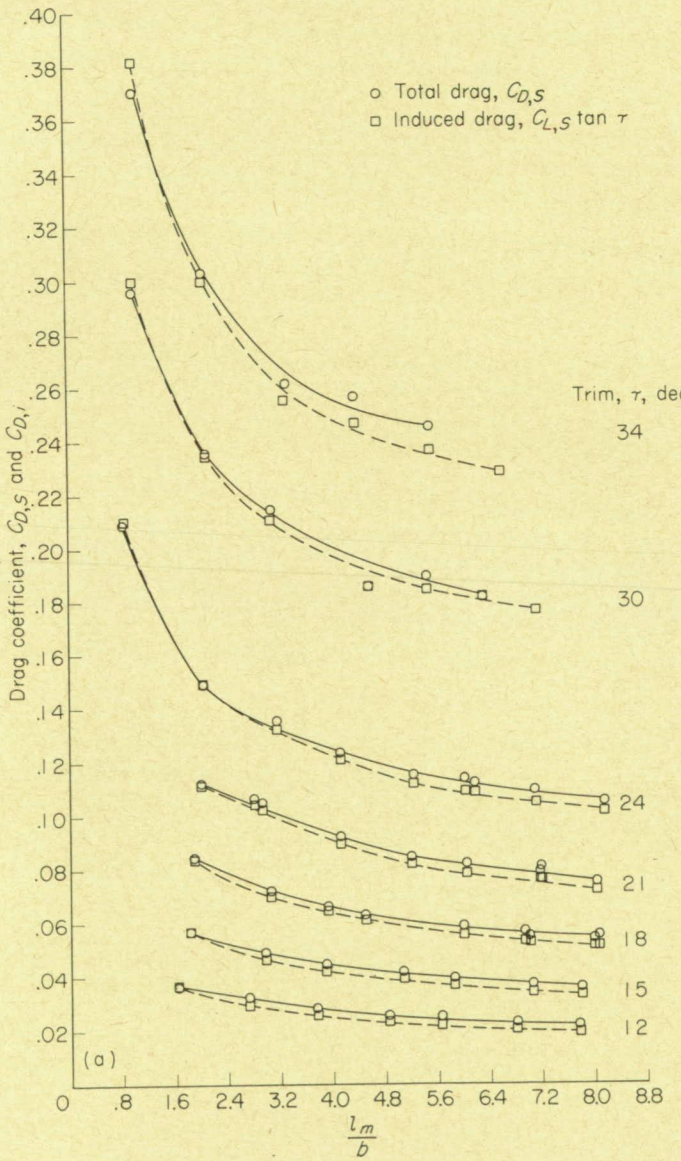


(b) Dead rise, 20°.

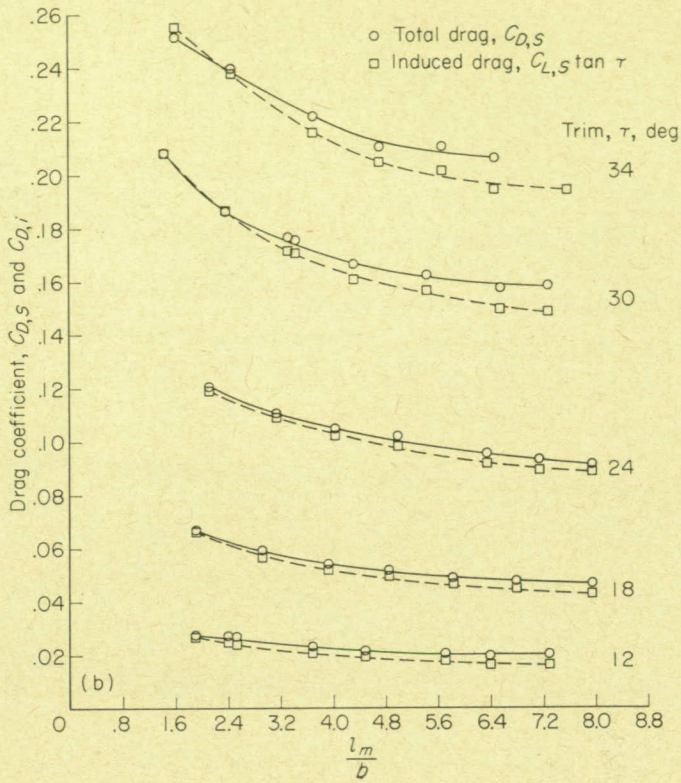
FIGURE 15.—Continued



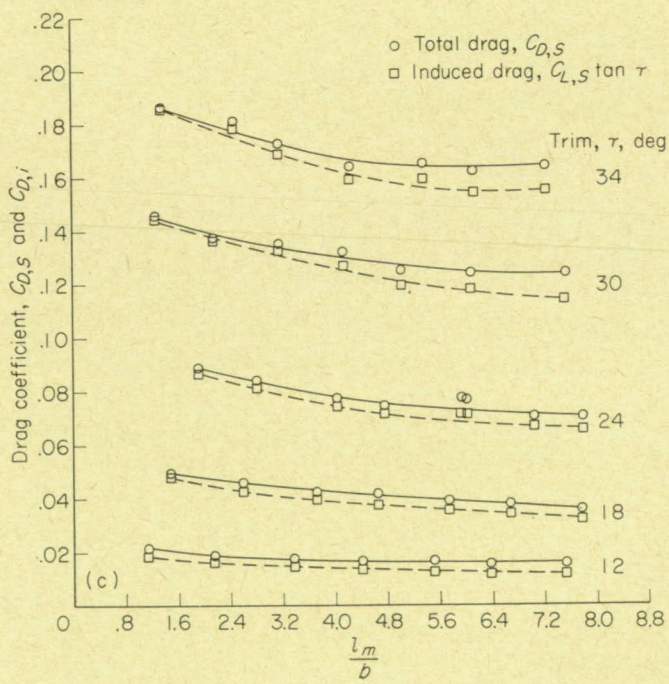
(c) Dead rise, 40°.
FIGURE 15.—Concluded.



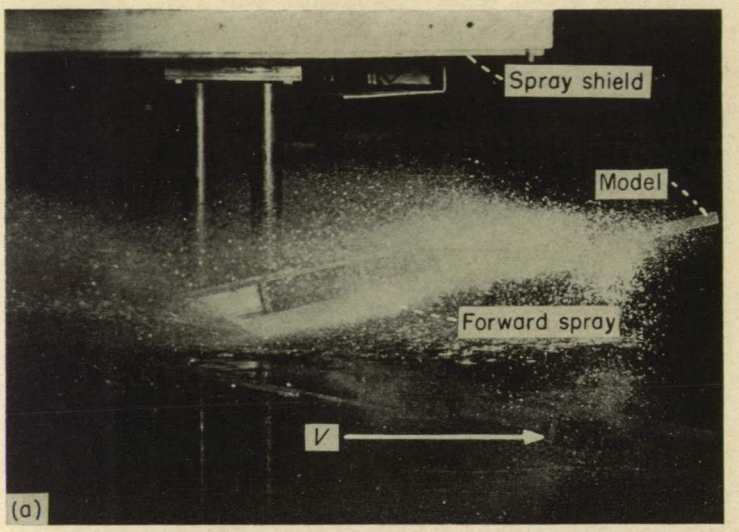
(a) Flat plate.
FIGURE 16.—Comparison of total drag with induced drag.

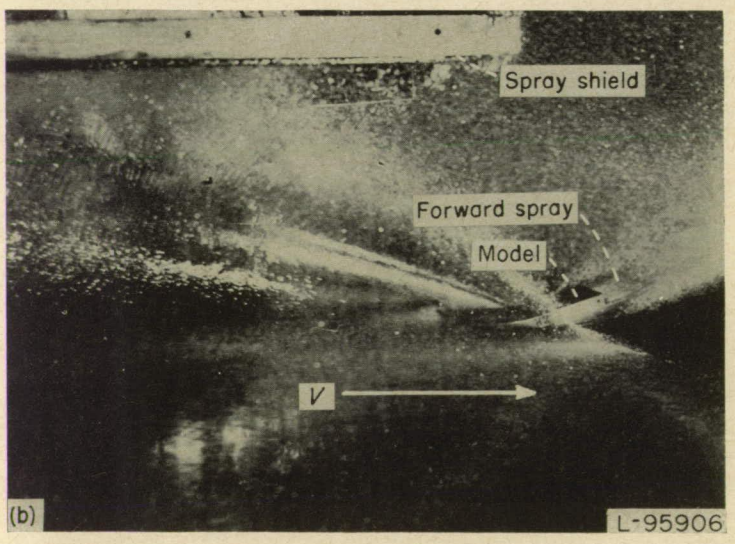


(b) Dead rise, 20°.
FIGURE 16.—Continued.



(c) Dead rise, 40°.
FIGURE 16.—Concluded.

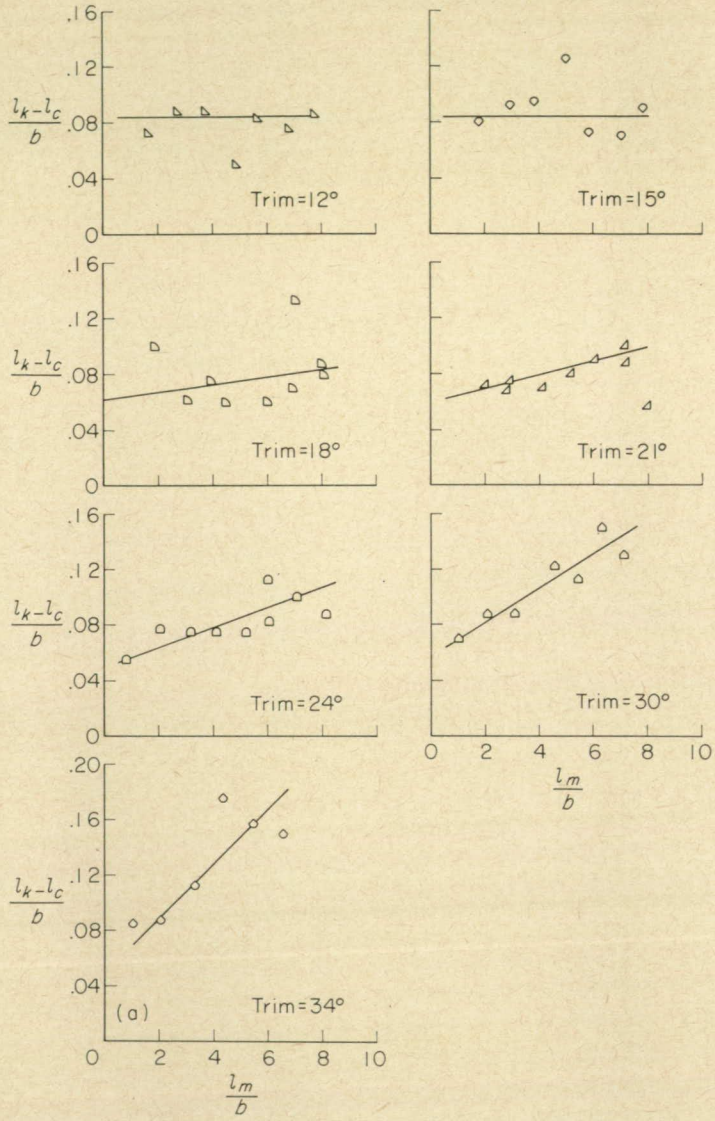




(a) $\frac{l_m}{b}=1.69$.

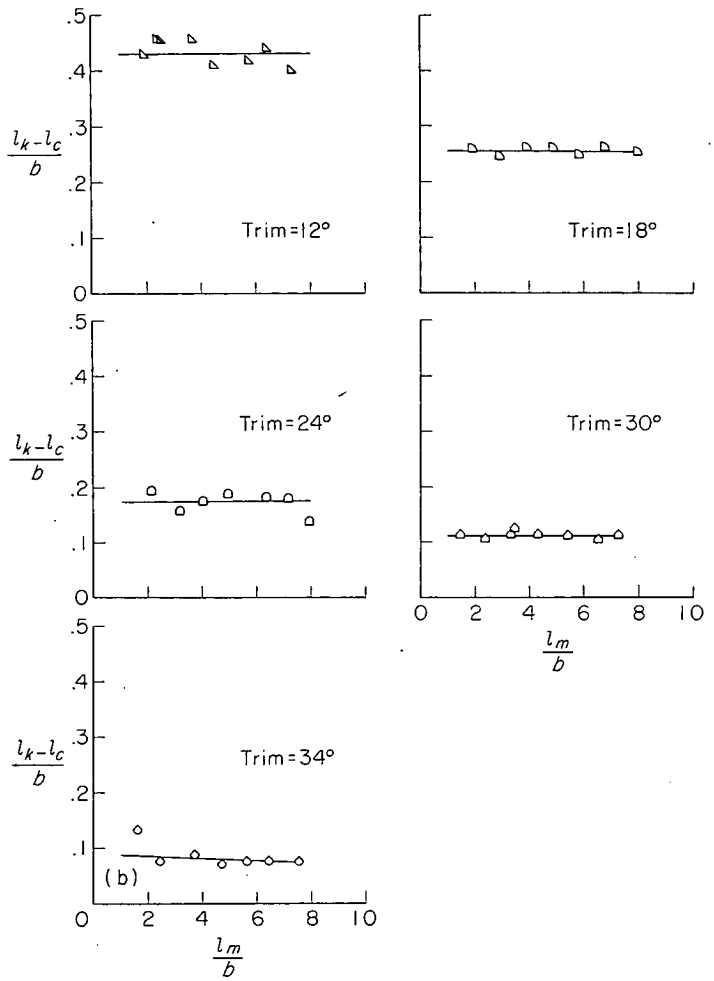
(b) $\frac{l_m}{b}=7.86$.

FIGURE 17.—Spray photographs of flat-plate model with wind screen removed. Trim, 12°.

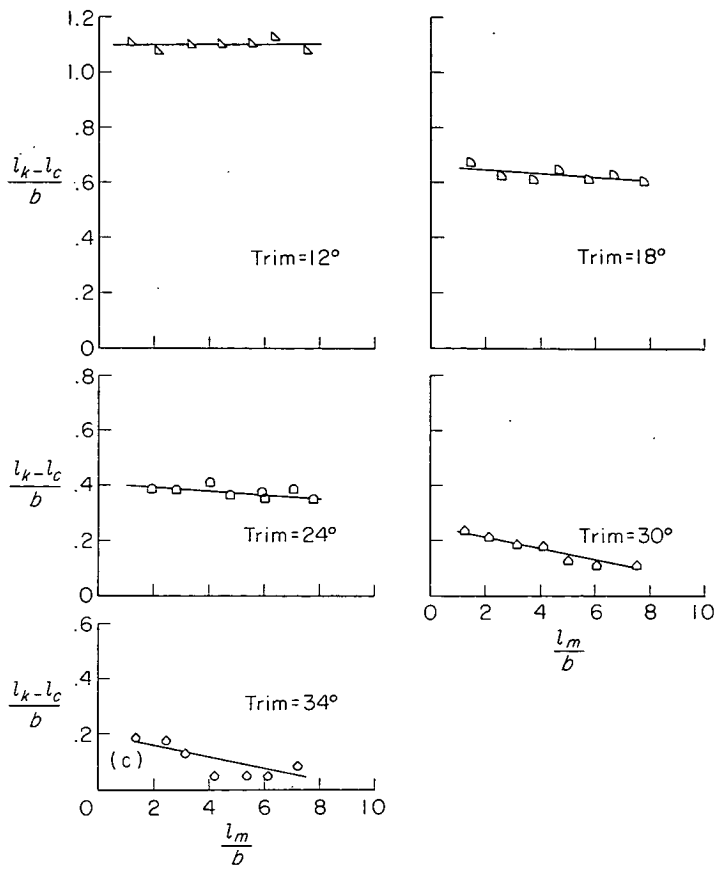


(a) Flat plate.

FIGURE 18.—Variation of $\frac{l_k-l_c}{b}$ with trim.



(b) Dead rise, 20°.
FIGURE 18.—Continued.



(c) Dead rise, 40°.
FIGURE 18.—Concluded.

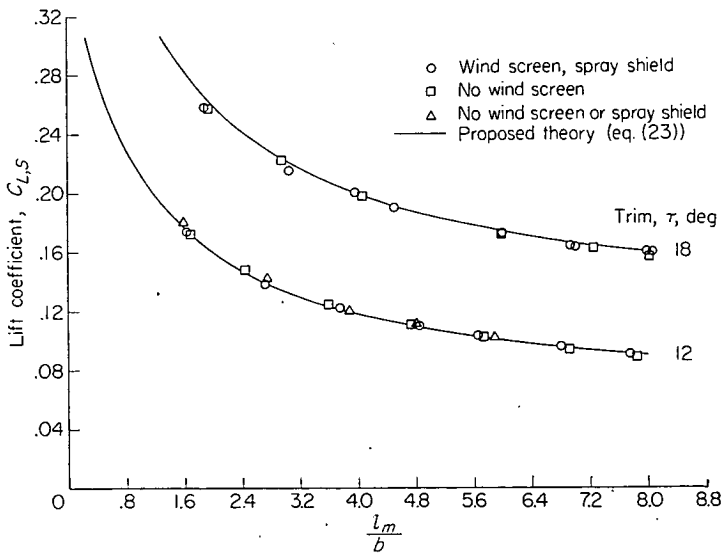


FIGURE 19.—Effect of wind screen and spray shield on the lift of a rectangular flat plate.

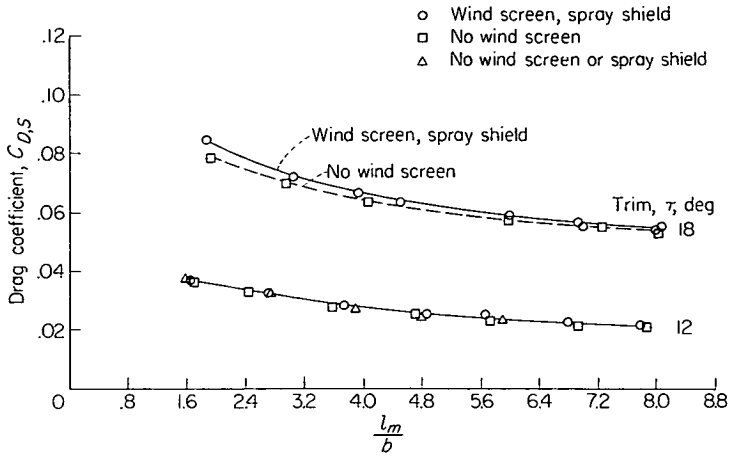


FIGURE 20.—Effect of wind screen and spray shield on the drag of a rectangular flat plate.

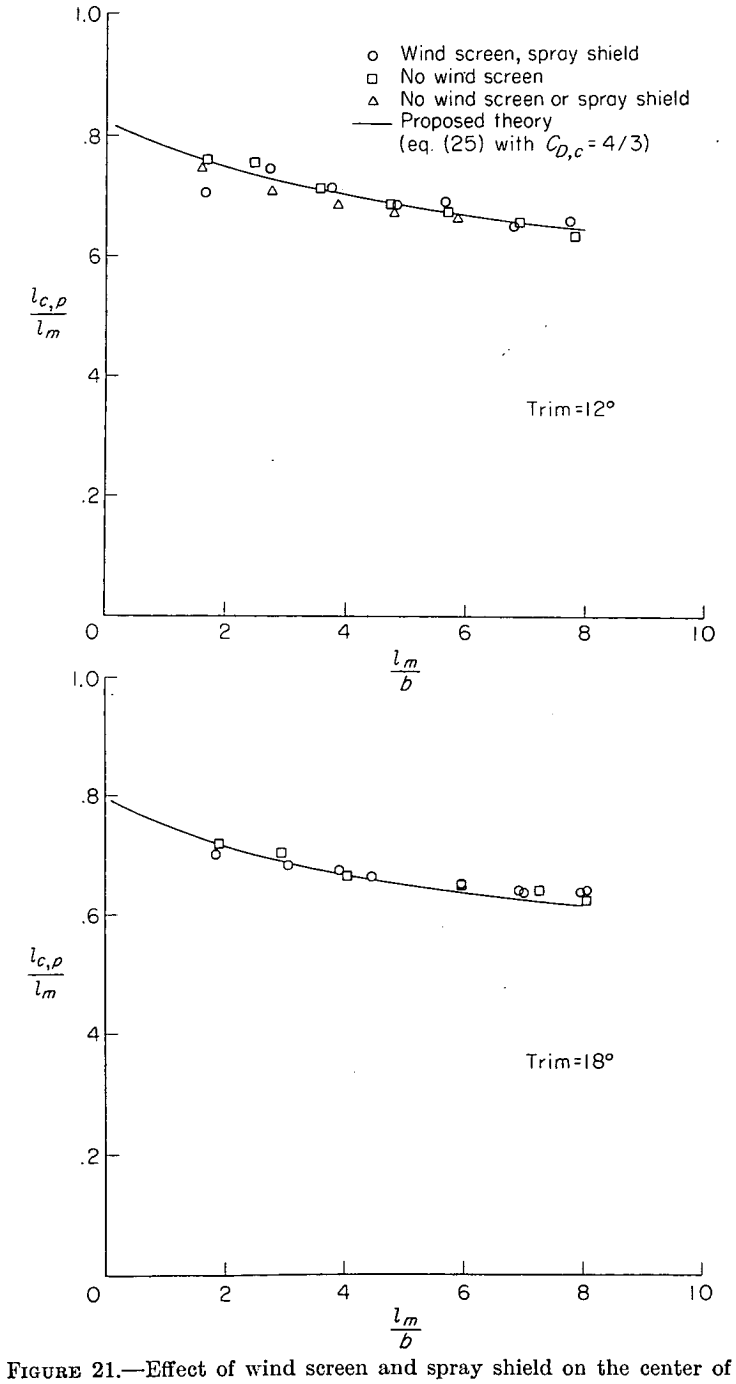
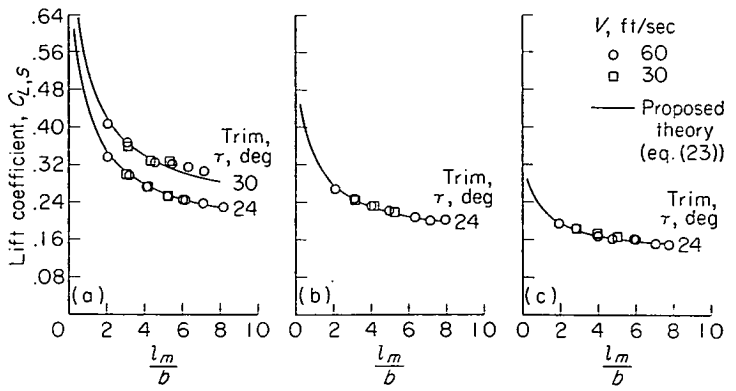
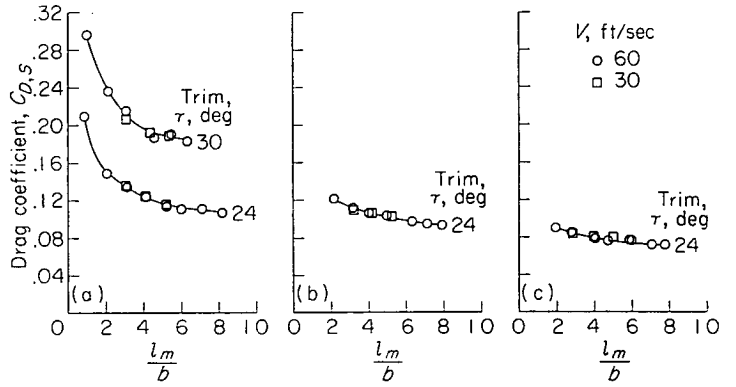


FIGURE 21.—Effect of wind screen and spray shield on the center of pressure of a rectangular flat plate.



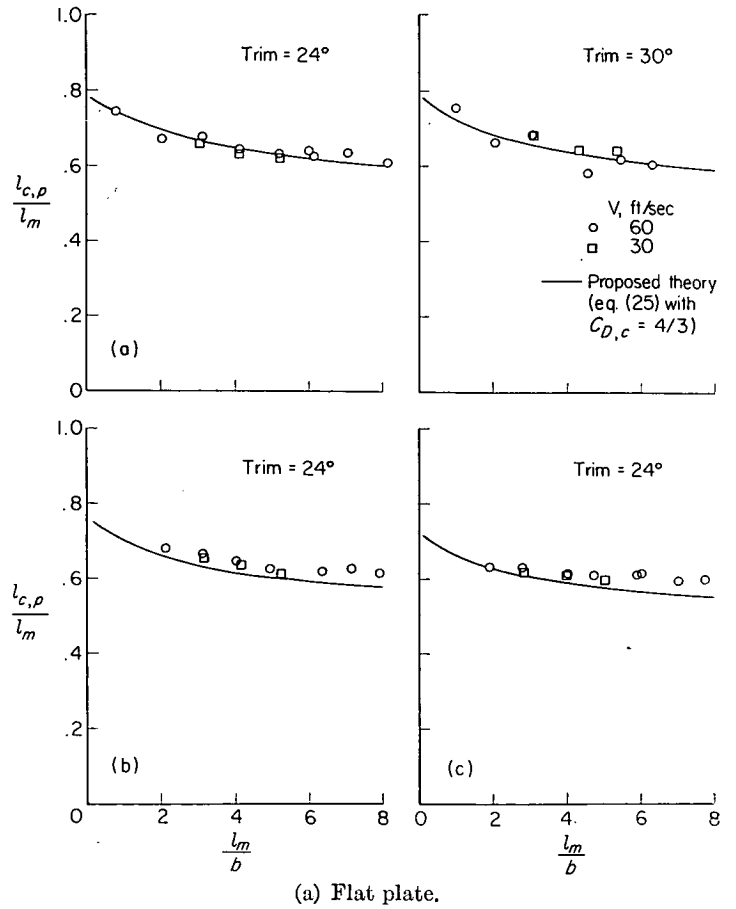
(a) Flat plate. (b) Dead rise, 20°. (c) Dead rise, 40°.

FIGURE 22.—The effect of speed on lift coefficient.



(a) Flat plate. (b) Dead rise, 20°. (c) Dead rise, 40°.

FIGURE 23.—The effect of speed on drag coefficient.



(a) Flat plate.

(b) Dead rise, 20°. (c) Dead rise, 40°.

FIGURE 24.—The effect of speed on center of pressure.

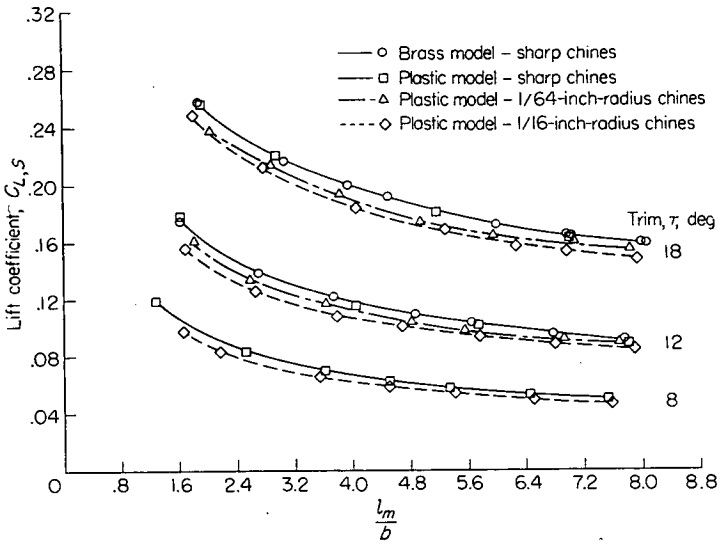


FIGURE 25.—The effect of rounded chines on the lift of a 4-inch-beam rectangular-flat-plate planing surface.

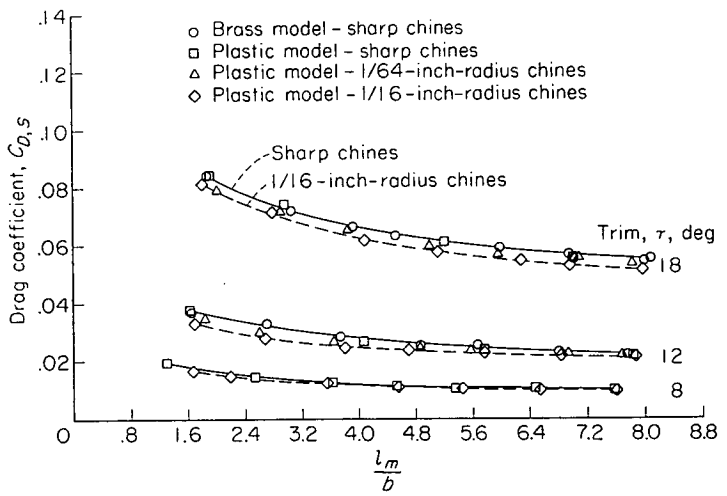


FIGURE 26.—The effect of rounded chines on the drag of a 4-inch-beam rectangular flat plate.

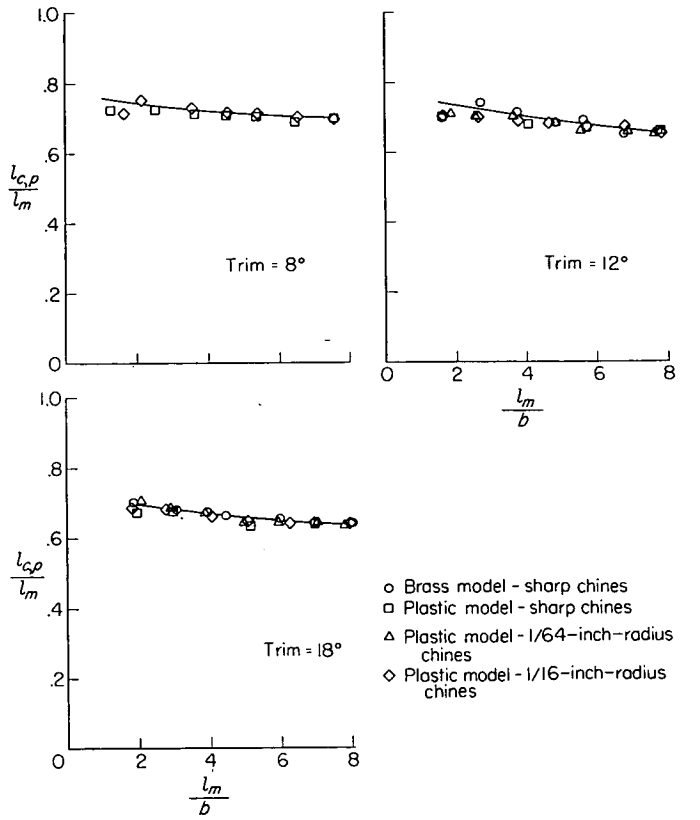
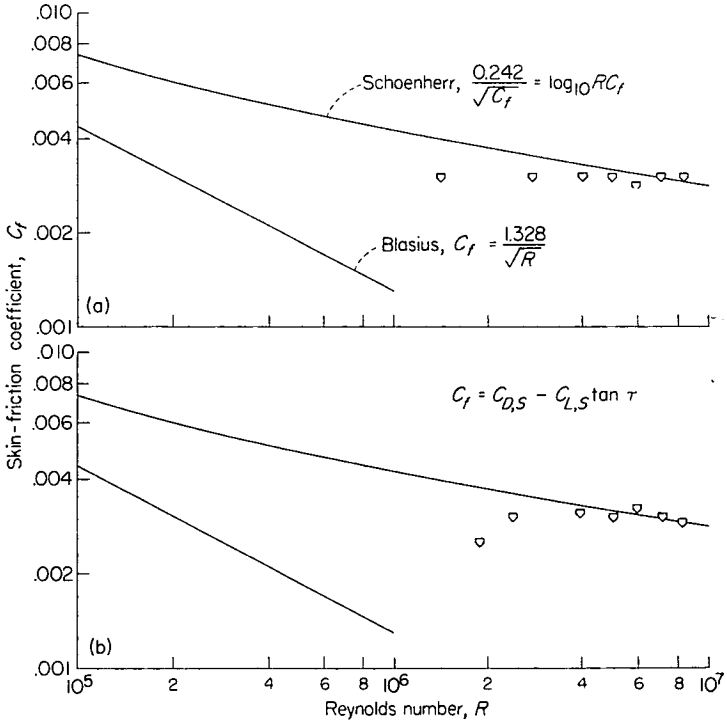


FIGURE 27.—The effect of rounded chines on the center of pressure of a 4-inch-beam rectangular flat plate.



(a) Sharp chines.
(b) 1/16-inch-radius chines.

FIGURE 28.—Variation of skin-friction coefficient with Reynolds number. Trim, 8°.

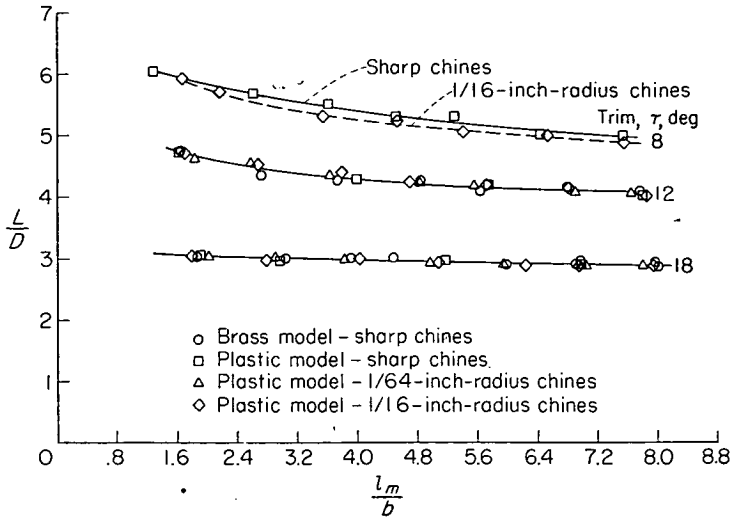


FIGURE 29.—Comparison of lift-drag ratios for flat-plate models having sharp chines with flat-plate models having rounded chines.

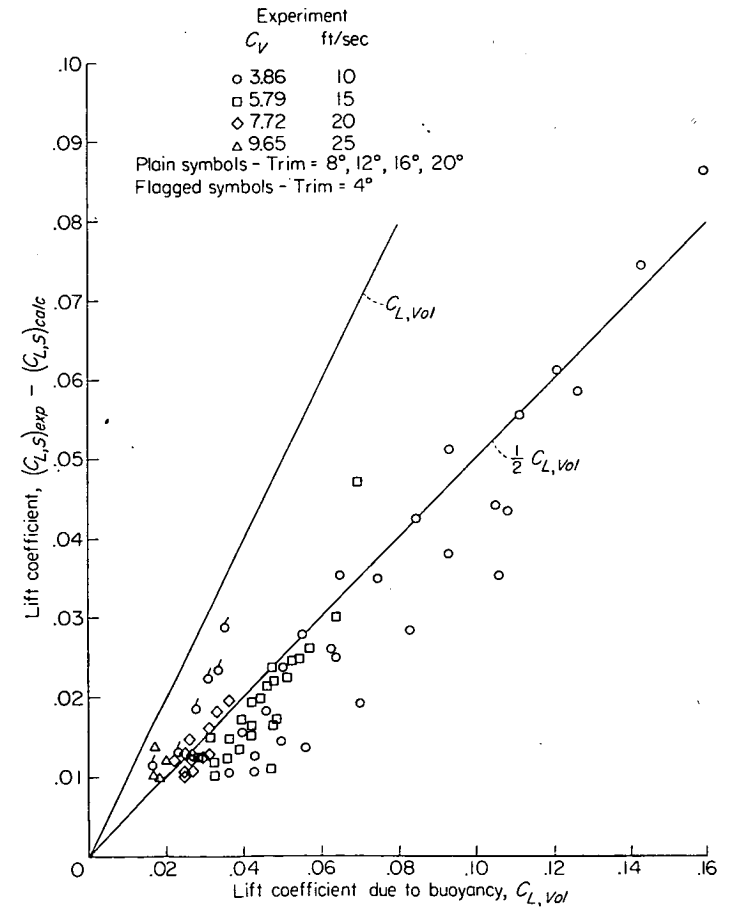
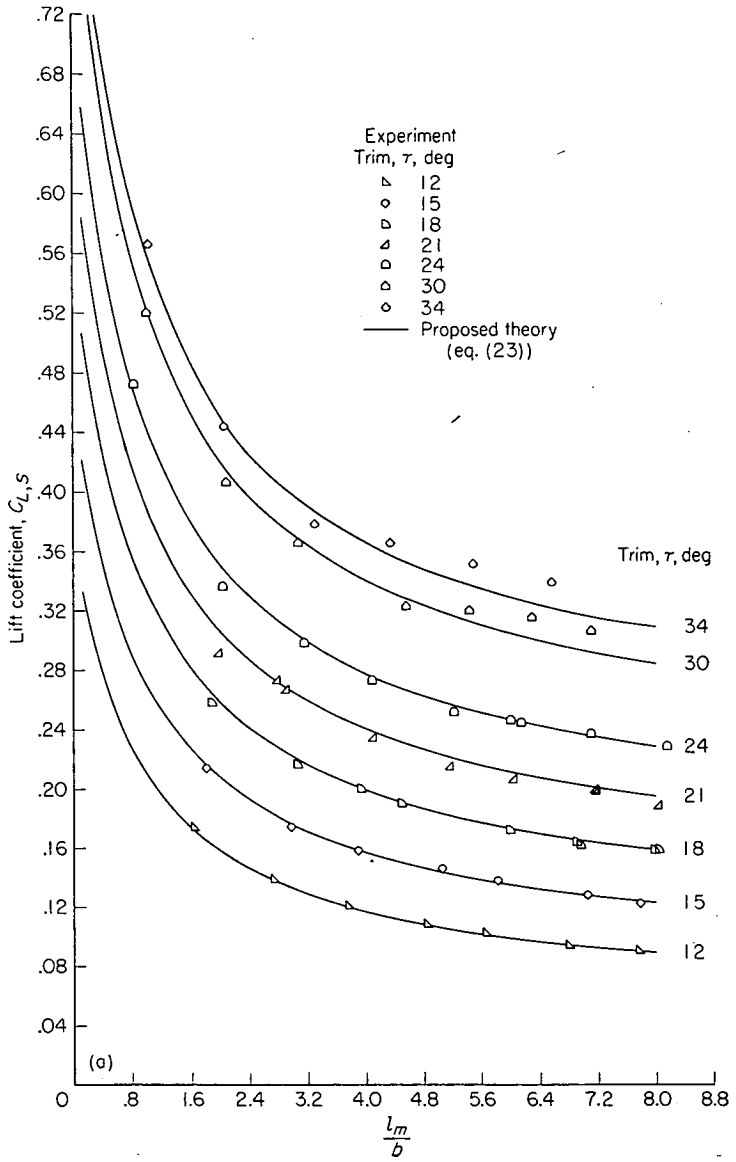
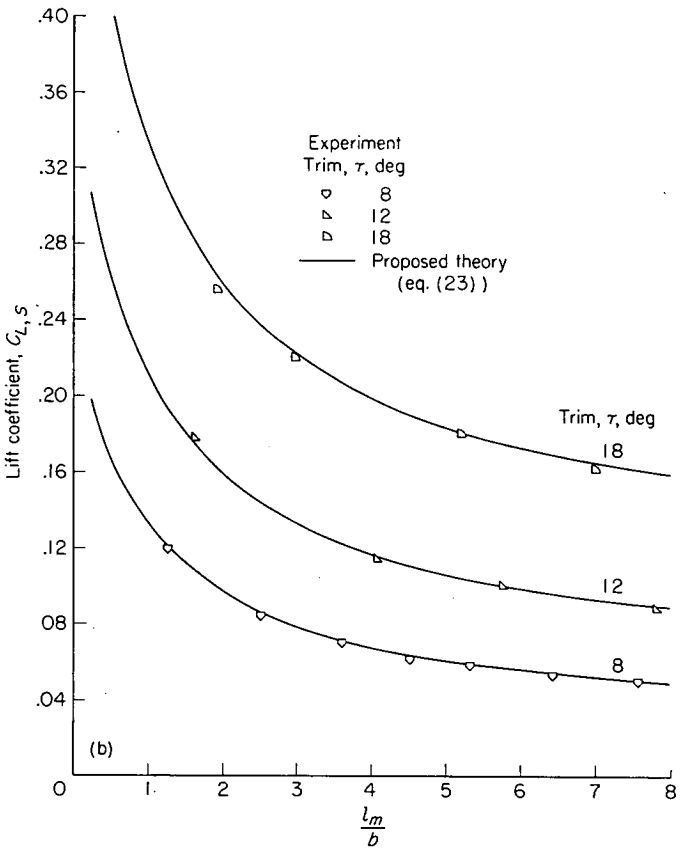


FIGURE 30.—Lift coefficient due to buoyancy for various speed coefficients. (Data of ref. 31.) Calculated value of $C_{L,\beta}$ was determined from equation (20) with $C_{D,c}=1.15$ (see fig. 32 (c)).

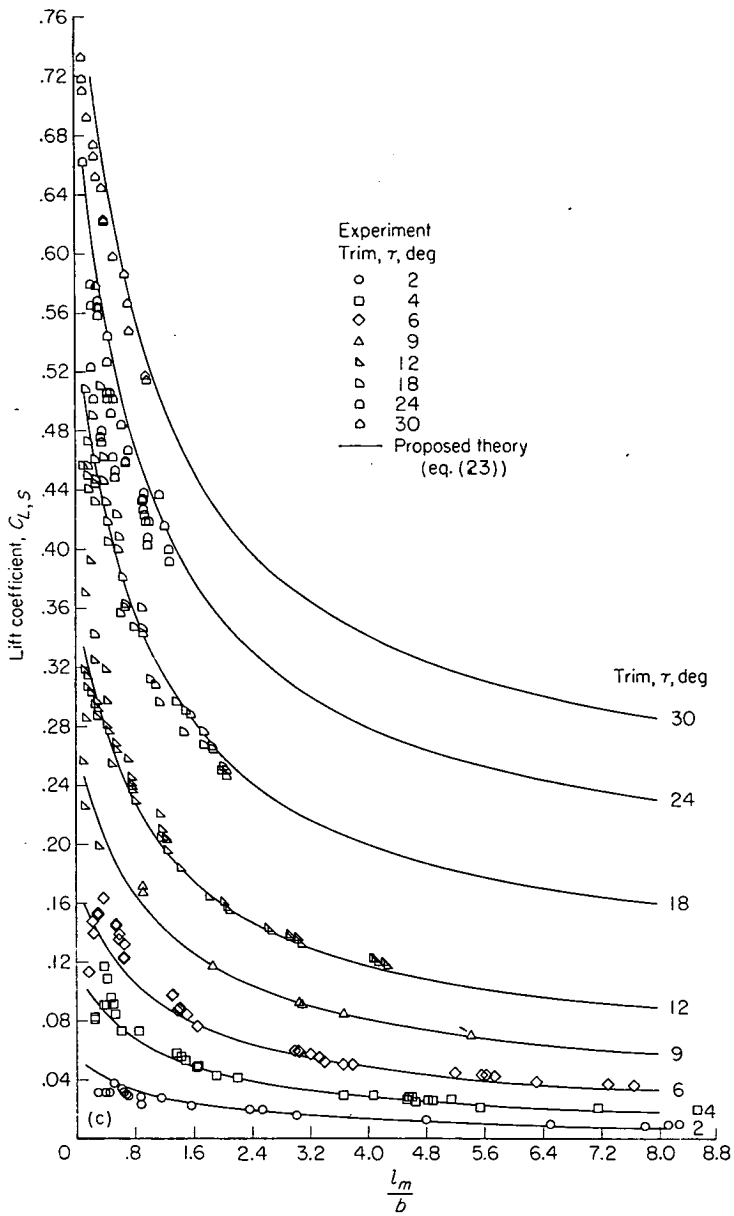


(a) Data of present report (brass model).

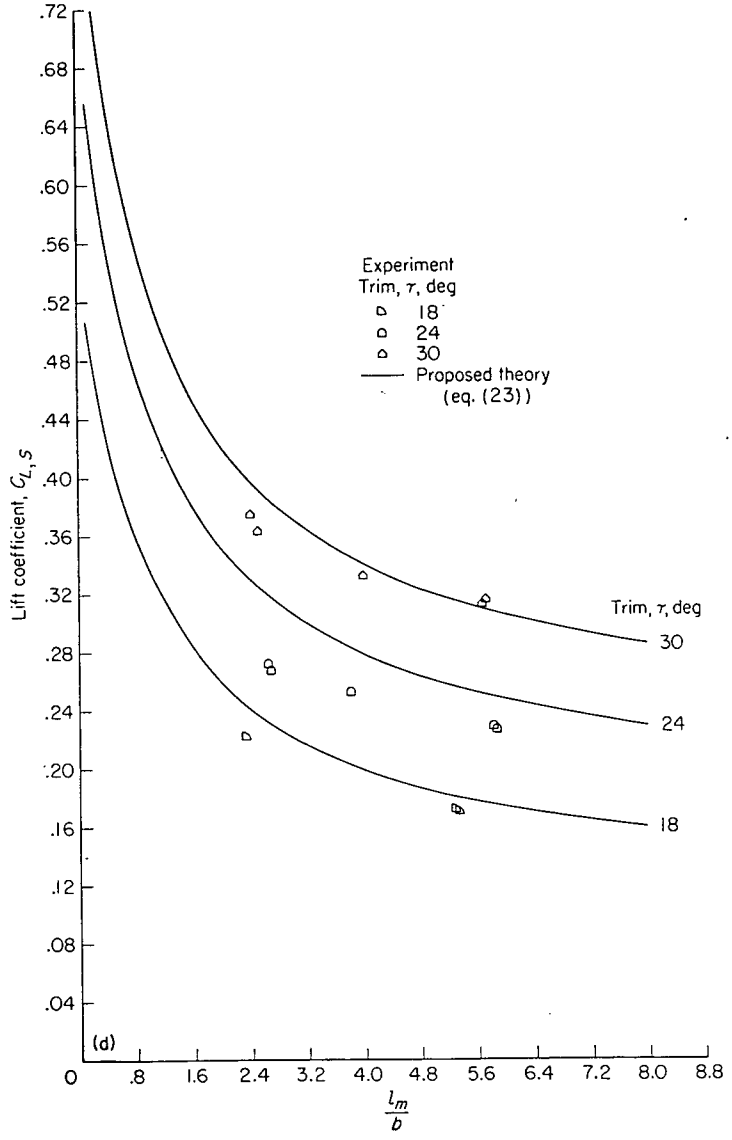
FIGURE 31.—Comparison of proposed theory with experimental lift coefficients for rectangular-flat-plate planing surfaces.



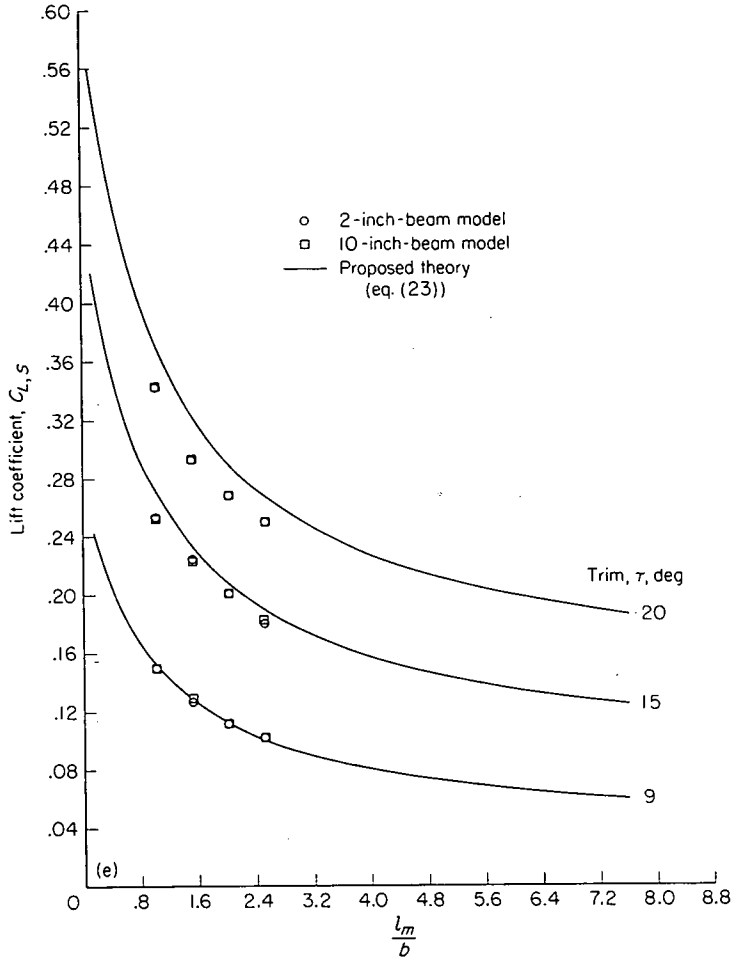
(b) Data of present report (sharp-chine plastic model).
FIGURE 31.—Continued.



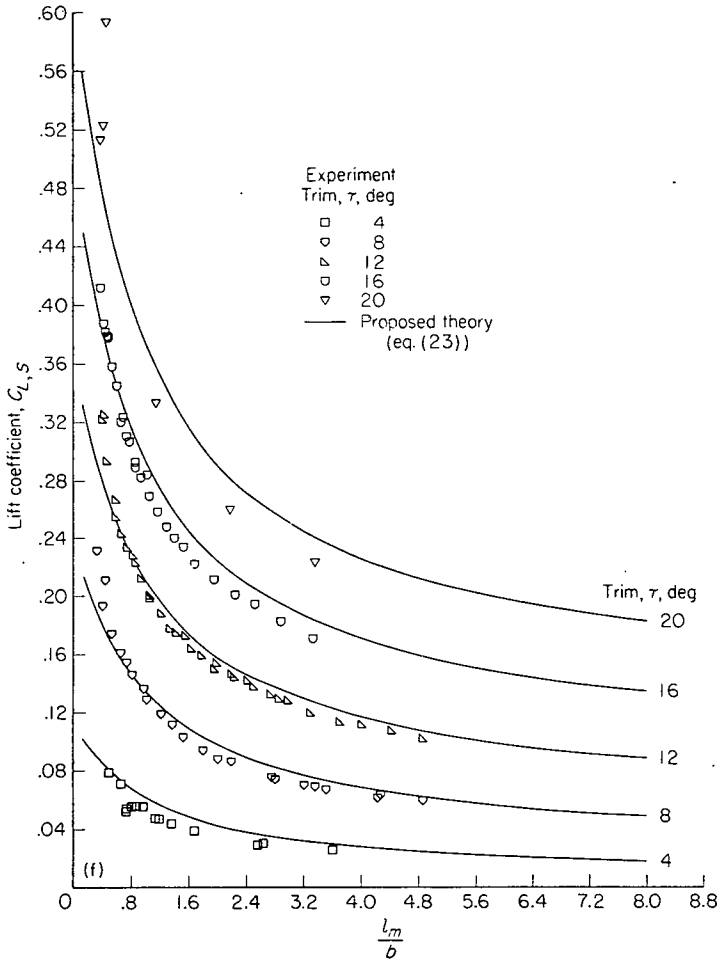
(c) Data of Weinstein and Kapryan (ref. 23).
FIGURE 31.—Continued.



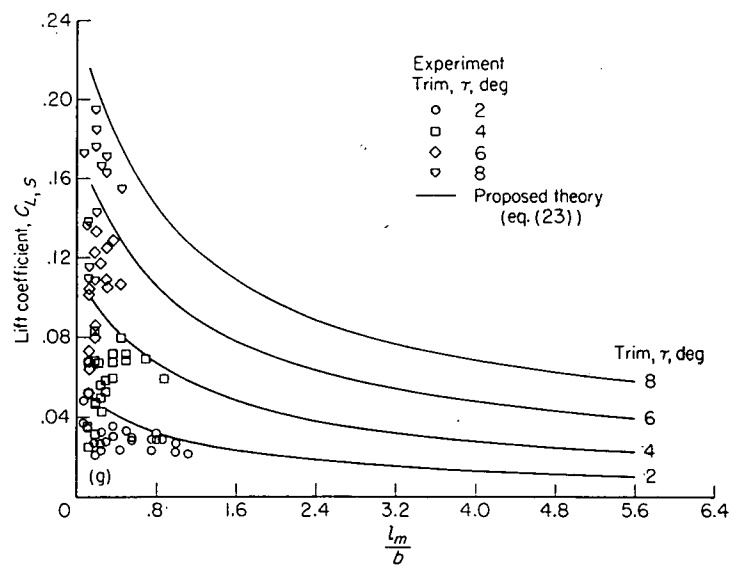
(d) Data of Farshing (ref. 12).
FIGURE 31.—Continued.



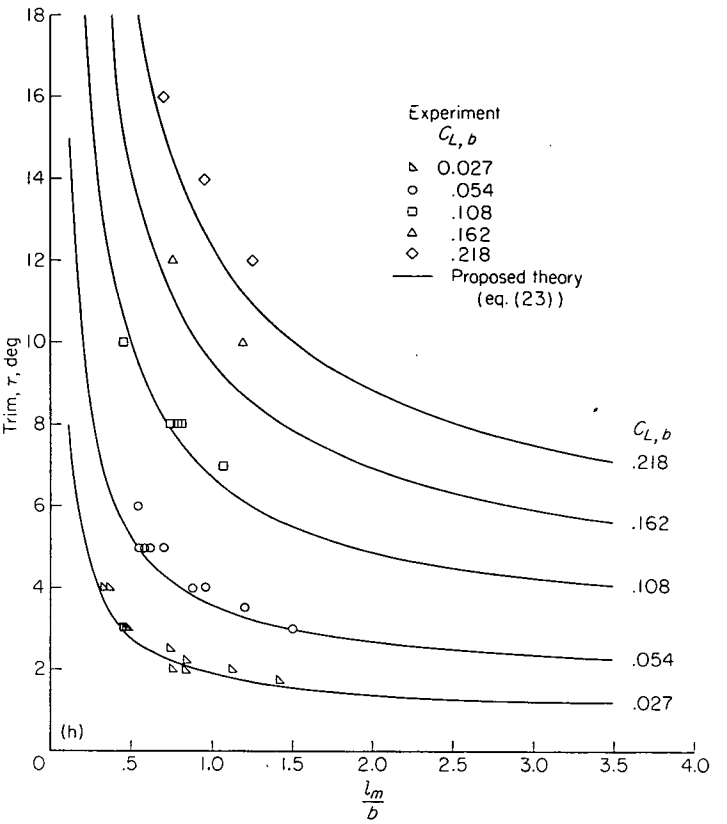
(e) Data of McBride (ref. 32).
FIGURE 31.—Continued.



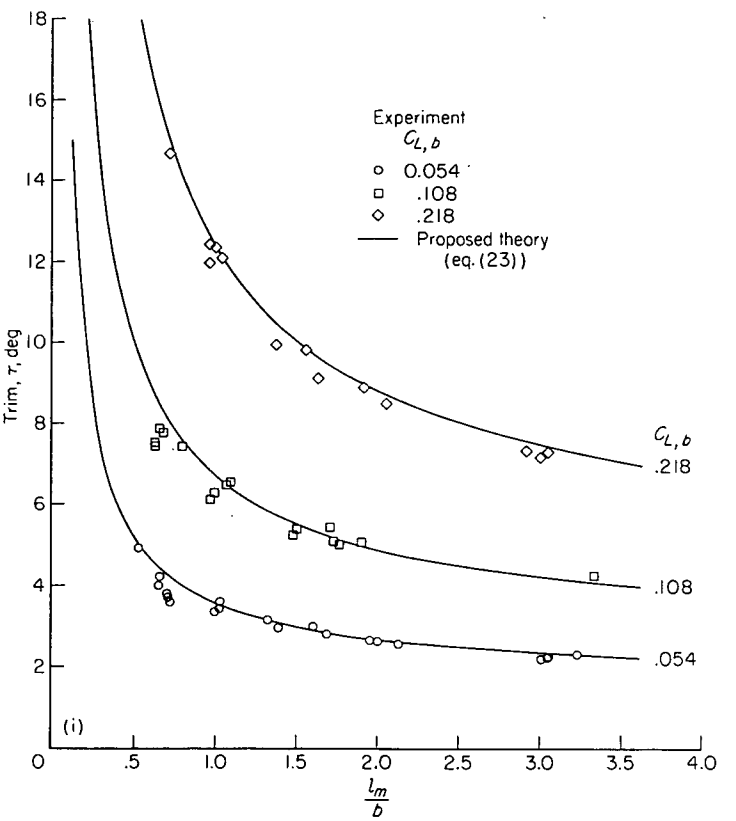
(f) Data of Wadlin and McGehee (ref. 31).
FIGURE 31.—Continued.



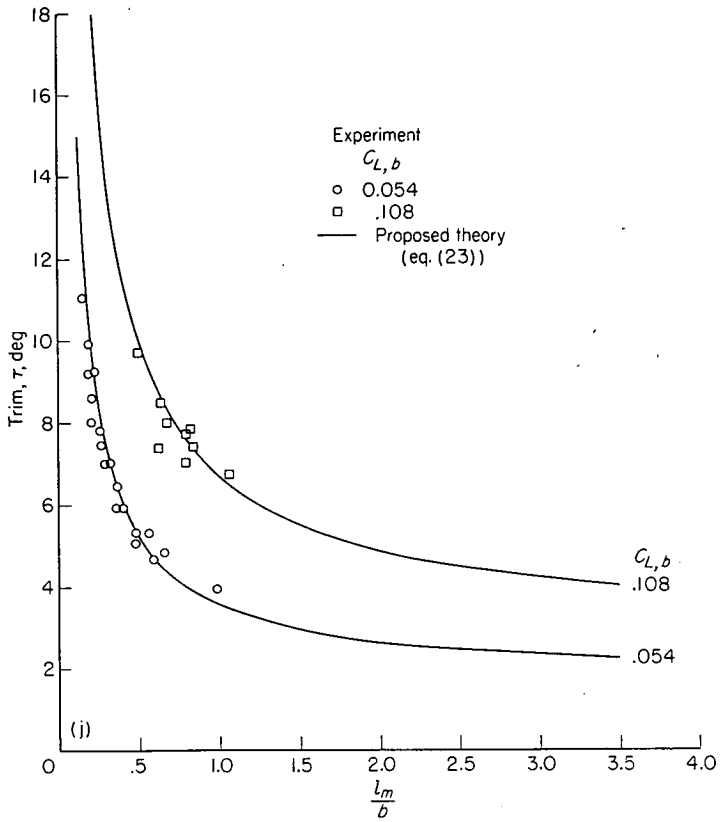
(g) Data of Shoemaker (ref. 33).
FIGURE 31.—Continued.



(h) Data of Locke (ref. 34).
FIGURE 31.—Continued.

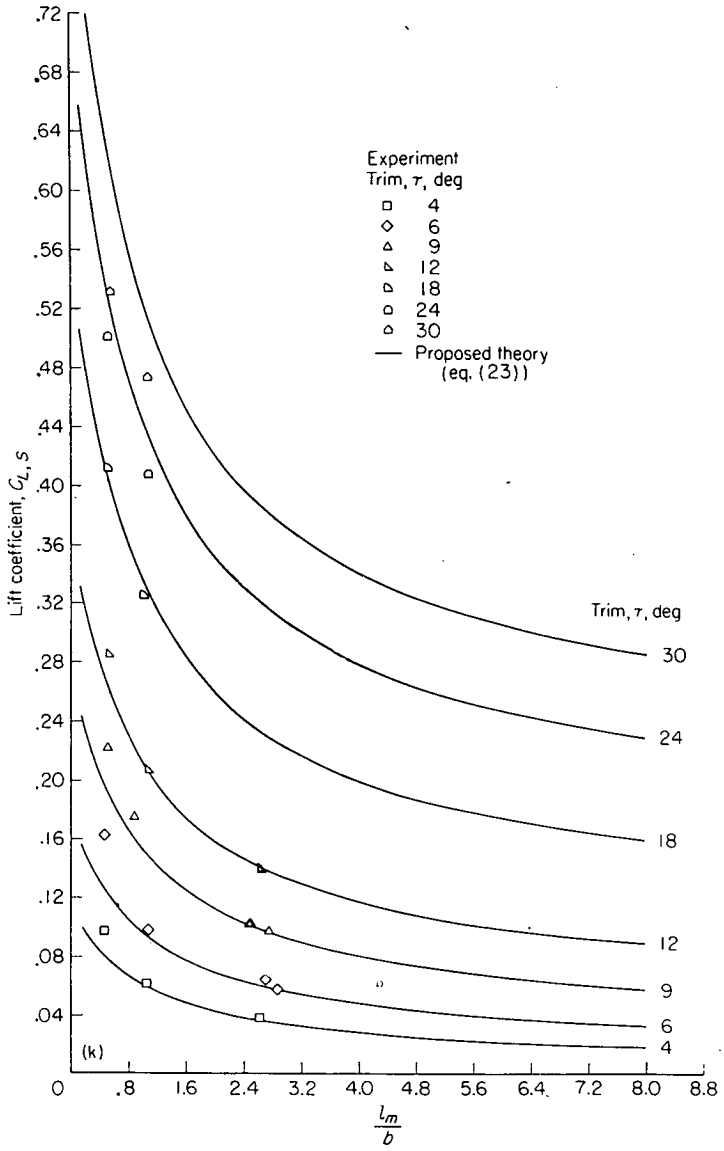


(i) Data of Sambraus (ref. 16).
FIGURE 31.—Continued.



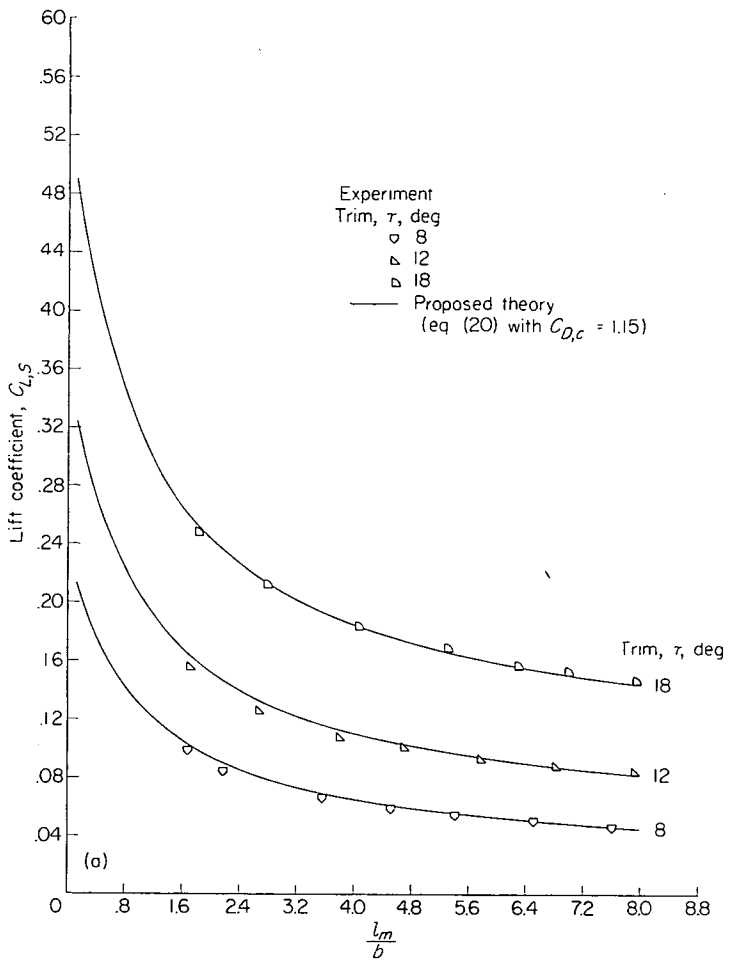
(j) Data of Sottorf (ref. 15).

FIGURE 31.—Continued.



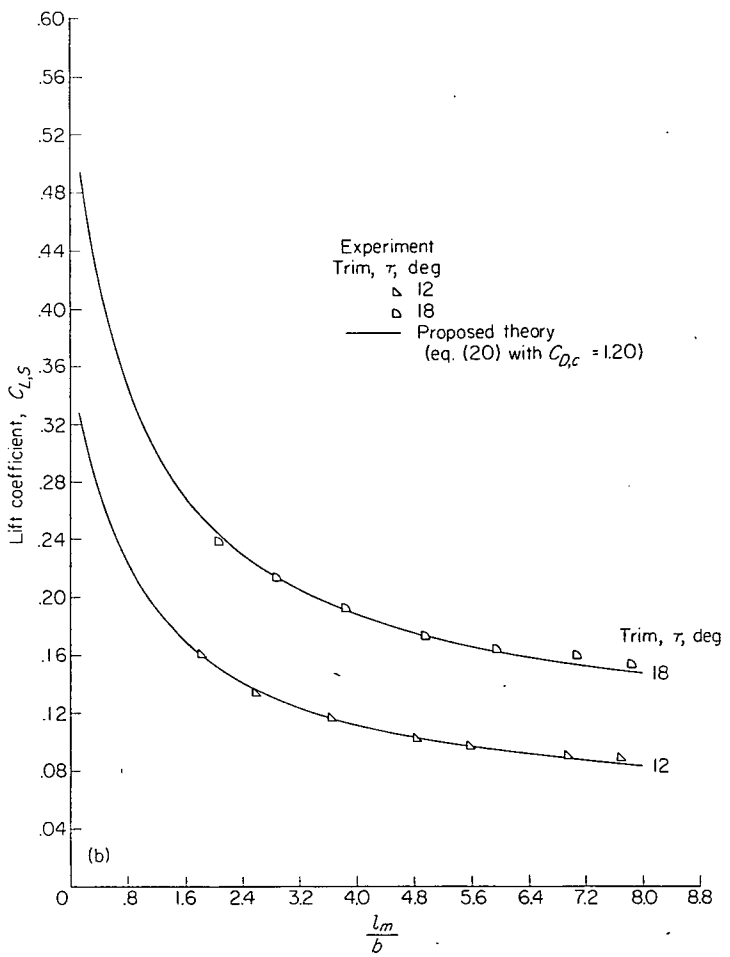
(k) Data of Kapryan and Boyd (ref. 25).

FIGURE 31.—Concluded.



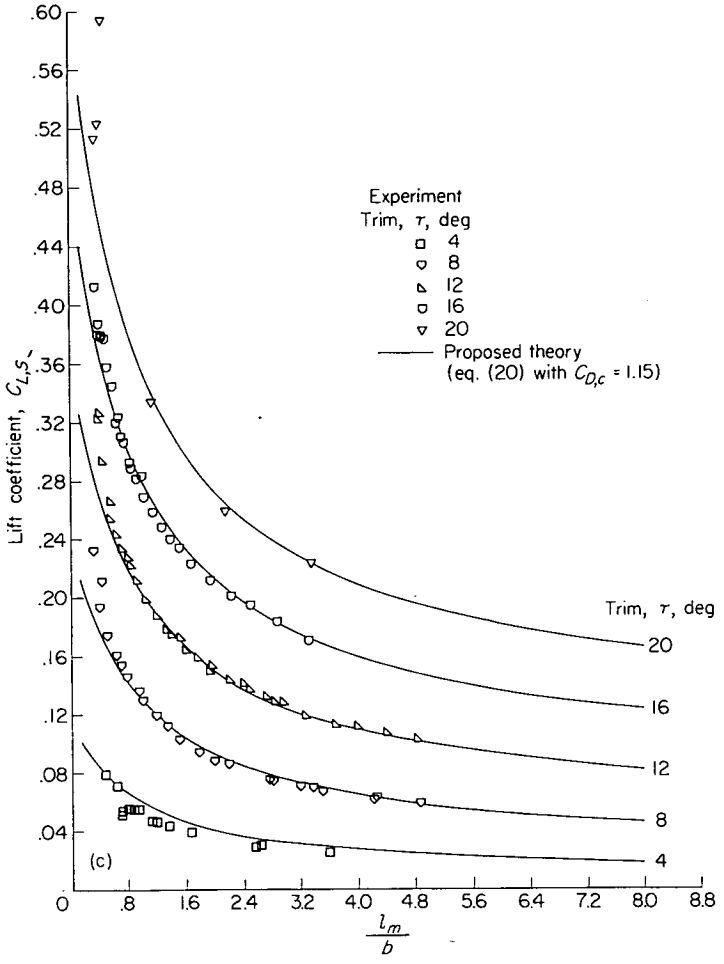
(a) Data of present report (1/16-inch-radius chines).

FIGURE 32.—Comparison of proposed theory with experimental lift coefficients for rectangular-flat-plate planing surfaces having rounded chines.

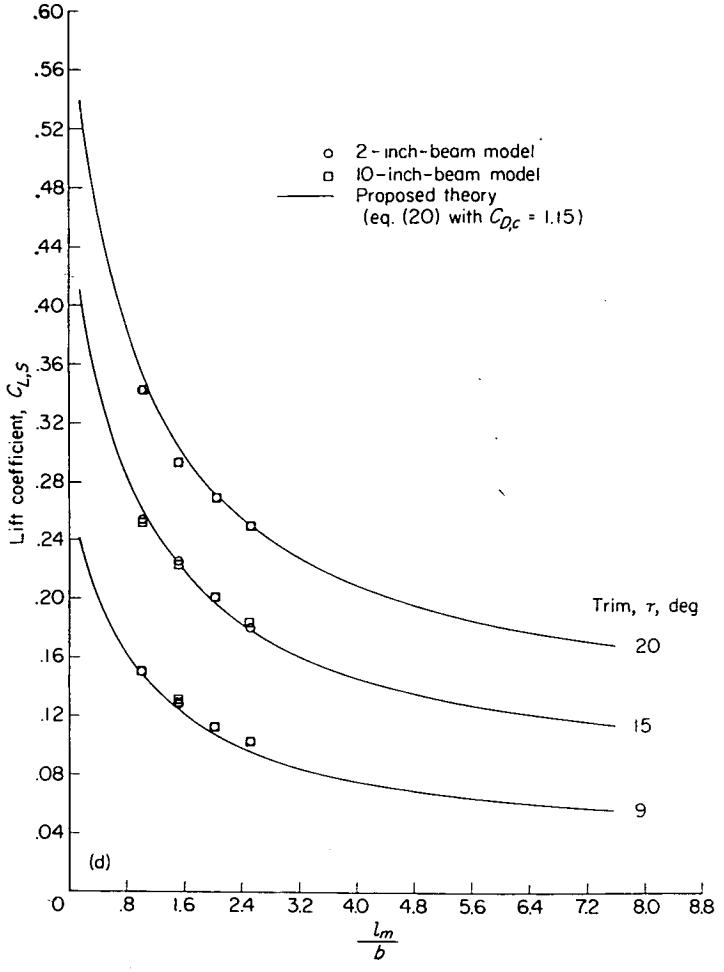


(b) Data of present report (1/64-inch-radius chines).

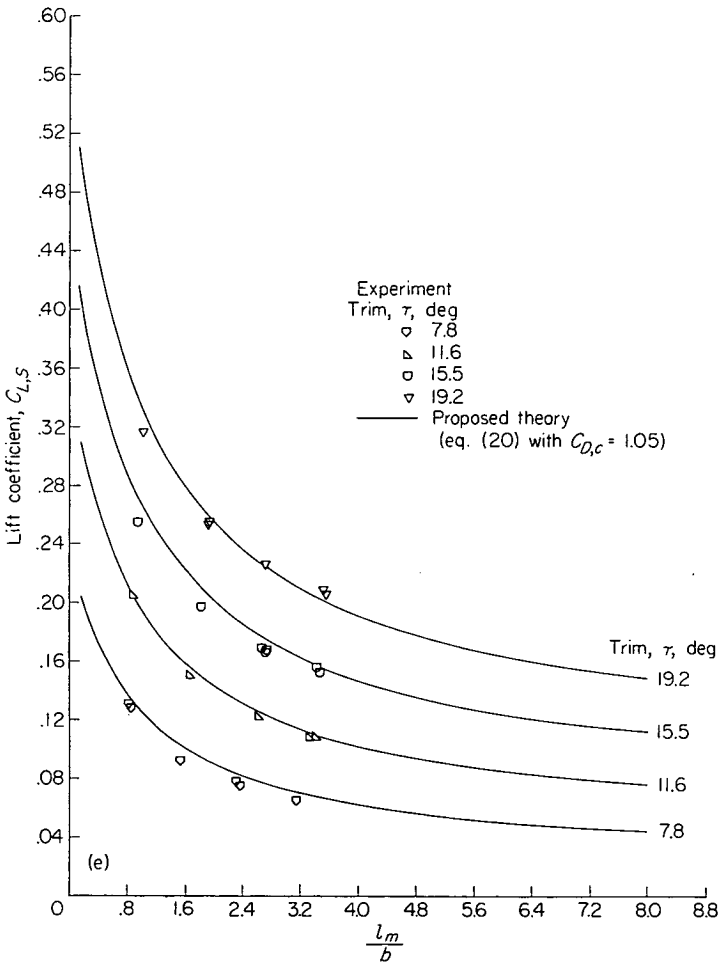
FIGURE 32.—Continued.



(c) Data of Wadlin and McGehee (ref. 31).
FIGURE 32.—Continued.

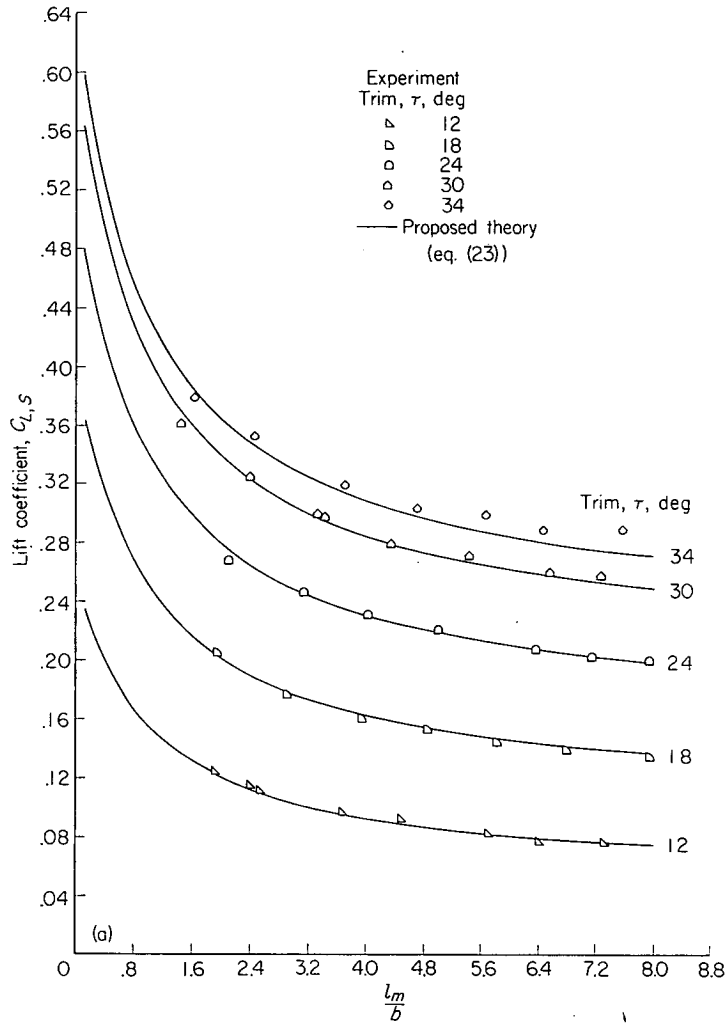


(d) Data of McBride (ref. 32).
FIGURE 32.—Continued.



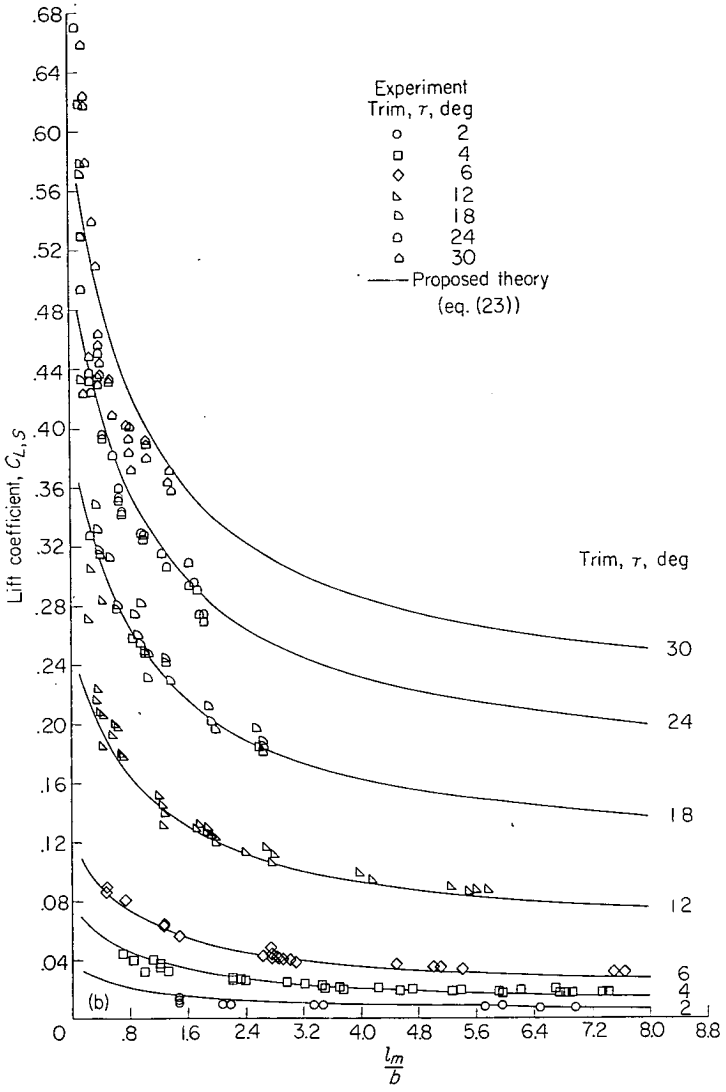
(e) Data of Christopher (ref. 35).

FIGURE 32.—Concluded.



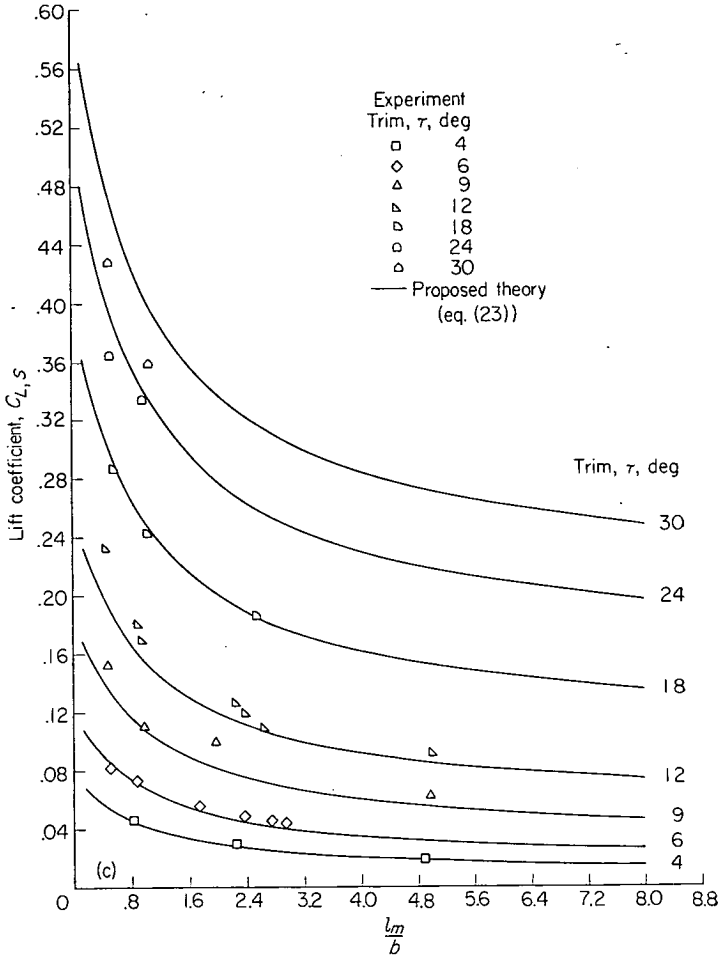
(a) Data of present report.

FIGURE 33.—Comparison of proposed theory with experimental lift coefficients for a surface having a 20° angle of dead rise.



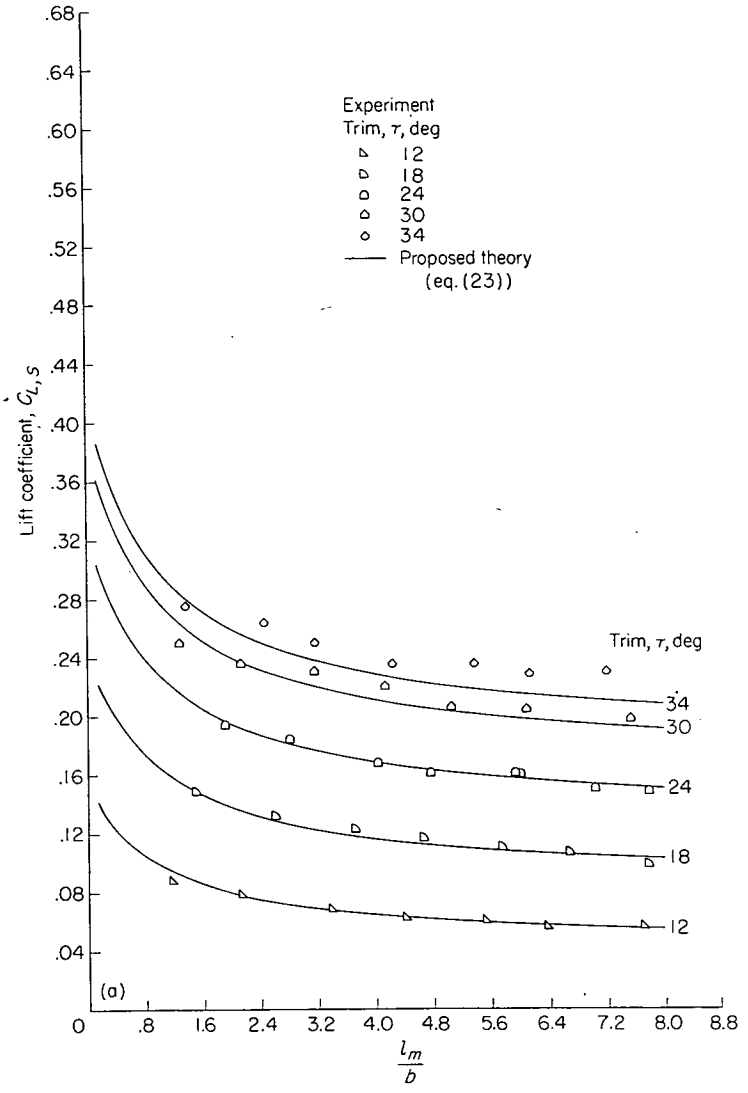
(b) Data of Chambliss and Boyd (ref. 28).

FIGURE 33.—Continued.



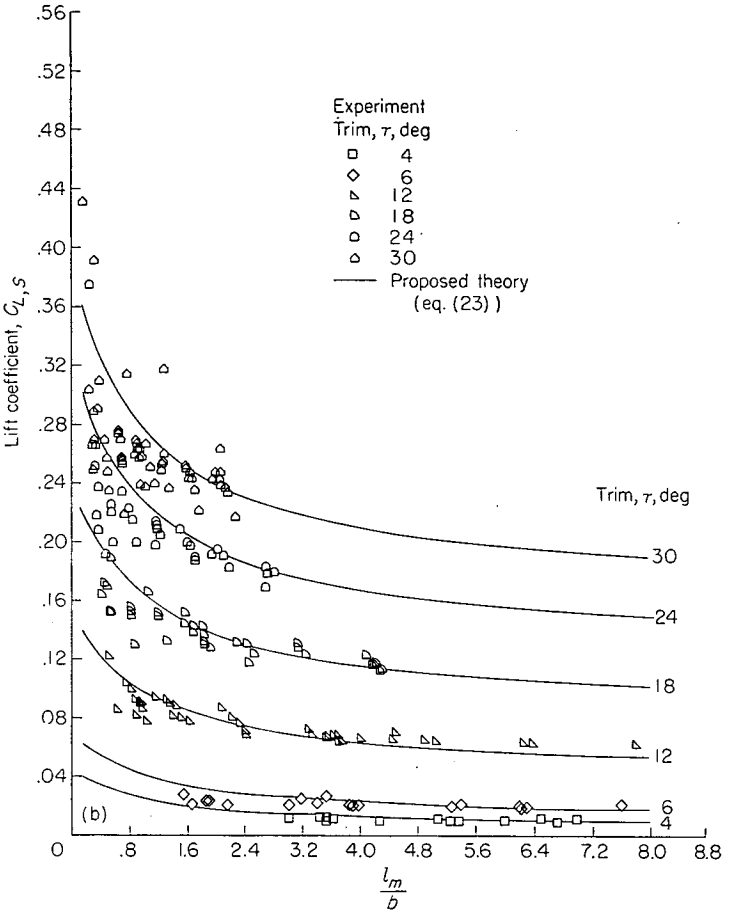
(c) Data of Kapryan and Boyd (ref. 25).

FIGURE 33.—Concluded.



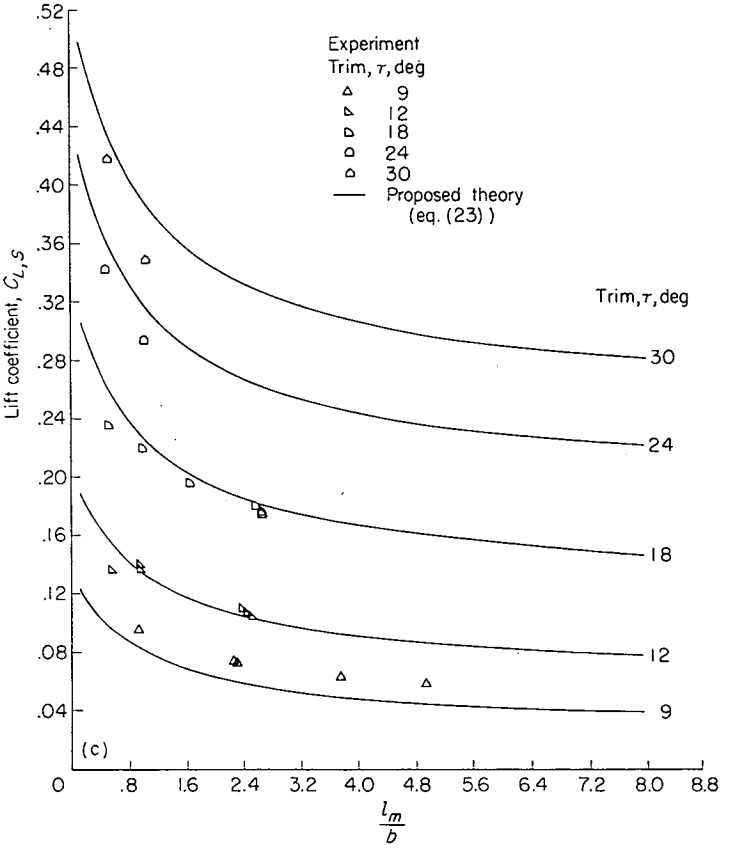
(a) Data of present report.

FIGURE 34.—Comparison of proposed theory with experimental lift coefficients for a surface having a 40° angle of dead rise.



(b) Data of Chambliss and Boyd (ref. 28).

FIGURE 34.—Continued.



(c) Data of Kapryan and Boyd (ref 25).

FIGURE 34.—Concluded.

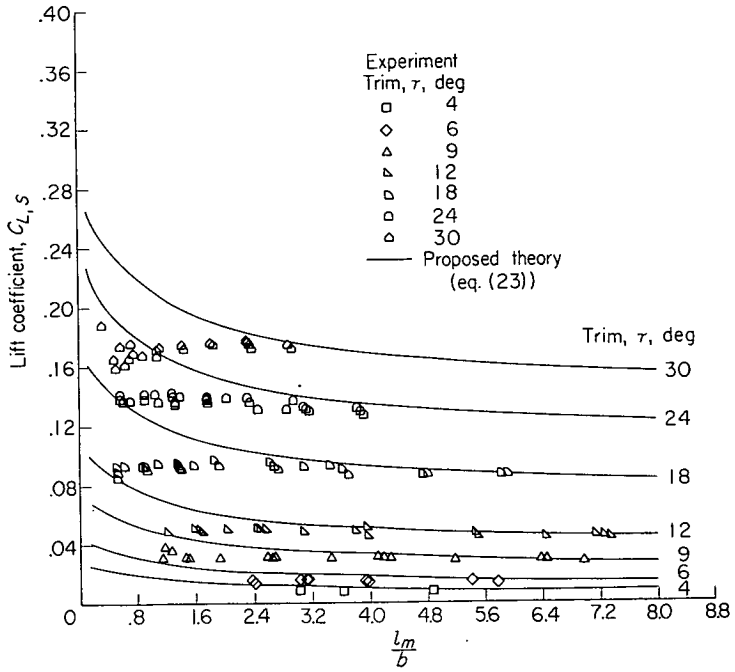
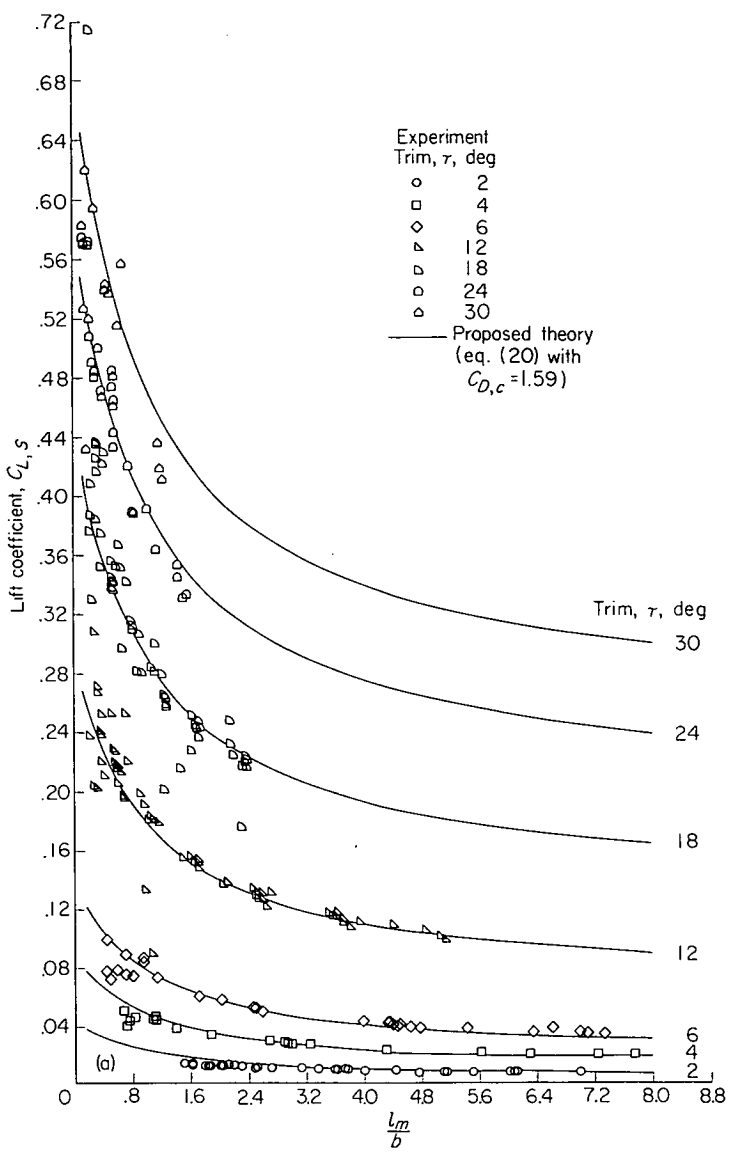
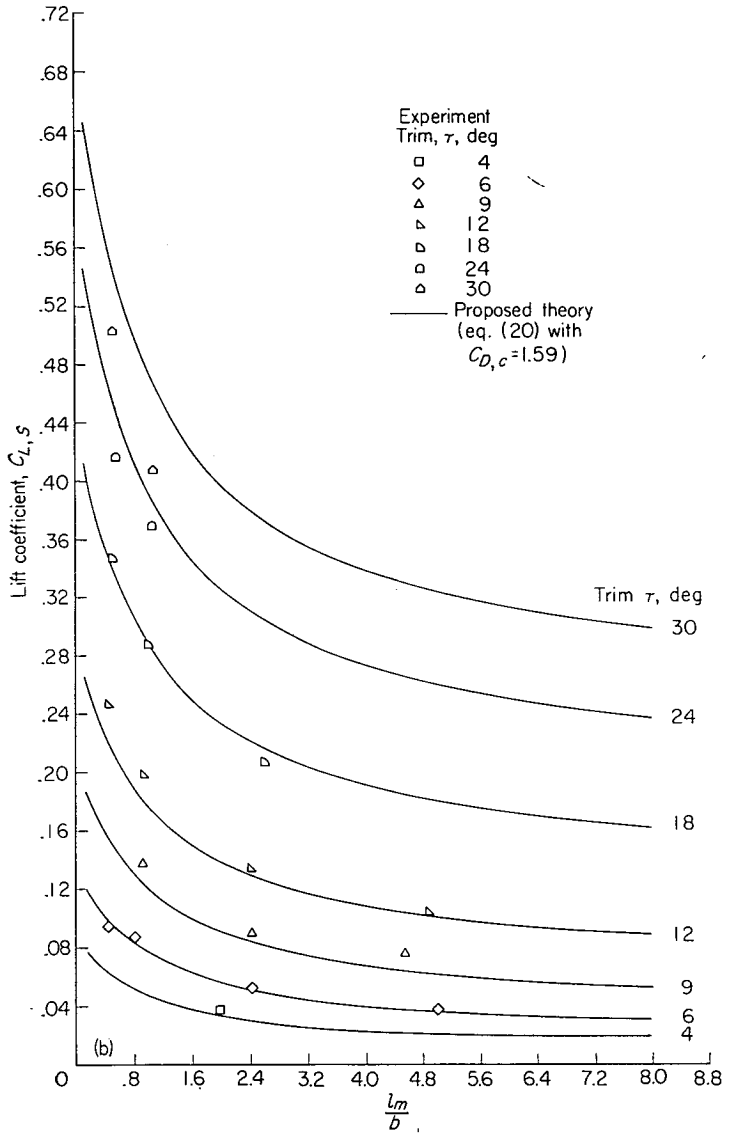


FIGURE 35.—Comparison of proposed theory with experimental lift coefficients for a model having a 50° angle of dead rise. (Data of Springston and Sayre (ref. 36).)



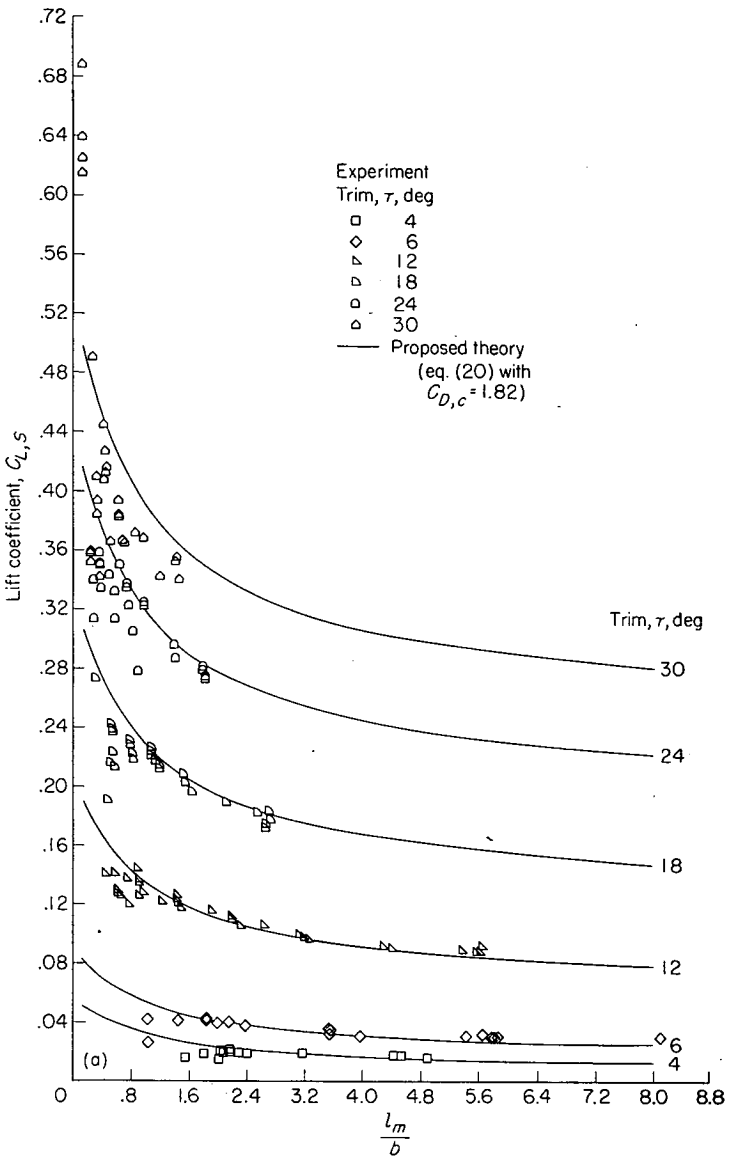
(a) Data of Kapryan and Weinstein (ref. 13).

FIGURE 36.—Comparison of proposed theory with experimental lift coefficients for a surface having a basic angle of dead rise of 20° and horizontal chine flare. (Effective angle of dead rise, 16°.)



(b) Data of Kapryan and Boyd (ref. 25).

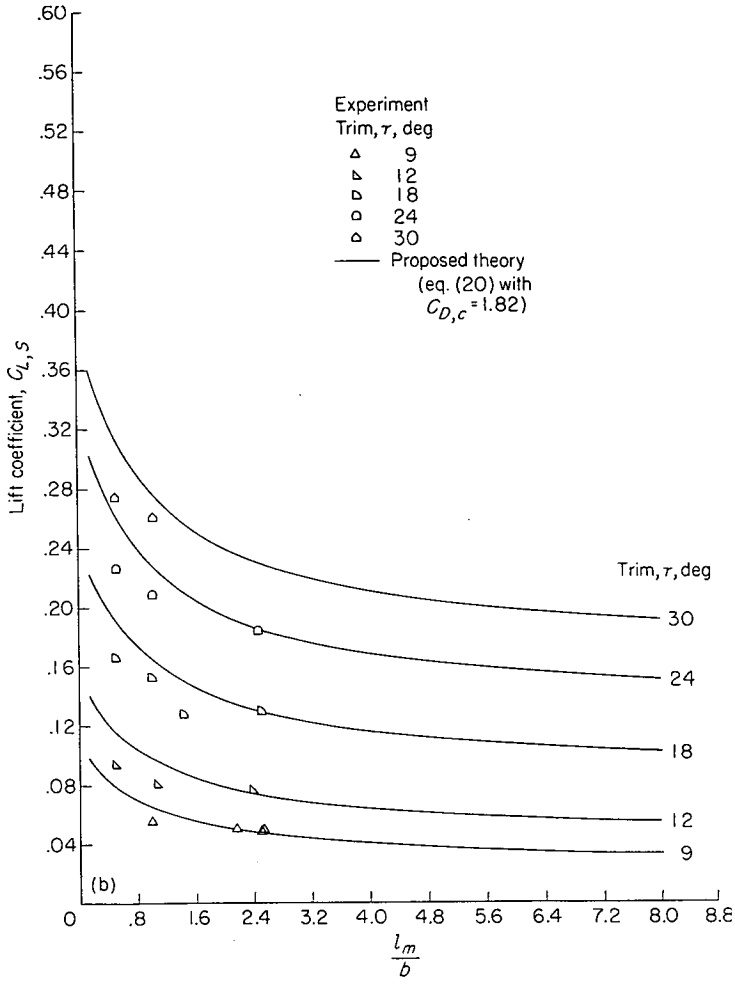
FIGURE 36.—Concluded.



(a) Data of Blanchard (ref. 24).

FIGURE 37.—Comparison of proposed theory with experimental lift coefficients for a surface having a basic angle of dead rise of 40° and horizontal chine flare. (Effective angle of dead rise, 32°47′.)

526597—60——27



(b) Data of Kapryan and Boyd (ref. 25).

FIGURE 37.—Concluded.

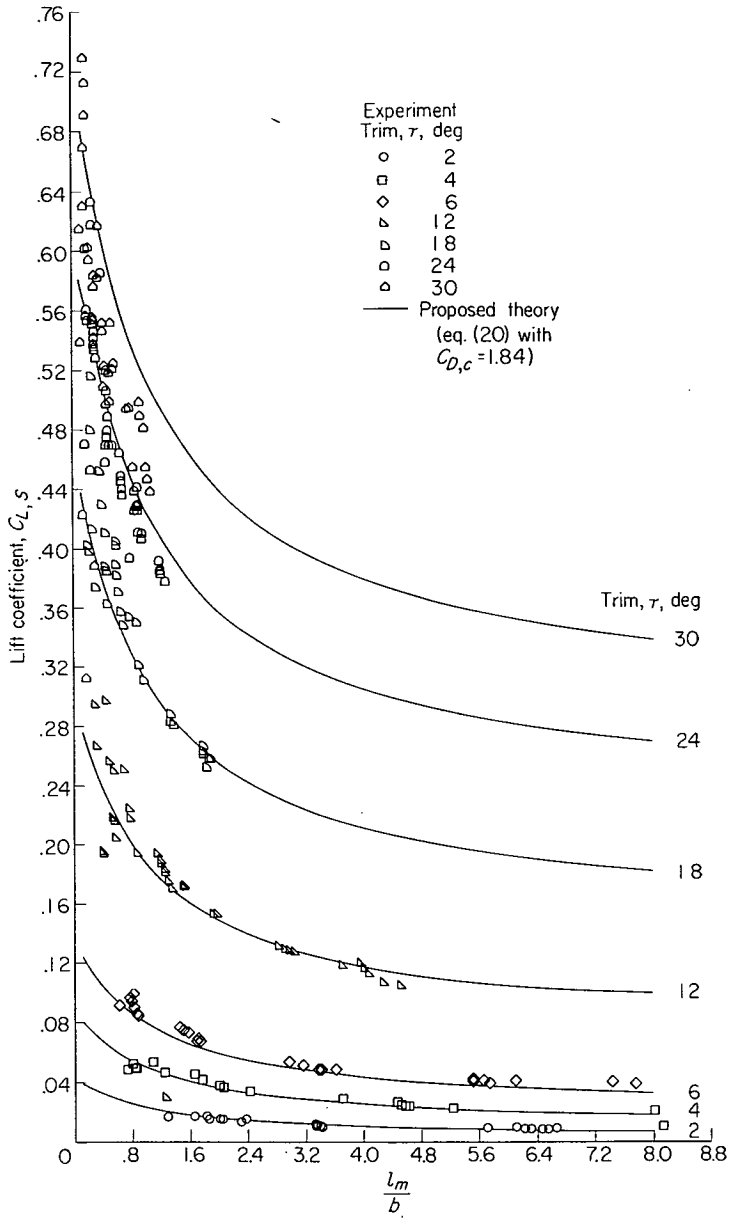


FIGURE 38.—Comparison of proposed theory with experimental lift coefficients for a surface having a basic angle of dead rise of 20° and vertical chine strips. (Effective angle of dead rise, 15°33′.) (Data of Kapryan and Boyd (ref. 26).)

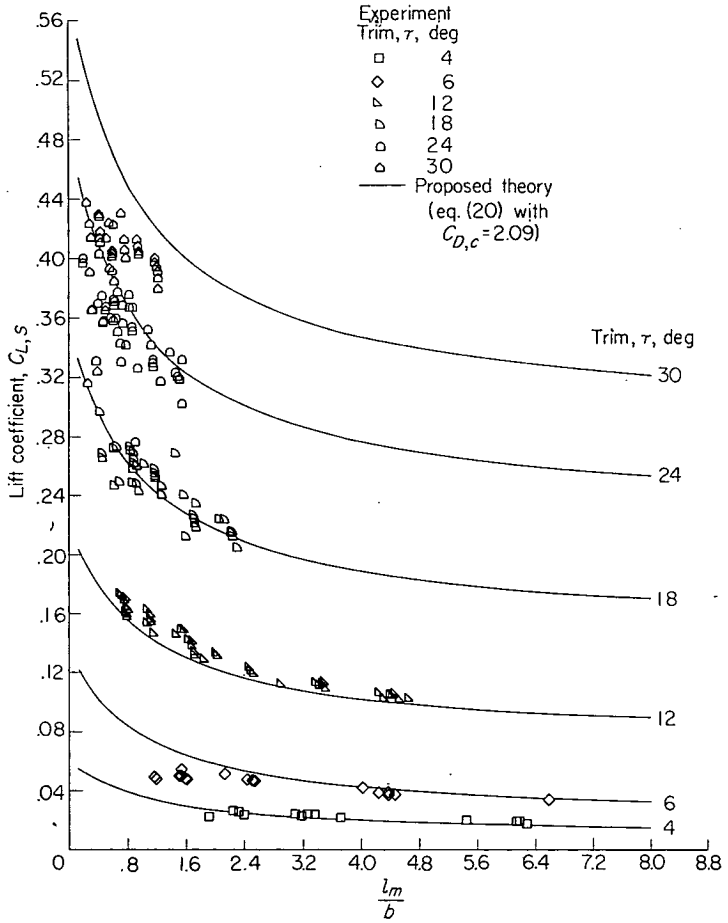
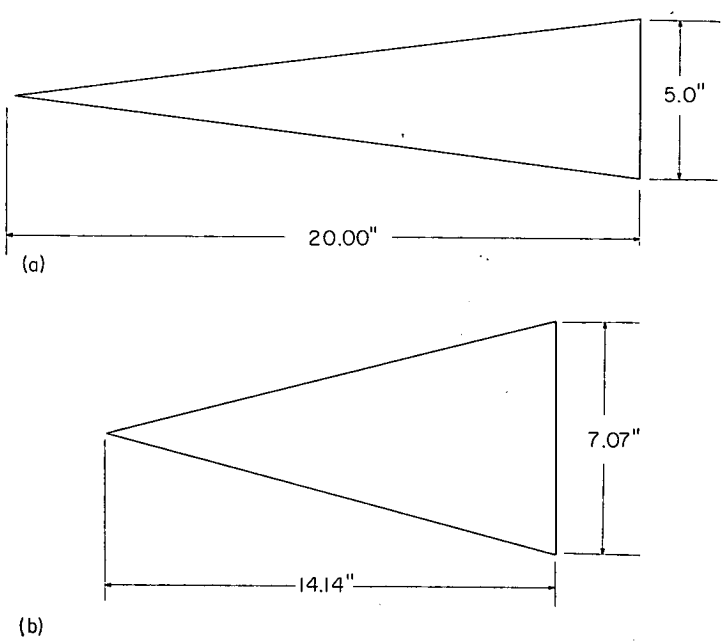


FIGURE 39.—Comparison of proposed theory with experimental lift coefficients for a surface having a basic angle of dead rise of 40° and vertical chine strips. (Effective angle of dead rise, 31°59′.) (Data of Kapryan and Boyd (ref. 26).)



(a) Triangular flat plate; $\frac{l}{b}=4$; $A_t=\frac{1}{4}$.

(b) Triangular flat plate; $\frac{l}{b}=2$; $A_t=\frac{1}{2}$.

FIGURE 40.—Plan forms of triangular-flat-plate models (wooden) planing with base forward.

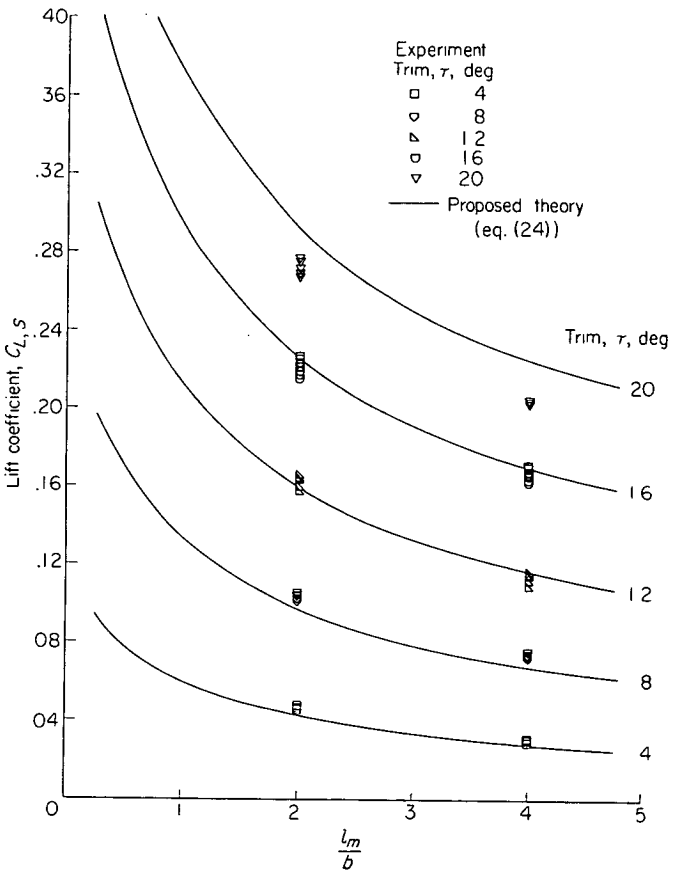
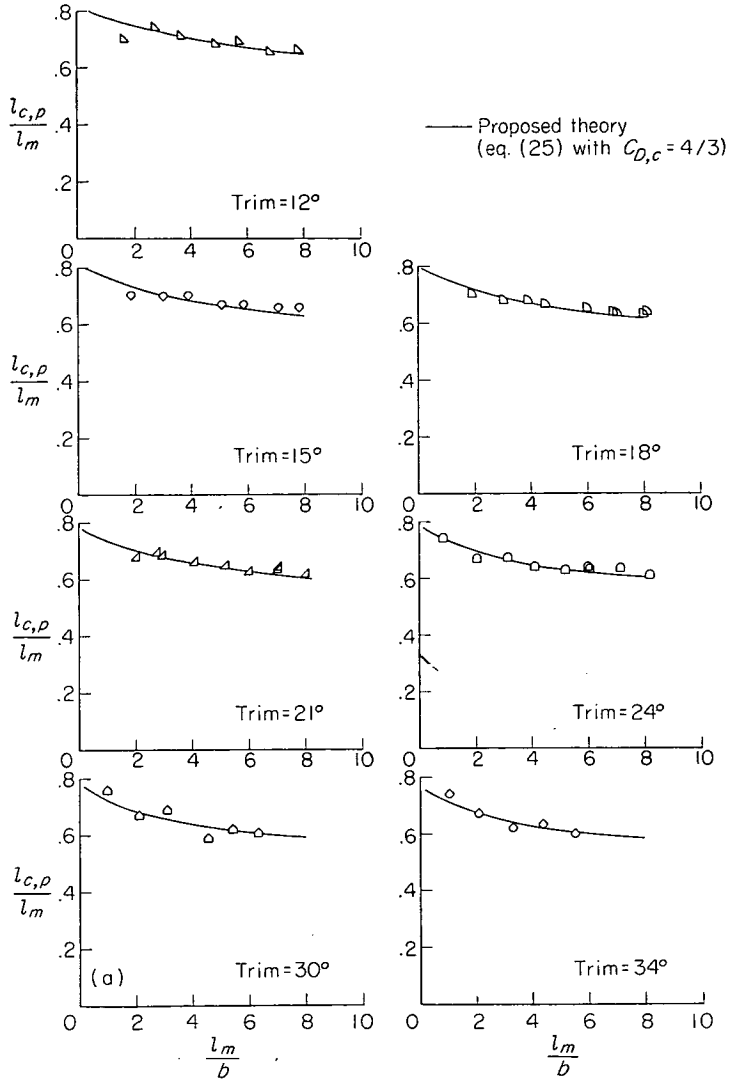
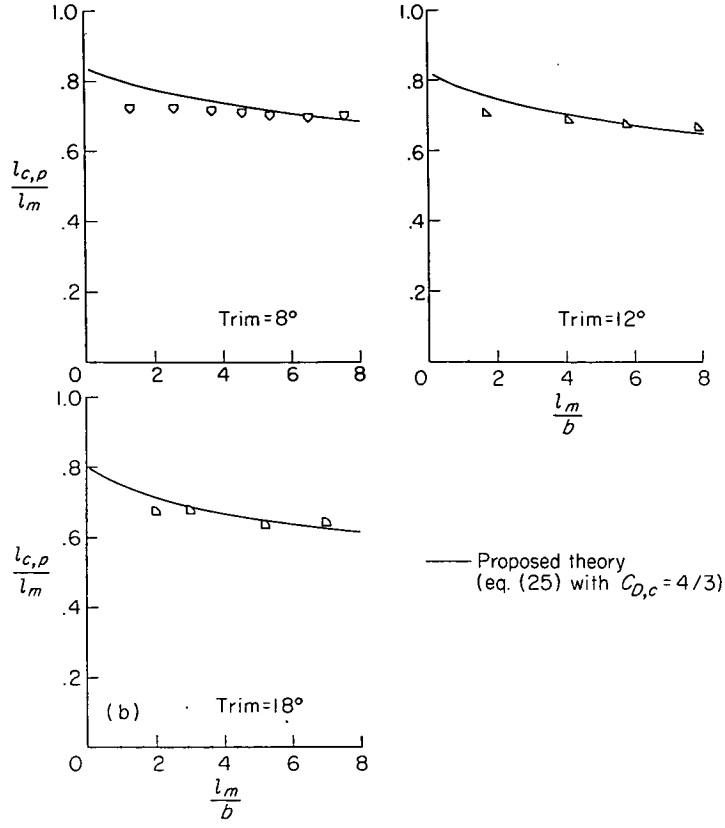


FIGURE 41.—Comparison of proposed theory with experimental lift coefficients for triangular-flat-plate surfaces planing with base forward. (Data of Wadlin and McGehee (ref. 31) and unpublished tank no. 2 data.)



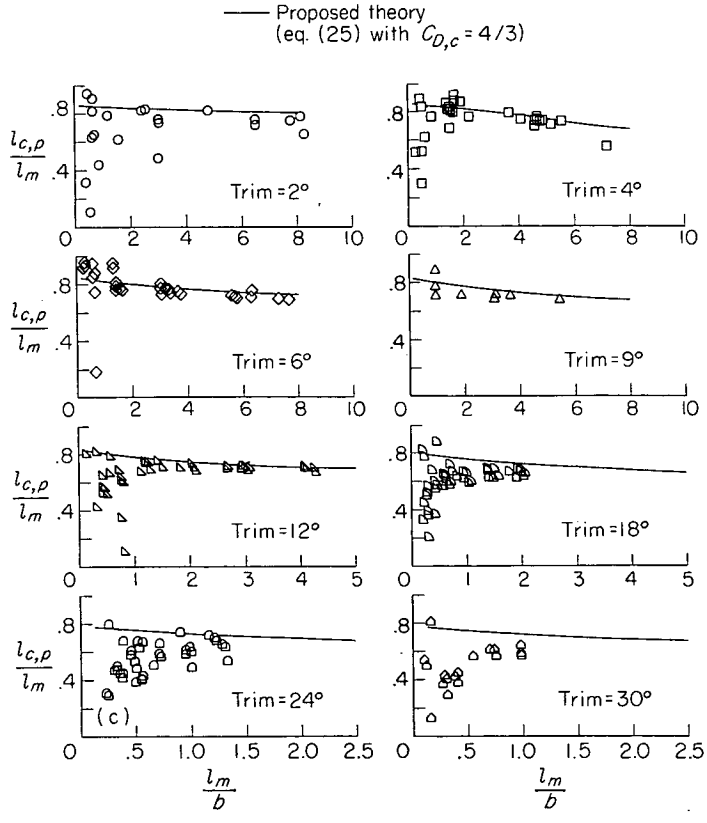
(a) Data of present report (brass model).

FIGURE 42.—Variation of center-of-pressure location with mean wetted-length-beam ratio for rectangular-flat-plate planing surfaces.



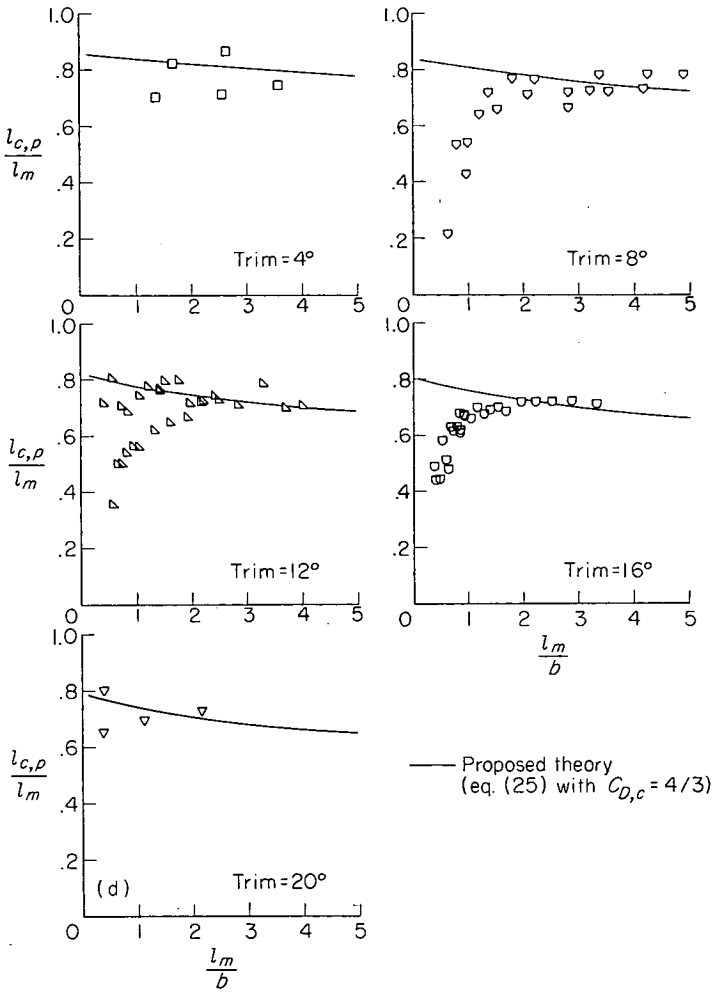
(b) Data of present report (sharp-chine plastic model).

FIGURE 42.—Continued.

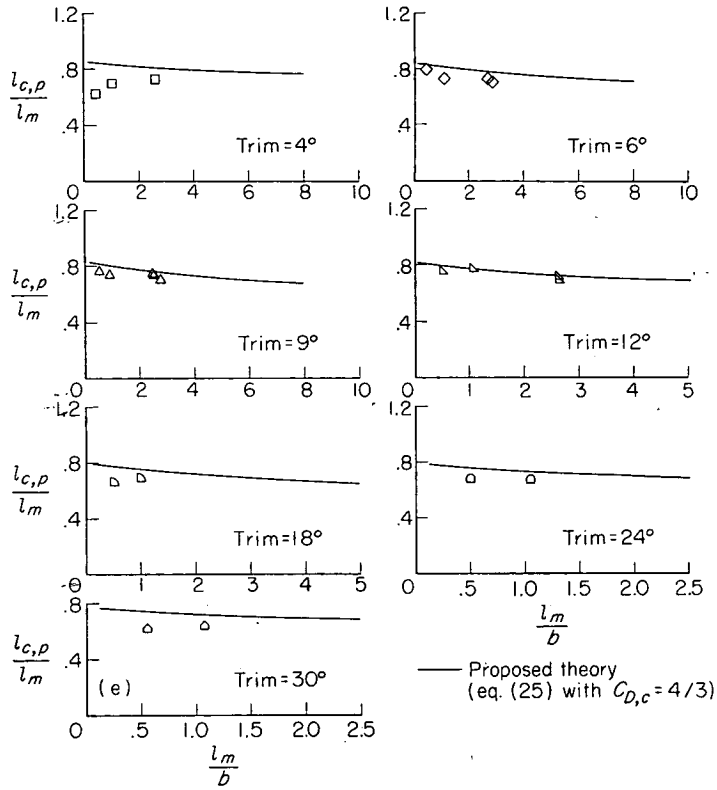


(c) Data of Weinstein and Kapryan (ref. 23).

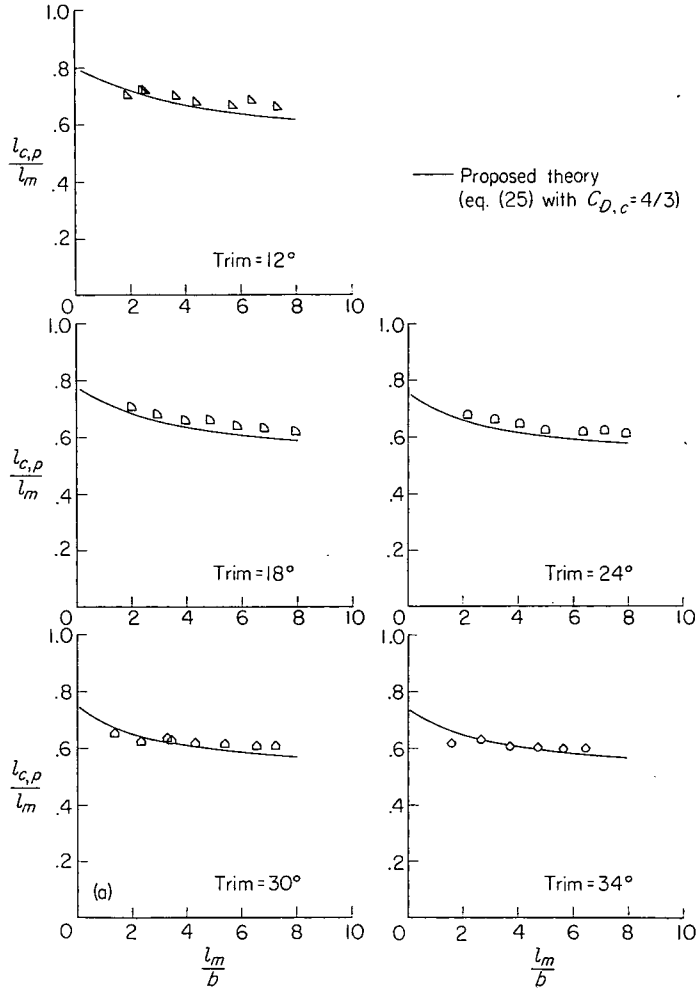
FIGURE 42.—Continued.



(d) Data of Wadlin and McGehee (ref. 31).
FIGURE 42.—Continued.

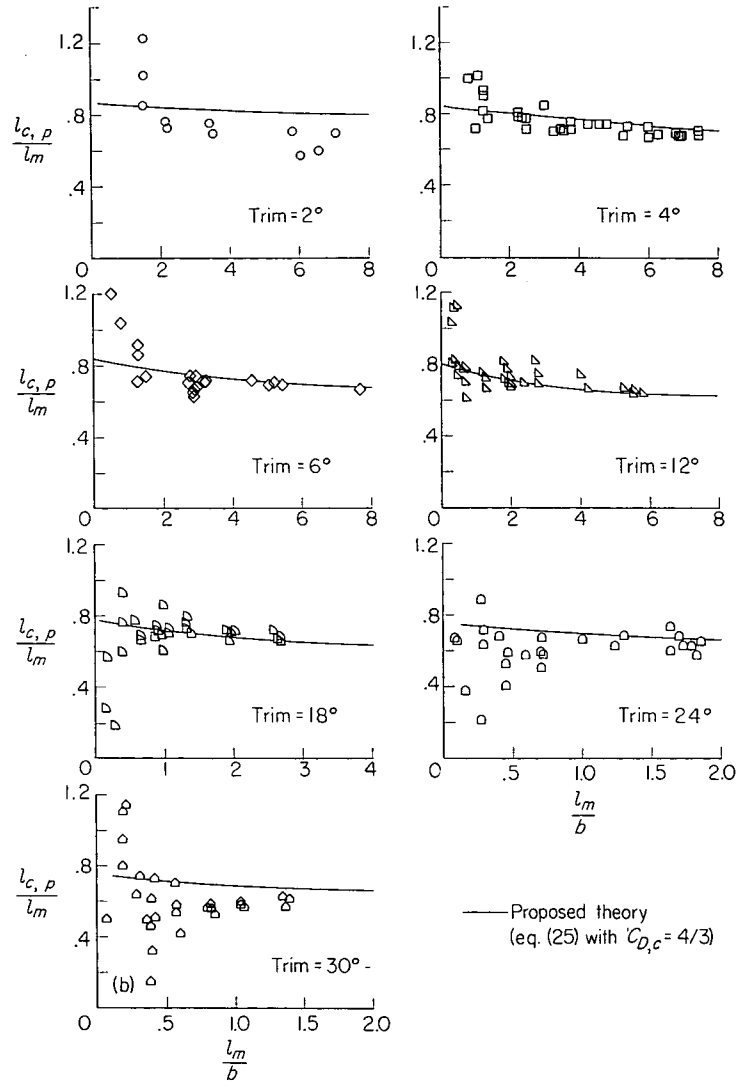


(e) Data of Kapryan and Boyd (ref. 25).
FIGURE 42.—Concluded.



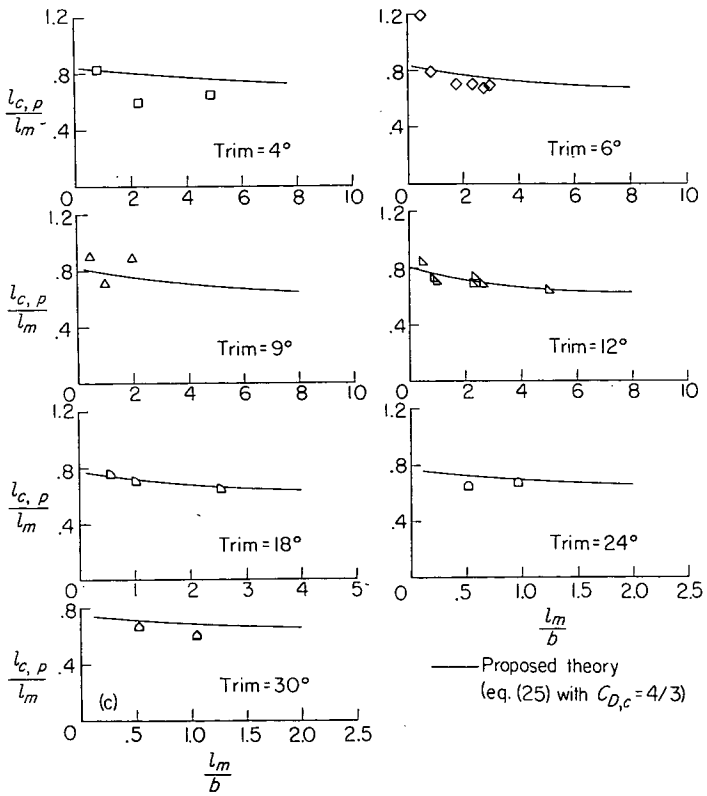
(a) Data of present report.

FIGURE 43.—Variation of center-of-pressure location with mean wetted-length-beam ratio for a surface having a 20° angle of dead rise.



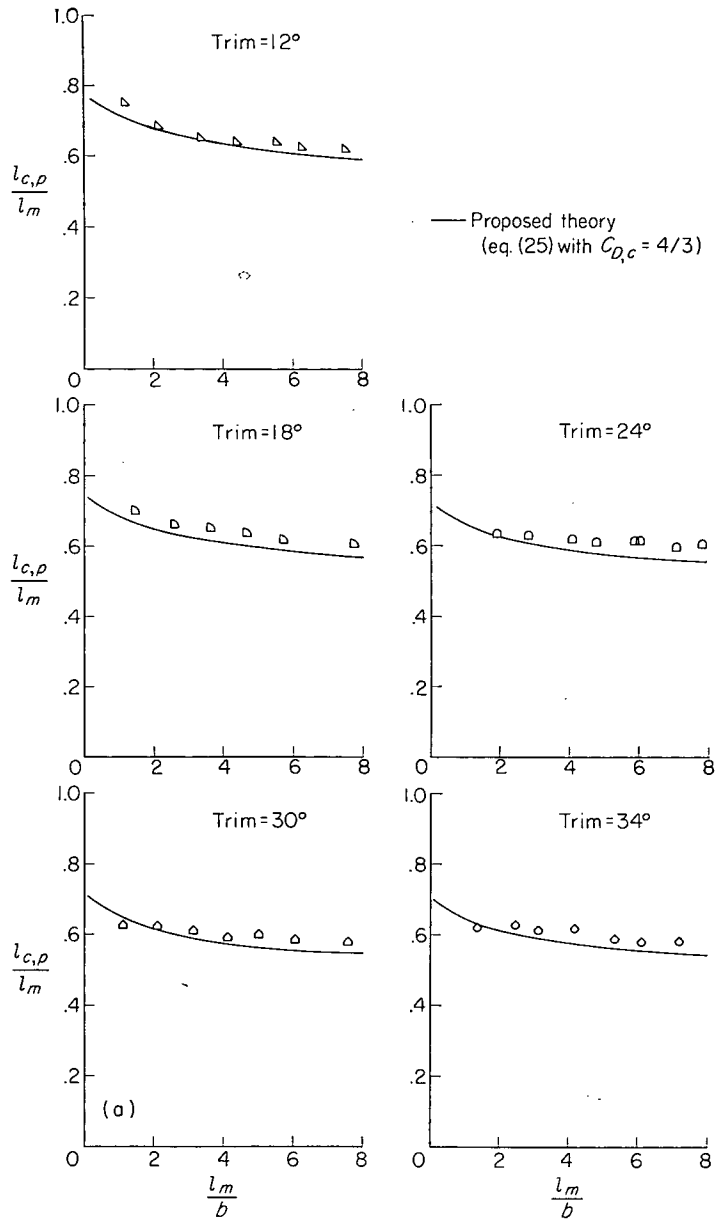
(b) Data of Chambliss and Boyd (ref. 28).

FIGURE 43.—Continued.



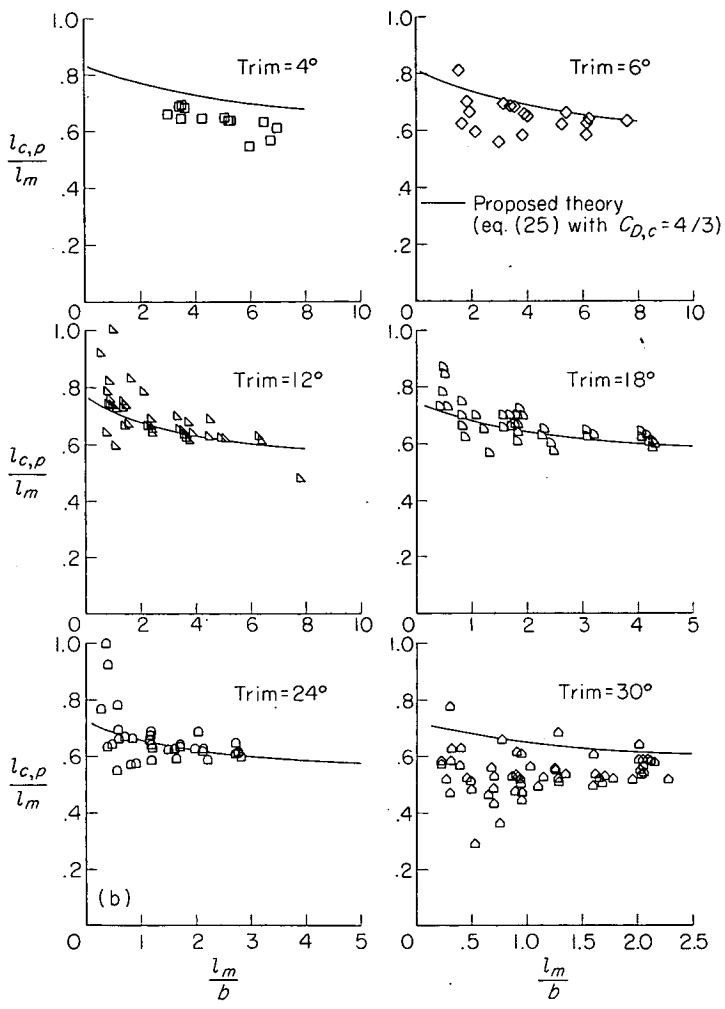
(c) Data of Kapryan and Boyd (ref. 25).

FIGURE 43.—Concluded.



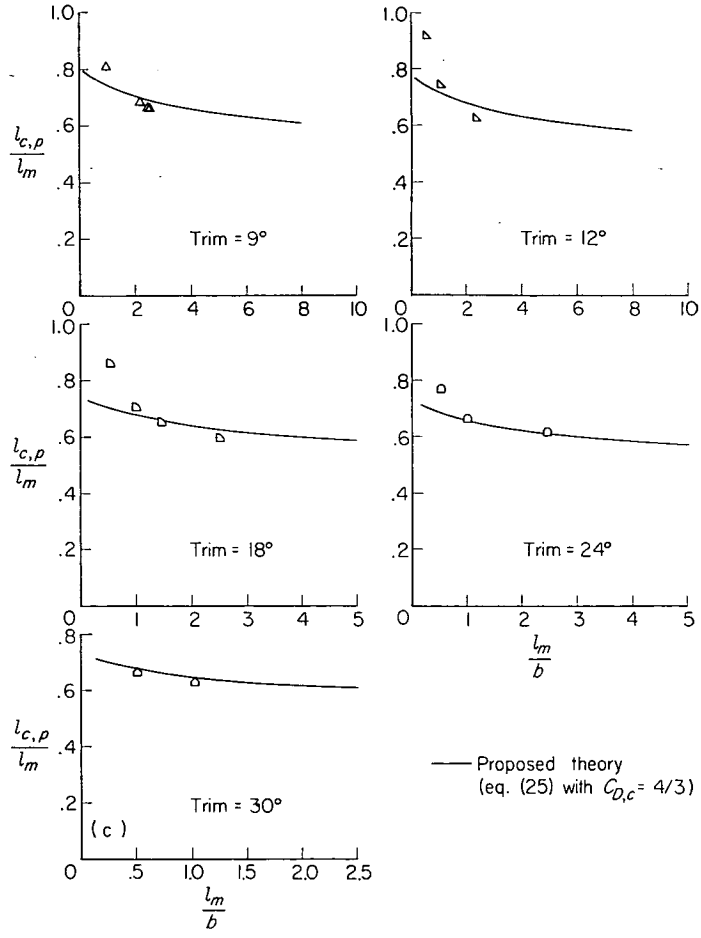
(a) Data of present report.

FIGURE 44.—Variation of center-of-pressure location with mean wetted-length-beam ratio for a surface having a 40° angle of dead rise.



(b) Data of Chambliss and Boyd (ref. 28).

FIGURE 44.—Continued.



(c) Data of Kapryan and Boyd (ref. 25).

FIGURE 44.—Concluded.

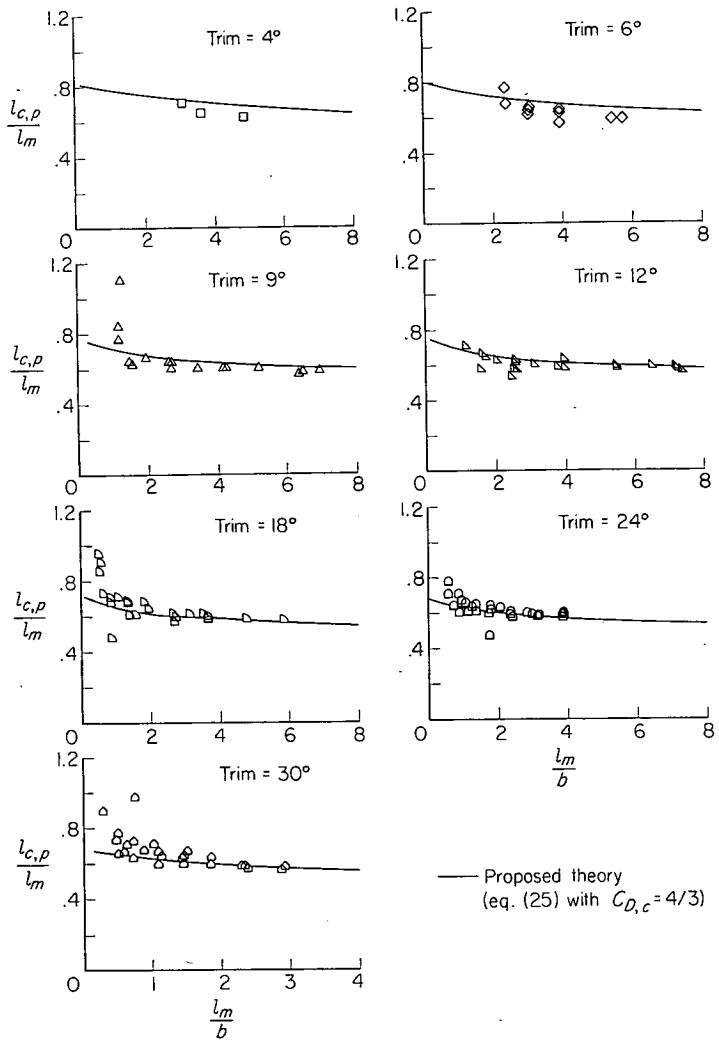
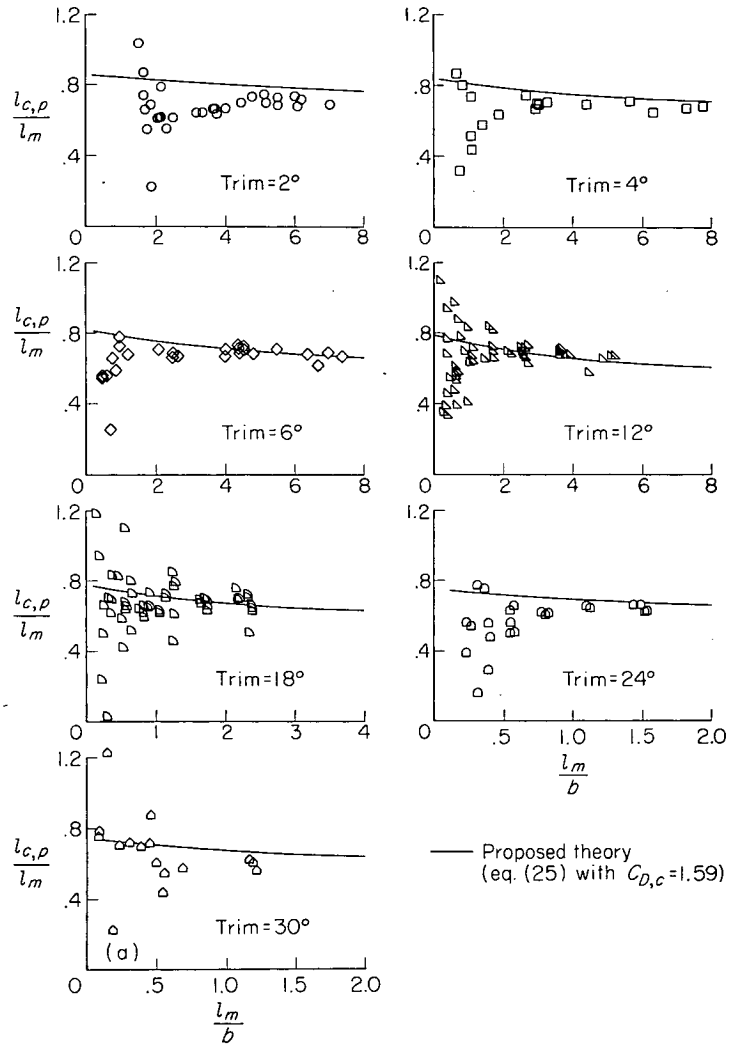
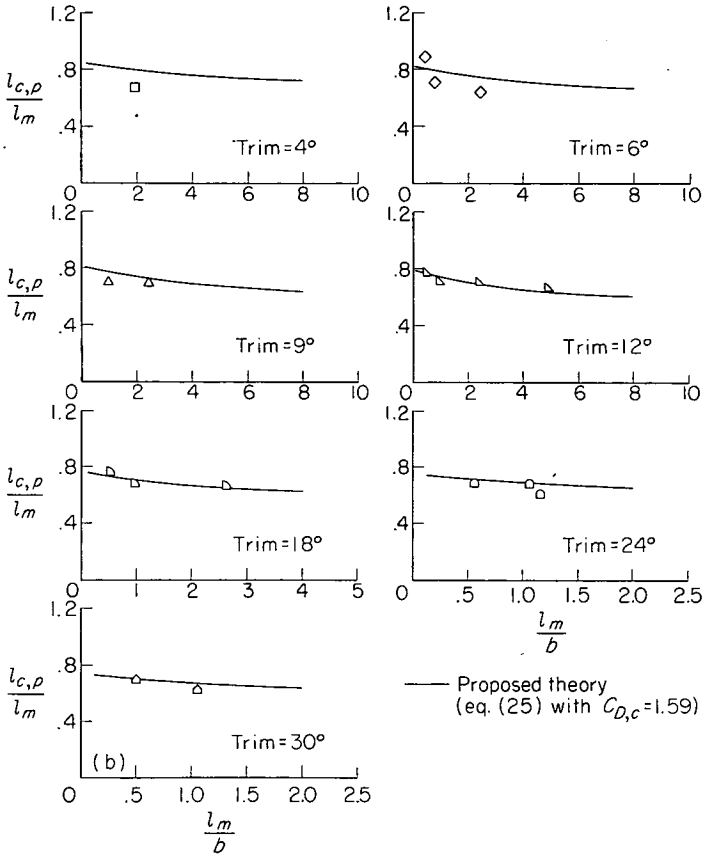


FIGURE 45.—Variation of center-of-pressure location with mean wetted-length-beam ratio for a model having a 50° angle of dead rise. (Data of Springston and Sayre (ref. 36).)



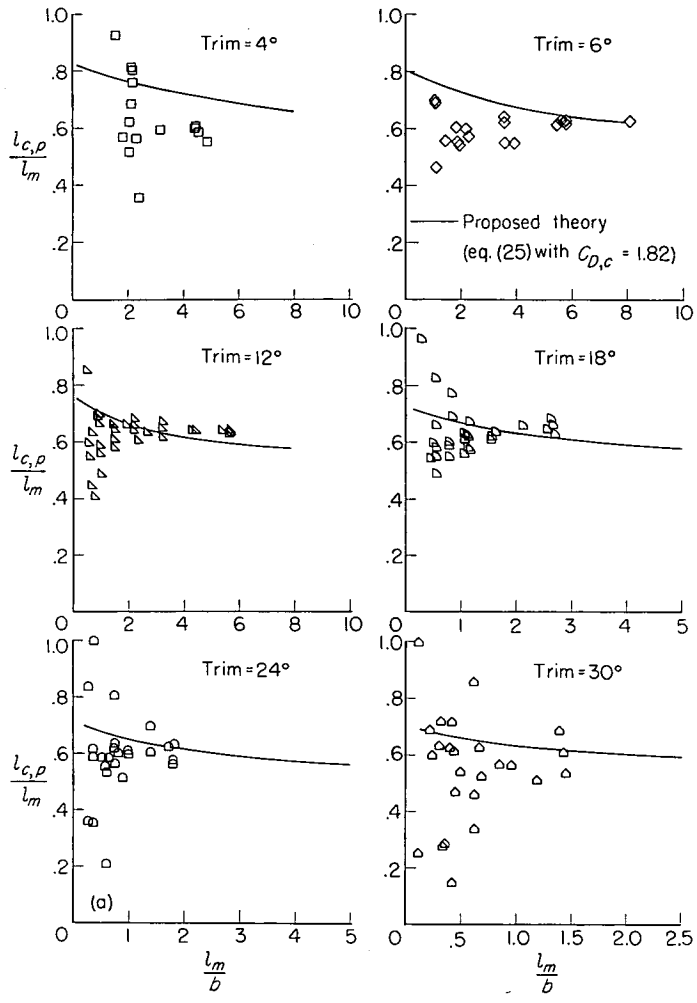
(a) Data of Kapryan and Weinstein (ref. 13).

FIGURE 46.—Variation of center-of-pressure location with mean wetted-length-beam ratio for a surface having a basic angle of dead rise of 20° and horizontal chine flare. (Effective angle of dead rise, 16°.)



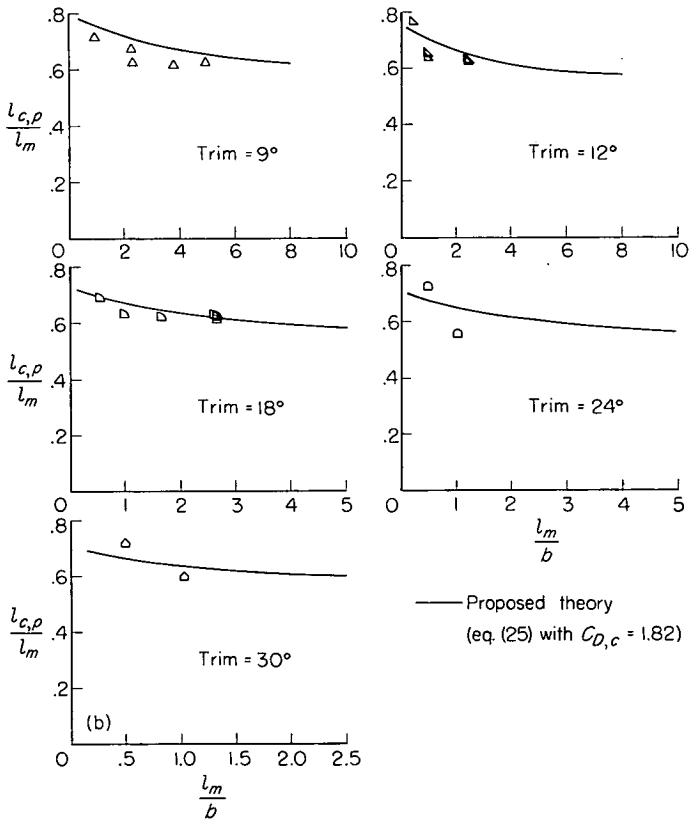
(b) Data of Kapryan and Boyd (ref. 25).

FIGURE 46.—Concluded.



(a) Data of Blanchard (ref. 24).

FIGURE 47.—Variation of center-of-pressure location with mean wetted-length-beam ratio for a surface having a basic angle of dead rise of 40° and horizontal chine flare. (Effective angle of dead rise, 32°47′.)



(b) Data of Kapryan and Boyd (ref. 25).

FIGURE 47.—Concluded.

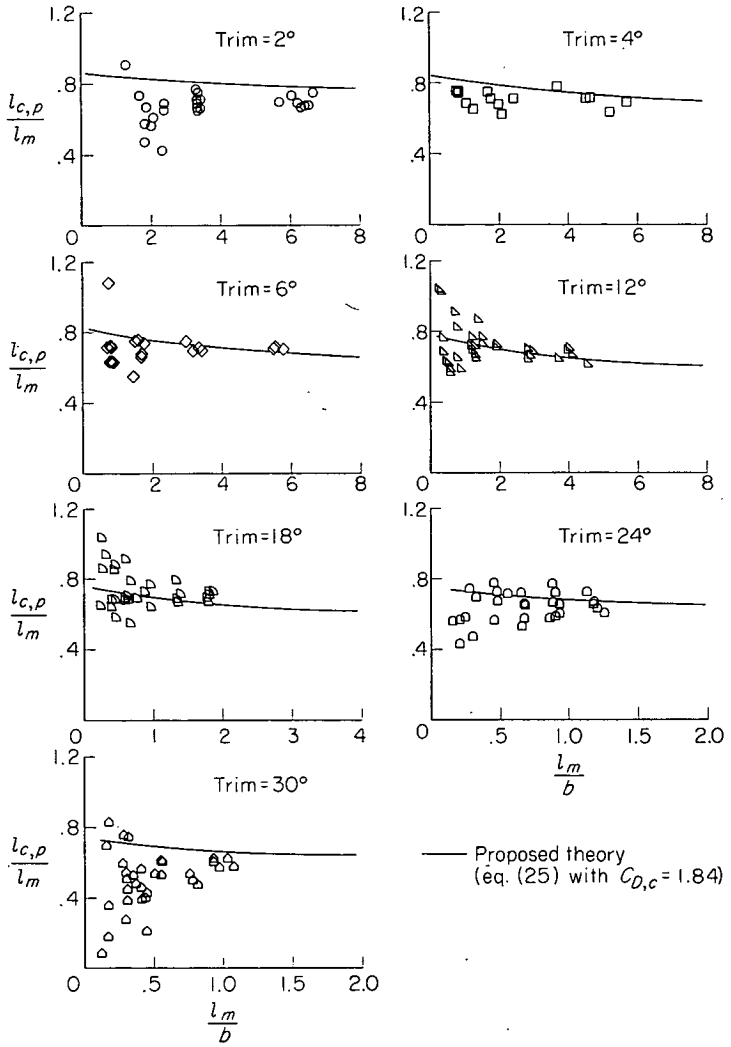


FIGURE 48.—Variation of center-of-pressure location with mean wetted-length-beam ratio for a surface having a basic angle of dead rise of 20° and vertical chine strips. (Effective angle of dead rise, 15°33′.) (Data of Kapryan and Boyd (ref. 26).)

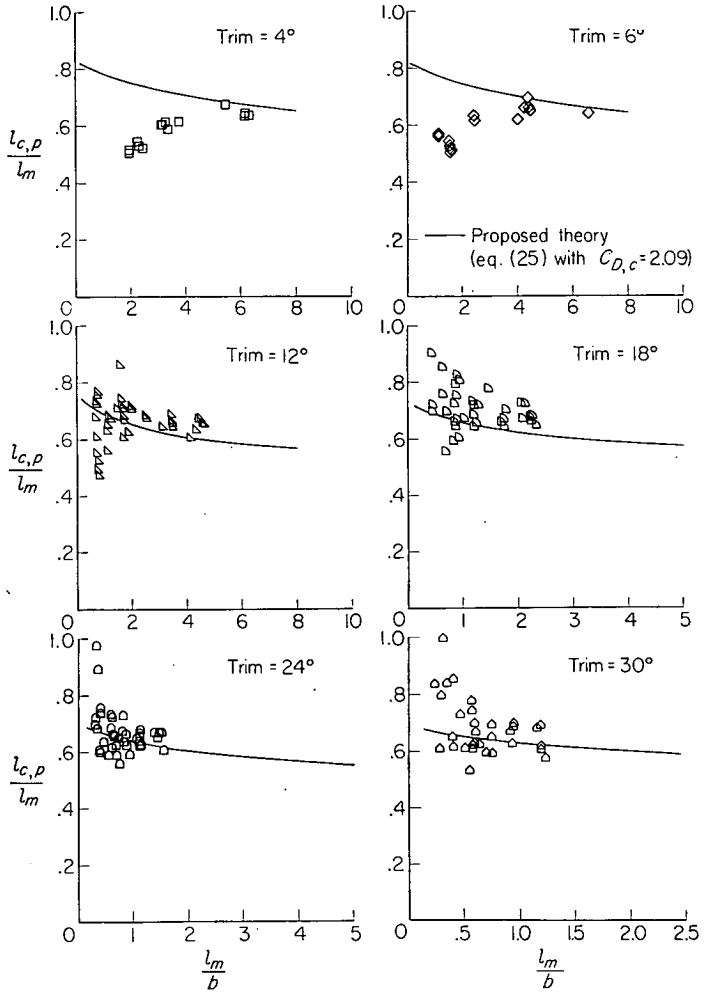


FIGURE 49.—Variation of center-of-pressure location with mean wetted-length-beam ratio for a surface having a basic angle of dead rise of 40° and vertical chine strips. (Effective angle of dead rise, 31°59′.) (Data of Kapryan and Boyd (ref. 26).)

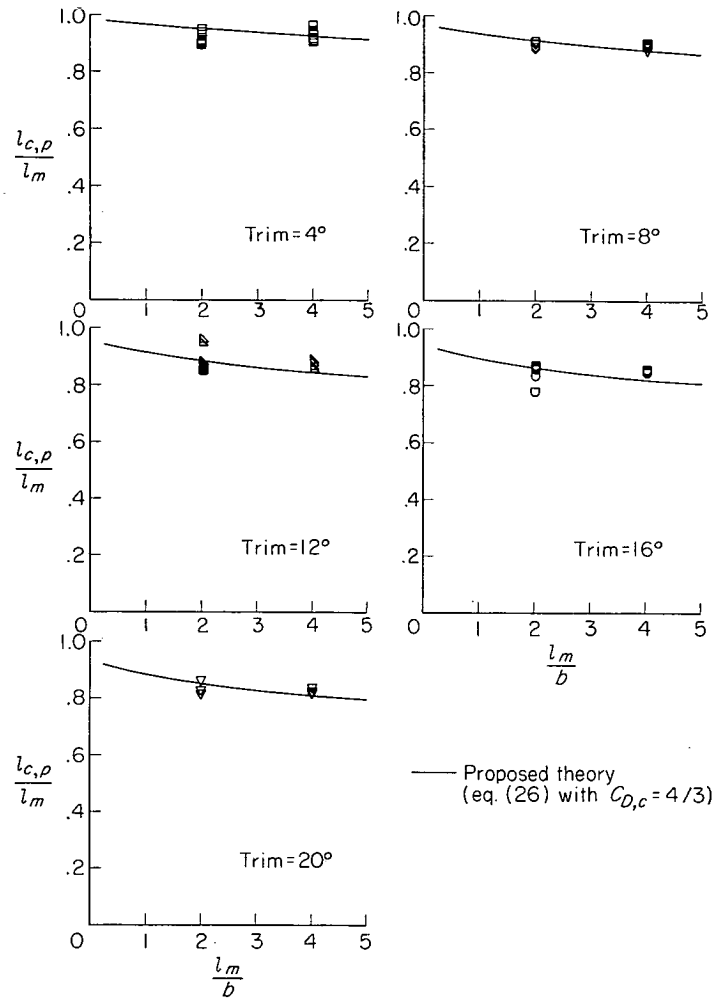


FIGURE 50.—Variation of center-of-pressure location with length-beam ratio for triangular-flat-plate surfaces planing with base forward. (Data of Wadlin and McGehee (ref. 31) and unpublished tank no. 2 data.)

REPORT 1356

CONTENTS

	Page
SUMMARY	421
INTRODUCTION	421
NOTATION	423
Subscripts	423
Superscripts	423
APPARATUS AND TEST METHODS	423
Wind Tunnel	423
Models and Supports	423
Test Methods and Techniques	424
Variation in Mach number	424
Optical techniques	424
Transition determination from shadowgraphs	426
Boundary-layer trips	427
Surface oil-film technique	427
RESULTS AND DISCUSSION PERTAINING TO RELATIVE TRANSITION LOCATION	428
General Survey Illustrating Dominant Importance of Relative Transition Location	428
Results of initial experiments	428
Correlation between transition and occurrence of abrupt pressure rise	428
Representative pressure distributions for the three regimes and results of high-speed motion picture studies	432
Representative Reynolds number effects for the three regimes	436
Representative Mach number effects for the three regimes	438
Significance to wind-tunnel testing	438
REYNOLDS NUMBER RANGE FOR PURE LAMINAR SEPARATIONS	441
MECHANISM DETERMINING PRESSURE IN SEPARATED REGIONS AND THEORETICAL EXPLANATION FOR IMPORTANCE OF TRANSITION LOCATION RELATIVE TO REATTACHMENT	443
Theoretical Analysis of Leading-Edge Separation	443
Experimental Results for Flows With Negligible Boundary-Layer Thickness at Separation	445
An Explanation of the Importance of Transition Location Relative to Reattachment	447
CHARACTERISTICS INDEPENDENT OF THE MODE OF INDUCING SEPARATION (FREE INTERACTIONS)	448
Results for Various Separated Flows	448
Difference between subsonic and supersonic separations	448
Simplified analysis for free-interaction regions	449
Experiments on effects of geometry, Reynolds number, and Mach number for laminar separation	450
Experiments on effects of geometry, Reynolds number, and Mach number for turbulent separation	452
CONCLUSIONS	457
APPENDIX A—ANOMALOUS OIL-FILM OBSERVATIONS	458
APPENDIX B—SPECIAL EXPERIMENTS PERTAINING TO THE CROCCO-LEES THEORY	459
REFERENCES	460

REPORT 1356

INVESTIGATION OF SEPARATED FLOWS IN SUPERSONIC AND SUBSONIC STREAMS WITH EMPHASIS ON THE EFFECT OF TRANSITION [1]

By Dean R. Chapman, Donald M. Kuehn, and Howard K. Larson

SUMMARY

Experimental and theoretical research has been conducted on flow separation associated with steps, bases, compression corners, curved surfaces, shock-wave boundary-layer reflections, and configurations producing leading-edge separation. Results were obtained from pressure-distribution measurements, shadowgraph observations, high-speed motion pictures, and oil-film studies. The maximum scope of measurement encompassed Mach numbers between 0.4 and 3.6, and length Reynolds numbers between 4,000 and 5,000,000.

The principal variable controlling pressure distribution in the separated flows was found to be the location of transition relative to the reattachment and separation positions. Classification is made of each separated flow into one of three regimes: "pure laminar" with transition downstream of reattachment, "transitional" with transition between separation and reattachment, and "turbulent" with transition upstream of separation. By this means of classification it is possible to state rather general results regarding the steadiness of flow and the influence of Reynolds number within each regime.

For certain pure laminar separations a theory for calculating dead-air pressure is advanced which agrees well with subsonic and supersonic experiments. This theory involves no empirical information and provides an explanation of why transition location relative to reattachment is important. A simple analysis of the equations for interaction of boundary-layer and external flow near either laminar or turbulent separation indicates the pressure rise to vary as the square root of the wall shear stress at the beginning of interaction. Various experiments substantiate this variation for most test conditions. An incidental observation is that the stability of a separated laminar mixing layer increases markedly with an increase in Mach number. The possible significance of this observation is discussed.

INTRODUCTION

Flow separation often is considered as a scourge to many technical devices which depend upon the dynamics of fluids for successful operation, inasmuch as separation often limits the usefulness of these devices. For example, the maximum lift of an airfoil and the maximum compression ratio of a compressor are limited by the occurrence of separation. Separated regions can also occur near a deflected flap, around a spoiler control, in an overexpanded rocket nozzle, behind a blunt base, on the leeward side of an object inclined at large angle of attack, and near the impingement of a shock wave from one body upon the boundary layer of another. Such occurrences make flow separation a very common phenomenon warranting much research effort.

Of the numerous experimental results on separated flows, a few have proved to be applicable throughout the subsonic, transonic, and supersonic speed ranges. The first and most important result involves the phenomenon of boundary-layer transition. In 1914 Prandtl (ref. 1) demonstrated that the pronounced effects of flow separation on the low-speed drag of a bluff body, such as were observed earlier by Eiffel (ref. 2), are determined by the type of boundary-layer flow approaching the separation point; that is, whether it is laminar or turbulent. In the initial post-war years, a number of independent investigations (refs. 3, 4, 5, and 6) were conducted in transonic and supersonic wind tunnels which revealed similar marked effects on compressible flow fields when the boundary layer approaching separation was changed from laminar to turbulent. These experiments leave little doubt that separated flows with transition upstream of separation are fundamentally different from those with transition downstream.

From various experiments on separated flows, a second general result can be detected which may not have been evident at the time the various experiments were conducted, but which is perceptible now through the medium of hindsight coupled with the findings of more recent research. This second result concerns the importance of the location of transition within a separated layer relative to the position of laminar separation. Schiller and Linke (ref. 7) found that even under conditions where the boundary-layer flow remains laminar at separation, the pressure distribution about a circular cylinder depends significantly on how near transition is to the separation position. They observed that an increase in either Reynolds number or turbulence level moved transition upstream in the separated layer to a position closer to separation, and that such movement considerably affected the drag and pressure distribution. Closely related to these findings are some isolated observations that transition location often correlates with an abrupt pressure

[1] Supersedes NACA TN 3869 by Dean R. Chapman, Donald M. Kuehn, and Howard K. Larson, 1957.

Preceding Page Blank

rise when the separated layer is laminar. This correlation is found within "separation bubbles" on airfoils (ref. 8), and in many other cases, both at low speed and supersonic speed, as is discussed in detail later. Thus with a separated layer remaining laminar, a variation in Reynolds number changes the location of transition relative to the separation point and this varies the pressure rise associated with transition; the consequence is an effect of Reynolds number on pressure distribution which is especially pronounced in the separated flow behind a base. (See refs. 5 and 6.) An initial approach to the computation of such effects has been made by Crocco and Lees (ref. 9) who consider explicitly the movement of transition along a separated layer. The synoptic result of these various investigations is that the location of transition relative to separation is a variable generally important to separated flows wherein the boundary layer is laminar at separation.

In most previous experiments attention generally has been directed to the type of boundary-layer flow existing at separation and to the relative distance between transition and separation; less attention has been given to the type of boundary-layer flow existing at reattachment and to the relative distance between transition and reattachment. ("Reattachment" is taken herein to mean the localized zone wherein a separated layer either meets a surface or another separated layer.) At sufficiently low Reynolds numbers, a type of separation can exist where transition is downstream of the reattachment zone, or perhaps even nowhere in the flow field. In order to achieve this pure laminar [2] type of separation in a low-speed flow, however, the Reynolds number must be very low (e. g., the order of several thousand for a circular cylinder). In view of the unusually low Reynolds number required, and the fact that the reattachment position is not steady in a subsonic wake, it is understandable that conditions at reattachment previously have received relatively little emphasis in investigations of separated flow. An isolated example of pure laminar separation was observed by Liepmann and Fila (ref. 10) behind a small, half-cylinder, roughness element placed within a subsonic laminar boundary layer.

The present investigation, which is concerned in considerable part with flow conditions near reattachment, was conducted in three phases differing greatly in purpose and scope. Such division was not planned but was dictated by some rather surprising and encouraging results obtained during the initial phase of experimentation, coupled with some major revisions in the wind-tunnel facility made during the interval over which the research was conducted. The initial experiments (conducted in 1953) were concerned with the manner in which Reynolds number variation at supersonic speed affects the separated-flow region upstream of two-dimensional steps of various height. Comparison of the results of the initial experiments with those of other experiments revealed several intriguing similarities among various separated flows on presumably unrelated configurations. These similarities (discussed in detail later) suggested that the location of transition relative to reattachment might be just as fundamental to any separated flow as is the location of transition relative to separation. In order to explore this possibility, a second phase of experiments was conducted with a variety of model shapes rather than just a step. A third phase of experiments was conducted after modifications were made to the wind tunnel which enabled operation over an extended Mach number and Reynolds number range. Inasmuch as an ultimate hope was to improve the understanding of separated flows, it was thought mandatory to include measurements at subsonic as well as supersonic speeds as an integral part of the research. All measurements were made on two-dimensional models.

This report covers three subjects: (1) a general survey of the experimental results grouped according to whether transition is downstream of reattachment, between separation and reattachment, or upstream of separation; (2) a description and experimental test of a theory of the fundamental mechanism near reattachment which governs the dead-air pressure in a separated region (this theory is used to provide an explanation of why transition location relative to reattachment is of importance to separated flows); (3) a simple analysis and pertinent experiments on "free interaction" type flows wherein the boundary layer interacts freely with an external supersonic flow in the manner originally pictured by Oswatitsch and Wieghardt (ref. 11). A preliminary report presenting briefly some of the salient results of this investigation has been published as reference 12.

In the three-year interim over which the present experiments and theoretical research were conducted, various results of other studies appeared which benefited and influenced the course of this research. A thorough investigation of turbulent separation induced by steps and by interaction of oblique shock waves with the turbulent boundary layer on a wind-tunnel wall was published by Bogdonoff (ref. 13) and by Bogdonoff and Kepler (ref. 14). As a result it was deemed unnecessary to investigate turbulent separations for these two cases, except to provide incidental comparisons and checks with their data. Similarly, extensive results of Gadd, Holder, and Regan (ref. 15) became available for the case of shock-wave-induced separation. In these latter experiments, separated flows with transition downstream of reattachment were observed as were fully turbulent flows and flows with transition between separation and reattachment. The importance of transition location relative to reattachment is clearly recognized by Gadd, et al. More recently, the research of Korst, Page, and Childs (ref. 16) became available, in which nearly the same fundamental theoretical mechanism was employed in their calculations of base pressure for thin turbulent boundary layers as that mechanism described and experimentally tested herein for thin laminar boundary layers. Comparison of results from these various recent and independent researches is made later in the report.

[2] For reasons explained later, many flows commonly designated as "laminar" separations in previous investigations really are affected significantly by the presence of transition locally in the reattachment zone; such flows are referred to herein as "transitional" separations. Consequently, it is desirable for purposes of emphasis and contradistinction to use an unambiguous terminology, such as "pure laminar," for those flows which truly are unaffected by transition.

NOTATION

c_f local skin-friction coefficient, $\frac{\tau}{q}$

$\bar{c}_f$ ratio of c_{f_o} at a given R_{x_o} to corresponding value $R_{x_o}=10^6$

h height of step or base

l_i characteristic streamwise length over which interaction takes place

L body length (see fig. 2)

m mass-flow rate per unit span

M Mach number

p pressure

Pr Prandtl number

q dynamic pressure, $\frac{\rho u^2}{2}$

R reattachment point

R_L, R_{x_o} Reynolds number, $\frac{u_0 L}{\nu_0}$ and $\frac{u_0 x_0}{\nu_0}$, respectively

S separation point

T absolute temperature

u velocity

x distance along model measured from leading edge

α angle of attack relative to surface having length L

γ ratio of specific heats, 1.40 for air

δ mixing-layer or boundary-layer thickness

δ^* displacement thickness of boundary layer

μ viscosity coefficient

ν kinematic viscosity, $\frac{\mu}{\rho}$

ρ density

τ shear stress

SUBSCRIPTS

o conditions at beginning of interaction in supersonic flow, or at location of minimum pressure in subsonic flow

∞ test-section stream conditions

d dead air

e outer edge of mixing layer, or edge of boundary layer

p plateau conditions (for laminar separation), or peak conditions (for turbulent separation)

r reattachment point

s separation point

t total conditions $\left(\text{e. g., } \frac{T_t}{T}=1+\frac{\gamma-1}{2}M^2\right)$

$*$ ratio of quantity to corresponding value at edge of mixing layer $\left(\text{e. g., } T_*\equiv\frac{T}{T_e}, \mu_*\equiv\frac{\mu}{\mu_e}, \text{etc.}\right)$

w wall

SUPERSCRIPTS

$'$ conditions downstream of reattachment region

$-$ conditions along dividing streamline of mixing layer.

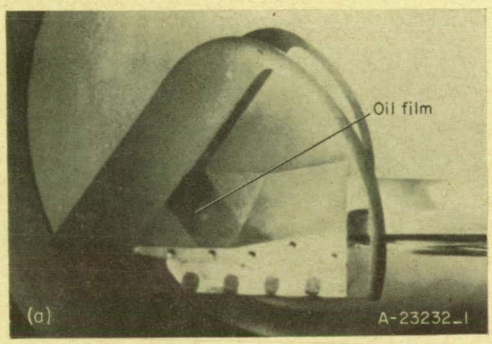
APPARATUS AND TEST METHODS

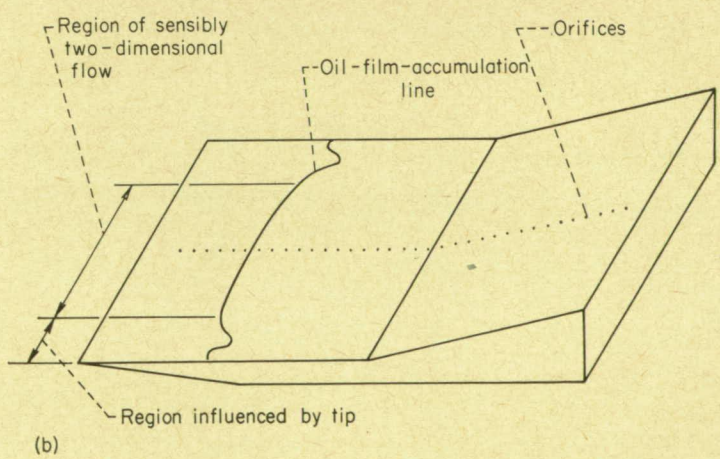
WIND TUNNEL

Experiments were conducted in the Ames 1- by 3-foot supersonic wind tunnel No. 1. This tunnel operates continuously with dry air over a range of reservoir pressures. For the initial portion of experiments, the range of tunnel pressures available was limited to between 2.5 and 30 pounds per square inch absolute, and the Mach number was limited to about 2.4. Revisions to the tunnel structure, flexible-plate nozzle, and drive motors were made in 1955 so that subsequent experiments could be made over the range of pressures between about 2 and 60 psia and at Mach numbers up to about 3.6. Subsonic speed control ($0.4 \leq M_\infty \leq 0.8$) was obtained by choking the flow downstream of the test section with the flexible, supersonic diffuser.

MODELS AND SUPPORTS

Several types of models with different supports and end plates were employed, each being designed to provide two-dimensional flow conditions. Pressure orifices were located at stations near the center span, and, in most cases, were spaced either 0.05 or 0.10 inch apart. The initial experiments were conducted on step models in an 8-inch-wide two-dimensional channel placed within the 1- by 3-foot test section (see ref. 17 for description of channel). Since use of the channel made model changes and observation rather cumbersome, subsequent experiments were conducted without the channel apparatus by mounting the 8-inch span models on a sting from the rear, and by attaching at both tips relatively small, transparent (lucite), end plates. The photograph in figure 1 (a) illustrates the latter method of



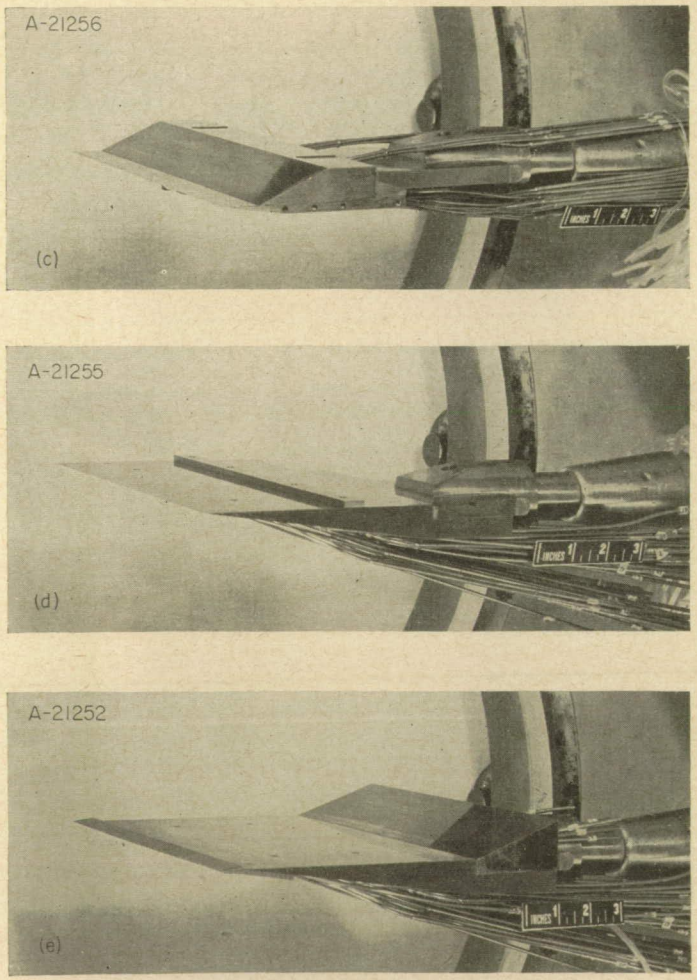


(a) Photograph showing oil-film accumulation taken during a run of model CC10°—2 with end plates.
(b) Sketch of typical oil-film-accumulation line.

FIGURE 1.—Typical model installations.

sting mounting. Since comparison of results obtained with the two methods of mounting showed no significant difference, all subsequent measurements were taken with this latter method of mounting. For those data presented, the flow over the center portion of the model was judged essentially two-dimensional according to three indications: (1) several pressure orifices located spanwise 2 inches off center revealed only small variations of static pressure; (2) the pattern formed by oil film on a model surface (see fig. 1 (b)) was normal to the flow direction over a sizable center portion of span; and (3) at all Mach numbers, changing from triangular-shaped to rectangular-shaped end plates had no effect on midspan pressure distribution, and at Mach numbers above about 2.3, even the removal of end plates had no effect. End plates often were not used at the higher Mach numbers, as this enabled better shadowgraphs to be obtained.

Photographs of several models mounted without end plates are presented in figures 1 (c), 1 (d), and 1 (e). The



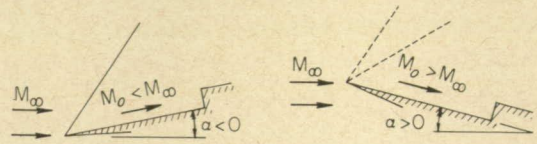
(c) Model CC25°—2. (d) Model S–4. (e) Model CC25°—5 (trip 4).

FIGURE 1.—Concluded.

geometry, dimensions, and designations of the various models are given in figure 2. Most of the models of figure 2 consist of a basic flat plate to which various wedges and steps were fastened to form additional models. This basic flat plate also was used for measurements of boundary-layer-transition Reynolds number to give an indication of wind-tunnel disturbance level. The leading-edge thickness of the flat plate was determined optically to be 0.005 inch. The leading-edge thickness of the other models (for which the surface contour is an integral part of the basic plate) is believed to be approximately the same.

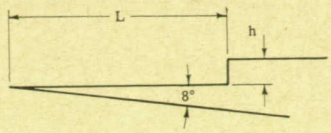
TEST METHODS AND TECHNIQUES

Variation in Mach number.—The Mach number M_o approaching an interaction region was varied in several ways. At subsonic speed, the angle of attack was held fixed while adjustment of the diffuser minimum area provided variation in test-section Mach number M_∞. At supersonic speed, the angle of attack was changed to provide variation in M_o, as illustrated, and the flexible nozzle walls occasionally were repositioned to provide additional varia-



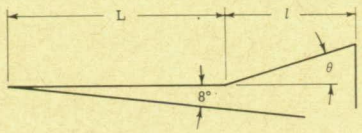
tion in M_∞. Only a few test-section Mach numbers were required to achieve variation in M_o from values near 1 to about 3.6, inasmuch as the angle of attack for some of the models could be varied by $\pm 16°$. Thus a given M_o could be obtained with either an expansion wave or a shock wave occurring at the model leading edge. It was found in most cases that for a given M_o both types of settings would yield the same pressure distribution over the center-span portion of the model. In several cases, though, detached bow waves at $\alpha > 0$ resulted from excessive flow deflection over the lower surface, and this caused transition to occur prematurely on the upper surface. Under such conditions, the pressure distribution in transitional-type separations differed from that obtained at the same M_o, but with an expansion wave at the leading edge. In some cases of laminar separation, small differences in the shape of pressure distribution—but not in the pressure rise to separation—were observed at the same M_o for the two types of settings. These small differences are attributed to known differences in tunnel-empty pressure distribution at the different nozzle settings.

Optical techniques.—One or more shadowgraphs were taken for each pressure distribution in order to determine the location of transition. Relatively long exposure times were used ($\frac{1}{25}$ to $\frac{1}{100}$ sec) since the mean position of transition was desired rather than an instantaneous position. In the first two phases of experimentation, film was placed next to a side window which intercepted near-parallel light passing through the test section. Polaroid-Land film was used. In the third phase of experimentation, the film was placed on a parallel-motion mechanism surrounded by light-proof bellows (see fig. 3). This enabled the distance from the model to the film to be adjusted in order to take advantage of focusing effects induced by the refraction of parallel light as it passes through the boundary layer (for an explanation of the focusing effects, see ref. 18). Comparison of figures 4 (b) with 4 (a) reveals the improvement achieved by increasing the distance between the film and



Model designation	L (inches)	h (inches)	$\frac{L}{h}$
S-1	1.14	0.041	27.8
S-2	6.55	0.237	27.7
S-3	2.60	0.094	27.7
S-4	2.73	0.150	18.2
S-5	5.14	0.150	34.3
S-6	2.73	0.300	9.1
S-7	4.70	0.100	47.0
S-8	4.43	0.040	110.8
S-9	3.30	0.150	22.0
S-10	6.05	0.200	30.3

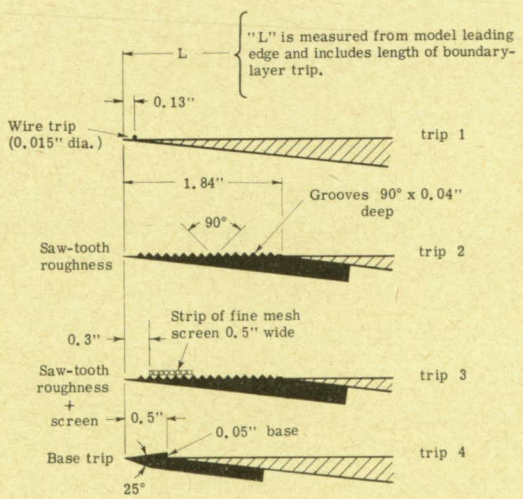
(a)



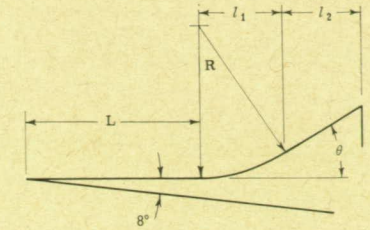
Model designation	θ (degrees)	L (inches)	l (inches)
CC10°-1	10	0.75	2.50
CC10°-2	10	2.25	1.75
CC10°-3	10	2.60	1.50
CC10°-4	10	5.00	2.00
CC15°-1	15	0.35	1.10
CC15°-2	15	0.76	1.10
CC15°-3	15	1.72	1.10
CC20°-1	20	0.34	0.80
CC20°-2	20	5.50	2.00
CC25°-1	25	0.28	1.40
CC25°-2	25	0.76	1.40
CC25°-3	25	3.34	0.66
CC25°-4	25	5.00	2.00
CC25°-5	25	5.50	2.00
CC35°-1	35	0.056	2.70
CC35°-2	35	0.166	2.70

(b)

Crosshatched-----Clean model
Solid---------- Detachable boundary-layer trip

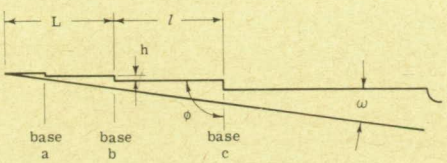


(c)



Model designation	θ (degrees)	L (inches)	R (inches)	l_1 (inches)	l_2 (inches)
CS15°-1	15	5.00	3.25	0.84	1.16
CS20°-1	20	5.50	2.00	0.68	1.32
CS25°-1	25	2.63	3.25	1.37	0
CS30°-1	30	5.50	1.00	0.50	1.50

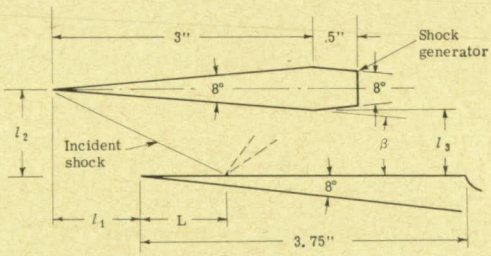
(d)



One model has 3 bases in series--others have only a single base. "L" is always measured from the model leading edge to the particular base. "l" is always the length of the unbroken surface downstream of the particular base.

Model designation	L (inches)	h (inches)	l (inches)	ω (degrees)	ϕ (degrees)
B-1-a	0.20	0.01	0.47	8	90
-b	0.67	0.03	1.61	8	90
-c	2.28	0.10	2.22	8	90
B-2	2.00	0.10	2.22	8	90
B-3	0.20	0.09	3.30	35	145

(e)



(l_1 is positive when leading edge of shock generator is ahead of leading edge of flat plate)

Model designation	L (inches)	l_1 (inches)	l_2 (inches)	l_3 (inches)	β (degrees)	α (degrees)
I 3°-1	1.1	1.00	1.14	0.93	4.0	-1.0
I 5°-1	1.0	1.00	1.14	0.93	4.0	+1.0
I 6.5°-1	0.9	1.00	1.14	0.93	4.0	+2.5
I 8°-2	1.8	-0.25	0.96	0.75	4.0	+4.0

(f)

(a) Step models.
(b) Compression corners.
(c) Boundary-layer trips.
(d) Curved surfaces.
(e) Base models.
(f) Incident shock models.

FIGURE 2.—Model configurations and dimensions.

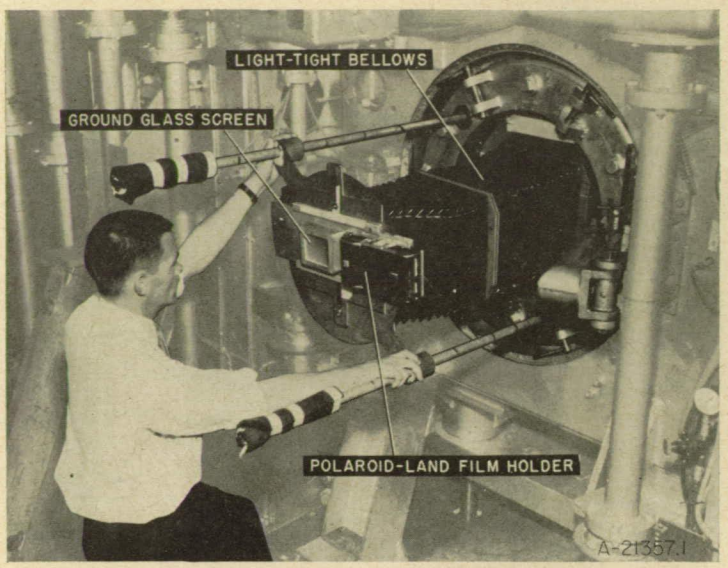
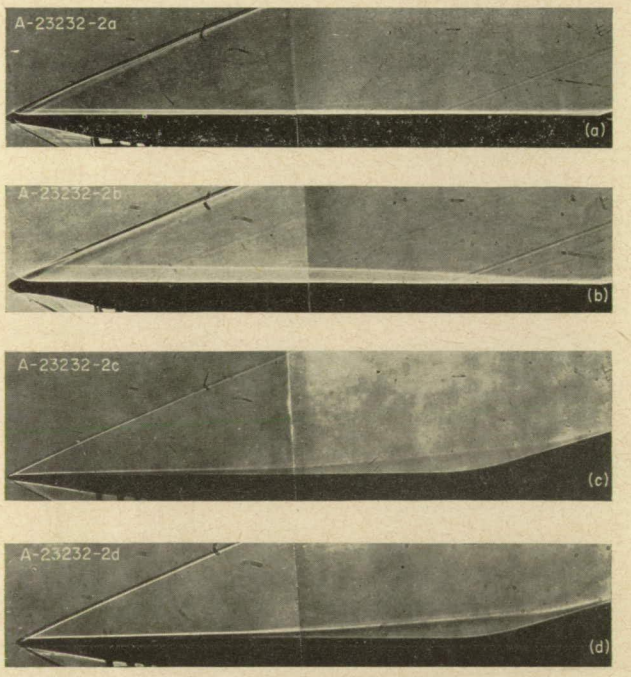


FIGURE 3.—Adjustable shadowgraph mount with light-tight bellows.



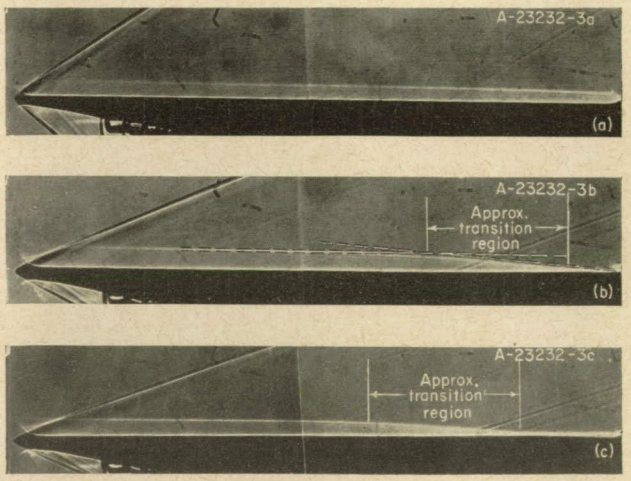
(a) Shadowgraph next to tunnel window. Flat plate model; $M_o=3.0$; $p_t=24.5$ psia.
(b) Shadowgraph 30 inches from tunnel window. Flat plate model; $M_o=3.0$; $p_t=24.5$ psia.
(c) Shadowgraph next to tunnel window. CS15°−1; $M_o=3.0$; $p_t=3$ psia.
(d) Shadowgraph 42 inches from tunnel window. CS15°−1; $M_o=3.0$; $p_t=3$ psia.

FIGURE 4.—Effect on shadowgraph appearance of variation in distance between model and shadowgraph film.

the flat-plate model. The white line, indicating the nature of boundary-layer flow, is displaced from the surface where it can be better observed. Comparison of figures 4 (d) with 4 (c) reveals the improvement achieved in visualizing the separated flow over a curved surface model by increasing the film-to-model distance.

High-speed motion pictures (Fastax) were taken of the shadowgraph field in order to ascertain the relative steadiness of various separated flows. The parallel light was of sufficient intensity to permit pictures of several thousand frames per second to be taken from the shadowgraph pattern cast on a ground-glass screen. Runs at various frame speeds up to 6000 frames per second showed that flow unsteadiness could be detected readily at speeds near 2000 frames per second.

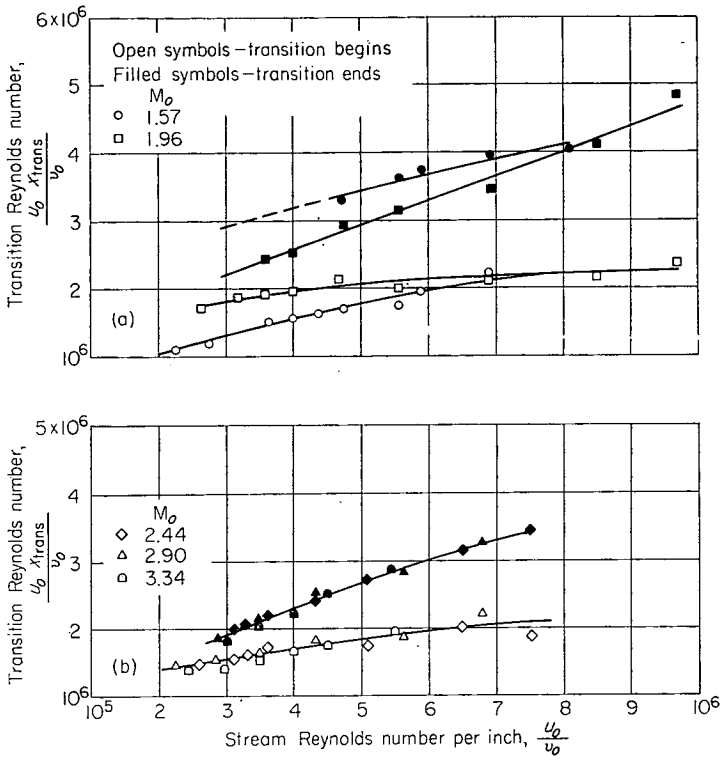
Transition determination from shadowgraphs.—Two methods, depending upon tunnel pressure, were used to detect transition from the shadowgraphs. At low tunnel static pressures, with small film-to-model distances, transition location appeared as the "end" of the laminar (white) line on the shadowgraphs. At high tunnel static pressures, with small film-to-model distances, or at arbitrary pressure with large film-to-model distances, optical refraction effects are large, and a technique used by Pearcey (ref. 18) was employed to locate transition. Under these conditions the white laminar line appears displaced from the surface by a distance large compared to the boundary-layer thickness. For flow over a flat plate, the apparent displacement is nearly constant from the surface as long as the layer remains laminar, since the density profiles are nearly similar along the plate length. An example is illustrated in figure 5 (a).



(a) Transition beginning near rear of plate. $M_o=2.0$; $R_L=1.9\times10^6$.
(b) Transition region on plate. $M_o=2.9$; $R_L=2.3\times10^6$.
(c) Transition region on plate. $M_o=3.3$; $R_L=2.8\times10^6$.

FIGURE 5.—Shadowgraphs indicating type of boundary-layer flow and location of transition on the flat plate model.

When the Reynolds number is increased so that transition is completed on the plate, the white line converges to the surface in the transition region. Examples of this are illustrated in figures 5 (b) and 5 (c). The beginning of convergence represents the beginning of transition effects on the density profile and is taken as the beginning of transition itself. The end of convergence, where the white line practically meets the surface, represents the first position where the density profile has its maximum gradient close to the surface (compared to a laminar profile) and is taken as the end of transition. Under high refraction conditions, therefore, both the beginning and end of transition often could be ascertained approximately. As an example, the results of transition determinations by this method for the flow over a flat plate (leading-edge thickness 0.005 in.) are presented in figure 6. The method employed in determining



(a) Lower supersonic Mach number range.
(b) Higher supersonic Mach number range.

FIGURE 6.—Reynolds number of transition on a flat plate in the Ames 1- by 3-foot wind tunnel No. 1. (Leading edge approximately 0.005 in. thick.)

the beginning and end of transition for these data is illustrated in figure 5 (b). The transition Reynolds number is plotted as a function of the Reynolds number per unit length, inasmuch as this variable appears to be more significant than the Mach number. For example, at stream Mach numbers above 2.0, the curves for both beginning and end of transition are independent of Mach number when plotted in this fashion. These curves will be used later in comparison with other data.

Boundary-layer trips.—A common experience in supersonic wind-tunnel operation is that larger and more severe trips are required as the supersonic Mach number is increased. This trend is reported in detail by Winter, Scott-Wilson, and Davies (ref. 19) who find that the required wire diameter for tripping the boundary layer increases roughly exponentially with Mach number (an interpretation of this trend is given later as it involves a result from the present research). Moreover, merely placing a disturbance at some streamwise position on a model does not insure a fixed transition location. For example, in the present investigation, at Mach numbers near 3 the wire trips often did not effect transition until a short distance before the separation position. Under these conditions the effective origin of the turbulent layer varied with tunnel pressure in an unknown manner over the plate length between the wire and the separation position. Data obtained on the effects of Reynolds number variation are uncertain under such conditions.

In the course of experimentation various full-span boundary-layer trips were used depending primarily on the Mach number. At subsonic and moderate supersonic Mach numbers a 0.015-inch-diameter wire (trip 1) placed 0.13 inch from the leading edge, as sketched in figure 2 (c), was adequate to effect transition near the wire. At the higher supersonic Mach numbers a trip more severe than a small wire was needed. On several models tested in this higher Mach number range during the second phase of experiments, the upstream portion of the model plate was corrugated by sawtoothed machining (see trip 2 in fig. 2 (c)) and on one model a section of wire screen also was added (trip 3). During the third phase of research a "base trip," consisting of a small wedgelike attachment to the leading edge, was employed (see trip 4 in fig. 2 (c) and photograph in fig. 1 (e)). A pressure orifice was installed in this base in order to determine when the trip fixed transition. A plot of the base pressure as a function of tunnel pressure revealed the tunnel pressure above which transition was fixed near the trip.

Surface oil-film technique.—A useful technique employed in the course of research was an oil-film method for determining quantitatively the location of separation (and hence the pressure rise to a separation point). It is known that liquids coated on a surface will accumulate along a line of separation. The flow upstream of separation washes liquid downstream, whereas reverse flow downstream of separation washes liquid upstream. In order to make this technique quantitative and to minimize interference, very small amounts of liquid are required. To detect minute accumulations of liquid, light at glancing incidence was employed. This enabled an accumulation to be detected of height much smaller, for example, than the mouth of a pitot tube. Silicone oil (Dow Corning DC 200–10) was employed, sometimes mixed with regular hydrocarbon oil. Thin films of this oil were mobile yet would not evaporate even after four or five hours of continuous tunnel operation. It was found possible either to coat portions of a model before a run or to emit oil from an orifice during a run. The minute, threadlike lines of accumulation, which were observed readily, could not be photographed well during tunnel operation. For photographic purposes, the surface oil film for the model in figure 1 (a) (possibly not visible in half-tone reproduction) was allowed to accumulate in larger amounts than for most quantitative measurements. A typical accumulation pattern is sketched in figure 1 (b).

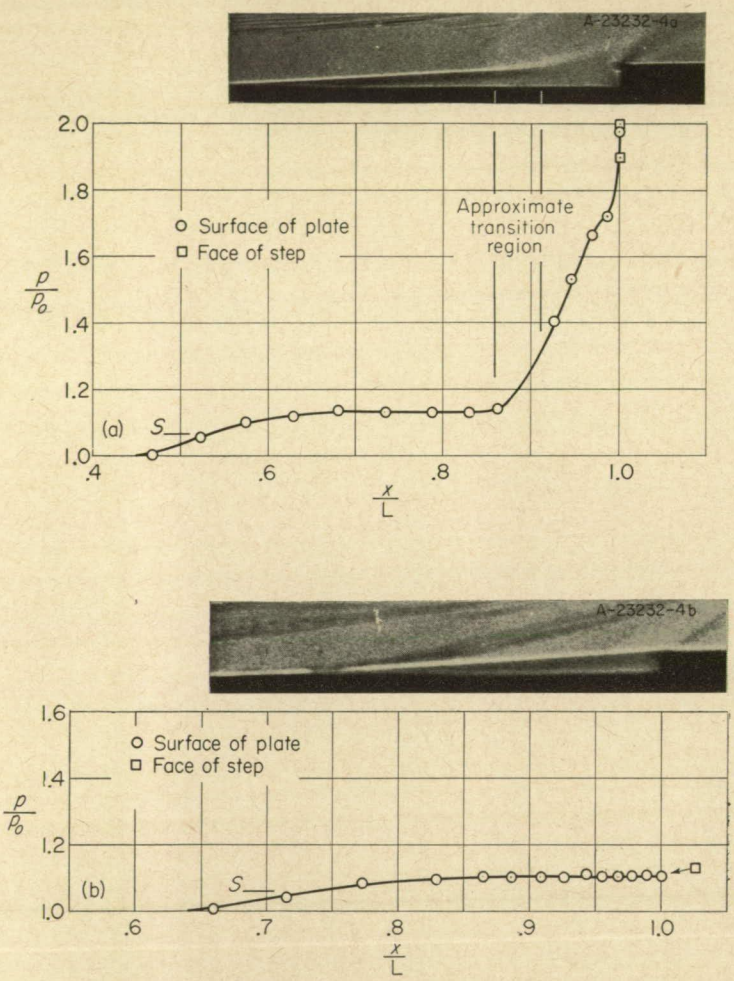
The oil-film technique for determining the separation point is believed to be more sensitive than the pitot-probe technique. Using a Stanton tube 0.005 inch high, for example, Gadd, et al., (ref. 15) could determine only roughly the laminar separation point and, hence, were unable to detect any Reynolds number dependence on the pressure rise to separation. As will be seen later, the oil-film technique readily enables the Reynolds number dependence to be determined as well as quantitative values of rather good accuracy for the pressure rise.

Extensive use of the oil-film technique revealed, under certain test conditions, an anomalous, double-accumulation pattern which was difficult to interpret. Some details of the research conducted to resolve this anomalous behavior are described in Appendix A.

RESULTS AND DISCUSSION PERTAINING TO RELATIVE TRANSITION LOCATION

GENERAL SURVEY ILLUSTRATING DOMINANT IMPORTANCE OF RELATIVE TRANSITION LOCATION

Results of initial experiments.—As noted previously, the initial experiments were conducted on step models in a two-dimensional-channel apparatus; they clearly revealed the basic importance of transition location relative to a reattachment position. Transition location was found to correlate closely with an abrupt rise in pressure when transition was between separation and reattachment. A typical example of this is illustrated in figure 7 (a). The pressure distribution in this type of separation was affected markedly by variations in Reynolds number. In contradistinction, no abrupt rise in pressure was observed when transition was downstream of the reattachment point (step shoulder); figure 7 (b) represents a typical example of this. The step height in figure 7 (b) is smaller than that in figure 7 (a) and is sufficiently small so as not to bring about transition. The pressure distribution for this pure laminar type of separation was affected only slightly by variations in Reynolds number.



(a) Transition upstream of reattachment. S–7; $M_o=1.9$; $R_L=0.92\times10^6$.

(b) Transition downstream of reattachment. S–8; $M_o=1.9$; $R_L=0.87\times10^6$.

FIGURE 7.—Typical results from two-dimensional channel illustrating importance of transition location relative to reattachment.

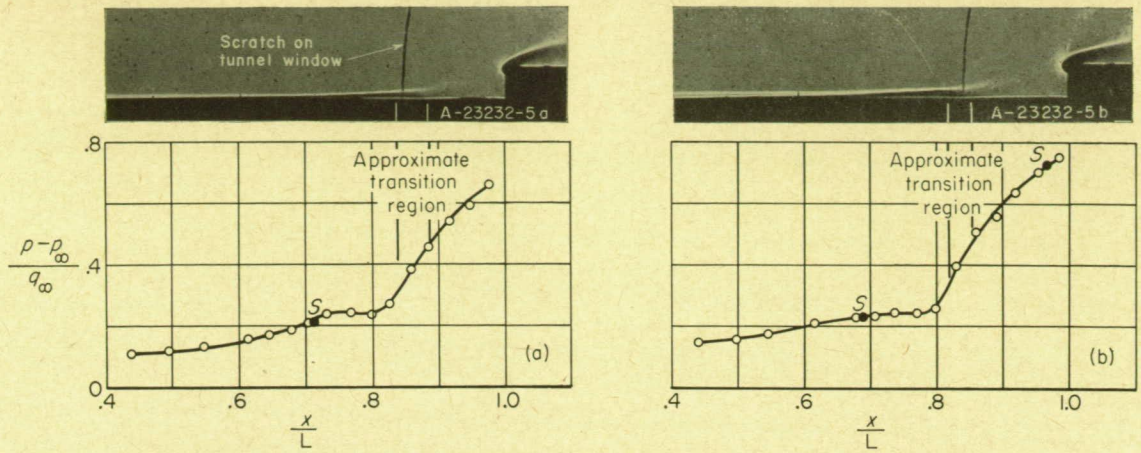
These contrasting characteristics show that the location of transition relative to reattachment is of critical importance at least to the separated flow ahead of a step.

The results of the initial experiments revealed some intriguing similarities between various results of experiments on separated flow from several other sources involving entirely different object shapes. The trend observed, of a slight influence of Reynolds number on pure laminar separations, was the same as the trend which could be interpreted from the base-pressure experiments of Reller and Hamaker (ref. 20). Also, the trend of large influences of Reynolds number for transitional separations was the same as that which could be interpreted from many previous measurements of base pressure. Crocco and Lees (ref. 9) make essentially this interpretation, only with reference to transition upstream of a "critical" location in the wake rather than upstream of reattachment. Consequently, it seemed possible that transition location relative to reattachment might be generally important to separated flows and that there might be some characteristics common to a variety of separated flows having the same relative transition location. The second phase of experiments was conducted with various model shapes in order to investigate this possibility. Some of the more salient results are surveyed below; they relate to the correlation between transition and abrupt pressure rise, to the relationship between type of pressure distribution and relative transition location, and to the effect of Reynolds number variation on separated flows.

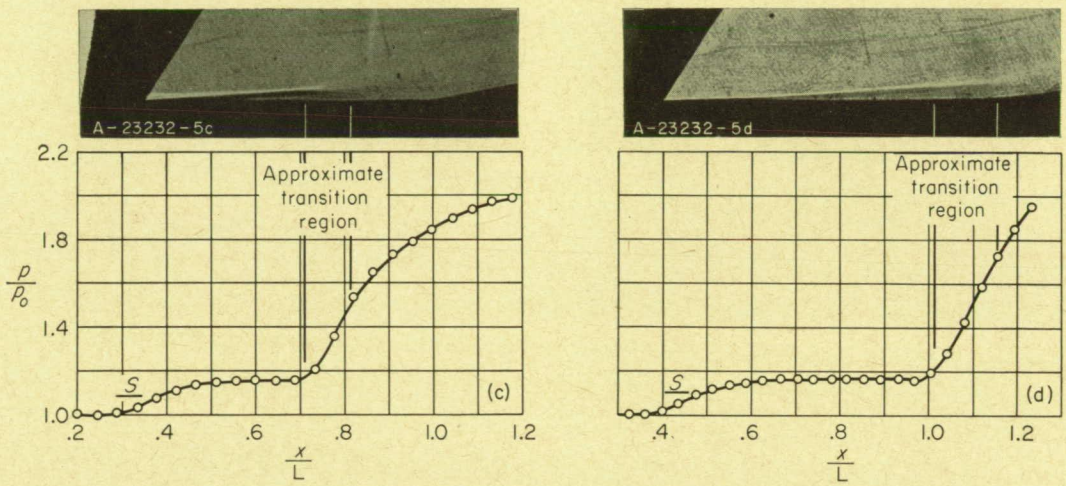
Correlation between transition and occurrence of abrupt pressure rise.—Transition was determined from shadowgraphs in two different ways (described in the section APPARATUS AND TEST METHODS). Under conditions of low pressure and low optical refraction, the mean location of transition was taken as the end of the familiar white line adjacent to a surface. Altogether about 170 cases of this type were examined corresponding to different combinations of Mach number, Reynolds number, and model shape. Figure 7 (a) represents one example, and various others are shown in figure 8 [3] for subsonic as well as supersonic flow. The terminal location of the white line is near an abrupt pressure rise in each case. There is sufficiently close coincidence of the two locations to associate the location of transition with that of a rapid rise in pressure. Emphasis is placed on the fact that the correlation for subsonic flow (figs. 8 (a) and 8 (b)) is much the same as that for supersonic flow. This attests to the fundamental importance of transition for separated flows.

As explained previously, both the beginning and the end of transition could often be determined, when optical refraction was high, by the beginning and end of convergence of the white line toward a solid surface. Altogether, about 95 cases of this type were examined for various combinations of Mach number, Reynolds number, and model shape. Some typical examples are shown in figure 9. In most of these examples transition occurs in an adverse pressure gradient, and the streamwise extent of the transition region

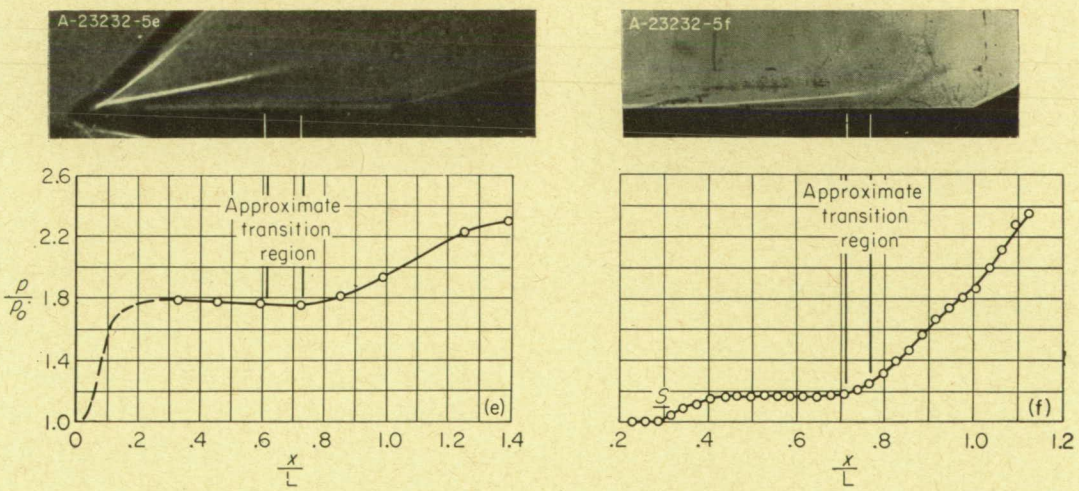
[3] In these and other figures, a separation point determined from an oil film observation is represented by a filled symbol. Separation pressure rises determined from a correlation (presented later) of measurements on a variety of model shapes are represented by a short line.



(a) S–9; $M_\infty = 0.47$; $\alpha = -4°$; $R_L = 0.47 \times 10^6$.
(b) S–9; $M_\infty = 0.76$; $\alpha = -4°$; $R_L = 0.50 \times 10^6$.



(c) CC10°–2; $M_o = 1.4$; $R_L = 0.33 \times 10^6$.
(d) CS25°–1; $M_o = 1.7$; $R_L = 0.26 \times 10^6$.



(e) CC15°–2; $M_o = 1.7$; $R_L = 0.058 \times 10^6$.
(f) CC25°–3; $M_o = 2.0$; $R_L = 0.44 \times 10^6$.

FIGURE 8.—Correlation of transition with abrupt pressure rise; low tunnel pressures.

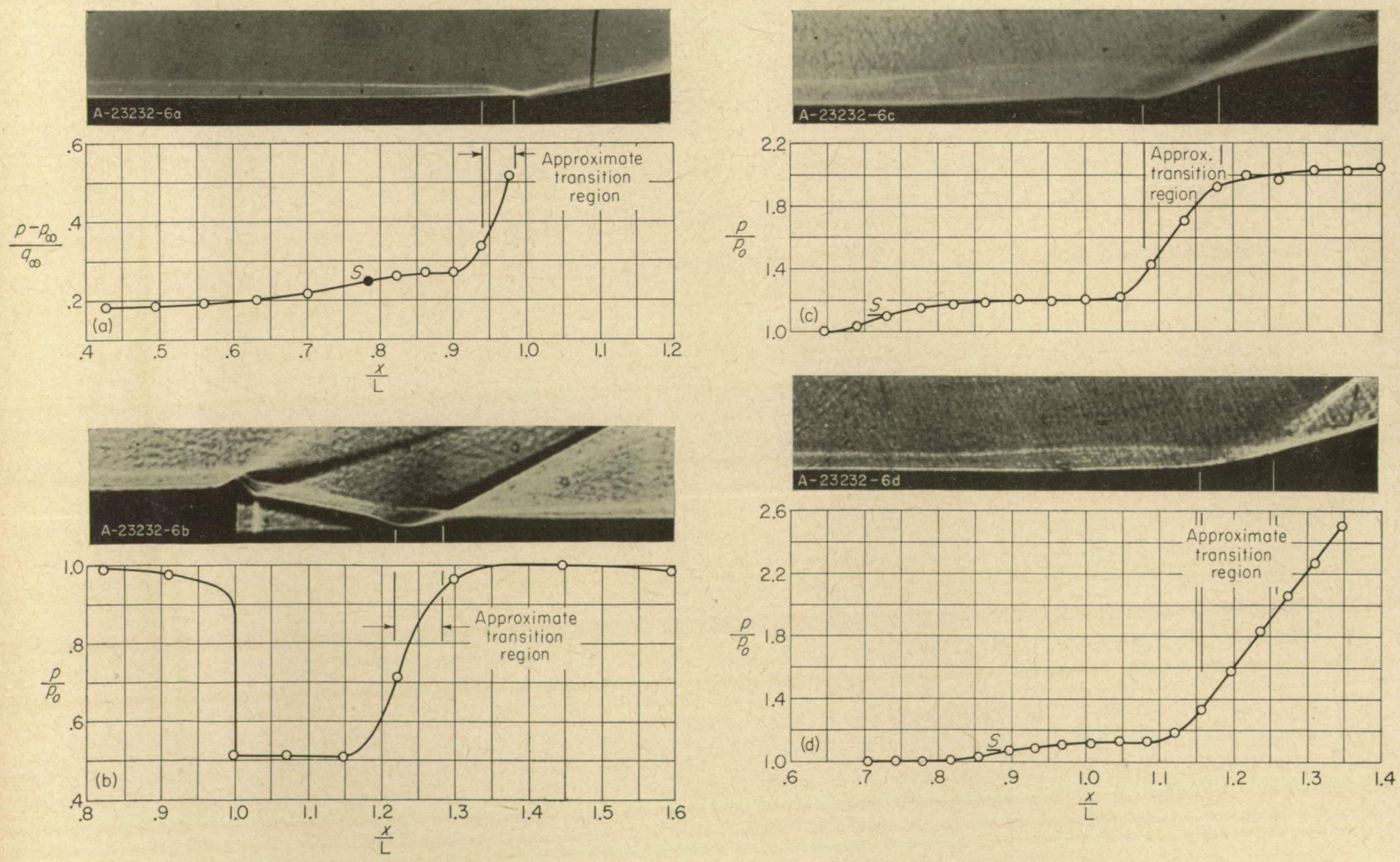
is much shorter than on a flat plate. In all cases the abrupt pressure rise occurs near the transition region, so that a marked pressure rise again is associated with transition.

It is interesting that, in subsonic flow over step models, separation bubbles often were observed on the flat surface well upstream of the step. An example is illustrated in figure 8 (b). In such cases, oil film accumulated at two streamwise locations; the upstream separation is that of a laminar layer and locates the upstream portion of the bubble; the downstream separation (not evident in shadowgraph) is that of a turbulent layer as it approaches the step. Turbulent reattachment presumably occurs somewhere between the two experimentally determined positions of separation.

The correlation of the location of transition with that of an abrupt pressure rise has been observed previously in many isolated cases. Experiments at low subsonic speeds conducted on circular cylinders, spheres, and airfoils, as reported by Fage (ref. 21), showed similar close correlation of transition location (determined by surface shear data from a Stanton tube) with an inflection point in pressure distribution which just preceded an abrupt pressure rise.[4] Analogous correlation also was noticed in transonic flow by Ackeret, Feldmann, and Rott (ref. 4), in supersonic shock-induced separations by Gadd, Holder, and Regan (ref. 15), and in subsonic separation bubbles on airfoils by Gault (ref. 8).

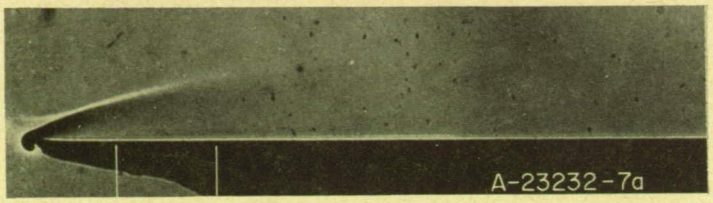
In spite of the many observations of correlation between transition location and abrupt pressure rise—as evidenced in figures 7 to 9 and in previous experiments—it is not necessary that transition in a separated layer be accompanied by a rapid pressure rise, or that abrupt rises in pressure necessarily indicate transition. If transition is far upstream of reattachment, and only slightly downstream of separation, then transition can occur in the mixing layer under conditions of nearly constant pressure. An example of this is shown in figure 10 (a) in which transition is com-

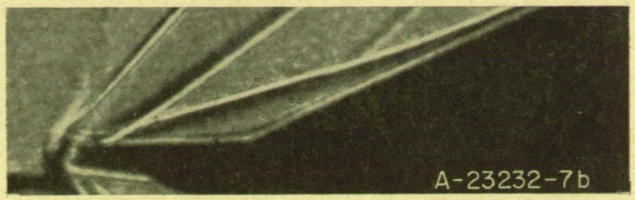
[4] In retrospect, it would be expected that for such correlation to have existed, transition would have occurred within a small "separation bubble" in these early experiments. This expectation was indicated by Bursnall and Loftin (ref. 22). Such bubbles have been observed frequently on airfoils but rarely on a sphere or circular cylinder. A direct confirmation of the existence, not often appreciated, of a small separation bubble on the upstream half of a circular cylinder in the supercritical Reynolds number range is reported by Gault (ref. 8) who used a liquid film to detect separation.

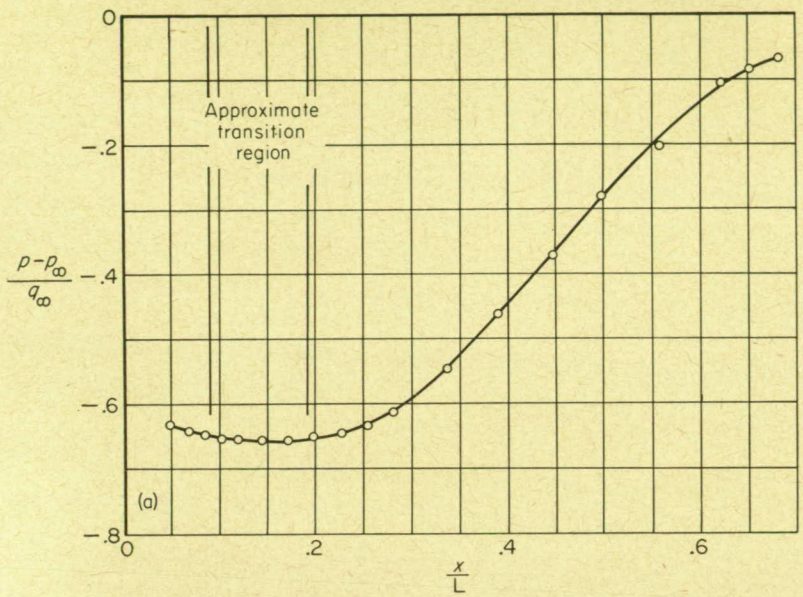


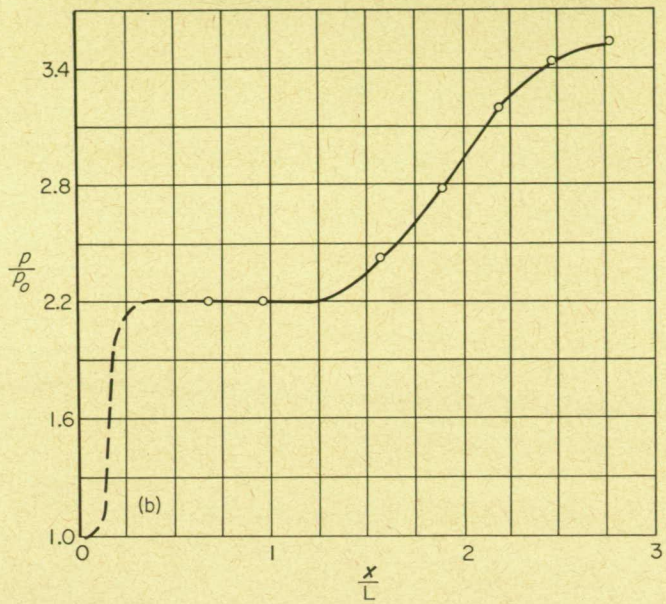
(a) CC10°−3; $M_\infty=0.78$; $\alpha=-4°$; $R_L=0.75\times10^6$.
(b) B–2; $M_o=1.7$; $R_L=0.57\times10^6$.
(c) CC10°−2; $M_o=2.7$; $R_L=1.05\times10^6$.
(d) CS25°−1; $M_o=2.1$; $R_L=1.13\times10^6$.

FIGURE 9.—Correlation of transition with abrupt pressure rise; high tunnel pressures.





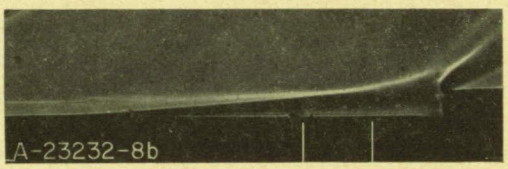


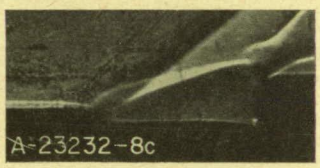


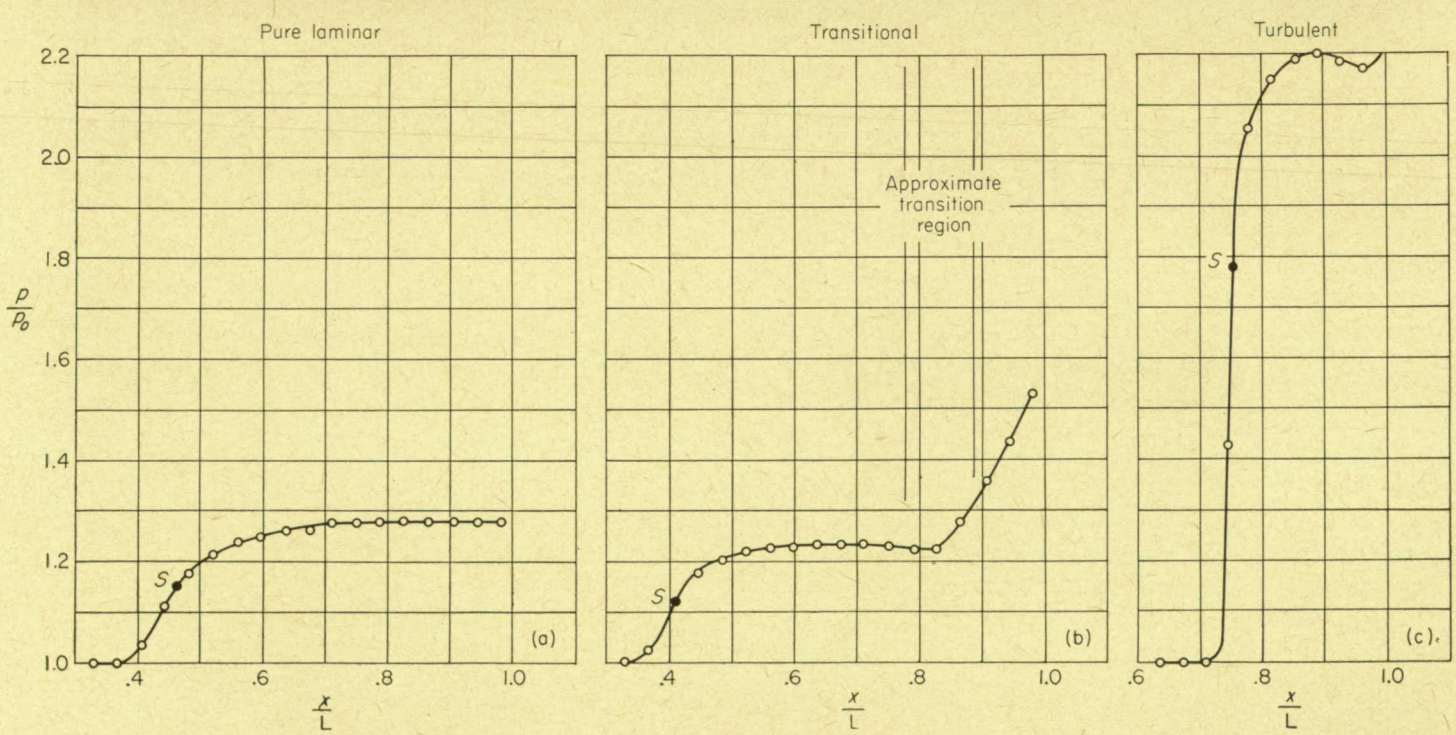
(a) Abrupt rise near reattachment of turbulent layer. S–9; $M_\infty=0.47$; $\alpha=3°$; $R_L=0.68\times10^6$.
(b) Abrupt rise near reattachment of thin laminar layer. CC20°−1; $M_o=3.0$; $R_L=0.018\times10^6$.

FIGURE 10.—Examples of abrupt pressure rise not correlated with the location of transition.



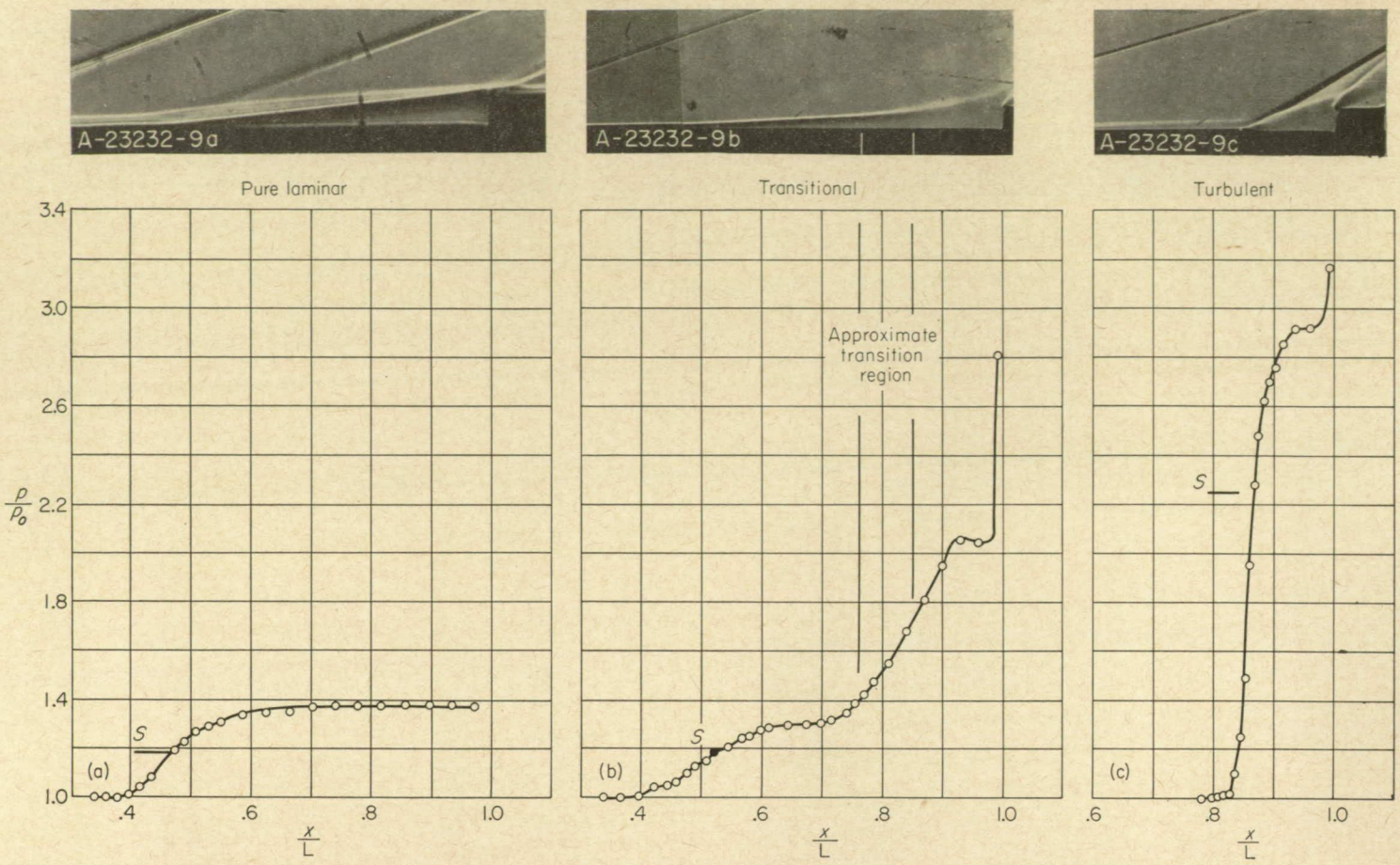






(a) S–3; $M_o=2.3$; $R_L=0.20\times10^6$. (b) S–3; $M_o=2.3$; $R_L=0.46\times10^6$. (c) S–4 (trip 1); $M_o=2.3$; $R_L=1.52\times10^6$.

FIGURE 11.—The three regimes for a step; $M_o=2.3$.



(a) S–3; $M_o=3.5$; $R_L=0.65\times10^6$.
(b) S–2; $M_o=3.6$; $R_L=1.53\times10^6$.
(c) S–10 (trip 4); $M_o=3.3$; $R_L=2.12\times10^6$.

FIGURE 12.—The three regimes for a step; $M_o\approx3.5$.

pleted well upstream of reattachment and the pressure rise is brought about by a fully turbulent layer as it reattaches. If a reattaching layer is laminar and very thin, it also can bring about an apparent rapid rise in pressure and not be indicative of transition. An example of this is presented in figure 10 (b) for which transition is downstream of the field of view. (A theory for the pressure rise of a thin, pure laminar, reattaching layer is given later.) In view of these observations, the pertinent conclusions drawn from the close correlation often observed between transition and an abrupt pressure rise is as follows: Once transition is between separation and reattachment—and is relatively close to reattachment—there is an abrupt pressure rise associated with transition; hence, any change in a parameter which experience has shown to affect transition (such as Reynolds number, surface roughness, turbulence level, etc.) can also change pressure distribution directly through its change in the location and magnitude of the steep pressure rise.

Representative pressure distributions for the three regimes and results of high-speed motion picture studies.—As the importance of transition location relative to reattachment is now manifest, and the importance of transition location relative to separation has long been known, it is clear that distinction should be made for any given object shape between the three regimes of flow separation; "pure laminar" where transition is downstream of reattachment, "transitional" where transition is between reattachment and separation, and "turbulent" where transition is upstream of separation. Within the scope of this study, all three regimes were observed for most of the model shapes, as the following table illustrates:

Regimes observed in present study			
Model	Pure laminar	Transitional	Turbulent
Step	$M>1$, $M<1$	$M>1$, $M<1$	$M>1$, $M<1$
Compression corner	$M>1$, $M<1$	$M>1$, $M<1$	$M>1$, $M<1$
Base	$M>1$	$M>1$	$M>1$
Curved surface	$M>1$	$M>1$	$M>1$
Oblique shock	$M>1$	$M>1$	
Leading-edge separation	$M>1$	$M>1$	

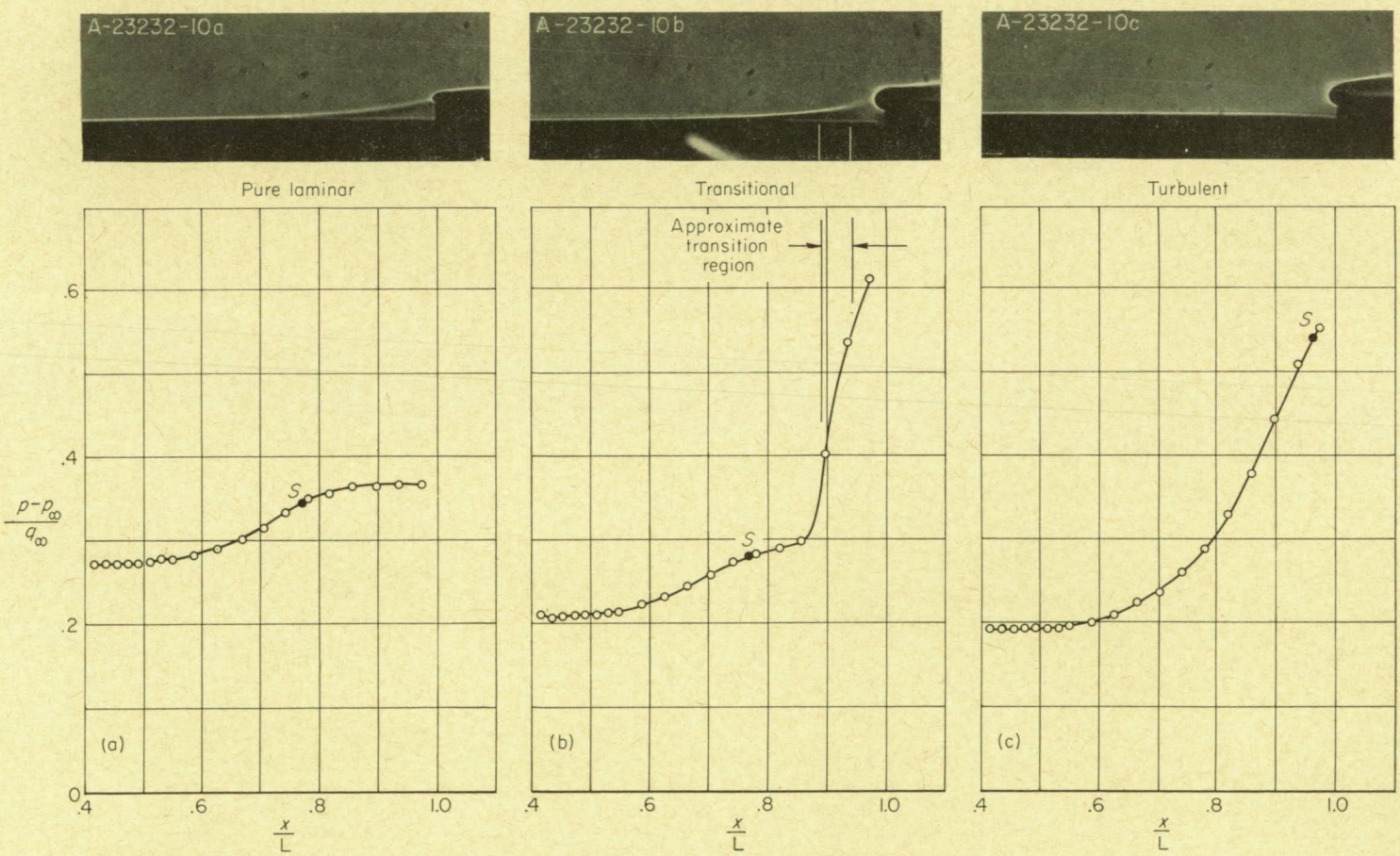
Studies were not conducted with the turbulent regime for leading-edge separation, or with the turbulent regime for oblique-shock-induced separation. Much data are available for this latter case in references 14 and 15.

Shadowgraphs and corresponding pressure distributions for the three regimes, at both supersonic and subsonic speeds, are illustrated in figures 11 through 17 for various models and various Mach numbers. Figure 11, which shows the

step in supersonic flow, reveals as well as any the basic differences between the three regimes. The pure laminar regime (fig. 11 (a)) has a plateau of nearly constant pressure representing a dead-air region. The separation-point pressure, p_s, and the plateau pressure, p_p, are of the order of 15 and 30 percent greater, respectively, than the pressure p_o just upstream of the separated region. For some step models, pressures were measured at a few points on the step face and were usually found—for the pure laminar regime—to be the same as the dead-air pressure (see fig. 7 (b) for example). In a few cases, a very small pressure rise was observed in the corner and on the step face. It is thought that there always is a small region near the step shoulder where pressures on the face locally are higher than the dead-air pressure, since a portion of the separated layer presumably must be brought to rest on the step face. If the separated layer at separation is thick, then the expected magnitude of pressure increase would be small, and if it is very thin, then the area over which the pressure increase would occur would be confined to a small area near the shoulder. This may explain why a significant pressure variation over the step face is not often measured. High-speed motion pictures (taken at $M_o=2.3$ with 2000 to 6000 frames per sec.) indicated the pure laminar separation over a step to be steady.

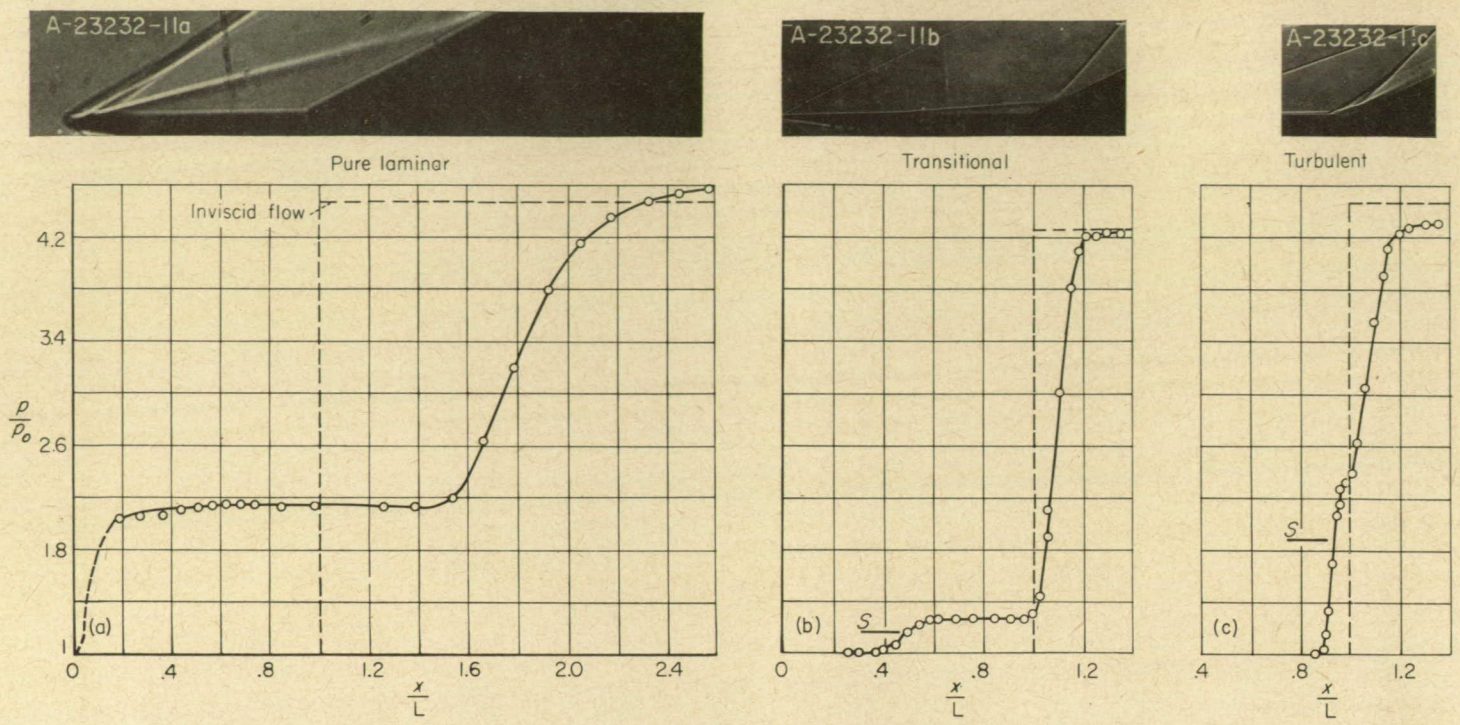
Most of these characteristics for pure laminar separation over a step differ from those for transitional separation illustrated in figure 11 (b). In the transitional regime the boundary layer is still laminar at separation so the pressure rise to separation remains about the same as for pure laminar separation, but the role of transition is to bring about much greater pressure rises before reattachment occurs at the step. Pressure variation on the step face, now easily measurable, amounts to the order of 0.1 p_o (see fig. 7 (a) for example). As Lange (ref. 23) has noticed previously, this variation implies that sizable subsonic velocities exist within the reverse flow region just upstream of the step. High-speed motion pictures indicated the flow to be unsteady in the region between transition and reattachment on the step. Such unsteadiness might be expected since transition itself is fundamentally a nonstationary phenomenon. In spite of this unsteadiness, the white line indicative of laminar flow appeared reasonably steady over most of its length whenever transition was relatively far from separation and relatively close to reattachment. At higher Reynolds number, though, where transition was close to separation, the angle of separation appeared unsteady in the motion pictures as did the flow downstream of transition.

These qualitative flow conditions again alter on passing



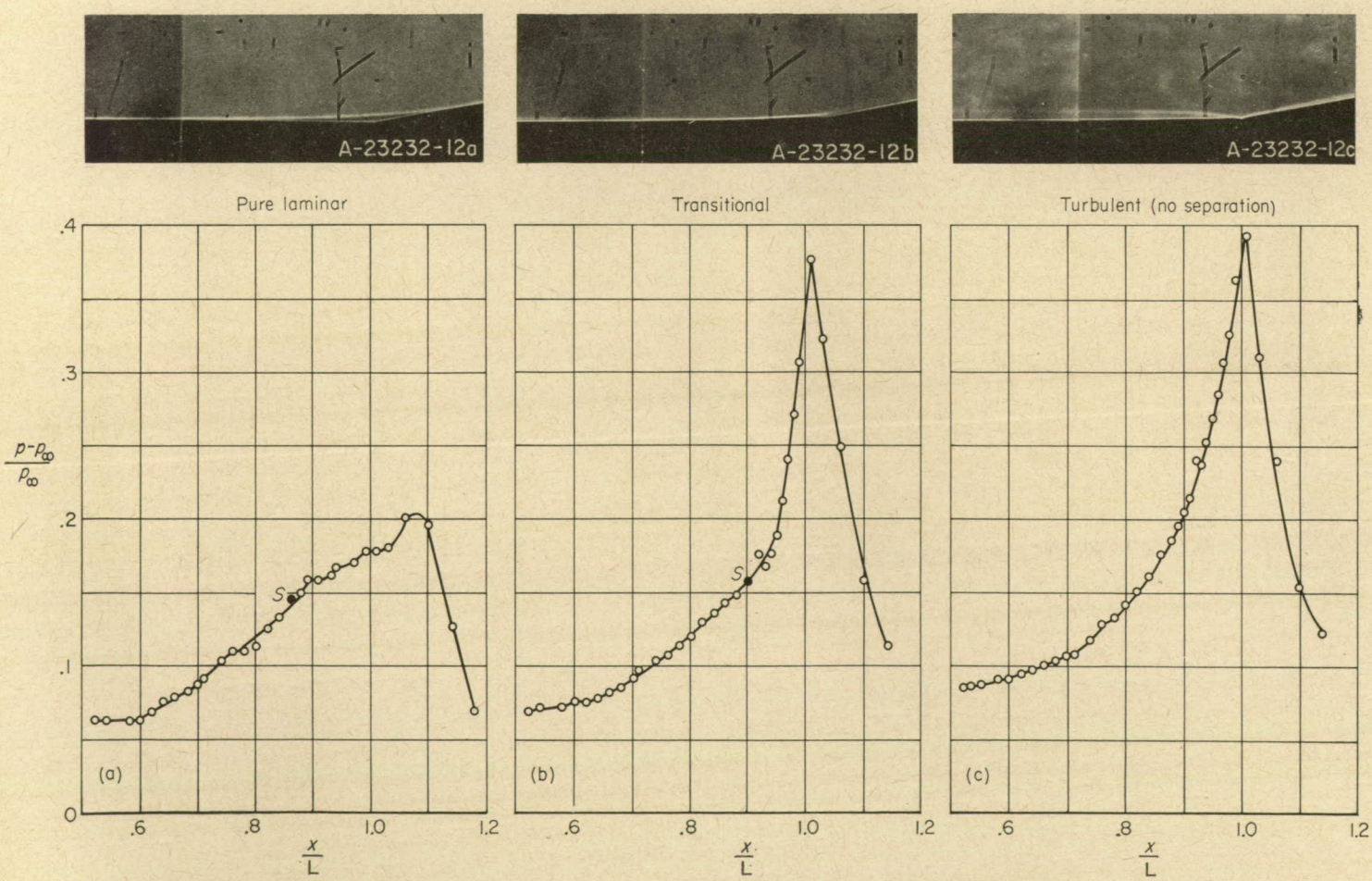
(a) S–3; $M_\infty=0.61$; $\alpha=-4.5°$; $R_L=0.106\times10^6$.
(b) S–3; $M_\infty=0.61$; $\alpha=-4.5°$; $R_L=0.358\times10^6$.
(c) S–3 (trip 1); $M_\infty=0.61$; $\alpha=-4.5°$; $R_L=0.407\times10^6$.

FIGURE 13.—The three regimes for a step in subsonic flow; $M_\infty=0.61$.



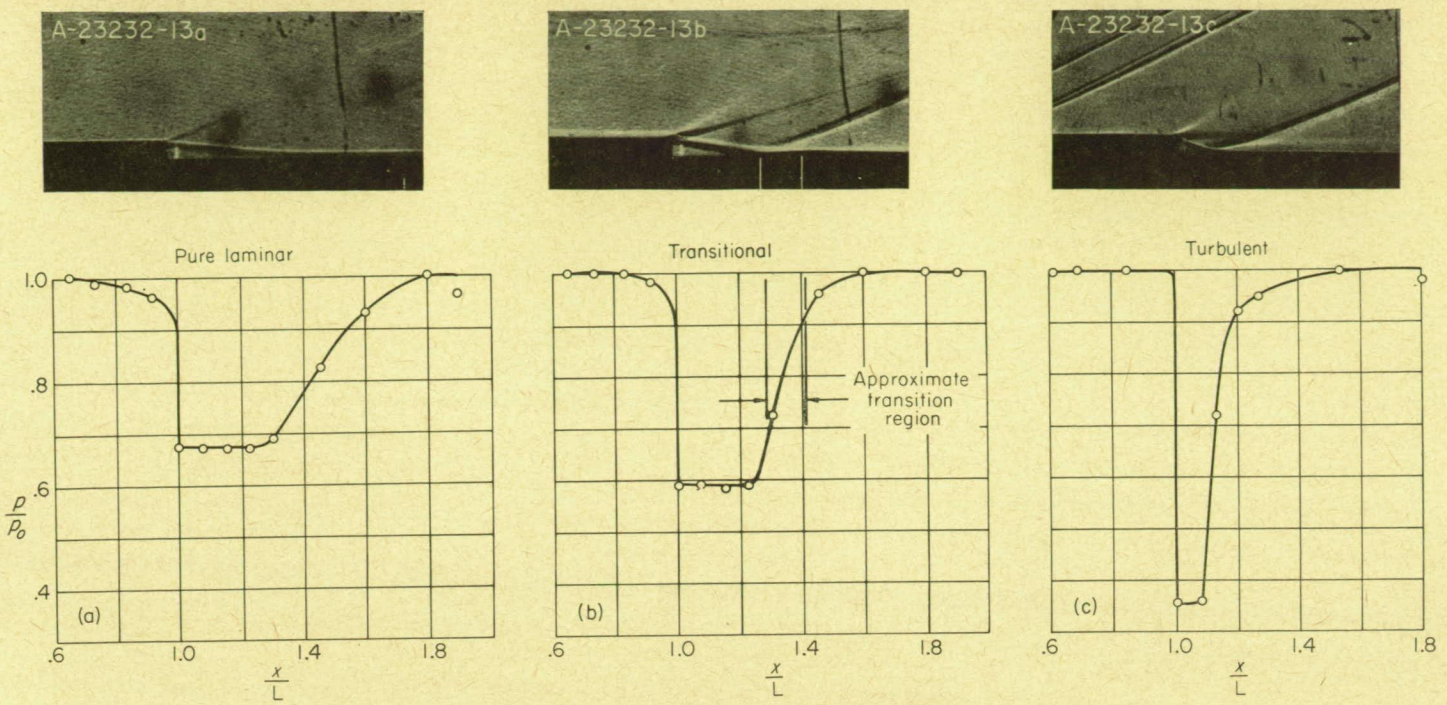
(a) CC25°−2; M_o=2.7; R_L=0.033×10⁶. (b) CC25°−4; M_o=2.6; R_L=0.33×10⁶. (c) CC25°−5 (trip 4); M_o=2.7; R_L=1.65×10⁶.

FIGURE 14.—The three regimes for a compression corner; $M_o \approx 2.7$.



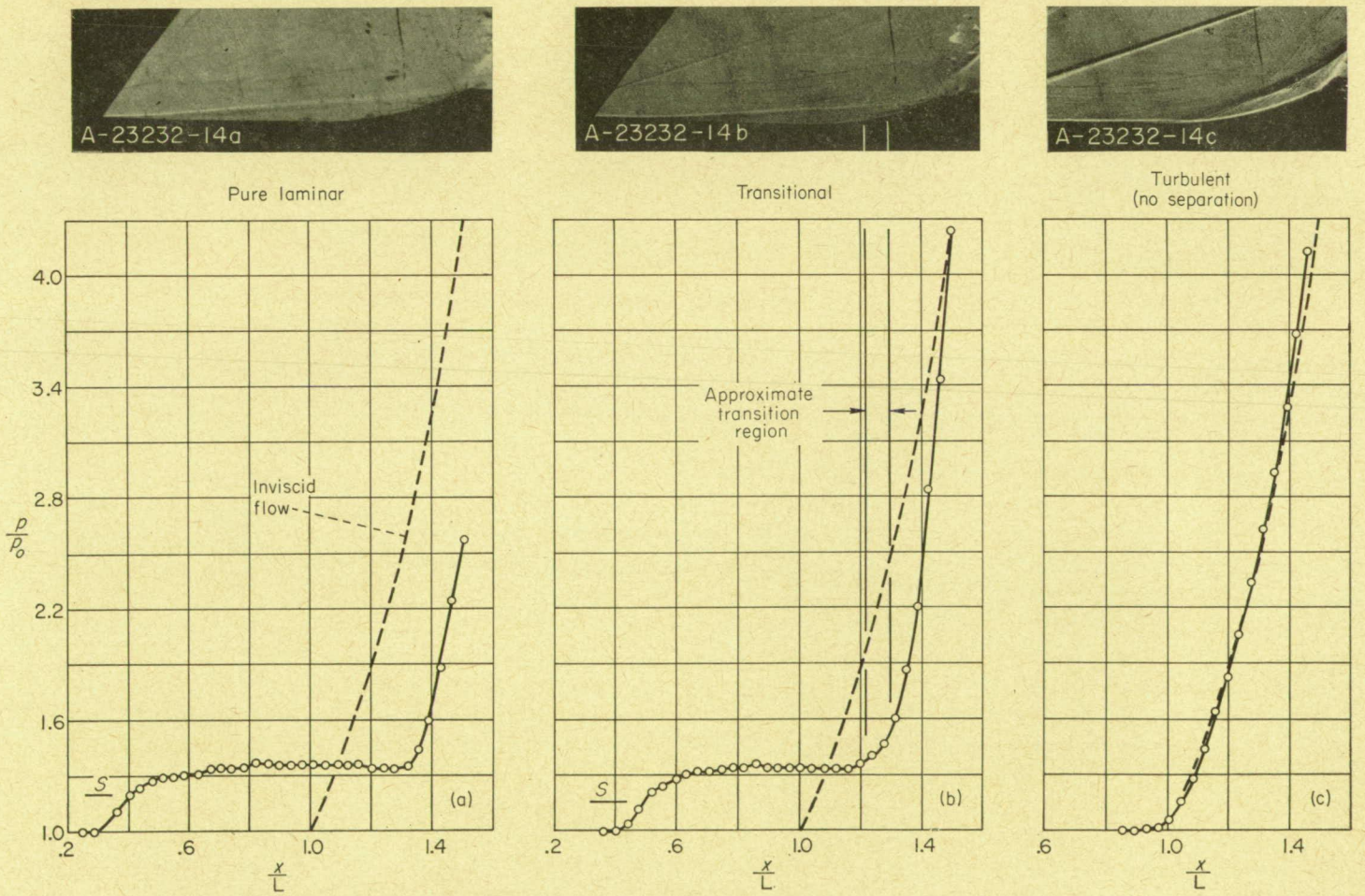
(a) CC10°−4; M_∞=0.5; α=−4°; R_L=0.17×10⁶. (b) CC10°−4; M_∞=0.5; α=−4°; R_L=0.43×10⁶.
(c) CC10°−4; M_∞=0.5; α=−4°; R_L=1.22×10⁶.

FIGURE 15.—The three regimes for a compression corner in subsonic flow; M_∞=0.5.



(a) B–2; $M_o=2.0$; $R_L=0.17\times10^6$. (b) B–2; $M_o=2.0$; $R_L=0.50\times10^6$. (c) B–1–c (trip 1); $M_o=2.0$; $R_L=0.39\times10^6$.

FIGURE 16.—The three regimes for a base; $M_o=2.0$.



(a) CS25°−1; $M_o=2.7$; $R_L=0.16\times10^6$. (b) CS25°−1 (trip 1); $M_o=2.7$; $R_L=0.21\times10^6$. (c) CS25°−1 (trip 1); $M_o=2.7$; $R_L=0.96\times10^6$.

FIGURE 17.—The three regimes for a curved surface; $M_o=2.7$.

to the turbulent regime illustrated in figure 11 (c). The pressure rise to separation now is much larger (about five times larger), as should be expected. A plateau in pressure (characteristic of dead air) does not occur since the eddying motion of the turbulent layer energizes the air. Pressures on the step face were found to vary in much the same manner as for the transitional regime. The flow field observed in high-speed motion pictures was not perfectly steady like the laminar separation was, but, compared to the transitional separation, the turbulent separation was relatively steady. Shock waves occasionally appeared to move slightly but no appreciable movement of the separated layer could be detected. This degree of steadiness of turbulent separation upstream of a step appears much the same as that observed by Bogdonoff and Kepler (ref. 14).

The data in figures 12 through 17 for steps, compression corners, bases, and curved surfaces show several similarities within a given regime to the characteristics just described for a step at $M_o=2.3$. It is emphasized that certain qualitative similarities exist irrespective of model shape or Mach number, or whether the flow is subsonic or supersonic (cf., e. g., figs. 11 and 13). Pure laminar separations ((a) portions of figs. 11 through 17) usually involve small pressure changes and relatively gradual pressure gradients. They are steady when observed in motion pictures at several thousand frames per second.[5] The transitional separations for the different configurations ((b) portions of figs. 11 to 17) involve severe pressure gradients near transition and usually were observed to be unsteady. The only transitional-type separation of those investigated which appeared steady was that over the base(e. g., fig. 16 (b)). The various turbulent separations (figs. 11 (c) to 17 (c)) are associated with abrupt pressure variation near both separation and reattachment. They were observed to be relatively steady flows except for the compression corners, which were rather unsteady in several cases at Mach numbers near shock detachment.

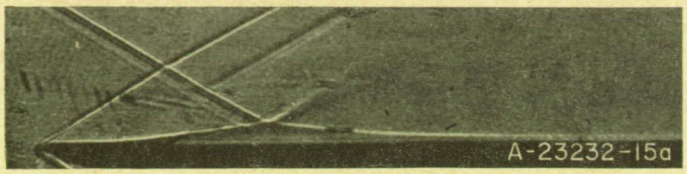
A general feature worth noting concerns the proximity of shock waves to the boundary layer in the various types of separated flow. For pure laminar separations the shock wave associated with separation, as well as the shock wave associated with reattachment on a flat surface, does not enter or originate within the boundary layer (see figs. 14 (a), 16 (a), and 18 (a)). The coalescence of compression wavelets into a shock wave occurs at a considerable distance from the boundary layer. In these cases, there obviously is no direct interaction of shock wave and boundary layer; there is, however, strong interaction of the supersonic external flow and the boundary layer. When pure laminar separation is induced by the reflection of an incident shock wave from a laminar boundary layer, the incident wave necessarily enters and locally interacts with the viscous layer near the station of impingement, but the shock waves formed near separation and reattachment do not originate within the viscous layer (see fig. 18 (a)). It is only after transition moves upstream of a reattachment position, thereby bringing about a steep pressure rise, that a shock wave originates partially within the boundary-layer flow near reattachment on a surface (see figs. 11 (b) through 18 (b)). Similarly, only after transition moves upstream of separation does a shock wave originate partially within the boundary-layer flow near separation.

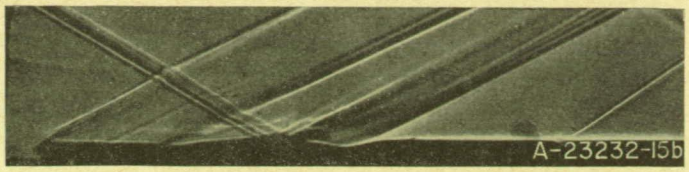
In the process of varying tunnel pressure, the conversion from transitional-type to turbulent-type separation often was observed to be irregular and unsteady. During such conversion, shadowgraphs were blurred since relatively long exposure times were used. The pressure distribution was not smooth since the various orifice-tube connections were not identical, and thus responded differently to the fluctuating pressure. An example illustrating these characteristics is shown in figure 19 (a) in comparison to an example of steady turbulent flow (fig. 19 (b)). Also, during such conversion between transitional and turbulent regimes, oil film did not accumulate along a threadlike line as it otherwise did. Instead, oil wandered irregularly over the plate in a jagged, random fashion. It is interesting, perhaps, to note that similar unsteady conversions have long been observed. In the fundamental paper on spheres by Prandtl (ref. 1) wherein smoke was used to determine the line of separation, the same type of unsteady flow with jagged separation line was observed during the conversion from the transitional regime to the turbulent regime. It is possible that certain of the unsteady flow phenomena sometimes found on various practical devices are intimately related to the unsteadiness found on these models of simple shape when conditions were such that the flow was on the verge of conversion between transitional-type and turbulent-type separation.

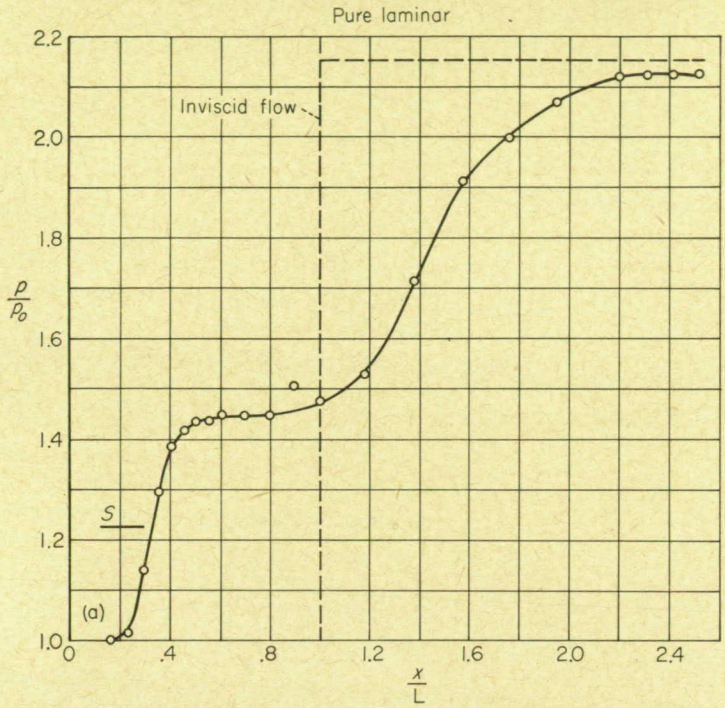
Representative Reynolds number effects for the three regimes.—As previously remarked, a variation in Reynolds number was found to have only a minor effect on pure laminar separations. This is illustrated in figure 20 (a). The ordinate is the pressure rise $|p'-p|$ across the reattachment region divided by the pressure p' just downstream of reattachment. The quantity p is measured at an arbitrary fixed point in the separated region. Some of the pure laminar separations are seen to be affected to a negligible extent by variation in Reynolds number. This is consistent with a theory to be developed shortly which indicates that the lack of dependence on Reynolds number is a characteristic of pure laminar separations for which the boundary-layer thickness at separation is zero or negligible. Other curves in figure 20 (a) show a small Reynolds number effect which amounts at the most to about a $\frac{1}{4}$-power variation. In these cases the boundary-layer thickness at separation is not negligible. Generally speaking, though, the pure laminar separations investigated are affected only to a small extent by variation in Reynolds number.

As might be anticipated, transitional-type separations behave differently than the pure laminar separations when subjected to variation in the Reynolds number. The effect of Reynolds number on various transitional-type separations is shown in figure 20 (b). Some of these flows are affected markedly by variation in Reynolds number. When such large variations were found, it was observed that transition was relatively near reattachment. For example, the lower Reynolds number portion of the filled-circle data points

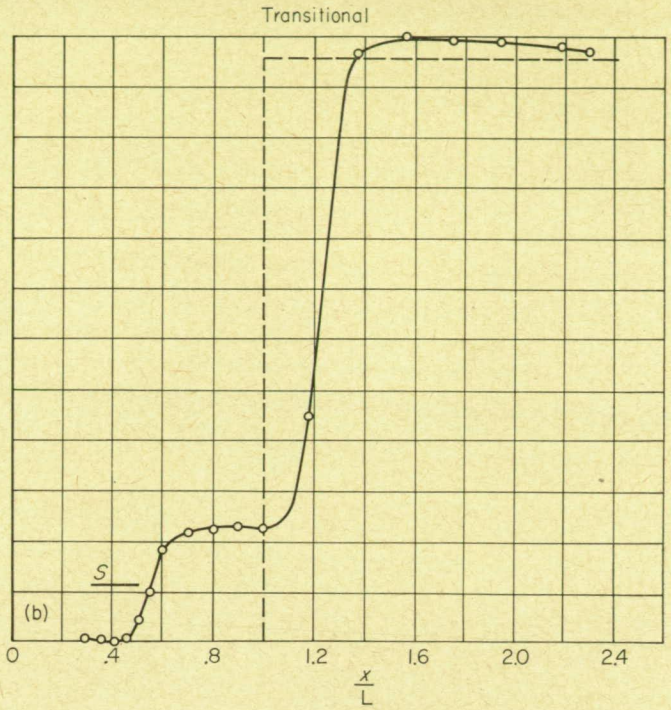
[5] Obviously, not all pure laminar separations are steady in subsonic flow. It is well known that the separated flow behind a cylinder develops into an unsteady vortex trail even at Reynolds numbers near 100 where the separated flow is entirely laminar.





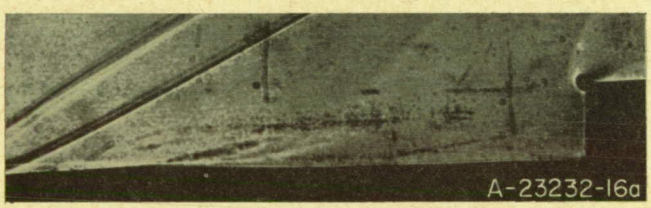


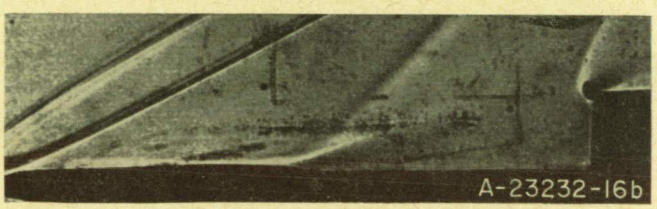
(a) I6.5°−1; M_o=2.4; R_L=0.054×10⁶.

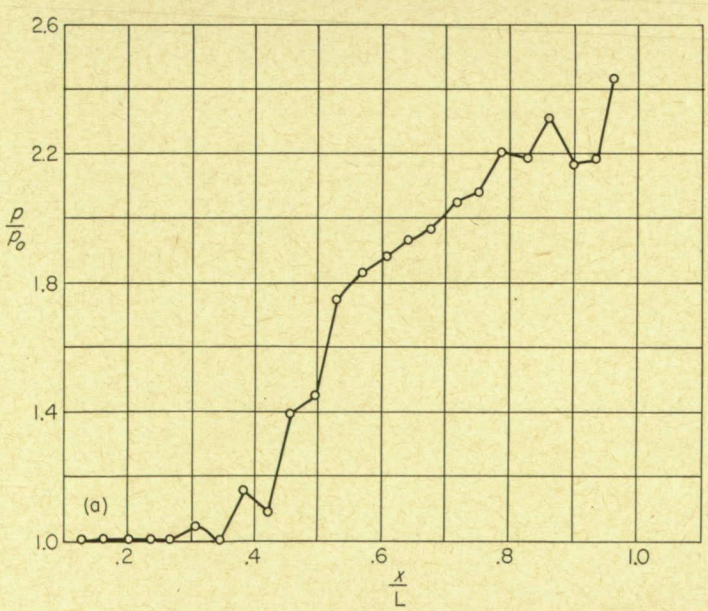


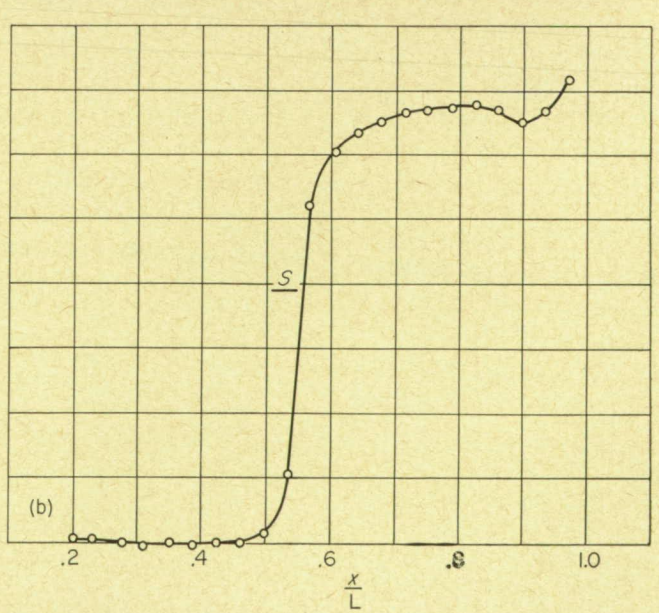
(b) I6.5°−1; M_o=2.4; R_L=0.176×10⁶.

FIGURE 18.—Pure laminar and transitional separations induced by an incident shock wave; M_o=2.4.









(a) Conversion from transitional to turbulent separation; S–6 (trip 1); M_o=2.1; R_L=0.39×10⁶.
(b) Turbulent separation established; S–6 (trip 1); M_0=2.1; R_L=0.51×10⁶.

FIGURE 19.—Example of unsteady flow during conversion from transitional to turbulent flow.

shows large effects and corresponds to transition relatively near reattachment, whereas the higher Reynolds number portion corresponds to transition relatively near separation and shows much less effect. In most cases, a movement of transition upstream of reattachment (brought about by an increase in Reynolds number) increases the pressure rise through the reattachment region.

Turning now to turbulent flows for which transition is upstream of separation, the characteristic influence of Reynolds number again changes rather strikingly. The effect of the variation in Reynolds number on various turbulent separations is shown in figure 20 (c). For this type of separation, the effects of Reynolds number are either small or negligible.

The typical effects of Reynolds number variation for the three separation regimes also can be clearly seen from complete pressure distributions. Some example pressure distributions for pure laminar separations over a compression corner at various Reynolds numbers are shown in figure 21 (a). These pressure distributions are only slightly affected by variation in Reynolds number, as would be anticipated from the trend illustrated in figure 20 (a). Some example pressure distributions for transitional separations over a curved surface at various Reynolds numbers are shown in figure 21 (b). These data show a large effect of variation in Reynolds number just as do the data in figure 20 (b). For example, the pressure drag coefficient of the curved surface would change by a factor of about 4 over the range of Reynolds numbers (0.16 to 0.81×10^6) represented. Also in agreement with the trend of figure 20 (b) for transitional separations, it is seen from figure 21 (b) that the changes in final pressure rise with Reynolds number are larger when transition is relatively near reattachment (Reynolds numbers from 0.16 to 0.36×10^6) than when transition is relatively near separation (Reynolds numbers from 0.36 to 0.81×10^6). Some example pressure distributions in turbulent separation at various Reynolds numbers are shown in figure 21 (c). As previously noted in figure 20 (c), the observed dependence on Reynolds number is small.

The characteristic influences of Reynolds number variation as illustrated for these different models also can be illustrated by a single model. A special model consisting of three bases in series was investigated on which all three separation regimes were found to occur simultaneously at 21 psia tunnel pressure, as may be deduced from study of figure 22. Although the results obtained with this special model are instructive, they do not reveal any new feature over and above those already illustrated in figures 11 through 17.

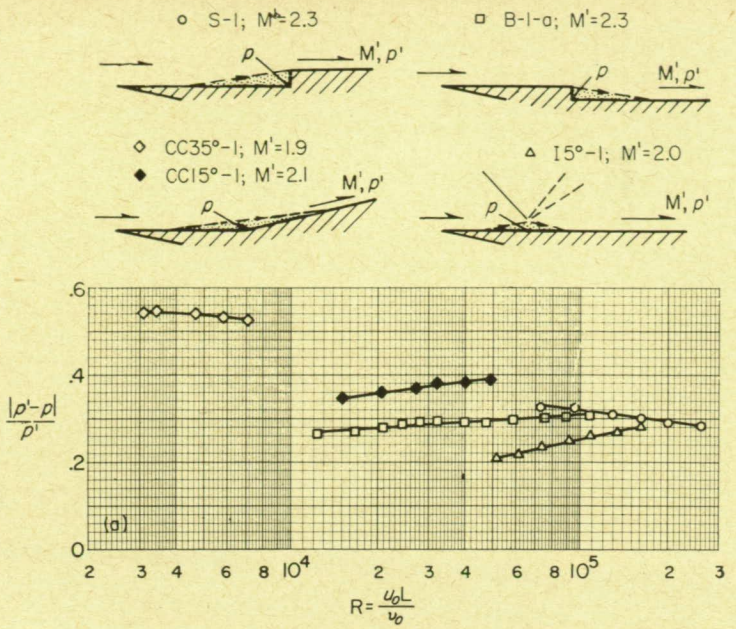
Representative Mach number effects for the three regimes.—Pressure-distribution curves for pure laminar separation over a step in the Mach number range between 1.3 and 3.1 are presented in figure 23 (a). These curves are for $R_L=0.13\times10^6$. The various curves qualitatively are similar, and exhibit only a small effect of Mach number on the streamwise length of dead-air region.

Pressure-distribution curves for transitional separation over a step in the Mach number range between 1.3 and 3.3 are presented in figure 23 (b) for $R_L\approx0.6\times10^6$. These curves show that transition moves downstream as the Mach number is increased. At $M_o=1.3$ the separated laminar layer is relatively unstable, resulting in transition near separation and a large pressure rise above the plateau pressure; at $M_o=3.3$ the separated laminar layer is much more stable, resulting in transition near reattachment and only a small pressure rise above the plateau.

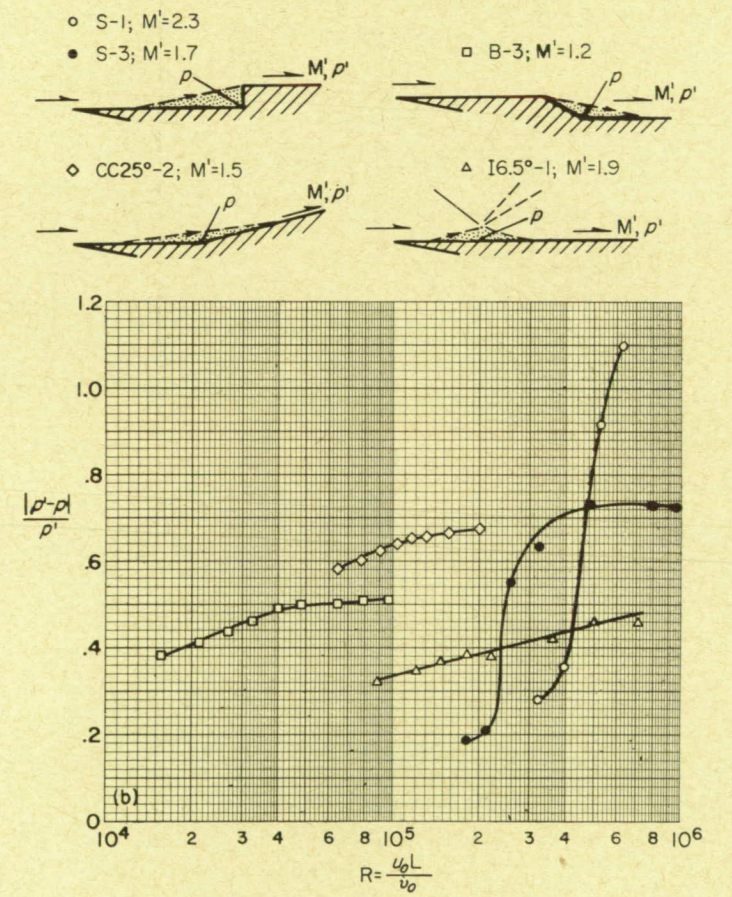
The effect of Mach number on the pressure distribution over a step in turbulent flow at Mach numbers between 2.0 and 3.4 is presented in figure 23 (c). These data correspond to $R_L\approx2.6\times10^6$. The streamwise extent of the interaction region is seen to be not significantly affected by variations in Mach number over the range investigated. The peak pressures, though, are strongly dependent on Mach number.

Significance to wind-tunnel testing.—From one viewpoint it is fortunate that a variety of separated flows, such as supersonic flow behind a base, or subsonic flow in a corner, or the flow induced by a strong shock wave impinging on a boundary layer, turn out actually to be dominated largely by a single variable, namely, the location of transition relative to reattachment and separation positions. On the other hand, from the viewpoint of wind-tunnel testing of prototype models, it is unfortunate that a variable like transition, which is so elusive to control and difficult to predict, turns out to be so important. Nevertheless, merely an understanding of the dominating influence of transition on separated flows can be helpful. For example, it is clear that the proper simulation in a wind tunnel of any flow involving separation in flight, such as large-deflection control effectiveness, buffeting, or high angle-of-attack force characteristics, would require the relative transition location to be duplicated between wind tunnel and flight. If the relative transition location is either downstream of reattachment (pure laminar separation) or upstream of separation (turbulent separation), then the precise position of transition does not critically affect the pressure distribution provided the relative location is duplicated; but, if transition is between separation and reattachment (transitional-type separation), then the precise position is important.

The requirement of matching relative transition location between wind tunnel and flight appears particularly important at hypersonic speeds. Inasmuch as a separated laminar mixing layer is relatively stable at hypersonic Mach numbers (see next section), transition can often occur near reattachment in this speed range. Under such conditions, the type of separation could be transitional in the wind tunnel yet pure laminar in flight, or vice versa. Even if a separation is transitional both in wind tunnel and in flight, the type of flow field can be sensitive to variations in Reynolds number when transition is near reattachment, as was illustrated by figures 20 (b) and 21 (b). In the past, interest has focused more on flow at lower Mach numbers where transition is relatively near separation, under which conditions a close matching of relative transition location for transitional separations is not so important.

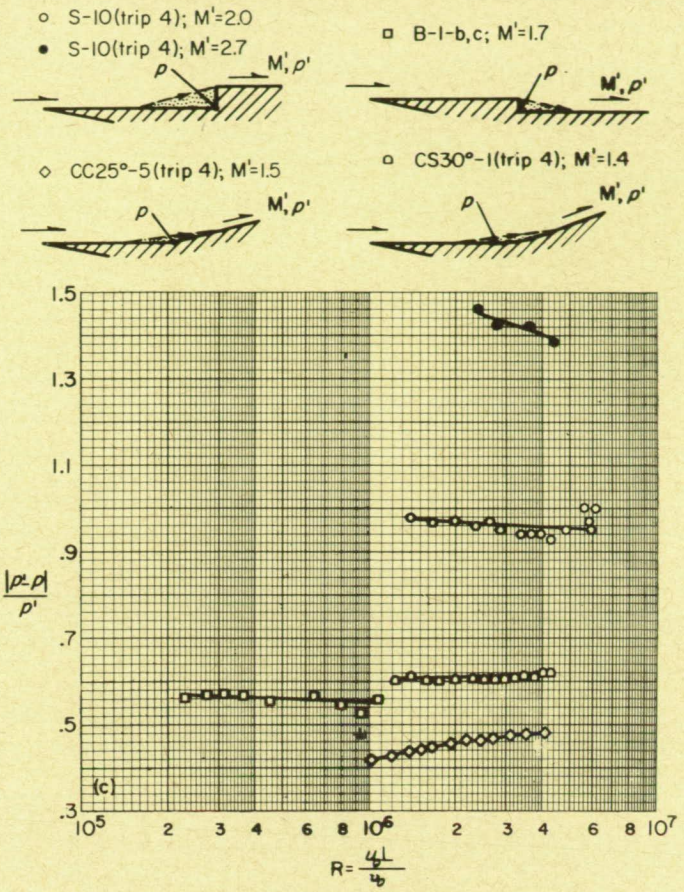


(a) Pure laminar separation.



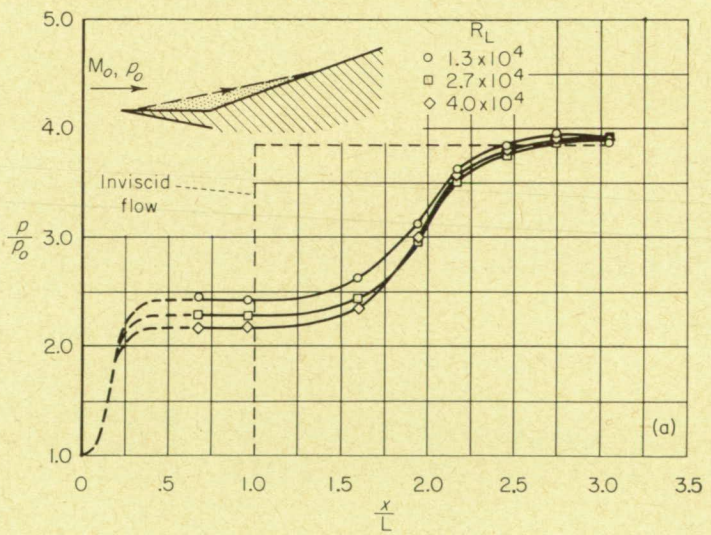
(b) Transitional separation.

FIGURE 20.—Characteristic effect of Reynolds number variation on pressure differential for the three regimes.



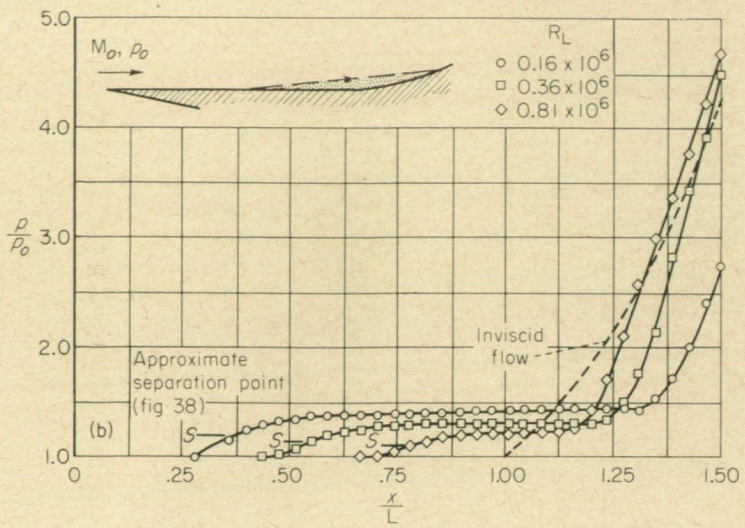
(c) Turbulent separation.

FIGURE 20.—Concluded.

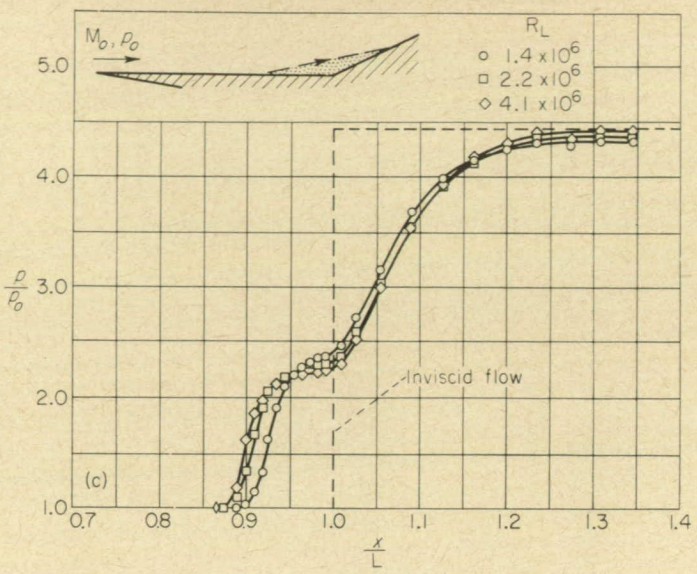


(a) Pure laminar separation; CC20°–1; $M_o=3.0$.

FIGURE 21.—Reynolds number effect on pressure distribution for the three flow regimes.

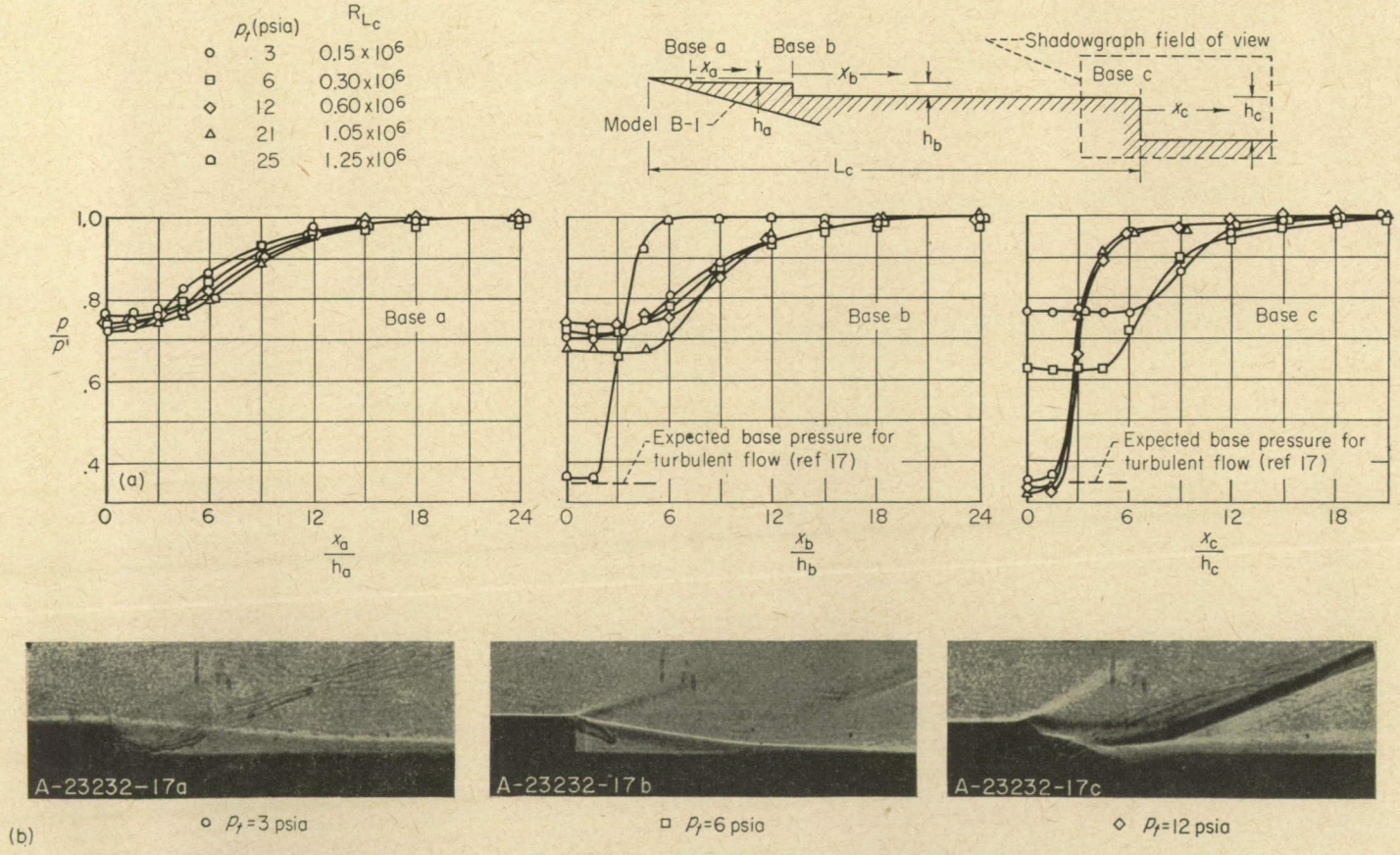


(b) Transitional separation; CS25°−1; M_o=2.7.



(c) Turbulent separation; CC25°−5 (trip 4); M_o=2.7.

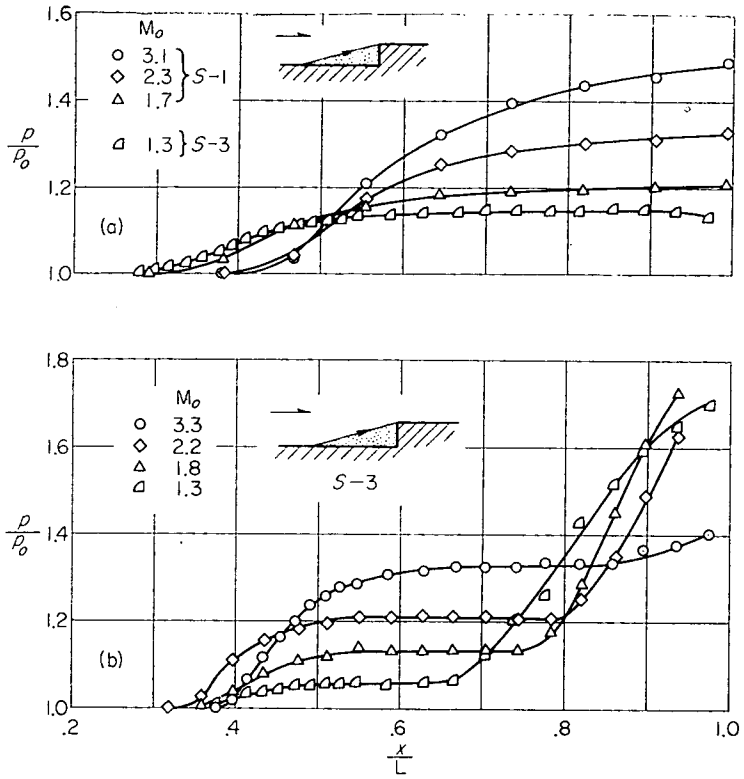
FIGURE 21.—Concluded.



(a) Pressure distribution; M_o=2.0.

(b) Representative shadowgraphs of flow over base c; M_o=2.0.

FIGURE 22.—Model having three bases in series illustrating characteristic Reynolds number effect for each flow separation regime.



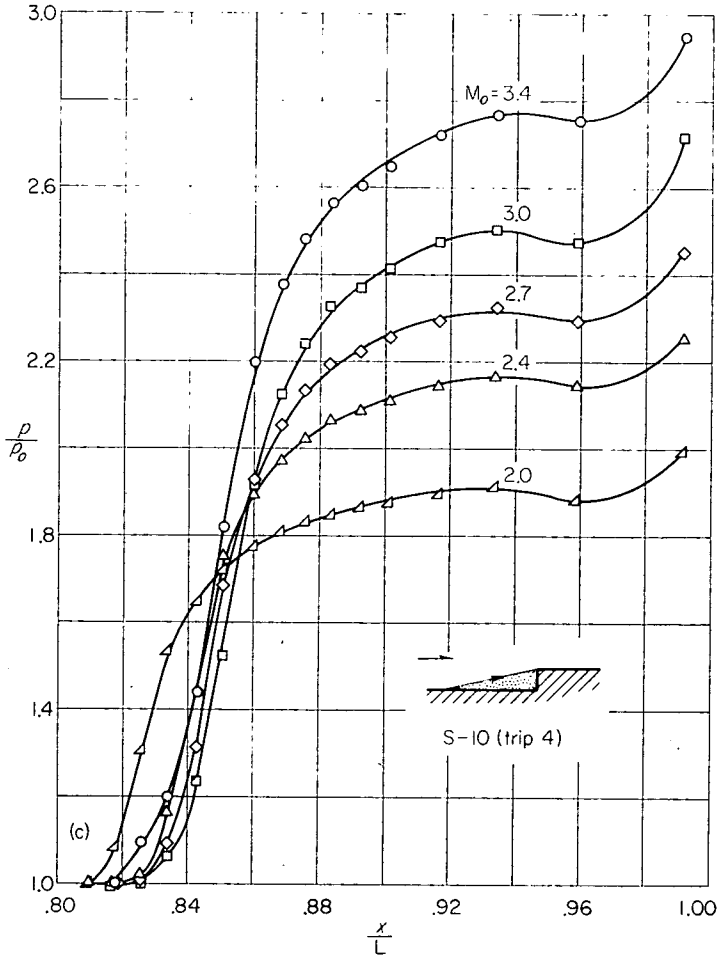
(a) Pure laminar separation; $R_L \approx 0.13 \times 10^6$.

(b) Transitional separation; $R_L \approx 0.60 \times 10^6$.

FIGURE 23.—Effect of Mach number on the pressure distribution on a step for the three flow regimes.

REYNOLDS NUMBER RANGE FOR PURE LAMINAR SEPARATIONS

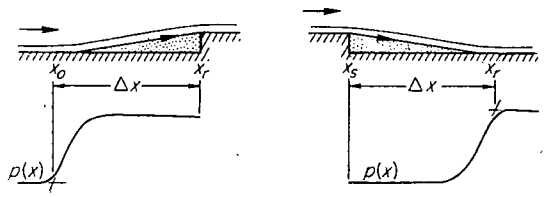
As the investigation progressed, it became evident that the prevalence of pure laminar-type separations increased as the Mach number was increased. In order to put these qualitative observations on a quantitative basis, data from various models were examined to determine the maximum Reynolds number up to which pure laminar separation was found at each Mach number. Such determinations from shadowgraphs agreed well with corresponding determinations from a break in the curves of dead-air pressure plotted against u_oL/ν_o. The values so obtained for $(u_oL/\nu_o)_{max}$ were different for various models, but for each model they consistently showed strong dependence on Mach number as illustrated in figure 24 (a) for various step and base models. Also included in this figure are two data points (at $M_o=4$ and $M_o=4.5$) determined from an examination of various unpublished spark photographs obtained by Reller and Hamaker during their investigation (ref. 20) of base pressure on bodies of revolution, and one data point determined from Kavanau's experiments on base pressure (ref. 24). The close agreement of data from bodies of revolution with that from two-dimensional models is regarded as accidental. Also shown in figure 24 (a) for purposes of comparison are two curves representing the Reynolds number for the beginning and the end of transition on an attached boundary layer over a flat plate. These two curves correspond to a Reynolds number per inch of 0.3×10^6, as obtained from a cross plot of the data of figure 6.



(c) Turbulent separation; $R_L \approx 2.6 \times 10^6$.

FIGURE 23.—Concluded.

Since models of different geometry have different lengths of separated layer relative to the model length, it would seem more significant to consider a Reynolds number based on some typical length of separated layer, rather than on model length. A pertinent length easy to determine from

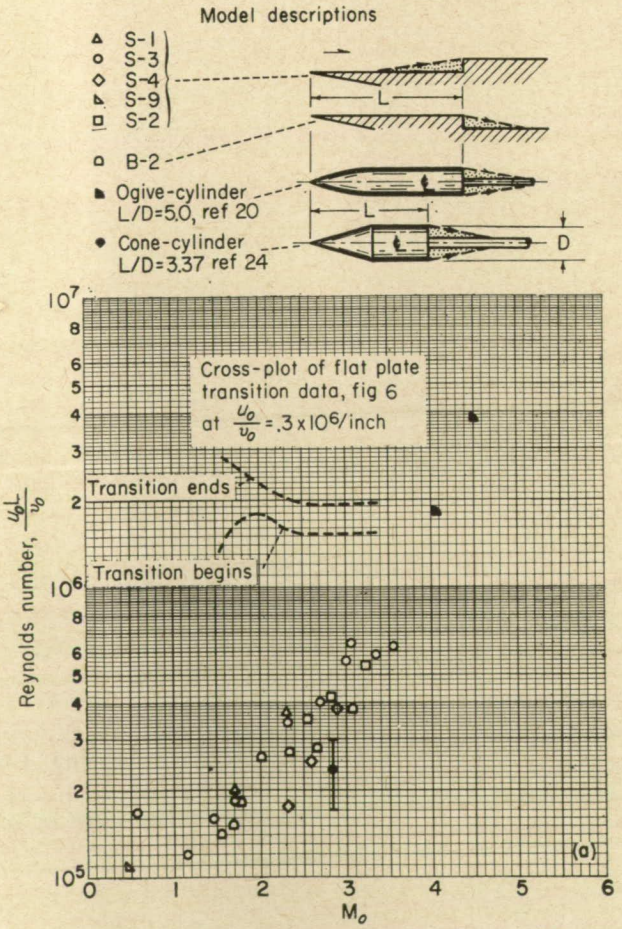


pressure distributions is the length Δx as shown. The maximum Reynolds number for the pure laminar regime $(u_o\Delta x/\nu_o)_{max}$ is plotted as a function of Mach number in figure 24 (b).[6] It is evident from figure 24 (b) that the stability of a laminar mixing layer increases markedly with an increase in Mach number. In subsonic flow the separated laminar layer is stable only to about a Reynolds number $u_o\Delta x/\nu_o$ of 60,000, whereas at Mach numbers near 4 it is stable to a Reynolds number of about a million.

[6] In a preliminary report of this research (ref. 12) a slightly different length, x_r-x_s, between the reattachment location, x_r, and separation location, x_s, was used in place of Δx. The length Δx can be precisely determined; the length x_r-x_s was only approximate.

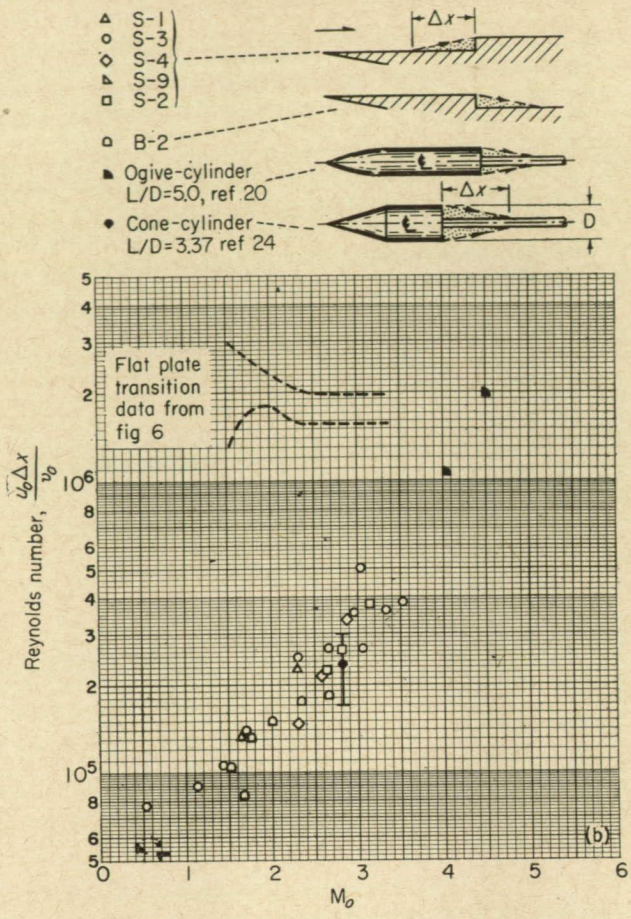
For purposes of comparison in figure 24 (b), the two curves are shown which represent the Reynolds numbers for beginning and end of transition on a flat plate. These transition data are directly comparable to the separated-flow data from the present experiments, inasmuch as they were obtained in the same wind tunnel, with essentially the same model leading-edge thickness, at approximately the same tunnel pressures, and under identical conditions of essentially constant pressure and zero heat transfer. The data are not comparable, however, to flight conditions. Flight conditions involve different rates of heat transfer, and different levels of external disturbance. Consequently, the quantitative values for Reynolds number in figure 24 (b) are not of central importance. Instead the important item is that, compared to an attached laminar boundary layer, the stability of a separated laminar mixing layer increases markedly with an increase in Mach number.

It is noted that the data of figure 24 correspond to models having relatively extensive regions of separated flow; that is, they represent separated flows wherein the length of separated layer Δx is roughly 0.5 to 0.7 of the model length L. If a separated flow extends over only a small portion of the model length, then the data in figure 24 might not be closely applicable. An example illustrating this is presented in figure 25. Here the step height is $0.009L$ and Δx is the order



(a) Reynolds number based on model length.

FIGURE 24.—Maximum Reynolds number for pure laminar type separation.



(b) Reynolds number based on length of separated layer.

FIGURE 24.—Concluded.

of $0.3L$. Over the Mach number range investigated, these pure laminar separations extend to higher Reynolds numbers than for the main body of data representing relatively extensive separated regions.

Although the conventional neutral stability theory—which considers only infinitesimal two-dimensional disturbances—is not a theory for transition, it has indicated certain trends which transition also follows in some cases. For example, surface cooling stabilizes a laminar boundary layer according to both neutral stability calculations and transition experiments. Neutral stability calculations for the laminar mixing layer in compressible flow have been made by Lin (ref. 25) who finds complete stability at Mach numbers above 2.5 for conditions of zero heat transfer. It can be said then that neutral stability theory for certain restricted types of disturbances indicates a strong stabilizing effect of Mach number on laminar mixing layers in accordance with the present experiments.

The experimental result that the stability of a separated laminar mixing layer increases markedly with an increase in Mach number provides an explanation of an experimental characteristic commonly encountered in conducting wind-tunnel tests. In attempting to trip the laminar boundary layer for certain wind-tunnel tests, it has been found that the diameter of wire required increases markedly at the higher Mach numbers. This can be attributed directly to the increase in stability of separated laminar mixing layers.

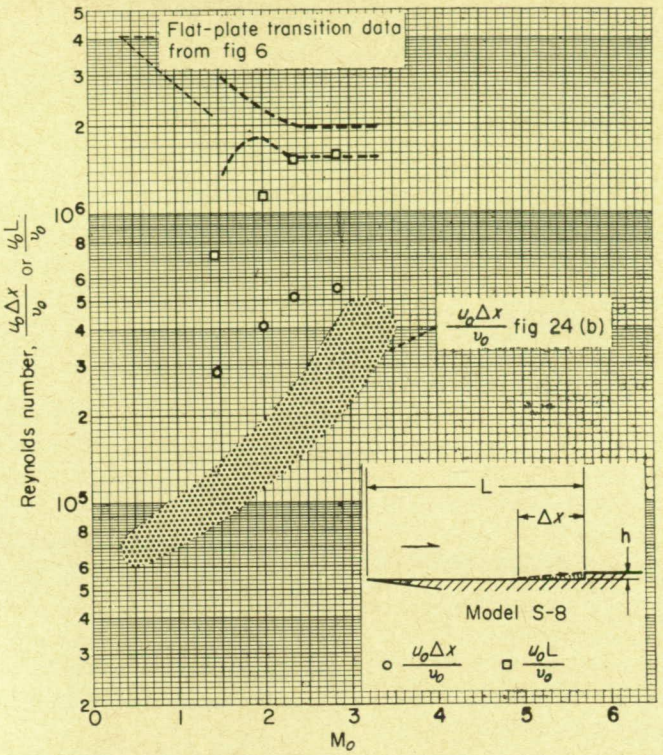


FIGURE 25.—Maximum Reynolds number for pure laminar separation on step of small height; $h/L=0.009$.

If a given wire does not effectively trip the boundary layer, then the baselike separated flow downstream of the wire, as well as the steplike separated region upstream of the wire, are of the pure laminar type. As soon as transition moves upstream of reattachment in the baselike separation downstream of the wire, then the wire trip has effectively promoted transition. Thus, the maximum Reynolds number for pure laminar-type separation downstream of the wire corresponds precisely to the minimum Reynolds number required to fix transition. Winter, Scott-Wilson, and Davies (ref. 19) have determined quantitatively from experiments with different wire diameters the critical Reynolds number (based on wire diameter) which will fix transition for various Mach numbers. If their data are converted to a Reynolds number based on Δx, the length of separated laminar layer upstream and downstream of the wire (Δx is roughly $20d$ for conditions of their experiments), then a direct comparison can be made with the data shown in figure 24. Their data have the same trend as the data in figure 24, but fall about a factor of 4 below. This situation is consistent with observations from the present experiments, inasmuch as the data in figure 24 represent only certain configurations and the data for other configurations are different (as in fig. 25). A wire trip represents one configuration which is not conducive to the promotion of extensive laminar separation.

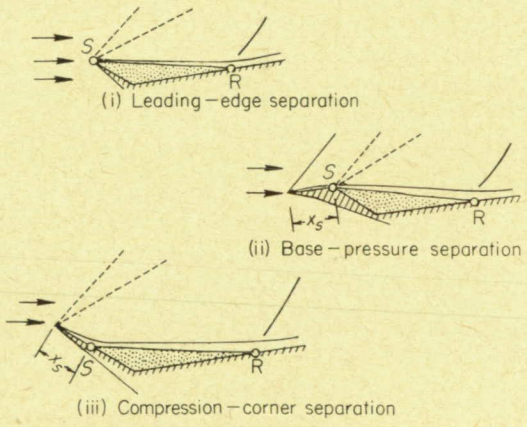
The trend of increasing stability of separated laminar layers with increasing Mach number may be practically significant inasmuch as separated laminar flows have certain uncommon characteristics which might be advantageous. After the trend evident in figure 24 was observed, it appeared desirable to investigate theoretically the heat-transfer and skin-friction characteristics of certain simple pure laminar separations. Such analysis is presented in a separate report (ref. 26) which indicates that the heat transfer and skin friction are less than those of a comparable attached laminar boundary layer.

MECHANISM DETERMINING PRESSURE IN SEPARATED REGIONS AND THEORETICAL EXPLANATION FOR IMPORTANCE OF TRANSITION LOCATION RELATIVE TO REATTACHMENT

Prior to further discussion of experimental results, a digression is made here in order to develop a theory of the mechanism which determines the dead-air pressure in a separated region. This theory is used subsequently to provide an explanation of the principal experimental result of the preceding section; namely, that transition location relative to a reattachment position is of crucial importance to separated flows.

THEORETICAL ANALYSIS OF LEADING-EDGE SEPARATION

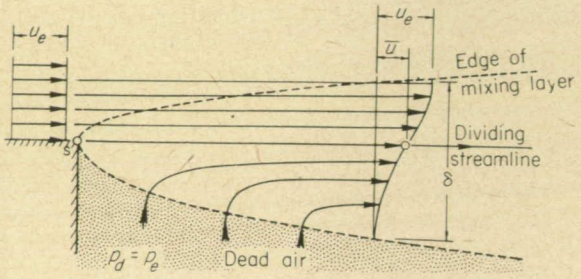
In order to establish a separated flow amenable to a simple theoretical calculation which requires no empirical knowledge, and which would thereby be helpful in analyzing the mechanism governing pressure in separated regions, a special type of model was investigated which produced leading-edge separation. This type of separation actually represents a limiting case both of separations behind a base and of separations in a compression corner, the limit being taken in each case as the distance x_s, from leading edge to



separation, approaches zero. Leading-edge separation is relatively easy to analyze because the complicated course of boundary-layer development in the region of pressure variation between the boundary-layer origin and its position of separation need not be considered. Also, calculations of the laminar mixing layer already are available (ref. 27) for flows of this type wherein the boundary-layer thickness at separation, δ_s, is zero, and the pressure is essentially constant. These theoretical calculations would apply directly, provided that transition is excluded from consideration.

Before developing the basic idea for calculating dead-air pressure, it is advantageous to outline the results of the laminar-mixing-layer theory which forms the basis for such calculations. Typical streamlines in the viscous mixing

region and a representative velocity profile are depicted below. A uniform stream of velocity u_e, Mach number M_e, and pressure p_e mixes with a dead-air region (of pressure $p_d=p_e$) having dimensions large compared to the thickness δ of the mixing layer. The mixing-layer thickness grows



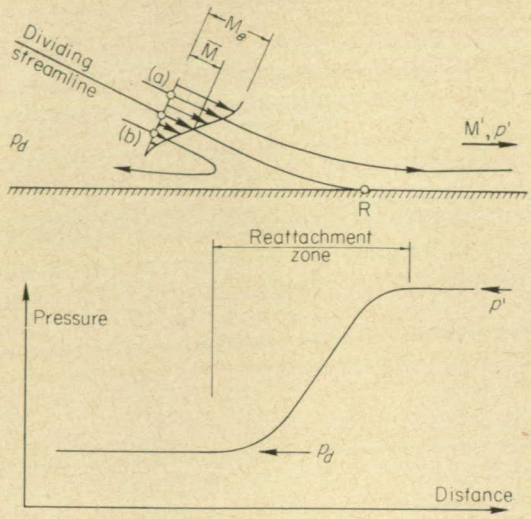
parabolically with distance from the origin of mixing just as a laminar boundary layer grows, but the rate of growth is roughly three times that of a corresponding boundary layer. The velocity profiles at different streamwise stations are similar; hence, the velocity ratio $\overline{u}/u_e$ along the dividing streamline does not change with Reynolds number or with distance from separation. One consequence of this fact soon will appear. Moreover, this velocity ratio changes only slightly with variation in Mach number and in temperature-viscosity relationship. Computed values, reference 27, of $\overline{u}/u_e$ are obtained by solving the familiar nonlinear differential equation of Blasius with unfamiliar boundary conditions. Some values are tabulated as follows:

Computed values of $\overline{u}_*\equiv\overline{u}/u_e$ (ref. 27)

Mach number, M_e	for $\mu_*\sim T_*$	for $\mu_*\sim T_*^{0.76}$
0	0.587	0.587
1	.587	.588
2	.587	.591
3	.587	.593
5	.587	.597

In subsequent calculations, the ratio $\overline{u}/u_e\equiv\overline{u}_*$ appears often. From the table, it is clear that the single value $\overline{u}_*=0.587$, corresponding to the linear temperature-viscosity relationship, is a reasonable approximation for all conditions. It is noted that the tabulated values of $\overline{u}_*$ involve no empirical constants and are exact within the framework of the boundary-layer equations.

In the calculation of dead-air pressure, the essential mechanism is considered to be a balance between mass flow scavenged from the dead-air region by the mixing layer and mass flow reversed back into the dead-air region by the pressure rise through the reattachment zone. For steady flow the dividing streamline at separation as calculated from mixing-layer theory must also be a dividing streamline at reattachment. If this were not the case air would be either continually removed from or continually injected into the dead-air region, and the scavenged mass flux would not balance the reversed mass flux. The pertinent conditions are illustrated of the reattachment zone and of the corresponding pressure distribution.



In order for a particle along a streamline within the mixing layer to be able to overcome the pressure rise through the reattachment zone and to pass downstream, its total pressure p_t must be greater than the terminal static pressure p' at the end of the reattachment zone. As sketched above, particle (a) passes downstream in this manner. Particle (b), however, has a low velocity with corresponding low total pressure and is reversed before the pressure rises from p_d to p'. The dead-air pressure is determined by requiring [7] that the total pressure along the dividing streamline as it approaches the reattachment zone

$$p_t\equiv p_e\left(1+\frac{\gamma-1}{2}\overline{M}^2\right)^{\gamma/(\gamma-1)}$$

$$=p_d\left(1+\frac{\gamma-1}{2}\overline{M}^2\right)^{\gamma/(\gamma-1)} \tag{1}$$

be equal to the terminal static pressure p'. Thus the flow is divided into two regions: a viscous layer wherein the pressure is assumed to be constant, and a reattachment zone wherein the compression is assumed to be such that not much total pressure is lost along the dividing streamline. This yields

$$p_d=\frac{p'}{\left(1+\frac{\gamma-1}{2}\overline{M}^2\right)^{\gamma/(\gamma-1)}} \tag{2}$$

To cast this equation into a convenient form, it is necessary to relate $\overline{M}$ to the terminal Mach number M', or to the Mach number M_e along the outer edge of the mixing layer. From the mixing-layer calculations in which the Prandtl number is assumed to be unity,[8] the Mach number $\overline{M}$ along the dividing streamline is related to the corresponding velocity $\overline{u}$ by the Busemann isoenergetic integral of the energy equation if the

[7] As is discussed later, essentially the same idea also has been employed effectively to calculate base pressure for turbulent boundary layers in a recent paper by Korst, Page, and Childs (ref. 16).

[8] As long as temperature profiles or heat-transfer characteristics are not considered, the assumption $Pr=1$ provides a satisfactory approximation for air. For example, at $M'=2$ the calculated value of p_d/p' for $Pr=0.72$ (the approximate value for air) is only 0.025 below that for $Pr=1$. Consequently, the analysis for $Pr=0.72$ is not presented here as it is much more complex, and does not yield a final equation in closed form.

dead-air temperature T_d is equal to the outer stream total temperature.

$$T_{te} \equiv T_e\left(1+\frac{\gamma-1}{2}M_e^2\right) \tag{3}$$

and by the Crocco integral if T_d differs from T_{te}. (See ref. 27.) At present, the dead-air temperature is considered equal to the recovery temperature (T_{te} for $Pr=1$), so that Busemann's integral for a perfect gas yields

$$\overline{M}^2=\frac{(\bar{u}/u_e)^2 M_e^2}{1+\frac{\gamma-1}{2}M_e^2\left(1-\frac{\bar{u}^2}{u_e^2}\right)} \tag{4}$$

Combining the above two equations gives an equation for dead-air pressure

$$\frac{p_d}{p'}=\left[\frac{1+(1-\bar{u}_*^2)\frac{\gamma-1}{2}M_e^2}{1+\frac{\gamma-1}{2}M_e^2}\right]^{\gamma/(\gamma-1)} \tag{5}$$

where $\bar{u}_*=0.587$. Since $\bar{u}_*$ is independent of Reynolds number, p_d also is independent of Reynolds number. Body shape affects p_d only through its effect on p', the reference pressure.

A more convenient equation for p_d/p' can be obtained by expressing M_e in terms of the Mach number M' which exists just downstream of the reattachment zone. Because the outer edge of the laminar viscous layer curves smoothly, the trailing shock wave does not form within or near this viscous layer, and the flow along this outer edge is isentropic. Hence the values of M' and p' for two-dimensional flow are, in the terminology of reference 28, the same as the "equivalent free-stream conditions" approaching separation. For isentropic flow along the outer edge of the viscous layer

$$\frac{p'}{p_d}=\frac{p'}{p_e}=\left(\frac{1+\frac{\gamma-1}{2}M_e^2}{1+\frac{\gamma-1}{2}M'^2}\right)^{\gamma/(\gamma-1)} \tag{6}$$

By combining this with equation (5), there results

$$M'^2=(1-\bar{u}_*^2)M_e^2 \tag{7}$$

which yields the simple physical interpretation that the Mach number ratio across the laminar reattachment zone M'/M_e is a constant equal to $(1-\bar{u}_*^2)^{1/2}=0.81$. Equations (5) and (7) provide an explicit equation for dead-air pressure.

$$\frac{p_d}{p'}=\left[\frac{1+\frac{\gamma-1}{2}M'^2}{1+\frac{\gamma-1}{2}\frac{M'^2}{(1-\bar{u}_*^2)}}\right]^{\gamma/(\gamma-1)} \tag{8}$$

This equation was presented in reference 12 without derivation.

The foregoing theory also would apply to low-speed flow. By taking the limit of equation (8) as $M'\to 0$, there results

$$\frac{p_d-p'}{q'}=\frac{p_d-p'}{\frac{\gamma}{2}p'M'^2}=\lim_{M'\to 0}\frac{2}{\gamma M'^2}\left\{\left[\frac{1+\frac{\gamma-1}{2}M'^2}{1+\frac{\gamma-1}{2}\frac{M'^2}{(1-\bar{u}_*^2)}}\right]^{\gamma/(\gamma-1)}-1\right\}$$

$$=-\frac{\bar{u}_*^2}{1-\bar{u}_*^2} \tag{9}$$

or, since $\bar{u}_*=0.587$,

$$\frac{p_d-p'}{\frac{1}{2}\rho u'^2}=-0.526 \tag{10}$$

Equation (10) for incompressible flow, just like equation (8) for compressible flow, would apply irrespective of the Reynolds number or the shape of the dead-air region.

The chief approximations and restricting assumptions made in the foregoing analysis should be noted. One essential approximation is that the compression is isentropic along the dividing streamline through the reattachment zone. Actually there would be some change in total pressure. Another approximation is that the dividing streamline terminates at a point where the pressure is p' rather than at the reattachment point where the pressure is p_r. Considering these two facts, the fundamental equation corresponding to equation (2) would be

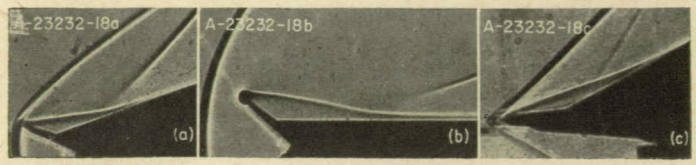
$$p_d=\frac{p_r}{\eta\left(1+\frac{\gamma-1}{2}\overline{M}^2\right)^{\gamma/(\gamma-1)}}$$

where $\eta \equiv p_r/\bar{p}_t$ is a factor (not necessarily less than unity) representing the "efficiency" of compression relative to that of an isentropic process. It is evident that the use of p' in equation (2)—rather than the use of p_r/η—entails the disregard of two factors: the pressure rise downstream of reattachment and the viscous effects on the compression along the dividing streamline. Aside from these approximations it is to be remembered that the substitution $\bar{u}_*=0.587$ in equation (8) is restricted to steady, two-dimensional, pure laminar, separated flows having zero boundary-layer thickness at the separation point. If the boundary-layer thickness at separation were sizable, equation (8) would still apply, but the velocity profiles at different stations along the mixing layer would not be similar and $\bar{u}_*$ would not be 0.587. The value of $\bar{u}_*$ would have to be calculated by solving the partial differential equations of viscous flow for each case.

EXPERIMENTAL RESULTS FOR FLOWS WITH NEGLIGIBLE BOUNDARY-LAYER THICKNESS AT SEPARATION

There are two features of the theory which can be tested quantitatively by present experiments: the absence of a dependence on Reynolds number, and the calculated dependence on Mach number. Three typical shadowgraphs from the experiments on leading-edge separation are shown in figure 26. Unless specified otherwise, the measurements correspond to an attached bow wave as in figures 26 (a) and 26 (c) rather than to a detached wave as in figure 26 (b).

In principle, equation (8) should apply equally well to both types of bow wave, as long as M' and p' are known. In figure 27 the measured variation of p_d/p' with Reynolds numbers at $M'=1.8$, where the bow wave is detached, is compared with the value calculated from equation (8). There



(a) CC35°−2; $M_\infty=2.3$; $\alpha=15°$; $M'\approx1.5$; $R=\dfrac{u'L}{\nu'}=10.9\times10^3$.

(b) CC35°−2; $M_\infty=2.3$; $\alpha=35°$; $M'\approx2.0$; $R=\dfrac{u'L}{\nu'}=9.2\times10^3$.

(c) CC20°−1; $M_\infty=2.3$; $\alpha=-5°$; $M'\approx1.3$; $R=\dfrac{u'L}{\nu'}=22.8\times10^3$.

FIGURE 26.—Pure laminar separations with negligible boundary-layer thickness at separation.

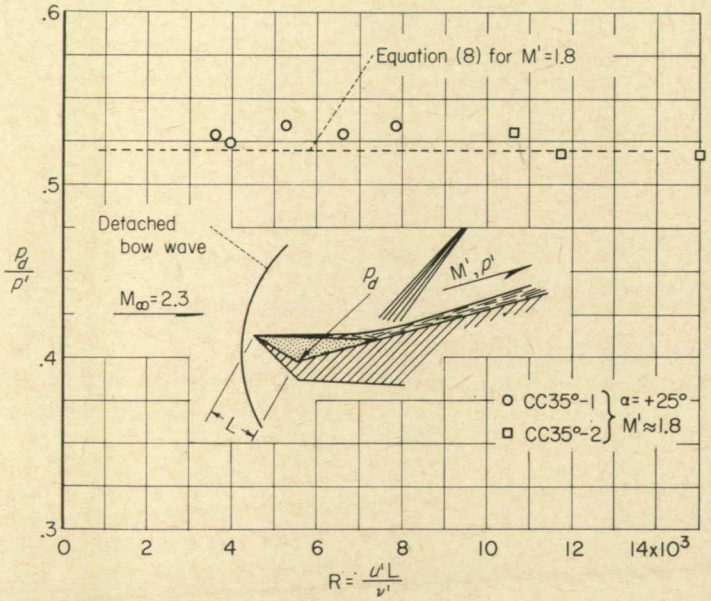


FIGURE 27.—Absence of significant Reynolds number effect on dead-air pressure for wedge models with leading-edge laminar separation.

is seen to be no marked variation with Reynolds number. A similar absence of such variation also was observed at other Mach numbers investigated (1.3 to 2.0). It is apparent also from figure 27 that the calculated and experimental values agree rather well. Agreement of this nature extends to the other Mach numbers investigated, as is shown in figure 28 where the various data points plotted at each Mach number represent measurements at different Reynolds numbers. The several data points corresponding to a detached bow wave fall somewhat below the general trend, but not far below. Considering the simple nature of the theory and the fact that the calculation involves no empirical information or adjustable constants, the observed correspondence of theory and experiment is quite satisfactory. This establishes considerable confidence in the mechanism postulated for the calculations.

Although the present experiments did not include cases of pure laminar leading-edge separation at low speeds, some recent experiments of Roshko (ref. 29) approximate such conditions and provide further test of the theory. In order largely to avoid the usual unsteadiness of subsonic wakes, Roshko employed the splitter-plate technique. His data for cylinders and a flat plate normal to the flow are shown in figure 29. These data do not show any significant dependence either on body shape or Reynolds number. This lack of dependence is in accord with the theory. For quantitative comparison with the theory, it is assumed that $p'=p_\infty$ which is indicated to be closely the case by several streamwise wake pressure distributions presented by Roshko. The agreement exhibited in figure 29 is quite good. The close agreement should be viewed with reservation inasmuch as the splitter plates did not always render the flow perfectly steady, and the mixing layer may not be entirely laminar. The Reynolds numbers are low enough though (5,000 to 17,000), so that extensive laminar flow would be expected along the mixing layer.

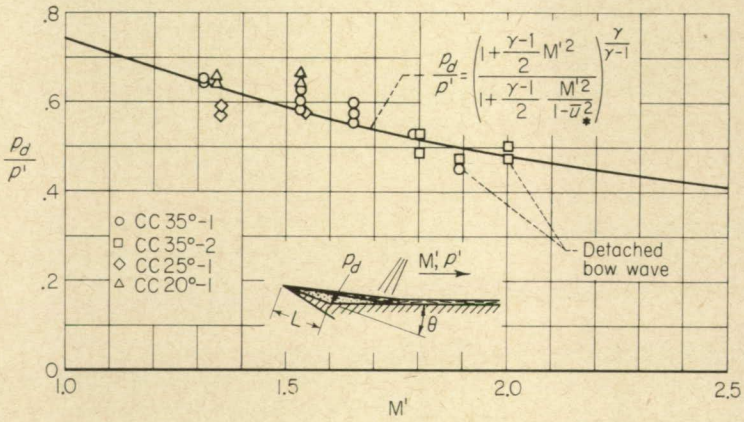


FIGURE 28.—Comparison of theory and experiment for pure laminar separations with negligible boundary-layer thickness at separation.

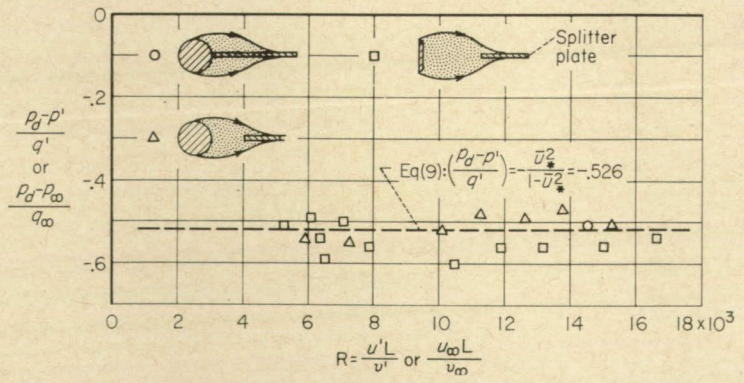


FIGURE 29.—Comparison of theory with experiments of Roshko conducted at low speed; $M'\approx0$.

For incompressible flow, a comparison of the present theory can be made with a numerical solution to the full Navier-Stokes equations obtained by Kawaguti (ref. 30) for the steady flow over a circular cylinder at Reynolds number 40. His solution yields a value of −0.55 for the pressure coefficient at the rear of the cylinder. The corresponding experimental value (ref. 30) is about the same. This is surprisingly close to the value −0.526 obtained from the present theory.

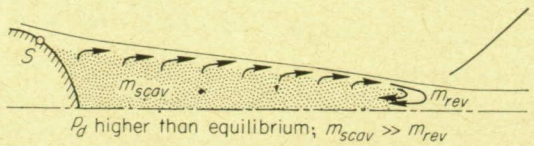
Additional evidence as to the soundness of the basic calculation method is provided by an independent theoretical analysis of Korst, Page, and Childs (ref. 31), which became available during preparation of reference 12. In their analysis, the same basic method is used for calculating dead-air pressure. Since they were concerned with fully turbulent flow rather than with pure laminar flow, their results complement the results of the present research. A direct comparison of their equations with equation (8) cannot be made since they did not present an explicit equation for dead-air pressure, but a comparison can be made of the various assumptions employed in the two analysis. Such comparison indicated only small, relatively unimportant differences in the two calculation methods. For calculating the velocity ratio $\overline{u}_*$ along the dividing streamline they employed a simplified equation since the rigorous equations for turbulent flow are unsolvable. They obtain values of $\overline{u}_*$ for turbulent flow ranging between 0.62 at zero Mach number to apparently 1.00 at infinite Mach number, whereas the corresponding value for laminar flow is 0.59, as noted earlier. They used the oblique shock equations across the reattachment region, whereas the isentropic equations are applied above for pure laminar flow. The dead-air pressure was calculated by equating the total pressure along the dividing streamline to the static pressure downstream; this is the essential idea common to both analyses. They obtain very close agreement with base pressure measurements for turbulent flow over a wide range of conditions, and this strengthens further the simple idea common to the two calculations.

It is noted that the values of p_d/p' in figure 28 for pure laminar separations with $\delta_s \approx 0$ are not much greater than for turbulent base pressure measurements (ref. 17) with $\delta_s \approx 0$. From the theoretical viewpoint, this arises because the corresponding values of $\overline{u}_*$ are not greatly different. Thus, a thin reattaching laminar layer can undergo a pressure rise comparable to that of a thin reattaching turbulent layer. Hence, with $\delta_s \approx 0$, the movement of transition from downstream to upstream of reattachment would not markedly alter such flows. Experiments confirm this. For example, at Reynolds numbers beyond those shown in figure 27, at which the separations on both CC35°—1 and CC35°—2 were transitional, the values of p_d/p' were only slightly smaller. On the other hand, when δ_s is relatively large and $\overline{u}_*$ for laminar flow is much less than 0.587 (corresponding to $\delta_s=0$), then the movement of transition from downstream to upstream of reattachment can markedly alter flow conditions.

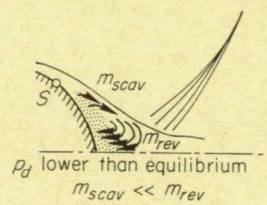
In regard to theoretical methods for calculating dead-air pressure in a separated flow, it is noted that there is one aspect of the Crocco-Lees theory (ref. 9) which appears to be at variance with both the present theory and with certain experiments. This aspect is discussed in Appendix B.

AN EXPLANATION OF THE IMPORTANCE OF TRANSITION LOCATION RELATIVE TO REATTACHMENT

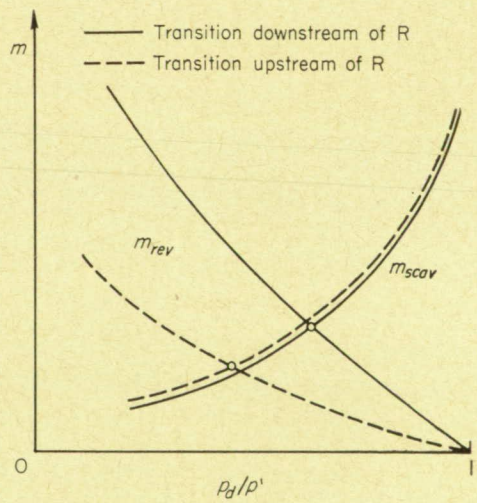
The basic mechanism assumed in the calculations of dead-air pressure appears well confirmed and thus can be used now to provide an explanation of one of the main experimental results described earlier, namely, an explanation of why a separated flow changes markedly when transition moves upstream of the reattachment position. For equilibrium, the basic requirement is that the mass flow scavenged (m_{scav}) from the dead-air region by the mixing layer balance the mass flow reversed (m_{rev}) by the pressure rise through the reattachment zone. This can be made clear by considering the variation of m_{scav} and m_{rev} with dead-air pressure for conditions removed from equilibrium. It is assumed temporarily that transition is slightly downstream of reattachment. For simplicity the external flow is assumed to be supersonic and two-dimensional. If p_d/p' is near unity the mixing layer is long and m_{scav} is large



since it depends on the product $\rho_e u_e$ as well as the length of mixing; but if p_d/p' is near zero, the mixing layer is short, $\rho_e u_e$ is small,



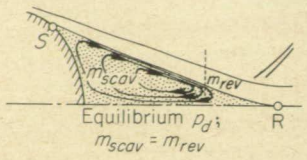
and m_{scav} is small. Thus the scavenged air increases as p_d increases, as illustrated. The reversed flow, however, follows an opposite trend;



if p_d/p' is near unity, the pressure rise $p'-p_d$ is small and m_{rev} is small, but if p_d/p' is near zero the pressure rise is large and m_{rev} is large; hence, m_{rev} decreases as p_d increases, as illustrated in the mass-flow curves. Intersection of the curves determines p_d for equilibrium (provided no mass flow is injected or removed by external means). If transition were now to move suddenly to a new position slightly upstream of reattachment, say, to the position of the dotted

526597—60——30

line in the lower right portion of the following sketch representing the equilibrium



condition, then m_{scav} would be affected only negligibly since the distance between transition and reattachment is negligible compared to the distance between separation and transition. The new m_{scav} curve (dotted line in the above mass-flow curves) would be close to the corresponding m_{scav} representing transition slightly downstream of reattachment (solid line in the above mass-flow curves). Because of the turbulence, however, the m_{rev} curve would be much lower. The energy imparted to the low-velocity portion of the mixing layer would be much increased by the transport of eddies from the outer stream and this energizing process would greatly reduce the amount of air reversed for a given pressure ratio p_d/p'. The new equilibrium dead-air pressure would be represented by the intersection of dotted mass-flow curves. As transition moves upstream of reattachment, therefore, the ratio p_d/p' would be expected to decrease substantially. This agrees with the experimental observations described earlier, irrespective of whether the separation is induced by a base, compression corner, curved surface, step, or an incident shock wave.

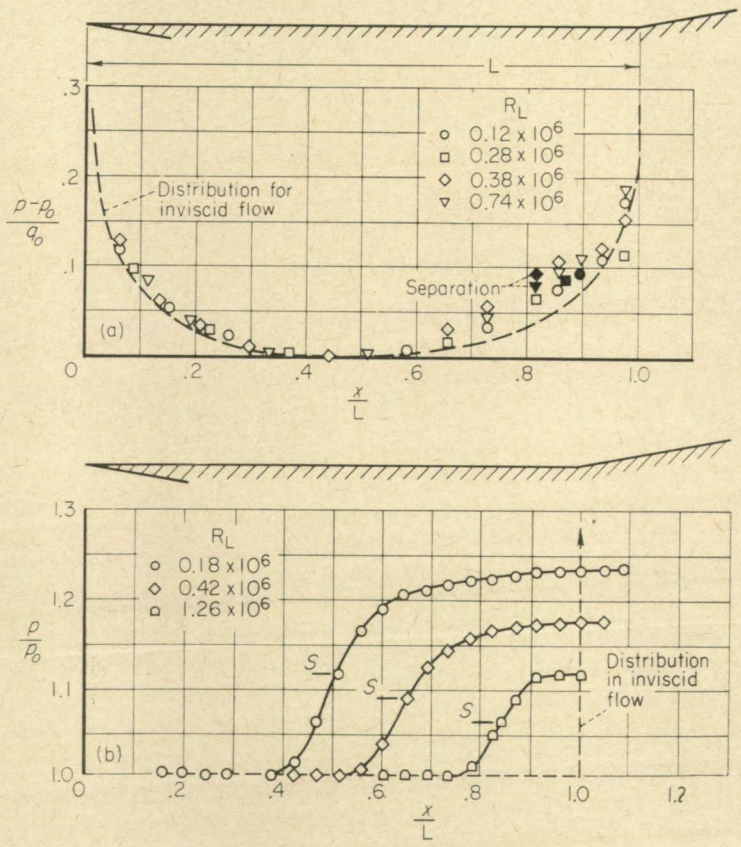
Transition actually should begin to affect a separated flow as soon as it occurs in the small recompression region downstream of the reattachment point, even if negligible turbulence exists upstream of the reattachment point. In this region, where the pressure is between p_r and p', the introduction of turbulence would permit a greater pressure rise $p'-p_r$ to occur after the reattachment point, and this would change the dead-air pressure. Obviously transition is not a steady, point phenomenon, but is spread over some distance. Strictly speaking then, the pure laminar regime would end as soon as appreciable turbulence occurs in the downstream portion of a reattachment zone. A separated flow that is laminar only to the reattachment *point* could be quite different from the pure laminar type, which is defined as being laminar through the reattachment zone.

CHARACTERISTICS INDEPENDENT OF THE MODE OF INDUCING SEPARATION (FREE INTERACTIONS)

During the course of experimentation, it was observed that certain characteristics of separated flows did not depend on the object shape or on the mode of inducing separation. Similar observations previously have been made in the researches of Gadd, Holder, and Regan (ref. 15) and of Bogdonoff and Kepler (ref. 14). Any phenomenon near separation which is independent of object shape would not depend on geometric boundary conditions which describe the flow downstream, but would depend only on the simultaneous solution of the equations for flow in the boundary layer together with the equations for flow external to the boundary layer. Such flows that are free from direct influences (though not free from indirect influences) of downstream geometry, and are free from complicating influences of the mode of inducing separation, arbitrarily will be termed "free interactions" for brevity. In the present section, some pressure distributions are compared first for a given body in supersonic and in subsonic flow. Free interaction is observed in supersonic separation, though not in subsonic separation on this body. A simple analysis is then made of the Reynolds number dependence of free interactions in supersonic flow. Subsequent to this analysis, various experimental results are presented and compared with the analysis where possible.

RESULTS FOR VARIOUS SEPARATED FLOWS

Difference between subsonic and supersonic separations.—A fundamental difference between subsonic and supersonic separations can be seen from pressure distributions obtained at various Reynolds numbers in subsonic and in supersonic flow for a given model geometry. Measured distributions for laminar separation ahead of a 10° compression corner in subsonic flow are shown in figure 30 (a)



(a) Subsonic; CC10°−3; $0.4<M_\infty<0.8$; $\alpha=-4°$.

(b) Supersonic; CC10°−2; $M_o=2.0$.

FIGURE 30.—Comparison of subsonic and supersonic flows at various Reynolds numbers.

together with the calculated distribution that would exist in an incompressible, inviscid fluid (dotted line).[9] At these subsonic speeds ($0.4\leq M_\infty\leq 0.8$) variation in Reynolds number brings about only small changes in pressure dis-

[9] These calculations were made with small-disturbance theory by superimposing the appropriate thickness pressure distributions for wedges with the appropriate lift pressure distribution for an inclined flat plate.

tribution and no measurable change in pressure rise to separation ($(p_s-p_o)/q_o$ is equal to 0.08 ± 0.005 for all R). Moreover, the distribution is roughly that which would exist in an inviscid flow, as represented by the dotted line. In contrast, the pressure distributions shown in figure 30 (b), which also were obtained on a 10° compression corner, in the same wind tunnel, and over the same Reynolds number range, exhibit relatively large changes in pressure distribution as well as easily measurable changes in the position of and the pressure rise to separation. Further contrast is exhibited by the disparity between the measured distributions at supersonic speed and the calculated distribution for inviscid flow (a constant pressure with discontinuous jump as indicated by the dotted line). These data illustrate how the pressure distribution in subsonic flow near and upstream of separation is determined primarily by the inviscid flow pressure distribution about the object shape, and only secondarily by the Reynolds number dependent interaction between boundary layer and external flow; whereas, in supersonic flow, the pressure distribution near separation is determined primarily by a Reynolds number dependent interaction (free interaction) and only secondarily by the inviscid flow pressure distribution.

Only in supersonic flow were free interactions commonly observed in the present experiments. The fact that they were not observed at subsonic speed does not necessarily mean that free interactions cannot occur at such speeds. Lighthill (ref. 32) has made an analysis of the incompressible flow upstream of a step, which, in effect, assumes that the pressure distribution is determined by interaction of boundary layer and external flow. In the present experiments, relatively small steps were employed and the pressure distribution was determined primarily by the geometry of the model, and only secondarily by interaction phenomena. Consequently, the present experiments and Lighthill's theory for incompressible flow upstream of a step are not comparable. It would appear possible, by using a step with larger ratio of step height to plate length, and a model with smaller leading-edge angle, that the pressure distribution in subsonic flow might be determined primarily by interaction phenomena and only secondarily by external constraints imposed through model geometry.

Simplified analysis for free-interaction regions.—If a pressure distribution is determined locally by free interaction of boundary layer and external supersonic flow, then the applicable equations are the momentum equation for steady flow in the viscous layer coupled with the following equation for external supersonic flow:

$$p=p_{inviscid}+\frac{\rho_e u_e^2}{\sqrt{M_e^2-1}}\frac{d\delta^*}{dx} \tag{11}$$

This equation would apply for both laminar and turbulent flow. For the special case of free interaction in regions where the inviscid pressure distribution (first term in eq. (11)) is constant or is small compared to the interaction term, certain information about the effects of Reynolds number can be extracted from order-of-magnitude arguments alone. Since the rate of boundary-layer growth is small, equation (11) for a free interaction is written as

$$\frac{p-p_o}{q_o}=\frac{2}{\sqrt{M_o^2-1}}\frac{d\delta^*}{dx} \tag{12}$$

The subscript o designates conditions at the beginning of interaction, that is, at the downstream-most point upstream of which the pressure is sensibly the same as the inviscid flow. If l_i is a length characteristic of the streamwise extent of free interaction, then order-of-magnitude considerations applied to equation (12) yield

$$\frac{p-p_o}{q_o}\sim\frac{\delta^*}{l_i\sqrt{M_o^2-1}} \tag{13}$$

Turning now to the equation for viscous flow, the usual boundary-layer momentum equation

$$\rho u\frac{\partial u}{\partial x}+\rho v\frac{\partial u}{\partial y}=-\frac{dp}{dx}+\frac{\partial \tau}{\partial y} \tag{14}$$

would apply provided the transverse pressure gradients within the layer are small compared to the streamwise gradients. This would be the case for laminar flow but is questionable for turbulent flow, since the detailed surveys of Bogdonoff and Kepler (ref. 14) at $M_o=2.9$ reveal the *average* transverse gradient near separation to be larger, in fact, than the streamwise gradient. Since large curvature of streamlines is required for large transverse pressure gradients, and since the streamlines must approach straight lines in the immediate vicinity of a straight wall, it follows that only in the outer part of a boundary layer is the streamline curvature large near separation and the turbulent boundary-layer equations locally questionable. For this reason, the boundary-layer equation is applied at the wall where it becomes

$$\frac{dp}{dx}=\left(\frac{\partial \tau}{\partial y}\right)_w \tag{15}$$

This application places emphasis on the low-velocity part of the boundary layer, which appears desirable in analyzing the flow approaching separation. By applying order-of-magnitude considerations to equation (15) there results for constant Mach number M_o,

$$\frac{p-p_o}{l_i}\sim\frac{\tau_w}{\delta}\sim\frac{\tau_{wo}}{\delta^*} \tag{16}$$

In this last step, the wall shear τ_{wo} at the beginning of interaction has been taken as a measure of the variable wall shear τ_w. What this and the previous steps amount to is the consideration of a family of similar flows having a fixed Mach number, but differing in the Reynolds number.

Mach number dependent factors have been omitted from equation (16) since they arise from density variations across the boundary layer and would be smoothly varying functions of M_o. In contrast, the factor $(\sqrt{M_o^2-1})^{-1}$ arising from density variations along the edge of the boundary layer was retained in equation (13) since it is a singular function at $M_o=1$, and would be the dominant factor if M_o is only

slightly greater than 1. By multiplying equations (16) and (13) there results

$$\frac{p-p_o}{q_o}\sim\left(\frac{\tau_{wo}}{q_o\sqrt{M_o^2-1}}\right)^{1/2}\sim\frac{\sqrt{c_{f_o}}}{(M_o^2-1)^{1/4}} \tag{17}$$

and, by dividing them, there results

$$\frac{l_i}{\delta^*}\sim\left(\frac{q_o}{\tau_{wo}\sqrt{M_o^2-1}}\right)^{1/2}\sim\frac{1}{\sqrt{c_{f_o}}(M_o^2-1)^{1/4}} \tag{18}$$

For convenience, the ratio $\tilde{c}_f$ of skin friction at a given Reynolds number to skin friction at a Reynolds number of one million, is introduced

$$\tilde{c}_f\equiv\frac{(c_{f_o})}{(c_{f_o})_{R=10^6}} \tag{19}$$

At constant M_o, then, equations (17) and (18) become

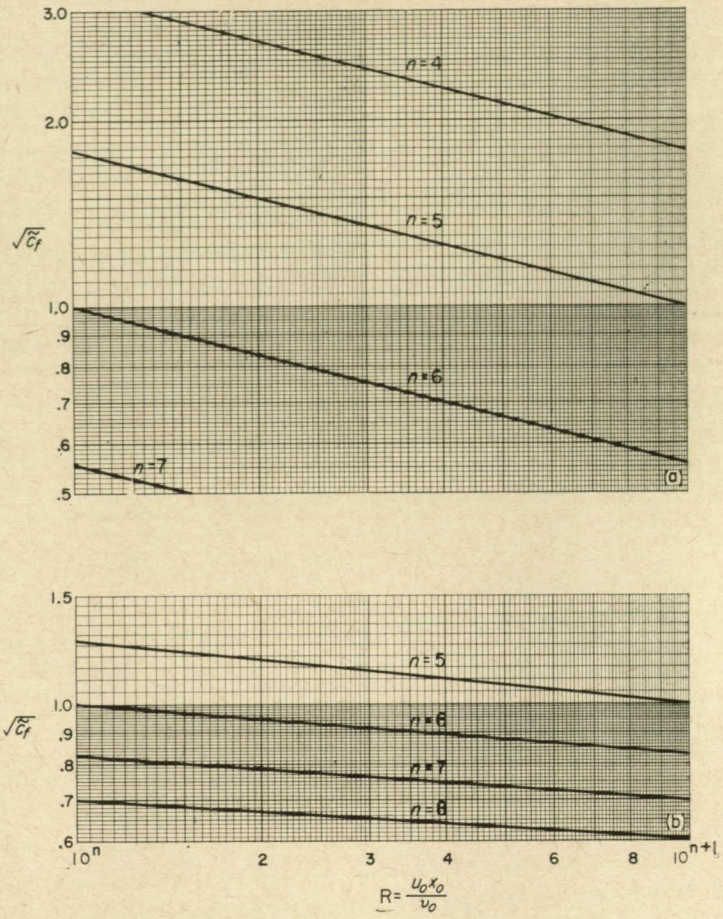
$$\frac{p-p_o}{p_o}\sim\sqrt{\tilde{c}_f} \tag{17a}$$

$$\frac{l_i}{\delta^*}\sim\frac{1}{\sqrt{\tilde{c}_f}} \tag{18a}$$

Equation (17a) was originally presented in reference 12 without derivation. Curves of $\sqrt{\tilde{c}_f}$ as a function of Reynolds number are shown in figure 31 for both laminar and turbulent boundary layers. The curves for laminar layers represent a $(R_{x_o})^{-1/4}$ variation. The curves for turbulent layers represent the variation indicated by the Kármán-Schoenherr equation applicable to incompressible flow. A more accurate variation applicable to compressible turbulent flow is unknown at present.

The above results, as regards variation with Reynolds number, would apply to the pressure rise in either laminar or turbulent flow, provided the flow is determined by free interaction and not complicated by influences of downstream geometry; they would apply to the separation pressure rise (p_s-p_o), to the peak or plateau pressure rise (p_p-p_o), and to the over-all configuration pressure rise for incipient separation if such rises were determined by free interaction. For the particular case of pressure rise to a laminar separation point, equation (17a) agrees with the first analysis of this problem made by Lees (ref. 33), who obtained a $R_{x_o}{}^{-1/4}$ variation. Subsequent analyses have obtained different results (e. g., $R_{x_o}{}^{-2/5}$ variation in ref. 34). It should be noted that the approach used above considers interaction of boundary layer and external flow to be the heart of the problem (as also is considered, though in more detail, in refs. 9, 33, and 35). Other approaches to the problem of boundary-layer separation in supersonic flow have disregarded this interaction (e. g., refs. 36, 37, and 38).

Experiments on effects of geometry, Reynolds number, and Mach number for laminar separation.—Inasmuch as the pressure distribution in laminar separation depends on Reynolds number and Mach number, it is necessary in assessing the effects of model geometry to hold these numbers fixed. Some pressure distributions obtained with four different models—a step, a compression corner, a curved surface, and an incident shock model—are presented in figure 32 for the fixed conditions of $M_o=2.3$ and $R_{x_o}=0.20\times10^6$. The dotted lines rising from terminal data points designate the eventual rise in pressure observed as the separated laminar layer either begins to reattach or to be affected by transition. It is evident that the pressure distribution does not depend significantly on the mode of inducing laminar separation (this independence will be further substantiated



(a) Laminar flow.

(b) Turbulent flow.

FIGURE 31.—Square root of local skin friction as function of Reynolds number.

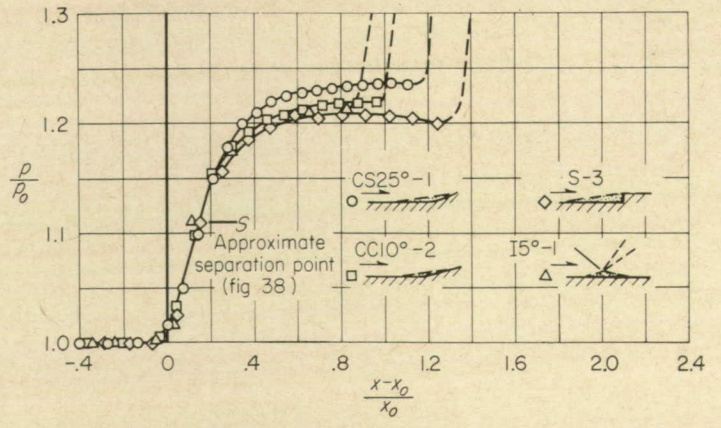


FIGURE 32.—Independence of pressure distribution and method of inducing laminar separation; $M_o=2.3$; $R_{x_o}=0.20^{\pm.01}\times10^6$.

in subsequent figures). Such pressure distributions represent free interactions.

To assess the influence of Reynolds number, only the Mach number is held fixed. As is illustrated by the data in figure 33 for $M_o=2.3$, the curves for various Reynolds

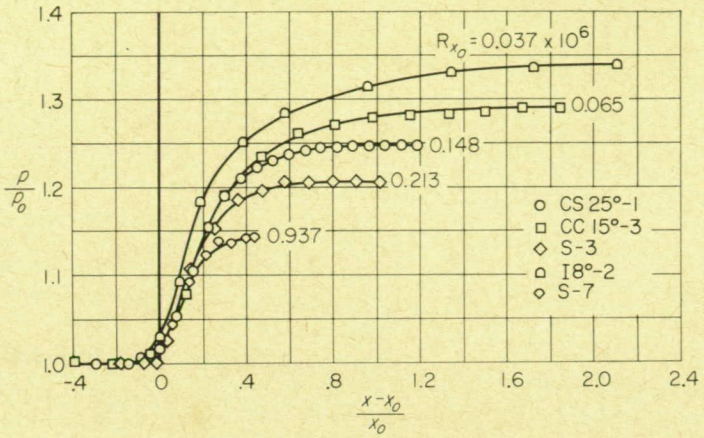
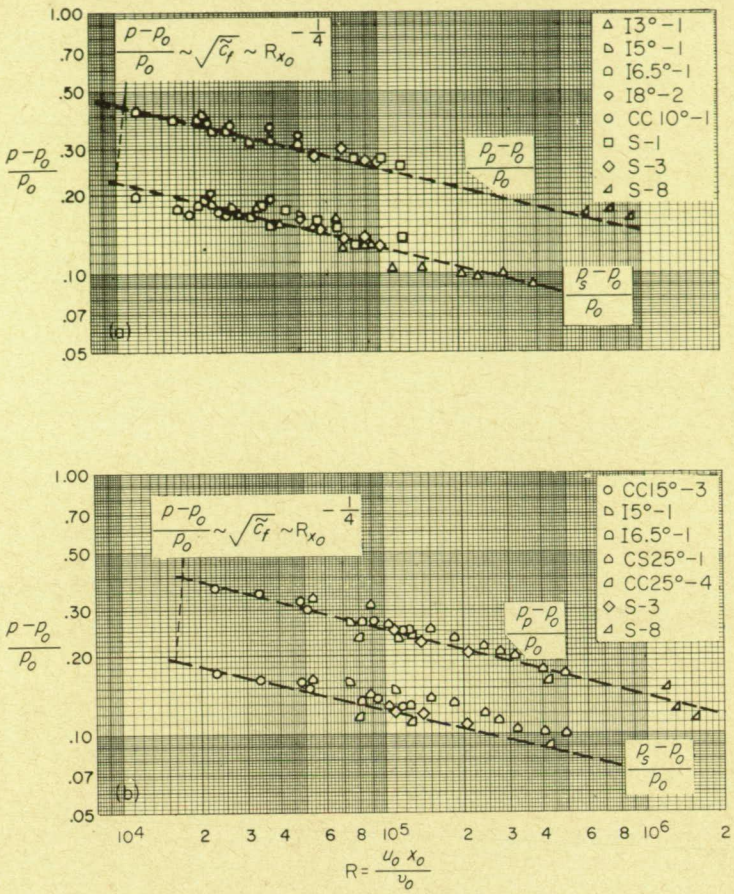


FIGURE 33.—Effect of Reynolds number on pressure distribution in laminar separation; $M_o=2.3$.

numbers are qualitatively similar but quantitatively quite different. An analogous spread of the curves was observed at the other supersonic Mach numbers investigated. For quantitative comparison with results from the simple dimentional analysis, the pressure at separation, p_s, and the plateau pressure, p_p, are plotted in figure 34 as a function of R_{x_o}. Common reference lines (dashed) are shown in both figures 34 (a) and 34 (b), from which it appears that both p_s and p_p approximately follow the same curve irrespective of whether transition is upstream or downstream of reattachment. Actually, when the type of separation changes from pure laminar to transitional, the distance x_o changes, but not the relation between pressure and R_{x_o}. It is noteworthy that the result from the simple order-of-magnitude analysis of free interactions ($\Delta p/p_o \sim \sqrt{\bar{c}_f} \sim (R_{x_o})^{-1/4}$ for laminar flow) is in good agreement with the experimental data over the wide range of R_{x_o} investigated (1.2×10^4 to 1.2×10^6).

Attention is called to several restrictions pertinent to the correlation of the laminar pressure rise data of figure 34. One such restriction is to two-dimensional flow. The oil-film technique revealed readily any flow that was not two-dimensional. Shadowgraphs likewise indicated occasional departures from two-dimensional flow. An example of this, where the shadowgraph indicates multiple separation lines (and the oil film similarly indicated lack of two-dimensionality) is shown in figure 35. The downstream geometry of this particular model was not uniform across the span. Under such conditions the peak-pressure rise was found to be less (up to about 30 percent) than for the correlated data of figure 34. In figure 36 some data are presented which illustrate an additional restriction for correlation of transitional data, namely, that transition not be too close to separation. In this figure the pressure at three different points is plotted for a step model: the pressure at separation p_s, the plateau pressure p_p, and the pressure measured in the step corner p_c. At Reynolds numbers below 10^5 the



(a) Pure laminar separation; $M_o=2.3$.

(b) Transitional separation; $M_o=2.3$.

FIGURE 34.—Effect of Reynolds number on pressure rise to separation and plateau pressure.

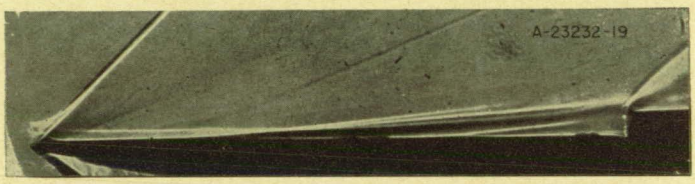


FIGURE 35.—Shadowgraph indicating lack of two-dimensional flow; S−3; $M_o=3.0$; $R_L=0.57\times10^6$.

separation is of the pure laminar type, since p_c does not differ from p_p; both p_s-p_o and p_p-p_o are close to the dashed lines representing the correlation of figure 34. Between Reynolds numbers of 10^5 and about 2.5×10^5, the separation is of the transitional type since p_c rises well above p_p, but both p_s-p_o and p_p-p_o still follow the same $R_{x_o}^{-1/4}$ variation as the correlated data. Above $R_{x_o}=2.5\times10^5$, the separation type remains transitional, and the pressure distributions (not shown) reveal transition to be approaching closely the separation point. Both p_s and p_p depart from the correlated data above this Reynolds number. When transition is close to separation, the flow in the neighborhood of separation would not be expected to be steady and often was not. Examination of various data obtained in the present experiments revealed two sufficient conditions for correlation: (1) that the pressure distribution have a length of sensibly constant plateau pressure not less than about 1.5 times the

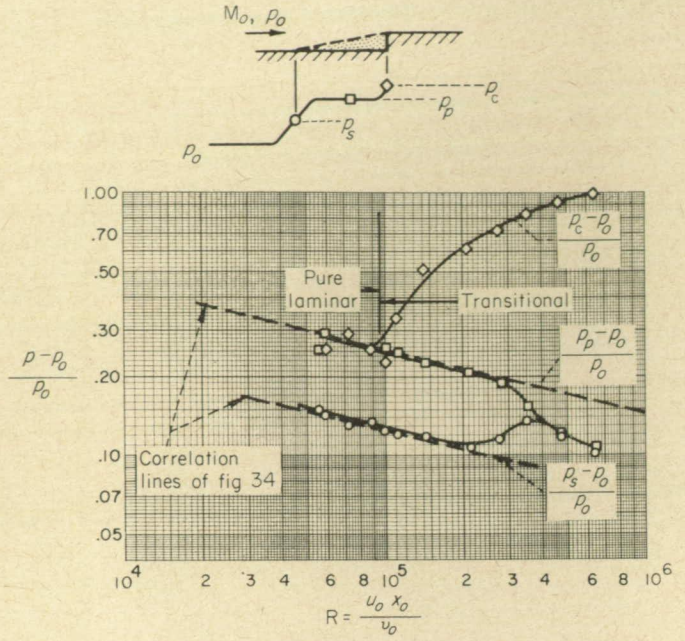


FIGURE 36.—Data illustrating restriction for correlation of transitional data; S−3; $M_o=2.3$.

length over which it takes the pressure to rise from p_o to p_p; (2) that the disturbance due to transition—as measured by the magnitude of pressure rise above the laminar plateau—not exceed two to three times the pressure rise to the laminar plateau. No necessary conditions for correlation could be observed from the data obtained, but it would be expected from theoretical considerations that the laminar separation should be steady and have at least a short length of plateau. These various restrictions may account for the lack of consistency in some previous measurements of pressure rise in laminar separation.

The fact that $(p_s-p_o)/p_o$ and $(p_p-p_o)/p_o$ in laminar flow vary nearly as $\sqrt{\bar{c}_f}\sim R_{x_o}{}^{-1/4}$, in agreement with the simple dimensional analysis, encourages a further test of the analysis by examination of the entire pressure distribution. In laminar flow $\delta^*\sim x(R_x)^{-1/2}\sim x\bar{c}_f$, so that equation (18a) for the characteristic interaction distance l_i becomes

$$l_i\sim\frac{\delta^*}{\sqrt{\bar{c}_f}}\sim\frac{x_o\bar{c}_f}{\sqrt{\bar{c}_f}}\sim x_o\sqrt{\bar{c}_f} \tag{19}$$

Since $\Delta p/p_o\sim\sqrt{\bar{c}_f}$, it follows that correlation of the pressure-distribution curves would be expected by plotting $[(p-p_o)/p_o](\bar{c}_f)^{-1/2}$ versus $[(x-x_o)/x_o](\bar{c}_f)^{-1/2}$. A plot of the data in figure 33 using these special coordinates is shown in figure 37. Data from a compression corner, a curved surface, two steps, and an incident shock-wave-induced separation are included in this figure. The various pressure distributions in the special coordinate system appear independent of Reynolds number as well as independent of object shape in conformity with the simple analysis of free interactions.

In view of the correlation observed for Reynolds number effects on the pressure distribution in laminar separation, it follows that the essential results pertaining to pressure rises can be obtained from a plot of the quantities $[(p_s-p_o)/p_o](\bar{c}_f)^{-1/2}$ and $[(p_p-p_o)/p_o](\bar{c}_f)^{-1/2}$ as functions of Mach number. Such a plot is shown in figure 38. Near $M_o=1$ the

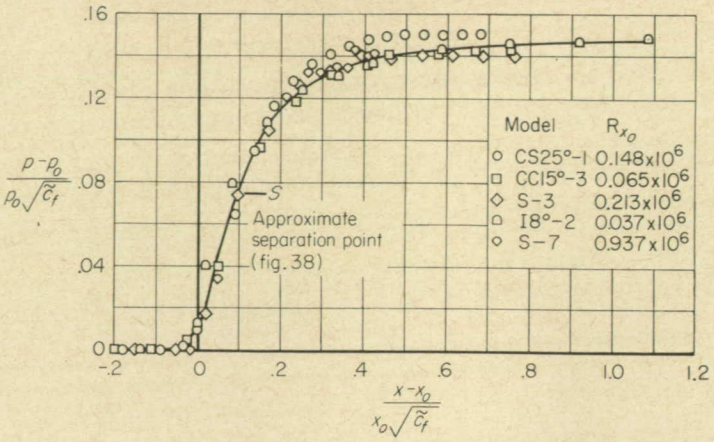


FIGURE 37.—Correlation of pressure distribution for laminar separation for various model configurations and Reynolds numbers; $M_o=2.3$.

singularity $(M_o^2-1)^{-1/4}$ should dominate in equation (17) and the plateau pressure rise $(p_p-p_o)/q_o$ should asymptotically follow a $(M_o^2-1)^{-1/4}$ variation as M_o approaches unity. Hence $(p_p-p_o)/p_o$ should asymptotically follow a $M_o^2(M_o^2-1)^{-1/4}$ variation. The dotted line in figure 38 represents

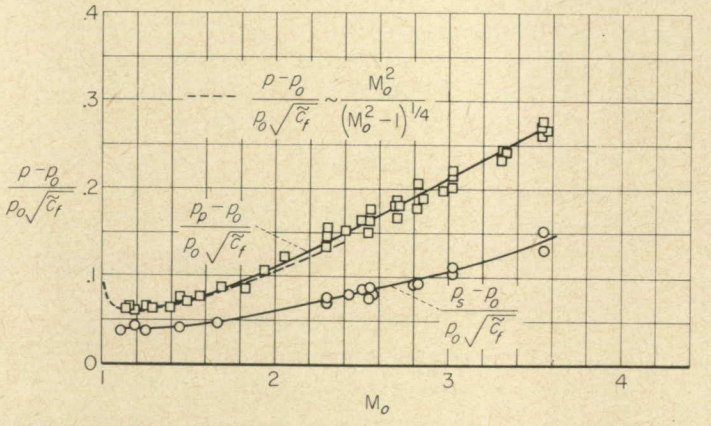


FIGURE 38.—Effect of Mach number on characteristics of laminar separation for a series of model configurations and Reynolds numbers.

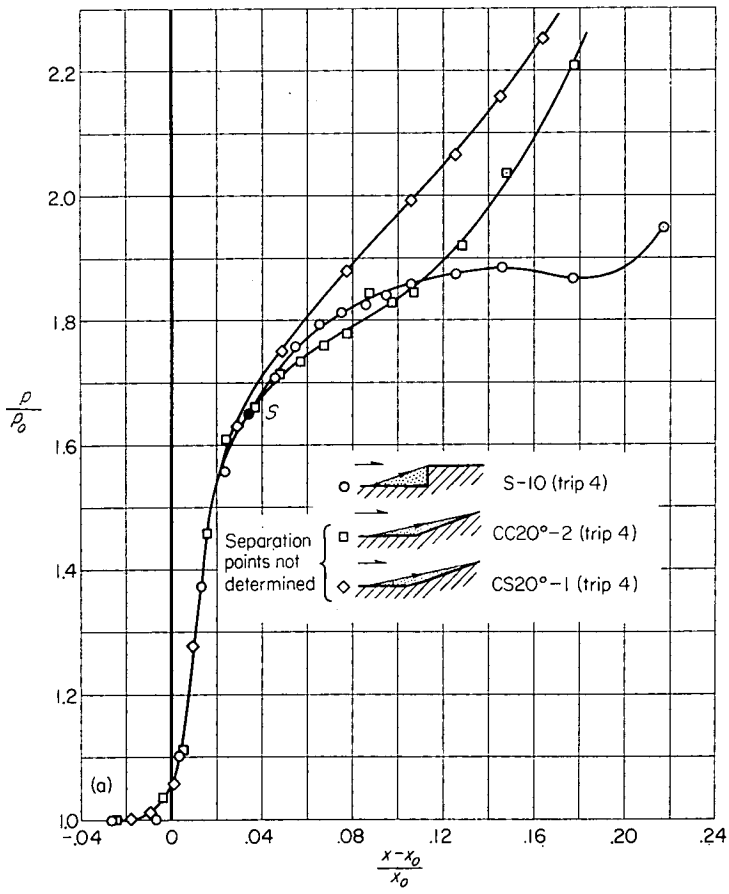
such a variation. Unfortunately the data do not extend to sufficiently low Mach numbers to test critically the predicted increase in pressure rise near $M_o=1$. Over the range of data obtained, however, there is surprising consistency with the theoretical variation. This consistency accidentally extends to supersonic Mach numbers much higher than could be expected from a knowledge of the assumptions made in the analysis.

Experiments on effects of geometry, Reynolds number, and Mach number for turbulent separation.—The pressure distributions for turbulent separation over a step, a compression corner, and a curved surface are shown in figure 39 (a). These distributions are for a constant Mach number of 2.0 and a constant Reynolds number of 3.1×10^6. Only the model shape differs for these three pressure distributions. The three curves are essentially the same up to the separation point, but beyond this they begin to depart from each other. It is evident also from figure 39 (a) that the separated flow over a step is the only flow of those investigated which exhibits a definite peak in the pressure distribution within

the separated region. Analogous results are presented in figure 39 (b) for three similar configurations at a Mach number of 3.0. In this case the three curves practically coincide for a short distance downstream of separation, but do not coincide at the station where the peak in pressure occurs for the step. This result is similar to one of Bogdonoff and Kepler (ref. 14) who compared distributions for a step and a strong incident shock.

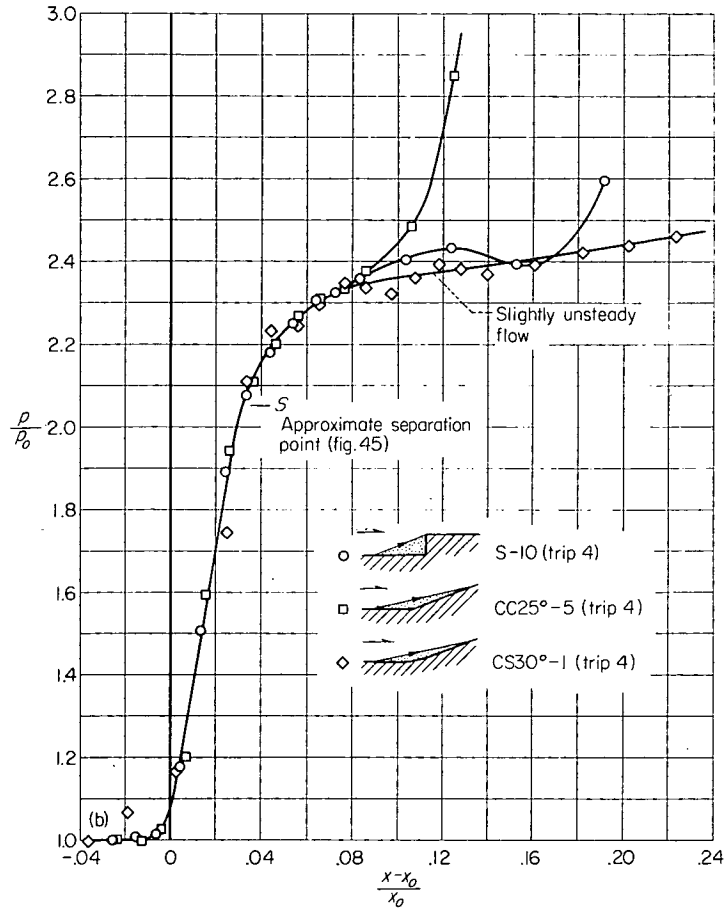
It is evident already that there is an essential difference between the qualitative characteristics of laminar separations and turbulent separations. Since turbulent separations follow a single curve only as far downstream as the separation point (or perhaps a little farther), only the flow up to the separation point would represent free interaction; the flow downstream of separation, and hence the peak pressure, would not. A possible exception might be the step which shows a definite peak pressure, but the other configurations investigated definitely do not represent free interaction phenomena downstream of the point of separation. In contrast, for laminar separations the pressure distribution well downstream of separation—including the plateau pressure—represents a free-interaction-type flow for all of the various configurations tested.

In order for the pressure distributions up to separation to represent a free interaction independent of the mode of inducing separation, it is necessary that the flow be steady.



(a) $M_o=2.0$; $R_{x_0}=3.1\times10^6$

FIGURE 39.—Effect of body shape on the pressure distribution for turbulent separation at a fixed Mach number and Reynolds number.

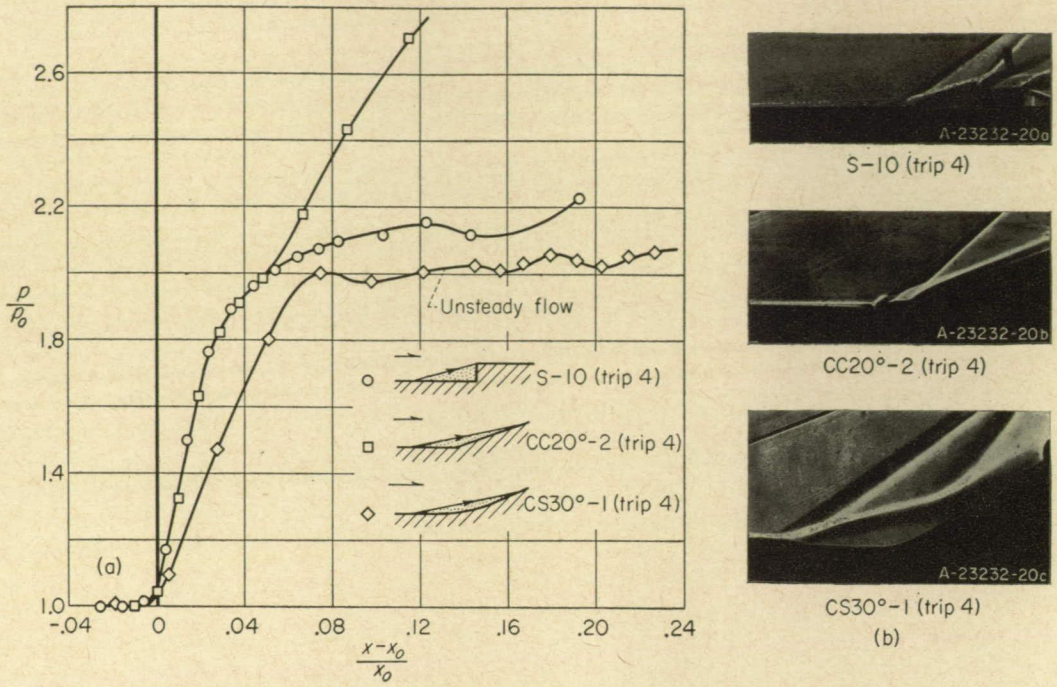


(b) $M_o=3.0$; $R_{x_0}=3.1\times10^6$

FIGURE 39.—Concluded.

Actually, the curved-surface model (represented by diamond symbols) in figure 39 (b) shows a little irregularity in pressure distribution which is attributed to a slight unsteadiness of the turbulent separation over this particular model. At Mach numbers lower than that represented in figure 39 (b), the turbulent separation on this model was sufficiently unsteady to bring about both irregularities in pressure distribution as well as sizable departures from the mean curves representing steady turbulent separations. An example is illustrated in figure 40 (a) which corresponds to a Mach number of 2.4. Since the turbulent separation on the curved-surface model is unsteady, the interaction takes place over a much larger streamwise distance that for the steady turbulent separations (on the step and the compression corner). Evidence of the unsteadiness is provided by the jagged pressure distribution and by the lack of sharpness in the corresponding shadowgraph in figure 40. It should be emphasized that most of the turbulent separations were relatively steady and unsteadiness to the degree illustrated in figure 40 was more an exception than a rule.

In assessing the effects of variation in Reynolds number on turbulent separations it is necessary to keep the model shape and the Mach number fixed. This requirement is unlike the case for laminar separation where only the Mach number needed to be held fixed. Some pressure distributions at various Reynolds numbers are shown in figure 41 for turbulent separation over a step at a Mach number of 2.0.



(a) Pressure distribution. (b) Shadowgraphs.

FIGURE 40.—Effects of flow unsteadiness on the pressure distribution and the corresponding shadowgraphs for turbulent separation; $M_o=2.4$; $R_{x_o}=2.7\times10^6$.

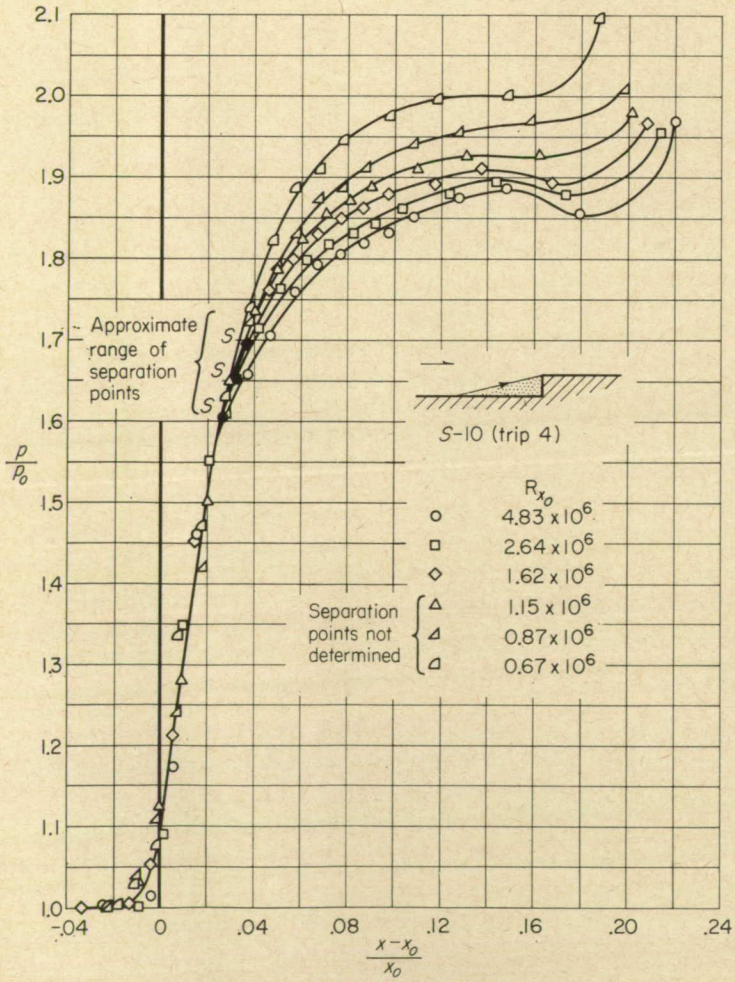


FIGURE 41.—Effect of Reynolds number on the pressure distribution for a step with turbulent separation; $M_o=2.0$.

The step model is selected inasmuch as it is the only model of those investigated which exhibits a clearly defined peak in pressure distribution. The data of figure 41 cover a range in Reynolds number corresponding to a variation by a factor of about 7 to 1, and show no large effect of such variation. These particular data do show, however, a small but consistent effect in the direction of decreasing peak pressure with increasing Reynolds number. The trend of decreasing pressure rise with increasing Reynolds number is the same as that predicted by the simple analysis for free interactions which indicates the pressure rise to vary as $\sqrt{\bar{c}_f}$. A quantitative comparison of this theoretical result with the measurements on step model S–10 (trip 4) over the M_o range between 2.0 and 3.4 is presented in figure 42. The various lines shown represent a variation proportional to $\sqrt{\bar{c}_f}$ for turbulent flow. At a Mach number of 2.0 the data indicate somewhat less variation than $\sqrt{\bar{c}_f}$, but at Mach numbers near 3 they indicate somewhat greater variation. Part of the experimental variation, particularly at the higher Mach numbers, is due to the fact that the effective origin of the turbulent boundary layer was not always at the boundary-layer trip. At low tunnel pressures, where the boundary-layer trip was not completely effective, transition could be anywhere between the trip and the beginning of separation. Data points taken under these conditions are represented by filled symbols in figure 42. For such points the Reynolds number plotted is somewhat greater than the effective Reynolds number of the turbulent boundary layer; consequently, small arrows have been attached to these points, indicating the direction in which they would move if plotted as a function of the true effective Reynolds number. It is noted that these points with arrows correspond to a pure-laminar-type separation

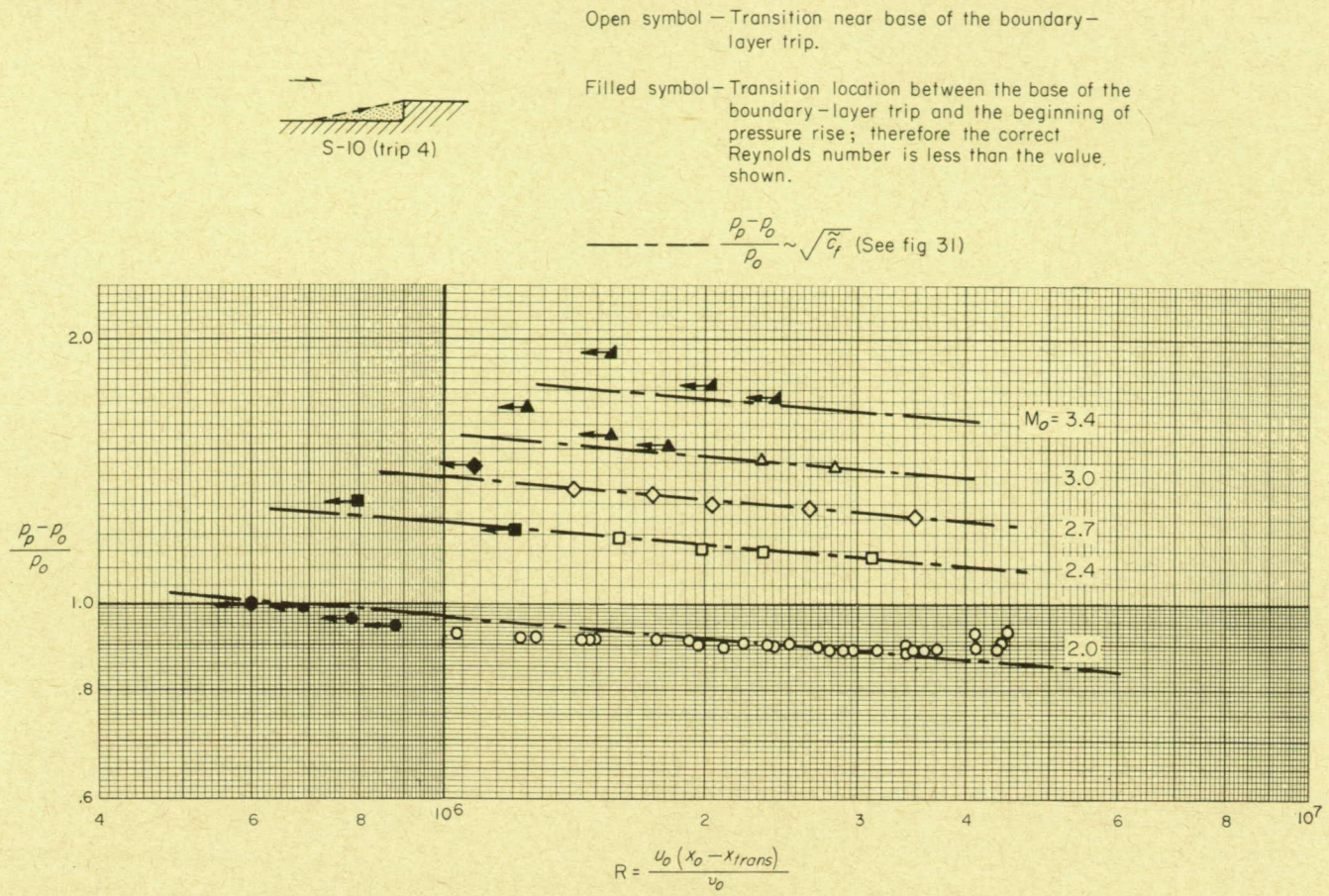


FIGURE 42.—Reynolds number effect on the peak pressure ratio for a step with turbulent separation at various Mach numbers.

behind the base of the trip (as determined by measurements of base pressure on the trip) but to a fully turbulent separation over the step.

Although the data in figures 41 and 42 for model S–10 (trip 4) show a consistent decrease in peak pressure rise with increasing Reynolds number, not all of the data for turbulent separations showed this trend. Model S–5 (trip 2) revealed no appreciable variation in p_p-p_o with R_{x_o} over the range of M_o and R_{x_o} investigated. Similarly, Love (ref. 39) found no appreciable variation of p_p-p_o with R_{x_o} over a wide range of M_o and R_{x_o}. On the other hand, the several compression-corner and curved-surface models investigated herein exhibited essentially the same trend of decreasing p_p-p_o with increasing R_{x_o} as model S–10 (trip 4). The reason for these different results is not known. These apparent discrepancies, however, are consistent with the interpretation that the flow downstream of supersonic turbulent separation—unlike the flow downstream of supersonic laminar separation—usually is not a free-interaction phenomenon, and, thus should not necessarily follow a variation approximately as $\sqrt{\bar{c}_f}$.

In figure 43 a comparison is made between the measured variation with Reynolds number of the pressure rise to a turbulent separation point and the theoretical variation predicted by the analysis. In this comparison, various model shapes are employed inasmuch as p_s-p_o (unlike p_p-p_o) is regarded as being determined by free interaction. Experimental data of Gadd, Holder, and Regan (ref. 15) are shown in figure 43 by the dashed lines. The calculated trend proportional to $\sqrt{\bar{c}_f}$ is seen to be in approximate, though not accurate, agreement with the various measurements.

As a further test of the dimensional analysis for turbulent free interactions, pressure measurements can be plotted in coordinates which should make the pressure distributions—at least up to the separation point—independent of both Reynolds number and object shape. According to equations (17) and (18), the quantity $[(p-p_o)/p_o]\bar{c}_f^{-1/2}$ should be plotted against $(x-x_o)/(\delta^*\bar{c}_f^{-1/2})$, just as in the case of laminar separation. In the absence of better information, δ^*/x_o for turbulent flow is taken as proportional to $\bar{c}_f$.[10] The appropriate longitudinal coordinate is then $[(x-x_o)/x_o]\bar{c}_f^{-1/2}$. A replot of the data of figure 41 in these appropriate coordinates is presented in figure 44. By observing that p/p_o is plotted in figure 41 and $\Delta p/p_o$ in figure 44, it is seen that the small spread due to variation of Reynolds number is approximately, though not entirely, accounted for by the simple analysis. The same coordinates which correlate the pressure distribution in laminar separation up to the plateau pressure, also correlate reasonably well the turbulent separation data up to at least the separation pressure.

The effect of Mach number on the pressure rise to the

[10] Approximate formulae for incompressible turbulent flow with 1/7-power velocity profile are: $\delta^*\sim\delta\sim x(R_x)^{-1/5}$ and $\bar{c}_f\sim R_x^{-1/5}$. These combine to give $\delta^*/x\sim\bar{c}_f$. If more refined analysis is made, such as by combining the wall law with the velocity defect law for incompressible flow, then δ^*/x is proportional to about the 1.2 power of $\bar{c}_f$. At present, appropriate formulae for compressible flow are not accurately known; hence the simplest relation $\delta^*/x\sim\bar{c}_f$ is used.

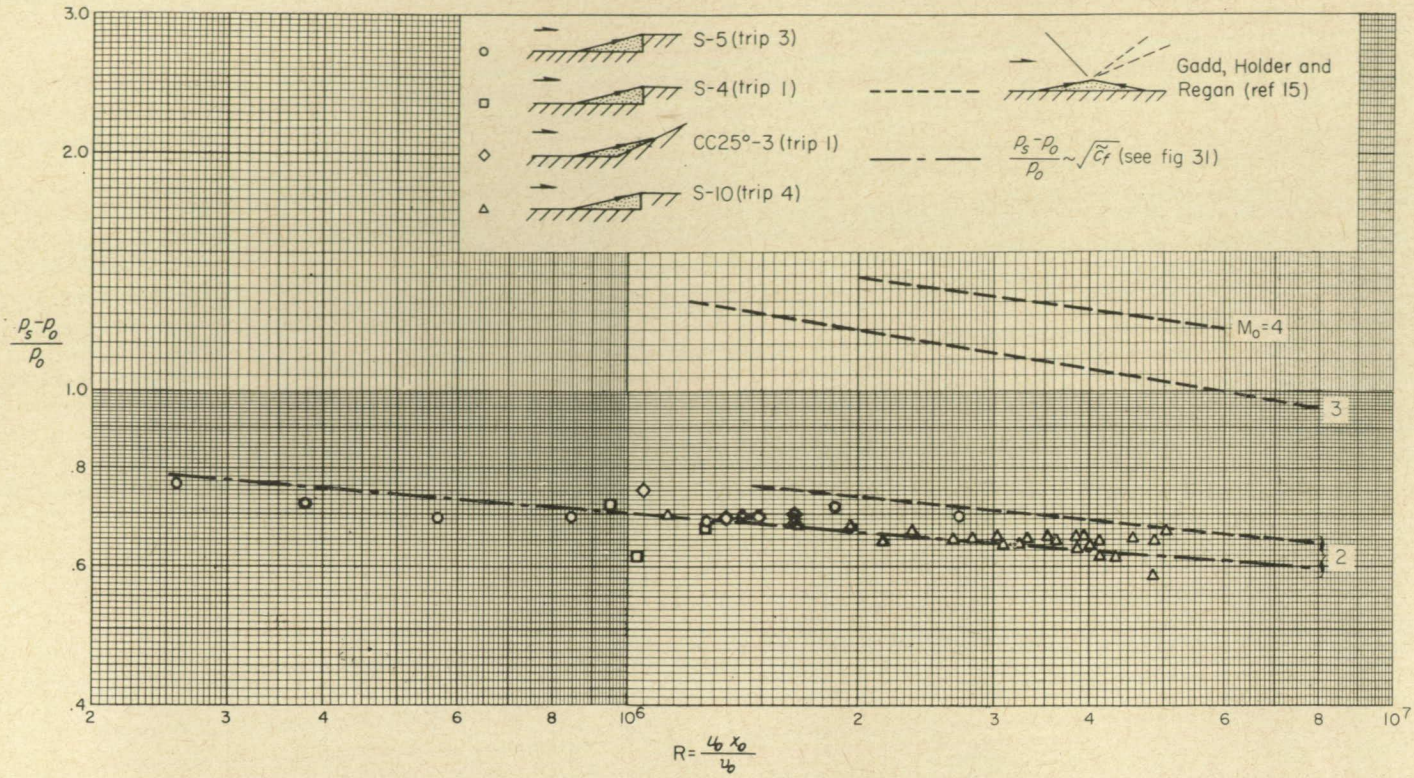


FIGURE 43.—Reynolds number effect on pressure rise to turbulent separation for various Mach numbers.

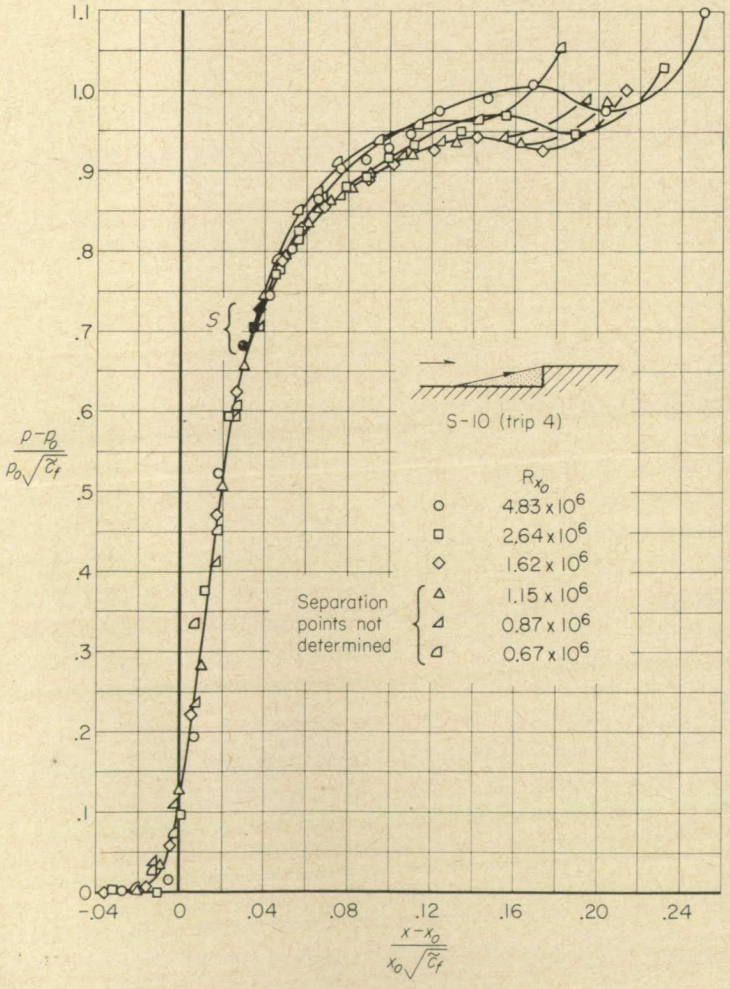


FIGURE 44.—Correlation of pressure distribution at various Reynolds numbers for turbulent separation over a step; M_0=2.0.

turbulent separation point of various models is shown in figure 45. The pressure rise $(p_s-p_0)/p_0$ is divided by $\sqrt{\bar{c}_f}$ as this would roughly account for the influence of Reynolds number. Data from various sources for steps, compression corners, and incident shock reflections are included in this figure. Two different techniques were employed in measuring the separation point as indicated in the figure legend. The Reynolds number range for the data from the present investigation is 0.3 to 6.0×10^6; whereas for the data of Bogdonoff it is approximately 8 to 36×10^6 and for the

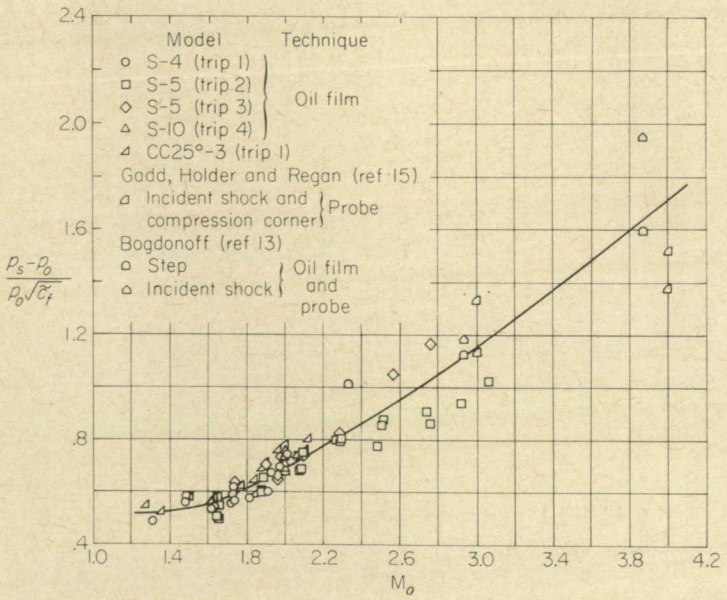


FIGURE 45.—Effect of Mach number on pressure rise to separation point for turbulent flow for steps, compression corners, and incident shocks.

data of Gadd, Holder, and Regan it is from 2 to 8×10^6. Although there is considerable scatter in the measurements (since the pressure rise to the separation point is a difficult quantity to measure accurately), there is no systematic trend discernible between the various configurations. This is consistent with the view that the pressure rise to a separation point in supersonic turbulent flow is a free-interaction phenomenon and should be independent of the mode of inducing separation.

The effect of Mach number on peak pressure rise for steps in turbulent flow is shown in figure 46. Data from experiments of Bogdonoff (ref. 13) and Love (ref. 39) are included in this figure. Two extremes are represented for Bogdonoff's data at each Mach number; they correspond to the smallest and largest step heights used in his experiments. At Mach numbers above about 2.6 the present measurements for S–6 (trip 1) show considerably higher values of p_p-p_o than do the measurements of Bogdonoff and Love. The large spread of data, as represented by the crosshatched area, is attributed primarily to the effect of boundary-layer thickness on p_p-p_o. Models for which the step height h is considerably smaller than δ_o (e. g., the lower data points of Bogdonoff in fig. 46) yield peak pressure values only slightly greater than the separation pressure, whereas the model with the largest ratio h/δ (model S–6 with trip 1 for which $h/\delta\approx6$) yields the largest values for peak pressure. The upper limit of Bogdonoff's data corresponds to an intermediate case of $h/\delta\approx2$.

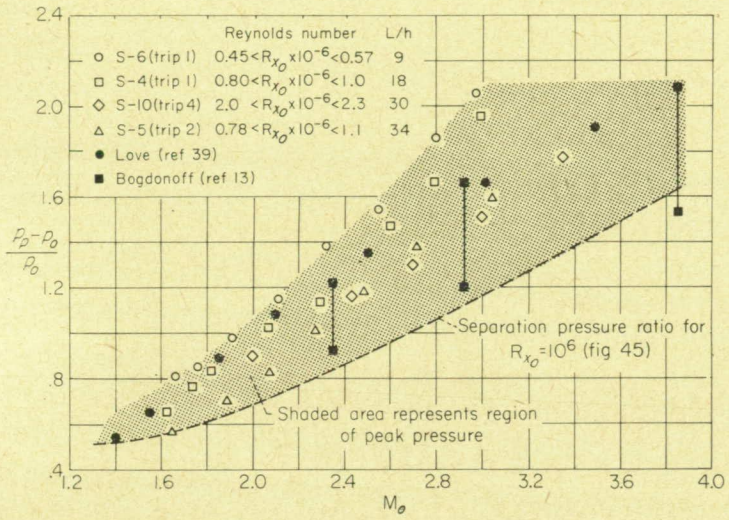


FIGURE 46.—Effect of Mach number on peak pressure ratio for steps with turbulent separation.

CONCLUSIONS

The conclusions which follow were drawn mainly from experiments with boundary layers of essentially constant pressure preceding a two-dimensional separated region. Sufficiently wide variations in model geometry (steps, bases, compression corners, curved surfaces, shock reflections) were covered to regard the conclusions as rather general, although some of these conclusions may not apply for an initial boundary-layer history of strongly rising or falling pressure.

1. For a given model shape, the location of transition relative to the reattachment and separation positions is dominant in controlling the characteristic features of pressure distribution irrespective of Mach number and Reynolds number. This dominance leads to classification of each separated flow into one of three types: pure laminar, transitional, and turbulent.

2. Pure laminar separations (transition downstream of reattachment zone) were steady in a supersonic stream and depended only to a relatively small extent on Reynolds number. The dead-air pressure for pure laminar separations having negligible boundary-layer thickness at separation can be calculated from a simple theory involving no empirical information; the theory is applicable to both subsonic and supersonic flow.

3. Transitional separations (transition between separation and reattachment) generally were unsteady and often depended markedly on Reynolds number. In transitional separations an abrupt pressure rise often occurs at the location of transition, especially when transition is only a short distance upstream of reattachment.

4. Turbulent separations (transition upstream of separation) depended only to a minor extent on Reynolds number. Most of the supersonic turbulent separations were relatively steady compared to transitional separations.

5. The stability of a separated laminar mixing layer increases markedly with an increase in Mach number. As a result, pure laminar separations, which are uncommon at subsonic speed, may become of some practical interest at hypersonic speed. Because of this marked increase in stability, laminar separations warrant additional research in hypersonic flow.

6. In a region where boundary layer and external flow interact freely, a simple analysis indicates that pressure rises vary as the square root of the skin friction. Experiments at supersonic speed substantiated this result accurately for laminar separation, and approximately for turbulent separation.

7. The pressure rise to separation is independent of the mode of inducing separation for either laminar or turbulent separation in supersonic flow. The plateau pressure rise in laminar separation is similarly independent, but the peak pressure rise in turbulent separation depends significantly on model geometry.

AMES AERONAUTICAL LABORATORY
NATIONAL ADVISORY COMMITTEE FOR AERONAUTICS
MOFFETT FIELD, CALIF., *Nov. 29, 1956*

APPENDIX A

ANOMALOUS OIL-FILM OBSERVATIONS

When the oil-film technique was used, two threadlike lines of accumulation sometimes occurred simultaneously. They were never observed in laminar separation, but only in turbulent separation, and only over a certain Mach number range. Both lines of accumulation were stable, repeatable, and normal to the stream direction of flow. They were displaced streamwise a distance equivalent to several boundary-layer thicknesses. Depending upon test conditions, the downstream line could appear by itself, the two lines could appear simultaneously, or the upstream line could appear by itself. The upstream line corresponded to a pressure rise of about 0.3 p_o, whereas the downstream line corresponded to between 0.6 p_o and 1.0 p_o rise, depending on the Mach number. Comparable measurements of Bogdonoff and of Gadd, derived from a different technique of location of separation (near-surface pitot-pressure surveys) corresponded to the downstream line. To determine directly whether the two techniques inherently produce different results, Professor S. M. Bogdonoff volunteered cooperation by trying the oil-film technique with the Princeton apparatus on which the pitot-pressure surveys previously had been made. He immediately confirmed his earlier result on pressure rise to separation at $M_o=2.9$ (corresponding to the downstream line in the present experiments), and did not find any evidence of a second line. Although this left unexplained the simultaneous occurrence of two lines, it did remove suspicion of excessive probe interference and place suspicion on the physical significance of the upstream line of oil accumulation. It appeared possible that the upstream line did not accumulate at a separation position, but actually represented a second, stable, equilibrium position, due to wind forces acting downstream and buoyancy forces acting upstream. Sizable buoyancy forces arise from the large streamwise pressure gradients near turbulent separation. (The gradients near laminar separation are an order of magnitude smaller.)

By regarding the thread of oil as a cylinder of fixed dimensions in a wind stream of density ρ_w and velocity proportional to $(\partial u/\partial y)_w$, the drag per unit span would be proportional to $\rho_w(\partial u/\partial y)_w^2$. The upstream-acting buoyancy force would be proportional to $(dp/dx)\sim(p_o/\delta_o)$, so that

$$\hat{r}\equiv\frac{\text{buoyance forces}}{\text{wind forces}}\sim\frac{p_o}{(\delta_o)\rho_w\left(\frac{\partial u}{\partial y}\right)_w^2}\sim\frac{p_o}{\left(\frac{x_o}{R_{x_o}^{1/5}}\right)\rho_w\left(\frac{c_f\rho_o u_o^2}{\mu_w}\right)^2}$$

or, since $\rho_w=\rho_e T_e/T_w\sim\rho_o T_o$ (approximately),

$$\hat{r}\sim\frac{R_{x_o}^{1/5}}{x_o\rho_o^2 c_f^2 u_o^4}$$

For fixed M_o and x_o, $\hat{r}\sim p_o^{1/5}/p_o^2(p_o^{-1/5})^2\sim p_o^{-7/5}$. From this brief analysis three inferences can be drawn: first, an increase in tunnel pressure for fixed M_o and x should decrease the importance of buoyancy forces; second, an increase in model length for fixed M_o and p_o should decrease the importance of buoyancy forces since $\hat{r}\sim x_o^{1/5}/x_o\sim x_o^{-4/5}$; third, for fixed x_o and p_o, the variation of $\hat{r}$ with an increase in M_o is dominated by the decrease in ρ_o and c_f; hence an increase in Mach number should increase the importance of buoyancy forces. In view of these inferred trends, a special model (S–5 with trip 2) having double the length x_o was constructed. Whereas the regular models exhibited the upstream line above about $M_o=1.9$, the larger model exhibited such lines above about $M_o=2.5$. This is consistent with both the second and third inferences above. It was found also that increasing tunnel pressure caused the upstream line to disappear. This is consistent with the first inference. Consequently, it is deduced that the upstream line, which corresponded to a pressure rise of $\Delta p/p_o=0.3\pm0.1$, is not a separation line but represents a second position for stable equilibrium of buoyancy forces and wind forces.

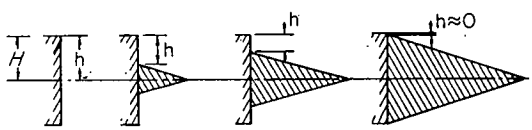
APPENDIX B

SPECIAL EXPERIMENTS PERTAINING TO THE CROCCO-LEES THEORY

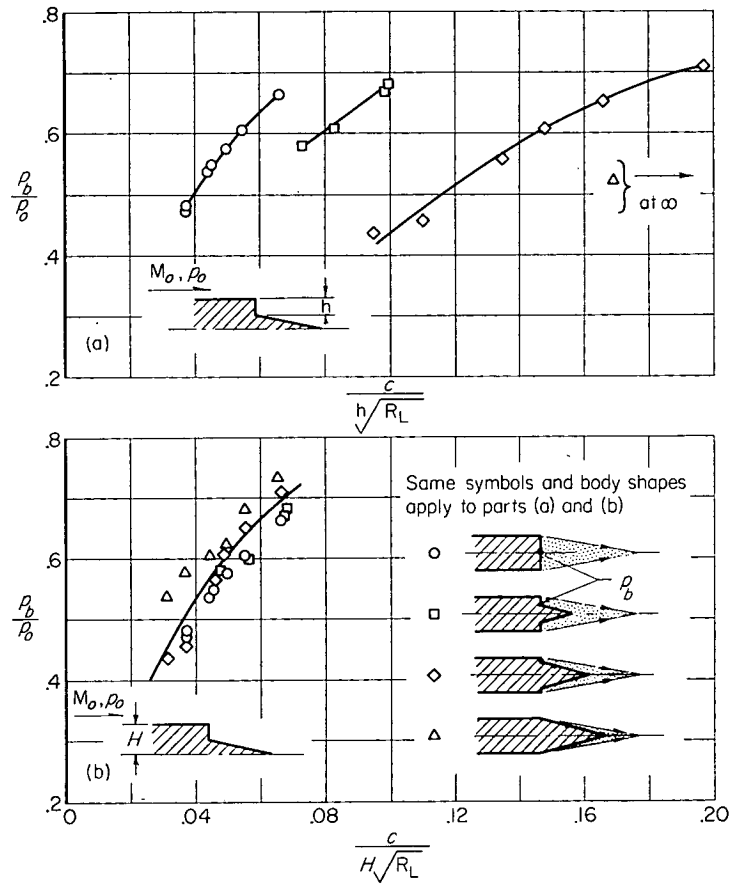
The Crocco-Lees theory (ref. 9) is unusually broad in scope, covering laminar-, transitional-, and turbulent-type separations. Because of this extensiveness, many untested approximations are introduced in their analysis where appropriate experimental data are missing and cannot provide a guide. Also, because of the broad scope, it is important to supplement this theory wherever possible with pertinent experimental information. The present experiments suggest a way in which the Crocco-Lees theory for base pressure might be improved. This possible improvement may have no bearing, however, on the Crocco-Lees theory for other types of separation.

In the Crocco-Lees analysis the wake thickness is an important variable appearing throughout their analysis; it determines, among other things, the initial condition for integration of their differential equation which governs the dead-air pressure. On the other hand, the theory of this report indicates that the total wake thickness of a separated region would not influence the dead-air pressure.

The special experiments designed to provide a decisive test of the importance of the thickness of wake were conducted during the initial experiments (1953) on models with triangular inserts as is illustrated. The two-dimensional channel appratus was employed.



The experimental test conditions were especially selected to be in a Reynolds number range where in the separation was of the transitional type, and wherein the Crocco-Lees theory would indicate the dead-air pressure to be sensitive to changes in the initial wake thickness $h+\delta$. If the total thickness of wake were dominant in determining base pressure, then the dead-air pressure for a fixed Reynolds number R (based on the chord length c of the airfoil) should correlate roughly as a function of the parameter h/δ, or as a function of the equivalent parameter $c/(h\sqrt{R})$ where c is the model length. On the other hand, if the thickness of wake is totally unimportant, it would be expected that the dead-air pressure would be unaffected by the triangular-shaped inserts and would correlate much better when plotted as a function of H/δ, or of the equivalent parameter $c/(H\sqrt{R})$. The experimental data plotted in figure 47 are definitive in



(a) h as characteristic length.
(b) H as characteristic length.

FIGURE 47.—Base pressure measurements for transitional type separation with various wedge inserts in the dead-air region; $M_0=2.0$.

showing that H is the essential characteristic length in the problem; and hence that the total wake thickness is not important in determining base pressure. It is believed that in the Crocco-Lees theory the base height should more appropriately be introduced in a way which determines the length of mixing layer, rather than in a way which determines the initial thickness of the wake.

REFERENCES

1. Prandtl, L.: Der Luftwiderstand von Kugeln: Nachrichten von der Koniglichen Gesselschaft der Wissenschaften zu Gottingen Math. Phys. Klass, 1914, pp. 177–190.
2. Eiffel, G.: Sur la resistance des spheres dans l'air en mouvement. Comptes Rendus de l'Academie de Sciences, vol. 155, 1912, pp. 1597–1599.
3. Liepmann, H. W.: The Interaction Between Boundary Layer and Shock Waves in Transonic Flow. Jour. Aero. Sci., vol. 13, no. 12, Dec. 1946, pp. 623–637.
4. Ackeret, J., Feldmann, F., and Rott, N.: Investigations of Compression Shocks and Boundary Layers in Gases Moving at High Speed. NACA TM 1113, 1947.
5. Chapman, Dean R., and Perkins, Edward W.: Experimental Investigation of the Effects of Viscosity on the Drag of Bodies of Revolution at a Mach Number of 1.5. NACA RM A7A31a, 1947. (Also available as NACA Rep. 1036).
6. Hankins, G. A.: Experiments of Reynolds Number Effect on Projectiles at Supersonic Speeds. Rep. Engr. Div. N. P. L. No. 221/46, as reported in: Howarth, L., ed., Modern Developments in Fluid Mechanics, High Speed Flow, vol. II, p. 702, Oxford Press, 1953.
7. Schiller, L., and Linke, W.: Pressure and Frictional Resistance of a Cylinder at Reynolds Numbers 5,000 to 40,000. NACA TM 715, 1933.
8. Gault, Donald E.: An Experimental Investigation of Regions of Separated Laminar Flow. NACA TN 3505, 1955.
9. Crocco, Luigi, and Lees, Lester: A Mixing Theory for the Interaction Between Dissipative Flows and Nearly Isentropic Streams. Jour. Aero. Sci., vol. 19, no. 10, Oct. 1952, pp. 649–676.
10. Liepmann, Hans W., and Fila, Gertrude H.: Investigations of Effects of Surface Temperature and Single Roughness Elements on Boundary-Layer Transition. NACA Rep. 890, 1947.
11. Oswatitsch, K., and Wieghardt, K.: Theoretical Analysis of Stationary Potential Flows and Boundary Layers at High Speed. NACA TM 1189, 1948.
12. Chapman, Dean R., Kuehn, Donald M., and Larson, Howard K.: Preliminary Report on a Study of Separated Flows in Supersonic and Subsonic Streams. NACA RM A55L14, 1956.
13. Bogdonoff, Seymour M.: Some Experimental Studies of the Separation of Supersonic Turbulent Boundary Layers. Papers presented at the Heat Transfer and Fluid Mechanics Institute, Univ. of Calif. at Los Angeles, June 23–25, 1955, sec. V, pp. 1–23.
14. Bogdonoff, S. M., and Kepler, C. E.: Separation of a Supersonic Turbulent Boundary Layer. Rep. 249, Princeton Univ., Dept. Aero. Engr., Jan. 1954.
15. Gadd, G. E., Holder, D. W., and Regan, J. D.: An Experimental Investigation of the Interaction Between Shock Waves and Boundary Layers. Proc. Roy. Soc. of London, ser. A, vol. 226, 1954, pp. 227–253.
16. Korst, H. H., Page, R. H., and Childs, M. E.: Compressible Two-Dimensional Jet Mixing at Constant Pressure. TN 392–1, Univ. of Ill., Engr. Exp. Sta., Mech. Engr. Dept., 1954.
17. Chapman, Dean R., Wimbrow, William R., and Kester, Robert H.: Experimental Investigation of Base Pressure on Blunt-Trailing-Edge Wings at Supersonic Velocities. NACA TN 2611, 1952.
18. Pearcey, H. H.: The Indication of Boundary-Layer Transition on Aerofoils in the N. P. L. 20 in. × 8 in. High Speed Wind Tunnel. British A. R. C. 11,991, Dec. 14, 1948.
19. Winter, K. G., Scott-Wilson, J. B., and Davies, F. V.: Methods of Determination and of Fixing Boundary Layer Transition on Wind Tunnel Models at Supersonic Speeds. British R. A. E. TN Aero 2341, Sept. 1954.
20. Reller, John O., Jr., and Hamaker, Frank M.: An Experimental Investigation of the Base Pressure Characteristics of Nonlifting Bodies of Revolution at Mach Numbers From 2.73 to 4.98. NACA TN 3393, 1955. (Formerly NACA RM A52E20)
21. Fage, A.: On Reynolds Numbers of Transition. R. & M. 1765, British A. R. C., June 6, 1936.
22. Bursnall, William J., and Loftin, Laurence K.: Experimental Investigation of the Pressure Distribution About a Yawed Circular Cylinder in the Critical Reynolds Number Range. NACA TN 2463, 1951.
23. Lange, Roy H.: Present Status of Information Relative to the Prediction of Shock-Induced Boundary-Layer Separation. NACA TN 3065, 1954.
24. Kavanau, L. L.: Results of Some Base Pressure Experiments at Intermediate Reynolds Numbers with M=2.84. TR No. HE–150–117, Univ. of Calif., Inst. of Engr. Res., Oct. 22, 1953.
25. Lin, C. C.: On the Stability of the Laminar Mixing Region Between Two Parallel Streams in a Gas. NACA TN 2887, 1953.
26. Chapman, Dean R.: A Theoretical Analysis of Heat Transfer in Regions of Separated Flow. NACA TN 3792, 1956.
27. Chapman, Dean R.: Laminar Mixing of a Compressible Fluid. NACA Rep. 958, 1950. (Formerly NACA TN 1800)
28. Chapman, Dean R.: An Analysis of Base Pressure at Supersonic Velocities and Comparison With Experiment. NACA Rep. 1051, 1951.
29. Roshko, Anatol: On the Drag and Shedding Frequency of Two-Dimensional Bluff Bodies. NACA TN 3169, 1954.
30. Kawaguti, Mitutosi: Numerical Solution of the Navier-Stokes Equations for the Flow Around a Circular Cylinder at Reynolds Number 40. Phys. Soc. of Japan Journal, vol. 8, no. 6, Nov.-Dec. 1953, pp. 747–757.
31. Korst, H. H., Page, R. H., and Childs, M. E.: A Theory for Base Pressures in Transonic and Supersonic Flow. TN 392–2, Univ. of Ill., Engr. Exp. Sta., Mech. Engr. Dept., Mar. 1955.
32. Lighthill, M. J.: On Boundary Layers and Upstream Influence. I. A Comparison Between Subsonic and Supersonic Flows. Proc. Roy. Soc. of London, ser. A., vol. 217, no. 1130, 1953.
33. Lees, Lester: Interaction Between the Laminar Boundary Layer Over a Plane Surface and an Incident Oblique Shock Wave. Rep. 143, Princeton Univ., Aero. Engr. Lab., Jan. 24, 1949.
34. Stewartson, K.: On the Interaction Between Shock Waves and Boundary Layers. Proc. Camb. Phil. Soc., vol. 47, pt. 3, July 1951 pp. 545–553.
35. Gadd, G. E.: Interactions Between Wholly Laminar or Wholly Turbulent Boundary Layers and Shock Waves Strong Enough to Cause Separation. Jour. Aero. Sci., vol. 20, no. 11, Nov. 1953, pp. 729–739.
36. Tyler, Robert D., and Shapiro, Ascher H.: Pressure Rise Required for Separation in Interaction Between Turbulent Boundary Layer and Shock Wave. Jour. Aero. Sci., vol. 20, no. 12, Dec. 1953, pp. 858–860.
37. Mager, Artur: Prediction of Shock-Induced Turbulent Boundary-Layer Separation. Jour. Aero. Sci., vol. 22, no. 3, Mar. 1955, pp. 201–202.
38. Schuh, H.: On Determining Turbulent Boundary-Layer Separation in Incompressible and Compressible Flow. Jour. Aero. Sci., vol. 22, no. 5, May 1955, pp. 343–345.
39. Love, Eugene S.: Pressure Rise Associated With Shock-Induced Boundary-Layer Separation. NACA TN 3601, 1955.

REPORT 1357

EXPERIMENTAL DETERMINATION OF EFFECTS OF FREQUENCY AND AMPLITUDE ON THE LATERAL STABILITY DERIVATIVES FOR A DELTA, A SWEPT, AND AN UNSWEPT WING OSCILLATING IN YAW [1]

By Lewis R. Fisher

SUMMARY

Three wing models were oscillated in yaw about their vertical axes to determine the effects of systematic variations of frequency and amplitude of oscillation on the in-phase and out-of-phase combination lateral stability derivatives resulting from this motion. The tests were made at low speeds for a 60° delta wing, a 45° swept wing, and an unswept wing; the swept and unswept wings had aspect ratios of 4.

The results indicate that large changes in the magnitude of the stability derivatives due to the variation of frequency occur at high angles of attack, particularly for the delta wing. The greatest variations of the derivatives with frequency take place for the lowest frequencies of oscillation; at the higher frequencies, the effects of frequency are smaller and the derivatives become more linear with angle of attack.

Effects of amplitude of oscillation on the stability derivatives for the delta wing were evident for certain high angles of attack and for the lowest frequencies of oscillation. As the frequency became high, the amplitude effects tended to disappear.

The algebraic addition of the component derivatives determined in separate investigations were generally in good agreement with the combination derivatives obtained herein. The major contributions to the out-of-phase derivatives are made by the sideslipping acceleration derivatives, whereas the contribution to the in-phase derivatives are made chiefly by the sideslipping velocity derivatives.

INTRODUCTION

Recent investigations have shown that stability derivatives of large magnitude exist at high angles of attack for wings undergoing rotary accelerations in yaw or transverse accelerations in sideslip. The results of one such investigation are presented in reference 1 for which wing models were forced to oscillate in a pure yawing motion (zero sideslip) at a constant frequency of oscillation. The stability derivatives resulting from this investigation include the rate of change of yawing- and rolling-moment coefficients with yawing velocity $C_{n_{r,\omega}}$ and $C_{l_{r,\omega}}$ and the rate of change of yawing- and rolling-moment coefficients with yawing acceleration $C_{n_{\dot{r},\omega}}$ and $C_{l_{\dot{r},\omega}}$, where the subscript ω indicates oscillatory derivatives. These derivatives were measured for a 60° delta wing, a 45° sweptback wing, and an unswept wing; the swept and unswept wings had aspect ratios of 4.

The same wing models were oscillated in a pure sideslipping motion for the investigation of reference 2. The measured stability derivatives resulting from this type of motion included the yawing- and rolling-moment coefficients due to sideslipping velocity $C_{n_{\beta,\omega}}$ and $C_{l_{\beta,\omega}}$ and the yawing- and rolling-moment coefficients due to sideslipping acceleration $C_{n_{\dot{\beta},\omega}}$ and $C_{l_{\dot{\beta},\omega}}$. These derivatives were measured primarily at one frequency of oscillation; however, some limited data involving a variation of oscillation frequency in reference 2 indicated that the sideslipping derivatives at high angles of attack were dependent upon frequency. The results presented in reference 3 substantiated these effects of frequency at high angles of attack on the lateral stability derivatives for a similar set of wings. Reference 3 also includes a comprehensive discussion of the probable origin of the acceleration derivatives of large magnitude, and reference 4 points out the importance of including these derivatives in dynamic stability calculations, particularly at high angles of attack where the derivatives assume large magnitudes.

A reasonably simple oscillation-test technique for extracting the lateral stability derivatives for a model is the method of oscillating the model in yaw about its vertical wind axis. Since the motion of the model is then a combination of yawing and sideslipping, the stability derivatives measured by this technique are the combination derivatives $C_{n_{r,\omega}}-C_{n_{\dot{\beta},\omega}}$, $C_{l_{r,\omega}}-C_{l_{\dot{\beta},\omega}}$, $C_{n_{\beta,\omega}}+k^2C_{n_{\dot{r},\omega}}$, and $C_{l_{\beta,\omega}}+k^2C_{l_{\dot{r},\omega}}$, where k is the reduced frequency parameter $\omega b/2V$. The present investigation employed this technique for the purpose of determining the effects of a systematic variation of frequency and amplitude of oscillation on the resulting combination stability derivatives. Furthermore, in order to establish the relative importance of the individual derivatives which form the combination derivatives, the results of the investigation of reference 1 and of additional tests similar to those of reference 2 are compared individually and as an algebraic sum with the results of the present investigation. These comparisons provide an indication of the degree to which the results of the individual sideslipping and yawing tests are additive and attest to the linearity of the aerodynamic phenomena responsible for the large-magnitude derivatives.

[1] Supersedes recently declassified NACA Research Memorandum L56A19 by Lewis R. Fisher, 1956.

SYMBOLS

The data are referred to the system of stability axes and are presented in the form of standard coefficients of forces and moments about the quarter-chord point of the mean aerodynamic chord of each wing tested. (See fig. 1.) The coefficients and symbols used herein are defined as follows:

b	span, ft
c	local chord, ft
$\bar{c}$	mean aerodynamic chord, ft
C_D	drag coefficient, Drag/qS
C_L	lift coefficient, Lift/qS
C_l	rolling-moment coefficient, Rolling moment/qSb
C_m	pitching-moment coefficient, Pitching moment/$qS\bar{c}$
C_n	yawing-moment coefficient, Yawing moment/qSb
k	reduced-frequency parameter, $\omega b/2V$
q	dynamic pressure, $\frac{1}{2}\rho V^2$, lb/sq ft
r	rate of change of yaw angle, $\dot{\psi}$, radians/sec
$\dot{r}$	yawing acceleration, $\partial\dot{\psi}/\partial t$
S	wing area, sq ft
t	time, sec
V	free-stream velocity, ft/sec
α	angle of attack, deg
β	angle of sideslip, radians or deg
$\dot{\beta}$	rate of change of sideslip angle, $\partial\beta/\partial t$
β_0	amplitude of sideslip, deg
ρ	mass density of air, slugs/cu ft
ψ	angle of yaw, radians or deg
$\dot{\psi}$	rate of change of yaw angle, $\partial\psi/\partial t$

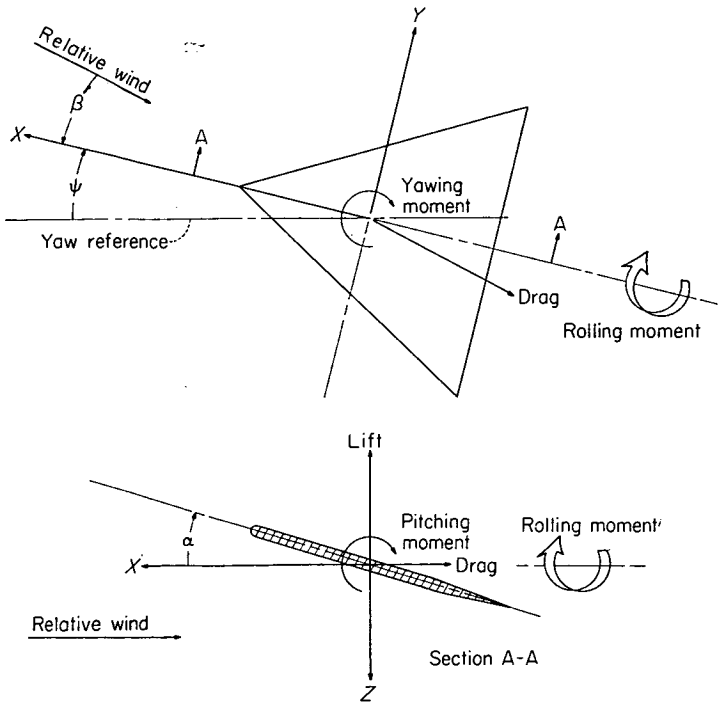


FIGURE 1.—System of stability axes. Arrows indicate positive forces, moments, and angular displacements. Yaw reference is generally chosen to coincide with initial relative wind.

ψ_0	amplitude of yawing oscillation measured from zero yaw, deg
ω	circular frequency of oscillation, radians/sec

Derivatives: Following are formulas for the lateral stability derivatives used in presenting the results. All derivatives are nondimensionalized (1/radians).

$$C_{n_\beta}=\frac{\partial C_n}{\partial\beta} \qquad C_{n_r}=\frac{\partial C_n}{\partial\left(\frac{rb}{2V}\right)}$$

$$C_{n_{\dot{\beta}}}=\frac{\partial C_n}{\partial\left(\frac{\dot{\beta}b}{2V}\right)} \qquad C_{n_{\dot{r}}}=\frac{\partial C_n}{\partial\left(\frac{\dot{r}b^2}{4V^2}\right)}$$

$$C_{l_\beta}=\frac{\partial C_l}{\partial\beta} \qquad C_{l_r}=\frac{\partial C_l}{\partial\left(\frac{rb}{2V}\right)}$$

$$C_{l_{\dot{\beta}}}=\frac{\partial C_l}{\partial\left(\frac{\dot{\beta}b}{2V}\right)} \qquad C_{l_{\dot{r}}}=\frac{\partial C_l}{\partial\left(\frac{\dot{r}b^2}{4V^2}\right)}$$

The subscript ω used with a derivative denotes the oscillatory derivative.

APPARATUS AND MODELS

OSCILLATION APPARATUS

The equipment used to oscillate the models consisted of the motor-driven flywheel, connecting rod, crank arm, and model-support strut shown schematically in figure 2 and photographically in figures 3 and 4. The connecting rod was pinned to an eccentric center on the flywheel and transmitted a sinusoidal yawing motion to the support strut by means of the crank arm. Because the models were mounted to the support strut at their assumed centers of gravity, the oscillation was forced about the vertical wind (or stability) axis of the models. The apparatus was driven by a 1-horsepower direct-current motor through a geared speed reducer.

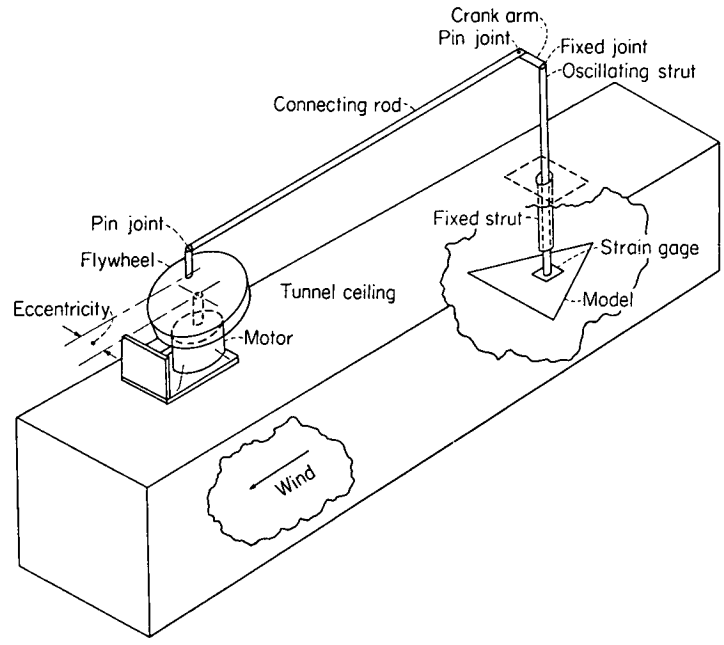


FIGURE 2.—Sketch of oscillation-in-yaw equipment.

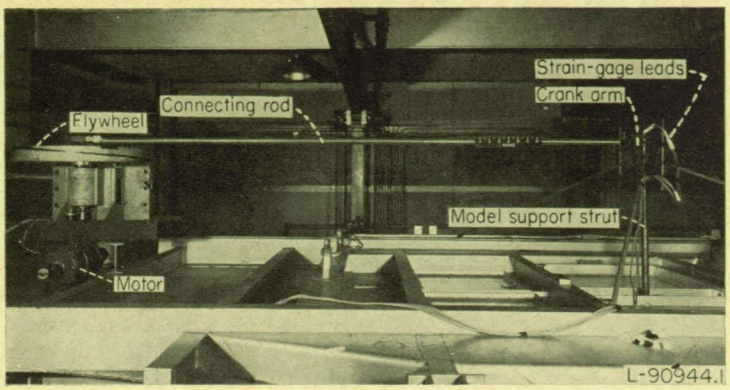


FIGURE 3.—Oscillation-in-yaw equipment on top of tunnel test section.

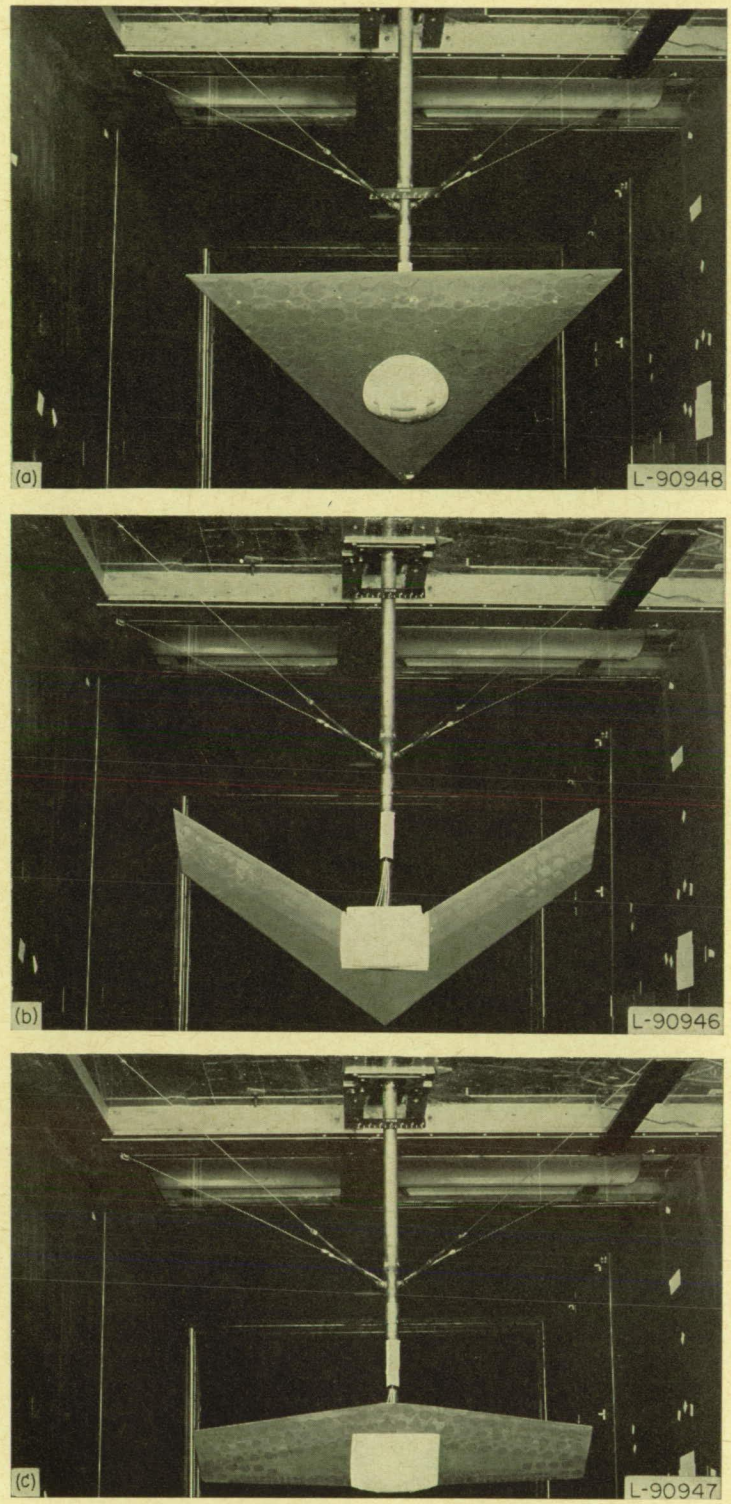
The frequency of oscillation was varied by changing the voltage supplied to the motor, and the amplitude of oscillation was varied by adjusting the throw of the eccentric on the flywheel.

Because the reduced frequency of the tests of reference 2 differed from that of reference 1, some additional tests similar to those of reference 2 were made for this investigation at a reduced frequency which corresponded to that of reference 1. The results in reference 2 were obtained from freely damped sideslipping oscillation tests in which the motion was forced by a set of coil springs. For these additional tests, however, the coil springs were replaced by a flywheel and crank mechanism similar to that used for the yawing-oscillation tests. The resulting motion, therefore, was a continuous sideslipping oscillation of constant amplitude. Check tests for comparable frequencies indicated that the derivatives measured by either technique were about the same.

MODELS

The models tested were the three wings used for the investigations of references 1 and 2 and are shown in figure 4. These models included a 60° delta wing, a 45° sweptback wing, and an unswept wing (fig. 5). The swept and unswept wings had aspect ratios of 4, taper ratios of 0.6, and rounded tips. Each of the three wings was constructed from ¾-inch plywood and had essentially a flat-plate airfoil section with a circular leading edge and a beveled trailing edge (fig. 5 (d)). The trailing edges of all wings were beveled to provide a trailing-edge angle of 10° that was constant across the span. Model dimensions are shown in the sketches of the three wings presented in figure 5, and other pertinent parameters are listed in the following table:

Item	Delta Wing	Swept wing	Unswept wing
Aspect ratio	2. 31	4. 0	4. 0
Taper ratio	0	0. 6	0. 6
Sweep angle, deg	(At L. E.) 60	(At $c/4$) 45	(At $c/4$) 0
Dihedral angle, deg	0	0	0
Twist, deg	0	0	0
Airfoil section	Flat plate	Flat plate	Flat plate
Area, sq in.	561. 20	324	324
Span, in.	36. 00	36	36
Mean aerodynamic chord, in.	20. 79	9. 19	9. 19

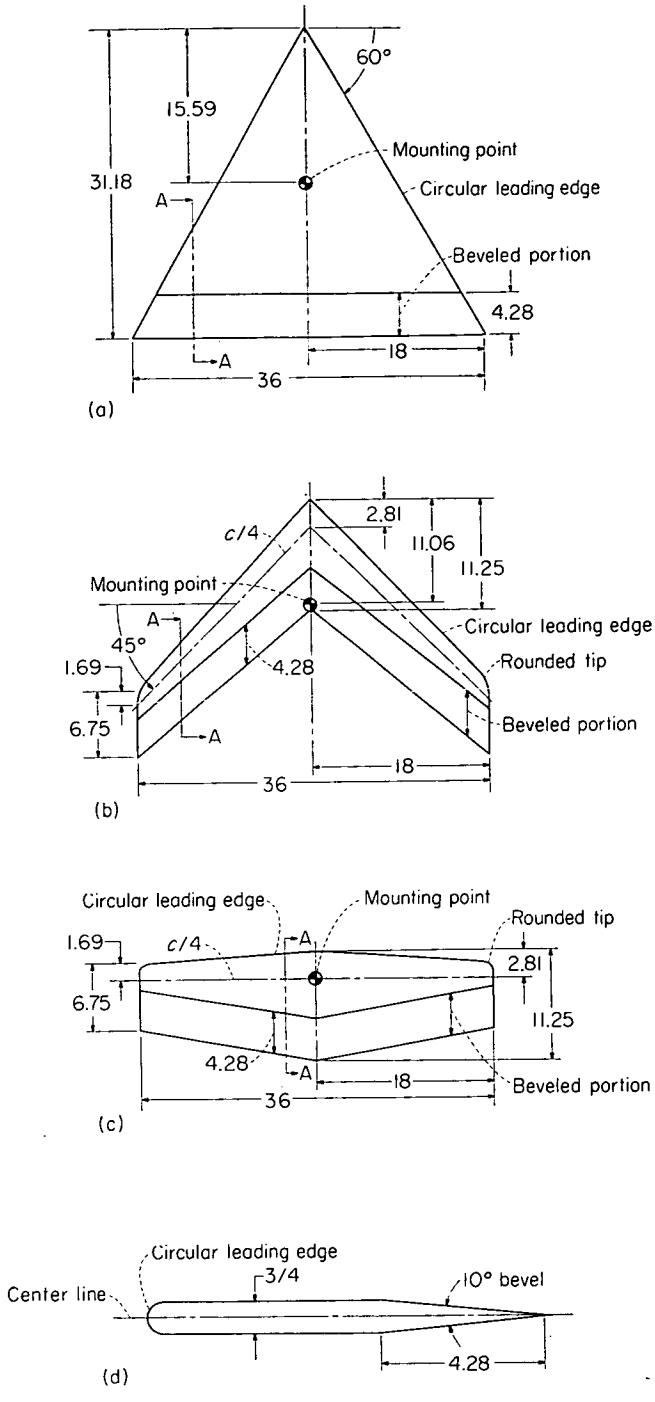


(a) 60° delta wing.
(b) 45° swept wing.
(c) Unswept wing.

FIGURE 4.—Models in tunnel test section.

RECORDING OF DATA

The data obtained in this investigation were recorded by means of the equipment described in the appendix of reference 1. Briefly, the rolling and yawing moments acting on the model during oscillation were measured by means of resistance-type strain gages mounted on the oscillating strut to which the model was attached. The moments were modified by a sine-cosine resolver driven by the oscillating



(a) Delta wing.
(b) Swept wing.
(c) Unswept wing.
(d) Airfoil section (all models).

FIGURE 5.—Sketches of the three wing models investigated. All dimensions are in inches.

mechanism so that the out-put signals of the strain gages were proportional to the in-phase and out-of-phase components of the strain-gage signals. These signals were read visually on a highly damped direct-current meter and the aerodynamic coefficients were obtained by multiplying the meter readings by the appropriate constants, one of which was the system calibration constant. The additional sideslipping oscillation tests required for the present investigation made use of this new equipment rather than the equipment used in the investigation of reference 2.

TESTS

All tests were conducted in the 6- by 6-foot test section of the Langley stability tunnel at a dynamic pressure of 24.9 pounds per square foot which corresponds to a Mach number of 0.13. The Reynolds number based on the mean aerodynamic chord was approximately 1.6×10^6 for the 60° delta wing and 0.71×10^6 for the swept and unswept wings.

The oscillation tests with the delta wing were conducted for nominal frequencies of oscillation of 0.5, 1.0, 2.0, 3.0, and 3.3 cycles per second. These frequencies correspond to values of the reduced-frequency parameter k of 0.033, 0.065, 0.130, 0.195, and 0.215. The amplitudes of oscillation ψ_0 for each of these frequencies was $\pm2°$, $\pm4°$, $\pm6°$, $\pm8°$, and $\pm10°$ for the delta wing. For the swept and unswept wings, the reduced frequency of 0.195 and the amplitude of 8° were omitted from the tests.

The in-phase and out-of-phase yawing and rolling moments were measured for the delta wing in angle-of-attack increments of 4° from $\alpha=0°$ to $\alpha=16°$ and thereafter in 2° increments up to $\alpha=32°$. For the swept wing, these measurements were taken in increments of 4° from $\alpha=0°$ to $\alpha=20°$ and also at $\alpha=10°$, 18°, and 22°. For the unswept wing, the measurements were taken in increments of 2° from $\alpha=0°$ to $\alpha=16°$.

For each amplitude, frequency, and angle-of-attack condition, both a wind-on test and a wind-off test were made. The effects of the inertia of the model were eliminated from the data by subtracting the results of the wind-off tests from those of the wind-on tests.

The value of reduced-frequency parameter k of 0.215 (or 3.3 cycles per second) was selected because it corresponded to the reduced frequency of the tests of reference 1. The tests of reference 2 were made at lower values of the reduced frequency. In order to arrive at a better basis of comparison for frequency, the additional tests made by the method similar to that of reference 2 were for $k=0.22$ and $\beta_0=\pm6°$. These tests, however, were made by the forced-oscillation method rather than the free-oscillation method used in reference 2.

RESULTS AND DISCUSSION

PRESENTATION OF RESULTS

In figure 6 are shown the lift, drag, and pitching-moment coefficients as functions of angle of attack for the three wings tested. These data are taken from reference 2 and are for a dynamic pressure of 39.8 pounds per square foot, which is somewhat higher than the dynamic pressure used for the present tests. The static variations of rolling moment and yawing moment with sideslip angles up to $\pm10°$ are presented in figure 7 for given angles of attack. These data exhibit no extreme nonlinearities in the range of sideslip angles being considered.

The data measured during these oscillation tests are presented for the delta wing in figure 8, for the swept wing in figure 9, and for the unswept wing in figure 10. These data are for four combination lateral stability derivatives resulting from the combined oscillatory yawing and sideslipping motion employed for the tests. The derivatives are shown as functions of angle of attack for five frequencies of oscillation of the delta wing and four frequencies of oscillation for the

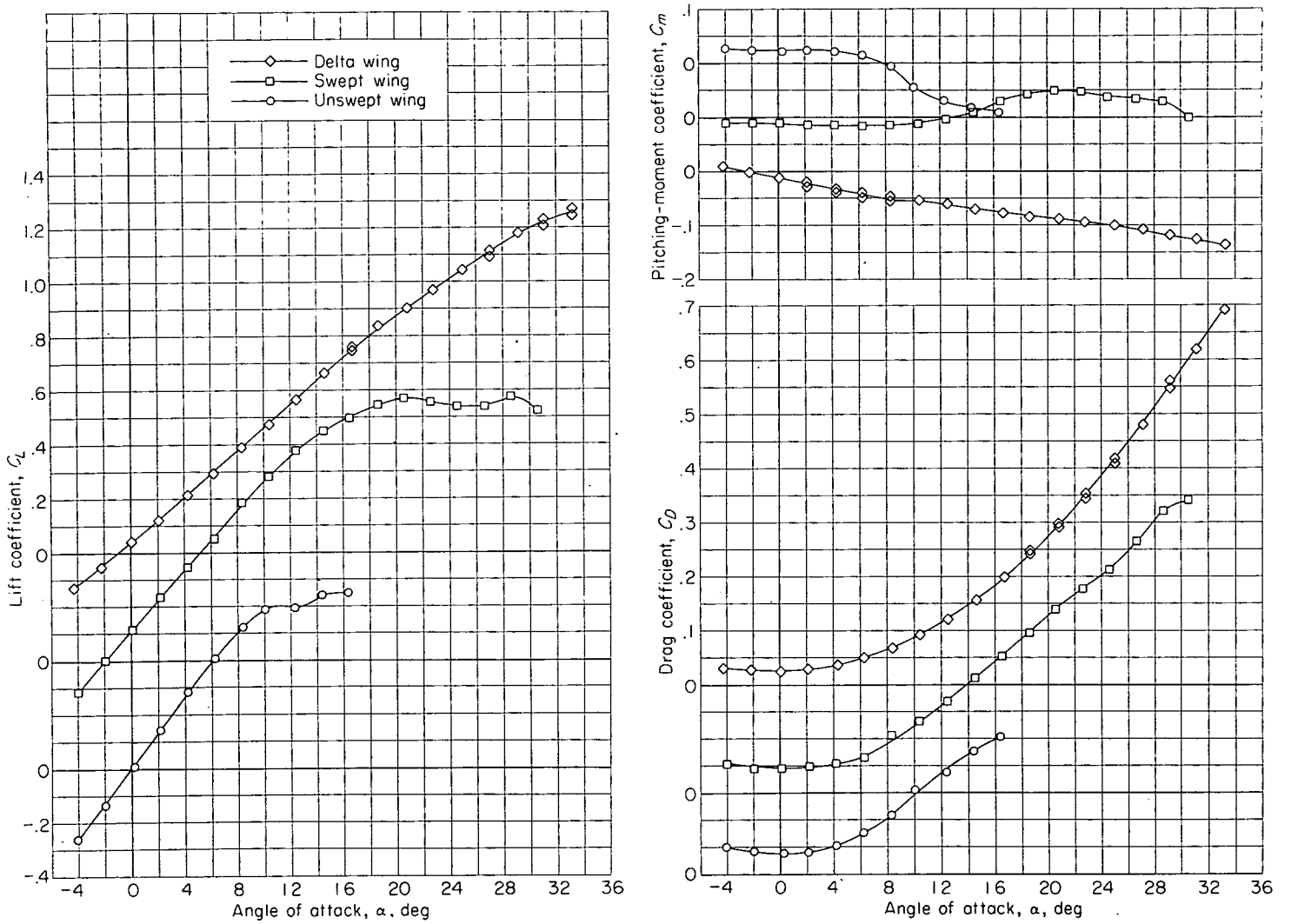


FIGURE 6.—Lift, drag, and pitching-moment characteristics as a function of angle of attack for the unswept, the 45° swept, and the 60° delta wings. $q=40$ lb/sq ft.

swept and unswept wings. Each part of figures 8, 9, and 10 presents the data for a different amplitude of oscillation from $\psi_0=\pm 2°$ to $\psi_0=\pm 10°$. In these figures the static derivatives C_{n_β} and C_{l_β} are also shown for comparison with the oscillatory derivatives $C_{n_{\beta,\omega}}+k^2C_{n_{\dot{r},\omega}}$ and $C_{l_{\beta,\omega}}+k^2C_{l_{\dot{r},\omega}}$, respectively. The static derivatives were taken from reference 2 and were measured at Reynolds numbers slightly higher than those for the present tests.

The effects of the reduced-frequency parameter k on the measured stability derivatives are shown for the three wings in figures 11 to 14. These cross-plotted data are given for four angles of attack for each wing. The measured stability derivatives are also cross-plotted as functions of amplitude of oscillation for the three wings in figures 15 to 18 for the same angles of attack given in figures 11 to 14.

In figure 19, the values of the derivative $C_{n_{r,\omega}}$ measured during the tests of reference 1 are added algebraically to the values of the derivative $C_{n_{\dot{\beta},\omega}}$ measured by means of tests similar to those of reference 2. The sums of these derivatives are compared with experimental values of $C_{n_{r,\omega}}-C_{n_{\dot{\beta},\omega}}$ for a corresponding frequency and amplitude of oscillation. Figures 20, 21, and 22 present similar comparisons for the derivatives $C_{l_{r,\omega}}-C_{l_{\dot{\beta},\omega}}$, $C_{n_{\beta,\omega}}+k^2C_{n_{\dot{r},\omega}}$, and $C_{l_{\beta,\omega}}+k^2C_{l_{\dot{r},\omega}}$, respectively.

Although the following discussion has been divided into sections on the effects of angle of attack, of frequency, and of amplitude, it should be pointed out that, because of the apparent interrelationship among all three quantities, it is not possible to isolate the discussion concerning these parameters without discussing the related quantities as well. However, each of the following sections concerns itself primarily with the effect of the parameter being considered.

EFFECT OF ANGLE OF ATTACK

In the discussion of the effects of angle of attack on the measured stability derivatives, it is convenient to separate the low range of angle of attack from the high range of angle of attack. This division takes place at $\alpha\approx 18°$ for the delta wing, at $\alpha\approx 10°$ for the swept wing, and at $\alpha\approx 8°$ for the unswept wing. These are the angles, for the respective wings, below which frequency effects appear to be relatively small and above which frequency effects are relatively large. (See figs. 8, 9, and 10.) In figure 6, these angles of attack are shown to correspond to the angles at which initial changes take place in the lift-curve slopes for each wing; this change in slope indicates that these are the angles of attack at which flow separation has begun. Reference 3 shows that the

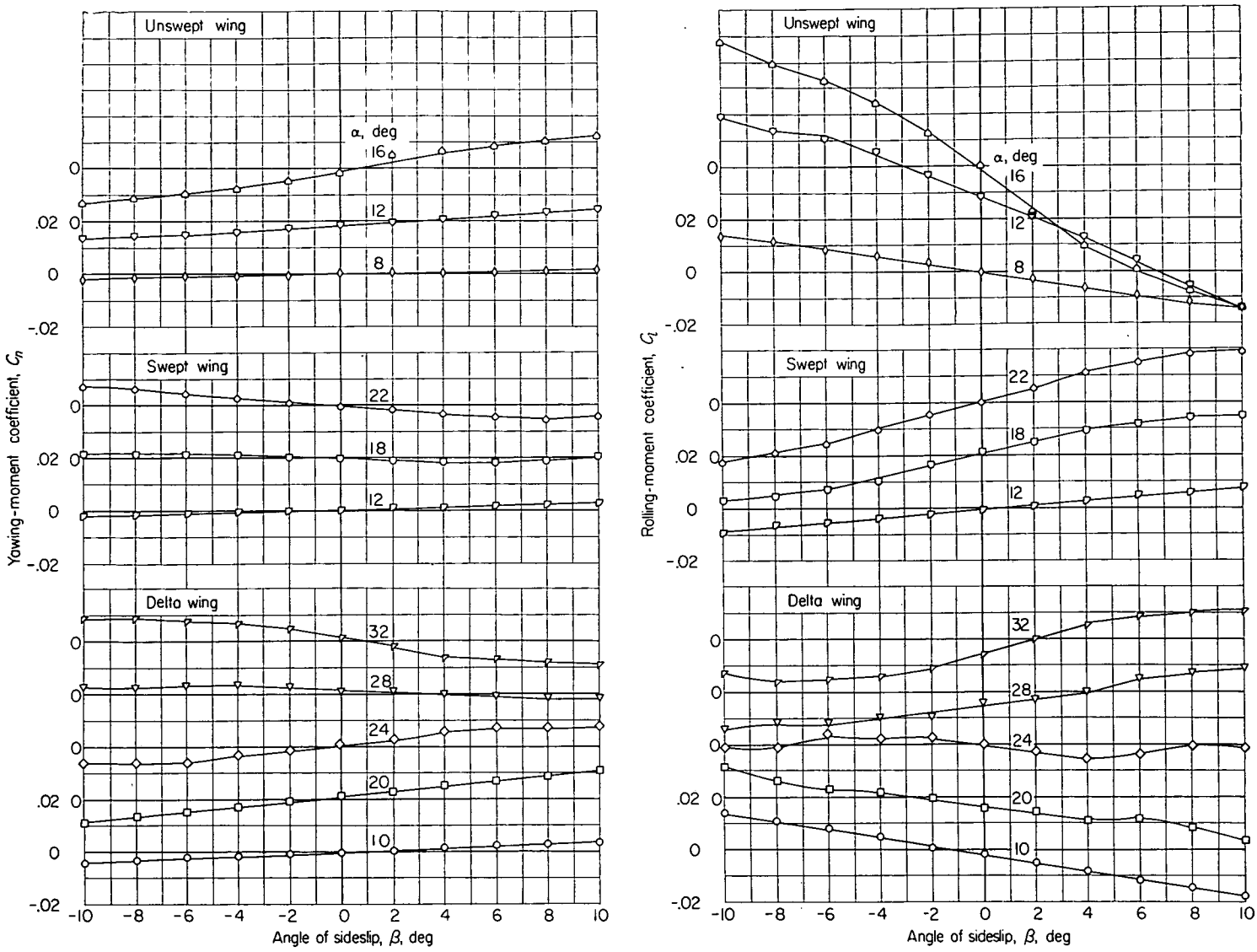


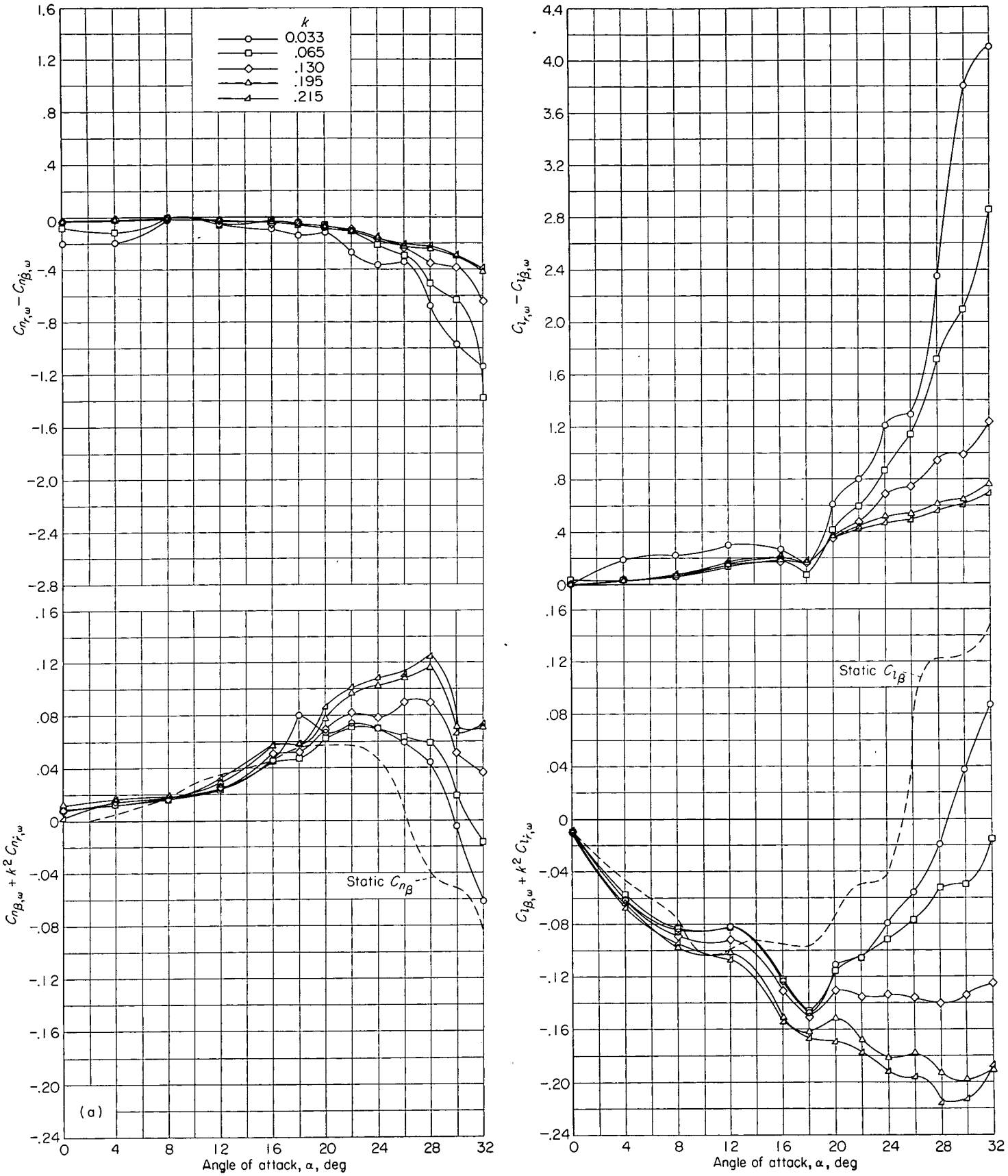
FIGURE 7.—Variation of yawing-moment and rolling-moment coefficients with angle of sideslip for $q=25$ lb/sq ft.

magnitude of these stability derivatives depends substantially upon the degree of separation present on the wing.

The data shown in figures 8, 9, and 10 are presented as functions of the nominal values of the uncorrected angle of attack. The same angles of attack corrected for jet-boundary effects are shown in figure 6. The largest effects of frequency on the stability derivatives take place in the high angle-of-attack range for each wing. At low angles of attack, a variation of reduced frequency had a slight effect on the magnitude of the derivatives but, at high angles of attack, frequency had a determining effect on the magnitude and, in some instances, on the sign of the derivatives. These results are, generally, in agreement with the effects of angle of attack and frequency presented in reference 3 for a set of wings of similar plan form as those tested for this investigation.

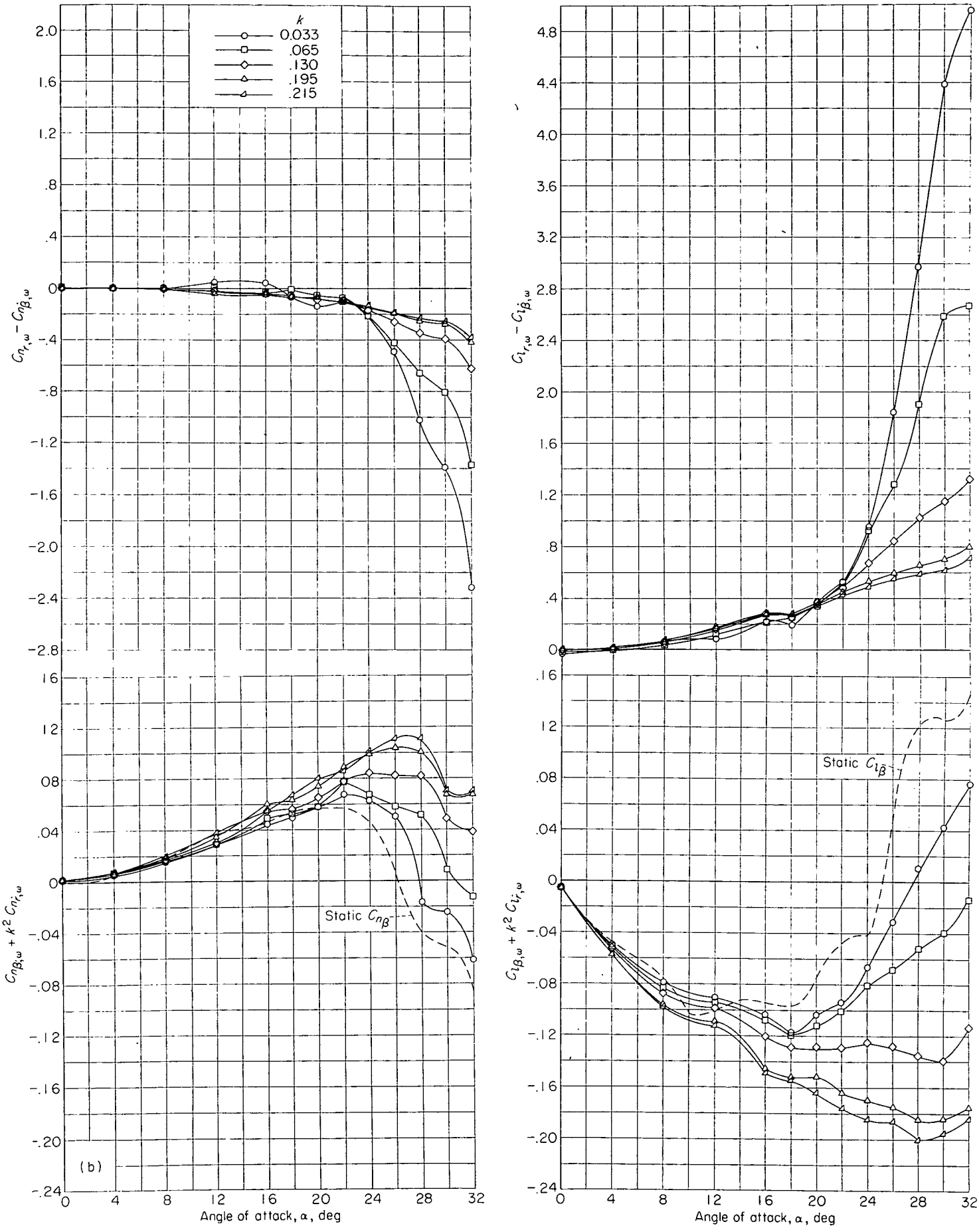
Damping in yaw.—The damping-in-yaw derivative $C_{n_{r,\omega}}-C_{n_{\dot{\beta},\omega}}$ has small negative values at low angles of attack for each of the three wings tested (figs. 8, 9, and 10). At high angles of attack, the derivative becomes large and negative for the delta and swept wings (figs. 8 and 9), with the largest negative values resulting for the lowest frequencies of oscillation. For the unswept wing (fig. 10), the derivative becomes positive at high angles of attack, with the largest positive values resulting for the lowest frequencies of oscillation. The derivatives obtained for the swept wing at its highest angle of attack are substantially smaller than those measured for the delta wing at its highest angle of attack. The absolute magnitudes of $C_{n_{r,\omega}}-C_{n_{\dot{\beta},\omega}}$ for the unswept wing are likewise much smaller than for the swept wing at the highest angle of attack for each wing.

Rolling moment due to yawing.—The parameter representative of the rolling moment due to yawing $C_{l_{r,\omega}}-C_{l_{\dot{\beta},\omega}}$ is small and generally positive at low angles of attack for the delta and swept wings (figs. 8 and 9). As the angle of attack is increased, the derivative increases positively for these wings, with the largest values being realized for the lowest frequencies of oscillation. With an increase in frequency, the derivative tends to become more nearly linear with increasing angle of attack. The magnitudes of the derivative reached for the swept wing are not so large as those for the delta wing at the highest angle of attack for each wing.



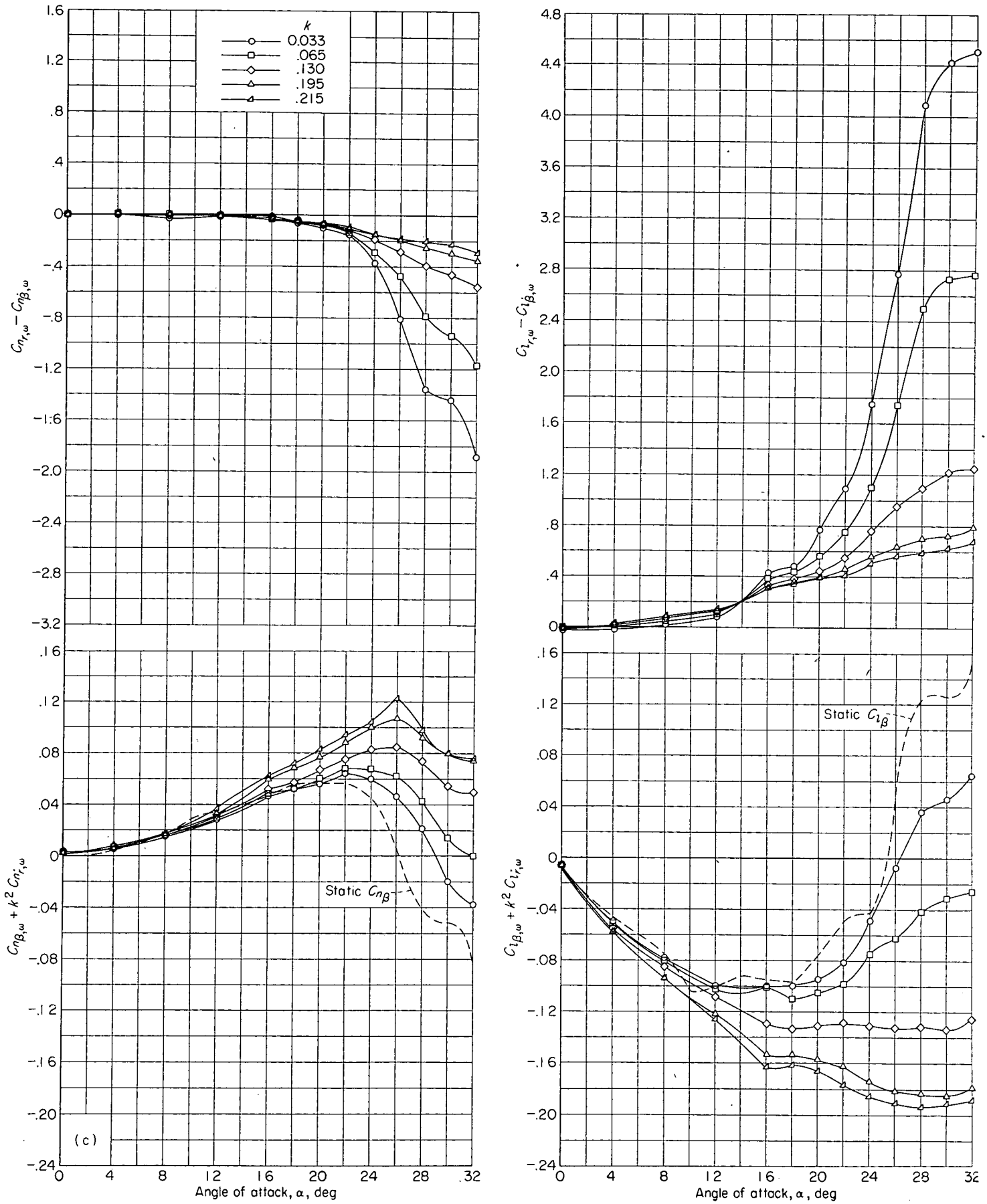
(a) $\psi_0 = \pm 2°$.

FIGURE 8.—Stability derivatives measured during oscillation for delta wing.



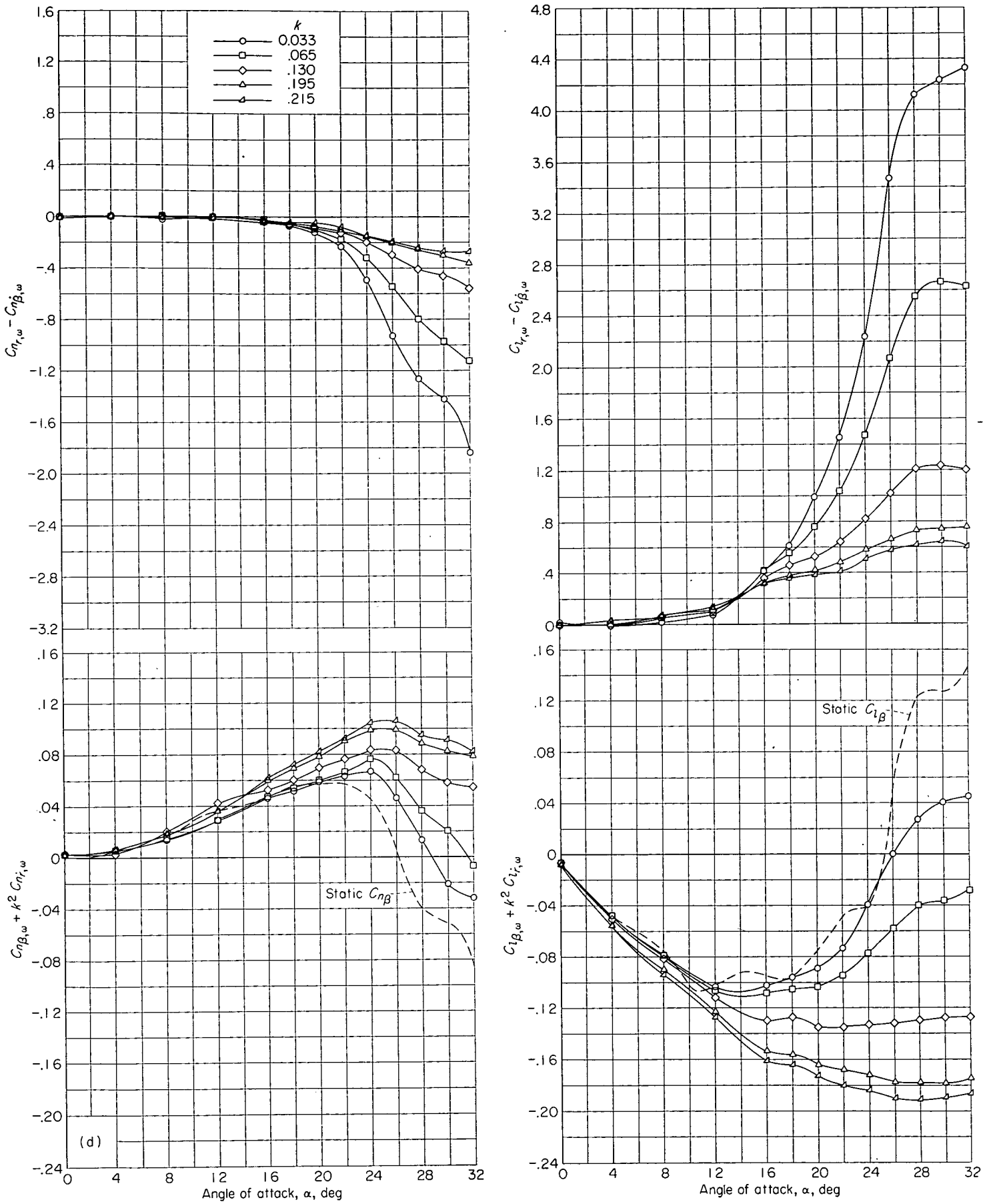
(b) $\psi_0 = \pm 4°$.

FIGURE 8.—Continued.



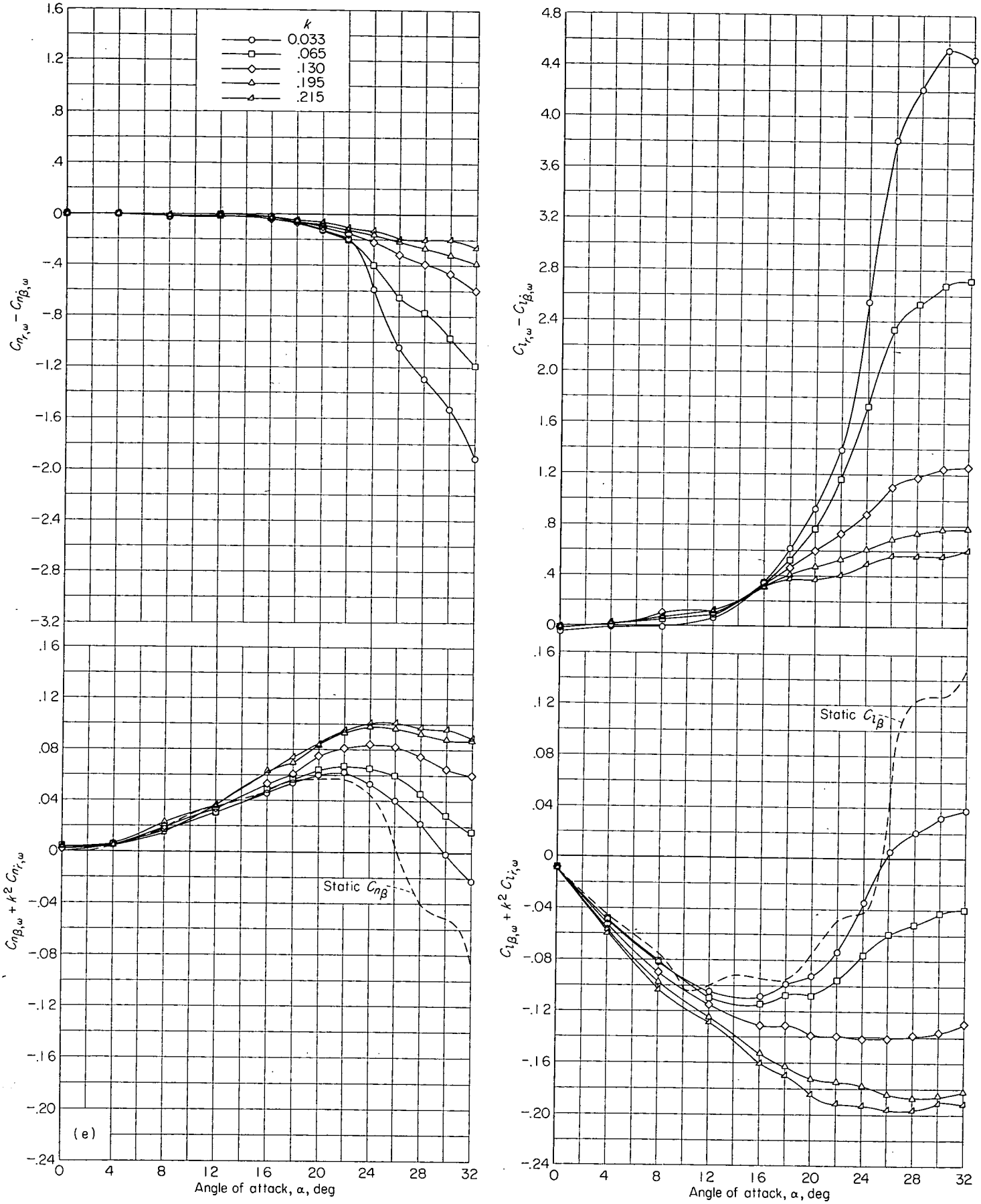
(c) $\psi_0 = \pm 6°$.

FIGURE 8.—Continued.



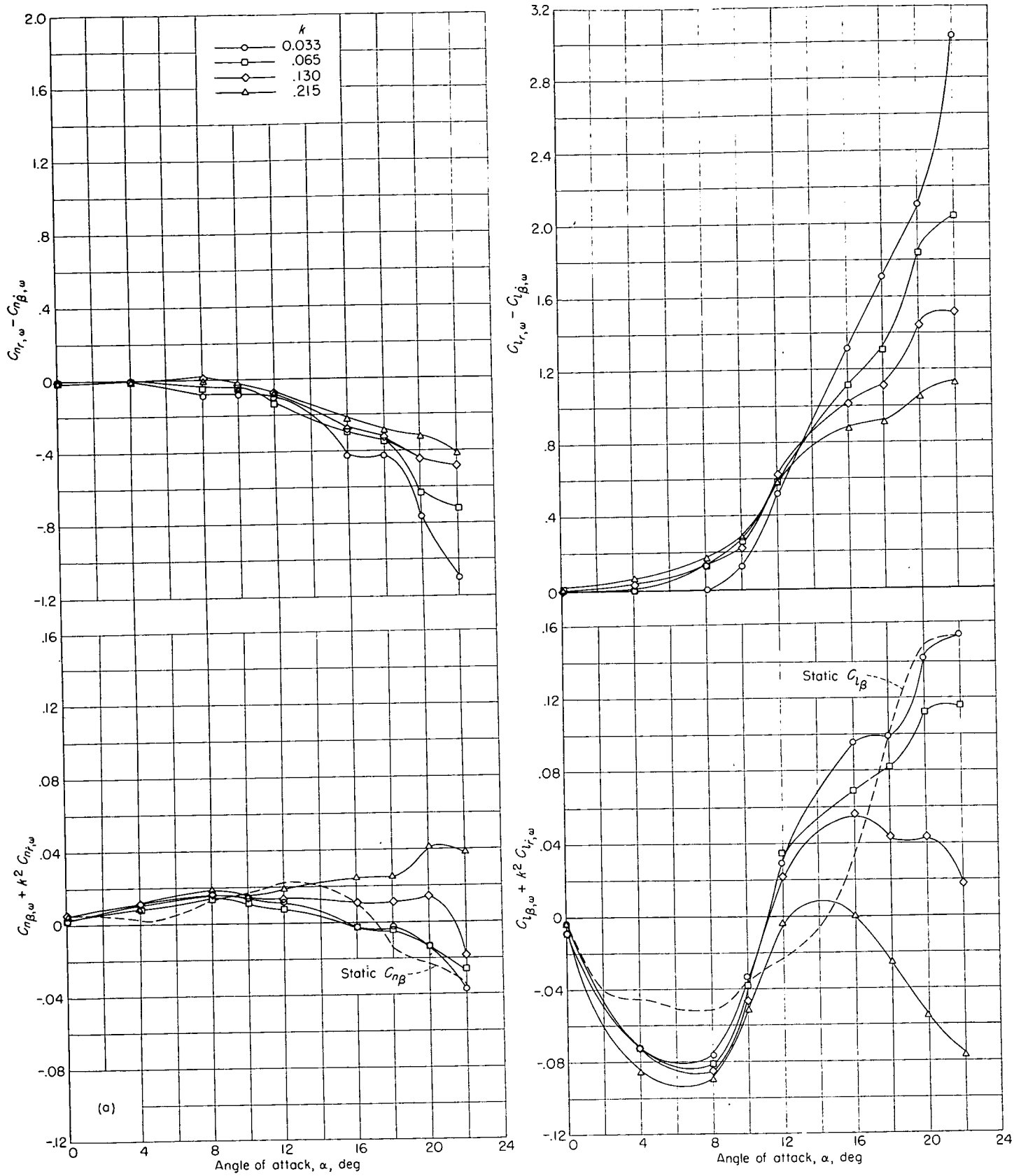
(d) $\psi_0 = \pm 8°$.

FIGURE 8.—Continued.



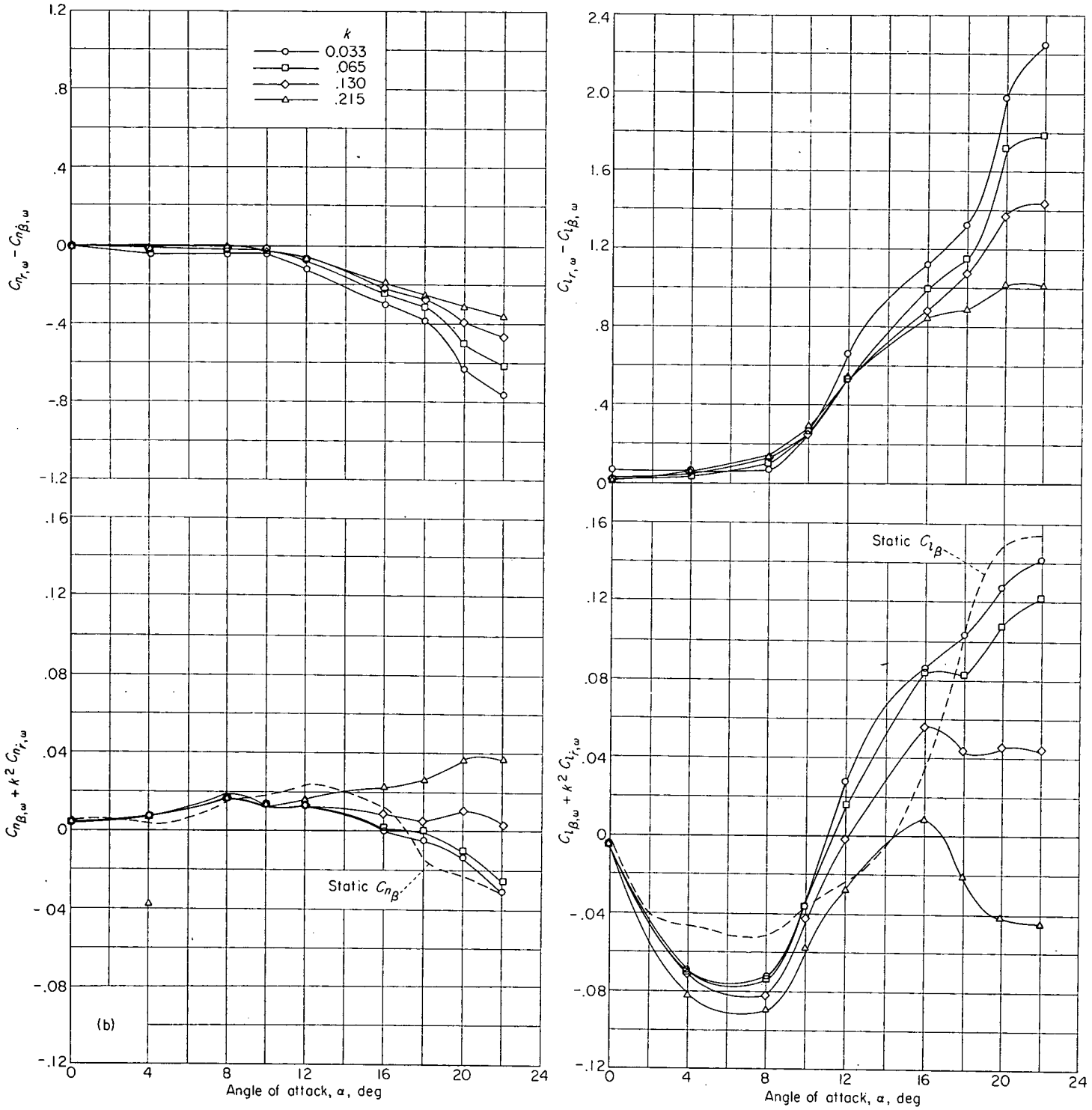
(e) $\psi_0 = \pm 10°$.

FIGURE 8.—Concluded.



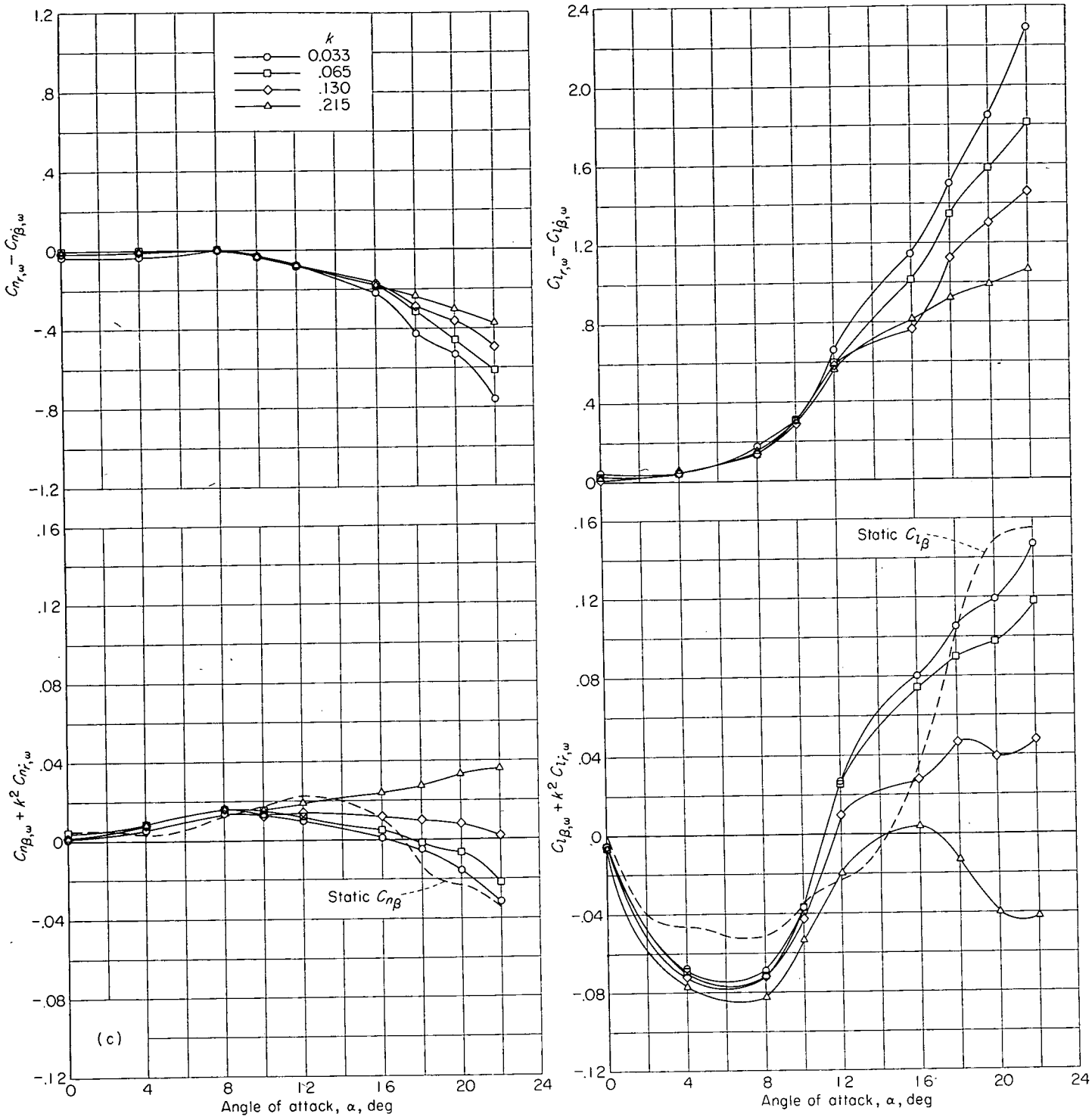
(a) $\psi_0 = \pm 2°$.

FIGURE 9.—Stability derivatives measured during oscillation for swept wing.



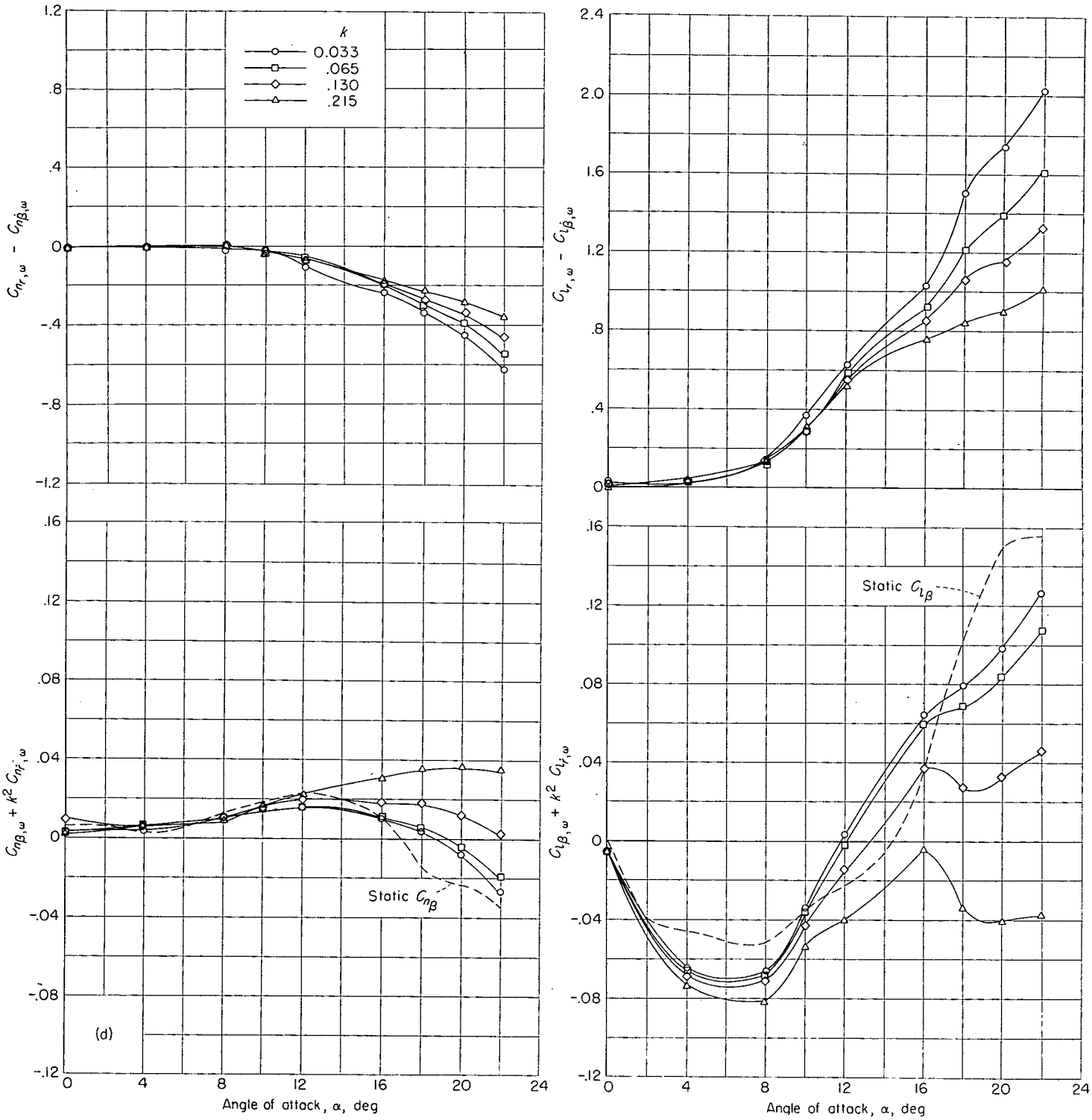
(b) $\psi_0 = \pm 4°$.

FIGURE 9.—Continued.



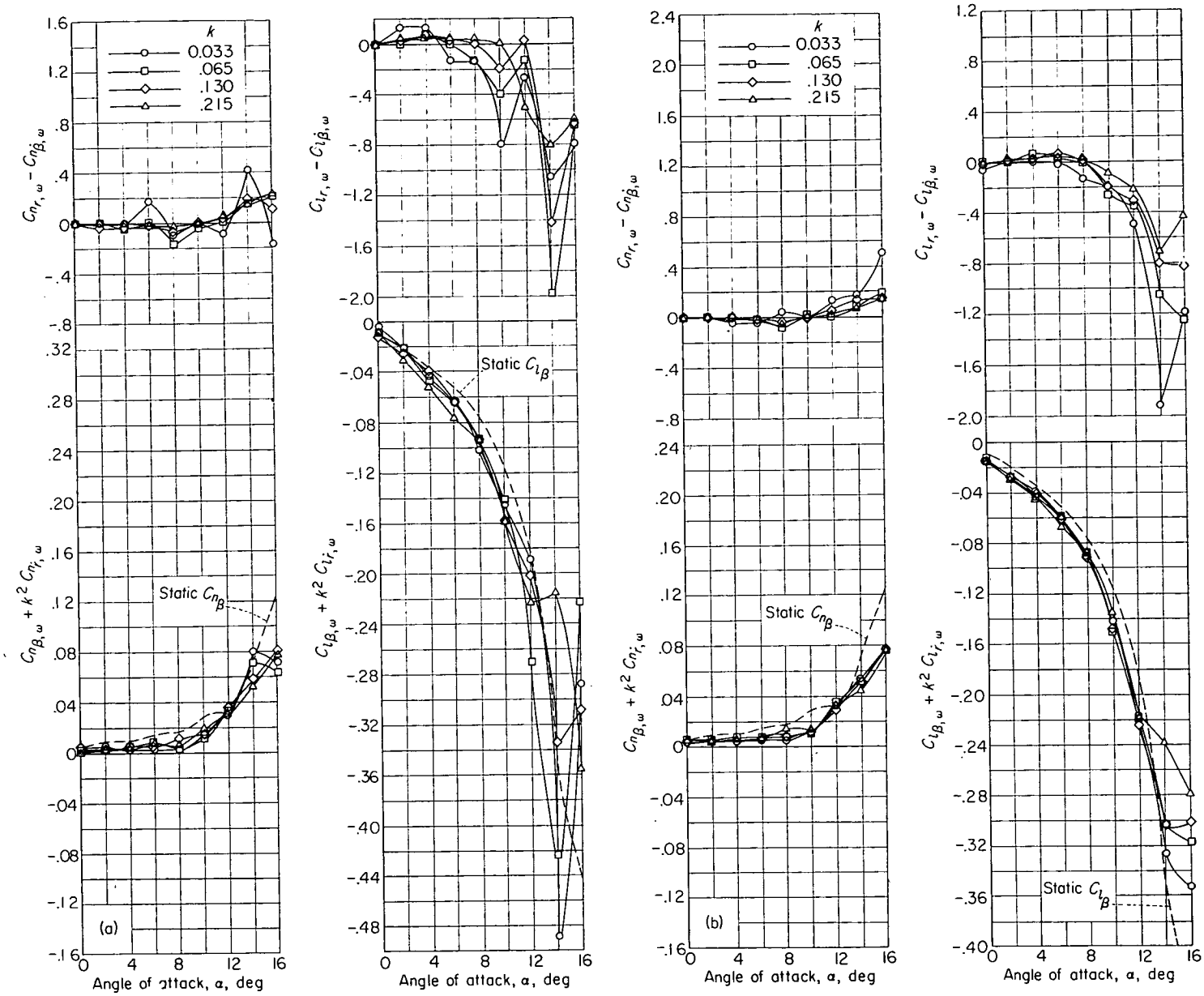
(c) $\psi_0 = \pm 6°$.

FIGURE 9.—Continued.



(d) $\psi_0 = \pm 10°$.

FIGURE 9.—Concluded.



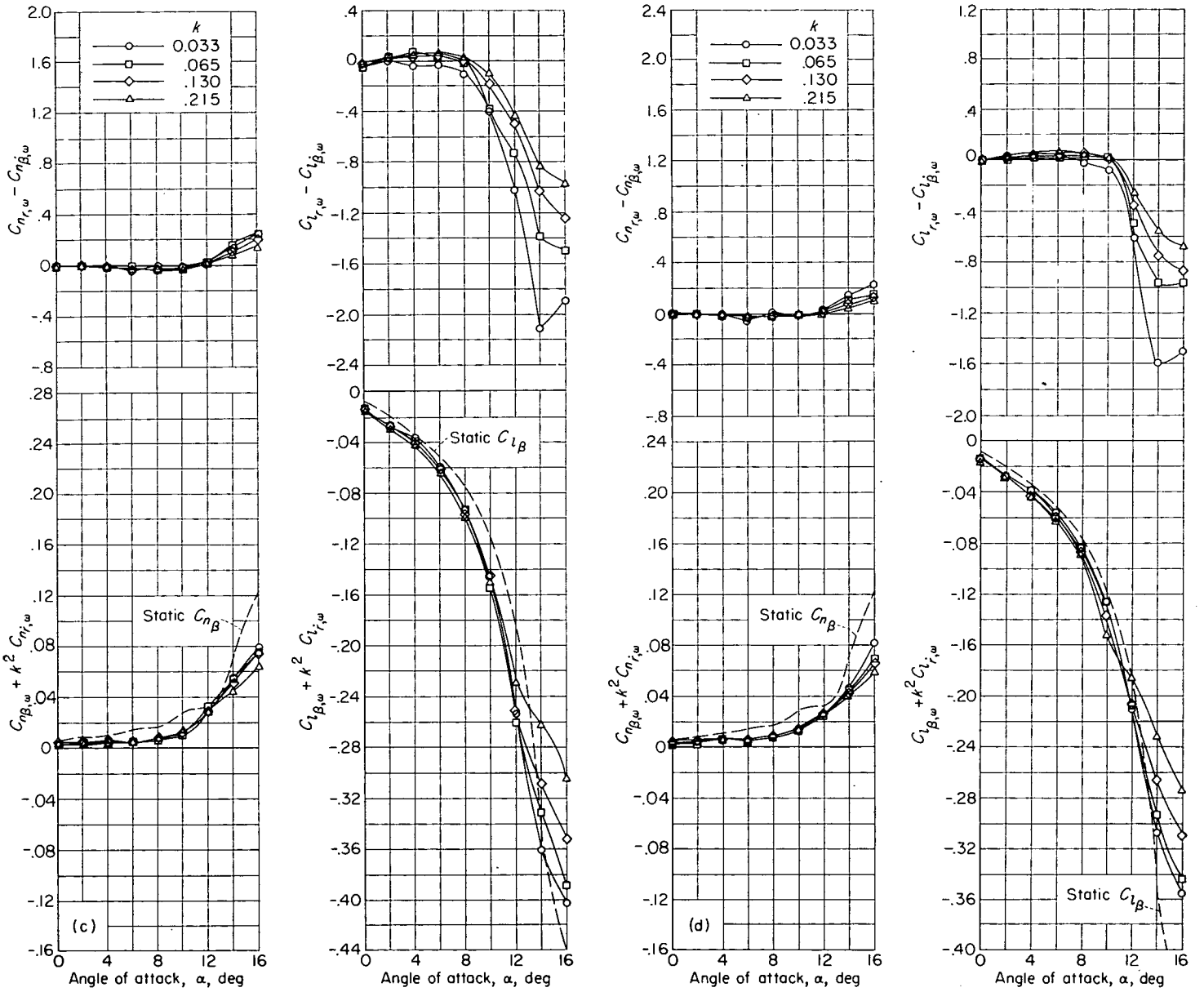
(a) $\psi_0 = \pm 2°$. (b) $\psi_0 = \pm 4°$.

FIGURE 10.—Stability derivatives measured during oscillation for unswept wing.

In the case of the unswept wing (fig. 10), $C_{l_{r,\omega}} - C_{l_{\dot{\beta},\omega}}$ is generally small and positive at low angles of attack, except for perhaps the lowest frequency of oscillation for which some small negative values were measured. At high angles of attack, $C_{l_{r,\omega}} - C_{l_{\dot{\beta},\omega}}$ for the unswept wing becomes large and negative with the magnitude of the derivative again depending upon frequency. At $\alpha = 14°$ for this wing, the variation of the derivative with angle of attack tends to reverse itself. At this angle of attack, figure 6 indicates this wing to be completely stalled.

Directional stability.—The directional-stability parameter $C_{n_{\beta,\omega}} + k^2 C_{n_{\dot{r},\omega}}$ for the delta and the swept wings is positive and increases with angle of attack at low angles of attack (figs. 8 and 9). At the high angles of attack, and for the lowest frequencies of oscillation, the derivative decreases and, for certain conditions, reverses sign and becomes negative. The higher frequencies reduce this trend toward the negative direction and make the variation of the derivative with angle of attack more nearly linear. The derivative for the unswept wing is a small positive value at low angles of attack and increases positively as the angle of attack is increased through the high range (fig. 10). Frequency has only a small effect on this derivative for this wing at high angles of attack but, again, the lower test frequencies produce the largest values of the derivative.

The values of the static derivative C_{n_β} are also shown in figures 8, 9, and 10 for comparison with the oscillatory values of $C_{n_{\beta,\omega}} + k^2 C_{n_{\dot{r},\omega}}$. These static derivatives were measured for the investigation of reference 2 at slightly higher Reynolds numbers than those for the present tests. The values of



(c) $\psi_0 = \pm 6°$. (d) $\psi_0 = \pm 10°$.

FIGURE 10.—Concluded.

C_{n_β} exhibit the same trend with angle of attack as is shown by the oscillatory derivative at the lowest frequencies.

Effective dihedral.—The effective dihedral parameter $C_{l_{\beta,\omega}} + k^2 C_{l_{\dot{r},\omega}}$ is negative at zero angle of attack and increases negatively as the angle of attack is increased in the low angle-of-attack range for all three wings. For the delta and swept wings (figs. 8 and 9), the variation with angle of attack tends to reverse itself at high values of α and, for the lowest frequencies of oscillation, the reversal causes a definite reduction in the derivative and a change of sign under certain conditions. As the frequency is increased, the derivative tends to become more nearly linear with angle of attack, at least for the delta wing (fig. 8). In the case of the swept wing (fig. 9), the derivative becomes positive at high angles of attack for all frequencies with the possible exception of the highest frequency for which the derivative approaches zero magnitude at $\alpha \approx 16°$ and then increases in the negative direction at higher angles of attack. The derivative for the unswept wing continues increasing in the negative direction as the angle of attack is increased to its largest value (fig. 10). The largest negative values of the derivative were obtained for the lowest frequency of oscillation.

The values of the static derivative C_{l_β} from reference 2 are shown in figures 8, 9, and 10 for comparison with the oscillatory derivatives $C_{l_{\beta,\omega}} + k^2 C_{l_{\dot{r},\omega}}$. The static values of C_{l_β} had about the same variation with angle of attack as is shown by the oscillatory derivatives. The change of sign of C_{l_β} for the swept wing occurred at a somewhat higher angle of attack than it did for the oscillatory deriviatve.

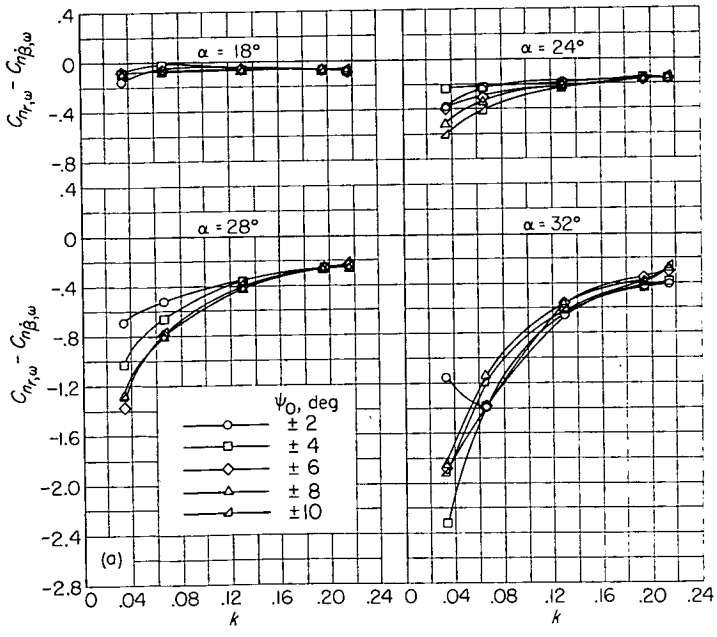
Check tests, however, indicated that the proper Reynolds number would shift this angle of attack to the lower value shown by the oscillation data.

EFFECT OF FREQUENCY

Damping in yaw.—The effect of frequency on the damping in yaw $C_{n_{r,\omega}}-C_{n_{\dot{\beta},\omega}}$ is shown in figure 11 for the delta, swept, and unswept wings. These cross plots are presented for four angles of attack for each wing and for all amplitudes of oscillation. At $\alpha=18°$ for the delta wing, frequency has little or no effect on the damping (fig. 11 (a)) but, for each succeedingly higher angle of attack, the effect of frequency is to make the overall variation of $C_{n_{r,\omega}}-C_{n_{\dot{\beta},\omega}}$ greater as the angle of attack is increased. The largest values of the derivative result for the smallest values of the reduced frequency for each angle of attack. For the swept wing (fig. 11 (b)), frequency has only a slight effect on the derivative at $\alpha=18°$ and a somewhat larger effect at $\alpha=22°$. These curves show trends with frequency similar to those for the delta wing with the difference being that the frequency effects are much smaller. The results for the unswept wing in figure 11 (c), in general, indicate no frequency effects on $C_{n_{r,\omega}}-C_{n_{\dot{\beta},\omega}}$ up to the highest angle of attack at which tests were made.

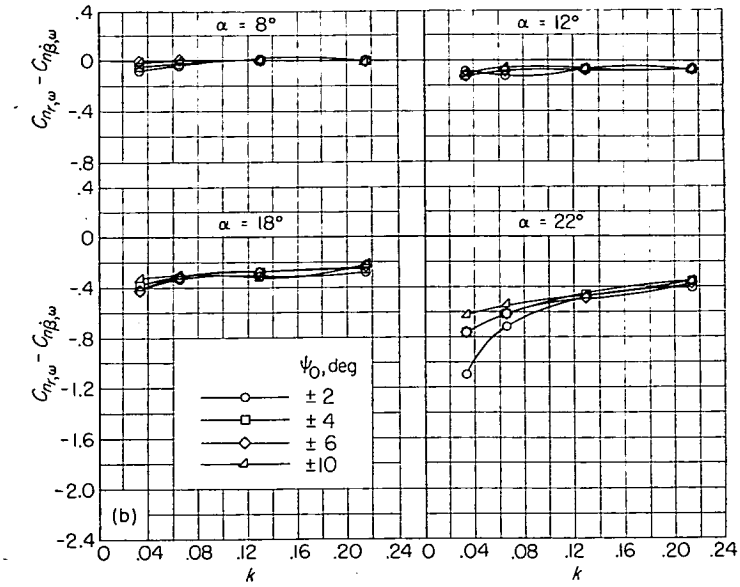
Rolling moment due to yawing.—The parameter for the rolling moment due to yawing $C_{l_{r,\omega}}-C_{l_{\dot{\beta},\omega}}$ is shown as a function of reduced frequency in figure 12 for the three wings. There is little effect of frequency indicated for the delta wing at $\alpha=18°$ but, as the angle of attack increases thereafter, the variation due to frequency became greater for each successive angle of attack. The largest effects of frequency were found at the lower frequencies of oscillation for each angle of attack.

A small frequency effect on the derivative is indicated for the swept wing in figure 12 (b) at $\alpha=18°$ and a somewhat larger effect at $\alpha=22°$. These changes due to frequency



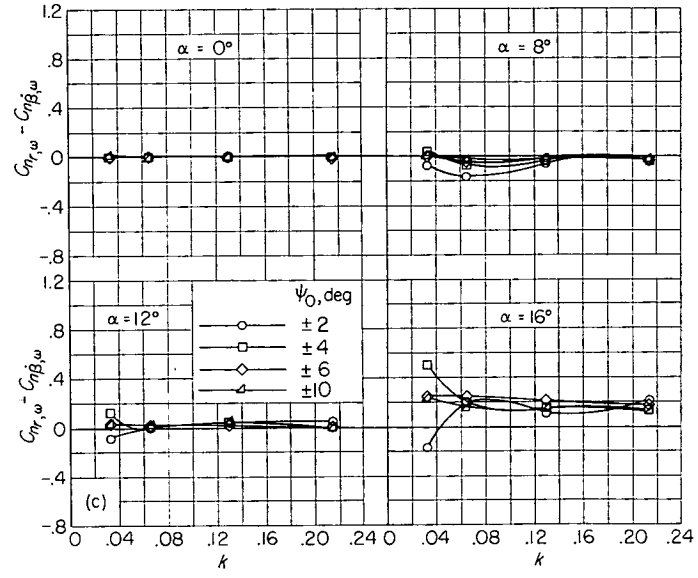
(a) Delta wing.

FIGURE 11.—The effect of reduced-frequency parameter on damping in yaw.



(b) Swept wing.

FIGURE 11.—Continued.

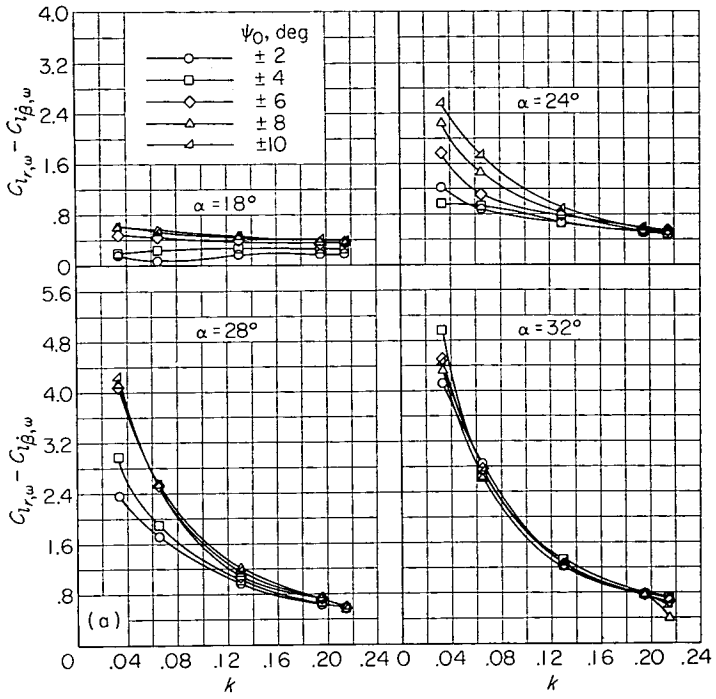


(c) Unswept wing.

FIGURE 11.—Concluded.

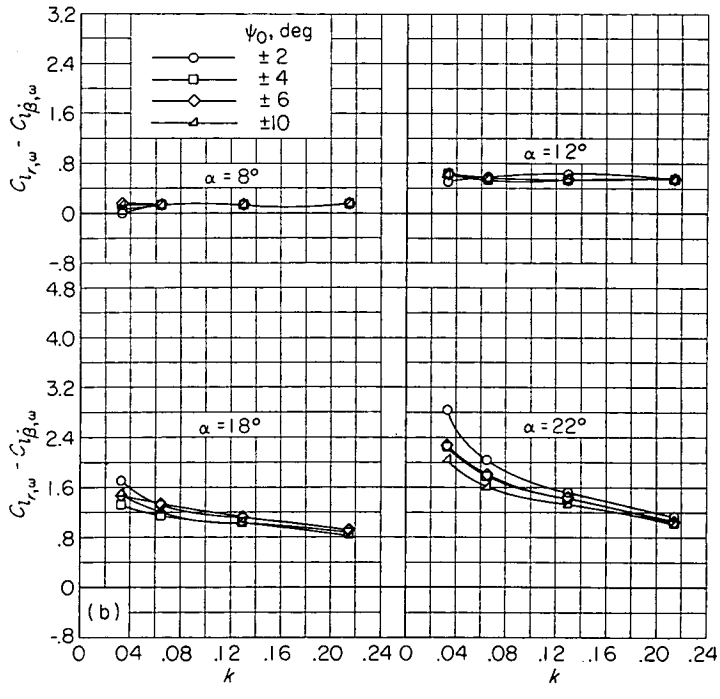
are similar to but are much smaller than those indicated for the delta wing in figure 12 (a). The unswept wing in figure 12 (c) exhibits values of $C_{l_{r,\omega}}-C_{l_{\dot{\beta},\omega}}$ which vary slightly with frequency at the two higher angles of attack in a manner opposite to the variations shown by the delta and swept wings. The derivative becomes less negative as the frequency is increased rather than more negative as in the plots for the delta and swept wings.

Directional stability.—The derivative $C_{n_{\beta,\omega}}+k^2C_{n_{\dot{r},\omega}}$ is shown in figure 13 as a function of the reduced frequency for four angles of attack for each of the three wings. As the frequency parameter is increased from its lowest value at $\alpha=18°$ for the delta wing (fig. 13 (a)), a slight positive increase in the derivative occurs. This effect of frequency becomes larger at the higher angles of attack until, at $\alpha=32°$, $C_{n_{\beta,\omega}}+k^2C_{n_{\dot{r},\omega}}$ may be either negative (at the lowest frequencies) or positive depending on the frequency. For



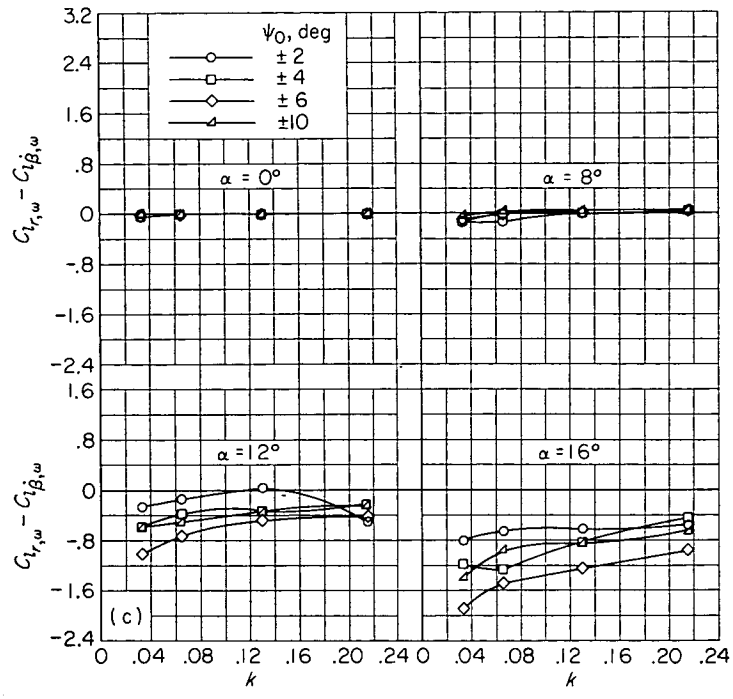
(a) Delta wing.

FIGURE 12.—The effect of reduced-frequency parameter on rolling moment due to yawing.



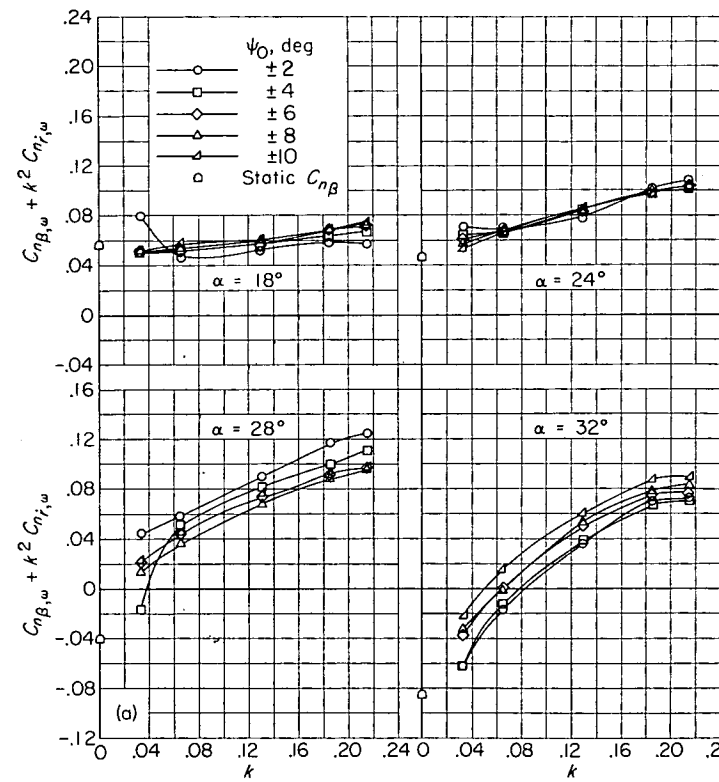
(b) Swept wing.

FIGURE 12.—Continued.



(c) Unswept wing.

FIGURE 12.—Concluded.



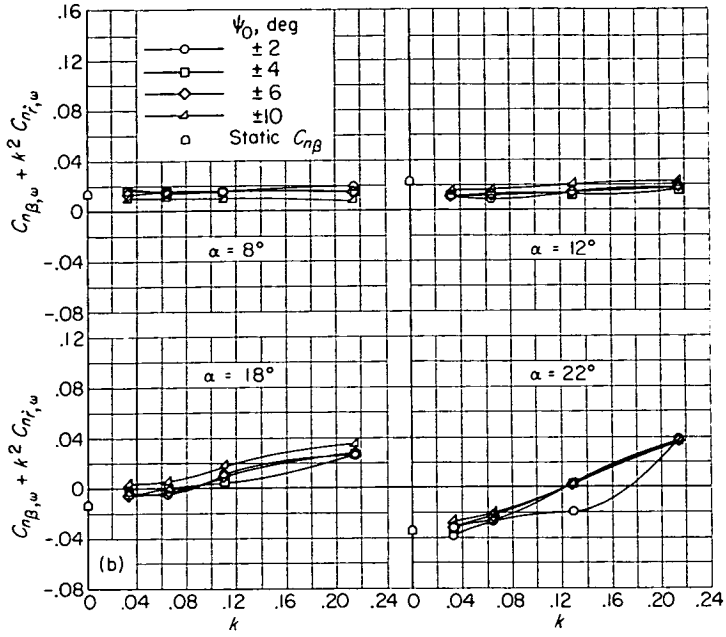
(a) Delta wing.

FIGURE 13.—The effect of reduced-frequency parameter on directional-stability derivative.

the swept wing in figure 13 (b), the directional stability varies with frequency at the higher angles of attack in the manner of, but not as much as for, the delta wing. No particular effects of frequency on this derivative are indicated for the unswept wing in figure 13 (c) at any angle of attack.

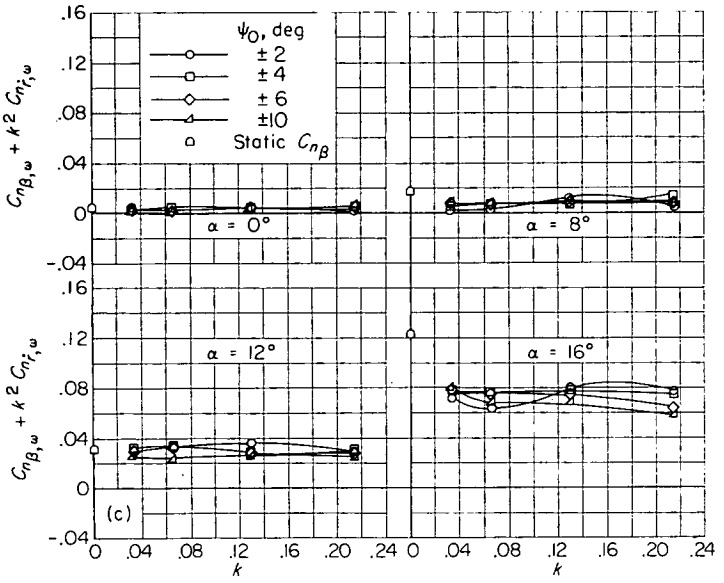
The values of the static stability derivative C_{n_β} appear in figure 13 as the value of $C_{n_{\beta,\omega}}+k^2C_{n_{\dot{r},\omega}}$ for $k=0$. In general, the variation of the oscillatory derivative with the frequency parameter approaches the static C_{n_β} for each angle of attack for all wings. This approach to zero frequency appears to be somewhat smoother for the larger amplitudes of oscillation than for the smaller amplitudes.

Effective dihedral.—The effect of the frequency parameter on $C_{l_{\beta,\omega}}+k^2C_{l_{\dot{r},\omega}}$ is shown in figure 14. The frequency effect



(b) Swept wing.

FIGURE 13.—Continued.

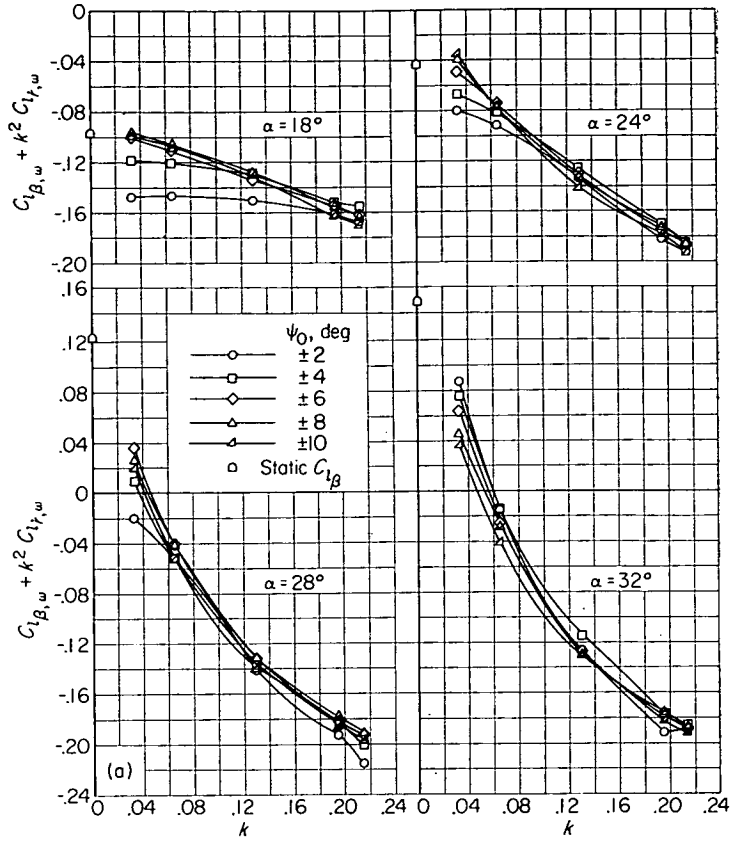


(c) Unswept wing.

FIGURE 13.—Concluded.

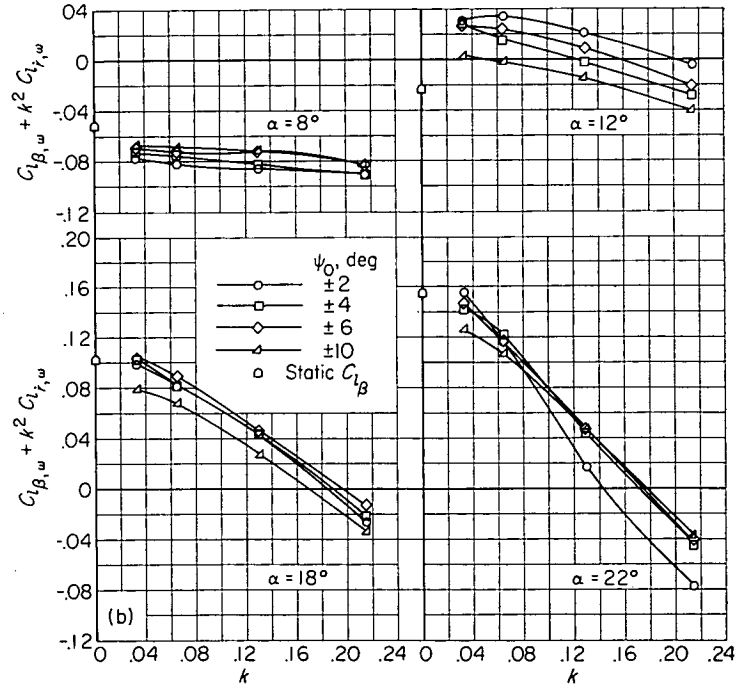
that is indicated at $\alpha=18°$ for the delta wing (fig. 14 (a)) becomes larger for each angle as the angle of attack is increased. At high frequencies of oscillation, the derivative has about the same magnitude regardless of the angle of attack but, at the low frequencies, the derivative becomes more nearly positive as the angle of attack grows larger. For the two highest angles of attack, the derivative becomes positive at the lowest frequency of oscillation.

The results for the swept wing in figure 14 (b) indicate that the effective dihedral derivative generally has higher positive values than for the delta wing but that the effect of frequency is roughly the same. The unswept wing in figure 14 (c) shows little effect of frequency except at $\alpha=16°$ where the frequency effect appears to be somewhat dependent upon amplitude of oscillation. For the largest amplitudes, the derivative becomes less negative as the frequency is



(a) Delta wing.

FIGURE 14.—The effect of reduced-frequency parameter on effective-dihedral derivative.

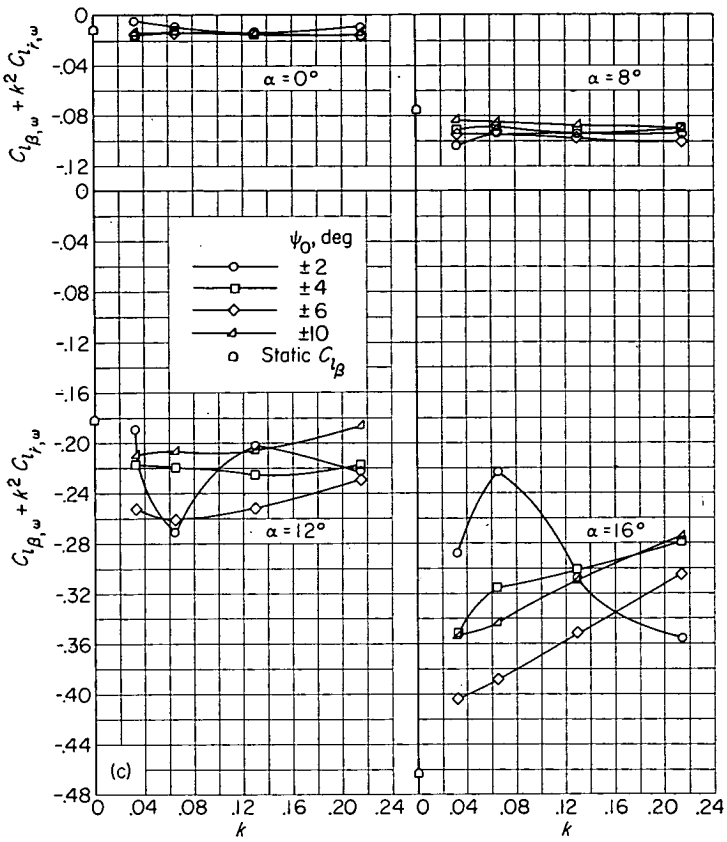


(b) Swept wing.

FIGURE 14.—Continued.

increased; for the smallest amplitude, however, the derivative in general becomes more negative at the higher frequencies of oscillation.

The extreme nonlinearities which occur, particularly for low-frequency and small-amplitude oscillations such as are shown for the unswept wing in figure 14 (c), may be at least



(c) Unswept wing.

FIGURE 14.—Concluded.

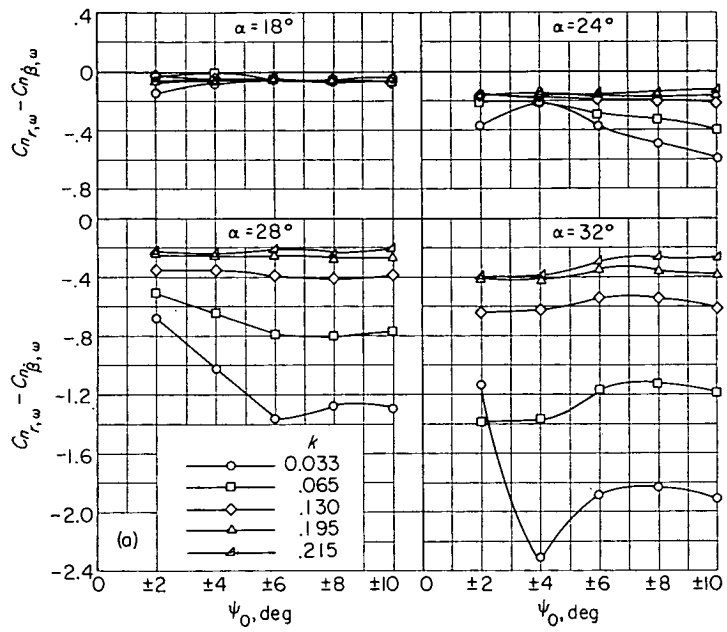
partially the fault of the data-reduction process employed. Because the measured moments were divided by the frequency and the amplitude in order to evolve the derivative form, small errors of measurement tend to be exaggerated for low-frequency and small-amplitude conditions of oscillation.

The oscillatory values of $C_{l_{\beta,\omega}}+k^2C_{l_{\dot{r},\omega}}$, in general, tend to approach the static values of C_{l_β} for all wings, especially for the higher amplitudes of oscillation. The static C_{l_β} is shown in figure 14 as the $k=0$ value of the oscillation derivative.

EFFECT OF AMPLITUDE

The effect of the variation of amplitude on the oscillatory derivatives under consideration is not as clear cut or consistent as is the effect previously discussed of the variation of frequency. The amplitude effects that appear in the data are interdependent with both frequency and angle of attack in that certain trends with amplitude may appear at one angle or one range of amplitude variation, whereas reverse trends may appear at a slightly different angle of attack or another range of the amplitude variation.

Damping in yaw.—The effects of amplitude ψ_0 on the damping-in-yaw derivative $C_{n_{r,\omega}}-C_{n_{\dot{\beta},\omega}}$ are presented in figure 15. When amplitude effects on the damping in yaw do occur, they appear to be most important at the lowest values of k. For those angles of attack at which an amplitude effect is in evidence, this effect diminishes as the k is increased and generally disappears at the highest frequencies. For example, in figure 15 (a) where $C_{n_{r,\omega}}-C_{n_{\dot{\beta},\omega}}$ is shown as a function of oscillation amplitude for the delta wing, certain effects of amplitude are indicated. For the

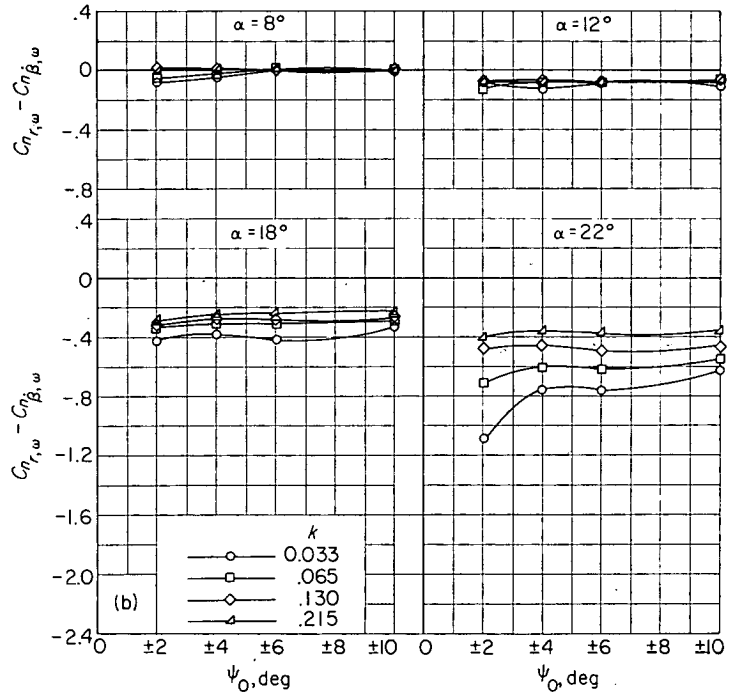


(a) Delta wing.

FIGURE 15.—The effect of amplitude on damping-in-yaw derivative.

lowest frequency ($k=0.033$) at $\alpha=18°$ a slight reduction in damping takes place as the amplitude is increased from $\psi_0=2°$ to $\psi_0=6°$, but as the amplitude is increased further the damping remains constant. At $\alpha=24°$ for the lowest frequency, the damping increases as the amplitude becomes larger than 4°, whereas at $\alpha=28°$ and $\alpha=32°$ the damping generally increases at low amplitudes but decreases and then levels off at the larger amplitudes. Higher frequencies of oscillation tend to diminish the amplitude effect until at the highest frequency the damping shows a variation with amplitude only at $\alpha=32°$, and this effect is small.

The swept wing in figure 15 (b) exhibits an effect of amplitude on the damping only at $\alpha=22°$ for the lower frequencies

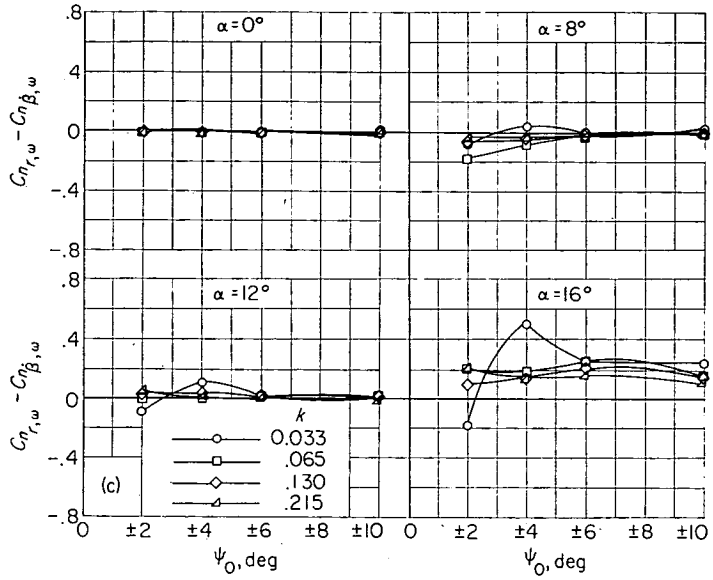


(b) Swept wing.

FIGURE 15.—Continued.

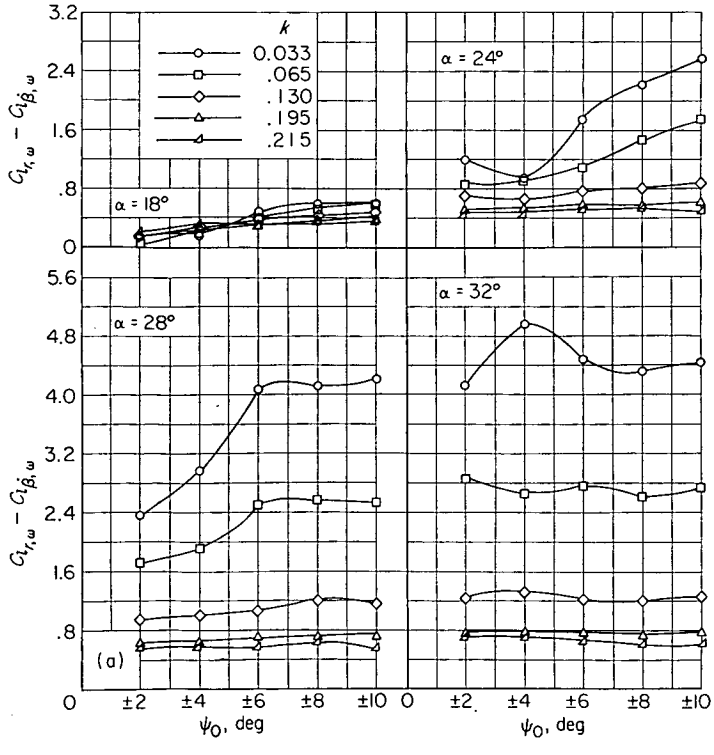
of oscillation. The unswept wing in figure 15 (c) shows some effects at low frequencies and small amplitudes of oscillation.

Rolling moment due to yawing.—The effects of the oscillation amplitude ψ_0 on $C_{l_{r,\omega}}-C_{l_{\dot{\beta},\omega}}$, which are indicated in figure 16, are similar to those described for $C_{n_{r,\omega}}-C_{n_{\dot{\beta},\omega}}$. For the delta wing at $\alpha=18°$, the derivative has higher positive values with increased amplitude, although as the frequency is increased, this effect is diminished. At $\alpha=24°$, the greatest change in the derivative takes place at the large amplitudes and the lowest frequency, whereas at $\alpha=28°$, the greatest change takes place at the small amplitudes and the lowest frequency.



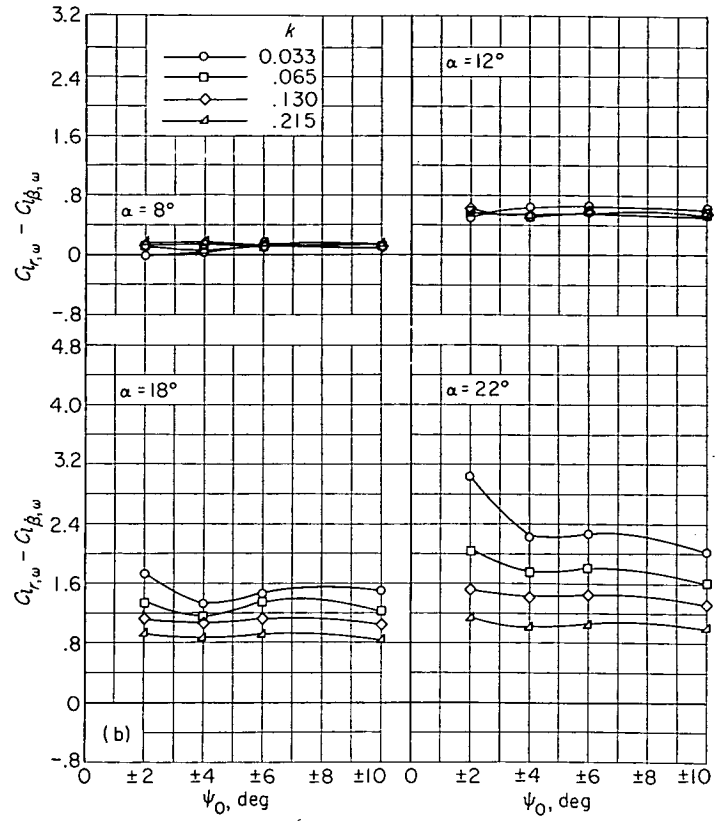
(c) Unswept wing.

FIGURE 15.—Concluded.



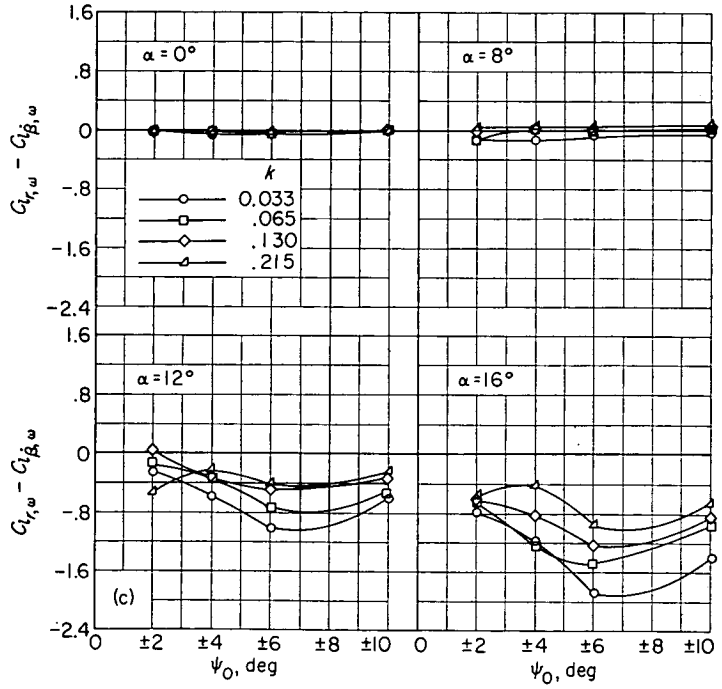
(a) Delta wing.

FIGURE 16.—The effect of amplitude on rolling moment due to yawing.



(b) Swept wing.

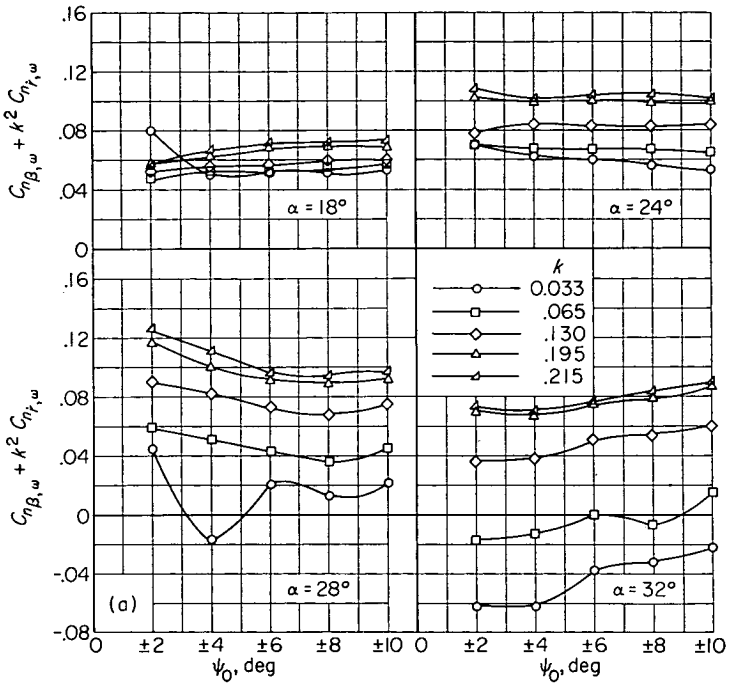
FIGURE 16.—Continued.



(c) Unswept wing.

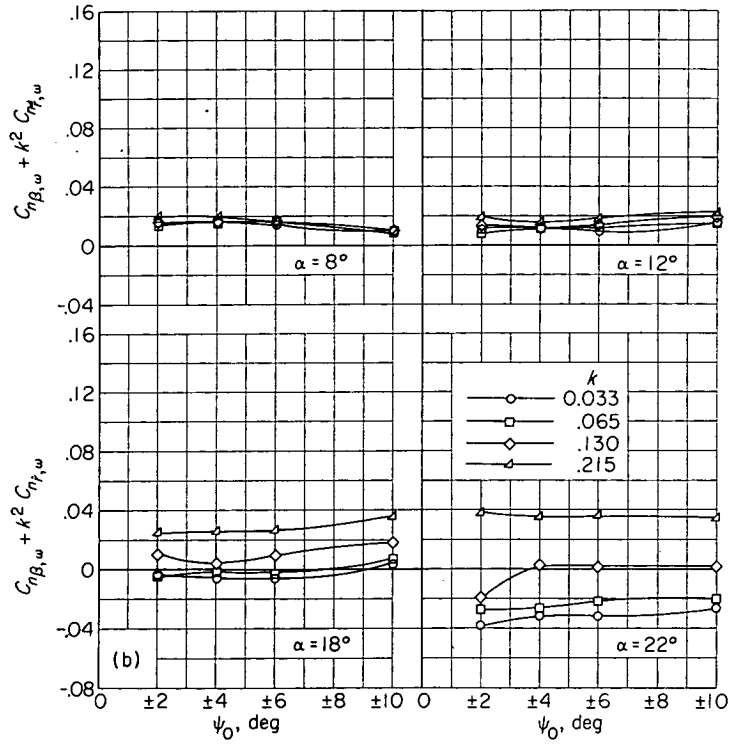
FIGURE 16.—Concluded.

Directional stability.—The variation of the directional-stability derivative $C_{n_{\beta,\omega}}+k^2C_{n_{\dot{r},\omega}}$ with amplitude is shown in figure 17. The delta wing (fig. 17 (a)) exhibits amplitude effects for all frequencies of oscillation at $\alpha=28°$ and $\alpha=32°$ which are about equal in magnitude but opposite in direction. At $\alpha=28°$, an increase in amplitude generally reduces the derivative, whereas at $\alpha=32°$, an increase in amplitude increases the positive values of the derivative.



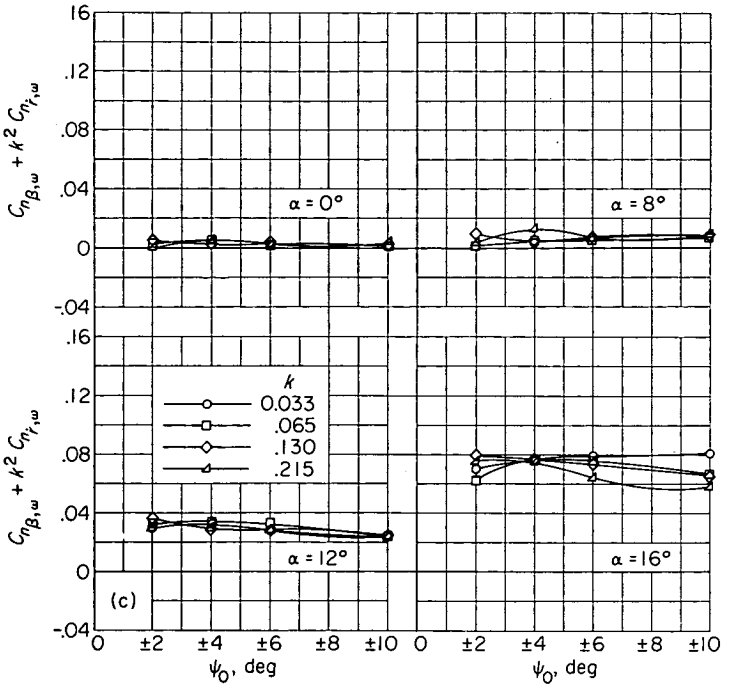
(a) Delta wing.

FIGURE 17.—The effect of amplitude on directional-stability derivative.



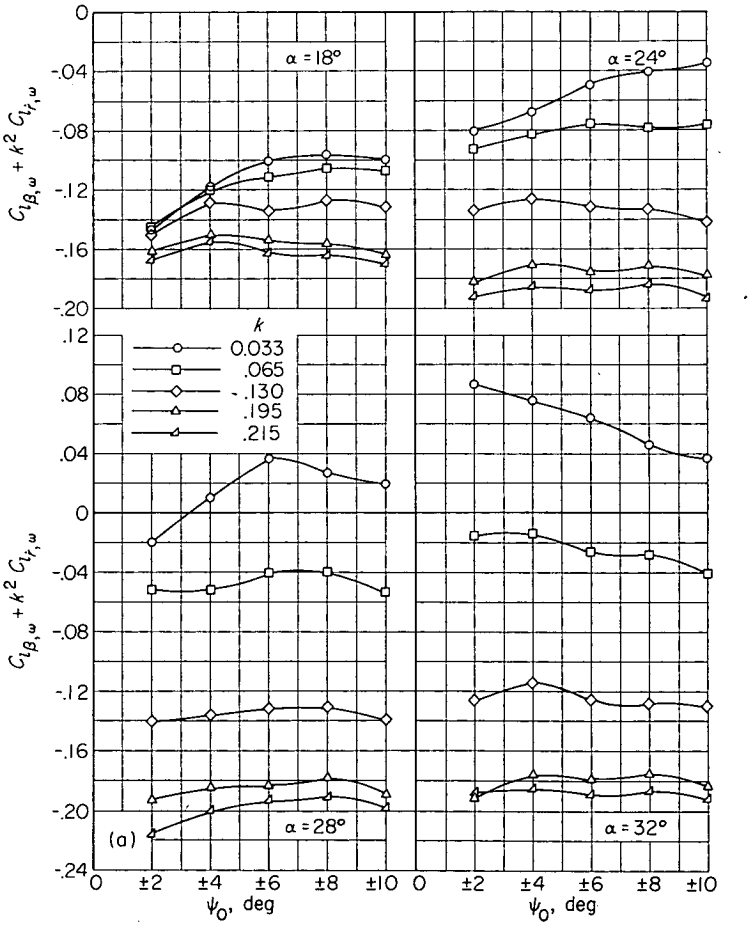
(b) Swept wing.

FIGURE 17.—Continued.



(c) Unswept wing.

FIGURE 17.—Concluded.

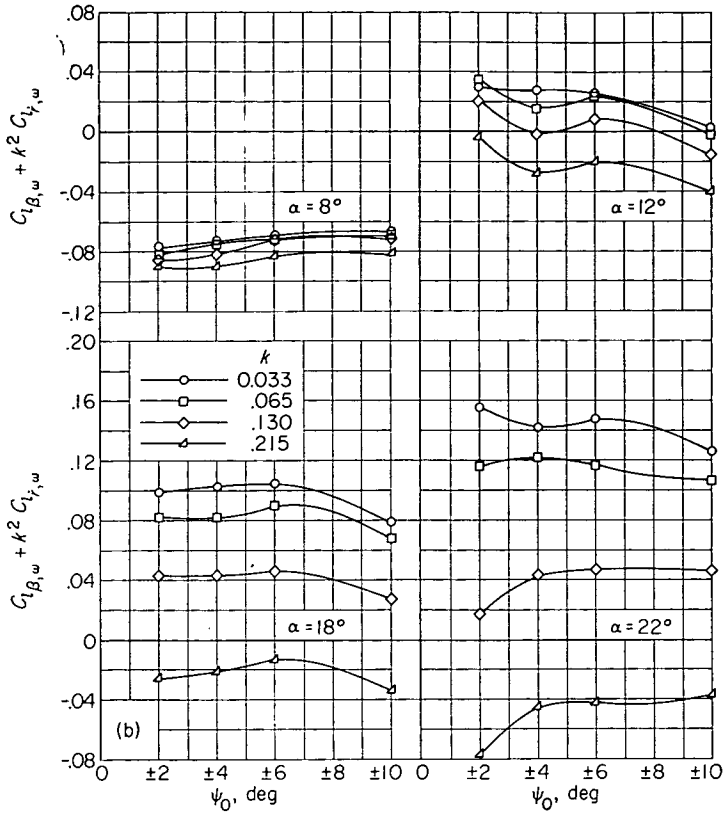


(a) Delta wing.

FIGURE 18.—The effect of amplitude on effective-dihedral derivative.

For the swept wing at $\alpha=22°$ (fig. 17 (b)), an increase of amplitude gives slightly higher positive values of the derivative for the lowest frequency; for the highest frequency a reverse effect, although slight, is indicated.

Effective dihedral.—The effect of amplitude on the effective-dihedral parameter $C_{l_{\beta,\omega}}+k^2C_{l_{\dot{r},\omega}}$ is shown in figure 18. For the delta wing at $\alpha=18°$, and for the lowest frequency of oscillation, an increase in amplitude reduces the magnitude of the derivative at low amplitudes, whereas at the higher amplitudes, the magnitude of the derivative remains about constant with amplitude. At $\alpha=24°$, for the lowest frequency ($k=0.033$), increasing the amplitude reduces the derivative. A reversal in the variation with amplitude is



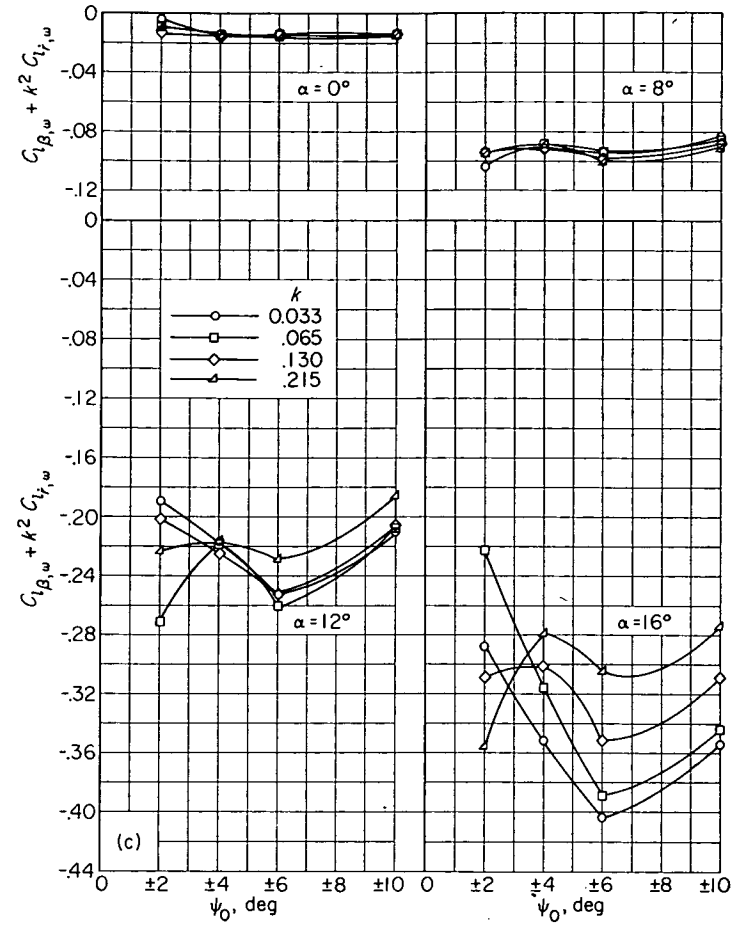
(b) Swept wing.
FIGURE 18.—Continued.

indicated at $\alpha=28°$ for this frequency; and at $\alpha=32°$ the derivative increases in magnitude throughout the amplitude range.

The data for the swept wing at $\alpha=22°$ (fig. 18 (b)) shows a reversal in trend with amplitude between the lowest and highest frequencies of oscillation. The derivative for the unswept wing at the higher angles of attack (fig. 18 (c)) exhibits large variations due to amplitude and reversals in trend between the low and high amplitudes of oscillation. These variations with amplitude are strongly dependent upon frequency.

COMPARISON OF EXPERIMENTAL DERIVATIVES AND ADDITION OF COMPONENT DERIVATIVES

The derivatives $C_{n_{r,\omega}}$, $C_{n_{\dot{r},\omega}}$, $C_{l_{r,\omega}}$, and $C_{l_{\dot{r},\omega}}$ were measured at $k=0.22$ and at an amplitude $\psi_0=8°$ for the investigation of reference 1. The derivatives $C_{n_{\beta,\omega}}$, $C_{n_{\dot{\beta},\omega}}$, $C_{l_{\beta,\omega}}$, and $C_{l_{\dot{\beta},\omega}}$ were determined by a series of tests similar to those of reference 2. The latter were forced-oscillation tests with $k=0.22$ and an amplitude of sideslip $\beta_0=6°$. These individual derivatives, and the appropriate algebraic additions thereof, are compared in figures 19 to 22 with the corresponding combination derivatives measured in the present investigation for $k=0.22$ and $\psi_0=6°$. In general, the comparisons are good. In figure 19, the experimentally combined damping-in-yaw derivative for the delta wing is just a little smaller than the sum of the individual derivatives through the angle-of-attack range. The comparisons for the swept and unswept wings are also generally in good agreement. Figure 19 indicates for these wings that the $C_{n_{\dot{\beta},\omega}}$ derivative



(c) Unswept wing.
FIGURE 18.—Concluded.

is larger in absolute magnitude than the $C_{n_{r,\omega}}$ derivative at high angles of attack and therefore is the major contributor to the damping in yaw as determined in these tests.

For the delta wing, the algebraic sum of the individual derivatives $C_{l_{r,\omega}}$ and $C_{l_{\dot{\beta},\omega}}$ (fig. 20) appears to have somewhat higher positive values by an almost constant increment through the angle-of-attack range than the experimentally obtained combination derivative. For the swept wing, the added derivatives also have higher positive values than the experimental derivatives up to $\alpha=16°$, and for the unswept wing at all angles of attack greater than zero. Figure 20 indicates that, at least for the delta and swept wings, $C_{l_{\dot{\beta},\omega}}$ contributes a greater portion to the combination derivative than does $C_{l_{r,\omega}}$.

The algebraically added derivatives $C_{n_{\beta,\omega}}$ and $k^2C_{n_{\dot{r},\omega}}$ are presented in figure 21 as a function of angle of attack and are compared with the experimental combination derivatives. Although $C_{n_{\dot{r},\omega}}$ can have large magnitudes of its own, as demonstrated by the investigation of reference 1, the multiplication of this derivative by k^2 would be expected to reduce the significance of this term in the determination of the directional stability parameter except for, perhaps, extremely large values of the reduced frequency or the derivative $C_{n_{\dot{r},\omega}}$. Figure 21 shows this $k^2C_{n_{\dot{r},\omega}}$ contribution to be small relative to the large $C_{n_{\beta,\omega}}$ contributions for the delta and the

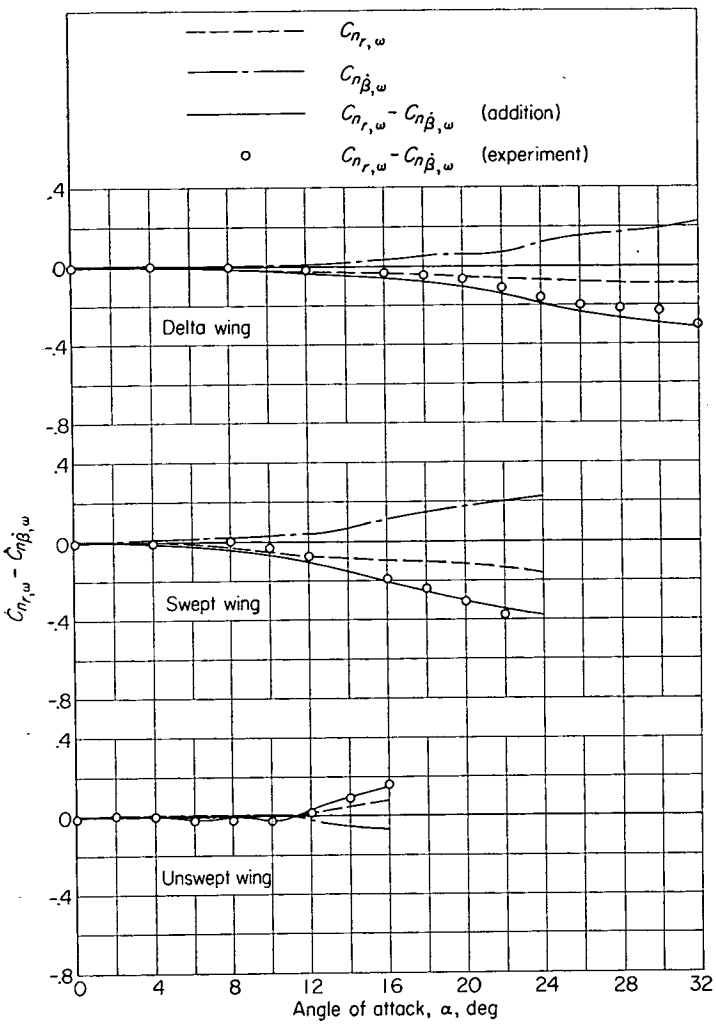


FIGURE 19.—Comparison of the component and the combination derivatives making up the damping in yaw. $k=0.22$; $\psi_0=\pm 6°$ or $\pm 8°$.

unswept wings at high angles of attack. The swept wing has relatively small values of $C_{n_{\beta,\omega}}$ which are of about the same magnitude as $k^2C_{n_{\dot r,\omega}}$ for most of the high-angle-of-attack range.

The contribution of $k^2C_{l_{\dot r,\omega}}$ to the effective dihedral derivative is also small relative to $C_{l_{\beta,\omega}}$ for the delta and the unswept wings (fig. 22). At lower frequencies of oscillation, the $k^2C_{l_{\dot r,\omega}}$ contribution to the derivative would be of less significance still, since the k^2 factor would reduce to relative unimportance even $C_{l_{\dot r,\omega}}$ derivatives of very large magnitude as k approached zero. The nonlinear variation with angle of attack shown by $C_{l_{\beta,\omega}}+k^2C_{l_{\dot r,\omega}}$ for the swept wing can be attributed to the $C_{l_{\beta,\omega}}$ portion of the derivative.

The particular model yawing motion employed for these tests was such that the amplitude of the sideslipping motion was the negative of the amplitude of the yawing motion so that $\beta_0/\psi_0=-1$. Airplane lateral motions may be made up of any ratio of these amplitudes, although motions wherein $\beta_0/\psi_0\approx -1$ occur quite frequently. When this ratio is close to -1 and when the phase relationship between the separate motions is small, then the stability derivatives may be combined in the airplane lateral equations of motion in the forms

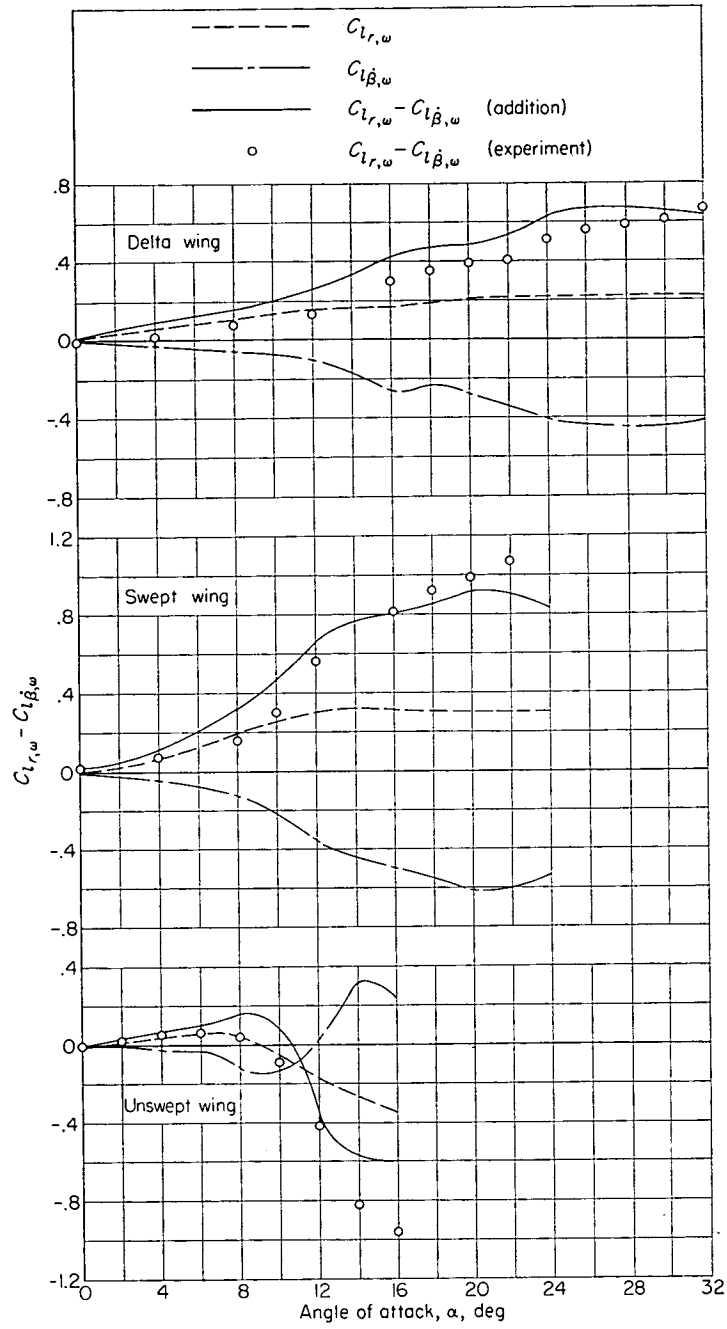


FIGURE 20.—Comparison of the component and the combination derivatives making up the rolling moment due to yawing. $k=0.22$; $\psi_0=\pm 6°$ or $\pm 8°$.

used herein. The resulting agreement between the addition of the separately determined β and ψ derivatives and the combination derivatives measured herein indicates that for $\beta_0/\psi_0=-1$, at least, and for $k=0.22$, the aerodynamic phenomena responsible for the individual derivatives are linear to a large degree in that the individual derivatives are approximately additive. For low values of the reduced frequency, however, it is possible that the individual derivatives may not add up quite as well as at the high reduced frequency because of the large effects of frequency and amplitude which exist at low frequencies and which indicate lessening linearity.

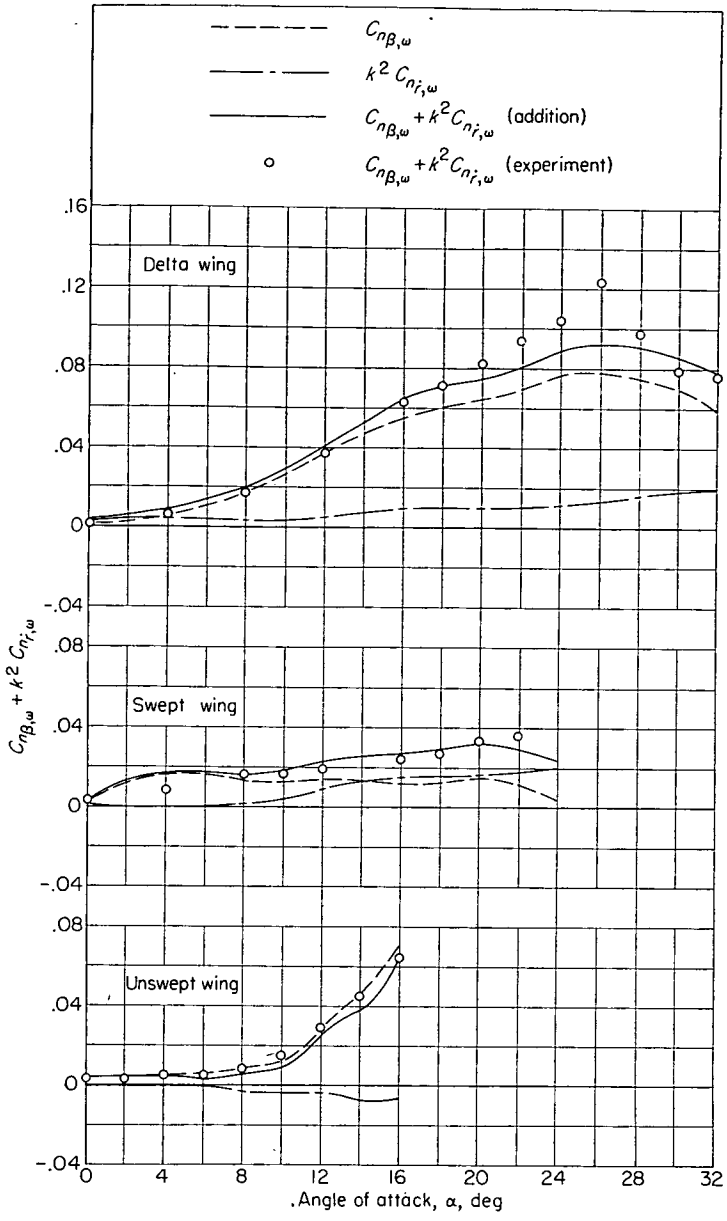


FIGURE 21.—Comparison of the component and the combination derivatives making up the directional stability. $k=0.22$; $\psi_0=\pm 6°$ or $\pm 8°$.

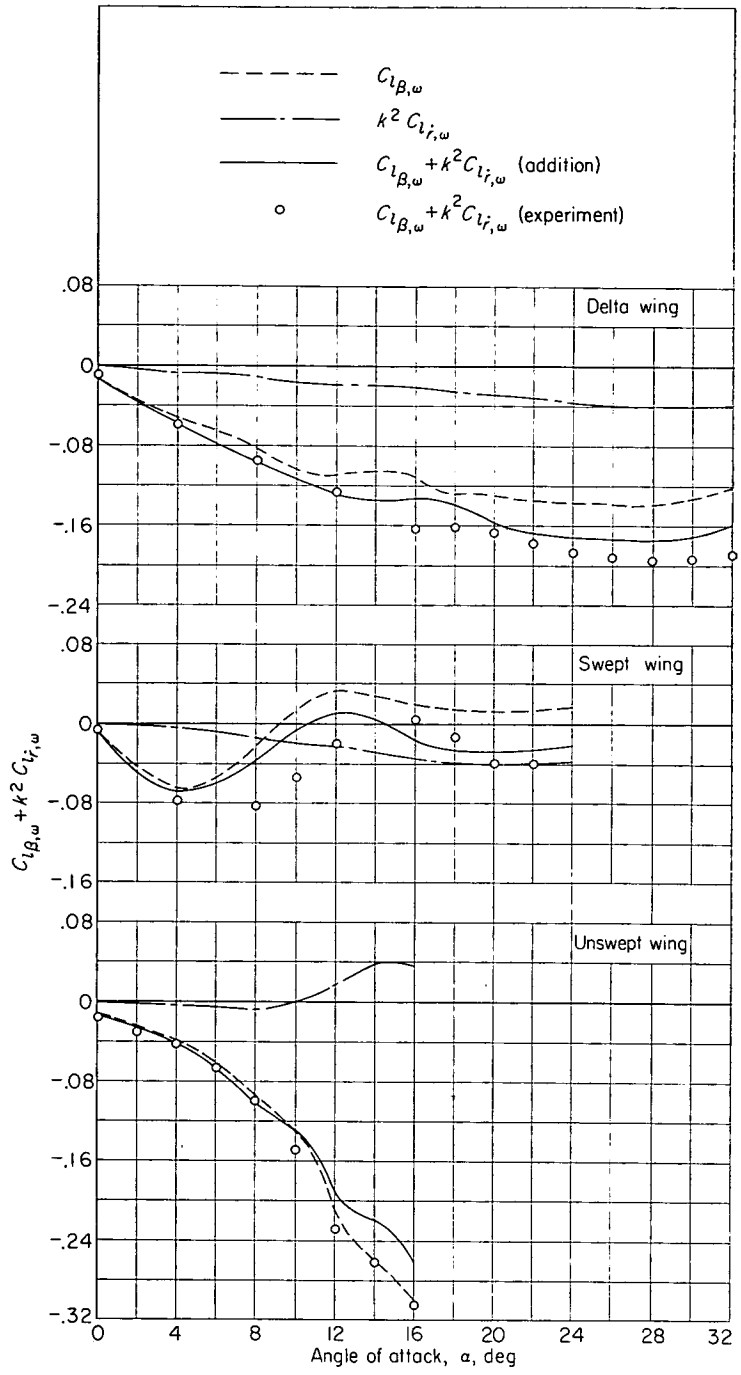


FIGURE 22.—Comparison of the component and the combination derivatives making up the effective dihedral. $k=0.22$; $\psi_0=\pm 6°$ or $\pm 8°$.

CONCLUSIONS

A delta wing, a swept wing, and an unswept wing were oscillated in yaw about their quarter-chord points in order to determine the separate effects of frequency and amplitude on the combination lateral stability derivatives resulting from this motion. The results of this investigation indicate the following conclusions:

1. The frequency of oscillation had a determining influence on the lateral stability derivatives for the delta wing at high angles of attack. The largest changes in the variations of the derivatives with angle of attack took place for the lowest frequencies of oscillation; as the frequency increased, the effects of frequency became smaller, and the curves of the derivatives plotted against angle of attack became more linear. Similar effects of frequency, but to a smaller extent, were shown for the derivatives of the swept wing. The derivatives for the unswept wing were apparently influenced only slightly by frequency.

2. The effect of amplitude of oscillation on the lateral stability derivatives appears to depend substantially upon the angle of attack of the wing and upon the frequency of oscillation. Some large effects of amplitude were shown on

the derivatives for the delta wing at high angles of attack and for the lowest frequency of oscillation. As the frequency was increased to its highest value, these effects of amplitude, in general, disappeared. Similar amplitude effects were indicated for the swept wing to a lesser degree, but, in general, did not appear for the unswept wing.

3. A comparison of the present results with the results of previous investigations for a corresponding frequency and amplitude indicated that the derivatives taken with respect to sideslip angular velocity $\dot{\beta}$ are somewhat larger in absolute magnitude than the derivatives taken with respect to yawing angular velocity r, with which they are generally combined. The derivatives taken with respect to yawing angular acceleration $\dot{r}$, although of large magnitude themselves, lose significance when combined with the derivatives taken with respect to sideslip β because of their multiplication by the square of the reduced-frequency parameter. Hence, in the range of frequencies being considered, the in-phase stability derivatives are determined primarily by the β derivatives. As the frequency of oscillation became smaller, the combination in-phase derivatives approached the static (zero frequency) β derivatives.

4. The algebraic addition of the component derivatives gave results which were generally in good agreement with the derivatives obtained in combination for the present investigation. These results indicate that the aerodynamic phenomena responsible for these derivatives are linear to a large degree.

LANGLEY AERONAUTICAL LABORATORY,
NATIONAL ADVISORY COMMITTEE FOR AERONAUTICS,
LANGLEY FIELD, VA., *January 6, 1956.*

REFERENCES

1. Queijo, M. J., Fletcher, Herman S., Marple, C. G., and Hughes, F. M.: Preliminary Measurements of the Aerodynamic Yawing Derivatives of a Triangular, a Swept, and an Unswept Wing Performing Pure Yawing Oscillations, With a Description of the Instrumentation Employed. NACA RM L55L14, 1956.
2. Riley, Donald R., Bird, John D., and Fisher, Lewis R.: Experimental Determination of the Aerodynamic Derivatives Arising From Acceleration in Sideslip for a Triangular, a Swept, and an Unswept Wing. NACA RM L55A07, 1955.
3. Campbell, John P., Johnson, Joseph L., Jr., and Hewes, Donald E.: Low-Speed Study of the Effect of Frequency on the Stability Derivatives of Wings Oscillating in Yaw With Particular Reference to High Angle-of-Attack Conditions. NACA RM L55H05, 1955.
4. Campbell, John P., and Woodling, Carroll H.: Calculated Effects of the Lateral Acceleration Derivatives on the Dynamic Lateral Stability of a Delta-Wing Airplane. NACA RM L54K26, 1955.

REPORT 1358

ON FLOW OF ELECTRICALLY CONDUCTING FLUIDS OVER A FLAT PLATE IN THE PRESENCE OF A TRANSVERSE MAGNETIC FIELD [1]

By VERNON J. ROSSOW

SUMMARY

The use of a magnetic field to control the motion of electrically conducting fluids is studied. The incompressible boundary-layer solutions are found for flow over a flat plate when the magnetic field is fixed relative to the plate or to the fluid. The equations are integrated numerically for the effect of the transverse magnetic field on the velocity and temperature profiles, and hence, the skin friction and rate of heat transfer.

It is concluded that the skin friction and the heat-transfer rate are reduced when the transverse magnetic field is fixed relative to the plate and increased when fixed relative to the fluid. The total drag is increased in all of the cases studied.

INTRODUCTION

It has been said that a fluid at a very high temperature is like a universal solvent which cannot be contained. A possible method of containing this fluid is suggested when it is noted that at such a high temperature it would surely contain ions and quite probably also free electrons. The fluid would then be an electrical conductor. The invisible hand of electrical and magnetic fields can then be used to induce forces on the fluid such that it is prevented from coming in direct contact with a wall which it would dissolve.

A somewhat similar technique has been in use for some time in the metal purification industry. It employs a high-frequency magnetic field which causes eddy currents in a lump of molten metal which in turn react with the imposed magnetic field. The metal is thereby suspended in space if the imposed magnetic field is made strong enough.

Another example is the so-called "perhapsatron" described briefly in reference 1. A gas in a doughnut shaped container is heated to a high temperature by an electrical current discharge. Through the use of the interaction of the resulting ion current and a magnetic field, the hot gas is prevented from coming in contact with the surface of the vessel. An application of similar principles was used in thermonuclear fusion experiments in the Soviet Union. The techniques and results described very briefly in reference 2 indicate that it was possible to keep the hot fluid from the walls and to concentrate the hot gases quickly so as to generate a focusing shock wave.

These examples indicate the possibilities which may be realized through the use of a magnetic-field force on a flowing conducting fluid. A number of situations exist in aerodynamics wherein a magnetic or electrical field might be used to alleviate high convective heat-transfer rates to a wall. Such problems arise in the flow of air in the boundary layer and in the vicinity of stagnation regions of an aircraft moving at very high speeds. If the velocity is high enough the air is ionized and, therefore, electrically conducting. See, for example, references 3 and 4. Other examples are those associated with the flow of the combustion products (which are hot and generally electrically conducting, refs. 5 through 7) in the propulsion units of aircraft.

The extent to which a given heating problem can be alleviated is as yet difficult to determine. It would be well if a few theoretical results were available to evaluate the effect of a magnetic field on the drag and heat-transfer rate. An attempt to include all the aerodynamic features of the flow of air over or inside an aircraft plus the magneto-hydrodynamic (or more correctly, magneto-aerodynamic) effects would render the problem so complicated as to make its solution difficult if not impossible. It is felt that a few simple basic theoretical solutions would point out the advantages or disadvantages and yield a rough estimate of the various quantities entering the problem. It is the purpose of this report to present the results of several such solutions which, it is hoped, will extend the information already available so that such estimates can be made. Several applications of the results are indicated.

PRINCIPAL SYMBOLS

$\vec{b},\vec{B}$	magnetic induction, lines/sq in.
c_f	local skin-friction coefficient
C_p	heat capacity of air at constant pressure, Btu/slug °F
$\vec{E}$	electric field intensity, volts/in.
E	total energy, $C_pT+\frac{u^2}{2}$
erf	error function
$erfc$	complementary error function, 1-erf
f_o	dimensionless Blasius boundary-layer stream function

[1] Supersedes NACA TN 3971 by Vernon J. Rossow, 1957.

Preceding Page Blank

$f_1, f_2, f_3 \ldots$ dimensionless stream function, equation (26)
F force, lb
h local heat-transfer coefficient, Btu/sec ft² °F
$\vec{H}$ magnetic intensity, $\frac{\vec{B}}{\mu}$, (ampere)(turns)/in.
i electric current, amp
$\vec{j}$ electric current density in the fluid, amp/sq in.
$\vec{J}$ electric current density associated with generation of magnetic field, amp/sq in.
k thermal conductivity, Btu/sec ft² °F/ft
l characteristic length
m magnetic parameter, $\frac{\sigma B_o^2}{\rho u_\infty}$, per in.
m_1 $\frac{\sigma B_o^2}{\rho}$, per sec
$\overline{M}$ magnetic Hartmann number, $\sqrt{\frac{\sigma B^2 l^2}{\mu}}$
p pressure, lb/sq in.
Q $\frac{B^2 \sigma l}{\rho U}$
Re Reynolds number
s Laplace transform variable
time, sec
T temperature, °R
u,v,w velocity components in x,y,z directions
$\overline{u}$ Laplace transform of velocity u (see eq. (14))
$\vec{U}$ velocity, ft/sec
x,y,z coordinate axes, x alined with free stream
η $y\sqrt{\frac{u_\infty}{\nu x}}$
θ excess charge density, coulomb/cu in.
λ magnetic viscosity, $\frac{1}{4\pi\sigma\overline{\mu}}$
μ coefficient of viscosity, slugs/ft sec
$\overline{\mu}$ magnetic permeability, (volt)(second)/(ampere)(inch)
ν kinematic viscosity, $\frac{\mu}{\rho}$, ft²/sec
ξ x
ρ density of fluid, slugs/cu ft
σ conductivity, mhos/in.
τ shear stress, lb/sq in.
ψ stream function

SUBSCRIPTS

o basic quantity
∞ free stream
B magnetic induction
e electron
w at plate, $\eta=y=0$

SUPERSCRIPTS

$(\vec{\ })$ vector quantity
$(\ )', (\ )'', (\ )'''$ derivatives

HISTORICAL REVIEW OF MAGNETO-HYDRODYNAMICS

The earliest known published works treating a problem in the flow of an electrically conducting fluid through a magnetic field are those of Hartmann and of Hartmann and Lazarus in references 8 and 9. Since that time a number of theoretical and experimental studies have been carried out. Some of these pertain to the flow of a conducting fluid but a larger number relate to the dynamics of ionized clouds or stars. No attempt will be made here to include a complete discussion of the latter group. However, much can be learned by studying the papers on the flow of conducting fluids. These papers will be divided into several groups according to the type of problem treated.

1. Flow in a channel (refs. 8 through 19).
2. Flow about bodies of various shapes (refs. 20 through 22).
3. Related papers on astronomy (refs. 23 through 26).

The various papers will be reviewed briefly on a group basis and reference to particular papers given only in special instances.

FLOW IN CHANNEL

Following his invention of the electromagnetic pump [2] in 1918, Hartmann, reference 8, developed equations which describe the steady-state flow inside a channel in the presence of a magnetic field or a magnetic and electrical field. Interest was stimulated in problems of this type when it was found in reference 9 that a turbulent stream could be stabilized to the extent that it could be forced to return to a laminar flow. Such a sequence of events is opposite to the usual form of transition when a magnetic field is not present. Further investigations by other authors, references 10 through 19, substantiated these results and led to the introduction of terms such as "magnetic viscosity," $\lambda=\frac{1}{4\pi\sigma\overline{\mu}}$, "magnetic Hartmann number," $\overline{M}=Bl\sqrt{\frac{\sigma}{\mu}}$ and $Q=\frac{\sigma B^2 l}{\rho U}$.

A rigidity of the fluid is brought about by a coplanar magnetic field so that stabilization is achieved because the conducting fluid experiences a force which resists the motion across the magnetic lines of force (ref. 13). For example, if the main fluid flow direction is parallel to the magnetic lines of force, no interaction takes place unless some deviation or instability arises. In this event, a restraining force will be induced which is proportional and opposite to the velocity component perpendicular to the lines of force, tending to damp out the initial instability.

When the magnetic field is perpendicular to the flow direction, a change is brought about in the velocity distribution. This may make the fluid flow more stable or unstable to transition to turbulence. In the case of flow of an electrically conducting fluid through a transverse magnetic field in a two-dimensional channel (refs. 9 and 14), the change in the velocity profile had a very favorable effect on transition. Such is not always expected to be the case in other flow problems.

[2] Electromagnetic pumps are used in atomic energy plants to transfer radioactive solutions from one place to another (e. g., see p. 32 of Atomic Power—a Scientific American book, Simon and Schuster Inc., New York, 1955).

These two techniques which increase the stability of fluid flowing in a two-dimensional channel were studied theoretically in references 13 and 14. The transition boundaries are given in graphical form for a range of the magnetic parameter. It was observed that a considerable increase in laminar run could be achieved at the higher values of the magnetic parameter.

FLOW ABOUT BODIES OF VARIOUS SHAPES

The papers describing the external flow of a conducting fluid about bodies are small in number. The three references listed, 20 through 22, describe the flow of a conducting fluid around a circular cylinder and a sphere in the presence of a magnetic field; the third paper treats the stability of the flow between rotating cylinders. Streamlines are shown in the first two cases and the stability boundary for the latter case. Problems in this category are naturally more difficult than the unidirectional channel flow problems discussed in the previous section.

RELATED PAPERS ON ASTRONOMY

A need for understanding the motion of electrically conducting fluids (ionized clouds) has been felt by astronomers for some time. The dimensions and quantities considered are generally not reproducible in the laboratory or in the earth's atmosphere; however, some of the equations and results may be applied to aerodynamic problems.

In reference 23, Batchelor investigated the possibility of spontaneous magnetic fields arising in a conducting medium as a result of turbulence. He found that unless $4\pi\bar{\mu}\sigma\nu > 1$ such fields cannot occur. In all foreseeable problems in aerodynamics $4\pi\bar{\mu}\sigma\nu$ is many orders of magnitude less than 1, ruling out spontaneous magnetic fields in a fluid due to turbulence.

The manner and velocity at which pressure waves are propagated in an ionized fluid and other cosmic problems are treated in references 24 through 26. The results of these studies on wave propagation may be useful in studying interference problems on high-velocity aircraft.

MAGNETO-AERODYNAMIC EQUATIONS

The equations which describe the flow of an electrically conducting fluid in the presence of magnetic and electrical fields will now be discussed. The equations are simplified to the extent that the flow is assumed to be incompressible and to have constant properties (C_p, μ, k) throughout the flow field. In all cases except one, the electrical conductivity of the fluid is assumed to be constant.

MOMENTUM-TRANSPORT EQUATIONS

The momentum-transport equations for the flow of a viscous incompressible fluid consist of a combination of the force terms arising from the excess charge density θ, and induced magnetic effect due to the motion of the conducting fluid through magnetic lines of force (see, e. g., refs. 23 and 27) and the usual Navier-Stokes relations (see, e. g., ref. 28). In equation form, these force terms are,

$$\vec{F}=\theta\vec{E}+\vec{j}\times\vec{B}$$

where the term $\theta\vec{E}$ results from the electrostatic force on the excess charges due to the presence of an imposed electric field $\vec{E}$. The second term describes the force on the fluid due to the interaction of the electric current, $\vec{j}$, in the fluid and the magnetic induction $\vec{B}$. The differential equation can be written in vector notation as

$$\frac{D\vec{U}}{Dt}=\frac{\theta\vec{E}}{\rho}+\frac{\bar{\mu}}{\rho}\vec{j}\times\vec{H}+\frac{1}{\rho}\text{grad}\,p=\nu\nabla^2\vec{U} \tag{1}$$

where ρ is the fluid density, θ is the excess charge density, and $\bar{\mu}$ is the magnetic permeability. The substantial derivative D/Dt is associated with the use of spatial coordinates. A simplified version of Maxwell's equations appropriate for the present problem is

$$\text{div}\,\vec{H}=0;\ \text{div}\,\vec{J}=0;\ \bar{\mu}\vec{H}=\vec{B} \tag{2a}$$

$$\text{curl}\,\vec{H}=4\pi\vec{J} \tag{2b}$$

A reduced form of the generalized Ohm's law is, from reference 29,

$$\vec{j}=\sigma(\vec{E}+\bar{\mu}\vec{U}\times\vec{H}) \tag{2c}$$

The more complete form given as equation 2–22 in reference 29 includes additional terms accounting for gravity and pressure gradient effects. Both of these factors will be assumed negligible in this analysis. It will also be assumed that the conductivity, σ, does not have directional properties.

The continuity equation is

$$\text{div}\,\vec{U}=0 \tag{3}$$

Equation (2b) expresses the relation between the magnetic intensity $\vec{H}$ and the total electric current density $\vec{J}$. The distinction between the current densities $\vec{j}$ and $\vec{J}$ lies in their location and action. Consider first the situation when the fluid is stationary and the electric field intensity $\vec{E}$ is zero. The current density in the fluid is then zero. The magnetic field strength $\vec{H}_o$ or magnetic induction $\vec{B}_o=\mu\vec{H}_o$ is a result of an electric current $\vec{J}_o$ outside of the fluid. The current density $\vec{J}_o$ could be thought of as an electric current in a coil or electromagnet outside the flow region producing a magnetic field of a given number of lines of force per unit area. The relation between $\vec{J}_o$ and $\vec{H}_o$ is given by equation (2b). The basic magnetic field strength will be designated as $\vec{H}_o$.

When a conducting fluid moves through the magnetic lines of force, $\vec{B}_o$, the positive and negative charges are each accelerated in such a way that their average motion gives rise to an electric current $\vec{j}=\sigma\vec{U}\times\vec{B}$, where $\vec{B}=\vec{B}_o+\vec{b}$. The quantity $\vec{b}$ is the magnetic induction resulting from the electric current $\vec{j}$ in the fluid. In this analysis $\vec{b}$ will be con-

sidered as a perturbation on the basic field strength and negligible in comparison with $\vec{B}_o$; that is, from equation (2b),

$$\text{curl } (\vec{B}_o+\vec{b})=4\pi\bar{\mu}(\vec{J}_o+\vec{j})=4\pi\bar{\mu}\vec{J}$$

or

$$\text{curl } \vec{B}_o=4\pi\bar{\mu}\vec{J}_o$$

$$\text{curl } \vec{b}=4\pi\bar{\mu}\vec{j}$$

where $\vec{B}_o \gg \vec{b}$.

If an electric potential $\vec{E}$ were to be imposed across the flow field, the current density would be changed by $\vec{j}=\sigma\vec{E}$. However, the boundary conditions will be taken so that the impressed potential, $\vec{E}$, is zero. Therefore, $\vec{j}=\sigma\vec{U}\times\vec{B}_o$; that is, the electric current is proportional to the voltage generated by the relative motion of the fluid and magnetic field.

The fluid is assumed to be ionized and thereby an electrical conductor. However, within any small but finite volume the number of particles with positive and negative charges are nearly equal. The total excess charge, θ, in this small but finite volume will be taken as equal to zero. It has been shown in reference 17 that a very small increase in viscosity is realized due to the increased ordered-migration velocities of positive and negative ions in the presence of the electric field. This effect will be neglected and the electrostatic force term, $\theta\vec{E}$ will be assumed to be identically zero.

The induced electromagnetic force term, $\vec{j}\times\vec{B}_o$ will now be related to the local velocity vector. The procedure used in references 10, 19, and 22 which results in the magnetic parameter $\frac{\bar{\mu}H^2}{\rho U^2}$ (ratio of electromagnetic and inertia forces) and the magnetic viscosity $\lambda=\frac{1}{4\pi\sigma\bar{\mu}}$ will not be used. Instead a procedure will be followed which will lead to the magnetic parameter, $Q=\frac{\sigma B^2 l}{\rho U}$, used by references 7, 9, 11, 12, and 13.

A relation between $\vec{j}\times\vec{B}$ and the velocity is obtained from equation (2). It will be assumed that:

(1) Magnetic field lines are perpendicular to free-stream velocity.

(2) Permeability $\bar{\mu}$ is constant throughout the fluid.

(3) The assumptions already made are that the excess charge density θ and imposed electric field intensity $\vec{E}$ are assumed to be zero.

(4) Induced magnetic field $\vec{b}$ is negligible, linearizing the induced magnetic force term.

The first assumption is not highly restrictive since the perpendicular component of the magnetic field is the only part contributing a force which will change the laminar velocity profile. The other assumptions are reasonable physical approximations.

If these assumptions are used together with equation (2c), the induced magnetic force term becomes

$$-\frac{\vec{j}\times\vec{B}_o}{\rho}=-\frac{\sigma}{\rho}\left(\vec{U}\times\vec{B}_o\right)\times\vec{B}_o \tag{5}$$

From vector relations,

$$-\frac{\vec{j}\times\vec{B}_o}{\rho}=-\frac{\sigma}{\rho}\left(\vec{U}\times\vec{B}_o\right)\times\vec{B}_o=\frac{\sigma}{\rho}\left[\vec{U}\left(\vec{B}_o\cdot\vec{B}_o\right)-\vec{B}_o\left(\vec{B}_o\cdot\vec{U}\right)\right]$$

However, it has been assumed that $\vec{B}_o$ is perpendicular to the free-stream velocity $\vec{U}_\infty$ (assumption (1)). In the problems treated, the local velocity direction differs a negligible amount from the free-stream direction so that $\vec{B}_o\cdot\vec{U}=0$ and the linearized magneto-hydrodynamic force term becomes

$$-\frac{\vec{j}\times\vec{B}_o}{\rho}=\frac{\sigma B_o^2\vec{U}}{\rho}=mU_\infty\vec{U} \tag{6}$$

The parameter [3] m is related to the viscous Reynolds number and the Hartmann number of references 8 through 12 by

$$ml=\frac{\sigma B_o^2 l}{\rho U_\infty}=\frac{\sigma B_o^2 l^2}{\mu}\frac{1}{\frac{\rho U_\infty l}{\mu}}=\frac{\overline{M}^2}{Re}$$

Equation (1) may then be written as

$$\frac{D\vec{U}}{Dt}+\frac{\sigma B_o^2}{\rho}\vec{U}+\frac{1}{\rho}\text{grad } p=\nu\nabla^2\vec{U} \tag{7}$$

In the development of equation (7), it was assumed that the velocity of the magnetic field is zero. Since only the inductive force is being considered, the second term becomes $\frac{\sigma B_o^2}{\rho}\left(\vec{U}-\vec{U}_B\right)$ for a magnetic field in uniform translation, where $\vec{U}_B$ is the velocity of the magnetic field.

When electrical currents flow in a plasma it is well to define the conditions at the solid boundaries of the flow field. The problems treated are assumed to be two-dimensional with the electric current flowing from and to infinity parallel to a flat plate and perpendicular to the stream direction. The configuration may also be thought to consist of flow in a wide channel with the two side walls as conductors connected by a conductor of negligible resistance located outside of the influence of the flow field. The flow in the middle of such a channel should approximate the two-dimensional type of flow being analyzed. Such phenomena as charge accumulation and boundary effects at the walls will be assumed negligible.

THERMAL ENERGY TRANSPORT EQUATION

The differential equation describing the relationship between the convection and conduction of thermal energy and the work done on an electrically conducting fluid in the presence of a magnetic field is found by considering the

---

[3] From electric motor equations, it can be shown that

$$\sigma B_o^2=\frac{\text{force}}{j^3\times\text{velocity}}$$

and therefore

$$\frac{\sigma B_o^2 l}{\rho U_\infty}=\left(\frac{\bar{\mu}H_o^2}{\rho U_\infty^2}\right)(\sigma\bar{\mu}U_\infty l)=\left(\frac{\text{magnetic pressure}}{\text{dynamic pressure}}\right)\left(\text{magnetic Reynolds number}\right)$$

energy entering and leaving an elementary cubic box. The result is given by

$$\rho C_p \frac{DT}{Dt}=k\nabla^2 T+\frac{j^2}{\sigma}+\frac{Dp}{Dt}+\mu\left\{2\left[\left(\frac{\partial u}{\partial x}\right)^2+\left(\frac{\partial v}{\partial y}\right)^2+\left(\frac{\partial w}{\partial z}\right)^2\right]+\left(\frac{\partial v}{\partial x}+\frac{\partial u}{\partial y}\right)^2+\left(\frac{\partial w}{\partial y}+\frac{\partial v}{\partial z}\right)^2+\left(\frac{\partial u}{\partial z}+\frac{\partial w}{\partial x}\right)^2\right\} \quad (8)$$

The derivation of equation (8), with the exception of the second term on the right of the equal sign, can be found, for example, in reference 28. The term on the left of the equal sign takes account of the enthalpy transported by the motion of the fluid or by convection. The first term on the right represents heat conducted from one element of fluid to the next by molecular motion. The expression, j^2/σ, is the heat added by the electrical current produced by the motion of the fluid through magnetic lines of force or by an imposed electrical field (see eq. (2c)). The remaining terms arise when work is done on the fluid by either pressure or shear forces. The symbol D/Dt is the substantial derivative of the particular quantity and ∇^2 denotes the Laplacian.

If the general expression for the electric current density, as given by equation (2c), is inserted into the expression for the heat added by electrical means, the result is

$$\frac{j^2}{\sigma}=\sigma\left(\vec{E}+\vec{U}\times\vec{B}\right)^2 \quad (9)$$

It has been assumed that the electric field $\vec{E}$ is zero and that the magnetic field lines are perpendicular to the free-stream direction. To a good approximation in the problems to be considered, equation (9) can then be written as

$$\frac{j^2}{\sigma}=\sigma U^2 B_o^2 \quad (10)$$

where U^2 must be written as $(U-U_B)^2$ when relative motion exists between the magnetic field and the plate. Equation (8) is then

$$\rho C_p \frac{DT}{Dt}=k\nabla^2 T+\sigma U^2 B_o^2+\frac{Dp}{Dt}+\mu\left\{2\left[\left(\frac{\partial u}{\partial x}\right)^2+\left(\frac{\partial v}{\partial y}\right)^2+\left(\frac{\partial w}{\partial z}\right)^2\right]+\left(\frac{\partial v}{\partial x}+\frac{\partial u}{\partial y}\right)^2+\left(\frac{\partial w}{\partial y}+\frac{\partial v}{\partial z}\right)^2+\left(\frac{\partial u}{\partial z}+\frac{\partial w}{\partial x}\right)^2\right\} \quad (11)$$

IMPULSIVE MOTION OF A FLAT PLATE

The impulsive motion of an infinite flat plate [4] in a viscous fluid serves as a model for the boundary layer on a semi-infinite flat plate. The advantages of working the problem of the impulsive motion of a flat plate are that it is simple enough to yield a result in closed form and suggests the proper choice of parameters to be used on the more complicated problem of a semi-infinite flat plate.

The velocity profiles will be found for two cases. In the first it will be assumed that the magnetic lines of force are fixed relative to the plate, and the second relative to the fluid. In both cases the fluid is of uniform density and viscosity, and has the same electrical conductivity throughout. A third case, in which the magnetic field is fixed on the plate and a compensating pressure gradient exists in the fluid, will be shown to be equivalent to the case wherein the magnetic field is fixed relative to the fluid. The problem wherein the fluid conductivity varies will not be considered. The fluid and plate will be assumed to be initially at rest. At time $t=0$, the plate will move impulsively with a given velocity.

MAGNETIC FIELD FIXED RELATIVE TO THE PLATE

At time $t<0$, the fluid, plate, and magnetic field are assumed to be everywhere stationary. At time $t=0$ and for all later times the plate and magnetic field are moving at velocity $u=u_\infty$ (fig. 1). The problem is to find the velocity-time history of the fluid.

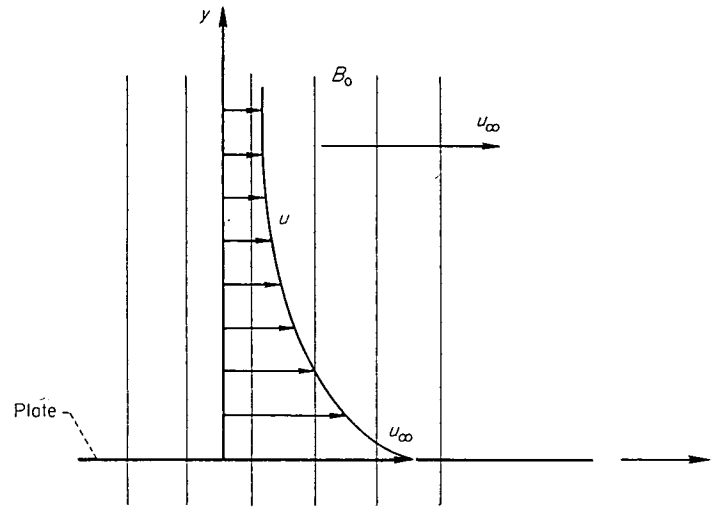


FIGURE 1.—Flat plate moving impulsively through a fluid in the presence of a transverse magnetic field.

The velocity in a given y=constant plane does not change with x. It can then be reasoned that the vertical, v, and transverse, w, velocities are zero or negligible together with the pressure gradients in all directions. Equation (7) then reduces to

$$\frac{\partial u}{\partial t}+\frac{\sigma B_o^2}{\rho}u=\nu\frac{\partial^2 u}{\partial y^2} \quad (12)$$

Since the magnetic field is moving and the fluid is initially at rest the relative motion must be accounted for. Equation (12) is then

$$\frac{\partial u}{\partial t}+\frac{\sigma B_o^2}{\rho}(u-u_\infty)=\nu\frac{\partial^2 u}{\partial y^2} \quad (13)$$

The boundary conditions are

$$u=u_\infty,\ y=0,\ t\geq 0$$

$$u=0,\quad y>0,\ t=0$$

The Laplace transform of the velocity u is defined as

$$\bar{u}=\int_0^\infty e^{-st}u\,dt \quad (14)$$

[4] This problem is often referred to as the "Rayleigh problem" when the fluid is incompressible and nonconducting.

Applying the Laplace transformation (see, e. g., refs. 30 and 31) to the first term in equation (13) gives

$$L\left(\frac{\partial u}{\partial t}\right)=\int_0^\infty e^{-st}\frac{\partial u}{\partial t}dt=+ue^{-st}\Big|_0^\infty+s\int_0^\infty e^{-st}u\,dt$$

$$\equiv s\bar{u}$$

If the other terms of equation (13) are treated similarly, the transformed equation is

$$s\bar{u}=\nu\frac{d^2\bar{u}}{dy^2}+\frac{m_1u_\infty}{s}-m_1\bar{u}$$

or

$$\frac{d^2\bar{u}}{dy^2}=\bar{u}\left(\frac{s+m_1}{\nu}\right)-\frac{m_1u_\infty}{\nu s} \tag{15}$$

The solution to equation (15) is the sum of the solution of the homogeneous equation plus the particular solution, that is,

$$\bar{u}=\frac{m_1u_\infty}{s(s+m_1)}+\frac{m_1u_\infty}{s(s+m_1)}\left[C_1(s)e^{-y\sqrt{\frac{s+m_1}{\nu}}}+C_2e^{+y\sqrt{\frac{s+m_1}{\nu}}}\right]$$

The constant C_2 is chosen equal to zero to fit the boundary condition that $\bar{u}$ must be finite at $y=\infty$. The integration constant $C_1(s)$ is found from the boundary condition at $y=0$; that is, on the plate

$$u_{y=0}=u_\infty$$

The Laplace transform of u_∞ is u_∞/s. Therefore

$$C_1(s)=\frac{s}{m_1}$$

and

$$\bar{u}=\frac{m_1u_\infty}{s(s+m_1)}+\frac{u_\infty}{s+m_1}e^{-y\sqrt{\frac{s+m_1}{\nu}}} \tag{16}$$

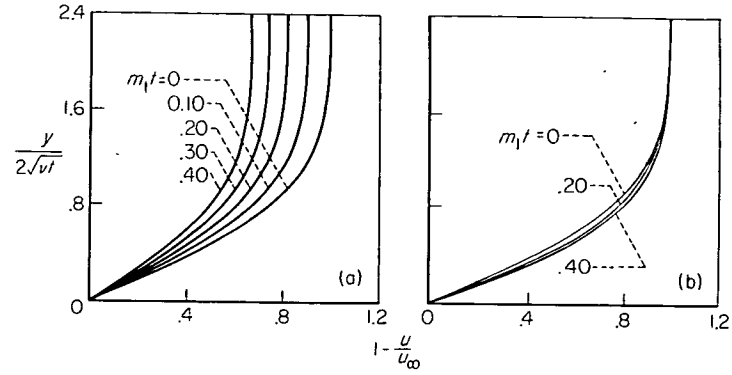
Equation (16) can be inverted with the aid of reference 30. Combining several terms gives

$$u=u_\infty\left(1-e^{-m_1t}erf\frac{y}{2\sqrt{\nu t}}\right) \tag{17}$$

The symbol *erf* denotes the error function of the argument. The error function is discussed in reference 31 and tabulated extensively in reference 32. Typical velocity profiles are shown in figure 2 (a). If m_1 is set equal to zero, equation (17) reduces to the result for the Rayleigh problem; that is,

$$u=u_\infty\left(1-erf\frac{y}{2\sqrt{\nu t}}\right)$$

The velocity is a function of $y/2\sqrt{\nu t}$ only and therefore a single profile suffices. However, when a magnetic field is acting on the fluid, the velocity profiles are not similar because they change with time according to e^{-m_1t}. The fluid at infinity is accelerated by the magnetic field so that the entire mass of fluid is accelerated by the magnetic field. It is, in fact, accelerated more rapidly than when the only force is the viscous action between layers.



(a) Magnetic field fixed relative to plate. (b) Magnetic field fixed relative to fluid.

FIGURE 2.—Boundary-layer velocity profiles on a flat plate set into motion impulsively.

The skin-friction coefficient is expressed as

$$c_f=\frac{\mu(\partial u/\partial y)|_{y=0}}{\rho u_\infty{}^2/2} \tag{18}$$

so that, from equation (17),

$$c_f=\frac{2\nu}{u_\infty\sqrt{\pi\nu t}}e^{-m_1t} \tag{19a}$$

Values of c_f are shown in graphical form in figure 3. When m_1 is zero, equation (19a) reduces to the skin friction for the nonelectromagnetic Rayleigh problem.

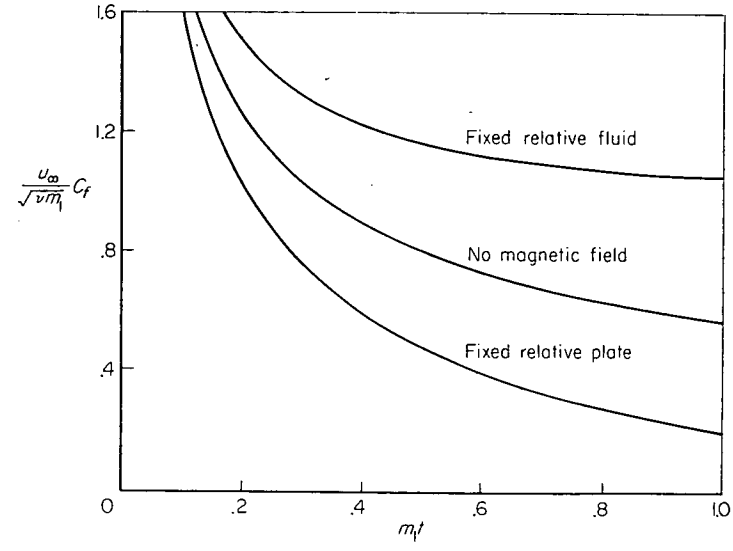


FIGURE 3.—Skin friction parameter as a function of a magnetic parameter.

The change in the velocity profile is a result of the force exerted by the magnetic field on the fluid. The reaction on the unit generating the magnetic field is expressed as

$$F/\text{unit area}=\int\sigma B_o{}^2(u_\infty-u)\,dy=\sigma B_o{}^2e^{-m_1t}\int_0^{y\to\infty}erf\frac{y}{2\sqrt{\nu t}}dy \tag{19b}$$

The force per unit area goes to infinity as the upper limit of integration goes to infinity because the magnetic field extends

undiminished an infinite distance from the plate. Thereby, an infinite amount of fluid is accelerated, resulting in an infinite force.

MAGNETIC FIELD FIXED RELATIVE TO THE FLUID

At all times less than zero the fluid, magnetic field, and plate are assumed to be at rest. At time $t=0$ the plate begins moving with velocity $u=u_\infty$ but the magnetic field remains at rest. The differential equation is the same as equation (12) because there is no relative motion between the fluid at $y=\infty$ and the magnetic field.

$$\frac{\partial u}{\partial t}+m_1 u=\nu\frac{\partial^2 u}{\partial y^2} \tag{20}$$

The boundary conditions are

$$u=u_\infty \quad \text{at } y=0\ t\geq 0$$

$$u=0 \quad \text{at } y>0\ t=0$$

Applying the Laplace transformation to equation (20), as was done in the previous section, yields the transformed equation

$$\nu\frac{d^2\bar{u}}{dy^2}=\bar{u}(s+m_1)$$

The solution to this ordinary differential equation is

$$\bar{u}=C_1(s)e^{-y\sqrt{\frac{s+m_1}{\nu}}}+C_2 e^{+y\sqrt{\frac{s+m_1}{\nu}}}$$

where the constant C_2 is set equal to zero because of the requirement of a finite velocity at $y=\infty$. The integration constant, $C_1(s)$, is found from the boundary condition at $y=0$, $t\geq 0$, as

$$C_1(s)=\frac{u_\infty}{s}$$

Equation (20) can be written as

$$\bar{u}=\frac{u_\infty}{(s+m_1)-m_1}e^{-\sqrt{s+m_1}\frac{y}{\sqrt{\nu}}}$$

This equation can be inverted with the aid of reference 30 as

$$u=\frac{u_\infty}{2}\left[e^{-y\sqrt{\frac{m_1}{\nu}}}erfc\left(\frac{y}{2\sqrt{\nu t}}-\sqrt{m_1 t}\right)+e^{+y\sqrt{\frac{m_1}{\nu}}}erfc\left(\frac{y}{2\sqrt{\nu t}}+\sqrt{m_1 t}\right)\right] \tag{21}$$

The symbol *erfc* denotes the complementary error function defined as $1-erf$ (see, e. g., p. 370 of ref. 31). The velocity is once again dependent on more than one parameter so that a single similar profile cannot be drawn. Several profiles are shown in figure 2 (b). The fluid at $y=\infty$ is not disturbed in this case because the velocity across the magnetic lines is zero. In the vicinity of the plate the induced magnetic force counteracts the acceleration force of viscosity resulting in an increased rate of shear at the walls as expressed by the skin-friction coefficient.

$$c_f=\frac{2\nu}{u_\infty}\left(\sqrt{\frac{m_1}{\nu}}\,erf\sqrt{m_1 t}+\frac{e^{-m_1 t}}{\sqrt{\pi\nu t}}\right) \tag{22}$$

Even at time, $t=\infty$, a friction force acts on the plate—a situation contrary to the previous case and the Rayleigh problem. Values computed by equation (22) are shown in figure 3.

The force on the magnetic field is given by

$$F/\text{unit area}=\int_0^\infty \sigma B_o^2 u\,dy \tag{23}$$

where u is given by equation (21). The force is finite in this case.

Another case which may be of interest arises when the magnetic field is fixed on the plate but a pressure gradient compensates for the action of the magnetic field at $y=\infty$. A flow of this character may be imagined to exist in the early stages of boundary-layer formation on the walls of a two-dimensional channel. The conducting fluid is assumed to be pumped through a channel containing a stationary transverse magnetic field. A pressure gradient arises automatically to compensate for the resistance of the magnetic field. The equations then describe the boundary layer as a function of time, after the pump has started. For this case equation (7) reduces to

$$\frac{\partial u}{\partial t}+m_1(u-u_\infty)+\frac{1}{\rho}\frac{\partial p}{\partial x}=\nu\frac{\partial^2 u}{\partial y^2}$$

The pressure gradient $\frac{1}{\rho}\frac{\partial p}{\partial x}$ is found by examining the boundary condition mentioned above at $y=\infty$. At $y=\infty$

$$\frac{\partial u}{\partial t}=\frac{\partial^2 u}{\partial y^2}=u=0$$

Therefore, at $y=\infty$,

$$-m_1 u_\infty+\frac{1}{\rho}\frac{\partial p}{\partial x}=0$$

and the above equation becomes equation (12). Since the boundary conditions are the same as when the magnetic field was fixed relative to the fluid, the results shown in figures 2 (b) and 3 apply here also.

BOUNDARY LAYER ON A SEMI-INFINITE FLAT PLATE

In the analysis of the boundary layer on a flat plate moving impulsively, it was found that the shape of the boundary-layer velocity profile changes with time, necessitating a new calculation at each instant. Therefore, a simple transformation of the coordinates would not yield a similar solution wherein all profiles could be drawn as one. It is then to be expected that in the flow of an incompressible fluid over a semi-infinite flat plate in the presence of a magnetic field, a similar solution will not exist. Since the boundary-layer solution of Blasius is not known in closed form and the velocity profiles at two different stations along the plate are not similar, a numerical solution to a series expansion is found by the method used in reference 33. The first or zero-order term is found to be the same as the Blasius solution which is well known and is tabulated, for example, on page 103 of reference 28. The first nonzero term will be calculated for the cases studied here.

The boundary-layer velocity and temperature profiles will be found for three cases. The conductivity of the fluid is assumed to be uniform throughout the flow field in the first

and second cases. A particular variation is assumed in the third case. The magnetic field is fixed relative to the plate in the first and third cases and relative to the fluid in the second case. A fourth case is shown to be equivalent to the second. In all cases the fluid will be assumed to be incompressible and to have a Prandtl number of 1.[5]

MAGNETIC FIELD FIXED RELATIVE TO THE PLATE

Velocity profile.—The magnetic field lines of force are assumed to be perpendicular to the free-stream direction and to begin at the leading edge of the plate as indicated in figure 4. An experimental setup may be imagined to consist of a wing or flat plate in a stream of conducting fluid such as mercury, sodium, or salt water. A magnetic field is impressed across the flow field using either a permanent or electromagnet.

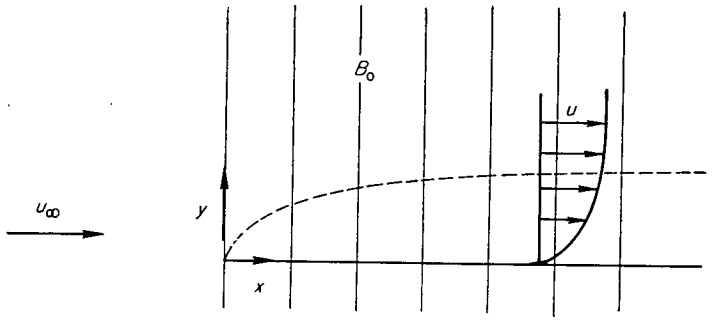


FIGURE 4.—Fluid flowing past a semi-infinite flat plate in the presence of a transverse magnetic field.

On the basis of the usual boundary-layer assumptions, equation (7) reduces to

$$u\frac{\partial u}{\partial x}+v\frac{\partial u}{\partial y}+m_1u=\nu\frac{\partial^2 u}{\partial y^2} \tag{24}$$

The boundary conditions are that $u=0$ at $y=0$ and $u=u_\infty$ upstream of the plate. At $y=\infty$, $\partial u/\partial y=0$ and $\partial u/\partial x=-m_1$. Outside of the boundary layer the continuity equation requires that $\partial v/\partial y=m_1$; therefore, $v\to\infty$ as $y\to\infty$. If the flow field is restricted to the vicinity of the surface of the flat plate, no real difficulty arises. In an actual problem the magnetic field will not extend uniformly to large distances from the plate. At the location where the magnetic field strength dies out another viscous layer will develop. This slip layer will be ignored. Equation (24) is the same as the incompressible boundary-layer equation except for the additional term m_1u. As was done in the Blasius boundary-layer solution, the transformation,

$$\left.\begin{aligned}\xi&=x\\ \eta&=y\sqrt{\frac{u_\infty}{\nu x}}\end{aligned}\right\} \tag{25}$$

is introduced. The stream function, ψ, is defined as

$$\psi=\sqrt{u_\infty\nu x}\,[f_o+\sqrt{mx}f_1+mxf_2+(mx)^{3/2}f_3+(mx)^2f_4\ \ldots] \tag{26}$$

where the functions f_o, f_1, f_2, . . . are functions of η only. The series expansion in $\sqrt{mx}$ is suggested by equation (21), where the exact form of m is yet to be determined. If the expression (21) is expanded in a power series in m_1t, the odd power terms contributed by the first and second parts cancel each other. Also, if these terms are carried along in the following analysis, the corresponding functions are found to be zero. Therefore, only whole powers of mx will be considered in what follows.

The velocity components and their derivatives are found from equations (25) and (26) as

$$u=\frac{\partial\psi}{\partial y}=\frac{\partial\psi}{\partial\xi}\frac{\partial\xi}{\partial y}+\frac{\partial\psi}{\partial\eta}\frac{\partial\eta}{\partial y}$$

$$u=u_\infty\,[f_o'+mxf_2'+(mx)^2f_4'\ \ldots] \tag{27}$$

$$v=-\frac{\partial\psi}{\partial x}=-\frac{\partial\psi}{\partial\xi}\frac{\partial\xi}{\partial x}-\frac{\partial\psi}{\partial\eta}\frac{\partial\eta}{\partial x}$$

$$v=\frac{1}{2}\sqrt{\frac{u_\infty\nu}{x}}\,[f_o'+mxf_2'+(mx)^2f_4'+\ \ldots]-$$

$$\frac{1}{2}\sqrt{\frac{u_\infty\nu}{x}}\,[f_o+3mxf_2+5(mx)^2f_4+\ \ldots] \tag{28}$$

Similarly,

$$\frac{\partial u}{\partial x}=-\frac{\eta}{2}\frac{u_\infty}{x}\,[f_o''+mxf_2''+(mx)^2f_4''+\ \ldots]+$$

$$\frac{u_\infty}{2x}\,[2mxf_2'+4(mx)^2f_4'+\ \ldots] \tag{29a}$$

$$\frac{\partial u}{\partial y}=u_\infty\sqrt{\frac{u_\infty}{\nu x}}\,[f_o''+mxf_2''+(mx)^2f_4''+\ \ldots] \tag{29b}$$

$$\frac{\partial^2 u}{\partial y^2}=\frac{u_\infty^2}{\nu x}[f_o'''+mxf_2'''+(mx)^2f_4'''+\ \ldots] \tag{29c}$$

When equations (27) through (29) are substituted into equation (24) and the like powers of

$$mx=\frac{\sigma B_o^2}{\rho u_\infty}x=\frac{\overline{M}^2}{Re_x} \tag{30}$$

are equated, the following differential equations result:

$$2f_o'''=-f_o''f_o \tag{31}$$

$$f_2'''=f_o'f_2'-\frac{1}{2}f_of_2''-\frac{3}{2}f_2f_o''+f_o' \tag{32a}$$

$$f_4'''=2f_o'f_4'+f_2'f_2'-\frac{1}{2}f_of_4''-\frac{3}{2}f_2f_2''-\frac{5}{2}f_4f_o''+f_2' \tag{32b}$$

etc.

The boundary conditions are

$$f_o=f_2=f_4=\ \ldots\ =0 \text{ at } \eta=0$$

$$f_o'=f_2'=f_4'=\ \ldots\ =0 \text{ at } \eta=0$$

$$f_o'=1 \text{ and } f_2'=-1 \text{ at } \eta=\infty$$

$$f_4'=f_6'=\ \ldots\ =0 \text{ at } \eta=\infty$$

[5] Recent theoretical computations by Hansen (ref. 34) indicate that when the air is ionized up to 20 or 25 percent, a more realistic value for the Prandtl number would be about 0.3. When the gas becomes fully ionized, the Prandtl number drops off to the order of 0.01.

The differential equations for f_2 and f_4 are linear ordinary differential equations with variable coefficients. Since the coefficients (Blasius solution) are not known in closed form, the equations must be integrated numerically. Only the functions f_2 and f_4 of the series will be found because the work involved is sizable and it is the intent of this study to find the over-all trends and gross effects rather than precise results.

The Runge-Kutta method was used to integrate both the homogeneous and nonhomogeneous forms of equations (32a) and (32b). The integration is started at the surface of the plate using two boundary conditions and then assuming a value for f_2'' and f_4''. The correct solution is found by a proper combination of the numerical solutions to the homogeneous and nonhomogeneous equations. The factor by which the homogeneous equation is to be multiplied is found from the boundary condition at $\eta=\infty$. The numerical results for f_2 and f_4 are tabulated in table I (a). The velocity profiles shown in figure 5 (a) indicate that the flow separation at $mx=0.5$ will probably not be predicted if a sufficient number of terms are taken in the series (27). The first three terms (f_o', f_2', and f_4') describe the velocity in the boundary layer quite well up to at least $mx=0.2$.

The skin-friction coefficient and the displacement δ^* of an incoming streamline are

$$c_f=\frac{0.664-1.789\ mx+0.706\ m^2x^2-\ \cdots\ +\ \cdots}{\sqrt{Re_x}} \tag{33a}$$

$$\delta^*=mxy+(1.73+0.54\ mx+1.34\ m^2x^2+\ \cdots\ )\sqrt{\frac{\nu x}{u_\infty}} \tag{33b}$$

The unit generating the magnetic field is assumed to be carried by the aircraft. The drag on this unit caused by the magnetic-field-fluid interaction is

$$F/\text{unit area}=\int_0^{y\to\infty}\sigma B_o^2 u\,dy$$

Substituting equation (27),

$$F/\text{unit area}=\sigma B_o^2\sqrt{u_\infty \nu x}\int_0^{\eta\to\infty}(f_o'+mxf_2'+\ \cdots\ )d\eta$$

$$=\sigma B_o^2\sqrt{u_\infty \nu x}\,(f_o+mxf_2+\ \cdots\ )_0^{\eta\to\infty} \tag{33c}$$

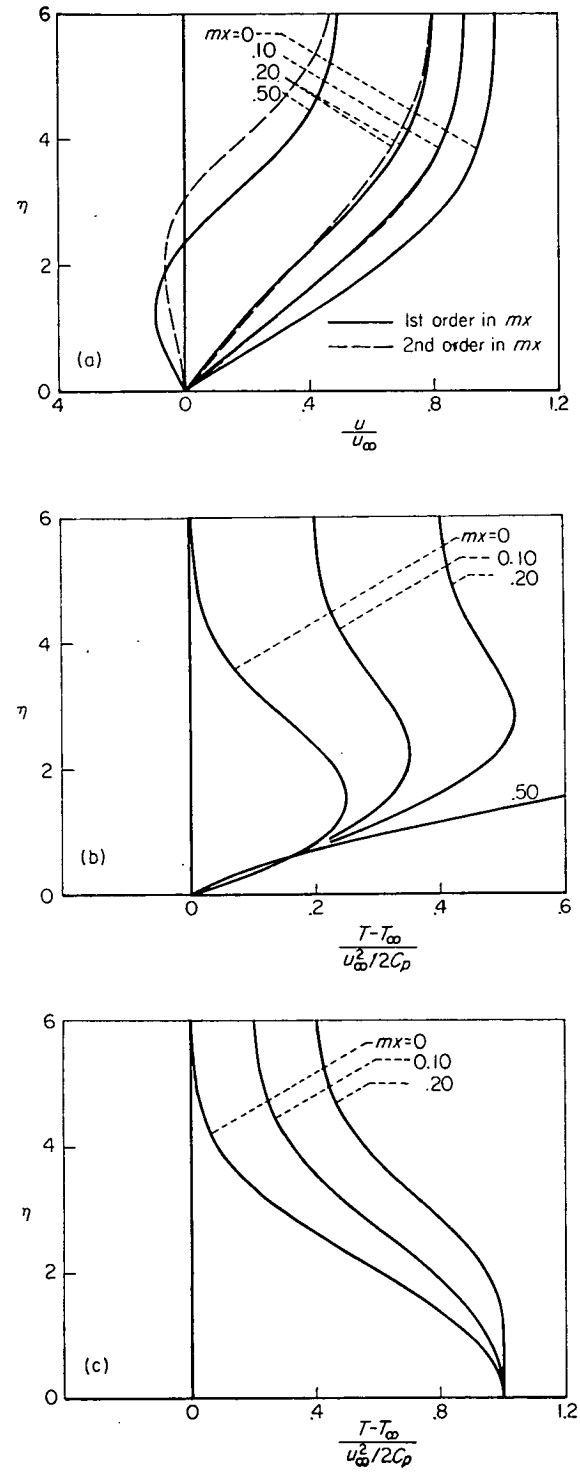
The force is finite only for a conducting layer of finite thickness.

Temperature profile.—When the pressure gradients are reasoned to be everywhere zero and the usual two-dimensional boundary-layer assumptions are made, equation (11) reduces to

$$\rho u C_p\frac{\partial T}{\partial x}+\rho v C_p\frac{\partial T}{\partial y}-\sigma B_o^2u^2=\frac{C_p\mu}{Pr}\frac{\partial^2 T}{\partial y^2}+\mu\left(\frac{\partial u}{\partial y}\right)^2 \tag{34}$$

If total energy is defined as

$$E=C_pT+\frac{u^2}{2} \tag{35}$$



(a) Velocity.
(b) Temperature distribution for a cool wall, $T_w=T_\infty$.
(c) Temperature distribution for an insulated wall.

FIGURE 5.—Boundary-layer profiles for fluid flowing over a semi-infinite flat plate with a transverse magnetic field fixed relative to the plate.

equations (24) and (34) can be combined to yield a differential equation for the transport of total energy E; that is, if equation (24) is multiplied by u, added to equation (34), and the Prandtl number, Pr, is assumed to be 1,

$$u\frac{\partial E}{\partial x}+v\frac{\partial E}{\partial y}=\nu\frac{\partial^2 E}{\partial y^2} \tag{36}$$

TABLE I.—MAGNETIC FIELD FIXED RELATIVE TO PLATE

(a) Stream function							(b) Temperature function for cold plate		(c) Temperature function for insulated plate	
η	f_2	f_2'	f_2''	f_4	f_4'	f_4''	$\frac{T_2}{u_\infty^2/2C_p}$	$\frac{T_2'}{u_\infty^2/2C_p}$	$\frac{T_2}{u_\infty^2/2C_p}$	$\frac{T_2'}{u_\infty^2/2C_p}$
0	0	0	−0.894	0	0	0.353	0	−0.352	0	0
.2	−.018	−.178	−.888	.007	.069	.336	−.047	−.115	.024	.236
.4	−.071	−.354	−.868	.027	.132	.287	−.046	.116	.094	.465
.6	−.159	−.525	−.835	.059	.183	.213	−.001	.336	.209	.679
.8	−.281	−.687	−.789	.099	.216	.117	.087	.538	.364	.867
1.0	−.433	−.839	−.730	.144	.228	.068	.213	.715	.554	1.024
1.2	−.615	−.978	−.660	.189	.218	−.111	.370	.859	.771	1.139
1.4	−.824	−1.102	−.579	.230	.184	−.228	.553	.965	1.006	1.207
1.6	−1.055	−1.209	−.489	.261	.127	−.338	.754	1.028	1.250	1.224
1.8	−1.306	−1.298	−.394	.279	.050	−.431	.962	1.047	1.492	1.187
2.0	−1.573	−1.367	−.296	.280	−.044	−.500	1.169	1.020	1.722	1.102
2.2	−1.852	−1.416	−.197	.261	−.148	−.539	1.367	.954	1.930	.973
2.4	−2.138	−1.446	−.103	.221	−.257	−.544	1.549	.854	2.108	.811
2.6	−2.429	−1.458	−.017	.159	−.363	−.514	1.707	.730	2.253	.628
2.8	−2.720	−1.454	.059	.076	−.460	−.450	1.840	.593	2.359	.440
3.0	−3.010	−1.435	.121	−.024	−.541	−.358	1.944	.453	2.429	.259
3.2	−3.294	−1.406	.168	−.139	−.602	−.247	2.021	.321	2.464	.096
3.4	−3.572	−1.369	.201	−.264	−.640	−.125	2.074	.205	2.469	−.039
3.6	−3.841	−1.327	.218	−.393	−.653	−.005	2.105	.108	2.451	−.143
3.8	−4.102	−1.283	.222	−.523	−.642	.106	2.118	.033	2.414	−.213
4.0	−4.354	−1.239	.216	−.649	−.611	.199	2.119	−.020	2.367	−.253
4.2	−4.598	−1.197	.200	−.767	−.564	.269	2.112	−.054	2.315	−.267
4.4	−4.833	−1.159	.180	−.874	−.505	.314	2.099	−.072	2.262	−.260
4.6	−5.062	−1.125	.156	−.968	−.440	.335	2.083	−.078	2.212	−.239
4.8	−5.284	−1.097	.131	−1.049	−.373	.334	2.068	−.075	2.167	−.210
5.0	−5.501	−1.073	.107	−1.117	−.307	.316	2.054	−.068	2.128	−.177
5.2	−5.713	−1.054	.085	−1.173	−.247	.285	2.041	−.058	2.096	−.144
5.4	−5.923	−1.039	.065	−1.217	−.194	.248	2.030	−.047	2.070	−.113
5.6	−6.129	−1.028	.049	−1.251	−.148	.208	2.022	−.037	2.050	−.087
5.8	−6.334	−1.019	.036	−1.277	−.111	.168	2.016	−.028	2.035	−.064
6.0	−6.537	−1.013	.026	−1.296	−.081	.132	2.011	−.021	2.024	−.047
6.2	−6.739	−1.009	.018	−1.309	−.057	.101	2.007	−.015	2.016	−.033
6.4	−6.940	−1.006	.012	−1.319	−.040	.075	2.005	−.010	2.011	−.022
6.6	−7.141	−1.004	.008	−1.326	−.027	.054	2.003	−.007	2.007	−.015
6.8	−7.342	−1.002	.005	−1.330	−.018	.038	2.002	−.004	2.005	−.010
7.0	−7.542	−1.001	.003	−1.333	−.012	.026	2.001	.003	2.003	−.006
7.2	−7.743	−1.001	.002	−1.335	−.008	.017	2.001	.002	2.002	−.004
7.4	−7.943	−1.001	.001	−1.336	−.005	.011	2.000	.001	2.002	−.002
7.6	−8.143	−1.0	.001	−1.337	−.003	.007	2.000	.001	2.001	−.001
7.8	−8.343	−1.0	0	−1.337	−.002	.004	2.000	0	2.000	−.001
8.0	−8.543	−1.0	0	−1.338	−.001	.002	2.000	0	2.000	0
8.2	−8.743	−1.0	0	−1.338	0	.001	2.000	0	2.000	0
8.4	−8.943	−1.0	0	−1.338	0	0	2.000	0	2.000	0
8.6	−9.143	−1.0	0	−1.338	0	0	2.000	0	2.000	0

Although the temperature distribution is altered by the presence of the magnetic field because u and v are affected, the total energy of the conducting fluid is not. The kinetic energy removed by the force of the magnetic field is exactly equal to the heat generated by the electric current, independent of the field strength B_o and the conductivity σ. An analogy may be drawn by considering a similar situation for an electric motor. Assume the motor to be rotating at a given speed. The power is then turned off and the armature is short-circuited. The motor will decelerate at a given rate depending on the field strength, resistance of the circuit, and rotational speed, just as in the fluid flow problem. The temperature rise of the wires, insulation, etc., however, depends only on the initial kinetic energy of the rotor. If the conductivity of the wires (or fluid) is reduced, the time required to stop the motion will be increased but the total j^2/σ or joule heat is not changed.

A first-order estimate of the influence of the magnetic field on the temperature profile can be found from equation (34) together with equations (25) through (29) and table I (a). Assume that

$$T=T_o(\eta)+T_2(\eta)mx+T_4(\eta)m^2x^2+\ldots \tag{37}$$

where, T_2, T_4, . . . are functions only of $\eta=y\sqrt{\frac{u_\infty}{\nu x}}$ and $T_1=T_3=T_5\ldots=0$ as in the part of the problem dealing with the velocity profile. The derivatives of the temperature with respect to x and y are found as

$$\frac{\partial T}{\partial x}=\frac{\partial T}{\partial \xi}\frac{\partial \xi}{\partial x}+\frac{\partial T}{\partial \eta}\frac{\partial \eta}{\partial x}$$

$$\left.\begin{aligned}\frac{\partial T}{\partial x}&=\frac{1}{x}\left[mxT_2+2m^2x^2T_4+\ldots-\right.\\&\qquad\left.\frac{\eta}{2}(T_o'+mxT_2'+m^2x^2T_4'+\ldots)\right]\\\frac{\partial T}{\partial y}&=\frac{\partial T}{\partial \eta}\frac{\partial \eta}{\partial y}=\sqrt{\frac{u_\infty}{\nu x}}(T_o'+mxT_2'+m^2x^2T_4'+\ldots)\end{aligned}\right\} \tag{38}$$

When the various expressions are inserted into equation (34) and terms containing like powers of mx are equated, the differential equations for T_o and T_2 are

$$\frac{T_o''}{Pr}+\frac{T_o'f_o}{2}+\frac{u_\infty^2(f_o'')^2}{C_p}=0 \tag{39}$$

$$\frac{T_2''}{Pr}+\frac{T_2'f_o}{2}-f_o'T_2+\frac{3}{2}f_2T_o'+\frac{u_\infty^2}{C_p}(f_o'^2+2f_o''f_2'')=0 \tag{40}$$

The boundary conditions are

$$\begin{aligned}T_o&=T_w &&\text{at } \eta=0\\T_o&=T_\infty &&\text{at } \eta=\infty\\T_2''&=T_2'=0 &&\text{at } \eta=\infty\\T_2&=0 &&\text{at } \eta=0\end{aligned}$$

The solution to equation (39) was first found by Pohlhausen and is discussed on page 246 ff. of reference 28. The function $T_o(\eta)$ is the temperature profile for a boundary layer on a flat plate and is given by (assuming $Pr=1$)

$$T_o=T_\infty+\left(T_w-T_\infty-\frac{u_\infty^2}{2C_p}\right)(1-f_o')+\frac{u_\infty^2}{2C_p}(1-f_o'^2) \quad (41)$$

The derivative of T_o to be inserted into equation (40) becomes

$$T_o'=-f_o''\left(T_W-T_\infty-\frac{u_\infty^2}{2C_p}+\frac{u_\infty^2}{C_p}f_o'\right) \quad (42)$$

For simplicity, the temperature of the plate will be assumed to be the same as that of the fluid far from the plate; that is, $T_W=T_\infty$. Equation (40) then becomes ($Pr=1$)

$$T_2''+\frac{f_o}{2}T_2'-f_o'T_2+\frac{u_\infty^2}{C_p}\left[\frac{3}{2}f_2f_o''\left(\frac{1}{2}-f_o'\right)+(f_o')^2+2f_o''f_2''\right]=0 \quad (43)$$

Equation (43) was integrated numerically by the same method used for equation (32a) and the results are tabulated in table I (b). Several temperature profiles are shown in figure 5 (b). The quantity of heat transferred to the plate per unit time is

$$q=k\left(\frac{\partial T}{\partial y}\right)_{y=0} \quad (44a)$$

The local convective heat-transfer rate is ($Pr=1$)

$$h=\frac{q}{u_\infty^2/2C_p}=\frac{\rho u_\infty C_p}{2\sqrt{Re_x}}(0.664-0.704\,mx-\ \ldots\ +\ \ldots) \quad (44b)$$

In the limit as the conductivity or field strength vanishes ($m\to 0$), equation (44b) reduces to

$$h)_{m=0}=\frac{f_o''u_\infty\rho C_p}{\sqrt{Re_x}} \quad (45a)$$

or by virtue of equation (33a)

$$h)_{m=0}=\frac{1}{2}c_f\rho u_\infty C_p \quad (45b)$$

Equation (45b) is often identified as Reynolds analogy. A similar relation of equal simplicity was not found for the problems treated in this paper.

The differential equation for flow over an insulated plate is obtained from equation (40) by introducing the proper expression for T_o'. The solution of equation (39) for the insulated plate case is (see, e. g., ref. 28)

$$T_o=T_\infty+\frac{u_\infty^2}{2C_p}(1-f_o'^2) \quad (46a)$$

and therefore,

$$T_o'=-\frac{u_\infty^2}{C_p}f_o'f_o'' \quad (46b)$$

Equation (40) then becomes, for the insulated plate case ($Pr=1$),

$$T_2''+\frac{T_2'f_o}{2}-f_o'T_2-\frac{u_\infty^2}{C_p}\left[\frac{3}{2}f_2f_o'f_o''-(f_o')^2-2f_o''f_2''\right]=0 \quad (46c)$$

The temperature profiles (table I (c)) for several values of mx are shown in figure 5 (c). It is to be noted that the recovery temperature is not altered by the magnetic field. Such a result is to be expected since the magnetic field and the fluid at the wall do not interact.

MAGNETIC FIELD FIXED RELATIVE TO THE FLUID

Velocity profile.—In this case the magnetic lines of force move past the plate at the free-stream velocity. The fluid, which is decelerated by the viscous action of the plate, receives a push from the magnetic field which counteracts the viscous effect. Such a situation exists when a plate, vane, or wing moves through a stationary electrically conducting fluid and magnetic field. The boundary layer on a wing of an aircraft flying in the ionosphere over the magnetic poles of the earth could be considered to correspond to this case. Under these circumstances, equation (7) reduces to

$$u\frac{\partial u}{\partial x}+v\frac{\partial u}{\partial y}+\frac{\sigma B_o^2}{\rho}(u-u_\infty)=\nu\frac{\partial^2 u}{\partial y^2} \quad (47)$$

If the transformation of coordinates and the stream function described by equations (25) and (26) are introduced into equation (47), a set of ordinary linear differential equations with variable coefficients is found for f_2, f_4, . . .

$$f_2'''=f_o'f_2'-\frac{1}{2}f_o'f_2''-\frac{3}{2}f_2f_o''+f_o'-1 \quad (48a)$$

$$f_4'''=2f_o'f_4'+f_2'f_2'-\frac{1}{2}f_of_4''-\frac{3}{2}f_2f_2''-\frac{5}{2}f_4f_o''+f_2' \quad (48b)$$

The boundary conditions are

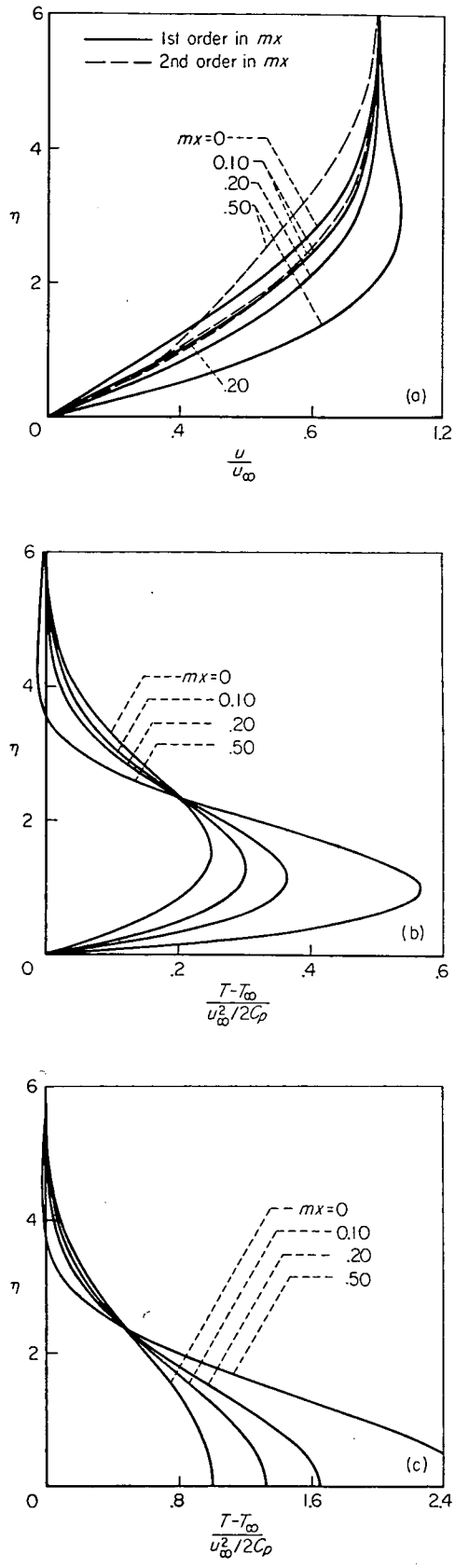
$$f_o=f_2=f_4=\ \ldots\ =0 \qquad \text{at } \eta=0$$

$$f_o'=f_2'=f_4'=\ \ldots\ =0 \qquad \text{at } \eta=0$$

$$f_o'=1 \text{ and } f_2'=f_4'=\ \ldots\ =0 \text{ at } \eta=\infty$$

The integration for f_2 and f_4 was carried out by the same method described in the previous section and the results are tabulated in table II (a). Several velocity profiles are shown in figure 6 (a). The difference between the first- and second-order curves is small at small values of mx. However, the separation of the $mx=0.5$ curves indicates that the series expression (27) does not converge rapidly. More than two terms in the series must then be used if the velocity profile is to be predicted accurately at values of mx higher than about 0.2. The local skin-friction coefficient is

$$c_f=\frac{0.664+2.293\,mx-2.768\,m^2x^2+\ \ldots\ -\ \ldots}{\sqrt{Re_x}} \quad (49a)$$



(a) Velocity.
(b) Temperature distribution for a cool wall, $T_w = T_\infty$.
(c) Temperature distribution for an insulated wall.

FIGURE 6.—Boundary-layer profiles for fluid flowing over a semi-infinite flat plate with a transverse magnetic field fixed relative to the fluid.

and the displacement thickness is

$$\delta^* = (1.73 - 2.21\,mx + 5.22\,m^2x^2 - \ldots + \ldots)\sqrt{\frac{\nu x}{u_\infty}} \tag{49b}$$

The disturbance caused by viscous action on the plate results in a force on the magnetic field, which is given by

$$F/\text{unit area} = \int_0^{y\to\infty} \sigma B_o^2 (u_\infty - u)\,dy$$

From equations (27), (66), and table II (a),

$$\left.\begin{aligned} F/\text{unit area} &= \sigma B_o \sqrt{u_\infty \nu x} \int_0^{\eta\to\infty} (1 - f_o' - mx f_2' - \ldots)\,d\eta \\ &= (1.73 - 2.21\,mx + 5.22\,m^2x^2 - \\ &\quad \ldots + \ldots)\sigma B_o^2 \sqrt{u_\infty \nu x} \\ &= \sigma u_\infty \delta^* B_o^2 \end{aligned}\right\} \tag{49c}$$

The force would appear as a reaction on the unit generating the magnetic field and not on the model which disturbs the fluid.

Equation (47) is identical with the differential equation for the case when the magnetic field is fixed with respect to the plate and a pressure gradient exists just strong enough to compensate for the electromagnetic effects at $\eta = \infty$. The boundary conditions and, hence, also the numerical results of table II (a) and figure 6 (a) can be applied to this problem.

Temperature profile.—Since the magnetic field lines are now moving relative to the plate, the expression for the electric current in the fluid is

$$j = \sigma B_o (u - u_\infty)$$

The equation for the transport of thermal energy in the boundary layer then becomes

$$\rho u C_p \frac{\partial T}{\partial x} + \rho v C_p \frac{\partial T}{\partial y} - \sigma B_o^2 (u - u_\infty)^2 = \frac{\mu C_p}{Pr} \frac{\partial^2 T}{\partial y^2} + \mu \left(\frac{\partial u}{\partial y}\right)^2 \tag{50}$$

If equations (47) and (50) are combined to describe the transport of total energy in the boundary layer ($Pr = 1$)

$$\rho u \frac{\partial E}{\partial x} + \rho v \frac{\partial E}{\partial y} + u_\infty (u - u_\infty)\sigma B_o^2 = \mu \frac{\partial^2 E}{\partial y^2} \tag{51}$$

where, as before, $E = C_p T + \frac{u^2}{2}$. It is seen that the presence of the magnetic field adds energy to the local element by doing work on the fluid retarded by viscosity. The magnitude of the work depends on the velocity, electrical conductivity, and field strength.

When the transformation of coordinates, equation (25), and the series expansion, equation (37), are inserted into equation (50), a set of differential equations is obtained for T_o, T_2, T_4, . . . The relation for T_o is the same as equation (39) and that for T_2 is

$$\frac{T_2''}{Pr} + \frac{f_o}{2} T_2' - f_o' T_2 + \frac{3}{2} f_2 T_o' + \frac{u_\infty^2}{C_p} [(1 - f_o')^2 + 2 f_o'' f_2''] = 0 \tag{52a}$$

TABLE II.—MAGNETIC FIELD FIXED RELATIVE TO FLUID

(a) Stream function							(b) Temperature function for cold plate		(c) Temperature function for insulated plate	
η	f_2	f_2'	f_2''	f_4	f_4'	f_4''	$\frac{T_2}{u_\infty^2/2C_p}$	$\frac{T_2'}{u_\infty^2/2C_p}$	$\frac{T_2}{u_\infty^2/2C_p}$	$\frac{T_2'}{u_\infty^2/2C_p}$
0	0	0	1.147	0	0	−1.384	0	2.022	3.228	0
.2	.022	.210	.953	−.028	−.275	−1.362	.337	1.370	3.163	−.631
.4	.081	.382	.773	−.110	−.542	−1.300	.555	.821	2.985	−1.121
.6	.172	.520	.606	−.243	−.793	−1.205	.672	.370	2.723	−1.477
.8	.287	.626	.453	−.425	−1.022	−1.080	.709	.014	2.403	−1.710
1.0	.420	.702	.312	−.650	−1.224	−.932	.684	−.253	2.047	−1.830
1.2	.566	.752	.186	−.913	−1.394	−.765	.613	−.438	1.677	−1.851
1.4	.719	.777	.072	−1.205	−1.529	−.584	.513	−.549	1.312	−1.786
1.6	.876	.781	−.028	−1.522	−1.626	−.394	.398	−.596	.967	−1.652
1.8	1.031	.767	−.113	−1.854	−1.686	−.202	.279	−.589	.654	−1.466
2.0	1.181	.737	−.184	−2.193	−1.708	−.014	.165	−.541	.383	−1.245
2.2	1.325	.694	−.241	−2.534	−1.692	.165	.064	−.464	.158	−1.006
2.4	1.458	.642	−.282	−2.868	−1.643	.327	−.019	−.369	−.019	−.766
2.6	1.581	.582	−.310	−3.189	−1.563	.467	−.083	−.269	−.149	−.539
2.8	1.691	.519	−.323	−3.492	−1.458	.580	−.127	−.172	−.237	−.337
3.0	1.788	.454	−.324	−3.771	−1.333	.663	−.153	−.087	−.286	−.166
3.2	1.873	.390	−.314	−4.024	−1.195	.713	−.163	−.016	−.305	−.030
3.4	1.944	.329	−.296	−4.248	−1.050	.732	−.161	.036	−.301	.069
3.6	2.004	.272	−.270	−4.444	−.904	.722	−.149	.072	−.280	.134
3.8	2.054	.221	−.240	−4.610	−.763	.687	−.133	.092	−.249	.171
4.0	2.093	.176	−.208	−4.749	−.630	.632	−.114	.099	−.213	.184
4.2	2.124	.138	−.176	−4.863	−.511	.565	−.094	.097	−.177	.180
4.4	2.149	.105	−.145	−4.954	−.405	.490	−.075	.089	−.142	.166
4.6	2.167	.079	−.117	−5.026	−.315	.413	−.058	.077	−.111	.144
4.8	2.181	.058	−.092	−5.081	−.240	.339	−.044	.064	−.084	.120
5.0	2.191	.042	−.071	−5.123	−.179	.271	−.033	.051	−.063	.097
5.2	2.198	.030	−.053	−5.154	−.130	.212	−.024	.040	−.045	.076
5.4	2.203	.021	−.039	−5.176	−.093	.161	−.017	.030	−.032	.057
5.6	2.206	.014	−.028	−5.192	−.065	.120	−.012	.022	−.022	.042
5.8	2.209	.009	−.020	−5.203	−.045	.087	−.008	.016	−.015	.030
6.0	2.210	.006	−.013	−5.210	−.030	.061	−.005	.011	−.010	.021
6.2	2.211	.004	−.009	−5.215	−.020	.043	−.003	.007	−.006	.014
6.4	2.212	.002	−.006	−5.218	−.013	.029	−.002	.005	−.004	.010
6.6	2.212	.001	−.004	−5.220	−.008	.019	−.002	.003	−.003	.006
6.8	2.212	.001	−.002	−5.222	−.005	.012	−.001	.002	−.002	.004
7.0	2.213	0	−.002	−5.522	−.003	.008	0	.001	−.001	.002
7.2	2.213	0	−.001	−5.223	−.002	.005	0	.001	−.001	.002
7.4	2.213	0	−.001	−5.223	−.001	.003	0	0	0	.001
7.6	2.213	0	0	−5.223	−.001	.002	0	0	0	.001
7.8	2.213	0	0	−5.223	0	.001	0	0	0	0
8.0	2.213	0	0	−5.223	0	.001	0	0	0	0
8.2	2.213	0	0	−5.224	0	0	0	0	0	0
8.4	2.213	0	0	−5.224	0	0	0	0	0	0
8.6	2.213	0	0	−5.224	0	0	0	0	0	0

When the expression (42) is inserted into equation (52a) and it is assumed that $T_w=T_\infty$ and $Pr=1$, the result is

$$T_2''+\frac{f_o}{2}T_2'-f_o'T_2+\frac{u_\infty^2}{C_p}\left[\frac{3}{2}f_2f_o''\left(\frac{1}{2}-f_o'\right)+(1-f_o')^2+2f_o''f_2''\right]=0 \tag{52b}$$

The boundary conditions are

$$T_2=0 \text{ at } \eta=0$$

$$T_2=0 \text{ at } \eta=\infty$$

The numerical integration of equation (52b) was carried out by the method used earlier and the results are tabulated in table II (b). The temperature profiles shown in figure 6 (b) correspond to the same values of mx shown for the velocity profiles in figure 6 (a). The temperature gradient and the heat transfer to the wall are, respectively,

$$\left(\frac{\partial T}{\partial y}\right)_{y=0}=\frac{u_\infty^2}{2C_p}\sqrt{\frac{u_\infty}{\nu x}}\,(0.332+2.022\,mx+\ldots)$$

$$h=\frac{q}{u_\infty^2/2C_p}=\frac{\rho u_\infty C_p}{2\sqrt{Re_x}}\,(0.664+4.044\,mx+\ldots) \tag{53}$$

The recovery temperature for an insulated plate is altered by the relative motion between the magnetic field and the fluid at the plate. The differential equation for the perturbation profiles are obtained by inserting equation (46b) into equation (52a).

$$T_2''+\frac{f_o}{2}T_2'-f_o'T_2-\frac{3u_\infty^2}{2C_p}f_2f_o'f_o''+\frac{u_\infty^2}{C_p}[(1-f_o')^2+2f_o''f_2'']=0 \tag{54a}$$

Several typical temperature profiles (table II (c)) are shown in figure 6 (c). The recovery temperature at the wall is changed due to the j^2/σ or joule heating caused by the relative motion between the magnetic field and the fluid at the plate; that is, the recovery temperature at the wall is given by

$$T_r)_{y=0}=T_o+1.614\,\frac{u_\infty^2}{C_p}\,mx+\ldots-\ldots$$

$$T_r)_{y=0}=T_\infty+\frac{u_\infty^2}{2C_p}\,(1+3.228\,mx+\ldots-\ldots) \tag{54b}$$

The heat transferred to the plate may also be written as $q=h(T_r-T_w)$, where T_r is the recovery temperature given by equation (54b) and T_w is the wall temperature. Since the magnetic field increases T_r as well as τ, the heat-transfer rate is increased in two ways.

MAGNETIC FIELD FIXED RELATIVE TO PLATE—FLUID OF VARIABLE CONDUCTIVITY

Velocity profile.—Numerous problems in fluid dynamics exist wherein the electrical conductivity of the fluid or the strength of the magnetic field changes with distance from

the surface. The magnetic field strength can be varied somewhat by the design of the apparatus. It is possible to adjust not only the strength of the field but also the variation with distance from or along the surface within certain physical limits. A first approximation to the shape and magnitude of most magnetic fields would be a uniform magnetic field of constant magnitude throughout the flow field. Such a magnetic system will once again be chosen for this case.

The electrical conductivity of the fluid would be expected to vary in a complicated manner in directions along and perpendicular to the surface and from one situation to the next. The constant value chosen for the conductivity in the two previous cases is not realistic. The conductivity will vary under actual conditions of flow in a boundary layer. This will surely change the skin friction and heat transfer from that found in the last two cases. A logical variation will be studied in this section to see how large an effect a variable conductivity will have on c_f and h.

It is to be expected that the conductivity will vanish at the outer edge of the boundary layer and reach a maximum somewhere near the surface. The equations which can be used to determine the number of ions (and hence conductivity) in a stream at high temperature or under circumstances wherein combustion is taking place, are cumbersome. Therefore, a simple, approximate, analytical relation for the electrical conductivity as a function of temperature between the plate and outer edge of the boundary layer was not found. The conductivity of air after the passage of a normal shock wave has been measured in a shock tube and reported on page 339 of reference 3. The conductivity is reproduced in figure 7. At Mach numbers above 20, the results are approximated by a straight line.

In view of the lack of knowledge of the variation of σ in the boundary layer, a linear relation between the velocity

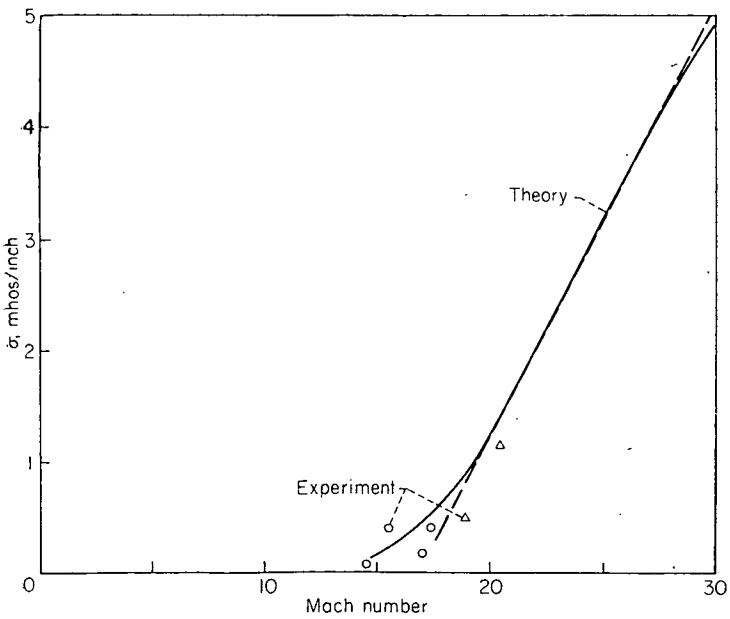


FIGURE 7.—Electrical conductivity of air as a function of shock wave Mach number as found in reference 3.

decrement and the conductivity will be chosen for this case. Therefore, it will be assumed that

$$\sigma=\sigma_o\left(\frac{u_\infty-u}{u_\infty}\right) \tag{55}$$

where σ_o is the conductivity at the surface, where $u=0$. Whether equation (55) is realistic is uncertain. Inserting the expression (55) into equation (24) gives

$$u\frac{\partial u}{\partial x}+v\frac{\partial u}{\partial y}+\frac{m_1 u}{u_\infty}(u_\infty-u)=\nu\frac{\partial^2 u}{\partial y^2} \tag{56}$$

As before, an ordinary differential equation for each of the functions $f_2, f_4, \ldots$ results when the variables in equations (25) and (26) are inserted into equation (56) and like powers of mx are equated.

$$f_2'''=f_o'f_2'-\frac{3}{2}f_2f_o''-\frac{1}{2}f_of_2''+f_o'(1-f_o') \tag{57a}$$

$$f_4'''=2f_o'f_4'+f_2'f_2'-\frac{1}{2}f_of_4''-\frac{3}{2}f_2f_2''-\frac{5}{2}f_4f_o''+f_2'-2f_2'f_o' \tag{57b}$$

The boundary conditions are,

$f_o=f_2=f_4=\ldots=0$ when $\eta=0$

$f_o'=f_2'=f_4'=\ldots=0$ when $\eta=0$

$f_o'=1, f_2'=f_4'=\ldots=0$ when $\eta=\infty$

The numerical integration of equation (57a) was carried out for f_2 by the method used in the other cases and the results are tabulated in table III(a). Typical boundary-layer velocity profiles are shown in figure 8(a). The local skin-friction coefficient is

$$c_f=\frac{0.664-0.627\,mx\pm\ldots}{\sqrt{Re_x}} \tag{58a}$$

and the displacement thickness is

$$\delta^*=(1.73+0.97\,mx+\ldots)\sqrt{\frac{\nu x}{u_\infty}} \tag{58b}$$

The force on the unit generating the magnetic field is expressed by

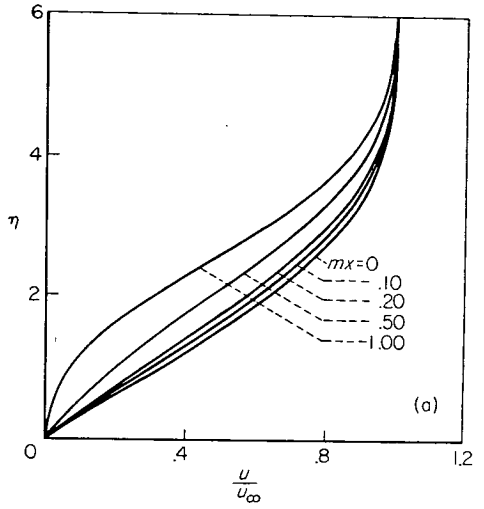
$$F=\sigma B_o^2\sqrt{u_\infty\nu x}\int_0^{\eta\to\infty}(1-f_o'-mxf_2'-\ldots)(f_o'+mxf_2'+\ldots)d\eta/\text{unit area}$$

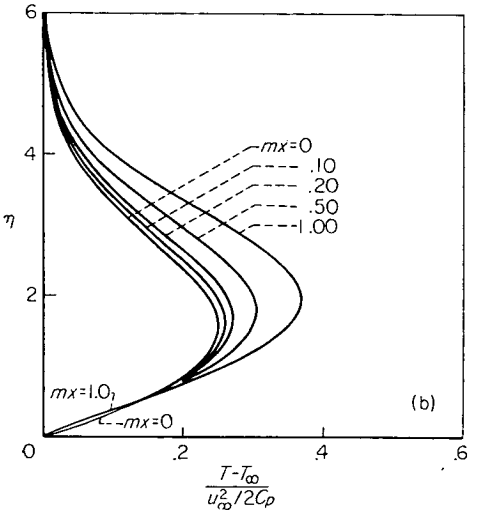
The integral is evaluated through the use of equation (57a) and table III (a) as

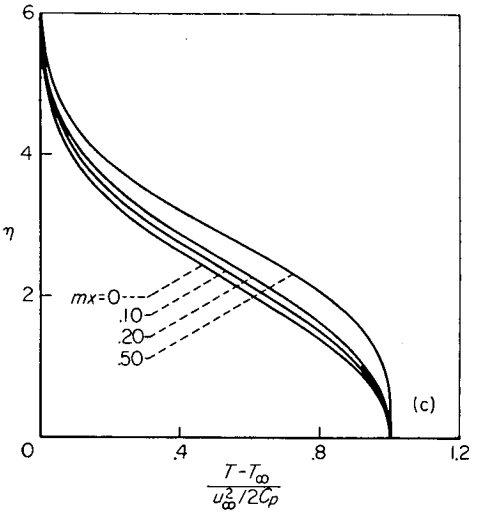
$$F=\sigma B_o^2\sqrt{u_\infty\nu x}\,(0.664+0.649\,mx+\ldots)\text{lb/unit area} \tag{59a}$$

or, integrating from the leading edge to x,

$$F=\frac{2}{3}x\sigma_o B_o^2\sqrt{u_\infty\nu x}\,(0.664+0.390\,mx+\ldots)\text{lb/unit width} \tag{59b}$$







(a) Velocity.
(b) Temperature distribution for a cool wall, $T_w = T_\infty$.
(c) Temperature distribution for an insulated wall.

FIGURE 8.—Boundary-layer profiles for fluid flowing over a semi-infinite flat plate with a transverse magnetic field fixed relative to the plate-fluid of variable conductivity.

Equation (59a) or (59b) expresses a drag force on the plate which is to be added to the friction drag. In coefficient form, the local drag per unit area on the plate due to the magnetic field is

$$c_B = \frac{mx}{\sqrt{Re_x}} (1.328 + 1.299\, mx + \ldots) \tag{60a}$$

When equations (58a) and (60a) are added, the net local force coefficient to a first order in mx is

$$c_D = \frac{1}{\sqrt{Re_x}} (0.664 + 0.701\, mx + \ldots) \tag{60b}$$

The interference of the magnetic field reduces the skin friction at the expense of a higher drag.

Temperature profile.—The thermal-energy transport equation is reduced in the manner used in the previous cases. The electrical or joule heating is now described by

$$\frac{j^2}{\sigma} = \sigma_o B_o^2 \left(\frac{u_\infty - u}{u_\infty}\right) u^2$$

Equation (11) is then

$$\rho C_p u \frac{\partial T}{\partial x} + \rho v C_p \frac{\partial T}{\partial y} - \frac{\sigma_o B_o^2}{u_\infty}(u_\infty - u)u^2 = \frac{\mu C_p}{Pr}\frac{\partial^2 T}{\partial y^2} + \mu \left(\frac{\partial u}{\partial y}\right)^2 \tag{61}$$

If equation (56) is multiplied by u and added to equation (61), the resulting equation for the transport of total energy is identical with equation (36). Once again, the temperature distribution is changed but the total energy of the fluid is not altered by the presence of a magnetic field.

The change of variables ξ, η, the stream function, ψ, and temperature expansion given by equations (25), (26), and (37), respectively, are now introduced into equation (61). A set of linear ordinary differential equations for T_o, T_2, T_4, . . . is obtained for this case when like powers of mx are equated. The expression for T_o is once again the same as equation (39). The differential equation for T_2 is

$$\frac{T_2''}{Pr} + \frac{f_o T_2'}{2} - f_o' T_2 + \frac{3}{2} f_2 T_o' + \frac{u_\infty^2}{C_p}[(1 - f_o')f_o'^2 + 2f_o'' f_2''] = 0 \tag{62}$$

If it is assumed that $Pr = 1$ and the expression for T_o' is inserted into equation (62), the result is

$$T_2'' + \frac{f_o T_2'}{2} - f_o' T_2 + \frac{u_\infty^2}{C_p}\left[\frac{3}{2} f_2 f_o''\left(\frac{1}{2} - f_o'\right) + (1 - f_o')f_o'^2 + 2f_o'' f_2''\right] = 0 \tag{63}$$

Numerical integration of equation (63) was carried out by the method used for the previous cases. The results are presented in table III (b) and several temperature profiles are shown in figure 8 (b). The coefficient for the convective heat-transfer rate is given by

$$h = \frac{\rho u_\infty C_p}{2\sqrt{Re_x}} (0.664 - 0.206\, mx - \ldots + \ldots) \tag{64}$$

TABLE III.—MAGNETIC FIELD FIXED RELATIVE TO PLATE—VARIABLE CONDUCTIVITY

(a) First-order stream function				(b) Temperature function for cold plate		(c) Temperature function for insulated plate	
η	f_2	f_2'	f_2''	$\frac{T_2}{u_\infty^2/2C_p}$	$\frac{T_2'}{u_\infty^2/2C_p}$	$\frac{T_2}{u_\infty^2/2C_p}$	$\frac{T_2'}{u_\infty^2/2C_p}$
0	0	0	−0.313	0	−0.103	0	0
.2	−.006	−.062	−.307	−.012	−.021	.008	.082
.4	−.025	−.122	−.289	−.009	.056	.032	.158
.6	−.055	−.177	−.262	.009	.122	.071	.221
.8	−.095	−.226	−.226	.039	.173	.120	.268
1.0	−.145	−.267	−.185	.077	.207	.176	.295
1.2	−.202	−.300	−.139	.121	.223	.236	.300
1.4	−.264	−.323	−.092	.165	.220	.295	.283
1.6	−.330	−.337	−.045	.208	.199	.348	.246
1.8	−.398	−.341	0	.244	.163	.392	.193
2.0	−.466	−.337	.004	.272	.117	.424	.128
2.2	−.532	−.325	.077	.290	.064	.443	.056
2.4	−.596	−.307	.106	.298	.010	.447	−.015
2.6	−.655	−.283	.128	.294	−.041	.437	−.081
2.8	−.709	−.256	.143	.282	−.085	.415	−.138
3.0	−.757	−.226	.150	.261	−.118	.383	−.180
3.2	−.799	−.196	.150	.235	−.140	.344	−.208
3.4	−.835	−.167	.144	.206	−.151	.301	−.221
3.6	−.866	−.139	.134	.175	−.152	.256	−.221
3.8	−.891	−.113	.121	.146	−.145	.213	−.210
4.0	−.911	−.090	.106	.118	−.132	.173	−.191
4.2	−.927	−.071	.090	.093	−.115	.137	−.167
4.4	−.940	−.054	.075	.072	−.097	.106	−.141
4.6	−.949	−.041	.060	.054	−.079	.080	−.116
4.8	−.956	−.030	.047	.040	−.063	.060	−.092
5.0	−.961	−.022	.036	.029	−.048	.043	−.072
5.2	−.965	−.015	.027	.020	−.036	.031	−.054
5.4	−.968	−.011	.020	.014	−.027	.021	−.040
5.6	−.970	−.007	.014	.009	−.019	.015	−.029
5.8	−.971	−.005	.010	.006	−.013	.010	−.020
6.0	−.972	−.003	.007	.004	−.009	.006	−.014
6.2	−.972	−.002	.005	.003	−.006	.004	−.009
6.4	−.972	−.001	.003	.002	−.004	.003	−.006
6.6	−.973	−.001	.002	.001	−.003	.002	−.004
6.8	−.973	0	.001	.001	−.002	.001	−.002
7.0	−.973	0	.001	0	−.001	.001	−.001
7.2	−.973	0	0	0	−.001	0	−.001
7.4	−.973	0	0	0	0	0	0
7.6	−.973	0	0	0	0	0	0
7.8	−.973	0	0	0	0	0	0
8.0	−.973	0	0	0	0	0	0
8.2	−.973	0	0	0	0	0	0
8.4	−.973	0	0	0	0	0	0
8.6	−.973	0	0	0	0	0	0

The influence of the magnetic field on the heat-transfer rate and skin friction is not so large in this case as in either of the two previous cases (eqs. (33a), (44b), (49a), and (53)). From these results it is apparent that the change in the heat-transfer rate and the skin friction is strongly dependent on the manner in which the conductivity (or magnetic field strength) vary through the boundary layer. A magnetic field which changes in strength with distance from the surface and a variable conductivity are to be expected in the real physical situation.

The differential equation for flow over an insulated plate is obtained by substitution of equation (46b) into equation (62).

$$T_2''+\frac{f_o T_2'}{2}-f_o' T_2-\frac{3u_\infty^2}{2C_p} f_2 f_o' f_o''+\frac{u_\infty^2}{C_p}\left[(1-f_o')f_o'^2+2f_o''f_2''\right]=0$$

The temperature profiles for several values of mx are shown in figure 8 (c) and tabulated in table III (c). As would be expected, the recovery temperature at the wall is not altered by the magnetic field because there is no relative motion between the fluid at the wall and the magnetic field.

MAGNETIC PARAMETER

UNITS

The importance of the magneto-hydrodynamic effect depends on the size of the magnetic parameter $m=\sigma B_o^2/\rho u_\infty$. The usual engineering units are: σ in mhos/inch; B_o in lines/square inch; ρ in slugs/cubic foot; and u_∞ in feet/second. If each of these quantities is expressed as such, the parameter mx will be dimensionless only if multiplied by a factor which relates the various dimensional quantities. When the correct conversion factors are inserted, reference 27,

$$m=1.529\times10^{-12}\frac{\sigma\left(\frac{\text{mhos}}{\text{in.}}\right)\left[B_o\left(\frac{\text{lines}}{\text{in.}^2}\right)\right]^2}{\rho\left(\frac{\text{slugs}}{\text{ft}^3}\right)u_\infty\left(\frac{\text{ft}}{\text{sec}}\right)}\text{ per inch} \quad (65a)$$

or

$$m=6.432\times10^{-10}\frac{\sigma\left(\frac{\text{mhos}}{\text{in.}}\right)\left[B_o\left(\frac{\text{lines}}{\text{in.}^2}\right)\right]^2}{\left(\frac{\rho}{\rho_o}\right)u_\infty\left(\frac{\text{ft}}{\text{sec}}\right)}\text{ per inch} \quad (65b)$$

where $\rho_o=0.002378$ slugs/ft^3 is the air density at sea level.

Another method of finding the conversion factor for m is to combine the electric motor equations (ref. 35)

$$F=8.8507\times10^{-8}B_o l i \text{ lb} \quad (66a)$$

$$E=B_o l u\times10^{-8}\text{ volts}=\frac{i}{\sigma l} \quad (66b)$$

so that

$$\frac{\text{Force}}{ul^3}=8.8507\times10^{-16}\sigma B_o^2\frac{\text{lb sec}}{\text{in.}^4}$$

or

$$m=\frac{\text{force}/l^3}{\rho_o(\rho/\rho_o)u^2}=\frac{(8.8507)(1728)10^{-16}}{0.002378}\frac{\sigma B_o^2}{(\rho/\rho_o)u}\text{ per inch}$$

$$=6.432\times10^{-10}\frac{\sigma B_o^2}{(\rho/\rho_o)u_\infty}\text{ per inch}$$

In words, the parameter m expresses the ratio of electromagnetic force density to dynamic pressure.

The value of m can easily vary over many orders of magnitude. However, the density ρ and velocity u associated with a particular vehicle are generally fixed within relatively narrow limits. It remains, then, to adjust the conductivity and magnetic field strength so that the desired characteristics are achieved. The limits for the magnetic field strength lie between zero and a maximum (discounting astrophysical possibilities) of about 10^5 lines/sq in. The electrical conductivity depends on the fluid considered and can vary over wide limits from very small values for insulators to approximately 10^5 mhos/inch for metals. The results of several investigations of the conductivity of gases will be discussed in the next section.

ELECTRICAL CONDUCTIVITY

The information on the electrical conductivity[6] of gases under the special conditions of this report is not large. However, it is known that the air around a missile will be a conductor if: (1) the energy imparted to the air is great enough to ionize it; (2) metal is ablated from the missile; (3) the missile is in the ionosphere where the air is ionized by radiation from the sun; or (4) other special devices are used to ionize the air, such as irradiation by high energy particles.

The electrical conductivity of air behind a normal shock wave has been measured in a shock tube and is reported on page 339 of reference 3. The results, replotted in figure 7, indicate conductivities of the order of 1 to 5 mhos/inch for air behind strong shock waves.

Firings of ultraspeed pellets, references 36 through 39, indicate that another phenomenon will enter the problem of conductivity. Photographs and spectrographs taken with special cameras show that metal is eroded or ablated from the pellet and swept off the model into the wake where it burns. Since the metal is in a liquid spray or vapor form while it is in the vicinity of the pellet, the conductivity there would be increased by a sizable amount. It would be difficult to estimate the orders of magnitude to be expected. The tests show that the air can be made a conductor by ionization of its molecules and atoms and/or by metal vapor or spray eroded from the surface of the vehicle. It is pointed out in reference 40 that the latter effect predominates when meteors enter the earth's atmosphere.

The air in the ionosphere is partially ionized by radiation from the sun so that it is a conductor without addition of energy from the aircraft. The amount of ionization at various altitudes and the total number of particles are listed in tables 2 and 9 of reference 41. A rough estimate of the conductivity is found from reference 7 as

$$\sigma=\frac{ne^2l_e}{m_eU_e}\approx 3\times 10^{-16}\, n\,\frac{N_o}{N}\ \text{mhos/inch} \qquad (67)$$

[6] Good electrical conductors are always good heat conductors. The ratio may be expressed approximately as (ref. 7),

$$\frac{k}{\sigma T}=\frac{\pi^2}{3}\left(\frac{\kappa}{e}\right)^2$$

where k is the coefficient of thermal conductivity, κ is Boltzmann's constant, and e is the charge on an electron

where e, l_e, m_e, and U_e are the charge, mean free path length, mass, and velocity, respectively, of the electron and N_o and N are the particle density at sea level and the altitude in question. The factor n is the electron density. The values for σ range from 10^{-4} mhos/in. at 62 miles altitude to about 32 mhos/in. at 250 miles altitude.

The large variety in fuels makes it difficult to bracket the magnitude of the conductivity of combustion products but information is available for several cases. It was reported in reference 5 that the conductivity of the jet from a 50-pound thrust acid-aniline rocket motor was measured as being about 10^{-6} mhos/in. It was added, however, that the addition of a small amount of an impurity such as sodium would strikingly increase the electron density.

A discussion is given in reference 6 of similar experiments and theory on the combustion of hydrocarbon fuels. The experimental evidence required that the number of electrons in the combustion products (10^{11} to 10^{14} per cc) be several orders of magnitude greater than predicted theoretically (10^8 to 10^9 per cc). The maximum conductivity can be estimated by equation (67) to be roughly 10^{-2} mhos/inch.

Although the conductivities discussed are low compared with those of metals, they appear to be large enough so that appreciable magneto-hydrodynamic forces can be exerted. If the conductivity is too low for a specific case, it may be possible that alkaline salts or some other additive can be used to increase the number of free electrons and ions.

APPLICATIONS

The possibility of using a magnetic field to prevent a hot fluid from coming in contact with a wall which it would dissolve or destroy was discussed in the introduction. The extent to which this can be accomplished is measured directly by the parameter $m=(\sigma B_o^2/\rho u_\infty)$. The larger the parameter m is, the more effectively the "fluid suspension" process can be carried out. The influence of the magnetic field on the fluid is expressed in equations (33), (44), (49), (53), (58), . . . by the product mx. The distance x represents an "adjustment distance" required before the fluid responds a given amount or adjusts to the magnetic lines of force. If the magnetic parameter is very large, the adjustment distance will be very small and the fluid will follow the magnetic lines of force quite closely as indicated in figure 9. The magnetic force restrains any motion across the lines of force because the inertia forces are insignificant in comparison. In this limit the magnetic lines of force are the same as invisible solid boundaries.

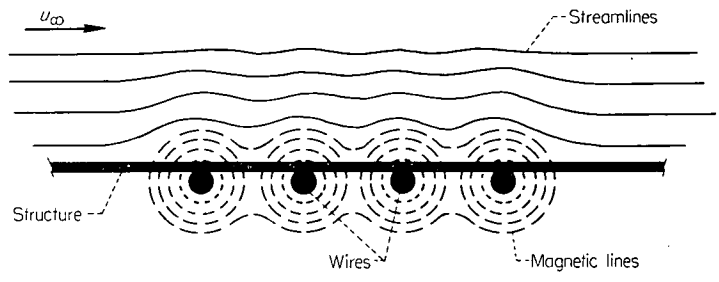


FIGURE 9.—Sketch of fluid of high electrical conductivity flowing over a surface.

If the parameter m is very small the adjustment distance x becomes very large and the influence of the magnetic field becomes negligible.

The numbers quoted in the last section for the conductivity and field strength indicate that most of the applications will lie between the two extreme limits.

FLOW OVER A HIGH-SPEED VEHICLE

Magneto-aerodynamic effects may be used to alter the external flow over aircraft. Examples which illustrate the changes in the boundary layer will now be discussed. It will be pointed out that the skin friction on an aircraft might be reduced by judicious use of a magnetic field either to inhibit transition to turbulent flow or to alter the boundary-layer profile.

It has been shown in reference 13 that the Reynolds number of transition is raised when a coplanar magnetic field is applied. The results of reference 13 can be used as a rough estimate for flows of the boundary-layer type when the particular velocity distribution may be approximated by a parabolic profile. This is permissible since a coplanar magnetic field does not change the velocity profile, which is not so for the cases considered in this paper.

The results of reference 14 for a transverse magnetic field apply to a two-dimensional channel and should not be used for flows of the boundary-layer type because of the change induced by the magnetic field on the velocity profile. For the flow in the two-dimensional channel the change in the velocity profile was largely responsible for the resistance to turbulence. The same will not always be true for other types of flow fields. It will then in general be necessary to carry out a stability calculation in order to determine whether a transverse magnetic field tends to stabilize or destabilize the boundary layer. A situation wherein the magnetic field destabilizes the flow field is presented in reference 26, warning one that the presence of a magnetic field does not always decrease the likelihood of transition.

The numerical results of table I and the equations (33) and (44) may be used to estimate the effects of a magnetic field attached to an aircraft on boundary layers of uniform electrical conductivity. The model analyzed theoretically will probably never be duplicated in a physical situation. However, circumstances may arise wherein the conductivity and magnetic field are such that they vary only slightly or are almost uniform in a layer of finite depth. This might occur, for example, (1) in the boundary layer of high-speed aircraft; (2) in the region between the surface of a blunt body and its shock wave; (3) in local regions near an aircraft when material is being ablated from the surface; or (4) in the ionosphere wherein air is ionized by radiation from the sun (ref. 41) and is then a uniform conductor, provided the influence of the aircraft is small. The fact that the layer is of finite thickness causes the equations to be in error at the interface. However, if the conducting layer is relatively thick the equations would serve as a good estimate in the vicinity of the surface.

The second semi-infinite flat plate case which was analyzed, equations (49) and (53), could be thought to correspond to flight over the magnetic poles of the earth or through some other magnetic field. The electrically conducting fluid could come about by the same processes mentioned in the previous paragraph. As before, the magnetic field strength and electrical conductivity will probably not correspond exactly to the model analyzed. A close approximation is obtained when an aircraft flies through the ionosphere over one of the magnetic poles of the earth (provided the influence of the aircraft on the electrical conductivity of the air and on the magnetic field is small). Since the earth's magnetic field is small ($B_o \approx 4$ lines/sq in. from ref. 42), effects of this type are generally negligible in the lower reaches of the ionosphere. At the higher altitudes the magnetic parameter is large enough to cause a change in the heat-transfer rate but at those altitudes the mean free path is so large that the continuum flow analysis of this report is no longer applicable.

If the air in the boundary layer is ionized by frictional heating, the conductivity of the air will change with distance from the surface (fig. 10). The actual variation to be expected would be difficult to predict theoretically. The

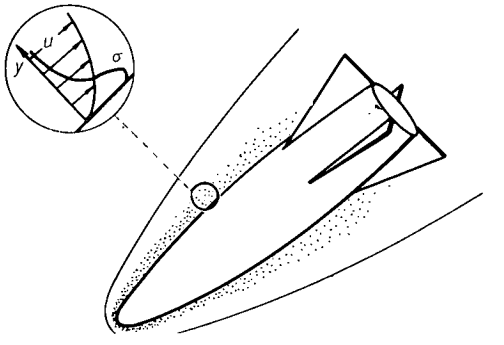


FIGURE 10.—Aircraft moving through the atmosphere at high speed.

solution for a boundary layer with variable electrical conductivity found in a previous section of this paper (eqs. (58), (59), (60), and (64)) and tabulated in table III can be used as an approximate answer. Equation (58) shows that the skin friction can be reduced by a sizable amount at the expense of increased total drag (see eq. (60)). The advantages of using a magnetic field lie in the possibility of reducing the aerodynamic heating, as expressed by equation (64).

The preceding discussion dealt with the advantages that may be achieved by reducing the skin friction, heat transfer, or turbulence. Favorable effects may also be obtained by increasing the displacement thickness of the boundary layer. Such a device, figure 11, could be used on the lower surface of a wing or body to induce forces for lift, control purposes, or drag. The magnitude of these forces is easily changed by increasing or decreasing the field strength which in turn increases or decreases the displacement thickness.

Several additional problems arise when magneto-hydrodynamic effects are used. The system generating the magnetic field will need to be cooled since its parts will dissipate power. Also, the weight of the unit required to generate a magnetic field of sufficient strength may be too large to consider, or of such a size that any advantages are nullified. If the slow moving fluid is hot enough to radiate energy, a sizable quantity of heat may be transferred even though the hot fluid is not in contact with the surface. An

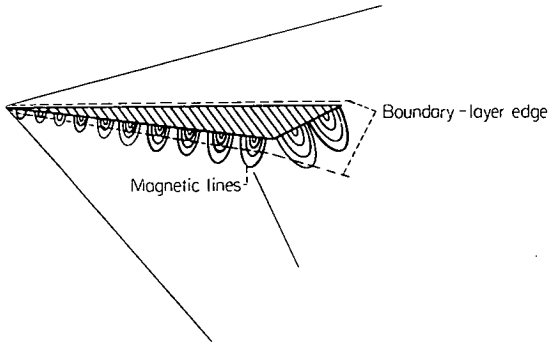


FIGURE 11.—Schematic diagram indicating use of magnetic field to build up the boundary layer on a wing for lift or control purposes.

evaluation of this effect would require a more complete analysis than the solutions developed in this paper.

Whether the applications just discussed can actually be made depends on the magnitude of the quantities entering the parameter m. Consider, for example, an aircraft moving through the upper atmosphere at 25,000 feet per second. From figure 7, a conductivity of not over 5 mhos/inch is to be expected. If ρ/ρ_o is taken as 10^{-4}, and the above values are inserted into equation (65b),

$$m=6.43\times10^{-10}\frac{5B_o^2}{2.5}\approx10^{-9}B_o^2$$

In figures 5, 6, and 8, it is seen that the product mx should be of the order of 0.1 for a notable magneto-aerodynamic effect to be brought about. If x is taken as about 100 inches, the magnetic field strength, B_o, should be around 1000 lines per square inch so that the product mx is equal to 0.1. A magnetic field of such a strength is not unreasonable.

FLOW IN PROPULSION UNITS

The discussion on the reduction of skin friction and heat-transfer rate to the walls of an aircraft by electromagnetic forces applies as well to the internal flow of reaction engines. It may be added that a uniform magnetic field across the jet stream corresponds to the channel flow problems studied in references 8 to 12 and 14. In general, imposing such a field increases the skin friction, equation (49a), and lowers the thrust because of the interference of the magnetic field. A compensating influence is realized through a reduction in turbulence in the stream (see, e. g., refs. 9 and 14) which lowers the skin friction, heat transfer, and probably the noise level of jet engines. Shallow magnetic fields appear to be the most promising for reducing the heat transfer if the flow is nearly laminar.

The cases and illustrations considered so far have assumed that an electric potential E has not been applied across the fluid. To do so would add another force term (see eq. (2)) to equations (7) and (11). If a source of power is available, a combined electric and magnetic field can be used to maneuver the fluid. A possible application would be to use the combined fields to induce an electric motor action to obtain very high exhaust velocities.

CONCLUDING REMARKS

The laminar boundary-layer solutions presented in this paper for the flow of an incompressible electrically conducting fluid over a flat plate indicate the changes that will be brought about by a transverse magnetic field. It has been found that the skin friction and heat-transfer rate are reduced if there is no relative motion between the plate and the magnetic field. The skin friction and heat-transfer rate increased in the case where relative motion was assumed. In all the cases studied the total drag was increased.

The product of the magnetic parameter m and an adjustment distance x is the quantity which determines the effectiveness of the magnetic field to change the heat-transfer rate. Other studies have shown that a magnetic field will in certain cases inhibit transition to turbulent flow and thereby retain a lower heat-transfer rate.

All the cases studied, except one, assume that the conductivity and magnetic field did not change with distance from the surface. A more realistic case of a variable conductivity was considered in one example where a special variation was chosen. The reduction in heat-transfer rate and skin friction for a given value of mx was not as large as when the conductivity was constant. This points out the importance of considering the way in which the conductivity and magnetic field strength change with distance from the surface.

AMES AERONAUTICAL LABORATORY
NATIONAL ADVISORY COMMITTEE FOR AERONAUTICS
MOFFETT FIELD, CALIF., *Mar. 13, 1957*

REFERENCES

1. Anon.: Pinch Effect. Scientific American, vol. 194, no. 2, Feb. 1956, p. 54.
2. Kurchatov, I. V.: Thermonuclear Fusion, Gas Discharge Research in the Soviet Union. Engineering, London, vol. 181, no. 4705, May 11, 1956, pp. 322–325.
3. Kantrowitz, Arthur: A Survey of Physical Phenomena Occurring in Flight at Extreme Speeds. Proceedings of the Conference on High-Speed Aeronautics. Polytechnic Institute of Brooklyn, Jan. 20–22, 1955, pp. 335–339.
4. Gilmore, F. R.: Equilibrium Composition and Thermodynamic Properties of Air to 24,000° K. The RAND Corp., RM–1543, Aug. 24, 1955.
5. Adler, Fred P.: Measurement of Conductivity of a Jet Flame. Jour. of Appl. Phys., vol. 25, no. 7, July 1954, pp. 903–906.
6. Sänger, E., Goercke, P., and Bredt, I.: On Ionization and Luminescence in Flames. NACA TM 1305, 1951.
7. Chapman, Sydney, and Cowling, T. G.: The Mathematical Theory of Non-Uniform Gases. Second ed., Cambridge Univ. Press, 1952.
8. Hartmann, Jul.: Hg-Dynamics I—Theory of the Laminar Flow of an Electrically Conductive Liquid in a Homogeneous Magnetic Field. Kgl. Danske Videnskabernes Selskab, Mathematisk-Fysiske Meddelelser, vol. 15, no. 6, Copenhagen, 1937.
9. Hartmann, Jul., and Lazarus, Freimut: Hg-Dynamics II—Experimental Investigations on the Flow of Mercury in a Homogeneous Magnetic Field. Kgl. Danske Videnskabernes Selskab, Mathematisk-Fysiske Meddelelser, vol. 15, no. 7, Copenhagen, 1937.
10. Shercliff, J. A.: Steady Motion of Conducting Fluids in Pipes Under Transverse Magnetic Field. Proc. Cambridge Philos. Soc. vol. 49, pt. 1, Jan. 1953, pp. 136–144.

11. Michael, D. H.: Stability of Plane Parallel Flows of Electrically Conducting Fluids. Proc. Cambridge Philos. Soc., vol. 49, pt. 1, Jan. 1953, pp. 166–168.
12. Murgatroyd, W.: Experiments on Magneto-Hydrodynamic Channel Flow. Philosophical Magazine, vol. 44, seventh series, no. 358, Nov. 1953, pp. 1348–1354.
13. Stuart, J. T.: On the Stability of Viscous Flow Between Parallel Planes in the Presence of a Co-Planar Magnetic Field. Proc. Roy. Soc. of London, ser. A, vol. 221, no. 1145, 21 Jan. 1954, pp. 189–206.
14. Lock, R. C.: Stability of the Flow of an Electrically Conducting Fluid Between Parallel Planes Under a Transverse Magnetic Field. Proc. Roy. Soc. of London, ser. A, vol. 233, no. 1192, 6 Dec. 1955, pp. 105–125.
15. Chandrasekhar, S.: The Invariant Theory of Isotropic Turbulence in Magneto-Hydrodynamics. Proc. Roy. Soc. of London, ser. A, vol. 204, no. 1079, 9 Jan. 1951, pp. 435–449.
16. Lehnert, B.: The Decay of Magneto-Turbulence in the Presence of a Magnetic Field and Coriolis Force. Quart. Appl. Math., vol. XII, no. 4, Jan. 1955, pp. 321–341.
17. Andrade, E. N. DaC., and Dodd, D.: The Effect of an Electric Field on the Viscosity of Liquids, II. Proc. Roy. Soc. of London, ser. A, vol. 204, no. 1079, 9 Jan. 1951, pp. 449–464.
18. Thompson, W. B.: Thermal Convection in a Magnetic Field. Philosophical Magazine, vol. 42, seventh series, no. 335, Dec. 1951, pp. 1417–1432.
19. Chandrasekhar, S.: On the Inhibition of Convection by a Magnetic Field. Philosophical Magazine, vol. 43, seventh series, no. 340, May 1952, pp. 501–532.
20. Michael, D. H.: Two-Dimensional Magnetic Boundary Layer Problems. Mathematika, vol. I, pt. 2, no. 2, Dec. 1954, pp. 131–142.
21. Stewartson, K.: Motion of a Sphere Through a Conducting Fluid in the Presence of a Strong Magnetic Field. Proc. Cambridge Philos. Soc., vol. 52, pt. 2, Apr. 1956, pp. 301–316.
22. Chandrasekhar, S.: The Stability of Viscous Flow Between Rotating Cylinders in the Presence of a Magnetic Field. Proc. Roy. Soc. of London, ser. A, vol. 216, Feb. 1953, pp. 293–309.
23. Batchelor, G. K.: On the Spontaneous Magnetic Field in a Conducting Liquid in Turbulent Motion. Proc. Roy. Soc. of London, ser. A, vol. 201, no. 1066, 26 Apr. 1950, pp. 405–416.
24. Elsasser, Walter M.: Dimensional Relations in Magneto-Hydrodynamics. The Physical Review, vol. 95, no. 1, July 1, 1954, pp. 1–5.
25. Lundquist, S.: Experimental Investigation of Magneto-Hydrodynamic Waves. The Physical Review, vol. 76, no. 12, Dec. 15, 1949, pp. 1805–1809.
26. Bullard, Edward (Moderator) and others: A Discussion on Magneto-Hydrodynamics. Proc. Roy. Soc. of London, ser. A, vol. 233, no. 1194, Dec. 29, 1955, pp. 289–427.
27. Stratton, Julius Adams: Electromagnetic Theory. McGraw-Hill Book Co., Inc., 1941.
28. Schlichting, Hermann: Grenzschicht-Theorie. G. Braun, Karlsruhe, 1951.
29. Spitzer, Lyman, Jr.: Physics of Fully Ionized Gases. Interscience, 1956.
30. Erdelyi, A., ed.: Tables of Integral Transforms. Vol. II, McGraw-Hill Book Co., Inc., 1954.
31. Carslaw, H. S., and Jaeger, J. C.: Conduction of Heat in Solids. Clarendon Press, Oxford, 1947.
32. Anon.: Tables of the Error Function and Its Derivative. National Bureau of Standards Applied Mathematics, ser. no. 41, 1954.
33. Howarth, L.: Steady Flow in the Boundary Layer Near the Surface of a Cylinder in a Stream. R. & M. No. 1632, British A. R. C., July 1934.
34. Hansen, C. Frederick: Approximations for the Thermodynamic and Transport Properties of High-Temperature Air. NACA TN 4150, 1958.
35. Kloeffler, R. G., Kerchner, R. M., and Brenneman, J. L.: Direct-Current Machinery. The Macmillan Co., 1948.
36. Allen, William A., Rinehart, John S., and White, W. C.: Phenomena Associated With the Flight of Ultra-Speed Pellets. Part I. Ballistics. Jour. Appl. Phys., vol. 23, no. 1, Jan. 1952, pp. 132–137.
37. White, W. C., Rinehart, John S., and Allen, William A.: Phenomena Associated With the Flight of Ultra-Speed Pellets. Part II. Spectral Character of Luminosity. Jour. Appl. Phys., vol. 23, no. 2, Feb. 1952, pp. 198–201.
38. Rinehart, John S., Allen, William A., and White, W. C.: Phenomena Associated With the Flight of Ultra-Speed Pellets. Part III. General Features of Luminosity. Jour. Appl. Phys., vol. 23, no. 3, Mar. 1952, pp. 297–299.
39. Allen, William A., and Mayfield, Earle B.: Time-Resolved Spectroscopy of Ultra-Speed Pellet Luminosity. Jour. Appl. Phys., vol. 24, no. 2, Feb. 1953, pp. 131–133.
40. Öpik, E. J.: Meteor Radiation, Ionization and Atomic Luminous Efficiency. Proc. Roy. Soc. of London, ser. A, vol. 230, no. 1183, 12 July 1955, pp. 463–501.
41. Hulbert, E. O.: Advances in the Physics of the Upper Air Since 1950. Naval Res. Lab. Rep. 4600, Oct. 25, 1955.
42. Anon.: International Critical Tables. Vol. VI, McGraw-Hill Book Co., Inc., 1929, pp. 445 ff.

REPORT 1359

THIN AIRFOIL THEORY BASED ON APPROXIMATE SOLUTION OF THE TRANSONIC FLOW EQUATION [1]

By JOHN R. SPREITER and ALBERTA Y. ALKSNE

SUMMARY

The present paper describes a method for the approximate solution of the nonlinear equations of transonic small disturbance theory. Although the solutions are nonlinear, the analysis is sufficiently simple that results are obtained in closed analytic form for a large and significant class of nonlifting airfoils. Application to two-dimensional flows with free-stream Mach number near 1 leads, for instance, to general expressions for the determination of the pressure distribution on an airfoil of specified geometry and for the shape of an airfoil having a prescribed pressure distribution and gives, furthermore, the correct variation of pressure with Mach number at Mach number 1. For flows that are subsonic everywhere, the method yields a pressure-correction formula that is more accurate than the Prandtl-Glauert rule and compares favorably with existing higher approximations. For flows that are supersonic everywhere, the method yields the equivalent, in transonic approximation, of simple wave theory. Results obtained by application of these general expressions are shown to correspond closely to existing solutions and to experimental data for a wide variety of airfoils.

INTRODUCTION

The difficulty of solving the nonlinear equations of motion of a compressible inviscid gas has led to widespread use of approximate methods in the practical solution of the problems of airfoil theory. The simplest and most versatile approximate method is that based on a complete linearization of the equations and stems from the pioneering work of Munk, Prandtl, Glauert, Ackeret, and others (see refs. 1 and 2 for a résumé). Although this linear theory of compressible flow has been extensively developed in recent years and is widely used in aeronautical applications, it has two limitations that are of significance in the present discussion. First, linearized theory gives only a first approximation that is correct for airfoils of small thickness ratio. This limitation is, in some respects, of continually diminishing significance as the aeronautical engineer is forced to use thin wings and slender bodies to avoid heavy penalties in wave drag. If the airfoil is not sufficiently thin, however, corrections are necessary and higher order theories have been developed to fill the need (see ref. 3 for a résumé). Second, and more important for the present discussion, linearized theory requires, in general, that the Mach number be sufficiently removed from unity that the flow is either purely subsonic or purely supersonic. If both subsonic and supersonic velocities occur in different parts of a single flow field, the flow is said to be transonic and the results of neither linear theory nor the existing higher order theories are, even qualitatively, in agreement with the experimentally observed flows.

Transonic flows have been studied successfully by consideration of a simplified, although still nonlinear, theory that was originally conceived in an effort to provide a useful first approximation for the pressures and forces on thin wings and slender bodies in inviscid flows with free-stream Mach number very near unity (see ref. 4 for a short résumé). More recent developments described in references 5, 6, 7, 8, and elsewhere have shown that the useful range of this theory can be extended to include subsonic and supersonic flows if slightly different approximations are employed in the derivation of the fundamental equations. Although the resulting theory is commonly designated as transonic small disturbance theory, or more briefly as transonic flow theory, it is actually a unified theory for subsonic, supersonic, or transonic flow around thin wings and slender bodies, and is moreover, the simplest theory proposed to date that is capable of yielding reliable results throughout that Mach number range.

This formulation of transonic flow theory provides a set of equations that differs from that of linear theory by the addition of one nonlinear term in the differential equation for the perturbation potential and in the shock relation. If the flow is purely subsonic or purely supersonic, solutions of the equations of transonic flow theory can be sought by application of existing methods for approximating the solutions of the exact equations of compressible inviscid flow. If the flow is transonic, however, the results obtained by application of these methods are at wide variance with those observed experimentally and it is necessary to devise new and appropriate methods of solution. Although methods of the successive approximation type have recently been developed that can be applied to transonic flows (e. g., refs. 9 and 10), the principal method that has been employed in the theoretical analysis of such flows involves the use of the hodograph transformation by means of which the nonlinear equation for the perturbation potential is transformed into a linear differential equation of mixed elliptic-hyperbolic type, the Tricomi equation. Although the resulting boundary-value problem is still very difficult to solve, this method has been applied with considerable success in the study of transonic flow around wedge and flat-plate airfoils and a

[1] Supersedes NACA TN 3970 by John R. Spreiter and Alberta Y. Alksne, 1957.

number of specific results have been given in recent years by Guderley and Yoshihara, Vincenti and Wagoner, Cole, and others (see ref. 11 for a résumé). Extension of this method to permit calculation of transonic flows around arbitrary airfoils with curved boundaries appears, however, to be a difficult task.

The present analysis is based on a novel method of approximation that avoids most of the difficulties of existing procedures while still preserving much of the nonlinear effects in the solution. Sufficient simplicity is gained by restricting attention to surface pressures and to flows that are either purely subsonic, purely supersonic, or have a free-stream Mach number near 1, that results can be obtained in closed analytical form for both the direct problem of calculating the pressure distribution on an airfoil of given shape, and the inverse problem of calculating the shape of an airfoil associated with a given pressure distribution. Inasmuch as the magnitude of the errors introduced by use of the approximation procedures is not evaluated in all cases by mathematical considerations, the usefulness and accuracy of the results are demonstrated by the calculation of the pressure distribution and drag for many different airfoil shapes and by comparison with existing theoretical and experimental results.

Of the theoretical results available for comparison, only two are exact. They are the simple-wave solution for supersonic flows without shock waves, and the variation of pressure with Mach number at Mach number 1. The present method yields both of these results exactly within the framework of transonic small disturbance theory.

Although the existing results mentioned above for wedge airfoils at Mach number 1 contain certain approximations beyond those implicit in the use of the equations of transonic flow theory, the influence of these approximations appears to be minor and the results are generally considered to be very nearly exact solutions of these equations. The present method produces results for this case that are in substantial agreement with these previous theoretical results. In contrast to the hodograph methods, the necessary steps are sufficiently simple, moreover, that results can also be obtained for sonic and near sonic flow around arbitrary airfoils with curved boundaries. Since previous theoretical information for such cases is meager, comparisons are made with a large number of experimental results. In general, the theoretical results found by application of the present method lie within the range of experimental scatter of the data.

In the subsonic range, no exact solutions are available for flow around a thin airfoil. Comparisons are made, therefore, with pressure correction formulas, such as that of Kármán-Tsien, and with higher approximations obtained by iteration methods.

A simple heuristic account of the general method and extensive discussion of the results are contained in the main text. Additional details concerning the underlying basis for the general procedures are contained in the Appendix.

PRINCIPAL SYMBOLS

a	speed of sound
a_∞	speed of sound in the free stream
C_p	pressure coefficient, $\frac{p-p_\infty}{\frac{\rho_\infty}{2}U_\infty^2}$
$\overline{C}_p$	$\frac{[M_\infty^2(\gamma+1)]^{1/3}}{\tau^{2/3}}C_p$
c	chord
c_d	section pressure drag coefficient, $\frac{d}{\frac{\rho_\infty}{2}U_\infty^2 c}$
$\bar{c}_d$	$\frac{[M_\infty^2(\gamma+1)]^{1/3}}{\tau^{5/3}}c_d$
d	pressure drag
k	$\frac{M_\infty^2(\gamma+1)}{U_\infty}$
M	local Mach number
M_∞	free-stream Mach number
n	exponent in the relations for airfoil ordinates given by equations (56) and (61)
p	static pressure
p_∞	free-stream static pressure
q	resultant local velocity
t	maximum thickness of profile
U_∞	free-stream velocity
u,w	perturbation velocity components parallel to x and z axes, respectively
u_E	value of u obtained by solution of equation (21)
u_H	value of u obtained by solution of equation (8)
u_P	value of u obtained by solution of equation (39)
X	value of x at which parabolic and hyperbolic solutions are joined
x,z	Cartesian coordinates where x extends in the direction of the free-stream velocity
x^*	value of x at which the local velocity is sonic
Z	ordinates of the upper surface of the airfoil
Γ	gamma function
γ	ratio of specific heats, for air $\gamma=1.4$
θ	semiapex angle of wedge airfoil
Λ	pressure gradient, $\frac{dC_p}{d(x/c)}$
λ_E	$1-M_\infty^2-ku$
λ_H	M_∞^2-1+ku
λ_P	$k\frac{\partial u}{\partial x}$
ξ_∞	$\frac{M_\infty^2-1}{[M_\infty^2(\gamma+1)\tau]^{2/3}}$
ρ_∞	free-stream density of air
τ	thickness ratio, t/c
φ	perturbation velocity potential

SUBSCRIPTS

cr	values associated with critical Mach number
i	values associated with incompressible flow or with $M_\infty=0$
L	values given by linearized compressible flow theory

$M_\infty=1$ values associated with $M_\infty=1$
Z_{max} values associated with maximum ordinate of airfoil
$\xi_\infty=0$ values associated with $\xi_\infty=0$, or with $M_\infty=1$

FUNDAMENTAL EQUATIONS AND BOUNDARY CONDITIONS

Consider the steady flow of an inviscid compressible gas past an arbitrary thin symmetrical nonlifting airfoil, and introduce Cartesian coordinates x and z with the x axis parallel to the direction of the free-stream, as illustrated in figure 1.

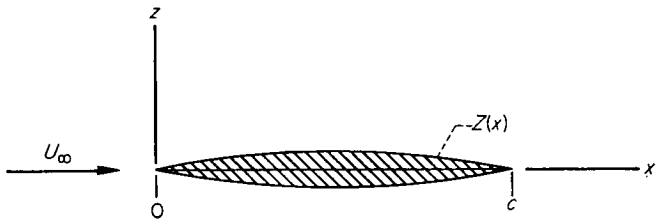


FIGURE 1.—View of airfoil and coordinate system.

Let the free-stream velocity and density be U_∞ and ρ_∞, the perturbation potential be φ, and the perturbation velocity components parallel to the x and z axes be φ_x, or u, and φ_z, or w, where the subscript indicates differentiation. The boundary conditions require that the perturbation velocities vanish at infinity, and that the flow be tangential to the wing surface. The first condition indicates that φ is constant at infinity. The latter condition can be approximated for thin wings by

$$(\varphi_z)_{z=0}=U_\infty \frac{dZ}{dx} \tag{1}$$

where Z represents the ordinates of the airfoil upper surface. The pressure coefficient C_p is likewise approximated to first order by

$$C_p\equiv\frac{p-p_\infty}{\frac{\rho_\infty}{2}U_\infty^2}=-2\frac{\varphi_x}{U_\infty}=-2\frac{u}{U_\infty} \tag{2}$$

These relations are familiar from linear theory, but apply equally for transonic thin airfoil theory. The differential equation for φ is not the same as in linear theory, however, but is

$$\left(1-M_\infty^2-M_\infty^2\frac{\gamma+1}{U_\infty}\varphi_x\right)\varphi_{xx}+\varphi_{zz}=0 \tag{3}$$

where M_∞ is the Mach number of the undisturbed flow and γ is the ratio of specific heats (1.4 for air). It is useful to note that the coefficient of φ_{xx} corresponds, in the present approximation, to $1-M^2$ where M is the local Mach number.

Knowledge of methods for obtaining solutions of equation (3) is meager, not only because the equation is nonlinear, but because it can change type (elliptic, hyperbolic), depending on the value of M_∞ and φ_x. This change of type is an essential feature of transonic flow, since subsonic flows are represented by elliptic equations and supersonic flows by hyperbolic equations. If both types of flow occur in a single flow field, it is apparent that the differential equation must change type. In the present case, the type of the equation is recognized by the sign of the total coefficient of φ_{xx}, as follows:

$$1-M_\infty^2-M_\infty^2\frac{\gamma+1}{U_\infty}\varphi_x\begin{cases}>0 & \text{elliptic (subsonic)}\\ <0 & \text{hyperbolic (supersonic)}\end{cases} \tag{4}$$

An important quantity in the discussion of compressible flows is the critical pressure coefficient $C_{p_{cr}}$ associated with the local occurrence of sonic velocity. The appropriate relation is found by combination of equation (2) and the relation obtained by equating the coefficient of φ_{xx} in equation (3) to zero, and is

$$C_{p_{cr}}=-\frac{2(1-M_\infty^2)}{M_\infty^2(\gamma+1)} \tag{5}$$

In transonic and supersonic flows, it is also necessary, in general, to provide an additional equation for the discontinuous changes in velocity that occur at shock surfaces. The necessary equations, when simplified to the form consistent with the approximations of transonic flow theory, reduce to

$$\left.\begin{aligned}&\left[1-M_\infty^2-M_\infty^2\frac{\gamma+1}{U_\infty}\left(\frac{u_a+u_b}{2}\right)\right](u_a-u_b)^2+(w_a-w_b)^2=0\\ &\varphi_a=\varphi_b\end{aligned}\right\} \tag{6}$$

where the subscripts a and b refer to the values on the two sides of the shock surface. With the exception of the Appendix and minor references in the main text, equation (6) is not employed explicitly in the following analysis and discussion because attention is confined to (a) purely subsonic flows in which no shocks occur, (b) purely supersonic flows in which shock waves can be approximated with good accuracy by isentropic compressions, and (c) flows with free-stream Mach number near 1 in which the shock waves are situated either downstream or far upstream of the airfoil.

The remainder of the present paper is concerned with the approximate solution of the preceding equations and with comparison of the results obtained in specific applications with existing theoretical and experimental results. Purely supersonic flows are discussed first because the method of approximation yields the exact equivalent, in transonic approximation, of simple wave theory. Purely subsonic flows are discussed next because of the close relationship between the results for this and the preceding case. Flows with free-stream Mach number near 1 are treated last.

SUPERSONIC FLOWS

APPROXIMATE SOLUTION OF EQUATIONS

It is convenient in the analysis of supersonic flows to introduce the symbol λ_H as an abbreviation for the negative of the coefficient of φ_{xx}

$$\lambda_H=M_\infty^2-1+M_\infty^2\frac{\gamma+1}{U_\infty}\varphi_x=M_\infty^2-1+ku>0 \tag{7}$$

and rewrite equation (3) in the form:

$$-\lambda_H\varphi_{xx}+\varphi_{zz}=0 \tag{8}$$

It is now assumed that λ_H is neither zero nor infinite and that it varies sufficiently slowly that its derivatives can be disregarded so that it can be considered, temporarily, as a constant. At this stage, the problem is equivalent to that encountered in linearized supersonic airfoil theory (it is identical if λ_H is replaced by M_∞^2-1) and the solution u_H at the airfoil surface is

$$u_H=-\frac{U_\infty}{\sqrt{\lambda_H}}\frac{dZ}{dx} \tag{9}$$

Differentiation yields

$$\frac{du_H}{dx}=-\frac{U_\infty}{\sqrt{\lambda_H}}\frac{d^2Z}{dx^2} \tag{10}$$

If, now, M_∞^2-1+ku is restored in place of λ_H so that, in effect, the local value for λ_H is used at each point and the subscript H on u is dropped, equation (10) becomes

$$\frac{du}{dx}=-\frac{U_\infty}{\sqrt{M_\infty^2-1+ku}}\frac{d^2Z}{dx^2} \tag{11}$$

It is immediately apparent that a certain degree of arbitrariness is displayed in the preceding steps and that different results will be obtained depending, for instance, on whether M_∞^2-1+ku is substituted for λ_H in equation (10) as above, or in equation (9), or in other equations obtained by further differentiation or integration of equation (9). It is shown in the Appendix, however, that the error involved in the preceding steps can be assessed exactly by examination of the remainder terms that have been omitted in writing equations (9) and (10). The advisability of using equation (11) is assured by the fact that the error is shown to vanish, in the absence of shock waves, if λ_H is replaced by M_∞^2-1+ku in equation (10), but not in equation (9). This conclusion becomes immediately evident, furthermore, upon recognition of the fact that equation (11) is the counterpart, in transonic small disturbance theory, of a fundamental differential equation that occurs in the analysis of Prandtl-Meyer and simple wave flows (see, e. g., ref. 12, p. 87 or ref. 13, pp. 190 and 212). Equation (11) is a nonlinear ordinary differential equation for u that can be solved easily by separation of variables. The result is

$$\frac{2}{3k}\left(M_\infty^2-1+ku\right)^{3/2}=-U_\infty\frac{dZ}{dx}+C \tag{12}$$

where C is a constant of integration. In applications of equation (12) to flows that are supersonic everywhere, perhaps the most logical method for the evaluation of this constant is to use the expression between u and dZ/dx provided at the leading edge by the transonic approximation to the shock relation, that is by equation (6) with u_a and w_a equated to zero, u_b to $(u)_{x=0}$, and w_b to $U_\infty(dZ/dx)_{x=0}$. The result given by equation (12) with C evaluated in this way corresponds, to the degree of approximation afforded by use of transonic small disturbance theory, to shock-expansion theory. An alternative procedure that leads to a somewhat simpler result possessing very nearly equal accuracy is to evaluate C by use of the result indicated by equation (9) that $u=0$ where $dZ/dx=0$ for any nonsingular λ_H thus

$$C=\frac{2}{3k}(M_\infty^2-1)^{3/2} \tag{13}$$

whence

$$u=\frac{1}{k}\left\{-(M_\infty^2-1)+\left[(M_\infty^2-1)^{3/2}-\frac{3}{2}kU_\infty\frac{dZ}{dx}\right]^{2/3}\right\} \tag{14}$$

The corresponding relation for the pressure coefficient C_p is obtained by combination of equations (2) and (14), and is

$$C_p=\frac{2}{M_\infty^2(\gamma+1)}\left\{(M_\infty^2-1)-\left[(M_\infty^2-1)^{3/2}-\frac{3}{2}M_\infty^2(\gamma+1)\frac{dZ}{dx}\right]^{2/3}\right\} \tag{15}$$

It should be noted that the restriction to supersonic flow imposed in the evaluation of C and in the inequality of equation (7) requires that equation (15) is to be applied only to cases for which the quantity in square brackets, that is, $[(M_\infty^2-1)^{3/2}-(3/2)M_\infty^2(\gamma+1)\ (dZ/dx)]$, is positive.

COMPARISON WITH EXISTING HIGHER APPROXIMATIONS

Equation (15) is recognized, by comparison with equation (3-15) of reference 3, page 387,[2] as the precise equivalent, in the transonic small disturbance approximation, of simple wave theory for the surface pressure on an airfoil in supersonic flow. Exact simple wave theory is known, moreover, to be perfectly adequate for all practical purposes up to a Mach number of 3, which is considerably in excess of the present range of interest. Within this Mach number range, the results obtained by use of simple wave theory are almost identical with those obtained by use of shock-expansion theory. Comparisons of the variations of C_p with dZ/dx indicated by exact simple wave theory and by equation (15) are shown in figure 2 for several Mach numbers from 1 to 2. As might be anticipated, the two sets of results are in close agreement for Mach numbers near 1, and differ by an increasing amount with increasing Mach number.

Although the necessary calculations are very easy to accomplish in any given case, simple wave theory is not always used in actual practice. Many calculations are based on linear theory or Busemann's second-order theory. Consequently, an additional set of graphs is shown in figure 3 in which the curves of figure 2 are repeated together with the corresponding curves calculated by use of first- and second-order theory. No comparisons are shown for $M_\infty=1$ because the latter theories indicate infinite pressures. It can be seen that equation (15) furnishes a better approximation than linear theory throughout the entire range of variables shown on figure 3 and a better approximation than second-order theory for Mach numbers less than about 1.4. It can be

[2] Comparison discloses that the quantity $M_\infty^2(\gamma+1)$ that appears in equation (15) is represented by $\gamma+1$ in equation (3-15) of reference 3. The difference is associated with a corresponding difference in the coefficient k of the nonlinear term of equation (3). Although the two coefficients are identical at $M_\infty=1$, and might appear to be equally consistent with the other assumptions of transonic flow theory, it has been shown in references 5, 6, 7, 8, and elsewhere that the approximation obtained by use of $M_\infty^2(\gamma+1)$ is much the better of the two for Mach numbers other than 1.

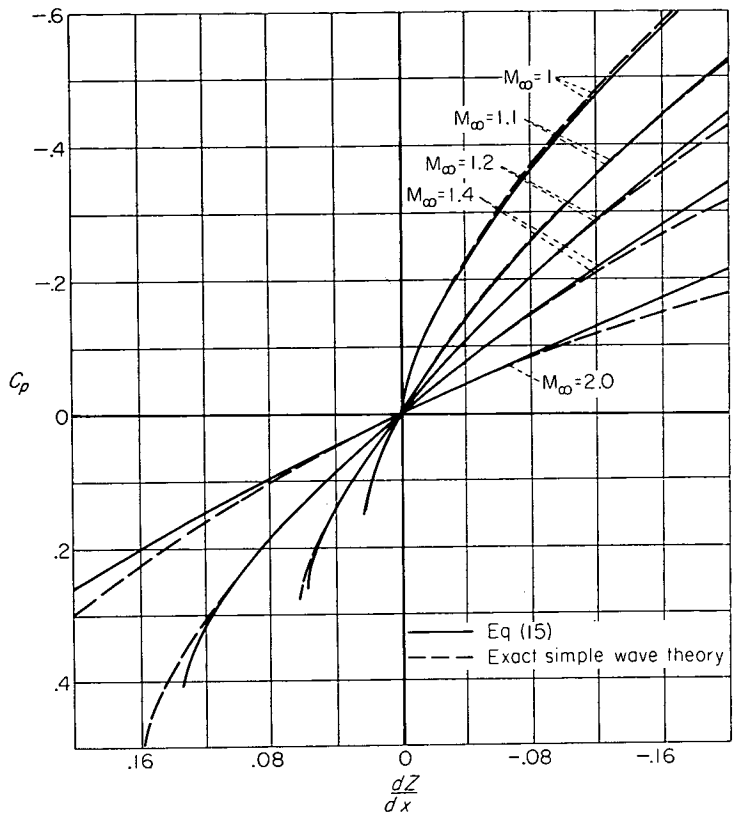


FIGURE 2.—Comparison of results indicated by present theory and by exact simple wave theory.

seen that second-order theory furnishes a very poor approximation for C_p at Mach numbers approaching unity.

In order to explore this behavior further, two additional curves labeled "third order" and "fourth order," calculated using the formulas of references 14 and 15,[3] are included on the graph of figure 3, even though they must be interpreted in a somewhat more restricted sense than the other curves. To be more precise, the third-order curve is restricted to airfoils for which dZ/dx is zero at the leading edge, and the fourth-order curve to airfoils for which both dZ/dx and d^2Z/dx^2 are zero there. It is clear from this sketch that the accuracy of second-order theory at Mach numbers near unity is not improved by addition of higher order terms. The explanation resides in the fact that the larger values of $|dZ/dx|$ shown on the graphs of figure 3 exceed the radius of convergence of the power series expansion for C_p for all but the highest Mach number shown. With the noted restrictions on the leading edge, the higher order results of figure 3 are equivalent to the first few terms of a power series expansion, in terms of dZ/dx, of the expression for C_p indicated by exact simple wave theory. The radius of convergence of the series depends, of course, on the Mach number and is given by the value of $|dZ/dx|$ associated with the occurrence of sonic flow or, in terms of the curves shown on figures 2 and 3, with the termination of the left end of the exact curve. The failure of higher order theories at negative dZ/dx is thus of purely mathematical origin and has no direct physical significance.

[3] Attention of those who refer to reference 15 is called to the fact that the first term appearing in the fourth-order coefficient a_4 of equation (29) should be 2/3 rather than 1/3. This term is written correctly in the numerical example given in equation (135).

ADDITIONAL PROPERTIES OF APPROXIMATE SOLUTION

Equation (15) has some additional interesting properties worth noting. Of the two major components of the right-hand side, the first is recognized upon comparison with equation (5) as the expression for $C_{p_{cr}}$. Since the remaining term is zero when $C_p=C_{p_{cr}}$, it follows that the expression for the critical value for dZ/dx associated with the occurrence of sonic velocity at a given Mach number M_∞ is

$$\left(\frac{dZ}{dx}\right)_{cr}=\frac{2(M_\infty^2-1)^{3/4}}{3M_\infty^2(\gamma+1)} \tag{16}$$

It follows, furthermore, that a curve representing the variation of C_p with M_∞ for a given dZ/dx, and hence a given point on the airfoil, approaches infinite slope as C_p approaches $C_{p_{cr}}$.

An alternative form for equation (15) that is useful for some purposes is the following which expresses C_p in terms of the linear-theory solution C_{p_L} rather than dZ/dx.

$$C_p=\frac{2(M_\infty^2-1)}{M_\infty^2(\gamma+1)}\left\{1-\left[1-\frac{3}{4}\frac{M_\infty^2(\gamma+1)}{M_\infty^2-1}C_{p_L}\right]^{4/3}\right\} \tag{17}$$

where

$$C_{p_L}=\frac{2}{\sqrt{M_\infty^2-1}}\frac{dZ}{dx}$$

This relation can be written in somewhat more concise form if expressed in terms of the transonic similarity parameters $\overline{C}_p$ and ξ_∞, thus

$$\overline{C}_p=2\xi_\infty\left[1-\left(1-\frac{3}{4}\frac{\overline{C}_{p_L}}{\xi_\infty}\right)^{4/3}\right] \tag{18}$$

where

$$\overline{C}_p\equiv\frac{[M_\infty^2(\gamma+1)]^{1/4}}{\tau^{3/4}}C_p, \qquad \xi_\infty\equiv\frac{M_\infty^2-1}{[M_\infty^2(\gamma+1)\tau]^{2/3}}$$

and τ refers to the thickness ratio. Critical values for $\overline{C}_p$ and $\overline{C}_{p_L}$ corresponding to the local occurrence of sonic velocity are easily recognized to be the following:

$$\overline{C}_{p_{cr}}=2\xi_\infty, \qquad \overline{C}_{p_{L_{cr}}}=\frac{4}{3}\xi_\infty \tag{19}$$

SUBSONIC FLOWS

APPROXIMATE SOLUTION OF EQUATIONS

The procedure described in the preceding section will now be applied to the analysis of subsonic flows. Thus, introduce the symbol λ_E as an abbreviation for the coefficient of φ_{xx}

$$\lambda_E=1-M_\infty^2-M_\infty^2\frac{\gamma+1}{U_\infty}\varphi_x=1-M_\infty^2-ku>0 \tag{20}$$

and rewrite equation (3) as follows:

$$\lambda_E\varphi_{xx}+\varphi_{zz}=0 \tag{21}$$

If it is again assumed that λ_E is neither zero nor infinite and that it varies sufficiently slowly that its derivatives can be disregarded, the problem is equivalent to that encountered

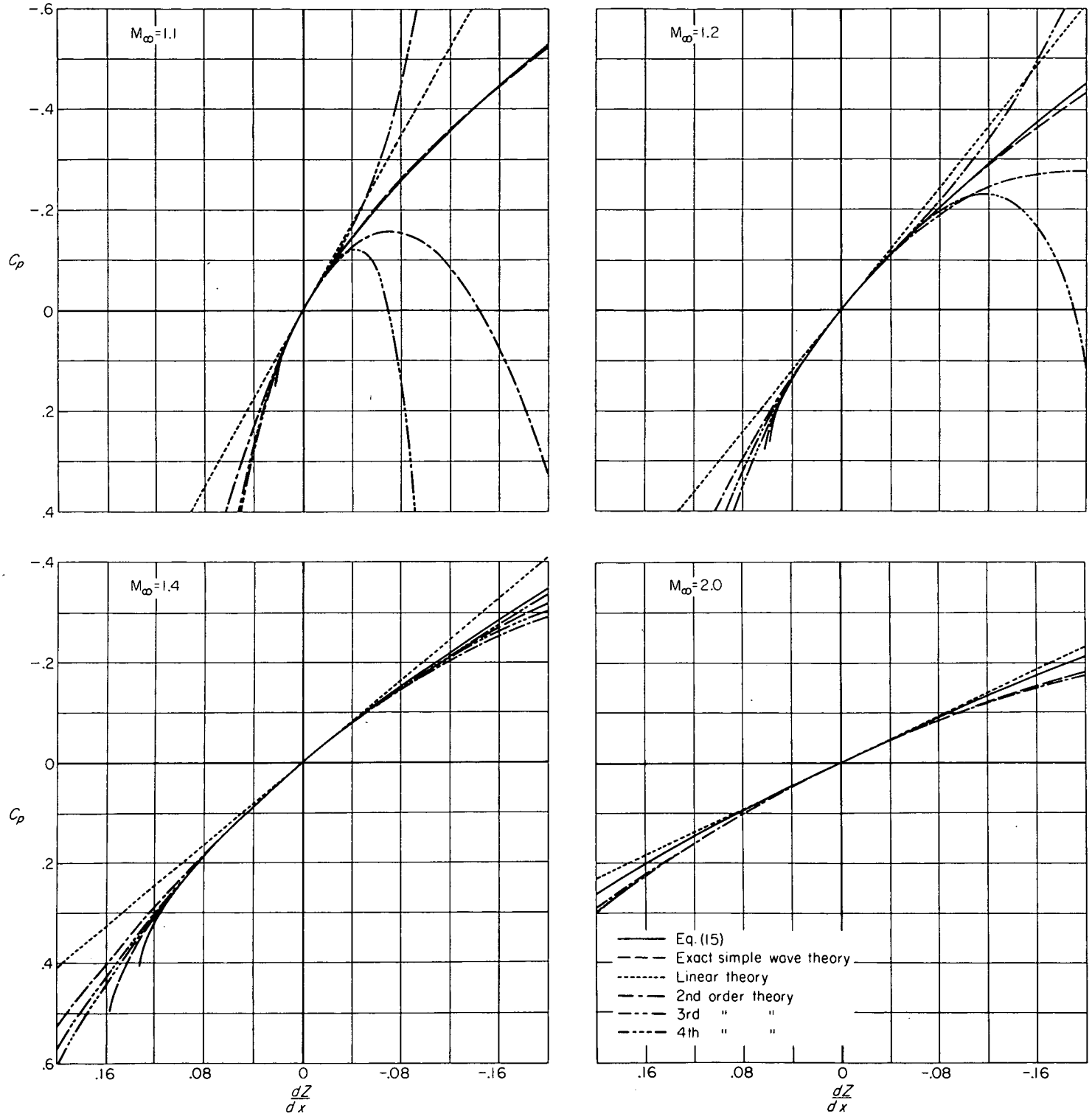


FIGURE 3.—Comparison of results indicated by present theory and by the method of successive approximations for supersonic flow.

in linearized subsonic airfoil theory and the solution u_E at the airfoil surface is

$$u_E=\frac{U_\infty}{\pi\sqrt{\lambda_E}}\int_0^c \frac{dZ/d\xi}{x-\xi}\,d\xi=\frac{u_i}{\sqrt{\lambda_E}} \tag{22}$$

where the subscript i refers to the values for $M_\infty=0$. Differentiation yields

$$\frac{du_E}{dx}=\frac{1}{\sqrt{\lambda_E}}\frac{du_i}{dx} \tag{23}$$

If, in the same manner as described for the supersonic case, $1-M_\infty{}^2-ku$ is restored in place of λ_E so that, in effect, the local value for λ_E is used at each point, and the subscript E on u is dropped, equation (23) becomes

$$\frac{du}{dx}=\frac{1}{\sqrt{1-M_\infty{}^2-ku}}\frac{du_i}{dx} \tag{24}$$

As in the previous discussion of supersonic flows, the error terms are omitted in writing the preceding relations, but are included in a more complete presentation of the equations

given in the Appendix. Once again, the resulting relation is a nonlinear ordinary differential equation that can be solved readily by separation of variables

$$-\frac{2}{3k}(1-M_\infty^2-ku)^{3/2}=u_i+C \tag{25}$$

In applications to flows that are subsonic everywhere, the constant of integration C is evaluated by use of the result indicated by equation (22) that $u=0$ where $u_i=0$ for any nonsingular λ_E, thus

$$C=-\frac{2}{3k}(1-M_\infty^2)^{3/2} \tag{26}$$

In this way, the following relation is obtained between u and u_i

$$u=\frac{1}{k}\left\{1-M_\infty^2-\left[(1-M_\infty^2)^{3/2}-\frac{3}{2}ku_i\right]^{2/3}\right\} \tag{27}$$

The corresponding relation for the pressure coefficient C_p is obtained by combination of equations (2) and (27) and is [4]

$$C_p=-\frac{2}{M_\infty^2(\gamma+1)}\left\{(1-M_\infty^2)-\left[(1-M_\infty^2)^{3/2}+\frac{3}{4}M_\infty^2(\gamma+1)C_{p_i}\right]^{2/3}\right\} \tag{28}$$

where

$$C_{p_i}=-2\frac{u_i}{U_\infty}=-\frac{2}{\pi}\int_0^c\frac{dZ/d\xi}{x-\xi}d\xi$$

In the same way as noted for supersonic flows following equation (15), the restriction to subsonic flow imposed in the evaluation of C and by the inequality of equation (20) requires that equation (28) be applied only to cases where the quantity in the square bracket is positive.

This result possesses several simple, but interesting, properties. First of all, the leading term of an expansion of equation (28) in a series involving ascending powers of C_{p_i} is precisely the familiar Prandtl-Glauert rule of linearized subsonic compressible flow theory

$$C_{p_L}=\frac{C_{p_i}}{\sqrt{1-M_\infty^2}} \tag{29}$$

The coefficients of succeeding terms, however, do not agree with those given by the method of successive approximation. Next, the first of the two major components of the right-hand member of equation (28) is recognized, just as in the supersonic case, as the expression for the critical pressure coefficient $C_{p_{cr}}$. Since the remaining term is zero when $C_p=C_{p_{cr}}$, it follows that the expression for the critical value for C_{p_i} associated with the occurrence of sonic velocity at a given Mach number M_∞ is

$$C_{p_{i_{cr}}}=-\frac{4}{3}\frac{(1-M_\infty^2)^{3/2}}{M_\infty^2(\gamma+1)} \tag{30}$$

[4] Attention is called to the fact that this same relation, except for replacement of $M_\infty^2(\gamma+1)$ by $\gamma+1$ for the same reasons as noted in footnote 2, has been found independently by Kusukawa by application of the WKB method of approximation to the equations of transonic flow theory. This result, together with a number of applications, is published in the September 1957 issue of the Journal of the Physical Society of Japan.

It may be noted that this value is just two-thirds of that obtained by use of equation (5) together with the Prandtl-Glauert rule. It follows, furthermore, that a curve illustrating the variation of C_p with M_∞ for a given C_{p_i}, and hence a given point on the airfoil surface, approaches infinite slope as C_p approaches $C_{p_{cr}}$. This latter behavior signifies that a power series expansion of the result will only converge for Mach numbers less than the critical. Last, the following result is obtained if equation (28) is expressed in terms of the subsonic linear theory solution C_{p_L} rather than C_{p_i}

$$C_p=\frac{-2(1-M_\infty^2)}{M_\infty^2(\gamma+1)}\left\{1-\left[1+\frac{3}{4}\frac{M_\infty^2(\gamma+1)}{1-M_\infty^2}C_{p_L}\right]^{2/3}\right\} \tag{31}$$

where

$$C_{p_L}=\frac{C_{p_i}}{\sqrt{1-M_\infty^2}}$$

Note that the relation between C_p and C_{p_L} indicated by equation (31) for subsonic flows is precisely the same as given by equation (17) for supersonic flows. It follows immediately that the corresponding expression in terms of the transonic similarity parameters $\overline{C}_p$ and ξ_∞ given by equation (18) applies to subsonic, as well as supersonic flows. In order to illustrate the nature of the results indicated by equation (18), a plot of the variation of $\overline{C}_p$ with ξ_∞ for various $C_{p_L}\sqrt{|\xi_\infty|}$ is shown in figure 4. Although the remarkable symmetry about $\xi_\infty=0$ is a consequence of expressing the results in terms of the transonic similarity parameters, the general symmetry remains, although in somewhat distorted form, when C_p is plotted as a function of M_∞ for constant $C_{p_L}\sqrt{|1-M_\infty^2|}$. Such a plot is shown in figure 5.

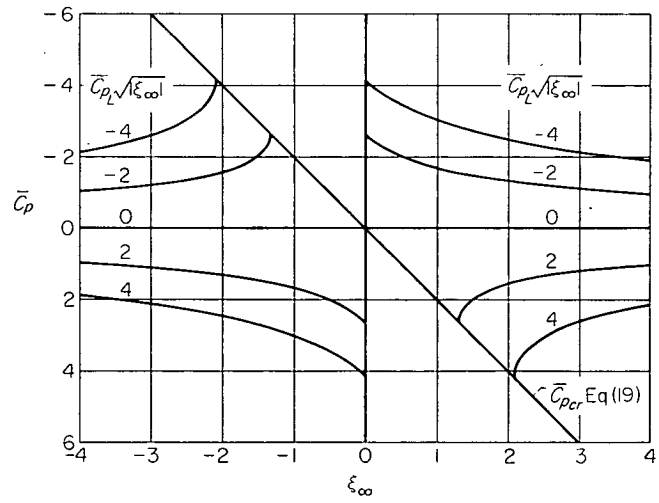


FIGURE 4.—Variation of reduced pressure coefficient, $\overline{C}_p$, with the similarity parameter, ξ_∞, for various values of $\overline{C}_{p_L}\sqrt{|\xi_\infty|}$.

COMPARISON WITH EXISTING HIGHER APPROXIMATIONS

The remainder of the present section on subsonic flows is concerned with an evaluation of the degree of accuracy achieved by use of equation (28). This discussion is handicapped somewhat by the fact that all other theories for subsonic flows around airfoils are also approximate and that no exact solutions are known. Perhaps the most widely

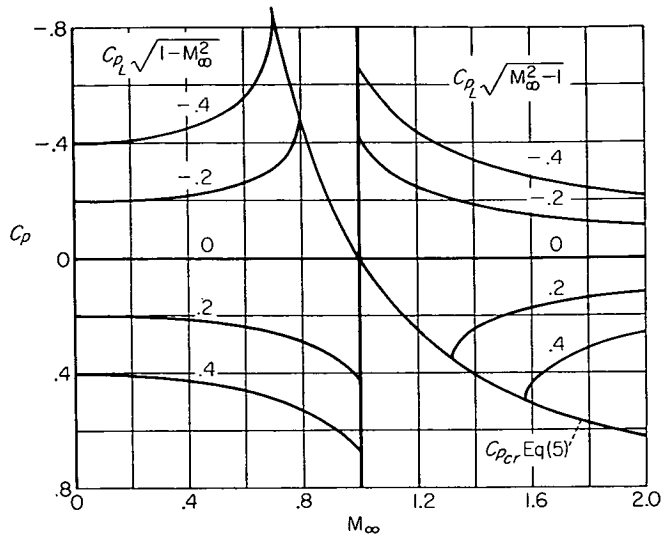


FIGURE 5.—Variation of C_p with M_∞ for various values of $C_{p_L}\sqrt{|M_\infty^2-1|}$.

used higher approximation is the Kármán-Tsien rule. (See refs. 3 and 16 for a résumé.) Although the traditional derivation of the Kármán-Tsien rule is based on the hodograph method, it is not without interest to observe that the Kármán-Tsien rule can be obtained by use of the present procedures together with the three assumptions introduced in the original derivation. These are: (a) that γ can be approximated by -1 in the expression for the speed of sound, (b) that the perturbation velocities are small, and (c) that the Mach number can be considered small in the evaluation of additional effects of compressibility beyond those indicated by linear theory. The starting point is equation (3) with the coefficient of φ_{xx} replaced by the approximate relation for $1-M^2$, where M is the local Mach number, afforded by use of assumptions (a) and (b). The necessary relation can be derived from the energy equation

$$\frac{a^2}{\gamma-1}+\frac{q^2}{2}=\frac{a_\infty^2}{\gamma-1}+\frac{U_\infty^2}{2} \tag{32}$$

where

$$q^2=(U_\infty+u)^2+w^2$$

by setting $\gamma=-1$, whence

$$a^2=a_\infty^2-U_\infty^2+q^2$$

and

$$1-M^2=1-\frac{q^2}{a^2}=\frac{1-M_\infty^2}{1-M_\infty^2+M_\infty^2(q^2/U_\infty^2)}\approx\frac{1-M_\infty^2}{1+2M_\infty^2(u/U_\infty)} \tag{33}$$

Note that this approximation does not permit the attainment of $M=1$ with finite q/U_∞ and with M_∞ different from unity. Substitution of this relation for $1-M^2$ in place of λ_E in equation (23) and integration yields

$$\sqrt{1+2M_\infty^2(u/U_\infty)}=\frac{M_\infty^2}{\sqrt{1-M_\infty^2}}\frac{u_i}{U_\infty}+C \tag{34}$$

The constant of integration is again evaluated by setting $u=0$ where $u_i=0$, whence C equals unity. Solution for u and introduction of the relation between u and C_p given by equation (2) yields

$$C_p=\frac{C_{p_i}}{\sqrt{1-M_\infty^2}}\left(1-\frac{M_\infty^2}{4\sqrt{1-M_\infty^2}}C_{p_i}\right)\approx\frac{C_{p_i}}{\sqrt{1-M_\infty^2}+(1/4)M_\infty^2C_{p_i}} \tag{35}$$

Replacement of M_∞^2 in the second term in the denominator by $2(1-\sqrt{1-M_\infty^2})$ is consistent with assumption (c) and leads directly to the familiar expression for the Kármán-Tsien rule

$$C_p=\frac{C_{p_i}}{\sqrt{1-M_\infty^2}+(1-\sqrt{1-M_\infty^2})(C_{p_i}/2)} \tag{36}$$

This rule, in common with the Prandtl-Glauert rule and the present result given in equation (28), is termed a pressure correction formula because C_p is given in terms of C_{p_i} and M_∞ with no further dependence on airfoil shape. A comparison of the variations of C_p with M_∞ indicated by these three relations is shown in figure 6. A great many other pressure-correction formulas having widely varying properties have also been proposed in recent years. One that yields results in closer agreement with equation (28) than the Prandtl-Glauert or the Kármán-Tsien rule has been given by Garrick and Kaplan in reference 17. A curve illustrating their results is included on figure 6.

A second important method that has been used to obtain higher approximations for subsonic pressure distributions on thin airfoils is the method of successive approximation in which the solution is expressed in a power series in thickness ratio. In this method, the first term is the result given by linear theory, and the coefficients of successive terms are determined by iteration. Higher approximations cannot be expressed in terms of C_{p_i} and M_∞ in such a simple and uni-

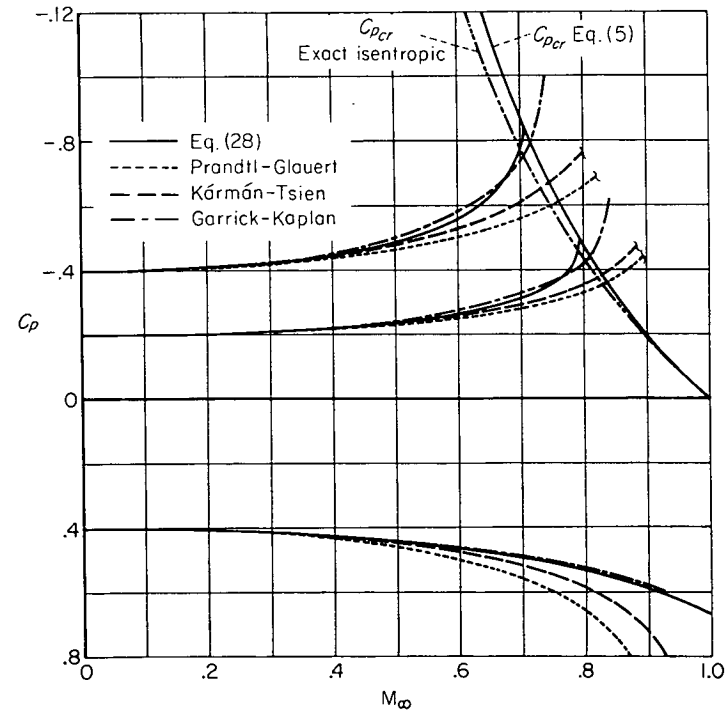


FIGURE 6.—Comparison of results indicated by present theory and by various pressure correction formulas for subsonic flow.

versal manner as with the pressure-correction formulas, but depend on the airfoil shape in a more explicit manner. Although a relatively simple and general procedure for the evaluation of the second approximation has recently been given by Van Dyke (ref. 18), the determination of the third approximation has been accomplished for only a few special shapes. One of these is the nonlifting symmetrical circular-arc section for which the second approximation has been given by Hantzsche and Wendt (ref. 19) and the third approximation by Asaka (refs. 20, 21, and 22).[5] Figure 7 shows a comparison of the variations of C_p with M_∞ at the midpoint of such an airfoil having a thickness ratio τ of 0.10, as indicated by equation (28) and by the first, second, and third approximations. It can be seen that the results obtained by use of equation (28) are identical to those given by the first approximation (or linear theory) for small Mach numbers, but depart therefrom with increasing Mach number and are much closer to the higher approximations for Mach numbers near the critical. It should be noted that the curves labeled first, second, and third order represent the results indicated by successive approximations to the solution of the exact equation for inviscid compressible flow. It is also of interest to compare the results indicated by equation (28) with those indicated by successive approximations to the solution of the simplified equations of transonic small disturbance theory. The latter results can be calculated by use of the following expression, which is readily derived from Asaka's result by taking the limiting form consistent with the approximations of transonic flow theory:

$$C_p=-\frac{8}{\pi}\frac{\tau}{\sqrt{1-M_\infty^2}}-\left(\frac{10}{\pi^2}-\frac{1}{2}\right)\frac{(\gamma+1)M_\infty^2}{(1-M_\infty^2)^2}\tau^2-\left[\frac{1}{\pi}\left(-\frac{281}{108}+\frac{7}{6}ln2\right)+\frac{1}{\pi^3}\left(\frac{292}{9}+4.908\right)\right]\frac{(\gamma+1)^2M_\infty^4}{(1-M_\infty^2)^{7/2}}\tau^3+\ldots$$

$$=-2.5465\frac{\tau}{\sqrt{1-M_\infty^2}}-0.5132\frac{(\gamma+1)M_\infty^2}{(1-M_\infty^2)^2}\tau^2-0.6339\frac{(\gamma+1)^2M_\infty^4}{(1-M_\infty^2)^{7/2}}\tau^3+\ldots \quad (37)$$

It can be seen that the curve in figure 8 indicated by equation (28) is somewhat higher than even that representing the third approximation, but evaluation of its accuracy remains difficult because neither the exact solution nor an upper bound for the results is provided by the classical method of successive approximation. Attention is called to the fact that recent developments in transonic flow theory permit the establishment of an upper bound by application of an alternative method of successive approximation that involves the solution of quadratic, rather than linear, equations at each step of the iteration process. This process, based on the methods employed in reference 9. is described in the Appendix, and additional results are given for the specific case considered in figure 8.

[5] The results for the third approximation given in the present report differ from those obtainable directly from the expressions given in either reference 20 or 21 and 22 due to the correction of some misprints. These corrections have been verified by correspondence with the author, and are published in the January 1958 issue of the Journal of the Physical Society of Japan.

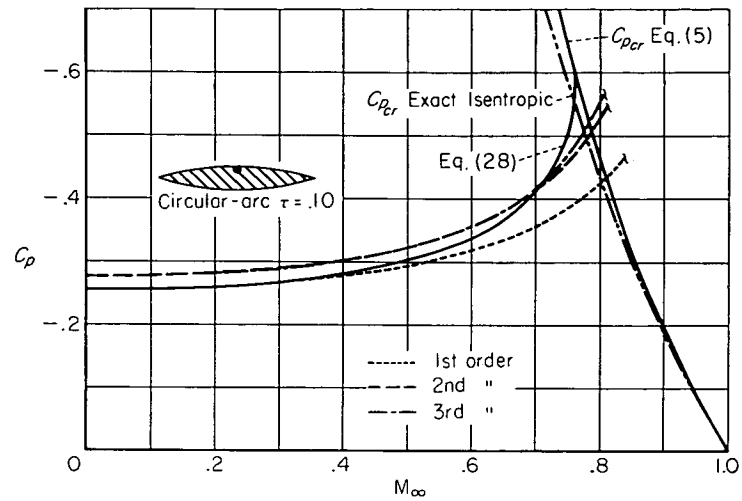


FIGURE 7.—Comparison of the variation of C_p with M_∞ at the midpoint of a circular-arc airfoil, as indicated by present theory and by application of the method of successive approximations to the exact equations for inviscid subsonic flow.

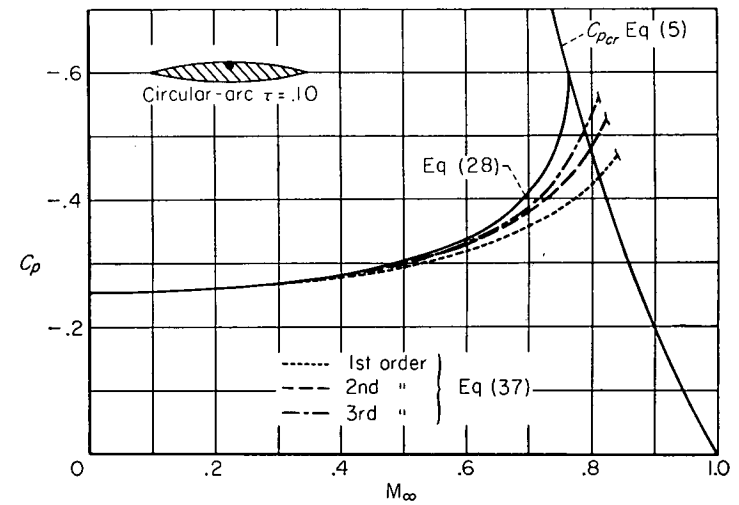


FIGURE 8.—Comparison of the variation of C_p with M_∞ at the midpoint of a circular-arc airfoil in subsonic flow, as indicated by present theory and by application of the method of successive approximations to the transonic equation.

FLOWS WITH FREE-STREAM MACH NUMBER NEAR 1

The analyses of supersonic and subsonic flows given in the preceding sections have started by introduction of a symbol λ for the coefficient of φ_{xx} and the assumption that λ is nonsingular and varies sufficiently slowly that it can be regarded as a constant in the initial stages of the analysis. Since the results so obtained terminate if $\lambda=0$, or physically if sonic velocity occurs in the flow field, it is immediately clear that some change is necessary to study flows with free-stream Mach number near 1 where the transition from subsonic to supersonic flow is an essential feature. The technique adopted is to introduce the symbol λ_P as an abbreviation for the coefficient of φ_x rather than φ_{xx}, thus

$$\lambda_P=M_\infty^2\frac{\gamma+1}{U_\infty}\varphi_{xx}=k\frac{\partial u}{\partial x} \quad (38)$$

whence equation (3) may be written as follows:

$$\varphi_{zz}-\lambda_P\varphi_x=-(1-M_\infty^2)\varphi_{xx}=f_P \quad (39)$$

If attention is confined to flows with free-stream Mach number 1 so that the right-hand side of equation (39) vanishes and if λ_P is replaced by a constant, the resulting relation given by equation (39) is a linear partial differential equation of parabolic type that is familiar from the study of one-dimensional unsteady conduction of heat. If approximate solutions for flows with free-stream Mach number 1 are sought in this way, the analysis proceeds through considerations that are generally applied to parabolic differential equations, and is, in some sense, intermediate between the mixed elliptic-hyperbolic type of the transonic equation. The idea of using the equation for heat conduction for the study of transonic flows in this way is not new, but apparently originated with Oswatitsch, who suggested it to Behrbohm for the analysis of internal flows of nozzles (refs. 23 and 24) The same idea has been applied more recently by Oswatitsch and Keune (refs. 25, 26, and 27) to calculate the flow around the forepart of slender bodies of revolution at free-stream Mach number 1, and they have shown that the results are in remarkable agreement with those measured on the front half of a circular-arc body of revolution. Although the parameter λ_P is regarded throughout as a constant, and various means are proposed for the selection of an appropriate value, it develops that the numerical result for the pressures on the forward part of typical smooth bodies of revolution depends so slightly on the actual choice that almost any reasonable value can be used for λ_P.

If flows with free-stream Mach number different from unity are considered so that the right-hand side of equation (39) remains, and if λ_P is again replaced by a constant, the resulting differential equation is linear and is of elliptic or hyperbolic type depending on whether the free-stream Mach number, rather than the local Mach number, is less than or greater than unity. Maeder and Thommen (ref. 28) have suggested that this linearized equation, or its counterpart in three dimensions, be applied, together with a new and arbitrary rule for the selection of a value for λ_P, to calculate the pressure distribution on complete bodies of revolution and on airfoils in two-dimensional flows. The selection of an appropriate value for λ_P is much more critical for these problems than for those discussed originally by Oswatitsch and Keune, however, and the replacement of λ_P by a constant results not only in serious loss of accuracy in many applications, but also in loss of certain essential general features of the solution. In general, results obtained by replacing λ_P, or $\partial u/\partial x$, with a constant appear to be remarkably accurate if the resulting values calculated for $\partial u/\partial x$ are, indeed, nearly constant over most of the chord. If, on the other hand, $\partial u/\partial x$ varies substantially over the chord, no choice of a single value for λ_P will suffice to provide a useful result. This point is developed further in the course of the following discussion and in the Appendix. Some criticisms of the above procedure, although principally from a different point of view, have appeared in a note by Miles (ref. 29).

In the present analysis, it is assumed once again that λ_P is nonsingular and that it varies sufficiently slowly that it can be considered as a constant in the initial stages of the analysis in which a nonlinear ordinary differential equation is established for u on the airfoil surface. The final result for u is determined by integration of this differential equation and restores, to a large degree, the effects of the variation of λ_P along the chord. The result for the first stage of the analysis requires the solution of equation (39) subject to the boundary conditions given in equation (1) and can be obtained by application of standard procedures. The solution has two distinct forms depending on the sign of λ_P. The form associated with positive λ_P is appropriate for application to regions where the flow is accelerating, whereas that associated with negative λ_P may be appropriate for application to regions where the flow is decelerating. The analysis of accelerating flow will be developed first. The direct problem in which the airfoil shape is specified and the pressure distribution is sought, and the inverse problem in which the pressure distribution is specified and the associated airfoil shape is sought are discussed for each case.

ACCELERATING FLOWS, DIRECT PROBLEMS

Approximate solution of equations for arbitrary airfoil shape.—A relation for u at the airfoil surface derived by consideration of equation (39) with positive λ_P, the boundary conditions stated in equation (1), and the form of Green's theorem associated with the left side of equation (39) (see Appendix) is

$$u_P=-\frac{U_\infty}{\sqrt{\pi\lambda_P}}\frac{d}{dx}\int_0^x\frac{dZ/d\xi}{\sqrt{x-\xi}}d\xi-\frac{1}{\lambda_P}\frac{\partial}{\partial x}\int_{-\infty}^{+\infty}d\zeta\int_{-\infty}^{x}\sigma_P f_P d\xi$$

$$=-\frac{U_\infty}{\sqrt{\pi\lambda_P}}\left[\left(\frac{dZ}{dx}\right)_{x=0}\frac{1}{\sqrt{x}}+\int_0^x\frac{d^2Z/d\xi^2}{\sqrt{x-\xi}}d\xi\right]-\frac{1}{\lambda_P}\frac{\partial}{\partial x}\int_{-\infty}^{+\infty}d\zeta\int_{-\infty}^{x}\sigma_P f_P d\xi \qquad (40)$$

where

$$f_P=-(1-M_\infty^2)\varphi_{\xi\xi},\ \sigma_P=\sqrt{\frac{\lambda_P}{4\pi(x-\xi)}}\,e^{\left[-\frac{\lambda_P(x-\xi)^2}{4(x-\xi)}\right]}$$

The two alternative expressions for u_P are completely equivalent. The first is more concise and will be used in the following equations, but the second is often somewhat simpler to evaluate. If the free-stream Mach number is unity, the double integral vanishes and u_P can be calculated directly. The result so obtained corresponds to that found by application of Maeder and Thommen's proposal of reference 28. (It should be noted, however, that the general expression for φ given in reference 28 is incorrect owing to improper treatment of plus and minus signs.)

If the free-stream Mach number is not unity, equation (40) is an integral equation, and it might appear that little progress toward a solution has been made. If attention is confined to the vicinity of the airfoil and to Mach numbers near unity, however, it is only necessary to approximate $\varphi_{\xi\xi}$ well locally and it is sufficient to substitute λ_P/k for $\varphi_{\xi\xi}$ or $\partial u/\partial\xi$ in the double integral. The integral can then be evaluated and the following relationship results:

$$u_P=\frac{(1-M_\infty^2)U_\infty}{M_\infty^2(\gamma+1)}-\frac{U_\infty}{\sqrt{\pi\lambda_P}}\frac{d}{dx}\int_0^x\frac{dZ/d\xi}{\sqrt{x-\xi}}d\xi \qquad (41)$$

If, once again, ku_x is restored in place of λ_P so that, in effect, the local value is used at each point, and the subscript P on

u is dropped, a simple nonlinear ordinary differential equation is obtained for u

$$u=\frac{(1-M_\infty^2)U_\infty}{M_\infty^2(\gamma+1)}-\frac{U_\infty}{\sqrt{\pi k(du/dx)}}\frac{d}{dx}\int_0^x\frac{dZ/d\xi}{\sqrt{x-\xi}}d\xi \tag{42}$$

Equation (42) can be written in the following form upon rearranging the terms and squaring both sides.

$$\left[u-\frac{(1-M_\infty^2)U_\infty}{M_\infty^2(\gamma+1)}\right]^2\frac{du}{dx}=\frac{U_\infty^3}{\pi M_\infty^2(\gamma+1)}\left(\frac{d}{dx}\int_0^x\frac{dZ/d\xi}{\sqrt{x-\xi}}d\xi\right)^2 \tag{43}$$

As in the other cases, equation (43) can be solved readily by separation of variables, and the constant of integration can be evaluated by introduction of the additional condition that equation (41) provides the correct location $x=x^*$ for the sonic point, or point where $u=(1-M_\infty^2)U_\infty/M_\infty^2(\gamma+1)$. The result is

$$\left[u-\frac{(1-M_\infty^2)U_\infty}{M_\infty^2(\gamma+1)}\right]^3=\frac{3U_\infty^3}{\pi M_\infty^2(\gamma+1)}\int_{x^*}^x\left(\frac{d}{dx_1}\int_0^{x_1}\frac{dZ/d\xi}{\sqrt{x_1-\xi}}d\xi\right)^2dx_1 \tag{44}$$

where x^* is the value for x for which

$$\frac{d}{dx}\int_0^x\frac{dZ/d\xi}{\sqrt{x-\xi}}d\xi=0 \tag{45}$$

This method of evaluation of the constant of integration is completely analogous to that employed in the analysis of subsonic and supersonic flows, and is necessary in the analysis of flows with free-stream Mach number near 1 in order to avoid infinite pressure gradients at the point of sonic velocity on smooth airfoils. This method, moreover, provides a mechanism for the introduction of direct upstream dependence on airfoil shape in the subsonic region, and its exclusion in the supersonic region. The corresponding relation for the pressure coefficient C_p is obtained by combination of equations (2) and (44) and is

$$C_p=\frac{-2(1-M_\infty^2)}{M_\infty^2(\gamma+1)}-2\left[\frac{3}{\pi M_\infty^2(\gamma+1)}\int_{x^*}^x\left(\frac{d}{dx_1}\int_0^{x_1}\frac{dZ/d\xi}{\sqrt{x_1-\xi}}d\xi\right)^2dx_1\right]^{1/3} \tag{46}$$

An alternative expression in terms of the transonic similarity parameter is

$$\overline{C}_p\equiv\frac{[M_\infty^2(\gamma+1)]^{1/3}}{\tau^{2/3}}C_p=2\xi_\infty-2\left\{\frac{3}{\pi}\int_{x^*}^x\left[\frac{d}{dx_1}\int_0^{x_1}\frac{d(Z/\tau)/d\xi}{\sqrt{x_1-\xi}}d\xi\right]^2dx_1\right\}^{1/3}=2\xi_\infty+\overline{C}_{p_{\xi_\infty=0}} \tag{47}$$

The variation of $\overline{C}_p$ with ξ_∞ expressed by equation (47) is exact, within the approximation of transonic small disturbance theory, for flows with free-stream Mach numbers very near unity, and is associated with the fact that the local Mach number distribution on an airfoil is independent of the free-stream Mach number at values of the latter near unity. This phenomenon has been discussed previously in references 30, 31, 6, and elsewhere.

Once C_p is known, the pressure drag d can be readily calculated by use of the following relation

$$c_d\equiv\frac{d}{\frac{\rho_\infty}{2}U_\infty^2c}\equiv\frac{2}{c}\int_0^c C_p\frac{dZ}{dx}dx \tag{48}$$

Application to single-wedge airfoils.—Sufficient theoretical and experimental results are available at the present time to provide considerable insight into the accuracy and usefulness of equation (46) or (47). The shape for which the greatest amount of information is available is the single-wedge profile for which both theoretical and experimental pressure distributions are available. Thus, consider a single-wedge profile of maximum thickness t and chord $c/2$ as illustrated in figure 9. The ordinates of the airfoil upper surface are

$$\left.\begin{aligned}Z=t\frac{x}{c}=\tau x \quad &\text{for } 0<x<c/2\\ Z=t/2=\tau c/2 \ &\text{for } x>c/2\end{aligned}\right\} \tag{49}$$

and the semiapex angle θ is equal, to the order of accuracy of thin airfoil theory, to τ. Substitution of equation (49) for Z into equations (45) and (46) provides that the sonic point is at the shoulder ($x^*=c/2$) and that the pressure distribution on the surface of the wedge at free-stream Mach numbers near 1 is

$$\overline{C}_p\equiv\frac{[M_\infty^2(\gamma+1)]^{1/3}}{\tau^{2/3}}C_p=2\xi_\infty-2\left(\frac{3}{\pi}\ln\frac{x}{c/2}\right)^{1/3} \tag{50}$$

A plot of the results for Mach number 1 is shown in figure 10 together with the corresponding theoretical results given by Guderley and Yoshihara in reference 32. Although some approximations are introduced in the course of the latter analysis, the results are generally regarded as virtually an exact solution of the equations of transonic small disturbance

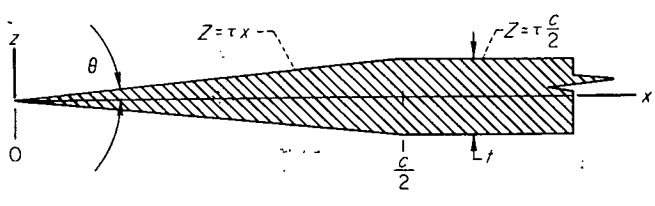


FIGURE 9.—View of single-wedge airfoil and principal dimensions.

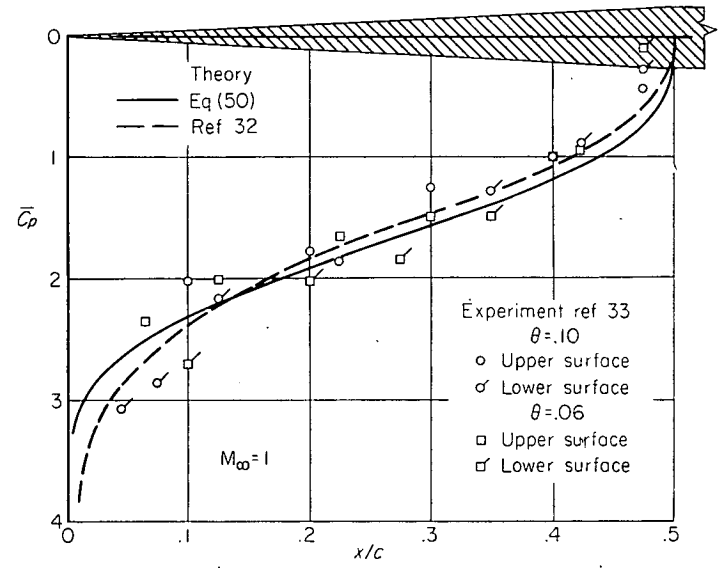


FIGURE 10.—Theoretical and experimental pressure distributions for single-wedge airfoils at free-stream Mach number 1.

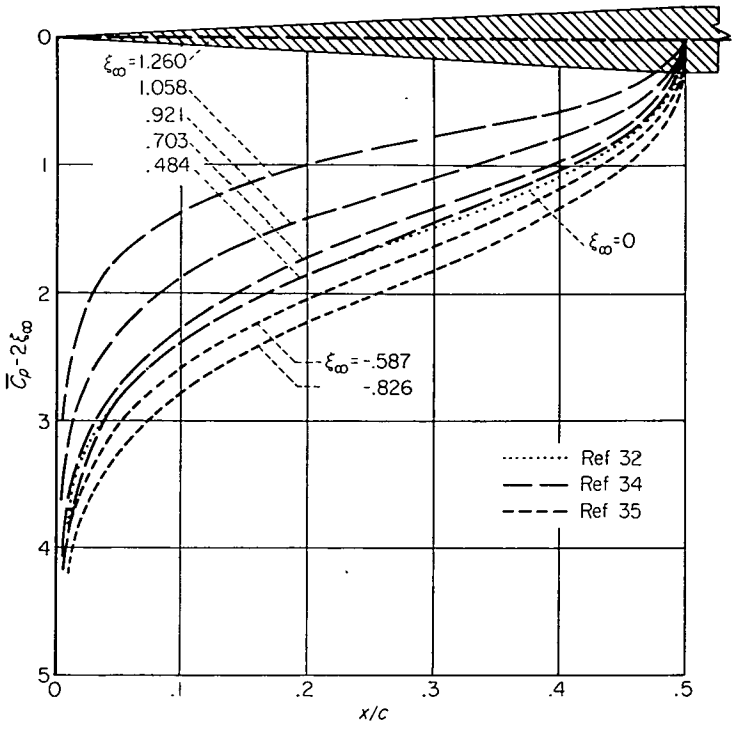


FIGURE 11.—Summary of other theoretical results for transonic flow past single-wedge airfoils.

theory. Also included in figure 10 are experimental results for $M_\infty=1$ obtained in the Langley annular transonic wind tunnel and reported by Habel, Henderson, and Miller in reference 33.

Since the comparisons shown in figure 10 indicate that equation (50) provides an approximate solution for the pressure distribution on a single-wedge profile at $M_\infty=1$ that is probably satisfactory for most purposes, and since the variation of $\overline{C}_p$ with ξ_∞ given by equation (47) or (50) is exact, within the framework of transonic small disturbance theory, at $M_\infty=1$, the principal question remaining in the evaluation of the degree of approximation afforded by use of equation (50) is to define the range of ξ_∞, or Mach number, over which it applies. Accordingly, figure 11 has been prepared to summarize the results given previously by Guderley and Yoshihara for Mach number 1 (ref. 32), by Vincenti and Wagoner for Mach numbers slightly greater than unity (ref. 34), and by Yoshihara for Mach numbers slightly less than unity (ref. 35). The latter two sets of results were obtained by lengthy numerical calculations and, together with the results for Mach number 1, are generally regarded as being very close to those that would be given by exact solutions of the equations of transonic small disturbance theory. The results are plotted in terms of $\overline{C}_p-2\xi_\infty$ so that the pressure distributions for Mach numbers very near unity should determine a single line. It can be seen that the variation of $\overline{C}_p$ with ξ_∞ indicated by equation (47) or (50) holds until the absolute value of ξ_∞ is nearly one-half. At greater values, the results begin to tend toward those associated with purely subsonic or purely supersonic flows, and equations (47) and (50) are no longer applicable.

Experimental measurements of the flow around single-wedge profiles at free-stream Mach numbers both less than and greater than unity have been made by Liepmann and Bryson and reported in references 30 and 31. Results were obtained for three different profiles having semiapex angles of 4½°, 7½°, and 10°. Plots of the experimental pressure distributions for the test Mach numbers closest to unity for each profile are shown in figure 12 together with the theoretical pressure distribution calculated by use of equation (50). Additional experimental data for other Mach numbers are not included on figure 12 since those shown are already for values of ξ_∞ that are somewhat outside the range of validity of equation (50). Only the theoretical results given by equation (50) are included since examination of the data reveals that these results differ less from the theoretical results shown on figure 11, for Mach numbers near unity, than the experimental curves differ from either set of theoretical curves, or even than the experimental curves differ among themselves. Perhaps the most prominent discrepancy is that which occurs near the shoulder. Theory indicates that sonic velocity ($\overline{C}_p-2\xi_\infty=0$) occurs at the shoulder, whereas the experimental data, particularly that of Liepmann and Bryson, consistently indicate that sonic velocity occurs forward of the shoulder. It is interesting to observe that this discrepancy is greatest for the thinnest airfoil tested.

The foregoing results may be contrasted with those obtained by direct use of equation (41) in which case $\overline{C}_p-2\xi_\infty$

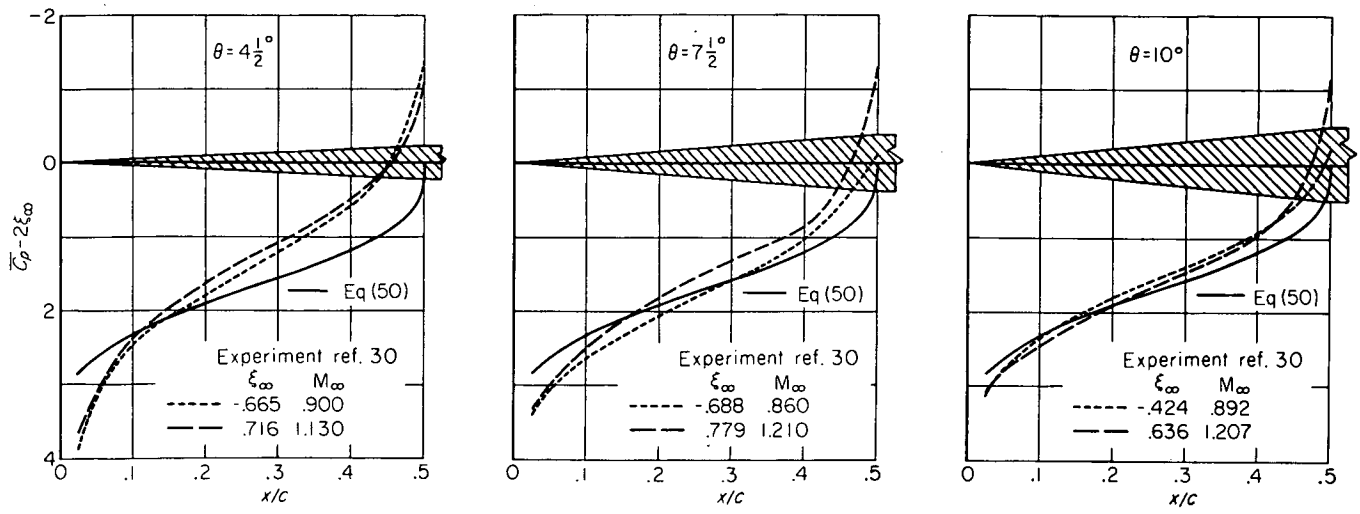


FIGURE 12.—Theoretical and experimental pressure distributions for three single-wedge airfoils at free-stream Mach numbers near 1.

is found to be proportional to $1/\sqrt{\lambda_P x}$. It is clear from this comparison that there is no constant with which λ_P can be replaced that would provide a satisfactory solution for the pressure distribution on a single-wedge airfoil at free-stream Mach numbers near unity.

The pressure drag of single-wedge profiles at Mach numbers near 1 can be found easily by integration of equation (48) with the relations given by equations (49) and (50) substituted for Z and C_p. The result is

$$\frac{[M_\infty^2(\gamma+1)]^{1/3}c_d}{\tau^{5/3}} \equiv \bar{c}_d = 2\xi_\infty + 2\left(\frac{3}{\pi}\right)^{1/3}\Gamma\left(\frac{4}{3}\right) = 2\xi_\infty + 1.758 \quad (51)$$

where Γ represents the gamma function. This result compares very favorably with the value of 1.75 for $\xi_\infty = 0$, or Mach number 1, given by Cole in reference 36 as that obtained by numerical integration of the pressure distribution given by Guderley and Yoshihara in reference 32. Cole's own theory for the drag of a single-wedge airfoil at high subsonic speeds, which is fundamentally somewhat less accurate than Guderley and Yoshihara's theory, gives the value 1.67 for $\xi_\infty = 0$.

Application to biconvex circular-arc airfoils.—In addition to data for three single-wedge profiles, Bryson also gives in reference 30 experimental results for transonic flow around the front half of an 8.8-percent thick biconvex circular-arc airfoil followed by a straight section as illustrated in figure 13. Since the pressure distribution on the curved portion

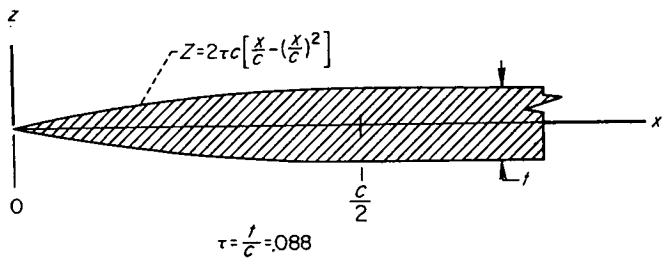


FIGURE 13.—View of a half-circular-arc airfoil and principal dimensions.

of this profile is the same at Mach numbers near unity as that on the front half of a complete circular-arc airfoil having the same thickness ratio, and additional experimental data are available for the latter airfoil although for other thickness ratios, the following analysis is developed for a complete biconvex circular-arc airfoil. It is moreover sufficient, in thin airfoil theory, to approximate the ordinates Z for a circular-arc airfoil by those for a parabolic-arc airfoil, thus

$$\frac{Z}{c} = 2\tau\left[\frac{x}{c} - \left(\frac{x}{c}\right)^2\right] \quad (52)$$

where τ is the thickness ratio as indicated in figure 14. Substitution of this relation for Z into equations (45) and (47) yields the following result for the pressure distribution on the airfoil surface.

$$\bar{C}_p \equiv \frac{[M_\infty^2(\gamma+1)]^{1/3}}{\tau^{2/3}} C_p = 2\xi_\infty - 2\left\{\frac{12}{\pi}\left[ln\left(4\frac{x}{c}\right) - 8\frac{x}{c} + 8\left(\frac{x}{c}\right)^2 + \frac{3}{2}\right]\right\}^{1/3} \quad (53)$$

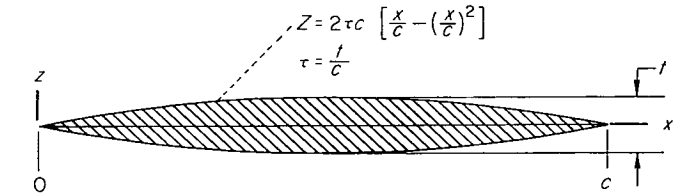


FIGURE 14.—View of a complete circular-arc airfoil and principal dimensions.

Figure 15 shows a comparison of the pressure distributions for Mach numbers near unity calculated by use of equation (53) with those obtained from Bryson's experiments with the half airfoil. As for the single-wedge profile, the results are again plotted in terms of $\bar{C}_p - 2\xi_\infty$ since experimental results are available only for Mach numbers somewhat different from unity. It can be seen by comparison of figures 12 and 15 that the theoretical and experimental results are in much better agreement for the front half of a circular-arc airfoil than for single-wedge profiles. Experimental pressure distributions for transonic flow past four complete biconvex circular-arc airfoils having thickness ratios of 6, 8, 10, and 12 percent have been given by Michel, Marchaud, and Le Gallo in reference 37. Their results for Mach number 1 are plotted in figure 16 together with the theoretical results calculated by use of equation (53). These results are presented in terms of $\bar{C}_p$ because transonic theory indicates that the pressure distributions for all four airfoils should then define a single curve independent of the thickness ratio. Results for Mach numbers other than unity are not included on this plot because the variation of $\bar{C}_p$ with ξ_∞ for small ξ_∞ indicated by equation (47) and subsequent relations is not only simple but is amply verified by the preceding comparisons

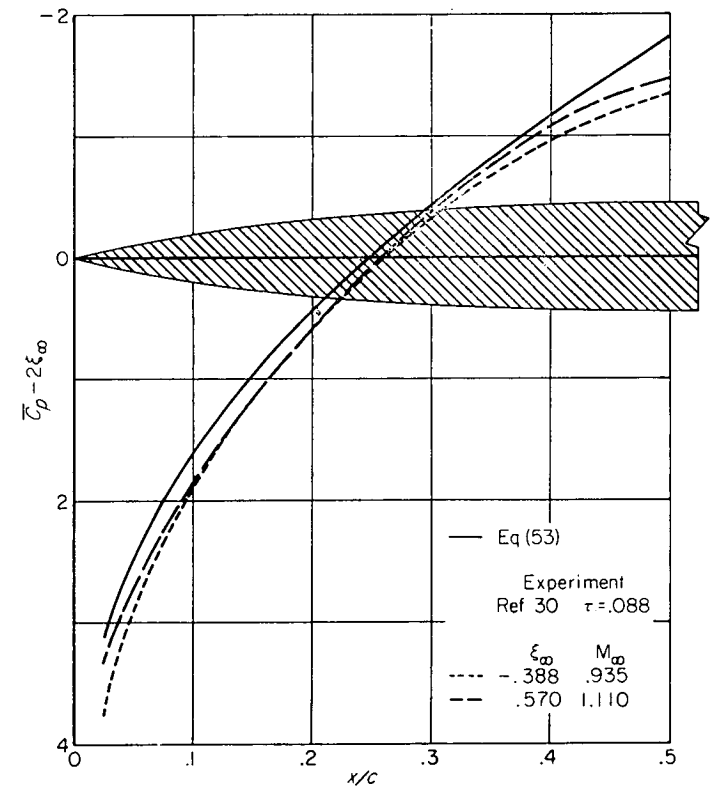


FIGURE 15.—Theoretical and experimental pressure distributions for half-circular-arc airfoils at free-stream Mach numbers near 1.

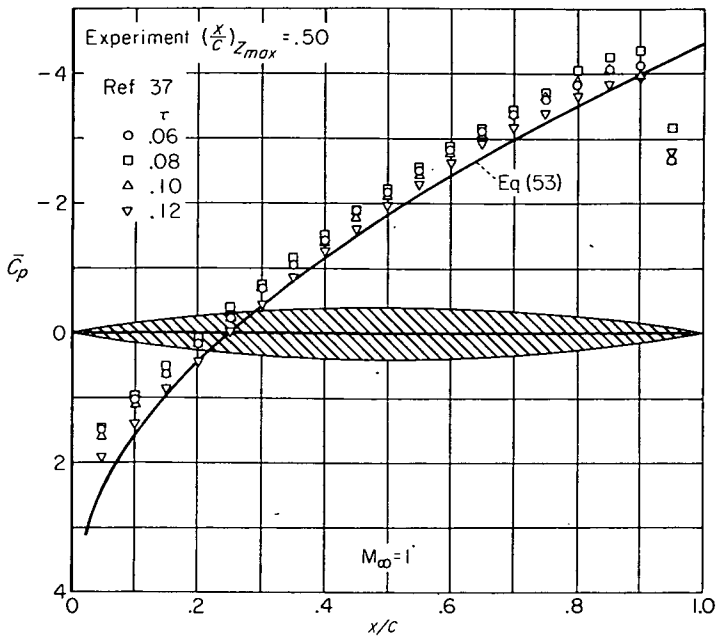


FIGURE 16.—Theoretical and experimental pressure distributions for circular-arc airfoils; $M_\infty = 1$.

and by similar discussions elsewhere in the literature of transonic flow. It can be seen that the theoretical and experimental results are in substantial agreement. The most notable discrepancy is that found near the trailing edge, and can be attributed to flow separation induced by boundary-layer shock-wave interaction. It can also be seen that the agreement between theory and experiment is not so good for the complete airfoils, particularly the thinner ones, as for the half airfoil. Part of the discrepancy for the complete airfoils may possibly be attributed to the experimental technique in which the airfoil is simulated by a bump on the tunnel wall and is hence imbedded in the wall boundary layer. Some comments on this method of testing have been given recently by Carroll and Anderson in reference 38.

The pressure drag of circular-arc airfoils at Mach numbers near 1 has been found by numerical integration of equation (48) with the relations given by equations (52) and (53) substituted for Z and C_p and is

$$\frac{[M_\infty^2(\gamma+1)]^{1/3}c_d}{\tau^{5/3}} \equiv \bar{c}_d = 4.77 \tag{54}$$

The pressure drag of the front half can be evaluated in the same way by changing the upper limit in equation (48) to $c/2$ and is

$$\bar{c}_d = 2\xi_\infty + 1.13 \tag{55}$$

The integrations required to determine the drag results given in equations (54) and (55) were evaluated numerically using Simpson's rule together with an analytic determination of the contribution of the region in the immediate vicinity of the leading-edge singularity. Sufficiently fine intervals were used that the resulting values are estimated to be accurate to within about one digit in the third significant figure, as judged by comparison with the results of similar calculations made with wider intervals. It is necessary to use very fine intervals, particularly near the nose, to achieve such accuracy, and intervals as small as $0.00005c$ were used in some cases.

Application to a family of airfoils having the point of maximum thickness displaced aft of the midchord station.—The primary object of this present section is to present some comparisons of calculated and measured pressure distributions at Mach number 1 on a number of specific airfoils that have the point of maximum thickness aft of the midchord station. The experimental data are from reference 39 by Michel, Marchaud, and Le Gallo, and are for members of the family of airfoils having ordinates given by

$$\frac{Z}{c} = A\left[\frac{x}{c} - \left(\frac{x}{c}\right)^n\right] \tag{56}$$

where A and n are constants for each airfoil and n is greater than unity. The values selected for A and n determine the thickness ratio τ and the location $(x/c)_{z_{max}}$ of the point of maximum thickness according to the relations

$$\left(\frac{x}{c}\right)_{z_{max}} = \left(\frac{1}{n}\right)^{\frac{1}{n-1}} \tag{57}$$

$$\tau = 2A\left[\left(\frac{1}{n}\right)^{\frac{1}{n-1}} - \left(\frac{1}{n}\right)^{\frac{n}{n-1}}\right] = \frac{2A(n-1)}{n^{n/(n-1)}} \tag{58}$$

The biconvex circular-arc airfoils discussed in the preceding section are special cases of the present family that correspond to $n=2$. The point of maximum thickness is located forward or aft of the midchord station depending on whether n is less than or greater than 2. The particular airfoils tested by Michel, Marchaud, and Le Gallo are special cases that correspond to either $n=3.38$ or 6.05 and have the point of maximum thickness at 0.60 or 0.70 chord. As in the earlier work by the same investigators on biconvex circular-arc airfoils, the results were obtained by simulating the airfoil by a bump on the tunnel wall and are again subject to criticism regarding the influence of the wall boundary layer.

Substitution of equation (56) for Z into equations (45) and (46) yields the following result for the pressure distribution on the airfoil surface for Mach number near unity:

$$\bar{C}_p \equiv \frac{[M_\infty^2(\gamma+1)]^{1/3}}{\tau^{2/3}} C_p$$

$$= 2\xi_\infty - 2\left\{\frac{3}{4\pi}\left[\frac{n^{n/(n-1)}}{n-1}\right]^2\right\}^{1/3}\left\{ln\frac{x}{c} - \right.$$

$$\left.\frac{2\sqrt{\pi}\Gamma(n+1)}{(n-1)\Gamma\left(n-\frac{1}{2}\right)}\left(\frac{x}{c}\right)^{n-1} + \frac{\pi[\Gamma(n+1)]^2}{2(n-1)\left[\Gamma\left(n-\frac{1}{2}\right)\right]^2}\left(\frac{x}{c}\right)^{2(n-1)} + \right.$$

$$\left.\frac{1}{n-1} ln\frac{\sqrt{\pi}\Gamma(n+1)}{\Gamma\left(n-\frac{1}{2}\right)} + \frac{3}{2(n-1)}\right\}^{1/3} \tag{59}$$

where Γ represents the gamma function. If m is any positive integer greater than unity, the following relations are useful for evaluation of the gamma function:

$$\left.\begin{aligned} &\Gamma(m)=1\cdot2\cdot3\ldots(m-1)=(m-1)!, \qquad \Gamma(1/2)=\sqrt{\pi} \\ &\Gamma\left(m+\frac{1}{2}\right)=\sqrt{\pi}\,\frac{1}{2}\cdot\frac{3}{2}\cdot\frac{5}{2}\cdot\cdot\left(m-\frac{1}{2}\right), \qquad \Gamma\left(\frac{3}{2}\right)=\frac{\sqrt{\pi}}{2} \end{aligned}\right\} \quad (60)$$

Substitution of $n=2$ in equation (59) reproduces equation (53) for the pressure distribution on biconvex circular-arc airfoils as a special case. Equation (50) for the pressure distribution on a single-wedge airfoil can also be obtained as a limiting case by setting $n=\infty$ and noting that the chord of the wedge is designated here as c rather than $c/2$. Theoretical pressure distributions on the airfoils tested by Michel, Marchaud, and Le Gallo are obtained from equation (59) by substitution of the values 3.38 and 6.05 for n. Figures 17 and 18 show comparisons of the theoretical and experimental pressure distributions for $M_\infty=1$ for the two groups of airfoils. Except for the discrepancy near the trailing edge which can again be attributed to boundary-layer shock-wave interaction, it can be seen that the theoretical and experimental results are in at least qualitative agreement. Some differences occur, however, in the levels of the pressure distribution curves. Comparison with the results for the circular-arc airfoils shown in figure 16 reveals that the same trend is in evidence for those airfoils, although to a lesser degree, and that the difference between the theoretical and experimental results increases as the point of maximum thickness moves rearward. It is not clear at the present time whether this discrepancy is to be attributed principally to the shortcomings of the theoretical or the experimental results.

Application to a family of airfoils having the point of maximum thickness forward of midchord station.—The test program of Michel, Marchaud, and Le Gallo reported in reference 39 and discussed in the preceding section also included tests of each of the airfoils reversed in the wind tunnel so that the point of maximum thickness is located forward of the midchord station. The particular airfoils tested are thus specific cases of the family of profiles described by equation (56) with x/c replaced by $1-(x/c)$; that is, the ordinates are

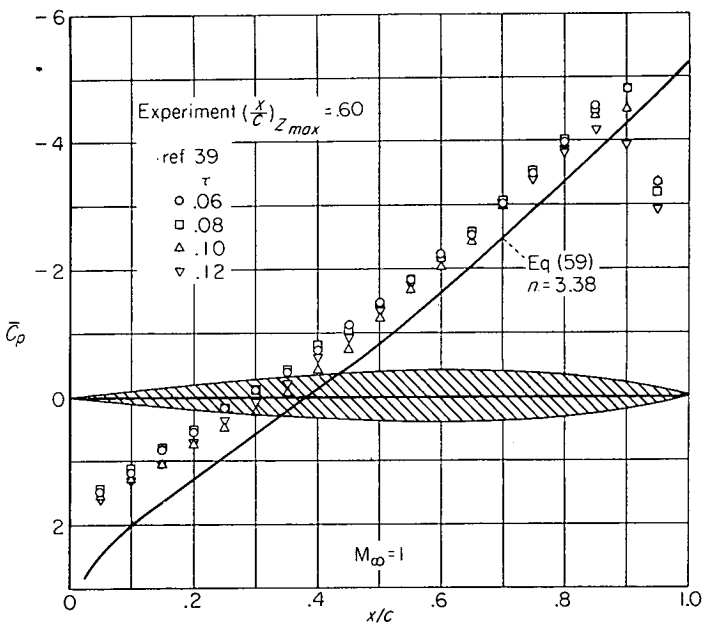


FIGURE 17.—Theoretical and experimental pressure distributions for airfoils having maximum thickness at 0.60 chord; $M_\infty=1$.

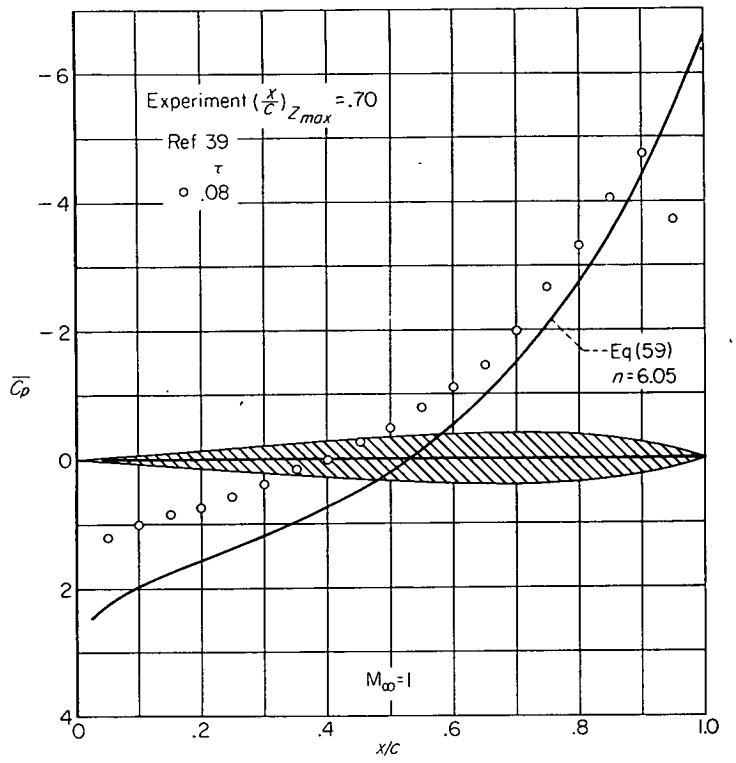


FIGURE 18.—Theoretical and experimental pressure distributions for airfoils having maximum thickness at 0.70 chord: $M_\infty=1$.

$$\frac{Z}{c}=A\left[1-\frac{x}{c}-\left(1-\frac{x}{c}\right)^n\right] \quad (61)$$

where A and n are again constants for each airfoil and n is greater than unity. The values selected for A and n determine the thickness ratio τ and the location $(x/c)_{z_{max}}$ of the point of maximum thickness according to the relations

$$\left(1-\frac{x}{c}\right)_{z_{max}}=\left(\frac{1}{n}\right)^{\frac{1}{n-1}} \quad (62)$$

$$\tau=\frac{2A(n-1)}{n^{n/(n-1)}} \quad (63)$$

Biconvex circular-arc airfoils are special cases of the present family that correspond to $n=2$. The point of maximum thickness is located forward or aft of the midchord station depending on whether n is greater or less than 2. The particular airfoils tested by Michel, Marchaud, and Le Gallo are special cases that correspond to either $n=3.38$ or 6.05 and have the point of maximum thickness at 0.40 or 0.30 chord.

Since the integrations encountered when equation (61) is substituted in equations (45) and (46) for the determination of C_p are more difficult than those encountered in any of

the preceding examples, no general formula will be given for arbitrary n. Two formulas of more restricted generality are given, however. One is applicable when n is any integer greater than unity, the other when n is one-half plus any positive integer. The first is

$$\overline{C}_p=2\xi_\infty-2\left[\frac{3}{4\pi}\left(\frac{n^{\frac{n}{n-1}}}{n-1}\right)^2\right]^{1/3}\left\{\left\{(n-1)^2 ln\frac{x}{c}+2(n-1)\Gamma(n+1)\sqrt{\pi}\sum_{\nu=1}^{n-1}\frac{1}{\Gamma(n-\nu)\Gamma\left(\nu+\frac{1}{2}\right)}\frac{(-x/c)^\nu}{\nu}+[\Gamma(n+1)]^2\pi\sum_{\nu=1}^{n-1}\frac{1}{\Gamma(n-\nu)\Gamma\left(\nu+\frac{1}{2}\right)}\sum_{\mu=1}^{n-1}\frac{1}{\Gamma(n-\mu)\Gamma\left(\mu+\frac{1}{2}\right)}\frac{(-x/c)^{\nu+\mu}}{\nu+\mu}\right\}\Bigg|_{x^*}^{x}\right]^{1/3} \tag{64}$$

where the symbol $|_{x^*}^{x}$ is used to denote the difference between the preceding expression with first x and then x^* substituted for x, that is,

$$f(x)\Big|_{x^*}^{x}=f(x)-f(x^*)$$

where x^*, the location of the sonic point, is found from

$$n-1+\Gamma(n+1)\sqrt{\pi}\sum_{\nu=1}^{n-1}\frac{(-x^*/c)^\nu}{\Gamma(n-\nu)\Gamma\left(\nu+\frac{1}{2}\right)}=0$$

and Γ refers again to the gamma function. The second is

$$\overline{C}_p=2\xi_\infty-2\left[\frac{3}{4\pi}\left(\frac{n^{\frac{n}{n-1}}}{n-1}\right)^2\right]^{1/3}\left\{\left\{(n-1)^2 ln\frac{x}{c}-\frac{B^2\left(1-\frac{x}{c}\right)^{2n-2}}{2n-2}\left(ln\frac{1+\sqrt{x/c}}{1-\sqrt{x/c}}\right)^2+\left[\left(1+\sqrt{\frac{x}{c}}\right)ln\left(1+\sqrt{\frac{x}{c}}\right)+\left(1-\sqrt{\frac{x}{c}}\right)ln\left(1-\sqrt{\frac{x}{c}}\right)\right]\left[-2n(n-1)+\frac{B^2\sqrt{\pi}}{n-1}F(2n-2)\right]+\left[\frac{x}{c}+\left(1+\frac{x}{c}\sqrt{\frac{x}{c}}\right)ln\left(1+\sqrt{\frac{x}{c}}\right)+\left(1-\frac{x}{c}\sqrt{\frac{x}{c}}\right)ln\left(1-\sqrt{\frac{x}{c}}\right)\right]\left[B^2\pi\sum_{\nu=1}^{n-\frac{3}{2}}\frac{F\left(n-\frac{1}{2}-\nu\right)F\left(n-\frac{3}{2}+\nu\right)}{n-1+\nu}\right]-\frac{2n(n-1)}{\sqrt{\pi}}\left(1-\frac{x}{c}\right)\sum_{\nu=1}^{n-\frac{3}{2}}\frac{\left(1-\frac{x}{c}\right)^{n-\frac{3}{2}-\nu}}{\left(n-\frac{1}{2}-\nu\right)F\left(n-\frac{1}{2}-\nu\right)}\left(\frac{1}{n-\frac{1}{2}-\nu}+\sqrt{\frac{x}{c}}\,ln\frac{1+\sqrt{x/c}}{1-\sqrt{x/c}}\right)+\frac{B^2}{n-1}\left(1-\frac{x}{c}\right)F(2n-2)\sum_{\nu=1}^{2n-3}\frac{\left(1-\frac{x}{c}\right)^{2n-3-\nu}}{(2n-2-\nu)F(2n-2-\nu)}\left(\frac{1}{2n-2-\nu}+\sqrt{\frac{x}{c}}\,ln\frac{1+\sqrt{x/c}}{1-\sqrt{x/c}}\right)+2B^2\sqrt{\pi}\left(1-\frac{x}{c}\right)\sum_{\nu=1}^{n-\frac{3}{2}}\frac{F\left(n-\frac{1}{2}-\nu\right)F\left(n-\frac{3}{2}+\nu\right)}{n-1+\nu}\sum_{\mu=1}^{n-\frac{5}{2}+\nu}\frac{\left(1-\frac{x}{c}\right)^{n-\frac{5}{2}+\nu-\mu}}{F\left(n-\frac{1}{2}+\nu-\mu\right)}\left[\frac{1}{n-\frac{3}{2}+\nu-\mu}-\frac{\left(1-\frac{x}{c}\right)}{n-\frac{1}{2}+\nu-\mu}+\frac{x}{c}\sqrt{\frac{x}{c}}\,ln\frac{1+\sqrt{x/c}}{1-\sqrt{x/c}}\right]+2(n-1)B\sqrt{\pi}\sum_{\nu=1}^{n-\frac{3}{2}}F\left(n-\frac{1}{2}-\nu\right)\frac{\left(1-\frac{x}{c}\right)^\nu}{\nu}-B^2\pi\sum_{\nu=1}^{n-\frac{3}{2}}F\left(n-\frac{1}{2}-\nu\right)\sum_{\mu=1}^{n-\frac{3}{2}}F\left(n-\frac{1}{2}-\mu\right)\left(1-\frac{x}{c}\right)^{\nu+\mu-1}\left[\frac{1}{\nu+\mu-1}-\frac{\left(1-\frac{x}{c}\right)}{\nu+\mu}\right]\right\}\Bigg|_{x^*}^{x}\right]^{1/3} \tag{65}$$

where $B=\dfrac{n}{\sqrt{\pi}F\left(n-\frac{1}{2}\right)}$, and $F(\zeta)=\dfrac{\Gamma(\zeta)}{\Gamma\left(\zeta+\frac{1}{2}\right)}$

Attention is called to the fact that ν and μ are positive integers so that when n=(3/2) all the summations drop out.

Again x^* is the location of the sonic point and it is found from

$$n-1-B\left(1-\frac{x^*}{c}\right)^{n-\frac{3}{2}}\sqrt{\frac{x^*}{c}}ln\frac{1+\sqrt{x^*/c}}{1-\sqrt{x^*/c}}-B\sum_{\nu=1}^{n-\frac{3}{2}}F\left(n-\frac{1}{2}-\nu\right)\frac{x^*}{c}\left(1-\frac{x^*}{c}\right)^{\nu-1}=0$$

Substitution of $n=2$ in equation (64) again reproduces equation (53) for the pressure distribution on biconvex circular-arc airfoils. Figures 19 and 20 show comparisons of the pressure distributions measured at Mach number 1 by Michel, Marchaud, and Le Gallo with those calculated by use of equations (64) and (65). The experimental results shown in sketch (s) are for airfoils that have the point of maximum thickness located at 0.40 chord corresponding to a value for n of 3.38. Since results could not be calculated analytically for this value for n, theoretical results are shown for both $n=3.0$ and $n=3.5$. The corresponding locations for the point of maximum thickness can be readily calculated using equation (62) and are 0.423 and 0.394 chord. Similarly, the experimental results shown in figure 20 are for an

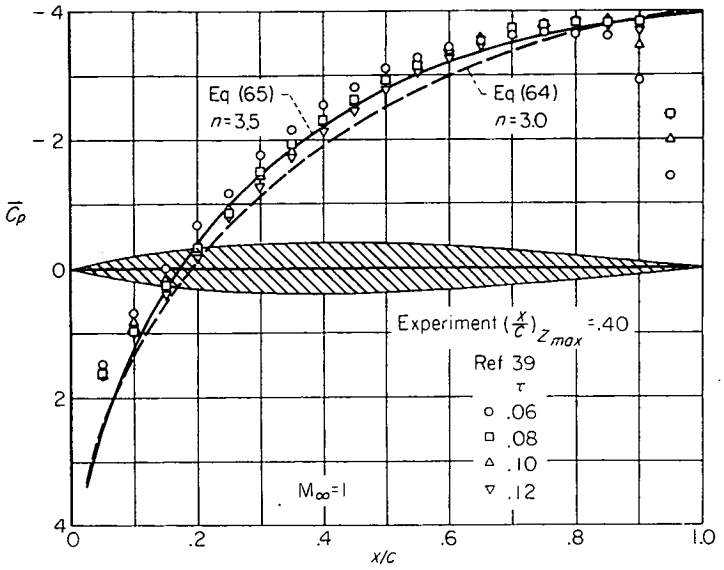


FIGURE 19.—Theoretical and experimental pressure distributions for airfoils having maximum thickness near 0.40 chord; $M_\infty = 1$.

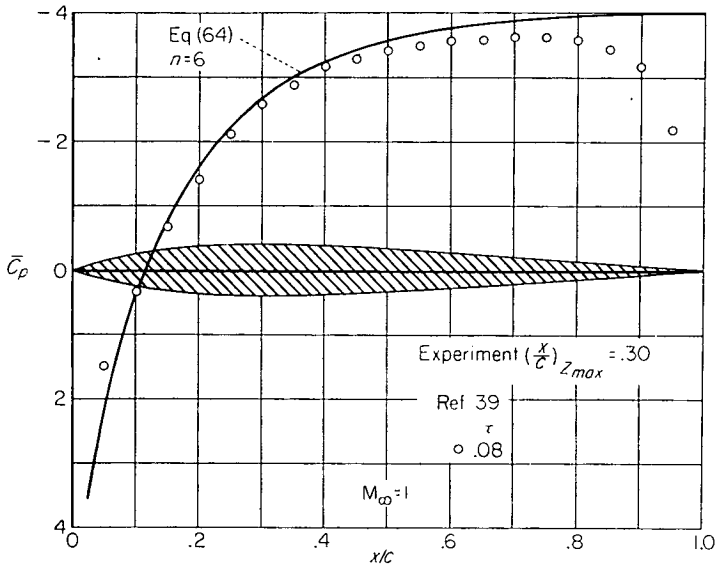


FIGURE 20.—Theoretical and experimental pressure distributions for airfoils having maximum thickness at 0.30 chord: $M_\infty = 1$.

airfoil that has the point of maximum thickness located at 0.30 chord corresponding to a value for n of 6.05; whereas the theoretical results are for airfoils that have the point of maximum thickness located at 0.301 chord corresponding to a value for n of 6.00. These results continue the trend noted in the preceding section that the agreement between the present experimental and theoretical results improves as the location of the point of maximum thickness moves forward along the chord. The principal discrepancy remaining is, in fact, reduced to that near the trailing edge associated with boundary-layer shock-wave interaction, and is therefore beyond the scope of any inviscid theory.

ACCELERATING FLOWS, INVERSE PROBLEMS

Approximate solution of equations for given pressure distribution.—Although all of the preceding discussion is concerned with the calculation of the pressure distribution on an airfoil of specified geometry, an equally important problem in many engineering situations is the design of an airfoil to have a specified pressure distribution at a given Mach number. This poses no new problem in the analysis of purely subsonic or purely supersonic flows by the present methods because the specification of C_p permits the determination of C_{p_L} through application of equation (31) or (17), and the inversion problem is reduced to the familiar inversion problem of linear theory. The necessary relation for flows with free-stream Mach number near 1 can be derived from consideration of equation (42) as an integral equation in which u and du/dx are given and the unknown appears in the integrand of a definite integral. This equation can be inverted readily since it has the same form as the relation encountered in the solution of Abel's integral equation (see, e. g., ref. 40, pp. 483–484). The inversion thus has the form of Abel's integral equation, and is the following in the present application:

$$\frac{dZ}{dx} = -\frac{1}{U_\infty}\sqrt{\frac{k}{\pi}}\int_0^x \left[u - \frac{(1-M_\infty^2)U_\infty}{M_\infty^2(\gamma+1)}\right]\sqrt{\frac{du}{d\xi}}\frac{d\xi}{\sqrt{x-\xi}} \tag{66}$$

The desired relation for the ordinates $Z(x)$ of the airfoil can now be found by a second integration, and is the following if it is assumed that Z is zero at the leading edge ($x=0$).

$$Z = Z^* - \frac{1}{U_\infty}\sqrt{\frac{k}{\pi}}\int_{x^*}^x dx_1 \int_0^{x_1}\left[u - \frac{(1-M_\infty^2)U_\infty}{M_\infty^2(\gamma+1)}\right]\sqrt{\frac{du}{d\xi}}\frac{d\xi}{\sqrt{x_1-\xi}}$$

$$= -\frac{1}{U_\infty}\sqrt{\frac{k}{\pi}}\int_0^x dx_1 \int_0^{x_1}\left[u - \frac{(1-M_\infty^2)U_\infty}{M_\infty^2(\gamma+1)}\right]\sqrt{\frac{du}{d\xi}}\frac{d\xi}{\sqrt{x_1-\xi}} \tag{67}$$

where Z^* is the ordinate at the point x^* where u is zero. It is interesting to note that the two alternative expressions for Z lead to identical results although the apparent regions of dependence, as indicated by the limits on the integrals, are quite different. The same result expressed in terms of C_p or $\bar{C}_p$ is

$$Z = \frac{1}{2}\sqrt{\frac{M_\infty^2(\gamma+1)}{2\pi}}\int_0^x dx_1 \int_0^{x_1}\left[C_p + \frac{2(1-M_\infty^2)}{M_\infty^2(\gamma+1)}\right]\sqrt{-\frac{dC_p}{d\xi}}\frac{d\xi}{\sqrt{x_1-\xi}} \tag{68}$$

or

$$Z = \frac{\tau}{2\sqrt{2\pi}}\int_0^x dx_1 \int_0^{x_1}(\bar{C}_p - 2\xi_\infty)\sqrt{-\frac{d\bar{C}_p}{d\xi}}\frac{d\xi}{\sqrt{x_1-\xi}} \tag{69}$$

A simple application or check of these relations is furnished by substitution for $\bar{C}_p$ of the relation given in equation (50) for single-wedge profiles, whence Z is found to be equal to θx between $x=0$ and $x=c/2$. In the same way, substitution of equation (53) for $\bar{C}_p$ leads directly to equation (52) for the ordinates of a circular-arc airfoil, etc.

Application to airfoils with constant pressure gradient.—An example that permits an additional comparison with an existing theoretical result given by Guderley in reference 41, is furnished by consideration of the problem of determining the shape of an airfoil having a constant negative pressure gradient at $M_\infty = 1$, thus

$$C_p = \frac{dC_p}{d(x/c)}\left(\frac{x}{c} - \frac{x^*}{c}\right) = -\Lambda\left(\frac{x}{c} - \frac{x^*}{c}\right) \tag{70}$$

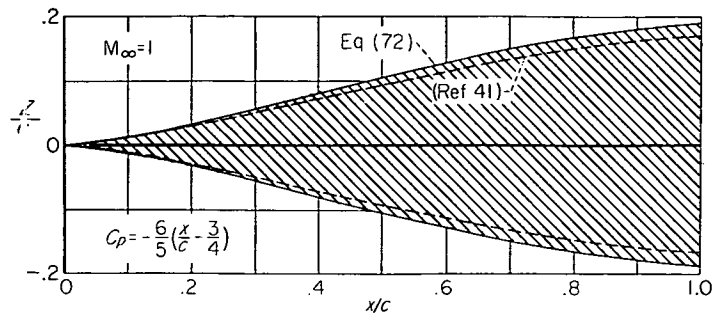


FIGURE 21.—Shape of the forward part of an airfoil having a constant pressure gradient at free-stream Mach number 1, as indicated by present theory and by Guderley.

where $\Lambda = -dC_p/d(x/c)$ is a positive constant. Substitution of this relation for C_p in equation (68) and integration leads directly to the following result:

$$\frac{Z}{c} = \frac{2}{3}\sqrt{\frac{\gamma+1}{2\pi}}\,\Lambda^{3/2}\left[\left(\frac{x}{c}\right)^{3/2}\left(\frac{x^*}{c} - \frac{2}{5}\frac{x}{c}\right)\right] \tag{71}$$

The special case considered by Guderley is obtained by insertion of the values $x^*/c = 3/4$ and $\Lambda = 6/5$, whence equation (71) reduces to

$$\frac{Z}{c} = \left(\frac{3}{5}\right)^{3/2}\sqrt{\frac{\gamma+1}{\pi}}\left[\left(\frac{x}{c}\right)^{3/2}\left(1 - \frac{8}{15}\frac{x}{c}\right)\right] \tag{72}$$

Figure 21 shows a scale drawing of the profile calculated by use of equation (72) and of that given by Guderley. It is evident from the sketch that the present theory indicates larger values for the ordinates Z than are given by Guderley. Although the latter results are given only in graphical form, and are hence difficult to determine with precision, the two sets of values for Z appear to be related by a constant ratio of approximately 9 to 8.[6]

The case considered by Guderley and discussed above results in a shape that does not close at the stern. It can be seen immediately from equation (71), however, that a closed airfoil will result if x^*/c is equated to 2/5, in which case equation (71) reduces to

$$\frac{Z}{c} = \frac{4}{15}\sqrt{\frac{\gamma+1}{2\pi}}\,\Lambda^{3/2}\left[\left(\frac{x}{c}\right)^{3/2}\left(1 - \frac{x}{c}\right)\right] \tag{73}$$

A plot of the results is shown in figure 22.

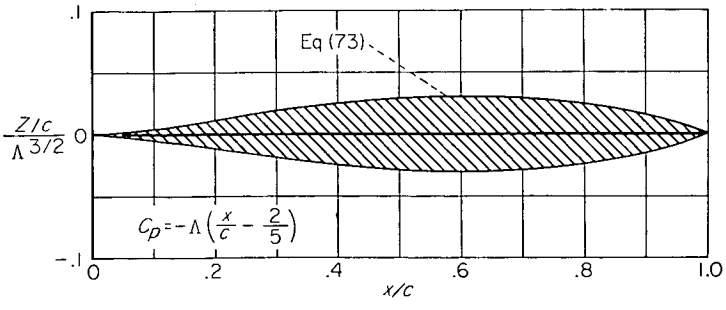


FIGURE 22.—Shape of complete airfoil having a constant pressure gradient at free-stream Mach number 1.

[6] This conclusion is confirmed by a new solution in closed analytic form given by Guderley on page 239 of his book "Theorie Schallnaher Strömungen" published by Springer-Verlag in 1957. Guderley's result has the same functional form as equation (72), but the coefficient in the latter result is greater by a factor $2/\sqrt{\pi} \approx 9.027/8$, after correcting an obvious slip in Guderley's final equation.

DECELERATING FLOWS

Although it is clear that the preceding relations are not appropriate for the analysis of flows with free-stream Mach number near 1 that decelerate smoothly through sonic velocity, it might appear that the proper expressions could be derived by formal application of the procedures described in the preceding section for positive λ_P to the approximate solution of equation (39) for negative λ_P. The analysis leads, in the absence of contributions from shock waves, to the following relation for u at the airfoil surface instead of equation (40)

$$u_P = -\frac{U_\infty}{\sqrt{-\pi\lambda_P}}\frac{d}{dx}\int_x^c \frac{dZ/d\xi}{\sqrt{\xi - x}}\,d\xi + \frac{1}{\lambda_P}\frac{\partial}{\partial x}\int_{-\infty}^{+\infty} d\zeta \int_x^\infty \sigma_P f\,d\xi \tag{74}$$

where

$$f = -(1 - M_\infty^2)\varphi_{\xi\xi}, \qquad \sigma_P = \sqrt{\frac{-\lambda_P}{4\pi(\xi - x)}}\,e^{\left[\frac{\lambda_P(x-\zeta)^2}{4(\xi-x)}\right]}$$

The principal difference between the results for the two cases is that the value of $u(x)$ indicated by equation (74) depends on conditions downstream of the point x, whereas that indicated by equation (40) for positive λ_P depends on conditions upstream of x. This difference is a fundamental property of equation (39) and necessitates a change in the argument required to disregard additional contributions from shock waves, because now it is the oblique shock waves situated downstream, rather than upstream of x, that furnish a contribution to $u(x)$. If, however, there are no oblique shock waves downstream of x, or if the contributions resulting from additional integrals over the shock surfaces are disregarded so that equation (74) can be used as a starting point in the analysis, the following result is obtained by proceeding in a fashion analogous to that employed in the derivation of equation (47) from (40):

$$\overline{C}_p = 2\xi_\infty + 2\left\{\frac{3}{\pi}\int_{x^*}^x \left[\frac{d}{dx_1}\int_{x_1}^c \frac{d(Z/\tau)/d\xi}{\sqrt{\xi - x_1}}\,d\xi\right]^2 dx_1\right\}^{1/3} \tag{75}$$

The symbol x^* again refers to the location of the sonic point and is equal to the value for x for which

$$\frac{d}{dx}\int_x^c \frac{dZ/d\xi}{\sqrt{\xi - x}}\,d\xi = 0 \tag{76}$$

The corresponding relation for the shape of an airfoil associated with a given pressure distribution at some free-stream Mach number near unity can also be found and is the following, again assuming that Z is zero at the leading edge:

$$Z = -\frac{\tau}{2\sqrt{2\pi}}\int_0^x dx_1 \int_{x_1}^c \frac{(\overline{C}_p - 2\xi_\infty)\sqrt{d\overline{C}_p/d\xi}}{\sqrt{\xi - x_1}}\,d\xi \tag{77}$$

No further use is made in this paper of equations (74) through (77) for decelerating flows at free-stream Mach numbers near 1. As will become more evident at a later point in the present discussion, it would appear necessary to use such formulas for the analysis of flows decelerating through sonic velocity, but the region of dependence in these relations is such as either to cast suspicions on their applicability or to require the occurrence of exceptional coincidences. On the other hand, two-dimensional flows that

decelerate smoothly through sonic velocity appear to be very exceptional physically. Further investigation is needed before additional remarks can be made regarding the role of the parabolic case with negative λ_P in the analysis of transonic flows.

The next section will be concerned with an alternative analysis of certain cases in which decelerating flows occur.

COMBINATION OF ACCELERATING AND DECELERATING FLOWS

The calculation of the pressure distribution at Mach numbers near 1 on an airfoil having such a shape that the velocity increases over part of the chord and decreases over the remainder cannot be accomplished by direct application of any of the relations developed in the preceding sections. On the one hand, the parabolic method described for flows with free-stream Mach number near 1 permits the analysis of flows that pass through sonic velocity, but fails when the velocity gradient is zero. On the other hand, the elliptic and hyperbolic methods described for subsonic and supersonic flows permit the analysis of flows with zero velocity gradient, but fail if the local velocity is sonic. The breakdown in each case is associated with the fact that the basic partial differential equation for each case, that is, equation (8), (21), or (39), assumes a degenerate form when λ is zero. Such cases are, nevertheless, interesting and important since they can occur in practical applications, and the present section is concerned with their discussion. The procedure adopted is based on the idea of joining together various of the results derived in the preceding sections in such a way that the failings associated with vanishing λ are avoided, rather than on a complete re-analysis of the problem from a sufficiently general point of view to encompass the entire problem in a single sweep.

In order to fix the ideas, consider the problem of calculating the pressure distribution at Mach number 1 on the airfoil with cusped trailing edge illustrated in figure 23 for which experimental data are available from reference 42 by Michel, Marchaud, and Le Gallo. The front half of this airfoil is the same as that of a biconvex circular-arc airfoil having a thickness ratio of 0.10, but the rear half is shaped in such a manner that an inflection point is located at 0.75 chord and that the trailing edge angle is zero. The ordinates

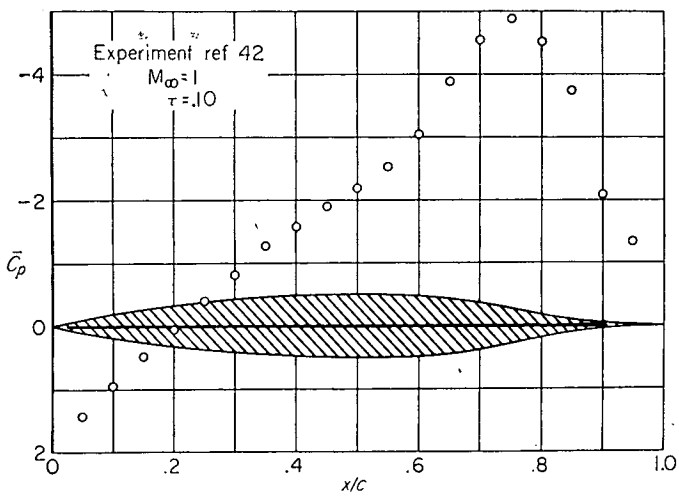


FIGURE 23.—Experimental pressure distribution for an airfoil with cusped trailing edge; $M_\infty = 1$.

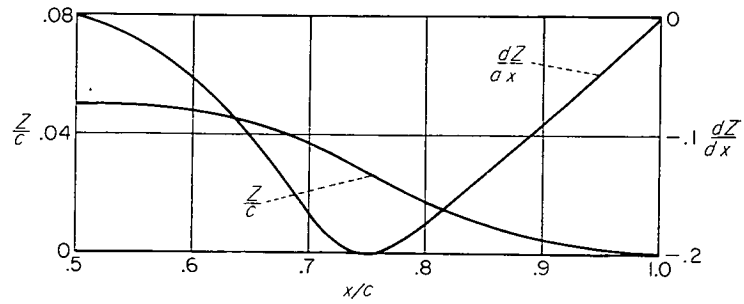


FIGURE 24.—Chordwise variation of ordinate, Z, and slope, $\frac{dZ}{dx}$, for the rear half of the airfoil shown in figure 23.

and slopes of the rear half of this airfoil are shown graphically in figure 24. No analytic expression is given in reference 42 for the ordinates of the rear half.

The pressure distribution on the front part of the airfoil where the passage through sonic velocity occurs can be calculated by use of equations (45) and (46), since it does not depend on the shape of the rear half of the airfoil. This means that the pressure distribution on the front half of the airfoil described above is given specifically by equation (53) for x/c between 0 and ½. It is clear that the pressure distribution on the entire rear half of the airfoil cannot be determined by use of equations (45) and (46) because the results so calculated indicate a point of zero pressure gradient in the vicinity of the inflection point. Although this detail, in itself, is not incorrect, it signals the breakdown of the parabolic method that occurs when λ is zero. Positive evidence of the breakdown is provided by the fact that the calculated pressures decrease downstream of the point of zero pressure gradient rather than increase as indicated by the experimental data shown on sketch (w) or by simple considerations of supersonic flow. These results, furthermore, cannot be joined to those obtained by use of equations (75) and (76) for the part of the airfoil downstream of the point of zero pressure gradient because the two sets of equations do not indicate the same location for this point. This situation should not be too surprising since the procedures should not be expected to fail abruptly when λ is precisely zero, but gradually as λ approaches zero.

There exists another possibility for the determination of the pressure distribution on the rear half of the present airfoil by joining together solutions. It is to use the formulas developed for supersonic flow, but with the final constant of integration adjusted so that the pressure is equal, at the point of connection, to that given by the solution for the forward part of the airfoil. This procedure corresponds to the use of simple wave theory for the calculation of the difference in pressure between an arbitrary point on the rear of the airfoil and the point of connection. In this way, the following equation results for the pressures on the rear of the airfoil at Mach numbers near unity:

$$\bar{C}_p - 2\xi_\infty = -2\left\{\left[-\left(\frac{\bar{C}_p(X) - 2\xi_\infty}{2}\right)\right]^{3/2} - \frac{3}{2\tau}\left[Z'(x) - Z'(X)\right]\right\}^{2/3} \tag{78}$$

where Z' refers to dZ/dx, and $\bar{C}_p(X)$ is the value of $\bar{C}_p$ at $x = X$.

The most convenient point for joining the two solutions in the application described in figures 23 and 24 is at $x/c=0.50$. Then the pressures on the forward half of the airfoil can be calculated directly by use of equation (53), the values of $(\overline{C}_pX)$ and $Z'(X)$ are

$$\overline{C}_p(X)=\overline{C}_p\left(\frac{c}{2}\right)=2\xi_\infty-2\left[\frac{6}{\pi}(-1+ln4)\right]^{1/3},\ Z'\left(\frac{c}{2}\right)=0 \quad (79)$$

and the following expression results for the pressures on the rear half of the airfoil at Mach numbers near unity:

$$\overline{C}_p\equiv\frac{[M_\infty{}^2(\gamma+1)]^{1/3}}{\tau^{2/3}}C_p=2\xi_\infty-2\left[\sqrt{\frac{6}{\pi}(-1+ln4)}-\frac{3}{2\tau}\frac{dZ}{dx}\right]^{2/3} \quad (80)$$

Figure 25 shows a comparison of the experimental pressure distribution for Mach number 1 given by Michel, Marchaud, and Le Gallo in reference 42 and the corresponding theoretical values calculated using equations (53) and (80) together with the values for dZ/dx given in figure 24. The theoretical and experimental results bear about the same relationship to each other as those shown previously for biconvex circular-arc airfoils although effects of boundary-layer shock-wave interaction extend over a larger fraction of the chord of the cusped airfoil. This difference is in agreement with the results obtained from schlieren photographs and given in reference 42 that indicate that the shock wave meets the airfoil, at Mach number 1, at 78-percent chord for the cusped airfoil and at 95-percent chord for the biconvex circular-arc airfoil of the same thickness ratio.

It is apparent that the pressures computed over the rear half of the airfoil by using equation (80) will tend to be somewhat too negative because the use of this relation corresponds to the use of simple wave theory and hence disregards the influence of a family of incoming compression waves arising from the sonic line. Some idea of the magnitude of this effect can be gained by examination of figure 26 which shows a comparison of the pressure distribution on biconvex circular-arc airfoils at Mach number 1 calculated using equation (53) for the entire airfoil, with those calculated using equation (78) for various fractions of the chord.

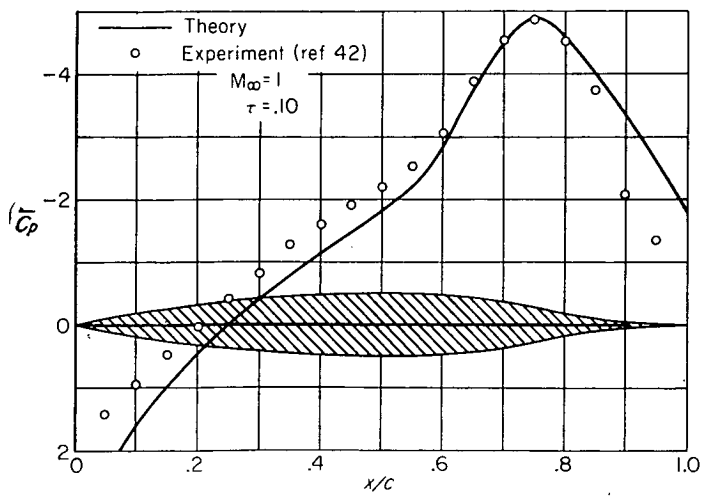


FIGURE 25.—Theoretical and experimental pressure distribution for the airfoil shown in figure 23; $M_\infty=1$.

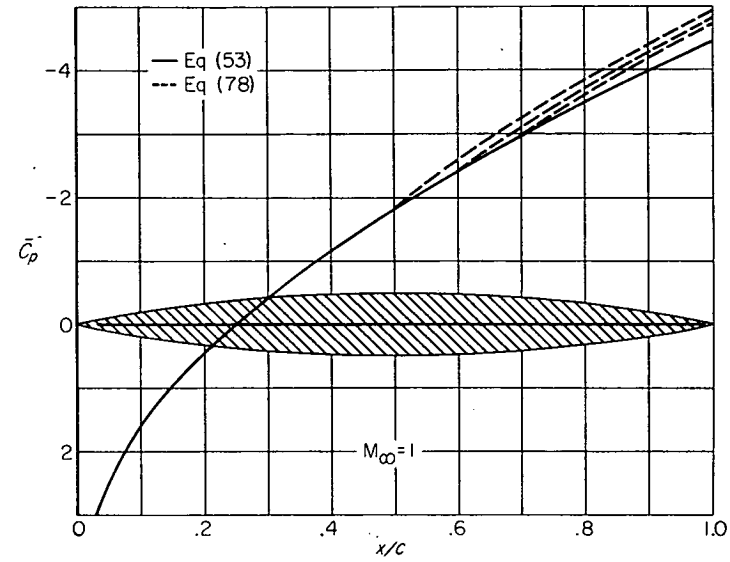


FIGURE 26.—Comparison of pressure distributions for the rear part of a circular-arc airfoil as indicated by the parabolic and hyperbolic methods; $M_\infty=1$.

A further example involving accelerating and decelerating flows at Mach number 1 is furnished by examining the case of the symmetrical double-wedge airfoil of arbitrary thickness ratio for which a solution has been given by Guderley and Yoshihara in reference 32. Figure 27 shows a plot of their result together with the corresponding result calculated by the procedures described above. The result for $0<x<c/2$ is calculated by use of equation (50). That for $c/2<x<c$ is calculated by use of the following equation which is obtained from equation (78) by equating $\overline{C}_p(X)$ to 0, $Z'(X)$ to $\bar{\tau}$, and $Z'(x)$ to $-\tau$.

$$\overline{C}_p=-2(3)^{2/3} \quad (81)$$

The difference between the two pressure distributions on the rear half of the airfoil is again the result of the neglect,

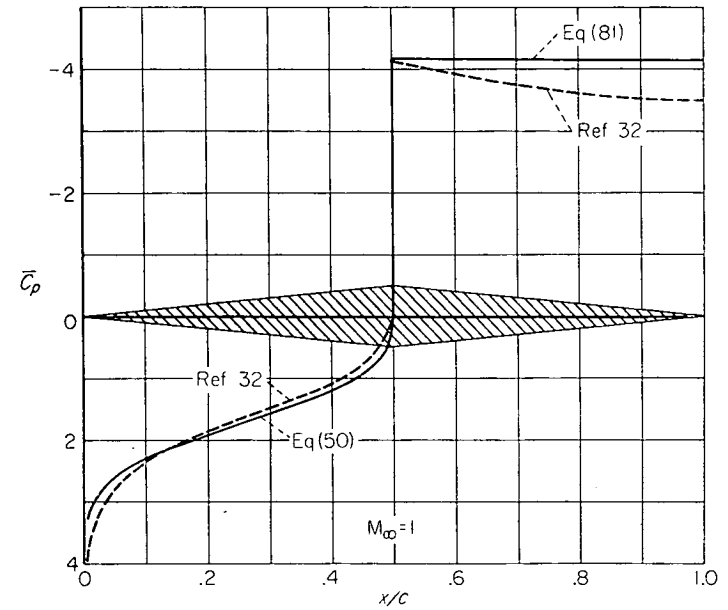


FIGURE 27.—Comparison of the pressure distributions for a double-wedge airfoil as indicated by the present theory and by Guderley and Yoshihara; $M_\infty=1$.

in the present analysis, of the contribution of the family of incoming compression waves arising from the sonic line.

It is evident from these three examples that the present procedure of joining solutions is capable of yielding results that are at least qualitatively correct and that, although somewhat greater accuracy is undoubtedly desired, this procedure may be useful until such time as a more general analysis of accelerating-decelerating flows is accomplished.

COMPARISON OF RESULTS FOR MACH NUMBER 1 WITH THOSE FOR OTHER MACH NUMBERS

The remainder of this report is concerned with the discussion of some selected examples that illustrate the relation between results for Mach number 1 and those for other Mach numbers. This discussion is divided into two parts. The first is concerned with comparisons of pressure distributions on the same airfoil at different Mach numbers, and the second with pressure drag.

PRESSURE DISTRIBUTION

Attention is directed in this section to comparisons, for a number of airfoils, of the theoretical pressure distribution for Mach number 1 with that for the highest Mach number for purely subsonic flow and that for the lowest Mach number for purely supersonic flow. Pressure distributions for these two Mach numbers, designated more briefly as the lower and upper critical Mach numbers, respectively, are of particular significance not only because they represent the results associated with the bounds of the transonic range, but also because they are typical of the pressure distributions for all purely subsonic or purely supersonic flows. All of the theoretical results shown are calculated by application of the general expressions derived in the present paper. The results for Mach number 1 are the same as discussed in detail in the preceding section. Subsonic pressure distributions are calculated by use of equation (28), and supersonic pressure distributions by use of equation (15). The lower critical Mach number is determined from equation (30) by replacing $C_{p_{i_{cr}}}$ with the most negative value of C_{p_i} that occurs in each case, and solving for M_∞. The upper critical Mach number is determined from equation (16) by replacing $(dZ/dx)_{cr}$ with the value of dZ/dx at the leading edge and solving for M_∞.

Consider, first, the single-wedge airfoil for which the pressure distribution at Mach number 1 is given by equation (50) and illustrated graphically in figure 10. Figure 28 shows a comparison of this result for the specific case of a wedge having a semiapex angle θ of 0.10 radians with those for the upper and lower critical Mach numbers. The lower critical Mach number is, of course, zero because the velocity is sonic at the corner for all free-stream Mach numbers less than the upper critical. The pressure distribution for Mach number 0 is given by

$$C_p=C_{p_i}=-\frac{2\theta}{\pi}\,ln\,\frac{2x/c}{1-2x/c} \tag{82}$$

The three curves shown on figure 28 suffice to show that the pressure distribution on a single-wedge airfoil at Mach

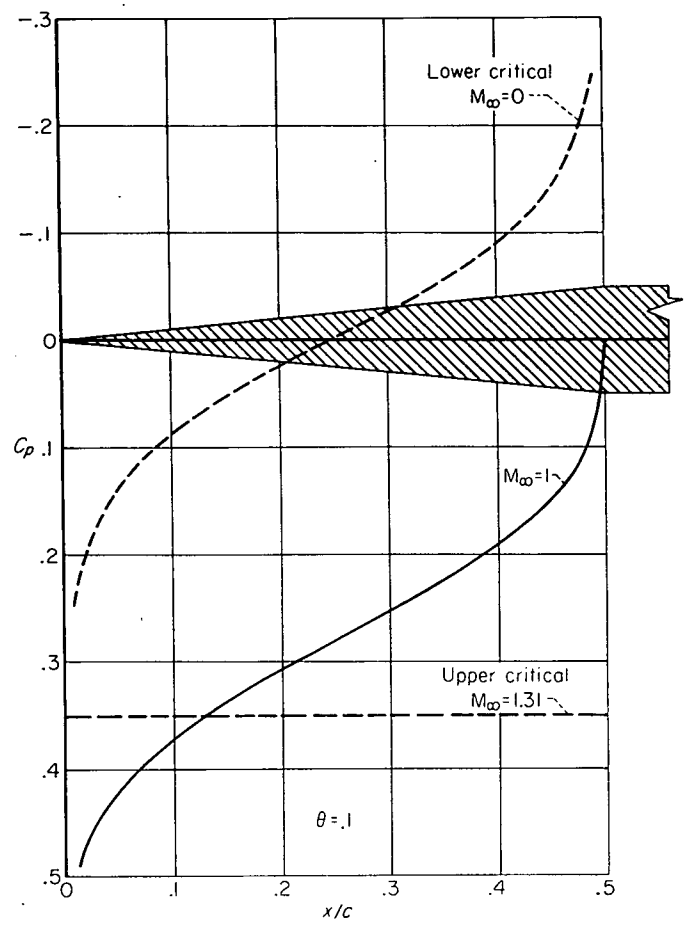


FIGURE 28.—Summary of pressure distributions for upper and lower critical Mach numbers and for Mach number 1. Single-wedge airfoil with a semiapex angle, θ, of 0.10 radian.

number 1 bears a much closer resemblance to that at the lower critical Mach number than to that at the upper critical Mach number. It is interesting to note, moreover, that the difference between the pressure distribution at Mach number 1 and that at Mach number 0 is very nearly constant across the chord.

Consider, next, the half circular-arc airfoil for which the pressure distribution at Mach number 1 is given by equation (53) and illustrated graphically in figure 15. Figure 29 shows a comparison of this result with those for the upper and lower critical Mach numbers. The computation of the pressure distribution for the lower critical Mach number involves the use of the following expression for C_{p_i} which is obtained by integration of the auxiliary relation of equation (28) with Z replaced by the expression given in equation (52) for $0<x<c/2$ and by $\tau c/2$ for $x>c/2$:

$$C_{p_i}=-\frac{4}{\pi}\tau\left[1+\left(1-\frac{2x}{c}\right)ln\,\frac{2x/c}{1-2x/c}\right] \tag{83}$$

The results illustrated in figure 29 display a remarkable property that the subsonic part of the pressure distribution at Mach number 1 differs from the pressure distribution at the lower critical Mach number by nearly a constant, and that the supersonic part of the pressure distribution differs from the pressure distribution at the upper critical Mach number by nearly the same constant, although of opposite sign.

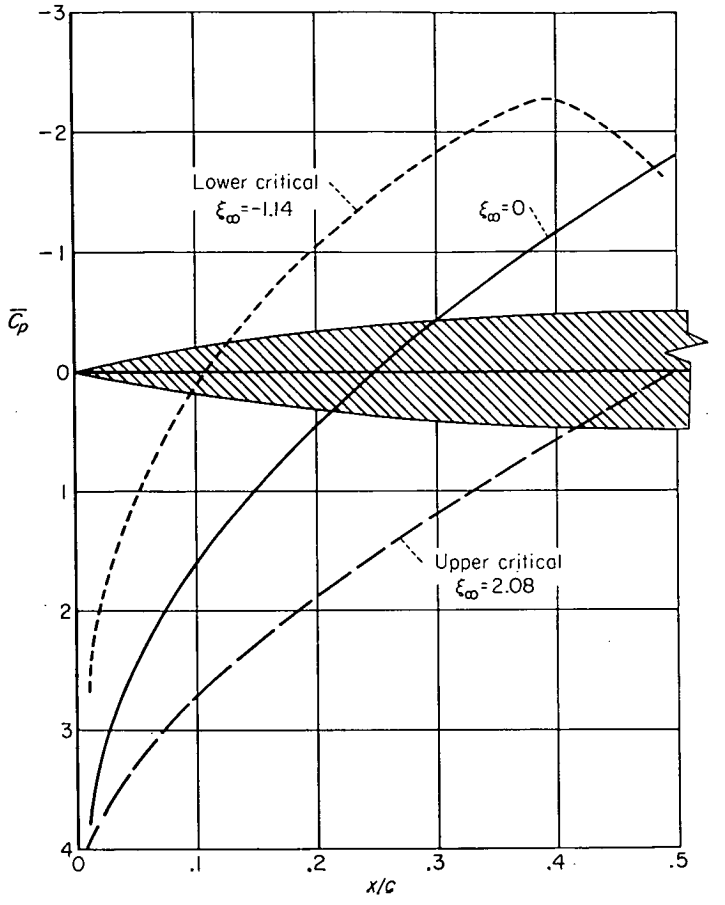


FIGURE 29.—Summary of pressure distributions for upper and lower critical Mach numbers and for Mach number 1 for half-circular-arc airfoils.

In order to investigate this difference further, the pressure distributions at the upper and lower critical Mach numbers have been calculated for the complete biconvex circular-arc airfoil and each of the four related airfoils having maximum thickness forward and aft of the midchord station for which the results for Mach number 1 are shown in figures 16 through 20. The results are shown in figure 30. It can be seen that the three pressure distributions for each airfoil bear the same general relationship to each other as noted above, although the difference between the pressure distributions is not always quite so constant as is observed for the wedge and circular-arc profiles.

PRESSURE DRAG

Once the pressure distribution is known for a given airfoil, the pressure drag can be obtained directly by integration of equation (48). The corresponding expression in terms of $\bar{c}_d$ and $\bar{C}_p$ is

$$\bar{c}_d \equiv \frac{[M_\infty^2(\gamma+1)]^{1/3}}{\tau^{5/3}} c_d \equiv 2\int_0^1 \bar{C}_p \frac{d(Z/t)}{d(x/c)} d\left(\frac{x}{c}\right) \qquad (84)$$

Although the present theoretical results only permit the calculation of pressure drag for Mach numbers near 1 and for Mach numbers greater than the upper critical, these results, together with existing theoretical and experimental results, can be used to sketch the variation of pressure drag with Mach number throughout the transonic range. The airfoil for which the most information is available is, of course, the single-wedge profile for which an approximate solution for Mach numbers less than 1 has been given by Cole (ref. 36) and improved recently by Yoshihara (ref. 35), that for Mach number 1 by Guderley and Yoshihara (ref. 32), and that for Mach numbers greater than 1 by Vincenti and Wagoner (ref. 34), and experimental data have been given by Liepmann and Bryson (refs. 30 and 31). Figure 31 shows a plot of these results, all in terms of the reduced parameters $\bar{c}_d$ and ξ_∞ and recast into the form consistent with the present formulation of the basic equations for transonic flow (see ref. 5, 6, or 9 for additional information on this point), together with the results computed by use of the present theory. The new results are indicated by the solid lines, the former by dashed lines and by data points. The short vertical lines on the data points indicate Bryson's estimate of the experimental accuracy of the data. As can be seen, the only point of difference between the present results and the previously existing results is at Mach numbers slightly in excess of the upper critical, and results from the error incurred in approximating the pressure jump through the bow shock wave by simple wave theory (i. e., by eq. (15) rather than eq. (6)). The positive slope of the drag curve at $\xi_\infty=0$, or Mach number 1 is in agreement with the result indicated by equation (51) and is typical for airfoils that do not close at the rear.

Figure 32 shows a summary of the comparable information for the front half of a biconvex circular-arc airfoil followed by a straight section, for which experimental data have been given by Bryson in reference 30. The theoretical values are again indicated by a solid line, and the experimental values by data points.[7] Although the amount of information available is much less than for the single-wedge airfoil, the results for both cases show striking similarity.

Results for half airfoils are not typical of those for complete airfoils, however, as can be seen by comparison of the preceding results with the corresponding theoretical and experimental results illustrated in figure 33 for complete biconvex circular-arc airfoils. The experimental results are those given by Michel, Marchaud, and Le Gallo in reference 37 and are obtained by integration of equation (48) together with experimental values for the pressure distribution. The most prominent difference concerns the slope of the curve of $\bar{c}_d$ versus ξ_∞ at $\xi_\infty=0$, or Mach number 1, for which the same procedures that led to positive values for a half airfoil, lead to zero slope for a complete airfoil. It can be seen that the experimental data support these values of the slope in both cases. Although the calculated values for drag are somewhat greater than those measured in the wind tunnel, most of the discrepancy can be attributed to the local effects of shock-wave boundary-layer interaction that occur near the trailing edge. Because this phenomenon depends on Reynolds number and may be of greatly diminished importance at full-scale conditions, Michel, Marchaud, and Le Gallo in-

[7] The experimental values shown in figure 32 differ somewhat from those given originally in figure 21 of reference 30 because of the correction of some inaccuracies in the calculation of the drag from the experimental pressure distributions given in figure 20 of reference 30. Although no explanation is known for the substantial negative drag indicated at subcritical Mach numbers and its existence must be indicative of some shortcomings of the experimental technique, its occurrence is an unmistakable consequence of the measured pressure distribution. That this is so can be seen at a glance by comparison of the measured pressure distribution with that indicated by linearized compressible flow theory, for which the drag is zero.

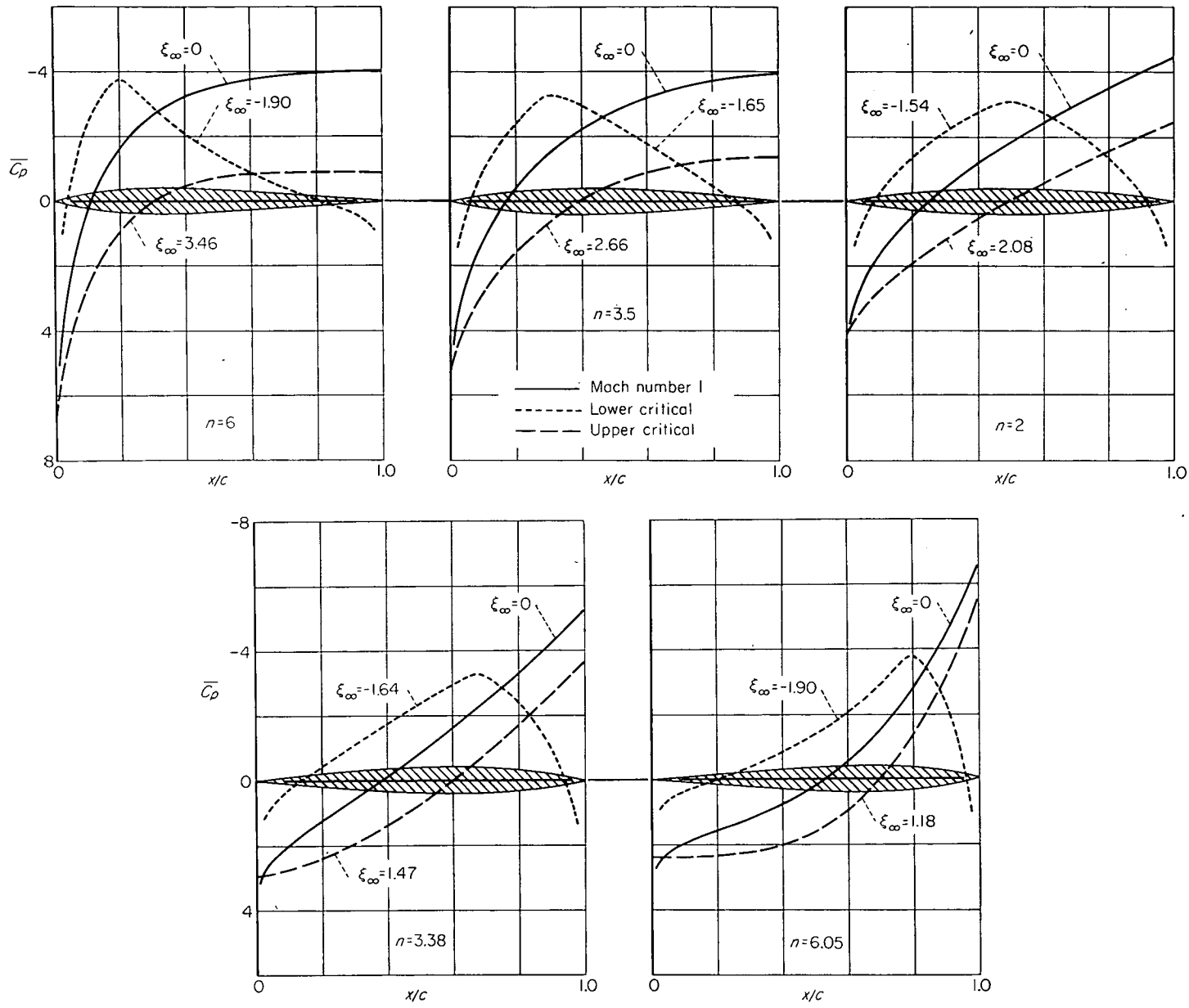


FIGURE 30.—Summary of pressure distributions for upper and lower critical Mach numbers and for Mach number 1 for a series of airfoils with different positions of maximum thickness.

troduced, in the discussion of their experimental results, the concept of "extrapolated drag" to represent the drag that would occur in the absence of separation. This quantity is calculated by consideration of a pressure distribution that differs from the experimental pressure distribution in the vicinity of the trailing edge as a result of the replacement of the pressures actually measured by those obtained by extrapolation of the trends indicated at stations upstream of the separation point. Accordingly, the values for "extrapolated drag" given by Michel, Marchaud, and Le Gallo are also shown on figure 33. As might be expected, the theoretical values for drag are in better agreement with the values for "extrapolated drag" than with those obtained directly from the actual measurements.

The results for biconvex circular-arc airfoils are typical of those for other complete airfoils. Attention is called, however, to the fact that the experimental values given by Michel, Marchaud, and Le Gallo in reference 39 for the airfoils that have the point of maximum thickness located forward of the midchord station are not so reliable as those they give for airfoils that have a more rearward location of the point of maximum thickness. This reduction in accuracy results from the facts that the method of testing and the fixed spacing of the orifices tend to diminish the accuracy with which the contribution of the region near the leading edge can be evaluated, and that the contribution of this region is, at the same time, of increased importance.

Figure 34 shows a summary of the calculated results for the pressure drag of the two families of airfoils described by equations (56) and (61) with values for n ranging from 1.5 to 6. For this range of n the airfoils described by equation (61) have a range of location for the point of maximum thickness that extends from about 0.30 to 0.55 chord, and those described by equation (56) have a range of locations extending from about 0.45 to 0.70 chord. In addition to lines for

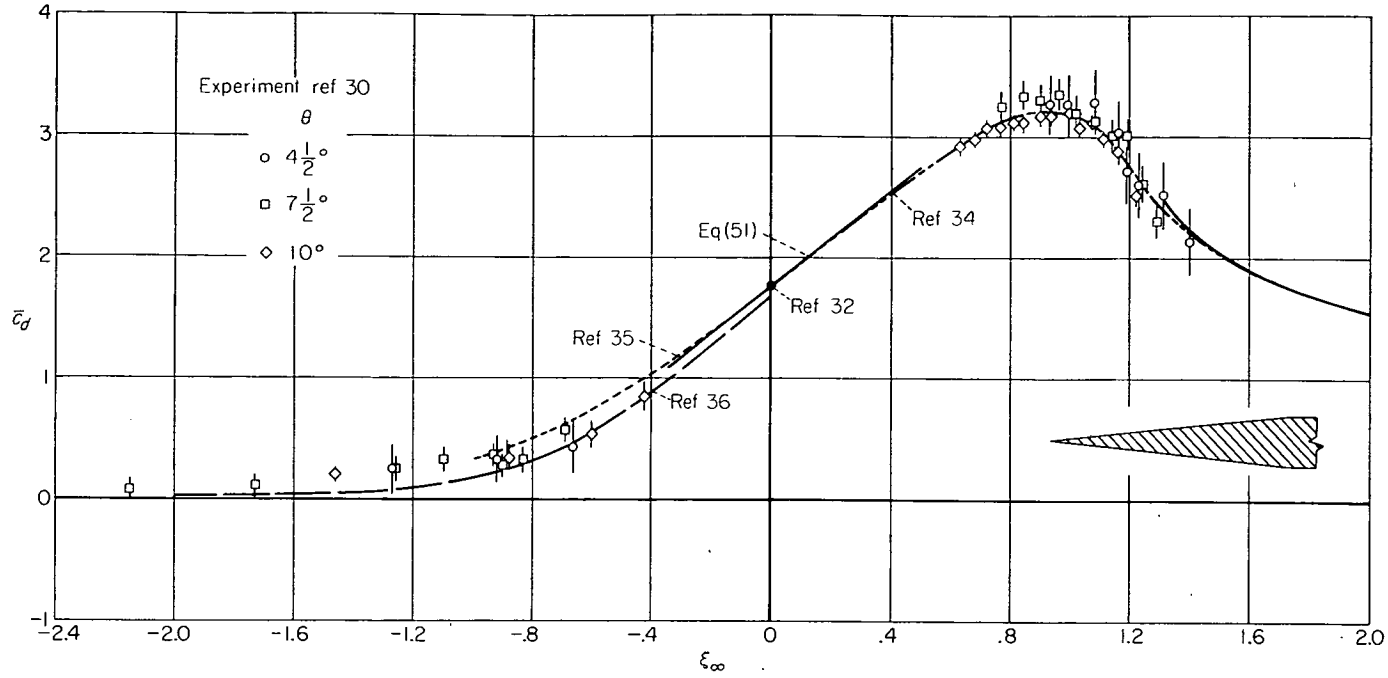


FIGURE 31.—Summary of theoretical and experimental results for the drag of single-wedge airfoils.

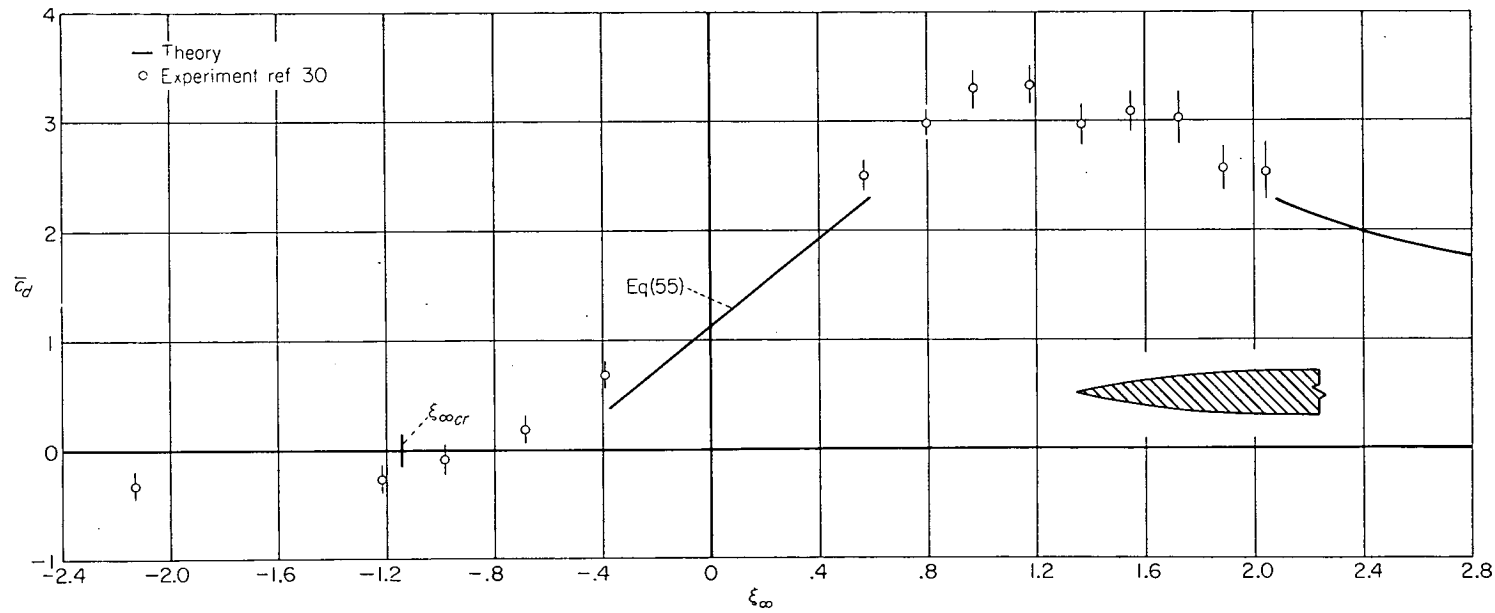


FIGURE 32.—Summary of theoretical and experimental results for the drag of half-circular-arc airfoils.

constant ξ_∞, which correspond to lines of constant Mach number for a group of airfoils having the same thickness ratio, a line is also shown for $\xi_{\infty cr}$, which corresponds to the line for the lowest Mach number for which the flow is purely supersonic. It can be seen that the variation of pressure drag with the location of the point of maximum thickness at Mach number 1 is quite different from that indicated by lines of constant ξ_∞, or Mach number, for purely supersonic flows, but is rather similar to that indicated by the line for $\xi_{\infty cr}$. An interesting feature of the results for purely supersonic flow is that the drag is not the same in forward and reverse flow, as is indicated by linearized compressible flow theory (see ref. 43 or 44).

CONCLUDING REMARKS

It appears worthwhile, in conclusion, to summarize and contrast the alternative discussions presented in the main text and in the Appendix of the general procedures involved in the approximate solution of all the problems treated in this paper. The arguments presented in the Appendix are based essentially on the idea of diminishing the importance of the higher order terms, and hence concentrate on the

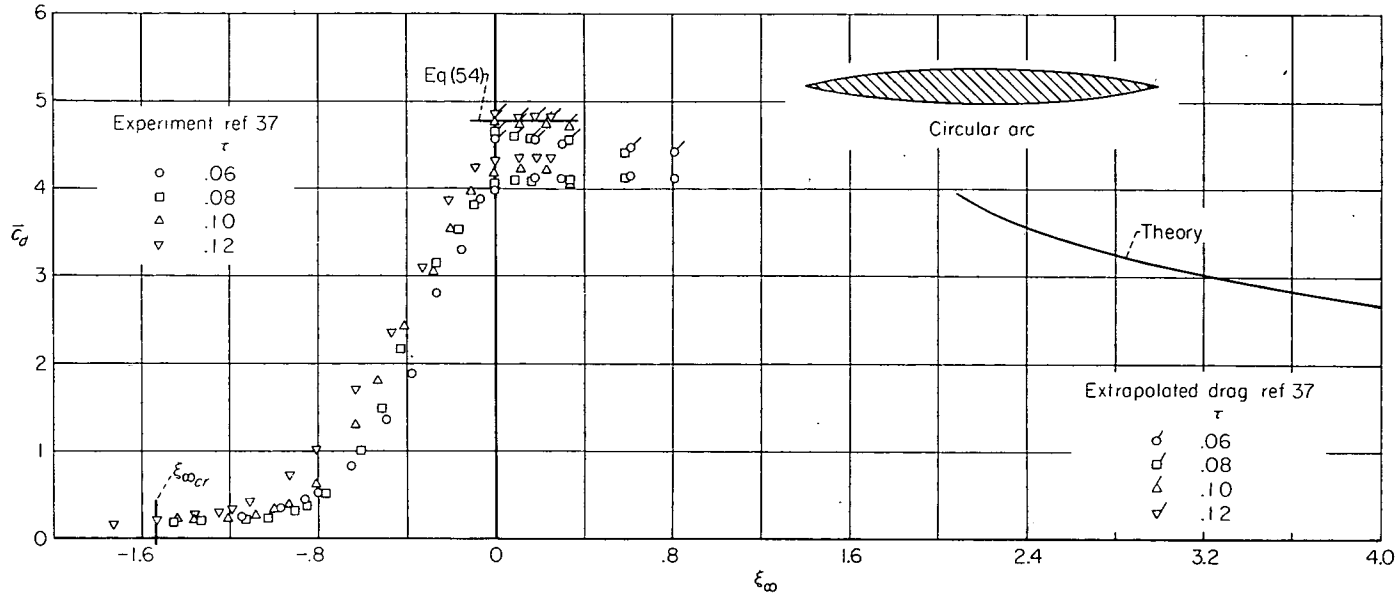


FIGURE 33.—Summary of theoretical and experimental results for the drag of complete circular-arc airfoils.

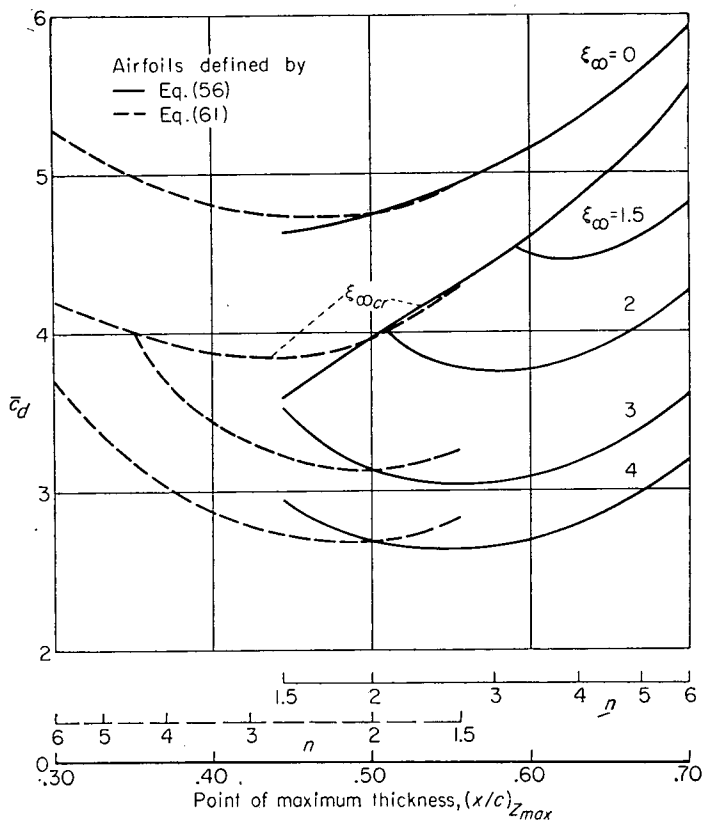


FIGURE 34.—Summary of theoretical results for the drag of two families of airfoils having various positions for the point of maximum thickness.

contributions stemming from the double integral of the integral equation appropriate for each case. The arguments presented in the main text lead to the same conclusions, but are based essentially on the idea of linearizing the transonic equation in a small region by replacing part of the nonlinear term by a constant λ, and then introducing different values for λ for different points in the field. This procedure might be considered equivalent, in some sense, to the replacement of the original nonlinear equation by a different linear differential equation for each point. Results obtained by solution of the equations at this stage depend, of course, on the choice of λ and must be assembled in order to determine the final results. This step is accomplished in each case by putting the results into such a form that a first-order nonlinear ordinary differential equation is obtained upon substituting for λ the quantity it originally replaced. At this point, the equations encountered coincide with those obtained following the procedures described in the Appendix and the remainder of the analysis proceeds in identical manner. In the cases considered herein, the differential equation is always of sufficiently simple form that it can be integrated analytically and the result expressed in closed analytic form. This integration implicitly introduces the assumption of continuity of the velocity or pressure distribution and leads, upon evaluation of a single constant of integration, to the final result.

AMES AERONAUTICAL LABORATORY
NATIONAL ADVISORY COMMITTEE FOR AERONAUTICS
MOFFETT FIELD, CALIF., *Mar. 11, 1957*

APPENDIX A

REINSPECTION AND ANALYSIS OF METHOD OF APPROXIMATION

INTRODUCTION

The methods used in the main text of this paper are appealing for their brevity and for the efficiency with which approximate solutions of the nonlinear equations of transonic flow theory are found. These methods are not entirely satisfying to the critical reader, however, because certain elements appear to be arbitrary and there is no a priori way in which the accuracy of the approximations can be judged. Both the virtue and weakness of these procedures are the result of introducing the essential simplifications at the beginning of the analysis. If the introduction of approximations is deferred to the end, the relations that occur in the initial stages of the analysis are, of course, more complicated than those presented in the main text. Consideration of these relations is, however, essential for an understanding of the basis for the method of approximation.

The following discussion of the approximate solution of problems of transonic flow theory is based on consideration of integral equations derived from the differential equations of transonic flow theory by standard application of Green's theorem. Since the details of each of the three cases, hyperbolic, elliptic, and parabolic, are somewhat different, each case is considered separately. In each case, exact relations are retained as long as possible and the approximations, when introduced, are seen to be closely related to those employed in the method of successive approximations commonly used in the determination of higher approximations in compressible flow theory. The following paragraphs will be concerned at the outset with the derivation of integral equations for each of the three cases, and subsequently with the discussion of the simplification and approximate solution of these equations.

DERIVATION OF INTEGRAL EQUATIONS

All of the subsequent analysis proceeds from Green's theorem. There are many forms of Green's theorem, but a sufficiently general form for all of the present purposes is that associated with the linear operator $\overline{L}(\Omega)$ defined as follows (ref. 45, pp. 244–247):

$$\overline{L}(\Omega)=\overline{A}\Omega_{xx}+\Omega_{zz}+\overline{B}\Omega_x \tag{A1}$$

where $\overline{A}$ and $\overline{B}$ are constants. Green's theorem states that the following relation holds between any two arbitrary functions Ω and ψ having continuous first and second derivatives:

$$\iint_{\overline{R}}[\psi\overline{L}(\Omega)-\Omega\overline{M}(\psi)]\,d\overline{R}=-\oint_{\overline{C}}\left[\overline{\Lambda}\left(\psi\frac{\partial\Omega}{\partial\nu}-\Omega\frac{\partial\psi}{\partial\nu}\right)+\overline{B}\psi\Omega\cos(n,x)\right]ds \tag{A2}$$

in which $\overline{R}$ refers to the interior of an arbitrary region bounded by the curve $\overline{C}$, as shown in figure 35, $\overline{M}$ is called the adjoint differential operator

$$\overline{M}(\psi)=\overline{A}\psi_{xx}+\psi_{zz}-\overline{B}\psi_x$$

$\overline{\Lambda}$ represents the quantity

$$\Lambda=\sqrt{\overline{A}^2\cos(n,x)+\cos^2(n,z)}$$

and $\partial/\partial\nu$ stands for a derivative in the direction ν, and can be written as a linear differential operator.

$$\frac{\partial\Omega}{\partial\nu}=\Omega_x\cos(\nu,x)+\Omega_z\cos(\nu,z)$$

The direction ν is called the conormal, and its direction cosines are related to those of the normal n according to

$$\overline{\Lambda}\cos(\nu,x)=\overline{A}\cos(n,x)$$

$$\overline{\Lambda}\cos(\nu,z)=\cos(n,z)$$

HYPERBOLIC CASE

The initial step in the present derivation of the integral equation appropriate for the discussion of the hyperbolic case is to subtract $\lambda_H\varphi_{xx}$ from both sides of equation (3), and to write the resulting equation as follows:

$$-\lambda_H\varphi_{xx}+\varphi_{zz}=(M_\infty{}^2-1+ku-\lambda_H)\varphi_{xx}=f_H \tag{A3}$$

The symbol λ_H refers to any positive finite constant. The form of Green's theorem associated with the linear operator

$$\overline{L}(\varphi)=\overline{L}_H(\varphi)=-\lambda_H\varphi_{xx}+\varphi_{zz} \tag{A4}$$

will now be applied, whence

$$\overline{A}=-\lambda_H,\qquad \overline{B}=0,\qquad \overline{M}_H(\varphi)=\overline{L}_H(\varphi) \tag{A5}$$

The quantity Ω is now identified with the perturbation potential φ, and ψ with an elementary solution of $\overline{M}_H(\psi)=0$,

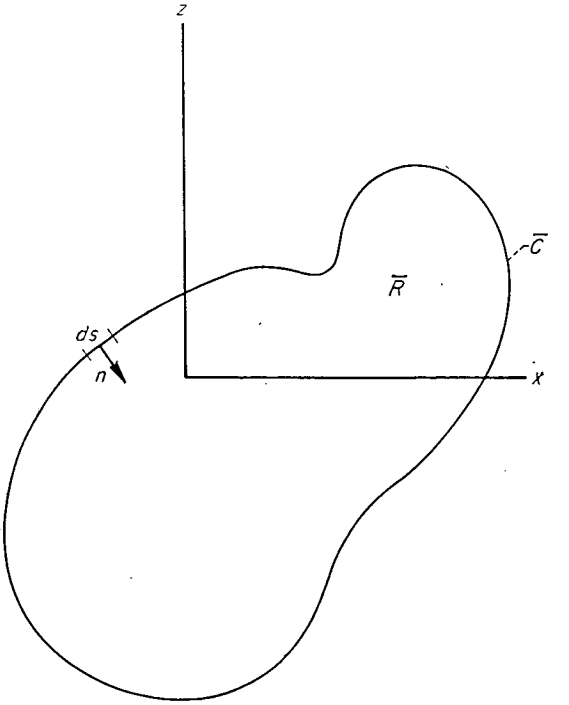


FIGURE 35.—Region of integration.

in particular with the unit supersonic source σ_H defined as follows:

$$\psi=\sigma_H=\begin{cases}-\dfrac{1}{2\sqrt{\lambda_H}} & \text{for } (x-\xi)^2\geq\lambda_H(z-\zeta)^2 \quad \text{(A6a)}\\ 0 & \text{for } (x-\xi)^2<\lambda_H(z-\zeta)^2 \quad \text{(A6b)}\end{cases}$$

If the region $\overline{R}$ is so selected that the inequality expressed in equation (A6a) holds throughout, equation (A2) reduces to

$$-\int_{\overline{C}}\overline{\Lambda}_H\frac{\partial\varphi}{\partial\nu_H}ds=\iint_{\overline{R}}\overline{L}_H(\varphi)d\overline{R}=\iint_{\overline{R}}f_Hd\overline{R} \qquad \text{(A7)}$$

in which $\overline{\Lambda}_H$ and ν_H refer to the special forms of $\overline{\Lambda}$ and ν consistent with equation (A4) or (A5), the running coordinates of integration are ξ,ζ, and the field point at which φ is to be evaluated is x,z. Equation (A7) is now applied to the region indicated in figure 36. Note that the wing, wake, and shock waves must be excluded from the region of integration. It should be noted that figure 36 is only a schematic illustration to help define the quantities involved in equation (A7), and that the shock wave, indicated as a detached bow wave, might instead be attached to the leading edge, to the trailing edge, or situated somewhere along the chord. The single shock wave illustrated in figure 36 could, moreover, be replaced by a complicated system of shock waves. The region $\overline{R}_H$ may likewise be considered to consist of a single region, or as the sum of a number of regions as typified by adding to $\overline{R}_H$ the region situated upstream of the bow wave

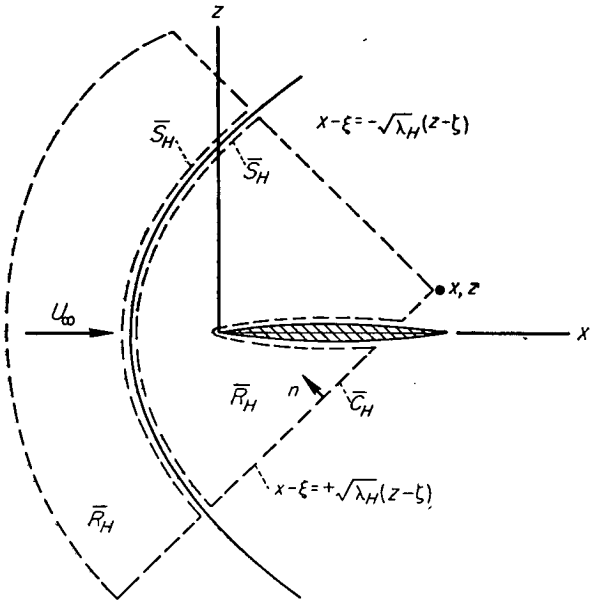


FIGURE 36.—Region of integration for the hyperbolic case.

and within the dotted lines of figure 36. In any case, the general considerations remain the same, and the following integral equation is obtained for φ at an arbitrary point x,z:

$$\varphi(x,z)=\left[\frac{1}{-2\sqrt{\lambda_H}}\int_0^{x-\sqrt{\lambda_H}|z|}\Delta\frac{\partial\varphi}{\partial\zeta}d\xi+\frac{\Delta\varphi(x-\sqrt{\lambda_H}|z|)}{2}\right]-\frac{1}{2\sqrt{\lambda_H}}\int_{\overline{S}_H}\overline{\Lambda}_H\delta\frac{\partial\varphi}{\partial\nu_H}d\overline{S}_H-\frac{1}{2\sqrt{\lambda_H}}\iint_{\overline{R}_H}f_Hd\overline{R}_H \qquad \text{(A8)}$$

where

$$\Delta\frac{\partial\varphi}{\partial\zeta}=\frac{\partial\varphi_u}{\partial\zeta}-\frac{\partial\varphi_l}{\partial\zeta}, \qquad \Delta\varphi=\varphi_u-\varphi_l$$

in which u and l refer to conditions on the upper and lower sides of the wing and wake, where

$$\delta\frac{\partial\varphi}{\partial\nu_H}=\frac{\partial\varphi_a}{\partial\nu_H}+\frac{\partial\varphi_b}{\partial\nu_H}$$

in which a and b refer to conditions on the two sides of the shock wave $\overline{S}_H$, and where

$$\overline{\Lambda}_H\frac{\partial\varphi}{\partial\nu_H}=-\lambda_H\frac{\partial\varphi}{\partial\xi}\cos(n,x)+\frac{\partial\varphi}{\partial\zeta}\cos(n,z)$$

ELLIPTIC CASE

The integral equation appropriate for the discussion of the elliptic case can be derived by use of procedures analogous to those described in the preceding paragraph for the hyperbolic case. The initial step is to add $\lambda_E\varphi_{xx}$ to both sides of equation (3), and to write the resulting equation as follows:

$$\lambda_E\varphi_{xx}+\varphi_{zz}=[\lambda_E-(1-M_\infty{}^2-ku)]\varphi_{xx}=f_E \qquad \text{(A9)}$$

As in the hyperbolic case, the symbol λ_E refers to any positive finite constant. The form of Green's theorem associated with the linear operator

$$\overline{L}(\varphi)=\overline{L}_E(\varphi)=\lambda_E\varphi_{xx}+\varphi_{zz} \qquad \text{(A10)}$$

will now be applied, whence

$$\overline{A}=\lambda_E, \qquad \overline{B}=0, \qquad \overline{M}_E(\varphi)=\overline{L}_E(\varphi) \qquad \text{(A11)}$$

The quantity Ω is now identified with φ, and ψ with an elementary solution of $\overline{M}_E(\psi)=0$, in particular the unit subsonic source defined by the function

$$\psi=\sigma_E=\frac{1}{2\pi\sqrt{\lambda_E}}ln\sqrt{(x-\xi)^2+\lambda_E(z-\zeta)^2} \qquad \text{(A12)}$$

In this way equation (A2) reduces to

$$-\int_{\overline{C}}\overline{\Lambda}_E\left(\sigma_E\frac{\partial\varphi}{\partial\nu_E}-\varphi\frac{\partial\sigma_E}{\partial\nu_E}\right)ds=\iint_{\overline{R}}\sigma_E\overline{L}_E(\varphi)d\overline{R}=\iint_{\overline{R}}\sigma_Ef_Ed\overline{R} \qquad \text{(A13)}$$

in which $\overline{\Lambda}_E$ and ν_E refer to the special forms of $\overline{\Lambda}$ and ν consistent with equation (A10) or (A11), the running coordinates of integration are ξ,ζ, and the field point at which φ is to be determined is x,z. If equation (A13) is now applied to the region $\overline{R}_E$ surrounding the wing, wake, and shock waves, as illustrated in figure 37, and the a priori assumption is made that the perturbation field attenuates sufficiently fast with distance to negate the contribution of the surface integral over the large circle in the limit as the radius goes to infinity, the following integral equation is obtained for φ at an arbitrary point x,z:

$$\varphi(x,z)=\int_0^\infty\left(\sigma_E\Delta\frac{\partial\varphi}{\partial\zeta}-\Delta\varphi\frac{\partial\sigma_E}{\partial\zeta}\right)d\xi+\int_{\overline{S}_E}\sigma_E\overline{\Lambda}_E\delta\frac{\partial\varphi}{\partial\nu_E}d\overline{S}_E+\iint_{\overline{R}_E}\sigma_Ef_Ed\overline{R}_E \qquad \text{(A14)}$$

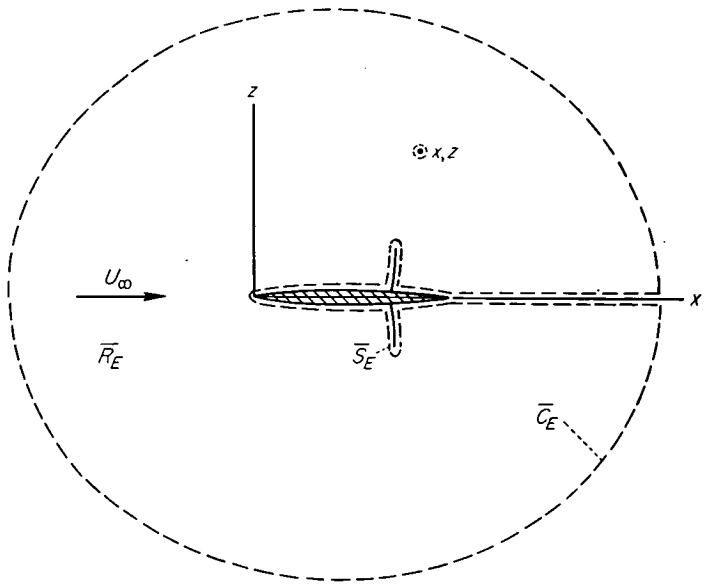


FIGURE 37.—Region of integration for the elliptic case.

where $\Delta\varphi$ and $\Delta(\partial\varphi/\partial\zeta)$ have the same meaning as in equation (A8), but where

$$\delta\frac{\partial\varphi}{\partial\nu_E}=\frac{\partial\varphi_a}{\partial\nu_E}+\frac{\partial\varphi_b}{\partial\nu_E}$$

in which a and b refer to conditions on the two sides of the shock wave $\bar{S}_E$, and where

$$\bar{\Lambda}_E\frac{\partial\varphi}{\partial\nu_E}=\lambda_E\frac{\partial\varphi}{\partial\xi}\cos(n,x)+\frac{\partial\varphi}{\partial\zeta}\cos(n,z)$$

PARABOLIC CASE

The initial step in the derivation of the integral equations appropriate for the discussion of the parabolic case is to subtract $\lambda_P\varphi_x$ from both sides of equation (3), and to write the resulting equation as follows:

$$\varphi_{zz}-\lambda_P\varphi_x=(M_\infty^2-1)\varphi_{xx}+(k\varphi_{xx}-\lambda_P)\varphi_x=f_P \qquad \text{(A15)}$$

The symbol λ_P refers again to a finite constant, which may be either positive or negative. The form of Green's theorem associated with the linear operator

$$\bar{L}(\varphi)=\bar{L}_P(\varphi)=\varphi_{zz}-\lambda_P\varphi_x \qquad \text{(A16)}$$

will now be applied, whence

$$\bar{A}=0, \quad \bar{B}=-\lambda_P, \quad \bar{M}_P(\varphi)=\varphi_{zz}+\lambda_P\varphi_x \qquad \text{(A17)}$$

The quantity Ω is again identified with φ, and ψ with an elementary solution of $\bar{M}_P(\psi)=0$, in particular with the function

$$\psi=\sigma_P=\begin{cases}\sqrt{\dfrac{\lambda_P}{4\pi(x-\xi)}}\,e^{\left[-\frac{\lambda_P(z-\zeta)^2}{4(x-\xi)}\right]} & \text{for } \dfrac{\lambda_P}{x-\xi}\geq 0 \qquad \text{(A18a)}\\ 0 & \text{for } \dfrac{\lambda_P}{x-\xi}<0 \qquad \text{(A18b)}\end{cases}$$

This function assumes a role in the analysis of the parabolic case that is analogous to that of the unit subsonic and supersonic sources in the elliptic and hyperbolic cases. In mathematical literature, the linear partial differential equation $\bar{L}_P(\varphi)=0$ with positive λ_P arises in the study of heat conduction, and the function σ_P is often referred to as a unit heat source. If the region $\bar{R}$ is so selected that the inequality expressed in equation (A18a) holds throughout, equation (A2) reduces to

$$-\int_{\bar{C}}\left[\bar{\Lambda}_P\left(\sigma_P\frac{\partial\varphi}{\partial\nu_P}-\varphi\frac{\partial\sigma_P}{\partial\nu_P}\right)-\lambda_P\sigma_P\varphi\cos(n,x)\right]ds$$
$$=\iint_{\bar{R}}\sigma_P\bar{L}_P(\varphi)d\bar{R}=\iint_{\bar{R}}\sigma_P f_P d\bar{R} \qquad \text{(A19)}$$

in which $\bar{\Lambda}_P$ and ν_P refer to the special forms of $\bar{\Lambda}$ and ν consistent with equation (A16) or (A17), the running coordinates of integration are ξ,ζ, and the field point at which φ is to be determined is x,z. It is apparent from the condition imposed on $\bar{R}_P$, that $\lambda_P/(x-\xi)$ is greater than or equal to zero, that two distinct subcases result depending on the sign of λ_P.

Positive λ_P.—If λ_P is positive, the region $\bar{R}_P$ appropriate for the application of equation (A19) is that part of space upstream from the point x,z. Again the wing, wake, and shock must be excluded from the region of integration, as illustrated schematically in figure 38. If equation (A19) is

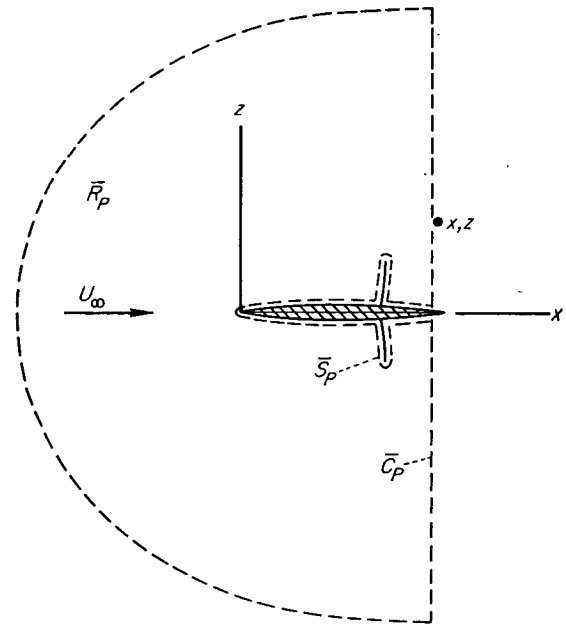


FIGURE 38.—Region of integration for the parabolic case with $\lambda_P>0$.

now applied to the region $\bar{R}_P$, and it is assumed that the perturbation field attenuates sufficiently fast with distance to negate the contribution of the surface integral over the outer boundary in the limit as the radius is increased to infinity, the following integral equation is obtained for φ at an arbitrary point x,z:

$$\varphi(x,z)=-\frac{1}{\lambda_P}\int_0^x\left(\sigma_P\Delta\frac{\partial\varphi}{\partial\zeta}-\Delta\varphi\frac{\partial\sigma_P}{\partial\zeta}\right)d\xi-\frac{1}{\lambda_P}\int_{\bar{S}_P}\sigma_P\bar{\Lambda}_P\delta\left(\frac{\partial\varphi}{\partial\nu_P}\right)d\bar{S}_P-$$
$$\frac{1}{\lambda_P}\iint_{\bar{R}_P}\sigma_P f_P d\bar{R}_P \qquad \text{(A20)}$$

where $\Delta\varphi$ and $\Delta(\partial\varphi/\partial\zeta)$ have the same meaning as in equation (A8), but where

$$\delta\frac{\partial\varphi}{\partial\nu_P}=\frac{\partial\varphi_a}{\partial\nu_P}+\frac{\partial\varphi_b}{\partial\nu_P}$$

in which a and b refer to conditions on the two sides of the shock wave $\overline{S}_P$, and where

$$\overline{\Lambda}_P\frac{\partial\varphi}{\partial\nu_P}=\frac{\partial\varphi}{\partial\zeta}\cos(n,z)$$

Negative λ_P.—If λ_P is negative, the region $\overline{R}_P$ appropriate for the application of equation (A19) is that part of space downstream from the point x, z. If equation (A19) is applied to the region $\overline{R}_P$ surrounding the appropriate part of the wing, wake, and shock waves, as illustrated in figure 39, and the contribution of the surface integral over the outer boundary vanishes as the radius is increased to infinity, the following integral equation is obtained for φ at an arbitrary point x,z:

$$\varphi(x,z)=\frac{1}{\lambda_P}\int_x^\infty\left(\sigma_P\Delta\frac{\partial\varphi}{\partial\zeta}-\Delta\varphi\frac{\partial\sigma_P}{\partial\zeta}\right)d\xi+\frac{1}{\lambda_P}\int_{\overline{S}_P}\sigma_P\overline{\Lambda}_P\delta\left(\frac{\partial\varphi}{\partial\nu_P}\right)d\overline{S}_P+\frac{1}{\lambda_P}\iint_{\overline{R}_P}\sigma_P f_P d\overline{R}_P \qquad \text{(A21)}$$

where the symbols have the same meaning as in equation (A20), except that $\overline{S}_P$ and $\overline{R}_P$ now refer to those portions of the shock waves and space situated downstream from x,z.

SOME PROPERTIES OF THE INTEGRAL EQUATIONS

Although the four integral equations derived in the preceding paragraphs and written explicitly in equations (A8), (A14), (A20), and (A21) are quite different in most respects, they do possess a number of properties in common that are of concern in the present discussion. Perhaps the most obvious similarity is that each integral equation consists of a term that involves integration over the wing and wake, another term that involves integration over the shock waves, and a third term that involves integration over the surrounding space. The integrals extend over all space in the elliptic case, but only over part of space in the parabolic and hyperbolic cases. It is important to realize that there is no direct connection between the region of integration in each of the integral equations and the region of dependence in the solution, or in the physical flow, and that these two regions may, in fact, be distinctly different in some applications.

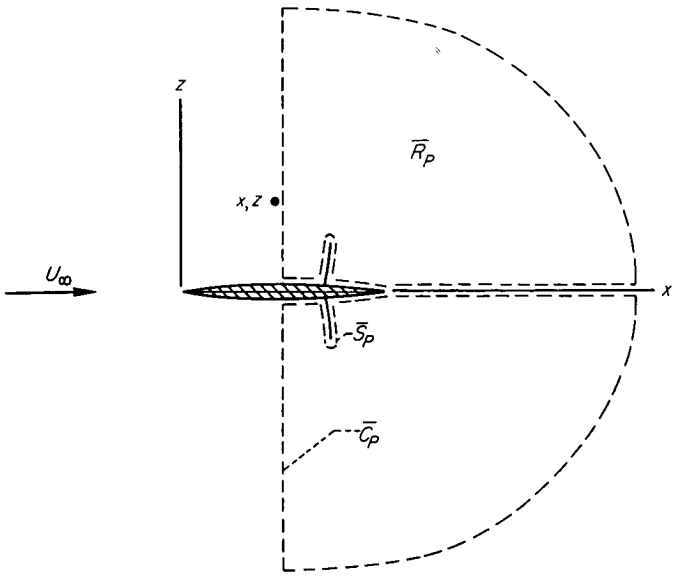


FIGURE 39.—Region of integration for the parabolic case with $\lambda_P<0$.

The first term in each integral equation involves a distribution of sources σ proportional to $\Delta(\partial\varphi/\partial\zeta)$ and doublets $\partial\sigma/\partial\zeta$ proportional to $\Delta\varphi$. Since $\Delta(\partial\varphi/\partial\zeta)$ is equal, according to the boundary condition given in equation (1), to $U_\infty\Delta(dZ/dx)$ and $\Delta\varphi$ is proportional to an x-wise integration of the lift, it follows that the part of the term containing sources is associated with the thickness distribution, and that part containing doublets, with the effects of camber and angle of attack. The latter part of the first term is zero for all of the nonlifting airfoils discussed in the main text of this paper. The first term in the elliptic and hyperbolic cases is familiar in compressible flow theory because, upon equating λ_E to $1-M_\infty^2$ or λ_H to M_∞^2-1, it reduces to the well-known solution for φ in the linearized theory of subsonic and supersonic flow around thin airfoils.

The second term in each integral equation involves a distribution of sources σ proportional to $\overline{\Lambda}\delta(\partial\varphi/\partial\nu)$ over any part of the shock waves that is situated in what otherwise would be part of the region of integration $\overline{R}$. There is no doublet distribution on the shock wave, as on the wing and wake, because φ is continuous across the shock wave. Although the contribution of the integral over the shock waves is often difficult to evaluate because $\delta(\partial\varphi/\partial\nu)$ is unknown and must be determined as part of the solution, there are a number of important applications in which this term either vanishes completely, or contributes nothing to the values for φ along the chord of the airfoil. The simplest class of problems for which this term vanishes is, of course, that in which the flow is subsonic everywhere and is hence shock-free. The contribution of this term will also vanish in parts of the field even if shock waves are present, provided they are situated entirely downstream of the region of integration in the hyperbolic case or the parabolic case with positive λ_P, or entirely upstream of the region of integration in the parabolic case with negative λ_P. The contributions of the shock wave vanish in the above situations because the complete term disappears from the integral equation. If the term remains, however, each element of the shock wave provides a contribution to φ that depends upon its strength and orientation. There are, moreover, certain directions in which an element of a shock wave can be oriented that result in no contribution to φ in the parabolic and hyperbolic cases. Thus, in the parabolic case, the contribution vanishes when the element of the shock wave extends perpendicular to the x axis, so that $\cos(n,z)$ in the second term of equation (A20) or (A21) is zero. It is similarly evident from equation (A8) that an element of a shock wave contributes nothing to φ in the hyperbolic case if the direction cosines and velocity components on the two sides of the shock wave satisfy the relationship

$$\frac{\cos(n_b,z)}{\cos(n_b,x)}=\lambda_H\frac{u_a-u_b}{w_a-w_b} \qquad \text{(A22)}$$

This relation can be expressed completely in geometric terms by combining it with the following equation that can be derived from consideration of the fact that φ is continuous across the shock

$$\frac{\cos(n_b,z)}{\cos(n_b,x)}=\frac{w_a-w_b}{u_a-u_b} \tag{A23}$$

Thus, the contribution to φ vanishes if the element of the shock wave is oriented so that

$$\left[\frac{\cos(n_b,z)}{\cos(n_b,x)}\right]^2=\tan^2(n_b,x)=\lambda_H \tag{A24}$$

If the same line of reasoning is applied to the elliptic case, relations analogous to equations (A22) through (A24) occur in which λ_H is replaced by $-\lambda_E$. From such considerations it would appear that the contribution to φ vanishes if the element of the shock wave is oriented so that

$$\left[\frac{\cos(n_b,z)}{\cos(n_b,x)}\right]^2=-\lambda_E \tag{A25}$$

Since λ_E is required to be a positive quantity, however, it is clear that there is no orientation for which the contribution vanishes. In the hyperbolic case, on the other hand, λ_H is required to be positive and there are always two particular orientations for which an element of a shock wave contributes nothing to φ. It is interesting to note, before leaving the discussion of the second term of each of the integral equations, that the particular orientation for which an element of a shock wave provides no contribution to φ coincides in all three cases, elliptic, parabolic, and hyperbolic, with the directions of the characteristic lines of the associated form of the linear partial differential equation, $\overline{L}(\varphi)=0$. The reader should observe, however, that these characteristic lines have no particular physical significance, inasmuch as their existence and direction depend on an arbitrary choice of a value for λ.

The third term in each integral equation involves integration of the effects of a distribution of sources σ proportional to f over that part of space surrounding the airfoil that is enclosed within the region of integration $\overline{R}$. The contribution of this term does not vanish, except in almost trivial circumstances such as occur, for example, in the hyperbolic case for points upstream of a bow wave provided λ_H is equated to M_∞^2-1 so that f_H is zero. Discussion of the contribution of the third term in each integral equation will consequently constitute the subject of much of the remainder of this Appendix. An interesting property of each of the integral equations that is worth noting before proceeding to the more specific discussion of each case is that the integrated strength of the sources in all space exterior to the airfoil, including those distributed along the shock waves, is equal, but opposite in sign, to the integrated strength of the sources distributed along the entire chord of the airfoil.

SIMPLIFICATION AND APPROXIMATE SOLUTION OF THE INTEGRAL EQUATIONS

No general methods are known for the analytical solution of the integral equations given in equations (A8), (A14), (A20), and (A21). Although certain simplifications can be made by restricting attention to nonlifting cases, and to cases in which the shock waves are not in the region of dependence, the essential difficulties remain because the integral equations are nonlinear, just as is the differential equation from which they are derived. The principal method that has been employed in the past for the solution of similar problems is that of successive approximation in which φ is expanded in a power series of some parameter such as the thickness ratio, and the coefficients in this series are determined as the solution develops. The first approximation in these methods is generally either the solution for linearized compressible flow theory or for incompressible flow, and the second and higher approximations are determined by iteration procedures in which linear equations are solved at every step. In practice, these methods have been found very difficult to apply to problems of compressible flow, and calculations of higher approximations than the second have, in most cases, proved prohibitively lengthy. (See ref. 3 for a résumé.) Serious questions of convergence remain in the existing solutions of this type, and it is doubtful if the results apply when mixed subsonic-supersonic flow occurs.

Another type of successive approximation procedure which involves the solution of quadratic equations with every iteration step is described in reference 9 and applied to the calculation of pressure distributions on circular-arc airfoils for all Mach numbers up to unity. Although the calculations could only be accomplished after the introduction of certain approximations, whose influence on the result is difficult to ascertain, the general procedure appears to succeed even with the occurrence of mixed flow.

The methods applied in the main text of this paper can be considered as the first step of still another type of successive approximation procedure in which certain nonlinear features are incorporated into even the first approximation. This procedure possesses the advantage of yielding results that disclose much of the nonlinear effects in the first approximation, and of making unnecessary, in many applications, the difficult task of iteration to determine higher approximations. A simple heuristic description of the analysis is given in the main text. The following paragraphs are concerned with a more detailed examination of the approximations involved in the analysis, and of the relationship between the present approximation and the approximations previously employed in the solution of problems of compressible flow. Although it is apparent that much of the discussion could be applied to lifting airfoils, attention is confined, as in the main text, to symmetrical nonlifting airfoils for which the following relations are to be applied in the first term of each integral equation:

$$\Delta\varphi=0, \qquad \Delta\frac{\partial\varphi}{\partial\zeta}=2U_\infty\frac{dZ}{d\xi} \tag{A26}$$

HYPERBOLIC CASE

The first problem to be discussed is the approximate solution of the integral equation given in equation (A8) for the hyperbolic case under the restrictions that the flow is purely supersonic so that

$$M_\infty^2-1+ku>0 \tag{A27}$$

Equation (A8) contains both a line integral over the shock wave $\overline{S}_H$ and a double integral over the surrounding region $\overline{R}_H$. The double integral can be integrated x-wise, however, because the integrand is a perfect differential. This partial integration results in a term that exactly cancels the line integral on the shock wave and equation (A8) can be rewritten as follows:

$$\varphi(x,z)=-\frac{U_\infty}{\sqrt{\lambda_H}}\int_0^{x-\sqrt{\lambda_H}|z|}\frac{dZ}{d\xi}\,d\xi-\frac{1}{2\sqrt{\lambda_H}}\int_>u\left(M_\infty{}^2-1+\frac{ku}{2}-\lambda_H\right)d\zeta \quad \text{(A28)}$$

The symbol $>$ below the integral sign of the second term indicates that the integration is to be carried over the lines $\xi=x-\sqrt{\lambda_H}(|z-\zeta|)$ extending upstream from x,z. Differentiation yields the following relations for u and $\partial u/\partial x$:

$$u(x,z)=-\frac{U_\infty}{\sqrt{\lambda_H}}Z'(x-\sqrt{\lambda_H}|z|)-\frac{1}{2\sqrt{\lambda_H}}\frac{\partial}{\partial x}\int_>u\left(M_\infty{}^2-1+\frac{ku}{2}-\lambda_H\right)d\zeta \quad \text{(A29)}$$

$$\frac{\partial u(x,z)}{\partial x}=-\frac{U_\infty}{\sqrt{\lambda_H}}Z''(x-\sqrt{\lambda_H}|z|)-\frac{1}{2\sqrt{\lambda_H}}\frac{\partial^2}{\partial x^2}\int_>u\left(M_\infty{}^2-1+\frac{ku}{2}-\lambda_H\right)d\zeta \quad \text{(A30)}$$

It should be noted that equations (A28), (A29), and (A30) are all integral equations and that each is an exact relation valid for any positive value of λ_H.

The results of linearized supersonic flow theory, as well as those of the counterpart, in the small disturbance theory of transonic flow, of higher approximations can be reproduced from any of the above equations upon equating λ_H to $M_\infty{}^2-1$. In this way, all contributions of first order are included in the first term on the right and the contribution of the second term on the right is, at most, of second order. Thus, the familiar expression of linearized supersonic flow theory follows immediately upon disregarding the contribution of the second term

$$u(x,z)=-\frac{U_\infty}{\sqrt{M_\infty{}^2-1}}Z'\,(x-\sqrt{M_\infty{}^2-1}|z|)+0(u^2) \quad \text{(A31)}$$

Its counterpart, correct to second order in Z', can be determined by application of the method of successive approximations in which the contribution of the second term is approximated by replacing the unknown u by the first-order approximation provided by equation (A31) and integrating. In this way, the following result is obtained for points on the airfoil.

$$u(x,0)=-\frac{U_\infty}{\sqrt{M_\infty{}^2-1}}\frac{dZ}{dx}-\frac{kU_\infty{}^2}{4(M_\infty{}^2-1)^2}\left(\frac{dZ}{dx}\right)^2+0\left(\frac{dZ}{dx}\right)^3 \quad \text{(A32)}$$

Note that although the first- and second-order approximations for u are different in general, first-order theory is sufficient to determine to second-order accuracy the point where u vanishes, that is where $dZ/dx=0$. First-order theory, moreover, provides the exact location for the point of zero u in the absence of shock waves, but this simple result is true only to second order if there are shock waves situated within the Mach forecone of the point $(x,0)$. Although the difficulties of integration are such that only the first few steps of the method of successive approximation can be evaluated in all but the simplest examples, the method can, in principle at least, be repeated indefinitely to establish the result accurate to any desired order. The result for u on the airfoil surface appears in the form of a power series involving ascending powers of $(dZ/dx)/(M_\infty{}^2-1)^{3/2}$. It is clear that a valid approximation is obtained provided the absolute value of dZ/dx is sufficiently small at all points, and the Mach number is not too close to unity. The failure associated with excessive positive values for dZ/dx usually occurs near the leading edge of the airfoil and is associated physically with detachment of the bow wave and the occurrence of local regions of subsonic flow. The failure associated with excessive negative values for dZ/dx, and clearly illustrated in figure 3 of the main text, usually occurs near the trailing edge of the airfoil and is purely mathematical in origin. In actual practice where only the first term or two may be evaluated, the result fails to provide adequate information regarding the ultimate convergence or divergence of the series and the question must be settled in each application by appeal to more exact solutions. It is important to realize that these uncertainties are not inherent in the integral equations given in equations (A28) through (A30), but enter the analysis with the assumption that the solution can be approximated satisfactorily by application of the particular form of the method of successive approximation described above.

The method of analysis employed throughout the main text is equivalent, from the present point of view, to the first step of a slightly different method of successive approximation that proceeds from consideration of the infinite set of relations that result if different values are selected for λ_H in the determination of conditions at different points in space. Analyses based on such a system of equations are more complex, in general, than those based on a single equation, but this increase in complexity is counterbalanced, in the present applications, by the fact that approximations can be introduced on the basis of local, rather than global, considerations. This fact makes possible the incorporation of some of the higher order or nonlinear contributions, as well as all of the first-order contributions, into the first term on the right in each relation of the infinite set, thereby reducing the contribution of the term containing the unknown u (ξ,ζ). If a rule for the selection of λ_H can be found that achieves this effect and if it can be expressed in analytic form, the infinite set of relations can be expressed once again in the form of a single equation; and the remainder of the analysis can proceed in a manner analogous to that described in the preceding paragraph for the classical method of successive approximation.

The method employed in the analysis of the hyperbolic case in the main text of this paper is equivalent to the first step of a successive approximation procedure based on the infinite set of equations for $\partial u/\partial x$ typified by equation (A30)

with λ_H equated to the local value of $M_\infty^2-1+ku(x,z)$ in each relation. Although it would appear from cursory examination of equation (A30) that the error incurred in so doing would be of second order, it will be demonstrated below that the result is actually accurate to second order and that the error is, at most, of third order. Although equations (A29) and (A30), upon which the remainder of the discussion of the hyperbolic case is based, are exact within the approximations of transonic flow theory, they are not in the most advantageous form for the following discussion because of the presence of the integral in the second term of each relation. If, however, attention is confined to the evaluation of the result at the airfoil surface to second-order accuracy, and to cases for which λ_H is restricted to values that differ from M_∞^2-1 by, at most, a quantity proportional to $u(x,z)$, that is $\lambda_H=M_\infty^2-1+au(x,z)$, the integrals can be integrated and the following relations result:

$$u(x,0)=-\frac{U_\infty}{\sqrt{\lambda_H}}\frac{dZ}{dx}-\frac{u\left(M_\infty^2-1+\frac{ku}{2}-\lambda_H\right)}{2(M_\infty^2-1)}+0(u^3) \quad \text{(A33)}$$

$$\frac{\partial u(x,0)}{\partial x}=-\frac{U_\infty}{\sqrt{\lambda_H}}\frac{d^2Z}{dx^2}-\frac{u_x(M_\infty^2-1+ku-\lambda_H)}{2(M_\infty^2-1)}+0(u^3) \quad \text{(A34)}$$

It is now clear that the substitution of M_∞^2-1+ku for λ_H in equation (A34) yields

$$\frac{\partial u(x,0)}{\partial x}=-\frac{U_\infty}{\sqrt{M_\infty^2-1+ku}}\frac{d^2Z}{dx^2}+0(u^3) \quad \text{(A35)}$$

This result corresponds to equation (11) of the main text and leads, upon integration and insertion of the auxiliary relation that u vanishes where dZ/dx is zero, to equation (15) relating C_p and dZ/dx. This relationship is commonly designated as that of simple wave theory. From the above discussion, it is clear that equation (15) must be correct to at least second order, as indeed simple wave theory is known to be for the pressures on the surface of an airfoil. If there are no shock waves in the region influencing conditions at the point $(x,0)$, the flow field is characterized by a single family of waves; and it can be shown that the error term indicated in equation (A35) vanishes completely. The resulting relation is thus exact within the approximation of transonic flow theory. It is interesting to observe that the use of the same relation for λ_H in equation (A29) for u leads to

$$u=-\frac{U_\infty}{\sqrt{M_\infty^2-1+ku}}\frac{dZ}{dx}+\frac{ku^2}{4(M_\infty^2-1)}+0(u^3) \quad \text{(A36)}$$

and results in errors of second order if only the first term is used.

There is another choice for λ_H that is not mentioned in the main text that will remove the second-order error if only the first term of equation (A29) or (A33) for u is used and that is $\lambda_H=M_\infty^2-1+(ku/2)$, since then

$$u=-\frac{U_\infty}{\sqrt{M_\infty^2-1+\frac{ku}{2}}}\frac{dZ}{dx}+0(u^3) \quad \text{(A37)}$$

This result is not the same as that of simple wave theory, but is recognized upon rearranging so that

$$u\sqrt{M_\infty^2-1+\frac{ku}{2}}=-U_\infty\frac{dZ}{dx} \quad \text{(A38)}$$

as being the square root, with appropriate choice of sign, of the shock relation given in equation (6) with u_a and w_a equated to zero. The result obtained by use of equation (A38) is thus equivalent to that obtained by equating the pressure at each point of the airfoil surface to that on a tangent wedge. Such a procedure has been proposed previously and is sometimes called "tangent-wedge theory." Although the first two terms of the formal expansion of either equation (A38) of tangent-wedge theory or equation (14) of simple wave theory agree with the second-order result obtained by use of the method of successive approximations and given in equation (A32), the results of either simple wave theory or tangent-wedge theory are to be preferred in applications because they approximate the proper termination of the solution when dZ/dx becomes too large, and do not fail spuriously at larger negative values of dZ/dx.

ELLIPTIC CASE

The second problem to be discussed is the approximate solution of the integral equation given in equation (A14) under the restriction that the flow is purely subsonic so that

$$1-M_\infty^2-ku>0 \quad \text{(A39)}$$

This restriction implies that the integral over $\overline{S}_E$ is zero, since there are no shock waves in a purely subsonic flow. Thus, equation (A14) reduces to

$$\varphi(x,z)=2U_\infty\int_0^c\sigma_E\frac{dZ}{d\xi}d\xi+\int_{-\infty}^{+\infty}\int f_E\sigma_E d\xi\,d\zeta \quad \text{(A40)}$$

Differentiation yields the following relations for u and $\partial u/\partial x$

$$u(x,z)=2U_\infty\int_0^c\frac{\partial\sigma_E}{\partial x}\frac{dZ}{d\xi}d\xi+\int_{-\infty}^{+\infty}\int f_E\frac{\partial\sigma_E}{\partial x}d\xi\,d\zeta \quad \text{(A41)}$$

$$\frac{\partial u(x,z)}{\partial x}=2U_\infty\int_0^c\frac{\partial^2\sigma_E}{\partial x^2}\frac{dZ}{d\xi}d\xi+\int_{-\infty}^{+\infty}\int f_E\frac{\partial^2\sigma_E}{\partial x^2}d\xi\,d\zeta \quad \text{(A42)}$$

where

$$\sigma_E=\frac{1}{2\pi\sqrt{\lambda_E}}ln\sqrt{(x-\xi)^2+\lambda_E(z-\zeta)^2}$$

$$\frac{\partial\sigma_E}{\partial x}=\frac{1}{2\pi\sqrt{\lambda_E}}\frac{x-\xi}{[(x-\xi)^2+\lambda_E(z-\zeta)^2]}$$

$$\frac{\partial^2\sigma_E}{\partial x^2}=-\frac{1}{2\pi\sqrt{\lambda_E}}\frac{(x-\xi)^2-\lambda_E(z-\zeta)^2}{[(x-\xi)^2+\lambda_E(z-\zeta)^2]^2}$$

$$f_E=\left\{\lambda_E-[1-M_\infty^2-ku(\xi,\zeta)]\right\}\frac{\partial u}{\partial\xi}$$

Equations (A40), (A41), and (A42) are all integral equations and each is exact for any positive value for λ_E. The solution of any of these integral equations is complicated not only because the relations are nonlinear, but also because the kernel, designated by σ_E or its derivative, is infinite at the point $\xi=x$, $\zeta=z$.

The familiar result of linearized subsonic flow theory can be obtained from any of the above equations by replacing λ_E by $1-M_\infty^2$ and disregarding the contribution of the double integral as being of higher order. The corresponding result, correct to second order, can be obtained by application of the method of successive approximations in which the contribution of the double integral is approximated by means of the first-order result to evaluate f_E at each point. Higher approximations can be obtained, at least in principle, by repeated application of the same procedure except that f_E is evaluated at each step by use of the results of the next lower approximation. In this way, an approximate expression for the solution is determined in the form of a truncated power series. Although the difficulties of integration are so great that few cases have been evaluated beyond the second approximation, it appears that the process converges to the desired solution for thin airfoils provided that certain well-known difficulties associated with stagnation points are properly accounted for and that, as in the hyperbolic case, the Mach number is not too close to unity. Again the results provided by the method of successive approximation indicate no definite limit for the Mach number. Comparison with experimental results shows that the trends displayed by the results are generally confirmed for Mach numbers less than the critical Mach number, but are essentially refuted for greater Mach numbers.

It is interesting and informative to compare the results obtained in the manner described above with those obtained by application of an alternative version of the method of successive approximations described in reference 9 that involves the solution of quadratic rather than linear algebraic equations at each step of the iteration process. The equation fundamental to this discussion is obtained from equation (A41) by again equating λ_E to $1-M_\infty^2$ and integrating the double integral by parts. In this way the following integral equation is determined for u:

$$u-\frac{k}{1-M_\infty^2}\frac{u^2}{2}=2U_\infty\int_0^c\frac{\partial\sigma_E}{\partial x}\frac{dZ}{d\xi}\,d\xi-k\int_{-\infty}^{+\infty}\int\frac{u^2(\xi,\zeta)}{2}\frac{\partial^2\sigma_E}{\partial x^2}\,d\xi\,d\zeta \tag{A43}$$

Although equation (A43) is completely equivalent to equation (A41), it is, in certain respects, superior from the point of view of obtaining approximate solutions. This is because the predominant effects of the region near the point x,z, which form a major contribution to the value of the integral in equation (A41), are furnished in equation (A43), by the term involving the square of u standing outside the integral. Although the difficulties of integration are as great or greater than encountered in the classical method of successive approximations and only the first few steps can be evaluated without approximation in any specific application, certain general features of the solution are clearly defined. In particular, it is shown in the report version of reference 9 that the results obtained for flows that are subsonic everywhere converge, in the limit of an infinite number of iteration steps, to the same result as ultimately obtained by application of the classical method of successive approximation. Whereas there is considerable doubt about the precise range of convergence of the latter result, the result obtained by application of the quadratic method of successive approximation clearly terminates with the occurrence of sonic velocity somewhere in the flow. The termination of the solution is recognized by the disappearance of real roots of the quadratic equation and is apparent at every step of the iteration process. It is evident, moreover, from comparison of the two sets of results that the series expansion for the solution obtained by the classical method of successive approximation converges only for purely subsonic flows and that the results indicated for mixed or transonic flows are false. These properties of the result obtained by the quadratic method of successive approximation are consistent with the numerous arguments and proofs for the nearly nonexistence of continuous shock-free transonic flows that have been advanced in recent years. (See ref. 46 for a brief résumé.)

This difference in behavior can be readily illustrated if one considers the expressions for the pressure coefficient at the midpoint of a symmetrical circular-arc airfoil that are obtained following the completion of the first two steps of each iteration process. The result provided by use of the classical method can be readily obtained from the third-order result quoted in equation (37) of the main text and is

$$C_P=-\frac{8}{\pi}\frac{\tau}{\sqrt{1-M_\infty^2}}-\left(\frac{10}{\pi^2}-\frac{1}{2}\right)\frac{(\gamma+1)M_\infty^2}{(1-M_\infty^2)^2}\tau^2+0(\tau^3) \tag{A44}$$

The first term represents the result obtained if one considers equation (A41) and disregards completely the contribution of the double integral. The result is precisely that of linearized compressible flow theory for the particular point under discussion. The second term represents an approximation for the contribution of the double integral obtained by replacing f_E for each point in space with the result provided by linearized theory. The results obtained by application of equation (A44) indicate that $-C_p$ increases indefinitely with increasing value of $\tau/(1-M_\infty^2)^{3/2}$ and appear to apply for mixed, or transonic, flows as well as for purely subsonic flows. The corresponding results obtained by use of the quadratic method of successive approximation are found by consideration of equation (A43). A first approximation obtained by disregarding completely the contribution of the double integral is

$$C_P=-\frac{2(1-M_\infty^2)}{M_\infty^2(\gamma+1)}\left[1-\sqrt{1-\frac{8}{\pi}\frac{M_\infty^2(\gamma+1)}{(1-M_\infty^2)^{3/2}}\tau}+0(\tau^2)\right] \tag{A45}$$

and a second approximation obtained from the evaluation of the contribution of the double integral by use of the result provided by linearized theory for f_E at each point is

$$C_p=-\frac{2(1-M_\infty^2)}{M_\infty^2(\gamma+1)}\left[1-\sqrt{1-\frac{8}{\pi}\frac{M_\infty^2(\gamma+1)}{(1-M_\infty^2)^{3/2}}\tau+\left(\frac{6}{\pi^2}+\frac{1}{2}\right)\frac{M_\infty^4(\gamma+1)^2}{(1-M_\infty^2)^3}\tau^2+0(\tau^3)}\right] \tag{A46}$$

The results obtained by application of either equation (A45) or (A46) also indicate that $-C_p$ increases with increasing values of $\tau/(1-M_\infty^2)^{3/2}$, but that this trend terminates when C_p reaches the critical value associated with the occurrence of sonic velocity, that is, when

$$C_p=-\frac{2(1-M_\infty^2)}{M_\infty^2(\gamma+1)}=C_{p_{cr}} \tag{5}$$

At this point, the slope of a curve representing the variation of C_p with M_∞ is infinite. In spite of these distinct differences in behavior, it is important to note that a formal power series expansion of equation (A46) in terms of τ agrees to second order with equation (A44), and that this agreement increases by one order of τ upon the completion of each additional iteration step. Results obtained following completion of additional iteration steps continue to follow the same trends. Those indicated by the classical method never provide any information regarding the precise range of convergence, and those indicated by the quadratic method always terminate with the occurrence of sonic velocity.

The method employed in the main text can be considered as an alternative procedure devised in any attempt to improve the quality of the first approximation and to diminish thereby some of the necessity for the evaluation of higher approximations. Before proceeding, it is important to recall that equations (A40), (A41), and (A42) are all integral equations valid for any positive value for λ_E; and that each can be considered, in the same way as described for the hyperbolic case, as a typical member of an infinite set of relations that result if different values are selected for λ_E in the determination of conditions at different points in space. It appears plausible that an increase in the accuracy, although not the mathematical order, of the first approximation might occur if λ_E is equated not to simply $1-M_\infty^2$, but to $1-M_\infty^2-ku(x,z)$ because then the function f_E in the double integral of each integral equation reduces to $k[u(x,z)-u(\xi,\zeta)](\partial u/\partial\xi)$ and hence vanishes at the point $\xi=x$, $\zeta=z$ where σ_E, $\partial\sigma_E/\partial x$, or $\partial^2\sigma_E/\partial x^2$ are infinite. If this procedure is applied to equation (A40) or (A41) for φ or u, and only the contribution of the single integral is retained, it is clear that the desired improvement will not be obtained for all Mach numbers up to the critical because the function $\sqrt{1-M_\infty^2-ku}$ that appears in the denominator of each term vanishes with the occurrence of sonic velocity, and the numerator does not vanish simultaneously. It is interesting to note, nevertheless, that the result for the pressure coefficient on the airfoil surface that is obtained in this way from equation (A41), that is,

$$C_p(x,0)=\frac{C_{p_i}(x,0)}{\sqrt{1-M_\infty^2+\frac{kU_\infty}{2}C_p}}=\frac{C_{p_i}(x,0)}{\sqrt{1-M^2}} \tag{A47}$$

corresponds to the use of the local, rather than free-stream, Mach number in the Prandtl-Glauert rule; and that this result is the counterpart, in transonic small disturbance theory, of an approximation proposed by Laitone, Szebehely, and Truitt (refs. 47 through 51). It is immediately apparent that although this result differs from the Prandtl-Glauert rule in the same direction as the higher order approximations, the effects of compressibility are greatly overestimated at points where the local velocity approaches sonic velocity. A typical set of results illustrating this statement is shown in figure 40 in which are repeated the curves of figure 8 showing the variation of C_p with M_∞ at the midpoint of a 10-percent-thick circular-arc airfoil together with the corresponding curve calculated by use of equation (A47).

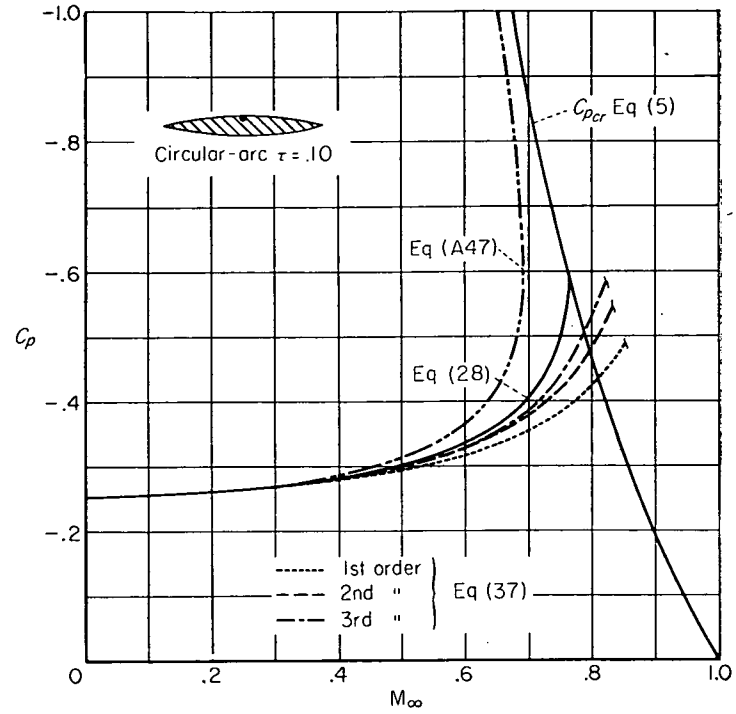


FIGURE 40.—Variation of C_p with M_∞ at the midpoint of a circular-arc airfoil, as indicated by equation (A47), by present theory, and by the method of successive approximations.

The relations developed in the discussion of the elliptic case in the main text do not encounter any such difficulties as the local Mach number approaches unity. The difference in behavior is a consequence of the fact that the latter results are based on the equation for $\partial u/\partial x$ rather than that for φ or u. That such a difference might occur can be seen by examination of equation (A42). The denominator again approaches zero as the local Mach number approaches 1, but the numerator is always zero at the point of maximum velocity. Since sonic velocity is first encountered with increasing Mach number at the point of maximum velocity, it is apparent that an indeterminate form occurs at the critical Mach number and the possibility at least exists that the gain sought by forcing f_E to be zero at the point where $\partial^2\sigma_E/\partial x^2$ is infinite will be realized. That a gain in accuracy, although not the mathematical order, of the solution is actually attained by this procedure is shown in the main text by comparison with existing higher approximations. Further confirmation of this conclusion is shown by the comparison illustrated in figure 41 in which the curves of figure 8 showing the variation with M_∞ of C_p at the midpoint of a 10-percent-thick circular-arc airfoil are repeated together with the curves calculated by use of equations (A45) and (A46) representing the first two approximations furnished by the quadratic method of successive approximations.

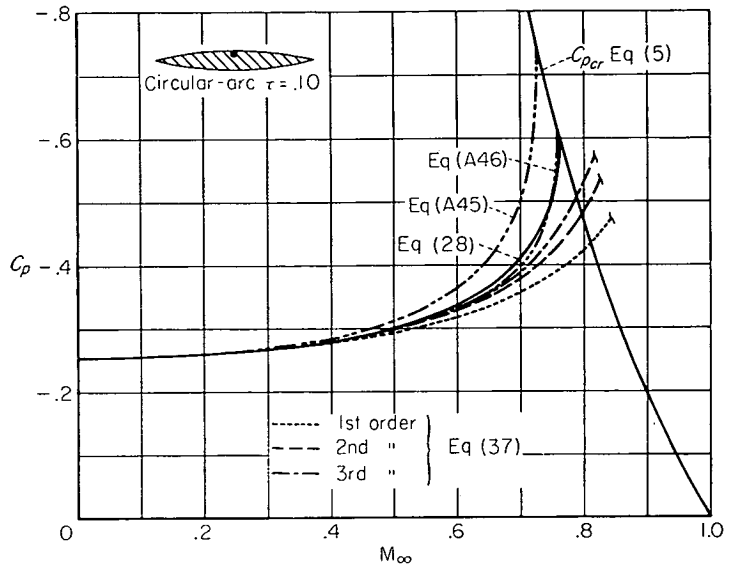


FIGURE 41.—Variation of C_p with M_∞ at the midpoint of a circular-arc airfoil, as indicated by present theory and by two alternative methods of successive approximations.

PARABOLIC CASE

The third problem to be discussed is the approximate solution of the integral equations for the parabolic case under the restriction that the free-stream Mach number is near unity. Two integral equations are given depending on whether λ_P is positive or negative. Inasmuch as no use is made in the main text of the equation for negative λ_P, the following remarks will be confined to the case for positive λ_P, for which the integral equation is given by equation (A20):

$$\varphi(x,z)=-\frac{2U_\infty}{\lambda_P}\int_0^x \sigma_P \frac{dZ}{d\xi}d\xi-\frac{1}{\lambda_P}\iint_{\bar{R}_P}\sigma_P f_P d\bar{R}_P-$$

$$\frac{1}{\lambda_P}\int_{\bar{S}_p}\sigma_P\left(\frac{\partial\varphi_b}{\partial\zeta}-\frac{\partial\varphi_a}{\partial\zeta}\right)\cos(n_b,z)dS \quad \text{(A48)}$$

where

$$\sigma_P=\sqrt{\frac{\lambda_P}{4\pi(x-\xi)}}\,e^{\left[-\frac{\lambda_P(z-\zeta)^2}{4(x-\xi)}\right]}$$

$$f_P=(M_\infty{}^2-1)\varphi_{\xi\xi}+(k\varphi_{\xi\xi}-\lambda_P)\varphi_\xi$$

The third term of equation (A48) represents the contribution of sources distributed along the surface of any part of the shock system that is situated upstream of the point x,z. This term has the property of effectively continuing the source distribution of the first term smoothly through a concave corner when the adjacent flow is supersonic. In this way, the singularities in the velocity and pressure that occur at such corners when the adjacent flow is subsonic are replaced, when the adjacent flow is supersonic, by the discontinuous, but finite, jump associated with an oblique shock wave. The contribution of this term vanishes if no part of the shock system is situated upstream of x,z or if the shock wave is parallel to the z axis. In that which follows attention is confined to cases in which it is presumed that one or both of these conditions are satisfied for all points situated upstream of the trailing edge. The integral over the shock waves thus contributes nothing to φ at any point on the airfoil surface, and the remainder of the discussion will proceed with considerations involving only the first two terms of equation (A48), and with the corresponding equation for u obtained therefrom by differentiation with respect to x. These two equations reduce to the following forms for points on the airfoil surface (i. e., $z=0$):

$$\varphi(x,0)=-\frac{U_\infty}{\sqrt{\pi\lambda_P}}\int_0^x\frac{dZ/d\xi}{\sqrt{x-\xi}}d\xi-\frac{1}{\lambda_P}\iint_{\bar{R}_P}\sigma_P f_P d\bar{R}_P \quad \text{(A49)}$$

$$u(x,0)=-\frac{U_\infty}{\sqrt{\pi\lambda_P}}\frac{\partial}{\partial x}\int_0^x\frac{dZ/d\xi}{\sqrt{x-\xi}}d\xi-\frac{f_P}{\lambda_P}-\frac{1}{\lambda_P}\iint_{\bar{R}_P}f_P\frac{\partial\sigma_P}{\partial x}d\bar{R}_P \quad \text{(A50)}$$

where

$$\sigma_P=\sqrt{\frac{\lambda_P}{4\pi(x-\xi)}}\,e^{\left[-\frac{\lambda_P\zeta^2}{4(x-\xi)}\right]}$$

$$\frac{\partial\sigma_P}{\partial x}=\sqrt{\frac{\lambda_P}{4\pi(x-\xi)^3}}\left[\frac{1}{2}+\frac{\lambda_P\zeta^2}{4(x-\xi)}\right]e^{\left[-\frac{\lambda_P\zeta^2}{4(x-\xi)}\right]}$$

It can be seen from examination of the preceding relations that the integral equations for the parabolic case are nonlinear and singular just as are the integral equations for the elliptic case. The following discussion of the approximate solution of the equations for the parabolic case will proceed, therefore, through applications of considerations that are very similar to those described in the discussion of the elliptic case in the preceding section.

The results found by application of the linearized theory for sonic flow described in references 23 through 28 follow from equation (A49) or (A50) by equating f_P to zero so that

$$u(x,0)=-\frac{U_\infty}{\sqrt{\pi\lambda_P}}\frac{\partial}{\partial x}\int_0^x\frac{dZ/d\xi}{\sqrt{x-\xi}}d\xi \quad \text{(A51)}$$

and selecting a value for λ_P. Various means have been proposed for the selection of an appropriate value for λ_P. In reference 28, the only one of the above references that pertains directly to two-dimensional flows, Maeder and Thommen suggest that λ_P be determined by equating it to the value for $k\partial u/\partial x$, obtained by differentiating equation (A51), that occurs at the point along the chord at which u is a maximum in incompressible flow. As noted in the main text in the discussion of the solution for the wedge, the results obtained by application of this linearized theory for sonic flow past thin airfoils may be at considerable variance with other theoretical and experimental results. A further illustration of this statement is provided in figure 42 in which the results given in figures 16, 18, and 19 for the circular-arc airfoil and the two related airfoils that have the point of maximum thickness at 30- and 70-percent chord are repeated together with the corresponding results obtained by application of the procedures described in reference 28. It can be seen upon comparison of these results with the experimental results shown in figures 16, 18, and 19 that the agreement between the pressure distribution calculated by application of the linearized theory for sonic flow and that measured experimentally deteriorates as the pressure gradient departs from a constant. It is apparent from equation (A51) that the accuracy cannot be improved

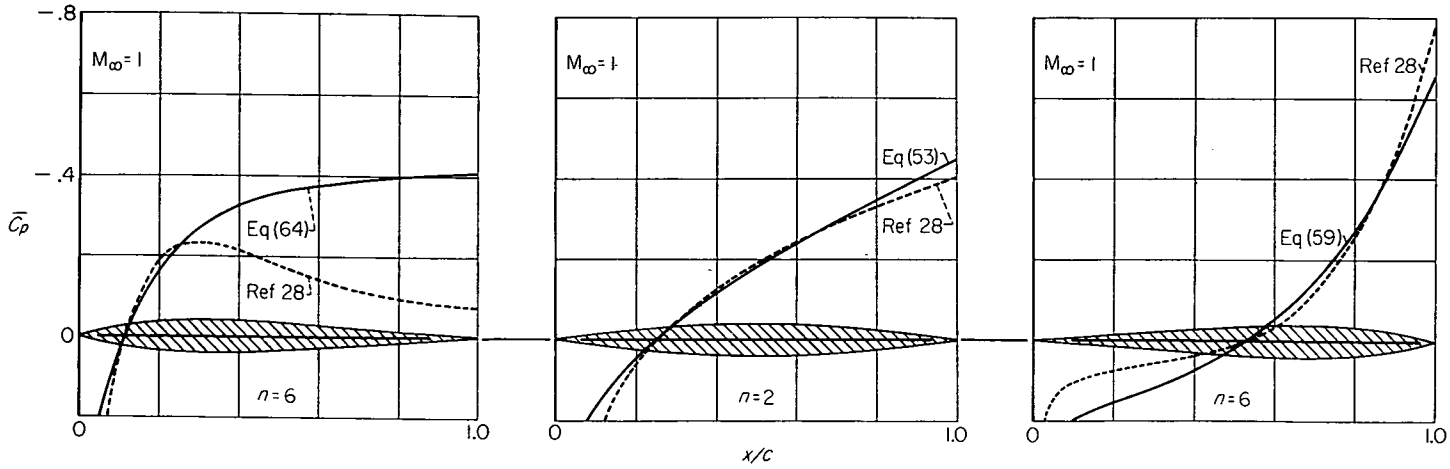


FIGURE 42.—Comparison of pressure distributions as indicated by present theory and by linearized transonic flow theory; $M_\infty = 1$.

in any essential manner by the adoption of a different rule for the selection of an appropriate value for λ_P. This follows from the fact that the entire curve representing the pressure distribution is proportional to $1/\sqrt{\lambda_P}$ and can be altered in scale, but not in form, by use of other values for λ_P. Possibilities for iteration always exist, and it is conceivable that improvements in accuracy could be attained by inserting the solution of linearized sonic flow theory into the terms involving f_P in equation (A49) or (A50) to obtain a second approximation, etc. To do so would be a laborious task and there is always present a grave danger that the process will diverge, or not converge sufficiently rapidly to be useful, when the first approximation is as far from the proper solution as may be inferred from figure 42 for the airfoil with maximum thickness at 30-percent chord.

The procedures employed in the main text for the approximate solution of the equations for the parabolic case closely parallel those used for the approximate solution of the equations for the hyperbolic and elliptic cases. It is, consequently, not surprizing that the following discussion of these procedures from the point of view of the integral equations given in equations (A49) and (A50) is very similar to that in the preceding sections of the Appendix. The general considerations are the same in all three cases, but the parabolic case more closely resembles the elliptic case than the hyperbolic case because of the singular nature of the kernel in the double integral; that is, σ_P and σ_E approach infinity at the point $\xi = x$, $\zeta = z$. The expressions applied in the main text follow from consideration of equation (A50) as a typical member of an infinite set of relations that result if λ_P is replaced with the local value of $k\partial u/\partial x$ and the contribution of the double integral is disregarded. At free-stream Mach number 1, the function f_P thus reduces to zero at the point where σ_P is infinite, and it again appears plausible that less loss in accuracy is incurred by disregarding the contribution of the double integral than in alternative procedures in which f_P is not zero at this point. At free-stream Mach numbers different from unity, f_P is not zero although it can be made as small as desired by approaching sufficiently closely to free-stream Mach number 1. The results obtained by solution of the remaining relation, which is a first-order nonlinear ordinary differential equation, are completely consistent with the above remarks. The pressure distributions calculated by use of only the first approximation are indeed in good accord with existing theoretical and experimental results, and the initial variation of C_p with M_∞ at free-stream Mach number 1 is given exactly; but no indication is provided of the subsequent variation of C_p with M_∞ at Mach numbers considerably removed from unity.

If, on the other hand, the pressure distribution is calculated by substitution of $k\varphi_{xx}$ for λ_P in equation (A49) and differentiation of the resulting expression to obtain an equation for u, the function in the double integral that corresponds to f_P in the above discussion does not vanish at the point $\xi = x$, $\zeta = z$ where the kernel is infinite. If the preceding discussion can be considered to imply that the effective removal of the singularity is important in the approximate solution of singular integral equations, it may be anticipated that the results obtained using equation (A49) will not, in general, be so good as those obtained following the procedure employed in the main text.

REFERENCES

1. Heaslet, Max. A., and Lomax, Harvard: Supersonic and Transonic Small Perturbation Theory. Sec. D of General Theory of High Speed Aerodynamics. Vol. VI of High Speed Aerodynamics and Jet Propulsion, W. R. Sears, ed., Princeton Univ. Press, 1954.
2. Ward, G. N.: Linearized Theory of Steady High-Speed Flow. Cambridge Univ. Press, 1955.
3. Lighthill, M. J.: Higher Approximations. Sec. E of General Theory of High Speed Aerodynamics. Vol. VI of High Speed Aerodynamics and Jet Propulsion, W. R. Sears, ed., Princeton Univ. Press, 1954.
4. von Kármán, Th.: On the Foundation of High Speed Aerodynamics. Sec. A of General Theory of High Speed Aerodynamics. Vol. VI of High Speed Aerodynamics and Jet Propulsion, W. R. Sears, ed., Princeton Univ. Press, 1954.
5. Spreiter, John R.: On Alternative Forms for the Basic Equations of Transonic Flow Theory. Jour. Aero. Sci., vol. 21, no. 1. Jan. 1954, pp. 70–72.
6. Spreiter, John R.: On the Application of Transonic Similarity Rules to Wings of Finite Span. NACA Rep. 1153, 1953.
7. Vincenti, Walter G., Dugan, Duane W., and Phelps, E. Ray: On Experimental Study of the Lift and Pressure Distribution on a Double-Wedge Profile at Mach Numbers Near Shock Attachment. NACA TN 3225, 1954.
8. Heaslet, Max. A., and Fuller, Franklyn B.: Particular Solutions for Flows at Mach Number 1. NACA TN 3868, 1956.

9. Spreiter, John R., and Alksne, Alberta Y.: Theoretical Predictions of Pressure Distributions on Nonlifting Airfoils at High Subsonic Speeds. NACA Rep. 1217, 1955. (Formerly NACA TN 3096.)
10. Heaslet, Max A., and Spreiter, John R.: Three-Dimensional Transonic Flow Theory Applied to Slender Wings and Bodies. NACA TN 3717, 1956.
11. Spreiter, John R.: Theoretical and Experimental Analysis of Transonic Flow Fields. NACA—University Conference on Aerodynamics, Construction and Propulsion. Vol. II, Aerodynamics. A compilation of the papers presented, Lewis Flight Propulsion Laboratory, Cleveland, Ohio, Oct. 20–22, 1954.
12. Sauer, Robert: Instroduction to Theoretical Gas Dynamics. J. W. Edwards, Ann Arbor, Mich., 1947.
13. Liepmann, Hans Wolfgang, and Puckett, Allen E.: Introduction to Aerodynamics of a Compressible Fluid. John Wiley and Sons, Inc., 1947.
14. Donov, A. E.: Ploskoe Krylo s Ostrymi Kromkami v Sverkhzvukovom Potoke. Izvestiia Akademii NAUK, USSR, 1939, pp. 603–626.
15. Donov, A. E.: A Flat Wing with Sharp Edges in a Supersonic Stream. NACA TM 1394, 1956.
16. Kuo, Y. H., and Sears, W. R.: Plane Subsonic and Transonic Potential Flows. Sec. F of General Theory of High Speed Aerodynamics. Vol. VI of High Speed Aerodynamics and Jet Propulsion. W. E. Sears, ed., Princeton Univ. Press, 1954.
17. Garrick, I. E., and Kaplan, Carl: On the Flow of a Compressible Fluid by the Hodograph Method. I—Unification and Extension of Present-Day Results. NACA Rep. 789, 1944.
18. Van Dyke, Milton D.: Second-Order Subsonic Airfoil Theory Including Edge Effects. NACA Rep. 1274, 1956.
19. Hantzsche, W., and Wendt, H.: Der Kompressibilitätseinfluss für dünne wenig gekrümmte Profile bei Unterschallgeschwindigkeit. Z. a. M. M., Bd. 22, Nr. 2, Apr. 1942, pp. 72–86.
20. Asaka, Saburo: On the Velocity Distribution over the Surface of a Symmetrical Airfoil at High Speeds, II. National Science Report of the Ochanomizu University, vol. 5, no. 1, 1954, pp. 59–78.
21. Asaka, Saburo: Application of the Thin-Wing-Expansion Method to the Flow of a Compressible Fluid Past a Symmetrical Circular Arc Aerofoil. Jour. Phy. Soc. Japan, vol. 10, no. 6, June 1955, pp. 482–492.
22. Asaka, Saburo: Errata: Application of the Thin-Wing-Expansion Method to the Flow of a Compressible Fluid Past a Symmetrical Circular Arc Aerofoil. Jour. Phy. Soc. Japan, vol. 10, no. 7, July 1955, p. 593.
23. Behrbohm, H.: Näherungstheorie des unsymmetrischen Schalldurchgangs in einer Lavaldüse. Z. a. M. M., Bd. 30, Nr. 4, Apr. 1950, pp. 101–112.
24. Behrbohm, H.: Schalldurchgang in zwei-und dreidimensionalen Düsenstromungen. Z. a. M. M., Bd. 30, Nr. 8/9, Aug./Sept. 1950, pp. 268–269.
25. Oswatitsch, K., and Kuene, F.: The Flow Around Bodies of Revolution at Mach Number 1. Proc. Conf. on High-Speed Aeronautics, Polytechnic Institute of Brooklyn, Brooklyn, N. Y., Jan. 20–22, 1955, pp. 113–131.
26. Keune, F.: Bericht über eine Näherungstheorie der Strömung um Rotationskörper ohne Anstellung bei Machzahl Eins. DVL Bericht Nr. 3. Westdeutscher Verlag, Köln und Opladen, 1955.
27. Keune, F.: Über den Kompressibilitätseinfluss bei und nahe Machzahl Eins für Körper kleiner Streckung und schlanke Rotationskörper. Zs. f. Flugwiss. 4 Jahr., Heft 1/2, Jan./Feb. 1956, pp. 47–53.
28. Maeder, P. F., and Thommen, H. U.: Some Results of Linearized Transonic Flow About Slender Airfoils and Bodies of Revolution. Jour. Aero, Sci., vol. 23, no. 2, Feb. 1956, pp. 187–188.
29. Miles, John W.: On Linearized Transonic Flow Theory for Slender Bodies. Jour. Aero. Sci., vol. 23, no. 7, July 1956, pp. 704–705.
30. Bryson, Arthur Earl, Jr.: On Experimental Investigation of Transonic Flow Past Two-Dimensional Wedge and Circular-Arc Sections Using a Mach-Zehnder Interferometer. NACA Rep. 1094, 1952. (Formerly NACA TN 2560.)
31. Liepmann, H. W., and Bryson, A. E., Jr.: Transonic Flow Past Wedge Sections. Jour. Aero. Sci., vol. 17, no. 12, Dec. 1950, pp. 745–755.
32. Guderley, Gottfried, and Yoshihara, Hideo: The Flow Over a Wedge Profile at Mach Number 1. Jour. Aero. Sci., vol. 17, no. 11, Nov. 1950, pp. 723–735.
33. Habel, Louis W., Henderson, James H., and Miller, Mason F.: The Langley Annular Transonic Tunnel. NACA Rep. 1106, 1952.
34. Vincenti, Walter G., and Wagoner, Cleo B.: Transonic Flow Past a Wedge Profile With Detached Bow Wave. NACA Rep. 1095, 1952. (Supersedes NACA TN's 2339 and 2588)
35. Yoshihara, Hideo: On the Flow Over a Finite Wedge in the Lower Transonic Region. WADC Tech. Rep. 56–268, June 1956.
36. Cole, Julian D.: Drag of Finite Wedge at High Subsonic Speeds. Jour. Math. and Phys., vol. 30, no. 2, July 1951, pp. 79–93.
37. Michel, R., Marchaud, F., and Le Gallo, J.: Étude des écoulements transsoniques autour des profils lenticulaires, a incidence nulle. O. N. E. R. A. Pub. No. 65, 1953.
38. Carroll, James B., and Anderson, Gordon F.: Boundary-Layer Effect on Local Mach Number Measurements on a Circular Arc Half Profile. Jour. Aero. Sci., vol. 23, no. 6, June 1956, pp. 604–605.
39. Michel, R., Marchaud, F., and Le Gallo, J.: Influence de la position du maitre-couple sur les écoulements transsoniques autour de profils a pointes. O. N. E. R. A. Pub. No. 72, 1954.
40. Frank, Philip, and v. Mises, Richard: Die Differential-und Integralgleichungen der Mechanik und Physik. Mary S. Rosenberg, New York, 1943.
41. Güderley, K. Gottfried: Singularities at the Sonic Velocity. Tech. Rep. F-TR-1171-ND, Air Materiel Command, U. S. Air Force, June 1948.
42. Michel, R., Marchaud, F., and Le Gallo, J.: Influence d'un point d'inflexion a l'arriere d'un profil en écoulement transsonique. La Recherche Aéronautique, No. 40, Juillet, Aout, 1954, pp 15–19.
43. von Kármán, Th.: Supersonic Aerodynamics—Principles and Applications. Jour. Aero. Sci., vol. 14, no. 7, July 1947, pp. 373–409.
44. Heaslet, Max. A., and Spreiter, John R.: Reciprocity Relations in Aerodynamics. NACA Rep. 1119, 1953.
45. Webster, Arthur Gordon: Partial Differential Equations of Mathematical Physics. G. E. Stechert and Co., New York, 1933.
46. von Kármán, Theodore: Solved and Unsolved Problems of High Speed Aerodynamics. Proc. Conf. on High-Speed Aeronautics, Polytechnic Institute of Brooklyn, Brooklyn, N. Y., Jan. 20–22, 1955, pp. 11–39.
47. Laitone, E. V.: New Compressibility Correction for Two-Dimensional Subsonic Flow. Jour. Aero. Sci., vol. 18, no. 5, May 1951, p. 350.
48. Szebehely, V. G.: Local Compressible Pressure Coefficient. Jour. Aero. Sci., vol. 18, no. 11, Nov. 1951, pp. 772–773.
49. Laitone, E. V.: Use of the Local Mach Number in the Prandtl-Glauert Method. Jour. Aero. Sci., vol. 18, no. 12, Dec. 1951, pp. 842–843.
50. Truitt, Robert Wesley: Analogy of the Special Theory of Relativity to the Study of Compressible Fluid Flow. Bulletin No. 44, Dept. of Engineering Research, North Carolina State College, June 1949.
51. Truitt, Robert Wesley: Prediction of Subsonic Pressure Distributions by the Sound-Space Theory. Bulletin No. 47, Dept. of Engineering Research, North Carolina State College, Sept. 1950.

REPORT 1360

CONTENTS

	Page
SUMMARY	547
ACKNOWLEDGMENTS	547
INTRODUCTION	547
Dependence of Turbulent Flame Speed on Disturbances Originating in Shear Regions	547
Effect of Combustor Oscillations in Increasing Rate of Flame Propagation	548
SYMBOLS	548
THEORY: STABILITY OF FLOW FOR A FLAME IN A DUCT	549
Introduction	549
Steady-State Flow Field of a Flame Anchored in a Duct	549
Stability Problem	549
Interpreting Results of Stability Analysis	551
Stability Analysis	551
Steady-State Solution	551
First-Order Disturbance Problem	552
Boundary Conditions	552
Solution of the Boundary-Value Problem	553
Results	555
Construction of Stability Map	557
Phase Velocity	557
Disturbance Growth	558
Disturbance Velocity Distribution in y-Direction	560
Relation of Theoretical Results to Measurable Quantities	561
Effect of Flameholder	563
Summary of Theoretical Results	565
EXPERIMENT: EXAMINATION OF DISTURBANCE GROWTH IN A V-FLAME	565
Introduction	565
Apparatus	566
Burner Test Section	566
Auxiliary Equipment	567
Properties of System	568
Calibration of Disturbance Amplitude With Speaker Input	570
Ratio of Turbulent to Laminar Flame Speed Determined by Photomultiplier Probe	571
Results	572
Examination of Method	572
Comparison of Flame Speed with Flame Appearance	573
Distribution of Local V_T/V_L Values with Respect to Various Frequencies	575
Disturbance-Displacement Growth	576
Disturbance Phase Velocities	576
Effect of Test-Section Depth	578
Effect of Amplitude	579
Effect of Flameholder Size	579
Effect of Velocity	579
Symmetric Disturbances	581
DISCUSSION	581
SUMMARY OF RESULTS	588
Theory	588
Experiment	588
CONCLUDING REMARKS	588
APPENDIX—AXISYMMETRIC DISTURBANCES IN AXISYMMETRIC FLOW WITH DENSITY JUMPS	589
Disturbance Equation	589
Boundary Conditions	589
Boundary-Value Problem	590
REFERENCES	591

REPORT 1360

GROWTH OF DISTURBANCES IN A FLAME-GENERATED SHEAR REGION [1]

By Perry L. Blackshear, Jr.

SUMMARY

The growth of transverse velocity disturbances in the shear region caused by a flame in a duct was examined theoretically and experimentally. In the theoretical stability analysis, a flow field arising from a flame in a duct was analyzed. The flow was neutrally stable to symmetric disturbances and unstable to antisymmetric ones. As a disturbance of given frequency moves downstream from the flameholder, a most-amplified frequency is found that is equal to flow velocity divided by duct width. Disturbances at frequencies greater or less than this are less amplified. The amount that an incoming disturbance is amplified depends on the flame slope. For the most-amplified frequency, the ratio of terminal to initial transverse disturbance velocity is equal to $(1.1)^{1/\text{slope}}$*, where the slope is roughly turbulent flame speed divided by flow velocity. This ratio of terminal to initial transverse disturbance velocity depends on inlet velocity and flame speed only in the stated manner and is essentially independent of density ratio.*

The critical wavelength separating disturbances that grow from those that do not grow varies as a constant times flame width. The constant is 2½ for flames that are narrow compared with duct width and becomes infinite as the flame reaches the wall. The flow is unstable to disturbances having wavelengths greater than critical. Thus, short-wavelength (i. e., high-frequency) disturbances achieve their terminal amplifications near the flameholder, while long-wavelength disturbances achieve theirs farther downstream. The most-amplified disturbance achieves its terminal amplification when the flame fills 0.60 of the duct. The results are related to measurable quantities in the form of (1) flame-front displacement, (2) phase velocity, and (3) to a first approximation, the effect of disturbance frequency on flame-propagation velocity.

In the experimental part of the program disturbances of various frequencies were imposed on a flame stabilized in a duct, and the effects were measured by shadow photography and photomultiplier-probe surveys. Efforts to verify elements of the theory are encouraging but not conclusive. Reasonable agreement is achieved in the comparison of flame-front displacement and phase velocity. In the measurements of the effect of frequency of disturbance on flame speed, there appeared to be a most-effective frequency, which was twice the most amplified frequency given by theory. There is no direct evidence of transition due to the amplified disturbances. The flow was turbulent in all cases owing to transition in the flameholder boundary layer, either on the flameholder or near the point of separation. There was some evidence of an increased small-scale turbulence in the flame when long-wavelength disturbances were present. In other words, the large-amplitude, long-wavelength disturbances cause a sort of transition in the already turbulent flow and amplify the smaller-scale disturbances.

ACKNOWLEDGMENTS

The information presented herein was originally submitted as a thesis in partial fulfillment of the requirements for the degree of Doctor of Philosophy, Case Institute of Technology, Cleveland, Ohio, June 1956. The project represented a cooperative effort wherein the experimental work was carried out at the Lewis laboratory with Professor Harold G. Elrod of the Case Institute of Technology acting as the author's faculty advisor. The author is also indebted to Professors Ray. E. Bolz and Gustav Kuerti for discussions and suggestions that were of great help in the successful completion of this investigation.

INTRODUCTION

The stability of the flow field arising from an anchored flame in a duct is of interest for two reasons: (1) Experimental investigations have shown that the turbulent flame speeds attained in a flame anchored in a duct depend more on the turbulence originating in the shear regions generated by the flameholder and flame than on the turbulence in the incident gas stream; and (2) some transverse modes of burner resonance encountered have been accompanied by an increase in the rate of flame propagation.

DEPENDENCE OF TURBULENT FLAME SPEED ON DISTURBANCES ORIGINATING IN SHEAR REGIONS

The problem of describing the flow field that arises when a flame is anchored in a duct was first posed and solved by Scurlock (ref. 1). One result of this work was the relation between the fraction of mixture burned and the local flame width. Scurlock used this result to measure turbulent flame speeds in an experiment originally designed to give the effect of inlet turbulence on flame speeds. He found that turbulence associated with two regions of shear flow masked, to a great extent, the effect of imposed stream turbulence. These

[1] Supersedes NACA Technical Note 3830 by Perry L. Blackshear, Jr., 1956.

two regions are the near wake of the flameholder and the shear region associated with the fully developed flame in a duct. The latter shear region is caused by the pressure gradient acting on gases of different densities. Scurlock calculated the velocity profile in this region.

In flow past cylinders without flames, eddies are encountered. Scurlock found that the flame seated on a cylindrical flameholder prevented eddies from shedding from the flameholder over the range of Reynolds numbers investigated (up to approximately 15,000). Haddock (ref. 2) and Zukoski and Marble (ref. 3), in investigating the mechanism of flames seating on cylindrical rods, found that the boundary layer separating from either side of the rod underwent transition from laminar to turbulent flow. The transition point approached the point of separation at a Reynolds number of about 10^4. References 2 and 3 show that transition in the flameholder boundary layer is one mechanism for producing turbulence in the shear region near the flameholder.

The role played by the second shear region cited by Scurlock as a source of turbulence has not been directly investigated. After obtaining experimental results similar to those of Scurlock, several investigators [e. g., refs. 4 (Wohl) and 5] concluded that turbulence is generated in this region. The arguments leading to this conclusion are briefly indicated in the following discussion.

Theories of turbulent flame propagation have been postulated for two types of turbulence: (1) turbulence with a scale that is small compared with laminar flame-front thickness, and (2) turbulence with a scale that is large compared with laminar flame-front thickness (refs. 6 to 8). Experiments conducted in the absence of shear regions yielded flame speeds in good agreement with values predicted by the large-scale-turbulence theory (refs. 9 to 12). Experiments conducted in the presence of shear regions (refs. 4, 5, and 8) gave flame speeds higher than those predicted by theory. The interpretation of this difference is the subject of a current controversy (refs. 4, 5, 8, 13, and 14). It is generally agreed that, when an existing shear region is of the type associated with an anchored flame in a duct, the higher flame speed is due in part to turbulence amplified by or originating in this shear region.

Rayleigh (ref. 15) observed that some jets and diffusion flames are sensitive to certain imposed transverse disturbances. From an inviscid stability analysis, he found a $_/\!\!\diagup\!\!\diagdown\!\!_$ velocity profile unstable to antisymmetric disturbances but neutrally stable to symmetric wavy disturbances. This result agreed with his observations on sensitive flames and jets. Some of the limitations of Rayleigh's work are considered in the theoretical section of this report. The analytical method used by Rayleigh is applied in the present examination of the instability of flame-zone flow to imposed disturbances.

EFFECT OF COMBUSTOR OSCILLATIONS IN INCREASING RATE OF FLAME PROPAGATION

A great variety of combustion-chamber resonances have been observed in jet-engine combustors (refs. 16 to 19). These resonances most often involve some mode of acoustic oscillation in the combustion chamber. Reference 16 discusses modes that involve longitudinal gas and flame motion and reports a deterioration in combustor performance when these oscillations occur. Reference 17 discusses a type of resonance identified as a transverse mode of oscillation in the combustion chamber. Accompanying this type of oscillation was an apparent increase in combustion efficiency (ref. 17) and in the rate of flame spreading (ref. 18). This type of oscillation, with an acoustic wavelength controlled by duct dimensions, could possibly excite a wavy disturbance that would subsequently be amplified by the flame-generated shear region.

Unfortunately, these transverse modes (called screech) also cause the destruction of the burner walls when the screech becomes severe enough (ref. 18). Reference 19 shows pictures of the flame near the flameholder when a combustor was resonating in a transverse mode. A strong interaction was apparent in the form of flame wrinkles forming at the flameholder and growing in amplitude as they moved downstream. It seems apparent that at least one of the ways the transverse oscillation increases the rate of flame spreading is by wrinkling and hence extending the interface between the burned and unburned gases.

If the oscillation that disturbs the flame at the flameholder is supplied locally (by some suitable exciting mechanism) and not by the sometimes destructive combustor resonance, some of the benefits of screech can be realized without its penalties. The gains in flame speed should be greatest for those frequencies of excitation that are amplified by the flame. It is hoped that, by examining the sensitivity of a flame in a duct to imposed disturbances, an excitation frequency may be found that gives the optimum increase in flame speed.

This report is divided into three parts—theory, experiment, and discussion. Separate introductions are given for the first two parts describing the purpose of each. The discussion weighs the results of the other parts and includes some extrapolations.

SYMBOLS

A, B, C, D	constants of integration
b	width of shear region in Rayleigh's problem
b'	width of plateau in $_/\!\!\diagup\!\!\diagdown\!\!_$ velocity profile
c	complex phase velocity, ft/sec
d	flameholder width
E	voltage
F	fraction burned
f	frequency, cps
G	gain; $v'=v'_o G^{1/K_2}$
G'	gain; $v'=v'_o (G')^{1/K_1}$
h	flame-front displacement from mean, ft
h_1	duct half-width, ft
h_2	flame half-width, ft
K_1	constant, $\mathrm{d}F/[\mathrm{d}(x/h_1)]$
K_2	constant, $\mathrm{d}h_2/\mathrm{d}x$, for an assumed flame-spreading mechanism
$\mathscr{K}$	proportionality factor
k	constant
L	Eulerian scale of turbulence, ft
l	length, ft
l_F	length of flame measured from wake, ft
l_w	length of flameholder wake, ft

P	mean pressure, lb/sq ft
p	pressure, lb/sq ft
p'	perturbation pressure, lb/sq ft
Re	Reynolds number
S	flame surface area
t	time, sec
U	flow velocity in x-direction, ft/sec
U_1	flow velocity in x-direction in cold gas, ft/sec
U^*	flow velocity in x-direction at apex of hot-gas velocity profile, ft/sec
u'	disturbance velocity in x-direction, ft/sec
V	flame speed, ft/sec
v'	disturbance velocity in y-direction, ft/sec
x	coordinate in direction of duct axis, ft
y	coordinate perpendicular to duct axis, ft
α	wave number of disturbance, ft^{-1}
α_o	wave number of disturbance based on initial velocity and frequency, $f2\pi/U_o$
α_s	wave number for neutral stability based on inviscid analysis, ft^{-1}
β	hot-gas velocity gradient, $(U^*-U_1)/h_2$, sec^{-1}
γ_y	$e^{-\alpha y}$
γ_1	$e^{-\alpha h_1}$
γ_2	$e^{-\alpha h_2}$
ζ	$\frac{\gamma_2^2+\gamma_1^2}{\gamma_2^2-\gamma_1^2}$
λ	wavelength, ft
λ_s	$2\pi/\alpha_s$, ft
ξ	$\frac{1+\gamma_2^2}{1-\gamma_2^2}$
ρ	density, $lb\text{-}sec^2/ft^4$
ρ_1	density of cold gas, $lb\text{-}sec^2/ft^4$
ρ_2	density of hot gas, $lb\text{-}sec^2/ft^4$
ρ'	perturbation density, $lb\text{-}sec^2/ft^4$
$\varphi(y)$	y-distribution of disturbance amplitude, ft^2/sec

Subscripts:

cr	critical
d	disturbed
f	frequency
i	imaginary part
L	laminar
max	maximum
o	initial; plane of flameholder
pg	measured from flame photographs
pm	measured by photomultiplier
r	real part
T	turbulent
t	total
u	undisturbed

THEORY: STABILITY OF FLOW FOR A FLAME IN A DUCT

INTRODUCTION

STEADY-STATE FLOW FIELD OF A FLAME ANCHORED IN A DUCT

The problem of describing the flow field that exists when a flame is anchored in a duct was first posed and solved by Scurlock in 1948 (ref. 1). Subsequently, Tsien (ref. 20) and others (ref. 21) elaborated on the problem. The following table summarizes Scurlock's and Tsien's assumptions and results as they pertain to the present work:

Scurlock	Common	Tsien
Assumptions		
(1) Fluid is incompressible.	(1) Fluid is steady-state, two-dimensional, inviscid, non-heat-conducting, non-turbulent.	(1) Two cases are treated, compressible and incompressible. In the incompressible, Scurlock's assumption (2) holds; in the compressible, density is allowed to vary in the direction of flow.
(2) Density jumps from ρ_1 to ρ_2 across the flame front and is constant in each region.	(2) Velocity, density, and pressure are uniform at combustor inlet. (3) Static pressure is uniform at any cross section. (4) The flameholder is of negligible size and spans the combustor. (5) The flame front is of negligible thickness. (6) The chamber is of constant width.	(2) Density ratio is constant across flame front at any station. (3) The velocity profile is composed of four straight-line segments.
Results		
(1) Velocity profile as a function of flame width: ⌒ slightly concave to incoming gas). (2) Momentum pressure drop as a function of flame width (i. e., of fraction burned).	(1) Fraction burned as a function of flame width. (2) Cold-gas velocity as a function of flame width.	(1) Peak hot-gas velocity as a function of flame width. (2) Limiting inlet velocity beyond which complete combustion cannot occur as a function of density ratio (for compressible case).

A stability analysis is made herein of a parallel flow having a velocity profile approximating the one found by Scurlock by means of straight-line segments and a density distribution as taken by Scurlock (i. e., constant ρ_1/ρ_2).

STABILITY PROBLEM

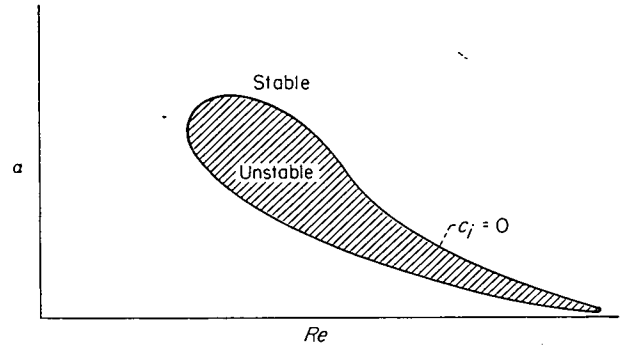
The study of the origins of turbulent motion has received considerable attention in the past, particularly with respect to turbulence occurring in boundary layers. One way of treating the problem is to assume the existence of infinitesimal wavy disturbances in the flowing stream and to seek the conditions under which these disturbances are amplified (refs. 22 and 23). In the application of this method to the study of the stability of the laminar boundary layer, a major objective is to determine a minimum Reynolds number below which all disturbances decay and to determine the effect of velocity profile on this minimum Reynolds number.

The amplification of wavy disturbances supposedly leads to the transition to turbulence under certain circumstances. The desirability of maintaining laminar flow on airfoils makes an understanding of transition an important practical problem. In 1941, Schubauer and Skramstad conducted an experiment in which the disturbances introduced into a laminar boundary layer were carefully controlled (ref. 24). They found a relation between the wave numbers of amplified, neutral, and damped disturbances and the Reynolds number that confirmed the predictions of the infinitesimal wavy disturbance theory in almost every important respect.

The practical value of learning about the stability of a flow field created by a flame in a duct is in furnishing information that will enable combustor designers to encourage the growth of disturbances in this region, because turbulence generally aids flame spreading. The information needed is (1) a range of Reynolds numbers over which the flow is unstable and (2) the kind of disturbance that possesses the greatest rate of amplification within this range. In the following qualitative discussion most flames of practical interest appear to be in a Reynolds number range where amplified disturbances always exist and where the wavelengths of disturbances that will be amplified may be obtained when viscosity is neglected.

If the disturbance varies as $v'=\varphi(y)e^{i\alpha(x-ct)}$, where the wave number α is real and the phase velocity c is generally complex, then the stability of boundary-layer flows (or of flows with symmetric profiles in a two-dimensional channel) can be illustrated by a graph of values for α for neutral stability (i. e., where the imaginary part of c vanishes) against Reynolds number Re (ref. 22).

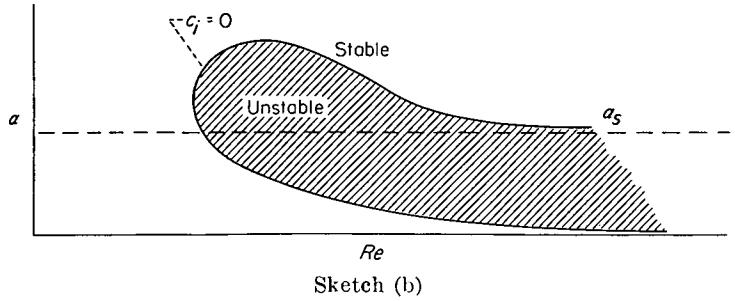
A profile without a point of inflection would possess the following plot of α against Re for $c_i=0$:



Sketch (a)

This curve is called the neutral envelope for the profile in question. Inside the envelope, disturbances are amplified ($c_i>0$); outside, disturbances are damped ($c_i<0$). Proceeding to the right from the minimum Reynolds number attained by the $c_i=0$ curve are two branches of the curve $c_i=0$ As Re becomes indefinitely great, both curves asymptotically approach $\alpha=0$.

For the profile with a point of inflection, a similar relation $\alpha(c,Re)$ is obtained:



Sketch (b)

The significant difference between this plot for a profile with an inflection point and sketch (a) for a profile without an inflection point is that the asymptotic values of the two branches approach different limits for large values of Re. The upper branch approaches $\alpha=\alpha_s$, the wave number for neutral stability obtained by neglecting viscosity, and the lower branch approaches $\alpha=0$. The Reynolds number range over which the flow with an inflection point is unstable extends to indefinitely large Reynolds numbers. The flow generated by a flame in a duct has, in effect, an inflection point.

It is desirable either by example or direct calculation to determine the order of magnitude of the Reynolds number range over which the neutral α departs from α_s; that is, where viscosity has a dominating influence. In two examples in the literature, Pretsch (ref. 25) and Lessen (ref. 26) examined a flow with a flex for stability. In both instances the minimum Reynolds number for $c_i=0$ was of the order of 10; the maximum Re, where α for $c_i=0$ differed from α_s calculated from inviscid theory by more than 2 percent, was of the order of 10^3. The profile of reference 25 is for a boundary layer with pressure rise; that of reference 26 is for the free boundary layer between streams of differing velocities.

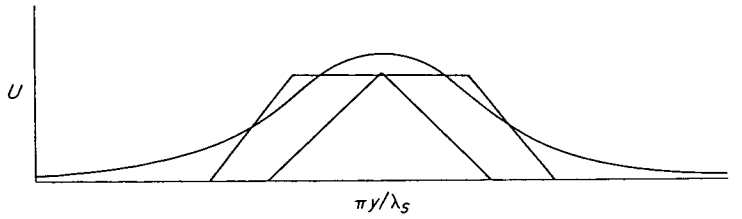
If these values are taken to suggest the order of Reynolds number where the stability of a profile with a flex is sensitive to the effects of viscosity, some idea of flame-zone sizes can be estimated for the range of velocities encountered in jet engines (i. e., 50 to 500 ft/sec). For example, at 50 feet per second, the range of flame width where viscous forces are important is 1/3000 to 1/30 inch. At 500 feet per second, the range is 1/30,000 to 1/300 inch. Most of the flame zones of practical interest are much wider than these dimensions and may be considered well within the range of Reynolds numbers where disturbances are amplified and where viscosity effects are small. Therefore, the following inviscid stability analysis may give meaningful information on the value of the wave numbers α where amplification can occur.

Lin (ref. 22) and Heisenberg (ref. 27) have criticized the use of broken-line profiles because there is a separate solution for c for each corner of the profile. These objections might be met by the following observations:

(1) The steady-state flow field solved by Scurlock possesses corners (places where the velocity gradient jumps) and can be very closely approximated by straight-line segments without introducing new corners into the profile. The jumps in velocity gradient that occur at the corners result from the assumption that the flame front is of negligible thickness compared with the width of the flame zone.

(2) The following results show that the flame zone is unstable to disturbances having wavelengths 2.5 times the flame-zone width and greater. Thus, any rounding of the corners over a distance that is small compared with the flame-zone width should not affect the results; to the long-wavelength disturbances that are amplified, the corners will still appear sharp.

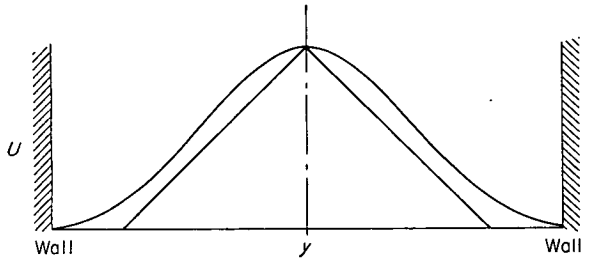
In order to examine the effect of corners in a velocity profile, three profiles of a similar shape are shown in the following sketch:



Sketch (c)

Each of these profiles has been examined for instability, and a wavelength for neutral stability has been computed. The scale of the abscissa is chosen so that the value of the neutral wavelength is the same for the three profiles. The two broken-line profiles are from Rayleigh (ref. 15); the continuous profile, from Savic (ref. 28). These solutions correspond to the antisymmetric disturbance. The flow in each case is inviscid.

A similar comparison can be made between the velocity profile $U=1+\sin[(2\pi y/l)-(\pi/2)]$ treated briefly by Lin (ref. 22) and a corresponding broken-line approximation. Lin's result yields $\alpha_s l=\pi\sqrt{3}$ for the sine profile. Equation (37) in the following analysis was used to obtain the dimensions of a profile having the same $\alpha_s l$. The following two profiles are given for flow between parallel walls, v' vanishing at the walls:



Sketch (d)

Since the widths of the profiles composed of broken-line segments are so nearly equal to those with continuous velocity gradients (having identical neutral wave numbers), it is believed that the broken-line profile used herein does not involve the introduction of extraneous solutions.

INTERPRETING RESULTS OF STABILITY ANALYSIS

The stability analysis gives an amplification rate αc_i and a phase velocity c_r for disturbances as functions of the wave number α and the fraction of duct occupied by flame h_2/h_1 for any one station along the axis of the duct. From this information a stability map is constructed, consisting of a plot of contours of constant αc_i on a grid of αh_1 against h_2/h_1. This is a generalized map, with no assumption regarding the rate of change of flame width with distance. Lines of constant frequency are shown on the stability map calculated from the phase velocity c_r. From the map and an assumption of the nature of flame-spreading rates, the total amplification of a disturbance of given frequency is calculated.

Some aspects of this information are reduced to measurable quantities that can subsequently be compared with experimental results. These quantities include

(1) Qualitative dependence of turbulent flame-spreading rate on disturbance frequency
(2) Relation between critical wave number and flame width
(3) Qualitative behavior of amplified disturbances as affected by the steady-state condition (velocity, fuel-air ratio)

One section of the analysis deals with the effect of a flameholder of finite size on the steady-state profile and hence on the stability analysis.

STABILITY ANALYSIS

STEADY-STATE SOLUTION

The equations for incompressible flow derived by Tsien (ref. 20) relating U_1, U_o, U^*, ρ_1/ρ_2, h_2/h_1, and F are listed first; these relations are based on the assumption that the velocity profile can be approximated by straight-line segments:

Apex velocity:

$$\frac{U^*}{U_o}=\sqrt{1+\frac{\rho_1}{\rho_2}\left[\left(\frac{U_1}{U_o}\right)^2-1\right]} \tag{1}$$

Hot-gas velocity distribution:

$$\frac{U}{U_o}=\sqrt{1+\frac{\rho_1}{\rho_2}\left[\left(\frac{U_1}{U_o}\right)^2-1\right]}-\left\{\sqrt{1+\frac{\rho_1}{\rho_2}\left[\left(\frac{U_1}{U_o}\right)^2-1\right]}-\frac{U_1}{U_o}\right\}\frac{y}{h_2} \tag{2}$$

Flame width:

$$\frac{h_2}{h_1}=\frac{\frac{U_1}{U_o}-1}{\left(1-\frac{1}{2}\frac{\rho_2}{\rho_1}\right)\frac{U_1}{U_o}-\frac{1}{2}\frac{\rho_2}{\rho_1}\sqrt{1+\frac{\rho_1}{\rho_2}\left[\left(\frac{U_1}{U_o}\right)^2-1\right]}} \tag{3}$$

Fraction burned:

$$F=1-\frac{U_1}{U_o}\left(1-\frac{h_2}{h_1}\right) \tag{4}$$

The hot-gas distribution (eq. (2)) and the relation between h_2/h_1 and U_1/U_o (eq. (3)) are used in interpreting the results of the stability analysis. In the analysis the hot-gas velocity distribution (eq. (2)) is represented by

$$U=U_1+(h_2-y)\beta \qquad (y>0)$$

$$U=U_1+(h_2+y)\beta \qquad (y<0)$$

where

$$\beta=\frac{U^*-U_1}{h_2}$$

Tsien's analysis says nothing about the distribution of h_2/h_1 with distance x. This must come from further assumptions

regarding flame slope, flame speed, or rate of change of F with x. For the present it is sufficient to say that the rate of change of h_2/h_1 with x is small; that is,

$$\frac{\partial(h_2/h_1)}{\partial x}\lambda \ll \frac{h_2}{h_1}$$

where λ is the wavelength of a disturbance of interest.

The stability of the profile assumed by Tsien, which closely approximates that calculated by Scurlock, is treated as a parallel-flow problem.

FIRST-ORDER DISTURBANCE PROBLEM

Two excellent summary papers are available on the stability of parallel flows (refs. 22 and 23). No attempt to review the field is made herein. The method employed here dates back to some of Rayleigh's early work (ref. 15) with very slight modification. The development of the disturbance equation that follows is from reference 29.

The flow is assumed parallel, inviscid, incompressible, plane, and non-heat-conducting. Gravity is neglected. The equations of motion are

$$\frac{\partial p}{\partial x}=-\rho\left(\frac{\partial u}{\partial t}+u\frac{\partial u}{\partial x}+v\frac{\partial u}{\partial y}\right) \tag{5}$$

$$\frac{\partial p}{\partial y}=-\rho\left(\frac{\partial v}{\partial t}+u\frac{\partial v}{\partial x}+v\frac{\partial v}{\partial y}\right) \tag{6}$$

The fluid is assumed incompressible (but the density is allowed to vary with y), so that

$$\frac{\partial \rho}{\partial t}+u\frac{\partial \rho}{\partial x}+v\frac{\partial \rho}{\partial y}=0 \tag{7}$$

and the equation of continuity is

$$\frac{\partial u}{\partial x}+\frac{\partial v}{\partial y}=0 \tag{8}$$

Let

$$\left.\begin{aligned} u&=U(y)+u'(x,y,t)\\ v&=v'(x,y,t)\\ p&=P+p'(x,y,t)\\ \rho&=\bar{\rho}(y)+\rho'(x,y,t)\end{aligned}\right\} \tag{9}$$

where primed quantities are of first order of smallness. Assume u', v', p', and ρ' to vary with x and t as $e^{i\alpha(x-ct)}$, where α is real and c, in general, is complex.

By substituting equation (9) in equations (5) to (8) and retaining terms of the first order, equations (5) to (8) become

$$\bar{\rho}\left[i\alpha(U-c)u'+\frac{dU}{dy}v'\right]=-i\alpha p' \tag{10}$$

$$\bar{\rho}[i\alpha(U-c)v']=-\frac{\partial p'}{\partial y} \tag{11}$$

$$i\alpha(U-c)\rho'+v'\frac{d\bar{\rho}}{dy}=0 \tag{12}$$

$$\frac{\partial v'}{\partial y}+i\alpha u'=0 \tag{13}$$

Eliminating p', ρ', and u' from equations (10) to (13) yields an equation for v':

$$(U-c)\left(\frac{\partial^2 v'}{\partial y}-\alpha^2 v'\right)-v'\frac{\partial^2 U}{\partial y^2}+\frac{1}{\bar{\rho}}\frac{d\bar{\rho}}{dy}\left[(U-c)\frac{\partial v'}{\partial y}-v'\frac{\partial U}{\partial y}\right]=0 \tag{14}$$

It is apparent that, though equations (7) and (12) are useful in defining the type of incompressible flow field assumed, they are not required to obtain the disturbance equation (14) unless it becomes necessary to specify ρ'.

Defining

$$v'=-i\alpha\varphi(y)e^{i\alpha(x-ct)}$$

equation (14) becomes

$$(U-c)\left(\frac{d^2\varphi}{dy^2}-\alpha^2\varphi\right)-\varphi\frac{d^2U}{dy^2}+\frac{1}{\bar{\rho}}\frac{d\bar{\rho}}{dy}\left[(U-c)\frac{d\varphi}{dy}-\varphi\frac{dU}{dy}\right]=0 \tag{15}$$

In regions where $\bar{\rho}$ and dU/dy are constant, equation (15) reduces to

$$\frac{d^2\varphi}{dy^2}-\alpha^2\varphi=0 \tag{16}$$

with the solution

$$\varphi=A_1e^{\alpha y}+A_2e^{-\alpha y} \tag{17}$$

The disturbance velocities given by definition and equation (13) are the real parts of

$$\left.\begin{aligned} u'&=(A_1\alpha e^{\alpha y}-A_2\alpha e^{-\alpha y})e^{i\alpha(x-ct)}\\ v'&=-i\alpha(A_1e^{\alpha y}+A_2e^{-\alpha y})e^{i\alpha(x-ct)}\end{aligned}\right\} \tag{18}$$

BOUNDARY CONDITIONS

The geometry of the flow field is shown in figure 1. Equation (16) and the solutions (eqs. (18)) apply to each of the regions 1 to 4 considered separately. The establishment of the boundary-value problem consists in assigning suitable

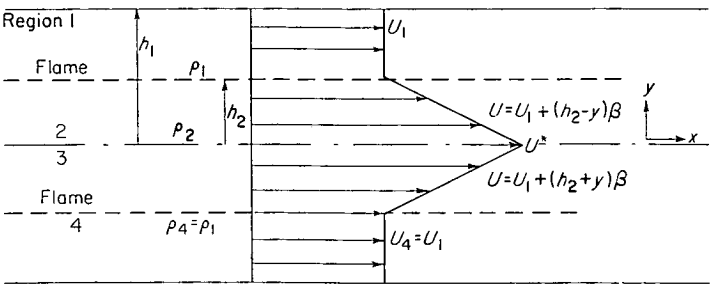


FIGURE 1.—Geometry of flow field.

boundary conditions at the walls and at the boundaries of regions 1 to 4. These boundary conditions are:

(1) v' vanishes at $y=\pm h_1$.

(2) v' is continuous at interfaces.

(3) p' is continuous at interfaces (or, equivalently, the complete eq. (14) integrated across each interface is satisfied).

Let the equation of the interface at $y=h_m$ be

$$y=h_m+h(x,t) \tag{19}$$

(In the following derivation the subscripts m and n represent conditions evaluated in a region m or n.) Then, to the first order of approximation, at the interface,

$$v'=\frac{\partial h}{\partial t}+U\frac{\partial h}{\partial x} \tag{20}$$

where U is the mean velocity at the interface. In order for the pressure to be continuous at the interface, it is necessary that

$$\frac{\mathrm{d}p_m}{\mathrm{d}x_1}=\frac{\mathrm{d}p_n}{\mathrm{d}x_1}$$

where x_1 is along the interface, or equivalently in the x,y-system,

$$\frac{\partial p_m}{\partial x}+\frac{\partial p_m}{\partial y}\frac{\partial h}{\partial x}=\frac{\partial p_n}{\partial x}+\frac{\partial p_n}{\partial y}\frac{\partial h}{\partial x} \tag{21}$$

where at the interface

$$\frac{\partial y}{\partial x}=\frac{\partial h}{\partial x}$$

From the equation of motion,

$$\frac{\partial p}{\partial x}=-\rho\left(\frac{\partial u}{\partial t}+u\frac{\partial u}{\partial x}+v\frac{\partial u}{\partial y}\right) \tag{5}$$

$$\frac{\partial p}{\partial y}=-\rho\left(\frac{\partial v}{\partial t}+u\frac{\partial v}{\partial x}+v\frac{\partial v}{\partial y}\right) \tag{6}$$

where

$$\left.\begin{aligned} u&=U+u'\\ v&=v'\\ p&=P+p'\end{aligned}\right\} \tag{9}$$

By retaining terms of zero- and first-order approximations,

$$\left.\begin{aligned}\frac{\partial p}{\partial x}=\frac{\partial p'}{\partial x}&=-\rho\left(\frac{\partial u'}{\partial t}+U\frac{\partial u'}{\partial x}+v'\frac{\mathrm{d}U}{\mathrm{d}y}\right)\\ \frac{\partial p}{\partial y}=\frac{\partial p'}{\partial y}&=-\rho\left(\frac{\partial v'}{\partial t}+U\frac{\partial v}{\partial x}\right)\end{aligned}\right\} \tag{22}$$

or $\partial p/\partial x$ and $\partial p/\partial y$ are first-order terms. But, from equation (20), it is clear that $\partial h/\partial x$ is of the first order so that the products $(\partial p/\partial y)(\partial h/\partial x)$ are of the second order, and equation (21) becomes

$$\frac{\partial p_m}{\partial x}=\frac{\partial p_n}{\partial x} \tag{23}$$

or

$$\rho_m\left(\frac{\partial u_m'}{\partial t}+U_m\frac{\partial u_m'}{\partial x}+v_m\frac{\partial U_m}{\partial y}\right)=\rho_n\left[\frac{\partial u_n'}{\partial t}+U_n\frac{\partial u_n'}{\partial x}+v_n'\frac{\partial U_n}{\partial y}\right] \tag{24}$$

at the interface between the regions m and n. Equation (24) results from a necessary condition for the pressure to be continuous at surfaces where either $\bar{\rho}$ or $\mathrm{d}U/\mathrm{d}y$ jumps.

In order to show that this condition is equivalent to requiring that the integrated equation (14) be satisfied at the interface, equation (14) is written

$$\frac{\partial}{\partial y}\left\{\bar{\rho}\left[(U-c)\frac{\partial v'}{\partial y}-v'\frac{\partial U}{\partial y}\right]\right\}-\bar{\rho}(U-c)\alpha^2v'=0 \tag{25}$$

Integrating equation (25) across the interface gives

$$\bar{\rho}_m\left[(U_m-c)\frac{\partial v_m'}{\partial y}-v_m'\frac{\partial U_m}{\partial y}\right]=\bar{\rho}_n\left[(U_n-c)\frac{\partial v_n'}{\partial y}-v_n'\frac{\partial U_n}{\partial y}\right]$$

which, with the insertion of the continuity equation, becomes

$$\bar{\rho}_m\left[(U_m-c)\frac{\partial u_m'}{\partial x}+v_m'\frac{\partial U_m}{\partial y}\right]=\bar{\rho}_n\left[(U_n-c)\frac{\partial u_n}{\partial x}+v_n'\frac{\partial U_n}{\partial y}\right] \tag{26}$$

But u' varies as $e^{i\alpha(x-ct)}$, so that equation (26) can be recognized as another way of writing equation (24).

The boundary conditions can be written

$$v_1'=0 \quad \text{at} \quad y=h_1 \tag{27a}$$

$$v_1'=v_2' \quad \text{at} \quad y=h_2 \tag{27b}$$

$$\frac{\partial p_1'}{\partial x}=\frac{\partial p_2'}{\partial x} \quad \text{at} \quad y=h_2 \tag{27c}$$

$$v_2'=v_3' \quad \text{at} \quad y=0 \tag{27d}$$

$$\frac{\partial p_2'}{\partial x}=\frac{\partial p_3'}{\partial x} \quad \text{at} \quad y=0 \tag{27e}$$

$$v_3'=v_4' \quad \text{at} \quad y=-h_2 \tag{27f}$$

$$\frac{\partial p_3'}{\partial x}=\frac{\partial p_4'}{\partial x} \quad \text{at} \quad y=-h_2 \tag{27g}$$

$$v_4'=0 \quad \text{at} \quad y=-h_1 \tag{27h}$$

where the subscripts 1 to 4 denote flow regions (fig. 1).

SOLUTION OF THE BOUNDARY-VALUE PROBLEM

The solutions of equation (16) for regions 1 to 4 (fig. 1) are written as follows:

$$\left.\begin{aligned}\text{Region 1:}\quad &\varphi_1=A_1e^{\alpha y}+A_2e^{-\alpha y}\\ \text{Region 2:}\quad &\varphi_2=B_1e^{\alpha y}+B_2e^{-\alpha y}\\ \text{Region 3:}\quad &\varphi_3=C_1e^{\alpha y}+C_2e^{-\alpha y}\\ \text{Region 4:}\quad &\varphi_4=D_1e^{\alpha y}+D_2e^{-\alpha y}\end{aligned}\right\} \tag{28}$$

Inserting equations (28) into equations (27) results in eight equations in the eight unknowns A_1, A_2, . . . D_2. The requirement that A_1, A_2, . . . D_2 have nontrivial solutions is

$$\begin{vmatrix} 1 & \gamma_1^2 & 0 & 0 & 0 & 0 & 0 & 0 \\ 1 & \gamma_2^2 & -1 & -\gamma_2^2 & 0 & 0 & 0 & 0 \\ \frac{\rho_1}{\rho_2}(U_1-c) & -\frac{\rho_1}{\rho_2}(U_1-c)\gamma_2^2 & -\left[(U_1-c)+\frac{\beta}{\alpha}\right] & \left[(U_1-c)-\frac{\beta}{\alpha}\right]\gamma_2^2 & 0 & 0 & 0 & 0 \\ 0 & 0 & 1 & 1 & -1 & -1 & -1 & -1 \\ 0 & 0 & (U^*-c)+\frac{\beta}{\alpha} & -\left[(U^*-c)-\frac{\beta}{\alpha}\right] & -\left[(U^*-c)-\frac{\beta}{\alpha}\right] & (U^*-c)+\frac{\beta}{\alpha} & 0 & 0 \\ 0 & 0 & 0 & 0 & \gamma_2^2 & 1 & -\gamma_2^2 & 1 \\ 0 & 0 & 0 & 0 & \left[(U_1-c)-\frac{\beta}{\alpha}\right]\gamma_2^2 & -\left[(U_1-c)+\frac{\beta}{\alpha}\right] & -\frac{\rho_1}{\rho_2}(U_1-c)\gamma_2^2 & \frac{\rho_1}{\rho_2}(U_1-c) \\ 0 & 0 & 0 & 0 & 0 & 0 & \gamma_2^2 & 1 \end{vmatrix} = 0 \tag{29}$$

Where $\gamma_1 \equiv e^{-\alpha h_1}$ and $\gamma_2 \equiv e^{-\alpha h_2}$. By assigning $U_1=0$ (this merely alters the real part of c) and operating on rows 1, 2, 3, 6, 7, and 8, equation (29) can be reduced to the determinant

$$\begin{vmatrix} c-\frac{\beta}{\alpha}+\zeta\frac{\rho_1}{\rho_2}c & \left[\zeta\frac{\rho_1}{\rho_2}c-\left(c+\frac{\beta}{\alpha}\right)\right]\gamma_2^2 & 0 & 0 \\ 1 & 1 & -1 & -1 \\ h_2\beta-c+\frac{\beta}{\alpha} & -\left(h_2\beta-c-\frac{\beta}{\alpha}\right) & -\left(h_2\beta-c-\frac{\beta}{\alpha}\right) & h_2\beta-c+\frac{\beta}{\alpha} \\ 0 & 0 & \left(\zeta\frac{\rho_1}{\rho_2}c-c-\frac{\beta}{\alpha}\right)\gamma_2^2 & \zeta\frac{\rho_1}{\rho_2}c+c-\frac{\beta}{\alpha} \end{vmatrix} = 0 \tag{30}$$

where

$$\zeta \equiv \frac{\gamma_2^2+\gamma_1^2}{\gamma_2^2-\gamma_1^2}$$

On expanding and simplifying, equation (30) becomes

$$\left[c-\frac{\beta}{\alpha}\left(\zeta\frac{\rho_1}{\rho_2}+\xi\right)^{-1}\right]\left[c^2\left(\zeta\frac{\rho_1}{\rho_2}\xi+1\right)-c\left(h_2\beta-\zeta\frac{\rho_1}{\rho_2}\frac{\beta}{\alpha}+h\beta\zeta\frac{\rho_1}{\rho_2}\xi\right)+\frac{h\beta^2}{\alpha}\xi-\frac{\beta^2}{\alpha^2}\right]=0 \tag{31}$$

where

$$\xi \equiv \frac{1+\gamma_2^2}{1-\gamma_2^2}$$

One root can be seen to be wholly real:

$$c=\frac{\beta}{\alpha}\left(\zeta\frac{\rho_1}{\rho_2}+\xi\right)^{-1} \tag{32}$$

This can be identified as the root belonging to a symmetric disturbance by assigning $v_2'=v_3'=0$ at $y=0$ in equation (27). In this case equation (30) reduces to

$$\begin{vmatrix} c-\frac{\beta}{\alpha}+\zeta\frac{\rho_1}{\rho_2}c & \zeta\frac{\rho_1}{\rho_2}c-\left(c+\frac{\beta}{\alpha}\right)\gamma_2^2 \\ 1 & 1 \end{vmatrix} = 0 \tag{33}$$

which yields equation (32) as before. The remaining two roots,

$$c=\frac{\beta}{\alpha}\left\{\frac{h_2\alpha+\zeta\frac{\rho_1}{\rho_2}(\xi\alpha h_2-1)\pm\sqrt{\left[h_2\alpha+\zeta\frac{\rho_1}{\rho_2}(\xi\alpha h_2-1)\right]^2-4\left(\zeta\frac{\rho_1}{\rho_2}\xi+1\right)(\alpha h_2\xi-1)}}{2\left(\zeta\frac{\rho_1}{\rho_2}\xi+1\right)}\right\} \tag{34}$$

can similarly be identified as roots belonging to an antisymmetric disturbance. One way of doing this is to set v_2' at $y=h_2$ equal to v_3' at $y=-h_2$ or (from eq. (28))

$$B_1+B_2\gamma_2^2-C_1\gamma_2^2-C_2=0 \tag{35}$$

Using equation (35) in place of equations (27f), (27g), and (27h) gives for the determinantal equation

$$\begin{vmatrix} 1 & \gamma_2^2 & 0 & 0 & 0 & 0 \\ 1 & \gamma_2^2 & -1 & -\gamma_2^2 & 0 & 0 \\ \frac{\rho_1}{\rho_2}(-c) & \frac{\rho_1}{\rho_2}c\gamma_2^2 & \left(c-\frac{\beta}{\alpha}\right)\gamma_2^2 & -\left(c+\frac{\beta}{\alpha}\right)\gamma_2^2 & 0 & 0 \\ 0 & 0 & 1 & 1 & -1 & -1 \\ 0 & 0 & -c+\frac{\beta}{\alpha} & c+\frac{\beta}{\alpha} & c+\frac{\beta}{\alpha} & -c+\frac{\beta}{\alpha} \\ 0 & 0 & 1 & \gamma_2^2 & -\gamma_2^2 & -1 \end{vmatrix}=0 \tag{36}$$

with roots of equation (34) for c as before. That the root for the symmetric disturbance $c=(\beta/\alpha)[\zeta(\rho_1/\rho_2)+\xi]^{-1}$ is wholly real implies neutral stability. For the symmetric disturbance, then, the inviscid analysis does not yield information on wave numbers where amplification occurs, but merely suggests that the profile is relatively stable to symmetric disturbances and neutrally stable in the limit of infinite Reynolds number.

The roots corresponding to the antisymmetric disturbances (eq. (34)) are complex when

$$4\left(\zeta\frac{\rho_1}{\rho_2}\xi+1\right)(\alpha h_2\xi-1)>\left[h_2\alpha+\zeta\frac{\rho_1}{\rho_2}(\xi\alpha h_2-1)\right]^2 \tag{37}$$

The complex root having the positive imaginary part corresponds to an amplified disturbance. The denominator of the right side of equation (34), $2[\zeta(\rho_1/\rho_2)\xi+1]$, when written in full,

$$2\left(\frac{\rho_1}{\rho_2}\frac{e^{-2\alpha h_2}+e^{-2\alpha h_1}}{e^{-2\alpha h_2}-e^{-2\alpha h_1}}\frac{1+e^{-2\alpha h_2}}{1-e^{-2\alpha h_1}}+1\right)$$

is positive for $h_2<h_1$; that is, for the flame zone contained within the duct. Therefore, the amplified root of equation (34) is

$$c=\frac{\beta}{\alpha}\left\{\frac{h_2\alpha+\zeta\frac{\rho_1}{\rho_2}(\xi\alpha h_2-1)+\sqrt{\left[h_2\alpha+\zeta\frac{\rho_1}{\rho_2}(\xi\alpha h_2-1)\right]^2-4\left(\zeta\frac{\rho_1}{\rho_2}\xi+1\right)(\alpha h_2\xi-1)}}{2\left(\zeta\frac{\rho_1}{\rho_2}\xi+1\right)}\right\} \tag{38}$$

Since this is an inviscid analysis, the damped root of equation (34) can have no meaning (ref. 22) and is consequently ignored.

RESULTS

The disturbance amplitude grows with time as $e^{\alpha c_i t}$, where αc_i is (from eq. (38))

$$\alpha c_i=\frac{\Delta U}{2h_2}\sqrt{\left[\frac{h_2\alpha+\zeta\frac{\rho_1}{\rho_2}(\xi\alpha h_2-1)}{\zeta\frac{\rho_1}{\rho_2}\xi+1}\right]^2-4\frac{\alpha h_2\xi-1}{\zeta\frac{\rho_1}{\rho_2}\xi+1}} \tag{39}$$

since

$$\beta=\frac{U^*-U_1}{h_2}=\frac{\Delta U}{h_2}$$

The quantity under the radical in equation (39) is independent of local $(U^*-U)/h_2$ values. This quantity is plotted in figure 2 as a function $2\alpha h_2$ for the following conditions:

$$\frac{\rho_1}{\rho_2}=1 \qquad \lim_{h_1\to\infty}\frac{h_2}{h_1}=0$$

$$\frac{\rho_1}{\rho_2}=5,\ 7 \qquad \frac{h_2}{h_1}=0.25,\ 0.50,\ 0.75$$

The first set of conditions corresponds to Rayleigh's solution for the stability of an unconfined jet. The second set of conditions represents density ratios that are expected in a flame in a duct for three flame widths. The values of the parameter $\alpha c_i(2h_2/\Delta U)$ in figure 2 go from 0 at $2\alpha h_2=0$ through a maximum, then to 0 again at a finite value of $2\alpha h_2$. For a given value of $2h_2/\Delta U$, this parameter behaves as the amplification rate αc_i.

It is clear from figure 2 that, for constant density, the flow is more unstable the smaller h_2/h_1 becomes. For constant h_2/h_1, the flow is more unstable the smaller ρ_1/ρ_2 becomes. The influence of density ratio and wall proximity on the stability of the subject profile is in keeping with experimental observations of another type of profile with a flex—namely, the wake of a cylindrical rod. The stabilizing effect of density ratio is illustrated in reference 1, which notes that a flame anchored in the wake of the rod inhibits vortex shedding. The stabilizing effect of wall proximity is illustrated in reference 30, which shows that wall proximity increases the minimum Reynolds number for the occurrence of shed vortices.

The stabilizing influence of the walls is further illustrated in figure 3. Figures 3(a) and (b) show the values of $2\alpha h_2$ for neutral stability and maximum instability plotted against

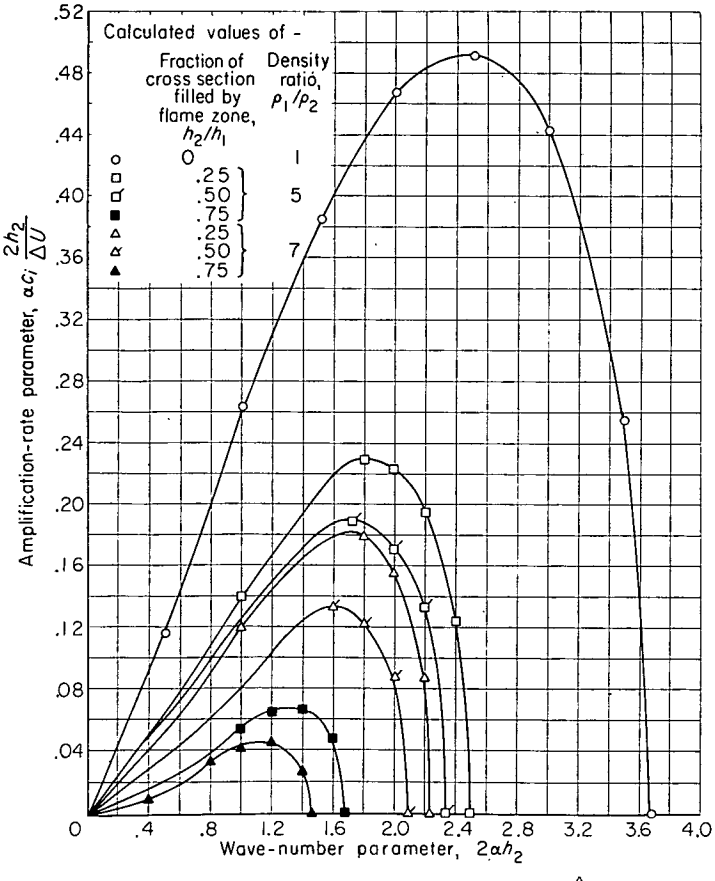
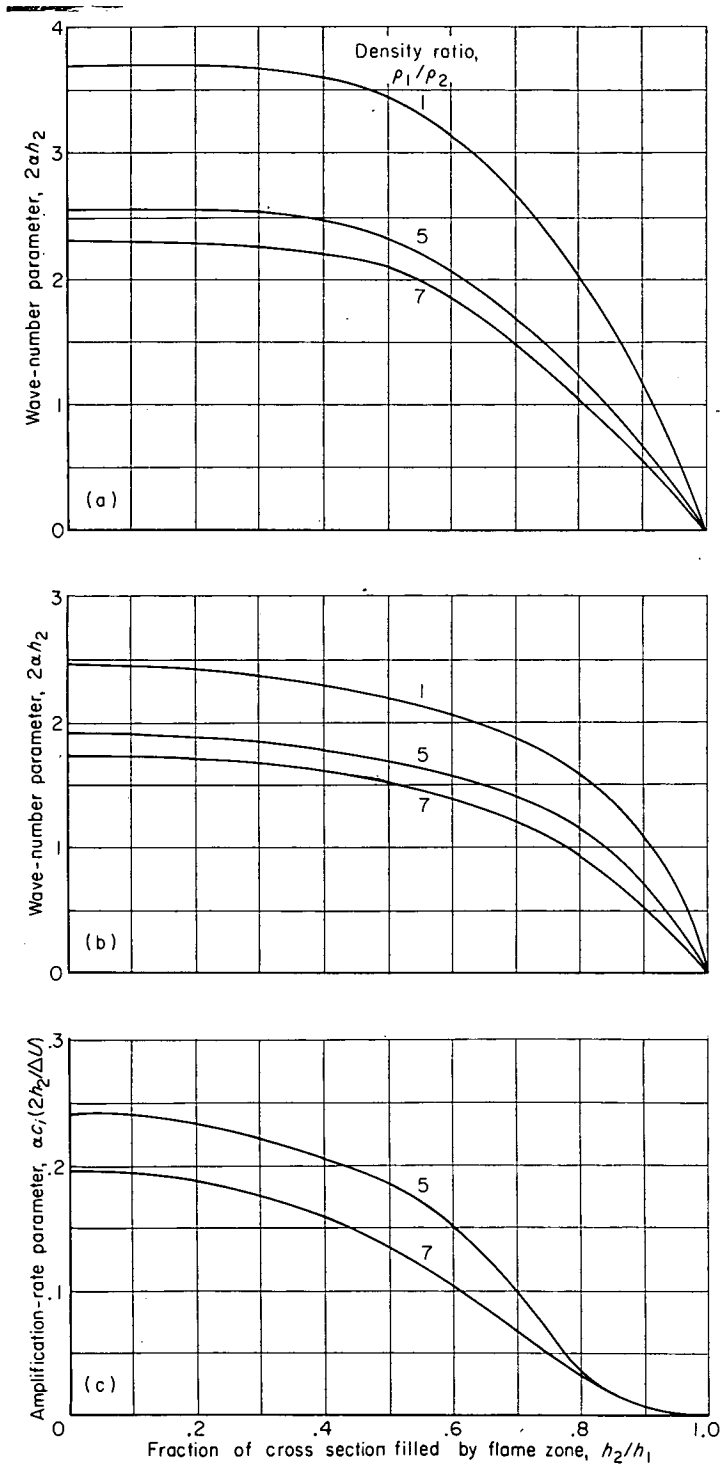
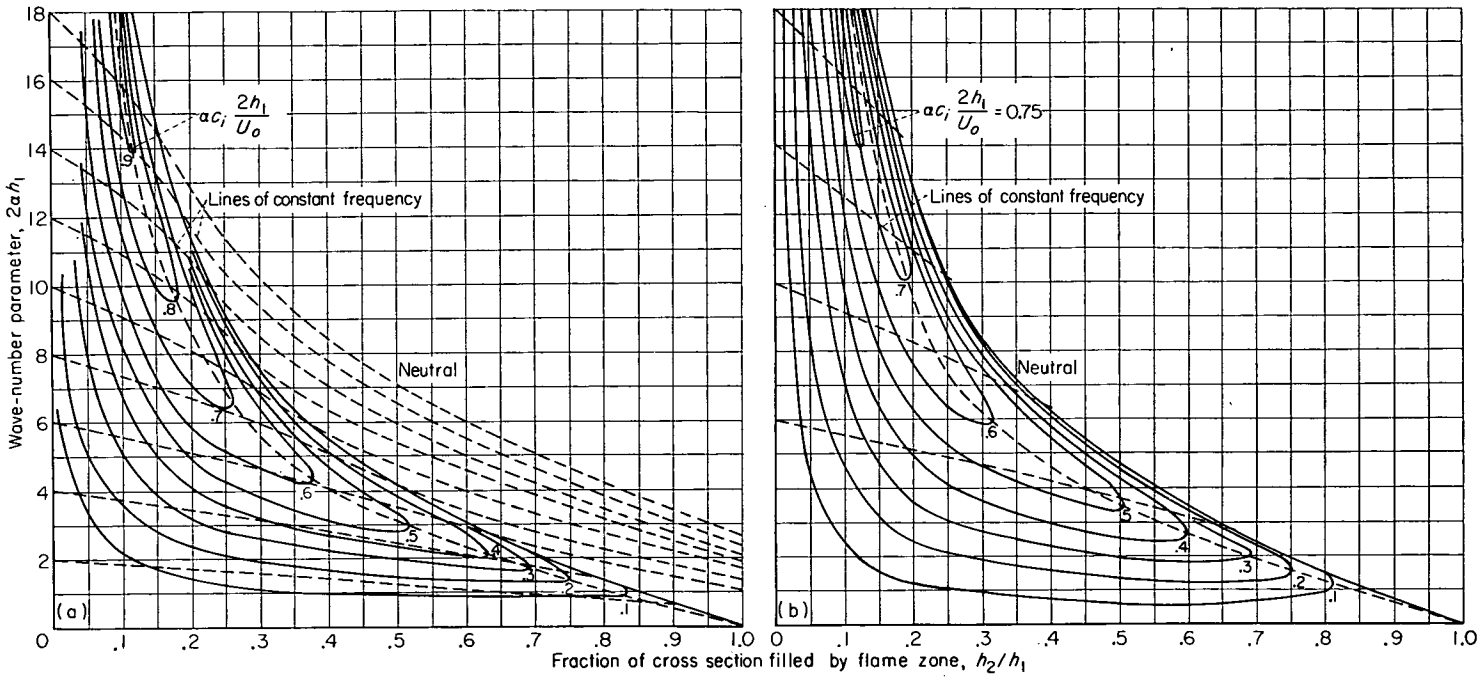


FIGURE 2.—Amplification-rate parameter for ⎯⎯ profile.



(a) Wave-number parameter for neutral stability.
(b) Wave-number parameter for maximum instability.
(c) Amplification-rate parameter for maximum instability.

FIGURE 3.—Wave-number parameter for neutral stability and maximum instability, and amplification-rate parameter at maximum instability for ⎯⎯ profile.



(a) Density ratio, 7. (b) Density ratio, 5.

FIGURE 4.—Stability map for flame in a duct. Contours of constant amplification rate are given by lines of constant $\alpha c_i(2h_1/U_o)$. Lines of constant frequency show path a given disturbance originating at flameholder takes as it propagates along flame zone at phase velocity.

h_2/h_1. Figure 3(c) shows the amplification parameter $\alpha c_i(2h_2/\Delta U)$ for maximum amplification rate plotted against h_2/h_1. Both the amplification rate and the range of the parameter $2\alpha h_2$ diminish as the flame fills the duct.

CONSTRUCTION OF STABILITY MAP

In considering the effect of disturbance amplification in the flame zone, local growth-rate contours as a function of wave number and flame-width ratio h_2/h_1 present nearly all the important information. Such a plot is called the stability map of a flame in a duct. The map is constructed from the data of figures 2 and 3 and from the steady-state relation of U^*/U_o and U_1/U_o as functions of h_2/h_1 (eqs. (1) and (3)) in the following manner. Given: $(U_1/U_o)(h_2/h_1)$, (U^*/U_o) (h_2/h_1), and $[\alpha c_i(2h_2/\Delta U)](2\alpha h_2, h_2/h_1)$ for a given ρ_1/ρ_2. The quantity desired is $[\alpha c_i(2h_1/U_o)]$ $(2\alpha h_1, h_2/h_1)$. This quantity is obtained through suitable cross plots of figures 2 and 3 and equations (1) and (3) by setting $2\alpha h_1 = 2\alpha h_2/(h_2/h_1)$:

$$\alpha c_i \frac{2h_1}{U_o} = \alpha c_i \frac{2h_2}{U^* - U_1} \left(\frac{\frac{U^*}{U_o} - \frac{U_1}{U_o}}{h_2/h_1} \right) \tag{40}$$

The resulting stability map is shown in figure 4. Contours of constant dimensionless amplification rates $\alpha c_i(2h_1/U_o)$ are shown as functions of the dimensionless wave number $2\alpha h_1$ and dimensionless flame width h_2/h_1 for ρ_1/ρ_2 of 7 and 5. These contours are in a region bounded by $2\alpha h_1 = \infty$, 0; $h_2/h_1 = 0$; and the line of $2\alpha h_1$ for neutral stability (i.e., the critical $2\alpha h_1$ as a function of h_2/h_1).

PHASE VELOCITY

A disturbance that distorts the flow and therefore distorts the flame front has a wavelength $\lambda = 2\pi/\alpha$. Such a disturbance if introduced at the flameholder travels along the flame front at the phase velocity c_r. This can be seen from the variation of the disturbance with x distance and time; that is,

$$v' \approx e^{i\alpha(x-ct)} = e^{\alpha c_i t} e^{i\alpha(x-c_r t)}$$

In order to follow the amplification rate of a given disturbance, it is necessary to follow a disturbance of constant frequency. The relation between frequency and wavelength is

$$f = \frac{c_r}{\lambda} = \frac{\alpha c_r}{2\pi} \tag{41}$$

The quantity $\frac{c_r - U_1}{U^* - U_1}$ from equation (38) is given by

$$\frac{c_r - U_1}{U^* - U_1} = \frac{1}{\alpha h_2} \frac{h_2\alpha + \zeta \frac{\rho_1}{\rho_2}(\xi\alpha h_2 - 1)}{2\left(\zeta \frac{\rho_1}{\rho_2}\xi + 1\right)} \tag{42}$$

for

$$\left[h_2\alpha + \zeta \frac{\rho_1}{\rho_2}(\xi\alpha h_2 - 1)\right]^2 - 4\left(\zeta \frac{\rho_1}{\rho_2}\xi + 1\right)(\alpha h_2 \xi - 1) < 0$$

and by

$$\frac{c_r - U_1}{U^* - U_1} = \frac{1}{\alpha h_2} \frac{h_2\alpha + \zeta \frac{\rho_1}{\rho_2}(\xi\alpha h_2 - 1) + \sqrt{\left[h_2\alpha + \zeta \frac{\rho_1}{\rho_2}(\xi\alpha h_2 - 1)\right]^2 - 4\left(\zeta \frac{\rho_1}{\rho_2}\xi + 1\right)(\alpha h_2 \xi - 1)}}{2\left(\zeta \frac{\rho_1}{\rho_2}\xi + 1\right)} \tag{43}$$

for

$$h_2\alpha+\zeta\frac{\rho_1}{\rho_2}(\xi\alpha h_2-1)-4\left(\zeta\frac{\rho_1}{\rho_2}\xi+1\right)(\alpha h_2\xi-1)\geq 0$$

A plot of this quantity against αh_2 is given for $\rho_1/\rho_2=7$ at $h_2/h_1=0.25$, 0.50, and 0.75 in figure 5(a). Also shown in figure 5(a) for comparison is $(c_r-U_1)/(U^*-U_1)$ for $\rho_1/\rho_2=5$, $h_2/h_1=0.25$ and for $\rho_1/\rho_2=1$, $h_2/h_1=0$.

Note that

$$\lim_{\alpha h_2\to 0}\frac{c_r-U_1}{U^*-U_1}=0$$

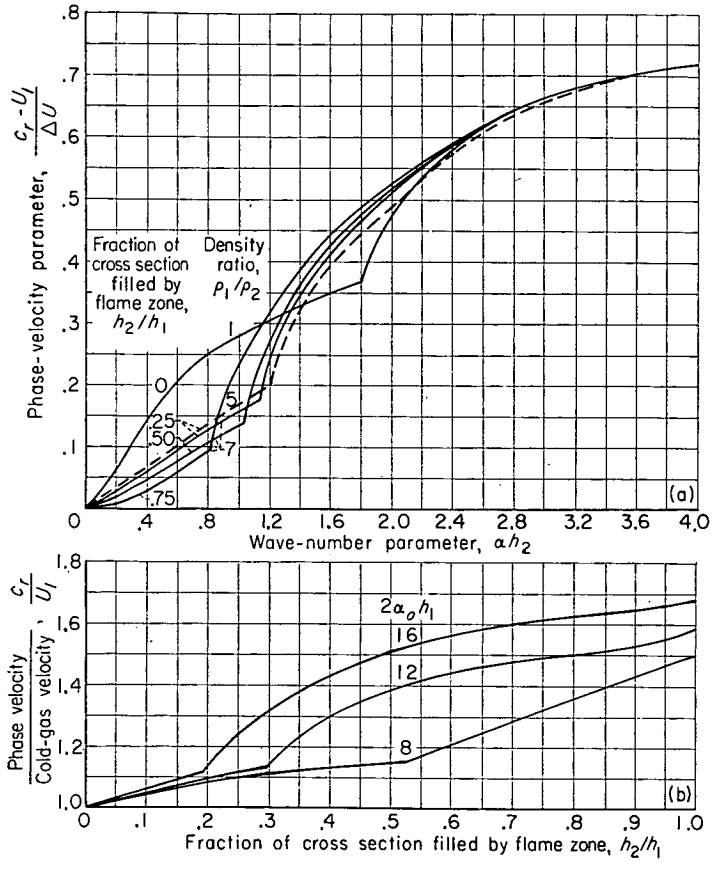
From the steady-state solutions,

$$\lim_{h_2/h_1\to 0}(U^*-U_1)=0$$

Therefore, at the flameholder $c_r=U_1=U_o$. Then it is convenient to relate the local wave number to the wave number at the flameholder by

$$\alpha=\alpha_o\frac{U_o}{c_r} \tag{44}$$

where α_o is the wave number at the flameholder, which is related to the frequency of the disturbance f and U_o by $\alpha_o=f2\pi/U_o$. By means of equations (42), (43), (44), (1), and (3), values of $\alpha(\alpha_o, h_2/h_1)$ were calculated; these are shown in figure 4 as lines of constant frequency. These lines enable one to follow the local amplification rate of a disturbance of given frequency from the flameholder to some station downstream and are so employed in a later section.



(a) Phase-velocity parameter for amplified and neutral disturbances as function of wave-number parameter.

(b) Ratio of phase velocity to cold-gas velocity at three frequencies as function of h_2/h_1 for density ratio of 7.

FIGURE 5.—Phase-velocity parameters.

An additional calculation for the phase velocity was made for later comparison with experimental data. In figure 5(b) is shown a plot of c_r/U_1 against h_2/h_1 for ρ_1/ρ_2 of 7 and $2\alpha_o h_1$ of 8, 12, and 16. These data enable direct comparison of measured values of phase velocity with values predicted from the stability analysis.

DISTURBANCE GROWTH

A qualitative picture of the nature of the disturbances propagating at phase velocity is shown in figure 6. The streamline distributions are given for a neutral disturbance in a reference plane moving at the phase velocity c_r; in this frame of reference, the streamlines are no longer a function of time. Motion is relative to the "eyes" of the disturbance centers. In the hot flame core, the gas moves faster than c_r; in the colder gas outside the flame, the gas moves slower than c_r.

To picture what happens to an amplified disturbance, imagine the y-amplitude of the wrinkles in figure 6 to be

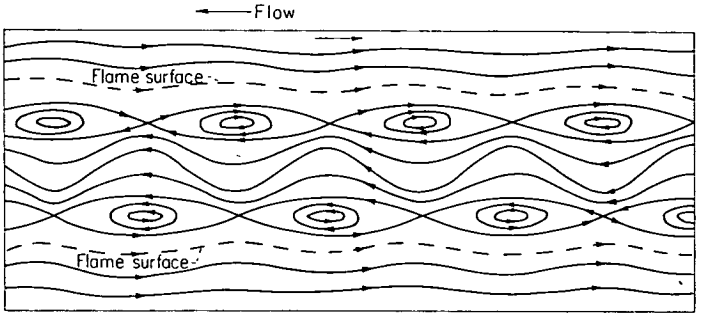


FIGURE 6.—Streamlines of neutral disturbance moving at phase velocity.

growing from right to left. In addition, the flame width is increasing gradually, as is the phase velocity; and therefore the x- and y-spacing of the "eyes" is increasing in the direction of flow until a neutral situation is reached. At each x-station the disturbance has a local growth rate αc_i that acts over a short time Δt. Then (since x is related to time by $dx=c_r dt$), at any time t after the disturbance originated at the flameholder, the amplitude is

$$v'=v'_o e^{\int_0^t \alpha c_i dt} \tag{45}$$

where v'_o is the amplitude of the disturbance at the flameholder on the centerline of the profile.[2]

Up to this point, the independent variables have been the dimensionless wave number $2\alpha h_2$ and flame width h_2/h_1. In order to evaluate equation (45), it is necessary to use the relation

$$\frac{dx}{dt}=c_r \tag{46}$$

and some assumption concerning the variation of h_2/h_1 with x. Two simple assumptions are used that bracket the variation of h_2/h_1 with x found by experiment and facilitate the integra-

[2] The linking of the parallel-flow solutions by conserving v' along the centerline is the simplest but not necessarily the best of several available choices.

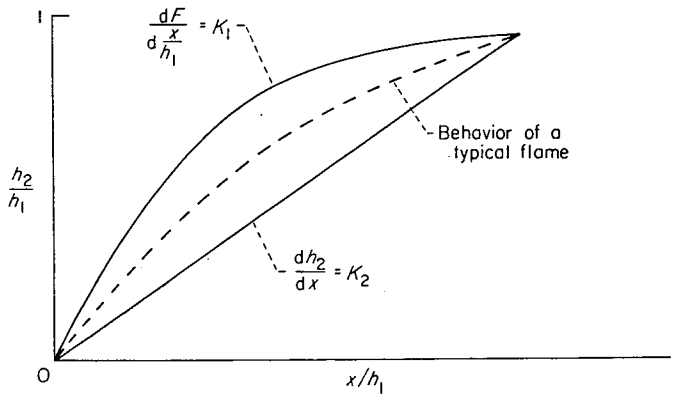
tion of equation (45). These assumptions are (1) that the flame is linear:

$$\frac{\mathrm{d}\frac{h_2}{h_1}}{\mathrm{d}\frac{x}{h_1}}=K_2 \tag{47}$$

and (2) that the change in fraction burned with distance is linear:

$$\frac{\mathrm{d}F}{\mathrm{d}\frac{x}{h_1}}=K_1 \tag{48}$$

A qualitative comparison of the way these assumptions describe a flame surface is given in the following sketch:



Sketch (e)

Inserting equations (46) and (47) in equation (45) results in

$$v'=v_o'\left(e^{\frac{1}{2}\int_0^{h_2/h_1}\alpha c_i\frac{2h_1}{U_o}\frac{U_o}{c_r}\mathrm{d}\frac{h_2}{h_1}}\right)^{1/K_2} \tag{49}$$

The term in parentheses is called the gain G, which is independent of the value of the propagation rate K_2.

A similar derivation can be made for the alternative form of heat release; that is, for

$$\frac{\mathrm{d}F}{\mathrm{d}\frac{x}{h_1}}=K_1$$

which yields

$$v'=v_o'\left(e^{\frac{1}{2}\int_0^{F}\alpha c_i\frac{2h_1}{U_o}\frac{U_o}{c_r}\mathrm{d}F}\right)^{1/K_1} \tag{50}$$

where the term in parentheses G' is independent of the value of K_1.

The values of G and G' can be obtained by graphical integration. They give relative values of amplification of a disturbance of given frequency when integrated along a constant-frequency line in figure 4. Figure 7 gives the results of such an integration carried from h_2/h_1 of 0 to 1 for a range of $2\alpha_o h_1$ and for the following conditions: G is given as a function of $2\alpha_o h_1$ for ρ_1/ρ_2 of 5 and 7, and G' is given as a function of $2\alpha_o h_1$ for ρ_1/ρ_2 of 7. It is apparent that, for the conditions examined, there is a most-amplified frequency

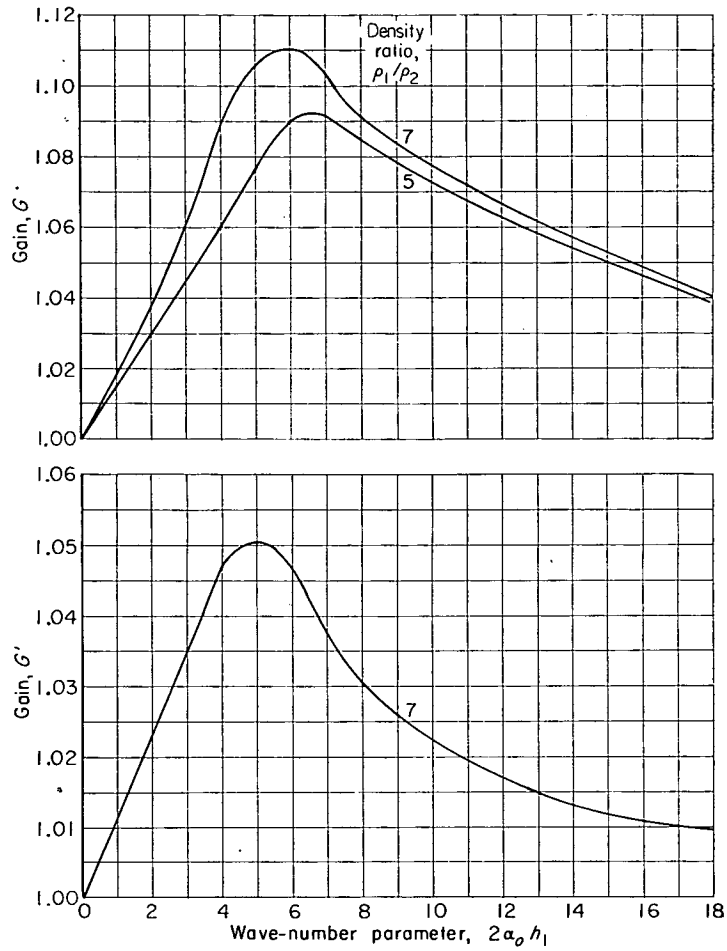


FIGURE 7.—Gains for flame filling the duct.

corresponding to a value of $2\alpha_o h_1 \approx 6$. Recall that $f=2\alpha_o h_1 U_o/2\pi 2h_1$ or the most-amplified frequency is approximately $f \approx U_o/2h_1$. This frequency does not depend upon a rate of flame spreading; it was obtained by assuming that a mode of flame spreading is specified. Approximately the same frequency obtains for the two modes of flame spreading specified.

Not only is the most-amplified frequency in figure 7 at ρ_1/ρ_2 of 5 very near that for ρ_1/ρ_2 of 7, but also the numerical values of the gains are very nearly the same. This latter occurrence is due to two opposing influences: For a given U^*-U_1, the profile having the lower value of ρ_1/ρ_2 has a higher amplification rate, and a disturbance of given frequency is amplified over a wider range of h_2/h_1. On the other hand, at any value of h_2/h_1, U^*-U_1 is smaller for the smaller ρ_1/ρ_2.

The growth of the disturbances for fractional values of h_2/h_1 (or F) was calculated by taking the integral in equation (49) or (50) to fractional values of h_2/h_1 (or F). The results are shown in figure 8, in which the gains G and G' are plotted against h_2/h_1 or F for values of $2\alpha_o h_1$ from 2 to 18. For some values of $h_2/h_1 < 5$, there are frequencies higher than those corresponding to $2\alpha_o h_1 \approx 6$ that locally exhibit a maximum gain. The fact that for values of $h_2/h_1 < 0.5$ there is a local amplification that depends on frequency is used later in comparing analysis with experiment. As h_2/h_1 decreases, the frequency that is most amplified increases.

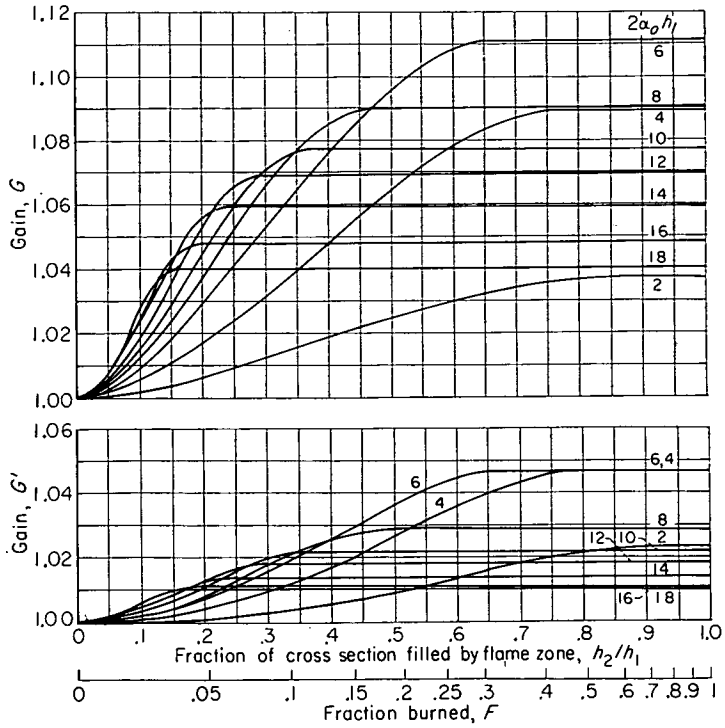


FIGURE 8.—Gains as function of h_2/h_1 for family of initial wave-number parameters. Density ratio, 7.

DISTURBANCE VELOCITY DISTRIBUTION IN y-DIRECTION

The way the disturbance velocity v' varies along the axis of the duct is shown in figure 8. In reducing the results of this analysis to measurable quantities, a qualitative picture of the way the disturbance velocity v' varies across the duct is needed. Such a picture can most easily be obtained by considering a neutrally stable disturbance.

From equations (18) and (28),

$$\frac{v'_{2,y}}{v'_o}=\frac{1}{\gamma_y}\frac{\frac{B_1}{B_2}+\gamma_y^2}{\frac{B_1}{B_2}+1} \quad 0\leq y\leq h_2 \tag{51}$$

where $v'_{2,y}$ is the disturbance velocity at y in region 2, v'_o is the disturbance velocity at the centerline, and $\gamma_y\equiv e^{-\alpha y}$. In the region $h_2\leq y\leq h_1$, $v'_{1,y}/v'_{2,h_2}$ can be obtained from equations (18), (27), and (28) in the form

$$\frac{v'_{1,y}}{v'_{2,h_2}}=\frac{-\gamma_1^2+\gamma_y^2\gamma_2}{-\gamma_1^2+\gamma_2^2\gamma_y} \tag{52}$$

The ratio B_1/B_2 can be obtained from the equation represented by the first row in the determinantal equation (30)

$$\left(c-\frac{\beta}{\alpha}+\zeta\frac{\rho_1}{\rho_2}c\right)B_1+\left(-c-\frac{\beta}{\alpha}+\zeta\frac{\rho_1}{\rho_2}c\right)\gamma_2^2B_2=0$$

or

$$\frac{B_1}{B_2}=-\gamma_2^2\left[\frac{\left(\zeta\frac{\rho_1}{\rho_2}-1\right)-\frac{\beta}{\alpha c}}{\left(\zeta\frac{\rho_1}{\rho_2}+1\right)-\frac{\beta}{\alpha c}}\right] \tag{53}$$

Recall that $\beta/\alpha c$ in equation (30) is the same as $(1/\alpha h_2)[(U^*-U_1)/(c-U_1)]$, which for real values of c is given in equations (42) and (43).

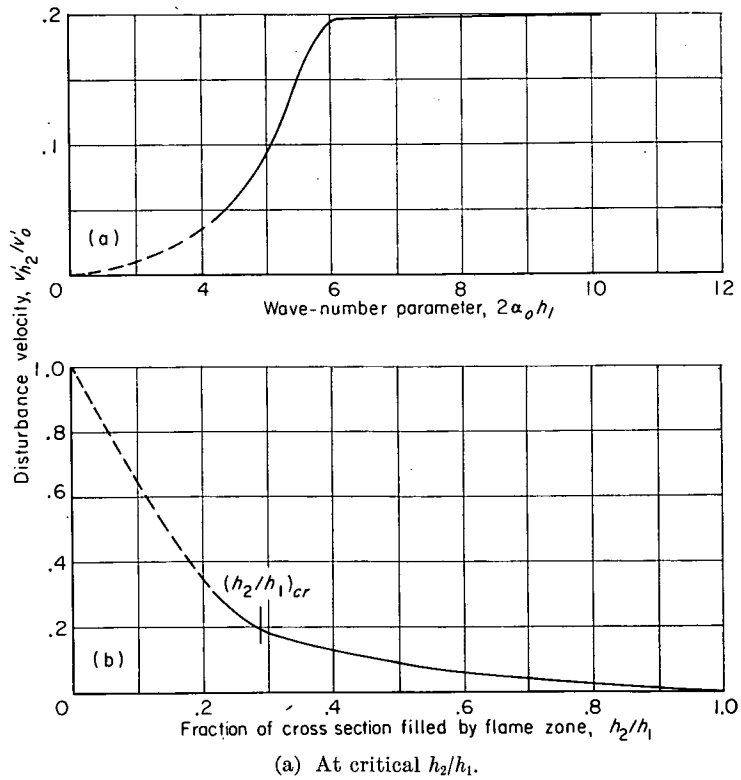
A series of calculations was made to obtain the representative behavior of v'_{h_2}/v'_o across the duct, and the results are shown in figure 9 for ρ_1/ρ_2 of 7. The critical h_2/h_1 is taken as the value where for a given frequency the imaginary part of c becomes 0. Figure 9(a) shows the value of v'_{h_2}/v'_o at the critical h_2/h_1 plotted against initial wave number $2\alpha_o h_1$. For $2\alpha_o h_1>8$ (i. e., for $(h_2/h_1)_{cr}<0.46$) the value of $v'_{h_2}/v'_o\approx 0.2$. The ratio decreases at $2\alpha_o h_1<8$ (i. e., for $(h_2/h_1)_{cr}>0.46$) as the flame approaches the wall.

In figure 9(b) the value v'_{h_2}/v'_o is given for a fixed frequency corresponding to $2\alpha_o h_1=12$ following a disturbance along the duct from the flameholder ($h_2/h_1=0$) to the station where the flame touches the wall. The dashed portion is interpolated between $h_2/h_1=0$ (where $v'_{h_2}=v'_o$) and $h_2/h_1=(h_2/h_1)_{cr}$ (where the calculation starts). It is obvious from this curve that, if v'_{h_2} is measured instead of v'_o, the apparent growth rate is not as rapid for $h_2/h_1<(h_2/h_1)_{cr}$ as for v'_o, simply because of the velocity distribution. Also, for $h_2/h_1>(h_2/h_1)_{cr}$ there is an apparent decay in v'_{h_2} owing to this distribution, despite the fact that the value of v'_o is neutrally stable. This latter point is employed in comparing the analytical with the experimental results.

The significance of figure 9 is summarized as follows:

(1) Although the inviscid treatment eliminates consideration of damping, it is clear that at the flame front the velocity amplitude diminishes at $h_2/h_1>(h_2/h_1)_{cr}$ because of the velocity distribution.

(2) In some instances, even though the flow is unstable and the disturbance velocity amplitude is increasing along



(a) At critical h_2/h_1.
(b) For wave-number parameter of 12.

FIGURE 9.—Disturbance-velocity distributions. Density ratio, 7.

the center of the flame, the disturbance-velocity amplitude at the flame front may not necessarily be increasing.

(3) The disturbance that is most amplified at the center of the profile (i.e., $2\alpha_o h_1=6$) is not necessarily the most amplified at the flame front, owing to the velocity distribution; the frequency of the latter is somewhat greater than that of the former.

RELATION OF THEORETICAL RESULTS TO MEASURABLE QUANTITIES

In the experimental phase, current instrumentation techniques impose limitations on what can be measured. For example, the velocity v'_o cannot be measured directly by hot-wire techniques because the flame temperature is too high ($\approx$4000° R). The purpose of this section is to collect certain results of the foregoing analysis that lend themselves to direct measurement.

Flame slope.—In equations (49) and (50) the growth of a disturbance v'/v'_o is found to be proportional to a calculable quantity, gain, raised to a power $1/K$. The quantity K is alternatively $K_2=\mathrm{d}(h_2/h_1)/\mathrm{d}(x/h_1)$ or $K_1=\mathrm{d}F/\mathrm{d}(x/h_1)$, depending on the mode of flame propagation assumed. For both modes, K is smaller the more gradual the rate of flame spreading. To a first approximation, then, the amplification of a disturbance increases as the ratio of propagation velocity to flow velocity decreases. This trend can be verified experimentally.

Phase velocity.—One quantity that can be measured immediately is the phase velocity c_r. A plot of c_r/U_1 for three frequencies is given in figure 5(b). Thus, for a given flow setting, the absolute magnitudes of c_r/U_1 can be compared and the variation with frequency and with h_2/h_1 can be examined.

Flame-front displacement.—The transverse velocity v' acting at the flame surface $y=h_2$ causes a wavy wrinkle to appear in the surface. If a quantity h is defined as the distance from crest to valley of these wrinkles, this quantity equals twice the y amplitude of the streamlines of the flow at the flame front. If a neutral case is considered and the distribution of v' in the flame zone is approximated by

$$v'=v'_c+(v'_o-v'_c)\left(1-\frac{y}{y_c}\right)$$

the equations of the streamlines are given by

$$\frac{y}{y_c}\approx 1-\epsilon\cos\alpha x\pm\sqrt{1-2\Psi^*+2k\cos\alpha x}$$

where

k $\dfrac{v'_c}{(U^*-c)\alpha y_c}$

v'_c amplitude of disturbance velocity at y_c

v'_o amplitude of disturbance velocity at centerline

y_c coordinate where $U=c$

ϵ $\dfrac{v'_o-v'_c}{(U^*-c)\alpha y_c}$

Ψ^* dimensionless stream function, $\dfrac{1}{(U^*-c)y_c}\displaystyle\int_0^y U\,\mathrm{d}y$

At $h_2\leqq h_{2,cr}$, $2\Psi^*$ varies between 0.96 and 0.99. Because $2k$ can be taken arbitrarily small, for $2k/(1-2\Psi^*)\ll 1$,

$$\frac{y}{y_c}=1-\epsilon\cos\alpha x\pm\sqrt{1-2\Psi^*}\left[1+\frac{k\cos\alpha x}{(1-2\Psi^*)}\right]$$

Because $y>y_c$, the plus sign is chosen so that

$$\frac{y}{y_c}=1+\sqrt{1-2\Psi^*}+\left(\frac{k}{\sqrt{(1-2\Psi^*)}}-\epsilon\right)\cos\alpha x$$

$$\approx 1+0.2+\frac{1}{\alpha y_c}\left[\frac{\dfrac{v'_c}{U_o}}{\dfrac{U^*-U_c}{U_o}(0.2)}-\frac{\dfrac{v'_o}{U_o}-\dfrac{v'_c}{U_o}}{\dfrac{U^*-U_o}{U_o}}\right]\cos\alpha x$$

$$\approx 1.2+\frac{\dfrac{v'_o}{U_o}}{\alpha y_c\dfrac{U^*-c}{U_o}}\left(\frac{6v'_c}{v'_o}-1\right)\cos\alpha x$$

But v'_c/v'_o is a weak function of α and h_2/h_1 and is approximately 0.2.

Employing the identity

$$\frac{U^*}{U_o}-\frac{c}{U_o}=\left(\frac{U^*}{U_o}-\frac{U_1}{U_o}\right)\left(1-\frac{c-U_1}{U^*-U_1}\right)$$

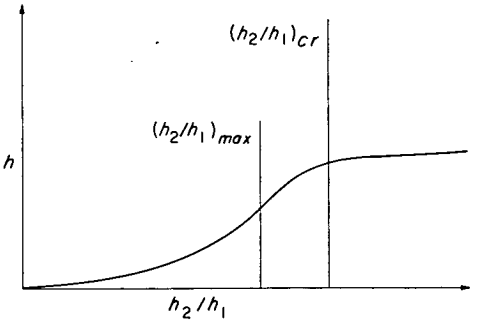
and a value of $(c-U_1)/(U^*-U_1)$ from figure 5(a),

$$\frac{U^*}{U_o}-\frac{c}{U_o}\approx\left(\frac{U^*}{U_o}-\frac{U_1}{U_o}\right)(0.85)$$

where the quantity $(U^*/U_o)-(U_1/U_o)$ is a function of ρ_1/ρ_2 and h_2/h_1 only. Thus,

$$\frac{y}{y_c}\approx 1.2+\frac{0.2\dfrac{v'_o}{U_o}}{0.85\,\alpha y_c\dfrac{U-U_o}{U_o}}\cos\alpha x$$

at the flame front. The coefficient of cos αx is $\frac{1}{2}h$, the flame-front wrinkle amplitude. It can be seen that h will behave qualitatively like v'. Without going into further detail, then, some predictions can be made from the theory that may be verified by experiment. First, h may be expected to behave qualitatively as shown in the following sketch:

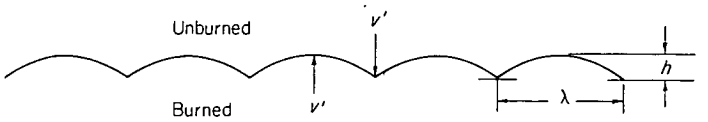


Sketch (f)

The shape of the curve in sketch (f) can be used to locate the approximate x-position of $(h_2/h_1)_{cr}$. There is a point of inflection where v'_{h_2/h_1} reaches a maximum and a knee as v'_{h_2/h_1} ceases to grow. The knee position falls between the h_2/h_1 for maximum amplification and $(h_2/h_1)_{cr}$. Thus, the data that can be sought are the absolute values of h_2/h_1 where the knee occurs for a given frequency and the relative

positions of the knee for different frequencies.

Flame propagation.—As stated in the introduction, one of the reasons for pursuing the stability analysis is to find a disturbance frequency that permits the greatest increase in flame spreading with the smallest expenditure of energy. In this section a model of flame propagation is constructed that permits extrapolating the behavior of v' from the stability analysis to a measurable behavior of flame propagation. The flame front is assumed to be a zone in which the density goes from ρ_1 to ρ_2 in a distance that is short compared with the disturbance wavelength. This front is propagating into the gas of density ρ_1 at a rate $V_{T,u}$; that is, the undisturbed turbulent flame speed. Owing to the normal propagation of the front, an initially wavy surface becomes a cusped surface. Assuming such a surface composed of cylindrical arcs



Sketch (g)

permits a calculation of the flame-front stretching due to a displacement h. If the undisturbed area $S_u=\lambda$ and the disturbed area S_d are approximately equal to arc length,

$$\frac{S_d}{S_u}\approx\sqrt{1+\left(\frac{2h}{\lambda}\right)^2} \tag{54}$$

An equilibrium h is reached when

$$\frac{S_d}{S_u}=\sqrt{\frac{1+\frac{2v'}{V_{T,u}}}{1+\frac{v'}{V_{T,u}}}} \tag{55}$$

Then S_d/S_u behaves roughly as $\left(1+\frac{1}{2}\frac{v'}{V_{T,u}}\right)$ for small amplitude. Equation (54) contains a nonlinear term $4h^2/\lambda^2$. The development so far as been a linear one. The linear development would be expected to furnish only a first approximation for amplitudes large enough so that $4h^2/\lambda^2$ is no longer negligible compared to unity.

The sequence of events that leads to a prediction of S_d/S_u is as follows:

(1) The flame is initially wrinkled by the velocity v' acting at the flame surface.

(2) As the wrinkles grow, the flame shape shifts from a sine wave to a cusped surface, owing to normal propagation.

(3) After a certain time an equilibrium is reached between the disturbance velocity v' and the undisturbed propagation velocity $V_{T,u}$.

The ratio of the disturbed surface to the undisturbed surface when equilibrium is reached is, for small disturbances,

$$\frac{S_d}{S_u}=\left(1+\frac{1}{2}\frac{v'}{V_{T,u}}\right)=\frac{V_{T,d}}{V_{T,u}} \tag{56}$$

Before this equilibrium value of S_d/S_u is reached, the flame surface is given by (again for the neutral case)

$$\frac{y_{h_2}}{y_c}\approx 1.2+\frac{0.2\,v_o'}{\Delta U\alpha y_c}\cos\alpha x$$

But $2h/\lambda$ of equation (54) is given by

$$\frac{2h}{\lambda}\approx\left(\frac{y_{h_2}}{y_c}-1.2\right)\frac{y_c 2\alpha}{\pi}$$

$$\approx\frac{v_o'}{\Delta U}\frac{0.4}{\pi}\cos\alpha x$$

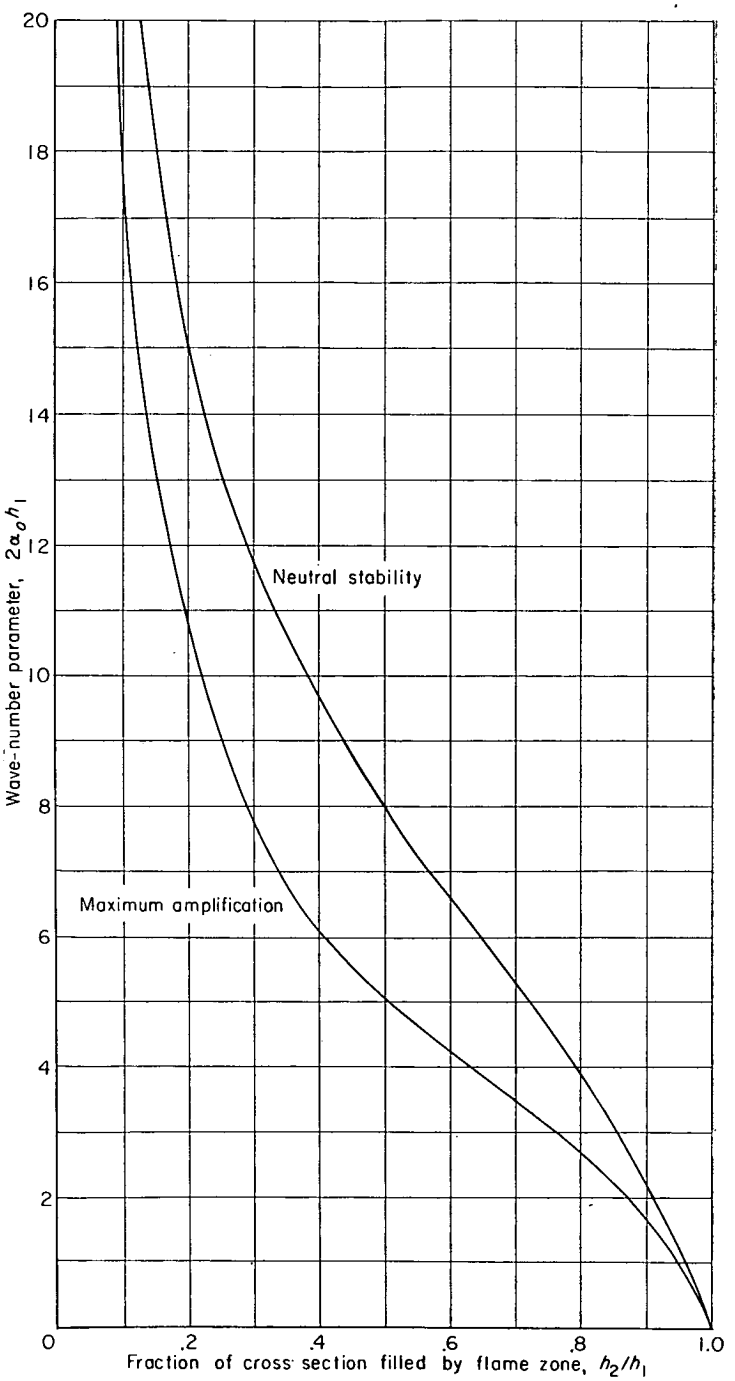


FIGURE 10.—Frequencies that give maximum increase in local flame speed. Density ratio, 7.

Thus, in the transient case as in the equilibrium case (eq. (55)), S_d/S_u behaves as v'. The quantity S_d/S_u when measured locally should behave like G in figure 8, if the effect of distribution is neglected. When the latter effect is taken into account, v' for fixed $2\alpha_o h_1$ measured at h_2 achieves a maximum value somewhere between h_2/h_1 for maximum amplification and neutral stability.

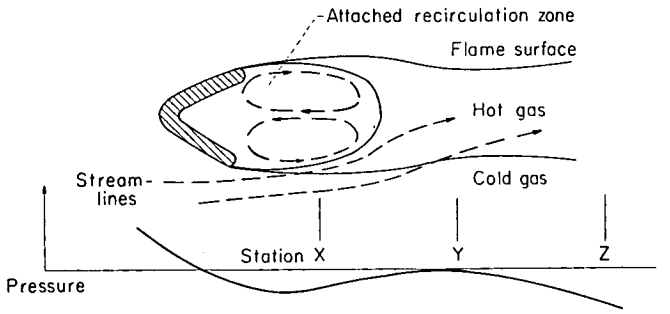
Thus, at any station h_2/h_1, there should be a frequency of disturbance that would cause the greatest increase in flame speed, and at this station the increase in flame speed should be greater for greater values of $v'/V_{T,u}$.

Figure 10 gives a plot of $2\alpha_o h_1$ against h_2/h_1 for maximum amplification and for neutral stability. For any value of h_2/h_1, the frequency giving the greatest $v'/V_{T,u}$ (at the flame surface) has a value of $2\alpha_o h_1$ that falls between these curves. The lag in time required for the flame to become wrinkled initially will move the curve for maximum S_d/S_u to slightly higher $2\alpha_o h_1$ values. The curves given should be considered the lower limits of $2\alpha_o h_1$ for maximum S_d/S_u, and they serve as a basis for comparison with the experimental data.

EFFECT OF FLAMEHOLDER

When a flame is anchored in a duct, some form of flameholder must be used. The most common form of flameholder studied in recent years is the cylinder with axis normal to the stream. The cross section of the cylinder has assumed many different shapes. Properties of the flow in the wake are common to all the shapes studied. In this section some of these properties are used to deduce the effect of a flameholder on the flow field and on its stability far from the flameholder.

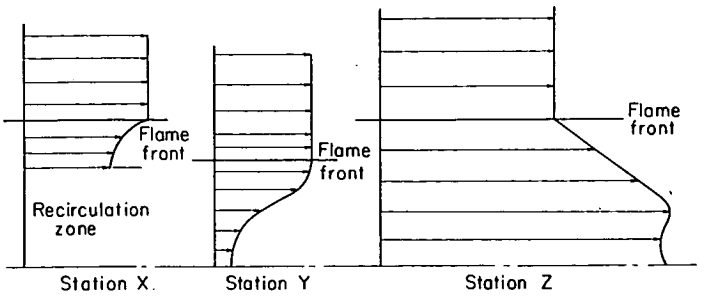
Steady-state velocity distribution.—The properties of the flow field in the immediate wake of the flameholder as described in references 1 and 31 are shown in sketch (h):



Sketch (h)

Two eddies are attached in the wake of the flameholder. The gas in this zone is hot; it acquires energy from the downstream hot gas and delivers energy to the outside cold gas by diffusion. At some position on the surface of the recirculation zone, sufficient energy is acquired by the cold gas for ignition to occur and a flame to propagate into the cold-gas stream as shown in sketch (h). The pressure measured at the walls has an axial distribution that is shown qualitatively in sketch (h) (refs. 1 and 31).

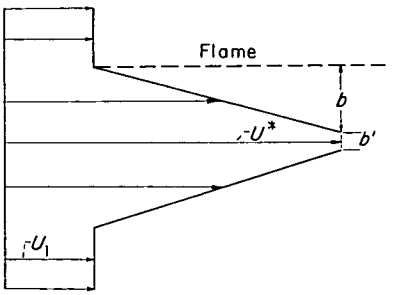
If the static pressure is assumed constant across the duct at any axial station, the effect of the first positive, then vanishing, then negative pressure gradient upon gases of unlike densities permits an estimation of the velocity profile downstream of the flameholder. The velocity profiles at stations X, Y, and Z of sketch (h) are shown in sketch (i):



Sketch (i)

At station X the pressure gradient in the axial direction has been positive for a small distance and is still positive at X. This fixes the sense of the velocity difference between cold and hot gases on either side of the flame and the sense of the velocity gradient of the hot gas at the flame front. At station Y the gas has a positive-pressure-gradient history, again fixing the sense of the velocity difference, and at Y the pressure gradient vanishes, causing the velocity gradient at the flame front to vanish. At station Z the gas has a negative-pressure-gradient history from Y sufficient to cause the sense of velocity difference and gradient at the flame front as shown. The gas particle at the position of the velocity maximum passed through the flame at station Y.

If the profile is approximated by straight-line segments with a corner at this velocity maximum as shown in sketch (j),



Sketch (j)

some quantitative relation based on the continuity equation and experimental observations can be obtained. From continuity,

$$\frac{1}{2} b'U^* = V_w l_w \frac{\rho_1}{\rho_2} \tag{57}$$

and

$$b \frac{U^* + U_1}{2} = V_F l_F \frac{\rho_1}{\rho_2} \tag{58}$$

where

l_F axial length from station Y to station of interest downstream of Y (sketch (h))
l_w axial length of wake to station Y
V_F mean flame speed over l_F
V_w mean flame speed over l_w

Combining equations (57) and (58) gives

$$\frac{b'}{2b} = \frac{U^* + U_1}{2U^*} \frac{V_w l_w}{V_F l_F} \tag{59}$$

In order to obtain an order of magnitude of $b'/2b$ of interest in the stability analysis, the terms on the right side of equation (59) are given the following values: $(U^*+U_1)/U^*=1.5$ (from ref. 1 for $F=0.25$, $\rho_1/\rho_2=6$); $V_w/V_F \approx 1/(V_T/V_L) \approx 1/2.5$; and $l_w \approx 4d$ (from ref. 1). Defining l as l_w+l_F,

$$\frac{l_w}{l_F}=\frac{1}{\frac{l}{l_w}-1}=\frac{4}{\frac{l}{d}-4}$$

equation (59) becomes

$$\frac{b'}{2b}=\frac{1.2}{\frac{l}{d}-4} \qquad \left(\frac{l}{d}>4\right) \tag{60}$$

At a station $l/d=8$ (from eq. (60)),

$$\frac{b'}{2b}=0.6$$

Farther downstream, at $l/d=24$, for example,

$$\frac{b'}{2b}=0.06$$

The foregoing stability analysis is for a profile in which $b'=0$.

From this section it can be seen that, near the flameholder ($l/d=8$), the hot-gas velocity distribution differs in shape from the _/_ profile neglecting the flameholder. At this station, 60 percent of the flame-zone width has a flat distribution. Remote from the flameholder ($l/d=24$), 6 percent of the hot-gas width has a flat velocity distribution. The magnitude and direction of the error incurred in neglecting this flattening are estimated in the following section.

Comparison of stability of _/_ and _/‾_ profiles.—Amplification rates as a function of $2\alpha h_2$ are compared in figure 2 for several values of ρ_1/ρ_2 and h_2/h_1. The effect of increasing ρ_1/ρ_2 and h_2/h_1 is stabilizing; that is, the magnitude of the amplification rates and the range of $2\alpha h_2$ over which positive values exist are reduced. The plots of amplification rate against $2\alpha h_2$ are affine. It appears reasonable that, in examining the effect of truncating the profile, an examination at a single value of ρ_1/ρ_2 and h_2/h_1 would yield representative results.

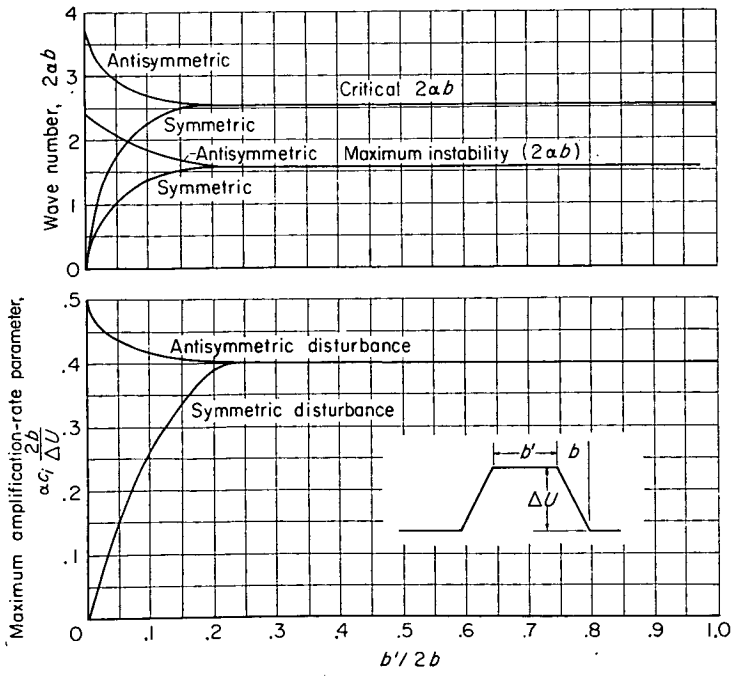


FIGURE 11.—Effect of velocity profile on amplification-rate parameter and on wave-number parameters for neutral stability and maximum instability.

The conditions considered here are the ones formulated by Rayleigh in equations (24) and (25) (p. 387, ref. 15), which correspond to $\rho_1/\rho_2=1$ and $h_2/h_1=0$ (or $h_1=\infty$). Calculations were made in which $b'/2b$ was taken as a parameter in such a way that the results yield values of $\alpha c_i(2b/\Delta U)$ and $2\alpha b$ at maximum instability and a critical value of $2\alpha b$ where αc_i vanishes. The results of these calculations are shown in figure 11. When $b'\neq 0$, the results correspond to those of figure 2; the flow is unstable to antisymmetric disturbances and neutrally stable to symmetric disturbances. As $b'/2b$ increases, the amplification rate and the critical values of $2\alpha b$ decrease for the antisymmetric disturbances. The flow gradually becomes unstable to symmetric disturbances as $b'/2b$ increases. At $b'/2b<0.2$, the flow is as unstable to symmetric as to antisymmetric disturbances and possesses the same critical values of $2\alpha b$. The values of $b'/2b$ of interest here are of the order 0.6 to 0.06. The flame half-width h_2 is $b'/2+b$. In the following table the values of the important parameters $\alpha c_i(2h_2/\Delta U)$, $(2\alpha h_2)_{max\ c_i}$, and $(2\alpha h_2)_{cr}$ are compared for $b'/2b=0$, 0.06, and 0.6 for antisymmetric disturbances:

$\frac{b'}{2b}$	$\alpha c_i\left(\frac{2h_2}{\Delta U}\right)_{max}$	$(2\alpha h_2)_{max\ c_i}$	$(2\alpha h_2)_{cr}$
0	0.492	2.44	3.69
.06	.508	2.49	3.71
.6	.688	3.28	4.57

For a given $2h_2/\Delta U$, the amplification rate is increased as the hot-gas velocity is progressively truncated. The wave-number range over which the flow is unstable is widened. Both of these effects bespeak a greater instability of flow. On the other hand, it can be easily demonstrated that, for a given ΔU, h_2/h_1 is greater when the profile is truncated, so that the destabilizing effect of the flameholder is partially but not completely attenuated.

The difference between the parameters calculated at $b'/2b=0$ and 0.6 shows that near the flameholder the amplification rates may be of the order of 20 percent higher for some wave numbers than were those previously found. Because the flame zone must start with a finite width dependent upon the flameholder width, those frequencies having wave numbers $2\alpha d\mathcal{K}$ that exceed $2\alpha d\mathcal{K}_{cr}$ are suppressed. Here, $\mathcal{K}$ is some proportionality factor less than unity. Certainly, neglect of the effect of a finite-size flameholder facilitates generalizing the results of the stability analysis. The investigations of this section indicate that, for flameholders small compared with duct width, such neglect appears warranted in a large part of the flame zone.

SUMMARY OF THEORETICAL RESULTS

1. The flow field of a flame in a duct is unstable to antisymmetric disturbances having wavelengths of the order of 2.5 times the local flame width and greater. As h_2/h_1 approaches unity, this critical wavelength approaches ∞.

2. The amplification rate depends directly upon the magnitude of the velocity difference (apex velocity minus cold-gas velocity) and inversely upon the flame width. For fixed values of these quantities, the maximum amplification rate decreases with increasing values of ρ_1/ρ_2 and h_2/h_1, going to zero for $h_2/h_1=1$.

3. When the history of a disturbance is followed through the course of an entire flame, a wave number for maximum disturbance growth is found. This maximum growth is for such a wave number at the flameholder that $2\alpha_o h_1=6$, which corresponds to a frequency $f=U_o/2h_1$. The actual growth is substantially independent of density ratio because of two compensating factors:

(a) The amplification rate is lower for a higher density and given velocity difference.

(b) The velocity difference is greater for a higher density ratio.

4. The disturbances achieve their terminal amplification at a value of h_2/h_1 roughly inversely proportional to the frequency of the disturbance. Thus, higher frequencies achieve their amplification near the flameholder; lower frequencies, remote from the flameholder.

5. The magnitude of the terminal amplification depends upon the inverse of flame slope or roughly $(V_T/U_o)^{-1}$. The amplification that can be achieved for the maximum of $2\alpha_o h_1=6$ is about $(1.1)^{U_o/V_T}$. For example, for $V_T/U_o=1/20$, amplification is eightfold. For $V_T/U_o=1/100$, amplification is 14,000-fold.

6. The disturbance propagates with a phase velocity up to 60 percent greater than the cold-gas velocity.

7. The flameholder inhibits the growth of antisymmetric disturbances having higher frequencies but permits symmetric disturbances to be amplified near the flameholder. At 8 diameters downstream of the flameholder, the stability picture is substantially that obtained by neglecting the flameholder.

EXPERIMENT: EXAMINATION OF DISTURBANCE GROWTH IN A V-FLAME

INTRODUCTION

The effect of imposing controlled disturbances on a V-flame anchored in a duct was investigated experimentally for two reasons:

(1) To gain quantitative information on the mechanism of the breakdown of the flame-generated shear region that would explain the occurrence of flame-amplified turbulence

(2) To find a type of excitation that promotes flame propagation without causing the sort of shell failure that combustor resonance causes

The method of excitation consists in exciting a column of gas in the flameholder support tube. This method offers a control on the amplitude when excitation is accomplished with a speaker, but could be accomplished by means of an edge tone excited by the flowing stream for application in an engine. Only the speaker excitation is used here. The sound issues from a port at the flameholder and disturbs the flame at the flameholder. The two types of ports used operated as follows:

(1) Sound issued from a port just upstream of one flameholder edge, causing the fluctuating flow about the flameholder to be quasi-antisymmetric.

(2) Sound issued from the center of the flameholder, causing the fluctuating flow at the flameholder to be symmetric.

The principal disadvantage in this form of excitation is that, for some frequencies, modes of burner cavity resonance are excited. An objective in the experimental work, therefore, was to determine whether an observed flame-front distortion accompanying an imposed disturbance was due to flame-zone instability or to some form of duct resonance.

No effort was made to determine effects of variations in fuel-air ratio or fuel type. The primary variable investigated was the frequency of excitation. The only attempts at correlating the results are the comparison with the results of the preceding stability analysis. The chief frustration encountered is the impossibility of obtaining a laminar V-flame at velocities where values of V_T/U_o are sufficiently low for the preceding theory to be valid. The reason for this

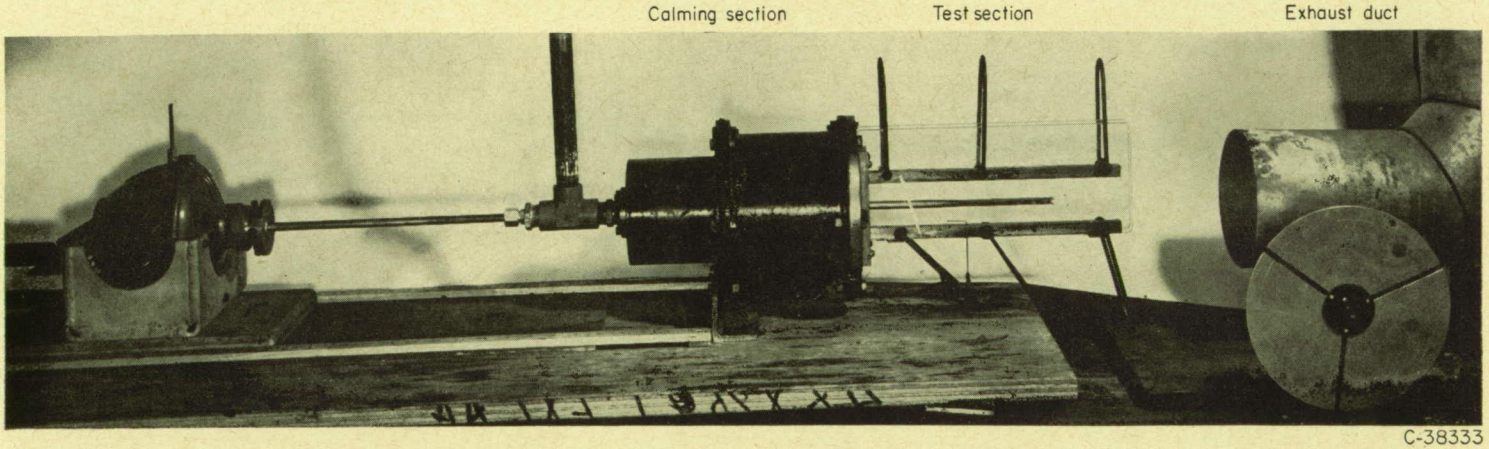


FIGURE 12.—Combustor.

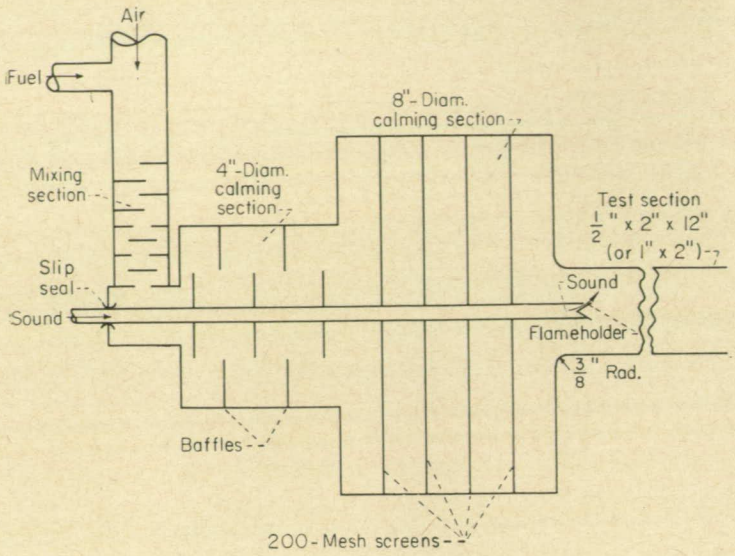


FIGURE 13.—Schematic drawing of combustor.

difficulty is the instability of the boundary layer, which separates from the flameholder and undergoes transition to turbulent motion quite close to the point of separation. All the results are obtained with the flow already somewhat turbulent.

The principal instrument used in measuring flame speeds is the photomultiplier probe, first applied in a rigorous way to the study of turbulent flame speeds by Clark and Bittker (ref. 32). An independent confirmation of the method is obtained by comparing combustion efficiency measured by the photomultiplier probe and by momentum pressure drop.

APPARATUS

BURNER TEST SECTION

A photograph of the burner (fig. 12) shows the important components. Air and propane were filtered, metered, and mixed before entering the two-stage calming section (fig. 13). In this section the mixture passed through six banks of 200-mesh screen and then through a ⅜-inch-radius nozzle plate into the ½- by 2-inch (or alternatively 1- by 2-in.) rectangular glass-walled test section. The top and bottom walls of this test section were ½- by ½-inch (alternatively ½- by 1-in.) brass stock. The side walls were ¼-inch Vycor plates resting on brackets and held against the ½-inch top and bottom pieces by clamps.

The exhaust system consisted of a 6-inch-diameter pipe connected to a hood and a blower to force the gases out. A 4- to 6-inch spacing was maintained between the test section and the exhaust duct, and between the exhaust duct and the hood; there was no indication of resonance due to the exhauster.

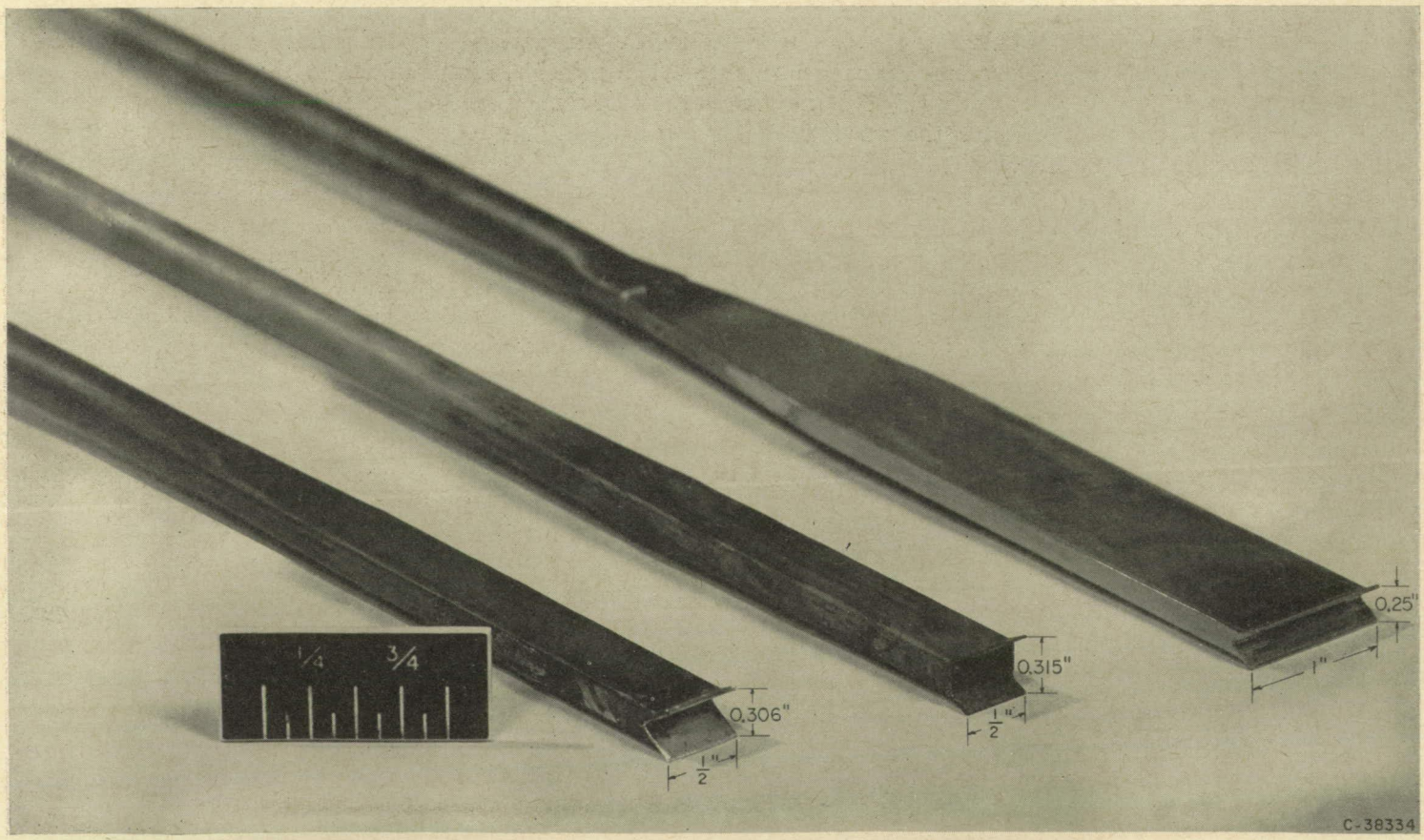


FIGURE 14.—Flameholders.

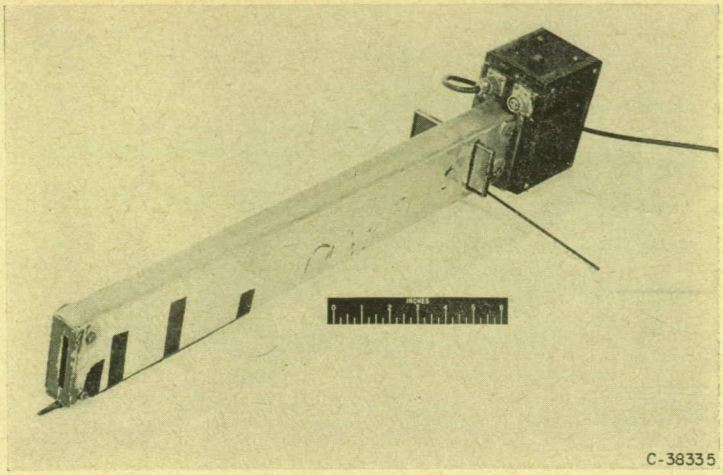


FIGURE 15.—Photomultiplier probe.

The flameholder was a flat hollow paddle 36 to 38 inches long with a 60° gutter on one end and a ⅜-inch tube leading to a piston-type loudspeaker on the other. The three flameholders used in this program are shown in figure 14. The flameholders used to supply the disturbances were resonators that had resonant frequencies every 190 to 200 cycles when coupled to the speaker. The flameholder designed to produce antisymmetric disturbances allowed the sound to issue from a slot just upstream of one edge of the flameholder; the one designed to give symmetric disturbances allowed the sound to issue from the center. The flameholders pictured were approximately 0.25 to 0.30 inch thick. In one test a 0.50-inch gutter was tacked onto the 0.306-inch antisymmetric flameholder to examine the effect of flameholder size.

In no case was the distribution of v' downstream of the flameholder measured. It is not known how much the experimental distribution differs from the measured theoretical distribution. The essential features in both experimental and theoretical disturbances are that antisymmetric disturbances cause the flow to flap back and forth at the centerline of the duct, while symmetric disturbances cause it to dilate about the centerline.

AUXILIARY EQUIPMENT

Sound-producing system.—The speaker was supplied a sinusoidal signal from a signal generator through a power amplifier. The speaker and flameholder could be positioned as desired.

Flow metering.—Air and propane were metered through rotameters.

Hot-wire equipment.—An NACA constant-temperature, frequency-compensated, hot-wire anemometer was used (ref. 33). Spectra and u' were measured at various locations in the duct. Measurements of u' were made primarily with a vacuum-tube voltmeter. Two spot checks were made against a root-mean-square computer, and the correction factor was found to be approximately unity. Spectra were measured with a wave analyzer.

Pressure measurements.—Velocity surveys were made using 0.018-inch hypodermic tubing, or 0.030-inch stainless tubing, for impact tubes. Measurements were read on a water micromanometer. Velocity measurements were made at the plane of exhaust with room pressure as static.

Photomultiplier probe.—The photomultiplier tube was installed in a probe as shown in figure 15. Light reached the photomultiplier tube after passing through two vertical slots, which were ¼ and 1/16 inch wide and 2 feet apart, and through filters when desired. Photomultipliers were supplied by a ripple-free regulated d-c source.

Alternating-current and direct-current voltmeters having identical input resistances were used where indicated.

Shadowgraph system.—The optical arrangement used in taking shadowgraph pictures is shown in figure 16. The light source could be used continuously or as a 4-microsecond flash. The camera was focused 1.5 feet in front of the test section. The shutter and flash were manually synchronized.

Stroboscope.—A stroboscope consisting of a slotted aluminum disk and a synchronous motor was used to view the disturbed flame in the preliminary phases of the investigation. The stroboscope can be seen in the lower right corner of figure 12.

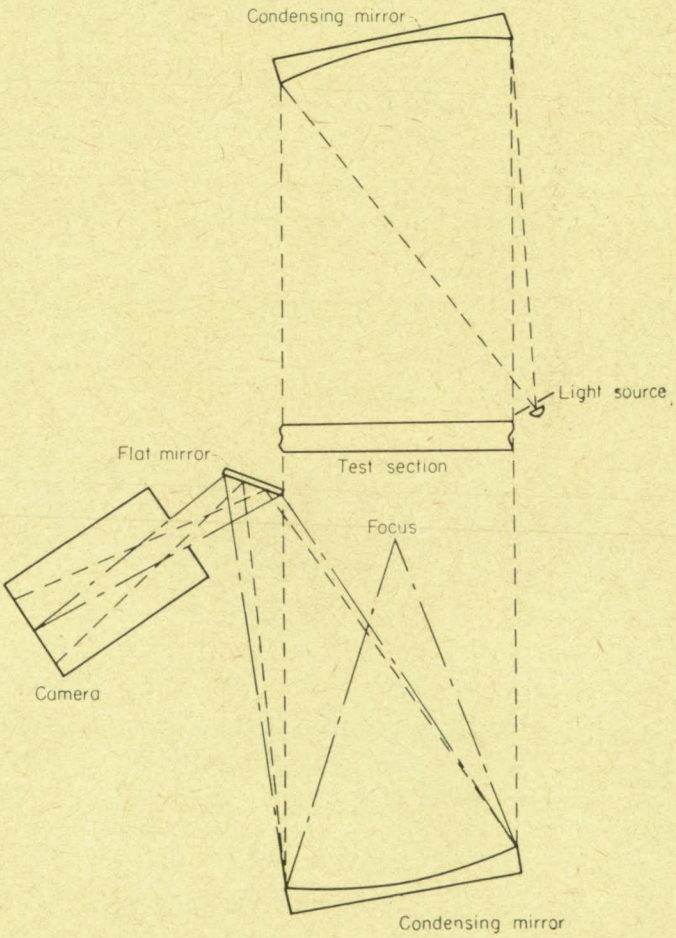


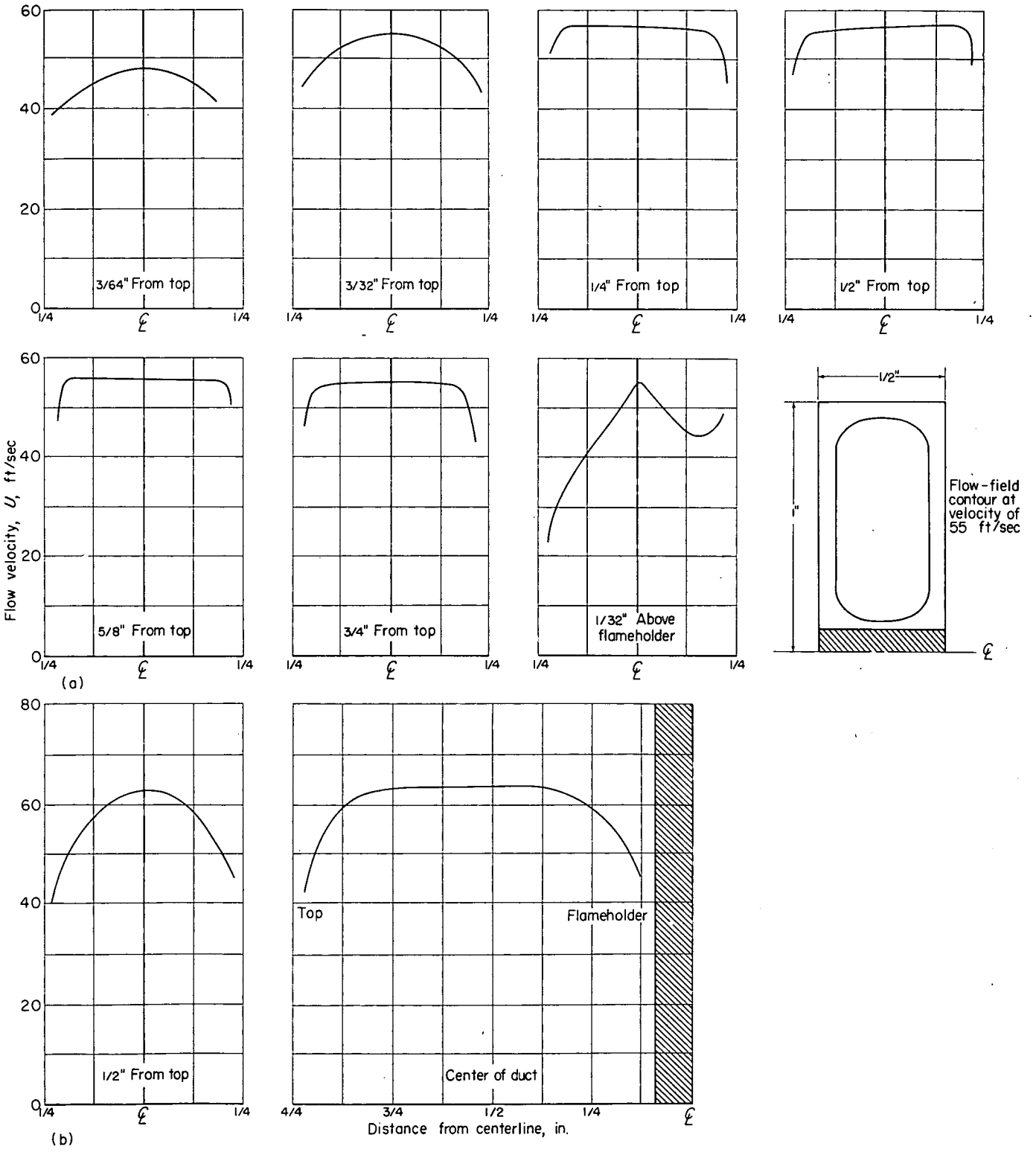
FIGURE 16.—Schematic drawing of shadowgraph apparatus.

PROPERTIES OF SYSTEM

Velocity profiles upstream of flameholder.—Velocity profiles measured 3 and 12 inches downstream of the nozzle are shown in figure 17. The flameholder was positioned so that each measurement was taken upstream of the gutter. Measurements were also taken at the plane of the nozzle, and no variation greater than ½ foot per second from 55 feet per second was found. These measurements are for a nominal flow setting of 50 feet per second.

Flame photographs and flame-speed measurements were made at nominal velocities of 50 and 100 feet per second in ½- and 1-inch-wide test sections; the profiles of figure 17 therefore represent the highest percentage of boundary layer encountered.

Velocity profile in wake; no flame.—Velocity profiles in the wake of a 0.306-inch-wide, 60° gutter at a nominal



(a) Profiles 3 inches downstream of nozzle.
(b) Profiles 12 inches downstream of nozzle.

FIGURE 17.—Time-averaged velocity profiles with cold flow. Nominal velocity, 50 feet per second.

velocity of 46 feet per second are shown in figure 18. This set of profiles shows a comparison of the spreading of a wake with and without an antisymmetric disturbance at 200 cycles per second. The only amplitude measurement available for this disturbance is a root-mean-square u' of 5 feet per second, measured ⅛ inch above the lip of the flameholder.

The effect of other frequencies on wake spreading was examined by placing total-pressure tubes 3 inches downstream of the flameholder at the center of the wake and varying the frequencies. The results are interpreted in the following manner. The velocity is read while disturbances are being introduced. The distance from the wake at which this velocity is attained without the sound (say x) is found. An index of the lengths required to accomplish equal degrees of mixing without and with the disturbance is then the ratio $x/3$. This ratio is plotted against frequency in figure 19.

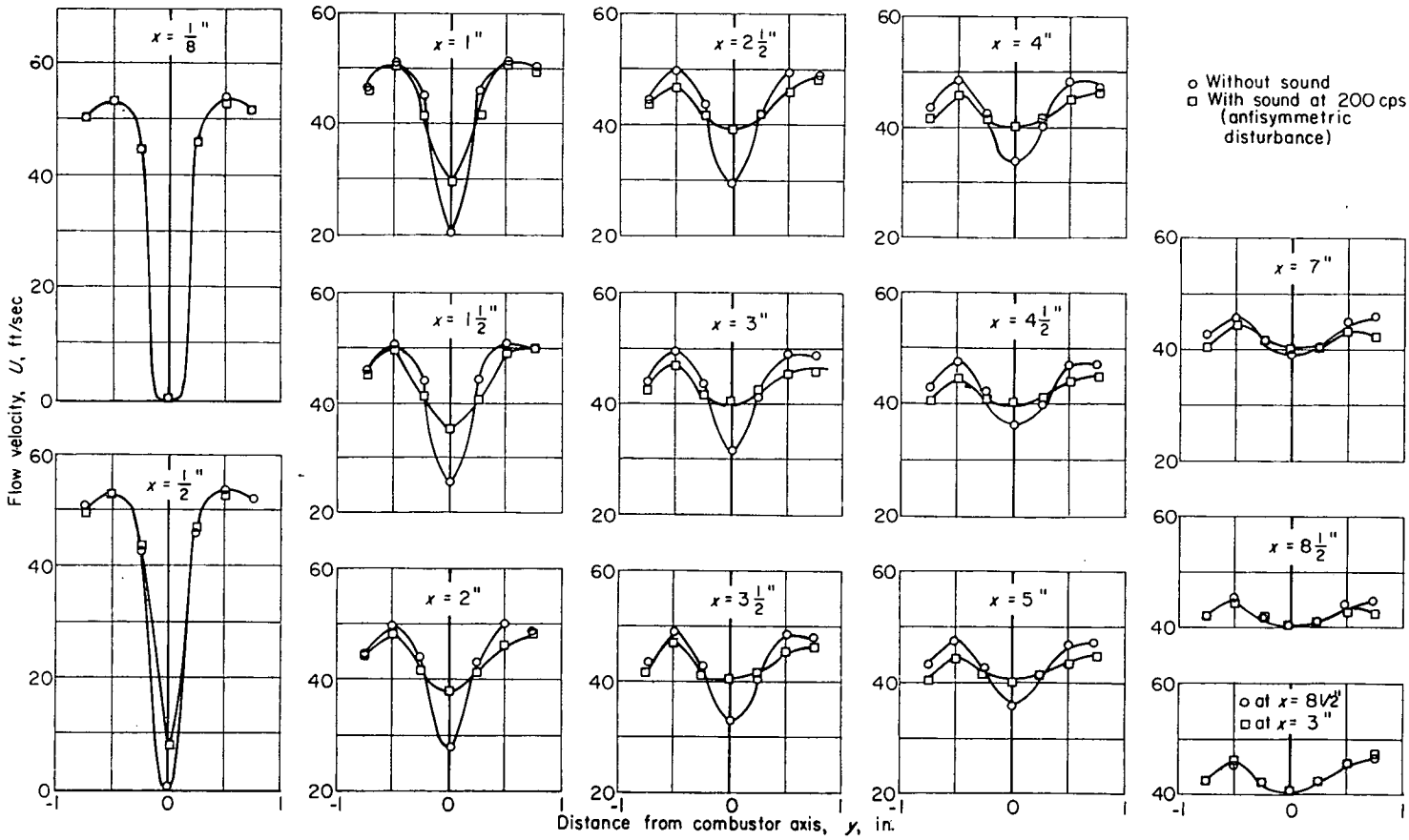


FIGURE 18.—Velocity profiles in wake of 0.306-inch flameholder.

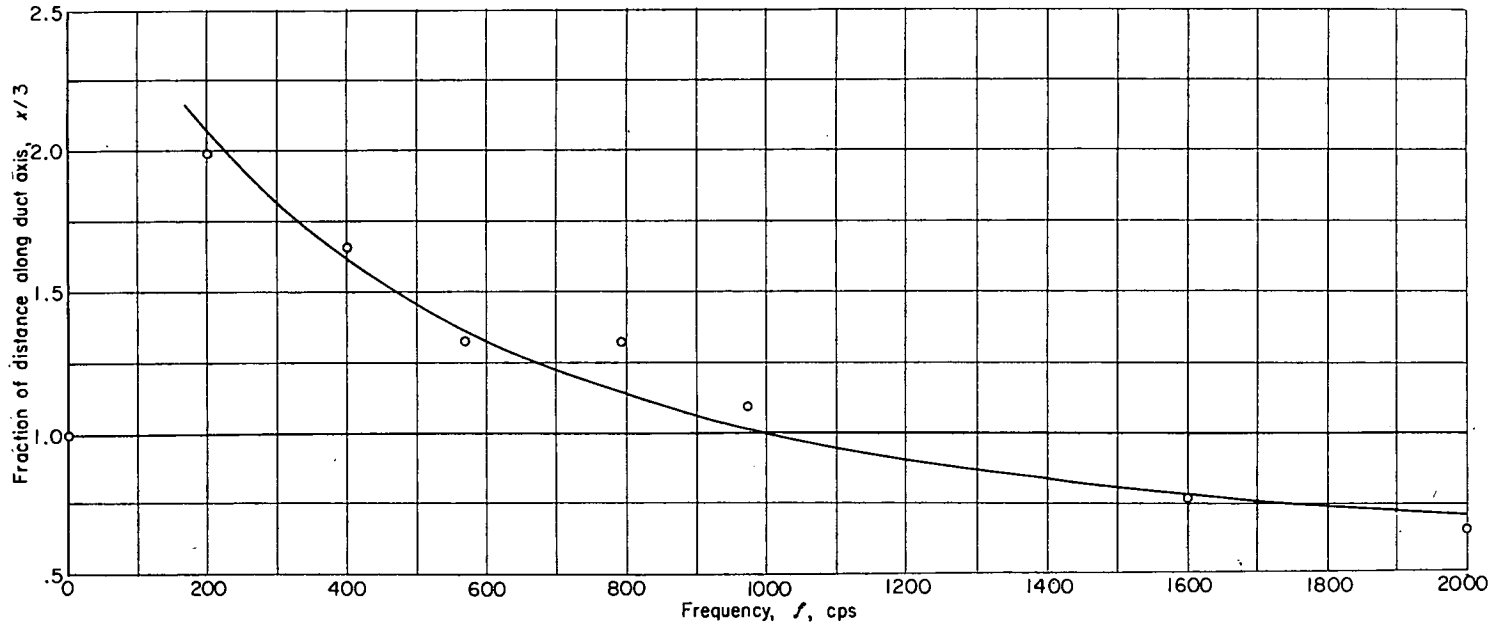


FIGURE 19.—Axial length required to achieve mixing to arbitrary extent.

The fact that the apparent diffusion rate decreased at frequencies greater than 1000 cycles per second indicated a decrease in form drag for frequencies greater than 1000 cycles per second. Static measurements at the base of the gutter showed no change in base pressure for the higher-frequency disturbances. Those lower frequencies that increased mixing also decreased base pressure (i. e., increased form drag). This probably means that the velocity is increased in the wake for frequencies less than 1000 cycles per second. There seems little hope, however, of reducing flameholder drag by imposing high-frequency disturbances of this kind.

Turbulence intensity and spectra.—The turbulence component u' in the direction of flow was measured with 0.0002- by 0.08-inch tungsten wires, using the NACA constant-temperature anemometer amplifier. The wire was oriented parallel to the flameholder tips. No flame was present for these measurements. The results are presented in the following table:

Distance from nozzle lip, x, in.	Nominal velocity, U, ft/sec	Distance from top wall, y, in. [a]	Vertical distance from station, in.	Turbulence component, u', ft/sec	Scale of turbulence, L, in.
0	50	½	¼	0.306	----------
	100	½	¼	.420	----------
6	50	⅛	¼	1.38	0.2
		⅛	⅛	1.68	----------
		¼	¼	.818	.15
		¼	⅛	.978	----------
		½	¼	1.021	.15
		¾	¼	3.35	.17
	100	⅛	¼	2.44	----------

[a] At $x=0$, y measured from centerline; at $x=6$, y measured from flameholder lip.

The spectra measured at several stations were compared with spectra found representative for isotropic turbulence (refs. 33 and 34). A typical plot is shown in figure 20. The scale L is estimated as the one whose spectrum most nearly corresponds to the measured spectrum (refs. 33 and 34). This scale [3] where determined is given in the preceding table.

The apparent transition from laminar to turbulent flow in the boundary layer on the flameholder surface occurred if the flameholder was about 1 inch or more from the test-section nozzle; the disturbance velocity in the boundary was roughly that in the nozzle itself. With the flameholder within 1 inch of the nozzle, eddies were shed at 420 cycles per second when no flame was present. With the flameholder 1 inch or more from the nozzle, transition occurred upstream of the flameholder lip, and no clearly defined eddy-shedding frequency was found in the wake.

With a flame anchored on the flameholder, no eddy shedding was observed without external excitation. The flame appeared turbulent for flameholder positions greater and less than 1 inch from the nozzle. Therefore, the transition

[3] This is the scale that would be used for calculating a turbulent burning velocity from existing theory (ref. 8). It is of interest herein because of the scale of disturbance the flame amplifies: $L \approx 1$.

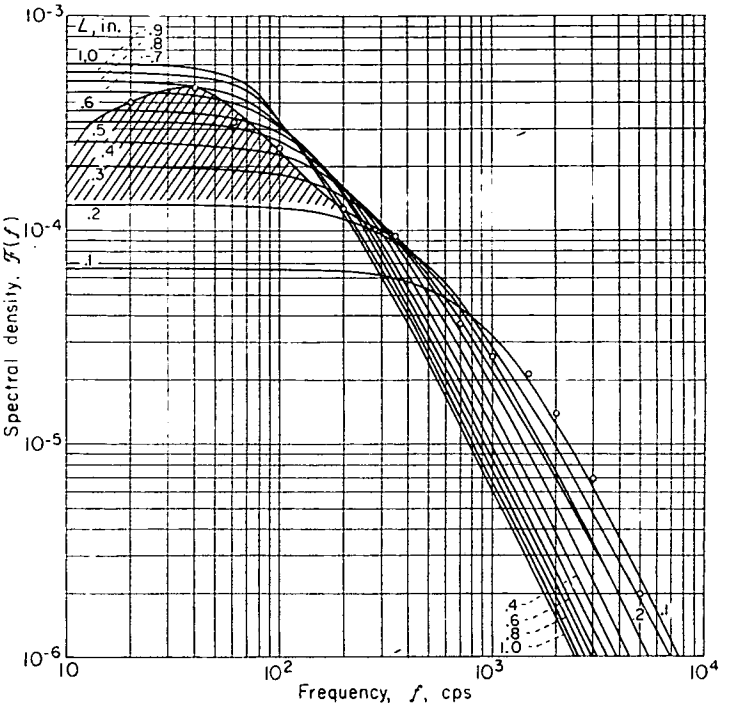


FIGURE 20.—Turbulence spectra for flow velocity of 50 feet per second; $\mathcal{F}(f)=(4L/U)/\{1+[(2\pi/U)L]^2f^2\}$, measured ⅛ inch above flameholder lip.

to turbulence in the separated boundary evidently affects the turbulent flame appearance in about the same manner as transition in the attached boundary layer. The lean-blowout fuel-air ratio was adversely affected when the transition was moved from the attached to the free boundary layer.

In an effort to obtain a laminar flame zone, some exploratory work was done to move the transition point farther downstream of the point of separation from the flameholder. Small unheated cylindrical rods (as in ref. 3) placed about 1 inch from the nozzle entrance were used as flameholders. It was possible to move the transition point about 1 inch downstream of the flameholder (at 50 ft/sec). Lean blowout, however, was moved to a fuel-air ratio so rich that excessive heating occurred in the glass walls, which impaired the use of the shadowgraph system. In the transient period immediately after ignition while the walls were still cool, a clear picture of the flame could be observed. Studying the flame for a length of time was not possible with this arrangement. Therefore, turbulent transition at or upstream of the flameholder lip was accepted.

CALIBRATION OF DISTURBANCE AMPLITUDE WITH SPEAKER INPUT

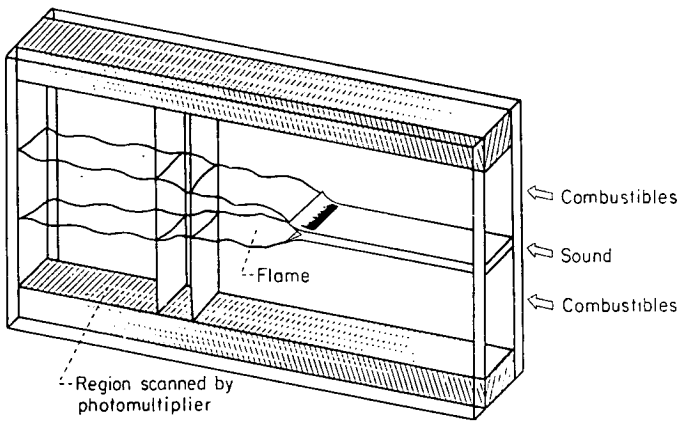
Because of the interaction between the standing-wave tube supplying the sound to the flameholder and the standing waves in the test section, it was necessary to calibrate the sound input with the flameholder at the position and velocity to be used in the burning tests. For most runs the flameholder was placed midway between acoustically open ends in the test section in order to suppress velocity disturbances at the flameholder due to all even modes of vibration of the test section.

The inputs were set in the following manner: The flameholder position and flow velocity to be used in a burning run were set. The hot wire was placed 1/8 inch above and 1/8 inch upstream of the flameholder lip, to center it over the port from which the sound issued. Resonant frequencies were excited in the flameholder support tube. The input to the speaker required to give the desired u' at the wire was recorded for each frequency. The wire was removed, fuel was introduced and ignited, and the burning run was made. The distribution of v' resulting from this sort of excitation was not explored. The change in the nature of interaction between test sections and the standing-wave tube with and without combustion was not explored but was presumed to be small, since only about 30 percent of the combustible mixture was burned in the test section.

RATIO OF TURBULENT TO LAMINAR FLAME SPEED DETERMINED BY PHOTOMULTIPLIER PROBE

Photomultiplier tubes have been used to sense transient area changes in a laminar flame distorted by sound (refs. 35 and 36) and to study Bunsen flames that were alternately laminar and turbulent by comparing the average intensity of light emitted from the flame (ref. 32). Turbulent and laminar flames having identical mixture ratios and feed rates produced identical quantities of light (ref. 32). Therefore, it appears that the photomultiplier tube, if used with caution, can become an average-heat-release-rate meter.

In the following discussion, the local heat-release rate is characterized by the ratio of turbulent to laminar flame speed V_T/V_L. This ratio is defined as the heat released per unit time divided by the heat that a pair of laminar flames alined with the axis of the duct would release per unit length per unit time. The relation is illustrated by considering the way the quantities are measured:



Sketch (k)

In the test section shown in sketch (k), flame fronts are anchored on the top and bottom of the flameholder and appear to span from wall to wall. The photomultiplier scans a narrow region of the test section. The voltages read from the photomultiplier-tube output are recorded at the same fuel-air ratio for a turbulent flame and for a laminar flame. The flame-front half-angle is measured, and each voltage is multiplied by the cosine of the half-angle. The ratio of the resulting product for the turbulent flame to that for the laminar flame is defined as V_T/V_L. In the region of interest, the cosine of the half-angle was approximately 1 for the turbulent flames, so that, in effect, the unit length of the flame fronts becomes the unit length of the combustor.

In obtaining the laminar flame, the same fuel and air rotameter settings were used as for the turbulent flame, but a large fraction of the mixture was bled off upstream of the flameholder. Three banks of 200-mesh screen were installed just upstream of the flameholder, and the resulting flame appeared laminar. The flame did not span from wall to wall near the flameholder; therefore, the voltage recorded for this region was quite low. Far downstream of the flameholder the flame front became twisted so that it represented a flame depth greater than the wall-to-wall depth. In between these two regions was one in which the flame appeared to touch the walls and to have negligible twist. The voltage recorded by the photomultiplier probe as it scanned this region was nearly constant. The extreme voltages recorded in this region envelop a band within which the true voltage corresponding to a pair of laminar flames was thought to lie.

In order to pinpoint an exact value for the laminar voltage as well as to verify the method (the zone of uncertainty is quite small), an auxiliary determination of V_T/V_L was made. Photomultiplier-probe voltages were read at seven equally spaced stations along the combustor from flameholder to exhaust nozzle, and an average voltage was calculated. Simultaneously, the momentum pressure drop across the flame zone was measured. With the help of Scurlock's results (ref. 1), the fraction of combustible burned F was determined from the measured momentum pressure drop. Then an average V_T was calculated from

$$F=\frac{(\text{Length})\ (2)\ (V_T)\ (\text{depth})}{(U_o)\ (\text{depth})\ (\text{height})}$$

where length, depth, and height are the dimensions of the combustor. With this V_T, the measured average voltage, and the value for laminar flame speed V_L taken from reference 37, voltage corresponding to a laminar flame was obtained from

$$\frac{E_L}{V_L}=\frac{E_T}{V_T}$$

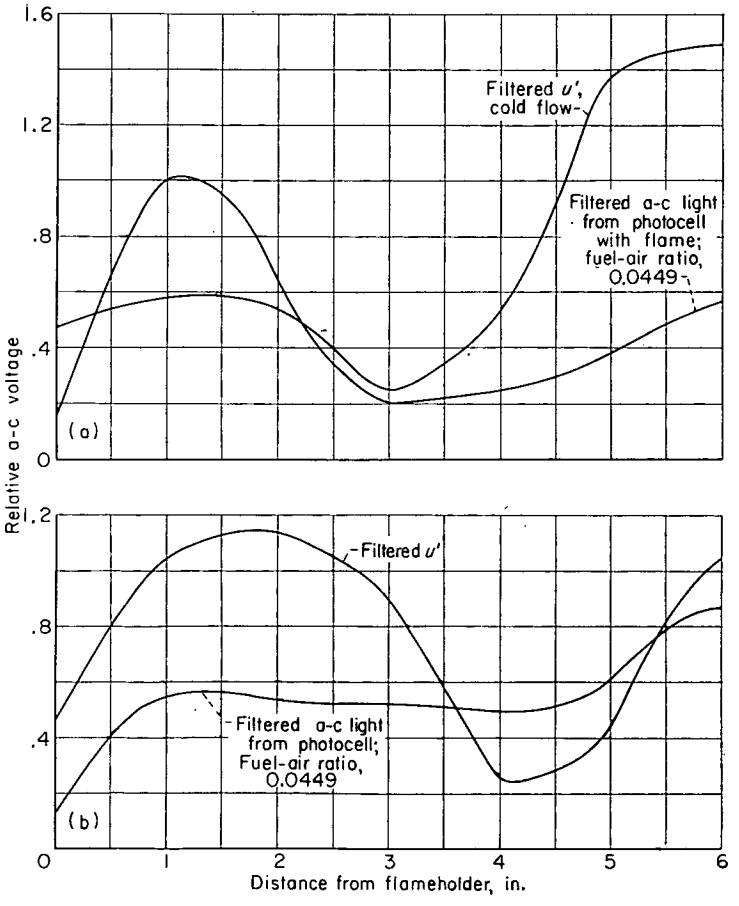
where E_L and E_T are the photomultiplier voltages for laminar and turbulent flames. This voltage lies within the zone of uncertainty found by direct viewing of the laminar flame. These results are reported more fully in the section Examination of Method.

The fact that reference 32 was cited does not mean that any photomultiplier calibration was obtained from that work. Reference 32 established that (for a given combustor at a given composition and flow rate) a photomultiplier voltage is proportional to the heat released within sight of the photomultiplier tube and is independent of the existence or nonexistence of turbulence. The agreement of the two methods

for determining V_T/V_L justifies this use of the photomultiplier probe.

It was hoped initially to follow the amplitude of a flame wrinkle by measuring the a-c component of the photomultiplier signal. The reasoning was that the flame would be wrinkled sufficiently for its local instantaneous slope to serve as a detectable index of flame-wrinkle amplitude. This slope, of course, would appear as an increased voltage at the photomultiplier because the length of the flame cutting across the field of view would be increased. The data showed an amplitude more dependent on the distance from the duct exhaust than on the distance from the flameholder. The sound waves introduced as the source of excitation at the flameholder reflected from the exhaust of the combustor. Therefore, the a-c component read by the probe was largely influenced by the time-varying displacement of local flame zones due to plane waves of sound. The filter a-c signals for two frequencies as a function of distance from the flameholder are compared in figure 21. One set was obtained from the photomultiplier probe with burning, the other set from a hot-wire anemometer without burning.

The photomultiplier probe was used only to survey for the



(a) Frequency, 570 cps.
(b) Frequency, 1500 cps.

FIGURE 21.—Comparison of hot-wire and photomultiplier measurements showing effect of plane waves near exhaust of duct. Flow velocity, 50 feet per second.

effect of disturbances on local V_T/V_L values on a time-average basis.

RESULTS

The analytical part of this paper suggests certain beha ior that can be examined experimentally. Accordingly, tests are included that furnish the necessary data for a comparison with the results of the analysis. One of the primary variables studied was the effect of the frequency of excitation on disturbance growth. The frequency range of interest happened to include some of the resonant frequencies of the combustion-gas volume as well as the spontaneous eddy-shedding frequency of the flameholder in cold flow. The effect of combustor resonance or spontaneous eddy-shedding was also examined.

Certain precautionary measures were taken in choosing geometry and operating conditions. To guard against burner resonance, the combustor was kept short, so that only about 30 percent of the combustible was consumed. Spontaneous burner resonance sometimes occurred when this value was exceeded. The conditions were kept within the Reynolds number reported in reference 1 to be free of spontaneous eddy-shedding when a flame is anchored on the flameholder. Although these measures precluded the occurrence of spontaneous oscillations due to these two causes, they could not prevent the system from favoring certain frequencies within the range of interest. These influences, then, received special attention.

Markstein has shown that instabilities of a laminar flame front cause the front to assume a cellular structure under certain conditions (ref. 4). The occurrence of such cells clearly could confuse an interpretation of the results. Consequently, the data were taken solely at conditions where the cells do not spontaneously arise.

EXAMINATION OF METHOD

With the flameholder 6 inches from the open end of the duct and 6 inches from the tunnel entrance, runs were made at three fuel-air ratios at 50 feet per second over a range of disturbance frequencies. The 0.306-inch-wide gutter with antisymmetric disturbances was used. The change in impact pressure with and without combustion was measured by a single impact tube upstream of the flameholder. Since the difference is of the order of inches of water and the rate of mass flow is constant, it is assumed that the difference is entirely due to a change in static pressure. The fraction burned was calculated from Scurlock's results (ref. 1) and the measured pressure drop. Concurrently, the light intensity at seven stations along the flame was measured and averaged.

The fraction burned is compared with the average voltage (which is proportional to the average intensity) in figure 22 by plotting both against the frequency of disturbance for the three fuel-air ratios examined. The following table indicates the amount of scatter in the ratio of fraction burned to mean voltage:

Fuel-air ratio	F/E_T for frequency, f, cps, of—					Average F/E_T
	0	380	470	760	1500	
0.0444	0.137	0.131	0.134	0.137	0.131	0.134
.0515	.1017	.1070	.1055	.1063	.1035	.105
.0580	.0818	.0817	.0863	.0858	.0852	.084

From the relation

$$\frac{F}{E_T}=\frac{2V_T\times\text{length}\times\text{depth}}{U_o\times\text{height}\times\text{depth}\times E_T}$$

(where length, height, and depth are dimensions of the combustor), an average value of V_T/E_T is calculated. From the average values in the preceding table for F/E_T at each fuel-air ratio, the following values of V_T/E_T were obtained:

Fuel-air ratio	V_T/E_T, (ft/sec)/volt
0.0444	1.115
.0515	.880
.0580	.709

For these fuel-air ratios and the inlet temperature and pressure used, a laminar flame speed was obtained from reference 37. Then the voltage that would correspond to a laminar flame was calculated from

$$E_L=\frac{V_L}{V_T/E_T}$$

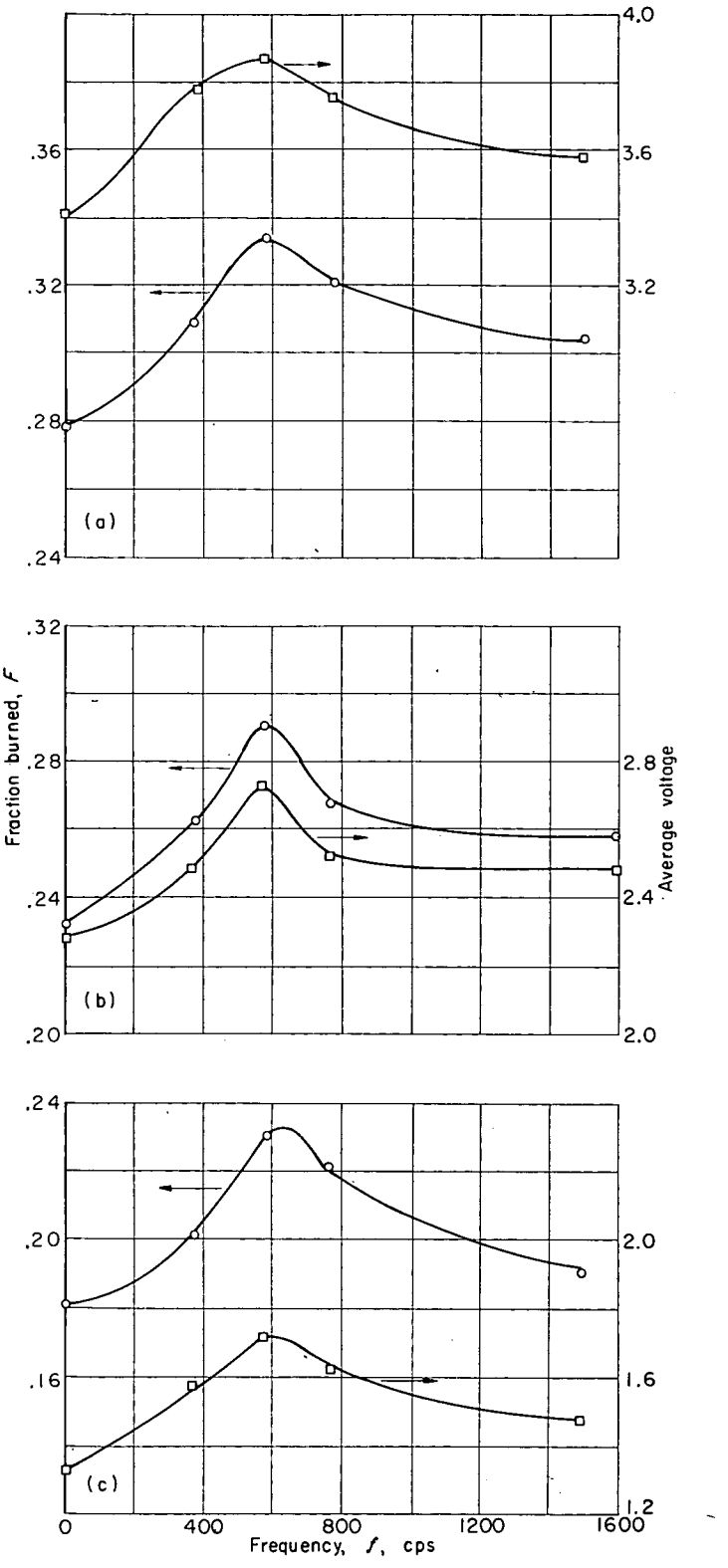
The values of V_L from reference 37, the value of E_L calculated from the preceding relation, and the zone of E_L measured directly by viewing a pair of laminar flames in the test section are as follows:

Fuel-air ratio	V_L (ref. 37)	$E_L=\frac{V_L}{V_T/E_T}$	E_L by direct measurement
0.0444	0.74	0.663	0.658 to 0.682
.0515	1.10	1.25	1.15 to 1.39
.0580	1.32	1.852	----------

The E_L taken from values of $V_L/(V_T/E_T)$ that resulted from momentum-pressure-drop measurements fall within the limits of E_L by direct measurement and are used as the calibration of the photomultiplier probe. Local values of V_T/V_L reported subsequently are defined by the ratio of voltage read at that station to this E_L for the applicable fuel-air ratio.

COMPARISON OF FLAME SPEED WITH FLAME APPEARANCE

Shadowgraphs were taken at the same conditions used in the preceding comparison between average voltage and Δp. Some of these shadowgraphs, along with the distribution of



(a) Fuel-air ratio, 0.0580.
(b) Fuel-air ratio, 0.0515.
(c) Fuel-air ratio, 0.0444.

FIGURE 22.—Comparison of fraction burned obtained by momentum-pressure-drop measurement with average voltage obtained by photomultiplier survey. Flow velocity, 50 feet per second; length, 6 inches; disturbance velocity, 2.38 feet per second; antisymmetric disturbance.

V_T/V_L for each, are presented in figure 23. In most of these photographs the gross disturbance caused by the input sound can be identified. If a line drawn along the turbulent flame front is faired through all but these gross wrinkles, its length divided by the length of a line faired along the undisturbed surface should be equal to

$$\left(\frac{S_d}{S_u}\right)_{pg} \equiv \frac{\text{Area of flame disturbed at frequency } f}{\text{Area of undisturbed flame surface}}$$

A similar ratio is available from the average voltages obtained by the photomultiplier survey in figure 22, defined by

$$\left(\frac{S_d}{S_u}\right)_{pm} = \frac{(E_T)_d}{(E_T)_u}$$

The $(S_d/S_u)_{pg}$ obtained by the former method and the $(S_d/S_u)_{pm}$ obtained from the photomultiplier readings are compared in the following table:

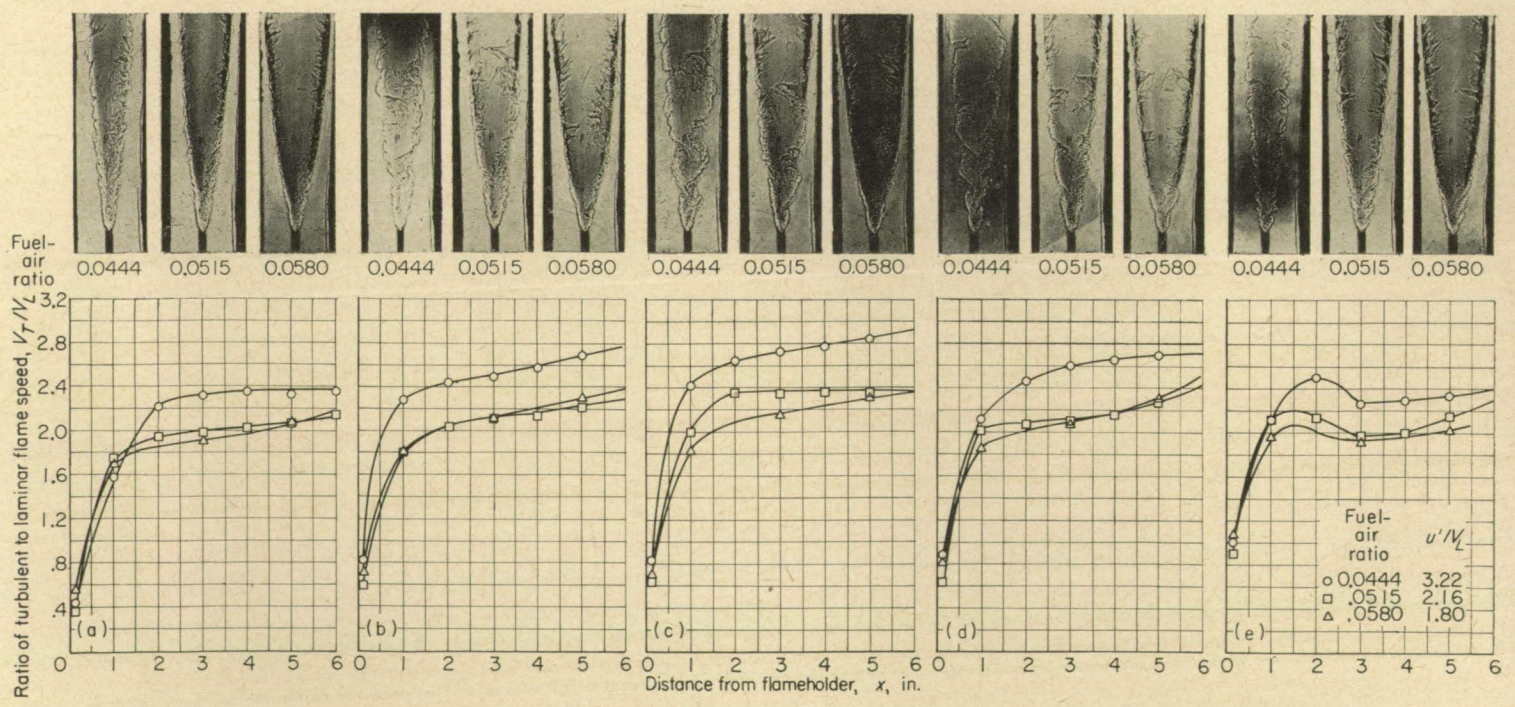
Frequency, f, cps	Fuel-air ratio			
	0.0444		0.0515	
	$\left(\frac{S_d}{S_u}\right)_{pm}$	$\left(\frac{S_d}{S_u}\right)_{pg}$	$\left(\frac{S_d}{S_u}\right)_{pm}$	$\left(\frac{S_d}{S_u}\right)_{pg}$
0	1	1	1	1
380	.18	1.15	1.09	1.11
570	1.304	1.185	1.19	1.12
770	1.23	1.23	1.10	1.18
1500	1.10	1.085	1.09	1.07

In general, the correlation is good. It may be significant that, at 570 cps, $(S_d/S_u)_{pm}$ is about 10 percent greater than $(S_d/S_u)_{pg}$. At this frequency, it is relatively easy to measure the area; that is, experimental scatter should not be as great as 10 percent. The evidence suggests the generation of additional turbulence in the flame, other than the growth of the low-frequency-imposed disturbance. It is regrettable that a laminar stabilized flame could not be obtained in this equipment, because this frequency could conceivably cause a transition point from laminar to turbulent flow.

For each plot in figure 23, u' is a constant, so that u'/V_L decreases with increasing fuel-air ratio. Also, V_T/V_L decreases, for the most part, with increasing fuel-air ratio and, therefore, with decreasing u'/V_L.

At a given distance x, the ratio $(S_d/S_u)_{pm}$ defined by $\frac{(V_T/V_L)_d}{(V_T/V_L)_u}$ descends with ascending fuel-air ratio. This is in keeping with the interpretation in the stability analysis. The following table gives the values of S_d/S_u at 570 cps for the three fuel-air ratios:

x, in.	Fuel-air ratio					
	0.0444		0.0515		0.0580	
	$\frac{S_d}{S_u}$	$\frac{u'}{V_{T,u}}$	$\frac{S_d}{S_u}$	$\frac{u'}{V_{T,u}}$	$\frac{S_d}{S_u}$	$\frac{u'}{V_{T,u}}$
1	1.522	2.025	1.129	1.220	1.076	1.055
2	1.183	1.437	1.205	1.107	1.122	.962
3	1.166	1.376	1.175	1.08	1.119	.937
4	1.177	1.358	1.151	1.058	1.147	.913
5	1.197	1.352	1.129	1.038	1.116	.873



(a) No disturbance.
(b) Antisymmetric disturbance at 380 cps.
(c) Antisymmetric disturbance at 570 cps.
(d) Antisymmetric disturbance at 760 cps.
(e) Antisymmetric disturbance at 1500 cps.

FIGURE 23.—Comparison of flame appearance and V_T/V_L for three fuel-air ratios for 0.306-inch flameholder. Flow velocity at plane of flameholder, 50 feet per second.

DISTRIBUTION OF LOCAL V_T/V_L VALUES WITH RESPECT TO VARIOUS FREQUENCIES

The ratio of turbulent to laminar flame speed V_T/V_L is plotted against distance from the flameholder in figure 24(a), and V_T/V_L is cross-plotted against frequency at several stations in figure 24(b). Great care was taken in keeping fuel-air ratio, velocity, and plate voltage to the photocell constant throughout the run. The 0.306-inch flameholder, modified to prevent leakage about the edges, was used. The disturbance velocity measured as described earlier gave u' of 2.16 feet per second for all frequencies.

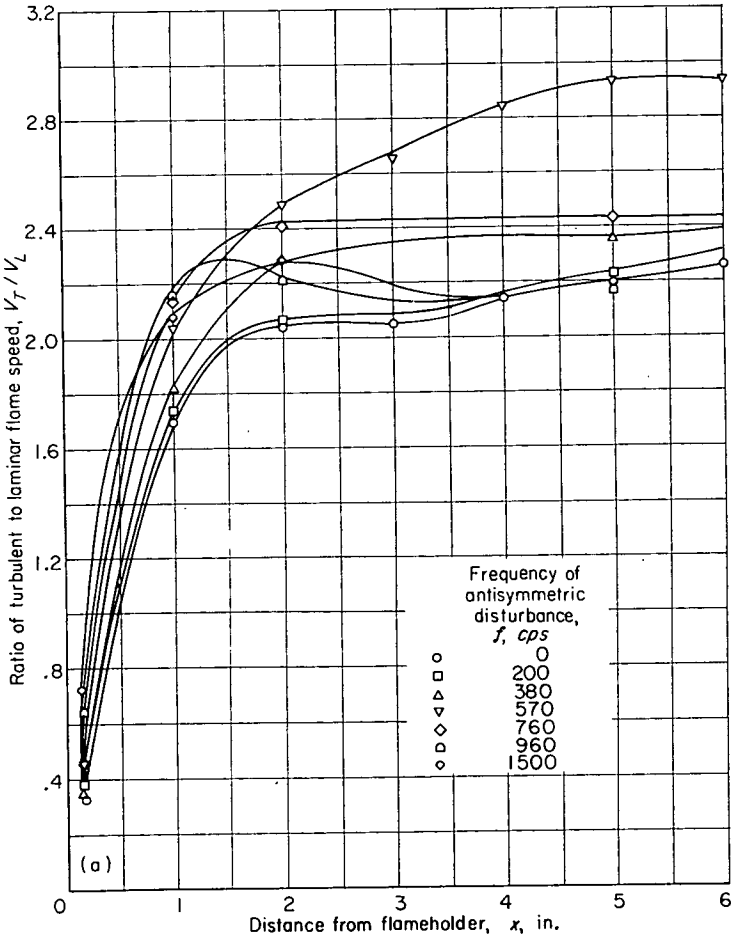
In order to compare these data with theory, the following computations were made:

(1) From the preceding calibration the fraction burned was calculated as a function of combustor length for the upper envelope of the V_T/V_L curves for the disturbed flames.

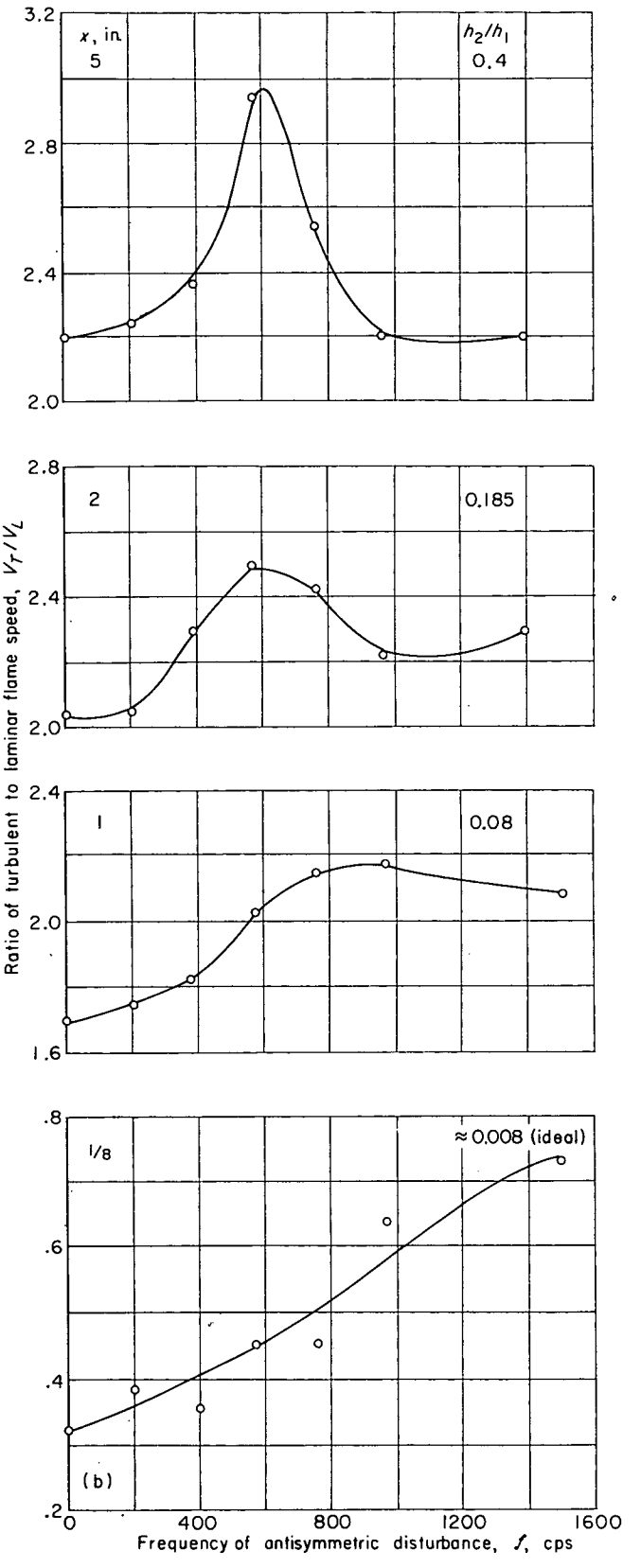
(2) An idealized h_2/h_1 against length was obtained from this fraction burned using Scurlock's results (ref. 1).

(3) Increments of length over which a given frequency has a maximum V_T/V_L were read from figure 24(a).

(4) These increments were plotted against h_2/h_1 and compared with the theoretical plot taken from figure 10. Recall



(a) Variation of flame-speed ratio with distance from flameholder. Test-section depth, ½ inch.



(b) Variation of flame-speed ratio with frequency for various distances from flameholder. Test-section depth, 1½ inches.

FIGURE 24.—Effect of antisymmetric-disturbance frequency on flame-speed distribution with 0.306-inch flameholder. Flow velocity, 50 feet per second; fuel-air ratio, 0.0444; disturbance velocity, 2.16 feet per second.

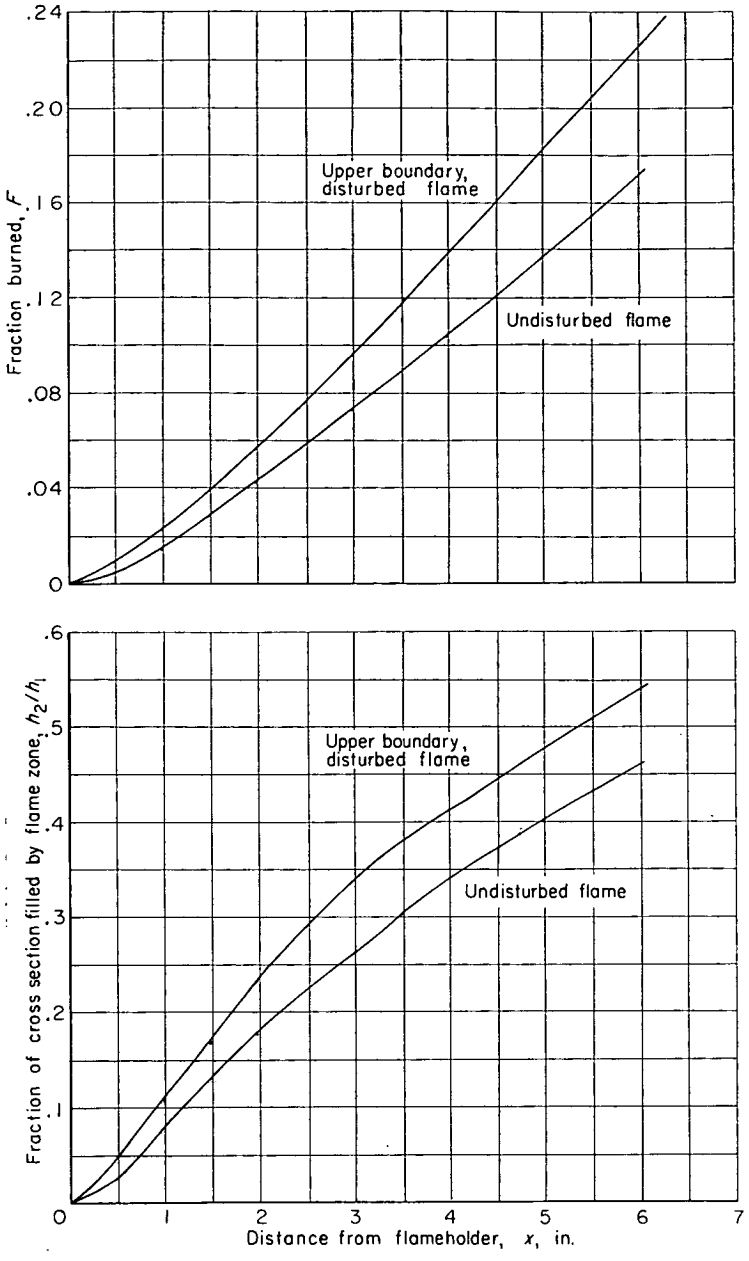


FIGURE 25.—Distribution of fraction burned and idealized h_2/h_1 for data of figure 24(a).

that $f=\frac{2\alpha_o h_1 U_o}{2\pi 2h_1}$. Results of steps (1) and (2) are shown in figure 25, and steps (3) and (4) in figure 26.

Similar data taken at the lower amplitude ($u'=1.44$ ft/sec) gave similar results.

DISTURBANCE-DISPLACEMENT GROWTH

In this section the actual disturbance-displacement growth is compared with that of qualitative theory (sketch (f)).

In an effort to produce low disturbance amplitudes, the glass walls of the test section were reduced to 6 inches in length and the flameholder was moved to ⅝ inch downstream of the nozzle entrance. At this position the speaker inputs were calibrated with the hot wire as previously discussed, and shadowgraphs were taken for several low amplitudes. As mentioned in the section on turbulence intensity and spectra, the flameholder boundary layer underwent

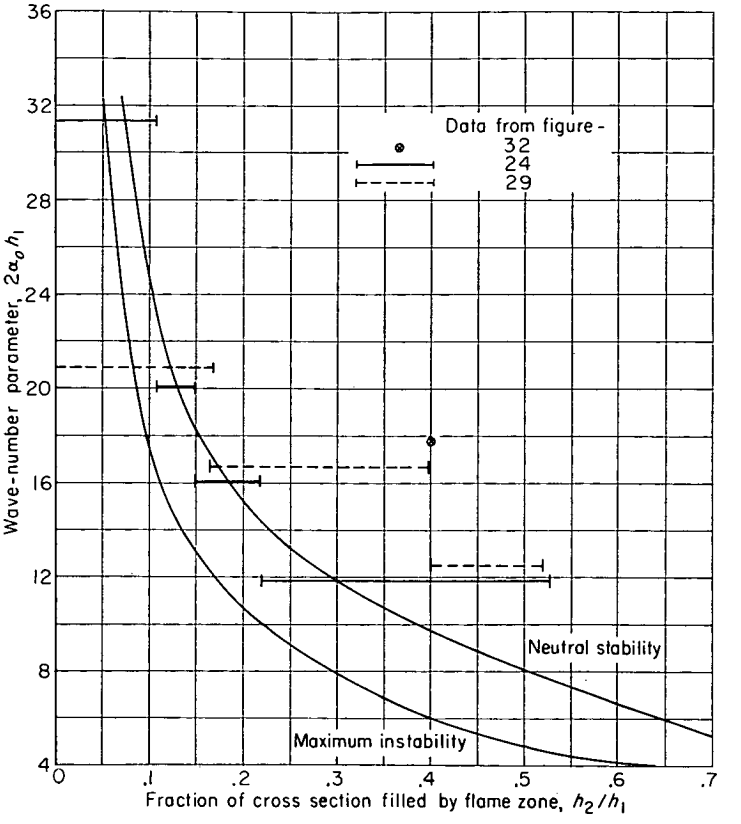


FIGURE 26.—Frequency giving maximum increase in flame speed as function of h_2/h_1 compared with results of stability analysis.

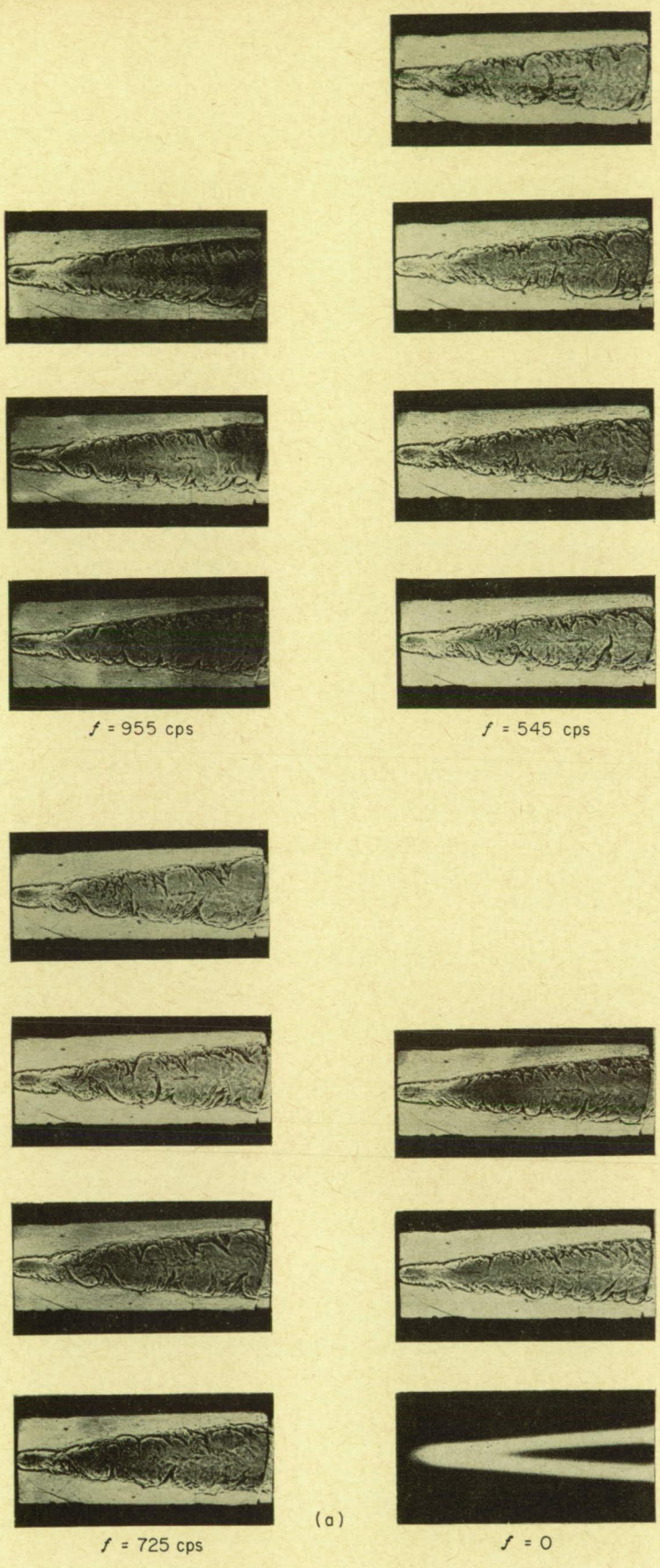
transition in the separated layer. The photographs of figure 27(a) show that, at these low intensities, the apparent width of the flame was not appreciably altered. The mean flame width measured from a direct photograph was used to determine h_2/h_1.

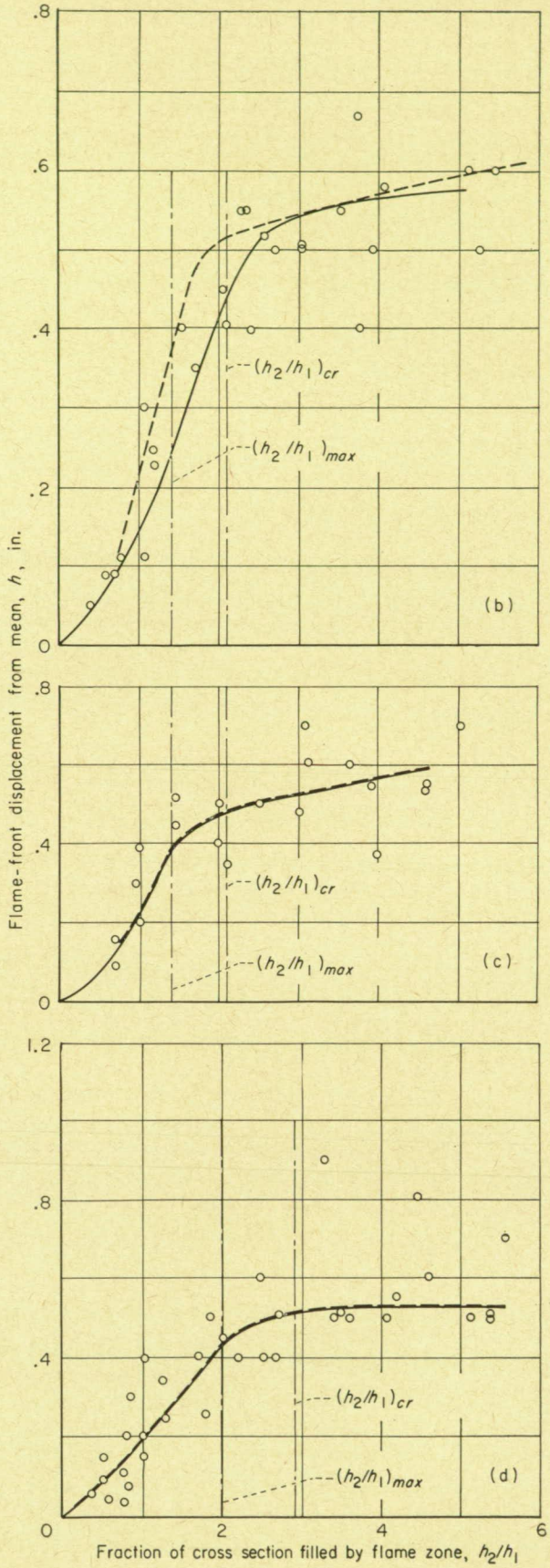
The displacement h was measured as the distance from surrounding crests to a given trough in the flame surface. Measurements were made on both sides of the flame for each photograph. The data for two amplitudes and two frequencies obtained in this manner are shown in figures 27(b) to (d). The dashed curve is the qualitative curve from sketch (f).

The knee should occur between $(h_2/h_1)_{max}$ and $(h_2/h_1)_{cr}$ as discussed in the section Relation of Theoretical Results to Measurable Quantities. The vertical lines in figure 27 are drawn through these two values. With the general shape of the qualitative curve known, it can be seen that a line faired through the data points would exhibit a knee in the region bounded by $(h_2/h_1)_{max}$ and $(h_2/h_1)_{cr}$. Comparison of figures 27(c) and (d) shows that the knee moves to increased values of h_2/h_1 as frequency is reduced. Both the value of h_2/h_1 where the knee occurs and the variation of this value with frequency agree with the results of the analysis.

DISTURBANCE PHASE VELOCITIES

From the photographs of figure 27(a), values of c_r/U_1 were determined, again using the mean flame width to furnish h_2/h_1. The quantity U_1/U_o was then determined from Tsien's results (eq. (3)). Wavelengths were measured from trough to trough, and the mean position of a pair of troughs located





(a) Flame shadowgraphs for disturbance velocity of 0.75 foot per second at various frequencies.

(b) Disturbance velocity, 0.60 foot per second; frequency, 725 cps.
(c) Disturbance velocity, 0.75 foot per second; frequency, 725 cps.
(d) Disturbance velocity, 0.75 foot per second; frequency, 545 cps.

FIGURE 27.—Displacement measure on flame front for small-amplitude disturbances. Flow velocity, 50 feet per second; fuel-air ratio, 0.0484; turbulent disturbance velocity, 0.303 foot per second.

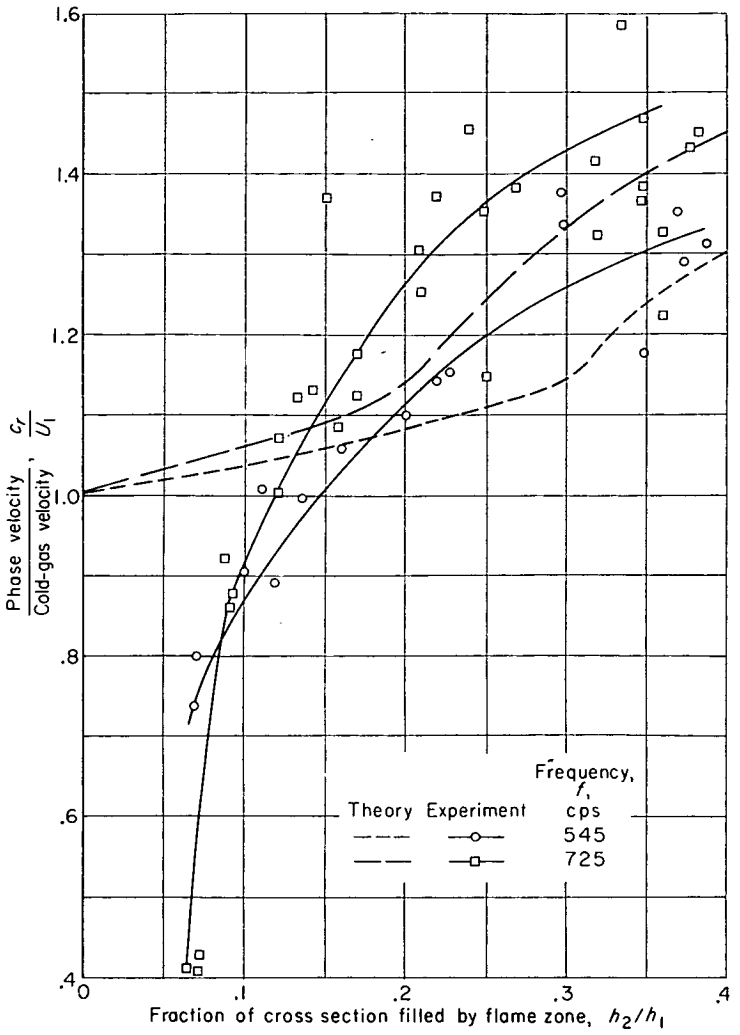


FIGURE 28.—Propagation velocities for small-amplitude disturbance.

the applicable value of h_2/h_1. The results are shown for two frequencies in figure 28.

The dashed lines are the values of c_r/U_1 obtained from figure 5(b), which is based on the results and interpretation of the stability analysis. The scatter of the experimental data is wide, but the magnitude and trends of the data remote from the flameholder are quite good. Values of c_r/U_1 less than unity are obtained for values of $h_2/h_1 < 1.5$, which implies flow reversal within this region.

EFFECT OF TEST-SECTION DEPTH

A single run was made to determine the effect of the test-section depth on the results. The data obtained with the 1-inch-deep combustor at a velocity of 50 feet per second and a fuel-air ratio of 0.0493 are shown in figure 29. The turbulence at the center of the duct was half that of the ½-inch duct. Combustor depth seems to have some influence on the turbulent flame speed but not on the effect of imposed disturbances.

The undisturbed flame speed in the 1-inch duct reached almost twice laminar flame speed in a longer time than in the ½-inch duct. The effect of imposed disturbance on amplification as a function of frequency remains the same,

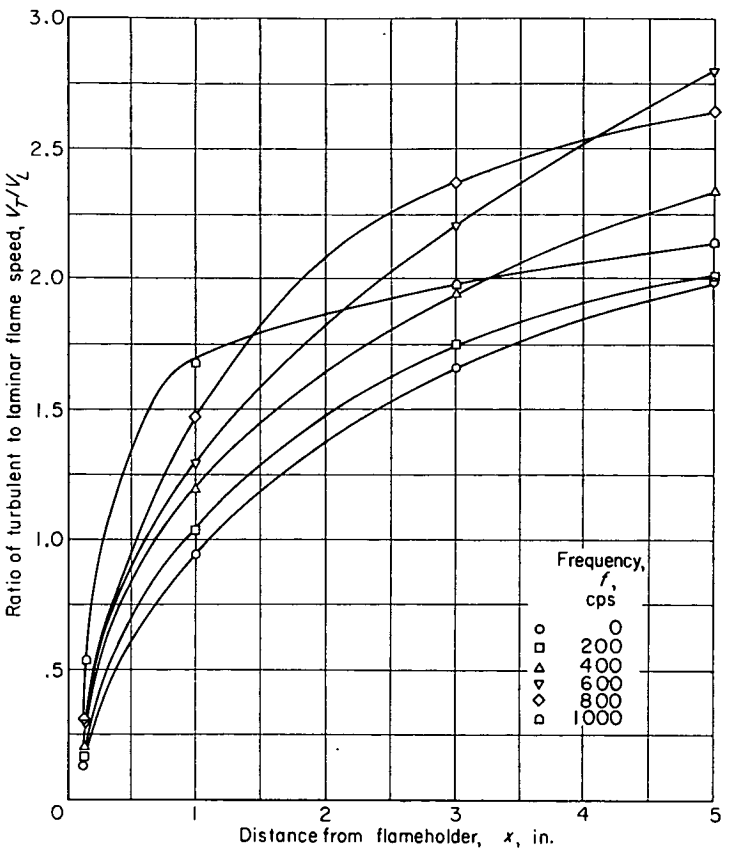


FIGURE 29.—Flame-speed distribution in 1-inch-deep test section. Flow velocity at plane of flameholder, 50 feet per second; fuel-air ratio, 0.0493; ¼-inch flameholder.

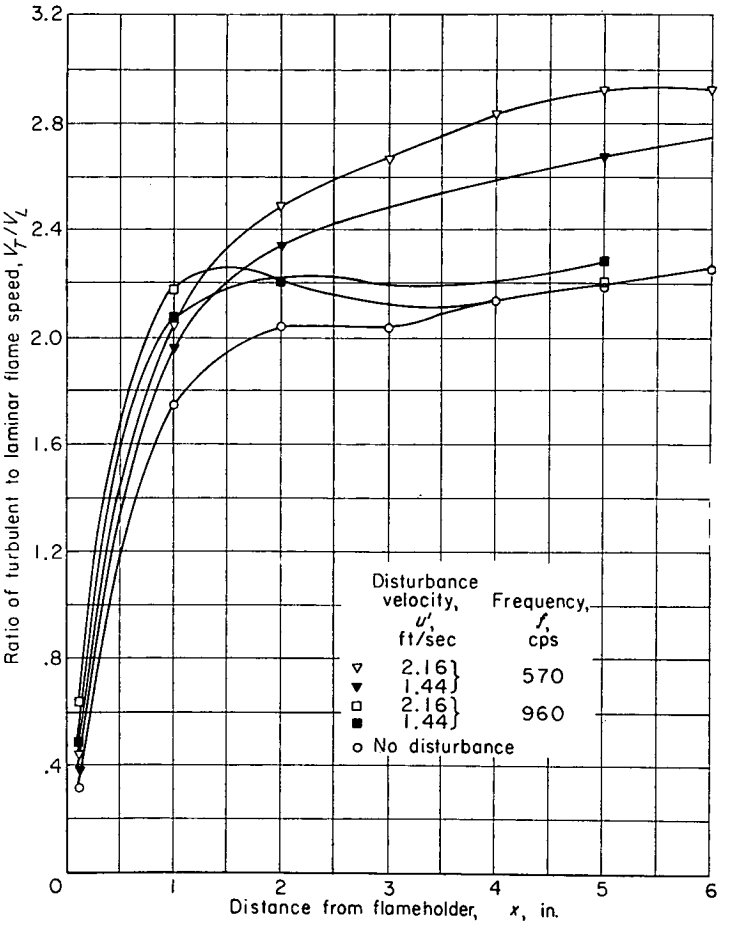


FIGURE 30.—Effect of amplitude on flame-speed distribution. Flow velocity, 50 feet per second; fuel-air ratio, 0.0444. ⟶

however. This can be seen from a comparison of figures 29 and 24(a). The range over which a given frequency dominates, taken from this run, is also plotted in figure 26.

EFFECT OF AMPLITUDE

The effect of amplitude on single frequencies is shown in figure 30, where flame speeds for two levels of excitation (570 and 960 cps) are compared. For the lower frequency, the increase $\Delta(V_{T,d}/V_{T,u})$ varies directly as u'. For the higher frequency, the curves cross. Thus, the effect of low excitation is felt farther along the flame than that of higher excitation. This behavior is not data scatter and was checked repeatedly. The same sort of thing occurs at 1500 cps, although not so markedly. The reason for this anomalous behavior is not immediately apparent.

EFFECT OF FLAMEHOLDER SIZE

Flame appearance and V_T/V_L are compared for two flameholder sizes at a velocity of 50 feet per second and a fuel-air ratio of 0.0444 in figure 31. The data for a ½-inch flameholder and a variety of excitation frequencies (fig. 31(a)) show that the 570-cps excitation is again the dominant one, but not so markedly as before. The effect of flameholder size can be summarized from figures 31(b) to (d) as follows:

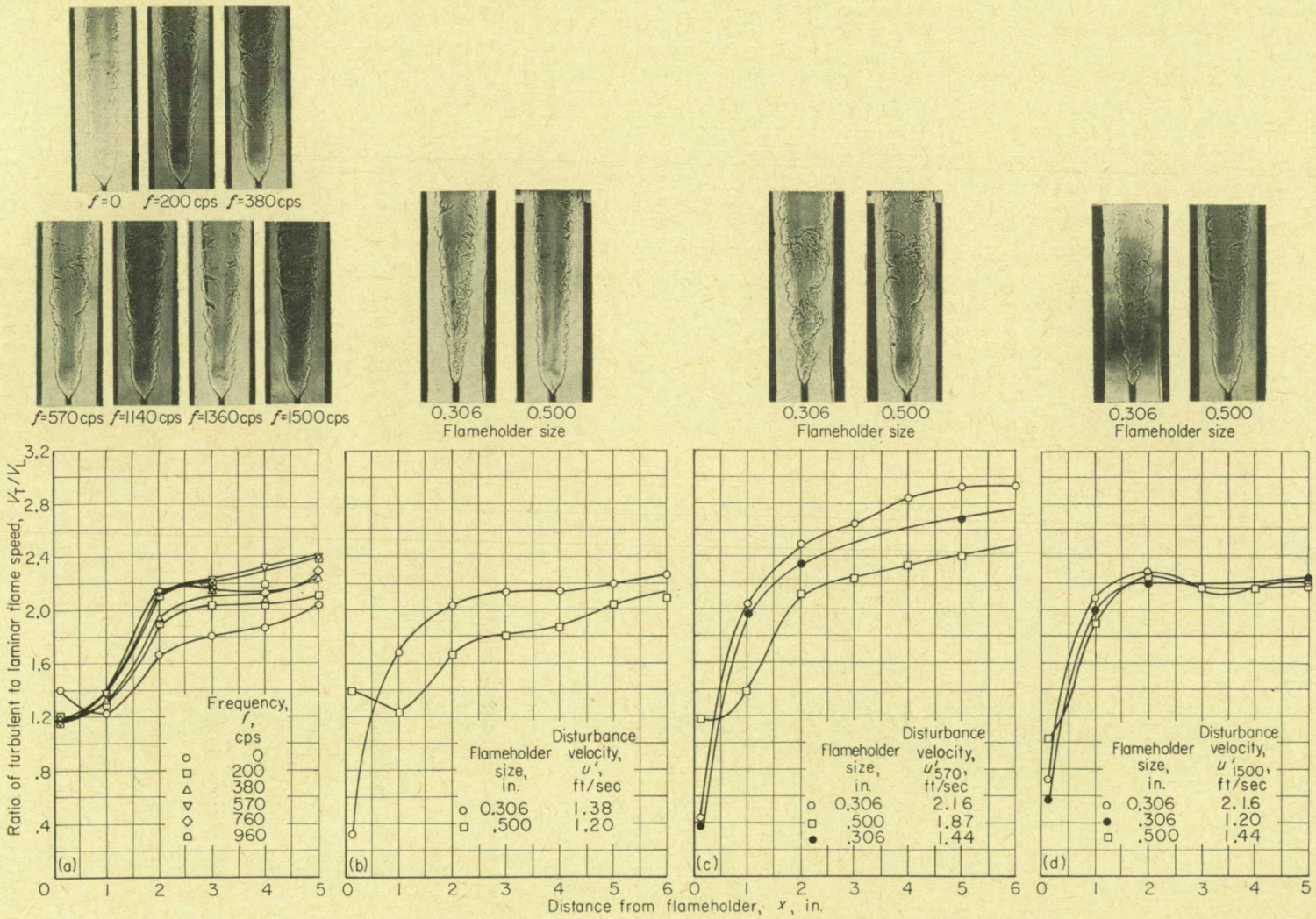
(1) Flame speed is noticeably decreased with the larger flameholder.

(2) The impact of the 570-cps frequency is not nearly so great in the ½-inch flameholder as in the 0.306-inch flameholder.

The decrease in flame speed with increase in flameholder size might be explained by the theory that (1) the wake region is longer and (2) the growth of the higher frequencies is therefore somewhat inhibited by this long, relatively stable wake.

EFFECT OF VELOCITY

Momentum-pressure-drop and flame-speed readings were taken over a range of frequencies, using a 0.306-inch flameholder, a velocity of 100 feet per second, and fuel-air



(a) ½-Inch flameholder with antisymmetric disturbances. Disturbance velocities, feet per second: u'_t, 2.22; u'_T, 1.2; and u'_f, 1.87.

(b) Both flameholders without disturbance.

(c) Both flameholders with disturbance at 570 cps.

(d) Both flameholders with disturbance at 1500 cps.

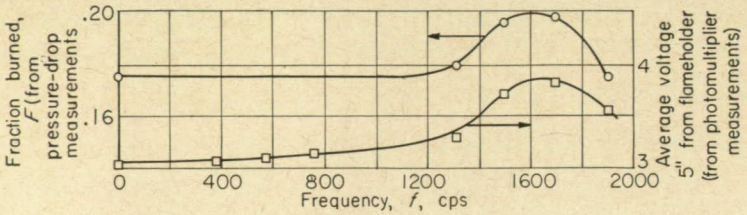
FIGURE 31.—Comparison of flame appearance and V_T/V_L for ½- and 0.306-inch flameholders. Flow velocity, 50 feet per second; fuel-air ratio, 0.0444.

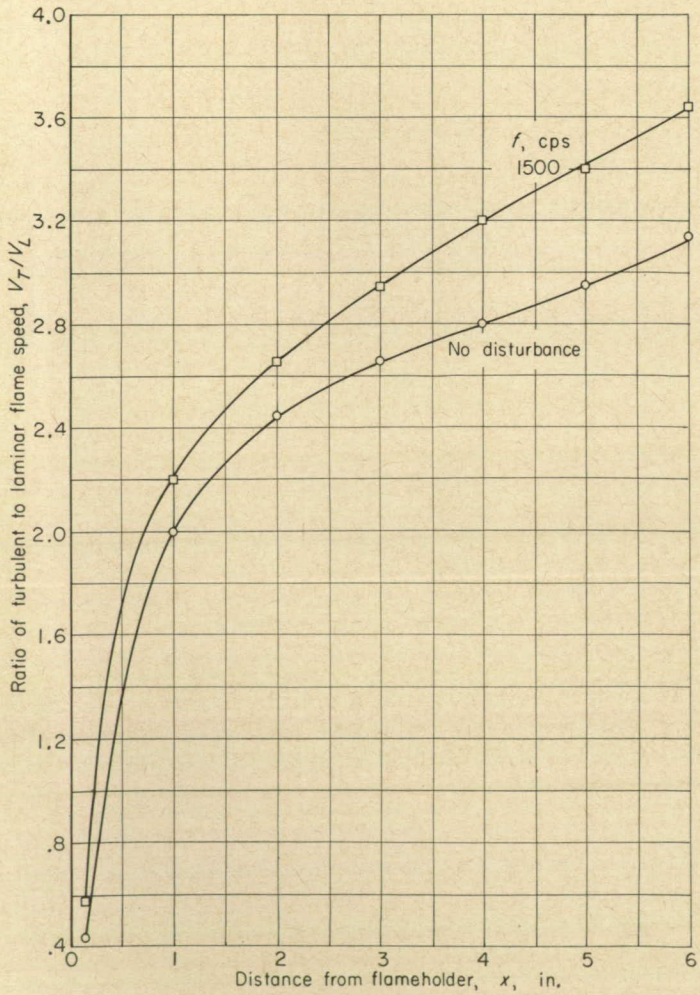
ratio of 0.0493. The results are shown in figure 32. The metering systems drifted slightly at this setting, making it difficult to hold fuel flow steady and causing some scatter in the determination of V_L.

The most sensitive frequency at 100 feet per second was 1700 cps, which is about three times the frequency observed at 50 feet per second. Clearly the effect is not allied with a spontaneous eddy-shedding frequency. The fraction burned is not so great as at 50 feet per second. Also, the flame speed increased sharply up to the end of the duct. These two factors tend to emphasize the higher frequencies within the limited duct length, and seem to be directly related to the instability of the flame zone. The single data point at 1700 cps is included in figure 26. This run was directed toward finding a frequency other than 570 cps for maximum effect, mainly to prevent duct resonance. Shadowgraph photographs of the flames show the antisymmetric disturbance.

The possible effect of duct resonance on these results must be considered. The modes of resonance likely to occur in a combustor are the "organ-pipe" or longitudinal modes, the transverse modes, and a single mode coupling the combustion chamber with the volume upstream of the nozzle. In the configuration studied, the longitudinal modes have frequencies, roughly, of 250 or 500 cps plus multiples of 500. The transverse modes have a minimum frequency of 3000 cps, so they are not considered here. The last type of oscillation gives a frequency of the order of 45 to 90 cps and is below the range of interest.

A longitudinal mode could affect the results in two dis-





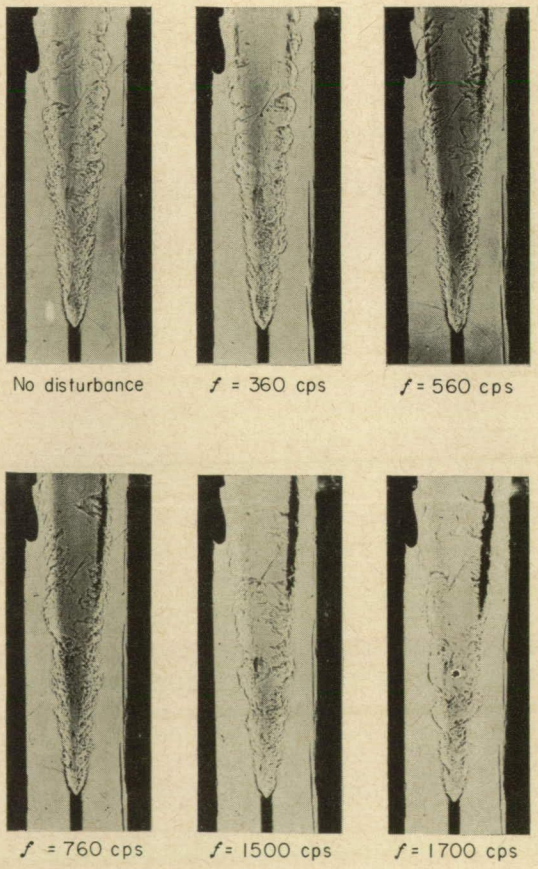


FIGURE 32.—Comparison of fraction burned with average voltage, distribution of V_T/V_L, and shadowgraphs with 0.306-inch flameholder. Flow velocity, 100 feet per second; fuel-air ratio, 0.0493; antisymmetric disturbance.

tinct ways: (1) If the flameholder were placed in a standing wave system at a pressure node, the time-varying velocity past the flameholder would cause large initial disturbances that would be symmetric with respect to the duct axis. (2) If the flameholder were placed at a pressure loop, there would be a coupling between the combustor and flameholder resonance that would be initially compensated for by the input calibration already discussed. If the nature of cuct resonance shifts the resonant frequencies so that this dompensation is no longer adequate, the input u' is no longer constant for all the frequencies.

Since the photographs of figure 32 show the disturbances to be antisymmetric, the first manner of coupling is rejected. To explore the second manner of coupling, the input u' for the frequencies on either side of the most sensitive ones (i. e., 1500 to 1700 cps; see fig. 32) was increased by a factor of 3. In no case was it possible to increase the fraction burned as much as the 1500- to 1700-cps disturbances increased it. Thus, the results shown in figure 32 are due to the sensitivity of the flame zone to the imposed disturbance and are not due to duct resonance.

SYMMETRIC DISTURBANCES

A symmetric disturbance was used for tests with a 0.315-inch flameholder, velocity of 50 feet per second, and a fuel-air ratio of 0.0444. No separate calibration of input sound was attempted, the inputs of the antisymmetric-disturbance tests being used. The results are shown in figure 33. Comparisons with flame speeds obtained with antisymmetric disturbances are given. There was a leak of approximately $\frac{1}{16}$ inch past one edge, which provided an additional flame surface and increased the apparent mean flame speed near the flameholder but did not disturb the results at some distance from the flameholder. In general, symmetric and antisymmetric disturbances gave roughly comparable shifts in flame speed near the flameholder. At a distance from the flameholder, antisymmetric disturbances increased the flame speed more than symmetric disturbances. These results are in accordance with sketch (f).

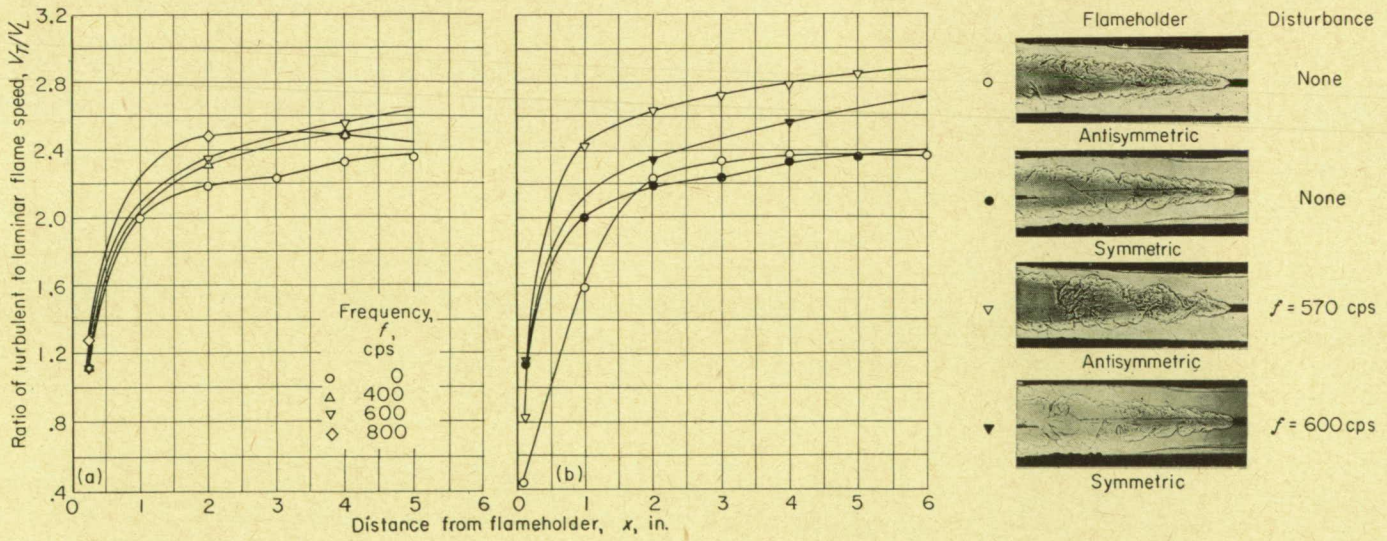
DISCUSSION

Ten questions raised by the analytical and experimental phases of the investigation are discussed in this section.

1. In what respects do the experimental results and the interpretations of the stability analysis agree?—The areas of agreement are summarized in the following table:

Interpretation of stability analysis	Investigation of sensitivity of a flame in a duct to transverse velocity disturbance
(1) The flow is stable to symmetric disturbances, unstable to antisymmetric disturbances. A qualification is made near a flameholder where the two types of disturbances are equally unstable.	(1) The flame seems about equally unstable to symmetric and antisymmetric disturbances near flameholder, is more unstable to antisymmetric disturbances far from flameholder.
(2) In moving along the flame at phase velocity, a disturbance of given frequency grows until the flame width becomes about 0.4 of the wavelength; then an apparent decay of the disturbance begins.	(2) A disturbance of given frequency first grows, then decays. The critical flame width where decay starts is slightly smaller than that predicted.
(3) There is a most-amplified frequency having a wave number of $5<2\alpha_0 h_1<7$.	(3) There is a most-amplified frequency which, for the lengths investigated, corresponds to $2\alpha_0 h_1 \approx 12$.
(4) The phase velocity ranges from a velocity equal to the cold-gas velocity at the flameholder up to 1.5 times the cold-gas velocity far from the flameholder.	(4) The phase velocity behaves much as predicted except near the flameholder, where it is lower than the cold-gas velocity.
(5) The amplification depends on $v'/V_{T,u}$ for a given dh_2/dx.	(5) The amplification depends on $v'/V_{T,u}$ for a given dh_2/dx.

The details of the system that would define more exactly the shortcomings of the stability analysis as well as the adequacies await the development of a transient-velocity



(a) Symmetric disturbances. Disturbance amplitude, unknown; input same as for figure 24 (a).

(b) Comparison of symmetric and antisymmetric flameholders with and without disturbance.

FIGURE 33.—Comparison of V_T/V_L obtained with flameholders for producing symmetric and antisymmetric disturbances. Flow velocity, 50 feet per second; fuel-air ratio, 0.0444.

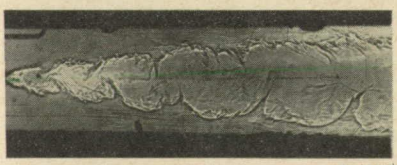
measuring technique that can be used in a flame zone. In at least one instance there was evidence that a form of transition took place (see Comparison of Flame Speed with Flame Appearance). The stability analysis cannot indicate when this takes place.

2. Would the same distribution of displacement and V_T/V_L with distance from the flameholder obtain if no growth occurred in the flame zone?—This seems unlikely. For example, if the input disturbance distribution simulates a source at the corner of the flameholder, only near the flameholder would there be a marked transverse velocity component. The highest frequencies would show the greatest increase in flame speed.

3. Do eddies shed?—They certainly seem to. In figure 34 photographs of a lean flame, both shadowgraphs and direct



Direct photograph of flame through stroboscope; frequency, f, 600 cps



Shadowgraph of excited flame; frequency, f, 760 cps



C-41538

Eddy trail

FIGURE 34.—Comparison of photographs of excited flame with eddy trail.

photographs taken through the stroboscope, are compared with a smoke-trace photograph of eddies shedding from a rod at a Reynolds number of 73 (ref. 30). The appearance of flame clearly indicates that eddy-shedding is present.

As the fuel-air ratio is increased, the range over which these eddies appear near the flameholder narrows. Figure 35 shows a plot of frequencies at which eddies appeared against fuel flow from lean to rich blowout. These data were obtained by exciting the flame at frequencies at which the constant-speed stroboscope would permit observation; that is, approximately every 100 cps.

Eddies are characterized by lobes of flame of about equal size on either side of the flameholder. These are contrasted to mere sinuosity of the flame. At 700 cps the lobes appeared symmetric, indicating duct resonance at this frequency. At 800 cps the lobes were antisymmetric and were observed throughout the fuel-air-ratio range. At the lean fuel-air ratios, most of the disturbances produced eddy-shedding.

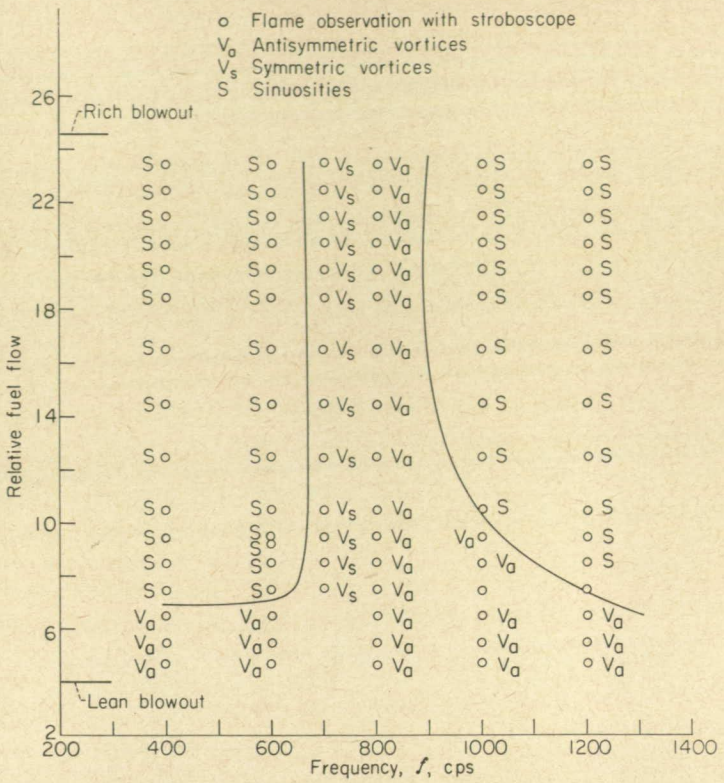
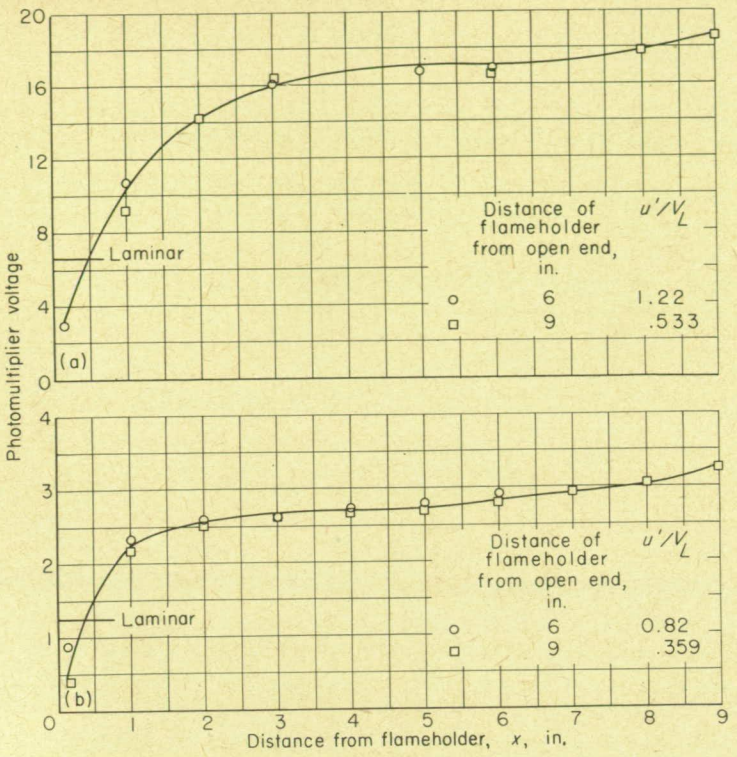


FIGURE 35.—Observations of vortex shedding excited by antisymmetric disturbances.

4. Does the turbulent-flame propagation velocity depend upon upstream turbulence?—It should. Bolz and Burlage (ref. 11) and Mickelsen and Ernstein (ref. 12) have shown turbulent flame speeds to be in fair agreement with Scurlock's theory (ref. 8), omitting flame-generating turbulence effects. These data were obtained in turbulent "soap-bubble" flames. Thus, in addition to the effect of the instabilities mentioned here, the incident turbulence should have an effect.

The most important point, however, is that the instability merely acts as an amplifier for a relatively narrow range of frequencies, the output within limits of the linearized theory being proportional to the input. Part of the input is, of course, the turbulent motion. The other, and in some cases the most important part, is the role played by the sound in the duct which, upon hitting the flameholder, produces a transverse velocity that may be subsequently amplified. In that this sound is related to the incident turbulence, the turbulence has an effect.

Some data on an effect of incident turbulence were obtained while exploring the properties of the system. Figure 36 shows a plot of E_T against distance from the flameholder x for two flameholder positions and two fuel-air ratios. The table in the section on turbulence intensity and spectra shows that the turbulence intensity increases from inlet nozzle to exhaust and from the wall to the interior of the test section. Taking as representative the value of u' measured $\frac{3}{16}$ inch above the flameholder lip, the values of the turbulence parameter u'/V_L vary over a factor of 2 for the two flameholder positions. It is apparent that, everywhere except near the flameholder, there is little effect of the initial u'/V_L values measured. The data are insufficient for pin-



(a) Fuel-air ratio, 0.0444.
(b) Fuel-air ratio, 0.0515.

FIGURE 36.—Comparison of relative flame speeds at two flameholder positions. Flow velocity, 50 feet per second.

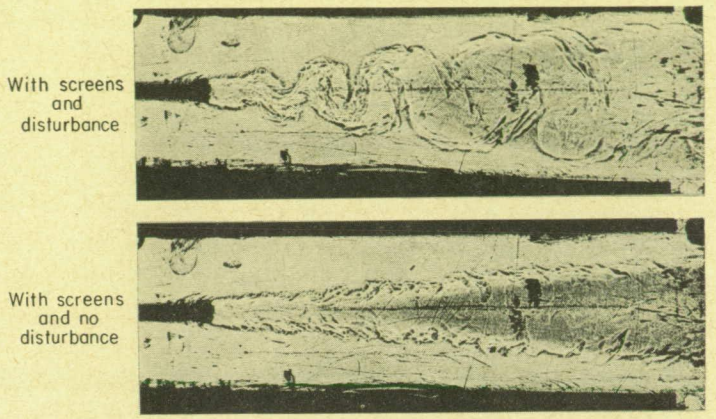
pointing the cause of this lack of effect. Two surmises appear warranted:

(1) The flame was noisier at the 9-inch position than at the 6-inch position because of flame-duct interaction; u' was measured in the absence of a flame.

(2) The turbulence found upstream of the flameholder was due to transition in the boundary layer. The u' in the boundary layer was growing for both positions measured. It is thought that the growth of this u' is accelerated when the boundary layer separates from the flameholder and quite rapidly achieves a value that would be relatively insensitive to u' prior to separation.

Additional data on the effect of upstream turbulence were obtained by putting three banks of 200-mesh screen just upstream of the flameholder. Shadowgraphs of the flame in this case with and without a 560-cps disturbance are shown in figure 37. Also plotted in this figure is V_T/V_L measured with and without screens. In the absence of imposed disturbances, V_T/V_L is lower with the screens than without. Although the conditions were set for 50 feet per second, leaks were found between the mixing section and the flameholder for this run so that the velocity was not known. The reduction in V_T/V_L is thought to be primarily due to the reduction in u' by the presence of the screens.

It is of interest to compare the flame-speed data obtained in this investigation with data taken in a similar apparatus. Figure 38 shows a comparison of V_T/V_L obtained by photomultiplier tube with V_T/V_L obtained by Scurlock (ref. 8) by measuring a mean flame width. Because V_L was taken as a property of the mixture, the values of V_T/V_L near the flameholder are low. The values of V_T/V_L obtained with the relatively high turbulence appear higher than those obtained by Scurlock. The possible displacement of the absolute magnitudes of V_T/V_L due to the different methods used would not warrant interpreting these data to give a quantitative dependence on turbulence intensity.



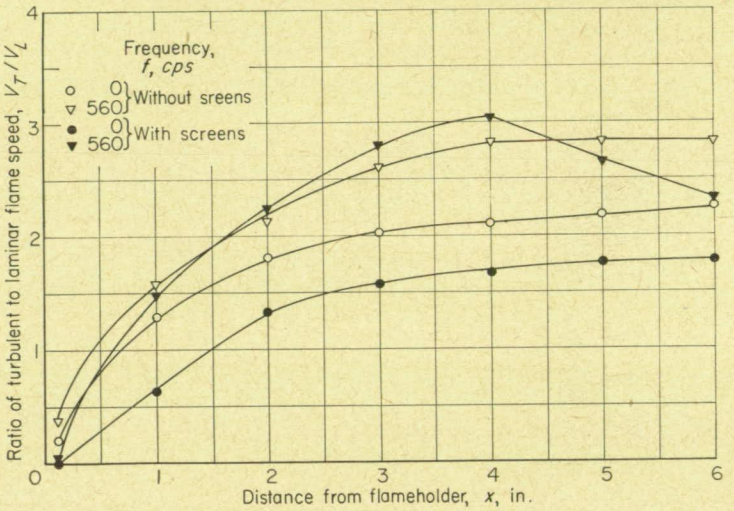


FIGURE 37.—Comparison of flame speeds with and without banks of 200-mesh screens upstream of flameholder.

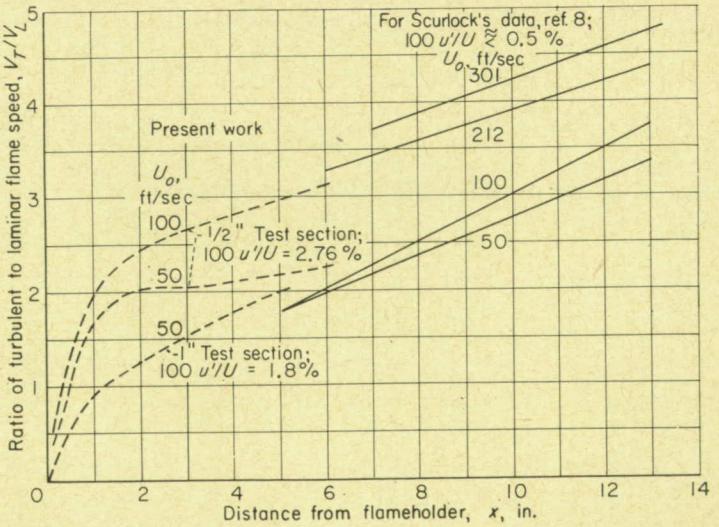


FIGURE 38.—Comparison of V_T/V_L taken in ½-inch- and 1-inch-wide ducts with Scurlock's data.

5. How does V_T/V_L obtained from area measurements compare with V_T/V_L taken from photomultiplier data?—The shadowgraphs indicate considerable wrinkling of the flame surface. In addition, it appears that density gradients exist within the outer envelope of flame surface, implying heat release there.

Since no single continuous flame surface is apparent, measuring flame area from these pictures seems impossible. For the sake of comparison, however, some relative surface extension should be of interest to those who would formulate a theory of turbulent flame propagation. Such measurements were made in the following manner: The negatives of a group of photographs were used to project an image of the flame on a screen. The image of a 6-inch test section was 2½ feet long. A map measure was used to find the length of the outer envelope of the group of flame images, ignoring the obvious density gradients within the outer envelope. Lengths were measured on the top and bottom surface of each flame, averaged, and divided by projected length. The resulting quotient is defined as $\overline{(V_T/V_L)}_{pg}$.

In the following table, the ratios so obtained are compared with the average V_T/V_L obtained from a photomultiplier survey $\overline{(V_T/V_L)}_{pm}$:

U_o, ft/sec	Flame-holder size, in.	Fuel-air ratio	Excitation frequency, f, cps	$\overline{(V_T/V_L)}_{pm}$	$\overline{(V_T/V_L)}_{pg}$	$\frac{\overline{(V_T/V_L)}_{pm}}{\overline{(V_T/V_L)}_{pg}}$	Photograph from figure
50	0.305	0.0444	0	2	1.436	1.39	23(a)
			570	2.54	1.77	1.43	23(c)
		0.0515	0	1.82	1.40	1.30	23(a)
	0.500	0.0444	0	1.735	1.36	1.28	31(a)
100	0.306	0.0493	0	2.46	1.65	1.49	32(b)

In general, the trends indicated by the $\overline{(V_T/V_L)}_{pm}$ are followed by the $(V_T/V_L)_{pg}$. In view of the obvious internal structure and three-dimensional nature of the wrinkles, no argument for or against the wrinkled flame as an adequate turbulent flame model can be introduced.

6. How can flame speeds be predicted on the basis of these results?—The most promising method of predicting flame speeds would be based on an incident and amplified spectra, as recommended by Markstein (ref. 4). For example: If the incident v' spectrum corresponds to a scale of turbulence L of 0.15 inch and each frequency is amplified as the theory states, the spectra at $h_2/h_1=0.5$ and 0.25, for $1/K_2 \approx 20$ would correspond to the ones shown in figure 39. Between the two spectra would be a continuously shifting spectrum. What is needed, then, is a model of flame propagation that would allow for a continuously shifting spectrum of turbulence. This model should have the advantage of allowing for the appearance of discrete frequencies that dominate the rest of the spectrum.

An interesting point comes up in regard to spectra. It is seen experimentally as well as theoretically that very little effect is derived from exciting the flame at a frequency less than $(2/3)(U/2h_1)$ or greater than $4U/2h_1$ (see figs. 22, 32, and 7). Therefore, for the present conditions (i. e., velocity of 50 ft/sec, 2-in. duct) the energy in the spectrum of turbulence below 200 cps apparently will not increase flame spreading.

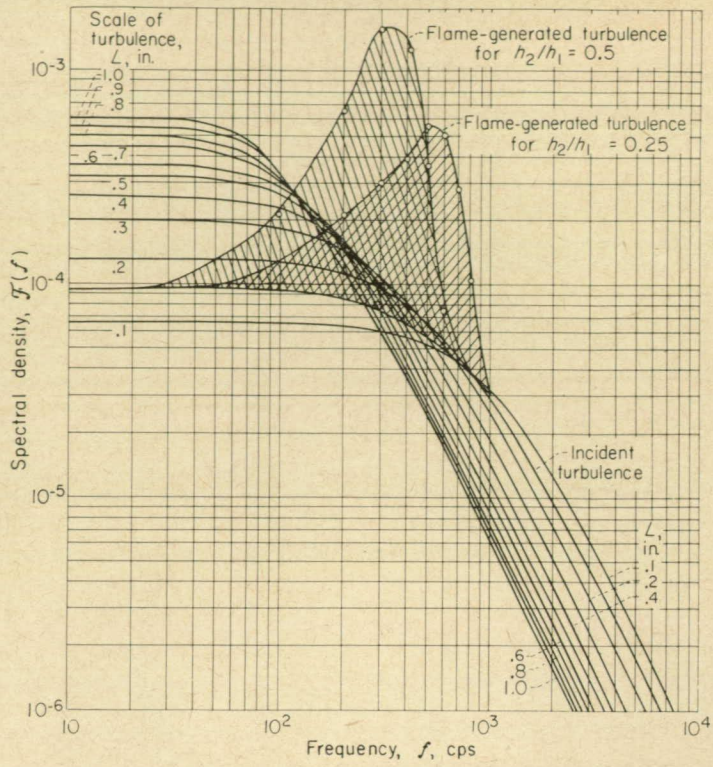


FIGURE 39.—Spectra of incident and flame-amplified turbulence; $\mathcal{F}(f)=(4L/U)/\{1+[(2\pi/U)Lf]^2\}$.

A plot of the percentage of energy in the turbulence at all frequencies below f against fL/U from reference 38 is shown in figure 40. For an assumed scale $L=(1/6)2h_1$, the frequency below the frequency $(2/3)(U/2h_1)$ represents about 35 percent of the total turbulence energy. This amount of energy is contained in disturbances with frequency too low to be amplified to any usable extent by the flame zone. Similarly from figure 40, the energy in the spectrum below the frequency $f=4U/2h_1$ [or $f(L/U)\approx 0.66$] is 85 percent of the total turbulence energy. Thus, about 15 percent of the turbulence energy is at frequencies too high to be appreciably amplified by the flame zone.

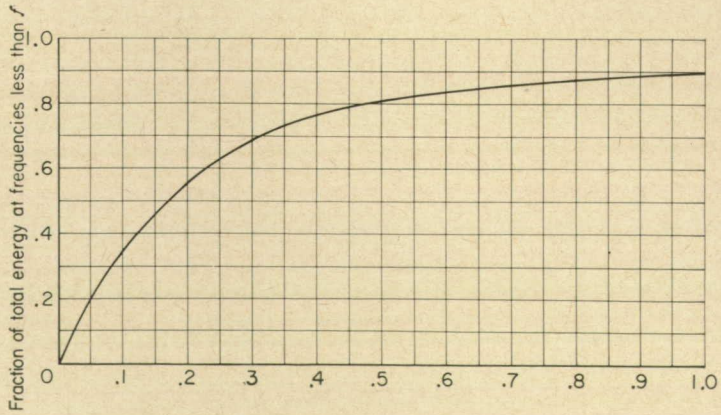


FIGURE 40.—Turbulence energy distribution for exponential correlation coefficient (ref. 38).

The scale of isotropic turbulence that would put the largest percentage of energy in the frequency range $(2/3)(U/2h_1)< f<4U/2h_1$ can be found from the extreme of the quantity (ref. 36)

$$\tan^{-1}\left(2\pi\frac{4U}{2h_1}\frac{L}{U}\right)-\tan^{-1}\left(2\pi\frac{2}{3}\frac{U}{2h_1}\frac{L}{U}\right)$$

or

$$L=\frac{1}{10}2h_1$$

In this case the amount of energy within the frequency range is 55 percent of the total as compared with 50 percent for $L=(1/6)2h_1$, 40 percent for $L=(1/3)2h_1$, and 45 percent for $L=(1/20)2h_1$.

7. Can the results concerning frequency be applied to multiple flameholders?—If n flameholders are arranged so that the flow field can be divided into n identical segments, Scurlock's results hold for each segment. The results in the theoretical sections of this report for the stability of the flow field apply to each segment and rely on the condition that v' vanishes at the boundary of each segment. Although one of several modes of instability may satisfy this condition, it is obvious that the foregoing results do not give any information about the other modes.

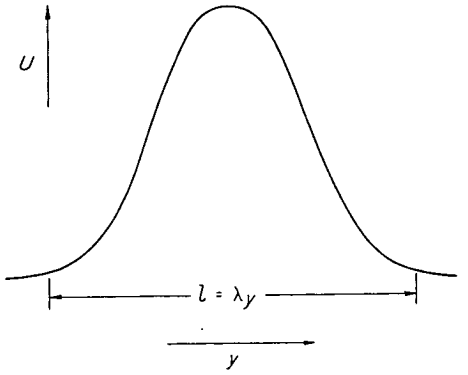
To illustrate the occurrence of multiple modes, consider a profile examined by Lin (ref. 22, pp. 219–220) where

$$U=A+B\sin\frac{2\pi}{\lambda_y}y$$

Lin shows that the wave numbers for neutral stability of the different modes available depend on the number of inflection points in the flow and can be given by

$$(\alpha l)^2=\left(\frac{2\pi l}{\lambda_y}\right)^2-(n\pi)^2$$

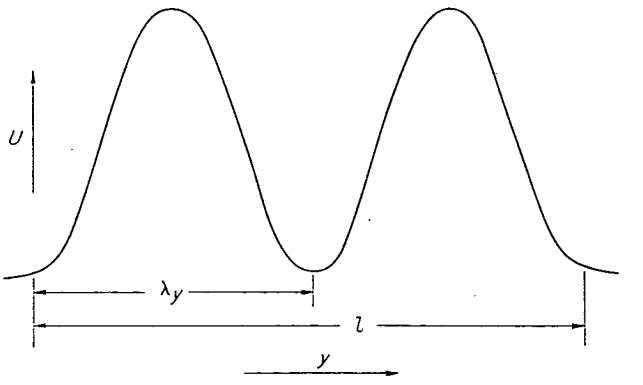
The choice of $l=\lambda_y$ yields the following profile, which is similar to the one studied earlier in this report for a single flameholder:



Sketch (l)

For this case neutral stability occurs at $\alpha\lambda_y=\alpha l=\pi\sqrt{3}, 0$.

If two flameholders are present, the following profile may be approximated by setting $l=2\lambda_y$:



Sketch (m)

For this case the wave numbers for neutral stability of the four modes obtained are

$$\alpha\lambda_y=\alpha\frac{l}{2}=\pi\frac{\sqrt{15}}{2},\ \pi\sqrt{3},\ \pi\frac{\sqrt{7}}{2},\ 0$$

Two new modes appear in addition to the two for the single profile.

Similarly, for three flameholders,

$$a\lambda_y=\alpha\frac{l}{3}=\pi\frac{\sqrt{35}}{3},\ \pi\frac{\sqrt{32}}{3},\ \pi\sqrt{3},\ \pi\frac{\sqrt{20}}{3},\ \pi\frac{\sqrt{\pi}}{3},\ 0$$

that is, there appear four roots in addition to the two for $l=\lambda_y$.

In short, the single mode investigated in this report is applicable to multiple flameholders, but only as one of several modes that combine to give the entire instability.

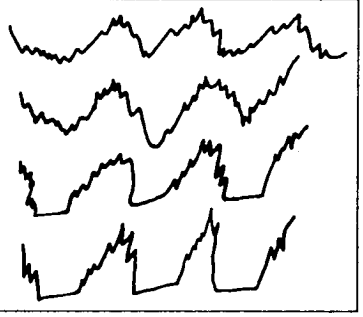
8. Can the excitation at the flameholder permit increased combustion rates without destroying the burner walls?—Yes. In these tests the sound level at the exhaust plane was only 93 decibels with the flame excited. When the flame is excited by the destructive duct resonance, the sound level is of the order of 200 decibels (ref. 17).

In order to apply this type of excitation to an engine, the control exerted herein (a speaker system) would not be needed. Instead, the disturbance can be introduced by suitably placed whistles, mounted on the flameholder and driven by the flowing stream. The whistle ideally should have a number of strong overtones and a fundamental equal to the most sensitive frequency $U_o/2h$. The overtones would serve to increase the heat-release rate near the flameholder, while the fundamental would increase the heat-release rate far from the flameholder.

9. What would be the sacrifice in stability and pressure drop for such an excitation?—Both these penalties require further investigation, but from work that has been done the sacrifice does not seem great. For example, when the flameholder was placed ⅝ inch from the nozzle entrance and a 6-inch-long test section was installed, lean blowout at 50 feet per second occurred at a fuel-air ratio of 0.042. At a fuel-ar ratio of 0.0453, the disturbance amplitudes required to cause blowout were found for several frequencies. The results are shown in figure 41. Minimum disturbance velocity was required at 780 cps. At this condition the

flameholder without flame had an eddy-shedding frequency of 420 cps. The Strouhal number is thus 0.206, agreeing well with the results of Roshko (ref. 34). The cold-duct resonance fundamental was 1000 cps. The reason for this result is not known. The main point here, however, is to show the effect of disturbances to be used for promoting flame propagation upon flameholder stability. At a fuel-air ratio of 0.047, it was impossible to induce blowout with speaker inputs as much as 10 times those used in the earlier tests. The imposed disturbances will probably narrow the stability range slightly but not prohibitively, the amount of narrowing depending on the frequencies imposed.

An interesting observation was made in the study of lean blowout. As the lean-blowout fuel-air ratio was approached, the flame emitted a low-frequency noise at 87 cps. The average heat-release rate dropped abruptly. A survey with the photomultiplier probe showed the flame to be intermittently extinguished for all positions greater than ⅞ inch downstream of the flameholder. Typical wave forms observed at several stations downstream of the flameholder are shown in the following sketch:

Distance downstream of flameholder, in.	Wave form of photomultiplier signal
$\frac{7}{8}$	
$1\frac{1}{8}$	
2	
4	

Sketch (n)

Random photographs taken at this condition show intervals during which no flame was present in part of the combustor (fig. 42).

It is curious that the flame surface facing upstream at the break in the flame is strong and well-defined both in the photomultiplier and the shadowgraph observations. The flame surface facing downstream is conversely ill-defined in both methods of observation. Near the point of rupture the photomultiplier signal is approximately symmetric. No explanation for this is apparent. The most significant feature of these data is that this form of resonance accompanied by intermittent blowoff downstream of the sheltered zone was the only form of excitation that reduced the heat-release rate in the combustor. On this basis it is tempting to generalize that all oscillations that do not cause flame parting must increase the heat-release rate in the combustor.

For the frequency of maximum amplification (570 cps), an increase of as much as 30 percent in heat release or about 0.2 percent of the kinetic energy of the flowing stream was obtained in the 6-inch-long combustor for an energy flux

$$\frac{\text{Sound energy}}{\text{Kinetic energy of stream}} \approx \frac{6}{2500}$$

In this case the noise level at the exhaust was 93 decibels.

Another way of increasing the heat-release rate that is indirectly suggested is to accelerate the flow locally or alter the profile to a more unstable one by use of a convergent-divergent combustion chamber. One way these can be combined with the introduction of a v' at the desired frequency is to construct a combustor with a wavy wall. Using this method of excitation would require a new experimental determination of the desired wavelength and amplitude of the waves in the wall, but would eliminate any effect on flame anchoring.

10. Can the behavior of axisymmetric flames in cylindrical ducts be predicted?—First, the steady-state problem, solved by Scurlock, of the cylindrical flame in a cylindrical duct yielded a _⌒_ profile as opposed to the _/_ profile for plane flow. If the arc part of the curved profile is assumed parabolic, the cylindrically symmetric disturbance equation can be solved by elementary functions for symmetric disturbances. This, however, accomplishes nothing, because the profile is neutrally stable to symmetric disturbances. The same result is obtained for the _/_ profile in the plane case. For antisymmetric disturbances, the problem is more complicated, and no simple solution is apparent.

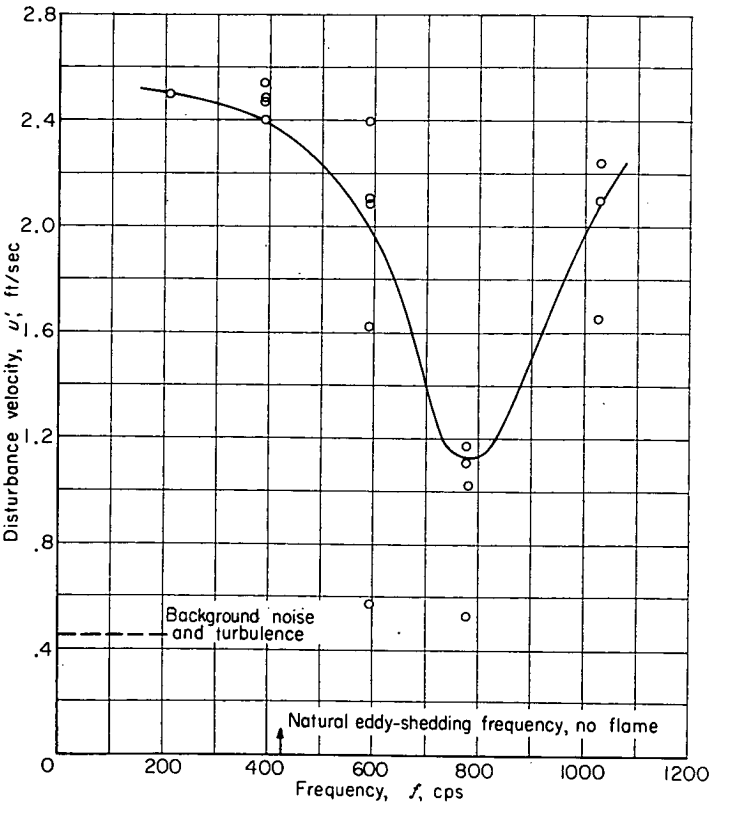


FIGURE 41.—Distribution with frequency of disturbance velocities required to produce blowout at fixed velocity and fuel-air ratio with 0.306-inch flameholder placed ⅝ inch from nozzle. Flow velocity at plane of flameholder, 50 feet per second; duct length, 5.7 inches; antisymmetric disturbances.

If the profile is affected by a flameholder in such a way that it may more nearly be approximated by a ⎽⎍⎽ profile composed of three straight-line segments and two parabolic arcs, a range of instability for symmetric disturbances is obtained. This profile can be compared with the corresponding profile in plane flow ⎽/‾\⎽. Such an analysis is given in the appendix. A few calculations are given to permit comparison with the data of figure 11, for conditions that h_1 approaches infinity and ρ is constant throughout. The results are compared in the following table:



Sketch (o)

$\frac{b'}{2b}$	$2\alpha b$	
	Plane flow	Cylindrical flow
0.1	2.26	2.08
.2	2.55	2.42
1.0	2.55	2.54

The critical wave numbers agree quite closely. At first glance, the results for plane flow seem to be a fair approximation for cylindrical flow. In order to obtain a rough experimental verification of this supposition, a 1½-inch-inside-diameter glass tube and its accommodating nozzle were installed in place of the rectangular test section. The ½- by 0.306-inch antisymmetric flameholder was retained. At 50 feet per second and a fuel-air ratio of 0.047, resonance-free operation was obtained at a combustor length of 4½ inches or less. With the flameholder set to give this length, the disturbance inputs were calibrated as before to give a disturbance velocity of 1.8 feet per second. Then the burning run was made with the settings indicated by calibration. The flame speeds were measured by the photomultiplier probe plus a measurement of an average local flame diameter. The results are shown in the following table:

Frequency, f, cps	V_T/V_L		
	1″ From flameholder	2″ From flameholder	4″ From flameholder
0	2.27	3.31	3.58
200	------	3.56	3.77
385	2.59	3.56	3.95
580	2.68	3.56	3.95
770	2.82	3.65	4.25
980	2.89	3.70	3.80
1170	2.89	3.70	3.73
1360	2.96	3.65	3.73
1740	3.09	3.65	3.99

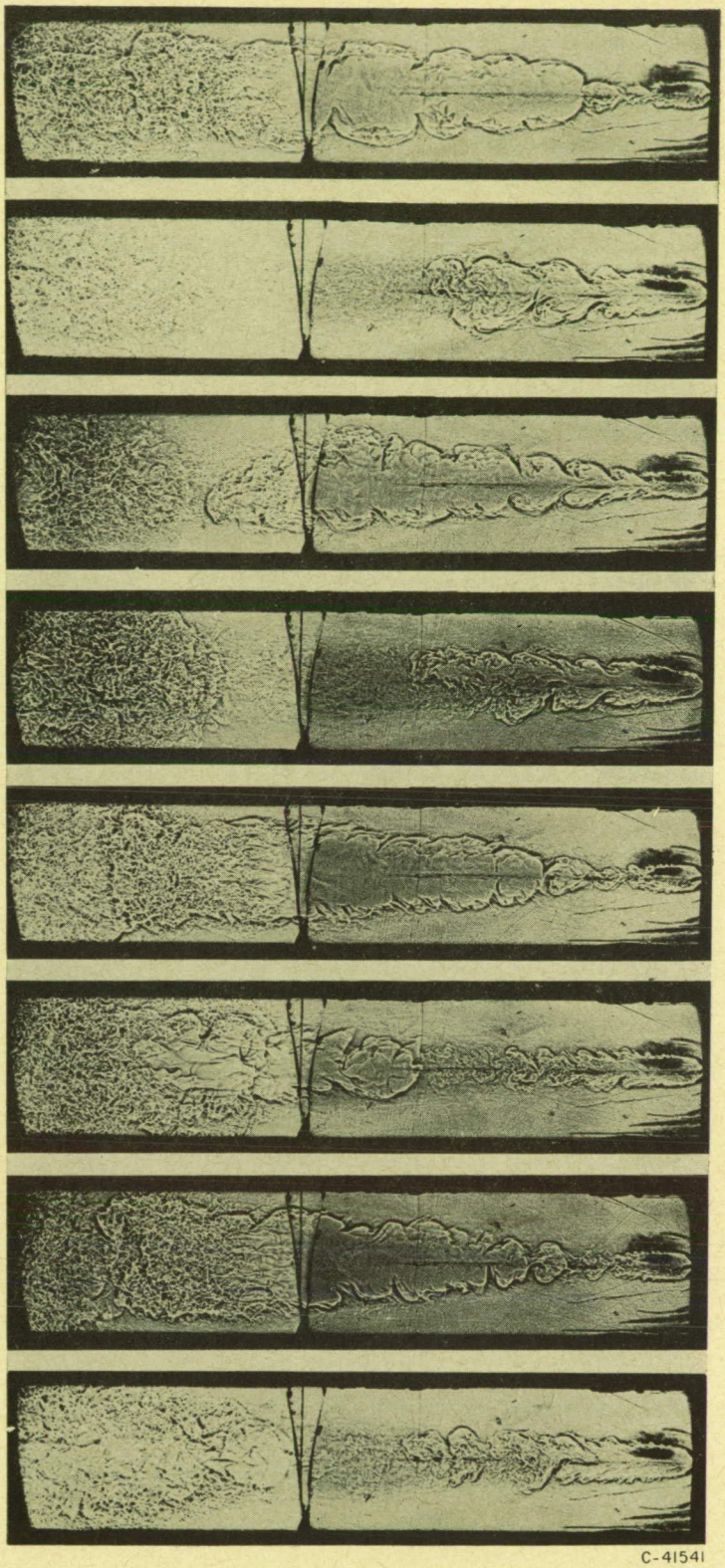


FIGURE 42.—Spontaneous oscillations showing intermittent flame interruption. Flow velocity, 50 feet per second; frequency, 85 cps; fuel-air ratio, 0.0444.

The flame speed with this arrangement is almost twice as high as with the plane burner. Part of this increase is undoubtedly due to the disturbances introduced by the corners of the flameholder. The fraction burned is 20 percent at the position 4 inches from the flameholder, corresponding to $h_2/h_1=0.7$. Therefore, the frequencies in 4 inches of this duct may be compared with those obtained in 6 inches or more of the rectangular duct. The values of $2\alpha_o h_1$ giving the greatest increase in flame speed at the termini of the respective ducts are, for U_o of 50 feet per second,

Geometry	Frequency, f, cps	$2h_1$, in.	$2\alpha_o h_1$ for $(V_T/V_L)_{max}$
Plane	570	2	11.95
Cylindrical	770	1.5	12.10

Of course, these data were obtained in a single test, performed to satisfy curiosity. The agreement does make it seem likely that a carryover of about 1:1 would be feasible in going from plane to cylindrically symmetric flow.

SUMMARY OF RESULTS

THEORY

The flow field of a flame in a duct is unstable to transverse disturbances having wavelengths 2.5 times the local flame width.

The amount a given frequency disturbance will grow varies directly as the frequency and inversely as the rate of flame spreading dh/dx and is independent of velocity and density ratio across the flame front. The frequency f where maximum velocity-disturbance growth obtains is $f=(2.8/\pi)(U_o/2h_1)$, where U_o is approach velocity and $2h_1$ is duct width. This maximum growth occurs by the time the flame fills 64 percent of the duct and implies an amplification $v'/v_o=(1.108)^{1/K_2}$, where $K_2=dh_2/dx$. Frequencies higher or lower than this are amplified less. Higher frequencies achieve their terminal amplification at smaller values of h_2/h_1. For example, a frequency of $(1.5/\pi)(U_o/2h_1)$ has an amplification of $v'/v_o=(1.07)^{1/K_2}$ by the time the flame fills 28 percent of the duct.

By using a crude model of flame propagation, it is possible to predict the qualitative effect that amplified disturbances of discrete frequencies will have upon turbulent flame speed.

EXPERIMENT

The effects of disturbances imposed at the flameholder are in substantial agreement with those predicted by theory. In addition, the results show:

1. Eddies shed from the flameholder with flame when suitably excited.
2. The ratio of turbulent to laminar flame speed varies inversely as flameholder size and directly as the ratio of flow velocity to flame speed or the ratio of disturbance velocity to flame speed.
3. Potentially, the most useful theory of turbulent flame propagation would be based on an incident and locally shifting spectrum of turbulence.
4. Gains in local heat-release rates can be obtained without damage to walls or excessive energy expenditure by using acoustic disturbances at a flameholder.

CONCLUDING REMARKS

In formulating a theory of turbulent flame propagation, the form of instability that is discussed in this paper must be taken into account, as must plane-combustion-wave instability and flameholder boundary-layer instability. At present it is not known whether the latter two forms of instability can be encouraged to influence turbulent flame propagation more than they encourage it spontaneously; from the little evidence that is available, it appears that they cannot.

The type of instability discussed herein is of additional significance because its effect on the ratio of turbulent to laminar flame speed can be increased in some important applications. Several methods of increasing this ratio are as follows:

(1) Increase the disturbance velocity at the frequency that the flame zone can amplify.

(2) Increase the amplification rate by locally raising the mean velocity in the combustor.

(3) Increase the amplification rate by locally varying the velocity profile.

A method of employing all three of these improving factors would be to build a combustor having a wavy wall. Although the second and third methods listed will clearly cause an increase in pressure drop, the first method substantially increases the heat-release rate at the cost of a very small fraction of the kinetic energy in the approach-stream flow and a slight reduction in the operating range of the flameholder.

LEWIS FLIGHT PROPULSION LABORATORY
NATIONAL ADVISORY COMMITTEE FOR AERONAUTICS
CLEVELAND, OHIO, *October 14, 1957*

APPENDIX

AXISYMMETRIC DISTURBANCES IN AXISYMMETRIC FLOW WITH DENSITY JUMPS

This appendix examines the stability of the flow field arising from a flame in a duct for axial symmetry. The results are used in the body of the text to compare wave numbers for neutral stability of comparable plane and axisymmetric flow fields. The symbols are defined where used.

DISTURBANCE EQUATION

Pillow (ref. 23) defines the quantity ψ as

$$\psi=\varphi(r)e^{i\alpha(z-ct)} \tag{A1}$$

The velocity in the z-direction is

$$u=U+u'$$

and in the r-direction,

$$v=v'$$

where

$$v'=-\frac{\partial\psi}{\partial z},\ u'=\frac{1}{r}\frac{\partial(r\psi)}{\partial r} \tag{A2}$$

and the continuity equation is satisfied identically. Pillow shows that the disturbance equation then becomes

$$\left[(U-c)-\frac{1}{i\alpha Re}(M-\alpha^2)\right](M-\alpha^2)\varphi-\varphi\left(U''-\frac{1}{r}U'\right)=0 \tag{A3}$$

where

$$M\equiv\frac{\mathrm{d}^2}{\mathrm{d}r^2}+\frac{1}{r}\frac{\mathrm{d}}{\mathrm{d}r}-\frac{1}{r^2} \tag{A4}$$

If the study is restricted to cases where $Re\to\infty$ and $U''=\frac{1}{r}U'$ (i. e., parabolic profiles or flat profiles), then equation (A3) becomes

$$(M-\alpha^2)\varphi=0$$

or

$$\frac{\mathrm{d}^2\varphi}{\mathrm{d}r^2}+\frac{1}{r}\frac{\mathrm{d}\varphi}{\mathrm{d}r}-\frac{1}{r^2}+\alpha^2=0 \tag{A5}$$

with solutions

$$\varphi=A_1I_1(\alpha r)+A_2K_1(\alpha r) \tag{A6}$$

where I_1 and K_1 are modified Bessel functions of the first and second kind. Therefore,

$$v'=\frac{\partial\psi}{\partial z}=-i\alpha\varphi(r)e^{i\alpha(z-ct)}$$
$$=-i\alpha e^{i\alpha(z-ct)}[A_1I_1(\alpha r)+A_2K_1(\alpha r)] \tag{A7}$$

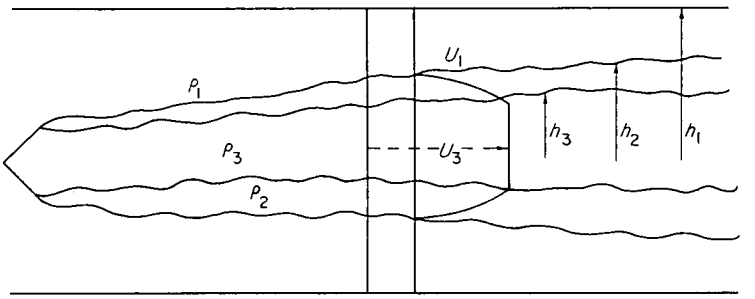
and

$$u'=\frac{1}{r}\frac{\partial(r\psi)}{\partial r}$$
$$=\frac{\partial\psi}{\partial r}+\frac{1}{r}\psi$$
$$=\varphi'+\frac{1}{r}\varphi e^{i\alpha(z-ct)}$$
$$=e^{i\alpha(z-ct)}\left\{A_1\left[\alpha I_1(\alpha r)+\frac{1}{r}I_1(\alpha r)\right]+A_2\left[\alpha K_1(\alpha r)+\frac{1}{r}K_1(\alpha r)\right]\right\} \tag{A8}$$

where the prime denotes differentiation with respect to the argument.

BOUNDARY CONDITIONS

Consider the following profile and density distribution:



Sketch (p)

Let solutions to equation (A5) be denoted by φ_1, φ_2, φ_3 for regions 1, 2, and 3 with densities ρ_1, ρ_2, and ρ_3, respectively.

As in the plane case, the requirements are

$$\left.\begin{aligned}\varphi_1&=0 \text{ at } h_1\\ \varphi_1&=\varphi_2 \text{ at } h_2\\ \varphi_2&=\varphi_3 \text{ at } h_3\end{aligned}\right\} \tag{A9}$$

and, because of symmetry,

$$\varphi_3=0 \text{ at } r=0$$

Similarly,

$$\left.\begin{aligned}\left(\frac{\mathrm{d}p}{\mathrm{d}z}\right)_1&=\left(\frac{\mathrm{d}p}{\mathrm{d}z}\right)_2 \text{ at } h_2\\ \left(\frac{\mathrm{d}p}{\mathrm{d}z}\right)_2&=\left(\frac{\mathrm{d}p}{\mathrm{d}z}\right)_3 \text{ at } h_3\end{aligned}\right\} \tag{A10}$$

Since, at $r=h_1$,

$$\varphi_1=A_1I_1(\alpha h_1)+A_2K_1(\alpha h_1)=0$$

then

$$A_1=-A_1\frac{I_1(\alpha h_1)}{K_1(\alpha h_1)} \tag{A11}$$

At $r=h_2$, $\varphi_1=\varphi_2$ or, with equation (A11),

$$\left.\begin{aligned}\varphi_1&=\alpha_1\left[I_1(\alpha h_2)-\frac{I_1(\alpha h_1)}{K_1(\alpha h_1)}K_1(\alpha h_2)\right]\\&=\varphi_2=B_1I_1(\alpha h_2)+B_2K_1(\alpha h_2)\end{aligned}\right\} \tag{A12}$$

At $r=h_3$, $\varphi_2=\varphi_3$ or

$$\left.\begin{aligned}\varphi_2&=B_1I_1(\alpha h_3)+B_2K_1(\alpha h_3)\\&=\varphi_3=C_1I_1(\alpha h_3)+C_2K_1(\alpha h_3)\end{aligned}\right\} \tag{A13}$$

Since $K_1(\alpha r)\to\infty$ as $\alpha r\to 0$, $I_1(\alpha r)\to 0$ as $\alpha r\to 0$, and at $r=0$, $\varphi_3=0$,

$$C_2=0 \tag{A14}$$

Since

$$\frac{\partial p}{\partial z}=-\rho\left(\frac{\partial u'}{\partial t}+U\frac{\partial u'}{\partial z}+v'\frac{dU}{dr}\right)$$

the pressure conditions yield at h_2 (from eqs. (A7) and (A8))

$$-\rho_1\left[(-\alpha c+i\alpha U_1)\left(\alpha\varphi_1'+\frac{1}{h_2}\varphi_1\right)\right]=-\rho_2\left[(-i\alpha c+\alpha U_1)\left(\alpha\varphi_2'+\frac{1}{h_2}\varphi_2\right)-i\alpha\varphi_2\frac{dU}{dr}\right] \tag{A15}$$

and at h_3

$$\rho_3\left\{[-i(\alpha c)+i(\alpha U_3)]\left(\varphi_3'+\frac{1}{h_3}\varphi_3\right)\right\}=\rho_2\left\{[-i(\alpha c)+i(\alpha U_3)]\left(\varphi_2'+\frac{1}{h_3}\varphi_2\right)-i(\alpha)\varphi_2\frac{dU}{dr}\right\} \tag{A16}$$

BOUNDARY-VALUE PROBLEM

The following notation is used:

$$\left.\begin{aligned}
\alpha_1&=I_1(\alpha h_2)-\frac{I_1(\alpha h_1)}{K_1(\alpha h_1)}K_1(\alpha h_2)\\
\alpha_2&=\frac{\rho_1}{\rho_2}\left\{\alpha I_1'(\alpha h_2)+\frac{1}{h_2}I_1(\alpha h_2)-\frac{I_1(\alpha h_1)}{K_1(\alpha h_1)}\left[\alpha K_1'(\alpha h_2)+\frac{1}{h_2}K_1(\alpha h_2)\right]\right\}\\
\beta_1&=I_1(\alpha h_2)\\
\beta_2&=K_1(\alpha h_2)\\
\beta_3&=I_1(\alpha h_3)\\
\beta_4&=K_1(\alpha h_3)\\
\beta_5&=\alpha I_1'(\alpha h_2)+\frac{1}{h_2}I_1(\alpha h_2)\\
\beta_6&=I_1(\alpha h_2)\left(\frac{dU}{dr}\right)_{h_2}\\
\beta_7&=\alpha K_1'(\alpha h_2)+\frac{1}{h_2}K_1(\alpha h_2)\\
\beta_8&=K_1(\alpha h_2)\left(\frac{dU}{dr}\right)_{h_2}\\
\beta_9&=\frac{\rho_2}{\rho_3}(\alpha I_1')(\alpha h_3)+\frac{1}{h_3}I_1(\alpha h_3)\\
\beta_{10}&=\frac{\rho_2}{\rho_3}(\alpha K_1')(\alpha h_3)+\frac{1}{h_3}K_1(\alpha h_3)\\
\beta_{11}&=\frac{\rho_2}{\rho_3}I_1(\alpha h_3)\left(\frac{dU}{dr}\right)_{h_2}\\
\beta_{12}&=\frac{\rho_2}{\rho_3}K_1(\alpha h_3)\left(\frac{dU}{dr}\right)_{h_3}
\end{aligned}\right\} \tag{A17}$$

and

$$\gamma_1=I_1(\alpha h_3)=\beta_3$$

$$\gamma_2=\alpha I_1'(\alpha h_3)+\frac{1}{h_3}I_1(\alpha h_3)$$

Setting $U_1=0$ (this merely alters the real part of c by U_1), the determinantal equation for A_1, B_1, B_2, and C_1 is

$$\begin{vmatrix}\alpha_1 & -\beta_1 & -\beta_2 & 0\\ 0 & \beta_3 & \beta_4 & -\gamma_1\\ -c\alpha_2 & c\beta_5+\beta_6 & c\beta_7+\beta_8 & 0\\ 0 & (U_3-c)\beta_9-\beta_{11} & (U_3-c)\beta_{10}-\beta_{11} & -(U_3-c)\gamma_2\end{vmatrix}=0 \tag{A18}$$

One immediate result of equation (A18) is to show that, if dU/dr vanished at either h_2 or h_3 in region 2, c is real for all α_s'. This can be seen by setting

$$\beta_6=\beta_8=\left(\frac{dU}{dr}\right)_{h_2}=0$$

and factoring c from the third row of equation (A18), or setting

$$\beta_{11}=\beta_{12}=\left(\frac{dU}{dr}\right)_{h_3}=0$$

and factoring $U_3=c$ from the fourth row of equation (A18). Either operation leaves a determinantal equation in which c is wholly real.

If

$$\left.\begin{aligned}\left(\frac{dU}{dr}\right)_{h_2}&=g_2\\ \left(\frac{dU}{dr}\right)_{h_3}&=g_3\end{aligned}\right\} \tag{A19}$$

and

$$\left.\begin{aligned}g_2\beta_1&=\beta_6\\ g_2\beta_2&=\beta_8\\ \frac{\rho_2}{\rho_3}g_3\beta_3&=\beta_{11}\\ \frac{\rho_2}{\rho_3}g_3\beta_4&=\beta_{12}\end{aligned}\right\} \tag{A20}$$

then equation (A18) can be reduced to

$$\begin{bmatrix} -\frac{c\alpha_2-g_2\alpha_1}{\alpha_1}\beta_1+c\beta_5 & & \\ \frac{(U_3-c)\gamma_2+\frac{\rho_2}{\rho_3}g_3\gamma_1}{\gamma_1}\beta_3+(U_3-c(\beta_9- & -\frac{c\alpha_2-g_2\alpha_1}{\alpha_1}\beta_2+c\beta_7 & \\ & \frac{(U_3-c)\gamma_2+\frac{\rho_2}{\rho_3}g_3\gamma_1}{\gamma_1}\beta_4+(U_3-c)\beta_{10} & \end{bmatrix}=0 \quad \text{(A21)}$$

This is in the form

$$\begin{vmatrix} jc+k & mc+n \\ oc+q & sc+w \end{vmatrix}=0$$

or

$$jsc^2-moc^2+c(jw+ks-mq-on)+kw-nq=0$$

and the discriminant of c is

$$D\equiv j^2w^2+k^2s^2+m^2q^2+o^2n^2+-2jwks-2mqon-2jwmq-2jwon-2ksmq-2kson+4mokw+4jsnq \quad \text{(A22)}$$

If $D<0$, then c is complex and an unstable mode exists. The symbols of equation (A22) are defined

$$\left.\begin{aligned} j&=\beta_5-\beta_1\frac{\alpha_2}{\alpha_1} \\ k&=\beta_1 g_2 \\ m&=\beta_7-\beta_2\frac{\alpha_2}{\alpha_1} \\ n&=\beta_2 g_2 \\ o&=\beta_3\frac{\gamma_2}{\gamma_1}-\beta_9 \\ q&=U_3\beta_9-\frac{\rho_2}{\rho_3}g_3\beta_3-U_3\frac{\gamma_2}{\gamma_1}\beta_3 \\ s&=\beta_4\frac{\gamma_2}{\gamma_1}-\beta_{10} \\ w&=U_3\beta_{10}-\frac{\rho_2}{\rho_3}g_3\beta_4-U_3\frac{\gamma_2}{\gamma_1}\beta_4 \end{aligned}\right\} \quad \text{A(23)}$$

REFERENCES

1. Scurlock, A. C.: Flame Stabilization and Propagation in High-Velocity Gas Streams. Meteor Rep. 19, Fuels Res. Lab., M. I. T., May 1948. (Contract NOrd 9661.)
2. Haddock, Gordon W.: Flame-Blowoff Studies of Cylindrical Flameholders in Channeled Flow. Prog. Rep. 3-24, Jet Prop. Lab., C. I. T., May 14, 1951.
3. Zukoski, Edward E., and Marble, Frank E.: The Role of Wake Transition in the Process of Flame Stabilization on Bluff Bodies. Combustion Res. and Rev., Butterworths Sci. Pub., 1955, pp. 167–180.
4. Karlovitz, Béla: A Turbulent Flame Theory Derived from Experiments. AGARD Selected Combustion Problems, Butterworths Sci. Pub. (London), 1954, pp. 248–262. (Discussion by K. Wohl, pp. 268–274, and by G. H. Markstein, pp. 263–265.)
5. Berl, W. G., Rice, J. L., and Rosen, P.: Flames in Turbulent Streams. Jet Prop., vol. 25, no. 7, July 1955, pp. 341–346.
6. Damköhler, Gerhard: The effect of Turbulence on the Flame Velocity in Gas Mixtures. NACA TM 1112, 1947.
7. Shelkin, K. I.: On Combustion in a Turbulent Flow. NACA TM 1110, 1947.
8. Scurlock, Arch C., and Grover, John H.: Experimental Studies on Turbulent Flames. AGARD Selected Combustion Problems, Butterworths Sci. Pub. (London), 1954, pp. 215–247.
9. Leason, D. B.: Turbulence and Flame Propagation in Premixed Gases. Fuel, vol. XXX, no. 10, Oct. 1951, pp. 233–238; discussion, pp. 238–239.
10. Mickelsen, William R.: The Propagation of a Free Flame Through a Turbulent Gas Stream. M. S. Thesis, Case Inst. Tech., 1953.
11. Bolz, Ray E., and Burlage, Henry, Jr.: The Influence of Turbulence on Flame Propagation Rates. Jet Prop., vol. 25, no. 6, June 1955, pp. 265–275: con. p. 283.
12. Mickelsen, William R., and Ernstein, Norman E.: Propagation of a Free Flame in a Turbulent Gas Stream. NACA Rep. 1286, 1956. (Supersedes NACA TN 3456.)
13. Tucker, Maurice: Interaction of a Free Flame Front with a Turbulence Field. NACA Rep. 1277, 1956. (Supersedes NACA TN 3407.)
14. Summerfield, Martin, Reiter, Sydney H., Kebely, Victor, and Mascolo, Richard W.: The Structure and Propagation Mechanism of Turbulent Flames in High Speed Flow. Jet Prop., vol. 25, no. 8, Aug. 1955, pp. 377–384.
15. Rayleigh: The Theory of Sound. Vol. II. Dover Pub., 1945.
16. Fenn, J. B., Forney, H. B., and Garmon, R. C.: Burners for Supersonic Ram-Jets. Ind. and Eng. Chem., vol. 43, no. 7, July 1951, pp. 1663–1671.
17. Blackshear, Perry L., Rayle, Warren D., and Tower, Leonard K.: Study of Screeching Combustion in a 6-Inch Simulated Afterburner. NACA TN 3567, 1955.
18. Truman, John C., and Newton, Roger T.: Why Do High-Thrust Engines Screech? Aviation Age, vol. 23, no. 5, May 1955, pp. 136–143.
19. Kaskan, W. E., and Noreen, A. E.: High-Frequency Oscillations of a Flame Held by a Bluff Body. Trans. ASME, vol. 77, no. 6, Aug. 1955, pp. 885–891; discussion, pp. 891–895.
20. Tsien, H. S.: Influence of Flame Front on the Flow Field. Jour. Appl. Mech., vol. 18, no. 2, June 1951, pp. 188–194.
21. Fabri, J., Siestrunck, R., and Fouré, C.: On the Aerodynamic Field of Stabilized Flames. Fourth Symposium (International) on Combustion, The Williams & Wilkins Co. (Baltimore), 1953, pp. 443–450.
22. Lin, C. C.: On the Stability of Two-Dimensional Parallel Flows, pt. I. Quarterly Appl. Math., vol. III, no. 2, July 1945, pp. 117–142; pt. II, vol. III, no. 3, Oct. 1945, pp. 218–234; pt. III, vol. III, no. 4, Jan. 1946, pp. 277–301.
23. Pillow, A. F.: A Review of Hydrodynamic Stability and Its Bearing on Transition to Turbulent Flow in the Boundary Layer. Rep. A.35, Div. Aero., Council Sci. & Ind. Res. (Australia), May 1945.
24. Schubauer, G. B., and Skramstad, H. K.: Laminar-Boundary-Layer Oscillations and Transition on a Flat Plate. NACA Rep. 909, 1948. (Supersedes NACA WR W-8.)
25. Pretsch, J.: The Stability of Two-Dimensional Laminar Flow with Pressure Drop and Pressure Rise. Joint Intelligence Objectives Agency (Wash., D. C.), July 23, 1946.
26. Lessen, Martin: On Stability of Free Laminar Boundary Layer Between Parallel Streams. NACA Rep. 979, 1950. (Supersedes NACA TN 1929.)
27. Heisenberg, Werner: On Stability and Turbulence of Fluid Flows. NACA TM 1291, 1951.
28. Savic, P.: On Acoustically Effective Vortex Motion in Gaseous Jets. Phil. Mag., ser. 7, vol. 32, Sept. 1941, pp. 245–252.

29. Goldstein, S.: On The Stability of Superposed Streams of Fluids of Different Densities. Proc. Roy. Soc. (London), ser. A, vol. 132, Aug. 1, 1931, pp. 524–548.

30. Goldstein, Sydney, ed.: Modern Developments in Fluid Dynamics. Vols. I and II. Clarendon Press (Oxford), 1938.

31. Mestre, André: Étude des Limites de Stabilite en Relation avec la Résistance des Obstacles à l'Écoulement. Combustion Res. and Rev., Butterworths Sci. Pub., 1955, pp. 72–86.

32. Clark, Thomas P., and Bittker, David A.: A study of the Radiation from Laminar and Turbulent Open Propane-Air Flames as a Function of Flame Area, Equivalence Ratio, and Fuel Flow Rate. NACA RM E54F29, 1954.

33. Mickelsen, William R., and Laurence, James C.: Measurement and Analysis of Turbulent Flow Containing Periodic Flow Fluctuations. NACA RM E53F19, 1953.

34. Roshko, Anatol: On the Development of Turbulent Wakes from Vortex Streets. NACA Rep. 1191, 1954. (Supersedes NACA TN 2913.)

35. Blackshear, Perry L., Jr.: Driving Standing Waves by Heat Addition. NACA TN 2772, 1952. (See also Fourth Symposium (International) on Combustion, The Williams & Wilkins Co., 1953, pp. 553–566.)

36. Kaskan, W. E.: An Investigation of Vibrating Flames. Fourth Symposium (International) on Combustion, The Williams & Wilkins Co., 1953, pp, 575–591.

37. Dugger, Gordon L.: Effect of Initial Mixture Temperature on Flame Speed of Methane-Air, Propane-Air, and Ethylene-Air Mixtures. NACA Rep. 1061, 1952. (Supersedes NACA TN's 2170 and 2374.)

38. Dryden, Hugh L.: A Review of the Statistical Theory of Turbulence. Quarterly Appl. Math., vol. I, no. 1, Apr. 1943, pp. 7–42.

REPORT 1361

APPROXIMATE ANALYSIS OF EFFECTS OF LARGE DEFLECTIONS AND INITIAL TWIST ON TORSIONAL STIFFNESS OF A CANTILEVER PLATE SUBJECTED TO THERMAL STRESSES [1]

By Richard R. Heldenfels and Louis F. Vosteen

SUMMARY

An approximate analysis of the nonlinear effects of initial twist and large deflections on the torsional stiffness of a cantilever plate subjected to a nonuniform temperature distribution is presented. The Von Kármán large-deflection equations are satisfied through the use of a variational principle. The results show that initial twist and applied moments can have significant effects on the changes in stiffness produced by nonuniform heating, particularly in the region of the buckling temperature difference. Results calculated by this approximate analysis are in satisfactory agreement with measured torsional deformations and changes in natural frequency.

INTRODUCTION

One of the structural problems of high-speed flight is the reduction of effective stiffness of structures due to the thermal stresses produced by aerodynamic heating. A reduction in torsional stiffness can be an important factor in aeroelastic problems as indicated in references 1 and 2. A similar reduction in stiffness produced by thermal stresses presumably caused the flutter and failures of some structural models described in reference 3. A simple method for calculating the reduction in torsional stiffness of thin wings is presented in reference 4. In reference 5 the results calculated from a small-deflection plate theory are compared with experimentally determined changes in the torsional stiffness of a cantilever plate rapidly heated along the longitudinal edges. The theory used in reference 5 predicted the general effect of thermal stresses on the torsional stiffness, as indicated by measurements of torsional deformation and changes in natural frequency of vibration, but overestimated the magnitude of the changes.

The purpose of this paper is to present the results of an approximate analysis to show that the differences between theory and experiment noted in reference 5 are due to the nonlinear effects of large deflections and initial deformations not included in the small-deflection analysis. The analytical approach used to account for large deflections and initial deformations is presented, the general significance of the results is discussed, and calculated values are compared with the experimental data of reference 5.

SYMBOLS

a	plate length in x-direction
$A_1,A_2, \ldots A_i$	coefficients of series expansion for plate deflection
b	half-plate width in y-direction
C	coefficient of stress function
D	plate flexural stiffness, $\frac{Et^3}{12(1-\mu^2)}$
E	modulus of elasticity
F	stress function defining stress distribution in plate
$f_1,f_2, \ldots f_i$	selected functions of x and y
$I_1,I_2, \ldots I_i$	values obtained from definite integrals
GJ	torsional stiffness
$(GJ)_0$	torsional stiffness of flat, unstressed plate
$\Delta(GJ)$	incremental torsional stiffness
$\Delta(GJ)_i$	initial incremental torsional stiffness before heating
$\Delta(GJ)_{min}$	minimum incremental torsional stiffness
m	nondimensional moment
M	applied moment (positive in direction of positive twist)
p	pressure
t	plate thickness
T	temperature
ΔT	particular temperature difference
ΔT_{cr}	critical value of ΔT
w	total plate deflection
w_i	initial plate deflection
x,y	coordinate axes
α	coefficient of thermal expansion
ϵ	small dynamic perturbation
ζ	exponential parameter of temperature distribution function
θ	twist at plate tip
θ_i	initial twist at plate tip
λ	temperature ratio, $\Delta T/\Delta T_{cr}$
λ_{min}	value of λ corresponding to $\Delta(GJ)_{min}$
μ	Poisson's ratio
ρ	density

[1] Supersedes NACA Technical Note 4067 by Richard R. Heldenfels and Louis F. Vosteen, 1957.

σ_x, σ_y normal stresses in plane of plate in x- and y-directions, respectively, positive for tension

τ_{xy} shear stress in plane of plate

τ time

φ nondimensional twist

φ_i initial nondimensional twist

ω circular frequency

ω_0 circular frequency of unheated perfect plate

ω_i initial circular frequency

ω_{min} minimum circular frequency

∇^2 differential operator, $\frac{\partial^2}{\partial x^2}+\frac{\partial^2}{\partial y^2}$

∇^4 differential operator, $\frac{\partial^4}{\partial x^4}+2\frac{\partial^4}{\partial x^2\partial y^2}+\frac{\partial^4}{\partial y^4}$

Double dot indicates second derivative with respect to time.

ANALYSIS

STATEMENT OF PROBLEM

The studies presented herein are primarily concerned with the twist of a uniformly thick rectangular cantilever plate shown in figure 1. The equations are derived to consider the effects of initial twist, applied moments, and thermal stresses on the torsional deformations and natural frequencies of plates. The analysis involves an approximate solution of the Von Kármán large-deflection equations which have been modified to include the effects of initial imperfections and nonuniform temperature distributions. The modified equations are (from ref. 6)

$$\nabla^4 F=-E\alpha\nabla^2 T+E\left[\left(\frac{\partial^2 w}{\partial x\,\partial y}\right)^2-\frac{\partial^2 w}{\partial x^2}\frac{\partial^2 w}{\partial y^2}-\left(\frac{\partial^2 w_i}{\partial x\,\partial y}\right)^2+\frac{\partial^2 w_i}{\partial x^2}\frac{\partial^2 w_i}{\partial y^2}\right] \tag{1a}$$

$$\nabla^4(w-w_i)=\frac{p}{D}+\frac{t}{D}\left(\frac{\partial^2 F}{\partial y^2}\frac{\partial^2 w}{\partial x^2}+\frac{\partial^2 F}{\partial x^2}\frac{\partial^2 w}{\partial y^2}-2\frac{\partial^2 F}{\partial x\,\partial y}\frac{\partial^2 w}{\partial x\,\partial y}\right) \tag{1b}$$

where F is the stress function such that

$$\sigma_x=\frac{\partial^2 F}{\partial y^2} \tag{2a}$$

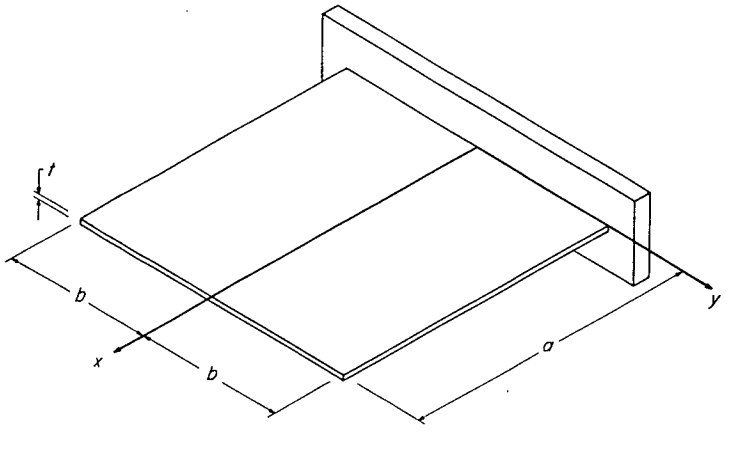


FIGURE 1.—Dimensions and coordinate system of cantilever plate.

$$\sigma_y=\frac{\partial^2 F}{\partial x^2} \tag{2b}$$

$$\tau_{xy}=-\frac{\partial^2 F}{\partial x\,\partial y} \tag{2c}$$

Equation (1a) is the differential equation for compatibility in the plane of the plate and equation (1b) is the differential equation for equilibrium of forces acting perpendicular to the plane of the plate. The solution of equations (1), subject to the proper boundary conditions on the deflections and stresses, describes the behavior of the plate under the applied loads p and the temperature distribution T. For the purpose of this paper the assumption is made that no external loads are applied in the plane of the plate so that the inplane stresses defined by the stress function F are zero at the free boundaries (stress-free edges). Equations (1) apply to both the dynamic and the static problem if p includes the dynamic loads as well as static loads.

APPROXIMATE SOLUTION OF EQUATIONS

Exact solutions of the Von Kármán large-deflection equations are difficult to obtain, but approximate solutions can be obtained to any desired accuracy by several methods. For the analysis herein equations (1) will be satisfied through the use of the following variational principle:

$$\delta\left(\iint\frac{D}{2}\left\{[\nabla^2(w-w_i)]^2-2(1-\mu)\left[\frac{\partial^2(w-w_i)}{\partial x^2}\frac{\partial^2(w-w_i)}{\partial y^2}-\left(\frac{\partial^2(w-w_i)}{\partial x\,\partial y}\right)^2\right]\right\}dx\,dy+\iint\frac{t}{2}\left\{\frac{\partial^2 F}{\partial y^2}\left[\left(\frac{\partial w}{\partial x}\right)^2-\left(\frac{\partial w_i}{\partial x}\right)^2\right]+\frac{\partial^2 F}{\partial x^2}\left[\left(\frac{\partial w}{\partial y}\right)^2-\left(\frac{\partial w_i}{\partial y}\right)^2\right]-2\frac{\partial^2 F}{\partial x\,\partial y}\left(\frac{\partial w}{\partial x}\frac{\partial w}{\partial y}-\frac{\partial w_i}{\partial x}\frac{\partial w_i}{\partial y}\right)\right\}dx\,dy-\iint\frac{t}{2E}\left[\left(\frac{\partial^2 F}{\partial x^2}\right)^2+\left(\frac{\partial^2 F}{\partial y^2}\right)^2-2\mu\frac{\partial^2 F}{\partial x^2}\frac{\partial^2 F}{\partial y^2}+2(1+\mu)\left(\frac{\partial^2 F}{\partial x\,\partial y}\right)^2\right]dx\,dy-\iint t\alpha T\left(\frac{\partial^2 F}{\partial x^2}+\frac{\partial^2 F}{\partial y^2}\right)dx\,dy-\iint p(w-w_i)dx\,dy\Bigg)=0 \tag{3}$$

This principle is essentially a particularization of one given by Reissner (ref. 7) and also has been modified to include the effects of initial deformations and a nonuniform temperature distribution. The deflection w must satisfy the geometrical boundary conditions, that is, the conditions imposed on slopes and deflections. Variation of equation (3) with respect to F yields equation (1a) and the associated natural boundary conditions, and variation with respect to w yields equation (1b) and the associated natural boundary conditions.

The following assumptions for stress, deflection, and temperature are made:

$$\left.\begin{aligned} F&=Cf_1\\ w&=b\theta f_2\\ w_i&=b\theta_i f_2\\ T&=\Delta T f_3\end{aligned}\right\} \tag{4}$$

where the stress coefficient C and the tip twist θ are to be determined by means of the variational principle. The functions f_1, f_2, and f_3, the initial tip twist θ_i, and the temperature coefficient ΔT are presumed to be known. Selection of these quantities is discussed in appendix A. It should be noted here that, although the temperature distribution is considered to vary with time, the shapes of the plate deflection and of the stress function are assumed to remain constant during heating or loading.

The unknown coefficient of the stress function C is obtained by substituting equations (4) into equation (3) and taking the variation with respect to C. The result is

$$C=-E\alpha\,\Delta T\left(\frac{I_2}{I_1}\right)+Eb^2(\theta^2-\theta_i^2)\left(\frac{I_3}{I_1}\right) \tag{5}$$

where

$$I_1=\iint\left[\left(\frac{\partial^2 f_1}{\partial y^2}\right)^2+\left(\frac{\partial^2 f_1}{\partial x^2}\right)^2-2\mu\frac{\partial^2 f_1}{\partial x^2}\frac{\partial^2 f_1}{\partial y^2}+2(1+\mu)\left(\frac{\partial^2 f_1}{\partial x\,\partial y}\right)^2\right]dx\,dy \tag{6}$$

$$I_2=\iint f_3\left(\frac{\partial^2 f_1}{\partial x^2}+\frac{\partial^2 f_1}{\partial y^2}\right)dx\,dy \tag{7}$$

$$I_3=\iint\frac{1}{2}\left[\frac{\partial^2 f_1}{\partial y^2}\left(\frac{\partial f_2}{\partial x}\right)^2+\frac{\partial^2 f_1}{\partial x^2}\left(\frac{\partial f_2}{\partial y}\right)^2-2\frac{\partial^2 f_1}{\partial x\,\partial y}\frac{\partial f_2}{\partial x}\frac{\partial f_2}{\partial y}\right] \tag{8}$$

The relation between the twist, the load, and the temperature is obtained by performing the variation on equation (3) with respect to the twist θ with C held constant. The resulting relationship is

$$Db^2(\theta-\theta_i)I_4+2tCb^2\theta I_3-b\iint pf_2\,dx\,dy=0 \tag{9}$$

where

$$I_4=\iint\left[\left(\frac{\partial^2 f_2}{\partial x^2}\right)^2+\left(\frac{\partial^2 f_2}{\partial y^2}\right)^2+2\mu\frac{\partial^2 f_2}{\partial x^2}\frac{\partial^2 f_2}{\partial y^2}+2(1-\mu)\left(\frac{\partial^2 f_2}{\partial x\,\partial y}\right)^2\right]dx\,dy \tag{10}$$

The pressure loading p now will be considered to consist of a static loading p_s and a dynamic or inertia loading $\rho t\,\ddot{w}$ so that

$$p=p_s-\rho t\,\ddot{w} \tag{11}$$

For this analysis the lateral static load p_s will be restricted to two equal concentrated loads P applied at the corners $x=a$, $y=\pm b$ in such a way as to form a couple about the x-axis. Then

$$\iint pf_2\,dx\,dy=\frac{M}{2b}I_5-\rho tb\ddot{\theta}I_6 \tag{12}$$

where

$$I_5=\iint\delta(x-a)[\delta(y-b)-\delta(y+b)]f_2\,dx\,dy \tag{13}$$

$$I_6=\iint f_2^2\,dx\,dy \tag{14}$$

$$M=2bP \tag{15}$$

and δ is the Dirac delta function.

If the value of C from equation (5) is substituted into equation (9) and the terms are rearranged, the resulting expression is

$$b^2(\theta-\theta_i)I_4=\frac{M}{2D}I_5-\rho\frac{tb^2}{D}\ddot{\theta}I_6+\frac{2tb^2\theta}{D}E\alpha\,\Delta T\frac{I_3I_2}{I_1}-\frac{2tb^4}{D}E\theta(\theta^2-\theta_i^2)\frac{(I_3)^2}{I_1} \tag{16}$$

which gives the relationship between twist, applied moment, inertia loading, and temperature.

DEFINITION OF PARAMETERS

It is convenient to define certain parameters which can be obtained from equation (16) when the large-deflection effects are neglected and the initial twist θ_i is 0. Then, from equation (16)

$$b^2\theta I_4=\frac{M}{2D}I_5-\rho\frac{tb^2}{D}\ddot{\theta}I_6+\frac{2tb^2\theta}{D}E\alpha\,\Delta T\frac{I_3I_2}{I_1} \tag{17}$$

If the plate is not vibrating and no loads are applied, the critical, or buckling, temperature difference is obtained from equation (17) as

$$\Delta T_{cr}=\frac{D}{2E\alpha t}\frac{I_1I_4}{I_2I_3} \tag{18}$$

Similarly, when the plate is not vibrating and the temperature is uniform ($\Delta T=0$) but the load is acting, the moment-twist relation is given by

$$\theta=\frac{Ma}{(GJ)_0} \tag{19}$$

where $(GJ)_0$ is the torsional stiffness of the flat plate given by

$$(GJ)_0=2ab^2D\frac{I_4}{I_5} \tag{20}$$

In the absence of heating and loading the frequency may be found to be

$$\omega_0^2=\frac{D}{\rho t}\frac{I_4}{I_6} \tag{21}$$

When equations (18), (19), (20), and (21) are substituted into equation (16) the result may be written as

$$\theta-\theta_i=\frac{Ma}{(GJ)_0}-\frac{1}{\omega_0^2}\ddot{\theta}+\frac{\Delta T}{\Delta T_{cr}}\theta-\theta(\theta^2-\theta_i^2)\frac{2Etb^2}{D}\frac{(I_3)^2}{I_1I_4} \tag{22}$$

If a "nondimensional" twist is defined so that

$$\varphi=\theta\sqrt{\frac{2Etb^2}{D}\frac{(I_3)^2}{I_1I_4}} \tag{23}$$

along with a nondimensional moment

$$m=\frac{Ma}{(GJ)_0}\sqrt{\frac{2Etb^2}{D}\frac{(I_3)^2}{I_1I_4}} \tag{24}$$

and a temperature ratio

$$\lambda=\frac{\Delta T}{\Delta T_{cr}} \tag{25}$$

equation (22) may be written simply as

$$\varphi-\varphi_i=m+\lambda\varphi-\varphi(\varphi^2-\varphi_i^2)-\frac{1}{\omega_0^2}\ddot{\varphi} \tag{26}$$

APPLICATION TO STATIC PROBLEM

The relationship between twist, moment, and temperature is given by equation (26) when the dynamic term $\frac{1}{\omega_0^2}\ddot{\varphi}$ is 0. Equation (26) then becomes

$$\varphi-\varphi_i=m+\lambda\varphi-\varphi(\varphi^2-\varphi_i^2) \tag{27}$$

The incremental stiffness of the plate, defined as the rate of change of moment with respect to twist, is given by

$$\frac{\Delta(GJ)}{(GJ)_0}=\frac{a}{(GJ)_0}\frac{\partial M}{\partial\theta}$$

or, from equation (27),

$$\frac{\Delta(GJ)}{(GJ)_0}=\frac{\partial m}{\partial\varphi}=1-\lambda+3\varphi^2-\varphi_i^2 \tag{28}$$

APPLICATION TO DYNAMIC PROBLEM

In order to determine the effect of temperature, moment, and initial twist on the natural frequency of torsional vibration, the quantity φ in equation (26) is replaced by $\varphi+\epsilon\sin\omega\tau$ where φ is considered to be the static solution obtained from equation (27) and ϵ represents a small dynamic perturbation about the static equilibrium position. Subtracting equation (27) from the perturbated relation, neglecting higher order terms in ϵ, and dividing by $\epsilon\sin\omega\tau$ yields

$$1=\lambda-3\varphi^2+\varphi_i^2+\left(\frac{\omega}{\omega_0}\right)^2$$

The frequency may then be written in terms of the twist and temperature as

$$\left(\frac{\omega}{\omega_0}\right)^2=1-\lambda+3\varphi^2-\varphi_i^2 \tag{29}$$

which is identical to the incremental stiffness (eq. (28)). This identity results from assuming similar deflection mode shapes for thermal buckling, twist due to applied moment, and torsional vibration and would not be expected to apply if the mode shapes involved were different.

RESULTS AND DISCUSSION

GENERAL RESULTS OF EQUATIONS

The behavior of the plate as determined by equation (26) is discussed in the following sections for several combinations of conditions. In most cases the calculations include large values of initial twist and applied moment and have been carried well into the region where the temperature difference ΔT exceeds the critical value. Although some of the results may be beyond the range for which the analysis is accurate, these results have been presented to illustrate the trends indicated by the equations despite the fact that they may not be quantitatively correct in some regions.

Twisting due to an applied moment.—The twisting of the plate due to an applied moment is given by equation (27) if the temperature ratio λ is set equal to 0. The results from this expression are presented in figure 2 for various values of the initial twist.

In figure 2, small-deflection results would plot as lines at 45° to the coordinate axes. The large-deflection results become increasingly different as the moment or initial twist is increased and indicate that the plate becomes substantially stiffer as the twist is increased.

Buckling due to nonuniform heating.—The twist of the plate (assuming that the buckling mode is a twisting action) is given by equation (27) when the moment m is 0; for the initially flat plate φ_i would also be 0. The initially flat, or perfect, plate begins to deform only after the critical temperature difference is reached, whereas, as indicated by equation (27), the plate with initial twist begins to deform immediately upon heating. The results obtained from evaluation of equation (27) are given in figure 3 for several values of the initial twist.

If the initial twist is large, a plot of twist against temperature ratio, like figure 3, does not give an accurate indication of the buckling temperature. Only if the initial twist is small is there a definite knee in the curve as the buckling temperature is approached, but this knee occurs below the buckling temperature of the perfect plate.

Combined action of applied moment and nonuniform heating.—Equation (27) applies directly to this case but may be more conveniently written as

$$\varphi-\varphi'-\lambda'\varphi+\varphi(\varphi^2-\varphi'^2)=0 \tag{30}$$

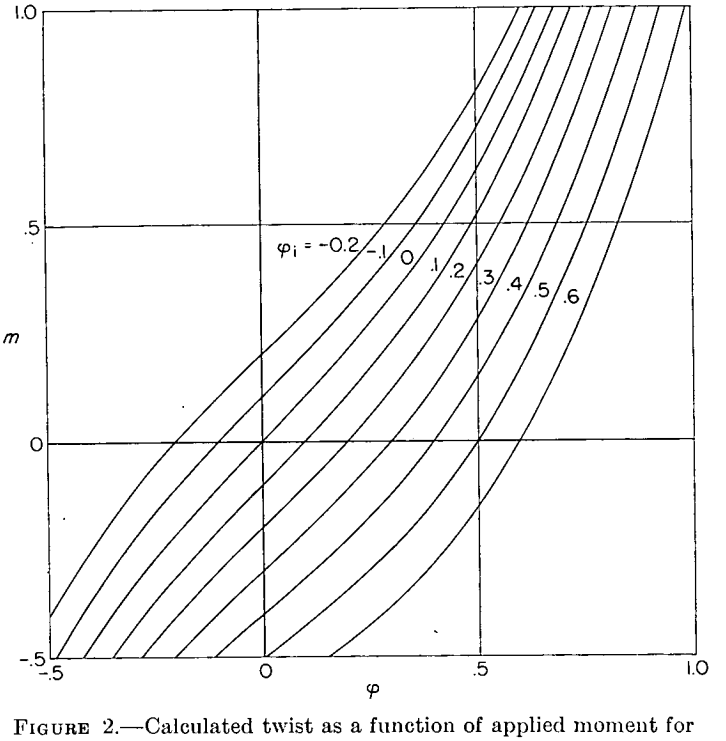


FIGURE 2.—Calculated twist as a function of applied moment for several values of the initial twist.

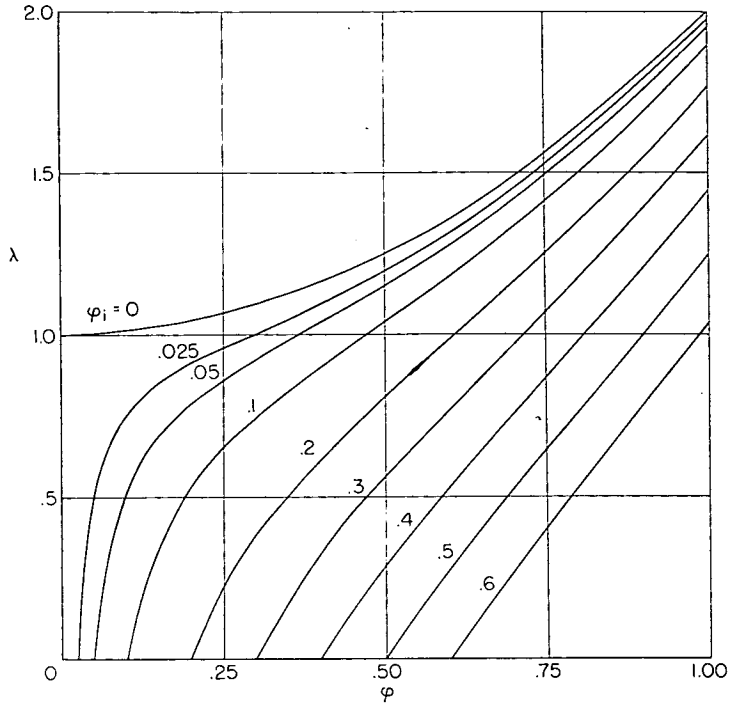


FIGURE 3.—Calculated twist as a function of temperature ratio for several values of initial twist.

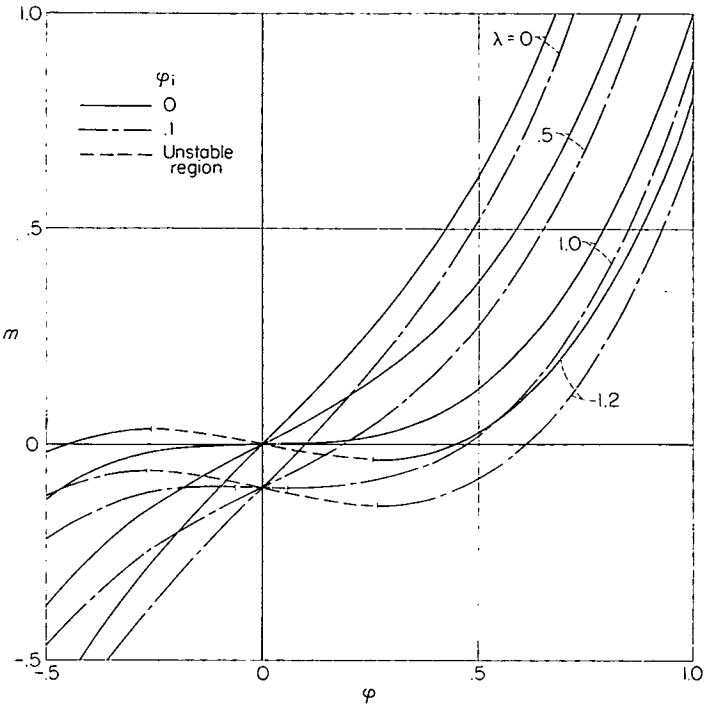


FIGURE 4.—Calculated twist as a function of applied moment for several combinations of temperature ratio and initial twist.

where

$$\varphi' = \varphi_i + m \tag{31a}$$

and

$$\lambda' = \lambda - (m^2 + 2m\varphi_i) \tag{31b}$$

Equation (30) now has the same form as equation (27) when m is set equal to 0. The results plotted in figure 3 then apply to this case also if φ_i is replaced by φ' and λ by λ'. The moment then effectively acts the same as an initial twist if the temperature ratio is reduced by the quantity $m^2+2m\varphi_i$.

In figure 4 the relation between moment and twist has been indicated for two values of initial twist and several values of λ. These curves show the characteristic increase in stiffness as the twist increases but also show a reduction in stiffness as the temperature ratio increases. These changes in stiffness are examined further in the following section. The portions of the curves where the slope is negative have been shown as dashed lines and are regions of unstable equilibrium which would not exist in the physical problem. The unstable portion of the curve exists whenever $\lambda+\varphi_i^2-3\varphi^2>1$.

Frequency and incremental stiffness.—As has been noted, the square of the frequency ratio (eq. (29)) varies in the same manner as the incremental stiffness (eq. (28)) and, therefore, any of the following discussion pertaining to stiffness applies directly to the square of the frequency. Also, the figures which are presented for the incremental stiffness have been labeled with the square of the frequency ratio as well as with the stiffness ratio.

The variation in incremental stiffness with temperature given by equation (28) is shown in figure 5 for several values of initial twist when m is equal to 0. The results show that, when the perfect plate is heated, the stiffness decreases linearly as the thermal stresses develop and becomes zero

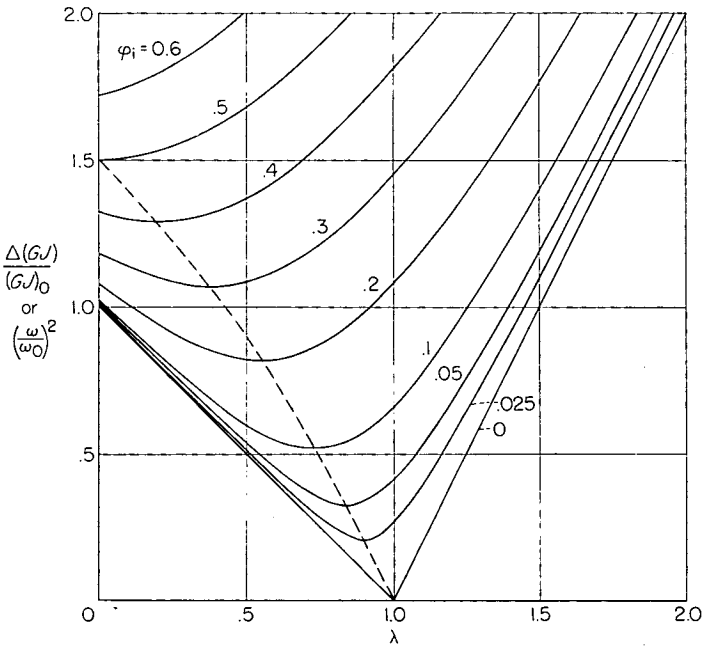


FIGURE 5.—Calculated incremental stiffness as a function of temperature ratio for several values of initial twist.

when the buckling temperature difference is reached Further heating causes the plate to twist and the twisting in turn leads to an increase in stiffness at a rate twice that of the initial decrease.

If the plate has an initial twist, the heating causes the twist to increase as the heating progresses. This twist leads to an increase in stiffness that tends to counteract the reduction produced by thermal stresses and, as a result, the stiffness first decreases and then increases without going to zero. The points of minimum stiffness occur at temperatures lower than the buckling temperature. The locus

of points of minimum stiffness has been indicated in figure 5 by the dashed line. If the initial twist is sufficiently large, the stiffness does not decrease but increases with heating.

When a moment is applied to the plate, figure 5 will indicate the incremental stiffness of the plate if φ_i is replaced by φ' and λ by λ' (as defined by eqs. (31a) and (31b)).

The locus of points where the incremental stiffness is a minimum is given by the equations

$$\frac{\Delta(GJ)_{min}}{(GJ)_0}=6\left(\frac{\varphi_i+m}{4}\right)^{2/3} \tag{32}$$

$$\lambda_{min}=1-\varphi_i^2-3\left(\frac{\varphi_i+m}{4}\right)^{2/3} \tag{33}$$

or

$$\frac{\Delta(GJ)_{min}}{(GJ)_0}=2(1-\lambda_{min}-\varphi_i^2) \tag{34}$$

Equations (33) and (34) show that the nonuniform heating will increase the stiffness of the plate if the initial twist is geater than that given by

$$3\left(\frac{\varphi_i+m}{4}\right)^{2/3}+\varphi_i^2=1$$

The initial incremental stiffness of the plate is given by equation (28) when λ is 0. The ratio of the minimum to the initial incremental stiffness therefore may be written as

$$\frac{\Delta(GJ)_{min}}{\Delta(GJ)_i}=\frac{6\left(\frac{\varphi_i+m}{4}\right)^{2/3}}{1+3\varphi^2-\varphi_i^2} \tag{35}$$

Some results from equation (35) have been plotted in figure 6. This figure indicates that small changes in the initial twist may cause large changes in the minimum incremental stiffness. The effects of applied moment are again similar to those of initial twist and certain combinations of the two can lead to drastic stiffness changes. For negative values of φ_i the curves would be similar, with the stiffness ratio going to zero whenever $\varphi_i=-m$.

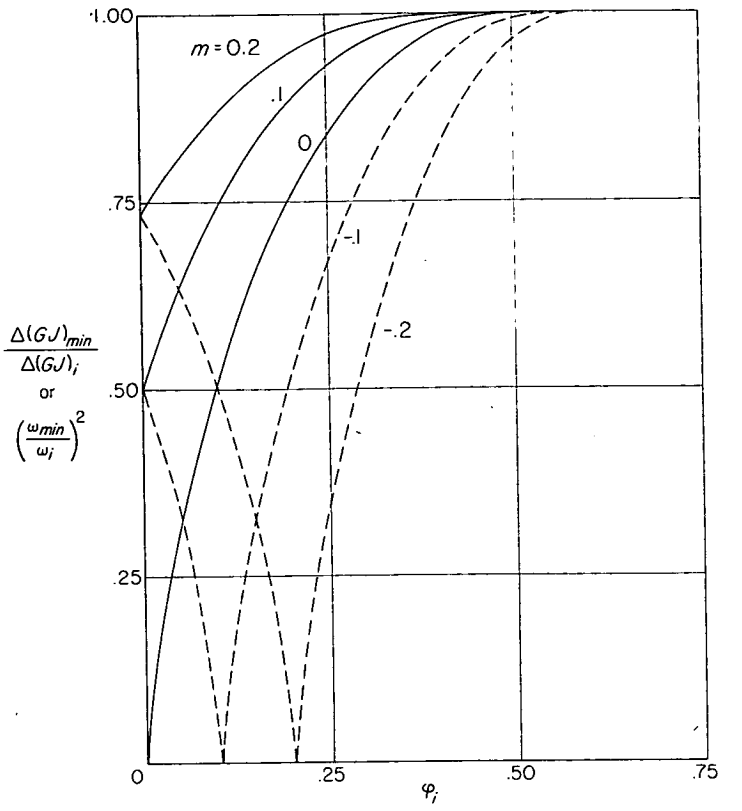


FIGURE 6.—Calculated ratio of minimum incremental stiffness to initial incremental stiffness as a function of initial twist for several values of applied moment.

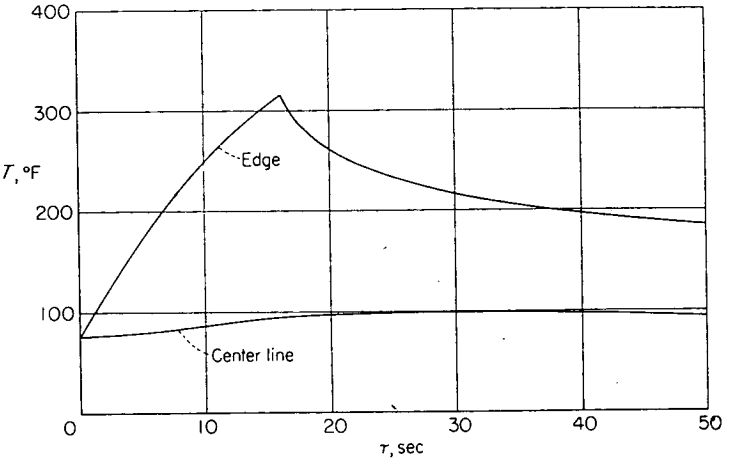


FIGURE 7.—Measured temperature histories for a heated edge and the center line of the plate test specimen.

COMPARISON WITH EXPERIMENT

Results calculated with the previously derived equations are compared in the following sections with the experimental results reported in reference 5. The results given in reference 5 are for a square cantilever plate which was heated along the two longitudinal edges by carbon-rod radiators. Typical temperature histories of points on the heated edge and on the longitudinal center line are given in figure 7. Heat was supplied to the plate edges for 16 seconds; then the plate was allowed to cool. The deformations of the plate under the influence of nonuniform heating were determined for the conditions of no load and applied positive and negative tip moments. The changes in natural frequency of the first torsion mode were also measured during a heating test.

The expressions used in reference 5 for stresses, deflections, and temperature are retained except that herein only three terms are used for the deflections. In nondimensional form these expressions are

$$f_1=\left[\left(\frac{x}{a}\right)^2-1\right]^2\left[\left(\frac{y}{b}\right)^2-1\right]^2 \tag{36}$$

$$f_2=\frac{\frac{y}{b}\left[\left(\frac{x}{a}\right)^2+A_1\left(\frac{x}{a}\right)^3+A_2\left(\frac{x}{a}\right)^4\right]}{1+A_1+A_2} \tag{37}$$

and

$$f_3=\left(\frac{y}{b}\right)^r \tag{38}$$

The function f_1 satisfies the condition of zero stress on the free edges and f_2 specifies zero slope and deflection along the root. The two undetermined coefficients of equation (37) are established from the small-deflection buckling analysis and carried through the large-deflection analysis as constants. Their values are given in appendix A along with data on the influence of the number of terms in the deflection function on the accuracy with which the buckling temperature difference, natural frequency, and ratio of twist to an applied moment can be calculated. The exponential parameter ζ of the temperature function is adjusted to approximate the variation in the temperature distribution during a test.

The numerical evaluation of the integrals and related functions required for comparison of theory and experiment are given in appendix B.

Initial plate shape.—The initial shape of the plate of reference 5 was measured and is indicated in figure 8. In the selection of a value of initial twist, the higher order shapes (which are unlikely to have much influence on the twisting) have been ignored. The free corners were connected by a straight line in order to obtain a value of initial twist of $\theta_i=0.35°$ which was used for comparison of theory and experiment.

Twist due to an applied moment.—The deformations resulting from heating for three values of applied tip moment are presented in figure 9 and compared with curves calculated by use of a value of $\theta_i=0.35°$. The agreement between theory and experiment is satisfactory, although the theory overestimates the twist in the vicinity of the maximum temperature difference (about 16 seconds). No theoretical results are presented past 20 seconds because, beyond this time, the actual temperature distribution cannot be represented very well by the one-parameter temperature function.

Another comparison of measured and calculated deformations is shown in figure 10 where the abscissa is the temperature difference instead of time. Because the shape of the temperature distribution changes with time, the portion of the curve for decreasing ΔT does not retrace the heating portion.

Natural frequency.—The changes in natural frequency during a heating test are shown in figure 11 and compared

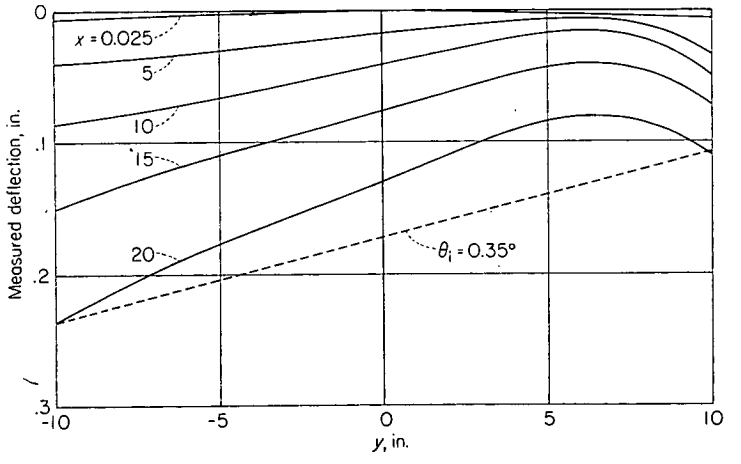


FIGURE 8.—Initial shape of plate test specimen.

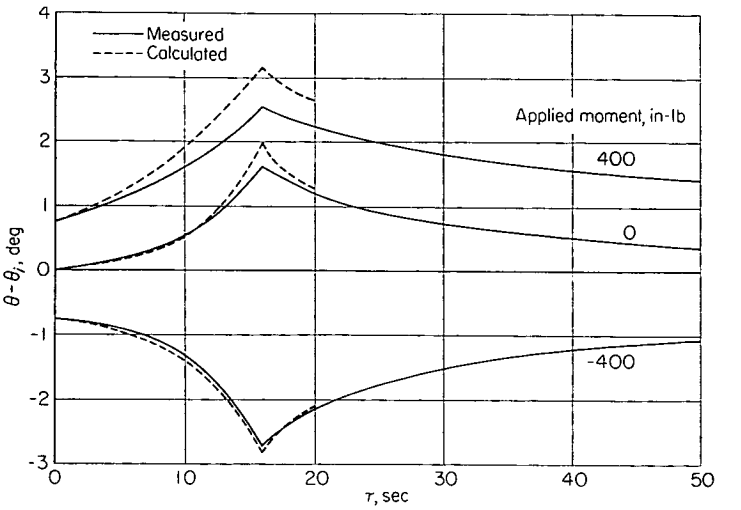


FIGURE 9.—Comparison of measured and calculated values of twist as a function of time for the rapidly heated plate for three values of applied moment.

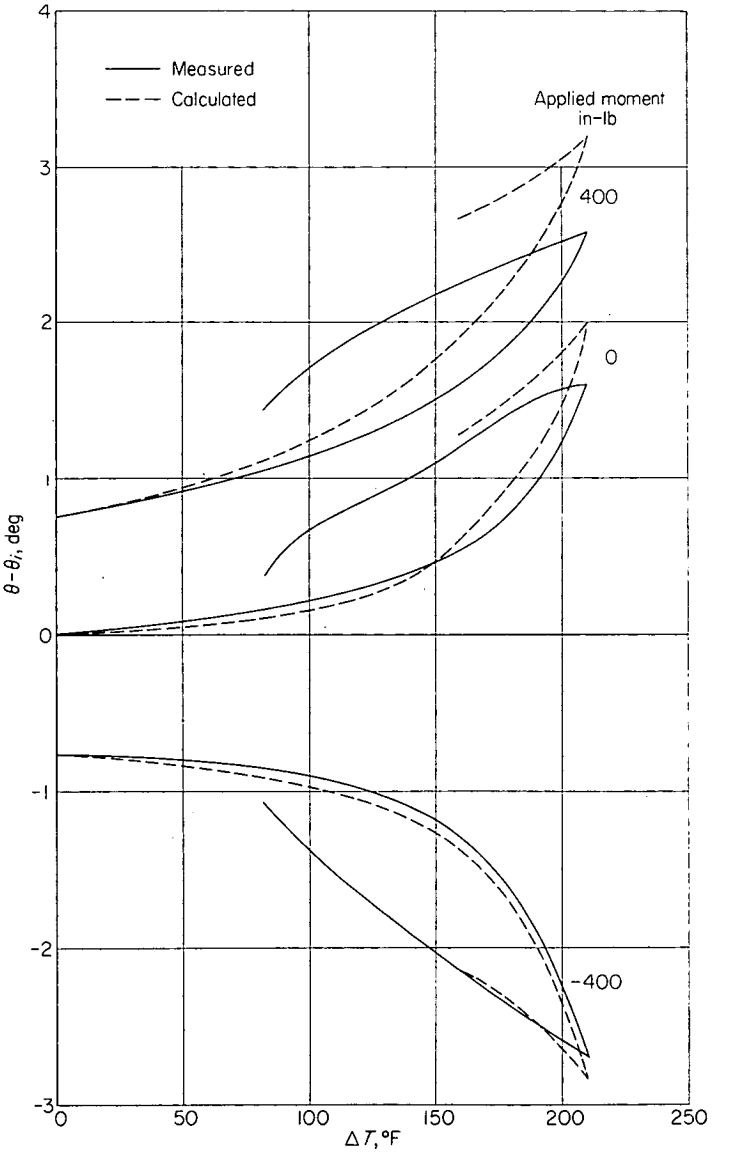


FIGURE 10.—Comparison of measured and calculated values of twist as a function of temperature difference for three values of the applied moment.

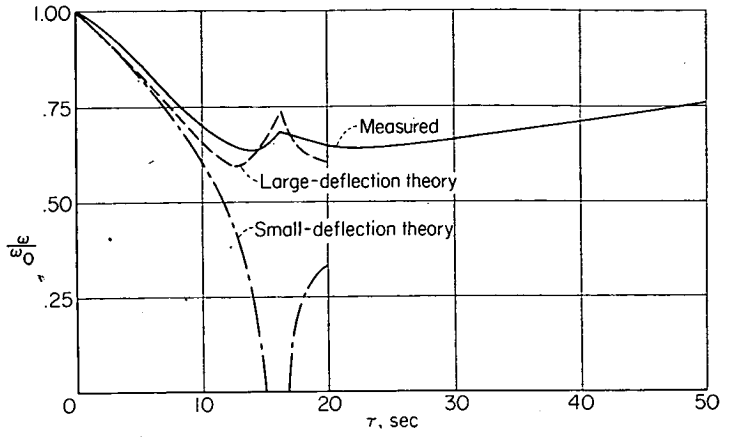


FIGURE 11.—Comparison of measured and calculated values of frequency ratio as a function of time for the rapidly heated plate.

with a calculated curve for $\theta_i = 0.35°$ and with the small-deflection results of reference 5. The results calculated by the use of the large-deflection equations are in good agreement with experimental values and account for the frequency increase measured in the vicinity of the buckling temperature. A substantial improvement is noted over the predictions of small-deflection theory. In figure 12 the frequency ratio is shown as a function of temperature difference.

CONCLUDING REMARKS

An approximate analysis of the effects of initial twist and large deflections on the torsional stiffness of a cantilever plate subjected to nonuniform heating shows that for a perfectly flat plate the effective stiffness, and thus the torsional frequency, decreases with increasing thermal stress, just as predicted by small-deflection theory, and goes to zero when the buckling temperature difference is reached. Beyond the buckling temperature, however, the stiffness, and thus the frequency, increases as the plate twists. If the plate has an initial twist, it begins to deform immediately upon heating and the stiffness decreases in much the same way as that of the perfect plate. The incremental stiffness of the initially twisted plate, however, reaches a minimum greater than zero before the theoretical buckling temperature difference is reached; further heating then increases the stiffness. The minimum incremental stiffness is a function of the initial twist and, if the initial twist is sufficiently large, no reductions in stiffness are obtained and nonuniform heating then always increases the stiffness.

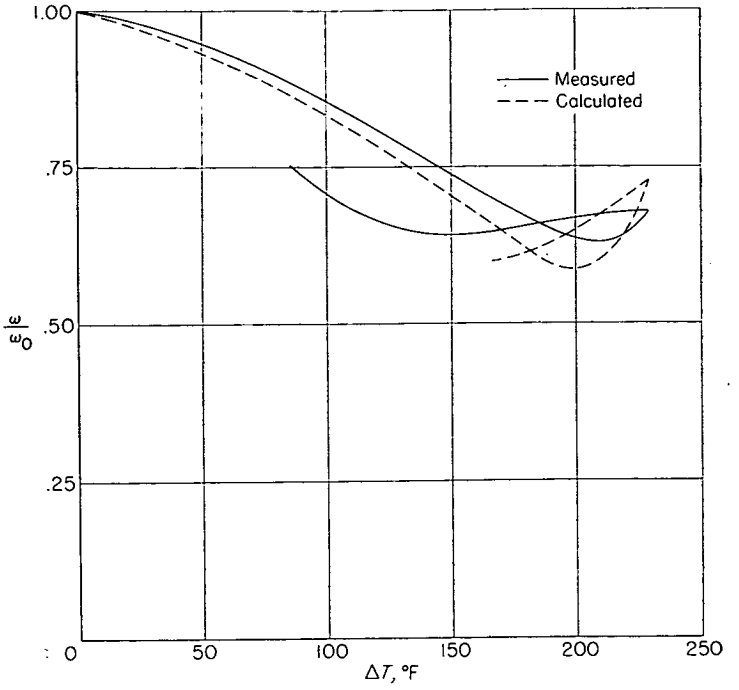


FIGURE 12.—Comparison of measured and calculated values of the frequency ratio as a function of temperature difference.

These results for stiffness changes associated with the torsional frequency are also applicable to the stiffness of the plate with respect to small changes in the applied moment. In this case the applied moment has an effect similar to the effect of an initial twist. If the applied moment exactly counteracts the initial twist, the plate behaves in much the same way as the perfect plate.

Calculated results were compared with available experimental data and were found to be in satisfactory agreement in view of the approximate nature of the calculations.

LANGLEY AERONAUTICAL LABORATORY,
NATIONAL ADVISORY COMMITTEE FOR AERONAUTICS,
LANGLEY FIELD, VA., *May 15, 1957.*

APPENDIX A

DISCUSSION OF MODAL FUNCTIONS USED IN THE ANALYSIS

In the analysis of the torsional deformations of the cantilever plate by small-deflection theory, a deflection function containing six terms antisymmetrical in the coordinate y was used. The function (eq. (8) in ref. 5) is

$$w=A_{12}x^2y+A_{14}x^2y^3+A_{22}x^3y+A_{24}x^3y^3+A_{32}x^4y+A_{34}x^4y^3 \quad \text{(A1)}$$

The effect of various combinations of terms on the calculated critical temperature difference, torsional frequency, and moment-twist relation was investigated for a square cantilever plate ($a/b=2$) by use of the small-deflection theory of reference 5. The following table shows the results obtained by starting with a single term A_{12} and then progressing through other combinations to six terms:

Terms used	$\frac{\Delta T_{cr}}{K_1}$	$\frac{\omega_0^2}{K_2}$	$\frac{M}{\theta}$
A_{12}	103.9	127.0	0.324×10^6
A_{12}, A_{22}	57.7	77.5	.278
A_{12}, A_{22}, A_{32}	50.4	71.3	.273
A_{12}, A_{22}, A_{14}, A_{24}	57.2	77.4	.278
A_{12}, A_{22}, A_{32}, A_{14}, A_{24}, A_{34}	50.0	70.1	.273

where K_1 and K_2 represent constants that include the plate dimensions and material properties.

Inasmuch as the tabulated values were obtained from an application of the Rayleigh-Ritz procedure, the lowest value is the most accurate. The use of six terms improves the accuracy less than 2 percent over three terms and, consequently, is not worth the extra complication. The large-deflection analysis thus can be made by use of only three terms. The deflection function is nondimensionalized for this analysis and expressed in the form

$$f_2=\frac{\frac{y}{b}\left[\left(\frac{x}{a}\right)^2+A_1\left(\frac{x}{a}\right)^3+A_2\left(\frac{x}{a}\right)^4\right]}{1+A_1+A_2} \quad \text{(A2)}$$

The relative values of these coefficients for the conditions given in the preceding table were obtained from the small-deflection analysis of reference 5 for the square cantilever plate ($a/b=2$) with the following results:

Condition	$\frac{1}{1+A_1+A_2}$	$\frac{A_1}{1+A_1+A_2}$	$\frac{A_2}{1+A_1+A_2}$
Thermal buckling ($\lambda=1$, $\omega/\omega_0=0$)	4.61	−5.75	2.14
Torsional vibration ($\lambda=0$, $\omega/\omega_0=1$)	3.63	−4.06	1.42
Applied moment ($\lambda=0$)	2.36	−2.01	0.65
Applied moment ($\lambda=0.5$)	3.10	−3.20	1.10

The variation of f_2 with x/a for these four conditions has been plotted in figure 13. The table indicates a wide variation in the relative values of the coefficients but the plotted data show that the deflection shapes are all approximately the same. Then, so long as the calculations are used to indicate changes from the initial conditions, any of the modes indicated should be satisfactory.

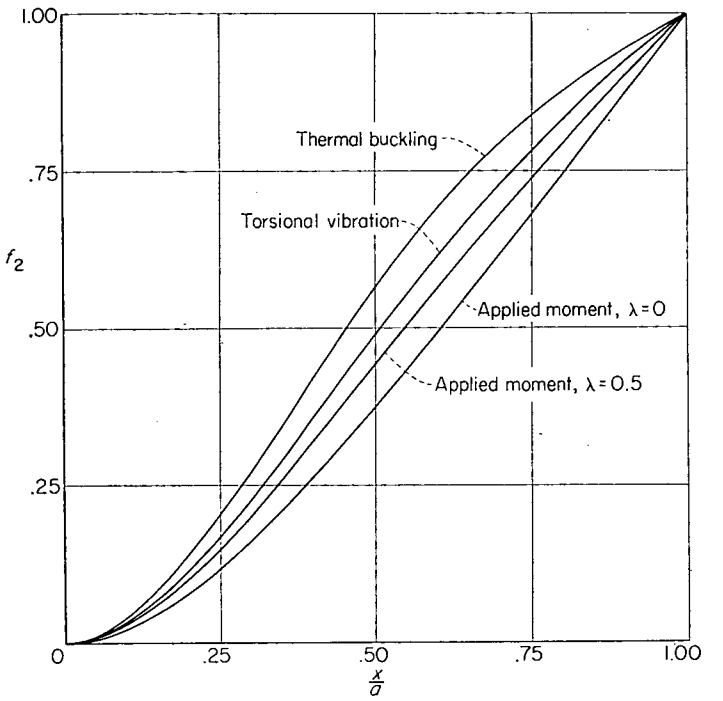


FIGURE 13.—Comparison of deflected shapes for thermal buckling, torsional vibration, and twist due to an applied moment as given by small-deflection theory.

In addition to the deflection function of equation (A2), a stress function and a temperature function are required in the analysis and have been selected to correspond to those of reference 5. For convenience, the functions are expressed in nondimensional form as follows:

$$f_1=\left[\left(\frac{x}{a}\right)^2-1\right]^2\left[\left(\frac{y}{b}\right)^2-1\right]^2 \quad \text{(A3)}$$

$$f_3=\left(\frac{y}{b}\right)^\zeta \quad \text{(A4)}$$

The exponent ζ must be selected to describe best the measured temperature distribution at the time of interest. Note that equation (A4) requires that the specified temperature difference ΔT be the difference between temperatures at the heated edges and the longitudinal center line. The function f_1 has been chosen so that the stresses vanish on the free boundaries. Along the root ($x=0$) the function requires that the plate be free to expand parallel to the y-axis. Although this requirement does not indicate a "built-in" condition, it probably resembles the actual test condition.

APPENDIX B

EVALUATION OF INTEGRALS AND RELATED FUNCTIONS

The integrals indicated in the analysis have been evaluated in terms of the plate dimensions and the nondimensional functions given in appendix A. The integrals are as follows:

$$I_1=\int_0^a\int_{-b}^b\left[\left(\frac{\partial^2 f_1}{\partial y^2}\right)^2+\left(\frac{\partial^2 f_1}{\partial x^2}\right)^2-2\mu\,\frac{\partial^2 f_1}{\partial x^2}\,\frac{\partial^2 f_1}{\partial y^2}+2(1+\mu)\left(\frac{\partial^2 f_1}{\partial x\,\partial y}\right)^2\right]dx\,dy=\left(\frac{128}{105}\right)^2\frac{b}{a^3}\left[7\left(\frac{a}{b}\right)^4+4\left(\frac{a}{b}\right)^2+7\right] \tag{B1}$$

$$I_2=\int_0^a\int_{-b}^b f_3\left(\frac{\partial^2 f_1}{\partial x^2}+\frac{\partial^2 f_1}{\partial y^2}\right)dx\,dy=\frac{128}{15}\,\frac{a}{b}\,\frac{\zeta}{(\zeta+3)(\zeta+1)} \tag{B2}$$

$$I_3=\int_0^a\int_{-b}^b\frac{1}{2}\left[\frac{\partial^2 f_1}{\partial y^2}\left(\frac{\partial f_2}{\partial x}\right)^2+\frac{\partial^2 f_1}{\partial x^2}\left(\frac{\partial f_2}{\partial y}\right)^2-2\,\frac{\partial^2 f_1}{\partial x\,\partial y}\,\frac{\partial f_2}{\partial x}\,\frac{\partial f_2}{\partial y}\right]dx\,dy=\frac{128}{15ab\,(1+A_1+A_2)^2}\left(\frac{4}{105}+\frac{A_1^2}{35}+\frac{16A_2^2}{693}+\frac{A_1}{16}+\frac{16A_2}{315}+\frac{A_1A_2}{20}\right) \tag{B3}$$

$$I_4=\int_0^a\int_{-b}^b\left[\left(\frac{\partial^2 f_2}{\partial x^2}\right)^2+\left(\frac{\partial^2 f_2}{\partial y^2}\right)^2+2\mu\left(\frac{\partial^2 f_2}{\partial x^2}\,\frac{\partial^2 f_2}{\partial y^2}\right)+2(1-\mu)\left(\frac{\partial^2 f_2}{\partial x\,\partial y}\right)^2\right]dy\,dx=\frac{b}{a^3(1+A_1+A_2)^2}\left[\frac{8}{3}+8A_1^2+\frac{96}{5}A_2^2+8A_1+\frac{32A_2}{3}+24A_1A_2+2(1-\mu)\left(\frac{a}{b}\right)^2\left(\frac{8}{3}+\frac{18A_1^2}{5}+\frac{32A_2^2}{7}+6A_1+\frac{32A_2}{5}+8A_1A_2\right)\right] \tag{B4}$$

$$I_5=\int_0^a\int_{-b}^b\delta(x-a)\,[\delta(y-b)-\delta(y+b)]f_2\,dy\,dx=2 \tag{B5}$$

$$I_6=\int_0^a\int_{-b}^b f_2^2\,dy\,dx=\frac{2ab}{3(1+A_1+A_2)^2}\left(\frac{1}{5}+\frac{A_1^2}{7}+\frac{A_2^2}{9}+\frac{A_1}{3}+\frac{2A_2}{7}+\frac{A_1A_2}{4}\right) \tag{B6}$$

For the square cantilever plate ($a/b=2$) and the values of A_1 and A_2 given in appendix A for the thermal-buckling mode, the integrals I_1 to I_4 reduce to the following when Poisson's ratio μ equals 0.33:

$$I_1=\left(\frac{128}{105}\right)^2\frac{135}{2a^2} \tag{B7}$$

$$I_2=\frac{256}{15}\,\frac{\zeta}{(\zeta+3)(\zeta+1)} \tag{B8}$$

$$I_3=\frac{1.520}{a^2} \tag{B9}$$

$$I_4=\frac{9.567}{a^2} \tag{B10}$$

The integrals I_5 and I_6 have not been included but are discussed subsequently.

The critical temperature difference given by equation (18) then becomes

$$\Delta T_{cr}=18.5\,\frac{D}{E\alpha t a^2}\left[\frac{(\zeta+1)(\zeta+3)}{\zeta}\right] \tag{B11}$$

The twist and applied moment are related to their corresponding nondimensional quantities by equations (23) and (24) and may now be expressed as

$$\varphi=0.035\theta\sqrt{\frac{Eta^2}{D}} \tag{B12}$$

$$m=0.035\frac{Ma}{(GJ)_0}\sqrt{\frac{Eta^2}{D}} \tag{B13}$$

Use of the thermal-buckling mode yields incorrect values for the natural frequency and the twist due to applied moment. In addition, the measured values differ slightly from the correct calculated values as a result of the imperfect clamping at the root of the cantilever plate. For these reasons, the measured initial values of torsional frequency and twist due to an applied moment are used in the calculations and the changes produced by the heating cycle are calculated from the following equations:

$$\lambda=1-\frac{\varphi_i+m}{\varphi}+\varphi^2-\varphi_i^2 \tag{B14}$$

$$\left(\frac{\omega}{\omega_0}\right)^2=1-\lambda+3\varphi^2-\varphi_i^2 \tag{B15}$$

The integrals I_5 and I_6 are needed only to calculate the initial natural frequency and twist due to applied moment and, thus, have not been evaluated for the mode shape of thermal buckling.

In the calculations, results of which are presented in figures 9, 10, 11, and 12, the following quantities were used:

$E=10.6\times10^6$ psi
$\alpha=12.8\times10^{-6}$ °F^{-1}
$\mu=0.33$
$t=0.25$ in.
$a=20$ in.
$b=10$ in.
$\theta_i=0.35°$

REFERENCES

1. Dryden, Hugh L., and Duberg, John E.: Aeroelastic Effects of Aerodynamic Heating. Proc. of the Fifth AGARD General Assembly (Canada), June 15–16, 1955, pp. 102–107.
2. Bisplinghoff, R. L.: Some Structural and Aeroelastic Considerations of High-Speed Flight—The Nineteenth Wright Brothers Lecture. Jour. Aero. Sci., vol. 23, no. 4, Apr. 1956, pp. 289–329, 367.
3. Heldenfels, Richard R., and Roseerans, Richard: Preliminary Results of Supersonic-Jet Tests of Simplified Wing Structures. NACA RM L53E26a, 1953.
4. Budiansky, Bernard, and Mayers, J.: Influence of Aerodynamic Heating on the Effective Torsional Stiffness of Thin Wings. Jour. Aero. Sci., vol. 23, no. 12, Dec. 1956, pp. 1081–1093, 1108.
5. Vosteen, Louis F., and Fuller, Kenneth E.: Behavior of a Cantilever Plate Under Rapid-Heating Conditions. NACA RM L55E20c, 1955.
6. Gossard, Myron L., Seide, Paul, and Roberts, William M.: Thermal Buckling of Plates. NACA TN 2771, 1952.
7. Reissner, Eric: On a Variational Theorem for Finite Elastic Deformations. Jour. Math. and Phys., vol. XXXII, nos. 2–3, July-Oct. 1953, pp. 129–135.

REPORT 1362

THEORETICAL COMBUSTION PERFORMANCE OF SEVERAL HIGH-ENERGY FUELS FOR RAMJET ENGINES [1]

By Leonard K. Tower, Roland Breitwieser, and Benson E. Gammon

SUMMARY

An analytical evaluation of the theoretical ramjet performance of magnesium, magnesium—octene-1 slurries, aluminum, aluminum—octene-1 slurries, boron, boron—octene-1 slurries, carbon, hydrogen, α-methylnaphthalene, diborane, pentaborane, and octene-1 is presented herein. Combustion temperature, air specific-impulse, and fuel specific-impulse data are presented for each fuel over a range of equivalence ratios at an inlet air temperature of 560° R and a combustion pressure of 2 atmospheres.

It was assumed that chemical equilibrium was attained during the combustion but that the expansion in the exhaust nozzle occurred with composition fixed. Thermal and velocity equilibrium was assumed between gases and condensed phases at all times.

Magnesium, magnesium—octene-1 slurries, aluminum, aluminum—octene-1 slurries, boron, boron—octene-1 slurries, pentaborane, diborane, and hydrogen provide air specific impulses exceeding those of octene-1. At any fixed air specific impulse below 152 seconds, the fuel weight specific impulses of hydrogen, diborane, pentaborane, boron, and boron—octene-1 slurries are superior to octene-1. The fuel volume specific impulses of boron, aluminum, carbon, boron—octene-1 slurries, magnesium, pentaborane, α-methylnaphthalene, and magnesium—octene-1 slurries are superior to octene-1.

The effects of inlet air temperature and combustion pressure are investigated for some of the fuels. Because of the limited range of inlet conditions considered, means of extending these data to other inlet conditions are presented.

Determination of air specific-impulse efficiency and combustion efficiency for experimental combustion by means of the theoretical data herein is discussed. The use of the theoretical performance data in determining the relative flows of the various fuels to an engine operating at a fixed thrust level is described.

INTRODUCTION

The ever increasing performance required of high-speed aircraft places new demands upon the propulsion system. Improved range, thrust, combustion efficiency, and combustion stability characteristics may possibly be obtained by the use of the special jet-engine fuels. These materials promise advantages over conventional hydrocarbon fuels because of their higher heating values and because of the ease and stability of their combustion.

The use of special fuels is warranted for high-speed flight because the cost of the fuel is often only a small part of the total cost of aircraft operation. This is particularly true in the case of nonreturn guided missiles.

Various fuels of interest for air-breathing engines are certain light elements such as boron and aluminum, alloys and hydrides of these elements, and slurries or paintlike suspensions of the solid materials in a liquid hydrocarbon. The heating values of these substances are higher than those of the ordinary jet fuels on either a gravimetric or a volumetric basis. Hydrocarbons having a high volumetric heating value have also been of interest. Table I presents the heating values and certain physical properties for some of the fuels.

Considerable experimental work, summarized in reference 1, has been conducted with certain high-energy fuels to determine their suitability for selected applications in aircraft. The NACA Lewis laboratory has determined some of the physical properties and combustion properties of diborane, boron, magnesium, and aluminum (refs. 1 to 7). The metals were burned in the form of powder, wire, and slurries.

The theoretical performance of high-energy ramjet fuels is of interest both in evaluating experimental results and in judging the potentialities of proposed but untested materials. Theoretical comparisons of fuels burned in a great excess of cool air may be based upon conventional heating values of the fuel. However, when the temperatures obtained in the combustion process exceed about 3500° R, the mean molecular weight of gaseous products changes, and considerable energy is absorbed by dissociation, vaporization, and fusion. Thus, the theoretical performance of a fuel must be determined by an analytical method which can account for as many thermal effects as possible.

This report contains the theoretical performance for several potential ramjet fuels determined by such an analytical method. The combustion process was assumed to result in chemical equilibrium at the combustor outlet or exhaust-nozzle inlet. However, the composition throughout the expansion process was assumed to be fixed. It is customary in computing the theoretical thrust produced by a jet to assume either that equilibrium composition exists throughout the exhaust nozzle or that the composition is fixed. In real expansions, partial recombination of dissociated materials is obtained, but the reaction rates are insufficiently known for inclusion of this effect in theoretical calculations. In this

[1] Supersedes NACA Research Memorandums E51C12 by Benson E. Gammon, 1951; E51C23 by Benson E. Gammon, 1951; E51D25 by Benson E. Gammon, 1951; E51F05 by Benson E. Gammon, 1951; E52L08 by Roland Breitwieser, Sanford Gordon, and Benson E. Gammon, 1953; and E53G14 by Leonard K. Tower and Benson E. Gammon, 1953.

Preceding Page Blank

TABLE I.—HEATING VALUES AND PHYSICAL PROPERTIES OF SOME HIGH-ENERGY FUELS

[Except as noted, heats of combustion calculated from heats of formation at 25° C from ref. 15; melting and boiling points obtained from ref. 16.]

Fuel	Melting point, °F	Boiling point, °F	Specific gravity	Stoichiometric fuel-air ratio	Oxides (a)	Heat of combustion		
						Btu/lb	Btu/cu ft	Btu/lb air
Acetylene	−115.2	−118.5 (sublimes)	0.6208 (−119° F)	0.0755	CO_2, H_2O	20,734	803,556	1565
Aluminum	1219.5	4442	2.702	0.2608	Al_2O_3	13,309	2,244,979	3471
Beryllium	2332.4	5378	1.85	0.1307	BeO	29,140	3,365,447	3809
Boron	4172	4622	2.34	0.1046	B_2O_3	[b] 25,381	3,707,695	2655
Carbon (graphite)	6606–87 (sublimes)	7592	2.25	0.0871	CO_2	14,087	1,978,712	1227
Diborane	−265.9	−134.5	[c] 0.4315 (−134.3° F)	0.0669	B_2O_3, H_2O	[b] 31,591	850,988	2113
Hydrogen	−434.5	−423.0	0.070 (liquid)	0.0292	H_2O	51,571	225,364	1506
Lithium	367	2437±9	0.534	0.2013	Li_2O	18,460	615,396	3716
Lithium hydride	1256	----------	0.82	0.1152	Li_2O, H_2O	17,760	909,156	2046
Magnesium	1204	2025	1.74 (41° F)	0.3527	MgO	10,639	1,155,664	3752
Octene-1	−152.3	250.3	0.716 (68° F)	0.0678	CO_2, H_2O	[d] 18,999	848,606	1288
Pentaborane	−51.9	32 (66 mm Hg)	[c] 0.6233 (77° F)	0.0763	B_2O_3, H_2O	[d] 29,362	1,142,516	2240
Silicon	2588	4271	2.4	0.2035	SiO_2	13,170	1,973,234	2680
Silane	−301	−169.2	0.68 (−301° F)	0.1164	SiO_2, H_2O	17,160	728,463	1997
Titanium	3272	5432	4.5 (68° F)	0.3473	TiO_2	8,187	2,299,952	2843
α-Methylnaphthalene	−22.90	471.96	1.020	0.0764	CO_2, H_2O	17,015	1,083,462	1300

[a] CO_2 and H_2O gaseous at 77° F; other products condensed at 77° F.
[b] Computed from data in ref. 17.
[c] Data from ref. 18.
[d] Data from refs. 19 and 20.

report, the assumption of expansion with fixed composition results in conservatively low air specific impulse.

The theoretical performance for the following potential ramjet engine fuels is reported herein: octene-1, magnesium, magnesium—octene-1 slurries, aluminum, aluminum—octene-1 slurries, diborane, pentaborane, boron, boron—octene-1 slurries, hydrogen, α-methylnaphthalene, and carbon. A combustor-inlet air temperature of 560° R and a pressure of 2 atmospheres were chosen.

An extended range of combustor-inlet conditions was chosen for the performance calculations of some of the fuels to facilitate the evaluation of experimental data. Some examples are given of the manner in which this theoretical information can be used in the operation of engines and in the evaluation of experimental data.

SYMBOLS

A area, sq ft
C constant used in computing the stoichiometric fuel-air ratio of a slurry
F stream thrust, lb
g acceleration due to gravity, 32.17 ft/sec²
H_t° sum of sensible enthalpy and chemical energy at temperature t and at standard conditions, kcal/mole
M Mach number
m molecular weight of a constituent
$\overline{m}$ mean molecular weight
n number of moles of a constituent
p static pressure, lb/sq ft
R universal gas constant, 1545.33 ft-lb/(mole) (°R)
r weight fraction of solid fuel in slurry
S_a air specific impulse, lb-sec/lb air
$S_{f,v}$ fuel-volume specific impulse, lb-sec/cu ft fuel
$S_{f,w}$ fuel-weight specific impulse, lb-sec/lb fuel
T total temperature, °R
t static temperature, °R
V velocity, ft/sec
w weight flow, lb/sec
γ ratio of specific heats
η efficiency
η_{S_a} air-specific-impulse efficiency
ρ density, lb/cu ft
$\Phi(M)$ stream thrust correction factor to $M=1$
φ equivalence ratio, ratio of actual to stoichiometric fuel-air ratio

Subscripts:
a air
c combustion, combustor outlet
e exhaust-nozzle outlet
exp experimental
f fuel
g gas
i denotes i^{th} constituent of combustion products
in engine inlet
l liquid
n net
s solid
st stoichiometric
t theoretical
v volume
w weight

Superscript:
* denotes a station having a Mach number of unity

ANALYTICAL METHOD

Suitable thrust parameters for both theoretical and actual jet-engine fuel performance have been found to be air specific impulse and fuel specific impulse or total stream momentum per pound of air and per pound of fuel, respectively. Air specific impulse, defined for choked flow, is

$$S_a=\frac{1}{w_a}\left(pA+\frac{wV}{g}\right)^* \tag{1}$$

where

$$w=w_a+w_f$$

Fuel-weight specific impulse is defined as

$$S_{f,w}=\frac{1}{w_f}\left(pA+\frac{wV}{g}\right)^*=\frac{S_a}{\frac{w_f}{w_a}} \tag{2}$$

and fuel-volume specific impulse is defined as

$$S_{f,v}=\rho S_{f,w} \tag{3}$$

The density of slurries for use in equation (3), relating fuel-weight and fuel-volume specific impulse, was calculated thus:

$$\frac{1}{\rho_{\text{slurry}}}=\frac{\text{Fraction metal}}{\rho_{\text{metal}}}+\frac{\text{Fraction octene-1}}{\rho_{\text{octene-1}}} \tag{4}$$

Magnesium and aluminum slurries follow this relation up to about 80 percent metal by weight, and boron follows up to 60 percent metal by weight for metal powders now available.

Air specific impulse can also be expressed as

$$S_a=\left(1+\frac{w_f}{w_a}\right)\sqrt{\frac{2(\bar{\gamma}+1)RT_c}{\bar{\gamma}g\bar{m}}} \tag{5}$$

where $\bar{\gamma}$ is an effective ratio of specific heats. The net internal thrust of an engine can be determined from the relation

$$F_n=\Phi(M_e)w_aS_a-\left(pA+\frac{wV}{g}\right)_{in} \tag{6}$$

where $\Phi(M)$ is a function relating stream thrust at any station to stream thrust at a station having a Mach number of unity (see eqs. (A2) and (A3)). The significance and the utility of these concepts are discussed in more detail in reference 8.

The theoretical determination of air specific impulse and fuel specific impulse for the fuels considered herein involved two principal steps: (1) the combustion temperature and burned-product composition were determined at the assigned combustion pressure, and (2) an isentropic expansion in the exhaust nozzle to a throat Mach number of unity determined the exhaust-nozzle-outlet static temperature and velocity. The results of step (2) were used to compute air and fuel specific impulses.

The method of computing combustion temperature and composition was that of reference 9. A set of simultaneous equations was solved which involved mass balance, heat balance, pressure, phase changes, and dissociation of solid, liquid, and gaseous molecules. The necessary thermodynamic properties of almost all the dissociated and undissociated combustion products were taken from tables included in reference 9. An empirical equation given in reference 10 for the specific heat of magnesium oxide was used to obtain values of specific heat, enthalpy, and entropy for magnesium oxide; the standard-state entropy of magnesium oxide was taken from reference 11. The thermal properties for boric oxide (B_2O_3) were obtained from reference 12.

The following assumptions were made concerning the combustion process in order to simplify the analysis: (1) all fuels were pure; (2) the air was composed of 3.78 moles of nitrogen to every mole of oxygen; (3) combustor-inlet air velocity was negligible so that the combustion static and total temperatures were equal; (4) all gases were ideal; (5) combustion was adiabatic and complete, that is, chemical equilibrium was assumed; (6) when solids or liquids were present in the combustion products, the volume occupied by the condensed material was negligible; and (7) thermal and velocity equilibrium existed between the different phases.

The products of adiabatic combustion of each fuel which were considered possible in the computations of composition are listed in table II. They were gaseous except as noted. The nitrides of boron, magnesium, and aluminum were neglected because of inadequate thermodynamic data. For the same reason, dissociation, fusion, and vaporization of magnesium oxide were neglected.

The exhaust-nozzle-outlet temperature was determined by computing an isentropic expansion from the combustion temperature and pressure to a pressure giving a Mach number of unity. It was assumed that in the nozzle (1) composition was fixed during the expansion process, (2) the volume occupied by condensed materials was negligible, and (3) condensed materials were in thermal and velocity equilibrium with the gas phase. The jet velocity was then calculated by using the following equation (ref. 13):

$$\frac{V_e^*}{g}=294.98\sqrt{\left[\frac{\Sigma n_i(H_t^\circ)_i}{\Sigma n_i m_i}\right]_c-\left[\frac{\Sigma n_i(H_t^\circ)_i}{\Sigma n_i m_i}\right]_e} \tag{7}$$

The air specific impulse was then

$$S_a=\left(1+\frac{w_f}{w_a}\right)\left(\frac{V_e}{g}+\frac{Rt_e}{\bar{m}V_e}\right)^* \tag{8}$$

RESULTS AND DISCUSSION

The combustion performance of several high-energy fuels is presented in figures 1 to 6 for a combustor-inlet air temperature of 560° R and a pressure of 2 atmospheres.

MAGNESIUM, MAGNESIUM—OCTENE-1 SLURRIES, AND OCTENE-1

The combustion temperatures for magnesium, magnesium—octene-1 slurries, and octene-1 are shown in figure 1(a). The data are limited to a maximum combustion temperature of about 5500° R because of the lack of thermodynamic data as previously discussed.

Increasing the magnesium concentration in a magnesium—octene-1 slurry increased the combustion temperature at all equivalence ratios investigated. It is significant that the maximum combustion temperature for the magnesium slurries occurs at progressively higher equivalence ratios as the magnesium concentration is increased. In order to show this effect, the data were calculated at equivalence ratios exceeding 1.0. This effect is a result of the high heating

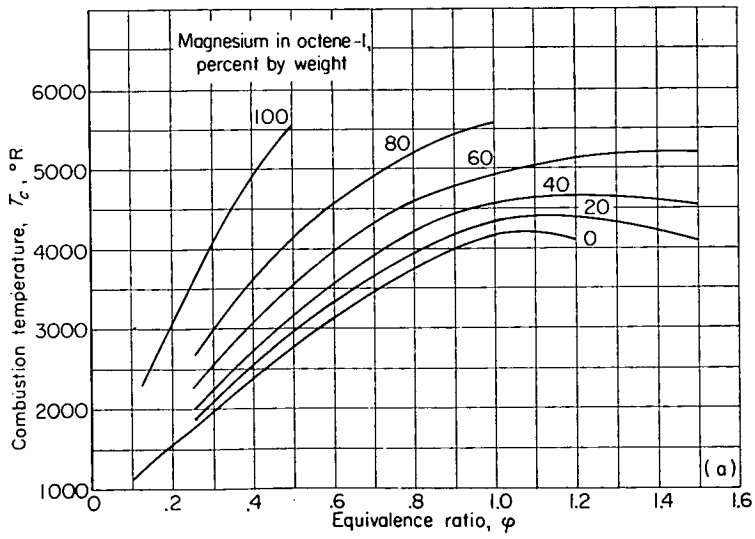
TABLE II.—PRODUCTS CONSIDERED POSSIBLE AS A RESULT OF ADIABATIC COMBUSTION

Product	Fuel										
(a)	Octene-1, α-methyl-naphthalene	Boron	Penta-borane	Diborane	Hydrogen	Carbon	Magnesium slurry	Aluminum	Boron—octene-1 slurries	Aluminum—octene-1 slurries	Magnesium
O_2	x	x	x	x	x	x	x	x	x	x	x
N_2	x	x	x	x	x	x	x	x	x	x	x
CO_2	x	-----	-----	-----	-----	x	x	-----	x	x	-----
H_2O	x	-----	x	x	x	-----	x	-----	x	x	x
H_2	x	-----	x	x	x	-----	x	-----	x	x	-----
CO	x	-----	-----	-----	-----	x	x	-----	x	x	-----
C	x	-----	-----	-----	-----	x	x	-----	x	x	-----
H	x	-----	x	x	x	-----	x	-----	x	x	-----
O	x	x	x	x	x	x	x	x	x	x	x
N	x	x	x	x	x	x	x	x	x	x	x
OH	x	-----	x	x	x	-----	x	-----	x	x	-----
NO	x	x	x	x	x	x	x	x	x	x	x
$(MgO)_s$	-----	-----	-----	-----	-----	-----	x	-----	-----	-----	x
$(Al_2O_3)_s, l, g$	-----	-----	-----	-----	-----	-----	-----	x	-----	x	-----
Al	-----	-----	-----	-----	-----	-----	-----	x	-----	x	-----
AlO	-----	-----	-----	-----	-----	-----	-----	x	-----	x	-----
$(B_2O_3)_s, l, g$	-----	x	x	x	-----	-----	-----	-----	x	-----	-----
B	-----	x	x	x	-----	-----	-----	-----	x	-----	-----
BO	-----	x	x	x	-----	-----	-----	-----	x	-----	-----
BH	-----	-----	x	x	-----	-----	-----	-----	x	-----	-----

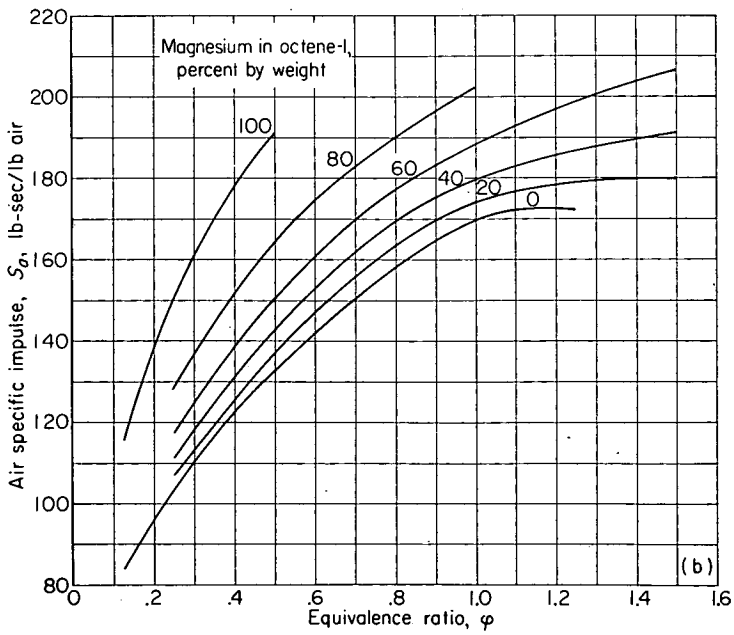
[a] Gaseous except as noted.

value of magnesium per pound of air since it was assumed that all magnesium combined with the oxygen present to form magnesium oxide. The tendency of high-concentration magnesium slurries to burn at equivalence ratios greater than 1.0 and to exhibit a higher heat release per pound of reactants than at an equivalence ratio of 1.0 has been experimentally established in reference 2. Reference 2 indicates that, for a slurry consisting of finely powdered magnesium suspended in a hydrocarbon fuel, magnesium burned preferentially with the oxygen present and hence permitted the high heat release.

Air specific-impulse values for pure magnesium, several magnesium—octene-1 slurries, and octene-1 are presented in figure 1(b). Higher air specific-impulse values can be achieved as the percent magnesium in the slurry is increased.



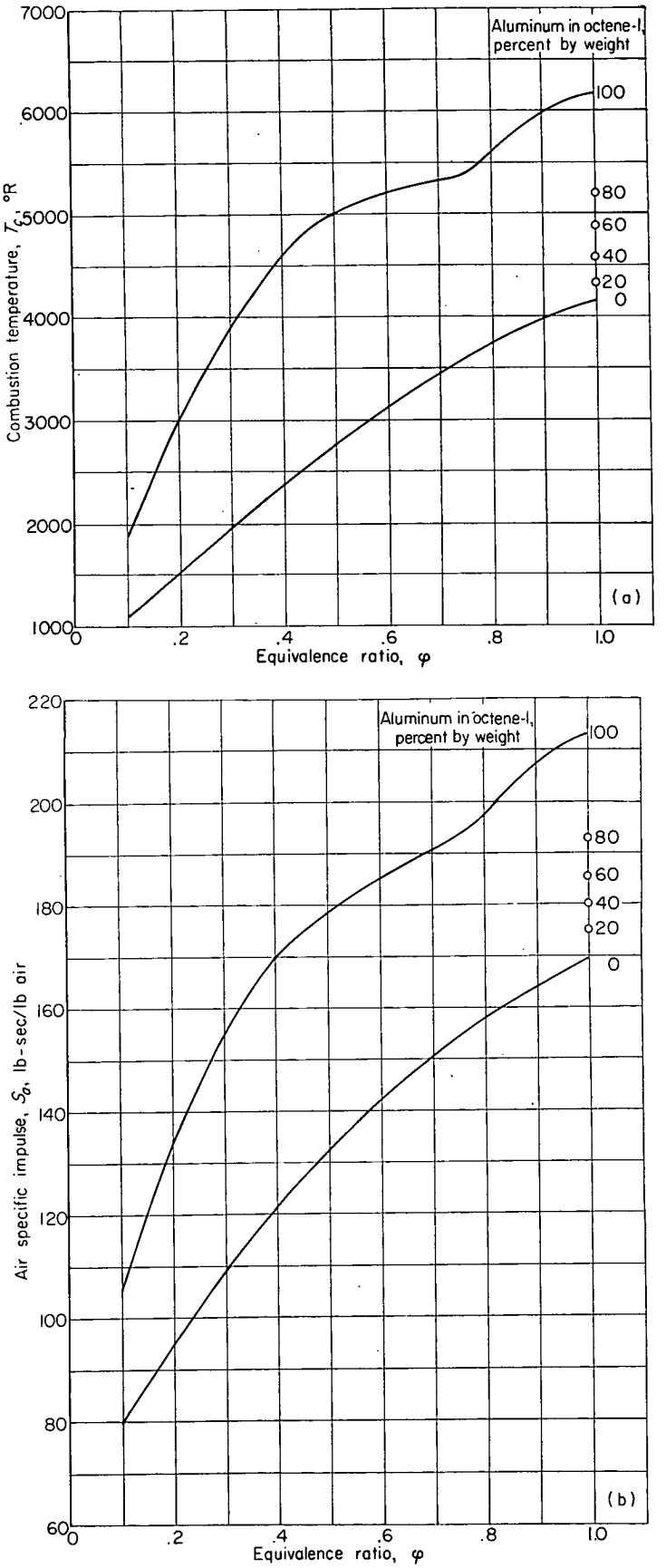
(a) Variation of combustion temperature with equivalence ratio.



(b) Variation of air specific impulse with equivalence ratio.

FIGURE 1.—Theoretical combustion performance for magnesium, magnesium—octene-1 slurries, and octene-1. Combustor-inlet air temperature, 560° R; inlet air pressure, 2 atmospheres.

FIGURE 1.—Concluded.



(a) Variation of combustion temperature with equivalence ratio.

(b) Variation of air specific impulse with equivalence ratio.

FIGURE 2.—Theoretical combustion performance for aluminum, aluminum—octene-1 slurries, and octene-1. Combustor-inlet air temperature, 560° R; inlet air pressure, 2 atmospheres.

ALUMINUM AND ALUMINUM—OCTENE-1 SLURRIES

The combustion temperatures for aluminum, aluminum—octene-1 slurries, and octene-1 are shown in figure 2(a). Included in figure 2(a) are the theoretical combustion temperatures for several concentrations of metal in aluminum—octene-1 slurries at an equivalence ratio of 1.0. The irregular nature of the temperature curve for aluminum is due to a phase transition of aluminum oxide Al_2O_3 from liquid to gas.

The variation of air specific impulse with equivalence ratio for aluminum and octene-1 is presented in figure 2(b). Included in this figure are values of air specific impulse for several aluminum slurries evaluated at an equivalence ratio of 1.0. The air specific impulse increases as the metal concentration in the slurry is increased.

BORON AND BORON—OCTENE-1 SLURRIES

The combustion temperatures for boron and several boron—octene-1 slurries are shown in figure 3(a). The variation of air specific impulse with equivalence ratio for boron, boron—octene-1 slurries, and octene-1 is presented in figure 3(b). Between about 3500° and 4050° R the slope of the combustion temperature curve for boron changes rapidly. At 4050° R there is a discontinuity in the slope of the curve. These effects are caused by the vaporization of boric oxide which absorbs heat. A similar trend is noted in the air specific-impulse curve for boron.

CARBON, HYDROGEN, AND α-METHYLNAPHTHALENE

The combustion temperatures for carbon, hydrogen, α-methylnaphthalene, and octene-1 are shown in figure 4(a). The variation of air specific impulse with equivalence ratio for carbon, hydrogen, α-methylnaphthalene, and octene-1 is presented in figure 4(b). Since the combustion temperatures for carbon, α-methylnaphthalene, and octene-1 are sufficiently close together, a single curve has been drawn for the data.

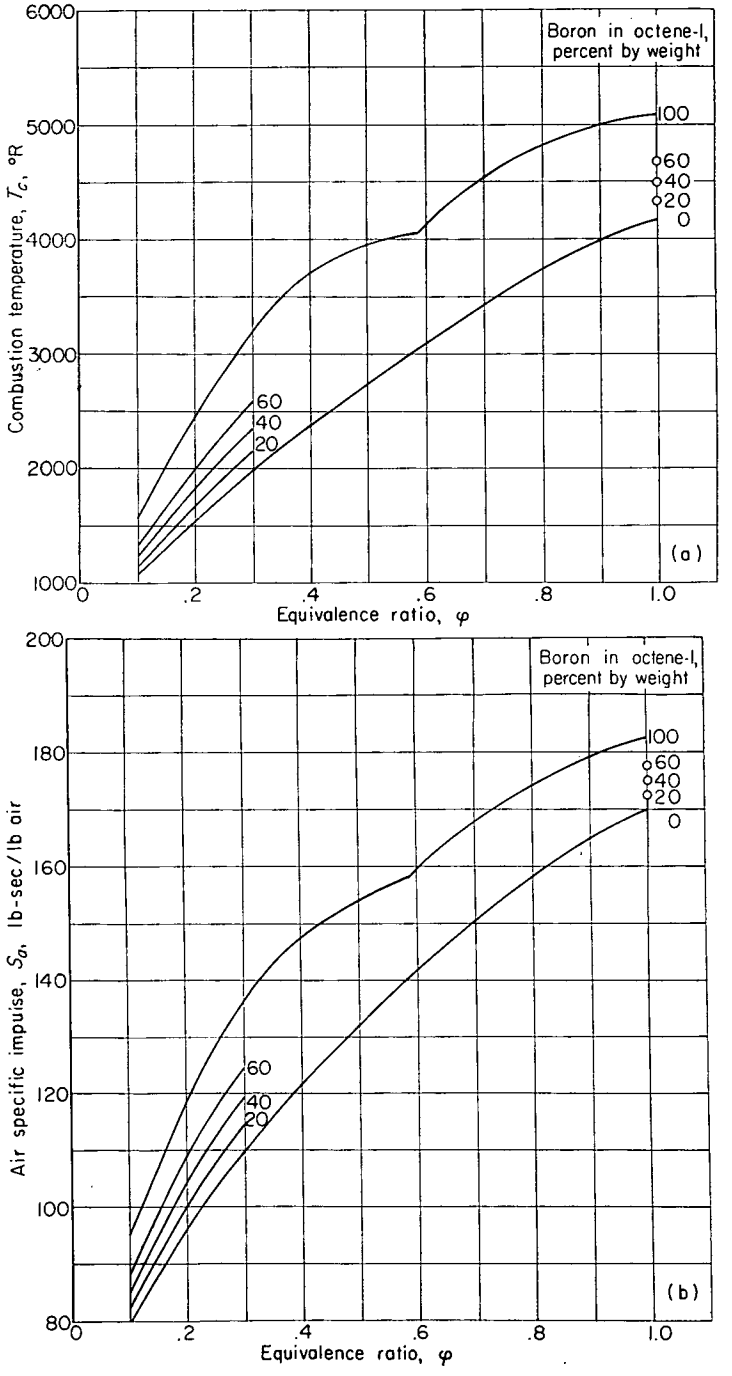
DIBORANE AND PENTABORANE

The combustion temperatures for diborane and pentaborane are compared with those of hydrogen and boron in figure 5(a). The variation of air specific impulse with equivalence ratio for diborane, pentaborane, hydrogen, and boron is presented in figure 5(b). Between about 3500° and 4000° R, the combustion temperature curves for diborane and pentaborane show a trend caused by the vaporization of boric oxide, which is similar to that previously noted for boron. This trend is also present in the curves of air specific impulse for diborane and pentaborane.

Boron, pentaborane, diborane, and hydrogen comprise a sequence in which boron is combined with increasing percentages of hydrogen. In the following table are shown the mole fractions of boron and hydrogen in the fuels and the approximate heat absorbed by vaporizing the boric oxide formed from a pound of each fuel. Also shown is the approximate heat absorbed by vaporizing the boric oxide formed from a pound of stoichiometric fuel-air mixture. These heats of vaporization have been evaluated at a temperature of 3600° R for convenience.

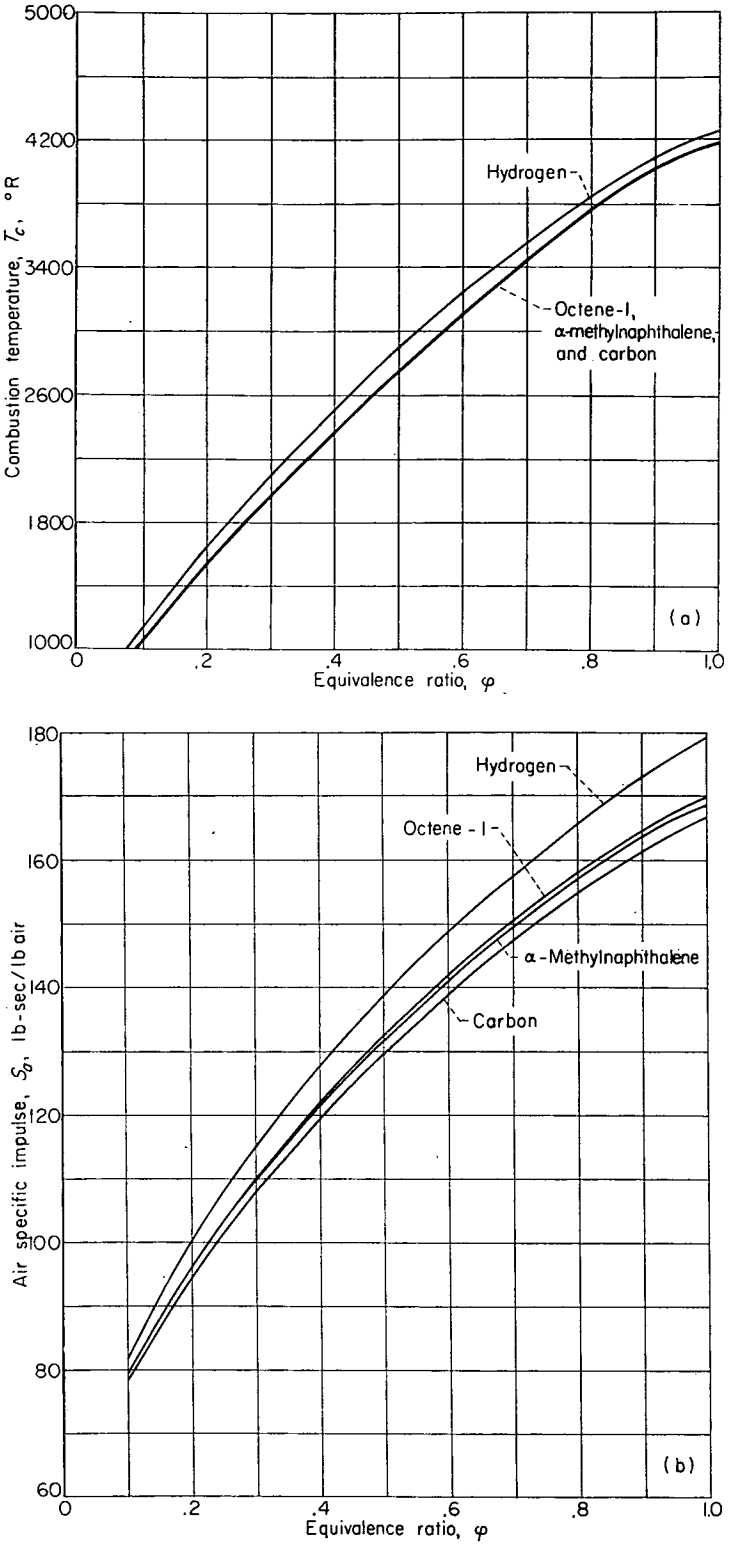
Fuel	Atom fraction of constituents		Heat absorbed by vaporization of boric oxide	
	Boron	Hydrogen	Btu/lb fuel	Btu/lb stoichiometric fuel-air mixture
Boron	1.0	0	6240	591
Pentaborane	.357	.643	5344	379
Diborane	.250	.750	4877	306
Hydrogen	0	1.00	0	0

As suggested by the table, the irregularities in the curves of figure 5 become less severe as the hydrogen content of the fuel is raised because of the decreasing amount of heat absorbed by vaporization of boric oxide.



(a) Variation of combustion temperature with equivalence ratio.
(b) Variation of air specific impulse with equivalence ratio.

FIGURE 3.—Theoretical combustion performance for boron, boron—octene-1 slurries, and octene-1. Combustor-inlet air temperature, 560° R; inlet air pressure, 2 atmospheres.

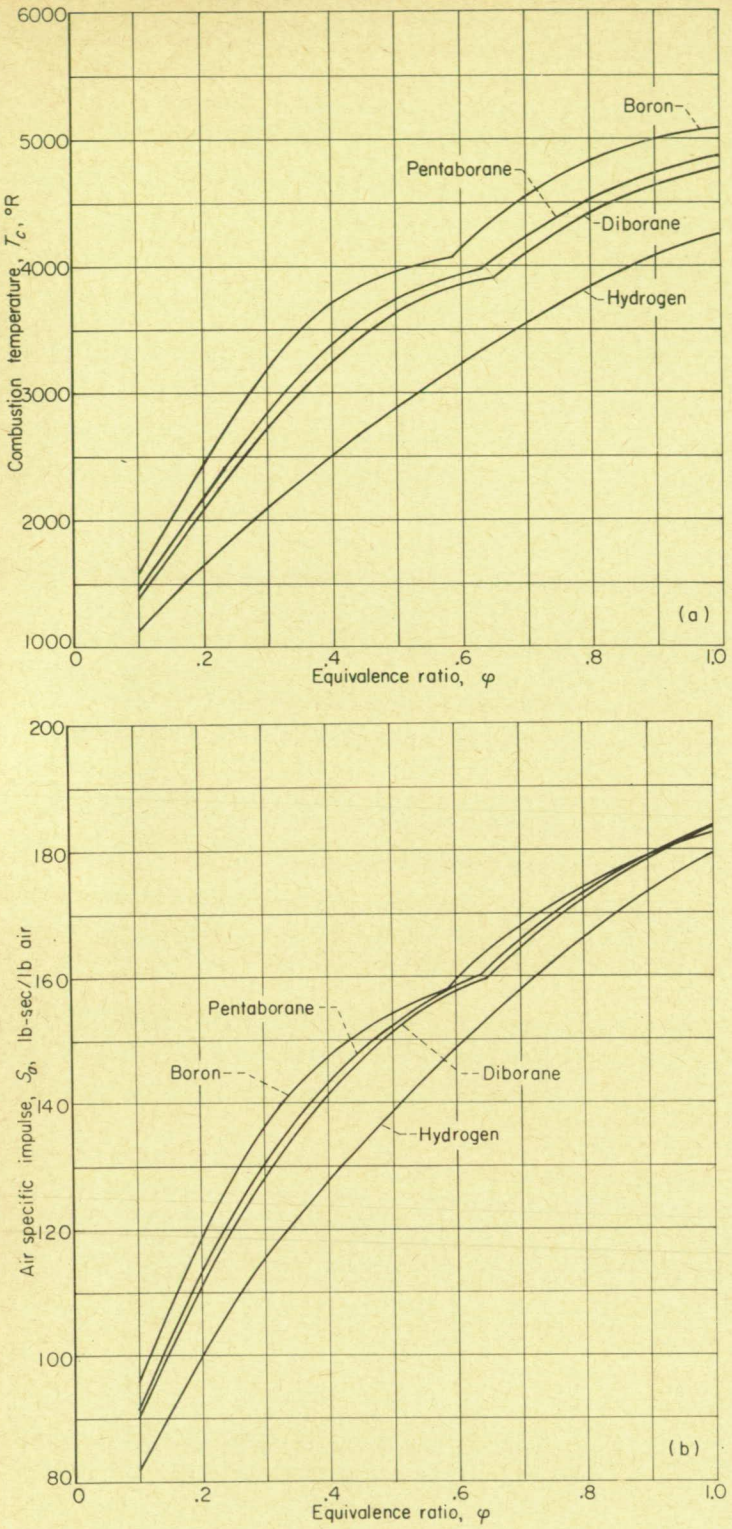


(a) Variation of combustion temperature with equivalence ratio.
(b) Variation of air specific impulse with equivalence ratio.

FIGURE 4.—Theoretical combustion performance for hydrogen, carbon, α-methylnaphthalene, and octene-1. Combustor-inlet air temperature, 560° R; inlet air pressure, 2 atmospheres.

SUMMARY COMPARISONS

The adiabatic constant-pressure combustion temperature and impulse characteristics of magnesium, 50 percent magnesium—octene-1 slurry, aluminum, boron, 50 percent boron—octene-1 slurry, hydrogen, carbon, α-methylnaphtha-



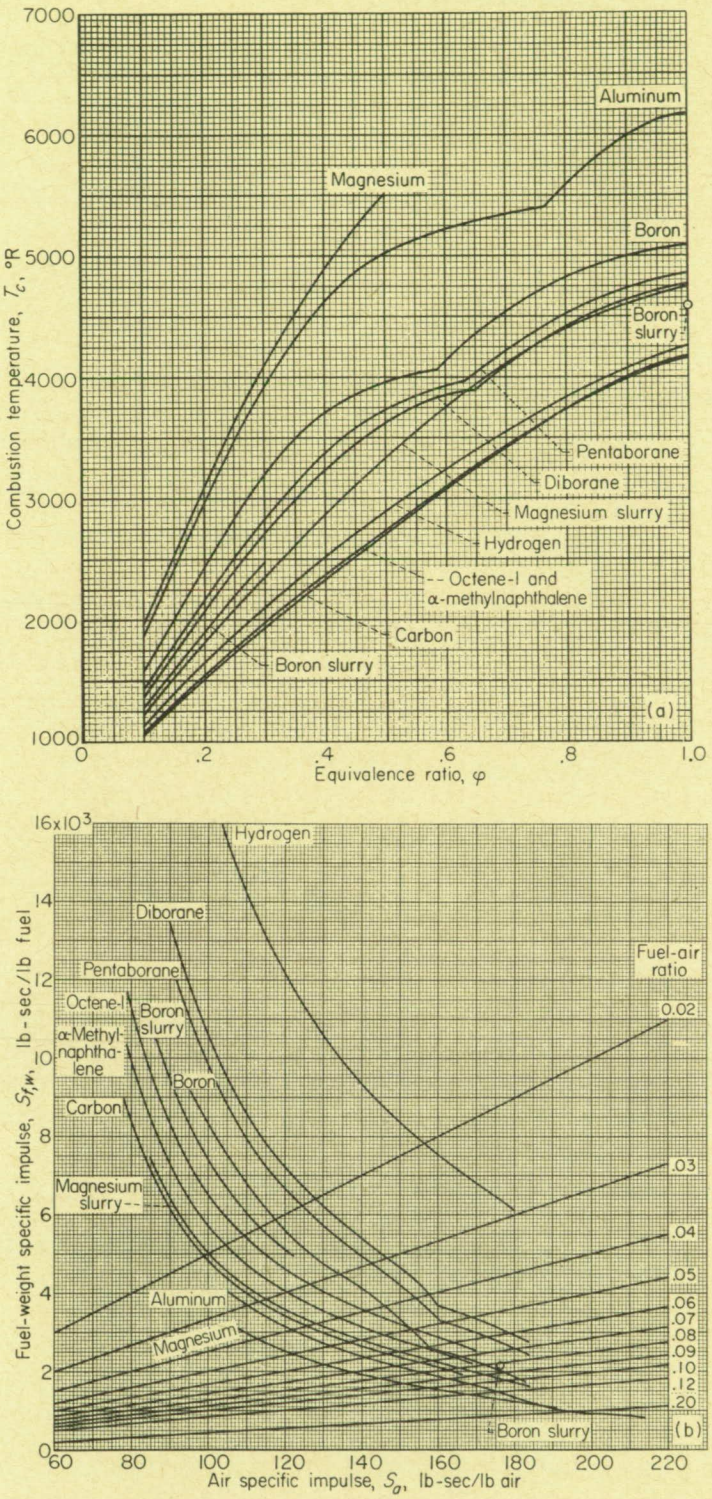
(a) Variation of combustion temperature with equivalence ratio.

(b) Variation of air specific impulse with equivalence ratio.

FIGURE 5.—Theoretical combustion performance for boron, pentaborane, diborane, and hydrogen. Combustor-inlet air temperature, 560° R; inlet air pressure, 2 atmospheres.

lene, diborane, pentaborane, and octene-1 are compared in figure 6. In order to reduce the congestion of the figures, only slurries containing 50 percent metal by weight are included in the summary comparisons.

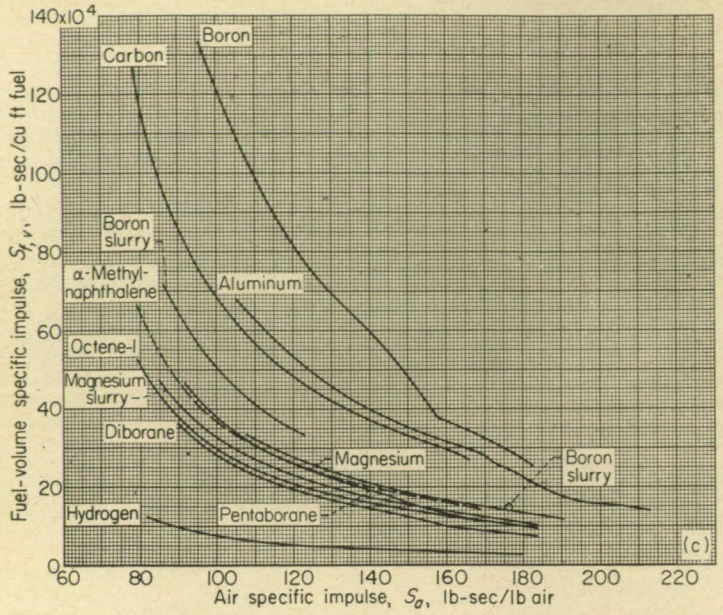
The combustion temperatures for the aforementioned fuels are presented in figure 6(a). The fuels, listed in order of decreasing combustion temperature at equivalence ratios below 0.5, are: magnesium, aluminum, boron, pentaborane, diborane, 50 percent boron—octene-1 slurry, 50 percent magnesium—octene-1 slurry, hydrogen, α-methylnaphthalene, octene-1, and carbon.



(a) Variation of combustion temperature with equivalence ratio.

(b) Variation of fuel-weight specific impulse with air specific impulse.

FIGURE 6.—Summary of combustion performance for representative high-energy fuels. Combustor-inlet air temperature, 560° R; inlet air pressure, 2 atmospheres. (Slurry fuels, 50 percent metal by weight in octene-1.)



(c) Variation of fuel-volume specific impulse with air specific impulse.

FIGURE 6.—Concluded.

These fuels are compared on the basis of fuel-weight specific impulse, an index of fuel economy, and air specific impulse, an index of thrust in figure 6(b). The data in figure 6(b) are presented because comparison of fuel economy for various fuels should be made at the same level of air specific impulse. Also, the relative air specific impulse of several fuels at a fixed value of fuel economy or fuel-weight specific impulse may be of interest. This information and the corresponding fuel-air ratios may be readily obtained from figure 6(b).

The following fuels, evaluated below an air specific-impulse value of 152 seconds, are listed in order of decreasing fuel-weight specific impulse: hydrogen, diborane, pentaborane, boron, 50 percent boron—octene-1 slurry, octene-1, α-methylnaphthalene, 50 percent magnesium—octene-1 slurry, carbon, aluminum, and magnesium. While this order is retained in general above an air specific impulse of 152 seconds, the fuel specific impulse of octene-1 exceeds that of boron above this air specific impulse because of the vaporization of boric oxide B_2O_3.

The maximum obtainable air specific impulse, occurring generally at equivalence ratios exceeding 1.0, was not calculated. However, all fuels except carbon and α-methylnaphthalene appear to have a maximum air specific impulse exceeding that of octene-1, which is 172.8 seconds.

Representative fuels were also evaluated in terms of fuel-volume specific impulse at various air specific-impulse values as shown in figure 6(c). The curves for pure magnesium, aluminum, and boron are based upon the solid densities of the metal. The densities of pentaborane, diborane, and hydrogen were those of the liquids at 536.7°, 325.1°, and 36.6° R, respectively.

The fuels evaluated in order of decreasing fuel-volume specific impulse (increasing volumetric fuel consumption) at an air specific impulse below 152 seconds are as follows: boron, aluminum, carbon, 50 percent boron—octene-1 slurry, magnesium, pentaborane or α-methylnaphthalene, 50 percent magnesium—octene-1 slurry, octene-1, diborane, and hydrogen.

APPLICATIONS OF DATA

The theoretical performance data of figures 1 to 6 can be used for the determination of air specific-impulse efficiency and combustion efficiency. They can also be used in estimating the relative amounts of the various fuels required to maintain a fixed level of thrust in an engine. For these purposes the single combustor-inlet condition of a temperature of 560° R and a pressure of 2 atmospheres will often be too limited. Some of the fuels such as diborane seemed, on the basis of the theoretical performance shown in figures 1 to 6, to be likely candidates for further theoretical and experimental investigation. Other fuels such as carbon, hydrogen, and boron were of interest because they are the elemental constituents of some of the high-performance fuels.

To facilitate the application of the theoretical performance data to the evaluation of experimental data it seemed desirable to extend the range of inlet conditions of these fuels: octene-1, slurry of 50 percent magnesium in octene-1, carbon (graphite), boron (crystal), pentaborane (liquid), diborane (liquid), and hydrogen (liquid). Inlet air temperatures from 560° to 1360° R and combustion pressures from 0.2 to 2 atmospheres were considered. The data are presented in figures 7 to 13.

Parts (a) and (b) of figures 7 to 13 present combustion temperature and air specific impulse, respectively, plotted against equivalence ratio for inlet air temperatures of 560°, 960°, and 1360° R at a combustion pressure of 2 atmospheres. Examination of parts (a) and (b) reveals that a given increase in inlet air temperature results in a diminishing gain in combustion temperature and air specific impulse as equivalence ratio is raised. The higher combustion temperatures associated with increasing equivalence ratio result in increased specific heat and more dissociation of the combustion products. Much of the heat made available by an increase in inlet air temperature is absorbed without a corresponding gain in combustion temperature or air specific impulse.

Parts (c) and (d) present combustion temperature and air specific impulse, respectively, plotted against combustion pressure for an inlet air temperature of 560° R and equivalence ratios from 0.7 to 1.0. At the lower equivalence ratios (below 0.7) the effect of pressure is usually negligible. An exception to this arises with materials containing boron, where the vaporization of boric oxide in the vicinity of an equivalence ratio of 0.4 is pressure dependent. A direct computation is then necessary.

Although the data of parts (c) and (d) of figures 7 to 13 were computed at pressures of only 0.2 and 2 atmospheres, a straight line of combustion temperature or air specific impulse plotted against the logarithm of combustion pressure has been drawn between these pressures for each equivalence ratio. This convenient procedure has been verified for several cases. For instance, combustion temperature and air specific impulse at an equivalence ratio of 1.0 were computed for octene-1 at two additional combustion pressures of 0.6 and 10 atmospheres. These data are represented in figures 7(c) and (d) by the circled points.

This semilogarithmic relation between combustion temperature or air specific impulse and combustion pressure is expected to be valid for all eight fuels reported herein at equivalence ratios from 0.7 to 1.0. Extrapolation of the lines from combustion pressures of 2 to 10 atmospheres is less satisfactory than interpolation between 0.2 and 2 atmospheres. All lines have therefore been dashed above 2 atmospheres. Extrapolation below 0.2 atmosphere may also be less satisfactory.

In parts (c) and (d) the combustion temperature and air specific impulse at a combustion pressure of 0.2 atmosphere are less than those at a combustion pressure of 2 atmospheres within the range of equivalence ratios shown. Moreover, the loss in combustion temperature and air specific impulse with this decrease in combustion pressure is greatest at the richer equivalence ratios. These effects result from the increasing dissociation caused by an increase in temperature or a decrease in pressure.

DETERMINATION OF COMBUSTION TEMPERATURE AND AIR SPECIFIC IMPULSE AT COMBUSTOR-INLET CONDITIONS OTHER THAN THOSE REPORTED

In many instances it is desired to know the combustion temperature and air specific impulse at inlet conditions other than those for which the data of figures 1 to 13 were computed. When the effects of inlet air temperature and combustion pressure are known for a fuel over a range of inlet conditions as in figures 7 to 13, approximate values of air specific impulse at other inlet conditions may be determined as follows.

At equivalence ratios below 0.7 these data can be read directly from the curves of part (a) or (b) without consideration of pressure, with the exception of boron-containing fuels. At equivalence ratios exceeding 0.7 the effect of combustion pressure on combustion temperature and air specific impulse becomes important for all fuels. The effect of combustion pressure on combustion temperature or air specific impulse in this region can be determined in the following manner: The combustion pressure or air specific impulse at the desired inlet air temperature, determined from part (a) or (b) of figures 7 to 13, is entered in part (c) or (d) at a pressure of 2 atmospheres. The combustion temperature or air specific impulse is then corrected to the desired pressure along a line of constant equivalence ratio. For example, the air specific impulse of boron at an equivalence ratio of 0.8, an inlet air temperature of 1260° R, and a combustion pressure of 0.3 atmosphere can be found as follows: From figure 10(b) the air specific impulse is determined as 178.8 seconds for the conditions stated, but at a combustion pressure of 2 atmospheres. The value obtained is entered in figure 10(d) at this pressure and air specific impulse (point A), and a line of constant equivalence ratio is followed to a pressure of 0.3 atmosphere. The desired air specific impulse is found to be 174.9 seconds. This is very close to the value of 175.2 seconds determined by direct computation for a pressure of 0.3 atmosphere.

In making a pressure correction, it may be necessary occasionally to enter data in a figure such as figure 10(d) at an air specific impulse or combustion temperature exceeding the highest line of air specific impulse or combustion temperature plotted against combustion pressure. For example, figure 10(b) indicates an air specific impulse of 186.6 seconds for an equivalence ratio of 1.0, an inlet air temperature of 1360° R, and a combustion pressure of 2 atmospheres. Point C is thus located on figure 10(d) which is above the highest line already present. A correction to a combustion pressure of 0.2 atmosphere, made along a dashed line converging toward existing lines at the same rate at which they converge toward each other, locates an air specific impulse of 181.2 seconds at point D. By direct computation, the value sought is 180.9 seconds.

DETERMINATION OF AIR SPECIFIC-IMPULSE EFFICIENCY AND COMBUSTION EFFICIENCY

Both air specific-impulse efficiency and combustion efficiency may be found for experimental data by the use of the curves presented herein. Air specific-impulse efficiency is defined as the ratio of the experimental air specific impulse to the theoretical air specific impulse at the same equivalence ratio:

$$\eta_{S_a}=\left(\frac{S_{a,exp}}{S_{a,t}}\right)_{\varphi} (\varphi=\text{const.}) \tag{9}$$

The experimental air specific impulse must be computed from experimental measurements as discussed in the appendix; the theoretical air specific impulse is read from the curves of air specific impulse plotted against equivalence ratio for a pressure of 2 atmospheres at the combustor-inlet temperature and equivalence ratio applying to the experimental data. This value may then be corrected to the combustion pressure used in the actual engine by the method described previously.

A combustion efficiency which is often useful can be defined as the ratio of the theoretical equivalence ratio to the experimental equivalence ratio required to produce a given air specific impulse or combustion temperature:

$$\eta_c=\left(\frac{\varphi_t}{\varphi_{exp}}\right)_{T_c} (T_c=\text{const.}) \tag{10}$$

and

$$\eta_c=\left(\frac{\varphi_t}{\varphi_{exp}}\right)_{S_a} (S_a=\text{const.}) \tag{11}$$

Fuel-air ratios may replace equivalence ratios. These definitions are valid only for equivalence ratios of 1.0 or less. When the experimental data are obtained at pressures other than 2 atmospheres, a pressure correction may be applied conveniently to the theoretical equivalence ratio as follows: The experimental combustion temperature or air specific impulse, together with the combustion pressure, is entered on the semilogarithmic graph of theoretical combustion temperature or air specific impulse plotted against combustion pressure (part (c) or (d) of figs. 7 to 13), and a line of constant composition is followed to a combustion pressure of 2 atmospheres. The combustion temperature or air specific impulse, adjusted to the 2-atmosphere standard, and the experimental inlet air temperature are then used on the plots of combustion temperature or air specific impulse plotted against inlet air temperature and equivalence ratio to find the theoretical equivalence ratio. For example,

suppose that boron burned at an inlet air temperature of 960° R, a combustion pressure of 0.2 atmosphere, and an equivalence ratio of 1.0 produces an experimental air specific impulse of 176 seconds, which locates point E on figure 10(d). Following the dashed line of constant composition to point F determines a pressure-adjusted air specific impulse of 180.9 seconds. Locating a point in figure 10(b) at 180.9 seconds and at an inlet air temperature of 960° R determines a theoretical equivalence ratio of 0.89. A combustion efficiency of 0.89 is then found by means of equation (11).

In equations (9) and (11), experimental air specific-impulse data are compared with theoretical data in which expansion at fixed composition is assumed. If the recombination rates are such that some adjustment of composition is obtained in the nozzle, efficiencies computed from these equations will tend to be high when the data of figures 7 to 13 are used since these data are for expansion at fixed composition.

DETERMINATION OF RELATIVE FUEL-FLOW REQUIREMENTS FOR GIVEN ENGINE

In instances where several fuels are being considered for an engine, it may be desired to know the relative amounts of each fuel required to obtain a fixed thrust level. The curves of air specific impulse plotted against equivalence ratio may conveniently be used for determining the amounts of fuel if advantage is taken of the following assumptions: The combustion efficiency is the same for each fuel, and momentum and other internal pressure losses are nearly the same for each fuel at a given thrust level.

For example, a ramjet engine is operated with octene-1 or any other reasonably similar hydrocarbon at an equivalence ratio of 0.737, an inlet air temperature of 560° R, and a combustion pressure of 2 atmospheres. From figure 7(b), the air specific impulse for octene-1 at this equivalence ratio and inlet air temperature is 153.4 seconds. By the use of figures 8(b), 10(b), 11(b), and (12b) for 50 percent magnesium slurry, boron, pentaborane, and diborane, the equivalence ratios required to produce an air specific impulse of 153.4 seconds are determined. These are converted to fuel-air ratios by the formula

$$\frac{w_f}{w_a}=\varphi\left(\frac{w_f}{w_a}\right)_{st} \tag{12}$$

The required equivalence ratios and fuel-air ratios are presented in the following table:

Fuel	Equivalence ratio	Fuel-air ratio	Relative fuel flow
Octene-1	0.737	0.0500	1.00
50 Percent magnesium slurry	.57	.0648	1.30
Boron	.49	.0513	1.03
Pentaborane	.515	.0393	.79
Diborane	.525	.0351	.70

The relative fuel flow is defined in this case as the ratio of the fuel-air ratio of the substitute fuel to that of octene-1.

The stoichiometric fuel-air ratio of slurry is calculated from the expression

$$\left(\frac{w_f}{w_a}\right)_{st}=\frac{0.06781}{1-Cr} \tag{13}$$

where C is 0.8078 for magnesium slurry. The value of C is 0.3519 for boron slurry, 0.7401 for aluminum slurry, and 0.11189 for pentaborane blends.

A correction of fuel-air ratios for combustion pressures other than 2 atmospheres can be made in the manner previously described for equivalence ratios used to determine combustion efficiency.

CONCLUDING REMARKS

An analytical evaluation of the air and fuel specific-impulse characteristics of magnesium, magnesium—octene-1 slurries, aluminum, aluminum—octene-1 slurries, boron, boron—octene-1 slurries, carbon, hydrogen, α-methylnaphthalene, diborane, pentaborane, and octene-1 is presented herein. While chemical equilibrium was assumed in the combustion process, the expansion was assumed to occur at fixed composition.

At a fixed air specific impulse below 152 seconds, the fuel weight specific impulses of hydrogen, diborane, pentaborane, boron, and boron—octene-1 slurries were superior to octene-1 for a combustor-inlet air temperature of 560° R and a pressure of 2 atmospheres. At air specific-impulse values of about 152 seconds and higher, the vaporization of boric oxide B_2O_3 for the fuels containing boron reduced the fuel specific impulse relative to octene-1.

The fuel-volume specific impulses of boron, aluminum, carbon, slurries of 50 percent boron and 50 percent octene-1 by weight, magnesium, pentaborane, α-methylnaphthalene, and slurries of 50 percent magnesium and 50 percent octene-1 by weight were superior to octene-1 for an inlet air temperature of 560° R and a combustion pressure of 2 atmospheres.

The effects of inlet air temperature and combustion pressure were investigated for the following fuels: octene-1, 50 percent magnesium slurry, boron, pentaborane, diborane, hydrogen, and carbon. Because a limited range of inlet air temperatures and combustion pressures was considered, methods of extending the data to other inlet conditions were presented.

Determination of air specific-impulse efficiency and combustion efficiency for experimental combustion by means of the theoretical data herein was considered. The use of the theoretical performance data in determining the relative flows of the various fuels to an engine operating at a fixed thrust level was discussed.

LEWIS FLIGHT PROPULSION LABORATORY
NATIONAL ADVISORY COMMITTEE FOR AERONAUTICS
CLEVELAND, OHIO, *September 14, 1953*

APPENDIX—COMPUTATION OF AIR SPECIFIC IMPULSE FROM EXPERIMENTAL DATA

The determination of air specific-impulse efficiency requires that the experimental air specific impulse be computable. Suitable measurements of pressure, drag, and thrust must be made on the experimental engine or combustor to permit computation of the stream thrust at the end of the exhaust nozzle:

$$F_e=\left(pA+\frac{wV}{g}\right)_e \tag{A1}$$

This equation is then reduced to the stream thrust function at a condition of sonic flow:

$$F_e^*=\frac{\left(pA+\frac{wV}{g}\right)_e}{\Phi(M_e)} \tag{A2}$$

where

$$\Phi(M_e)=\frac{1+\gamma_e M_e^2}{M_e\sqrt{2(\gamma_e+1)\left(1+\frac{\gamma_e-1}{2}M_e^2\right)}} \tag{A3}$$

The experimental air specific impulse is then

$$S_a=\frac{F_e^*}{w_a} \tag{A4}$$

The Mach number at the exhaust-nozzle outlet can be estimated from the equation

$$M_e=\sqrt{\frac{w_{g,e}V_e}{\gamma_e g p_e A_e}} \tag{A5}$$

For convenience, $\Phi(M_e)$ may be found from tables 30 to 35 of reference 14 as the term F/F^*. The expression $\Phi(M)$ is relatively insensitive to γ, in the neighborhood of M equal to 1.0, as shown in the following table:

M	$F/F^*=\Phi(M)$	
	$\gamma_e=1.1$	$\gamma_e=1.4$
0.7	1.0599	1.0451
.8	1.0231	1.0185
.9	1.0051	1.0034
1.0	1.0000	1.0000
1.1	1.0041	1.0030
1.2	1.0148	1.0108
1.3	1.0305	1.0217

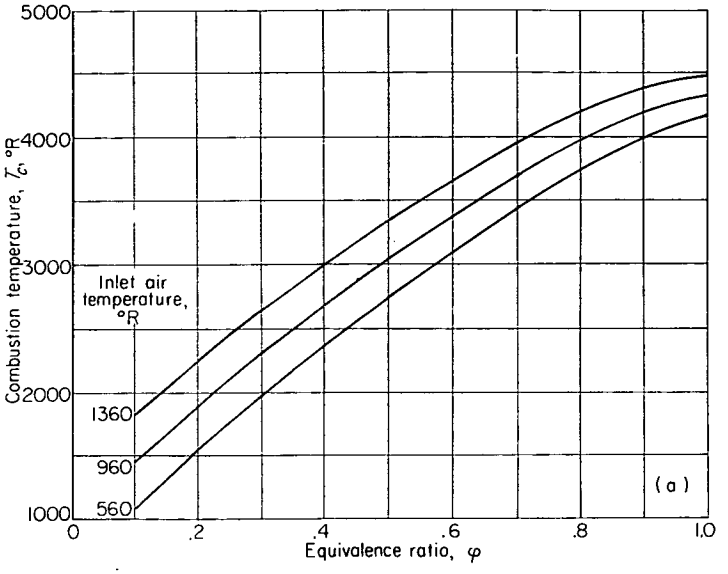
It must be observed that, if M_e is determined by equation (A5), the error in $\Phi(M_e)$, which results from an incorrect choice of γ_e, will exceed that shown in the preceding table. Data in reference 5 show that a satisfactory value of γ_e at high combustion temperatures (or high air specific impulse) would be 1.2 to 1.3; at low air specific impulse or combustion temperature, values of 1.3 to 1.4 can be employed.

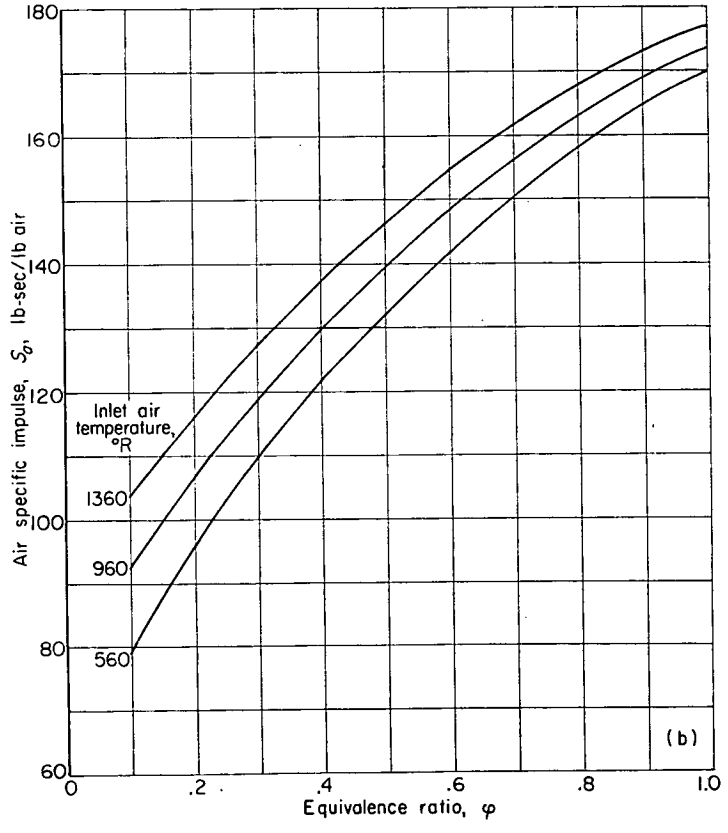
Because equation (A3) is based on the assumption of expansion at fixed composition, it cannot be used to correct experimental data to sonic conditions when there is reason to believe that appreciable recombination has occurred.

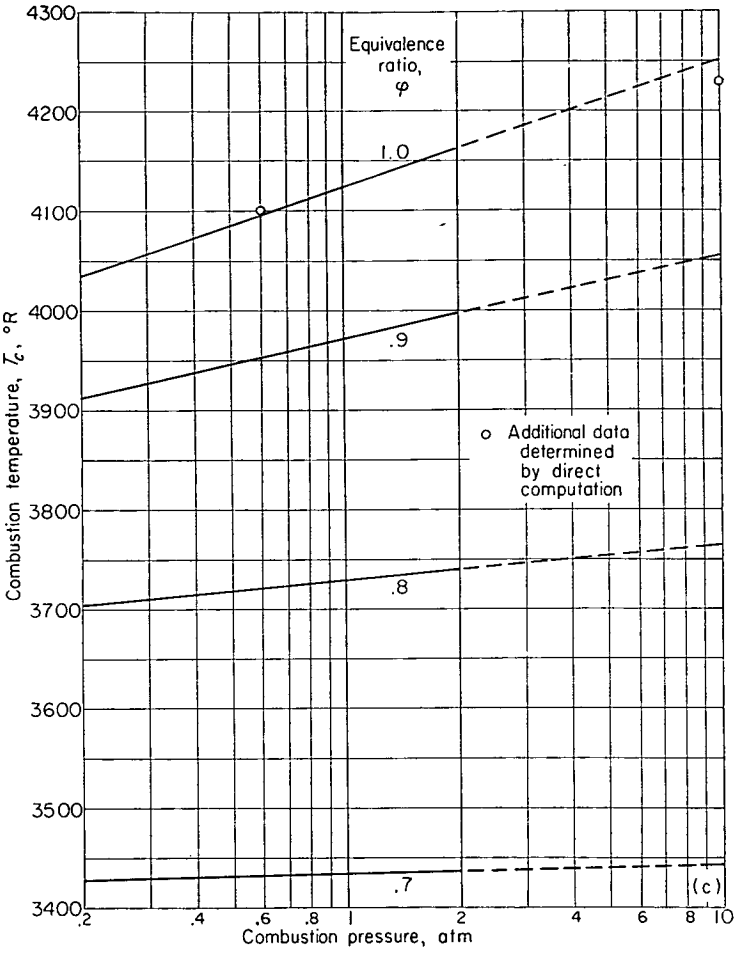
REFERENCES

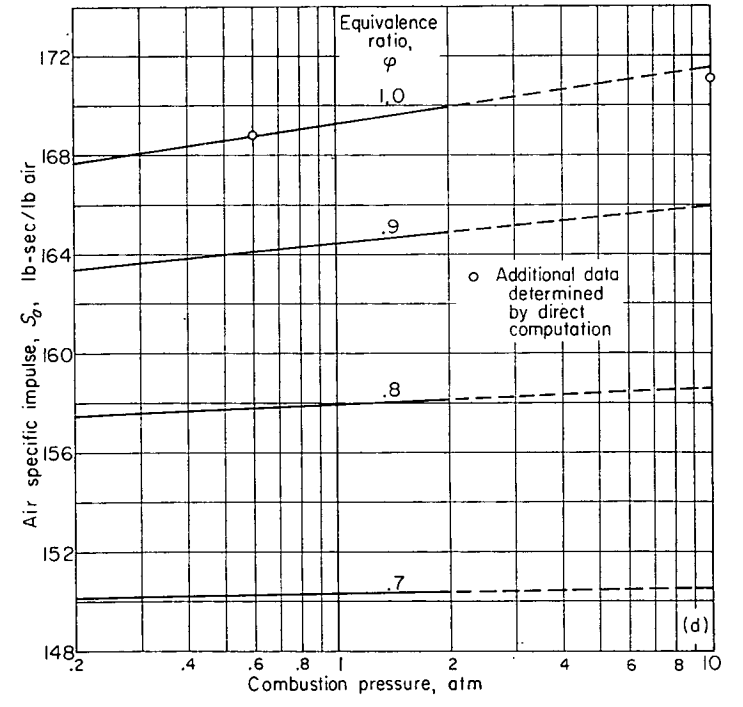
1. Olson, Walter T., and Gibbons, Louis C.: Status of Combustion Research on High-Energy Fuels for Ram Jets. NACA RM E51D23, 1951.
2. Lord, Albert M.: An Experimental Investigation of the Combustion Properties of a Hydrocarbon Fuel and Several Magnesium and Boron Slurries. NACA RM E52B01, 1952.
3. Branstetter, J. Robert, Lord, Albert M., and Gerstein, Melvin: Combustion Properties of Aluminum as Ram-Jet Fuel. NACA RM E51B02, 1951.
4. Gibbs, James B., and Cook, Preston N., Jr.: Preparation and Physical Properties of Metal Slurry Fuels. NACA RM E52A23, 1952.
5. Tower, Leonard K.: Effect of Water Vapor on Combustion of Magnesium-Hydrocarbon Slurry Fuels in a Small-Scale Afterburner. NACA RM E52H25, 1952.
6. Lord, Albert M., and Evans, Vernida E.: Effect of Particle Size and Stabilizing Additives on the Combustion Properties of Magnesium Slurry. NACA RM E52K12, 1953.
7. Branstetter, J. Robert, Gibbs, James B., and Kaufman, Warner B.: Magnesium-Slurry Combustion Performance in 6.5-Inch-Diameter Ram-Jet Engine Mounted in Connected-Pipe Facility. NACA RM E53E27, 1953.
8. Rudnick, Philip: Momentum Relations in Propulsive Ducts. Jour. Aero. Sci., vol. 14, no. 9, Sept. 1947, pp. 540–544.
9. Huff, Vearl N., Gordon, Sanford, and Morrell, Virginia E.: General Method and Thermodynamic Tables for Computation of Equilibrium Composition and Temperature of Chemical Reactions. NACA Rep. 1037, 1951. (Supersedes NACA TN's 2113 and 2161.)
10. Perry, John H., ed.: Chemical Engineers' Handbook. Third ed., McGraw-Hill Book Co., Inc., 1950.
11. Kelley, K. K.: Contributions to the Data on Theoretical Metallurgy. IX—The Entropies of Inorganic Substances. Bull. 434, Bur. Mines, 1941.
12. Setze, Paul C.: A Review of the Physical and Thermodynamic Properties of Boric Oxide. NACA RM E57B14, 1957.
13. Huff, Vearl N., Calvert, Clyde S., and Erdmann, Virginia C.: Theoretical Performance of Diborane as a Rocket Fuel. NACA RM E8I17a, 1949.
14. Keenan, Joseph H., and Kaye, Joseph: Gas Tables—Thermodynamic Properties of Air, Products of Combustion and Component Gases, Compressible Flow Functions. John Wiley & Sons, Inc., 1948.
15. Rossini, Frederick D., et al.: Selected Values of Chemical Thermodynamic Properties. Cir. 500, NBS, Feb. 1952.
16. Hodgman, Charles D., ed.: Handbook of Chemistry and Physics Thirty-eighth ed., Chem. Rubber Pub. Co., 1957.
17. Southard, J. C.: The Thermal Properties of Crystalline and Glassy Boron Trioxide. Vol. 63, no. 11, Nov. 1941, pp. 3147–3150.
18. Smith, S. H., Jr., and Miller, R. R.: Some Physical Properties of Diborane, Pentaborane and Aluminum Borohydride. Jour. Am. Chem. Soc., vol. 72, no. 4, Apr. 1950, pp. 1452–1458.
19. Rossini, Frederick D., et al.: Selected Values of Properties of Hydrocarbons. Cir. 461, NBS, Nov. 1947.
20. Smith, Marion L., and Stinson, Karl W.: Fuels and Combustion. McGraw-Hill Book Co., Inc., 1952.

526597—60——40









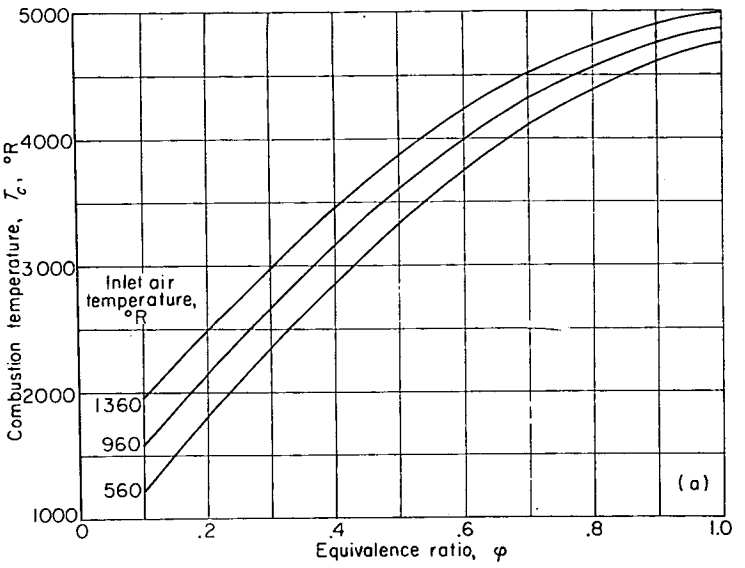
(a) Variation of combustion temperature with equivalence ratio and inlet air temperature. Combustion pressure, 2 atmospheres.

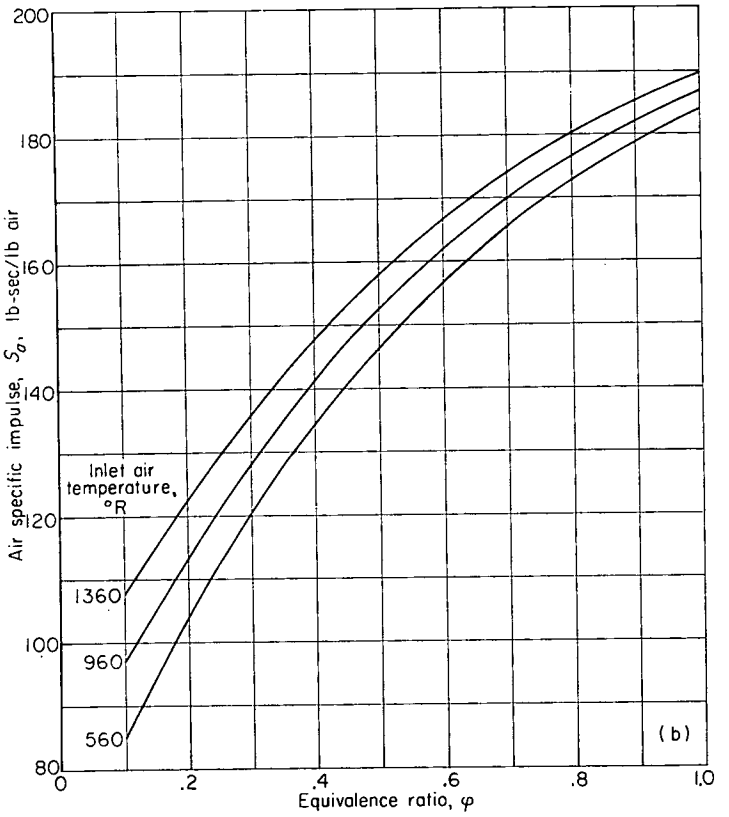
(b) Variation of air specific impulse with inlet air temperature and equivalence ratio. Combustion pressure, 2 atmospheres.

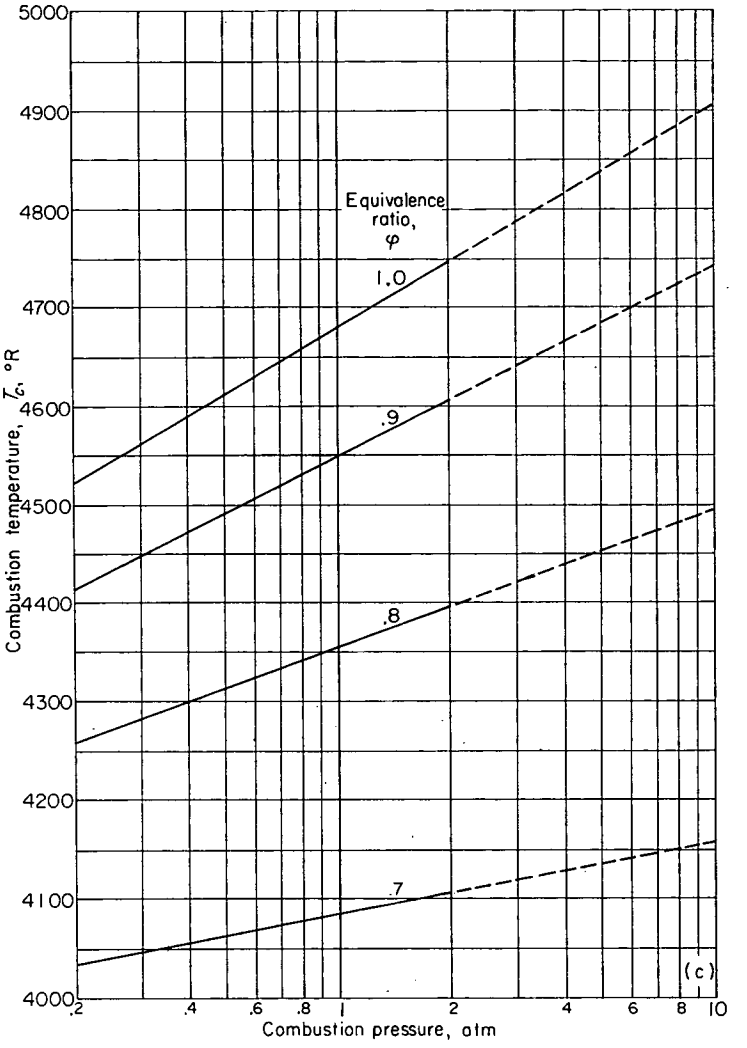
(c) Variation of combustion temperature with combustion pressure at selected equivalence ratios. Inlet air temperature, 560° R.

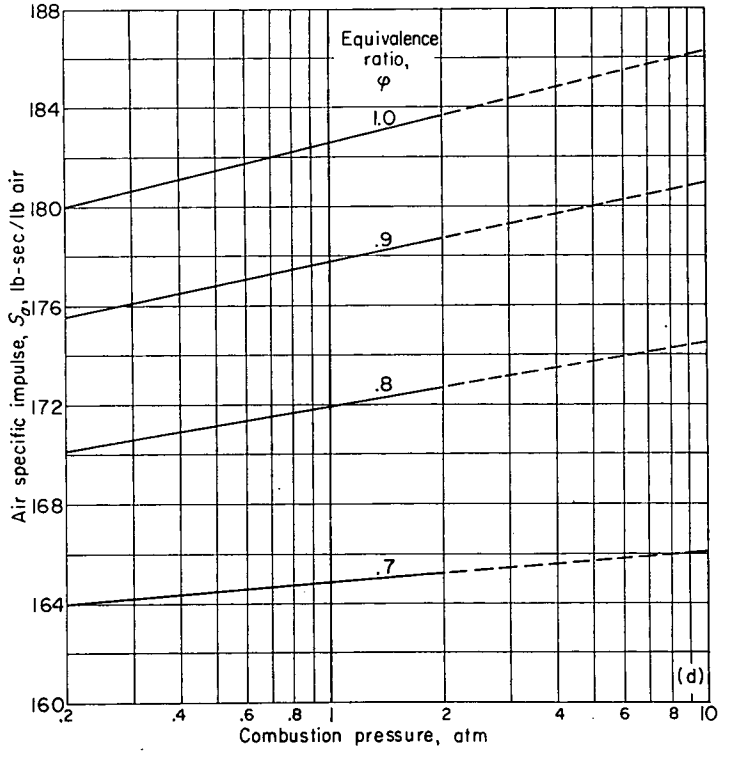
(d) Variation of air specific impulse with combustion pressure at selected equivalence ratios. Inlet air temperature, 560° R.

FIGURE 7.—Effect of ramjet combustor-inlet conditions on theoretical combustion performance of liquid octene-1.









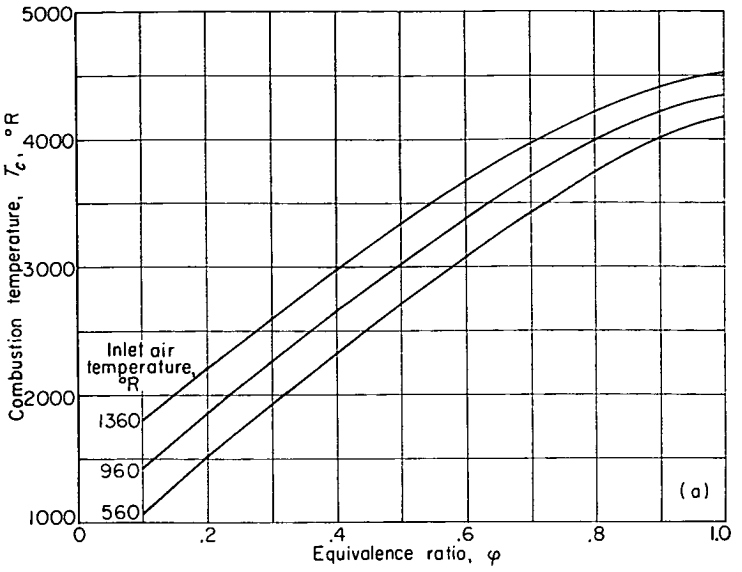
(a) Variation of combustion temperature with equivalence ratio and inlet air temperature. Combustion pressure, 2 atmospheres.

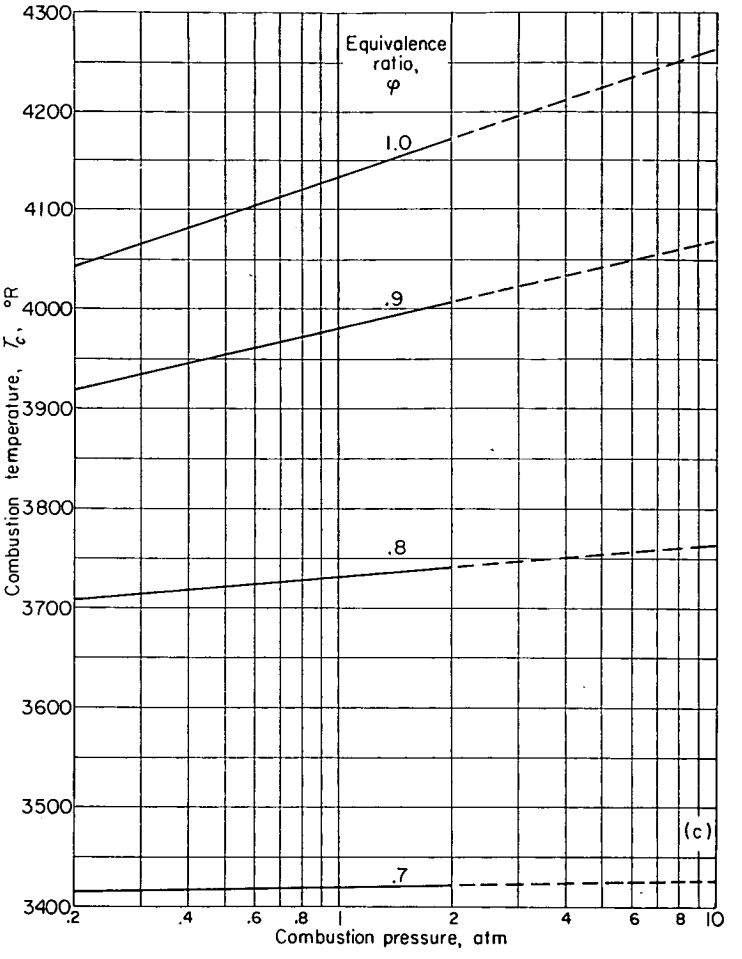
(b) Variation of air specific impulse with inlet air temperature and equivalence ratio. Combustion pressure, 2 atmospheres.

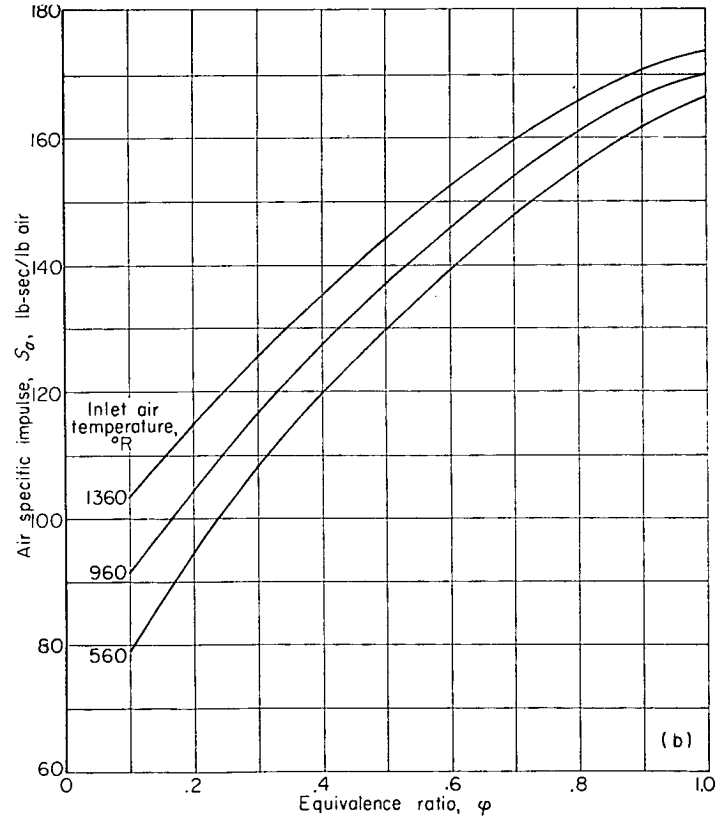
(c) Variation of combustion temperature with combustion pressure at selected equivalence ratios. Inlet air temperature, 560° R.

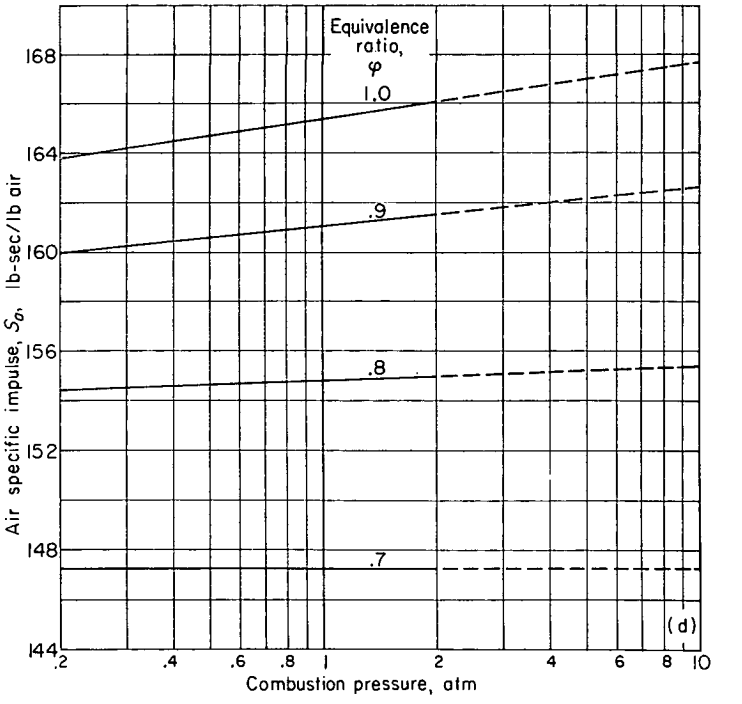
(d) Variation of air specific impulse with combustion pressure at selected equivalence ratios. Inlet air temperature, 560° R.

FIGURE 8.—Effect of ramjet combustor-inlet conditions on theoretical combustion performance of 50 percent magnesium slurry.









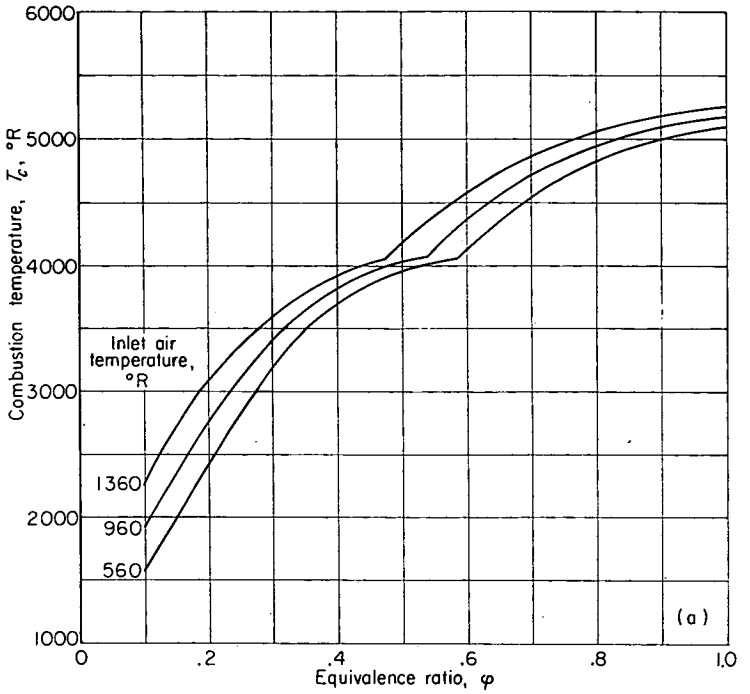
(a) Variation of combustion temperature with equivalence ratio and inlet air temperature. Combustion pressure, 2 atmospheres.

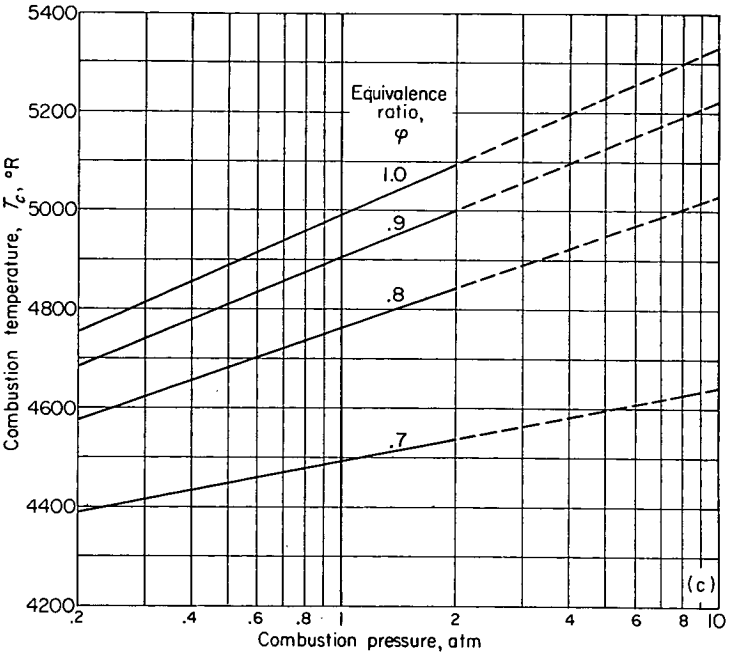
(b) Variation of air specific impulse with equivalence ratio and inlet air temperature. Combustion pressure, 2 atmospheres.

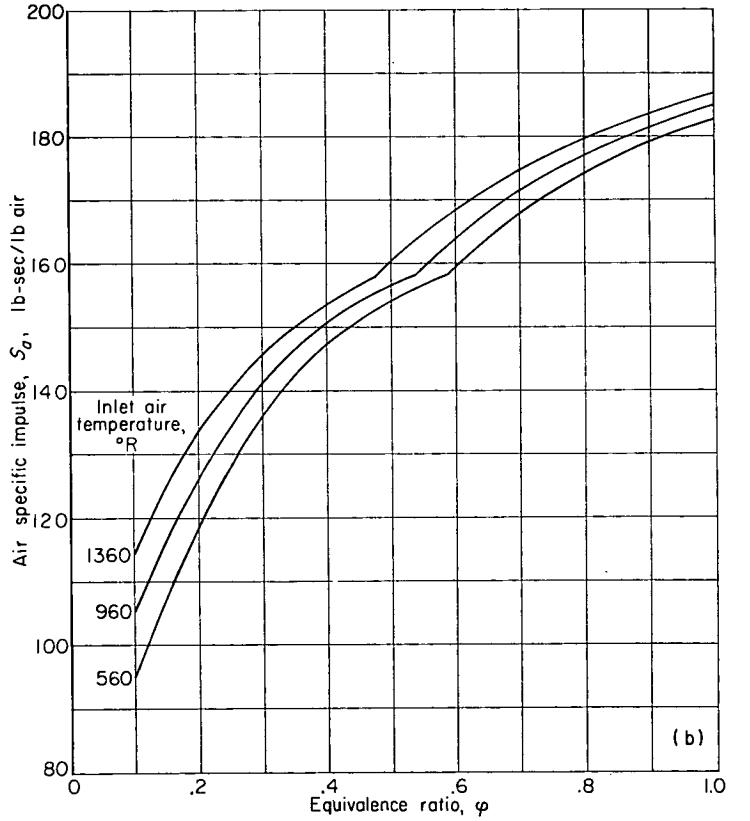
(c) Variation of combustion temperature with combustion pressure at selected equivalence ratios. Inlet air temperature, 560° R.

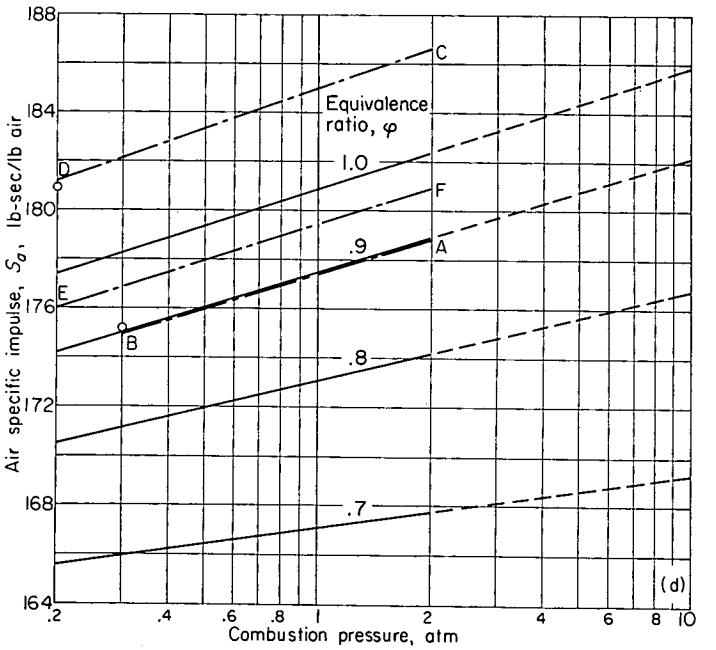
(d) Variation of air specific impulse with combustion pressure at selected equivalence ratios. Inlet air temperature, 560° R.

FIGURE 9.—Effect of ramjet combustor-inlet conditions on theoretical combustion performance of carbon (graphite).









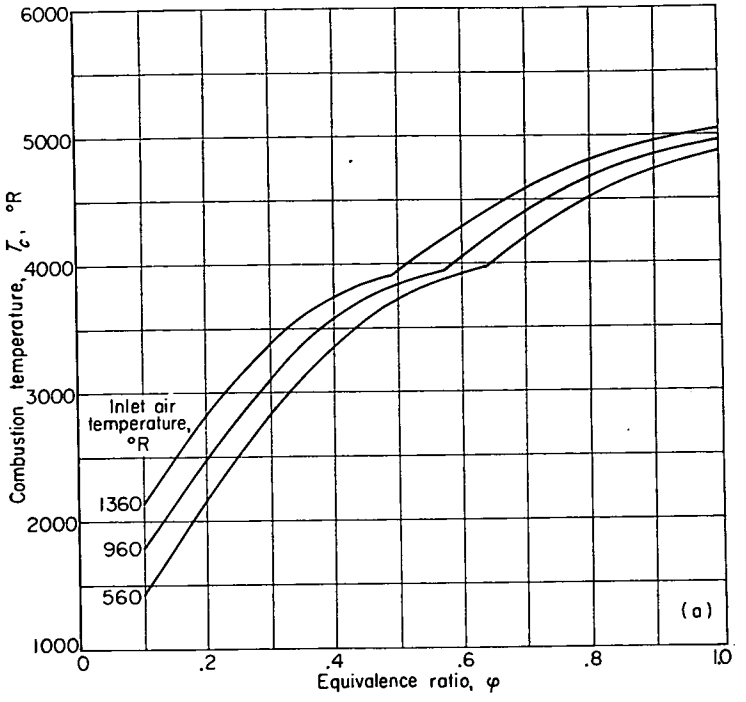
(a) Variation of combustion temperature with inlet air temperature and equivalence ratio. Combustion pressure, 2 atmospheres.

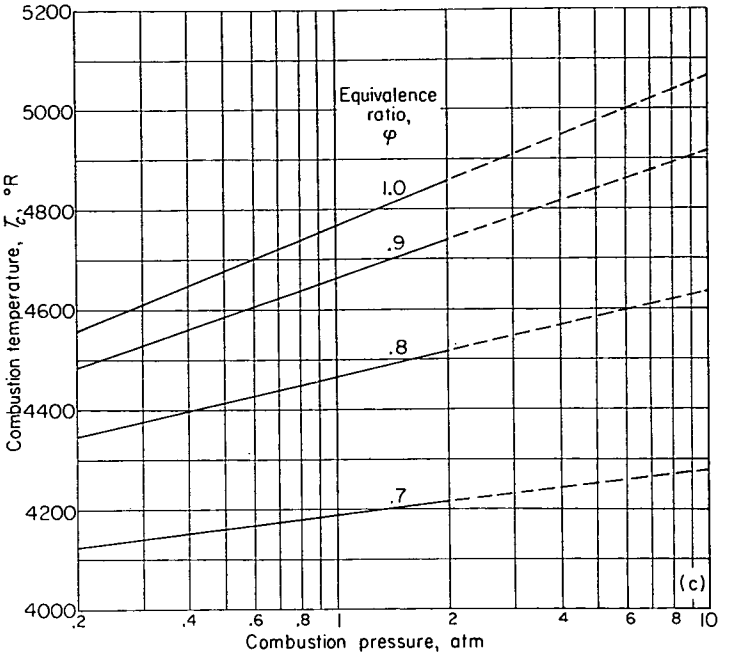
(b) Variation of air specific impulse with inlet air temperature and equivalence ratio. Combustion pressure, 2 atmospheres.

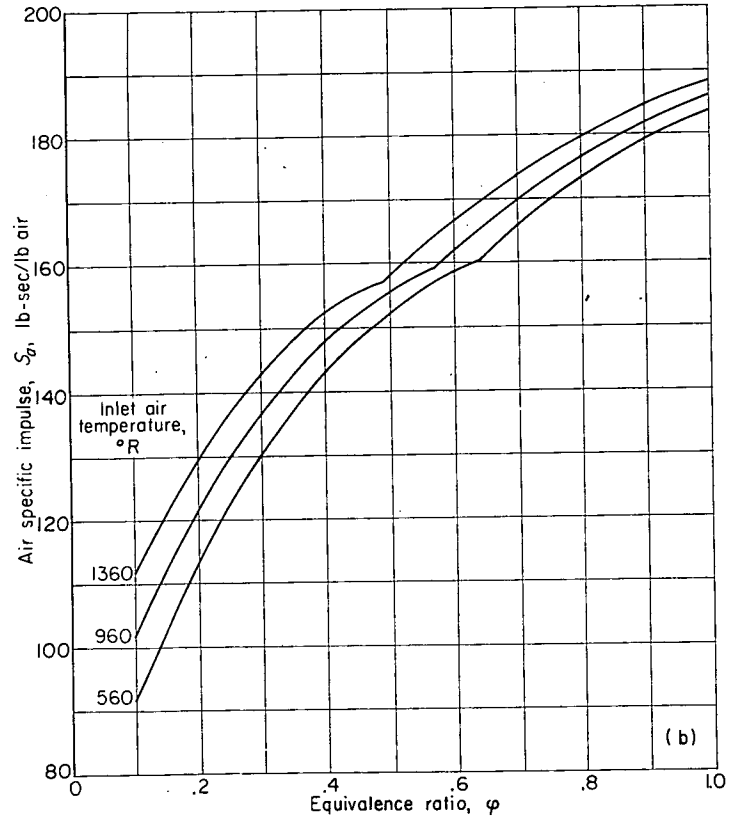
(c) Variation of combustion temperature with combustion pressure at selected equivalence ratios. Inlet air temperature, 560° R.

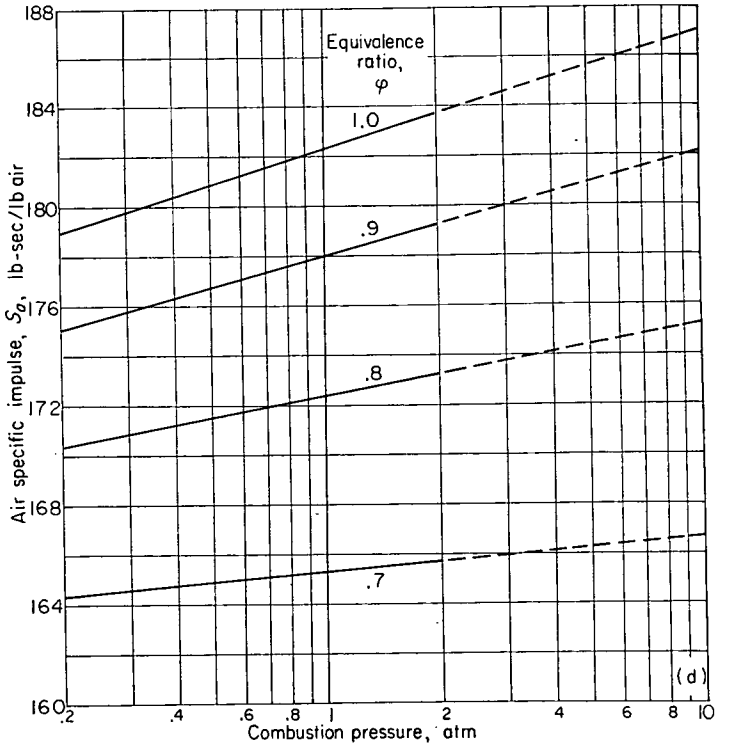
(d) Variation of air specific impulse with combustion pressure at selected equivalence ratios. Inlet air temperature, 560° R.

FIGURE 10.—Effect of ramjet combustor-inlet conditions on theoretical combustion performance of crystalline boron.









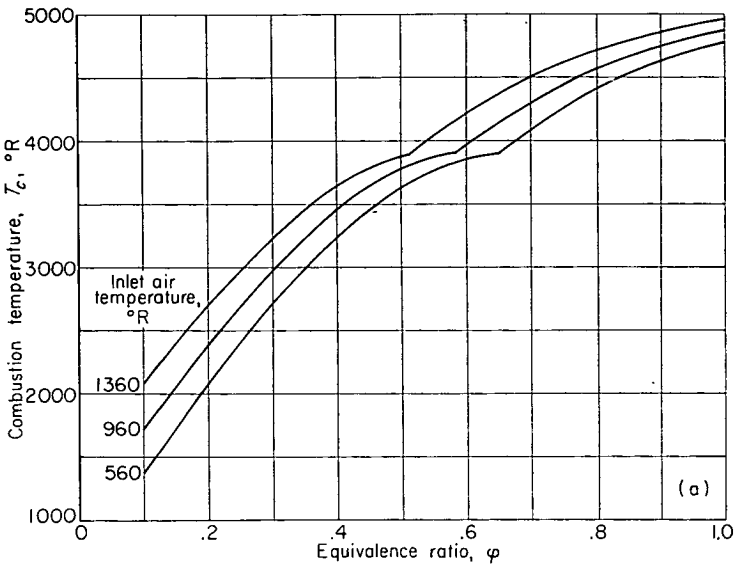
(a) Variation of combustion temperature with equivalence ratio and inlet air temperature. Combustion pressure, 2 atmospheres.

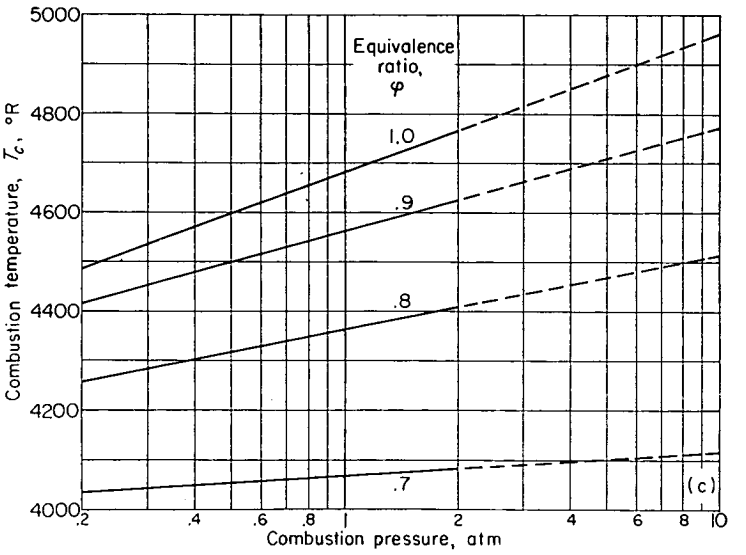
(b) Variation of air specific impulse with inlet air temperature and equivalence ratio. Combustion pressure, 2 atmospheres.

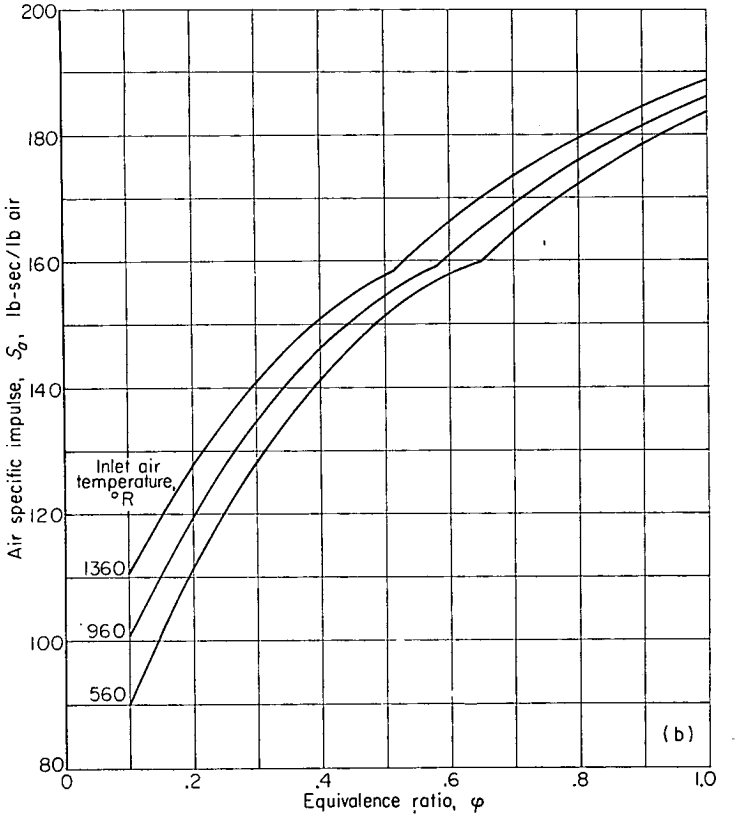
(c) Variation of combustion temperature with combustion pressure at selected equivalence ratios. Inlet air temperature, 560° R.

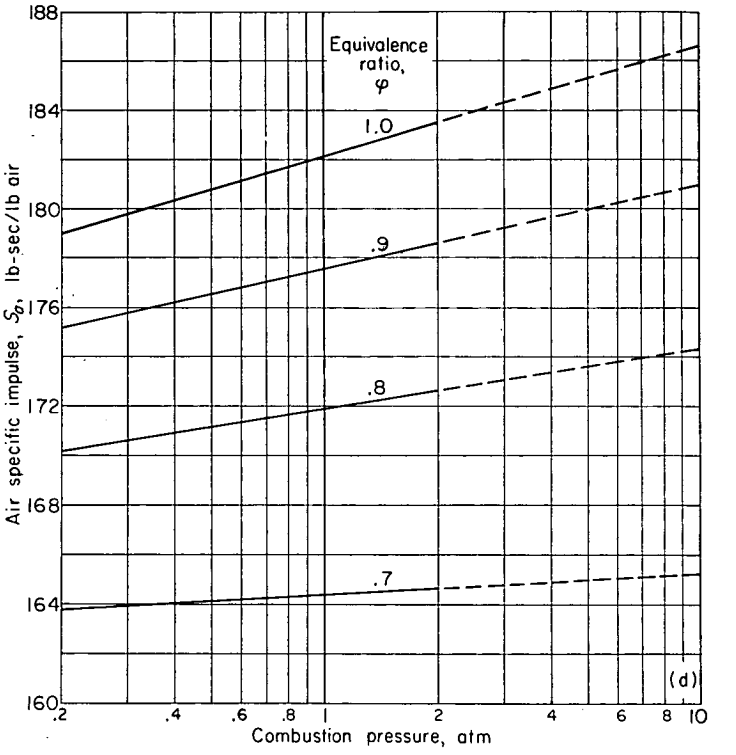
(d) Variation of air specific impulse with combustion pressure at selected equivalence ratios. Inlet air temperature, 560° R.

FIGURE 11.—Effect of ramjet combustor-inlet conditions on theoretical combustion performance of liquid pentaborane.









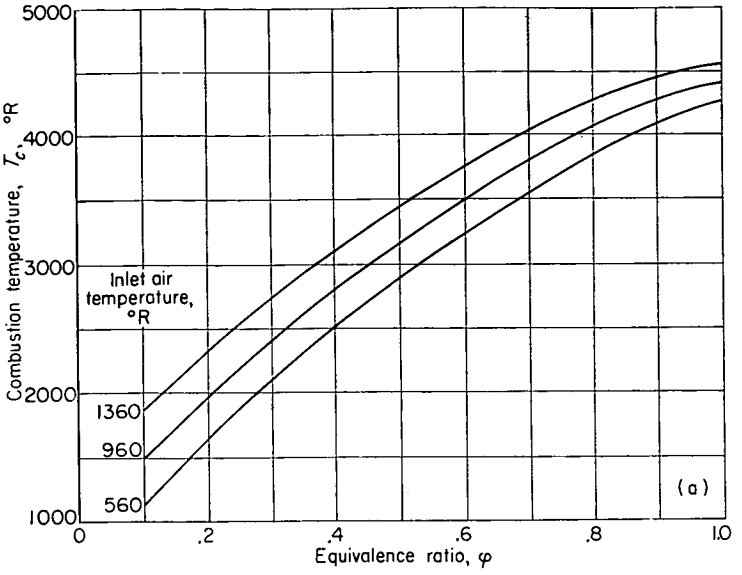
(a) Variation of combustion temperature with equivalence ratio and inlet air temperature. Combustion pressure, 2 atmospheres.

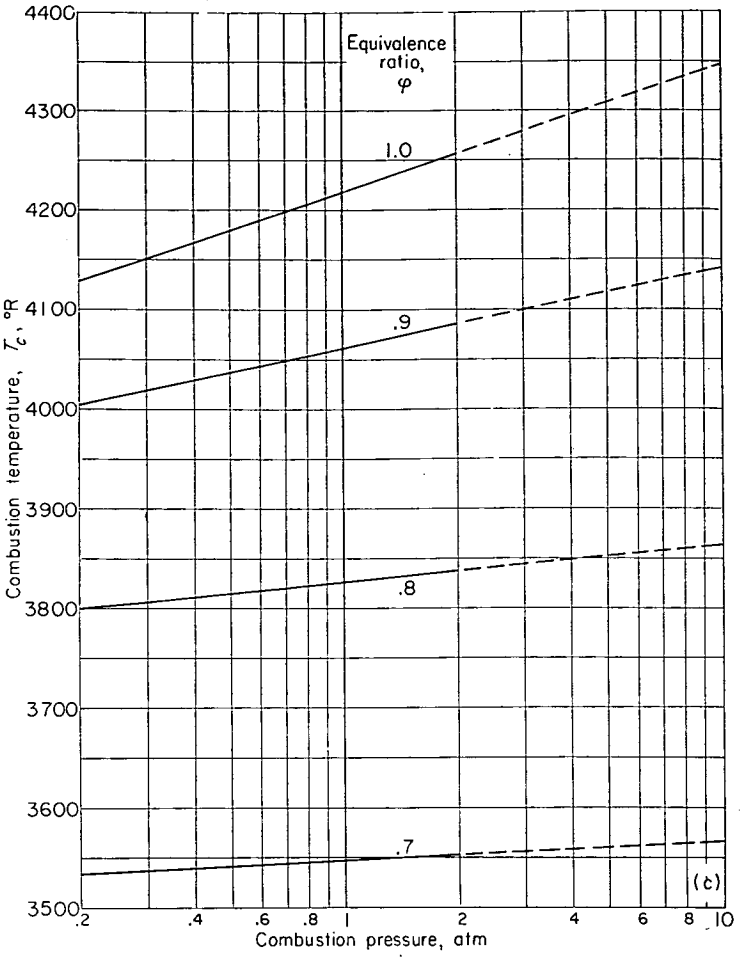
(b) Variation of air specific impulse with inlet air temperature and equivalence ratio. Combustion pressure, 2 atmospheres.

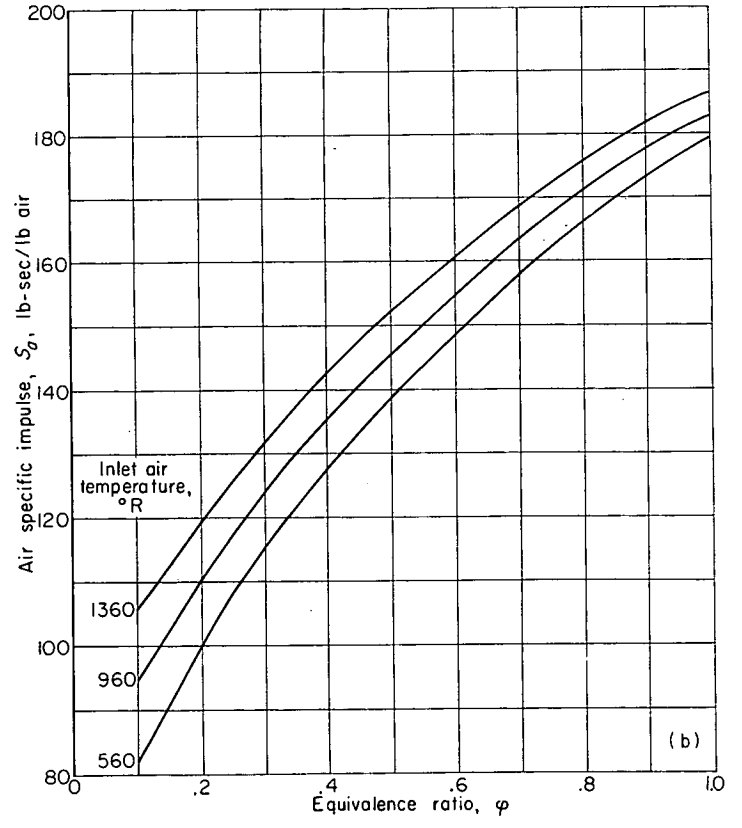
(c) Variation of combustion temperature with combustion pressure at selected equivalence ratios. Inlet air temperature, 560° R.

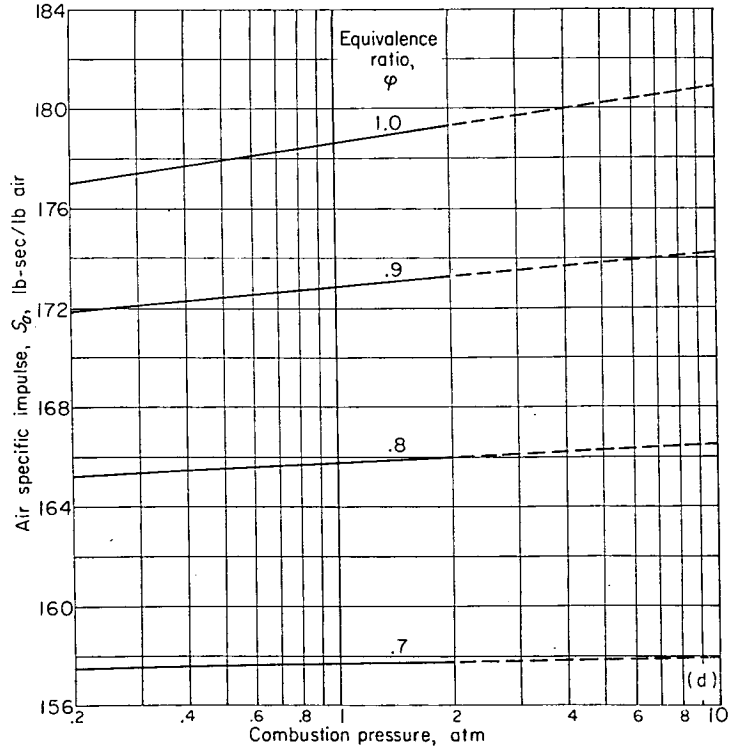
(d) Variation of air specific impulse with combustion pressure at selected equivalence ratios. Inlet air temperature, 560° R.

FIGURE 12.—Effect of ramjet combustor-inlet conditions on theoretical combustion performance of liquid diborane.









(a) Variation of combustion temperature with equivalence ratio and inlet air temperature. Combustion pressure, 2 atmospheres.

(b) Variation of air specific impulse with inlet air temperature and equivalence ratio. Combustion pressure, 2 atmospheres.

(c) Variation of combustion temperature with combustion pressure at selected equivalence ratios. Inlet air temperature, 560° R.

(d) Variation of air specific impulse with combustion pressure at selected equivalence ratios. Inlet air temperature, 560° R.

FIGURE 13.—Effect of ramjet combustor-inlet conditions on theoretical combustion performance of liquid hydrogen.

REPORT 1363

ORIGIN AND PREVENTION OF CRASH FIRES IN TURBOJET AIRCRAFT [1]

By I. Irving Pinkel, Solomon Weiss, G. Merritt Preston, and Gerard J. Pesman

SUMMARY

The tendency for the jet engine rotor to continue to rotate after crash presents the probability that crash-spilled combustibles suspended in the air or puddled on the ground at the engine inlet may be sucked into the engine. Studies with jet engines operating on a test stand and full-scale crashes of turbojet-powered airplanes showed that combustibles drawn into the engine in this way ignite explosively within the engine. Flames that could set the major fire appear at the engine tailpipe and often at the inlet when this explosive ignition occurs. This ignition may occur on the hot metal of the engine interior even after the combustor flame is extinguished and the engine rotor is coasting to rest.

Experiment showed that the gas flow through the engine is too rapid to permit the ignition of ingested combustibles on the hot metal in contact with the main gas stream. Ignition will occur on those hot surfaces not in the main gas stream. A portion of the engine airflow is diverted for cooling and ventilation to these zones where the gas moves slowly enough for ignition to occur.

The limited extent of the hot-metal zones that may start a fire permitted an approach to inerting the engine that involved the simultaneous initiation of the following actions immediately upon crash impact: (1) Shut off fuel flow to engine; (2) spray coolant (water) on those hot surfaces found to be ignition sources; (3) disconnect airplane electrical system at the battery and generator.

The effectiveness of this approach was evaluated by crashing airplanes powered by jet engines. Pylon-mounted engines attached to the wings were used to simulate airplanes with exposed pod nacelles. Fighters represented airplane types whose engines are contained within the main airplane structure. The quantity of water required as a coolant ranged from 9 to 12 gallons for each engine, depending on the engine and the length of the attached tailpipe. No fires occurred in six crashes in which the inerting system was used. Two airplanes crashed without protection caught fire.

INTRODUCTION

NACA research on the origin of crash fires, begun in 1949, has been extended to include jet aircraft. The work performed with jet aircraft followed an extensive program with piston-engine airplanes (ref. 1) which was documented with motion pictures (ref. 2). The objective of this work is to learn how turbojet crash fires start and to study means for reducing their likelihood. This report discusses the results of the study and describes a method developed to reduce the probability of such crash fires.

Since jet airplanes have the same gross configuration and assortment of components as piston-engine airplanes, much of what was learned about the start of crash fires in piston-engine airplanes applies to the turbojet. In the jet phase of the research new elements of the problem, peculiar to the jet airplane, were emphasized. These include the jet engine, jet fuel, increased fuel quantity, and differences in fuel location. Of these new elements, the jet engine is most important. Ignition hazards presented by friction and electrostatic sparks, electrical arcs and sparks, and air heaters remain substantially the same for piston-engine and jet airplanes. Some safety advantage is obtained from the lower volatility of jet fuels, but some of this advantage is counteracted by the increased quantity of fuel and its broader distribution on the airplane.

In this report interest is centered on the part the turbojet engine plays in setting crash fires. Because of the knowledge gained about combustible spillage and movement in crashes with piston-engine airplanes, this combustible spillage could be simulated for a jet engine on a test stand. Therefore, the crash-fire hazard presented by the jet engine could be assessed by test-stand studies. At appropriate times, airplanes with jet engines were crashed to verify important results obtained on the test stand.

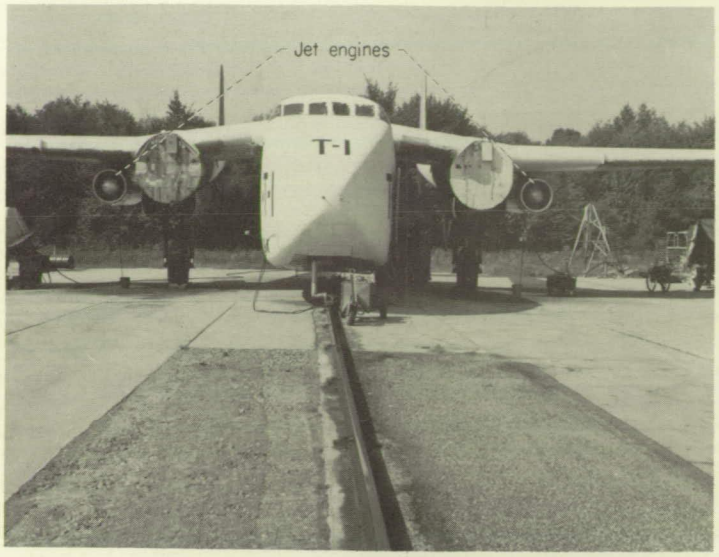
MECHANISM OF TURBOJET-AIRCRAFT CRASH FIRE

The start of a crash fire involves three major steps: movement of the crash-spilled combustibles to an ignition source, ignition of the combustible at the source, and spread of fire to the main body of fuel on the airplane. The movement of crash-spilled fuel to ignition zones and the spread of the fire were observed in the work with piston engines and are reported in detail in reference 1. There remains, then, the matter of understanding how the turbojet acts as an ignition source.

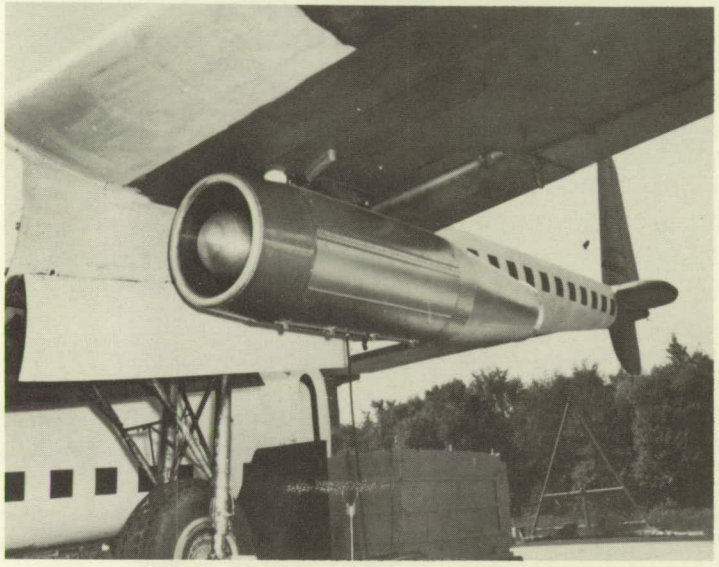
In order to observe how crash fires start with jet aircraft, two experimental full-scale crashes were conducted with turbojet aircraft having different engine installations. One of the aircraft was a C–82 airplane. The piston engines normally carried were replaced with either J35 or J47 engines, pylon-mounted to each wing to simulate a bomber-type engine installation. The airplane with turbojets is shown in figure 1. A fighter-type engine installation was

[1] Supersedes NACA Technical Note 3973 by I. Irving Pinkel, Solomon Weiss, G. Merritt Preston, and Gerard J. Pesman, 1957.

526597 O—60——41



(a)



(b)

(a) Front view.
(b) Side view.

FIGURE 1.—Jet engines pylon-mounted to wing of cargo airplane.

represented by an F–84 airplane whose J35 engine is submerged in its fuselage.

These crashes simulated takeoff or landing accidents, which occur at low airplane speed where the chance for human survival of the crash impact is high. In the experimental C–82 crash, turbojets accelerated the airplane from rest to a speed of about 90 miles per hour along a 1700-foot runway. A crash abutment (ref. 3) at the end of the runway was arranged to rip off the landing gear, while a pair of poles on each side of the wing tore open the fuel tanks containing 1000 gallons of JP–4 fuel.

The airplane as it struck the barrier is shown in figure 2(a). The cloud of fuel mist (liquid droplets suspended in air) that appeared when fuel spillage occurred while the airplane was in motion is evident at the breach in both wings (fig. 2(b)). Red dye in the fuel accounts for the bright color of the fuel cloud. As the crashed airplane slowed, the fuel mist moved forward of the wing and reached the air inlet on the left engine (fig. 2(c)). A strong cross wind swept the fuel mist away from the engine on the right wing.

Fuel mist ingested by the left engine was ignited somewhere within the engine. The ignited fuel mist produced the flames at the tailpipe and inlet shown in figure 2(d). These exposed engine flames ignited the fuel spilling from the wing (fig. 2(e)). The flame spread through this fuel to the wing to produce the stable fire shown in figure 2(f).

The F–84 fighter (fig. 3), carrying its turbojet submerged in the fuselage structure, caught fire in a similar crash. In this crash the fuel that entered the engine inlet was spilled from a fuselage tank adjacent to the engine-inlet duct. Arrangements for ensuring the failure of this tank in the crash are shown in figure 4. A driving strut was attached at one end to the nose wheel strut. The free end of the driving strut carried a spear-like tank cutter aimed at the fuselage fuel tank, whose wall is adjacent to that of the air duct. When the nose wheel strut failed rearward in crash, the driving strut cut the duct and tank walls. Fuel in liquid form poured into the air duct and was drawn into the engine.

A crash of the F–84 is shown in the sequence in figure 5. Upon passing through the crash barrier the airplane flew over a ditch toward rising ground. The fuel spilled from the damaged wing tanks in mist form and moved to the rear of the airplane (fig. 5(a)), which was traveling about 100 miles per hour. When the nose gear collapsed upon contact with the ground, the fuselage fuel tank was pierced. Fuel poured from this tank into the engine-inlet duct. Ignition of this fuel within the engine provided a succession of flame puffs issuing from the tailpipe, one of which is shown in figure 5(b). These flame puffs moved into the wake of the airplane and continued to burn as isolated masses. Fuel spilling from the wing was ignited by these flames at the rear of the airplane (fig. 5(c)). The resulting fire moved forward through the fuel spilling from the wing and reached the slowing airplane to produce the fire shown in figure 5(d).

The fire that occurred in these crashes of the cargo airplane with externally mounted engines and the fighter with a submerged engine showed that fuel ingested with the engine air can ignite within the engine. The flames produced may reach out of the engine tailpipe and inlet to ignite combustibles spilled around the crashed airplane.

ROLE OF TURBOJET ENGINE IN SETTING CRASH FIRES

The crash fires just described show that the turbojet plays a threefold role in setting the crash fires. First, because the turbojet has no propeller to strike the ground and stop the compressor and turbine rotation when crash occurs, the engine continues to operate. The large air mass flow into the engine is drawn from a broad zone ahead of the engine inlet. Combustibles spilled into this zone are sucked into the engine with this air. This ingestion of combustibles is the first step leading to the start of fire by the engine. Second, combustibles drawn into the engine as liquid are well mixed with air by the compressor. Wetting of the compressor blades, particularly those of the rotor, promotes the evaporation of the liquid combustible in the air. Evaporation is further promoted by the heating of the



(a) Airplane contacting barrier.



(b) Fuel-mist cloud, 0.8 second after initial impact.



(c) Fuel mist entering left engine, 2.5 seconds after initial impact.



(d) Fire at engine inlet and tailpipe of left engine, 2.6 seconds after initial impact.



(e) Fire spread to fuel mist issuing from left wing, 2.8 seconds after initial impact.



(f) Spread of fire, 4.0 seconds after initial impact.

FIGURE 2.—Development of crash fire in simulated jet bomber.



FIGURE 3.—F–84 Fighter airplane used in crash-fire investigation.

air in the compressor. The ingested fuel, favorably conditioned for ignition, then moves into zones in the hot end of the engine containing combustor flame and metal above the ignition temperature of petroleum fuels where ignition occurs. Third, the resulting flame propagates out of the engine to spread the fire.

Even if a pylon-mounted engine is torn free in a crash, its essential role in setting fires is unchanged. The normal fuel flow to the combustor is cut off upon engine separation, but the kinetic energy stored in the rotor maintains the compressor airflow. The inlet air velocity remains high enough for about 5 seconds after combustor fuel cutoff for appreciable entrainment of spilled combustibles with the inlet air. The probability of fuel ingestion is increased when the engine tumbles into the fuel deposited under or behind the airplane.

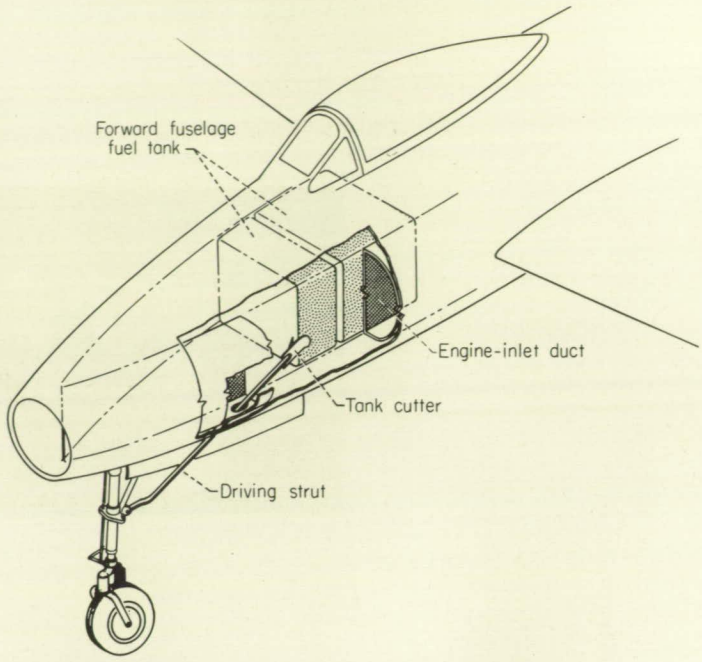


FIGURE 4.—Schematic diagram of F–84 tank-cutting mechanism.

A turbojet disintegrating in a crash could scatter hot-metal parts and burning combustor fuel into fuel-wetted areas. The resulting fire hazard is obvious and is not considered a subject for research. Experience gained in experimental crashes of turbojet aircraft in this and related programs has shown that there is little likelihood that the engine will come apart in a crash impact that is survivable. In no case did the engine break in crashes involving a total



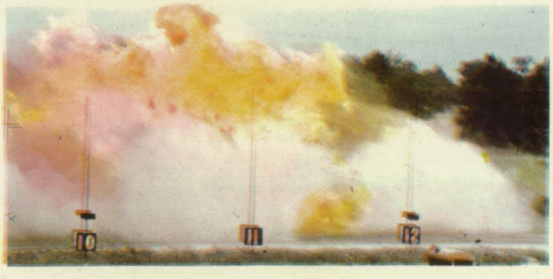
(a) Wing-tank fuel spillage, 0.35 second after initial impact.



(b) Flames at engine tailpipe, 0.75 second after initial impact.



(c) Wing-tank fuel mist, 1.10 seconds after initial impact.



(d) Spread of fire, 2.15 seconds after initial impact.

FIGURE 5.—Development of crash fire in jet fighter.

of 23 engines, yet some of these crashes produced airplane decelerations well beyond human endurance.

The characteristics of the engine as a source of ignition received the most attention in this work. Understanding the ignition process within the engine was considered the key to any useful approach to reducing this crash-fire hazard.

FUEL INGESTION

An operating turbojet draws its air from a stream tube of diameter less than that of the engine inlet when the airplane is flying. When the engine is moving with low forward speed on the ground, the static pressure at the inlet is less than atmospheric and the stream-tube diameter is greater than the engine-inlet diameter. This condition exists when the airplane slows in crash. This stream tube broadens further if the engine comes close to the ground as the airplane breaks up.

Liquid combustibles sprayed into areas of low velocity in the inlet stream tube may drop to the ground before they reach the engine inlet. Liquid suspended in air (mist) entering the same zones is drawn into the inlet. Streams or jets of liquid combustibles projected into the high-velocity air within a few inlet diameters of the engine are also drawn into the inlet. As the velocity of the inlet air decreases with engine rotor speed, the distance at which ingestion of these streams or jets occurs shortens correspondingly.

Liquid fuel may be sucked into the engine from pools of fuel on the ground in front of the inlet. If the engine is on the ground, this fuel is drawn into the engine with the inlet air. If the engine is above the ground, a vortex that sometimes develops at the inlet and extends to the ground may raise liquid fuel from the ground into the intake airstream (ref. 4). Also, fuel stored in tanks adjacent to engine air-intake ducts could pour into the duct when walls separating them are breached.

Evaporation of liquid pools of fuel or fuel from wetted surfaces is a relatively slow process. This is particularly true for jet fuels with volatilities lower than aviation gasoline. Therefore, the vapors emanating from liquid fuel, spilled in the zone of influence of the inlet stream tube, rarely will be sufficient to produce a combustible mixture with the large mass airflow into the engine. Usually, ignitible concentrations of combustibles will enter the engine only when liquids are ingested. These liquids may be in solid streams or mist form.

ENGINE IGNITION SOURCES

The two principal engine ignition sources, combustor flames and hot-metal surfaces, are sufficiently different in their behavior to merit separate discussion. These differences relate to the time these sources persist after crash, the manner in which ignition occurs, and the mode of propagation of the resulting fire out of the engine.

Combustor flames.—If normal combustor fuel flow continues after crash, the combustor flame persists as long as fuel remains in the tank. Combustibles ingested with the engine intake air are ignited immediately upon contact with this flame. Since this ingested fuel enters the combustor through air openings in its liner, which extend to the downstream end of the combustor, the burning of this fuel is not completed in the combustor. The fuel continues to burn in the tailpipe downstream of the turbine. Exposed flames that could start the crash fire might appear at the tailpipe exit, particularly if the tailpipe is short. Ignition of the ingested fuel-air mixture will occur even if it is somewhat leaner than the conventional lower combustible limit, because it is intimately mixed with the combustor flame.

If the fuel flow to the combustor is cut off by intent or accident, the main combustor flame is extinguished at once. However, the fuel manifold continues to drain slowly through the lower fuel nozzles to support small adjacent residual fires. These fires were observed in test-stand engine studies through windows in the combustor. The flames were visible up to 8 seconds after combustor fuel shutoff when the engine was operated at rated sea-level conditions. The ignition hazard provided by these residual flames compares with that of the full combustor flame. However, the ingested fuel would have to produce mixtures within the conventional combustible limits for the small residual flames to produce ignition.

Flames originating within the engine may also appear at the engine inlet as observed in figure 2(d). The appearance of this inlet flame may be explained in the following way. Burning of ingested fuel in the combustor flame reduces the turbine-inlet gas density. A higher pressure in the combustor is required to pass the gas through the turbine. When an abrupt change in over-all combustor fuel-air ratio is provided by the ingested fuel, the pressure in the combustor required to pass the combustor gas through the turbine may exceed the capability of the compressor at the existing rotor speed. The compressor flow may stall before the turbine can accelerate the rotor to a speed that will provide the necessary pressure. At this moment the combustor flame may propagate upstream through the ingested combustible mixture that fills the stalled compressor and exit at the engine inlet.

Hot-metal surfaces.—If combustor fuel shutoff is provided upon crash and residual flames are avoided, the hot engine metal may be a potential ignitor. Consequently, the temperatures of characteristic engine parts downstream of the compressor were measured on test-stand engines at locations shown in figure 6 for a period following combustor fuel shutoff. Thermocouples reading temperatures on rotating engine

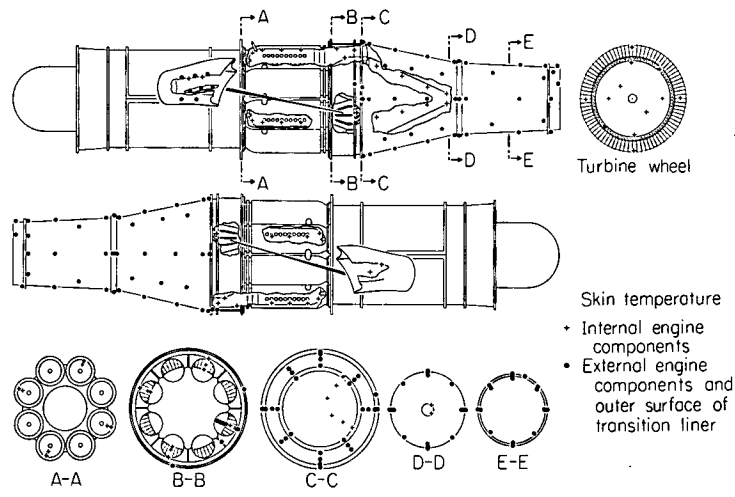


FIGURE 6.—Thermocouple locations on J47 engine.

parts were connected to recorders through slip rings on the engine shaft.

Maximum temperatures obtained with the J47 and J35 engines running on the test stand were comparable (fig. 7). Temperatures of similar locations in the J30 engine, which are not given here, were also comparable to those recorded on the J47 and J35 engines.

The engine metal temperatures aft of the compressor are discussed in detail in appendix A. These temperature measurements showed that all the metal downstream of the compressor was above the laboratory measured ignition temperature of jet fuels and lubricants. These parts were at dangerous temperatures for varying periods of time after the combustor fuel was shut off. However, temperature alone is an insufficient measure of the ignition potential of a hot surface.

In contrast with flame ignition, which is instantaneous in terms of time intervals significant in this problem, ignition of combustible atmospheres by hot surfaces is not instantaneous. An appreciable contact time is required between the combustible atmosphere and the hot surface in order for ignition to occur. The contact time required for ignition on hot surfaces has been the subject of some recent experiments. Unfortunately, much of the experimental data on ignition of combustible atmospheres flowing over hot surfaces was obtained with single-constituent hydrocarbon fuels under conditions that hardly approximate those in a jet engine. Some data obtained with jet fuels, however, show the important trends and the orders of magnitude involved.

The relation between surface temperature and contact time required for ignition is shown by data given in figure 8(a) for JP–4 fuel (refs. 5 and 6 and unpublished NACA data). Two main trends are evident. (1) The required contact time decreases with increasing surface temperature. (2) When the combustible atmosphere is at high pressure, which exists within an engine during the initial stages of a crash, ignition is possible at a lower surface temperature for a given contact time. As the pressure decreases to atmospheric, ignition occurs at higher temperatures for a particular contact time.

The corresponding curves for kerosene and 115/145 and 100/130 aviation gasolines (refs. 7 and 8) show the same trends as the curves for JP–4 fuel (fig. 8(b)). The fact that a contact time of more than 0.1 second is required to ignite a combustible atmosphere of JP–4 fuel on a 1000° F surface and a combustible atmosphere of gasoline on a 1400° F surface is important in the problem being investigated herein.

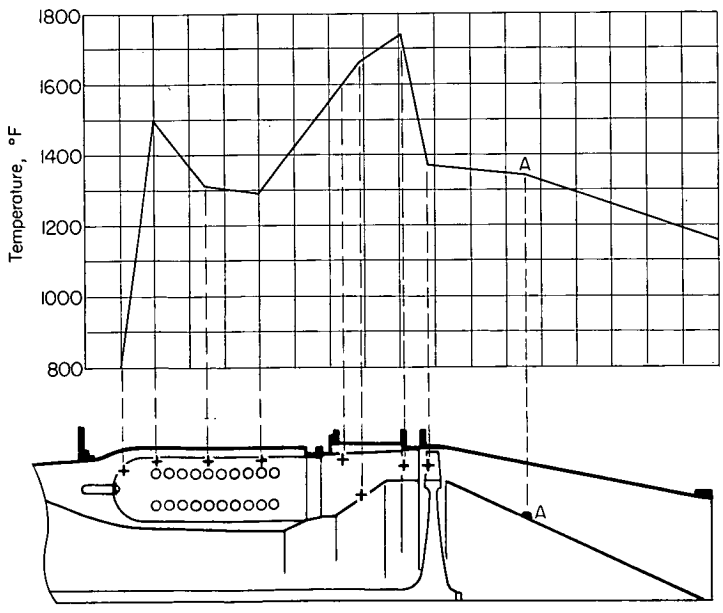
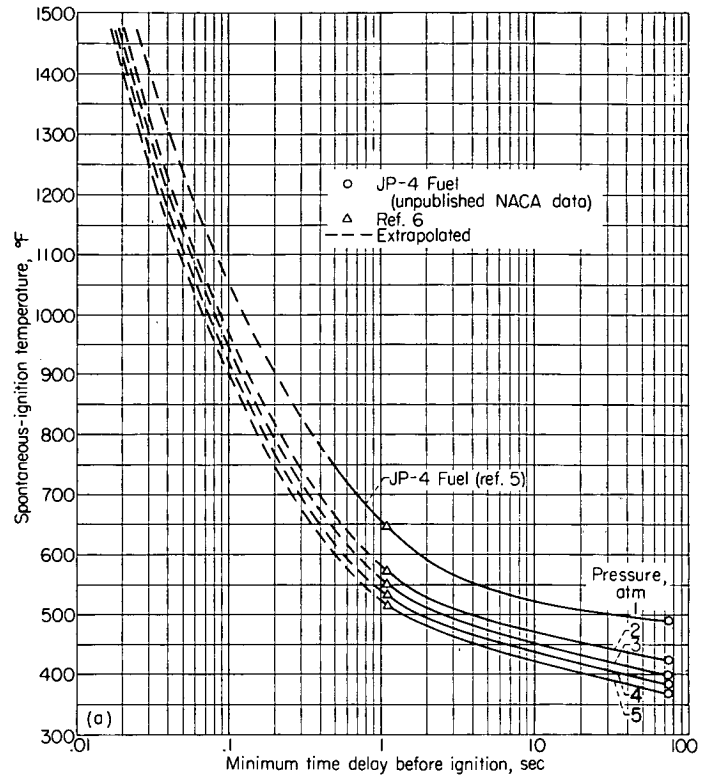
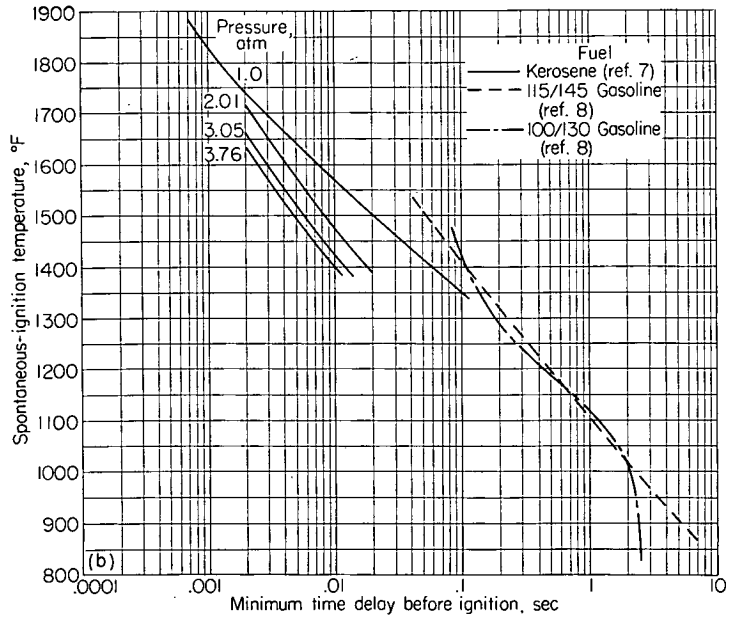


FIGURE 7.—Maximum temperatures of metal components in main gas stream of J47 and J35 engines.



(a) JP–4 Fuel.



(b) Kerosene and 115/145 and 100/130 aviation gasolines.

FIGURE 8.—Ignition characteristics of aviation fuels.

A study of the gas velocity through the hot zones of the engine in the main gas stream showed that combustibles pass through these zones too rapidly to ignite. This is true for approximately 20 seconds following engine combustor fuel shutoff. After this period, the probability of fuel ingestion is quite low. The engine temperature and velocity data used in this study are discussed in appendix B for the J35 engine. In these studies the engine temperature and air velocity data provided in figures 9 and 10 were used. Similar studies which led to the same result were made for the J30 and J47 engines. The method of analysis discussed in appendix B provides a first appraisal of the possibility of ignition of ingested combustibles by components in the main gas stream.

While the analysis showed the J30, J35, and J47 engines safe in this regard, it is conceivable that, with larger engines, ignition on the hot metal in the main gas stream may be possible. The longer components of the larger engines provide a longer transit time for the combustible atmosphere moving by. Minimum contact times for ignition may then exist for components in the main gas stream. The method discussed in appendix B is useful in determining when this may occur.

While ignition by hot surfaces is unlikely in the main gas streams of the engines studied, there are other zones in the engine where hot-metal ignition is likely. The hot-metal ignition zones within the engines studied were found to be in those areas where the gas velocity is less than that of the main gas stream. A small portion of the engine gas flow is diverted to hot zones in the engine where sufficient contact

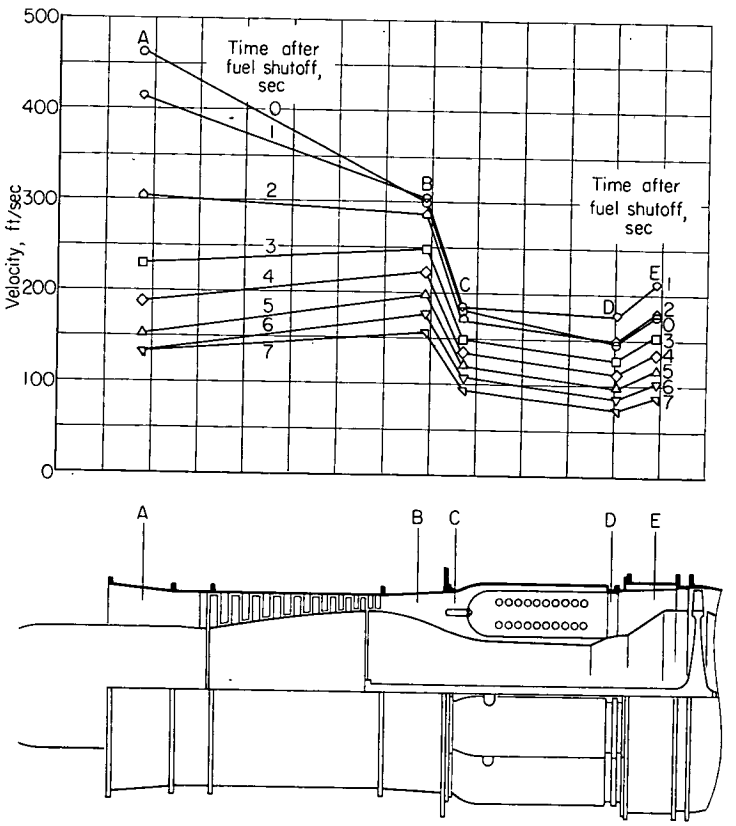


FIGURE 9.—Air velocity through J35 engine after combustor fuel shutoff.

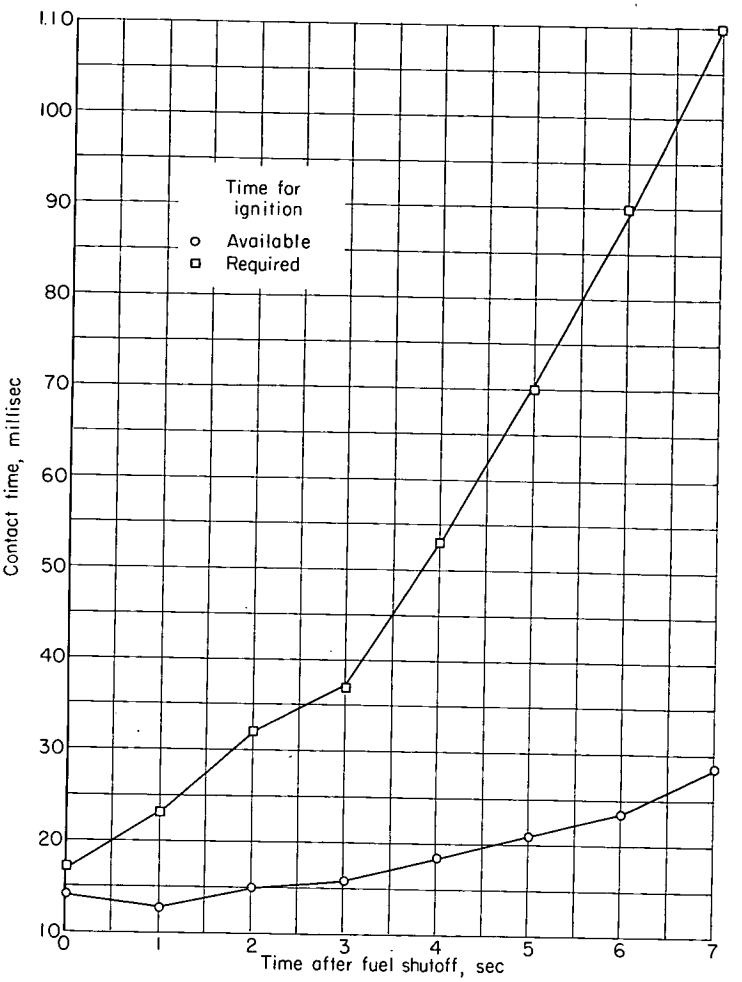


FIGURE 10.—Analysis of ignition probability in J35 combustor.

time for ignition exists. The quantity of gas diverted is sometimes unknown, and the geometry of the flow in the diversion zones is uncertain. For these reasons the period over which these diversion zones were hazardous was difficult to define based upon an analysis involving surface temperature and contact time.

The ignition zones were identified in test-stand engines by the method discussed in detail in appendix C. The technique employed involved the use of fuel sprays local to the engine zone suspected as an ignition source. Following engine operation at rated conditions for a time sufficient to establish temperature equilibrium, the fuel flow to the combustor was turned off and the fuel spray was turned on local to the zone under study. The fuel flow was programmed to maintain a combustible atmosphere in the zone. If ignition occurred, inerting means were installed to prevent the ignition in subsequent tests of upstream zones. By starting at the downstream end of the engine and proceeding upstream in this way, each ignition zone was identified and inerted in turn. As a final check after all the zones were inerted, fuel was injected into the main gas stream to determine whether ignition would occur. In this manner, ignition zones were found on the combustor liner, transition liner, turbine, inner cone, and tailcone and tailpipe (fig. 11).

Combustor liner: The ignition zone found on the combustor liner was the dome, which lies close to the primary

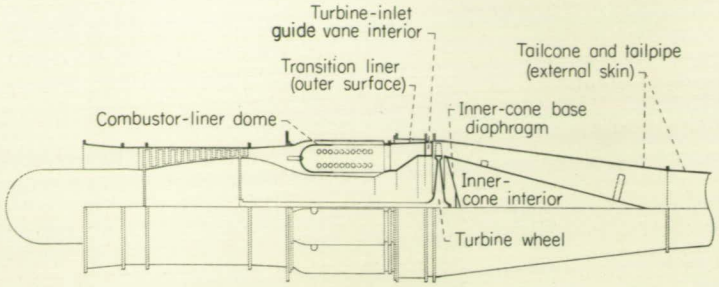


FIGURE 11.—Hot-metal ignition sources found in J35 engine.

combustion zone. The metal adjacent to the dome is heated by the combustor flame and attains unsafe temperatures in spite of the cooling provided by the adjacent air. Also, in this region the engine air is caused to recirculate by design to provide a zone of low transitional speed and promote good combustion. Both the hot metal of the combustor liner adjacent to the dome and the residual flames previously discussed make this zone particularly hazardous. The size of this zone is difficult to define, since it depends on the air temperature at the compressor outlet, the combustor design, and the ignition characteristics of the combustibles sucked into the engine.

Transition liner: The outside surface of the transition liner, which joins the combustor to the turbine, is another ignition zone. A small quantity of air flows continuously from the combustor over the outer surface of the transition liner. Combustibles sucked into the engine inlet are brought to the outside surface of the liner with this air. In some engines this air is drawn through the hollow turbine-inlet guide vanes for cooling. These vanes are at the same high temperature as the transition liner and must be counted as an ignition source in this engine zone.

Turbine: The cavity containing the turbine wheel is a zone of low gas velocity. The combustibles sucked into the engine inlet are delivered to each face of the turbine wheel with the cooling air drawn from the higher compressor stages. This air moves slowly enough for ignition to occur on the turbine-wheel faces and on the inner-cone base diaphragm.

Inner cone: Combustible atmospheres delivered to the turbine wheel from the compressor can enter the interior of the inner cone through vent holes. In some engines these vent holes are located at the base of the tailcone as shown

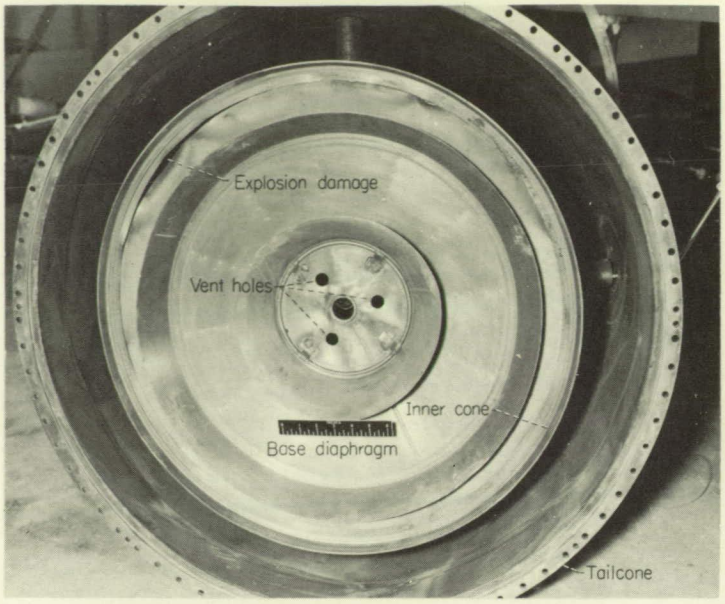


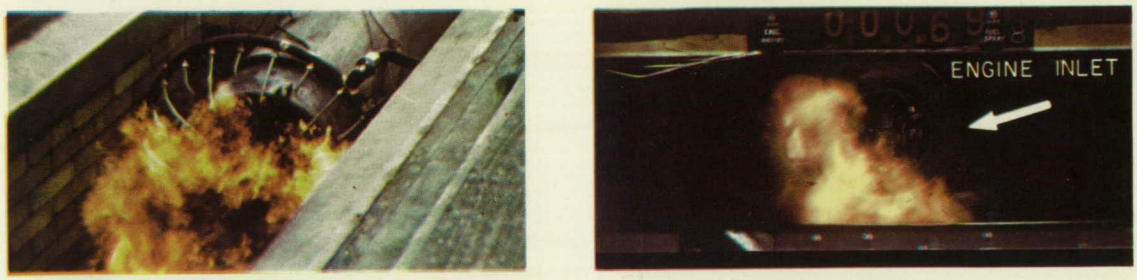
FIGURE 12.—J35 Inner-cone base diaphragm.

in figure 12. The plane of the inner-cone base is parallel to the turbine wheel. Combustibles entering the cone could ignite on the hot walls of its quiescent interior. The slight damage to the base diaphragm, indicated in the figure, followed ignition in the interior. The resulting flame might ignite the combustible atmosphere streaming through the engine to produce the dangerous flames at the engine inlet and tailpipe shown in figure 13.

Tailcone and tailpipe: The ignition zones discussed previously were all that were found within these engines. Experiments showed that fires could also be obtained when fuels or lubricants contacted the outside surface of the tailcone and tailpipe. The fire produced by jet fuel on an engine tailpipe is shown in figure 14. For engines having a pressure ratio of 5 or less, the unsafe exterior surfaces were confined to the tailcone and tailpipe.

CRASH-FIRE INERTING SYSTEM FOR TURBOJET AIRPLANES

If fuel ingestion could be prevented, a study of the engine ignition would not be necessary. A review of possible methods and means for employing closures at the inlet, outlet, or within the engine to prevent fuel ingestion on crash indicated little hope for this approach. Unacceptable



(a) Tailpipe (b) Inlet.

FIGURE 13.—Flames issuing from engine following explosive ignition of fuel within engine.



FIGURE 14.—Fuel ignition on tailcone surface.

weight and complexity were required in the closure equipment necessary to meet the stringent specifications of fast actuation and strength to support the pressure differences developed by the compressor.

Previous crash research with piston-engine airplanes showed that a marked reduction in the crash-fire hazard could be realized by controlling potential ignition sources (ref. 1). Most of the ignition sources carried on the airplane are associated with the electrical system and the engine. By de-energizing the electrical system and inerting the engine ignition zones upon crash, most of the fire hazard is overcome.

The electrical system can be de-energized by opening the generator and battery circuits. The armatures of main electrical components likely to generate dangerous voltages as they coast to a stop are grounded close to these components. In this way these armatures are brought to a rapid stop, and the length of electrical wiring at dangerous voltages is shortened considerably. Ignition sources associated with the engine consist of combustor flames and hot engine metal discussed previously.

COMBUSTOR FLAMES

In crash the combustor flame can be put out by shutting off the combustor fuel flow. Residual combustor flames can be avoided if the fuel manifold can be vented to an overboard drain at the time the main fuel valve is closed. Dribbling of fuel from the nozzles into the combustors is avoided in this way.

HOT ENGINE METAL

The problem of inerting the hot engine metal was solved during the search for these dangerous zones. The method employed for locating ignition zones within the engine, described in appendix C, involved the inerting of known ignition zones as the search for others proceeded. Water, applied to the dangerous hot surfaces, was chosen as the inerting agent because its high heat of vaporization made possible the cooling of ignition zones with small quantities. A blanket of steam generated by the water evaporating from the hot surfaces inerted these zones, thus preventing ignition while the surfaces cooled to safe temperatures.

The quantities of water required to inert the separate ignition zones within the J30, J35, and J47 engines are shown in table I. These quantities do not represent mini-

TABLE I.—WATER QUANTITIES USED FOR INERTING ENGINE COMPONENTS

Internal engine components	Engine					
	J30		J35		J47	
	Water quantity, gal	Duration of flow, sec	Water quantity, gal	Duration of flow, sec	Water quantity, gal	Duration of flow, sec
Combustor domes	0. 25	0. 5–1. 8	3	3	3	3
Transition liners and hollow turbine-inlet guide vanes	0. 03	0. 5–1. 8	1	14	1	14
Turbine wheel and inner-cone base diaphragm:						
Rapid flow	None	None	1	5	1	5
Slow flow	0. 89	2. 5	2	30	2	30
Inner-cone interior	0. 2	2. 5	0. 35	39	None	None
External engine components	Engine (airplane installation)					
	J30		J35 (F–84)		J47 Pylon installation (C–82)	
	Water quantity, gal	Duration of flow, sec	Water quantity, gal	Duration of flow, sec	Water quantity, gal	Duration of flow, sec
Tailcone and tailpipe	0. 7	6	[a]2 [b]2. 5	[a]7 [b]3. 6	2	5
Total water required, gal	2. 07	------	11. 85	------	9	------

[a]Tailcone. [b]Tailpipe.

mums but provide for a margin of safety. The water quantities listed cover all of a given class of components. For example, the 3 gallons of water for the J35 combustor include the eight combustors carried on each engine. The time duration of the water flow is given as well.

Combustor liner.—The method of introducing the water into each J47 combustor is shown in figure 15. A toroidal

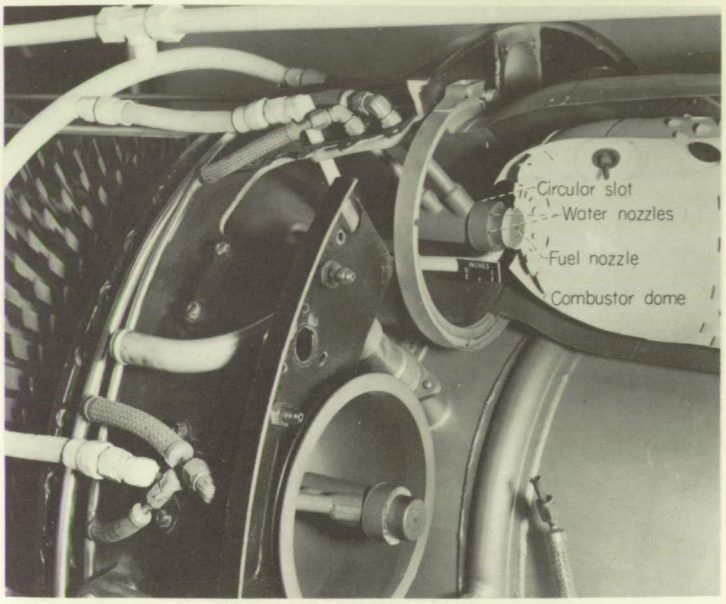


FIGURE 15.—Combustion-chamber water spray nozzle (J47 engine).

water manifold surrounded each fuel nozzle. Eight 0.082-inch holes on the downstream face of the manifold directed water at the combustor dome and its louvers leading into the combustion space. A continuous circumferential slot, 0.020-inch wide, on the perimeter of the manifold provided a sheet of water spreading radially. This water was directed downstream by the airflow to impinge and wash along the outside surfaces of the combustor liner. The 3 gallons of water delivered to the combustors of the J35 and J47 engines were divided equally among the combustors. The water discharge lasted for 3 seconds.

Transition liner.—Water was delivered to each transition liner in a fan-shaped sheet from nozzles arranged as shown in figure 16. Adequate cooling was obtained with three nozzles for each liner by directing the water at glancing incidence to the outside surfaces of the transition liner. One pint of water was discharged onto each transition liner of the J35 and J47 engines.

The water applied to the transition liner was sufficient to fill the hollow turbine-inlet guide vanes with steam for the 14 seconds the water flowed. During this period the space was inerted with steam. No additional water for the turbine-inlet guide vanes was required, since the main gas stream through the engine cooled the vanes to safe temperature in this time.

Turbine.—Cooling water to the turbine was applied as shown in figure 17. Several streams of water issued from the ring-type water manifold at the hub and spread centrifugally over the rotating wheel. The J35 and J47 engines contained an inner-cone base diaphragm that was hot enough to be dangerous. Cooling was effected by discharging an additional gallon of water over a 5-second period on the downstream face of the turbine wheel through the turbine cooling-air tube (fig. 17). A portion of this water rebounded from the spinning wheel and sprayed onto the base diaphragm.

Because the turbine wheel had large mass and thickness, reheating of the wheel surface to unsafe temperatures occurred after the applied cooling water was expended. An example of the reheating of the hottest part of the wheel is shown in figure 18. In early experiments, when 2 gallons of water were sprayed over a 2-second period onto the aft

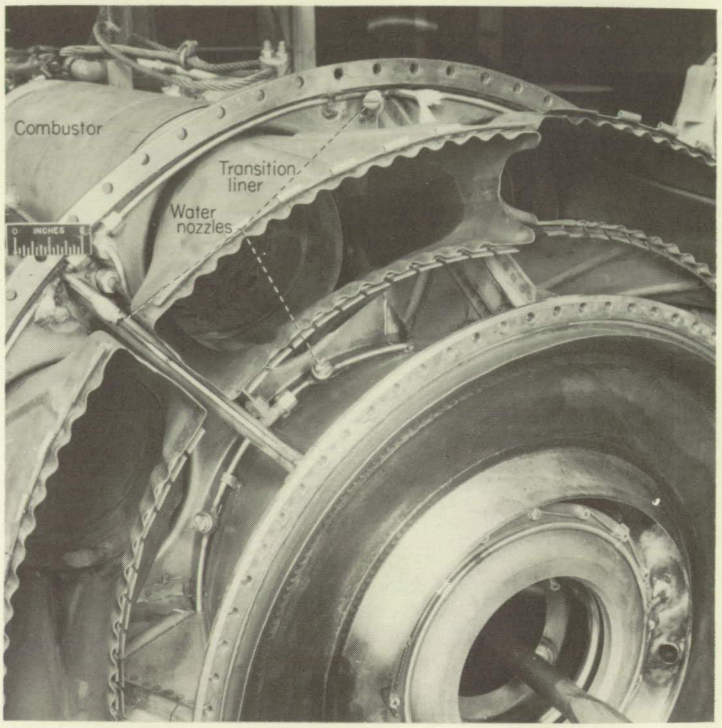


FIGURE 16.—Transition-liner water spray system (J35 and J47 engines).

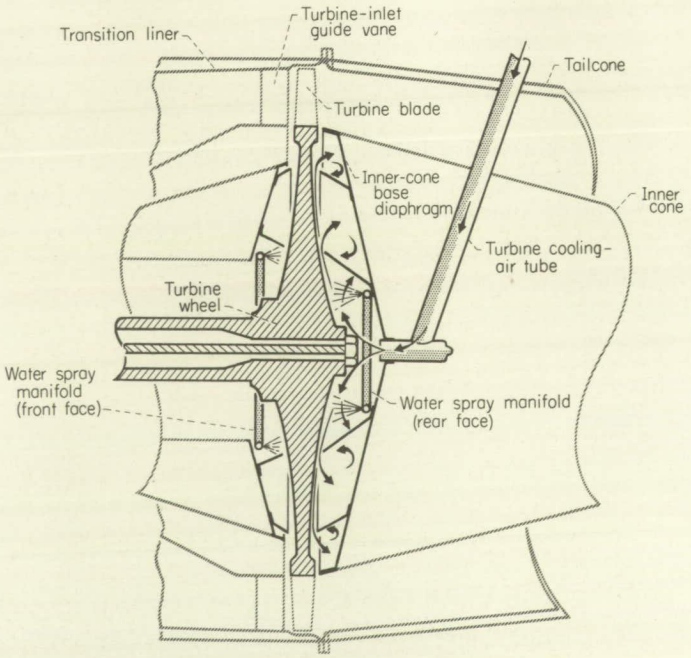


FIGURE 17.—Schematic diagram of turbine-cooling system.

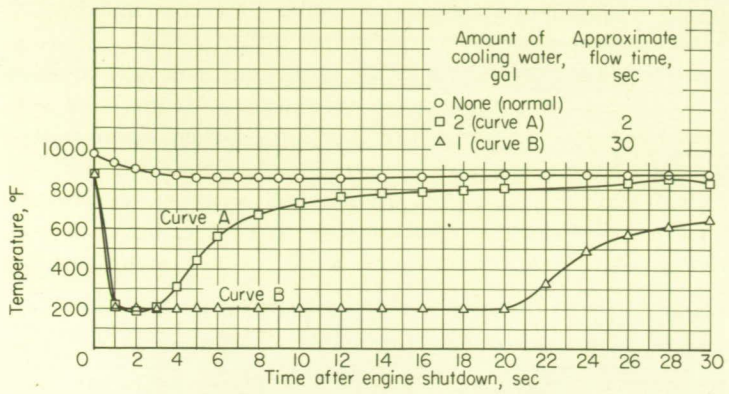


FIGURE 18.—Comparison of turbine-wheel cooling with short- and long-duration water sprays.

face of the turbine at the hub, the surface temperature dropped rapidly to the boiling temperature of water (curve A, fig. 18). Shortly after the water was expended, the surface of the wheel reheated by conduction from the hot interior. Unsafe temperatures above 600° F were established in less than 7 seconds. In order to avoid reheating to unsafe temperatures, the water discharge period was extended to 30 seconds. Experiments indicated that the quantity of water necessary could be reduced from 2 to 1 gallon for each face of the turbine disk. The wheel temperatures obtained are shown by curve B in figure 18. The time interval before reheating began was increased from 3 to 20 seconds. Reheating to temperatures above 600° F occurred after 27 seconds, at which time, however, the chance for fuel ingestion was remote.

This problem of reheating must always be considered in the use of water for cooling unsafe zones. The chance for fuel ingestion by the engine is greatest just before the airplane comes to rest in the first 5 seconds after crash impact. At this time fuel spilling from torn tanks has its broadest distribution forward of the wings in areas adjacent to the engines. Reheating after this time is not as serious within the engine as it would be on the outside surfaces which could be wetted by fuel that continues to drip and flow around the engine after the airplane comes to rest.

Inner cone.—The cavity of the inner cone was inerted by diluting the air with steam produced by the evaporation of water from spray nozzles within the inner cone. The initial water flow rate to the inner-cone cavity should be rapid enough to reduce the oxygen concentration within the cavity below 10 percent in 1 second. This was the approximate time latitude that existed between the start of fuel ingestion in the engine inlet and the entrance of dangerous amounts of fuel into the tailcone. The effectiveness of these arrangements was enhanced by directing the water sprays at the openings through which the fuel could enter. In this way the steam diluted the air local to the fuel entering the inner cone and provided protection, while the steam concentration developed throughout the cavity. The chamber was maintained inert until its walls were cooled to safe temperatures by the main gas stream. For engine cavities having the low ventilation rates found in the inner tailcone, the quantity of water required for protection could be calculated from the volume of the cavity and volumes of steam generated per unit mass of water. Allowance was made, of course, for steam loss due to ventilation.

For the J35 engine, which has an inner-cone volume of 5.8 cubic feet, 0.35 gallon of water was required to provide an inert atmosphere. In contrast, the inner cone of the J30 engine, which has no base diaphragm and contains a volume of only approximately 0.7 cubic foot, required 0.2 gallon of water to achieve an inert atmosphere. This relatively larger amount of water was necessary because of the higher ventilation rates existing in the open-base inner cone of the J30 engine.

Tailcone and tailpipe.—The uniform distribution and efficient utilization of the cooling water on the tailcone and tailpipe posed some problems. Because the tailcone and tailpipe were circular in section and mounted with the axis horizontal, an unduly large number of water sprays had to be used to obtain complete wetting of the outside surface. The tendency of the water sprayed on the tailpipe to form thin rivulets reduced the area wetted by each spray. Water sprayed on the tailpipe above the equator provided rivulets that ran by gravity to the equator where they dripped off. Water sprayed on the tailpipe below the equator dripped off the tailpipe a short distance from the impingement area.

Effective water distribution and wetting were promoted by wrapping a 100-mesh stainless-steel screen around the entire exhaust system. This screen was spotwelded to the tailcone and tailpipe. Water sprayed on the screen penetrated to the surface of the tailpipe and tailcone. The screen promoted wetting and discouraged the formation of rivulets.

Water distribution over the screen-covered exhaust system was provided by a network of flattened tubes mounted axially in contact with the screen. Water sprayed through orifices drilled into the flattened side of the manifold facing the tailcone and tailpipe. The discharge orifices were 0.040 inch in diameter and spaced so that each would distribute water over approximately 50 square inches. Additional holes were drilled where experiment showed them to be necessary to provide uniform wetting. The tubes were also covered with ribbons of stainless-steel screen and spaced around the tailcone and tailpipe in order to provide a uniform water distribution. Three circular water manifolds connected the tubes to form a single interconnected unit. This water system is shown partially installed on the J35 tailpipe in figure 19. Some of the flattened manifolds, which are uncovered,

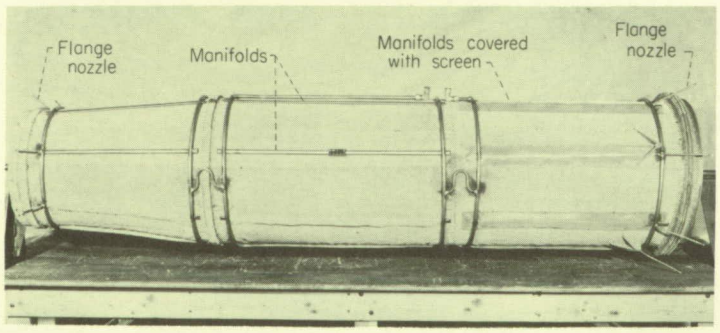


FIGURE 19.—Typical water distribution system for F–84 tailpipe.

are visible. The waffled appearance of the screen was produced by two sets of mutually perpendicular grooves that were rolled into the screen. These grooves permitted the screen to be tightly wound to the tailpipe and yet allowed water to flow under the screen.

Direct water sprays were provided through orifices and nozzles placed on the local circular manifolds in order to provide cooling of the massive flanges joining the tailcone to the engine and the tailpipe to the tailcone.

The quantity of water required for cooling the tailcone and tailpipe (table I) depended upon its diameter and length and the thickness of the metal. For the J35 engine with a long tailcone and tailpipe (157 in.) sized for the F–84 airplane, 4½ gallons of water were required. Two gallons of water were required for cooling the corresponding parts in a pod-mounted nacelle with a short tailcone and tailpipe (63 in.).

The total water requirement for protecting J35 and J47 engines ranged from 9 to approximately 12 gallons depending on the size of the tail sections. The J30 engine required approximately 2 gallons of water.

CRASH STUDY OF INERTING SYSTEMS FOR JET AIRPLANES

Two types of airplanes were used in the study of the use of water for reducing the likelihood of crash fires. Cargo airplanes (C–82) were fitted with pylon-mounted engine nacelles to simulate a jet bomber with pod-installed engines as shown in figure 1. Fighters (F–84) were used to represent airplanes having engines submerged within their structures (fig. 3).

INSTALLATION OF CRASH-FIRE SYSTEM

The complete crash-fire protection system used in this crash study is shown schematically in figure 20. The system comprised a water storage and distribution system, a shutoff valve for the combustor fuel, an electric switch for de-energizing the battery and generator circuits, and a crash-actuated switch for turning on the protection system. In these tests this switch was exposed on the airplane. The switch struck a target at the crash barrier which operated the switch shortly after major airplane damage had begun. While this arrangement was suited for these experiments, more elaborate means would be required for actual airplane installations. A comprehensive discussion of initiating systems for actuating crash-fire inerting systems is presented in reference 9.

In order to ensure that known quantities of water were applied at each engine ignition zone, the water for each zone was carried in a separate reservoir. Compressed gas for

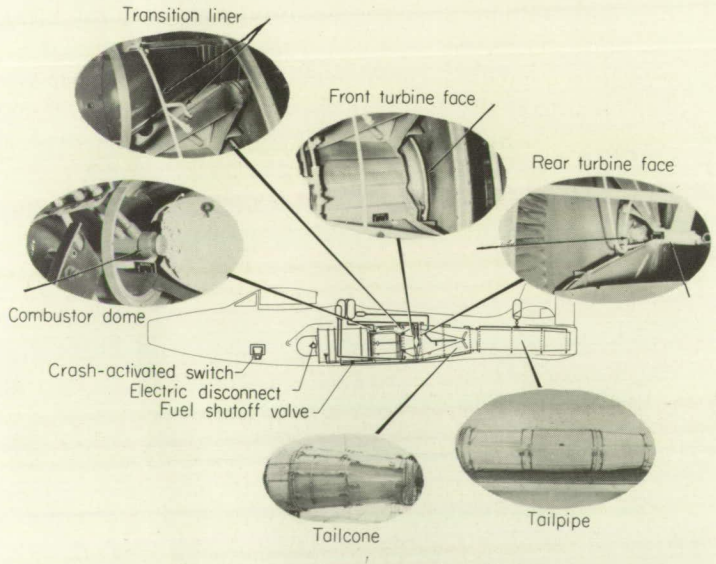
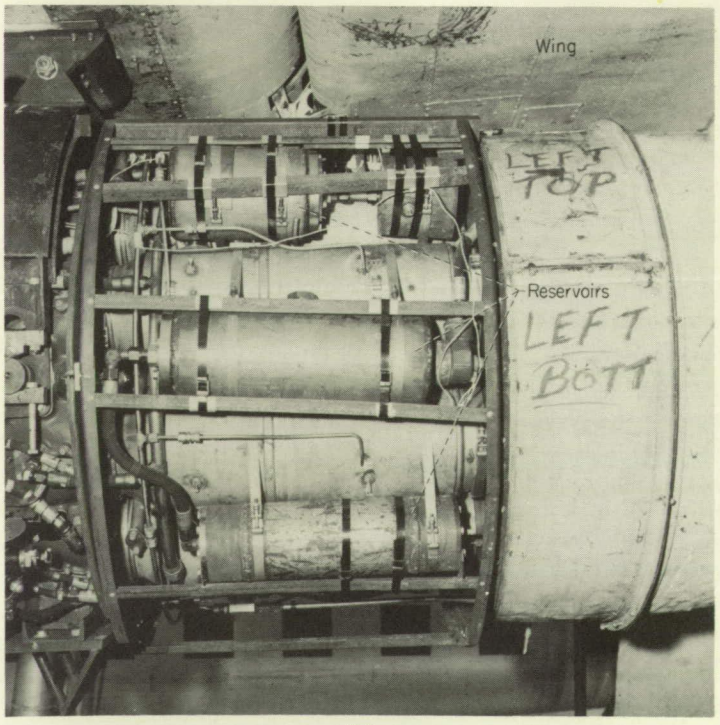


FIGURE 20.—Complete inerting system installed in F–84 airplane.



(a)



(b)

(a) Located in wing root of C–82 cargo airplane.
(b) Secured to J47 engine.

FIGURE 21.—Water reservoirs.

propelling the water was contained in the reservoir. The gas space and pressure were designed to give an initial water flow rate with a subsequent decline in the flow rate that was found experimentally to provide effective use of the water. Design compromises involving reservoir location, length of water distribution lines, reservoir pressure, and required quantity of water were made in order to stay within a 0.2-second time limit (after crash impact) for the application of the water at the ignition zones. This time limit was dictated by the normal lag involved in the functioning of the hardware components of the inerting system. Considerations of rate of fuel spread in the crash indicate that it is unlikely that combustible atmospheres will contact the engine ignition zones within this short interval of time.

In three of the crashes of cargo airplanes fitted with J47 engines, the water reservoirs were carried in the wing root as shown in figure 21(a). Flexible lines joined these reservoirs to the engines. In one crash in which arrangements were made to rip the engine from the wing, the water reservoirs were strapped between the engine combustors as shown in figure 21(b).

FULL-SCALE CRASHES

The first crash in which this inerting system was evaluated was conducted with a C–82 equipped with J47 engines. Shortly after the airplane passed through the crash barrier, the right wing tore free to produce the large volume of fuel mist shown in figure 22(a). Entry of fuel mist into the left engine occurred 3.0 seconds after barrier impact just as the airplane began to ground-loop (fig. 22(b)). The condensed water vapor pouring from the engine tailpipe indicated that the fire-prevention system was working. The pool of fuel at the inlet lips of the left engine (shown in fig. 22(c)) represents some of the fuel that entered the engine inlet and then drained forward when the engine stopped. In spite of the fuel that entered the engines and that which poured over the nacelles (fig. 22(d)), no fire occurred. No fires occurred in two additional crashes conducted under the same circumstances.

It is evident that pylon-mounted engines on jet airplanes may part from the supporting wings in a crash. To determine whether fire protection could be provided to the engine after separation, a crash was arranged in which the left engine nacelle was torn free. The entire nacelle inerting system was built into the nacelle and designed to function regardless of the attitude assumed by the nacelle after separation from the airplane.

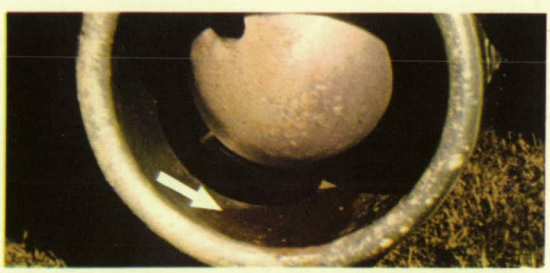
For this crash special water reservoirs were made that would fit in the spaces between the combustors on the J47 engines. Some of the water reservoirs held to the combustors by metal bands are shown in figure 21(b). To ensure complete expulsion of the water regardless of the nacelle orientation, reservoirs of the type shown in figure 23 were employed. Each consisted of a steel cylinder with a



(a) Fuel mist discharging from torn wing, 0.9 second after initial impact.



(b) Entry of fuel mist into left engine, 3.0 seconds after initial impact.



(c) Pool of fuel left in inlet cowl indicating fuel entry into engine.



(d) Fuel spillage on nacelle.

FIGURE 22.—Crash of C–82 with jet engines equipped with inerting system.

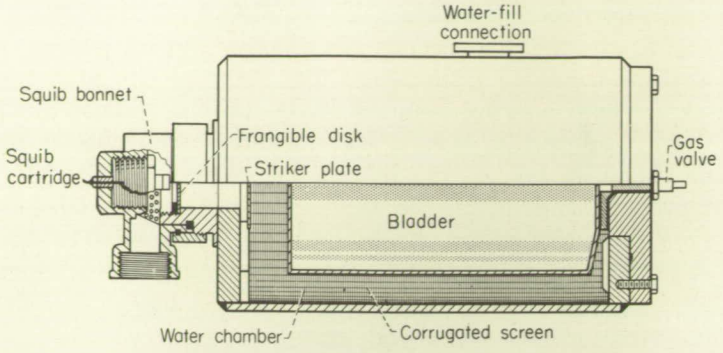


FIGURE 23.—Bladder-type water reservoir.

neoprene-fabric bladder insert. Water was retained in the steel cylinder while the volume of the bladder was filled with nitrogen gas at a pressure necessary to give the desired water discharge rate. When the outlet valve was opened, the bladder expanded, forcing the water to flow.

The airplane used in the crash in which engine separation was to occur differed from the previous airplanes only in the changes in the water system, just described, for the left engine. A blade rigidly attached to the bottom of the left nacelle was arranged to drag through an earth mound at the crash barrier and pull the engine from the wing.

Separation of the engine from the wing is shown in the picture sequence of the crash in figure 24. After separation (fig. 24(a)) the engine tumbled in the fuel spraying into the wake of the damaged wing (figs. 24(b) and (c)) and came to rest in the fuel-wetted slide path of the airplane (fig. 24(d)). The plume of condensed water vapor at the tailpipe (fig. 24(b)) shows that the water inerting system was actuated. No fire occurred.

The crash technique for the F–84 with protected engines was identical with that used in the crash with the unprotected engine discussed in connection with figure 5. The crash-fire protection system for the engine was the same as that for the cargo airplanes fitted with jet pods.

The sequence of events following crash was the same for the F–84 as for the cargo airplanes. Poles at the crash barrier ripped open the wing fuel tanks and produced the fuel mist shown in figure 25(a). Collapse of the nose gear allowed fuel from the torn forward fuselage tank to enter the engine inlet. Vapor issuing from the tailpipe (fig. 25(b)) was provided in part by the fuel that passed through the engine from the damaged fuel tank adjacent to the engine inlet. Evaporation of water from the fire protection system contributed a large part of the vapors formed (fig. 25(b)). Inspection of the engine after crash showed the telltale dye stains left by the red-dyed fuel flowing through the compressor (fig. 26). No fire occurred.

A second crash of an F-84 airplane equipped with the fire protection system was conducted, again with no fire occurring. When the airplane came to rest beyond the crash barrier, complete wetting of the airplane by the red-dyed fuel was observed (fig. 27).



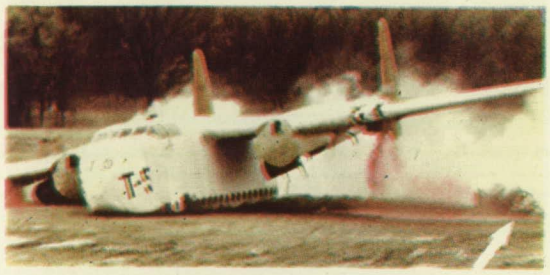
(a) 1.3 Seconds after initial impact.



(b) 1.8 Seconds after initial impact.



(c) 3.1 Seconds after initial impact.

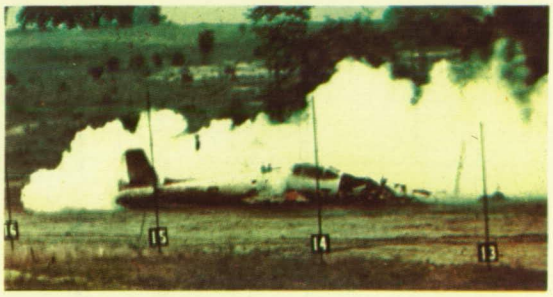


(d) 4.4 Seconds after initial impact.

FIGURE 24.—Separation of J47 engine from C–82 wing in crash.



(a) Fuel mist, 1.1 seconds after initial impact.



(b) Water and fuel vapors issuing from tailpipe, 3.6 seconds after initial impact.

FIGURE 25.—Crash of F–84 with J35 inerting system installed.

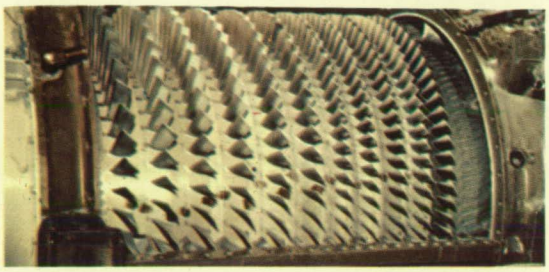


FIGURE 26.—Fuel-dye stains on J35-engine compressor following F–84 crash.

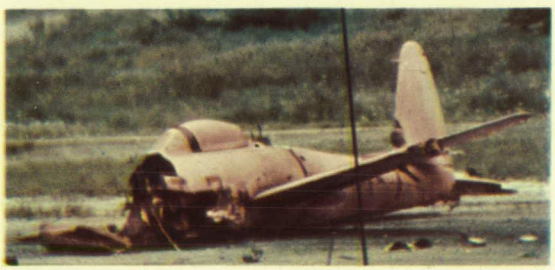


FIGURE 27.—Extensive fuel wetting of F–84 following crash with inerting system.

SUMMARY OF RESULTS

A study of the ignition of combustibles sucked into the inlets of turbojet engines having a size and compression ratio of the J35, J47, and J30 engines gave the following results:

1. The main gas stream through the engine moved too rapidly for ignition to occur on the hot metal within the engine.

2. Ignition may occur on the hot surfaces within the engine downstream of the compressor in those zones not in the main gas stream. For the engines studied, these zones included the combustor-liner dome, the transition-liner outer surfaces, the turbine-inlet guide vane interior, both faces of the turbine wheel, the inner-cone base diaphragm, and the interior of the inner cone.

3. Outside surfaces of the tailcone and tailpipe can ignite jet-engine fuels and lubricants.

4. A crash-fire protection system which de-energizes the electrical system, shuts off the fuel flow to the engine, and sprays coolant (water) over these hot surfaces proved effective in preventing fires. Fighter aircraft with submerged engines and simulated bomber configurations with pylon-mounted nacelles were used in these studies. No fire occurred in the six crashes when the engine fire-prevention system was used. Fires did occur in the two crashes in which no engine protection was provided. Coolant requirements ranged from about 9 to approximately 12 gallons of water per engine (J35 and J47 engines) depending on the length of tailpipe to be cooled.

LEWIS FLIGHT PROPULSION LABORATORY
NATIONAL ADVISORY COMMITTEE FOR AERONAUTICS
CLEVELAND, OHIO, *January 18, 1957*

APPENDIX A

ENGINE TEMPERATURE SURVEY

A first appraisal of the ignition potential of a surface is its temperature. Therefore, a complete temperature survey of the engine was made in order to determine where temperatures were high enough to cause ignition of aircraft-type combustibles.

The hottest parts of the engine, when operated at rated conditions, were those which lay in the main gas stream downstream of the compressor. The highest temperatures (fig. 7) were measured on the primary zone of the combustor liner, on the bend in the transition liner where the hot gases leaving the combustor impinge, and on the turbine-inlet guide vanes. Temperatures as high as 1660° and 1740° F were found on the transition liner and the adjacent turbine-inlet guide vanes, respectively. The stagnation gas temperature at the moving turbine blades was less than the stagnation temperature at stationary engine members in the same gas stream. The temperature of the blades was correspondingly lower, being about 1370° F for the hottest parts of the blade. The gases leaving the turbine were reduced in temperature because of the turbine work that had been done. Therefore, the temperature of the inner tailcone at location A in figure 7 was about 400° cooler than the turbine-inlet guide vanes. The temperature was about 1350° F at the hottest point of the inner cone and about 1150° F at its coolest point.

The largest temperature gradients occurred within the combustor (fig. 7) where some metal was in contact with the relatively cool combustor-inlet air and other metal was heated by the combustor flame. The maximum temperatures recorded were about 800° F on the dome, about 1500° F on the primary section of the combustor liner, and about 1300° F at the outlet. The lower temperatures at the combustor-liner outlet were produced by the cooler secondary combustor air.

Engine parts not in the main gas stream were heated mostly by conduction. The turbine wheel was the most massive engine part heated this way. The radial variation in temperature on the surface of the turbine wheel, shown in figure 28, resulted from the fact that the heat conduction was from the wheel rim to the relatively cool hub. The data shown were obtained with the engine operating at rated sea-level conditions. The turbine-wheel surface temperature varied from approximately 980° F at the rim to about 605° F at a point midway between the rim and hub. Cooling air from the compressor applied to the hub to protect the engine bearings maintained this temperature pattern.

The inner-cone base diaphragm, lying opposite the turbine, was also heated by conduction. In general, the temperature decreased from the rim toward the diaphragm center, which also received some cooling by the air applied to the turbine hub.

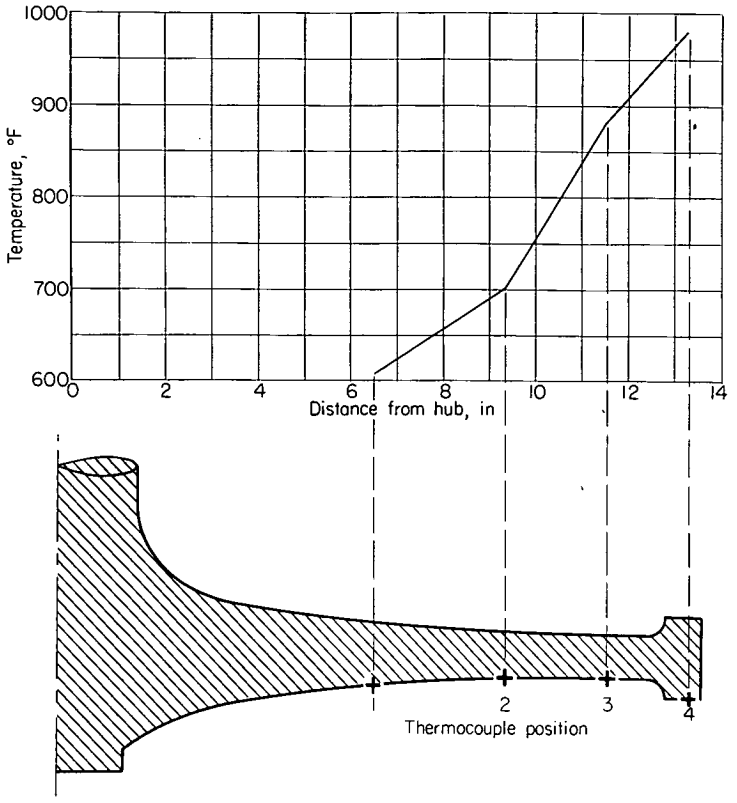


FIGURE 28.—Maximum temperatures recorded on J47-engine turbine wheel.

When the fuel flow to the operating engine combustor was shut off, the engine parts declined in temperature. Those components which lay in the main gas stream cooled more rapidly than those which did not. This rapid decline in temperature was due to the cooler air now flowing through the engine and the generally low heat capacity of these parts.

A history of the temperature of engine parts lying in the main gas stream is shown in figure 29. Fuel shutoff occurred at zero second, and the temperatures indicated were the maximum recorded anywhere on the component at the time noted. The hottest section of the combustion-chamber liner cooled from 1500° to 600° F in 24½ seconds. It took over 30 seconds for the transition-liner temperature to decline from 1660° to 600° F. In 30 seconds the turbine-inlet guide vane temperature dropped from a maximum temperature of 1750° to 645° F. The rotating turbine blade temperature fell from 1370° to 600° F in 16 seconds. Inner-cone skin temperatures declined from 1350° to 640° F in 30 seconds.

Engine parts not located in the main gas stream declined in temperature at much slower rates (fig. 30). The hottest part of the turbine wheel was initially at 980° F and dropped only 100° F in 30 seconds after fuel flow to the engine had stopped. The turbine wheel remained above the ignition

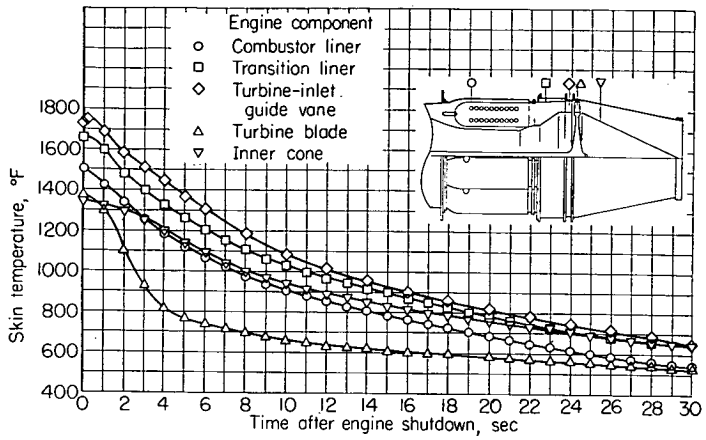


FIGURE 29.—History of maximum skin temperatures on engine components in main gas streams.

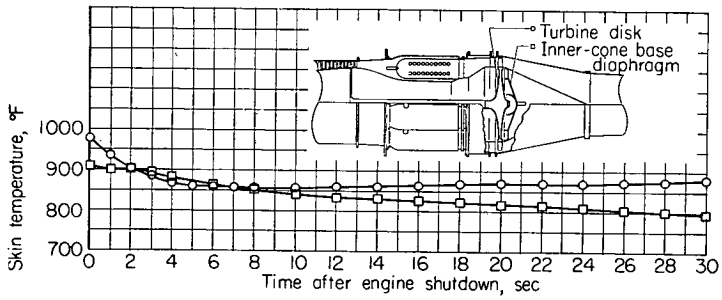


FIGURE 30.—History of maximum skin temperatures on turbine disk and inner-cone base diaphragm.

temperature of JP–4 fuel for 30 minutes after the engine was shut down. The large mass of the turbine disk contributed to its slow cooling rate. The inner-cone base diaphragm exhibited the same slow rate of cooling. Its maximum temperature was 910° F and cooled only approximately 115° F in 30 seconds.

Experimental crashes conducted with piston- and jet-engine airplanes showed that fuel mists that might be drawn into the engine inlet exist during the first 15 seconds after impact with the barrier. In this time the airplane decelerates to a stop and the wind clears the fuel mist from the crash zone. During this hazardous period these engine temperature data show that practically all the metal downstream of the combustor inlet is above the laboratory measured ignition temperature of jet fuels and hydrocarbon lubricants.

External surfaces of the tailcone and tailpipe were the only unsafe zones found in engines with compression ratios of 5 or less. Airplane combustibles that contact this section of the engine can ignite. In engines of higher compression ratios unsafe engine case temperatures may extend downstream from the last compressor stages. Temperatures must exceed 600° F for ignition to occur readily on the engine case, because it is moderately ventilated. This fact was established by many ignition trials on the external engine surfaces.

Temperature measurements made on the external skin of the J47 engine (fig. 31) indicated that the tailcone and tailpipe temperatures remained above 600° F for more than 30 seconds after the fuel to the combustor was shut off. Temperatures of the engine case upstream of the tailcone and tailpipe were usually below 600° F (fig. 32). Although the turbine case reached a maximum temperature of 600° F and remained so for 10 seconds after the fuel was shut off (fig. 31), no ignitions were experienced here.

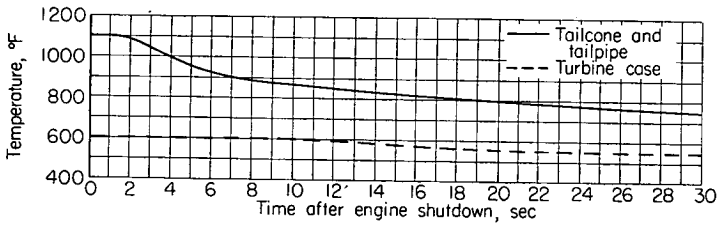


FIGURE 31.—History of maximum external skin temperatures on J47 turbine case and tailcone and tailpipe.

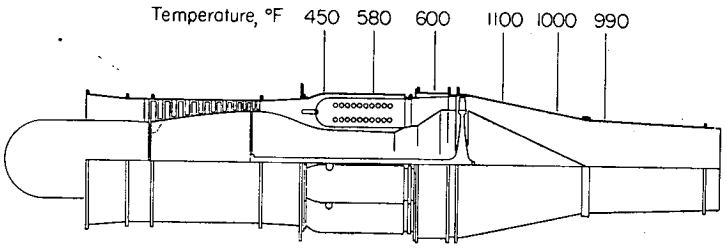


FIGURE 32.—Maximum external skin temperatures on J47 engine.

APPENDIX B

PRELIMINARY EVALUATION OF PROBABILITY OF HOT-SURFACE IGNITION

The data on contact time required for ignition (fig. 8) can be used to obtain an approximation of the probability of hot-metal ignition of combustibles sucked into the engine inlet. The engine metal temperatures are known from the measurements given in figures 29 and 30. The contact time can be computed from the known mass airflow through the engine (fig. 33). From the airflow data for the J35

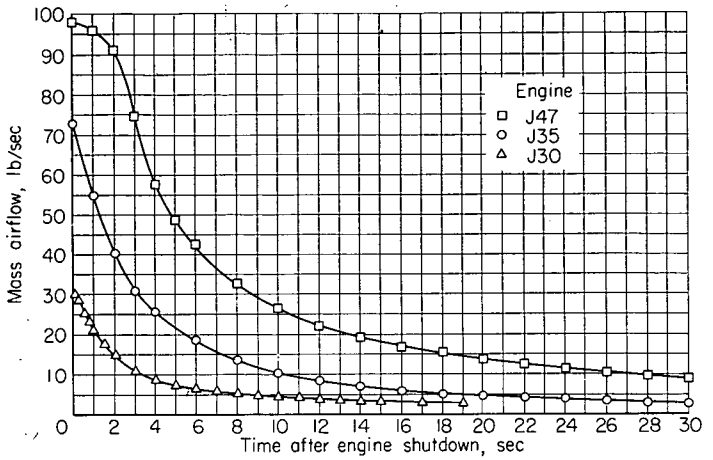


FIGURE 33.—Mass airflow after combustor fuel has been stopped.

engine and the engine geometry, the local air velocity through the engine upstream of the turbine inlet was plotted and appears in figure 9. Velocities were calculated only at the engine stations marked on the sketch. Each line connecting the symbols provides the velocity distribution through the engine at the time indicated. It is interesting to note that at 3 seconds after fuel shutoff the velocity at the compressor exit was slightly higher than at the compressor inlet. This was due to the fact that the turbine-inlet total temperature had fallen to the point where it caused a large drop in compressor-exit static pressure. The lower static pressure was the dominant influence on the speedup in airflow.

This analysis does not consider the increase in contact time resulting from recirculation of gases in the combustor-dome area or approximately the first 30 percent of the combustor. However, the contact time available in the aft 70 percent of the combustor might be considered conservative, since the indicated contact time was based on the total length of the combustor. A required contact time may be picked from the data in figure 8(a), if the entire combustor liner is considered to be at the maximum temperature shown in figure 29. A crude analysis of this type for the first 7 seconds after fuel shutoff is shown in figure 10, which indicates that the gas stream moved through the combustor liner too quickly to allow a sufficient contact time for ignition from the hot metal. Ignition is considered likely when the available contact time equals or exceeds the required contact time.

A similar analysis for the other engine components showed that the contact time of the main gas stream in each component was too short for ignition to occur. This analysis by components was based on the assumption that the fuel-air mixture in contact with the hot metal in passage through one component is no longer in contact in passage through the next.

APPENDIX C

METHOD OF LOCATING IGNITION ZONES WITHIN ENGINE

Inspection of most turbojets shows that the engine interior is divided into well-defined cavities, some of which are in flow communication. The airflow direction through these cavities is also well defined, so that they can be considered to be arranged in order. Each can be recognized to be upstream or downstream with respect to another. For this reason each of the cavities could be explored separately by the following technique for the ignition hazard it presents.

The ignition hazard presented by each cavity was studied by installing a fuel spray system in each cavity to produce a combustible atmosphere as desired. A separate system was also installed to apply cooling water to the hot surfaces in the cavity or to provide a water spray in the cavity space.

The engine cavity farthest downstream, the inner cone, was studied first. The arrangements used for the J30 tailcone are shown schematically in figure 34. A fuel system,

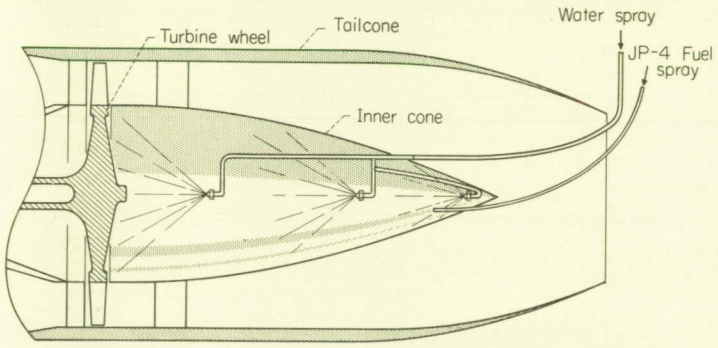


FIGURE 34.—Typical equipment used to study ignition hazard (J30 inner tailcone).

consisting of a single tube and nozzle, was arranged to spray fuel in measured quantities into the cavity of the inner cone to produce a combustible atmosphere. In addition, three water spray nozzles were installed facing the upstream direction. Since the J30 engine has no base diaphragm, the downstream face of the turbine wheel must be taken as a bounding surface of this cavity. The upstream water nozzle was arranged to spray water on the turbine wheel to avoid ignition from this source.

In this study of internal ignition zones the engine was run at rated conditions until temperature equilibrium was established. The fuel flow to the combustor was stopped, and 0.2 second later the fuel spray in the inner-cone cavity was turned on. Ignition of this fuel occurred. The process was repeated with increasing intervals between engine combustor fuel shutoff and the beginning of fuel spray into the inner-cone cavity. Ignitions were obtained up to 20 seconds after the combustor fuel was shut off.

Following this evaluation of the inner-cone interior as an ignition hazard the runs were repeated, but this time the water sprays were also turned on with the fuel spray in the inner cone. Initially, sufficient water was used to ensure absence of ignition. By progressively reducing the water quantity in repeated runs a minimum water requirement was established below which ignition would sometimes occur.

The next upstream ignition zone is the cavity of the engine containing the turbine wheel. In order to provide positive identification of the ignition surfaces in the turbine-wheel cavity, a fuel spray was installed to fill the cavity with a combustible atmosphere. Runs were made similar to those described for studying the inner cone. The water spray system in the inner cone was always used to ensure that no ignition would occur in this zone. Repeated runs were made in which fuel was sprayed into the turbine-wheel cavity following fuel shutoff to the engine combustor. Evaluation of the smallest quantity of cooling water for the turbine that was required to prevent ignition was obtained in the manner described for the inner cone. These quantities may be influenced by the method of water distribution employed. In order to provide a margin of safety for crash experiments, quantities of water above the minimum were used. These are tabulated in table I.

Each of the engine cavities was studied in turn by proceeding upstream in this way. The zones that presented ignition potential were identified and inerted.

REFERENCES

1. Pinkel, I. Irving, Preston, G. Merritt, and Pesman, Gerard J.: Mechanism of Start and Development of Aircraft Crash Fires. NACA Rep. 1133, 1953. (Supersedes NACA RM E52F06.)
2. Pinkel, I. Irving, and Preston, G. Merritt: NACA Crash Fire Research. NACA Tech. Film 26, May 1953.
3. Black, Dugald O.: Facilities and Methods Used in Full-Scale Airplane Crash-Fire Investigation. NACA RM E51L06, 1952.
4. Rodert, Lewis A., and Garrett, Floyd B.: Ingestion of Foreign Objects into Turbine Engines by Vortices. NACA TN 3330, 1955.
5. Jones, G. W., Zabetakis, M. G., Scott, G. S., and Furno, A. L.: Research on the Flammability Characteristics of Aircraft Fuels. WADC Tech. Rep. 52–35, Supp. 1, Feb. 1, 1952–Feb. 1, 1953, Wright Air Dev. Center, Wright-Patterson Air Force Base, Jan. 1954. (Contract AF–18(600)–151.)
6. Smith, Maxwell: Technical Curiosities: "Oleodieseling." Shell Aviation News, no. 183, Sept. 1953, pp. 8–9.
7. Mullins, B. P.: Studies on the Spontaneous Ignition of Fuels Injected Into a Hot Air Stream: Pt. II—The Effect of Physical Factors upon the Ignition Delay of Kerosine-Air Mixtures. Rep. No. R.90, British N.G.T.E., Sept. 1951.
8. Jones, G. W., Zabetakis, M. G. Scott, G. S., and Furno, A. L.: Research on the Flammability Characteristics of Aircraft Fuels. WADC Tech. Rep. 52–35, Supp. 2, Feb. 1, 1953–Feb. 1, 1954, Wright Air Dev. Center, Wright-Patterson Air Force Base, Aug. 1954. (Contract AF–18(600)–151.)
9. Moser, Jacob C., and Black, Dugald O.: Proposed Initiating System for Crash-Fire Prevention Systems. NACA TN 3774, 1956.

REPORT 1364

CONTENTS

	Page
SUMMARY	645
INTRODUCTION	645
SYMBOLS	645
STATIC-PRESSURE MEASUREMENT	646
STATIC-PRESSURE ERRORS OF TUBES	646
Tubes at Zero Angle of Attack	646
Axial location of orifices rearward of the nose	646
Axial location of orifices ahead of protuberances	647
Tubes at Angles of Attack	648
Orifices at $\pm 30°$ location	648
Orifices on top and bottom of tube	649
Conical Static-Pressure Tubes	650
Orifice Size and Configuration	650
STATIC-PRESSURE ERRORS OF INSTALLATIONS	651
Static-Pressure Errors Ahead of Fuselage Nose	651
Effect of nose shape	651
Effect of Mach number	651
Effect of angle of attack	653
Effect of nose inlet	655
Static-Pressure Errors Ahead of Wings	655
Effect of location of orifices	656
Effect of Mach number (unswept wings)	656
Effect of angle of attack (unswept wings)	656
Effect of Mach number (swept wings)	657
Effect of angle of attack (swept wings)	657
Static-Pressure Errors Ahead of Vertical Tail Fin	657
Static-Pressure Errors of Vents on Fuselage (Models)	658
Effect of axial location of vents	659
Effect of Mach number	659
Effect of circumferential location of vents	659
Static-Pressure Errors of Vents on Fuselage (Airplane)	660
Vent Configuration	660
Conversion Factors	661
COMPARISON OF INSTALLATIONS	661
FLIGHT CALIBRATION METHODS	663
Speed-Course Method	663
Trailing-Static-Pressure-Tube Method	663
Aneroid Method	663
Reference landmark	663
Photographic	664
Geometric	664
Reference airplane	664
Radar phototheodolite	664
Radio altimeter	665
Accelerometer	665
Radar-Temperature Method	665
Temperature Method	665
Formation-Flight Method	666
CONCLUSIONS	666
REFERENCES	666

Preceding Page Blank

REPORT 1364

MEASUREMENT OF STATIC PRESSURE ON AIRCRAFT[1]

By William Gracey

SUMMARY

Existing data on the errors involved in the measurement of static pressure by means of static-pressure tubes and fuselage vents are presented. The errors associated with the various design features of static-pressure tubes are discussed for the condition of zero angle of attack and for the case where the tube is inclined to the flow. Errors which result from variations in the configuration of static-pressure vents are also presented. Errors due to the position of a static-pressure tube in the flow field of the airplane are given for locations ahead of the fuselage nose, ahead of the wing tip, and ahead of the vertical tail fin. The errors of static-pressure vents on the fuselage of an airplane are also presented.

A comparison of the calibrations of the four static-pressure-measuring installations indicates that, for an airplane designed to operate at supersonic speeds, a static-pressure tube located ahead of the fuselage nose will, in general, be the most desirable installation. If the operating range is confined to speeds below sonic, a static-pressure tube located ahead of the wing tip may, for some airplane configurations, prove more satisfactory than a fuselage-nose installation. For operation at Mach numbers below 0.8, a static-pressure tube ahead of the vertical tail fin or fuselage vents, properly located and installed, should prove satisfactory.

Various methods of calibrating static-pressure installations in flight are briefly discussed.

INTRODUCTION

The proper functioning of fire-control and guidance systems for airplanes and missiles depends fundamentally on the accurate measurement of total and static pressures. For each of these measurements the basic problem is that of determining what type of sensing device to use and where to locate it on the flight vehicle.

The National Advisory Committee for Aeronautics has been studying this problem for many years. A comprehensive survey of the subject, based on information obtained at subsonic speeds, was published in 1948 (ref. 1). Since that time additional data have been obtained from wind tunnel, rocket-model, and flight tests in the transonic and low supersonic speed ranges. Because of current interest in this information, it appeared appropriate at this time to present these data and to review the overall problem in the light of this new knowledge.

The measurement of total pressure is not discussed in this report because this measurement can be accomplished quite accurately with little or no difficulty and because the subject has been adequately treated in other reports. The problems involved in the design and location of a total-pressure tube on the airplane are discussed in reference 1. The only error of any consequence in the measurement of total pressure is that due to the inclination of the tube to the airstream. This error can be avoided by using a swiveling tube or a suitably designed rigid tube. Information required for designing a rigid tube which will measure total pressure correctly over a wide range of angle of attack at both subsonic and supersonic speeds may be found in reference 2.

SYMBOLS

p	free-stream static pressure
p'	indicated static pressure
Δp	static-pressure error, $p'-p$
p_t	total pressure
q	dynamic pressure, $\frac{1}{2}\rho V^2$
q_c	impact pressure, p_t-p
M	free-stream Mach number
M'	measured Mach number
T	ambient temperature, absolute units
T'	measured temperature, absolute units
K	temperature recovery factor, $\frac{T'-T}{0.2M^2T}$
ρ	mass density of air
R	gas constant, 53.3
N_{Re}	Reynolds number
r	radius of curvature
C_L	lift coefficient
C_N	normal-force coefficient
h	altitude
d	diameter of static-pressure tube; diameter of orifice
D	diameter of collar on static-pressure tube; maximum diameter of model or fuselage
t	maximum thickness of stem on static-pressure tube; maximum thickness of wing or vertical tail fin
l	length of model
l'	twice distance from nose of model to maximum-diameter station
x	axial position of static-pressure orifice from reference point
y	height of protuberance near static-pressure orifice
α	angle of attack
φ	circumferential position of static-pressure orifices
γ	ratio of specific heats, 1.4 for air

Subscripts:

1	lower limit
2	upper limit

[1] Supersedes NACA Technical Note 4184 by William Gracey, 1957.

Preceding Page Blank

STATIC-PRESSURE MEASUREMENT

The sensing device which has been universally used for the measurement of static pressure is a surface orifice oriented parallel to the flight path. Orifices are installed either in the walls of the body of the aircraft or on a tube attached to some part of the aircraft. In either case the pressure at the point in the airstream where the orifice is located usually differs from the free-stream value because the air flowing over the aircraft creates a flow field in which the pressures vary widely from one point to another. At subsonic speeds the flow field extends in all directions for a considerable distance from the aircraft. At supersonic speeds the field is confined to the regions behind the shock waves which form ahead of the aircraft.

The amount by which the local static pressure at a given point in the flow field differs from free-stream static pressure is called the "position error" of the installation. If the static-pressure source is a static-pressure tube, there may be an additional error due to the flow field created by the tube. The flow field around the aircraft as well as that around the tube changes primarily with Mach number and angle of attack and, secondarily, with Reynolds number. The pressure developed at the static-pressure orifice is, therefore, a function of these variables.

The most difficult problem in designing a static-pressure installation is that of locating the static-pressure source (tube or vent) on the aircraft, because the flow field of each aircraft configuration is unique. Because of the impossibility of finding a location on or close to the aircraft where the static-pressure error is zero for all flight conditions, the problem becomes one of choosing a location where the error is of sufficiently small magnitude or where it varies uniformly with Mach number and angle of attack. Generally, the greater the distance from the aircraft that the static-pressure source can be located (preferably ahead of the aircraft), the more nearly will this objective be realized. For such remote locations of the static-pressure source, the magnitude and variation of the static-pressure error can be predicted with some success from the calibrations of similar installations on other aircraft.

The actual errors of a given installation, however, can be determined only by a calibration in flight. Such a flight calibration establishes the overall static-pressure error, that is, the error due to the location of the static-pressure source and the error due to the source itself. If the resulting errors are higher than desired, corrections may be applied either before or after the pressure indication is displayed. Even when corrections can be applied, however, it is advisable to choose an installation with as small an error as practical because, in general, the greater the magnitude of the corrections the more they will change with each change in flight condition and the more inaccurate and involved will be the calibration and correction procedure.

Inaccuracies in static-pressure measurement may also arise from instrument errors and from errors due to pressure lag of the tubing that connects the instrument to the static-pressure source. A general discussion of instrument and pressure-lag errors may be found in reference 1. Other aspects of the pressure-lag problem are treated in references 3 and 4.

STATIC-PRESSURE ERRORS OF TUBES

The flow field around an isolated static-pressure tube is determined by the shape of the nose section, the size and shape of any protuberance on the rear portion of the tube, the Mach number, the angle of attack, and the Reynolds number.

TUBES AT ZERO ANGLE OF ATTACK

For the condition of zero angle of attack, the pressure registered by a static-pressure tube at a given Mach number depends on the axial location of the orifices along the tube and the size and configuration of the orifices.

Axial location of orifices rearward of the nose.—The variation of static pressure along a static-pressure tube may be illustrated by two examples of theoretical pressure distributions over the forward portions of tubes at zero angle of attack. Figure 1 presents a subsonic (incompressible flow) pressure distribution for a tube with a parabolic nose (ref. 5) and a typical supersonic pressure distribution for a tube with a conical nose.

The symbol Δp in this figure denotes the static-pressure error, which is defined by the relation $\Delta p = p' - p$, where p' is the static pressure measured by the tube and p is free-stream static pressure. For the theoretical case considered in figure 1, Δp is expressed as a fraction of the dynamic pressure q; for most of the experimental data presented subsequently, Δp is expressed as a fraction of the impact pressure q_c. With a few exceptions, the values of $\Delta p/q$ and $\Delta p/q_c$ are in all cases plotted to the same scale.

The two curves in figure 1 show that, downstream from the end of the nose sections, the pressures at subsonic and supersonic speeds are below free-stream static pressure. With increasing distance from the nose, the pressures in both speed ranges approach the free-stream value. At supersonic

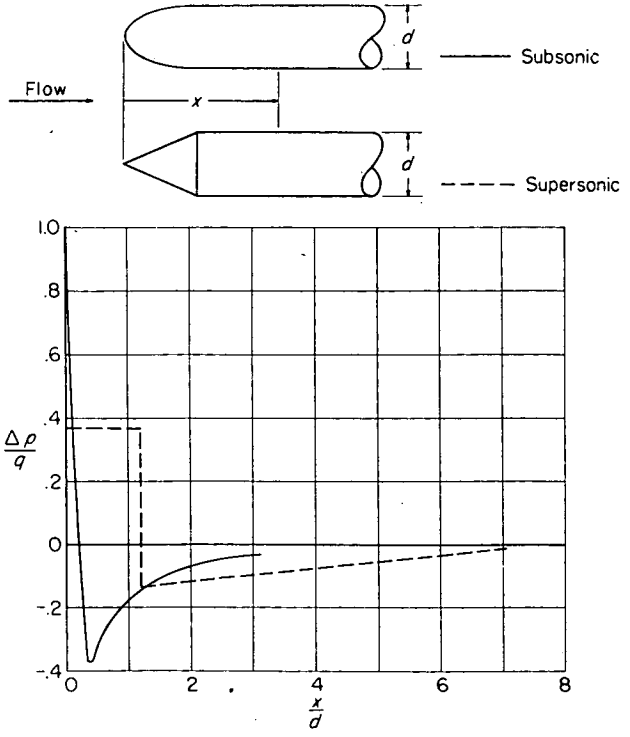


FIGURE 1.—Theoretical pressure distribution along cylindrical bodies (subsonic data from ref. 5).

speeds, however, the return to free-stream pressure occurs farther downstream. The axial location of orifices on a tube designed to function at both subsonic and supersonic speeds would, therefore, be determined by the pressure distribution at supersonic speeds.

Experimental data showing the variation of static-pressure error with axial location of orifices on three tubes are presented in figure 2. The subsonic data were obtained with a tube with a truncated ogival nose (ref. 6), whereas the supersonic data were determined with tubes having a more elongated truncated ogival nose (ref. 7) and a conical nose (ref. 8). Note that the axial locations of the orifices on these tubes are referenced to the end of the nose section rather than the tip of the nose as in figure 1. The data from investigations conducted with these tubes show that at subsonic speeds (M=0.6 to 0.9) a static-pressure error of ½ percent of q_c is reached at a distance of 4 tube diameters behind the end of the nose section. At supersonic speeds (M=1.55 to 2.87) an error of ½ percent of q_c is reached at 5 to 7 diameters rearward of the nose section.

The effect of varying the shape of the nose of a static-pressure tube has also been determined at both subsonic and supersonic speeds. Subsonic tests (M=0.3 to 0.95) of tubes having hemispherical, ogival, and truncated ogival noses showed that, when the orifices were located 6 or more tube diameters behind the end of the nose section, the static-pressure errors of the three tubes were in close agreement (ref. 6). Supersonic tests (M=1.61) of tubes having cylindrical, hemispherical, 30° conical, short ogival, and long ogival noses showed that, for orifice locations at least 10 diameters rearward of the nose section, the measured pressures were substantially independent of the shape of the nose (ref. 9).

From all of these results, it may be concluded that a tube with orifices located 10 or more diameters behind the end of the nose section measures free-stream static pressure with small error at both subsonic and supersonic speeds and that for this axial location of the orifices the measured pressure is unaffected by the shape of the nose.

The investigations referred to in the previous paragraphs were conducted with small-scale tubes in small-throated tunnels. Tests of a larger (0.97-inch-diameter) tube in the Langley 8-foot transonic tunnel provide full-scale confirmation of this work at subsonic speeds. This tube had a truncated ogival nose with orifices located 7.8 diameters rearward of the end of the nose section. The calibration of this tube (fig. 3) shows the static-pressure error to be within ±½ percent of q_c up to M=0.95.

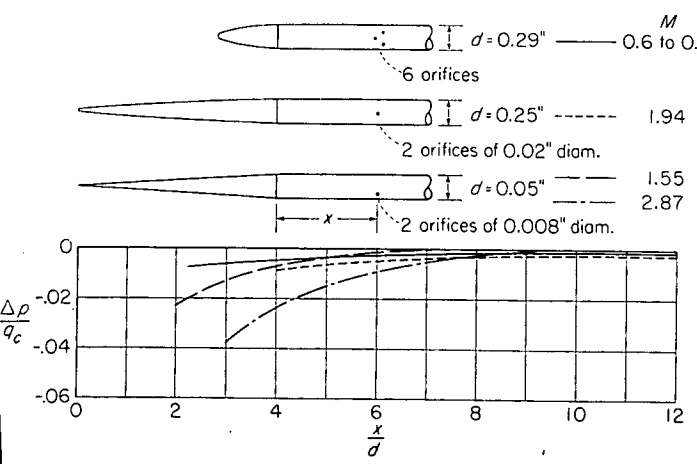


FIGURE 2.—Experimental pressure distribution along static-pressure tubes (refs. 6, 7, and 8).

526597—60——43

Axial location of orifices ahead of protuberances.—The pressure developed by a static-pressure tube depends not only on the axial location of the orifices behind the nose but also on the location ahead of protuberances on the rear of the tube. Protuberances may be either transverse stems or collars (expansion of tube to accommodate a support or boom of larger diameter than tube).

The effect of a transverse stem may be seen from figure 4, which presents the theoretical pressure distribution (incompressible flow) ahead of a body of infinite span (ref. 5). The static-pressure errors shown by this curve would apply to a tube with a stem extending from two sides; for a stem extending from only one side, the values would be halved. It will be seen from figure 4 that the static-pressure error due to the stem ("blocking effect") is positive and decreases rapidly with increasing distance from the stem.

Experimental effects at subsonic speeds of a streamlined stem extending on one side of a tube (ref. 6) are given in figure 5. These data show that the static-pressure error decreases with distance ahead of the stem and increases, at high subsonic speeds, with Mach number. For orifices located a distance of about 10 times the stem thickness ahead of the stem, the static-pressure error will be within ½ percent of q_c for Mach numbers up to 0.7. The fact that the error caused by protuberances is positive is often used in the

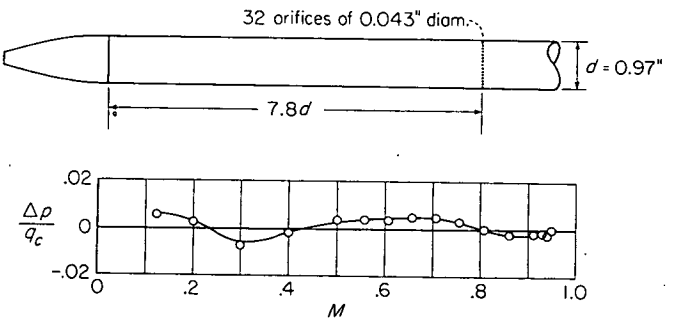


FIGURE 3.—Calibration of a static-pressure tube at α=0°.

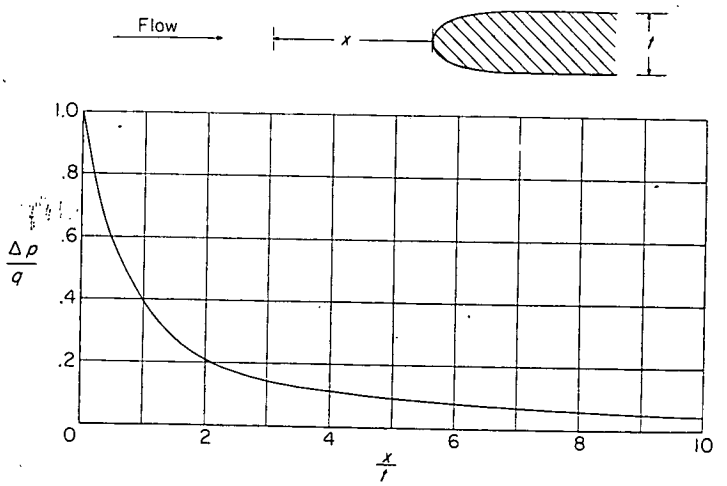


FIGURE 4.—Theoretical pressure distribution ahead of a body of infinite length transverse to the flow (incompressible-flow theory, ref. 5).

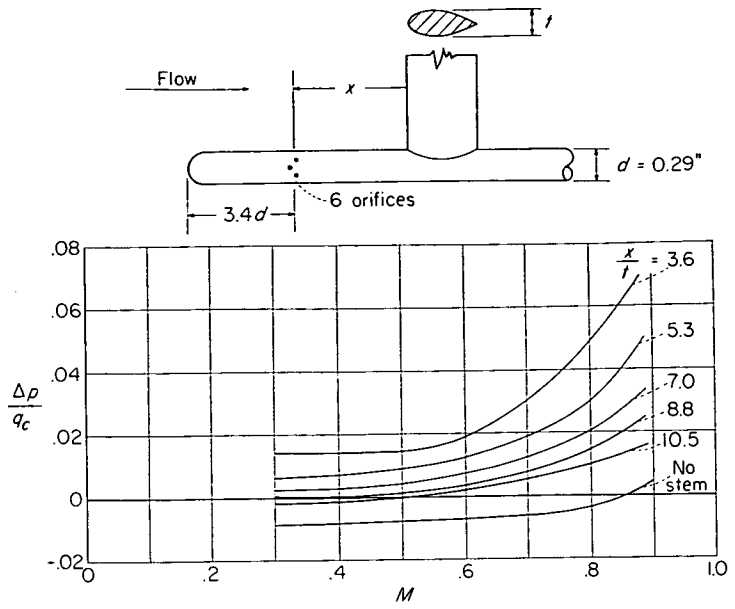


FIGURE 5.—Effect of transverse stem on the pressure developed by a static-pressure tube at $\alpha=0°$ (ref. 6).

design of a static-pressure tube to compensate for the negative error due to the pressure distribution along the forward portion of the tube.

Data from reference 6 on the blocking effect of collars at subsonic speeds are presented in figure 6. In these tests the ratio of collar diameter to tube diameter was fixed and the position of the collar with respect to the orifices was varied. The distance of the orifices from the nose section (12 tube diameters) was such that the error of the tube without the collar was essentially zero. The results indicate that the static-pressure error decreases with distance of the collar from the orifices and that, for x/D greater than 3.2, the variation of static-pressure error with Mach number is negligible up to $M=0.95$ with $\alpha=0°$. The data shown in this figure apply to a ratio of collar to tube diameter D/d of 1.43; for larger values of D/d, the blocking effect of the collar will be greater.

The calibration of a 0.91-inch-diameter tube with a collar behind the orifices and $\alpha=0°$ is given in figure 7. These data, obtained from tests in the Langley 8-foot transonic tunnel, show the static-pressure error to be about $+\frac{1}{2}$ percent of q_c up to $M=0.9$. Tests of similar tubes in other wind tunnels (refs. 10 and 11) showed the errors below $M=0.9$ to be as high as 2 percent of q_c.

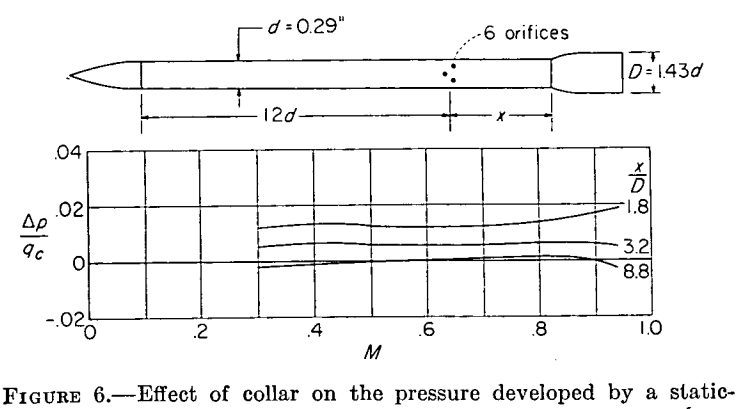


FIGURE 6.—Effect of collar on the pressure developed by a static-pressure tube at $\alpha=0°$ (ref. 6).

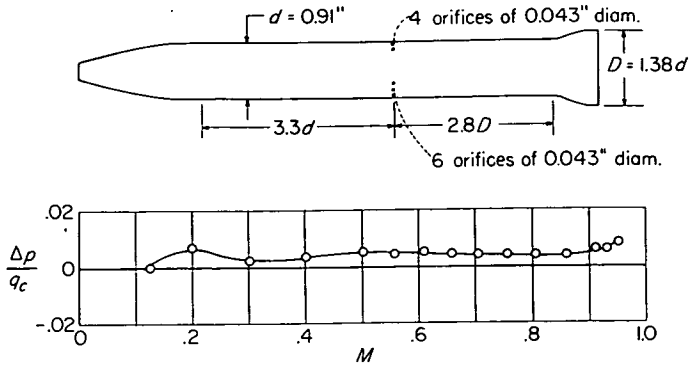


FIGURE 7.—Calibration at $\alpha=0°$ of a static-pressure tube with collar.

TUBES AT ANGLES OF ATTACK

The pressure developed by a static-pressure tube at an angle of attack other than 0° depends not only on the axial location of the orifices but also on their circumferential positions. When orifices encircle the tube, the measured static pressure decreases with inclination of the tube, and the variation of static-pressure error with inclination is the same for angles of attack and angles of yaw. The static-pressure error of a tube with this orifice configuration remains within 1 percent of q_c of the value at $\alpha=0°$ over an angular range of about $\pm5°$ (ref. 12). The additional error resulting from the inclination of the tube can be avoided by pivoting the tube so that it always alines itself with the airstream. Because of the relative fragility of swiveling tubes, however, attempts have been made to devise rigid tubes which would remain insensitive over an appreciable range of angle of attack.

The basis of these attempts is the pressure distribution around a cylinder. Figure 8 presents the results of pressure distribution tests of a 2-inch-diameter cylinder at angles of attack of 30° and 45° and at low subsonic speeds ($M<0.2$). These curves show the static-pressure error to be positive on the bottom of the cylinder, negative on the top, and zero at a circumferential position of about 30° from the bottom. It would appear, therefore, that insensitivity to inclination might be accomplished either by locating orifices at a circumferential position of about $\pm30°$ or by placing orifices along the top and bottom of the tube to achieve compensation of the positive and negative pressures. The application of both of these methods will be discussed.

The data from reference 13, as exemplified in figure 8, show that, at low subsonic speeds and at $\alpha>30°$, the pressure distribution at circumferential positions greater than 30° varies appreciably with the Reynolds number. In another investigation (ref. 14) in which cylinders at $\alpha=90°$ were tested at higher Mach numbers (0.3 to 2.9), the effect of Reynolds number on the pressure distribution was found to be negligible at supersonic speeds.

Orifices at $\pm30°$ location.—The effect of angle of attack at subsonic speeds for a 1-inch-diameter tube with orifices located on the bottom of the tube 30° on either side of the vertical radius is reported in reference 15. Sample results of these tests (fig. 9) show that the static-pressure error remains within 1 percent of q_c of the value at $\alpha=0°$ for angles of attack up to at least 20° at $M=0.30$ and to 9° at $M=0.65$. At angles of yaw the angular range for an error

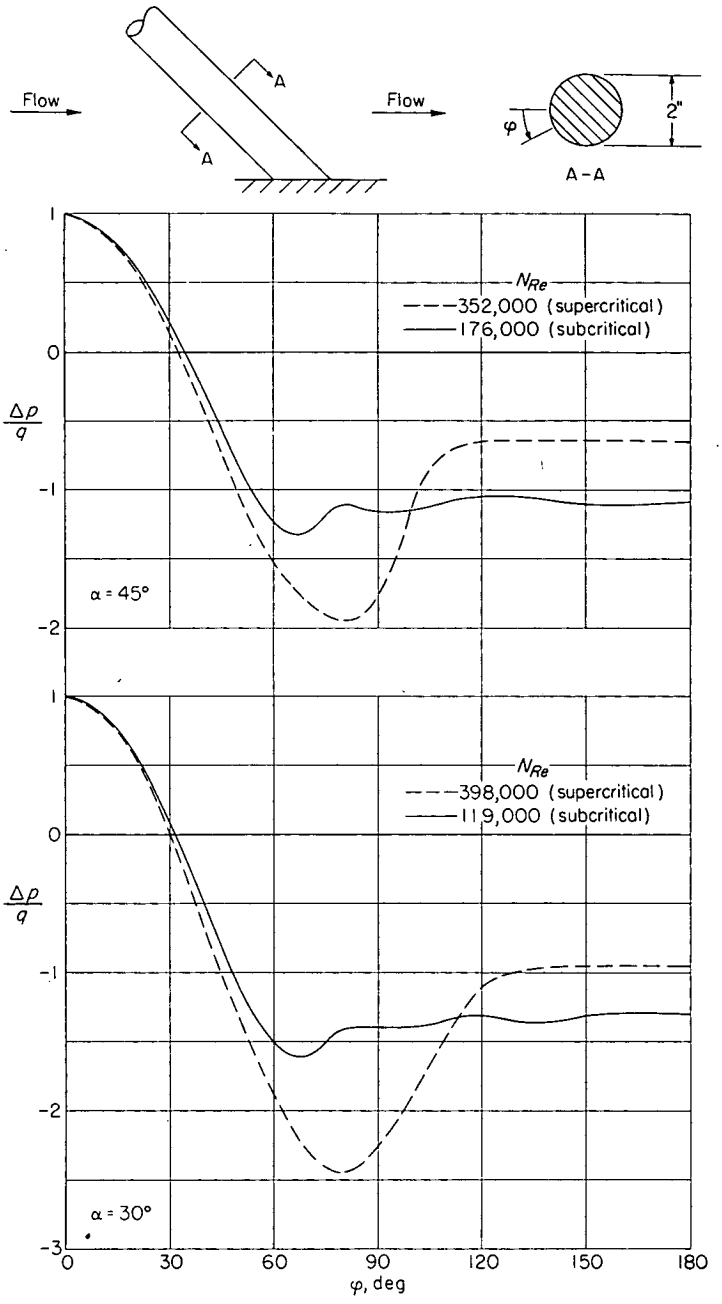


FIGURE 8.—Pressure distribution around a cylinder at angles of attack of 30° and 45° (ref. 13). $M<0.2$.

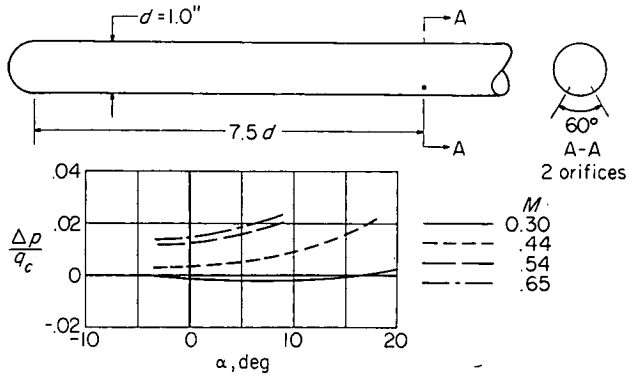


FIGURE 9.—Calibration at angles of attack of a static-pressure tube with orifices at circumferential stations of 30° and −30° (ref. 15).

of 1 percent of q_c is about ±5° (ref. 15).

Supersonic tests of a 0.05-inch-diameter probe with orifices at a circumferential position of ±33° are reported in reference 8. The calibrations of this tube (fig. 10) show that the static-pressure error remains within 1 percent of q_c for angles of attack up to 17° at $M=1.56$ and up to at least 8° at $M=2.92$.

Supersonic tests of a 0.63-inch-diameter tube with orifices at a circumferential position of ±37.5° are reported in reference 16. The results of these tests (fig. 11) show the static-pressure error to remain within 1 percent of q_c for angles of attack up to at least 12° at $M=1.57$ and at least 15° at $M=1.88$.

Orifices on top and bottom of tube.—Calibrations at angles of attack of a 0.91-inch-diameter tube with four orifices on the top of the tube and seven on the bottom were determined at several Mach numbers between 0.20 and 0.68 (ref. 17). Data for these two Mach numbers (fig. 12) show that the static-pressure error remains within 1 percent of q_c of the value at $\alpha=0°$ for angles of attack up to 40° at $M=0.20$ and to 18° at $M=0.68$. At some angle of attack above 30° and at M above 0.3 the static pressure registered by the tube increases abruptly and fluctuates erratically. For angles of attack between 15° and 30° and Mach numbers between 0.2 and 0.68 the static-pressure error was found to increase as much as 2 percent of q_c for a change in Reynolds number (based on the local velocity and the diameter of the tube) of from 100,000 to 250,000. Because of the unsymmetric arrangement of the orifices, the sensitivity of the tube at angles of

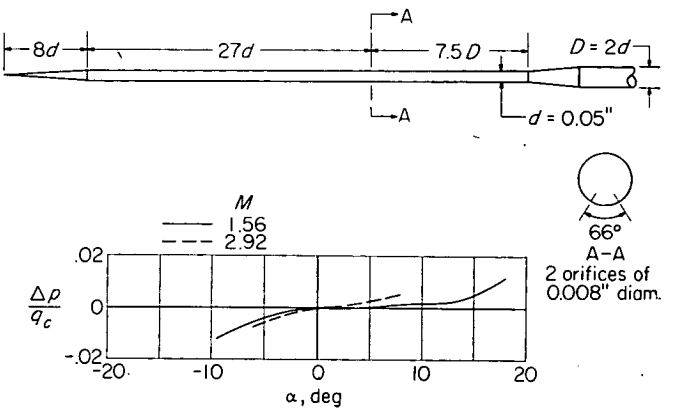


FIGURE 10.—Calibration at angles of attack of a static-pressure tube with orifices at circumferential stations of 33° and −33° (ref. 8).

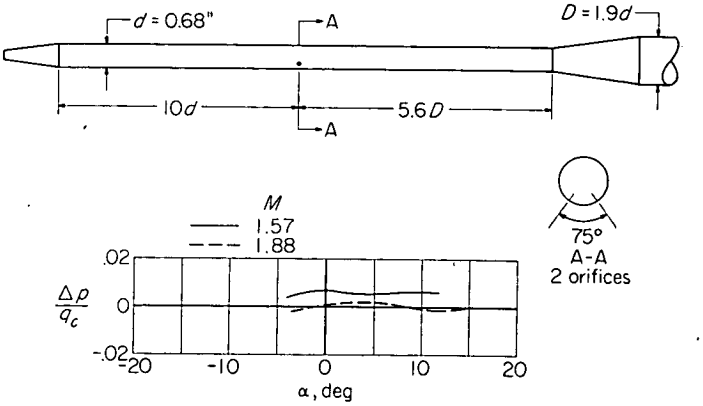


FIGURE 11.—Calibration at angles of attack of a static-pressure tube with orifices at circumferential stations of 37.5° and −37.5° (ref. 16).

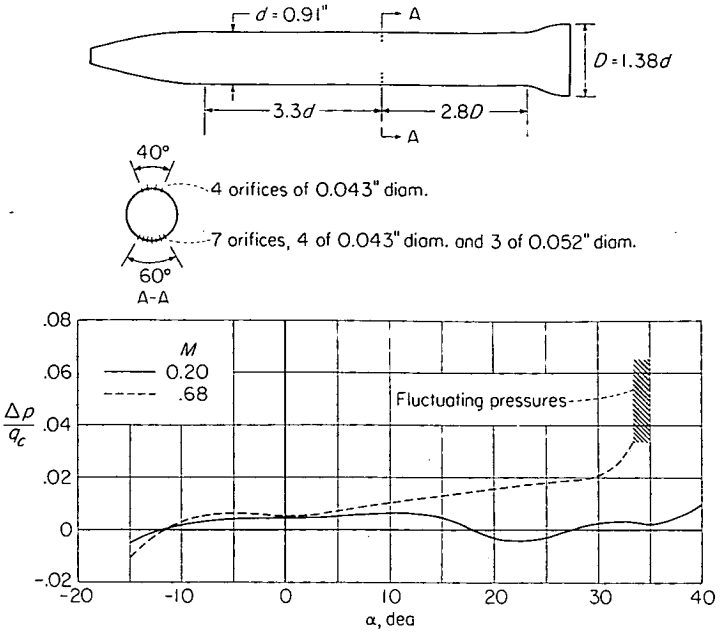


FIGURE 12.—Calibration at angles of attack of a static-pressure tube with an unsymmetrical orifice arrangement (ref. 17).

yaw is, like that of the $\pm 30°$ orifice arrangement, much greater than at angles of attack. At angles of yaw the error remained within 1 percent of q_c over an angular range of $\pm 5°$ at $M=0.2$.

Tests of an 0.88-inch-diameter static-pressure tube with four orifices on the top of the tube and seven on the bottom were conducted at $M=0.6$ to 1.10 (ref. 18). The calibrations of this tube at $M=0.6$, 0.8, and 1.0 (fig. 13) show the static-pressure errors to remain within 1 percent of q_c of the value at $\alpha=0°$ for angles of attack up to 11° at M between 0.6 and 1.0.

The effect of angle of attack on a 0.91-inch-diameter tube with four orifices on the top of the tube and six on the bottom was determined at supersonic speeds through an angle-of-attack range of $\pm 7°$. The results, as presented in reference 7, showed that, for this range of angle of attack, the static-pressure error remained within about 0.4 percent of q_c of the value at $\alpha=0°$ at $M=1.62$ and 1.93.

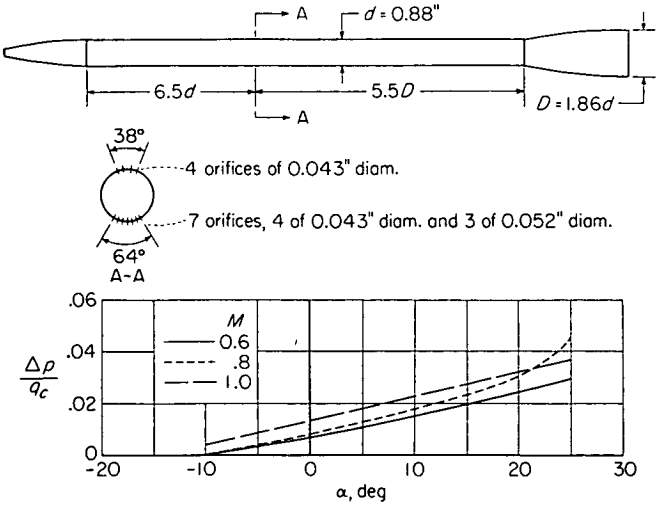


FIGURE 13.—Calibration at angles of attack of a static-pressure tube with an unsymmetrical orifice arrangement (ref. 18).

CONICAL STATIC-PRESSURE TUBES

Orifices on the surface of a cone have been proposed for the measurement of static pressure at supersonic speeds.

Experimental data for an orifice at two locations near the nose of a 3° cone are presented in figure 14. These data were obtained from tests in the Langley 8-foot transonic tunnel at values of α between 1° and −1° and $M=0.20$ to 1.13. The calibrations show the static-pressure errors for the two orifice locations to remain within about 1 percent of q_c over the range of Mach number tested.

Tests of orifices on a conical-nose body of revolution at $M=1.59$ are reported in reference 19. In these tests four orifices were located 0.29 maximum body diameter from the front of a parabolic body of revolution with an apex angle of 15°. For the test Mach number (1.59) the results indicate that the static-pressure error is about 6 percent of q at an angle of attack of 0°.

ORIFICE SIZE AND CONFIGURATION

The static-pressure errors due to the axial and circumferential location of the orifices, as discussed in the previous sections, apply to tubes with orifices which are accurately drilled and free from burs, protuberances, or depressions. Variations in the diameter and edge shape of the orifices can result in additional errors in the static-pressure measurements.

The influence of orifice diameter on the measured static pressure has been investigated with orifices on the inside wall of a cylindrical test section (ref. 20). The tests were conducted for orifice diameters of 0.006 to 0.125 inch over a Mach number range of about 0.4 to 0.8. The results of the tests at these two Mach numbers (fig. 15(a)) show the static-pressure error to increase with both orifice diameter and Mach number.

The effect of orifice diameter has also been determined for two orifice diameters on a 0.5-inch-diameter static-pressure tube at $M=1.45$ in an investigation made at the Douglas Aircraft Co., Inc., by T. W. Buquoi, L. E. Lundquist, and J. M. Stark. The results of these tests showed that an increase of 0.025 to 0.052 inch in the orifice diameter caused the static-pressure error to increase by 0.6 percent of q_c at $\alpha=0°$.

In other tests of reference 20, the effect of varying the cross-sectional shape of the orifice edge was investigated with 0.032-inch-diameter orifices on the inside wall of a

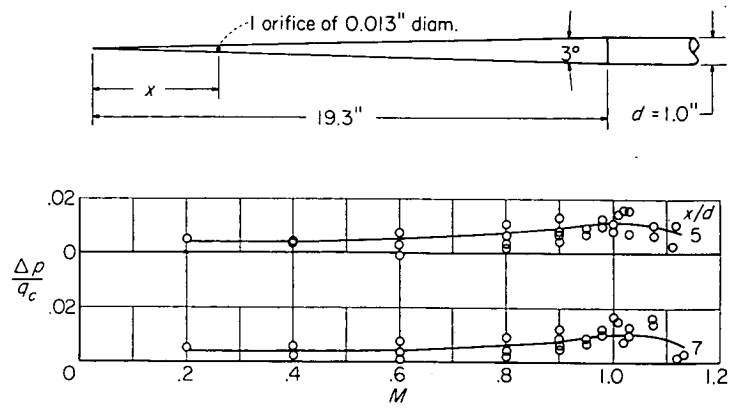


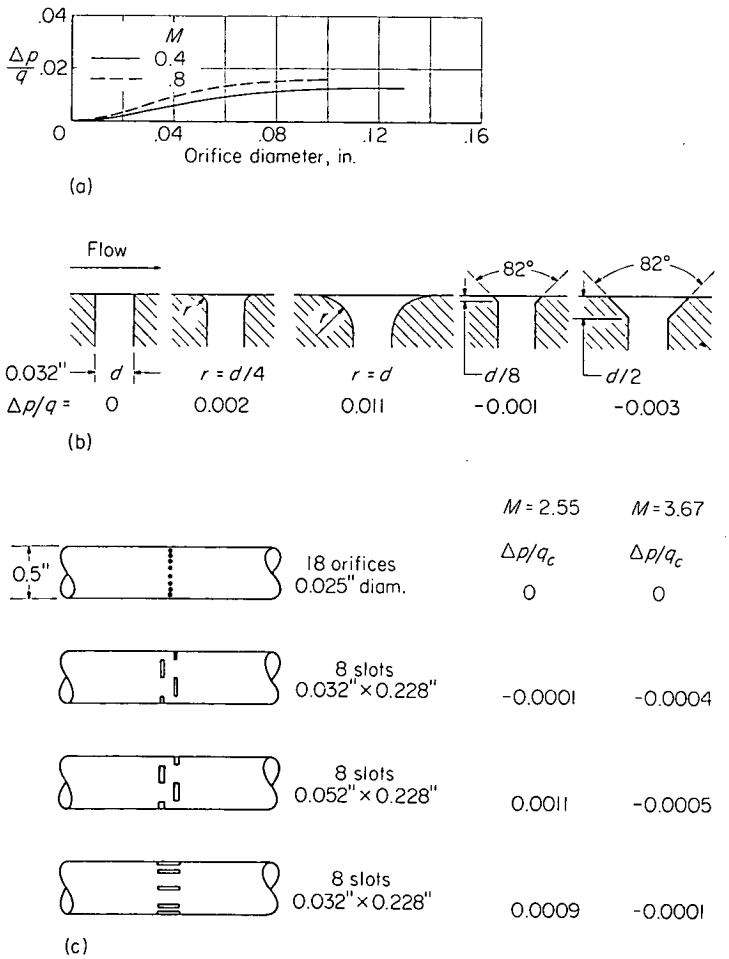
FIGURE 14.—Calibration of orifices on the nose section of a conical static-pressure tube at $\alpha=1°$ to −1°.

cylindrical test section. Sample results of these tests are presented in figure 15(b), which gives the difference between the static-pressure error of each orifice configuration and that of a sharp-edge orifice of the same diameter.

In the previously mentioned investigation of Buquoi, Lundquist, and Stark at Douglas Aircraft Co., Inc., the effect of elongating the orifices in a 0.5-inch diameter static-pressure tube was also investigated. The three configurations tested are shown in figure 15(c); the differences in the static-pressure errors of the configurations, as referenced to a tube with 0.025-inch-diameter orifices encircling it, are given for the tubes at $\alpha=0°$ and $M=2.55$ and 3.67.

STATIC-PRESSURE ERRORS OF INSTALLATIONS

Static-pressure sources (tubes and vents) have been located at numerous positions on or near the aircraft. Static-pressure tubes have been located ahead of the fuselage nose, ahead of the wing, and ahead of the vertical tail fin. Static-pressure vents have generally been located on the fuselage between the nose and the wing or between the wing and the tail surfaces. The choice of type and location



(a) Effect of orifice diameter (ref. 20).

(b) Effect of edge shape of orifices. Static-pressure error of each edge shape referenced to square-edge orifice of 0.032-inch diameter (ref. 20). $M=0.4$ to 0.8.

(c) Effect of elongating orifices. Static-pressure error of slotted orifices referenced to 18-orifice configuration (data from Douglas Aircraft Co., Inc.).

FIGURE 15.—Effect of orifice size and configuration on static-pressure measurements.

of the static-pressure source will depend on numerous considerations, such as the configuration and speed range of the aircraft, the accuracy required, pressure lag, icing, and the possibility of damage due to ground handling.

For any practical location of the static-pressure source, the installation will have a position error which will vary to some degree with Mach number and angle of attack. The position error will, therefore, vary with impact pressure, static pressure, aircraft weight, and normal acceleration. The error may also vary with changes in the configuration, and thus the flow field, of the airplane—for example, changes in flap setting and landing-gear extension. As the flow field about an airplane is markedly different for the subsonic, transonic, and supersonic speed ranges, the position errors for locations near the airplane may be expected to be quite different in each of the three speed ranges.

In the discussion to follow, the static-pressure errors of the various installations are presented as a function of Mach number or lift coefficient. Wherever possible, the effects of Mach number and lift coefficient have been separated. In those cases where the static-pressure errors of level-flight calibrations are plotted as a function of Mach number, the lift coefficient varies throughout the Mach number range. At the high subsonic and transonic Mach numbers at which these calibrations were performed, however, the variation of lift coefficient was small.

The static-pressure errors represent the overall static-pressure errors of the installation, that is, the sum of the position errors and the static-pressure errors of the pressure source. Diagrams of the static-pressure tubes used for the airplane installations are presented in figure 16, and the type of tube used with each installation is noted in the calibration figures.

STATIC-PRESSURE ERRORS AHEAD OF FUSELAGE NOSE

At Mach numbers below that at which a shock passes the static-pressure orifices, the position error at a given distance ahead of the fuselage nose is determined by the shape of the nose and the maximum diameter of the body.

Effect of nose shape.—The effect of nose shape was investigated in wind-tunnel tests of bodies of revolution (fineness ratio, 8.3) with circular, elliptical, and elongated ogival noses (ref. 21). The tests were conducted at a Mach number of about 0.2 and at $\alpha=0°$. The results of the tests (fig. 17) show that, for a given distance ahead of the body, the position errors were greatest for the circular nose and least for the elongated ogival nose. At a distance of 1 diameter, for example, the errors were about 9, 4, and 1 percent, respectively, for the circular, elliptical, and elongated ogival noses. At 2 diameters the effect of variations in nose shape had diminished considerably.

The static-pressure errors at three distances (½, 1, and 1½ fuselage diameters) ahead of a fuselage were measured on an airplane with an elliptical nose section (ref. 22). The results of these tests at small angles of attack ($C_L=0.2$) are shown in figure 18 together with the data for the elliptical nose model taken from figure 17.

Effect of Mach number.—The effect of Mach number on the static-pressure errors ahead of two bodies of revolution at transonic speeds was determined by wing-flow tests

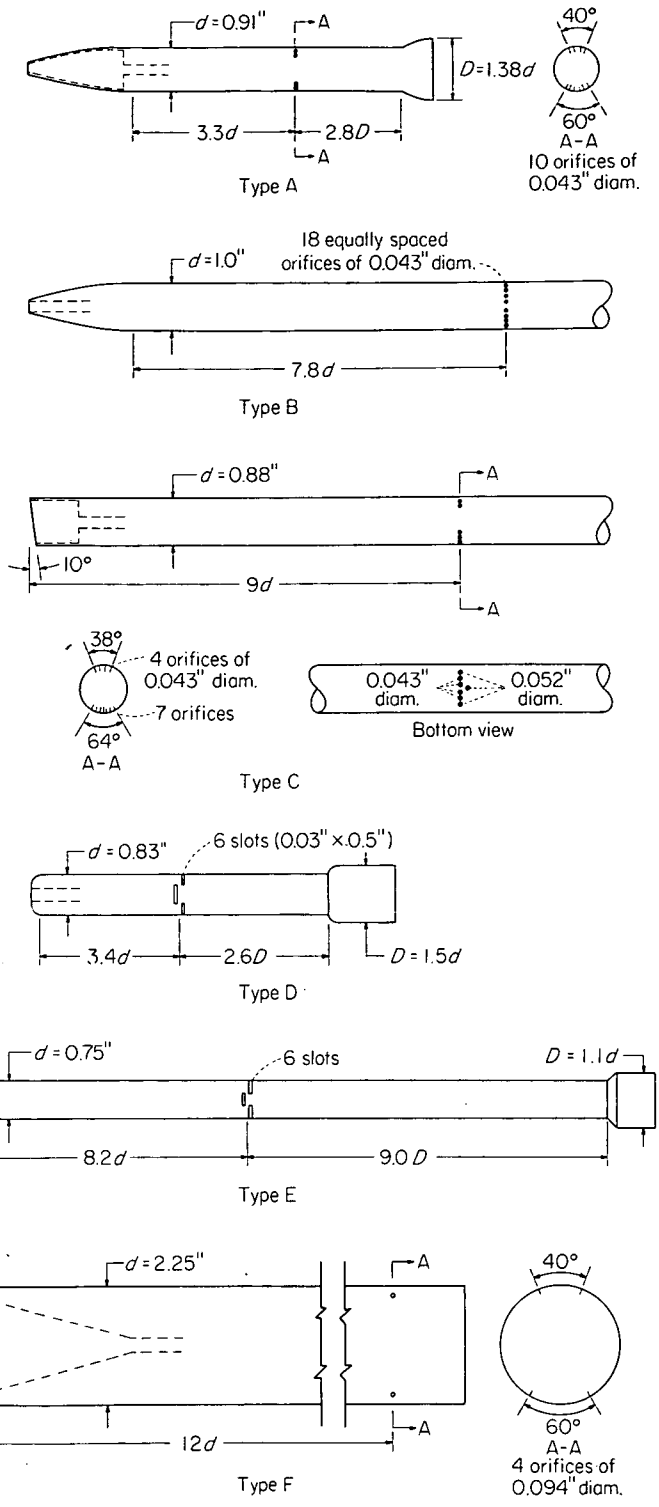


FIGURE 16.—Diagrams of static-pressure tubes used on airplane installations (½ scale).

(ref. 23). The nose shapes (that portion ahead of the maximum-diameter station) of the two bodies (fig. 19(a)) were similar. The nose shape of body A was developed from a circular arc, whereas the shape of body B was based on that of an actual airplane. The calibration of three installations on body B (fig. 19(a)) shows that, when the critical Mach number of the body is reached, the error begins to increase because the effect of negative pressures on the rear of the body are then diminished by the shock which forms around the maximum body diameter. When the free-stream Mach

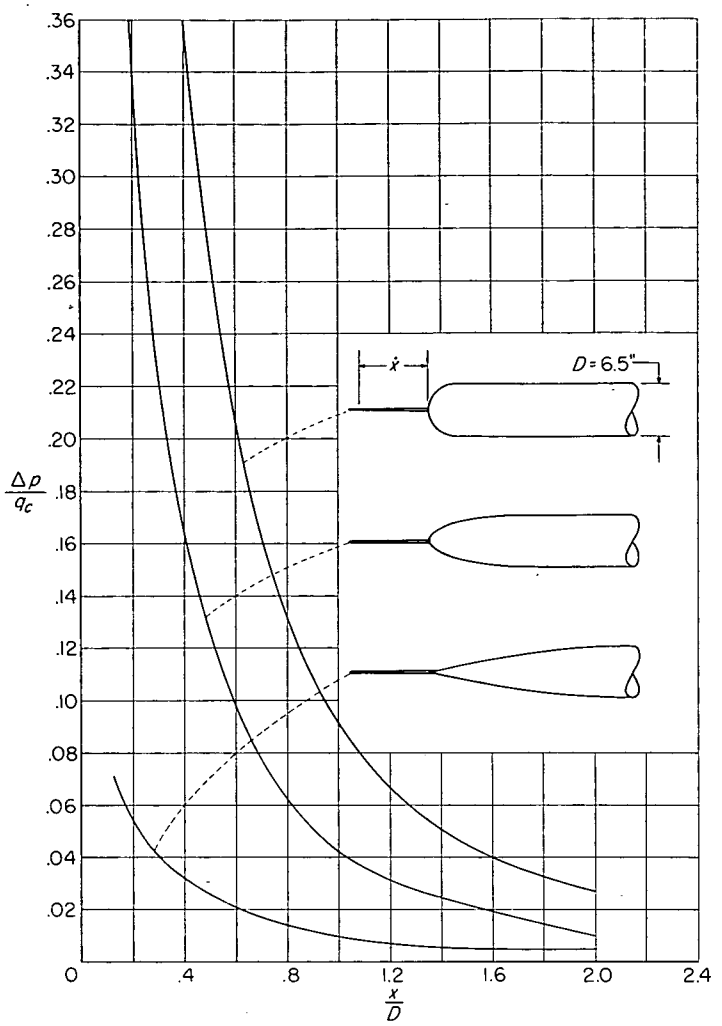


FIGURE 17.—Static-pressure errors at various distances ahead of three bodies of revolution with different nose shapes. $M=0.21$; $\alpha=0°$ (ref. 21).

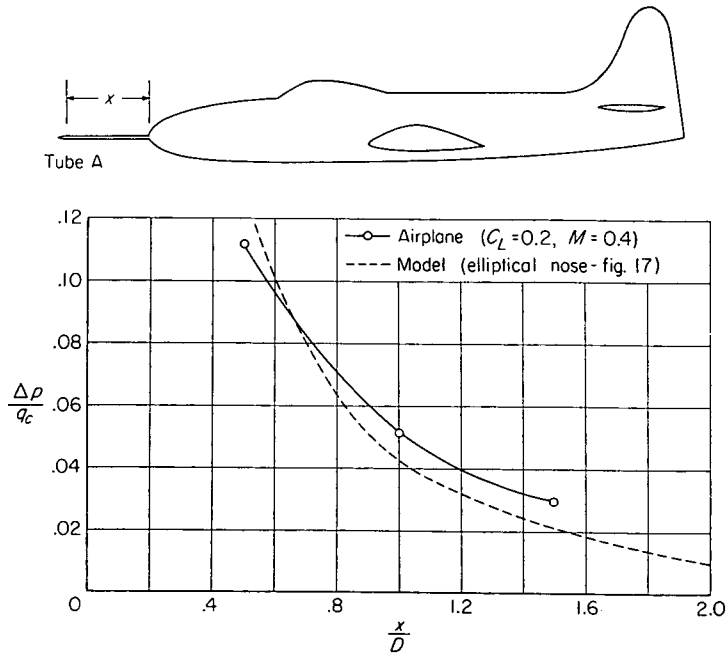
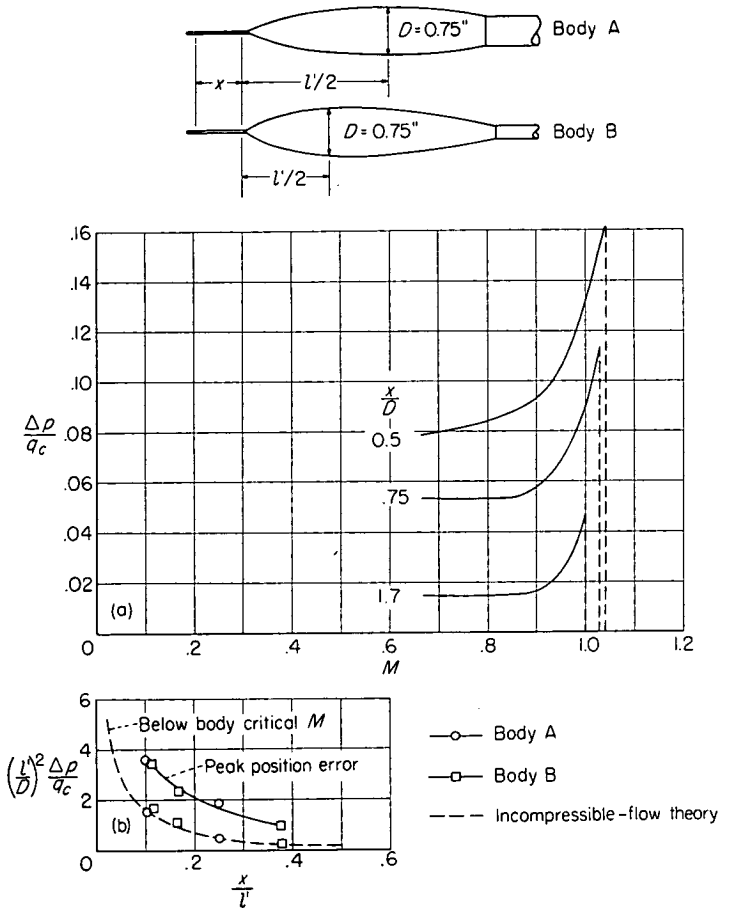


FIGURE 18.—Static-pressure errors at three distances ahead of an airplane fuselage with an elliptical nose shape (ref. 22).

number becomes supersonic, a shock wave forms ahead of the body and the static-pressure error continues to increase as the shock moves toward the body. When the shock wave passes the orifices on the tube, the error falls to a value near zero, because the pressure field of the body is then isolated from the orifices. At the Mach number at which the shock wave passes the orifices, and at all higher Mach numbers, the pressure registered by the orifices should be that of the isolated tube. However, if the shock, after passing the orifices, interacts with the boundary layer to form a complex shock pattern in the vicinity of the orifices, the static-pressure error following the drop from the peak error will be slightly higher than that of the isolated tube. In this case, the static-pressure error will not return to that of the isolated tube until some higher Mach number has been reached.

In reference 23 it was shown that, for slender bodies having similar nose shapes, the position errors below the critical Mach number of the body and the peak errors just prior to the shock passage can both be correlated by the use of parameters which include the length as well as the diameter of the body. The manner in which the data of reference 23 correlate is shown in figure 19(b), which includes a theoretical curve for a parabolic-arc body calculated on the basis of the linearized subsonic theory. For the bodies considered, the peak errors are about twice the subsonic errors.



(a) Variation of static-pressure error with Mach number for body B.
(b) Variation of static-pressure-error parameter with distance ahead of nose.

FIGURE 19.—Static-pressure errors at various distances ahead of two bodies of revolution at $\alpha=0°$ (ref. 23).

The calibration at transonic speeds of a static-pressure tube ahead of the nose of the airplane of which body B of figure 19 was a model (ref. 24) is presented in figure 20. These data confirm the results of the model tests by showing (1) the rapid increase in the static-pressure error at Mach numbers near 1.0 and (2) the discontinuity which occurs in the calibration when the fuselage bow wave passes the static-pressure orifices. The static-pressure errors of this airplane at values of M between 0.8 and 1.0 and those of a number of other airplanes with somewhat similar nose shapes are plotted in figure 21 as a function of x/D. For a fuselage with a more elongated nose, the static-pressure errors will, as shown in figure 22, be considerably lower.

The calibrations of fuselage-nose installations up to low supersonic speeds indicate that, after the body bow wave and any boundary-layer—shock interaction have passed downstream of the orifices, the static-pressure error becomes that of the isolated tube and should remain at this value for all higher Mach numbers. That the static-pressure error remains small at higher supersonic speeds has been shown by calibration tests of a nose-boom installation on a free-flight rocket model. In this calibration, the error dropped to zero when the free-stream Mach number became supersonic and remained zero up to $M=4.5$.

Effect of angle of attack.—The variation of static-pressure error with angle of attack for a number of positions ahead of bodies of revolution was investigated during the tests reported in reference 21. The results of these tests (fig. 23) show the error to decrease with increasing angle of attack. The change in static-pressure error for a given change in angle of attack is greatest near the nose and decreases with distance from the nose. At a distance of 1 diameter ahead of the nose,

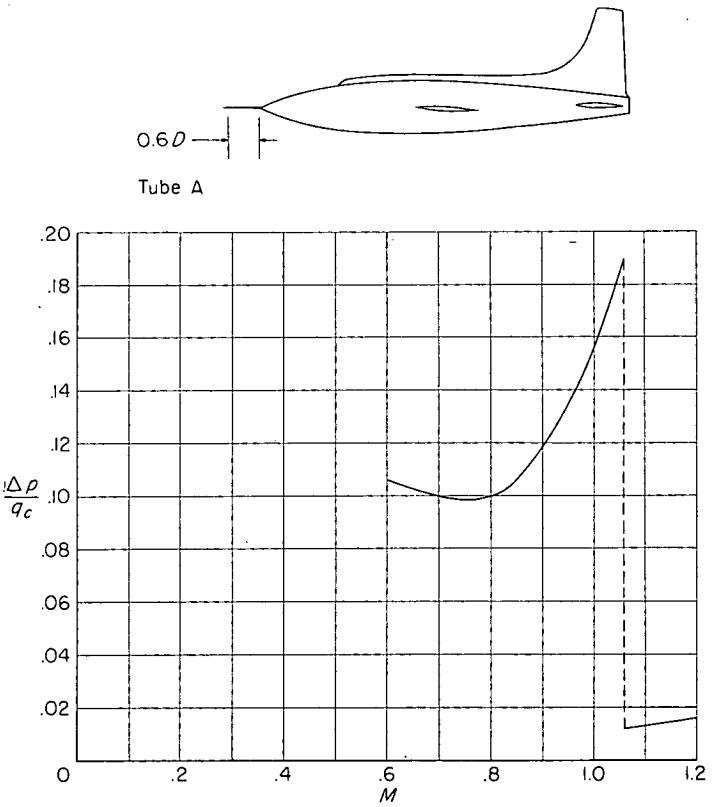


FIGURE 20.—Calibration in level flight of a static-pressure tube ahead of an airplane fuselage with a pointed nose (ref. 24).

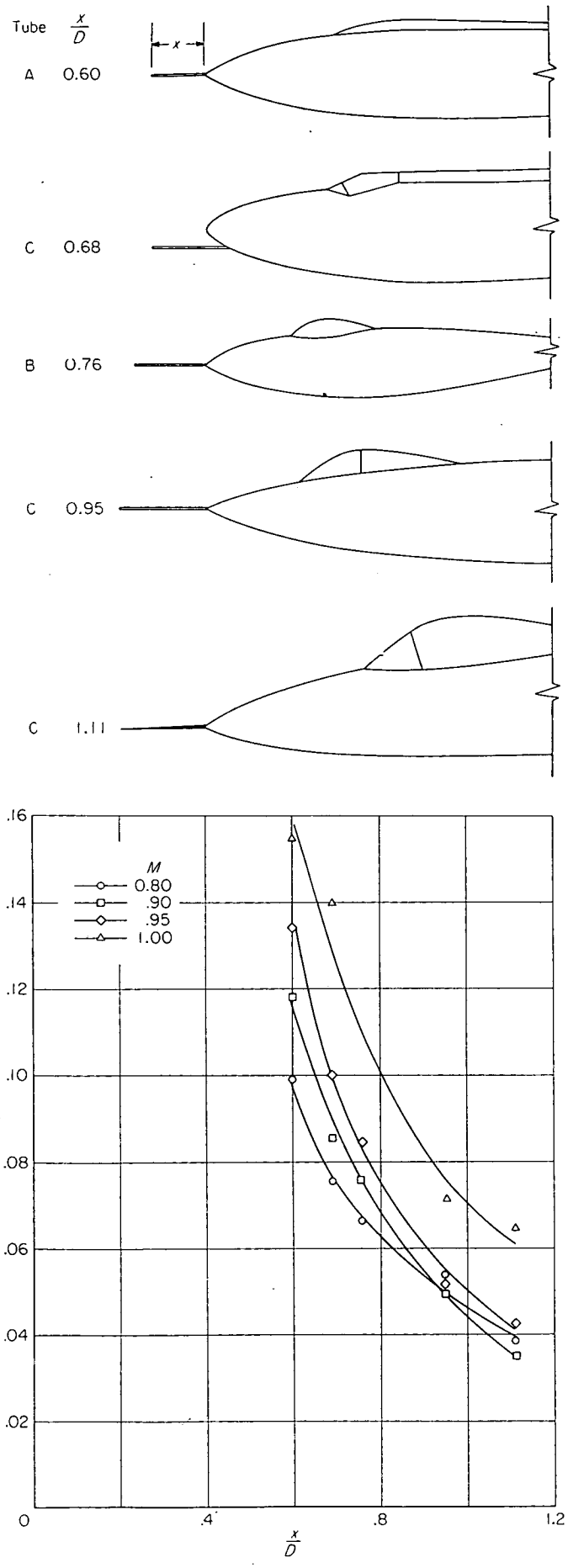


FIGURE 21.—Static-pressure errors ahead of five airplane fuselages with pointed noses.

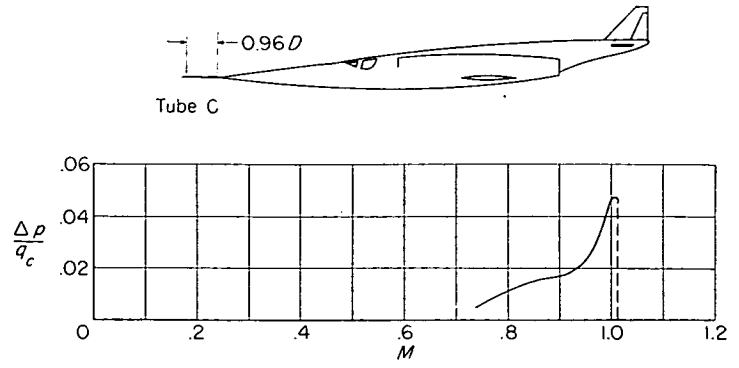


FIGURE 22.—Calibration in level flight of a static-pressure tube ahead of a fuselage with an elongated pointed nose.

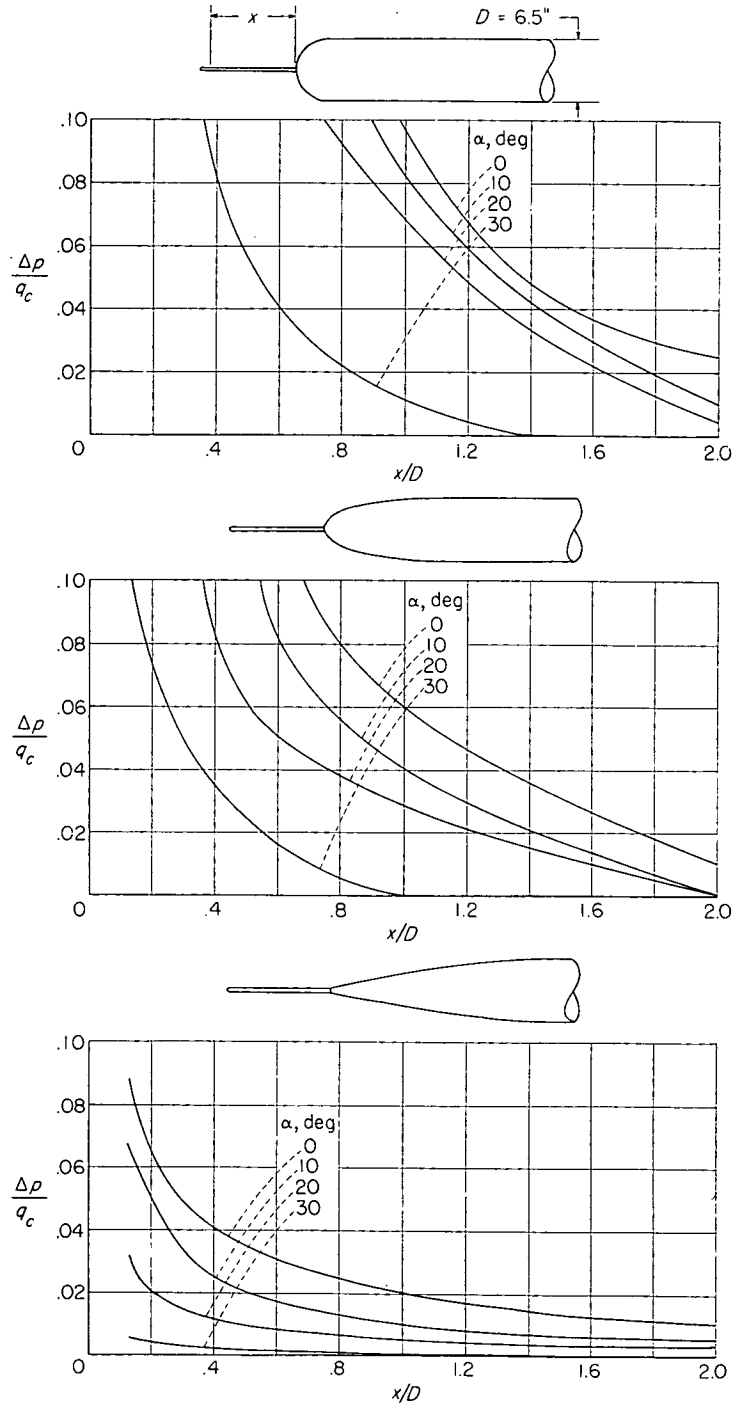


FIGURE 23.—Effect of angle of attack on the pressures at various distances ahead of three bodies of revolution with different nose shapes, $M=0.16$ (ref. 21).

the change in static-pressure error for a change in angle of attack of 30° is about 8 percent of q_c for the circular nose, and 2 percent of q_c for the elongated ogival nose.

In reference 25, the position errors ahead of slender parabolic-arc bodies of revolution at angles of attack were calculated on the basis of the subsonic linearized theory. Comparison between the theoretical and measured values for a body of revolution with a fineness ratio of 6 at a Mach number of 0.2 showed the theory to be valid for distances greater than 0.5 body diameter ahead of the body and for angles of attack less than 20°.

The effect of angle of attack on the static-pressure errors of fuselage-nose installations on airplanes at low and high subsonic speeds (refs. 22 and 24) is presented in figure 24. For lift coefficients up to 0.5, the effect of angle of attack is negligible. At C_L above 0.5 the static-pressure errors of the installations on airplane A decrease with increasing C_L. However, for other combinations of fuselage-nose shape, boom length, orientation of orifices on static-pressure tube, and Mach number, the static-pressure error may increase at high angles of attack.

Effect of nose inlet.—The position errors at various distances ahead of a body of revolution with a nose inlet were determined by wing-flow tests (ref. 23). The tests were conducted at transonic speeds and at $\alpha=0°$. The inlet velocity ratio varied from about 0.68 at $M=0.7$ to 0.57 at $M=1.0$. The results of the tests (fig. 25(a)) show the same general variation of static-pressure error with Mach number as the installations on sharp-nose bodies (fig. 19(a)). The variation of the static-pressure error at subsonic speeds

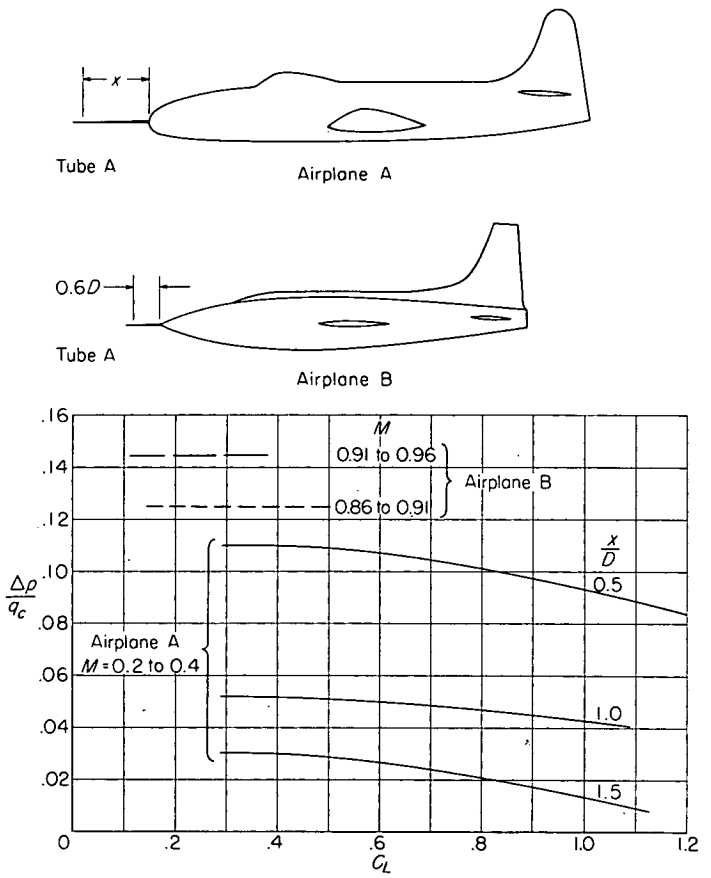


FIGURE 24.—Variation of static-pressure error with lift coefficient of fuselage-nose installations on two airplanes (refs. 22 and 24).

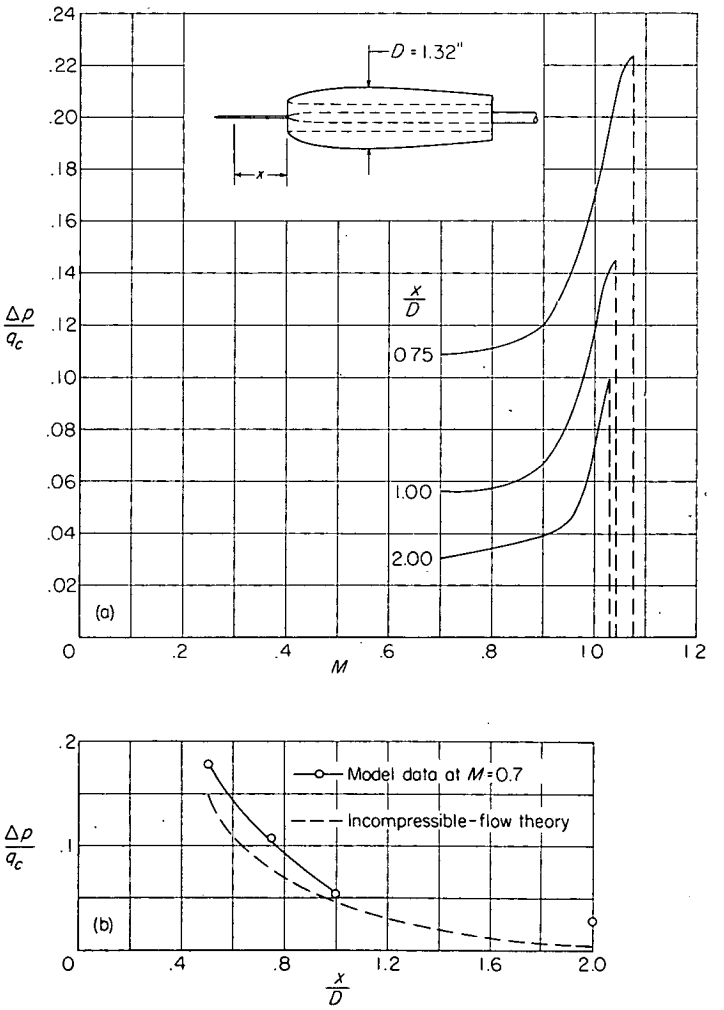
526597—60——44

($M=0.7$) with distance ahead of the body (fig. 25(b)) is also similar to that of the sharp-nose bodies. In other tests to determine the effect of inlet velocity, it was found that the static-pressure error increased when the inlet velocity ratio decreased.

Calibrations of nose-boom installations ahead of an airplane having a nose inlet (ref. 26) are given in figure 26. For these tests the orifices were located at various distances along a boom extending from the upper lip of the inlet. The calibrations of these installations exhibit the same variation of static-pressure error with Mach number as an installation ahead of a pointed-nose fuselage (fig. 20). The variation of the static-pressure errors with orifice location for a number of other airplanes with nose inlets is shown in figure 27 for $M=0.80$ to 1.00.

STATIC-PRESSURE ERRORS AHEAD OF WINGS

Prior to the passage of the shock over the static-pressure orifices, the position error at a given distance ahead of the wing of an airplane depends on the shape of the airfoil section, the maximum thickness of the airfoil, the sweepback angle of the wing, and the spanwise location of the static-pressure tube. In order to avoid the influence of the fuselage and the wake of any propellers, static-pressure tubes are usually



(a) Variation of static-pressure error with Mach number (inlet-velocity ratio 0.68 at $M=0.7$; 0.57 at $M=1.0$).
(b) Variation of static-pressure error with distance ahead of nose.

FIGURE 25.—Static-pressure errors at three distances ahead of a body of revolution with a nose inlet (ref. 23).

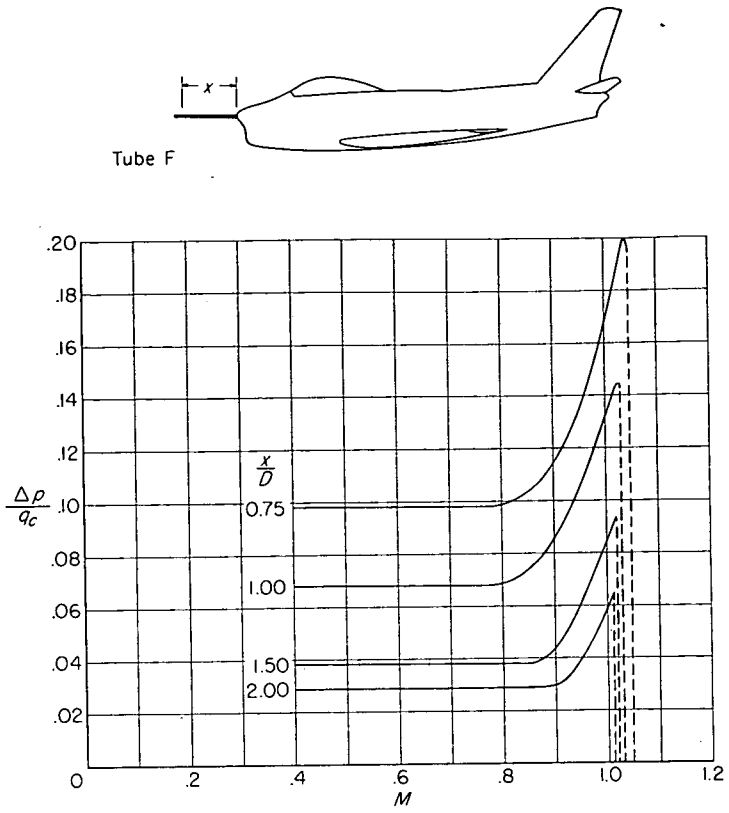


FIGURE 26.—Calibration in level flight of static-pressure orifices at four distances ahead of an airplane fuselage with a nose inlet (ref. 26).

installed on the outboard span of the wing. The lengths of tubing between the static-pressure tube and the instruments, however, may create undesirable problems as regards the pressure lag of the installation.

Effect of location of orifices.—Calibrations of static-pressure installations at various distances ahead of the leading edge of the wing tip of an unswept-wing airplane were determined at low subsonic speeds (ref. 22). The variation of static-pressure error of these installations (at small angles of attack) with distance ahead of the wing, expressed as a multiple of the maximum wing thickness, is given in figure 28. At $x/t=10$ (or 1 chord length for a 10-percent-thick airfoil), the error is about 1 percent, and it decreases only slightly with increasing distance ahead of the wing. The static-pressure errors of wing-tip installations on nine other unswept-wing airplanes with similar airfoil sections are also plotted in figure 28. This variation of static-pressure error with distance ahead of a wing tip is similar to that ahead of a transverse stem shown in figures 4 and 5.

Effect of Mach number (unswept wings).—The variation of static-pressure error with Mach number for a static-pressure tube located ahead of the wing tip of an unswept-wing airplane at transonic speeds (ref. 24) is presented in figure 29. The calibration of this installation is similar to that of the fuselage-nose installations up to the Mach number at which the discontinuity due to shock passage occurs. At this point, however, the error falls to a negative value and then, with increasing Mach number, begins to increase to positive values. The explanation for this behavior may best be illustrated by diagrams of the shock waves ahead of the airplane (fig. 30). At a Mach number of about 1.03, the wing bow wave has passed the orifices, thus effectively isolating

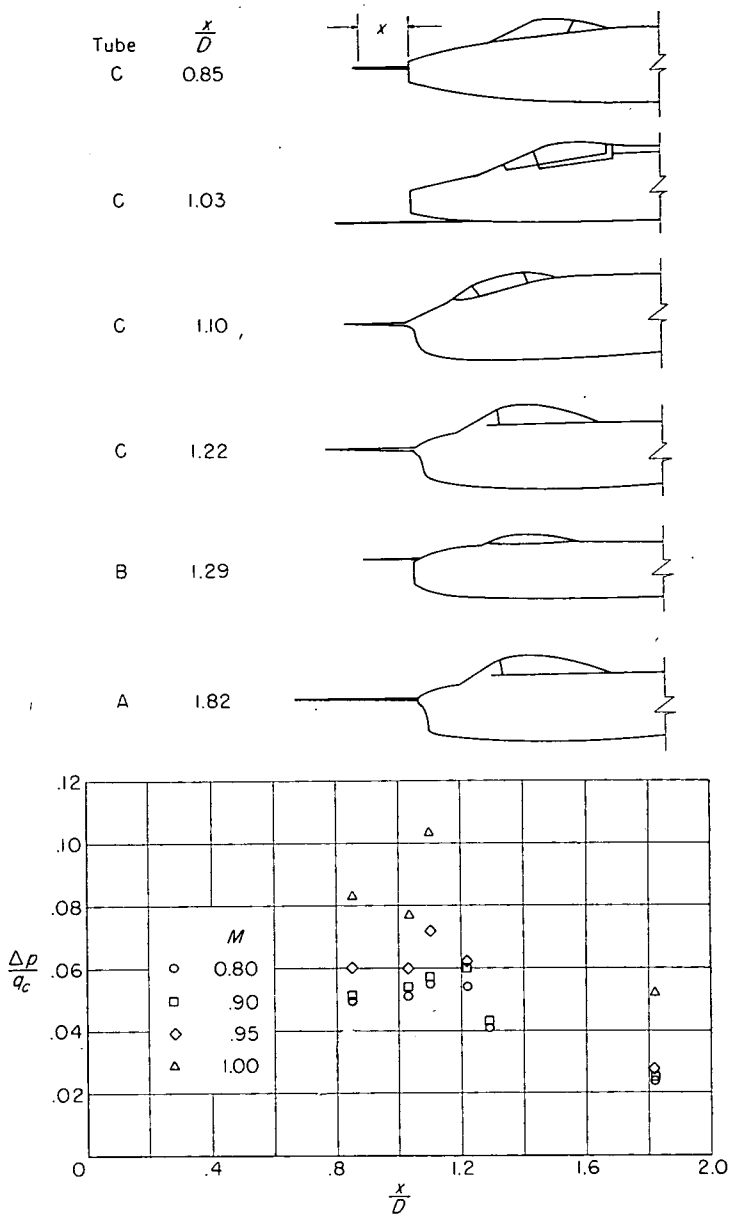


FIGURE 27.—Static-pressure errors ahead of six airplane fuselages with nose inlets.

them from the pressure field of the wing. At this Mach number, the pressure at the orifices is influenced by the negative pressures around the rear portion of the fuselage nose, the effect of which extends outward along Mach lines from the surface of the fuselage. As the Mach number increases, the Mach lines slant backward, and the orifices come under the influence of the positive pressures around the forward portion of the fuselage nose and behind the fuselage bow wave. At some higher Mach number, the fuselage bow wave will traverse the orifices, which will then be isolated from the flow fields of both wing and fuselage. At this and all higher Mach numbers, the static-pressure error will, in the absence of any boundary-layer—shock interaction, be that of the tube itself. It should be noted that, when the wing or fuselage bow shock is in the vicinity of the static-pressure orifices, the static-pressure error may vary considerably with angle of sideslip. For this reason a wing-tip installation at $M>1.0$ is much more sensitive to angle of sideslip than a fuselage-nose installation.

Effect of angle of attack (unswept wings).—The variation

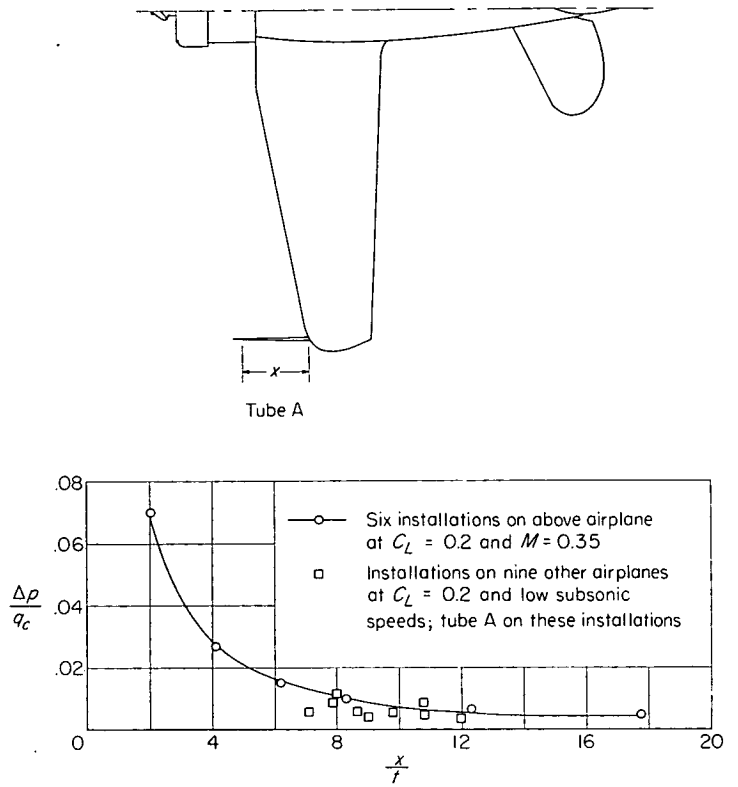


FIGURE 28.—Static-pressure errors at various distances ahead of the wing tips of unswept-wing airplanes (ref. 22).

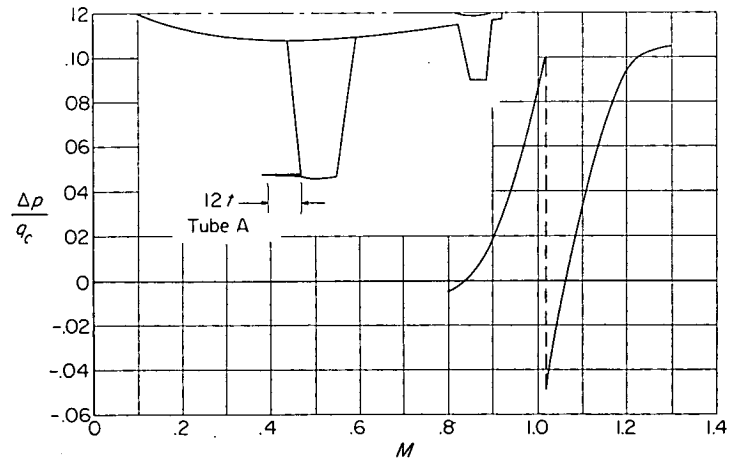


FIGURE 29.—Calibration in level flight of a static-pressure tube ahead of the wing tip of an unswept-wing airplane (ref. 24).

of static-pressure error with lift coefficient at low subsonic Mach numbers (0.1 to 0.36) for various distances ahead of the wing tip of an unswept-wing airplane (ref. 22) is given in figure 31. These data show that, for lift coefficients up to 0.7, the effect of angle of attack is small for distances of x/t=4.2 or greater. At higher lift coefficients, however, the effect of angle of attack is appreciable even for values of x/t as large as 16.8.

The effect of angle of attack on the static-pressure errors of a wing-tip installation with x/t=4.1 (ref. 27) at higher subsonic speeds (up to M=0.80) is presented in figure 32. For the range of C_L covered by the tests, the curves show that, at Mach numbers between 0.30 and 0.60, the static-pressure error decreases with lift coefficient. At M=0.70, the effect of angle of attack is negligible, and with increasing

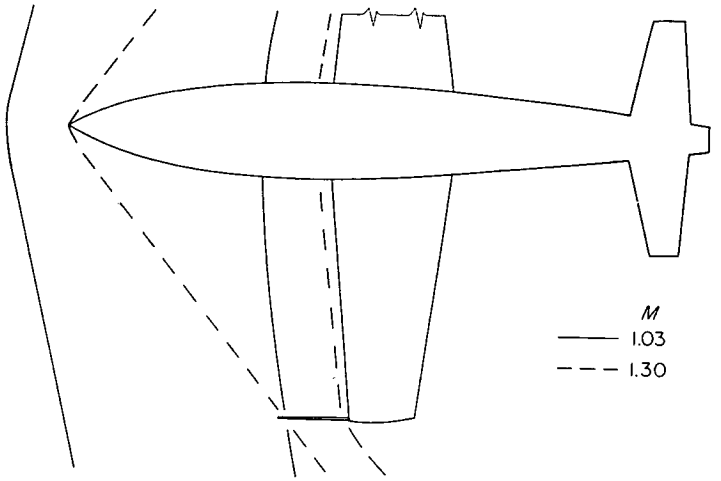


FIGURE 30.—Diagram showing position of shock waves with respect to a wing-tip installation on an unswept-wing airplane.

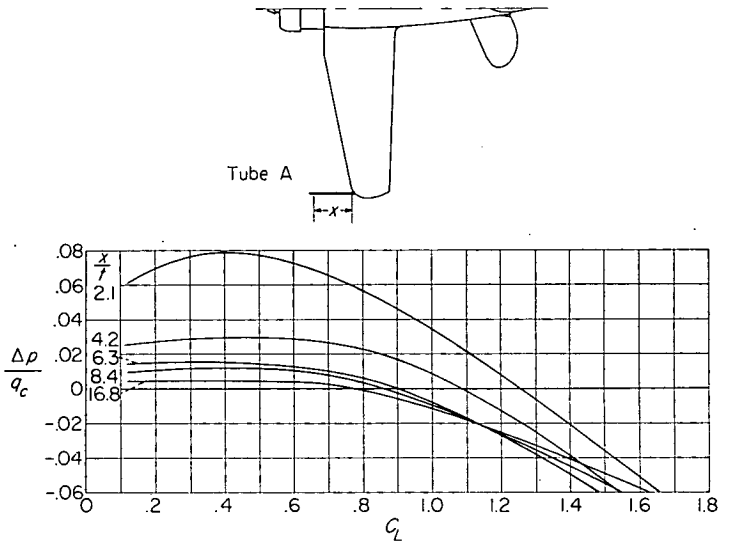


FIGURE 31.—Variation of static-pressure error with lift coefficient at five distances ahead of the wing tip of an unswept-wing airplane. M= 0.1 to 0.36 (ref. 22).

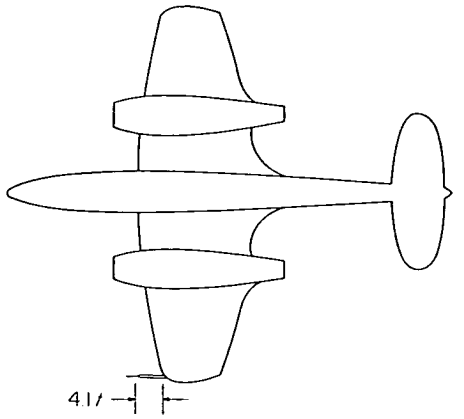
Mach number (up to M=0.80), the static-pressure error increases with lift coefficient.

Effect of Mach number (swept wings).—Calibrations of static-pressure tubes ahead of the wing tips of two swept-wing airplanes (refs. 28 and 29) are presented in figure 33. In one case the static-pressure tube was located 16t ahead of a 35° swept wing; in the other the tube was located 8.4t ahead of a 40° swept wing. The calibrations of these installations differ from those of wing-tip installations on unswept wings in that the static-pressure errors do not drop abruptly after the peak error is reached, but decrease toward zero at a more gradual rate.

Effect of angle of attack (swept wings).—The variation of static-pressure error with normal-force coefficient for a wing-tip installation on a swept-wing airplane at transonic speeds (ref. 28) is presented in figure 34. These data show that at M=0.75 to 0.90 the static-pressure errors increase with angle of attack as in the case of the unswept-wing installation at M=0.75 to 0.80 (fig. 32).

STATIC-PRESSURE ERRORS AHEAD OF VERTICAL TAIL FIN

Calibrations at transonic speeds of static-pressure tubes



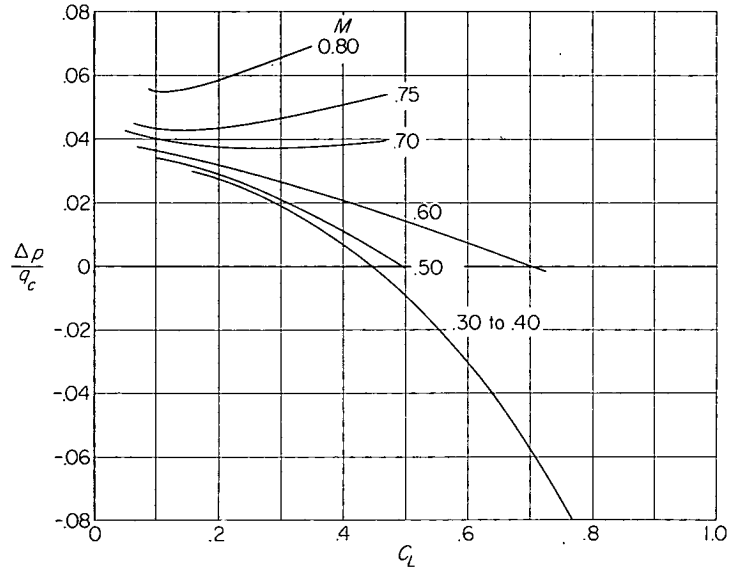
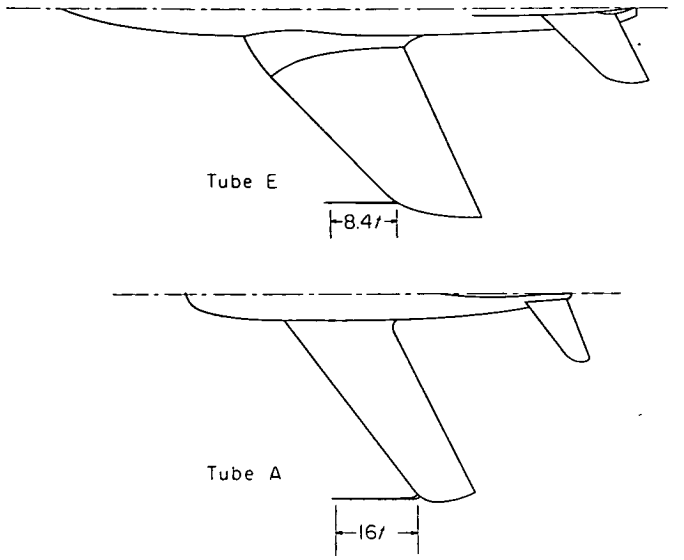


FIGURE 32.—Variation of static-pressure error with lift coefficient for a wing-tip installation on an unswept-wing airplane (ref. 27).



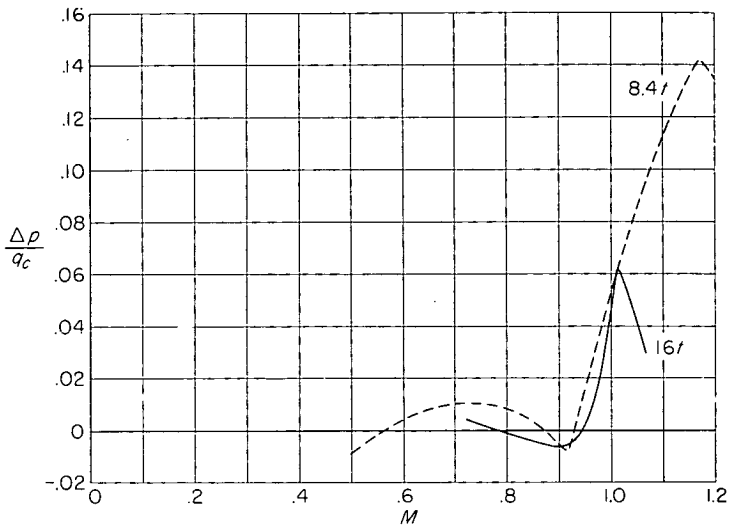


FIGURE 33.—Calibration in level flight of wing-tip installations on two swept-wing airplanes (refs. 28 and 29).

ahead of the tip of the vertical tail fins of two free-flight models are given in figure 35. One of these was a free-fall model of a canard airplane with the static-pressure orifices located 13.5t ahead of the tail fin. The other was a rocket-propelled model of an airplane configuration with the orifices 16.7t ahead of the tail fin. Although the magnitudes of the errors of both the installations are open to question (because of uncertainties in the telemetered measurements), the curves may be accepted as an approximate indication of the type of static-pressure-error variation to be expected for a vertical-tail-fin installation in the transonic speed range.

STATIC-PRESSURE ERRORS OF VENTS ON FUSELAGE (MODELS)

For the purpose of locating a fuselage static-pressure vent, the fuselage may, in a very general way, be likened to a static-pressure tube. As with the static-pressure tube, the pressure at a fuselage vent at zero angle of attack is determined by the axial location of the orifice along the body. The pressure at a given point on the body may, of course, be modified by the blocking effect or the wake of any protuberances extending from the body. At angles of attack other than 0°, the pressure at a fuselage vent is, as with the static-pressure tube, determined by the circumferential orientation of the orifice.

Static-pressure vents have generally been located on opposite sides of the fuselage in order to minimize angle-of-sideslip effects. Calibrations, at angles of sideslip, of a vent installation in which two vents were located at approximately ±67° from the bottom of a circular fuselage are reported in reference 30. The results showed that at an angle of sideslip of 4°, the maximum angle reached in the tests, the static-pressure error varied by 0.2 percent of q_c from the value at zero angle of sideslip. When the cross section of the fuselage is circular, the orifices may also be located at approximately ±30° from the bottom of the body to minimize angle-of-attack effects.

Because of the complex nature of the pressure distribution along the fuselage of an airplane, it is difficult to predict, with any degree of certainty, those locations where the static-pressure error will be minimum. It is customary, therefore, to make pressure-distribution tests in a wind tunnel with a detailed replica of the airplane, and to choose from the results a number of locations that appear promising for static-pressure vents. These locations are then calibrated on the full-scale airplane and the best location is chosen for the operational installation. In reference 31, the calibrations of fuselage-vent installations on a number of airplanes are

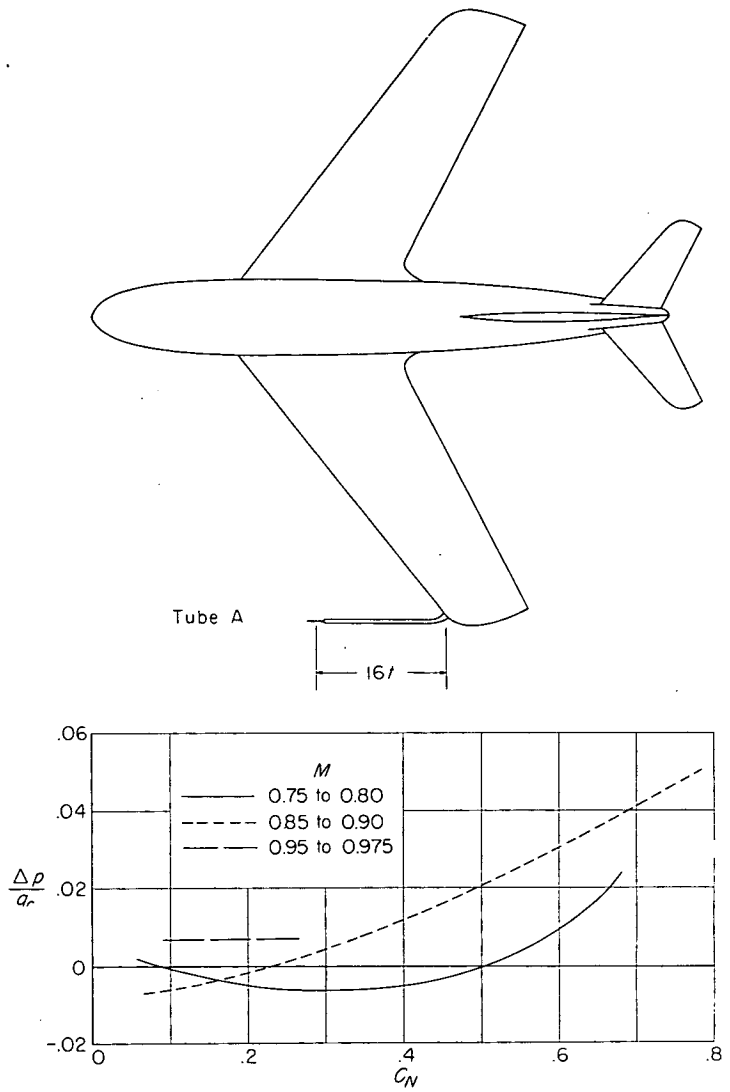


FIGURE 34.—Variation of static-pressure error with normal-force coefficient for a wing-tip installation on a swept-wing airplane (ref. 28).

compared with comparable installations on wind-tunnel models of these airplanes. For the low speeds at which these tests were conducted (below 175 knots), the results showed that the errors of the airplane installations could be predicted from the model tests to within ±2 percent of q_c.

Effect of axial location of vents.—Pressure-distribution studies of a body of revolution (ref. 32) provide a generalized indication of the pressure variation which might be expected along the fuselage of an airplane or missile. Sample results of these tests, which were conducted with a body of revolution with a fineness ratio of 12 at transonic speeds and at $\alpha=0°$, are presented in figure 36. These curves show that for any given Mach number there are at least two axial locations, one on the forward portion and the other on the rearward portion of the fuselage, where the static-pressure error equals zero. It is evident, however, that these axial locations vary appreciably with Mach number.

Pressure-distribution tests of prolate spheroids (with aspect ratios of 6 and 10) and of a typical transonic body are reported in reference 33. In these tests the pressures over the forward half of the bodies were measured at $M=0.3$ to 0.95 and at $\alpha=0°$ to 7.7°.

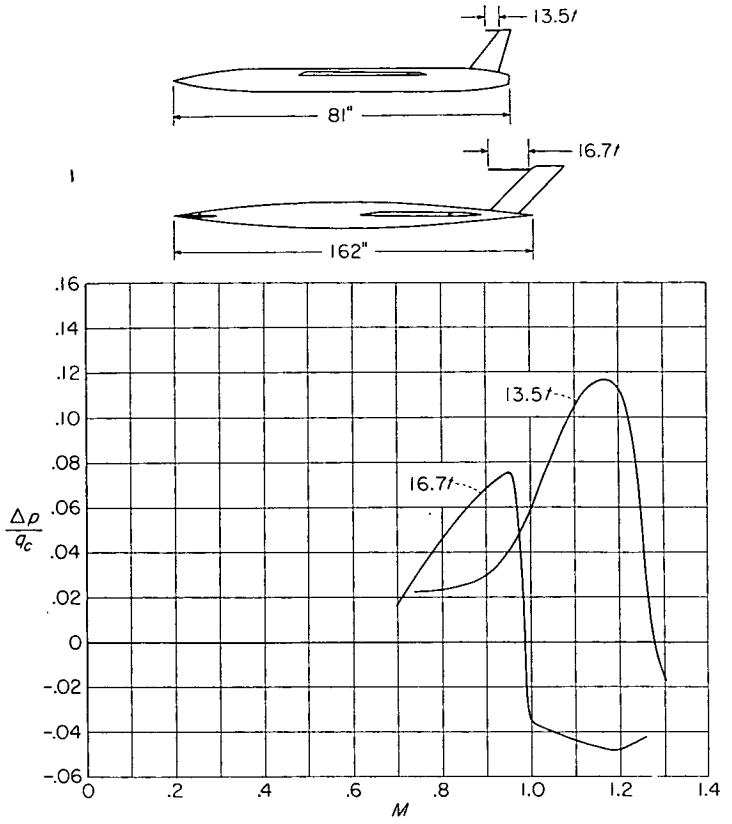


FIGURE 35.—Calibrations of vertical-tail-fin installations on free-flight models.

Effect of Mach number.—The variation with Mach number of the static-pressure error of orifices at three axial locations along a body of revolution (ref. 32) is given in figure 37. These curves show that the magnitude and variation of static-pressure error change considerably along the body. In contrast to most of the static-pressure-tube installations, the variation of static-pressure error with Mach number for these vent installations is comparatively irregular. These variations, it must be remembered, apply to a simple body without protuberances of any kind. For an actual flight vehicle with wings, tail surfaces, external stores, and so forth, the pressure variation with Mach number can be expected to be much more complex.

The calibration of a vent on the cylindrical portion of the fuselage of a rocket-propelled model of an aircraft configuration at transonic and supersonic speeds is presented in figure 38. The single orifice was located on the top of the fuselage at 0.28 of the fuselage length behind the nose.

Effect of circumferential location of vents.—The possibility of minimizing the effect of angle of attack by properly locating the orifices around the circumference of a fuselage was investigated in reference 34. This study was based on tests with a body of revolution of fineness ratio 12.2 at $M=1.59$ and at angles of attack up to 36° (ref. 35). In this investigation (ref. 35) complete circumferential pressure distributions were obtained with orifices located at 12 stations along the body. The circumferential pressure distribution for an orifice located at the maximum-diameter station is given in figure 39 as a typical example of the results obtained. From these curves it would appear that the optimum location for static-pressure vents at this station would be about ±40° from the bottom of the body.

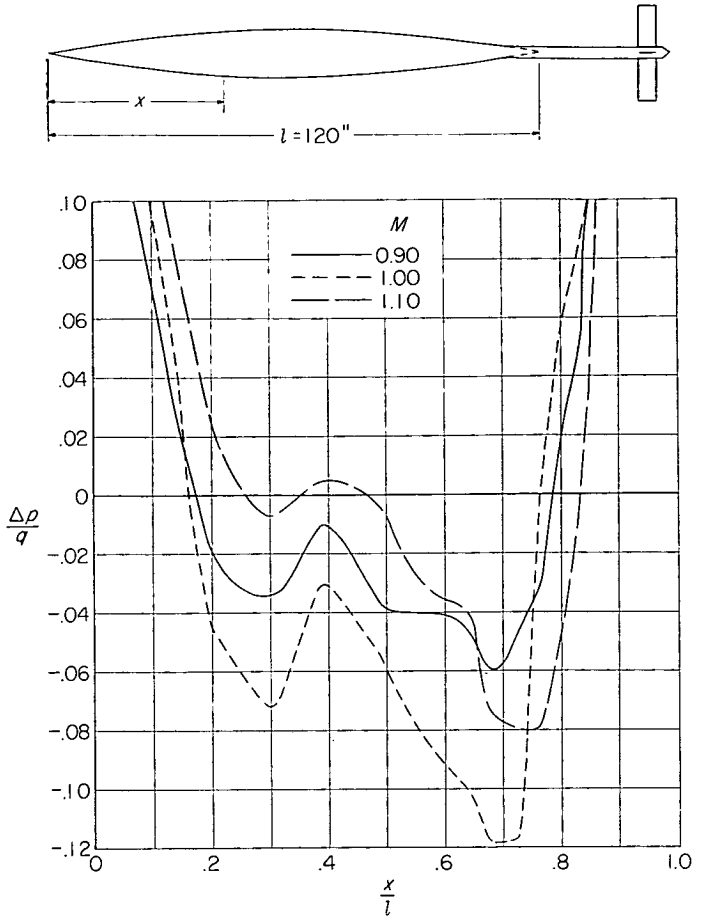


FIGURE 36.—Pressure distribution along a body of revolution at $\alpha=0°$ (ref. 32).

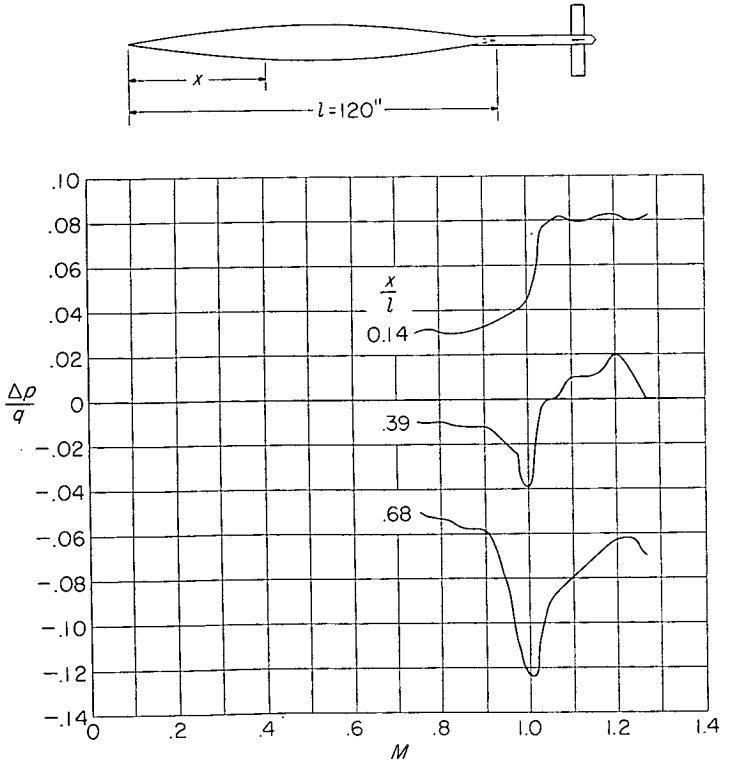


FIGURE 37.—Calibrations of orifices at three positions along a body of revolution at $\alpha=0°$ (ref. 32).

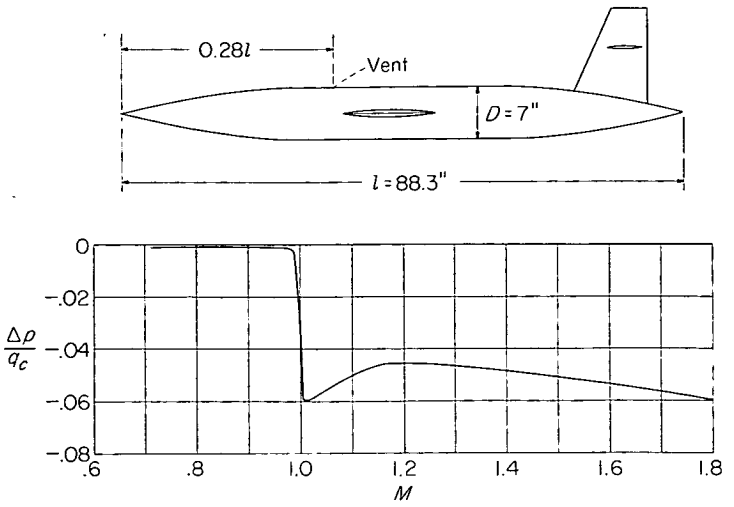


FIGURE 38.—Calibration of an orifice on a free-flight model.

For this orientation of the orifices, the static-pressure error remains within about ½ percent of q of the value at $\alpha=0°$ (-3 percent of q) for angles of attack up to 20°. For the other axial locations tested, the optimum circumferential location and the range of angle of attack over which the error remained small differed from those at the maximum-diameter station.

STATIC-PRESSURE ERRORS OF VENTS ON FUSELAGE (AIRPLANE)

An example of the type of calibration which may be expected for a static-pressure-vent installation at transonic speeds (ref. 28) is given in figure 40(a). The static-pressure vents of this installation were on each side of the nose of a jet fighter with a nose inlet and 35° swept wings. The calibration of this installation showed the static-pressure error to change abruptly at a Mach number of about 0.98. This abrupt change is believed to be caused by passage of shock waves, which form in the local supersonic flow field around the nose of the fuselage, over the vents. The fact that the variations occur over a range of Mach number (0.97 to 0.99) is probably due to asymmetry of the shock waves on each side of the fuselage which results from variations in angle of sideslip.

The effect of angle of attack on a fuselage vent (ref. 28) is shown in figure 40(b). At a Mach number of 0.75, the error begins to vary with normal-force coefficient at values of C_N above 0.3. At the higher Mach numbers ($M=0.95$) the effect of normal-force coefficient becomes evident at values of C_N below 0.1. In comparison with the data of fuselage-nose and wing-tip boom systems on the same airplane (ref. 28), the fuselage-vent installation was shown to be affected to a much greater extent by angle of attack.

VENT CONFIGURATION

The pressure registered by a fuselage static-pressure vent depends not only on its location on the fuselage but also on any protuberances or skin-contour variations in the vicinity of the orifice. The error of a vent installed on a pressurized fuselage may also change if the skin on which the vent is mounted flexes with pressurization.

Model tests of the effect of protuberances in the vicinity of a vent, waviness of the skin, and proximity of rivets are reported in reference 36. The results of these tests showed

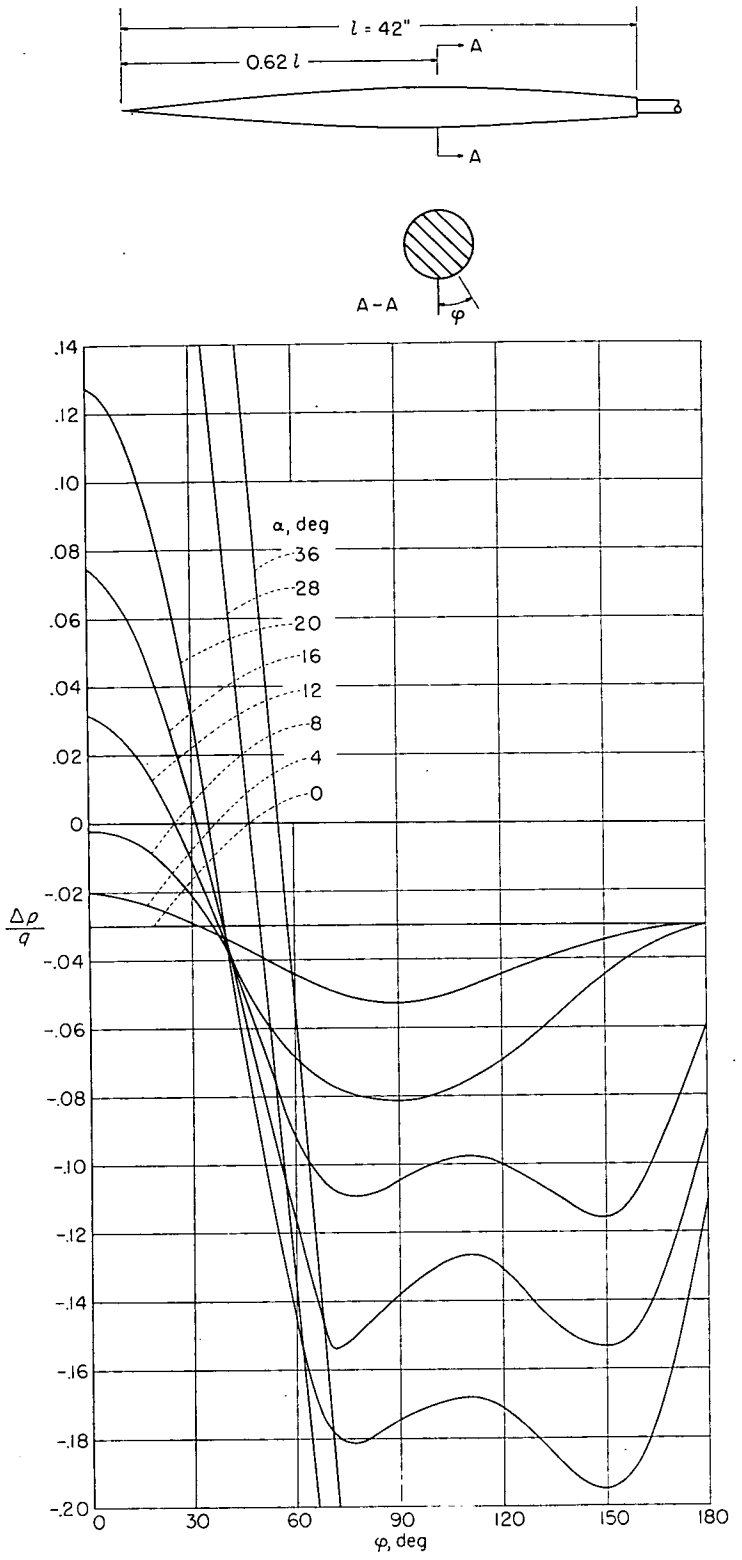
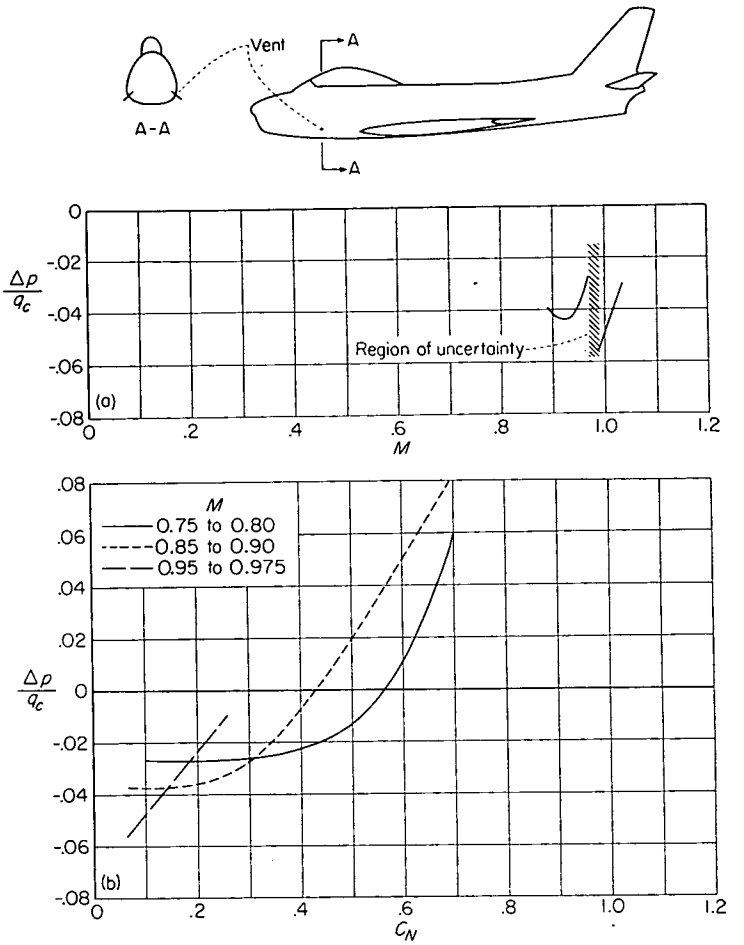


FIGURE 39.—Variation of the circumferential pressure distribution with angle of attack at the maximum diameter of a body of revolution at $M=1.59$ (ref. 35).

that relatively small imperfections in the surface surrounding the orifice can produce sizable changes in the position error. Sample data showing the effect of protuberances and skin waviness on the pressure of a 0.23-inch-diameter orifice at a speed of 175 knots are presented in figure 41.

For some fuselage-vent installations, specially designed protuberances have been installed near the vents in an attempt to compensate for the position errors at the vent location. Tests of several types of protuberances and indentations intended as aerodynamic compensators for fuselage vents are reported in reference 37.



(a) Variation of static-pressure error with Mach number.
(b) Variation of static-pressure error with normal-force coefficient.

FIGURE 40.—Calibration of a static-pressure vent on an airplane fuselage (ref. 28).

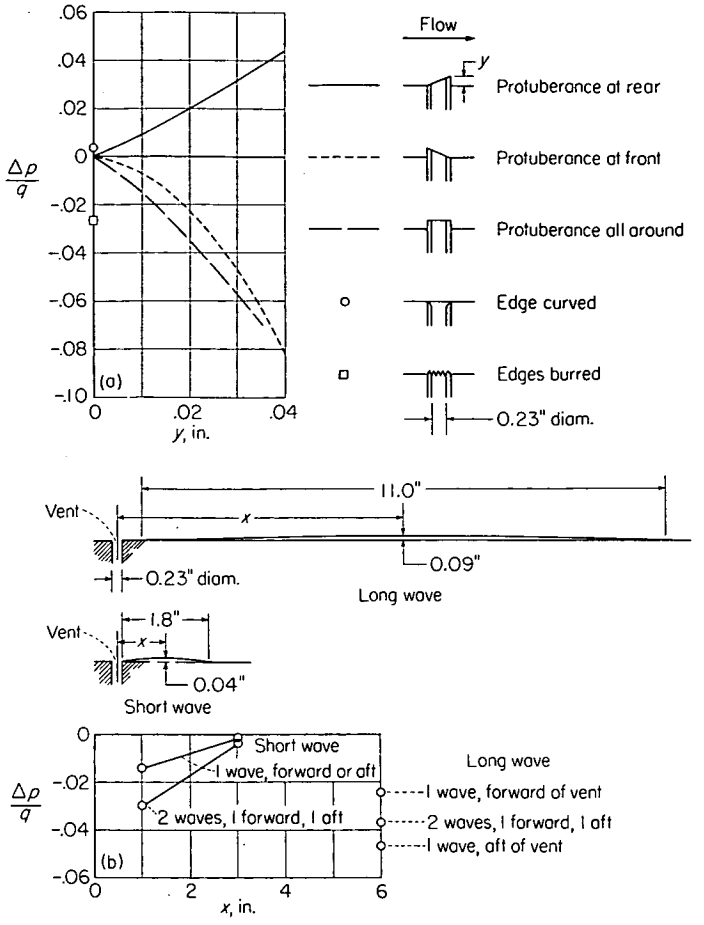
CONVERSION FACTORS

The static-pressure errors in this report have in most cases been expressed as a fraction of the impact pressure q_c. The errors are sometimes expressed in other nondimensional forms such as $\Delta p/p$ or $\Delta M/M$. For the convenience of the reader, a chart for converting $\Delta p/q_c$ to $\Delta p/p$ is given in figure 42. Charts from reference 38 for converting $\Delta p/q_c$ and $\Delta p/p$ to $\Delta M/M$ are presented in figure 43.

COMPARISON OF INSTALLATIONS

As stated earlier, the choice of type and location of the static-pressure tube or vent depends on a number of factors. If the magnitude of the static-pressure error is the prime consideration, the selection will depend largely on the configuration of the aircraft and the speed range through which it is expected to operate.

A comparison of the calibrations of the various installations presented in this report indicates that, for an airplane designed to fly at supersonic speeds, a static-pressure tube located ahead of the fuselage nose will, in general, be the most desirable installation. This selection is based on the fact that the calibration has only one discontinuity (when the



(a) Effect of protuberances and indentations.
(b) Effect of waviness of skin in vicinity of vent.

FIGURE 41.—Variation of static-pressure error with configuration of static-pressure vents at a speed of 175 knots (ref. 36).

fuselage bow wave passes the orifices) and that at higher supersonic speeds the error will, for the usual case, be that of the isolated tube. In addition, the sensitivity of this installation to angle of sideslip at supersonic speeds will be that of the isolated tube. At subsonic and transonic speeds, the errors at a given distance ahead of the nose (in terms of fuselage diameters) depends on the shape of the nose section. As these errors decrease with increasing fineness ratio of the nose section, the static-pressure error of an installation ahead of a fuselage with a long pointed nose will be comparatively small throughout the speed range. An illustration of this fact may be seen from the calibration in figure 22. For installations ahead of blunter fuselage-nose sections, the errors at subsonic and transonic speeds will be considerably higher.

If the operating range of the airplane is confined to speeds below sonic, a static-pressure tube ahead of the wing tip may, for some airplane configurations, prove more satisfactory than a fuselage-nose installation. At equal distances ahead of the wing and fuselage nose, for example, the static-pressure error (at subsonic speeds) of the wing-tip installation will ordinarily be smaller than that of the fuselage-nose installation. The relative magnitudes of the errors of the two installations will, of course, depend on the relative values of the wing thickness and fuselage diameter and on the shape of the fuselage-nose section.

At speeds above sonic, a wing-tip installation will generally be less desirable than a fuselage-nose installation because of

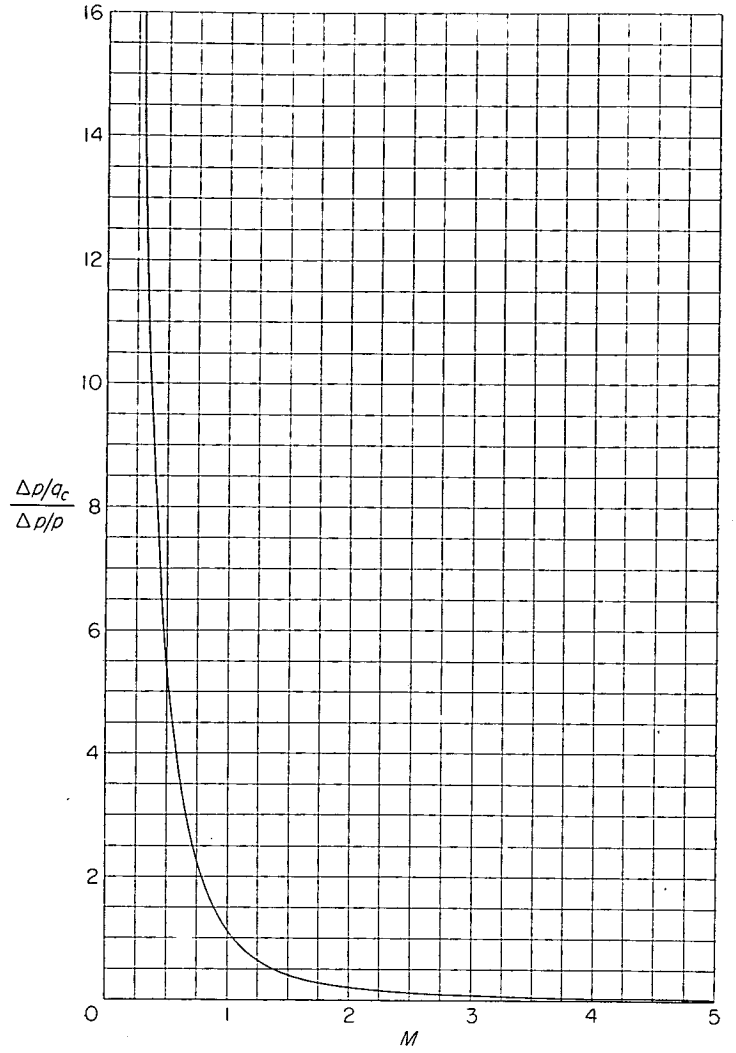


FIGURE 42.—Chart for converting $\Delta p/q_c$ to $\Delta p/p$ (based on calculations in ref. 38).

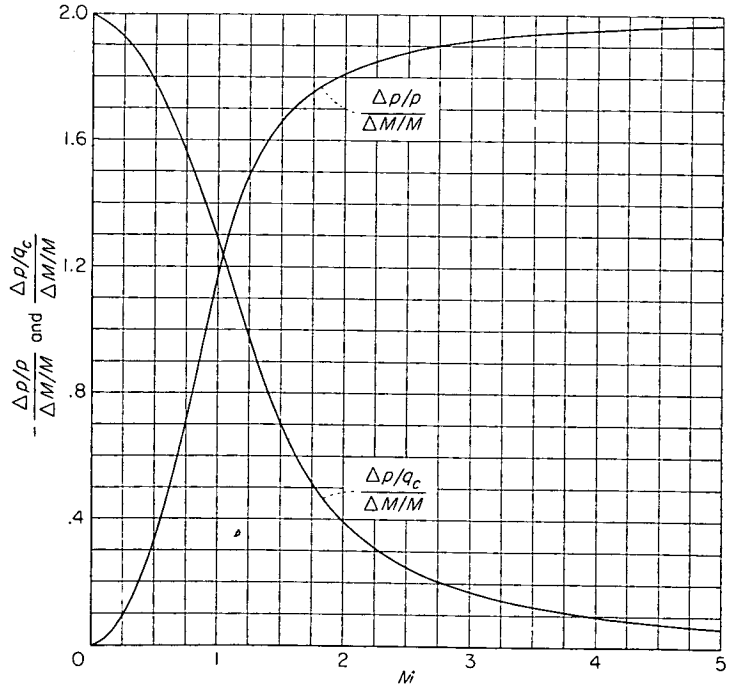


FIGURE 43.—Chart for converting $\Delta p/q_c$ or $\Delta p/p$ to $\Delta M/M$. A $M>1$ the value of q_c includes loss through normal shock (ref. 38)

the relatively high sensitivity of the wing-tip installation to angle of sideslip, particularly at the Mach numbers at which the wing or fuselage shock waves are near the static-pressure orifices. In addition, the calibrations of wing-tip installations at supersonic speeds are more difficult to apply because of the two discontinuities which occur when the wing and fuselage bow waves pass the orifices.

For operation in the subsonic speed range, a static-pressure-tube installation ahead of a vertical tail fin may, for some configurations, offer certain advantages. In comparison with a wing-tip installation, for example, the thinner sections of vertical tail fins permit the use of shorter booms to achieve an equivalent static-pressure error. Because of the complex nature of the shock waves which form on the wing and fuselage, however, it would appear advisable to limit the use of vertical-tail-fin installations to Mach numbers below approximately 0.8.

Subsonic calibrations of numerous fuselage-vent installations on airplanes (not included in this report) have demonstrated that acceptable static-pressure errors can be obtained through a Mach number range up to about 0.8. The model tests presented in figure 37, however, showed irregular variations of static-pressure error with Mach number at transonic speeds. Furthermore, if the vents are near the fuselage nose, the static-pressure errors, as shown in figure 40, are apt to fluctuate erratically because of variations in angle of sideslip. It may be concluded, therefore, that fuselage vents, properly located and installed, may provide satisfactory calibrations at subsonic speeds up to $M=0.8$.

FLIGHT CALIBRATION METHODS

The calibration of an airspeed installation is usually accomplished by determining the errors in the pitot and static systems independently. The pitot system can be calibrated quite simply by comparison with a free-swiveling total-pressure tube or a shielded tube (of the type described in ref. 2) installed on the test airplane. The total-pressure error of the system being calibrated can be determined with a high degree of accuracy, since the difference between the total pressures of the two tubes can be measured directly with a differential pressure indicator or recorder.

The calibration of the static-pressure system may be performed by any one of a number of methods of varying degrees of complexity and accuracy. The choice of the calibration method will, in general, depend on the instrumentation available, the accuracy required, and the ranges of speed and lift coefficient over which the airplane is to be calibrated. As the procedure and instrumentation of most of the methods are quite involved, only a general description of each of the methods will be given here. Detailed information may be obtained by reference to the original reports.

SPEED-COURSE METHOD

In the speed-course method, the true airspeed of the airplane is determined by measuring the time required for the airplane to fly at constant speed and constant altitude between two landmarks (ref. 39). The effects of winds must be accounted for either by direct measurement or by elimination (by flying a triangular course or by flying in opposite directions along a straight-line course). The static-pressure error is determined by comparing the measured indicated airspeed with the correct indicated airspeed (as computed from the measured true speed). The method is limited to speeds above the stall region and to the maximum speed of the airplane in level flight. The accuracy of the method is largely dependent on the accuracy of the measurement of time, the constancy of the wind speed, and the degree to which constant airspeed is maintained throughout the test.

TRAILING-STATIC-PRESSURE-TUBE METHOD

The static pressure of the static-pressure installation is compared directly with free-stream static pressure as measured by a static-pressure tube suspended on a long cable below the airplane (ref. 40). The cable must, of course, be long enough to place the trailing tube at a distance below the airplane where the pressure is approximately ambient. In reference 40, it was shown that the cable length should be approximately 1½ to 2 wing spans. The advantage of this calibration method is that the calibration can be conducted at altitude and at speeds down to the stall. The maximum speed at which the tests may be conducted is limited by the speed at which the trailing tube encounters instability. The unstable motions of the towed body which develop above this limiting airspeed have been attributed to cable oscillations which originate near the airplane and are amplified by aerodynamic forces as they travel down the cable (ref. 41). Simple trailing tubes which depend on the weight of the body to keep them below the airplane have a maximum usable speed of approximately $M=0.4$. A more complex trailing tube with wings set at a negative angle of incidence to keep it below the airplane has been towed to a Mach number of 0.85 (ref. 27). The accuracy which can be achieved by this method is relatively high because the difference between the system and free-stream pressures can be measured directly with a differential pressure instrument.

ANEROID METHOD

Basically, the aneroid method consists in measuring the static pressure developed by the static-pressure system of the airplane at a known height and measuring the free-stream static pressure at the same height. The static-pressure error of the installation is then determined as the difference between these two pressures. The pressure developed by the static-pressure tube may be measured either with an absolute-pressure gage or with an altimeter. The measurement of the reference height and of the free-stream static pressure at this height may be accomplished by any one of a variety of methods to be described.

Reference landmark.—The simplest form of the aneroid method is that in which the reference height is established as the top of a tall tower or building of known height (ref. 42). The free-stream static pressure at the reference height may be determined directly with an absolute-pressure gage or altimeter located at the top of the landmark. This measurement may also be determined by measuring the atmospheric pressure and temperature at the ground and computing the pressure at the reference height on the basis of the standard lapse rate. The flight calibration procedure consists in measuring the static pressure of the airplane installation as the airplane flies past the landmark in level flight at constant

speed. Any deviations in the height of the airplane above or below the reference height may be determined either by visual observation or by photographing the airplane from the landmark. The speed range of the calibration is limited to speeds above the stall and below the maximum level-flight speed of the airplane. Because of the ease and precision with which the reference height and the free-stream static pressure can be measured, the static-pressure error of the installation may be determined with a relatively high degree of accuracy. The principal disadvantages of this method are the fact that the calibration is limited to level-flight speeds and the hazards involved in flying the airplane near the ground.

Photographic.—The height of the airplane may be determined either by photographing the airplane as it passes over a camera directed vertically upward from the ground or by photographing reference landmarks on the ground with a camera pointed vertically downward from the airplane. In either case, the height of the airplane is calculated from the focal length of the camera and a comparison of the size of the image on the film with the true dimensions of the object. For accurate measurements, corrections must be applied for any deviations of the airplane from zero angle of bank. The free-stream static pressure at the reference height is computed by using the standard lapse rate and measurements of pressure and temperature at the ground. Because the accuracy of the determination of free-stream static pressure by means of these computations decreases as the altitude of the airplane is increased, it may be advisable in some cases to determine the stream pressure by flying the airplane at a speed for which the installation has been previously calibrated by another method, for example, the reference-landmark method.

The calibration procedure consists in flying the airplane at constant speed and altitude over the ground station. Although the speed range of the calibration is the same as that of the reference-landmark method, this method is less hazardous because the tests can be conducted at higher altitudes. In one application of this method, satisfactory calibrations have been made at heights of 300 to 800 feet (ref. 43). An attempt to use the method at much higher altitudes (25,000 to 30,000 feet) did not prove very successful (ref. 44).

Geometric.—In the first of two forms of the geometric method (described in ref. 45), the height of the airplane is determined by flying the airplane at constant speed and altitude over a predetermined ground course such as a line down a runway, and in measuring the elevation angle of the airplane from a ground station that is a known distance from the ground course. For best results, the distance of the ground station from the ground course should be about the same as the height at which the airplane is expected to fly. The elevation angle of the airplane may be determined with either a visual indicator (sighting stand of ref. 45) or a phototheodolite. Lateral deviations of the flight path of the airplane from the ground course must be estimated and corrected.

A second, and more accurate, form of this method involves the determination of the elevation angle of the airplane from two ground stations located a known distance apart and preferably an equal distance on each side of the ground course (ref. 45). This method has an advantage in that the flight path of the airplane may deviate from the ground course without affecting the accuracy of the height measurement. In either of these methods the free-stream static pressure at the reference height is calculated by using the standard lapse rate and measurements of pressure and temperature at some reference point on the ground, or it is measured by flying the airplane at a speed for which the calibration has been determined by other means.

Reference airplane.—The reference height may be established by another airplane flying at a low and constant speed and at constant pressure altitude (refs. 42 and 46). The static-pressure system of the reference airplane must have been previously calibrated for the speed at which it is flown in order to determine the free-stream static pressure at the reference height. The test airplane is then flown at a series of constant speeds past the reference airplane. Corrections for any differences between the height of the two airplanes can be determined most accurately by photographing the test airplane as it flies past the reference airplane.

Radar phototheodolite.—In another form of the aneroid method, the height of the airplane is calculated from the slant range and elevation angle of the airplane as measured by a radar-phototheodolite assembly located at a ground station (ref. 38). The radar antenna is directed at the test airplane by a separate optical tracking unit operated through a servosystem. The radar-phototheodolite assembly consists of a radar unit which has been modified by the addition of (1) an elevation scale on the radar antenna and a camera to photograph this scale and (2) a camera with a long-focal-length lens mounted at the center of, and boresighted with, the radar antenna. The scale camera provides a measure of the elevation angle of the optical axis of the antenna camera, and the antenna camera provides a means of correcting for any deviations of the position of the airplane from the optical axis of the antenna camera. A third camera is installed in the radar unit to photograph the range scope. The three cameras, together with the pressure-recording instruments in the airplane, are all synchronized by means of radio time signals transmitted from the airplane.

As this method permits calibrations of the airplane in dives and maneuvers as well as in level flight, the tests are usually conducted over a range of altitude. The free-stream static pressure at the reference altitudes must, therefore, be determined by measuring the variation of pressure with height over the test altitude range. This variation of pressure with height may be determined by any of the following methods:

(1) The test airplane is tracked by the radar phototheodolite as the airplane climbs through the test altitude range at a low, constant speed for which the static-pressure error has been determined by other means. The airplane is then flown through the same atmosphere at the higher speeds at which the installation is to be calibrated. For best results it is advisable to repeat the survey after the calibration runs have been made.

(2) For cases in which the airplane cannot be flown through the test altitude range at flight conditions (Mach number and lift coefficient) for which the calibration is known, the free-stream static pressure at one height (as

measured by the radar phototheodolite) is first determined for one flight condition for which the static-pressure error is known (ref. 47). The airplane is then tracked by radar at other speeds through the test altitude range. From measurements of temperature and pressure during this ascent, the pressure p_2 at any given height h_2 may be determined by means of the following equation:

$$\left(\frac{p_2}{p_1}\right)^n = 1 - n\int_{h_1}^{h_2}\left(\frac{p'}{p_1}\right)^{n}\frac{1+\frac{\gamma-1}{2}K(M')^2}{RT'}\,dh \qquad (1)$$

where p_1 is the free-stream pressure at the start of the test (at altitude h_1), p' and T' are the measured pressure and temperature at altitude h, and M' is the Mach number determined from the measured total pressure and the static pressure p'. The value of n depends on the temperature recovery factor K of the thermometer and on the Mach number. For $K=1$, a value of n of $\frac{\gamma-1}{\gamma}$ (or 0.286) gives satisfactory results at subsonic and low supersonic speeds. Computations of n for other values of K and M are given in reference 47.

(3) A radiosonde transmitting pressure measurements is tracked by the radar phototheodolite through the test altitude range. Although this method appears attractive because of its simplicity, calibration tests have shown that the radiosonde measurements are not sufficiently accurate to establish the static-pressure error of an installation to the accuracy required for most research tests.

(4) The variation of pressure with height at the test altitudes is computed from measurements of temperature and pressure transmitted from a radiosonde. The height at any given pressure level may be computed from the equation

$$h = -\int_0^h \frac{RT}{p}\,dp \qquad (2)$$

where p and T are simultaneous radiosonde measurements. This equation indicates that an error in static pressure results in an error in altitude of opposite sign. Therefore, in a plot of pressure against altitude, the error in altitude tends to compensate for the error in static pressure. As a consequence, the variation of static pressure with altitude obtained by this method will be closer to the actual variation than that obtained when the static pressure is measured by by the radiosonde and the height of the radiosonde is measured by a radar theodolite.

Radio altimeter.—The reference height is determined by means of a radio altimeter installed in the airplane (ref. 48). The variation of free-stream static pressure with height is first determined by flying the airplane through the test altitude range at a low constant speed for which the static-pressure error is known. The calibration tests are then performed through the same atmosphere, the height of the airplane being measured by the radio altimeter.

Like the radar-phototheodolite method, this method allows the calibrations to be conducted at high altitude. The instrumentation required for this method, however, is much simpler and has the advantage of being entirely contained within the airplane. The method has the disadvantage of requiring a level ground-reference plane, and thus it is restricted to flight over a large body of water. From the tests reported in reference 48, the accuracy of this method was found to be of the same order as that of the radar-phototheodolite method.

Accelerometer.—In the accelerometer method (ref. 47), the free-stream static pressure at a given height is determined by flying the airplane in level flight at a speed for which the static-pressure error has previously been determined by another method. The airplane is then flown in level flight or in vertical-plane maneuvers at the higher speeds for which a calibration is desired. From measurements of normal and longitudinal acceleration and the attitude angle of the airplane, a calculation is made of the vertical velocity which, when integrated, provides a measure of the change in height. The height increment is then combined with temperature measurements to determine the variation of free-stream static pressure with height during the calibration run. An evaluation of this method (ref. 47) as compared with the radar-phototheodolite method showed the accuracy of the two methods to be comparable.

RADAR-TEMPERATURE METHOD

In the radar-temperature method, the variation of ambient temperature with height is first determined by (1) tracking a radiosonde (transmitting temperature measurements) with a radar phototheodolite or (2) computing the height of the radiosonde from equation (2) using values of pressure and temperature transmitted from the radiosonde. The test airplane is then tracked by the theodolite as the airplane is flown through the atmosphere surveyed. During the calibration runs continuous measurements are made of the total temperature developed by a probe on the airplane. From a knowledge of the total temperature T' and the ambient temperature T at a given height, the true Mach number at this height may be determined from the equation

$$\frac{T'}{T} = 1 + 0.2KM^2 \qquad (3)$$

From a comparison of the true Mach number with the Mach number measured by the airplane installation at this height, the static-pressure error may be calculated.

TEMPERATURE METHOD

This method is based on the assumption that the temperature and pressure at a given point in the atmosphere remains unchanged over a short period of time. The method, as described in reference 49, consists in measuring the temperature, static pressure, and total pressure from the airplane as it is flown through the test altitude range at a speed for which the calibration is known. This survey establishes the relation between the ambient temperature and the free-stream static pressure. The airplane is then flown through the altitude range surveyed, and the same measurements are repeated. The values of the indicated temperature and total pressure at a given instant in the calibration run, together with the temperature recovery factor of the thermometer, define the relation between the ambient temperature and the indicated static pressure at that instant. From a comparison of this temperature with the temperature-pressure variation determined in the survey, the free-stream

static pressure at that instant is determined. The static-pressure error is then found as the difference between the indicated and free-stream static pressures. Although the instrumentation required for this method is comparatively simple, the measurement of temperature must be very precise. The accuracy which may be obtained with this method was determined in the tests reported in reference 50.

FORMATION-FLIGHT METHOD

In the formation-flight method, the test airplane is flown in formation with another airplane that has a calibrated airspeed system. The static-pressure error may be determined by comparing either the altimeter or the airspeed indicator readings of the two airplanes. If airspeed readings are compared, the errors, if any, in the total-pressure systems of the two airplanes must be taken into account. This method is limited to the altitude and speed capabilities of the reference airplane. An evaluation of the accuracy which may be achieved with this method at speeds between 200 and 400 knots is reported in reference 51.

CONCLUSIONS

From a comparison of the calibrations of four types of static-pressure-measuring installations (fuselage nose, wing-tip, vertical tail fin, and fuselage vent) the following conclusions may be drawn:

1. For an airplane designed to operate at supersonic speeds, a static-pressure tube located ahead of the fuselage nose will, in general, be the most desirable installation.

2. If the operating range is confined to speeds below sonic, a static-pressure tube located ahead of the wing tip may, for some airplane configurations, prove more satisfactory than a fuselage-nose installation.

3. For operation at Mach numbers below 0.8, a static-pressure tube ahead of the vertical tail fin or fuselage vents, properly located and installed, should prove satisfactory.

LANGLEY AERONAUTICAL LABORATORY,
NATIONAL ADVISORY COMMITTEE FOR AERONAUTICS,
LANGLEY FIELD, VA., *December 17, 1956.*

REFERENCES

1. Huston, Wilber B.: Accuracy of Airspeed Measurements and Flight Calibration Procedures. NACA Rep. 919, 1948. (Supersedes NACA TN 1605.)
2. Gracey, William: Wind-Tunnel Investigation of a Number of Total-Pressure Tubes at High Angles of Attack—Subsonic, Transonic, and Supersonic Speeds. NACA Rep. 1303, 1957. (Supersedes NACA TN 3641.)
3. Taback, Israel: The Response of Pressure Measuring Systems to Oscillating Pressures. NACA TN 1819, 1949.
4. Smith, Keith: Pressure Lag in Pipes With Special Reference to Aircraft Speed and Height Measurements. Rep. No. Aero 2507, British R.A.E., Nov. 1954.
5. Kumbruch, H.: Pitot-Static Tubes for Determining the Velocity of Air. NACA TM 303, 1925.
6. Lock, C. N. H., Knowler, A. E., and Pearcey, H. H.: The Effect of Compressibility on Static Heads. R. & M. No. 2386, British A.R.C., Jan. 1943.
7. Hasel, Lowell E., and Coletti, Donald E.: Investigation of Two Pitot-Static Tubes at Supersonic Speeds. NACA RM L8I02, 1948.
8. Walter, L. W., and Redman, E. J.: Needle Static-Pressure Probes Insensitive to Flow Inclination in Supersonic Air Streams. NAVORD Rep. 3694 (Aeroballistic Res. Rep. 231), U. S. Naval Ord. Lab. (White Oak, Md.), Mar. 15, 1954.
9. Holder, D. W., North, R. J., and Chinneck, A.: Experiments With Static Tubes in a Supersonic Airstream—Parts I and II. R. & M. No. 2782, British A.R.C., July 1950.
10. Hensley, Reece V.: Calibrations of Pitot-Static Tubes at High Speeds. NACA WR L-396, 1942. (Formerly NACA ACR, July 1942.)
11. Stivers, Louis S., Jr., and Adams, Charles N., Jr.: High-Speed Wind-Tunnel Investigation of the Effects of Compressibility on a Pitot-Static Tube. NACA RM A7F12, 1947.
12. Merriam, Kenneth G., and Spaulding, Ellis R.: Comparative Tests of Pitot-Static Tubes. NACA TN 546, 1935.
13. Bursnall, William J., and Loftin, Laurence K., Jr.: Experimental Investigation of the Pressure Distribution About a Yawed Circular Cylinder in the Critical Reynolds Number Range. NACA TN 2463, 1951.
14. Gowen, Forrest E., and Perkins, Edward W.: Drag of Circular Cylinders for a Wide Range of Reynolds Numbers and Mach Numbers. NACA TN 2960, 1953.
15. Smith, W. E.: Wind Tunnel Calibration of Two Static-Pressure Sensing Devices. Rep. No. AF-682-A-6 (WADC Contract No. AF 33(038)-10709), Cornell Aero. Lab., Inc., Dec. 1952.
16. Ziegler, Norman G.: Wind-Tunnel Calibration of the Given High-Speed Pitot-Static Probe at Mach Numbers of 1.57 and 1.88. Aero Data Rep. 33, David W. Taylor Model Basin, Navy Dept., Sept. 1955.
17. Gracey, William, and Scheithauer, Elwood F.: Flight Investigation at Large Angles of Attack of the Static-Pressure Errors of a Service Pitot-Static Tube Having a Modified Orifice Configuration. NACA TN 3159, 1954.
18. Pearson, Albin O., and Brown, Harold A.: Calibration of a Combined Pitot-Static Tube and Vane-Type Flow Angularity Indicator at Transonic Speeds and at Large Angles of Attack or Yaw. NACA RM L52F24, 1952.
19. Cooper, Morton, and Webster, Robert A.: The Use of an Uncalibrated Cone for Determination of Flow Angles and Mach Numbers at Supersonic Speeds. NACA TN 2190, 1951.
20. Rayle, Roy E., Jr.: An Investigation of the Influence of Orifice Geometry on Static Pressure Measurements. M. S. Thesis, M.I.T., 1949.
21. Letko, William: Investigation of the Fuselage Interference on a Pitot-Static Tube Extending Forward From the Nose of the Fuselage. NACA TN 1496, 1947.
22. Gracey, William, and Scheithauer, Elwood F.: Flight Investigation of the Variation of Static-Pressure Error of a Static-Pressure Tube With Distance Ahead of a Wing and a Fuselage. NACA TN 2311, 1951.
23. O'Bryan, Thomas C., Danforth, Edward C. B., and Johnston, J. Ford.: Error in Airspeed Measurement Due to the Static-Pressure Field Ahead of an Airplane at Transonic Speeds. NACA Rep. 1239, 1955. (Supersedes NACA RM's L9C25 by Danforth and Johnston, L50L28 by Danforth and O'Bryan, and L52A17 by O'Bryan.)
24. Goodman, Harold R., and Yancey, Roxanah B.: The Static-Pressure Error of Wing and Fuselage Airspeed Installations of the X-1 Airplanes in Transonic Flight. NACA RM L9G22, 1949.
25. Letko, William, and Danforth, Edward C. B., III: Theoretical Investigation at Subsonic Speeds of the Flow Ahead of a Slender Inclined Parabolic-Arc Body of Revolution and Correlation With Experimental Data Obtained at Low Speeds. NACA TN 3205, 1954.
26. Roe, M.: Position Error Calibration of Three Airspeed Systems on the F-86A Airplane Through the Transonic Speed Range and in Maneuvering Flight. Rep. No. NA-51-864, North American Aviation, Inc., Oct. 5, 1951.
27. Smith, K. W.: The Measurement of Position Error at High Speeds and Altitude by Means of a Trailing Static Head. C.P. No. 160, British A.R.C., 1954.

28. Thompson, Jim Rogers, Bray, Richard S., and Cooper, George E.: Flight Calibration of Four Airspeed Systems on a Swept-Wing Airplane at Mach Numbers up to 1.04 by the NACA Radar-Phototheodolite Method. NACA TN 3526, 1955. (Supersedes NACA RM A50H24.)
29. Andrews, D. R., and Nethaway, J. E.: Flight Measurements of the Pressure Errors of a Nose and a Wing Boom Airspeed System on a Swept-Wing Aircraft (Hunter, F. Mk. I) at Mach Numbers up to 1.2. Tech. Note No. Aero 2354, British R.A.E., Jan. 1955.
30. Chilton, Robert G., and Brown, B. Porter: Flight Investigation of the Effect of Sideslip on the Pressure at the Static Orifices of the Boeing B–29 Airplane. NACA RM L50J30, 1951.
31. Somerville, T. V., Kirk, F. N., and Jefferies, R. L.: Comparison of Model and Full Scale Tests on a Fuselage Vent for Measurements of Static Pressure. Rep. No. Aero 1806, British R.A.E., Mar. 1943.
32. Thompson, Jim Rogers: Measurements of the Drag and Pressure Distribution on a Body of Revolution Throughout Transition From Subsonic to Supersonic Speeds. NACA RM L9J27, 1950.
33. Matthews, Clarence W.: A Comparison of the Experimental Subsonic Pressure Distributions About Several Bodies of Revolution With Pressure Distributions Computed by Means of the Linearized Theory. NACA Rep. 1155, 1953. (Supersedes NACA TN 2519.)
34. Cooper, Morton, and Hamilton, Clyde V.: Orientation of Orifices on Bodies of Revolution for Determination of Stream Static Pressure at Supersonic Speeds. NACA TN 2592, 1952.
35. Cooper, Morton, Gapcynski, John P., and Hasel, Lowell E.: A Pressure Distribution Investigation of a Fineness-Ratio-12.2 Parabolic Body of Revolution (NACA RM–10) at M=1.59 and Angles of Attack up to 36°. NACA RM L52G14a, 1952.
36. Sommerville, T. V., and Jefferies, R. L.: Note on Model Tests of Static Vents. Effect of Degrees of Flushness, Waviness of Skin and Proximity of Rivets. B. A. Dept. Note—Wind Tunnels No. 531, British R.A.E., Sept. 1941.
37. Howard, J. R.: Wind Tunnel Tests of Alternate Static Source Protuberances for the F–86A Airplane. Rep. No. NA–49–449, North American Aviation, Inc., June 16, 1949.
38. Zalovcik, John A.: A Radar Method of Calibrating Airspeed Installations on Airplanes in Maneuvers at High Altitudes and at Transonic and Supersonic Speeds. NACA Rep. 985, 1950. Supersedes NACA TN 1979.)
39. Thompson, F. L.: Procedure for Determining Speed and Climbing Performance of Airships. NACA TN 564, 1936.
40. Thompson, F. L.: The Measurement of Air Speed of Airplanes. NACA TN 616, 1937.
41. Phillips, William H.: Theoretical Analysis of Oscillations of a Towed Cable. NACA TN 1796, 1949.
42. Thompson, F. L., and Zalovcik, John A.: Airspeed Measurements in Flight at High Speeds. NACA ARR, Oct. 1942.
43. Hesse, W. J.: Position Error Determination by Stadiametric Ranging With a 35mm Movie Camera. Tech. Rep. No. 2–55, Test Pilot Training Div., U. S. Naval Air Test Center (Patuxent River, Md.), June 24, 1955.
44. Lang, D. W., and Charnley, W. J.: Measurement of Aircraft Height and Speed in High Speed Dives by a Photographic Method and by Radar Tracking. R. & M. No. 2351, British A.R.C., Jan. 1946.
45. Schoenfeld, L. I., and Harding, G. A.: Report on the Dual Sighting Stand and Other Methods of Calibrating Altimeter and Airspeed Installations. Rep. No. NAES–INSTR–16–44 (Project No. TED NAM 3335), NAES, Philadelphia Navy Yard, Bur. Areo., Aug. 15, 1944.
46. Fuhrman, R. A., Wheatley, J. P., Lytle, W. J., and Doyle, G. B.: Preliminary Report on Airspeed-Altimeter System Calibration at High Mach Numbers. Phase A—The Altimeter Depression Method Using a Base Airplane at Altitude. Test Pilot Training Div., U. S. Naval Air Test Center (Patuxent River, Md.), Mar. 3, 1952.
47. Zalovcik, John A., Lina, Lindsay J., and Trant, James P., Jr.: A Method of Calibrating Airspeed Installations on Airplanes at Transonic and Supersonic Speeds by the Use of Accelerometer and Attitude-Angle Measurements. NACA Rep. 1145, 1953. (Supersedes NACA TN 2099 by Zalovcik and NACA TN 2570 by Lina and Trant.)
48. Thompson, Jim Rogers, and Kurbjun, Max C.: Evaluation of the Accuracy of an Aircraft Radio Altimeter for Use in a Method of Airspeed Calibration. NACA TN 3186, 1954.
49. Zalovcik, John A.: A Method of Calibrating Airspeed Installations on Airplanes at Transonic and Supersonic Speeds by Use of Temperature Measurements. NACA TN 2046, 1950.
50. Lina, Lindsay J., and Ricker, Harry H., Jr.: Measurements of Temperature Variations in the Atmosphere Near the Tropopause With Reference to Airspeed Calibration by the Temperature Method. NACA TN 2807, 1952.
51. Levon, K. C.: Pressure Error Measurement Using the Formation Method. C.P. No. 126, British A.R.C., 1953.

REPORT 1365

A CORRELATION OF RESULTS OF A FLIGHT INVESTIGATION WITH RESULTS OF AN ANALYTICAL STUDY OF EFFECTS OF WING FLEXIBILITY ON WING STRAINS DUE TO GUSTS [1]

By C. C. Shufflebarger, Chester B. Payne, and George L. Cahen

SUMMARY

An analytical study of the effects of wing flexibility on wing strains due to gusts has been made for four spanwise stations of a four-engine bomber airplane, and the results have been correlated with results of a previous flight investigation. The measured bending-strain amplification factors due to wing flexibility (ratio of strain for the flexible airplane to strain for the "rigid" airplane) at a station near the wing root were 1.09 when based on the ratio of root-mean-square values and approximately 1.19 when based on the ratio of strains obtained from distributions of strain peaks. The amplification factors decreased with each successive outboard station and then increased slightly at the tip station. When the airplane was considered to have three degrees of freedom (vertical motion and wing bending in the first and second symmetric bending modes), calculated amplification factors were in reasonable agreement with the measured results.

INTRODUCTION

The current trend toward thinner wings, higher speeds, and larger concentrations of mass in the wings has led to increased concern regarding the effects of wing flexibility on the aircraft structural loads in flight through atmospheric turbulence. A number of investigations have dealt with the development of analytical methods for calculating structural responses of airplanes to gusts (refs. 1 to 6). Also, a number of flight investigations of the effect of transient response associated with wing flexibility of present-day airplanes have been made by the National Advisory Committee for Aeronautics to determine the amplification of wing strain and accelerations induced by gusts (refs. 7 to 10), and correlations of these results with the results of analytical studies have been made.

In the initial studies the correlations of calculated and measured values were based primarily on the response of the airplane to simple and discrete gust disturbances and, although this approach has proven useful, it has not provided a clear description of the response of an airplane to continuous turbulence. The recent application of the method of generalized harmonic analysis to the problem of gust loads has, however, provided a technique that gives a more complete description of the response of an airplane to continuous turbulence. This approach has been applied in reference 1 in analytical studies, and the results obtained show good correlation with flight-test results evaluated on a "selected peak" basis for the overall effects of wing flexibility on the strains at the wing root stations of three airplanes.

In this paper the techniques of generalized harmonic analysis are applied in both the analytical calculations and in the analysis of the wing-strain measurements made on a four-engine bomber airplane during flight through rough air. (An evaluation of the data for the flight investigation on the basis of selected peaks is reported in ref. 10.) The use of generalized harmonic analysis techniques for both the calculated and measured values enables correlations to be made on the same basis and in more detail than in reference 1. Strain spectra, root-mean-square strain values, and the distribution of strain peaks were determined for each of four spanwise measuring stations, and the analytical methods of reference 1 are applied in order to calculate the same quantities. The method of reference 1 was extended to include the second symmetrical bending mode, in addition to the fundamental bending mode, as it appeared particularly pertinent for the outboard stations.

SYMBOLS USED IN BODY, TABLE, AND FIGURES

a	slope of lift curve of wing
b	span of wing
c	chord of wing
c_0	chord of wing at midsemispan
E	Young's modulus of elasticity
f	frequency, cps
g	acceleration due to gravity
I	bending moment of inertia
k	statistical number of degrees of freedom
L	scale of turbulence, ft
l	distance from neutral axis to the extreme fiber
M_{c_0}	moment of wing area about spanwise station under consideration, $\int_{y_j}^{b/2} c(y-y_j)dy$

$$M_{c_1}=\int_{y_j}^{b/2} cw_1(y-y_j)dy$$

[1] Supersedes NACA Technical Note 4071 by C. C. Shufflebarger, Chester B. Payne, and George L. Cahen, 1957.

Preceding Page Blank

$$M_{c_2}=\int_{y_j}^{b/2} cw_2(y-y_j)dy$$

$$M_{m_0}=\int_{y_j}^{b/2} m(y-y_j)dy$$

$$M_{m_1}=\int_{y_j}^{b/2} mw_1(y-y_j)dy$$

$$M_{m_2}=\int_{y_j}^{b/2} mw_2(y-y_j)dy$$

M_n generalized mass of nth mode
m mass per unit span of wing (except in eq. (4))
$N(y)$ number of strain peaks per second greater than a given strain level y
Δn incremental normal acceleration, g units

$$r_1=\frac{2\int_0^{b/2} cw_1dy}{2\int_0^{b/2} cdy}$$

$$r_2=\frac{2\int_0^{b/2} cw_1^2dy}{2\int_0^{b/2} cdy}$$

$$r_4=\frac{2\int_0^{b/2} cw_2dy}{2\int_0^{b/2} cdy}$$

$$r_5=\frac{2\int_0^{b/2} cw_1w_2dy}{2\int_0^{b/2} cdy}$$

$$r_6=\frac{2\int_0^{b/2} cw_2^2dy}{2\int_0^{b/2} cdy}$$

S wing area
s distance traveled, $\frac{2V}{c_0}t$, half-chords
T arbitrary value of t, sec
$T(f)$ amplitude of airplane frequency-response function
t time (zero at beginning of gust penetration)
V forward velocity of flight
W total weight of airplane
w_n deflection of elastic axis in nth mode, given in terms of unit tip deflection, positive upward
y distance along wing measured from airplane center line
$y(t)$ stationary random disturbance (strain amplitude)
ϵ strain

$$\lambda_1=\frac{\omega_1 c_0}{2V}$$

$$\lambda_2=\frac{\omega_2 c_0}{2V}$$

$$\mu_0=\frac{8M_0}{a\rho c_0 s}$$

$$\mu_1=\frac{8M_1}{a\rho c_0 s}$$

$$\mu_2=\frac{8M_2}{a\rho c_0 s}$$

ρ mass density of air
σ root-mean-square value of output response
σ_U root-mean-square gust velocity
$\Phi_i(\ )$ input power-spectral-density function
$\Phi_o(\ )$ output power-spectral-density function
Ω frequency, radians/ft
ω_n natural circular frequency of vibration of nth mode

Primes denote derivatives with respect to s or σ.

Subscripts:
F flexible case
j spanwise station
n natural modes of vibration
R rigid case

APPARATUS, TESTS, AND ACCURACY OF MEASUREMENTS

The experimental data used in the present investigation were obtained from the flight investigation reported in reference 10. The airplane, flight conditions, and test procedures are described in detail in reference 10, and the description is partially repeated herein for completeness of this paper.

The characteristics of the test airplane are given in table I, and a three-view drawing of the test airplane is shown in figure 1. The estimated spanwise stiffness distribution is given in figure 2, and the estimated weight distribution for the test run considered herein is shown in figure 3.

The instrumentation used in this investigation consisted of electrical strain-gage bridges for measuring wing bending strains at the front and rear spars of wing stations 126, 255, 432, and 590, and an accelerometer mounted in each wing near the elastic axis at the estimated nodal point of the fundamental bending mode (station 278). All strain indications were recorded on a multichannel oscillograph. The outputs of the strain-gage installations at the inboard stations were recorded separately, whereas the gages on the front and rear spars of stations 432 and 590 were combined electrically to give a single output for each station. The natural frequency of the nodal-accelerometer recording system was approximately 9 cps. All recorders were correlated in time by means of an NACA ½-second chronometric timer.

The investigation was made at a speed of 250 mph for a weight of 105,900 pounds. In the course of the actual flight test, small variations from the specific test conditions occurred in the airspeed, altitude, and airplane weight. These variations were too small to be significant. A pull-up which was made at the same weight and speed was also analyzed for use in determining the equivalent "rigid" airplane strains.

The instrumentation, the character of the records, and the method of record reading were such that the overall accuracy

TABLE I

AIRPLANE LOADING, PHYSICAL CONSTANTS, AND BASIC PARAMETERS

(a) Terms that apply to all wing stations

W, lb	105, 900
V, mph	250
S, sq ft	1, 739
b, in.	1, 700
Aspect ratio	11. 6
Mean aerodynamic chord, ft	12. 9
Center-of-gravity position (approximate), percent mean aerodynamic chord	22
a	5. 00
c_0, in.	205
ρ, slugs/cu ft	0. 00238
ω_1, radians/sec	15. 6
ω_2, radians/sec	40. 8
μ_0	74. 4
μ_1	1. 422
μ_2	0. 181
λ_1	0. 362
λ_2	0. 953
r_1	0. 190
r_2	0. 131
r_4	0. 082
r_5	0. 068
r_6	0. 054

(b) Terms that apply to specific wing stations

Wing station, in.	$\frac{M_{m_0}}{M_{c_0}}$	$\frac{M_{m_1}}{M_{m_0}}$	$\frac{M_{m_2}}{M_{m_0}}$	$\frac{M_{c_1}}{M_{c_0}}$	$\frac{M_{c_2}}{M_{c_0}}$	l, in.
126	0. 834	0. 154	−0. 015	0. 455	0. 205	16. 9
255	. 562	. 230	−. 0015	. 536	. 262	15. 3
432	. 155	. 496	. 179	. 661	. 388	13. 1
590	. 089	. 700	. 452	. 786	. 571	11. 3

of the individual measurements was estimated to be as follows:

Strain indications, percent	±5
Accelerations, g units	±0.05

The strain measurements in pull-ups and in laboratory load calibrations were linear within the accuracy of the measurements.

BASIS OF ANALYSIS

The object of the present study is to correlate data for analytically determined effects with data for experimentally determined effects of wing bending flexibility on the wing strains during flight through rough air. The overall effects of wing bending flexibility can be conveniently expressed in terms of amplification factors which are ratios of the strains for the flexible airplane to the strains for the rigid airplane condition. Two strain amplification factors are used in the analysis, one based on root-mean-square strains and the other on strains that a given number of peak strains equal or exceed.

The flexibility measures used involve comparison of actual incremental wing strains with the strains that would be obtained if the airplane were rigid. Since it is, of course, not possible to obtain the rigid-body reference strains in flight,

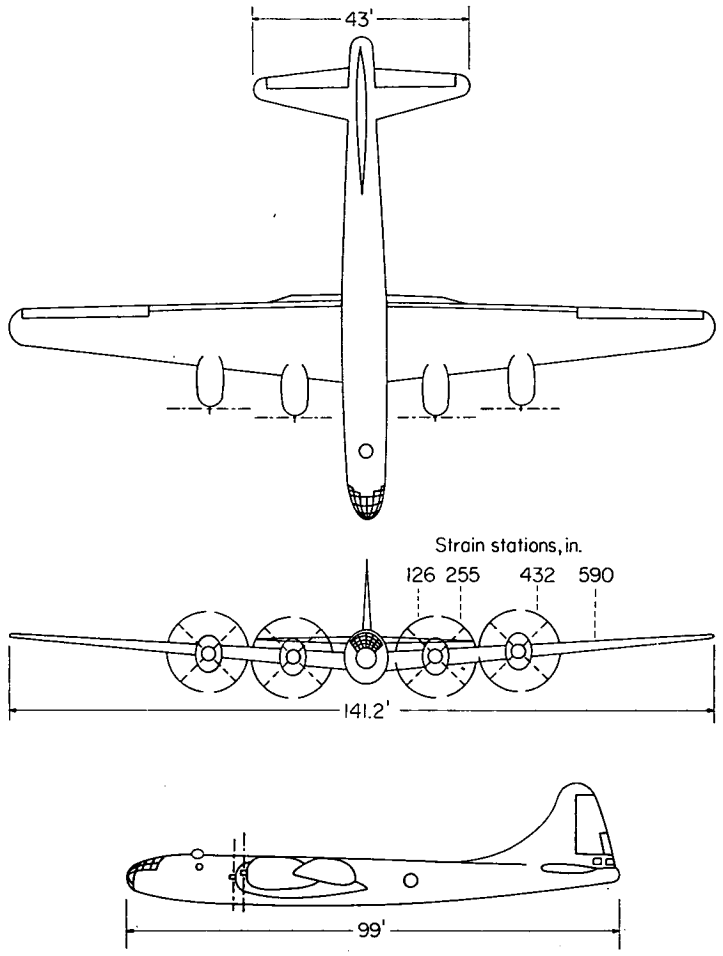


FIGURE 1.—Three-view drawing of test airplane.

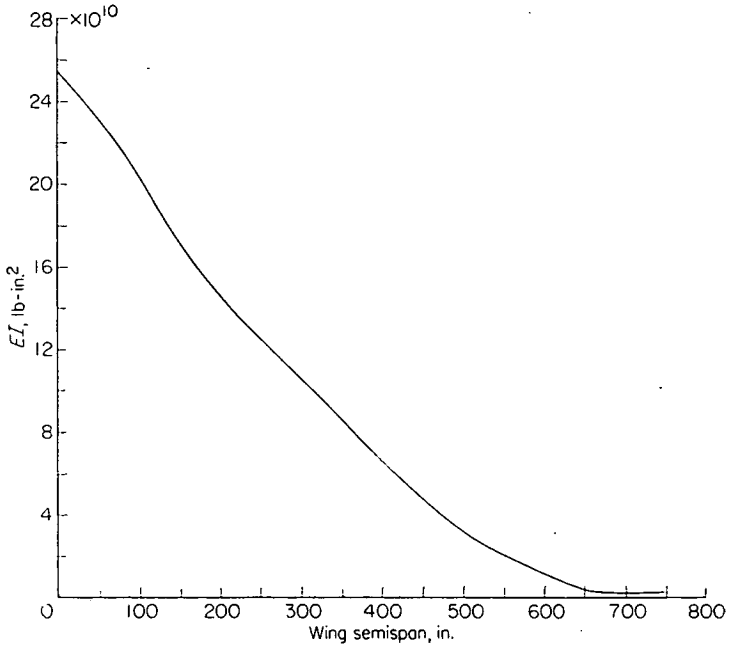
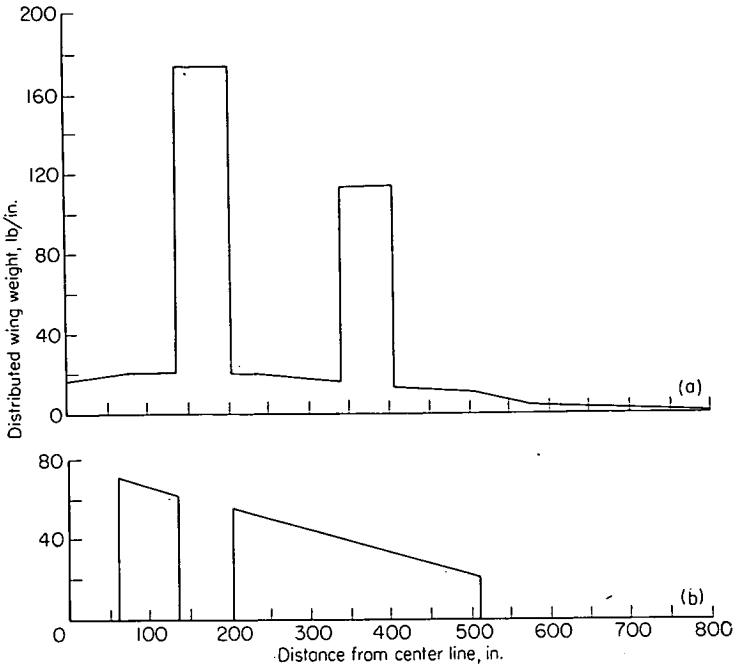


FIGURE 2.—Estimated spanwise stiffness distribution.

some nearly equivalent strain must be used. The general practice, as in reference 1, has been to assume that the rigid-body strains are equal to the strains that would develop during pull-ups at accelerations equal to the accelerations that are measured at the nodal points during rough-air



(a) Wing structure and nacelles.
(b) Fuel load.

FIGURE 3.—Estimated spanwise weight distribution for a gross weight of 105,900 pounds.

flights, and this practice has been followed herein. In utilizing the pull-up as the reference condition, the effects of quasi-static elastic twist and other aerodynamic features of the airplane are represented. The quasi-static elastic twist is, however, small for the test airplane and is neglected in this analysis. The acceleration values obtained from the nodal accelerometers in the left and right wings are averaged to give a single time history which is used as the rigid-body acceleration in rough air. The use of the average of the two nodal accelerometers largely eliminates the effects of roll and of unsymmetrical vibrations on the measured accelerations.

Inasmuch as the evaluation of the results of the flight investigation and the associated analytical results are based on the techniques of generalized harmonic analysis, a few basic concepts and relations that are needed are given here. One of the more important and useful characteristics of a stationary random disturbance is its power-spectral-density function. If $y(t)$ is a stationary random disturbance, the power-spectral-density function or power spectrum of $y(t)$ is defined by

$$\Phi(f)=\lim_{T\to\infty}\frac{1}{T}\left|\int_{-T}^{T}y(t)e^{-2\pi ift}dt\right|^2 \tag{1}$$

where the bars designate the modulus of the complex quantity and T is an arbitrary value of t in seconds. The power spectrum $\Phi(f)$ can essentially be considered to describe the contributions of the various frequencies to the total power or mean-square value of the disturbance.

The power spectrum of a disturbance and the power spectrum of the response of the airplane to the disturbance are, for a linear system, related simply by

$$\Phi_o(f)=\Phi_i(f)|T(f)|^2 \tag{2}$$

where $\Phi_i(f)$ is the power spectrum of the input, $\Phi_o(f)$ is the power spectrum of the output response, and $|T(f)|$ is the amplitude of the system frequency-response function which, in the present application, is the amplitude of the airplane wing bending-strain response to a unit sinusoidal gust disturbance of frequency f. In a subsequent section of this paper, the frequency-response functions $T(f)$ are determined analytically and applied in equation (2) in order to determine the expected strain spectra for comparison with the measured results.

The spectrum of the output response permits the determination of the mean square of the response and other statistical characteristics of the disturbance that are of interest. The root-mean-square value provides a simple and direct measure of the overall response intensity. Also, as in reference 1, the spectra for a Gaussian random process may be used to derive the average number of peaks per second $N(y)$ that exceed a given strain level y. The expression for obtaining the average number of peaks per second exceeding given values, as given in reference 1, is

$$N(y)=\left[\frac{\int_0^\infty f^2\Phi_o(f)df}{\int_0^\infty \Phi_o(f)df}\right]^{1/2} e^{-y^2/2\sigma^2} \tag{3}$$

where

$N(y)$ number of strain peaks per second greater than y

y strain amplitude

σ^2 mean-square value of the strain response, $\int_0^\infty \Phi_o(f)df$

Thus, equation (3) may also be written as

$$N(y)=\frac{\sigma_1}{\sigma}e^{-y^2/2\sigma^2}$$

where

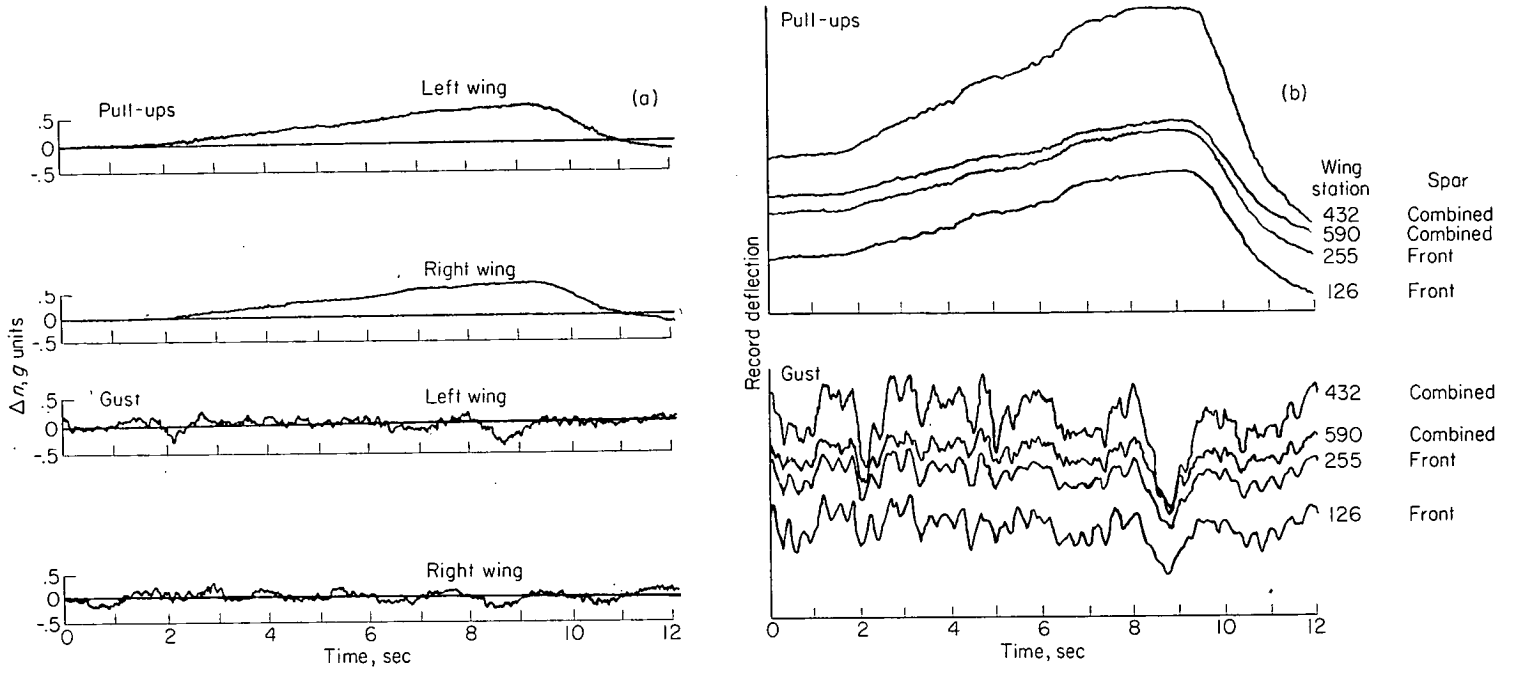
$$\sigma_1^2=\int_0^\infty f^2\Phi_o(f)df$$

RESULTS

EXPERIMENTAL

Time histories of strain indications and nodal-point accelerations for a portion of a gust record and a pull-up are shown in figure 4. A preliminary check of the strain indications for the front and rear spars of stations 126 and 255 indicated that the strains in rough air relative to the strains in pull-ups were essentially the same for the front and rear spars at these stations and, therefore, only the front-spar strains were used to represent these stations.

Power spectra.—Power-spectral-density functions for the wing bending strains and rigid-body accelerations were computed from the time-history data for a 2-minute section of records by Tukey's calculation procedure for spectra estimation as presented in references 11 and 12. In determining



(a) Nodal accelerations. (b) Wing-strain indications.

FIGURE 4.—Time histories of nodal accelerations and wing-strain indications.

the strain spectra from the measurements, the nature of the records made impractical the reading of the records at time intervals of less than 0.1 second; therefore, the range of the spectra was limited to 5 cps. The nodal-acceleration records, however, were read at intervals of 0.05 second; thus the spectra for the rigid condition covered the frequency range from 0 to 10 cps. Forty estimates of the power, equally spaced over the frequency range from 0 to 5 cps, were obtained for the strain histories, and 20 estimates (due to a difference in reading intervals) were obtained for the rigid-body acceleration.

Since the wing strains in a pull-up are different at the various wing stations (fig. 4) the spectra of rigid-body strains also differ from station to station. To permit direct comparison between amplification effects at the various stations, the time histories of wing bending strain ϵ_j in rough air were normalized in the following manner:

$$\text{Normalized } \epsilon_j = \epsilon_j \frac{(\epsilon/g) \text{ at station 126 in a pull-up}}{(\epsilon_j/g) \text{ in a pull-up}}$$

The rigid-body acceleration history was also converted to a normalized rigid-body strain by multiplying by the strain per g at station 126 in a pull-up. This normalization permits direct comparison of all strain spectra with a single rigid-body strain spectrum. The normalized strain spectra obtained in the foregoing manner are shown in figure 5 for the frequency range from 0 to 5 cps. Because of the normalization the actual numerical values have no real significance, except at station 126, and do not reflect the actual strain variations between the different stations.

Peak counts.—A direct count of the strain peaks for all cases was not considered practical; therefore, the number of strain peaks per mile greater than a given strain level was

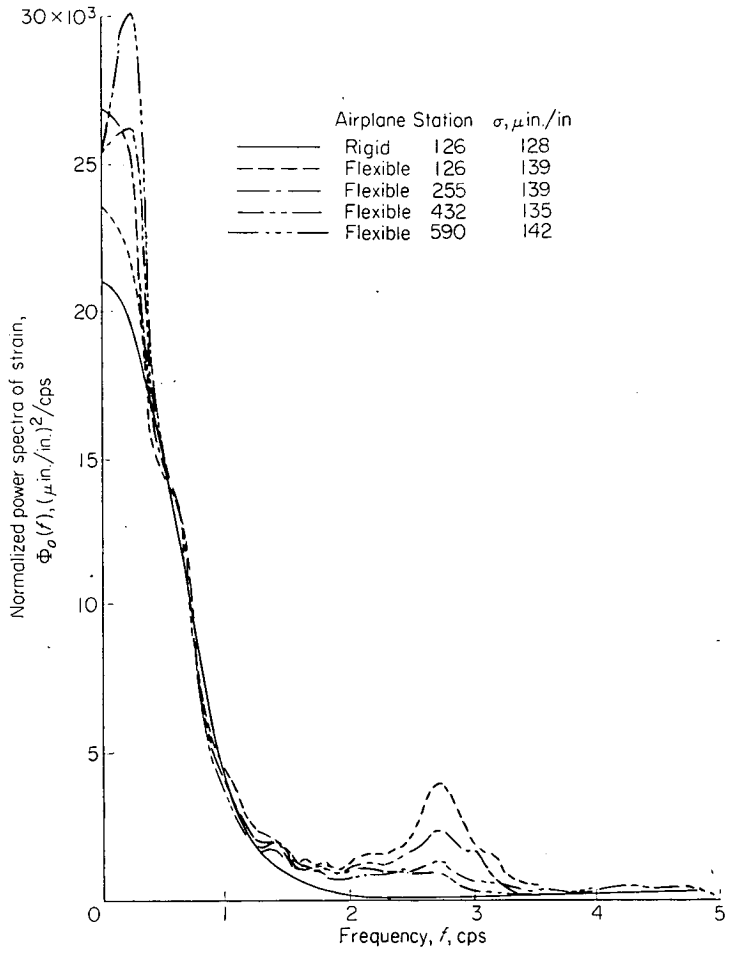


FIGURE 5.—Measured strain spectra (normalized to strain at station 126).

estimated from the measured spectra of figure 5 by means of equation (3). The results are plotted in figure 6 as a function of strain level for the flexible and rigid cases at station 126.

In the evaluation of the integrals in equation (3), the spectra of figure 5 were used. Inasmuch as these spectra cover only the frequency range of 0 to 5 cps, the integrals could be determined only for this region. This approximation does not affect the reliability of the root-mean-square values, inasmuch as the numerical procedures used result in no loss of power but only in a distortion of the true spectrum; the power at frequencies above 5 cps appears as power at lower frequencies. The number of peaks exceeding given values is somewhat underestimated, however, as a result of this approximation, as is indicated in a subsequent section.

Amplification factors.—The magnitude of the flexibility effects can be shown by strain ratios, that is, the ratio of a measure of the strain for the flexible case to the comparable measure of strain for a reference rigid case. Inasmuch as the root-mean-square strains provide a simple measure of the strain levels, the ratios of the root-mean-square values for the flexible case to the corresponding values for the rigid case give one measure of the strain amplification factor (obtained from the root-mean-square values given in fig. 5) and are plotted as a function of wing station in figure 7 (a).

Another measure of the strain amplification due to flexibility that is frequently of interest is the ratio of the strain for the flexible airplane to the strain for the rigid airplane that has the same frequency of occurrence. This ratio may be more significant for fatigue studies than the ratio of the root-mean-square values and is determined as illustrated in figure 6 from the distributions of strain peaks for the flexible and rigid airplanes. Figure 6 shows that the ratio of the strain for the flexible airplane to the strain for the rigid airplane that has the same frequency of occurrence varies with strain level; the ratio is highest at the low strain values and, as can be shown analytically, approaches the ratio of the root-mean-square values at the higher strain levels. As in reference 1, the frequency of occurrence selected for determining the strain ratios was the frequency for the flexible airplane at a strain equal to twice the root-mean-square strain for the flexible airplane. This strain ratio for each of the four measuring stations is shown in figure 7 (b).

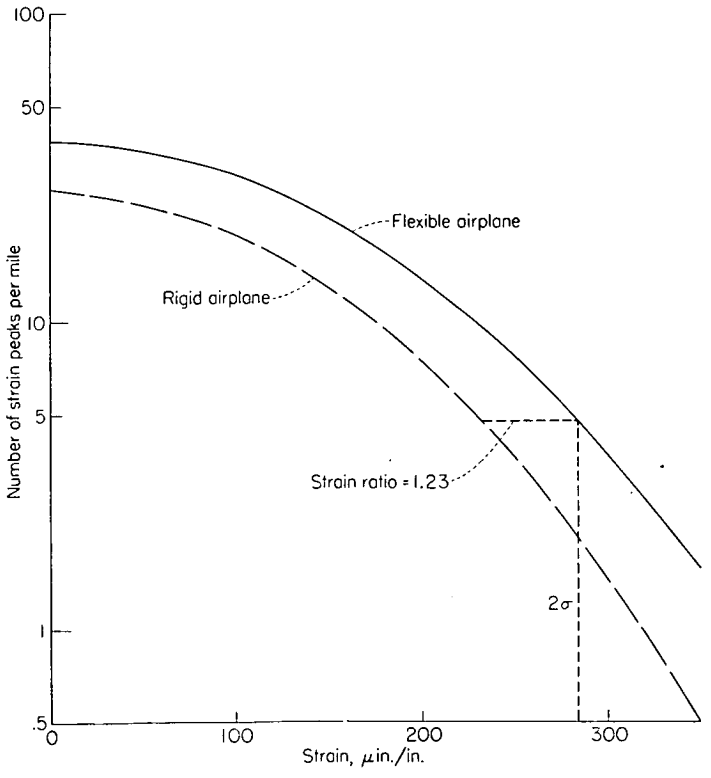


FIGURE 6.—Variation of the number of strain peaks with strain level for the rigid and flexible conditions at station 126 (estimated from measured spectra and eq. (3)).

Statistical reliability.—The statistical reliability of the power spectra determined from the 2-minute section of record was determined by the method of reference 11. The reliability of each power estimate for relatively flat spectra is expressed in terms of the statistical number of degrees of freedom k, where

$$k=\frac{n-\frac{m}{5}}{\frac{m}{2}}=\frac{1200-\frac{40}{5}}{\frac{40}{2}}=59.6 \qquad (4)$$

and

m number of uniformly spaced points over frequency range for which power estimates are obtained

n number of equally spaced observations taken over the length of the time history, $T/\Delta t$

For this value of k, figure 2 of reference 11 shows each individual power estimate to have 95-percent confidence limits from 0.68 to 1.35 of the value measured. Small peaks in the measured spectra may, therefore, be merely statistical fluctuations. The statistical reliability of the root-mean-square value, which is based on the integrated power, is considerably higher and is estimated to be reliable to within approximately ±10 percent.

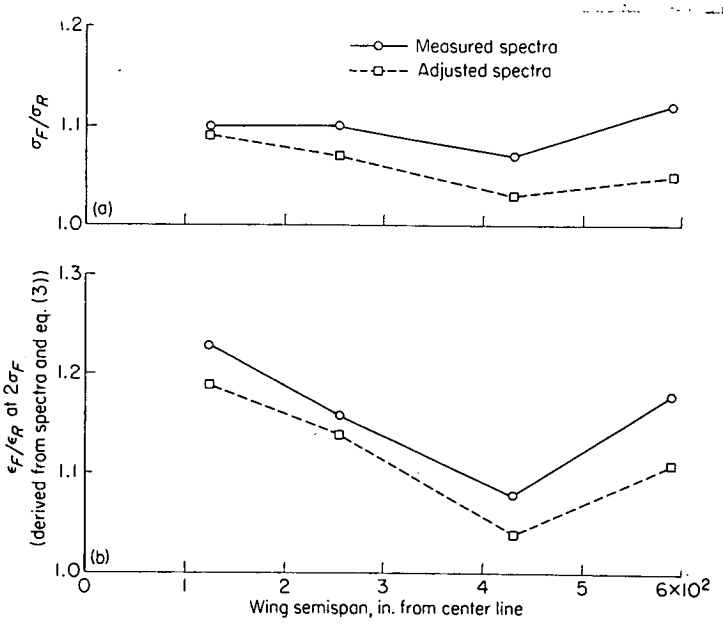


FIGURE 7.—Measured strain amplification factors.

ANALYTICAL

The results obtained in the analytical phase of this investigation were based on the relation of the random input disturbance (for a uniform spanwise gust), the output response of the airplane, and the frequency-response characteristics of the airplane as given in equation (2). Selection of a suitable input disturbance, calculation of the airplane frequency-response function, and determination of the output response by means of equation (2) was required. Inspection of the wing strain indications, as in figure 4, revealed that the second bending mode of vibration was of some importance at the outboard wing stations; the method of reference 1 was therefore extended to include the second symmetrical bending mode. The determination of the input gust disturbance, the airplane frequency-response or transfer functions, and the output responses are discussed in the following sections.

Input disturbance.—Recent theoretical studies, such as reference 13, have used the following expression to approximate the spectrum of vertical gust velocity:

$$\Phi_i(\Omega)=\sigma_U^2\frac{L}{\pi}\frac{1+3\Omega^2L^2}{(1+\Omega^2L^2)^2} \tag{5}$$

where

σ_U^2 mean-square gust velocity, $(\text{ft/sec})^2$

L scale of turbulence, ft

Ω frequency, $2\pi/\lambda$ (where λ is gust wave length in feet), radians/ft

For present purposes it is convenient to express the gust spectrum in terms of the frequency argument f in cycles per second, where

$$f=\frac{V}{2\pi}\Omega$$

and $V=368$ ft/sec. In terms of this frequency argument, the gust power spectrum is given by

$$\hat{\Phi}_i(f)=\Phi_i(\Omega)\frac{d\Omega}{df}$$

$$=\sigma_U^2\frac{2L}{V}\frac{1+3\left(\frac{2\pi Lf}{V}\right)^2}{\left[1+\left(\frac{2\pi Lf}{V}\right)^2\right]^2}$$

Representative values of L for atmospheric turbulence are believed to vary from several hundred feet to more than 1,000 feet. The spectra for values of L of 400, 1,000 and 2,000 feet are shown in figure 8 for a value of σ_U^2 of 1. The value of L equal to 1,000 feet was selected for the present analysis as being of the correct order, on the basis of measured data (ref. 12), although calculations were also made for other values of L.

Frequency-response functions.—The frequency-response characteristics were obtained for the airplane bending-strain response to continuous sinusoidal gust encounters on the basis of the method of reference 1. In addition to calculations for the rigid condition, the frequency-response functions were calculated for two separate flexible conditions: (1) the airplane with two degrees of freedom (as in ref. 1), vertical motion and wing bending in the fundamental mode, and

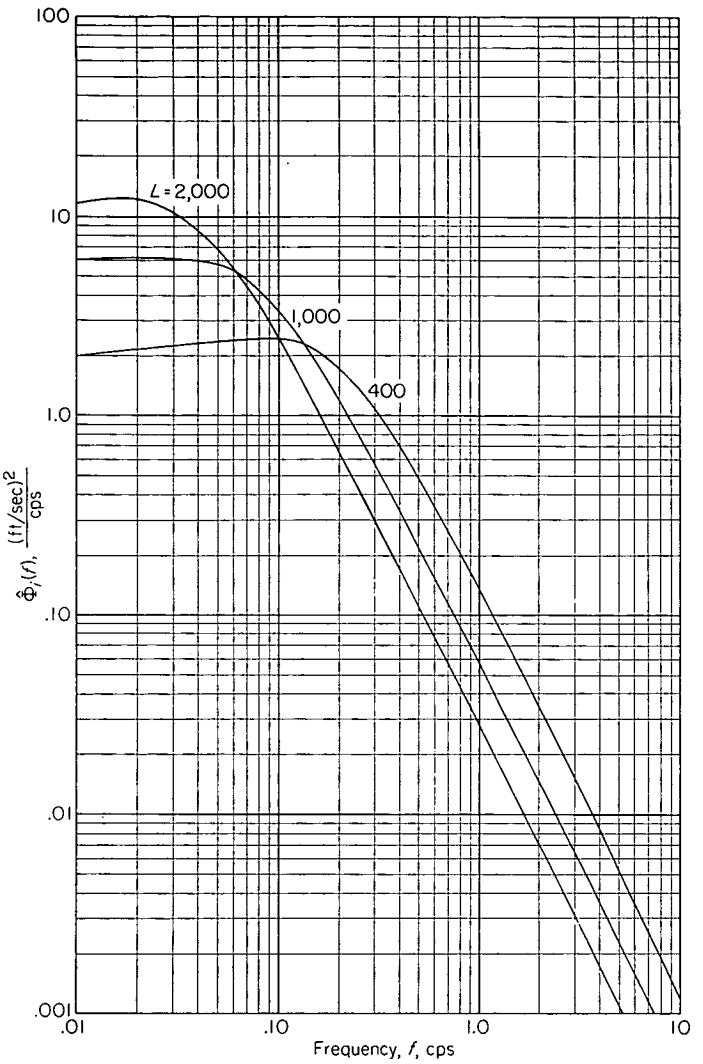


FIGURE 8.—Assumed gust input spectrum.

$$\hat{\Phi}_i(f)=\sigma_U^2\frac{2L}{V}\frac{1+3\left(\frac{2\pi Lf}{V}\right)^2}{\left[1+\left(\frac{2\pi Lf}{V}\right)^2\right]^2};\ \sigma_U^2=1.$$

(2) the airplane with three degrees of freedom, vertical motion and wing bending in the fundamental mode and second mode (first and second symmetrical bending modes).

Although airplane pitch may be important in the response of an airplane to gusts and rough calculations for the rigid airplane with pitch were made, pitch response was not included in the calculations presented herein because of increased complexity. The equations necessary for including the second symmetrical mode are derived in the appendix, and the airplane loading, physical constants, and basic parameters are given in table I. The slope of the lift curve a was estimated to be 5.00 per radian for the test airplane, and this value was used as being more appropriate in the calculations than the value of 6.28 used in reference 1. In using the method of reference 1 to obtain the amplitude of the airplane bending response, the results were obtained in terms of a bending-moment coefficient per foot per second. The equations necessary for converting the bending-moment coefficients to strains are given in the appendix of the present

report. The frequency-response functions obtained for the wing stations at which flight measurements were made are shown in figure 9.

Output response.—Output-response spectra were obtained for each wing station by using in equation (1) the calculated frequency-response functions and the assumed input spectrum of equation (5) for $\sigma_U^2=1$. The output spectra were calculated for a frequency range of 0 to 10 cps in order to include the effect of the second symmetrical mode that peaks at approximately 7 cps. For convenience in making comparisons, the calculated output spectra for the rigid airplane and the flexible airplane (three degrees of freedom) for the wing stations at which the flight measurements were made and a value of L of 1,000 feet were normalized in the manner used in obtaining figure 5 (so that direct comparisons could be made) and are shown in figure 10. The results for frequencies of only 0 to 5 cps are shown in this figure because of the very low values at the higher frequencies. In order to show the results for the higher frequencies, and in particular to indicate the effect of the second bending mode, the complete frequency-response functions for frequencies of 0 to 10 cps are shown in figure 11 with a logarithmic ordinate scale.

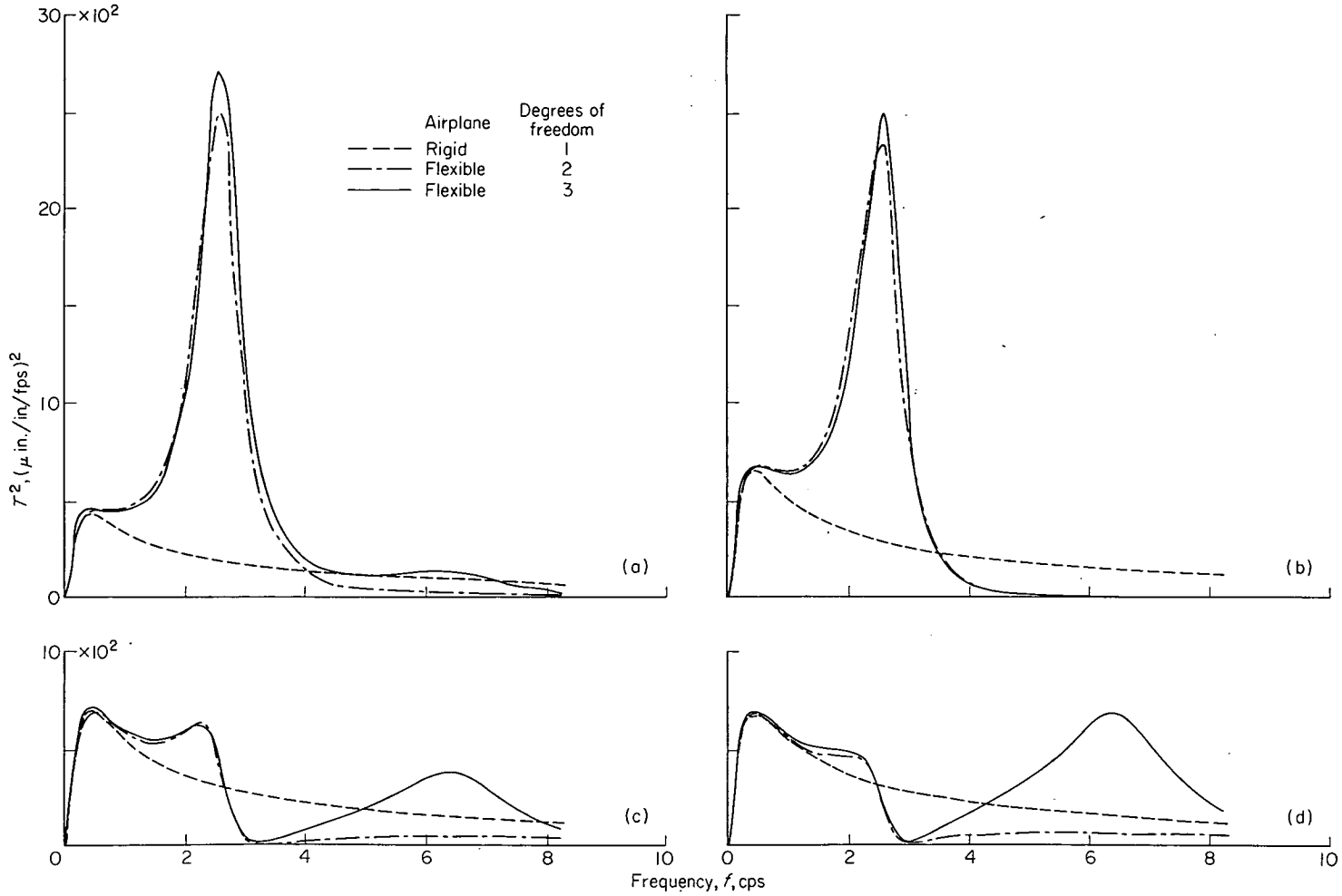
Amplification factors.—The amplification factors or strain ratios based on the ratio of the root-mean-square strain for the flexible airplane to that for the rigid airplane were obtained from spectra such as those in figure 10 (square root of area under spectra). These calculated values for both two degrees and three degrees of freedom are shown in figure 12 (a), plotted as a function of wing station for a value of L of 1,000 feet, along with the measured values from figure 7 (a).

The number of strain peaks per mile greater than given strain levels were obtained for each wing station by use of equation (3) in order to determine amplification factors or strain ratios based on the distribution of peak strain values, as was done for the experimental results shown in figure 6. The calculated values for both two degrees and three degrees of freedom are shown in figure 12 (b) for a value of L of 1,000 feet, along with the measured values from figure 7 (b).

DISCUSSION

EXPERIMENTAL RESULTS

Power spectra.—Inspection of the spectra of wing strains in flight through turbulence (fig. 5) reveals two features of interest. In the frequency range below approximately 0.5 cps, an amplification of wing strains that increases roughly in proportion to the distance from the center line is apparent. It is felt that this increase is primarily due to factors such



(a) Station 126.
(b) Station 255.
(c) Station 432.
(d) Station 590.

FIGURE 9.—Theoretical transfer functions. $a=5.00$.

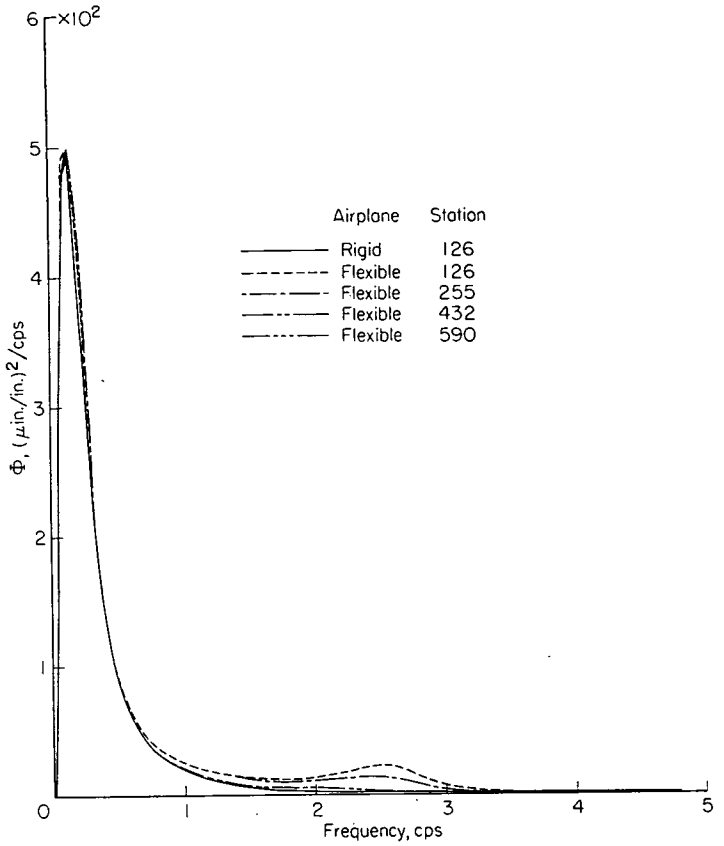


FIGURE 10.—Power spectra of strain at four wing stations normalized to strain at station 126. L=1,000 feet.

as spanwise gust variations and airplane rolling motions rather than wing flexibility. At the fundamental bending-mode frequency of 2.7 cps, the effects of wing flexibility are evidenced by the bump that appears in the spectra. The spectra indicate that flexibility effects near the fundamental bending-mode frequency are greatest at the most inboard station and least at the two outboard stations.

The effects of the second symmetrical bending mode are not evident in the measured spectra, inasmuch as the frequency of the second bending mode is about 7 cps and the spectra in figure 5 are shown to only 5 cps. Because of the method of obtaining the spectra, however, the power at higher frequencies is not lost but is reflected and appears as power at frequencies of less than 5 cps; in particular, the power associated with the second symmetric mode at approximately 7 cps may be expected to appear at 3 cps. This characteristic of reflection of the power above the highest resolved frequency (5 cps in the present case) has been termed "aliasing" (ref. 12). The measured spectra are distorted to the extent of this reflection. The power expected at the higher frequencies is small, however, as indicated by inspection of the strain records, and the distortion expected is also small.

The measured spectra also show a slight tendency to increase in power at frequencies above approximately 3.5 cps. This tendency may be a reflection of the first antisymmetrical mode, believed to be at about 5 cps, as indicated in reference 10.

Amplification factors.—The ratios of the measured values

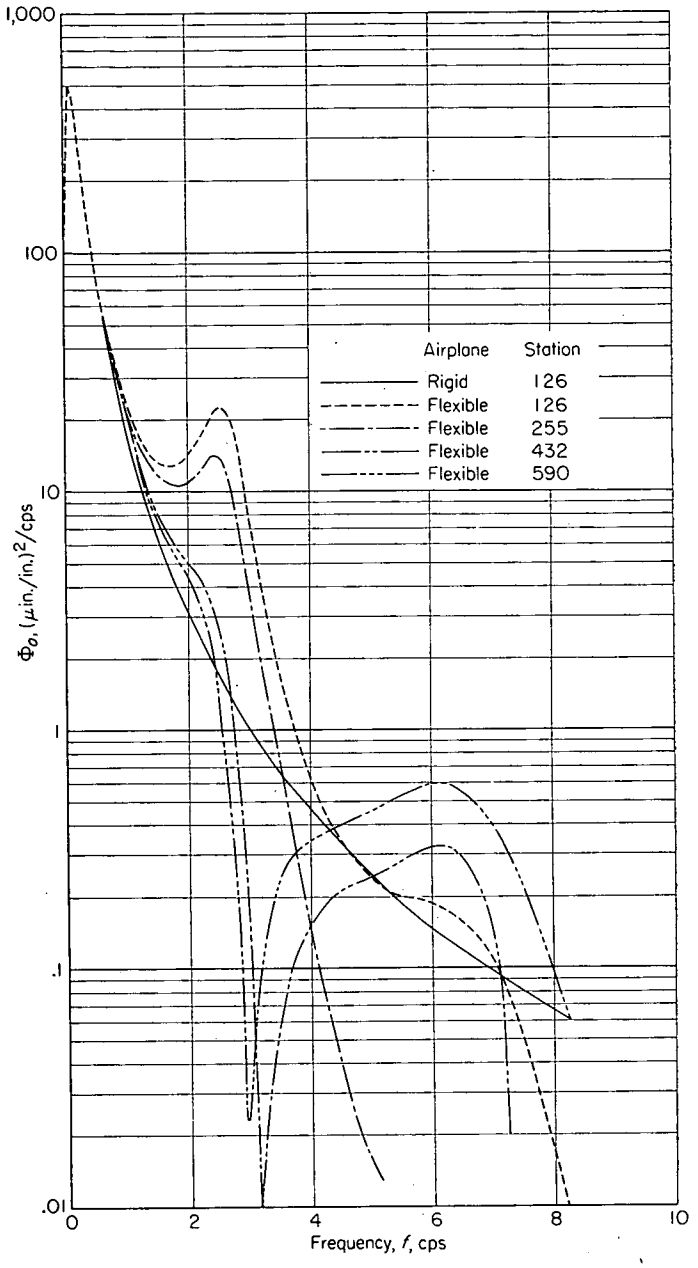


FIGURE 11.—Power spectra of strain to 10 cps at four wing stations normalized to strain at station 126. L=1,000 feet.

of root-mean-square strain for the flexible airplane to those for the rigid airplane (fig. 7 (a)) indicate that an amplification factor of approximately 1.1 applies for all wing stations. However, part of the amplification (especially at the outboard stations) is due to differences in the spectra of figure 5 at frequencies below approximately 0.5 cps that, as previously noted, are felt to result from factors such as spanwise gust variations and rolling motions rather than from wing flexibility. In order to obtain amplification factors that, insofar as possible, reflect only the amplification due to flexibility, the spectra for the flexible condition in figure 5 were reduced to the same values as the spectrum for the rigid condition in the frequency range from 0 to 0.5 cps on the assumption that these differences between the spectra were not due to flexibility. The amplification factors obtained from these adjusted spectra are also shown in figure 7 (a) and indicate that the amplification factor due to flexibility decreased

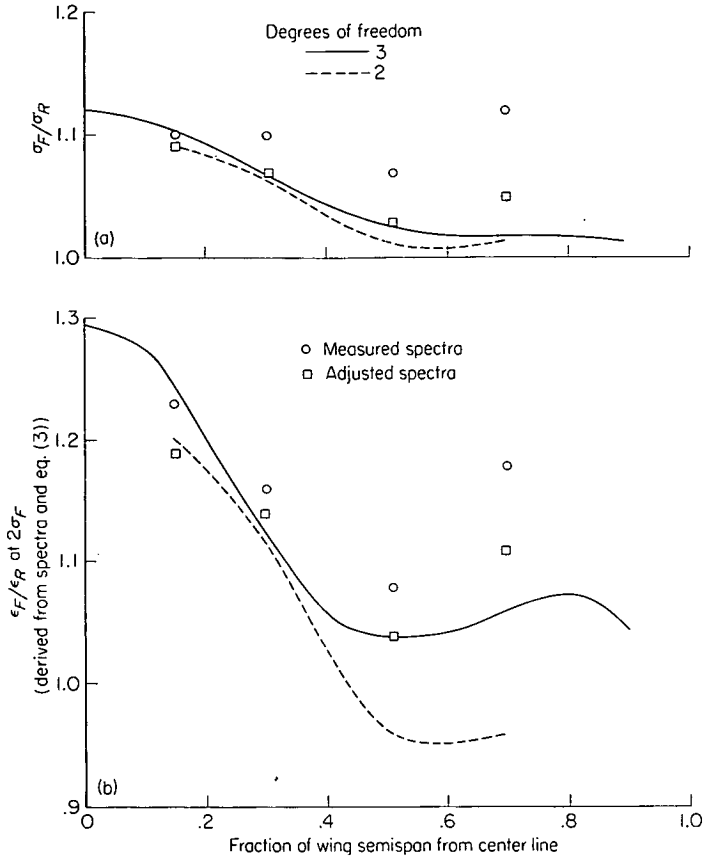


FIGURE 12.—Calculated and measured strain and amplification factors. L=1,000 feet.

from a value of 1.09 at station 126 to a value of 1.03 at station 432 and then increased to a value of 1.05 at station 590.

Amplification factors based on distributions of strain peaks as in figure 6 are shown in figure 7 (b) for both the measured and adjusted spectra of figure 5. These amplification factors are, in general, considerably higher than those based on root-mean-square values but indicate the same trend of flexibility effects; that is, the amplification factor based on the adjusted spectra of figure 5 decreased from a value of 1.19 at station 126 to a value of 1.03 at station 432, and then increased to a value of 1.11 at station 590. The amplification factors based on the measured spectra are greater than those based on the adjusted spectra by an increment of 0.02 to 0.07. All the amplification factors in figure 7 (b) determined from the spectra of figure 5 and by the use of equation (3) are believed to be somewhat too low because they are based on spectrum measurements which cover only the frequency range from 0 to 5 cps. A few checks of these ratios were made by actual counts of strain peaks and they yielded values that were greater by an increment of about 0.05 than those obtained from the spectra and the use of equation (3). It would thus appear that amplification effects due to flexibility, as obtained from the measured spectra, may be underestimated by this amount in figure 7 (b).

The preceding discussion indicates that both the amplification factors used—the ratio of root-mean-square values and the factor determined from distributions of strain peaks—show the largest effects of flexibility at the most inboard station and the smallest at station 432. It is also of interest to note that increasing the amplification factors obtained from distributions of strain peaks (fig. 7) by an increment of 0.05 (the approximate amount by which the strain peaks are believed to be underestimated) results in substantial agreement between the results from the spectra of figure 5 and the amplification factors obtained in reference 10 on a basis of selected peaks.

COMPARISON OF CALCULATED AND EXPERIMENTAL RESULTS

Frequency-response functions.—Inspection of the calculated frequency-response functions in figure 9 indicates that the amplification of a wing bending strain due to fundamental bending-mode response at approximately 2.5 cps is largest at the inboard wing stations while the amplification of a wing bending strain due to second bending-mode response at approximately 6.5 cps is largest at the outboard stations. The calculated frequency-response functions for two degrees and three degrees of freedom in figure 9 are approximately the same for frequencies below about 4 cps. When the rapid decrease of input power with frequency is considered (fig. 8), it is evident that the output power will be little changed by the effect of the second bending mode. The differences in the frequency-response functions at frequencies above 4 cps, however, will result in a larger number of peak strains above a given value because of the fact that the number of peaks depends more heavily on the higher frequencies of the spectrum (eq. (3)).

Power spectra.—Direct comparison of the output spectra of figures 5 and 10 on the basis of the ordinate values is not justified because the intensity of the input for the measured spectra is not known and because a value of 1 was used for σ_U^2 in the calculations. The calculated output spectra of figure 10 for a value of L of 1,000 feet, however, resemble the measured spectra of figure 5 except for the differences in the frequency range below approximately 0.5 cps which, as previously noted, are believed to be due to factors not related to wing flexibility. Both the measured and calculated spectra show a large peak power due to rigid-body motions at a frequency below 1.0 cps and a secondary small peak (indicating response of first bending mode) around 2.5 cps, with the secondary peak decreasing in both cases as the stations become more outboard. The measured spectra, however, show greater power in the secondary peak relative to that in the primary peak than do the calculated spectra. Results from the rough calculations made for the rigid airplane with pitch indicate that this discrepancy is due primarily to the effects of pitching motions on the measured spectra at low frequencies. The use of an assumed turbulence spectrum in the calculations may also account for a part of the discrepancy. In addition, there is a greater decrease in power of the secondary peak, as the stations become more outboard, for the calculated spectra than for the measured spectra, and part of this decrease (although possibly only a small part) is a reflection (due to the aliasing effect) of the power associated with the second symmetrical bending mode at about 7 cps (see outboard stations, fig. 4). It should be noted that although the calculated spectra shown in figure 10 are for the three-degree-of-freedom case (two structural modes), the spectra are essentially the same as for the two-degree-of-freedom case (see transfer functions in fig. 9) for frequencies below 4.0 cps.

The calculated and measured spectra of figures 5 and 10 cannot be compared directly to determine the effects of the second symmetrical mode in bending on the strains, since the measurements covered only the frequency range from 0 to 5 cps. An indication of the very low power due to this mode is shown in the plot of the calculated spectra for the three-degree-of-freedom condition on a logarithmic scale in figure 11, where the peak power of the spectra is approximately one thousand times as great as the peak power at 6 cps for the outboard wing stations.

Amplification factors.—Comparisons of the adjusted and calculated effects of flexibility in figure 12 (a), based on the ratio of root-mean-square values of the adjusted spectra of figure 5 and the results for both two and three degrees of freedom for a value of L of 1,000 feet, indicate that the adjusted values of amplification factors are in substantial agreement with the calculated values except at the most outboard station where the value is 1.05 compared with the calculated value of approximately 1.02. The calculated factors shown in figure 12 (a) decrease from a value of 1.12 at the center line to a value of 1.02 at 0.6 of the semispan from the center line, and the value is about 1.02 or less for stations outboard of this point. Measurements and calculations therefore agree and show the largest effects of flexibility at the most inboard stations, but a discrepancy between the calculated and adjusted results is apparent at the most outboard stations.

Comparison of the effects of flexibility (fig. 12 (b)) on the basis of amplification factors determined from distributions of peak strains, as in figure 6, indicates that in general the calculated results for the three-degree-of-freedom condition and a value of L of 1,000 feet are in relatively good agreement with the results derived from the adjusted spectra of figure 5 (shown in fig. 7 (b)) except at the most outboard stations. The calculated amplification factors shown in figure 12 (b) decrease from a value of 1.29 at the center line to a value of 1.04 at 0.5 of the semispan from the center line, increase to a value of 1.07 at 0.8 of the semispan, and then decrease. The calculated amplification factors for the two- and three-degree-of-freedom conditions (fig. 12 (b)) are in substantial agreement at the inboard stations, but the results for two degrees of freedom show much lower amplification factors at the outboard stations and indicate that the second symmetric bending mode has a large effect on the amplification factors at these stations. The higher amplification factors for the calculated results at the two outboard stations when the second symmetric bending mode is taken into account are, as previously mentioned, the result of differences in the spectra at the higher frequencies that have small effects on the root-mean-square values.

The effect of the choice of gust input, slope of the lift curve, and frequency range on the calculated amplification factors is of interest. A lower value of L in equation (5) will result in a higher amplification factor; for example, the use of a value of L of 400 feet yields an amplification factor based on root-mean-square values of approximately 1.16 for station 126, compared with approximately 1.10 for a value of L of 1,000 feet. A higher lift-curve slope reduces the amplification factor, and for these calculations the use of a lift-curve slope of 6.28 instead of 5.00 would have approximately the same effect as the use of a value of L of 1,000 feet instead of 400 feet. The calculated amplification factors obtained from distributions of strain peaks are dependent on the upper limit of integration used in equation (3) because it is not practical to integrate to infinity, and the effect of a change in the upper limit on the amplification factor depends upon the frequency-response functions. In the present case, however, both analytic considerations and the recorded data place the upper limit of the integration at about 10 cps.

In assessing the reliability of the analytic calculations it was noted that although the measured and calculated results are in relatively good agreement, some discrepancies are present. Inaccuracies in the calculations can, of course, arise from a large number of sources and will require further study. In the present case an assumed gust input was used, and the effect of factors such as airplane pitching motions, spanwise gust effects, and the antisymmetric bending mode were neglected. Although uncertainties in the calculations may arise from the factors mentioned, the present results indicate that the methods used provide reasonable first-order estimates of the magnitude and character of the effects of flexibility on the bending strains at the various spanwise stations for unswept-wing airplanes.

CONCLUSIONS

The effects of wing flexibility on the wing strains that result from gust encounter have been examined on a power-spectral basis. Both flight results and analytical results have been considered for a four-engine bomber airplane, and correlations between the measured and analytical results have been made. The effects of wing flexibility on the wing strains were measured in terms of amplification factors based on the ratio of the strain for the flexible condition to the strain for the "rigid" condition, and results were obtained for four spanwise stations of the wing. The effect of including the second symmetric bending mode in addition to the fundamental bending mode in the calculations was also evaluated. The study led to the following results:

1. Comparison of the measured strain spectra for the flexible and rigid conditions showed strain amplifications in the frequency range below 0.5 cps, especially at the outboard wing stations, that are attributed to the effect of factors such as spanwise gust variations and airplane rolling motions rather than to flexibility effects.

2. The measured strain amplification factors due to wing flexibility at a station near the wing root were 1.09, on the basis of the ratio of root-mean-square strains, and approximately 1.19 on the basis of the ratio of strains derived from distributions of strain peaks. The amplification factors decreased with each successive outboard station and then increased slightly at the most outboard measuring station.

3. The calculated output spectra were in reasonable agreement with the measured spectra except at low frequencies, where the differences are attributed to extraneous factors. At the outboard stations it was necessary to include the effect of the second symmetric bending mode in the calculations in order to estimate adequately the effect of flexibility on the distributions of strain peaks.

526597—60——45

4. Both calculations and measurements indicated that the second symmetric bending mode had a very small effect on the root-mean-square strains but that, for strain amplification factors determined from distributions of strain peaks, the second symmetric bending mode had a pronounced effect at the outboard wing stations.

5. Although uncertainties in the calculations may arise from a number of factors, the present results indicate that calculations based on power-spectral techniques may provide reliable estimates of the magnitude and character of wing flexibility effects on wing strains in gusts for unswept-wing airplanes.

LANGLEY AERONAUTICAL LABORATORY,
NATIONAL ADVISORY COMMITTEE FOR AERONAUTICS,
LANGLEY FIELD, VA., *May 27, 1957.*

APPENDIX

DERIVATION OF THE FREQUENCY-RESPONSE FUNCTIONS INCLUDING VERTICAL MOTION AND FIRST AND SECOND SYMMETRICAL MODES OF WING BENDING

In order to include the effects of a higher mode in the analytical results of this paper, the gust-response analysis of reference 1 was extended to include the second symmetrical wing bending mode. Addition of the second symmetrical wing bending mode simply adds a term to each of the response equations of reference 1, and an additional equation is obtained for the second mode. This appendix shows the effect of the additional mode on the pertinent equations but does not attempt to present the complete derivation, which should be self-evident.

SYMBOLS USED IN APPENDIX

a slope of lift curve of wing

a_n deflection coefficient for nth mode, function of time alone

b span of wing

c chord of wing

c_0 chord of wing at midsemispan

E Young's modulus of elasticity

I bending moment of inertia

K_j nondimensional bending-moment factor, $\dfrac{M_j}{\frac{a}{2}\rho UVM_{c_0}}$

k reduced-frequency parameter, $\dfrac{\omega c_0}{2V}$

l distance from neutral axis to extreme fiber

M_{c_0} moment of wing area about spanwise station under consideration, $\displaystyle\int_{y_j}^{b/2} c(y-y_j)dy$

$$M_{c_1}=\int_{y_j}^{b/2} cw_1(y-y_j)dy$$

$$M_{c_2}=\int_{y_j}^{b/2} cw_2(y-y_j)dy$$

M_j net incremental bending moment at wing station j, $K_j\dfrac{a}{2}\rho UVM_{c_0}$

$$M_{m_0}=\int_{y_j}^{b/2} m(y-y_j)dy$$

$$M_{m_1}=\int_{y_j}^{b/2} mw_1(y-y_j)dy$$

$$M_{m_2}=\int_{y_j}^{b/2} mw_2(y-y_j)dy$$

M_n generalized mass of nth mode

m mass per unit span of wing

$$r_1=\frac{2\displaystyle\int_0^{b/2} cw_1dy}{2\displaystyle\int_0^{b/2} cdy}$$

$$r_2=\frac{2\displaystyle\int_0^{b/2} cw_1^2dy}{2\displaystyle\int_0^{b/2} cdy}$$

$$r_4=\frac{2\displaystyle\int_0^{b/2} cw_2dy}{2\displaystyle\int_0^{b/2} cdy}$$

$$r_5=\frac{2\displaystyle\int_0^{b/2} cw_1w_2dy}{2\displaystyle\int_0^{b/2} cdy}$$

$$r_6=\frac{2\displaystyle\int_0^{b/2} cw_2^2dy}{2\displaystyle\int_0^{b/2} cdy}$$

s, o distance traveled, $\dfrac{2V}{c_0}t$, half-chords

$T(f)$ amplitude of airplane frequency-response function

t time (zero at beginning of gust penetration)

U gust velocity

u vertical velocity of gust

V forward velocity of flight

w_n deflection of elastic axis in nth mode, given in terms of unit tip deflection, positive upward

y distance along wing measured from airplane center line

z_n response coefficient based on a_n, $\dfrac{V}{Uc_0}a_n$

ϵ strain, normal

$$\lambda_1=\frac{\omega_1c_0}{2V}$$

$$\lambda_2=\frac{\omega_2c_0}{2V}$$

$$\mu_0=\frac{8M_0}{a\rho c_0s}$$

$$\mu_1=\frac{8M_1}{a\rho c_0s}$$

$$\mu_2=\frac{8M_2}{a\rho c_0s}$$

ρ mass density of air

$1-\varphi$ function which denotes growth of lift on an airfoil following a sudden change in angle of attack (Wagner function)

ψ function which denotes growth of lift on rigid wing entering a sharp-edge gust (Küssner function)

ω_n natural circular frequency of vibration of nth mode

Subscripts:

j spanwise station

n natural modes of vibration

By following the procedure used in reference 1 for obtaining the response equations (eqs. (16) and (17) of ref. 1) for only two degrees of freedom, vertical motion and wing fundamental bending, the following response equations are obtained for the addition of the second symmetrical mode:

$$\mu_0 z_0'' = -2\int_0^s (z_0''+r_1 z_1''+r_4 z_2'')[1-\varphi(s-\sigma)]d\sigma + \int_0^s \frac{u'}{U}\psi(s-\sigma)d\sigma \quad \text{(A1)}$$

$$\mu_1 z_1''+\mu_1\lambda_1^2 z_1 = -2\int_0^s (r_1 z_0''+r_2 z_1''+r_5 z_2'')[1-\varphi(s-\sigma)]d\sigma + r_1\int_0^s \frac{u'}{U}\psi(s-\sigma)d\sigma \quad \text{(A2)}$$

$$\mu_2 z_2''+\mu_2\lambda_2^2 z_2 = -2\int_0^s (r_4 z_0''+r_5 z_1''+r_6 z_2'')[1-\varphi(s-\sigma)]d\sigma + r_4\int_0^s \frac{u'}{U}\psi(s-\sigma)d\sigma \quad \text{(A3)}$$

The equation that defines a bending-moment factor K_j at wing station y_j (from eq. (22) of ref. 1) takes the following form:

$$K_j = \frac{-8M_{m_0}}{a\rho c_0 M_{c_0}}\left(z_0''+\frac{M_{m_1}}{M_{m_0}}z_1''+\frac{M_{m_2}}{M_{m_0}}z_2''\right) - 2\int_0^s\left(z_0''+\frac{M_{c_1}}{M_{c_0}}z_1''+\frac{M_{c_2}}{M_{c_0}}z_2''\right)[1-\varphi(s-\sigma)]d\sigma + \int_0^s \frac{u'}{U}\psi(s-\sigma)d\sigma \quad \text{(A4)}$$

In order to reduce the response equations (A1) to (A4) to the special case of sinusoidal gust encounter where the gust has a frequency ω, the quantities u, z_0, and z_1 may all be taken proportional to e^{iks}, where $k=\frac{\omega c_0}{2V}$, as shown in reference 1. By following the procedure used in reference 1, equations (A1) to (A4) are reduced to the following form:

$$-\mu_0 k^2 z_0 = -2ik(z_0+r_1 z_1+r_4 z_2)(F+iG)+(P+iQ) \quad \text{(A5)}$$

$$-\mu_1 k^2 z_1+\mu_1\lambda_1^2 z_1 = -2ik(r_1 z_0+r_2 z_1+r_5 z_2)(F+iG)+r_1(P+iQ) \quad \text{(A6)}$$

$$-\mu_2 k^2 z_2+\mu_2\lambda_2^2 z_2 = -2ik(r_4 z_0+r_5 z_1+r_6 z_2)(F+iG)+r_4(P+iQ) \quad \text{(A7)}$$

$$K_j = \frac{8M_{m_0}}{a\rho c_0 M_{c_0}}k^2\left(z_0+\frac{M_{m_1}}{M_{m_0}}z_1+\frac{M_{m_2}}{M_{m_0}}z_2\right) - 2ik(F+iG)\left(z_0+\frac{M_{c_1}}{M_{c_0}}z_1+\frac{M_{c_2}}{M_{c_0}}z_2\right)+(P+iQ) \quad \text{(A8)}$$

where $F(k)$ and $G(k)$ are the in-phase and out-of-phase oscillatory lift coefficients and $P(k)$ and $Q(k)$ are the similar in-phase and out-of-phase lift components on a rigid wing subjected to a sinusoidal gust. In equation (A8), K_j represents the bending-moment transfer function $T(f)$ per unit gust velocity at station y_j. By solving equations (A5), (A6), and (A7) simultaneously for values of z_0, z_1, and z_2 and substituting these values into equation (A8), values of K_j may be obtained for any frequency k.

For the present analysis, the bending-moment factor K_j was expressed as strain by use of the following relation:

$$\epsilon = \frac{M_j l}{EI} = \frac{l}{EI}\frac{a}{2}\rho U V M_{c_0} K_j \quad \text{(A9)}$$

The airplane loading, physical constants, and basic paramenters used in this analysis are listed for each wing station in table I.

REFERENCES

1. Houbolt, John C., and Kordes, Eldon E.: Structural Response to Discrete and Continuous Gusts of an Airplane Having Wing-Bending Flexibility and a Correlation of Calculated and Flight Results. NACA Rep. 1181, 1954. (Supersedes NACA TN 3006; also contains essential material from TN 2763 and TN 2897.)
2. Houbolt, John C., and Kordes, Eldon E.: Gust-Response Analysis of an Airplane Including Wing Bending Flexibility. NACA TN 2763, 1952.
3. Houbolt, John C.: A Recurrence Matrix Solution for the Dynamic Response of Aircraft in Gusts. NACA Rep. 1010, 1951. (Supersedes NACA TN 2060.)
4. Bisplinghoff, R. L., Isakson, G., Pian, T. H. H., Flomenhoft, H. I., and O'Brien, T. F.: An Investigation of Stresses in Aircraft Structures Under Dynamic Loading. Contract No. NOa(s) 8790, M.I.T. Rep., Bur. Aero., Jan. 21, 1949.
5. Goland, M., Luke, Y. L., and Kahn, E. A.: Prediction of Wing Loads Due to Gusts Including Aero-Elastic Effects. Part I—Formulation of the Method. AF TR No. 5706, Air Materiel Command, U. S. Air Force, July 21, 1947.
6. Bisplinghoff, R. L., Isakson, G., and O'Brien, T. F.: Report on Gust Loads on Rigid and Elastic Airplanes. Contract No. NOa(s) 8790, M.I.T. Rep., Bur. Aero., Aug. 15, 1949.
7. Shufflebarger, C. C., and Mickleboro, Harry C.: Flight Investigation of the Effect of Transient Wing Response on Measured Accelerations of a Modern Transport Airplane in Rough Air. NACA TN 2150, 1950.
8. Mickleboro, Harry C., and Shufflebarger, C. C.: Flight Investigation of the Effect of Transient Wing Response on Wing Strains of a Twin-Engine Transport Airplane in Rough Air. NACA TN 2424, 1951.
9. Mickleboro, Harry C., Fahrer, Richard B., and Shufflebarger, C. C.: Flight Investigation of Transient Wing Response on a Four-Engine Bomber Airplane in Rough Air With Respect to Center-of-Gravity Accelerations. NACA TN 2780, 1952.
10. Murrow, Harold N., and Payne, Chester B.: Flight Investigation of the Effect of Transient Wing Response on Wing Strains of a Four-Engine Bomber Airplane in Rough Air. NACA TN 2951, 1953.
11. Press, Harry, and Houbolt, John C.: Some Applications of Generalized Harmonic Analysis to Gust Loads on Airplanes. Jour. Aero. Sci., vol. 22, no. 1, Jan. 1955, pp. 17–26, 60.
12. Press, Harry, and Tukey, John W.: Power Spectral Methods of Analysis and Their Application to Problems in Airplane Dynamics. Vol. IV of AGARD Flight Test Manual, Pt. IVC, Enoch J. Durbin, ed., North Atlantic Treaty Organization (Paris), pp. IVC:1—IVC:41.
13. Press, Harry, and Meadows, May T.: A Reevaluation of Gust-Load Statistics for Applications in Spectral Calculations. NACA TN 3540, 1955.

REPORT 1366

THE MECHANISM OF THERMAL-GRADIENT MASS TRANSFER IN THE SODIUM HYDROXIDE—NICKEL SYSTEM [1]

By Charles E. May

SUMMARY

"Thermal-gradient mass transfer" was investigated in the molten sodium hydroxide—nickel system. Possible mechanisms (physical, electrochemical, and chemical) are discussed in terms of experimental and theoretical evidence. Experimental details are included in appendixes. The following mechanism is found to be the most probable:

$$Na_2NiO_2 + 2Na \underset{\text{Hot zone}}{\overset{\text{Cold zone}}{\rightleftharpoons}} 2Na_2O + Ni$$

Kinetic equations are theoretically derived considering separately the following three factors as controlling the overall rate of mass transfer: the chemical reaction, the diffusion process, and the forced circulation (if present). If the above mechanism is the true one, the chemical reaction is the rate-determining step in dynamic systems, and the diffusion process is the rate-controlling step in static systems. The beneficial and detrimental effects of additives are interpreted in terms of the probable mechanism.

Evidence is also presented to show that thermal-gradient mass transfer in the molten sodium hydroxide—copper system occurs by a similar mechanism.

INTRODUCTION

Sodium hydroxide is in many ways an attractive choice as a high-temperature heat-transfer fluid. Unfortunately, only a few materials are suitable for containing it in the molten condition at the temperatures desired, 1500° to 1700° F. Among these are nickel (refs. 1 to 3), copper, silver, gold (ref. 4), and some nickel-base alloys recently produced at the Lewis laboratory. Even these materials exhibit corrosion termed "thermal-gradient mass transfer", although they do not show intergranular attack or rapid solution. Thermal-gradient mass transfer is the phenomenon by which the metal is removed (either chemically or physically) from the hotter regions of a system and deposited in colder regions. With the previously listed metals the deposit is in the form of needlelike crystals, the size of which depends on the experimental conditions.

In order to find ways of inhibiting this type of corrosion, an investigation was conducted concerning the possible mechanisms for mass transfer. Although mass transfer also occurs in liquid metal systems (ref. 5; e.g., molten sodium in copper), the mechanism in such cases is undoubtedly purely physical in nature, being due to solution of the container material in the molten metal. In systems using sodium hydroxide, transfer is probably chemical in nature, and the process is believed to be similar for all the container materials previously mentioned. The purpose of this report is to establish the most probable mechanism for mass transfer in this system. This report discusses methods of measurement, choice of mechanism, kinetics, effect of additives, and alternate mechanisms. Many of the proofs require the use of previously unpublished experimental data, the details of which are included in the appendixes.

METHODS OF MEASUREMENT

At the Lewis laboratory two methods have been used to study the phenomenon of mass transfer; they are the static capsule test and the dynamic toroid test. Previous reports (refs. 1 to 3) describe these in detail. In the static test a vertical temperature gradient exists in nickel capsules (crucibles) with the hot zone at the bottom. This type of gradient was intended to produce thermal convection. The nickel dissolves from the bottom of the capsule and precipitates as a narrow ring at the liquid level of the sodium hydroxide. From radiographs of such capsules the relative amounts of transfer can be estimated qualitatively. The loss in weight of a nickel specimen placed in the hot zone (bottom) is found to be proportional to the amount of transfer in the cold zone (ref. 1).

In the circulating liquid runs made in toroids, radiographs of the cold sections also supply a convenient method for measuring mass transfer. Since the transferred nickel is spread over an extended area, the average reduction in internal diameter of the cold section of the toroid gives a quantitative measure of transfer.

CHOICE OF MECHANISM

In the study of the mechanism of thermal-gradient mass transfer, a most general case can be considered. In the cold

[1] Supersedes NACA Technical Note 4089 by Charles E. May, 1957.

zone all of the reactants R_j's combine to produce nickel and all of the other products P_i's:

$$\sum_j n_j R_j \rightarrow \mathrm{Ni} + \sum_i m_i P_i$$

where n_j and m_i are the number of moles of R_j and P_i, respectively. The reverse reaction must occur at the hot zone to maintain the process. The requirements for such a cyclic reaction to occur are that at each temperature reaction occurs toward the attainment of equilibrium and that the equilibrium constant varies significantly with temperature. Thus, the concentrations are slightly displaced in one direction from equilibrium at the higher temperatures and in the other direction at the lower temperatures. Obviously, at some "mean temperature" the concentrations of the materials involved are in chemical equilibrium.

As a consequence, three major processes are involved in any proposed mechanism: (1) the chemical reactions that occur at the hot and cold zones, (2) the migration (diffusion or circulation) of the species from the hot to the cold zone and vice versa, and (3) the initial adjustment of concentrations to "mean-temperature" equilibrium, which sometimes requires additional chemical reactions. The evidence for or against a particular mechanism depends primarily on the nature of the first process, the zone reactions.

POSSIBLE REACTIONS

The first step in determining the mechanism of transfer was to enumerate all the possible reactions that could be envisioned (table I). A similar list is suggested in reference 6. These mechanisms were divided into three primary groups: physical, electrochemical, and chemical. The chemical mechanisms have been subdivided as to whether the oxidizing-reducing pair in the equation

$$\mathrm{Na_2NiO_2} + \mathrm{Reductant} \underset{\text{Hot zone}}{\overset{\text{Cold zone}}{\rightleftharpoons}} \mathrm{Oxidant} + \mathrm{Ni}$$

arises from an impurity, the disproportionation of nickel, or the sodium hydroxide. If the sodium hydroxide supplies the redox pair, the element actually involved in the oxidation could be either oxygen, hydrogen, or sodium. In the subsequent discussion, the oxidized form of nickel is generally represented as sodium nickelite ($\mathrm{Na_2NiO_2}$), since this compound in the form of olive-green needlelike crystals has recently been isolated at the Lewis laboratory (appendix A) as well as at other laboratories (refs. 6 to 9). It likewise appears that this is the only oxidized form of nickel stable in molten sodium hydroxide (appendix A).

MEANS OF SELECTION

The requirements for the actual mechanism are the following:

(1) The existence of chemical species involved in the reactions should be feasible. Their presence should be supported either experimentally or theoretically.

(2) The mechanism should explain the apparent difference in the kinetics between static and dynamic tests. Since in static tests hydrogen simultaneously decreases the rate of transfer and the nickelite concentration (appendix B), it appears that the rate of transfer depends upon nickelite concentration. However, in dynamic toroid tests, even though the nickelite concentration increases with time (appendix C), the rate of transfer is independent of time. This indicates that the rate of transfer is independent of nickelite concentration.

(3) The mechanism should explain the effect of additives upon the rate of transfer. Special attention should be devoted to the compounds of chromium (appendixes D and E), since both metallic chromium and chromium sesquioxide ($\mathrm{Cr_2O_3}$) inhibit transfer in static tests, while only chromium inhibits it in dynamic tests.

(4) There should be no experimental data in direct contradiction to the mechanism. However, all mechanisms except the last (reaction (7)) are contradictory to one or more experimental facts. These discrepancies are discussed later.

SODIUM MECHANISM

The following mechanism is considered to be the most probable one (table I, reaction (7)):

$$\mathrm{Na_2NiO_2} + 2\mathrm{Na} \underset{\text{Hot zone}}{\overset{\text{Cold zone}}{\rightleftharpoons}} 2\mathrm{Na_2O} + \mathrm{Ni}$$

The sodium oxide is presumed to arise exclusively from dissociation of sodium hydroxide, which generates water at the same time. Theoretically, sodium oxide should exist in sodium hydroxide; thermodynamic calculations (appendix F) show that its equilibrium concentration can be as high as 2.7 mole percent. Its presence has also been supported experimentally (ref. 10). Sodium nickelite (appendix A) and metallic sodium (ref. 7) have definitely been found experimentally in the sodium hydroxide—nickel system. Metallic sodium has likewise been detected in the sodium hydroxide—copper system (appendix G). Sodium, as well as sodium nickelite, is formed by the hot-zone reaction. Since, however, the concentration of sodium nickelite does not reach a constant value (appendix C), undoubtedly most of it is formed by the reaction

$$\mathrm{Ni} + 2\mathrm{NaOH} \rightarrow \mathrm{H_2} + \mathrm{Na_2NiO_2}$$

KINETICS

In order to explain the apparent differences between the results in static and dynamic tests, one must first derive the kinetic equations which are applicable to the mass transfer process. Any one of the following three factors can be considered to control the over-all rate of transfer: the rate of the chemical reaction, the rate of the diffusion process, and the rate of the circulation (if present). The equations in the next sections are developed in terms of the general reaction as written for the cold zone

$$\sum_j n_j R_j \rightarrow \mathrm{Ni} + \sum_i m_i P_i$$

CHEMICAL REACTION

When the chemical reaction is relatively slow, the molten material is essentially homogeneous with respect to the con-

centrations of all the chemical species. The rate of transfer r_t is obtained by considering the net rate of reaction in a unit area of the cold zone (denoted by the subscript c):

$$r_t=k_{f,c}\prod_j[R_j]^{n_i}-k_{r,c}\,a\prod_i[P_i]^{m_i} \tag{1}$$

where k_f is the rate constant of the forward reaction, k_r is the rate constant of the reverse reaction, a is the activity of the nickel metal, and [ ] indicates the concentration of the species. Rearranging gives

$$r_t=k_{f,c}\left(\prod_j[R_j]^{n_i}\right)\left(1-\frac{k_{r,c}}{k_{f,c}}\frac{a\prod_i[P_i]^{m_i}}{\prod_j[R_j]^{n_i}}\right) \tag{2}$$

Since at some "mean temperature" (mentioned previously) the species involved are in chemical equilibrium, their concentrations are related to each other by the equilibrium constant K_e of that "mean temperature":

$$K_e=\frac{a\prod_i[P_i]^{m_i}}{\prod[R_j]^{n_j}} \tag{3}$$

The equilibrium constant K_c for the cold zone is given by the equation

$$K_c=k_{f,c}/k_{r,c} \tag{4}$$

Substituting equations (3) and (4) into equation (2) yields

$$r_t=k_{f,c}\left(\prod_j[R_j]^{n_i}\right)\left(1-\frac{K_e}{K_c}\right) \tag{5}$$

From temperature-coefficient considerations,

$$\frac{K_e}{K_c}=e^{\Delta H/RT_c-\Delta H/RT_e} \tag{6}$$

where ΔH is the enthalpy of the reaction as written for the cold zone, R is the gas constant, T_c is the temperature of the cold zone, and T_e is the equilibrium temperature. Substituting equation (6) into equation (5) gives

$$r_t=k_f\left(\prod_j[R_j]^{n_i}\right)\left(1-e^{\Delta H/RT_c-\Delta H/RT_e}\right) \tag{7}$$

Finally, by expanding the exponential and assuming T_e-T_c (ΔT in eq. (8)) to be small, the rate of mass transfer is obtained for a chemical-reaction-controlled process:

$$r_t=-k_f\left(\prod_j[R_j]^{n_i}\right)\frac{\Delta H\Delta T}{RT^2} \tag{8}$$

or similarly

$$r_t=-k_r a\left(\prod_i[P_i]^{m_i}\right)\frac{\Delta H\Delta T}{RT^2} \tag{9}$$

DIFFUSION PROCESS

If the chemical reactions concerned are relatively fast, diffusion of the products and reactants may become the governing factor for the rate process. The resulting rate equation can be most easily derived for two nickel plates, each of unit area, at different temperatures, and placed parallel to each other at a distance l apart in molten sodium hydroxide. The temperature difference and the speed of the chemical reaction give rise to concentration differences ΔP_i and ΔR_j for the species surrounding the two plates. These plates are designated by the subscripts h for hot and c for cold.

The rate of transfer, being equal to the rate of diffusion of each species, is given by

$$r_t=\frac{m_i k_i}{l}([P_{i,c}]-[P_{i,h}])=\frac{n_j k_j}{l}([R_{j,h}]-[R_{j,c}]) \tag{10}$$

or simply

$$r_t=\frac{m_i k_i\Delta P_i}{l}=\frac{n_j k_j\Delta R_j}{l} \tag{11}$$

where the k_i's and k_j's are diffusion constants for the ith and and jth species. Multiplication of equations (10) and (11) by $l/k_i[P_i]$ and $l/k_j[R_j]$, respectively, and then summation over all i's and j's result in

$$r_t l\left(\sum_i\frac{1}{k_i[P_i]}+\sum_j\frac{1}{k_j[R_j]}\right)=\sum_i\frac{m_i\Delta P_i}{[P_i]}+\sum_j\frac{n_j\Delta R_j}{[R_j]} \tag{12}$$

or

$$r_t=\left(\sum_i\frac{m_i\Delta P_i}{[P_i]}+\sum_j\frac{n_i\Delta R_j}{[R_j]}\right)\Big/ l\left(\sum_i\frac{1}{k_i[P_i]}+\sum_j\frac{1}{k_j[R_j]}\right) \tag{13}$$

The numerator can be evaluated from equilibrium considerations as follows. Since chemical equilibrium exists at the hot and cold zones, the respective equilibrium constants K_h and K_c are

$$K_h=\frac{a\prod_i[P_{i,h}]^{m_i}}{\prod_j[R_{j,h}]^{n_j}} \tag{14}$$

and

$$K_c=\frac{a\prod_i[P_{i,c}]^{m_i}}{\prod_j[R_{j,c}]^{n_j}} \tag{15}$$

From temperature-coefficient considerations,

$$\frac{K_h}{K_c}=e^{\Delta H/RT_c-\Delta H/RT_h} \tag{16}$$

where T_h is the temperature of the hot zone. Combining equations (14), (15), and (16) gives

$$e^{\Delta H/RT_c-\Delta H/RT_h}=\prod_i\left(\frac{[P_{i,h}]}{[P_{i,c}]}\right)^{m_i}\Big/\prod_j\left(\frac{[R_{j,h}]}{[R_{j,c}]}\right)^{n_j} \tag{17}$$

The concentrations at the hot zone expressed in terms of the concentrations at the cold zone are

$$e^{\Delta H/RT_c-\Delta H/RT_h}=\frac{\prod_i\left(1-\frac{\Delta P_i}{[P_{i,c}]}\right)^{m_i}}{\prod_j\left(1+\frac{\Delta R_j}{[R_{j,c}]}\right)^{n_j}} \tag{18}$$

Expanding $\prod_i$ and $\prod_j$ and assuming that the ΔR_j's and ΔP_i's are small with respect to the corresponding R_j's and P_i's yield

$$e^{\Delta H/RT_c-\Delta H/RT_h}=1-\sum_i\frac{m_i\Delta P_i}{[P_{i,c}]}-\sum_j\frac{n_j\Delta R_j}{[R_{j,c}]} \tag{19}$$

Expanding the exponential with ΔT, $T_h - T_c$, assumed to be small gives

$$\frac{-\Delta H \Delta T}{RT^2} = \sum_i \frac{m_i \Delta P_i}{[P_i]} + \sum_j \frac{n_j \Delta R_j}{[R_j]} \tag{20}$$

Combining equations (13) and (20), one obtains

$$r_t = -\Delta H \Delta T / \left(\sum_i \frac{1}{k_i[P_i]} + \sum_j \frac{1}{k_j[R_j]} \right) RT^2 l$$

$$= -k_a \Delta H \Delta T / \left(\sum_i \frac{k_a}{k_i[P_i]} + \sum_j \frac{k_a}{k_j[R_j]} \right) RT^2 l \tag{21}$$

where k_a is the average-diffusion-rate constant.

CIRCULATION

In a system with force flow the rate of transfer may be controlled by the rate of circulation k_{cir} (in cps). In a static system with thermal convection a value for k_{cir} might be difficult to assign. Nevertheless, the rate of transfer in a circulation-controlled system can be expressed as

$$r_t = Ck_{cir} m_i \Delta P_i = Ck_{cir} n_j \Delta R_j \tag{22}$$

where C expresses the dependence of r_t on the volume of the melt. The following equation can then be obtained in a similar manner to that for equation (13):

$$r_t = Ck_{cir} \left(\sum_i \frac{m_i \Delta P_i}{[P_i]} + \sum_j \frac{n_j \Delta R_j}{[R_j]} \right) \Big/ \left(\sum_i \frac{1}{[P_i]} + \sum_j \frac{1}{[R_j]} \right) \tag{23}$$

Since chemical equilibrium exists at the higher and lower temperatures, equation (20) is again valid. Upon substituting equation (20) into equation (23),

$$r_t = -Ck_{cir} \Delta H \Delta T / \left(\sum_i \frac{1}{[P_i]} + \sum_j \frac{1}{[R_j]} \right) RT^2 \tag{24}$$

It is readily noted that in all three cases (eqs. (9), (21), and (24)) the rate of transfer (to the first approximation) is proportional to the change in enthalpy of the reaction as written for the cold zone. Inasmuch as the rate r_t is positive as written, the enthalpy must be negative. To the first approximation, the transfer is proportional to the difference in temperature; this point has been supported experimentally (ref. 1).

APPLICATION OF EQUATIONS

For the sodium mechanism the three kinetic equations would be:

$$r_t(\text{chemical}) = \frac{-k_r a \Delta H \Delta T}{RT^2 \left(\frac{1}{[\text{Na}_2\text{O}]} \right)^2} \tag{25}$$

$$r_t(\text{diffusion}) = \frac{-k_a \Delta H \Delta T}{RT^2 l \left(\frac{k_a}{k_1[\text{Na}_2\text{O}]} + \frac{k_a}{k_2[\text{Na}]} + \frac{k_a}{k_3[\text{Na}_2\text{NiO}_2]} \right)} \tag{26}$$

$$r_t(\text{circulation}) = \frac{-k_{cir} C \Delta H \Delta T}{RT^2 \left(\frac{1}{[\text{Na}_2\text{O}]} + \frac{1}{[\text{Na}]} + \frac{1}{[\text{Na}_2\text{NiO}_2]} \right)} \tag{27}$$

In a chemically controlled process the rate of transfer is constant as long as the equilibrium concentration of sodium oxide is not disturbed significantly by the zone reaction

$$\text{Na}_2\text{NiO}_2 + 2\text{Na} \underset{\text{Hot zone}}{\overset{\text{Cold zone}}{\rightleftharpoons}} 2\text{Na}_2\text{O} + \text{Ni}$$

If the equilibrium constant for the zone reaction has a value which keeps the sodium concentration low with respect to that of sodium oxide, the latter is not appreciably affected.

In a diffusion-controlled process, the effect of the sodium concentration may be ignored if k_2 is relatively large, as would be predicted from the uncharged nature and the small size of an atom of metallic sodium. Thus, the rate of transfer should depend upon the nickelite concentration, since it is of the same order of magnitude as the sodium oxide concentration ($[\text{Na}_2\text{NiO}_2] = 0.2$ mole percent at 24 hr, calculated from data in table VIII; $[\text{Na}_2\text{O}] = 0.02$ to 2.7 mole percent, appendix F).

The rate of circulation-controlled transfer (eq. (27)) can be considered next. Since the sodium concentration is less than the nickelite concentration, the term $1/[\text{Na}]$ affects the rate of transfer more than the term $1/[\text{Na}_2\text{NiO}_2]$. Therefore, since $1/[\text{Na}]$ is proportional to the nickelite concentration, the rate of mass transfer must decrease as the nickelite concentration increases.

One therefore concludes that the rate of transfer in dynamic systems is chemically controlled, since it is independent of sodium nickelite concentration. However, transfer in static systems must be diffusion controlled, since its rate increases with nickelite concentration (appendix B). In static tests the rate of transfer should then increase with time. The increased rate of specimen weight loss with time in capsule tests (table VIII, column 9) is an indication of this increased rate of transfer.

EFFECT OF ADDITIVES

In a chemically controlled mechanism (dynamic system) additives may affect the rate of transfer in the following ways:

(1) By changing the concentration of the sodium oxide
(2) By supplying an auxiliary transfer mechanism
(3) By changing the activity of the nickel metal

The first two methods of affecting the rate of transfer are also valid in a diffusion-controlled mechanism (static system). However, the third method, changing the activity of the nickel, should have no effect; instead changing the concentration of sodium nickelite should affect the rate of transfer as stated previously.

SODIUM OXIDE

One would predict that the addition of sodium oxide and sodium metal (which would effectively increase the sodium oxide concentration) to either a static or dynamic system should increase the rate of mass transfer. This has been verified experimentally (ref. 3). Adding calcium, sodium hydride, lithium hydride, or calcium nitride (being equivalent to adding metallic sodium) should likewise increase

the rate of transfer. For example, the reaction with calcium is

$$Ca+2NaOH \rightarrow Ca(OH)_2+2Na$$

This also is demonstrated in references 2 and 3. The fast decomposition of the sodium hydride and lithium hydride should allow all the hydrogen thus generated to diffuse rapidly through the nickel and thus to produce no beneficial effect.

In cases in which metallic additives react with sodium hydroxide to produce sodium oxide, an increased rate of transfer should again be expected. This point is perhaps illustrated in the increased rate of transfer caused by addition of manganese, iron, titanium, vanadium, or molybdenum:

$$Mo+6NaOH \rightarrow Na_2MoO_4+2Na_2O$$

WATER

Additions of water in small amounts should suppress the sodium oxide concentration and inhibit transfer. In static tests where gas saturated with water vapor was passed over the sodium hydroxide in the nickel crucible being tested, transfer was decreased (ref. 3).

Additions of certain oxides may be equivalent to adding water, as is evident from the equation

$$CoO+2NaOH \rightarrow Na_2CoO_2+H_2O$$

This may be the case when inhibition of transfer results from the use of the following: cobalt oxide, cupric oxide, cuprous oxide, stannous oxide, manganese monoxide, and zirconium dioxide (ref. 11). The effectiveness of stannous oxide, manganese monoxide, and cuprous oxide may be partially due to their reducing action. In order for beneficial effects due to water to be observed, the additive must either be added after purging or react only at temperatures higher than the purging temperature.

It is possible that too much water might result in an auxiliary reaction such as

$$Na_2NiO_2+2Na+2H_2O \underset{\text{Hot zone}}{\overset{\text{Cold zone}}{\rightleftharpoons}} Ni+4NaOH$$

This may account for the case of unpurged sodium hydroxide in which the rate of transfer was increased (ref. 2). This reaction may also account for the fact that any beneficial effects attributable to the presence of water are always slight.

METALLIC CHROMIUM

Metallic chromium is an inhibitor of mass transfer (ref. 2). The method by which chromium works is not by decreasing the nickelite concentration (appendix D).

Experiments show that metallic chromium reacts rapidly with molten sodium hydroxide to form sodium chromite (Cr^{+3}), which then reacts more slowly (for 20 hr) to form perhaps sodium hypochromate (Cr^{+5}) (appendix E). This chromite-hypochromate reaction is in equilibrium with the hydrogen pressure (appendix E). Since the nickel-nickelite reaction is not in equilibrium with hydrogen (appendix C), a reaction similar to the following one cannot be at "mean-temperature" equilibrium:

$$Ni+Na_5CrO_5 \underset{\text{Hot zone}}{\overset{\text{Cold zone}}{\rightleftharpoons}} Na_3CrO_3+Na_2NiO_2$$

The chromium is therefore not effective by means of this auxiliary mechanism. In some way the chromite and hypochromate form a complex in an approximate ratio of 1 to 1 at 1500° F. Therefore, it is not unreasonable that one of the species might partially complex with sodium oxide and thus inhibit mass transfer (in both static and dynamic tests).

The question which now arises is why the chromite formed from metallic chromium reacts differently from the chromite formed from chromium sesquioxide (appendix D). Even though both may form sodium chromite, the coordination of the oxygen atoms about the chromium might be different; this is quite common among water-soluble salts of chromium. If the mechanism by which transfer is inhibited using metallic chromium involves coordination (complex formation), chromium sesquioxide obviously need not inhibit transfer in the same manner as metallic chromium.

REDUCING AGENTS

Since chromium sesquioxide reduces the sodium nickelite concentration (appendix D) presumedly by the generation of hydrogen, it should inhibit mass transfer when the transfer is a diffusion-controlled process. Indeed, transfer is inhibited in static tests by chromium sesquioxide (appendix D) but not in dynamic tests recently performed at the Lewis laboratory. Another reducing agent, calcium hydride, also inhibits transfer in static tests but not in dynamic tests (ref. 3). Hence, directly applied hydrogen pressure which inhibits transfer in static tests should not necessarily be effective in dynamic tests. Published work on this effect is inconclusive (ref. 11). Hydrogen could inhibit transfer in dynamic tests if its poisoning action were sufficient to reduce the activity of the nickel. (Calcium hydride increases the rate of transfer in dynamic systems, because its decomposition produces "detrimental" calcium metal as well as "beneficial" hydrogen.)

OXIDIZING AGENTS

Oxidizing agents should have the opposite effect of reducing agents upon the rate of transfer, since they should increase the sodium nickelite concentration. This is the effect found in static systems for materials such as sodium peroxide, ferric oxide, potassium chlorate, potassium chromate, sodium chromate, calcium chromate, cobaltous-ic oxide, manganese dioxide, sodium bromate, and lead sesquioxide (refs. 2 and 11). This effect is not expected in dynamic tests, but none of these additives have ever been studied under such conditions.

INSOLUBLE COMPOUNDS

Apparent inhibition of transfer resulted in static tests from additions of aluminum, aluminum oxide, sodium aluminate, aluminum fluoride, magnesium oxide, calcium chloride, or strontium peroxide (refs. 2, 3, and 11). This has been attributed to the formation of protective insoluble

526597—60——46

layers over the specimens, sodium aluminate in the case of aluminum compounds, and insoluble oxides from the others.

INERT MATERIALS

Since silver, gold, and copper do not react rapidly with sodium hydroxide, no effect is produced by using these metals as additives (ref. 11). Other materials, such as salts that are inert to sodium hydroxide (sodium chloride, sodium fluoride, and sodium iodide) and ceramic materials stable at 1500° and 1700° F (tantalum nitride and columbium nitride), should not and do not have any effect upon mass transfer (refs. 2 and 11).

CONSIDERATION OF ALTERNATIVE MECHANISMS

PHYSICAL MECHANISM

In considering the physical mechanism (table I, reaction (1))

$$\mathrm{Ni^{o}(dissolved)} \underset{\text{Hot zone}}{\overset{\text{Cold zone}}{\rightleftharpoons}} \mathrm{Ni^{o}(metal)}$$

one may admit that nickel is soluble in molten sodium hydroxide and that as soon as saturation is reached transfer could occur.

Although mass transfer might be attributable to this mechanism, experiments with hydrogen atmospheres show its contribution to be quite small, since the presence of hydrogen reduces the rate of transfer by a large factor (appendix B and ref. 3). In no way is it conceivable that hydrogen reduces the solubility of nickel in molten sodium hydroxide. A large variety of other materials in small quantities do affect the rate of transfer (appendixes D and E and refs. 2 and 3). It does not seem plausible that such materials would affect transfer if it were just a problem of physical solubility.

ELECTRICAL MECHANISM

The second possible mechanism for transfer involves the electrochemical half-cell reactions (table I, reaction (2))

$$\mathrm{Na_2NiO_2 + 2Na^+ + 2e^-} \underset{\text{Hot zone}}{\overset{\text{Cold zone}}{\rightleftharpoons}} \mathrm{2Na_2O + Ni}$$

This mechanism requires the existence of an electromotive force between nickel at the hot zone and nickel at the cold zone. Such a potential has been observed experimentally (appendix H and ref. 12); it is probably attributable to reaction (2). Moreover, this potential is sufficient to sustain a current of measurable magnitude for 6 hours (appendix H). The electrochemical reaction requires that, since the sodium nickelite concentration builds up with time (appendix C), the electromotive force as well as the actual rate of transfer should decrease with time. This is contrary to fact. Also, in the presence of hydrogen, the mass transfer should occur from the cold zone to the hot zone in accordance with the reversal of polarity observed with a hydrogen atmosphere (appendix H).

The conclusions are that the electrochemical process may be occurring, but that its contribution to the mass transfer actually observed is small and as time progresses becomes less and less. In the presence of a hydrogen atmosphere this process cannot occur at all. An additional proof is the fact that crystals of nickel plate out on a ceramic material in cold regions (ref. 6); in this case an electrochemical process is impossible.

The latter conclusions are of course valid even though the half-cell reactions might involve nickel with a valence of +3:

$$\mathrm{NaNiO_2 + 3Na^+ + 3e^-} \underset{\text{Hot zone}}{\overset{\text{Cold zone}}{\rightleftharpoons}} \mathrm{2Na_2O + Ni}$$

IMPURITY MECHANISM

Of the impurities present in sodium hydroxide (table II) and nickel (table III), only iron, cobalt, or manganese could contribute to the impurity mechanism, since the element involved must exist in two oxidized valence states:

$$\mathrm{Na_2NiO_2 + 2Na_2FeO_2} \underset{\text{Hot zone}}{\overset{\text{Cold zone}}{\rightleftharpoons}} \mathrm{2Na_3FeO_3 + Ni}$$

$$\mathrm{Na_2NiO_2 + 2Na_2CoO_2} \underset{\text{Hot zone}}{\overset{\text{Cold zone}}{\rightleftharpoons}} \mathrm{2Na_3CoO_3 + Ni}$$

$$\mathrm{2Na_2NiO_2 + Na_2MnO_2} \underset{\text{Hot zone}}{\overset{\text{Cold zone}}{\rightleftharpoons}} \mathrm{Na_2MnO_4 + 2Na_2O + 2Ni}$$

The probability that a sulfate, a phosphate, silver, or copper would exist in two ionic valences is exceedingly small. Because of the small concentrations of all the impurities, this type mechanism, although possible, is still not probable.

The concentration of impurities arising from the nickel increases in the sodium hydroxide with time (ref. 6), and thus the rate of transfer should increase. The rate of transfer does not increase with time in dynamic tests.

Finally, all these impurities were deliberately added (in some form) to the sodium hydroxide, and although some apparently increase transfer (perhaps fivefold by qualitative estimate) (table IV), this increase is not proportional to the thousandfold increase of the impurity concentration.

DISPROPORTIONATION MECHANISM

The next mechanism to consider is the disproportionation reaction of nickel (table I, reaction (4))

$$\mathrm{3Na_2NiO_2} \underset{\text{Hot zone}}{\overset{\text{Cold zone}}{\rightleftharpoons}} \mathrm{2Na_3NiO_3 + Ni}$$

Again reference is made to the fact that the sodium nickelite concentration increases with time (appendix C). Since the nickelite and nickelate must be in "mean-temperature" equilibrium, the concentration of the nickelate must also increase. Therefore, the transfer rate should depend on the nickelite concentration regardless of how the rate process is controlled. The same is true even if the chemical equation is

$$\mathrm{3Na_2NiO_2} \underset{\text{Hot zone}}{\overset{\text{Cold zone}}{\rightleftharpoons}} \mathrm{2NaNiO_2 + 2Na_2O + Ni}$$

Since the transfer rate in dynamic systems is experimentally independent of nickelite concentration, the actual mechanism cannot involve disproportionation of nickel.

Furthermore, the higher valences of nickel should not exist in the presence of a hydrogen pressure (ref. 6) such as has been reported to exist above the nickel—sodium hydroxide system at 800° C (4 mm Hg, ref. 7).

OXYGEN MECHANISM

The possibility that oxygen is the "redox" material according to the equation

$$Na_2NiO_2 \underset{\text{Hot zone}}{\overset{\text{Cold zone}}{\rightleftharpoons}} Na_2O + \tfrac{1}{2}O_2 + Ni$$

is nil, since the pressure of hydrogen of 4-millimeters of mercury (ref. 7) eliminates the possibility that oxygen is present at all.

HYDROGEN MECHANISM

The mechanism that for a long time seemed the most logical involves hydrogen as the redox material; the reaction is (table I, reaction (6))

$$Na_2NiO_2 + H_2 \underset{\text{Hot zone}}{\overset{\text{Cold zone}}{\rightleftharpoons}} 2NaOH + Ni$$

The reaction between nickel and sodium hydroxide is known to occur, since both hydrogen and sodium nickelite are found as products; the problem is whether this reaction can go in reverse. This seemed possible, since nickel oxide (assumed to be the oxidized form of nickel) is easily reduced by hydrogen. Experiments under isothermal conditions with a constant imposed hydrogen pressure (appendix C) showed that the rate of formation of sodium nickelite is constant even up to times of 600 hours. Thus, equilibrium is not reached, the reverse reaction never occurs, and this mechanism could never account for transfer. Even with no added hydrogen, equilibrium is not reached, inasmuch as the concentration of sodium nickelite does not reach a constant value (table VIII, column 7). The decrease in the rate of formation of sodium nickelite caused by hydrogen must be due to its direct poisoning action upon the nickel.

Since the concentration of species of nickel other than Ni^{+2} (e.g., Ni^{+3}) which might be in equilibrium with the hydrogen present is extremely low (ref. 6), the corresponding reactions involving this concentration need not be considered.

SUMMARY OF RESULTS

The following zone reactions are the probable ones occurring in thermal-gradient mass transfer of nickel in molten sodium hydroxide:

$$Na_2NiO_2 + 2Na \underset{\text{Hot zone}}{\overset{\text{Cold zone}}{\rightleftharpoons}} 2Na_2O + Ni$$

The diffusion of the molecular species in the melt allows the process to continue indefinitely. The sodium oxide arises from the dissociation of sodium hydroxide at high temperatures. The sodium nickelite (Na_2NiO_2) is formed primarily from the following reaction and at a constant rate with any given pressure of hydrogen:

$$2NaOH + Ni \rightarrow H_2 + Na_2NiO_2$$

In dynamic tests, the rate of transfer is controlled by the rate of the zone reactions and thus is constant with time. In static tests, the rate of transfer is controlled by the rate of diffusion and thus increases with time.

The effects of additives upon the rate of transfer can be explained in terms of this mechanism. Additives which effectively increase the sodium oxide concentration increase the rate of transfer; those which decrease this concentration decrease the rate of transfer. Reducing agents decrease the rate of transfer in static tests and have no effect in dynamic tests. Oxidizing agents have the opposite effect in static tests.

LEWIS FLIGHT PROPULSION LABORATORY
NATIONAL ADVISORY COMMITTEE FOR AERONAUTICS
CLEVELAND, OHIO, *June 20, 1957*

APPENDIX A

EXISTENCE OF SODIUM NICKELITE IN SODIUM HYDROXIDE—NICKEL SYSTEM

An investigation was made to demonstrate the existence of sodium nickelite in the sodium hydroxide—nickel system. The existence of this or a similar compound is necessary for six of the seven possible mechanisms of mass transfer (table I). The nature of the hydrolysis product of sodium nickelite was also studied in order to substantiate the theory that nickel was present in the +2 valence state. The reaction between nickel oxide and sodium hydroxide was investigated to show the relative instability of this compound with respect to sodium nickelite.

MATERIALS AND PROCEDURE

The "L" nickel crucibles as well as the procedure were identical to those used in the standard static capsule test at the Lewis laboratory (fig. 1 and refs. 2 and 3). The crucibles were 5 inches long and had an outside diameter of ⅝ inch and 1/16-inch-thick walls. All the crucible components except the vent tube were fabricated from the same length of tubing.

Before the crucibles were assembled, the components were cleaned in a modified aqua regia solution for 2 minutes. Heliarc welding with an atmosphere containing 15 percent hydrogen in helium was used in fabrication. A flow of argon was maintained in the tube during welding. Sodium hydroxide (13.0 ± 0.1 g) was weighed into each crucible in the dry box. The top and vent tube were then welded into place. The moisture and air were removed by evacuation to 5 microns of mercury at 580° F (in 16 hr) and then to 5 microns of mercury at 720° F (in 4 hr). After evacuation and cooling, a cover gas of helium at about 2 pounds per square inch gage was admitted. Crimping and welding at

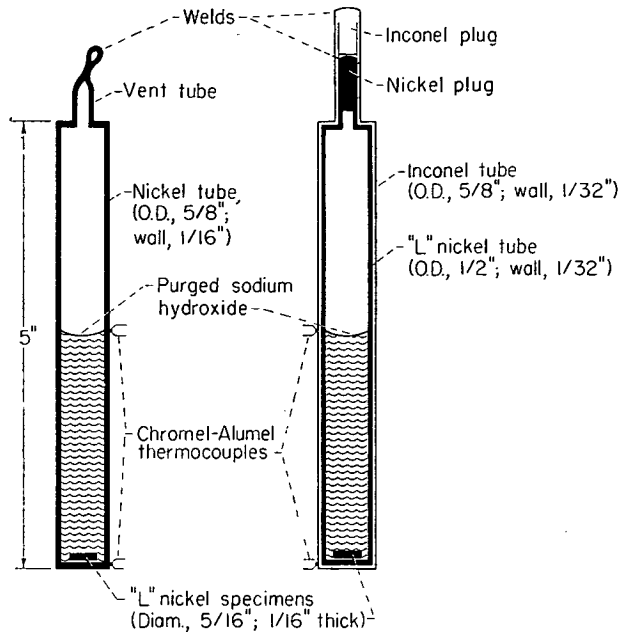


FIGURE 1.—Comparison of standard crucible (left) and crucible with Inconel shell.

the crimp served to seal the crucible. Thermocouples were spot-welded to the crucibles ⅛ inch from the bottom and also at the liquid level. A special furnace (ref. 2) was used.

ISOLATION AND IDENTIFICATION OF SODIUM NICKELITE

Four crucibles were heated to 1700° F for 24 hours. After cooling, they were cut into sections about ½ inch long in a dry helium atmosphere. Olive to dark-green needlelike crystals about ⅛ inch long were visible throughout the white sodium hydroxide matrix. Similar crystals are reported in reference 6. The sodium hydroxide was dissolved away from the crystals with absolute methyl alcohol. The X-ray powder diffraction pattern (table V) determined for the crystals matched the ones which have been reported by other laboratories (refs. 7 and 9) and assigned the formula Na_2NiO_2. No lines of nickel oxide or nickel hydroxide were found. The utmost care was used to keep air and moisture away from the crystals at all times. The chemical analysis reported for this compound (residue) in reference 9 roughly corresponds to the formula Na_2NiO_2. Reference 7 reports an X-ray pattern from a residue obtained by heating sodium hydroxide in nickel until all the hydrogen present was evolved as a gas; this would likewise correspond to the formula Na_2NiO_2. The fact that the pattern from this work matches the others indicates that sodium nickelite does not significantly react with absolute methyl alcohol.

No well defined crystals were obtained by heating sodium hydroxide in nickel at 1500° F, since the nickelite concentration was too small.

PREPARATION OF HYDROLYSIS PRODUCTS

In order to investigate the hydrolysis products, other crucibles were prepared in the way described previously. After the 24-hour treatment at 1700° F, the contents of the crucibles were washed out with distilled water and the crystals present were allowed to remain in the water about 3 days. Bright grass-green needlelike crystals were formed. There was also present a slight amount of fine black precipitate, which was probably formed from the hydrolysis of sodium nickelite dissolved in the sodium hydroxide. After removal of the black precipitate by decantation, the green crystals were washed and then dried in a desiccator containing Drierite. They were shown spectroscopically to contain no sodium, and their X-ray pattern matched that for nickel hydroxide ($Ni(OH)_2$). The individual crystals were hexagonal in shape as seen under a microscope. The crystals turned black upon drying at 120° C for 24 hours but still retained the same crystalline form and X-ray pattern. The crystals lost 11.8 percent of their weight during the heating process. The chemical analysis of the black crystals showed them to be nickel hydroxide ($Ni(OH)_2$). Although the green crystals correspond to the composition $Ni(OH)_2 \cdot H_2O$, they probably contain merely physically trapped water (inasmuch as the X-ray pattern was unchanged).

At 1500° F the reaction between sodium hydroxide and nickel did not yield a crystalline hydrolysis product (except in one isolated instance). The black to brown powder regularly obtained by filtering the water solution of the melt nevertheless gave the X-ray pattern for nickel hydroxide. This powder was probably the same as the slight amount of black powder obtained from the crucible run at 1700° F.

HYDROLYSIS PRODUCTS FROM REACTION OF SODIUM HYDROXIDE WITH NICKEL OXIDE

A nickel crucible containing 0.13 gram of nickel oxide and the usual 13 grams of sodium hydroxide was purged, sealed, and heated to 1700° F for 15 minutes. When the contents were washed out, large grass-green needlelike crystals were found. Only a trace of the nickel oxide X-ray pattern was detectable in the nickel hydroxide pattern found for these green crystals. X-ray patterns of individual crystals proved them to be actually polycrystalline.

CONCLUSIONS

The reaction between nickel and molten sodium hydroxide produces sodium nickelite (Na_2NiO_2). The sodium nickelite can be isolated as needlelike crystals if the reaction occurs at 1700° F but not if it occurs at 1500° F or lower; this is attributed to the greater concentration of the nickelite at 1700° F (table VIII) and to a probably large rate of change of solubility with temperature between 1500° and 1700° F.

The reaction between nickel oxide and sodium hydroxide at 1700° F (and likely below that temperature) also produces sodium nickelite (indicated by the presence of its hydrolysis product nickel hydroxide):

$$NiO + 2NaOH \rightarrow Na_2NiO_2 + H_2O$$

Since this reaction goes essentially to completion, very little possibility exists that the species NiO can be present in molten sodium hydroxide—nickel systems.

The reaction between sodium nickelite and water

$$Na_2NiO_2 + 2H_2O \rightarrow 2NaOH + Ni(OH)_2$$

results in the removal of the Na_2O component by leaching without disturbing the external shape of the crystals. Probably during this process single crystals of sodium nickelite convert to polycrystalline nickel hydroxide (containing physically trapped water).

APPENDIX B

THE EFFECT OF HYDROGEN UPON MASS TRANSFER AND NICKELITE CONCENTRATION

Experiments were conducted to show the simultaneous dependence of sodium nickelite concentration and rate of mass transfer upon the hydrogen pressure in nickel capsules containing sodium hydroxide. A more complete study of the rate of formation of sodium nickelite is presented in appendix C.

METHOD 1

Four standard "L" nickel crucibles containing weighed nickel specimens (1/16 in. thick and 5/16 in. in diam.) and sodium hydroxide (13.0±0.1 g) were prepared and sealed in the usual manner for standard capsule tests (appendix A and ref. 2). They were encased in Inconel chambers (fig. 2).

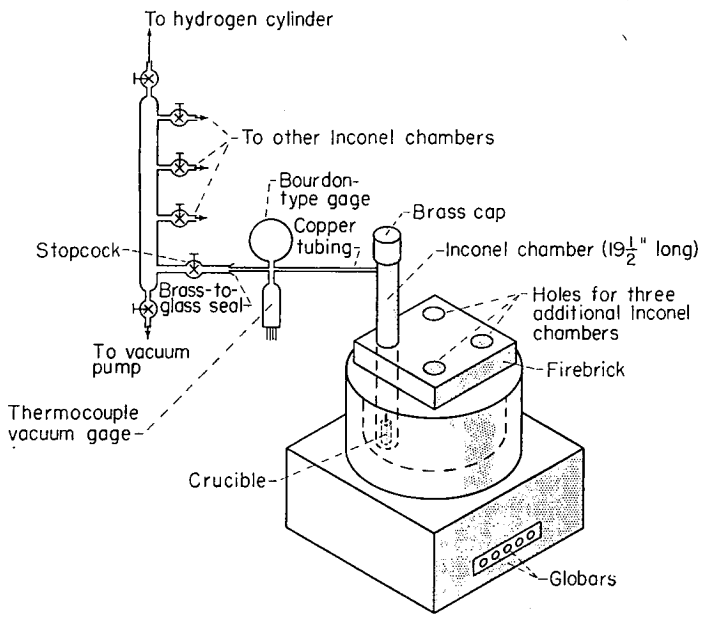


FIGURE 2.—Vacuum system and Inconel chamber.

The chambers were evacuated to a pressure of 5 microns of mercury and then connected to a supply of hydrogen at a constant pressure of 17 inches of mercury. The temperature of the crucibles was raised to 1500° F by means of a special Globar furnace (ref. 2). This furnace by supplying heat from the bottom maintained an 80° F difference between the bottom of the Inconel chambers and a position 2½ inches from the bottom (the sodium hydroxide liquid level). The pressure of hydrogen inside the nickel crucibles was also 17 inches of mercury because of the permeability of nickel toward hydrogen. After 80 hours at temperature the crucibles were cooled and were radiographed to detect the amount of transfer. The amount of sodium nickelite was determined as nickel +2, and the specimens were reweighed (table VI). The experiment was repeated with crucibles having no added hydrogen in the chambers. Even though no hydrogen was added to these control crucibles, a steady-state hydrogen pressure of about 4 millimeters of mercury was present (ref. 7). The steady-state pressure arises in a sealed container from the fact that hydrogen is generated by the reaction of nickel with sodium hydroxide and that hydrogen is lost by diffusion through the walls of the nickel container. The rates of these two processes become equal when a certain steady-state hydrogen pressure is reached.

As is obvious from the data of table VI, the added hydrogen simultaneously inhibited the formation of the nickelite and the rate of mass transfer.

METHOD 2

Tests were also run in which hydrogen was introduced directly into the hot zone (bottom of the crucible) (fig. 3).

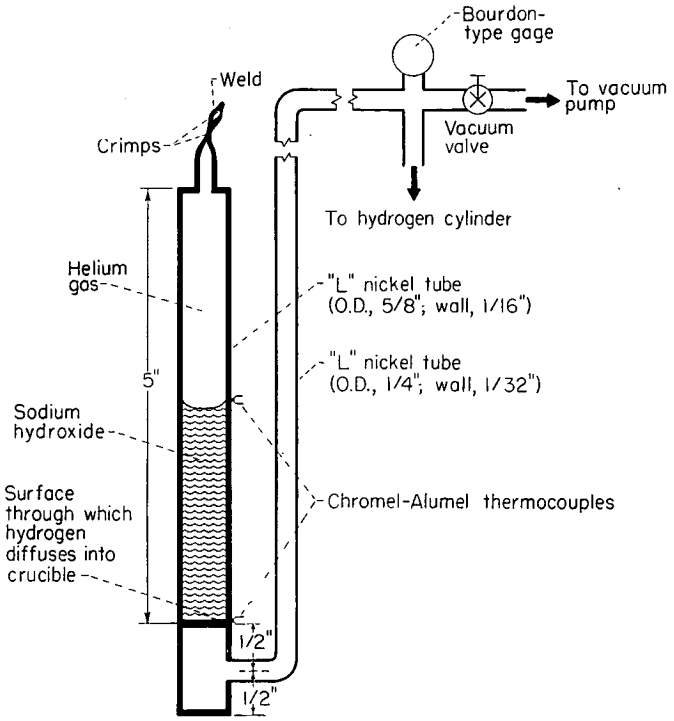


FIGURE 3.—Crucible for introduction of hydrogen at hot zone.

These tests again showed that added hydrogen simultaneously inhibited the formation of sodium nickelite and the rate of mass transfer.

METHOD 3

The third method was designed to determine whether inhibiting the loss of hydrogen normally formed in a crucible would likewise inhibit transfer. This was accomplished by placing a shell of Inconel around a standard nickel crucible (fig. 1), inasmuch as the rate of diffusion of hydrogen through Inconel is much less than through nickel.

The internal and external dimensions of the modified crucibles were as close as practicable to those of a standard one. Two standard crucibles were used for comparison (appendix A and ref. 2). Two Inconel-covered crucibles were prepared by first treating the inner nickel crucibles in essentially normal fashion. The top plugs were hammered into place in a dry box and then welded to seal the crucibles. The Inconel shells were then assembled

around the nickel and welded together. These four crucibles were heated at 1560° F (in the Globar furnace) for 24 hours; after this the crucibles were radiographed and the contents were analyzed chemically (table VI).

The Inconel shell inhibited transfer as expected. Reduction of the rate of formation of the nickelite was also detectable and was attributed to an increased hydrogen pressure caused by the decreased loss of hydrogen by diffusion.

APPENDIX C

RATE OF FORMATION OF SODIUM NICKELITE

A study was made to determine the rate of formation of sodium nickelite according to the equation

$$Ni+2NaOH \rightarrow Na_2NiO_2+H_2$$

If the reaction does not reach equilibrium in a reasonable time, the mechanism of mass transfer involving hydrogen as the "redox" material (table I, reaction (6)) is impossible.

PROCEDURE

Standard test nickel crucibles (fig. 1) containing 13.0 ±0.1 gram of sodium hydrozide were prepared (purged and crimped) in the usual manner (appendix A). They were in turn suspended in an Inconel tube by means of a long Nichrome loop spot-welded to the crimp of the nickel crucible (fig. 4). The top of the loop was placed over a nickel

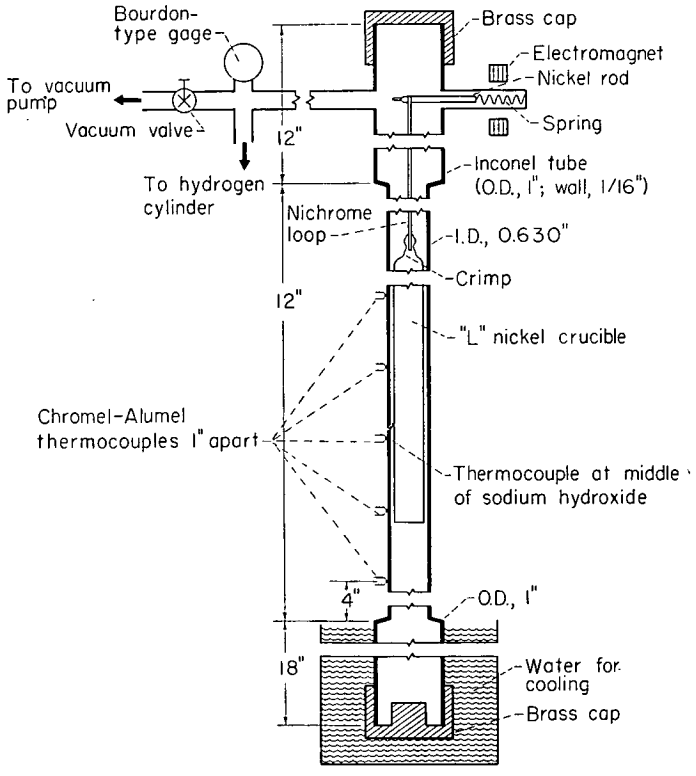


FIGURE 4.—Apparatus for kinetic and equilibrium studies.

plunger, which could be pulled out from under the loop by means of a magnet outside the vacuum system. Brass caps were soft soldered to the top and bottom of the Inconel tube so that the system could be evacuated. After evacuation, hydrogen gas was admitted and controlled at the desired pressure. The temperature was then raised as quickly as possible to 1500° F (±4° F). The temperature measurements along the outside of the Inconel tube showed that a temperature difference of at most 3° F existed between the top and the bottom of the molten sodium hydroxide. At the end of a run a magnetic field was applied to the plunger so that the nickel crucible was allowed to fall to the bottom of the Inconel tube. The nickel crucible was thereby rapidly cooled. The experiment was repeated for various times and various hydrogen pressures (table VII). After each run the crucible was cut open and its contents were analyzed for oxidized nickel (fig. 5 and table VII).

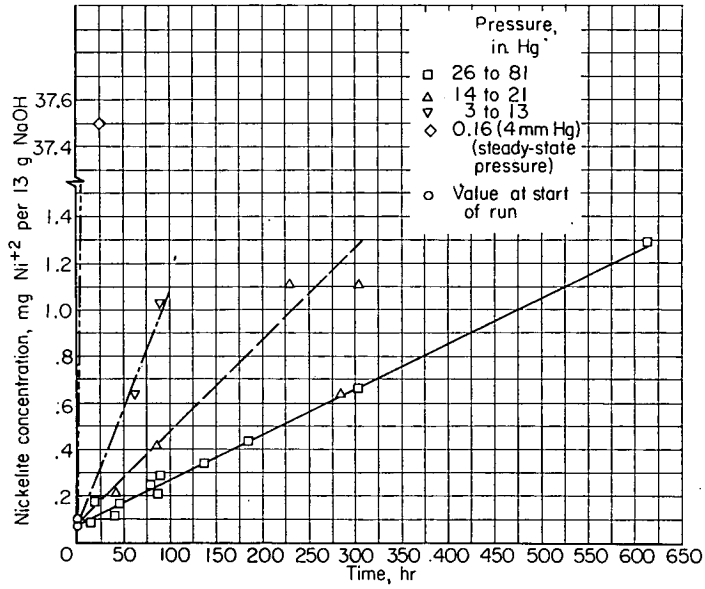


FIGURE 5.—Rate of formation of sodium nickelite from nickel and sodium hydroxide at 1500° F at various hydrogen pressures.

KINETICS

The sodium nickelite concentration appears to be a linear function of time (fig. 5) and to be independent of hydrogen pressures above 26 inches of mercury. The results, although scattered, indicate the rate of formation to be greater for lower pressures. The data for steady-state hydrogen pressure conditions (37.5 mg/24 hr (appendix D)) confirm this fact. To express this effect analytically, one must use a kinetic equation for reactions in which surfaces are easily poisoned (in this case by hydrogen):

$$r_{form}=k_1+k_2/(P_{H_2})^n$$

where r_{form} is the rate of formation of sodium nickelite, k_1, k_2, and n are constants, and P_{H_2} is the hydrogen pressure. Since r_{form} is equal to k_1 at high pressure, $k_1=64$ (mg/dm²)/yr (area=0.267 dm²). The values for the other constants are

$n=1.4$ and $k_2=360$ [(g)(mm of Hg)$^{1.4}$/dm^2]/yr. The kinetics are obviously independent of the reverse reaction.

CONCLUSIONS

Since the rate of the reaction under discussion is linear with time, the reaction itself never reaches equilibrium under the experimental conditions (at 1500° F, for times up to 600 hr, and with hydrogen pressures between 0.16 and 81 in. Hg). It follows that the mechanism of mass transfer cannot involve hydrogen as the "redox" material.

APPENDIX D

REACTIONS OF CHROMIUM AND ITS COMPOUNDS WITH MOLTEN SODIUM HYDROXIDE

An investigation was made to determine the chemical differences between the sodium chromites (or chromates) produced from the following three reactions:

$$Cr+NaOH \xrightarrow{1500^\circ F}$$

$$Cr_2O_3+NaOH \xrightarrow{1500^\circ F}$$

$$Na_2CrO_4+NaOH \xrightarrow{1500^\circ F}$$

This work was initiated because chromium metal was reported to be an inhibitor of mass transfer, while chromium sesquioxide and sodium chromate were originally interpreted to be detrimental as additives (ref. 2).

PROCEDURE

Standard static crucible corrosion (mass transfer) tests (appendixes A and B and ref. 2) were performed using chromium (325 mesh), chromium sesquioxide (Cr_2O_3), and sodium chromate (Na_2CrO_4) as additives in the sodium hydroxide—nickel system. These additives were added before purging. In order to accomplish a more thorough investigation, certain variations in the procedure were used for each group of crucibles, as indicated in the footnotes of table VIII.

CHROMIUM METAL

The ratio of chromate concentration [Cr^{+6}] to chromite concentration [Cr^{+3}] as found in water solutions is approximately 1 to 2 (table VIII, group I, column 6), being independent of the percentage of chromium metal used (column 3) and independent of time for relatively long periods (column 5). The composition is essentially uniform throughout the crucibles (table VIII, footnote (b)). For periods of time less than 1 hour, Cr^{+3} alone existed (group II). Group III results indicate that this apparent 1-to-2 ratio for [Cr^{+6}] to [Cr^{+3}] does not depend upon the steady-state hydrogen pressure that is present in closed (sealed) systems (ref. 7). These facts perhaps indicate the presence of Cr^{+4} in the sodium hydroxide.

Since, however, this [Cr^{+6}] to [Cr^{+3}] ratio perhaps depends somewhat upon temperature (table VIII, group IV), the 1-to-2 ratio may be only approximate, and thus the existence of Cr^{+4} is somewhat doubtful. For further discussion see appendix E.

The reaction forming the hypothetical Cr^{+4} is fast enough so that any hydrogen so produced is quickly lost (by diffusion) and is thus prevented from inhibiting significantly the production of sodium nickelite (table VIII, column 7).

CHROMIUM SESQUIOXIDE

The results with chromium sesquioxide (table VIII, group V) show that it is an inhibitor of transfer. This is indicated by comparison of the specimen weight changes (column 8) and was substantiated by the decrease in the rate of transfer apparent in radiographs of the crucibles (not shown). Chromium sesquioxide is not beneficial in dynamic tests. During the process the chromium converts slowly from Cr^{+3} to the Cr^{+6} as found in the water solution, but the reaction apparently stops when it is two-thirds complete. This perhaps indicates the presence of Cr^{+5}. The hydrogen produced from the oxidation of the chromium sesquioxide keeps the sodium nickelite concentration low (table VIII, column 7). The magnitude of this phenomenon depends upon the actual percent of chromium sesquioxide used. It seems possible that the Cr_2O_3 inhibits transfer by this property of keeping the nickelite concentration low (thus working in a different manner than chromium metal).

Group VI results (table VIII) compare the three additives used. These results confirm the previous data (groups I to V). The tests with sodium chromate indicate that the chromium converts to essentially the same oxidation state as it does in the chromium sesquioxide (table VIII, column 7). This results in the oxidation of metallic nickel (table VIII, footnote (f)).

SUMMARY

The following equations roughly summarize the information obtained:

(1) $$Cr+3NaOH \xrightarrow{\text{Very fast}} Na_3CrO_3+\frac{3}{2}H_2$$

$$Na_3CrO_3+NaOH \xrightarrow{\text{Moderately fast}} (\text{Perhaps})Cr^{+4}+H_2$$

(2) $$Cr_2O_3+2NaOH \rightarrow 2NaCrO_2+H_2O$$

$$NaCrO_2+2NaOH \xrightarrow{\text{Slow}} Na_3CrO_4+H_2$$

$$Ni+2NaOH \xrightarrow[\text{pressures}]{\text{Inhibited by hydrogen}} Na_2NiO_2+H_2$$

(3) $$2Na_2CrO_4+Ni+2NaOH \rightarrow 2Na_3CrO_4+H_2O+NiO$$

See appendix E for further discussion of chromium metal.

APPENDIX E

CHROMATE-CHROMITE EQUILIBRIUM IN MOLTEN SODIUM HYDROXIDE

A study was made concerning the equilibrium between the valences of chromium formed when the metal reacts with molten sodium hydroxide at 1500° F. It was hoped that such an investigation might uniquely define the valences of chromium.

PROCEDURE

Standard static-test nickel crucibles containing sodium hydroxide (13.0±0.1 g) and various amounts of chromium metal (325 mesh) were prepared in the usual manner (appendix A and ref. 2). They were then heated in a hydrogen atmosphere at 1500° F and quenched in the manner described in appendix C. After each crucible was opened, its content was immediately acidified with dilute sulfuric acid. Then the water phase was analyzed for Cr^{+3} and Cr^{+6} (table IX, columns 4 and 5). The insoluble material was assumed to contain only Cr^{+3}.

EQUILIBRIUM

Proof that equilibrium was actually reached is the fact that the "equilibrium constants" subsequently calculated are independent of test duration (table IX, column 3).

The equilibrium between the lower and higher oxidation states of chromium as it exists in molten sodium hydroxide (not necessarily as it exists in water) is expressible by the general equation

$$K_1=\frac{[Cr^{+y}]P_{H_2}^{\frac{y-x}{2}}}{[Cr^{+x}]}$$

where K_1 is the equilibrium constant. Since in fact the value of $P_{H_2}[Cr^{+6}]/[\text{total Cr}]$ is essentially constant (table IX, column 6), one might conclude that +3 and +5 are the valences present ($[Cr^{+5}]$ being proportional to $[Cr^{+6}]$; $[Cr^{+3}]$ being essentially equal to [total Cr]; and the dependence upon P_{H_2} being the first power). This selection is not unambiguous if chromium can exist as a dimer or trimer. Since in the case of a dimer the equilibrium constant K_2 can be expressed

$$K_2=\frac{[Cr_2^{+2y}]P_{H_2}^{y-x}}{[Cr_2^{+2x}]}$$

the valences would be +3 and +4. The valences +3 and +5 are in some ways the simpler explanation, being in agreement with the work in which chromium sesquioxide is oxidized to Cr^{+5} (appendix D).

COMPLEX FORMATION

When a compound containing Cr^{+5} is dissolved in water and acidified, the following disproportionation reaction should occur:

$$6Na_5CrO_5+29H_2SO_4\rightarrow Cr_2(SO_4)_3+2Na_2Cr_2O_7+26NaHSO_4+16H_2O$$

If all the resulting chromium compounds are water soluble, one would expect [soluble Cr^{+3}]/$[Cr^{+6}]$ to equal 0.5, not 3.3 (table IX, column 7). A value of 3.5 (almost 3.3) to 1 for this ratio is understandable, if the Cr^{+5} is assumed to be coordinated with Cr^{+3} according to the first formula in the equation

$$6Na_5CrO_5(Na_3CrO_3)_2+83H_2SO_4\rightarrow 7Cr_2(SO_4)_3+2Na_2Cr_2O_7+62NaHSO_4+52H_2O$$

Under conditions of low and varying hydrogen pressure (unsealed systems) one chromite (Cr^{+3}) apparently coordinates with one hypochromate, as indicated by the apparent +4 valence (appendix D and table VIII, group III).

APPENDIX F

EQUILIBRIUM CONCENTRATION OF SODIUM OXIDE IN SODIUM HYDROXIDE

The equilibrium constant for the reaction

$$2NaOH(\text{liquid})\rightleftarrows Na_2O(\text{solid})+H_2O(\text{gas})$$

was calculated from thermodynamic data (table X and refs. 13 and 14). It was found to be $10^{-3.96}$ atmosphere at 822° C. Since the partial pressure of water over sodium hydroxide is about 3 millimeters of mercury at 822° C (ref. 7), the molar concentration of sodium oxide must be about 2.7 percent. This is in general agreement with recent experimental work (ref. 10). This concentration seems more than sufficient for the oxide to take part in the chemical reactions involved in mass transfer.

The molar concentration of water must also be 2.7 percent, since very little water is in the vapor state (because of the low vapor pressure). This low pressure is indicated indirectly in static crucible tests using flowing atmospheres (appendix D and ref. 3). If pressures larger than several millimeters of mercury existed, large quantities of water would be removed by a flowing gas, and the sodium oxide concentration and mass transfer would thus be increased.

If one disregards the experimental evidence and assumes all the water formed from the dissociation to be contained in the free space (10 ml in a standard crucible), the molar concentration of sodium oxide would still be sufficient (0.02 percent) to take part in mass transfer. The resulting water pressure (400 mm Hg) would be, of course, in gross disagreement with the facts.

APPENDIX G

CORROSION AND MASS TRANSFER IN SODIUM HYDROXIDE—COPPER SYSTEM

In order to compare the mechanism of transfer in nickel with that in another metal, the sodium hydroxide—copper system was investigated.

PROCEDURE

Static corrosion tests in which copper crucibles were exposed to air for 24 hours resulted in excess oxidation and leaking. Therefore, static-capsule corrosion tests were performed with the copper crucibles protected from oxidation by being encased in Inconel chambers (fig. 2).

Four crucibles were fabricated from copper tubing in the same manner as the "L" nickel crucibles (appendix A and ref. 2). In three out of four cases during the 1500° F test, leaks occurred at the lower weld (below the sodium hydroxide level). Subsequent capsules were therefore fabricated from a single bar of copper to the same dimensions as the standard nickel crucibles. The specimens and tops were machined from the same bar stock, while the vent tubes were made from tubing in the usual manner. The loading and purging procedure was identical to that used for nickel crucibles. The conditions of the test were the same as those for method 1 in appendix B except that the Inconel chambers were continually evacuated. Nickel crucibles were used for comparison. After the crucibles were radiographed, the melts were analyzed chemically, and the weight losses of the specimens were determined (table XI).

PRESENCE OF SODIUM

Several days after the test, a white alkaline coating was detected around the crimp on some unopened copper crucibles (table XI, column 5). This phenomenon was interpreted as being due to the formation of metallic sodium in the melt and its diffusion through the copper metal at high temperature followed at room temperature by its reaction with the components of the air to form sodium carbonate. Photomicrographs of the crimped sections indicated that some foreign material had vaporized from the surface of the copper.

Furthermore, the extremely large weight losses of the copper crucibles (table XI, column 6) can be attributed only to the loss of metallic sodium. Radiographs of the copper crucibles show a loss of sodium hydroxide. Unfortunately the contents were not analyzed for sodium hydroxide. All this evidence indicates a reaction for copper which is similar to that for nickel:

$$Cu+2Na_2O \rightarrow Na_2CuO_2+2Na$$

EFFECT OF CHROMIUM

Radiographs (not shown) and the specimen weight changes (table XI, column 7) indicate that chromium is an inhibitor of transfer in the sodium hydroxide—copper system, as could be predicted from the proposed mechanism. However, another factor has to be considered here. The pressure of hydrogen generated by the chromium reaction is not easily eliminated, since copper is less permeable to hydrogen than is nickel. The resulting hydrogen pressure inhibits the chromite-to-chromate reaction (column 8) as well as the copper-to-cuprate reaction (column 9). This accounts for some of the effectiveness of the chromium in copper but not for that in nickel.

COMPARISON OF TRANSFER OF COPPER AND NICKEL

Radiographs of crucibles show little difference in the actual amount of transfer for copper and nickel. The fact that the specimens have relatively large weight losses is attributable to the large amount of copper (from the specimens as well as the crucibles) which reacts with sodium oxide to form metallic sodium and the sodium cuprate. It is the side reactions of copper (oxidation, sodium diffusion, and the rapid reaction with sodium hydroxide) which make it a far less favorable container material for molten caustic than nickel is.

APPENDIX H

THERMOELECTRIC POTENTIAL OF NICKEL IN MOLTEN SODIUM HYDROXIDE

This section describes the thermoelectric potential and current found to exist in the sodium hydroxide—nickel system and presents a tentative explanation for them.

APPARATUS

Although many types of apparatus were used (most of which had about the same degree of success and reproducibility), only the final apparatus is described here (fig. 6). The outside container was fabricated from Inconel and made vacuum tight by means of a water-cooled O-ring seal between the two brass plates on top. The cup inside (containing NaOH) and the electrodes were fabricated from "L" nickel tubing. The electrodes were vacuum sealed to the system by means of rubber tubing and electrically insulated from the Inconel supports by means of ceramic tubes. Heating was accomplished by means of ceramic-covered Nichrome heating wire wound around the Inconel container. Several layers of asbestos supplied sufficient heat insulation. The temperature was manually controlled through a Variac and measured by thermocouples contacting the tips of the electrodes.

THERMOELECTRIC POTENTIAL

While the temperature of the vessel and one electrode was held constant, the second electrode was cooled by passing a stream of air through it. The temperature difference between the two electrodes was measured as well as the electrical potential existing between them. Generally, the results were very scattered, although the hotter electrode was always negative with respect to the cooler electrode. Occasionally, the scatter was low (fig. 7).

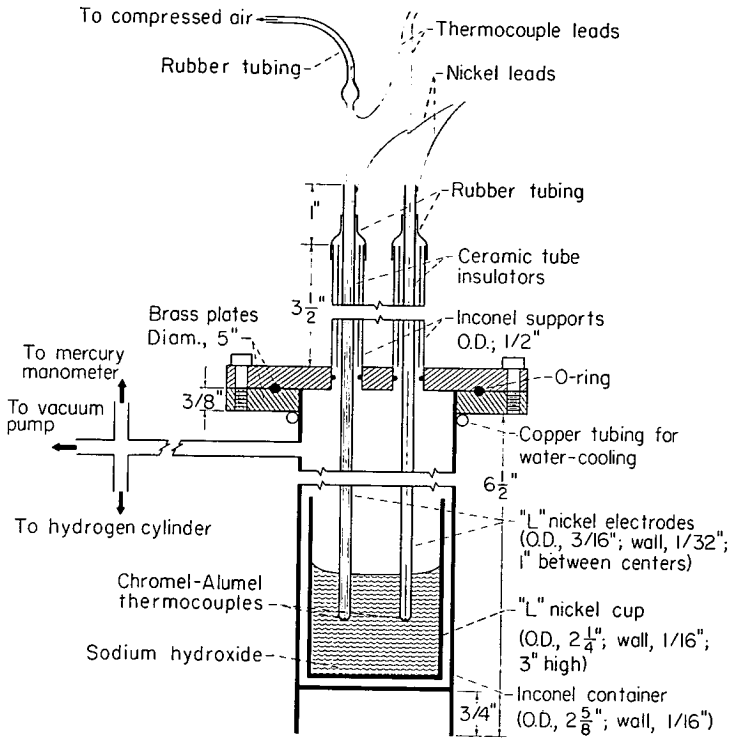


FIGURE 6.—Apparatus for measurement of thermoelectric potentials.

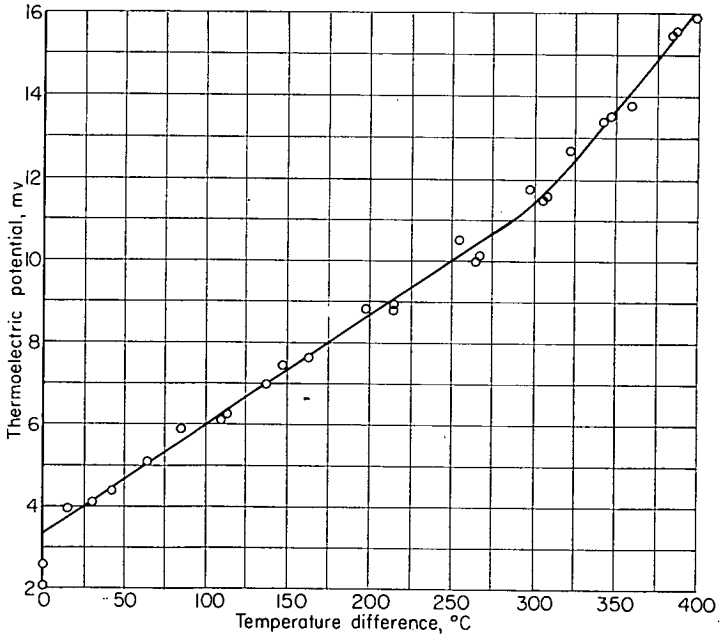


FIGURE 7.—Thermoelectric potential between two nickel electrodes at different temperatures in sodium hydroxide. Higher temperature, 670° C.

Values for electromotive force divided by the temperature difference ($emf/\Delta T$) for many trials ranged from 10 to 120 microvolts per degree. These values were essentially independent of whether a vacuum or a helium atmosphere was present above the sodium hydroxide. However, when a hydrogen pressure was used, the sign of $emf/\Delta T$ was reversed (i.e., the cooler electrode became negative with respect to the hotter one). Upon removal of the hydrogen pressure the original polarity was restored.

THERMOELECTRIC CURRENT

An experiment was also carried out to see whether this thermoelectric potential could sustain an electric current. The hot and cold electrodes were connected through a low resistance (2 ohms), and the potential drop across it was measured over a period of 6 hours. The current was quite unsteady.

INTERPRETATION

The measured potential could be due to the Seebeck effect or to one of the following half-cell reactions:

$$Na_2NiO_2+2Na^++2e^- \underset{\text{Hot zone}}{\overset{\text{Cold zone}}{\rightleftharpoons}} 2Na_2O+Ni$$

$$2H_2O+2e^- \underset{\text{Hot zone}}{\overset{\text{Cold zone}}{\rightleftharpoons}} 2OH^-+H_2$$

$$NaOH+e^- \underset{\text{Hot zone}}{\overset{\text{Cold zone}}{\rightleftharpoons}} OH^-+Na$$

$$Na^++NaNiO_2+e^- \underset{\text{Hot zone}}{\overset{\text{Cold zone}}{\rightleftharpoons}} Na_2NiO_2$$

The Seebeck (thermocouple) effect is not likely for the following reasons: Sodium hydroxide is probably a poor electronic conductor, and the effect of hydrogen is far too great for the potential to be due to simple thermocouple action. The effect of the hydrogen upon the thermoelectric potential is even difficult to explain in terms of any of the thermocell reactions listed. The presence of hydrogen should in all cases (by reducing the ratio of products to reactants) increase $emf/\Delta T$ (not decrease it past zero as is found experimentally) inasmuch as the value of $emf/\Delta T$ is determined by the equation (ref. 15)

$$n\mathcal{F}\frac{emf}{\Delta T}=\Delta S^\circ - R \ln\left(\frac{[\text{products}]}{[\text{reactants}]}\right)$$

where n is the number of electrons shown in the half-cell reaction, $\mathcal{F}$ is the Faraday conversion factor, and ΔS° is the standard entropy change for the reaction as written for the hot zone. The only reasonable way to explain the effect is to assume that the thermoelectric potential is produced by the nickel-nickelite reaction with the hydrogen poisoning the nickel. In appendix C another case is presented in which hydrogen apparently poisons nickel in the sodium hydroxide system.

REFERENCES

1. Mosher, Don R., and Lad, Robert A.: Kinetic Study of Mass Transfer by Sodium Hydroxide in Nickel Under Free-Convection Conditions. NACA RM E53K24, 1954.
2. Forestieri, Americo F.: Effects of Additives on Corrosion and Mass Transfer in Sodium Hydroxide—Nickel Systems Under Free-Convection Conditions. NACA RM E54E19, 1954.

3. Lad, Robert A., and Simon, Sidney L.: A Study of Corrosion and Mass Transfer of Nickel by Molten Sodium Hydroxide. Corrosion, vol. 10, no. 12, Dec. 1954, pp. 435–439.
4. Le Blanc, M., and Bergmann, L. (A. Pingell, trans.): The Effect of Metals on Molten Sodium Hydroxide. Trans. 393, Naval Res. Lab., 1952.
5. Manly, W. D.: Fundamentals of Liquid-Metal Corrosion. ORNL–2055, Metallurgy Div., Oak Ridge Nat. Lab. (Contract W–7405–eng–26.)
6. Smith, G. P.: Corrosion of Materials in Fused Hydroxides. ORNL–2048, Metallurgy Div., Oak Ridge Nat. Lab., Mar. 27, 1956. (Contract W–7405–eng–26.)
7. Williams, Dale D., and Miller, R. R.: Thermal and Related Physical Properties of Molten Materials. Pt. II—High Temperature Reactions of Sodium Hydroxide. Tech. Rep. 54–185, WADC, Feb. 1955. (MIPR No. 33(616)–54–102, Proj. No. 1252.)
8. Peoples, Robert S., Miller, Paul D., and Hannan, H. Dale: Reaction of Nickel in Molten Sodium Hydroxide. Rep. No. BMI–1041, Battelle Memorial Inst., Sept. 27, 1955. (Contract W–7405–eng–92.)
9. Anon.: High-Temperature Chemistry of Fused Substances. Prog. Rep., College of Arts and Sci., Univ. Ark., Nov. 1, 1954. (Subcontract 501, W–7405–eng–26.)
10. Smith, G. P.: Problems Pertaining to the Dehydration of Sodium Hydroxide by Volatization of Water. ORNL–2130, Metallurgy Div., Oak Ridge Nat. Lab., Sept. 10, 1956. (Contract W–7405–eng–26.)
11. Simons, Eugene M., Miller, Neil E., Stang, John H., and Weaver, C. Vernon: Corrosion and Component Studies on Systems Containing Fused NaOH. Rep. No. BMI–1118, Battelle Memorial Inst., July 30, 1956. (Contract W–7405–eng–92.)
12. Smothers, W. J.: Progress Report Jan. 1, 1953–Mar. 31, 1953. Inst. Sci. and Tech., Univ. Ark., Apr. 20, 1953. (Subcontract 501–Under W–7405–eng–26.)
13. Kubaschewski, O., and Evans, E. L.: Metallurgical Thermochemistry. Vol. I. Academic Press, Inc., 1951, pp. 274–275; 291.
14. Powers, W. D., and Blalock, G. C.: Enthalpies and Specific Heats of Alkali and Alkaline Earth Hydroxides at High Temperatures. ORNL–1653, Reactor Exp. Eng. Div., Oak Ridge Nat. Lab., Jan. 20, 1954. (Contract W–7405–eng–26.)
15. Eastman, E. D.: Thermodynamics of Non-Isothermal Systems. Jour. Am. Chem. Soc.. vol. 48, June 1926, pp. 1482–1493.

TABLE I.—PROPOSED MECHANISMS

Type of reaction	Reaction	Migration processes	Additional reactions required for initiation
Physical	(1) Ni^0(dissolved) $\underset{\text{Hot zone}}{\overset{\text{Cold zone}}{\rightleftharpoons}}$ Ni^0(metal)	Ni^0(hot) → (cold)	None
Electrochemical	(2) $Na_2NiO_2 + 2Na^+ + 2e^- \underset{\text{Hot zone}}{\overset{\text{Cold zone}}{\rightleftharpoons}} 2Na_2O + Ni$	Na_2NiO_2(hot) → (cold) Na^+(hot) → (cold) e^-(hot) → (cold) Na_2O(cold) → (hot)	$2NaOH \rightarrow Na_2O + H_2O$
Chemical	$Na_2NiO_2 + \text{Reductant} \underset{\text{Hot zone}}{\overset{\text{Cold zone}}{\rightleftharpoons}} \text{Oxidant} + Ni$		
Impurity	(3) $Na_2NiO_2 + 2Na_2FeO_2 \underset{\text{Hot zone}}{\overset{\text{Cold zone}}{\rightleftharpoons}} 2Na_3FeO_3 + Ni$	Na_2NiO_2(hot) → (cold) Na_2FeO_2(hot) → (cold) Na_3FeO_3(cold) → (hot)	None
Disproportionation	(4) $3Na_2NiO_2 \underset{\text{Hot zone}}{\overset{\text{Cold zone}}{\rightleftharpoons}} 2Na_3NiO_3 + Ni$	Na_2NiO_2(hot) → (cold) Na_3NiO_3(cold) → (hot)	$Ni + 2NaOH \rightarrow Na_2NiO_2 + H_2$
Element present in sodium hydroxide:			
Oxygen	(5) $Na_2NiO_2 \underset{\text{Hot zone}}{\overset{\text{Cold zone}}{\rightleftharpoons}} Na_2O + \frac{1}{2}O_2 + Ni$	Na_2NiO_2(hot) → (cold) Na_2O(cold) → (hot) O_2(cold) → (hot)	$Ni + 2NaOH \rightarrow Na_2NiO_2 + H_2$
Hydrogen	(6) $Na_2NiO_2 + H_2 \underset{\text{Hot zone}}{\overset{\text{Cold zone}}{\rightleftharpoons}} 2NaOH + Ni$	Na_2NiO_2(hot) → (cold) H_2(hot) → (cold) NaOH(cold) → (hot)	None
Sodium	(7) $Na_2NiO_2 + 2Na \underset{\text{Hot zone}}{\overset{\text{Cold zone}}{\rightleftharpoons}} 2Na_2O + Ni$	Na_2NiO_2(hot) → (cold) Na(hot) → (cold) Na_2O(cold) → (hot)	$2NaOH \rightarrow Na_2O + H_2O$

TABLE II.—ANALYSIS OF SODIUM HYDROXIDE PELLETS

[Ref. 2.]

Material	Percent
Sodium hydroxide	97.6
Chloride (Cl)	.005
Iron (Fe)	.001
Other heavy metals (as Ag)	0
Carbonate (Na_2CO_3)	.32
Phosphate	0
Silica and amonium hydroxide precipitate	0
Total nitrogen (as NH_3, NO_2)	.001
Sulfate (SO_4)	0

TABLE III.—COMPOSITION OF "L" NICKEL TUBING

[Ref. 2.]

Material	Percent
Manganese	0.149±0.015
Iron	.059±.006
Copper	.029±.006
Carbon	.024±.005
Silicon	.020±.002
Sulfur	.008±.001
Cobalt	.119±.013
Nickel	Balance

TABLE IV.—EFFECT UPON TRANSFER OF INCREASING IMPURITY CONTENT

[Refs. 2, 3, and 11.]

	Specimen weight change for various percents of added impurities, mg			
	0 Percent	1 Percent	3 Percent	5 Percent
Nickel impurities:				
Manganese	−4.7	−20.0	------	------
Iron	−5.1	−25.7	−28.4	−28.1
Copper	−5.1	−8.4	−6.7	−5.8
Carbon	−7.9	−78.6	−8.5	−7.8
Silicon (see sodium silicate below)	------	------	------	------
Sulfur (see sodium sulfate below)	------	------	------	------
Cobalt	−5.1	+0.6	+7.2	+8.2
Sodium hydroxide impurities:				
Sodium chloride	−7.9	−6.5	−6.6	------
Iron oxide	−5.1	−9.2	−11.1	−4.8
Silver metal	−5.1	−6.0	−4.8	−5.1
Sodium carbonate	−7.9	−17.5	−19.3	−22.0
Sodium phosphate	−5.1	−5.4	−5.2	−8.6
Sodium silicate	[a] −7	[a] −11	------	------
Nickel nitrate	[a] −7	[a] −11	------	------
Sodium sulfate	[a] −7	[a] −11	------	------

[a] Approximate (ref. 11).

TABLE V.—X-RAY DIFFRACTION DATA FOR SODIUM NICKELITE

Interatomic distances, *d*, Å	Intensity of line	*d* values from ref. 9 (Oak Ridge), Å	*d* values from ref. 9 (University of Arkansas), Å	*d* values from ref. 7, Å
8.48	Medium	------	------	--------
-------	----------	------	------	4.87
4.35	Strong	4.32	4.37	4.33
4.17	Strong	------	------	4.17
-------	----------	------	------	3.67
3.22	Weak	3.21	3.19	--------
-------	----------	2.71	------	--------
2.55	Medium	2.57	2.55	2.55
-------	----------	2.53	------	--------
2.43	Strong	2.42	2.44	--------
2.23	Weak	2.27	2.28	--------
2.17	Weak	2.14	2.16	--------
2.10	Weak	2.09	2.09	--------
1.92	Weak	1.93	1.92	1.91
1.87	Weak	1.87	------	--------
-------	----------	1.70	------	--------
1.65	Weak	1.64	------	1.65
-------	----------	1.61	------	--------
1.60	Weak	1.60	------	--------
1.57	Weak	1.56	------	--------
-------	----------	1.53	------	--------
-------	----------	1.49	1.49	--------
1.44	Medium	1.44	1.45	--------
-------	----------	1.41	1.43	1.41
1.38	Weak	1.38	------	--------
-------	----------	1.34	------	--------
-------	----------	1.31	------	--------
-------	----------	1.29	------	--------
1.27	Weak	1.27	------	--------
-------	----------	1.23	------	--------
-------	----------	1.22	1.22	--------

TABLE VI.—EFFECT OF HYDROGEN UPON MASS TRANSFER

Method	Total number of crucibles	Pressure of hydrogen, in. Hg	Temperature, °F	Time, hr	Specimen weight loss, mg	Amount Ni^{+2} in melt, mg	Appearance of transfer in radiograph
1	[a] 4	0.16 (Steady state)	1500	80	4.3±0.7	11.4±1.9	Clearly visible
	4	17	1500	80	2.8±0.6	0.41±0.05	Hardly visible
3	[a] 2	0.16 (Steady state)	1560	24	7.6±0.8	79.4±1.8	Clearly visible
	2	>0.16 (Slightly above steady state)	1560	24	4.6±0.3	8.3±0.1	Narrower band than in crucibles with steady-state hydrogen pressure

[a] Crucibles used for comparison.

TABLE VII.—KINETIC DATA FOR SODIUM NICKELITE FORMATION

Time, hr	Ni^{+2} in melt, mg	Hydrogen pressure, in. Hg
615	1. 40	81. 0
303	. 66	26. 5
303	1. 11	~16. 0
284	. 64	16. 5
228	1. 11	~15. 0
184	. 437	28. 3
138	. 343	28. 3
89	. 285	29. 1
89	1. 03	3. 5
88	. 21	38. 4
87	. 42	20. 7
82	. 25	38. 7
63	. 638	12. 7
45	. 167	70. 6
43	. 093	73. 2
41	. 115	37. 6
40	. 130	86. 5
26	. 080	60. 0
22	. 062	86. 1
21	. 218	20. 7
19	. 150	38. 4
18	. 175	28. 9
14	. 090	68. 4
0	. 100	--------
0	. 070	--------

TABLE VIII.—CORROSION DATA WITH CHROMIUM, CHROMIUM SESQUIOXIDE, AND SODIUM CHROMATE AS ADDITIVES

1	2	3	4	5	6	7	8	9
Group of crucibles	Additive	Amount of additive, percent	Temperature, °F	Time, hr	Percent of Cr as Cr^{+6} (remainder was Cr^{+3})	Ni^{+2} in melt, g	Specimen weight change, mg	Average rate of specimen weight change, mg/hr
[a, b, c] I	Cr	2. 5	1500	24	29. 9 32. 5 33. 3			
		7. 5		24	30. 1 30. 3 30. 7			
		5		24	30. 3			
		5. 8		96	33. 7			
		12		96	30. 8			
		15		240	30. 4			
		10		245	32. 0 33. 5 32. 6			
[a, b, c] II	Cr	12	1500	0. 33	0			
	Cr	[d]	1500	. 5	0			
	Cr	12	1500	5	1. 5			
[c, e] III	None	--------	1500	24	--------		−12. 9	
	None	--------			--------		−10. 5	
	Cr	3			33. 3		+4. 5	
	Cr	3			33. 9		+4. 5	

See footnotes at end of table.

TABLE VIII.—CORROSION DATA WITH CHROMIUM, CHROMIUM SESQUIOXIDE, AND SODIUM CHROMATE AS ADDITIVES—Continued

1	2	3	4	5	6	7	8	9
Group of crucibles	Additive	Amount of additive, percent	Temperature, °F	Time, hr	Percent of Cr as Cr^{+6} (remainder was Cr^{+3})	Ni^{+2} in melt, g	Specimen weight change, mg	Average rate of specimen weight change, mg/hr
IV	None	--------	1700	24	--------	0.251	−32.3	
	Cr	3			35.9	.255	+7.0	
	Cr	5			36.1	.195	+9.0	
	None	--------			--------	.232	−30.5	
	Cr	1			35.3	.235	−7.0	
	Cr	3	↓	↓	36.8	.207	+7.0	
V	None	--------	1500	24	--------	0.0375	−5.9	−0.25
	Cr_2O_3	1			43	.0109	+2.8	--------
	Cr_2O_3	3.2			16	.0180	+2.6	--------
	Cr_2O_3	5		↓	5.3	.0389	+2.1	--------
	None	--------		96	--------	.0830	−30.5	−.31
	Cr_2O_3	1			60	.0511	−24.1	--------
	Cr_2O_3	3			34	.0288	+3.8	--------
	Cr_2O_3	6.3		↓	22	.0511	−5.5	--------
	None	--------		168	--------	.1135	−81.2	−.48
	Cr_2O_3	1			58	.0945	−79.6	--------
	Cr_2O_3	2			61	.0485	−11.4	--------
	Cr_2O_3	4.9		↓	54	.0668	+.6	--------
	Cr_2O_3	1		240	57	.0914	−139.4	−.58
	Cr_2O_3	6.2	↓	240	57	.0931	−74.6	--------
[c] VI	None	--------	1500	67	--------	0.0834		
	Cr	1			32.0	.1053		
	Cr	3			37.0	.0669		
	Cr	5			32.5	.0802		
	Cr_2O_3	1.5			63.0	.0375		
	Cr_2O_3	4.4			24.2	.0227		
	Cr_2O_3	7.4			15.5	.0285		
	Na_2CrO_4	9.3		↓	66.1	[f]		
	None	--------		71	--------	.0748		
	Cr	1			42.8	.0780		
	Cr	3			37.2	.0772		
	Cr	5			33.2	.0784		
	Cr_2O_3	1.5			48.5	.0504		
	Cr_2O_3	4.4			24.6	.0244		
	Cr_2O_3	7.4			13.4	.0215		
	Na_2CrO_4	9.3	↓	↓	63.7	[f]		
	None	--------	1700	18.5	--------	.1591		
	Cr	3			39.8	.1640		
	Cr	3			38.2	.1859		
	Cr_2O_3	4.4			46.5	.0396		
	Cr_2O_3	7.4	↓	↓	28.0	.0423		

[a] These crucibles were cut into several sections; differences in analysis between sections were slight (column 6).
[b] No analysis was made for Ni^{+2}.
[c] No specimens.
[d] 10 percent 325 mesh plus 13 percent larger mesh.
[e] Flowing helium atmosphere over sodium hydroxide (ref. 3).
[f] Coating of oxide was found on inside surface of crucible.

TABLE IX.—CHROMITE-CHROMATE EQUILIBRIUM DATA

1	2	3	4	5	6	7
Total amount of chromium, g	Hydrogen pressure, P_{H_2}, in. Hg	Time, hr	Cr^{+6} in melt, g	Acid-soluble Cr^{+3} in melt, g	$\frac{P_{H_2}[Cr^{+6}]}{[\text{total Cr}]}$, in. Hg	$\frac{[\text{Soluble } Cr^{+3}]}{[Cr^{+6}]}$
0. 1300	79. 2	14	0. 0015	0. 0053	0. 91	3. 5
. 1310	68. 4	16	. 0016	. 0050	. 84	3. 1
. 1298	28. 3	16	. 0026	. 0083	. 56	3. 2
. 1296	22. 4	15	. 0039	. 0140	. 67	2. 8
. 1304	14. 8	32	. 0070	. 0177	. 80	3. 9
. 1307	10. 6	15	. 0088	[a]	. 71	---
. 3900	69. 2	18	. 0046	. 0135	. 81	3. 4
. 3903	63. 8	40	. 0049	. 0149	. 80	3. 3
. 3899	60. 1	65	. 0055	. 0175	. 85	3. 1
. 3900	40. 6	14	. 0103	[a]	1. 07	---
. 3901	40. 2	88	. 0094	. 0246	. 97	3. 8
. 3900	17. 5	14	. 0163	. 0447	. 73	2. 7
					Average 0. 81	Average 3. 3

[a] Not properly acidified.

TABLE X.—THERMODYNAMIC DATA FOR SODIUM HYDROXIDE, SODIUM OXIDE, AND WATER

[Refs. 13 and 14.]

	Heat of formation, ΔH_{form}, at 25° C, cal/mole	Entropy, S, at 25° C, cal/(mole)(°K)	Specific heat at constant pressure, C_p, cal/(mole)(°K)	Heat of transformation from alpha to beta, ΔH_{trans}, cal/mole	Heat of fusion, ΔH_{fusion}, cal/mole
Sodium hydroxide (α) (solid)	−102, 000	14. 2	17. 6	1000	---
Sodium hydroxide (β) (solid)	---	---	17. 6	---	1900
Sodium hydroxide (liquid)	---	---	19. 6	---	---
Sodium oxide (solid)	−102, 900	17. 4	$15.9+5.4\times10^{-3}T$	---	---
Water (gas)	−57, 800	45. 11	$7.19+2.83\times10^{-3}T-0.16\times10^{-6}T^2$	---	---

TABLE XI.—CORROSION DATA FOR SODIUM HYDROXIDE—COPPER SYSTEM

1	2	3	4	5	6	7	8	9
Crucible material	Chromium, percent	Temperature, °F	Time, hr	Alkalinity of coating on crucible, mg NaOH	Crucible weight change, mg	Specimen weight change, mg	Amount of Cr as Cr^{+6}, percent	Amount of Cu^{+2} or Ni^{+2} in melt, g
Nickel tubing	None	1500	24	None	−4. 4	−2. 1	---	---
Nickel tubing	None	1500	24	None	−4. 9	−3. 5	---	---
Copper tubing	None	1500	24	60	---	−3. 4	---	0. 0569
Copper bar	None	1500	24	0. 5	−45. 9	−9. 4	---	. 0852
Copper bar	None	1500	24	. 5	−25. 6	−9. 6	---	. 0846
Copper bar	3	1500	24	---	---	+5. 2	4. 4	0. 0172
Copper bar	3	1500	24	---	−945. 3	+6. 2	5. 7	. 0367
Nickel tubing	None	1500	80	None	+0. 7	−8. 1	---	0. 0625
Copper bar	None	1500	80	15. 8	−804. 1	−28. 5	---	. 533
Copper bar	None	1500	80	4. 8	−788. 2	−33. 7	---	. 670

REPORT 1367

CALCULATED AND MEASURED STRESSES IN SIMPLE PANELS SUBJECT TO INTENSE RANDOM ACOUSTIC LOADING INCLUDING THE NEAR NOISE FIELD OF A TURBOJET ENGINE [1]

By Leslie W. Lassiter and Robert W. Hess

SUMMARY

Flat 2024–T3 aluminum panels measuring 11 inches by 13 inches were tested in the near noise fields of a 4-inch air jet and turbojet engine. The stresses which were developed in the panels are compared with those calculated by generalized harmonic analysis. The calculated and measured stresses were found to be in good agreement.

In order to make the stress calculations, supplementary data relating to the transfer characteristics, damping, and static response of flat and curved panels under periodic loading are necessary and were determined experimentally. In addition, an appendix containing detailed data on the near pressure field of the turbojet engine is included.

INTRODUCTION

The problem of structural vibration due to acoustic loading has steadily become more severe particularly because of the widespread use of turbojet engines. Large areas such as wing and fuselage surfaces of the aircraft are exposed to intense random pressure fluctuations. These pressure fluctuations may induce many millions of loading cycles in a single flight and can thus cause fatigue of panels and secondary structure.

One of the prime needs in this problem is a means of determining, in the design stage, the magnitude of stresses that will be encountered by a given panel. The present paper, therefore, is concerned with the evaluation of the merits of a power-spectrum approach suggested by Miles as a means of predicting panel stresses. A family of simple test panels ranging in thickness from 0.032 inch to 0.081 inch was tested in the near sound field of an afterburner-equipped turbojet engine. These tests are an extension of reference 1 in that experimental and calculated stresses due to higher acoustic loadings are compared.

The presentation in reference 2 has been extended by a more complete description of the techniques used in obtaining calculated stresses. Also, because the calculation of stress for a given panel requires knowledge of the acoustic pressure loading and because very little data of this type are available in the literature, an appendix giving some detailed information on the near-field noise characteristics of the engine is included.

[1] Supersedes NACA Technical Note 4076 by Leslie W. Lassiter and Robert W. Hess, 1957

SYMBOLS

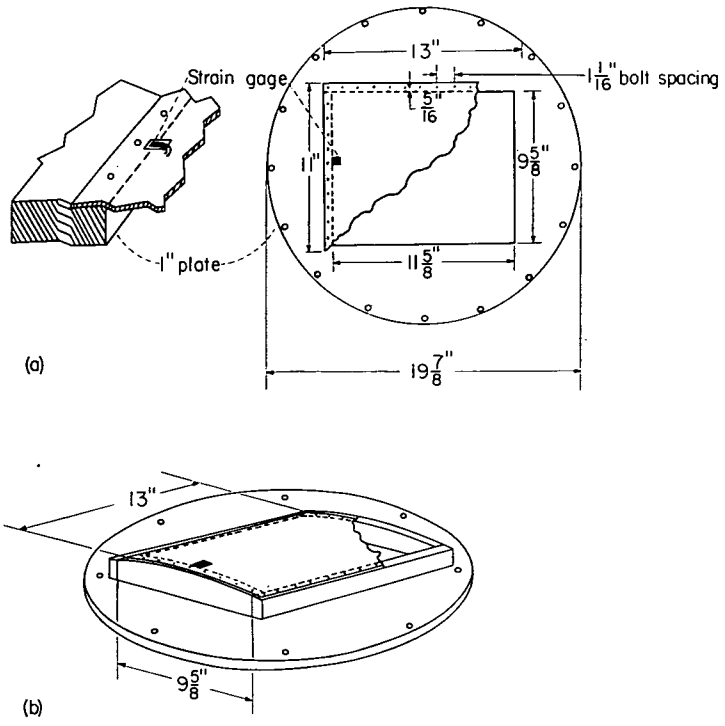
ω	frequency
ω_0	damped natural frequency
$Z(\omega)$	impedance of panel at frequency ω
$\Phi_N(\omega)$	power spectrum of noise input
$\Phi_N(\omega_0)$	power spectral density of noise at frequency ω_0
$\Phi_\sigma(\omega)$	power spectrum of stress response
$\overline{\sigma^2}$	mean-square stress
$\sqrt{\overline{\sigma^2}}$	root-mean-square stress
σ_{max}	stress amplitude
σ_{st}	static stress, positive in compression
S_0	static stress per unit static pressure
δ	damping as fraction of critical damping
p_1	root-mean-square acoustic siren pressure, psi
D	jet tailpipe diameter
z	axial distance from engine exit plane along lines 15° off jet center line
p	overall sound pressure, psi or dynes/cm^2
d	distance from jet 15° boundary
R	radius of curved panels
$db = 20 \log_{10}\left(\frac{p}{0.0002}\right)$	where p is in dynes/cm^2
t	thickness

APPARATUS

PANEL CONFIGURATIONS

Flat panel.—In this investigation the response of both flat and curved panels was studied. The tests were made on 2024–T3 aluminum panels with thicknesses of 0.032 inch, 0.040 inch, 0.064 inch, and 0.081 inch. The flat panels had overall dimensions of 11 inches by 13 inches and were attached to a rigid 1-inch-thick aluminum plate by round-head bolts. The main features of this configuration are shown in figure 1 (a). The use of the rigid frame for mounting the panels avoided the additional complications which might arise from support flexibility. The bolt fastening was used to facilitate the attachment of panels to the mounting frame.

Curved panels.—For the tests with curved panels, the configurations consisted of flat panels rolled to the desired radius of 4 feet and mounted on a curved steel frame of the same radius. As shown in figure 1 (b), this frame was attached to the same type of rigid aluminum plate as was used for the



(a) Flat panel.
(b) Curved panel.

FIGURE 1.—Details of test panels.

flat panels. The panel attachment to the frame was identical to that used with flat panels.

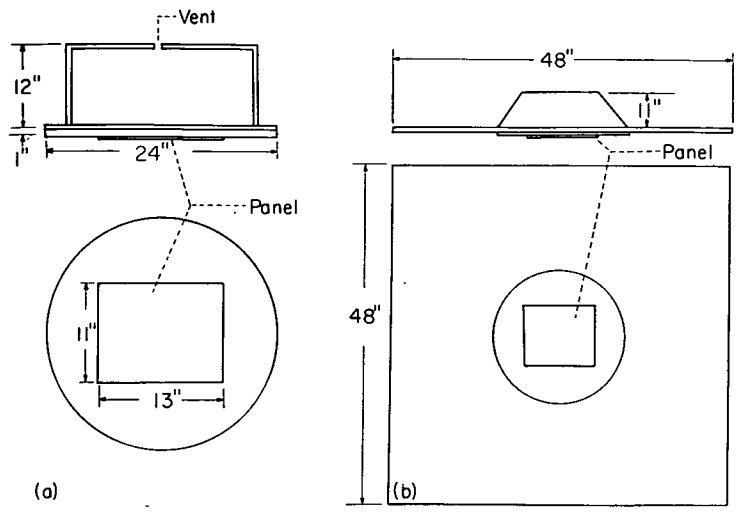
PANEL-MOUNTING CONDITIONS

Laboratory mounting.—The tests were divided into two parts—laboratory tests and field tests. Figure 2 shows schematically the two mounting conditions employed in the tests. Figure 2 (a) shows the laboratory mounting which consisted of a steel chamber, 18 inches in diameter and 12 inches deep, with a flange on the open end to permit attachment of the panel mounting plate. This chamber was convenient for applying either a positive or a negative pressure to the back side of the panel so that its static characteristics could be studied. During the laboratory tests this chamber behind the panels was filled with a porous material having rather poor sound-absorbing properties.

Field mounting.—Figure 2 (b) shows schematically the field mounting used for tests in the near sound field of a turbojet engine. The panel was mounted flush with a plywood surface in an attempt to simulate the acoustic environment of an isolated panel in a large reflecting surface. The backing chamber for this mount was also of plywood and had roughly twice the volume of that of the laboratory mount. This volume was filled to about 80 percent of its capacity with glass wool, which is more sound absorptive than the material used for the laboratory mount. Because this difference in mounting and backing or both was found to have a large effect on the panel damping, the terms "laboratory mount" and "field mount" will be used to differentiate between the test conditions throughout the report.

DISCRETE-FREQUENCY NOISE GENERATOR

For the determination of panel transfer characteristics and



(a) Laboratory mounting. (b) Field mounting.

FIGURE 2.—Panel mounts used in tests.

damping for which an intense discrete-frequency noise input was desired, the apparatus of figure 3 was used. This apparatus consisted of an air chopper or siren, which periodically interrupts an airstream to produce pressure pulsations. The siren is coupled by a short transition section to an acoustic horn with a length of 6 feet and a mouth diameter of 2 feet. The siren itself consists of a stator having 6 ports and 6 webs of equal width and a rotor of 6 ports of slightly less width. These rotor ports alternately cover and uncover the 6 stator ports at a rate determined by the speed of the rotor drive motor. The system was capable of generating sound levels up to 160 decibels at frequencies of 100 to 500 cycles per second.

INSTRUMENTATION

The measured data consisted mainly of panel stresses and frequencies and input pressure spectra. Figure 4 shows schematic diagrams of the instrument systems used to obtain these data. Figure 4 (a) shows the strain-gage setup. As is shown in figure 1, a Baldwin A–8 strain gage, which is roughly ⅛ inch long, was mounted at the middle of the short side of the panel in front of a bolt hole for all tests. A conventional strain-gage carrier and bridge system was used. Its output was channeled to a recording oscillograph for frequency observation and recording of time histories and to a thermocouple mean-square meter after filtering out the carrier with a 2,000 cycle per second low-pass filter. Calibration of the

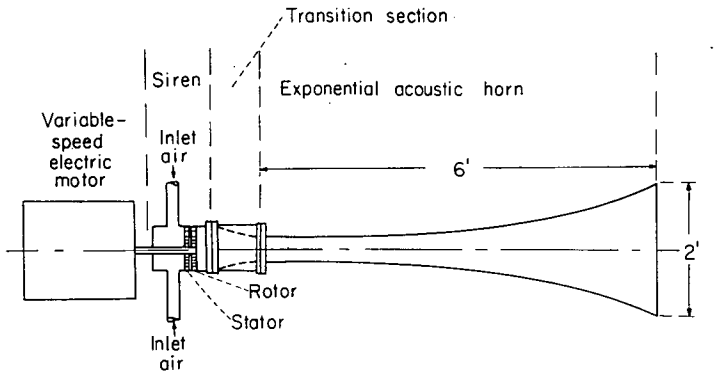


FIGURE 3.—Siren used in tests.

system for stress was made by statically loading a strain-gage cantilever beam and observing the oscillograph deflection and then assigning to that deflection the stress calculated for the system.

Figure 4 (b) shows schematically the instrumentation used for measurement of noise inputs. For periodic inputs (from the siren), the lower system of figure 4 (b) was used. It consisted of a dynamic-pressure gage, an associated carrier amplifier, and a panoramic frequency analyzer. Calibration of the system was made by comparison with a standard microphone of known sensitivity.

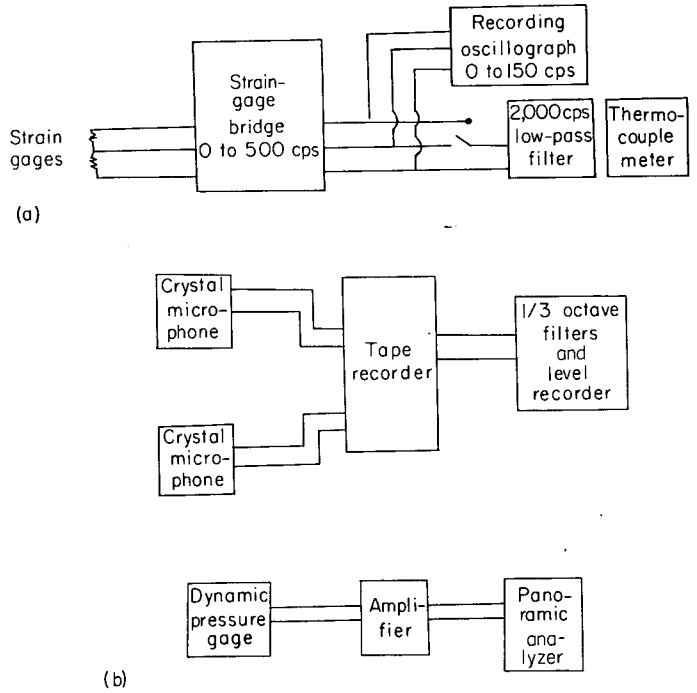
For random input, as from the 4-inch air jet and the turbojet engine, the system sketched at the top of figure 4 (b) was used. In this case a crystal microphone was used in conjunction with a tape recorder. For the spectrum analysis, playback of the tape records was made through a set of ⅓-octave filters. Since the results of such analyses depend upon the filter characteristics, they were corrected to spectrum-level values (band width of 1 cycle per second) from knowledge of the filter characteristics.

METHODS

In order to make calculations of stress for comparison with measured values, certain characteristics of the input acoustic loading and of the panel response were needed. For the loading, a representative spectrum of the pressure is involved; for the panels the determination of the static response to a given loading and the dynamic response to the equivalent sinusoidal loading is involved.

NOISE INPUTS

In all cases, for either periodic or random input, the input pressure that was used in calculations was measured at a point at the edge of the test panel. This practice was found to keep the measurement relatively free of the radiation field of the vibrating panel and results essentially in a value which corresponds to pressure at a rigid surface. Use of this pressure tacitly assumes unit correlation of pressure over the entire panel. This assumption seems to be justified for the fundamental frequencies of the panel models used in these tests as indicated by the correlation data of reference 3 for a similar engine. Further information on the noise pressure levels near turbojet engines is presented in reference 4 and in the appendix of this paper.



(a) Stress.
(b) Noise.

FIGURE 4.—Instrumentation used in panel tests.

PANEL CHARACTERISTICS

In order to calculate the stress response to random noise, the static-stress response and the panel-admittance characteristics are needed. The frequency-response curves for each panel at various input-pressure levels were obtained by positioning the panel in its mount (either laboratory or field) about 1½ feet outside the mouth of the siren and operating the latter at constant output pressure and various frequencies. From the resulting stress response curves, damping and resonant frequency were obtained. All static stress curves were obtained with the panels in the laboratory mount by either evacuating or pressurizing the backing chamber to various levels.

METHOD OF STRESS ANALYSIS

As Miles (ref. 5) has shown, the problem of random excitation of a structural panel can be handled by a power-spectrum procedure in the following manner:

Consider that the panel behaves as a simple single-degree-of-freedom linear system. Its response to an input at frequency ω is determined by the square of its transfer function $1/Z(\omega)^2$ where

$$|Z(\omega)|^2=\frac{1}{S_0^2}\left\{\left[1-\left(\frac{\omega}{\omega_0}\right)^2\right]^2+4\delta^2\left(\frac{\omega}{\omega_0}\right)^2\right\} \tag{1}$$

where

S_0 static stress per unit load
ω_0 resonant frequency
δ damping in terms of critical damping

If this system is excited by a random input which has the power spectrum $\Phi_N(\omega)$, the output stress response $\Phi_\sigma(\omega)$ is given as

$$\Phi_\sigma(\omega)=\frac{\Phi_N(\omega_0)}{|Z(\omega)|^2} \tag{2}$$

Integration of this relation throughout the width of the spectrum yields the following expression for the mean-square stress

$$\overline{\sigma^2}=\frac{\pi}{4\delta}\omega_0\Phi_N(\omega_0)S_0^2 \tag{3}$$

which is exact when the input spectrum is flat and is a good approximation for a system with low damping when the input spectrum is changing gradually in the vicinity of ω_0.

It is primarily with this latter relationship that the present report is concerned, inasmuch as measured stress data are

compared with values calculated from equation (3). In addition, it is proposed to apply this relationship, which assumes a strictly linear response, to panels which are driven into the nonlinear operating range and also to curved panels.

In addition to the root-mean-square stress response, there is interest also in the time history of stress, for this history undoubtedly affects fatigue life. As Miles discusses in reference 5, a linear single-degree-of-freedom system randomly excited is expected to respond at the natural frequency of the system and at stress amplitudes which vary as a function of time. The stress-amplitude envelope is expected to exhibit beats at more or less regular intervals and this condition was noted experimentally in reference 1. From the present tests, stress time histories were obtained at high random input levels where the panel response is somewhat nonlinear and also for the case where the loading spectrum contained a strong periodic component superposed on the random components.

Figure 5 presents sample stress time histories for various panels in the near noise field of the jet engine at the 100-percent engine-rotational-speed condition and at the afterburner condition. These sample stress records indicate the response frequency of the panels but the stress amplitudes as shown in the figure are not necessarily relative. At the 100-percent engine-rotational-speed condition of the engine, the noise inputs to the panels are essentially random in nature, whereas, for the afterburner condition, as is shown in figure 6, an additional intense discrete-frequency component is present in the input spectrum. It can be seen that, for the 100-percent engine-rotational-speed condition, the stress responses for these three panels exhibit a beating which was noted experimentally in reference 1 for much lower random input levels.

However, in the afterburner case the records for the most part lack this characteristic beating. This is believed to reflect the presence of the strong periodic component in the loading spectrum. The 0.032-inch panel, which has a natural frequency almost coincident with the periodic afterburner component, responds almost sinusoidally as might be expected.

RESULTS AND DISCUSSION

NOISE INPUTS

The panels tested in this investigation were loaded randomly by the near sound fields of a 4-inch cold air jet and a turbojet engine operated at three thrust settings in order to have a range of input pressures. The turbojet settings were (1) afterburner, (2) 100-percent engine rotational speed, and (3) a condition estimated as 95-percent rotational speed. Figure 6 gives sample spectra from the engine for the 100-percent rotational speed and for the afterburner condition. These particular spectra apply to a position 31.4 feet downstream of the tailpipe and 1.58 feet from the 15° jet boundary. The overall sound levels associated with these spectra are in the range of 146 to 155 decibels.

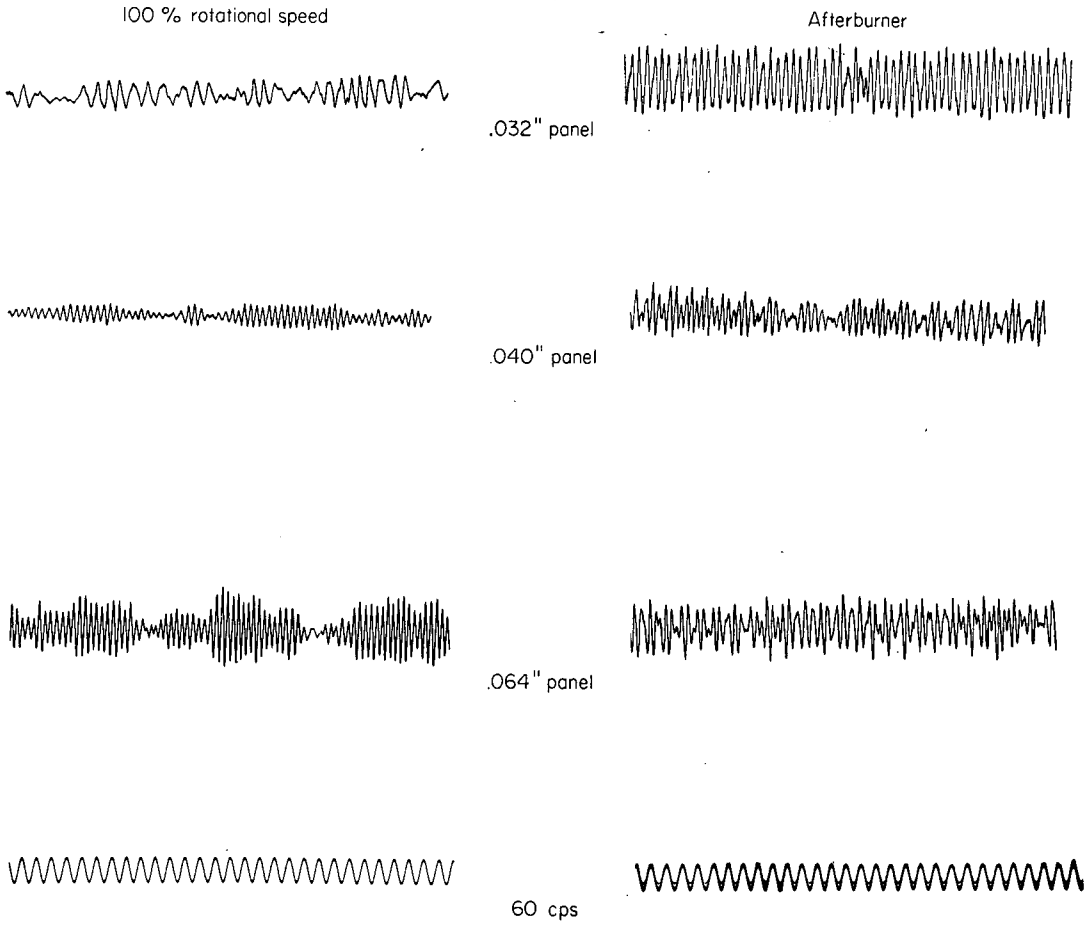


FIGURE 5.—Strain-gage response of panels to two different engine conditions.

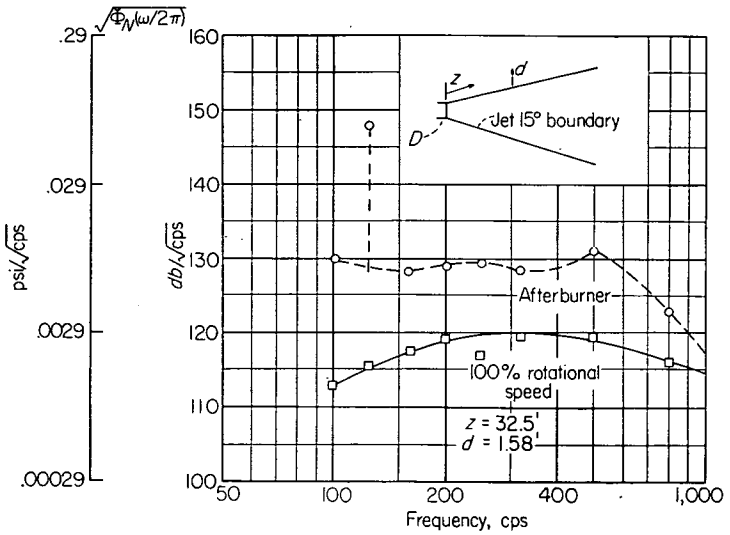


FIGURE 6.—Sample pressure spectra from the turbojet engine.

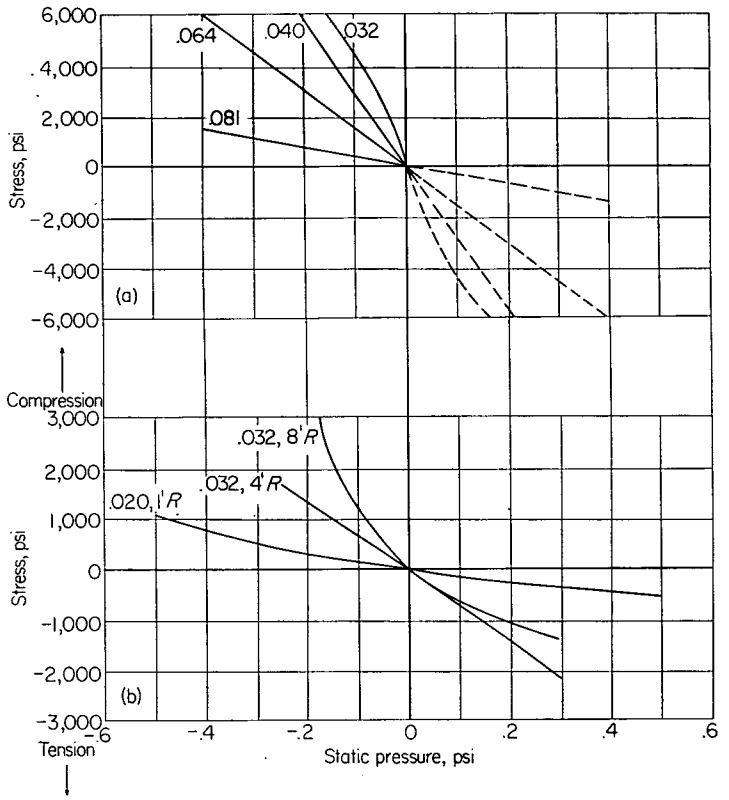
The shapes of the spectrum curves are typical of those measured heretofore in the near field of turbojets (ref. 2) and the increment in pressure between the 100-percent engine rotational speed and the afterburner condition is about that expected on the basis that the near-field pressure varies as the square of the velocity. (See ref. 6.) In addition to this increase there is also noted a very intense discrete frequency component at 125 cycles per second. This component is attributed to a resonant condition in the tailpipe and has also been observed on some other engines. (See ref. 7.) This discrete frequency lies below the resonant frequencies of the 0.040-inch panel and the 0.064-inch panel and was nearly coincident with the resonant frequency of the 0.032-inch panel.

The spectra obtained with the turbojet at the estimated 95-percent rotational speed and with the 4-inch air jet had, in general, acoustic pressure distributions similar to those of figure 6, except that the levels were lower. More detailed information on the spatial distribution of pressure at various frequencies is given in the appendix. With the 4-inch jet, overall levels were in the range of 125 to 135 decibels; with the 95-percent engine rotational speed, overall levels were in the range of 135 to 145 decibels.

PANEL CHARACTERISTICS

Stress calculations obtained by using equation (3) require experimental values for several of the panel-response characteristics, namely, (1) the static response per unit input pressure, (2) the resonant frequency, and (3) the damping. Figures 7 to 10 present a summary of data of this type obtained from the panels tested.

Static stress response.—Figure 7 presents the static stress response for the various test panels. Figure 7(a) groups the data for the flat panels with thicknesses of 0.032 inch to 0.081 inch; figure 7(b) gives the static-stress values of the curved panels. Differentiation is made between loading with pressure and loading with a vacuum on the back side of the panels. As used in this paper, a positive stress is associated with a vacuum on the back side of the panel. Although the



(a) Flat panel.
(b) Curved panel.

FIGURE 7.—Static stress characteristics of test panels.

method of mounting allows slightly different bending moments for a given pressure or vacuum loading, the stress differences were found to be negligible for the flat panels in the range of test pressures shown. Figure 7(a) indicates a linear increase of stress with pressure loading for pressures up to at least 0.2 pound per square inch for all panels except the 0.032-inch panel, which was linear only up to about 0.05 pound per square inch.

In the case of the curved panels, the direction of loading is a significant factor, as indicated in figure 7 (b) where it can be seen that the slopes of the respective stress curves change more rapidly as a function of pressure.

Frequency-response characteristics.—From the tests with the siren, in which frequency was varied systematically while the acoustic input pressure to the panel was held constant at various levels, frequency-response curves were obtained for the flat and curved panels of various thicknesses.

Figure 8 presents sample results for a flat panel of 0.040-inch thickness at three different input pressures. Peak stress amplitude in pounds per square inch is plotted as a function of driving frequency in cycles per second for root-mean-square values of fundamental siren pressure of 0.00184, 0.00366, and 0.0147 pound per square inch. At the lowest input pressure the response is fairly symmetrical about the resonant frequency which at that pressure is 148 cycles per second. This type of response is typical of a linear system. As the input pressure is increased to 0.00366 pound per square inch, the response curve takes on a skewed form, the peak now occurring at 163 cycles per second. As shown in reference 8 this increase in pressure reflects nonlinearities

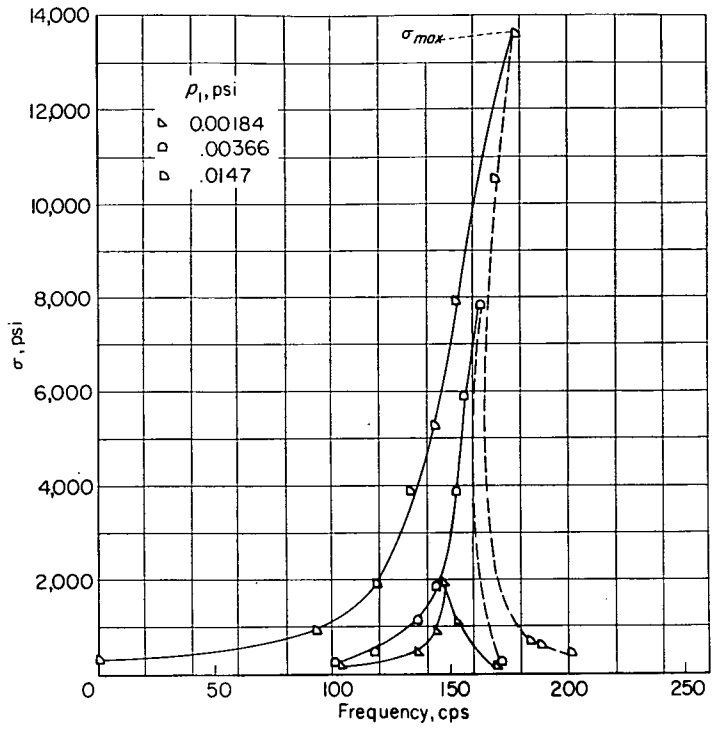


FIGURE 8.—Frequency-response characteristics of flat panels. $t=0.040$ inch.

of the system whereby the stiffness is increasing with panel deflections. Experimentally this type of response results in a triple-valued curve for a certain frequency range within which the curve is very difficult to define. For that reason a portion of the response curve is shown by a dashed line. At the input pressure of 0.0147 pound per square inch, the skewness is even more evident and the peak occurs at a still higher frequency.

The trends illustrated in figure 8 were found to be generally representative of all the flat panels tested, except, of course, that the resonant frequencies are higher for thicker panels.

Figure 9 presents similar results for a curved panel with a thickness of 0.032 inch and a radius of curvature of 4 feet. Response curves for input pressures of 0.00114, 0.0114, and 0.0229 pound per square inch are given. As was the case with flat panels, the curved-panel response is very nearly symmetrical about resonance at the lowest pressure and tends to skew to the right at intermediate pressures. Unlike the flat panels, however, the curved panel assumes a response which skews to the left at the highest pressures. As shown in reference 8, this type of nonlinear response is associated with a condition of decreasing stiffness with deflection increase. For a curved panel this condition is probably due to the tendency for the panel to dimple inward in response to a pressure on its convex surface.

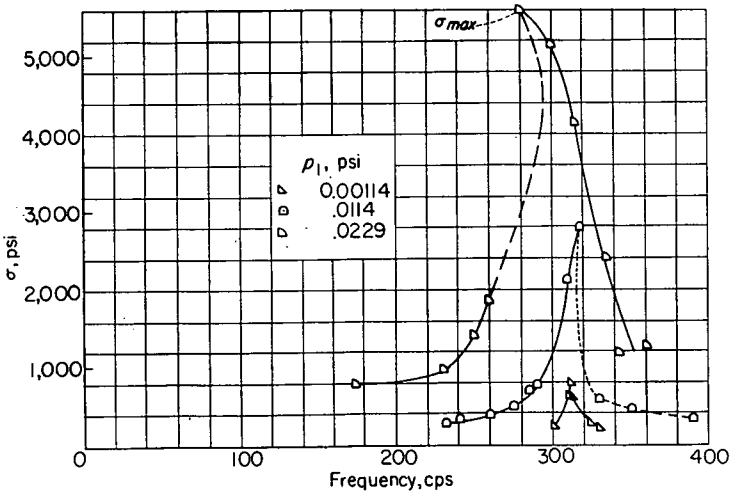


FIGURE 9.—Frequency-response characteristics of curved panels. $t=0.032$; $R=4$ feet.

Damping.—As is well known, either the height of the frequency-response curve or its width at the half-power points provides an indication of the panel damping. However, because of the unstable range involved just above or below the resonance of a nonlinear panel, the width is very difficult to obtain experimentally. Thus all damping data presented were obtained from the resonant amplification:

$$\delta=\frac{\sigma_{st}}{2(\sigma_{max})\,\omega_0}$$

Figure 10 illustrates the variation of damping δ as a function of the root-mean-square value of panel stress for flat panels of thickness 0.040 inch, 0.064 inch, and 0.081 inch. All data points shown are obtained from the resonant response of the panel in question at a particular level of acoustic pressure. In general, for the field mount it can be seen that at the higher stress conditions the damping increases very rapidly with stress (or deflection). Also apparent is some tendency for the damping to increase again at very low stresses. The reason for this increase is not known; however, this tendency was also apparent in the earlier tests (ref. 1) in which only low levels of excitation were employed.

The fact that the experimental points for all thicknesses tested fall on a common curve is a probable indication that, for the range of panel thicknesses tested, damping is primarily dependent upon stress level. The average damping curve for flat panels of 0.040 inch, 0.064 inch, and 0.081

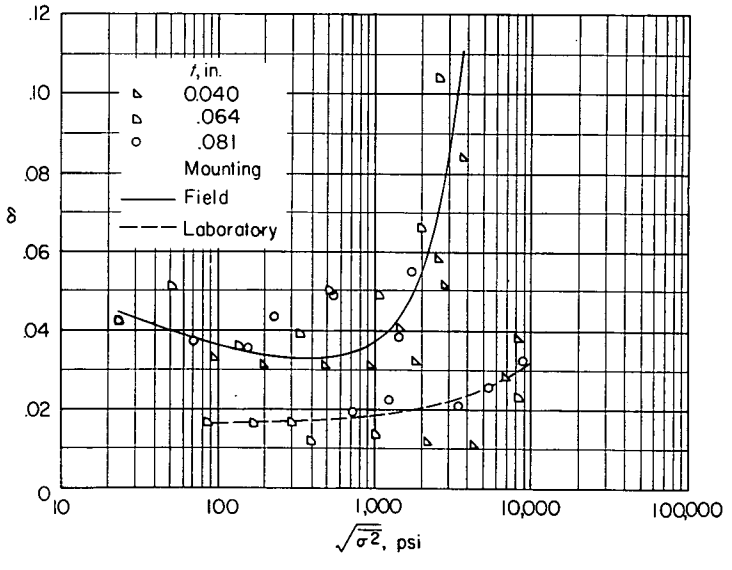


FIGURE 10.—Damping characteristics of flat panels.

inch in the laboratory mount is given by the dashed curve. (See fig. 10.) This curve illustrates clearly the significance of the mounting conditions since the laboratory mount with its less absorptive backing material yields appreciably lower values of damping. Damping for the curved panels was found to vary only slightly from that of the flat panels at the high stresses encountered with turbojet excitation.

PROCEDURE FOR CALCULATING STRESS

The success in using equation (3) to predict stress due to a random input depends to a large extent on the use of experimentally determined quantities. In order to facilitate these calculations, equation (3) can be rewritten as follows:

$$\sqrt{\Phi_N(\omega_0)}=\sqrt{\overline{\sigma^2}}\left(\frac{4\delta}{\pi\omega_0 S_0^2}\right)^{1/2}$$

where the quantities in parentheses have been shown to be a function of the stress level of the panel.

A curve of stress as a function of input acoustic pressure can be determined by solving the above equation for $\sqrt{\Phi_N\left(\frac{\omega_0}{2\pi}\right)}$ by using arbitrary values of $\sqrt{\overline{\sigma^2}}$ and the corresponding experimentally determined values of δ, S_0, and ω_0.

The data of figures 7, 8, 10, and 11 are used in conjunction with equation (3) to determine the curve of root-mean-square stress as a function of jet acoustic pressure $\sqrt{\Phi_N\left(\frac{\omega_0}{2\pi}\right)}$ shown in figure 12. For a given root-mean-square stress level, the value of S_0 is determined from figure 7 by using the relation

$$\sigma_{st}=2\delta\sqrt{2}\sqrt{\overline{\sigma^2}}$$

The damping δ at the appropriate stress level is obtained directly from the curves of figure 10. The natural frequency ω_0 is obtained from the response-curve data (such as that given in fig. 8) used in determining damping.

In addition to figures 7, 8, and 10, curves of mean-square stress as a function of siren acoustic pressure such as those

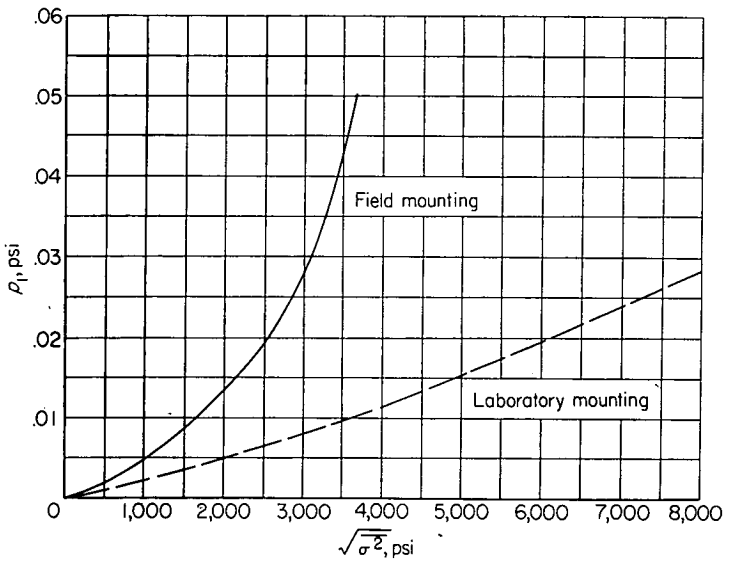
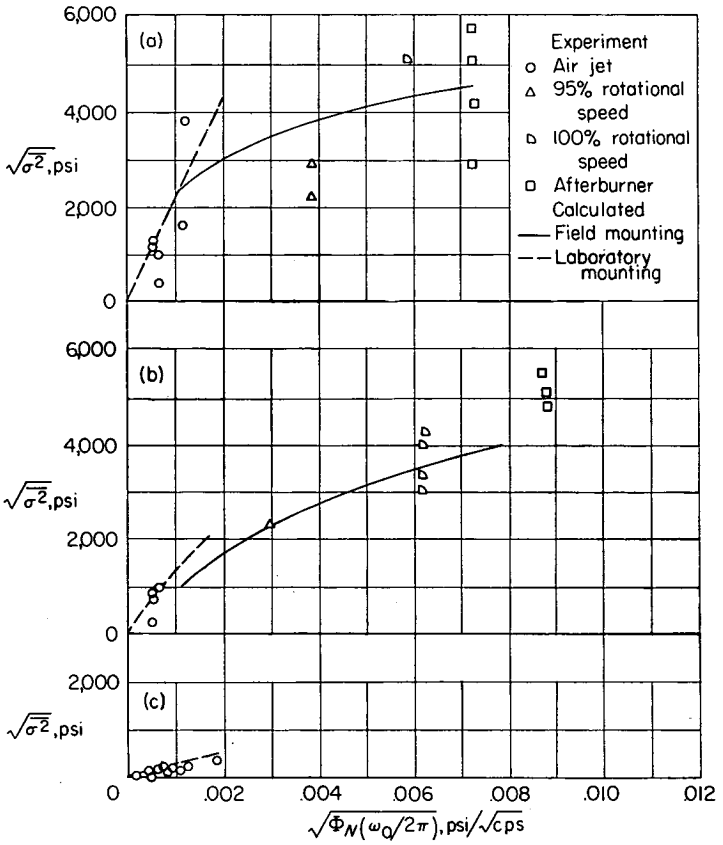


FIGURE 11.—Siren pressure as a function of root-mean-square stress for a 0.064-inch panel.



(a) $t=0.040$.
(b) $t=0.064$.
(c) $t=0.081$.

FIGURE 12.—Comparison of calculated and measured stresses for flat panels.

of figure 11 are useful in the calculation of $\sqrt{\Phi_N\left(\frac{\omega_0}{2\pi}\right)}$ when S_0 is in the nonlinear range. These curves are constructed from figure 7 and the average stress-damping curves of figure 10. For a given root-mean-square stress level, the associated siren acoustic pressure is first determined from a curve such as figure 11. The quantity S_0 was taken as the slope of a secant line drawn between two points on the curve of figure 7 at the appropriate pressure levels $\pm\sqrt{2}p_1$.

COMPARISON OF CALCULATED AND MEASURED STRESSES

A comparison of the measured and calculated stresses for flat panels of 0.032 inch, 0.040 inch, 0.064 inch, and 0.081 inch and for curved panels of 0.032 inch with radii of 8 feet and 4 feet is given in figures 12 and 13. Figure 12 relates to flat panels and presents calculated and measured root-mean-square stresses as a function of input spectrum-level pressure $\sqrt{\Phi_N\left(\frac{\omega_0}{2\pi}\right)}$ for thicknesses of 0.040 inch, 0.064 inch, and 0.081 inch. In each case the curve represents the calculated stress variation and the points are measured stress values from tests with both the 4-inch laboratory air jet and the turbojet.

For the 0.040-inch panel, the calculated and measured stresses are found to be in very good agreement at low pressures and the theory seems to be generally conservative

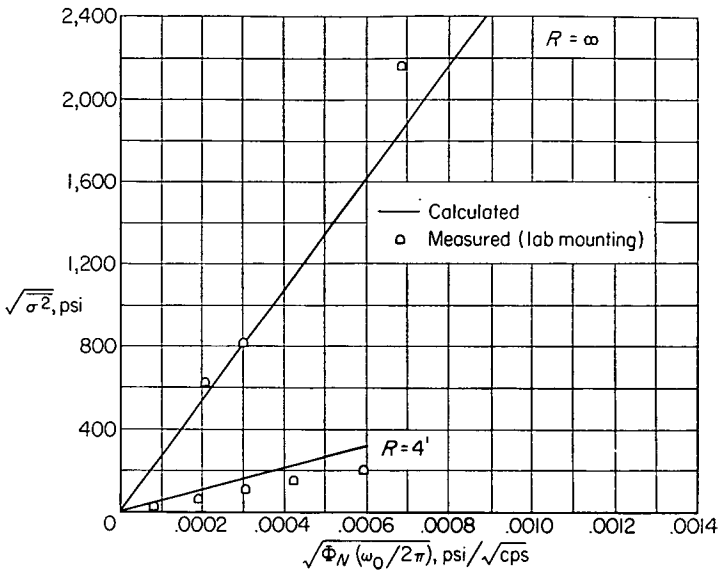


FIGURE 13.—Effect of curvature on calculated and measured stress of 0.032-inch 2024–T3 panels.

at the higher pressures. For the 0.081-inch panel only low-pressure data were obtained, but over the range tested the calculated and measured values are in excellent agreement. Thus it appears from figure 12 that equation (3) will yield stress values which are in fairly good agreement with measured values on flat panels over a wide range of input pressures and for a doubling of panel thickness.

The fact that the analysis is in such good agreement with experimental results for both the 4-inch air jet and the turbojet engine seems to indicate that the correlation length is a function of frequency and not of jet size.

Figure 13 compares calculated and measured stresses for a panel of given thickness (0.032 inch) having different radii of curvature. Again the root-mean-square stress $\sqrt{\overline{\sigma^2}}$ is plotted as a function of root-mean-square spectrum-level pressure $\sqrt{\Phi_N\left(\frac{\omega_0}{2\pi}\right)}$. The upper curve and associated points allow comparison of calculated and measured stresses for a flat panel ($R=\infty$). The agreement is similar to that of figure 12 for thicker panels, although the pressure range for the 0.032-inch panels is more limited. As the radius of curvature is decreased to 4 feet, the agreement between calculated and measured stresses is still rather good, the theory being consistently conservative.

CONCLUSIONS

An investigation was made of the stress response of simple flat and curved rectangular panels to random acoustic noise. In addition, this stress response was calculated by using general harmonic-analysis methods. This investigation indicated the following conclusions:

1. At input pressures of the order of those encountered in full-scale configurations, the panels are somewhat nonlinear. With flat panels this nonlinearity involves a stiffening spring constant; with curved panels the nonlinearity involves a decreasing spring constant.

2. Within reasonable limits in the stress range of the tests, the combined structural and radiation damping of flat panels is independent of panel thickness and depends only upon panel stress or deflection. Damping increases rapidly with stress at the higher stresses.

3. The generalized harmonic analysis predicts stresses which are in fair agreement with measured values for flat panels and for curved panels of radius 4 feet over the range of input pressures tested.

LANGLEY AERONAUTICAL LABORATORY,
NATIONAL ADVISORY COMMITTEE FOR AERONAUTICS,
LANGLEY FIELD, VA., *June 3, 1957.*

APPENDIX

NEAR NOISE FIELD OF THE TURBOJET ENGINE

Because of the rather limited near-field noise data from full-scale turbojets, particularly for afterburning conditions, it seems advisable to include more detailed results of the survey taken with an engine. The near field was explored along lines parallel to the theoretical 15° jet boundary at radial distances of 0.79 foot, 1.58 feet, and 3.16 feet for the engine under 100-percent rotational-speed conditions and for afterburner operation. The thrust and nozzle diameters for the 100-percent rotational-speed and for the afterburner conditions were 2,780 pounds at 15.38 inches and 3,390 pounds at 17.5 inches, respectively. In addition, data from another turbojet engine were obtained at a power condition estimated to be at 95-percent rotational speed for a thrust of approximately 2,300 pounds and a nozzle diameter of 15.38 inches. Figures 14 and 15 present some of the results obtained.

Figure 14 includes a plot of overall sound pressure as a function of slant distance z for 100-percent rotational-speed and afterburner conditions of the engine. Radial distances of 0.79 foot, 1.58 feet, and 3.16 feet are given for afterburner operation and radial distances of 1.58 feet and 3.16 feet are given for the 100-percent rotational-speed condition. In general, these curves indicate that the largest pressures occur farther downstream of the tailpipe as the radial distance is increased. This result is in agreement with the model-jet trends reported in reference 6. Also apparent is the fact that, at stations just downstream of the nozzle, the pressures decrease very rapidly with radial distance; whereas, at stations farther downstream there is only a slight decrease of pressure with radial distance. Comparison of the afterburner and 100-percent rotational-speed curves shows that operation of the afterburner increases the pressure fluctuations by as much as a factor of 5 in some locations. Of course, this particular engine is somewhat unique in that (as discussed previously) it resonates during afterburning and the periodic noise of that origin dominates the spectrum, particularly at stations near the tailpipe.

Figures 15 (a), 15 (b), and 15 (c) illustrate the spatial distribution of spectrum-level pressure at various frequencies

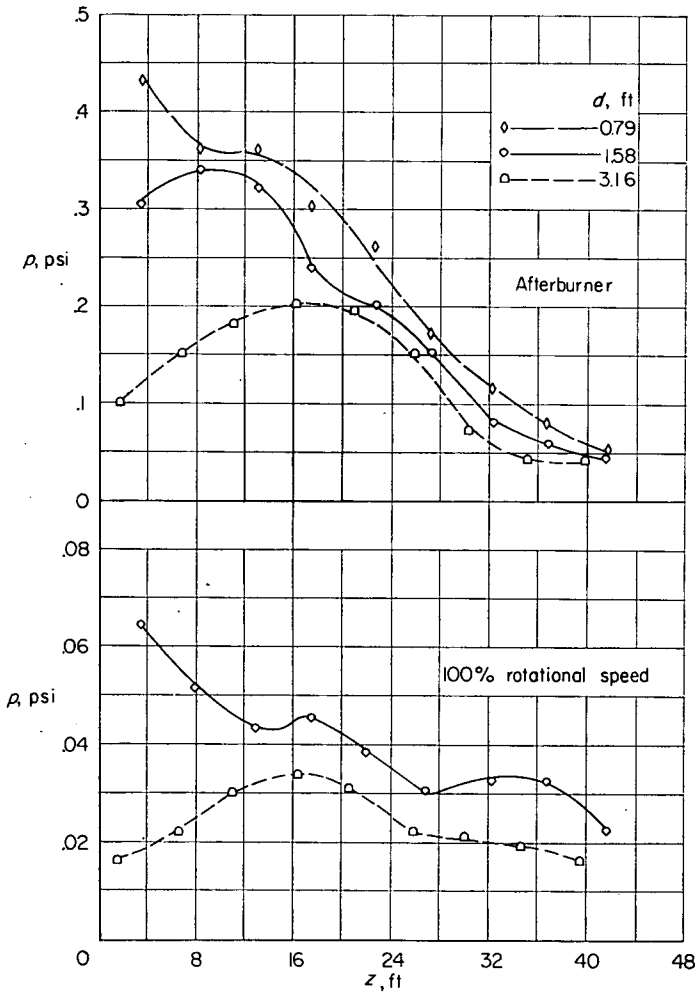
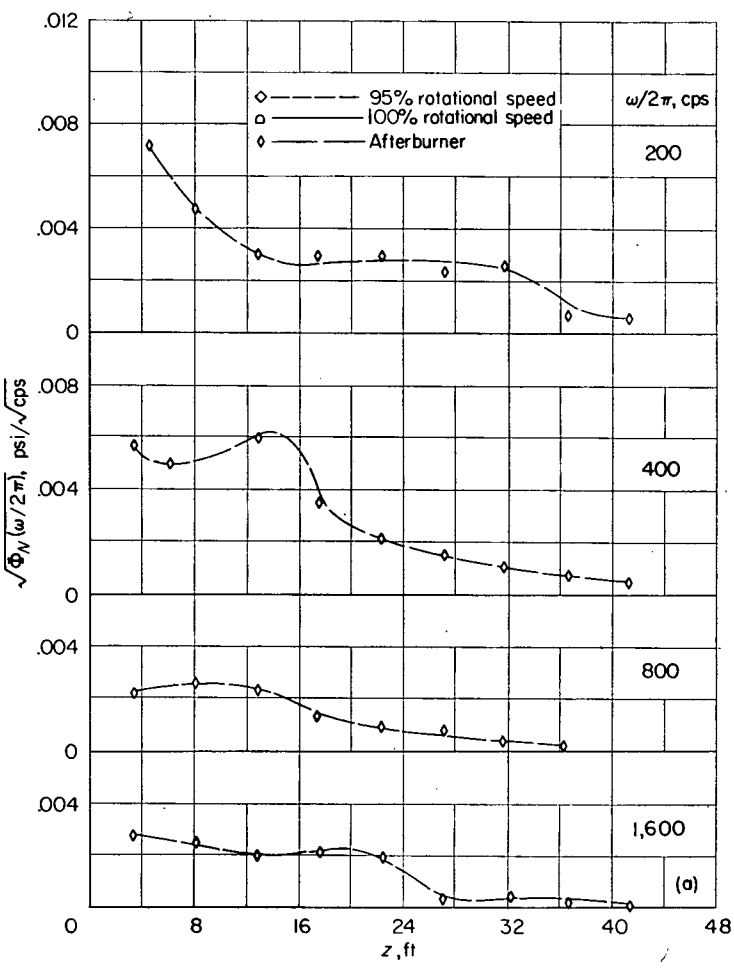
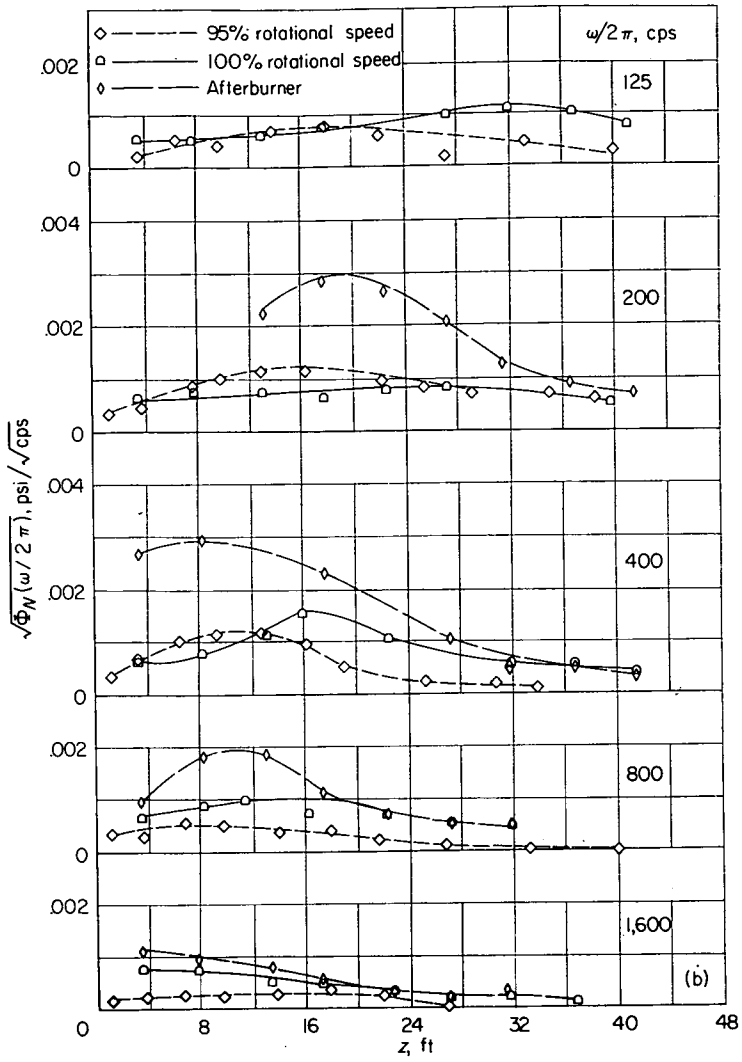


FIGURE 14.—Overall near-field sound pressures at various axial and radial distances from the turbojet engine.



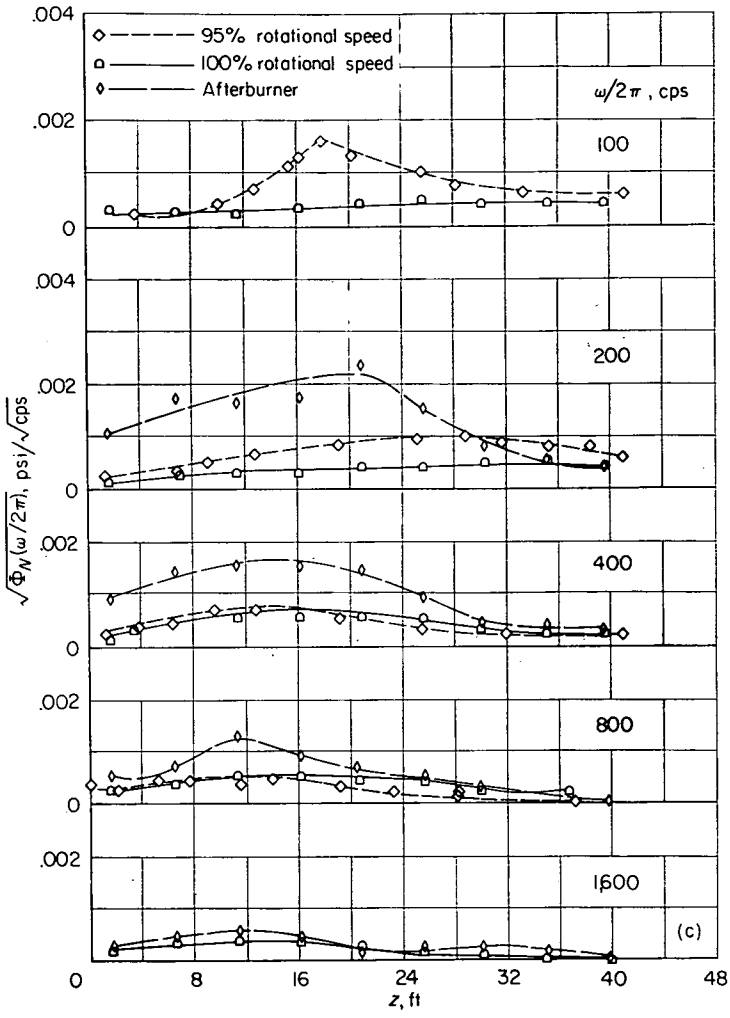
(a) d=0.79 foot.

FIGURE 15.—Near-field sound pressures of the turbojet engine at various frequencies as a function of axial and radial distances.



(b) $d=1.58$ feet.

FIGURE 15.—Continued.



(c) $d=3.16$ feet.

FIGURE 15.—Concluded.

for radial distances of 0.79 foot, 1.58 feet, and 3.16 feet, respectively. Figure 15 (a), for $d=0.79$ foot, presents only data from afterburner operation; figures 15 (b) and 15 (c) include data at the 95-percent and 100-percent rotational-speed conditions.

In general, these results indicate that the maximum pressure at a given frequency occurs at some distance downstream of the tailpipe. As the engine rotational speed (and thus jet velocity) is increased, the point of maximum pressure for any given frequency tends to occur somewhat near the tailpipe. Similarly, the high-frequency components tend to have maximum pressure values nearer the tailpipe than the low-frequency components. As shown in reference 6, this result is also in agreement with near-field results from unheated model jets.

REFERENCES

1. Hess, Robert W., Lassiter, Leslie W., and Hubbard, Harvey H.: A Study of the Response of Panels to Random Acoustic Excitation. NACA RM L55E13c, 1955.
2. Lassiter, Leslie W., Hess, Robert W., and Hubbard, Harvey H.: An Experimental Study of the Response of Simple Panels to Intense Acoustic Loading. Jour. Aero. Sci., vol. 24, no. 1, Jan. 1957, pp. 19–24, 80.
3. Callaghan, Edmund E., Howes, Walton L., and Coles, Willard D. (with appendix by Channing C. Conger and Donald F. Berg): Near Noise Field of a Jet-Engine Exhaust. II. Cross Correlation of Sound Pressures. NACA TN 3764, 1956.
4. Howes, Walton L., and Mull, Harold R.: Near Noise Field of a Jet-Engine Exhaust. I. Sound Pressures. NACA TN 3763, 1956.
5. Miles, John W.: On Structural Fatigue Under Random Loading. Jour. Aero. Sci., vol. 21, no. 11, Nov. 1954, pp. 753–762.
6. Lassiter, Leslie W., and Hubbard, Harvey H.: The Near Noise Field of Static Jets and Some Model Studies of Devices for Noise Reduction. NACA Rep. 1261, 1956. (Supersedes NACA TN 3187.)
7. Lassiter, Leslie W.: Noise From Intermittent Jet Engines and Steady-Flow Jet Engines With Rough Burning. NACA TN 2756, 1952.
8. Den Hartog, J. P.: Mechanical Vibrations. Second ed., McGraw-Hill Book Co., Inc., 1940.

REPORT 1368

SYSTEMATIC TWO-DIMENSIONAL CASCADE TESTS OF NACA 65-SERIES COMPRESSOR BLADES AT LOW SPEEDS [1]

By James C. Emery, L. Joseph Herrig, John R. Erwin, and A. Richard Felix

SUMMARY

The performance of NACA 65-series compressor blade sections in cascade has been investigated systematically in a low-speed cascade tunnel. Porous test-section side walls and, for high-pressure-rise conditions, porous flexible end walls were employed to establish conditions closely simulating two-dimensional flow. Blade sections of design lift coefficients from 0 to 2.7 were tested over the usable angle-of-attack range for various combinations of inlet-flow angle β_1 of 30°, 45°, 60°, and 70°, and solidity σ of 0.50, 0.75, 1.00, 1.25, and 1.50. Design points were chosen on the basis of optimum high-speed operation. A sufficient number of combinations were tested to permit interpolation and extrapolation of the data to all conditions within the usual range of application.

The results of this investigation indicate a continuous variation of blade-section performance as the major cascade parameters, blade camber, inlet angle, and solidity were varied over the test range. Summary curves of the results have been prepared to enable compressor designers to select the proper blade camber and angle of attack when the compressor velocity diagram and desired solidity have been determined.

At a few test conditions, an upper limit to the design lift coefficient that could provide satisfactory performance was found. These results provide information as to the maximum value of the loading parameter, expressed as the product of solidity and section lift coefficient based on the vector mean velocity, that can be used effectively in compressor design. Analysis of the trends indicated that the common practice of employing a constant maximum value of the loading parameter for all inlet angles and solidities fails to define the observed performance of the compressor blades studied in this investigation.

An index that the positive and negative limits of useful angle-of-attack range occurred when the section drag coefficient reached twice the minimum value was used to estimate the operating range of the compressor blade sections studied. A broad operating range for these sections was observed, except for conditions of highest pressure rise across the cascade corresponding to high cambers at high inlet angles. These conditions are not typical of usual design practice and no difficulty should ordinarily be encountered in employing these blade sections. In general, the observed performance of NACA 65-series compressor blades in cascade is considered to be very satisfactory.

INTRODUCTION

The design of an axial-flow compressor of high performance involves three-dimensional high-speed flow of compressible viscous gases through successive rows of closely spaced blades. No adequate theoretical solution for this complete problem has yet appeared nor, from consideration of the complexity of the problem, does it seem likely that complete relationships will be established for some time. Various aspects of the problem have been treated theoretically, and the results of those studies are quite useful in design calculations. All such studies, however, have been based on idealized flow, with effects of one or more such physical realities as compressibility, finite blade spacing, and viscosity neglected. Consideration of viscosity effects has been particularly difficult. It appears, therefore, that in spite of advances in theoretical methods, theory must be supplemented by experimental data for some time to come.

Some of the information required can be obtained only by experiment in single-stage and multistage compressors. Much of the information, however, can be obtained more easily by isolating the effects of each parameter for detailed measurement. The effects of inlet angle, blade shape, angle of attack, and solidity on the turning angle and drag produced can be studied by tests of compressor blades in two-dimensional cascade tunnels. Cascade tests can provide many basic data concerning the performance of compressors under widely varying conditions of operation with relative ease, rapidity, and low cost. A number of successful high-speed axial-flow compressors have been designed by using low-speed cascade data directly. A more refined procedure, however, would use cascade data, not as the final answer, but as a broad base from which to work out the three-dimensional relations.

Data from a large number of two-dimensional cascade tests have been available in this and other countries for

[1] Supersedes NACA Technical Note 3916 (formerly NACA RM L51G31) by L. Joseph Herrig, James C. Emery, and John R. Erwin, 1957, and NACA Technical Note 3913 (formerly NACA RM L54H18a) by A. Richard Felix, 1957.

some years. Although the cascade configurations used in these investigations were geometrically two dimensional, in no case except that of the porous-wall cascade of reference 1 was the flow believed to be two dimensional. This situation is ordinarily accepted on the grounds that the flow in the compressor is also subject to three-dimensional end effects. That similar end conditions would exist in stationary cascades and rotating blade rows seems unlikely. As discussed in reference 1, there is evidence, however, that the flow through typical axial compressor blades is more nearly like that in aerodynamically two-dimensional cascades than like that in cascades which are only geometrically two dimensional. Excellent correlation between porous-wall cascade and rotor-blade pressure-distribution and turning-angle values is shown for the design conditions of the compressor investigation reported in reference 2. The proper basic approach to the compressor design problem, therefore, would seem to be to separate the two-dimensional effects from the three-dimensional. This approach should also aid in the evaluation of the separate effects of tip clearance and secondary flow in axial compressors. Therefore, a systematic series of low-speed cascade tests of the NACA 65-series compressor blade sections were made by means of the porous-wall technique to insure two dimensionality of the flow. These results and an analysis of the data are presented, as well as summarized data in the form of carpet plots for use in specific design problems.

SYMBOLS

a mean-line loading designation
b blade height or span, feet
c blade chord, feet
c_d section drag coefficient
c_F resultant-force coefficient
c_l section lift coefficient
$c_{l,o}$ camber, expressed as design lift coefficient of isolated airfoil
c_N section normal-force coefficient
$c_{N,M}$ section normal-force coefficient obtained by calculation of momentum and pressure changes across blade row
$c_{N,P}$ section normal-force coefficient obtained by integration of blade-surface pressure distribution
c_w wake momentum difference coefficient
F force on blades, pounds
F_M force on blades due to momentum change through blade row, pounds
F_p force on blades due to pressure change through blade row, pounds
F_w force on blades due to momentum difference in wake, pounds
g tangential spacing between blades, feet
l/d ratio of section lift to section drag
M Mach number
P total pressure, pounds per square foot
p static pressure, pounds per square foot
Δp static pressure rise across cascade, pounds per square foot
q dynamic pressure, pounds per square foote
$\Delta p/q_1$ nondimensional static-pressure-rise paramter
R Reynolds number based on blade chord
S pressure coefficient $\left(\frac{P-p_1}{q_1}\right)$
U rotor-blade rotational speed, feet per second
V flow velocity, feet per second
W flow velocity relative to blades, feet per second
x chordwise distance from blade leading edge, feet
Y scaled value substituted for θ, $\theta+50(c_{l,o}-0.4)$
y perpendicular distance from blade chord line, feet
α angle between flow direction and blade chord, degrees
β angle between flow direction and a perpendicular to the cascade axis, degrees
θ flow turning angle, degrees $(\beta_2-\beta_1)$
γ angle between resultant-force direction and tangential direction, degrees
ρ mass density of flow, slugs per cubic foot
σ solidity, c/g

Subscripts:

a component in axial direction
d design value, except in drag coefficient
l local
m referred to vector-mean velocity, W_m
s flow outside wake
u component in tangential direction
1 upstream of blade row
2 downstream of blade row

APPARATUS, TEST PROGRAM, AND PROCEDURE

DESCRIPTION OF TEST EQUIPMENT

The test facility used in this investigation was the Langley 5-inch low-speed, porous-wall cascade tunnel described in reference 1 and shown in figures 1 and 2. During the course of this program some further improvements were required to establish proper testing conditions at higher pressure rise conditions. In particular, the boundary-layer buildup behind the slot on the convex flexible end wall with high pressure rise cascades was sufficient to cause separation and destroy simulation of the infinite cascade even though the blade flow was not separated. This condition was corrected by replacing the end wall with a porous flexible wall and suction chamber. In addition the large difference in flow length from the entrance cone to the side-wall slots between the tunnel ends at the higher inlet air angles gave quite different boundary-layer thickness along the length of the side-wall slots and made uniform flow entering the test section difficult to obtain. This condition was improved by making the changeable side plates porous and drawing a small amount of air through them. The concave flexible end wall was made porous to provide a further control of flow conditions through the test section.

The porous material found to be most satisfactory is commercial woven monel filter cloth. This cloth is available in various meshes in widths up to 36 inches and can be calendered at the factory to reduce porosity and improve surface smoothness. The combination found most suitable for the present work was a Dutch twill double weave of 30

by 250 mesh with warp wire diameter of 0.010 inch and fill wire diameter of 0.008 inch. The original thickness of about 0.026 inch was reduced to 0.018 inch by calendering. The resulting material has the porosity characteristics shown in figure 3. The primary advantages of this material over others tried previously are its uniformity, flexibility, strength, surface smoothness, and relatively low cost.

DESCRIPTION OF AIRFOILS

The blade family used in this investigation is formed by combining a basic thickness form with cambered mean lines. The basic thickness form used is the NACA 65(216)–010 thickness form with the ordinates increased by 0.0015 times the chordwise stations to provide slightly increased thickness toward the trailing edge. This thickness form has been designated the 65–010 blower blade section in references 3 and 4. It was not derived for 10-percent thickness but was scaled down from the NACA 65,2–016 airfoil given in reference 5. As discussed in reference 5, the scaling procedure gives the best results when it is restricted to maximum thickness changes of a few percent. Subsequent to the cascade studies of reference 3, in which the NACA 65–010 blower blade was first introduced, the basic thickness form for the NACA 65–010 airfoil section was derived and included in reference 5. The ordinates for the basic thickness form of the blower blade in reference 3 differ slightly from the airfoil ordinates in reference 5 but are considered interchangeable within the accuracy of the results reported herein. Ordinates for both the scaled thickness form (ref. 3) and derived thickness form (ref. 5) are given in table I.

TABLE I

ORDINATES FOR NACA 65-010 BASIC THICKNESS FORMS

[Stations and ordinates in percent chord]

Station, x	Ordinates, $\pm y$	
	65(216)–010 airfoil combined with $y=0.0015x$	Derived 65–010 airfoil
0	0	0
.5	.752	.772
.75	.890	.932
1.25	1.124	1.169
2.5	1.571	1.574
5.0	2.222	2.177
7.5	2.709	2.647
10	3.111	3.040
15	3.746	3.666
20	4.218	4.143
25	4.570	4.503
30	4.824	4.760
35	4.982	4.924
40	5.057	4.996
45	5.029	4.963
50	4.870	4.812
55	4.570	4.530
60	4.151	4.146
65	3.627	3.682
70	3.038	3.156
75	2.451	2.584
80	1.847	1.987
85	1.251	1.385
90	.749	.810
95	.354	.306
100	.150	0
L. E. radius	.666	.687

The basic mean line used is the $a=1.0$ mean line given on page 97 of reference 5. The amount of camber is expressed in reference 5 as design lift coefficient $c_{l,o}$ for the isolated airfoil, and that system has been retained. Ordinates and slopes for the $a=1.0$ mean line are given in table II for $c_{l,o}=1.0$. Both ordinates and slopes are scaled directly to obtain other cambers. Cambered blade sections are obtained by applying the thickness perpendicular to the mean line at stations laid out along the chord line. The blade sections tested are shown in figure 4. In the designation the camber $c_{l,o}$ is given by the first number after the dash in tenths. For example, the NACA 65–810 and NACA 65–(12)10 blade sections are cambered for $c_{l,o}=0.8$ and $c_{l,o}=1.2$, respectively.

TEST PROGRAM AND PROCEDURE

Test program.—The test program was planned to provide sufficient information to satisfy any conventional vector diagram of the type shown in figure 5. Tests of seven-blade cascades were run with various combinations of inlet air angle β_1 of 30°, 45°, 60°, and 70°, solidity σ of 0.50, 0.75, 1.00, 1.25, and 1.50, and cambers from $c_{l,o}$ of 0 to 2.7 over the useful angle-of-attack range. The most complete test series were run at solidities of 1.00 and 1.50; sufficient tests were made at the other solidities to guide interpolation and extrapolation. The combinations of β_1, σ, and blade section which were tested are tabulated in table III. The camber range covered at solidities of 1.00 and 1.50 was determined by one of two limitations. At the higher inlet angles progressively higher cambers were used until the limit loading had been reached, that is, until the design condition coincided with stall; at lower inlet angles, however, design turning angle exceeded inlet angle before the limit loading had been reached and the tests were terminated

TABLE II

ORDINATES FOR THE NACA $a=1.0$ MEAN LINE, $c_{l,o}=1.0$

[Stations and ordinates in percent chord]

Station, x	Ordinate, y	Slope, dy/dx
0	0	-------
.5	.250	0.42120
.75	.350	.38875
1.25	.535	.34770
2.5	.930	.29155
5.0	1.580	.23430
7.5	2.120	.19995
10	2.585	.17485
15	3.365	.13805
20	3.980	.11030
25	4.475	.08745
30	4.860	.06745
35	5.150	.04925
40	5.355	.03225
45	5.475	.01595
50	5.515	0
55	5.475	−.01595
60	5.355	−.03225
65	5.150	−.04925
70	4.860	−.06745
75	4.475	−.08745
80	3.980	−.11030
85	3.365	−.13805
90	2.585	−.17485
95	1.580	−.23430
100	0	-------

TABLE III

CASCADE COMBINATIONS TESTED

σ	NACA airfoil			
	$\beta_1=30°$	$\beta_1=45°$	$\beta_1=60°$	$\beta_1=70°$
0.50		65-410 65-(12)10 65-(18)10	65-410 65-(12)10 65-(18)10	
.75		65-410 65-(12)10 65-(18)10	65-410 65-(12)10 65-(18)10	
1.00	65-010 65-410 65-810 65-(12)10 65-(15)10 65-(18)10	65-010 65-410 65-810 65-(12)10 65-(15)10 65-(18)10 65-(21)10 65-(24)10 65-(27)10	65-010 65-410 65-810 65-(12)10 65-(15)10 65-(18)10 65-(21)10	65-010 65-410 65-810 65-(12)10 [a] 65-(15)10
1.25	65-410 65-(12)10 65-(18)10	65-410 65-(12)10 65-(18)10	65-410 65-(12)10 65-(18)10	65-410 65-810 65-(12)10 65-(15)10
1.50	65-010 65-410 65-810 65-(12)10 65-(15)10 65-(18)10	65-010 65-410 65-810 65-(12)10 65-(15)10 65-(18)10 65-(21)10 65-(24)10	65-010 65-410 65-810 65-(12)10 65-(15)10 65-(18)10 65-(21)10 65-(24)10	65-010 65-410 65-810 65-(12)10 65-(15)10

[a] No design point was obtained for this combination.

there. Limit conditions were attained at $\beta_1=70°$, $\sigma=1.00$, 1.25, and 1.50, and at $\beta_1=60°$, $\sigma=1.00$ and 1.50.

Test procedure.—It was shown in reference 1 that two-dimensional flow can be achieved by controlling the removal of boundary-layer air through porous test-section side walls so that the downstream static pressure equals the ideal value, corresponding to the turning angle, corrected for the blocking effect of the wake. This criterion was accordingly used in these tests. In addition, the flexible end-wall shapes and suction-flow quantities were adjusted to obtain uniform upstream flow direction and wall static pressures, criteria of two-dimensional flow simulating an infinite cascade. This procedure necessitated an approximate measurement of turning angle and wake size and an estimate of the correct pressure rise before the final settings could be made. Initially, this system required some cut-and-try procedure but after the initial tests at each combination of β_1 and σ a chart similar to figure 5 of reference 1 could be drawn to assist in estimating the pressure rise. An experienced operator could make the required estimates and settings very quickly by this procedure. Spot calculations of the correct pressure rises were made after completion of tests to check the accuracy of the values used.

Tests were made at each cascade combination shown in table III over a range of angles of attack at intervals of 2° to 3°. In general, the tests covered the interval from negative to positive stall, where stall was determined by a large increase in wake size. The principal exceptions occurred for low cambered blades where negative stall would have occurred at negative turning. It was found that the small wall boundary-layer buildup for negative turning angles and hence negative pressure rises would have required a less porous material than that normally used, to avoid excess air removal while maintaining sufficient suction pressure differential to avoid local reverse flow through the porous material. It was not deemed worthwhile to change the porous material to obtain data in this relatively uninteresting range. For the NACA 65-010 section at $\beta_1=30°$, however, the difficulty persisted well above 0° turning, and this combination was tested with both porous and solid walls.

The tests were entirely within a speed range considered incompressible. The bulk of the tests at solidities of 1.00 and 1.50 were run at an entering velocity of 95 feet per second. For the usual 5-inch blade chord, the Reynolds number was 245,000. Some information near the design point was obtained at higher effective Reynolds number for most cascade combinations by adding roughness to the blade leading edges in the form of ¼-inch-wide strips of masking tape draped around the leading edges from wall to wall. In addition, some tests near design conditions were run at a speed of 135 feet per second and a Reynolds number of 346,000 with and without roughness. Two cascade combinations were tested at design conditions over a range of Reynolds numbers from 160,000 to 470,000 to assist in estimating performance at Reynolds numbers other than the usual test value. In order to provide further information on scale effects, two cascade combinations were tested through the α range with leading-edge roughness at the standard Reynolds number and in the smooth conditions at a Reynolds number of 445,000. For solidities of 0.50 and 0.75 the tunnel could not accommodate seven blades of 5-inch chord; the blade chord was reduced to 2.5 inches and the Reynolds number to approximately 200,000 for those tests. Tests with roughness were made near the design point for solidities below 1.00, but Reynolds numbers higher than 200,000 could not be obtained with the existing equipment.

Test measurements.—The blade pressure distribution was measured at the midspan position of the central airfoil at each angle of attack. In addition, surveys of wake total-pressure loss and turning angle were made downstream of the cascade. The total-pressure surveys were made with a non-integrating multitube rake approximately 1 chord downstream of the blade trailing edges. Turning angle surveys were made by the "null method" with a claw-type yaw head; since the yaw device was mounted on a track at the rear of the tunnel the distance from the blades varied from about 1 to 3 chords in the flow direction depending upon the inlet- and turning-angle combination. Flow discharge angle readings were taken at a number of points downstream of several blade passages along the tunnel center line. These readings were averaged to obtain the final value. Since the angle readings in the wake deviated several degrees from the average reading, and the direction of the deviation varied consistently with the direction of the total pressure gradient, the accuracy of readings in the wake was questioned. Therefore, the values obtained when the wake readings were included and excluded in the averaging process were compared for a number of tests. The resulting turning-angle

curves compared very well, but scatter was considerably less when only the readings outside the wake were used to obtain the turning-angle value. This latter procedure has been adopted as the standard method of measuring the flow discharge direction. Static pressure and upstream flow angles were measured approximately 1 chord upstream of the blade row. Total pressure was measured in the settling chamber. Pressures were obtained by orifices with pressure leads to manometer boards. Angles of flow were again obtained by use of a claw-type yaw head by the null method.

Calculations.—Pressure distribution and wake-survey data were recorded and force values calculated nondimensionally as coefficients based numerically on the upstream dynamic pressure q_1. This choice was dictated partly for convenience in reducing the data (standardization of q_1 permits use of manometer scales which give nondimensional values directly) and partly because information based on entering flow was considered most convenient for design use, particularly when critical speed is important.

All forces due to pressure and momentum changes across the blade row were summed to obtain the resultant blade force coefficient $c_{F,1}$. In this process the wake total-pressure deficit was converted to an integrated momentum difference by the method given for the drag calculation in the appendix of reference 5. This wake momentum difference, expressed nondimensionally, is designated the wake coefficient $c_{w,1}$; it represents the momentum difference between the wake and the stream outside the wake, and is based on q_1 numerically. The wake coefficient is not considered to be a true drag coefficient, but is used merely for convenience in assessing the contribution of the wake in the summation of forces.

The resultant-force coefficient was resolved into components perpendicular and parallel to the vector mean velocity W_m (see fig. 5) to obtain the lift coefficient $c_{l,1}$ and the drag coefficient $c_{d,1}$, respectively. The mean velocity was calculated as the vector average of the velocities far upstream and far downstream. The velocity far downstream was obtained from measurements just behind the blades by using a momentum-weighted average of the velocity just behind the blades. This rather detailed method was found necessary to give consistent drag values. Since the resultant force is very nearly perpendicular to the mean velocity, the value of the component parallel to the mean velocity is quite sensitive to mean-velocity direction. Attempts at using the downstream velocity outside the wake for averaging rather than the momentum-average velocity gave very erratic drag results and indicated that mean velocity directions obtained in that manner were not reliable. In addition to the lift and drag, the section normal-force coefficient $c_{N,M,1}$ was obtained by computing the component of the resultant-force coefficient perpendicular to the blade chord line. This normal-force coefficient was compared with the normal-force coefficient $c_{N,P,1}$ obtained by integration of the blade surface pressure distribution as a check on the accuracy of individual tests. A detailed derivation of the method of calculating the force coefficients is given in appendix A.

Accuracy of results.—In general the turning-angle values measured are believed to be accurate within $\pm 0.5°$ near the design values. The correlation procedure used is believed to have improved further the accuracy of the design values in the final results. For tests far from design, that is, near positive or negative stall, the accuracy was reduced somewhat. In addition, at an inlet angle of 70° with sections of zero camber, satisfactory measurements were very difficult to obtain and the accuracy was reduced.

As noted in the section describing calculation methods, the blade normal-force coefficient $c_{N,M,1}$ calculated from pressure-rise and momentum considerations was compared with the normal-force coefficient $c_{N,P,1}$ obtained from the pressure distribution as a check on the overall accuracy of individual tests. Since these values would be affected by error in turning-angle, surface pressure or wake-survey readings, or by failure to achieve two dimensionality of the flow, this comparison is a check on the overall acceptability of the results. A difference of 5 percent between the two normal-force coefficients was set as the outside limit for acceptance of individual tests for lift coefficients above 0.2; below lift coefficients of 0.2 a direct numerical comparison was made using a limit of ± 0.01. The agreement was well within the 5-percent limit for most of the tests as originally run, and only a few conditions had to be repeated. The accuracy of the lift coefficients is directly comparable to that of the normal-force coefficients. The accuracy of wake-coefficient and drag-coefficient values will be discussed later under Reynolds number effects.

PRESENTATION OF RESULTS

Detailed blade-performance data for all cascade combinations tested are presented in the form of surface-pressure distributions and blade-section-characteristic plots in figures 6 to 84. The representative pressure distributions presented have been selected to illustrate the variation through the angle-of-attack range for each combination. The section characteristics presented through the angle-of-attack range are turning angle θ, lift coefficient $c_{l,1}$, wake coefficient $c_{w,1}$, drag coefficient $c_{d,1}$, and lift-drag ratio l/d. The effects of changes in Reynolds number and blade-surface condition on section characteristics are given in figure 85.

Trends of section operating range, in terms of angle-of-attack range, with camber for the four inlet angles of the tests are presented in figure 86. Variation of ideal and actual dynamic-pressure ratio across the cascade with turning angle and inlet angle is presented in figure 87. Figure 88 gives the relation between inlet dynamic pressure and mean dynamic pressure for convenience in converting coefficients from one reference velocity to the other. Limit loading information is summarized in figure 89. Comparison of the present porous-wall-cascade turning-angle data with those of the solid-wall cascade of reference 3 is made in figure 90 for a typical inlet angle and solidity combination.

The information which is most useful for choosing the blade sections to fulfill compressor design vector diagrams is summarized in figures 91 to 111. The variation of turning angle with angle of attack for the blade sections tested is presented for one combination of inlet angle and solidity in each of the figures 91 to 106. Trends of the slopes of the curves of turning angle against angle of attack near design are given in figure 107. Figures 108 to 111 are design and correlation charts; the variation of design turning angle and

design angle of attack with the parameters, camber, inlet angle, and solidity, is presented for several combinations of the parameters so that interpolation to the conditions of a design velocity diagram is relatively easy.

The selection of the blade section and the blade setting required to fulfill a given velocity diagram at design conditions requires several interpolations and cross plots of the data presented in figures 6 to 84. In order to facilitate these interpolations, a carpet plotting technique described in reference 6 has been used to correlate the data. This technique, for which details are explained in appendix B, permits a function of several variables to be presented on a single graph and such a graph lends itself readily to interpolations for intermediate values of the variables plotted. Carpet plots summarizing the present data are presented in figures 112 to 116, and an example illustrating their use is included in appendix B.

DISCUSSION

DESIGN CONDITIONS

The values and shape of the blade-surface pressure distribution are important criteria for predicting the conditions of best operation at high Mach numbers. Velocity peaks occurring on either surface in low-speed tests would be accentuated at high speeds, and supersonic velocities with attendant shock losses would occur at relatively low entering Mach numbers. The selection of the angle of attack designated as "design" for each combination of inlet angle, solidity, and camber is based on the premise that the blade section will be required to operate at Mach numbers near the critical value. The trend of pressure-distribution shape over the angle-of-attack range was examined for each cascade combination, and the angle for which no velocity peaks occurred on either surface was selected as being optimum from the standpoint of high-speed usage. In general, the design angle so selected is near the middle of the low-drag range thus indicating efficient section operation for angles a few degrees higher or lower than the design condition. The choices of design angle of attack are indicated by an arrow on the blade-section-characteristic plots of figures 6 to 84. The design angles are also shown by cross bars on the turning-angle summary curves in figures 91 to 106.

Correlation of the design angles of attack and design turning angles over the range of camber, solidity, and inlet angle is given by figures 108 to 111 in a manner convenient for design use. The correlation is excellent; smooth curves result when any two of the three parameters are used as independent variables.

The section-characteristic curves of figures 6 to 84 indicate that, in general, the design points chosen do not give maximum lift-drag ratios for low- and medium-speed operation. For designs which will not operate near critical speed, therefore, higher efficiency could be obtained by using angles of attack several degrees higher than the design points presented. This procedure must be used with caution, however, at the higher camber and inlet-angle combinations since the section operating range becomes quite narrow for combinations of highest camber and inlet angle corresponding to the highest values of $\triangle p/q_1$. It is recommended that the individual pressure distributions and section-characteristic curves be examined before departure from the specified design points is made.

REYNOLDS NUMBER EFFECTS

Pressure distribution and boundary layers.—For many of the tests at angles of attack near and below design, there is evidence that a region of laminar separation of the boundary-layer flow occurred on the convex blade surface; this separated boundary layer then became turbulent and reattached to the blade surface as a relatively thick turbulent boundary layer. The mechanism of such a flow sequence is described for the isolated airfoil in reference 7. The laminar separation is indicated by a relatively flat region in the pressure distribution on the convex surface and the turbulent reattachment is characterized by a rapid pressure recovery just downstream of the separated region. This flow pattern can be seen clearly in many of the figures but is particularly evident in figures 42 (a), 42 (c), 56 (b) to 56 (d), and 66 (a) to 66 (e). For some tests, laminar separation appeared to occur on the concave surface as well. This is noticeable in figures 42 (b), 42 (d), 42 (e), 66 (c), and 66 (d).

The extent of laminar boundary-layer flow which occurs on an airfoil surface is affected by Reynolds number, stream turbulence level, airfoil surface condition, and surface pressure gradient. Increases in Reynolds number, stream turbulence, and surface roughness would promote earlier transition. Qualitatively a gradient of decreasing surface pressure would be required to maintain laminar flow if the Reynolds number, stream turbulence, surface roughness, or the combination of these, which might be referred to as "effective Reynolds number," were high enough to favor transition. At the turbulence level of the 5-inch cascade tunnel, however, laminar flow and laminar separation on the convex surface persisted to Reynolds numbers up to 245,000 even when the surface pressure gradient was slightly unfavorable. The addition of leading-edge roughness, as described in the section "Test Procedure" reduced the extent of the laminar separation region, but did not eliminate it in some cases. In view of the thick boundary layer which results from laminar separation and reattachment, it appears that the minimum final boundary-layer thickness and section drag coefficient would result if the Reynolds number and turbulence values were such as to cause transition before laminar separation occurred. Use of leading-edge roughness to reduce an extended laminar separation region would probably result in a thinner final boundary layer than that for the smooth blade at the same Reynolds number but would probably result in a thicker boundary layer than that for the smooth blade at high Reynolds number. A thick turbulent boundary layer would be expected to promote turbulent separation near the trailing edge of compressor blades which produce a significant pressure rise.

Wake coefficient and drag coefficient.—As noted previously, the wake coefficient $c_{w,1}$ expresses the momentum difference between the wake flow and the downstream flow outside the wake in a manner convenient for use in summing blade forces. The wake coefficient is, of course, directly

dependent upon boundary-layer thickness and shape, and changes in the boundary layer with changes in effective Reynolds number are reflected in the wake-coefficient values. Furthermore, if the effective Reynolds number is near the condition where laminar separation may or may not occur, the change in surface pressure gradient with change in angle of attack would control the presence and extent of laminar separation on either blade surface. Obviously erratic variations in the value of the wake coefficients would result under those circumstances. The blade-section-characteristic curves of figures 6 to 84 show that in most cases the wake-coefficient values were irregular as the angle of attack was varied in the region near design at the usual test Reynolds number of 245,000. With either higher Reynolds number or leading-edge roughness, or both, the rapid local pressure recovery associated with boundary-layer reattachment was less evident in the surface pressure distributions and the wake coefficient usually was reduced. For a few cases, notably those of figures 34 (g), 35 (g), 68 (g), and 84 (g), leading-edge roughness increased the wake coefficient, however; in those cases the roughness apparently produced a more severe turbulent boundary layer than laminar separation and reattachment did.

The trend of drag coefficient $c_{d,1}$, defined as the component of resultant force parallel to the mean velocity, was similar to that of wake coefficient. The drag curves were quite irregular near design angle of attack and the values measured varied as much as 30 percent with Reynolds number and roughness. Obviously the values of both drag coefficient and lift-drag ratio near design are not sufficiently reliable to use directly in a design analysis. These values should be of some use for comparison purposes, however. The large drag rise associated with positive and negative stall should be relatively insensitive to Reynolds number effects, because the pressure gradients on the critical surfaces are then unfavorable to laminar flow and therefore should be useful for determining effective operating range.

The trend of drag coefficient with Reynolds number near the design condition for the NACA 65-(12)10 blade section at β_1 of 60°, σ of 1.00, and β_1 of 45°, σ of 1.50 shown in figure 85 (a) serves to indicate the magnitude of the Reynolds number effect. Increasing the stream turbulence by the use of a ½-inch-mesh screen upstream of the test section lowered the drag coefficients at low Reynolds number, and reduced the Reynolds number at which the drag coefficients become essentially constant with Reynolds number. The comparison of $c_{d,1}$ values through the angle-of-attack range for the same cascade combinations at two Reynolds numbers in figures 85 (b) and 85 (c) gives some further indication of Reynolds number effect. For R of 445,000, the drag coefficients are lower and the curves are smoother than for R of 245,000. The addition of leading-edge roughness in figure 85 (b) smoothed the drag curve but did not give the same decrease in drag that the high R did. There appears to be some effect on the angle of attack at which the drag rises rapidly in figure 85 (c) but since the effect was not the same in figure 85 (b) no conclusions can be drawn.

Turning angle and lift.—Figure 85 (a) shows that the effect of Reynolds number on turning angle near design α_1 is almost insignificant for R between 220,000 and 470,000. This is borne out by the fact that throughout figures 6 to 84 changes in θ with Reynolds number and roughness were, in general, within the limits of measuring accuracy. Below R of 220,000 a decrease of design turning angle can be expected. Reynolds number appears to have some effect on turning angle near stall in figure 85 (c), but again the effect has not been definitely established. It can be concluded that the design turning angles presented are correct for R above 220,000, but that the effect of R near stall is unknown.

Laminar separation had no appreciable effect on the measured lift. The lift-coefficient values for a given test agreed well at low and high Reynolds numbers and with and without roughness. The normal-force coefficients obtained by integration of the pressure distributions also changed very little with changes in Reynolds number and roughness.

OPERATING RANGE

In order to estimate the useful operating angle-of-attack range of the various sections at the several solidity and inlet angle conditions tested, Howell's index of twice the minimum drag (ref. 8) was used to select the upper and lower limits of angle of attack. As discussed previously in the section concerning Reynolds number effects, the accuracy of the measured values of drag coefficient near design angle of attack suffered due to laminar-flow separation. The minimum value of drag coefficient could not be determined exactly and an approximate value was used to determine the operating range. For most of the test configurations, the drag coefficient changed rapidly with angle of attack near the ends of the useful range, so an error in the value of minimum drag used would have only a small effect on the operating range value. Some scatter in the results was evident, however.

No significant effect of solidity was observed. Most values at constant camber and inlet angle fell within the scatter of the points. A tendency for the range to increase slightly as the solidity was increased was detectable at $\beta_1=45°$, but this was not evident for other inlet angles. The results plotted in figure 86 indicate that the major determinant of the operating range is inlet angle. As the inlet angle is increased, the usable range of angle of attack is decreased, with greater changes indicated for angles above design than for angles below design. The camber of the section affects the operating range in the following manner for angles of attack above design: at an inlet angle of 30°, the range increased with increasing camber; at inlet angles of 45°, 60°, and 70°, the opposite trend occurred. For values of α_1 less than design, little change in range with camber was indicated for $\beta_1=30°$; at higher inlet angles, the range decreased as the section camber increased.

With high entering velocities, the section operating range would be reduced because of a more rapid increase of drag at angles of attack well above or below design. Further, the comparison between sections of different camber, at constant inlet angle and solidity, would be altered as the flow velocities relative to the blade surfaces exceed the local velocity of sound.

526597—60——48

PRESSURE RISE

The ideal, nondimensional pressure rise $\Delta p/q_1$ across a two-dimensional cascade is specified when the inlet angle and turning angle are known, since the ratio of the flow areas determines the pressure rise. Since the mass flow is constant, the actual pressure rise is less than the ideal because of the "blocking" effect of the wake on the downstream flow area. For given inlet and turning angles, the blocking effect would be more severe for higher solidity, since the unaffected flow area is reduced. For incompressible flow the nondimensional pressure rise is equal to one minus the dynamic-pressure ratio, that is, $\frac{\Delta p}{q_1}=1-\frac{q_2}{q_1}$. The actual dynamic-pressure ratio becomes higher than the ideal because of the wake blocking effect. The ideal dynamic-pressure ratios, and the actual ratios at design turning angles for two solidities, are summarized in figure 87 for the range of inlet and turning angles of the tests. The dynamic-pressure ratios for individual tests are given by the short bars at the 100-percent points of the pressure-distribution plots in figures 6 to 84. Wake blocking effects would be changed by the same Reynolds number and roughness factors which change the wake coefficient; however, the percentage change in dynamic-pressure ratio would be small.

LIMIT LOADING

Information on the maximum loading which can be achieved in a compressor blade row is important in the design of high performance axial-flow compressors. As noted previously, the high pressure rise associated with large turning at high inlet angles promotes turbulent separation so that at inlet angles of 60° and 70° the stall angle of attack moved progressively closer to the design value with increasing section camber. The limit turning is reached when the maximum turning angle is no greater than design turning angle. The practical limit would be somewhat lower to give a reasonable operating range.

Approximate limit turning was reached at β_1 of 60°, σ of 1.00 and 1.50, and at β_1 of 70°, σ of 1.00, 1.25, and 1.50. Information from those tests is given in terms of a commonly used loading parameter, $\sigma c_{l,m}$, in figure 89. Both the actual test values of the parameter, and the ideal values calculated using the test inlet and turning angles are presented. Note that the lift coefficient is here based, numerically, on the mean velocity, to conform to the usual form of the parameter.

Arbitrarily chosen constant values of $\sigma c_{l,m}$ have often been used as maximum allowable values in design analyses. The fallacy of using any constant value as a limit is clearly shown in figure 89; the true limiting value increases with increasing solidity and decreases with increasing inlet angle. Since no limits were reached for inlet angles of 45° and 30°, it is clear that the limitation has very little significance there except, perhaps, at very low solidities. The phenomenon is not yet well enough understood to permit the choice of a parameter which could define the overall limitation as a single value.

COMPARISON WITH SOLID-WALL CASCADE DATA

The comparison between pressure-distribution and turning-angle data for a solid-wall cascade tunnel and for the present porous-wall cascade tunnel is given in reference 1 for the NACA 65–(12)10 blade section at β_1 of 60° and σ of 1.00. The comparison has been extended in figure 90 to include turning-angle data for all the cambers reported for β_1 of 60° and σ of 1.00 in reference 3. The turning-angle curves compare fairly well for cambers up to $c_{l,o}$ of 0.8, but for the airfoils of higher camber the data of reference 3 deviate significantly from the present results. Comparisons at other conditions would show similar trends.

RELATIONSHIPS BETWEEN TURNING ANGLE AND ANGLE OF ATTACK

Summaries of the relationships between turning angle and angle of attack through the camber range are given for each inlet angle and solidity in figures 91 to 106. The variations are quite consistent for most of the range. Some inconsistency in the shape of the curves at stall is a result of reduced accuracy of measurement there. For combinations giving moderate pressure rises straight-line relationships are indicated for considerable portions of the curves. For the highest pressure rises, however, no definite straight-line relationships exist. The variation of the slopes near design is given in figure 107 to assist in estimating relationships at conditions other than those tested. These slopes are average slopes for the camber range, and do not apply for the highest cambers. They must be used with particular caution for inlet angles near 70°, since very narrow straight-line regions are prevalent there.

CARPET PLOTS

The usual procedure in blade-section selection is to determine the camber $c_{l,o}$, which is required for a given design velocity diagram at a selected solidity. Figure 112 gives carpet plots of the data at five solidity conditions. The carpet plots indicate the variation of camber $c_{l,o}$, at design angle of attack $\alpha_{1,d}$ with required values of inlet-air angle β_1 and design turning angle θ_d. Each carpet plot is spaced from the next by a number of grid units proportional to the difference in solidities. Since design angle of attack is independent of inlet-air angle, it is possible to present a carpet plot (fig. 113) showing design angle of attack $\alpha_{1,d}$ as a function of camber $c_{l,o}$ and solidity σ.

The tests were made at fixed inlet-air angles with the angle-of-attack variation produced by changing the blade setting. Although data of this type facilitated the determination of design conditions for the various combinations of inlet-air angle, solidity, and camber, it does not lend itself easily, as presented, to obtaining off-design performance of a blade section as regards operation of this section in a compressor in which blade setting is fixed and the angle of attack varied by changing the inlet-air angle. However, if the data are plotted as an off-design carpet, it is a simple matter to draw in curves of constant blade setting and thus to predict the

variation in turning angle with angle of attack for all intermediate conditions of solidity, camber, and blade setting. Such off-design carpet plots showing turning angle as a function of solidity, inlet-air angle, angle of attack, and camber are presented in figure 114. Off-design data are presented for the following sections:

NACA 65–(4)10
NACA 65–(8)10
NACA 65–(12)10
NACA 65–(15)10
NACA 65–(18)10

Pressure rise as a percentage of inlet dynamic pressure $\Delta p/q_1$, called pressure-rise coefficient, has been used as a cascade loading-limit parameter. It is known that cascade losses increase rapidly above certain limiting values of $\Delta p/q_1$. However, in view of the physical meaning of the pressure-rise coefficient, particularly in reference to the inner and outer casings, it is considered to be a useful parameter. If the inlet-air angle, the turning angle, and the entering Mach number are known, calculations of an isentropic pressure-rise coefficient is possible, provided some relationship is assumed between the entering and leaving stream-tube areas. Therefore, two carpet plots were made in order to show the variation of the pressure-rise coefficient with inlet-air angle β_1, turning angle θ, and entering Mach number M_1. The first of these plots (fig. 116 (a)) was calculated by assuming constant stream-tube area; the second (fig. 116 (b)) was calculated by assuming that the stream-tube area varied so that constant axial velocity would be produced across the blade passage. Pressure-rise coefficients obtained from these two plots very often bracket the value associated with the actual three-dimensional condition being examined.

SUMMARY OF RESULTS

The systematic investigation of NACA 65-series compressor blade sections in a low-speed cascade tunnel has provided design data for all conditions within the usual range of application. The results of this investigation indicate a continuous variation of blade-section performance as the important cascade parameters blade camber, inlet angle, and solidity are varied over the useful range. Summary curves have been prepared to facilitate selection of blade sections and settings for compressor-design velocity diagrams for optimum high-speed operation.

Upper limits for the loading parameter $\sigma c_{l,m}$ have been established for some conditions, and the invalidity of using a constant value of the parameter has been shown.

The variation of the useful section operating range with camber, inlet angle, and solidity has been shown. The operating range was found to be broad except for the highest pressure-rise conditions.

Compressor-blade cascade data have been presented in the form of design carpet plots, which greatly facilitate the selection of compressor blade sections required to fulfill velocity diagrams. Plots of this type also are shown to increase greatly the usefulness of available cascade data by providing a simple method of obtaining the off-design variation in turning angle with angle of attack.

LANGLEY AERONAUTICAL LABORATORY,
NATIONAL ADVISORY COMMITTEE FOR AERONAUTICS,
LANGLEY FIELD, VA., *January 31, 1958.*

APPENDIX A

CALCULATION OF BLADE FORCE COEFFICIENTS

The two-dimensional resultant force on a blade in cascade is the vector sum of all the pressure and momentum forces exerted by the fluid. At any appreciable distance behind the blade row the static pressure is constant along a line parallel to the blade row, since any prior pressure gradients would have been converted to momentum changes. On the assumption that a pressure force acting in the upstream direction is positive,

$$F_p=(p_2-p_1)bg \tag{1}$$

sum the momentum forces in the axial and tangential directions. Assume that the axial momentum forces are positive if the force on the blade is in the upstream direction and that the tangential momentum forces are positive if the tangential velocity change is in the usual direction shown in figure 5. The axial momentum force then is

$$F_{M,a}=\int_g \rho_2 V_{a,2,l}(V_{a,2,l}-V_{a,1})b\,dg \tag{2}$$

and the tangential momentum force is

$$F_{M,u}=\int_g \rho_2 V_{a,2,l}(W_{u,1}-W_{u,2,l})b\,dg \tag{3}$$

Since momentum values in the wake can be obtained most easily as differences between the wake values and the downstream value outside the wake, it is convenient to rewrite equations (2) and (3)

$$F_{M,a}=\rho_1 V_{a,1}(V_{a,2,s}-V_{a,1})bg+\int_g \rho_2 V_{a,2,l}(V_{a,2,l}-V_{a,2,s})b\,dg \tag{4}$$

$$F_{M,u}=\rho_1 V_{a,1}(W_{u,1}-W_{u,2,s})bg+\int_g \rho_2 V_{a,2,l}(W_{u,2,s}-W_{u,2,l})b\,dg \tag{5}$$

However, the wake momentum force, as calculated from wake surveys, is

$$F_w=\int_g \rho_2 V_{a,2}(W_{2,s}-W_{2,l})b\,dg \tag{6}$$

If, now, the flow direction in the wake can be assumed to be the same as the average downstream flow direction, the wake force can be resolved into components in the axial and tangential directions. Using the same sign convention as before

$$F_{w,a}=-F_w\cos\beta_2=\int_g \rho_2 V_{a,2,l}(V_{a,2,l}-V_{a,2,s})b\,dg \tag{7}$$

$$F_{w,u}=F_w\sin\beta_2=\int_g \rho_2 V_{a,2,l}(W_{u,2,s}-W_{u,2,l})b\,dg \tag{8}$$

These are the integral terms in equations (4) and (5). Substituting equation (7) in equation (4) and equation (8) in equation (5) yields the axial and tangential force components, as follows:

$$F_a=F_p+F_{M,a}=(p_2-p_1)\,bg+\rho_1 V_{a,1}(V_{a,2,s}-V_{a,1})bg-F_w\cos\beta_2$$

$$F_u=F_{M,u}=\rho_1 V_{a,1}(W_{u,1}-W_{u,2,s})bg+F_w\sin\beta_2$$

For convenience coefficients based on q_1 are used and

$$c_{F,a,1}=\frac{F_a}{\frac{1}{2}\rho_1 W_1^2 bc}=\frac{1}{\sigma}\left[\frac{\Delta p}{q_1}+\frac{2V_{a,1}(V_{a,2,s}-V_{a,1})}{W_1^2}\right]-c_{w,1}\cos\beta_2$$

$$c_{F,u,1}=\frac{F_u}{\frac{1}{2}\rho_1 W_1^2 bc}=\frac{1}{\sigma}\left[\frac{2V_{a,1}(W_{u,1}-W_{u,2,s})}{W_1^2}\right]+c_{w,1}\sin\beta_2$$

The resultant-force coefficient is given by

$$c_{F,1}=\sqrt{c_{F,a,1}^2+c_{F,u,1}^2}$$

If γ is used to denote the angle between the resultant force and the tangential direction

$$\gamma=\tan^{-1}\frac{c_{F,a,1}}{c_{F,u,1}}$$

The lift coefficient $c_{l,1}$ and drag coefficient $c_{d,1}$ are the components of $c_{F,1}$ perpendicular and parallel, respectively, to the vector mean velocity W_m, where W_m is the vector average of the velocities far upstream and far downstream. The upstream velocity can be easily measured. The velocity far downstream is obtained by proper averaging of the velocities just behind the blades. Since the axial area controls the axial velocity, conservation of mass determines the axial component of the velocity far downstream. Inasmuch as there are no physical boundaries in the tangential direction to support pressure gradients, conservation of momentum controls the tangential component far downstream. The discussion up to this point applies to compressible as well as incompressible flow.

For compressible flow the effect of wake mixing on pressures and densities makes accurate determination of the axial velocity far downstream rather tedious. In the incompressible, two-dimensional case the downstream axial component is $V_{a,1}$, and the downstream tangential component is the momentum-weighted average of $W_{u,2}$. This tangential component can be obtained by adding to the tangential momentum of the discharge free stream the integrated tangential momentum of the wake. The integrated tangential momentum of the wake can be determined from the tangential component of the wake coefficient. Having the correct velocity far downstream, the vector mean-velocity direction W_m can be easily obtained. The direction of W_m should be determined accurately since $c_{F,1}$ is very nearly perpendicular to W_m, and the value of the drag component $c_{d,1}$ is sensitive to small changes in the direction of W_m.

APPENDIX B

CARPET-PLOTTING TECHNIQUE

CONSTRUCTION

Since the carpet-plotting technique is not too well known, a description of this technique will be helpful. Examine first figure 114 (a). It will be noted that this figure is composed of five similar and separate plots. Each of these plots shows the variation of the turning angle θ with the angle of attack α_1 and the inlet-air angle β_1 for a given solidity σ and a camber $c_{l,o}$ of 0.40. It might be here pointed out that the tests were made at four inlet-air angles, 30°, 45°, 60°, and 70°. The leftmost plot, which represents a solidity of 1.50, is constructed by plotting turning angle θ as ordinate against angle of attack α_1 as abscissa for $\beta_1=30°$. Then, for a β_1 of 45°, the α_1 scale is shifted to the right a number of grid units proportional to the 15° increment in β_1 and the turning angles are plotted as before. This procedure of shifting the α_1 scale is followed until the range of β_1 values for which test data are available has been completed. Curves of constant angle of attack may then be drawn between the several curves of α against θ, so that the removal of the α_1 abscissa scales is possible. At this point, curves of α_1 against θ may be filled in at 5° intervals of β_1 by using the proper abscissa increment. The plot thus constructed is called a θ,α_1,β_1 carpet.

A θ,α_1,β_1 carpet is constructed for the next solidity of 1.25 by shifting the angle-of-attack scales to the right a number of grid units proportional to the solidity increment of 0.25 and sufficient to keep any overlapping of the θ,α_1,β_1 carpets to a minimum. This procedure previously described in constructing the first θ,α_1,β_1 carpet is then repeated. The full range of solidities for which test data are available (0.50 to 1.50) may be presented by spacing and constructing the θ,α_1,β_1 carpets on this plot called a $\theta,\alpha_1,\beta_1,\sigma$ carpet plot. Similar $\theta,\alpha_1,\beta_1,\sigma$ carpet plots are then made for each of the other cambers, namely, $c_{l,o}=0.8$, 1.2, 1.5, and 1.8 shown in figures 114 (b), 114 (c), 114 (d), and 114 (e), respectively.

For intermediate camber conditions, linear interpolations between $\theta,\alpha_1,\beta_1,\sigma$ carpets could be used or these $\theta,\alpha_1,\beta_1,\sigma$ plots could be combined into a single carpet plot to make possible a single graphical interpolation. For example, figure 114 (a) may be combined with figure 114 (b) by again shifting the angle-of-attack scales to the right a number of grid units proportional to the camber increment of 0.40. Overlapping of the $\theta,\alpha_1,\beta_1,\sigma$ carpets can be avoided by shifting also the θ ordinate scale vertically a number of grid units proportional to the camber increment of 0.40. This combination of a vertical and a horizontal shift is facilitated by the use of register points labeled "AB" on both plots 114 (a) and 114 (b). The AB register points can be superimposed and the grids alined. In like manner, if all of the register points are used, figures 114 (a), 114 (b), 114 (c), 114 (d), and 114 (e) may be assembled into a single carpet plot. Figure 115 was made by combining plots 114 (a), 114 (c), and 114 (e) representing cambers $c_{l,o}$ of 0.4, 1.2, and 1.8, respectively. On this carpet, the design angle of attack is indicated by a dotted line and the approximate occurrence of twice minimum drag is indicated by a dashed line. Since the origins of the θ scales for cambers of 1.2 and 1.8 are shifted vertically a number of grid units proportional to the camber increment, the ordinate scale is no longer a true θ scale for these higher cambers and is called Y. When an interpolation is made for any camber above 0.4, the θ value may be obtained by substituting Y in the following expression:

$$\theta=Y-50(c_{l,o}-0.4)$$

Figures 114 (b) and 114 (d) representing cambers of 0.8 and 1.5 were omitted from figure 115 in order to reduce the size of the plot. It will also be noted that data are available for cambers of 0.8 and 1.5 at only two solidities, 1.00 and 1.50.

In view of the necessity for shifting the separate plots to provide for combinations of the several variables, as illustrated in figure 115, the carpet plots assembled in the present bound copy are useful only as a means of demonstrating this technique. For this reason, larger separate plots for use in compressor design have been prepared and are obtainable on request from NACA Headquarters, Washington, D. C.

ILLUSTRATIVE EXAMPLE

The use of the carpet plots presented can be shown best by use of an example. Generally, from a velocity-diagram calculation, the inlet-air angle, turning angle, and inlet Mach number are known, and some value of solidity has been decided upon. The problem is to find the camber $c_{l,o}$, the design angle of attack $\alpha_{1,d}$, the pressure-rise coefficient $\Delta p/q_1$ (one-dimensional flow being assumed), and the off-design variation in θ with α_1 at a constant blade setting. The following design conditions are assumed:

$$\beta_1=55°$$

$$\theta_d=15°$$

$$\sigma=1.10$$

$$M_1=0.65$$

Figure 112 is used to locate first the intersection of the curves for $\beta_1=55°$ and $\theta_d=15°$ on each of the four carpets representing solidities of 1.25, 1.00, 0.75, and 0.50; then a smooth curve is drawn connecting these four points which are labeled "A," "B," "C," and "D." If the β_1 and θ values had fallen between those represented on the curves, these intermediate values could be located by measuring the increments along the abscissa. Although the design solidity

of 1.10 falls between points A and B representing solidities of 1.25 and 1.00, respectively, points C and D for solidities of 0.75 and 0.50 are included to define more accurately the shape of the curve between points A and B. Since the horizontal interval from A to B represents a solidity increment of 0.25 from 1.25 to 1.00, the point corresponding to a solidity of 1.10 may be obtained by locating on the ABCD curve the point E, which has a horizontal distance from point B equal to a solidity increment of 0.10. Point E thus located indicates a camber $c_{l,o}$ of 0.87 on the ordinate scale.

Next, the solidity of 1.10 and the newly found camber $c_{l,o}$ of 0.87 are used in conjunction with figure 113 to find the design angle of attack. The point for a camber of 0.87 is located on the $\sigma=1.10$ curve between the camber of 0.8 and 0.9 curves by reading the proper horizontal increment of 0.07. This point indicates on the ordinate scale a design angle of attack of 10.5°.

The pressure-rise coefficient $\Delta p/q_1$ is found from figure 116 (a) by using the values $M_1=0.65$, $\beta_1=55°$, and $\theta=15°$. In figure 116 (a), the $\Delta p/q_1$ was calculated on a one-dimensional basis, whereas in figure 116 (b) the $\Delta p/q_1$ was calculated for a constant axial velocity. Since one-dimensional flow was assumed in this example, figure 116 (a) should be used. Employing the proper horizontal β_1 increment of 10° and starting at the $\beta_1=45°$ curve, locate the $\beta_1=55°$ point on the $\theta=15°$ curve for each of the carpet plots representing Mach numbers of 0.50, 0.60, 0.70, and 0.80. The four points thus located are designated "F," "G," "H," and "I" and are connected by a smooth curve. Next, locate on this curve point J whose horizontal distance from point G is equal to a Mach number increment of 0.05. Point J indicates on the ordinate scale a pressure-rise coefficient of 0.590.

The last step in this sample problem is the prediction of an α_1,θ curve at a constant blade setting. The off-design carpet (fig. 115) is used to predict this α_1,θ curve for the blade section having a camber $c_{l,o}$ of 0.87, a solidity σ of 1.10 and a blade setting of 44.5°. The blade setting is the difference between the inlet-air angle and the angle of attack, or 55°−10.5°=44.5° at the design condition. In figure 115, curves labeled "a" and "b" representing this constant blade setting of 44.5° are drawn on the θ,α_1,β_1 plots for $c_{l,o}$ of 0.4 at the solidities of 1.25 and 1.00, respectively. Curve c is then interpolated for the solidity of 1.10 by the use of the correct solidity increment along the abscissa. As can be seen in the example, this interpolation is aided by drawing between curves a and b lines of constant angle of attack at values of 6°, 8°, 10°, 12°, and 14°. A similar interpolation is then accomplished for a camber of 1.2, which produces curves d, e, and f. A linear interpolation for the intermediate camber of 0.87 is made between curves c and f to obtain curve g, which shows the variation of Y with α_1 for the design camber and solidity. The Y values may be converted to θ values by using the relationship

$$\theta=Y-50(c_{l,o}-0.4)$$

It has been found that linear interpolations between any two cambers of figure 115 produce design turning angles which agree with the design carpet plot within 1.0°. If greater accuracy is desired, a faired curve between the three cambers should be used. In figure 115, the design angle of attack is indicated by a short-dashed line and the approximate occurrence of twice minimum drag is indicated by a long-dashed line.

REFERENCES

1. Erwin, John R., and Emery, James C.: Effect of Tunnel Configuration and Testing Technique on Cascade Performance. NACA Rep. 1016, 1951. (Supersedes NACA TN 2028.)
2. Westphal, Willard R., and Godwin, William R.: Comparison of NACA 65-Series Compressor-Blade Pressure Distributions and Performance in a Rotor and in Cascade. NACA TN 3806, 1956. (Supersedes NACA RM L51H20.)
3. Bogdonoff, Seymour M., and Bogdonoff, Harriet E.: Blade Design Data for Axial-Flow Fans and Compressors. NACA WR L-635, 1945. (Formerly NACA ACR L5F07a.)
4. Bogdonoff, Seymour M., and Hess, Eugene E.: Axial-Flow Fan and Compressor Blade Design Data at 52.5° Stagger and Further Verification of Cascade Data by Rotor Tests. NACA TN 1271, 1947.
5. Abbott, Ira H., von Doenhoff, Albert E., and Stivers, Louis S., Jr.: Summary of Airfoil Data. NACA Rep. 824, 1945. (Supersedes NACA WR L-560.)
6. Yates, A. H.: 'Carpets' and 'Lattices.' Aircraft Engineering, vol. XVIII, no. 203, Jan. 1946, pp. 8–9.
7. Bursnall, William J., and Loftin, Laurence K., Jr.: Experimental Investigation of Localized Regions of Laminar-Boundary-Layer Separation. NACA TN 2338, 1951.
8. Howell, A. R.: Design of Axial Compressors. Lectures on the Development of the British Gas Turbine Jet Unit Published in War Emergency Issue No. 12 of the Institution of Mechanical Engineers. A.S.M.E. Reprint, Jan. 1947, pp. 452–462.

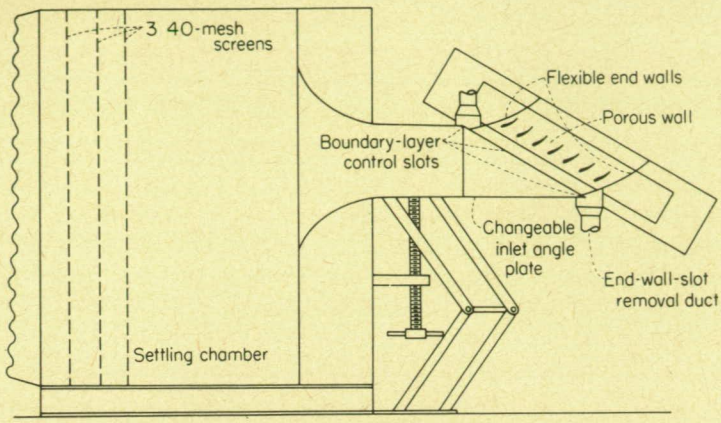


FIGURE 1.—Vertical cross section of two-dimensional low-speed cascade tunnel.

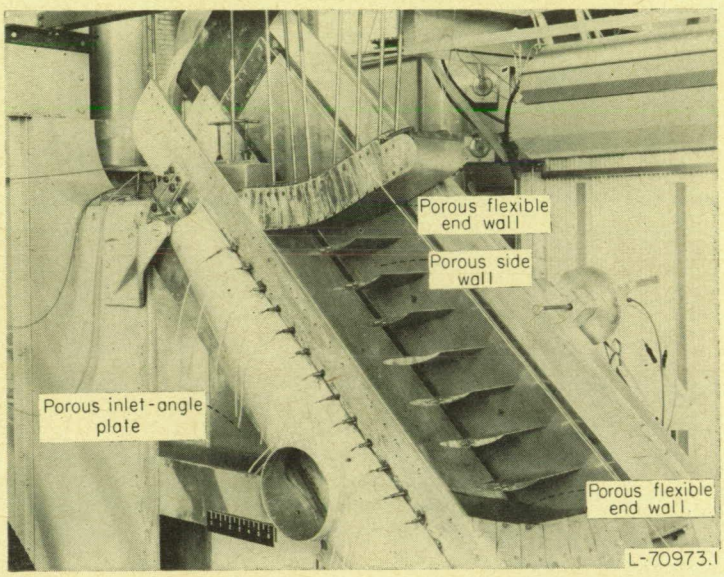


FIGURE 2.—Photograph of Langley 5-inch cascade tunnel with portions of one side removed to show porous surfaces.

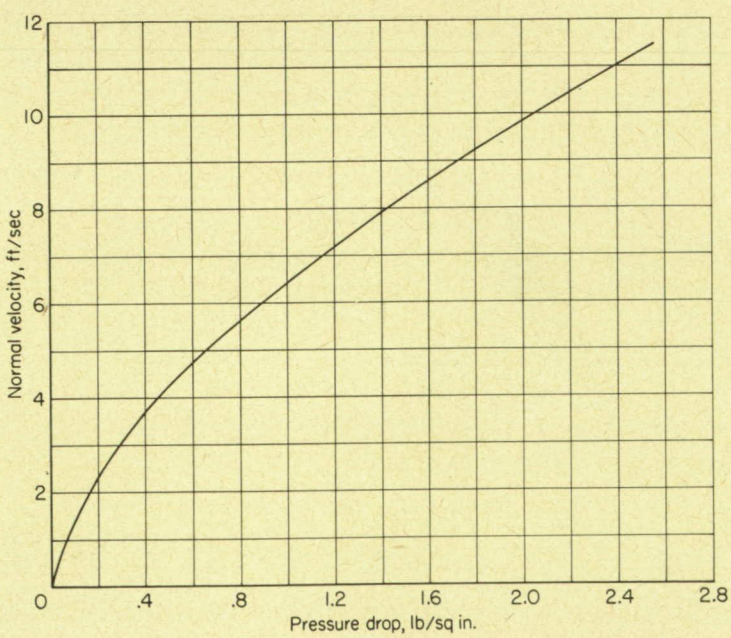
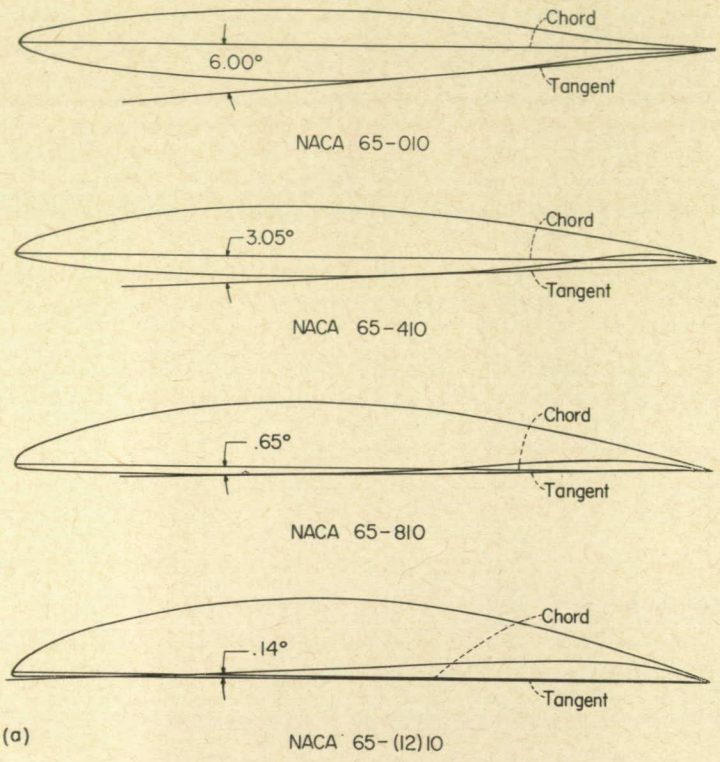
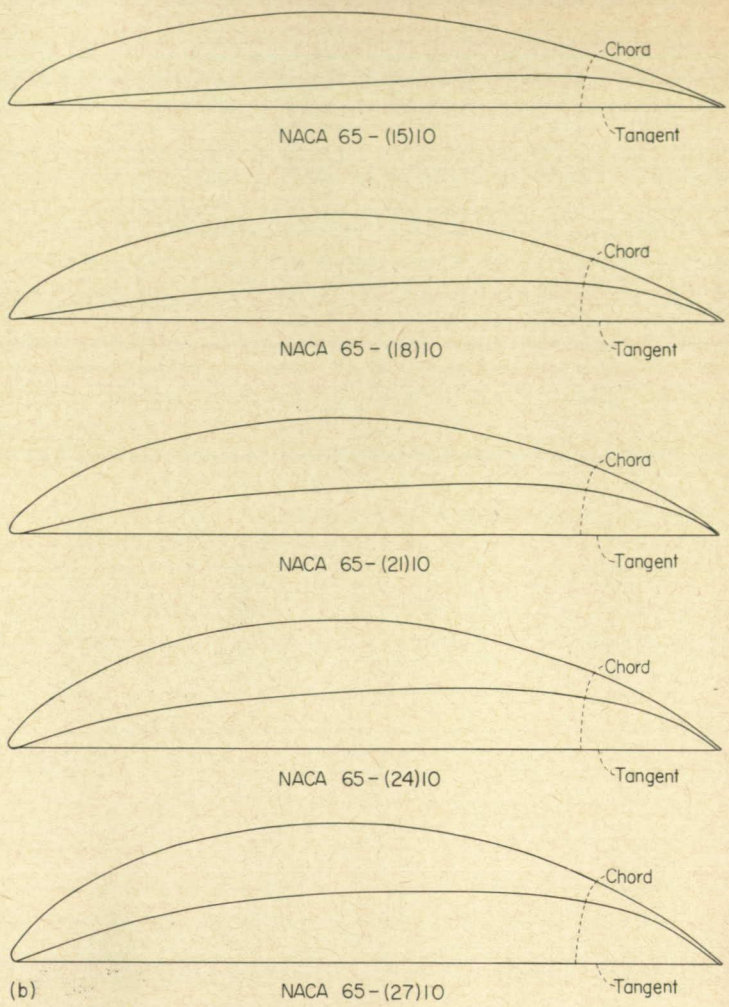


FIGURE 3.—Porosity characteristics of the calendered monel filter cloth used in this investigation.



(a) Lower cambered sections. Angle between chord line and tangent to lower surface as shown for the various sections.



(b) Higher cambered sections. Chord line and tangent line coincident.

FIGURE 4.—Blade sections tested in this investigation.

FIGURE 4.—Concluded.

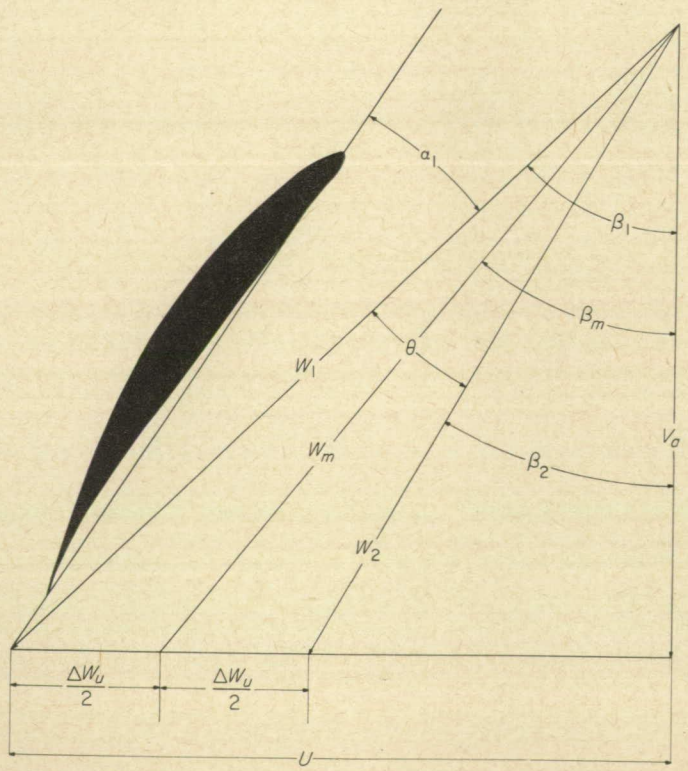
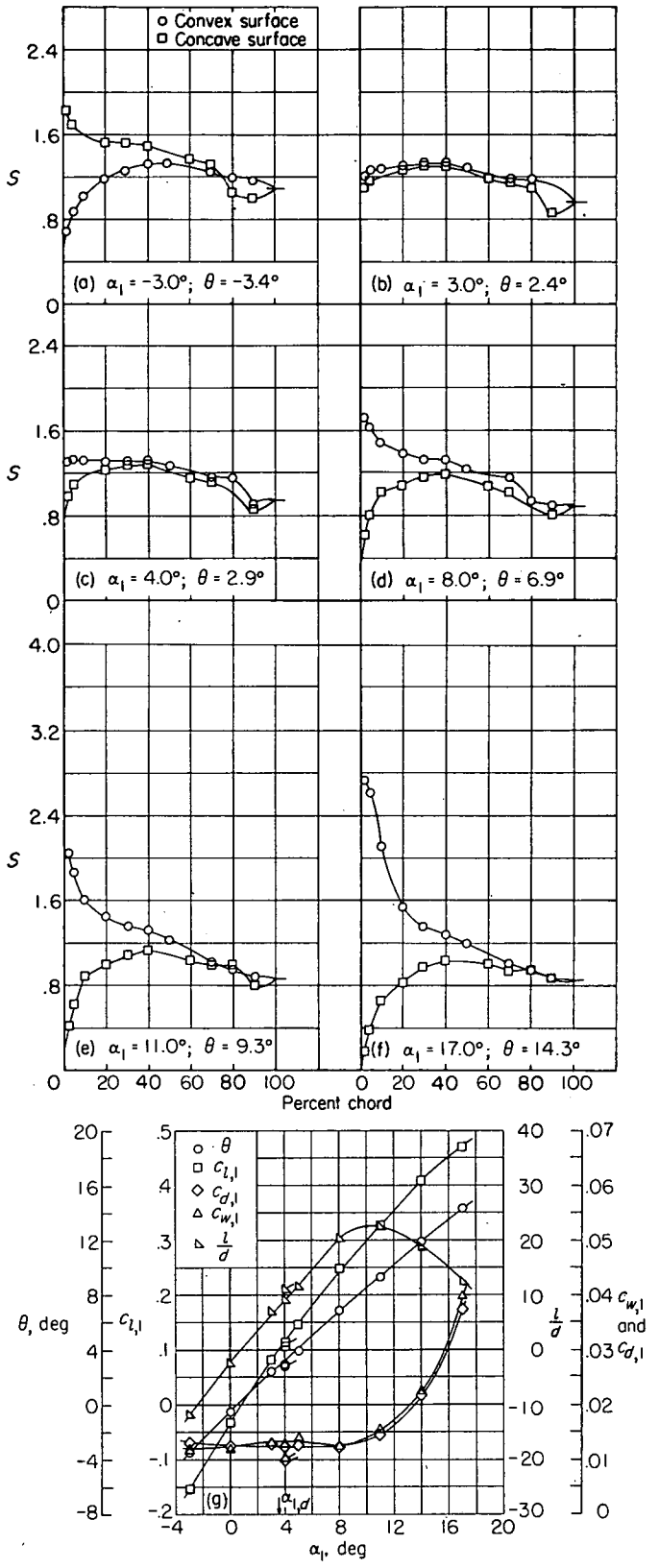
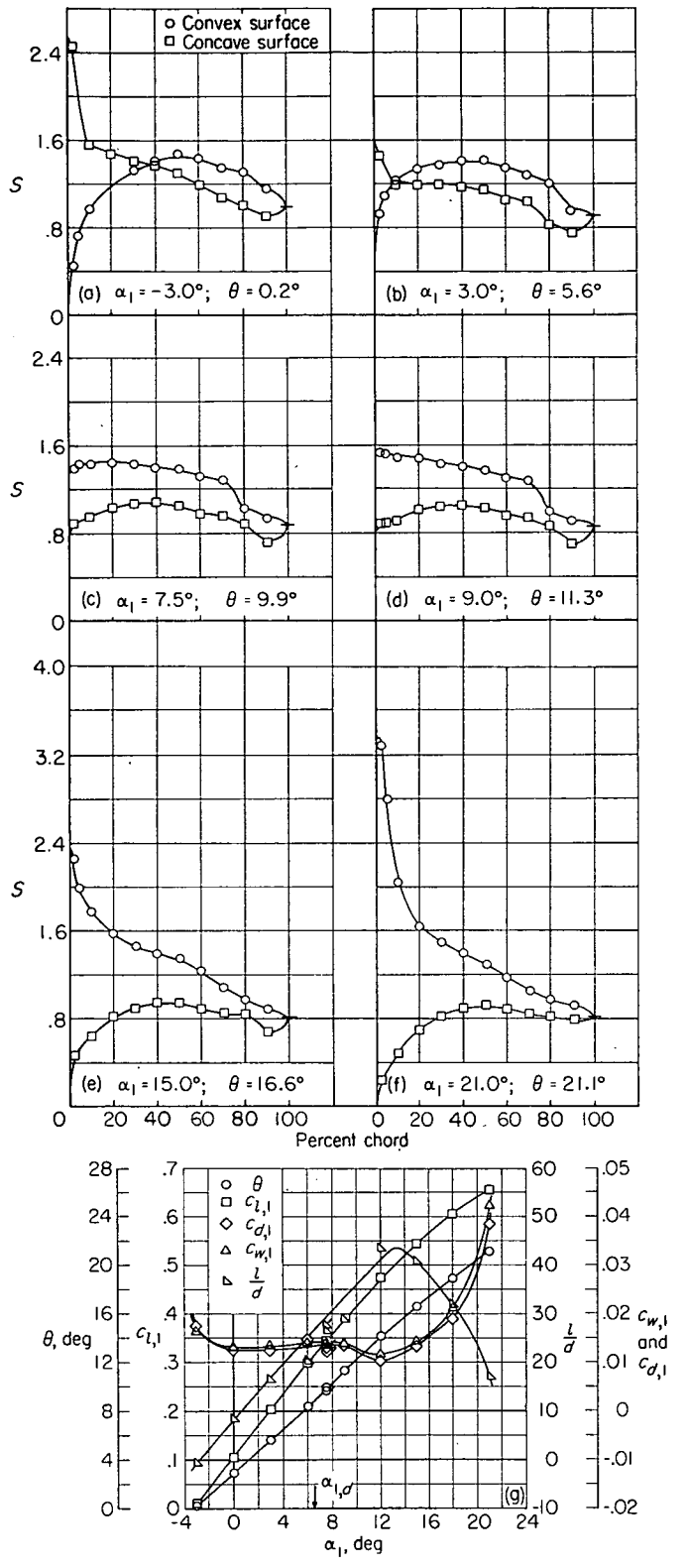


FIGURE 5.—Typical vector diagram for a compressor rotor.



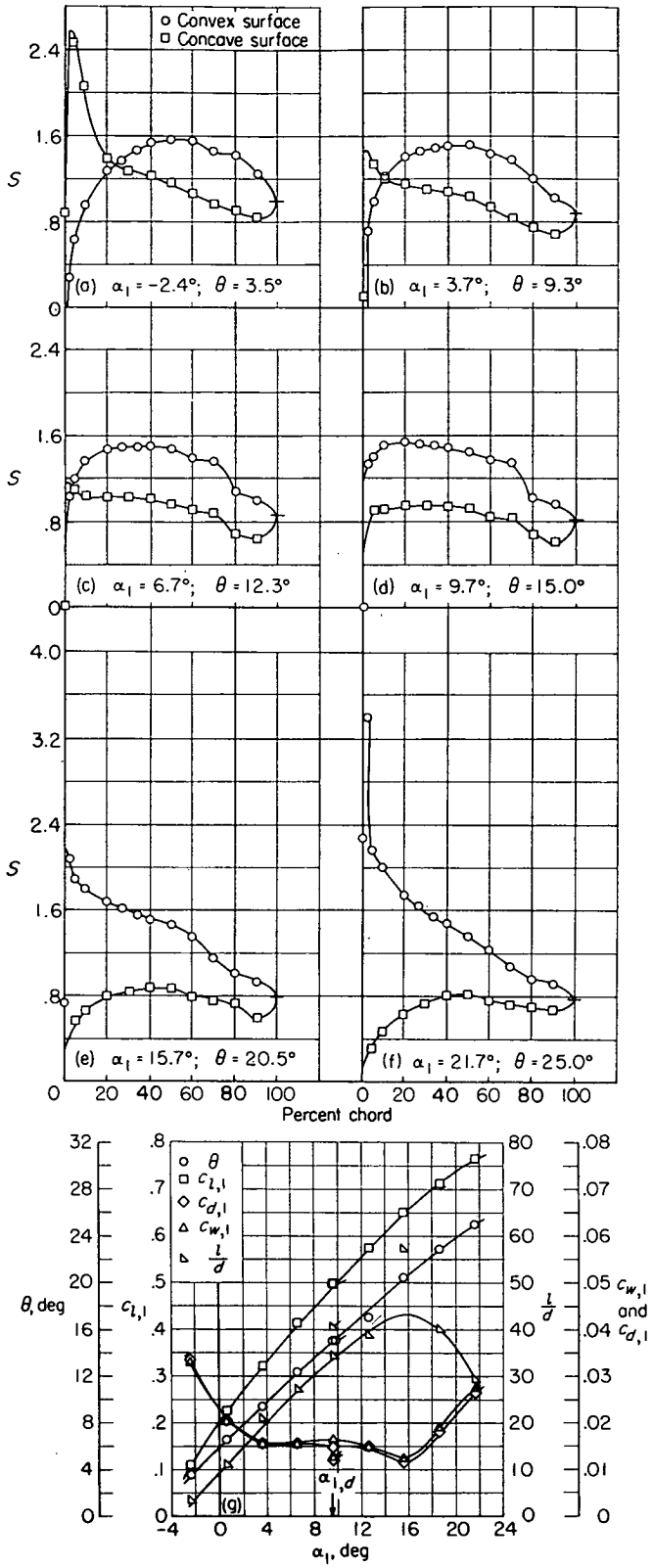
(g) Section characteristics; flagged symbol indicates leading-edge roughness.

FIGURE 6.—Blade-surface pressure distributions and blade section characteristics for the cascade combination, $\beta_1 = 30°$, $\sigma = 1.00$, and blade section, NACA 65-010.



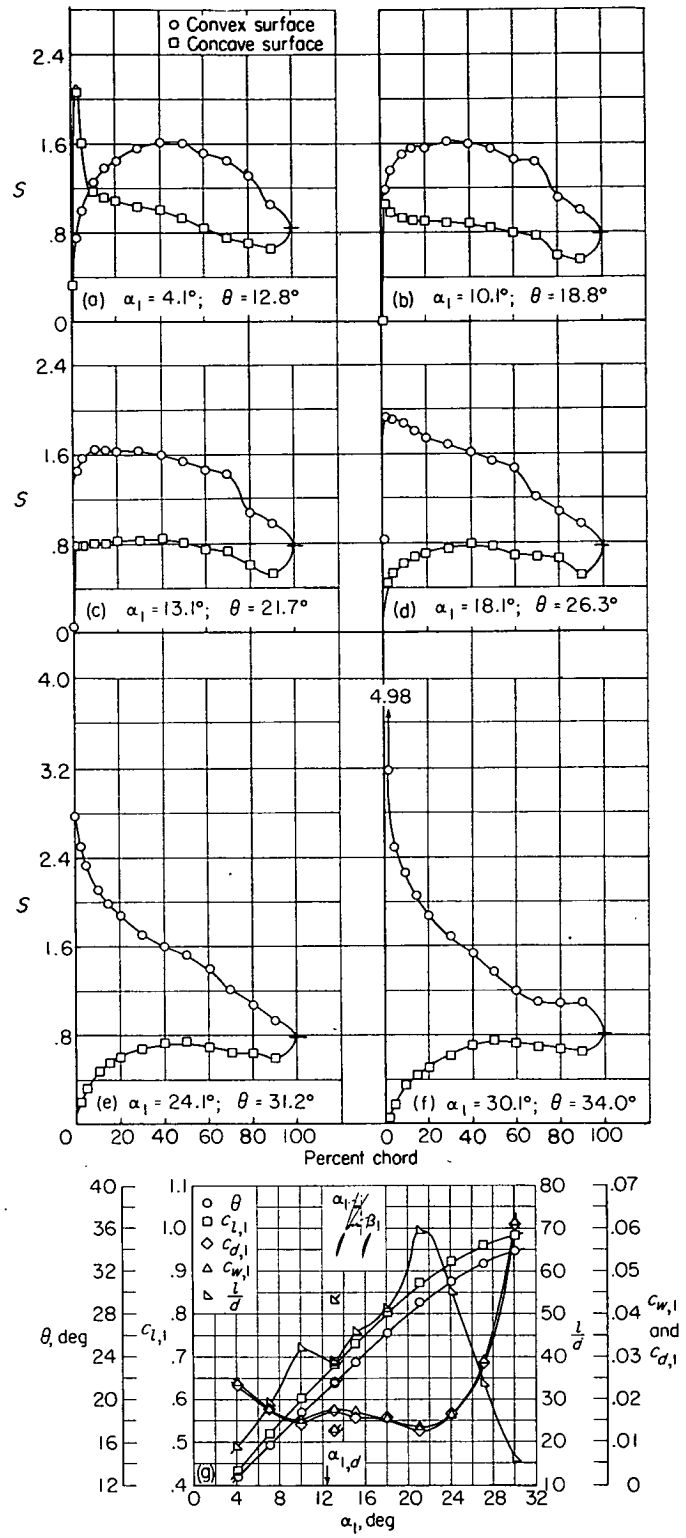
(g) Section characteristics; flagged symbol indicates leading-edge roughness.

FIGURE 7.—Blade-surface pressure distributions and blade section characteristics for the cascade combination, $\beta_1 = 30°$, $\sigma = 1.00$, and blade section, NACA 65-410.



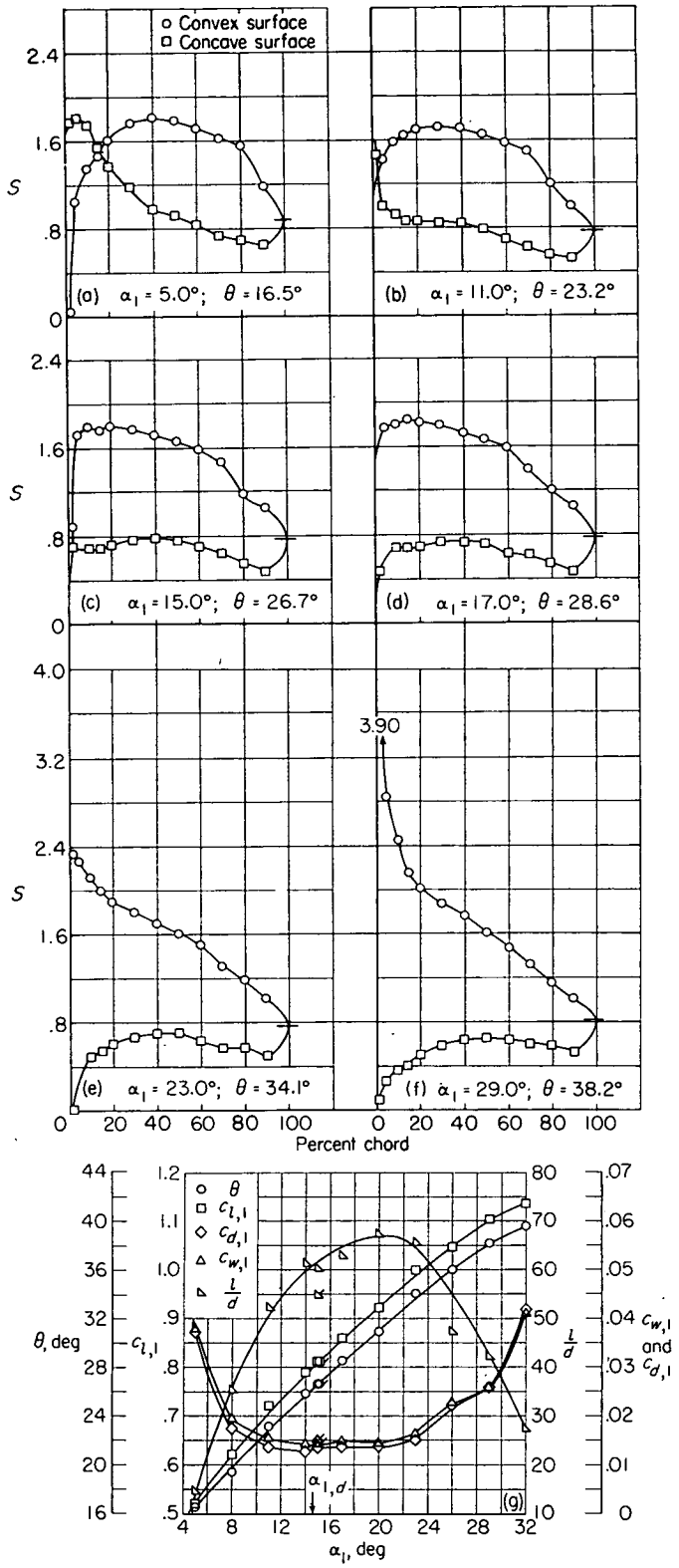
(g) Section characteristics; flagged symbol indicates leading-edge roughness.

FIGURE 8.—Blade-surface pressure distributions and blade section characteristics for the cascade combination, β_1=30°, σ=1.00, and blade section, NACA 65–810.



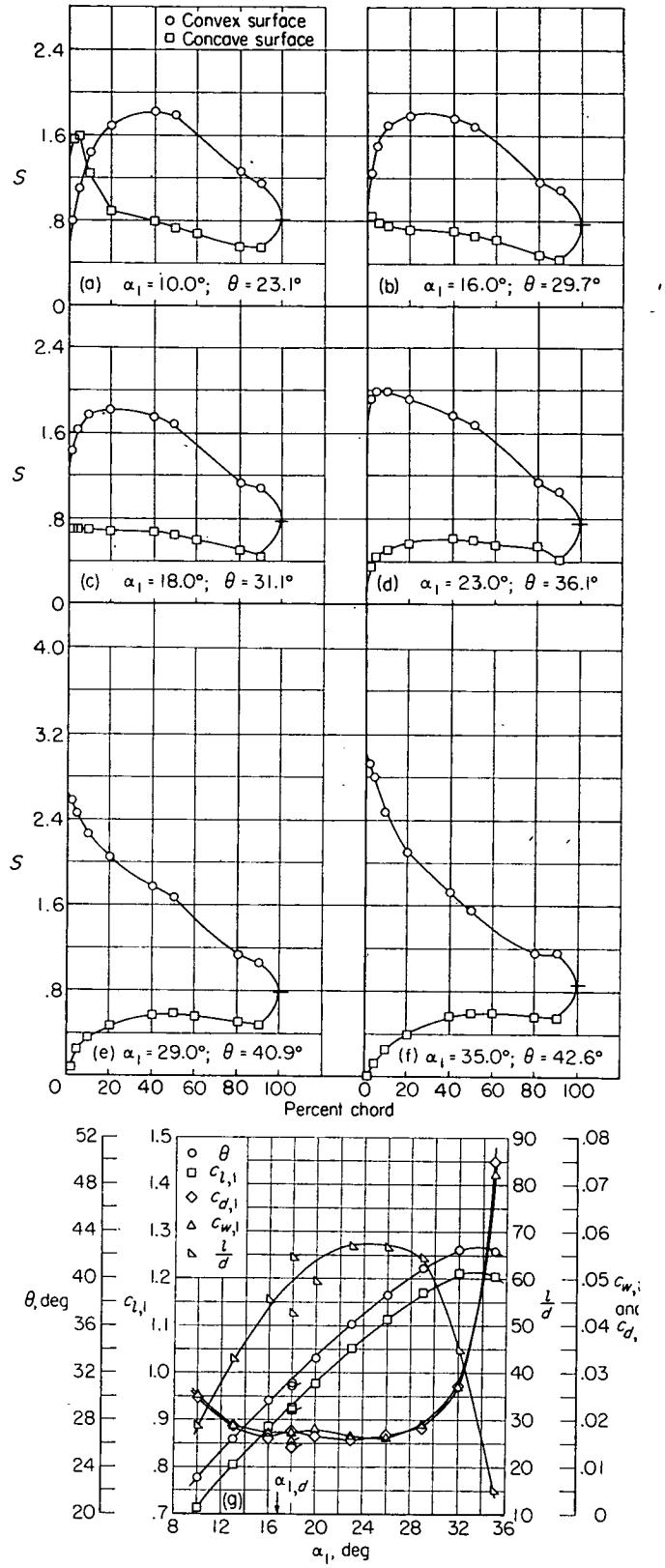
(g) Section characteristics; flagged symbol indicates leading-edge roughness.

FIGURE 9.—Blade-surface pressure distributions and blade section characteristics for the cascade combination, β_1=30°, σ=1.00, and blade section, NACA 65–(12)10.



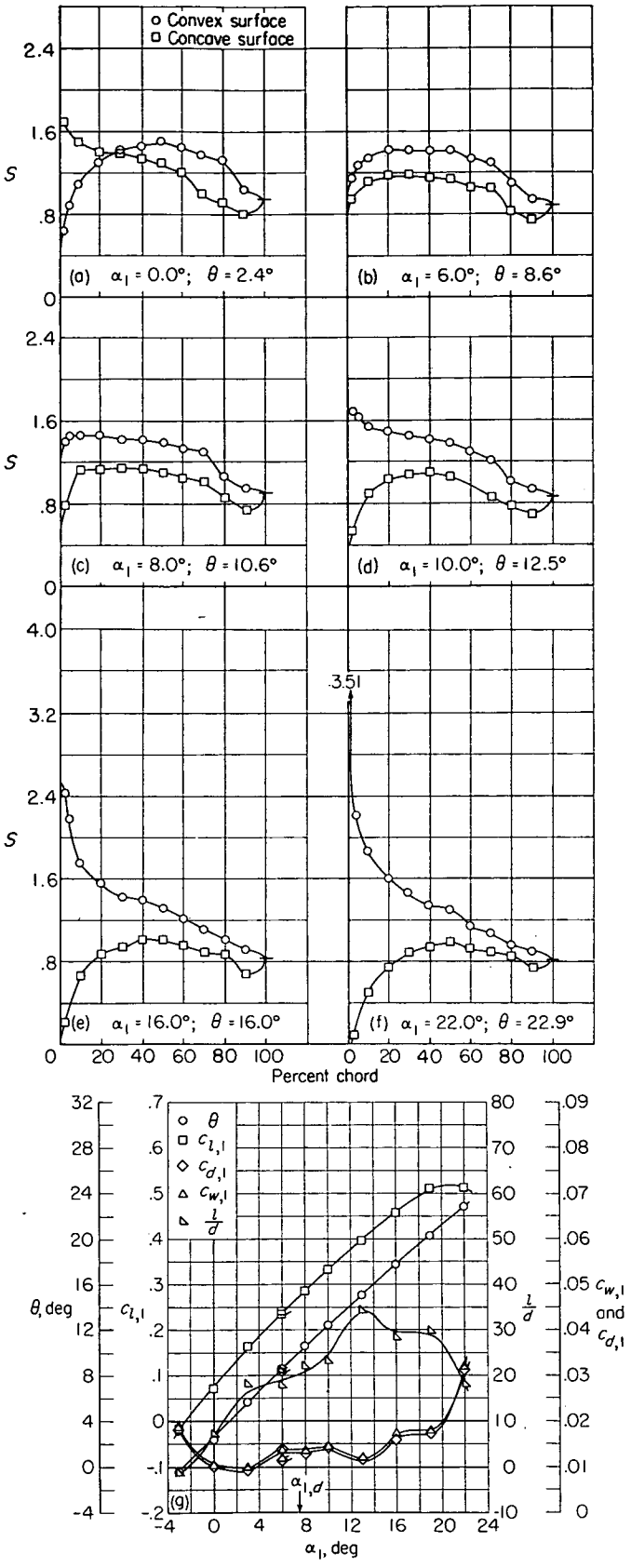
(g) Section characteristics; flagged symbol indicates leading-edge roughness.

FIGURE 10.—Blade-surface pressure distributions and blade section characteristics for the cascade combination, $\beta_1=30°$, $\sigma=1.00$, and blade section, NACA 65-(15)10.



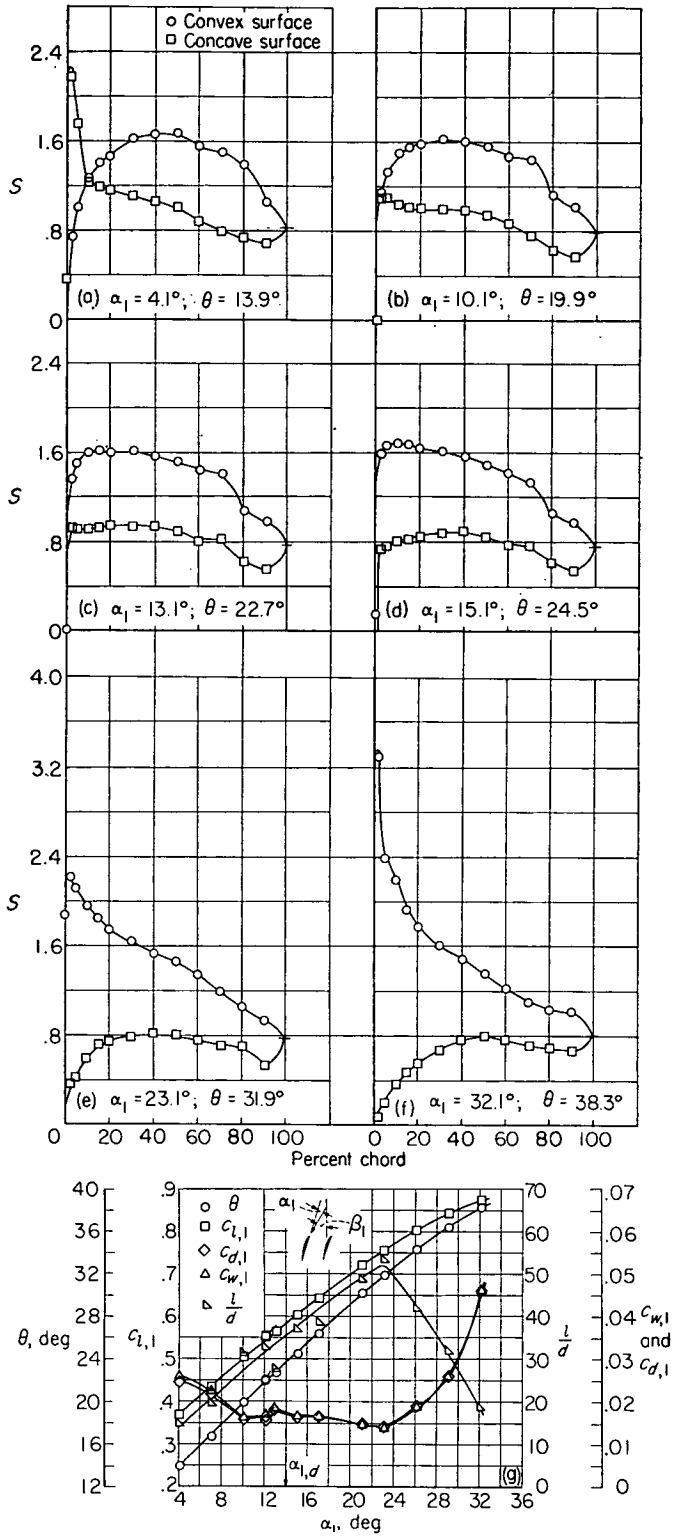
(g) Section characteristics; flagged symbol indicates leading-edge roughness.

FIGURE 11.—Blade-surface pressure distributions and blade section characteristics for the cascade combination, $\beta_1=30°$, $\sigma=1.00$, and blade section, NACA 65-(18)10.



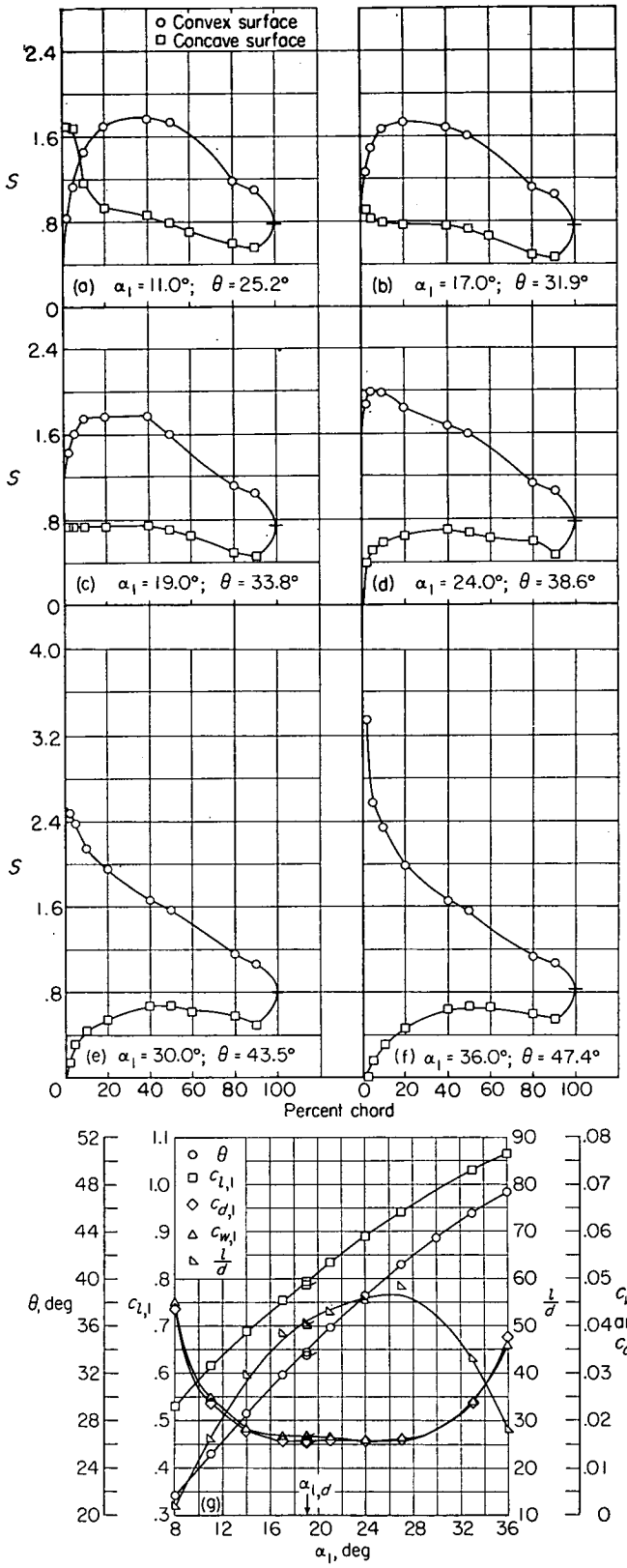
(g) Section characteristics; flagged symbol indicates leading-edge roughness.

FIGURE 12.—Blade-surface pressure distributions and blade section characteristics for the cascade combination, $\beta_1=30°$, $\sigma=1.25$, and blade section, NACA 65–410.



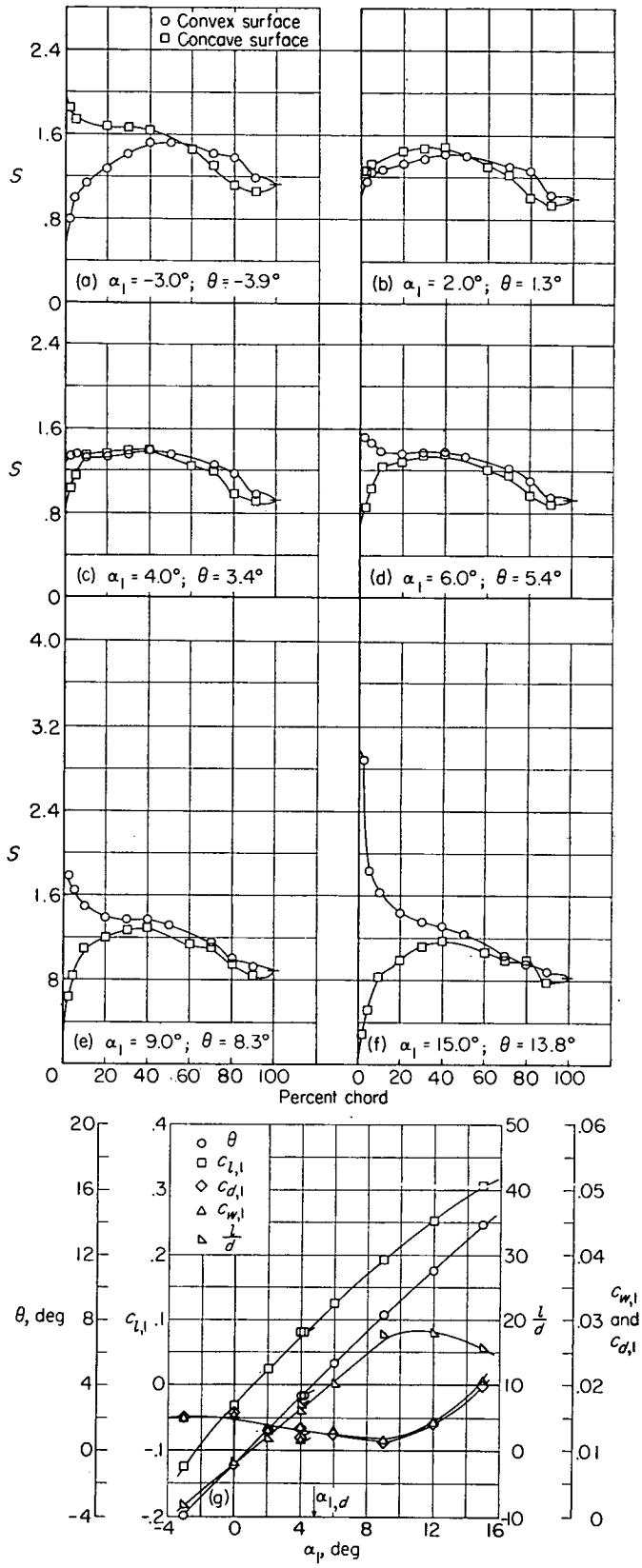
(g) Section characteristics; flagged symbol indicates leading-edge roughness.

FIGURE 13.—Blade-surface pressure distributions and blade section characteristics for the cascade combination, $\beta_1=30°$, $\sigma=1.25$, and blade section, NACA 65–(12)10.



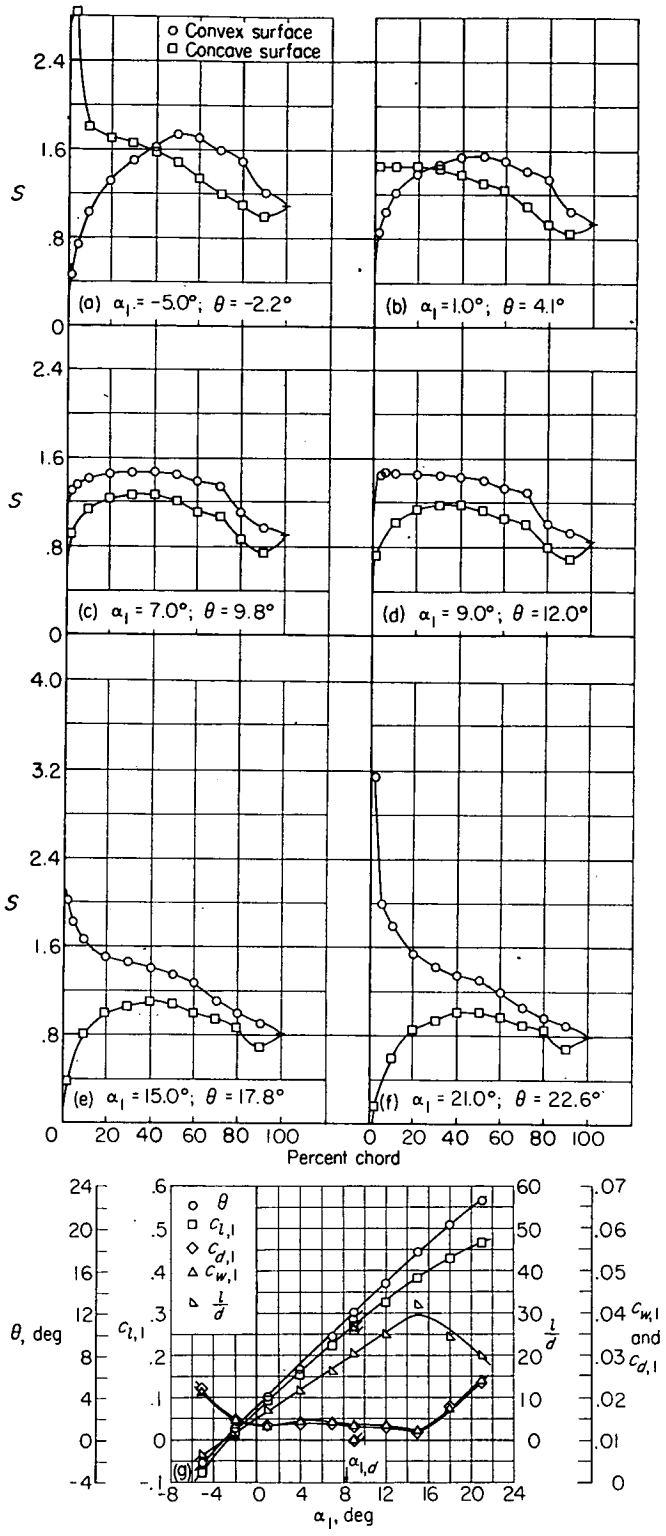
(g) Section characteristics; flagged symbol indicates leading-edge roughness.

FIGURE 14.—Blade-surface pressure distributions and blade section characteristics for the cascade combination, $\beta_1 = 30°$, $\sigma = 1.25$, and blade section, NACA 65-(18)10.



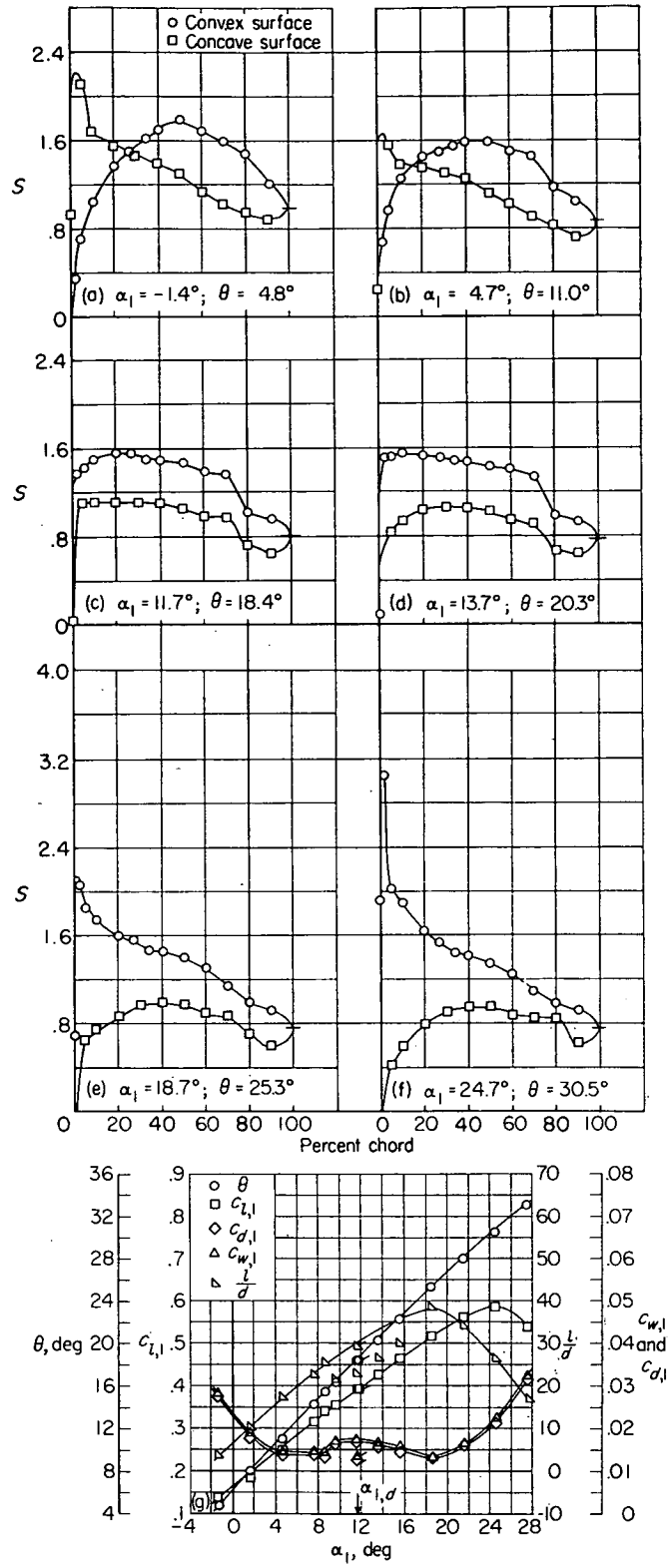
(g) Section characteristics; flagged symbol indicates leading-edge roughness.

FIGURE 15.—Blade-surface pressure distributions and blade section characteristics for the cascade combination, $\beta_1 = 30°$, $\sigma = 1.50$, and blade section, NACA 65-010.



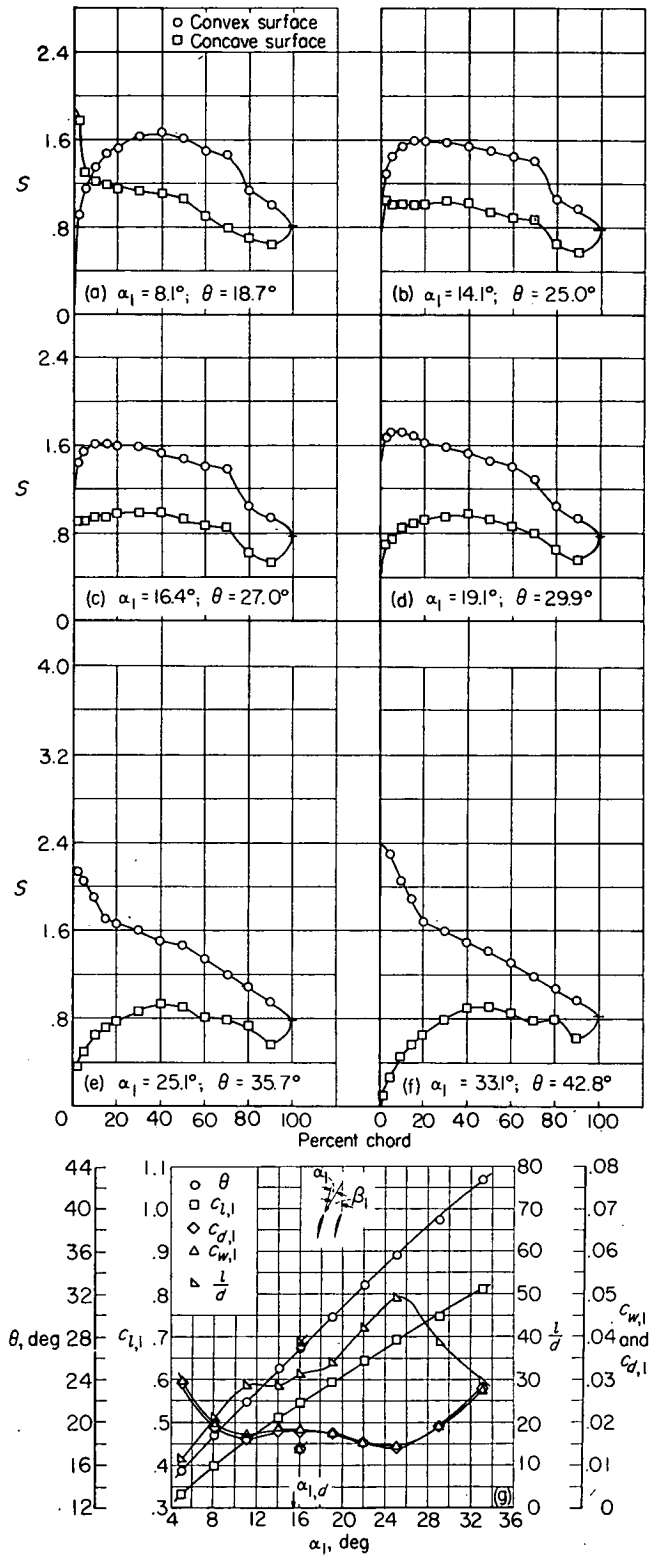
(g) Section characteristics; flagged symbol indicates leading-edge roughness.

FIGURE 16.—Blade-surface pressure distributions and blade section characteristics for the cascade combination, $\beta_1=30°$, $\sigma=1.50$, and blade section, NACA 65–410.



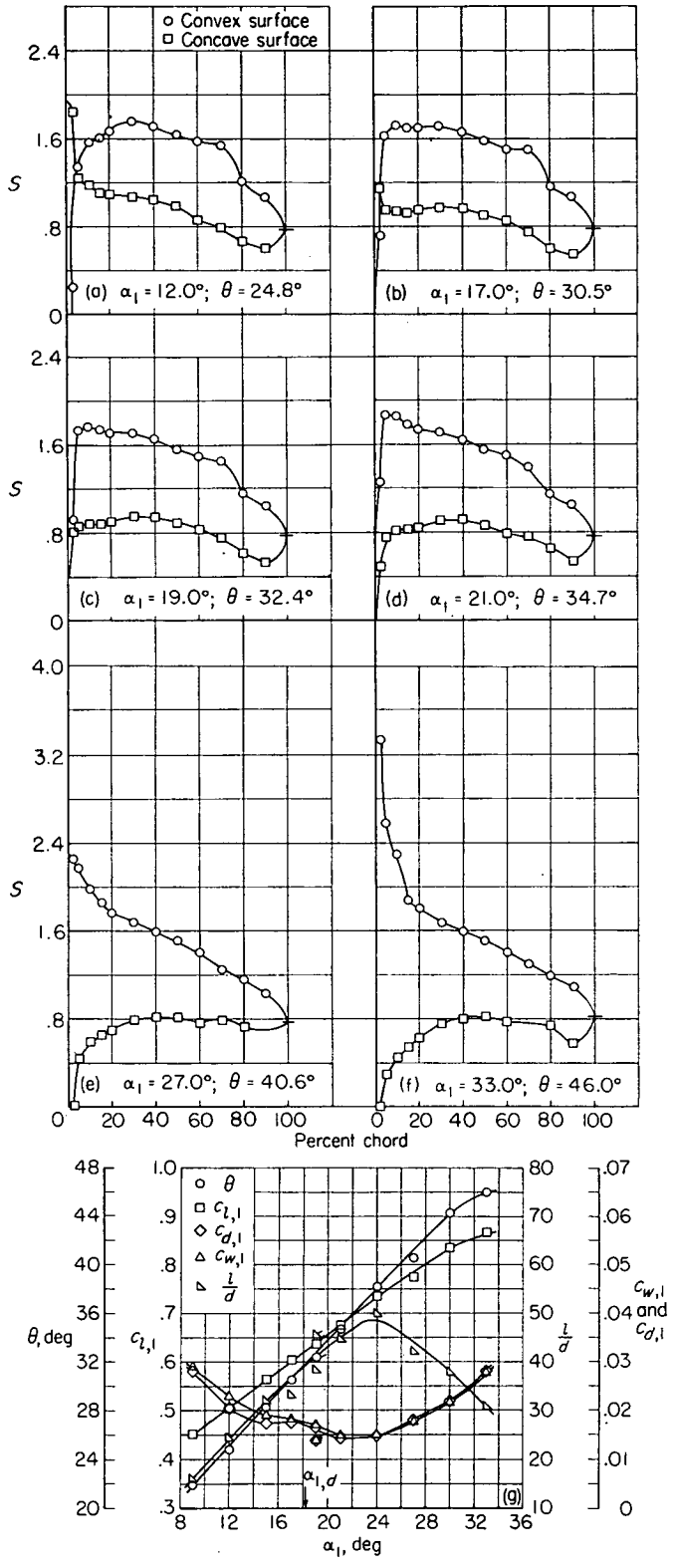
(g) Section characteristics; flagged symbol indicates leading-edge roughness.

FIGURE 17.—Blade-surface pressure distributions and blade section characteristics for the cascade combination, $\beta_1=30°$, $\sigma=1.50$, and blade section, NACA 65–810.



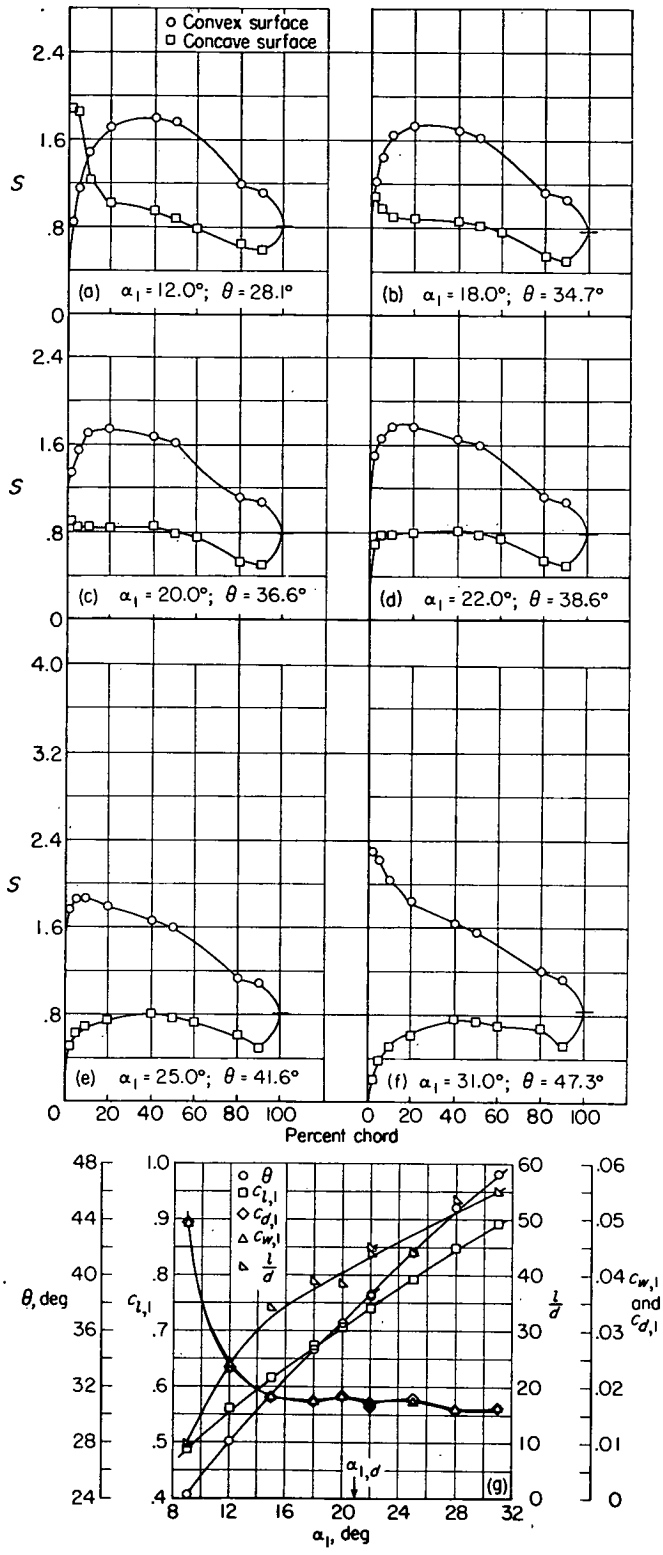
(g) Section characteristics; flagged symbol indicates leading-edge roughness.

FIGURE 18.—Blade-surface pressure distributions and blade section characteristics for the cascade combination, β_1=30°, σ=1.50, and blade section, NACA 65-(12)10.



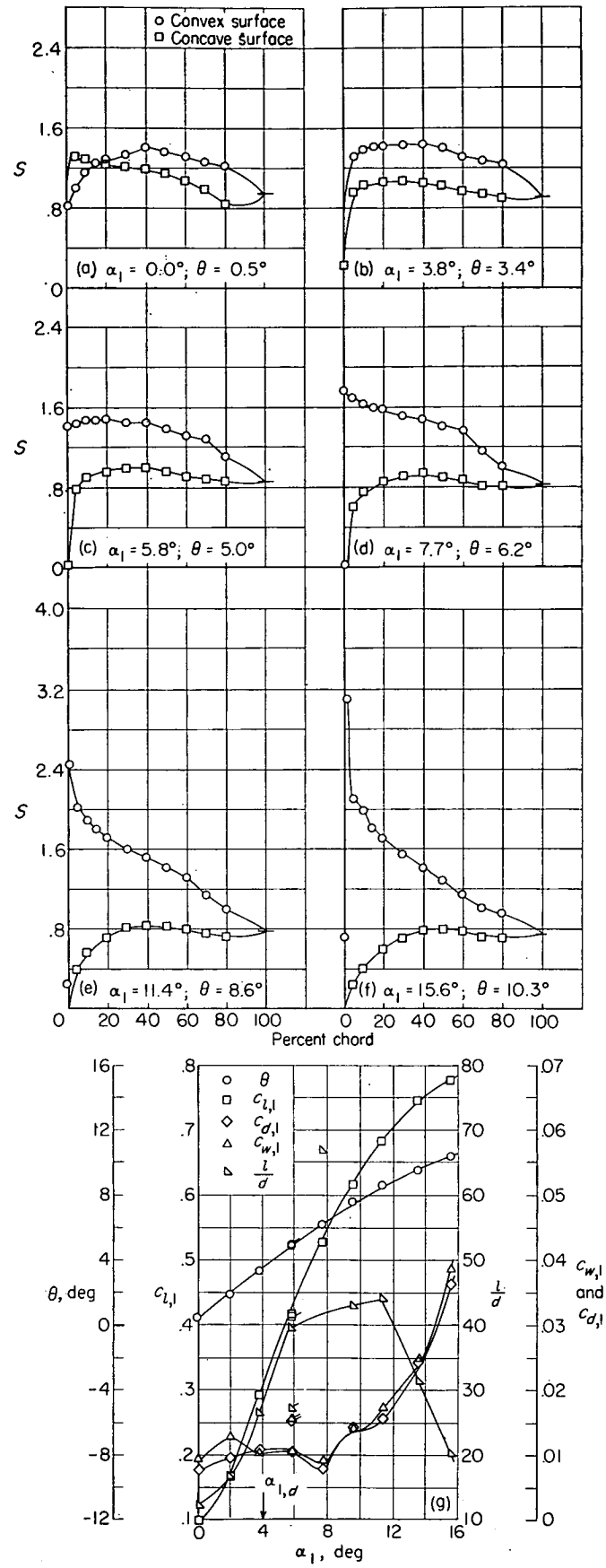
(g) Section characteristics; flagged symbol indicates leading-edge roughness.

FIGURE 19.—Blade-surface pressure distributions and blade section characteristics for the cascade combination, β_1=30°, σ=1.50, and blade section, NACA 65-(15)10.



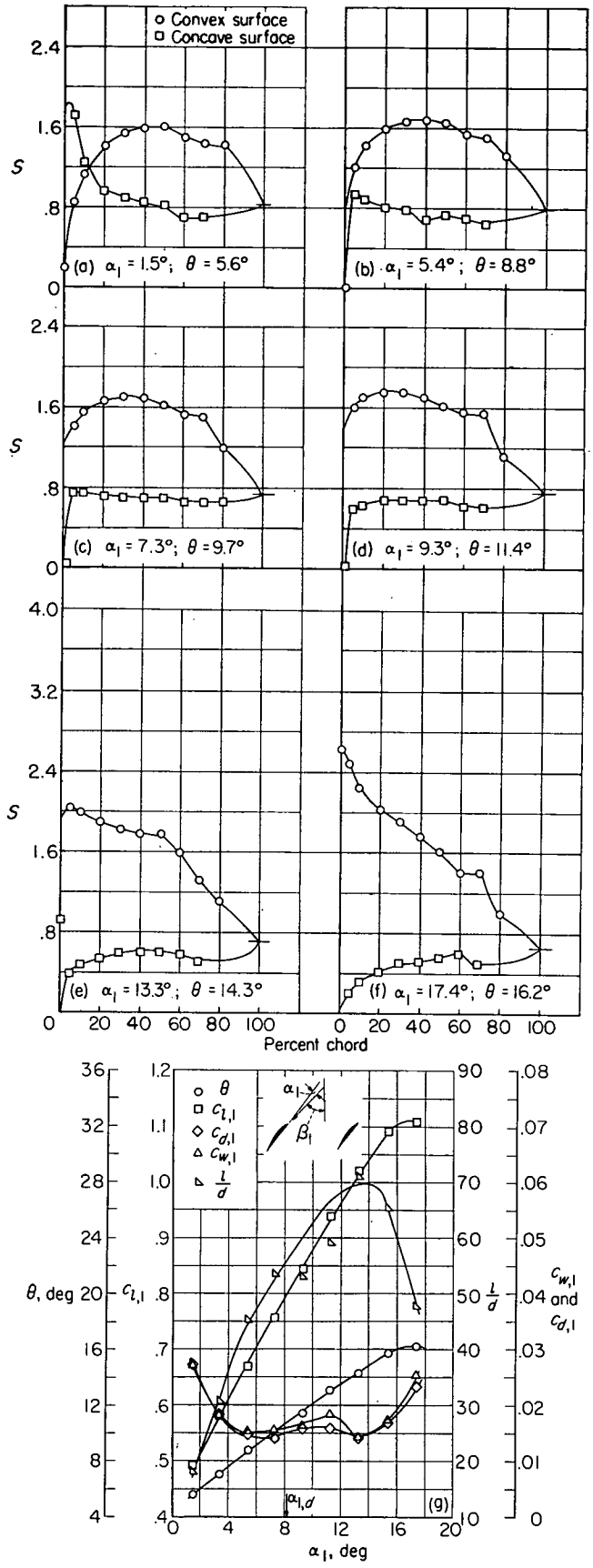
(g) Section characteristics; flagged symbol indicates leading-edge roughness.

FIGURE 20.—Blade-surface pressure distributions and blade section characteristics for the cascade combination, $\beta_1=30°$, $\sigma=1.50$, and blade section, NACA 65-(18)10.



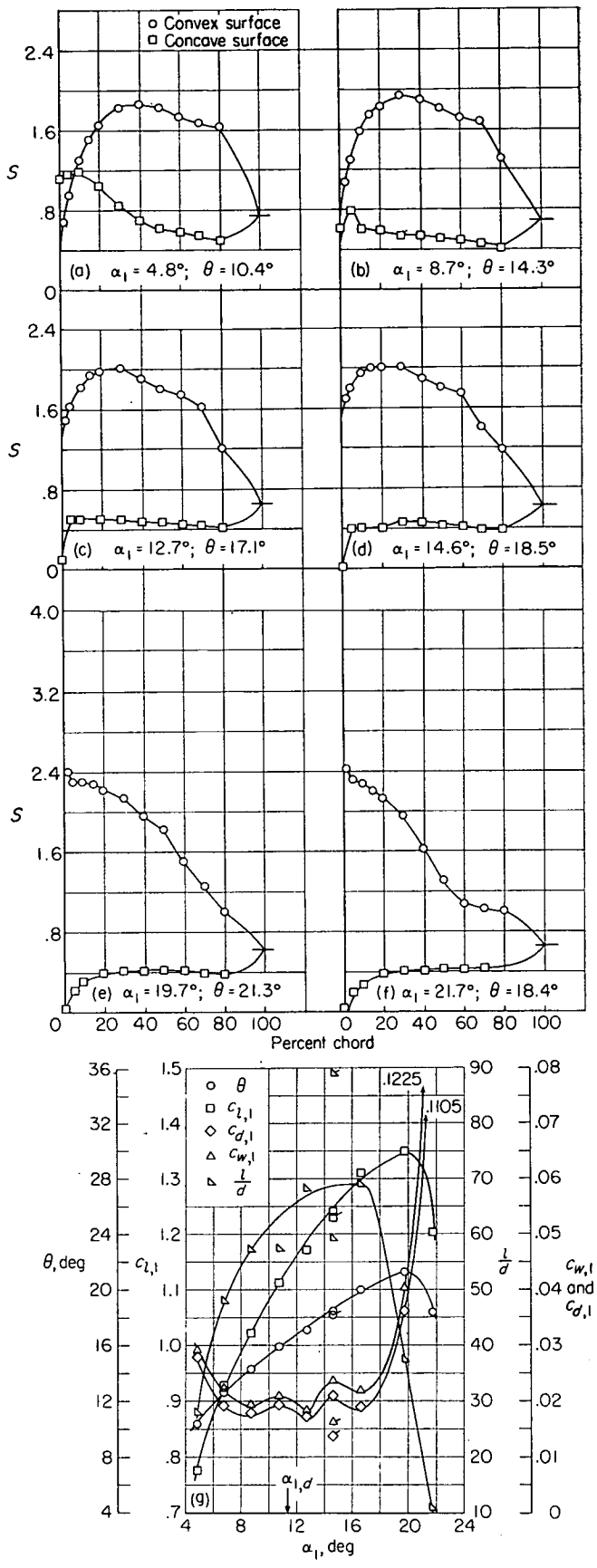
(g) Section characteristics; flagged symbol indicates leading-edge roughness.

FIGURE 21.—Blade-surface pressure distributions and blade section characteristics for the cascade combination, $\beta_1=45°$, $\sigma=0.50$, and blade section, NACA 65-410.



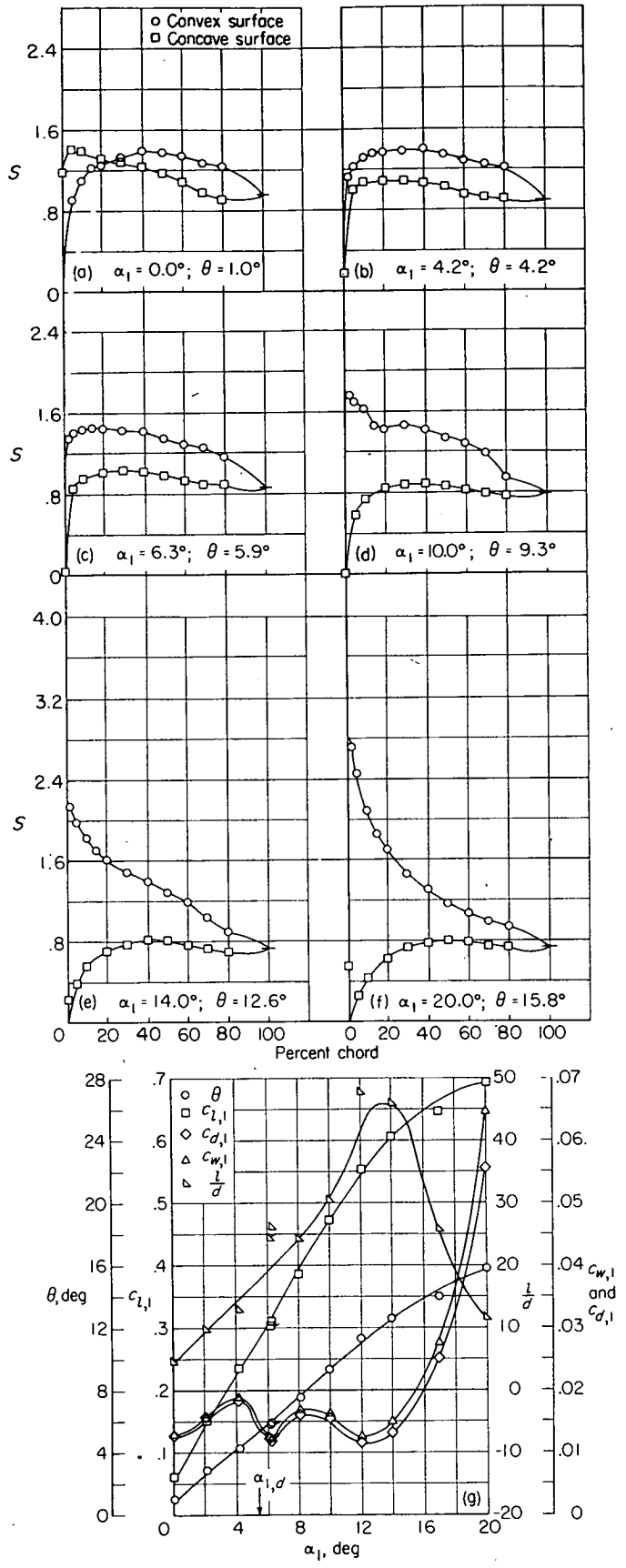
(g) Section characteristics.

FIGURE 22.—Blade-surface pressure distributions and blade section characteristics for the cascade combination, β_1=45°, σ=0.50, and blade section, NACA 65-(12)10.



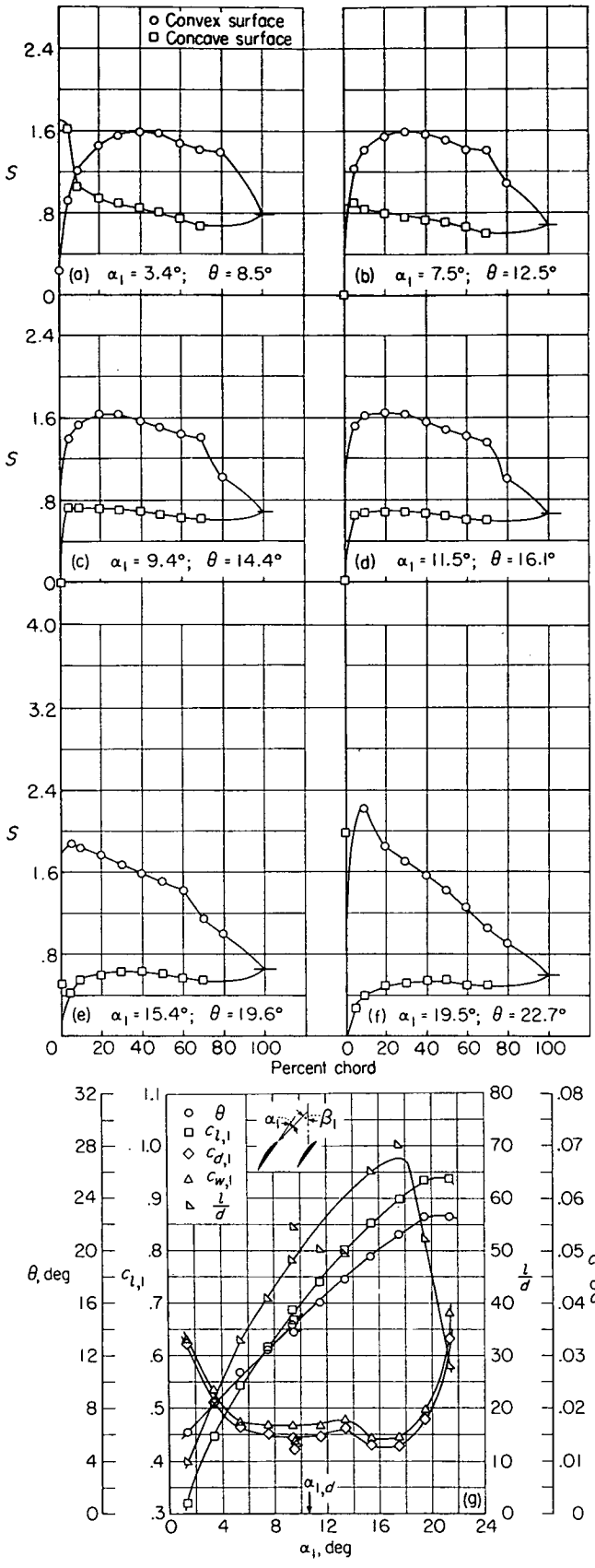
(g) Section characteristics; flagged symbol indicates leading-edge roughness.

FIGURE 23.—Blade-surface pressure distributions and blade section characteristics for the cascade combination, β_1=45°, σ=0.50, and blade section, NACA 65-(18)10.



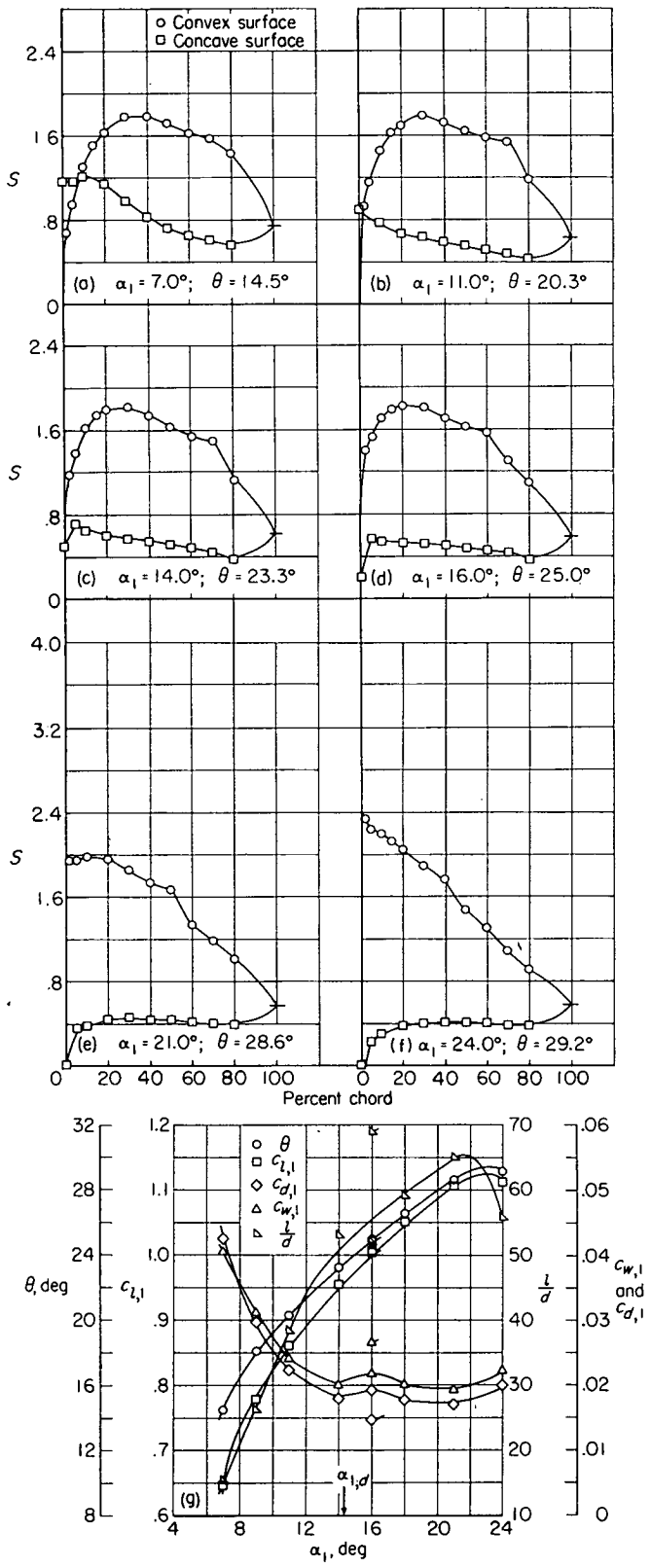
(g) Section characteristics; flagged symbol indicates leading-edge roughness.

FIGURE 24.—Blade-surface pressure distributions and blade section characteristics for the cascade combination, β_1=45°, σ=0.75, and blade section, NACA 65–410.



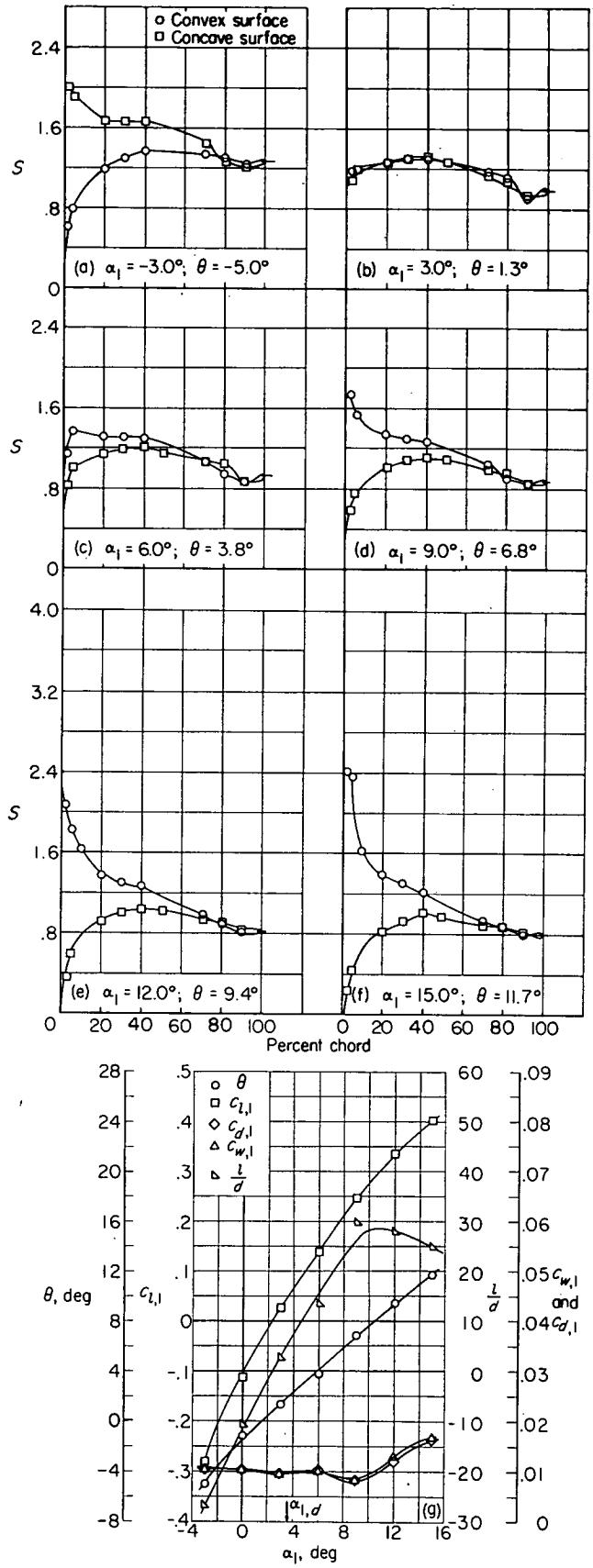
(g) Section characteristics; flagged symbol indicates leading-edge roughness.

FIGURE 25.—Blade-surface pressure distributions and blade section characteristics for the cascade combination, β_1=45°, σ=0.75, and blade section, NACA 65–(12)10.



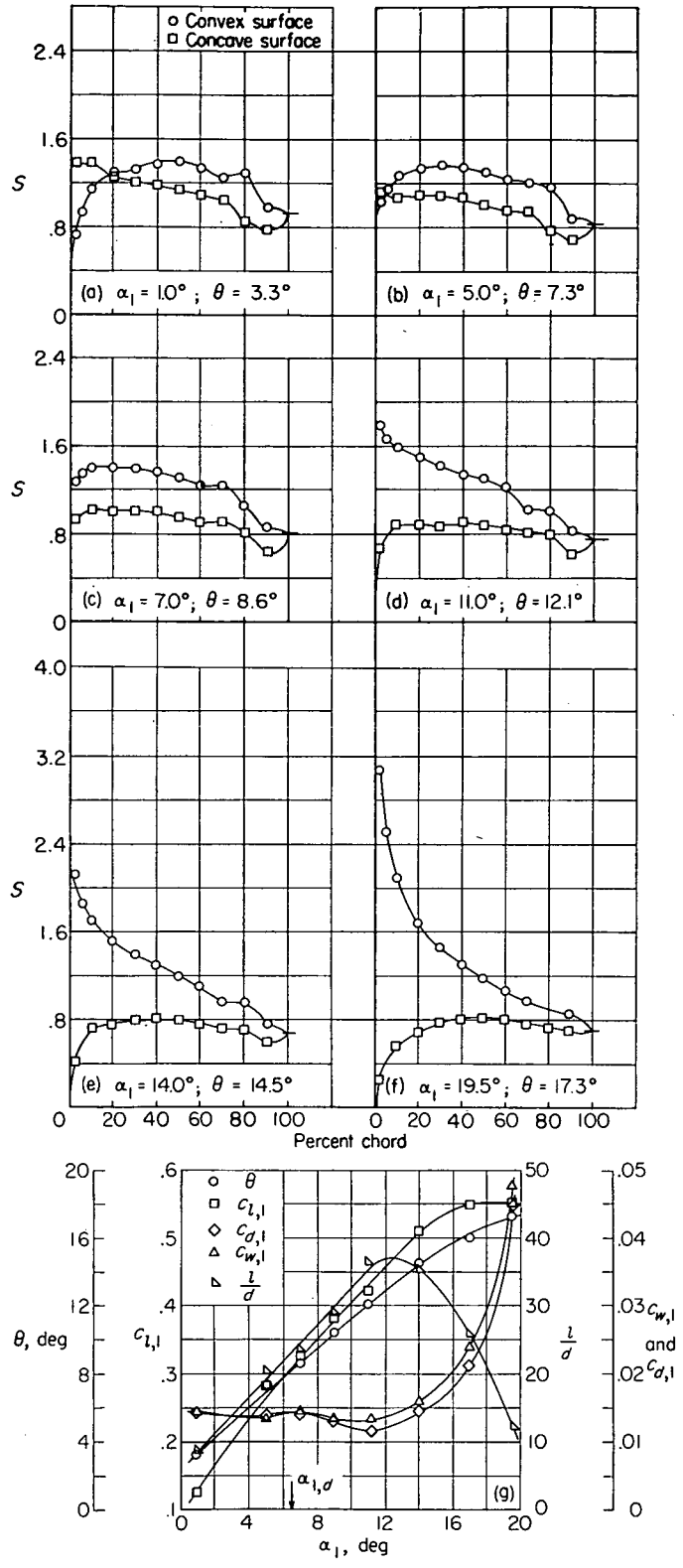
(g) Section characteristics; flagged symbol indicates leading-edge roughness.

FIGURE 26.—Blade-surface pressure distributions and blade section characteristics for the cascade combination, $\beta_1=45°$, $\sigma=0.75$, and blade section, NACA 65-(18)10.



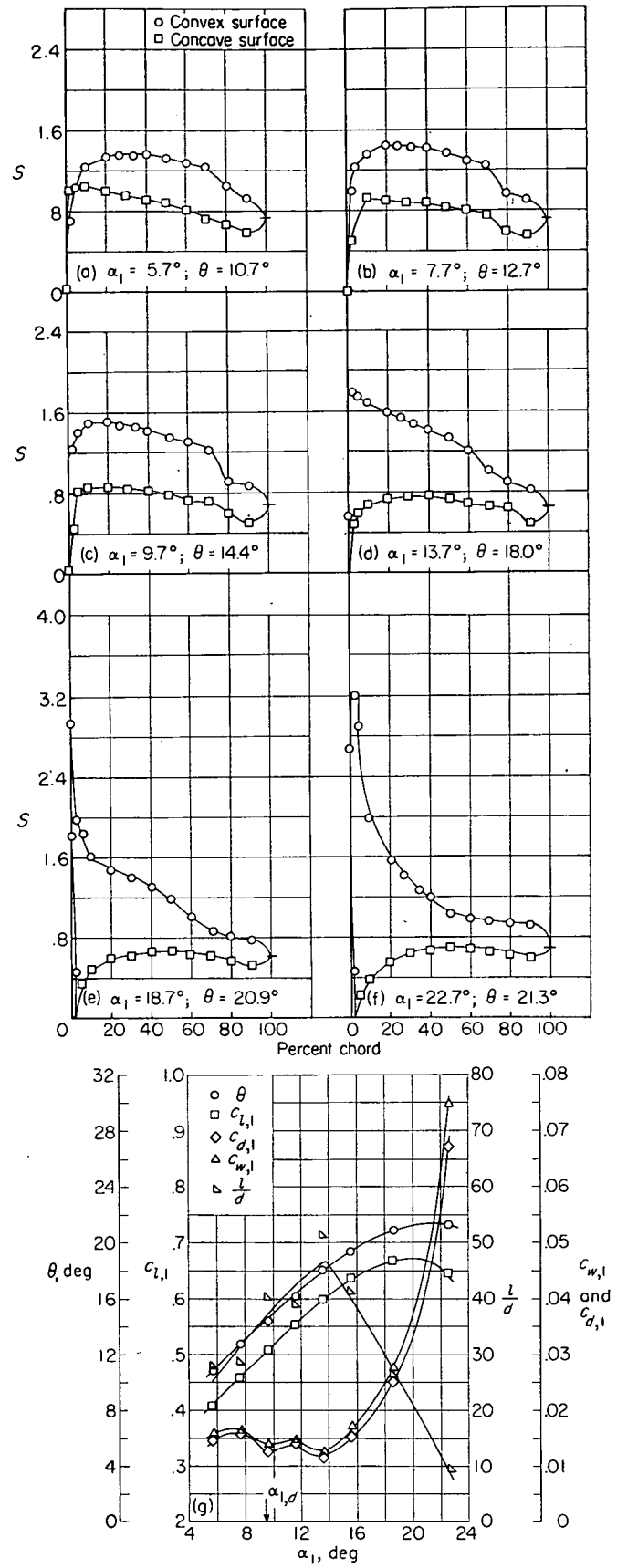
(g) Section characteristics.

FIGURE 27.—Blade-surface pressure distributions and blade section characteristics for the cascade combination, $\beta_1=45°$, $\sigma=1.00$, and blade section, NACA 65-010.



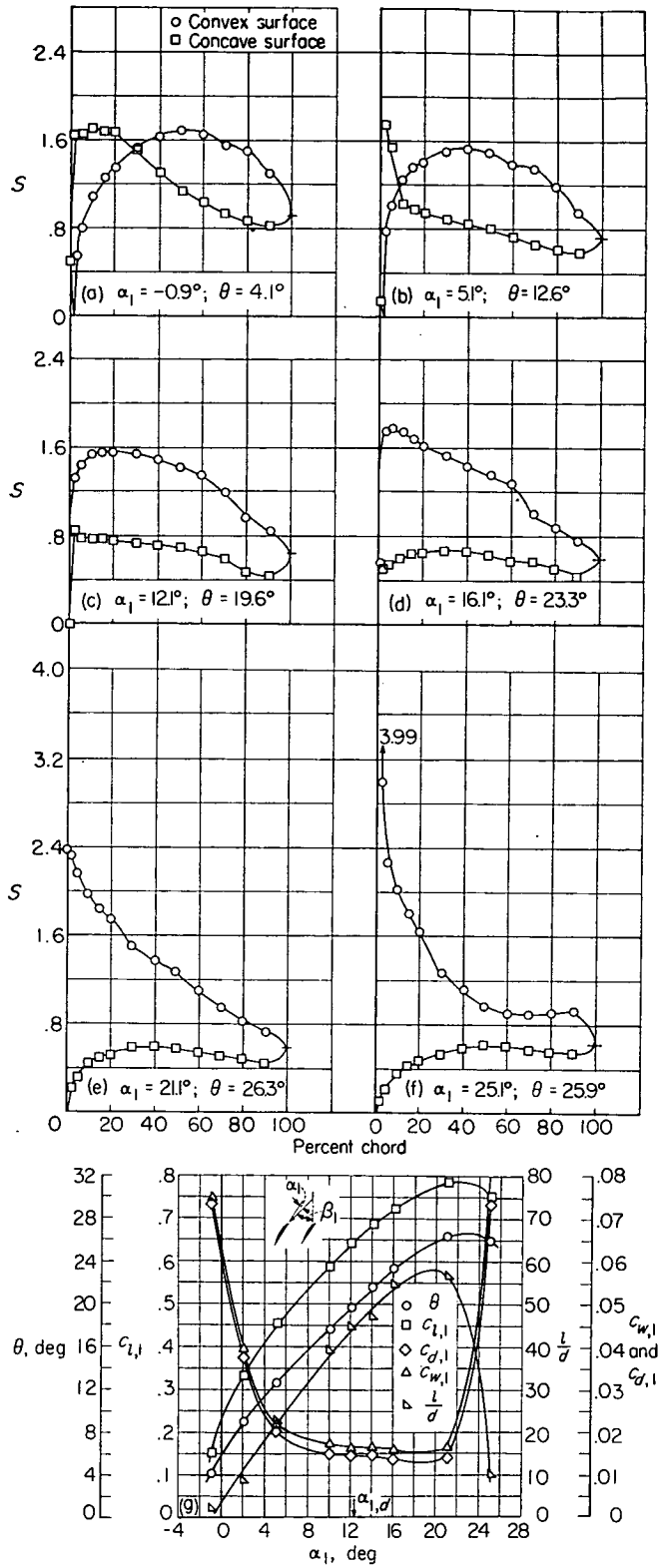
(g) Section characteristics.

FIGURE 28.—Blade-surface pressure distributions and blade section characteristics for the cascade combination, $\beta_1=45°$, $\sigma=1.00$, and blade section, NACA 65–410.



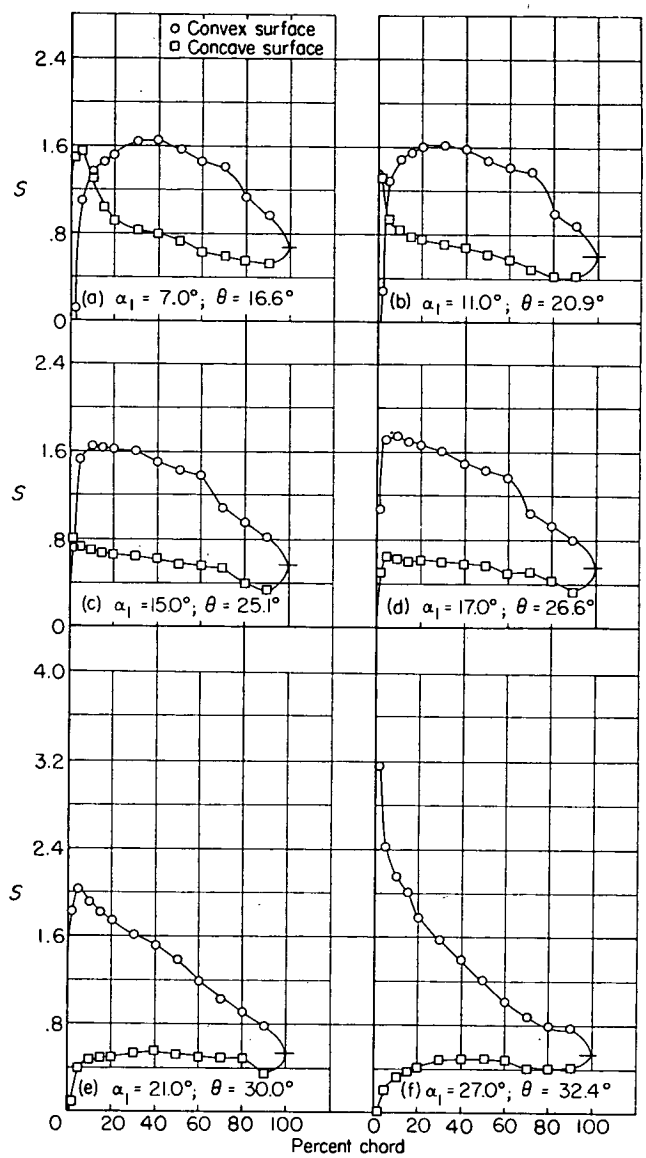
(g) Section characteristics.

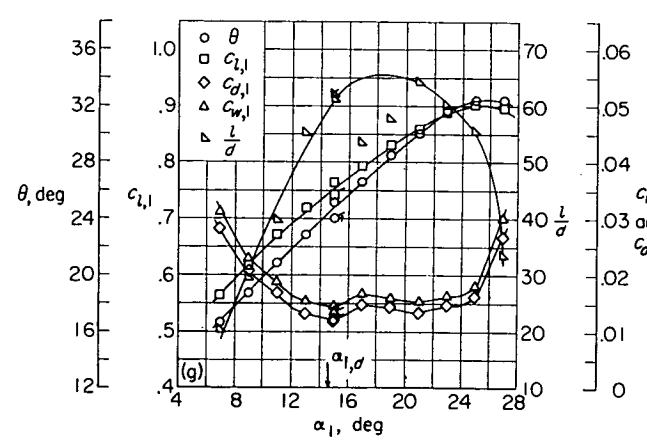
FIGURE 29.—Blade-surface pressure distributions and blade section characteristics for the cascade combination, $\beta_1=45°$, $\sigma=1.00$, and blade section, NACA 65–810.



(g) Section characteristics.

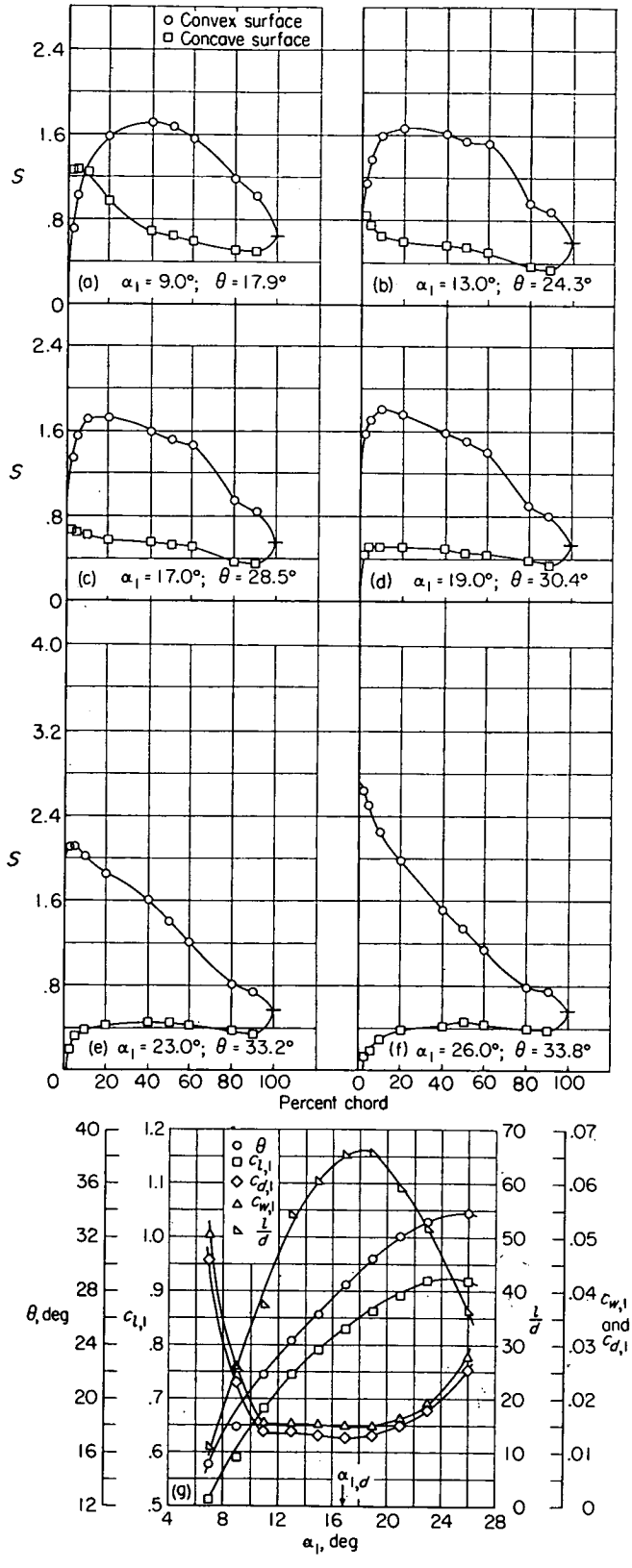
FIGURE 30.—Blade-surface pressure distributions and blade section characteristics for the cascade combination, $\beta_1 = 45°$, $\sigma = 1.00$, and blade section, NACA 65-(12)10.





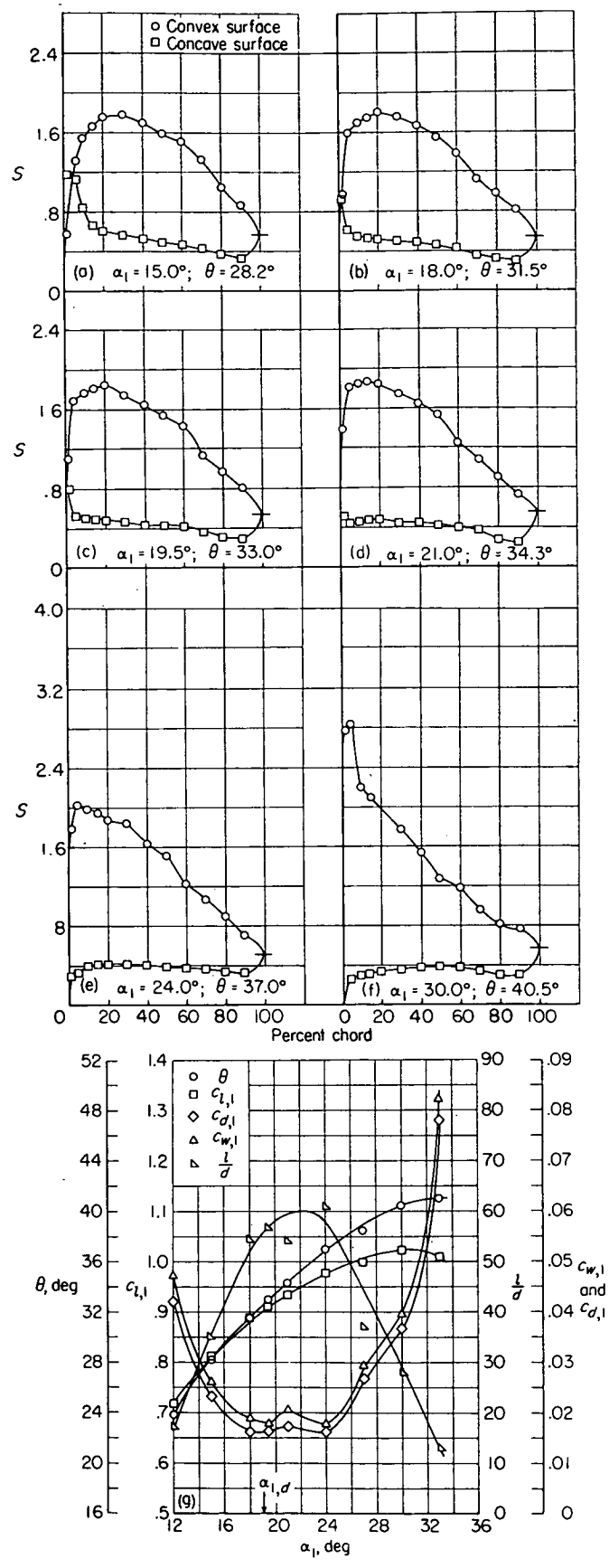
(g) Section characteristics; flagged symbol indicates leading-edge roughness.

FIGURE 31.—Blade-surface pressure distributions and blade section characteristics for the cascade combination, $\beta_1 = 45°$, $\sigma = 1.00$, and blade section, NACA 65-(15)10.



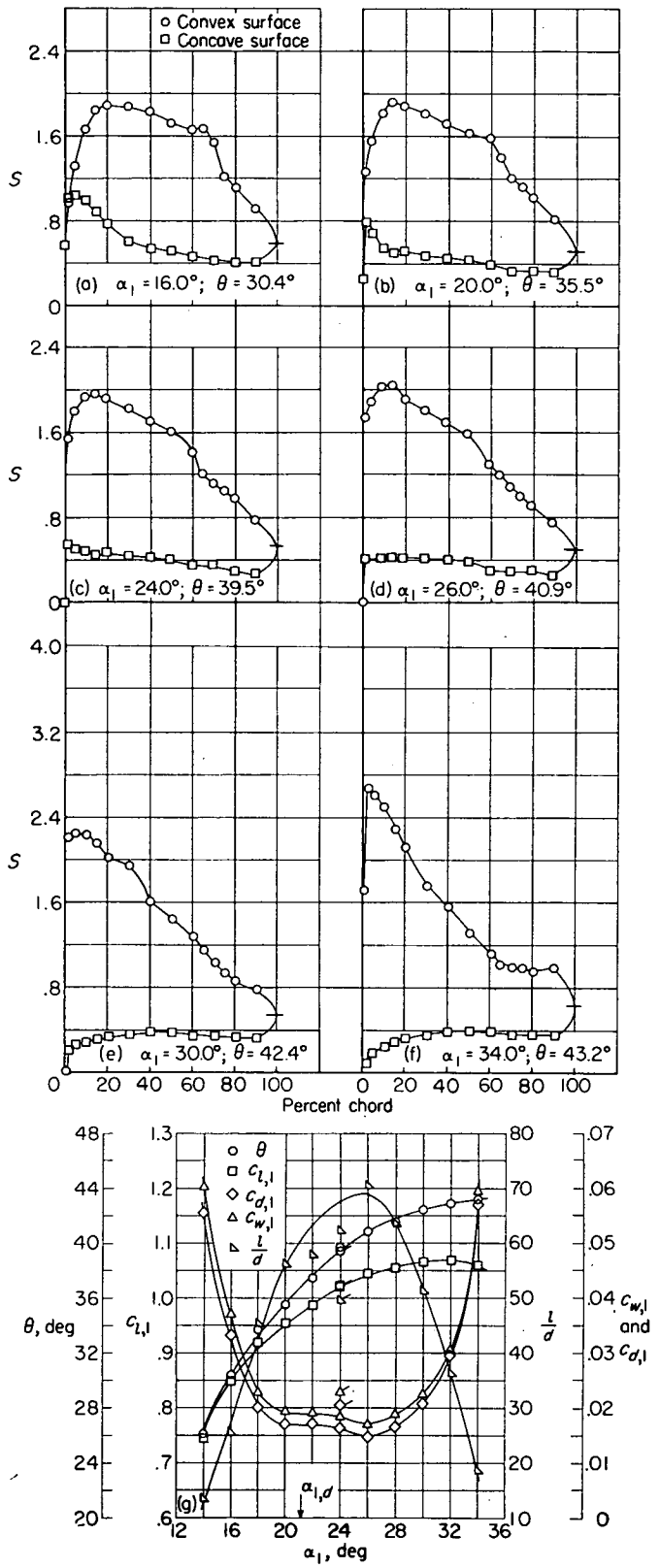
(g) Section characteristics.

FIGURE 32.—Blade-surface pressure distributions and blade section characteristics for the cascade combination, β_1=45°, σ=1.00, and blade section, NACA 65-(18)10.



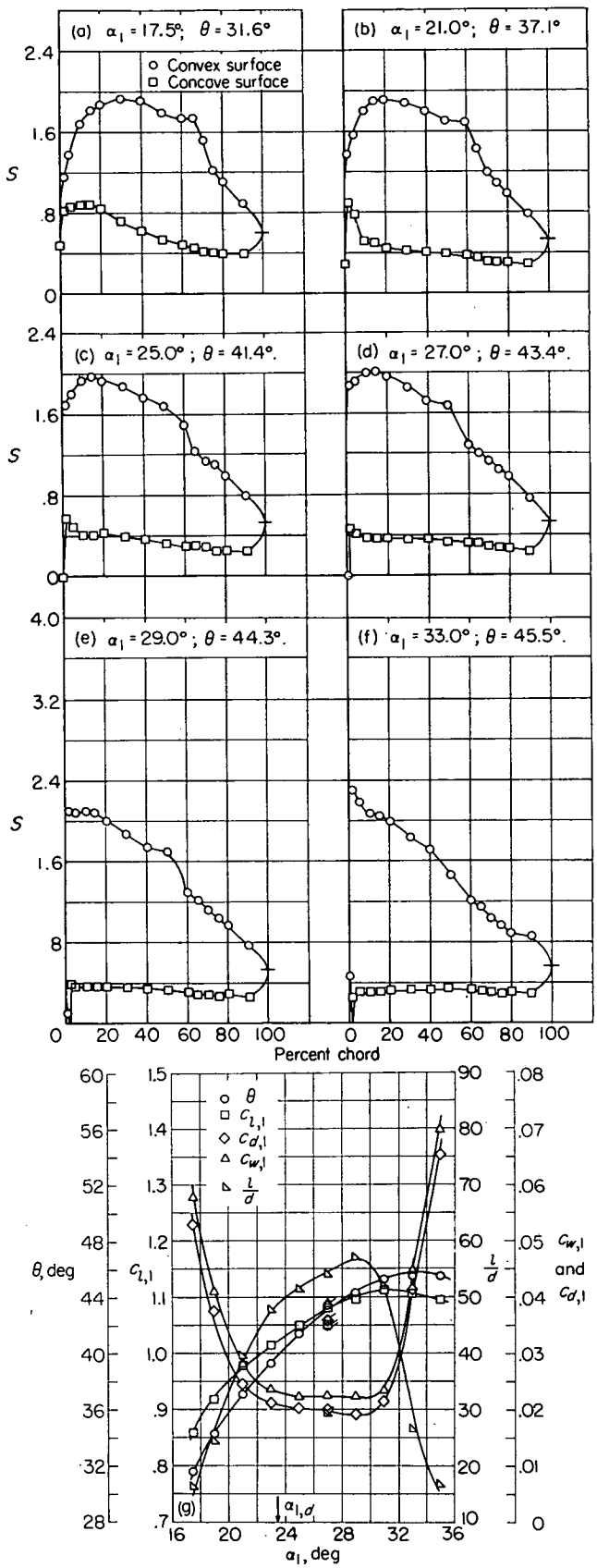
(g) Section characteristics.

FIGURE 33.—Blade-surface pressure distributions and blade section characteristics for the cascade combination, β_1=45°, σ=1.00, and blade section, NACA 65-(21)10.



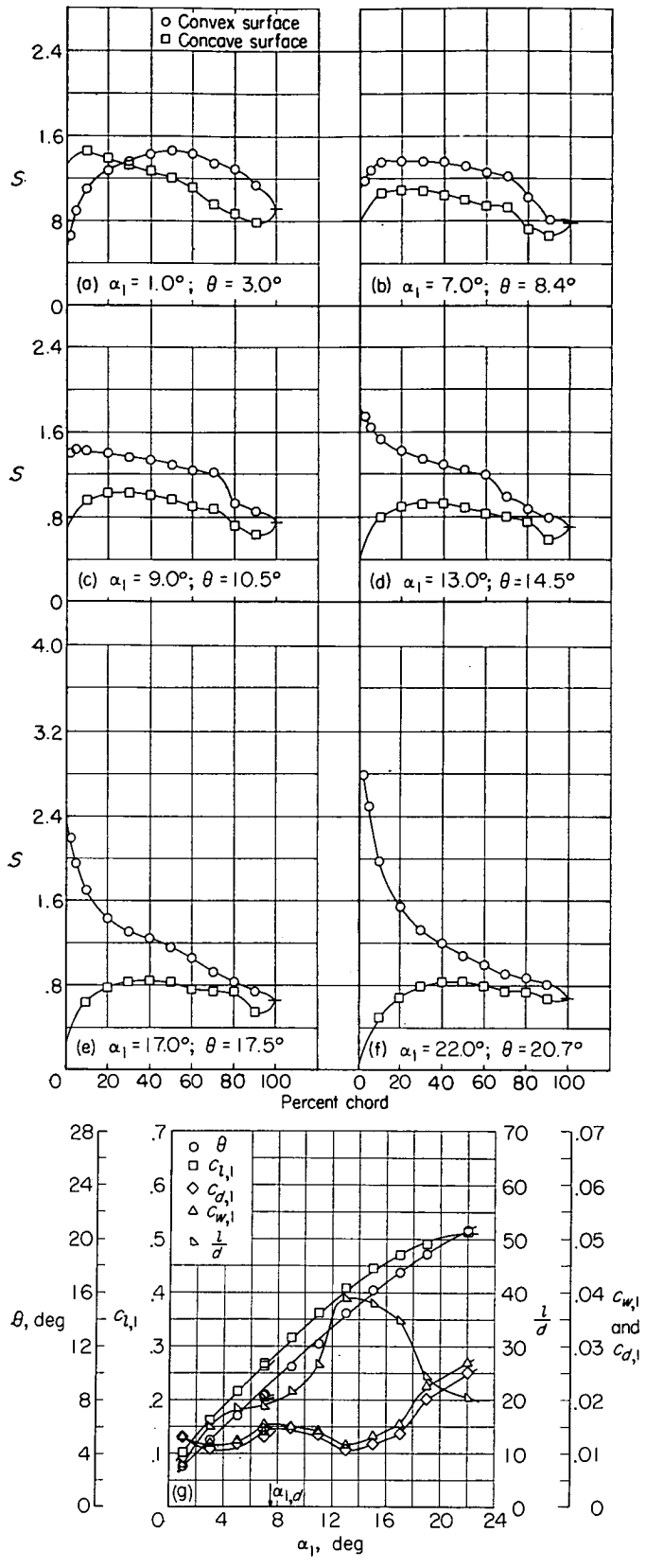
(g) Section characteristics; flagged symbol indicates leading-edge roughness.

FIGURE 34.—Blade-surface pressure distributions and blade section characteristics for the cascade combination, $\beta_1 = 45°$, $\sigma = 1.00$, and blade section, NACA 65-(24)10.



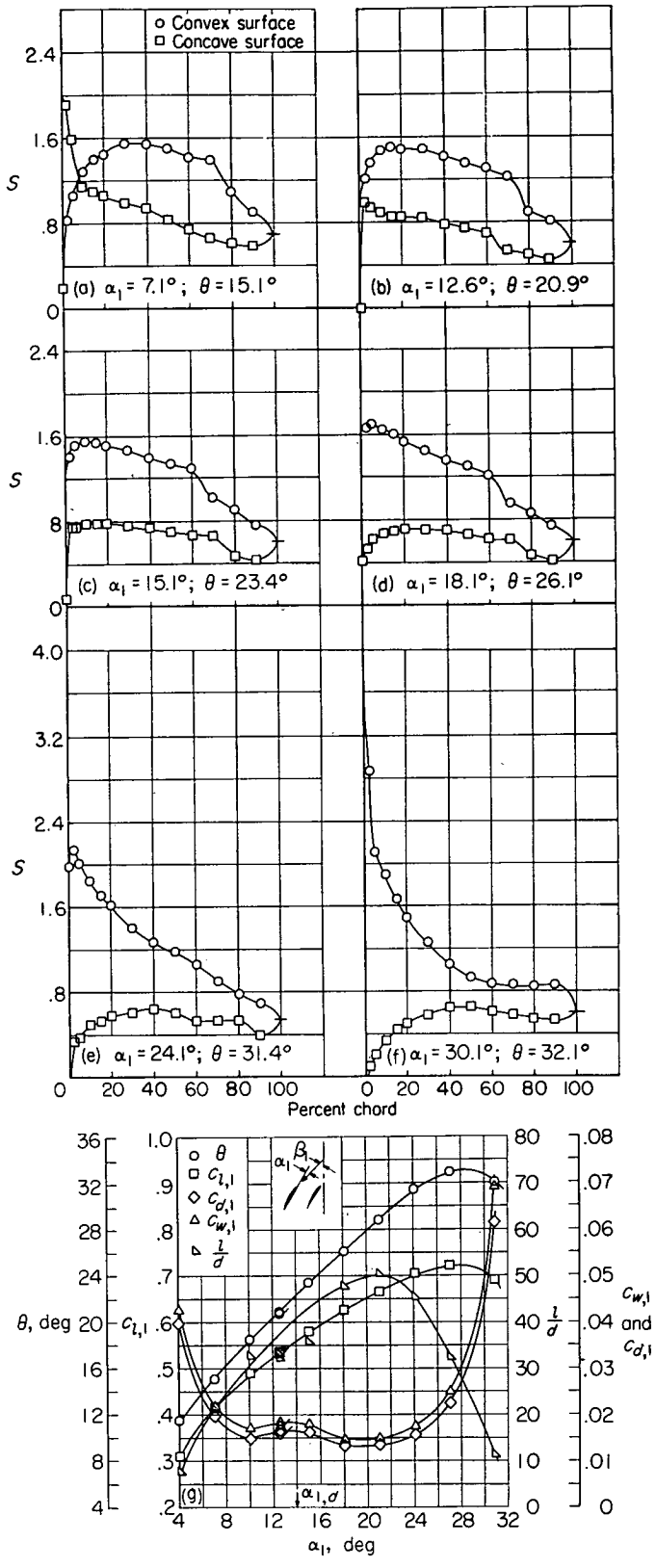
(g) Section characteristics; flagged symbol indicates leading-edge roughness.

FIGURE 35.—Blade-surface pressure distributions and blade section characteristics for the cascade combination, $\beta_1 = 45°$, $\sigma = 1.00$, and blade section, NACA 65-(27)10.



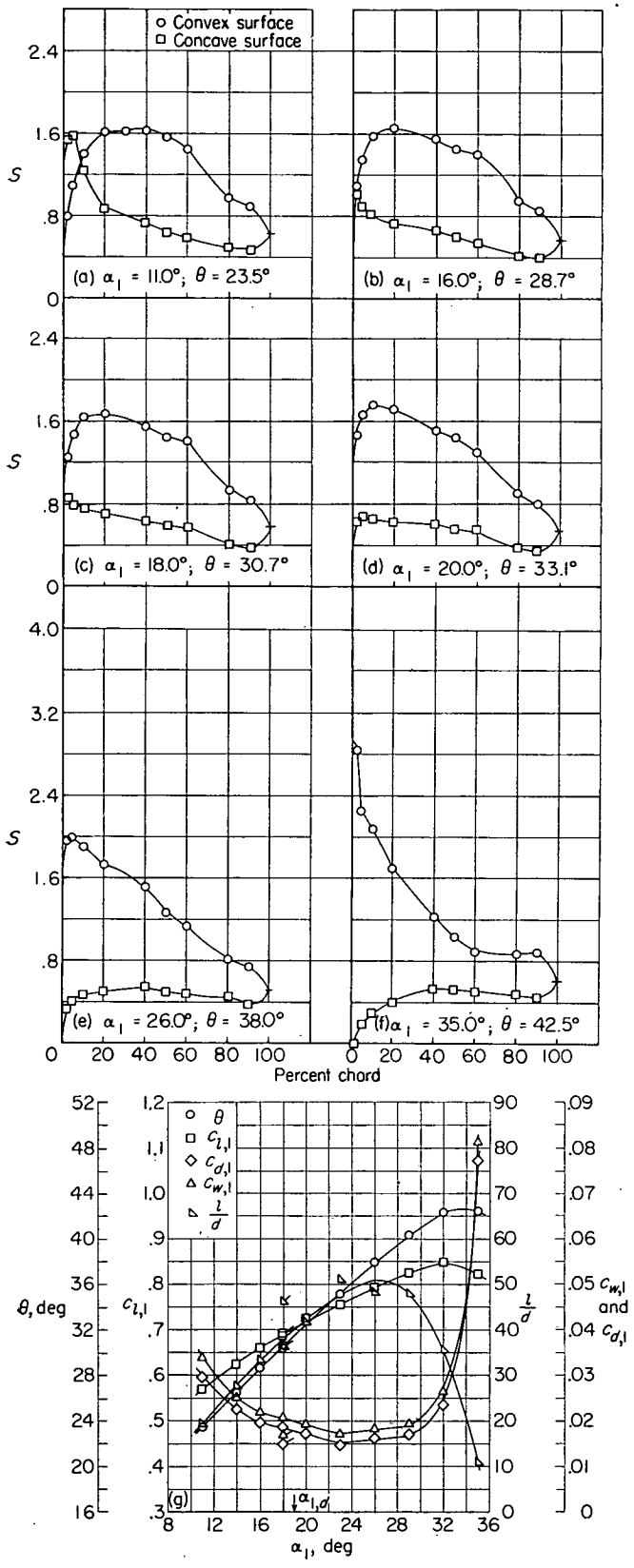
(g) Section characteristics; flagged symbol indicates leading-edge roughness.

FIGURE 36.—Blade-surface pressure distributions and blade section characteristics for the cascade combination, β_1=45°, σ=1.25, and blade section, NACA 65–410.



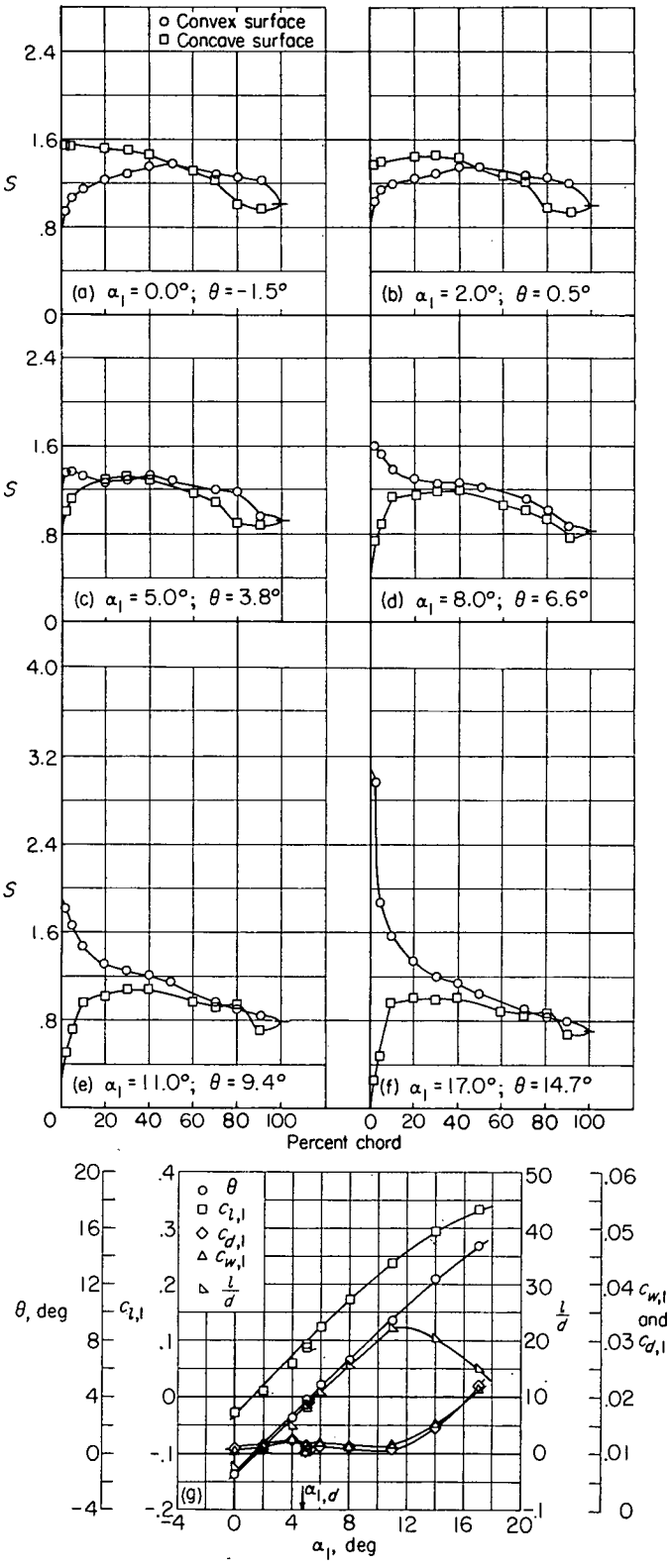
(g) Section characteristics; flagged symbol indicates leading-edge roughness.

FIGURE 37.—Blade-surface pressure distributions and blade section characteristics for the cascade combination, β_1=45°, σ=1.25, and blade section, NACA 65-(12)10.



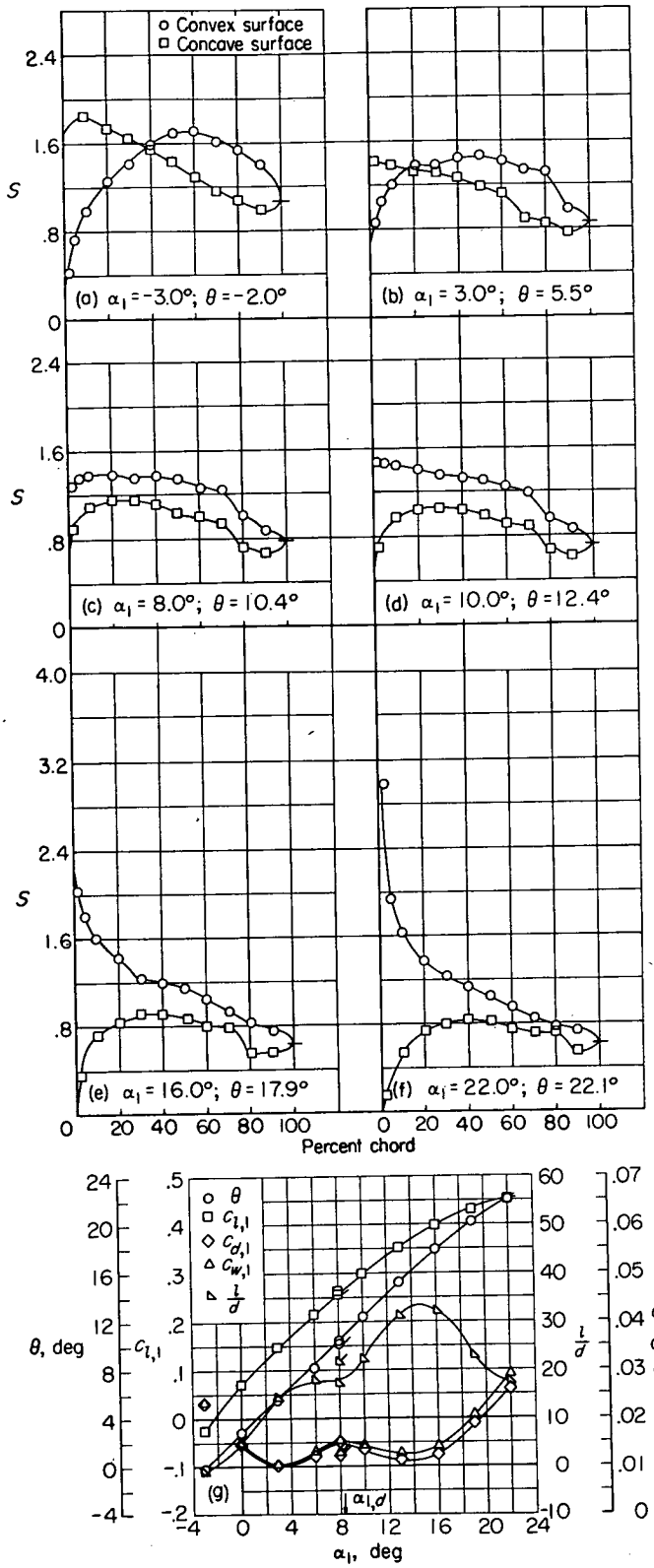
(g) Section characteristics; flagged symbol indicates leading-edge roughness.

FIGURE 38.—Blade-surface pressure distributions and blade section characteristics for the cascade combination, $\beta_1=45°$, $\sigma=1.25$, and blade section, NACA 65-(18)10.



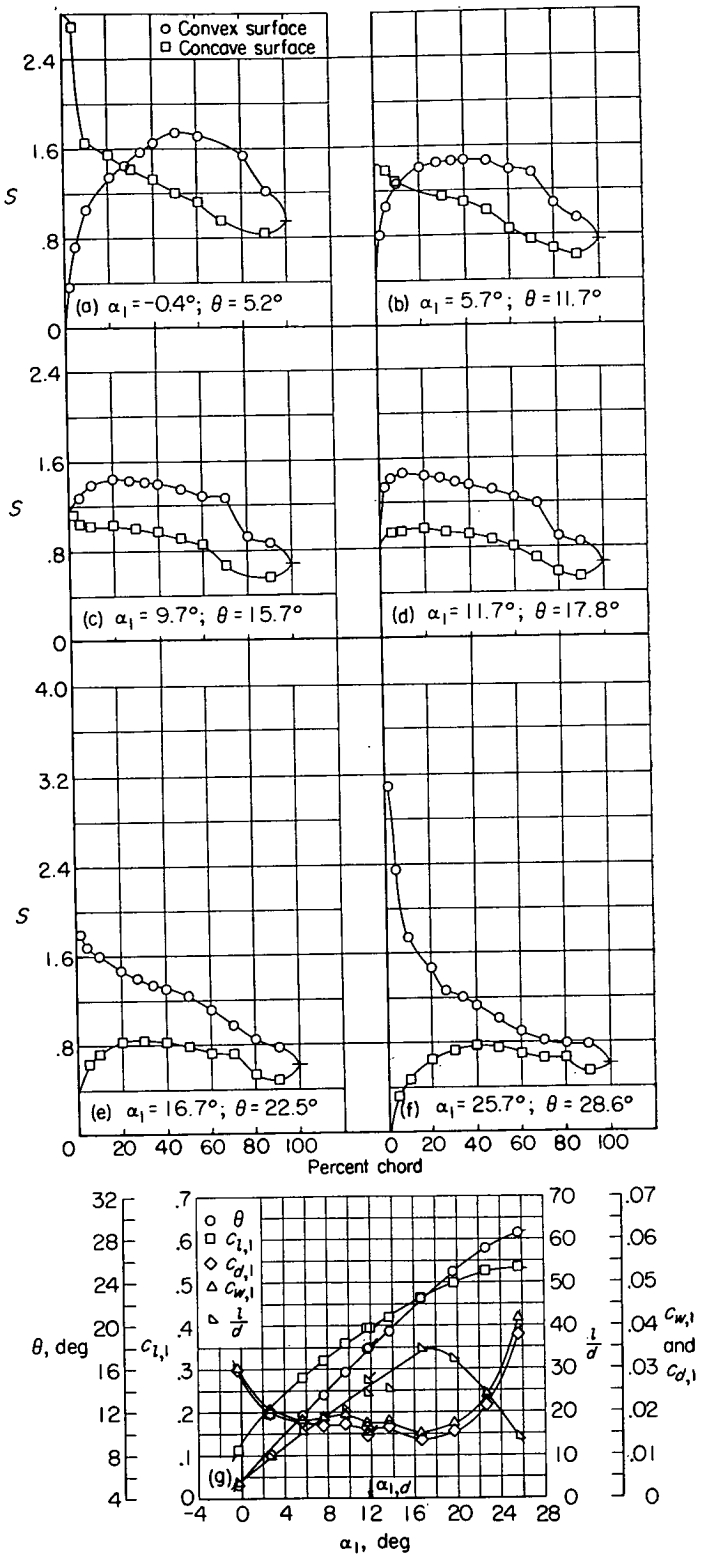
(g) Section characteristics; flagged symbol indicates leading-edge roughness.

FIGURE 39.—Blade-surface pressure distributions and blade section characteristics for the cascade combination, $\beta_1=45°$, $\sigma=1.50$, and blade section, NACA 65-010.



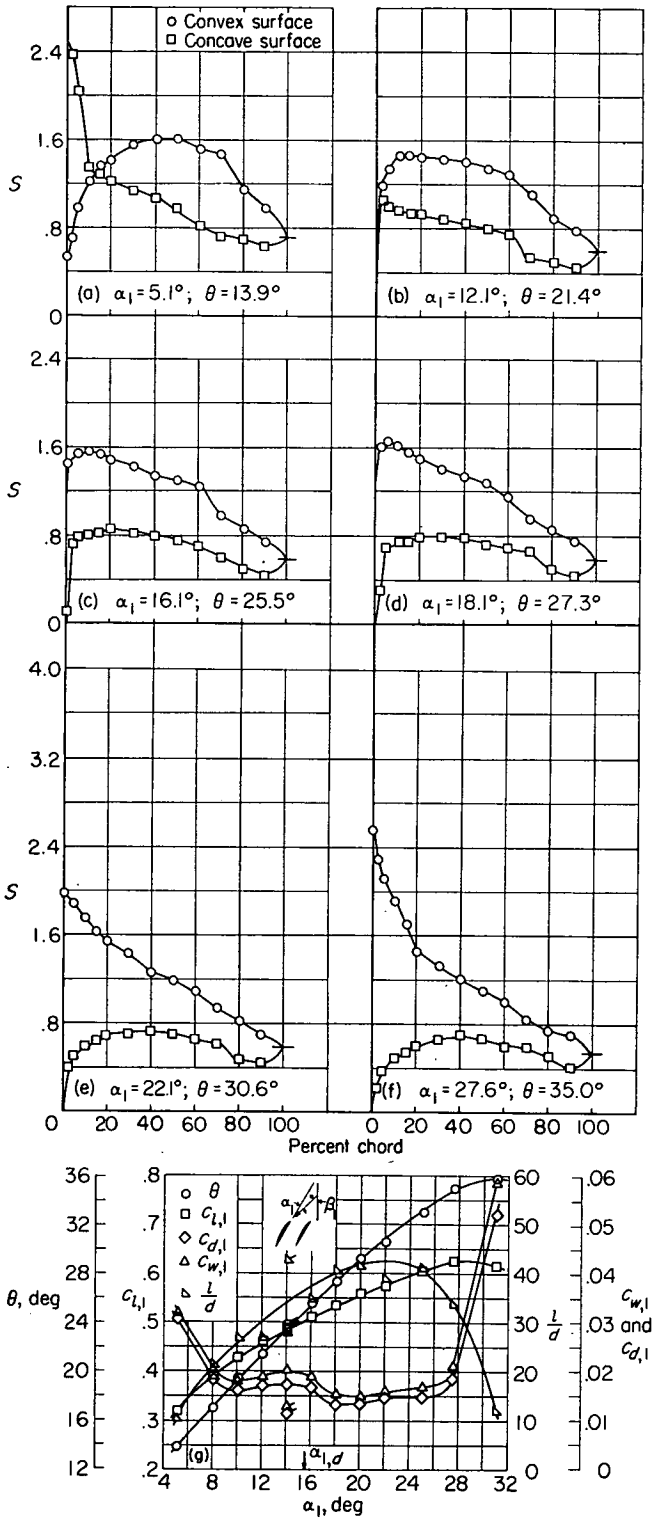
(g) Section characteristics; flagged symbol indicates leading-edge roughness.

FIGURE 40.—Blade-surface pressure distributions and blade section characteristics for the cascade combination, β_1=45°, σ=1.50, and blade section, NACA 65–410.



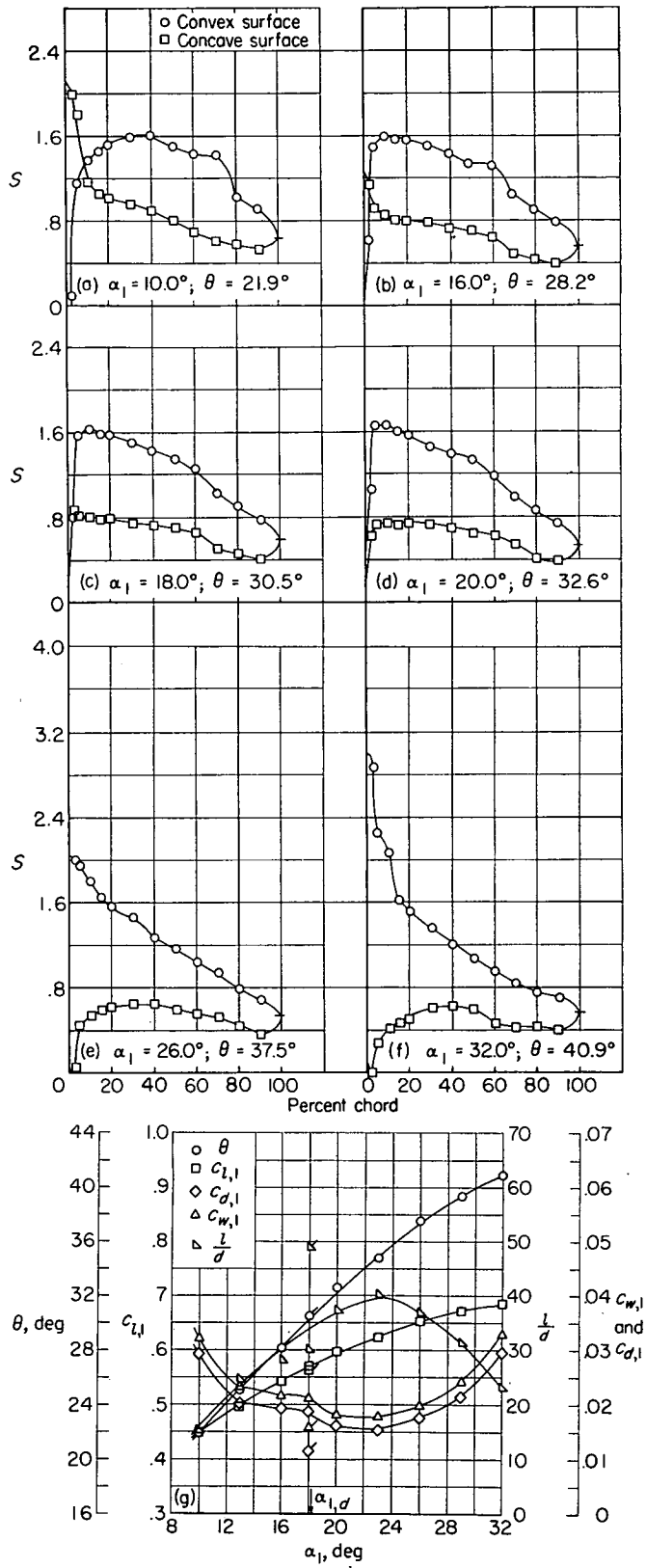
(g) Section characteristics; flagged symbol indicates leading-edge roughness.

FIGURE 41.—Blade-surface pressure distributions and blade section characteristics for the cascade combination, β_1=45°, σ=1.50, and blade section, NACA 65–810.



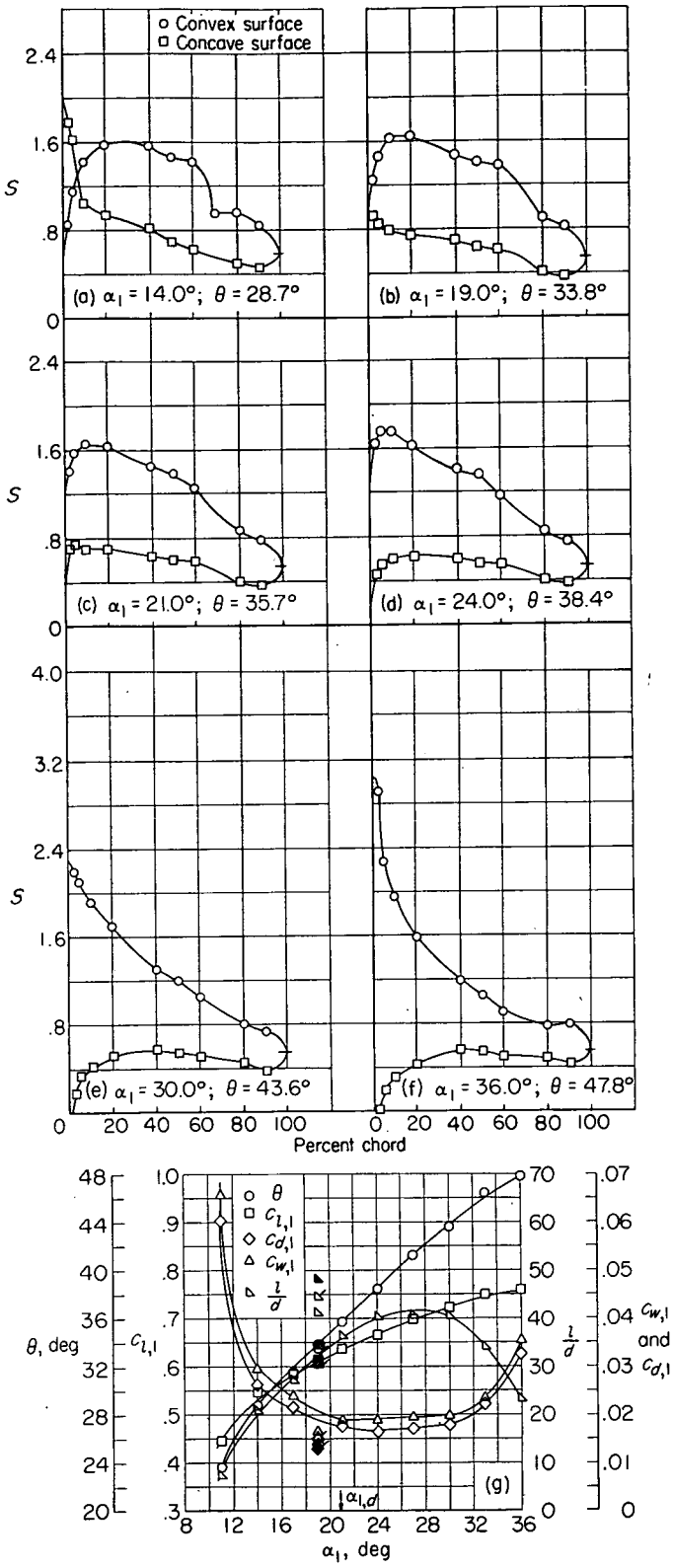
(g) Section characteristics; flagged symbol indicates leading-edge roughness.

FIGURE 42.—Blade-surface pressure distributions and blade section characteristics for the cascade combination, $\beta_1=45°$, $\sigma=1.50$, and blade section, NACA 65-(12)10.



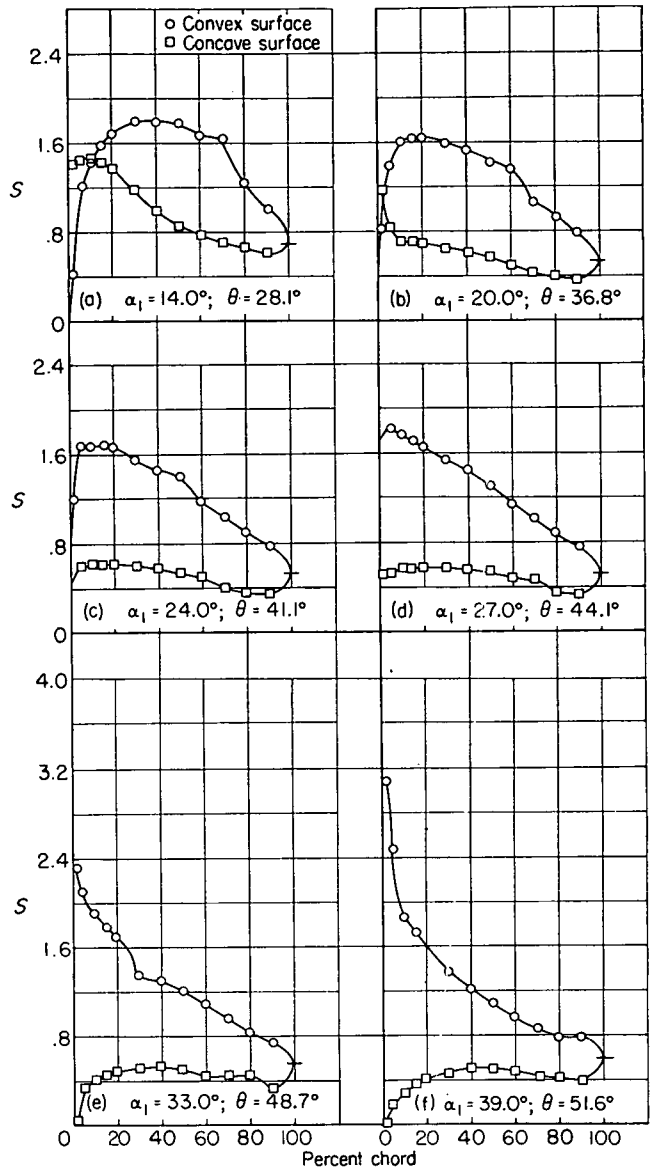
(g) Section characteristics; flagged symbol indicates leading-edge roughness.

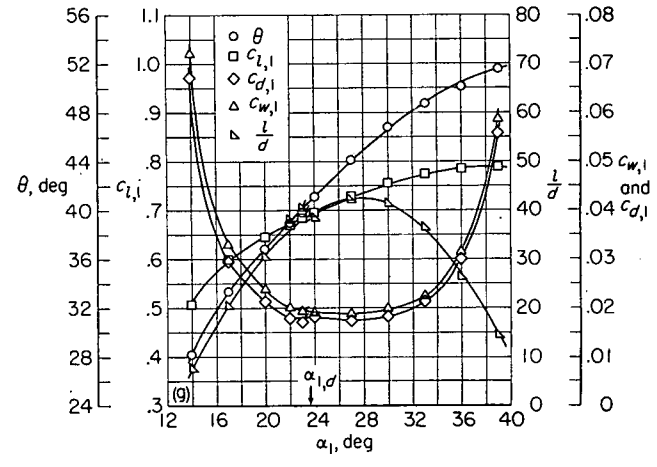
FIGURE 43.—Blade-surface pressure distributions and blade section characteristics for the cascade combination, $\beta_1=45°$, $\sigma=1.50$, and blade section, NACA 65-(15)10.



(g) Section characteristics; flagged symbol indicates leading-edge roughness; solid symbol indicates high Reynolds number.

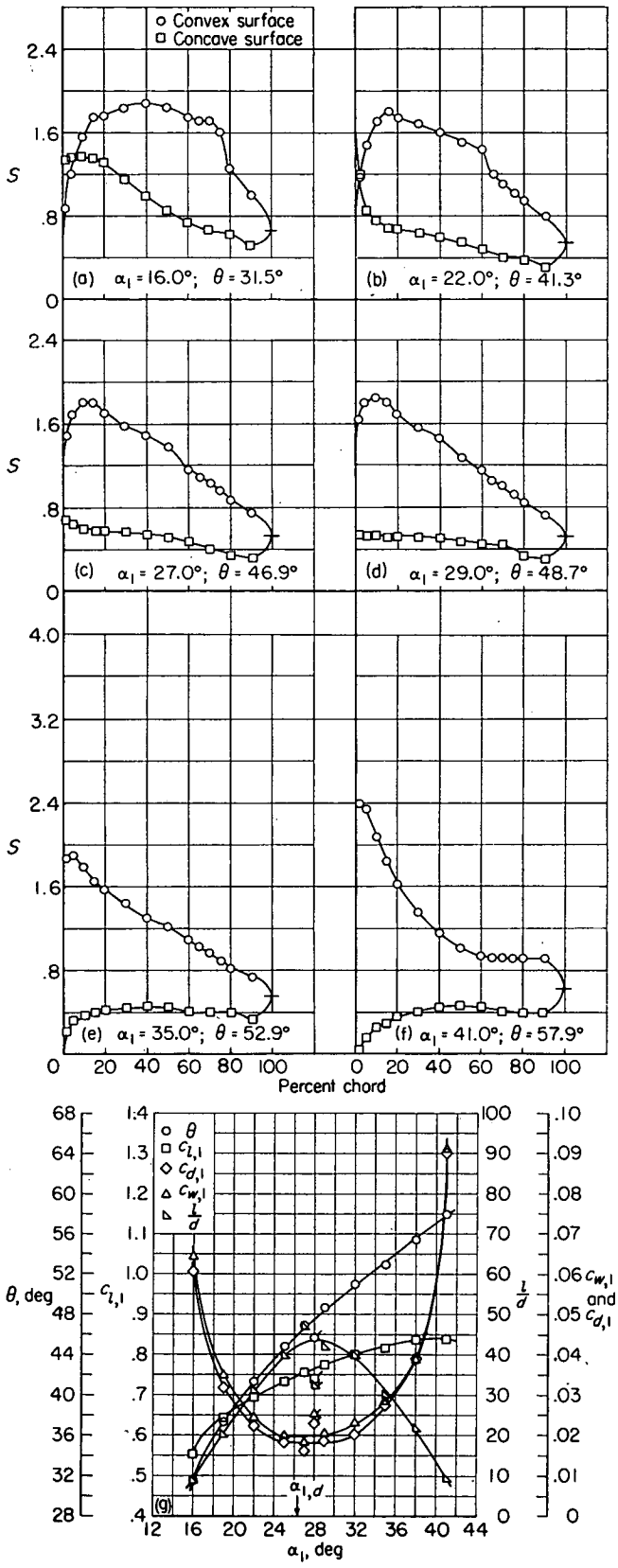
FIGURE 44.—Blade-surface pressure distributions and blade section characteristics for the cascade combination, β_1=45°, σ=1.50, and blade section, NACA 65–(18)10.





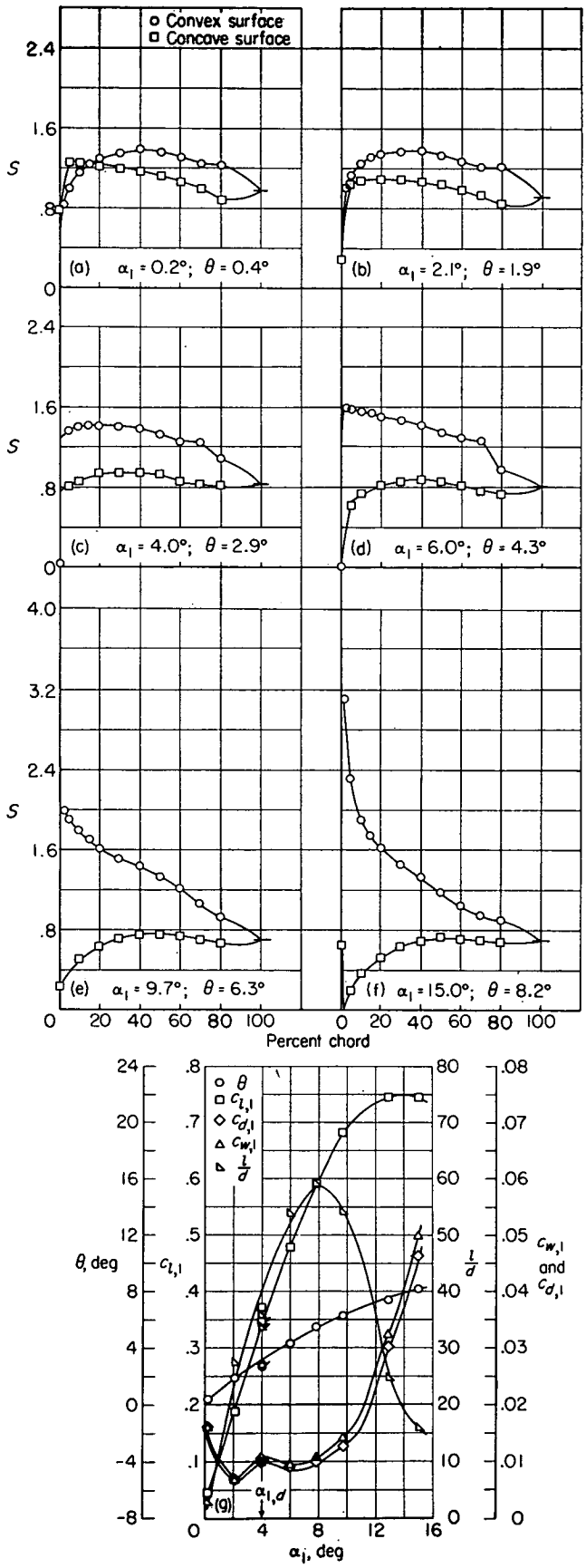
(g) Section characteristics; flagged symbol indicates leading-edge roughness.

FIGURE 45.—Blade-surface pressure distributions and blade section characteristics for the cascade combination, β_1=45°, σ=1.50, and blade section, NACA 65–(21)10.



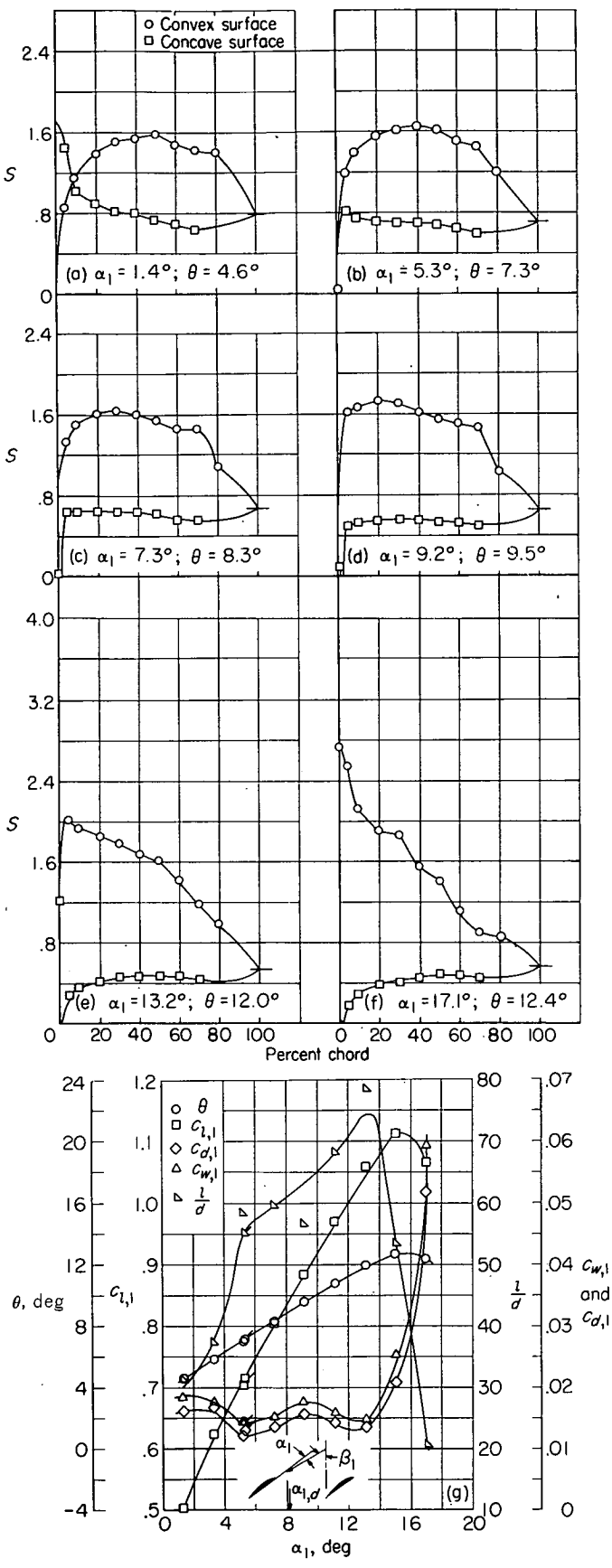
(g) Section characteristics; flagged symbol indicates leading-edge roughness.

FIGURE 46.—Blade-surface pressure distributions and blade section characteristics for the cascade combination, $\beta_1 = 45°$, $\sigma = 1.50$, and blade section, NACA 65-(24)10.



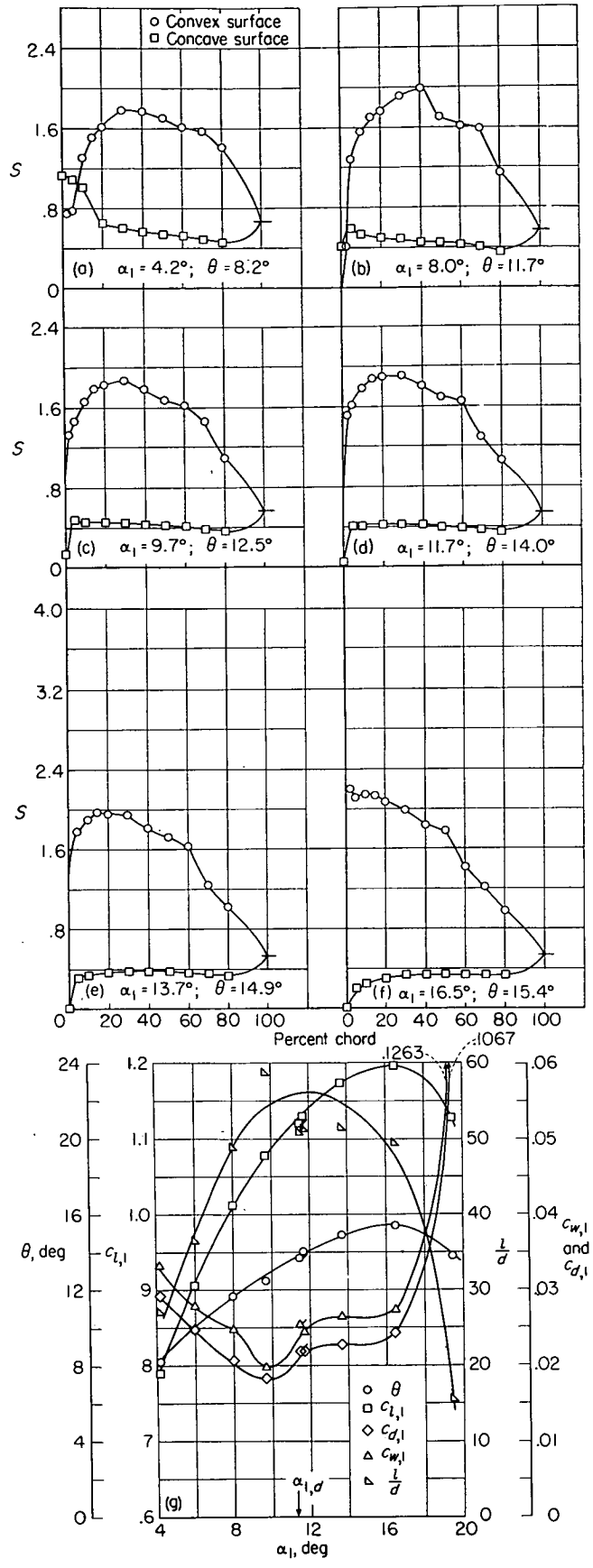
(g) Section characteristics; flagged symbol indicates leading-edge roughness.

FIGURE 47.—Blade-surface pressure distributions and blade section characteristics for the cascade combination, $\beta_1 = 60°$, $\sigma = 0.50$, and blade section, NACA 65-410.



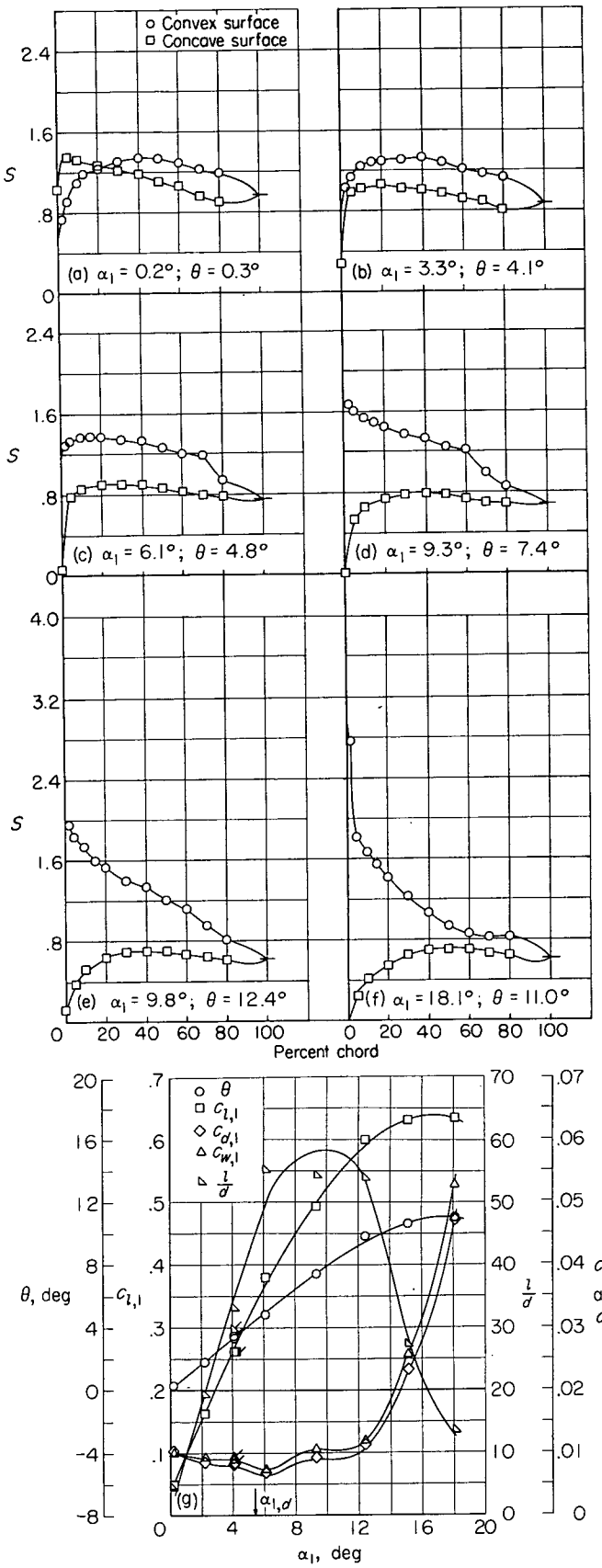
(g) Section characteristics; flagged symbol indicates leading-edge roughness.

FIGURE 48.—Blade-surface pressure distributions and blade section characteristics for the cascade combination, $\beta_1 = 60°$, $\sigma = 0.50$, and blade section, NACA 65-(12)10.



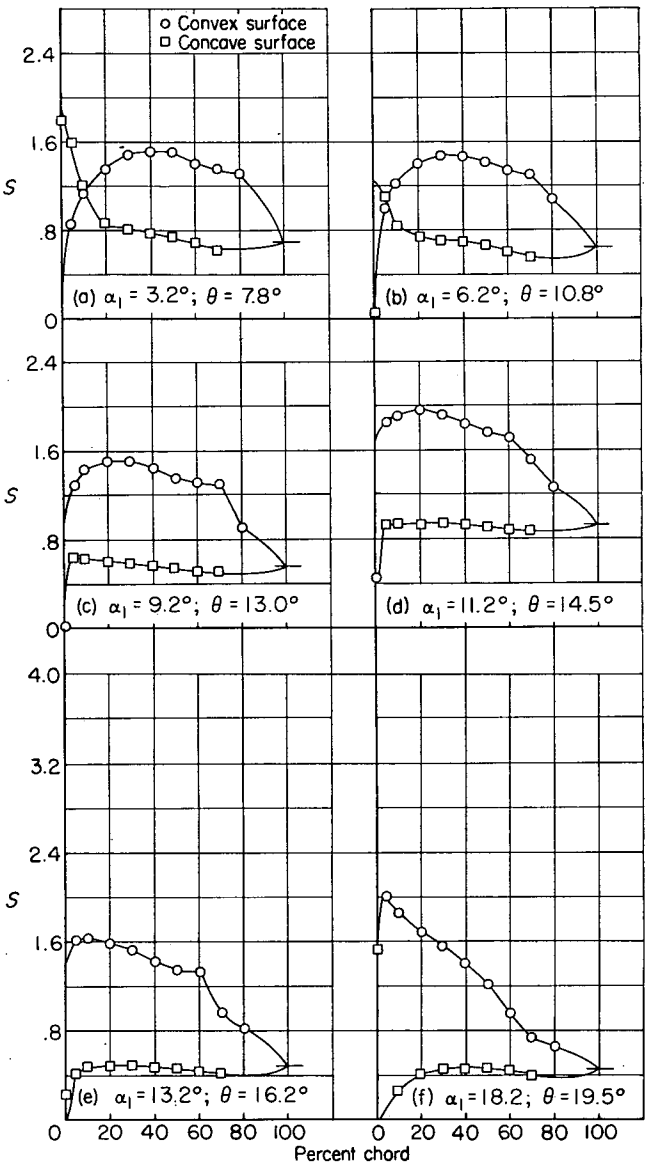
(g) Section characteristics; flagged symbol indicates leading-edge roughness.

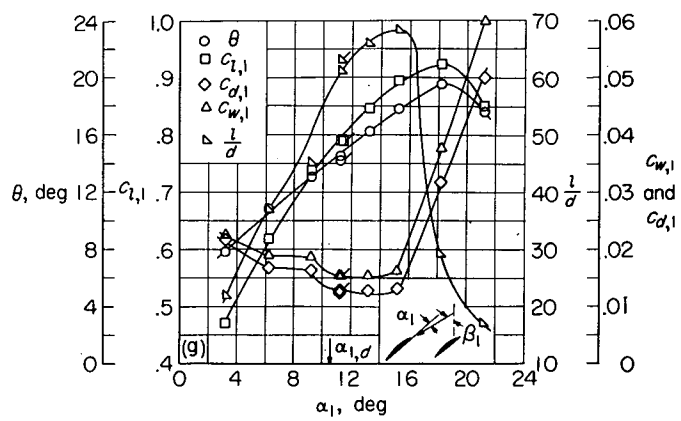
FIGURE 49.—Blade-surface pressure distributions and blade section characteristics for the cascade combination, $\beta_1 = 60°$, $\sigma = 0.50$, and blade section, NACA 65-(18)10.



(g) Section characteristics; flagged symbol indicates leading-edge roughness.

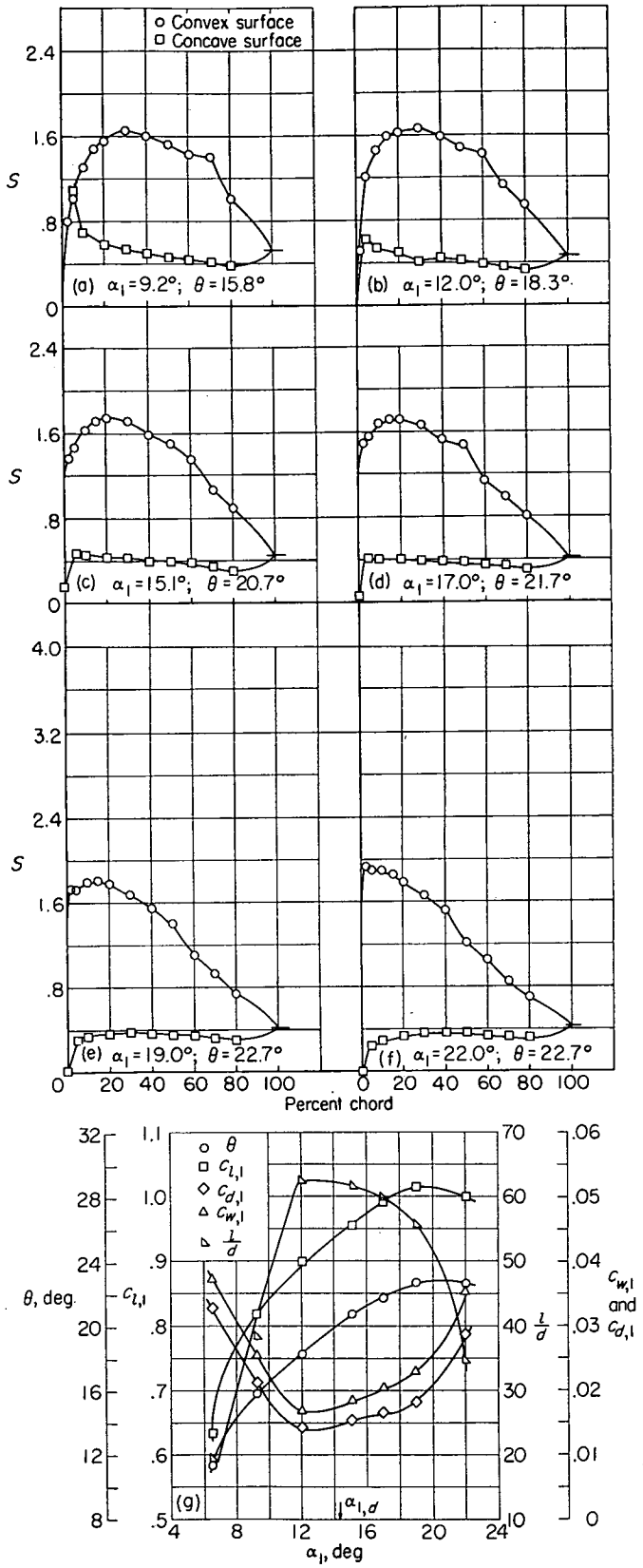
FIGURE 50.—Blade-surface pressure distributions and blade section characteristics for the cascade combination, $\beta_1 = 60°$, $\sigma = 0.75$, and blade section, NACA 65-410.





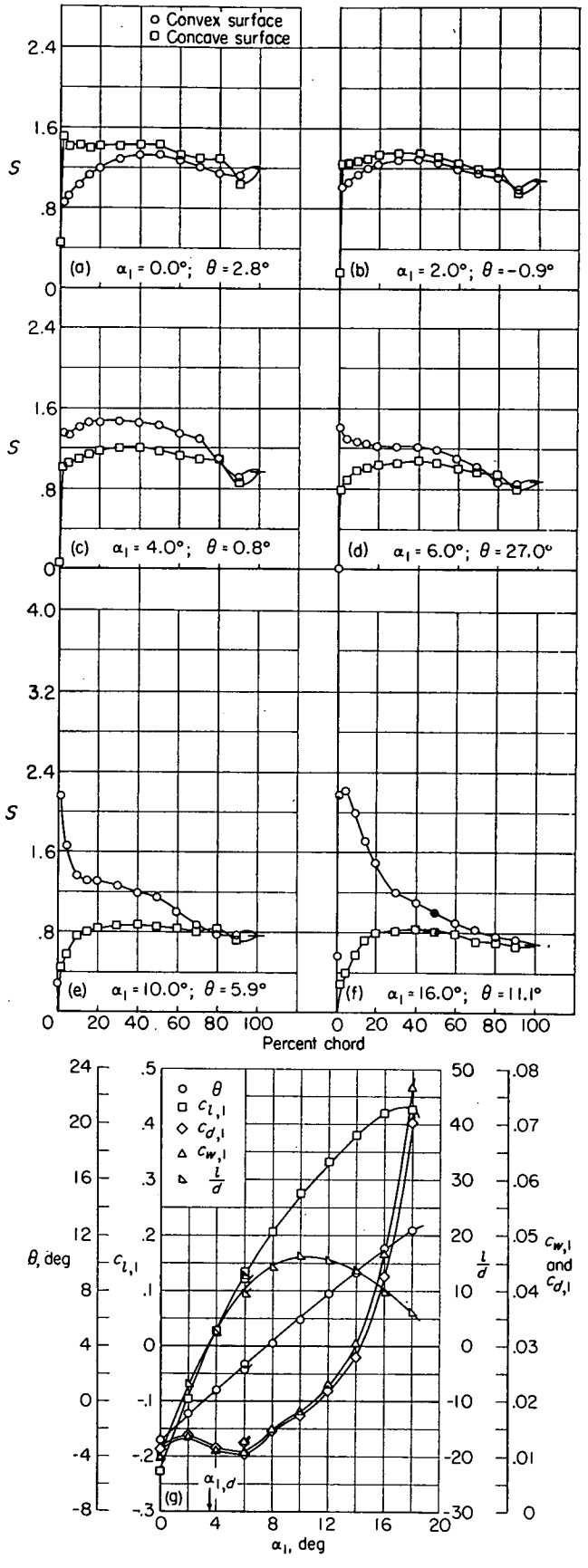
(g) Section characteristics; flagged symbol indicates leading-edge roughness.

FIGURE 51.—Blade-surface pressure distributions and blade section characteristics for the cascade combination, $\beta_1 = 60°$, $\sigma = 0.75$, and blade section, NACA 65-(12)10.



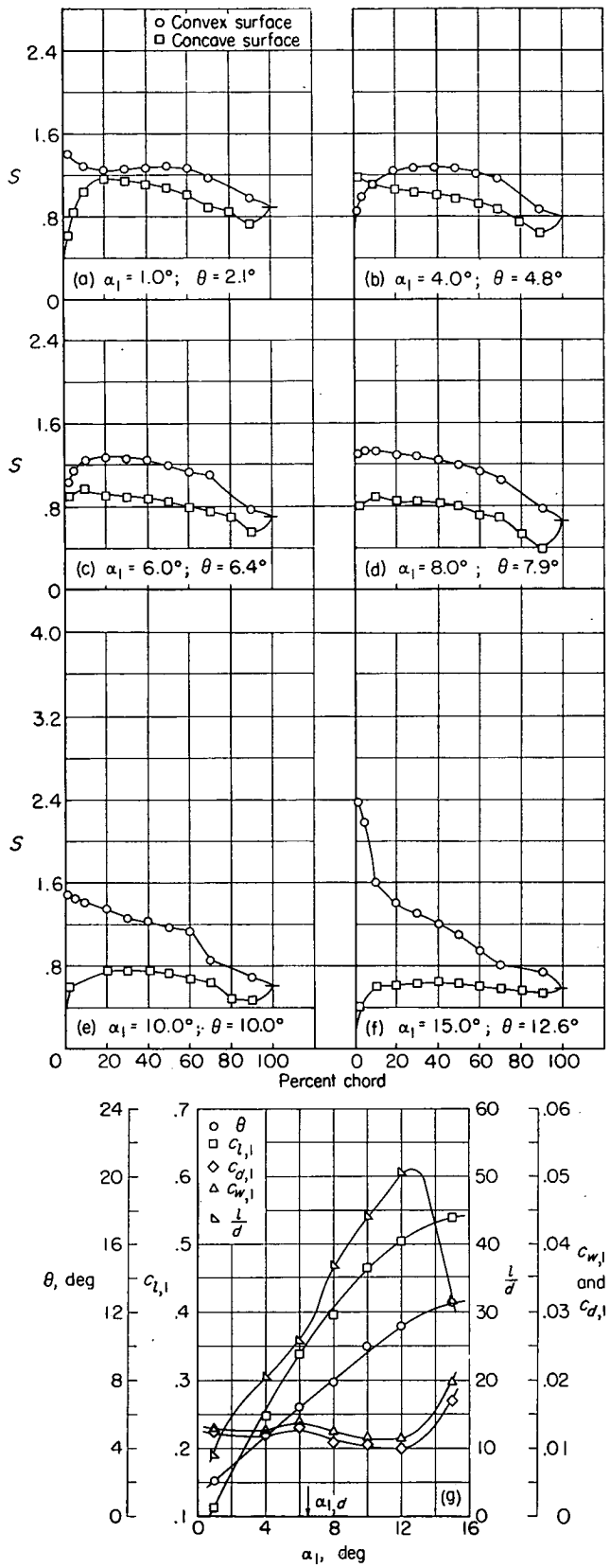
(g) Section characteristics.

FIGURE 52.—Blade-surface pressure distributions and blade section characteristics for the cascade combination, $\beta_1 = 60°$, $\sigma = 0.75$, and blade section, NACA 65–(18)10.



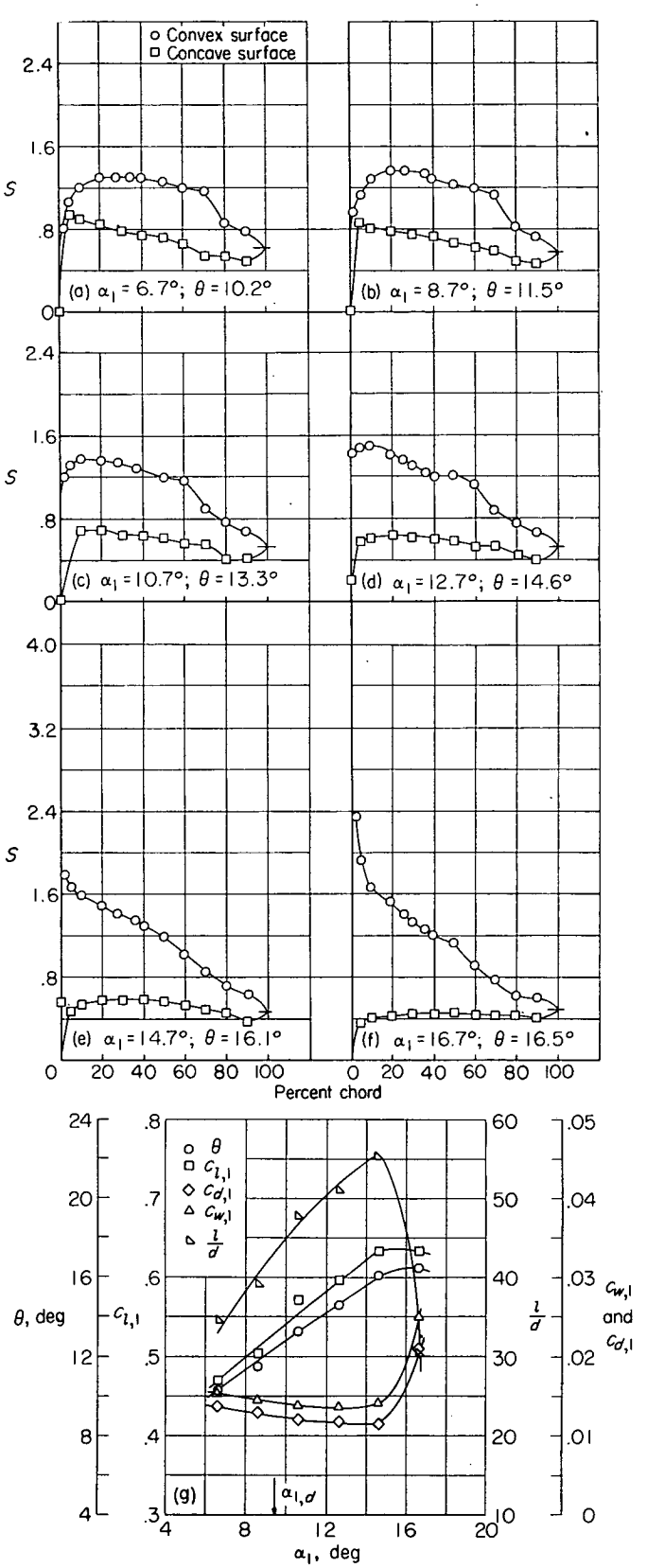
(g) Section characteristics; flagged symbol indicates leading-edge roughness.

FIGURE 53.—Blade-surface pressure distributions and blade section characteristics for the cascade combination, $\beta_1 = 60°$, $\sigma = 1.00$, and blade section, NACA 65–010.



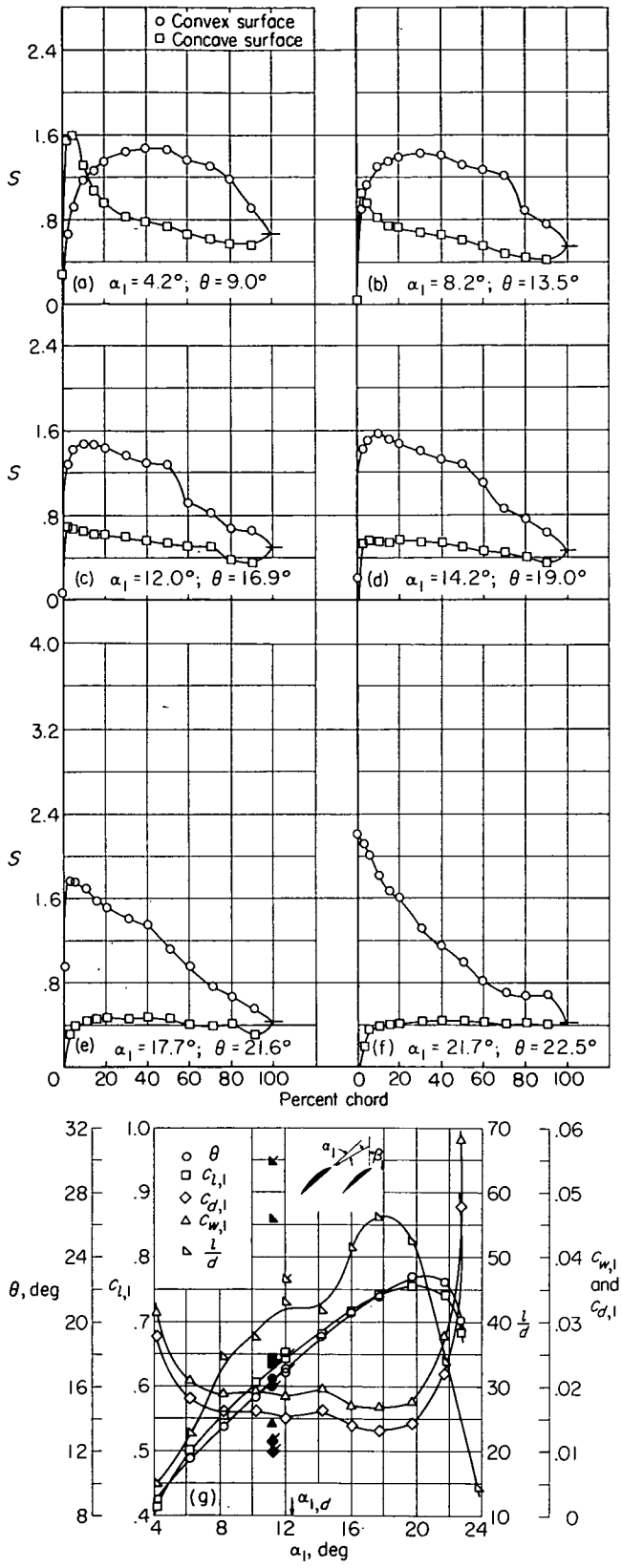
(g) Section characteristics.

FIGURE 54.—Blade-surface pressure distributions and blade section characteristics for the cascade combination, $\beta_1 = 60°$, $\sigma = 1.00$, and blade section, NACA 65–410.



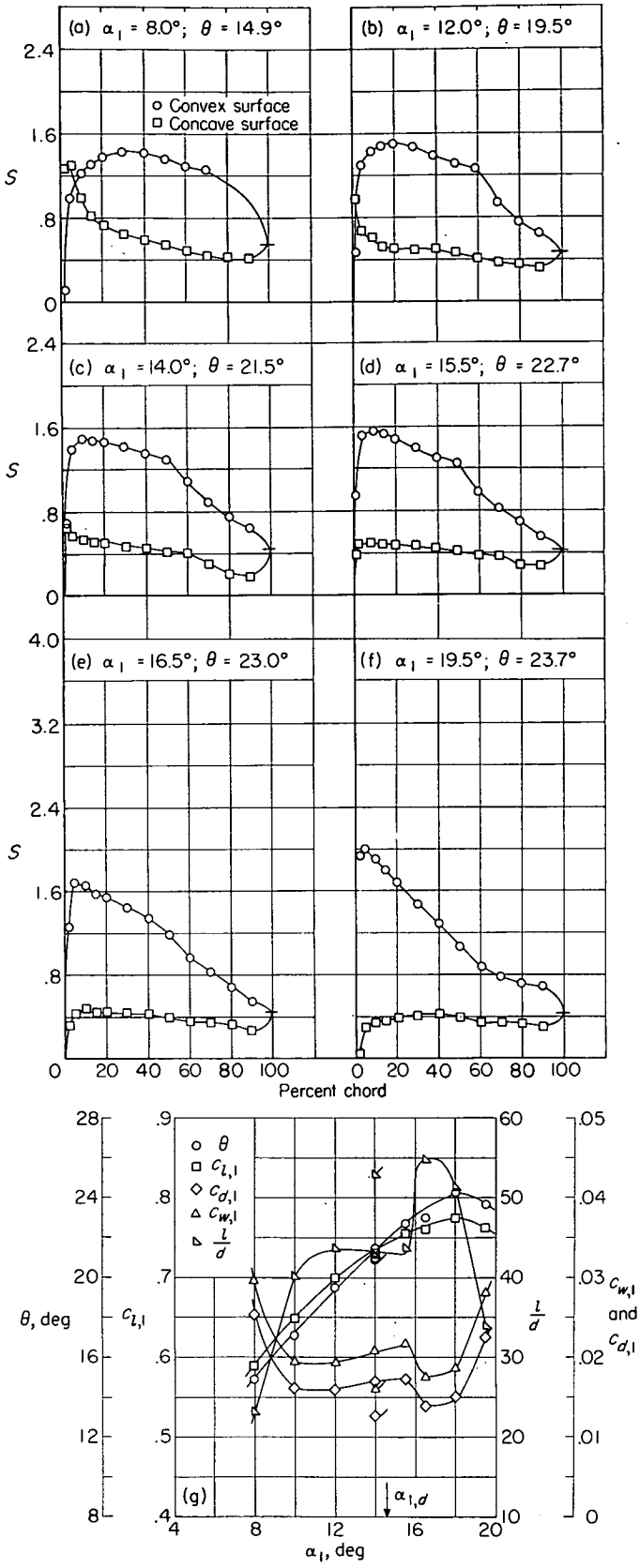
(g) Section characteristics.

FIGURE 55.—Blade-surface pressure distributions and blade section characteristics for the cascade combination, $\beta_1 = 60°$, $\sigma = 1.00$, and blade section, NACA 65–810.



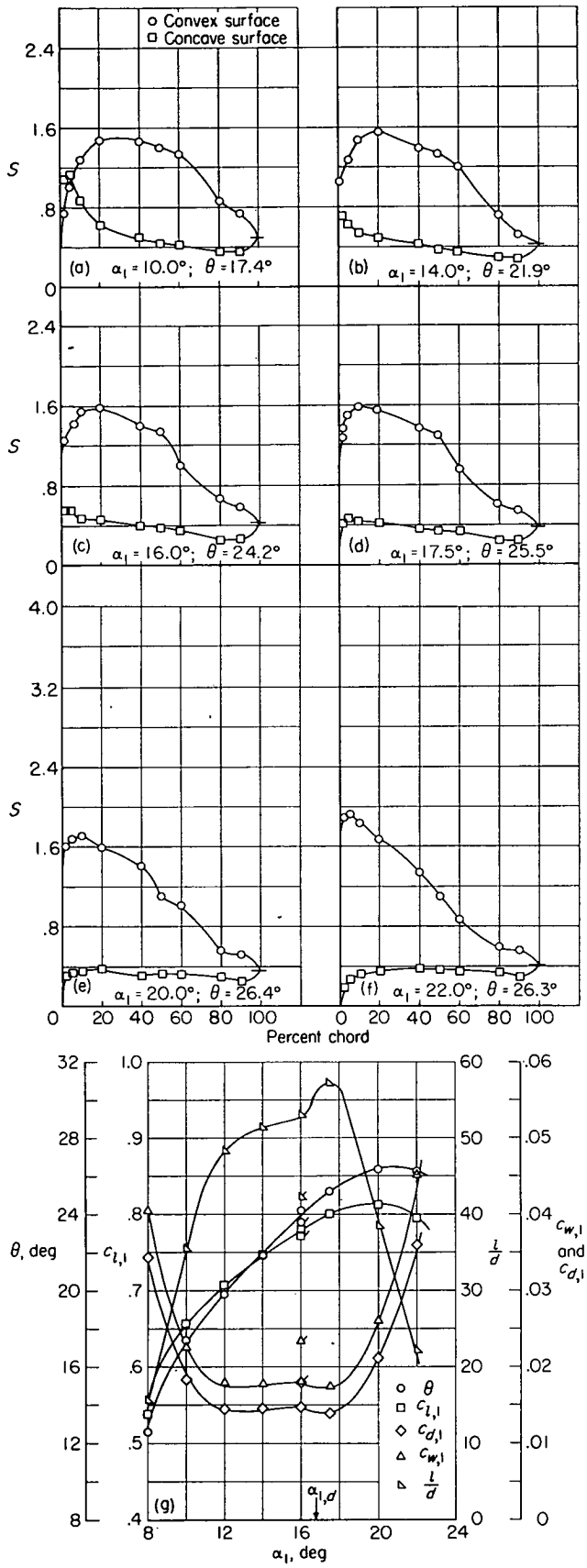
(g) Section characteristics; flagged symbol indicates leading-edge roughness; solid symbol indicates high Reynolds number.

FIGURE 56.—Blade-surface pressure distributions and blade section characteristics for the cascade combination, β_1=60°, σ=1.00, and blade section, NACA 65–(12)10.



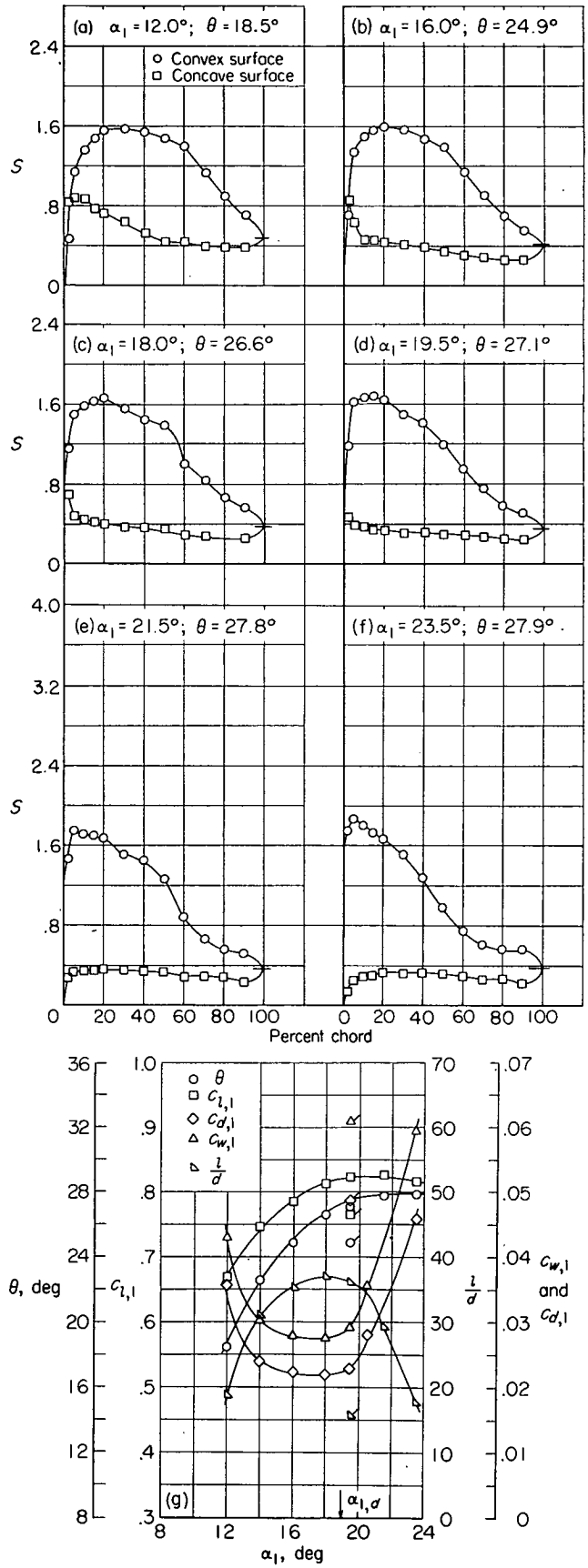
(g) Section characteristics; flagged symbol indicates leading-edge roughness.

FIGURE 57.—Blade-surface pressure distributions and blade section characteristics for the cascade combination, β_1=60°, σ=1.00, and blade section, NACA 65–(15)10.



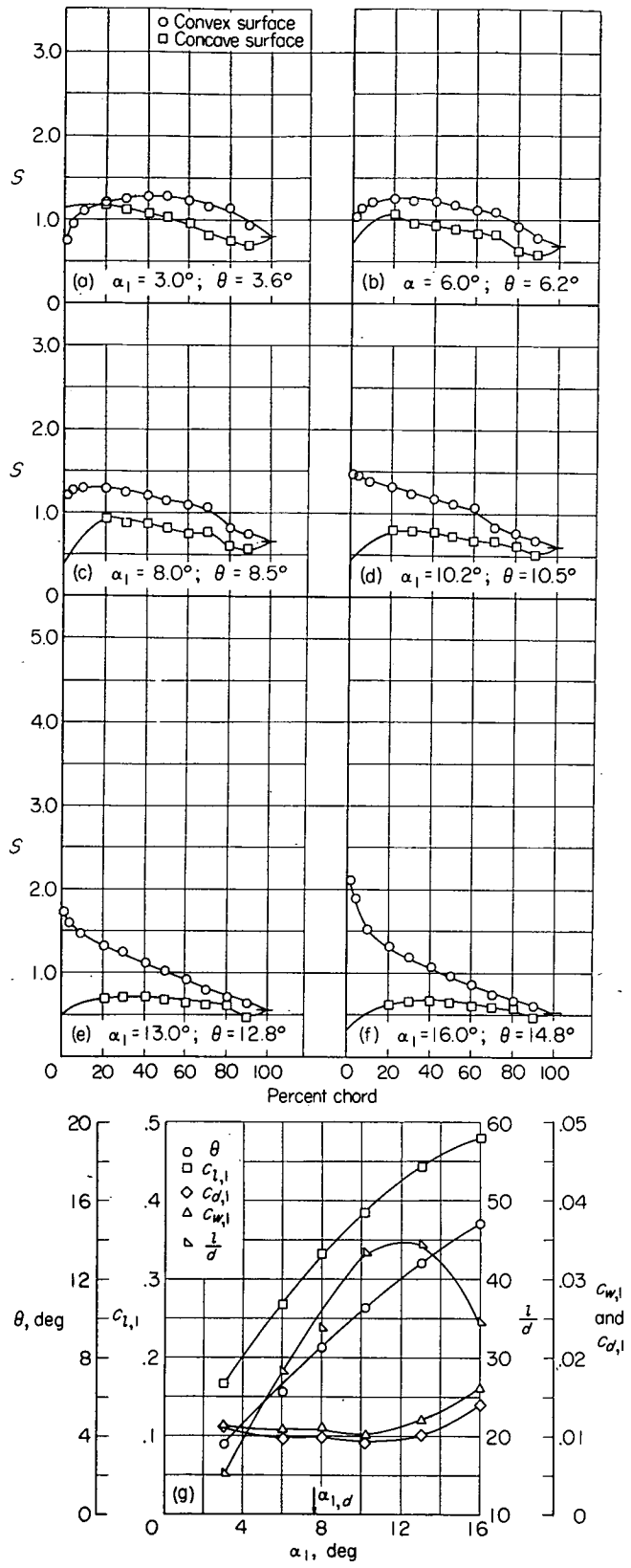
(g) Section characteristics; flagged symbol indicates leading-edge roughness.

FIGURE 58.—Blade-surface pressure distributions and blade section characteristics for the cascade combination, $\beta_1 = 60°$, $\sigma = 1.00$. and blade section, NACA 65-(18)10.



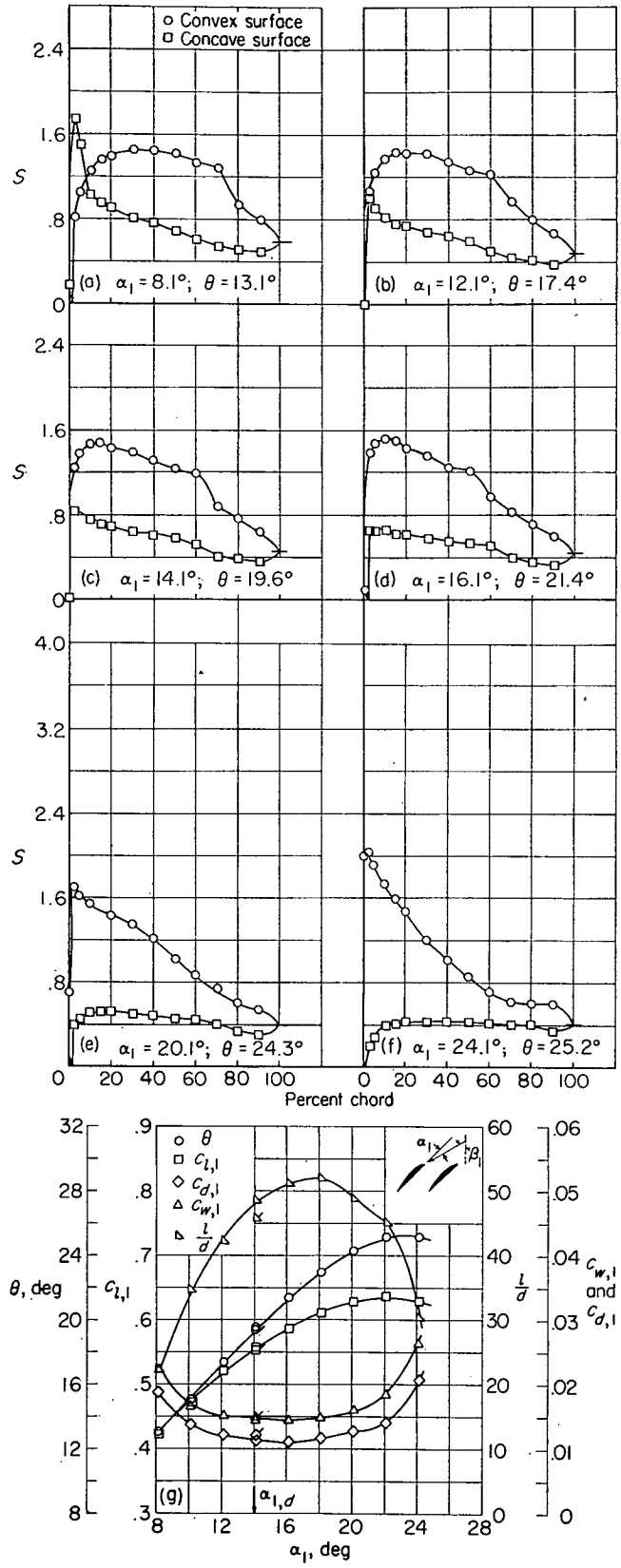
(g) Section characteristics; flagged symbol indicates leading-edge roughness.

FIGURE 59.—Blade-surface pressure distributions and blade section characteristics for the cascade combination, $\beta_1 = 60°$, $\sigma = 1.00$, and blade section, NACA 65-(21)10



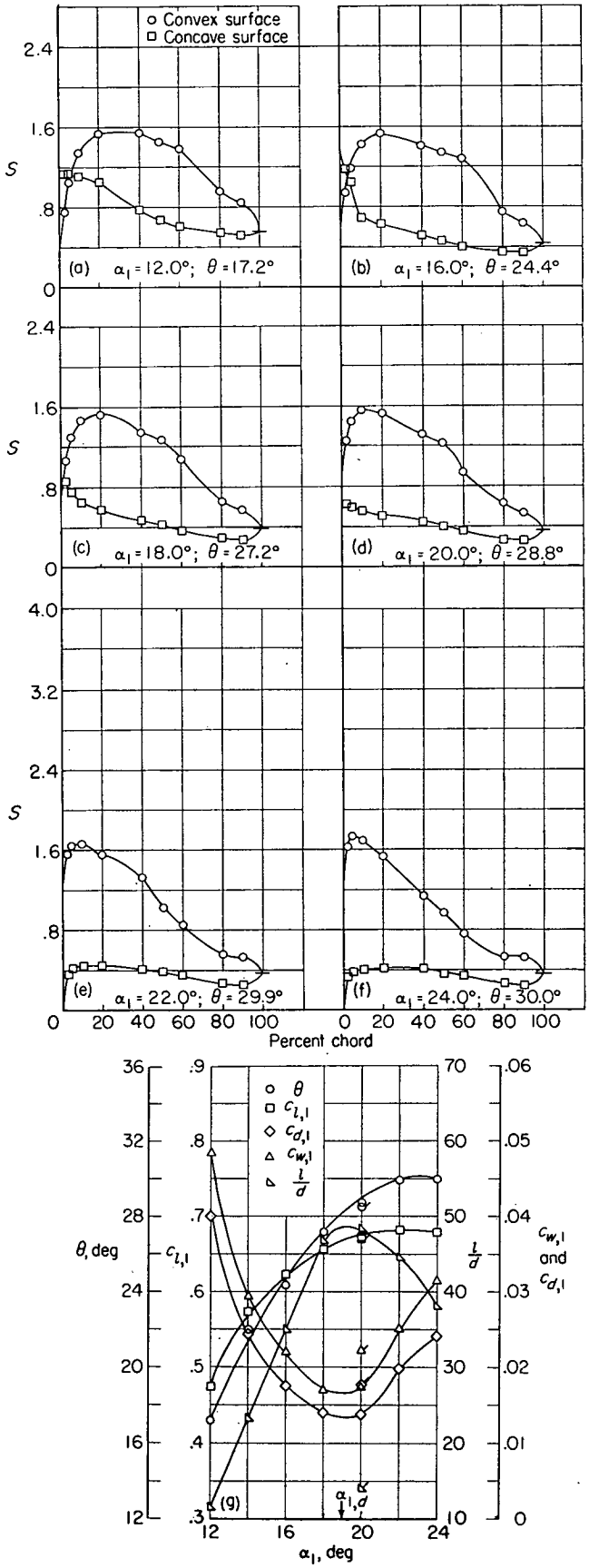
(g) Section characteristics; flagged symbol indicates leading-edge roughness.

FIGURE 60.—Blade-surface pressure distributions and blade section characteristics for the cascade combination, $\beta_1=60°$, $\sigma=1.25$, and blade section, NACA 65–410.



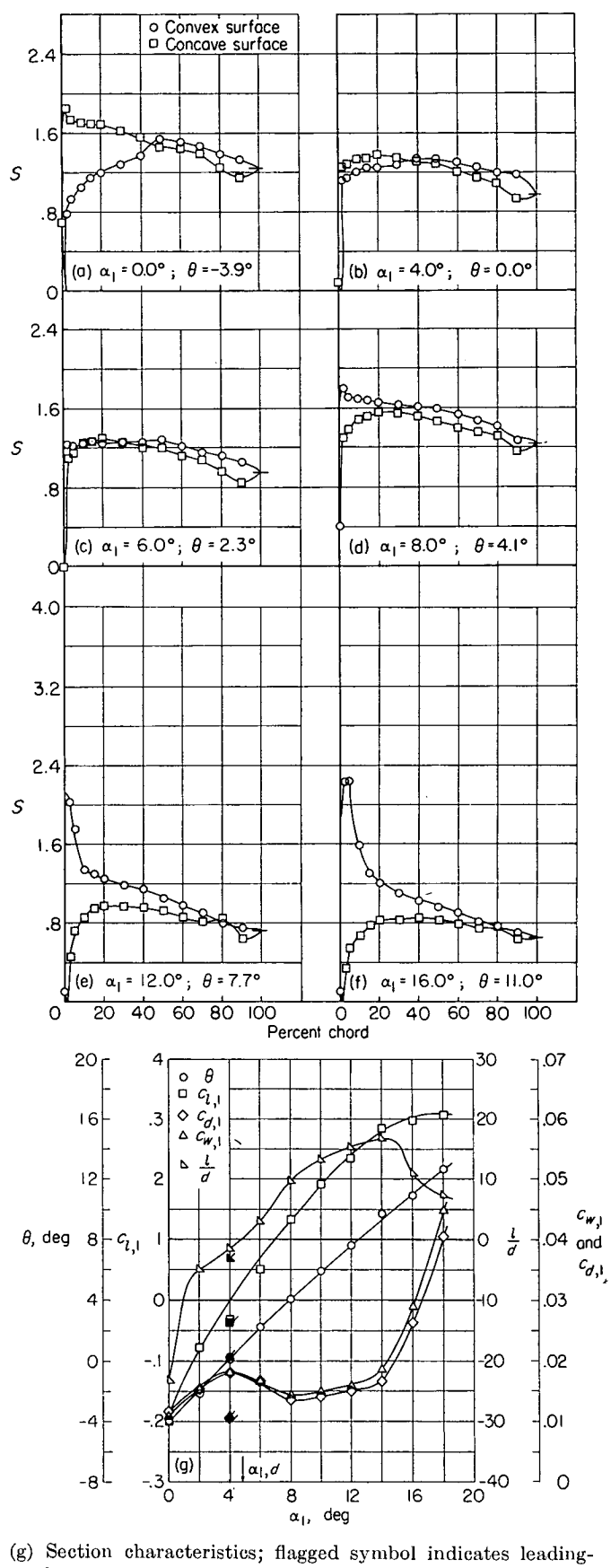
(g) Section characteristics; flagged symbol indicates leading-edge roughness.

FIGURE 61.—Blade-surface pressure distributions and blade section characteristics for the cascade combination, $\beta_1=60°$, $\sigma=1.25$, and blade section, NACA 65–(12)10.



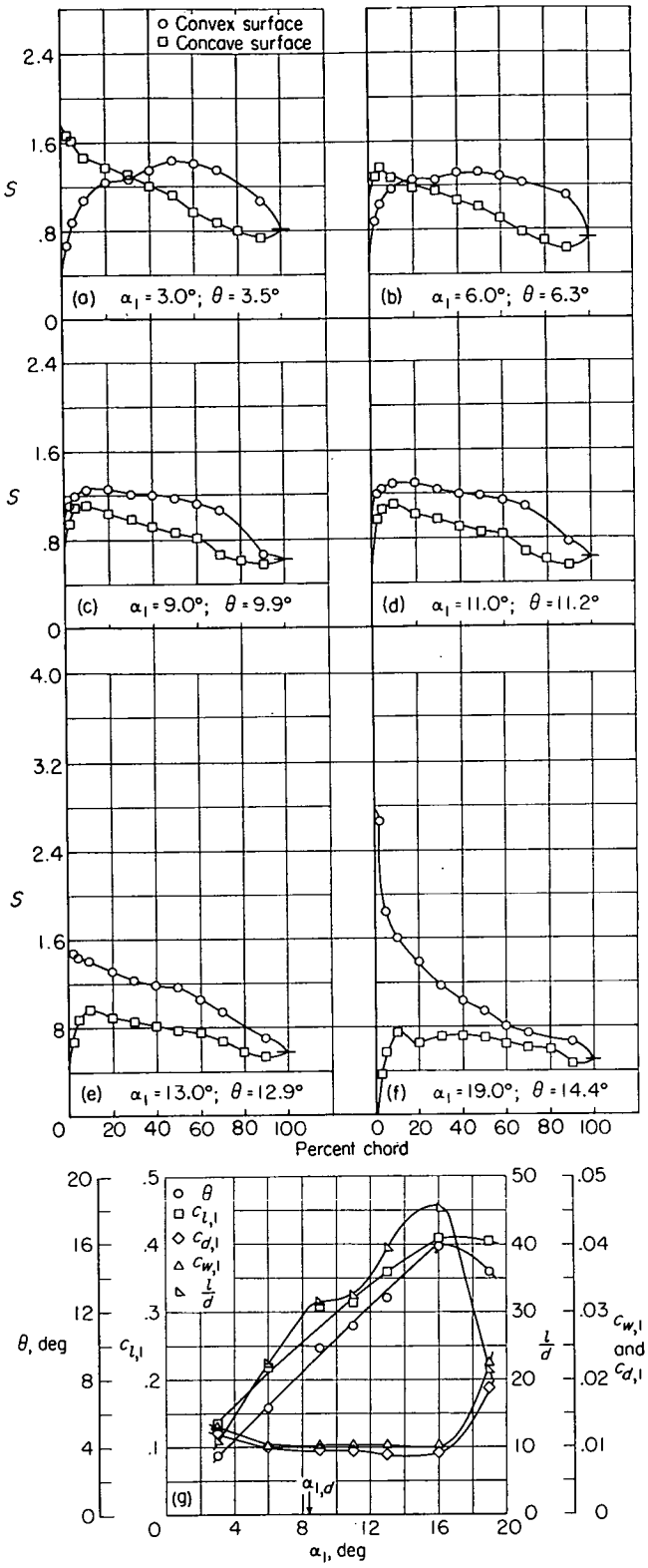
(g) Section characteristics; flagged symbol indicates leading-edge roughness.

FIGURE 62.—Blade-surface pressure distributions and blade section characteristics for the cascade combination, $\beta_1 = 60°$, $\sigma = 1.25$, and blade section, NACA 65-(18)10.



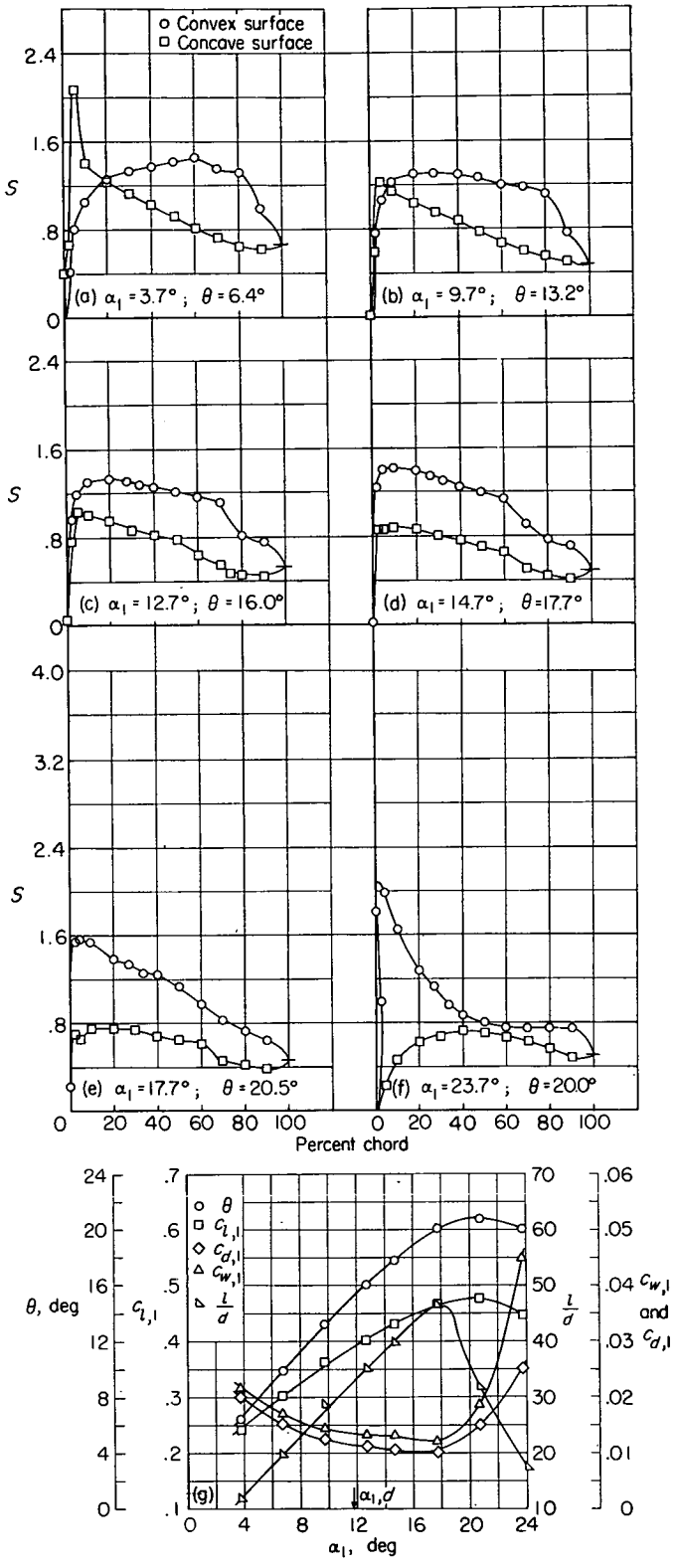
(g) Section characteristics; flagged symbol indicates leading-edge roughness; solid symbol indicates high Reynolds number.

FIGURE 63.—Blade-surface pressure distributions and blade section characteristics for the cascade combination, $\beta_1 = 60°$, $\sigma = 1.50$, and blade section, NACA 65-010.



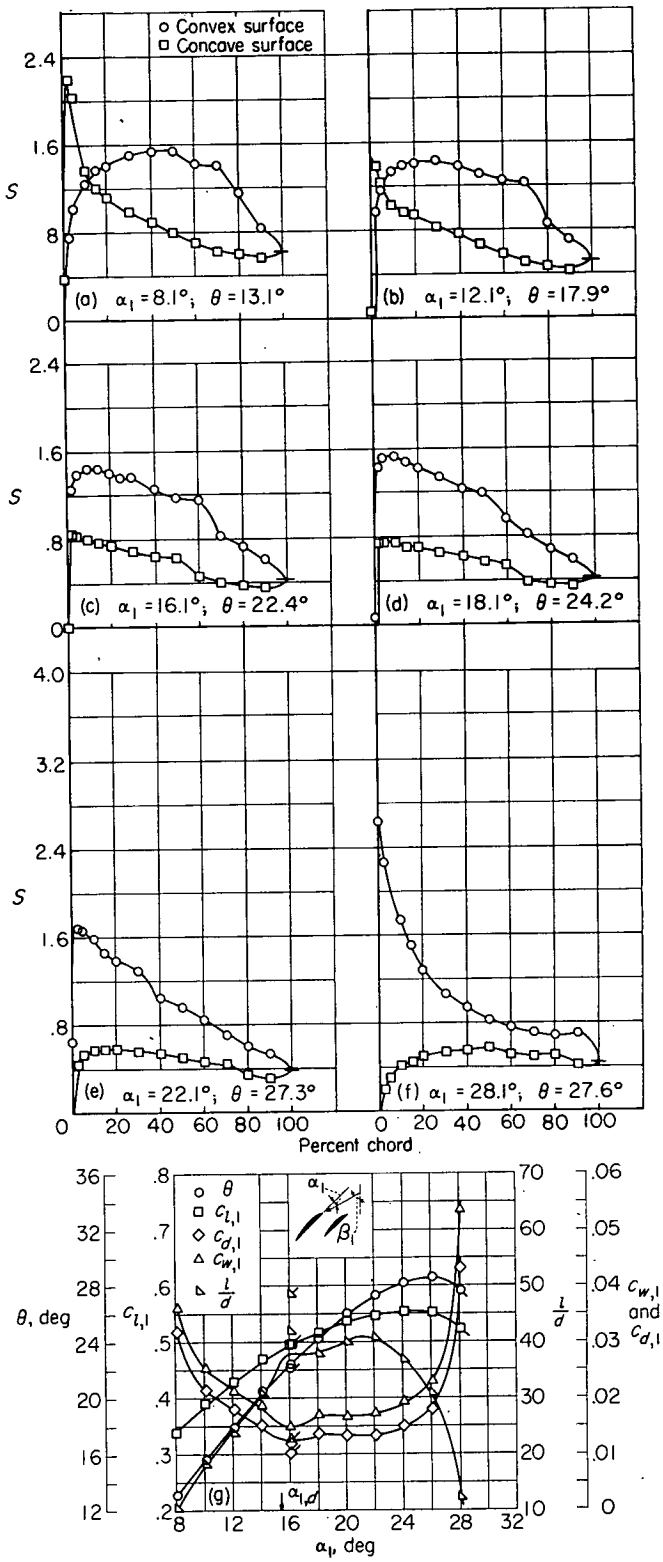
(g) Section characteristics.

FIGURE 64.—Blade-surface pressure distributions and blade section characteristics for the cascade combination, $\beta_1 = 60°$, $\sigma = 1.50$, and blade section, NACA 65-410.



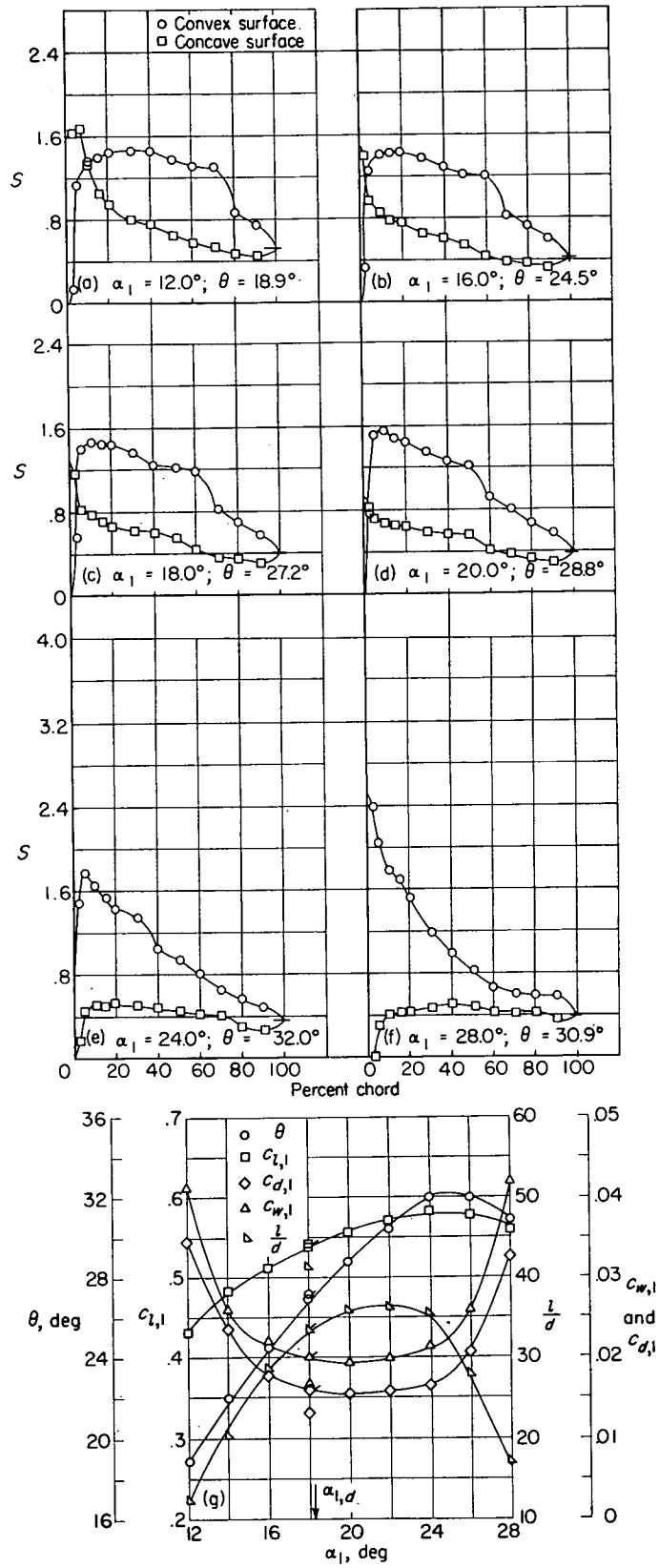
(g) Section characteristics.

FIGURE 65.—Blade-surface pressure distributions and blade section characteristics for the cascade combination, $\beta_1 = 60°$, $\sigma = 1.50$, and blade section, NACA 65-810.



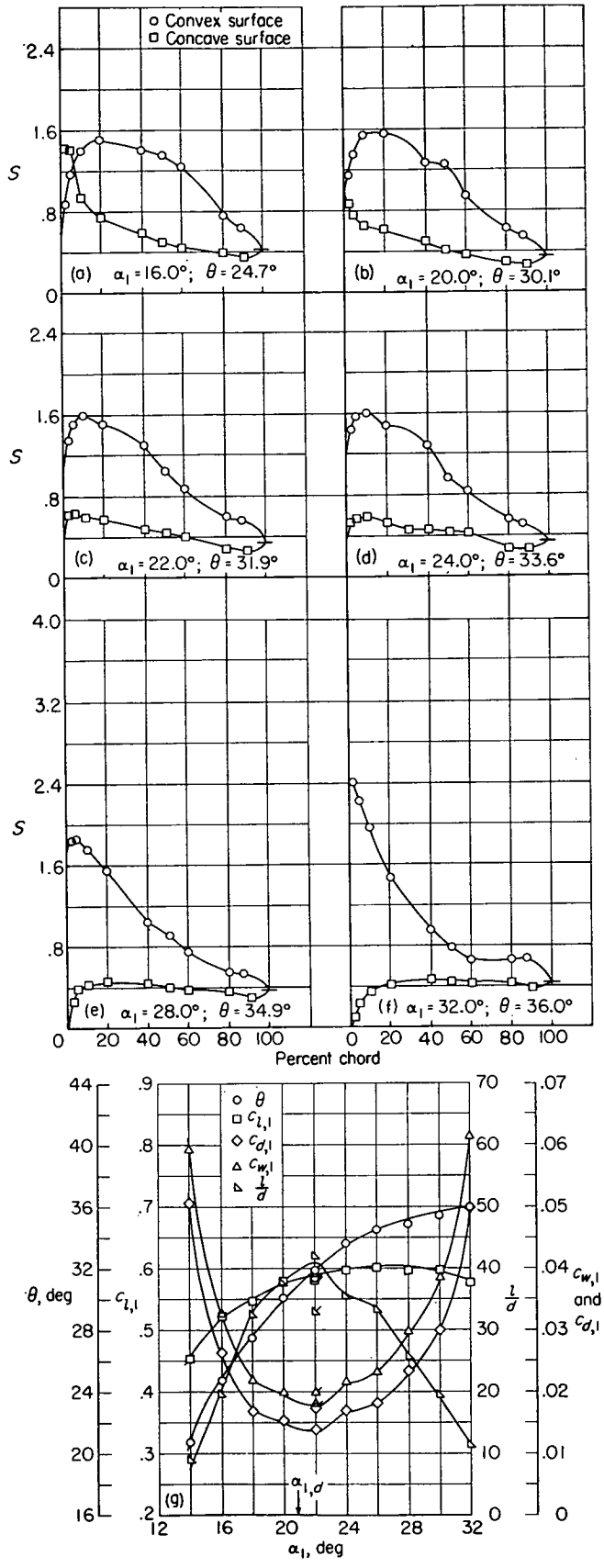
(g) Section characteristics; flagged symbol indicates leading-edge roughness.

FIGURE 66.—Blade-surface pressure distributions and blade section characteristics for the cascade combination, β_1=60°, σ=1.50, and blade section, NACA 65-(12)10.



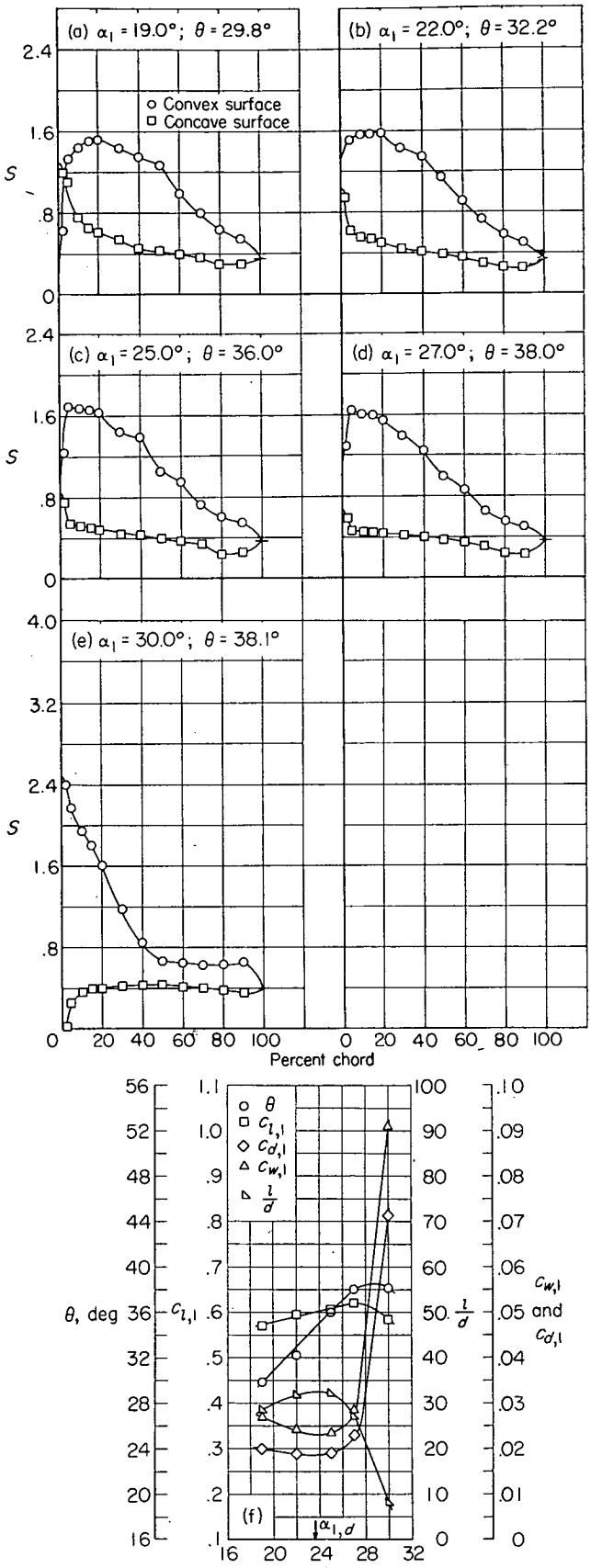
(g) Section characteristics; flagged symbol indicates leading-edge roughness.

FIGURE 67.—Blade-surface pressure distributions and blade section characteristics for the cascade combination, β_1=60°, σ=1.50, and blade section, NACA 65-(15)10.



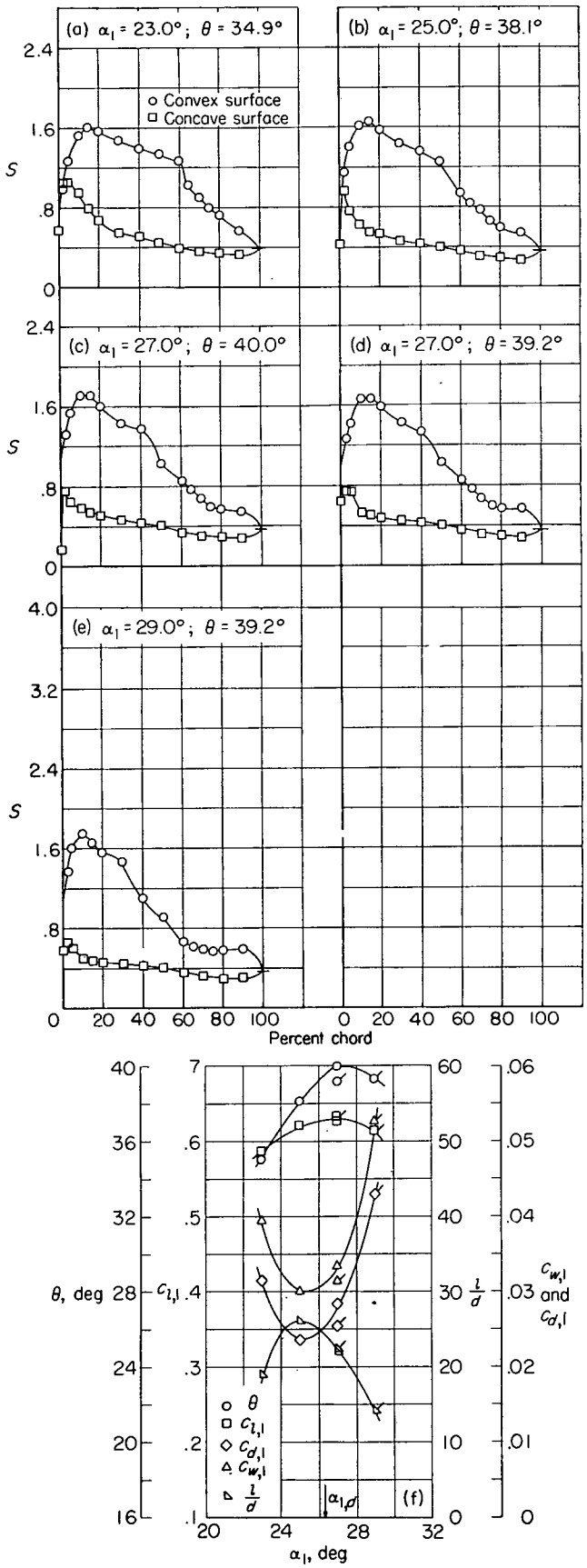
(g) Section characteristics; flagged symbol indicates leading-edge roughness.

FIGURE 68.—Blade-surface pressure distributions and blade section characteristics for the cascade combination, β_1=60°, σ=1.50, and blade section, NACA 65–(18)10.



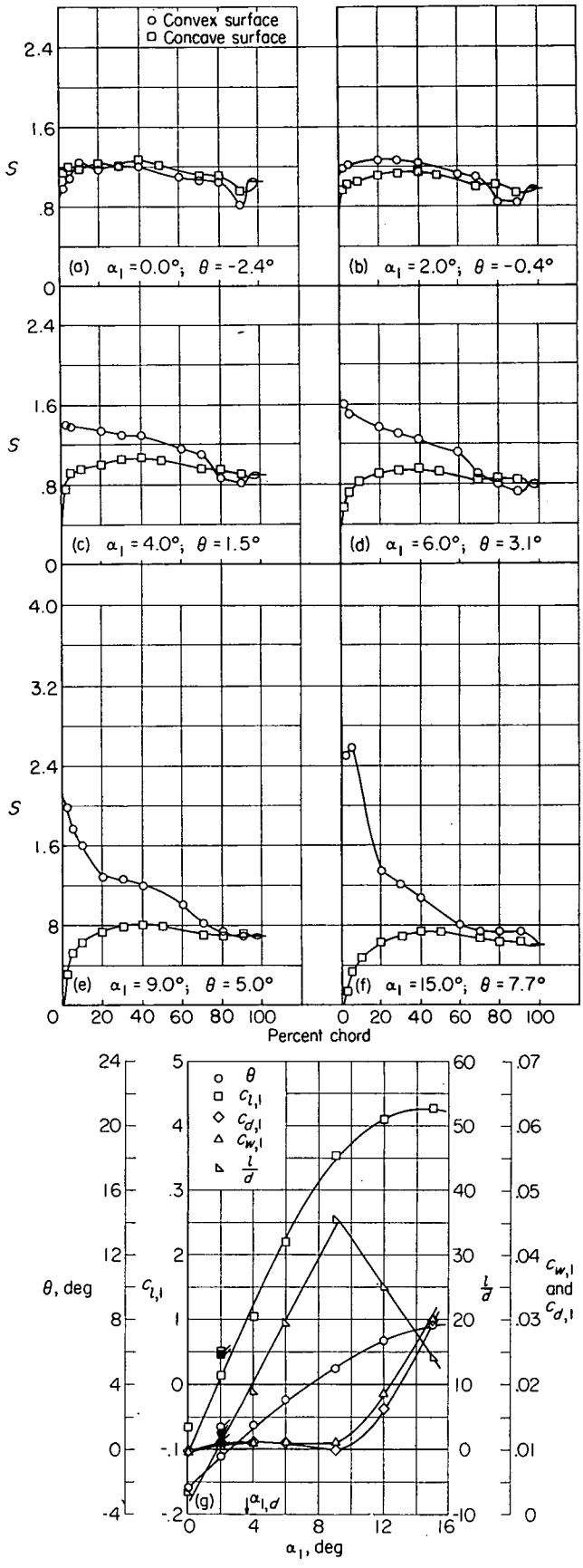
(f) Section characteristics.

FIGURE 69.—Blade-surface pressure distributions and blade section characteristics for the cascade combination, β_1=60°, σ=1.50, and blade section, NACA 65–(21)10.



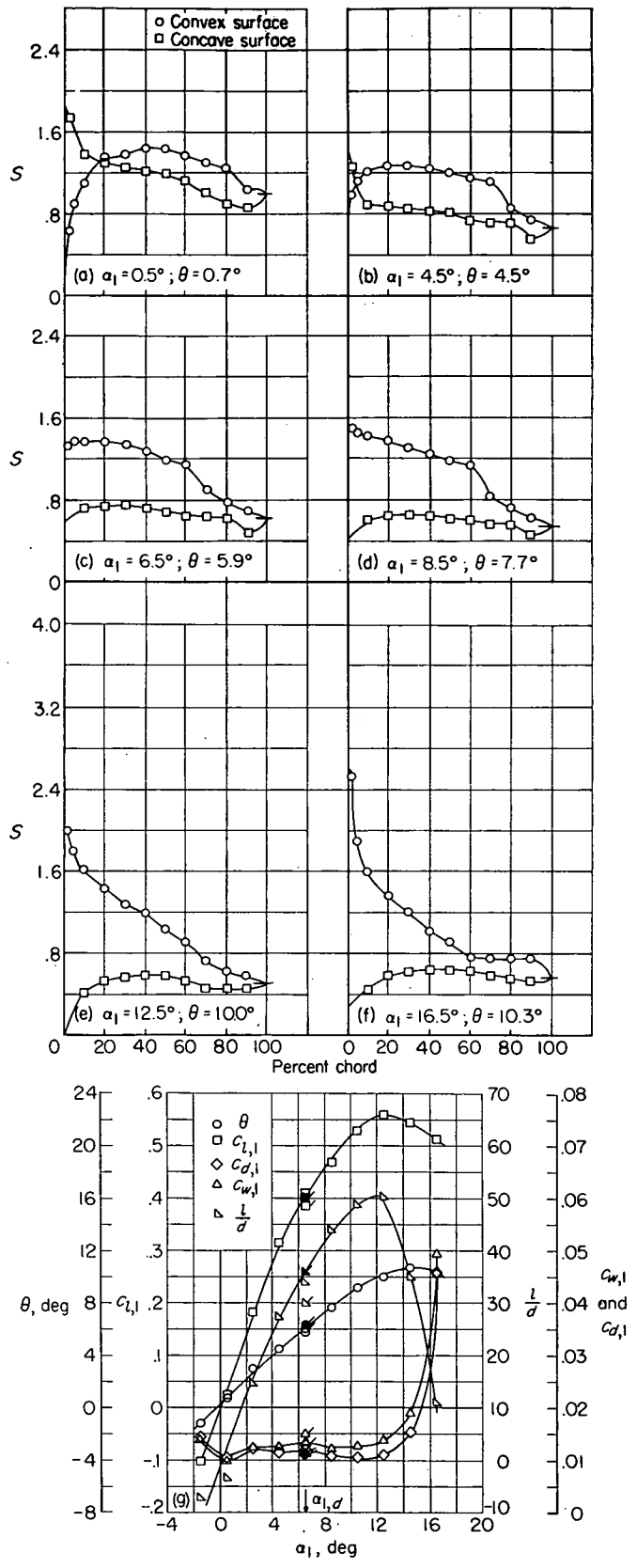
(f) Section characteristics; flagged symbol indicates leading-edge roughness.

FIGURE 70.—Blade-surface pressure distributions and blade section characteristics for the cascade combination, $\beta_1 = 60°$, $\sigma = 1.50$, and blade section, NACA 65-(24)10.



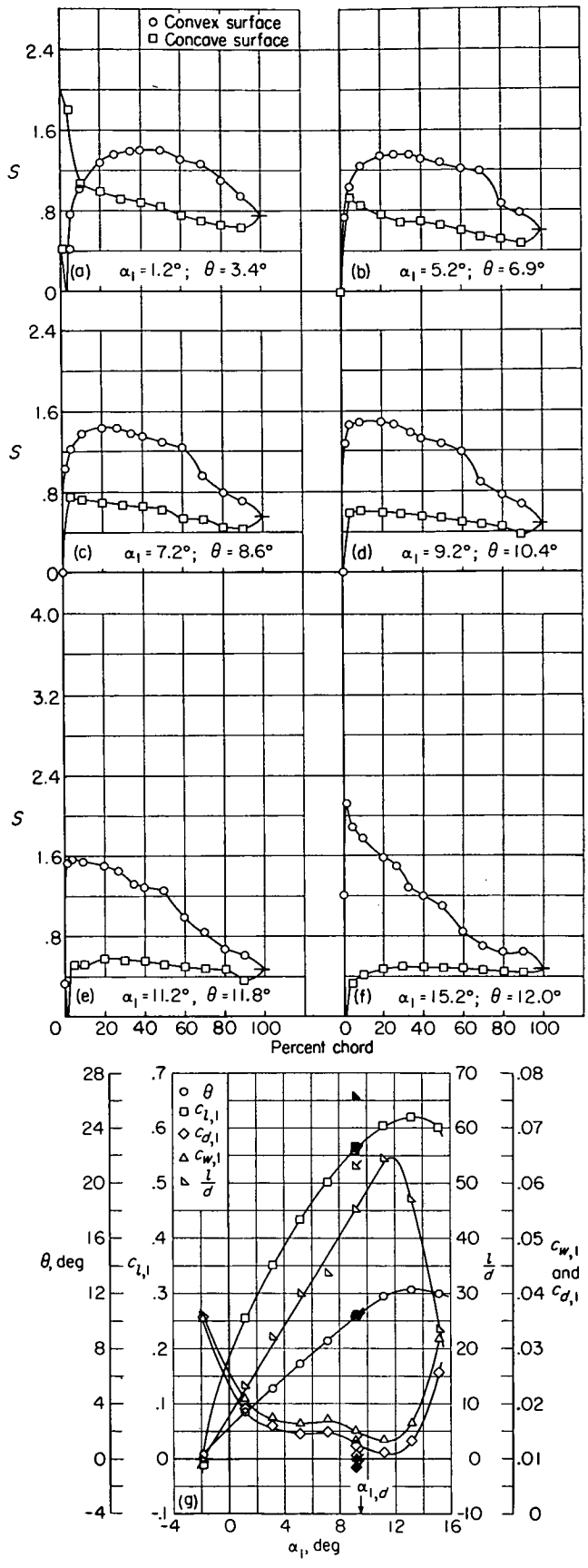
(g) Section characteristics; flagged symbol indicates leading-edge roughness; solid symbol indicates high Reynolds number.

FIGURE 71.—Blade-surface pressure distributions and blade section characteristics for the cascade combination, $\beta_1 = 70°$, $\sigma = 1.00$, and blade section, NACA 65-010.



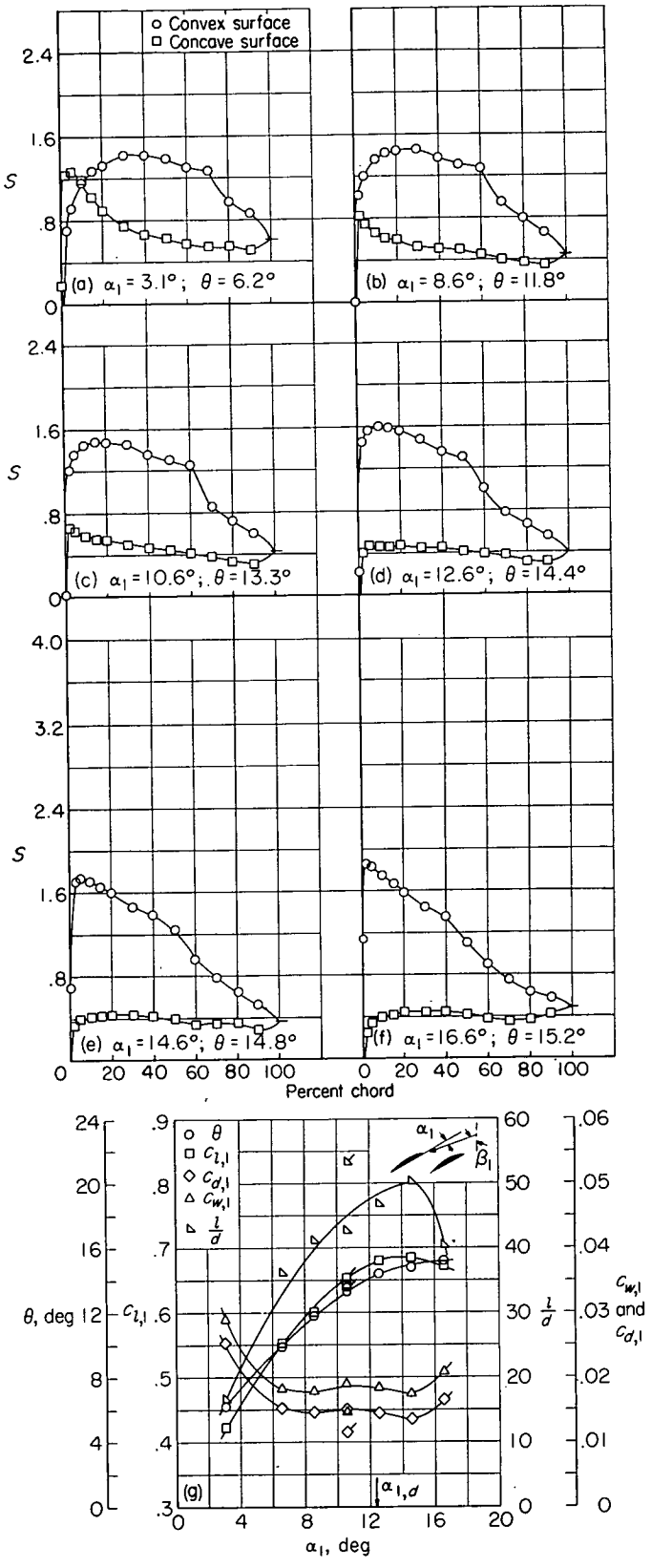
(g) Section characteristics; flagged symbol indicates leading-edge roughness; solid symbol indicates high Reynolds number.

FIGURE 72.—Blade-surface pressure distributions and blade section characteristics for the cascade combination, $\beta_1 = 70°$, $\sigma = 1.00$, and blade section, NACA 65-410.



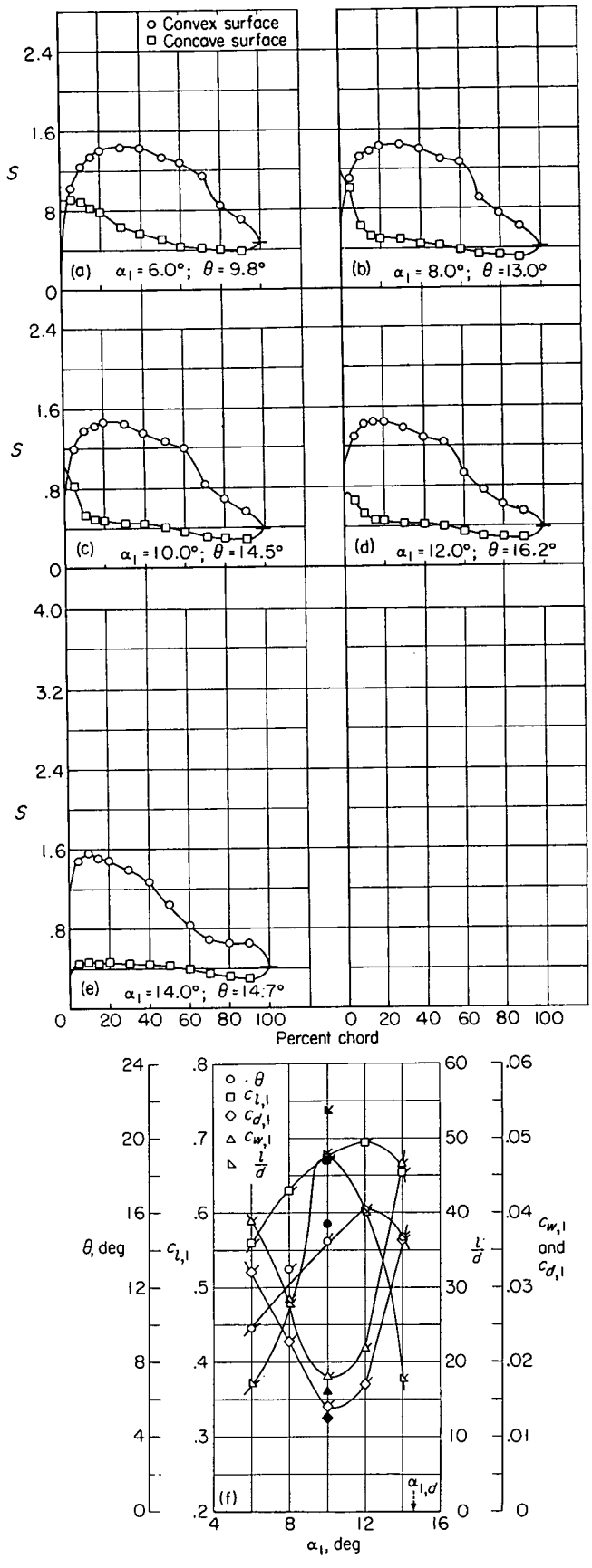
(g) Section characteristics; flagged symbol indicates leading-edge roughness; solid symbol indicates high Reynolds number.

FIGURE 73.—Blade-surface pressure distributions and blade section characteristics for the cascade combination, $\beta_1 = 70°$, $\sigma = 1.00$, and blade section, NACA 65-810.



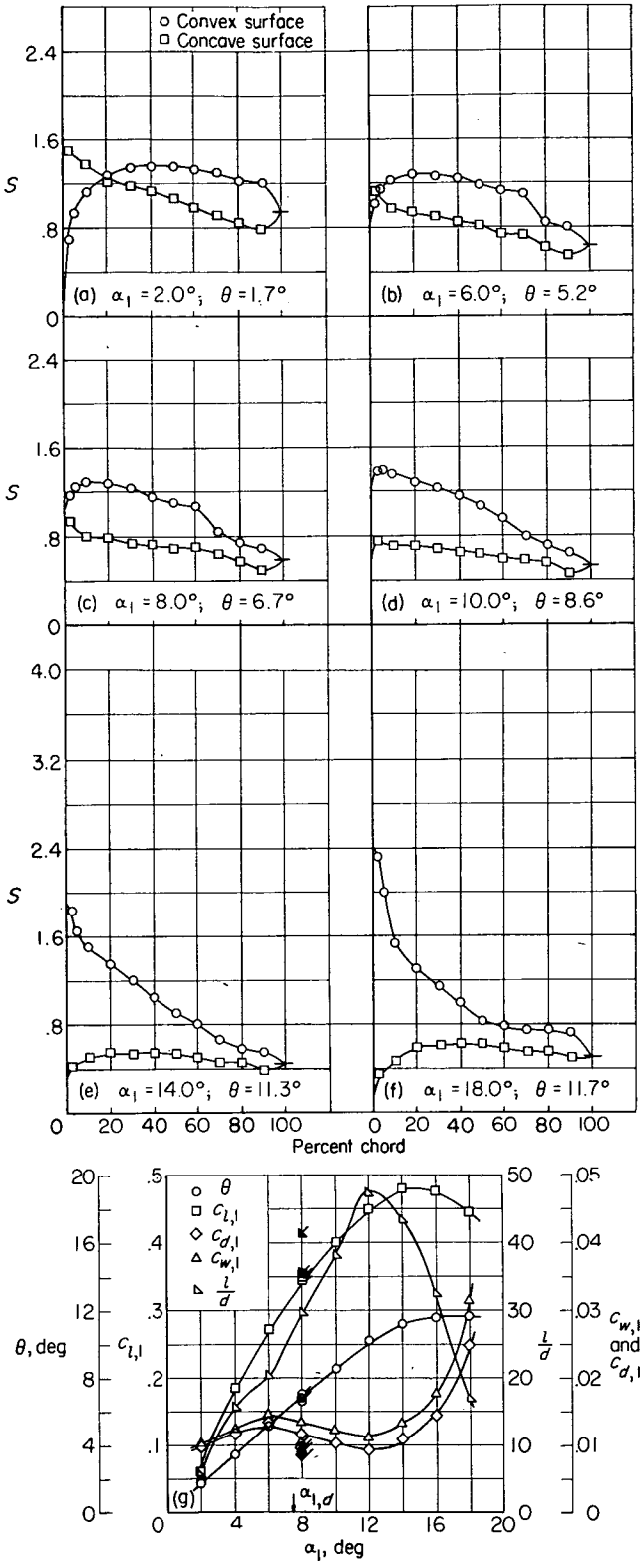
(g) Section characteristics; flagged symbol indicates leading-edge roughness.

FIGURE 74.—Blade-surface pressure distributions and blade section characteristics for the cascade combination, $\beta_1 = 70°$, $\sigma = 1.00$, and blade section, NACA 65-(12)10.



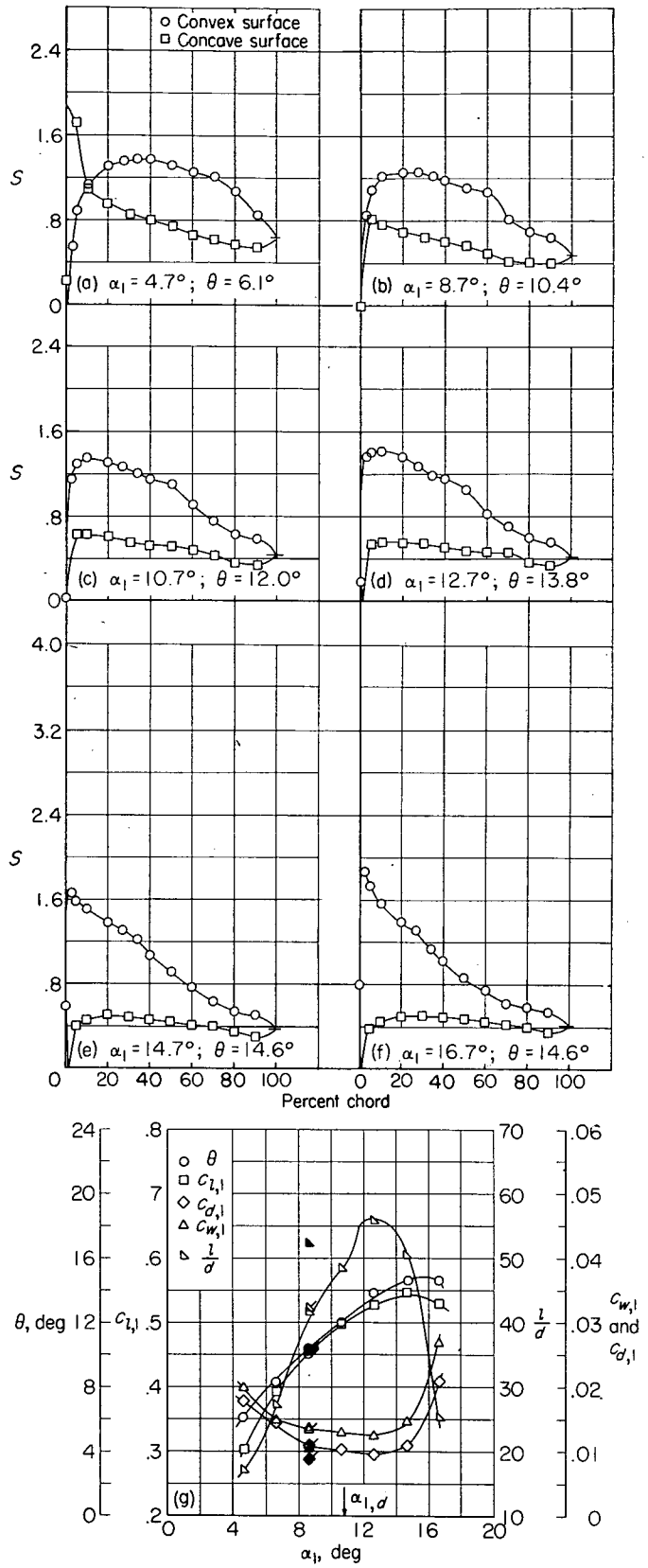
(f) Section characteristics; no design point was obtained; flagged symbol indicates leading-edge roughness; solid symbol indicates high Reynolds number.

FIGURE 75.—Blade-surface pressure distributions and blade section charactertistics for the cascade combination, $\beta_1 = 70°$, $\sigma = 1.00$, and blade section, NACA 65-(15)10.



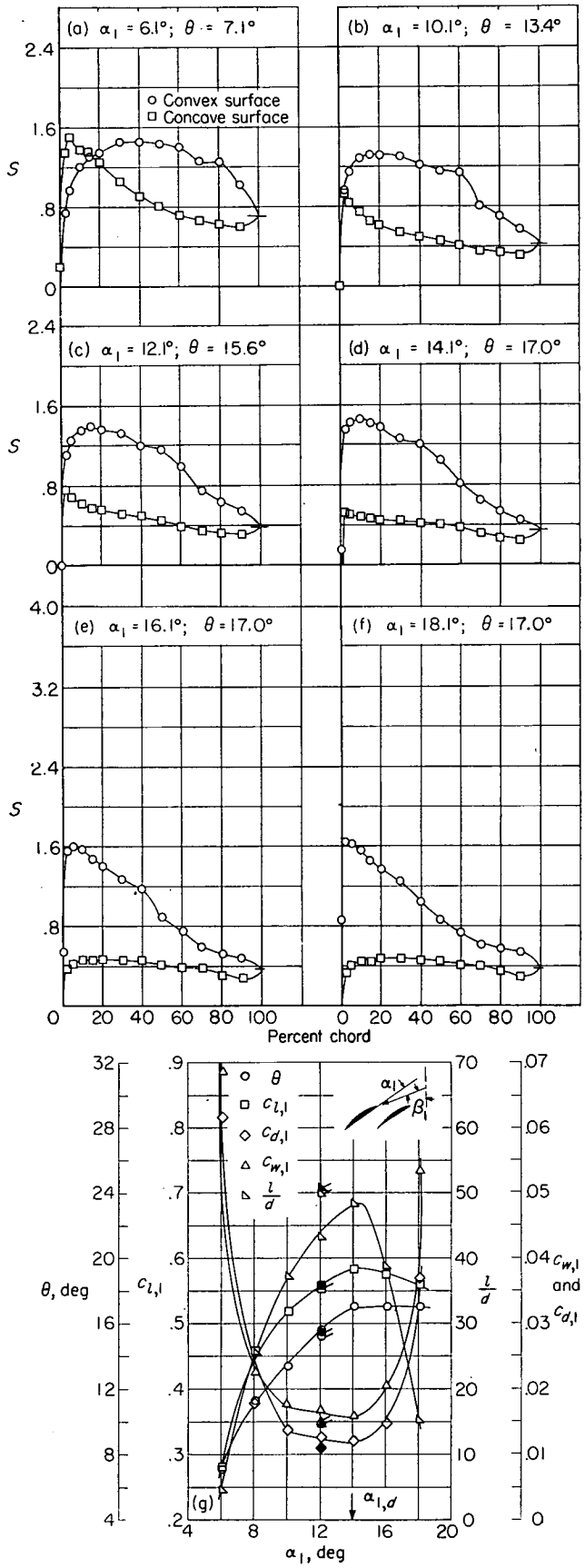
(g) Section characteristics; flagged symbol indicates leading-edge roughness; solid symbol indicates high Reynolds number.

FIGURE 76.—Blade-surface pressure distributions and blade section characteristics for the cascade combination, $\beta_1=70°$, $\sigma=1.25$, and blade section, NACA 65-410.



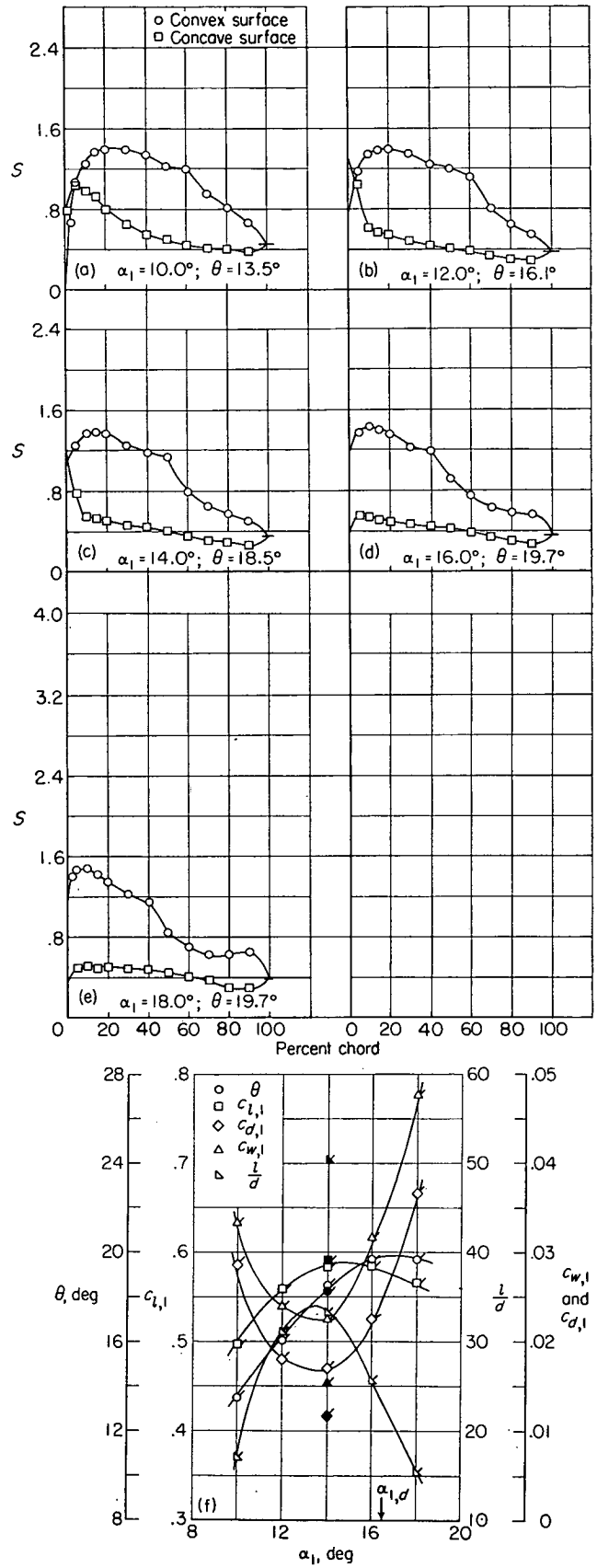
(g) Section characteristics; flagged symbol indicates leading-edge roughness; solid symbol indicates high Reynolds number.

FIGURE 77.—Blade-surface pressure distributions and blade section characteristics for the cascade combination, $\beta_1=70°$, $\sigma=1.25$, and blade section, NACA 65-810.



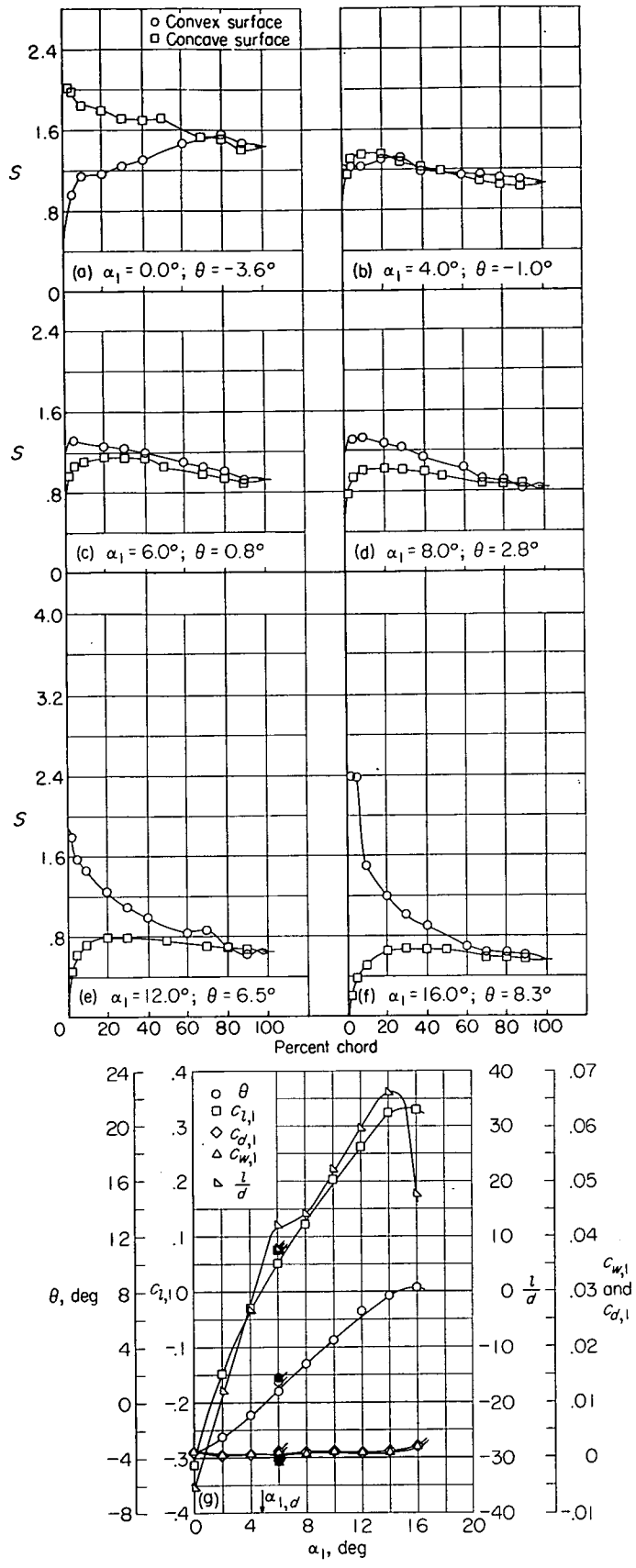
(g) Section characteristics; flagged symbol indicates leading-edge roughness; solid symbol indicates high Reynolds number.

FIGURE 78.—Blade-surface pressure distributions and blade section characteristics for the cascade combination, $\beta_1=70°$, $\sigma=1.25$, and blade section, NACA 65–(12)10.



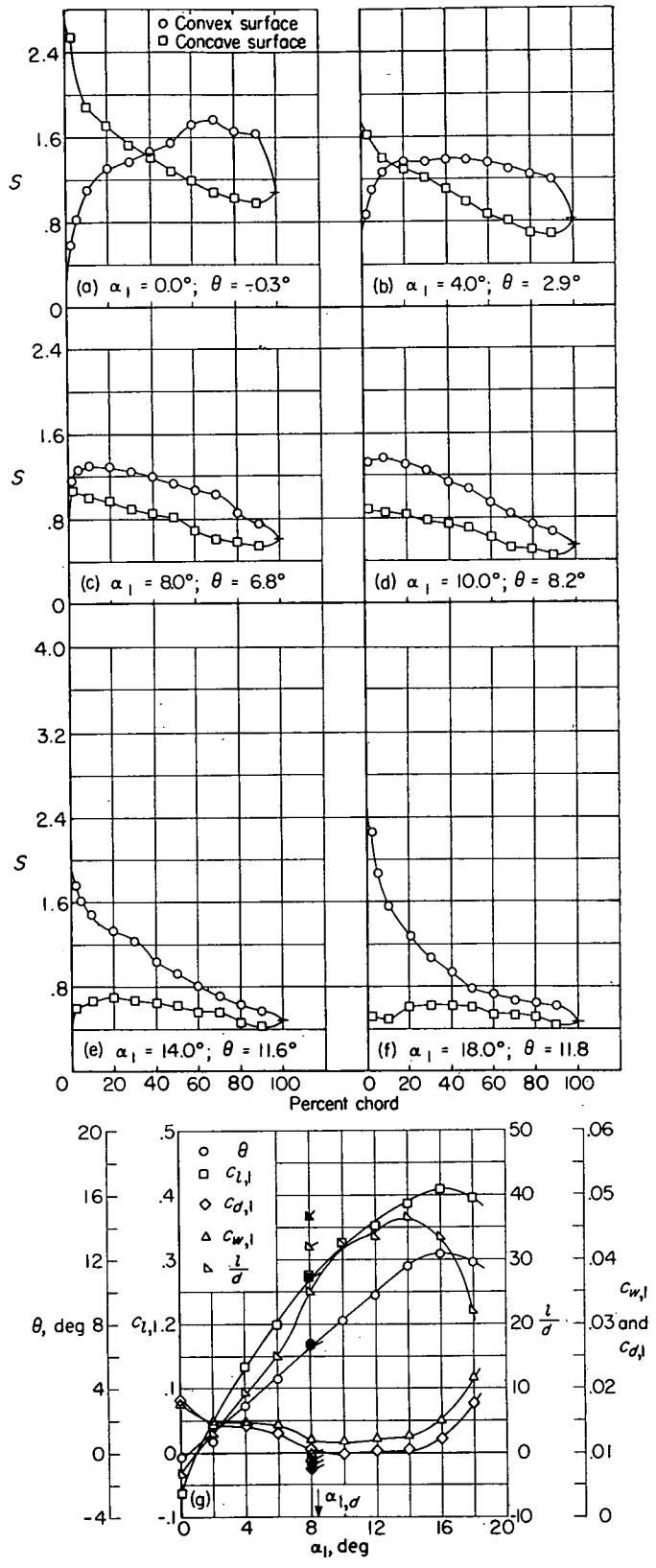
(f) Section characteristics; flagged symbol indicates leading-edge roughness; solid symbol indicates high Reynolds number.

FIGURE 79.—Blade-surface pressure distributions and blade section characteristics for the cascade combination, $\beta_1=70°$, $\sigma=1.25$, and blade section, NACA 65–(15)10.



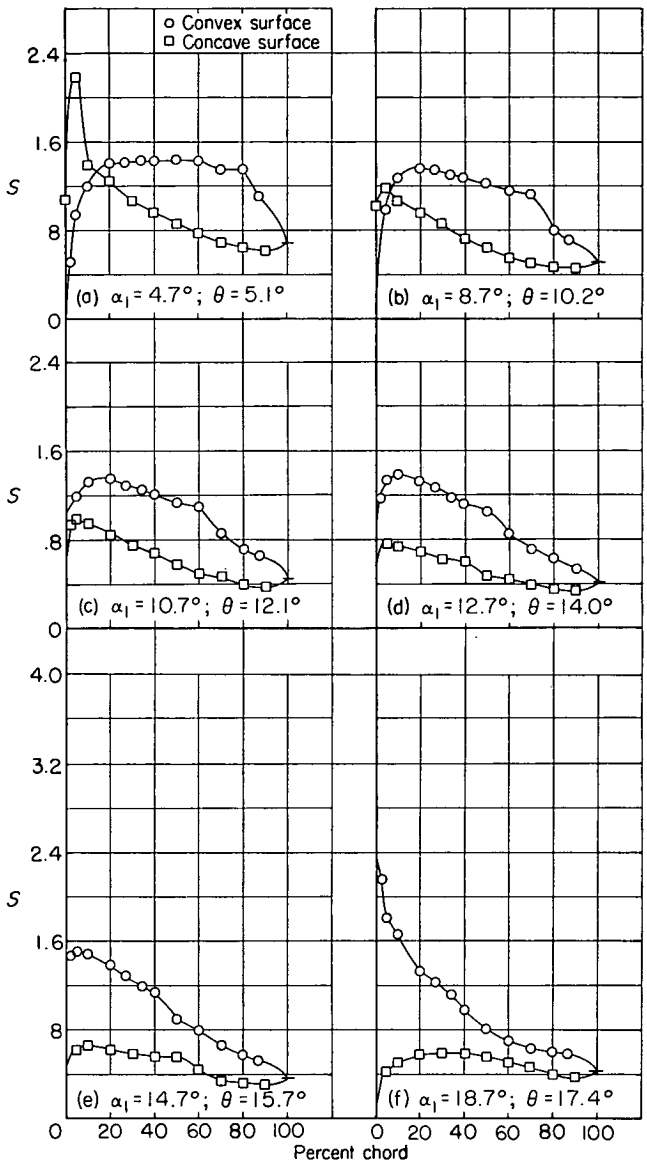
(g) Section characteristics; flagged symbol indicates leading-edge roughness; solid symbol indicates high Reynolds number.

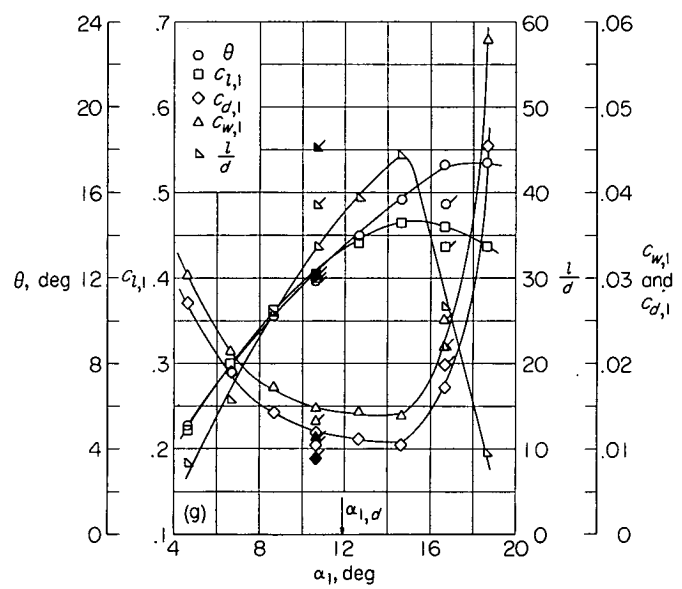
FIGURE 80.—Blade-surface pressure distributions and blade section characteristics for the cascade combination, β_1=70°, σ=1.50, and blade section, NACA 65-010.



(g) Section characteristics; flagged symbol indicates leading-edge roughness; solid symbol indicates high Reynolds number.

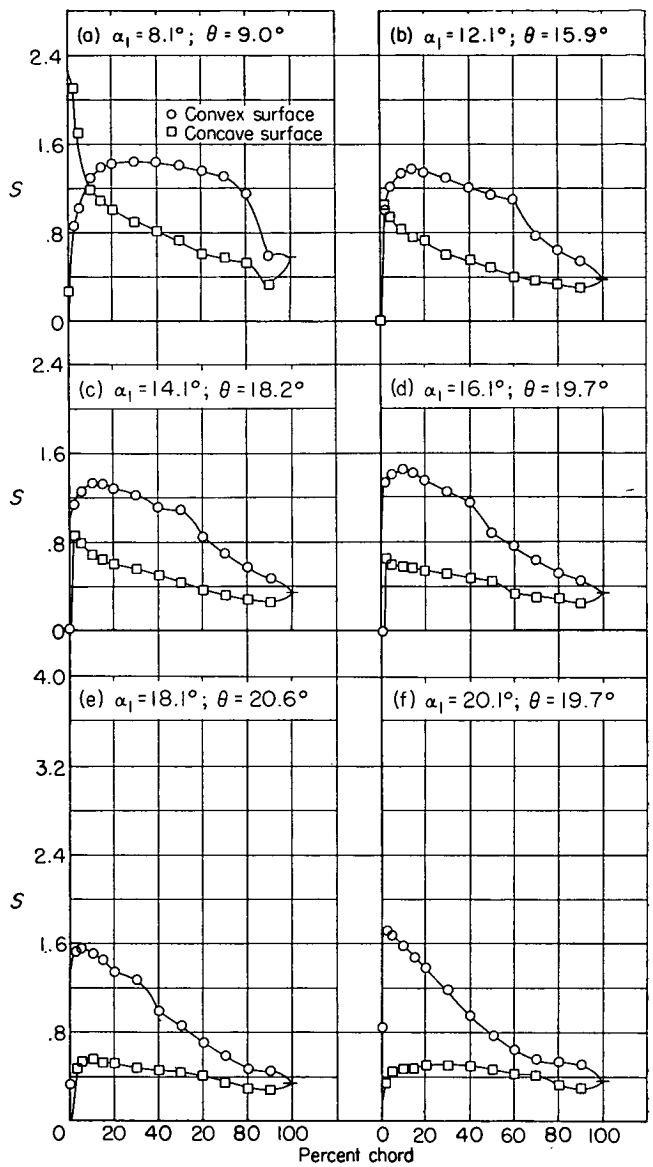
FIGURE 81.—Blade-surface pressure distributions and blade section characteristics for the cascade combination, β_1=70°, σ=1.50, and blade section, NACA 65-410.

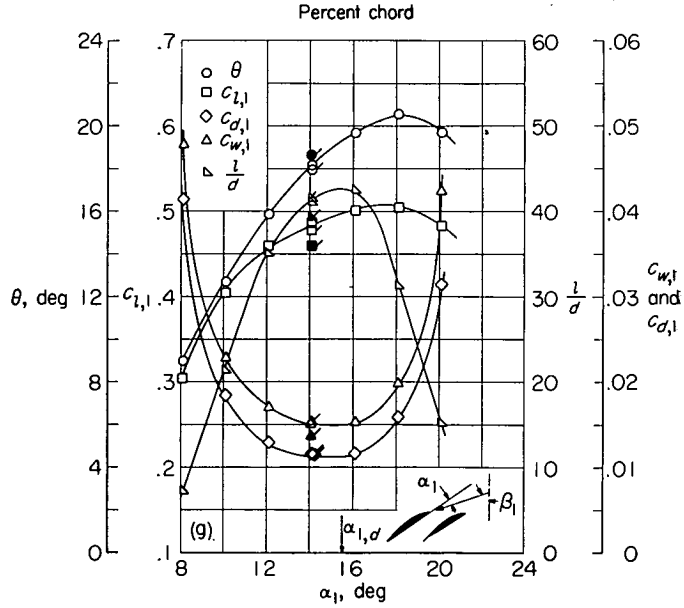




(g) Section characteristics; flagged symbol indicates leading-edge roughness; solid symbol indicates high Reynolds number.

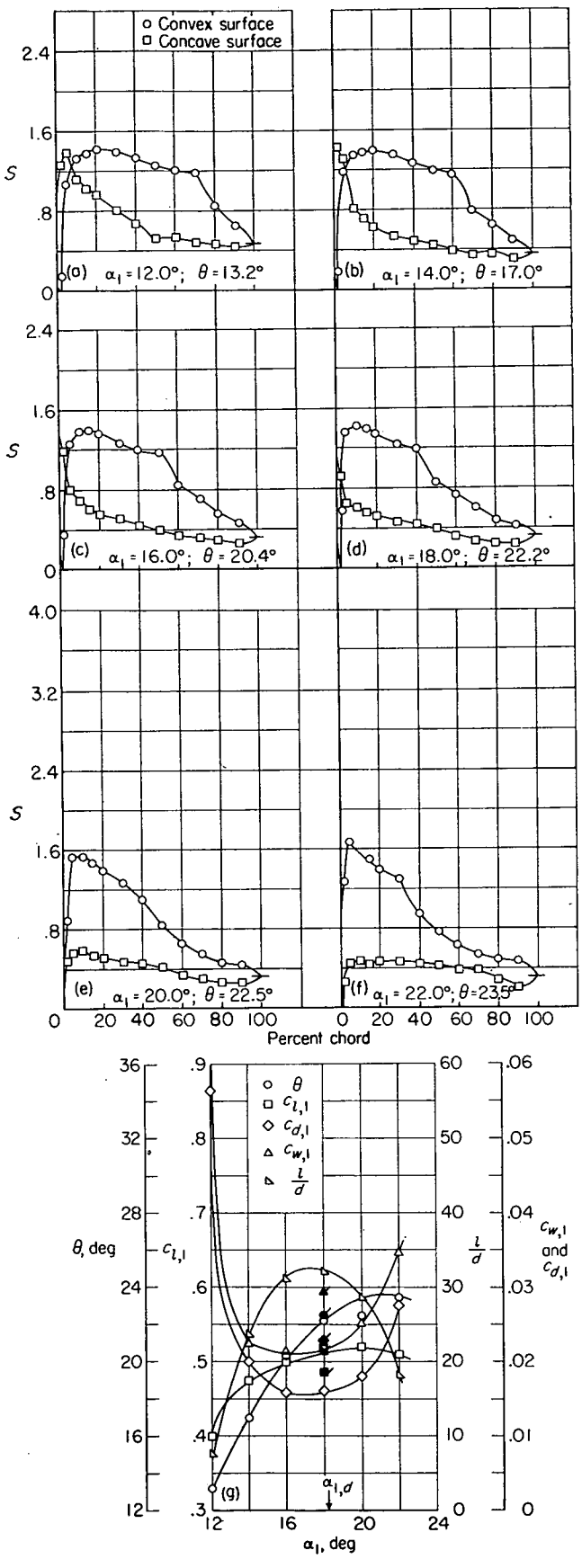
FIGURE 82.—Blade-surface pressure distributions and blade section characteristics for the cascade combination, $\beta_1 = 70°$, $\sigma = 1.50$, and blade section, NACA 65–810.





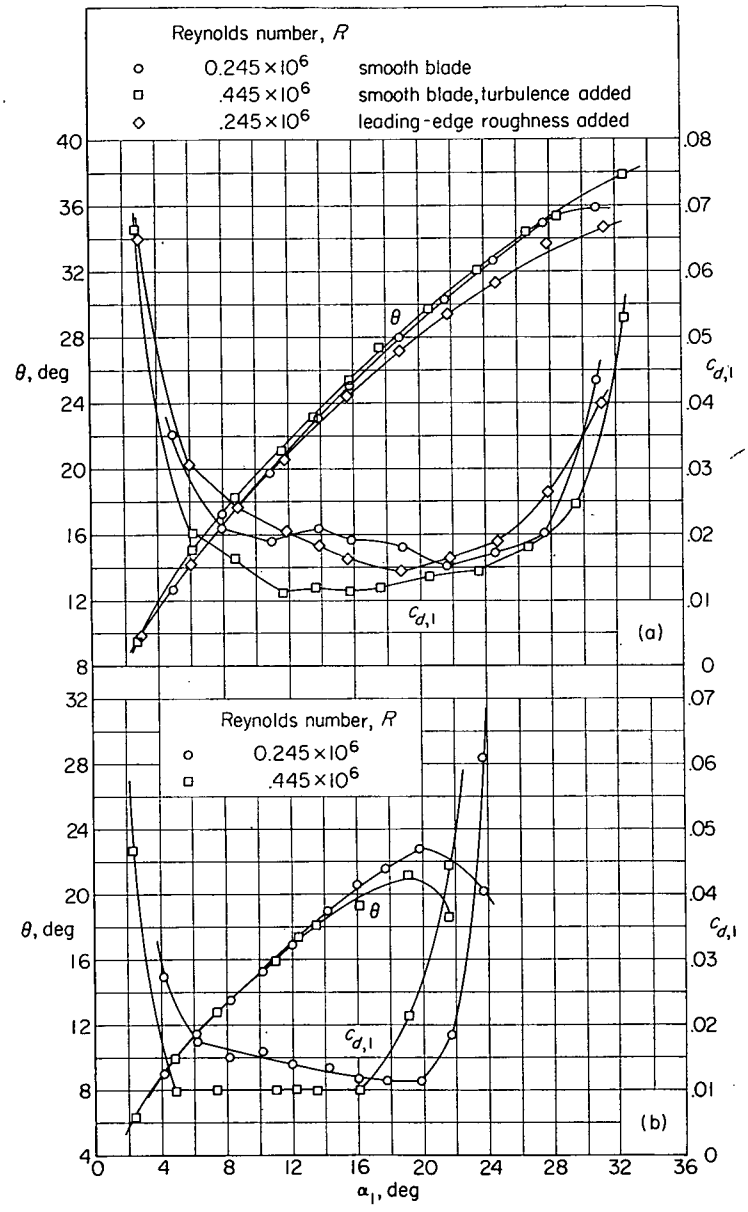
(g) Section characteristics; flagged symbol indicates leading-edge roughness; solid symbol indicates high Reynolds number.

FIGURE 83.—Blade-surface pressure distributions and blade section characteristics for the cascade combination, $\beta_1 = 70°$, $\sigma = 1.50$, and blade section, NACA 65–(12)10.



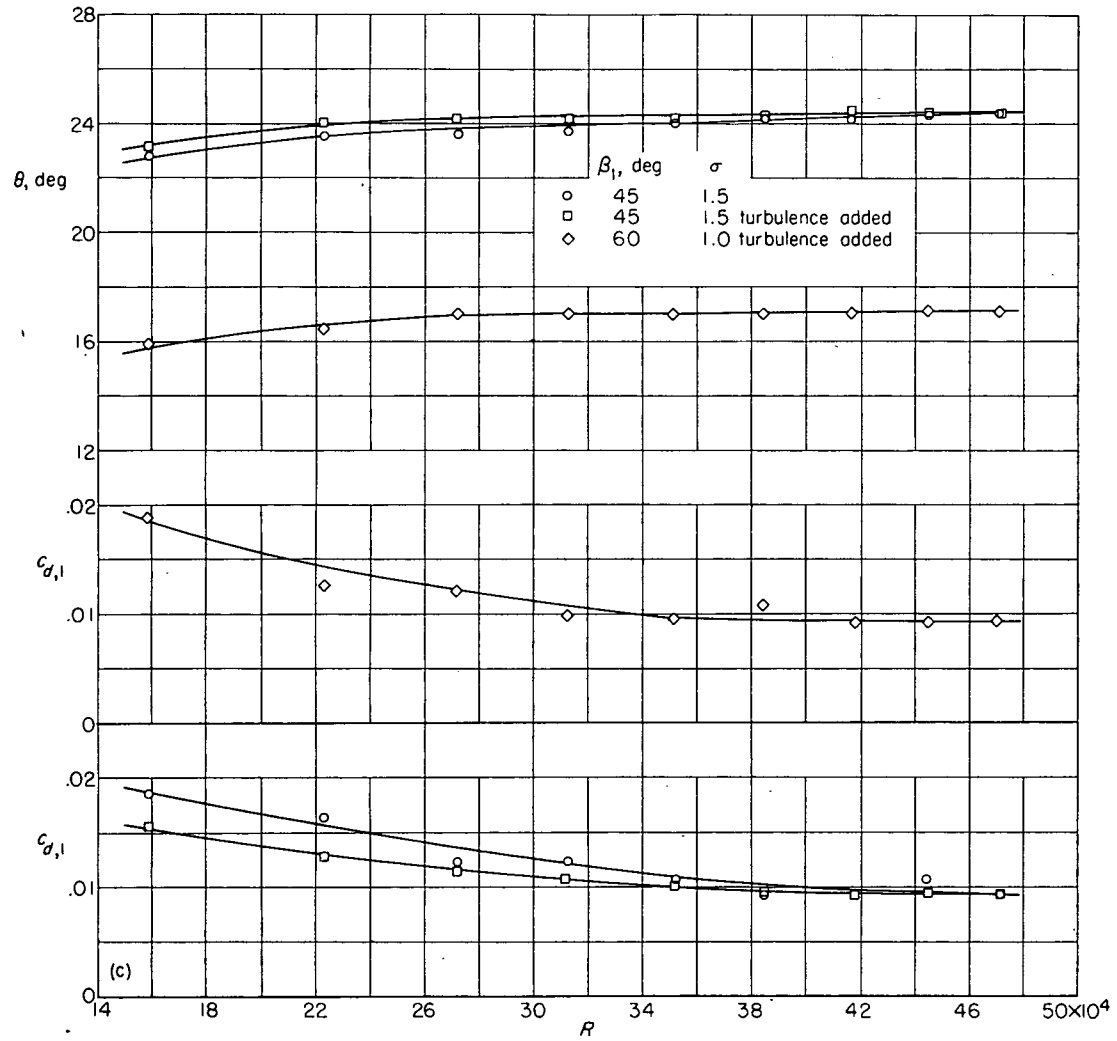
(g) Section characteristics; flagged symbol indicates leading-edge roughness; solid symbol indicates high Reynolds number.

FIGURE 84.—Blade-surface pressure distributions and blade section characteristics for the cascade combination, $\beta_1=70°$, $\sigma=1.50$, and blade section, NACA 65–(15)10.



(a) Comparison for the angle-of-attack range for $\beta_1=45°$, $\sigma=1.50$.
(b) Comparison for the angle-of-attack range for $\beta_1=60°$, $\sigma=1.00$. Smooth blade.

FIGURE 85.—Effect of Reynolds number on turning angle and drag coefficient of the NACA 65–(12)10 blade section for typical cascade combinations.



(c) Variation with R near design angle of attack.

FIGURE 85.—Concluded.

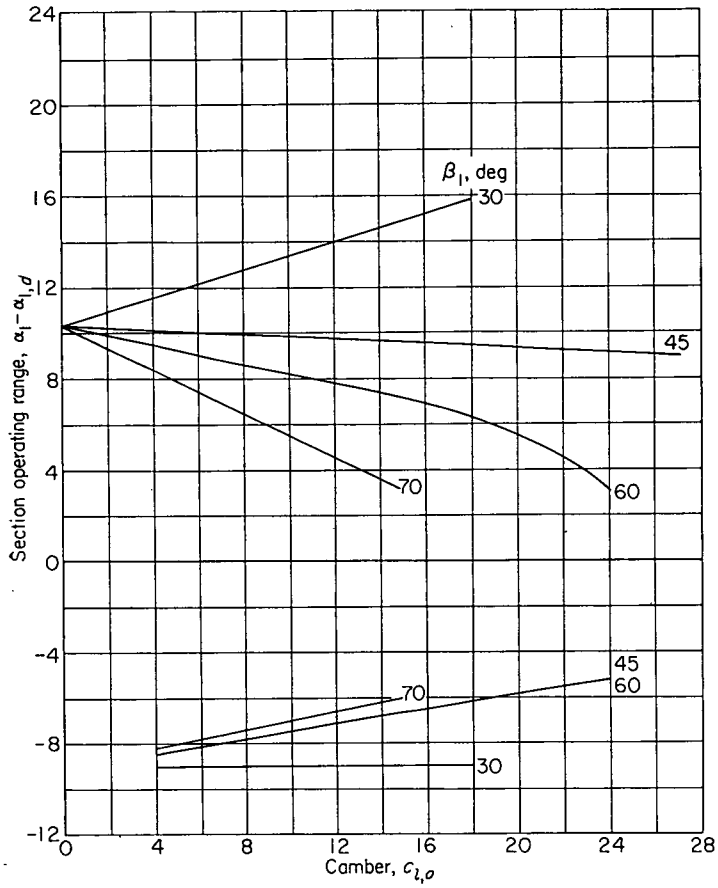


FIGURE 86.—Variation of estimated operating angle-of-attack range with camber for the inlet angles of the tests.

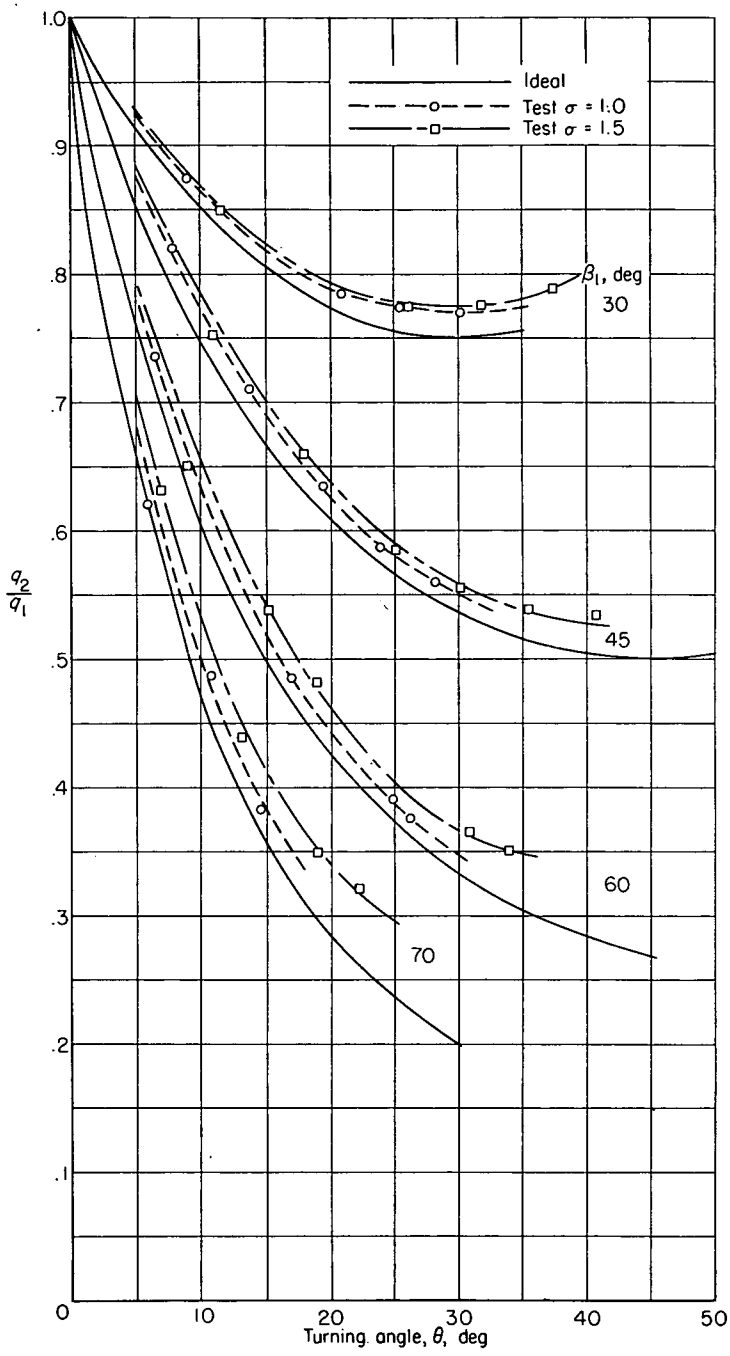


FIGURE 87.—Variation of ideal and test dynamic-pressure ratio across the cascade.

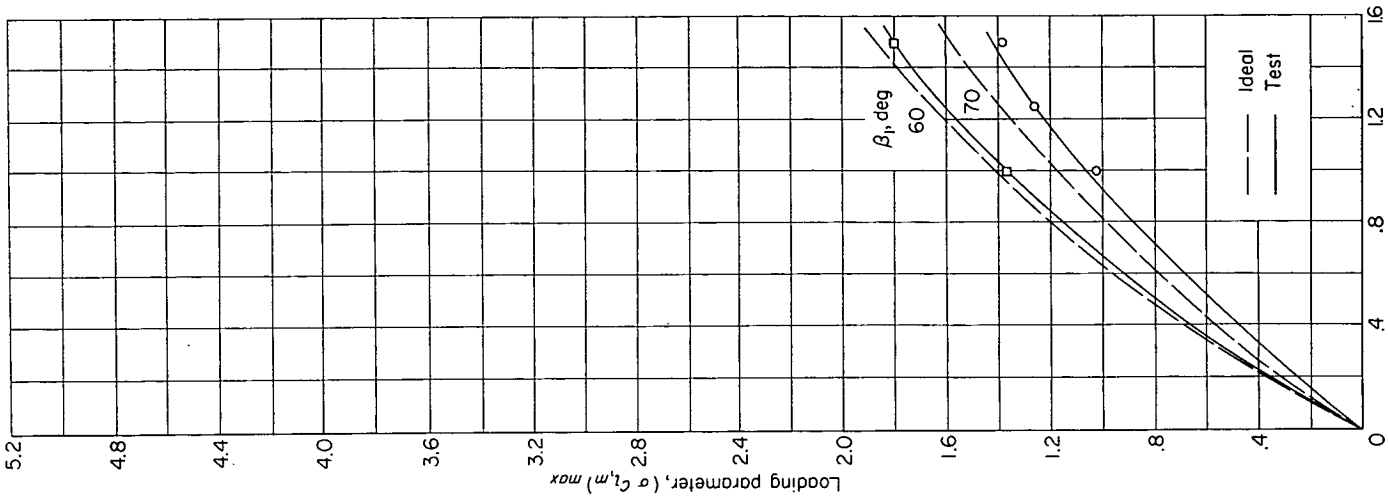


FIGURE 89.—Variation of the limit loading parameter, $(\sigma c_{l,m})_{max}$ with solidity for inlet angles of 60° and 70°.

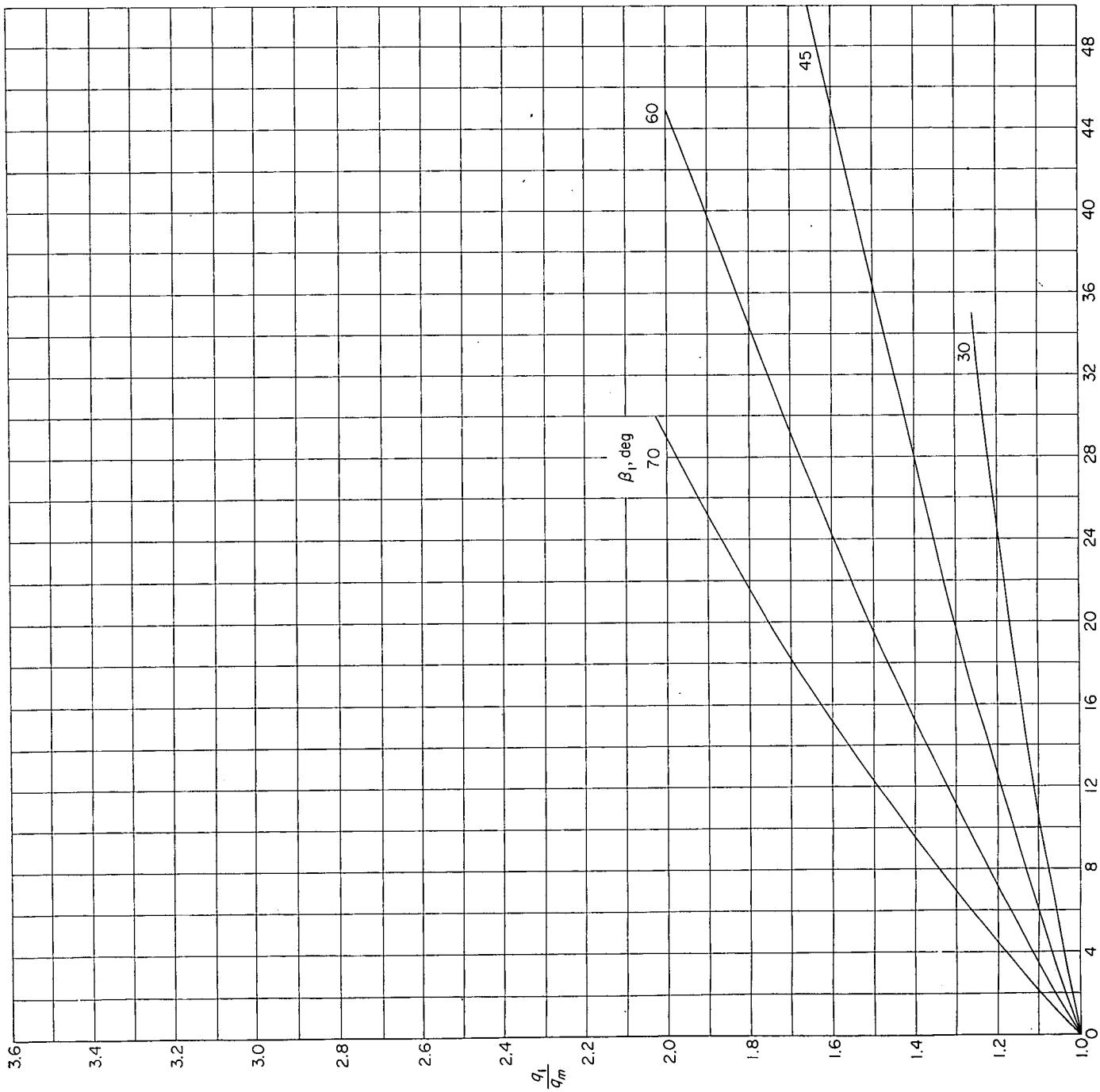


FIGURE 88.—Conversion chart showing the relation between entering and mean dynamic pressure as a function of turning angle and inlet angle.

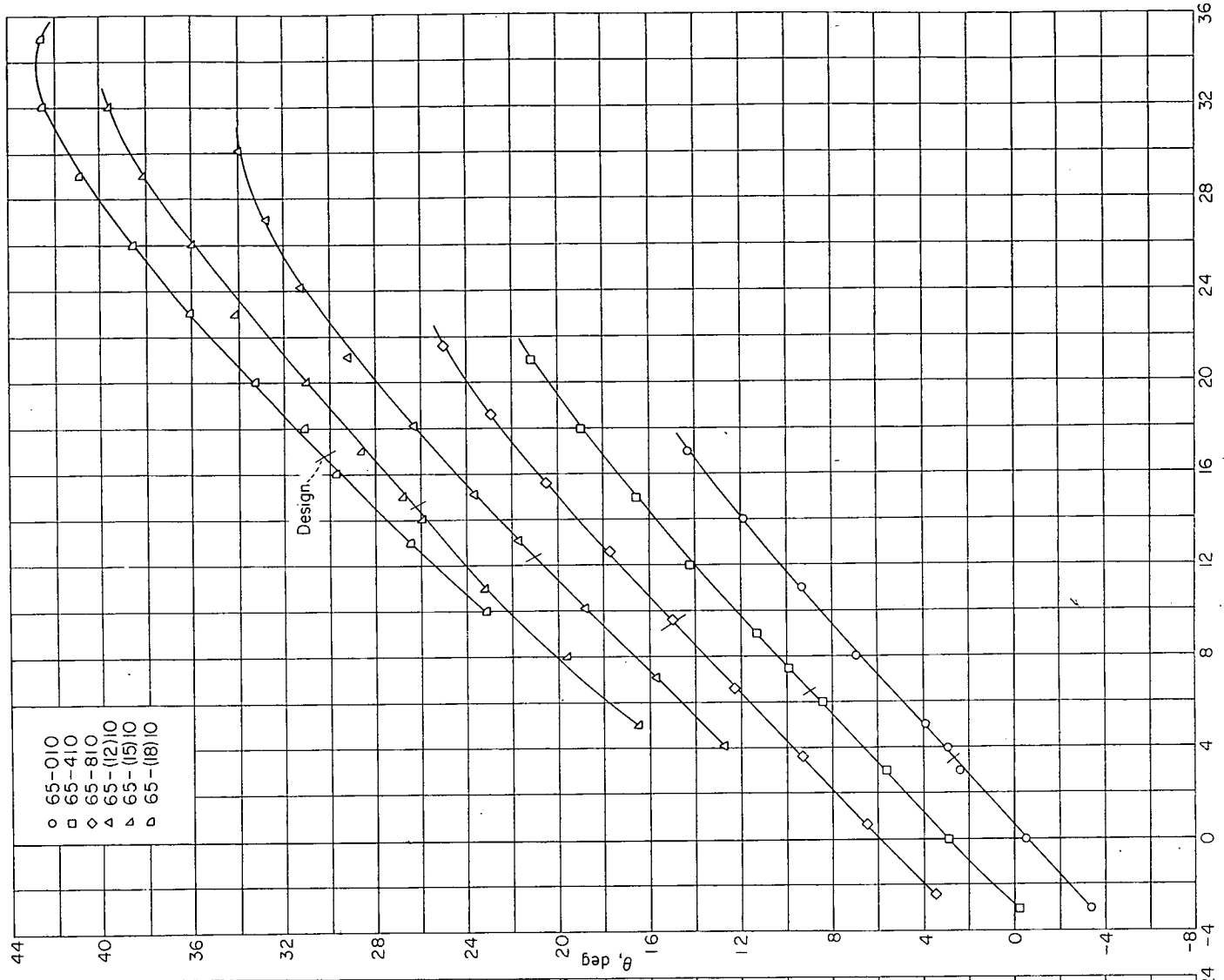


FIGURE 91.—Summary of relationship between turning angle θ and angle of attack α_1 for the blade sections tested at $\beta_1 = 30°$, $\sigma = 1.00$.

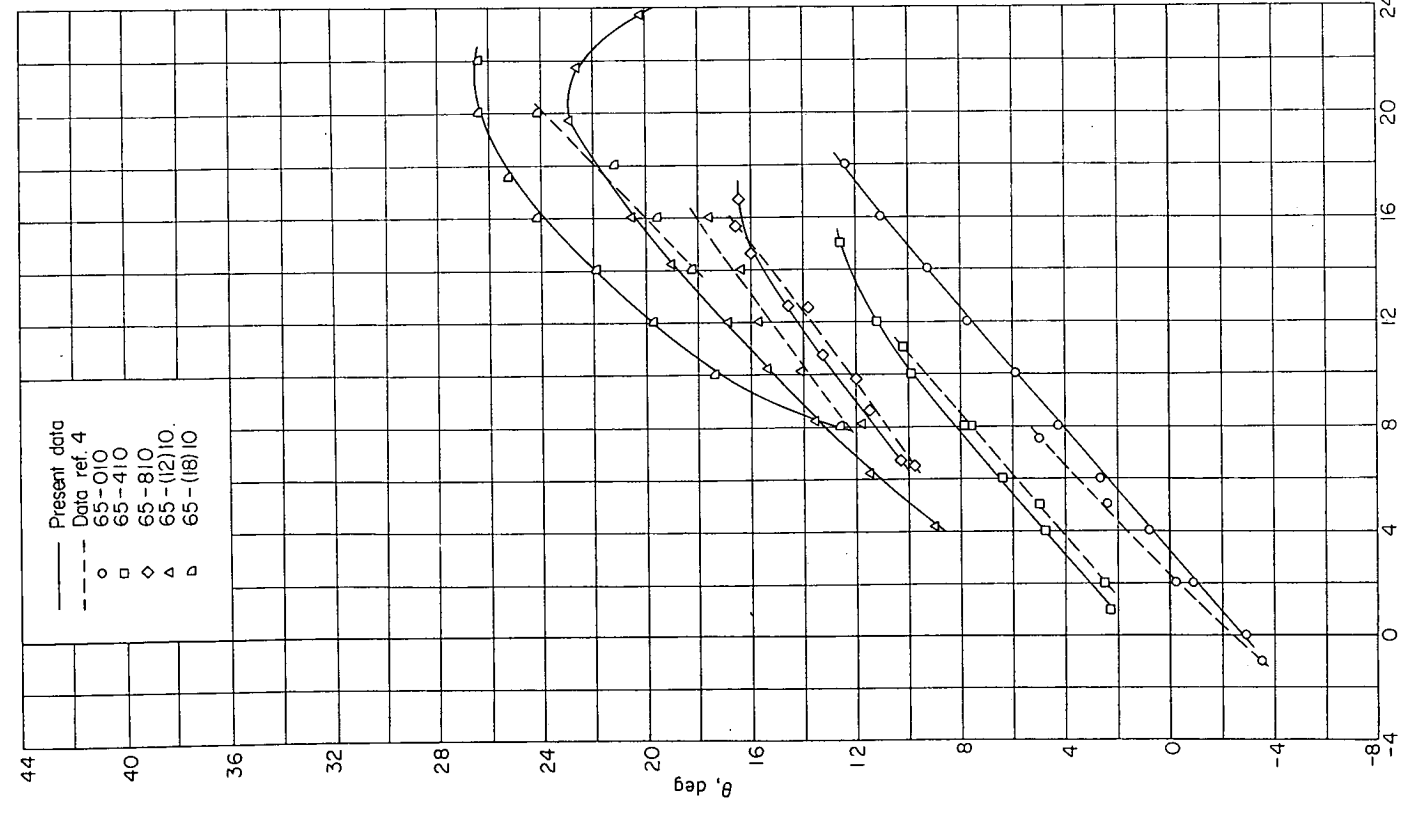


FIGURE 90.—Comparison of relationships between turning angle and angle of attack for the present porous-wall cascade results with those for the solid-wall cascade of reference 4 for a typical combination. $\beta_1 = 60°$; $\sigma = 1.00$.

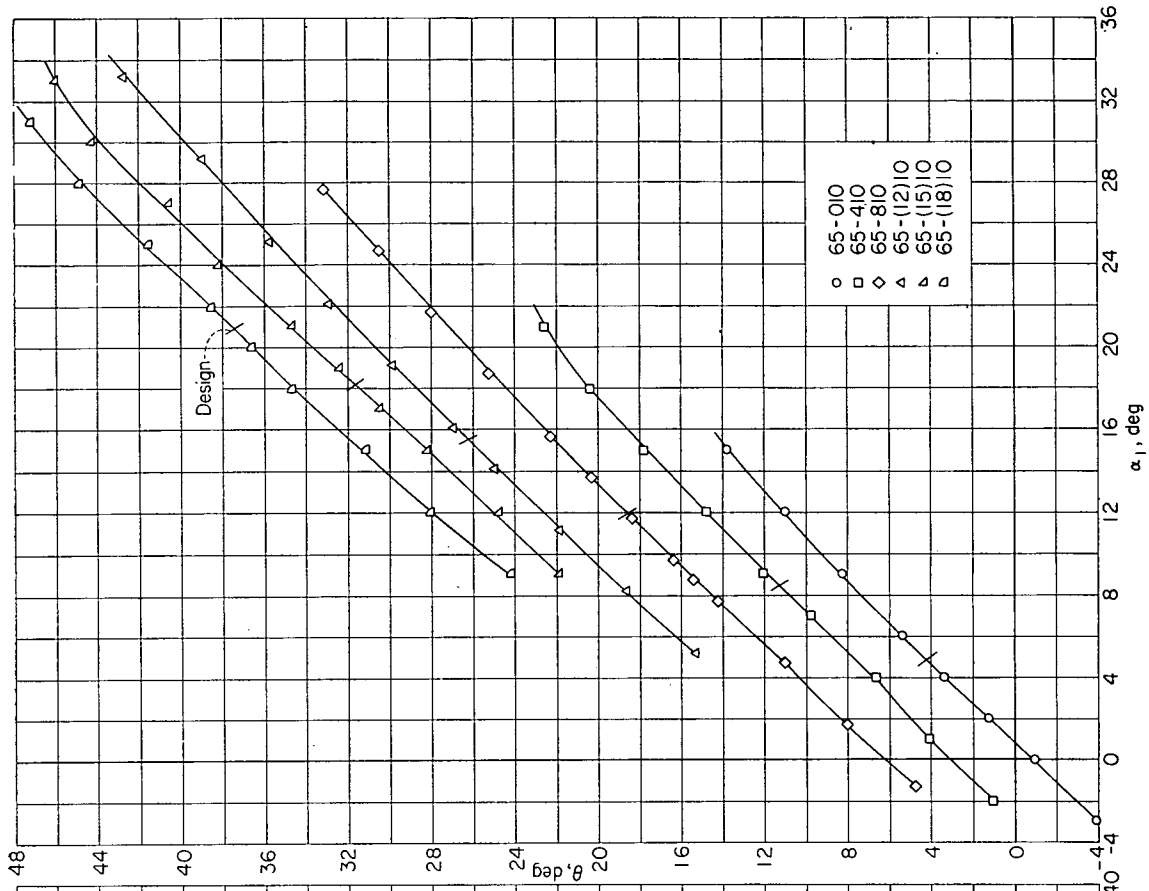


FIGURE 93.—Summary of relationship between turning angle θ and angle of attack α_1 for the blade sections tested at $\beta_1=30°$, $\sigma=1.50$.

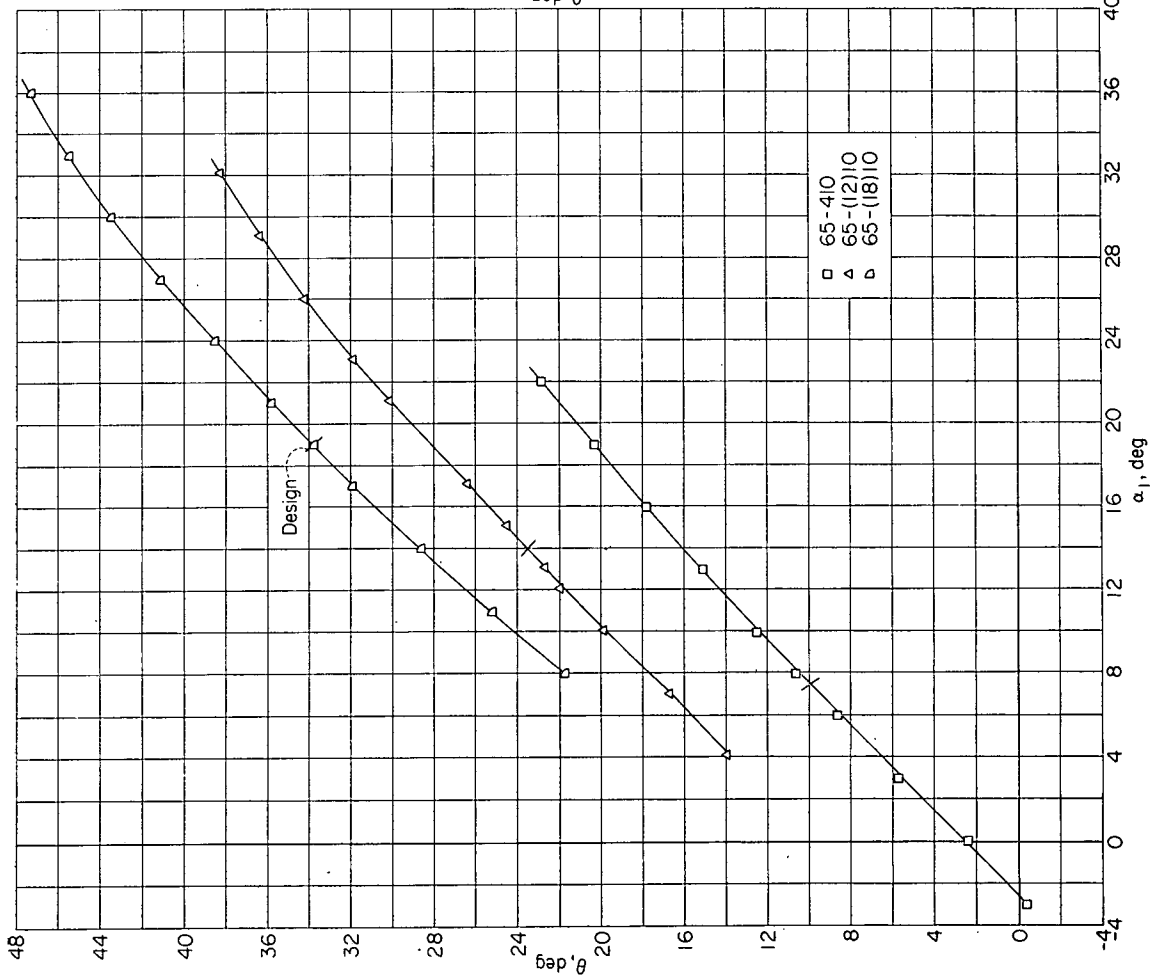


FIGURE 92.—Summary of relationship between turning angle θ and angle of attack α_1 for the blade sections tested at $\beta_1=30°$, $\sigma=1.25$.

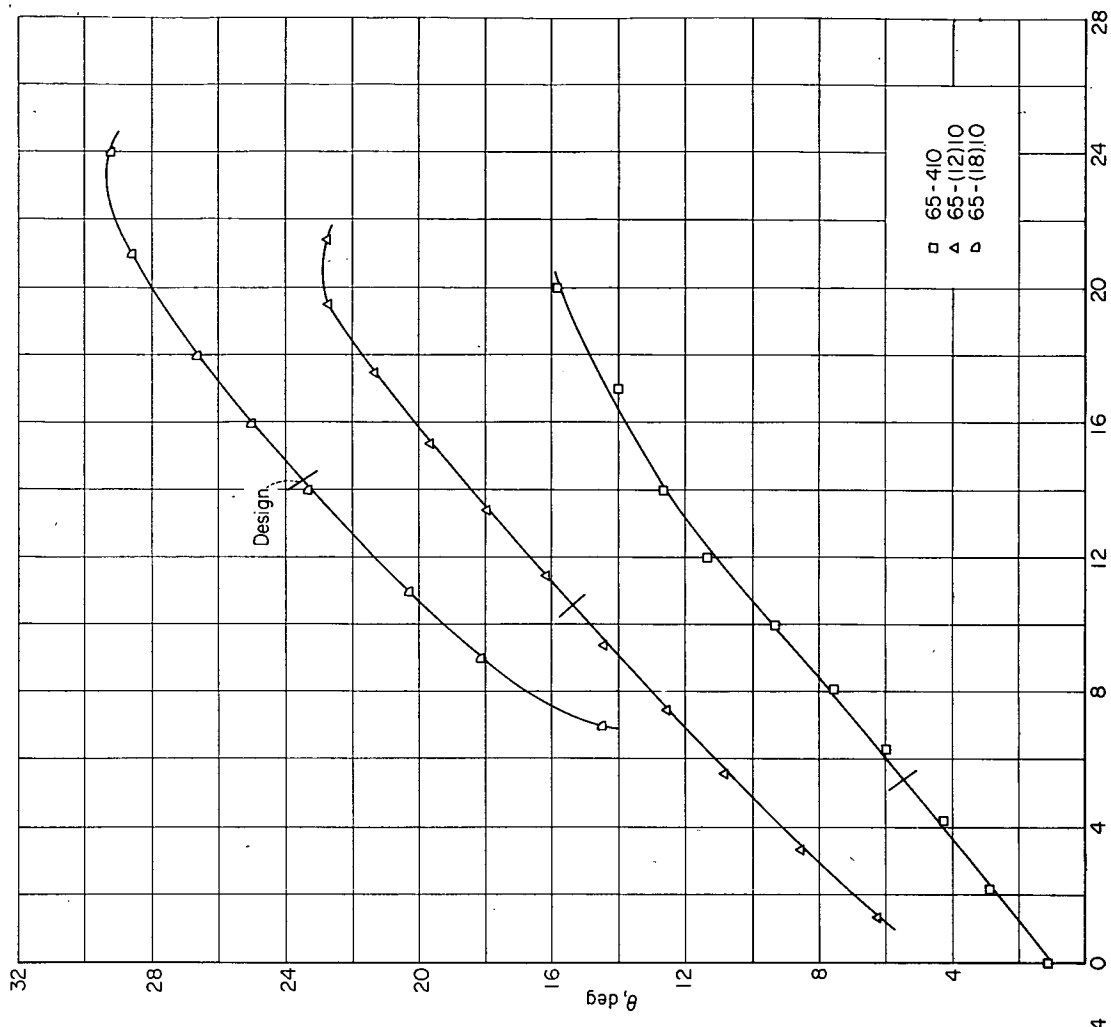


FIGURE 95.—Summary of relationship between turning angle θ and angle of attack α_1 for the blade sections tested at $\beta_1 = 45°$, $\sigma = 0.75$.

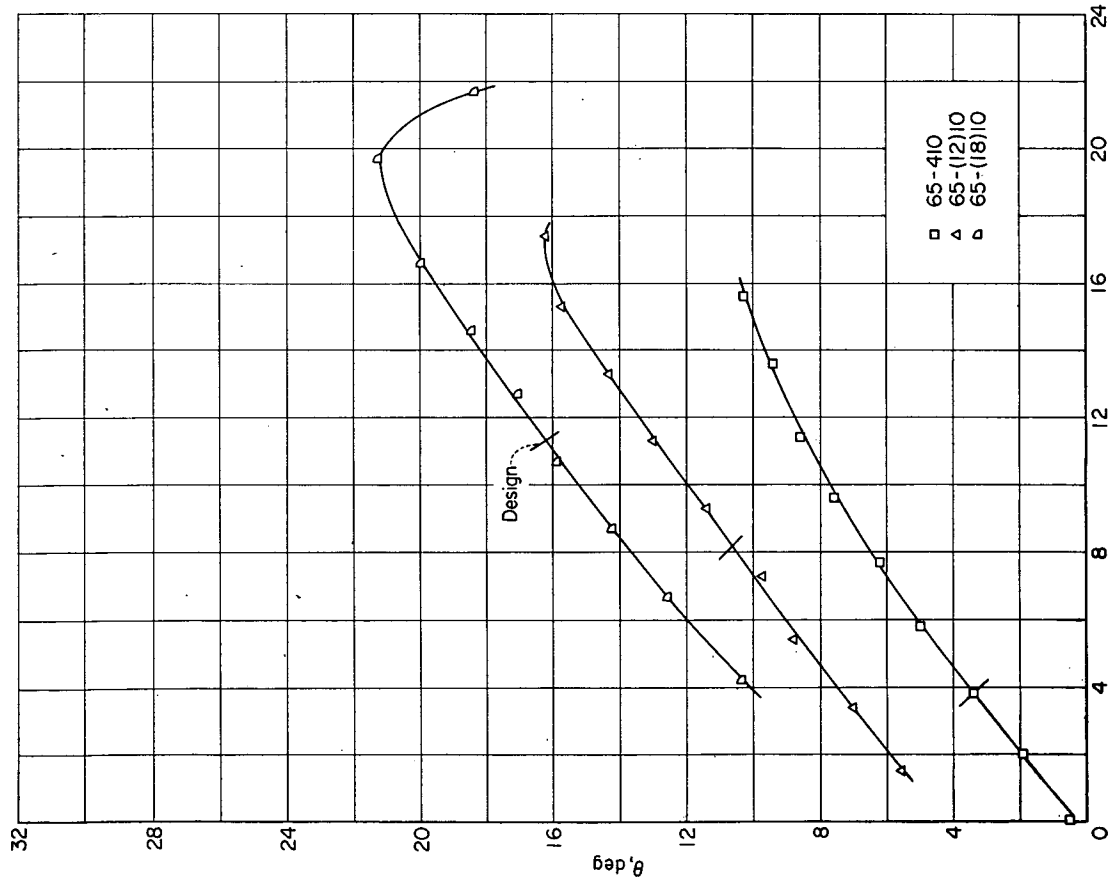


FIGURE 94.—Summary of relationship between turning angle θ and angle of attack α_1 for the blade sections tested at $\beta_1 = 45°$, $\sigma = 0.50$.

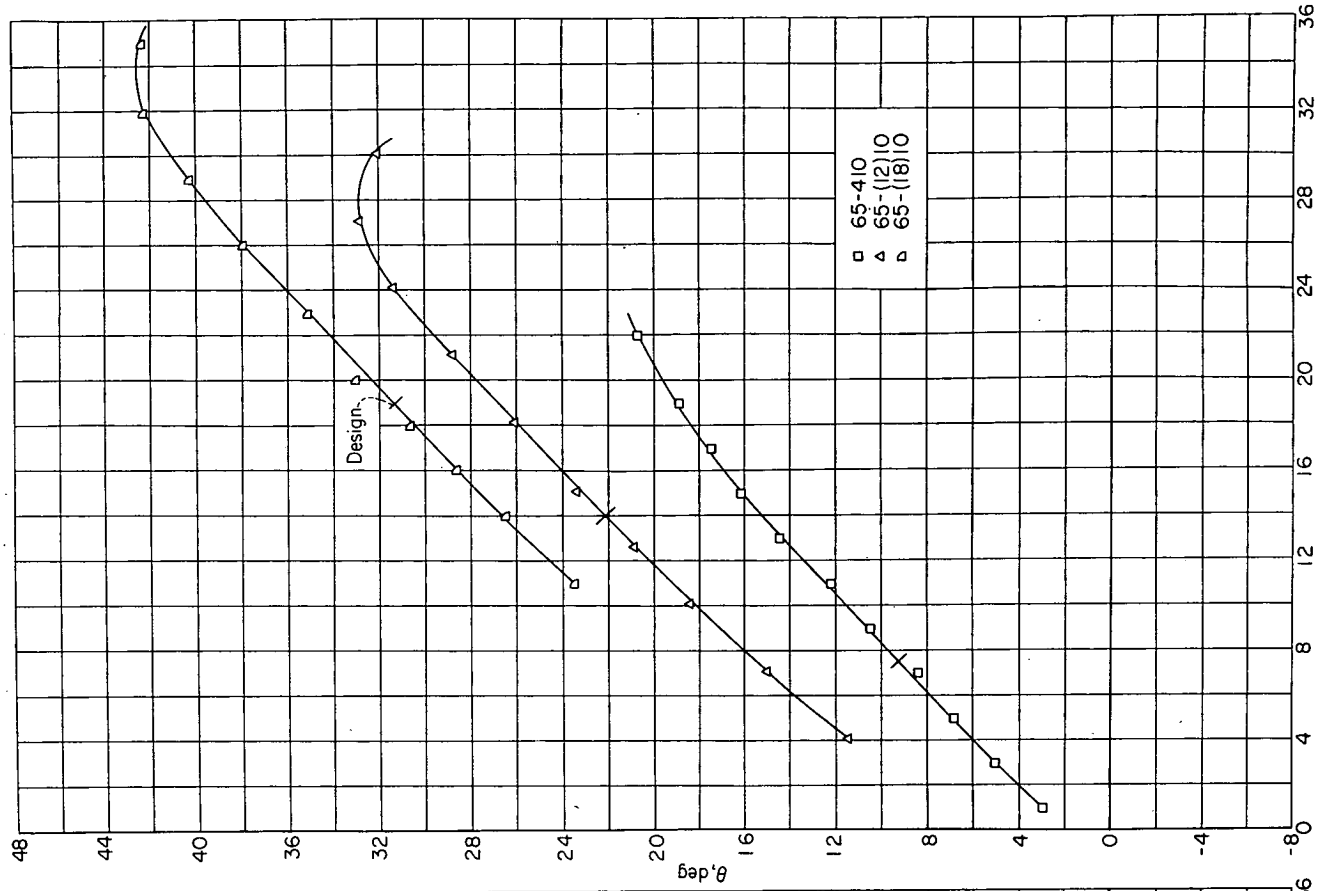


FIGURE 97.—Summary of relationship between turning angle θ and angle of attack α_1 for the blade sections tested at $\beta_1 = 45°$, $\sigma = 1.25$.

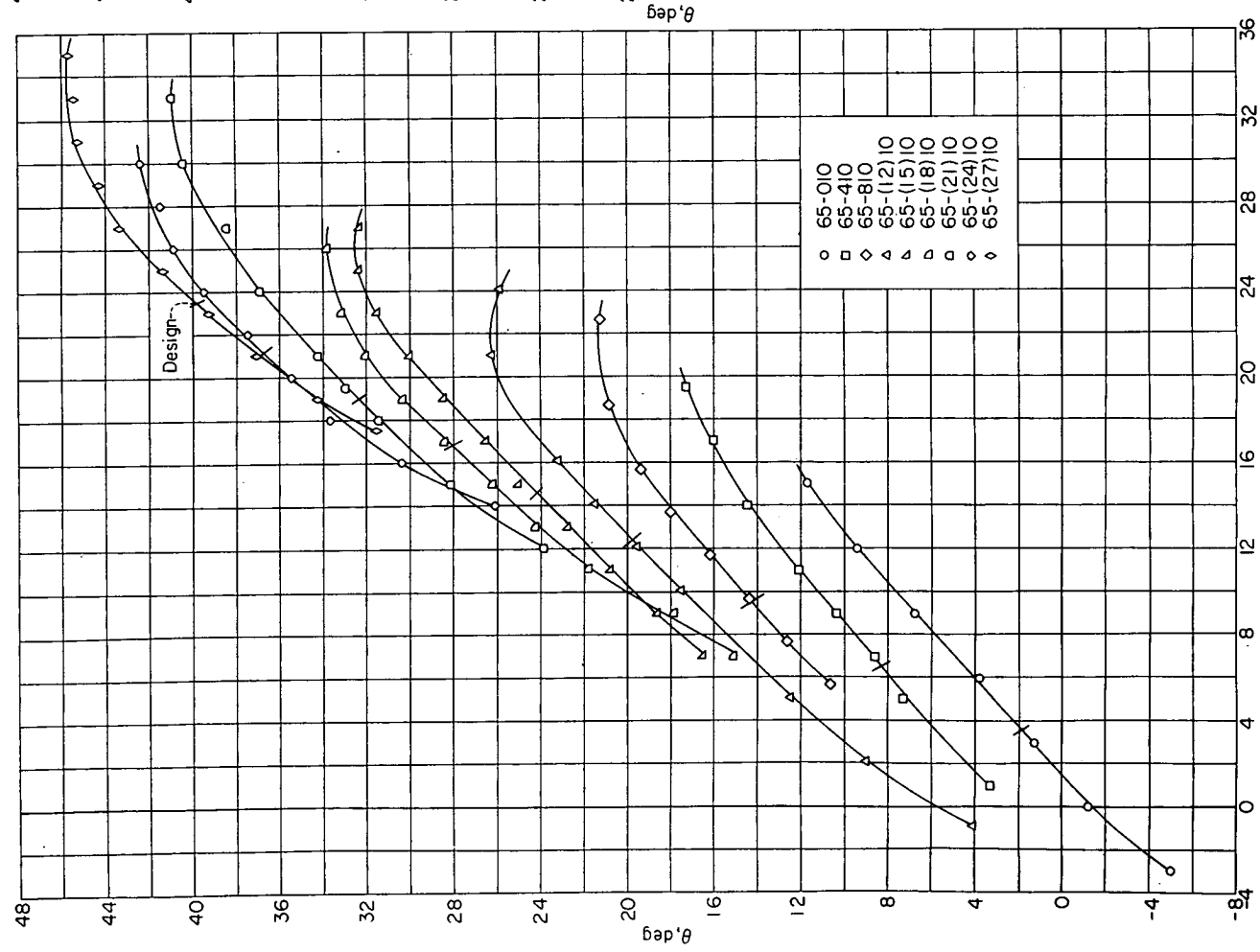


FIGURE 96.—Summary of relationship between turning angle θ and angle of attack α_1 for the blade sections tested at $\beta_1 = 45°$, $\sigma = 1.00$.

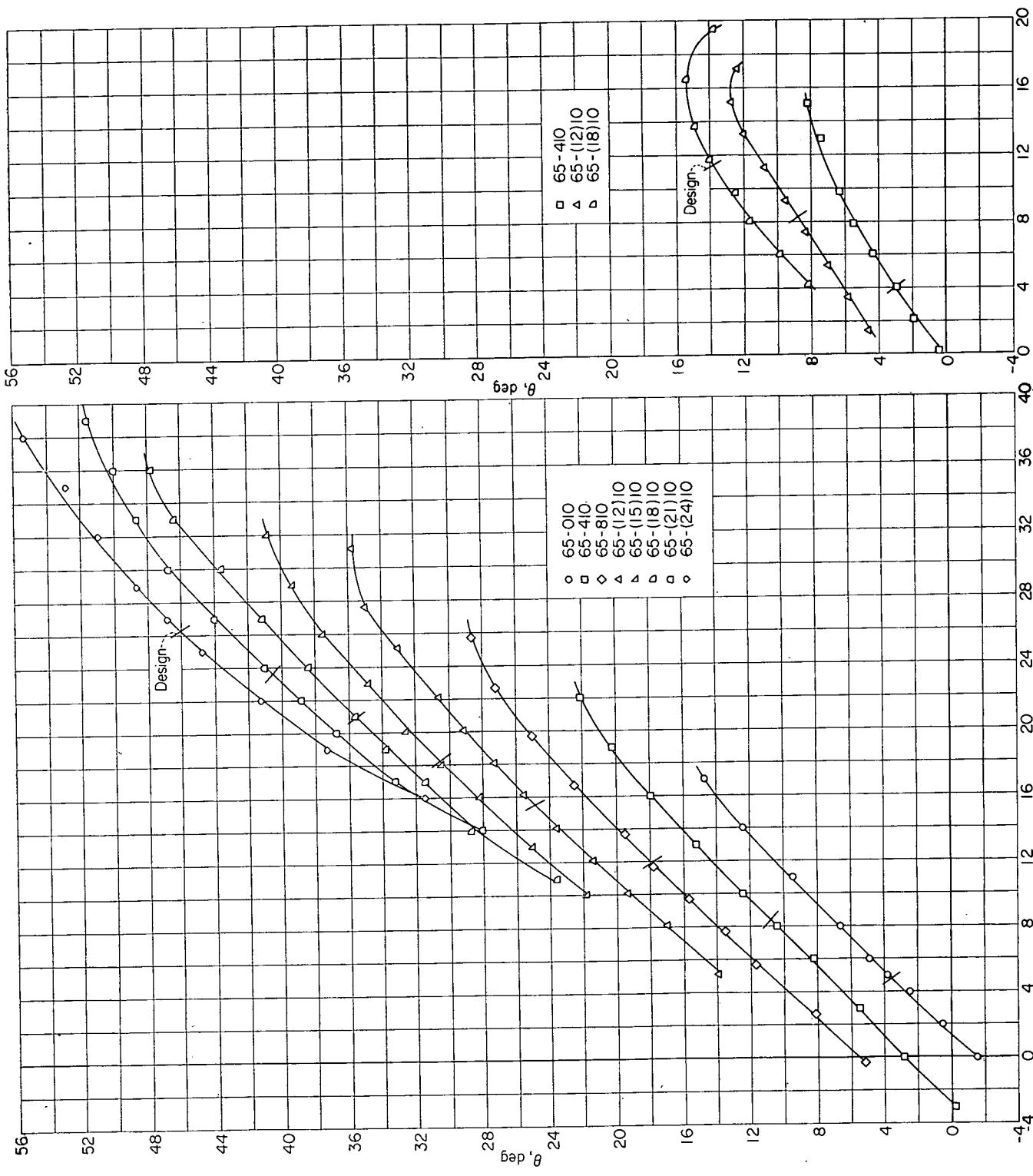


FIGURE 98.—Summary of relationship between turning angle θ and angle of attack α_1 for the blade sections tested at $\beta_1=45°$, $\sigma=1.50$.

FIGURE 99.—Summary of relationship between turning angle θ and angle of attack α_1 for the blade sections tested at $\beta_1=60°$, $\sigma=0.50$.

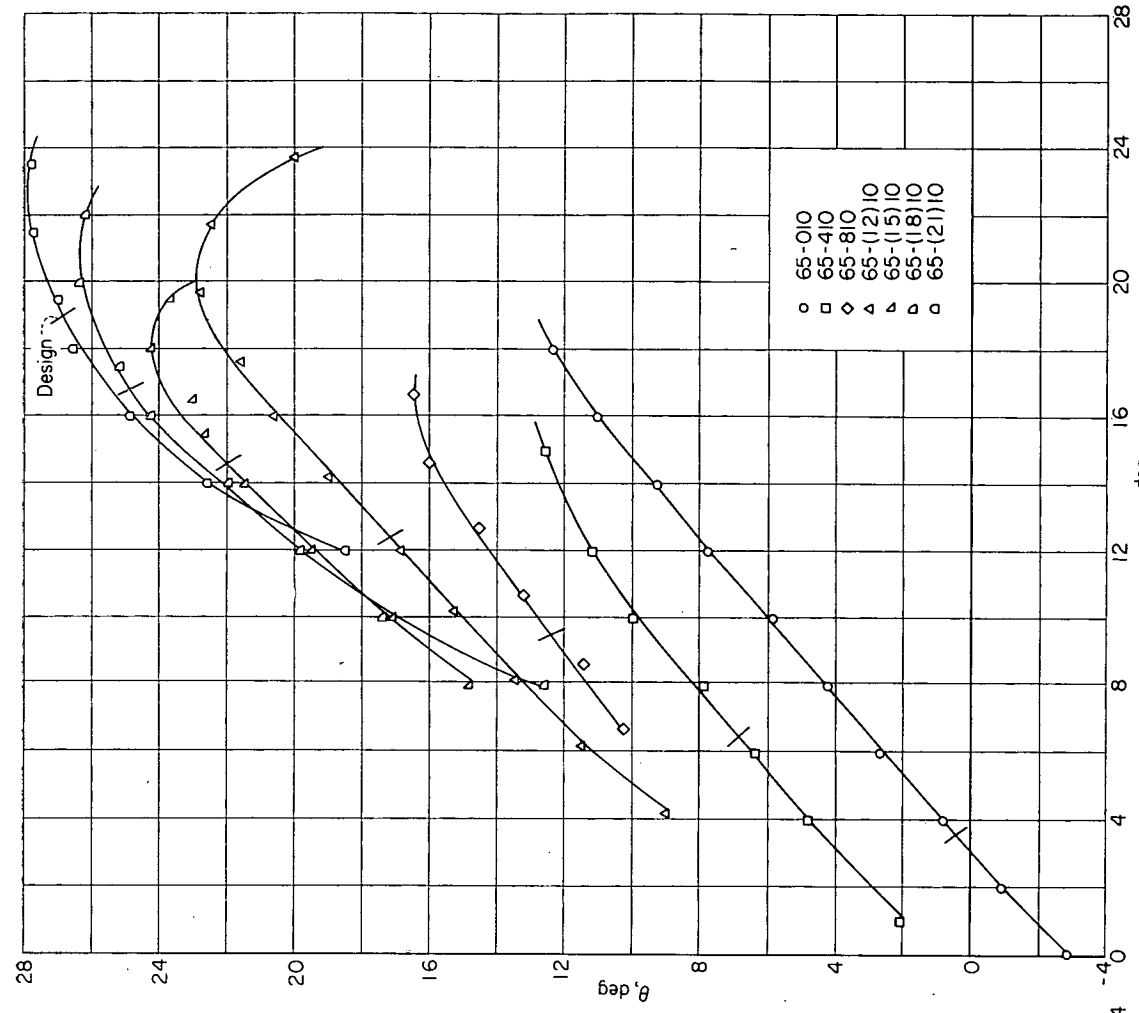


FIGURE 101.—Summary of relationship between turning angle θ and angle of attack α_1 for the blade sections tested at $\beta_1=60°$, $\sigma=1.00$.

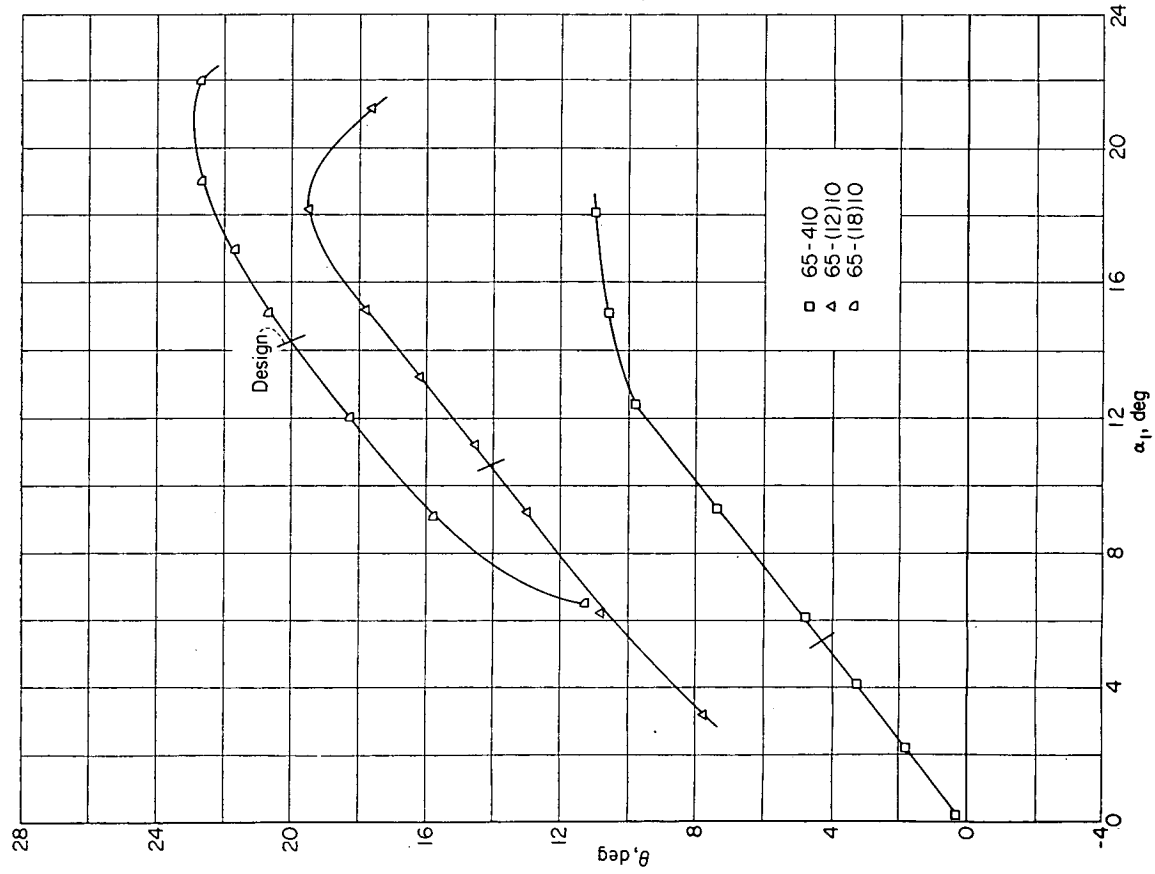


FIGURE 100.—Summary of relationship between turning angle θ and angle of attack α_1 for the blade sections tested at $\beta_1=60°$, $\sigma=0.75$.

526597—60——51

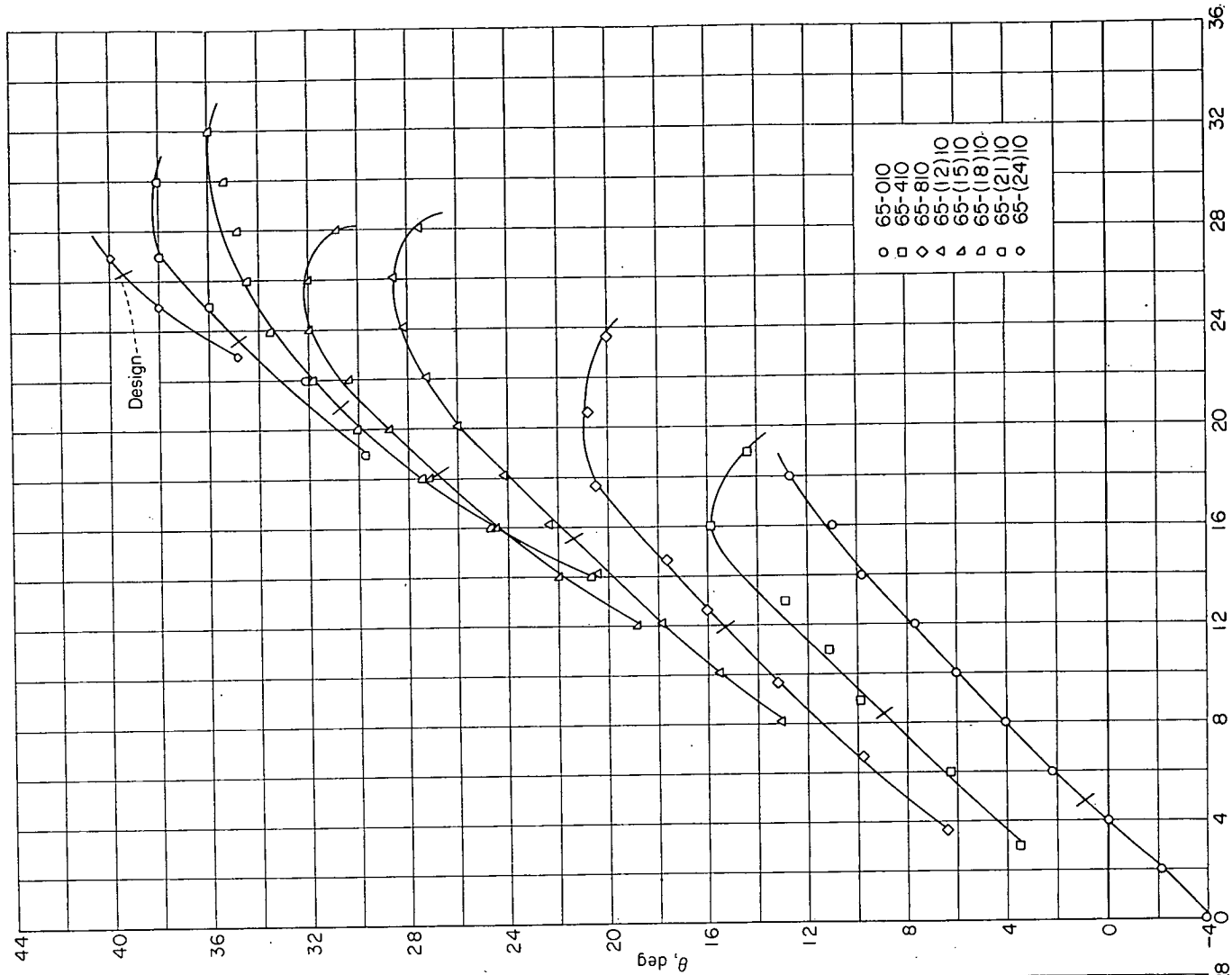


FIGURE 103.—Summary of relationship between turning angle θ and angle of attack α_1 for the blade sections tested at $\beta_1=60°$, $\sigma=1.50$.

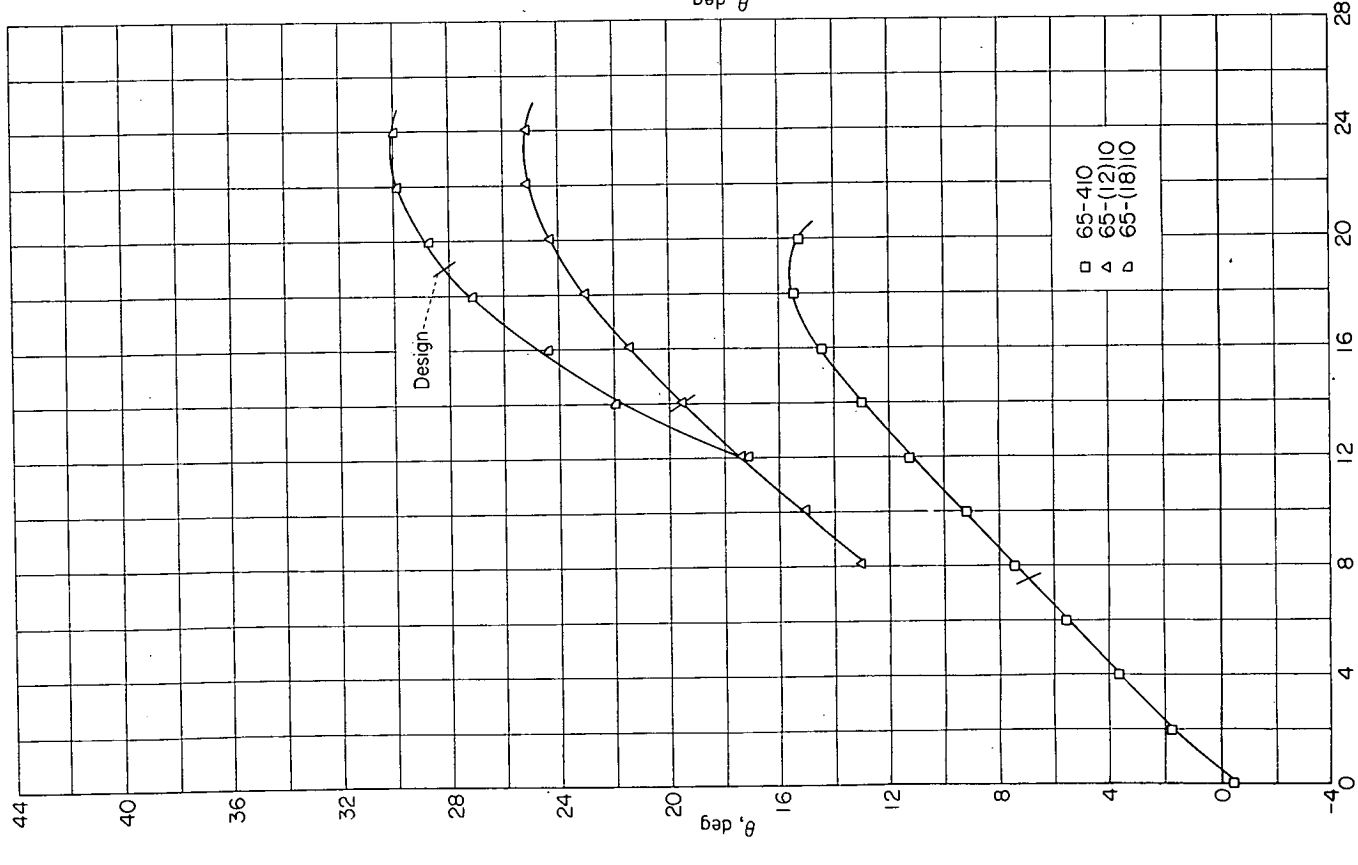


FIGURE 102.—Summary of relationship between turning angle θ and angle of attack α_1 for the blade sections tested at $\beta_1=60°$, $\sigma=1.25$.

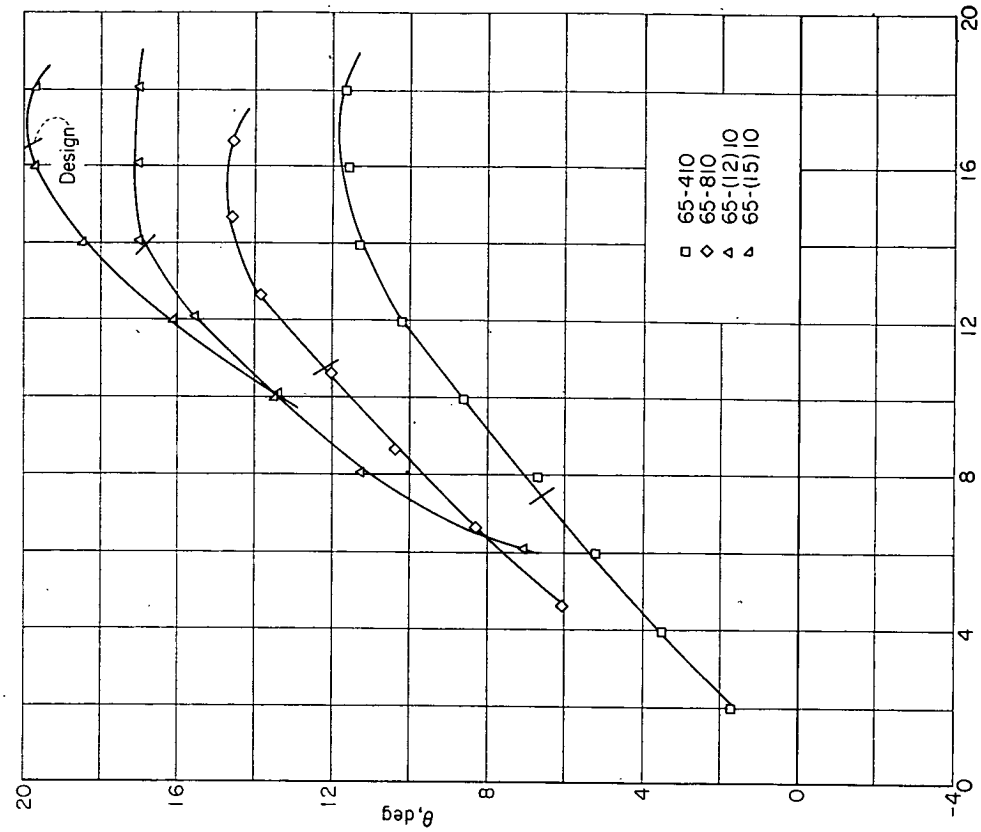


FIGURE 105.—Summary of relationship between turning angle θ and angle of attack α_1 for the blade sections tested at $\beta_1 = 70°$, $\sigma = 1.25$.

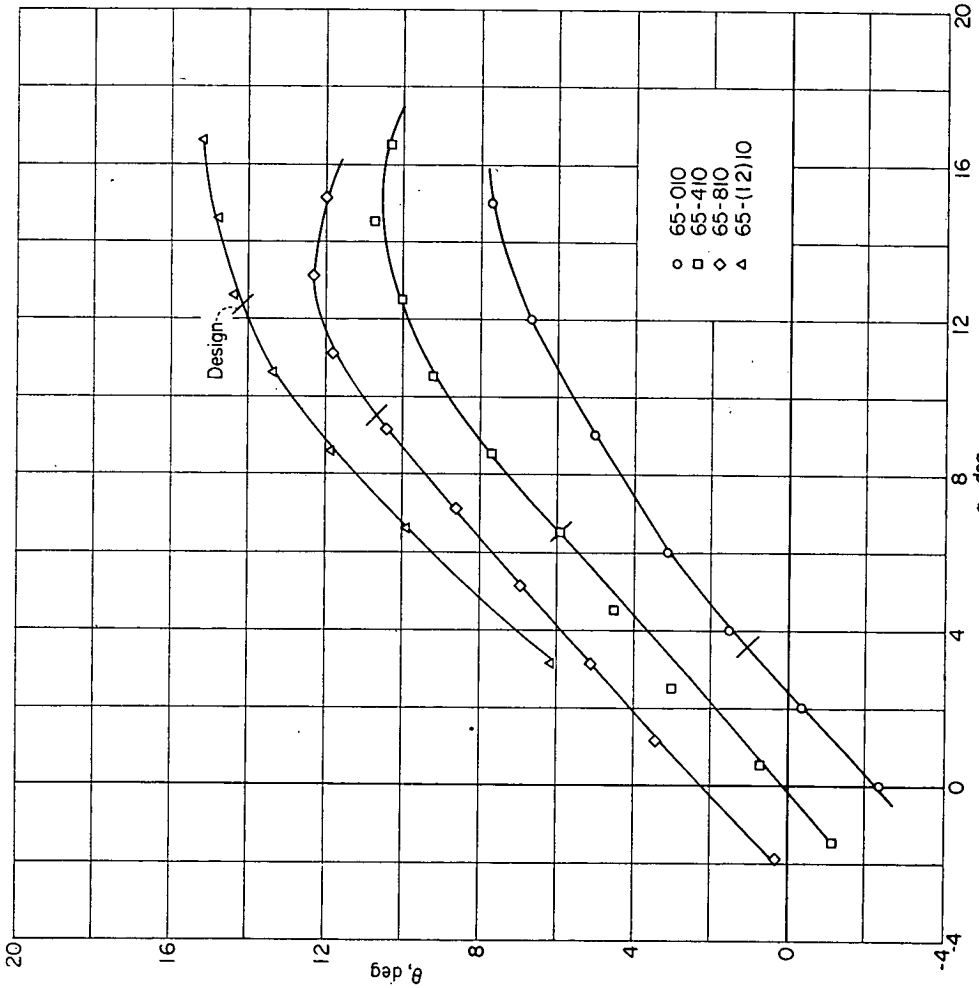


FIGURE 104.—Summary of relationship between turning angle θ and angle of attack α_1 for the blade sections tested at $\beta_1 = 70°$, $\sigma = 1.00$.

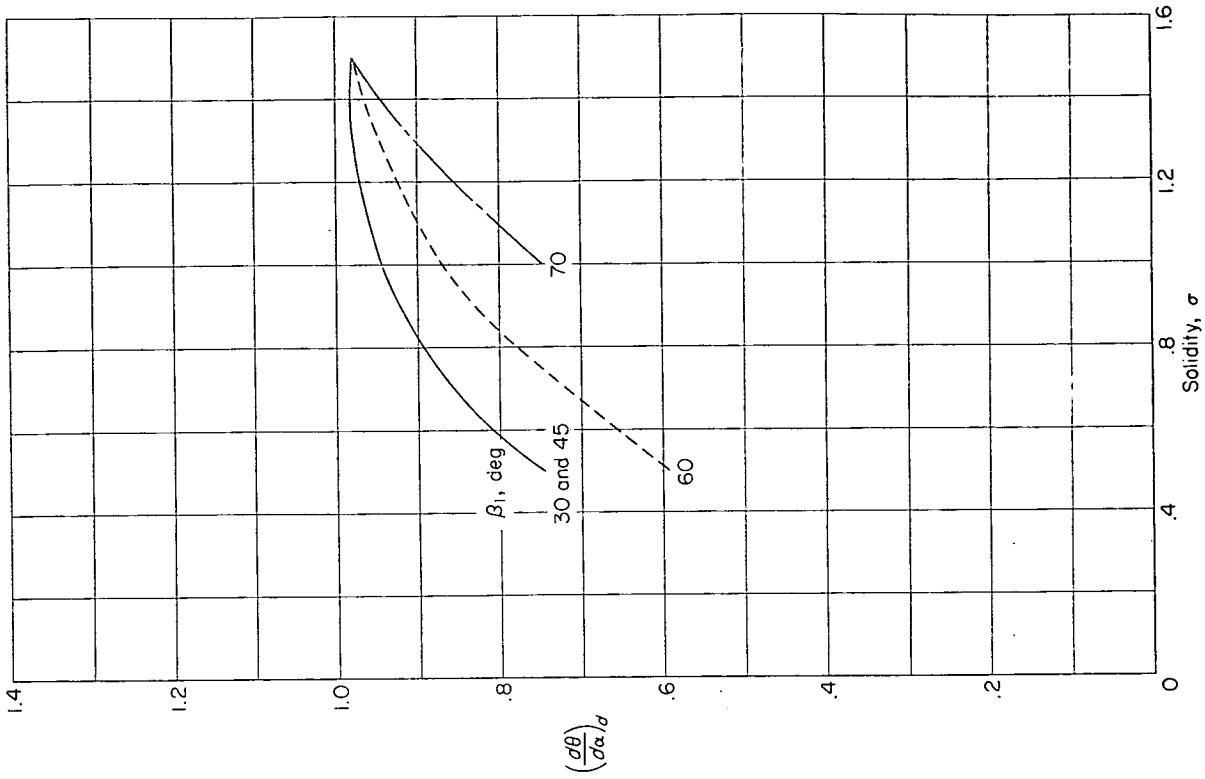


FIGURE 107.—Variation of slope of curves of turning angle against angle of attack at design conditions with solidity and inlet angle. The slopes are averages for the moderate camber range.

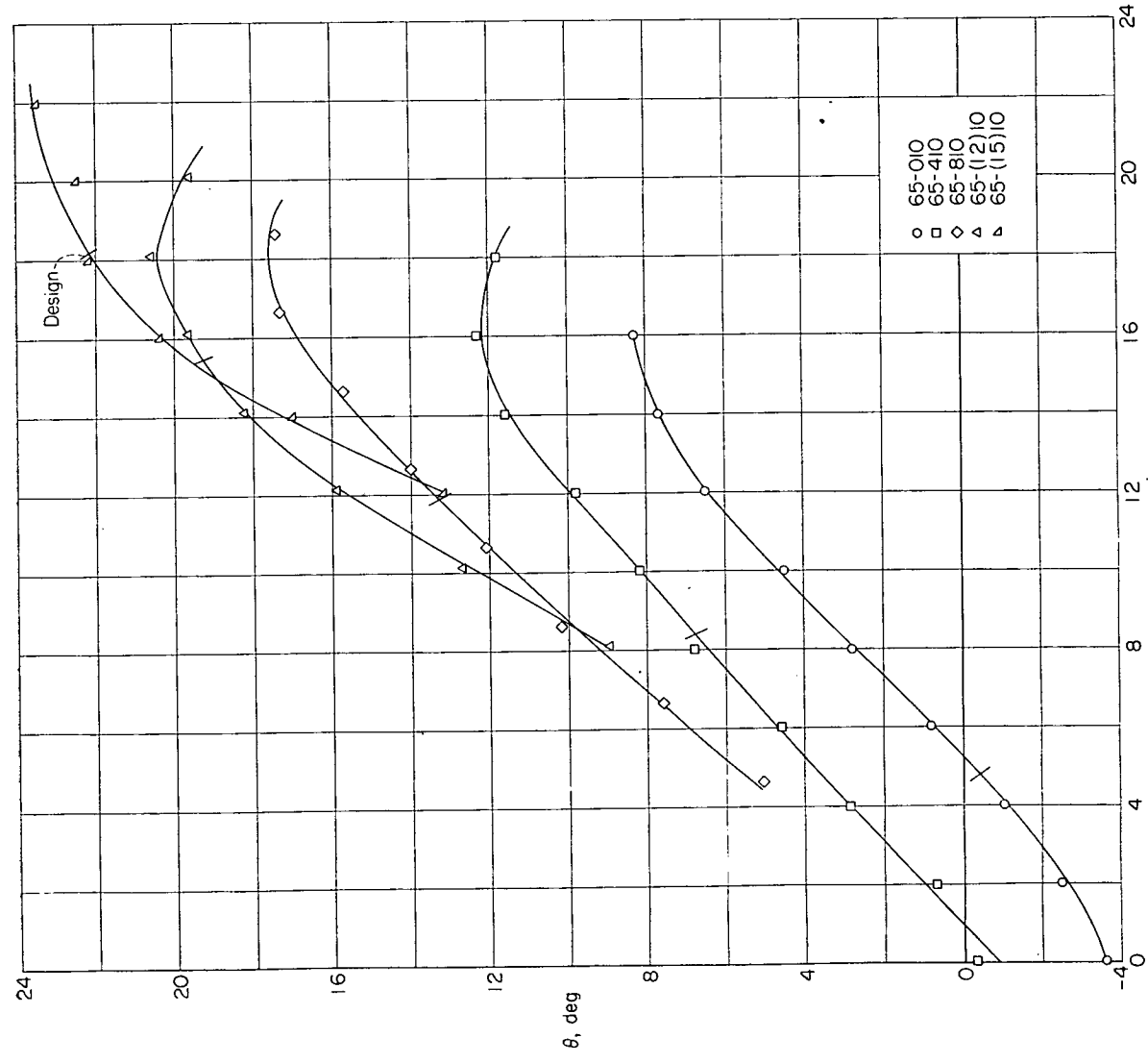


FIGURE 106.—Summary of relationship between turning angle θ and angle of attack α_1 for the blade sections tested at $\beta_1=70°$, $\sigma=1.50$.

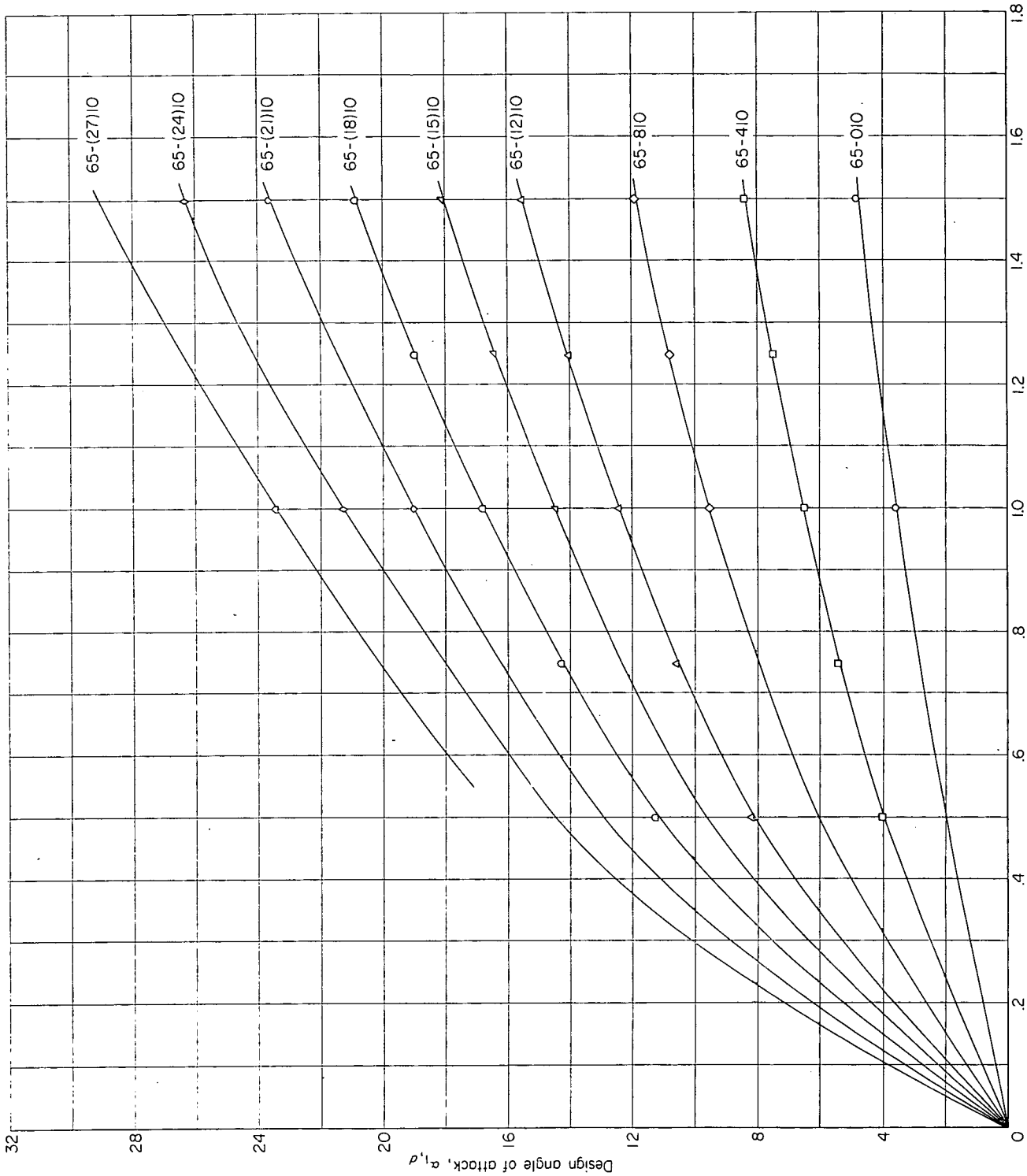
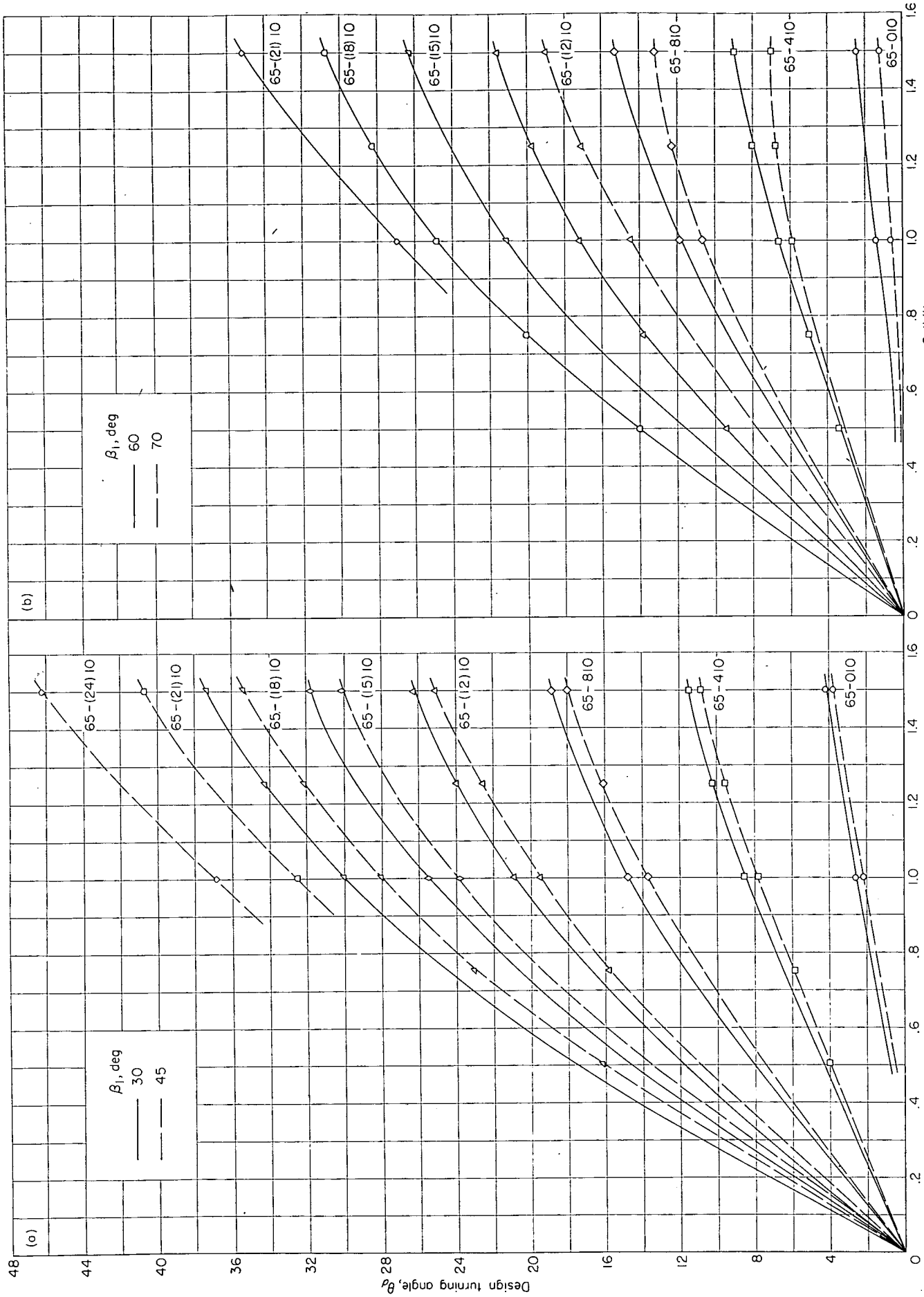


FIGURE 108.—Variation of design angle of attack with solidity for the sections tested.



(a) Inlet angles of 30° and 45°. (b) Inlet angles of 60° and 70°.

FIGURE 109.—Variation of design turning angle with solidity and inlet angle for the sections tested.

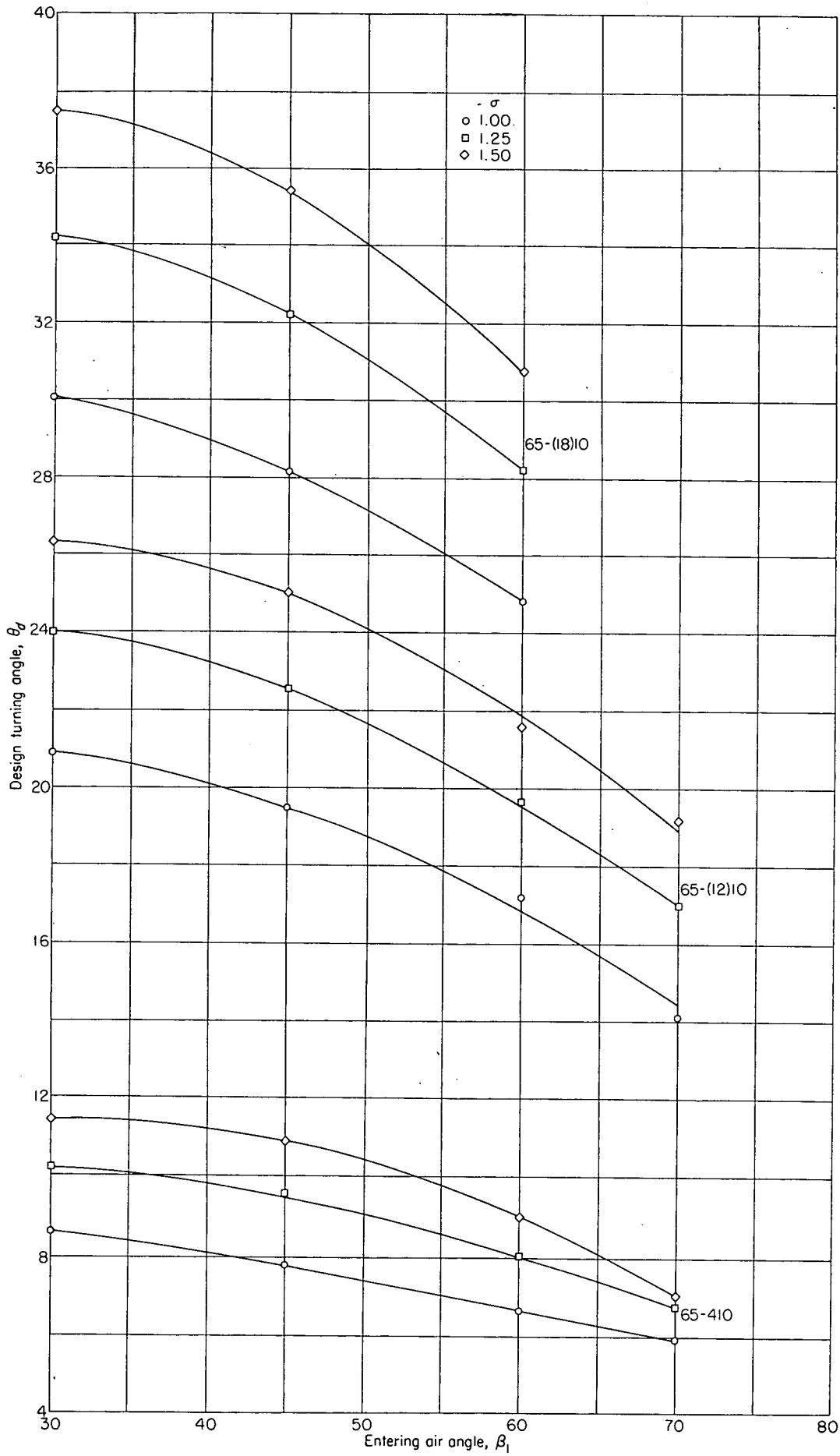
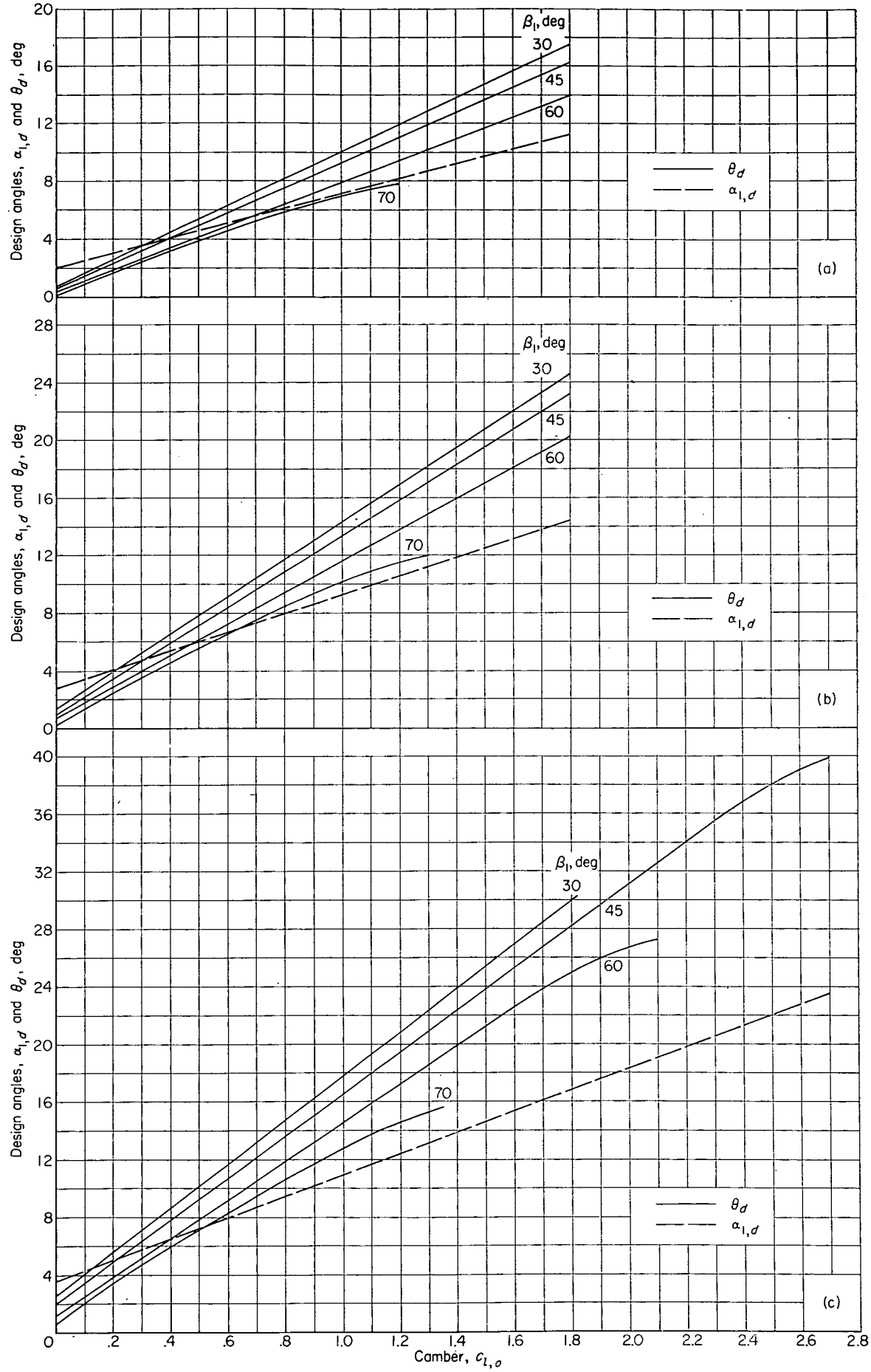
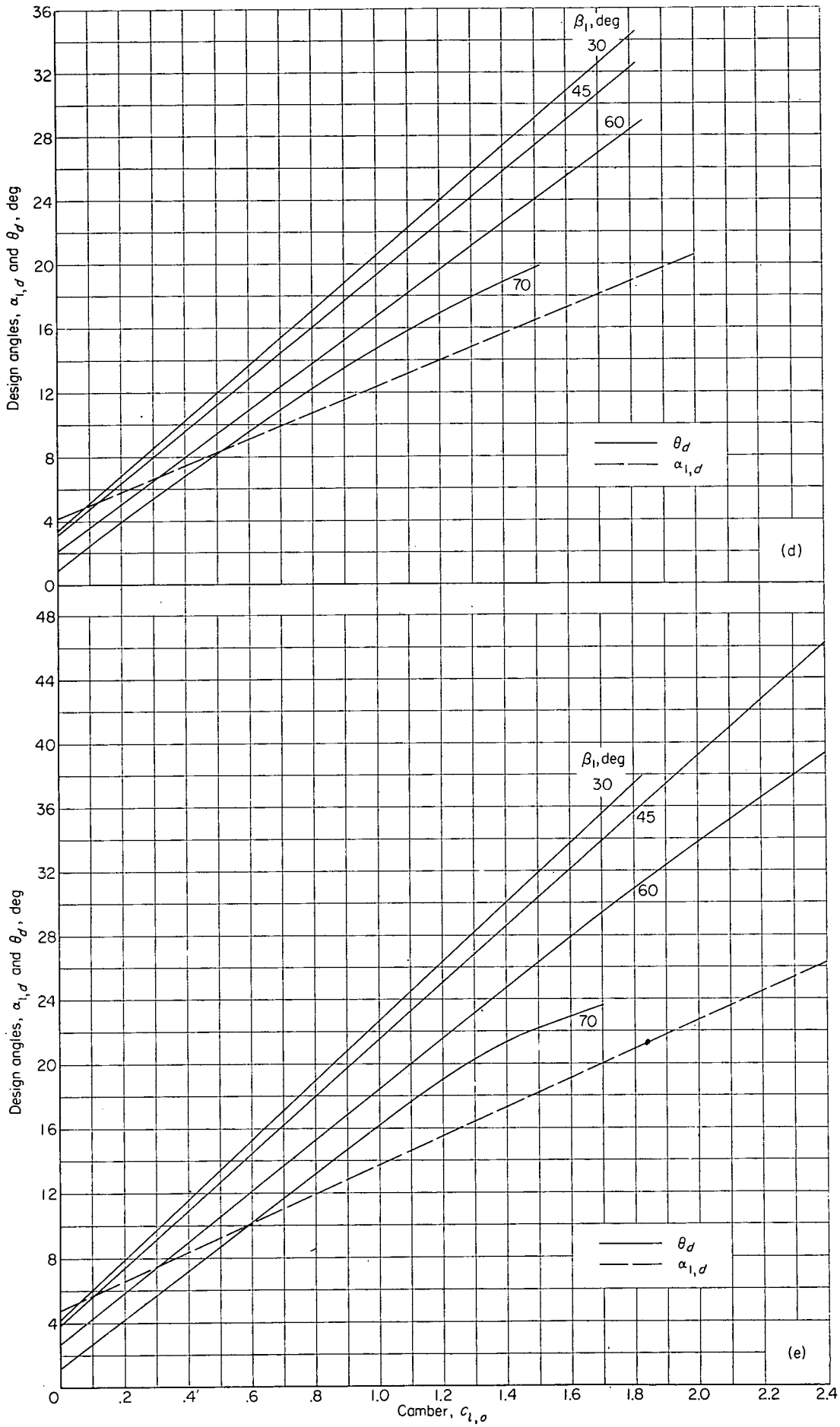


FIGURE 110.—Variation of design turning angle with inlet angle and solidity for typical sections.



(a) $\sigma=0.50$. (b) $\sigma=0.75$. (c) $\sigma=1.00$.

FIGURE 111.—Variation of design turning angle and design angle of attack with camber and inlet angle.



(d) $\sigma = 1.25$. (e) $\sigma = 1.50$.

FIGURE 111.—Concluded.

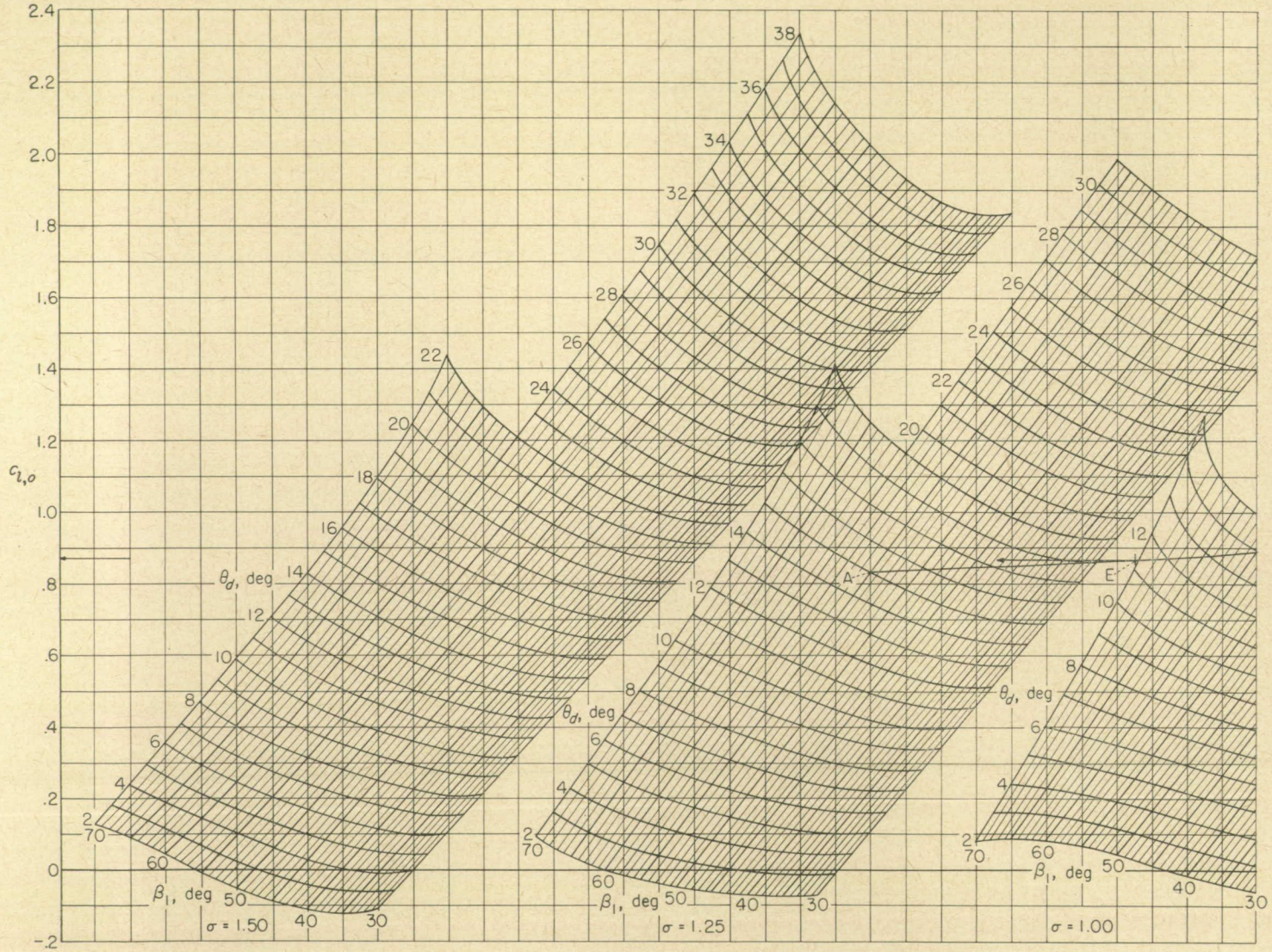


FIGURE 112.—Design-camber selection chart for NACA 65–($c_{l,o}$)10 sections.

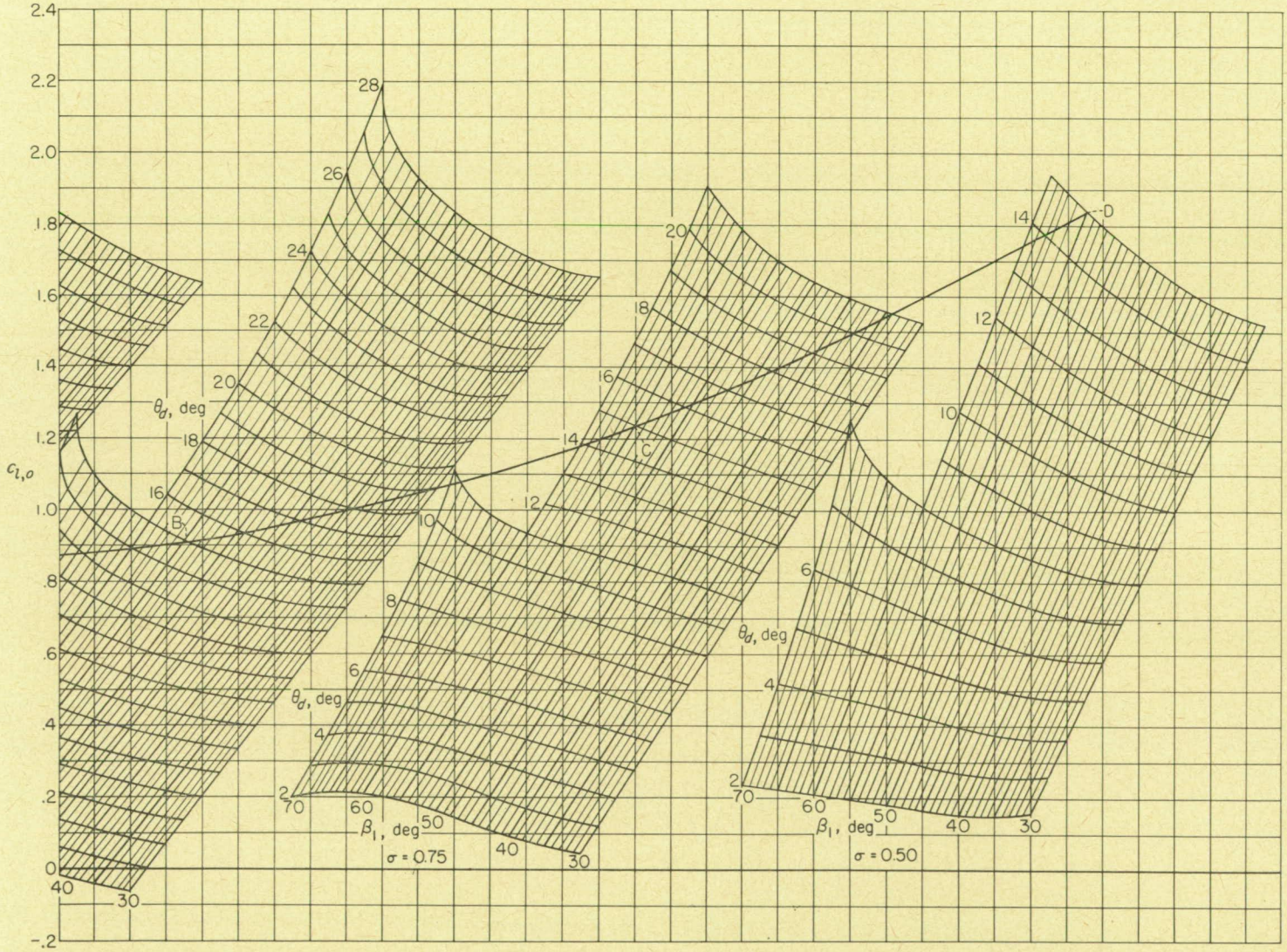


FIGURE 112.—Concluded.

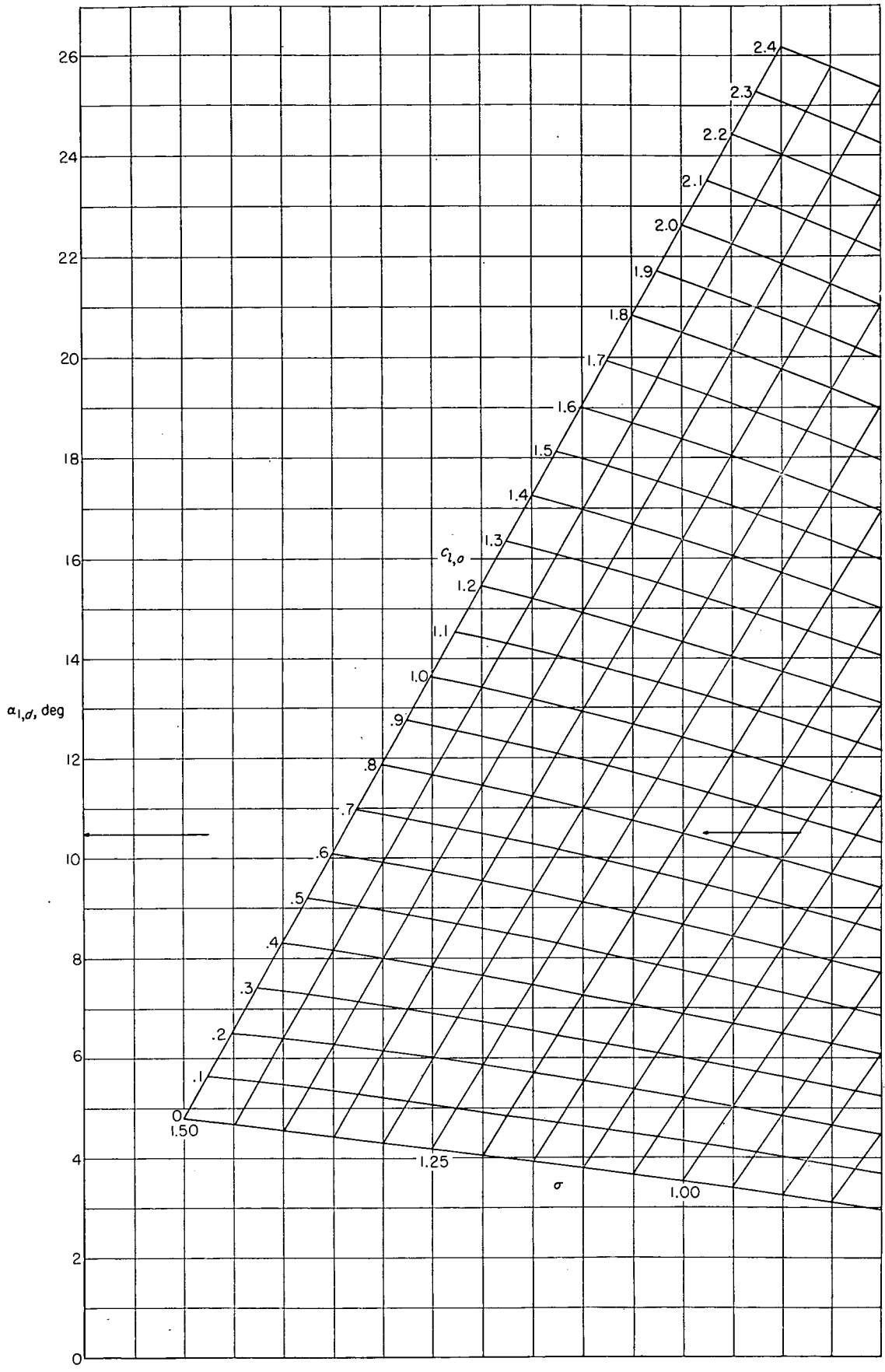


FIGURE 113.—Design angle-of-attack chart for NACA 65-($c_{l,o}$)10 sections.

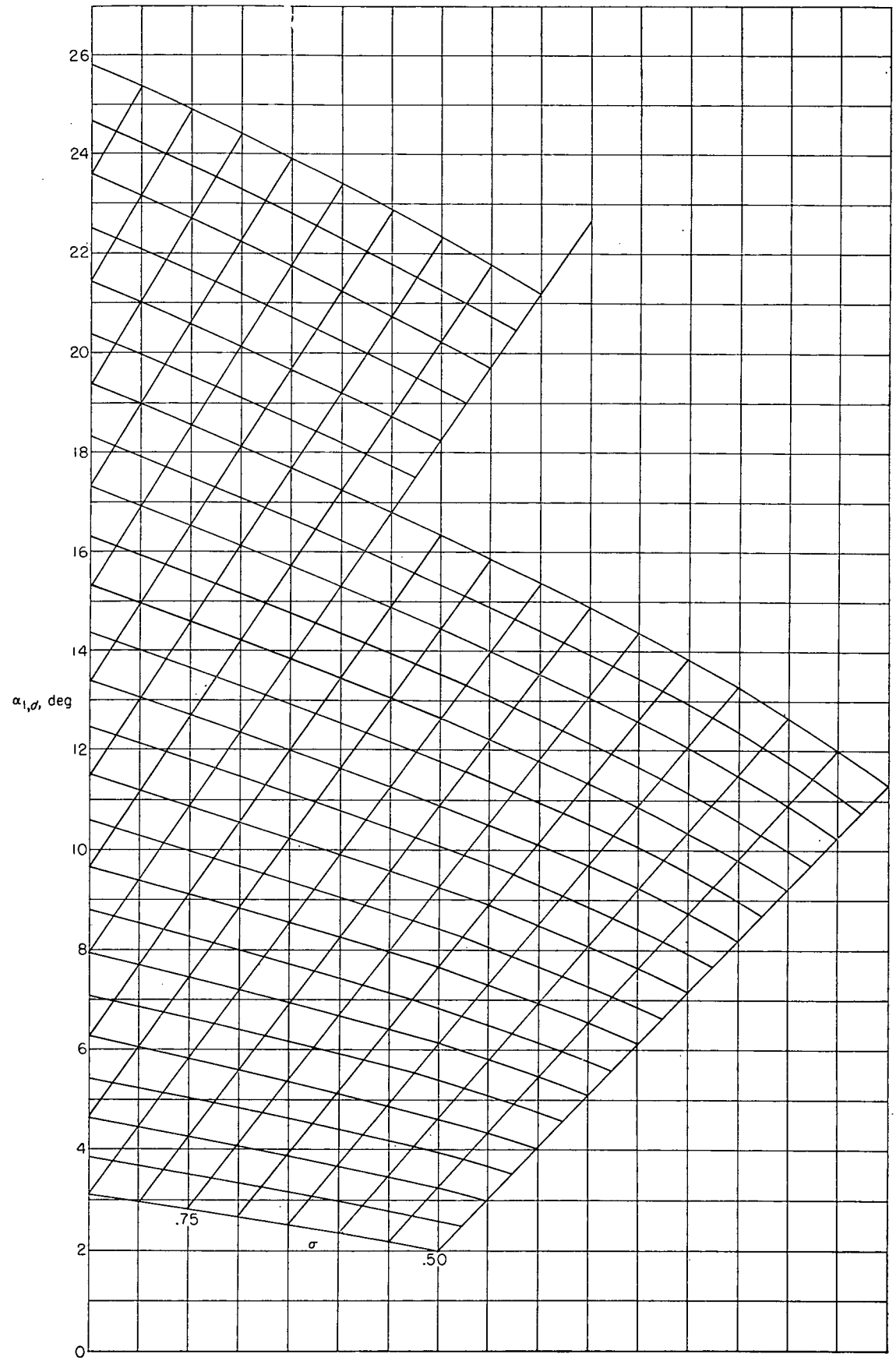


FIGURE 113.—Concluded.

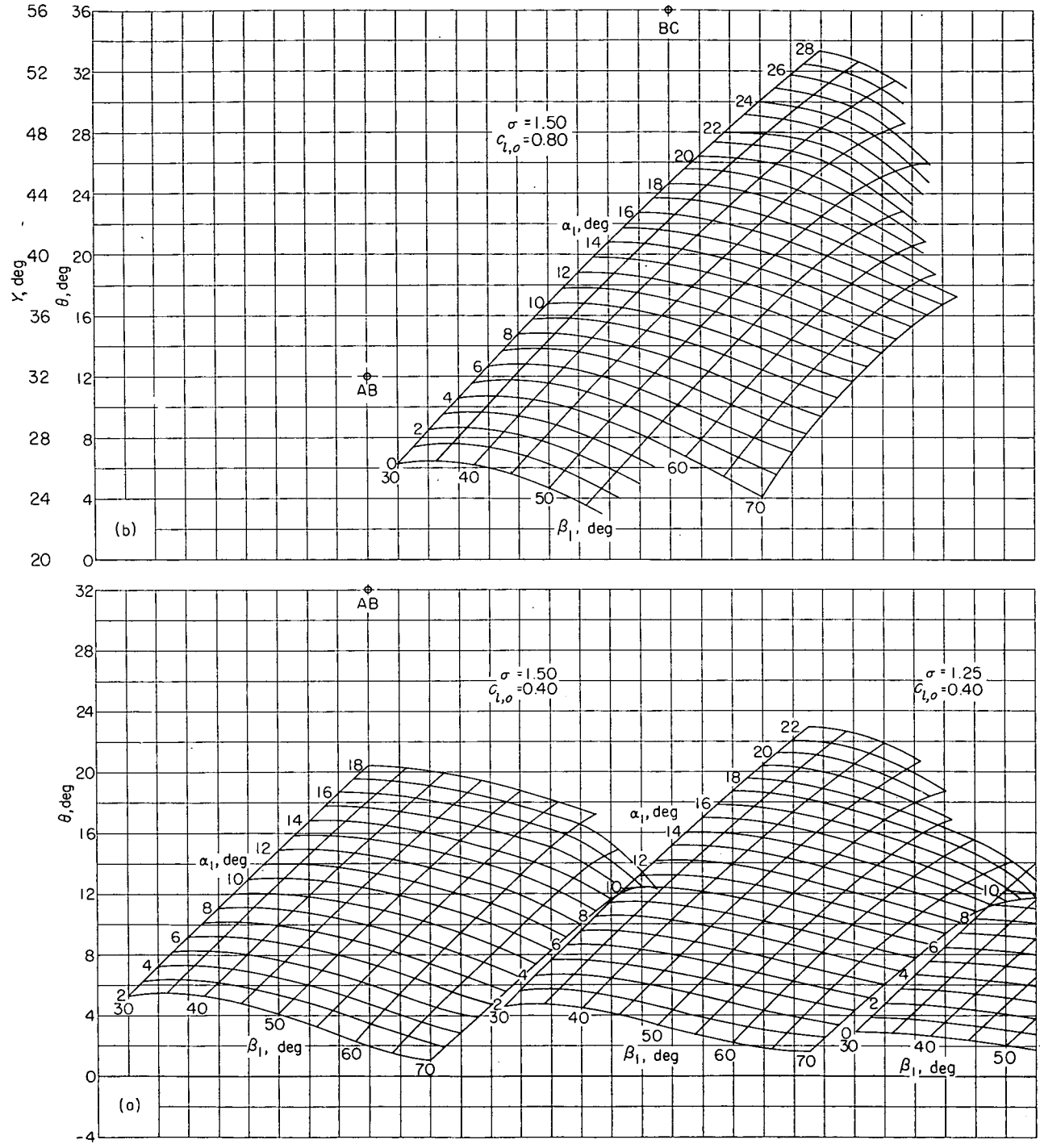


FIGURE 114.—Off-design turning-angle carpets for NACA 65-($c_{l,o}$)10 compressor blades.

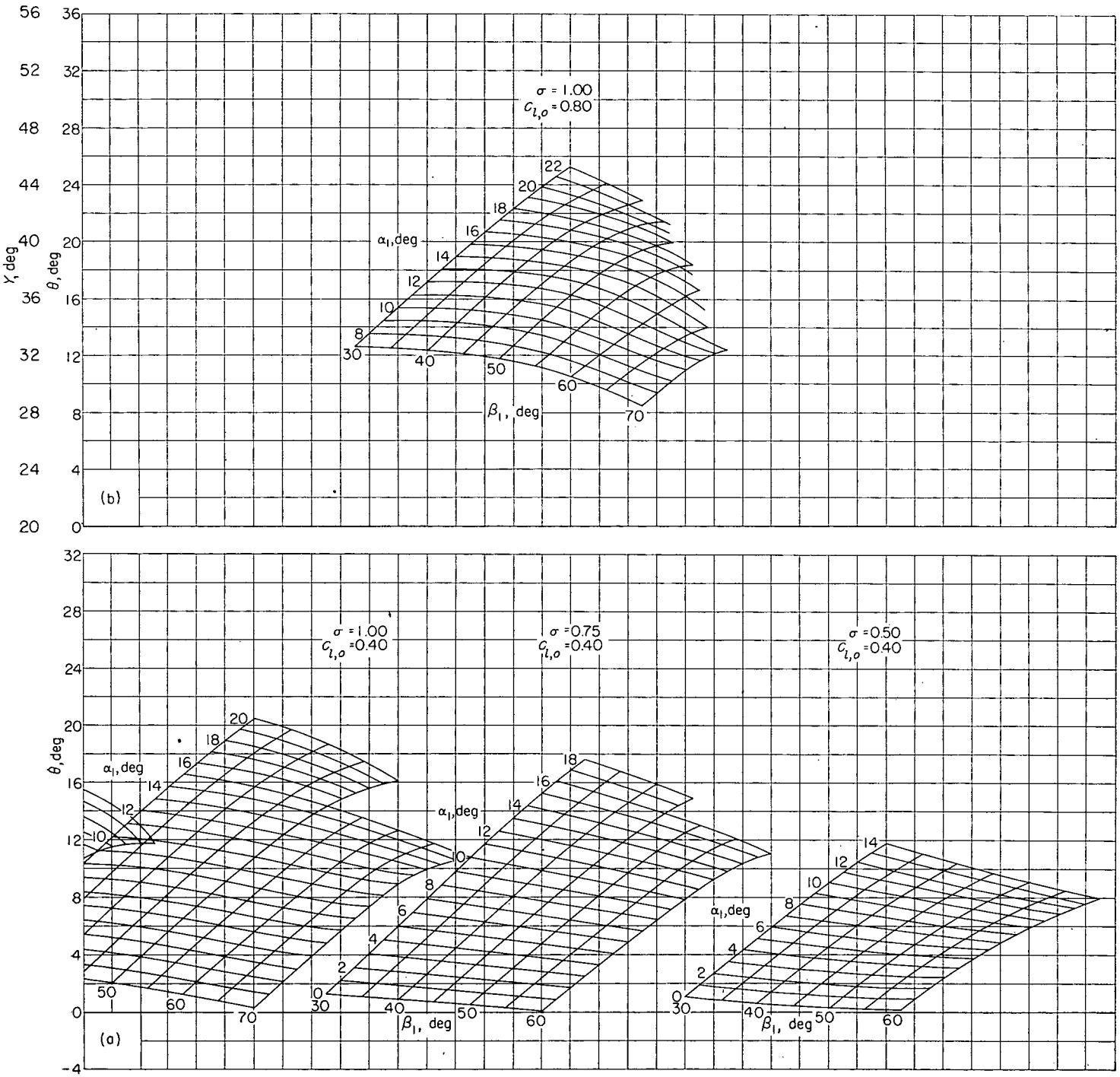


FIGURE 114.—Continued.

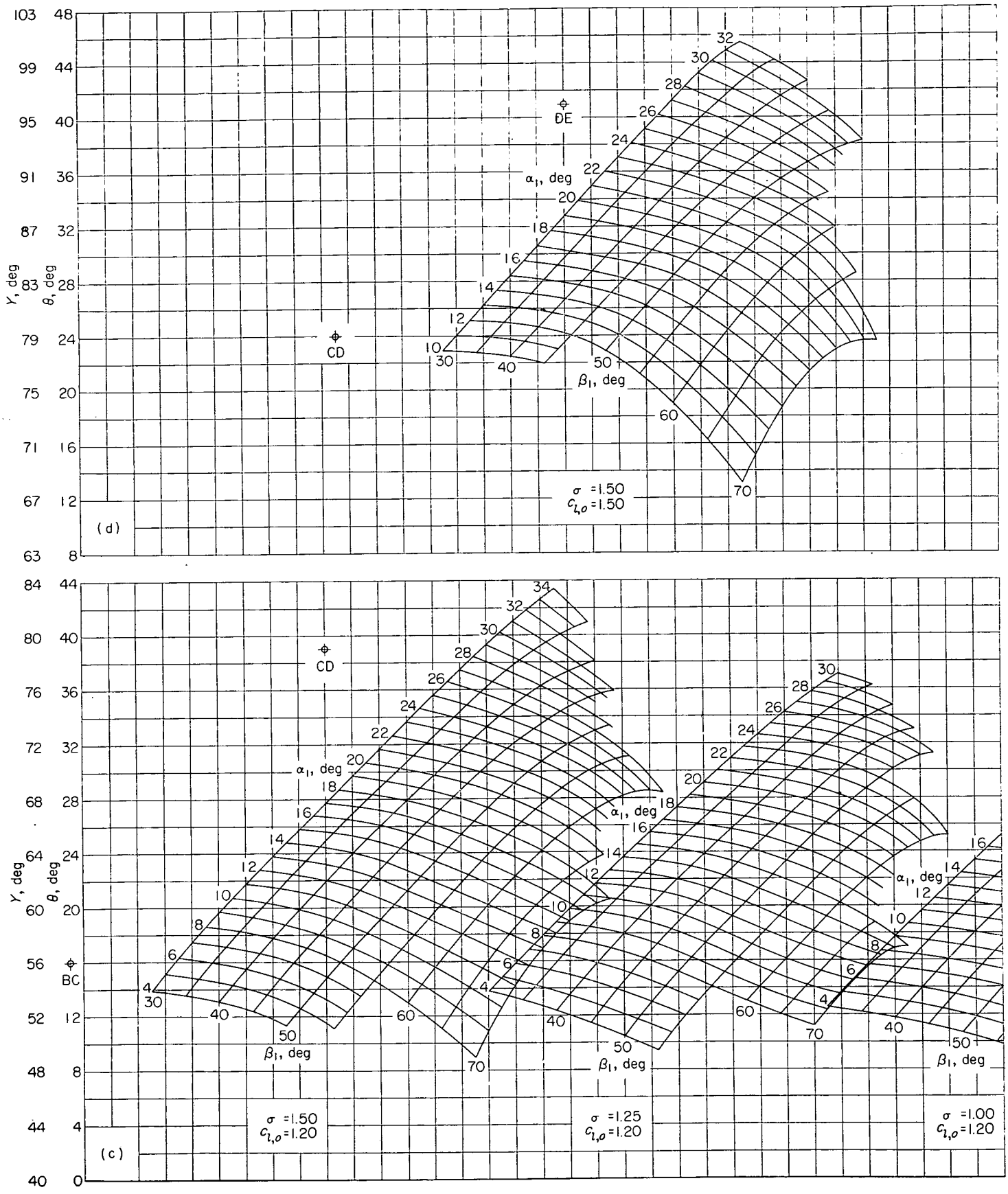


FIGURE 114.—Continued.

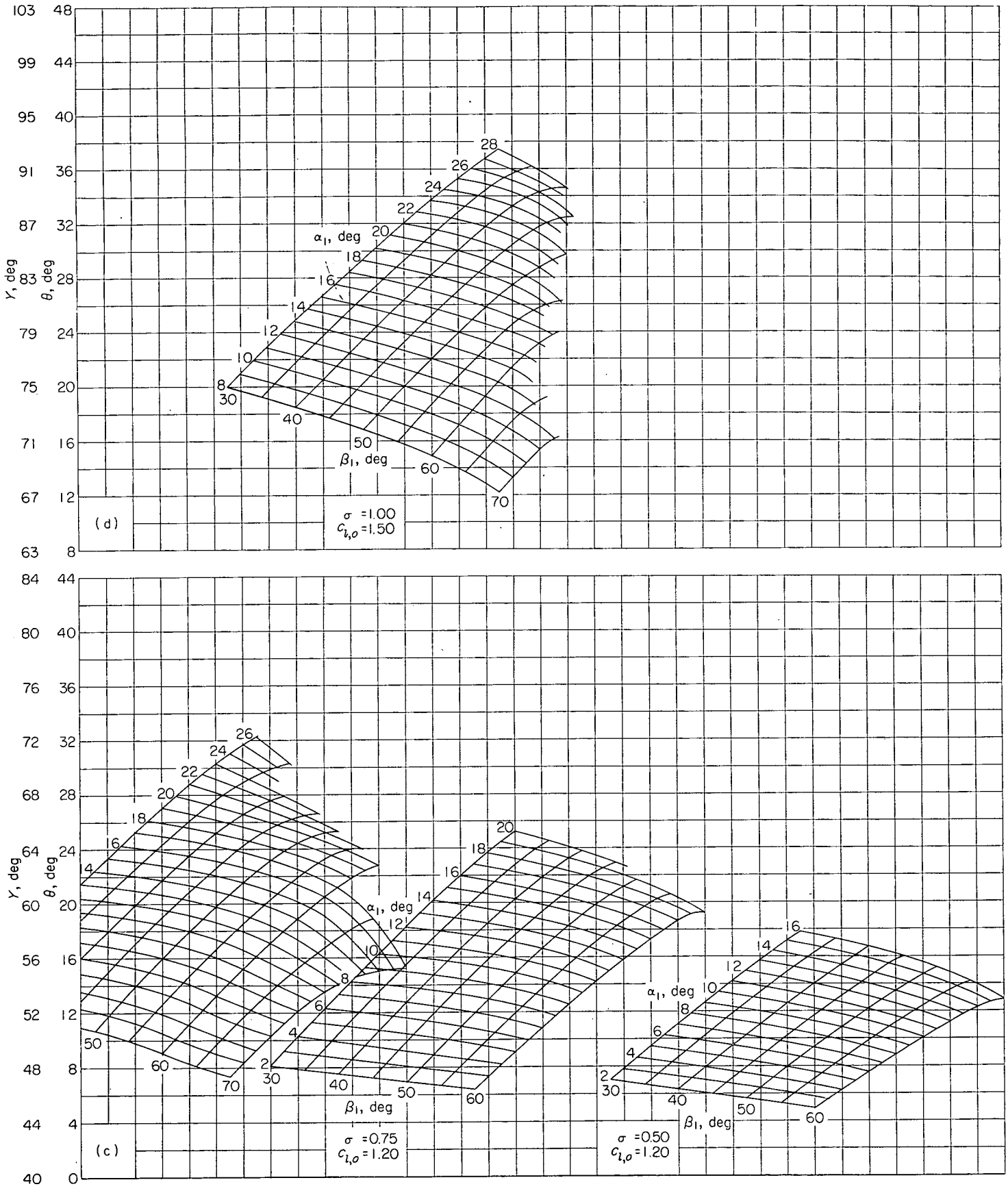


FIGURE 114.—Continued.

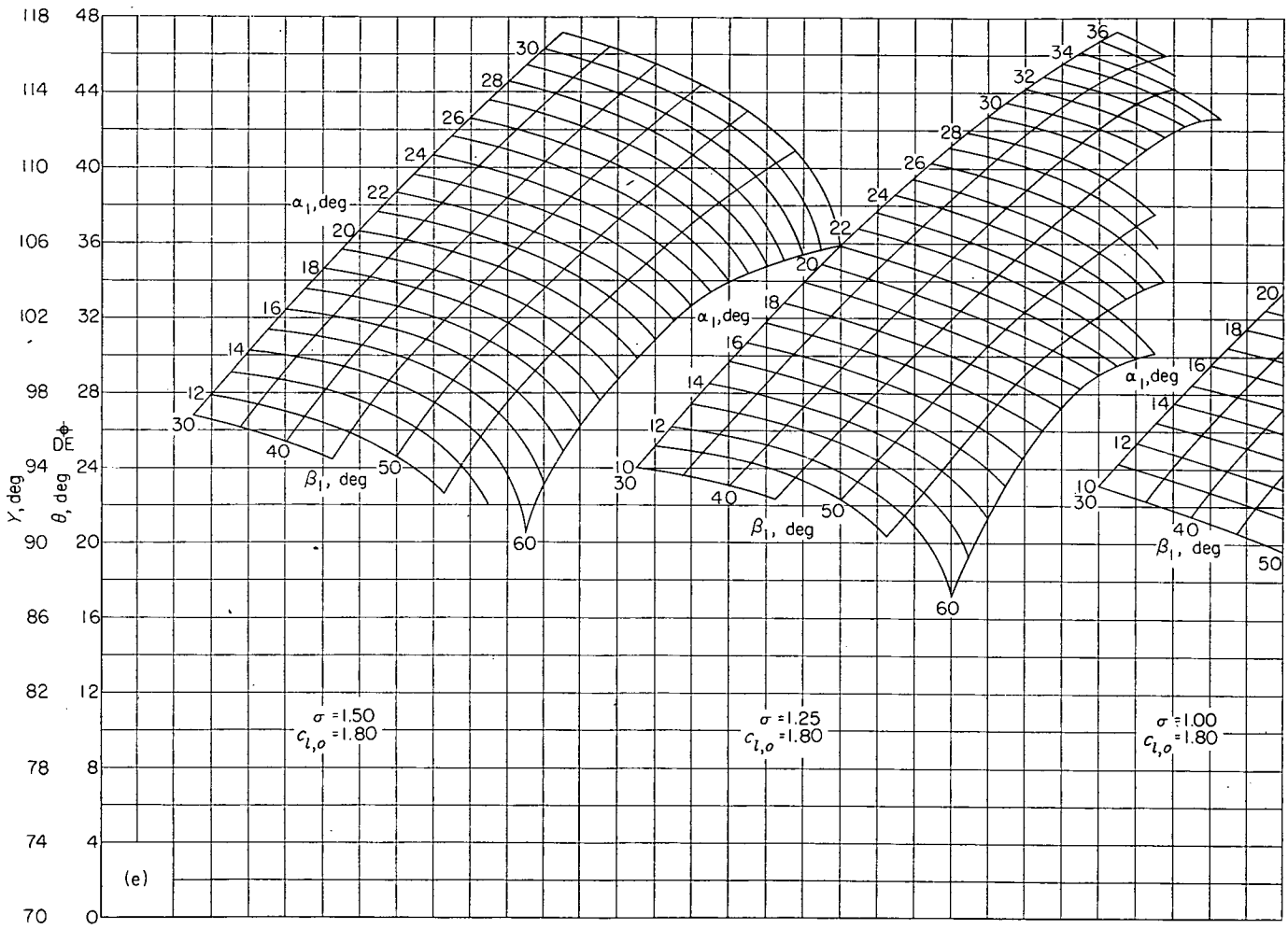


FIGURE 114.—Continued.

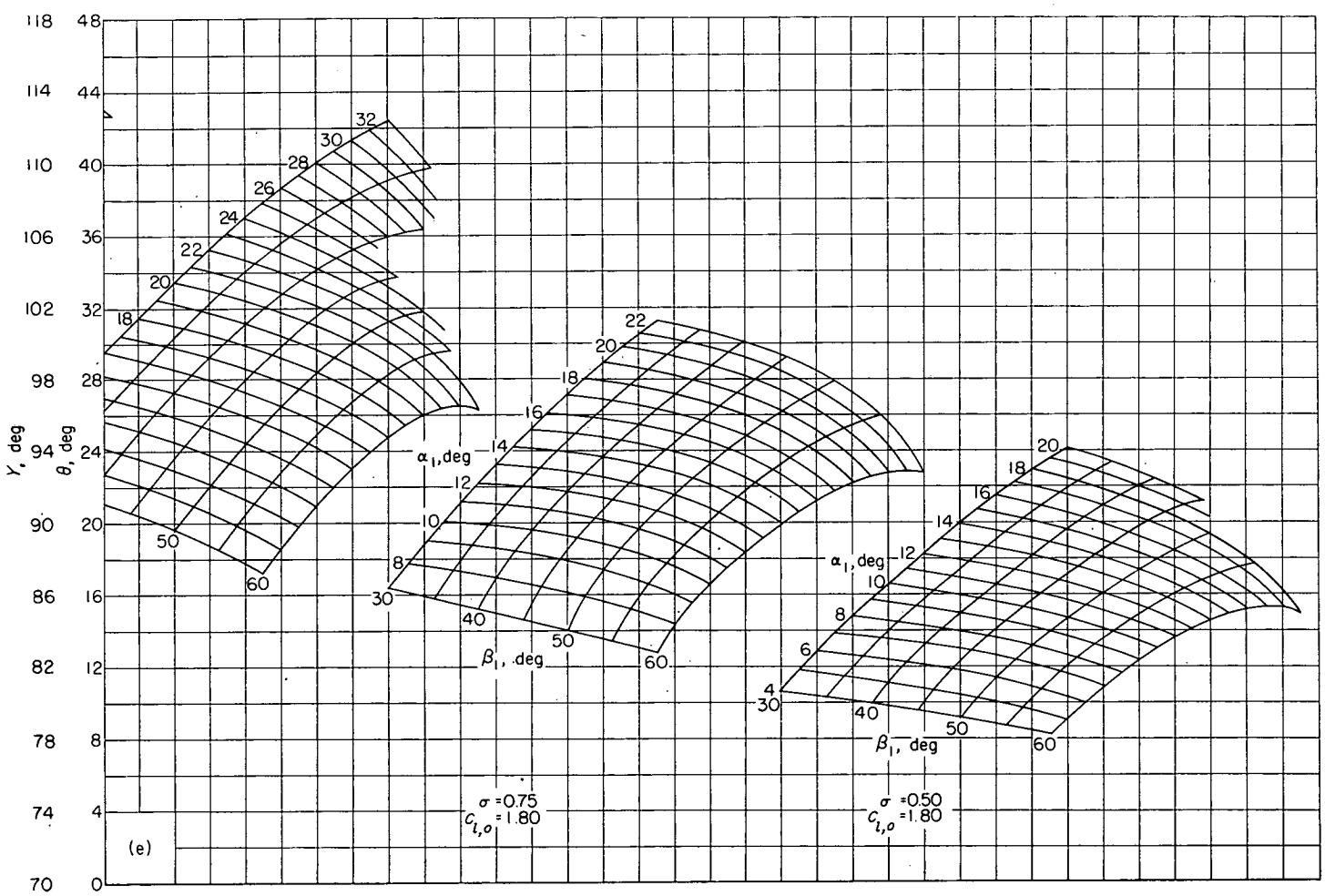


FIGURE 114.—Concluded.

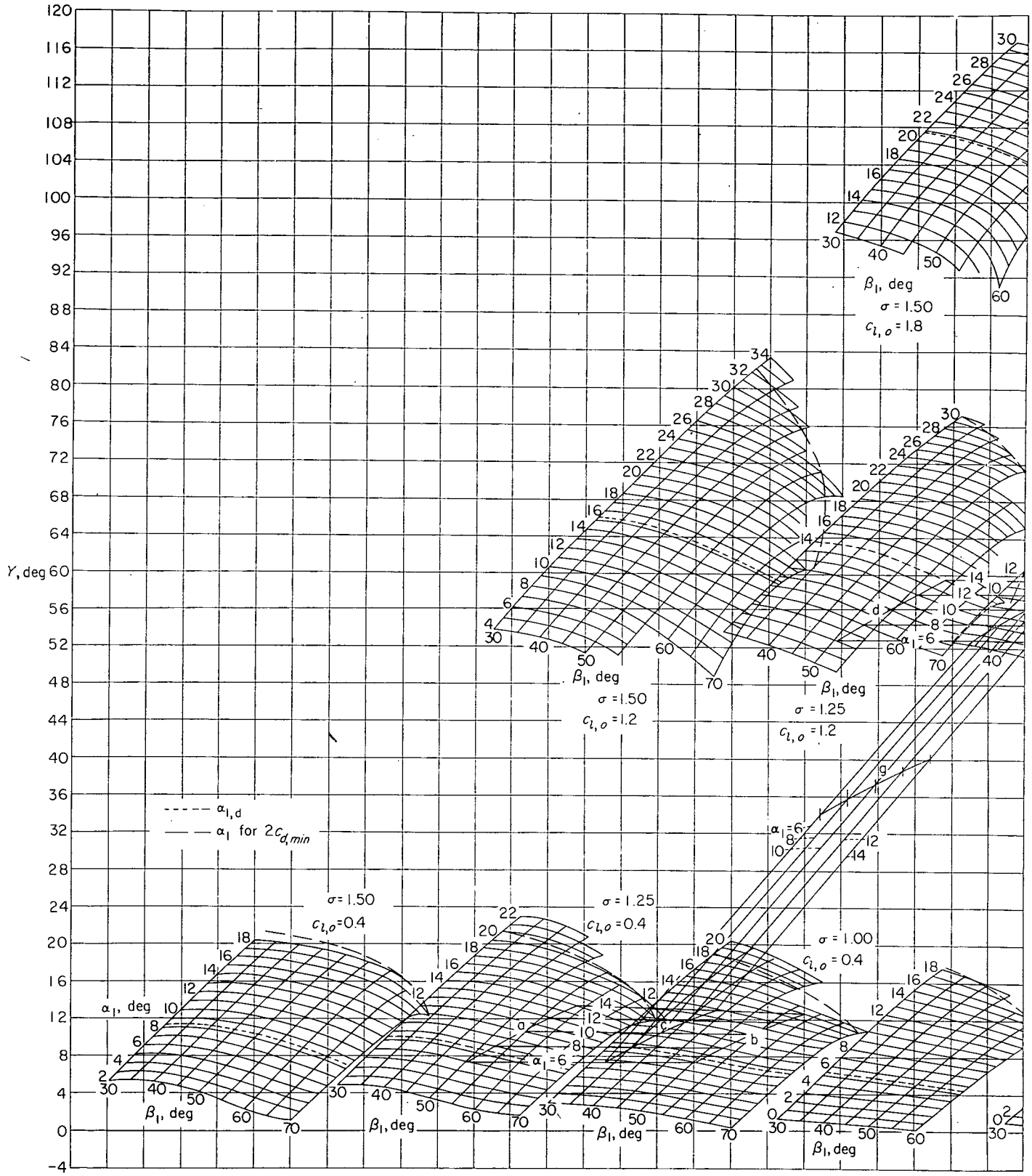


FIGURE 115.—Composite of off-design carpets for NACA 65-series sections for values of $c_{l,o}$ of 0.4, 1.2, and 1.8.

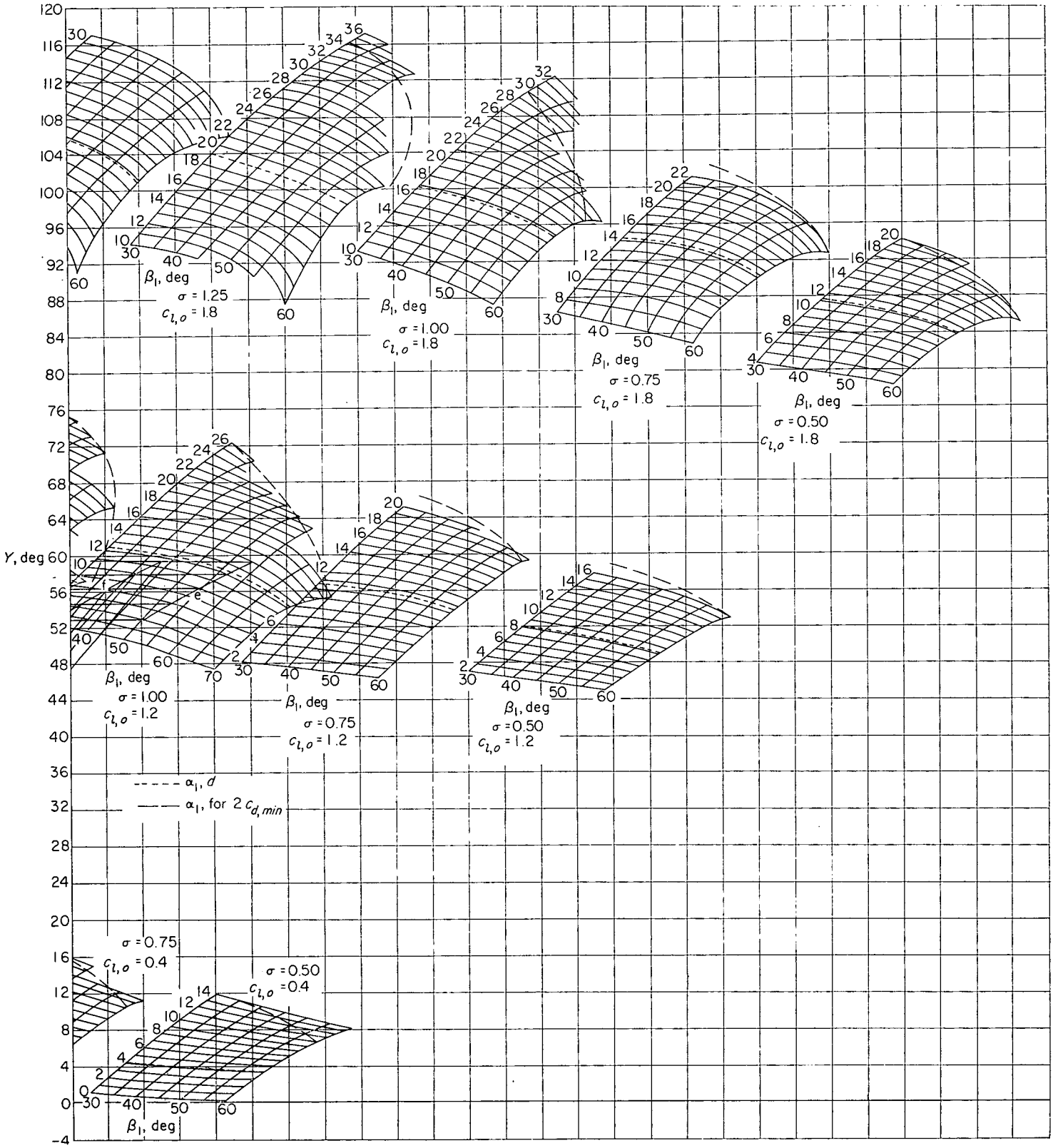
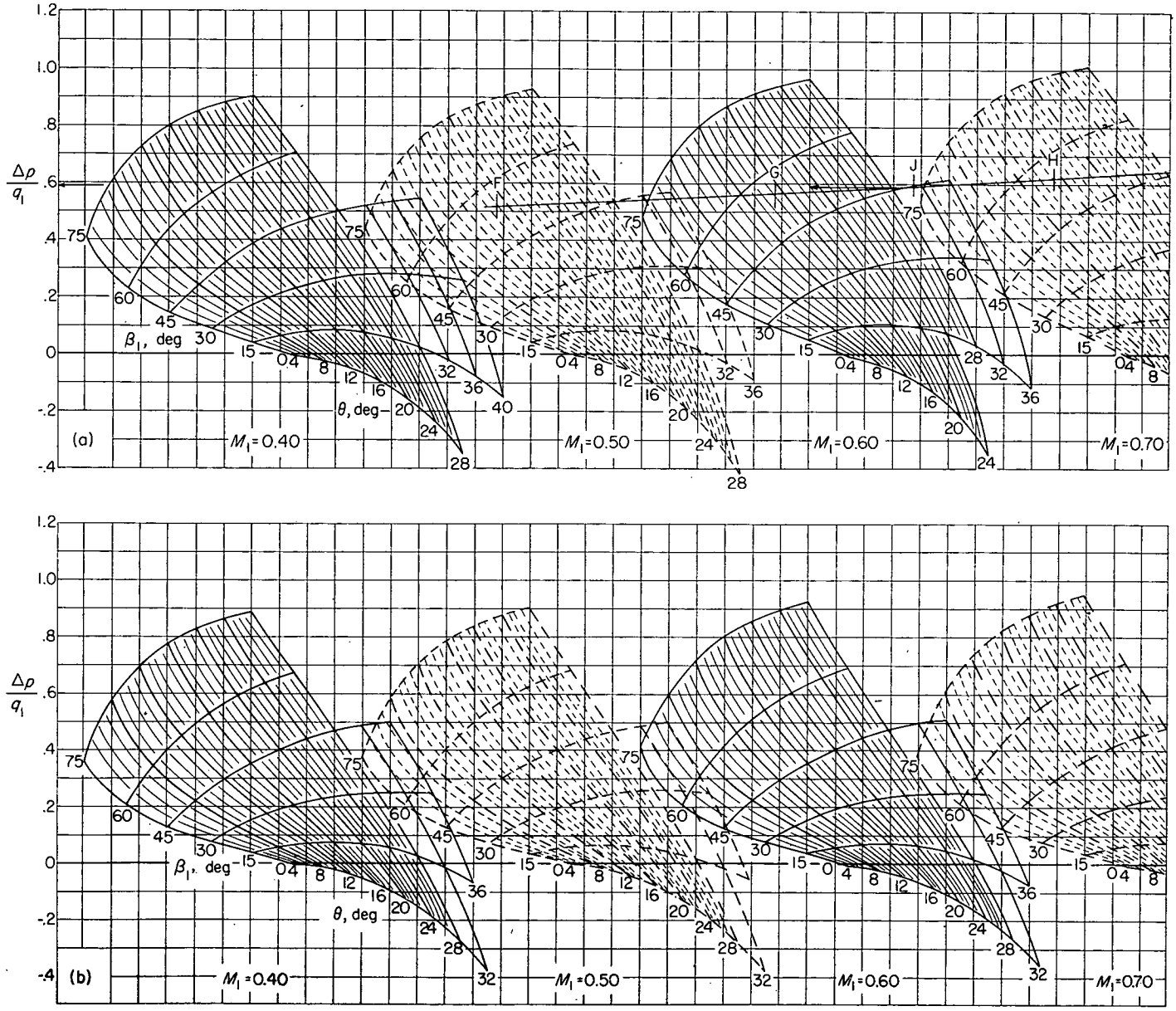
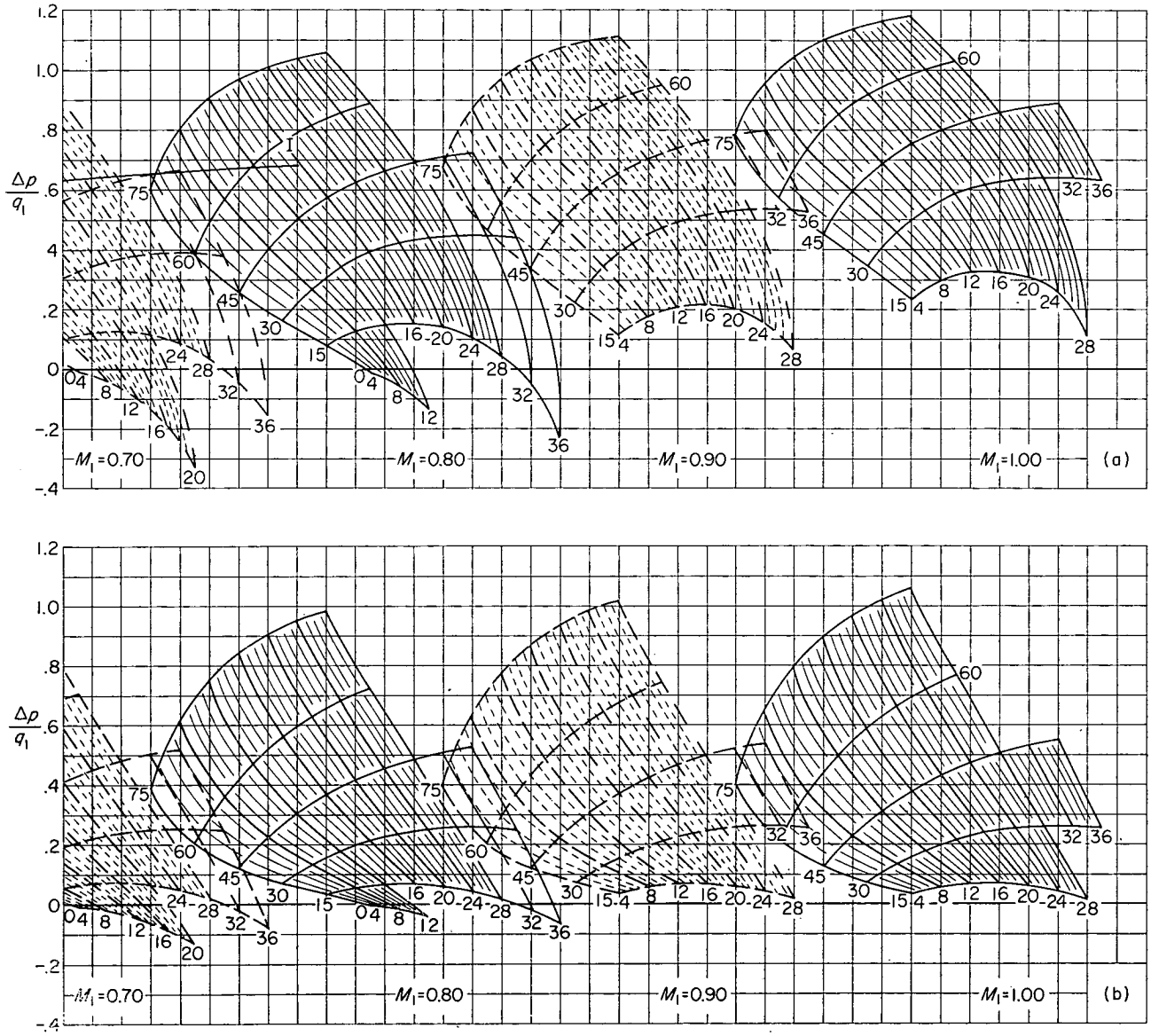


FIGURE 115.—Concluded.



(a) Constant stream-tube area.
(b) Constant axial velocity.

FIGURE 116.—Pressure-rise-coefficient carpets.



(a) Concluded.
(b) Concluded.

FIGURE 116.—Concluded.

REPORT 1369

BLOWING-TYPE BOUNDARY-LAYER CONTROL AS APPLIED TO THE TRAILING-EDGE FLAPS OF A 35° SWEPT-WING AIRPLANE[1]

By Mark W. Kelly, Seth B. Anderson, and Robert C. Innis

SUMMARY

A wind-tunnel investigation was made to determine the effects on the aerodynamic characteristics of a 35° swept-wing airplane of applying blowing-type boundary-layer control to the trailing-edge flaps. Flight tests of a similar airplane were then conducted to determine the effects of boundary-layer control on the handling qualities and operation of the airplane, particularly during landing and take-off.

The wind-tunnel and flight tests indicated that blowing over the flaps produced large increases in flap lift increment, and significant increases in maximum lift. The use of blowing permitted reductions in the landing approach speeds of as much as 12 knots.

INTRODUCTION

Numerous investigations have demonstrated that it is possible to significantly increase the lift of a wing by ejecting a high-velocity jet of air over the upper surface of a trailing-edge flap (e. g., refs. 1 and 2). These investigations have also indicated that the flow required to develop these lifts was so large that a powerful (and heavy) pumping system was required, and this deterred application of this system to actual aircraft. The introduction of the turbojet engine, which provided a convenient source of high-pressure air, and the trend of high-speed wing design to configurations having poor low-speed capabilities caused a renewal of interest in this method of obtaining high lift. The investigation reported in reference 3 indicated that the momentum of the jet, rather than the quantity flow, was the parameter which determined the effectiveness of blowing boundary-layer control, and that significant reductions in flow quantity requirements could be obtained by using highpressure air (i. e., high jet velocities). It was also pointed out in reference 3 that sufficient amounts of high-pressure air to satisfy the requirements of a blowing flap could be bled from the compressor of a turbojet engine. However, the thrust of a turbojet engine diminishes rapidly as the amount of bleed air is increased; it was therefore considered desirable to investigate the possibilities of reducing the flow requirements by careful design of the flap and nozzle itself, so that the desired lift would be obtained for a minimum expenditure of jet momentum.

The primary purpose of the full-scale wind-tunnel tests reported herein was to investigate a blowing flap configuration which preliminary small-scale tests had indicated should require less jet momentum to prevent flow separation than the arrangements previously investigated. Also, since the justification for presenting blowing flap effectiveness in terms of jet momentum was largely empirical, it was desired to verify this concept over the range of pressure ratios obtainable from current turbojet engines. Finally, it was desired to obtain sufficient data to design a blowing flap system into a research airplane for further study in flight.

The main purposes for conducting the flight tests were to investigate (1) the manner in which the pilots used the lift gains provided by the blowing flaps, and (2) the effects of boundary-layer control on the flying qualities and operation of the airplane.

This report presents results of both the wind-tunnel and flight investigations. Six-component force data showing the effects of blowing boundary-layer control on the longitudinal and lateral stability and control characteristics are discussed. Also presented are pilots' opinions of the effects of boundary-layer control on the handling qualities and operation of the airplane. Finally, the results of computations showing the effects of boundary-layer control on the landing and take-off performance are presented.

NOTATION

a	velocity of sound, ft/sec
A	area, sq ft
b	wing span, ft
c	wing chord parallel to plane of symmetry, ft
$\bar{c}$	mean aerodynamic chord, $\frac{2}{S}\int_0^{b/2} c^2 dy$
C_D	drag coefficient, $\frac{\text{drag}}{qS}$
C_L	lift coefficient, $\frac{\text{lift}}{qS}$
ΔC_L	increment of lift coefficient due to flaps
$C_{L_{max}}$	maximum lift coefficient
C_m	pitching-moment coefficient, $\frac{\text{pitching moment}}{qS\bar{c}}$
C_Q	flow coefficient, $\frac{W}{wVS}$
C_μ	momentum coefficient, $\frac{W/g}{qS}V_j$
$C_{L_{\delta_1}}$	rate of change of lift coefficient with flap deflection for full wing-chord flap (given as $C_{L_{\delta_1}}$ in ref. 5)

[1] Summarizes NACA Research Memorandums A55I09 by Mark W. Kelly and William H. Tolhurst, Jr., and A56G30 by Seth B. Anderson, Hervey C. Quigley, and Robert C. Innis.

Preceding Page Blank

d distance from engine thrust line to moment center, positive when thrust line is above moment center, ft

F_G gross thrust from engine, lb

F_N net thrust from engine, lb

g acceleration of gravity, ft/sec^2

h_s nozzle height, in.

M_j jet Mach number, $\frac{V_j}{a}$

N engine speed, rpm

p free-stream static pressure, lb/sq ft

p_d total pressure in flap duct, lb/sq ft

p_t compressor discharge total pressure, lb/sq ft

P_d duct pressure coefficient, $\frac{p_d-p}{q}$

q dynamic pressure, lb/sq ft

S wing area, sq ft

T temperature, °R

V free-stream velocity, ft/sec

V_i indicated airspeed, knots

V_j jet velocity assuming isentropic expansion, $\sqrt{\frac{2\gamma}{\gamma-1}RT_d\left[1-\left(\frac{p}{p_d}\right)^{\frac{\gamma-1}{\gamma}}\right]}$, ft/sec

V_s velocity at stall, knots

V_{s_G} velocity at stall in glide condition, knots

W bleed air flow, lb/sec

w specific weight of air at free-stream conditions, lb/cu ft

x distance along airfoil chord normal to wing quarter-chord line, in.

y spanwise distance perpendicular to plane of symmetry, ft

z height in inches above wing reference plane defined by quarter-chord line and the chord of the wing section at $0.663b/2$

Λ sweep angle, deg

α angle of attack of fuselage reference line, deg

δ ratio of total pressure at compressor inlet to standard pressure at sea level

δ_f flap deflection, measured normal to flap hinge line (given as δ in ref. 5), deg

$\underline{\delta}_f$ flap deflection, measured in plane parallel to plane of symmetry (given as δ in ref. 5), deg

δ_H horizontal-tail deflection, deg

ϵ angle between engine thrust axis and fuselage reference line, deg

γ ratio of specific heats for air, 1.4

θ ratio of total temperature at compressor inlet to standard temperature at sea level

φ angular distance between flap nozzle and a line drawn through the flap hinge line perpendicular to the wing chord plane (fig. 18)

SUBSCRIPTS

d flap duct

f flaps

j flap jet

u uncorrected

DESCRIPTION OF RESEARCH AIRPLANES, INSTRUMENTATION, AND TESTS

WIND-TUNNEL AIRPLANE AND INSTRUMENTATION

Airplane.—The wind-tunnel tests were conducted on a F–86D airplane on which the normal single-slotted flaps had been replaced by blowing flaps. A photograph showing the general arrangement of the airplane installed in the Ames 40- by 80-foot wind tunnel is presented in figure 1. The major dimensions and parameters of aerodynamic importance are shown in figure 2. The airfoil section at the wing root was an NACA 0012–64 (modified) and at the wing tip, an NACA 0011–64 (modified). The ordinates of the airfoil sections are given in table I. Detailed information for the wing and flaps is given in figure 3. Static-pressure orifices were installed in the afterportion of the flap upper surface so that the degree of flow separation could be estimated.

Flap nozzles.—Two flap and nozzle configurations were tested in the wind-tunnel investigation. The first of these was a plain flap arrangement in which the nozzle was essentially a slit in the flap upper surface extending over the full span of the flap. A section view of the nozzle is shown in figure 3. The nozzle blocks were machined from cold-rolled mild-steel stock and were fastened to the top wall of the flap duct with countersunk machine screws. Various nozzle heights were obtained by shimming the forward nozzle block. This assembly was made rigid enough to hold the nozzle deflections, under load, to acceptable values

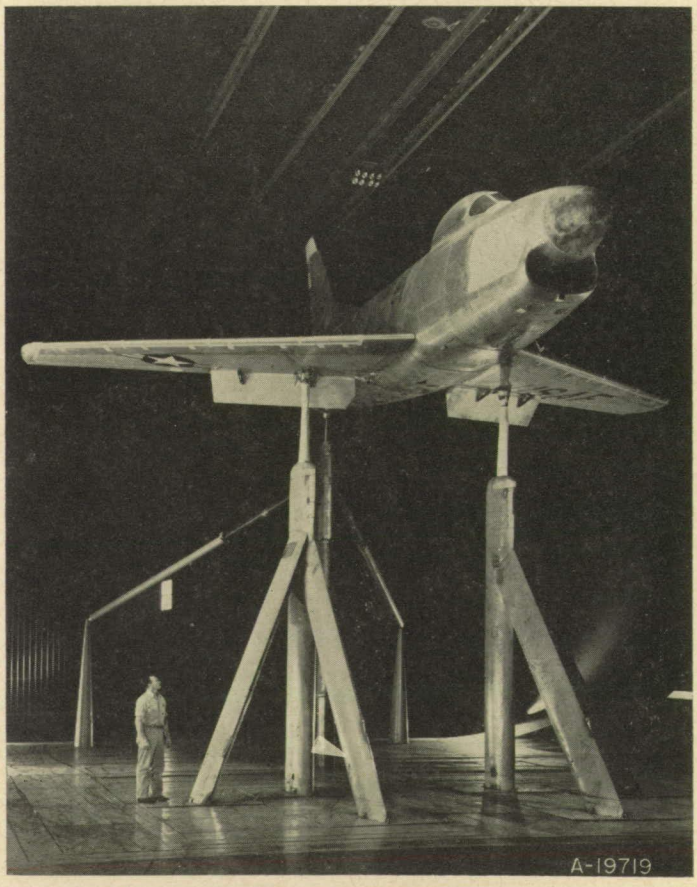
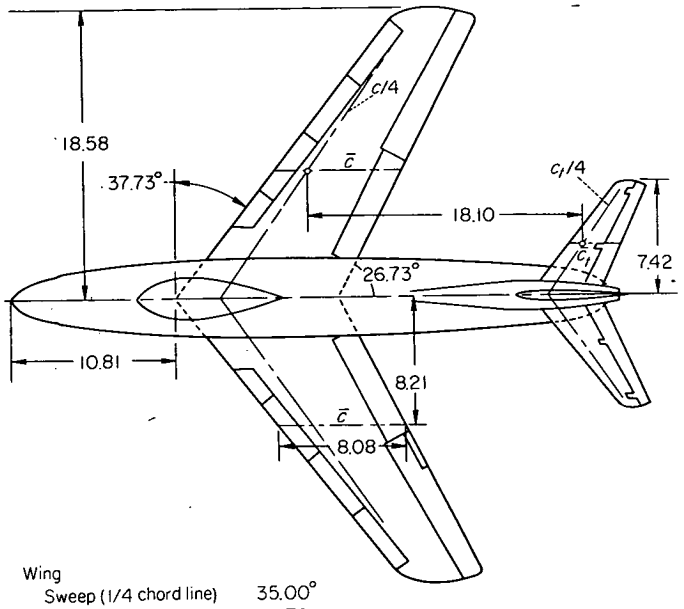


FIGURE 1.—Photograph of the F–86D airplane mounted in the Ames 40- by 80-foot wind tunnel.



Wing	
Sweep (1/4 chord line)	35.00°
Aspect ratio	4.79
Taper ratio	.51
Twist	2.0°
Dihedral	3.0°
Area	287.9 sq ft
Incidence (root)	1.0°
Horizontal tail	
Sweep	35.00°
Aspect ratio	4.73
Taper ratio	.45
Twist	0°
Dihedral	0°
Area	46.5 sq ft

All dimensions in feet unless otherwise noted

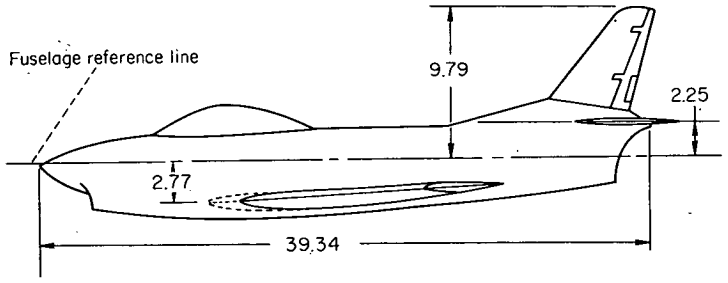


FIGURE 2.—General arrangement of the F-86D airplane.

without the use of fasteners or spacers in the high-velocity portion of the nozzle. For part of the investigation, spacers were simulated by cementing small rectangular pieces of gasket material at regular intervals in the nozzle.

In order to investigate the effects of chordwise location of the nozzle on the effectiveness of the flap, the flap duct was constructed so that it could be rotated about the flap hinge line independently of the flap itself. For most of the investigation the nozzle was located at an angular setting (φ) equal to one-half the flap deflection.

The second flap and nozzle arrangement investigated had a single-slotted flap and a nozzle located in the wing shroud ahead of the flap similar to the configuration investigated in reference 3. Details of this flap and nozzle are shown in figure 4.

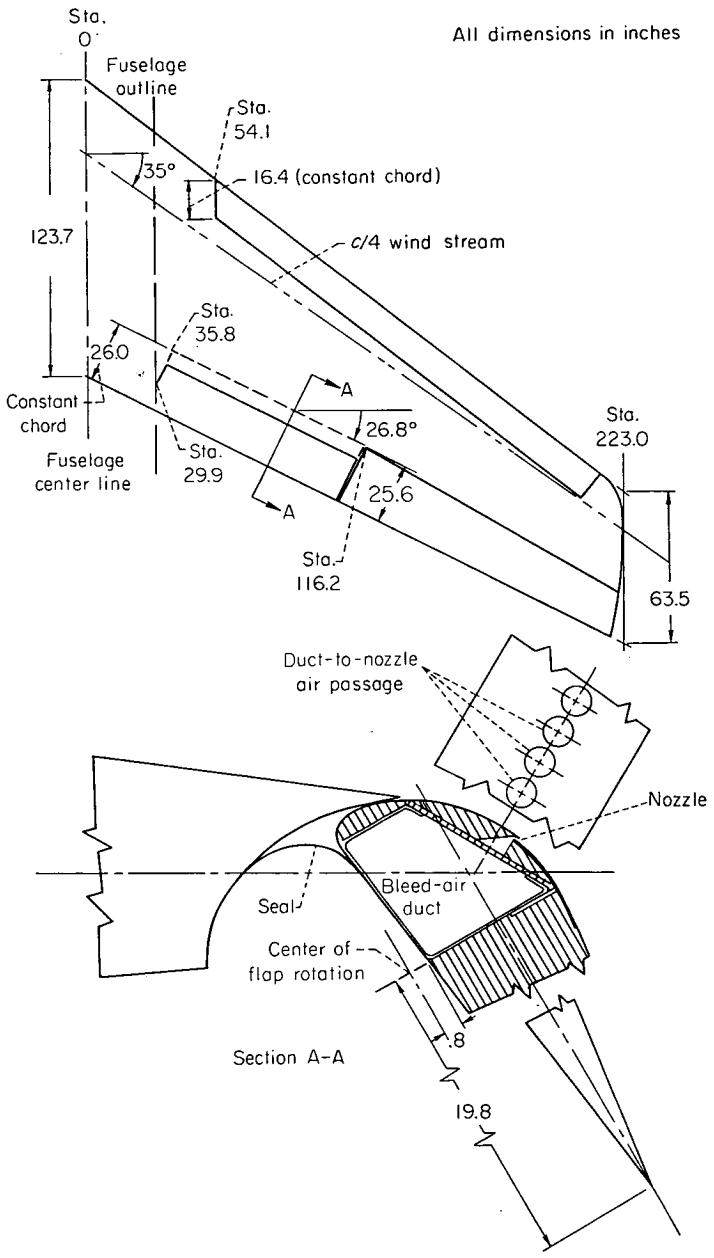


FIGURE 3.—Details of wing and plain blowing flap.

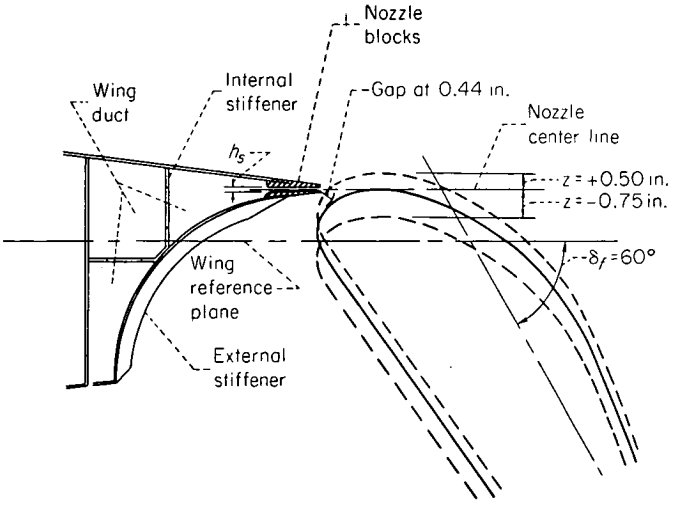


FIGURE 4.—Details of shroud blowing flap.

Engine and ducting.—For these tests the J–47 turbojet engine normally used in this airplane was replaced by a J–34 engine. (This was done only because spare J–47 engines were not available.) The amount of air delivered to the flaps was controlled by a butterfly valve in each duct.

The weight rate of flow to each flap was determined from total pressure, static pressure, and temperature measurements in the ducts. This system was calibrated using a thin plate orifice. The total-pressure and temperature measurements used for calculating the jet momentum were taken at the entrance of the flap duct. Static-pressure and temperature measurements were also made at the outboard end of the flap duct to obtain an estimate of the spanwise variation of the jet momentum.

TESTS

Range of variables.—The investigation covered a range of angles of attack from $-2°$ to $+23°$ and Reynolds numbers from 5.8 to 10.1×10^6. These Reynolds numbers were based on the mean aerodynamic chord of the airplane (8.08 ft) and correspond to free-stream dynamic pressures from 15 to 55 pounds per square foot. The range of flap deflections investigated was from 45° to 85°. The airplane was tested with and without the horizontal tail, and with and without the leading-edge slats extended.

Method of testing.—To define completely the aerodynamic characteristics of the airplane as a function of flap jet momentum, it would have been necessary to obtain data for various jet momentum flows throughout the angle-of-attack range. However, in order to expedite the tests, the momentum flow was varied at only three angles of attack, 0°, 8°, and 12°. (The angle of attack for maximum lift with leading-edge slats retracted was near 12°.) The additional information required to obtain typical lift, drag, and pitching-moment data for the airplane was obtained by testing at several other angles of attack with a constant jet momentum well above that required for flow attachment.

CORRECTIONS

The force data obtained from the wind-tunnel balance system were not corrected for support-strut interference but were corrected for the effects of the wind-tunnel-wall interference as follows:

$$\alpha=\alpha_u+0.611C_{L_u}$$

$$C_D=C_{D_u}+0.0107C_{L_u}{}^2$$

$$C_m=C_{m_u}+0.00691C_{L_u}\text{ (for tail-on tests only)}$$

The following corrections for the effects of the engine thrust were made:

$$C_L=\frac{\text{total lift}}{qS}-\frac{F_N}{qS}\sin(\alpha+\epsilon)$$

$$C_D=\frac{\text{total drag}}{qS}+\frac{F_N}{qS}\cos(\alpha+\epsilon)$$

$$C_m=\frac{\text{total moment}}{qS\bar{c}}+\frac{F_N d}{qS\bar{c}}$$

FLIGHT TEST AIRPLANE

The flight tests were conducted with an F–86F airplane on which the standard single-slotted flaps were replaced by blowing flaps. Pertinent dimensions of the airplane are given in table II. A general view of the airplane and a close-up of the flap are presented in figures 5 and 6, respectively. The blowing system consisted of a manifold to collect air from the last stage of the engine compressor of the J–47 engine, a butterfly valve controlled by the pilot, and a 3-inch-diameter ducting to each flap. The ducting was mounted on the underside of the fusealge to facilitate installation.

The flap used for the blowing system was a plain type made by reworking the nose section of the slotted flaps normally used on the airplane. The flap tracks were removed and external hinge brackets were installed on the undersurface of the wing, allowing flap deflections up to 66°. A rotating O-ring-type seal was used to supply air to the flap at a point on the center of flap rotation. A sketch of the



FIGURE 5.—General view of test airplane.

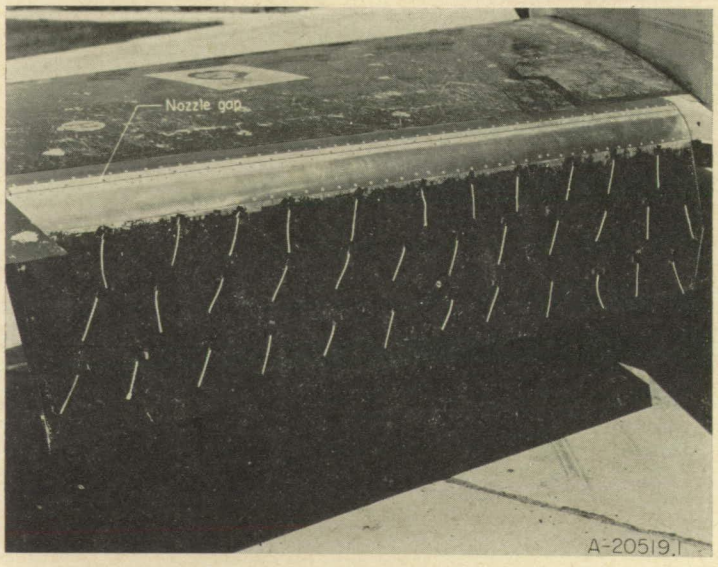


FIGURE 6.—Close-up of flap.

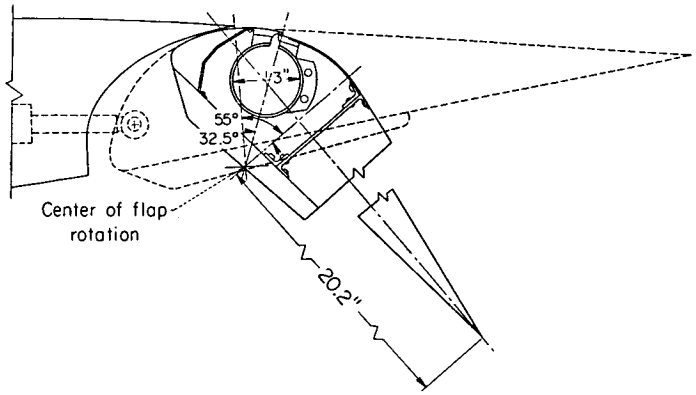


FIGURE 7.—Details of blowing flap construction for flight airplane.

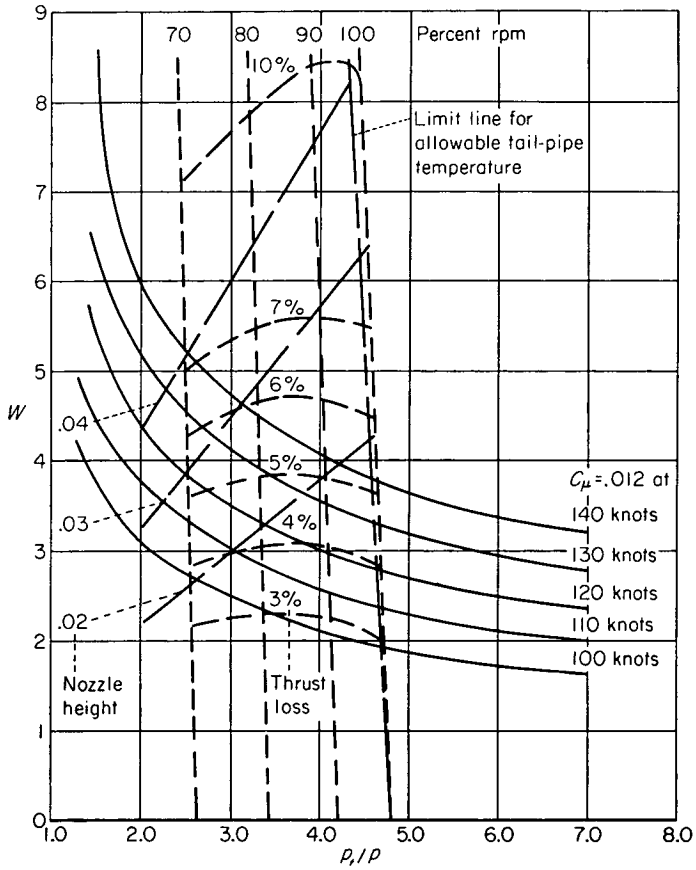


FIGURE 8.—Illustration of analysis for selecting proper nozzle size for blowing flap.

flap cross section is given in figure 7. All parts of the air-supply system were made of steel. The nozzle block was made in two parts, the lower part of steel welded to the 3-inch-diameter tubing, the upper part forming the nozzle exit of 2024–T aluminum, fastened by screws to the steel nozzle block. Spacers were used at 3-inch-span intervals to provide a 0.020-inch nozzle gap. The area of the nozzle was 0.0221 square feet.

It should be noted that the nozzle area was not selected arbitrarily, but was carefully chosen to meet the flow requirements of the blowing flaps and the limitations of bleed air from the engine. Figure 8 indicates graphically how this selection was made. First, the weight rate of flow available from the engine bleed air system was plotted as a function of pressure ratio for various engine speeds. These are the dashed lines in figure 8. Curves representing the jet momentum required to give the desired flap lift were then superimposed on this same plot. These are the hyperbolic-shaped solid curves in figure 8 and were obtained from the equation

$$W=\frac{C_\mu gqS}{M_j(a_j/a_d)\sqrt{\gamma RT_d}}$$

The value of C_μ used was 0.012, which the wind-tunnel investigation indicated to be about 14 percent above that required to prevent flow separation with the flap deflected 60°. The values of dynamic pressure used correspond to flight speeds of 100 to 140 knots, the range of interest in the landing approach. Finally, the weight rate of flow which can be driven through nozzles of various size was computed and is shown in figure 8 by the long dash lines. These were developed from the equation.

$$W=g\rho_d a_d\left(\frac{\rho}{\rho_d}\right)\left(\frac{a}{a_d}\right)A_j$$

where $\rho/\rho_d=0.634$ and $a/a_d=0.913$ for air flow in choked nozzles.

It is seen from figure 8 that, to have the flap fully effective for landing approach conditions (say 70- to 80-percent rpm and 100 to 120 knots) a nozzle height of 0.02 to 0.03 inch should be used. For a nozzle height of 0.02 inch, a loss of maximum thrust of between 5 and 6 percent due to bleeding air from the engine would be anticipated.

The weight of the boundary-layer-control equipment for this research-type installation was 175 pounds. In a production-type installation a considerable savings in weight should be possible.

The amount of engine bleed air actually used at various engine speeds is presented in figure 9. These values of bleed air correspond to approximately 3.5 percent of the primary engine air flow. The bleed flow quantity was calcu-

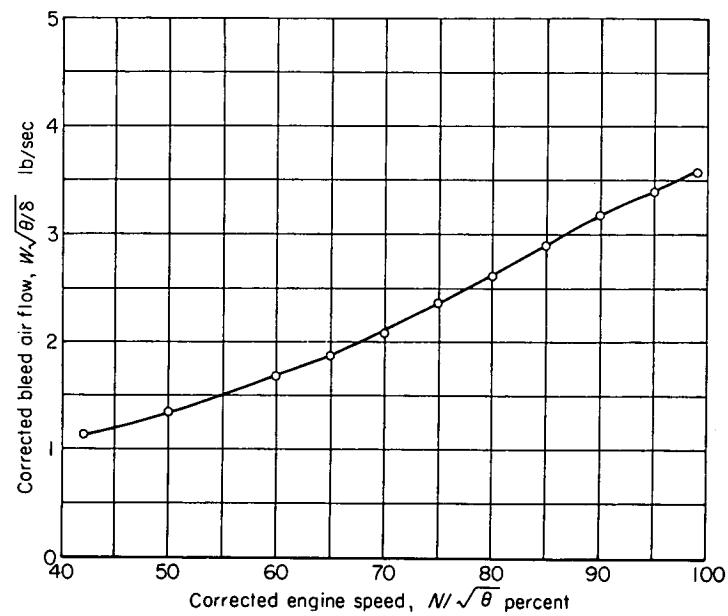


FIGURE 9.—Variation of engine bleed with engine speed; sea level, J–47 engine.

lated from one-dimensional flow equations using measured values of pressure, temperature, and nozzle area. The variation of static thrust (measured on a thrust stand) with percent engine speed is presented in figure 10 with and without bleed air extraction. It can be noted that for the blowing-on case there was a reduction in static thrust of approximately 5 percent. The variation of pressure ratio with percent engine speed is presented in figure 11. It will be noted that sonic flow would occur in the nozzle exit at approximately 63-percent rpm.

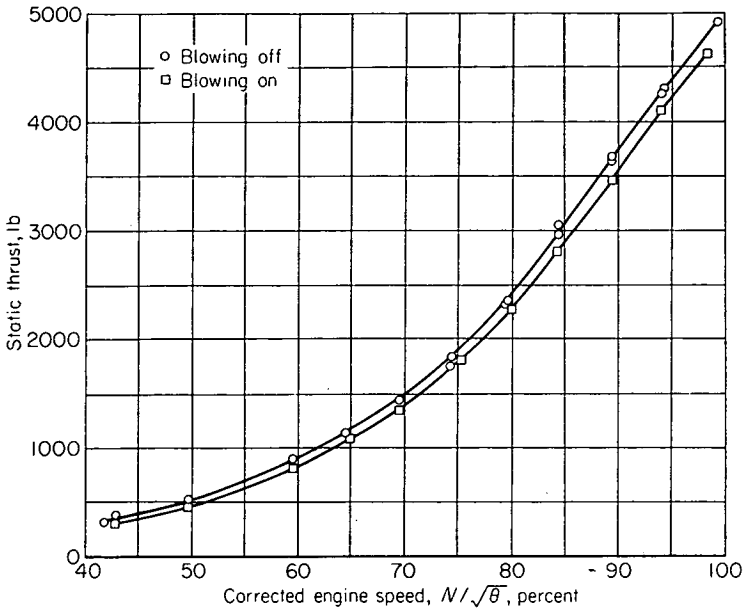


FIGURE 10.—Variation of static thrust with engine speed for blowing on and off; sea level, J–47 engine.

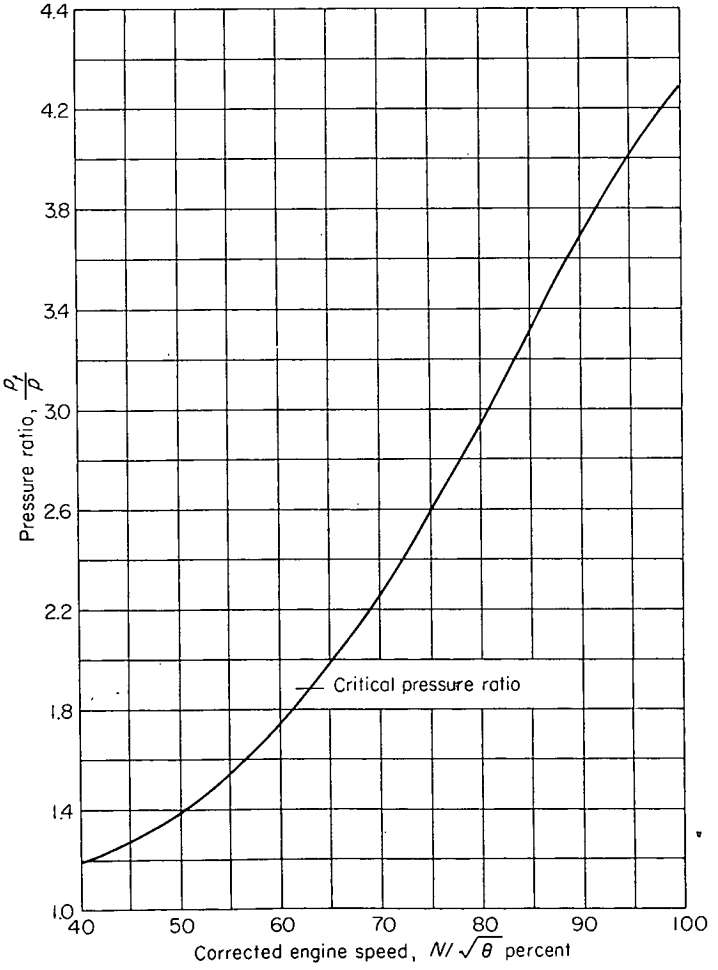


FIGURE 11.—Variation of pressure ratio at engine bleed ports with engine speed; J–47 engine.

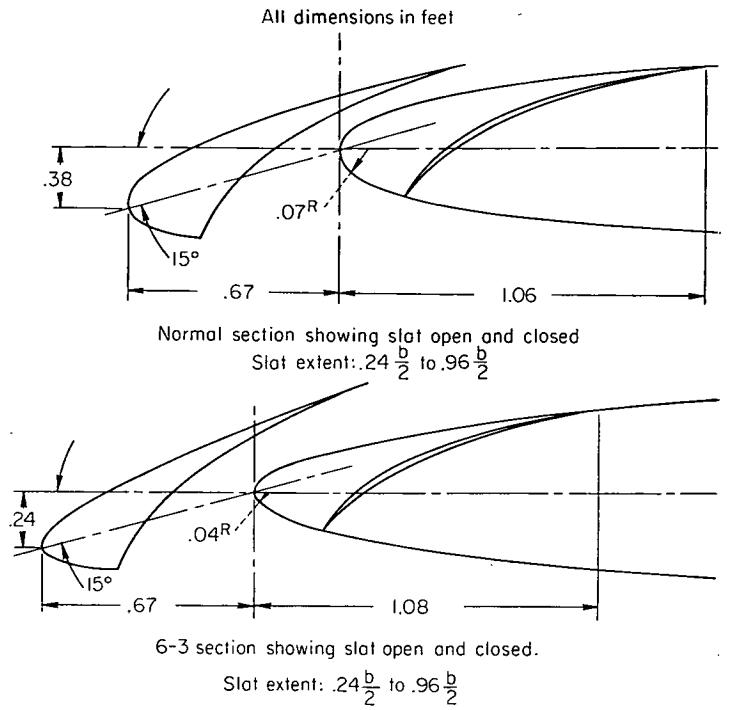


FIGURE 12.—Cross sections normal to wing leading edge of the normal slat and the 6–3 slat.

Standard NACA instruments were used to record airspeed, altitude, acceleration, duct pressures, and angle of attack. Values of airspeed, altitude, and angle of attack were measured approximately 8 feet ahead of the fuselage nose. Duct pressures in the flaps were measured at the midspan station of the flaps.

The flight tests were conducted with two wing leading-edge configurations, an F–86D type slat, and a 6–3 slat.[2] A sketch of the cross section of each leading-edge device is shown in figure 12. The majority of data obtained in the flight investigation was with the 6–3 slat, since this is the leading edge currently used with F–86F type airplanes.

Tests were conducted at sea level and 5,000 feet over a speed range from 170 knots to the stall. An average wing loading of 45.5 pounds per square foot was used with the take-off center of gravity at 24.1 and 26.6-percent mean aerodynamic chord for the airplane with the F–86D slatted leading edge and 6–3 leading edge, respectively. The engine rpm was held fixed for a given series of test runs. Tests were conducted at trailing-edge flap deflections of 38°, 45°, 55°, 60°, and 66°.

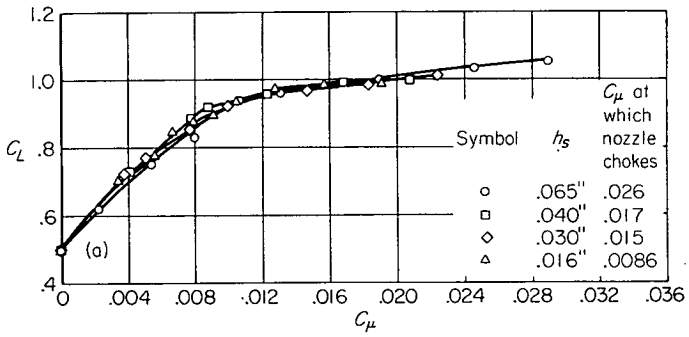
RESULTS AND DISCUSSION

WIND-TUNNEL TESTS

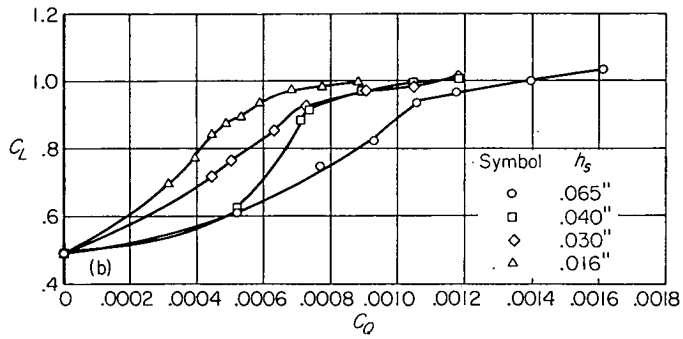
Correlation of blowing-flap performance with momentum coefficient.—One of the first objectives of the test programs was to establish whether the effectiveness of a partic-

[2] The designation "6–3" refers to a full-span chord extension of 6 inches at the wing root and 3 inches at the wing tip.

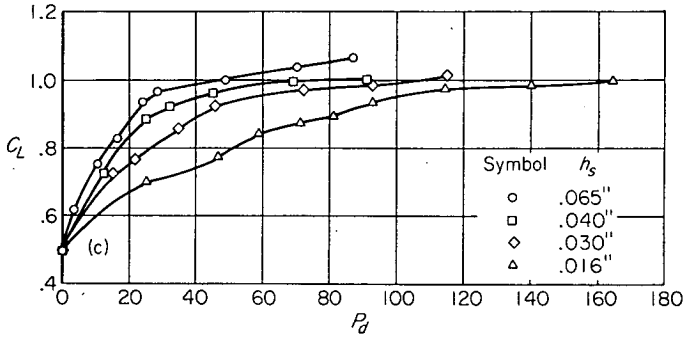
ular blowing-flap configuration was determined solely by the momentum of the air ejected over the flap. This was done by making a series of tests on the same basic flap configuration with various nozzle openings. Typical results of these tests are presented in figure 13 (a). It should be noted that, although the nozzle opening was changed from a value of 0.016 inch to 0.065 inch (corresponding to values of h_S/c from 0.00017 to 0.00067), good correlation with momentum coefficient is obtained. The data presented in figure 13 (a) cover a range of nozzle pressure ratios from subcritical up to 2.9, and therefore a range of expanded jet velocities from subsonic to supersonic. It should be noted that no particular aerodynamic difficulties or benefits are associated with either subsonic or supersonic jet velocities. Corresponding variations of lift coefficient with flow coefficient and duct pressure coefficient are shown in figures 13 (b) and 13 (c), respectively. Here it is seen that the effects of nozzle height are significant, and that values of flow coefficient or pressure coefficient have meaning only when the nozzle height is specified. While



(a) Variation of lift coefficient with momentum coefficient.



(b) Variation of lift coefficient with flow coefficient.



(c) Variation of lift coefficient with duct pressure coefficient.

FIGURE 13.—Effect of nozzle height on the flow requirements of the blowing flap; $\delta_f=60°$, $\alpha_u=0°$, $R=7.5\times10^6$, tail off.

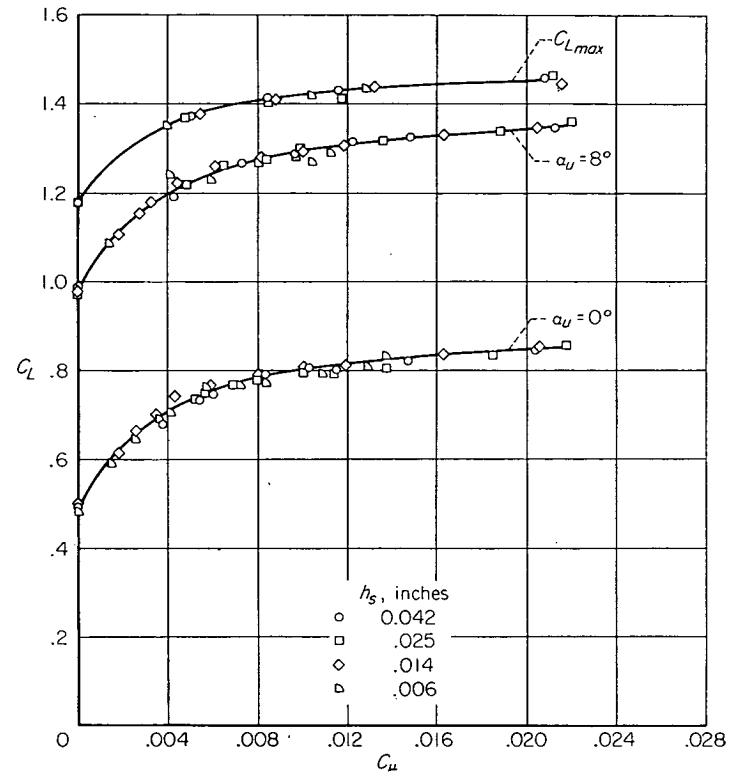
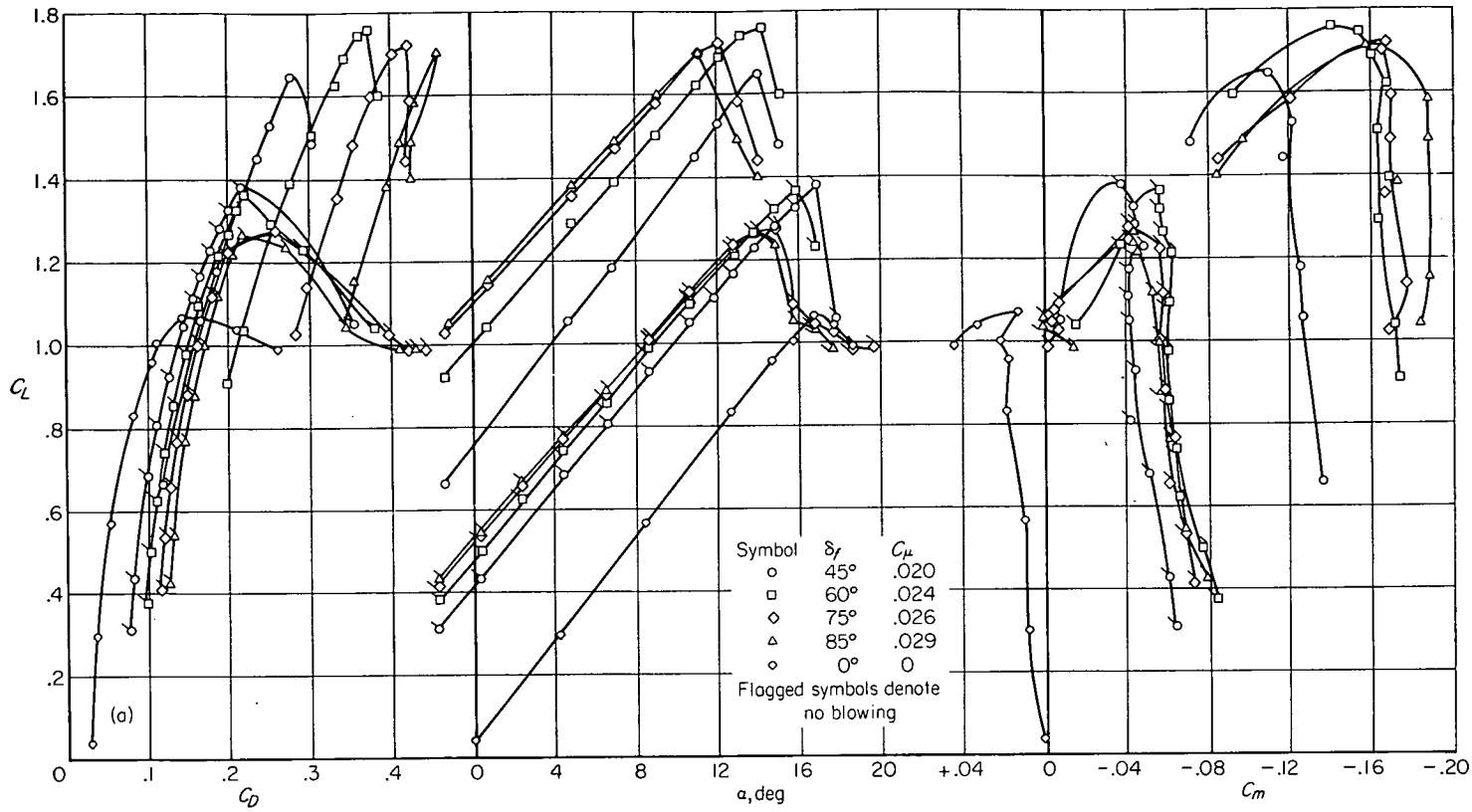


FIGURE 14.—Effect of nozzle height on the flow requirements of the blowing flap of reference 4; $\delta_f=60°$, $R=10.7\times10^6$.

the data presented in figure 13 are for 0° angle of attack only, similar results were obtained at 8° and 12° angle of attack. Figure 14 presents similar results obtained from later wind-tunnel tests of an F–93 airplane equipped with similar blowing flaps (ref. 4). Here the range of nozzle pressure ratios used was from subcritical up to 9.5, and good correlation of C_L with C_μ was again obtained. Thus, it appears that, for pressure ratios obtainable from turbojet engine bleed-air systems, the effects of blowing boundary-layer control on flap lift are adequately defined by the jet momentum.

Typical effects of blowing on aerodynamic characteristics.—Figure 15 (a) presents the tail-off lift, drag, and pitching-moment characteristics of the airplane with various flap deflections with and without blowing. The data obtained with blowing were taken at constant values of momentum coefficient which were more than sufficient to provide attached flow for each flap deflection. It is seen that blowing over the flap produced the type of lift and pitching-moment increments which would be expected from substantial increases in flap effectiveness. The drag coefficient for a given flap deflection was increased by blowing. This may be surprising in view of the fact that blowing over the flap should reduce the amount of flow separation and hence the profile drag of the flap. However, it must be remembered that the total airplane drag is the sum of both profile and induced drag. Since the total drag was increased by blowing, while the profile drag was decreased, it must be concluded that blowing over the flaps resulted in an increase in induced drag. The use of a short span, highly effective flap will usually cause a significant distortion of the wing span loading and a resulting increase in the induced drag of the wing. The order of magnitude of this induced drag can be

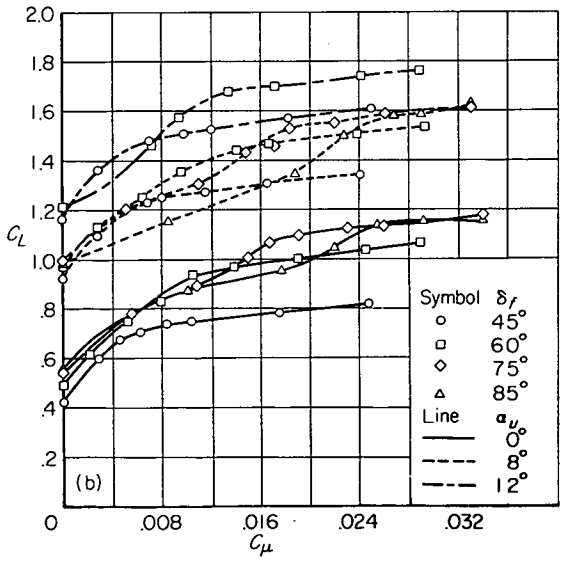


(a) Typical aerodynamic characteristics with and without blowing.

FIGURE 15.—Effects of blowing over the flaps on the aerodynamic characteristics of the airplane; $R=7.5\times10^6$, tail off, $h_s=0.065$ inch.

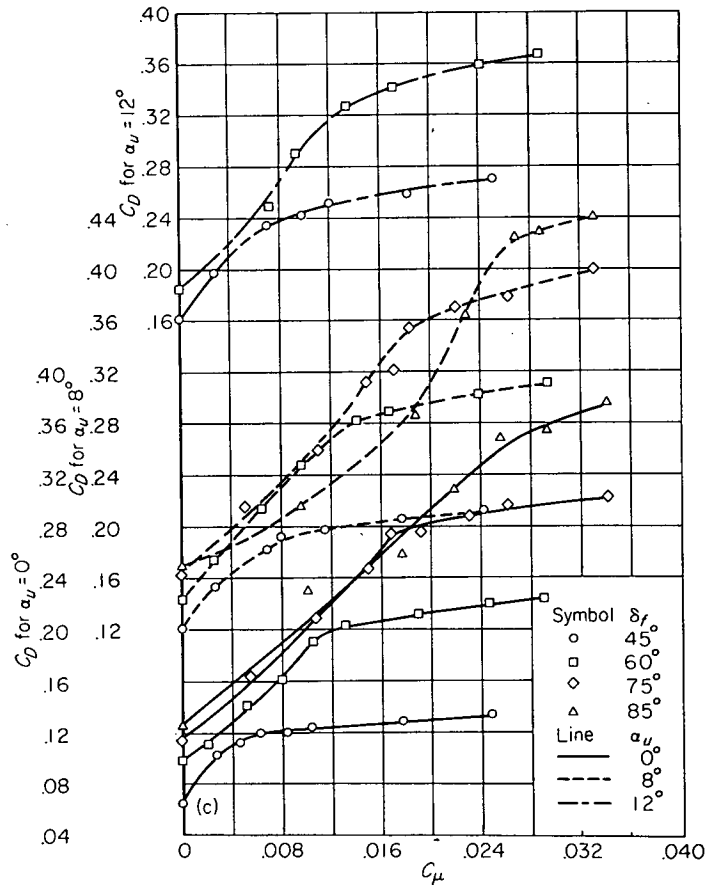
estimated from the theory of reference 5. It should be noted that this induced drag increment is a function of flap span and is more for small-span flaps than it is for large-span flaps.

The data presented in figure 15 were obtained with the flap nozzle located at an angular setting (φ) equal to one-half the flap deflection, as previously pointed out in the section "Wind-Tunnel Airplane and Instrumentation." This was done because previous research (ref. 6) had indicated that



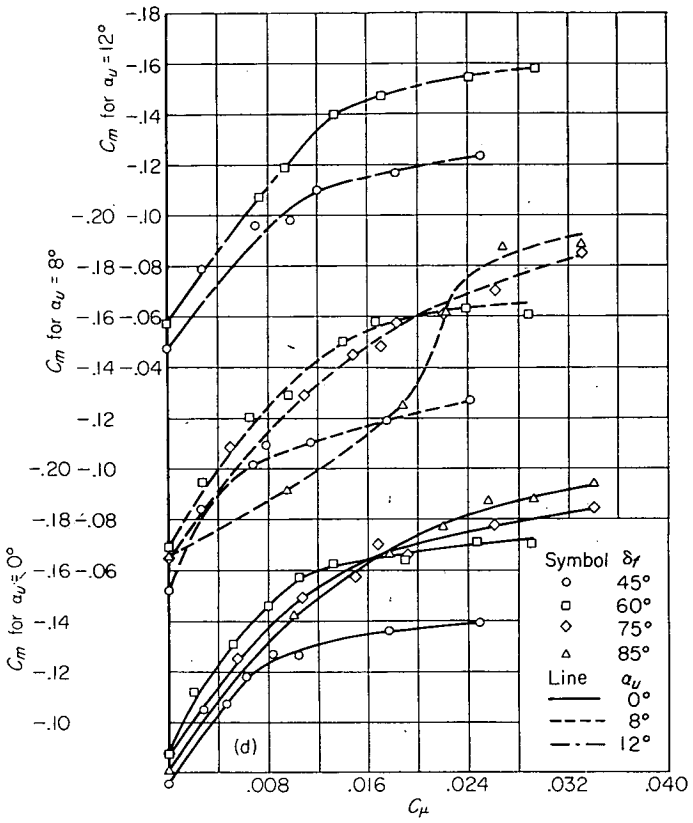
(b) Variation of lift coefficient with momentum coefficient.

FIGURE 15.—Continued.



(c) Variation of drag coefficient with momentum coefficient.

FIGURE 15.—Continued.



(d) Variation of pitching-moment coefficient with momentum coefficient.

FIGURE 15.—Concluded.

this setting would put the nozzle near the minimum-pressure point on the flap, and this was believed to be near the optimum location. Subsequent testing to determine the effects of nozzle location (see section entitled "Effect of Nozzle Location") indicated that this location was, in fact, near the optimum. However, the flap lift was relatively insensitive to nozzle position, and the data presented in figure 15 are typical of those which would be obtained with the nozzle located anywhere between the minimum-pressure point on the flap and the wing-flap juncture.

Figures 15 (b), (c), and (d) present the variation of lift, drag, and pitching-moment coefficient with momentum coefficient. As mentioned previously, the momemtum coefficient was varied only at uncorrected angles of attack of 0°, 8°, and 12°. (The momentum coefficient was not varied at 12° angle of attack for flap deflections of 75° and 85° since, with these flap deflections, the wing had already passed maximum lift.) Figure 15 (b) shows that, as the momentum coefficient was increased, the lift at first increased rapidly, but then the rate of increase fell off to a relatively low value. Static-pressure measurements on the upper surface of the flap indicated that the initial rapid increase in lift was associated with the control of the boundary layer on the flap. The additional lift obtained after the flow was attached is due to wing circulation induced by the jet flow over the flap. The data presented in figure 15 (b) indicate that the momentum coefficient required for a given flap lift increment is relatively low when the flap deflection is large enough so that the desired lift is obtained by using blowing primarily for boundary-layer control rather than to provide jet-induced circulation. It might be noted that the pitching moment per unit lift due to flap deflection is not significantly changed by blowing. This is shown in the following table which was obtained from the data presented in figures 15 (b) and 15 (d) for 0° uncorrected angle of attack:

δ_f	45°		60°		75°		85°	
C_μ	0	0.006	0	0.0105	0	0.0168	0	0.0255
$\frac{\Delta C_m}{\Delta C_L}$	−.20	−.18	−.20	−.18	−.18	−.17	−.16	−.17

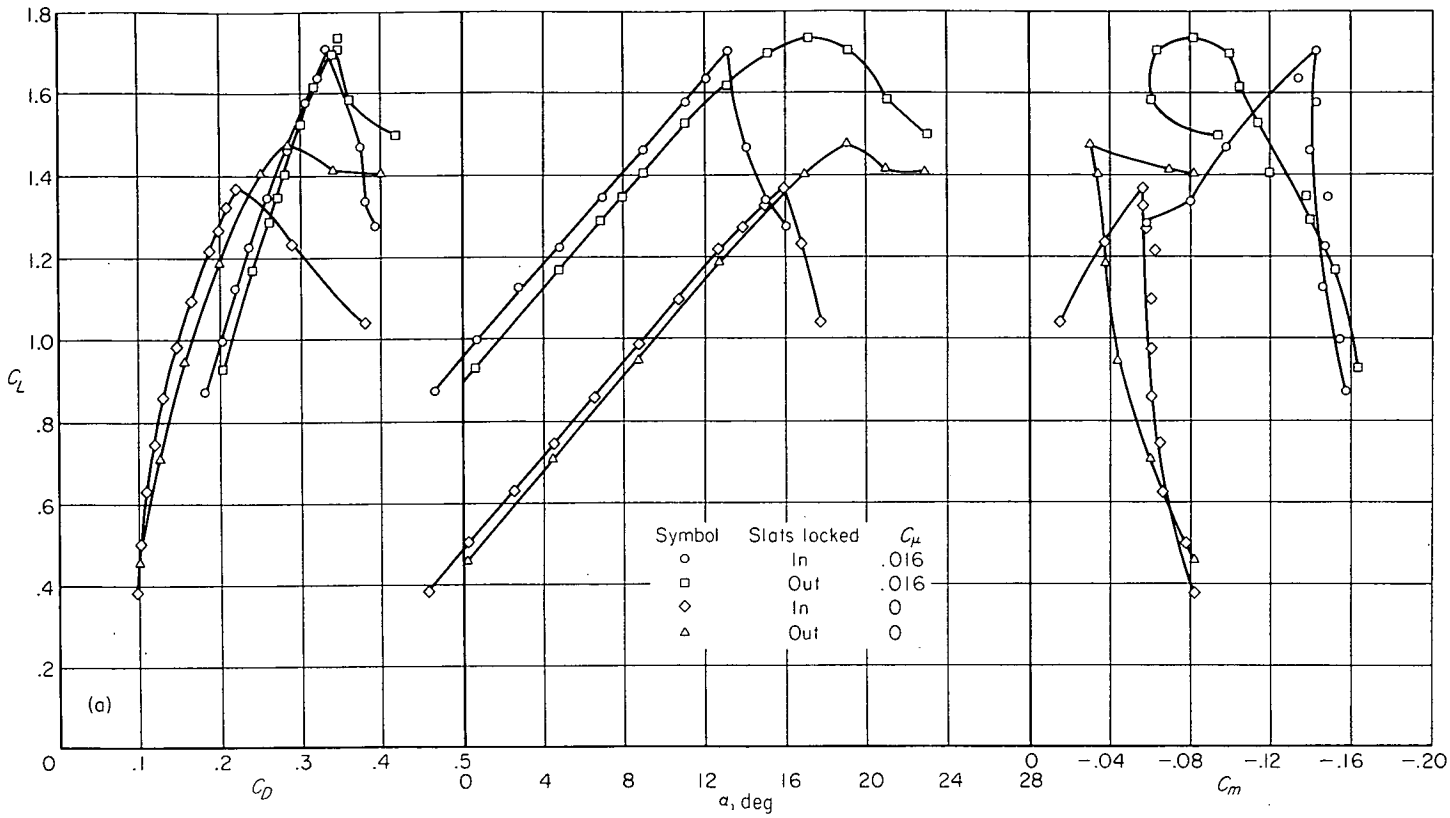
All of the preceding data were obtained at a Reynolds number of 7.5×10^6. Results of this investigation showed no effect of Reynolds number on the lift increment due to blowing from $R=5.8$ to 10×10^6.

Results of tests to determine the effects of blowing over the flaps on static lateral and directional stability indicated that both were slightly increased. It was also found that blowing over the flaps increased the aileron effectiveness by about 25 percent.

Effects of leading-edge slats.—Figures 16 (a) and (b) show the effects of extending the leading-edge slats on the aerodynamic characteristics of the airplane with and without blowing on the flaps. It is seen that extending the slats had no significant effect on the flap performance, that is, had no effect on the lift increment due to blowing or the required momentum coefficients. The loss in lift at angles of attack below maximum lift is due primarily to the nose camber effect of the slats. It should be noted that there is no nonlinearity in the lift curve such as that obtained with area-suction flaps in the investigation of reference 6, where the vortex shed from the slat root spoiled the flow over a portion of the flap. The leading-edge slats did not provide a significant increase in maximum lift, although they did change the type of stall from one that was very abrupt to one that was relatively gradual. The pitching-moment data show that, with blowing on, the leading-edge slats did not provide the stable variation in pitching moment at the stall that was obtained without blowing.

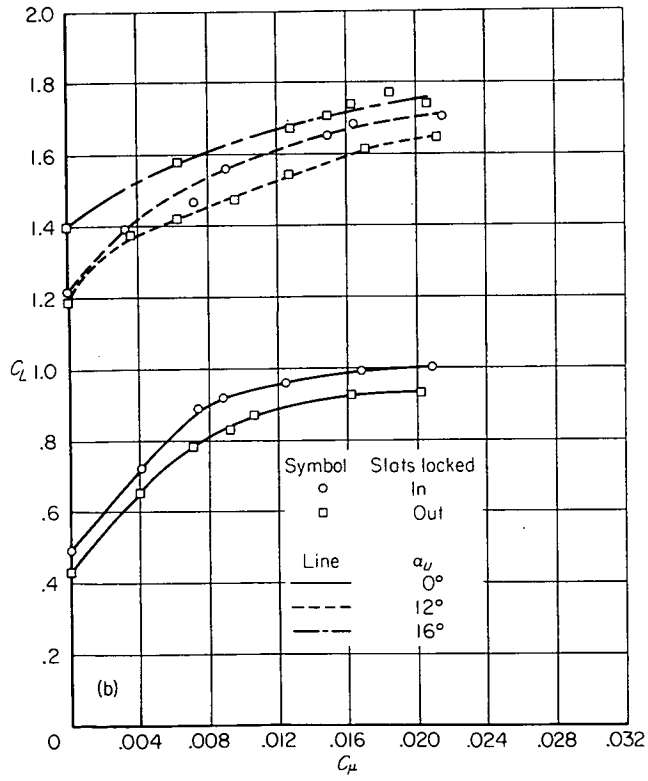
Effect of horizontal tail.—Lift and pitching-moment data for the airplane with and without the horizontal tail and with and without blowing on the flap are shown in figures 17 (a) and (b). It is seen that with the tail on and the airplane at a constant lift coefficient, blowing over the flap produced a positive pitching-moment change. This was caused by an increase in downwash in the vicinity of the horizontal tail. (The dynamic pressure at the tail was measured and found equal to free-stream dynamic pressure.)

Effect of nozzle location.—Figure 18 presents lift coefficient as a function of momentum coefficient for various nozzle locations on the flaps which were deflected 60°. The data indicate that, for the range of nozzle locations available with the flaps deflected 60°, no appreciable effect of nozzle location was found at angles of attack of 8° and 12°, which are in the range of most significance as far as landing and take-off of the airplane is concerned. Results from similar tests with the flaps deflected 85° showed that, with the nozzle behind the minimum pressure point ($\varphi=62.5°$), the flow could not be



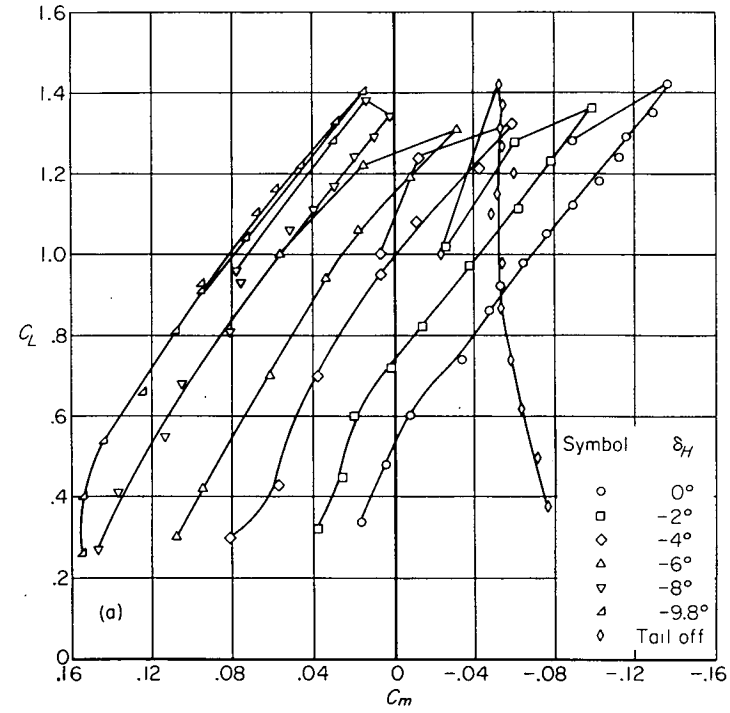
(a) Typical aerodynamic characteristics with and without leading-edge slats.

FIGURE 16.—Effects of leading-edge slats on the aerodynamic characteristics of the airplane with blowing over the flaps; $\delta_f=60°$, $R=7.5\times10^6$ tail off, $h_s=0.040$ inch.



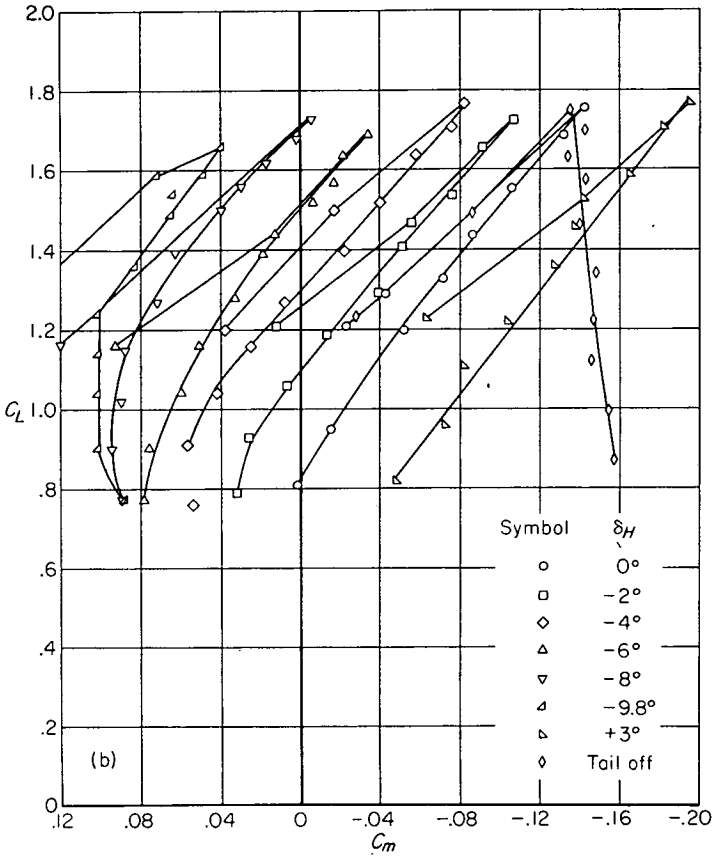
(b) Variation of lift coefficient with momentum coefficient.

FIGURE 16.—Concluded.



(a) Blowing off.

FIGURE 17.—Pitching-moment characteristics of the airplane with and without the horizontal tail.



(b) Blowing on.

FIGURE 17.—Concluded.

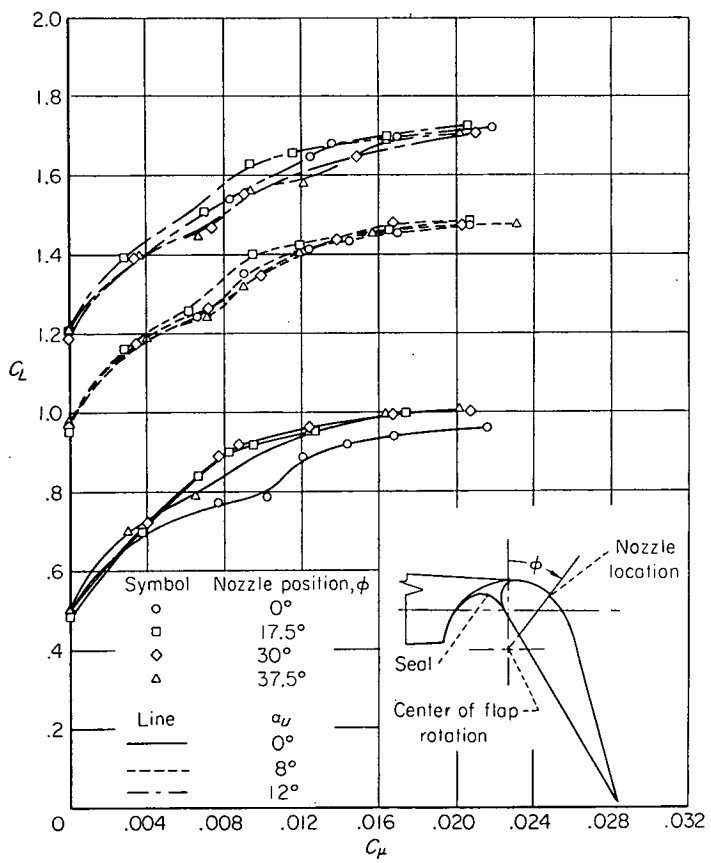


FIGURE 18.—Effect of nozzle position on the variation of lift coefficient with momentum coefficient with the nozzle in the flap upper surface; $\delta_f=60°$, tail off, $R=7.5\times10^6$.

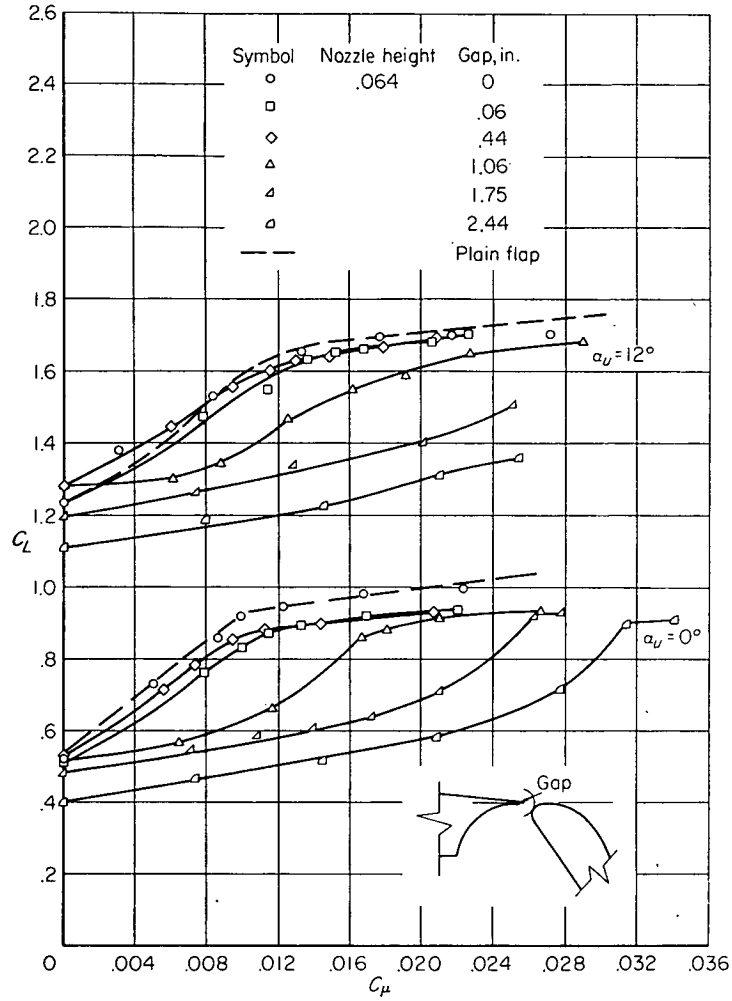


FIGURE 19.—Effects of flap position on the variation of lift coefficient with momentum coefficient for the nozzle located in the wing shroud; flap upper surface tangent to nozzle center line; $\delta_f=60°$, tail off, $R=7.5\times10^6$.

attached with the highest value of momentum coefficient available. In general, these data indicate that, as long as the nozzle is located between the wing-flap juncture and the minimum-pressure point on the flap, no significant effect on flow requirements will be obtained. It should be noted that, for the case where the nozzle is fixed with respect to the flap, the nozzle should be positioned approximately at the location of the minimum-pressure point on the flap for the maximum flap deflection contemplated. At lower flap deflections the nozzle will then be ahead of the minimum-pressure point on the flap and satisfactory performance should be obtained.

Figure 19 shows similar results obtained from subsequent tests of this airplane with a blowing flap with the nozzle in the wing shroud. With this arrangement, it was found that to obtain the minimum jet momentum requirements, the flap should be positioned close to the nozzle (within 0.44 inch for this flap). At this optimum position, the variation of lift coefficient with momentum coefficient for the shroud blowing flap compares favorably with that for the plain blowing flap.

Effect of spacers in nozzle.—For this phase of the investigation the nozzle was plugged with rectangular spacers at regular spanwise intervals to simulate an interrupted nozzle, that is, several discrete nozzles along the flap span. Data

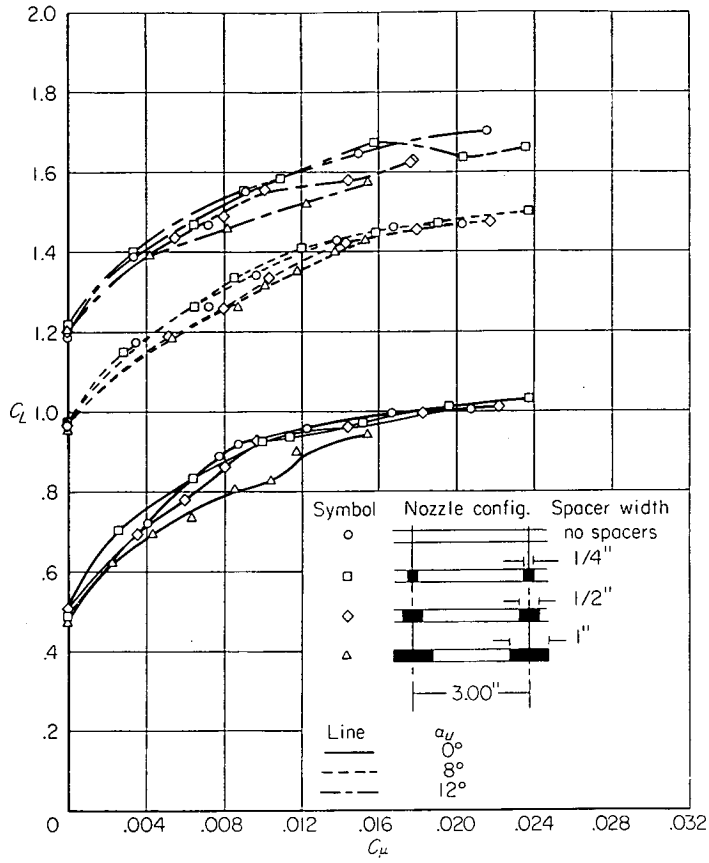


FIGURE 20.—Variation of lift coefficient with momentum coefficient for nozzles having various spacer arrangements; $\delta_f=60°$, $R=7.5\times10^6$, tail off, $h_s=0.040$ inch.

for various nozzle configurations are presented in figure 20. It is seen that no significant effect was obtained until nozzles 2 inches long separated by 1-inch spacers were simulated. For this arrangement, it was found that the required momentum coefficient for a given lift coefficient was somewhat increased.

Comparison with theory.—Usually any large discrepancies between the lift of a wing and that predicted from inviscid fluid theory can be attributed to flow separation. Since the application of boundary-layer control should reduce the amount of flow separation, it is reasonable to assume that the lift obtained by the use of boundary-layer control should approximate that predicted by inviscid fluid theory. Figure 21 shows a comparison of the flap lift increments due to boundary-layer control obtained in this investigation with those estimated by the theory of reference 5.[3] The experimental flap lift increments chosen were those existing when the flow over the flap first became attached, as indicated by static-pressure measurements near the flap trailing edge. The momentum coefficients required to eliminate flow separation for each flap deflection are also presented. It may be seen by referring to figure 15(b) that these momentum coefficients are in the region where the rate of increase of lift coefficient with momentum coefficient falls off to a relatively low value. This affords an alternative, but often less precise, method of selecting the point of flow attachment. It may be seen from figure 21 that, for flap deflections up to 60°, the estimated and experimental flap lift increments are in good agreement. The discrepancies between the predicted and experimental values at higher flap deflections are believed to be due more to the linearizing assumptions utilized in the theory rather than to an actual deterioration of the flow over the flap. Even at a flap deflection of 85° the static-pressure measurements on the flaps indicated that attached flow was obtained.

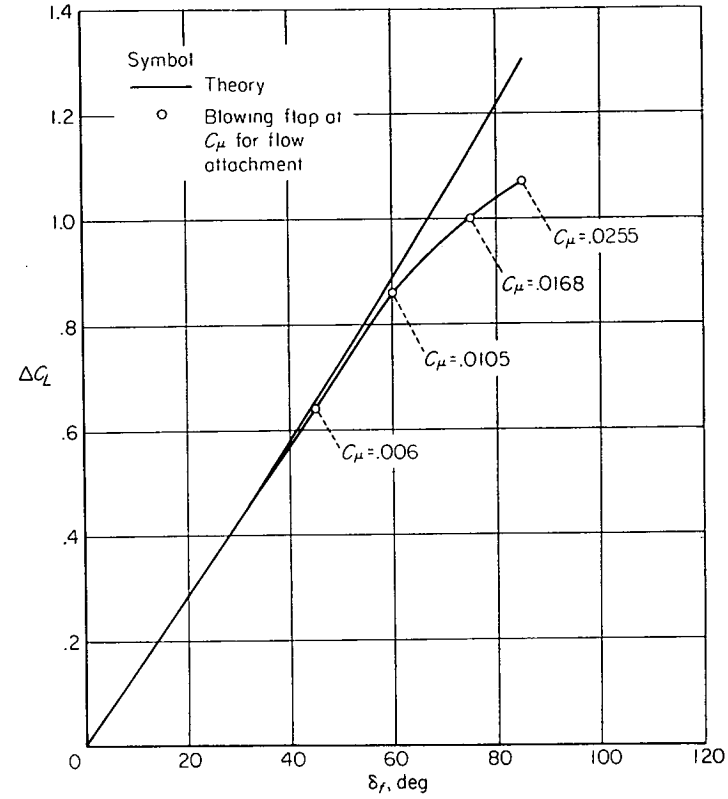


FIGURE 21.—Comparison of theoretical flap lift increments with those obtained experimentally on the blowing flap at the point of flow attachment; $\alpha=0°$.

FLIGHT TESTS

Aerodynamic characteristics with the 6–3 slatted leading edge.—Data are presented in figures 22 (a) and (b) for various flap deflections with blowing on and off for 100- and 80-percent engine rpm, and in figure 22 (c) for 60° flap deflection and various engine rpm's. The equations used to determine C_L and C_D are discussed in appendix A. The data in figure 22 indicate substantial increases in lift resulting from the application of blowing at all flap deflections. It will be noted that the angle of attack for maximum lift coefficient

[3] The theoretical flap effectiveness was estimated from $\Delta C_L=\frac{d\alpha}{d\alpha_f}C_{L_{\delta_1}}\frac{\delta_f}{57.3}$ (equivalent to eq. (7), ref. 5)

For the F-86D wing

$C_{L_{\delta_1}}=1.52$ (from cross plot of fig. 5, ref. 5)

$\frac{d\alpha}{d\delta_f}=0.58$ (from curve for theoretical flap effectiveness, fig. 3, ref. 5. Average $c_f/c=0.23$ perpendicular to flap hinge line)

$\tan\delta_f=\cos\Lambda_f\tan\delta_f=0.895\tan\delta_f$

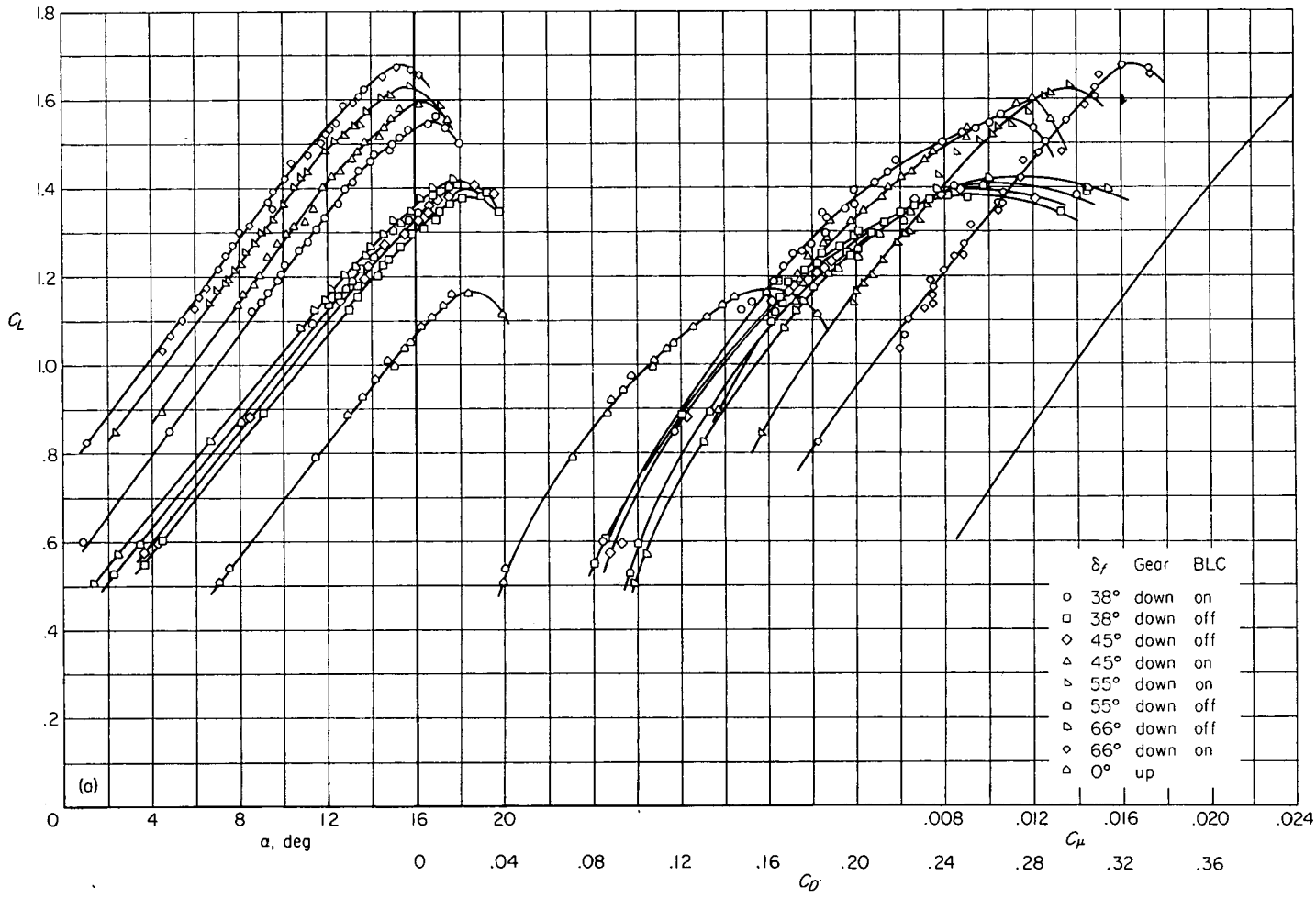
$\Delta C_L=\frac{(0.58)(1.52)}{57.3}\delta_f=0.0154\delta_f$

decreases with the amount of blowing, and with increase in flap deflection.

Flight tests of the airplane equipped with the standard 38° slotted flap normally used on this airplane gave essentially the same results as those shown for the plain flap deflected 38° without blowing. The improvement in C_L with blowing on the flaps deflected 55° over that obtained with the 38° flap was from 1.02 to 1.37 at the landing approach condition ($\alpha=11°$, 80-percent rpm). With the flaps deflected 66°, there was an increase in $C_{L_{max}}$ from 1.40 to 1.68 at maximum engine power.

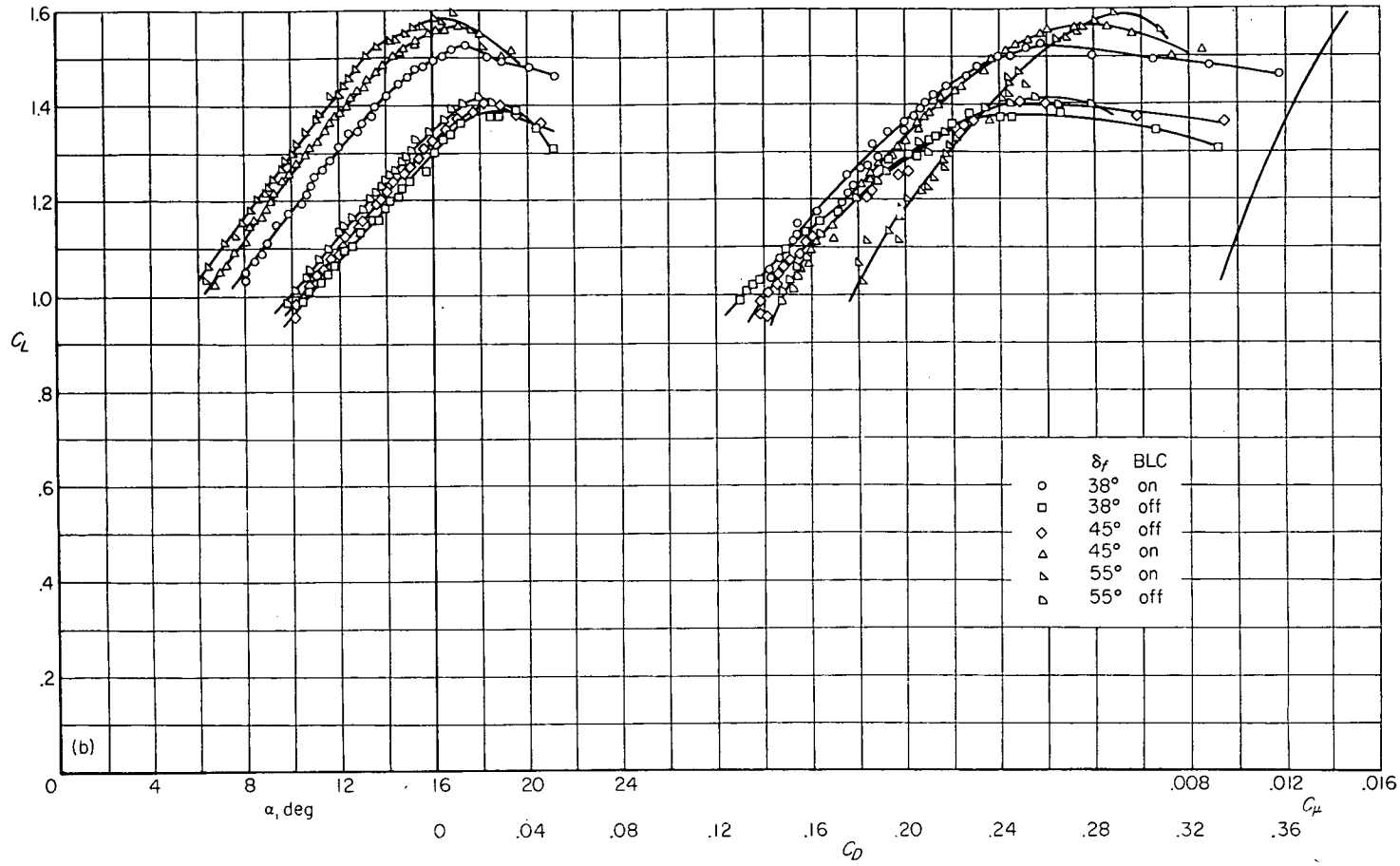
It can be observed from the data in figure 22 that the flap lift increment due to blowing varies over the angle-of-attack range. It is noteworthy that maximum flap lift increment occurs in the angle-of-attack range (10° to 12°) for the landing approach.

Aerodynamic characteristics with the standard F–86 leading-edge slats.—The lift and drag characteristics of the airplane equipped with the standard F–86 leading-edge slats are shown in figure 23. It is seen that, with blowing on, opening the leading-edge slats did not provide any increase in $C_{L_{max}}$. This same result was obtained in the wind-tunnel investigation. However, the leading-edge slats did improve the stalling characteristics of the airplane considerably.



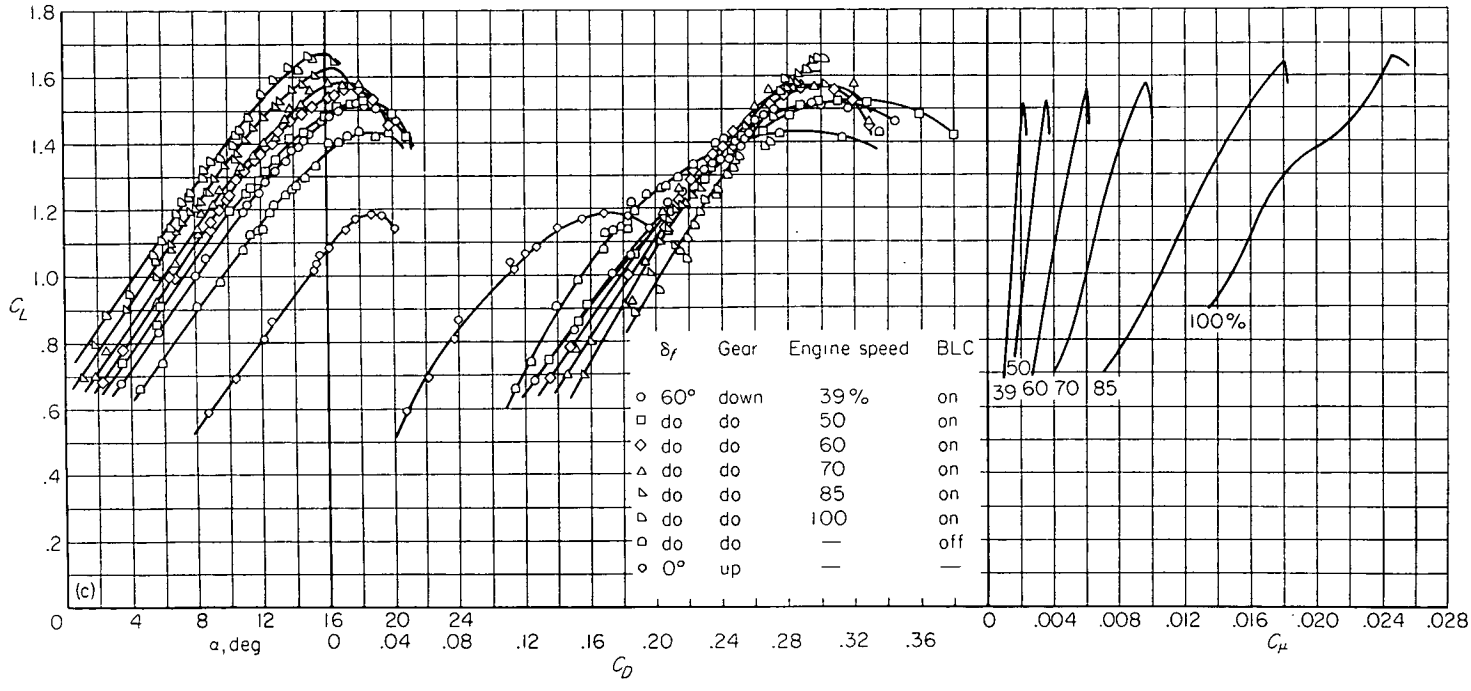
(a) 100-percent engine speed.

FIGURE 22.—Lift, drag, and momentum coefficient curves for various flap deflections; 6–3 slatted leading edge.



(b) 80-percent engine speed.

FIGURE 22.—Continued.



(c) $\delta_f = 60°$, various rpm.

FIGURE 22.—Concluded.

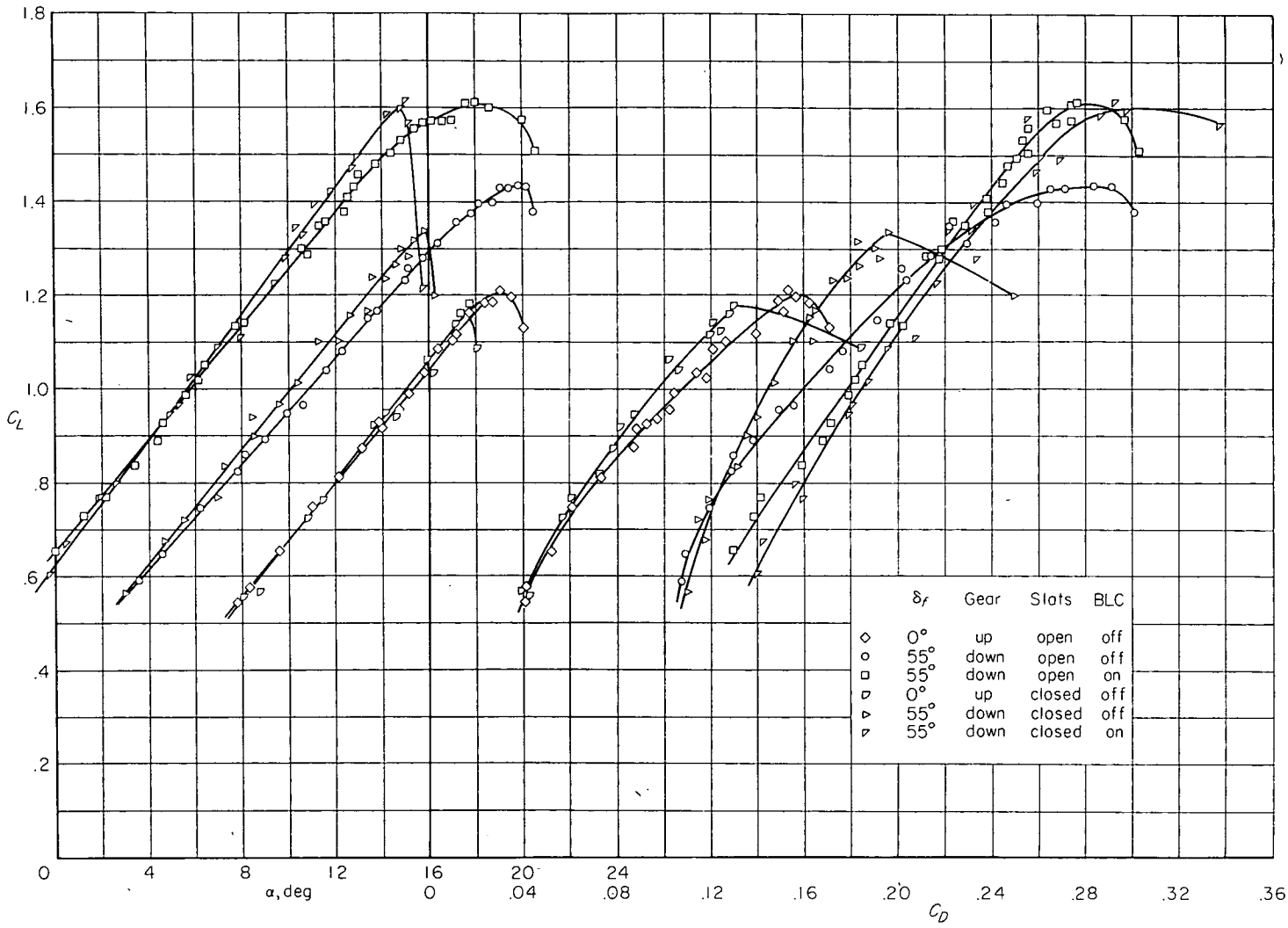


FIGURE 23.—Lift and drag curves for the airplane with the standard F–86D leading-edge slats; 80-percent engine speed.

Fig ure 24 shows a comparison between flight and wind-tunnel results for the flaps deflected 60° and at an angle of attack of 12°. The flight results are presented with the gear up to correspond to the configuration tested in the wind tunnel. These data show reasonably good correlation between the wind-tunnel results and the flight results over the C_μ range tested.

Pilot evaluation of the use of boundary-layer control.—A total of 48 flights were made by four Ames pilots, a number of company test pilots, and service pilots to evaluate the airplane with and without boundary-layer control. In particular, it was desired to know the effect of BLC on the landing-approach speeds, take-off characteristics, and flying qualities.

Approach speeds: The landing-approach speeds chosen by the NACA pilots for a carrier-type approach at 12,850 pounds, the stalling speeds, and the stalling characteristics are presented in table III for the airplane with various leading-edge devices for 55° flap deflection. Included in the table for comparison are the values for the slotted flap (δ_f=38°).

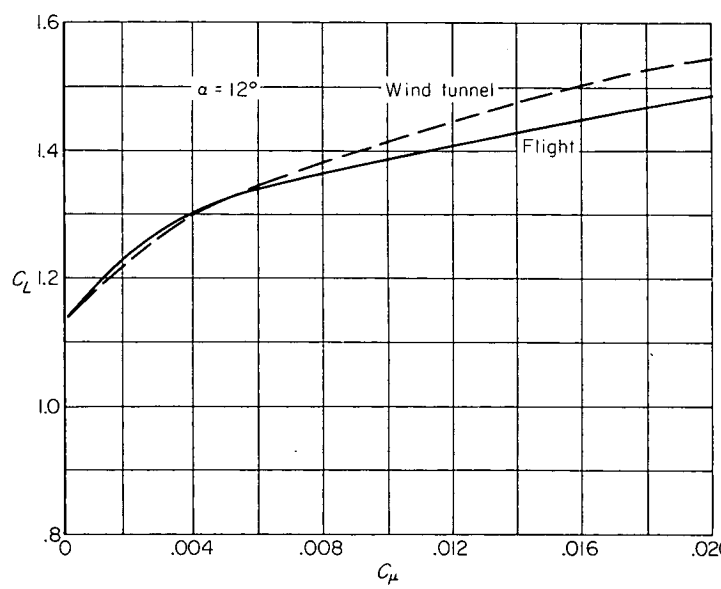


FIGURE 24.—Comparison of wind-tunnel and flight results; F-86D slatted leading edge, δ_f=60°, gear up.

These data indicate that substantial reductions in approach speed are realized with the boundary-layer control operating. For the normal type slatted leading edge, a 12-knot reduction in average approach speed over the slotted flap was obtained, while a 9-knot reduction was obtained with the 6–3 slatted leading edge. The variation of average approach speed with gross weight with the 6–3 leading edge for the 55° flap deflection, blowing on and off, and the slotted flap is presented in figure 25. These data were computed on the assumption that the pilot would approach at the same angle of attack regardless of gross weight.[4]

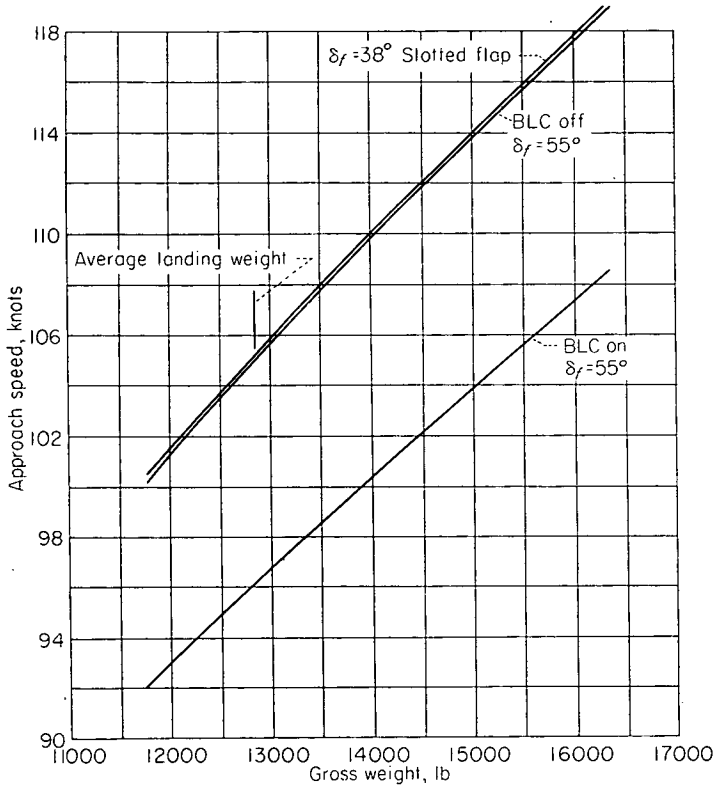


FIGURE 25.—Variation of approach speed with gross weight for various flap deflections; 6–3 slatted leading edge.

The reasons given by the pilots for selecting a minimum comfortable approach speed changed in most cases from the ability to arrest a sink rate or to control altitude without boundary-layer control to proximity to the stall with boundary-layer control on. The relationship between the pilots' selected approach speeds and the lift curves for the airplane with the 6–3 slatted leading edge is given in figure 26. These data indicate that the pilots did not make approaches at the same angle of attack with blowing on and off. Although the pilots felt that the ability to control altitude while maintaining a desired approach airspeed was greatly improved with blowing on, a reduction in angle of attack was necessary to maintain a safe margin below maximum lift.

Each pilot also made carrier approaches with the flaps deflected 66°. In this case the increased lift resulted in only small (1 to 2 knots) reductions in approach speed. The 66° flap deflection was not felt to be desirable for carrier approaches because of the increased drag causing poorer wave-off performance.

[4] Several pilots commented on the improvement in turning performance during landing approach by noting an increase in attainable angle of bank or normal acceleration with blowing on.

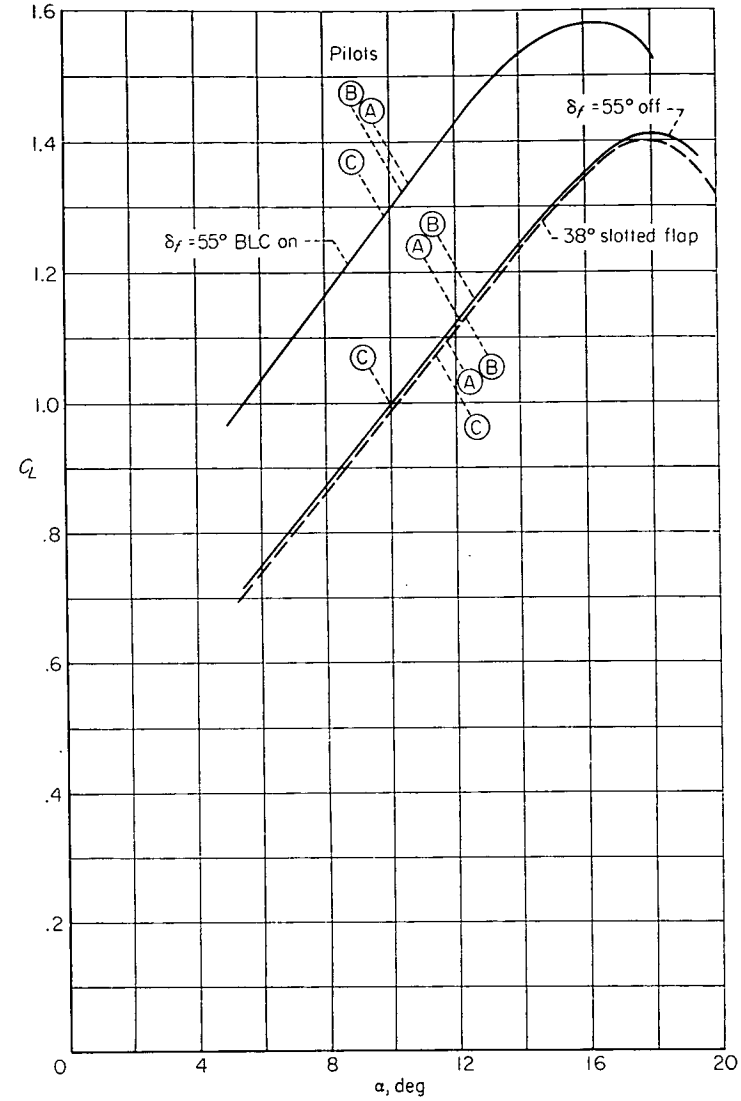


FIGURE 26.—Relationship of pilot's selected approach speeds to lift curves for various flap deflections; 6–3 slatted leading edge, 80-percent engine speed, $W/S=42.5$, $\delta_f=55°$.

The foregoing discussion has been concerned with carrier-type approaches which are made at essentially constant altitude with power for level flight. For normal field operation, a sinking-type approach is used at reduced engine powers. Because engine power has a direct effect on the amount of flap lift produced with blowing on, as well as affecting the steepness of the glide path, the approach speeds selected in a sinking-type approach will vary, depending on the amount of power used. The effect of engine power on flap lift increment is indicated by the data presented in figure 27 for a 55° flap deflection. The data show a smooth variation of flap lift with rpm. Figure 28 shows the variation of selected approach speed with engine rpm for a 55° flap deflection with boundary-layer control on and off. These approaches were made at constant power and constant airspeed with the throttle retarded after the flare (except for idle condition). Although an appreciable amount of lift due to blowing is present even at idle power, the data in figure 28 indicated that if the entire approach is made near idle power,

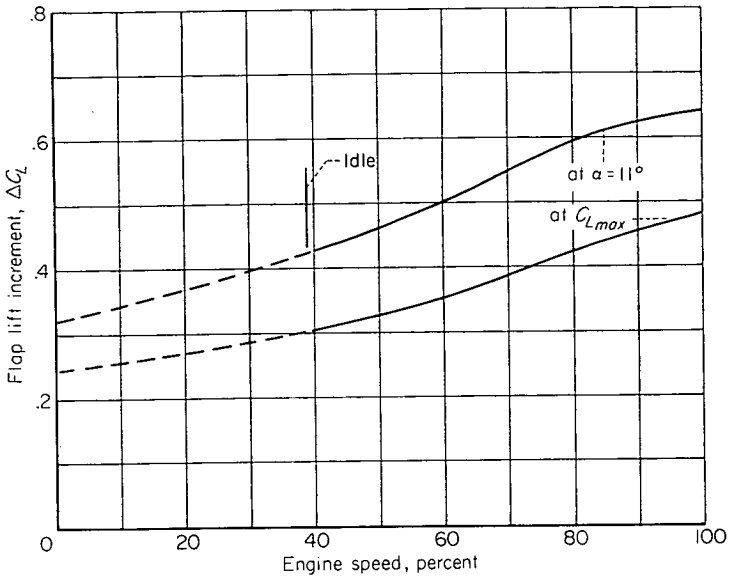


FIGURE 27.—Variation of flap lift increment with engine speed; 6–3 slatted leading edge, $\delta_f = 55°$.

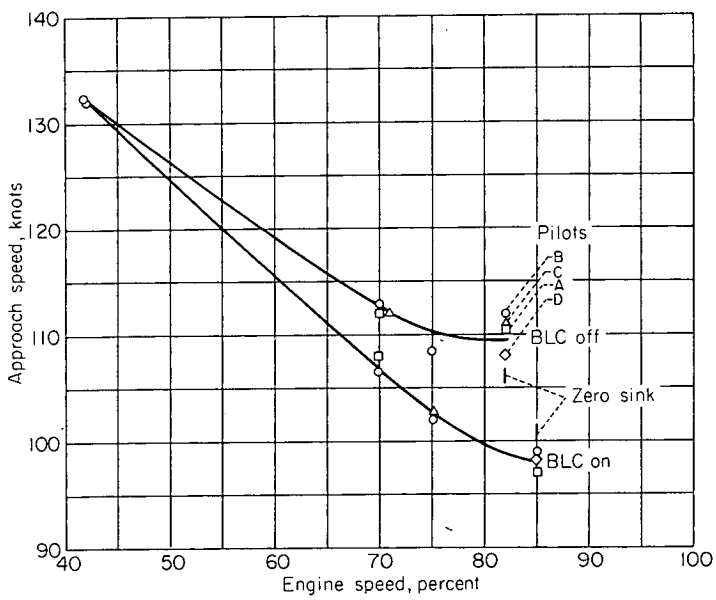


FIGURE 28.—Effect of engine speed on approach speed; blowing off and on, $\delta_f = 55°$, 6–3 slatted leading edge, sinking-type approach.

little or no reduction in approach speed would be realized. It should be noted that for modern jet-powered aircraft, approaches rarely are made at idle power. With the low values of L/D characteristic of modern aircraft, it is necessary in the interest of safety to use moderate amounts of engine power to prevent excessively high sink rates and provide satisfactory engine response in case of a wave-off. If idle power approaches are necessary for a particular design, a larger nozzle gap could be used to provide the required $C\mu$ values. There should be incorporated, however, a means of reducing the flow to avoid unnecessary loss of engine thrust at higher values of engine power. In order to get the maximum utilization of the boundary-layer control for a sinking-type approach, the NACA pilots modified their approach and used lower power to reduce airspeed and lose altitude in the early part of the landing pattern, and then increased power in the final approach, with a cut in power after the flare. Final approach speeds for landings made in this manner could be as slow as those obtained in the carrier-type approaches. In an approach where 70-percent rpm was maintained until the landing flare was initiated, due to windmilling action, the engine rpm dropped off only to 55 percent at touchdown. For the sinking-type approach, some pilots preferred a 66° flap deflection since the added drag permitted higher engine rpm and resulted in improved engine response and increased lift due to blowing.

In regard to instrument-type landings, several pilots commented that with blowing the airplane was held more easily at a desired approach speed. This effect is presumably tied in with the increased slope of the C_L—C_D curve with blowing on which results in smaller drag changes for a given lift change.

In order to investigate further the action of boundary-layer control in sinking-type approaches, several GCA (ground control approach) approaches were made using the Moffett Field GCA facilities. The pilot's comments were as follows:

"The first approach was made attempting to use the technique described in the pilot's handbook (i. e., power constant at 78 percent, 150 knots, on level portion of final approach, and upon reaching glide slope, opening speed brakes which is supposed to result in 500 feet per minute rate of descent at 150 knots). The flaps were set at 38°, blowing off. Altitude control was good; however, it seemed rather difficult to maintain the desired airspeed and a number of power corrections had to be made. Even so, rather large excursions from the desired airspeed occurred (10 to 15 knots). The second approach was made with 55° flap deflection with boundary-layer control off. The entire approach was made at 130 knots which seemed quite comfortable. Power required was about 80 percent, speed brakes were opened upon reaching the glide slope. In general, it seemed easier to hold close to the desired airspeed. Altitude control again was good. Two approaches were then made with the boundary-layer control on. On the first the flap deflection was left at 55° throughout the approach and the speed brakes were opened to start the rate of descent. On the second, 55° flap deflection was used to the glide slope, at which point the flaps were lowered to 66°, leaving the speed brakes retracted. This latter procedure seemed the most effective in commencing the 500 feet per minute rate of descent. The desirable approach speed seemed to be 115 knots which required about 83-percent rpm. Speed control with boundary-layer control on was excellent. Glide slope corrections were easily made with little effort, requiring only slight changes in power. Once the correct power and rate of descent were established the airplane seemed to ride down the glide slope as if it were on a track."

Other pilots made comments relative to the take-off characteristics. The fact that additional lift was available with no change in airplane attitude when the blowing was turned on was appreciated by some pilots and was felt to be desirable for instrument-type take-offs. Because of the high drag above 110 knots, a modified climb-out technique

was used to get maximum performance (i. e., climb initially at 100 to 110 knots, then turn the boundary-layer control off before acceleration to higher speeds).

Flying qualities: The following discussion will cover those items on which boundary-layer control had an effect. All other flying qualities were unaffected by boundary-layer-control operation.

The longitudinal trim changes due to the operation of the boundary-layer-control system on this airplane were considered to be excessive by the pilots. The measured control forces are presented in the following table:

Longitudinal stick force, lb	Initial trim condition					Configuration change	Parameter to be held constant
	Speed, knots	Gear	Flaps	Power, percent	BLC		
0	140 (1.4 V_{s_0})	Down	Up	80	Off		
7 pull	140	Down	55° down	80	Off	Flaps down	Altitude
18 pull	140	Down	55° down	87	On	BLC on	Altitude
0	140	Up	55° down	100	On		
15 push	-------	Up	55° down	100	Off	BLC off	Rate of climb
24 push	-------	Up	Up	100	Off	Flaps up	Rate of climb

Although the trim changes noted in the table are large, it is not felt that the boundary-layer-control operation in itself would represent a serious trim change problem. It can be noted that large trim changes were encountered in operation of the flaps alone and result from the type of force feel system (irreversible control system with a bungee-fixed spring gradient picked on the basis of high-speed flight) employed on this airplane. It is of interest to note that the pitching-moment change with the application of blowing measured in the wind tunnel for the F–86D airplane was in an opposite direction to that measured in flight in the present investigation. The reason for this is felt to be due to the difference in horizontal tail geometry between the two airplanes.

The effect of the boundary-layer control on the stalling characteristics was dependent somewhat on the type of leading-edge device employed with it. For the 6–3 slats and the slotted flap (δ_f=38°) the stall was characterized by a mild pitch-up coupled with a lateral unsteadiness which was controllable. The pitch-up was followed by a pitch-down. There was no stall warning. The stall in this configuration was considered satisfactory. With the plain flap deflected 55° and boundary-layer control off, the pitch-up was more pronounced. Applying boundary-layer control tended to increase the pitch-up and the stall itself was considered marginal to unsatisfactory due chiefly to the poor stall recovery characteristics. In order to recover from the stall, large forward stick displacements were necessary and the associated stick forces were objectionable. The pitch-up at the stall and the poor stall recovery characteristics were aggravated by the extreme rearward center-of-gravity location (approximately 27 percent) with the 6–3 slats installed. With the F–86D slats, the stall was considered satisfactory for all conditions; however, the application of boundary-layer control tended to reduce the stall warning and render it marginal to unsatisfactory.

Operational characteristics: In the evaluation of the performance of the airplane, actual measurements of landing and take-off distances, climb, and catapult launching were not made; but by the use of the lift and drag data obtained with the 6–3 slatted leading edge and engine thrust data, computations have been made of the performance. The methods used for computing performance are contained in appendix B and are felt to be adequate for comparative purposes.

Landing performance: The landing distance over a 50-foot obstacle and the ground roll distance were computed

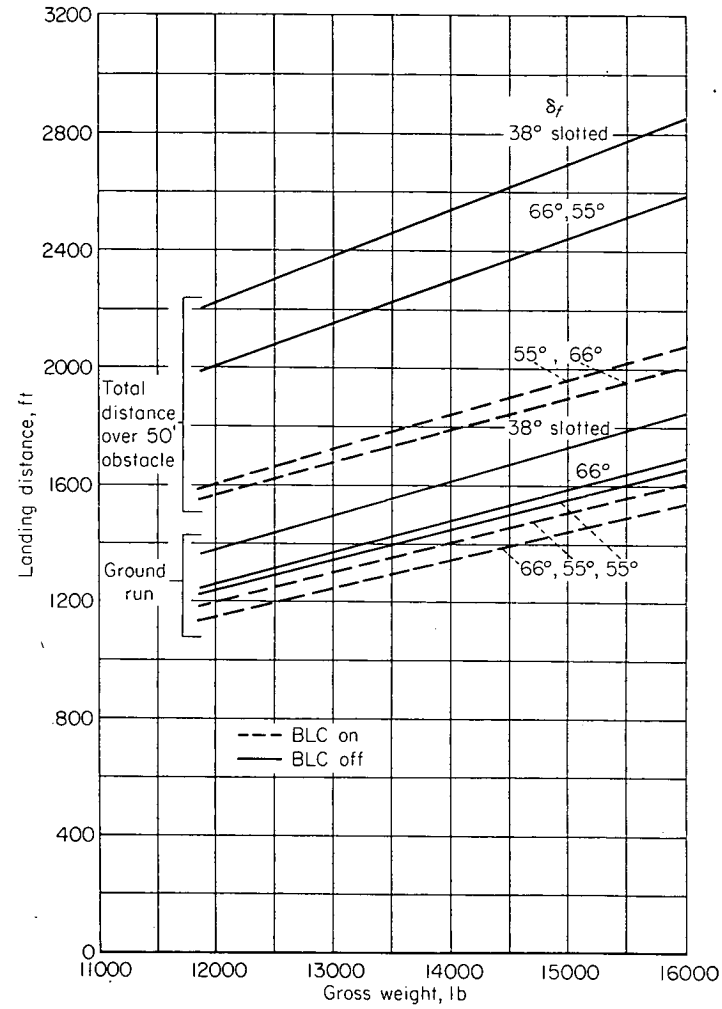


FIGURE 29.—Variation of landing distance with gross weight for various flap deflections; 6–3 slatted leading edge, sea level.

for the landing configuration using the average approach speeds selected by the pilots and are presented in figure 29 for flap deflections of 55° and 66°, blowing on and off. For comparison purposes the computed distances for the normal 38° slotted flap deflection are also presented in figure 29. These data indicate that a reduction of approximately 30 percent in total distance would be realized using the 66° flap deflection with blowing on at an airplane gross weight of 14,000 pounds.

Take-off performance: In the computations for take-off and climb, account is taken of the thrust loss incurred as a result of extracting air from the engine compressor. In order to operate the engine within the allowable tail-pipe tempera-

ture when extracting air for boundary-layer control, a reduced value of rpm is used. The thrust reduction was approximately 270 pounds at maximum power.

In considering a *catapult type take-off* this reduction in thrust is not too significant, since take-off acceleration is provided principally by the catapult itself. It is required, however, that sufficient engine thrust be available to accelerate the airplane after launch with a minimum longitudinal acceleration of approximately 0.065g.[5] Lift-off speed is selected as the speed at nine-tenths of $C_{L_{max}}$ or at the maximum ground attitude. The results of computations of the take-off speeds at the end of the catapult run as a function of gross weight for various flap deflections with blowing on and off are presented in figure 30. Indicated in this figure

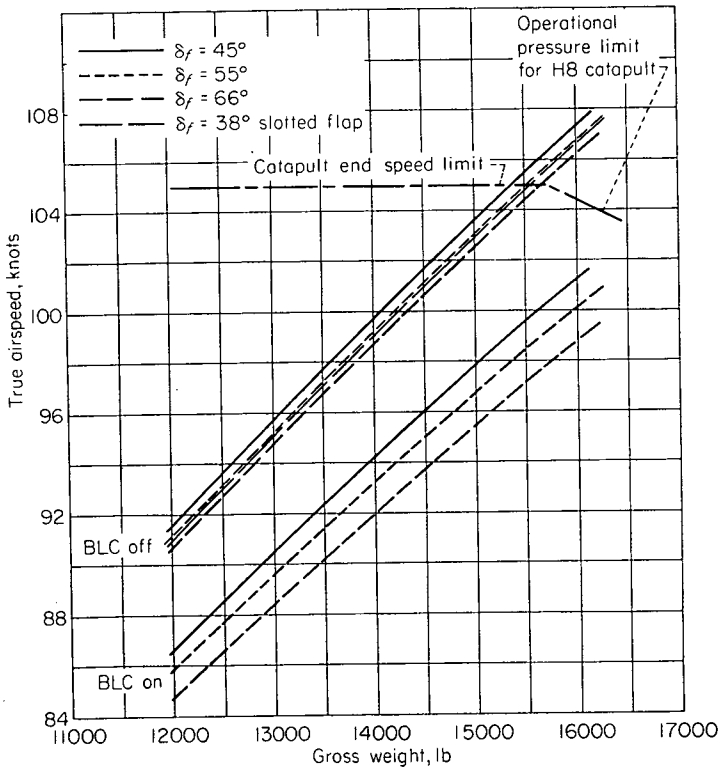


FIGURE 30.—Variation of catapult take-off velocity with gross weight for various flap deflections with blowing on and off; 6–3 leading edge, sea level.

are the H8–catapult characteristics. The results indicate significant improvements in performance with blowing on. Compared to the 38° deflection of the slotted flap, the 66° deflection of the flap with boundary-layer control would allow an 8-knot reduction in catapult take-off speed at a gross weight of 16,000 pounds. At this gross weight the longitudinal acceleration would be approximately 0.15g.

With regard to a *field take-off*, the assumption is made that the airplane accelerates on the ground in a level attitude, and at take-off speed the airplane is rotated to the angle of attack corresponding to a velocity of 1.2 V_s. For the transition distance, it is assumed that the airplane is in a steady rate of climb at the value for the 50-foot-height point. The results of the computations presented in figure 31 indicate

[5] Assumed minimum acceleration value used to assure that the airplane does not sink after launch.

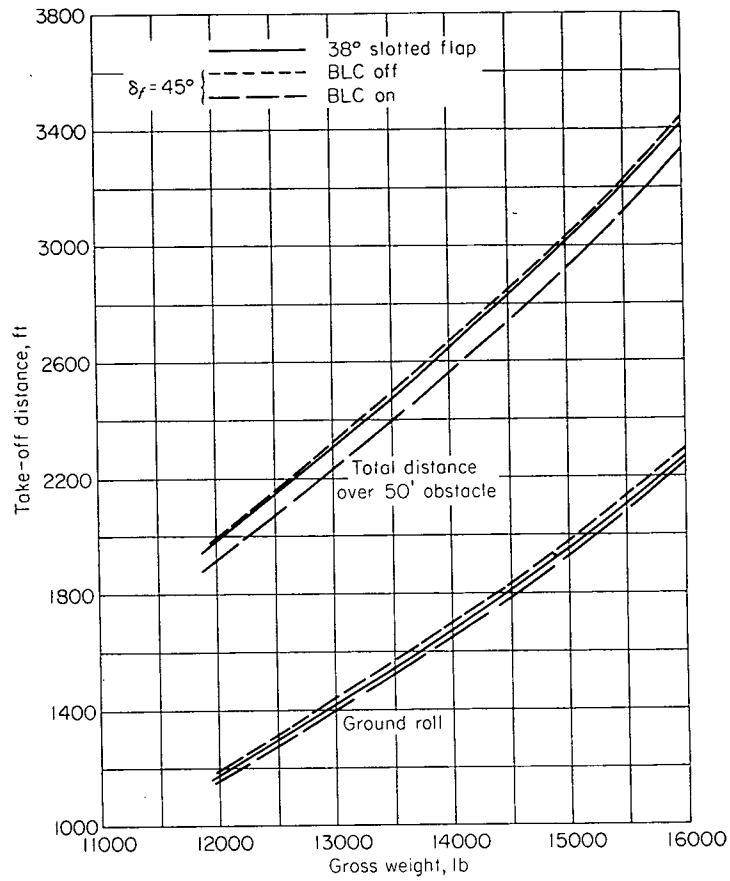


FIGURE 31.—Variation of take-off distance with gross weight for various flap deflections; blowing on and off, 6–3 slatted leading edge, sea level.

small improvements in total distance over a 50-foot obstacle with blowing on for the 45° flap deflection compared with the standard 38° slotted flap. The take-off performance was computed with the maximum possible C_μ available. Reducing the air flow to the flaps to reduce the thrust loss and thus operate at a lower C_μ made a further improvement in the take-off performance. By waiting until take-off speed is reached before turning on the boundary-layer control, a further reduction of 6 percent would be realized.

Climb characteristics: The rate of climb after a catapult take-off (at a speed of 1.05 V_s) is presented as a function of gross weight in figure 32. Although the rate of climb is reduced when blowing is used, it should be kept in mind that because of the lower stalling speed it is possible to climb at a lower airspeed with blowing on so that there is no significant change in climb angle.

SUMMARY OF RESULTS AND CONCLUSIONS

The following conclusions are based on wind-tunnel and flight investigations of F–86 type aircraft with blowing boundary-layer control on the trailing-edge flaps:

1. Correlation of flap lift with jet momentum coefficient was good for the range of pressure ratios obtainable from turbojet engine bleed air systems.
2. The lift increment obtained by preventing flow separation on the flap can be predicted up to 60° flap deflection by the linear inviscid fluid theory of NACA Rep. 1071.

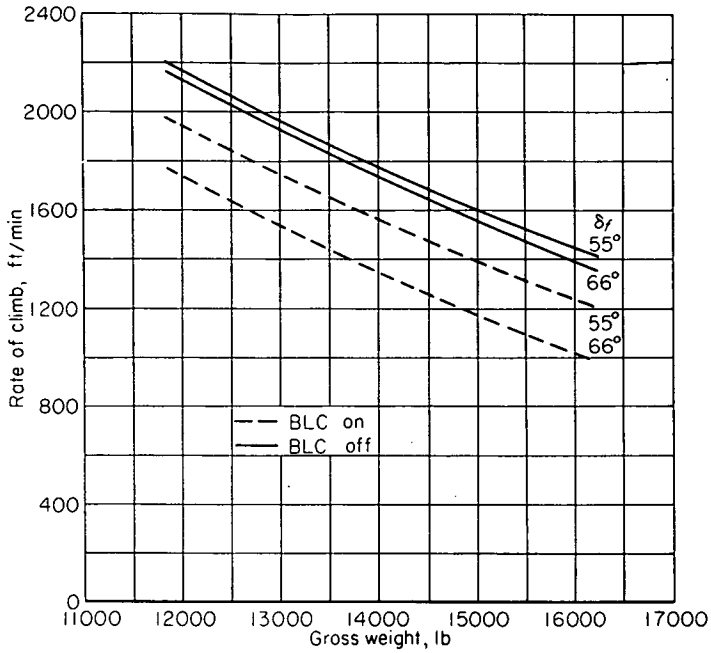


FIGURE 32.—Variation of rate of climb with gross weight for various flap deflections with blowing on and off; wave-off speed $= 1.05V_s$, 6–3 leading edge, sea level.

3. Higher lift increments than those obtained by preventing flow separation on the flaps can be achieved by further increasing the momentum coefficient to values above that required to prevent flow separation. However, once the flow is attached to the flap, large values of momentum coefficient are required to increase the lift significantly.

4. Lateral stability was increased slightly by blowing over the flaps, and the maximum roll power of the ailerons was increased by about 25 percent.

5. When the blowing nozzle was located in the upper surface of the flap, it was found that the chordwise position of the nozzle could be anywhere between the minimum pressure point on the flap and the wing-flap juncture without seriously affecting the flap lift. If the nozzle is located too far downstream of the minimum pressure point, large losses in flap lift may result.

6. When the blowing nozzle was located in the wing shroud ahead of the flap, it was necessary to position the flap close to the nozzle to obtain the same lift coefficients at low momentum coefficients as those for the plain-blowing-flap configuration.

7. The blowing flap lift is relatively insensitive to spacers or structural members in the nozzle throat. It is also insensitive to flow disturbances such as those caused by leading-edge slats.

8. Blowing with the flaps deflected 55° reduced the average approach speed by as much as 12 knots in a carrier-type approach compared to the slotted flap deflected 38°. In sinking-type approaches smaller reductions in speed were realized.

9. Blowing with the flaps deflected 66° reduced the calculated landing distance by 30 percent compared to the standard 38° slotted flap. In takeoff performance calculations, the catapult end speed required at a given gross weight was reduced by 8 knots due to blowing. For a field-type takeoff the gains calculated were relatively small.

10. Improvements were noted by the pilots in control of the glide path with blowing on. Improvements were noted also in take-off since the airplane would tend to fly off without as much rotation in attitude required.

11. The longitudinal trim changes due to flap deflection and application of blowing were considered excessive by the pilots.

12. In some cases the stalling characteristics were made less desirable with blowing on.

AMES AERONAUTICAL LABORATORY
NATIONAL ADVISORY COMMITTEE FOR AERONAUTICS
MOFFETT FIELD, CALIF., *April 30, 1958*

APPENDIX A

EQUATIONS USED FOR DETERMINING LIFT AND DRAG

The equations used to determine the lift coefficients and drag coefficients are as follows:

$$C_L=\frac{W}{qS}(A_z\cos\alpha+A_x\sin\alpha)-\frac{1}{qS}(F_G\sin\alpha)$$

$$C_D=\frac{W}{qS}(A_z\sin\alpha-A_x\cos\alpha)+\frac{1}{qS}(F_G\cos\alpha-wV)$$

where

$\frac{W}{S}$	airplane wing loading, lb/sq ft
q	dynamic pressure, lb/sq ft
A_z	normal acceleration factor, g units
A_x	longitudinal acceleration factor, g units
α	angle of attack, deg
w	engine air flow, lb sec/ft
V	free-stream velocity, ft/sec
F_G	engine gross thrust, lb

APPENDIX B

METHODS USED FOR PERFORMANCE EVALUATION

The following equations and assumptions were used in computing the performance:

Landing distance:

$$\text{Air distance}=\left(\frac{V_{50}^2-V_L^2+50}{64.4}\right)\frac{L}{D},\ \text{ft}$$

(ref. 7, p. 198) where V_{50} is pilots' average approach speed and the landing velocity

$$V_L=1.05V_s$$

$$\text{Ground run}=\frac{V_L^2}{64.4[\mu-(D/L)]}\log e\left(\frac{L}{D}\right)\mu,\ \text{ft}$$

and $\mu=0.4$ (ref. 8, p. 312).

Take-off distance:

$$\text{Ground run}=\frac{WV_{TO}^2}{64.4[T-\mu W-Sq(C_D-\mu C_L)]},\ \text{ft}$$

(from ref. 7, pp. 195–196)

$$\text{Air distance: }\frac{50W}{T-D}+\frac{V_{TO}^2}{g\sqrt{2}},\ \text{ft}$$

(ref. 9, p. 51) where take-off velocity

$$V_{TO}=1.2V_s$$

$$=1.2\sqrt{\frac{843(W-T\sin\alpha)}{SC_{L_{max}}}},\ \text{ft/sec}$$

and

T	thrust at 100-percent engine speed
q	$\frac{\rho}{2}(0.7V_{TO})^2$
W	airplane gross weight in pounds
α	angle of attack at $C_{L_{max}}$ or at maximum ground angle
μ	0.02

(The assumption is made that steady climb has been attained before reaching the 50 foot height.)

Catapult end speed:

$$V_{TO}=\sqrt{\frac{295(W-T\sin\alpha_{TO})}{SC_{L_{TO}}}},\ \text{knots}$$

where

$C_{L_{TO}}$	$0.9C_{L_{max}}$
α_{TO}	angle of attack at $C_{L_{TO}}$

Climb:

$$\text{Rate of climb}=\frac{60V_c(T-D)}{W},\ \text{ft/sec}$$

where

V_c	$1.05V_s$, ft/sec
T	thrust at climb power
D	drag at V_c

REFERENCES

1. Schwier, W.: Lift Increase by Blowing Out Air, Test on Airfoil of 12 Percent Thickness, Using Various Types of Flap. NACA TM 1148, 1947.
2. Schwier, W.: Lift Increase Produced by Blowing a Wing of a Profile Thickness of 9 Percent Equipped with a Slat and a Slotted Flap. Air Materiel Command Trans. Rep. F–TS–645–RE, Sept. 1946. (See also: R–30–18, pt. 9 (Ger–207), Goodyear Aircraft Corp. Trans. from: (ZWB, Berlin, FB 1622).
3. Harkleroad, E. L., and Murphy, R. D.: Two-Dimensional Wind-Tunnel Tests of a Model of an F9F–5 Airplane Wing Section Using a High-Speed Jet Blowing Over the Flap: Part I—Tests of a 6-Foot Chord Model. David Taylor Model Basin Aero. Rep. 845, May 1953.
4. Kelly, Mark W., and Tucker, Jeffrey H.: Wind-Tunnel Tests of Blowing Boundary-Layer Control With Jet Pressure Ratios Up to 9.5 on the Trailing-Edge Flaps of a 35° Sweptback Wing Airplane. NACA RM A56G19, 1956.
5. DeYoung, John: Theoretical Symmetric Span Loading Due to Flap Deflection for Wings of Abritrary Plan Form at Subsonic Speeds. NACA Rep. 1071. (Supersedes NACA TN 2278.)
6. Cook, Woodrow L., Holzhauser, Curt A., and Kelly, Mark W.: The Use of Area Suction for the Purpose of Improving Trailing-Edge Flap Effectiveness on a 35° Sweptback Wing. NACA RM A53E06, 1953.
7. Perkins, Courtland D., and Hage, Robert E.: Airplane Performance, Stability and Control. John Wiley & Sons, Inc., 1949.
8. Dwinnell, James H.: Principles of Aerodynamics. McGraw-Hill Book Co., 1949.
9. Lush, Kenneth J.: Standardization of Take-Off Performance Measurements for Airplanes. Tech. Note R–12, Edwards Air Force Base, Edwards, California (1954).

TABLE I.—COORDINATES OF THE WING AIRFOIL SECTIONS NORMAL TO THE WING QUARTER-CHORD LINE AT TWO SPAN STATIONS

[Dimensions given in inches]

Section at 0.467 semispan			Section at 0.857 semispan		
Distance from L. E.	Ordinate		Distance from L. E.	Ordinate	
	Upper	Lower		Upper	Lower
0	0.231	----------	0	−0.098	----------
.119	.738	−0.307	.089	.278	−0.464
.239	.943	−.516	.177	.420	−.605
.398	1.127	−.698	.295	.562	−.739
.597	1.320	−.895	.443	.701	−.879
.996	1.607	−1.196	.738	.908	−1.089
1.992	2.104	−1.703	1.476	1.273	−1.437
3.984	2.715	−2.358	2.952	1.730	−1.878
5.976	3.121	−2.811	4.428	2.046	−2.176
7.968	3.428	−3.161	5.903	2.290	−2.401
11.952	3.863	−3.687	8.855	2.648	−2.722
15.936	4.157	−4.064	11.806	2.911	−2.944
19.920	4.357	−4.364	14.758	3.104	−3.102
23.904	4.480	−4.573	17.710	3.244	−3.200
27.888	4.533	−4.719	20.661	3.333	−3.250
31.872	4.525	−4.800	23.613	3.380	−3.256
35.856	4.444	−4.812	26.564	3.373	−3.213
39.840	4.299	−4.758	29.516	3.322	−3.126
43.825	4.081	−4.638	32.467	3.219	−2.989
47.809	3.808	−4.452	35.419	3.074	−2.803
51.793	3.470	−4.202	38.370	2.885	−2.574
55.777	3.066	−3.891	41.322	2.650	−2.302
59.761	2.603	−3.521	44.273	2.374	−1.986
[a]63.745	2.079	−3.080	[a]47.225	2.054	−1.625
83.681	−.740	----------	63.031	.321	----------
Le. E. radius: 1.202, center at (1.201 0.216)			L. E. radius: 0.322, center at (0.822, −0.093)		

[a] Straight lines to trailing edge.

TABLE II.—DIMENSIONS OF TEST AIRPLANE

Wing:	
Total area, sq ft (with F–86D-type slats)	287.9
Total area, sq ft (with extended leading edge)	302
Span, ft	37.12
Aspect ratio	4.79
Taper ratio	0.51
Mean aerodynamic chord (wing station 98.7 in.), ft	8.1
Dihedral angle, deg	3.0
Sweepback of 0.25-chord line, deg	35.23
Geometric twist, deg	2.0
Root airfoil section (normal to 0.25-chord line)	NACA 0012–64 (modified)
Tip airfoil section (normal to 0.25-chord line)	NACA 0011–64 (modified)
Wing area affected by flap, sq ft	116.6
Horizontal tail:	
Total area, sq ft	35.0
Span, ft	12.7
Aspect ratio	4.65
Taper ratio	0.45
Dihedral angle, deg	10.0
Mean aerodynamic chord (horizontal-tail station 33.54 in.), ft	2.9
Sweepback of 0.25-chord line	34.58
Airfoil section (parallel to center line)	NACA 0010–64
Vertical tail:	
Total area, sq ft	34.4
Span, ft	7.5
Aspect ratio	1.74
Taper ratio	0.36
Sweepback of 0.25-chord line, deg	35.00
Flap:	
Total area, sq ft	23.7
Span (from 13.4 to 49.5-percent semispan), ft	7.27
Chord (constant), ft	1.67

TABLE III.—PILOTS' OBSERVED STALLING AND APPROACH CHARACTERISTICS FOR VARIOUS FLAP AND LEADING-EDGE DEVICES

Pilot	Configuration			Stall			Carrier approach 12,850 lb	
	Leading edge	Flap	BLC	Indicated air speed, knots	Gross weight, lb	Characteristics	Indicated air speed, knots	Reason for limiting approach speed
A	6-3 slat	38° slotted	None	89	12,750	Warning: Unsatisfactory Stall: No comment	105	Inadequate longitudinal control and visibility
	6-3 slat	55°	On	85	12,630	Warning: None—unsatisfactory Stall: Marginal—satisfactory	95	Proximity to stall, inadequate altitude control
	6-3 slat	55°	Off	90	12,720	Warning: None—unsatisfactory Stall: Marginal—satisfactory	103	Proximity to stall, inadequate altitude control and visibility
	F-86D slat	38° slotted	None	96	14.200	Warning: Satisfactory Stall: Satisfactory	106	Inadequate longitudinal control and visibility
	F-86D slat	55°	On	88	12,860	Warning: 93 knots, less than with BLC off Stall: Satisfactory	98	Proximity to stall
	F-86D slat	55°	Off	93	12,860	Warning: 103 knots, satisfactory Stall: Satisfactory	111	Inadequate longitudinal control and ability to arrest sink
B	6-3 slat	38° slotted	None	90	12,470	Mild pitch-up with roll-off	103-108	Proximity to pitch-up and roll-off
	6-3 slat	55°	On	86–88	12,860	Warning: Unsatisfactory Stall: Marginal, stall recovery unsatisfactory, mild pitch-up with lateral instability at $C_{L_{max}}$	93–98	Proximity to pitch-up
	6-3 slat	55°	Off	93	12,860	Warning: Unsatisfactory Stall: Marginal, satisfactory	98–103	Proximity to pitch-up
	F-86D slat	38° slotted	None	92	12,860	Warning: Satisfactory Stall: Satisfactory	103	Ability to arrest rate of sink, visibility
	F-86D slat	55°	On	88	12,860	Warning: 91 knots, satisfactory Stall: Satisfactory	96–98	Ability to control rate of sink
	F-86D slat	55°	Off	92	12,860	Warning: 96 knots; very mild; unsatisfactory Stall: Satisfactory	108–113	Ability to control rate of sink
C	6-3 slat	38° slotted	None	92	13,310	Smooth to 100 knots; yaw to left at 98 knots and fall through at 94 knots	106	Inadequate altitude control and proximity to stall
	6-3 slat	55°	On	86	12,860	Warning: Unsatisfactory Stall: Unsatisfactory due to pitch-up	97	Proximity to pitch-up
	6 3 slat	55°	Off	92	12,860	Warning: Unsatisfactory Stall: Marginal due to pitch-up	110	Ability to arrest rate of sink
	F-86D slat	38° slotted	None	98	14,300	Warning: Satisfactory Stall: Satisfactory	110	Ability to control rate of sink
	F-86D slat	55°	On	88	12,860	Stall: Satisfactory	98–100	Proximity to stall
	F-86D slat	55°	Off	92	12,860	Stall: Satisfactory	110–113	Ability to control altitude
D	F-86D slat	55°	On	90	12,960	Warning: 98 knots, unsatisfactory, light pitch-up Stall: Satisfactory	98	Inadequate altitude control
	F-86D slat	55°	Off	96	13,660	Warning: 99 knots, unsatisfactory Stall: No comment	108	Slow longitudinal control of flight path visibility

REPORT 1370

AREA-SUCTION BOUNDARY-LAYER CONTROL AS APPLIED TO THE TRAILING-EDGE FLAPS OF A 35° SWEPT-WING AIRPLANE [1]

By Woodrow L. Cook, Seth B. Anderson, and George E. Cooper

SUMMARY

A wind-tunnel investigation was made to determine the effects on the aerodynamic characteristics of a 35° swept-wing airplane of applying area-suction boundary-layer control to the trailing-edge flaps. Flight tests of a similar airplane were then conducted to determine the effect of boundary-layer control on the handling qualities and operation of the airplane, particularly during landing.

The wind-tunnel and flight tests indicated that area suction applied to the trailing-edge flaps produced significant increases in flap lift increment. Although the flap boundary-layer control reduced the stall speed only slightly, a reduction in minimum comfortable approach speed of about 12 knots was obtained.

INTRODUCTION

Reference 1 indicated that much less air flow and power were required to obtain boundary-layer control at a wing leading edge with suction through a porous area than through a slot. It was therefore reasoned that similar gains in suction requirements would be realized if boundary-layer control were applied by suction through a porous surface near the forward edge of trailing-edge flaps.

Because of the possibility of the power requirements with area suction being low enough to be of practical value, an investigation was conducted on the 35° sweptback wing F–86 airplane in flight and in the Ames 40- by 80-foot wind tunnel. Area suction was applied at several trailing-edge flap deflections through various chordwise extents and positions of porous surface. It was anticipated that maximum lift would be limited by leading-edge air-flow separation on the wing; thus, the investigations also included the use of the suction flap with (1) a modified wing leading having camber and increased leading-edge radius, and (2) a wing leading-edge slat.

In the flight tests, the landing approach with and without boundary-layer control was evaluated by 16 Air Force, Navy, contractor, and NACA pilots. The results of these evaluations are examined in this report to determine the relationship between the pilots' opinions of the several configurations flown and their choice of minimum comfortable landing-approach speed.

NOTATION

A_x	longitudinal acceleration
A_z	normal acceleration
BLC	boundary-layer control
b	wing span, ft
c	chord, measured parallel to the plane of symmetry, ft
$\bar{c}$	mean aerodynamic chord, $\frac{2}{S}\int_0^{b/2} c^2 dy$, ft
C_D	drag coefficient, $\frac{\text{drag}}{qS}$
C_L	lift coefficient, $\frac{\text{lift}}{qS}$
$C_{L_{max}}$	Maximum lift coefficient
C. L. E.	cambered leading edge
C_m	pitching-moment coefficient computed about the quarter-chord point of the mean aerodynamic chord, $\frac{\text{pitching moment}}{qS\bar{c}}$
C_Q	flow coefficient, $\frac{Q}{VS}$
d	chordwise extent of porous surface, measured in chord plane, ft
F_G	gross thrust
F_R	ram drag
I. A. S.	pilots' indicated airspeed as read from cockpit indicator, knots
$\frac{L}{D}$	lift-to-drag ratio
l	length of porous surface, measured along surface normal to leading edge, in.
p_∞	free-stream static pressure, lb/sq ft
p	static pressure, lb/sq ft
P	airfoil pressure coefficient, $\frac{p_l - p_\infty}{q}$
P_d	average duct pressure coefficient, $\frac{p_d - p_\infty}{q}$
P_p	plenum-chamber pressure coefficient, $\frac{p_p - p_\infty}{q}$
q	free-stream dynamic pressure, lb/sq ft

[1] Summarizes NACA Research Memorandums A53E06 by Woodrow L. Cook, Curt H. Holzhauser and Mark W. Kelly, A55K14 by George E. Cooper and Robert C. Innis, and A55K29 by Seth B. Anderson and Hervey C. Quigley.

Preceding Page Blank

Q	volume of air removed through porous surface, cu ft/sec, based on free-stream density at test attitude
R	Reynolds number, $\frac{V\bar{c}}{\nu}$
S	wing area, sq ft
t	thickness of porous material, in.
V	free-stream velocity, ft/sec
V_A	calibrated approach airspeed, knots
$V_{C_{L_{max}}}$	calibrated airspeed corresponding to maximum lift coefficient, knots
w	suction-air velocity, ft/sec
W	assumed weight of airplane, $C_L qS$
$\left(\frac{W}{S}\right)_A$	wing loading for approach condition (1000 lb of fuel remaining)
x	chordwise distance, parallel to plane of symmetry, ft
y	spanwise distance, perpendicular to plane of symmetry, ft
z	height above wing reference plane, ft
α	angle of attack of fuselage center line, deg
δ_f	flap deflection, measured in plane normal to the hinge line, deg
$\underline{\delta}_f$	flap deflection, measured in plane parallel to plane of symmetry (δ in ref. 2), deg
Δp	pressure drop across porous material, lb/sq ft
Λ	sweep angle, deg
ν	kinematic viscosity, ft²/sec

SUBSCRIPTS

crit	critical
d	duct
f	trailing-edge flap
L	leading edge
p	plenum chamber
R	reference conditions
l	local surface

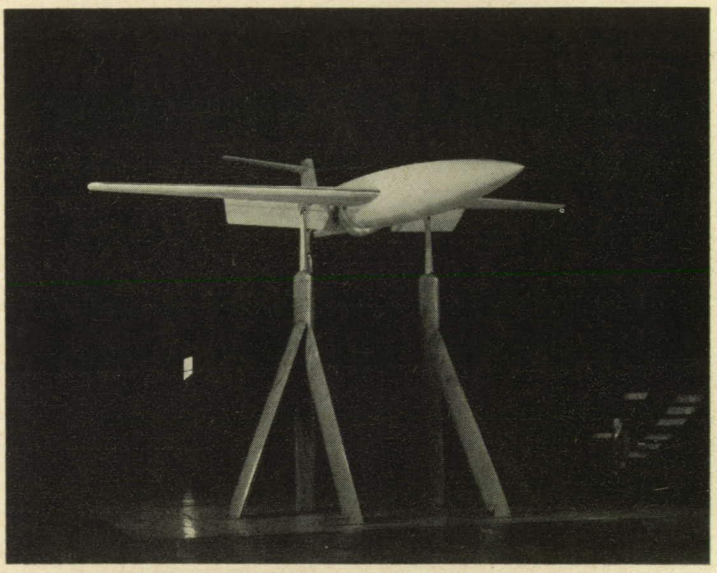
MODEL AND APPARATUS

WIND-TUNNEL MODEL

A general view of the model is shown in figure 1 (a). Except for the flaps, the model is the same as that used in the investigation of reference 1 where it is described completely. The geometric characteristics of the model are shown in figures 2 (a) and 3. Additional dimensions of the model are provided in table I. The wing panels and horizontal tail are from an F–86A airplane. The horizontal tail is in the same position relative to the wing as on the airplane. The coordinates for the airfoil section at two spanwise sections are given in table II.

The original trailing-edge flaps on the wing were removed and replaced with suction flaps that could be deflected to 45°, 55°, 64°, and 70°. The flaps has a constant chord and extended from 0.135 to 0.495 semispan. The flap chord of the wind-tunnel model was larger than that on the flight airplane, as is shown in figure 4. The flaps were constructed with the upper surface porous over the axis of rotation (fig. 4). The porous surface extended from a point ½ inch aft of the reference line to 8 inches aft of the reference line measured along the surface normal to the reference line. The reference line shown in figure 4 is a line on the upper surface of the wing in a vertical plane with the hinge line. The chordwise extent and position of porous surface was controlled with a nonporous tape of about 0.003-inch thickness. The various extents and positions of porous areas tested are listed in table III. The dimensions given are normal to the reference line and are measured along the curved porous surface. The chordwise extent of the porous surface for all configurations was constant across the span of the flap.

The porous material used for the flap was the same type used in the investigation of reference 1. The material was composed of a metal mesh sheet backed with a white wool felt material. The metal mesh sheet had 4,225 holes per square inch, and was 11 percent open and 0.008 inch thick. The flow resistance characteristics for the porous material are shown in figure 5 for two grades of wool felt, each having $\frac{1}{16}$-inch thickness. For other thicknesses of felt, the pressure

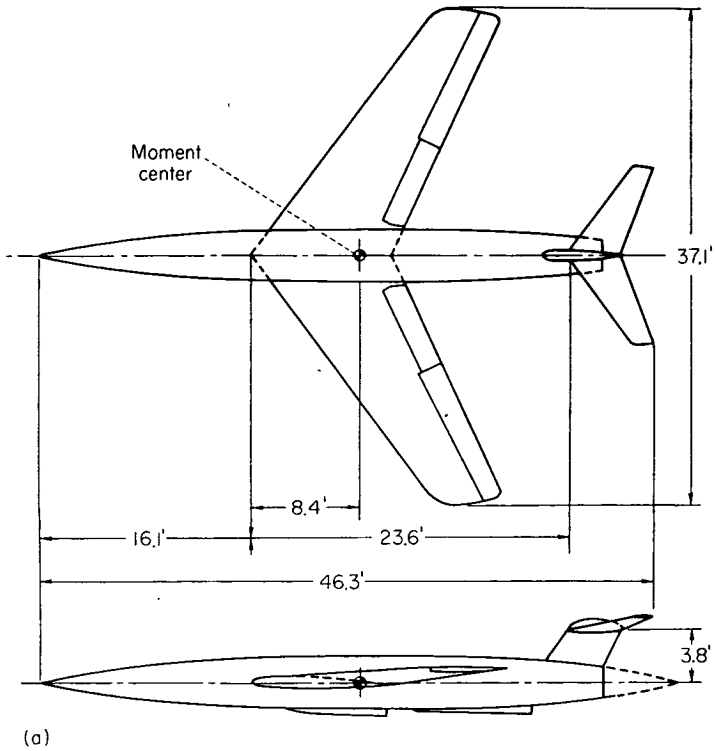


(a) The 35° sweptback wing wind-tunnel model.



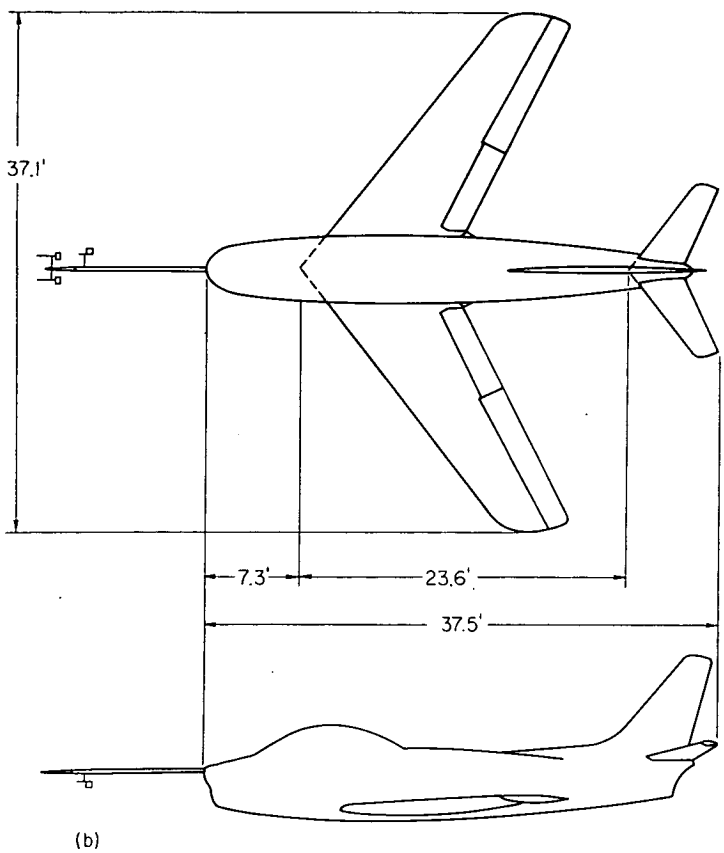
(b) The F86–A airplane.

FIGURE 1.—General arrangements of the test vehicles equipped with area suction flaps.



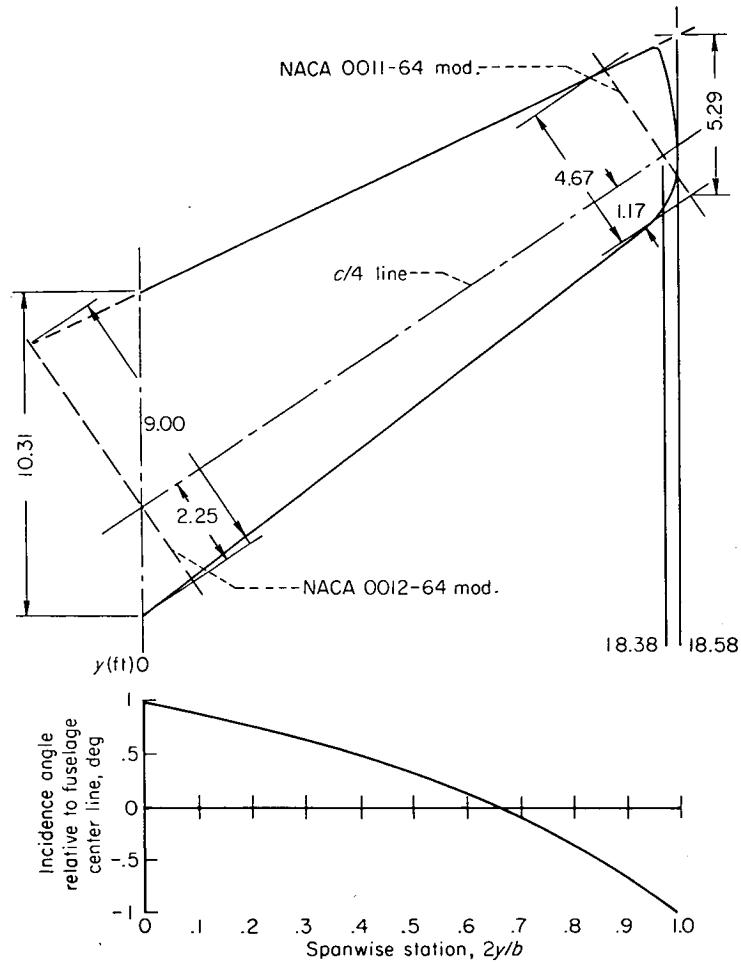
(a) 35° swept wing wind-tunnel model.

FIGURE 2.—Geometry of test vehicles.



(b) Flight-test airplane.

FIGURE 2.—Concluded.



Note: Coordinates of airfoil given in table II.
Sweep angle of quarter-chord line in plane of wing 34°58'
All dimensions in feet

FIGURE 3.—Wing geometry.

drop across the surface was directly proportional to thickness of the wool felt. The variation of thickness of a tapered felt is also shown in figure 5. Because of the external pressure variation over the flap, variations in thickness are used to give a more uniform chordwise distribution of suction-air velocity, as discussed in reference 1.

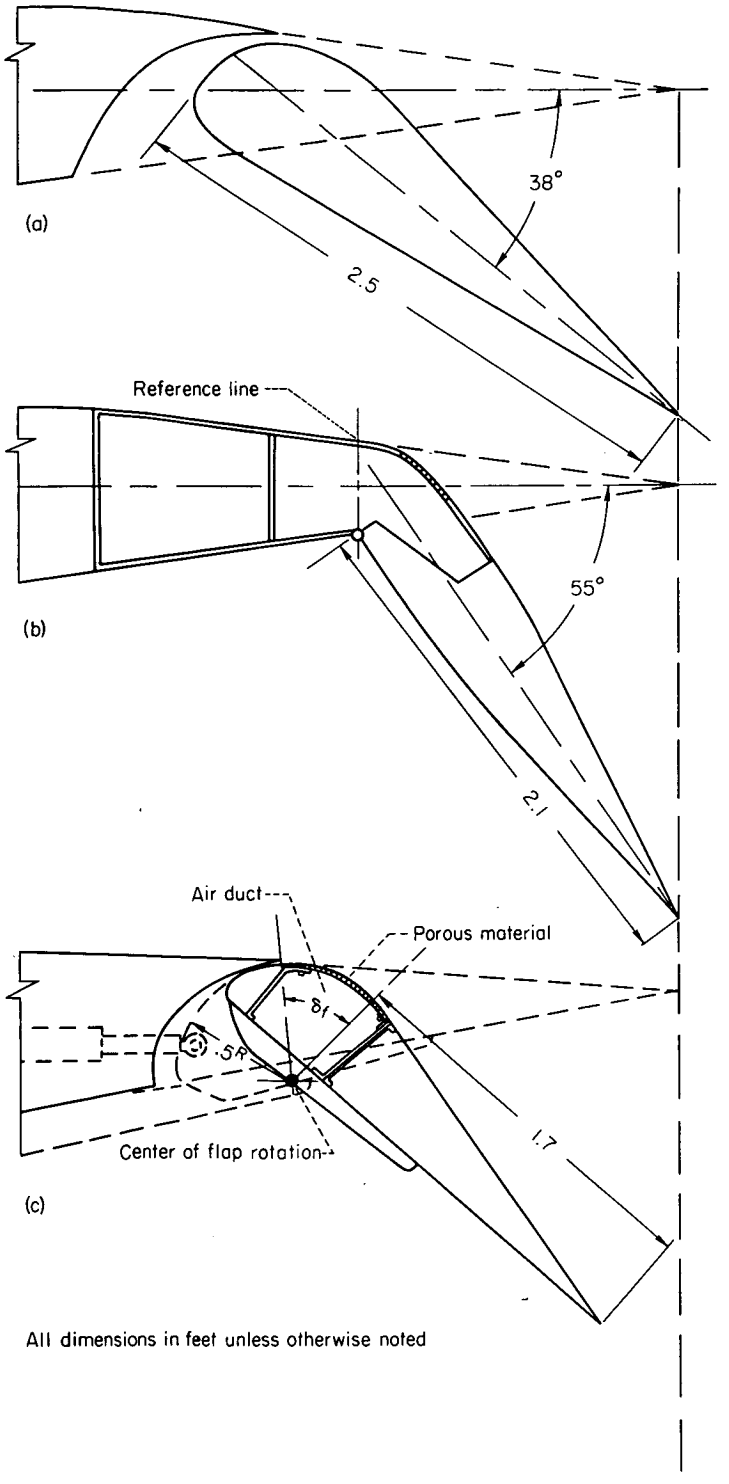
The model was tested with three wing leading-edge configurations. The majority of the tests were made with the normal F–86A leading edge for which the coordinates are given in table II. Two leading edges were used to enable studies of the area-suction flap at higher lift coefficients: (1) the modified leading edge which had camber added to the forward portion of the chord, and an increased leading-edge radius as shown in figure 6 (a) and table IV and (2) the F–86A leading-edge slat, shown in figure 6 (b), extending from 0.245 semispan to 0.94 semispan.

The fuselage used in the wind-tunnel tests was circular in cross section, and the radius, in feet, is defined by the equation

$$1.84\left[1-\left(\frac{x}{23}-1\right)^2\right]^{3/4}$$

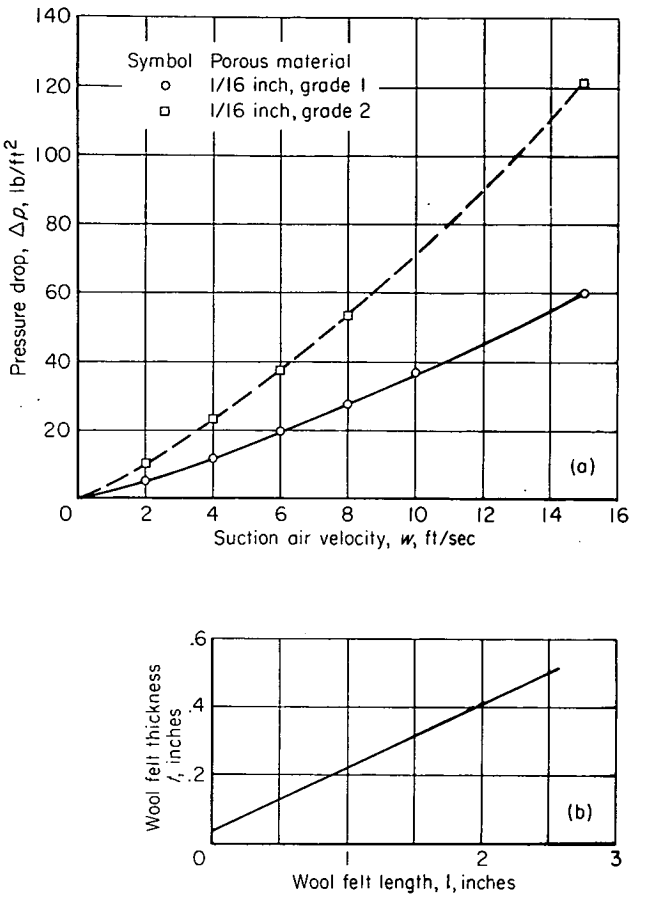
This fuselage has a larger fineness ratio (11.5) and smaller width (0.10 $b/2$) than the fuselage of the F–86 airplane (fineness ratio 6.9, and 0.13 $b/2$ width). With this fuselage the wing was mounted at a mid-fuselage position in contrast to the low wing position of the F–86 airplane.

The suction system consisted of a centrifugal compressor driven by an electric motor mounted in a plenum chamber in the fuselage. The air was drawn through the wing surface, into wing ducts, through the plenum chamber and the compressor, and out the exit duct at the bottom of the fuselage. The quantity of air removed was measured by survey rakes located at the exit of the system. The rakes were calibrated



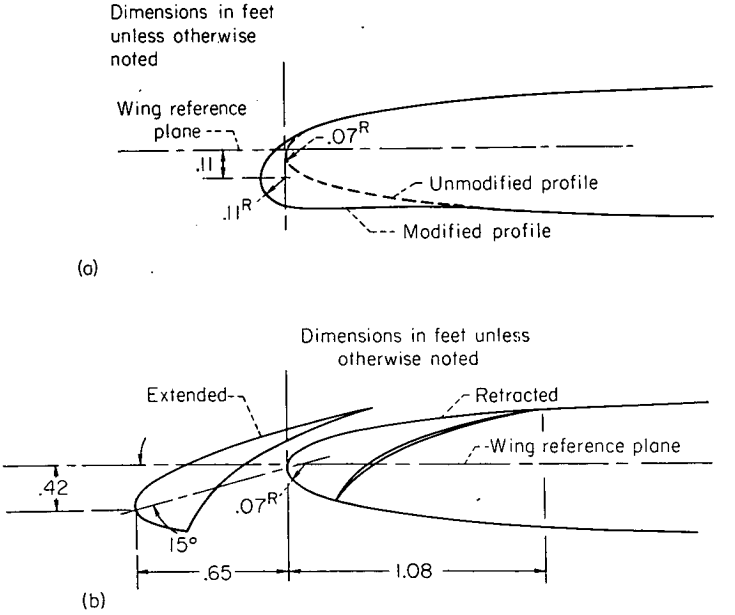
(a) Slotted flap.
(b) Area-suction flap, wind-tunnel model.
(c) Area-suction flap, airplane.

FIGURE 4.—Cross sections of various trailing-edge flaps.



(a) Flow characteristics.
(b) Chordwise distribution. Grade 1 felt.

FIGURE 5.—Chordwise distribution of porous surface and flow characteristics of two grades of porous material.



(a) Cambered leading edge.
(b) Slotted leading edge.

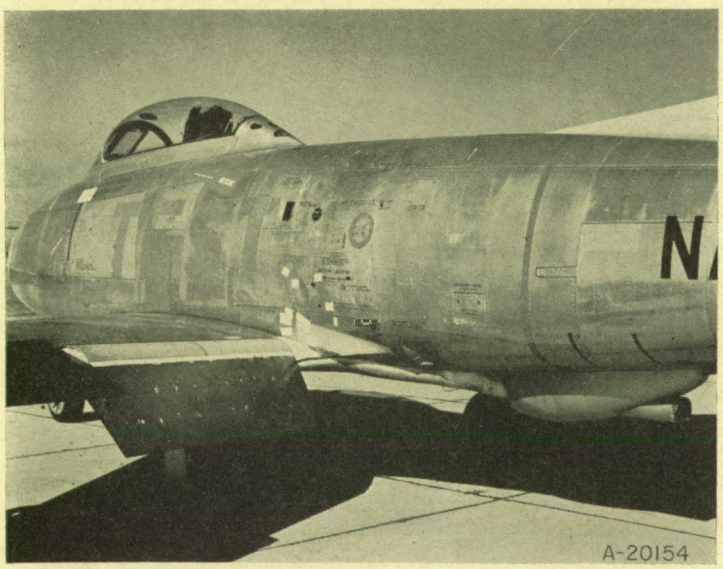
FIGURE 6.—Cross sections of the various leading edges.

with standard ASME orifice meters. Plenum-chamber and duct pressures were measured with static-pressure orifices and were assumed to be equal to the total pressure, since the suction-air velocities in the duct and plenum chamber were low. The spanwise and chordwise positions of surface-pressure orifices are listed in table V. The total suction power was measured with a wattmeter and included pump losses, duct losses, and the suction requirements.

FLIGHT-TEST AIRPLANE

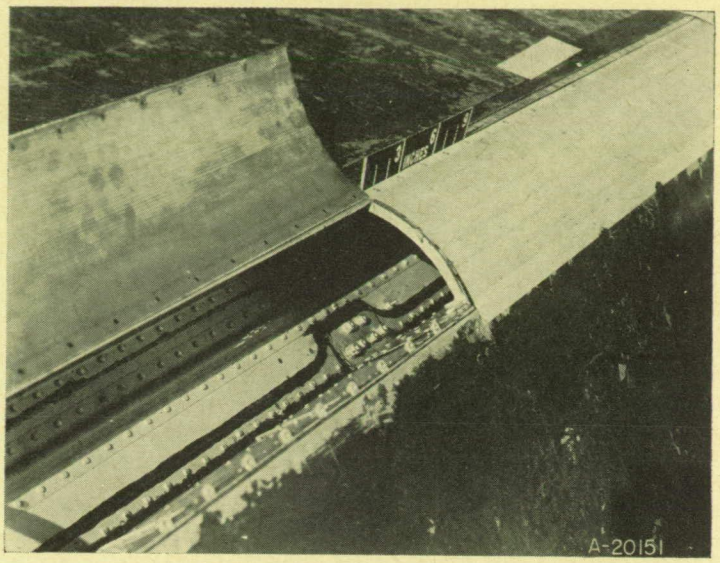
The installation of the area-suction flap was made on an F–86A–5 airplane. Figure 1 is a photograph showing the airplane with the boundary-layer-control equipment installed. The test airplane dimensions are presented in table I and a two-view drawing is shown in figure 2. Some of the boundary-layer-control equipment was mounted externally to facilitate installation. The external modifications to the airplane consisted of a faired pod, enclosng an ejector pump for supplying suction, and ducts on the underside of the fuselage for removing air from the flaps (see fig 7). Air was bled from the last stage of the compressor of the J–47 engine through a pilot-controlled butterfly valve to the primary nozzle of the ejector pump. The weight of the boundary-layer-control equipment for this research-type installation was 105 pounds. Considerable savings in weight should be possible in a production-type installation.

The F–86A slotted flap was modified to a plain type by reworking the nose section, removing the flap tracks, and mounting external hinge brackets on the under surface of the wing. This mounting allowed flap deflections up to 65°. The portion of the flap ahead of the flap spar was used as a duct and is shown in figure 7. A sketch of the flap cross section is given in figure 4 (c). Boundary-layer air was drawn in through a graded porous material of sintered stainless steel, which had the permeability characteristics shown in figure 8. It should be noted that the characteristics shown in figure 8 were not measured but were those specified to the manufacturer and were designed for a uniform inflow velocity of 3.75 feet per second (at $\delta_f=55°$) on the basis of pressure-distribution data obtained from the 40- by 80-foot wind-tunnel tests. The chordwise length and placement on the flap of the porous material were estimated also from the wind-tunnel tests. The porous material was formed easily, was readily adapted to the flap structure, and had a reported tensile strength of approximately 15,000 pounds per square inch.



(a) External flap duct and ejection pump.

FIGURE 7.—Close-up view showing area suction flap on airplane.



(b) Internal duct and porous material.

FIGURE 7.—Concluded.

The airplane was fitted with modified leading edges which replaced the slats for some of the flights. The modified leading edge consisted of a cambered leading edge having an increased radius similar to the leading edge used in the wind-tunnel tests. With this leading edge, tests were conducted both with and without a $0.20c$ wrap-around fence ($0.05c$ height) at 63-percent spanwise section.

Standard NACA instruments were used to record airspeed, altitude, acceleration, duct pressures, and angle of attack. Values of airspeed and angle of attack were measured

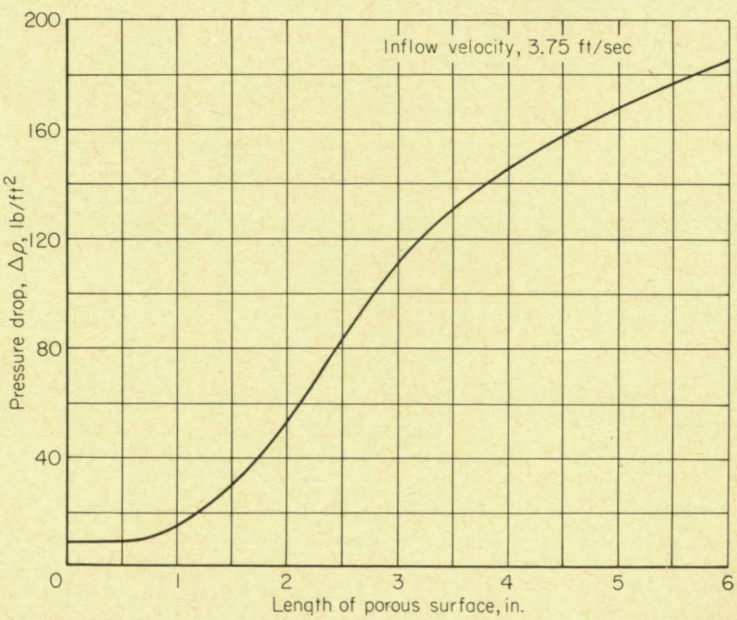


FIGURE 8.—Variation of pressure drop with chordwise length of porous surface for flight test airplane.

approximately 8 feet ahead of the fuselage nose. Duct pressures in the flap were measured at the midspan station of the flap. The flow quantity drawn through the porous material was measured by calibrated rakes in the ducts. Measurements taken on the ground with a flowmeter indicated uniform inflow velocities along the span of the flap.

TESTS AND CORRECTIONS

WIND TUNNEL

The primary purpose of the investigation was to determine the relation between the lift increments realized from the flap and the suction power and flow quantities required. Three-component force data were obtained at zero sideslip for all flap and wing configurations. For some conditions, pressure distributions over the wing were obtained. In addition, tests were made with the horizontal tail removed to show the effects on longitudinal stability.

Initial tests showed that as suction was increased, the lift increment first increased rapidly, then quite abruptly the rate of increase fell off to a very low value. The test procedure, therefore, was to determine for each model arrangement and angle of attack the power and suction quantities required to reach the point where further increases in these quantities gave little increase in lift increment. The values of flow coefficient and lift coefficient at this point are called $C_{Q_{crit}}$ and $C_{L_{crit}}$, respectively. In the tests the angle of attack and free-stream velocity were held constant and the suction quantity was varied.

For the model with the unmodified wing leading-edge profile, an extensive investigation was made for 45°, 55°, 64°, and 70° of flap deflections of the effect of position and extent of the porous area. Table III presents a summary of the porous area arrangements tested. Data were obtained at Reynolds numbers of 7.5×10^6 and 9.6×10^6. For the model with wing leading-edge modifications, only one flap deflection, 55°, and only one arrangement of porous area (config. 1) on the flap were tested.

The standard tunnel-wall corrections for a straight wing of the same area and span as the sweptback wing were applied to the angle of attack, pitching-moment, and drag-coefficient data. This procedure was followed since an analysis indicated that tunnel-wall corrections were approximately the same for straight and swept wings of the size under consideration. The following increments were added:

$$\Delta\alpha=0.61\ C_L$$
$$\Delta C_D=0.0107\ C_L^2$$
$$\Delta C_m=0.008\ C_L \text{ (tail-on data only)}$$

No corrections were made for strut interference. All flow coefficients were corrected to standard sea-level conditions. The effect of the thrust of the exhaust jets was found to be negligible.

FLIGHT

To obtain the lift and drag characteristics, tests were conducted at altitudes of 10,000 and 2,000 feet over a speed range of 150 knots to the stall. The tests were conducted at an average wing loading of 45 pounds per square foot except as noted, with the center of gravity at 22.5-percent mean aerodynamic chord. The engine rpm was held fixed for a given series of test runs. For the data presented in this report, an engine rpm of 70 percent was used (approximate rpm used in landing approach). In obtaining the data for the lift curves presented herein, no attempt was made to change the amount of bleed air to the primary nozzle of the ejector pump with airspeed so as to maintain a critical value of C_Q.

The initial phase of the landing-approach evaluation was flown by a total of 16 Air Force, Navy, contractor, and NACA pilots. For comparison purposes, most of the pilots also flew a standard F–86A–1 equipped with 38° flaps and 10° leading-edge slats. (For the major portion of the data reported herein, the normal (15°) F–86A–5 type slats were used on the wing leading edge.) Each pilot was requested to furnish the following information on each different configuration flown: stall speed, stall characteristics, and opinion of stall, the minimum comfortable approach speed at landing weight,[2] and the primary reasons for choosing that particular approach speed. The Navy and NACA pilots made their evaluation based on the requirements for a carrier approach and landing. The Air Force pilots, in general, made 360° overhead, partial power, sinking-type approaches, which started at approximately 1,000-feet altitude over the touchdown point. While the carrier-type approach may be defined by a single approach speed, it was noted that with the sinking approach at least three different speeds at different points in the pattern were considered necessary by most pilots to define adequately any given approach. For reasons of simplicity and comparison in those cases where three speeds were given, only the over-the-fence speed has been used as it was found to be more similar to the carrier-approach speed.

Another phase of the investigation comprised field carrier-landing evaluation flights of the suction-flap airplane with several leading-edge combinations. This phase of the evaluation was conducted by four NACA research pilots.

In the calculation of the measured stalling speeds and thrust-required curves, the value of wing loading used for each airplane was that corresponding to 1000 pounds of fuel remaining. This is given below for each test airplane.

Standard airplane	42.3 lb/sq ft
Suction-flap airplane	42.6 lb/sq ft

The value of gross weight for which many of the pilots reported stalling speeds was not accurately known. This factor undoubtedly contributed to the scatter in the reported stalling speeds, as well as to the differences between reported stalling speeds and the measured values based on $C_{L_{max}}$. For the standard airplane, this discrepancy is further aggravated by an unreliable but large error in indicated airspeed below about 102 knots. Consequently, the measured rather than reported value of stall speed has been used for all comparative purposes.

The airspeed covering the approach speed ranges was calibrated in flight for the airplanes. This made possible correlation between pilot-reported speeds of the airplanes, as well as between these speeds and the various measured

[2] Landing weight as used herein is defined as the gross weight with 1000 pounds of fuel remaining.

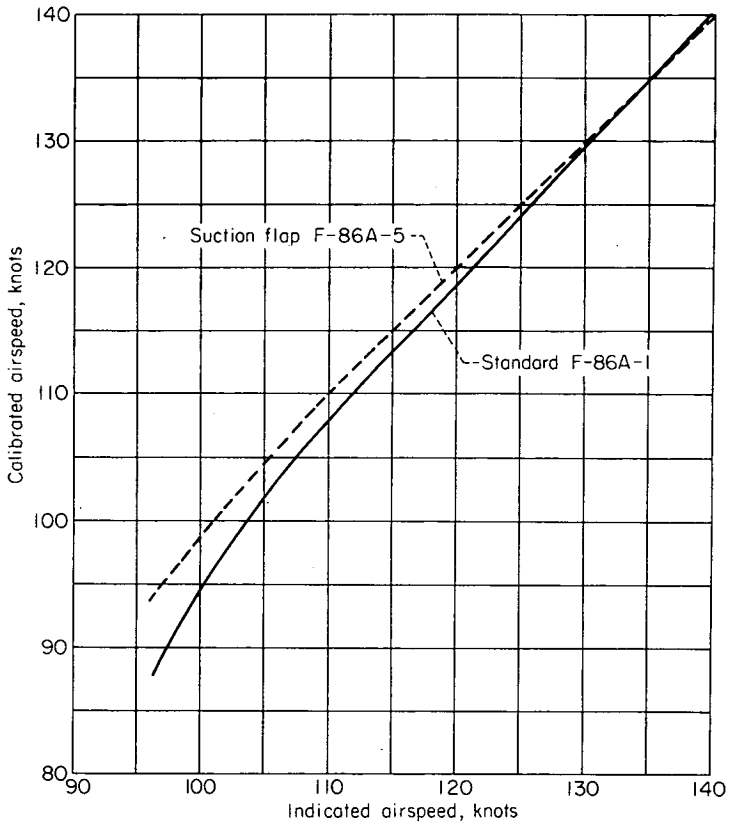


FIGURE 9.—Flight determined airspeed calibration curves.

quantities. With the exception of table VI, which gives pilot-reported stall and approach speeds in terms of the pilot's indicated airspeed, all other airspeed values are calibrated speeds and were obtained from pilots' indicated speeds using the flight-determined calibration curves of figure 9.

The equations used to determine the lift coefficients and drag coefficients are as follows:

$$C_L=\frac{W}{qS}(A_z\cos\alpha+A_x\sin\alpha)-\frac{1}{qS}(F_G\sin\alpha)$$

$$C_D=\frac{W}{qS}(A_z\sin\alpha-A_x\cos\alpha)+\frac{1}{qS}(F_G\cos\alpha-F_R)$$

In the equations above, the first portion is for the accelerations on the airplane, while the second portion is for the thrust force acting on the airplane. The gross thrust and engine air flow were determined from measurements of the total pressure and temperature in the tail pipe of the jet engine.

Measured stalling speeds were determined using the measured values of $C_{L_{max}}$ with a correction for thrust based on the thrust required at the approach airspeed.

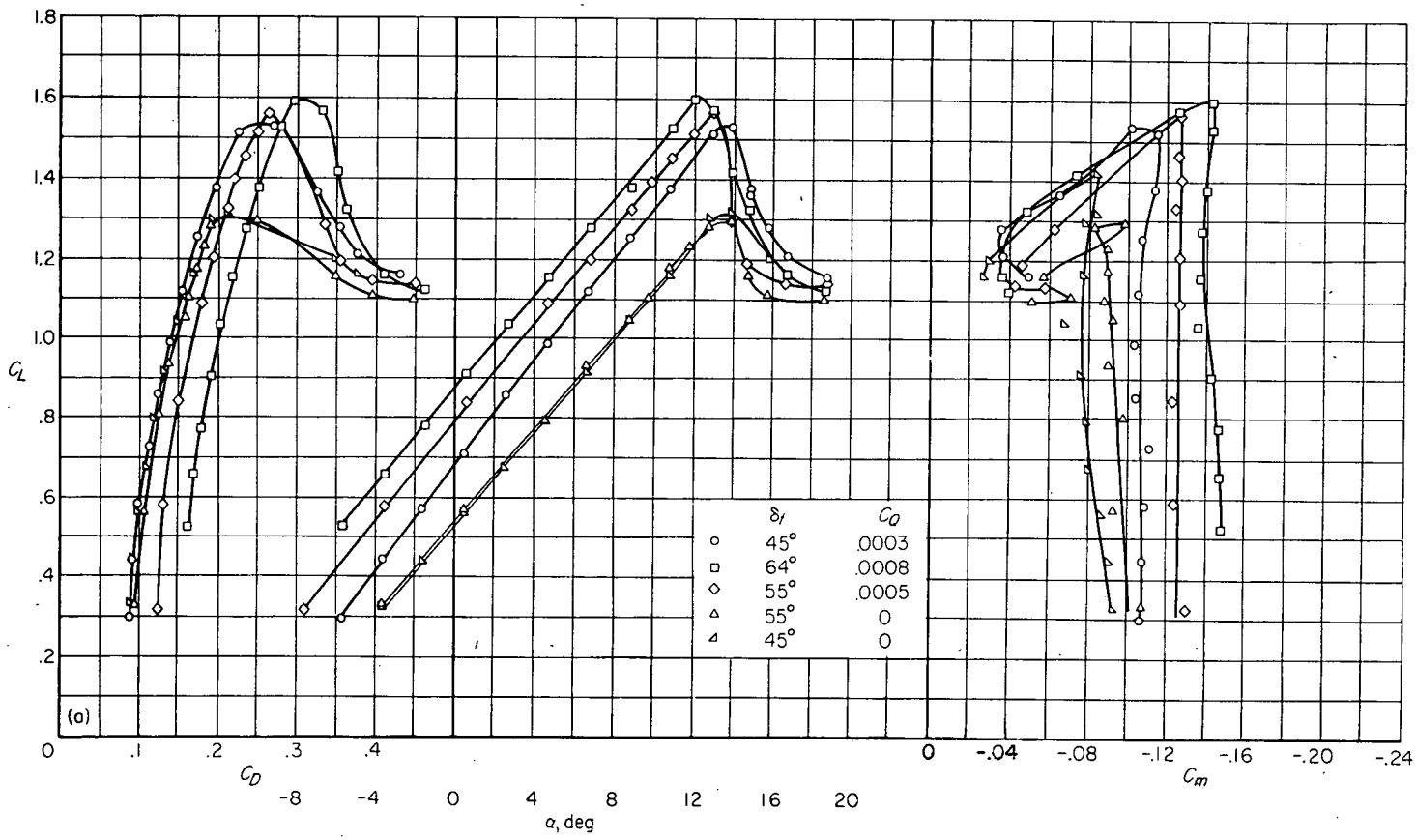
Thrust-required curves were determined at landing weight for each configuration by the following relationship:

$$\text{Net thrust from the engine required for level flight}=\frac{\text{drag}}{\cos\alpha}$$

RESULTS AND DISCUSSION

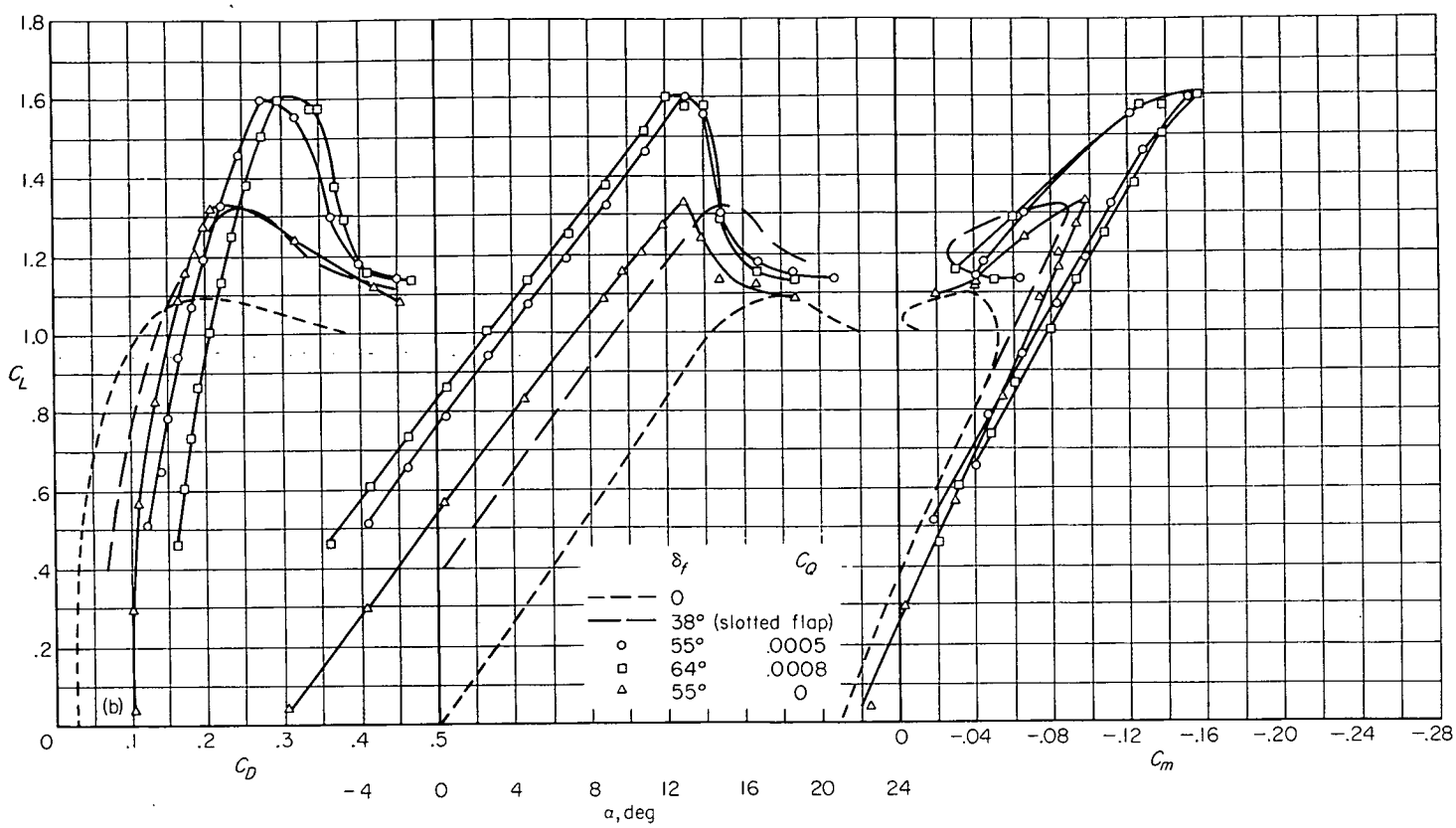
WIND-TUNNEL TESTS

Static-longitudinal characteristics with area suction applied to trailing-edge flaps.—The lift, drag, and pitching-moment data are shown in figure 10 with the trailing-edge flaps de-



(a) Horizontal tail off.

FIGURE 10.—Aerodynamic characteristics of the 35° swept wing model with area-suction trailing-edge flaps; plain leading edge.



(b) Horizontal tail on.

FIGURE 10.—Concluded.

flected 45°, 55°, and 64°. The results are shown with and without suction on the flap and are compared with the slotted flap deflected 38°. The results indicate that an appreciable increase in flap lift increment, ΔC_L, can be obtained up to 64° flap deflection with area suction applied throughout the angle-of-attack range up to the angle for maximum lift coefficient. Representative pressure distributions are shown in figure 11.

The flap lift increments obtained with suction applied at an angle of attack of 0° are compared in figure 12 to theoretical values [3] calculated by the method of reference 2. On this wing with area suction applied to the trailing-edge flaps, flap effectiveness above 90 percent of theoretical values is obtained to 64° of flap deflection. Although the theory is limited in its accuracy when wing-fuselage effects are considered, it is also known that some air-flow separation did exist on the trailing-edge flaps at all deflections, as indicated by tuft studies and by the pressure distribution shown in figure 11; and therefore higher flap lift increments possibly even greater than the theoretical values would be expected with more complete elimination of air-flow separation on the flaps. The use of 70° flap deflection with suction gave no more flap lift increment than the 64° flap deflection.

The gain in flap lift increment with area suction applied was retained at nearly a constant value to maximum lift coefficient with the normal wing leading edge. The maximum lift coefficient was established by leading-edge air-flow separation occurring on the wing from approximately mid-semispan to the tip, as indicated by the pressure distributions shown in figure 11, as well as by observations of the tufts on the wing. In order to study the effect of area suction on the flap at higher lift coefficients, tests were made with a modified wing leading edge and a wing leading-edge slat, both used to delay the occurrence of leading-edge air-flow separation. The effect of the leading-edge devices on the lift, drag, and pitching-moment characteristics is shown by a comparison of figures 13 and 10 (b). With the modified leading edge and flap deflection of 55°, the flap lift increment with area suction was almost constant to maximum lift; $C_{L_{max}}$ was 1.97, whereas with the normal leading edge it was 1.61. However, with the partial-span leading-edge slat, a reduction in flap lift increment occurred at about an angle of attack of 6° which was traced to rough air flow from the discontinuity, formed by the inboard end of the slat and the wing leading edge, causing air-flow separation to occur on the flap over an area directly aft of the discontinuity. With the slats, a value of $C_{L_{max}}$ of 1.7 was obtained. From these results, it is concluded that the major effect of applying area suction to trailing-edge flaps is to increase lift at a given attitude.

Suppression of air-flow separation on the flaps caused no particular change in pitching moment, with horizontal tail on, except to extend the linear range of pitching moment to higher lift coefficients. In the tail-off case, the increase in flap lift increment was accompanied by an increase in pitching moment. With area suction applied, the pitching

[3] The theoretical flap effectiveness was computed from reference 2.

$$\Delta C_L = \left(\frac{d\alpha}{d\delta_f}\right) C_{L_{\delta_f}} \frac{\delta_f}{57.3}, \text{ (equivalent to eq. (7), ref. 2)}$$

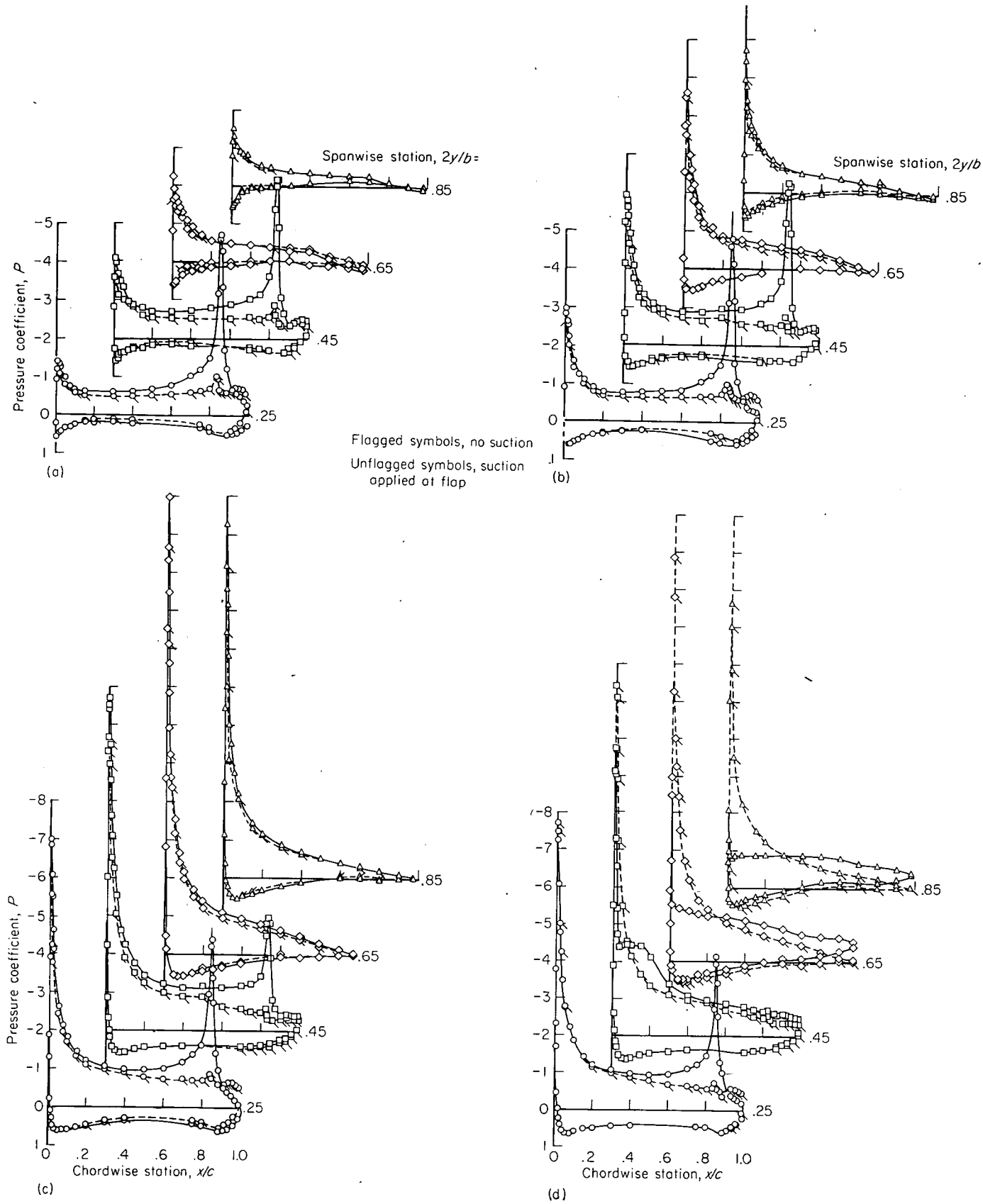
for the subject wing

$C_{L_{\delta_f}}$=1.52 (cross plot of fig. 5, ref. 2)

$d\alpha/d\delta_f$=0.61 (curve of theoretical flap effectiveness, fig. 3, ref 2; c_f/c=0.26, average value perpendicular to flap hinge line)

$\tan \delta_f = \cos \Lambda_f \tan \delta_f = 0.895 \tan \delta_f$

$$\Delta C_L = \frac{(0.61)(1.52)}{57.3} \delta_f = 0.0162 \delta_f$$



(a) $\alpha = 0.5°$ (b) $\alpha = 4.7°$
(c) $\alpha = 10.9°$ (d) $\alpha = 13.9°$

FIGURE 11.—Effect of area suction on the chordwise pressure distributions; $\delta_f = 55°$.

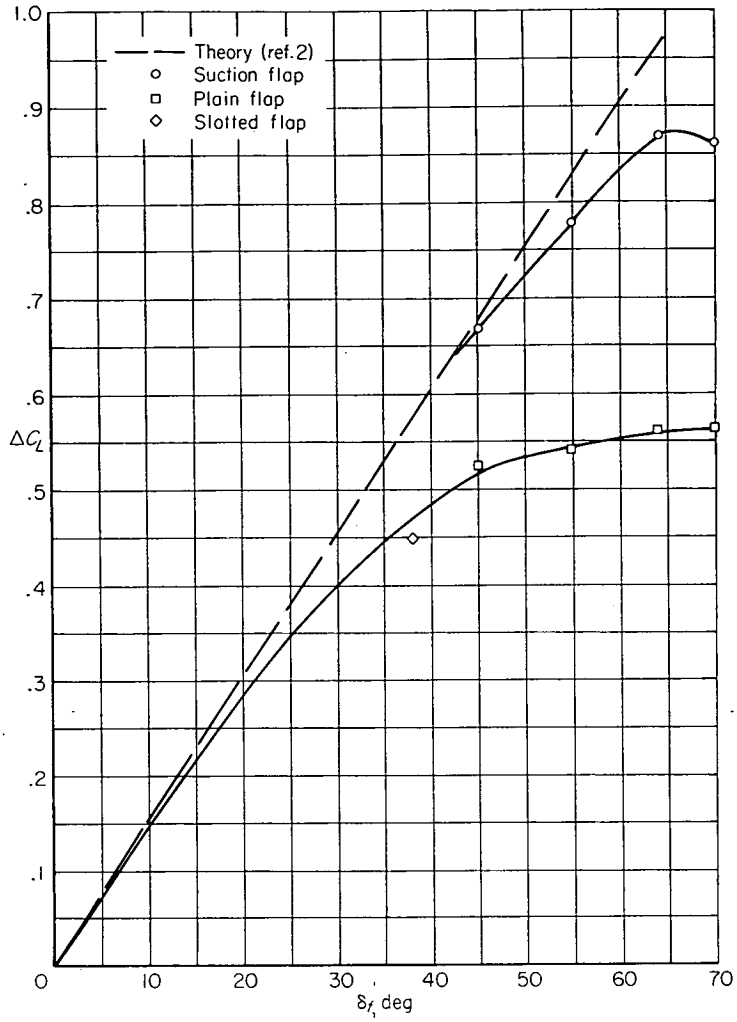


FIGURE 12.—Variation of flap lift increment with flap-deflection angle.

moment per unit of flap lift increment at a given angle of attack is 0.155, compared to a value of 0.185 for plain flap without suction. Presumably, this results from a forward movement of center of pressure at a given angle of attack as air-flow separation is suppressed on the flap. The increase in pitching moment with boundary-layer-control application may be of greater importance for larger flap lift increments, for example, with greater spanwise extent of flaps than studied herein the maximum lift of the horizontal tail would be approached for trimmed conditions.

With boundary-layer control applied to the flaps, the data in figure 10 indicate an increase in drag at a given lift coefficient or angle of attack. The increase in drag is due to the particular spanwise extent of flap which, with the application of suction, results in a span loading considerably more distorted from the ideal elliptical loading than the span loading obtained without boundary-layer control. It is deduced that the increase in induced drag due to the distorted loading is considerably greater than the reduction in profile drag due to suppression of air-flow separation and hence there is an over-all increase in drag. A decrease in drag with boundary-layer control would be expected with flaps of larger span.

Suction requirements of area-suction flap.—Figure 14 shows the variation of flap lift increment with flow coefficient for four flap deflections. These data were obtained at an angle of attack near 0° and for one location and chordwise extent of porous area. Similar data were obtained at other angles of attack and other configurations of porous area. Examination of all these data showed the following facts which are generally applicable to each flap deflection:

1. For any configuration of porous area, as flow coefficient was increased, an initial slow rise in lift was followed by an abrupt rise to a particular value which could be increased only slightly by further large increases in flow coefficient.

2. For any one configuration of porous area, the variation of lift increment with flow coefficient was essentially the same at all angles of attack, provided the angle of attack was less than that at which separation of flow appeared at the wing leading edge.

3. For nearly all configurations of porous area, nearly the same total increase in lift occurred as the flow coefficient was increased, but the abruptness of the rise and the flow coefficient at which it occurred were modified by the chordwise extent and location of the porous area.

For each flap deflection, a particular value of lift increment was obtained that was exceeded only slightly with large increases in flow coefficient; for example, with the 55° flap deflection (fig. 14), the ΔC_L increased from about 0.78 to 0.79 with a fourfold increase in flow coefficient from 0.0005 to 0.0020. These values of flap increment are also shown in figure 12, where a comparison is made between the measured values of lift increment for several flap deflection angles and values calculated by the method of reference 2.

The variation of flow coefficient required for a range of flap deflections is shown in figure 15 for three chordwise distributions of suction-air velocities. The required suction-air velocities can be controlled by two methods: first, by having porous surfaces of constant thickness with different pressure-drop characteristics and second, by having a porous surface with chordwise variation of pressure-drop characteristics, as described in reference 1. The pressure-drop characteristics of the materials used in these tests are shown in figure 5. The chordwise distributions of suction-air velocity for the three porous surfaces required to obtain equal values of $\Delta C_{L_{crit}}$ are shown in figure 16 for the flap deflection of 55°. For the least dense porous material (curve (a) of fig. 16), a pumping pressure coefficient of −4.5 was required for boundary-layer control, and the total air-flow coefficient was 0.00049. For a porous surface having twice the pressure drop (curve (b)), the pumping pressure coefficient was −4.9, and the total flow coefficient was 0.00036, about a 27-percent reduction in air flow. A further reduction in flow coefficient was obtained by using a tapered porous material which represented a porous surface with the pressure drop varying chordwise. The change in thickness of the porous material, shown in figure 5(b), varied as the external surface pressure with the thinnest or low-pressure-drop section at the forward edge near the peak negative pressure and the thick or high-pressure-drop section at the aft edge where the external surface pressure was less negative. With this tapered porous surface, the chordwise distribution of suction-air velocities required to prevent air-flow separation is shown by curve (c) in figure 16.

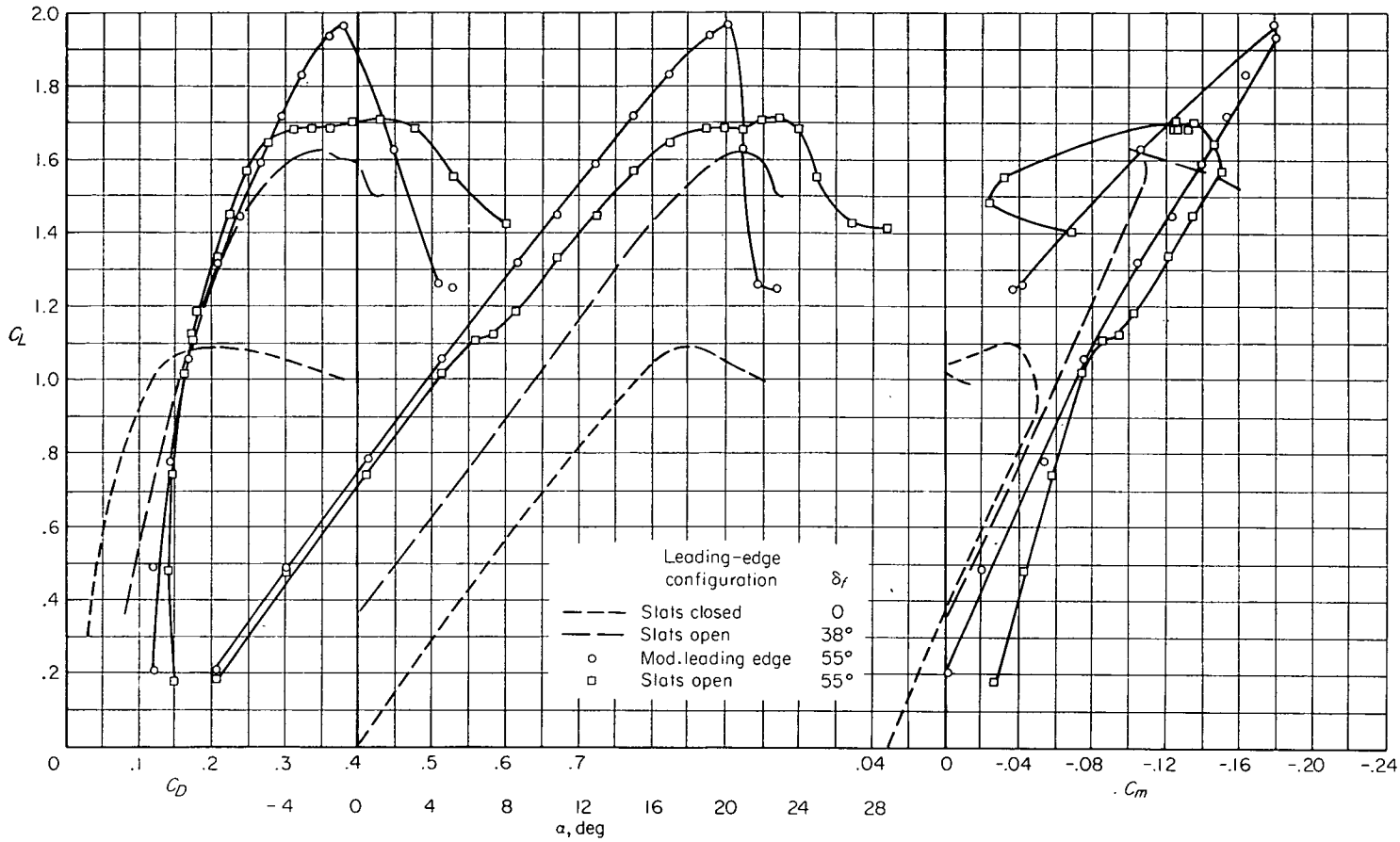


FIGURE 13.—Aerodynamic characteristics of the 35° swept-wing model with area-suction flaps and two wing leading-edge devices; horizontal tail on; $C_Q=0.0005$ for $\delta_f=55°$.

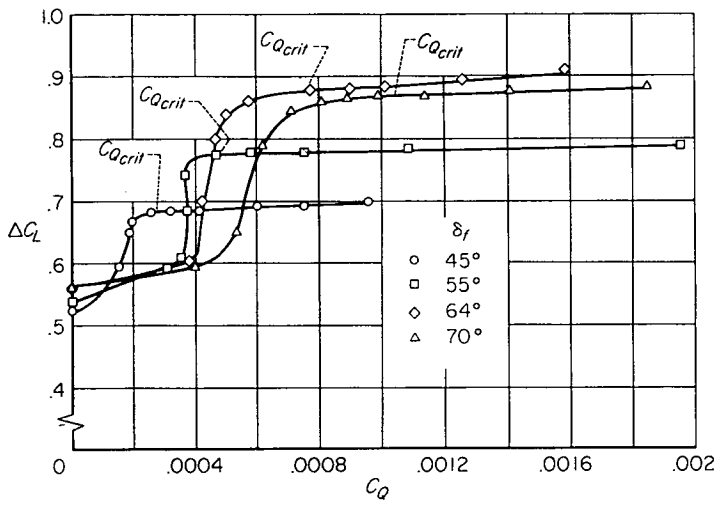


FIGURE 14.—Variation of flap lift coefficient increment with suction flow coefficient; $R=7.5\times10^6$.

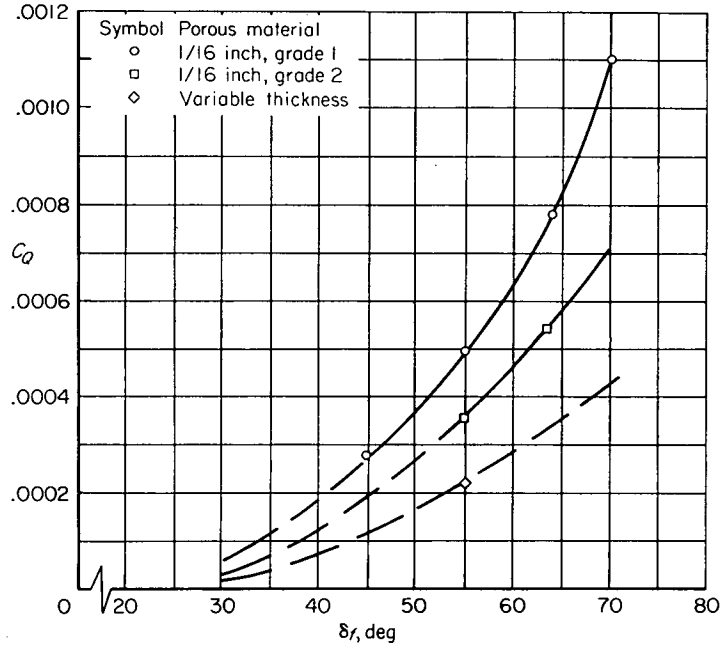


FIGURE 15.—Variation of flow-coefficient requirements with flap-deflection angle for three types of porous materials; $R=9.6\times10^6$.

A pumping pressure coefficient of −5.3 was required to obtain this distribution, resulting in a flow coefficient of 0.00022 or a 55-percent reduction of total flow from the first case of the constant thickness high-porosity material. It can be concluded that the proper distribution of suction-air velocities is required to obtain low flow coefficients.

A limited study was made of the effect of Reynolds number and angle of attack or wing lift coefficient on the flow coefficients required for boundary-layer control. These results shown in figure 17 indicate that within the range studied, there is essentially no effect of either Reynolds number or wing lift coefficient on the flow coefficients required for area-suction-type boundary-layer control. There is, however, a significant effect of angle of attack or

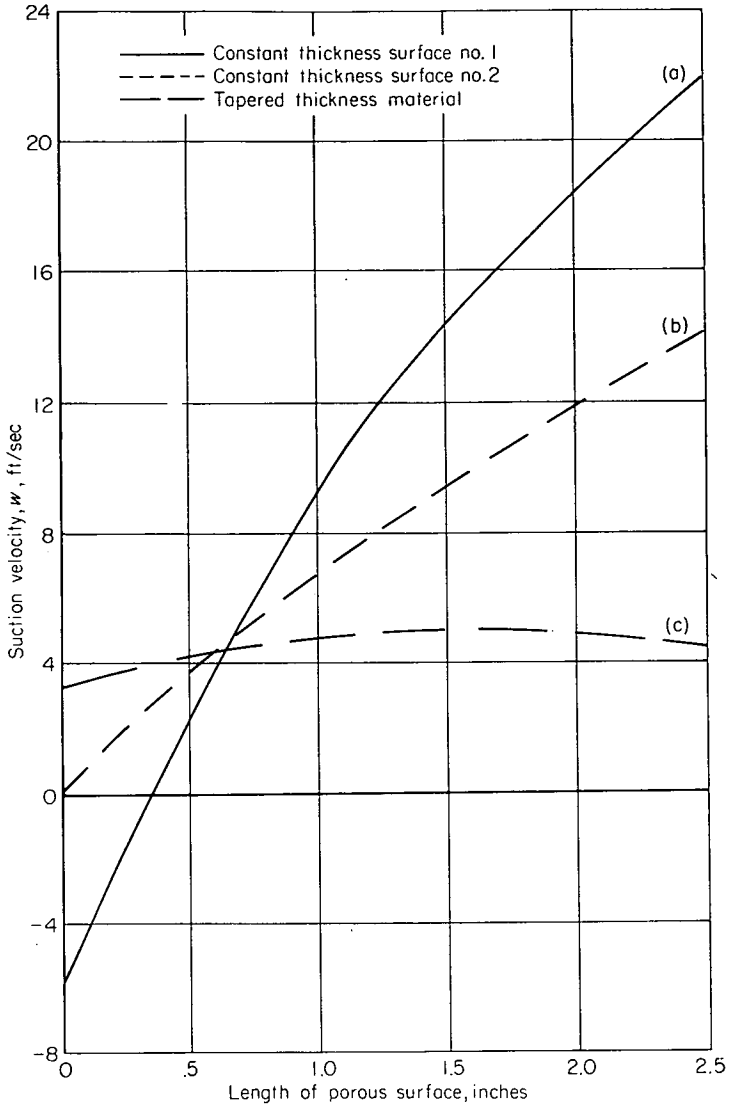


FIGURE 16.—Chordwise distribution of suction-air velocities for three types of porous material; $\delta_f=55°$, $R=9.6\times10^6$.

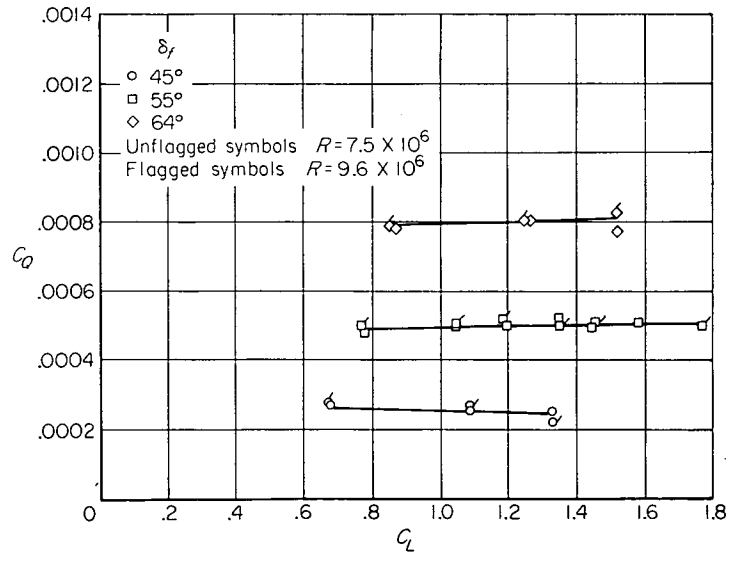


FIGURE 17.—Effect of wing lift coefficient and Reynolds number on flow-coefficient requirements.

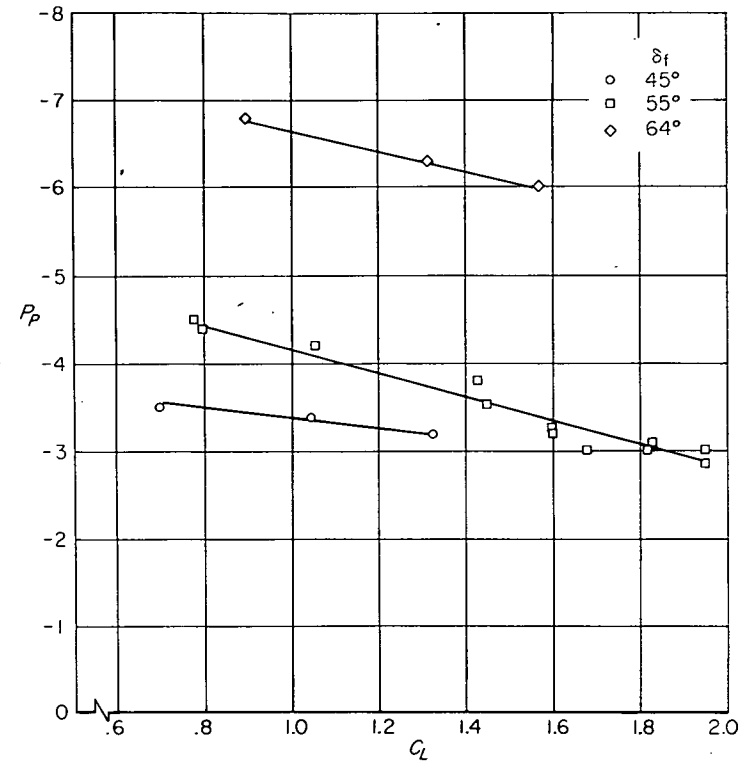
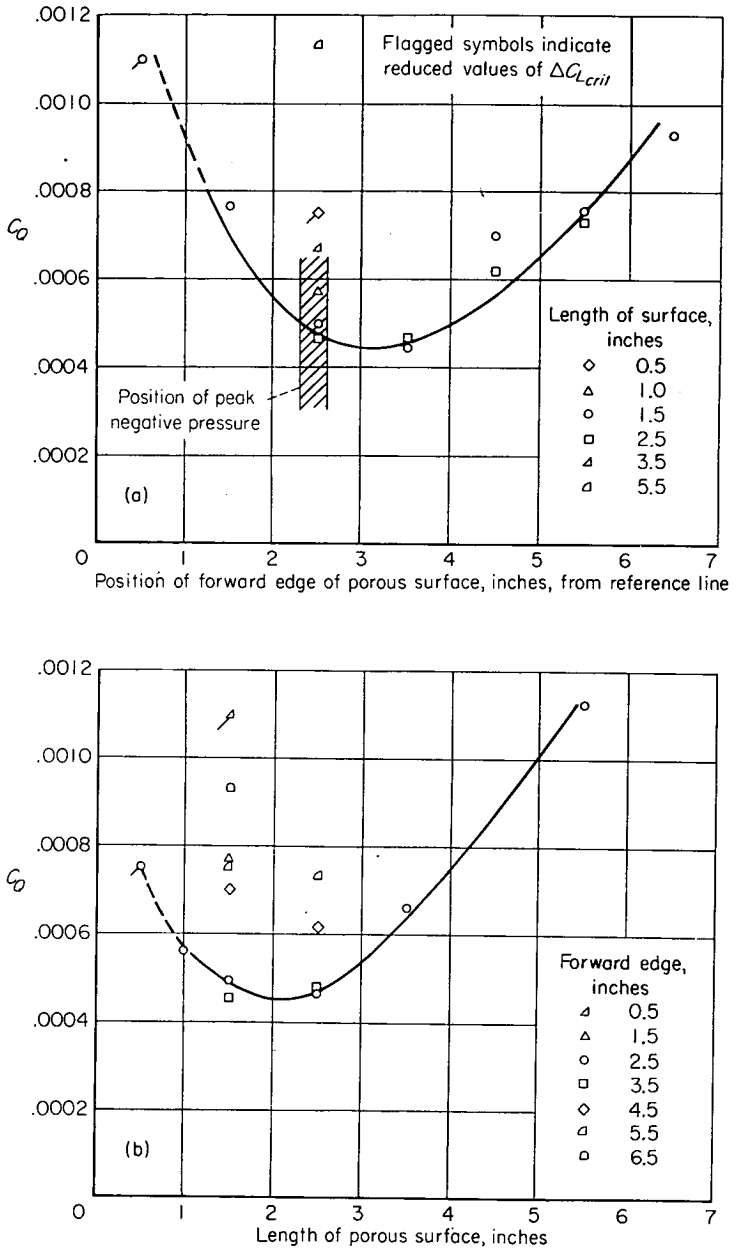


FIGURE 18.—Variation of plenum-chamber pressure coefficient with wing lift coefficient.

wing lift coefficient on the suction pressure coefficient (fig. 18). This effect, decreasing magnitude of pressure coefficient with increasing angle of attack, was due entirely to a reduction in magnitude of peak negative pressure coefficient over the porous surface with wing angle of attack. Such a drop in peak pressure is not compatible with potential theory. It was concluded that air-flow separation was not completely eliminated on the flaps and that more air-flow separation existed at the higher angles of attack. As in the case of flow coefficient, the suction pressure coefficient was independent of free-stream velocity.

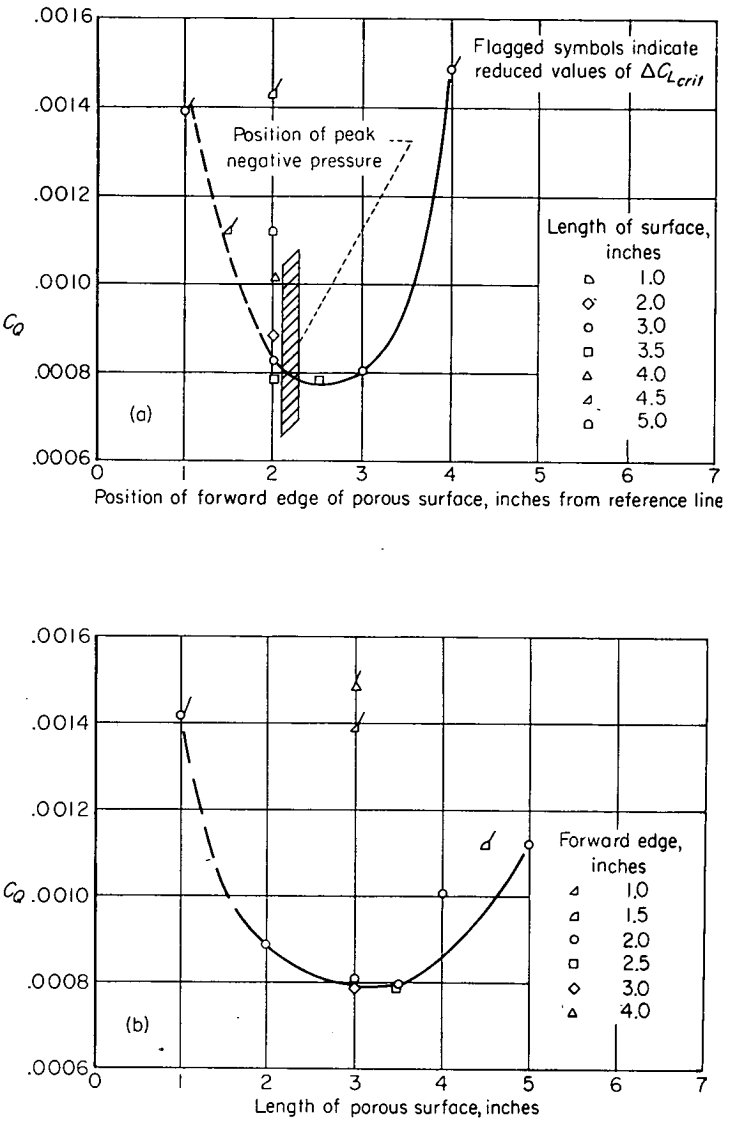
It was noted previously that the value of $\Delta C_{L_{crit}}$ could be obtained with numerous variations of porous surface position and extent. It was also noted that to obtain $\Delta C_{L_{crit}}$, the value of $C_{Q_{crit}}$ varied for each configuration of porous area. Figures 19, 20, and 21 have been prepared to show the variation of $C_{Q_{crit}}$ for several configurations of porous area for 55°, 64°, and 70° of flap deflection. The effects of two variables are shown in each figure, first, the effect of position of several extents of porous area, and second, the effect of the extent of porous opening with the forward edge at a fixed point.

The results shown in figures 19 (a), 20 (a), and 21 (a) indicate that there is a particular position for the forward edge of the porous opening which results in minimum $C_{Q_{crit}}$ and that this position is not greatly affected by the extent of opening—at least within the range tested. Figures 18 (b), 19 (b), and 20 (b) indicate that with the forward edge at the position for minimum $C_{Q_{crit}}$, for any of the extents, there is also a particular extent required to realize minimum $C_{Q_{crit}}$. These results were obtained with the



(a) Porous-surface position.
(b) Porous-surface extent.

FIGURE 19.—Variation of flow coefficient required for $\delta_f=55°$ with extent and position of porous area; $\Delta C_{L_{crit}}=0.78$, $R=7.5\times10^5$.



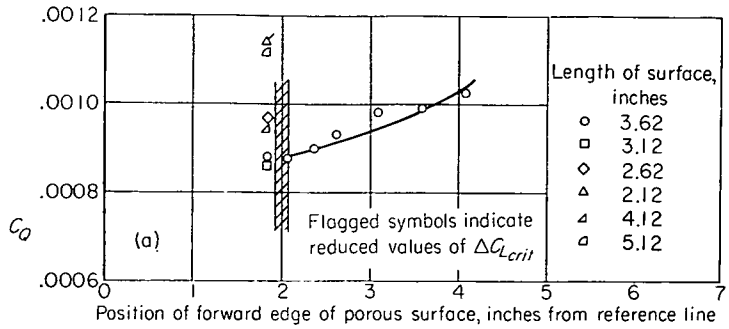
(a) Porous-surface position.
(b) Porous-surface extent.

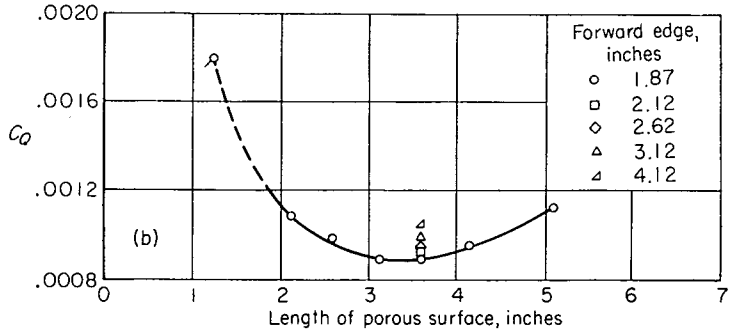
FIGURE 20.—Variation of flow coefficient required for $\delta_f=64°$ with extent and position of porous area; $\Delta C_{L_{crit}}=0.87$, $R=7.5\times10^5$.

low-pressure-drop porous surface, grade number 1, but the results shown indicating the chordwise location and extent of porous surface for minimum flow coefficient are typical of those for the other two porous surfaces studied. While the foregoing results serve to show trends, it would appear reasonable to assume they are not quantitatively applicable to other wing-flap arrangements.

It has been shown previously (ref. 1), in connection with application of area suction to control separation of air flow from the leading edge of a wing, that area suction is most effective when the forward edge of the porous area coincides with the point of maximum negative pressure. That this is also true in the case of the flap is indicated by the relative positions of the maximum negative pressure measured over the flap and the position of the forward edge of the porous area for minimum flow-coefficient requirement. Suction forward of this point results in needlessly withdrawing air in the region of a favorable pressure gradient. Moving the leading edge of the area suction progressively aft resulted in not only increased flow requirements but, as found during this investigation, instability of the flow and, finally, inability to attain the value of $\Delta C_{L_{crit}}$ obtained with the best positions and extents of porous area. It thus appears that the optimum location for the forward edge of the porous area will, for any plain flap, be at or very close to the point of maximum negative pressure.

General conclusions with regard to the extent of the porous area are not so readily reached. It can be conjectured from the results shown in figures 19, 20, and 21 that the position of the aft edge of the porous area for the minimum flow coefficient is at the point where the boundary layer is just sufficiently stable to withstand the subsequent pressure recovery without aid. If the porous area is not carried to this optimum point, then the boundary layer must be made





(a) Porous-surface position.
(b) Porous-surface extent.

FIGURE 21.—Variation of flow coefficient required for $\delta_f=70°$ with extent and position of porous area; $\Delta C_{L_{crit}}=0.86$, $R=7.5\times10^5$.

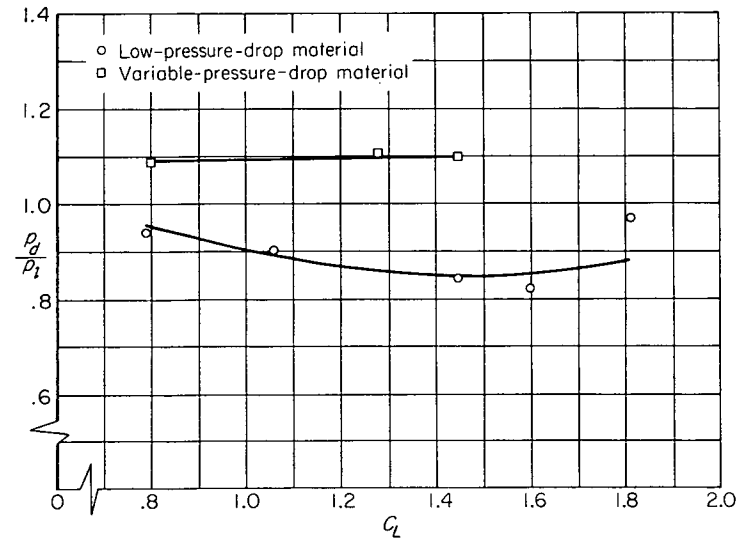


FIGURE 22.—Variation of suction pressure ratio (duct pressure to flap peak pressure) with wing lift coefficient for two types of porous surface.

more stable than in the case just mentioned; that is, larger flow coefficients would be required to suppress flow separation beyond the region of porous area. If the porous area is carried beyond the optimum point, air would be withdrawn needlessly. As yet, however, no method analogous to that shown in reference 1 is available for predicting the required extent of porous area in the case of the flap.

The total suction power required is a function of plenum-chamber pressure coefficient, as well as flow coefficient. The plenum-chamber coefficient P_P must have a sufficiently negative value to overcome duct losses, pressure drop through the porous material at the required flow rate, and the external negative pressure. In the present investigation, the duct losses and pressure drop through the material were negligible compared to the negative pressure peak over the flap; hence, the required values of P_P are almost entirely a result of the external surface pressure, especially for the least-dense constant-thickness porous material. The variations with lift coefficient of the ratio of plenum-chamber pressure to external surface pressure are shown in figure 22. A surprising feature for the low-pressure-drop constant-thickness material is that the ratio is less than 1.0 for a large part of the lift-coefficient range. For all the points shown, the forward edge of the porous area was at the location for minimum $C_{Q_{crit}}$; as noted previously, this location is near the peak negative pressure, indicating that some outflow of air occurred near the forward edge (curve (a), fig. 16). Such an occurrence does not seem favorable to any form of boundary-layer control, and it is probable that the outflow in these cases was possible only because excess air was being withdrawn through a major portion of the porous area (curve (a), fig. 16). With the airflow distribution controlled by chordwise porosity variation (curve (c), fig. 16), the value of the ratio of plenum-chamber pressure to peak negative pressure was significantly greater than 1.0, as shown in figure 22, which indicates that for near the minimum values of flow coefficient of the suction air, the required internal duct pressures will have to be somewhat greater than the peak negative pressures.

The actual power requirements for an airplane are specified in terms of wing loading and landing or take-off speeds. In order to determine these values without the uncertainties of estimating flow coefficient and pressure coefficient, wind-tunnel data were obtained and suction powers measured at conditions corresponding to level flight at wing loadings of 40 and 60 pounds per square foot for 55° and 64° flap deflection with the low-pressure-drop porous surface and at a wing loading of 40 pounds per square foot for 55° of flap deflection with the variable-pressure-drop porous surface. For 64° flap deflection, the measured powers were also obtained with the high-pressure-drop constant-thickness material at a wing loading of 40 pounds per square foot. The measured values of suction horsepower required to obtain $\Delta C_{L_{crit}}$ and the corresponding flow coefficients and plenum-chamber pressure coefficients are given in table VII. The measured suction horsepower shown in the table are the power required to drive the pump, as well as duct losses, system leakage, and the effect of pump efficiency. For most conditions, the duct losses and system leakage were very small and caused little increase in power. For all conditions, the pump efficiency ranged between 63 and 67 percent. The results obtained indicate that for this type of airplane, 10 to 25 horesepower would be required for landing approach and take-off, and that at the lower value of power required it is necessary to control the distribution of the suction-air velocities.

It is apparent that more horsepower is required to reach $\Delta C_{L_{crit}}$ at higher forward speeds. This does not appear to

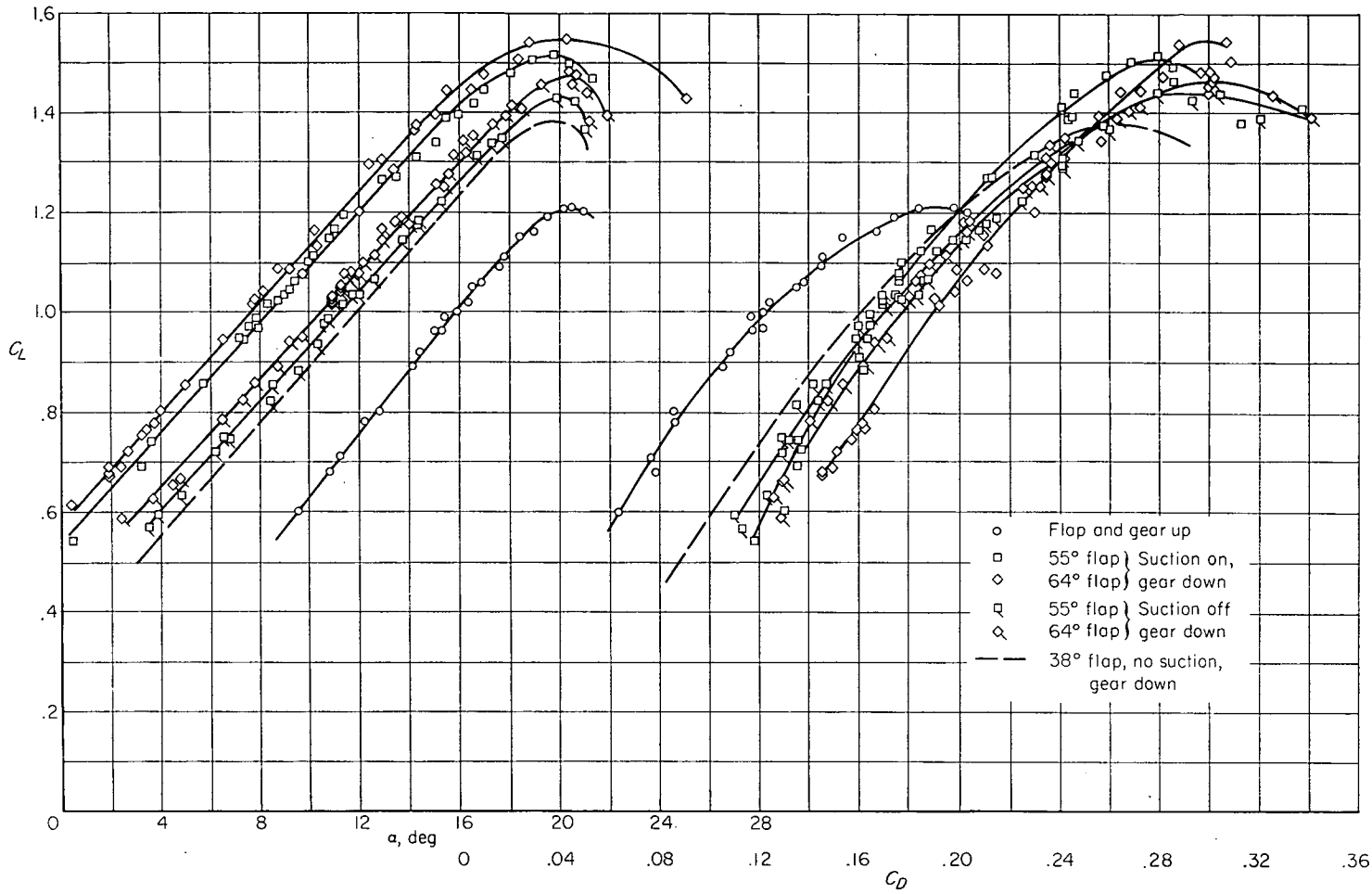


FIGURE 23.—Flight test lift and drag curves, area-suction flaps, and slatted leading edge.

be of particular importance, however, because it was demonstrated during the tests that area suction will cause reattachment of flow when applied where separation exists. Therefore, it would be necessary to supply only the power required to prevent separation at low landing approach speed; as this speed is approached from some higher speed, the flow will attach to the flap.

FLIGHT TESTS

Lift and drag characteristics of airplane with area-suction flaps.—The lift and drag data are presented in figure 23 for flap deflections of 55° and 64° for the flap, and gear-down configuration with boundary-layer control on and off. For comparative purposes, data for the 38° plain flap [4] with no suction are also shown in figure 23. The data in figure 23 indicate an increase in $C_{L_{max}}$ from 1.38 for the 38° flap to 1.54 for the 64° flap with suction. A comparison of the lift increment of the 64° flap deflection (suction on) with the 38° flap at a constant angle of attack of 11° (average angle of attack used in landing approach) indicates an approximate increase in C_L of 0.24. The lift increment due to suction flaps was essentially constant over the angle-of-attack range except near $C_{L_{max}}$ where there was a 50-percent reduction.

[4] The plain flap at a deflection of 38° was used as a basis for assessing the effectiveness of the suction flap since, at this deflection, the flap lift increment and lift curves were similar to that obtained with the normal 38° slotted flap on the unmodified airplane (ref. 3). The lift curves from reference 3 were not used directly since drag data, used for performance computation reported herein, were not available from reference 3.

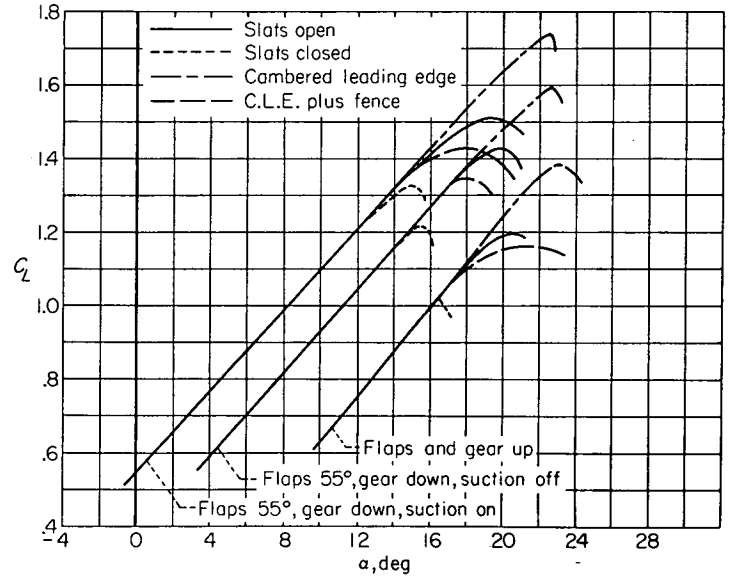


FIGURE 24.—Flight-test lift curves with various leading-edge configurations.

No marked loss in suction lift increment occurred at $\alpha=6°$ as in the tunnel tests. In the tunnel, this loss in lift was felt to be due to a vortex emanating from the inboard end of the slat flowing over the flap and causing an area of separated flow over a portion of the flap. In the flight tests, the duct structure at the wing-fuselage juncture caused flow separation

on the inboard end of the flap and the addition of the vortex flow from the inboard edge of the slat did not increase the amount of separated area at 6° angle of attack as it did in the tunnel.

The lift characteristics of the airplane equipped with various leading-edge devices are summarized in figure 24 for a flap deflection of 55°. These data indicate that the type of leading-edge configuration had no effect on the magnitude of the lift increment due to suction in the landing approach (α=11°). There was, however, a difference in magnitude at $C_{L_{max}}$ which was associated with the type of leading edge used. For the type of leading edge which produced a well-rounded lift-curve top and a satisfactory stall such as the cambered leading edge plus fence, less lift due to suction was realized. This was felt to result from the increased thickness of the boundary layer flowing over the flap at the higher C_L values. This increased boundary-layer thickness was the result of the action of the fence in tending to produce a stall in the area inboard of the fence. The significance of the decrease in lift due to suction at $C_{L_{max}}$ compared to that obtained at the approach angle of attack is not definitely known. Evidence is given later, however, that greater reductions in approach speed were realized than the reduction in stalling speed alone.

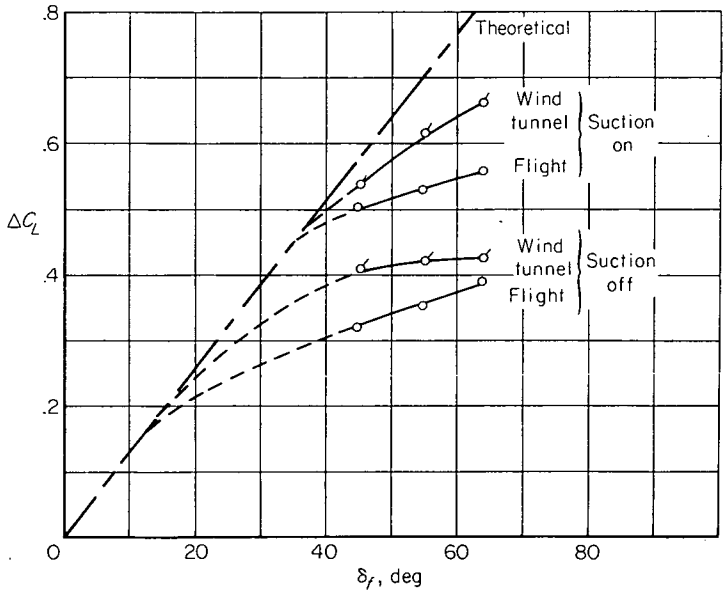


FIGURE 25.—Comparison of flight and wind-tunnel values of flap lift increment with flap deflection angle; α=6°.

The variation of flap lift increment with flap deflection is presented in figure 25 for the flight and wind-tunnel tests and compared with theory. The theoretical value was calculated by means of reference 2. The wind-tunnel results have been corrected to the flight airplane flap chord and corrected for trim. The results in figure 25 indicate that the flight flap lift values are less than the tunnel values for both suction on and off. The reason for this is not completely understood. Some of the differences in flap lift are felt to be associated with the effect of the type of wing-fuselage combination used on the flow at the inboard flap edge. In the tunnel tests, a midwing mounting was used in contrast to the low-wing position on the F–86A airplane. A limited

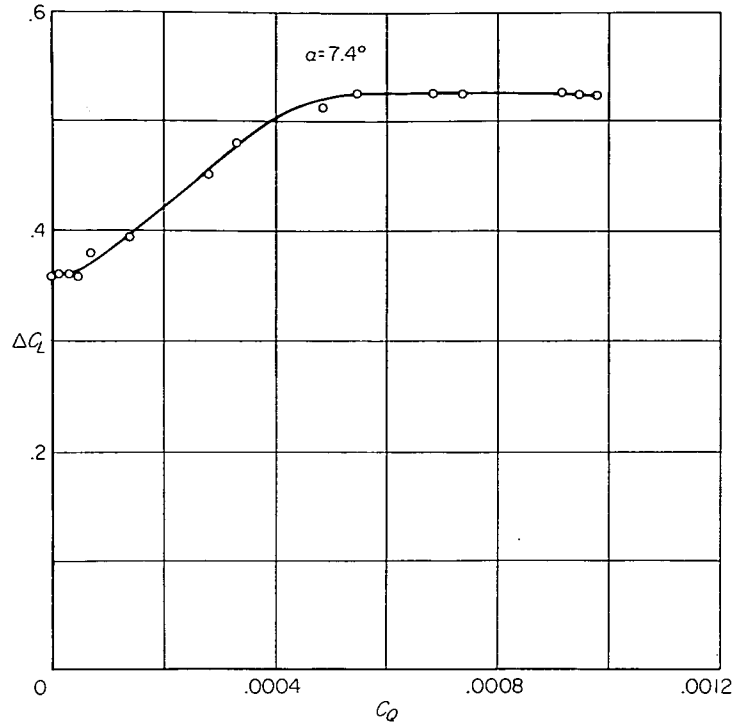


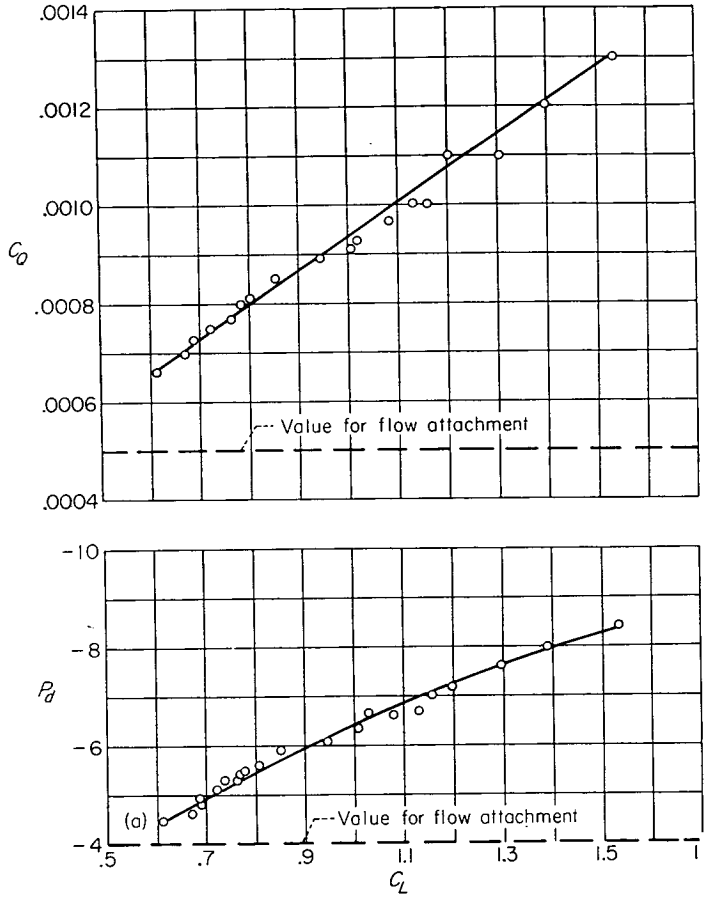
FIGURE 26.—Variation of flap lift increment with flow coefficient; δ_f=64°.

amount of fairing of the upper wing surface of the airplane at the fuselage trailing-edge juncture resulted in improvements in lift due to suction. Other attempts to increase the flap lift, such as a fence on the flap, a seal between the wing and the flap, and turning vanes to direct high energy air over the inboard area of the flap, did little or nothing to improve the lift increment due to suction.

Suction requirements.—Suction requirements are illustrated by the data presented in figure 26 in terms of flap lift increment, ΔC_L, and flow coefficient. These data indicate that the flap lift increased with flow coefficient up to a value of approximately 0.0005, beyond which no further increase in flap lift occurred. These data bear out the results of the wind-tunnel tests regarding the amount of flow coefficient required. A pressure coefficient of −4.0 was necessary to obtain the flow coefficient of 0.0005 at a C_L of 1.0. The values of flow coefficient and pressure coefficient in the flap duct used in the flight tests are shown in figure 27. These data indicate that sufficient flow coefficient and pressure coefficient were used over the speed range of these tests.

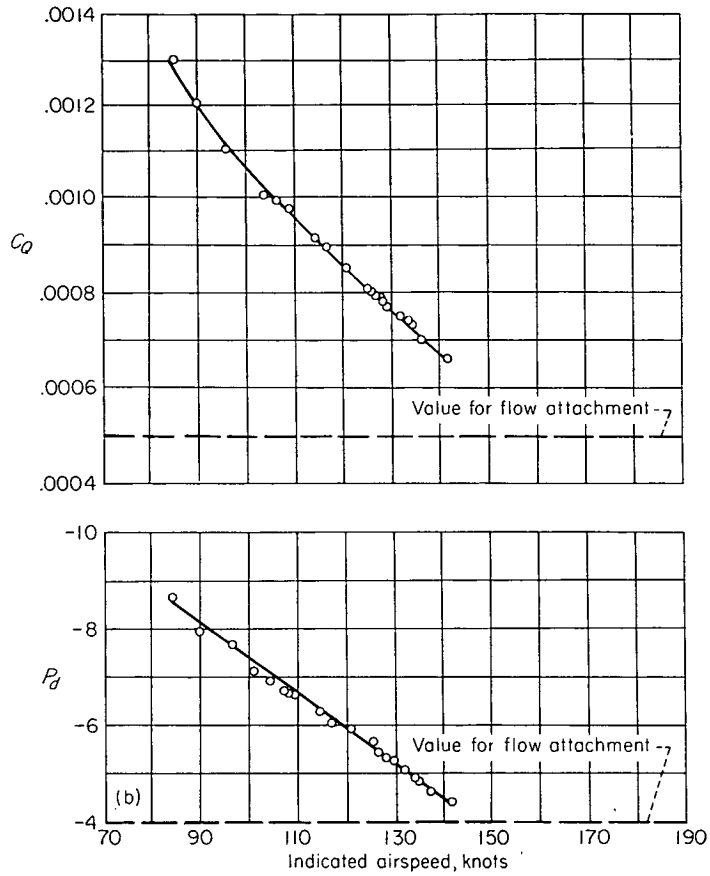
Operational characteristics of boundary-layer control.—One of the main points of interest in the use of boundary-layer control is the effect on the performance and handling characteristics of the airplane. Actual measurements were not made of landing distance, take-off distance, climb, and catapult launchings, but flight measurements of lift, drag, and engine thrust have been used to make computations of the various performance items for a range of gross weights and at standard sea-level conditions. The methods used for computing performance are noted in the appendix.

In evaluation of the landing performance of the airplane with area-suction flaps deflected 55°, the opinions of the 16 pilots, presented in table VI, were used in relating stalling and landing-approach characteristics for the airplane with



(a) Variation C_Q and P_d with C_L.

FIGURE 27.—Pump characteristics obtained over test range with $\delta_f = 64°$.



(b) Variation of C_Q and P_d with velocity.

FIGURE 27.—Concluded.

area-suction flaps as well as for the standard airplane with slotted flaps. The stall data for the two airplane configurations are shown in table VIII, while a compilation of minimum approach speed (or over-the-fence speeds) is shown in table IX. Comparative figures are listed showing the effects of suction alone and of increased flap deflection, as well as comparisons with the standard airplane. Additional data are shown in table X for other configurations of wing leading edge, the slatted leading edge and the cambered leading edge without fence for 55° and 64° deflection of area-suction flap, which were flown by the four research pilots (K, L, M, and N).

The lift coefficient and angle of attack corresponding to each pilot's approach speed are shown on the curves of figure 28 for three configurations of the airplane, with and without suction applied to the plain flaps and with the slotted flaps, and indicate the wide range of angles of attack used by various pilots. The maximum lift coefficient with boundary-layer control shown in this figure is for the configuration evaluated by the 16 pilots. Improvements to the installation later resulted in a slightly higher $C_{L_{max}}$ value, shown in figure 24. Curves of thrust required for level flight plotted against airspeed are presented in figure 29 for the various configurations tested and include the average approach speed chosen by the pilots.

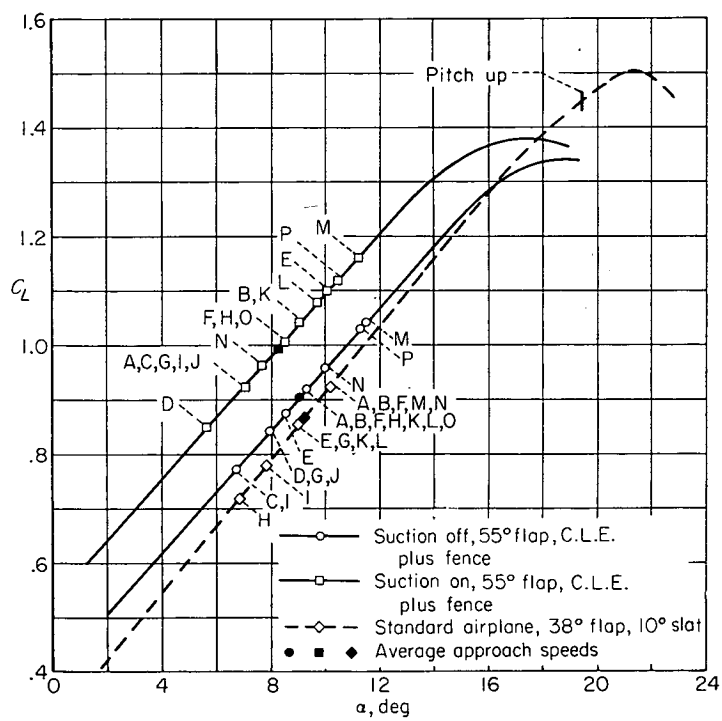
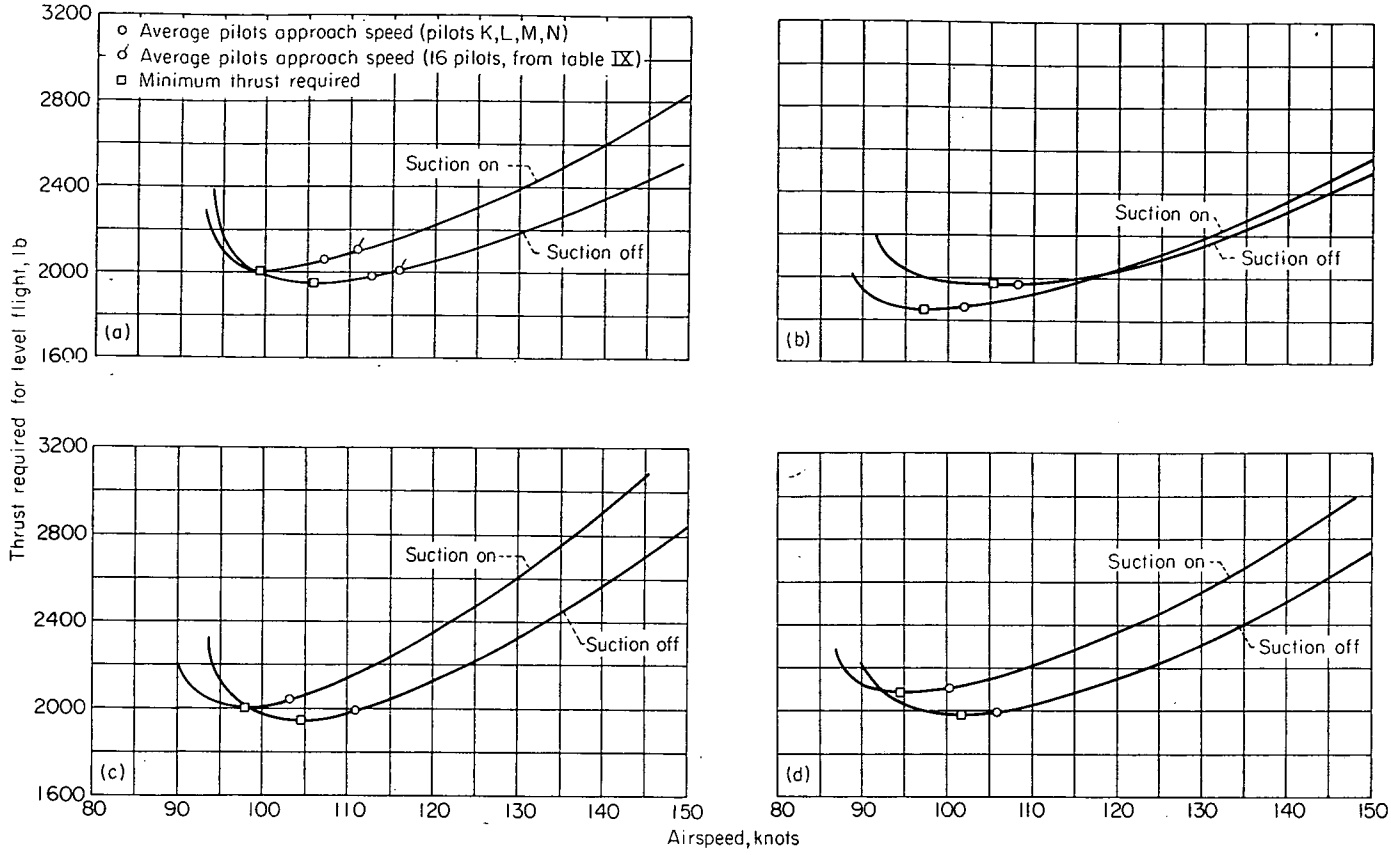


FIGURE 28.—Variation of lift coefficient with angle of attack for the test airplanes with values corresponding to individual pilot's approach speed shown.



(a) $\delta_f = 55°$, cambered leading edge with fence.
(b) $\delta_f = 55°$, slatted leading edge.
(c) $\delta_f = 64°$, cambered leading edge with fence.
(d) $\delta_f = 64°$, slatted leading edge.

FIGURE 29.—Thrust required for level flight for various configurations of test airplane, gear down and speed brakes out.

There is a wide variety of factors which may be considered by a pilot as affecting his choice of minimum comfortable approach speed. It is possible, and often the case, that several factors are present for one airplane, making selection of a single primary reason difficult because of complex interrelationships. An attempt has been made here, however, to isolate those factors considered of primary importance by the pilots.

Examination of table VI indicates that the pilots' reasons for limiting the approach speed of the various airplanes can be divided into three categories, as follows:

A. Reasons associated with stall characteristics: It would be expected that on airplanes limited by stall characteristics the most direct influence on the approach speed would result from an increase in $C_{L_{max}}$ or improvements in the stalling characteristics.

B. Reasons associated with attitude or visibility limitations: It would be expected that on an airplane limited by this characteristic the most direct influence on approach speed would result from an increase in lift at attitudes below $C_{L_{max}}$.

C. Reasons associated with longitudinal control, that is, ability to control altitude or flight path: A number of factors influence this characteristic. One expected to be of primary importance, which was varied on the test airplanes, was the variation of L/D with α. This variation is evident from the change in the shape of the curve of thrust required for steady level flight versus speed (fig. 29).

It is of interest to examine the above listed categories in comparison with the approach speed decrements realized from boundary-layer control.

The 16 pilots who flew the airplane with boundary-layer control inoperative gave reasons for limiting approach speed which were almost evenly divided between these categories (table XI).

On the basis of the lift curves presented in figure 28, it would be expected that application of boundary-layer control to the flap would tend to relieve attitude and visibility limitations but would not significantly change stall speed (a ΔV_s of only 1 knot). The pilots' comments are consistent with these changes in that, with boundary-layer control operating, only two considered the attitude or visibility the limiting factor. The average decrease in approach speed was 5.9 knots. Closer examination of this average, however, reveals that the pilots who previously considered Category B or C the limiting factor benefited most from the operation of boundary-layer control to the extent of a 7.9-knot decrease. The pilots who previously had considered proximity to the stall the limiting factor benefited the least to the extent of 3.0 knots. Thus, despite the lack of any dominant limiting factor on this airplane, there is a consistent relationship between the effect of aerodynamic change and the factors which the individual pilot considered limiting on choice of approach speed.

The aerodynamic factors which influence the ease with which the attitude or flight path of the airplane can be controlled are more complex than the Category A and B limitations. However, on all of the configurations tested the average minimum approach speed (fig. 29) lies slightly above the speed for minimum thrust required. For the configurations flown in this investigation, it would appear that the ability to flare or to arrest sink rates deteriorates below the minimum acceptable to the pilot at or near the speed for minimum thrust required and tends to result in his setting his approach speed accordingly. This surmise is not explicitly borne out by the pilots' comments, but it will be observed from table X that the decreases in average approach speed due to boundary-layer control on the flap are related very closely to the corresponding decreases in speed for minimum thrust required. It is noteworthy that the research pilots (K, L, M, and N) who had the most opportunity to fly the test airplanes were consistent in noting Category C (ability to control altitude) as the primary limiting factor establishing the approach speeds on all the configurations with flap boundary-layer control. Category C is also considered as the limiting factor for the standard F–86A–1 by 7 out of the 12 other pilots.

Of the additional configurations flown with flap boundary-layer control (table X), it is of interest to note that the airplane with cambered leading edge and no fence had an unsatisfactory roll-off at the stall but fell in Category C rather than Category A. The airplane with slats and 55° flap deflection, which had excellent stall characteristics, was also limited by Category C and was generally considered the most desirable configuration flown, although it did not result in any appreciable decrease in approach speed over the airplane with cambered leading edge and no fence. A slightly greater decrease in a approach speed resulted from increasing the flap deflection to 64°, but the increased drag resulted in less desirable wave-off characteristics.

From the foregoing results, it is apparent that the pilot utilized the increased lift offered by the 64° boundary-layer-control flap to decrease the approach speeds by flying at approximately the same attitude with suction off or on. These speeds correspond to 1.19 V_{stall} and 1.15 V_{stall} for suction off and on, respectively. Based on these values of approach speed and an assumed touchdown speed of 1.05 V_{stall}, the effect of boundary-layer control on the landing distance over a 50-foot obstacle was computed and is shown in figure 30 for various gross weights. These data indicate that a 14.5-percent reduction in landing distance due to boundary-layer control would be obtained at 64° flap deflection.

In the computations for take-off and climb, account is taken of the thrust loss incurred as a result of extracting air from the engine compressor. In order to operate the engine within allowable tail-pipe temperature limits with the suction system on, a reduction from 100-percent rpm was necessary for the type of engine tail pipe used in the F–86A airplane. The thrust loss associated with the decreased rpm was approximately 150 pounds. It is assumed that in take-off, the bleed-air valve would be opened only to that amount necessary to reach the C_Q value above which

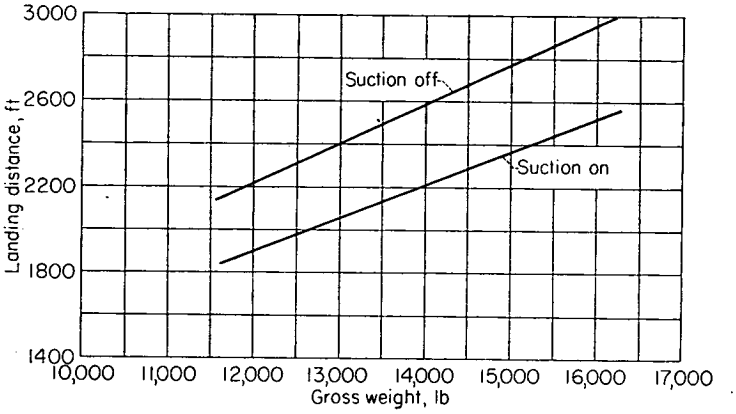


FIGURE 30.—Variation of landing distance over a 50-foot obstacle with gross weight for 64° flap deflection, slatted leading edge, speed brakes out.

no further increase in flap lift occurred (as shown in fig. 26) in order not to penalize unduly the suction system. With a more efficient pumping system (ejector pump used has an efficiency of approximately 15 percent) or a variable exit area type tail pipe, the thrust loss would be reduced appreciably with a resultant gain in performance with suction on.

Consider first catapult take-off. The following assumptions are used in computing the speed at the end of the catapult run. Lift-off speed is selected as the speed at nine-tenths of $C_{L_{max}}$ or at the maximum ground attitude. This speed has the additional restriction that the longitudinal acceleration shall be equal to or greater than 0.065g. [5] The results of computations of the take-off speeds at the end of the catapult run as a function of gross weight for various flap deflections with suction on and off are presented in figure 31. Indicated in this figure are the H8 catapult characteristics. The take-off speeds for the 55° and 64° flap-defection configurations with suction on were based on nine-tenths of $C_{L_{max}}$; the other configurations were limited in take-off speed by ground attitude to the C_L at α=16°. At 21,000 pounds or greater, the 0.065g acceleration requirement becomes limiting. The data in figure 31 indicate improvements in take-off performance with suction on. By use of the H8 catapult characteristics and the data in figure 31. computations were made of the wind required over the deck as a function of gross weight for the operational pressure limit of 3500 psi, a reduced pressure of 2950 psi, and the catapult end speed limit. These data are presented in figure 32. It can be noted in this figure that when the limit H8 catapult pressure is used, wind is required over the deck only for the very highest gross weights. The data in figure 32 indicate that approximately 6 knots less wind would be required for the flap deflected 64° with suction on, compared with the 38° flap with no suction.

Next, with regard to a field take-off, the assumption is made that the airplane accelerates on the ground in a level attitude, and at take-off speed the airplane is rotated to the angle of attack corresponding to a velocity of 1.2 V_{stall}. For the transition distance, it is assumed that the airplane

[5] Assumed minimum acceleration value used to assure that the aircraft does not sink after launch.

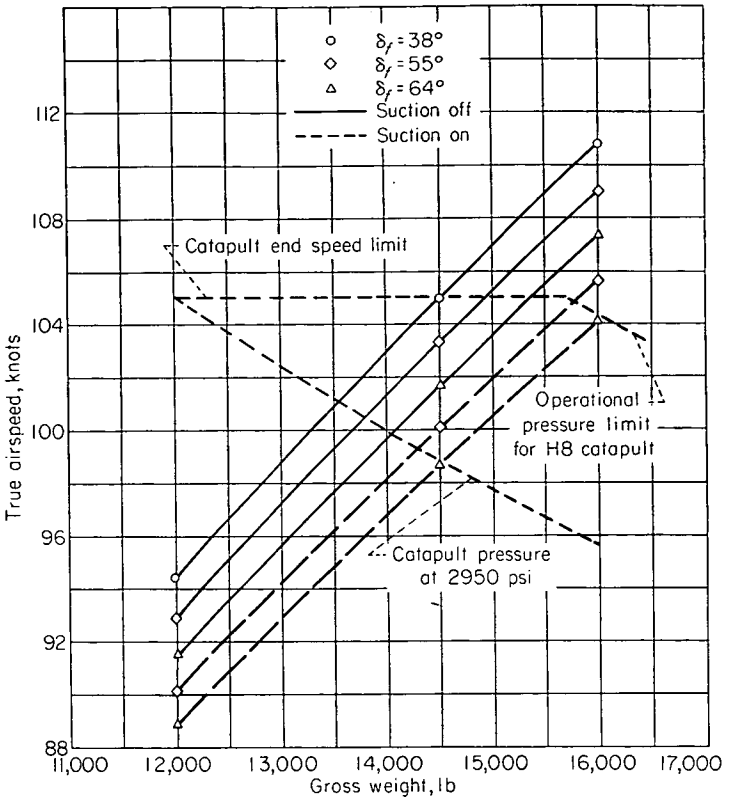


FIGURE 31.—Variation of catapult take-off velocity with gross weight for various flap deflections and boundary-layer control on and off.

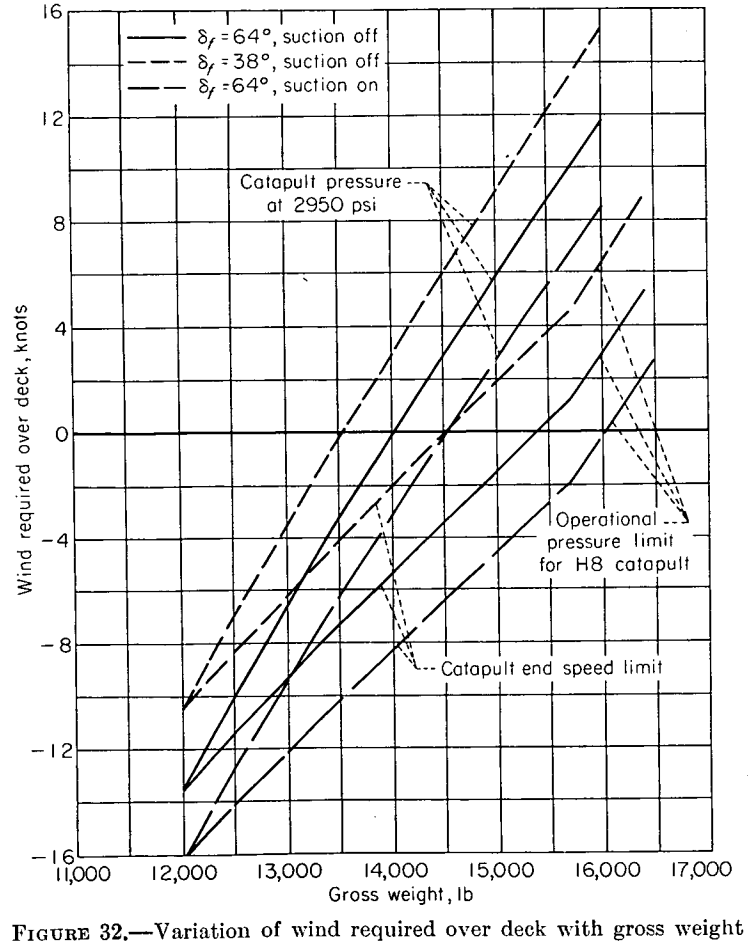


FIGURE 32.—Variation of wind required over deck with gross weight and boundary-layer control on and off.

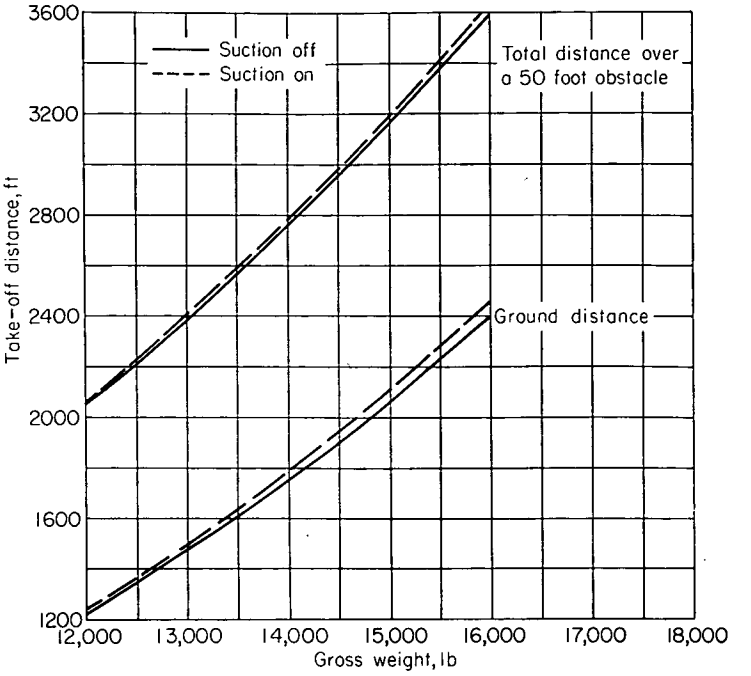
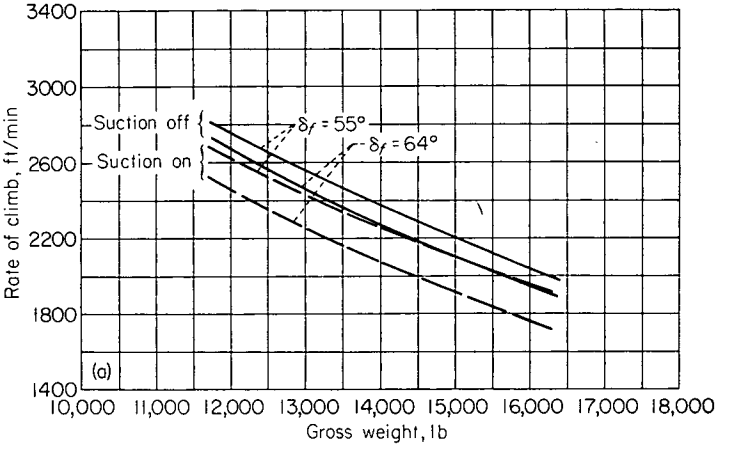


FIGURE 33.—Variation of take-off distance for boundary-layer control on and off; δ_f=55°, slatted leading edge.

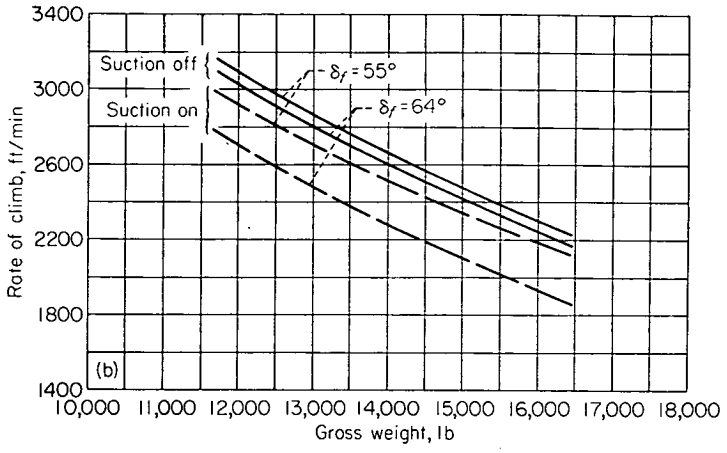


(a) Catapult speed, $V=1.05V_{stall}$.

FIGURE 34.—Variation of rate of climb with gross weight for various flap deflections and boundary-layer control on and off; slatted leading edge.

is in a steady rate of climb before attaining the 50-foot-height point. The results of the computations indicate very little change in take-off performance due to boundary-layer control or change in flap deflection. The effect of boundary-layer control on take-off performance is illustrated in figure 33 for 55° flap deflection. For this case, the gains in take-off performance which would result from the use of boundary-layer control are cancelled by the thrust loss associated with the type of pumping system used. The take-off performance could be improved by turning on the boundary-layer control after the airplane has accelerated to the take-off speed.

The rates of climb after a catapult take-off (1.05 V_{stall}) and after wave-off (1.15 V_{stall}) are presented in figure 34. These data indicate less rate of climb with the boundary-layer control on due to the loss in thrust previously men-



(b) Wave-off speed, $V=1.15V_{stall}$.

FIGURE 34.—Concluded.

tioned. The rate of climb should be adequate, however, over the gross-weight range covered.

Turning the suction off produced a nose-up pitch change which was considered small. No hazardous flight conditions were encountered in simulating loss of suction power at any airspeed. There was no marked change in stick-free stability as a result of the use of boundary-layer control.

Flight tests conducted in areas of moderate rain showed negligible effect of the rain on either the lift due to suction or the pumping requirements. No clogging of the porous material was evident after approximately 50 hours of flight testing. No particular effort was made to protect the porous area in the hangar. No detrimental effects on engine life due to the use of the air bleed (3 pounds per second, average) were noted for approximately 67 hours of flight testing.

CONCLUDING REMARKS

The results of wind-tunnel and flight tests of a 35° swept-wing airplane having area suction applied to trailing-edge flaps indicated that trailing-edge flap effectiveness could be improved to values approaching theory for flap deflections ranging from 45° to 64° of deflection. The primary effects of boundary-layer control applied to trailing-edge flaps was to increase lift at a given angle of attack. Although the flap boundary-layer control reduced the stall speed only slightly, a reduction in minimum comfortable approach speed of about 12 knots was obtained by a number of pilots, particularly those giving visibility and attitude or longitudinal control as the limiting factor. The improvements in flap effectiveness were accomplished with low values of flow quantity and suction horsepower; flow coefficients ranging from 0.0003 to 0.0008 were required; and suction power ranging from 10 to 25 horsepower would be required in the normal landing-approach and take-off speed ranges.

AMES AERONAUTICAL LABORATORY
NATIONAL ADVISORY COMMITTEE FOR AERONAUTICS
MOFFETT FIELD, CALIF., *May 6, 1958*

APPENDIX

METHODS USED FOR PERFORMANCE EVALUATION

The following equations and assumptions were used in computing the performance.

Take-off distance:

$$\text{Ground run}=\frac{WV_{TO}^2}{64.4[T-\mu W-Sq(C_D-\mu C_L)]}, \text{ ft}$$

(from ref. 4, pp. 195–196).

$$\text{Air distance}=\frac{50W}{T-D}+\frac{V_{TO}^2}{g\sqrt{2}}, \text{ ft}$$

(ref. 5, p. 51) where take-off velocity

$$V_{TO}=1.2\,V_{stall}$$

$$=1.2\left(1.71\sqrt{\frac{W-T\sin\alpha}{C_{L_{max}}}}\right), \text{ ft/sec}$$

and

T=engine thrust

$q=\frac{\rho}{2}(0.7\,V_{TO})^2$

W=gross weight in pounds.

α=angle of attack at $C_{L_{max}}$

μ=0.02

(The assumption is made that steady climb has been reached before the 50-foot height is attained.)

Climb:

$$\text{Rate of climb}=\frac{101.4\,VT_{EX}}{W}, \text{ ft/min}$$

where

T_{EX}=excess thrust at V

Landing distance:

$$\text{Air distance}=\left[\frac{(V^2_{50}-V_L^2)}{64.4}+50\right]\frac{L}{D}, \text{ ft}$$

$$\text{Ground run}=\frac{V_L^2}{64.4\left[\mu-\left(\frac{D}{L}\right)\right]}\log_e\left(\frac{L}{D}\right)\mu, \text{ ft}$$

(ref. 6, p. 312) where V_{50} is pilot's actual approach speed, and the landing velocity,

$$V_L=1.05\,V_{stall}$$

and

$$\mu=0.4$$

Catapult end speed:

$$V_{TO}=\sqrt{\frac{295(W-T\sin\alpha_{TO})}{SC_{L_{TO}}}}, \text{ knots}$$

where

T=thrust at 100-percent rpm

$C_{L_{TO}}=0.9\,C_{L_{max}}$

$\alpha_{TO}=\alpha$ at $C_{L_{TO}}$

REFERENCES

1. Holzhauser, Curt A., and Bray, Richard S.: Wind-Tunnel and Flight Investigations of the Use of Leading-Edge Area Suction for the Purpose of Increasing the Maximum Lift Coefficient of a 35° Swept Wing Airplane. NACA Rep. 1276, 1956. (Supersedes NACA RM A52G17 and RM A55C07)
2. DeYoung, John: Theoretical Symmetric Span Loading Due to Flap Deflection for Wings of Arbitrary Plan Form at Subsonic Speeds. NACA Rep. 1071, 1952.
3. Anderson, Seth B., Matteson, Frederick H., and Van Dyke, Rudolph D., Jr.: A Flight Investigation of the Effect of Leading-Edge Camber on the Aerodynamic Characteristics of a Swept-Wing Airplane. NACA RM A52L16a, 1953.
4. Perkins, Courtland D., and Hage, Robert E.: Airplane Performance Stability and Control. John Wiley & Sons, Inc., 1949.
5. Lush, Kenneth J.: Standardization of Take-Off Performance Measurements for Airplanes. Tech. Note R-12, USAF, ARDC, Air Force Flight Test Center, Edwards, Calif., 1954.
6. Dwinnell, James H.: Principles of Aerodynamics. McGraw-Hill Book Co., Inc., 1949.

TABLE I.—DIMENSIONS OF MODEL AND TEST AIRPLANE

Wing	
Total area, sq ft	287.9
Span, ft	37.12
Aspect ratio	4.79
Taper ratio	0.51
Mean aerodynamic chord (wing station 98.7 in.), ft	8.1
Dihedral angle, deg	3.0
Sweepback of 0.25-chord line	35°14′
Geometric twist, deg	2.0
Root airfoil section (normal to 0.25-chord line)	NACA 0012–64 modified
Tip airfoil section (normal to 0.25-chord line)	NACA 0011–64 modified
Wing area affected by flaps, sq ft	116.6
Flap	
Wind-tunnel model	
Flap area (total), sq ft	29.8
Flap span (from 13.5 to 49.5-percent semispan), ft	7.27
Flap chord (constant), ft	2.108
Test Airplane	
Flap area (total), sq ft	23.7
Flap span (from 13.5 to 49.5-percent semispan), ft	7.27
Flap chord (constant), ft	1.67

TABLE II.—COORDINATES OF THE WING AIRFOIL SECTIONS NORMAL TO THE WING QUARTER-CHORD LINE AT TWO SPAN STATIONS

[Dimensions given in inches]

Section at 0.467 semispan			Section at 0.857 semispan		
x	z		x	z	
	Upper surface	Lower surface		Upper surface	Lower surface
0	0. 231	--------	0	−0. 098	--------
. 119	. 738	−0. 307	. 089	. 278	−0. 464
. 239	. 943	−. 516	. 177	. 420	−. 605
. 398	1. 127	−. 698	. 295	. 562	−. 739
. 597	1. 320	−. 895	. 443	. 701	−. 879
. 996	1. 607	−1. 196	. 738	. 908	−1. 089
1. 992	2. 104	−1. 703	1. 476	1. 273	−1. 437
3. 984	2. 715	−2. 358	2. 952	1. 730	−1. 878
5. 976	3. 121	−2. 811	4. 428	2. 046	−2. 176
7. 968	3. 428	−3. 161	5. 903	2. 290	−2. 401
11. 952	3. 863	−3. 687	8. 855	2. 648	−2. 722
15. 936	4. 157	−4. 064	11. 806	2. 911	−2. 944
19. 920	4. 357	−4. 364	14. 758	3. 104	−3. 102
23. 904	4. 480	−4. 573	17. 710	3. 244	−3. 200
27. 888	4. 533	−4. 719	20. 661	3. 333	−3. 250
31. 872	4. 525	−4. 800	23. 613	3. 380	−3. 256
35. 856	4. 444	−4. 812	26. 564	3. 373	−3. 213
39. 840	4. 299	−4. 758	29. 516	3. 322	−3. 126
43. 825	4. 081	−4. 638	32. 467	3. 219	−2. 989
47. 809	3. 808	−4. 452	35. 419	3. 074	−2. 803
51. 793	3. 470	−4. 202	38. 370	2. 885	−2. 574
55. 777	3. 066	−3. 891	41. 322	2. 650	−2. 302
59. 761	2. 603	−3. 521	44. 273	2. 374	−1. 986
[a] 63. 745	2. 079	−3. 089	[a] 47. 225	2. 054	−1. 625
83. 681	−. 740	--------	63. 031	. 321	--------
L. E. radius: 1.202, center at 1.201, 0.216			L. E. radius: 0.822, center at 0.822, −0.093		

[a] Straight lines to trailing edge.

TABLE III.—SUMMARY OF EXTENT AND POSITIONS OF POROUS SURFACE TESTED ON SUCTION FLAP; DIMENSIONS NORMAL TO HINGE REFERENCE LINE

[Dimensions in inches]

Configuration no.	Extent of chordwise opening	Position of forward edge (aft of ref. line)	Flap deflection, deg	Configuration no.	Extent of chordwise opening	Position of forward edge (aft of ref. line)	Flap deflection, deg
1	2. 5	2. 5	45, 55	20	3. 0	1. 0	64
2	2. 5	3. 5	45, 55, 64	21	3. 0	2. 0	64
3	2. 5	1. 5	45	22	3. 0	3. 0	64
4	2. 5	4. 5	55	23	3. 0	4. 0	64
5	2. 5	4. 5	55	24	4. 0	2. 0	64
6	. 5	2. 5	55	25	4. 5	1. 5	64
7	1. 0	2. 5	55	26	5. 0	2. 0	64
8	1. 5	2. 5	55	27	1. 25	1. 87	70
9	3. 5	2. 5	55	28	2. 62	1. 87	70
10	5. 5	2. 5	55	29	3. 12	1. 87	70
11	1. 5	. 5	55	30	3. 62	1. 87	70
12	1. 5	1. 5	55	31	4. 12	1. 87	70
13	1. 5	3. 5	55	32	5. 12	1. 87	70
14	1. 5	4. 5	55	33	3. 62	2. 12	70
15	1. 5	5. 5	55	34	3. 62	2. 32	70
16	1. 5	6. 5	55	35	3. 62	2. 62	70
17	1. 0	2. 0	64	36	3. 62	3. 12	70
18	2. 0	2. 0	64	37	3. 62	3. 62	70
19	2. 0	2. 5	64	38	3. 62	4. 12	70

TABLE IV.—COORDINATES OF THE MODIFIED WING LEADING EDGE AT TWO SPAN STATIONS, NORMAL TO THE WING QUARTER-CHORD LINE

[Dimensions given in inches]

Section at 0.467 semispan			Section at 0.857 semispan		
x	z		x	z	
	Upper surface	Lower surface		Upper surface	Lower surface
−1. 692	−1. 445	-------	−1. 250	−1. 359	--------
−1. 273	−. 348	−2. 552	−. 934	−. 495	−2. 192
−. 855	. 222	−2. 898	−. 619	−. 099	−2. 454
−. 436	. 629	−3. 114	−. 304	. 197	−2. 609
−. 018	. 969	−3. 272	. 011	. 456	−2. 701
. 400	1. 266	−3. 391	. 326	. 675	−2. 769
. 819	1. 527	−3. 473	. 641	. 867	−2. 796
1. 237	1. 760	−3. 523	. 956	1. 040	−2. 813
1. 655	1. 952	−3. 549	1. 272	1. 189	−2. 821
1. 992	2. 104	-------	1. 476	1. 273	--------
2. 074	-------	−3. 552	1. 587	-------	−2. 813
2. 911	-------	−3. 531	2. 217	-------	−2. 787
4. 166	-------	−3. 481	3. 163	-------	−2. 742
6. 258	-------	−3. 472	4. 739	-------	−2. 709
8. 350	-------	−3. 542	6. 314	-------	−2. 712
10. 442	-------	−3. 657	7. 890	-------	−2. 751
14. 626	-------	−3. 956	9. 466	-------	−2. 808
15. 936	-------	−4. 064	11. 042	-------	−2. 885
			11. 806	-------	−2. 944
L. E. radius: 1.674, center at −0.018, −1.445			L. E. radius: 1.261, center at 0.011, −1.359		

TABLE V.—LOCATION OF SURFACE PRESSURE ORIFICES

[Position of orifices,[1] chordwise percent]

Orifice No.	0.25$b/2$ and 0.45$b/2$ station		0.65$b/2$ and 0.85$b/2$ station	
	Upper surface	Lower surface	Upper surface	Lower surface
1	0	--------	0	--------
2	.25	0.25	.25	0.25
3	.5	.5	.5	.15
4	1.0	1.0	1.0	1.0
5	1.5	1.5	1.5	1.5
6	2.0	2.0	2.0	2.0
7	2.5	2.5	2.5	2.5
8	3.5	3.5	3.5	3.5
9	5.0	5.0	5.0	5.0
10	7.5	7.5	7.5	7.5
11	10.0	10.0	10.0	10.0
12	15.0	15.0	15.0	15.0
13	20.0	20.0	20.0	20.0
14	30.0	30.0	30.0	30.0
15	40.0	40.0	40.0	40.0
16	50.0	70.0	50.0	60.0
17	60.0	75.0	60.0	70.0
18	70.0	80.0	70.0	80.0
19	75.0	88.0	80.0	90.0
20	80.0	90.5	90.0	97.5
21	83.3	93.2	97.5	--------
22	84.0	96.0	--------	--------
23	84.4	98.0	--------	--------
24	84.8	--------	--------	--------
25	85.4	--------	--------	--------
26	86.5	--------	--------	--------
27	87.7	--------	--------	--------
28	91.0	--------	--------	--------
29	93.0	--------	--------	--------
30	95.0	--------	--------	--------
31	97.0	--------	--------	--------
32	99.0	--------	--------	--------

[1] Upper surface orifices omitted:
Station 0.25$b/2$, no. 6.
Station 0.85$b/2$, nos. 2, 6, and 11.
Station 0.65$b/2$, no. 7.

Lower surface orifices omitted:
Station 0.25$b/2$, no. 16.
Station 0.65$b/2$, nos. 6, 7, and 8.
Station 0.85$t/2$, no. 10 above 12.8.

TABLE VI.—PILOTS' COMMENTS RELATING TO STALL AND APPROACH CHARACTERISTICS

(a) Configuration I: Standard F–86A–1; 38° flap; slats

Pilot	Suction B. L. C.	Stall speed, I. A. S., knots	Stall characteristics	Approach speed I. A. S., knots	Primary reasons for choosing approach speed
A	------	98–100	Warning: Lightening of stick forces. Stall: Satisfactory. Mild pitch-up and roll-off.	115----------	Visibility is limiting factor. Have good control down to 105, but attitude best at 115–120. At about 100 much larger stick movement is necessary for control. Approach speed dependent upon gustiness.
B	------	98	Warning: Marginally satisfactory. Force lightening at 105–102 and pitch-up at 102. No aerodynamic warning. Stall: Satisfactory. Mild buffet, left roll-off, easy to control. Ailerons more effective than elevator at stall.	115----------	115 chosen to give adequate speed above stall (in this case 105 where force lightening occurred). L. S. O. (Landing Signal Officer) would add 15 to stall for approach speed. Pilot chooses a minimum of 10. Airplane flyable at any speed above stall. Elevator control good at 110. At 110–115 visibility is a problem but would not be if seat could be raised. Considerable floating experienced at 115.
E	------	102	Warning: None. Stall: Slight pitch-up, left wing drop, incipient spin.	130 on final. 120 over fence.	Forward visibility.
F	------	97–101	Warning: Insufficient. Stall: Satisfactory. Moderate pitch-up and roll-off.	115----------	Poor lateral control and normal margin for flare out. Better lateral control and feel on suction flap airplane. Worse sink rate than suction flap airplane suction on.
G	------	99	Warning: Light buffet 110. Yaws left at 103 but controllable. Stall: Very good. Slow left wing drop.	130 on final. 120 over fence 110 touchdown.	Pattern felt comfortable by touching down at 110 with no buffet or yaw.
H	------	100	Warning: Good. Light buffet and pitch-up at 105. Stall: No comments.	130----------	Limited by visibility and feel of aircraft. Lack of adequate seat adjustment restricts visibility over nose more than on suction-flap airplane. Less able to rack around at 120 than suction-flap airplane.
I	------	100	Warning: Good. 3–6 above stall. Stall: Good to excellent.	125 over fence. 115–110 on touchdown.	Comfortable attitude, visibility. Not worried about hitting tailpipe.
K	------	100	Stall: Satisfactory.	120----------	Decrease in ability to control altitude by longitudinal control alone.
L	------	100	Stall: Satisfactory. Mild pitch-up and roll-off.	120----------	Loss of longitudinal control. No stick centering from trim at approach speed.
M	------	101–102	Stall: Unsatisfactory. Due to pitch-up.	115----------	Positive altitude control.
N	------	101	Warning: Unsatisfactory. Very little. Stall: Satisfactory.	115----------	No comment.

TABLE VI.—PILOTS' COMMENTS RELATING TO STALL AND APPROACH CHARACTERISTICS—Continued

(b) Configuration II: F–86A–5; 55° suction flap; C. L. E. plus fence

Pilot	Suction B. L. C.	Stall speed, I. A. S., knots	Stall characteristics	Approach speed I. A. S., knots	Primary reasons for choosing approach speed
A	Off	100	Warning: Weak buffet. Stall: Very satisfactory. Mild pitching, very gentle.	115	Proximity to stall. Good control 100 up. Good visibility 115–118. No noticeable difference between suction on and off.
	On	100		115	
B	Off	100	Warning: Too close but adequate. Stall: Mild, satisfactory.	115	Limited by visibility at 110. Control is satisfactory right down to stall. Longitudinal control too sensitive at approach speeds. More positive stick-free stability as on F–86F is more desirable.
	On	95–98	Warning: Too close but adequate. Stall: Mild, satisfactory.	108	Limited by nearness to stall. Visibility was not limiting at 110. Attitude is more desirable with suction on, but without lower stall speed, would not lower approach speed.
C	Off	100	Stall: Satisfactory.	125	Minimum positive control for gusts or emergency.
	On	95	Stall: Good.	115	Has better control and stability than with suction off. No visibility problem.
D	Off	100	Warning: Buffeting, slight wing roll. Stall: Satisfactory.	140 base. 120 over fence. 110 touchdown.	Adequate speed above stall. Feels comfortable at 110. Satisfactory stall allows coming to within 10 of stall.
	On	99	Warning: Buffeting and slight wing, roll. Stall: Satisfactory.	140 base. 120 over fence. 105 touchdown.	Adequate speed above stall. Decreased attitude allows lower touchdown speed. Visibility not a problem at base and final approach speeds used but noticeably improved on touchdown.
E	Off	98	Warning: High angle of attack, shaking and wallowing of airplane at 102 (more than suction on). Stall: Satisfactory, nose drops through.	125–130 on final. 115–120 over fences.	Optimum visibility with more than adequate airspeed. No control difficulties.
	On	97	Warning: None. Stall: Satisfactory. Consists of wing drop which is controllable but worse than suction off. Inconsistent: wing drops or stalls straight ahead.	115 on final. 105 over fence.	Decrease in approach speed due to better visibility. Not limited otherwise. Possibly could use 110 approach speed on final. Over fence speed limited by fear of dragging tail.
F	Off	92–97	Warning: Good (100–103). Stall: Satisfactory. Pitch-up followed by pitch-down.	115	Limited by concern about ability to flare and the time spent in transition-power off.
	On	90–94	Warning: Inadequate. Stall: Satisfactory.	110	Limited by lack of stall warning. Like increased visibility with suction. Suction also reduces rate of sink. Flared better than anticipated but may have been influenced by carrying more power than usual. Flies better 5–10 above stall than suction off.
G	Off	101	Warning: O. K. Burble at 115, slight left yaw at 102. Stall: Satisfactory. Slight left roll tendency.	130 on final. 120 over fence. 110 touchdown.	Limited by speed above yaw and stall. Sink rate higher than suction on.

TABLE VI.—PILOTS' COMMENTS RELATING TO STALL AND APPROACH CHARACTERISTICS—Continued

(b) Configuration II; F–86A–5; 55° suction flap; C. L. E. plus fence

Pilot	Suction B. L. C.	Stall speed, I. A. S., knots	Stall characteristics	Approach speed I. A. S., knots	Primary reasons for choosing approach speed
G	On	99	Warning: Satisfactory. Light buffet at 105. Stall: Satisfactory. Straight ahead.	120 on final. 115 over fence. 105 touchdown.	Limited by speed above stall. Speed on base and final very comfortable 120 kts. due to increased ability to turn. Feels better suction on, especially in jet wash (i. e., turbulence). Could tighten pattern suction on. Decrease in attitude very significant, may influence reduction in approach speed.
H	Off	99	Warning: Satisfactory. Light buffet. Stall: Satisfactory.	115	Limited by proximity to stall. Added flap deflection 55° over 38° quite apparent, gave large improvement, more than that due to effect of suction.
	On	94–97	Warning: Light to moderate buffet; more than suction off. Stall: Satisfactory.	110	Limited by general feel in approach. Decrease in sink rate with suction on. A more solid feel, especially in turns. Decrease in attitude quite noticeable. Not limited by nearness to stall.
I	Off	100–101	Warning: Good. Buffet 3 less than normal F–86.	125 (power on approach).	Comfortable attitude. Not worried about proximity to stall.
	On	98	Warning: Good. Buffet 3 less than normal F–86.	115 over fence 110 touchdown.	Speed above stall. Attitude improved. Maneuvering in approach felt better.
J	Off	100	Warning: Wing drop and buffet 2 or 3 above stall.	120	Attitude. Sufficient speed above stall.
	On	97	Warning: Sufficient. Right wing drop and buffet. 2 or 3 above stall.	115	Feels comfortable. Proximity to stall. With more power on would be comfortable at 110.
K	Off	95	Stall: Satisfactory.	115	Decrease in ability to control altitude by longitudinal control alone. Visibility.
	On	90	Stall: Satisfactory.	108	Decrease in ability to control altitude by longitudinal control alone. Visibility improved over suction off but becomes contributing factor again at this lower speed.
L	Off	95	Warning: Satisfactory. Buffet 3–4 before stall. Stall: Satisfactory. Mild pitch-up, straight ahead.	115	Loss of longitudinal control or ability to adequately control altitude.
	On	90	Warning: Marginal. Buffet 2–3 before stall. Stall: Satisfactory. Mild pitch-up, straight ahead.	105–107	Loss of longitudinal control or ability to adequately control altitude.
M	Off	95–97	Warning: Marginal. Buffet 98. Stall: Satisfactory.	105–110	Ability to stop sink rate.
	On	92–95	Warning: Marginal. Buffet 98. Stall: Satisfactory.	100–105	Ability to stop sink rate.
N	Off	98	Warning: Marginal. Buffet at 106. Stall: Good.	110–115	Adequate margin above stall.
	On	98	Warning: Marginal. Buffet at 106. Stall: Good.	110–115	Adequate margin above stall. Visibility good suction on. Pilot noted no difference in approach speed suction on or off but did note improved visibility.

TABLE VI.—PILOTS' COMMENTS RELATING TO STALL AND APPROACH CHARACTERISTICS—Concluded

(b) Configuration II; F-86A-5; 55 suction flap; C. L. E. plus fence

Pilot	Suction B. L. C.	Stall speed, I. A. S., knots	Stall characteristics	Approach speed I. A. S., knots	Primary reasons for choosing approach speed
O	Off	98	Warning: Mild aileron buffet 102. Stall: Good except for mild pitch-up.	120 on base. 115 over fence. 100 touchdown.	Ability to pull g.
	On	92	Warning: Mild aileron buffet 96. Stall: Good except for mild pitch-up.	110 on base. 110 over fence. 95 touchdown.	Ability to pull g.
P	Off	100	Satisfactory.	108	Proximity to stall.
	On	99	Satisfactory.	104	Proximity to stall.

TABLE VII.—SUCTION FLOW COEFFICIENT, PRESSURE COEFFICIENT, AND HORSEPOWER REQUIREMENTS

(a) Porous surfaces having low-pressure-drop characteristics

W/S, 40 lb/sq ft										
Flap deflection, 55°						Flap deflection, 64°				
α deg	C_L	V, ft/sec	C_{Q_f}	P_{v_f}	Measured suction, hp	C_L	V, ft/sec	C_{Q_f}	P_{v_f}	Measured suction, hp
0. 5	0. 79	206	0. 00047	−4. 4	23. 0	0. 92	191	0. 00078	−6. 8	44. 0
4. 6	1. 06	178	. 00050	−4. 2	15. 7	------	-------	--------	-------	--------
6. 6	------	-------	--------	-------	--------	1. 30	160	. 00082	−6. 3	24. 6
10. 9	1. 45	152. 5	. 00062	−3. 5	10. 1	1. 52	148	. 00082	−6. 0	18. 1
15. 1	1. 68	141. 5	. 00065	−3. 0	6. 7	------	-------	--------	-------	--------
W/S, 60 lb/sq ft										
0. 6	0. 78	255	0. 00049	−4. 5	43. 7	0. 92	237	0. 00079	−6. 9	87. 5
4. 6	1. 04	220	. 00052	−4. 2	28. 5	------	-------	--------	-------	--------
6. 6	------	-------	--------	-------	--------	1. 29	209	. 00082	−6. 4	56. 0
10. 9	1. 44	187. 6	. 00056	−3. 8	16. 9	1. 51	187	. 00080	−6. 0	33. 8
13. 0	1. 6	179. 5	. 00058	−3. 4	14. 0	------	-------	--------	-------	--------

TABLE VII.—SUCTION FLOW COEFFICIENT, PRESSURE COEFFICIENT AND HORSEPOWER REQUIREMENTS—Concluded

(b) Porous surface having variable- and high-pressure-drop characteristics

W/S, 40 lb/sq ft										
[1] Flap deflection, 55°						[2] Flap deflection, 64°				
α deg	C_L	V, ft/sec	C_{Q_f}	P_{v_f}	Measured suction, hp	C_L	V, ft/sec	C_{Q_f}	P_{v_f}	Measured suction, hp
0. 5	0. 83	202	0. 00022	−5. 3	12. 5	0. 92	191	0. 00054	−6. 8	28. 0
6. 6	------	-------	--------	-------	--------	1. 28	162	. 00050	−6. 3	15. 8
10. 9	1. 46	151. 5	. 00035	−4. 8	8. 3	1. 52	148. 5	. 00050	−6. 0	12. 4

[1] $\delta f = 55°$, variable-pressure-drop tapered-thickness porous material.

[2] $\delta f = 64°$, high-pressure-drop constant-thickness porous material.

TABLE VIII.—STALL DATA—LANDING APPROACH CONFIGURATION

Pilot	I. Standard F–86A–1; 38° flap; slats			II. F–86A–5; 55° suction flap; C. L. E. plus fence					
				Suction off			Suction on		
	V_{stall} knots [1]	Opinion of warning	Opinion of stall	V_{stall} knots [1]	Opinion of warning	Opinion of stall	V_{stall} knots [1]	Opinion of warning	Opinion of stall
A	91–95	Satisfactory	Satisfactory	99	Weak	Satisfactory	99	Weak	Satisfactory.
B	91	Marginal	Satisfactory	99	Adequate	Satisfactory	93–96	Adequate	Satisfactory.
C	---			99		Satisfactory	92		Good.
D	---			99		Satisfactory	98		Satisfactory.
E	97	No warning		96		Satisfactory	95	None	Satisfactory.
F	90–96	Insufficient	Satisfactory	89–95	Good	Satisfactory	87–91	Inadequate	Satisfactory.
G	93		Good	100	Satisfactory	Satisfactory	98	Satisfactory	Satisfactory.
H	95	Good		97	Satisfactory	Satisfactory	91–95		Satisfactory.
I	95	Good	Good	99–100	Good		96	Good	
J	---			99			95	Adequate	
K	95		Satisfactory	94		Satisfactory	90		Satisfactory.
L	95		Satisfactory	94	Satisfactory	Satisfactory	90	Marginal	Satisfactory.
M	96–97		Unsatisfactory	93–95	Marginal	Satisfactory	89–93	Marginal	Satisfactory.
N	96	Unsatisfactory	Satisfactory	97	Marginal	Good	97	Marginal	Good.
O	---			96		Good	89		Good.
P	---			99		Satisfactory	97		Satisfactory.
Average pilot's calibrated stall speed.	94. 6	Unsatisfactory to good.	Satisfactory to good.	97. 1	Marginal to satisfactory.	Satisfactory	94. 0	Marginal	Satisfactory to good.
Measured stall speed $V_{C_{L_{max}}}$ for $(W/S)_A$	88. 5			93. 9			92. 9		

[1] Extrapolation of the airspeed calibration curves of figure 9 has been required for some of these values.

TABLE IX.—APPROACH SPEEDS OR OVER-THE-FENCE SPEEDS CHOSEN

Configuration	Suction	Calibrated approach speed in knots for each pilot																Average
		A	B	C	D	E	F	G	H	I	J	K	L	M	N	O	P	
I. Standard F–86A–1; 38° flap; slats.	--------	114	114	---	---	118	114	118	130	125	---	118	118	114	114	---	---	117. 9
II. F–86A–5; 55° suction flap; C. L. E. plus fence.	Off----	115	115	126	121	115–121	115	121	115	126	121	115	115	105–110	110–115	115	108	116. 0
	On----	115	108	115	121	105	110	115	110	115	115	108	105–107	99–105	110–115	110	104	110. 8
Decrease in approach speed due to added flap deflection.	--------	−1	−1	---	---	+3–−2	−1	−2	15	−1	---	3	3	4–9	+4–−1	---	---	2. 1
Decrease in approach speed due to addition of flap BLC.	--------	0	7	11	0	10–16	5	6	5	11	6	7	8–10	5	0	5	4	5. 9

TABLE X.—COMPILATION OF CALIBRATED LANDING-APPROACH AIRSPEED DATA ON ALL CONFIGURATIONS FOR THE PILOTS FLYING THE COMPLETE EVALUATIONS

Pilot	Configuration I. Standard airplane	Configuration II. 55° flap; C. L. E. plus fence		Configuration III. 55° flap; C. L. E. no fence		Configuration IV. 55° flap; slats		Configuration V. 64° flap; C. L. E. and fence		Configuration VI. 64° flap; slats	
		Suction		Suction		Suction		Suction		Suction	
		Off	On	Off	On	Off	On	Off	On	Off	On
K	118	115	108	110	101–105	110	101–105	110	102	105	100
L	118	115	105–107	115	108	112	105	115	107	-----	-----
M	114	105–110	99–105	105	99	105	95–100	110–112	99–105	105–110	100
N	114	110–115	110–115	110–115	105	107–108	102–105	108–110	102	105	100–102
Average pilot's calibrated approach speed, knots	116. 0	112. 5	107. 1	110. 6	103. 7	108. 6	102. 2	111. 2	103. 2	105. 8	100. 3
Average decrease in approach speed due to added flap deflection, knots	------	3. 5		5. 4		7. 4		4. 8		9. 5	
Average decrease in approach speed due to addition of suction BLC, knots	------	5. 4		6. 9		6. 0		8. 0		5. 5	
Average decrease in approach speed below standard airplane, knots	------	8. 9		12. 3		13. 4		12. 8		15. 0	
Measured stall speed $V_{C_{L_{max}}}$ for $(W/S)_A$, knots	88. 5	93. 9	92. 9	85. 3	82. 1	90. 2	88. 4	91. 7	89. 4	89. 3	87. 3
Ratio of average approach speed to measured stall speed, knots	1. 31	1. 20	1. 15	1. 30	1. 26	1. 20	1. 16	1. 21	1. 16	1. 19	1. 15
Decrease in speed for minimum thrust required due to suction BLC, knots	------	6. 3		----------		8. 0		6. 7		7. 0	

TABLE XI.—PRIMARY REASONS FOR LIMITING APPROACH SPEEDS

Category	Reasons	I. Standard F–86A–1; 38° flap; slats	II. F–86A–5; 55° suction flap; C. L. E. plus fence		III–VII. F–86A; suction flap (all configurations)
			Suction off	Suction on	Suction on or off
A	Proximity to stall	B	A, D, G, H, J, N, P.	A, B, D, G, I, J, N, P.	
	Proximity to yaw				
	Poor stall characteristics			F	
	Number of pilots limiting because of stall characteristics.	1	7	8	
B	Visibility	A, B, E, H, I	B, E, L	E, L	
	Attitude	A, I	I, J		
	Concern for dragging tail			E	
	Number of pilots limiting because of attitude or visibility characteristics.	5	5	2	
C	Minimum positive longitudinal or altitude control	F, K, L, M, N	C, K, L	C, K, L	K, L, M, N.
	Ability to flare, maneuver or arrest sink	F	F, M, O	M, O	K, L, M, N.
	Feel	G, H		H	
	Number of pilots limiting for altitude or longitudinal control characteristics.	7	6	6	4.

REPORT 1371

INVESTIGATION OF SOME WAKE VORTEX CHARACTERISTICS OF AN INCLINED OGIVE-CYLINDER BODY AT MACH NUMBER 2 [1]

By Leland H. Jorgensen and Edward W. Perkins

SUMMARY

For an inclined body of revolution at a free-stream Mach number of 1.98, pitot-pressure distributions in the flow field, pressure distributions over the body, and downwash distributions through the shed vortices have been measured. The body consisted of a fineness-ratio-3, circular-arc, ogival nose tangent to a cylindrical afterbody 7.3 diameters long. The free-stream Reynolds numbers, based on body diameter, were 0.15×10^6 and 0.44×10^6, and the angle-of-attack range was from 5° to 20°. Pressure distributions on the body surface have been used in conjunction with flow-field contour plots of constant pitot pressure to determine the approximate locations at which the vortices left the body surface and their paths downstream.

To aid in the study of the experimental data, expressions have been written for the flow about a simple theoretical model in which the induced flow field in any crossflow plane along the cylindrical afterbody is represented by the incompressible steady potential flow around a cylinder in the presence of two symmetrical vortices of equal strength. By the use of velocity and vortex strength formulae resulting from consideration of this theoretical model, vortex paths which agree well with the experimental paths have been computed. However, in computing these paths, starting vortex positions and strengths determined from experiment were used, since there is no reliable theoretical method for determining these starting conditions.

Comparisons of theoretical and experimental downwash angle distributions along a line through the vortex centers illustrate the inadequacy of the sometimes-used potential flow about a cylinder which fails to account for the presence of vortices in the flow field. Except through and between the vortex cores, the downwash can be closely computed by assuming two symmetrical potential vortices in the flow field. If the sizes of the core radii are known, the agreement of theory with experiment both through and between the cores can be improved by the assumption of viscous rather than potential vortices in the field.

INTRODUCTION

One phase of the general problem of the interference between component parts of aircraft is the interference effects resulting from the vortices shed from a body of revolution at large angles of attack. Wind-tunnel tests have shown that these vortices can have a large effect upon the forces developed on wing and tail surfaces. Fortunately, techniques are available for estimating the forces developed on the wing and tail surfaces provided the strengths and positions of the body vortices are known (see, e. g., refs. 1 and 2). Although as yet, there is no rigorous theoretical method for predicting either the strengths or the positions of the vortices, certain simplified methods for estimating these characteristics can be suggested.

The purpose of this report is twofold: first, to present experimental results of flow-field characteristics about an inclined body of revolution and second, to assess the adequacy of a simplified method of estimating these characteristics. To this end an inclined body of revolution has been utilized for obtaining measurements of body pressure distributions, paths of the shed vortices, and downwash distributions through the vortex cores. Comparisons of computed vortex paths and downwash distributions are made with the results of the experimental measurements.

SYMBOLS

A	reference area, πa^2
a	radius of cylindrical portion of body
c	a constant of integration
C_N	normal-force coefficient, $\frac{N}{qA}$
C_{N_p}	normal-force coefficient by Tsien's potential theory
C_p	pressure coefficient, $\frac{p_l-p}{q}$
d	body diameter
l	body length
l_n	length of ogival nose
M	free-stream Mach number
N	normal force
p_l	local static pressure on body
p	free-stream static pressure
p_p	pitot pressure in body flow field (measured parallel to body axis)
p_t	free-stream total pressure
q	free-stream dynamic pressure
Re	free-stream Reynolds number per inch
r_*	core radius of viscous vortex
r_v	radial distance from vortex center to point y,z in crossflow plane
s	position of a point in crossflow plane, $y+iz$
t	time of vortex growth
v, w	induced velocities in y and z directions, respectively
V	free-stream velocity
V_c	crossflow velocity, $V \sin \alpha \approx V\alpha$

[1] Supersedes NACA RM A55E31 by Leland H. Jorgensen and Edward W. Perkins, 1955.

Preceding Page Blank

V_r vortex velocity in crossflow plane, $\sqrt{v^2+w^2}$

x,y,z Cartesian coordinates of point in space, origin at nose vertex, x axis coincident with body axis, z axis perpendicular to x axis in pitch plane

x,r,θ cylindrical coordinates of point in space, origin at nose vertex, x axis coincident with body axis, and $\theta=0°$ in crossflow plane on windward side

x_s distance from nose to vortex separation position

α angle of attack

Γ circulation strength

ϵ local flow (downwash) angle with respect to free-stream direction, $\alpha-\frac{w}{V}$ (Note that w is taken with respect to body axes.)

ζ position of vortex center in crossflow plane, $\xi+i\eta$

μ,ξ,η Cartesian coordinates of vortex filament position (referred to body axis with origin at nose)

ν kinematic viscosity of air

ρ free-stream air density

σ sidewash angle with respect to free-stream direction, $\frac{v}{V}$

φ potential function in crossflow plane

ψ stream function in crossflow plane

SUBSCRIPTS

x conditions at "x" distance from nose vertex

$n=1,2,3,4$ identifies real and image vortices

EXPERIMENTAL CONSIDERATIONS

APPARATUS

The experimental investigation was conducted in the Ames 1- by 3-foot supersonic wind tunnel No. 1. This tunnel is a closed-circuit variable-pressure tunnel in which the Reynolds number is changed by varying the total pressure within the approximate limits of one-fifth of an atmosphere to two atmospheres. Mach numbers between 1.2 and 2.5 are obtained by adjustment of the upper and lower flexible steel plates of the nozzle.

The model tested had a fineness-ratio-3, circular-arc, ogival nose tangent to a cylindrical afterbody 7.3 diameters long. A single row of 23 orifices extended longitudinally over both nose and afterbody. The model, which was constructed of steel, was sting supported from the rear and could be rotated 360° about its longitudinal axis by a mechanism operated from outside the tunnel. Pertinent model dimensions are shown in figure 1 (a).

Sketches of the pitot-survey rake and survey cone which were used to measure total pressures and local stream angles, respectively, are shown in figures 1 (b) and 1 (c). Photographs of the model and survey cone apparatus are presented in figures 1 (d) and 1 (e). The pitot-survey rake could be mounted on the body at various model length positions and could be rotated with the model about the model longitudinal axis. The survey cone was supported on a movable strut projecting from the steel side plate which replaced a tunnel window (fig. 1 (d)). The cone could be positioned laterally in the tunnel to within ±0.01 inch by the use of a hand crank and lateral position scale (fig. 1 (e)). In addition, the cone could be pitched about the lateral strut axis which passed midway between the top and bottom (downwash) orifices of the cone. The pitch angle could be set to within $\pm0.05°$.

Pressure leads from the body, pitot rake, and survey cone were connected to a liquid manometer system. The pressures were photographically recorded.

TESTS AND RESULTS

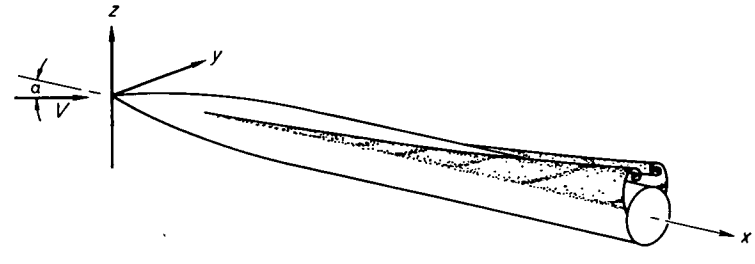
All data were obtained for a free-stream Mach number of 1.98. The model was tested at angles of attack of 5°, 10°, 15°, and 20° for a free-stream Reynolds number of 0.39×10^6 per inch and at an angle of attack of 15° for a Reynolds number of 0.13×10^6 per inch (Reynolds numbers of 0.44×10^6 and 0.15×10^6 based on body diameter). Circumferential pressure distributions were obtained by rotating the model through the desired range of circumferential angle (θ). At various model length stations (x/d) pitot-pressure distributions of the flow field were obtained also by rotating the model about its longitudinal axis.

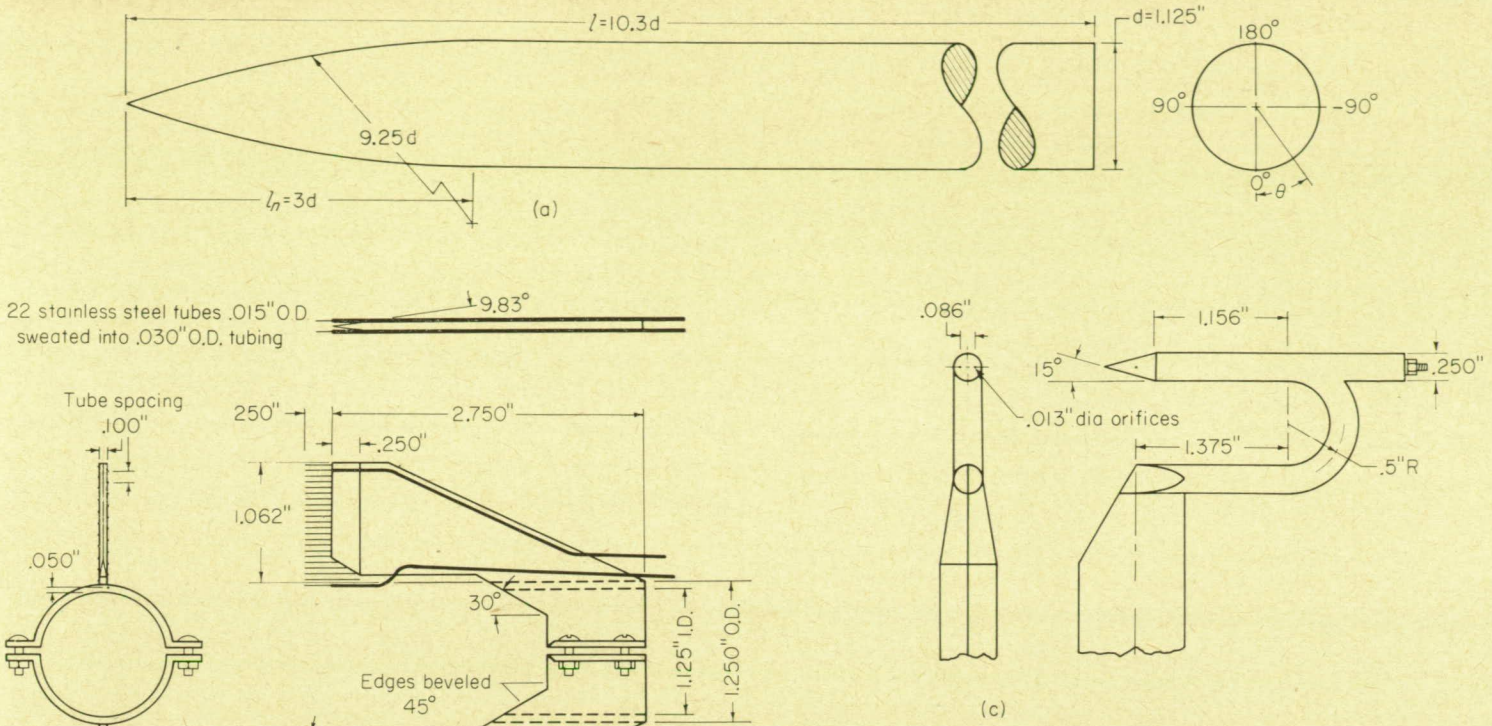
Downwash angle measurements were made along horizontal lines perpendicular to the model pitch plane and passing approximately through the vortex centers. The downwash angle surveys were made by the null-cone method in which the cone is pitched until the pressures measured at the top and bottom cone orifices indicate that the axis of the cone is alined with the local stream. The repeatability of the measurements was checked by making random reruns. Except at positions very close to the vortex centers where the induced velocity gradients were large, it was found that the downwash angles generally could be repeated to within $\pm0.2°$.

All of the pressure data for the model surface were reduced to coefficient form and are plotted in figures 2 through 6. (The data are tabulated in ref. 3.). The pitot-pressure data for the model flow field were reduced to the form of the ratio of local pitot pressure to free-stream total pressure, p_p/p_t. Contour plots of constant values of p_p/p_t are presented in figures 2 through 6. Downwash angles, measured in degrees with reference to the free-stream flow direction, are listed in tables I and II.

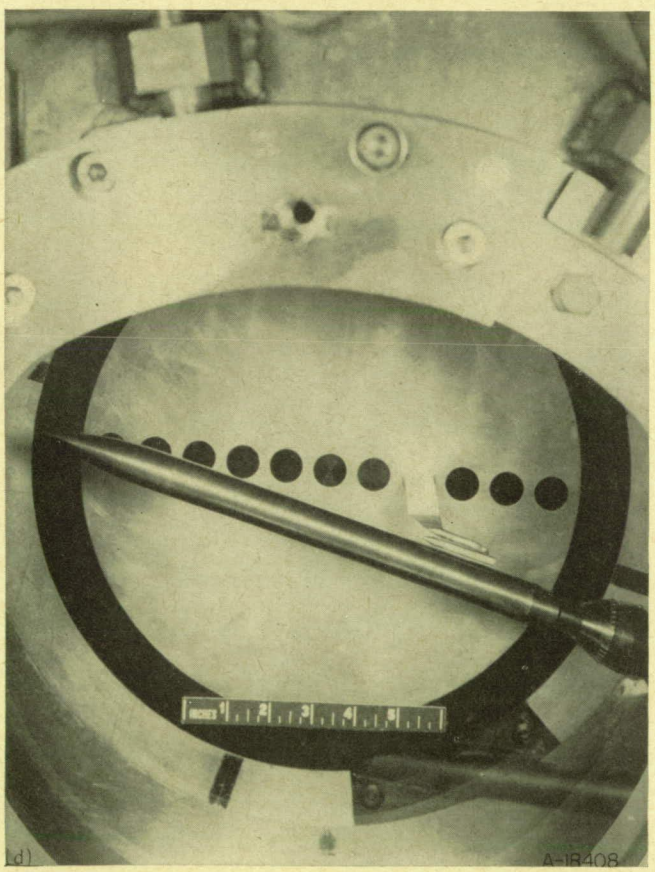
THEORETICAL CONSIDERATIONS

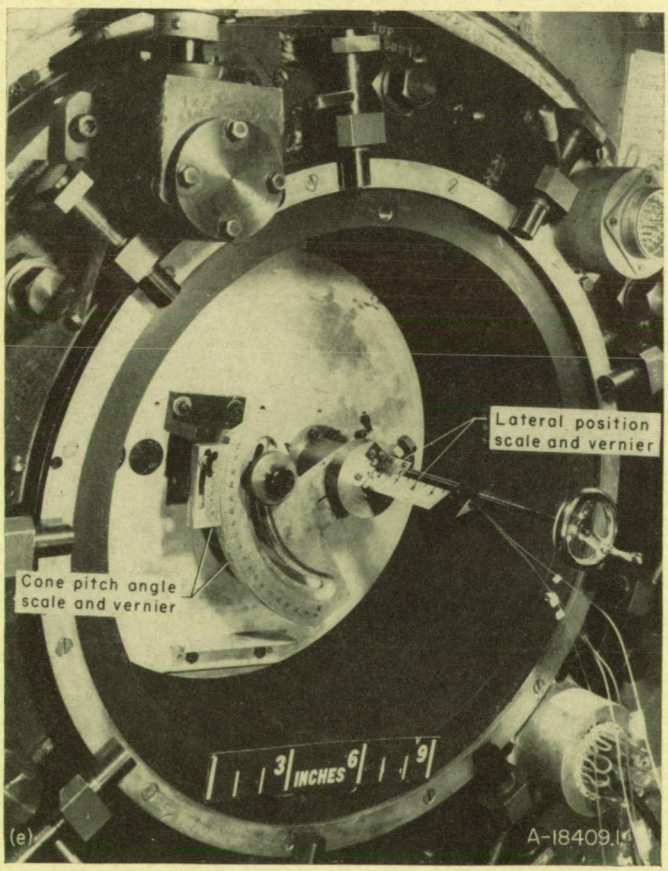
Calculation of the interference effects resulting from the vortices shed from a lifting body depends to a large extent upon an understanding of the manner in which the vorticity is discharged from the body and upon a satisfactory representation of the induced flow downstream of the body nose. From visual flow studies (e. g., ref. 4) it is known that the





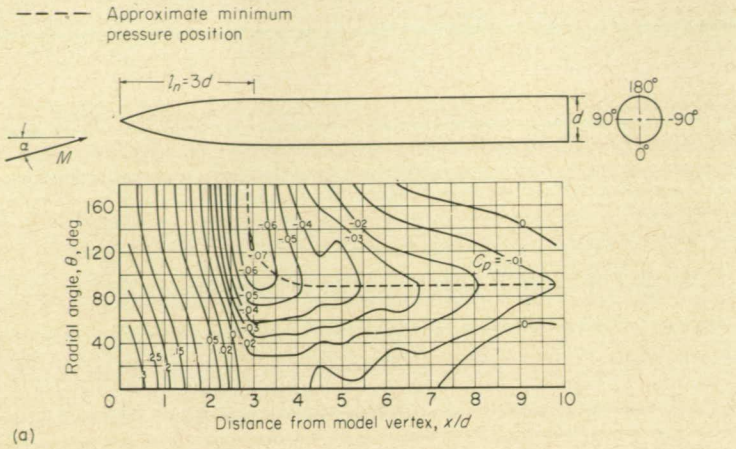
(a) Ogive-cylinder body.
(b) Pitot survey rake.
(c) Survey cone.

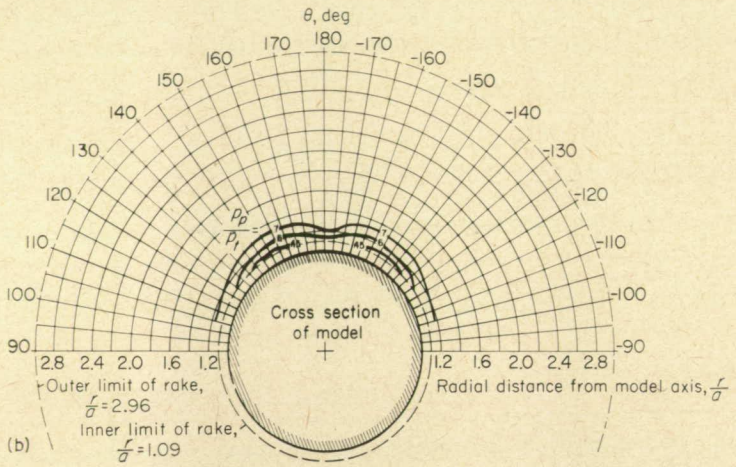


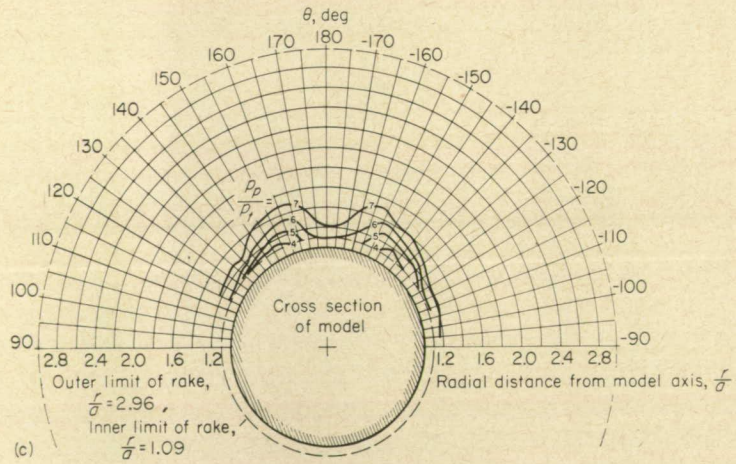


(d) Model and survey cone mounted in wind tunnel.
(e) Exterior view of side plate and cone survey apparatus.

FIGURE 1.—Model and survey apparatus.







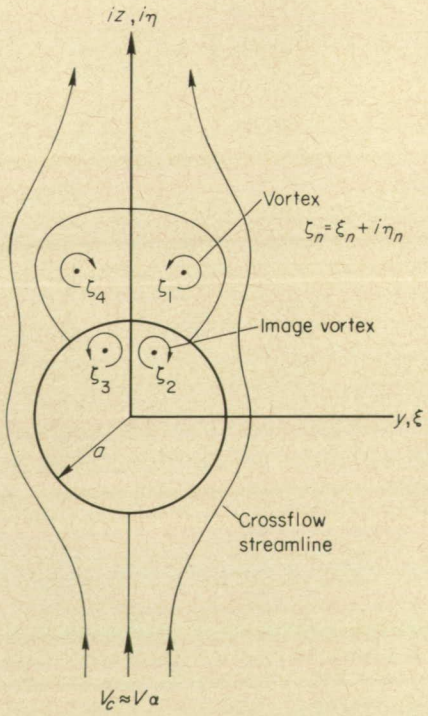
(a) Constant pressure-coefficient contours.
(b) Constant pitot-pressure ratio contours, $x/d=7.61$.
(c) Constant pitot-pressure ratio contours, $x/d=10.28$.

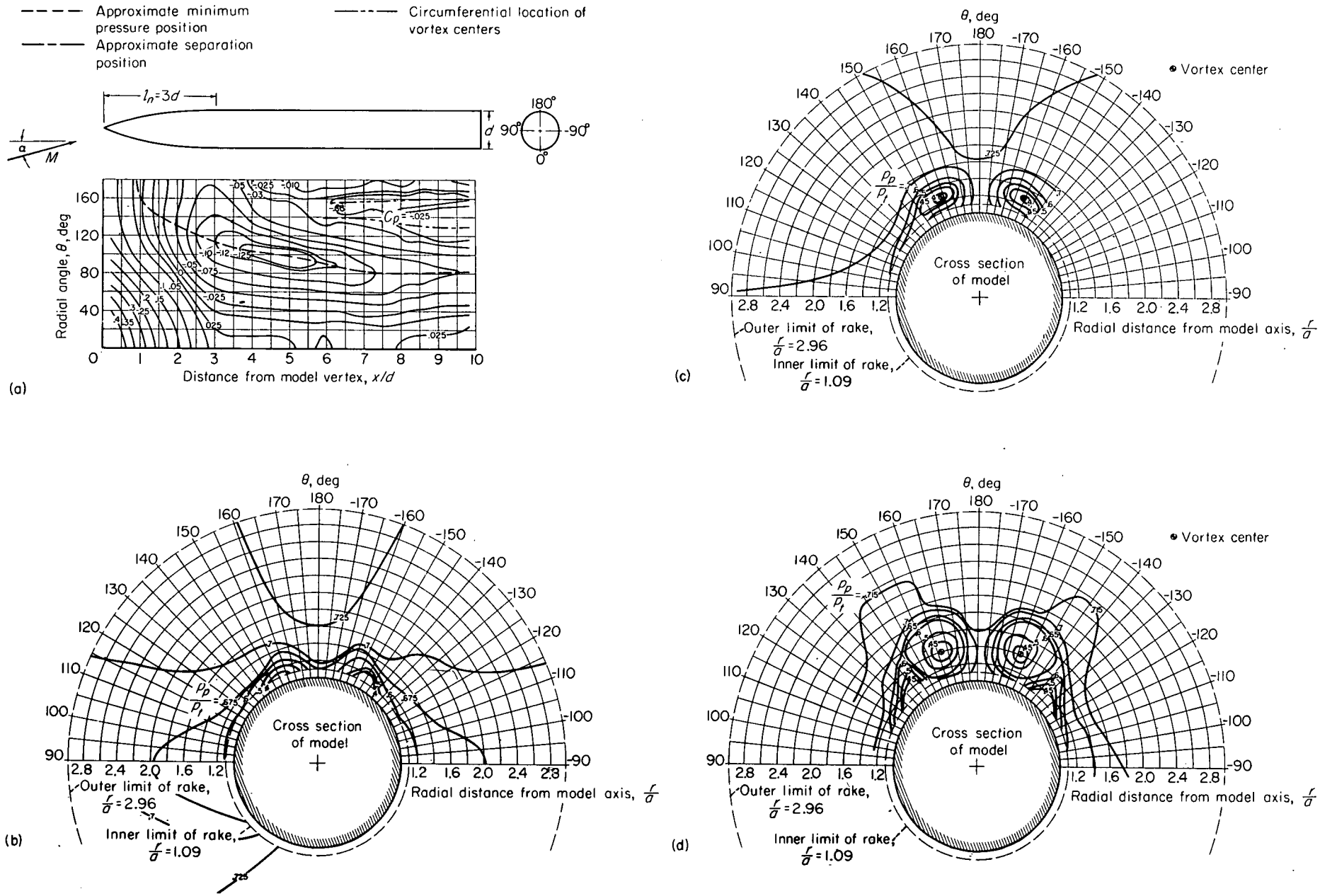
FIGURE 2.—Experimental contours of pressure coefficient on the body and pitot to free-stream total-pressure ratio in the flow field; $M=1.98$; $Re=0.39\times10^6$ per inch; $\alpha=5°$.

physical flow field for moderate angles of attack is approximately as indicated in the foregoing sketch. The vortex formation for the body is somewhat similar to that for the slender triangular plan-form wing considered by Brown and Michael (ref. 5). For both the body and the wing two spiral vortex sheets are produced, with flow separation occurring on the sides of the inclined body and on the leading edges of the wing. The sheets roll up to form two regions of concentrated vorticity. The large flow angles associated with these regions of vorticity are responsible for interference effects. The complex nature of the actual flow precludes an exact representation of the three-dimensional flow field; hence, a simplified model of the real flow must be chosen for study. In this section of the report expressions for the flow about a simple theoretical model are presented.

THEORETICAL MODEL AND BASIC FORMULAE FOR POTENTIAL AND VELOCITIES IN THE FLOW FIELD

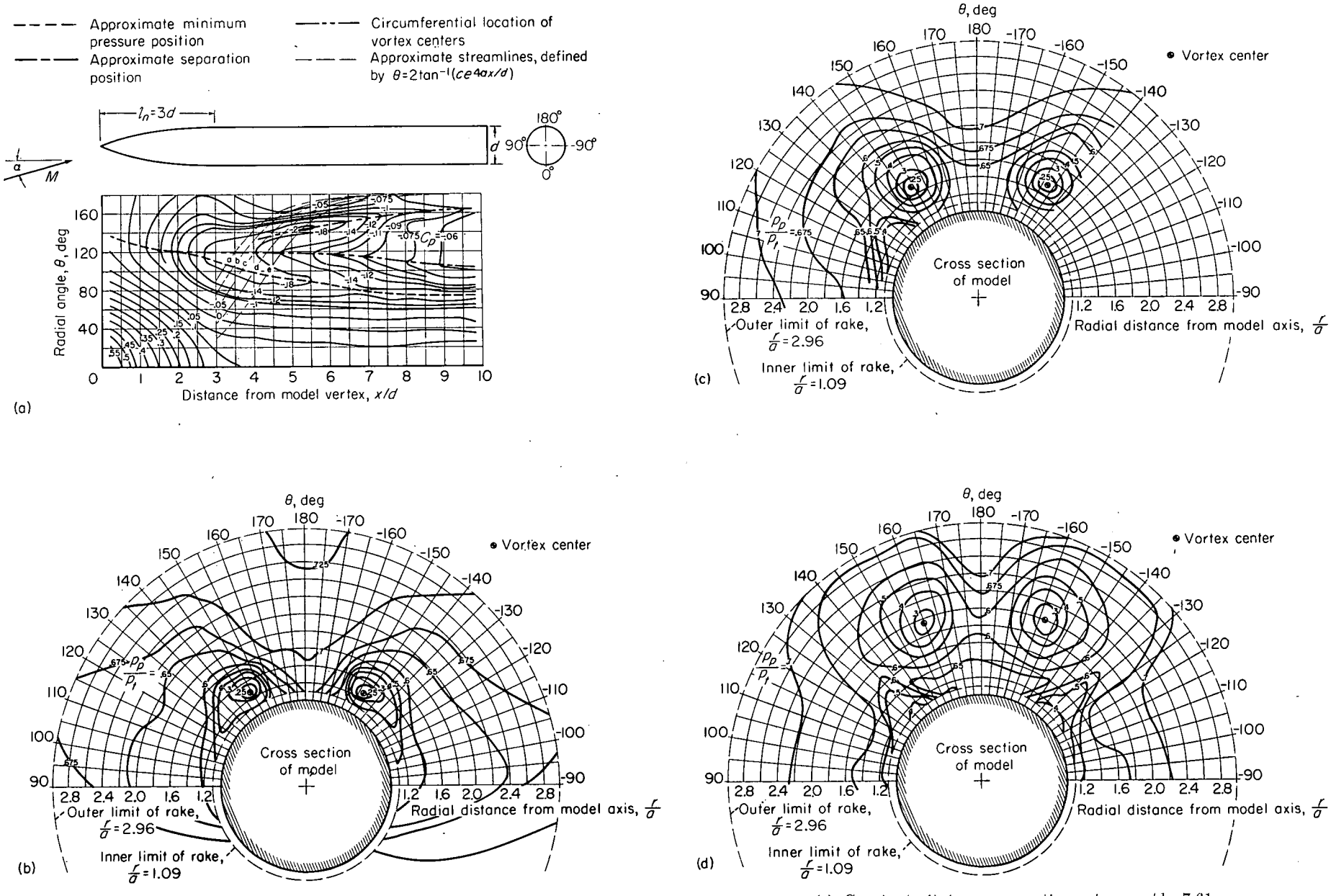
The assumption of slender-body theory that the flow is independent of Mach number is made. It is assumed that the induced flow field in any crossflow plane along the cylindrical afterbody can be adequately represented as the steady two-dimensional, incompressible potential flow around a circular cylinder in the presence of two symmetrical vortices of equal strength. This representation in a crossflow plane is shown in the following sketch. All of the vorticity is considered to be concentrated in the two external vortices, the effects of the feeding vortex sheets being omitted. In addition, it is assumed that the vortices need be considered only at positions downstream of the nose-cylinder junction. The boundary condition of tangential flow at the body surface is satisfied by placing image vortices within the body at the appropriate positions.





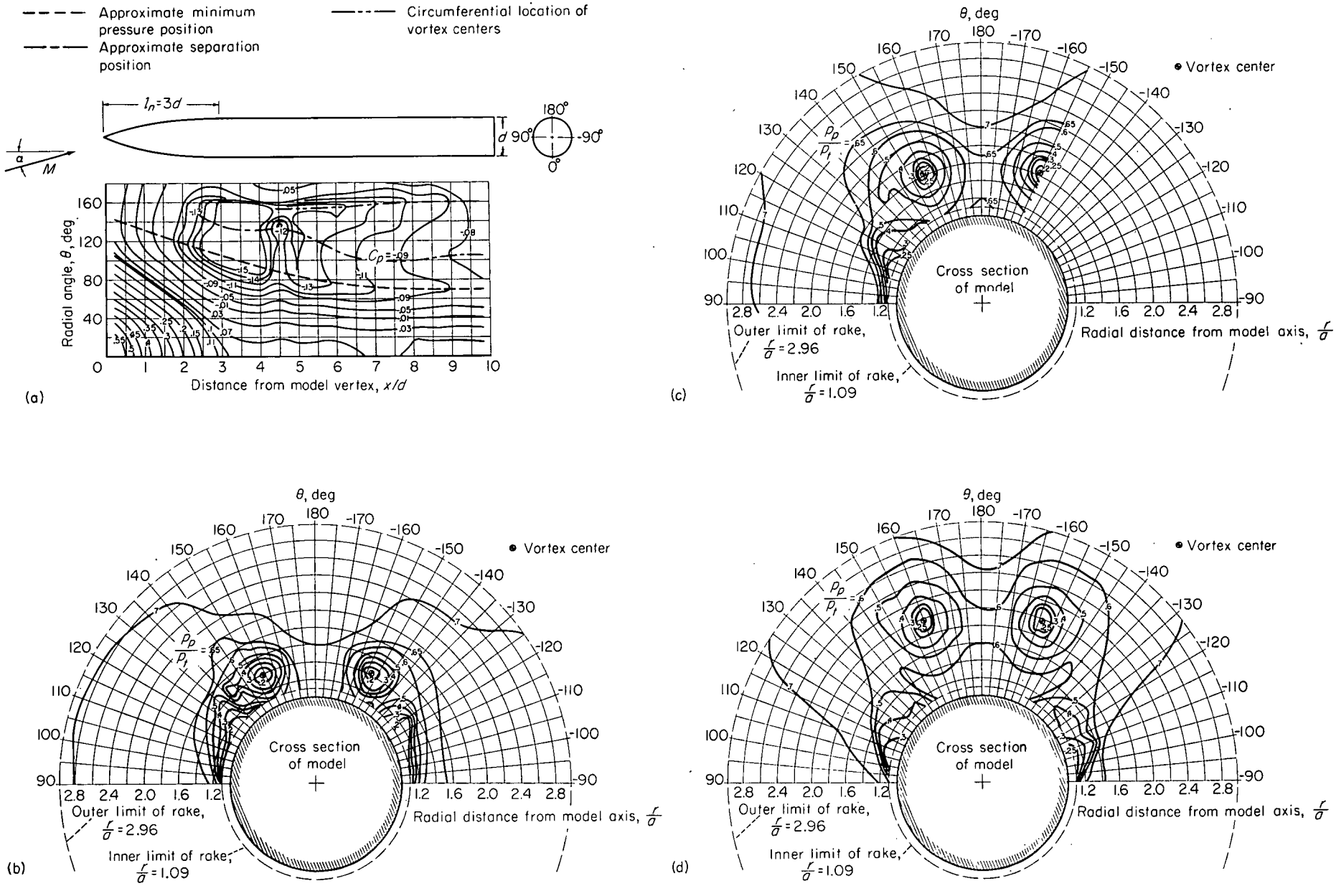
(a) Constant pressure-coefficient contours.
(b) Constant pitot-pressure ratio contours, $x/d=5.83$.
(c) Constant pitot-pressure ratio contours, $x/d=7.61$.
(d) Constant pitot-pressure ratio contours, $x/d=10.28$.

FIGURE 3.—Experimental contours of pressure coefficient on the body and pitot to free-stream total-pressure ratio in the flow field; $M=1.98$; $Re=0.39\times10^6$ per inch; $\alpha=10°$.



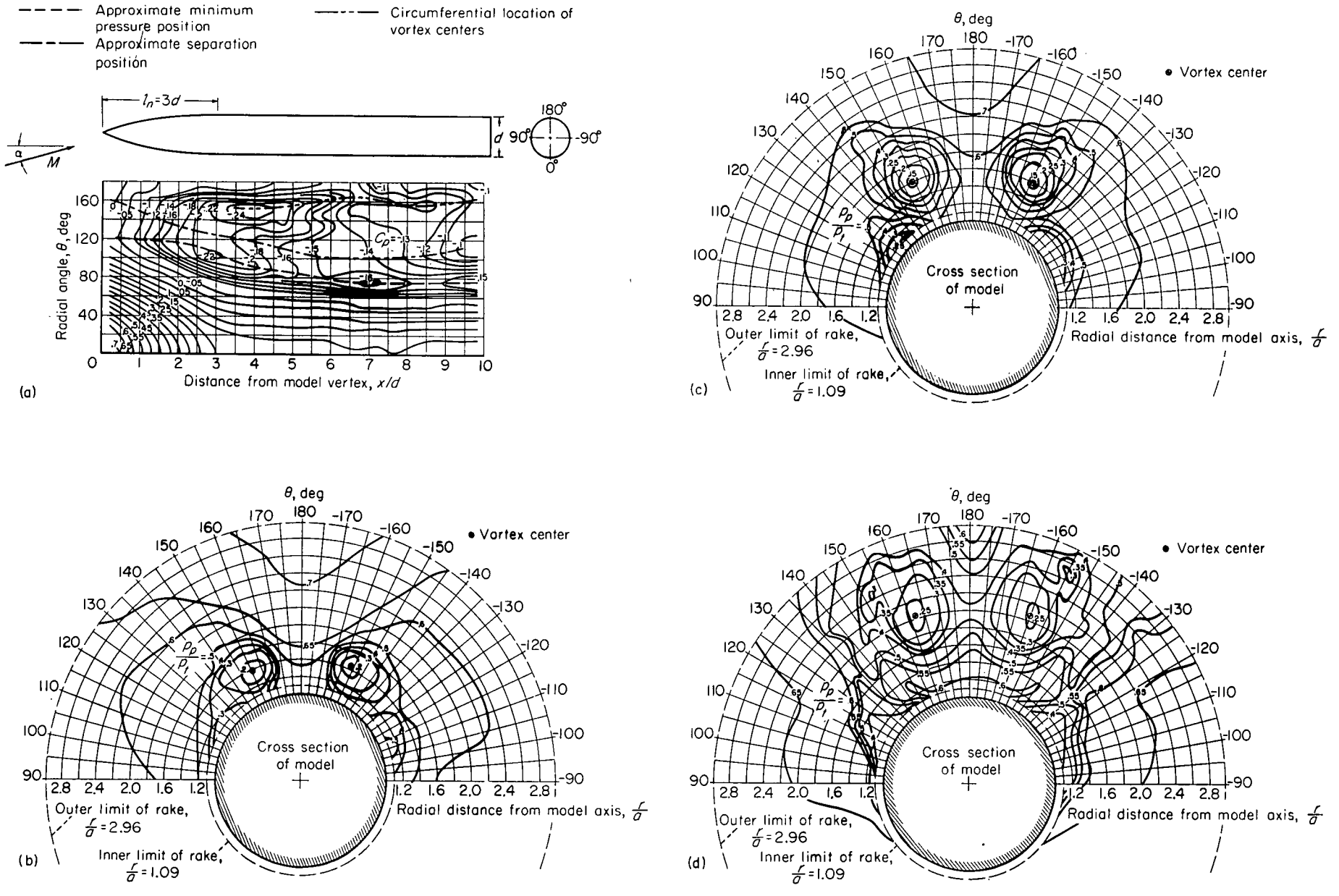
(a) Constant pressure-coefficient contours.
(b) Constant pitot-pressure ratio contours, $x/d=5.83$.
(c) Constant pitot-pressure ratio contours, $x/d=7.61$.
(d) Constant pitot-pressure ratio contours, $x/d=10.28$.

FIGURE 4.—Experimental contours of pressure coefficient on the body and pitot to free-stream total-pressure ratio in the flow field; $M=1.98$; $Re=0.39\times10^6$ per inch; $\alpha=15°$.



(a) Constant pressure-coefficient contours.
(b) Constant pitot-pressure ratio contours, $x/d=5.83$.
(c) Constant pitot-pressure ratio contours, $x/d=7.61$.
(d) Constant pitot-pressure ratio contours, $x/d=10.28$.

FIGURE 5.—Experimental contours of pressure coefficient on the body and pitot to free-stream total-pressure ratio in the flow field; $M=1.98$; $Re=0.13\times10^6$ per inch; $\alpha=15°$.



(a) Constant pressure-coefficient contours.
(b) Constant pitot-pressure ratio contours, $x/d=4.50$.
(c) Constant pitot-pressure ratio contours, $x/d=5.83$.
(d) Constant pitot-pressure ratio contours, $x/d=10.28$.

FIGURE 6.—Experimental contours of pressure coefficient on the body and pitot to free-stream total-pressure ratio in the flow field; $M=1.98$; $Re=0.39\times10^6$ per inch; $\alpha=20°$.

The complex potential equation for the crossflow is

$$\varphi+i\psi=-V_c i\left(s-\frac{a^2}{s}\right)-\frac{i\Gamma}{2\pi}\,ln\,\frac{(s-\zeta_1)(s-\zeta_3)}{(s-\zeta_2)(s-\zeta_4)} \tag{1}$$

where $|\Gamma|$ is the magnitude of the strength of each vortex; $s=y+iz$ is the position of a point in the field; and ζ_1, ζ_2, ζ_3, and ζ_4 are the positions of the real and image vortices, with $\zeta_n=\xi_n+i\eta_n$. Resulting expressions from which the velocities induced at any position (y, z) can be calculated are as follows:

$$w=V_c\left[1+\frac{a^2(y^2-z^2)}{(y^2+z^2)^2}\right]-\frac{\Gamma}{2\pi}\sum_{n=1}^{n=4}(-1)^n\left[\frac{y-\xi_n}{(z-\eta_n)^2+(y-\xi_n)^2}\right] \tag{2}$$

$$v=-\frac{2V_c a^2yz}{(y^2+z^2)^2}+\frac{\Gamma}{2\pi}\sum_{n=1}^{n=4}(-1)^n\left[\frac{z-\eta_n}{(z-\eta_n)^2+(y-\xi_n)^2}\right] \tag{3}$$

where

$$V_c\approx V\alpha$$

$$\xi_4=-\xi_1$$

$$\xi_3=-\xi_2=-\frac{a^2\xi_1}{\xi_1^2+\eta_1^2}$$

$$\eta_4=\eta_1$$

and

$$\eta_3=\eta_2=\frac{a^2\eta_1}{\xi_1^2+\eta_1^2}$$

Downwash and sidewash angles (with respect to the free-stream direction) are then given approximately by $\epsilon\approx\alpha-(w/V)$ and $\sigma\approx(v/V)$.

VELOCITY RELATIONSHIPS WITH VISCOUS VORTICES

Because of the effects of viscosity, downwash and sidewash distributions computed by equations (2) and (3) cannot be expected to agree closely with experiment near to and at the vortex centers. It is likely, however, that the agreement of theory with experiment can be improved by substituting theoretical viscous vortices for potential vortices in the flow field. For a single isolated viscous vortex it has been shown (ref. 6, p. 592) that the velocity varies according to the expression,

$$V_r=\frac{\Gamma}{2\pi r_v}\,(1-e^{-r_v^2/4\nu t}) \tag{4}$$

where

$$V_r=\sqrt{v^2+w^2}$$

$$r_v=\sqrt{(z-\eta)^2+(y-\xi)^2}$$

ν=kinematic viscosity

and

t=time of vortex growth

What is assumed to be a viscous vortex is, in essence, a vortex having a "solid" core with potential outer flow joined by a transition region. In this transition region, at some radial distance, r_*, from the vortex center the velocity reaches a maximum. Using equation (4) it can be shown (see, e. g., ref. 7) that r_* can be expressed as a simple function of time, t, by

$$r_*=2.24(\nu t)^{1/2} \tag{5}$$

In this report r_* is assumed to be the core radius of the viscous vortex.

For the complete flow field, if it is assumed that both the real and image vortices have core radii which are equal in magnitude, then approximate formulae for induced velocities in the field can be written as follows:

$$w=V_c\left[1+\frac{a^2(y^2-z^2)}{(y^2+z^2)^2}\right]-\frac{\Gamma}{2\pi}\sum_{n=4}^{n=1}(-1)^n\left[\frac{y-\xi_n}{(z-\eta_n)^2+(y-\xi_n)^2}\right](1-e^B) \tag{6}$$

$$v=-\frac{2V_c a^2yz}{(y^2+z^2)^2}+\frac{\Gamma}{2\pi}\sum_{n=1}^{n=4}(-1)^n\left[\frac{z-\eta_n}{(z-\eta_n)^2+(y-\xi_n)^2}\right](1-e^B) \tag{7}$$

where

$$B=-1.254(1/r_*)^2[(z-\eta_n)^2+(y-\xi_n)^2]$$

It is of note that these formulae, due to the linear superposition of a viscous onto a potential flow system, are not mathematically rigorous and do not satisfy the body boundary condition of zero normal velocity for all values of θ in the crossflow plane. However, at least for positions through and in the vicinity of the vortices, their use can be justified on the basis of good agreement between computed and experimental downwash distributions (discussed later in the report).

VORTEX STRENGTHS, ORIGINS, AND PATHS

Vortex strengths.—For a theoretical model in which two symmetrical vortices originate on and remain in the presence of an infinitely long circular cylinder, the strength of the vortices at a given station, x, can be related to the normal force on the portion of the cylinder between the origin of the vortices and station x by the Kutta-Joukowsky law (see, e. g., ref. 8). Thus,

$$(N_{cyl})_x=\rho\Gamma_x V(2\xi_1-2\xi_2)_x \tag{8}$$

For the considered theoretical model, which includes a slender ogival nose with a pair of symmetrical vortices originating on the cylinder or at the nose-cylinder junction, the total normal force at a given x station can be approximated by

$$N_x=(N_{cyl})_x+N_{nose}=\rho\Gamma_x V(2\xi_1-2\xi_2)_x+2\alpha qA \tag{9}$$

Thus,

$$\left(\frac{\Gamma}{V}\right)_x=\frac{(C_{N_x}-2\alpha)A}{4(\xi_1-\xi_2)_x} \tag{10}$$

where C_{N_x} is the coefficient of the total normal force developed from the nose vertex to the body-length station considered. The normal-force coefficient for the nose portion of the body is the slender-body result of $C_N=2\alpha$. For this theoretical model any so-called "lift carry-over" from the nose onto the cylinder is neglected. The lift on the cylinder is considered to be only that resulting from the motion of the vortices relative to the cylinder (the slender-body value of lift being zero over the cylinder). Experimental data (ref. 3), however, indicate that, even for the body at low angles of attack (of the order of 5°), there is a moderate

amount of lift carry-over from the nose onto the cylinder. Studies of these data have shown that this lift carry-over can be accounted for, at least in part, by the use of Tsien's potential theory (ref. 9). Hence, a preferred hybrid expression relating vortex strength and position to normal-force coefficient can be written as

$$\left(\frac{\Gamma}{V}\right)_x=\frac{(C_N-C_{N_p})_x A}{4(\xi_1-\xi_2)_x} \tag{11}$$

where C_{N_p} is the normal-force coefficient computed by Tsien's theory. The use of equation (10) or (11) is, of course, tantamount to assuming that only the so-called viscous crossflow component of the body normal force contributes to the vortex strength.

Vortex origins.—No theoretical procedure is known for predicting the positions of the origins of the vortices (that is, the positions at which the vortices leave the body surface). Qualitatively it is known that, as the angle of attack of the body is increased, the boundary layer first begins to thicken on the downstream lee side. This is followed by separation of the boundary layer and formation of two regions of concentrated vorticity in the wake on the lee side of the body. Moore (ref. 10) has studied the three-dimensional boundary-layer flow on inclined cones and has found that on the lee side of the cone, unique solutions to the classical boundary-layer-flow equations are limited to small angles of attack. Beyond a certain critical angle of attack, dependent on Mach number and cone angle, the boundary layer cannot remain thin. The critical angle of attack is of the same order as the semivertex angle of the cone. Moore presumes that, for angles of attack in excess of this critical value, the flat vortex bubbles which have formed on the lee side of the cone must be in the process of forming a symmetric pair of strong vortices. Similar considerations probably apply for the flow about inclined bodies other than cones. Consideration of pressure distributions along streamlines on an inclined cylinder indicate that, because of the adverse pressure gradient, there is a tendency toward separation and formation of a vortex bubble even at very low angles of attack. However, as yet there is no method for calculating the position on an inclined body at which coalescence of the vorticity has progressed to such a degree that a symmetric pair of steady vortices are formed. Hence, experimental measurements (some of which are presented in this report) must be relied upon entirely.

Vortex paths.—With the aid of equations (2) and (3) the paths of the vortex centers can be computed by stepwise procedures if the origins and strengths of the vortices are known. For example, if a vortex position (ξ,η) and strength (Γ/V) are known, values of w/V and v/V induced at the filament of the vortex can be computed by equations (2) and (3).[2] If in a given time interval Δt the vortex filament can be considered to move (with respect to the body) an axial distance $\Delta\mu\approx V\Delta t$, a vertical distance $\Delta\eta=w\Delta t$, and a lateral distance $\Delta\xi=v\Delta t$; then,

$$\Delta\eta\approx\Delta\mu(w/V) \tag{12}$$

and

$$\Delta\xi\approx\Delta\mu(v/V) \tag{13}$$

Hence, for a small incremental distance $\Delta\mu$, a new vortex center position can be estimated by the use of equations (12) and (13). Then if the strength of the vortex is known at this new body length station and at succeeding stations, this computation process may be repeated a sufficient number of times to determine the path. If the normal-force distribution over the body is known,[3] the vortex strength at each $\Delta\mu$ interval can be estimated by equation (11). The proper spacing $\Delta\mu$ of successive stations should be, of course, checked by trial and error. For the stepwise calculations made for this investigation the experimental normal-force distributions of reference 3 have been used.

DISCUSSION

In this section of the report the pressure distribution and pitot-pressure data are used to illustrate the flow conditions on the body which lead to the formation of the vortices and to isolate the positions along the body at which the vorticity is concentrated into two well-defined vortex centers. As an aid in assessing the usefulness of the simple theoretical flow model previously outlined, comparisons of computed vortex paths and downwash distributions are made with the results of the experimental measurements.

EXPERIMENTAL PRESSURE DISTRIBUTIONS AND VORTEX POSITIONS

From a study of the pressure distributions on the surface of the body and pitot-pressure distributions in the flow field on the lee side of the body, the positions at which the body vortices originated and the paths of the vortices downstream from the origin can be determined. The body pressure distribution data and the pitot-tube survey data have been plotted in figures 2 through 6 to show constant pressure contours for each of the test conditions.[4] On the contour plots of body pressure coefficient, lines are shown to indicate the circumferential positions of minimum pressure coefficient (C_p minimum with respect to θ), the approximate flow-separation positions, and the circumferential locations of the vortex centers. The minimum pressure positions, of course, are obvious. The flow-separation and vortex-center positions will be discussed in the following paragraphs.

The pitot-pressure plots are very useful for determining the positions of the vortex centers. The vortex center positions, indicated in figures 3 through 6, are assumed to be at the approximate centers of the smallest closed contours of p_p/p_t. It is interesting to note that these positions, when superimposed on schlieren photographs of the flow field taken with the knife edge horizontal, coincide with the inner edges of the dark vortex regions. (See, e. g., fig. 7.)

The conditions leading to flow separation and subsequent formation of the vortices are perhaps best illustrated by typical pressure distributions along approximate streamlines

[2] The more complex expressions, equations (6) and (7), also can be used; however, essentially the same results are obtained with equations (2) and (3).

[3] If the normal-force distribution is not known from experiment it can sometimes be computed by a semiempirical method (see, e. g., ref. 3).

[4] Since the pitot-pressure tubes were always alined with the body axis and not with the local stream direction, some of the indicated loss in pitot pressure results from the large inclination of the stream relative to the axes of the tubes.

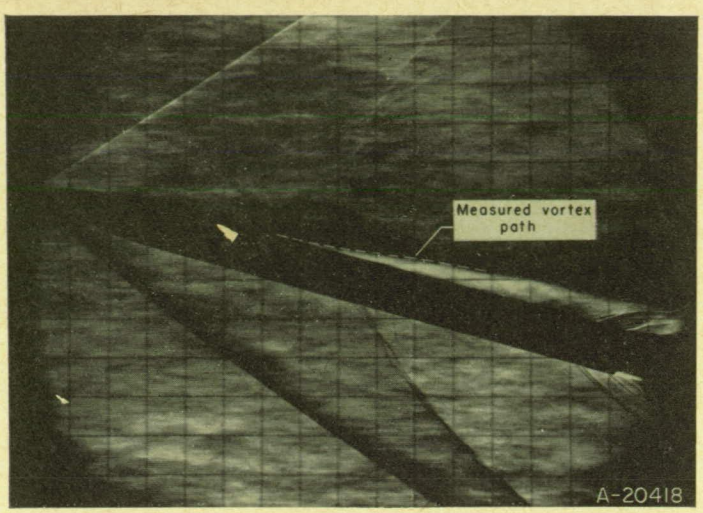


FIGURE 7.—Typical schlieren photograph of flow field with superimposed vortex path as measured from pitot-rake surveys; $\alpha=15°$; $Re=0.39\times10^6$ per inch; $M=1.98$.

on the cylindrical afterbody (fig. 4).[5] For $\alpha=15°$ and $Re=0.39\times10^6$ per inch, pressure distributions along the streamlines shown in figure 4 are plotted in figure 8. Along the streamlines the pressure decreases rapidly proceeding from the windward toward the leeward side of the body. A minimum pressure is reached near the side of the body. This is followed by a rising pressure (adverse pressure gradient) and eventual flow separation. The flow separation position is assumed to coincide with the point at which the pressure then begins to decrease. Following flow separation a second minimum pressure occurs (except for streamline *a*) at the approximate circumferential location of the vortex center. (Although the identity of the individual streamlines is lost beyond the flow separation point, these plots have been continued by dashed lines into the separated flow region to show the influence on the pressure distributions of the secondary flow associated with the vortices.)

From a study of the differences between the pressure distributions along the various streamlines coupled with a study of the pitot-pressure plots for various x/d positions, the approximate region of the origin of the vortices can be determined. For instance, for the pressure distribution along the streamline labeled "a" there is no clear indication of flow separation, nor is there any second minimum pressure that has been associated with the location of the vortex core. However, along the streamline labeled "b" there is an indication of a vortex forming at an x/d position of about 4. Since the pitot survey data (fig. 4) show that the vortices are clearly developed at $x/d=5.8$, it is reasonable to assume that the vortices originated at about 4 or 5 diameters from the nose. From similar studies of the data for the other angles of attack (5°, 10°, and 20°) additional information concerning the approximate origin of the vortices has been determined. In figure 9 the approximate length positions at which the effects of the vortices were first discernible in the pressure distributions are plotted as a function of angle of attack.

A considerable effect of Reynolds number upon the flow about the inclined body of this investigation was previously reported in reference 3. The changes in the pressure distribution and flow-separation characteristics at $\alpha=15°$ for an increase in Reynolds number from 0.13×10^6 to 0.39×10^6 per inch can be seen by comparing figures 5 and 4. Although there is a significant effect upon the pressure distributions, comparison of corresponding pitot-pressure plots reveal only a small effect upon the vortex positions. For the lower Reynolds number tests the positions of the vortex centers at $x/d=5.8$ were approximately 0.1 body radius farther from the body surface and about 5° closer to the vertical plane of symmetry than for the higher Reynolds number. At the base of the body, $x/d=10.3$, the locations

[5] These streamlines, which were derived simply from consideration of incompressible potential flow over an inclined circular cylinder (with no vortices considered), are defined by $\theta=2\tan^{-1}(ce^{i\alpha z/d})$.

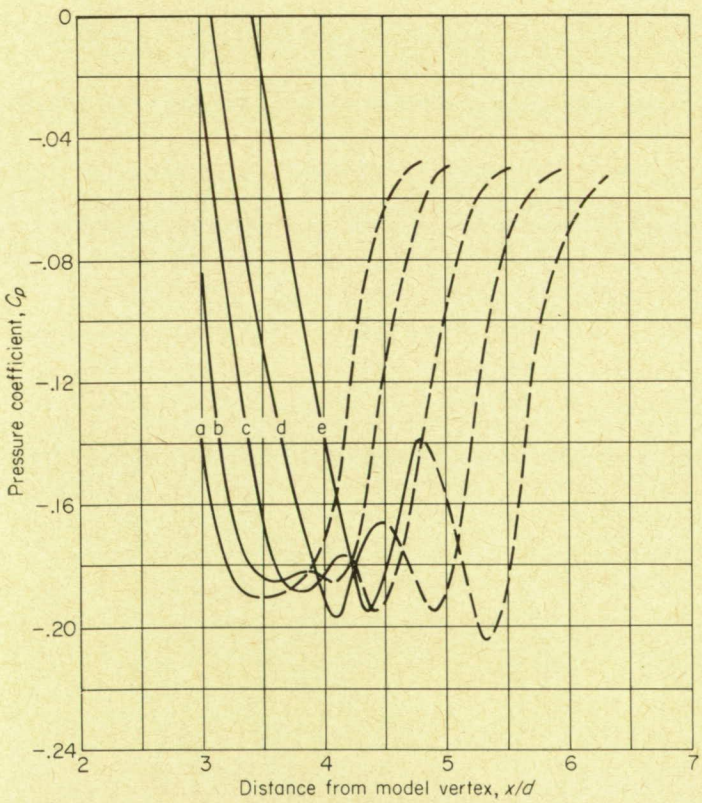


FIGURE 8.—Pressure distributions along the streamlines shown in figure 4; $M=1.98$; $Re=0.39\times10^6$ per inch; $\alpha=15$.

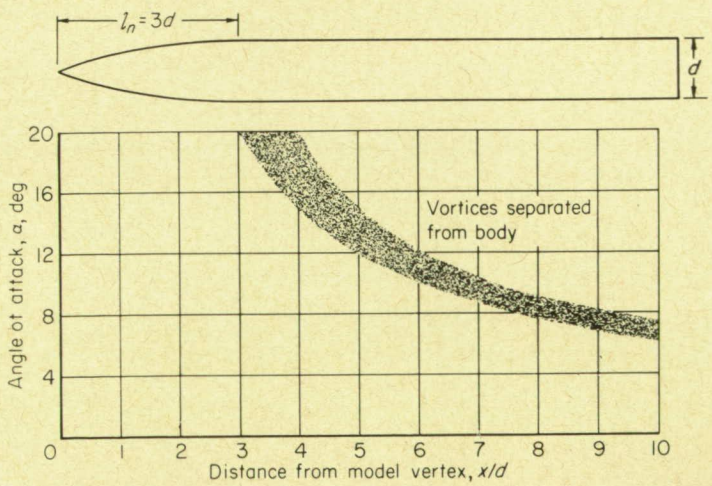
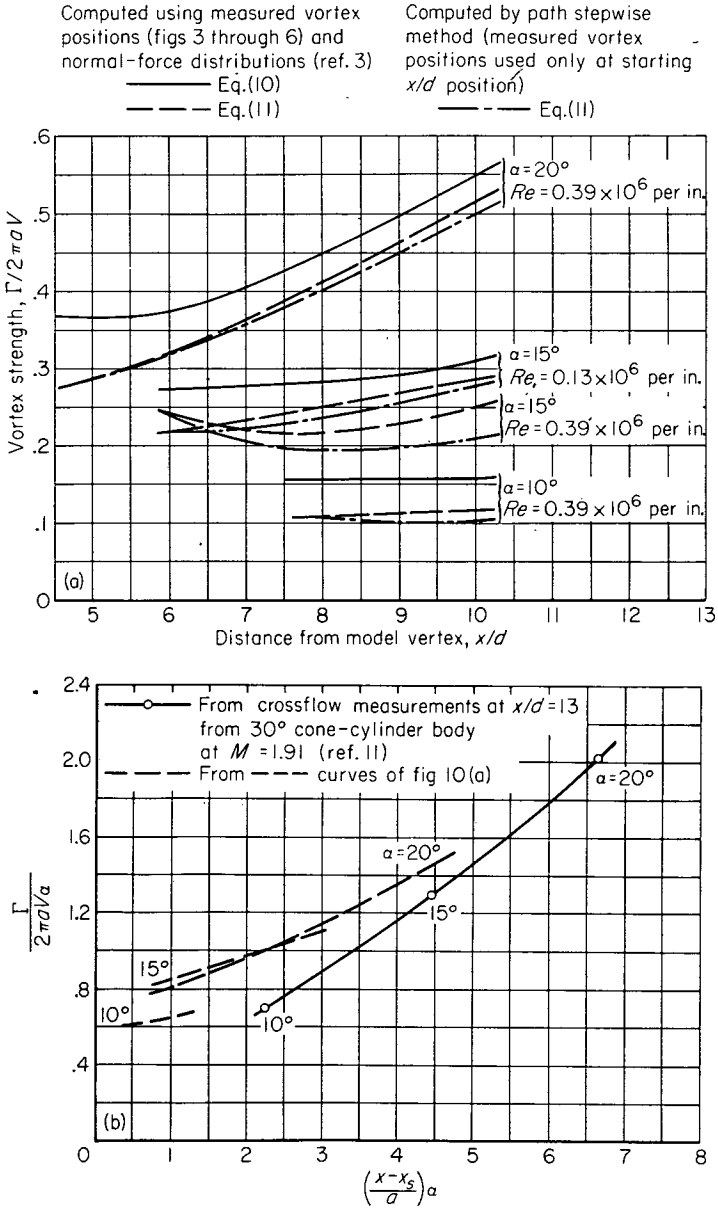


FIGURE 9.—Approximate body length positions at weich vortices separated frombody; $M=1.198$.

of the vortices were practically identical for both Reynolds numbers.

VORTEX STRENGTHS COMPUTED FROM EXPERIMENT

To provide values of vortex strength to aid in assessing the methods of computing the vortex paths and the downwash distributions, the strengths of the vortices at various body length positions have been computed by equations (10) and (11). They are presented nondimensionally in figure 10 (a) as $\Gamma/2\pi aV$ as a function of x/d. The calculations have been made using the experimental normal-force distributions of reference 3 with both measured and computed vortex positions taken at various body length stations. The measured vortex positions were obtained from figures 3 through 6. Where the vortices are shown to be slightly asymmetric, average values of the positions have been used. The strengths obtained using computed vortex positions (discussed later) result from application of the stepwise path calculation method previously outlined. In general, the strengths of the vortices would be expected to increase with distance downstream. It is believed that the small decreases in some of the computed vortex strengths with distance downstream are a result of approximations in the methods used and do not actually exist.



(a) Vortex strengths computed from measured vortex positions and normal-force distributions; $M=1.98$.

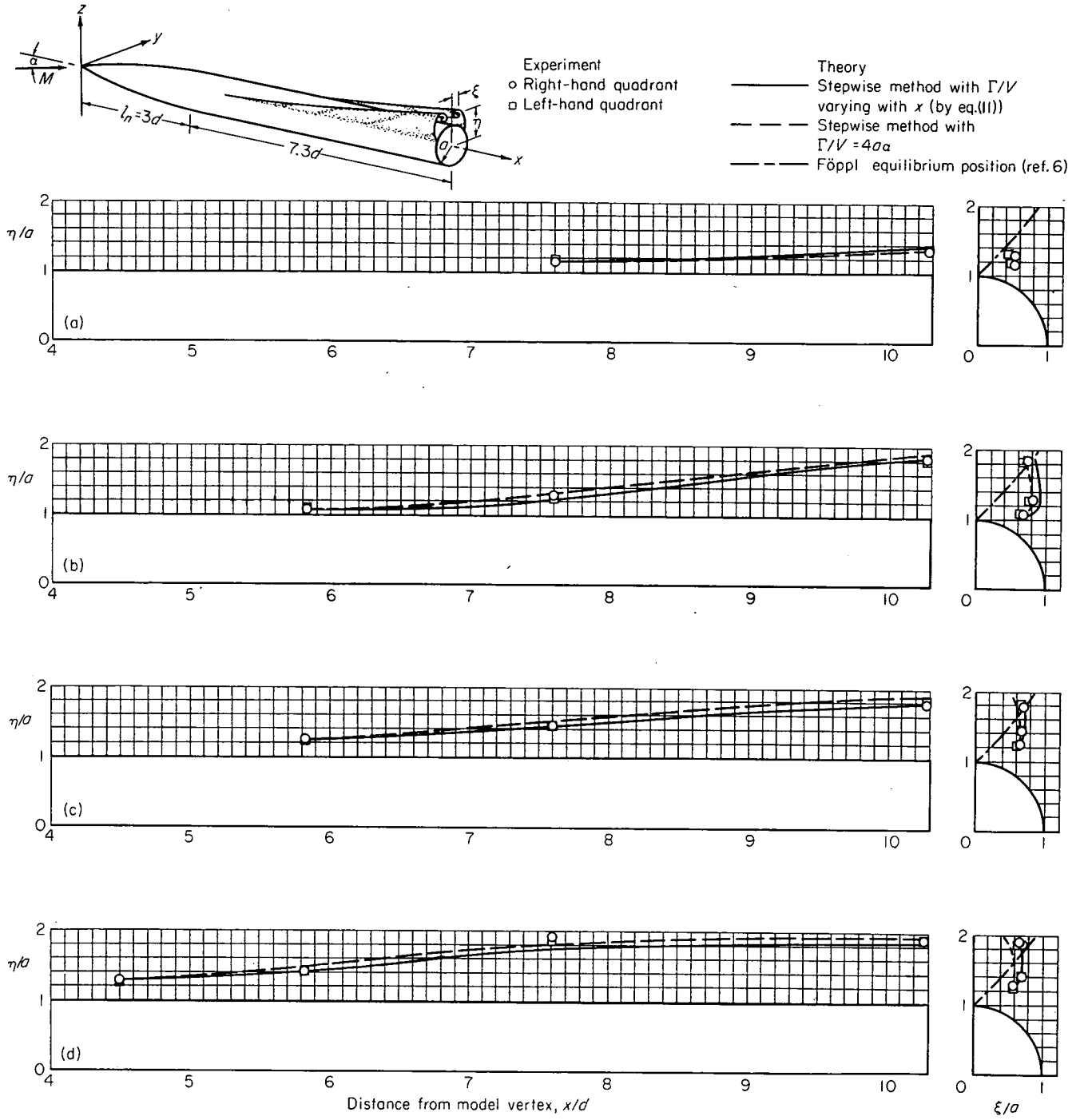
(b) Correlation and comparison of vortex strengths.

FIGURE 10.—Vortex strengths computed from experiment.

The data of figure 10 (a) have been replotted in figure 10 (b) with the vortex strength parameter $\Gamma/2\pi aV\alpha$ as a function of the quantity $(x-x_s)\alpha/a$. Also included in figure 10 (b) are vortex strengths computed from crossflow measurements around a cone-cylinder body at $\alpha=10°$, 15°, and 20° (ref. 11). The vortex strengths for the cone cylinder were determined by Raney (ref. 11) through adjusting theoretical crossflow velocities to match measured ones. As shown in figure 9, the precise location of the separation position x_s is not known. It lies within a band of about one diameter width. For the correlations in figure 10 (b), values of x_s were taken from figure 9, a mean position through the uncertainty band being assumed. Values of x_s for the ogive-cylinder body were used to correlate the data for the cone-cylinder body. For small values of $(x-x_s)\alpha/a$, the differences between the vortex strengths for the two bodies are appreciable. However, for larger values of the parameter where body vortex effects on stability are most important, the differences are not large. In reference 2 these strengths have been used in successfully predicting the effect of body vortices on the pitching moments of high-tail airplanes.

COMPARISONS OF THEORETICAL AND EXPERIMENTAL VORTEX PATHS

Theoretical and experimental vortex path positions are compared in figure 11. The experimental positions were taken from the pitot-pressure contour plots (figs. 3 through 6). The theoretical path positions were computed by the stepwise method (previously outlined) in which the vortex strength is computed by equation (11) and varies with distance x downstream (as shown in fig. 10 (a)). In addition, calculations were made by the stepwise procedure but with the vortex strength held constant over the path length and given by $\Gamma/V=4a\alpha$, an assumed relation to be mentioned later. The Föppl equilibrium positions for vortices in the crossflow plane of a two-dimensional cylinder (ref. 6, p. 223) are also presented in figure 11 merely for reference. All stepwise path calculations were started at the most forward body length positions at which pitot-pressure surveys revealed the presence of well-defined vortices. Incremental length spacings ($\Delta\mu$'s) of 25 percent of the body radius were used, although $\Delta\mu$'s of 50 percent of the radius were found to be satisfactory. For the stepwise method in which Γ/V varies with x, the initial vortex strengths at the starting positions were assumed to be the same as those computed using the measured vortex positions of this investigation and the normal-force distributions in figure 8 of reference 3. In general, the paths computed by this method are in very good agreement with experiment. However, for $\alpha=15°$ and $Re=0.39\times10^6$ per inch, it appears that the initial vortex strength calculated from experiment is too large, and as a result the computed vortex position initially moves too far in the ξ direction and not far enough in the η direction (as shown in the end view of fig. 11 (b)). However, with increase in



(a) $\alpha=10°$, $Re=0.39\times10^6$ per inch.
(b) $\alpha=15°$, $Re=0.39\times10^6$ per inch.
(c) $\alpha=15°$, $Re=0.13\times10^6$ per inch.
(d) $\alpha=20°$, $Re=0.39\times10^6$ per inch.

FIGURE 11.—Comparisons of computed and experimental vortex center positions; $M=1.98$.

distance downstream the strength computed by the stepwise method decreases at a sufficient rate (see fig. 10 (a)) so that the computed path agrees reasonably well with experiment even though the initial vortex strength seems much too large. For the other test conditions the initial strengths seem to be about right, and the agreement between the computed and measured path positions is very good.

Further investigation into the computation of the paths revealed that the vortex strengths only had to be approximated in order to compute the paths reasonably well. In fact, it was found that the strengths could be assumed to remain constant over the path lengths for each angle of attack. For example, at all α's the paths were satisfactorily computed (see fig. 11) by assuming the strengths to be given by $\Gamma/V=4a\alpha$, an expression which was merely chosen to given the correct value of strength (according to fig. 10 (a))

for $\alpha=10°$ but which underestimates the strengths for 15° and 20°.

It is interesting to note that, although there was a considerable effect on the body loading at 15° angle of attack due to change in Reynolds number from 0.13×10^6 to 0.39×10^6 per inch, there was only a small effect on the vortex positions, and the vortex paths for both Reynolds numbers can be computed reasonably well. Although there may be larger effects on the paths due to greater changes in Reynolds number, the data of this investigation indicate that the effect of Reynolds number on the paths need be considered only in determining the proper starting positions. As yet, no reliable solution to the starting problem has been determined.

COMPARISONS OF THEORETICAL AND EXPERIMENTAL DOWNWASH DISTRIBUTIONS THROUGH THE BODY VORTICES

Comparisons of theoretical and experimental downwash angle distributions along a line through the body vortices at various length stations and at angles of attack of 10°, 15°, and 20° are presented in figure 12. (Since the downwash surveys were made along horizontal lines passing just a little above or below the vortex centers, the z/a survey locations are not quite equal to the η/a vortex center locations shown in figure 12.) For the test conditions of this investigation the effect on the downwash distributions due to change in Reynolds number was small. Typical comparisons of downwash distributions for Reynolds numbers of 0.13×10^6 per inch and 0.39×10^6 per inch are shown in figure 13. Since the Reynolds number effects were small, only data for one Reynolds number ($Re=0.39\times10^6$ per inch) have been used for the comparisons with theory.

The comparisons of theory with experiment (fig. 12) show that the downwash distributions computed using only the potential flow around the cylinder with $\Gamma/V=0$ are completely erroneous; whereas, the distributions computed with the inclusion of a symmetrical pair of potential vortices (and images) superimposed in the flow field agree well with experiment except between and close to the vortex centers. The downwash distributions which include the effects of potential vortices (see eq. (2)) were computed with values of vortex strength taken from figure 10 (a) (eq. (11)) and also from the assumed relation $\Gamma/V=4a\alpha$. Except for $\alpha=20°$ at x/d's greater than 6.7 where the distributions computed with $\Gamma/V=4a\alpha$ differ appreciably from experiment, about the same agreement between theory and experiment is obtained with either method of estimating the strength. This, of course, is not surprising since the values of vortex strength from the assumed formula and from experiment only differ markedly for $\alpha=20°$.

Although the distributions computed with potential vortices superimposed in the flow field agree well with experiment at lateral positions (y's) greater than about 1.5 body radii from the vertical axis of symmetry, the agreement near the vortex cores is poor. Close to and through the vortex cores the experimental distributions can be more nearly duplicated by the assumption of viscous instead of potential flow vortices (see eq. (6)). This is demonstrated clearly in figure 12 (b) for $\alpha=15°$ at $x/d=8.8$. For the computed distributions in figure 12 (b) all of the core radii (including images) were assumed to be equal and of the same magnitude as the core radii estimated from the experimental distribution ($r_*/a=0.28$, the y/a distance from the vortex center to the maximum negative value of ϵ). Theoretically, the size of a core radius can be considered to be a simple function of the kinematic viscosity and the time of development of the vortex (see eq. (5)). However, without a clearer understanding of the time history and viscosity of the vortices, it is difficult to make a logical estimate of the core size. For example, the product νt computed from free-stream conditions indicates that viscosity is of minor importance, since the resulting magnitude of r_* by equation (5) is negligibly small compared to the value indicated by experiment.

At $\alpha=20°$ the agreement between theory and experiment is somewhat adversely affected because of the effect of wake shock waves (see figs. 12 (d), (e), (f), and (g)). These shock waves, which have been observed in previous visual studies of the wake shed from inclined flat-nosed cylinders (ref. 12) and pointed bodies apparently are formed when the cross-flow Mach number (M sin α) exceeds about 0.5. The downwash data indicate that these waves move outboard and toward the windward side of the body with increase in distance downstream.

CONCLUSIONS

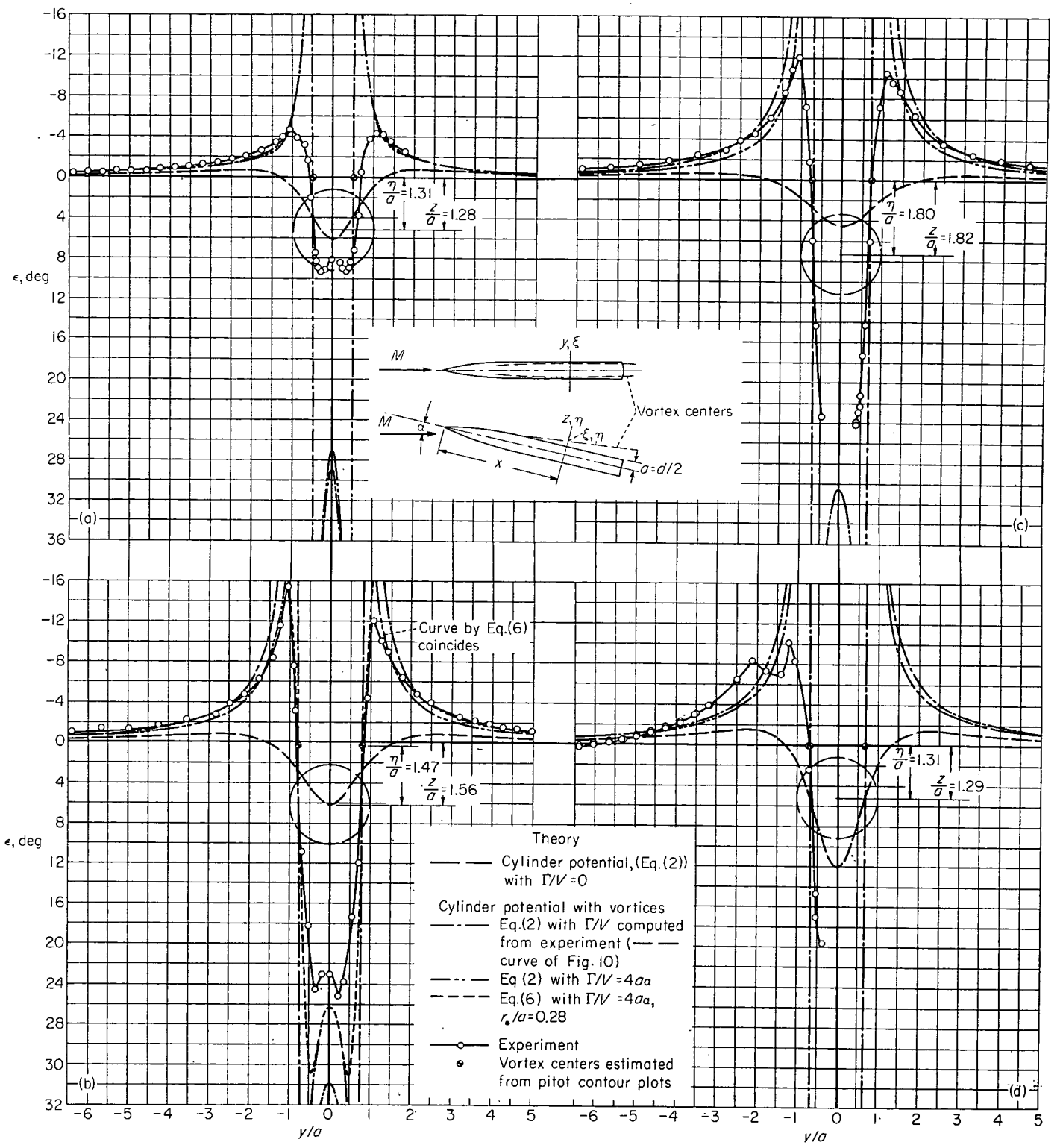
A body with a fineness-ratio-3, circular-arc, ogival nose tangent to a cylindrical afterbody 7.3 diameters long has been tested in the Ames 1- by 3-foot supersonic wind tunnel No. 1 at a free-stream Mach number of 1.98. Pitot-pressure distributions in the flow field, pressure distributions over the body, and downwash measurements through the body vortices have been obtained for angles of attack to 20°. Pressure distributions on the body surface and pitot-pressure contours in the flow field have been used to determine the approximate positions at which the vortices left the body surface and their paths downstream. An analysis of these data in conjunction with a simple theoretical flow model, which has been outlined in the report, has led to the following conclusions:

1. The paths of symmetrically shed body vortices can be computed quite accurately by the use of a simple stepwise method. However, in the application of this method, a knowledge of the body normal-force distribution and the starting positions and strengths of the vortices is required. Additional research on the problem of predicting the starting positions and strengths of the vortices is necessary.

2. Although not confirmed by detailed measurements of the flow field, it appears that the strengths of the concentrated body vortices can be estimated from the normal-force distributions and vortex positions.

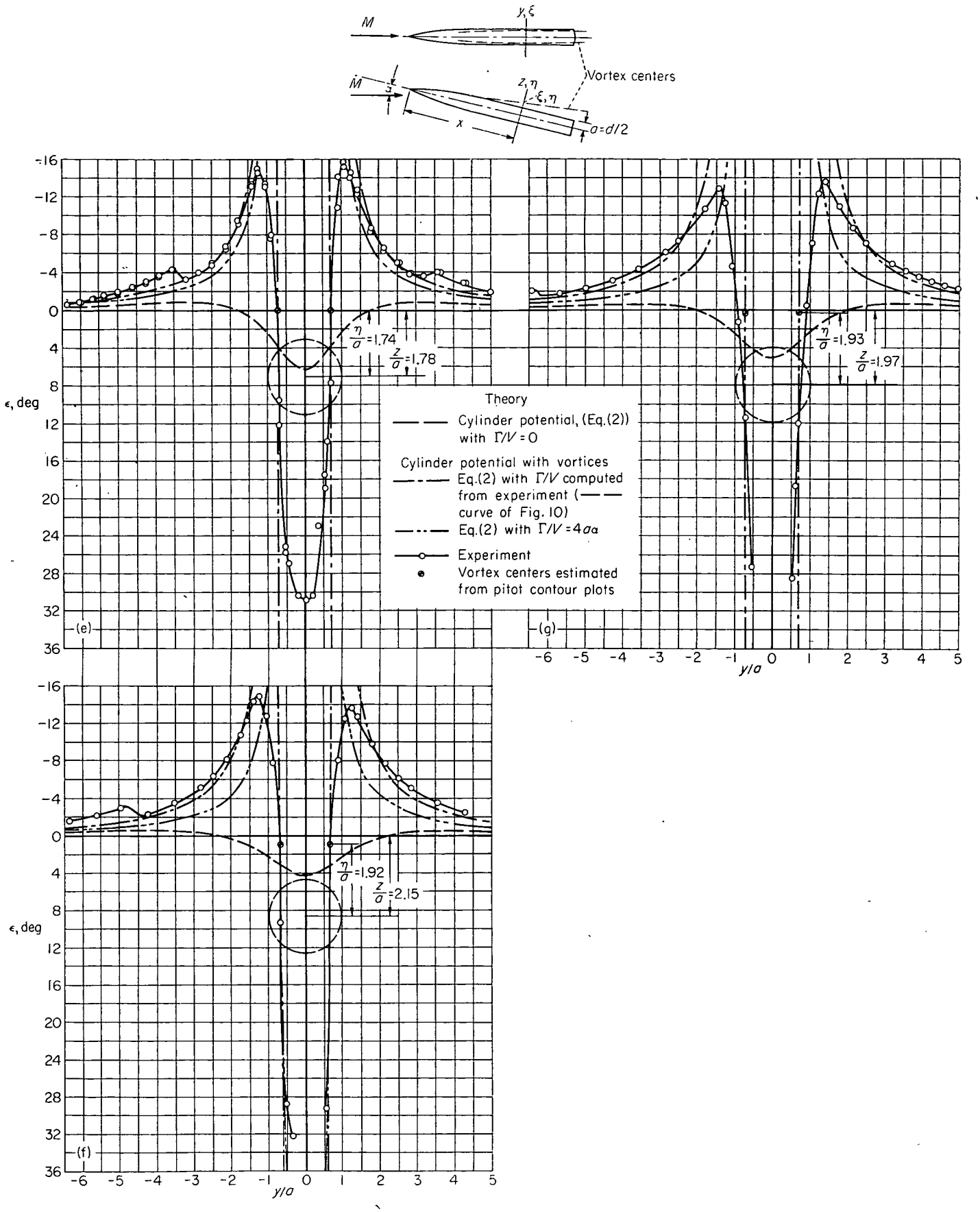
3. Flow angle distributions through the body vortex regions computed by assuming a pair of symmetric potential vortices (and images) superimposed in the flow field agree well with experiment, except between and through the vortex cores.

AMES AERONAUTICAL LABORATORY
NATIONAL ADVISORY COMMITTEE FOR AERONAUTICS
MOFFETT FIELD, CALIF., *May 31, 1955*



(a) $\alpha=10°$, $x/d=10.3$
(b) $\alpha=15°$, $x/d=8.8$
(c) $\alpha=15°$, $x/d=10.2$
(d) $\alpha=20°$, $x/d=5.1$

FIGURE 12.—Comparison of theoretical and experimental downwash distributions through body vortices for various α's and x/d stations; $M=1.98$; $Re=0.39\times10^6$ per inch.



(e) $\alpha=20°$, $x/d=6.7$
(f) $\alpha=20°$, $x/d=8.5$
(g) $\alpha=20°$, $x/d=10.2$

FIGURE 12.—Concluded.

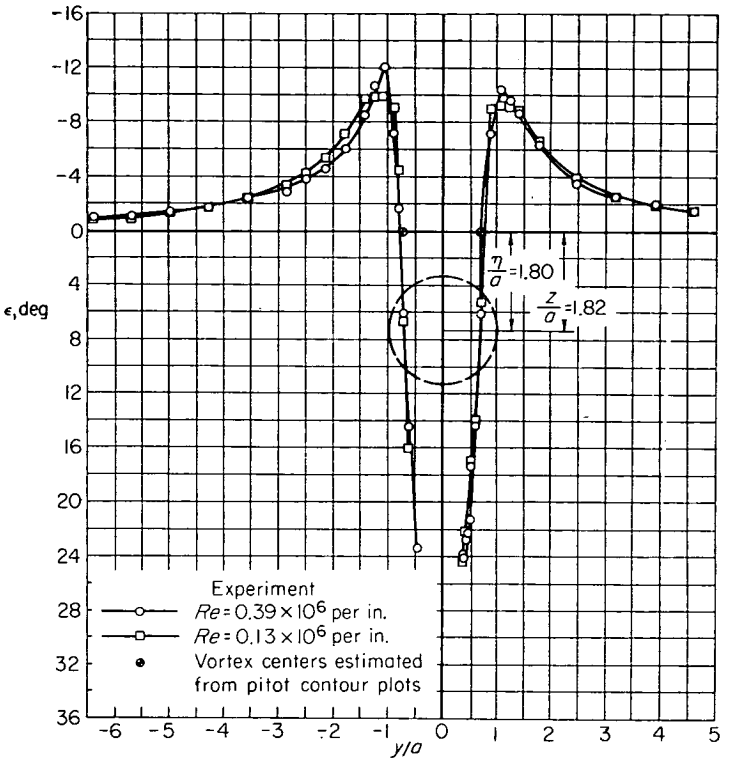


FIGURE 13.—Effect of Reynolds number on the downwash distributions through the body vortices for $\alpha=15°$ and $x/d=10.2$; $M=1.98$.

REFERENCES

1. Pitts, William C., Nielsen, Jack N., and Kaattari, George E.: Lift and Center of Pressure of Wing-Body-Tail Combinations at Subsonic, Transonic, and Supersonic Speeds. NACA Rep. 1307, 1957.
2. Nielsen, Jack N., and Kaattari, George E.: The Effects of Vortex and Shock-Expansion Fields on Pitch and Yaw Instabilities of Supersonic Airplanes. I. A. S. Preprint No. 743, June 17–20, 1957.
3. Perkins, Edward W., and Jorgensen, Leland H.: Comparison of Experimental and Theoretical Normal-Force Distributions (Including Reynolds Number Effects) on an Ogive-Cylinder Body at Mach Number 1.98. NACA TN 3716, 1956. (Supersedes NACA RM A54H23)
4. Gowen, Forrest E., and Perkins, Edward W.: A Study of the Effects of Body Shape on the Vortex Wakes of Inclined Bodies at a Mach Number of 2. NACA RM A53I17, 1953.
5. Brown, C. E., and Michael, W. H., Jr.: Effect of Leading-Edge Separation on the Lift of a Delta Wing. Jour. Aero. Sci., vol. 21, no. 10, Oct. 1954, pp. 690–694, 706.
6. Lamb, Sir Horace: Hydrodynamics. Sixth ed. Dover Pub., 1945
7. Roshko, Anatol: On the Development of Turbulent Wakes From Vortex Streets. NACA Rep. 1191, 1954. (Supersedes NACA TN 2913)
8. Lagerstrom, Paco A., and Graham, M. E.: Aerodynamic Interference in Supersonic Missiles. Rep. No. SM-13743, Douglas Aircraft Co., Inc., July 1950.
9. Tsien, Hsue-Shen: Supersonic Flow Over an Inclined Body of Revolution. Jour. Aero. Sci., vol. 5, no. 12, Oct. 1938, pp. 480–483.
10. Moore, Franklin K.: Laminar Boundary Layer on Cone in Supersonic Flow at Large Angle of Attack. NACA Rep. 1132, 1953. (Supersedes NACA TN 2844)
11. Raney, D. J.: Measurement of the Cross Flow Around an Inclined Body at a Mach Number of 1.91. R. A. E. TN Aero. 2357, British, Jan. 1955.
12. Hall, I. M.: Experiments on Supersonic Flow Over Flat-Nosed Circular Cylinders at Yaw. The Philosophical Magazine, ser. 7, vol. 45, Mar. 1954, pp. 333–343.

TABLE I.—EXPERIMENTAL DOWNWASH ANGLES MEASURED THROUGH MODEL VORTICES AT MACH NUMBER 1.98, $Re=0.39\times10^6$ PER INCH

(a) $\alpha=10°$; $x/d=10.3$; $z/a=1.28$		(b) $\alpha=15°$; $x/d=8.8$; $z/a=1.56$		(c) $\alpha=15°$; $x/d=10.2$; $z/a=1.82$		(d) $\alpha=20°$; $x/d=5.1$; $z/a=1.29$				(e) $\alpha=20°$; $x/d=6.7$; $z/a=1.78$				(f) $\alpha=20°$; $x/d=8.5$; $z/a=2.15$		(g) $\alpha=20°$; $x/d=10.2$; $z/a=1.97$	
								Check run				Check run					
y/a	ϵ, deg	y/a	ϵ, deg	y/a	ϵ, deg	y/a	ϵ, deg	y/a	ϵ, deg	y/a	ϵ, deg	y/a	ϵ, deg	y/a	ϵ, deg	y/a	ϵ, deg
−6.40	−0.40	−6.40	−1.05	−6.40	−0.95	−6.75	0.45	−6.75	0.40	−6.75	−0.45	−6.75	−0.40	−6.75	−1.25	−6.40	−2.10
−6.04	−.45	−5.67	−1.45	−5.70	−1.05	−6.40	.30	−6.40	.20	−6.04	−.90	−6.40	−.63	−6.40	−1.65	−5.67	−1.75
−5.67	−.45	−4.98	−1.27	−4.98	−1.40	−6.04	.10	−6.04	−.05	−5.67	−1.25	−6.04	−.90	−5.67	−2.20	−4.98	−2.35
−5.33	−.60	−4.27	−1.65	−4.27	−1.75	−5.67	−.15	−5.67	−.25	−5.33	−1.55	−5.67	−1.20	−4.98	−3.00	−4.27	−3.18
−4.98	−.60	−3.56	−2.25	−3.56	−2.40	−5.33	−.40	−5.33	−.45	−4.98	−2.00	−5.33	−1.50	−4.27	−2.30	−3.56	−4.35
−4.62	−.65	−2.84	−2.70	−2.85	−2.85	−4.98	−.75	−4.98	−.82	−4.62	−2.44	−4.98	−1.95	−3.56	−3.55	−2.84	−6.15
−4.27	−.80	−2.49	−3.75	−2.49	−3.80	−4.62	−1.20	−4.62	−1.30	−4.27	−3.04	−4.62	−2.40	−2.84	−5.17	−2.49	−7.35
−3.91	−1.00	−2.13	−4.70	−2.13	−4.55	−4.27	−1.60	−4.27	−1.75	−3.91	−3.67	−4.27	−2.94	−2.49	−6.45	−1.78	−10.75
−3.56	−1.10	−1.78	−6.20	−1.78	−6.00	−3.91	−2.20	−3.91	−2.30	−3.56	−4.36	−3.91	−3.57	−2.13	−8.20	−1.42	−12.85
−3.20	−1.30	−1.42	−8.40	−1.42	−8.56	−3.56	−3.00	−3.56	−3.00	−3.20	−3.25	−3.56	−4.31	−1.78	−10.75	−1.24	−11.35
−2.84	−1.50	−1.24	−11.65	−1.24	−10.77	−3.20	−3.85	−3.20	−3.90	−2.49	−4.80	−2.84	−3.97	−1.60	−12.39	−1.07	−4.65
−2.49	−1.80	−1.07	−15.50	−1.07	−12.13	−2.49	−6.45	−2.49	−6.30	−2.13	−6.73	−2.49	−4.90	−1.42	−14.38	−.89	1.25
−2.13	−2.10	−.89	−7.50	−.89	−7.20	−2.13	−8.35	−.71	2.40	−1.78	−9.40	−2.13	−6.63	−1.24	−14.92	−.71	11.50
−1.78	−2.70	−.71	10.95	−.80	−1.65	−1.73	−7.30	−.53	14.80	−1.42	−13.26	−1.78	−9.25	−1.07	−12.76	−.53	27.35
−1.42	−3.45	−.53	18.40	−.71	6.04	−1.42	−7.00	−.36	19.50	−1.24	−14.57	−1.42	−13.41	−.89	−7.75	.53	29.50
−1.24	−4.05	−.36	24.70	−.62	14.44	−1.24	−10.10			−1.07	−13.07	−1.24	−14.97	−.71	9.29	.62	18.70
−1.07	−4.75	−.18	23.10	−.45	23.38	−1.07	−8.25			−.89	−7.97	−1.07	−13.42	−.53	28.73	.71	12.05
−.89	−3.90	0	23.20	.41	24.15	−.71	.05			−.71	9.64	−.89	−7.67	−.36	32.27	.89	−.55
−.71	−3.25	.18	25.40	.39	23.85	−.53	17.10			−.53	25.24	−.71	12.29	.53	29.20	1.07	−7.05
−.62	−1.70	.36	23.90	.46	22.85	−.36	19.65			−.44	27.04	−.53	25.84	.89	−8.10	1.24	−12.25
−.53	1.95	.53	17.40	.48	22.35					−.18	30.45	.53	19.12	1.07	−12.55	1.42	−13.60
−.44	7.40	.71	12.00	.52	21.35					0	30.87	.71	7.73	1.24	−13.70	1.78	−10.88
−.41	8.30	.89	−4.40	.53	17.35					.53	17.62	.89	−14.22	1.42	−12.75	2.13	−8.72
−.36	8.85	1.07	−11.95	.62	14.40					.62	13.98	1.07	−15.72	1.78	−9.75	2.49	−7.15
−.27	9.25	1.24	−10.00	.71	6.15					.89	−10.92	1.24	−14.01	2.13	−7.75	3.20	−4.85
−.18	9.15	1.42	−9.00	.89	−7.15					1.07	−15.27	1.42	−12.26	2.49	−6.15	3.56	−4.20
0	8.05	1.78	−6.45	1.07	−10.45					1.24	−14.56	1.78	−8.25	2.84	−5.08	3.91	−3.59
.18	8.45	2.13	−4.80	1.24	−9.55					1.42	−12.76	2.13	−6.33	3.56	−3.60	4.27	−3.07
.41	9.00	2.49	−3.93	1.42	−8.65					1.78	−8.70	2.49	−4.96	4.27	−2.53	4.62	−2.70
.53	7.15	3.20	−2.56	1.78	−6.35					2.13	−6.58	2.84	−3.85			4.98	−2.35
.71	−.50	3.56	−2.25	2.49	−3.53					2.49	−5.06	3.56	−3.95			5.33	−2.00
.89	−3.80	3.91	−1.90	3.20	−2.51					2.84	−3.70	4.27	−2.85				
1.07	−4.35	4.27	−1.60	3.91	−2.00					3.20	−3.60	4.98	−1.86				
1.24	−4.25	4.62	−1.45	4.63	−1.55					3.56	−3.95	5.67	−1.27				
1.42	−3.55	4.98	−1.20	5.34	−1.10					4.27	−2.85						
1.78	−2.55	5.33	−1.07							4.98	−1.91						
										5.67	−1.27						

TABLE II.—EXPERIMENTAL DOWNWASH ANGLES MEASURED THROUGH MODEL VORTICES AT MACH NUMBER 1.98, $Re=0.13\times10^6$ PER INCH

(a) $\alpha=15°$; $x/d=8.8$; $z/a=1.61$		(b) $\alpha=15°$; $x/d=10.2$; $z/a=1.82$	
y/a	ϵ, deg	y/a	ϵ, deg
−6. 75	−0. 95	−6. 40	−0. 80
−6. 40	−1. 05	−5. 70	−. 80
−5. 67	−1. 25	−4. 98	−1. 30
−4. 98	−1. 50	−4. 27	−1. 70
−4. 27	−1. 75	−3. 56	−2. 40
−3. 56	−2. 45	−2. 85	−3. 38
−2. 84	−3. 20	−2. 49	−4. 20
−2. 49	−4. 02	−2. 13	−5. 38
−2. 13	−5. 19	−1. 78	−7. 10
−1. 78	−6. 90	−1. 42	−9. 73
−1. 42	−10. 06	−1. 24	−9. 90
−1. 24	−10. 83	−1. 07	−9. 96
−1. 07	−10. 84	−. 89	−9. 12
−. 89	−10. 15	−. 80	−4. 52
−. 71	6. 83	−. 71	6. 77
−. 71	6. 88	−. 62	16. 07
−. 57	21. 90	. 38	24. 33
−. 36	19. 91	. 44	22. 33
−. 18	24. 88	. 53	16. 82
0	24. 92	. 62	13. 92
. 18	25. 29	. 71	5. 31
. 36	19. 93	. 89	−9. 00
. 36	20. 48	1. 07	−9. 23
. 53	17. 62	1. 24	−9. 10
. 71	6. 31	1. 42	−8. 83
. 89	−7. 60	1. 78	−6. 60
1. 07	−9. 81	2. 49	−3. 86
1. 24	−10. 08	3. 20	−2. 57
1. 42	−9. 44	3. 91	−1. 88
1. 78	−6. 65	4. 63	−1. 44
2. 13	−5. 05	5. 34	−1. 05
2. 49	−3. 80		
2. 84	−3. 25		
3. 56	−2. 35		
4. 27	−1. 65		
4. 98	−1. 30		
5. 33	−1. 30		
5. 67	−1. 30		

and other data are substituted into explicit algebraic formulas to determine the temperature of the heated wall surface. If the heat-transfer coefficients are known, no guess or iteration procedure is required. As can be seen by the results of the example problems presented, the accuracy can be as good as is desired. For equal time-step sizes, the method is more accurate than more laborious numerical methods.

The simplicity of the results depends on two factors: One is the suppression of the variable x representing the distance into the wall by using an integrated form of Fourier's equation and assigning a value of x corresponding to the heated surface. The other is a mathematical device known as the time series introduced by Tustin (ref. 3). The time series is defined in appendix A. Reference 3 also introduced various manipulations of the series. The multiplication of two series is an important manipulation by means of which specific results can be generalized. Other writers (ref. 4, for example) have also presented various manipulations of the series.

The present paper is divided into two parts, analysis and application. The section on analysis includes a treatment of the determination of the temperature history for the special cases of the thermally thin wall and the infinitely thick wall as well as for the wall of intermediate thickness. The inverse problem of determining the heat flow corresponding to a known temperature history is also discussed. Although the method was set up for the purpose of predicting wall temperatures in engineering applications, it has also been found to be suitable for research applications wherein the transient skin temperature is measured and the heat-flow and heat-transfer-coefficient histories are deduced. Appendix A gives background material pertaining to the use of time series that may be an aid to a study of the analysis. Appendix B gives a summary of analytical temperature and heat-flow formulas used either as a basis of analysis or used in the solution of examples to test the accuracy of the present method. In the section on application the computing formulas are reviewed and several examples of their use are given. Because of the explicit nature of the temperature formulas, it is not necessary to study the analysis to use the results.

SYMBOLS

A dimensionless coefficient to determine heated-surface temperature history

b slope of adiabatic-wall temperature with respect to time, °F/hr

B dimensionless coefficient to determine inside-wall temperature history

c specific heat, Btu/lb-°F

e base of natural logarithms

$F(x,t)$ any function corresponding to reference slope $y=(1/\delta)t$

$F_y(t)$ any function corresponding to arbitrary control line $y=y(t)$

$F_\Delta(t)$ any function corresponding to unit triangle control line

G heat capacity of wall, ρcl, Btu/(sq ft)(°F)

ηh heat-transfer coefficient at $x=0$, Btu/(hr)(sq ft)(°F)

h heat-transfer coefficient at $x=l$, Btu/(hr)(sq ft)(°F)

H heat-transfer number, $h\delta\pi^2/16G$

H_∞ heat-transfer number for infinitely thick wall, $3h\sqrt{\pi k\delta}/8K$

k diffusivity, $K/c\rho$, sq ft/hr

K conductivity, (Btu)(ft)/(hr)(sq ft)(°F)

l wall thickness, ft

M memory coefficients, dimensionless

m term designating time in multiples of basic interval δ

n term number in infinite series

q instantaneous heat-transfer rate due to uniform temperature rise of heated wall surface of 1° in time δ, Btu/(hr)(sq ft)

$\bar{q}_m$ average heat-transfer rate from time $(m-1)\delta$ to $m\delta$ due to uniform temperature rise of heated wall surface of 1° in time δ, Btu/(hr)(sq ft)

q_Δ heat-transfer rate corresponding to unit triangle variation of surface temperature

$\bar{q}_{\Delta,m}$ average heat-transfer rate from time $(m-1)\delta$ to $m\delta$ due to unit triangle reference temperature variation of heated-wall surface, Btu/(hr)(sq ft)

$q_s(t)$ heat-flow history at heated surface due to unit temperature step of heated surface

r radiation rate, Btu/(hr)(sq ft)

R radiation term, $r\delta\pi^2/16G$, °F

R_∞ radiation term for infinitely thick wall, $3R\sqrt{\pi k\delta}/8K$, °F

t time, hr

T heated-wall-surface temperature, °F

T_S value of step in wall-surface temperature, °F

T_{aw} adiabatic-wall temperature or effective boundary-layer temperature, °F

T_i temperature of inside (unheated) surface or of any plane within wall, °F

$V(x,t)$ temperature response to unit step in T_{aw}, °F

x distance through wall, ft

y ordinate of control line or altitude of triangle

α_n positive roots of auxiliary equation in analytical solution of wall temperature

δ basic time interval in time series

η ratio of heat-transfer coefficient at cooler wall surface to heat-transfer coefficient at heated wall surface

θ difference in temperature between heated surface and any other plane due to unit triangle variation of heated surface, °F

θ_r difference in temperature between heated surface and any other plane due to uniform reference-temperature rise of 1° in time δ, °F

ρ weight density, lb/cu ft

τ dummy time variable, hr

Subscript or superscript:

m index denoting term number

A dot over a symbol denotes the derivative with respect to time.

ANALYSIS

TEMPERATURES ON OUTSIDE SURFACE

The wall considered in this paper is composed of a homogeneous material, and the temperature gradients and heat flow parallel to the surface are negligible. The transient temperatures of the heated or outside surface of the wall are determined by means of Fourier's equation which governs the heat flow through the wall:

$$\frac{\partial T}{\partial t}=k\frac{\partial^2 T}{\partial x^2} \tag{1}$$

The wall properties expressed by the diffusivity k are constant. The boundary conditions are given by the statements that the flow of heat at the unheated face of the wall (where x is taken as zero) is zero, that is,

$$\left(\frac{\partial T}{\partial x}\right)_{x=0}=0 \tag{2}$$

and that the heat transferred to the heated face is given by the relation

$$h(T_{aw}-T)=K(\partial T/\partial x)_{x=l} \tag{3}$$

For convenience, the initial temperature is taken as zero at zero time:

$$T=0 \qquad (t=0) \tag{4}$$

Since both h and T are functions of t and occur as a product in equation (3), the transform procedures of operational calculus do not apply. The problem may be stated in another form by means of an integral equation expressing the heat balance at the heated surface.

Let $q_s(t)$ be the heat-flow history at the heated wall surface at $x=l$ due to a unit step in that wall-surface temperature at $t=0$. Then the heat flow $q(t)$ due to a temperature history $T(t)$ of the heated surface that is continuous and is zero when $t=0$, but is otherwise an arbitrary variation, can be expressed by Duhamel's integral in the form indicated in the following equation, $\dot{T}$ represents $\frac{d}{dt}T(t)$ and τ is a dummy time variable:

$$q(t)=\int_0^t \dot{T}(t-\tau)q_s(\tau)d\tau \tag{5}$$

A heat balance is formed at $x=l$ by equating the integral in equation (5) to the left member of the boundary condition expressed by equation (3):

$$h(T_{aw}-T)=\int_0^t \dot{T}(t-\tau)q_s(\tau)d\tau \tag{6}$$

The determination of T from equation (6) establishes the solution.

The wall temperature T is determined, in general, from equation (6) for thermally thin, thick, and infinitely thick walls. The method first discussed is based on thick walls, and modifications of this method are introduced for the special cases of thermally thin and infinitely thick walls.

SOLUTION FOR THERMALLY THICK WALLS

Time series.—In the calculation of wall temperature T for thick walls, the right-hand member of equation (6) is replaced by the product of two time series. As explained in detail in appendix A, a time series is the value (here the ordinate) of a function of time at successive equal increments of time δ. Thus, any variation of wall surface temperature can be expressed as the series

$$T=T_1,\ T_2,\ T_3,\ \ldots\ T_m \tag{7}$$

When a wall surface has a unit triangle variation of surface temperature, the surface temperature increases from 0° at a constant rate to a value of 1° at the time $t=\delta$ and decreases at a constant rate to the value 0° at $t=2\delta$. The heat flow corresponding to a unit triangle variation of surface temperature can be expressed by the series

$$q_\Delta=q_{\Delta,1},\ q_{\Delta,2},\ q_{\Delta,3},\ \cdots\ q_{\Delta,m} \tag{8}$$

The product of equations (7) and (8) gives the instantaneous values of heat flow due to the temperature variation given by equation (7) and could be used to eliminate the integral in equation (6). However, a slight variation or refinement of the method is introduced which has been found to increase the accuracy of the results without increasing the labor involved.

If m represents the term number of a time series, the product $m\delta$ represents the corresponding time. The refinement consists in averaging the heat flow from the time $(m-1)\delta$ to the time $m\delta$. Let $\bar{q}_{\Delta,m}$ represent the average heat flow over this interval due to a triangular variation in surface temperature. Then the heat-flow history due to the triangular temperature variation can be represented by the series

$$\bar{q}_\Delta=\bar{q}_{\Delta,1},\ \bar{q}_{\Delta,2},\ \bar{q}_{\Delta,3},\ \cdots\ \bar{q}_{\Delta,m} \tag{9}$$

where $\bar{q}_{\Delta,1}$ is the average for the time 0 to δ, $\bar{q}_{\Delta,2}$ is the average for time δ to 2δ, and so forth.

The heat-flow history expressed as the average heat flow over successive increments δ, but due to the temperature variation (7), is given by the product of equations (7) and (9):

$$\bar{q}=(T_1,\ T_2,\ T_3,\ \ldots\ T_m)(\bar{q}_{\Delta,1},\ \bar{q}_{\Delta,2},\ \bar{q}_{\Delta,3},\ \cdots\ \bar{q}_{\Delta,m}) \tag{10}$$

Such a multiplication actually gives the result by forming the proper superpositions, as demonstrated in appendix A.

In order to adjust the boundary condition expressed by equation (3) or the left-hand side of equation (6) to represent an average flow of heat $\bar{q}_m$ over the interval δ, the average flow of heat from the boundary layer is approximated by the mean of the values at the beginning and end of the interval. Thus, for the interval ending at $t=m\delta$, $\bar{q}_m$ has the value

$$\bar{q}_m=\frac{1}{2}\left[h_m(T_{aw}-T)_m+h_{m-1}(T_{aw}-T)_{m-1}\right] \tag{11}$$

If radiation is important to the problem, it may be included. Let r_m be the rate of heat radiation per unit area at the time $m\delta$. Equation (11) may then be written

$$\bar{q}_m=\frac{1}{2}\left[h_m(T_{aw}-T)_m-r_m+h_{m-1}(T_{aw}-T)_{m-1}-r_{m-1}\right] \tag{11a}$$

526597—60——58

With or without radiation, the heating history, or variation of $\bar{q}$, may be expressed by the series

$$\bar{q}=\bar{q}_1, \bar{q}_2, \bar{q}_3, \ldots \bar{q}_m \tag{12}$$

wherein each term has the value given by equation (11) or (11a). Equating the average heat flow given by equation (12) to that given by equation (10) yields

$$\bar{q}_1, \bar{q}_2, \bar{q}_3, \ldots \bar{q}_m=(T_1, T_2, T_3, \ldots T_m)(\bar{q}_{\Delta,1}, \bar{q}_{\Delta,2}, \bar{q}_{\Delta,3}, \ldots \bar{q}_{\Delta,m}) \tag{13}$$

In order to evaluate equation (13), the product in the right-hand member is expanded by algebraic multiplication and values of both members of the equation pertaining to equal time are equated. The following set of equations results (for simplicity, the radiation terms are not written in):

$$\left.\begin{aligned}
&\frac{1}{2}[h_1(T_{aw}-T)_1+h_0(T_{aw}-T)_0]=T_1\bar{q}_{\Delta,1}\\
&\frac{1}{2}[h_2(T_{aw}-T)_2+h_1(T_{aw}-T)_1]=T_2\bar{q}_{\Delta,1}+T_1\bar{q}_{\Delta,2}\\
&\cdots\cdots\cdots\cdots\cdots\cdots\cdots\cdots\\
&\frac{1}{2}[h_m(T_{aw}-T)_m+h_{m-1}(T_{aw}-T)_{m-1}]=T_m\bar{q}_{\Delta,1}+T_{m-1}\bar{q}_{\Delta,2}+\ldots+T_1\bar{q}_{\Delta,m}
\end{aligned}\right\} \tag{14}$$

Equations (14) can be rearranged to obtain the equivalent equations for T:

$$\left.\begin{aligned}
&T_1=\frac{h_1T_{aw,1}+h_0T_{aw,0}}{2\bar{q}_{\Delta,1}+h_1}\\
&T_2=\frac{h_2T_{aw,2}+h_1T_{aw,1}-h_1T_1-2T_1\bar{q}_{\Delta,2}}{2\bar{q}_{\Delta,1}+h_2}\\
&\cdots\cdots\cdots\cdots\cdots\cdots\cdots\cdots\\
&T_m=\frac{(hT_{aw})_m+(hT_{aw}-hT)_{m-1}-2(\bar{q}_{\Delta,2}T_{m-1}+\bar{q}_{\Delta,3}T_{m-2}+\ldots+\bar{q}_{\Delta,m}T_1)}{2\bar{q}_{\Delta,1}+h_m}
\end{aligned}\right\} \tag{15}$$

The values of $\bar{q}_{\Delta,m}$ must be derived.

Average heat flow due to unit triangle variation of surface temperature.—In order to obtain the average heat flow due to a unit triangle variation of surface temperature, the average heat-flow rate $\bar{q}_m$ due to a uniform increase in the surface temperature of 1° in each unit time δ must be obtained. The average is taken over the time δ by integrating the instantaneous heat-flow rate from $t=(m-1)\delta$ to $t=m\delta$ and dividing by δ. This determination is carried out in appendix B. The result is

$$\bar{q}_m=\frac{8G}{\pi^2\delta}\left(\frac{\pi^2}{8}+A_m-A_{m-1}\right) \tag{16}$$

In equation (16), A_m and A_{m-1} are the summations

$$\left.\begin{aligned}
A_m&=\sum_{n=1}^{\infty}\frac{e^{-m(2n-1)^2\frac{\pi^2}{4}\frac{k\delta}{l^2}}}{\frac{\pi^2}{4}\frac{k\delta}{l^2}(2n-1)^4}\\
A_{m-1}&=\sum_{n=1}^{\infty}\frac{e^{-(m-1)(2n-1)^2\frac{\pi^2}{4}\frac{k\delta}{l^2}}}{\frac{\pi^2}{4}\frac{k\delta}{l^2}(2n-1)^4}
\end{aligned}\right\} \tag{17}$$

and G is the heat capacity of the wall per square foot per °F and is the product of weight density, specific heat, and wall thickness:

$$G=\rho cl \tag{18}$$

The average heat flow due to a unit triangle variation of surface temperature $\bar{q}_{\Delta,m}$ is obtained by the superposition of the heat flows $\bar{q}$ due to three linear variations of wall temperature as follows (for further details, see the development of equation (A1) in appendix A):

$$\bar{q}_{\Delta,m}=\bar{q}_m-2\bar{q}_{m-1}+\bar{q}_{m-2} \tag{19}$$

Expanding equation (19) by substituting for $\bar{q}_m$ from equation (16) gives

$$\bar{q}_{\Delta,m}=\frac{8G}{\pi^2\delta}\left[\left(\frac{\pi^2}{8}+A_m-A_{m-1}\right)-2\left(\frac{\pi^2}{8}+A_{m-1}-A_{m-2}\right)+\left(\frac{\pi^2}{8}+A_{m-2}-A_{m-3}\right)\right] \tag{20}$$

Substituting in equation (20) successive values of m, starting with $m=1$, ignoring any parenthetical group in which negative subscripts appear, and collecting terms result in the following equations:

$$\left.\begin{aligned}
\bar{q}_{\Delta,1}&=\frac{8G}{\pi^2\delta}\left(\frac{\pi^2}{8}+A_1-A_0\right)\\
\bar{q}_{\Delta,2}&=\frac{8G}{\pi^2\delta}\left(-\frac{\pi^2}{8}+A_2-3A_1+2A_0\right)\\
\bar{q}_{\Delta,3}&=\frac{8G}{\pi^2\delta}(A_3-3A_2+3A_1-A_0)\\
&\cdots\cdots\cdots\cdots\cdots\cdots\\
\bar{q}_{\Delta,m}&=\frac{8G}{\pi^2\delta}(A_m-3A_{m-1}+3A_{m-2}-A_{m-3})
\end{aligned}\right\} \tag{21}$$

For convenience, the quantities in parentheses can be tabulated. The quantities in parentheses usually retain significant values after the completion of the temperature triangle which created them. For this reason, in accordance with the notation of reference 4, they are called memory terms and are designated by the symbol M. With this notation, equations (21) become

$$\left.\begin{aligned}
\bar{q}_{\Delta,1}&=\frac{8G}{\pi^2\delta}M_1\\
\bar{q}_{\Delta,2}&=\frac{8G}{\pi^2\delta}M_2\\
\bar{q}_{\Delta,3}&=\frac{8G}{\pi^2\delta}M_3\\
&\cdots\cdots\\
\bar{q}_{\Delta,m}&=\frac{8G}{\pi^2\delta}M_m
\end{aligned}\right\} \tag{21a}$$

Hence, the following equations for memory terms are established:

$$\left.\begin{aligned}
M_1&=\frac{\pi^2}{8}+A_1-A_0\\
M_2&=-\frac{\pi^2}{8}+A_2-3A_1+2A_0\\
M_3&=A_3-3A_2+3A_1-A_0\\
&\cdots\cdots\cdots\cdots\cdots\\
M_m&=A_m-3A_{m-1}+3A_{m-2}-A_{m-3}
\end{aligned}\right\} \tag{22}$$

Obviously, the values of M are combinations of the values of A. Values of A and M were computed for a range of values of $k\delta/l^2$, and the memory coefficients M are listed in table I. The value of M decreases with increasing term number and sooner or later further terms can be neglected.

Resulting temperature formulas.—Equations (21a) give the value of $\bar{q}_{\Delta,m}$ sought to complete equations (15); therefore, equations (21a) are substituted into equations (15). The result can be simplified by dividing through by $16G/\pi^2\delta$ and letting

$$H=\frac{h}{\left(\frac{16G}{\pi^2\delta}\right)} \tag{23}$$

If radiation is important, the appropriate terms are included by using equation (11a) rather than equation (11). Since equations (15) are being divided through by $16G/\pi^2\delta$, the radiation term R is defined as

$$R=\frac{r}{\left(\frac{16G}{\pi^2\delta}\right)} \tag{24}$$

With the substitutions of equations (23) and (24) in equations (15), the final results, including terms for radiation, are

$$\left.\begin{aligned}
T_1&=\frac{H_1T_{aw,1}+H_0T_{aw,0}-R_1-R_0}{M_1+H_1}\\
T_2&=\frac{H_2T_{aw,2}+(HT_{aw}-HT)_1-M_2T_1-R_2-R_1}{M_1+H_2}\\
T_3&=\frac{H_3T_{aw,3}+(HT_{aw}-HT)_2-M_2T_2-M_3T_1-R_3-R_2}{M_1+H_3}\\
&\cdots\cdots\cdots\cdots\cdots\cdots\cdots\cdots\cdots\cdots\cdots\cdots\\
T_m&=\frac{(HT_{aw})_m+(HT_{aw}-HT)_{m-1}-M_2T_{m-1}-M_3T_{m-2}-\ \ldots\ -M_mT_1-R_m-R_{m-1}}{M_1+H_m}
\end{aligned}\right\} \tag{25}$$

SOLUTION FOR INFINITELY THICK WALLS

General considerations.—If a wall is thermally very thick and is heated rapidly so that the unheated side experiences little heating, it is convenient and accurate to assume that the wall is infinitely thick. The same formulas, equations (25), are used to compute the wall surface temperature. However, instead of the values of M for a particular wall or diffusion number, the values of M which are used are always a fixed set of numbers which are now derived. The values of H and R are also changed.

Determination of average heat flow due to unit triangle variation of surface temperature.—The determination of the heat flow due to a unit triangle variation of surface temperature of an infinitely thick wall depends upon the instantaneous heat flow into the surface due to a unit rise in surface temperature in unit time. From page 110 of reference 5, the instantaneous heat flow is equivalent to $2K\sqrt{t}/\sqrt{\pi k}$. Since the heat-flow rate is proportional to the surface-temperature slope, the instantaneous heat transfer due to unit rise of surface temperature in the time δ is $2K\sqrt{t}/\delta\sqrt{\pi k}$. This expression is integrated with respect to t between the

TABLE I.—VALUES OF M AND θ

m \ $k\delta/l^2$ [a]	0.01	0.02	0.05	0.1	0.2	0.5	1.0	2.0	5.0
	M								
1	0.09280547	0.13124675	0.20751933	0.29347652	0.41495535	0.64728198	0.85683719	1.02954117	1.15145420
2	−.01592290	−.02251838	−.03560496	−.05051887	−.07836507	−.22817155	−.51142924	−.82682869	−1.06920821
3	−.02683275	−.03794724	−.06002546	−.08722820	−.14861561	−.30052454	−.31662013	−.20127599	−.08224564
4	−.00957529	−.01354153	−.02166582	−.03696546	−.07338883	−.08405219	−.02634648	−.00142616	−.00000036
5	−.00553399	−.00782683	−.01320029	−.02628367	−.04463344	−.02447704	−.00223431	−.00001026	−.00000000
6	−.00373390	−.00528487	−.00983261	−.02025561	−.02724662	−.00712803	−.00018948	−.00000007	
7	−.00274116	−.00389296	−.00809228	−.01579610	−.01663399	−.00207577	−.00001607	−.00000000	
8	−.00212390	−.00304409	−.00695594	−.01233887	−.01015501	−.00060449	−.00000136		
9	−.00170890	−.00249270	−.00608368	−.00964054	−.00619962	−.00017604	−.00000012		
10	−.00141412	−.00211864	−.00535620	−.00753254	−.00378485	−.00005126	−.00000001		
11	−.00119615	−.00185533	−.00472749	−.00588550	−.00231065	−.00001493	−.00000000		
12	−.00103005	−.00166301	−.00417648	−.00459860	−.00141064	−.00000435			
13	−.00090058	−.00151702	−.00369098	−.00359308	−.00086120	−.00000127			
14	−.00079788	−.00140175	−.00326234	−.00280743	−.00052576	−.00000037			
15	−.00071529	−.00130717	−.00288362	−.00219357	−.00032097	−.00000011			
16	−.00064810	−.00122687	−.00254891	−.00171393	−.00019595	−.00000003			
17	−.00059290	−.00115666	−.00225306	−.00133917	−.00011963	−.00000001			
18	−.00054712	−.00109383	−.00199156	−.00104635	−.00007303	−.00000000			
19	−.00050883	−.00103658	−.00176041	−.00081756	−.00004459				
20	−.00047651	−.00098373	−.00155609	−.00063880	−.00002722				
21	−.00044899	−.00093448	−.00137549	−.00049912	−.00001662				
22	−.00042532	−.00088827	−.00121584	−.00038998	−.00001015				
23	−.00040477	−.00084473	−.00107473	−.00030471	−.00000619				
24	−.00038676	−.00080356	−.00094999	−.00023808	−.00000378				
25	−.00037081	−.00076455	−.00083973	−.00018603	−.00000231				
26	−.00035655	−.00072753	−.00074227	−.00014535	−.00000141				
27	−.00034368	−.00069237	−.00065612	−.00011357	−.00000086				
28	−.00033196	−.00065895	−.00057997	−.00008874	−.00000053				
29	−.00032119	−.00062716	−.00051265	−.00006933	−.00000032				
30	−.00031121	−.00059693	−.00045315	−.00005417	−.00000020				
	θ								
1	1.00000000	0.99999992	0.99956262	0.98873183	0.92596579	0.69945453	0.45623855	0.24814441	0.09999955
2	−.00000015	−.00019241	−.02166158	−.12553206	−.31355030	−.48643195	−.41618829	−.24630216	−.09999909
3	−.00002494	−.00333067	−.06963676	−.17636953	−.23787104	−.15098748	−.03665380	−.00182900	−.00000045
4	−.00033480	−.01195026	−.09012904	−.14882949	−.14587796	−.04396967	−.00310842	−.00001315	−.00000000
5	−.00144190	−.02167828	−.08988006	−.11749067	−.08906596	−.01280454	−.00026361	−.00000009	
6	−.00344276	−.02904775	−.08284990	−.09193126	−.05437468	−.00372885	−.00002236	−.00000000	
7	−.00595602	−.03361673	−.07435643	−.07184409	−.03319564	−.00108589	−.00000190		
8	−.00854573	−.03599626	−.06609621	−.05613647	−.02026587	−.00031622	−.00000016		
9	−.01092537	−.03687746	−.05854671	−.04386205	−.01237227	−.00009209	−.00000001		
10	−.01296010	−.03679326	−.05179171	−.03427135	−.00755325	−.00002682	−.00000000		
11	−.01461453	−.03611078	−.04579381	−.02677771	−.00461124	−.00000781			
12	−.01590635	−.03507183	−.04048318	−.02092260	−.00281516	−.00000227			
13	−.01687671	−.03383230	−.03578599	−.01634774	−.00171865	−.00000066			
14	−.01757370	−.03249148	−.03163302	−.01277320	−.00104923	−.00000019			
15	−.01804423	−.03111189	−.02796174	−.00998026	−.00064055	−.00000006			
16	−.01833036	−.02973243	−.02471645	−.00779802	−.00039106	−.00000002			
17	−.01846823	−.02837687	−.02184779	−.00609293	−.00023874	−.00000000			
18	−.01848809	−.02705931	−.01931206	−.00476067	−.00014575				
19	−.01841484	−.02578769	−.01707064	−.00371972	−.00008898				
20	−.01826874	−.02456607	−.01508936	−.00290638	−.00005432				
21	−.01806620	−.02339609	−.01333804	−.00227088	−.00003316				
22	−.01782042	−.02227782	−.01178998	−.00177434	−.00002025				
23	−.01754197	−.02121043	−.01042159	−.00138637	−.00001236				
24	−.01723931	−.02019254	−.00921203	−.00108323	−.00000755				
25	−.01691918	−.01922244	−.00814285	−.00084638	−.00000461				
26	−.01658695	−.01829828	−.00719776	−.00066131	−.00000281				
27	−.01624686	−.01741811	−.00636236	−.00051671	−.00000172				
28	−.01590229	−.01658000	−.00562392	−.00040373	−.00000105				
29	−.01555588	−.01578203	−.00497119	−.00031545	−.00000064				
30	−.01520972	−.01502236	−.00439422	−.00024648	−.00000039				

[a] For additional value of $k\delta/l^2$, see table II.

limits $(m-1)\delta$ and $m\delta$. Dividing by δ gives, for the average heat-flow rate $\bar{q}_m$ over the interval δ terminating at $m\delta$,

$$\bar{q}_m=\frac{4K}{3\sqrt{\pi k\delta}}\left[m^{3/2}-(m-1)^{3/2}\right] \tag{26}$$

The usual superposition required to change the result of the slope function to that of the unit triangle input function is accomplished by substituting equation (26) into equation (19):

$$\bar{q}_{\Delta,m}=\frac{4K}{3\sqrt{\pi k\delta}}\left[m^{3/2}-3(m-1)^{3/2}+3(m-2)^{3/2}-(m-3)^{3/2}\right] \tag{27}$$

Resulting temperature formulas.—If the bracketed quantity in equation (27) is designated as the memory coefficient M_m, then

$$M_m=[m^{3/2}-3(m-1)^{3/2}+3(m-2)^{3/2}-(m-3)^{3/2}] \quad (28)$$

A dimensionless heat-transfer coefficient (suggested by eq. (27)) is defined as

$$H_\infty=\frac{3h\sqrt{\pi k\delta}}{8K} \quad (29)$$

and a corresponding term for radiation is defined as

$$R_\infty=\frac{3r\sqrt{\pi k\delta}}{8K} \quad (30)$$

The substitution of equation (27) into equations (15) again results in equations (25). Hence, equations (25) are used to obtain the heated-surface temperature of the infinitely thick wall as well as of walls of intermediate thickness, except that M, H, and R for infinitely thick walls are defined by equations (28) to (30). Inspection of equations (28) to (30) indicates that the wall material properties and time-step size are expressed by equations (29) and (30), while the memory terms are invariant with wall properties or step size. Substituting successive integers for m from 1 to 20 into equation (28) gives the following corresponding values of M:

$$\left.\begin{array}{lll} M_1=1.0 & M_8=-0.022885 & M_{15}=-0.007580 \\ M_2=-0.171573 & M_9=-0.018412 & M_{16}=-0.006807 \\ M_3=-0.289129 & M_{10}=-0.015232 & M_{17}=-0.006157 \\ M_4=-0.103176 & M_{11}=-0.012874 & M_{18}=-0.005605 \\ M_5=-0.059630 & M_{12}=-0.011069 & M_{19}=-0.005130 \\ M_6=-0.040234 & M_{13}=-0.009650 & M_{20}=-0.004719 \\ M_7=-0.029536 & M_{14}=-0.008511 & \end{array}\right\} \quad (31)$$

These values of M, along with values of H_∞ and R_∞ from equations (29) and (30), can be used in all problems wherein the wall is so thick relative to the heating rates and times involved that the wall behaves as though it were infinitely thick.

THIN WALLS

When a wall is thermally thin, the temperature drop through the wall becomes negligible and the problem is simplified by assuming that all interior temperatures are equal to the surface temperature. The heat absorbed by the wall during any time interval δ must be equal to the gain in enthalpy or total heat during this time. Hence,

$$\bar{q}_m=\frac{1}{\delta}(G_mT_m-G_{m-1}T_{m-1}) \quad (32)$$

Equating the average rate of gain in enthalpy as given by equation (32) to the average rate of heat transfer through the boundary layer as given by equation (11a) results in the following heat balance:

$$h_m(T_{aw}-T)_m-r_m+h_{m-1}(T_{aw}-T)_{m-1}-r_{m-1}=\frac{2}{\delta}[(GT)_m-(GT)_{m-1}] \quad (33)$$

Solving for T_m gives

$$\left.\begin{aligned} T_1&=\frac{h_1T_{aw,1}+h_0T_{aw,0}-h_0T_0+\frac{2}{\delta}G_0T_0-r_1-r_0}{\frac{2}{\delta}G_1+h_1} \\ T_2&=\frac{h_2T_{aw,2}+h_1T_{aw,1}-h_1T_1+\frac{2}{\delta}G_1T_1-r_2-r_1}{\frac{2}{\delta}G_2+h_2} \\ &\cdots\cdots\cdots\cdots\cdots \\ T_m&=\frac{h_mT_{aw,m}+\left(hT_{aw}-hT+\frac{2}{\delta}GT\right)_{m-1}-r_m-r_{m-1}}{\frac{2}{\delta}G_m+h_m} \end{aligned}\right\} \quad (34)$$

Any variation of G with temperature is accounted for by equations (34). If the wall properties do not change over the temperature range covered, obviously, G is a constant. If G is considered to be constant, equations (34) can be derived from equations (25) as follows: As the diffusion number $k\delta/l^2$ becomes large, all values of A approach the value $\pi^2/8$, and from equations (22) it is seen that the only memory terms not identically equal to zero are M_1 and M_2, which have the values $\pi^2/8$ and $-\pi^2/8$. Eliminating M from equations (25) and utilizing definitions (23) and (24) yield equations (34).

In equations (34) the terms h_0, $T_{aw,0}$, and T_0 have been retained since in the thin-wall problem, unlike the thick-wall problem, it is convenient for T_0 to have any value. These equations have considerable advantage because the need for temperature extrapolation is reduced, if not eliminated. The equations tend to give accurate results and, as is shown subsequently, are suitable for the use of relatively large time increments.

INSIDE TEMPERATURES

If the heated wall surface is called the outside surface, the temperatures at other parallel planes may be called inside temperatures. In particular, this paper is concerned with the inside surface temperature. According to the notation used in this paper, the inside surface is designated by $x/l=0$, the outside surface by $x/l=1$, and other planes by values of x/l between 0 and 1.

Consider a wall, initially at zero temperature, which has the heated surface $x=l$ raised at a reference temperature slope $T=(1/\delta)t$, while the surface $x=0$ is insulated. The difference in temperature θ_r between the heated surface and any plane x is shown by equation (B11) of appendix B to be

$$\theta_r=\frac{16}{\pi^3}\frac{l^2}{k\delta}\left\{\sum_{n=1}^{\infty}\frac{(-1)^{n-1}}{(2n-1)^3}\cos\left[(2n-1)\frac{\pi}{2}\frac{x}{l}\right]-\sum_{n=1}^{\infty}\frac{(-1)^{n-1}}{(2n-1)^3}\cos\left[(2n-1)\frac{\pi}{2}\frac{x}{l}\right]e^{-(2n-1)^2\frac{\pi^2}{4}\frac{kt}{l^2}}\right\} \quad (35)$$

A set of terms is defined to represent the summations in equation (35):

$$\left.\begin{aligned}
B_0&=\frac{16}{\pi^3}\frac{l^2}{k\delta}\sum_{n=1}^{\infty}\frac{(-1)^{n-1}}{(2n-1)^3}\cos\left[(2n-1)\frac{\pi}{2}\frac{x}{l}\right]\\
B_1&=\frac{16}{\pi^3}\frac{l^2}{k\delta}\sum_{n=1}^{\infty}\frac{(-1)^{n-1}}{(2n-1)^3}\cos\left[(2n-1)\frac{\pi}{2}\frac{x}{l}\right]e^{-(2n-1)^2\frac{\pi^2}{4}\frac{k}{l^2}\delta}\\
B_2&=\frac{16}{\pi^3}\frac{l^2}{k\delta}\sum_{n=1}^{\infty}\frac{(-1)^{n-1}}{(2n-1)^3}\cos\left[(2n-1)\frac{\pi}{2}\frac{x}{l}\right]e^{-2(2n-1)^2\frac{\pi^2}{4}\frac{k}{l^2}\delta}\\
&\cdots\cdots\cdots\cdots\cdots\cdots\cdots\\
B_m&=\frac{16}{\pi^3}\frac{l^2}{k\delta}\sum_{n=1}^{\infty}\frac{(-1)^{n-1}}{(2n-1)^3}\cos\left[(2n-1)\frac{\pi}{2}\frac{x}{l}\right]e^{-m(2n-1)^2\frac{\pi^2}{4}\frac{k}{l^2}\delta}
\end{aligned}\right\}\quad(36a)$$

If the temperature difference across the entire wall is sought, then $x/l=0$ and equations (36a) become

$$\left.\begin{aligned}
B_0&=\frac{16}{\pi^3}\frac{l^2}{k\delta}\sum_{n=1}^{\infty}\frac{(-1)^{n-1}}{(2n-1)^3}=\frac{l^2}{2k\delta}\\
B_1&=\frac{16}{\pi^3}\frac{l^2}{k\delta}\sum_{n=1}^{\infty}\frac{(-1)^{n-1}}{(2n-1)^3}e^{-(2n-1)^2\frac{\pi^2}{4}\frac{k}{l^2}\delta}\\
B_2&=\frac{16}{\pi^3}\frac{l^2}{k\delta}\sum_{n=1}^{\infty}\frac{(-1)^{n-1}}{(2n-1)^3}e^{-2(2n-1)^2\frac{\pi^2}{4}\frac{k}{l^2}\delta}\\
&\cdots\cdots\cdots\cdots\cdots\\
B_m&=\frac{16}{\pi^3}\frac{l^2}{k\delta}\sum_{n=1}^{\infty}\frac{(-1)^{n-1}}{(2n-1)^3}e^{-m(2n-1)^2\frac{\pi^2}{4}\frac{k}{l^2}\delta}
\end{aligned}\right\}\quad(36b)$$

Regardless of whether equations (36a) or (36b) are used, equation (35) may be written

$$\theta_r=B_0-B_m \tag{37}$$

By the usual superposition, in order to change the result of the reference slope function to that of a unit triangular input function, the temperature difference between the plane of the heated wall and the plane being considered is

$$\theta=B_0-B_m-2(B_0-B_{m-1})+B_0-B_{m-2} \tag{38}$$

Assigning integral values to m and simplifying give the equations corresponding to successive values of time:

$$\left.\begin{aligned}
\theta_1&=-B_1+B_0\\
\theta_2&=-B_2+2B_1-B_0\\
\theta_3&=-B_3+2B_2-B_1\\
\theta_4&=-B_4+2B_3-B_2\\
&\cdots\cdots\cdots\cdots\\
\theta_m&=-B_m+2B_{m-1}-B_{m-2}
\end{aligned}\right\}\quad(39)$$

A sufficient number of values of θ for practical purposes are given in table I. According to equations (39), the temperature difference between the plane of the heated surface and any other plane due to a unit triangle temperature variation of the heated surface would be given by the time series $\theta_i=\theta_1, \theta_2, \theta_3, \ldots \theta_m$. In addition, any general temperature of the heated surface can be represented as $T=T_1, T_2, T_3, \ldots T_m$. The temperature difference due to this general temperature variation is obtained by formally multiplying these two time series, and the inside temperature is obtained by subtracting the product from the heated-surface temperature T. Hence

$$\left.\begin{aligned}
T_{i,1}&=T_1-\theta_1T_1\\
T_{i,2}&=T_2-(\theta_1T_2+\theta_2T_1)\\
T_{i,3}&=T_3-(\theta_1T_3+\theta_2T_2+\theta_3T_1)\\
&\cdots\cdots\cdots\cdots\cdots\\
T_{i,m}&=T_m-(\theta_1T_m+\theta_2T_{m-1}+\ \ldots\ +\theta_mT_1)
\end{aligned}\right\}\quad(40)$$

Computation of $T_{i,m}$ does not depend on prior computation of $T_{i,1}$, $T_{i,2}$, and so forth.

If the temperature distribution through the wall is required in a form which is analytical with respect to x and can be differentiated or integrated analytically with respect to x, the procedures outlined in appendix C should be followed.

CALCULATION OF HEAT FLOW FROM TEMPERATURE HISTORY

TEMPERATURE HISTORY OF OUTSIDE SURFACE KNOWN

If the heated-surface temperature history is known, the heat-flow history can be determined by substituting equations (21a) into equation (10) as follows:

$$\bar{q}=\frac{8G}{\pi^2\delta}(T_1, T_2, T_3, \ldots T_m)(M_1, M_2, M_3, \ldots M_m) \tag{41}$$

Multiplication shows that the mth term is given by

$$\bar{q}_m=\frac{8G}{\pi^2\delta}(M_1T_m+M_2T_{m-1}+\ \ldots\ +M_mT_1) \tag{42}$$

The heat-flow history can be determined readily from a given temperature history of the heated surface by means of equation (42). The average heat flow over a small interval δ can be assumed to give the instantaneous rate at the center of the interval.

TEMPERATURE HISTORY OF INSIDE SURFACE KNOWN

If the temperature history of the outer surface or of a plane near the outer surface is known, the feasibility of accurately determining the heat flow is excellent. If the temperature history of the inside surface for a thermally thin wall (kt/l^2 large and hl/K small) is known, it is also feasible to determine the history of the heat flow into the outer surface. However, if the wall is thermally thick, relatively small changes in temperatures at the inside surface may make it difficult to reconstruct the temperature history and heat flow at the outer surface.

A rearrangement of equations (40) may be used to determine the outside-surface-temperature history from the inside-surface-temperature history. Rearranging equations (40) gives

$$
\left.
\begin{aligned}
T_1 &= \frac{T_{i,1}}{1-\theta_1} \\
T_2 &= \frac{T_{i,2}+\theta_2 T_1}{1-\theta_1} \\
T_3 &= \frac{T_{i,3}+\theta_2 T_2+\theta_3 T_1}{1-\theta_1} \\
&\cdots\cdots\cdots\cdots\cdots\cdots \\
T_m &= \frac{T_{i,m}+\theta_2 T_{m-1}+\theta_3 T_{m-2}+\ \ldots\ +\theta_m T_1}{1-\theta_1}
\end{aligned}
\right\} \qquad (43)
$$

The rate of heat flow at any time is then determined from equation (42).

APPLICATION

GENERAL CONSIDERATIONS

The section on application is devoted to demonstrating the solution of two types of problems: In the first type the heat-transfer coefficient and adiabatic-wall-temperature histories are given and the wall-temperature solutions are obtained. In the second type the temperature history is known and the heating-rate history is computed. In each example, the problem chosen was a special case, selected so that its solution could be and was obtained by an exact analytical method. The degree of exactness of the present method is demonstrated by comparing each result with the solution calculated by exact theory.

With one exception, radiation was a negligible consideration in the examples given. Although the method presented is well suited to accounting for radiation and includes terms for that purpose, radiation was neglected in all cases to make possible an exact analytical solution for comparison.

EQUATIONS FOR HEATED SURFACE

If the temperature of the heated surface of the wall is required, equations (18) and (23) to (25) are used. Whether the objective is to compute wall temperature or to compute the heat flow from a known wall temperature, the first steps involve the determination of the required memory coefficients. In order to minimize the labor involved, the recommended procedure is as follows: First, choose a tentative time interval δ which seems appropriate to the particular problem. (A review of the examples presented herein will give an idea of a reasonable value.) Then compute a tentative value of the dimensionless diffusion number $k\delta/l^2$. From table I or II pick a diffusion number close to the one tentatively computed. The memory coefficients M and inside temperature coefficients θ given in the table for this diffusion number are to be used, and they do not therefore have to be computed. An adjustment in the value of δ is made by multiplying it by the ratio of the tabular value of $k\delta/l^2$ selected to the value of $k\delta/l^2$ tentatively computed. Then compute from equations (18) and (23) the value of G and the values of H; if the radiation is important, R must be computed also (eq. (24)). The temperature history of the heated-wall surface is then found from equations (25). If the heating rate is being determined from a known temperature history, the values of H and R are not required. The procedure for this case is discussed in the section entitled "Example 6."

The temperature formulas were derived with the assumption that the initial wall temperature was zero in order to avoid writing $T-T_0$ numerous times in the formula. The simplest way to handle most problems is to subtract the amount that the initial wall temperature is above zero from both the wall and the adiabatic-wall temperatures. The last step in the problem is to add this amount to the solution.

EQUATIONS FOR INSIDE SURFACE

If the temperature of the unheated side of the wall is required, equations (40) are used. Except for the case of the thermally thin wall, all equations were derived for constant material properties. For small changes in material properties with temperature, it appears reasonable to use an average value of the properties for the temperature range involved. For cases in which material properties vary, it seems possible that a more accurate solution might be obtained by varying the diffusion number or by varying the step size to keep the diffusion number constant; however, any consideration of such a technique is beyond the scope of this paper.

APPLICATION OF METHOD IN SPECIFIC EXAMPLES

The following illustrative examples were calculated before table I was prepared. Therefore, the values of the coefficients M and θ were computed for the particular walls and chosen time intervals δ of the examples. All values of M and θ used are listed in table II, which may be considered as being supplementary to table I.

EXAMPLE 1

Problem for example 1 (a).—A copper wall which is ½ inch (1/24 ft) thick is initially at a temperature of 0° F. One surface is heated by a boundary layer while the other side is insulated. The effective boundary-layer temperature T_{aw} is initially 0° F but increases linearly at the rate of 1,000° F per second for 10 seconds. The heat-transfer coefficient remains constant at $h=100$ Btu/(hr)(sq ft)(°F). The conductivity K and diffusivity k of copper are taken as

$$K=227\,(\text{Btu})(\text{ft})/(\text{hr})(\text{sq ft})(^\circ\text{F})$$

$$k=4.41 \text{ sq ft/hr}$$

Find the temperature history of both wall surfaces.

Solution for example 1 (a).—The material properties are usually given in terms of the hour unit. However, since fast heating conditions may be more easily understood in terms of seconds, time is referred to in seconds and is converted to hours for use in the equations. For example, if

$$\delta=1 \text{ sec}=\frac{1}{3600} \text{ hr}$$

then

$$\frac{k\delta}{l^2}=\frac{(4.41)(24)^2}{3600}=0.7056$$

By using this dimensionless diffusion number, the values of M in column 2 of the following table are obtained from table II. The values of T_{aw} are listed in column 4. The value of G is given by the equation

$$G=\frac{Kl}{k}=\frac{227}{(24)(4.41)}=2.1447 \text{ Btu/(sq ft)(°F)}$$

TABLE II.—VALUES OF M AND θ USED IN ILLUSTRATIVE EXAMPLES

m \ $k\delta/l^2$	0.00980	0.08820	0.17640	0.35280	0.70560
	M				
1	0.09187272	0.27561815	0.38974974	0.54911553	0.75160198
2	−.01576287	−.04735497	−.07101815	−.14414264	−.35255882
3	−.02656306	−.08094552	−.13303643	−.24244390	−.33055113
4	−.00947905	−.03275298	−.06587129	−.09447354	−.05648228
5	−.00547837	−.02295825	−.04229223	−.03955774	−.00990390
6	−.00369637	−.01799364	−.02736081	−.01656451	−.00173660
7	−.00271361	−.01440765	−.01770513	−.00693626	−.00030451
8	−.00210254	−.01158046	−.01145704	−.00290451	−.00005339
9	−.00169169	−.00931431	−.00741389	−.00121624	−.00000936
10	−.00139980	−.00749250	−.00479755	−.00050929	−.00000164
11	−.00118389	−.00602714	−.00310451	−.00021326	−.00000029
12	−.00101926	−.00484839	−.00200894	−.00008930	−.00000005
13	−.00089082	−.00390018	−.00129999	−.00003739	−.00000001
14	−.00078882	−.00313741	−.00084123	−.00001566	−.00000000
15	−.00070668	−.00252382	−.00054436	−.00000656	
16	−.00063977	−.00203023	−.00035226	−.00000275	
17	−.00058474	−.00163317	−.00022795	−.00000115	
18	−.00053905	−.00131377	−.00014751	−.00000048	
19	−.00050081	−.00105683	−.00009545	−.00000020	
20	−.00046851	−.00085014	−.00006177	−.00000008	
	θ				
1	1.00000000	0.99289947	0.94364543	0.80477935	0.58038199
2	−.00000012	−.09850808	−.27773216	−.44879472	−.47463257
3	−.00002053	−.15766415	−.23367386	−.20690977	−.08720676
4	−.00028945	−.14162795	−.15250956	−.08665088	−.01529129
5	−.00128807	−.11603872	−.09871526	−.03628441	−.00268126
6	−.00314564	−.09364233	−.06387947	−.01519382	−.00047015
7	−.00552973	−.07537042	−.04133662	−.00636230	−.00008244
8	−.00802789	−.06063594	−.02674906	−.00266417	−.00001446
9	−.01035556	−.04877804	−.01730940	−.00111560	−.00000253
10	−.01237062	−.03923850	−.01120097	−.00046715	−.00000044
11	−.01402862	−.03156453	−.00724818	−.00019562	−.00000008
12	−.01533940	−.02539137	−.00469032	−.00008191	−.00000001
13	−.01633809	−.02042551	−.00303512	−.00003430	−.00000000
14	−.01706855	−.01643084	−.00196404	−.00001436	
15	−.01757475	−.01321741	−.00127093	−.00000601	
16	−.01789689	−.01063245	−.00082243	−.00000252	
17	−.01806993	−.00855303	−.00053219	−.00000105	
18	−.01812340	−.00688029	−.00034438	−.00000044	
19	−.01808182	−.00553469	−.00022285	−.00000018	
20	−.01796529	−.00445226	−.00014421	−.00000008	

The value of $h=100$ Btu/(hr)(sq ft)(°F) is converted to $H=0.00800$. The use of columns 2 and 4 in equations (25) gives the heated-wall temperature in column 5. Using the inside-surface-temperature formulas, equations (40), and the values of θ in column 6 gives the values of T_i in column 7.

1	2	3	4	5	6	7
Term number	M	Time, sec	T_{aw}, °F	T, °F	θ, °F	T_i, °F
0	------	0	0	0	-------	0
1	0.75160	1	1,000	11	0.580382	4
2	−.35256	2	2,000	36	−.474632	21
3	−.33055	3	3,000	74	−.087207	50
4	−.05648	4	4,000	124	−.015291	91
5	−.00990	5	5,000	186	−.002681	144
6	−.00174	6	6,000	260	−.000470	210
7	−.00030	7	7,000	346	−.000082	288
8	−.00005	8	8,000	443	−.000015	377
9	−.00001	9	9,000	552	−.000002	478
10	−.00000	10	10,000	673	−.000000	591

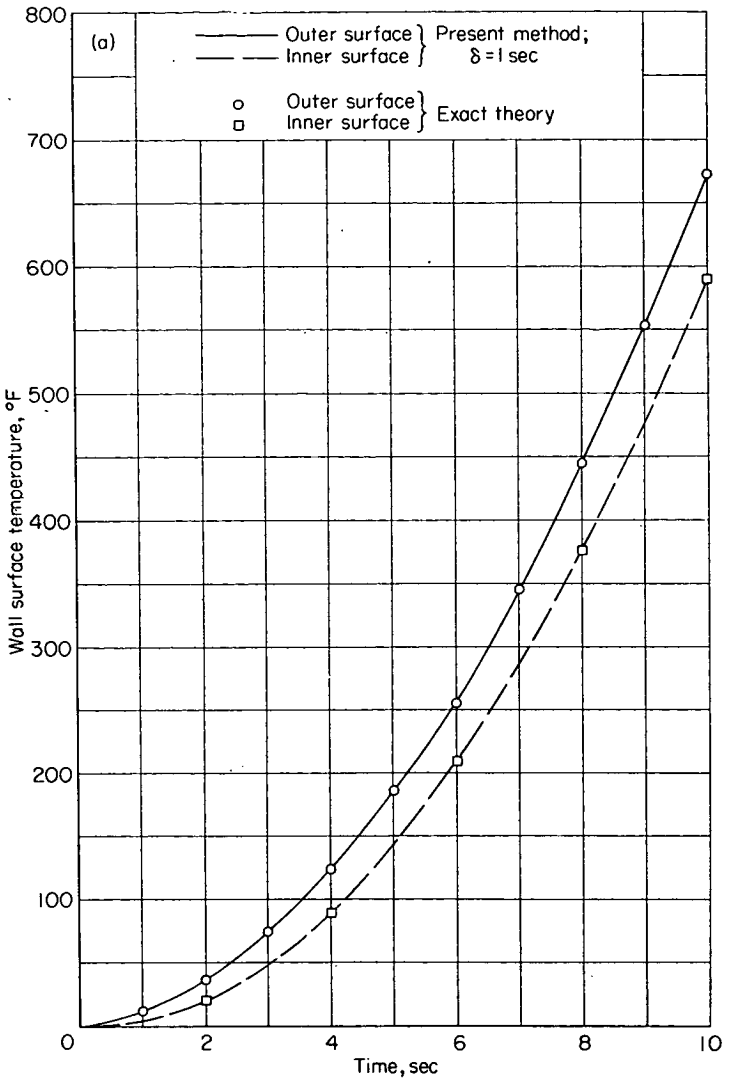
The wall-surface-temperature curves of T and T_i are shown in figure 1 (a). For comparison, the results calculated by the theoretically exact formula (eq. (B10) of appendix B) are shown. This formula is

$$T=bt-2b\frac{l^2}{k}\sum_{n=1}^{\infty}\frac{\cos\left(\frac{x}{l}\alpha_n\right)\left(1-e^{-\frac{kt}{l^2}\alpha_n^2}\right)}{\alpha_n^2\left(1+\frac{hl}{K}+\frac{K}{hl}\alpha_n^2\right)\cos\alpha_n} \tag{44}$$

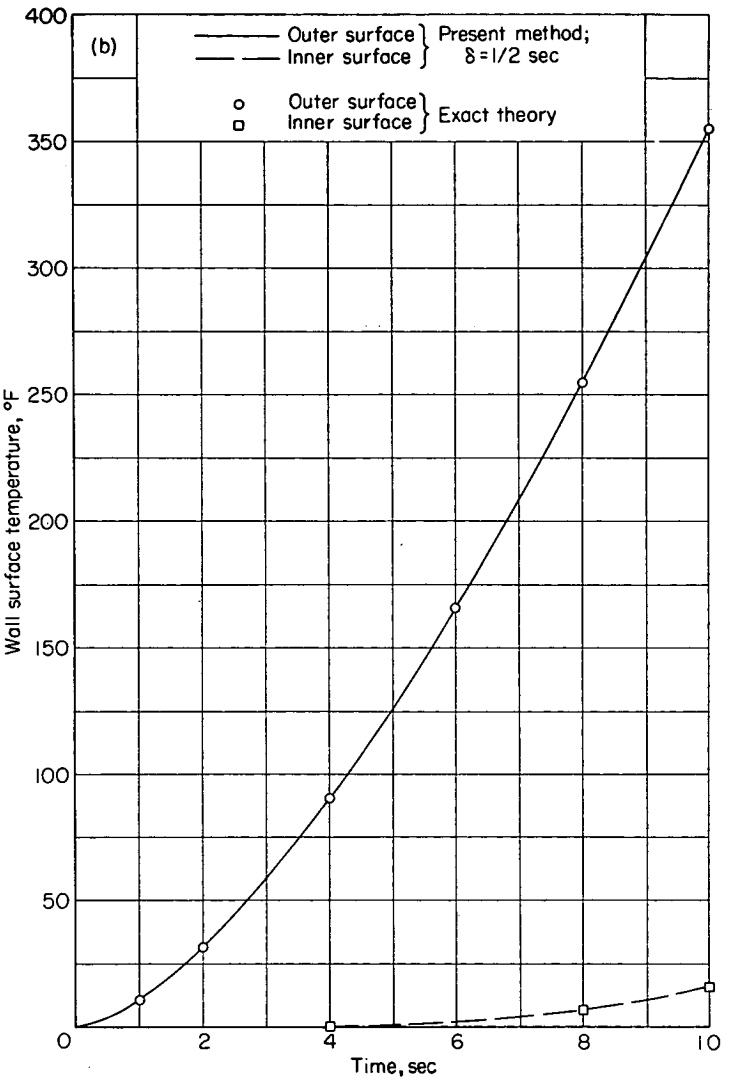
where b represents the slope of the adiabatic-wall-temperature curve and α_n represents the positive roots of the auxiliary equation

$$\alpha_n\tan\alpha_n=\frac{hl}{K} \tag{44a}$$

Setting $b=3{,}600{,}000$ °F/hr and setting $x=l$ and $x=0$ in equation (44) result in the values for outside and inside temperatures plotted as circles and squares in figure 1. The comparison shows that accurate results are obtained



(a) ½-inch-thick wall.



(b) 3-inch-thick wall.

FIGURE 1.—Example 1. Temperatures of copper-wall surfaces. Adiabatic-wall temperature varies linearly from 0° to 10,000° in 10 seconds; $h = 100$ Btu/(hr)(sq ft)(°F).

FIGURE 1.—Concluded.

by the present method, the maximum difference between methods being about 1°.

Problem for example 1 (b).—The conditions for example 1 (b) are the same as those for example 1 (a), except that the copper wall is 3 inches thick, or $l = \frac{1}{4}$ foot.

Solution for example 1 (b).—Since this wall is so thick, more highly transient conditions prevail throughout the heating period. A value of δ of ½ second or 1/7200 hour was therefore used. With the same procedure as used before, the results of the present method are given as continuous lines in figure 1 (b), while the results from equation (44) are given by the symbols. The agreement is evident.

EXAMPLE 2

Problem.—Example 2 illustrates the principal advantage of the present method; that is, its capability of handling arbitrary variations of T_{aw} and h. Neither is it necessary to know a mathematical formulation for these variations.

A ½-inch copper wall which is initially at a temperature of zero is aerodynamically heated on one side and insulated on the other. The time histories of T_{aw} and h are given at ½-second intervals in the following table:

Time, sec	T_{aw}, °F	h, Btu/(hr)(sq ft)(°F)	Time, sec	T_{aw}, °F	h, Btu/(hr)(sq ft)(°F)
0	0	36	5.5	5,391	68.4
.5	1,365	41.4	6.0	5,356	66.6
1.0	2,485	45.0	6.5	5,255	63.9
1.5	3,388	48.6	7.0	5,107	60.0
2.0	4,094	52.2	7.5	4,831	55.8
2.5	4,620	55.8	8.0	4,335	52.2
3.0	4,932	60.0	8.5	3,654	48.6
3.5	5,119	63.9	9.0	2,769	45.0
4.0	5,263	66.6	9.5	1,658	41.4
4.5	5,345	68.4	10.0	297.5	36.0
5.0	5,387	69.0			

The temperature history of both wall surfaces is to be found.

Solution.—The heating conditions are severe and continuously transient, with the boundary-layer temperature

rising and falling over 5,000° in 10 seconds. A computing interval δ smaller than that used in the first problem is therefore used. Let $\delta = \frac{1}{2}$ second $= 1/7200$ hour. The resulting wall-surface-temperature curves are drawn in figure 2. The circles and squares give the surface temperatures computed by a theoretically exact procedure. Comparison shows the present method to be accurate.

EXAMPLE 3

Problem.—Example 3 is the same as example 2 except that the wall is 3 inches thick and the effective boundary-layer temperatures are slightly different. The initial value of T_{aw} is 0. The subsequent values of T_{aw} are given at 0.5-second intervals by the following time series: $T_{aw} = 1{,}365$, 2,484, 3,386, 4,088, 4,609, 4,915, 5,094, 5,227, 5,296, 5,325, 5,315, 5,265, 5,149, 4,986, 4,694, 4,184, 3,489, 2,591, 1,471, 100. Find the temperature history of both wall surfaces.

Solution (a) (thick-wall solution).—The value of δ was taken as ½ second. By following the procedure previously presented, the wall-surface-temperature curves shown in figure 3 were obtained. Again the symbols give the results of exact theory.

It should be noted that the "exact solution" for examples 2 and 3 is not actually an alternate method of solution for any practical problem but gives a solution to the particular problems only. The "solution" was obtained by working in reverse; that is, a heat flow was assumed and the corresponding boundary-layer characteristics were computed. A truly alternate method of solution is now considered, however.

Solution (b) (infinitely thick-wall solution).—Since the thermal lag of a 3-inch copper wall is so great when subjected to the rapid heating specified by this problem, it appears reasonable to obtain the heated-surface temperature by assuming that the wall is infinitely thick. The memory coefficients are the same for all infinitely thick walls and are given by equations (31). The same temperature formulas, the same values of T_{aw}, and the same values of h are used as before, but the values of H_∞ are given by equation (29). The results calculated by this method are listed along with

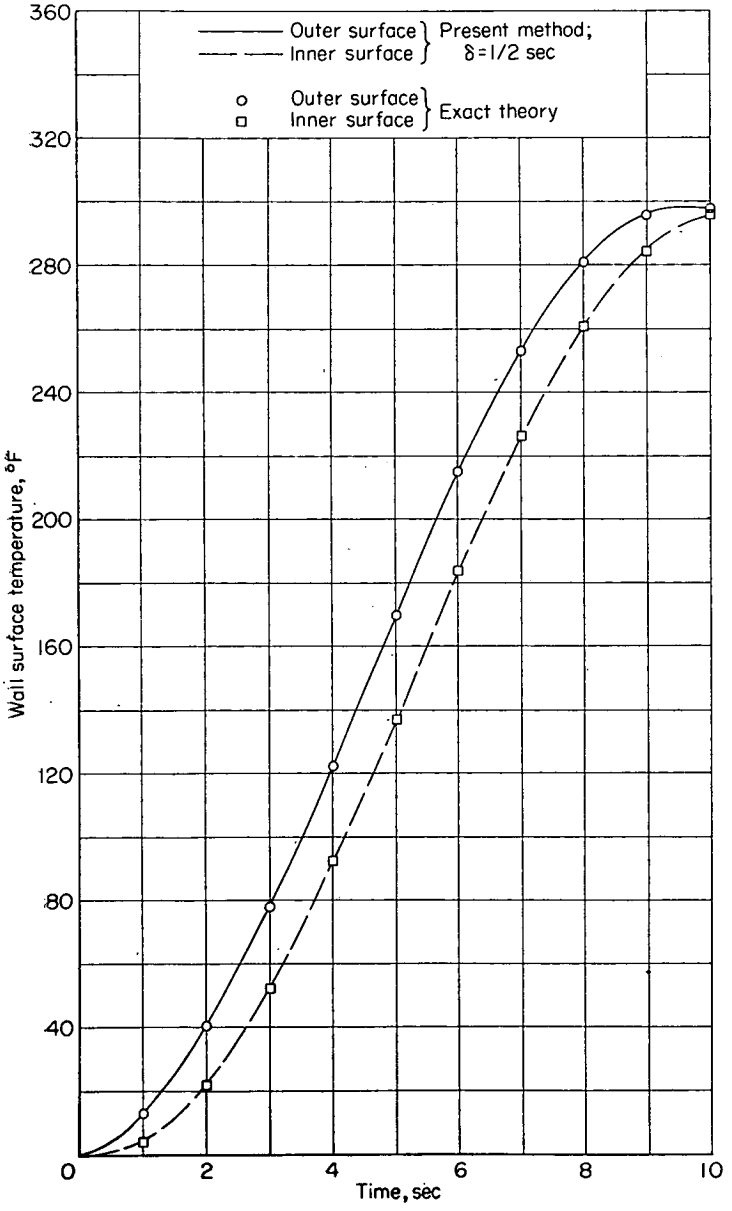


FIGURE 2.—Example 2. Temperatures of ½-inch copper wall heated according to assigned history of h and T_{aw}.

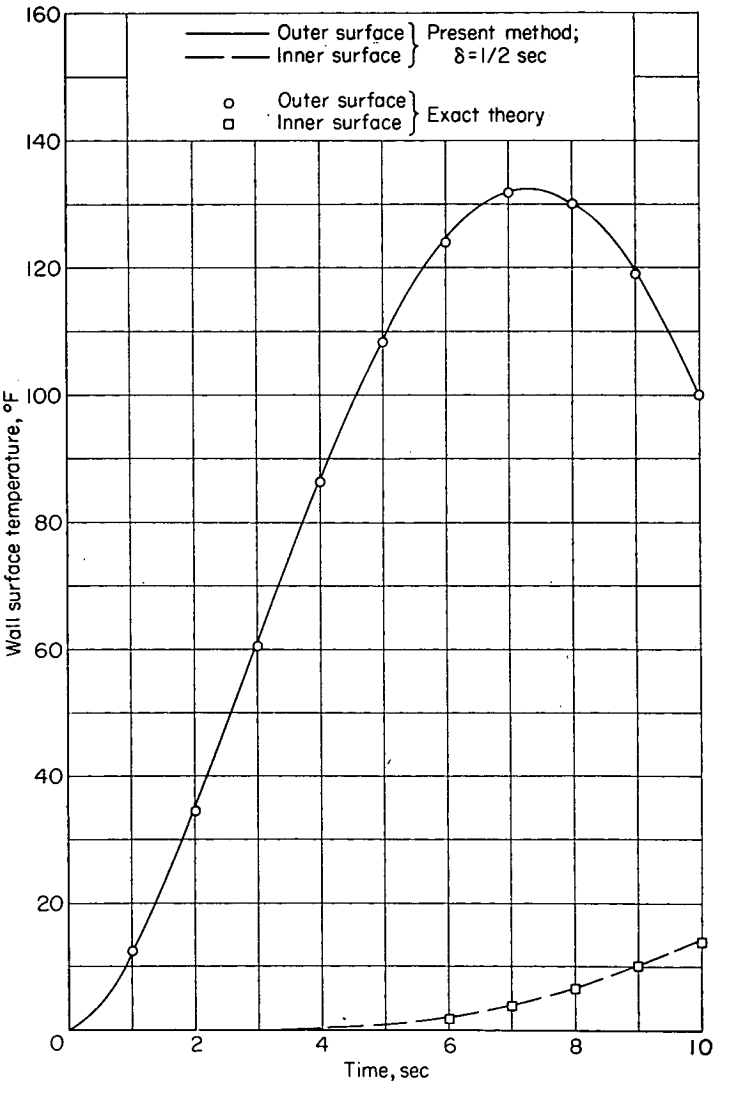


FIGURE 3.—Example 3. Temperatures of 3-inch copper wall heated according to assigned history of h and T_{aw}.

those from the thick-wall solution (a).

Time, sec	T, °F, calculated by—	
	Thick-wall solution	Infinitely thick-wall solution
1	12. 8	12. 8
2	35. 3	35. 3
3	61. 3	61. 3
4	87. 0	87. 0
5	109. 1	109. 1
6	124. 8	124. 8
7	132. 3	132. 3
8	130. 6	130. 6
9	119. 5	119. 4
10	100. 0	99. 8

The consistency of the alternate methods for a thermally thick wall is evident. The reason for the close agreement may be found in figure 3, which shows that the unheated surface of the 3-inch wall rose to only 14° F.

EXAMPLE 4

Problem.—The most severe test of the present method would occur if there were a large instantaneous increase of T_{aw}. While this condition could hardly happen in flight, it might happen if a research model were suddenly immersed in a high-stagnation-temperature jet. Let a ½-inch copper wall, initially at a temperature of zero, be instantly subjected to an effective boundary-layer temperature of 5,000° F on one surface while no heat transfer occurs on the other surface. The heat-transfer coefficient is 100 Btu/(hr)(sq ft)(°F). Solve for the temperature history of both wall surfaces for 10 seconds.

Solution.—In this case not only is there a very high transient-temperature condition initially but the instantaneous increase in T_{aw} does not lend itself to approximation by the unit triangle. The simplest procedure is to take small steps for the first few seconds to minimize the errors introduced. In order to help circumvent the difficulty of calculation, an excellent method of approximating the wall surface temperature for the first or first few small steps is to use the following formula from page 109 of reference 5, which gives the temperature on the surface of an infinitely thick wall for a constant flow of heat at the surface:

$$T=\frac{2hT_{aw}}{K}\sqrt{\frac{kt}{\pi}} \tag{45}$$

The values of δ used were $\delta=\frac{1}{8}$ second for 2 seconds, then $\delta=\frac{1}{2}$ second for 8 seconds. Since the use of an equation based on an infinite wall is permissible for a ½-inch copper wall for at least ¼ second, the values of T were computed by equation (45) for the first two ⅛-second steps, then by the usual equations. The results are presented in figure 4. Since the inside temperature T_i depends on the outside temperature T and not directly on T_{aw}, there is no particular difficulty of approximation in obtaining T_i. Accordingly, in obtaining T_i, ⅛-second steps were taken for 1 second to define the highly transient part of the curve, then ½-second steps for the remaining 9 seconds.

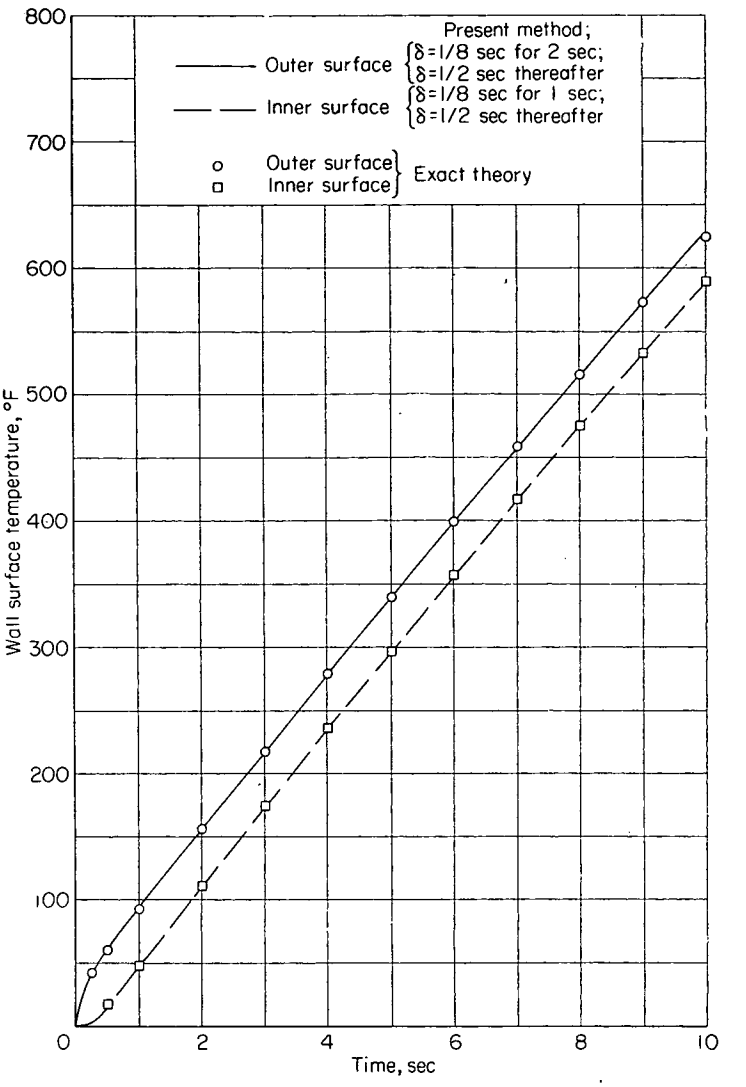


FIGURE 4.—Example 4. Temperatures of ½-inch copper wall after application of 5,000 °F jump in gas temperature. $h=100$ Btu/(hr)(sq ft)(°F).

A theoretically exact solution to this problem was obtained by equation (B7) of appendix B. The results of applying this equation are given by the symbols in figure 4, which shows that agreement was obtained.

EXAMPLE 5

Problem.—A $\frac{1}{16}$-inch Inconel wall is heated by a high-temperature jet. If $T_{aw}=5{,}000°$ F and $h=50$ Btu/(hr)(sq ft)(°F), determine the skin-temperature history for 15 seconds. Neglect radiation.

Solution.—The heat capacity of a $\frac{1}{16}$-inch Inconel wall was assumed to be $G=0.3229$ Btu/(sq ft)(°F). The example was worked three times with values of δ of 1, 2, and 5 seconds to show how sensitive the "thin wall" formula is to the time interval. Substituting the given constants into equation (34) yielded the results given by the symbols in figure 5. For this example the exact theory is shown by the solid line. Evidently, large time intervals are permissible with this formula.

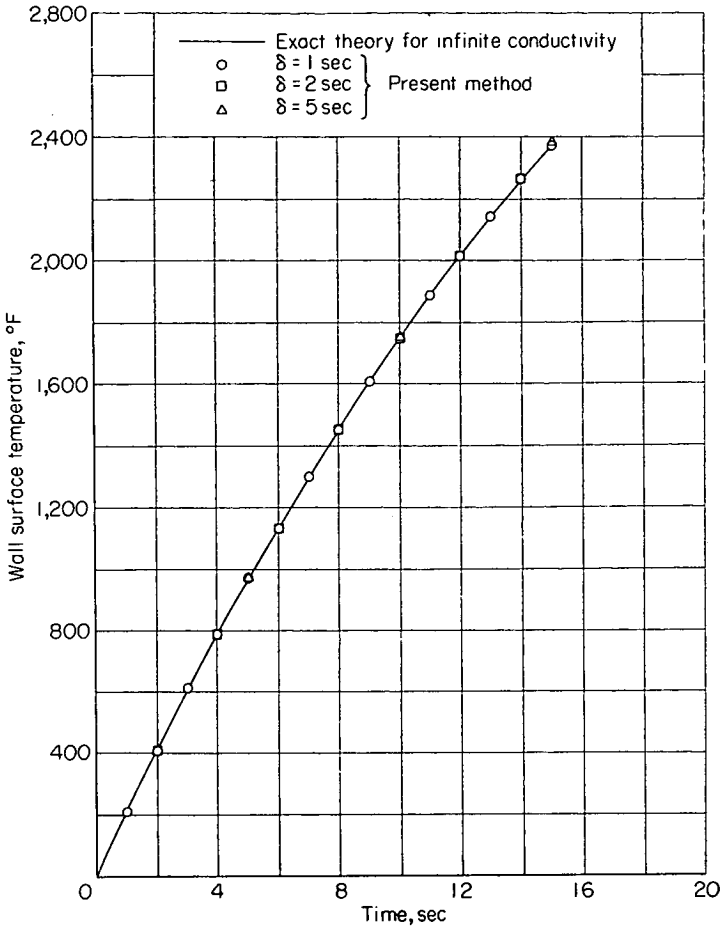


FIGURE 5.—Example 5. Temperatures of $\frac{1}{16}$-inch Inconel wall. T_{aw}=5,000 °F; h=50 Btu/(hr)(sq ft)(°F).

EXAMPLE 6

Problem for example 6 (a).—The temperature history of the heated surface of a ½-inch copper wall initially at zero temperature is given by the following time series in which the temperatures are for ½-second intervals: T=4.8, 13.2, 25.2, 40.2, 58.2, 77.9, 99.4, 122.6, 146.3, 169.8, 193.0, 214.8, 235.3, 253.2, 268.8, 281.5, 290.8, 296.7, 298.0, 297.5. The inside surface is insulated. Determine the history of heat flow into the heated surface from the given surface-temperature history.

Solution for example 6 (a).—If the time interval used is sufficiently small, the average rate of heat flow over the interval is a good approximation to the rate of heat flow at the center of the interval. Equation (42), which gives the average rate of heat flow over the interval ending at $t=m\delta$, may be used. For a value of δ of ½ second, the values of M are given in table II. Substituting in equation (42) gives the rate of heat flow plotted as circles in figure 6. The solid curve gives the theoretically exact instantaneous rate of heat flow for comparison. The results from equation (42) are seen to be precise. The system yielding instantaneous heat flow, mentioned previously, would seem to be a natural one for the present problem; however, the results obtained by that system were found to be inferior to those presented.

Problem for example 6 (b).—The corresponding inside-surface-temperature history of the same wall is given by

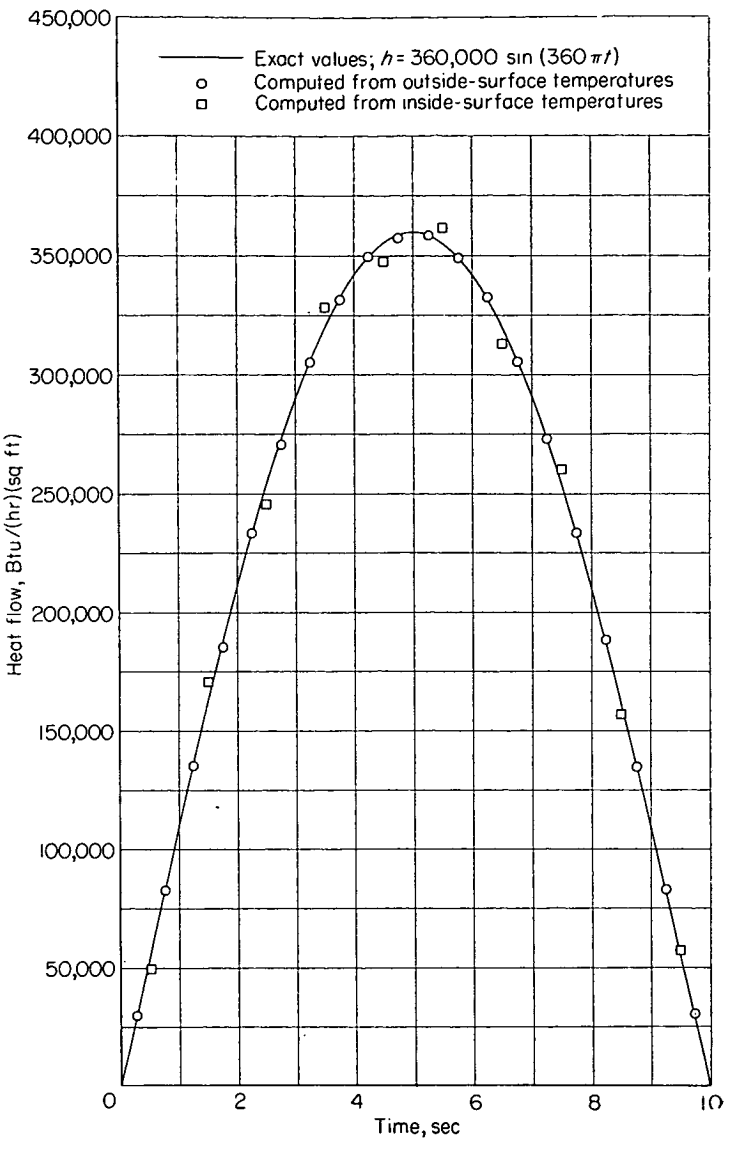


FIGURE 6.—Example 6. Rate of heat flow into heated (outer) surface of ½-inch copper wall computed from temperature history of outer surface and from temperature history of inner surface.

the following time series in which the temperatures are for ½-second intervals: T_i=0.8, 4.4, 11.7, 22.4, 36.0, 52.6, 71.6, 92.3, 114.2, 137.4, 160.6, 183.7, 205.4, 226.4, 245.3, 261.6, 275.2, 285.6, 292.4, 296.3. Determine the history of heat flow into the outer surface by using only the given inside temperatures.

Solution for example 6 (b).—Equations (43) may be used to determine the outside-surface-temperature history from the inside-temperature history. Then, the rate of heat flow at any time is determined as in the solution for example 6 (a). The factor $1/(1-\theta_1)$ in equations (43) may be thought of as a magnification factor. Large values of this factor tend to cause an instability in the computed temperatures. In this example, if δ is taken as ½ second or 1/7200 hour, the value of $k\delta/l^2$ is 0.3528, θ_1 is 0.80478, and the magnification factor is 5.1. On substitution in equations (43), an oscillation of period 2δ builds up in the values of T, very slowly at first and to either side of the correct answer as a mean value, but in a divergent manner so that by 4 seconds the amplitude is 6°. For a value of δ of 1 second, the value

of $k\delta/l^2$ is 0.7056, θ_1 is 0.58038, and the magnification factor is 2.4. In this instance, an oscillation in T of period 2δ and maximum amplitude of 1.5° occurred. Substituting these values of T, without fairing, into equation (42) gives the results shown by the square symbols in figure 6. If a larger value of δ were used, the oscillation would be damped out but the accuracy would suffer because of a lack of definition of the rapidly varying heating rate. The particular case demonstrated is therefore a marginal one for the determination of heat flow from the temperatures of the inside surface. The instability is found to disappear for thermally thinner walls and conversely to increase rapidly for thicker walls.

CONCLUDING REMARKS

Formulas to facilitate the determination of the transient surface temperatures of thick walls from an arbitrary variation of adiabatic-wall temperature and heat-transfer coefficient have been developed. Formulas to facilitate the determination of heat flow from an arbitrary variation of wall surface temperature were also obtained. The numerical applications given demonstrate a high degree of accuracy for the present method.

LANGLEY AERONAUTICAL LABORATORY,
NATIONAL ADVISORY COMMITTEE FOR AERONAUTICS,
LANGLEY FIELD, VA., *June 18, 1957*.

APPENDIX A

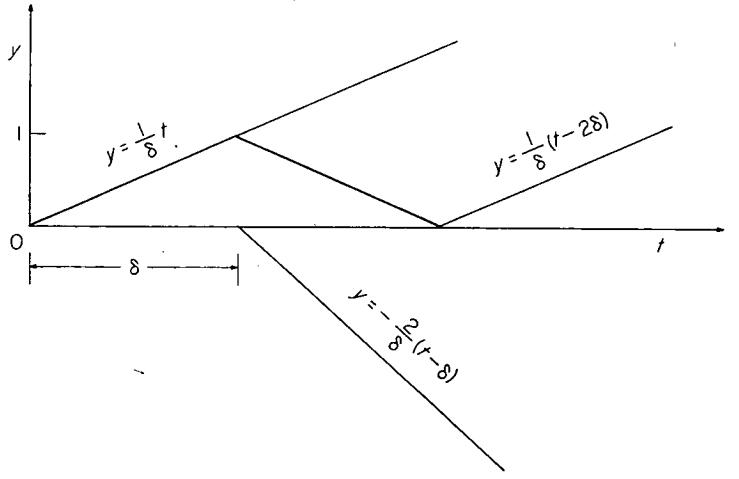
REVIEW OF SUPERPOSITION AND TIME SERIES

TIME SERIES

A time series may be defined as a series of numbers or quantities which represent the values of a function of time at successive equal intervals of time. According to the notation of Tustin (ref. 3), each quantity is separated from the others by a comma since the values corresponding to different times are not added together. The quantity at zero time is zero. The first quantity recorded represents the value of the function at the end of the first time interval. The time interval used is arbitrary and its size is selected to obtain the accuracy required in the solution of a specific problem. The symbol for the time interval is δ. Thus, the series $y=y_1, y_2, y_3, \ldots y_m$ represents the values of the function y at the times $\delta, 2\delta, 3\delta, \ldots m\delta$.

THE UNIT TRIANGLE

A unit triangle is an isosceles triangle which has an altitude of unit magnitude and a base of 2δ, or two time intervals. Since δ is an arbitrary time interval, the unit triangle is accordingly arbitrary. A plot of a unit triangle centered at $t=\delta$ is shown in sketch 1, where y represents magnitude



Sketch 1.

or altitude. The slopes of the sides of the triangle depend on the value of δ and are equal to $\pm 1/\delta$. Three lines may be superimposed to represent the unit triangle. The equations of the three lines which may be added to represent the unit triangle are $y=(1/\delta)t$, $y=-(2/\delta)(t-\delta)$, and $y=(1/\delta)(t-2\delta)$. Although the triangle terminates at $t=2\delta$, the values of t in the equations for y can go on to infinity since the values of y add to 0 beyond $t=2\delta$.

THE FUNCTION CORRESPONDING TO A REFERENCE LINE

Let $F(x,t)$ be the solution to a boundary-value problem specified by a linear partial differential equation and the linear boundary condition $y=(1/\delta)t$, where y is the value of F or one of its derivatives or integrals at some fixed value of x. Because of the linearity of the problem, the magnitude of the solution is directly proportional to the magnitude of the slope $1/\delta$ of the boundary condition. For example, if $y=(2/\delta)t$, the corresponding function representing the solution is $2F(x,t)$. Again, if $y=-(2/\delta)t$, the corresponding function is $-2F(x,t)$. The slope of the line $y=(1/\delta)t$ can thus be used as a reference magnitude. This slope is the same as that of the left side of the unit triangle.

The value of t in $F(x,t)$ is always identical with the value of t in the boundary condition $y=(1/\delta)t$. Thus, if the origin is shifted so that $y=(1/\delta)(t-2\delta)$, then the corresponding function is $F(x,t-2\delta)$. Particular solutions of a linear differential equation can always be added in linear combinations to satisfy more general boundary conditions. If a and b are constants, and $aF(x,t)$ corresponds to the boundary condition $y_1=(a/\delta)t$, and $bF(x,t-\delta)$ corresponds to $y_2=(b/\delta)(t-\delta)$, then the function corresponding to the sum of the two lines $y=y_1+y_2$ is $F=aF(x,t)+bF(x,t-\delta)$. Let an additional property of F, as well as of y, be that it assumes the value 0 for any time less than 0. The range of time of interest is therefore from 0 to ∞.

THE FUNCTION CORRESPONDING TO A TRIANGLE

Now consider a function $F_\Delta(t)$ dependent on the lines of the unit triangle in sketch 1 for its value just as $F(t)$ is related to the line $y=(1/\delta)t$. In consideration of the three lines by which the unit triangle may be replaced, $y=(1/\delta)t$, $y=-(2/\delta)(t-\delta)$, and $y=(1/\delta)(t-2\delta)$, the three corresponding solutions or functions of time are $F(t)$, $-2F(t-\delta)$, and $F(t-2\delta)$. Because of the additive nature of solutions, the solution corresponding to the complete triangle may be defined as the sum of the solutions for the lines which compose it:

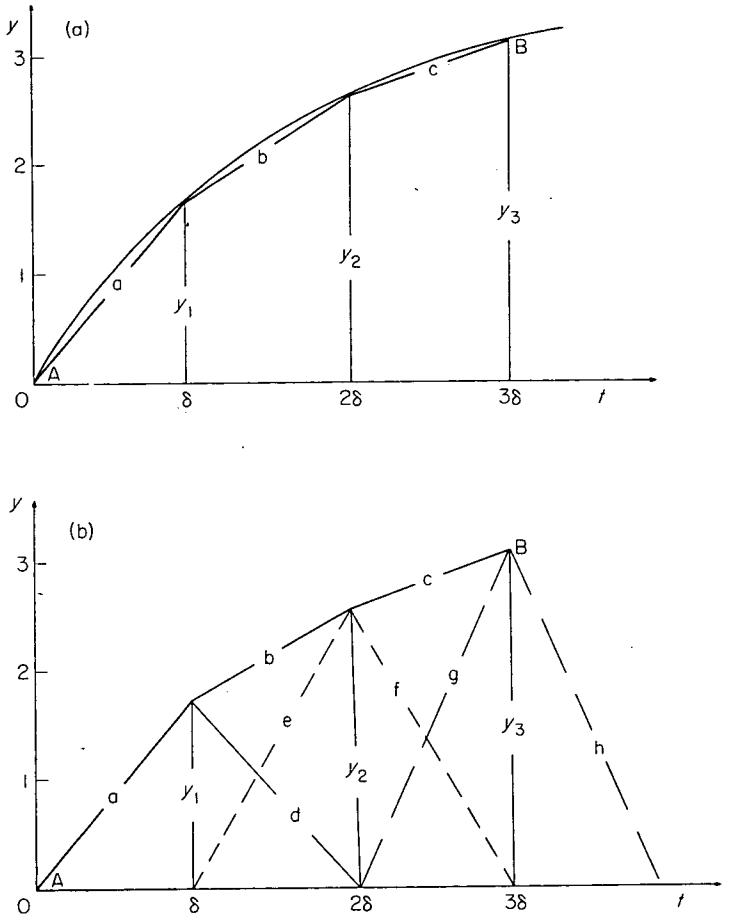
$$F_\Delta(t)=F(t)-2F(t-\delta)+F(t-2\delta) \qquad \text{(A1)}$$

In equation (A1) each term has a value of zero for negative values of its argument.

REPRESENTATION OF A GENERAL CURVE BY TRIANGLES

The curve A–B in sketch 2 (a) is any arbitrary continuous function in the plane y,t which can be faired through its

ordinate values 0, y_1, y_2, and y_3. The curve may be well approximated by a series of chords such as a, b, and c if a suitable spacing δ is used.



(a) Curve A–B.

(b) Synthesis of curve A–B.

Sketch 2.

Draw the lines d, e, f, g, and h of sketch 2 (b) to form the isosceles triangles with sides a and d, e and f, and g and h. Since the sum of two straight lines is a straight line, it is clear that, if the letters which designated the lines are now used to designate the equation of the line, then d+e=b and f+g=c. Of course, the line a is the first half of the first triangle as well as the first chord of the curve A–B. In designating the ordinates $y_1, y_2, y_3, \ldots y_m$, the altitudes of three triangles whose sides add up to the chords of the curve A–B are simultaneously designated. The ordinate series $y_1, y_2, y_3, \ldots y_m$, with spacing δ, is a time-series approximation of the curve A–B. In this case, as well as elsewhere in this report, each ordinate of a series is understood to represent the altitude of an isosceles triangle with a base width of 2δ.

ARBITRARY CONTROL FUNCTIONS

Suppose that the curve A–B, or $y(t)$, is to serve as an arbitrary reference or control function for a corresponding function $F_y(t)$. It is desired to determine $F_y(t)$ in terms of functions corresponding to unit triangles, such as $F_\Delta(t)$, given by equation (A1). The function $F_\Delta(t)$ is a function corresponding to a unit triangle centered at $t=\delta$. If $F_\Delta(t)$ is multiplied by y_1, there results the function corresponding to the triangle with sides a and d of sketch 2 (b). By superposition, the function corresponding to the three triangles centered at δ, 2δ, and 3δ is

$$F_y(t)=y_1F_\Delta(t)+y_2F_\Delta(t-\delta)+y_3F_\Delta(t-2\delta) \qquad \text{(A2)}$$

Then, since the three triangles add up to the chords of the curve A–B, this is the function, in ordinary algebraic form, corresponding exactly to the chords of the general reference curve $y=y_1, y_2, y_3, \ldots y_m$. In order to put equation (A2) in time-series form, let $F_\Delta(t)=a_1, a_2, a_3, \ldots a_m$, with spacing δ. Substituting in (A2) and placing terms for the same time in columns and adding yield

$$\begin{array}{lllll} y_1F_\Delta(t) & =y_1a_1, & y_1a_2, & y_1a_3, & \ldots \\ y_2F_\Delta(t-\delta) & = 0, & y_2a_1, & y_2a_2, & \ldots \\ y_3F_\Delta(t-2\delta) & = 0, & 0, & y_3a_1, & \ldots \\ \hline F_y(t) & =y_1a_1, & (y_1a_2+y_2a_1), & (y_1a_3+y_2a_2+y_3a_1), & \ldots \end{array} \qquad \text{(A3)}$$

The result shown by equation (A3) is obviously that which is obtained by formal algebraic multiplication of $a_1, a_2, a_3, \ldots$ by $y_1, y_2, y_3, \ldots$ as follows:

$$\begin{array}{lllll} F_\Delta(t)= & a_1, & a_2, & a_3, & \ldots \\ y(t)= & y_1, & y_2, & y_3, & \ldots \\ \hline & y_1a_1, & y_1a_2, & y_1a_3, & \ldots \\ & & y_2a_1, & y_2a_2, & \ldots \\ & & & y_3a_1, & \ldots \end{array}$$

$$F_y(t)=y_1a_1, (y_1a_2+y_2a_1), (y_1a_3+y_2a_2+y_3a_1), \ldots \qquad \text{(A4)}$$

Therefore,

$$F_y(t)_s=[F_\Delta(t)_s][y(t)_s] \qquad \text{(A5)}$$

where the subscript s denotes time-series form.

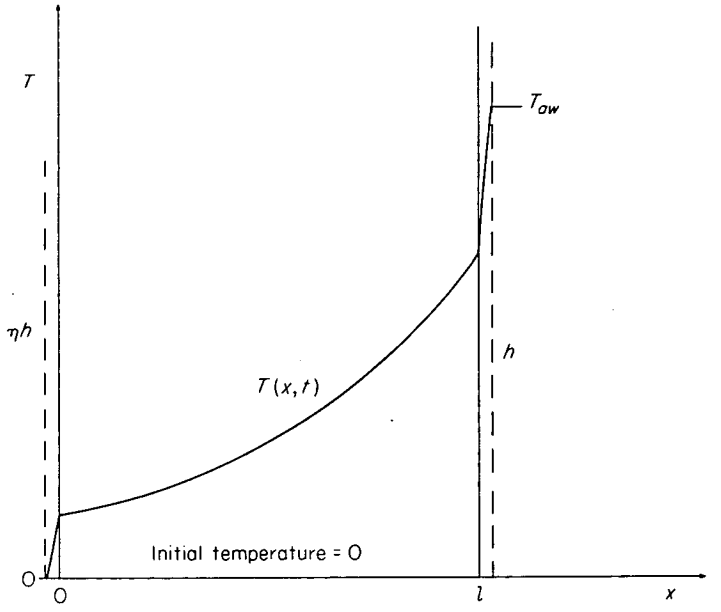
Equation (A5) states a simple theorem which was first given in reference 3. It was developed with $y(t)$ having a value of 0 at $t=0$ and $F_\Delta(t)$ also having a value of 0 at $t=0$. If either or both of the series had values other than 0 at $t=0$, multiplication as in equation (A5) would not be sufficient to obtain F_y.

APPENDIX B

SUMMARY OF ANALYTICAL TEMPERATURE FORMULAS FOR THICK WALLS

CONSTANT FLUID TEMPERATURES

Consider an infinite wall of thickness l and an initial temperature of zero. (See sketch 3.) Let the wall be suddenly



Sketch 3.

contacted at the face $x=l$ by a fluid of temperature T_{aw} while the face at $x=0$ remains exposed to a fluid of zero temperature. Let the heat-transfer coefficient at the face $x=l$ have the value h and the heat-transfer coefficient at the face $x=0$ have the value ηh. Let the wall have uniform physical properties which are invariant with time.

The flow of heat within the wall is governed by Fourier's equation for transient heat flow, which states that the rate of increase of temperature is proportional to the rate of change of temperature gradient:

$$\frac{\partial T}{\partial t}=k\frac{\partial^2 T}{\partial x^2} \tag{B1}$$

The constant of proportionality, called the diffusion coefficient, is equal to the ratio of the conductivity of the material to the heat capacity as represented by the product of specific heat and weight density as follows:

$$k=\frac{K}{c\rho}$$

The boundary equation for the wall at $x=l$ is obtained by equating the heat transfer between the fluid at temperature T_{aw} and the wall at temperature T to the rate of heat transfer in the wall at $x=l$:

$$h(T_{aw}-T_{x=l})=K\left(\frac{\partial T}{\partial x}\right)_{x=l} \tag{B2}$$

A similar boundary equation is written for $x=0$:

$$\eta h T_{x=0}=K\left(\frac{\partial T}{\partial x}\right)_{x=0} \tag{B3}$$

The initial condition specifies that the initial temperature of the wall is zero:

$$(T)_{t=0}=0 \tag{B4}$$

The simultaneous solution of partial differential equations (B1) to (B4) by operational methods yields the infinite series:

$$T=T_{aw}\frac{1+\eta\frac{hx}{K}}{1+\eta+\eta\frac{hl}{K}}-2T_{aw}\sum_{n=1}^{\infty}\frac{\left[\cos\left(\frac{x}{l}\alpha_n\right)+\frac{\eta}{\alpha_n}\frac{hl}{K}\sin\left(\frac{x}{l}\alpha_n\right)\right]e^{-\alpha_n^2\frac{kt}{l^2}}}{\left[\frac{K}{hl}\alpha_n^2-\eta\frac{hl}{K}-3(1+\eta)\right]\cos\alpha_n+\left[\left(\frac{4K}{hl}+1+\eta\right)\alpha_n-2\frac{\eta}{\alpha_n}\frac{hl}{K}\right]\sin\alpha_n} \tag{B5}$$

The parameters α_n are angles which are the positive roots of the equation

$$\tan\alpha_n=\frac{\alpha_n(1+\eta)}{\alpha_n^2\frac{K}{hl}-\eta\frac{hl}{K}} \tag{B5a}$$

Two dimensionless numbers of physical significance are present in equation (B5): the diffusion number kt/l^2, and the conductance or Nusselt number hl/K. The first term of equation (B5) gives the steady-state solution or equilibrium condition.

SPECIAL CASE $\eta=0$

The special case of a plate that is heated by convection on one face while the heat transfer on the other face is so small as to be negligible is important. Setting the heat-transfer coefficient at the unheated face equal to zero corresponds to making the assumption that the plate is perfectly insulated at that face. If the plate is perfectly in-

sulated at the face $x=0$, substitute $\eta=0$ in equations (B5) and (B5a) and utilize the following relation to eliminate $\sin \alpha_n$,

$$\alpha_n \tan \alpha_n = \frac{hl}{K} \tag{B6}$$

where α_n represents the positive roots of the equation. These substitutions yield the following expression for temperature:

$$T = T_{aw} - 2T_{aw} \sum_{n=1}^{\infty} \frac{\cos\left(\frac{x}{l}\alpha_n\right) e^{-\frac{kt}{l^2}\alpha_n^2}}{\left(1+\frac{hl}{K}+\frac{K}{hl}\alpha_n^2\right)\cos\alpha_n} \tag{B7}$$

Equations (B6) and (B7) may be found on page 100 of reference 1.

SPECIAL CASE $\eta=0$ AND $h=\infty$

The special case in which $\eta=0$ and $h=\infty$ corresponds physically to perfect insulation on one face and a known initial temperature on the other face. This case is developed by setting $h=\infty$ in equations (B6) and (B7). Equation (B6) becomes

$$\alpha_n \tan \alpha_n = \infty$$

$$\tan \alpha_n = \infty$$

or, since α_n assumes the sequence $\frac{\pi}{2}, \frac{3\pi}{2}, \frac{5\pi}{2}$, and so forth,

$$\alpha_n = (2n-1)\frac{\pi}{2}$$

Equation (B7) reduces to

$$T = T_S - \frac{4}{\pi} T_S \sum_{n=1}^{\infty} \frac{(-1)^{n-1}}{2n-1} \cos\left[(2n-1)\frac{\pi}{2}\frac{x}{l}\right] e^{-(2n-1)^2\frac{\pi^2}{4}\frac{kt}{l^2}} \tag{B8}$$

Equation (B8) may be found in standard references (ref. 5, page 196, problem 6, for example). In this equation, T_S is the step in wall-surface temperature used in place of T_{aw}.

VARIABLE FLUID TEMPERATURE

ARBITRARY VARIATION OF T_{aw}

Equation (B7) is an exact solution of a thick-wall boundary-layer heating problem which is suitable for checking the accuracy of the present method of computing wall temperatures. Another method, which is more general, can be obtained by letting the adiabatic-wall temperature vary in a known manner, $T_{aw}=F(t)$. Let $V(x,t)$ be the variation of wall temperature due to a 1° step in adiabatic-wall temperature. If the initial wall temperature is zero, the wall temperature is given by Duhamel's formula as

$$T(x,t) = \int_0^t \dot{F}(\tau) V(x, t-\tau) d\tau \tag{B9}$$

where $\dot{F}$ is the derivative of F with respect to t and τ is a dummy time variable.

LINEAR VARIATION OF T_{aw}

In the linear variation of T_{aw}, $T_{aw}=bt$, or, in the notation of Duhamel's formula, $F=bt$ and $\dot{F}=b$. Substituting T from equation (B7), with $T_{aw}=1$, into equation (B9) and performing the integration give

$$T(x,t) = bt - \frac{2bl^2}{k} \sum_{n=1}^{\infty} \frac{\cos\left(\frac{x}{l}\alpha_n\right)\left(1-e^{-\frac{kt}{l^2}\alpha_n^2}\right)}{\alpha_n^2\left(1+\frac{hl}{K}+\frac{K}{hl}\alpha_n^2\right)\cos\alpha_n} \tag{B10}$$

Equation (B6) is used to obtain α_n.

LINEAR VARIATION OF WALL SURFACE TEMPERATURE

One of the fundamental equations on which is based the time-series development of surface-temperature equations is one expressing the transient wall temperature due to an increase of 1° in temperature of one wall surface during each interval of time δ. The assumptions are made that the initial temperature is zero and that one wall is insulated. From these considerations, F in Duhamel's formula is $F=t/\delta$ and $\dot{F}=1/\delta$. Substituting this derivative and T from equation (B8), with $T_S=1$, into equation (B9) and performing the integration give the following equation for the temperature at any plane due to a surface temperature rise of 1° per unit of time δ:

$$T = \frac{t}{\delta} - \frac{16}{\pi^3}\frac{l^2}{k\delta} \sum_{n=1}^{\infty} \frac{(-1)^{n-1}\cos\left[(2n-1)\frac{\pi}{2}\frac{x}{l}\right]}{(2n-1)^3}\left(1-e^{-(2n-1)^2\frac{\pi^2}{4}\frac{k}{l^2}t}\right) \tag{B11}$$

The heat flow at any point within the wall due to 1° rise of wall surface temperature in the time δ is obtained by multiplying the conductivity by the temperature gradient. Differentiating equation (B11) with respect to x and multiplying by K yield

$$q = \frac{8}{\pi^2}\frac{lK}{k\delta} \sum_{n=1}^{\infty} \frac{(-1)^{n-1}\sin\left[(2n-1)\frac{\pi}{2}\frac{x}{l}\right]}{(2n-1)^2}\left(1-e^{-(2n-1)^2\frac{\pi^2}{4}\frac{k}{l^2}t}\right)$$

In order to eliminate k in the coefficient, substitute for k its definition $k=K/\rho c$. Then $lK/k\delta=\rho cl/\delta$. The product ρcl is the heat capacity of the wall per unit area per degree and is represented by the symbol G. In order to obtain the heat flow at the heated surface, where the heat balance is to be made, let $x=l$. Hence, the instantaneous heat flow due to a uniformly increasing surface temperature of 1° per unit of time δ is simplified to

$$q = \frac{8G}{\pi^2\delta} \sum_{n=1}^{\infty} \frac{1-e^{-(2n-1)^2\frac{\pi^2}{4}\frac{kt}{l^2}}}{(2n-1)^2} \tag{B12}$$

In order to find the average flow of heat over the interval δ, equation (B12) is integrated with respect to time between the limits $(t-\delta)$ and t. This integration gives the total heat flow through the surface during the interval. On dividing by δ, the average rate of flow for the interval is obtained. The result is

$$\bar{q}=\frac{8}{\pi^2}\frac{G}{\delta}\sum_{n=1}^{\infty}\left[\frac{1}{(2n-1)^2}+\frac{e^{-(2n-1)^2\frac{\pi^2}{4}\frac{k}{l^2}t}}{\frac{\pi^2}{4}\frac{k}{l^2}\delta(2n-1)^4}-\frac{e^{-(2n-1)^2\frac{\pi^2}{4}\frac{k}{l^2}(t-\delta)}}{\frac{\pi^2}{4}\frac{k}{l^2}\delta(2n-1)^4}\right] \tag{B13}$$

The summation $\sum_{n=1}^{\infty}\frac{1}{(2n-1)^2}$ is a constant with the value $\pi^2/8$. In working with time series only integral increments of time (δ, 2δ, 3δ, . . . $m\delta$) are used. In equation (B13), therefore, t may have any value $m\delta$, where m is an integer. For convenience, and to systematize results, the following identities are defined:

$$\left.\begin{aligned}
A_0&\equiv\frac{4l^2}{\pi^2k\delta}\sum_{n=1}^{\infty}\frac{1}{(2n-1)^4}\\
&\cdots\cdots\cdots\cdots\\
A_{m-1}&\equiv\frac{4l^2}{\pi^2k\delta}\sum_{n=1}^{\infty}\frac{e^{-(m-1)(2n-1)^2\frac{\pi^2}{4}\frac{k}{l^2}\delta}}{(2n-1)^4}\\
A_m&\equiv\frac{4l^2}{\pi^2k\delta}\sum_{n=1}^{\infty}\frac{e^{-m(2n-1)^2\frac{\pi^2}{4}\frac{k}{l^2}\delta}}{(2n-1)^4}
\end{aligned}\right\} \tag{B14}$$

Equation (B13) then becomes

$$\bar{q}_m=\frac{8}{\pi^2}\frac{G}{\delta}\left(\frac{\pi^2}{8}+A_m-A_{m-1}\right) \tag{B15}$$

for the time interval ending at $t=m\delta$. Equation (B15) is used in forming the heat balance at the heated wall surface in the derivation of wall temperature formulas.

APPENDIX C

ANALYTICAL TEMPERATURE DISTRIBUTION

Equations (40) are the formulas most convenient for determining the temperature of the inside surface or of any plane within the surface. For the determination of the temperature of planes within the wall, equations (36a) are ordinarily evaluated numerically to obtain θ for a given kt/l^2 and x/l. However, it may be necessary to obtain the temperature distribution through the wall at some instant of time due to an arbitrary surface-temperature history in a form that is analytical with respect to x and that can be differentiated or integrated with respect to x (for example, in the derivation of a general formula for the thermal stress distribution or maximum stress). This temperature distribution is obtained by substituting equations (36a) into equations (39), substituting equations (39) into equations (40), and collecting terms. The results are

$$T_{i,1}=T_1-\frac{16}{\pi^3}\frac{l^2}{k\delta}T_1\sum_{n=1}^{\infty}\frac{(-1)^{n-1}}{(2n-1)^3}\cos\left[(2n-1)\frac{\pi}{2}\frac{x}{l}\right]\left[1-e^{-(2n-1)^2\frac{\pi^2}{4}\frac{k\delta}{l^2}}\right]$$

$$T_{i,2}=T_2-\frac{16}{\pi^3}\frac{l^2}{k\delta}\sum_{n=1}^{\infty}\left\{\frac{(-1)^{n-1}\cos\left[(2n-1)\frac{\pi}{2}\frac{x}{l}\right]}{(2n-1)^3}\right\}\left[T_2-T_1+(2T_1-T_2)e^{-(2n-1)^2\frac{\pi^2}{4}\frac{k\delta}{l^2}}-T_1e^{-2(2n-1)^2\frac{\pi^2}{4}\frac{k\delta}{l^2}}\right]$$

$$T_{i,3}=T_3-\frac{16}{\pi^3}\frac{l^2}{k\delta}\sum_{n=1}^{\infty}\left\{\frac{(-1)^{n-1}\cos\left[(2n-1)\frac{\pi}{2}\frac{x}{l}\right]}{(2n-1)^3}\right\}\left[T_3-T_2+(-T_3+2T_2-T_1)e^{-(2n-1)^2\frac{\pi^2}{4}\frac{k\delta}{l^2}}+\right.$$
$$\left.(2T_1-T_2)e^{-2(n-1)^2\frac{\pi^2}{4}\frac{k\delta}{l^2}}-T_1e^{-3(2n-1)^2\frac{\pi^2}{4}\frac{k\delta}{l^2}}\right]$$

. . . . . .

$$T_{i,m}=T_m-\frac{16}{\pi^3}\frac{l^2}{k\delta}\sum_{n=1}^{\infty}\left\{\frac{(-1)^{n-1}\cos\left[(2n-1)\frac{\pi}{2}\frac{x}{l}\right]}{(2n-1)^3}\right\}\left[T_m-T_{m-1}+(-T_m+2T_{m-1}-T_{m-2})e^{-(2n-1)^2\frac{\pi^2}{4}\frac{k\delta}{l^2}}+\right.$$
$$\left.(-T_{m-1}+2T_{m-2}-T_{m-3})e^{-2(2n-1)^2\frac{\pi^2}{4}\frac{k\delta}{l^2}}+\ldots+(2T_1-T_2)e^{-(m-1)(2n-1)^2\frac{\pi^2}{4}\frac{k\delta}{l^2}}-T_1e^{-m(2n-1)^2\frac{\pi^2}{4}\frac{k\delta}{l^2}}\right]$$

Note that $T_{i,1}$, $T_{i,2}$, $T_{i,3}$, and $T_{i,m}$ can be computed independently. The use of these equations involves considerable labor, however, because all terms in the summation must be summed in unison.

REFERENCES

1. Carslaw, H. S., and Jaeger, J. C.: Conduction of Heat in Solids. The Clarendon Press (Oxford), 1947.
2. Schmidt, Ernst: Thermodynamics. The Clarendon Press (Oxford), 1949, pp. 428–436.
3. Tustin, A.: A Method of Analysing the Behavior of Linear Systems in Terms of Time Series. Jour. Inst. Elec. Eng. (British), vol. 94, pt. II–A, no. 1, 1947, pp. 130–142.
4. Bubb, Frank W.: Cardinal Spectrum Analysis of Physical Systems. AF Tech. Rep. No. 6300, Wright Air Dev. Center, U. S. Air Force, Mar. 1951.
5. Churchill, Ruel V.: Modern Operational Mathematics in Engineering. McGraw-Hill Book Co., Inc., 1944.

REPORT 1373

THEORETICAL ANALYSIS OF TOTAL-PRESSURE LOSS AND AIRFLOW DISTRIBUTION FOR TUBULAR TURBOJET COMBUSTORS WITH CONSTANT ANNULUS AND LINER CROSS-SECTIONAL AREAS [1]

By Charles C. Graves and Jack S. Grobman

SUMMARY

Compressible- and incompressible-flow calculations were made of the combustor total-pressure-loss coefficient and liner airflow distribution for tubular turbojet combustors having constant annulus and liner cross-sectional areas along the combustor axis. Information on static- and total-pressure distribution and liner air-jet entrance angles along the length of the combustor was obtained as an intermediate step in the calculations. The calculations include the effects of heat release, annulus wall friction, and variation in discharge coefficients of the liner wall openings along the combustor.

The combustor total-pressure-loss coefficient and liner airflow distribution are presented graphically in terms of the following dimensionless parameters: (1) combustor reference Mach number, (2) ratio of combustor-exit to -inlet total temperature, (3) fraction of total airflow passing through the liner dome, (4) ratio of total open hole area in liner wall to total combustor cross-sectional area, and (5) ratio of liner cross-sectional area to total combustor cross-sectional area.

INTRODUCTION

In the design of combustors for turbojet and ramjet engines, it is desirable to be able to predict the combustor total-pressure loss and liner airflow distribution from the combustor geometry and operating conditions. Low values of combustor total-pressure loss are desired since such losses reduce engine thrust and cycle efficiency (ref. 1). Airflow distribution and liner air-jet entrance angles are of direct interest to the combustor designer since they influence combustion efficiency and stability and combustor-outlet temperature profile (ref. 2). A combustion research program being conducted at the Lewis laboratory is concerned with these aerodynamic aspects of combustor design.

The loss in total pressure across a combustor may be attributed primarily to losses resulting from (1) mixing of high-velocity liner air jets with the liner gas stream, (2) heat release in the liner, and (3) annulus wall friction. The effects of these factors on combustor total-pressure loss are considered in the calculations of the present report. The liner airflow distribution and liner air-jet entrance angles are obtained in the course of the combustor total-pressure-loss calculations.

Previous analytical investigations of combustor total-pressure loss and liner airflow distribution have involved stepwise calculations in which the combustor is divided into an arbitary number of transverse sections. In a trial-and-error method presented in reference 3, the liner airflow distribution and combustor total-pressure loss are calculated for an assigned liner open hole area distribution. In a more rapid method presented in reference 4, the liner open hole area distribution is calculated for an assigned liner airflow distribution and combustor total-pressure loss. Both methods include the effects of heat release on the calculated values and could account for variation along the combustor of the discharge coefficient of the liner wall openings.

For particular combustor configurations, stepwise calculation methods such as presented in references 3 and 4 have been used to calculate the combustor flow conditions. However, there is a need for generalized curves that can be used to obtain preliminary estimates of combustor total-pressure loss, liner airflow distribution, and liner airjet entrance angles. Such curves are not intended as a substitute for the stepwise calculation methods, but would serve as a supplement. The curves would also be useful in indicating the relative effects of combustor geometry and operating conditions on combustor total-pressure loss and airflow distribution. The present report is concerned with the development of such generalized curves for tubular combustors having (1) constant annulus and liner cross-sectional areas along the combustor axis and (2) flush circular holes in the liner wall. The results should apply approximately to cannular combustors and to annular combustors having equal velocities in the inner and outer annuli at all stations along the combustor.

From compressible- and incompressible-flow calculations, the combustor total-pressure-loss coefficient and fractional liner airflow distribution are obtained in terms of the following dimensionless parameters: (1) combustor reference Mach number, (2) ratio of combustor-exit to -inlet total temperature, (3) fraction of total airflow passing through the liner dome, (4) ratio of total open hole area in liner wall to total combustor cross-sectional area, and (5) ratio of liner cross-sectional area to total combustor cross-sectional area. The calculations include the effects of heat release, annulus wall friction, and variation in the discharge coefficient of the liner wall openings along the combustor.

[1] Supersedes recently declassified NACA Research Memorandum E56I04 by Charles C. Graves and Jack S. Grobman, 1957.

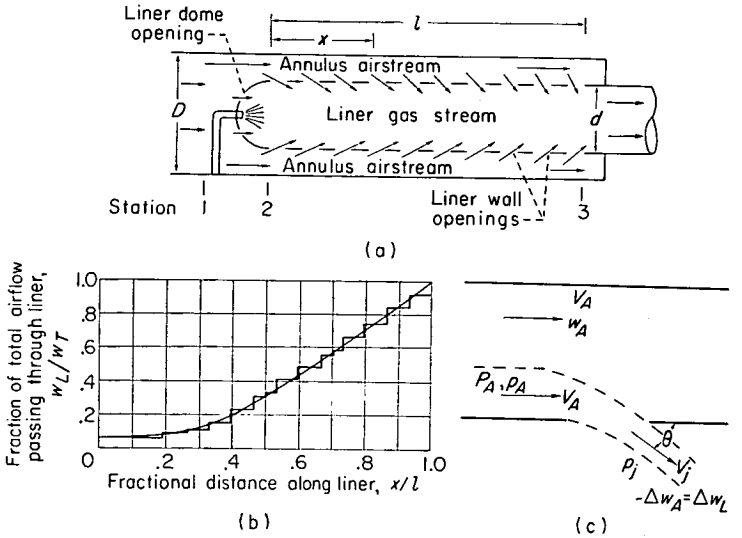
Preceding Page Blank

ANALYSIS

The present report considers the effect on combustor total-pressure loss of (1) mixing of high-velocity liner air jets with the liner gas stream, (2) heat release, and (3) annulus wall friction. The total-pressure loss resulting from these factors is calculated for tubular combustors having constant annulus and liner cross-sectional areas along the combustor axis and flush circular liner wall openings.

Values of the combustor total-pressure-loss coefficient for cold flow are presented for the cases of incompressible and compressible flow. Compressible-flow calculations were made for reference Mach numbers up to 0.15. All values of the combustor total-pressure-loss coefficient for flow with heat release were obtained from the incompressible-flow calculations. The liner airflow distribution and liner air-jet entrance angles are obtained in the course of the calculations of the total-pressure-loss coefficient. A list of the symbols used in the calculations is presented in appendix A.

A sketch of the tubular, parallel-wall combustor considered is presented in figure 1(a). In this figure, station 1 is the combustor inlet, station 2 is just upstream of the first air admission opening in the liner wall excluding openings in the liner dome, and station 3 is just downstream of the last air admission opening in the liner wall. The cross-sectional area at station 1 is the combustor reference cross-sectional area A_r, and inlet flow conditions are referenced at this station. If the air distribution along the combustor is directly proportional to liner open hole area, the liner airflow distribution for a representative turbojet combustor might correspond to the segmented curve of figure 1(b). The fraction of the total airflow passing through the liner at a given station w_L/w_T is plotted against the dimensionless parameter x/l, where l is the axial distance between stations 2 and 3 and x is the axial distance downstream of station 2. The segmented distribution curve corresponding to a finite number of liner wall openings may be replaced approximately by the continuous distribution curve corresponding to an infinite number of liner wall openings or, rather, to continuous slots between stations 2 and 3.



(a) Schematic sketch of parallel-wall combustor.
(b) Representative combustor airflow distribution.
(c) Schematic sketch of flow through liner wall opening.

FIGURE 1.—Air admission in tubular turbojet combustor with constant annulus and liner cross-sectional areas.

The orifice discharge equation for a given liner wall opening, such as is illustrated in figure 1(c), is given by

$$\Delta w_L = C \rho_{st,j} V_j \Delta A_h \tag{1}$$

For a differential portion of the air passing through the opening, equation (1) becomes

$$dw_L = C \rho_{st,j} V_j \, dA_h \tag{2}$$

In the use of equation (2), it is assumed that the flow in the jet from the annulus to the vena contracta is isentropic and that the static pressure in the vena contracta equals that within the liner at the station considered. The effect of cross-sectional area blockage of the liner gas stream by the air jet on the local static pressure at the vena contracta is neglected. The term $\rho_{st,j} V_j$ in equation (2) may then be determined from the annulus total pressure and temperature and the liner static pressure at the station considered. In the calculation of flow conditions in the parallel wall combustor, the airflow distribution in the liner was assumed to be of a continuous form such as illustrated by the smooth curve of figure 1(b), which thus allows the integration of equation (2).

INCOMPRESSIBLE-FLOW CALCULATIONS

Combustor total-pressure-loss coefficient.—As shown in appendix B, for incompressible flow, equation (2) may be rearranged and integrated between stations 2 and 3 to obtain the dimensionless equation

$$\int_{w_{L,2}/w_T}^{1} \frac{d\left(\frac{w_L}{w_T}\right)}{C\sqrt{\frac{P_A - p_L}{q_r}}} = \frac{A_{h,T}}{A_r} \tag{3}$$

In equation (3) the annulus total pressure P_A may be calculated from the combustor-inlet total pressure and the friction pressure drop along the annulus, while the liner static pressure p_L may be calculated from the momentum equation for the liner gas stream. For the case where the annulus and liner cross-sectional areas are constant along the combustor, the term $(P_A - p_L)/q_r$ of equation (3) is related to the combustor total-pressure-loss coefficient $\Delta P/q_r$ by

$$\frac{P_A - p_L}{q_r} = \frac{P_1 - P_{L,3}}{q_r} - \frac{P_1 - P_A}{q_r} - \left(\frac{A_r}{A_L}\right)^2 \left[\frac{T_{L,3}}{T_1} - 2\frac{T_L}{T_1}\left(\frac{w_L}{w_T}\right)^2\right] + \frac{A_r}{A_L}\frac{A_r}{A_A}\left(1 - \frac{w_L}{w_T}\right)^2 \tag{4}$$

where $(P_1 - P_{L,3})/q_r$ is the combustor total-pressure-loss coefficient $\Delta P/q_r$. The principal assumptions required in the derivation of equation (4) are:

(1) The actual flow can be approximated with sufficient accuracy by one-dimensional equations.

(2) The liner air jets mix instantaneously with the liner gas stream.

(3) The effect of fuel flow on molecular weight and weight w of the liner gas stream can be neglected.

(4) Heat transfer between the annulus and liner gas streams is negligible.

(5) Mixing losses in the annulus are negligible.

(6) Liner wall friction is negligible.

(7) Density is independent of pressure changes along the combustor and is affected only by the temperature changes along the combustor associated with heat release.

The relation between $\Delta P/q_r$ and $A_{h,T}/A_r$ is obtained from the solutions of equations (3) and (4). A value of $A_{h,T}/A_r$ is obtained for specified values of $\Delta P/q_r$ and A_L/A_r and values of $(P_1-P_A)/q_r$ and T_L/T_1 along the combustor. In equation (4), T_L and $T_{L,3}$ are the average temperatures of the liner gas stream at a given station and at the combustor exit, respectively. The evaluation of T_L with combustion would require knowledge of the fuel-air ratio and average combustion efficiency along the combustor. In typical combustors, the major portion of the inlet air is bypassed around the liner dome where all the fuel is injected. Accordingly, the average fuel-air ratio of the liner gas stream may vary from values well in excess of stoichiometric at the upstream end of the combustor to lean fuel-air ratios at the combustor exit. For the case where all the fuel is injected at the liner dome, the average fuel-air ratio F_L of the liner gas stream at various stations along the combustor is given by

$$F_L=\frac{F_{L,3}}{\frac{w_L}{w_T}} \tag{5}$$

where $F_{L,3}$ is the over-all fuel-air ratio of the combustor.

In the present calculations, the combustion efficiency was assumed to be 100 percent in the downstream portion of the combustor where the average fuel-air ratio of the liner gas stream is stoichiometric or leaner. In the upstream portion of the combustor where the overrich fuel-air ratios exist, the average temperature of the liner gas stream was assumed to be that corresponding to a stoichiometric fuel-air ratio and 100-percent combustion efficiency. The calculated hot-flow total-pressure-loss coefficient is limited by the accuracy in the determination of gas stream temperature T_L along the combustor.

Figure 2 presents values of T_L/T_1 for 100-percent combustion efficiency and a range of fuel-air ratios. The curve was calculated by the method of references 5 and 6 for T_1 equal to 728° R and for normal octane at an initial temperature of 540° R. From figure 2 and equation (5), the temperature ratio T_L/T_1 of equation (4) may be calculated for various values of w_L/w_T and $F_{L,3}$. Values of $F_{L,3}$ may be obtained from figure 2 and assigned values of the combustor over-all temperature ratio $T_{L,3}/T_1$.

The annulus total-pressure-loss term $(P_1-P_A)/q_r$ of equation (4) can be calculated from the relation

$$\frac{P_1-P_A}{q_r}=\frac{4f_A\frac{l}{D}}{\left(\frac{A_A}{A_r}\right)^2\left[1-\left(1-\frac{A_A}{A_r}\right)^{1/2}\right]}\int_0^{x/l}\left(1-\frac{w_L}{w_T}\right)^2 \mathrm{d}\left(\frac{x}{l}\right) \tag{6}$$

where the friction factor f_A is assumed to be constant. The

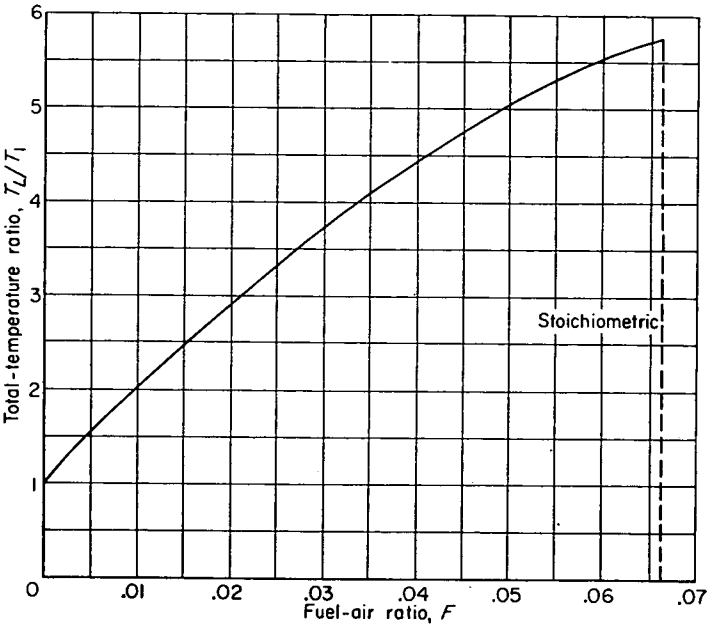


FIGURE 2.—Variation of exhaust to inlet temperature ratio with fuel-air ratio for combustion of n-octane fuel with 100-percent efficiency. Initial air temperature, 728° R; initial fuel temperature, 540° R; pressure, 1 atmosphere.

use of equation (6) requires an estimate of liner airflow distribution along the combustor axis. In the present calculations and for zero flow through the liner dome, the liner airflow distribution used in equation (6) was

$$\frac{w_L}{w_T}=\left(\frac{x}{l}\right)^2 \tag{7}$$

Values of f_A and l/D of 0.005 and 4, respectively, were used in equation (6).

Airflow distribution and air-jet entrance angles.—The liner airflow distribution is obtained as shown in appendix B from the relation

$$\frac{\int_{w_{L,2}/w_T}^{w_L/w_T}\frac{\mathrm{d}\left(\frac{w_L}{w_T}\right)}{C\sqrt{\frac{P_A-p_L}{q_r}}}}{\int_{w_{L,2}/w_T}^{1}\frac{\mathrm{d}\left(\frac{w_L}{w_T}\right)}{C\sqrt{\frac{P_A-p_L}{q_r}}}}=\frac{A_h}{A_{h,T}} \tag{8}$$

From equation (8), values for the fractional liner open hole area $A_h/A_{h,T}$ may be calculated for various values of w_L/w_T.

For thin-walled air admission openings in the liner, the entrance angle θ of the liner air jets (fig. 1) is calculated from the relation

$$\theta=\cos^{-1}\frac{V_A}{V_j} \tag{9}$$

where

$$\frac{V_A}{V_j}=\frac{1-\frac{w_L}{w_T}}{\frac{A_A}{A_r}\sqrt{\frac{P_A-p_L}{q_r}}} \tag{10}$$

COMPRESSIBLE-FLOW CALCULATIONS

The compressible-flow calculations of the combustor total-pressure-loss coefficient, airflow distribution, and liner air-jet entrance angles are similar to the incompressible-flow calculations. The assumptions made in the use of equation (2) as well as assumptions (1) to (6) made in the derivation of equation (4) are also made in the compressible-flow calculations. As a result of the complexity of the compressible-flow relations, however, the difference between annulus total pressure and liner static pressure along the combustor is not obtained directly as in equation (4) for incompressible flow. Details of the compressible-flow calculations are presented in appendix C. The compressible-flow calculations presented herein were made only for cold flow. However, the equations and procedure used for flow with combustion are presented in appendix C.

Combustor total-pressure-loss coefficient.—As shown in appendix C, equation (2) may be rearranged and integrated along the combustor between stations 2 and 3 to yield the following dimensionless equation:

$$\int_{w_{L,2}/w_T}^{1} \frac{M_1 \, \mathrm{d}\left(\frac{w_L}{w_T}\right)}{C\left(\frac{\rho_{st}V}{\rho_t a_t}\right)_j \frac{P_A}{P_1}} = \frac{A_{h,T}}{A_r} \tag{11}$$

The term M_1^* in equation (11) is related to the combustor reference Mach number M_r. The term $(\rho_{st}V/\rho_t a_t)_j$ is obtained from the momentum equation for the liner. As shown in appendix C, values of $(\rho_{st}V/\rho_t a_t)_j$ for cold flow may be calculated in terms of w_L/w_T for specified values of $\Delta P/q_r$, A_L/A_r, and M_r. As in the incompressible-flow calculations, the annulus total pressure P_A is obtained from friction pressure-drop relations and an estimate of the axial liner airflow distribution. For the compressible-flow calculations, the liner airflow distribution used to calculate friction pressure drop was also assumed to follow equation (7), and the values of f_A and l/D were also assumed to equal 0.005 and 4, respectively. Then from equation (11), values of $A_{h,T}/A_r$ for cold flow may be obtained for specified values of $\Delta P/q_r$, A_L/A_r, and M_r.

Airflow distribution and air-jet entrance angles.—The liner airflow distribution for the compressible-flow case is obtained as shown in appendix C from

$$\frac{\int_{w_{L,2}/w_T}^{w_L/w_T} \frac{M_1^* \, \mathrm{d}\left(\frac{w_L}{w_T}\right)}{C\left(\frac{\rho_{st}V}{\rho_t a_t}\right)_j \frac{P_A}{P_1}}}{\int_{w_{L,2}/w_T}^{1} \frac{M_1^* \, \mathrm{d}\left(\frac{w_L}{w_T}\right)}{C\left(\frac{\rho_{st}V}{\rho_t a_t}\right)_j \frac{P_A}{P_1}}} = \frac{A_h}{A_{h,T}} \tag{12}$$

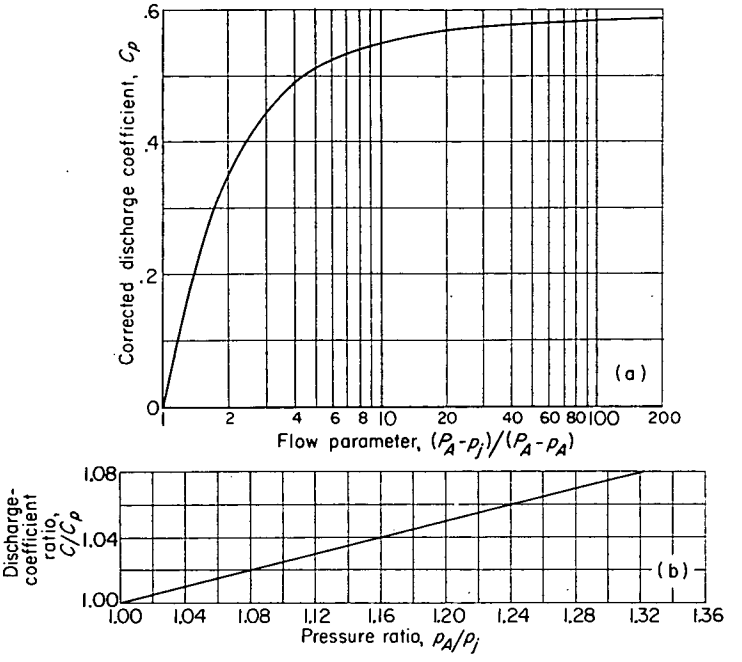
From equation (12), values of $A_h/A_{h,T}$ may be calculated for various values of w_L/w_T.

The entrance angle θ of the liner air jets (see fig. 1(c)) is obtained as shown in appendix C from the relation

$$\theta = \cos^{-1}\frac{M_A}{M_j} \tag{13}$$

DISCHARGE COEFFICIENT OF LINER WALL OPENINGS

Values of the liner wall opening discharge coefficient C required in the calculations of the combustor total-pressure-loss coefficient and airflow distribution may be obtained from correlations such as those presented in reference 7. The present calculations were based on the correlation from reference 7 for a ¾-inch-diameter hole in a 0.040-inch wall. The correlation curves for this opening are presented in figure 3. In figure 3(a), the discharge coefficient C_p corrected to a static-pressure ratio p_A/p_j of unity is plotted against the correlating parameter $(P_A-p_j)/(P_A-p_A)$. In figure 3(b), the ratio C/C_p is plotted against the static-



(a) Variation of corrected discharge coefficient with flow parameter.
(b) Effect of pressure ratio on discharge-coefficient ratio.

FIGURE 3.—Discharge coefficient of ¾-inch-diameter hole in 0.040-inch wall under external crossflow conditions (ref. 7).

pressure ratio p_A/p_j. The discharge coefficient C is obtained from the relation

$$C = C_p\left(\frac{C}{C_p}\right) \tag{14}$$

For incompressible-flow calculations, the correlation parameter $(P_A-p_j)/(P_A-p_A)$ of figure 3(a) may be taken equal to $(V_j/V_A)^2$ and the pressure-ratio correction C/C_p of figure 3(b) can be neglected; thus, the discharge coefficient C is obtained directly from figure 3(a) and the given value of $(V_j/V_A)^2$.

In theory, one would expect that the discharge coefficient C is related to the product of the discharge coefficient for flow normal to the hole C_n and the ratio of the normal component of velocity to the resultant jet velocity V_n/V_j. The term V_n/V_j is related to the air-jet entrance angle θ from the complementary function of equation (9) by

$$\frac{V_n}{V_j} = \sqrt{1-\frac{V_A^2}{V_j^2}} = \sin\theta \tag{15}$$

The relation between the experimental value of C taken from

the data of figure 3(a) and sin θ is shown in figure 4. The dashed curve represents the theoretical equation

$$C = C_n \sin \theta \tag{16}$$

where C_n was obtained from the experimental curve at sin $\theta = 1.0$. The experimental curve exhibited linearity only for values of sin θ greater than 0.45. For values of sin θ greater than 0.45, the experimental discharge-coefficient data

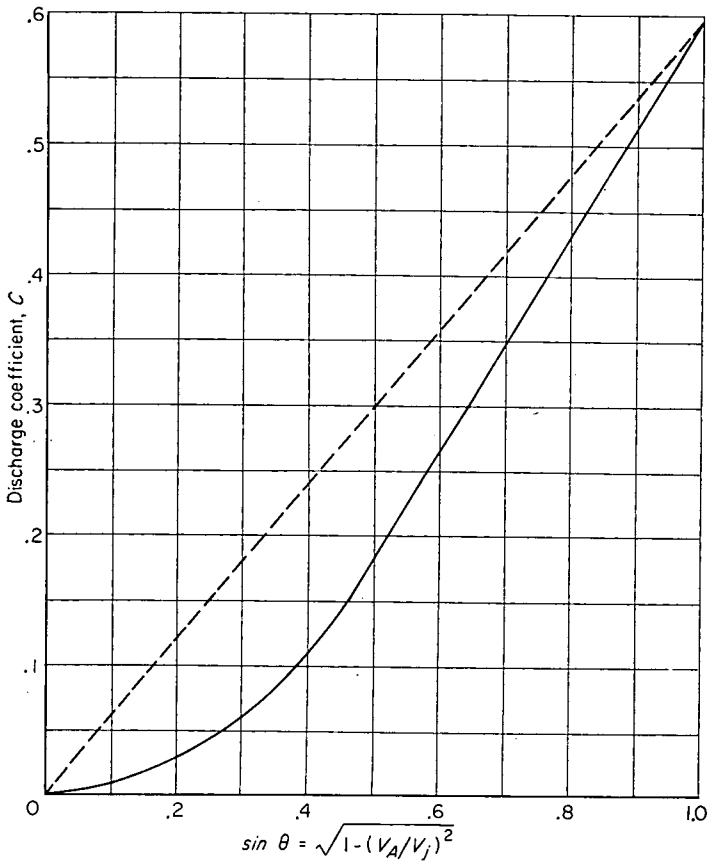


FIGURE 4.—Variation of discharge coefficient with sine of air-jet entrance angle θ.

of figure 3(a) can be represented by the following empirical equation:

$$C = 0.827 \sin \theta - 0.232 \tag{17}$$

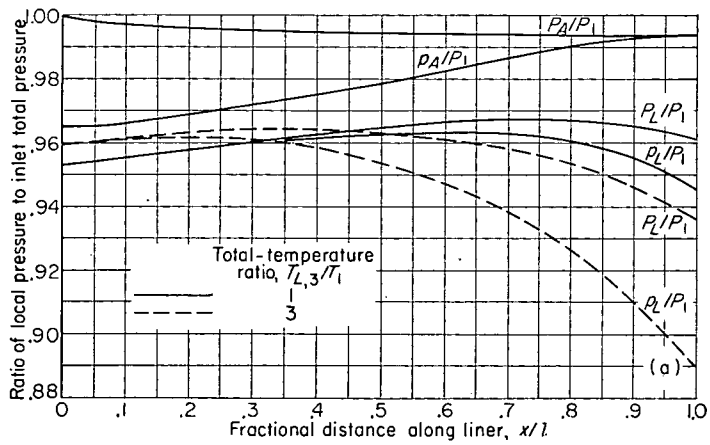
The data of figure 3, however, were used directly for calculations involving discharge coefficients in this report because of their wider range of application.

The correlation of figure 3 gives only the effect of annulus flow on the discharge coefficient. Data of references 8 and 9 indicate that there can also be a large effect of liner gas stream velocity on the discharge coefficient. However, provided the component of the jet velocity normal to the liner wall is larger than the local liner gas stream velocity, the effect of liner gas stream velocity on the discharge coefficient would appear to be small (refs. 8 and 9). Since such a condition existed for most of the calculations of the present report, the effect of liner gas stream velocity on the discharge coefficient was neglected.

RESULTS AND DISCUSSION

Results presented herein pertain only to parallel-wall combustors with flush liner hole openings. The results are considered representative of typical flush liner wall openings even though they are based on only one particular air admission hole geometry, since the data of reference 7 show that the effects of hole diameter and wall thickness on discharge coefficient are small compared to the effects of annulus flow shown in figure 3. The data may not be applicable to combustor liners having a substantial portion of the air admitted through louvers or through holes having intake scoops to direct the air through them.

The calculation of combustor total-pressure loss and airflow distribution requires a knowledge of static and total pressures in the annulus and in the liner along the axis of the combustor from station 2 to station 3 (fig. 1). Figure 5(a) shows the variation of calculated static and total pressures along the combustor expressed as a ratio of pressure at a given station to the inlet total pressure at station 1. This pressure ratio is plotted against the fractional distance along the combustor axis from station 2 to 3. The data for figure 5 were computed for a reference velocity V_r of 100



(a) Static and total pressures along length of combustor referenced to inlet total pressure.

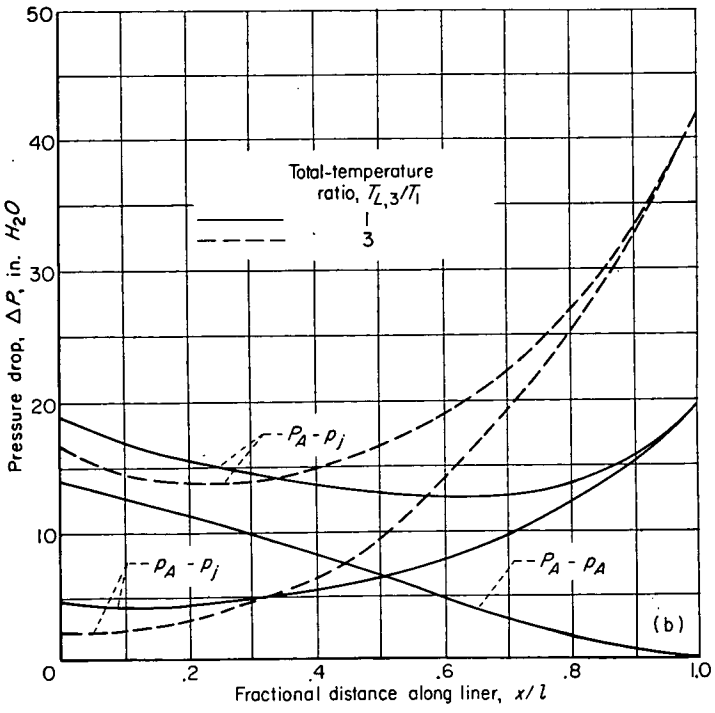
FIGURE 5.—Variation in total and static pressures in annulus and liner and in pressure drop across liner along combustor. Ratio of liner cross-sectional area to reference area A_L/A_r, 0.6; ratio of total liner open hole area to reference area $A_{h,T}/A_r$, 1.09; flow through liner dome $w_{L,2}/w_T$, 0; reference velocity, 100 feet per second; inlet total pressure, 1 atmosphere.

feet per second, an inlet total pressure P_1 of 30 inches of mercury absolute, and zero flow through the liner dome ($w_{L,2}/w_T = 0$) by using incompressible-flow equations including annulus wall friction. The calculations were made for a combustor with a ratio of liner cross-sectional area to reference area A_L/A_r of 0.6, a ratio of total liner open hole area to reference area $A_{h,T}/A_r$ of 1.09, and total-temperature ratios across the combustor $T_{L,3}/T_1$ of 1 (cold flow) and 3. The curves shown are for the case of uniformly distributed liner wall openings along the length of the combustor.

Figure 5(a) shows that the total pressure of the liner gas stream increases with an increase in x/l in the upstream

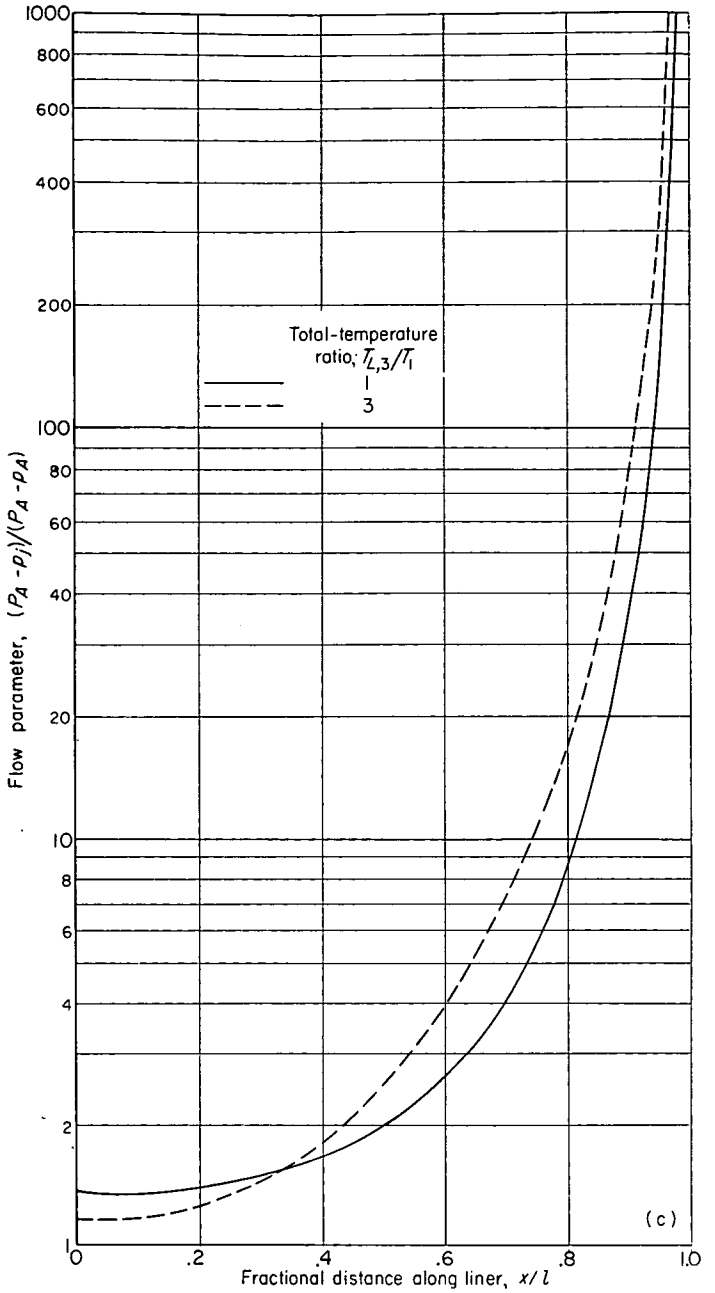
portion of the combustor, reaches a maximum, and then decreases in the downstream portion of the combustor. The variation in the total pressure of the liner gas stream for cold-flow conditions is a result of the difference in velocity of the annulus and liner gas streams. In the upstream portion of the combustor, annulus air at high axial velocity mixes with the low-velocity liner airstream and, hence, increases the total pressure of the liner airstream. In the downstream portion of the combustor, the mixing of the low-velocity annulus air with the high-velocity liner airstream results in a decrease in total pressure of the liner airstream. The maximum total pressure of the liner airstream for cold flow occurs at the station where the axial velocities of the two streams are equal. The curve for the static pressure of the liner airstream exhibits a similar trend although it differs in location of the maximum pressure and the magnitude of the pressure variation. The curves shown in figure 5(a) are intended only to illustrate typical trends in pressure along a combustor; actual values of pressure will vary with combustor geometry and operating conditions.

The static-pressure drop across the liner wall openings as shown in figure 5(b) reaches a minimum in the upstream portion of the combustor and then increases steadily along the axis of the combustor. The pressure-drop terms required for the determination of the flow parameter $(P_A - p_j)/(P_A - p_A)$ (fig. 3(a)) are also presented in figure 5(b). The calculated flow parameter is plotted against fractional liner distance in figure 5(c). A comparison of the curves of figures 3(a) and 5(c) shows that in a parallel-wall combustor the discharge



(b) Pressure drop along length of combustor.

FIGURE 5.—Continued. Variation in total and static pressures in annulus and liner and in pressure drop across liner along combustor. Ratio of liner cross-sectional area to reference area A_L/A_r, 0.6; ratio of total liner open hole area to reference area $A_{h,T}/A_r$, 1.09; flow through liner dome $w_{L,2}/w_T$, 0; reference velocity, 100 feet per second; inlet total pressure, 1 atmosphere.



(c) Variation in flow parameter along combustor.

FIGURE 5.—Concluded. Variation in total and static pressures in annulus and liner and in pressure drop across liner along combustor. Ratio of liner cross-sectional area to reference area A_L/A_r, 0.6; ratio of total liner open hole area to reference area $A_{h,T}/A_r$, 1.09; flow through liner dome $w_{L,2}/w_T$, 0; reference velocity, 100 feet per second; inlet total pressure, 1 atmosphere.

coefficients of the liner hole openings are a minimum at the upstream end of the combustor and a maximum at the exhaust end. Discharge coefficients range from about 0.1 for the upstream liner holes to about 0.6 for the holes at the extreme end of the liner. A variation in discharge coefficients along the liner such as is illustrated by these data would be expected in all parallel-wall combustors with flush liner hole openings; the actual values of discharge coefficients for any given combustor will vary, however, as the pressure distribution along the liner is altered. Since the discharge coefficient and static-pressure drop are indicative of the relative airflow through openings of a given size, it is evident

that the openings in the upstream region of the liner pass less flow per unit area than those in the downstream region of the liner.

COMBUSTOR TOTAL-PRESSURE-LOSS COEFFICIENT

Effect of liner cross-sectional area and liner total open hole area.—Figure 6 shows the effect of (1) the ratio of liner total open hole area to combustor reference area and (2) the ratio of the liner cross sectional area to combustor reference area on the combustor total-pressure-loss coefficient $\Delta P/q_r$. The data were calculated from incompressible-cold-flow relations described in appendix B with zero flow through the liner dome and with and without considering the effects of annulus wall friction. For any given value of A_L/A_r, the pressure-loss coefficient $\Delta P/q_r$ asymptotically approaches a minimum value as $A_{h,T}/A_r$ is increased over a value of about 1.5. For any given value of A_L/A_r, the pressure-loss coefficient

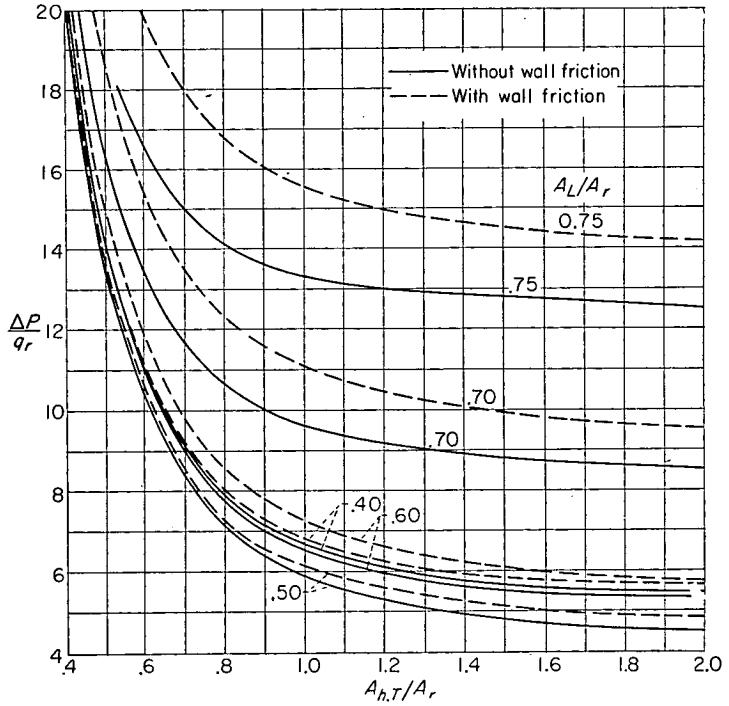


FIGURE 6.—Variation of total-pressure-loss coefficient $\Delta P/q_r$ with ratio of liner total open hole area to combustor reference area $A_{h,T}/A_r$ for various ratios of liner cross-sectional area to combustor reference area A_L/A_r. Data calculated from incompressible-cold-flow relations with zero flow through liner dome.

$\Delta P/q_r$ increases very rapidly as $A_{h,T}/A_r$ is decreased to values below about 1.0.

The consideration of annulus wall friction in the pressure-loss calculations tends to increase $\Delta P/q_r$ for given values of $A_{h,T}/A_r$ and A_L/A_r. The effect of annulus wall friction increased as the annulus area decreased, that is, as A_L/A_r increased. The importance of annulus wall friction on the calculations will, of course, vary with the combustor l/D and airflow distribution. The dashed curves of figure 6 were calculated for an l/D of 4, which is higher than that found in practice, and for an airflow distribution given by equation (7), which corresponds approximately to some fractional open hole area distributions found in practice. Values of $\Delta P/q_r$ for an l/D less than 4 and for the airflow distribution given by equation (7) may be estimated from linear interpolation between the solid curves (negligible wall friction) and the dashed curves of figure 6.

Figure 7 presents the variation of the minimum combustor total-pressure-loss coefficient $\Delta P/q_r$ with the ratio of liner cross-sectional area to reference area A_L/A_r. The data for figure 7 were calculated from incompressible-cold-flow relations assuming annulus wall friction negligible with zero flow through the liner dome ($w_{L,2}/w_T=0$). The minimum combustor total-pressure-loss coefficient is obtained by arbitrarily setting liner static pressure equal to annulus static pressure at station 2 and is calculated from equation (B24). The value obtained for the minimum total-pressure-loss coefficient for any given value of A_L/A_r is independent of the discharge coefficients of the liner wall openings and corresponds to relatively large values of liner total open hole area ($A_{h,T}/A_r>2.0$). Figure 7 shows that a minimum cold flow $\Delta P/q_r$ is obtained by using a liner that blocks 50 percent

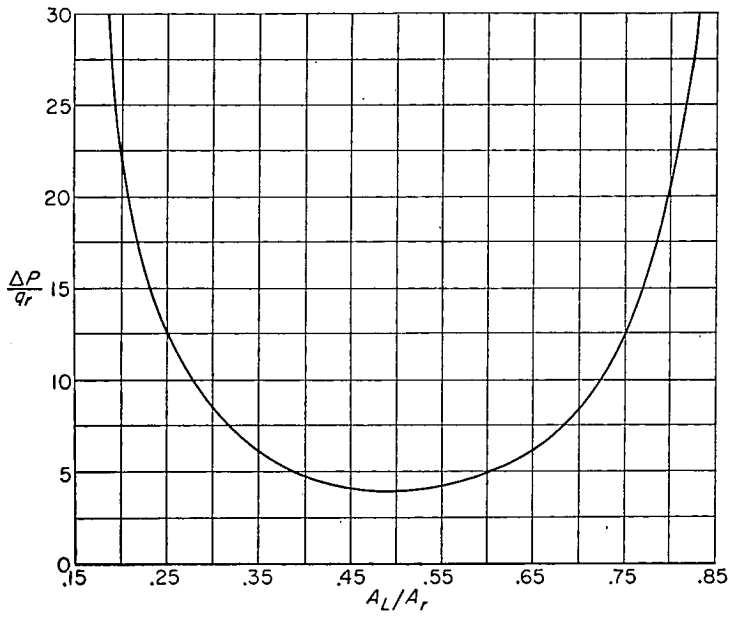


FIGURE 7.—Variation of minimum total-pressure-loss coefficient $\Delta P/q_r$ with ratio of liner cross-sectional area to combustor reference area A_L/A_r. Data calculated from incompressible-cold-flow relations assuming annulus wall friction negligible, zero flow through dome, and liner and annulus static pressures equal at station 2 (see fig. 1).

of the total cross-sectional area of the combustor. Either increasing or decreasing the percent blocked area from a mean of 50 percent tends to increase $\Delta P/q_r$. The data of figures 6 and 7 show that for a parallel-wall combustor an $A_{h,T}/A_r$ greater than 1.0 and an A_L/A_r between 0.4 and 0.6 are desirable in order to obtain a low cold-flow total-pressure loss.

Effect of airflow through liner dome.—The effects of the fraction of total airflow passing through the liner dome $w_{L,2}/w_T$ on the calculated combustor total-pressure-loss coefficient are illustrated in figure 8. The values were calculated from the incompressible-flow relations neglecting the effect of annulus wall friction. As would be expected, an increase in $w_{L,2}/w_T$ decreases the total-pressure-loss coefficient throughout the range of values of $A_{h,T}/A_r$ covered in the figure because the effective open hole area of the liner has been increased by opening holes in the liner dome. The

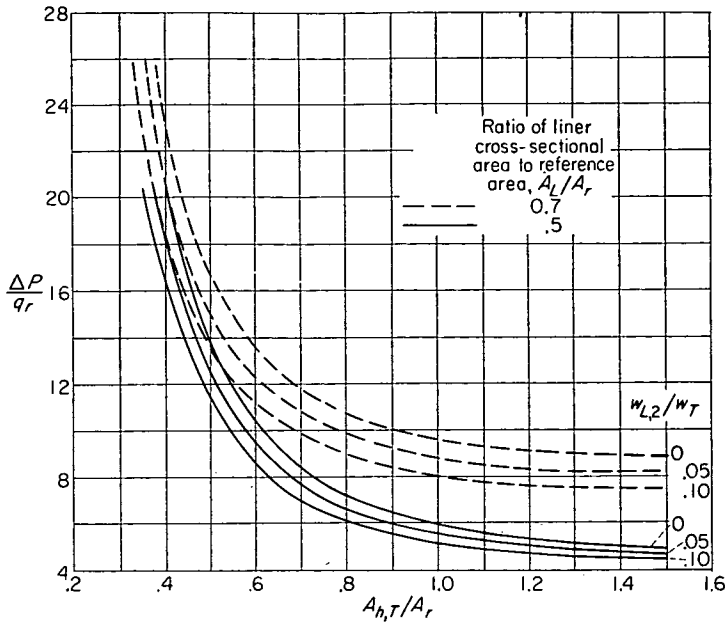
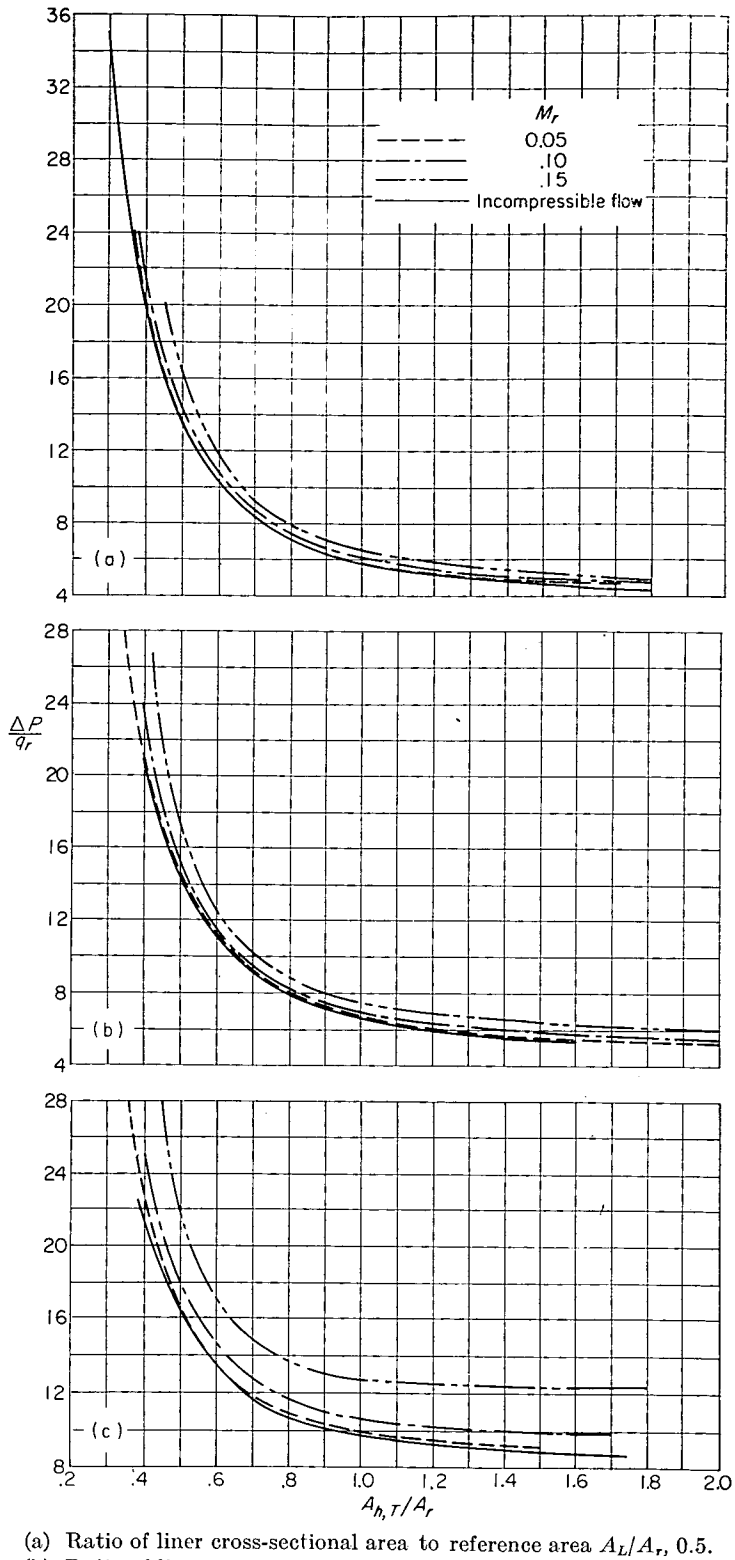


FIGURE 8.—Variation of total-pressure-loss coefficient $\Delta P/q_r$ with ratio of liner total open hole area to combustor reference area $A_{h,T}/A_r$ for various liner dome airflows $w_{L,2}/w_T$. Data calculated from incompressible-cold-flow relations assuming negligible annulus wall friction.

value of $A_{h,T}/A_r$ does not include the open hole area in the liner dome. The open hole area in the liner dome required to pass the specified $w_{L,2}/w_T$ may be calculated from the orifice discharge equation in conjunction with the total pressure upstream of the liner dome, values of the discharge coefficient of the liner dome openings, and the static pressure $p_{L,2}$ in the liner at station 2. Discharge coefficients for swirler-type liner dome openings are presented in reference 10. Values of $p_{L,2}$ may be obtained from equation (B18) for w_L/w_T equal to $w_{L,2}/w_T$.

Effect of combustor reference Mach number.—The effects of combustor reference Mach number M_r at station 1 (see fig. 1) on the calculated combustor total-pressure-loss coefficient are illustrated in figures 9, 10, and 11. The curves for M_r equal to 0.05, 0.10, and 0.15 were calculated from the compressible-flow relations of appendix C. The incompressible-flow data of figure 6 are also included in these figures for comparison with the compressible-flow data. The data were computed for an A_L/A_r of 0.5, 0.6, and 0.7 with cold flow and with zero flow through the liner dome. The data of figures 9 and 10 were computed neglecting annulus wall friction. A comparison of data calculated with and without the effects of annulus wall friction is shown in figure 11.

Figure 9 indicates that increasing M_r up to 0.10 results in a relatively small increase in $\Delta P/q_r$; therefore, at values of M_r below 0.1, the results of the incompressible-flow relations agree quite well with the results of the compressible-flow relations. The incompressible-flow relations are considered sufficiently accurate for design purposes for combustors operating below an M_r of 0.1. However, for M_r above approximately 0.10, there is an increase in $\Delta P/q_r$ with an increase in M_r, particularly at values of A_L/A_r over about 0.6. The effect of reference Mach number on $\Delta P/q_r$ is shown more



(a) Ratio of liner cross-sectional area to reference area A_L/A_r, 0.5.
(b) Ratio of liner cross-sectional area to reference area A_L/A_r, 0.6.
(c) Ratio of liner cross-sectional area to reference area A_L/A_r, 0.7.

FIGURE 9.—Variation of total-pressure-loss coefficient $\Delta P/q_r$ with ratio of liner total open hole area to combustor reference area $A_{h,T}/A_r$ for various combustor reference Mach numbers M_r. Data calculated for cold flow and zero liner dome flow assuming negligible annulus wall friction.

clearly in figure 10 in which the data of figure 9 are cross-plotted for a value of $A_{h,T}/A_r=1.0$. Figure 11 indicates the calculated increase in $\Delta P/q_r$ with M_r when annulus wall friction effects are included.

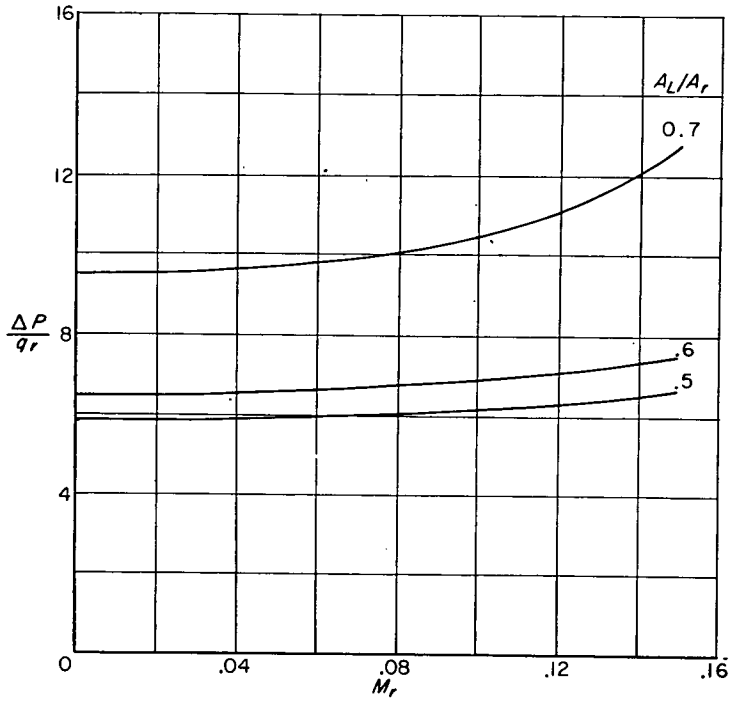
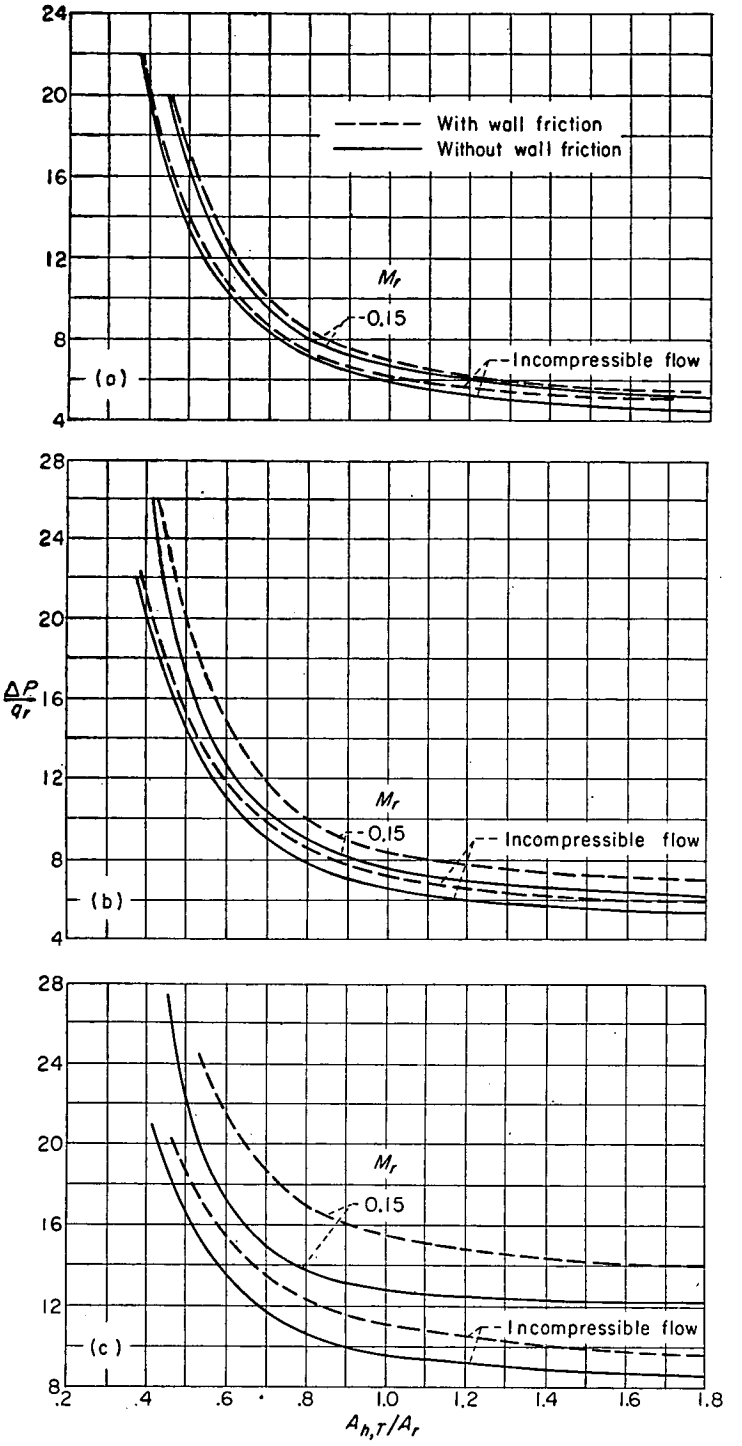


FIGURE 10.—Variation of total-pressure-loss coefficient $\Delta P/q_r$ with reference Mach number M_r for various ratios of liner cross-sectional area to reference area A_L/A_r. Data calculated for cold flow and zero liner dome flow assuming negligible annulus wall friction; ratio of total liner open hole area to reference area $A_{h,T}/A_r$, 1.0.

Effect of heat release.—The variation in $\Delta P/q_r$ with $A_{h,T}/A_r$ for various values of temperature ratio across the combustor $T_{L,3}/T_1$ and various values of A_L/A_r is presented in figure 12. The data for these curves were obtained from incompressible-flow relations including annulus wall friction for a $w_{L,2}/w_T$ of 0 and 0.1. The curves for a $w_{L,2}/w_T$ of 0.1 were obtained from the calculations for a $w_{L,2}/w_T$ of zero by the method presented in appendix B. Use of this method for the case where annulus wall friction effects are included in the calculations necessitated the preliminary estimation of the airflow distribution by the curves of figure 13 in the calculations of annulus total pressure. The curve for a $w_{L,2}/w_T$ of zero corresponds to that of equation (7). Approximate values of the combustor total-pressure-loss coefficient for values of $w_{L,2}/w_T$ between 0 and 0.1 may be obtained from linear interpolation between the solid and dashed curves of figure 12.

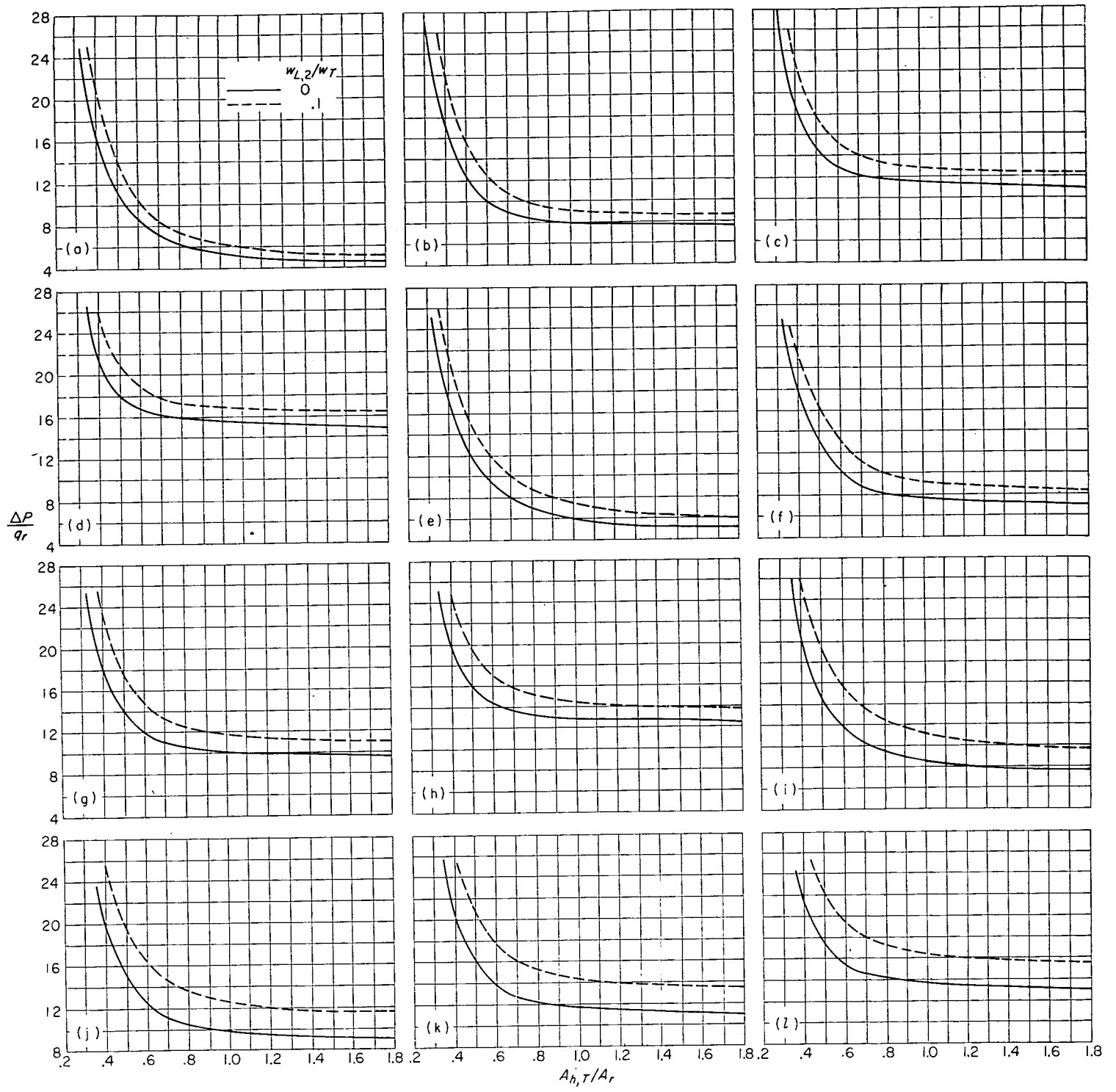
The combustor total-pressure-loss coefficient increases as combustor exhaust temperature is increased. The relative effect of airflow through the liner dome and annulus wall friction on $\Delta P/q_r$ is the same for hot flow as it was for cold flow. The data of figure 12 are cross-plotted in figure 14 to show the effect of the temperature ratio $T_{L,3}/T_1$ on $\Delta P/q_r$. Curves of $\Delta P/q_r$ against $T_{L,3}/T_1$ are shown for A_L/A_r values of 0.5, 0.6, and 0.7 and $A_{h,T}/A_r$ values of 0.6 and 1.6. For a given value of $A_{h,T}/A_r$ the total-pressure-loss coefficient increases with temperature ratio at a more rapid rate as A_L/A_r decreases. As a result, at higher values of temperature ratio, larger A_L/A_r values are required to minimize $\Delta P/q_r$. A value of A_L/A_r of 0.5 provided minimum $\Delta P/q_r$ under cold-flow conditions; a value of 0.6 provided the lowest total-pressure loss at temperature ratios above about 2.0. This



(a) Ratio of liner cross-sectional area to reference area A_L/A_r, 0.5.
(b) Ratio of liner cross-sectional area to reference area A_L/A_r, 0.6.
(c) Ratio of liner cross-sectional area to reference area A_L/A_r, 0.7.

FIGURE 11.—Variation of total-pressure-loss coefficient $\Delta P/q_r$ with ratio of liner total open hole area to combustor reference area $A_{h,T}/A_r$ calculated for combustor reference Mach number M_r of 0.15 and for incompressible flow with and without including effects of annulus wall friction.

effect is shown more clearly in figure 15 where $\Delta P/q_r$ is plotted against A_L/A_r for various temperature ratios across the combustor. These data were obtained from incompressible-flow relations including annulus wall friction with zero liner dome flow for values of $A_{h,T}/A_r$ of 0.6 and 1.6. For combustors with $A_{h,T}/A_r$ equal to 0.6 or 1.6 the value of A_L/A_r for a



(a) Total-temperature ratio across combustor $T_{L,3}/T_1$, 1; ratio of liner cross-sectional area to reference area A_L/A_r, 0.5.
(b) Total-temperature ratio across combustor $T_{L,3}/T_1$, 2; ratio of liner cross-sectional area to reference area A_L/A_r, 0.5.
(c) Total-temperature ratio across combustor $T_{L,3}/T_1$, 3; ratio of liner cross-sectional area to reference area A_L/A_r, 0.5.
(d) Total-temperature ratio across combustor $T_{L,3}/T_1$, 4; ratio of liner cross-sectional area to reference area A_L/A_r, 0.5.
(e) Total-temperature ratio across combustor $T_{L,3}/T_1$, 1; ratio of liner cross-sectional area to reference area A_L/A_r, 0.6.
(f) Total-temperature ratio across combustor $T_{L,3}/T_1$, 2; ratio of liner cross-sectional area to reference area A_L/A_r, 0.6.
(g) Total-temperature ratio across combustor $T_{L,3}/T_1$, 3; ratio of liner cross-sectional area to reference area A_L/A_r, 0.6.
(h) Total-temperature ratio across combustor $T_{L,3}/T_1$, 4; ratio of liner cross-sectional area to reference area A_L/A_r, 0.6.
(i) Total-temperature ratio across combustor $T_{L,3}/T_1$, 1; ratio of liner cross-sectional area to reference area A_L/A_r, 0.7.
(j) Total-temperature ratio across combustor $T_{L,3}/T_1$, 2; ratio of liner cross-sectional area to reference area A_L/A_r, 0.7.
(k) Total-temperature ratio across combustor $T_{L,3}/T_1$, 3; ratio of liner cross-sectional area to reference area A_L/A_r, 0.7.
(l) Total-temperature ratio across combustor $T_{L,3}/T_1$, 4; ratio of liner cross-sectional area to reference area A_L/A_r, 0.7.

FIGURE 12.—Variation of total-pressure-loss coefficient $\Delta P/q_r$ with ratio of liner total open hole area to combustor reference area $A_{h,T}/A_r$ for flow ratios through liner dome $w_{L,2}/w_T$ of 0 and 0.1. Data calculated from incompressible-flow relations including annulus wall friction.

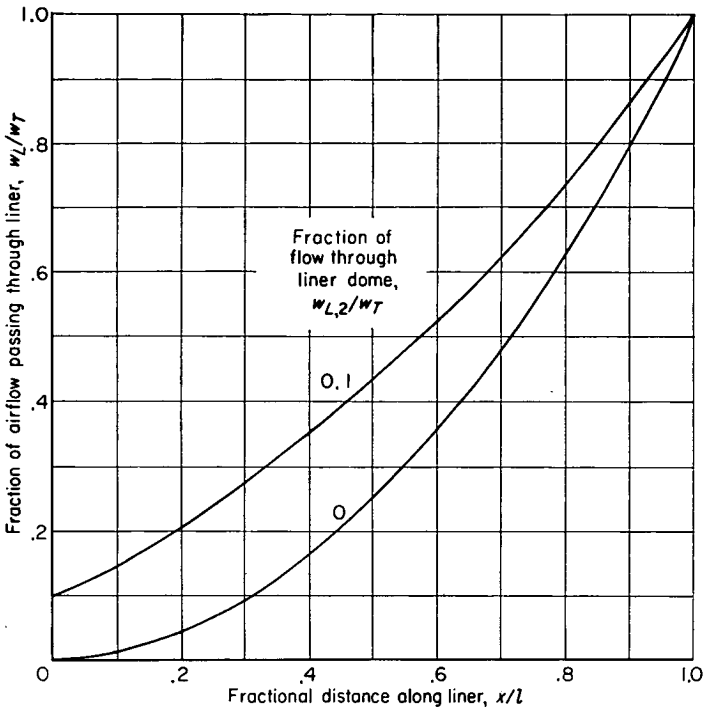


FIGURE 13.—Combustor airflow distributions assumed in calculations of variation in annulus total pressure along combustor.

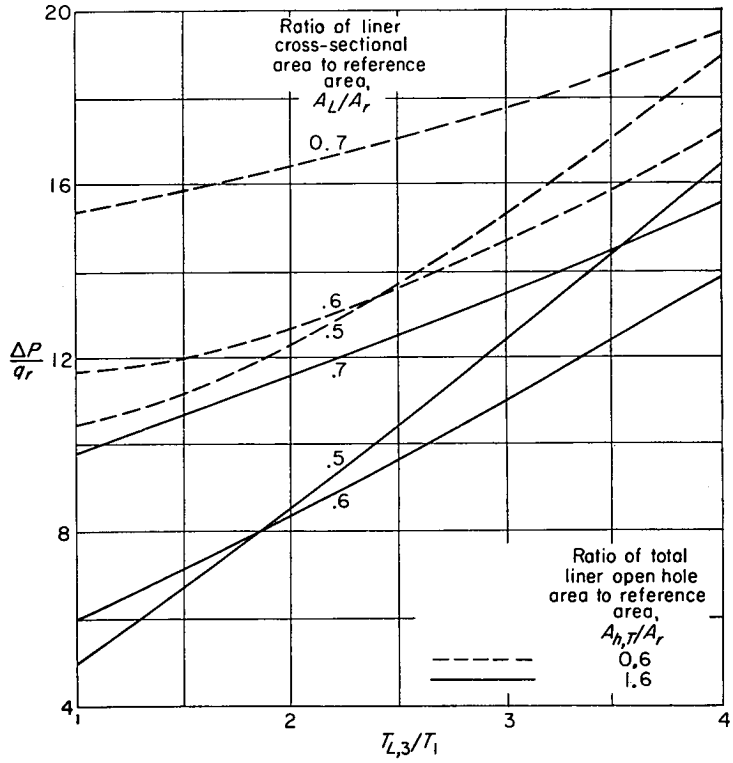
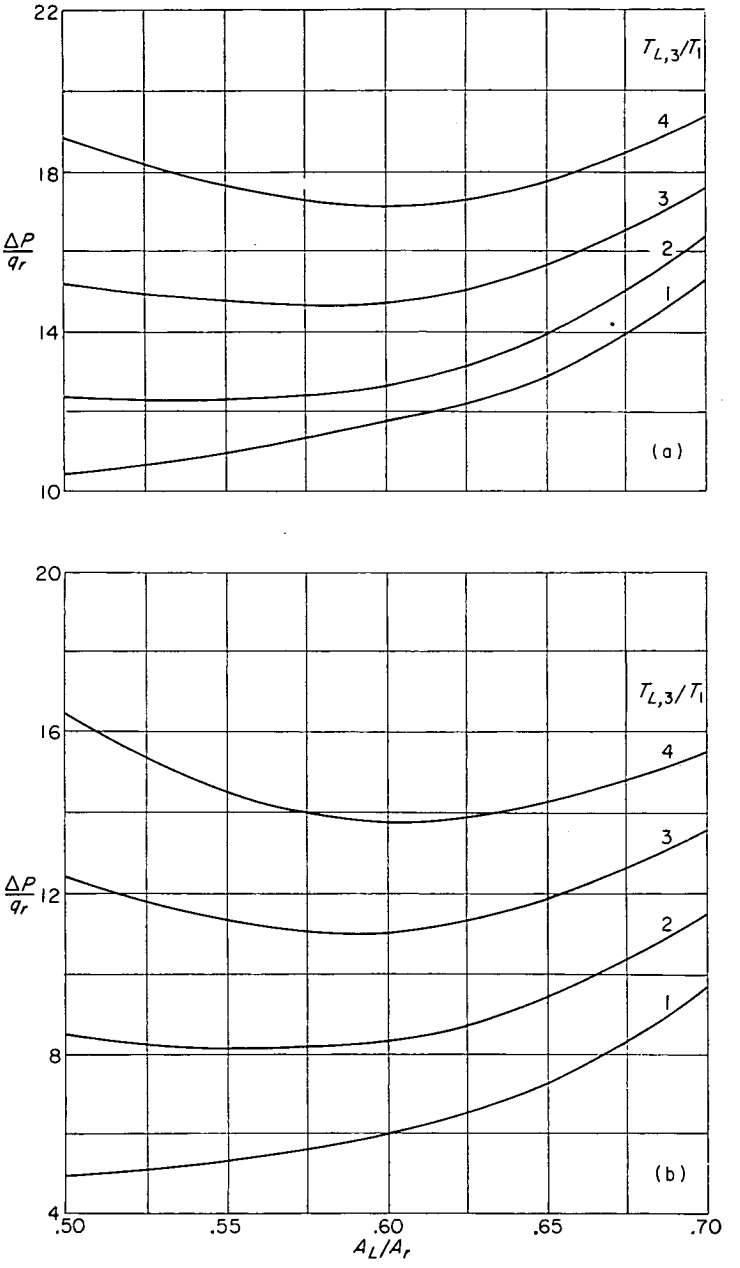


FIGURE 14.—Variation of total-pressure-loss coefficient $\Delta P/q_r$ with temperature ratio across combustor $T_{L,3}/T_1$. Data calculated from incompressible-flow relations including annulus wall friction with zero liner dome flow.

minimum $\Delta P/q_r$ shifts from 0.5 to 0.6 as combustor exhaust temperature is increased.

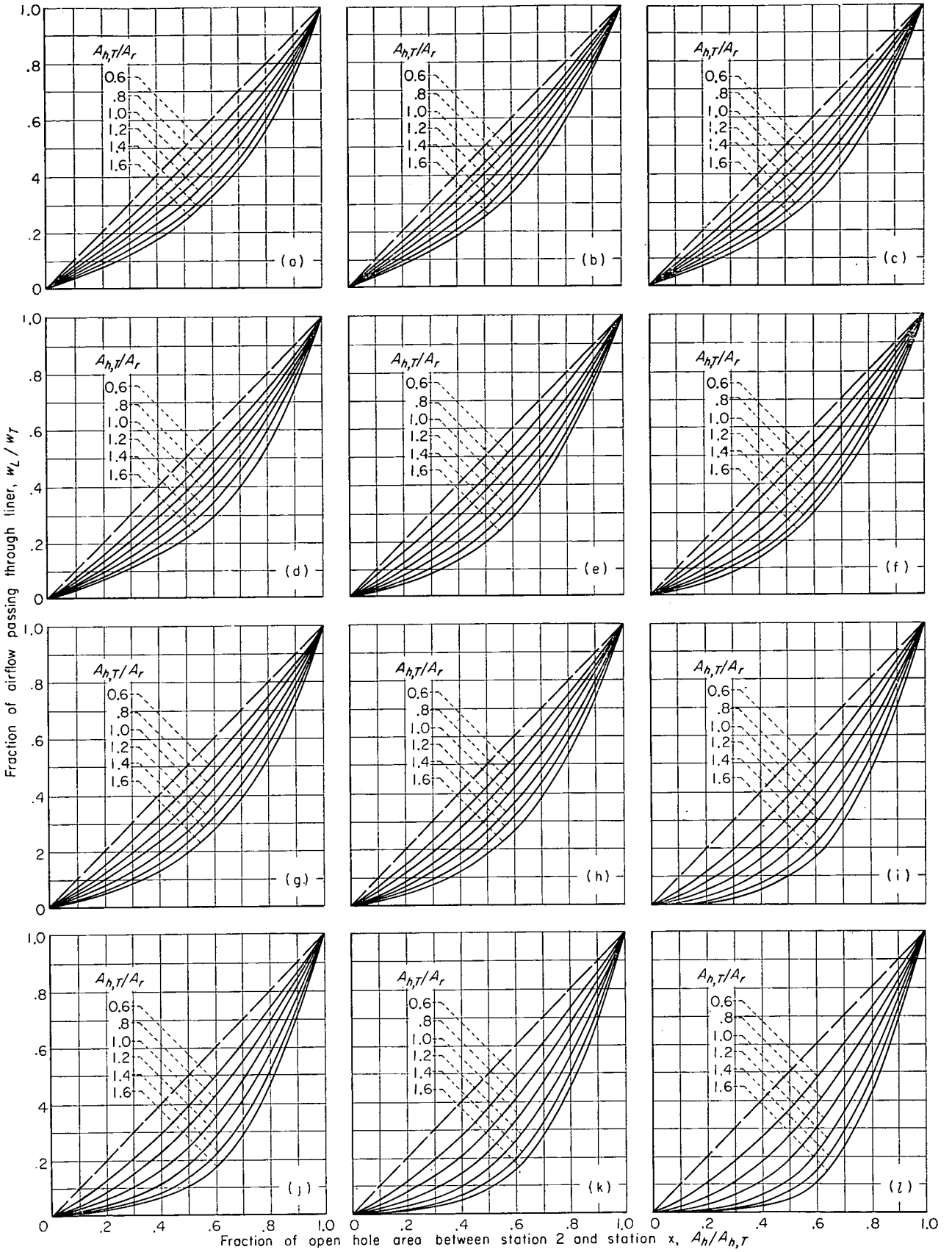
AIRFLOW DISTRIBUTION

The airflow distribution curves obtained from incompressible- and compressible-flow calculations are presented in figures 16 to 23. Except for the effects of variation in annulus wall friction with airflow distribution, the relations between w_L/w_T and $A_h/A_{h,T}$ presented in figures 16 to 23 are independent of the distribution of air entry holes along the liner. Accordingly, the variation of w_L/w_T along the combustor for a particular liner configuration may be estimated from the given values of $A_h/A_{h,T}$ along the combustor and the appropriate figure from figures 16 to 23. If, for example, there is a linear increase in liner open hole area along the combustor ($A_h/A_{h,T}=x/l$), the curves of figures 16 to 23 represent the variation in liner airflow with distance along the combustor. It is emphasized that the relations presented are representative only for parallel-wall combustors having flush liner air openings (see fig. 1).



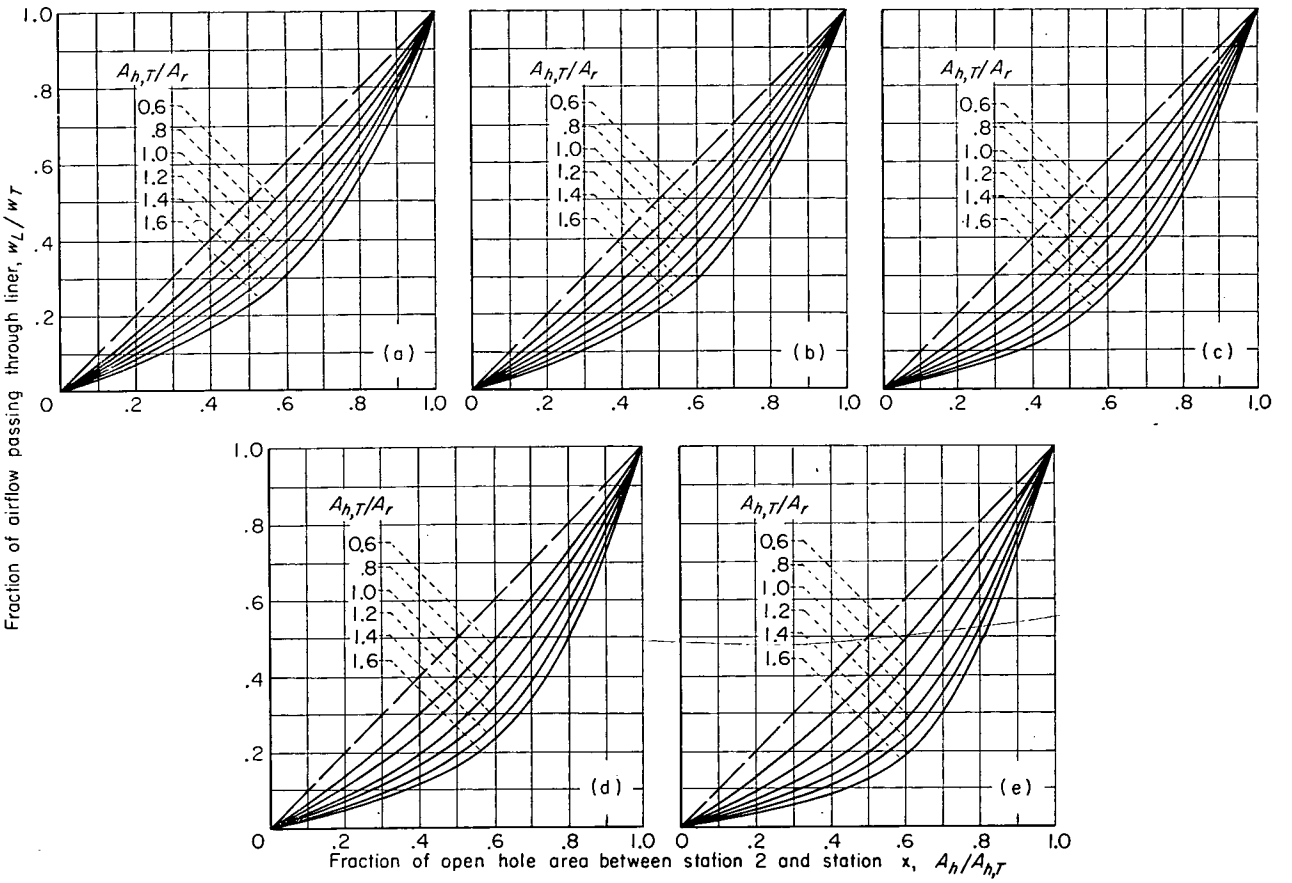
(a) Ratio of total liner open hole area to reference area $A_{h,T}/A_r$, 0.6.
(b) Ratio of total liner open hole area to reference area $A_{h,T}/A_r$, 1.6.

FIGURE 15.—Variation of total-pressure-loss coefficient $\Delta P/q_r$ with ratio of liner cross-sectional area to reference area A_L/A_r for various values of temperature ratio across combustor $T_{L,3}/T_1$. Data calculated from incompressible-flow relations including annulus wall friction with zero liner dome flow.



(a) Incompressible flow; ratio of liner cross-sectional area to reference area A_L/A_r, 0.5.
(b) Reference Mach number M_r, 0.05; A_L/A_r, 0.5.
(c) M_r, 0.10; A_L/A_r, 0.5.
(d) M_r, 0.15; A_L/A_r, 0.5.
(e) Incompressible flow; A_L/A_r, 0.6.
(f) M_r, 0.05; A_L/A_r, 0.6.
(g) M_r, 0.10; A_L/A_r, 0.6.
(h) M_r, 0.15; A_L/A_r, 0.6.
(i) Incompressible flow; A_L/A_r, 0.7.
(j) M_r, 0.05; A_L/A_r, 0.7.
(k) M_r, 0.10; A_L/A_r, 0.7.
(l) M_r, 0.15; A_L/A_r, 0.7.

FIGURE 16.—Effect of ratio of liner total open hole area to combustor reference area $A_{h,T}/A_r$ on airflow distribution. Incompressible- and compressible-cold-flow relations without annulus wall friction and with zero liner dome flow.



(a) Reference Mach number M_r, 0.15; ratio of liner cross-sectional area to reference area A_L/A_r, 0.5.
(b) Reference Mach number M_r, 0.15; ratio of liner cross-sectional area to reference area A_L/A_r, 0.6.
(c) Reference Mach number M_r, 0.05; ratio of liner cross-sectional area to reference area A_L/A_r, 0.7.
(d) Reference Mach number M_r, 0.10; ratio of liner cross-sectional area to reference area A_L/A_r, 0.7.
(e) Reference Mach number M_r, 0.15; ratio of liner cross-sectional area to reference area A_L/A_r, 0.7.

FIGURE 17.—Effect of ratio of liner total open hole area to combustor reference area $A_{h,T}/A_r$ on airflow distribution. Compressible-cold-flow relations including annulus wall friction with zero liner dome flow.

Effect of liner total open hole area.—The fraction of total air passing through the liner at any given station along the combustor w_L/w_T is plotted against the fraction of liner total open hole area $A_h/A_{h,T}$ in figure 16 for values of A_L/A_r of 0.5, 0.6, and 0.7. Curves are shown for various values of $A_{h,T}/A_r$, and the data were obtained from compressible-flow relations for reference Mach numbers of 0.05, 0.10, and 0.15. Data obtained from the incompressible-flow relations are also presented. Cold flow conditions with zero liner dome flow ($w_{L,2}/w_T=0$) and with negligible annulus wall friction were assumed. The 45° dashed line on the airflow distribution curves represents the airflow distribution that would be obtained if each hole in the liner admitted a quantity of air directly proportional to its area. Increasing the liner total open hole area $A_{h,T}$ decreases the fraction of total air entering the upstream region of the combustor liner. This decrease in upstream liner airflow becomes appreciable at large values of $A_{h,T}/A_r$. This reduction in w_L/w_T is a result of higher reductions in pressure drop and discharge coefficient for the holes at the upstream stations than for those at the downstream stations. The reduction becomes more critical as A_L/A_r is increased from 0.5 to 0.7. This effect is partially due to increased velocities in the upstream region of the annulus, which reduce the discharge coefficient of upstream holes in the liner (ref. 7).

Effect of combustor reference Mach number.—The effect of reference Mach number on combustor airflow distribution is shown in figure 16 for cold flow. Increasing reference Mach number decreases the fraction of the total airflow entering the liner through the upstream liner hole openings. The increased velocity in the upstream end of the annulus reduced the static-pressure drop and the discharge coefficient of upstream holes in the liner. The effect of Mach number becomes more pronounced as A_L/A_r is increased because of increased upstream velocities in the annulus. For the data presented in figure 16, annulus wall friction was neglected. Figure 17 shows the airflow distribution calculated from the compressible-flow relations with annulus wall friction included. The results are similar to those shown in figure 16 with the exception that annulus wall friction tends to increase the fraction of air entering the liner through the upstream holes in the liner. Friction reduced the total pressure in the downstream end of the annulus, which resulted in a lower pressure drop across the holes in this region and, hence, reduced airflow. The effect of reference Mach number on airflow distribution is shown more clearly in figure 18

526597—60——60

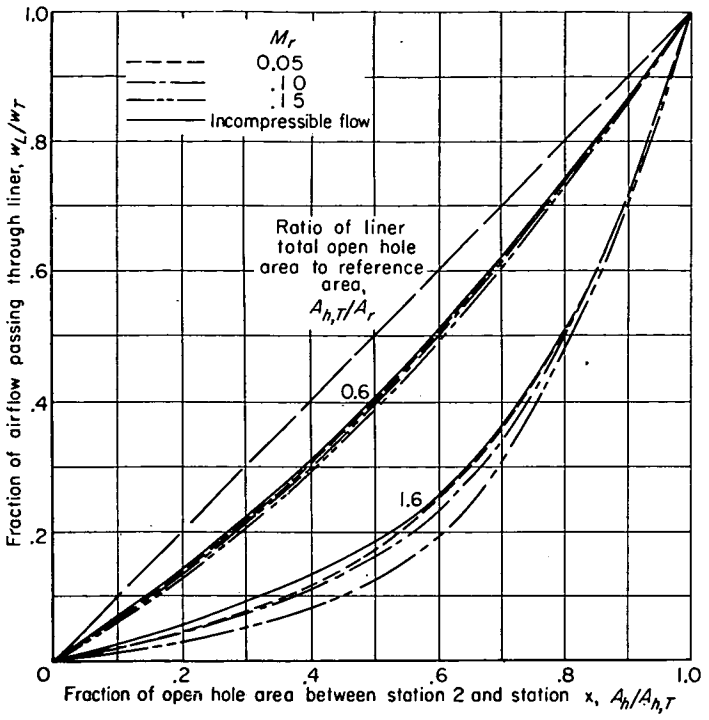
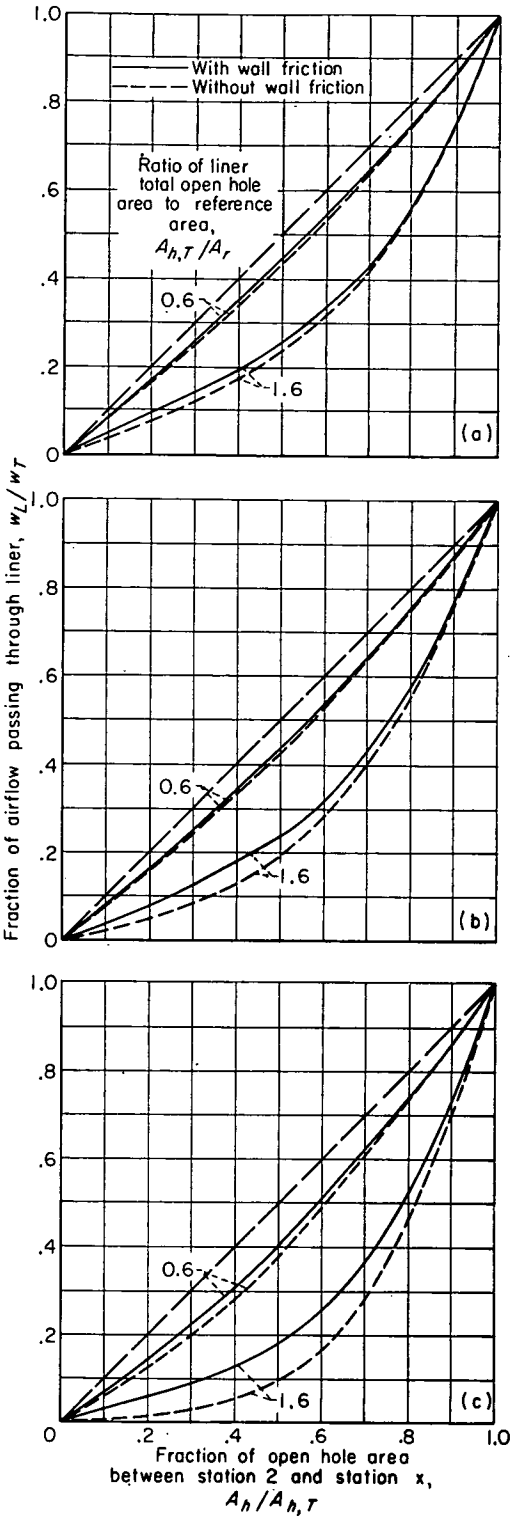


FIGURE 18.—Effect of reference Mach number M_r on airflow distribution. Compressible-cold-flow relations including annulus wall friction with zero liner dome flow; ratio of liner cross-sectional area to reference area A_L/A_r, 0.7.

where the data of figures 17(c) to (e) are replotted for $A_{h,T}/A_r$ equal to 0.6 and 1.6. Larger reductions in the fraction of total air entering the liner through the holes in the upstream region of the combustor occur at higher values of $A_{h,T}/A_r$ and at higher values of M_r.

The airflow distributions obtained from incompressible-flow relations with and without annulus wall friction are compared in figure 19 for $A_{h,T}/A_r$ equal to 0.6 and 1.6 and A_L/A_r equal to 0.5, 0.6, and 0.7. Including annulus wall friction in the computations tends to increase the fraction of total air entering the upstream region of the liner. The effect is more pronounced at higher values of A_L/A_r and $A_{h,T}/A_r$. The change in airflow distribution is a direct result of the added pressure loss in the annulus; increased A_L/A_r increases the velocity in the annulus, which in turn increases pressure loss due to friction.

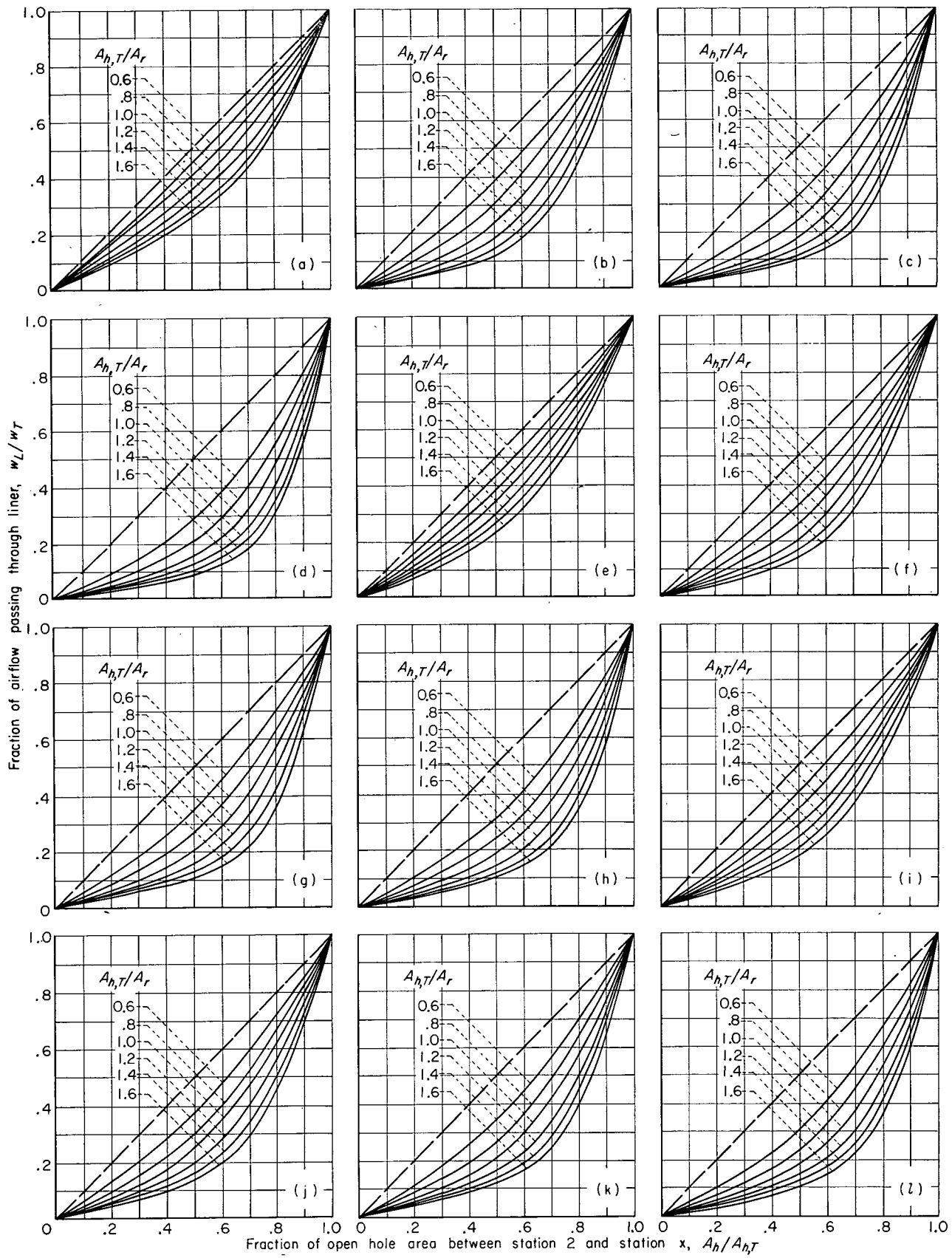
Effect of heat release.—The effect of heat release on airflow distribution is shown in figure 20 for A_L/A_r equal to 0.5, 0.6, and 0.7. These data were obtained from the incompressible-flow relations with annulus wall friction included and zero liner dome flow. Curves are shown for values of $T_{L,3}/T_1$ of 1, 2, 3, and 4. Increases in combustor temperature ratio tend to decrease the fraction of total air entering the upstream region of the liner. Heat release affects the liner pressures and velocities along the combustor, which in turn affect the static-pressure drop and the discharge coefficient of the liner wall openings. The data for $A_{h,T}/A_r$ equal to 0.6 and 1.6 are cross-plotted in figure 21 to show more clearly the effect of temperature ratio on airflow distribution. The decrease in upstream liner airflow with increasing combustor temperature ratio is more pronounced for larger values of $A_{h,T}/A_r$ and smaller values of A_L/A_r.



(a) Ratio of liner cross-sectional area to reference area A_L/A_r, 0.5.
(b) Ratio of liner cross-sectional area to reference area A_L/A_r, 0.6.
(c) Ratio of liner cross-sectional area to reference area A_L/A_r, 0.7.

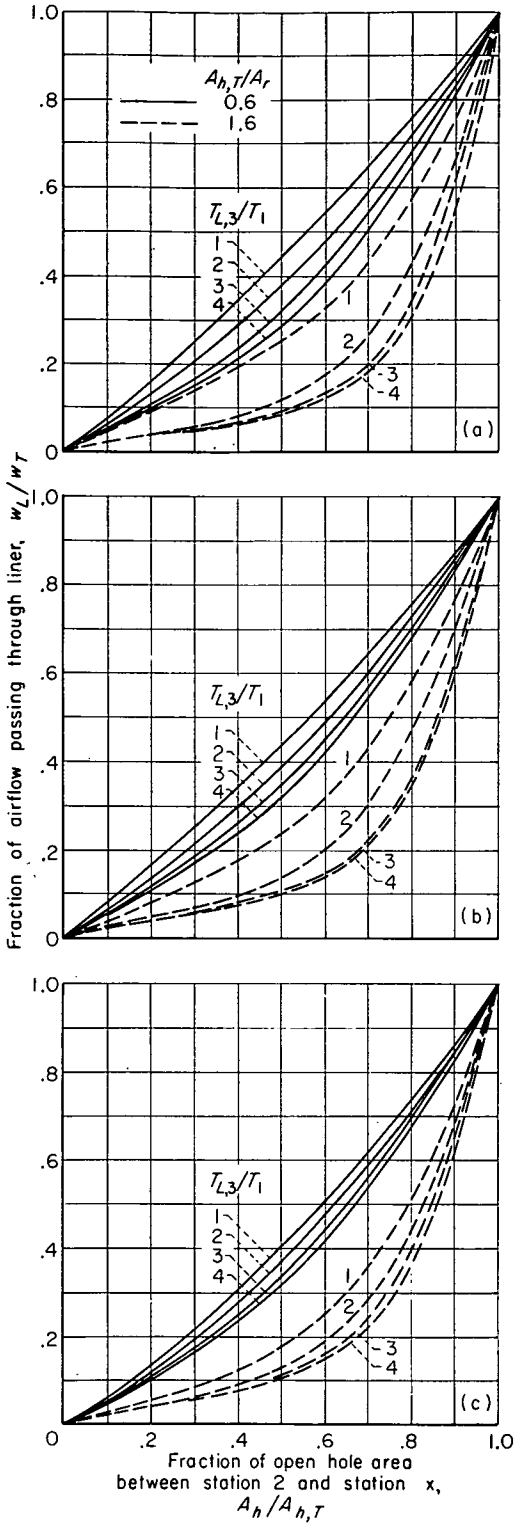
FIGURE 19.—Comparison of airflow distributions obtained from incompressible-cold-flow relations with and without annulus wall friction. Zero liner dome airflow.

Effect of liner cross-sectional area.—The effect of the ratio of liner cross-sectional area to reference area on airflow distribution is shown in figure 22 for flow with and without heat release. The data were obtained from incompressible-flow relations for values of $A_{h,T}/A_r$ of 0.6 and 1.6 with annulus



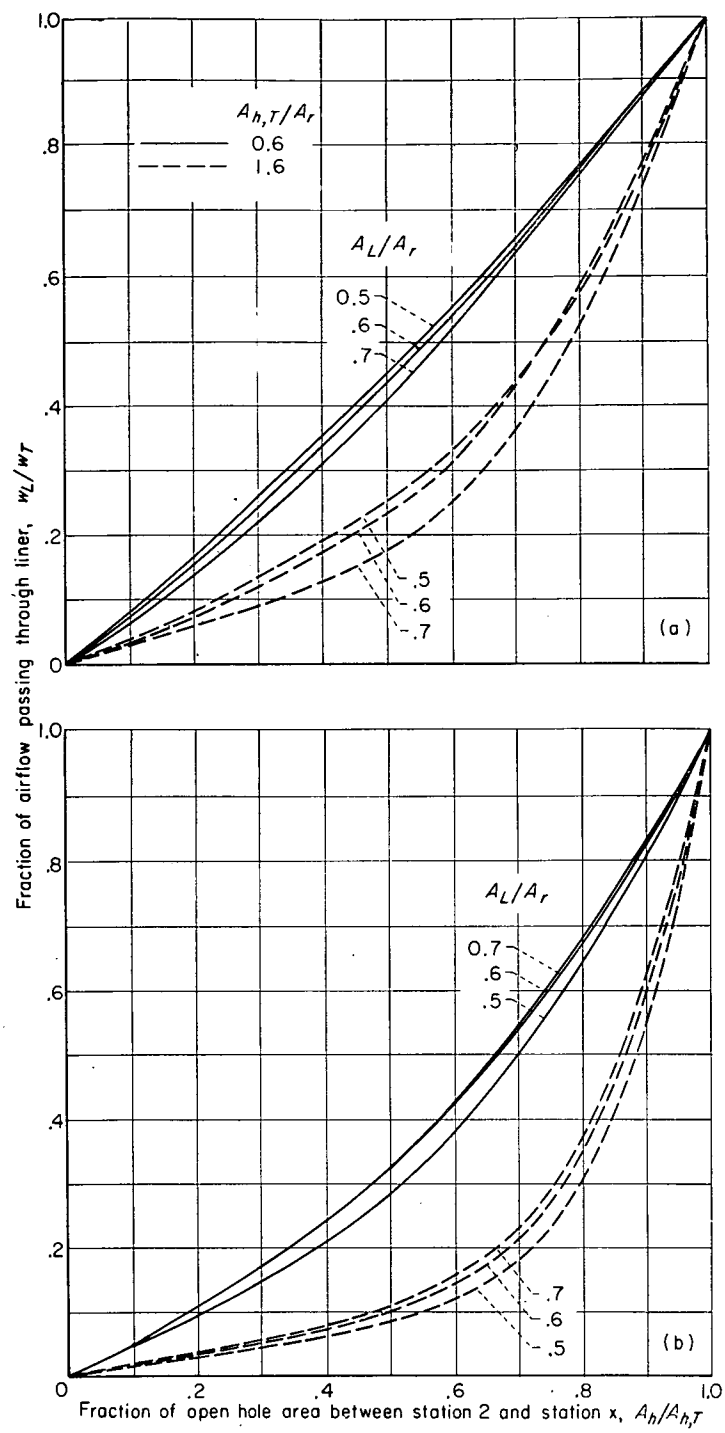
(a) Total-temperature ratio across combustor $T_{L,3}/T_1$, 1; ratio of liner cross-sectional area to reference area A_L/A_r, 0.5.
(b) $T_{L,3}/T_1$, 2; A_L/A_r, 0.5.
(c) $T_{L,3}/T_1$, 3; A_L/A_r, 0.5.
(d) $T_{L,3}/T_1$, 4; A_L/A_r, 0.5.
(e) $T_{L,3}/T_1$, 1; A_L/A_r, 0.6.
(f) $T_{L,3}/T_1$, 2; A_L/A_r, 0.6.
(g) $T_{L,3}/T_1$, 3; A_L/A_r, 0.6.
(h) $T_{L,3}/T_1$, 4; A_L/A_r, 0.6.
(i) $T_{L,3}/T_1$, 1; A_L/A_r, 0.7.
(j) $T_{L,3}/T_1$, 2; A_L/A_r, 0.7.
(k) $T_{L,3}/T_1$, 3; A_L/A_r, 0.7.
(l) $T_{L,3}/T_1$, 4; A_L/A_r, 0.7.

FIGURE 20.—Effect of ratio of liner total open hole area to reference area $A_{h,T}/A_r$ on airflow distribution. Incompressible-flow relations including annulus wall friction with zero liner dome flow.



(a) Ratio of liner cross-sectional area to reference area A_L/A_r, 0.5.
(b) Ratio of liner cross-sectional area to reference area A_L/A_r, 0.6.
(c) Ratio of liner cross-sectional area to reference area A_L/A_r, 0.7.

FIGURE 21.—Effect of temperature ratio across combustor $T_{L,3}/T_1$ on airflow distribution for values of ratio of liner total open hole area to reference area $A_{h,T}/A_r$ of 0.6 and 1.6. Incompressible-flow relations with annulus wall friction and zero liner dome flow.



(a) Total-temperature ratio across combustor $T_{L,3}/T_1$, 1.
(b) Total-temperature ratio across combustor $T_{L,3}/T_1$, 4.

FIGURE 22.—Effect of ratio of liner cross-sectional area to reference area on airflow distribution for values of ratio of liner total open hole area to reference area $A_{h,T}/A_r$ of 0.6 and 1.6. Incompressible-flow relations with annulus wall friction and zero liner dome flow.

wall friction and zero liner dome flow. The fraction of total air entering the upstream region of the combustor increases as the combustor liner area is reduced for cold flow (fig. 22(a)). The effect is similar to that of reference Mach number; that is, as velocity in the annulus is reduced by a reduction in reference Mach number or an increase in annulus area, the static-pressure drop and the orifice coefficients of the upstream liner holes increase. Calculations showed, however, that an A_L/A_r of 0.4 would have about the same cold-flow airflow distribution as an A_L/A_r of 0.6 despite the effect of reduced upstream annulus velocity. This reversal is attributed to high velocities in the downstream end of the

liner, which increase the static-pressure drop across the holes in the downstream region in the liner and thus increase the fraction of total air entering this region.

The effect of combustor-liner area on airflow distribution with a temperature ratio of 4 across the combustor is shown in figure 22(b). In this case the fraction of total air entering the upstream region of the combustor increases as A_L/A_r is increased from 0.5 to 0.7. The increased sensitivity of the airflow distribution to changes in $T_{L,3}/T_1$ for the smaller values of A_L/A_r causes a reversal in the effect of annulus area on airflow distribution. For cold flow ($T_{L,3}/T_1=1$) an increase in A_L/A_r from 0.5 to 0.7 reduces the flow to the upstream end of the combustor. However, the opposite trend is found for $T_{L,3}/T_1=4$.

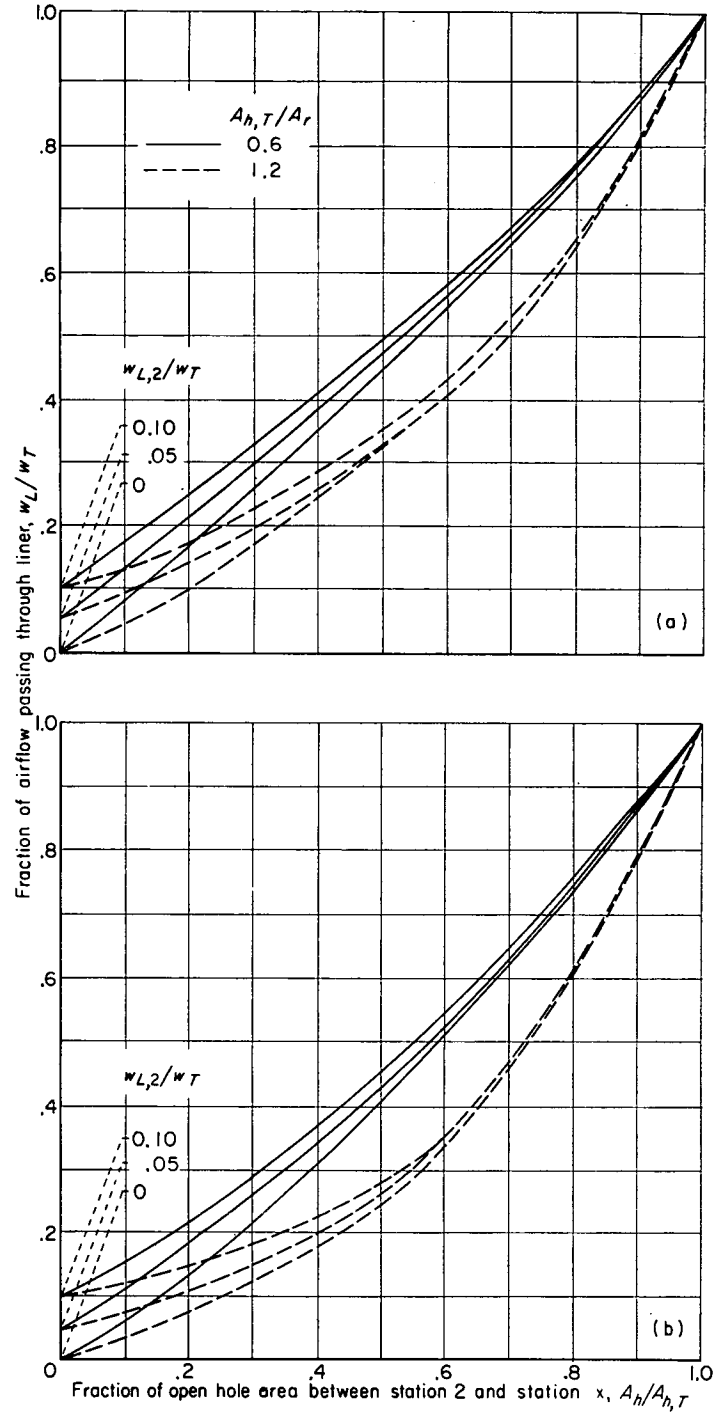
Effect of airflow through liner dome.—The effect of flow through the liner dome on the airflow distribution is illustrated in figure 23 for incompressible cold flow and negligible annulus wall friction. An increase in the flow through the liner dome for a given value of $A_{h,T}/A_r$ increases the flow through the upstream end of the combustor. Adding air through openings in the liner dome also tends to distribute the air in more direct proportion to the open area.

LINER AIR-JET ENTRANCE ANGLE

The variation of liner air-jet entrance angle θ with x/l for various values of $A_{h,T}/A_r$ and A_L/A_r is shown in figure 24. The calculations are for cold flow and include the effects of annulus wall friction. The curves shown are for liner wall openings uniformly distributed along the length of the combustor. The value of θ is a minimum at low values of x/l at the upstream end of the combustor where the static-pressure drop across the holes is lower and the annulus velocity is higher than corresponding values for the downstream liner openings. The air jet is not perpendicular to the plane of the hole until the last liner hole station is approached. Increasing $A_{h,T}/A_r$ from 0.6 to 1.6 and A_L/A_r from 0.5 to 0.7 decreases the relative value of θ, the reduction being more pronounced in the upstream portion of the combustor. It is to be noted that the data of figure 24 do not include the effect of liner air-jet deflection by the liner gas stream; this deflection can be appreciable in the downstream region of the combustor liner.

SIGNIFICANCE OF RESULTS TO TURBOJET COMBUSTOR DESIGN

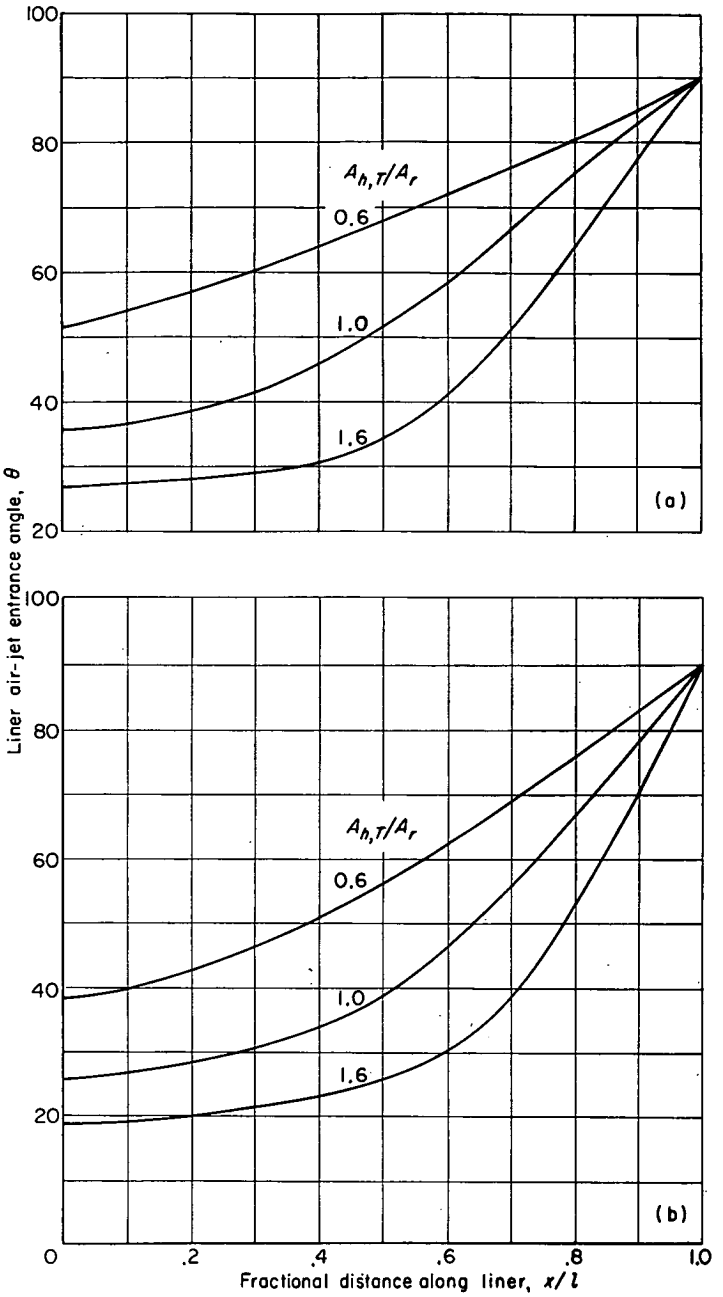
The thrust and cycle efficiency of a turbojet engine may be increased by reducing the total-pressure loss associated with the combustion chamber. Curves are presented in this report that show the effect of a number of combustor geometric and flow variables on the total-pressure-loss coefficient for a parallel-wall combustor. It is shown that the hot-flow pressure loss can be minimized by designing the combustor with a ratio of liner to total cross-sectional area of 0.6 and a total liner open hole area greater than the total cross-sectional area. The percent total-pressure loss of a combustor with a constant total-pressure-loss coefficient increases with the square of reference Mach number $\left(\frac{\Delta P}{P}=\frac{\Delta P}{q_r}\frac{\gamma_a}{2}\left(\frac{p}{P}\right)_r M_r^2\right)$. The total-pressure loss becomes even more severe when the total-pressure-loss coefficient $\Delta P/q_r$ also increases with reference Mach number. The severity of the increase in total-pressure loss can be minimized, however, by adequately designing the the liner cross-sectional area and total open hole area as suggested previously. Increasing the combustor frontal area is another means of reducing reference velocity and the pressure losses related to high velocity.



(a) Ratio of liner cross-sectional area to reference area A_L/A_r, 0.5.
(b) Ratio of liner cross-sectional area to reference area A_L/A_r, 0.7.

FIGURE 23.—Effect of airflow into liner dome $w_{L,2}/w_T$ on airflow distribution for values of ratio of liner total open hole area to reference area $A_{h,T}/A_r$ of 0.6 and 1.2. Incompressible-cold-flow relations with annulus wall friction.

It is shown that the percent of total air entering the upstream region of the liner where combustion of the fuel occurs is reduced as combustor exhaust temperature is increased.



(a) Ratio of liner cross-sectional area to reference area A_L/A_r, 0.5.
(b) Ratio of liner cross-sectional area to reference area A_L/A_r, 0.7.

FIGURE 24.—Variation of liner air-jet entrance angle along liner for various values of ratio of liner total open hole area to reference area $A_{h,T}/A_r$. Incompressible-cold-flow relations including annulus wall friction with zero liner dome flow.

The application of turbine-cooling techniques to turbojet engines will permit higher combustor exhaust gas temperatures for increased thrust output. These conditions will require the use of a larger percentage of the total airflow in the combustion process. If the combustion process is to occur in the same upstream region for high-temperature operation as for low-temperature operation, a larger percentage of air must be admitted into the upstream region. Future combustors may also be required to operate at higher reference Mach numbers because of the increased mass flow per unit frontal area that can be handled by the newer compressor designs. It was found that increasing reference Mach number also decreases the fraction of total air entering the upstream region of the liner.

Desirable decreases in pressure loss of the combustor may be obtained by increasing the liner total open hole area. This also entails reductions in the upstream liner airflow. Thus, providing for adequate air into the upstream primary combustion zone of combustors without inducing excessive pressure losses will be a big problem in future combustor development. Increasing the fraction of total open hole area in the upstream region of the liner may or may not alleviate the problem since the discharge coefficient of upstream liner holes can vary over a wide range as annulus flow conditions are varied. Providing adequate air admission for the severe operating conditions by increasing upstream total open hole area could result in excessive air admission for the less severe operating conditions. The use of scoops or shrouds in the primary or upstream end of the combustor may provide at least a partial solution to this problem.

This report illustrates the effects of geometric configurations and operating conditions on the distribution of air to the combustion chamber without considering the effects of these factors on combustor performance and stability. The effect of mass-flow distribution on the performance of a homogeneous ramjet combustor, based on theoretical calculations, is presented in reference 11. Also available are experimental design data for turbojet combustors which show the effects on performance of a number of geometric variables, including the open hole area distribution (ref. 12).

APPLICATION OF ANALYTICAL TECHNIQUE

The combustor total-pressure-loss coefficient and the airflow distribution of a given parallel-wall tubular combustor design can be estimated from the curves provided in the report by determining the dimensionless parameters M_r, $T_{L,3}/T_1$, $w_{L,2}/w_T$, $A_{h,T}/A_r$, A_L/A_r, and l/D. The curves based on compressible-flow relations are preferred over the incompressible-flow relations for all cases for determining the combustor total-pressure loss and the airflow distribution. However, the results comparing compressible- and incompressible-flow relations show that at reference Mach numbers below about 0.1 similar results should be obtained from both curves. Appreciable error can be introduced using incompressible-flow relations at higher reference Mach numbers, especially for combustors with small annulus air passages which have relatively high annulus velocities. Generalized curves are presented which both include and neglect the effect of annulus wall friction for a tubular combustor with an l/D of 4. For many combustor designs, this effect will be small. If the curves presented herein show appreciable effects of annulus wall friction, the choice between the curves will depend on the l/D of the design combustor. For example, the combustor aerodynamics of a design with an l/D of 2 could be determined by interpolating halfway between the curves calculated with and without annulus wall friction.

The curves presented herein can be applied to an annular combustor only if the velocities in the inner and outer annuli at any station are the same and if the walls are parallel. An

approach similar to that reported herein could be used to calculate total-pressure loss and airflow distribution for combustors with variable annulus and liner cross-sectional areas.

CONCLUSIONS

The effects of a number of geometric and operating variables of turbojet combustors on combustor total-pressure loss and airflow distribution were determined analytically from compressible- and incompressible-flow relations. The following conclusions were reached for combustors having a given maximum (reference) cross-sectional area, constant annulus and liner cross-sectional areas along the axis, and flush liner wall openings:

1. Combustor total-pressure loss increases rapidly as liner cross-sectional area is increased above 70 percent of reference area. For a given liner total open hole area, the minimum total-pressure loss is obtained when the liner cross-sectional area is 60 percent of the reference area for combustor temperature ratios from 3 to 4.

2. Combustor total-pressure loss increases rapidly as the liner total open hole area is decreased below 100 percent of the reference area. Increasing the liner total open hole area above about 200 percent has little effect on reducing the combustor total-pressure-loss coefficient.

3. The combustor total-pressure-loss coefficient increases with increasing reference velocities and annulus velocities and with increasing combustor exhaust temperature.

4. The distribution of air entering the combustor liner is approximately proportional to the open hole area distribution only for low values of total open hole area, which entail high pressure losses. Airflow distribution for larger total open hole area required for low pressure losses deviated appreciably from the open hole area distribution. For a given liner open hole area distribution, the fraction of total air entering the upstream region of the combustor under burning conditions decreased with an increase in liner total open hole area, reference Mach number, and combustor temperature ratio. The discharge coefficients of upstream holes are markedly lower than 0.6; the discharge coefficients of downstream holes approach 0.6.

5. The liner air-jet entrance angle in the upstream region of the liner is markedly reduced with increases in total open hole area. The jet entrance angle for holes in the downstream region of the liner approaches 90°.

LEWIS FLIGHT PROPULSION LABORATORY
NATIONAL ADVISORY COMMITTEE FOR AERONAUTICS
CLEVELAND, OHIO, *September 17, 1956*

APPENDIX A

SYMBOLS

A	cross-sectional area of any given flow passage, sq ft
A_A	cross-sectional area of annulus formed by outer diameter of liner d and inner diameter of combustor housing D, sq ft
A_h	liner open hole area from station 2 to station at x, sq ft
ΔA_h	liner open hole area from station at x to station at $x+\Delta x$, sq ft
$A_{h,T}$	total open hole area in liner wall (excluding liner dome openings), sq ft
A_L	cross-sectional area of liner, sq ft
A_r	total combustor cross-sectional area; reference area, sq ft
a_t	speed of sound at local total temperature
C	orifice discharge coefficient, ratio of measured to theoretical flow through hole
C_p	orifice discharge coefficient, corrected for pressure-ratio effect
D	inner diameter of combustor housing, ft
d	outer diameter of liner, ft
F	fuel-air ratio by weight
f	Fanning friction factor
g	gravitational constant, 32.2 ft/sec^2
l	length of combustor from station 2, just upstream of first row of holes in liner, to station 3, downstream of last row of holes at end of combustor
M	Mach number based on local average velocity and local static temperature
$M_{t,A}$	Mach number based on local average velocity and local total temperature in annulus of combustor, V/a_t
M^*	$\frac{w}{\rho_t a_t A}, \frac{\rho_{st} V}{\rho_t a_t}$
M_1^*	$\frac{w_T}{(\rho_t a_t)_1 A_r}, \left(\frac{\rho_{st} V}{\rho_t a_t}\right)_1$
P	local total pressure, lb/sq ft
$\Delta P/q_r$	combustor total-pressure-loss coefficient
p	local static pressure, lb/sq ft
q	dynamic pressure, lb/sq ft
q_r	reference dynamic pressure; $\frac{w_T^2}{2g\rho_{st,1}A_r^2}; \frac{\gamma_a}{2} p_1 M_r^2; \frac{\text{lb}}{\text{sq ft}}$
r_H	hydraulic radius, ft
T	local total temperature, °R
t	local static temperature, °R
V	local average velocity, ft/sec
w	weight-flow rate of air passing through any given flow passage, lb/sec
w_A	weight-flow rate of air passing through annulus at given station, lb/sec
w_L	weight-flow rate of air passing through liner at given station, lb/sec
$w_{L,2}/w_T$	fraction of total air passing through liner dome openings
Δw_L	weight-flow rate of air passing through liner from station at x to station at $x+\Delta x$, lb/sec
w_T	total weight-flow rate of air passing through combustor, lb/sec
x	distance along combustor measured from station 2 just upstream of first holes in liner, ft
β,β'	functions
γ_a	specific-heat ratio of air
γ_g	specific-heat ratio of combustion gases
θ	entrance angle of air issuing from liner wall openings, deg
ρ_{st}	density based on static pressure and static temperature, lb/cu ft
ρ_t	density based on total pressure and total temperature, lb/cu ft
φ	function
ψ,ψ'	functions

Subscripts:

A	annulus
j	jet issuing from liner wall opening
L	liner
n	flow normal to hole
r	reference
1	combustor inlet
2	station just upstream of first liner wall opening
3	combustor-exit station downstream of last liner wall opening

APPENDIX B

INCOMPRESSIBLE-FLOW CALCULATIONS FOR TUBULAR TURBOJET COMBUSTOR WITH CONSTANT ANNULUS AND LINER CROSS-SECTIONAL AREAS

The orifice discharge equation for a given liner wall opening such as illustrated in figure 1(c) is given by

$$\Delta w_L = C\rho_{st,j} V_j \, \Delta A_h \tag{1}$$

For a differential portion of the air passing through the opening, equation (1) becomes

$$\mathrm{d}w_L = C\rho_{st,j} V_j \, \mathrm{d}A_h \tag{2}$$

It is assumed that the static and total pressures in the vena contracta of the jet are equal to the liner static and annulus total pressures, respectively, at the station considered; then the term $\rho_{st,j}V_j$ in equations (1) and (2) can be determined from Bernoulli's equation for incompressible flow:

$$P_A = p_L + \frac{\rho_{st,j}V_j^2}{2g} = p_L + q_j \tag{B1}$$

If the density ρ_{st} is assumed to be independent of pressure changes along the combustor but to vary only with temperature changes resulting from combustion, equation (2) can be put in the following dimensionless form by the substitution of equation (B1) and the introduction of the reference dynamic-pressure term q_r:

$$\mathrm{d}\left(\frac{w_L}{w_T}\right) = C\sqrt{\frac{P_A - p_L}{q_r}}\,\mathrm{d}\left(\frac{A_h}{A_r}\right) \tag{B2}$$

Equation (B2) may be rearranged and integrated from station 2 (fig. 1) to a given station along the combustor to yield

$$\int_{w_{L,2}/w_T}^{w_L/w_T} \frac{\mathrm{d}\left(\frac{w_L}{w_T}\right)}{C\sqrt{\frac{P_A - p_L}{q_r}}} = \int_0^{A_h/A_r} \mathrm{d}\left(\frac{A_h}{A_r}\right) = \frac{A_h}{A_r} \tag{B3}$$

The combustor total open hole area $A_{h,T}$ for various combustor total-pressure losses is obtained from

$$\int_{w_{L,2}/w_T}^{1} \frac{\mathrm{d}\left(\frac{w_L}{w_T}\right)}{C\sqrt{\frac{P_A - p_L}{q_r}}} = \int_0^{A_{h,T}/A_r} \mathrm{d}\left(\frac{A_h}{A_r}\right) = \frac{A_{h,T}}{A_r} \tag{3}$$

while the fractional liner open hole areas $A_h/A_{h,T}$ for various fractional liner airflows w_L/w_T are obtained from

$$\frac{\displaystyle\int_{w_{L,2}/w_T}^{w_L/w_T} \frac{\mathrm{d}\left(\frac{w_L}{w_T}\right)}{C\sqrt{\frac{P_A - p_L}{q_r}}}}{\displaystyle\int_{w_{L,2}/w_T}^{1} \frac{\mathrm{d}\left(\frac{w_L}{w_T}\right)}{C\sqrt{\frac{P_A - p_L}{q_r}}}} = \frac{A_h}{A_{h,T}} \tag{8}$$

The term $(P_A - p_L)/q_r$ in equations (B3), (3), and (8) is obtained from the solution of the momentum equation. For a differential cross-sectional volume of the parallel-wall combustor of figure 1(a) it is assumed that (1) the flow is one dimensional, (2) the wall friction in the liner is negligible, and (3) the force exerted on the edge of the liner wall openings by the airstream is negligible. Then the differential momentum equation for both the annulus and liner is (see, e. g., ref. 13)

$$A_A\,\mathrm{d}p_A + \frac{w_A}{g}\,\mathrm{d}V_A + \frac{V_A}{g}\,\mathrm{d}w_A + \frac{f_A q_A A_A l}{r_{H,A}}\,\mathrm{d}\left(\frac{x}{l}\right) + A_L\,\mathrm{d}p_L + \frac{w_L}{g}\,\mathrm{d}V_L + \frac{V_L}{g}\,\mathrm{d}w_L = 0 \tag{B4}$$

For the annulus alone, the differential momentum equation is

$$A_A\,\mathrm{d}p_A + \frac{w_A}{g}\,\mathrm{d}V_A + \frac{f_A q_A A_A l}{r_{H,A}}\,\mathrm{d}\left(\frac{x}{l}\right) = 0 \tag{B5}$$

If it is assumed that the air crosses the plane of the liner wall opening with an axial component of velocity equal to V_A, subtracting equation (B5) from (B4) gives the differential momentum equation for the liner as

$$A_L\,\mathrm{d}p_L + \frac{w_L}{g}\,\mathrm{d}V_L + \frac{V_L}{g}\,\mathrm{d}w_L - \frac{V_A}{g}\,\mathrm{d}w_L = 0 \tag{B6}$$

since

$$\mathrm{d}w_A = -\mathrm{d}w_L \tag{B7}$$

For this case of constant A_L, equation (B6) may be expressed as

$$\mathrm{d}(p_L + 2q_L) - \frac{w_T}{gA_L}V_A\,\mathrm{d}\left(\frac{w_L}{w_T}\right) = 0 \tag{B8}$$

Equation (B8) may be integrated from the end of the combustor (station 3) to a given station to give

$$p_L + 2q_L - (p_{L,3} + 2q_{L,3}) - \frac{w_T}{gA_L}\int_1^{w_L/w_T} V_A\,\mathrm{d}\left(\frac{w_L}{w_T}\right) = 0 \tag{B9}$$

Again, by assuming density to be a function of temperature only,

$$\rho_{st,A} = \rho_{st,1} \tag{B10}$$

and

$$\rho_{st,L} = \rho_{st,1}\frac{T_1}{T_L} \tag{B11}$$

The relation between annulus and liner weight flows at any station is given by

$$\frac{w_L}{w_T} = 1 - \frac{w_A}{w_T} \tag{B12}$$

where the effect of fuel-flow rate on w_L is neglected. Then, from the continuity equation and equations (B10) and (B12),

$$V_A = \frac{w_A}{\rho_{st,A}A_A} = \frac{w_T}{\rho_{st,1}A_r}\frac{A_r}{A_A}\left(1 - \frac{w_L}{w_T}\right) \tag{B13}$$

and, for constant A_A, the integral term of equation (B9) becomes

$$\frac{w_T}{gA_L}\int_1^{w_L/w_T} V_A \, \mathrm{d}\left(\frac{w_L}{w_T}\right)=-\frac{w_T^2}{2g\rho_{st,1}A_r^2}\frac{A_r}{A_A}\frac{A_r}{A_L}\left(1-\frac{w_L}{w_T}\right)^2$$

$$=-q_r\frac{A_r}{A_A}\frac{A_r}{A_L}\left(1-\frac{w_L}{w_T}\right)^2 \tag{B14}$$

From the continuity equation and equation (B11) the dynamic pressures q_L and $q_{L,3}$ of equation (B9) can be related to the reference dynamic pressure q_r by

$$q_L=q_r\left(\frac{A_r}{A_L}\right)^2\frac{T_L}{T_1}\left(\frac{w_L}{w_T}\right)^2 \tag{B15}$$

and

$$q_{L,3}=q_r\left(\frac{A_r}{A_L}\right)^2\frac{T_{L,3}}{T_1} \tag{B16}$$

For incompressible flow,

$$P_{L,3}=p_{L,3}+q_{L,3} \tag{B17}$$

Then the substitution of equations (B14) to (B17) in equation (B9) gives

$$p_L=P_{L,3}+q_r\left(\frac{A_r}{A_L}\right)^2\left[\frac{T_{L,3}}{T_1}-2\frac{T_L}{T_1}\left(\frac{w_L}{w_T}\right)^2\right]-q_r\frac{A_r}{A_L}\frac{A_r}{A_A}\left(1-\frac{w_L}{w_T}\right)^2 \tag{B18}$$

Now,

$$\frac{P_A-p_L}{q_r}=\frac{P_1-p_L}{q_r}-\frac{P_1-P_A}{q_r} \tag{B19}$$

Combining equations (B18) and (B19) yields

$$\frac{P_A-p_L}{q_r}=\frac{P_1-P_{L,3}}{q_r}-\frac{P_1-P_A}{q_r}-\left(\frac{A_r}{A_L}\right)^2\left[\frac{T_{L,3}}{T_1}-2\frac{T_L}{T_1}\left(\frac{w_L}{w_T}\right)^2\right]$$

$$+\frac{A_r}{A_L}\frac{A_r}{A_A}\left(1-\frac{w_L}{w_T}\right)^2 \tag{4}$$

where the area ratios A_A/A_r and A_L/A_r are related by

$$\frac{A_A}{A_r}=1-\frac{A_L}{A_r} \tag{B20}$$

The annulus total-pressure-loss coefficient $(P_1-P_A)/q_r$ of equation (4) may be obtained by rearranging equation (B5), dividing through by the constants A_A and q_r, substituting the continuity relation, and integrating from station 2 to the station at x/l:

$$\frac{P_1-P_A}{q_r}=-\frac{1}{q_r}\int_{p_{A,2}}^{p_A}\mathrm{d}p_A-\frac{\rho_{st,A}}{q_r g}\int_{V_{A,2}}^{V_A}V_A\,\mathrm{d}V_A=\int_0^{x/l}\frac{f_A\frac{q_A}{q_r}l\,\mathrm{d}\left(\frac{x}{l}\right)}{r_{H,A}} \tag{B21}$$

The expression for the hydraulic radius of the annulus $r_{H,A}$ is

$$r_{H,A}=\frac{D-d}{4}=\frac{D}{4}\left[1-\left(\frac{A_L}{A_r}\right)^{1/2}\right]=\frac{D}{4}\left[1-\left(1-\frac{A_A}{A_r}\right)^{1/2}\right] \tag{B22}$$

The ratio of annulus dynamic pressure q_A to reference dynamic pressure q_r is given by

$$\frac{q_A}{q_r}=\left(\frac{w_A}{w_T}\right)^2\left(\frac{A_r}{A_A}\right)^2=\left(1-\frac{w_L}{w_T}\right)^2\left(\frac{A_r}{A_A}\right)^2 \tag{B23}$$

Substituting equations (B22) and (B23) into equation (B21) and assuming f_A to be constant along the combustor give

$$\frac{P_1-P_A}{q_r}=\frac{4f_A\frac{l}{D}}{\left(\frac{A_A}{A_r}\right)^2\left[1-\left(1-\frac{A_A}{A_r}\right)^{1/2}\right]}\int_0^{x/l}\left(1-\frac{w_L}{w_T}\right)^2\mathrm{d}\left(\frac{x}{l}\right) \tag{6}$$

The use of equation (6) requires an estimate of the airflow distribution along the combustor. For the present calculations and for zero airflow through the liner dome ($w_{L,2}/w_T=0$), the airflow distribution used in equation (6) was assumed to be

$$\frac{w_L}{w_T}=\left(\frac{x}{l}\right)^2 \tag{7}$$

For the calculations presented herein, the correlation of reference 7 for the discharge coefficient of flush circular holes was used (see fig. 3) to obtain values of C in equations (B3), (3), and (8). For incompressible flow, the correlation parameter $(P_A-p_j)/(P_A-p_A)$ of figure 3(a) is equal to $(V_j/V_A)^2$ and the correction of figure 3(b) is neglected. The velocity artio V_A/V_j may be obtained by relating q_j to q_A by equaitons (B1) and (B23), which gives

$$\frac{V_A}{V_j}=\frac{1-\frac{w_L}{w_T}}{\frac{A_A}{A_r}\sqrt{\frac{P_A-p_L}{q_r}}} \tag{10}$$

The liner air-jet entrance angle θ may be obtained from equation (10) and the relation

$$\theta=\cos^{-1}\frac{V_A}{V_j} \tag{9}$$

From equations (B3), (3), (8), (4), (B20) to (B23), (6), (7), and (10), the liner total open hole area and airflow distribution may be calculated for specified values of the combustor total-pressure-loss coefficient. However, if the specified value of the combustor total-pressure-loss coefficient in equation (4) is too low, the calculated liner static pressure p_L will be greater than the annulus static pressure p_A at some point in the combustor, and a solution for equations (B3), (3), and (8) will not be obtained. For the parallel-wall combustor and negligible annulus wall friction, the minimum difference between the annulus and liner static pressures occurs at the upstream end of the combustor where w_L/w_T is equal to $w_{L,2}/w_T$. From equation (4) the combustor total-pressure-loss coefficient is related to the difference between annulus and liner static pressures at this point by

$$\frac{P_1-P_{L,3}}{q_r}=\left(\frac{p_A-p_L}{q_r}\right)_2+\left(\frac{A_r}{A_L}\right)^2\left[\frac{T_{L,3}}{T_1}-2\frac{T_L}{T_1}\left(\frac{w_{L,2}}{w_T}\right)^2\right]-$$

$$\left[\frac{A_r}{A_L}\frac{A_r}{A_A}-\left(\frac{A_r}{A_A}\right)^2\right]\left(1-\frac{w_{L,2}}{w_T}\right)^2 \tag{B24}$$

The minimum combustor total-pressure-loss coefficient required for a solution of equations (B3), (3), and (8) is obtained from equation (B24) by setting $p_{A,2}-p_{L,2}$ equal to zero. It is noted that this minimum combustor total-pressure-loss coefficient is independent of the discharge coefficients of the liner wall openings. If annulus wall friction effects are included in the calculations, the minimum combustor total-pressure-loss coefficient will be somewhat greater than that given by equation (B24), and the minimum value of p_A-p_L will occur at values of w_L/w_T greater than $w_{L,2}/w_T$.

In the present report, the solutions of equations (B3), (3), and (8) were obtained for $w_{L,2}/w_T$ equal to zero. The combustor total-pressure-loss coefficient and airflow distribution curves for values of $w_{L,2}/w_T$ other than zero were obtained by correcting the curves where $w_{L,2}/w_T$ was equal to zero by the following procedure:

(1) For given values of $A_{h,T}/A_r$, A_L/A_r, and $T_{L,3}/T_1$, $\Delta P/q_r$ is obtained from the combustor total-pressure-loss coefficient curves computed with a $w_{L,2}/w_T$ of zero. The airflow distribution curve at corresponding conditions for a $w_{L,2}/w_T$ of zero is then used to obtain a value for $A_h/A_{h,T}$ at a value of w_L/w_T equal to the chosen finite value of $w_{L,2}/w_T$.

(2) A corrected value for $A_{h,T}/A_r$ is then obtained by multiplying the value of $A_{h,T}/A_r$ corresponding to the data for $w_{L,2}/w_T$ equal to zero by the quantity $1-(A_h/A_{h,T})$, where the value of $A_h/A_{h,T}$ was obtained by step (1).

(3) Values of $A_h/A_{h,T}$ are selected from the airflow distribution curve for $w_{L,2}/w_T$ equal to zero at various values of w_L/w_T greater than the chosen finite value of $w_{L,2}/w_T$. Corrected values of $A_h/A_{h,T}$ are then obtained by subtracting the value of $A_h/A_{h,T}$ obtained in step (1) from the selected value of $A_h/A_{h,T}$ and then dividing by the quantity $1-(A_h/A_{h,T})$ obtained in step (2).

With the preceding procedure the major portion of the combustor total-pressure-loss coefficient and airflow distribution curves may be obtained. However, for large values of $A_{h,T}/A_r$ the use of equations (B3), (3), and (8) for the given value of $w_{L,2}/w_T$ will be required. It is noted that the use of the preceding procedure for the cases where annulus wall friction effects are included requires the use of airflow distributions similar to those shown in figure 13.

APPENDIX C

COMPRESSIBLE-FLOW CALCULATIONS FOR TUBULAR TURBOJET COMBUSTOR WITH CONSTANT ANNULUS AND LINER CROSS-SECTIONAL AREAS

From application of the continuity equation, the flow at any station in the combustor may be related to the total airflow through the combustor by

$$\frac{w}{w_T}=\frac{1}{M_1^*}\frac{\rho_{st}V}{\rho_t a_t}\frac{A}{A_r}\frac{P}{P_1}\left(\frac{T_1}{T}\right)^{1/2} \tag{C1}$$

where

$$M_1^*=\frac{w_T}{\rho_{t,1}a_{t,1}A_r}=\left(\frac{\rho_{st}V}{\rho_t a_t}\right)_1 \tag{C2}$$

Transposing terms in equation (C1) gives

$$\frac{\rho_{st}V}{\rho_t a_t}=M^*=M_1^*\frac{A_r}{A}\frac{w}{w_T}\frac{P_1}{P}\left(\frac{T}{T_1}\right)^{1/2} \tag{C3}$$

Since

$$\frac{\rho_{st}V}{\rho_t a_t}=M\frac{p}{P}\left(\frac{T}{t}\right)^{1/2}=\beta\left(\frac{p}{P}\right) \tag{C4}$$

the relation between $\rho_{st}V/\rho_t a_t$ and local Mach number, local static to total temperature and pressure ratios, and other compressible-flow functions may be obtained from compressible-flow tables (e. g., ref. 14).

For any station in the liner,

$$M_L^*=M_1^*\frac{A_r}{A_L}\frac{w_L}{w_T}\frac{P_1}{P_L}\left(\frac{T_L}{T_1}\right)^{1/2} \tag{C5}$$

For the end of the liner,

$$M_{L,3}^*=M_1^*\frac{A_r}{A_L}\frac{P_1}{P_{L,3}}\left(\frac{T_{L,3}}{T_1}\right)^{1/2} \tag{C6}$$

For the annulus, where the total temperature is assumed equal to the combustor-inlet total temperature,

$$M_A^*=M_1^*\frac{A_r}{A_A}\frac{P_1}{P_A}\left(1-\frac{w_L}{w_T}\right) \tag{C7}$$

The dynamic pressure q is given by

$$q=\frac{\gamma_a}{2}pM^2=\frac{\gamma_a}{2}\frac{p}{P}M^2P=\beta'(M^*)P \tag{C8}$$

and the combustor total-pressure-loss coefficient by

$$\frac{\Delta P}{q_r}=\frac{P_1-P_{L,3}}{q_r}=\frac{1-\frac{P_{L,3}}{P_1}}{\beta'(M_1^*)} \tag{C9}$$

For the compressible-flow calculations, equation (B2) is put in the dimensionless form

$$\mathrm{d}\left(\frac{w_L}{w_T}\right)=\frac{C}{M_1^*}\left(\frac{\rho_{st}V}{\rho_t a_t}\right)_j\frac{P_j}{P_1}\left(\frac{T_1}{T_j}\right)^{1/2}\mathrm{d}\left(\frac{A_h}{A_r}\right) \tag{C10}$$

For isentropic flow through the liner wall openings to the jet vena contracta, P_j equals P_A, and, for T_j equal to T_1, equation (C10) may be rearranged and integrated from station 2 to a given station along the combustor to obtain

$$\int_{w_{L,2}/w_T}^{w_L/w_T}\frac{M_1^*\,\mathrm{d}\left(\frac{w_L}{w_T}\right)}{C\left(\frac{\rho_{st}V}{\rho_t a_t}\right)_j\frac{P_A}{P_1}}=\frac{A_h}{A_r} \tag{C11}$$

As in appendix B, the total liner open hole area is obtained from the integration from station 2 to station 3 where $w_{L,3}/w_T=1$:

$$\int_{w_{L,2}/w_T}^{1}\frac{M_1^*\,\mathrm{d}\left(\frac{w_L}{w_T}\right)}{C\left(\frac{\rho_{st}V}{\rho_t a_t}\right)_j\frac{P_A}{P_1}}=\frac{A_{h,t}}{A_r} \tag{11}$$

The airflow distribution is obtained from

$$\frac{\int_{w_{L,2}/w_T}^{w_L/w_T} \frac{M_1^* \, \mathrm{d}\left(\frac{w_L}{w_T}\right)}{C\left(\frac{\rho_{st}V}{\rho_t a_t}\right)_j \frac{P_A}{P_1}}}{\int_{w_{L,2}/w_T}^{1} \frac{M_1^* \, \mathrm{d}\left(\frac{w_L}{w_T}\right)}{C\left(\frac{\rho_{st}V}{\rho_t a_t}\right)_j \frac{P_A}{P_1}}} = \frac{A_h}{A_{h,t}} \tag{12}$$

If the static pressure at the jet vena contracta is assumed equal to the liner static pressure at the station considered, the term $(\rho_{st}V/\rho_t a_t)_j$ of equations (C11), (11), and (12) is obtained from the ratio of liner static to annulus total pressure p_L/P_A and equation (C4).

As in appendix B, the liner static pressure is obtained from the solution of the momentum equation. With the use of equation (C8) and the definition of $M_{t,A}$, the momentum equation (B9) can be put in the form

$$\frac{p_L}{P_L}(1+\gamma_g M_L^2)P_L - \frac{p_{L,3}}{P_{L,3}}(1+\gamma_g M_{L,3}^2)P_{L,3} - \gamma_a M_1^* \frac{A_r}{A_L} P_1 \int_1^{w_L/w_T} M_{t,A} \, \mathrm{d}\left(\frac{w_L}{w_T}\right) = 0 \tag{C12}$$

From equations (C4) to (C6),

$$\frac{p_L}{P_L}(1+\gamma_g M_L^2) = \varphi(M_L^*) \tag{C13}$$

and

$$\frac{p_{L,3}}{P_{L,3}}(1+\gamma_g M_{L,3}^2) = \varphi(M_{L,3}^*) \tag{C14}$$

In equations (C12) to (C14), the specific-heat ratio γ_g of the liner gas stream is assumed constant along the combustor.

Combining equations (C12) to (C14) and dividing through by $M_1^* \frac{A_r}{A_L}\left(\frac{T_L}{T_1}\right)^{1/2} \frac{w_L}{w_T}$ give

$$\frac{\varphi(M_L^*)}{M_L^*} = \frac{\left(\frac{T_{L,3}}{T_1}\right)^{1/2} \frac{\varphi(M_{L,3}^*)}{M_{L,3}^*} + \gamma_a \int_1^{w_L/w_T} M_{t,A} \, \mathrm{d}\left(\frac{w_L}{w_T}\right)}{\left(\frac{T_L}{T_1}\right)^{1/2} \frac{w_L}{w_T}} \tag{C15}$$

Equation (C15) may be written

$$\psi(M_L^*) = \frac{\psi(M_{L,3}^*)\left(\frac{T_{L,3}}{T_1}\right)^{1/2} + \gamma_a \int_1^{w_L/w_T} M_{t,A} \, \mathrm{d}\left(\frac{w_L}{w_T}\right)}{\left(\frac{T_L}{T_1}\right)^{1/2} \frac{w_L}{w_T}} \tag{C16}$$

where

$$\psi(M^*) = \frac{\varphi(M^*)}{M^*} \tag{C17}$$

From equation (C3), the integral in equation (C16) can be expressed as a function of M_A^*. For the present calculations, the total-pressure ratio P_A/P_1 required in the evaluation of M_A^* was obtained by using the following relation:

$$\frac{P_A}{P_1} = 1 - \frac{\gamma_a}{2}\left(\frac{p}{P}\right)_1 M_r^2 \left(\frac{P_1 - P_A}{q_r}\right) \tag{C18}$$

and the values of $(P_1 - P_A)/q_r$ were obtained from equations (6) and (7).

For the case of negligible annulus wall friction, the integral term of equation (C16) is given by

$$\gamma_a \int_1^{w_L/w_T} M_{t,A} \, \mathrm{d}\left(\frac{w_L}{w_T}\right) = \frac{-\gamma_a \left(\frac{A_A}{A_L}\right)[\varphi(M_A^*) - 1]}{M_1^*\left(\frac{A_r}{A_L}\right)} \tag{C19}$$

where

$$\varphi(M_A^*) = \frac{p_A}{P_A}(1+\gamma_a M_A^2) \tag{C20}$$

and equation (C16) reduces to

$$\psi(M_L^*) = \frac{\psi(M_{L,3}^*)\left(\frac{T_{L,3}}{T_1}\right)^{1/2} - \gamma_a\left(1 - \frac{w_L}{w_T}\right)\psi'(M_A^*)}{\frac{w_L}{w_T}\left(\frac{T_L}{T_1}\right)^{1/2}} \tag{C21}$$

where

$$\psi'(M_A^*) = \frac{\varphi(M_A^*) - 1}{M_A^*} \tag{C22}$$

In table I, φ, ψ, ψ', p/P, and M^* are presented for a range of values of M and for specific-heat ratios of 1.4 and 1.3.

If values of M_1^*, A_L/A_r, $P_1/P_{L,3}$, and T_L/T_1 are specified, the right side of equation (C16) or (C21) can be calculated for various values of w_L/w_T. From these values of $\psi(M_L^*)$, values for M_L^* and the pressure ratio p_L/P_L can be obtained from table I(a). Then

$$\frac{p_L}{P_A} = \left(\frac{p_L}{P_L}\right)\left(\frac{P_L}{P_1}\right)\left(\frac{P_1}{P_A}\right) = \frac{p_L}{P_L}\frac{P_1}{P_A}\frac{M_1^* \frac{A_r}{A_L}\frac{w_L}{w_T}\left(\frac{T_L}{T_1}\right)^{1/2}}{M_L^*} \tag{C23}$$

where P_1/P_A is obtained from equation (C18). From this value of p_L/P_A, the term $(\rho_{st}V/\rho_t a_t)_j$ of equations (11) and (12) is obtained.

In the present report, the orifice-discharge-coefficient correlation of reference 7 was used (see fig. 3). The pressure ratio p_A/P_A of the correlation parameter of figure 3(a) is obtained from table I(a) and M_A^*, while the pressure ratio p_A/p_L of figure 3(b) is obtained from

$$\frac{p_A}{p_L} = \frac{\frac{p_A}{P_A}}{\frac{p_L}{P_A}} \tag{C24}$$

where p_L/P_A is obtained from equation (23). With the above values of $C(\rho_{st}V/\rho_t a_t)_j$ and P_1/P_A, the integrals of equations (11) and (12) may be evaluated by trapezoidal or graphical integration.

The entrance angle θ of a liner air jet may be obtained from the relation

$$\theta = \cos^{-1}\frac{M_A}{M_j} \tag{13}$$

where M_A and M_j are obtained from table I(a) and values of M_A^* and $M_j^* = \left(\frac{\rho_{st}V}{\rho_t a_t}\right)$, respectively.

REFERENCES

1. Nichols, J. B.: An Energy Basis for Comparison of Performance of Combustion Chambers. Trans. A.S.M.E., vol. 75, Jan. 1953, pp. 29–33; discussion, p. 33.
2. Olson, W. T., Childs, J. Howard, and Jonash, E. R.: The Combustion-Efficiency Problem of the Turbojet at High Altitude. Trans. A.S.M.E., vol. 77, no. 5, July 1955, pp. 605–615.
3. Anon.: Quarterly Progress Report on Study of Combustors for Supersonic Ram-Jet for Period July 1–Sept. 30, 1949. Rep. No. PDN 5473, Process Div., Esso Labs., Standard Oil Dev. Co., Nov. 1, 1949. (Navy Bur. Ord. Contract NOrd–9233.)
4. Bader, Frank: A Convenient Method for Calculation of Flow Conditions within a Can-Type Burner Using Assigned Flow and Cross-Sectional Area Distributions. Rep. No. CM–642, Appl. Phys. Lab., The Johns Hopkins Univ., Sept. 28, 1950. (NOrd Contract 7386 with Bur. Ord., U. S. Navy.)
5. Turner, L. Richard, and Bogart, Donald: Constant-Pressure Combustion Charts Including Effects of Diluent Pressure. NACA Rep. 937, 1949. (Supersedes NACA TN's 1086 and 1655.)
6. Hottel, H. C., Williams, G. C., and Satterfield, C. N.: Thermodynamic Charts for Combustion Processes, pts. I and II. John Wiley & Sons, Inc., 1949.
7. Dittrich, Ralph T., and Graves, Charles C.: Discharge Coefficients for Combustor-Liner Air-Entry Holes. I—Circular Holes with Parallel Flow. NACA TN 3663, 1956.
8. Callaghan, Edmund E., and Bowden, Dean T.: Investigation of Flow Coefficient of Circular, Square, and Elliptical Orifices at High Pressure Ratios. NACA TN 1947, 1949.
9. Dewey, Paul E.: A Preliminary Investigation of Aerodynamic Characteristics of Small Inclined Air Outlets at Transonic Mach Numbers. NACA TN 3442, 1955. (Supersedes NACA RM L53C10.)
10. Knight, H. A., and Walker, R. B.: The Component Pressure Losses in Combustion Chambers. Rep. No. R.143, British N.G.T.E., Nov. 1953.
11. Rosen, Philip, and Hart, R. W.: A Constant-Area, Constant-Temperature Combustor. Jour. Aero. Sci., vol. 20, no. 8, Aug. 1953, pp. 549–554.
12. Fuels and Combustion Research Division: Adaptation of Combustion Principles to Aircraft Propulsion. Vol. II—Combustion in Air-Breathing Jet Engines. NACA RM E55G28, 1956.
13. Shapiro, Ascher H., and Hawthorne, W. R.: The Mechanics and Thermodynamics of Steady One-Dimensional Gas Flow. Jour. Appl. Mech., vol. 14, no. 4, Dec. 1947, pp. A317–A336.
14. Ames Research Staff: Equations, Tables and Charts for Compressible Flow. NACA Rep. 1135, 1953. (Supersedes NACA TN 1428.)

TABLE I.—SUBSONIC COMPRESSIBLE-FLOW PARAMETERS

(a) Specific-heat ratio γ_a, 1.4.

M	$\frac{p}{P}$	$M^*=\frac{\rho_{st}V}{\rho_t a_t}$	$\varphi=\frac{p}{P}(1+\gamma_a M^2)$	$\psi=\frac{\phi}{\frac{\rho_{st}V}{\rho_t a_t}}$	$\psi'=\frac{\varphi-1}{\frac{\rho_{st}V}{\rho_t a_t}}$
0	1.00	0	1.0	∞	0
.01	.9999	.0100	1.00004	100.004	.0040
.02	.9997	.0200	1.00026	50.013	.0130
.03	.9994	.0300	1.00065	33.355	.0217
.04	.9989	.0400	1.00114	25.028	.0285
.05	.9983	.0500	1.00179	20.036	.0358
.06	.9975	.0599	1.00252	16.737	.0421
.07	.9966	.0698	1.00344	14.376	.0493
.08	.9955	.0797	1.00442	12.603	.0555
.09	.9944	.0896	1.00568	11.224	.0634
.10	.9930	.0994	1.00690	10.130	.0694
.11	.9916	.1092	1.00840	9.2344	.0769
.12	.9900	.1190	1.00996	8.4871	.0837
.13	.9883	.1287	1.01168	7.8608	.0908
.14	.9864	.1384	1.01347	7.3228	.0973
.15	.9844	.1480	1.01541	6.8609	.1041
.16	.9823	.1576	1.01751	6.4563	.1111
.17	.9800	.1671	1.01965	6.1020	.1176
.18	.9776	.1765	1.02194	5.7900	.1243
.19	.9751	.1859	1.02438	5.5104	.1311
.20	.9725	.1953	1.02696	5.2584	.1380
.21	.9697	.2045	1.02957	5.0346	.1446
.22	.9668	.2137	1.03231	4.8306	.1512
.23	.9638	.2228	1.03518	4.6462	.1579
.24	.9607	.2319	1.03817	4.4768	.1646
.25	.9575	.2408	1.04128	4.3243	.1714
.26	.9541	.2497	1.04440	4.1826	.1778
.27	.9506	.2585	1.04762	4.0527	.1842
.28	.9470	.2672	1.05094	3.9332	.1906
.29	.9433	.2758	1.05436	3.8229	.1971
.30	.9395	.2844	1.05788	3.7197	.2035
.31	.9355	.2928	1.06136	3.6249	.2096
.32	.9315	.3011	1.06504	3.5371	.2160
.33	.9274	.3093	1.06879	3.4555	.2224
.34	.9231	.3175	1.07249	3.3779	.2283
.35	.9188	.3255	1.07637	3.3068	.2346
.36	.9143	.3334	1.08019	3.2399	.2405
.37	.9098	.3412	1.08417	3.1775	.2467
.38	.9052	.3489	1.08820	3.1189	.2528
.39	.9004	.3565	1.09213	3.0635	.2584
.40	.8956	.3640	1.09621	3.0116	.2643
.41	.8907	.3713	1.10032	2.9634	.2702
.42	.8857	.3785	1.10443	2.9179	.2759
.43	.8807	.3856	1.10868	2.8752	.2818
.44	.8755	.3926	1.11280	2.8344	.2873
.45	.8703	.3994	1.11703	2.7968	.2930
.46	.8650	.4062	1.12125	2.7603	.2985
.47	.8596	.4128	1.12544	2.7264	.3039
.48	.8541	.4193	1.12960	2.6940	.3091
.49	.8486	.4256	1.13385	2.6641	.3145
.50	.8430	.4319	1.13805	2.6350	.3196

(b) Specific-heat ratio γ_s, 1.3.

M	$\frac{p}{P}$	$M^*=\frac{\rho_{st}V}{\rho_t a_t}$	$\varphi=\frac{p}{P}(1+\gamma_s M^2)$	$\psi=\frac{\varphi}{\frac{\rho_{st}V}{\rho_t a_t}}$
0	1.0	0	1	∞
.01	.9999	.0100	1.00003	100.003
.02	.9997	.0200	1.00022	50.011
.03	.9994	.0300	1.00057	33.352
.04	.9990	.0400	1.00108	25.027
.05	.9984	.0499	1.00164	20.073
.06	.9977	.0599	1.00237	16.734
.07	.9968	.0698	1.00315	14.372
.08	.9959	.0797	1.00419	12.600
.09	.9948	.0896	1.00528	11.220
.10	.9935	.0994	1.00642	10.125
.11	.9922	.1092	1.00781	9.2290
.12	.9907	.1190	1.00925	8.4811
.13	.9891	.1287	1.01083	7.8542
.14	.9874	.1384	1.01256	7.3162
.15	.9855	.1481	1.01433	6.8490
.16	.9835	.1577	1.01623	6.4441
.17	.9814	.1672	1.01827	6.0901
.18	.9792	.1767	1.02044	5.7750
.19	.9769	.1861	1.02275	5.4957
.20	.9744	.1955	1.02507	5.2433
.21	.9718	.2048	1.02751	5.0171
.22	.9691	.2140	1.03008	4.8135
.23	.9663	.2231	1.03275	4.6291
.24	.9634	.2322	1.03554	4.4597
.25	.9604	.2412	1.03843	4.3053
.26	.9572	.2501	1.04132	4.1636
.27	.9540	.2590	1.04441	4.0325
.28	.9506	.2677	1.04749	3.9129
.29	.9471	.2764	1.05065	3.8012
.30	.9435	.2850	1.05389	3.6979
.31	.9399	.2935	1.05732	3.6024
.32	.9361	.3018	1.06071	3.5146
.33	.9322	.3101	1.06417	3.4317
.34	.9282	.3183	1.06769	3.3544
.35	.9241	.3264	1.07126	3.2820
.36	.9200	.3344	1.07500	3.2147
.37	.9157	.3423	1.07867	3.1512
.38	.9113	.3500	1.08237	3.0925
.39	.9069	.3577	1.08622	3.0367
.40	.9023	.3652	1.08998	2.9846
.41	.8977	.3727	1.09387	2.9350
.42	.8930	.3800	1.09778	2.8889
.43	.8882	.3872	1.10170	2.8453
.44	.8833	.3943	1.10561	2.8040
.45	.8784	.4012	1.10964	2.7658
.46	.8734	.4081	1.11365	2.7289
.47	.8683	.4148	1.11765	2.6944
.48	.8631	.4214	1.12162	2.6617
.49	.8579	.4279	1.12568	2.6307
.50	.8525	.4341	1.12956	2.6021

REPORT 1374

THE SIMILARITY RULES FOR SECOND-ORDER SUBSONIC AND SUPERSONIC FLOW [1]

By MILTON D. VAN DYKE

SUMMARY

The similarity rules for linearized compressible flow theory (Göthert's rule and its supersonic counterpart) are extended to second order. It is shown that any second-order subsonic flow can be related to "nearly incompressible" flow past the same body, which can be calculated by the Janzen-Rayleigh method.

INTRODUCTION

The linearized small-disturbance theory of steady compressible flow, based on the Prandtl-Glauert equation, yields a first approximation for thin objects moving at either subsonic or supersonic speeds. More precisely, it provides the first term in an asymptotic expansion of the solution for small disturbances, provided that the flight Mach number is not too close either to unity (transonic flow) or to infinity (hypersonic flow).

The similarity rule that governs linearized subsonic flow past general three-dimensional objects was first given correctly by Göthert (ref. 1). It has an obvious counterpart in supersonic flow, and the rules have rendered great service in both theoretical and experimental investigations.

Recently, various investigators have sought to improve on the linearized theory by finding higher approximations (see, e.g., refs. 2 to 5). The second step is commonly referred to as the second-order small-disturbance theory, or simply "second-order theory." It can be found in general by iterating upon the linearized solution, retaining all terms out of the full nonlinear equations of motion whose contribution is of the order of the square of the disturbances in linearized theory (ref. 3). In the simplest case of plane flow without stagnation points, the linearized disturbances are proportional to the thickness ratio τ of the airfoil, so that second-order theory adds terms in τ^2, and higher approximations extend the series in powers of τ^n. Stagnation points lead to the appearance of logarithmic terms, beginning with $\tau^4 ln\ \tau$ in the fourth approximation. The series diverges in the immediate vicinity of stagnation points, although it can be corrected there by simple techniques (ref. 6). Slender pointed objects, such as a smooth body of revolution, cause smaller disturbances than airfoils, but logarithmic terms always arise at the outset; hence the linearized solution contains terms of order $\tau^2 ln\ \tau$ and τ^2, and the second-order increment then consists of terms of order $\tau^4 ln^2 \tau$, $\tau^4 ln\ \tau$, and τ^4. Nothing is known of the convergence of these series; they are perhaps only asymptotic expansions for small thickness. Second-order theory, like linearized theory, breaks down in the transonic and hypersonic ranges, though it may penetrate somewhat farther into their fringes.

A similarity rule for second-order theory has recently been given in the special case of supersonic flow past thin flat wings by Fenain and Germain, who demonstrate its usefulness in theoretical studies (ref. 5). However, as in linearized theory, the rules for flat wings are only special cases of those for general three-dimensional shapes. The present paper is devoted to deducing the general rules for subsonic and supersonic flows, and examining their implications. In particular, it is shown how the rule for subsonic flow relates the second-order solution for any object to nearly incompressible flow past the same body, which can be calculated by the Janzen-Rayleigh method.

The author is indebted to Wallace D. Hayes for suggesting several improvements that have been incorporated in the present version of this paper. In particular, the procedure for recovering the second-order solution from the Janzen-Rayleigh solution (p. 930) is simpler and more logical than that originally given in NACA TN 3875.

DERIVATION OF RULES FOR BODIES OF REVOLUTION

A body of revolution is the simplest shape that is not a special case, but displays the full generality of the existing similarity rules for subsonic, supersonic, transonic, and hypersonic flows. The same can be shown to be true of the second-order rules to be discussed here. Hence for clarity of exposition, the second-order rules will be derived in detail only for an axisymmetric body at zero angle of attack. The rules for general three-dimensional thin or slender objects will thereafter be stated without proof. The subsonic and supersonic cases are so similar that they can be treated simultaneously.

Let the body be described by $r=\tau R(x)$, where τ is a thickness parameter or characteristic slope (say, the maximum slope, average slope, thickness ratio, or the like), and $R(x)$ is a function of order unity (fig. 1). As usual in similarity analysis, the characteristic slope τ is regarded as a parameter, so that different values of τ correspond to affinely related members of the same family of bodies.

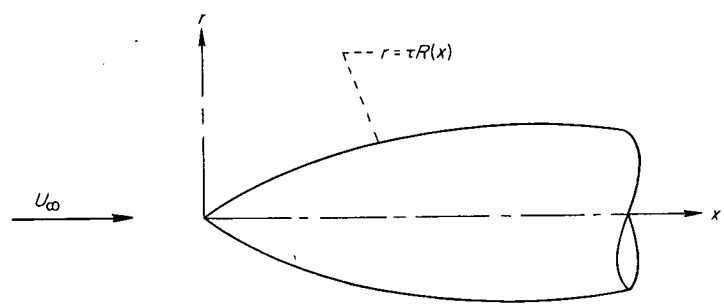


FIGURE 1.—Notation for body of revolution.

[1] Supersedes NACA TN 3875, by Milton D. Van Dyke, 1957.

To second order the flow is irrotational, so that there exists a velocity potential $\Phi(x, r; M, \gamma, \tau)$. This notation indicates that for each family of bodies (associated with a given function $R(x)$), the flow field is regarded as depending not only upon the two independent variables x and r but also upon the three parameters following the semicolon:

M free-stream Mach number
γ adiabatic exponent of gas [2]
τ characteristic slope of body

The aim of a similarity analysis is to transform the problem so as to reduce the number of parameters appearing in it. If that can be accomplished, flows having different values of the original parameters are related provided only that the reduced parameters are equal. The transformation to be used here consists in separating the dependent variable Φ into several components, and then stretching each component and the independent variables by factors that depend upon the original parameters. It is convenient, and involves no loss of generality, to leave streamwise coordinates unchanged, so that r is to be stretched but not x.

Perturbation potentials are first introduced by setting

$$\frac{\Phi}{U_\infty}=x+\phi+\varphi+\ldots \tag{1}$$

where ϕ is the potential of linearized theory, and φ the second-order increment.

RULES FOR LINEARIZED THEORY

The linearized problem is

$$\left.\begin{aligned} &\Box\phi\equiv(1-M^2)\phi_{xx}+\phi_{rr}+\frac{\phi_r}{r}=0 \\ &\phi\to 0 \qquad \text{at infinity} \\ &\phi_r=\tau R'(x) \quad \text{at } r=\tau R(x) \end{aligned}\right\} \tag{2}$$

The first relation is the linearized Prandtl-Glauert equation. The second is a statement, sufficiently definite for present purposes, of the requirement that the flow approach a uniform stream far from the body in almost all directions. The third is the linearized condition of tangent flow at the body surface.[3] The linearized problem is seen not to involve γ, so that the solution depends upon only the two parameters M and τ.

The similarity rules can be obtained by considering arbitrary scale transformations of ϕ and r. It is readily found that the only choice that reduces the number of parameters from two to one is (temporarily suppressing the dependence on parameters)

$$\phi(x,r)=\frac{1}{\beta^2}F(x,\rho) \tag{3a}$$

and

$$\rho=\beta r \tag{3b}$$

where

$$\beta=\begin{cases}\sqrt{1-M^2} & \text{for subsonic flow} \\ \sqrt{M^2-1} & \text{for supersonic flow}\end{cases} \tag{3c}$$

Then the problem becomes

$$\left.\begin{aligned} &\triangle F\equiv F_{\rho\rho}+\frac{F_\rho}{\rho}\pm F_{xx}=0 \\ &F\to 0 \qquad \text{at infinity} \\ &F_\rho=\beta\tau R'(x) \quad \text{at } \rho=\beta\tau R(x) \end{aligned}\right\} \tag{4}$$

where here and later the upper and lower signs apply, respectively, to the subsonic and supersonic problems.

The transformations of ϕ and r have been so chosen that the problem is reduced to one involving the two parameters M and τ not separately, but only in the combination $\beta\tau$. This is the similarity parameter. Two subsonic or supersonic flows past bodies of the same family are related if the corresponding Mach numbers are such that the parameter $\beta\tau$ is the same for both. The nature of the relationship is found by reintroducing the dependence on parameters into equation (3a), which gives the similarity rules

$$\phi(x,r;M,\tau)=\frac{1}{\beta^2}F(x,\beta r;\beta\tau) \tag{5}$$

SECOND-ORDER RULES

The second-order problem is found to be (ref. 3)

$$\left.\begin{aligned} &\Box\varphi=M^2\{[(\gamma+1)M^2+2(1-M^2)]\phi_x\phi_{xx}+2\phi_r\phi_{xr}+\phi_r{}^2\phi_{rr}\} \\ &\varphi\to 0 \qquad \text{at infinity} \\ &\varphi_r=\tau\phi_x R'(x) \quad \text{at } r=\tau R(x) \end{aligned}\right\} \tag{6}$$

Note that the first equation contains not only quadratic terms on the right-hand side, but also the triple product $\phi_r{}^2\phi_{rr}$ whose contribution is of second order in some cases.

The parameter γ appears only linearly in the combination $(\gamma+1)$ and can accordingly be separated out. Thus the appropriate transformation is found to be

$$\varphi(x,r)=\frac{1}{\beta^4}\left[f_1(x,\rho)+M^2f_2(x,\rho)+(\gamma+1)\frac{M^4}{\beta^2}f_3(x,\rho)\right] \tag{7}$$

Then equating like powers of M^2 yields the following set of three problems for f_1, f_2, f_3 in which the parameters M, γ, τ appear again only in the form of the single similarity parameter $\beta\tau$:

$$\left.\begin{aligned} &\triangle f_1=0 \\ &f_1\to 0 \qquad \text{at infinity} \\ &f_{1\rho}=\beta\tau F_x R'(x) \quad \text{at } \rho=\beta\tau R(x) \end{aligned}\right\} \tag{8a}$$

---

[2] Hayes has pointed out (ref. 7) that to second order an imperfect gas corresponds to a polytropic gas having a γ equal to the free-stream value of

$$\frac{2}{c}\left(\frac{\partial\rho c}{\partial\rho}\right)_s-1=1+\frac{\rho}{c}\left(\frac{\partial c^2}{\partial\rho}\right)_s$$

where c is the speed of sound and ρ the density, the partial derivative being taken at constant entropy s.

[3] In what is generally called the slender-body approximation, the body is assumed to be so smooth and slender that the tangency condition can be imposed on the axis rather than on the actual surface, for bodies of revolution in the form $\lim_{r\to 0} r\phi_r=\tau^2R(x)R'(x)$. Thus slender-body theory is a further approximation within linearized theory (being, in fact, the leading term in the asymptotic expansion of the linearized solution for small thickness τ). Consequently, the slender-body solution obeys the similarity rules of linearized theory, and he second-order slender-body solution likewise obeys the second-order similarity rules.

$$\left.\begin{aligned} \triangle f_2 &= \pm 2F_xF_{xx}+2F_\rho F_{x\rho}+F_\rho{}^2F_{\rho\rho} \\ f_2 &\to 0 \qquad \text{at infinity} \\ f_{2\rho} &= 0 \qquad \text{at } \rho=\beta\tau R(x) \end{aligned}\right\} \tag{8b}$$

$$\left.\begin{aligned} \triangle f_3 &= F_xF_{xx} \\ f_3 &\to 0 \qquad \text{at infinity} \\ f_{3\rho} &= 0 \qquad \text{at } \rho=\beta\tau R(x) \end{aligned}\right\} \tag{8c}$$

Then reintroducing the explicit dependence on parameters into the functions f_1,f_2,f_3 of equation (7) gives the similarity rules for the second-order increment in perturbation potential:

$$\varphi(x,r;M,\gamma,\tau)=\frac{1}{\beta^4}\left[f_1(x,\beta r;\beta\tau)+M^2f_2(\ )+(\gamma+1)\frac{M^4}{\beta^2}\ f_3(\ )\right] \tag{9}$$

where the arguments of f_2 and f_3 are the same as those of f_1. Hereafter the arguments of later terms will be omitted in this fashion when they are the same as for the leading term. It should be emphasized that, just as in linearized theory, the subsonic and supersonic rules are quite distinct, although they have the same form (9). Because of the different definitions of β, and the resulting $\pm$ signs in equations (4) and (8b), a supersonic flow is not related to a subsonic flow. Discussion of these results is deferred to the general case.

RULES FOR GENERAL BODIES

Consider a family of general three-dimensional bodies, whose members are derived from one another by a uniform magnification or reduction of all dimensions normal to the free stream (fig. 2). Each member of such a family can be characterized, as before, by some characteristic slope τ. It may be emphasized that τ can be identified with thickness, camber, or angle of attack, all of which vary together for related bodies.

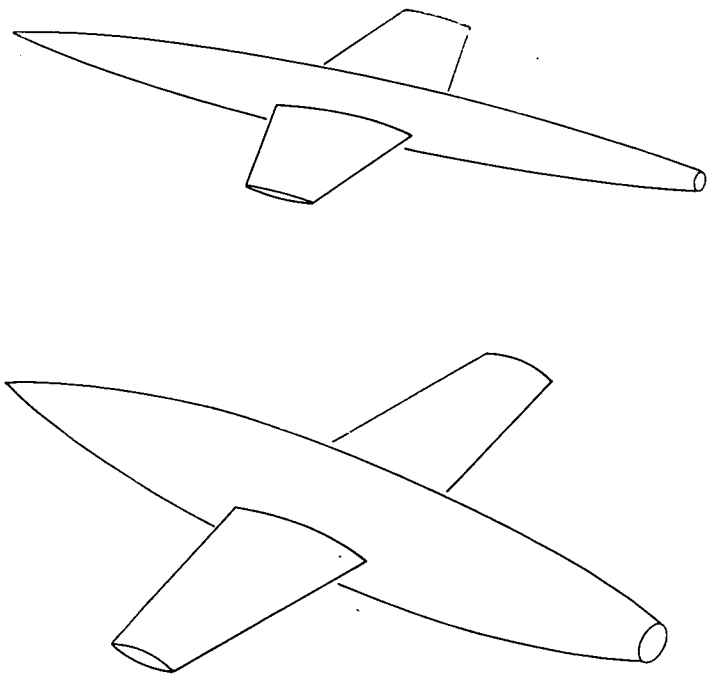


FIGURE 2.—Example of two related bodies.

The preceding analysis can be extended in a straightforward way to such general bodies, at the expense only of typographic complexity. Both cross-stream dimensions behave in the way that r did before. Hence the subsonic and supersonic second-order rules for the velocity potential, corresponding to equations (5) and (9), are, in Cartesian coordinates:

$$\frac{1}{U_\infty}\Phi(x,y,z;M,\gamma,\tau)=x+\frac{1}{\beta^2}F(x,\beta y,\beta z;\beta\tau)+\frac{1}{\beta^4}\left[f_1(x,\beta y,\beta z;\beta\tau)+M^2f_2(\ )+(\gamma+1)\frac{M^4}{\beta^2}f_3(\ )\right] \tag{10a}$$

Differentiation yields the corresponding rules for velocity components (those for w having the same form as for v):

$$\frac{u}{U_\infty}=1+\frac{1}{\beta^2}U(x,\beta y,\beta z;\beta\tau)+\frac{1}{\beta^4}\left[u_1(x,\beta y,\beta z;\beta\tau)+M^2u_2(\ )+(\gamma+1)\frac{M^4}{\beta^2}u_3(\ )\right] \tag{10b}$$

$$\frac{v}{U_\infty}=\frac{1}{\beta}V(x,\beta y,\beta z;\beta\tau)+\frac{1}{\beta^3}\left[v_1(x,\beta y,\beta z;\beta\tau)+M^2v_2(\ )+(\gamma+1)\frac{M^4}{\beta^2}v_3(\ )\right] \tag{10c}$$

(The functions appearing here are actually related to derivatives of the functions in equation (10a), but the connection is of little interest.) To second order the pressure coefficient is given by

$$C_p=-2\phi_x-(\phi_y{}^2+\phi_z{}^2)-2\varphi_x-2(\phi_y\varphi_y+\phi_z\varphi_z)+(M^2-1)\phi_x{}^2+M^2\phi_x(\phi_y{}^2+\phi_z{}^2)+\tfrac{1}{4}M^2(\phi_y{}^2+\phi_z{}^2)^2$$

where the terms in the second line may be significant for slender shapes. Substituting the expressions (10) for velocity components and simplifying shows that the similitude for pressure coefficient has the same form as that for the streamwise velocity increment $\Delta u/U_\infty$:

$$C_p(x,y,z;M,\gamma,\tau)=\frac{1}{\beta^2}P(x,\beta y,\beta z;\beta\tau)+\frac{1}{\beta^4}\left[p_1(x,\beta y,\beta z;\beta\tau)+M^2p_2(\ )+(\gamma+1)\frac{M^4}{\beta^2}p_3(\ )\right] \tag{10d}$$

The similarity rules for the perturbation stream function in plane flow are the same as those for v/U_∞ (eq. (10c)).

ALTERNATIVE FORMS

As with other similarity rules, an unlimited number of alternative forms can be produced by multiplying by powers of the similarity parameter. Thus, of the many possible alternatives to the second-order rules (10d) for pressure coefficient, two of the most useful are:

$$C_p=\frac{\tau}{\beta}\bar{P}(x,\beta y,\beta z;\beta\tau)+\frac{\tau^2}{\beta^2}\left[\bar{p}_1(\ )+M^2\bar{p}_2(\ )+(\gamma+1)\frac{M^4}{\beta^2}\bar{p}_3(\ )\right] \tag{10e}$$

$$C_p=\tau^2\tilde{P}(x,\beta y,\beta z;\beta\tau)+\tau^4\left[\tilde{p}_1(\ )+M^2\tilde{p}_2(\ )+(\gamma+1)\frac{M^4}{\beta^2}\tilde{p}_3(\ )\right] \tag{10f}$$

In addition, the first two second-order terms can be manipulated, using the connection between M^2 and β^2, to yield additional alternative forms such as the following, which correspond to the three forms above:

$$C_p=\frac{1}{\beta^2}P(x,\beta y,\beta z;\beta\tau)+\frac{1}{\beta^2}\left[p_1(\ )+\frac{M^2}{\beta^2}p_2'(\ )+(\gamma+1)\frac{M^4}{\beta^4}p_3(\ )\right] \tag{10g}$$

$$C_p=\frac{\tau}{\beta}\bar{P}(x,\beta y,\beta z;\beta\tau)+\tau^2\left[\bar{p}_1(\ )+\frac{M^2}{\beta^2}\bar{p}_2'(\ )+(\gamma+1)\frac{M^4}{\beta^4}\bar{p}_3(\ )\right] \tag{10h}$$

$$C_p=\tau^2\tilde{P}(x,\beta y,\beta z;\beta\tau)+\tau^4\left[\beta^2\tilde{p}_1(\ )+\tilde{p}_2'(\ )+(\gamma+1)\frac{M^4}{\beta^2}\tilde{p}_3(\ )\right] \tag{10i}$$

FORCE COEFFICIENTS

The rules for pressure imply rules for the lift and drag coefficients. For example, equation (10e) leads to

$$C_L(M,\gamma,\tau)=\frac{\tau}{\beta}L(\beta\tau)+\frac{\tau^2}{\beta^2}\left[l_1(\beta\tau)+M^2l_2(\beta\tau)+(\gamma+1)\frac{M^4}{\beta^2}l_3(\beta\tau)\right] \tag{10j}$$

$$C_D(M,\gamma,\tau)=\frac{\tau^2}{\beta}D(\beta\tau)+\frac{\tau^3}{\beta^2}\left[d_1(\beta\tau)+M^2d_2(\beta\tau)+(\gamma+1)\frac{M^4}{\beta^2}d_3(\beta\tau)\right] \tag{10k}$$

if the coefficients are referred to some plan-form area. If some cross-sectional area is used, each term is reduced by one power of τ. Various alternative forms are again useful. In the case of lift coefficient, one will ordinarily choose to identify τ with the angle of attack.

RULES FOR QUASI-CYLINDRICAL BODIES

A special class of objects must be distinguished, which will be termed quasi-cylindrical bodies. These are shapes that lie everywhere so close to some cylinder (not necessarily circular) parallel to the free stream that to a first approximation the condition of tangent flow can be imposed at the cylinder rather than on the actual body surface. Likewise, in second-order theory the tangency condition can be transferred to the cylinder by Taylor series expansion. The simplest example is an airfoil whose thickness, camber, and angle of attack are so small that the tangency condition can be transferred from the airfoil surface to a mean plane parallel to the stream (fig. 3). Another example is an open-nosed body of revolution whose radius varies only slightly. Others are biplanes, cruciform wings, any of these in an open or closed wind tunnel, in combination with one another, etc.

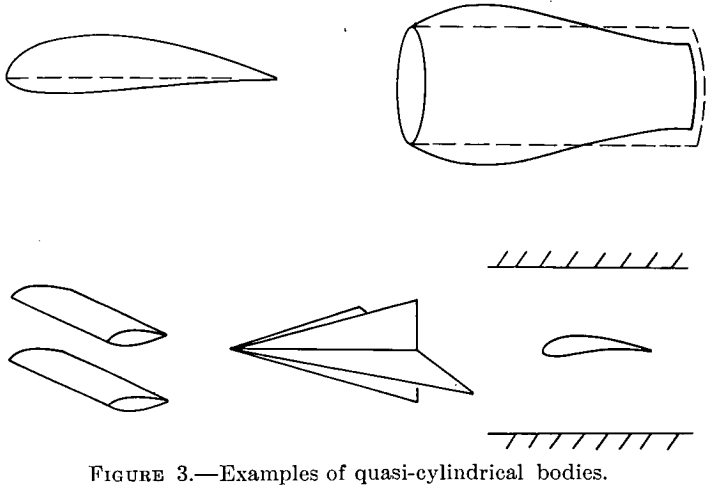


FIGURE 3.—Examples of quasi-cylindrical bodies.

A quasi-cylindrical body can be regarded as consisting of a skeleton upon which is superimposed a small slope distribution. The skeleton is simply the projection of the body onto the basic cylinder. For example, the skeleton of the quasi-cylindrical body of revolution is the circular tube shown dashed in figure 3.

The special place of quasi-cylindrical bodies in similarity theory arises from the fact that the skeleton and the slope distribution can be varied independently. This extra freedom is important. For example, it leads to a useful transonic similarity rule for quasi-cylindrical bodies whereas none exists for general shapes. It is convenient always to leave streamwise dimensions unaltered. Hence, we consider families of quasi-cylindrical bodies that are derived from one another by a lateral compression or expansion of the skeleton, and a quite independent magnification or reduction of all surface slopes. Two members of such a family are shown in figure 4.

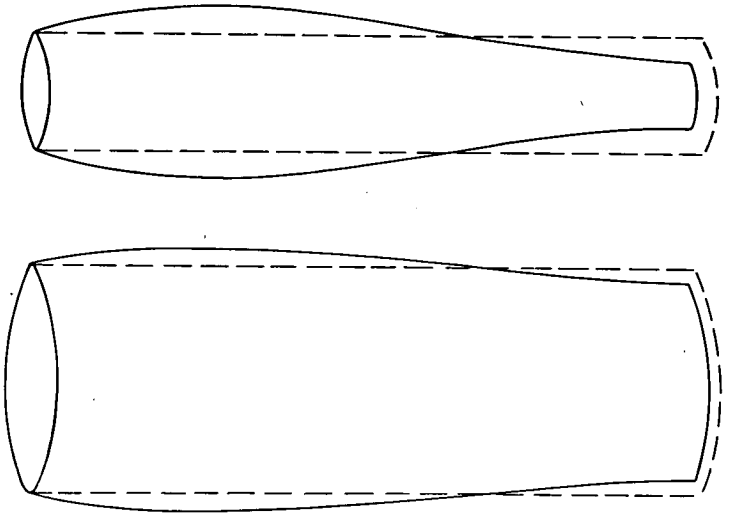


FIGURE 4.—Example of two related quasi-cylindrical bodies.

Distortions of the skeleton will be measured by some characteristic "aspect ratio" A. It is important to note that the term "aspect ratio" is used here in a very general sense to mean any typical ratio of gross cross stream to streamwise dimensions. For example, in the last shape in figure 3, the ratio of wind-tunnel height to airfoil chord is an appropriate characteristic aspect ratio. Changes of slope are measured, as before, by some characteristic slope τ.

The preceding similarity rules can be simplified for quasi-cylindrical bodies by using the facts that first-order perturbation quantities are directly proportional[4] to τ, and second-order terms to τ^2. The simplification can be carried out by first imagining the quasi-cylindrical body to be restricted to be a general body, which means that both βA and $\beta\tau$ must be the same for similarity. Then consider the preceding rules in the particular alternative forms in which τ appears explicitly outside the first-order term and

[4] This is by no means true for general bodies; as noted previously, the first-order pressure coefficient on a smooth slender pointed body of revolution varies as $\tau^2 ln\ \tau$ for small τ.

τ^2 outside the second-order terms. For the pressure coefficient, this form is that of equation (10e):

$$C_p=\frac{\tau}{\beta}\overline{P}(x,\beta y,\beta z;\beta\tau,\beta A)+\frac{\tau^2}{\beta^2}\left[\overline{p}_1(\ )+M^2\overline{p}_2(\ )+(\gamma+1)\frac{M^4}{\beta^2}\overline{p}_3(\ )\right]$$

So far the functions $\overline{P},\overline{p}_1,\overline{p}_2,\overline{p}_3$ have been supposed to depend parametrically upon both βA and $\beta\tau$. However, the first- and second-order terms can be proportional to τ and τ^2, respectively, only if the supposed dependence upon $\beta\tau$ is nonexistent. Hence, the similarity parameter is βA alone, and the rules for pressure are (dropping bars from the functional symbols):

$$C_p(x,y,z;M,\gamma,\tau,A)=\frac{\tau}{\beta}P(x,\beta y,\beta z;\beta A)+\frac{\tau^2}{\beta^2}\left[p_1(x,\beta y,\beta z;\beta A)+M^2p_2(\ )+(\gamma+1)\frac{M^4}{\beta^2}p_3(\ )\right] \quad (11a)$$

The corresponding rules for the potential and velocity components can, if desired, be written down by inspection from equations (10).

With $\hat{p}_2=p_2\pm p_1$ (where, as before, the upper sign applies to subsonic and the lower to supersonic flow), these rules can be rewritten as

$$C_p=\frac{\tau}{\beta}P(\ )+\tau^2\left[p_1(\ )+\frac{M^2}{\beta^2}\hat{p}_2(\ )+(\gamma+1)\frac{M^4}{\beta^4}p_3(\ )\right] \quad (11b)$$

and this is the result that Fenain and Germain found in their treatment of the flat diamond cone in supersonic flow (ref. 5).

CONNECTION WITH HAYES' RULE

For plane flow past a single body, Hayes has discovered a remarkable rule for the second-order surface pressure (ref. 7). It implies that, on the surface, the functions in equation (11a) are such that $p_2=0$ and $p_1=4p_3$. Hence,

$$C_{p_s}=\frac{\tau}{\beta}P(x)+\tau^2\frac{(\gamma+1)M^4+4(1-M^2)}{4(1-M^2)^2}p_1(x) \quad (12)$$

In supersonic flow this is simply Busemann's well-known second-order solution, P being twice the local slope of the surface and p_1 twice its square; in subsonic flow P and p_1 are more complicated (ref. 8). This rule implies a corresponding, but more complicated, rule for surface velocity (ref. 8).

In addition to the restriction to single bodies and plane flow, these rules are not similarity rules in the sense of the preceding results, because they apply only at the surface rather than throughout the field.

EXAMPLES

The rules will be illustrated by two simple examples, attention being confined to the surface pressure coefficient.

SLENDER CIRCULAR CONE IN SUPERSONIC FLOW

Broderick has derived the second-order slender-body solution for a circular cone at zero angle in a supersonic stream (ref. 2). The surface pressure coefficient on a cone of slope τ is

$$C_{p_s}=\tau^2\left(2\,ln\frac{2}{\beta\tau}-1\right)+\tau^4\left[3\beta^2\left(ln\frac{2}{\beta\tau}\right)^2-(5M^2-1)\,ln\frac{2}{\beta\tau}+\frac{13}{4}M^2+\frac{1}{2}+(\gamma+1)\frac{M^4}{\beta^2}\right] \quad (13)$$

This has the form of equation (10i) with

$$\tilde{P}=2\,ln\frac{2}{\beta\tau}-1 \qquad \tilde{p}_2'=-4\,ln\frac{2}{\beta\tau}+\frac{15}{4}$$

$$\tilde{p}_1=3\,ln^2\frac{2}{\beta\tau}-5\,ln\frac{2}{\beta\tau}+\frac{13}{4} \qquad \tilde{p}_3=1$$

WAVY WALL IN CLOSED SUBSONIC WIND TUNNEL

Consider the sinusoidal wall $y=\tau\sin x$ at a distance h from a flat wall (or a distance $2h$ from its mirror image) as indicated in figure 5. Subsonic flow between the walls at a mean

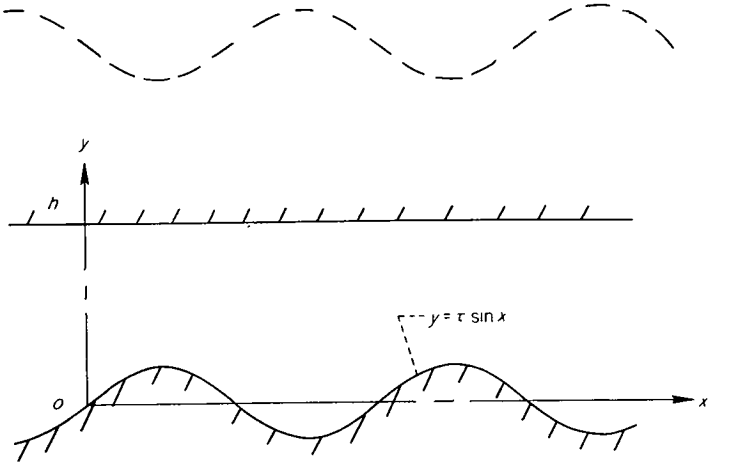


FIGURE 5.—Wavy wall in wind tunnel.

Mach number M can be readily calculated to second order by separation of variables. The resulting pressure coefficient on the surface of the wavy wall is

$$C_{p_s}=-\frac{2\tau}{\beta}\frac{1+e^{-2\beta h}}{1-e^{-2\beta h}}\sin x+\tau^2\frac{(\gamma+1)M^4+4(1-M^2)}{4(1-M^2)^2}\times\frac{1+4e^{-2\beta h}+e^{-4\beta h}}{(1-e^{-2\beta h})^2}\cos 2x-2\tau^2\frac{e^{-2\beta h}}{(1-e^{-2\beta h})^2}+2(\gamma+1)\frac{M^4}{\beta^4}\tau^2\frac{\beta h e^{-4\beta h}}{(1+e^{-2\beta h})(1-e^{-2\beta h})^3}\cos 2x \quad (14)$$

The relevant aspect ratio is the height h (which is really a multiple of the height-chord ratio, because of the choice of scale for the wavy wall). Thus the result is seen to have the similitude of equation (11a). As the tunnel height increases indefinitely, the last two terms disappear, and the remainder follows the similitude of equation (12) for the surface of a single plane body.

REDUCTION OF SUBSONIC PROBLEM TO NEARLY INCOMPRESSIBLE FLOW

In linearized theory, an important application of the similitude is Göthert's rule, which reduces any subsonic flow problem to a related incompressible flow (ref. 1). As the rule is usually stated, the incompressible flow is that past a thinner affinely related body. However, the incompressible solution for one member of an affinely related family of bodies determines that for all other members, so that the subsonic flow may, if desired, be related to the same body rather than a thinner one, and that viewpoint will be adopted here as being the simplest.

In second-order theory, the explicit appearance of terms in M^2 and $(\gamma+1)M^4$ in equations (10) means that reduction to an incompressible problem is impossible (except for the special case of the surface of a single plane body, where eq. (12) applies). The second-order problem can, however, be reduced to a nearly incompressible flow.

Flows at low Mach numbers can be calculated by the Janzen-Rayleigh method, which involves iterating on the incompressible solution to obtain a power series in M^2. Thus the velocity potential is approximated by

$$\frac{1}{U_\infty}\Phi(x,y,z;M,\gamma,\tau)=\Phi_0(x,y,z;\tau)+M^2\Phi_1(x,y,z;\tau)+(\gamma+1)M^4\Phi_2(\ )+M^4\Phi_3(\ )+\ldots \quad (15a)$$

The two terms in M^4 are ordinarily considered together, but for present purposes it is essential to separate them because only Φ_2 is required. This is fortunate because Φ_2 can be calculated almost as easily as Φ_1, whereas the determination of Φ_3 is much more difficult.

The small-disturbance and Janzen-Rayleigh series represent two different asymptotic expansions of the actual solution. They are believed to complement each other, so that an expansion of the Janzen-Rayleigh solution for small thickness must be identical with the expansion of the small-disturbance solution in powers of M^2, as has been verified in all worked examples. This fact permits the small-disturbance solution to be recovered from the Janzen-Rayleigh series. The converse is not true, however, except for bodies without stagnation points, because the small-disburbance expansion is not uniformly valid near a stagnation point.

PROCEDURE FOR RECOVERING SECOND-ORDER SOLUTION

Another alternative form for the second-order velocity potential of equation (10a), which is useful here, is

$$\frac{1}{U_\infty}\Phi(x,y,z;M,\gamma,\tau)=x+\tau^2F(x,\beta y,\beta z;\beta\tau)+\tau^2\left[f_1(\ )+\frac{M^2}{\beta^2}f_2(\ )+(\gamma+1)\frac{M^4}{\beta^4}f_3(\ )\right] \quad (10l)$$

(Here F and f_1, f_2, f_3 are not the same functions as in equation (10a) but related ones; in the notation of equations (10h) and (10i) they are actually $\tilde{F}$ and $\overline{f}_1$, $\overline{f}_2$, $\overline{f}_3$.)

For present purposes it is unnecessary to distinguish between the first-order term F and the second-order increment f_1; combining them as $F_1=F+f_1$ gives

$$\frac{\Phi-U_\infty x}{U_\infty\tau^2}=F_1(x,\beta y,\beta z;\beta\tau)+\frac{M^2}{\beta^2}f_2(\ )+(\gamma+1)\frac{M^4}{\beta^4}f_3(\ ) \quad (10m)$$

The Janzen-Rayleigh solution is now to be manipulated into this same form. The first three terms as given in equation (15a) are equivalent to

$$\frac{1}{U_\infty}\Phi(x,y,z;M,\gamma,\tau)=\Phi_0(x,y,z;\tau)+\frac{M^2}{\beta^2}\Phi_1(\ )+(\gamma+1)\frac{M^4}{\beta^4}\Phi_2(\ )+0\left(\frac{M^4}{\beta^4}\right) \quad (15b)$$

which may be rewritten as

$$\frac{\Phi-U_\infty x}{U_\infty\tau^2}=\varphi_0(x,y,z;\tau)+\frac{M^2}{\beta^2}\varphi_1(\ )+(\gamma+1)\frac{M^4}{\beta^4}\varphi_2(\ )+0\left(\frac{M^4}{\beta^4}\right) \quad (15c)$$

with

$$\left.\begin{aligned}\varphi_0&=\frac{\Phi_0-x}{\tau^2}\\ \varphi_1&=\frac{\Phi_1}{\tau^2}\\ \varphi_2&=\frac{\Phi_2}{\tau^2}\end{aligned}\right\} \quad (15d)$$

Finally, with the aid of

$$y=\beta y\sqrt{1+\frac{M^2}{\beta^2}}=\beta y\left[1+\frac{1}{2}\frac{M^2}{\beta^2}+0\left(\frac{M^4}{\beta^4}\right)\right] \quad (16)$$

and corresponding expansions for z and τ, this may be re-expressed as

$$\frac{\Phi-U_\infty x}{U_\infty\tau^2}=\varphi_0(x,\beta y,\beta z;\beta\tau)+\frac{M^2}{\beta^2}\left[\varphi_1(\ )+\frac{\beta y}{2}\varphi_{0_{\beta y}}(\ )+\frac{\beta z}{2}\varphi_{0_{\beta z}}(\ )+\frac{\beta\tau}{2}\varphi_{0_{\beta\tau}}(\ )\right]+(\gamma+1)\frac{M^4}{\beta^4}\varphi_2(\ ) \quad (15e)$$

which is the desired form. Here, for example, $\varphi_{0_{\beta y}}(x,\beta y,\beta z;\beta\tau)$ means $(\partial/\partial y)\varphi_0(x,y,z;\tau)$ evaluated at $x=x$, $y=\beta y$, $z=\beta z$, and $\tau=\beta\tau$.

The second-order solution is thus recovered from the Janzen-Rayleigh approximation simply by calculating in turn the expressions in equations (15d) and (15e). The procedure can actually be expressed by a single equation as follows. From the Janzen-Rayleigh approximation in the form of equation (15a), the second-order small-disturbance solution is recovered according to

$$\frac{\Phi}{U_\infty}=x+\tau^2\left\{\frac{\Phi_0(x,y,z;\tau)-x}{\tau^2}+\frac{M^2}{\beta^2}\left[\frac{\Phi_1}{\tau^2}+\frac{y}{2}\left(\frac{\Phi_0-x}{\tau^2}\right)_y+\frac{z}{2}\left(\frac{\Phi_0-x}{\tau^2}\right)_z+\frac{\tau}{2}\left(\frac{\Phi_0-x}{\tau^2}\right)_\tau\right]+(\gamma+1)\frac{M^4}{\beta^4}\frac{\Phi_2}{\tau^2}\right\}_{\substack{y\to\beta y\\ z\to\beta z\\ \tau\to\beta\tau}} \quad (17)$$

where Φ_n means $\Phi_n(x,y,z;\tau)$ throughout, and subscripts indicate differentiation.

APPLICATION TO PARABOLA

As an example, consider plane subsonic flow at zero angle of attack past the parabola described by $y=\tau\sqrt{x}$ (fig. 6).

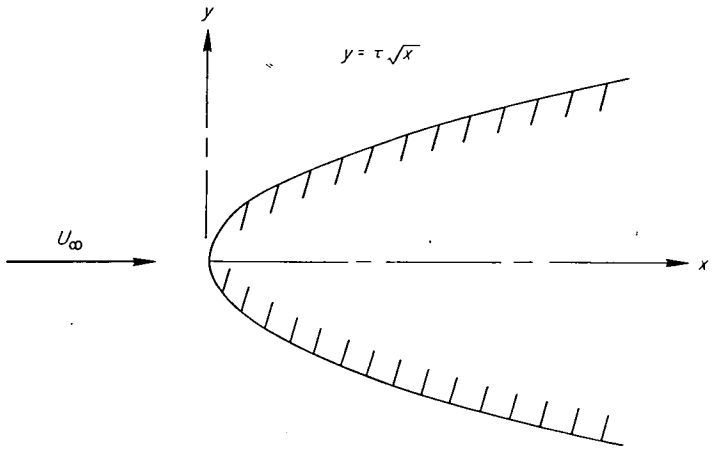


FIGURE 6.—Parabola at zero angle of attack.

The Janzen-Rayleigh solution including terms in $(\gamma+1)M^4$ has been calculated by Imai (ref. 9). Although the velocity potential is complicated, it simplifies when only second-order terms in τ are retained to

$$\frac{\Phi}{U_\infty}=x+\tau\eta+\frac{1}{2}M^2\tau\eta^2\frac{\eta-\tau}{\xi^2+\eta^2}-\frac{1}{8}M^2\tau^2\,ln\frac{\xi^2+\eta^2}{\tau^2}-\frac{\gamma+1}{32}M^4\tau^2\left[4\frac{\eta^4}{(\xi^2+\eta^2)^2}+ln\frac{\xi^2+\eta^2}{\tau^2}\right]+\cdots \quad (18a)$$

Here ξ,η are parabolic coordinates related to the Cartesian coordinates by

$$\left[\left(x-\frac{1}{4}\tau^2\right)+iy\right]=(\xi+i\eta)^2$$

so that to second order

$$\left.\begin{aligned}2\xi^2&=\sqrt{x^2+y^2}+x\\2\eta^2&=\sqrt{x^2+y^2}-x\end{aligned}\right\} \quad (18b)$$

In this case the expressions given by equation (15d) are

$$\left.\begin{aligned}\varphi_0&=\frac{\eta}{\tau}\\\varphi_1&=\frac{1}{8}\left[4\frac{\eta^2(\eta/\tau-1)}{\xi^2+\eta^2}+ln\frac{\xi^2+\eta^2}{\tau^2}\right]\\\varphi_2&=\frac{1}{32}\left[4\frac{\eta^4}{(\xi^2+\eta^2)^2}+ln\frac{\xi^2+\eta^2}{\tau^2}\right]\end{aligned}\right\} \quad (18c)$$

This example illustrates the fact that for planar systems these terms are not of order unity in τ. Then according to equation (15e) the second-order small-disturbance solution is

$$\frac{\Phi}{U_\infty}=x+\frac{\tau}{\beta}\bar{\eta}-\frac{1}{8}\frac{M^2}{\beta^2}\tau^2\left(4\frac{\bar{\eta}^2}{\bar{\xi}^2+\bar{\eta}^2}+ln\frac{\bar{\xi}^2+\bar{\eta}^2}{\beta^2\tau^2}\right)-\frac{\gamma+1}{32}\frac{M^4}{\beta^4}\tau^2\left[4\frac{\bar{\eta}^4}{(\bar{\xi}^2+\bar{\eta}^2)^2}+ln\frac{\bar{\xi}^2+\bar{\eta}^2}{\beta^2\tau^2}\right] \quad (19a)$$

where

$$\left.\begin{aligned}2\bar{\xi}^2&=\sqrt{x^2+\beta^2y^2}+x\\2\bar{\eta}^2&=\sqrt{x^2+\beta^2y^2}-x\end{aligned}\right\} \quad (19b)$$

This result is of interest because it apparently cannot be found directly. Plane small-disturbance flows can be calculated easily if one adopts the thin-airfoil approximation of transferring the boundary conditions to the line $y=0$ by Taylor series expansion, but that approximation fails near round noses in the second approximation and, as a consequence, divergent integrals arise (ref. 8). Instead, one can try to treat the round nose more carefully using conformal mapping (cf. ref. 11, pp. 361–367), but the result is found to be indeterminate to the extent of a multiple of $\ln(\bar{\xi}^2+\bar{\eta}^2)$. This is the potential of a point source at the origin, which is an eigensolution, the proper multiple of which (appearing in eq. (19a)) is not determined by the suggested method.

The second-order increment in equation (19a) is seen to include terms in $\tau^2 ln\,\tau$, whose function is to render the argument of the logarithm dimensionless. However, these terms are simply constants, so that no logarithms of thickness appear in the actual flow quantities such as velocity and pressure. As remarked in the introduction, logarithmic terms in thickness arise in the actual flow disturbances only in the fourth approximation.

The second-order small-disturbance solution for the stream function can in the same way be extracted from Imai's Janzen-Rayleigh solution, and the result is found to agree with that calculated directly by Kaplan (ref. 10) using conformal mapping. It contains no terms in $ln\,\tau$. (The direct approach succeeds for the stream function, although it fails for the velocity potential, because the tangency condition is imposed on the mass flux, which is affected by the above eigensolution.) Then using the connections between the stream function and velocity potential, one can verify the correctness of equations (19).

CONCLUDING REMARKS

UTILITY OF THE RULES

The second-order rules are scarcely suited for correlating experimental data, since tests on four related bodies would be needed in order to isolate the four functions involved. That they are, however, useful in theoretical analyses has already been pointed out by Fenain and Germain in the special case of supersonic flow past flat wings (ref. 5). Previous investigators had calculated (erroneously, as it turns out) the second-order solution for the flat diamond cone shown in figure 7, and carried out numerical computations

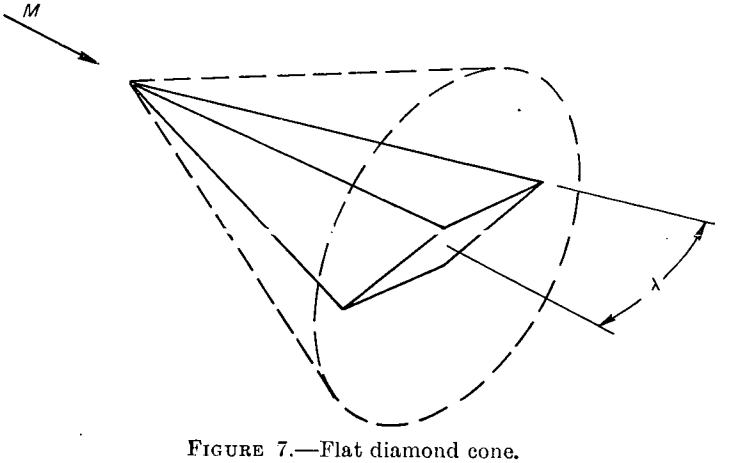


FIGURE 7.—Flat diamond cone.

for three different Mach numbers and four values of the parameter $\beta \tan \lambda$ (reported in ref. 11). Because the latter is the similarity parameter βA of equations (11), failure to take advantage of the similitude resulted in three fold unnecessary duplication of computing labor.

The reduction to nearly incompressible flow assumes importance for bodies with stagnation points. The small-disturbance assumption is violated, and, as was noted in the example of the parabola, the second-order solution consequently cannot be found directly. For bodies of revolution the difficulties appear to be even more severe. In such cases it is convenient to calculate the Janzen-Rayleigh solution, and from it extract the true second-order solution by the procedure outlined above. This process has been carried out for the paraboloid of revolution in reference 12.

NONUNIFORMITY IN SUPERSONIC FLOW

It should be noted that in supersonic flow the similarity rules may fail in localized regions. Shock waves or expansion fans spring from corners and edges, and in their vicinity the formal interation procedure is not uniformly valid. The similarity rules for surface pressure fail locally when such waves intersect other parts of the body, as in the case of a triangular wing with leading edges ahead of the Mach cone. The rules for integrated lift and drag are correct to first order, but may be in error in second-order terms. These difficulties can in principle be eliminated by straining the coordinates according to Lighthill's technique (ref. 13).

FURTHER EXTENSIONS

The similarity rules can readily be extended to third and higher order in the same fashion (except for additional complications in supersonic flow because of the ultimate appearance of significant vorticity engendered by curved shock waves). The similarity parameter remains unchanged; the complexity arising in a proliferation of functions multiplied by powers of $(\gamma+1)^m M^{2n}\beta^{-2p}$. Likewise, the small-disturbance solution to any order can be recovered from the nearly incompressible solution provided by an appropriate number of terms of the Janzen-Rayleigh solution.

AMES AERONAUTICAL LABORATORY
NATIONAL ADVISORY COMMITTEE FOR AERONAUTICS
MOFFETT FIELD, CALIF., *Oct. 18, 1956*

REFERENCES

1. Göthert, B. H.: Plane and Three-Dimensional Flow at High Subsonic Speeds (Extension of the Prandtl Rule). NACA TM 1105, 1946.
2. Broderick, J. B.: Supersonic Flow Round Pointed Bodies of Revolution. Quart. Jour. Mech. and Appl. Math., vol. 2, pt. 1, Mar. 1949, pp. 98–120.
3. Van Dyke, Milton D.: A Study of Second-Order Supersonic Flow Theory. NACA Rep. 1081, 1952.
4. Fell, J., and Leslie, D. C. M.: Second-Order Methods in Inviscid Supersonic Theory. Quart. Jour. Mech. and Appl. Math., vol. 8, pt. 3, Sept. 1955, pp. 257–265.
5. Fenain, Maurice, and Germain, Paul: Sur la résolution de l'équation régissant, en seconde approximation, les écoulements d'un fluide autour d'obstacles tridimensionnels. Comptes Rendus, vol. 241, no. 3, 18 July, 1955, pp. 276–278.
6. Van Dyke, Milton D.: Subsonic Edges in Thin-Wing and Slender-Body Theory. NACA TN 3343, 1954.
7. Hayes, Wallace D.: Second-Order Pressure Law for Two-Dimensional Compressible Flow. Jour. Aero. Sci., vol. 22, no. 4, Apr. 1955, pp. 284–286.
8. Van Dyke, Milton D.: Second-Order Subsonic Airfoil-Section Theory and Its Practical Application. NACA TN 3390, 1955.
9. Imai, Isao: Application of the M^2–Expansion Method to the Subsonic Flow of a Compressible Fluid Past a Parabolic Cylinder. Proc. 1st Japan Nat. Cong. for Appl. Math., 1952, pp. 349–352.
10. Kaplan, Carl: On the Small-Disturbance Iteration Method for the Flow of a Compressible Fluid With Application to a Parabolic Cylinder. NACA TN 3318, 1955.
11. Lighthill, M. J.: Higher Approximations. Section E of General Theory of High Speed Aerodynamics, vol. VI of High-Speed Aerodynamics and Jet Propulsion, Princeton Univ. Press, 1954, pp. 484–486.
12. Van Dyke, M. D.: The Paraboloid of Revolution in Subsonic Flow. Jour. Math. and Phys., vol. 37, no. 1, Apr. 1958, pp. 38–51.
13. Lighthill, M. J.: A Technique for Rendering Approximate Solutions to Physical Problems Uniformly Valid. Philos. Mag., ser. 7, vol. 40, Dec. 1949, pp. 1179–1201.

REPORT 1375

A WIND-TUNNEL INVESTIGATION OF THE AERODYNAMIC CHARACTERISTICS OF A FULL-SCALE SUPERSONIC-TYPE THREE-BLADE PROPELLER AT MACH NUMBERS TO 0.96†

By Albert J. Evans and George Liner

SUMMARY

An investigation of the characteristics of a full-scale supersonic-type propeller has been made in the Langley 16-foot transonic tunnel with the 6000-horsepower propeller dynamometer. The tests covered a range of blade angles from 20.2° to 60.2° at forward Mach numbers up to 0.96.

The results showed that envelope efficiency at an advance ratio of 2.8 decreased from 86 percent to 72 percent when the forward Mach number was increased from 0.70 to 0.96. A comparison of the experimental results with calculated results showed that maximum propeller efficiency can be calculated with good accuracy by using ordinary subsonic strip theory when the blade-section speeds are supersonic. The investigation also showed favorable power-absorption properties of the supersonic-type propeller at high speeds.

INTRODUCTION

The lack of airfoil data and adequate theory at transonic flight speeds makes the design and performance prediction of aircraft propellers uncertain for high-subsonic-speed aircraft. It is therefore necessary that the aerodynamic characteristics of propellers designed to operate at transonic speeds be determined experimentally. The experimental results not only are necessary to determine the characteristics of specific propellers but also to justify the assumptions that are necessary with respect to airfoil data and propeller theory in the transonic speed range.

Two facilities of the Langley Aeronautical Laboratory of the National Advisory Committee for Aeronautics, namely, the 6000-horsepower propeller dynamometer and the Langley 16-foot transonic tunnel, have made it possible to conduct full-scale propeller tests at transonic speeds. The tests of this investigation are the first full-scale propeller tests to be made in the transonic speed range and in a slotted wind-tunnel test section. The investigation included measurements of thrust and torque of the propeller, wake-pressure surveys to determine the blade thrust loadings, dynamic blade twist measurements, 1-P vibratory-stress measurements, and a determination of the effects of propeller thrust on the tunnel-airspeed calibration. The aerodynamic data are presented in the form of plots of efficiency and thrust and power coefficients against propeller advance ratio for a range of forward Mach numbers from 0.20 to 0.96. An airstream calibration of the Langley 16-foot transonic tunnel with the 6000-horsepower propeller dynamometer installed in the test section is also included herein.

SYMBOLS

A	propeller-disk area, sq ft
b	blade width (chord), ft
C_P	power coefficient, $\frac{P}{\rho n^3 D^5}$
C_T	thrust coefficient, $\frac{T}{\rho n^2 D^4}$
c_l	section lift coefficient
D	propeller diameter, ft
h	blade-section maximum thickness, ft
J	advance ratio, $\frac{V}{nD}$
M	forward Mach number
M_{prop}	forward Mach number with propeller installed and operating
$M_{no\ prop}$	forward Mach number with no propeller on dynamometer
M_t	helical tip Mach number, $M\sqrt{1+\left(\frac{\pi}{J}\right)^2}$
n	propeller rotational speed, rps
P	power, ft-lb/sec
P_C	power disk-loading coefficient, $\frac{P}{qAV}$
q	dynamic pressure, $\frac{1}{2}\rho V^2$
R	propeller tip radius, ft
r	radius to a blade element, ft
T	thrust, lb
V	forward velocity, fps
x	fraction of propeller tip radius, r/R
β	blade angle
$\beta_{0.75R}$	blade angle at $0.75R$, deg
η	efficiency
η_{max}	maximum efficiency
ρ	air density, slugs/cu ft

†Supersedes recently declassified NACA Research Memorandum L53F01 by Albert J. Evans and George Liner, 1953.

APPARATUS

LANGLEY 16-FOOT TRANSONIC TUNNEL

The investigation was made in the Langley 16-foot transonic tunnel. The test section is octagonal in cross section with longitudinal slots permitting interference-free testing with the propeller dynamometer installed to the top speed of the tunnel as limited by the maximum power. Additional details of the wind tunnel are given in reference 1.

THE 6000-HORSEPOWER PROPELLER DYNAMOMETER

The 6000-horsepower propeller dynamometer is described in reference 2. The two 3000-horsepower units of the dynamometer were coupled in tandem, and the propeller was mounted on the forward end for the present tests. In order to obtain a radially uniform axial flow field in the propeller plane, a long ($2.4D$) cylindrical fairing extended from a point upstream of the minimum area section of the tunnel to the propeller spinner. The boundary-layer thickness in the propeller plane caused by the cylindrical fairing was computed to be small enough in magnitude to produce no noticeable effect on the operating propeller. A sketch and photograph showing the arrangement of the dynamometer and the cylindrical fairing in the tunnel are shown in figures 1 and 2, respectively.

A variable-frequency power supply allows continuous speed control of the dynamometer. The rotational speed is set manually with the aid of an aircraft tachometer and measured to within ¼ rpm on a Stroboconn, which matches rotational frequency with the known frequency of a tuning fork.

Highly refined pressure gages convert pneumatic pressures from the thrust and torque capsules into direct readings of thrust and torque. Simultaneously, spinner-juncture pressures are measured on a micromanometer to correct thrust readings for effect of air-pressure difference on the ends of the rotating spinner.

The spinner diameter was 32 inches, the same as the forward cylindrical fairing and the dynamometer case. The propeller blade airfoil sections extended inboard to the spinner surface.

PROPELLER

The three-blade propeller used for this investigation had a diameter of 9.75 feet. The blades were made from solid

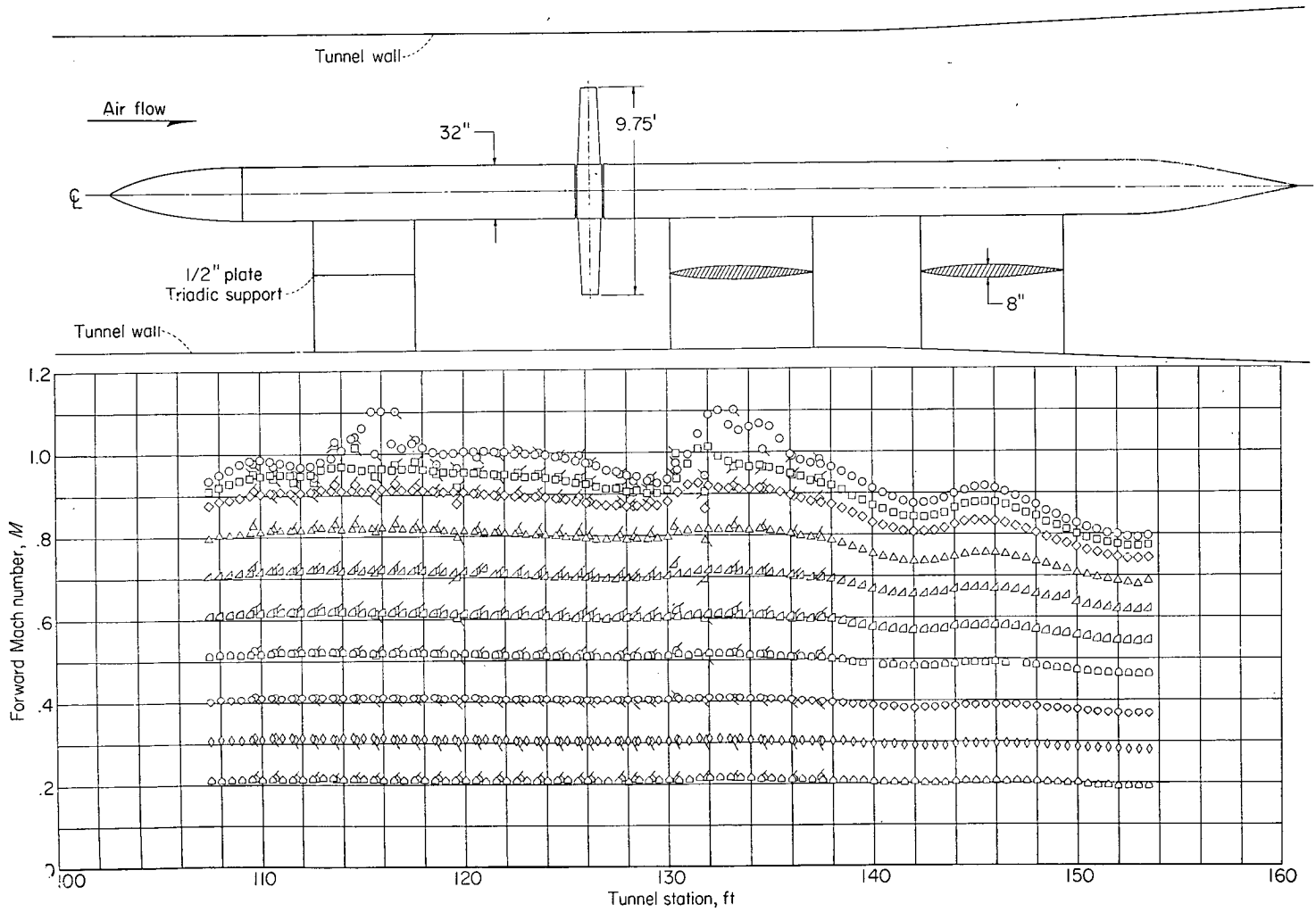


FIGURE 1.—Sketch of propeller dynamometer and Mach number distributions in the Langley 16-foot transonic tunnel with dynamometer but without propeller. Flagged symbols indicate dynamometer body measurements whereas symbols without flags represent tunnel-wall measurements.

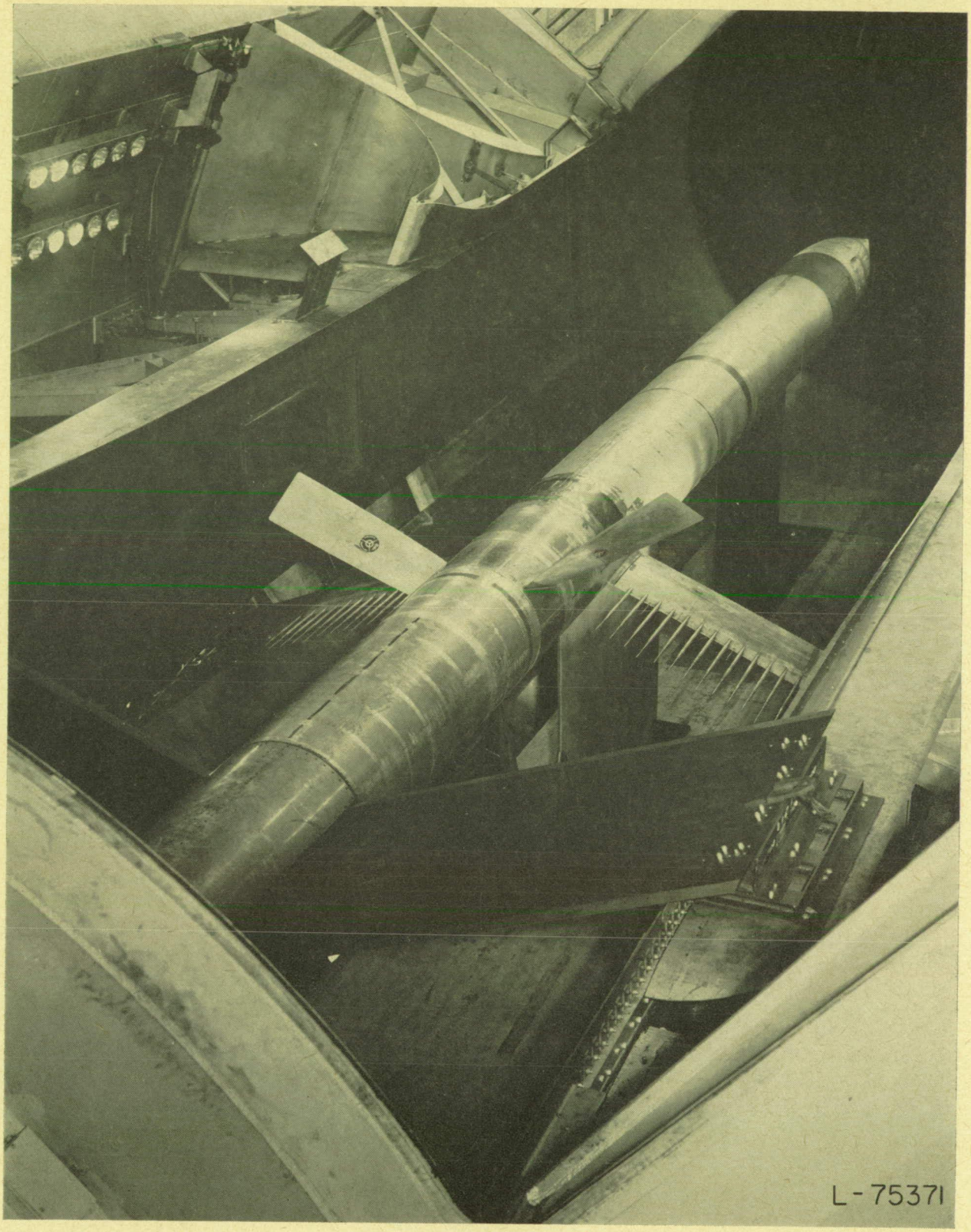


FIGURE 2.—Propeller mounted on the 6000-horsepower dynamometer in the Langley 16-foot transonic tunnel test section (tunnel open, view looking downstream).

6415 steel and had symmetrical 16-series airfoil sections. The blade-thickness ratio varied from 0.06 at the spinner to 0.02 at the tip, and the chord was constant for the length of the exposed blade. Blade-form characteristic curves are shown in figure 3. The propeller was designed to operate at a rotational speed of 2600 rpm at a forward Mach number of 0.95 at 35,000 feet altitude, corresponding to an advance ratio of 2.2.

526597—60——61

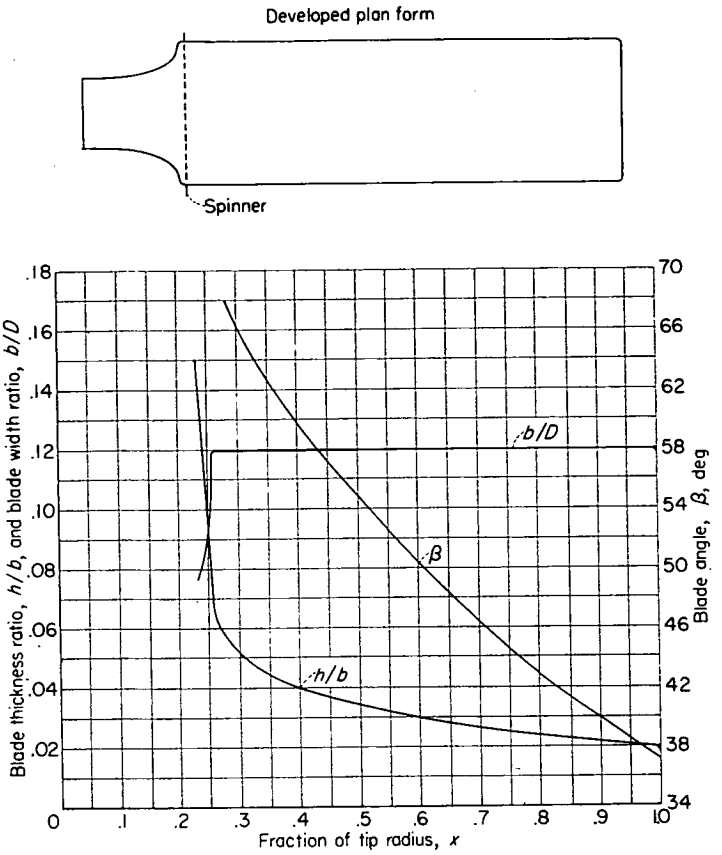


FIGURE 3.—Blade-form characteristics.

WAKE-SURVEY RAKES

The wake-survey rakes were constructed so that the orifices of the total-pressure and static-pressure probes were 2 feet ahead of the leading edge of the rake strut which was an 8-percent-thick circular-arc airfoil of constant 2-foot chord. The general arrangement of the dynamometer with the wake-survey rakes mounted with the orifices located 17 inches behind the propeller center line is shown in figures 2 and 4. Because of the difficulty of testing the propeller at high forward Mach numbers, as is explained subsequently, the rakes were set in the upper position for all tests except for rotational speeds of 1600 rpm.

TESTS

Most of the tests were made at constant values of forward Mach number, and a range of advance ratio was covered by varying the propeller rotational speed. One group of tests was made with the propeller operating at a rotational speed of 1600 rpm to cover a complete range of blade angles at low forward Mach numbers. For these tests, the advance ratio was varied by varying the tunnel airspeed. During the group of tests at 1600 rpm, the tunnel airspeed was lowered until flutter was audible at each blade angle tested and, although no data were recorded at flutter, the value of forward Mach number at which flutter occurred was determined.

In many cases the range of the tests was limited by the maximum dynamometer rotational speed and the available dynamometer power. These limitations did not permit the testing of the propeller at its design condition of operation and also did not permit testing at low values of advance ratio at the higher Mach numbers.

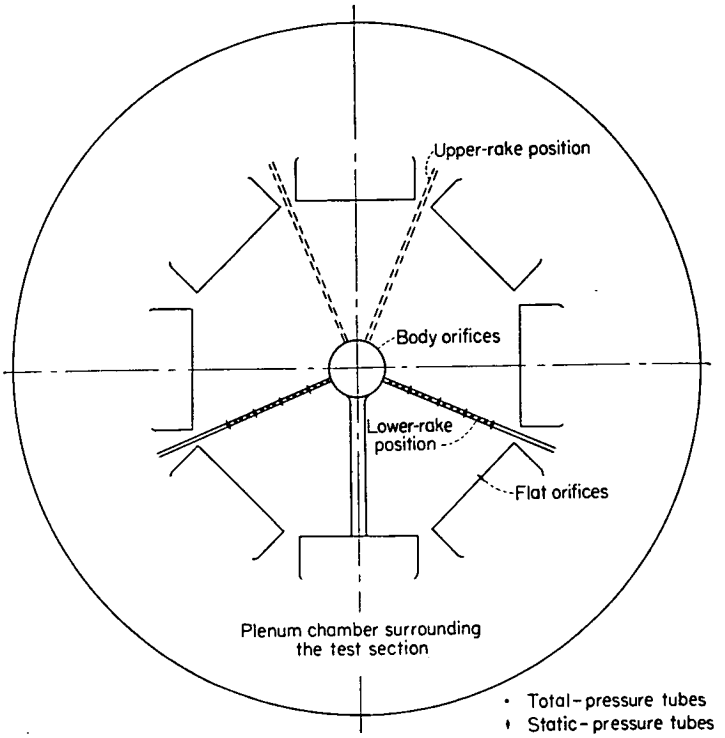


FIGURE 4.—Sectional view (looking downstream) of dynamometer and survey rakes mounted in the test section. Station 127.

CALIBRATIONS

TUNNEL AIRSPEED

The tunnel airstream was calibrated with the dynamometer installed in the test station with no propeller. The Mach number at which the propeller tests were run was set by a Mach number indicator that was referenced to static pressure in the plenum chamber surrounding the test section. The relationship between the Mach number at the propeller plane (without propeller) and the Mach number determined from the plenum static pressure was established in the same manner as in reference 1. Evidence that propeller operation has no significant effect on tunnel wall pressures is discussed in a subsequent section of this report.

A plot of the longitudinal Mach number distribution as measured by static-pressure orifices near the center line of one of the tunnel-wall flats and along the dynamometer body is shown in figure 1. At low speeds ($M=0.60$), the longitudinal Mach number distribution is uniform throughout the tunnel test section. At the higher values of Mach number, however, an acceleration of the tunnel airstream is indicated in the region of the dynamometer support struts. This acceleration, which is due to the partial blockage effect of the support struts, is accompanied by a deceleration of the airstream ahead of the struts in the region of the propeller plane. The velocity gradient through the propeller plane is small, however, except at the highest value of Mach number shown.

A comparison of the results obtained from the orifices on

the tunnel wall with those obtained from the dynamometer body orifices showed a negligible radial Mach number difference across the propeller plane (see fig. 1), the difference in Mach number being of the order of 0.005 at a stream Mach number of 0.95. Results from static probes of the wake-survey rakes in the lower position indicated a marked difference from the results shown in figure 1. The survey rakes indicated a gradually varying radial Mach number distribution which amounted to a difference in Mach number of about 0.05 from the dynamometer to the tunnel wall at the highest value of Mach number. However, the tests made at the constant rotational speed of 1600 rpm were the only tests made with the wake-survey rakes in the lower position. The stream Mach number for the tests at 1600 rpm did not exceed a value of about 0.70, and the nonuniform radial distribution up to $M=0.70$ is negligible.

It is believed that with the survey rakes in the lower position a partial stream blockage was caused by the proximity of the wake rake struts to the dynamometer support strut which caused the inboard static probes to record a low velocity. As shown in figure 4, the dynamometer body orifices were in the upper part of the test section, out of the area of influence of the struts, and the results did not indicate the low velocities indicated by the rake probes. In the plane of the operating propeller, the nonuniformity of the axial velocity distribution with the rakes in the lower position was further indicated by severe 1-P vibratory stresses at a Mach number of 0.70 which became worse as the Mach number was increased. In order to overcome these difficulties, it was necessary to move the wake-survey rakes to the upper position (fig. 4). Unfortunately, no tunnel calibration was made without the propeller with the wake-survey rakes in the upper position, although alleviation of the blockage effect was indicated by the absence of the 1-P vibration on the operating propeller even to the maximum speed of the tunnel.

With the wake-survey rakes in the upper position, the radial Mach number distribution was therefore presumed to agree with the results indicated by figure 1. From the foregoing considerations, it has been concluded that the propeller data presented in the present report do not include any detrimental effects that may be considered to arise from propeller operation in a nonuniform airstream and that the values of stream Mach number obtained from the tunnel-wall orifices are the values experienced by the operating propeller.

DYNAMOMETER CALIBRATION

Static calibrations of the thrust and torque meters were made in a manner similar to that for the 2000-horsepower propeller dynamometer described in reference 3. The calibrations were straight lines when the indicated loads were plotted against the applied loads and the slopes of the lines were determined by the method of least squares.

The probable error in the thrust scale readings was 5.6 pounds, which amounted to a maximum error of about 0.6 percent in the important operating range of the propeller. The probable error in the total torque readings was 4.9 foot-pounds, which was a maximum error of about 0.3 percent in the range of propeller operation for peak efficiency.

REDUCTION OF DATA

THRUST

Propeller thrust as used herein is defined as the shaft tension produced by the aerodynamic forces acting on the propeller blades from the spinner to the blade tips.

The aerodynamic forces on the rotating spinner were determined by running the tunnel and the dynamometer over a range of airspeed and rotational speed with no propeller installed and recording the readings of the thrust scales. The difference in pressure between the upstream face and the downstream face of the rotating spinner was recorded simultaneously with the thrust readings. The variation of thrust with the spinner-juncture pressure difference was one straight line for all combinations of tunnel airspeed and dynamometer rotational speed. With this relation determined, the spinner-juncture pressure difference was measured for test points with the propeller operating and the corresponding value of thrust was subtracted from the indicated scale readings as a tare thrust. Propeller thrust is, therefore, the indicated thrust of the propeller minus the spinner tare thrust created by the difference in spinner-juncture pressure between the upstream and downstream faces of the spinner, the spinner skin-friction drag being less than the accuracy of the thrust readings.

TORQUE

Torque tare readings were obtained simultaneously with the thrust tare readings during the tare runs. The torque tare forces varied with tunnel airspeed and to a slight extent with dynamometer rotational speed. The variation with rotational speed amounted to about 5 foot-pounds for the range of rotational speeds presented herein. The variation of torque with tunnel airspeed, however, was a straight-line variation which amounted to about 55 foot-pounds at a value of Mach number of 1.0. Inherent vibration of the dynamometer with the wind tunnel was believed to cause the variation of torque with tunnel airspeed.

The torque tare forces for all rotational speeds were plotted against a function of tunnel airspeed and a faired line was drawn through the points. This procedure neglected the small variation of torque with rotational speed so that there was an error of ± 2.5 foot-pounds. Propeller torque was the indicated torque reading minus the torque tare readings.

WIND-TUNNEL WALL CORRECTION

A theory was presented in reference 4 for the solid blockage interference effect in circular wind tunnels with walls slotted in the direction of flow. The theory indicated the possibility of obtaining zero blockage interference at high subsonic Mach numbers, and tests on a model tunnel reported in the same reference confirmed the theoretical results. Pressure measurements on a body of revolution in the Langley 16-foot transonic tunnel are compared with measurements

made on an identical body by the free-fall technique in reference 5. The results of reference 5 showed that the tunnel-wall interference effects were negligible up to and including Mach number 1.0.

In order to check the wall effect of a slotted test section on an operating propeller, pressure measurements were made along a region of the wind-tunnel wall extending from 1.3 feet ahead to 4.2 feet behind the propeller plane. The results of the pressure measurements are presented in figure 5 as the variation with tunnel station of the ratio of the Mach number with the propeller operating to the Mach number obtained from calibration tests without a propeller. The shaded area between the two curves includes representative data obtained throughout the entire Mach number and propeller-thrust-coefficient ranges covered in the investigation. The scatter of points in the enclosed area of figure 5 is within the accuracy of the tunnel-speed measurements. The Mach number with the propeller operating was within about ± 1.0 percent of the values obtained without the propeller, and the tunnel longitudinal Mach number gradient with the propeller operating was essentially the same as that obtained without the propeller (fig. 1). The variation of thrust coefficients from a negative value to a relatively high positive value did not appreciably affect the Mach number ratio. Since it is evident that the operating propeller had no significant effect on the tunnel wall pressures, it has been concluded that no wind-tunnel wall correction is necessary for the ranges of Mach number and thrust coefficient covered in the present tests.

ACCURACY

In the significant range of propeller operation the data are accurate to 1.3 percent based on the accuracy of the static calibrations. However, the accuracy of the faired curves is believed to be within 1.0 percent.

RESULTS AND DISCUSSION

PRESENTATION OF BASIC RESULTS

The aerodynamic data obtained during the tests are presented in figures 6 to 14 as faired curves of thrust coefficient, power coefficient, propeller efficiency, airstream Mach number, and helical tip Mach number plotted against propeller advance ratio. The data test points are included on the plots of thrust and power coefficients.

Many of the tests were extended into the negative thrust and power range of operation and the data have been included in figures 6 to 14. The curves indicate that data obtained in the positive range of operation can be extrapolated to small negative values with good accuracy.

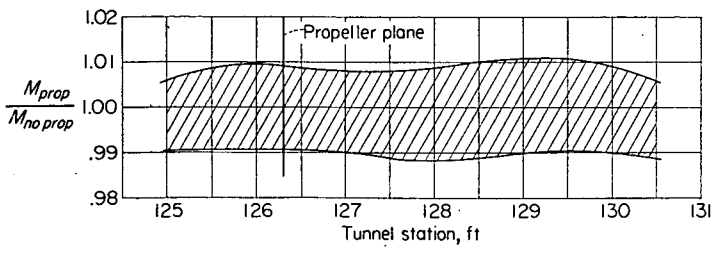


FIGURE 5.—Effect of propeller operation on the tunnel-wall measurements for the range of Mach numbers and thrust coefficients obtained in the tests.

The plot of thrust coefficient and efficiency in figure 14 for $\beta_{0.75R}=54.7°$ was obtained from wake-survey pressure data, since the thrust data obtained for this particular test were believed to be erroneous because of difficulties which were encountered in the operation of the thrust capsule.

In some cases the data have been extrapolated to define the efficiency peaks better. The extrapolated portions of the curves are shown in the figures as a dashed line. The values of peak efficiency obtained by extrapolation are considered to be within the experimental accuracy of the data.

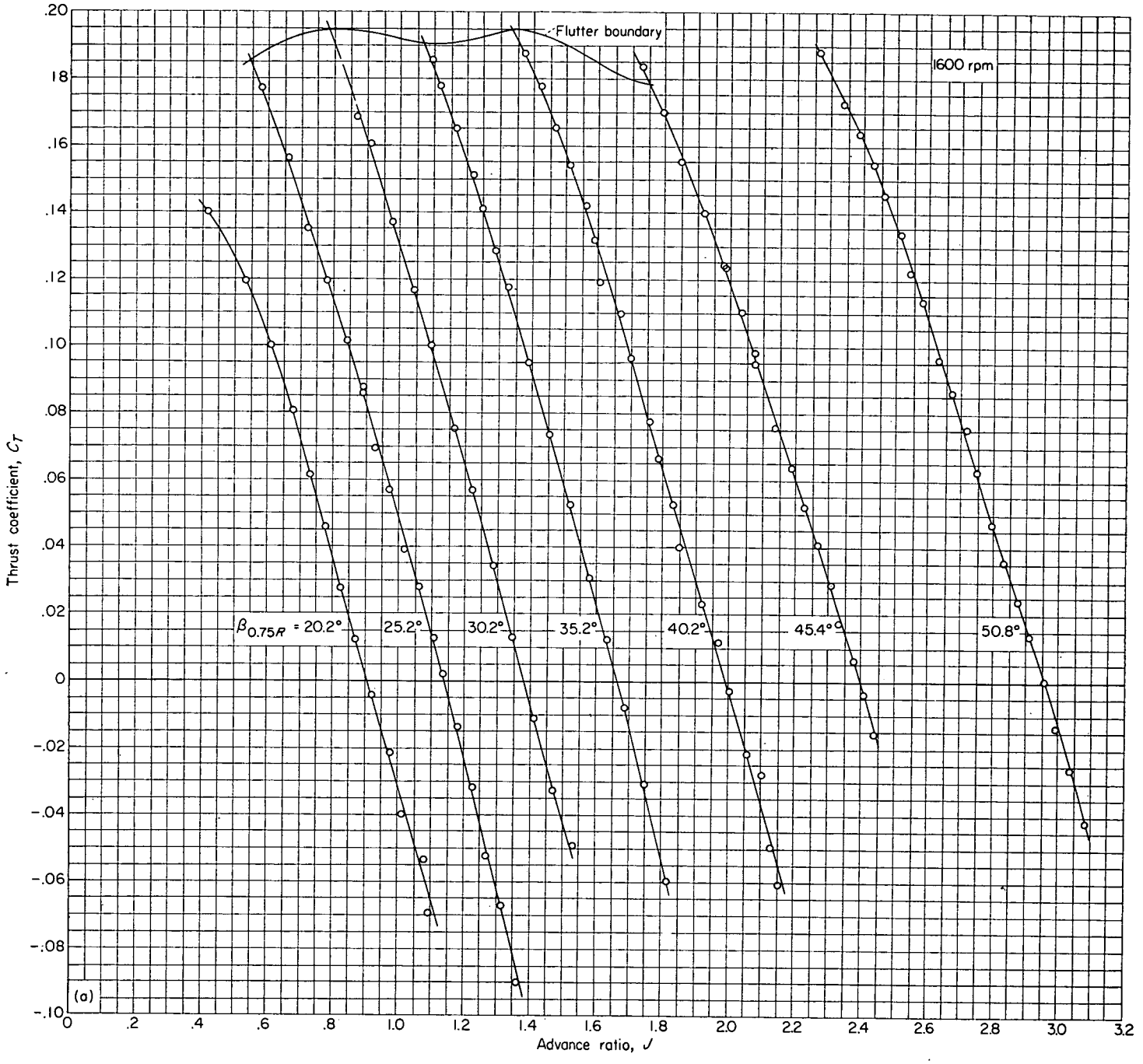
Discontinuities in some of the Mach number curves shown in figures 6 to 14 are attributed to changes in air temperature which occurred from day to day.

THE EFFECTS OF ADVANCE RATIO ON ENVELOPE EFFICIENCY

Figure 15 shows the variation of envelope efficiency with advance ratio for several values of forward Mach number. The most notable feature of the curves in figure 15 is that the loss in efficiency with an increase in advance ratio is small for any of the Mach numbers. Although the design value of advance ratio (2.2) could not be reached at the higher Mach numbers, the trend of the curves indicates that a supersonic propeller designed for an advance ratio of 2.2 will experience a loss in envelope efficiency of only about 1 percent when operated at an advance ratio of 3.2. As advance ratio is increased above 3.2 the drop in envelope efficiency is more rapid. The curves in figure 15 suggest the possibility that a supersonic propeller could be designed for advance ratios as high as 3.4. At these higher advance ratios the rotational speed would be much lower, and the structural problem caused by large centrifugal forces would be less severe; therefore, thinner blade sections might be used. Although there is an increase in the tendency to flutter, the use of thinner blade sections would be a definite advantage because of their higher lift-drag ratios at high Mach numbers. However, the use of a lower rotational speed would lower the power-absorption properties of the propeller with a given diameter, since the power varies as the cube of the rotational speed. Obviously, the selection of the proper advance ratio for a supersonic propeller involves a compromise between aerodynamic and structural requirements.

COMPARISON OF CALCULATED AND EXPERIMENTAL VALUES OF ENVELOPE EFFICIENCY

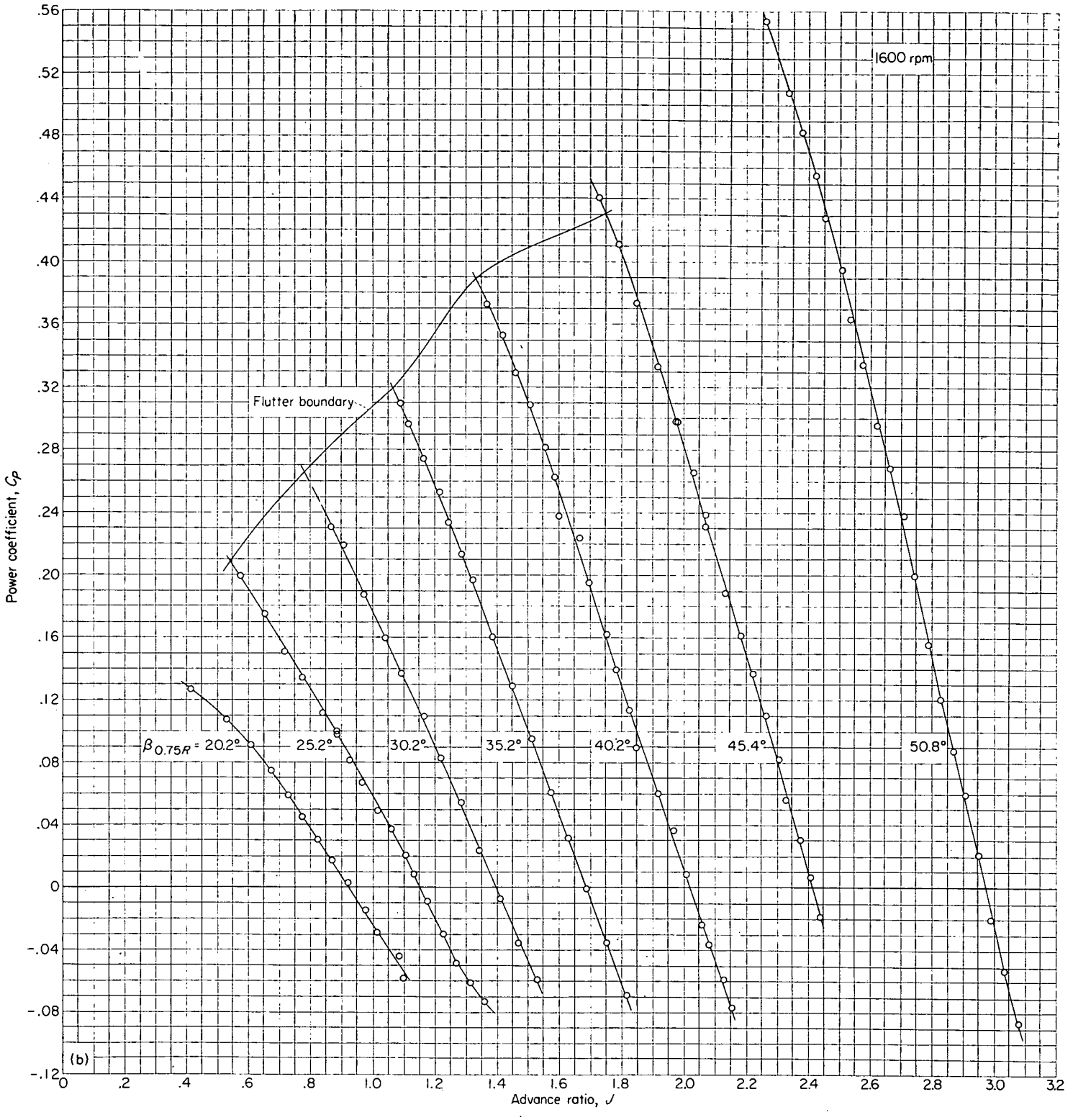
It was not possible to test the present propeller at the design operating conditions since the maximum rotational speed of the dynamometer (2300 rpm) did not permit operation at an advance ratio of 2.2 at a forward Mach number of 0.95. Strip-theory calculations, however, have been made for the efficiency of the propeller by using the method described in reference 3 and the results are plotted in figure 15. The airfoil data, which were cross-plotted and extrapolated for use with the blade-thickness ratios of the test propeller, were obtained for the calculations from reference 6.



(a) Thrust coefficient.

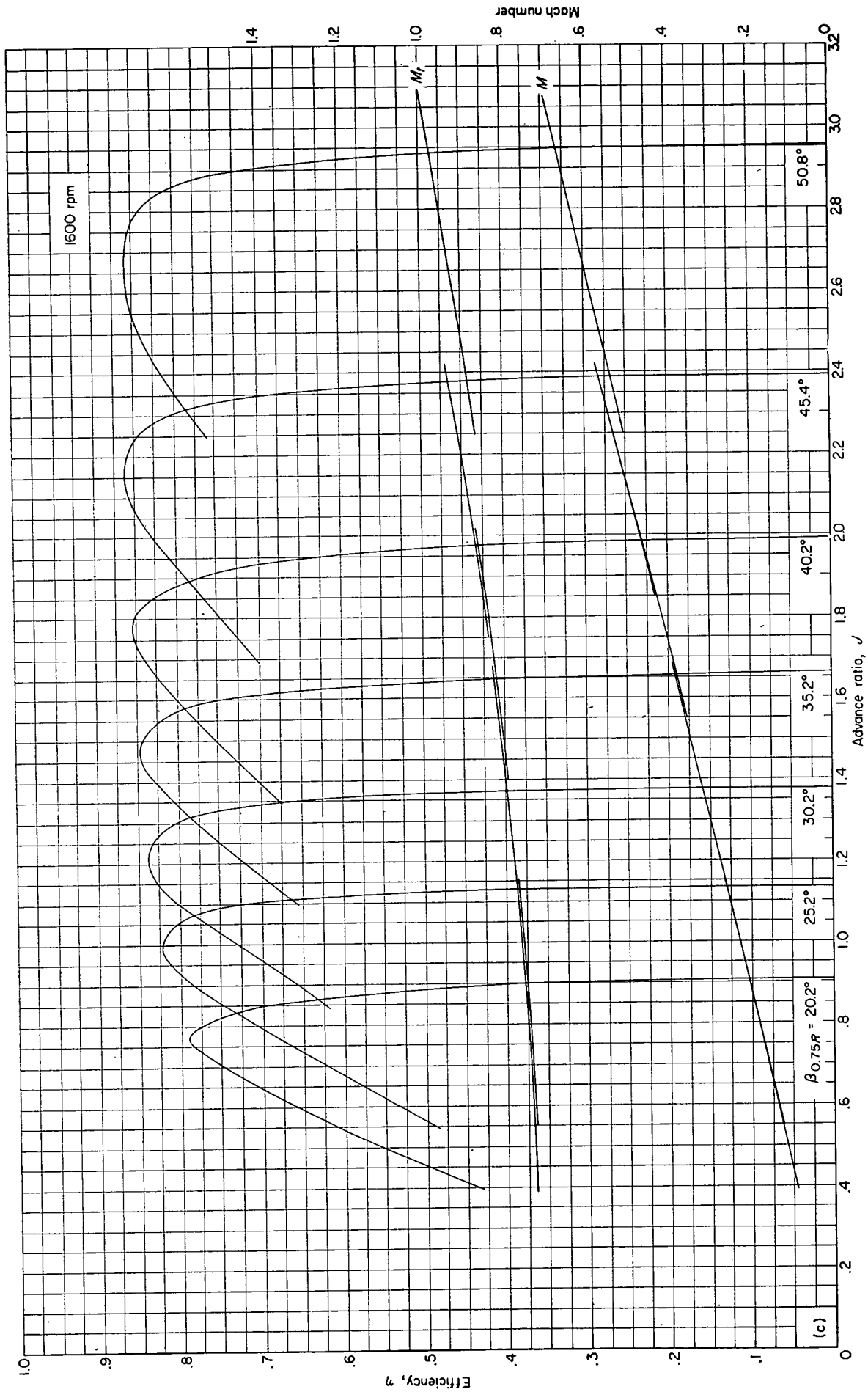
FIGURE 6.—Characteristics of propeller. Rotational speed, 1600 rpm; $M<0.67$.

On the basis of the nearly constant calculated values of efficiency between an advance ratio of 2.20 and 2.86, the experimental curve for a Mach number of 0.96 is faired to $J=2.2$ as shown in figure 15. This extrapolation of the experimental curve indicates an efficiency of the test propeller for $M=0.96$, $J=2.20$ of about 73 percent. There is remarkably close agreement shown between the calculated values of efficiency for this propeller and the experimental data in figure 15. In the worst case ($J=3.78$) the difference between the calculated efficiency and experimental efficiency is 0.025, whereas at $J=2.86$ the difference is 0.008. For the calculations at $J=3.78$, some of the effective blade sections were operating in a transonic speed range, where a small error of Mach number or angle of attack might result in a large error in drag. The agreement at the lower advance ratio shows that, when the blade section speeds are supersonic, maximum propeller efficiency can be calculated with good accuracy by using ordinary subsonic strip theory and the airfoil data compiled in reference 6. The calculations of thrust and torque coefficients, however, were about 20 percent below the experimental values. This result indicates that the lift-drag ratios used in the calculations were satisfactory but the values of both lift and drag were somewhat low.



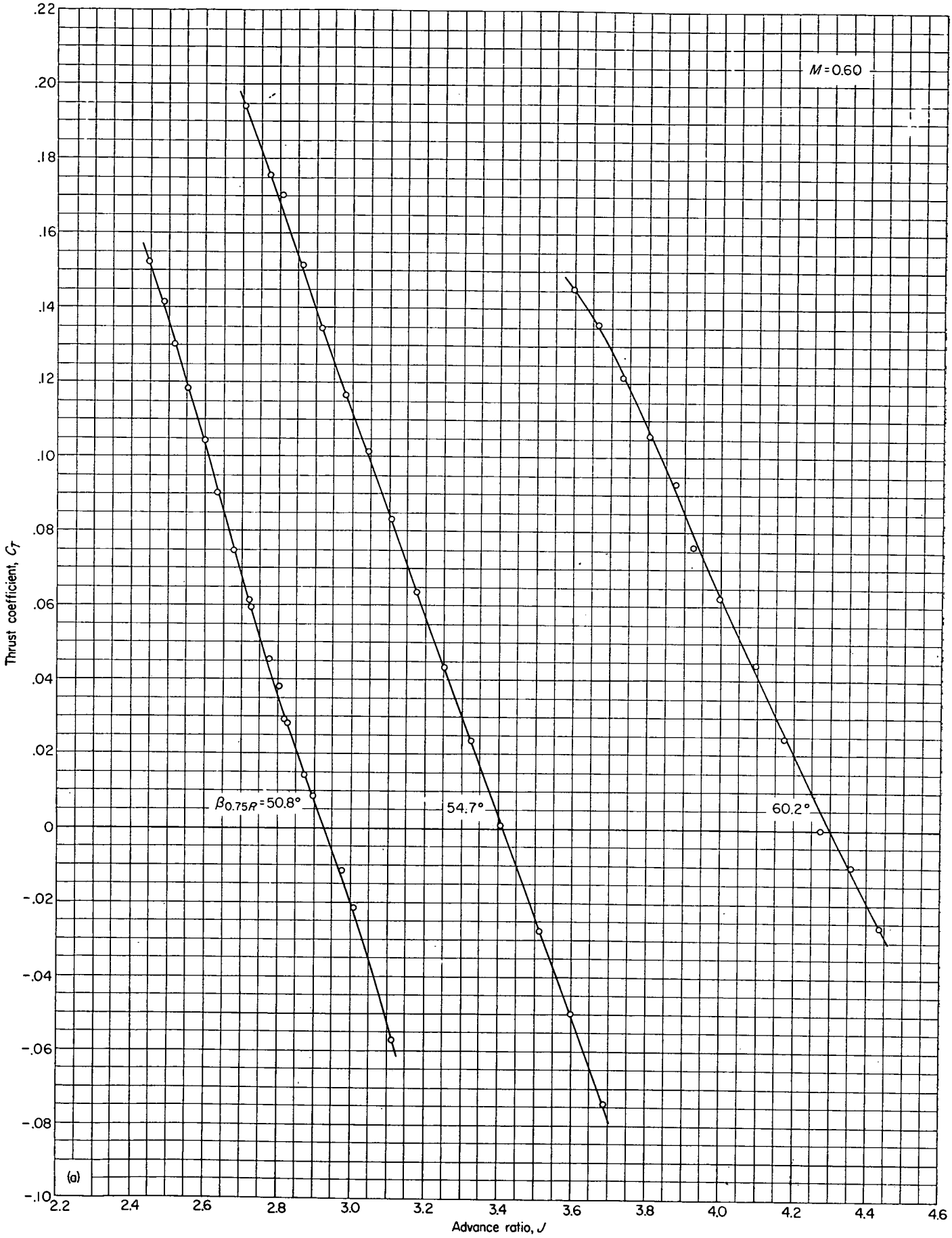
(b) Power coefficient.

FIGURE 6.—Continued.



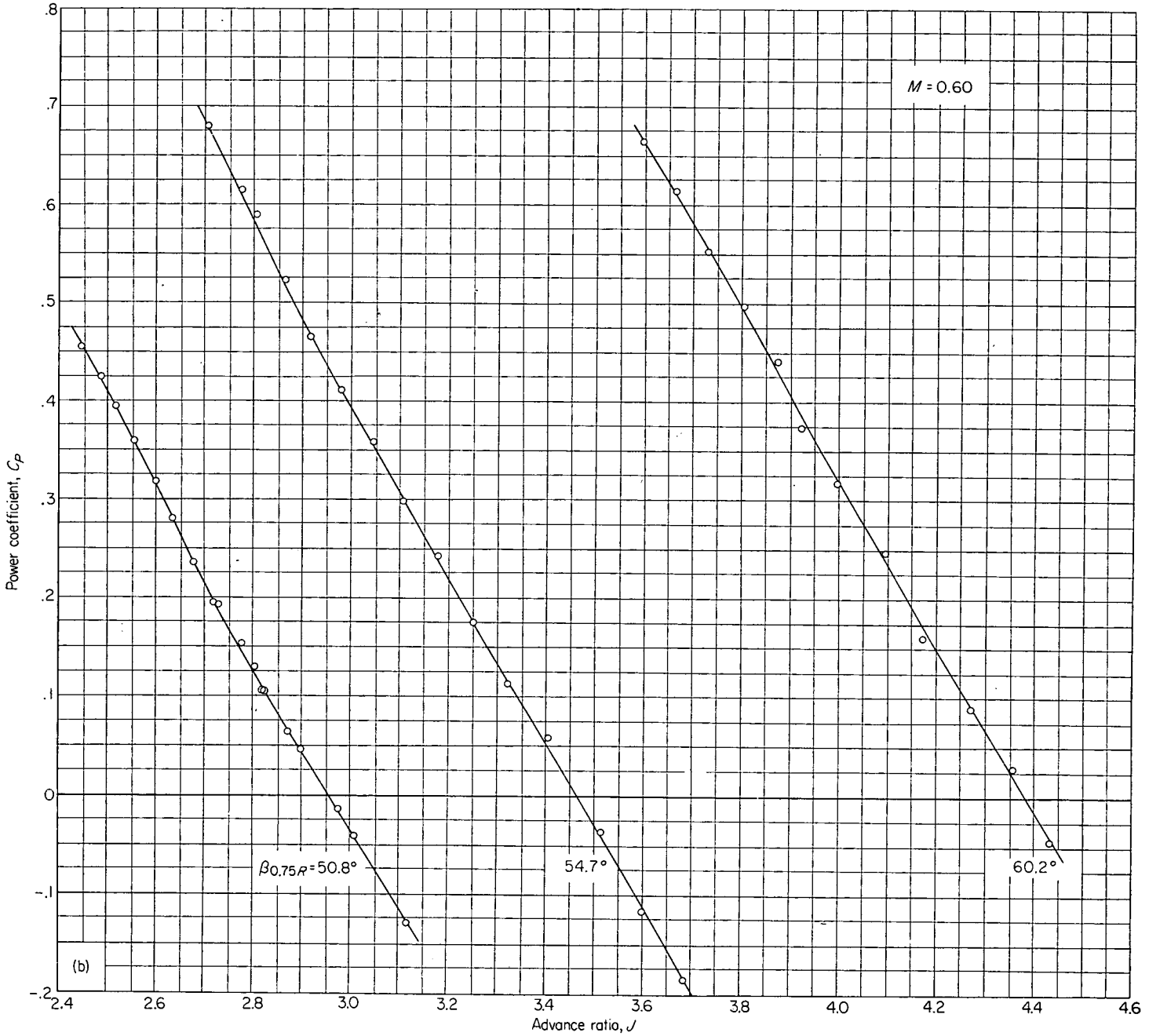
(c) Efficiency.

FIGURE 6.—Concluded.



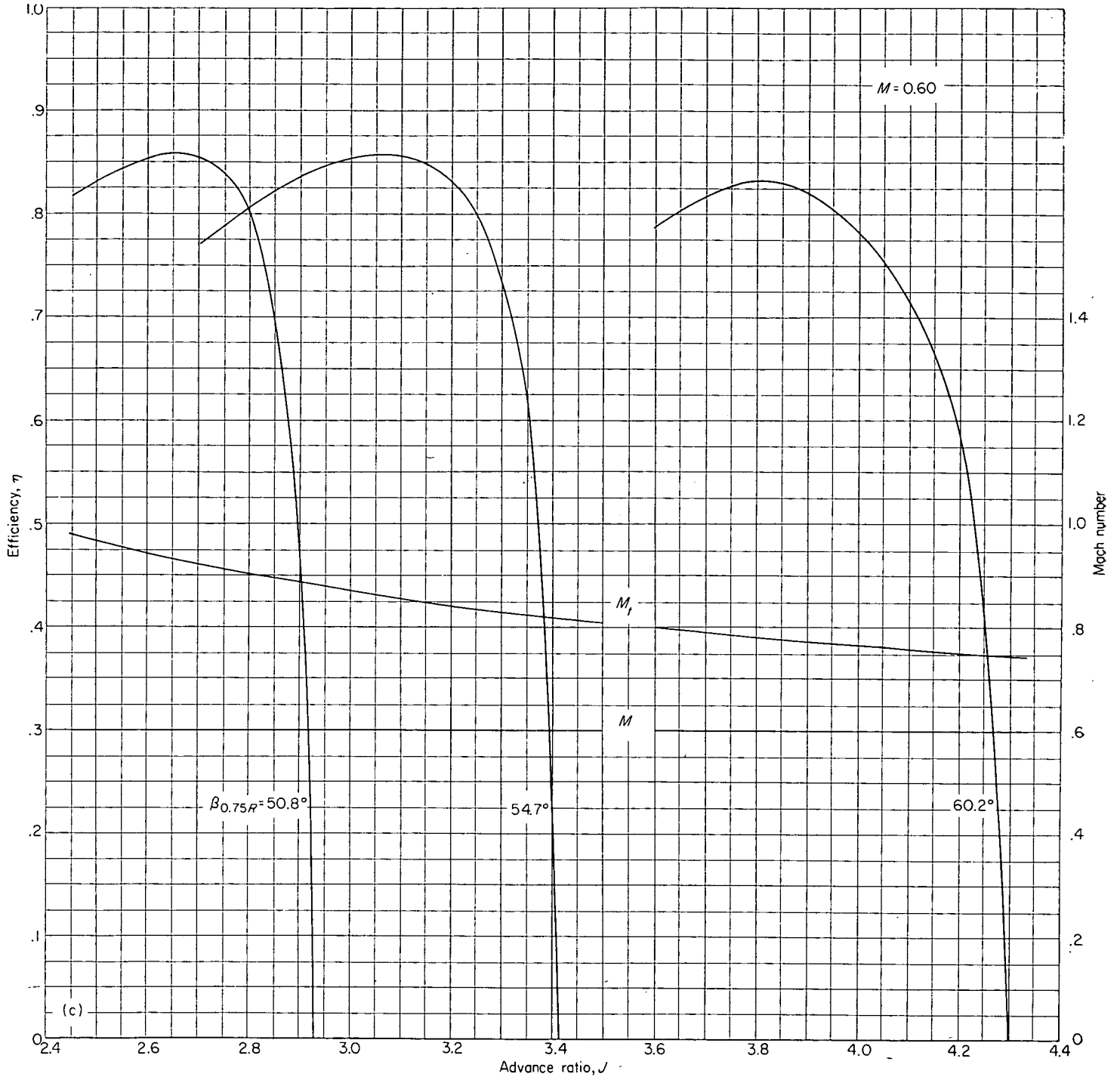
(a) Thrust coefficient.

FIGURE 7.—Characteristics of propeller. Forward Mach number 0.60.



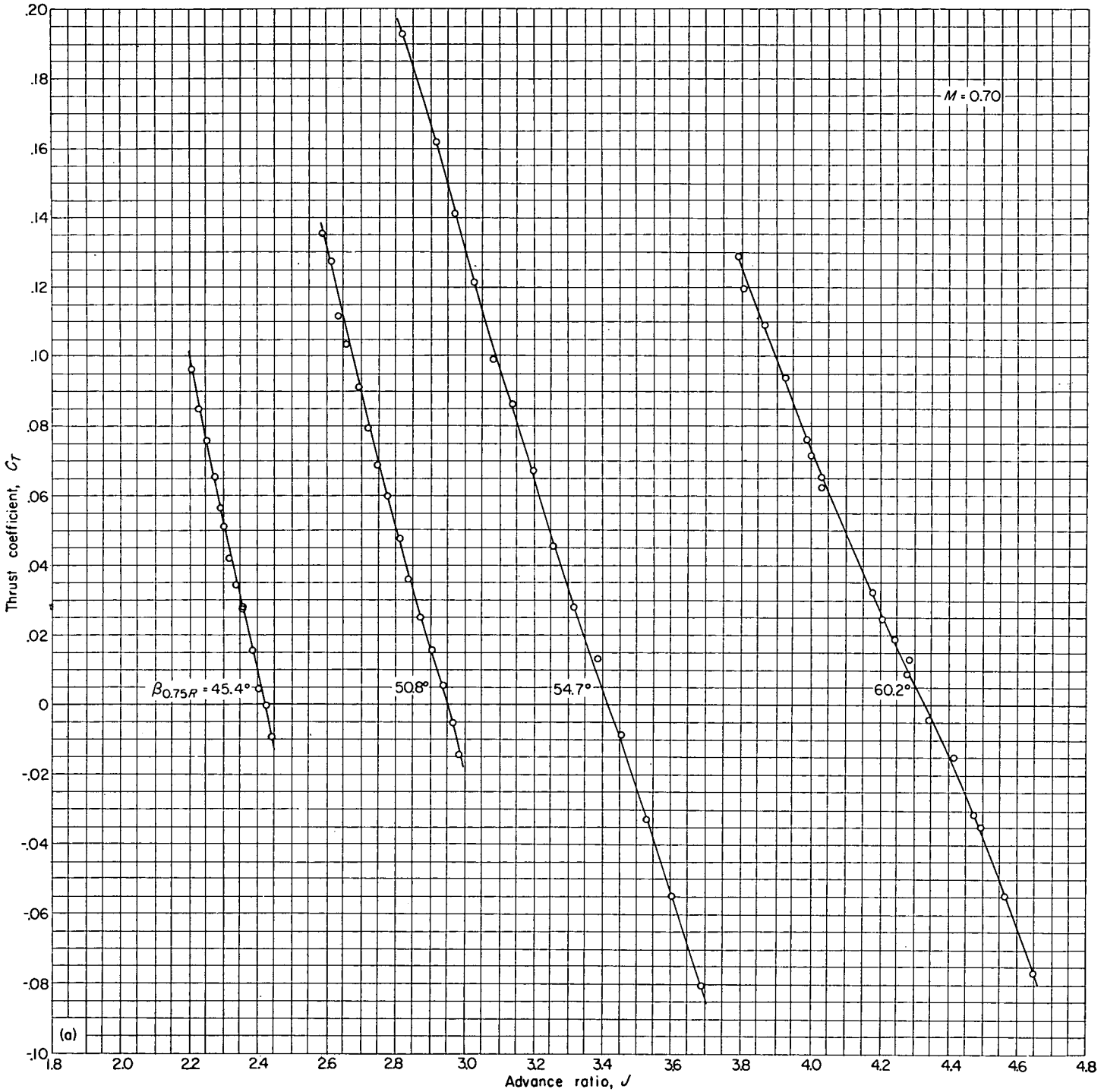
(b) Power coefficient.

FIGURE 7.—Continued.



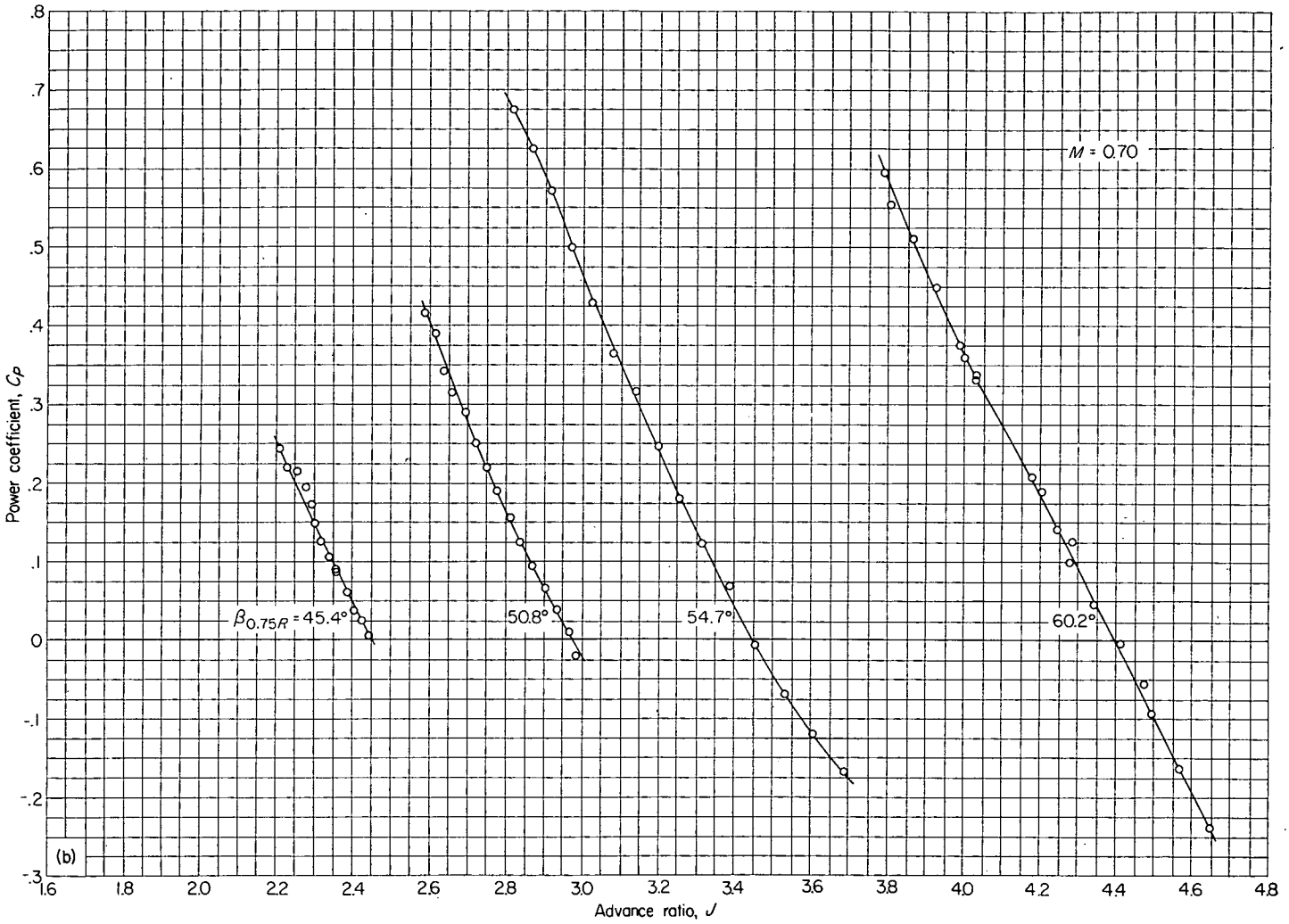
(c) Efficiency.

FIGURE 7.—Concluded.



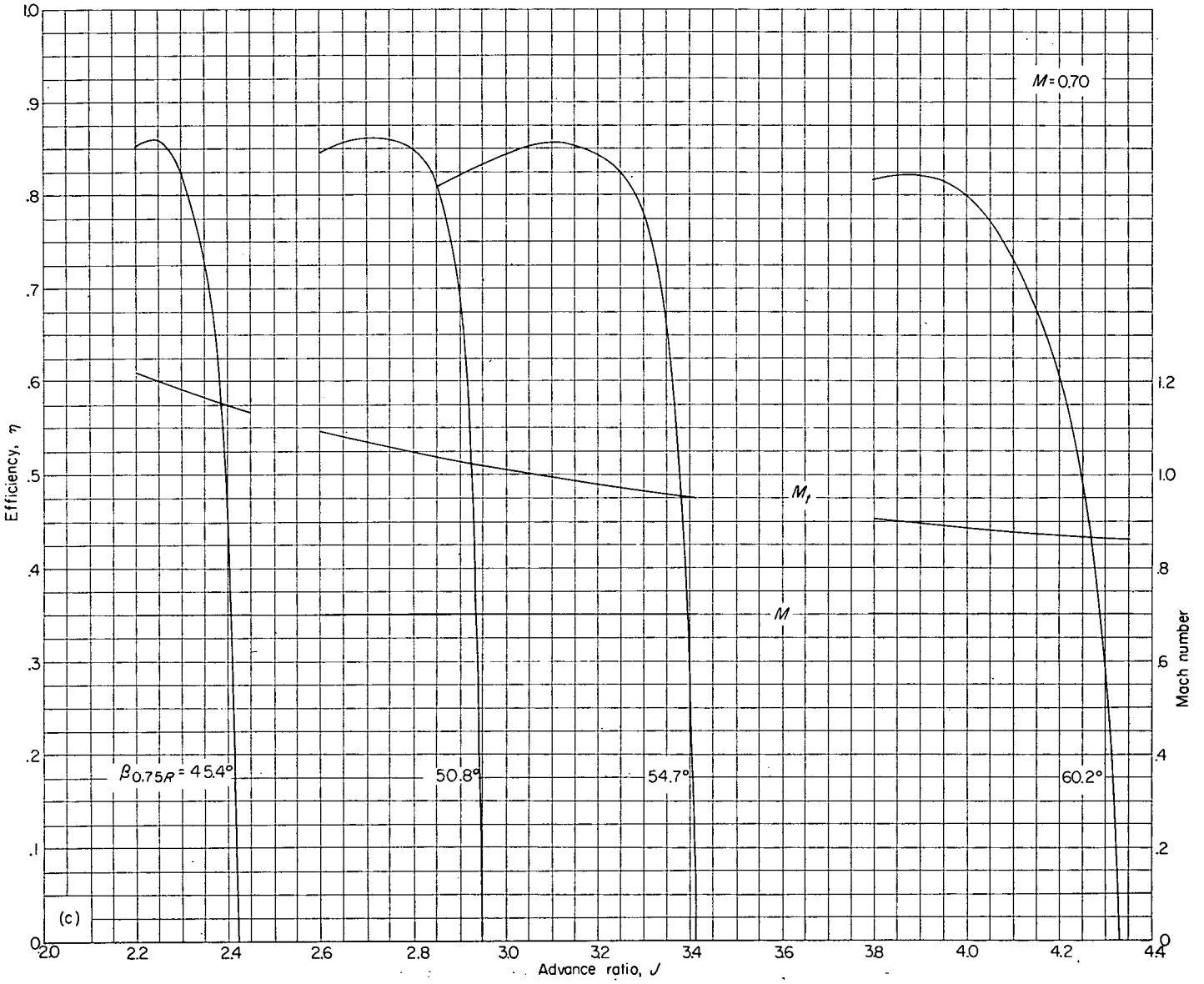
(a) Thrust coefficient.

FIGURE 8.—Characteristics of propeller. Forward Mach number 0.70.



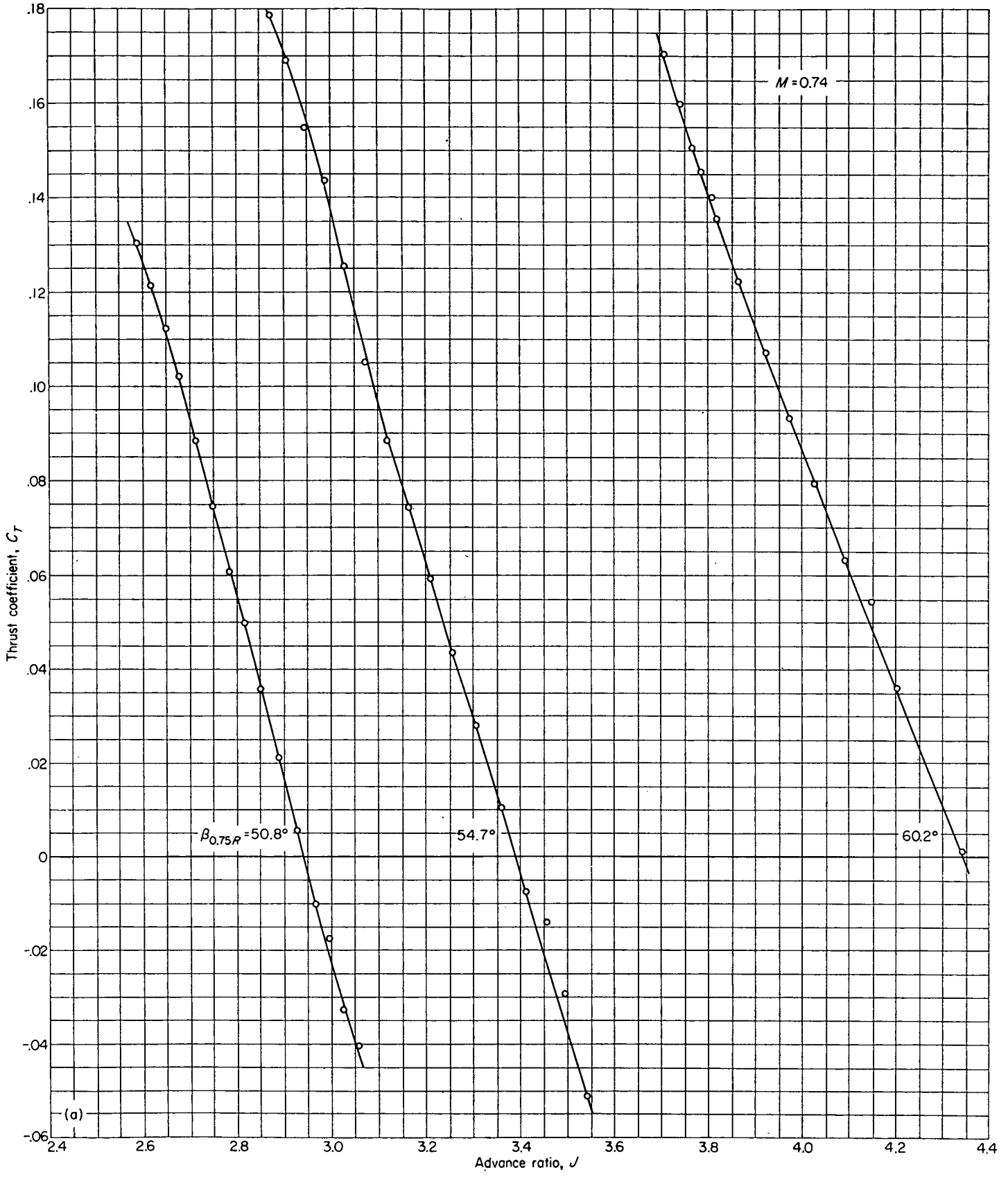
(b) Power coefficient.

FIGURE 8.—Continued.



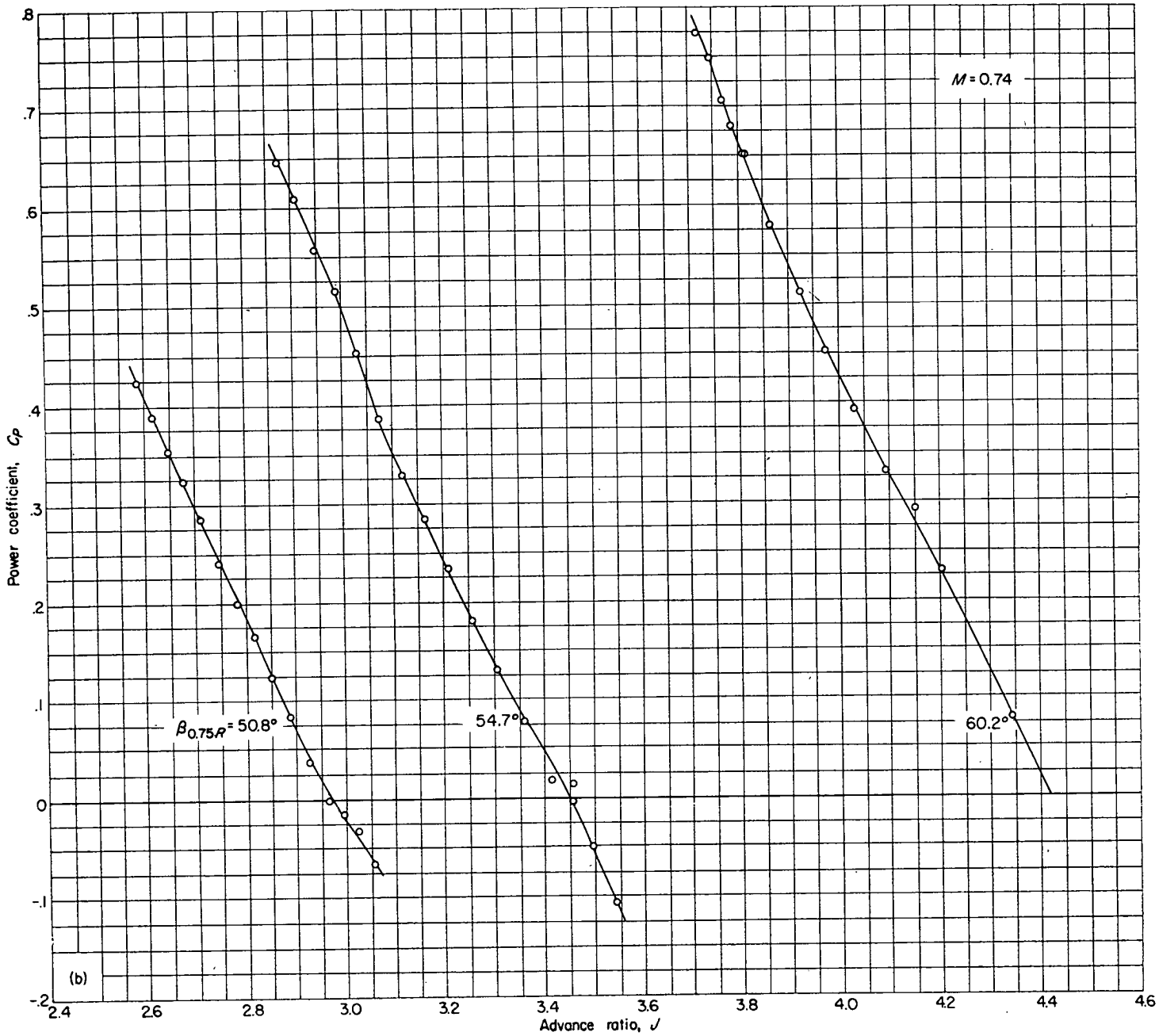
(c) Efficiency.

FIGURE 8.—Concluded.



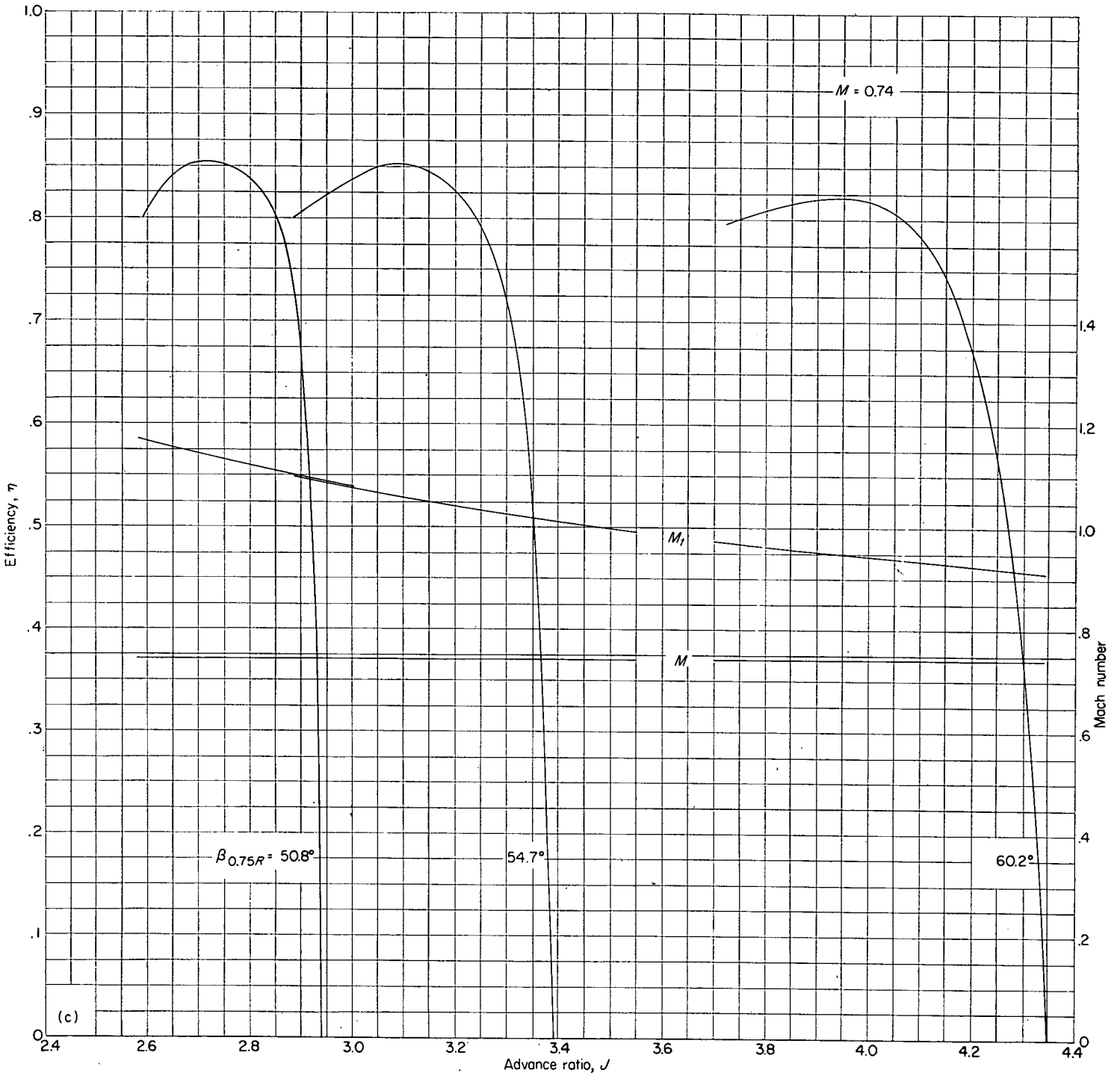
(a) Thrust coefficient.

FIGURE 9.—Characteristics of propeller. Forward Mach number 0.74.



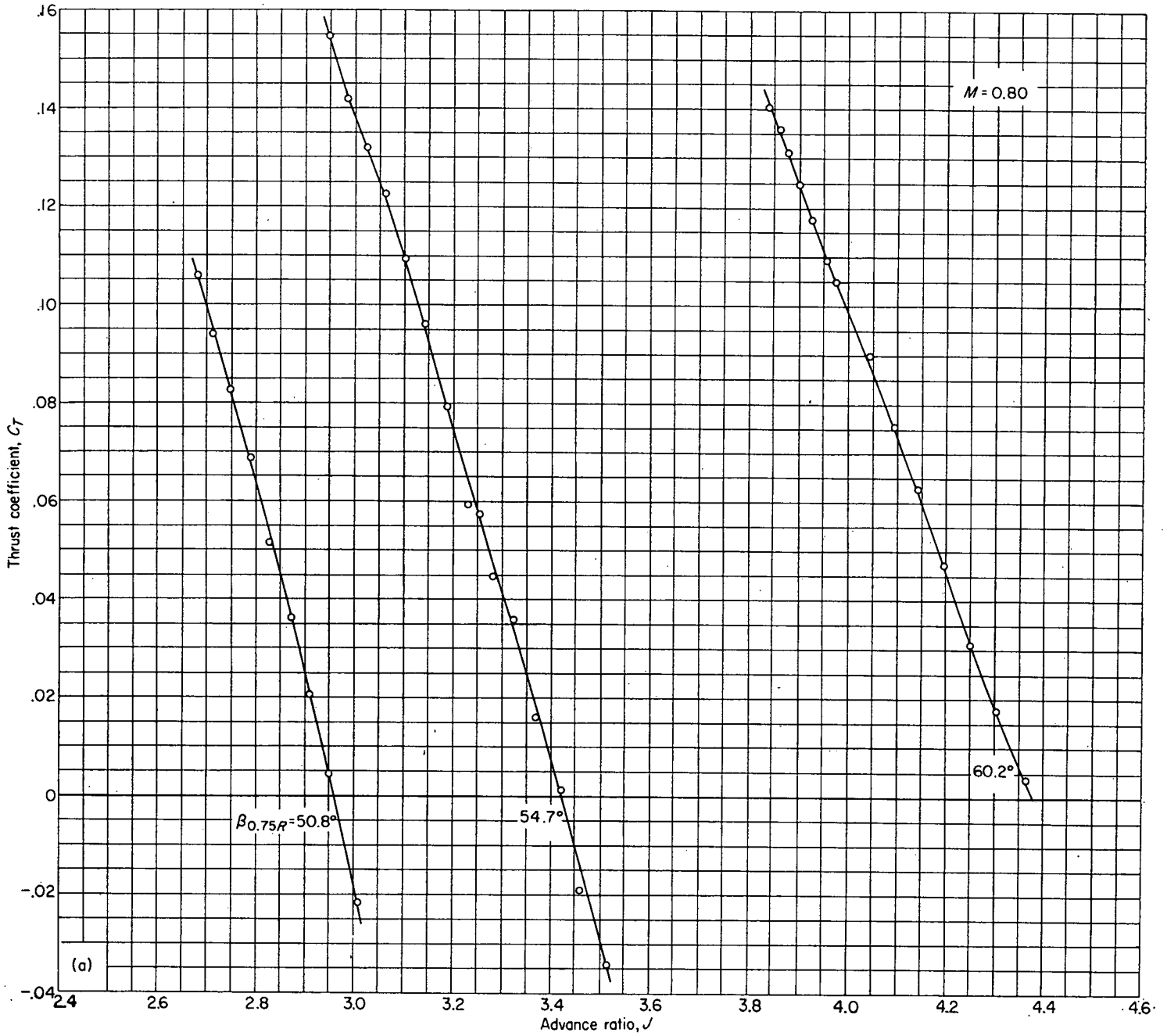
(b) Power coefficient.

FIGURE 9.—Continued.



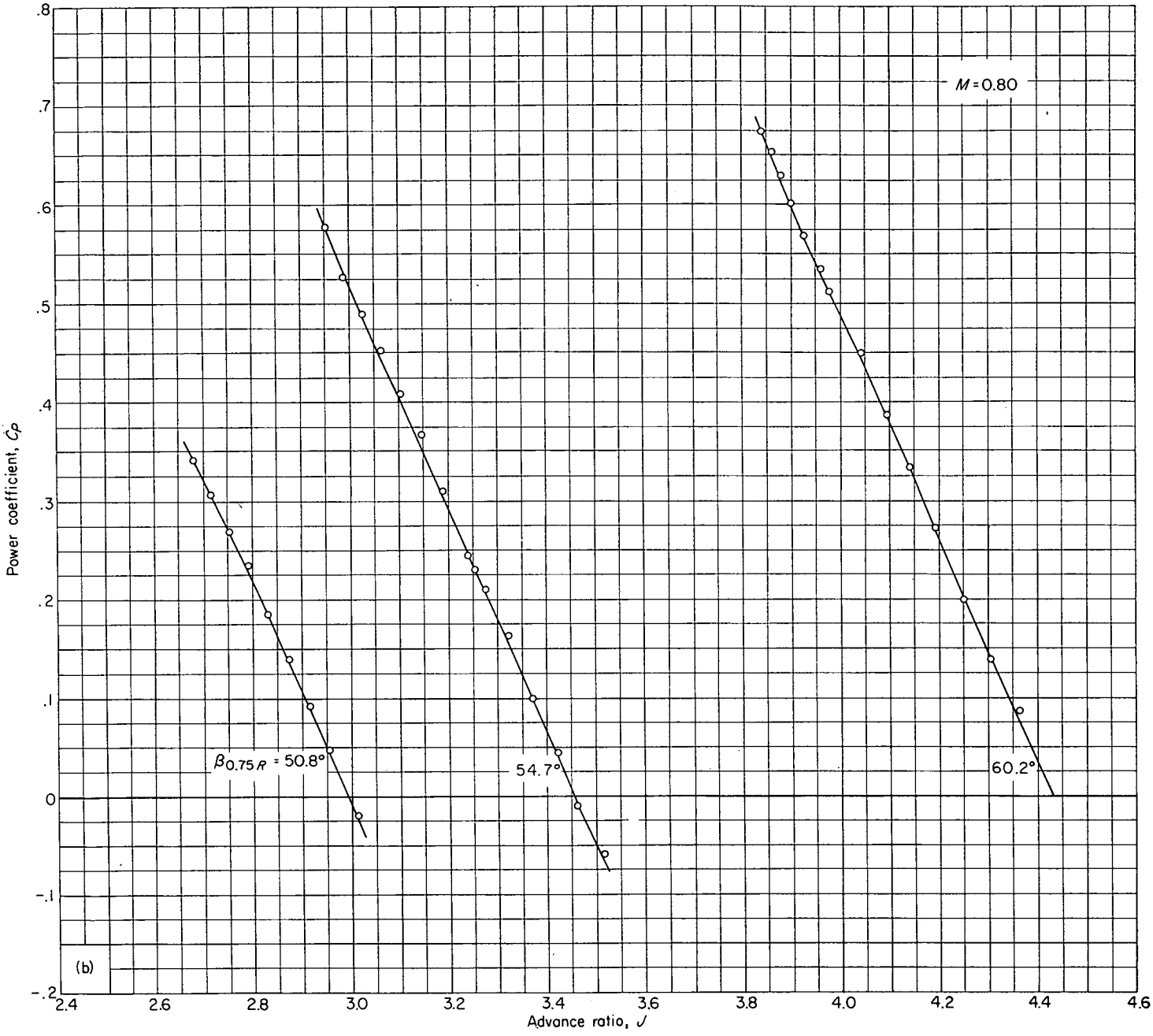
(c) Efficiency.

FIGURE 9.—Concluded.



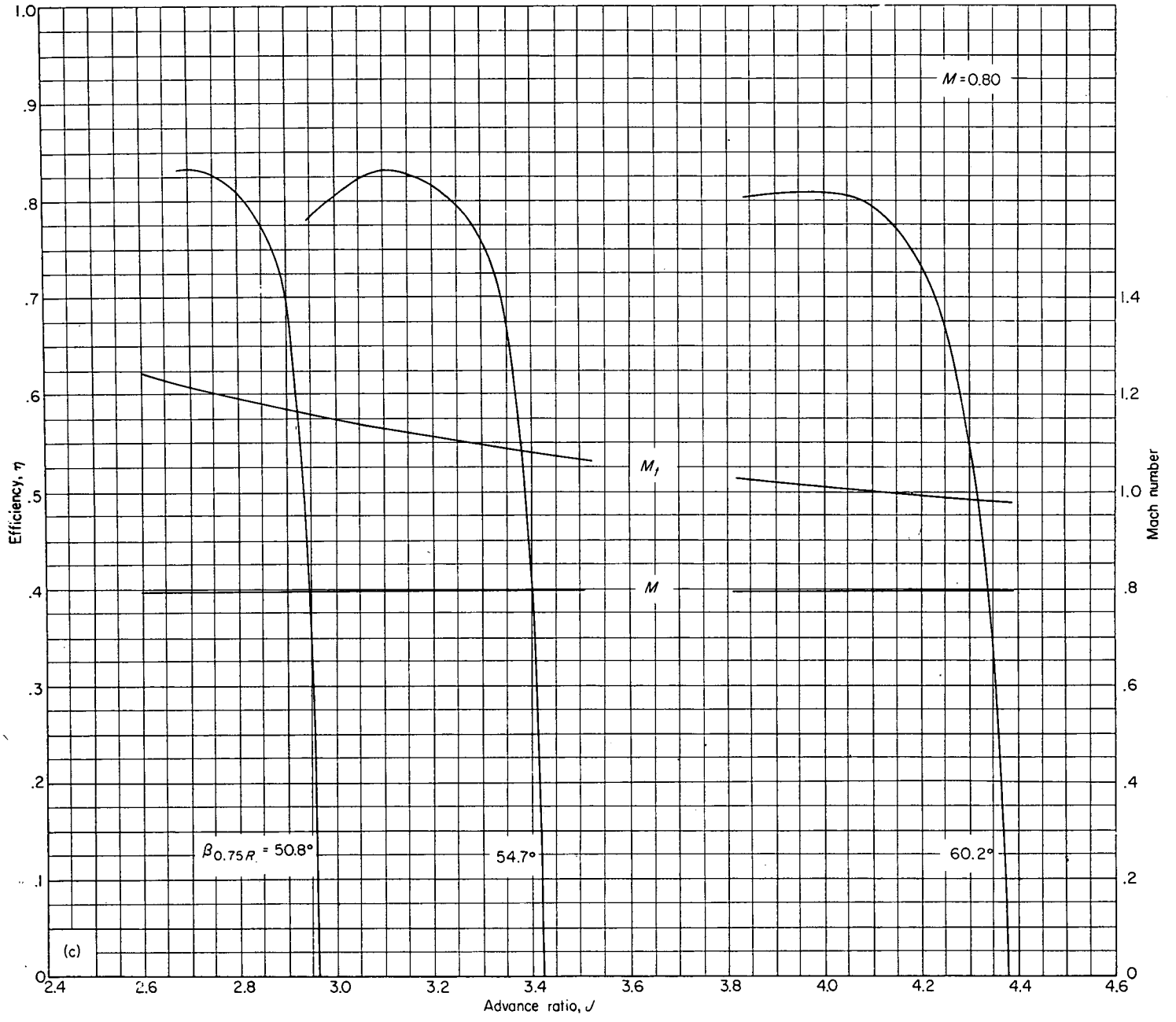
(a) Thrust coefficient.

FIGURE 10.—Characteristics of propeller. Forward Mach number 0.80.



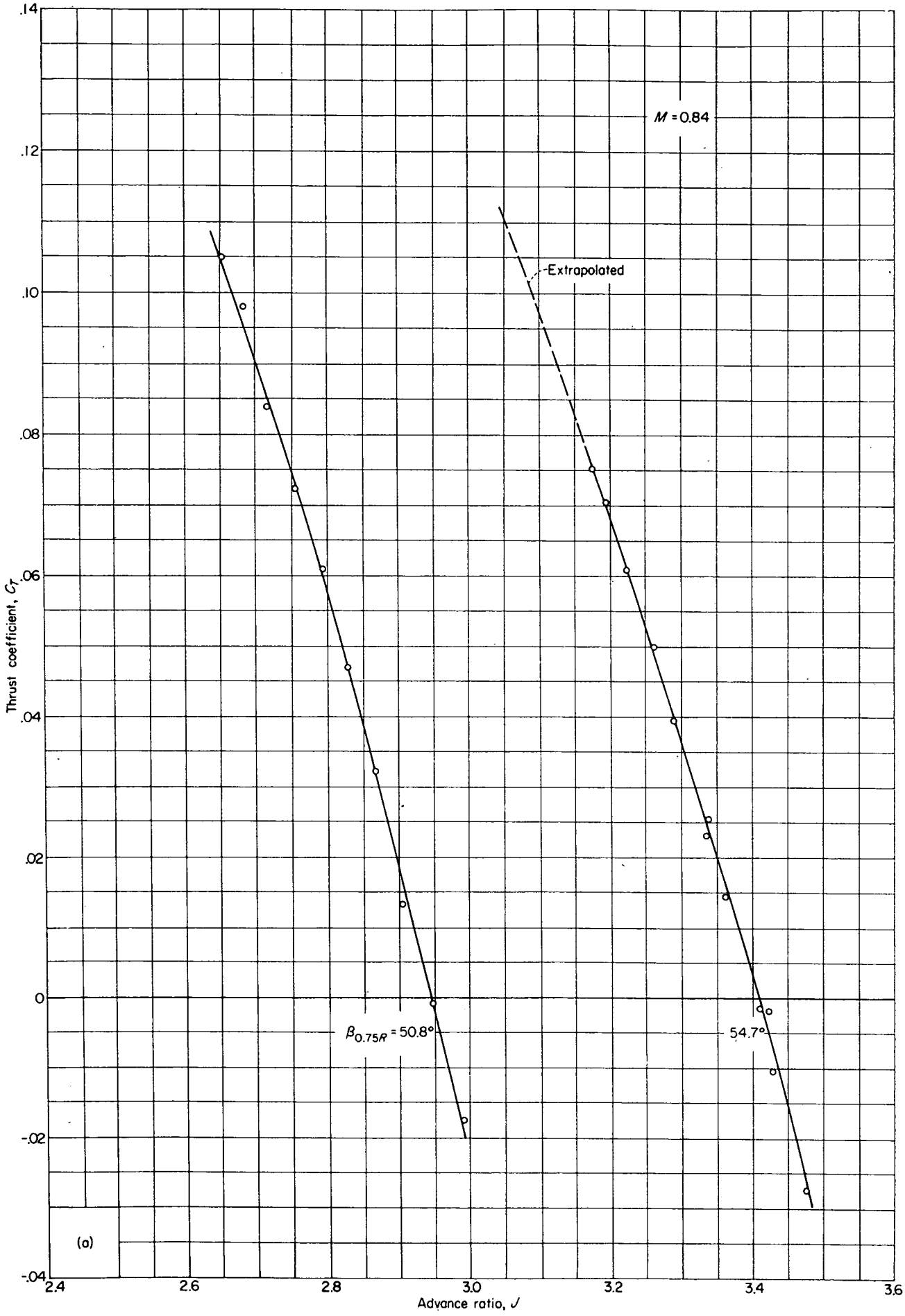
(b) Power coefficient.

FIGURE 10.—Continued.



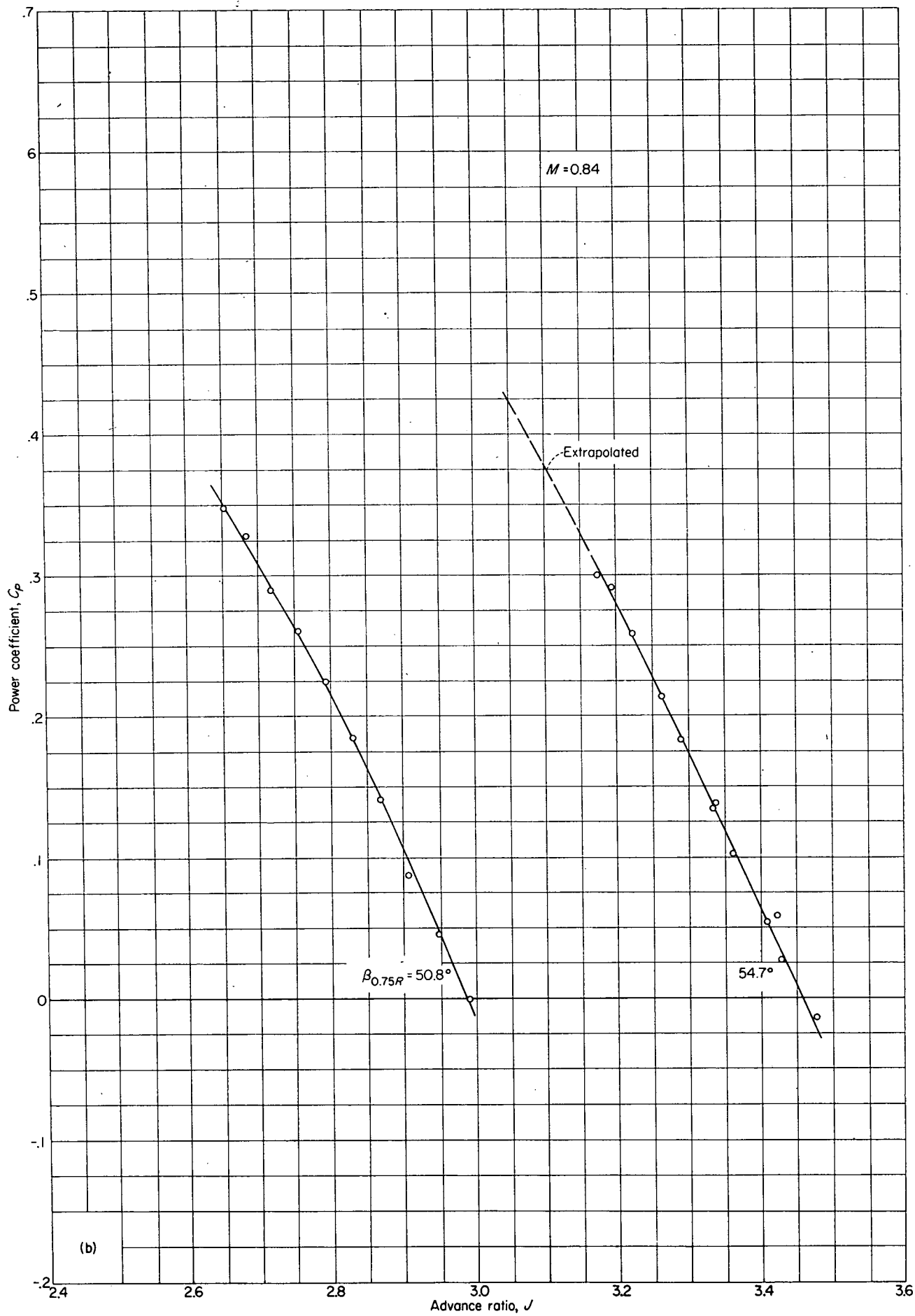
(c) Efficiency.

FIGURE 10.—Concluded.



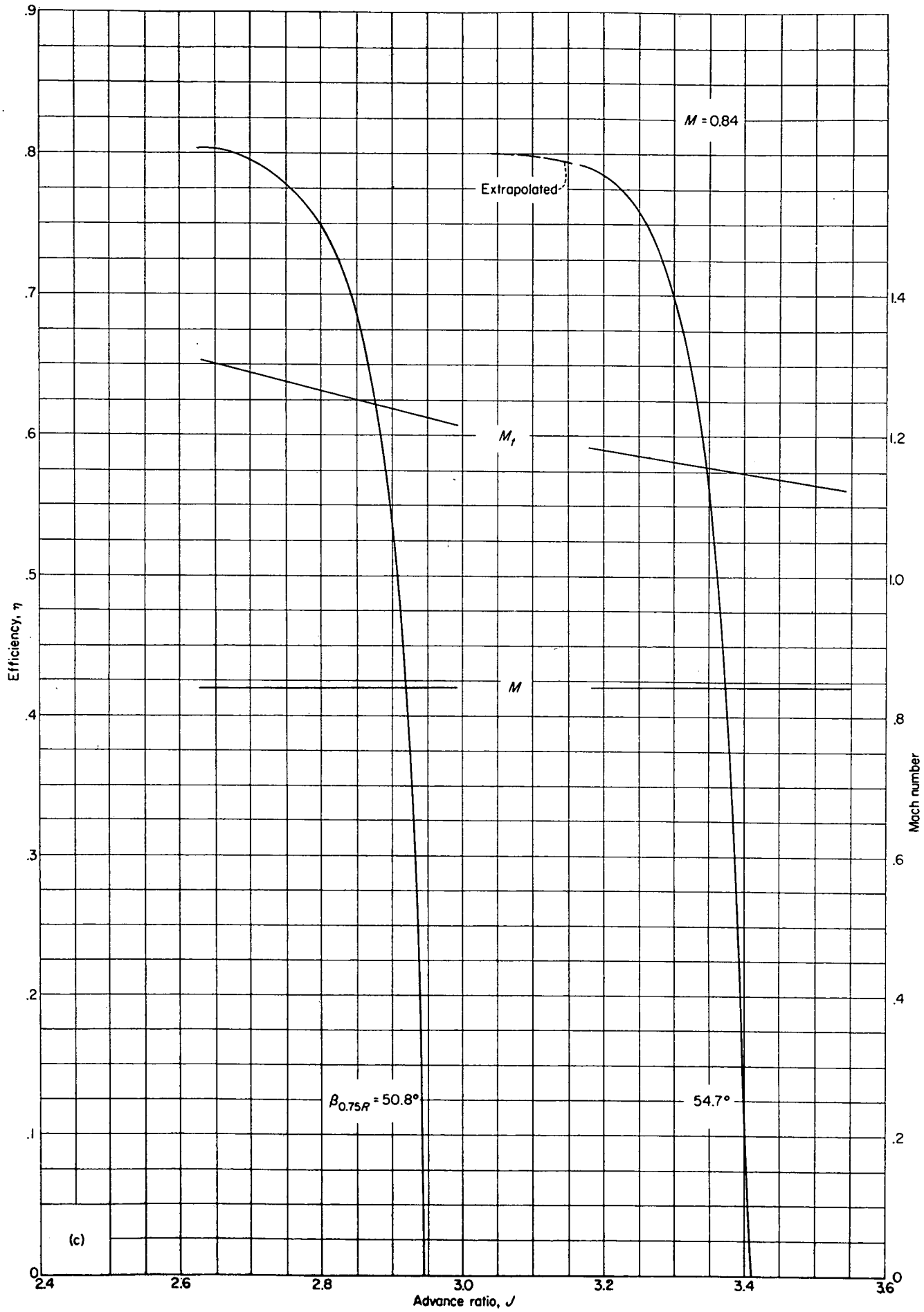
(a) Thrust coefficient.

FIGURE 11.—Characteristics of propeller. Forward Mach number 0.84.



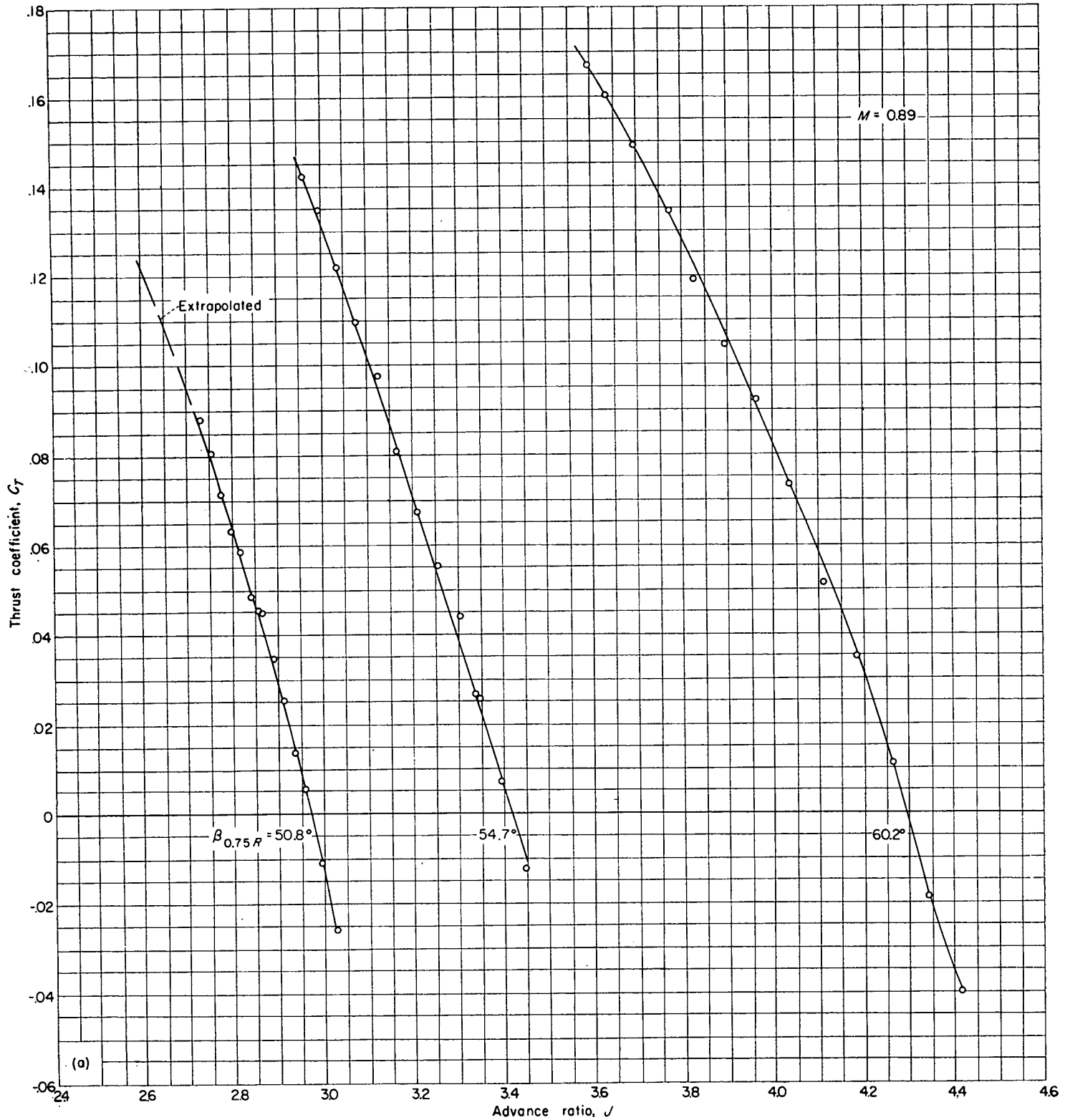
(b) Power coefficient.

FIGURE 11.—Continued.



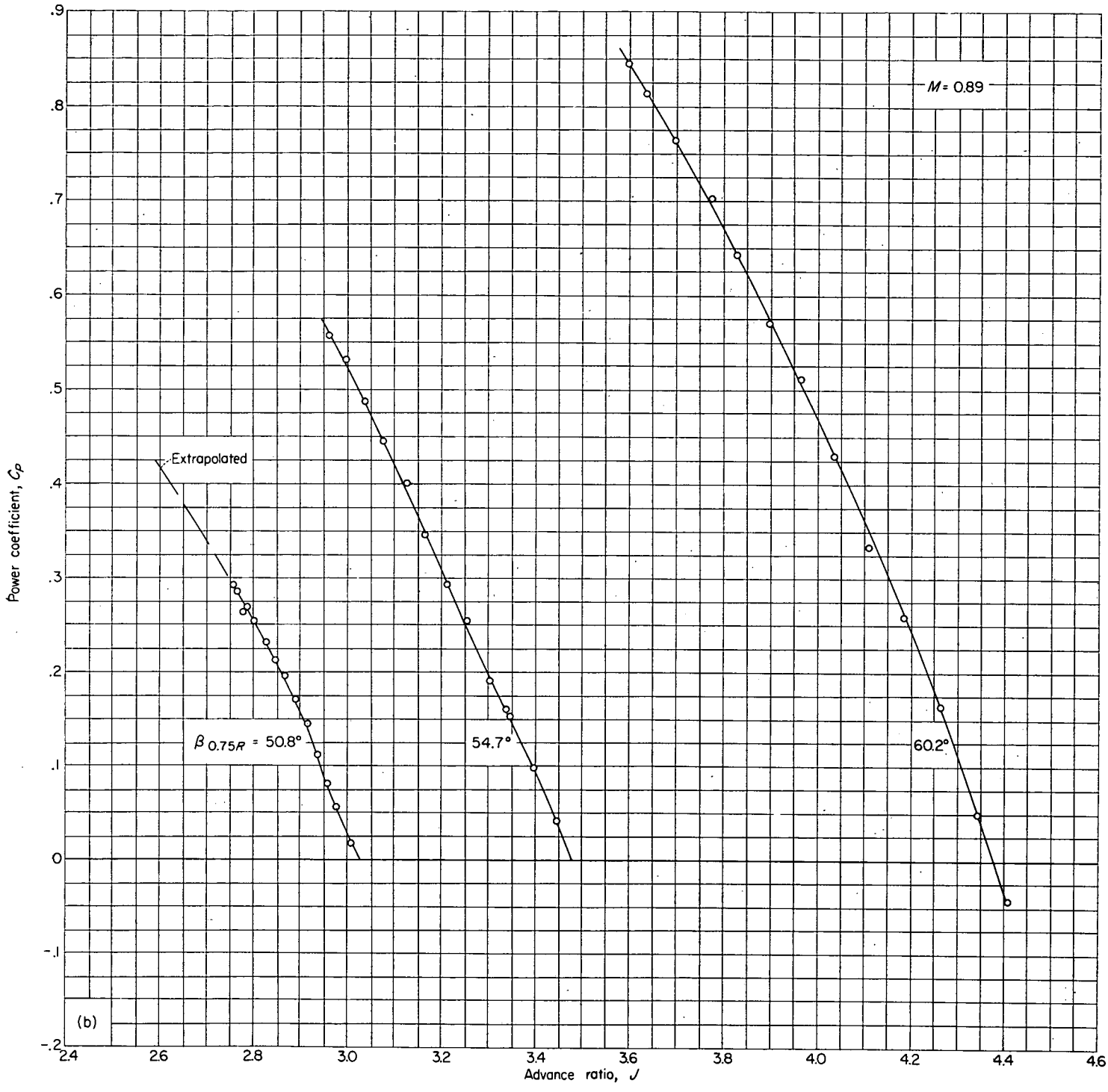
(c) Efficiency.

FIGURE 11.—Concluded.



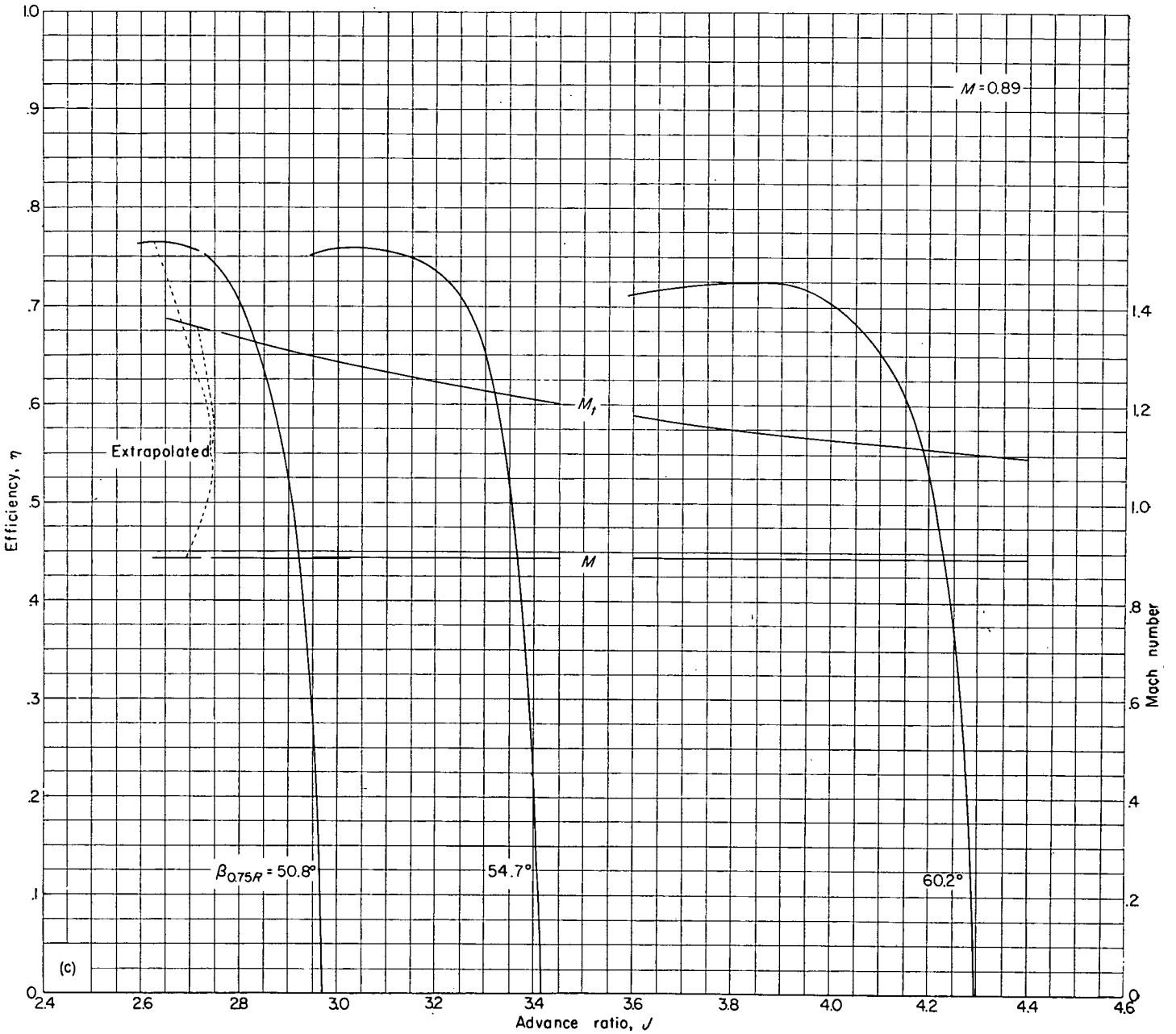
(a) Thrust coefficient.

FIGURE 12.—Characteristics of propeller. Forward Mach number 0.89.



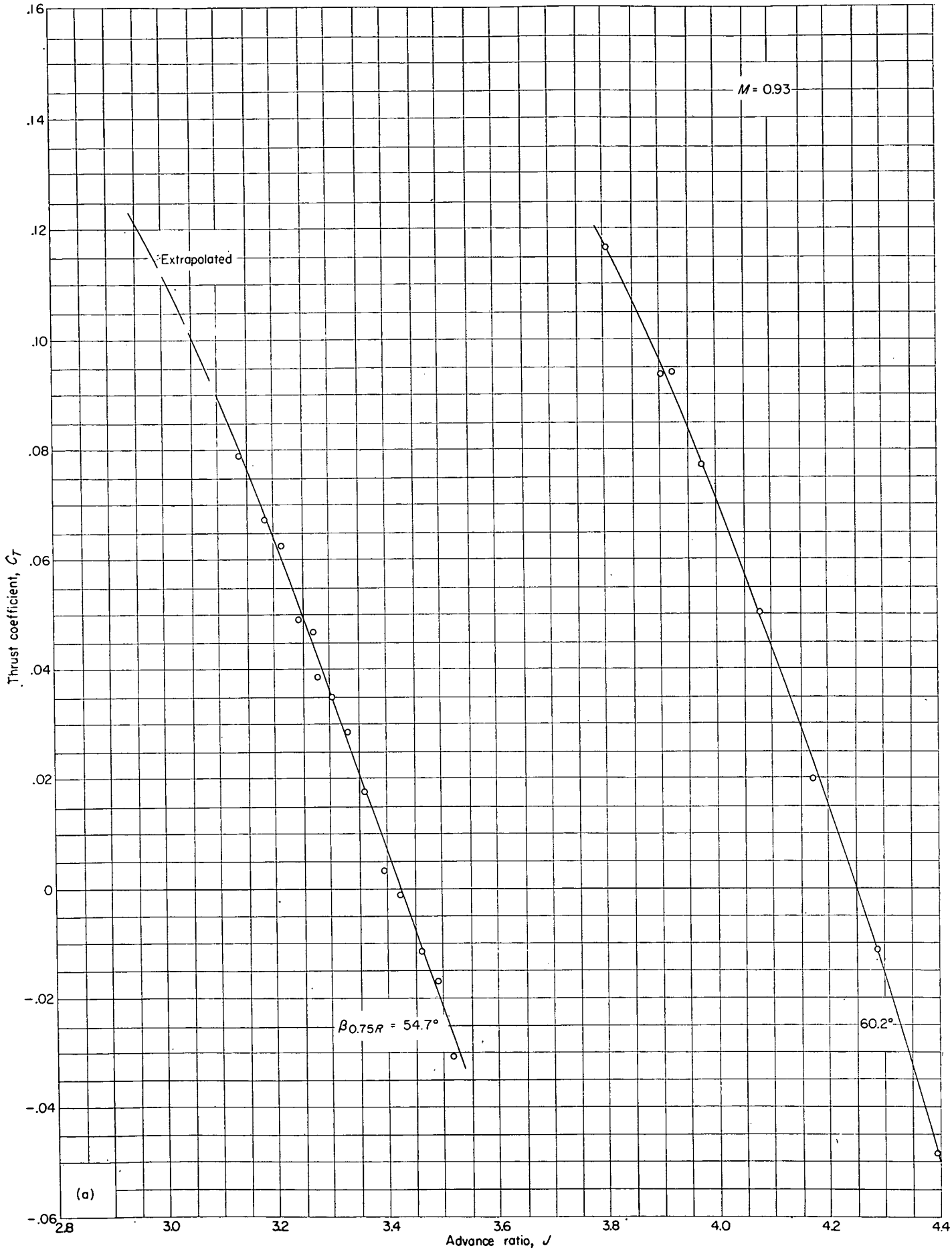
(b) Power coefficient.

FIGURE 12.—Continued.



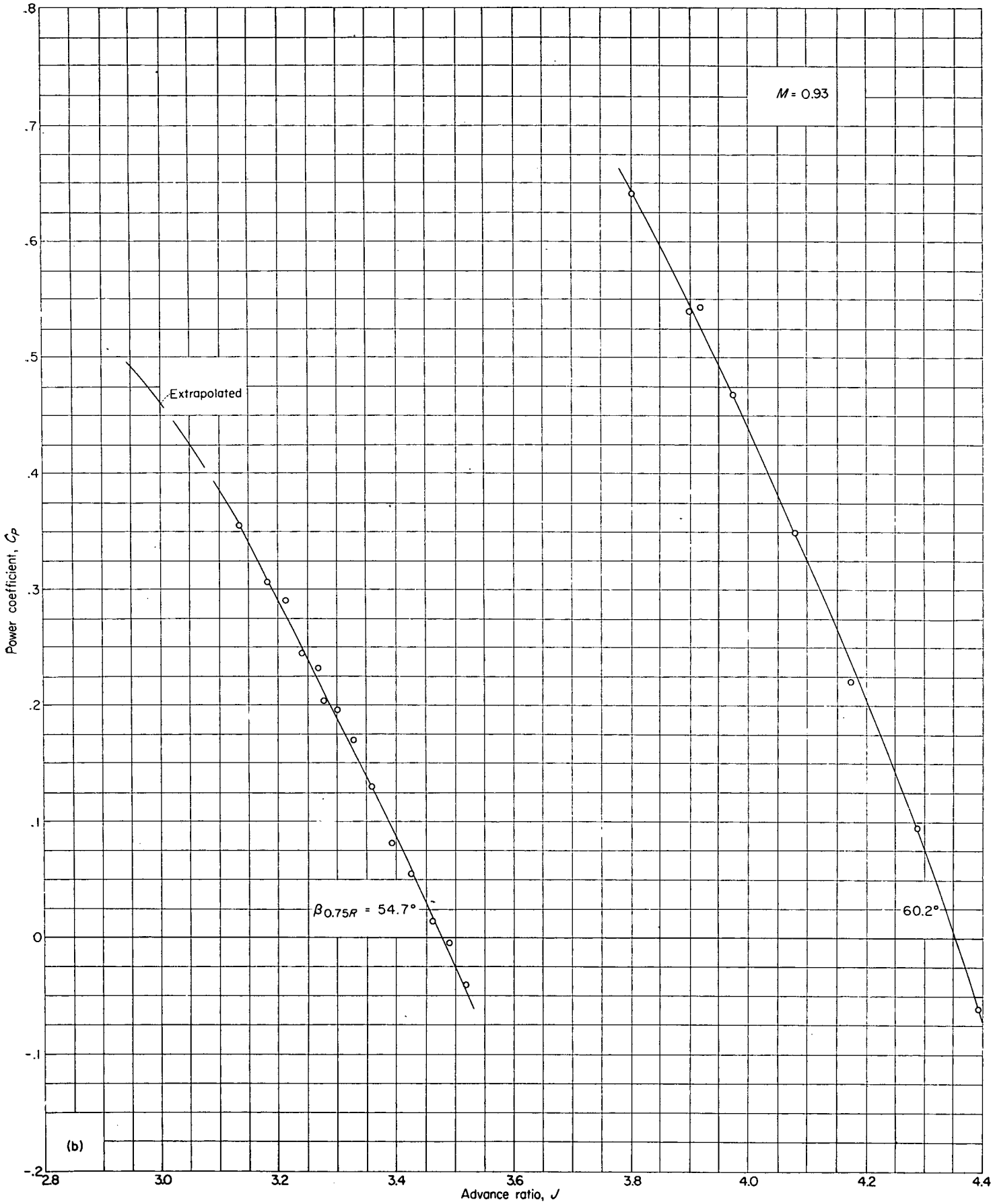
(c) Efficiency.

FIGURE 12.—Concluded.



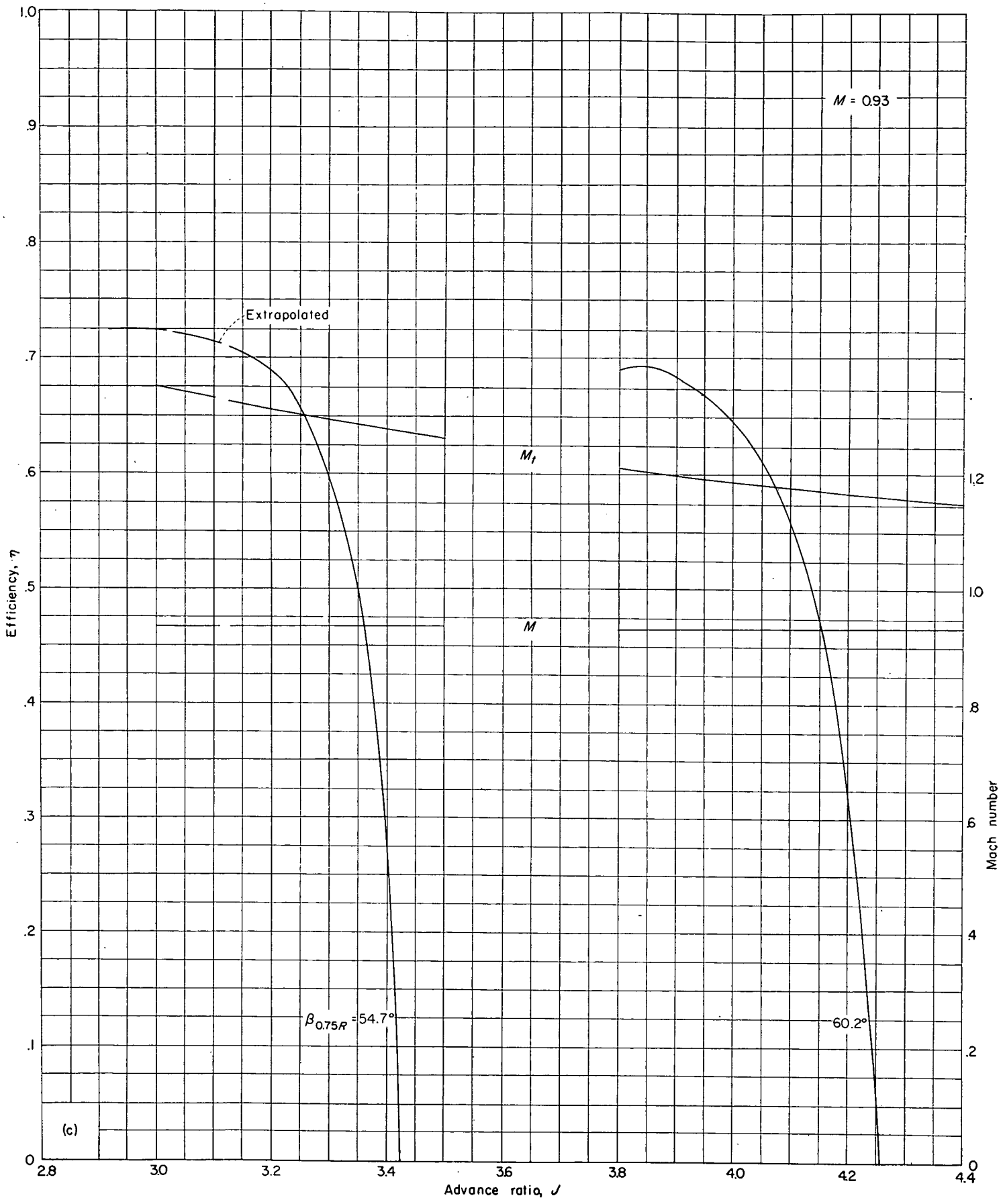
(a) Thrust coefficient.

FIGURE 13.—Characteristics of propeller. Forward Mach number 0.93.



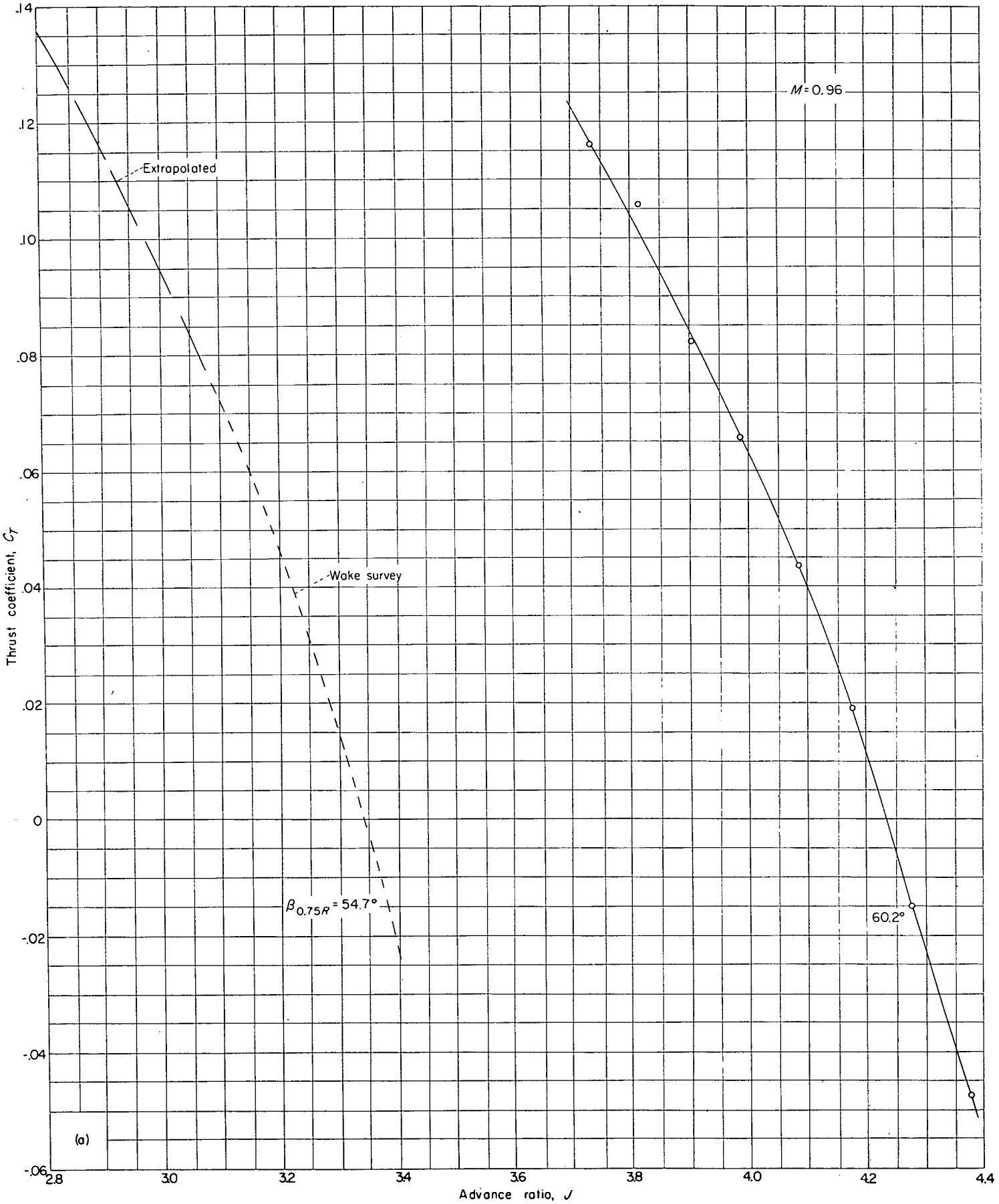
(b) Power coefficient.

FIGURE 13.—Continued.



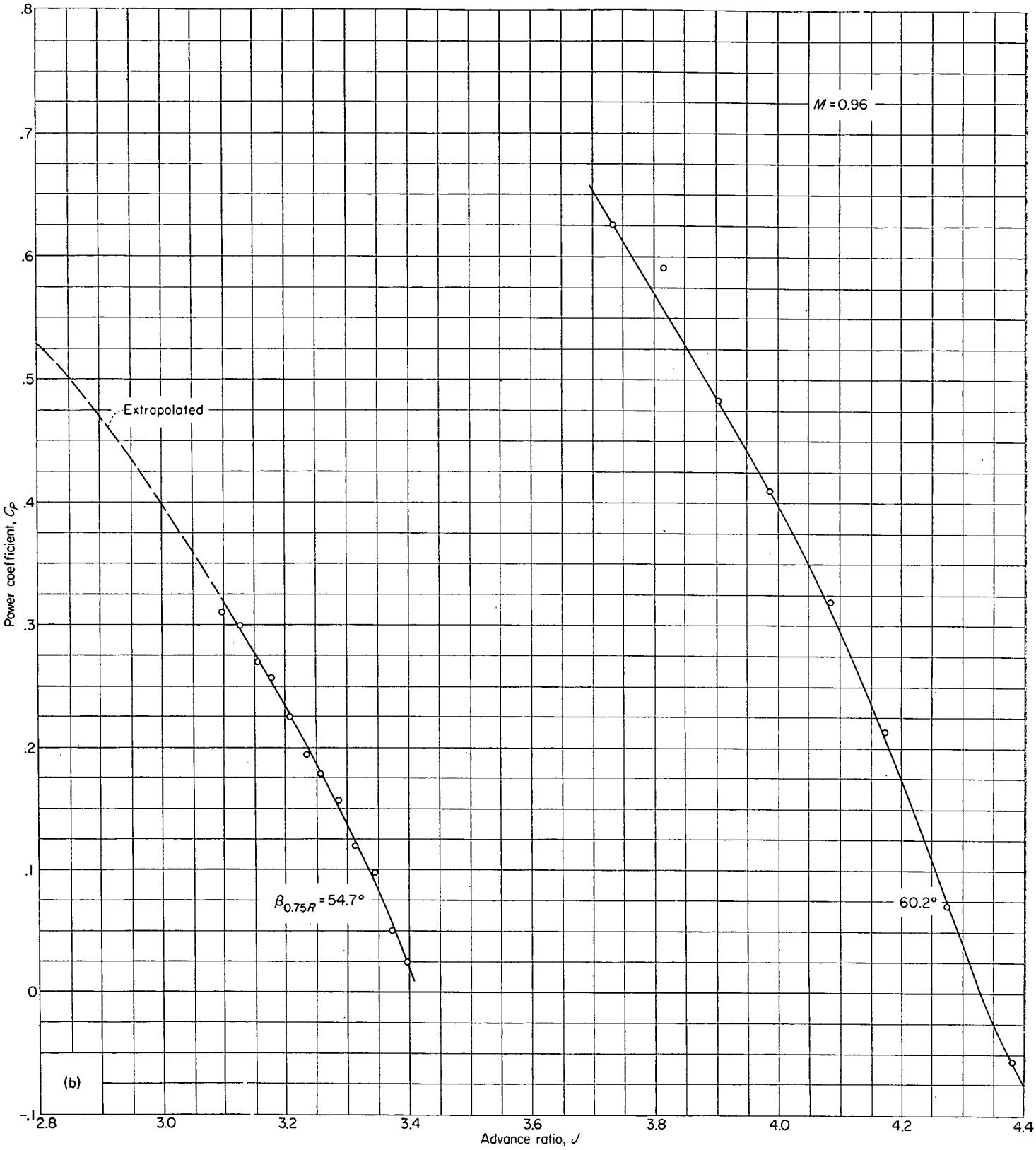
(c) Efficiency.

FIGURE 13.—Concluded.



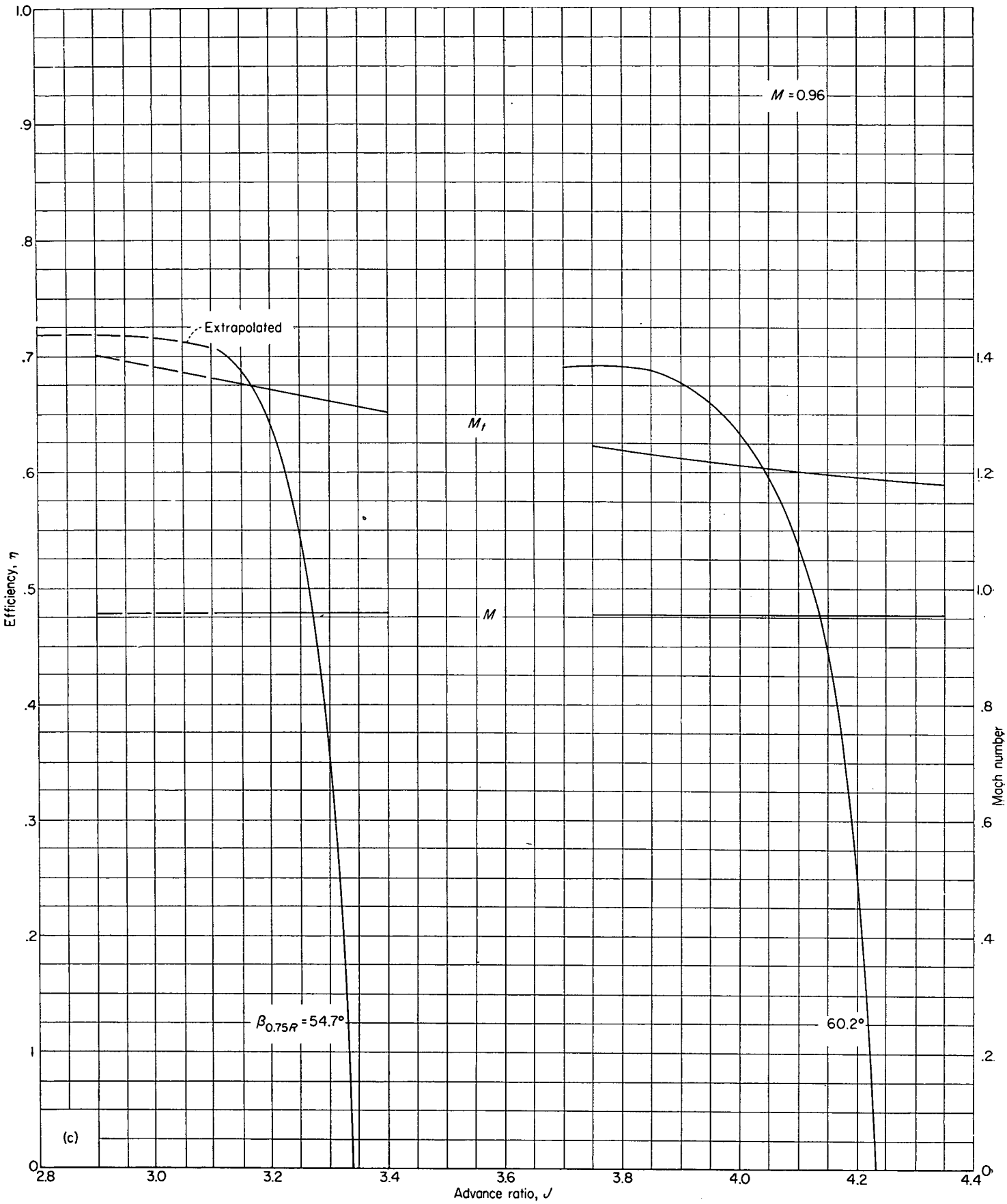
(a) Thrust coefficient.

FIGURE 14.—Characteristics of propeller. Forward Mach number 0.96.



(b) Power coefficient.

FIGURE 14.—Continued.



(c) Efficiency.

FIGURE 14.—Concluded.

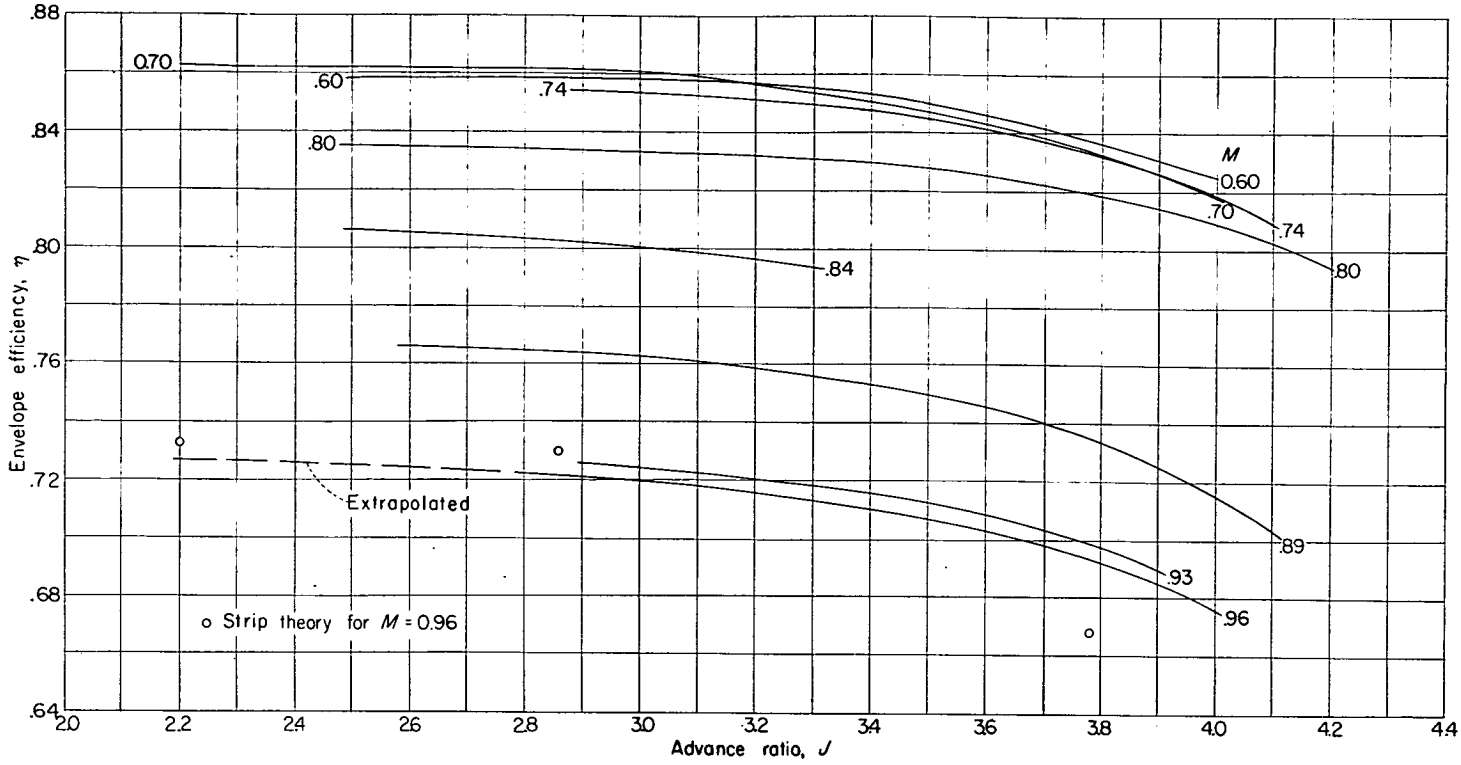


FIGURE 15.—Variation of envelope efficiency with advance ratio for various forward Mach numbers.

EFFECT OF FORWARD MACH NUMBER ON MAXIMUM EFFICIENCY

The variation of maximum propeller efficiency with forward Mach number is shown in figure 16 for advance-ratio values of 2.8, 3.4, and 4.0. These data show that the maximum efficiency attained during the tests was 86 percent between Mach numbers of 0.60 and 0.70 at an advance ratio of 2.8. Above $M=0.70$, the efficiency decreased gradually to a value of 72 percent at the Mach number of 0.96. At an advance ratio of 4.0, the maximum efficiency was 2.5 to 4.0 percent less than that for $J=2.8$ over the Mach number range from 0.60 to 0.96.[1]

Results of this investigation of the supersonic propeller agree with trends shown for model propellers designed for higher advance ratios (ref. 7) than 2.2. At a constant value of forward Mach number any increase in advance ratio decreases rotational speed and therefore results in lower values of blade-section Mach number. It is thus apparent that a propeller operating at high advance ratio will delay the onset of the adverse effects of compressibility on the blade sections and will operate to higher values of forward Mach number before the blade sections reach the critical speed. It is seen in figure 16 that the critical speed of the test propeller was delayed to higher Mach numbers as advance ratio was increased. At $J=2.8$ the point at which the efficiency began to decrease rapidly was $M=0.71$ and progressed to $M=0.75$ at $J=3.4$ and $M=0.80$ at $J=4.0$. Furthermore, as the value of forward Mach number is increased into the supercritical speed range, the present propeller and the model propellers of reference 7 will operate at a low advance ratio more efficiently than at a high advance ratio because of the more advantageous orientation of the blade force vectors.

Below the critical Mach number, there is a notable difference between the advance ratio at which maximum efficiency is attained for the model propeller tested in the investigation of reference 7 and the propeller used in the present investigation. Obviously, the model propeller operating at advance ratios lower than the design value of 3.36 will not have all blade sections at maximum lift-drag ratio, and a lower efficiency results. The present propeller will operate with efficiency decreasing as advance ratio is increased from the design value of 2.2 for the same reason.

POWER COEFFICIENT FOR MAXIMUM EFFICIENCY

The variation of power coefficient for maximum efficiency with advance ratio is shown in figure 17 for constant values of forward Mach number. These curves can be used to evaluate the power-absorption properties of the supersonic-type propeller designed for a low advance ratio. If a constant pressure altitude and a constant Mach number of 0.96 is assumed, the propeller operating at an advance ratio of 2.8 would absorb nearly twice as much power and, as shown in figure 15, would operate 3 percent more efficiently than a similar propeller operating at an advance ratio of 3.8. More power is absorbed when operating at the lower advance ratio because the power absorbed is inversely proportional to advance ratio, although the power coefficient is lower at the lower advance ratio. Another way to illustrate the

[1] In later tests of this same propeller in which forward Mach number was extended to 1.04, the values of propeller efficiency at speeds near Mach number 0.96 were slightly different from those presented in this report. The later tests indicate a continuing decrease of efficiency with increasing Mach number rather than the tendency for values of efficiency to level off in the region of Mach number 0.96 as indicated in figure 16. The actual differences in efficiency values between the two sets of data are generally less than one percent. The results of these tests were published in NACA Research Memorandum L56E10 entitled "Effect of Blade Section Camber on Aerodynamic Characteristics of Full-Scale Supersonic-Type Propellers at Mach Numbers to 1.04" by Julian D. Maynard, John M. Swihart, and Harry T. Norton, Jr.

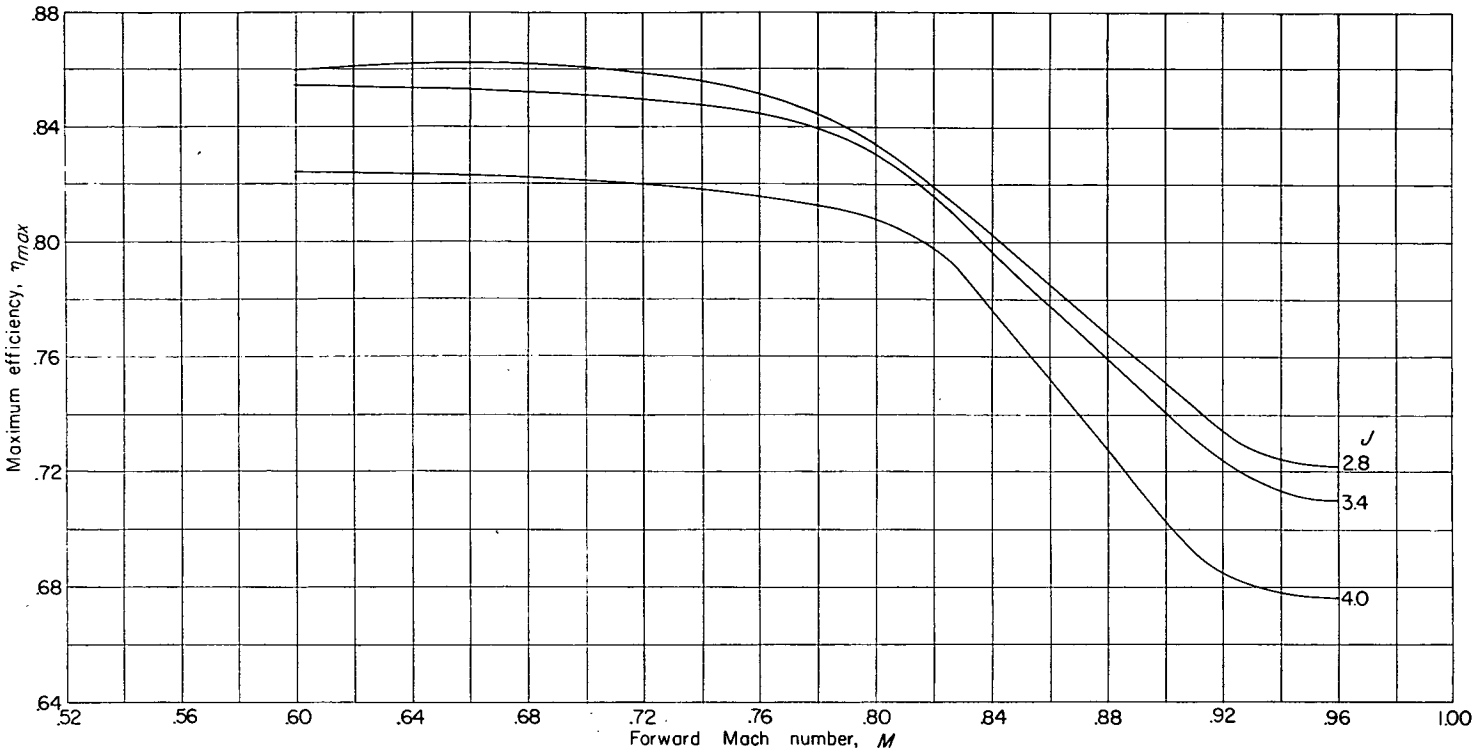


FIGURE 16.—Variation of maximum propeller efficiency with forward Mach number for several values of advance ratio.

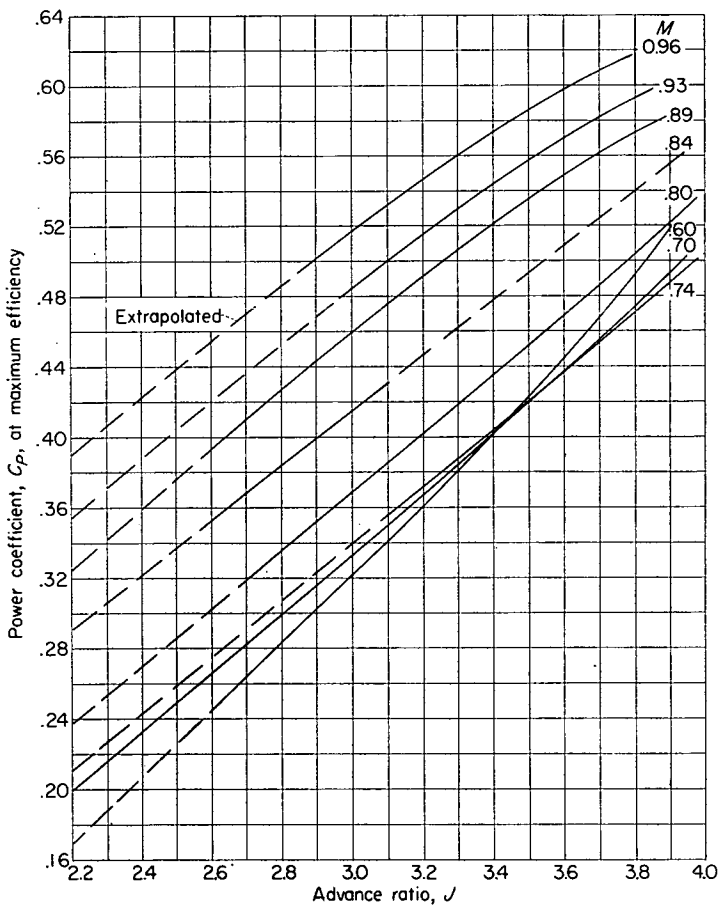


FIGURE 17.—Variation of power coefficient at maximum efficiency with advance ratio.

526597—60——63

advantages of operation at low advance ratios is to compare the diameters of propellers designed for a given power. In the foregoing example, the propeller operating at an advance ratio of 3.8 would have to be 40 percent greater in diameter to absorb the same power as the propeller operating at an advance ratio of 2.8. Therefore, the supersonic-type propeller with low design advance ratio has favorable power-absorption characteristics which permit the use of smaller propeller diameters.

COMPARISON OF DATA WITH COMPRESSIBLE-FLOW MOMENTUM-THEORY DATA

A compressible-flow momentum theory has been developed in reference 8, some results of which are reproduced in figure 18. Values of maximum efficiency obtained experimentally in the present tests are also plotted as data points in figure 18.

The compressible momentum theory based on the assumption of a subsonic slipstream indicates that, as the propeller power disk loading is increased beyond a certain value at a constant forward Mach number, the ideal efficiency decreases very rapidly and, if such were the case in practice, would preclude the use of propellers at Mach numbers above about 0.90. As pointed out in reference 8, however, the propeller slipstream can attain supersonic speeds when the power is increased, and the values of efficiency shown in figure 18 for the supersonic wake appear to be more reasonable. Although the calculated values of efficiency in figure 18 do not include any profile or rotational losses, most of the experimental data for the higher Mach numbers (0.93 and 0.96) are above the subsonic-wake curves. It appears, therefore, that the propeller slipstream must have attained supersonic velocities for at least a short distance behind the propeller for the tests at $M=0.93$ and $M=0.96$.

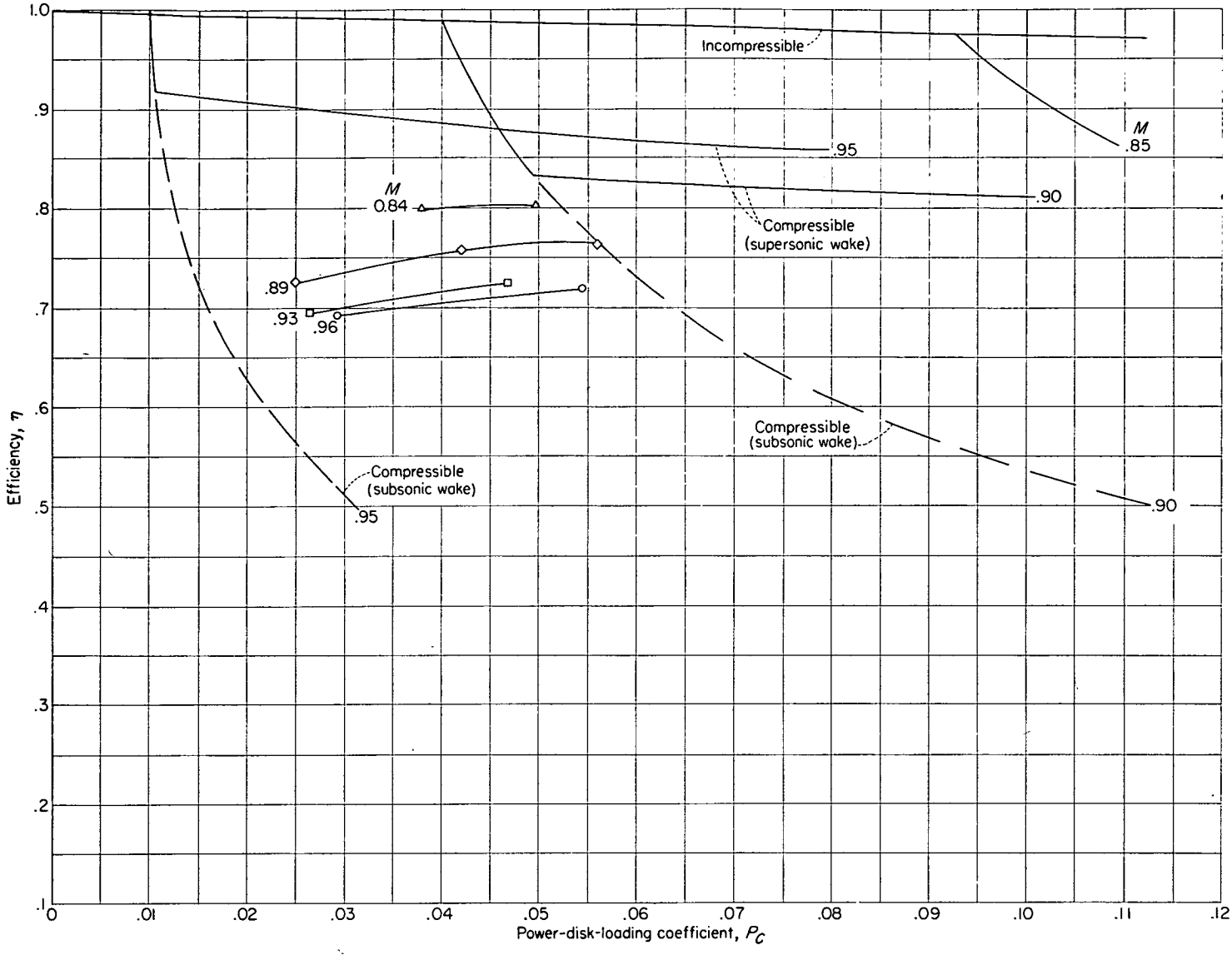


FIGURE 18.—Variation of maximum efficiency with power-disk-loading coefficient for several forward Mach numbers (from fig. 13 of ref. 8).

OPERATING CHARTS

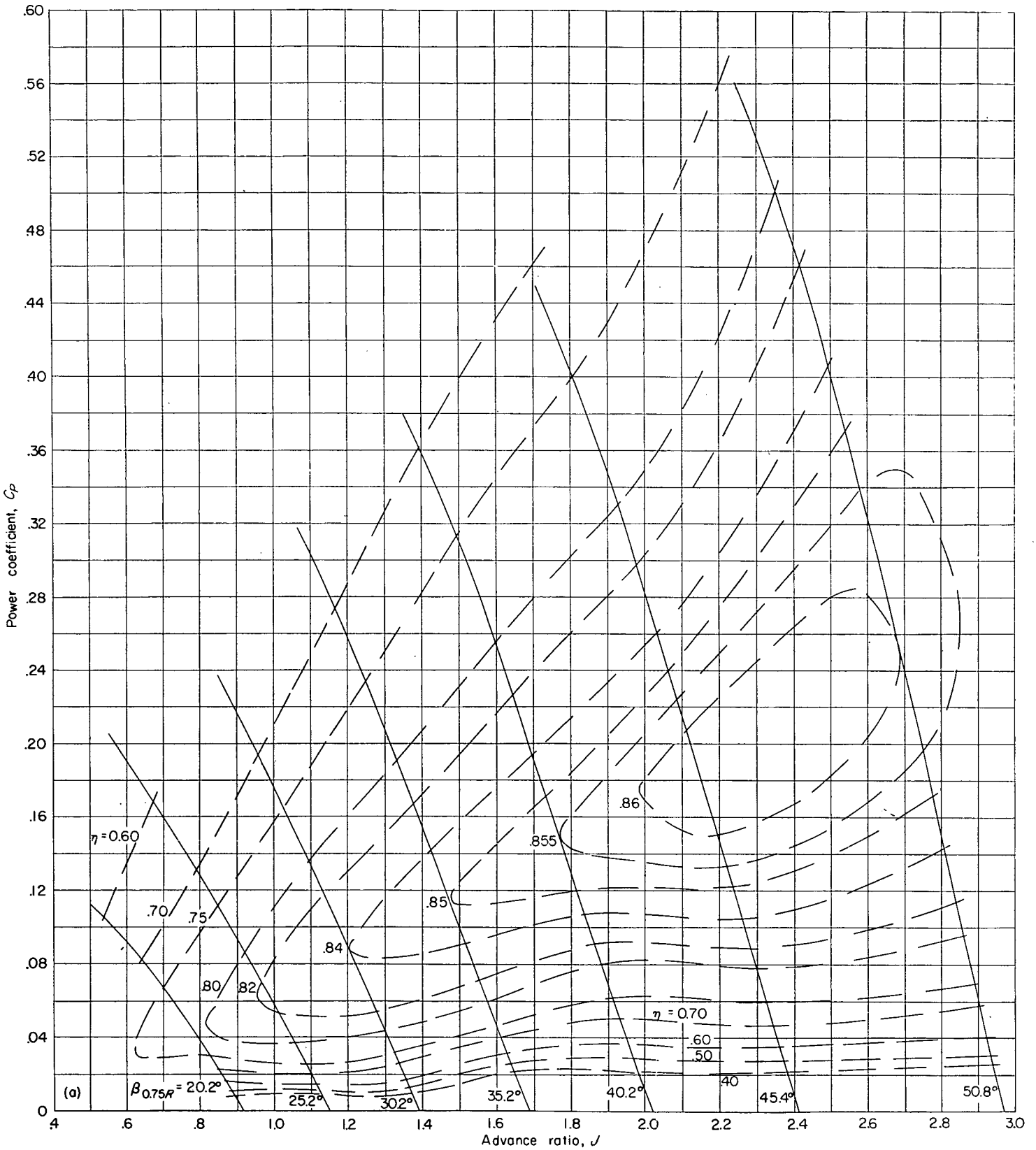
In order to facilitate the use of the data included herein for performance estimates, charts have been prepared and are included in figure 19. The charts consist of plots of power coefficient against advance ratio with lines of constant efficiency superimposed. Except for the first chart (fig. 19 (a)), which presents data obtained at a rotational speed of 1600 rpm ($M<0.67$), the charts are presented for the constant values of forward Mach number at which the tests were made. (See figs. 19 (b) to (i).)

STALL-FLUTTER DATA

The purpose of the present investigation was to determine the aerodynamic characteristics of the propeller tested, and the propeller was deliberately not operated at flutter since violent or sustained flutter would have been hazardous to the test equipment. Flutter was detected, however, both audibly and by strain gages during the tests at a constant rotational speed of 1600 rpm, during which propeller stall conditions were encountered. In some cases it was possible to record the value of forward Mach number at flutter whereas in other cases the dynamometer speed was dropped slightly before data were taken.

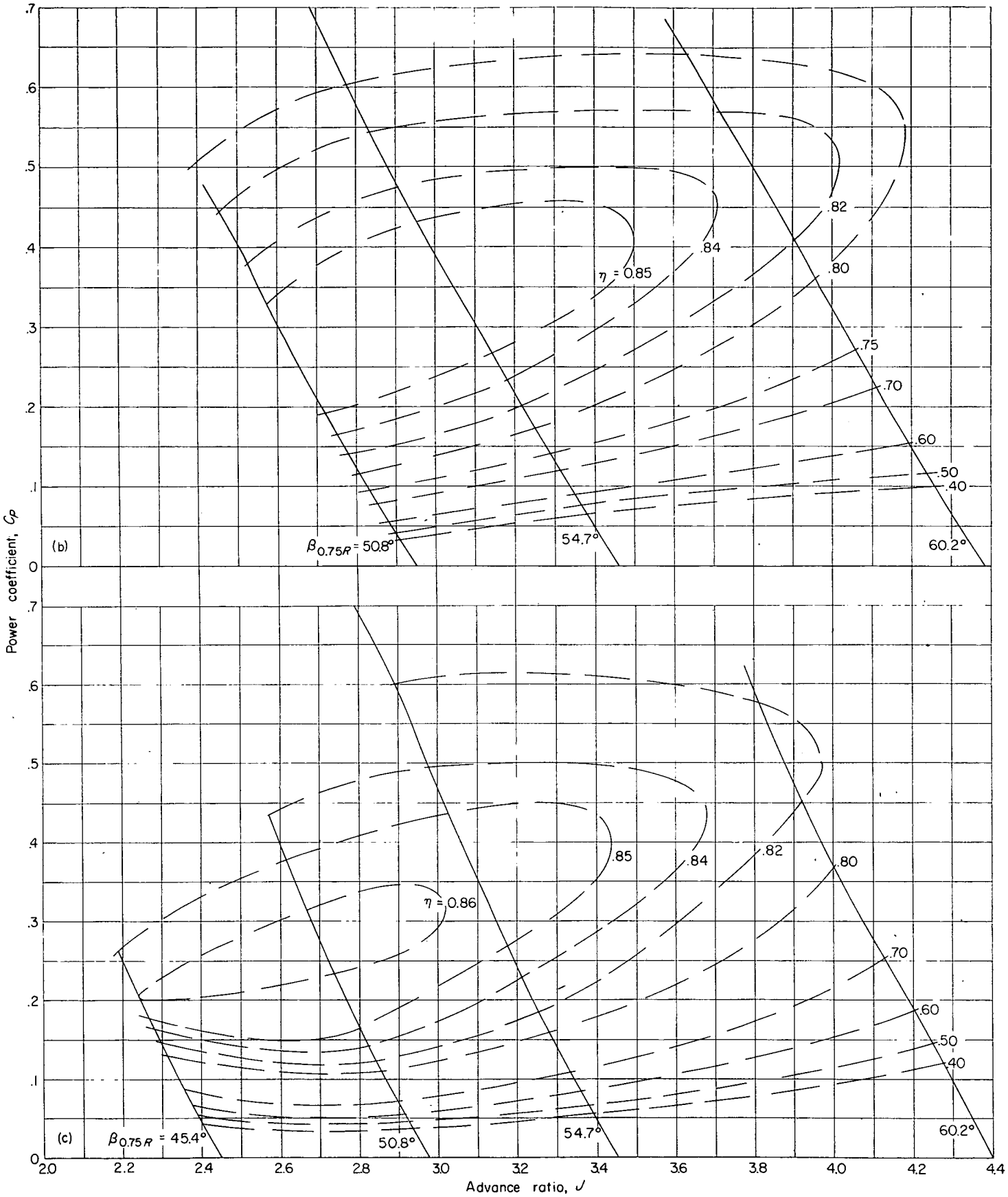
No analysis of the flutter data is presented, but the data obtained are included in figure 6. The values of advance ratio at which flutter occurred were spotted on the curves of thrust and power coefficient and a curve drawn through the points to mark the flutter boundary.

The flutter data, as replotted in figure 20, show the variation of the section lift coefficient and helical tip Mach number at flutter with advance ratio for the $x=0.60$ station as determined from wake pressure measurements. The values are shown for the $x=0.60$ station since the maximum value of lift coefficient along the propeller-blade radius occurred at approximately this station.



(a) 1600 rpm; $M<0.67$.

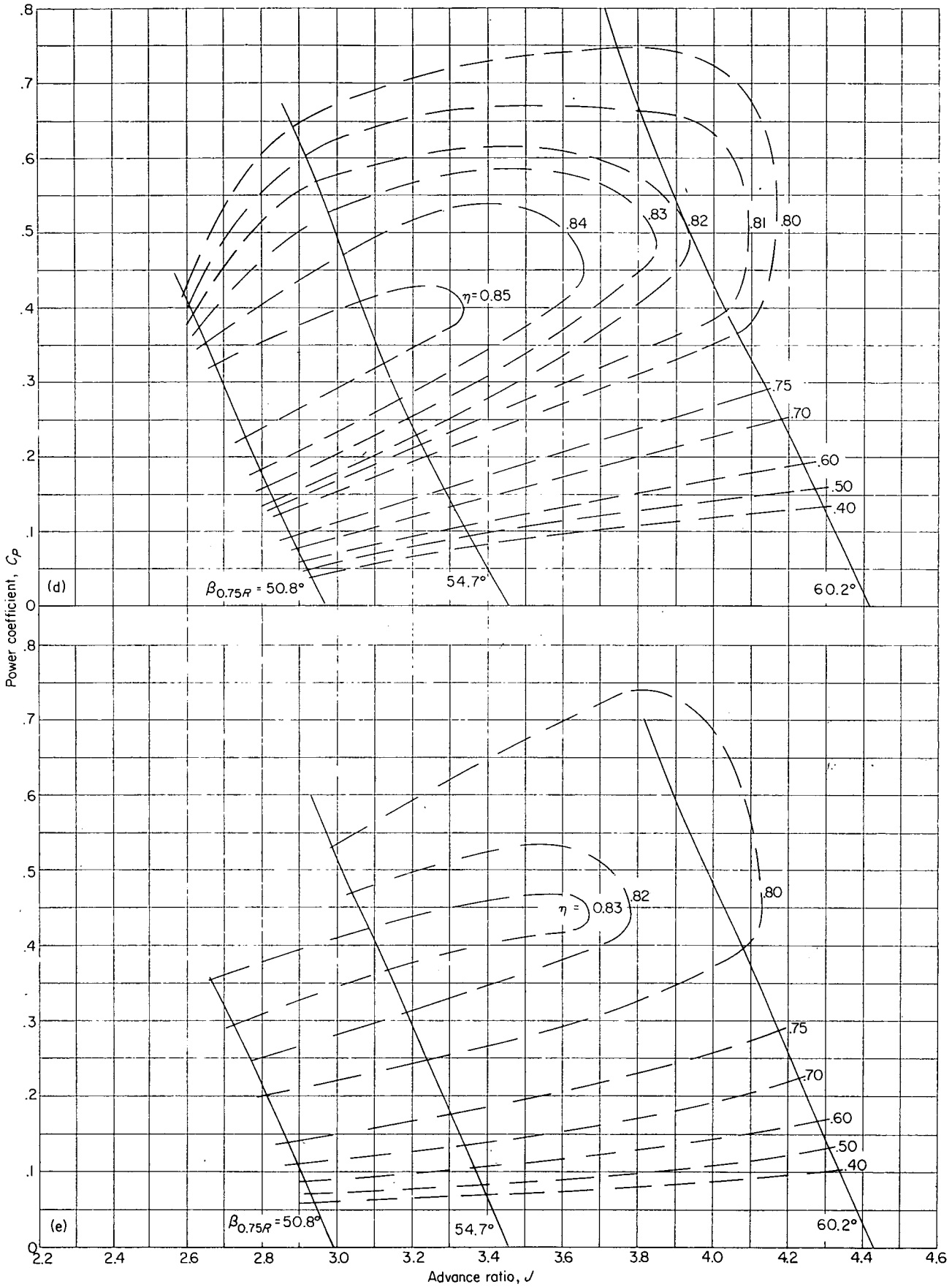
FIGURE 19.—Operating charts for three-blade propeller.



(b) $M=0.60$.

(c) $M=0.70$.

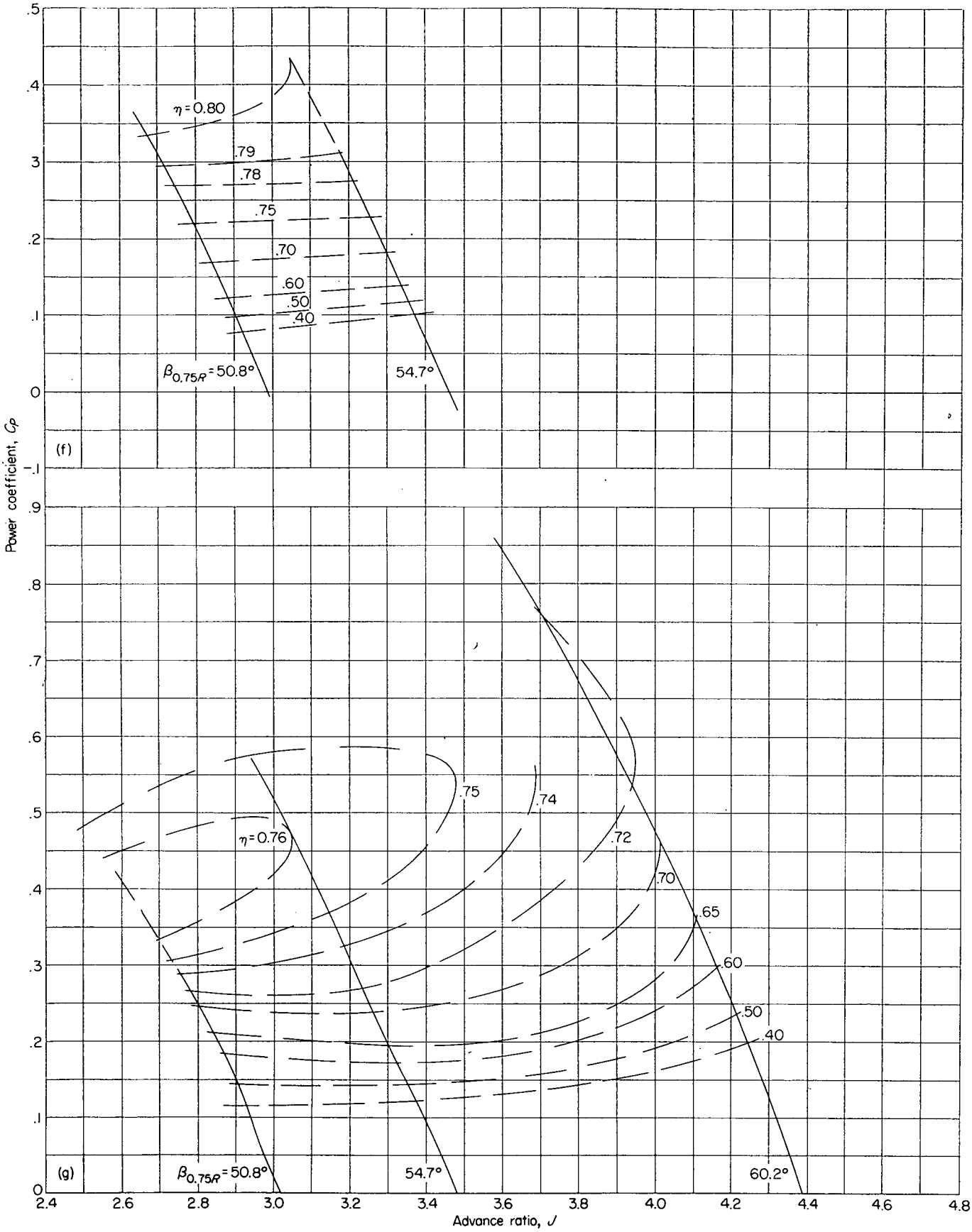
FIGURE 19.—Continued.



(d) $M=0.74$.

(e) $M=0.80$.

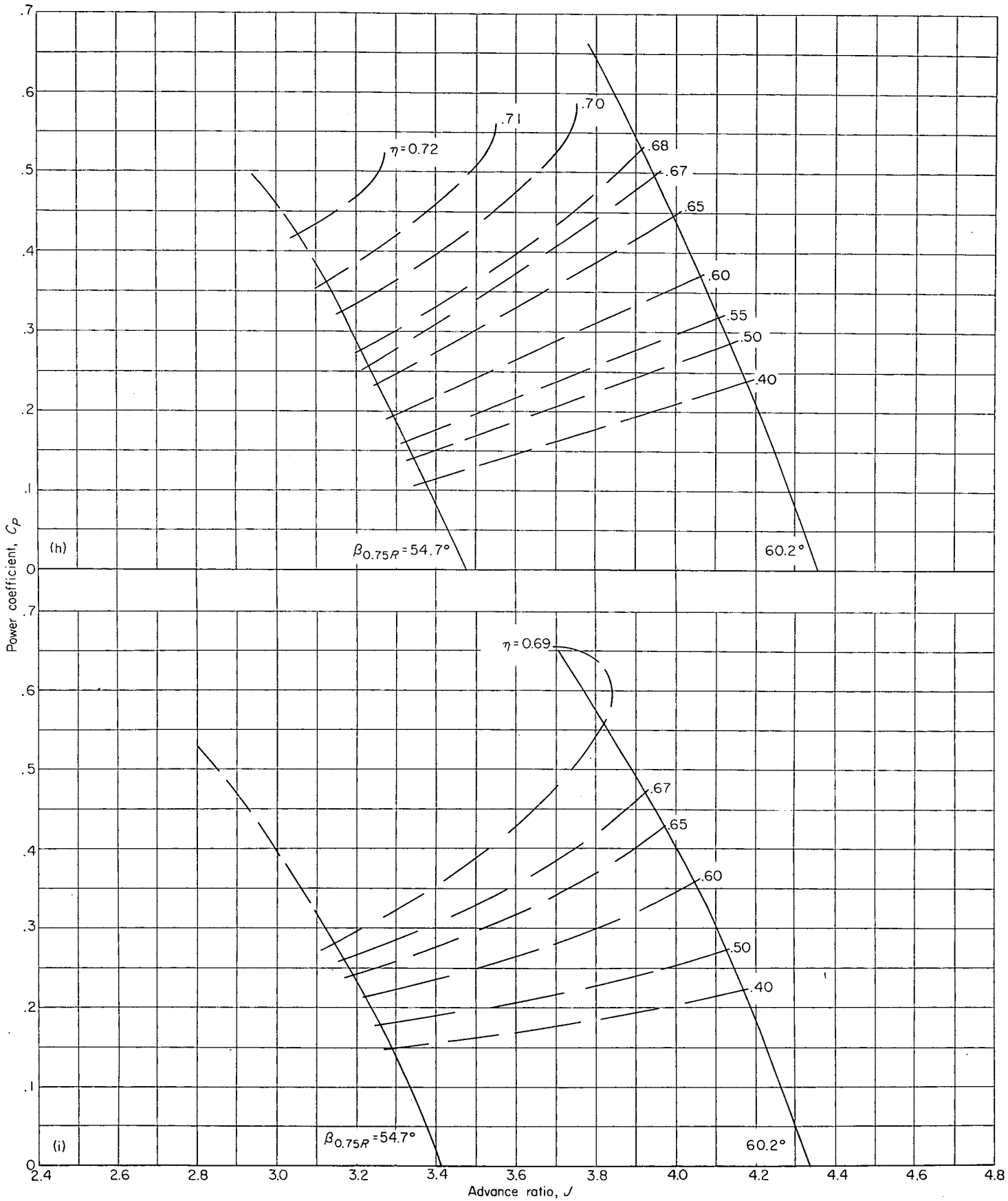
FIGURE 19.—Continued.



(f) $M=0.84$.

(g) $M=0.89$.

FIGURE 19.—Continued.



(h) M=0.93.

(i) M=0.96.

FIGURE 19.—Concluded.

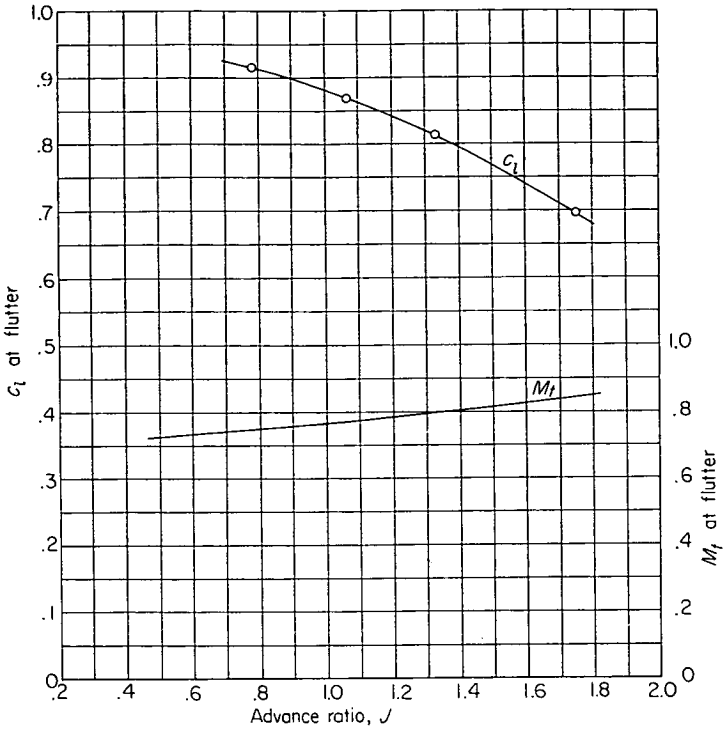


FIGURE 20.—Variation with advance ratio of lift coefficient and tip Mach number at flutter. $x=0.60$; rotational speed, 1600 rpm.

EFFECT OF STRAIN GAGES ON PROPELLER EFFICIENCY

Most of the tests for this were run with strain gages cemented to the surface of one of the propeller blades. Consideration of the effect of the strain gages on the aerodynamic characteristics led to the repeat tests with the strain gages removed from the propeller; thus, the propeller was aerodynamically clean. Data shown in figure 21 gave indication of no difference in maximum efficiency up to a Mach number of 0.88. Above $M=0.88$, the clean blades were slightly more efficient (about 2 percent at $M=0.96$) than the blades with gages attached.

It should be noted that the aerodynamic characteristics presented in this report at high Mach numbers were obtained with the clean propeller. At values of Mach number below 0.90, the differences in efficiency between the propeller with gages attached and the clean propeller were negligible.

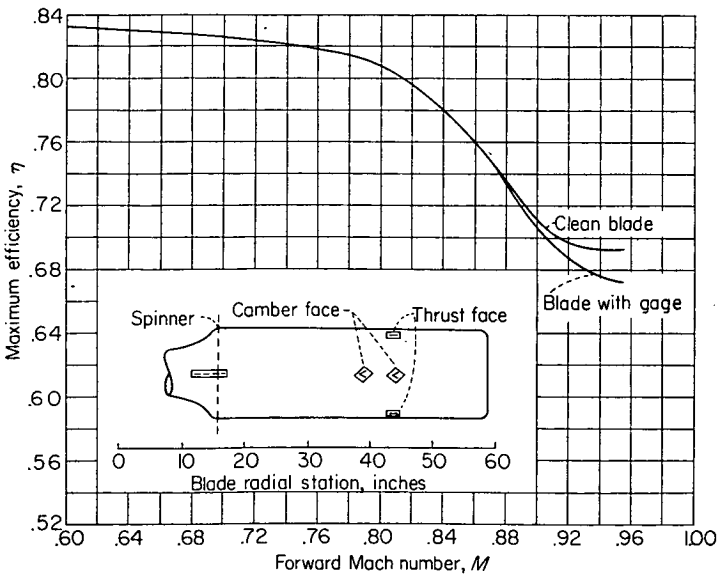


FIGURE 21.—Effect of strain gages on maximum efficiency.

CONCLUSIONS

Tests of a supersonic three-blade propeller have been made on the 6000-horsepower propeller dynamometer in the Langley 16-foot transonic tunnel over a range of blade angles at forward Mach numbers up to 0.96. The results of the investigation indicate the following conclusions:

1. In the range of the tests the tunnel-wall interference was found to be negligible for propeller operation in the slotted test section of the Langley 16-foot transonic tunnel.
2. Envelope efficiency at an advance ratio of 2.8 decreased from 86 percent to 72 percent when the forward Mach number was increased from 0.70 to 0.96.
3. Maximum propeller efficiency can be calculated with good accuracy by using ordinary subsonic strip theory when the blade-section speeds are supersonic.
4. The loss in envelope efficiency with increase in advance ratio is only about 1 percent between advance ratios of 2.2 and 3.2.
5. The supersonic-type propeller with a low design advance ratio has favorable power absorption characteristics which permit the use of smaller propeller diameters.
6. A comparison of the experimental data with compressible momentum theory indicates that the propeller slipstream attained supersonic velocities for at least a short distance behind the propeller at forward Mach numbers of 0.93 and 0.96.

LANGLEY AERONAUTICAL LABORATORY,
NATIONAL ADVISORY COMMITTEE FOR AERONAUTICS,
LANGLEY FIELD, VA., *May 18, 1953*.

REFERENCES

1. Ward, Vernon G., Whitcomb, Charles F., and Pearson, Merwin D.: Airflow and Power Characteristics of the Langley 16-Foot Transonic Tunnel With Slotted Test Section. NACA RM L52E01, 1952.
2. Wood, John H., and Swihart, John M.: The Effect of Blade Section Camber on the Static Characteristics of Three NACA Propellers. NACA RM L51L28, 1952.
3. Corson, Blake W., Jr., and Maynard, Julian D.: The Langley 2000-Horsepower Propeller Dynamometer and Tests at High Speed of an NACA 10-(3)(08)-03 Two-Blade Propeller. NACA TN 2859, 1952. (Supersedes NACA RM L7L29.)
4. Wright, Ray H., and Ward, Vernon G.: NACA Transonic Wind-Tunnel Test Sections. NACA Rep. 1231, 1955. (Supersedes NACA RM L8J06.)
5. Hallissy, Joseph M., Jr.: Pressure Measurements on a Body of Revolution in the Langley 16-Foot Transonic Tunnel and a Comparison With Free-Fall Data. NACA RM L51L07a, 1952.
6. Anon.: Propeller Performance Analysis. Aerodynamic Characteristics. NACA 16 Series Airfoils. Rep. No. C-2000, Curtiss-Wright Corp., Propeller Div. (Caldwell, N. J.), Dec. 2, 1948.
7. Delano, James B., and Carmel, Melvin M.: Investigation of the NACA 4-(0)(03)-045 and NACA 4-(0)(08)-045 Two-Blade Propellers at Forward Mach Numbers to 0.925. NACA RM L9L06a, 1950.
8. Delano, James B., and Crigler, John L.: Compressible-Flow Solutions for the Actuator Disk. NACA RM L53A07, 1953.

REPORT 1376

ELLIPTIC CONES ALONE AND WITH WINGS AT SUPERSONIC SPEEDS [1]

By LELAND H. JORGENSEN

SUMMARY

To help fill the gap in the knowledge of aerodynamics of shapes intermediate between bodies of revolution and flat triangular wings, force and moment characteristics for elliptic cones have been experimentally determined for Mach numbers of 1.97 and 2.94. Elliptic cones having cross-sectional axis ratios from 1 through 6 and with lengths and base areas equal to circular cones of fineness ratios 3.67 and 5 have been studied for angles of bank of 0° and 90°. Elliptic and circular cones in combination with triangular wings of aspect ratios 1 and 1.5 also have been considered. The angle-of-attack range was from 0° to about 16°, and the Reynolds number was 8×10^6, based on model length. In addition to the forces and moments at angle of attack, pressure distributions for elliptic cones at zero angle of attack have been determined.

The results of this investigation indicate that there are distinct aerodynamic advantages to the use of elliptic cones. With their major cross-sectional axes horizontal, they develop greater lift and have higher lift-drag ratios than circular cones of the same fineness ratio and volume. In combination with triangular wings of low aspect ratio, they also develop higher lift-drag ratios than circular cones with the same wings. For winged elliptic cones, this increase in lift-drag ratio results both from lower zero-lift drag and drag due to lift. Visual-flow studies indicate that, because of better streamlining in the crossflow plane, vortex flow is inhibited more for an elliptic cone with major axis in the plane of the wing than for a circular cone with the same wing. As a result, vortex drag resulting from lift is reduced. Shifts in center of pressure with changes in angle of attack and Mach number are small and about the same as for circular cones.

Comparisons of theoretical and experimental force and moment characteristics for elliptic cones indicate that simple linearized (flat plate) wing theory is generally adequate even for relatively thick cones. Zero-lift pressure distributions and drag can be computed using Van Dyke's second-order slender-body theory. For winged circular cones, a modification of the slender-body theory of NACA Rep. 962 results in good agreement of theory with experiment.

INTRODUCTION

Various theoretical studies have indicated that elliptical cones have important aerodynamic advantages over circular cones at supersonic speeds. At zero angle of attack, the pressure drag of a cone of given length and base area decreases as the cross section is changed from circular to flat elliptical (refs. 1 to 4). At angle of attack, it can be shown from theory that elliptic cones produce large gains in lift and lift-drag ratio compared to circular cones (refs. 1, 5, and 6).

Although there is a moderate amount of theoretical information applicable to elliptic cones (particularly for the case of zero incidence), relatively little experimental data have been obtained. There are some pressure-distribution data in references 7 and 8. Experimental results presented by Rogers and Berry (ref. 9) include pressure-distribution and force data for a series of relatively flat winglike elliptic cones having ratios of major-to-minor axes between 5.4 and 23.1.

In order to provide information for more bodylike shapes (shapes which might be adaptable for use for manned entry into planetary atmospheres), the present experimental investigation was performed. The aerodynamic characteristics of a family of elliptic cones having ratios of major-to-minor axes between 1 and 6 were measured. Also included in this investigation is a study of the effects of adding triangular wings to circular and elliptic cones of given length and base area. Tests were made for Mach numbers of 1.97 and 2.94. The purpose of the present report is to discuss the resulting aerodynamic data and to compare theoretical and experimental results.

SYMBOLS

A	aspect ratio, $\frac{4s^2}{A_w}$
A_b	base area of cone, πab
A_p	plan-form area of cone
A_w	total wing plan-form area (including the part within the body)
a	semimajor axis of elliptic cone
b	semiminor axis of elliptic cone
c	$\sqrt{a^2\cos^2\phi+b^2\sin^2\phi}$
C_{d_c}	crossflow drag coefficient of cylinder
C_D	drag coefficient, $\frac{D}{q_\infty A_b}$
C_{D_0}	drag coefficient at zero lift
C_L	lift coefficient, $\frac{L}{q_\infty A_b}$
$C_{L_{B_1}}$	lift coefficient for basic circular cone
C_m	pitching-moment coefficient about base of cone, $\frac{\text{pitching moment}}{q_\infty A_b l}$

[1] Supersedes NACA Technical Note 4045 by Leland H. Jorgensen, 1957.

526597—60——64

$C_{m_{B_1}}$ pitching-moment coefficient about base of basic circular cone

C_p pressure coefficient, $\frac{p-p_\infty}{q_\infty}$

D drag

d diameter of cone at base

E complete elliptic integral of second kind

l length of cone

L lift

$\left(\frac{L}{D}\right)_M$ maximum lift-drag ratio

$\left(\frac{L}{D}\right)_{M_{B_1}}$ maximum lift-drag ratio for basic circular cone

M_∞ free-stream Mach number

p_∞ free-stream static pressure

q_∞ free-stream dynamic pressure

s wing semispan, measured from body center line

x, y, z Cartesian coordinates as shown in figure 1

x_p center of pressure measured form cone vertex

y_s half the distance between flow separation lines on the cone at the base

y_v half the distance between vortex traces on the cone at the base

α angle of attack measured between body longitudinal axis and free-stream direction (see fig. 1)

β $\sqrt{M_\infty^2-1}$

ϵ wing semiapex angle

θ_s angle measured around base ellipse from horizontal base axis to flow separation line on cone

θ_v angle measured around base ellipse from horizontal base axis to vortex trace on cone

λ modification factor to take account of finite wing aspect ratios

ϕ angle of bank about body longitudinal axis (see fig. 1)

The positive directions of the angles and coefficients are shown in figure 1.

APPARATUS AND TESTS

WIND TUNNELS

The experimental investigation was conducted in the Ames 1- by 3-foot supersonic wind tunnels no. 1 and no. 2. Tunnel no. 1 is a closed-circuit, continuous-operation type and is equipped with a flexible-plate nozzle that provides a variation of Mach number from 1.4 to 4.0. The Reynolds number is changed by varying the total pressure within the approximate limits of 1/5 of an atmosphere to 4 atmospheres. Tunnel no. 2 is a nonreturn, intermittent-operation type and is also equipped with a flexible-plate nozzle that provides a variation of Mach number from 1.4 to 3.8. Air for this tunnel is obtained from the Ames 12-foot wind tunnel at a pressure of about 6 atmospheres and is expanded through the nozzle to the atmosphere. Changes in Reynolds number are obtained by varying the total pressure.

Except for vapor-screen tests, the water content of the air in the 1- by 3-foot wind tunnels is maintained at less than 0.0003 pound of water per pound of dry air. Consequently, the effect of humidity on the flow is negligible.

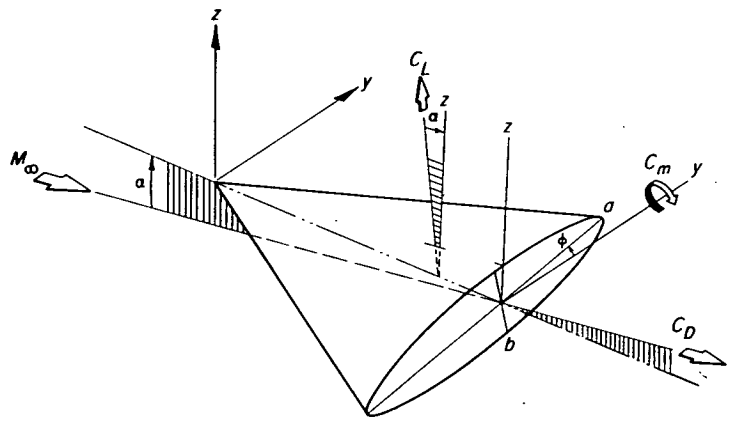


FIGURE 1.—Coordinate system and sign convention.

MODELS

Plan-form and end views of the models studied are shown in figure 2. Three elliptic-cone bodies (B_2, B_3, and B_4) with a/b ratios of 1.5, 3, and 6 had the same length and base area as the basic circular cone (B_1). Hence, the fineness ratio of $l/d=3.67$ for the circular cone was also the equivalent fineness ratio for these elliptic cones. In order to check the effect of fineness ratio on the aerodynamic characteristics, an additional elliptic cone body (B_5) with an a/b ratio of 1.5 and a fineness ratio of 5 was also studied.

In addition to being tested alone, bodies B_1 ($a/b=1$, $l/d=3.67$) and B_3 ($a/b=3$, $l/d=3.67$) were also tested with triangular wings (W_1 and W_2) of aspect ratio 1 and 1.5. With the major cross-sectional axis (a) of body B_3 mounted horizontally in line with the wings, the configurations are designated as $B_{3H}W_1$ and $B_{3H}W_2$. With the major axis of B_3 vertical to the wings, the configurations are designated as $B_{3V}W_1$ and $B_{3V}W_2$. The wing sections were flat plates with leading and trailing edges beveled as shown in figure 2.

All of the models were sting supported from the rear. Bodies B_3 and B_4 had pressure orifices distributed over the surfaces and were adaptable for both force and pressure-distribution tests.

TESTS

Force and pressure-distribution tests.—Force data were obtained in tunnel no. 2 for all the models at free-stream Mach numbers of 1.97 and 2.94. The Reynolds number, which was maintained constant for all tests, was 8×10^6 based on body length. Measurements of lift, drag, and pitching moment were taken for angles of attack from 0° to about 16°. The elliptic-cone bodies were tested at angles of bank of 0° and 90° (i. e., for $\phi=0°$ and 90° as shown in fig. 1). The winged elliptic cones were tested only with their wings at $\phi=0°$. Base pressures from eight orifices spaced around the inside of the base periphery of each body were measured by photographic recording from a multiple-tube manometer board.

Pressure-distribution data were obtained in tunnel no. 1 for bodies B_3 and B_4 at zero angle of attack and Mach number 1.97. The surface pressures were measured by photographic recording from a multiple-tube manometer system. The

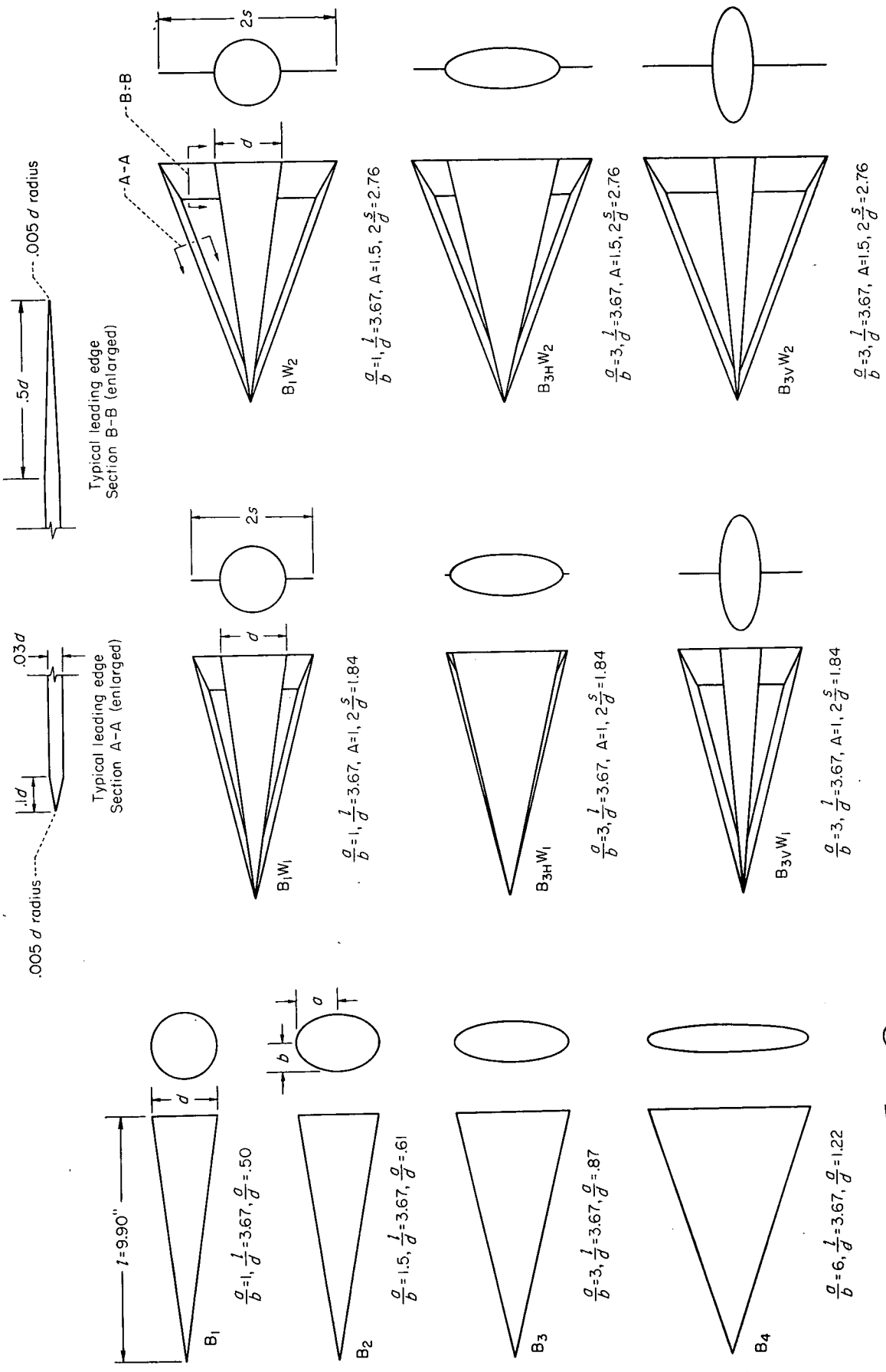


FIGURE 2.—Plan-form and end views of configurations

repeatability of both force and pressure measurements was checked by making reruns for several configurations.

Vapor-screen tests.—To make the vortices shed from the models at angle of attack visible, the "vapor-screen" method (ref. 10) was used. With this technique, water vapor is added to the tunnel air stream. This water vapor condenses in the wind-tunnel test section to produce a fine fog. A narrow sheet of bright light, produced by high-intensity mercury-vapor lamps, is projected through the tunnel window in a plane perpendicular to the model longitudinal axis. This plane of light appears as a uniformly lighted screen of fog particles in the absence of a model. However, with a model in the stream, the flow about the model affects the light scattered by the water particles, and vortices shed from the model are visible as dark spots.

Vapor-screen tests were made in tunnel no. 1 for various models at Mach number 1.97 and a Reynolds number of 8×10^6. With the models at several angles of attack, the vortex patterns were photographed with a camera mounted inside the wind tunnel 9 inches downstream from the base of the models.

Sublimation tests.—Another method of flow visualization that was used was the sublimation technique (ref. 11) for determining boundary-layer transition, flow separation, and vortex traces on the surfaces of the models. The models of this investigation, which were initially painted black, were sprayed with a 4-percent solution of acenaphthene in petroleum ether. This solution dries on contact with the model surface and presents a white appearance. The wind tunnel is operated, and as the process of sublimation takes place with the model in the tunnel, evidences of boundary-layer transition, separation, and vortex flow appear on the model. Regions of high surface shear, such as turbulent boundary layers and vortex traces, show up as dark areas, whereas regions of laminar flow and separation remain white. All sublimation tests were made in tunnel no. 1 at Mach number 1.97.

REDUCTION AND ACCURACY OF DATA

All of the pressure-distribution, force, and moment data have been reduced to coefficient form and are referred to the coordinate system shown in figure 1. The base drag was computed using the average base pressure and was subtracted from the total axial-force balance measurement, so that the data presented are for forces ahead of the body base.

The accuracy of the final data is affected by uncertainties in the measurement of the pressures, forces, and moments, and in the determination of the stream static and dynamic pressures used in reducing the data to coefficient form. These individual uncertainties led to estimated uncertainties which are listed in the following table:

Coefficient	Uncertainty
C_p	±0.004
C_L	±.02
C_D	±.004
C_m	±.02
x_p/l	±.02

The values of angle of attack are estimated to be accurate to within ±0.1°. The variation of the free-stream Mach number in the region of the test models was less than ±0.01 at Mach number 1.97 and less than ±0.02 at Mach number 2.94.

RESULTS AND DISCUSSION

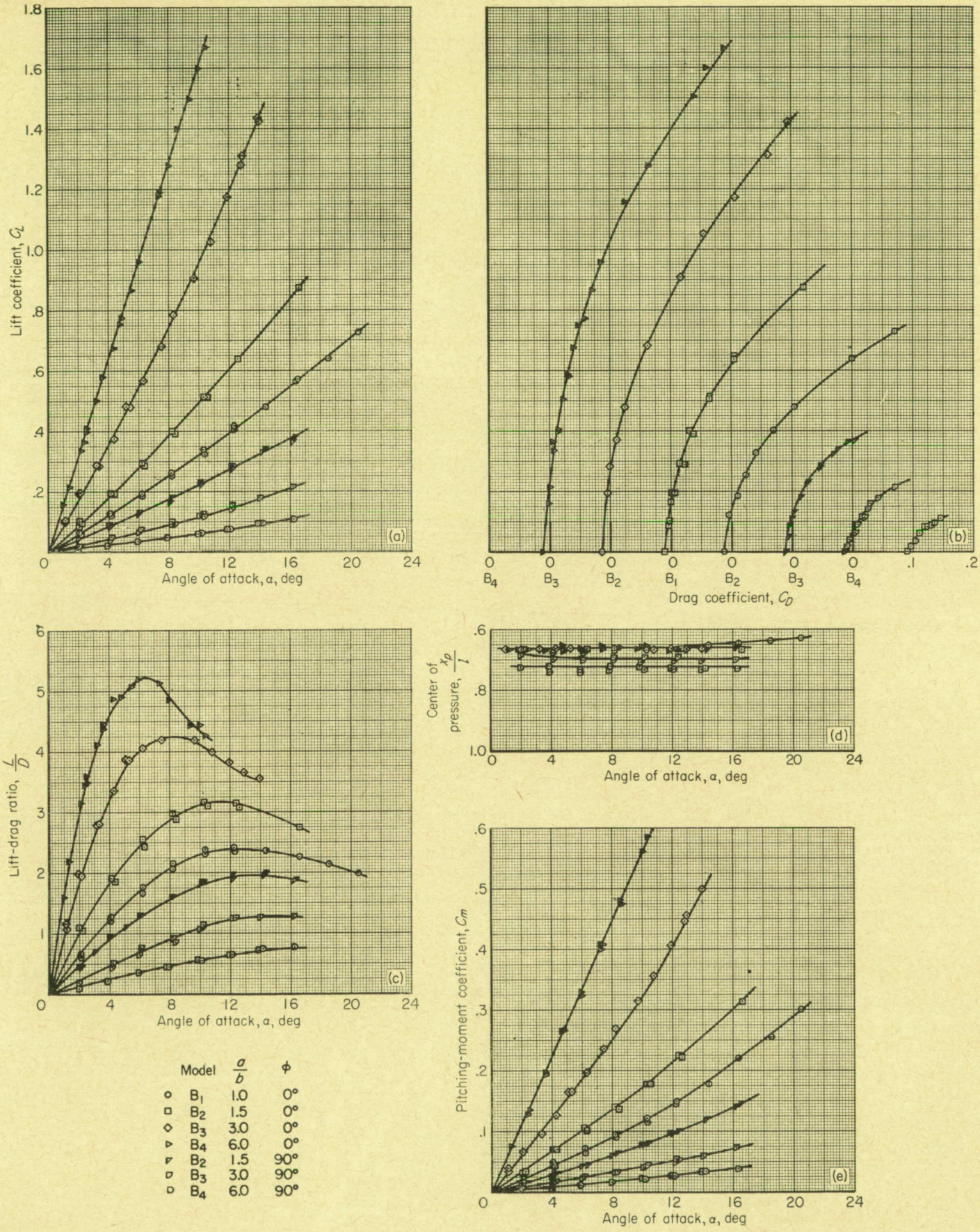
This section of the report is divided into three parts: (1) experimental force and moment characteristics; (2) comparisons of theoretical and experimental pressure distributions, forces, and moments; and (3) visual observations of the flow over various models. The experimental force and moment characteristics are presented in figures 3 through 9; comparisons of theory and experiment are presented in figures 10 through 17; and photographs and measurements from the visual-flow studies are presented in figures 18 through 22.

EXPERIMENTAL FORCE AND MOMENT CHARACTERISTICS

Effect of axis ratio (a/b).—The effect of change in cross-sectional axis ratio (a/b) on the aerodynamic characteristics of the elliptic cones of fineness ratio 3.67 is presented in figures 3 and 4 for Mach numbers 1.97 and 2.94. For the elliptic cones of figures 3 and 4 the lengths and base areas are constant; hence, increases in a/b result in increases in plan-form area with the major axis, a, horizontal ($\phi=0°$) and decreases in plan-form area with the major axis vertical ($\phi=90°$). In view of this fact, it is not surprising that with increase in a/b the lift coefficients (which are referred to base area) increase appreciably at all angles of attack for $\phi=0°$ and decrease for $\phi=90°$ (figs. 3(a) and 4(a)). The question arises, then, of whether or not the aerodynamic efficiency as determined by the lift-drag ratio also can be markedly increased by increasing a/b. From figures 3(c) and 4(c) it is clear that, at least throughout the angle-of-attack range investigated, significant gains in lift-drag ratio can be realized by increasing a/b from 1 to 6. In fact, by merely changing a/b from 1 to 1.5 a gain in maximum L/D of about 25 percent results. Furthermore, increasing a/b from 1 to 3 results in about a 75-percent increase in maximum L/D at Mach number 1.97 and in about a 60-percent increase at Mach number 2.94. It is clear that, in many cases where a body of given volume is required, it can be aerodynamically beneficial to deviate from a circular cross section.

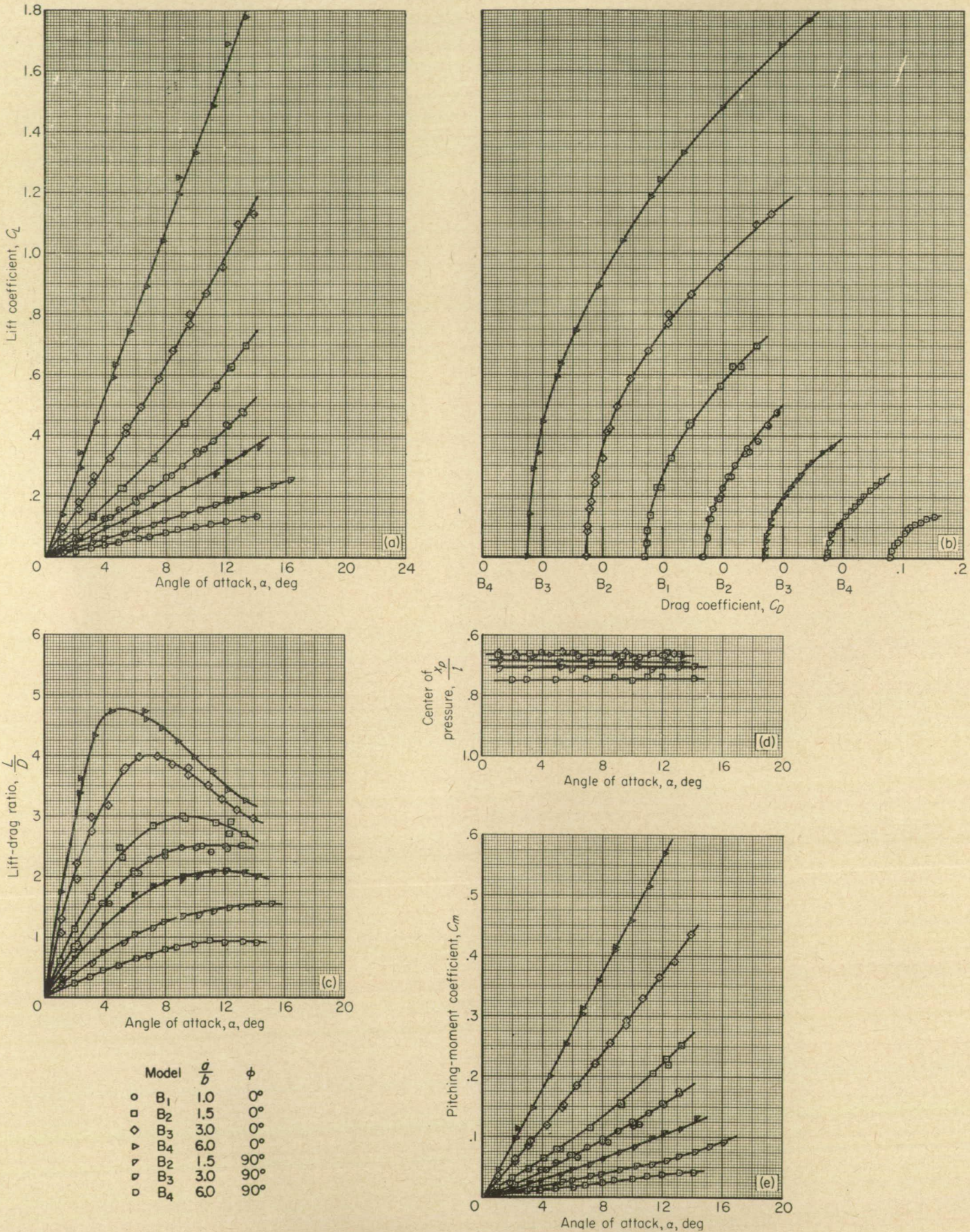
The effect of axis ratio on pitching moment and center of pressure is shown in figures 3(d), 3(e), 4(d), and 4(e). For all of the elliptic cones the center of pressure moves very little with angle of attack. With the major axis horizontal the center of pressure changes little with a/b and, as for the circular cone, is located at about the centroid of plan-form area for both Mach numbers 1.97 and 2.94. However, with the cones rotated to $\phi=90°$, the center of pressure moves rearward from the centroidal position with increase in a/b from 1 to 6.

Effect of fineness ratio.—The effect of change in fineness ratio on the aerodynamic characteristics of elliptic cones of $a/b=1.5$ is illustrated in figure 5. Data are compared for body B_2 of $l/d=3.67$ and body B_5 of $l/d=5$ tested at Mach numbers 1.97 and 2.94. For angles of attack to about 8°



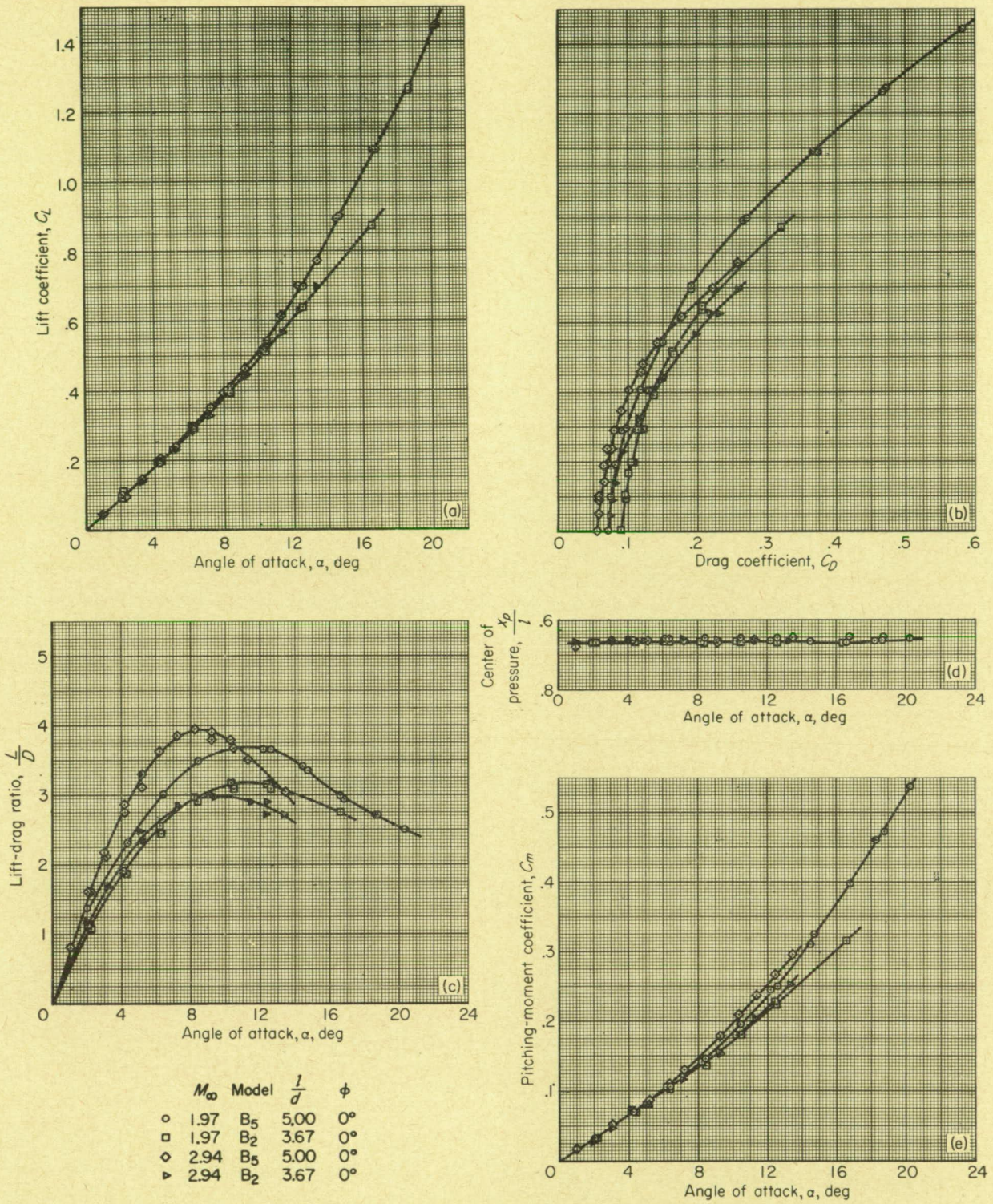
(a) Lift.
(b) Lift-drag polar.
(c) Lift-drag ratio.
(d) Center of pressure.
(e) Pitching moment.

FIGURE 3.—Effect of change in axis ratio (a/b) on the aerodynamic characteristics of elliptic cones; $l/d=3.67$, $M\infty=1.97$.



(a) Lift.
(b) Lift-drag polar.
(c) Lift-drag ratio.
(d) Center of pressure.
(e) Pitching Moment.

FIGURE 4.—Effect of change in axis ratio (a/b) on the aerodynamic characteristics of elliptic cones; $l/d=3.67$, $M_\infty=2.94$.



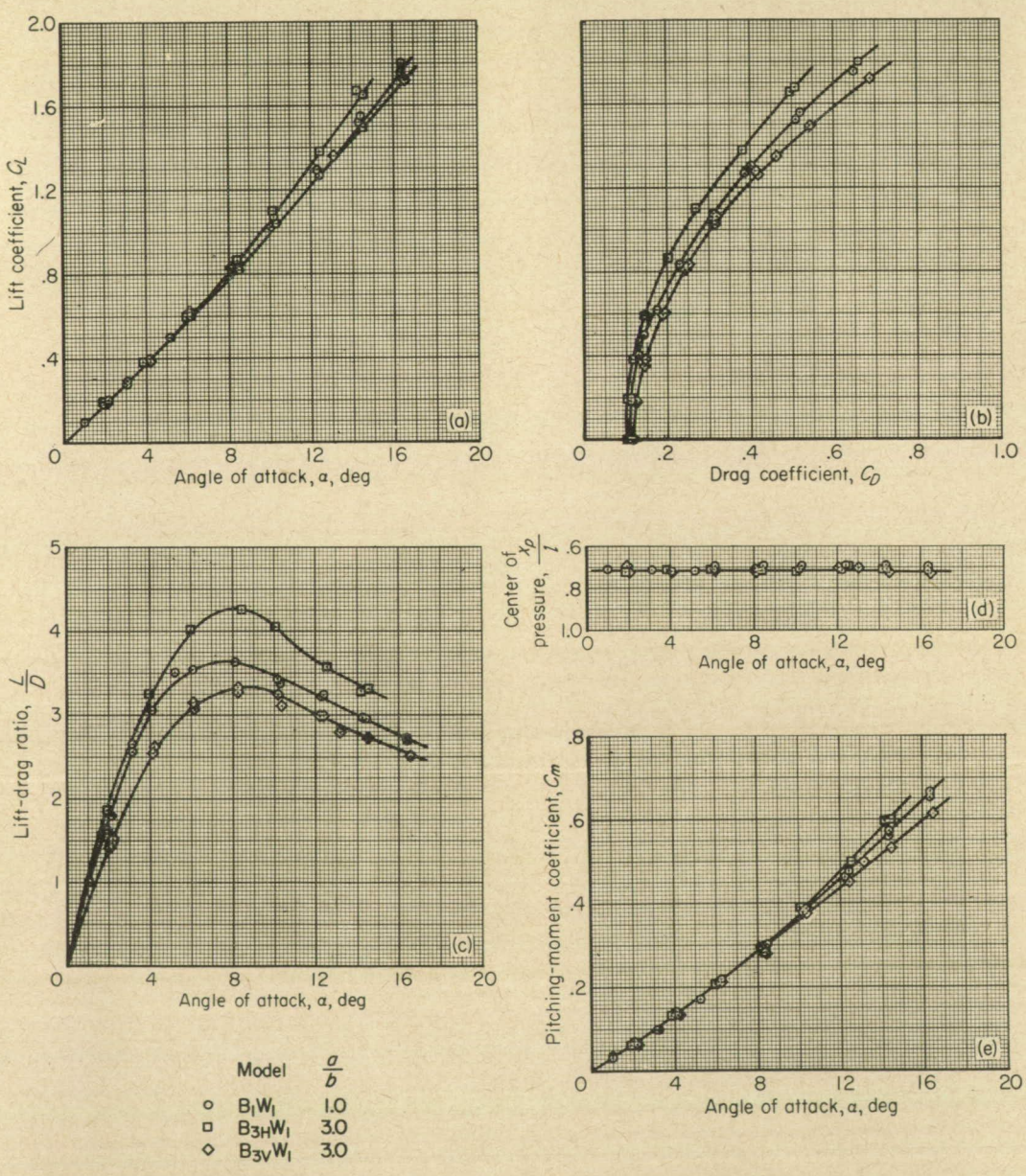
(a) Lift.
(b) Lift-drag polar.
(c) Lift-drag ratio.
(d) Center of pressure.
(e) Pitching moment.

FIGURE 5.—Effect of change in fineness ratio on the aerodynamic characteristics of elliptic cones of $a/b=1.5$.

there is little effect of fineness ratio on the lift (fig. 5 (a)). At higher angles, however, the lift coefficients are greater for the more slender cone (B_5). For all values of C_L the drag coefficients for B_5 were at least 20 percent lower than for B_2 (fig. 5 (b)). It is not surprising, then, that an increase in fineness ratio also results in substantially higher values of maximum lift-drag ratio. (See fig. 5 (c).) Although the lift, drag, and pitching-moment results were affected by change in fineness ratio, there was no effect on center of pressure, x_p/l (fig. 5 (d)).

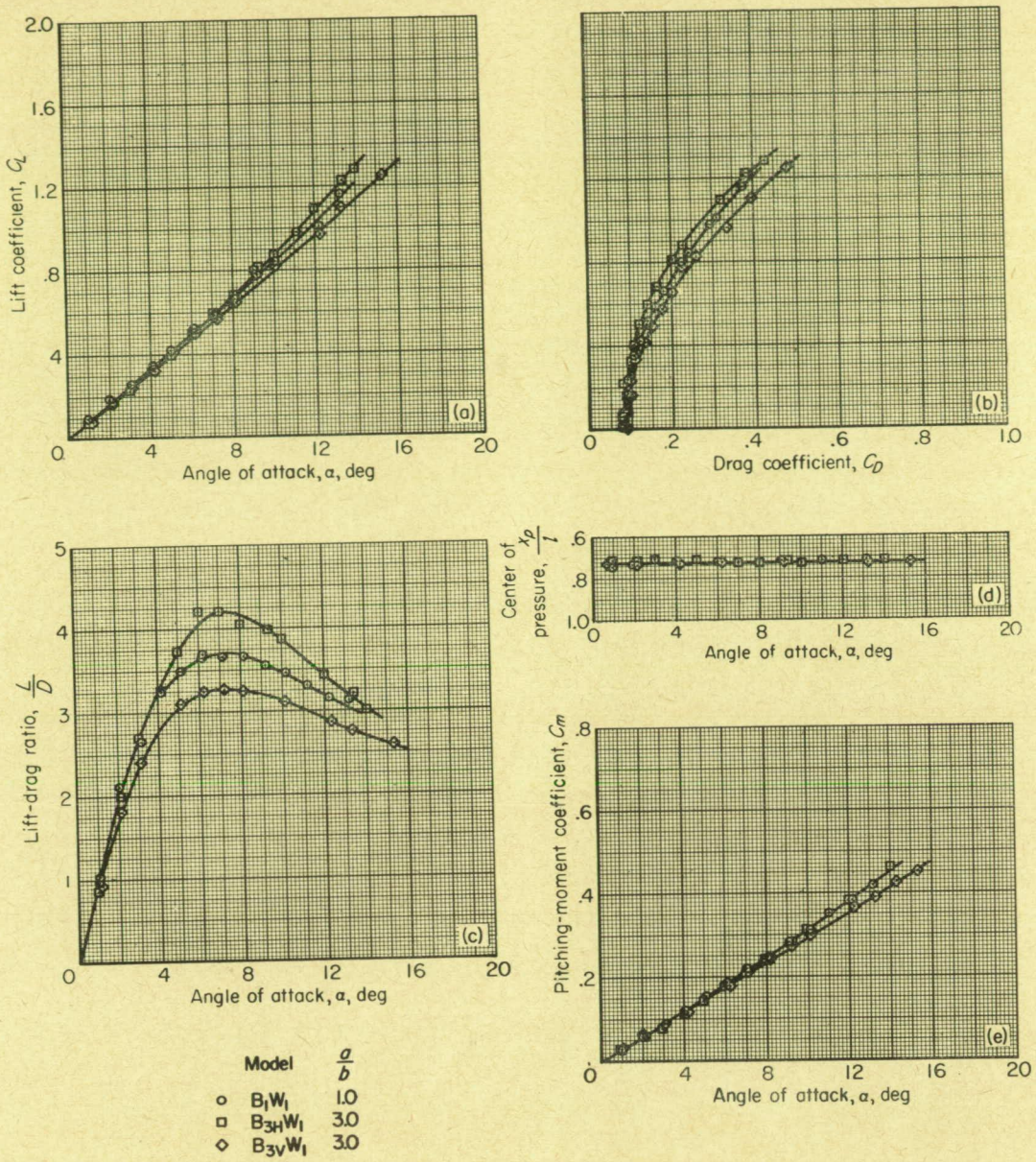
It is interesting to note that there is an effect of Mach number on maximum lift-drag ratio which depends upon fineness ratio. For body B_2 of $l/d=3.67$ the maximum value of L/D decreases with increase in Mach number from 1.97 to 2.94, whereas for body B_5 of $l/d=5$ the maximum value of L/D increases (fig. 5 (c)).

Effect of axis ratio (a/b) and arrangement for winged elliptic cones.—For conical bodies alone it has been shown that use of elliptic cross sections results in worthwhile gains in lift and lift-drag ratio. It is not clear, however, whether significant gains also can be realized through the use of elliptic cross sections for winged conical bodies. The test results presented in figures 6 through 9 demonstrate that important aerodynamic advantages can be obtained through proper arrangement of an elliptic body with a triangular wing. For instance, as shown in figures 6 and 7, gains in lift and large gains in lift-drag ratio result from using an elliptic body ($a/b=3$) with the major axis, a, in the plane of an aspect ratio 1 wing in preference to a circular body with the same wing. (Compare results for $B_{3H}W_1$ and B_1W_1.) However, with the elliptic body rotated 90° so that the minor axis is in the plane of the wing (model $B_{3V}W_1$), a loss in lift-drag ratio



(a) Lift.
(b) Lift-drag polar.
(c) Lift-drag ratio.
(d) Center of pressure.
(e) Pitching moment.

FIGURE 6.—Effect of change in axis ratio (a/b) and arrangement on the aerodynamic characteristics of elliptic cones with wings of aspect ratio 1; $M_\infty = 1.97$.

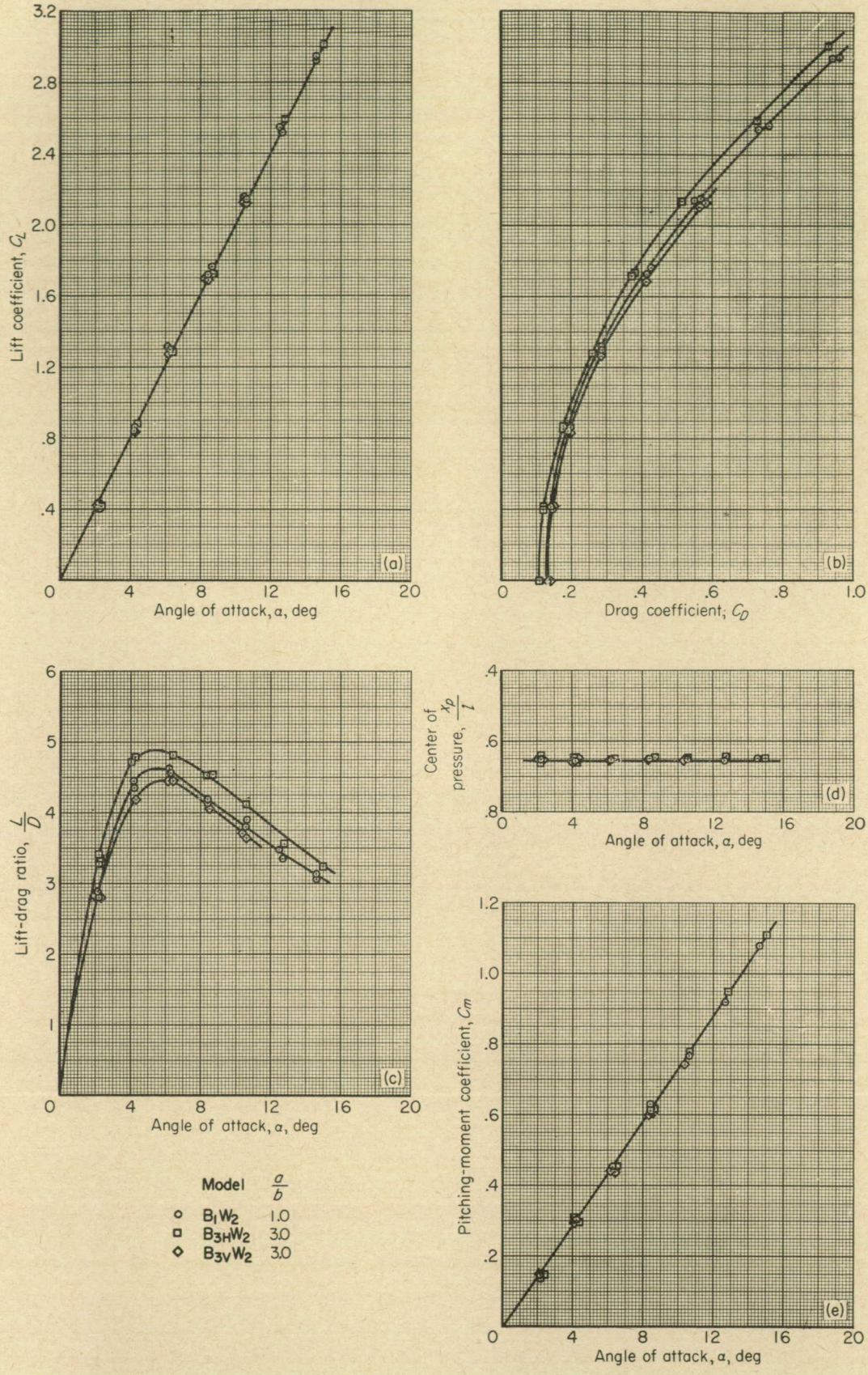


(a) Lift.
(b) Lift-drag polar.
(c) Lift-drag ratio.
(d) Center of pressure.
(e) Pitching moment.

FIGURE 7.—Effect of change in axis ratio (a/b) and arrangement on the aerodynamic characteristics of elliptic cones with wings of aspect ratio 1; $M_\infty = 2.94$.

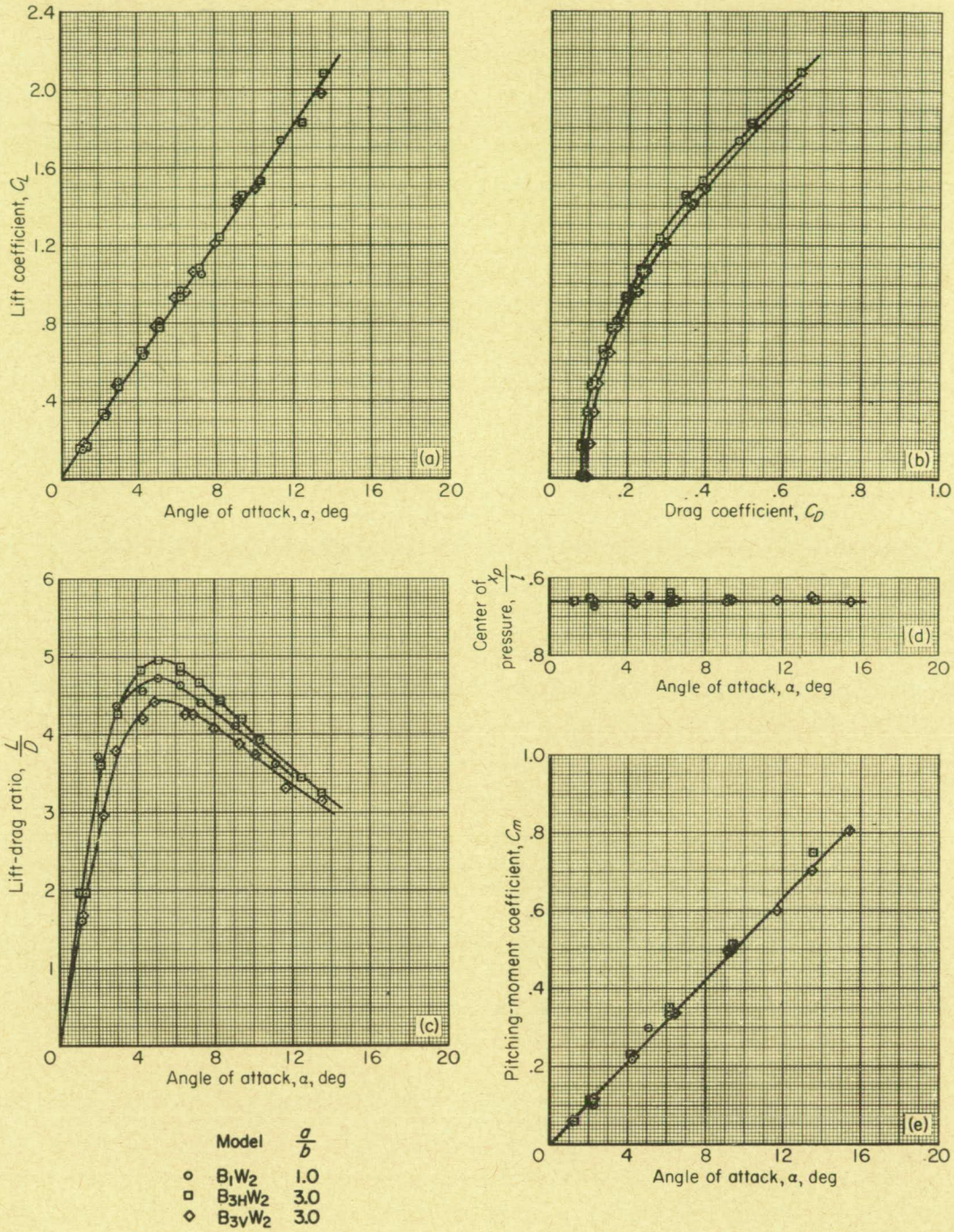
results. The gain in L/D for $B_{3H}W_1$ and loss in L/D for $B_{3V}W_1$ is primarily attributable to differences in drag (figs. 6 (b) and 7 (b)). Because of less wetted surface area and hence less skin friction, $B_{3H}W_1$ has slightly lower drag at zero lift than the other configurations. With increase in lift, $B_{3H}W_1$ still has the least drag, but the difference in drag between the models increases, resulting in a significantly higher value of maximum L/D for $B_{3H}W_1$ than for B_1W_1 or $B_{3V}W_1$. For the same bodies with a wing of aspect ratio 1.5 instead of 1, the differences between the maximum lift-drag ratios are diminished. (See figs. 8 (c) and 9 (c).) However, the results still significantly favor a body of elliptic cross section with the major axis in the plane of the wing.

The maximum lift-drag ratios were higher for the elliptic cones with major axes in line with the wings, primarily because they have less zero-lift drag and develop less drag due to lift. It is believed that the lower drag due to lift can be attributed to less vortex drag associated with the formation of vortices at angle of attack. From visual observations of the flow over the models by the vapor-screen technique, it was found that, at least for angles of attack from 0° to about 10°, the formation of vortices was inhibited more with the major axis of an elliptic cone in line with a wing (model $B_{3H}W_1$) than perpendicular to it (model $B_{3V}W_1$). Vortices appeared to separate from $B_{3V}W_1$ and B_1W_1 at lower angles of attack than from $B_{3H}W_1$. It is interesting to note that, as shown in the vapor-screen photographs of figure 20 (a) to be discussed later, the vortices shed from $B_{3V}W_1$ and B_1W_1 at $\alpha=10°$ appeared to be more completely formed and rolled up than those for $B_{3H}W_1$. As shown in figures 6 and 7, the drag due to lift is higher for $B_{3V}W_1$ and B_1W_1 at $\alpha=10°$ than for $B_{3H}W_1$. Apparently because of better streamlining in



(a) Lift.
(b) Lift-drag polar.
(c) Lift-drag ratio.
(d) Center of pressure.
(e) Pitching moment.

FIGURE 8.—Effect of change in axis ratio (a/b) and arrangement on the aerodynamic characteristics of elliptic cones with wings of aspect ratio 1.5; $M_\infty = 1.97$.



(a) Lift.
(b) Lift-drag polar.
(c) Lift-drag ratio.
(d) Center of pressure.
(e) Pitching moment.

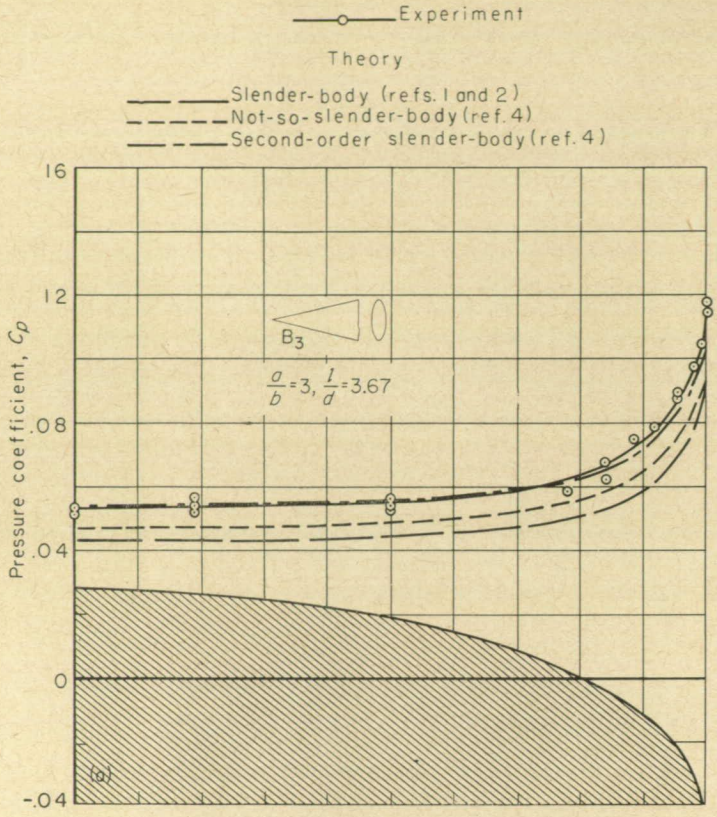
FIGURE 9.—Effect of change in axis ratio (a/b) and arrangement on the aerodynamic characteristics of elliptic cones with wings of aspect ratio 1.5; $M_\infty = 2.94$.

the crossflow plane, the vortex formation is inhibited and the drag due to lift is reduced with the major axis of the elliptic cone in line with the wing.

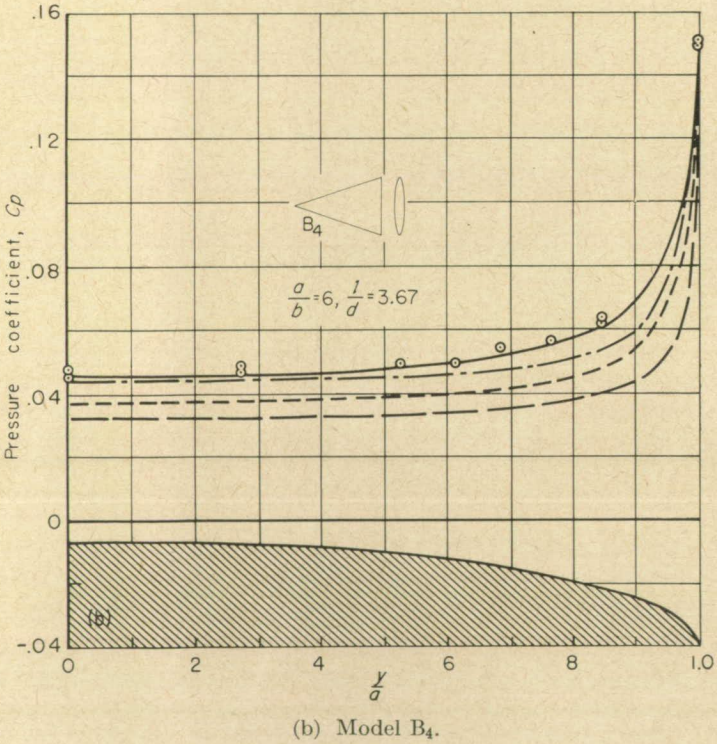
COMPARISONS OF THEORETICAL AND EXPERIMENTAL PRESSURE DISTRIBUTIONS, FORCES, AND MOMENTS

In this section of the report, theoretical methods of estimating the aerodynamic characteristics are assessed by comparison of theoretical results with experimental data. All comparisons are presented in figures 10 through 17 and are discussed in the following paragraphs.

Pressure distributions and drag of elliptic cones at zero angle of attack.—For elliptic cones of a/b of 3 and 6 (B_3 and B_4) theoretical and experimental pressure distributions for a Mach number of 1.97 are compared in figure 10. The pressure coefficients are plotted as a function of lateral distance, y/a, over a quadrant of each cone. The fact that the flow was conical is verified by the multiple experimental points at several y/a positions which were obtained at different longitudinal positions. The comparisons show that best agreement of theory with experiment is obtained through use



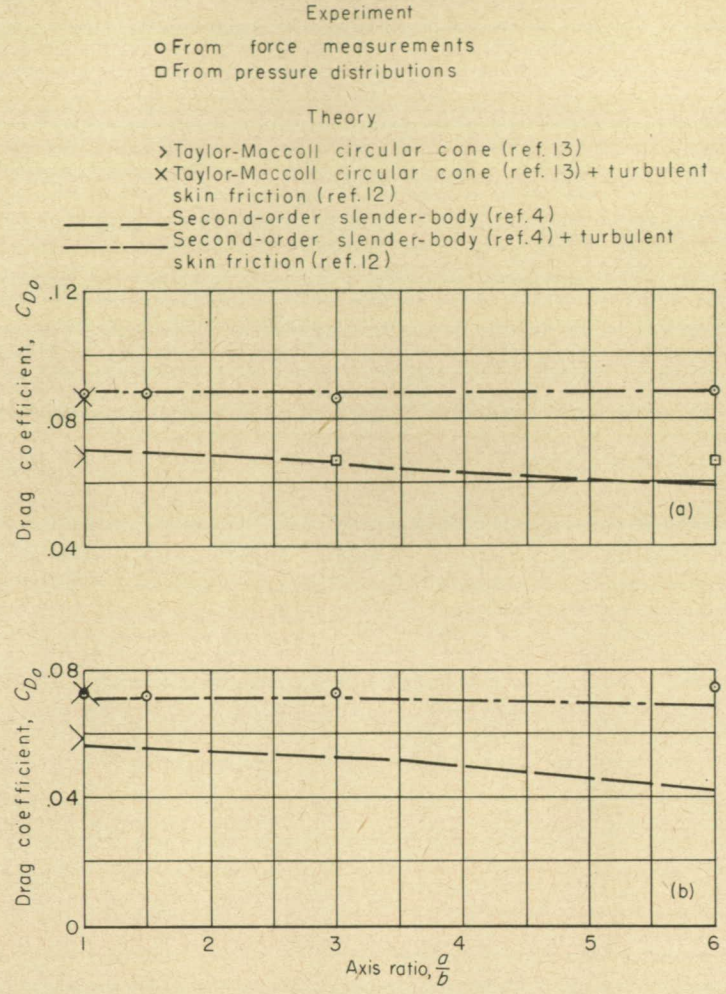
(a) Model B_3.



(b) Model B_4.

FIGURE 10.—Comparison of theoretical and experimental pressure distributions for elliptic cones at zero angle of attack; $M_\infty = 1.97$.

of the second-order slender-body theory of Van Dyke (ref. 4). Both the slender-body theory of references 1 and 2 and the not-so-slender-body theory of reference 4 result in pressure coefficients which are lower than those of experiment. Rogers and Berry (ref. 9) also found the agreement of second-order slender-body theory with experiment to be quite good for elliptic cones having even higher ratios of a/b.

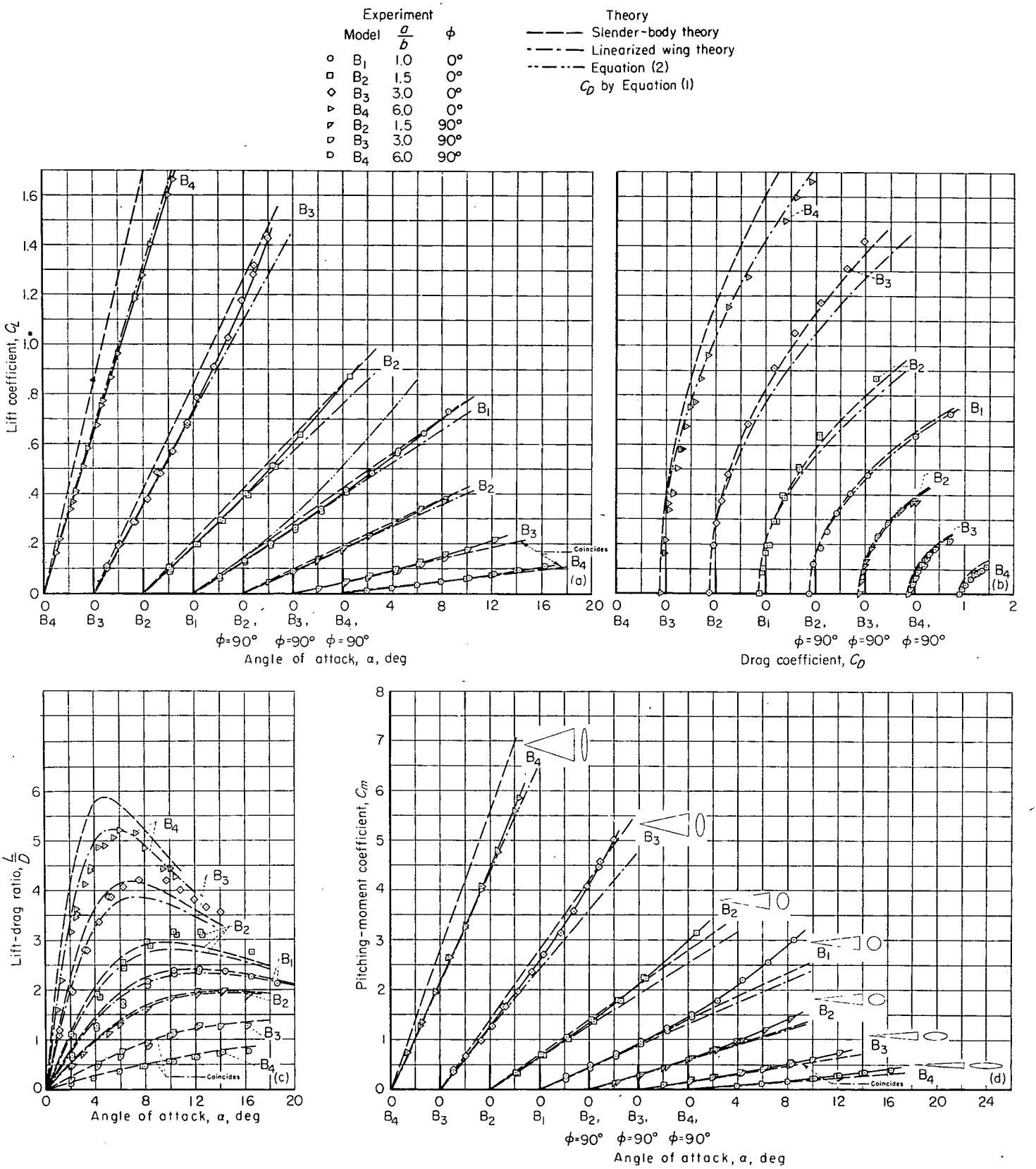


(a) $M_\infty = 1.97$.
(b) $M_\infty = 2.94$.

FIGURE 11.—Effect of change in axis ratio (a/b) on the zero-lift drag of elliptic cones.

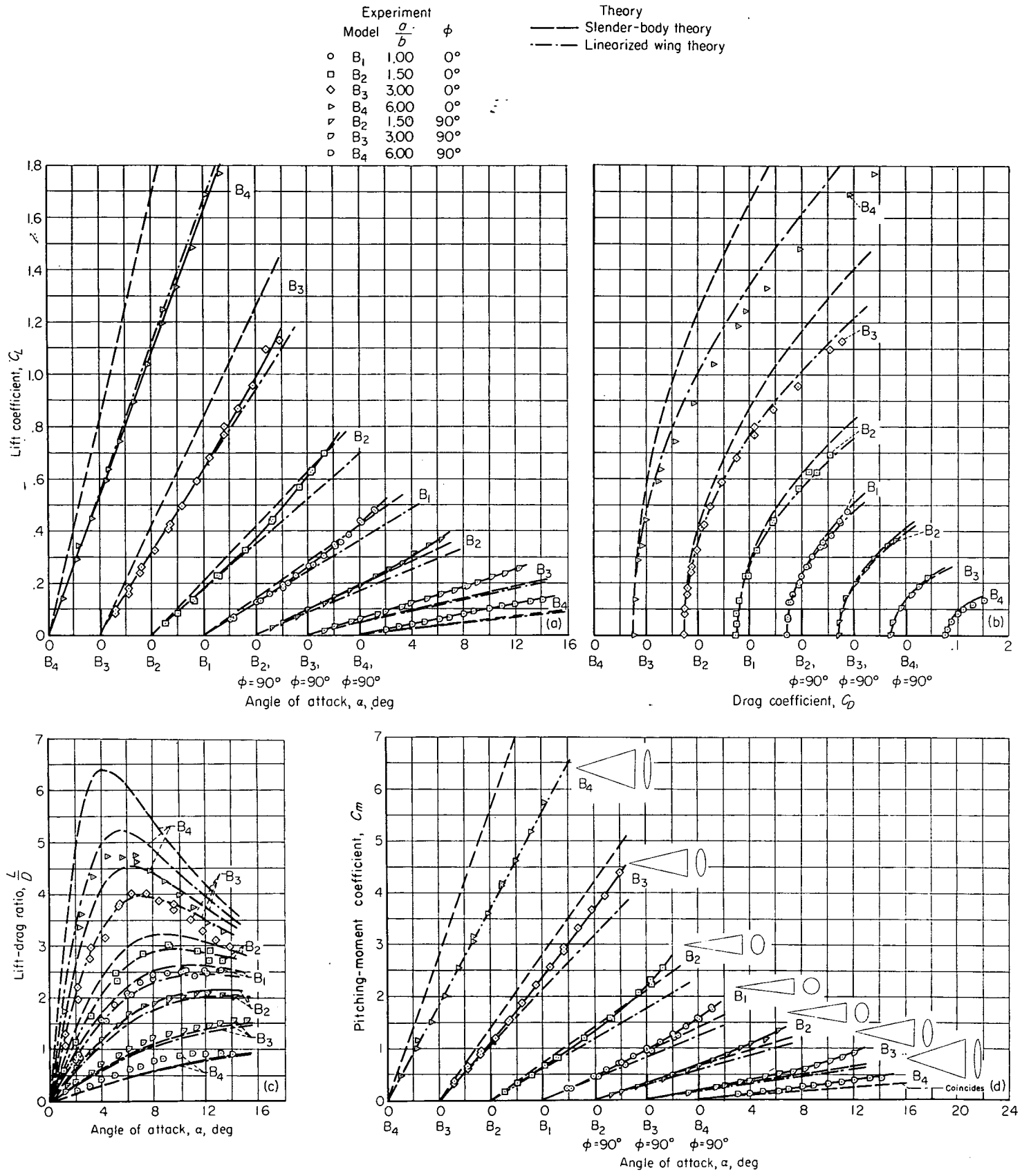
A study of the effect of change in axis ratio (a/b) on the zero-lift drag of elliptic cones is summarized in figure 11. The experimental results show that for these cones of equal volume and fineness ratio the drag remains essentially constant with change in axis ratio (a/b) at both Mach numbers 1.97 and 2.94. The boundary-layer flow over the models was mostly turbulent as shown by the sublimation results (to be discussed later) and as indicated by drag measurements with and without a transition ring at the nose of models B_1 and B_3. As seen in figure 11, the zero-lift drag is adequately predicted by the addition of turbulent skin friction (ref. 12) to pressure drag calculated by second-order slender-body theory (ref. 4). For the circular cone (B_1) the drag is also closely given by the addition of turbulent skin-friction drag (ref. 12) to pressure drag by Taylor-Maccoll cone theory (ref. 13). It is noted that the increase in skin-friction drag with increase in a/b (because of greater wetted surface area) is just large enough to nullify the drag saving from the decrease in pressure drag.

Forces and moments for elliptic cones.—Theoretical and experimental force and moment characteristics for elliptic cones at Mach numbers 1.97 and 2.94 are compared in figures 12 and 13. Both slender-body theory (refs. 1 and 5) and linearized wing theory (ref. 14) have been used in computing



(a) Lift.
(b) Lift-drag polar.
(c) Lift-drag ratio.
(d) Pitching moment.

FIGURE 12.—Comparison of theoretical and experimental aerodynamic characteristics of elliptic cones: $l/d=3.67$, $M_\infty=1.97$.



(a) Lift. (b) Lift-drag polar.
(c) Lift-drag ratio. (d) Pitching moment.

FIGURE 13.—Comparison of theoretical and experimental aerodynamic characteristics of elliptic cones; $l/d=3.67$, $M_\infty=2.94$.

the theoretical values of lift, drag, and pitching-moment coefficients shown. In computing the drag coefficient at angle of attack, the following expression has been used:

$$C_D = C_{D_0} + \left(\frac{dC_L}{d\alpha}\right)\alpha^2 \tag{1}$$

where

$$\frac{dC_L}{d\alpha} = \frac{C_L}{\alpha}$$

This relationship results from assuming that C_L varies linearily with α and that there is flow separation along the leading edges with complete loss of suction force. Theoretical values of C_D have been computed by assuming $dC_L/d\alpha$ to be given both by slender-body theory and by linearized wing theory. As discussed in the previous section, the drag coefficient at zero angle of attack (C_{D_0}) was computed from the addition of turbulent skin-friction drag (ref. 12) to pressure drag by second-order slender-body theory (ref. 4). As shown in figures 12 and 13, the agreement with experiment of the force and moment characteristics computed by means of linearized wing theory is generally quite good, especially for angles of attack from 0° to about 10°.

In figure 14 theoretical and experimental lift-curve slopes are compared. Results are correlated by plotting the parameter of lift-curve slope, $\frac{\beta}{4}\left(\frac{dC_L}{d\alpha}\right)\left(\frac{A_b}{A_p}\right)$, as a function of the ratio of leading-edge slope to Mach wave slope, $\beta \tan \epsilon$. Except for bodies B_3 and B_4 at $\phi=90°$ and $M_\infty=2.94$, the experimental data agree closely with linearized (flat plate) wing theory. Bodies $B_3(a/b=3)$ and B_4 $(a/b=6)$ banked to $\phi=90°$ are very thick in the lift direction, and at $M_\infty=2.94$ their lift-curve slopes are considerably higher than those given by either slender-body or linearized wing theory.

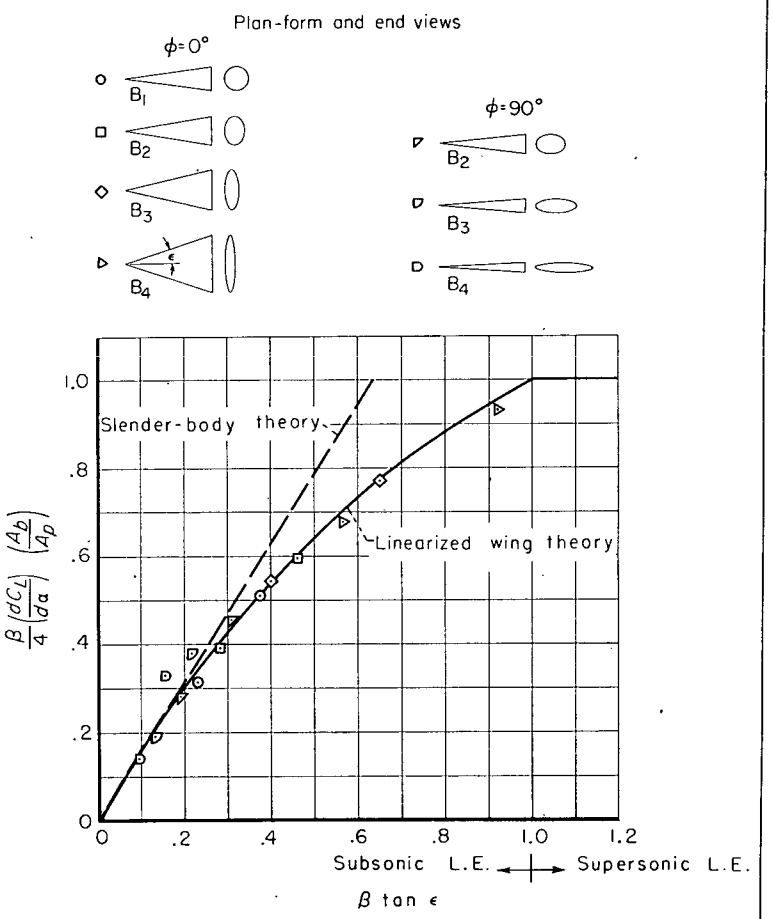


FIGURE 14.—Comparison of theoretical and experimental lift-curve slopes for elliptic cones at Mach numbers 1.97 and 2.94.

The nonlinearity of the experimental lift and pitching-moment curves (figs. 12 and 13), which becomes more evident at angles of attack greater than about 10°, probably results from viscous crossflow separation. Allen (ref. 10) has shown that for slender bodies of revolution an allowance for viscous effects can be computed. This is done by adding to the lift computed by slender-body or linearized theory an additional crossflow lift attributed to the separation effects of viscosity. Flax and Lawrence (ref. 15) have suggested the same procedure for low-aspect-ratio wings, and the resulting expression for lift coefficient is

$$C_L = \left(\frac{dC_L}{d\alpha}\right)_{\substack{linear\\theory}} \alpha + C_{d_c}\frac{A_p}{A_b}\alpha^2 \tag{2}$$

where C_{d_c} is the drag coefficient of a two-dimensional cylinder of equivalent cross section placed normal to a stream at a Mach number of $M_\infty \sin \alpha$. For the elliptic cones of this investigation, the lift is greatly overestimated by the use of equation (2). To illustrate this fact, the lift for the circular cone (B_1) computed using equation (2) is compared with experiment in figure 12 (a). The usual circular cylinder value of $C_{d_c}=1.2$ was used. Rogers and Berry (ref. 9) in their study of elliptic cones of higher ratios of a/b also found that equation (2) leads to lift coefficients larger than those given by experiment.

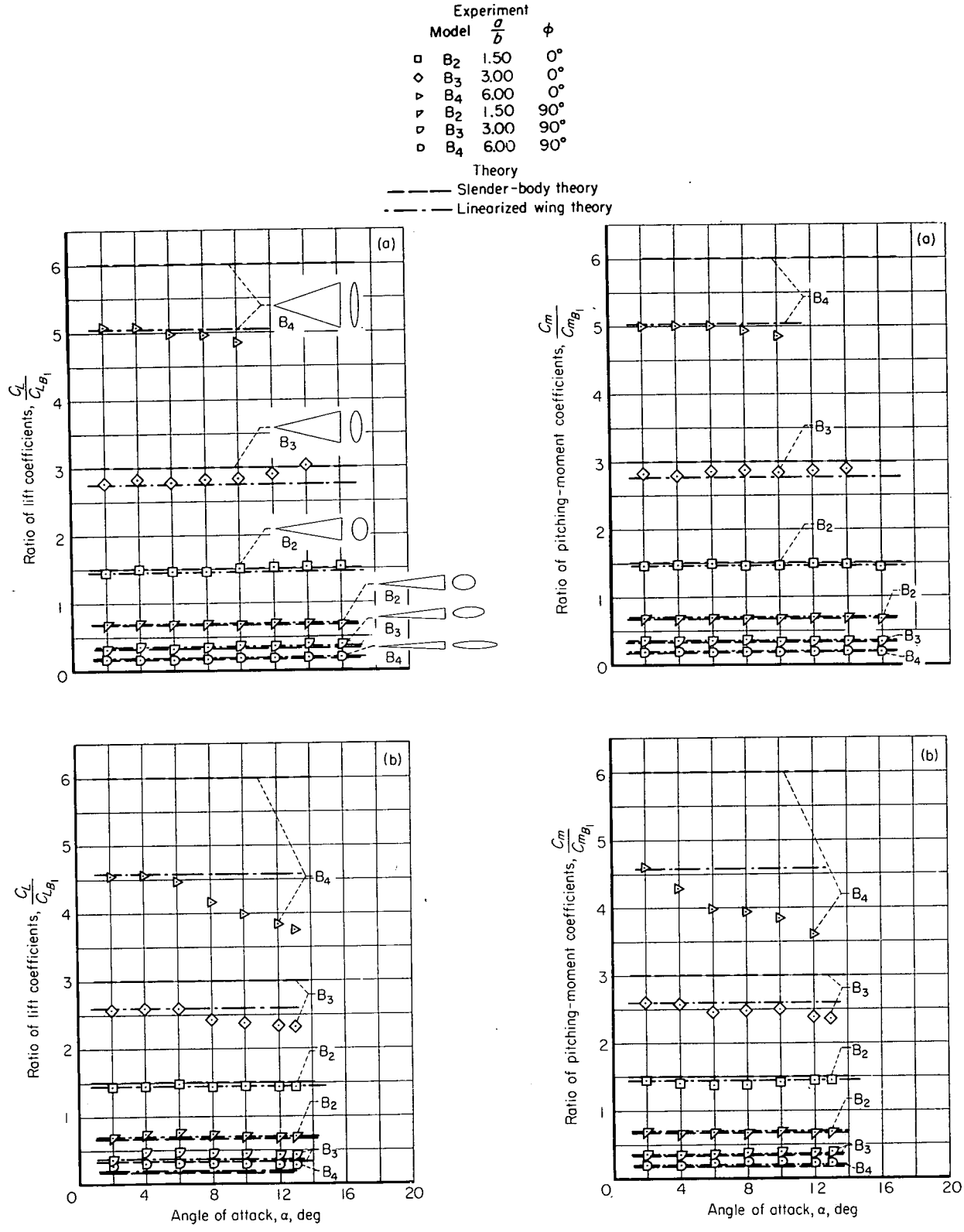
Although the lift and pitching-moment results of figures 12 and 13 show moderate nonlinearity with increase in α, the data can be simply correlated as shown in figure 15. Here the lift and pitching-moment coefficients for the elliptic cones are divided by the corresponding coefficients for the equivalent circular cone, and the ratios are plotted as a function of α. The results of the correlation demonstrate that, in general, $C_L/C_{L_{B_1}}$ and $C_m/C_{m_{B_1}}$ remain constant with change in α. Except for the elliptic cone of $a/b=6$ (B_4) at Mach number 2.94, the lift and moment ratios are given reasonably well by linearized wing theory.

Effect of axis ratio (a/b) on maximum lift-drag ratios of elliptic cones.—The effect of axis ratio (a/b) on the maximum lift-drag ratios of elliptic cones can be readily computed. From equation (1) the maximum lift-drag ratio is given by the relation

$$\left(\frac{L}{D}\right)_M = \frac{1}{2}\sqrt{\frac{C_L/\alpha}{C_{D_0}}} \tag{3}$$

If for cones of given fineness ratio it is assumed that C_{D_0} is constant with change in a/b (as suggested from the results of the present experiments), then the relative efficiency of an elliptic cone to a circular cone is expressed by the relation

$$\frac{(L/D)_M}{(L/D)_{M_{B_1}}} = \sqrt{\frac{C_L/\alpha}{(C_L/\alpha)_{B_1}}} \tag{4}$$



(a) $M_\infty = 1.97$.
(b) $M_\infty = 2.94$.

FIGURE 15.—Correlation of lift and pitching-moment data for elliptic cones.

For slender-body theory this ratio reduces to

$$\frac{(L/D)_M}{(L/D)_{M_{B_1}}}=\sqrt{\frac{a}{b}\cos^2\phi+\frac{b}{a}\sin^2\phi} \tag{5}$$

since

$$C_L=2\alpha\left(\frac{a}{b}\cos^2\phi+\frac{b}{a}\sin^2\phi\right)$$

In figure 16, computed values of $(L/D)_M$ and $(L/D)_M/(L/D)_{M_{B_1}}$ are compared with the experimental results for the cones of fineness ratio 3.67. The computations were made with values of C_L given both by slender-body theory and linearized wing theory. Since, as was shown in figure 11, the zero-lift drag was almost constant with change in a/b, average experimental values of C_{D_0} of 0.086 at $M_\infty=1.97$ and

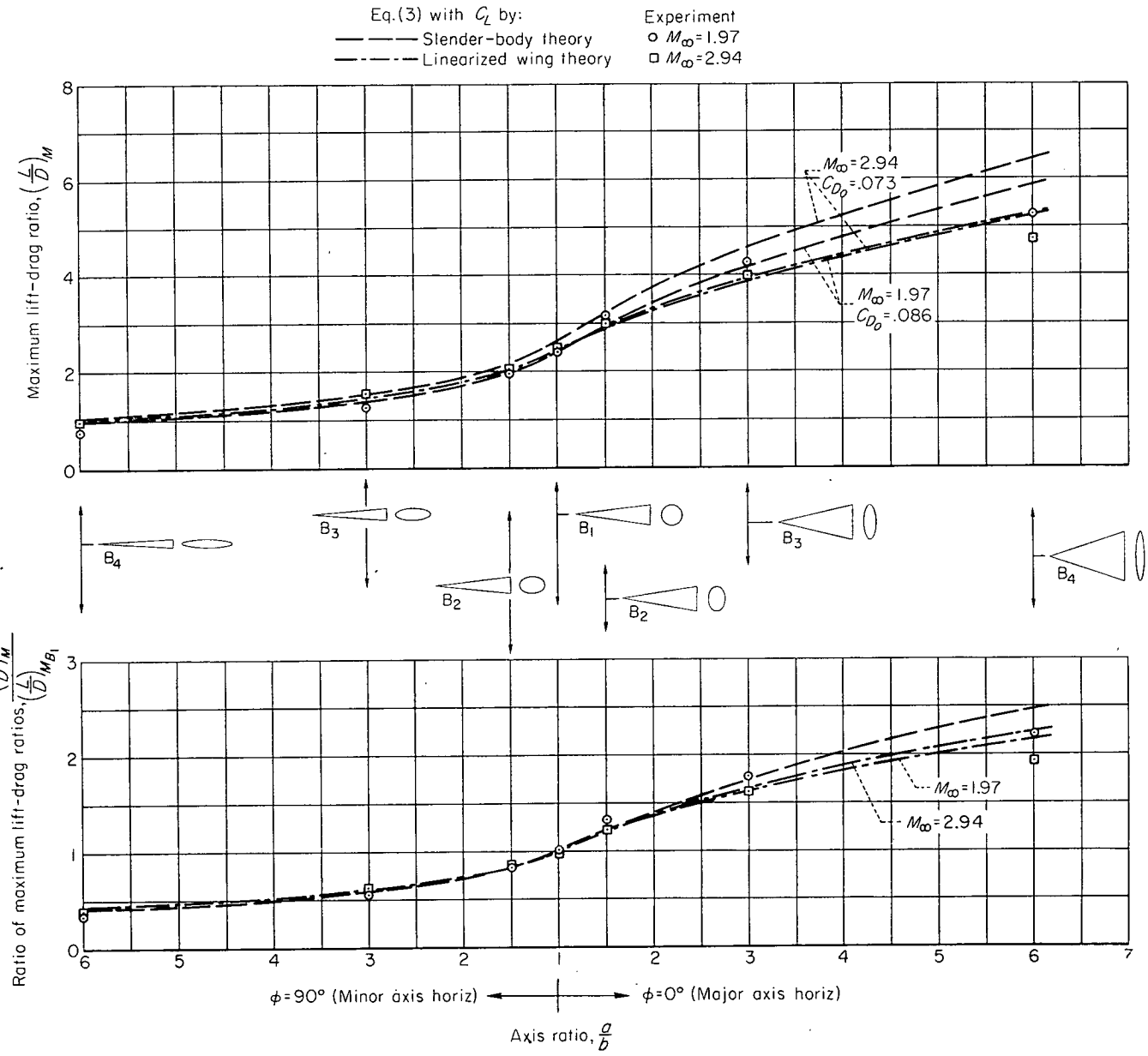


FIGURE 16.—Effect of axis ratio (a/b) on maximum lift-drag ratios of elliptic cones.

0.073 at $M_\infty=2.94$ have been used in the calculations. In general, the agreement of theory with experiment is good, the best agreement being obtained with linearized wing theory. In the lower plot of figure 16, however, the comparisons show that the relative efficiency of an elliptic to a circular cone can be closely estimated by means of slender-body theory (eq. (5)) for moderate values of a/b (of the order of 3 or less).

Forces and moments for winged circular cones.—For a slender wing-body combination consisting of a triangular wing mounted on a circular cone so that their vertices coincide, the lift coefficient is given by the slender-body method of Spreiter (ref. 16) as

$$C_L=\frac{\pi}{2}A\sigma\frac{A_w}{A_b}\alpha \tag{6}$$

where

$$\sigma=1+\left(\frac{d}{2s}\right)^4+\frac{1}{2\pi}\left\{\frac{d}{s}\left[1-\left(\frac{d}{2s}\right)^2\right]-\left[1+\left(\frac{d}{2s}\right)^2\right]^2\sin^{-1}\frac{\frac{d}{s}}{1+\left(\frac{d}{2s}\right)^2}\right\}$$

It has been shown (refs. 16 and 17) that the slender-body method of Spreiter can be modified so as to give results comparable to linearized theory. For winged circular cones this is accomplished merely by multiplying equation (6) by a modification factor λ. This factor is the ratio of the lift of the wing alone by linearized theory to the lift by slender-body theory and is given by

$$\left.\begin{aligned}\lambda&=\frac{1}{E\left(\sqrt{1-\beta^2\tan^2\epsilon}\right)};\ \beta\tan\epsilon\leq 1\\ \lambda&=\frac{2}{\pi\beta\tan\epsilon};\ \beta\tan\epsilon\geq 1\end{aligned}\right\} \tag{7}$$

By application of the factor λ to equation (6), there is obtained

$$C_L=\frac{\pi}{2}A\sigma\lambda\frac{A_w}{A_b}\alpha \tag{8}$$

Since the center of pressure is at the centroid of plan-form area, the pitching-moment coefficient is given by the relation

$$C_m=\frac{\pi}{6}A\sigma\lambda\frac{A_w}{A_b}\alpha \tag{9}$$

In figure 17, theoretical and experimental force and moment characteristics of winged circular cones are compared. Equations (8) and (9) were used to compute the lift and pitching-moment curves, and equations (1) and (8) to compute the lift-drag polars and ratios. The drag at zero lift was estimated by the addition of turbulent skin-friction drag (ref. 12) for the entire surface to the body pressure drag obtained by second-order slender-body theory (ref. 4). The agreement of the computed results with the experimental data is good for angles of attack below about 10°. As yet, the details of a theoretical method for computing the aerodynamic characteristics of winged elliptic cones have not been worked out. However, because of the close agreement of the experimental lift and moment characteristics for winged circular and elliptic cones at angles of attack to 10° (figs. 6 through 9), the method for winged circular cones can be used for winged elliptic cones.

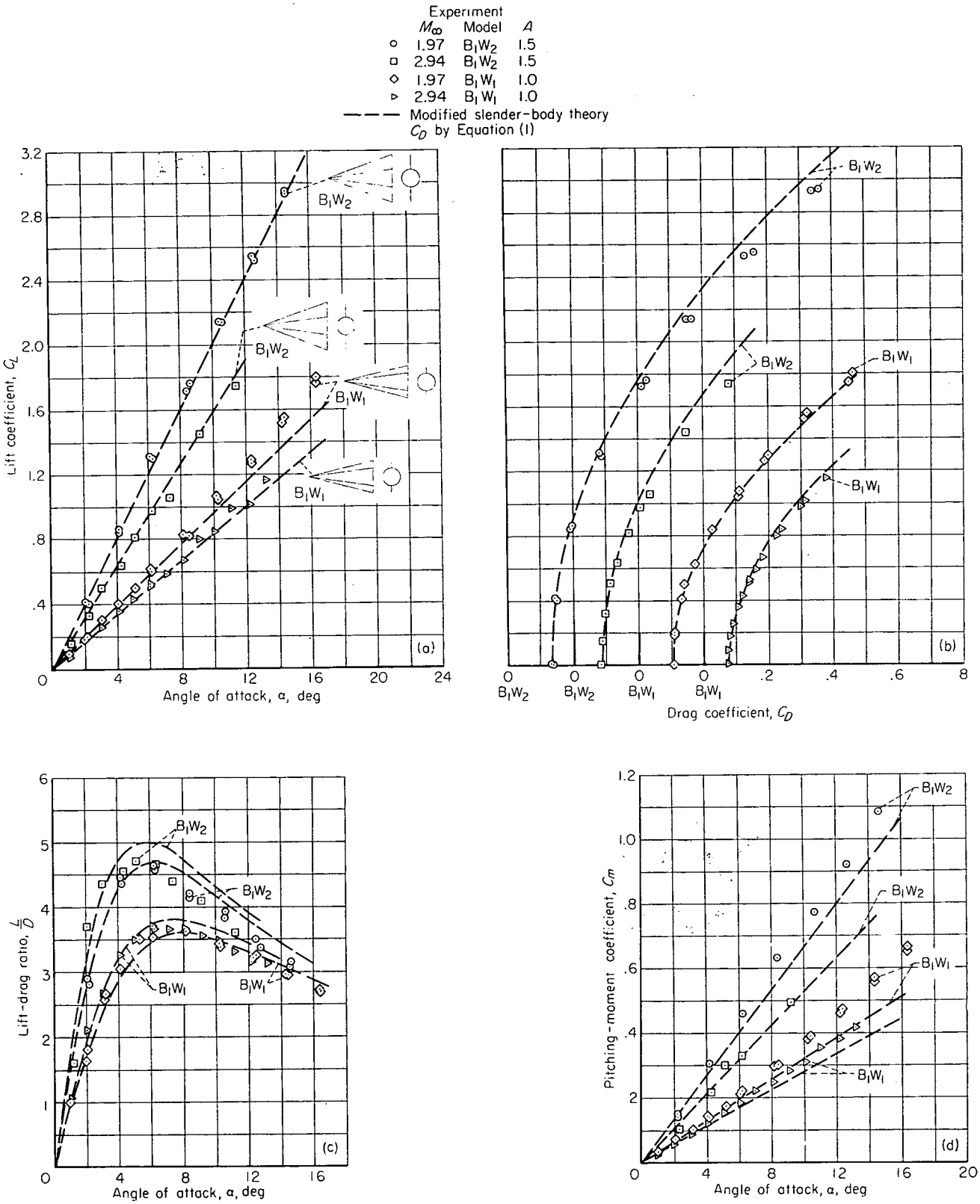
VISUAL OBSERVATIONS OF FLOW OVER MODELS

To supplement the force and moment results with studies that aid in giving a physical representation of the flow, vapor-screen and sublimation tests were made for the models at Mach number 1.97. Photographs and measurements of the resulting flow patterns are presented in figures 18 through 22. As mentioned previously, the vapor-screen pictures were taken with a camera mounted inside the tunnel just downstream of the models. The pictures of the models from the sublimation tests were taken immediately following tunnel shutdown.

Vapor-screen results.—In the photographs of figure 18, base views of bodies B_1, B_2, and B_3 showing vortices are presented for $\alpha=10°$, 15°, and 20°. For these pictures the light plane intersected the model axis at about $x=0.7\,l$, and part of the flow field was in the shadow of the model. In figure 18 a symmetrical pair of vortices is shown above each model. These vortices, which originate at the nose, were observed to grow in size (and presumably strength) with travel from the nose to the base. At each axial length position, it was found that the sizes and positions of the vortices relative to the body cross section were practically the same. In figure 18 it is seen that the sizes of the vortex regions increase with increase in α from 10° to 20°. The vortex regions also flatten out and move outboard relative to the body vertical center line with increase in a/b above 1.

The photographs of figures 19 (a) and 19 (b) are presented in order to demonstrate the effect of angle of bank on the vortex regions associated with elliptic cones at $\alpha=15°$ and 20°. For all cases studied, as the models were banked from $\phi=0°$ to $\phi=-45°$ the right vortex region appeared to flatten out and lie nearer to the body surface.

In figure 20 pictures of vortex patterns for the winged cones of aspect ratio 1 (B_1W_1, $B_{3H}W_1$, and $B_{3V}W_1$) are shown. These pictures were taken with the light plane at about the base of each model. As for the elliptic cones without wings, the vortex regions above the winged cones increase in size with increase in α from 10° to 15°. With α kept constant at 15°, the right vortex region flattens out and moves nearer to the model surface with change in ϕ from 0° to −45° (fig. 20 (b)). Comparison of these pictures with those for the bodies alone shows that the addition to a body of even low-aspect-ratio wings results in considerable outboard and downward movement of the vortex regions; for instance,



(a) Lift. (b) Lift-drag polar.
(c) Lift-drag ratio. (d) Pitching moment.

FIGURE 17.—Comparison of theoretical and experimental aerodynamic characteristics of winged circular cones.

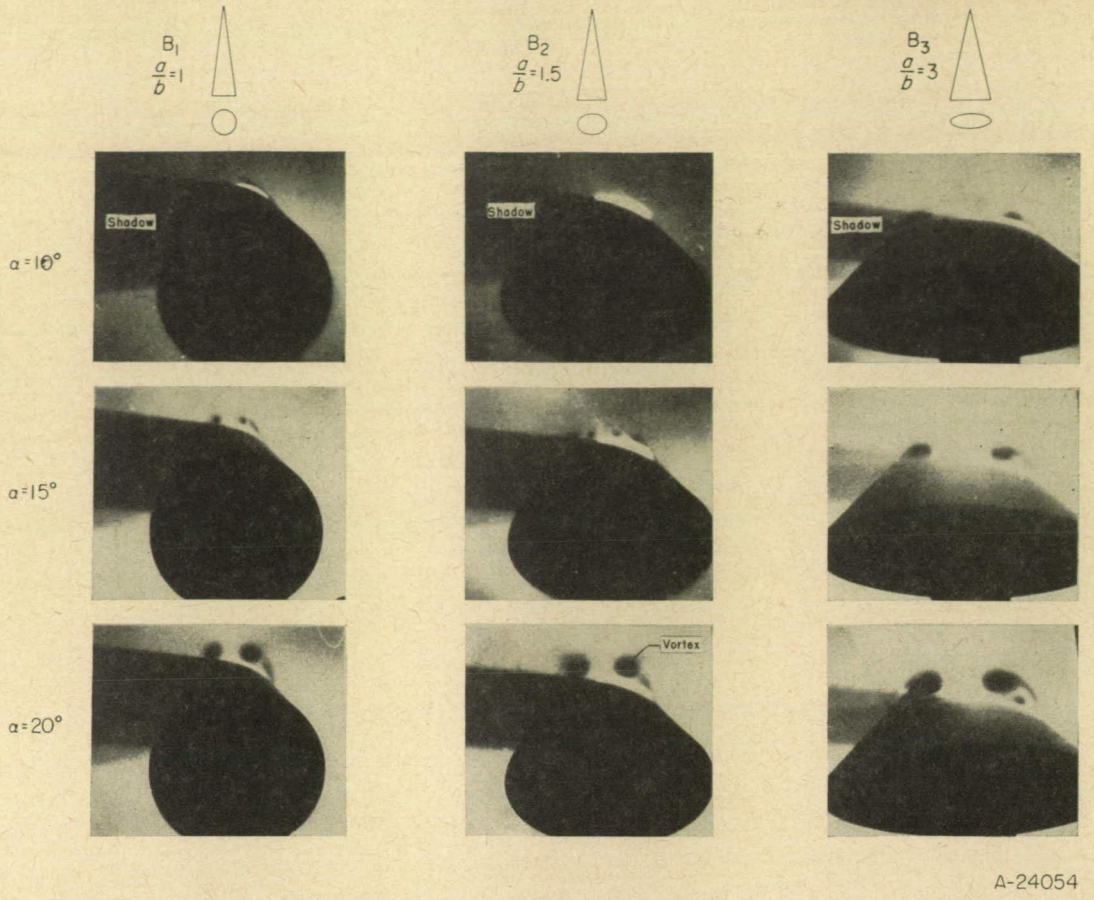
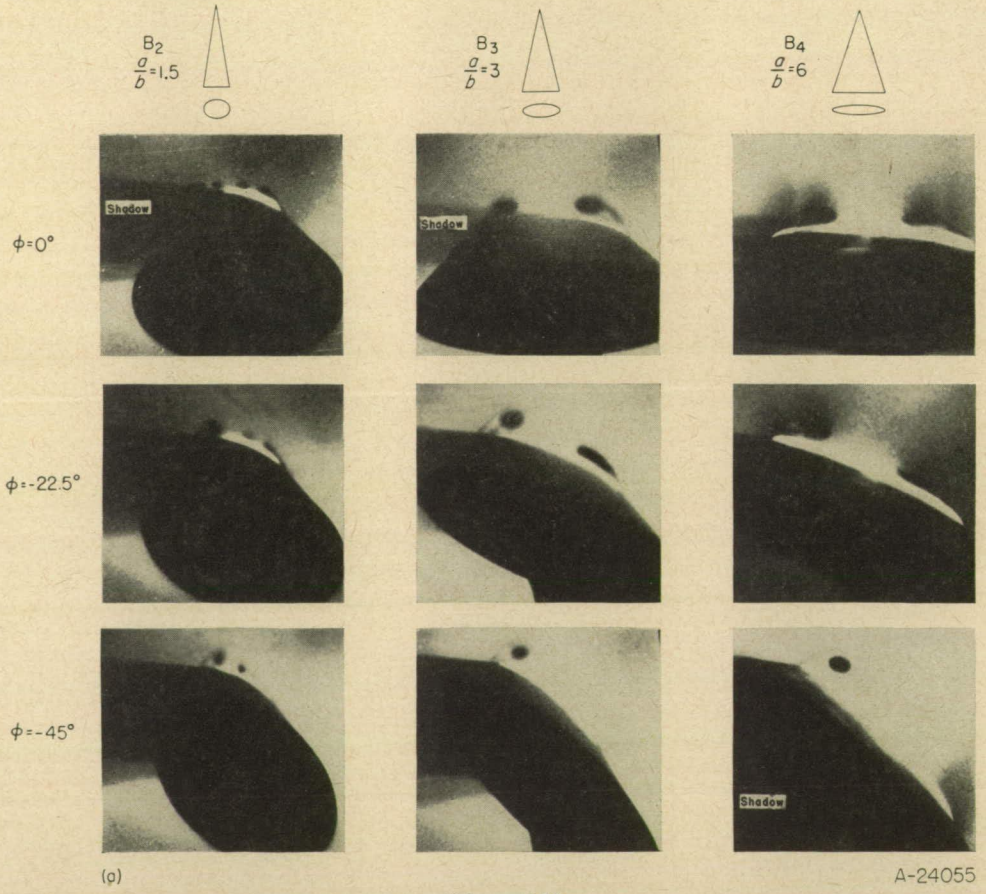
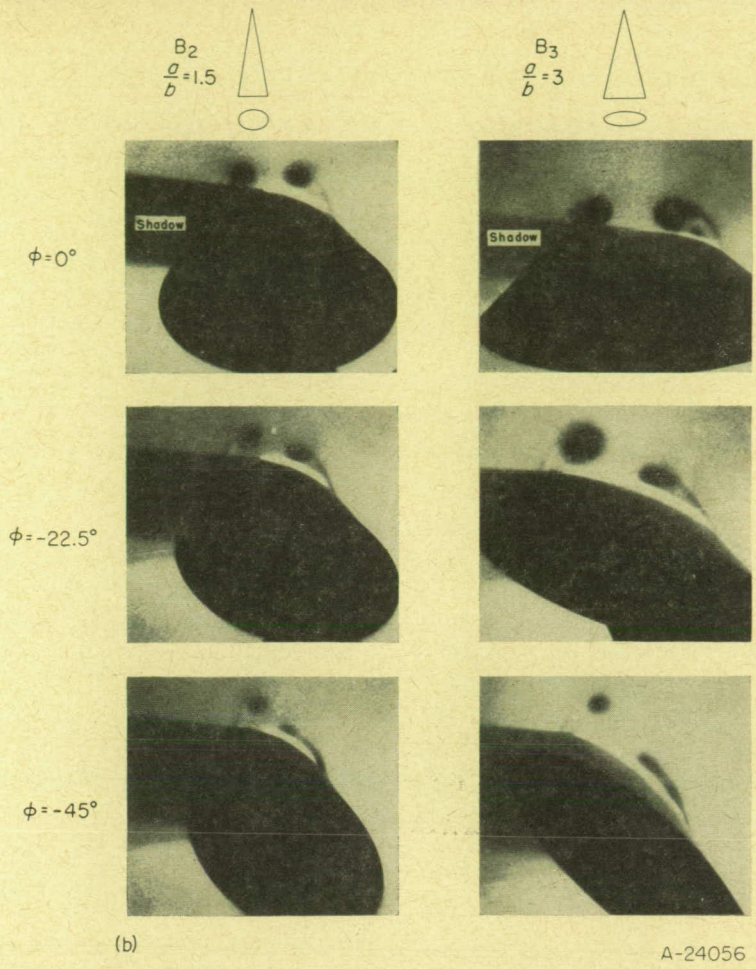


FIGURE 18.—Rear views of elliptic cones showing effect of angle of attack on vortex patterns (with vapor-screen light plane at $x=0.7\ l$); $M_\infty=1.97$.



(a) $\alpha=15°$.

FIGURE 19.—Rear views of elliptic cones showing effect of angle of bank on vortex patterns (with vapor-screen light plane at $x=0.7\ l$); $M_\infty=1.97$.



(*b*) $\alpha=20°$.

FIGURE 19.—Concluded.

compare the pictures for B_1 in figure 18 with those for B_1W_1 in figure 20. From these observations, it appears that body vortex interference with a vertical fin or air-breathing engine mounted above a body can be reduced by extending low-aspect-ratio wings all the way to the nose.

What is believed to be secondary vortex flow below and outboard of the main vortex regions is indicated in some of the photographs of the models at $\alpha=20°$. This is especially evident for model $B_{3H}W_1$ at $\alpha=20°$ in figure 20 (a). This secondary vortex flow also has been observed for delta wings at supersonic speeds by Drougge and Larson (ref. 18).

Sublimation technique results.—Transition, separation, and vortex regions for models B_1, B_2, and B_3 are shown in the photographs of figure 21. Top, side, and bottom views for the models at an angle of attack of 15° are presented. As seen in the bottom views, the boundary-layer flow over the models was mostly turbulent, the laminar region being limited to the white area near the nose. In the side views a line indicating flow separation is shown for each model, and in the top views symmetrical vortex traces are visible. Although not clearly evident in the pictures, the separation lines and vortex traces extended almost linearly from the nose to the base of each model. Measurements of the symmetrical separation and vortex positions at the base of all of the body models of $l/d=3.67$ were taken. In figure 22 the separation and vortex positions are plotted as a function of a/b. It is seen that for $a/b=1.5$ with the model banked 90° so that the minor axis is horizontal, the separation lines and vortex traces are close together and near the top of the body. With the model unbanked ($\phi=0°$) so that the major axis is horizontal, the separation and vortex positions are farther apart and nearer the sides of the body. For unbanked cones with a/b greater than 3, the flow separation positions are essentially at the sides of the body, and the vortex traces are about midway between the sides and the top.

CONCLUSIONS

Aerodynamic characteristics of elliptic cones alone and with triangular wings have been measured for Mach numbers 1.97 and 2.94 at a Reynolds number of 8×10^6, based on model length. Cones having fineness ratios (l/d) of 3.67 and 5 and cross-sectional axis ratios (a/b) from 1 through 6 have been considered for angles of bank of 0° and 90°. In addition, a study has been made of cones of l/d of 3.67 and a/b of 1 and 3 in combination with wings of aspect ratio 1 and 1.5. An analysis of the results has led to the following conclusions:

1. Pressure distributions over elliptic cones at zero incidence can be computed reasonably well by means of Van Dyke's second-order slender-body theory.

2. For a cone of given fineness ratio at zero lift, the pressure drag decreases with increase in cross-sectional axis ratio a/b. However, with a turbulent boundary layer, the skin friction increases enough that the pressure plus skin-friction drag remains practically constant with increase in a/b. The foredrag can be computed accurately by the addition of theoretical skin-friction drag to pressure drag predicted by second-order slender-body theory.

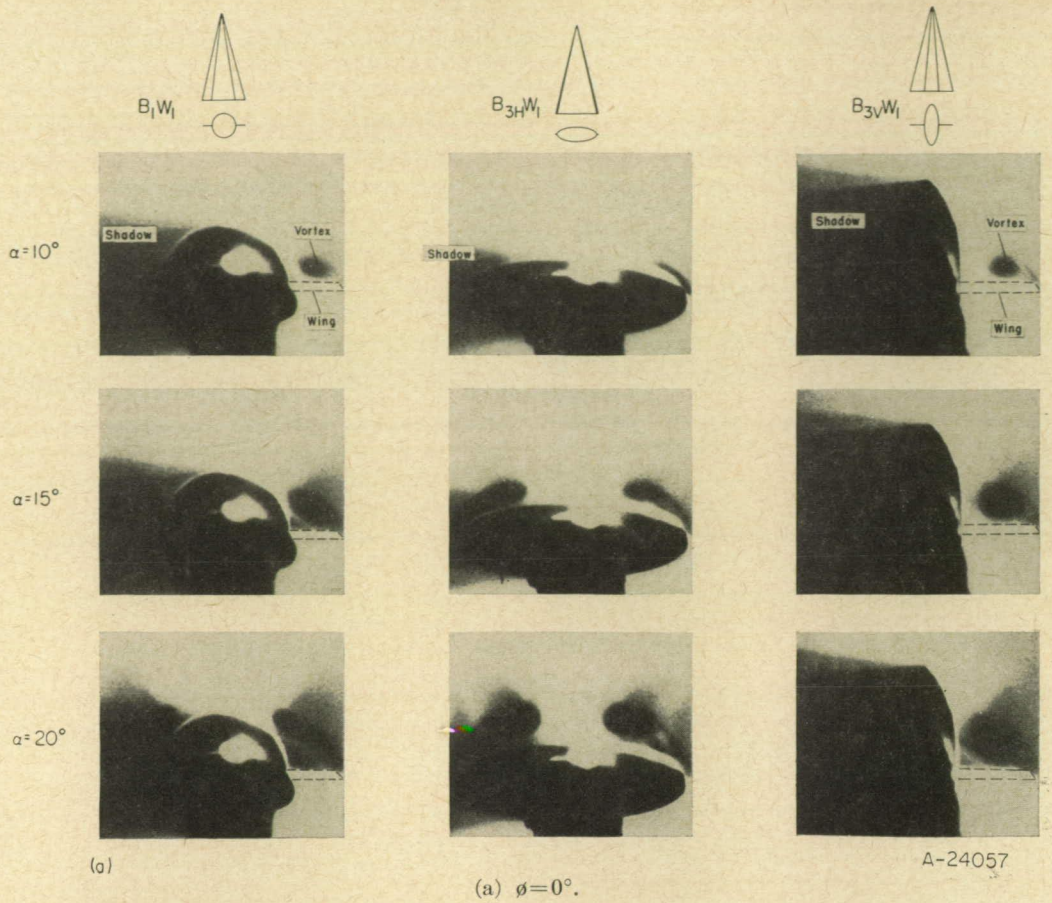
3. With the major cross-sectional axis horizontal, increases in axis ratio a/b result in large gains in lift and lift-drag ratio. These gains can be computed reasonably well by the use of linearized wing theory.

4. For a given cross-sectional axis ratio a/b, the lift-drag ratio increases with increase in equivalent fineness ratio.

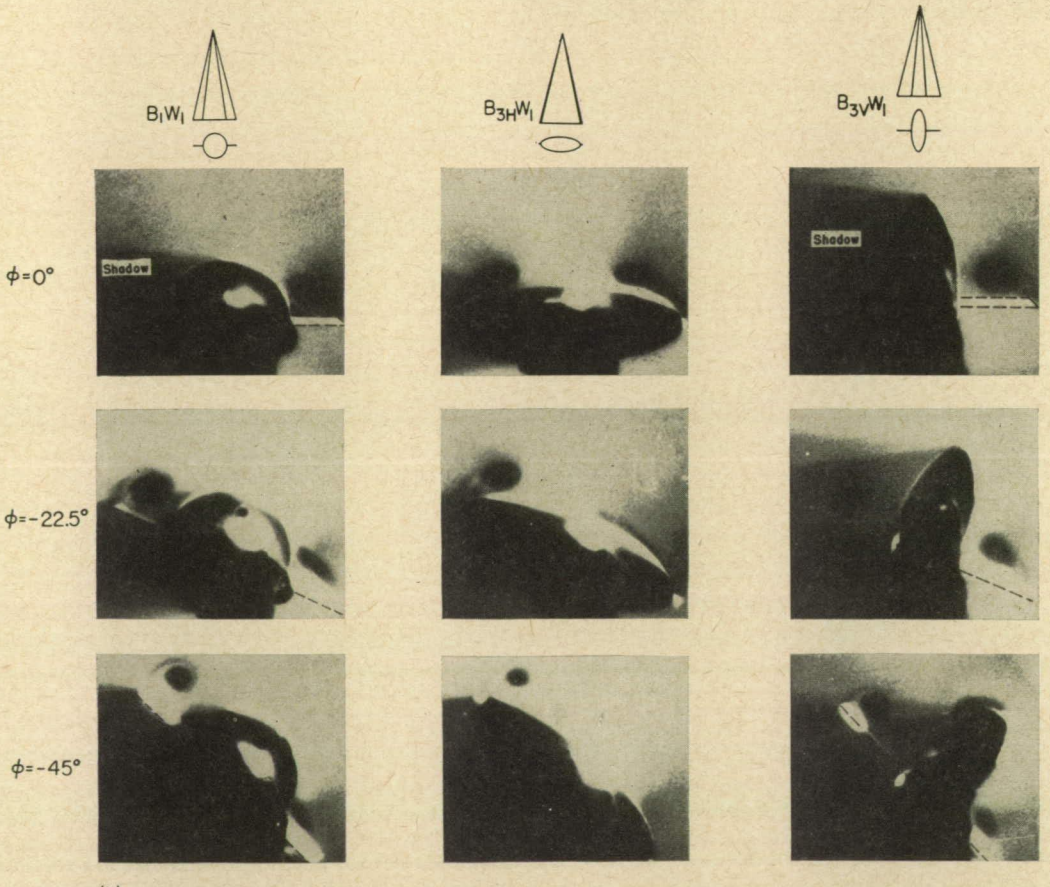
5. For wing-body combinations, a body with an elliptic cross section instead of a circular cross section appears aerodynamically advantageous. With triangular wings (aspect ratio=1, 1.5) mounted on cones ($l/d=3.67$) so that their vertices coincide, higher lift-drag ratios result from an elliptic cross section with major axis in line with the wings than from a circular cross section. However, a decrease in lift-drag ratio results from an elliptic cross section with the minor axis in line with the wing.

6. For the cones alone and with triangular wings, shifts in center of pressure with changes in angle of attack and Mach number are very small.

7. For winged circular cones, the theoretical results of NACA Rep. 962 can be modified to give good agreement with experimental results for angles of attack below about 10°.



(a) $\phi = 0°$.



(b) $\alpha = 15°$

FIGURE 20.—Rear views of winged elliptic cones ($A=1$) showing effects of angle of attack and angle of bank on vortex patterns (with vapor-screen light plane at base); $M_\infty = 1.97$.

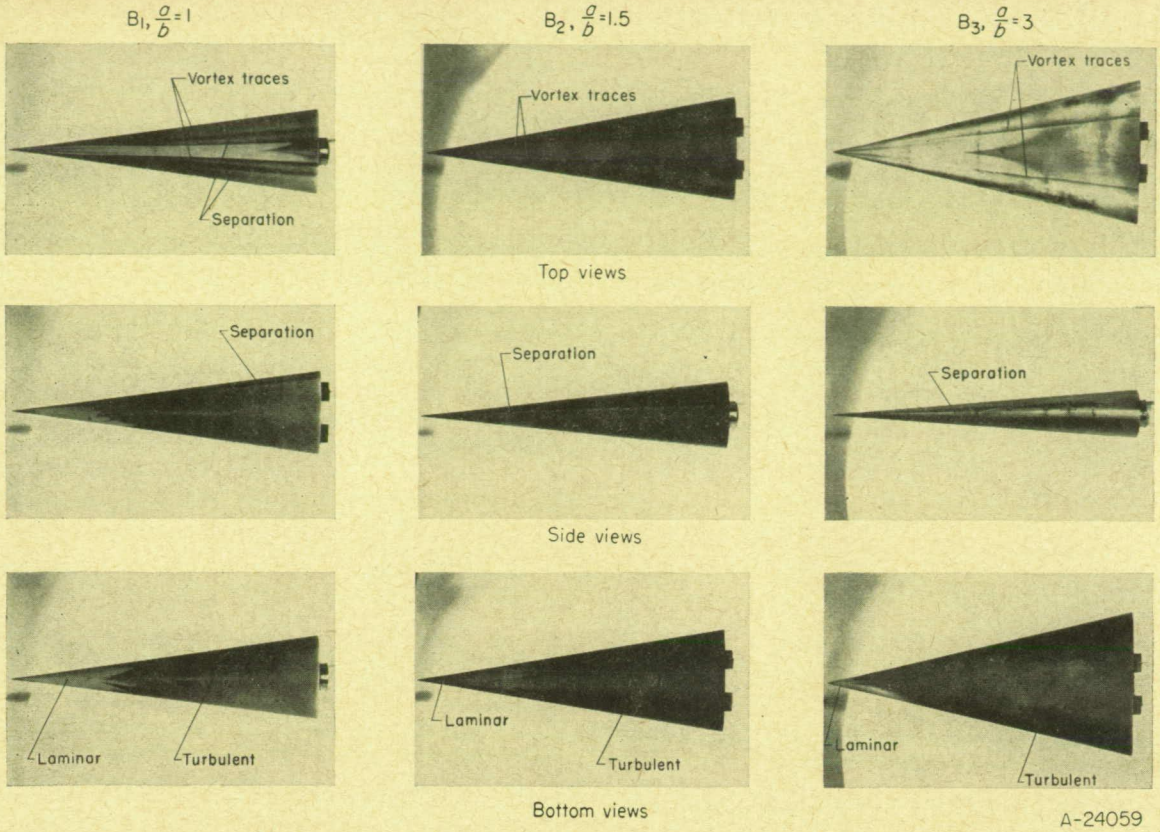


FIGURE 21.—Photographs of elliptic cones taken following sublimation tests of models at $\alpha=15°$; $M_\infty=1.97$.

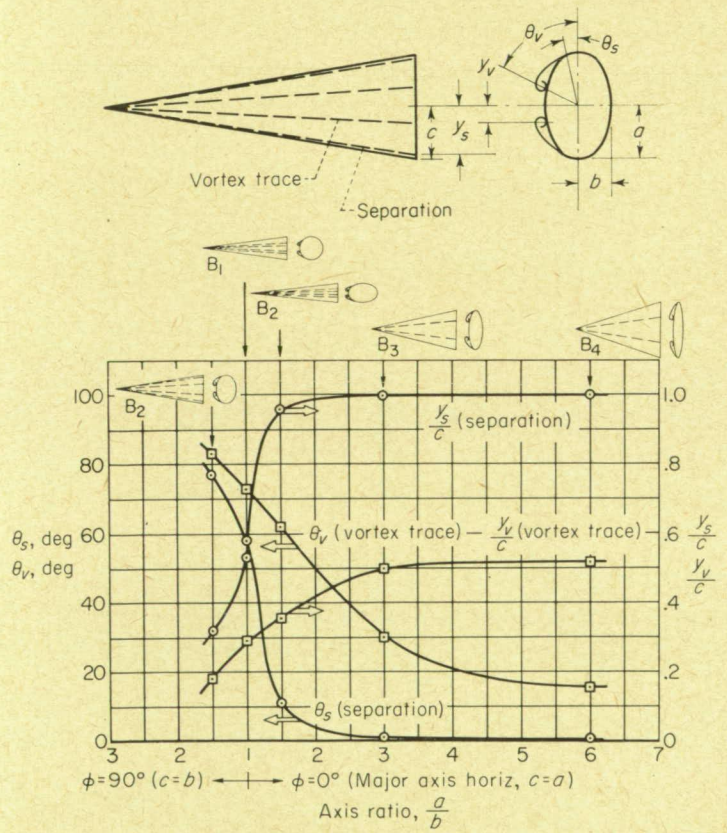


FIGURE 22.—Effect of axis ratio (a/b) on separation and vortex traces appearing on elliptic cones at $\alpha=15°$; $l/d=3.67$, $M_\infty=1.97$.

8. Visual boundary-layer flow studies indicate that, for unbanked elliptic cones at angle of attack, a pair of symmetrical vortices start at the nose and trace a linear path to the base. These vortices increase in size with travel from the nose to the base. The flow separation lines from which the vortices are fed also trace an essentially linear path along the model surface.

AMES AERONAUTICAL LABORATORY
NATIONAL ADVISORY COMMITTEE FOR AERONAUTICS
MOFFETT FIELD, CALIF., *July 17, 1957*

REFERENCES

1. Fraenkel, L. E : Supersonic Flow Past Slender Bodies of Elliptic Cross Section. R. & M. No. 2954, British A. R. C., 1955.
2. Kahane, A., and Solarski, A.: Supersonic Flow About Slender Bodies of Elliptic Cross Section. Jour. Aero. Sci., vol. 20, no. 8, Aug. 1953, pp. 513–524.
3. Ferri, Antonio, Ness, Nathan, and Kaplita, Thaddeus T.: Supersonic Flow Over Conical Bodies Without Axial Symmetry. Jour. Aero. Sci., vol. 20, no. 8, Aug. 1953, pp. 563–571.
4. Van Dyke, Milton D.: The Slender Elliptic Cone as a Model for Nonlinear Supersonic Flow Theory. Jour. Fluid Mech., vol. 1, no. 1, May 1956, pp. 1–15.
5. Ward, G. N.: Supersonic Flow Past Slender Pointed Bodies. Quart. Jour. Mech. and Appl. Math., vol. II, pt. 1, Mar. 1949, pp. 75–97.
6. Seaman, Donna Jean, and Dore, Frank J.: Force and Pressure Coefficients of Elliptic Cones and Cylinders in Newtonian Flow. Rep. ZA–7–004, Consolidated Vultee Aircraft Corp., San Diego, May 16, 1952.

7. Maslen, Stephen H.: Pressure Distributions on Thin Conical Body of Elliptic Cross Section at Mach Number 1.89. NACA RM E8K05, 1949.
8. Ferri, Antonio: The Linearized Characteristics Method and Its Application to Practical Nonlinear Supersonic Problems. NACA TN 2515, 1951.
9. Rogers, E. W. E., and Berry, C. J.: Experiments at M=1.41 on Elliptic Cones with Subsonic Leading Edges. British A. R. C. 17929, FM 2307, Perf. 1391, Oct. 11, 1955.
10. Allen, H. Julian, and Perkins, Edward W.: A Study of Effects of Viscosity on Flow Over Slender Inclined Bodies of Revolution. NACA Rep. 1048, 1951.
11. Main-Smith, J. D.: Chemical Solids as Diffusible Coating Films for Visual Indications of Boundary-Layer Transition in Air and Water. R. & M. No. 2755, British A. R. C., 1954.
12. Rubesin, Morris W., Maydew, Randall C., and Varga, Steven A.: An Analytical and Experimental Investigation of the Skin Friction of the Turbulent Boundary Layer on a Flat Plate at Supersonic Speeds. NACA TN 2305, 1951.
13. Ames Research Staff: Equations, Tables, and Charts for Compressible Flow. NACA Rep. 1135, 1953.
14. Stewart, H. J.: The Lift of a Delta Wing at Supersonic Speeds. Quart. Appl. Math., vol. IV, no. 3, Oct. 1946, pp. 246–254.
15. Flax, A. H., and Lawrence, H. R.: The Aerodynamics of Low-Aspect-Ratio Wings and Wing-Body Combinations. Third Anglo-American Aeronautical Conference, Brighton, 4th–7th September 1951. Convened by the R. A. S. and I. A. S., Joan Bradbrooke and E. G. Pike, eds., 1952, pp. 363–398. (Published also as Rep. CAL–37, Cornell Aeronautical Lab., Inc., Buffalo, 1951).
16. Spreiter, John R.: The Aerodynamic Forces on Slender Plane- and Cruciform-Wing and Body Combinations. NACA Rep. 962, 1950.
17. Nielsen, Jack N., Katzen, Elliott D., and Tang, Kenneth K.: Lift and Pitching-Moment Interference Between a Pointed Cylindrical Body and Triangular Wings of Various Aspect Ratios at Mach Numbers of 1.50 and 2.02. NACA TN 3795, 1956.
18. Drougge, G., and Larson, P. O.: Pressure Measurements and Flow Investigation on Delta Wings at Supersonic Speed. Flygtekniska Försöksanstalten, The Aeronautical Research Institute of Sweden, Rep. 57, Stockholm, Nov. 1956.

REPORT 1377

MEASUREMENTS OF FREE-SPACE OSCILLATING PRESSURES NEAR PROPELLERS AT FLIGHT MACH NUMBERS TO 0.72[†]

By Max C. Kurbjun and Arthur W. Vogeley

SUMMARY

In the course of a short flight program initiated to check the theory of Garrick and Watkins (NACA Rep. 1198), a series of measurements at three stations were made of the oscillating pressures near a tapered-blade plan-form propeller and a rectangular-blade plan-form propeller at flight Mach numbers up to 0.72. These measurements were made at a single radial station and at three axial positions (ahead of, in the plane of, and behind the propeller disk). Despite the limited scope of the tests, agreement with the theory was obtained to the extent that:

(a) The oscillating pressures near the propeller tend to decrease with increase in flight Mach number up to a Mach number of approximately 0.5 and to increase rather rapidly at higher Mach numbers.

(b) The sound-pressure levels of the higher harmonics of the propeller noise increase at a higher rate with increase in flight Mach number than the lower propeller harmonics.

In contradiction to the results found for the propeller studied in NACA Rep. 1198, the oscillating pressures in the plane and ahead of the propeller were found to be higher than those immediately behind the propeller. Factors such as variation in torque and thrust distribution, since the blades of the present investigation were operating above their design forward speed, may account for this contradiction.

The effect of blade plan form shows that a tapered-blade plan-form propeller will produce lower sound-pressure levels than a rectangular-blade plan-form propeller for the low blade-passage harmonics (the frequencies where structural considerations are important) and produce higher sound-pressure levels for the higher blade-passage harmonics (frequencies where passenger comfort is important).

INTRODUCTION

The effects of the near-field noise generated by propellers in flight are of continuously increasing concern to the aviation industry. With regard to air transportation, the oscillating pressures in the form of noise directly affect passenger comfort and the field of public relations. For the airplane structural engineer, these oscillating pressures are creating serious fatigue problems. The severity of the problems increases with the continual trend toward higher powers and higher flight speeds. Detailed knowledge of the pressure fields about propellers is necessary for design and also, it is hoped, will eventually indicate a means of reducing the oscillating pressures.

In the field of propeller-generated pressures, both the theoretical and experimental backgrounds are rather extensive. The Gutin theory (ref. 1) for the far-field pressures is well known. This theory has been extended in reference 2 to predict the pressures in the near field. Both references 1 and 2 deal strictly with stationary propellers but the results of investigations under static conditions have been applied with some success, as in reference 3, to low flight speeds. In reference 4, Garrick and Watkins have further extended Gutin's theory to take into account the effect of forward speed. This extended theory includes the stationary propeller and the far-field simplifications as special cases.

The purpose of the flight tests reported herein was to obtain in-flight measurements of propeller noise with which to check, if possible, the theory of reference 4 and to investigate parameters affecting propeller noise such as propeller-blade plan form, power, and tip speeds at a range of forward speeds up to the maximum permissible Mach number of 0.72.

SYMBOLS

b	blade width, ft
c_l	section design lift coefficient
D	propeller diameter, ft
h	blade thickness, ft
M_∞	flight Mach number
M_R	rotational tip Mach number
M_t	helical tip Mach number, $\sqrt{M_\infty^2+M_R^2}$
N	engine speed, rpm
P	power absorbed by propeller, hp
p	root mean square of oscillating pressure, lb/sq ft or decibels, as indicated
p_∞	static pressure, lb/sq ft
R	propeller tip radius, ft
r	radius to a blade element, ft
T	thrust of propeller, lb
t_∞	free-air temperature, °F
V	airspeed, ft/sec

[†] Supersedes NACA Technical Note 3417 by Arthur W. Vogeley and Max C. Kurbjun, 1955, and NACA Technical Note 4068 by Max C. Kurbjun, 1957.

526597—60——65

x longitudinal position of microphone, measured positive forward of propeller disk, ft

y radial position of microphone, measured from propeller center, ft

β section blade angle, deg

TEST EQUIPMENT

The airplane available for this investigation was a single-place fighter type equipped with a liquid-cooled inline engine. The engine was equipped with individual jet-ejector exhaust stacks.

Two types of propellers, differing principally in blade plan forms, were used in this investigation. The difference in the propeller-blade shapes is shown in the photographs of the two propellers mounted on the airplane (fig. 1). Figure 1 (a) shows the tapered blade and figure 1 (b), the rectangular blade. The characteristics of the two blade designs are shown in figures 2 (a) and 2 (b), respectively. Both propellers had a diameter of 11 feet 2 inches and were driven through a reduction gear providing a ratio of engine speed to propeller speed of 0.479.

The oscillating pressure pickup used was a commercial condenser-type microphone modified to operate under the rapidly varying static pressures encountered in the tests. A frequency-modulation system was used to transmit the pressure signals to a ground-located station where the signals were recorded with a magnetic-tape recorder. A complete description of the pickup, transmitter, receiver, and analyzer equipment is contained in reference 5.

The microphone was installed in a boom mounted in the center gunport of the right wing. This location placed the microphone at a radial distance of 7.31 feet from the propeller axis. The boom was constructed in such a manner that the microphone could be shifted forward and backward through a distance of approximately 4 feet before each flight. Figures 1 (a), 1 (b), and 3 show the microphone-boom installation.

Before the start of the flight-test program, the boom was tested in a wind tunnel to check for background noise over the anticipated flight speed range. It was found that the self-generated overall noise level of the microphone in the band width 80 to 1,000 cps was below 113 decibels. This level of self-generated random noise is considered acceptable in the measurement of sound-pressure levels as low as 100 decibels for discrete frequencies. The response of the system used was flat within ± 1 decibel between 80 to 1,000 cps.

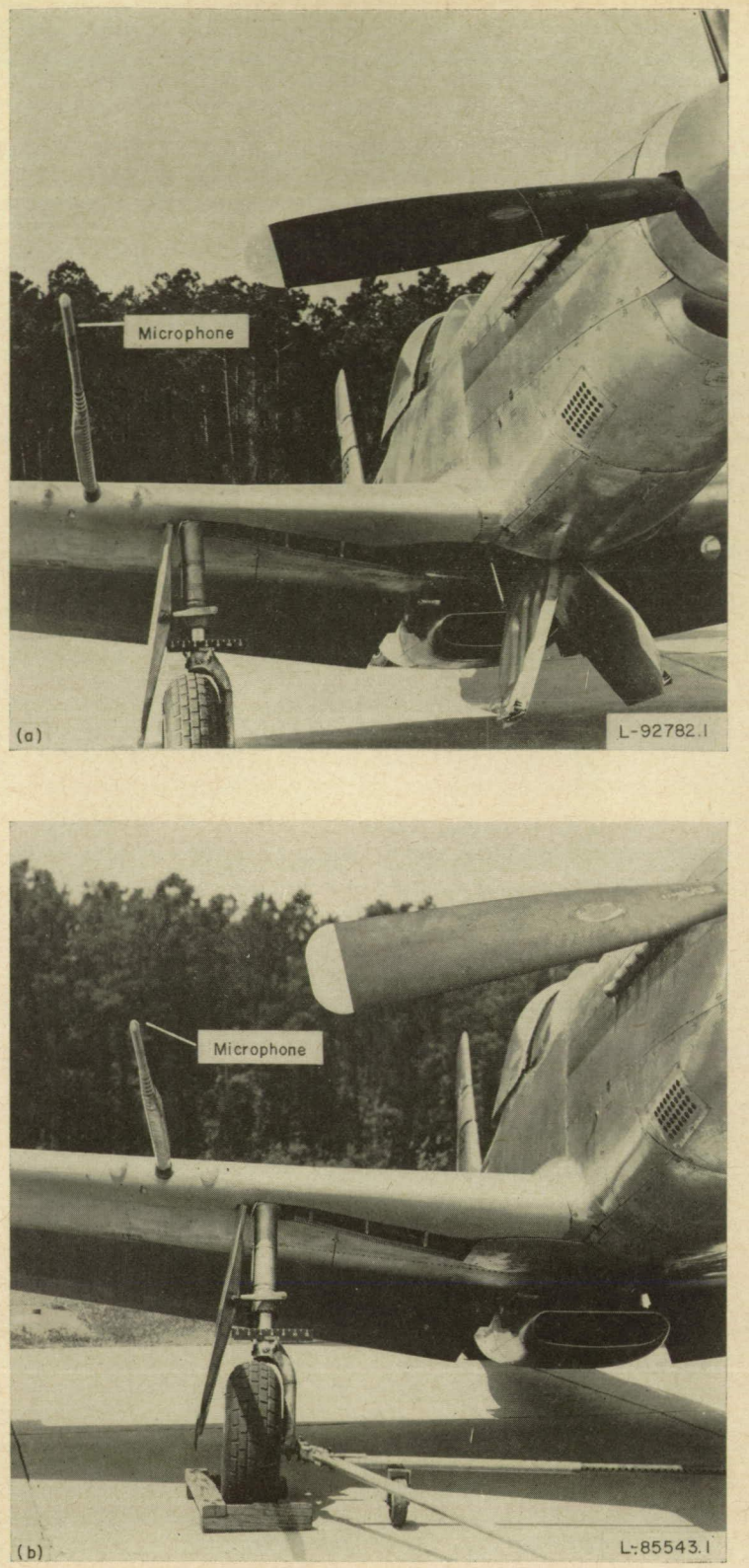
Standard NACA recording instruments were used to record dynamic pressure, altitude, free-air temperature, engine speed, and manifold pressure.

TEST PROCEDURE

All static ground tests and flight tests were made with the microphone located at a fixed radial distance of $y=0.655D$. Tests were made at three values of longitudinal distance $x=-0.125D$, 0, and $0.125D$. Flight tests were arranged to investigate the effects of flight Mach number, engine speed, and engine power on propeller noise, as follows:

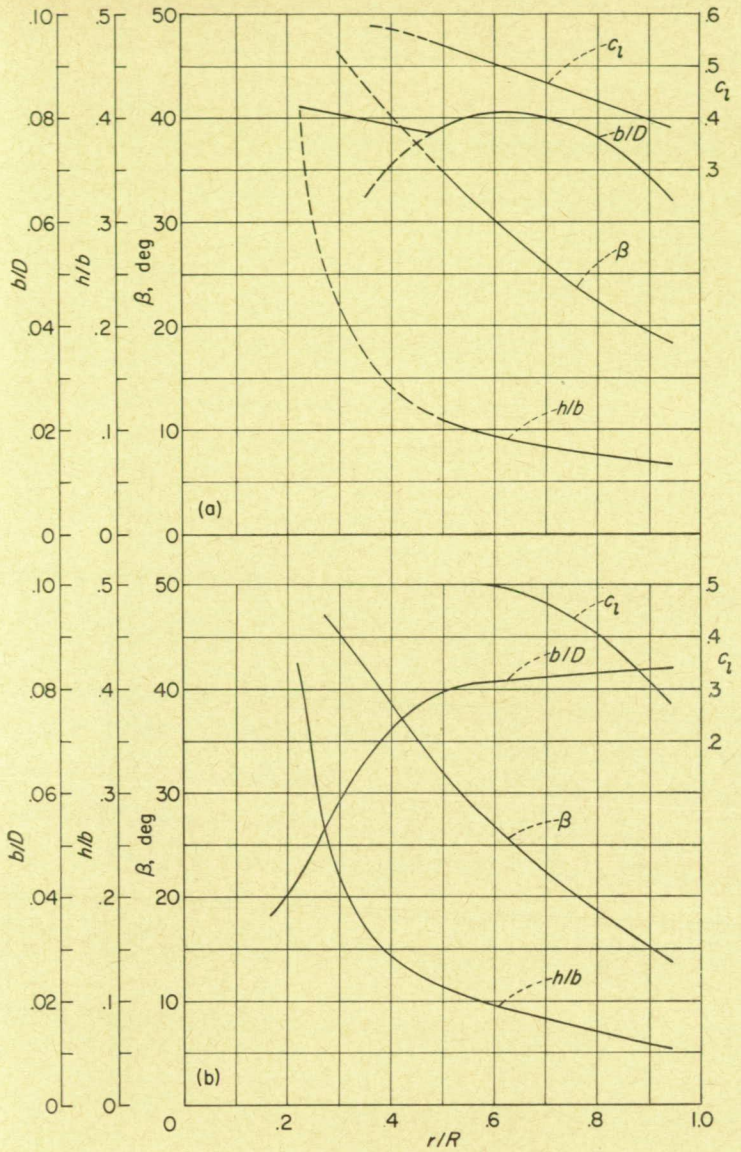
(1) Flight Mach number: At engine speeds of approximately 2,700 rpm with the manifold pressure adjusted to produce a power output of approximately 1,000 horsepower, flight tests were made on both propellers at flight Mach numbers from approximately 0.2 to 0.7 by varying the flight attitude. Static ground tests were also made at the same power and engine speed setting.

(2) Engine speed (rotational Mach number): At a flight Mach number of approximately 0.5 and engine output of approximately 1,000 horsepower, tests were made with the



(a) Tapered-blade plan form.
(b) Rectangular-blade plan form.

FIGURE 1.—Front view of the microphone installation showing the propeller-blade shape.



(a) Tapered-blade plan form.
(b) Rectangular-blade plan form.

FIGURE 2.—Characteristics of the propeller blades tested.

tapered-blade propeller at engine speeds of approximately 2,500, 2,600, 2,700, 2,800, 2,900, and 3,000 rpm.

(3) Engine power: At a flight Mach number of approximately 0.5 and engine speeds at approximately 2,700 rpm, tests were made with the tapered-blade propeller at engine powers of approximately 0, 500, 1,000, and 1,500 horsepower.

RESULTS AND DISCUSSION

Because it was necessary to make separate flights for each propeller and for each boom setting, it was impossible to repeat the test conditions exactly. All test conditions are given in tables I and II for the tapered and rectangular blades, respectively. In the discussion to follow, the small differences in test conditions are disregarded, and the data are compared and examined in only a general manner.

The effects of propeller-blade plan form are shown in a series of figures comparing the noise emitted from the two propellers tested with changes in operating parameters of flight Mach number, engine speed (rotational Mach number), and power. Correlation of theory with measured results follows the discussions of changes in the operating parameters.



FIGURE 3.—Three microphone locations used on the test airplane during the investigation. $y = 0.655D$ for all positions.

TABLE I.—RESULTS WITH TAPERED-BLADE PLAN-FORM PROPELLERS

[$y=0.655D$]

Test conditions											Sound-pressure level, db (Reference pressure level, 0.0002 dynes/cm²)									
											Order of harmonics									
x	T, lb	V, ft/sec	p_∞, lb/sq ft	t_∞, °F	P, hp	N, rpm	M_∞	M_R	M_t	Blade-passage frequency, cps	1st	2d	3d	4th	5th	6th	7th	8th	9th	10th
Ground tests																				
0.125D	2,800	0	2,110	81	1,030	2,693	0	0.66	0.66	86.0	[a]	[a]	[a]	[a]	[a]	[a]	[a]	[a]	[a]	[a]
.104D	2,800	0	2,110	81	1,030	2,693	0	.66	.66	86.0										
.089D	2,800	0	2,110	81	1,030	2,693	0	.66	.66	86.0										
.075D	2,800	0	2,110	81	1,030	2,693	0	.66	.66	86.0	128.6	122.6	116.7	110.0	109.3	108.7				
.060D	2,800	0	2,110	81	1,030	2,681	0	.66	.66	85.6	128.9	121.5	116.5	112.7						
.045D	2,800	0	2,110	81	1,030	2,681	0	.66	.66	85.6	128.7	122.3	117.1	112.9						
.030D	2,800	0	2,110	81	1,030	2,693	0	.66	.66	86.0	127.2	122.0	116.3	111.3	109.9					
.015D	2,800	0	2,110	81	1,030	2,693	0	.66	.66	86.0	127.5	121.0	116.3	111.3	108.0					
0	2,800	0	2,110	81	1,030	2,693	0	.66	.66	86.0	127.1	120.3	115.6							
−.015D	2,800	0	2,110	81	1,030	2,693	0	.66	.66	86.0	131.9	124.5	120.5	114.5						
−.030D	2,800	0	2,110	81	1,030	2,693	0	.66	.66	86.0	126.7	120.3	114.9	109.9						
−.045D	2,800	0	2,110	81	1,030	2,681	0	.66	.66	85.6	126.5	118.1	115.1	109.2						
−.060D	2,800	0	2,110	81	1,030	2,681	0	.66	.66	85.6	126.7	120.5	115.1	109.5						
−.075D	2,800	0	2,110	81	1,030	2,681	0	.66	.66	85.6	126.8	118.0	116.0	108.5						
−.089D	2,800	0	2,110	81	1,030	2,681	0	.66	.66	85.6										
−.104D	2,800	0	2,110	81	1,030	2,681	0	.66	.66	85.6	126.5	116.1	116.3			109.7				
−.125D	2,800	0	2,110	81	1,030	2,681	0	.66	.66	85.6	126.1	115.5	116.8							
.125D	1,490	0	2,110	81	570	2,418	0	.59	.59	77.2	126.1	116.2	110.8							
.125D	1,850	0	2,110	81	710	2,568	0	.63	.63	82.0	128.0	119.8	113.8							
.125D	2,500	0	2,110	81	960	2,681	0	.66	.66	85.6	128.6	120.8	116.0	110.0						
.125D	3,100	0	2,110	81	1,200	2,919	0	.72	.72	93.2	130.5	124.7	120.5	115.0						
0	1,490	0	2,110	81	570	2,405	0	.59	.59	76.8	122.1	113.2	109.5							
0	1,850	0	2,110	81	710	2,593	0	.64	.64	82.8	125.0	117.0	113.0	108.0						
0	2,500	0	2,110	81	960	2,693	0	.66	.66	86.0	127.8	121.5	117.7	112.0	110.5					
0	3,100	0	2,110	81	1,200	2,944	0	.72	.72	94.0	129.9	123.9	120.1	115.3	113.5					
−.125D	1,490	0	2,110	81	570	2,380	0	.58	.58	76.0	119.9	109.0	110.0	104.7	104.5					
−.125D	1,850	0	2,110	81	710	2,596	0	.64	.64	82.9	123.5	113.5	113.5							
−.125D	2,500	0	2,110	81	960	2,768	0	.68	.68	88.4	127.2	120.0	117.5	109.0						
−.125D	3,100	0	2,110	81	1,200	2,937	0	.72	.72	93.8	129.9	123.0	120.0	113.5						

[a] Lost due to infiltration of extraneous noise at receiving station.

TABLE I.—RESULTS WITH TAPERED-BLADE PLAN-FORM PROPELLERS—Concluded

[y=0.655D]

Test conditions											Sound-pressure level, db (Reference pressure level, 0.0002 dynes/cm²)									
											Order of harmonics									
x	T, lb	V, ft/sec	p_∞, lb/sq ft	t_∞, °F	P, hp	N, rpm	M_∞	M_R	M_t	Blade-passage frequency, cps	1st	2d	3d	4th	5th	6th	7th	8th	9th	10th
Flight tests																				
−0.125D	2,040	235	965	13	1,030	2,699	0.22	0.71	0.74	86.2	123.5	117.5	112.0	107.8	104.0	106.0				
−.125D	1,275	375	975	15	1,030	2,687	.35	.71	.79	85.8	118.3	111.7	107.5	107.0	102.0					
−.125D	1,240	385	945	14	1,030	2,699	.36	.71	.79	86.2	120.7	113.7								
−.125D	908	524	988	15	1,030	2,490	.49	.65	.82	79.5	118.3	113.5	108.2	109.3	105.5					
−.125D	914	530	970	14	1,050	2,584	.50	.68	.84	82.5	117.7	112.7	110.1	109.7	106.5					
−.125D	914	530	955	14	1,050	2,687	.50	.71	.86	85.8	117.2	114.2	111.5							
−.125D	914	530	948	14	1,050	2,787	.50	.73	.88	89.0	117.9	115.3	113.7	113.5						
−.125D	924	524	935	14	1,050	2,847	.49	.74	.89	90.9	118.0	116.0	117.0	116.2	115.0					
−.125D	924	524	935	13	1,050	2,951	.49	.74	.89	94.3	119.0	118.2	119.5	118.8	116.7	114.9	111.9	109.5	108.0	
−.125D	0	526	1,005	17	0	2,677	.49	.70	.85	85.5	118.1	114.9	111.8	108.3						
−.125D	545	526	1,014	17	600	2,687	.49	.70	.86	85.8		112.4	110.9	108.8	105.9					
−.125D	800	526	1,000	16	900	2,690	.49	.70	.86	85.9		111.5	109.5	108.5	110.5					
−.125D	1,280	526	990	15	1,400	2,701	.49	.71	.86	86.3	119.9	115.7	112.5	110.5	106.5	105.3				
−.125D	743	632	970	15	1,040	2,697	.59	.71	.92	86.1	119.0	116.7	115.1	113.0	110.0	108.5	106.0			
−.125D	575	775	1,040	20	1,040	2,672	.72	.70	1.00	85.3	132.1	134.0	133.2	132.0	129.7	127.2	124.0	121.0	120.5	
−.125D	568	785	1,010	20	1,040	2,682	.72	.70	1.00	85.6	132.7	135.5	134.5	132.8	130.0	127.3	124.0			
−.125D	698	785	960	26	1,280	2,926	.72	.77	1.05	93.5	133.8	136.9	136.7	134.5	133.5	127.8	123.8	121.2	118.0	117.0
0	2,050	231	938	−1	1,020	2,677	.22	.71	.75	85.5	124.8	121.1	117.6	113.8	109.5	106.3	102.0			
0	2,030	233	980	4	1,020	2,677	.22	.71	.74	85.5	123.8	119.6	115.7	110.0	108.2	106.4	104.0			
0	1,100	349	970	4	1,020	2,677	.33	.71	.78	85.5	123.6	119.5	116.1	112.8	109.0					
0	908	516	940	0	1,020	2,493	.49	.66	.82	79.6	121.6	118.3	114.9	111.9	109.7					
0	915	516	940	0	1,030	2,577	.49	.68	.84	82.3	122.5	120.1	117.3	114.6	110.3	108.7	103.0			
0	910	521	920	−2	1,040	2,681	.50	.71	.87	85.6	123.3	121.5	120.1	118.2	115.0	112.5	108.5	106.0		
0	915	525	900	−4	1,050	2,778	.50	.74	.89	88.7	124.3	123.3	122.5	121.3	119.1	116.9	114.1	110.5	108.0	105.0
0	920	522	880	−6	1,050	2,878	.50	.77	.91	91.9	125.4	126.3	126.3	126.2	125.7	124.4	122.4	119.9	117.3	114.0
0	945	507	860	−8	1,050	2,940	.49	.79	.93	93.9	125.9	127.6	128.3	128.1	127.2	125.0	123.3	120.7	117.5	
0	0	528	950	3	0	2,712	.50	.72	.88	86.6	120.3	120.9	119.7	117.3	114.7	111.5	107.1			
0	540	532	1,010	8	600	2,706	.50	.71	.87	86.4	120.7	120.5	119.3	117.0	113.6	116.8	108.5	105.0	103.0	
0	870	525	995	6	1,000	2,702	.50	.71	.87	86.3	121.6	120.6	119.3	116.8	114.1	111.4	108.0	105.5	100.0	
0	723	650	1,040	12	1,040	2,702	.61	.71	.94	86.3	126.9	127.7	127.7	126.8	125.4	123.0	120.5	117.9	114.9	113.0
0	652	702	850	−5	1,040	2,702	.67	.72	.99	86.3	131.2	134.4	135.2	134.1	131.2	127.0	121.8	119.8	119.8	118.8
0	808	707	860	0	1,300	2,928	.67	.78	1.02	93.5	134.8	139.5	140.3	138.0	131.9	120.0	125.5	125.9	123.4	119.0
.125D	2,170	222	965	3	1,030	2,702	.21	.72	.75	86.3	125.7	121.3	115.8	112.7	108.2	102.5				
.125D	1,295	370	960	3	1,030	2,702	.35	.72	.80	86.3	124.7	120.7	116.9	112.7	110.9					
.125D	900	528	970	4	1,030	2,493	.50	.66	.83	79.6	123.5	119.4	114.6	109.1	104.5	103.5	102.5			
.125D	912	528	960	3	1,000	2,587	.50	.69	.85	82.6	124.3	118.1	116.7	112.9	108.0	105.3				
.125D	920	528	955	2	1,050	2,690	.50	.71	.87	85.9	125.3	122.5	119.3	115.0	111.5	105.0				
.125D	910	532	940	1	1,050	2,778	.50	.73	.92	88.7	125.9	123.7	121.5	118.8	115.6	110.9	107.9	104.0	102.5	
.125D	912	527	928	−1	1,050	2,881	.50	.77	.92	92.0	126.6	124.0	122.8	120.1	117.0	113.7	111.0	108.0	106.0	
.125D	878	520	915	−3	1,050	2,953	.50	.79	.93	94.3	127.3	127.5	127.0	125.8	123.7	120.7	117.5	114.5	111.5	110.0
.125D	0	517	960	3	0	2,677	.49	.71	.86	85.5	119.5	119.3	116.7	112.9	109.7	107.3				
.125D	490	537	1,010	7	550	2,671	.51	.70	.87	85.3	122.2	120.2	117.6	113.6	109.8	106.0	103.5			
.125D	775	532	1,025	9	900	2,728	.50	.72	.87	87.1	123.4	120.7	117.5	113.5	109.9	105.6	103.5			
.125D	730	640	1,045	12	1,040	2,703	.60	.71	.94	86.3	128.2	126.3	125.5	122.9	119.7	116.2	111.7	107.0		
.125D	644	704	900	10	1,030	2,652	.66	.71	.97	84.7	131.3	133.0	132.0	129.7	125.6	126.9	119.3	118.3	116.5	114.5
.125D	643	698	950	5	1,020	2,702	.66	.71	.97	86.3	131.0	132.4	131.6	129.5	125.8	120.9	118.2	119.2	115.5	113.5
.125D	800	698	950	5	1,270	2,953	.66	.78	1.02	94.3	135.1	138.0	136.5	132.2	124.6	125.5	125.8	122.5	119.4	117.5

TABLE II.—RESULTS WITH RECTANGULAR-BLADE PLAN-FORM PROPELLERS

[$y=0.655D$]

Test conditions											Sound-pressure level, db (Reference pressure level, 0.0002 dynes/cm²)									
											Order of harmonics									
x	T, lb	V, ft/sec	p_∞, lb/sq ft	t_∞, °F	P, hp	N, rpm	M_∞	M_R	M_t	Blade-passage frequency, cps	1st	2d	3d	4th	5th	6th	7th	8th	9th	10th
Ground tests																				
0.125D	2,800	0	------	69	1,030	2,705	0	0.67	0.67	86.4	131.5	125.5	118.0	111.0	112.0					
0	2,800	0	------	69	1,030	2,700	0	.67	.67	86.2	129.5	123.0	118.5	113.0						
−.125D	2,800	0	------	69	1,030	2,700	0	.67	.67	86.2	129.0	120.0	119.0	108.0						
Flight tests																				
−0.125D	2,160	222	960	5	1,030	2,697	0.21	0.72	0.75	86.2	125.0	119.0	113.5	109.0						
−.125D	1,340	359	962	0	1,040	2,715	.34	.73	.80	86.7	123.5	117.8	112.5	109.5	107.0					
−.125D	915	520	947	−7	1,030	2,497	.50	.67	.84	79.5	120.5	115.6	109.5	107.5						
−.125D	942	513	969	−11	1,050	2,597	.49	.70	.86	82.9	120.5	116.0	112.0	109.5						
−.125D	946	522	961	−5	1,060	2,712	.49	.72	.88	86.6	121.5	116.5	112.5	108.0						
−.125D	960	515	961	−6	1,070	2,893	.49	.75	.92	92.3	122.5	118.5	116.0	112.5	107.5	104.5				
−.125D	963	516	966	−6	1,075	2,940	.49	.78	.93	94.0	122.0	120.0	118.0	114.5	110.4	106.5				
−.125D	756	628	980	−6	1,060	2,717	.60	.73	.94	86.6	124.5	121.5	118.0	112.5						
−.125D	583	757	1,075	0	1,030	2,730	.72	.72	1.02	87.2	135.0	136.5	134.0	131.0	126.0	121.5				
−.125D	738	747	1,040	−3	1,280	2,910	.71	.79	1.07	93.0	137.0	139.0	137.0	133.0	126.5					
0	1,830	270	947	9	1,048	2,710	.25	.71	.76	86.6	129.5	125.0	120.0	115.5						
0	1,310	374	943	9	1,048	2,710	.35	.72	.80	86.6	128.0	124.0	119.5	114.5						
0	955	523	951	10	1,080	2,705	.49	.71	.87	86.4	126.5	123.5	120.5	115.5	111.0					
0	1,350	524	955	10	1,530	2,945	.49	.77	.92	94.0	131.0	130.0	128.0	125.0	121.5	117.0	113.0			
0	774	633	983	11	1,080	2,700	.59	.71	.93	86.2	129.0	128.0	126.0	122.5	117.5	112.0	107.5			
0	574	767	1,000	13	1,030	2,685	.72	.71	1.01	85.8	138.5	142.0	141.5	138.0	131.0	124.5	128.5	127.0	123.5	121.5
0	710	768	1,030	18	1,270	2,910	.72	.76	1.04	92.9	143.5	146.0	142.0	129.5	128.5	129.5	123.0			
.125D	2,180	226	952	4	1,040	2,695	.21	.71	.74	86.0	129.5	124.5	120.0	115.0						
.125D	1,300	369	945	3	1,035	2,700	.35	.71	.78	86.2	128.0	123.0	119.0	113.5						
.125D	950	531	968	5	1,070	2,690	.50	.71	.87	85.8	128.5	125.5	122.0	117.5	114.0					
.125D	1,360	517	966	5	1,530	2,945	.49	.78	.92	94.0	131.0	130.5	129.0	126.5	123.0	119.5	114.5			
.125D	762	629	985	7	1,060	2,682	.59	.71	.92	85.6	130.5	129.5	127.0	123.5	119.5	115.0				
.125D	606	761	940	6	1,080	2,665	.72	.71	1.01	85.0	138.0	139.5	135.1	124.0	126.0	126.5	122.0	120.5	119.0	
.125D	890	744	940	5	1,530	2,920	.70	.77	1.04	93.2	142.5	143.5	133.5	132.5	133.0	121.0	128.0	123.5	124.5	125.0

EFFECTS OF FLIGHT MACH NUMBER

The effects of flight Mach number at the three axial microphone locations are shown in figure 4. A trend is shown for the lower blade-passage harmonics of both blade designs to decrease slowly in sound-pressure level as the flight Mach number increases to approximately 0.5 and to increase rapidly with further increase in flight Mach number. For the lower blade-passage harmonics the tapered blade shows a lower sound-pressure level than the rectangular blade.

The higher harmonics show a slight increase in sound-pressure level for both blade designs up to $M_\infty \approx 0.5$ with rapid increases for higher flight Mach numbers. Above $M_\infty = 0.5$ the tapered-blade design shows a more rapid increase in sound-pressure level with Mach number than the rectangular-blade design. This trend, which is more pronounced for the higher harmonics, produces higher sound-pressure levels in the higher harmonic range for the tapered-blade design than for the rectangular-blade design.

EFFECTS OF ENGINE SPEED (ROTATIONAL MACH NUMBER)

The effects of changing the engine speed (rotational Mach number) on the sound-pressure levels at a constant forward Mach number and power are shown in figures 5 and 6 for the tapered- and rectangular-blade designs, respectively. The results for both blade designs show small increases in the oscillating pressures with rotational Mach number for the first harmonic, but the increase for the higher harmonics becomes increasingly greater.

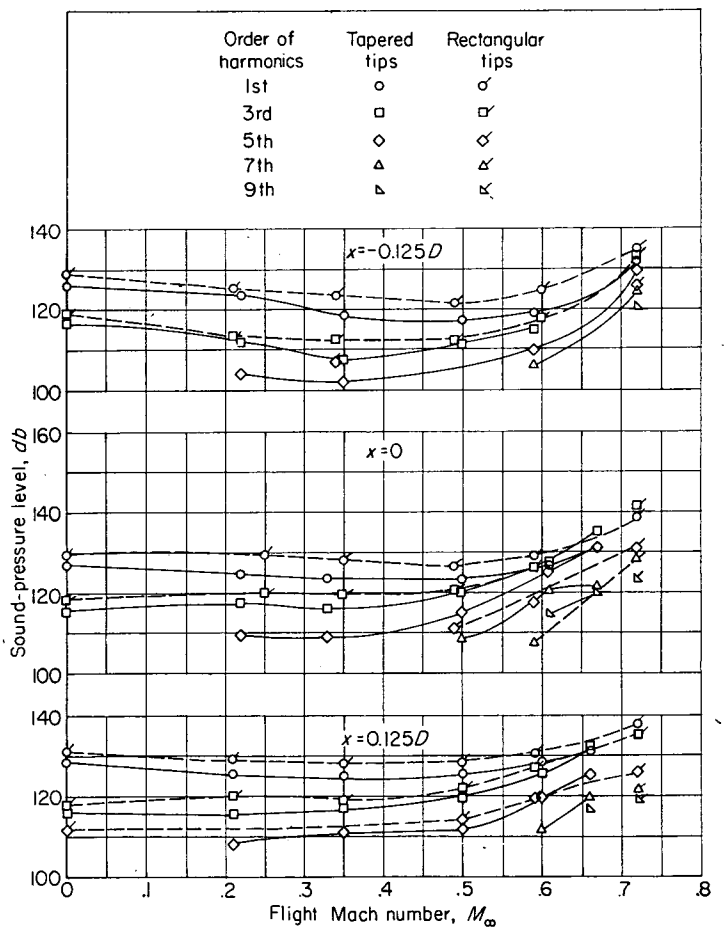


FIGURE 4.—Variation of propeller noise harmonic content with flight Mach number. $N \approx 2{,}700$ rpm; $P \approx 1{,}000$ hp; $y = 0.655D$.

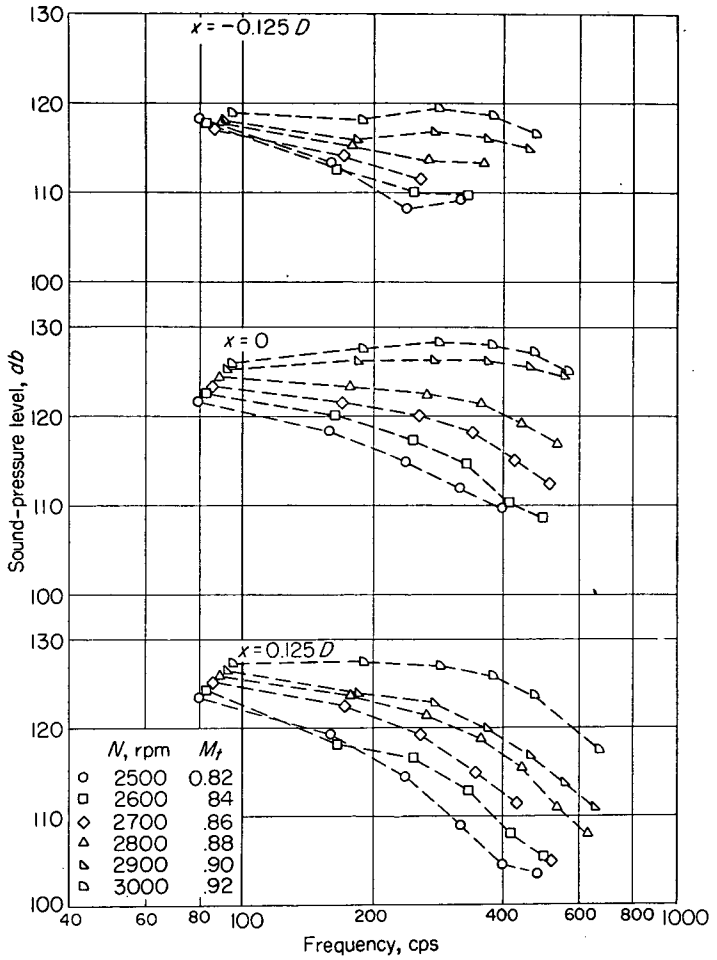


FIGURE 5.—Variation of sound-pressure levels with engine speed for the tapered-blade propeller. Blade-passage harmonics are connected with dashed lines for identification purposes only. $M_\infty \approx 0.5$; $P \approx 1{,}000$ hp; $y = 0.655D$.

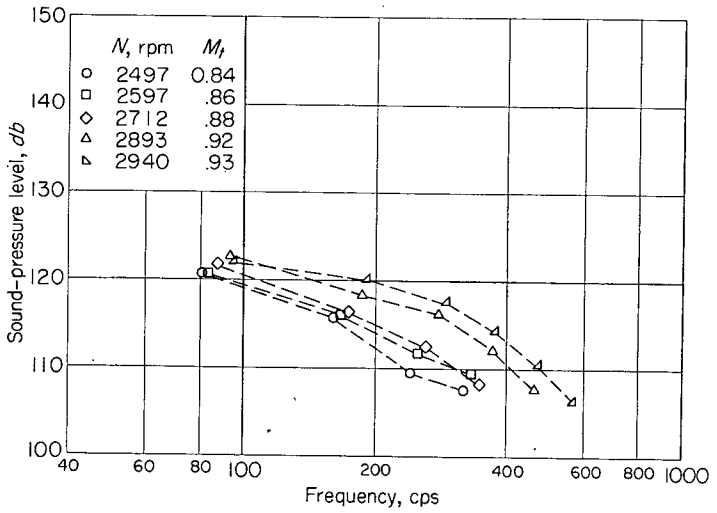
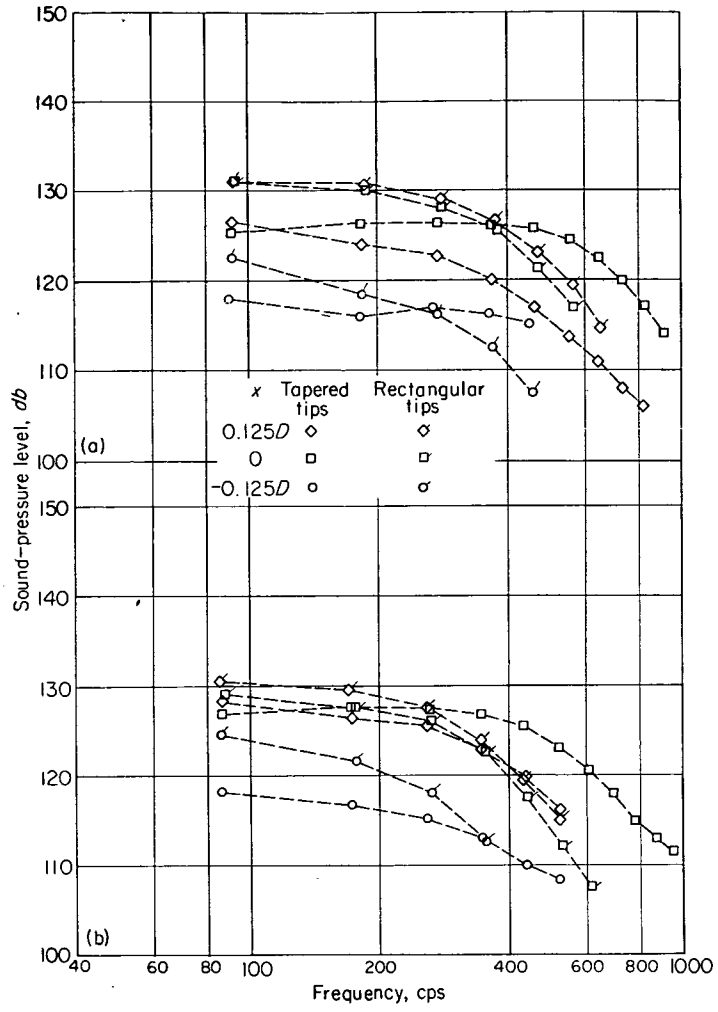


FIGURE 6.—Variation of sound-pressure levels with engine speed for the rectangular-blade propeller. Blade-passage harmonics are connected with dashed lines for identification purposes only. $M_\infty \approx 0.5$; $P \approx 1{,}050$ hp; microphone location, $x = -0.125D$.

Figures 7 (a) and 7 (b) show that the effects of flight Mach number are similar to those of rotational Mach number. Data for figure 7 (a) were obtained at a flight Mach number of approximately 0.5 and an engine speed of 2,900 rpm. Data for figure 7 (b) were obtained at a flight Mach number



(a) $M_\infty \approx 0.5$; $N \approx 2{,}900$ rpm; $P \approx 1{,}000$ hp; $y = 0.655D$.
(b) $M_\infty \approx 0.6$; $N \approx 2{,}700$ rpm; $P \approx 1{,}000$ hp; $y = 0.655D$.

FIGURE 7.—Variation of sound-pressure levels with axial microphone location. Blade-passage harmonics are connected with dashed lines for identification purposes only.

of approximately 0.6 and an engine speed of 2,700 rpm. The resultant tip Mach number for both conditions is approximately 0.95. The similarity of the two figures shows that in the range of the two conditions the effects of increase in flight Mach number are the same as increases in rotational speeds.

EFFECTS OF ENGINE POWER

The effects of engine power delivered to the tapered-blade propeller on the noise emitted from the propeller are shown in figure 8 for the three axial microphone locations. Data of this type were not obtained for the rectangular-blade propeller. The relatively small change in noise level with large changes in power displayed by the tapered-blade propeller seems to indicate that the propeller is also producing thickness noise of at least the same order of magnitude as the loading noise.

The power delivered to the propeller is seen to affect the noise emitted by the order of 6 decibels. This order of magnitude is far less than would be expected from consideration of only the blade-loading noise as was done in reference

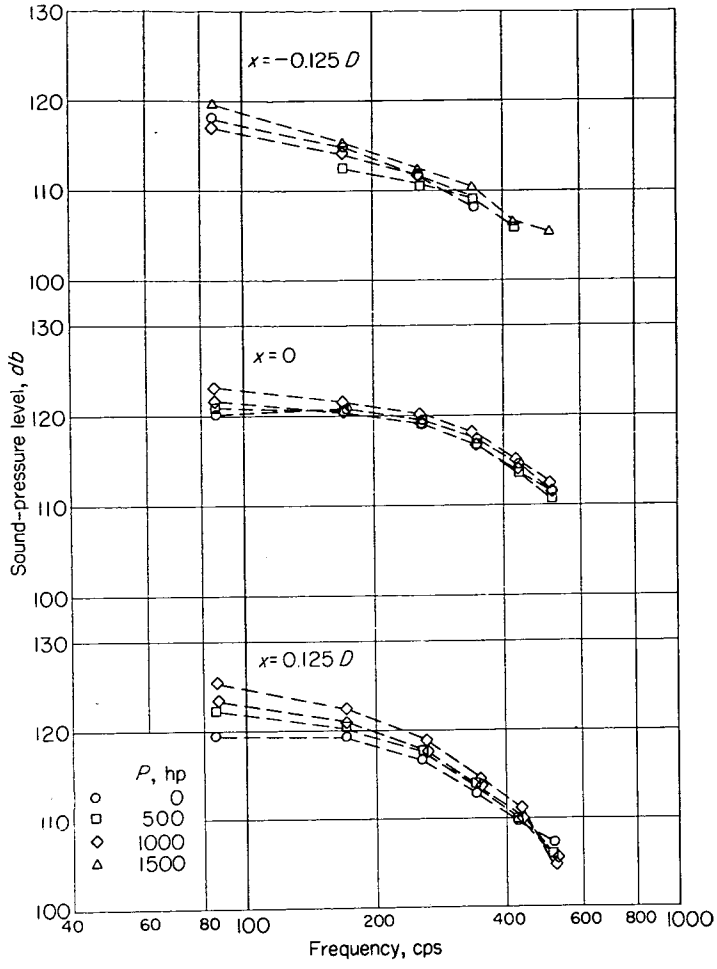


FIGURE 8.—Variation of sound-pressure levels with engine power for the tapered-blade propeller. Blade-passage harmonics are connected with dashed lines for identification purposes only. $M_\infty \approx 0.5$; $N \approx 2{,}700$ rpm; $y = 0.655D$.

4. However, calculations of thickness noise made in reference 6 show that the magnitude of the thickness noise, for the rectangular-blade propeller operating under the same flight conditions shown for figure 8, is within 6 decibels of the blade-loading noise.

It should be noted that the propellers used in the present investigation are designed for a flight Mach number of 0.5. At speeds above the design condition the outer portions of the blades tend to unload. Also, for a given horsepower input, the average thrust necessarily drops in proportion to the forward-speed increase. The combination of these two factors and the near location of the microphone to the tip would cause the results found in the present investigation to overemphasize the thickness noise in comparison with the loading noise at the higher speed conditions. This may be, in part, the reason that the results of the present investigation do not completely substantiate the theory of reference 4, as will be discussed subsequently.

CORRELATION WITH THEORY

Due to the nature and limitations of the present investigation, it was not possible to obtain a complete check of the theory of reference 4 for the effects of forward speed on the sound-pressure field around propellers. The results

obtained allow a few broad generalizations to be made which are as follows:

(1) In agreement with the theoretical results of reference 4, the results of the present investigation, as shown in figure 4, show an initial gradual decrease in the oscillating pressures with a more rapid increase at flight Mach numbers above 0.5. This was also shown in the results of reference 7, which utilizes the theory of reference 4. When account is taken of the differences between the flight-test configuration and the configuration examined theoretically in references 4 and 7, the pressure levels and changes in level with Mach number are also in rather satisfactory agreement.

(2) In agreement with the theory of reference 4, the test results show that the level of the higher harmonics of the propeller noise increases at a higher rate than that of the lower harmonics with increase in flight Mach number. This trend is shown in figure 5 of reference 8. The calculations of reference 8 utilize the theory of reference 4.

(3) For the propeller studied in reference 4, the oscillating pressures in the plane of the propeller disk and ahead of the disk were found to be lower than those immediately behind the disk. This theoretical result is contrary to the results found in the present tests, as is shown in figures 5 to 8. This contradiction does not, however, invalidate the theory. Rather it indicates that other effects such as variation in torque and thrust distribution should be investigated. As noted in the previous section, the outer portion of the blades was operating under unloaded condition for forward Mach numbers above 0.5.

CONCLUSIONS

As part of a brief flight program initiated to check the theory of Garrick and Watkins (NACA Rep. 1198), a brief set of measurements were made of the oscillating pressures in the vicinity of a blade of tapered plan form and a blade of rectangular plan form at flight Mach numbers up to 0.72. Measurements were made at a single radial station and at positions ahead of, in the plane of, and behind the propeller disk. The scope of the tests was found to be insufficient to obtain complete verification of the theory for the effect of forward speed on the sound-pressure field around propellers, but it was possible to substantiate the following two phenomena:

(a) The oscillating pressures near the tips of a propeller tend to decrease slowly with increase in flight Mach number up to a Mach number of approximately 0.5 and then to increase rather rapidly at higher Mach numbers.

(b) The sound-pressure levels of the higher harmonics of the propeller noise increase at a higher rate with increase in flight Mach number than do the lower propeller harmonics.

In contradiction to the results found for the propeller studied in NACA Rep. 1198, the oscillating pressures in the plane of and ahead of the propellers of the present investigation were found to be higher than those immediately behind the propeller. Factors such as variations in torque and thrust distributions, since the blades in the present investigation were operating above their design forward speed, may account for this contradiction.

The effect of blade plan form shows that a tapered-blade plan-form propeller will produce lower sound-pressure levels than a rectangular-blade plan-form propeller for the low blade-passage harmonics (the frequencies where structural considerations are important) and will produce higher sound-pressure levels for the higher blade-passage harmonics (frequencies where passenger comfort is important).

LANGLEY AERONAUTICAL LABORATORY,
NATIONAL ADVISORY COMMITTEE FOR AERONAUTICS,
LANGLEY FIELD, VA., *July 1, 1958.*

REFERENCES

1. Gutin, L.: On the Sound Field of a Rotating Propeller. NACA TM 1195, 1948.
2. Hubbard, Harvey H., and Regier, Arthur A.: Free-Space Oscillating Pressures Near the Tips of Rotating Propellers. NACA Rep. 996, 1950. (Supersedes NACA TN 1870.)
3. Vogeley, A. W.: Sound-Level Measurements of a Light Airplane Modified to Reduce Noise Reaching the Ground. NACA Rep. 926, 1949. (Supersedes NACA TN 1647.)
4. Garrick, I. E., and Watkins, Charles E.: A Theoretical Study of the Effect of Forward Speed on the Free-Space Sound-Pressure Field Around Propellers. NACA Rep. 1198, 1954. (Supersedes NACA TN 3018.)
5. Mace, William D., Haney, Francis J., and Brummer, Edmund A.: Instrumentation for Measurement of Free-Space Sound Pressures in the Immediate Vicinity of a Propeller in Flight. NACA TN 3534, 1956.
6. Arnoldi, Robert A.: Near-Field Computations of Propeller Blade Thickness Noise. Rep. R–0896–2, United Aircraft Corp., Res. Dept., Aug. 30, 1956.
7. Regier, Arthur A.: Why Do Airplanes Make Noise? SAE Preprint No. 284, SAE Nat. Aeronautic Meeting (New York), Apr. 12–15, 1954.
8. Schmey, Joern, and Clark, W. H.: Turboprop Propeller Noise Needn't Be a Bugaboo. SAE Journal, vol. 62, no. 4, Apr. 1954, pp. 44–47.

526597—60——66

REPORT 1378

A METHOD FOR SIMULATING THE ATMOSPHERIC ENTRY OF LONG-RANGE BALLISTIC MISSILES[1]

By A. J. Eggers, Jr.

SUMMARY

It is demonstrated with the aid of similitude arguments that a model launched from a hypervelocity gun upstream through a special supersonic nozzle should experience aerodynamic heating and resulting thermal stresses like those encountered by a long-range ballistic missile entering the earth's atmosphere. This demonstration hinges on the requirements that model and missile be geometrically similar and made of the same material, and that they have the same flight speed and Reynolds number (based on conditions just outside the boundary layer) at corresponding points in their trajectories. The hypervelocity gun provides the model with the required initial speed, while the nozzle scales the atmosphere, in terms of density variation, to provide the model with required speeds and Reynolds numbers over its entire trajectory. Since both the motion and aerodynamic heating of a missile tend to be simulated in the model tests, this combination of hypervelocity gun and supersonic nozzle is termed an atmosphere entry simulator.

INTRODUCTION

The aerodynamic heating of a long-range ballistic missile entering the earth's atmosphere poses problems of so serious a magnitude that the success or failure of the missile may well hinge on their solution. The extent to which these problems are solved can be fully determined only by flight tests, but such tests are, per se, very difficult, time consuming, and costly. It is appropriate to inquire, therefore, if a method can be devised for simulating with relatively simple equipment on the ground, the aerodynamic heating and resulting thermal stresses in a ballistic missile. This question forms the starting point of the present paper which undertakes first to establish conditions of simulation and then to determine a practical method of simulation. In the course of events it will be discovered that simulation of heating goes hand in hand with simulation of motion of a missile; accordingly, the subject of this paper is, more generally, an atmosphere entry simulator.

SYMBOLS

A	reference area for drag evaluation, sq ft
$C_1(T)$	rate constant (see eq. (A1)), sec^{-1}
$C_2(T)$	rate constant (see eq. (A2)), cu ft/sec
C_D	drag coefficient, dimensionless
C_{f_l}	local skin-friction coefficient based on conditions just outside of boundary layer, dimensionless
C_f'	equivalent skin-friction coefficient, $\frac{1}{S}\int_S C_{f_l}\left(\frac{\rho_l}{\rho}\right)\left(\frac{V_l}{V}\right) dS$, dimensionless
D	typical model or missile dimension, ft
E	Young's modulus, lb/sq ft
H	heat transferred per unit area, ft-lb/ft^2
K	diffusivity, sq ft/sec
k	thermal conductivity, ft-lb/sec ft^2(°R/ft)
L	length of nozzle, ft
M	flight Mach number, dimensionless
m	mass of missile or model, slugs
N	concentration of particles (i. e., number of particles per unit volume), ft^{-3}
n	distance normal to boundary, ft
$\bar{n}$	reduced normal distance, n/D, dimensionless
P_0	nozzle reservoir pressure, lb/sq ft
Q	total heat transferred, ft-lb
r	radius of curvature of body surface at stagnation point, ft
S	surface area, sq ft
T	temperature, °R
T_0	nozzle reservoir temperature, °F
t	time, sec
$\bar{t}$	reduced time, $\frac{t}{D^2}$, sec/sq ft
V	velocity, ft/sec
y'	altitude, ft
x,y,z	rectangular coordinates, ft (except when appearing as subscripts on stresses)
$\bar{x},\bar{y},\bar{z}$	reduced coordinates ($\bar{x}=x/D$, $\bar{y}=y/D$, $\bar{z}=z/D$), dimensionless
α	coefficient of thermal expansion, ft/ft-°R
β	constant in density-altitude relation, ft^{-1} (see eq. (1))
δ	typical flow deflection angle, deg
θ	angle of flight path with respect to horizontal, deg
ν	Poisson's ratio, dimensionless
ρ	air density, slugs/cu ft
ρ_0	reference density, slugs/cu ft (reservoir density in nozzle)
$\sigma_x,\sigma_y,\sigma_z$	tensile or compressive stresses, lb/sq ft (see sketch)
$\tau_{xy},\tau_{xz},\tau_{yz}$	shear stresses, lb/sq ft (see sketch and note $\tau_{xy}=\tau_{yx}$, $\tau_{xz}=\tau_{zx}$, and $\tau_{yz}=\tau_{zy}$)

[1] Supersedes NACA Research Memorandum A55I15 by A. J. Eggers, Jr., 1955.

Preceding Page Blank

ξ,η,ζ	direction cosines of normal to a boundary, dimensionless

SUBSCRIPTS

av	average conditions
e	conditions at "entrance" to earth's atmosphere or simulator
l	local conditions just outside of boundary layer
mi	missile
mo	model
s	stagnation conditions

ANALYSIS

In order to clarify the basic requirements of a simulator, this study is initiated with a review of some of the more important causes and effects of aerodynamic heating of long-range ballistic missiles. Following this review, the conditions of simulation will be set forth in a mathematical form designed to facilitate the choice of a practical simulator.

MOTION AND HEATING OF LONG-RANGE BALLISTIC MISSILES

It is a fundamental characteristic of ballistic missiles (see ref. 1) that speed begets range, with the result that hypervelocities in excess of 10,000 feet per second are required in order to obtain long ranges in excess of 1,000 miles. A long-range ballistic missile first attains hypervelocities near the end of powered flight. In this phase of flight and throughout the large majority of unpowered flight the vehicle should pass more or less unimpeded through the rarefied upper atmosphere of the earth, corresponding to altitudes in excess of several hundred thousand feet.[2] Its trajectory terminates, however, with a very rapid descent through all or part of the earth's relatively dense lower atmosphere. In this phase of flight, termed the atmospheric entry, retardation and severe aerodynamic heating of the missile can almost certainly be expected to occur (see ref. 2).

Retardation during atmospheric entry is caused by the combined action of pressure and viscous forces, while aerodynamic heating stems in the main from work done by viscous forces. In both cases it is aerodynamic rather than gravity forces which play the predominant role, with the result that motion and heating of the missile emerge as closely related phenomena. Thus changes in missile shape which affect motion will also affect heating. This fact can, as discussed in reference 2, be exploited in the design of missiles with reduced aerodynamic heating. The potential for excessive heating remains, however, as an unavoidable property of the long-range ballistic missile which enters the earth's atmosphere at hypervelocity.

Excessive heating can have several effects. First and perhaps most serious of these effects is the development of high thermal stresses in the structure of the missile. These stresses tend, for example, to far overshadow the pressure induced stresses. In addition, there is the natural weakening of the missile material at high temperatures, so that structural failure may occur during atmospheric entry. There is, of course, the further possibility that intense aerodynamic heating will, as with meteors, cause burning and the ultimate destruction of the missile.

These, then, are some of the important causes and effects of aerodynamic heating of a long-range ballistic missile entering the atmosphere. They suggest that an atmosphere entry simulator might logically include means of simulating missile velocity, missile configuration (e. g., shape), and the lower portion of the earth's atmosphere. We will proceed from this suggestion to formulate our conditions of simulation.

CONDITIONS OF SIMULATION

The analysis to follow tacitly presumes the validity of many time-tested assumptions of aerodynamics, thermodynamics, and solid mechanics. In addition, however, it is predicated on the assumptions that during atmospheric entry (1) radiation has a secondary effect on missile heating, (2) gravity has a secondary effect on missile motion, (3) the flow-field freeze principle of Oswatitsch (ref. 3) holds for the missile, and (4) the thermal properties (e. g., specific heats) and transport properties (e. g., thermal conductivity and viscosity) of air are functions of temperature only. The first two assumptions are suggested by the calculations of references 1 and 2,[3] while the third assumption hinges essentially on the requirement that the square of the hypersonic similarity parameter for a missile be large compared to 1 during entry (i. e., $M^2 \sin^2 \delta >> 1$). For missiles of normal slenderness, the hyperspeed of entry tends to insure the satisfying of this requirement with the result that flight Mach number loses its significance as an important similarity parameter.[4] The last assumption is restrictive only in the event air tends to dissociate (or possibly ionize) and it will therefore be treated in a discussion of these phenomena later in the paper (see section on "Performance Limitations").

Now it is convenient in discussing similitude to imagine a model counterpart to the missile and a test chamber counterpart to the atmosphere. Furthermore it is permissible for our purposes to proceed from the simplified equations of reference 2 for the convective heating of ballistic missiles. Thus for an isothermal atmosphere (which closely approximates the earth's lower atmosphere, see ref. 2)

$$\frac{\rho}{\rho_0} = e^{-\beta y'} \tag{1}$$

and there follows:

(a) Heat absorbed per unit mass at altitude y'

$$\frac{Q}{m} = \frac{1}{4}\left(\frac{C_f' S}{C_D A}\right)(V_e^2 - V^2) \tag{2}$$

where

$$V^2 = V_e^2 e^{-\frac{C_D \rho_0 A}{\beta m \sin \theta_e} e^{-\beta y'}} \tag{3}$$

[2] It is presumed that the missile is, unlike the usual meteor, so large (say of the order of feet in typical dimension) that free molecule phenomena play a minor role in its motion and heating.

[3] The first assumption is, of course, best suited to "relatively light" missiles which are designed on the so-called "heat sink" principle, or, more generally, which are designed to maintain relatively cool surfaces.

[4] It is demonstrated in reference 3 that Mach number and stream angle in the disturbed flow are independent of flight Mach number, provided $M^2 \sin^2 \delta >> 1$, and provided the air behaves ideally. In the event nonideal behavior, like changes in the specific heats, occurs as a result of high temperatures in the disturbed flow, then flight velocity tends to replace flight Mach number as the important index of motion since it is through this velocity (via kinetic energy) that high disturbed air temperatures are created.

(b) Average rate of heat transfer per unit area

$$\frac{dH_{av}}{dt}=\frac{C_f'\rho_0 V_e^3}{4}\,e^{-\beta y'}e^{-\frac{3}{2}\frac{C_D\rho_0 A}{\beta m\sin\theta_e}e^{-\beta y'}} \tag{4}$$

(c) Rate of heat transfer to stagnation point

$$\frac{dH_s}{dt}=\text{const}\,\sqrt{\frac{\rho_0}{r}}\,V_e^3 e^{-\frac{\beta y'}{2}}e^{-\frac{3}{2}\frac{C_D\rho_0 A}{\beta m\sin\theta_e}e^{-\beta y'}} \tag{5}$$

According to equation (1) the density of the air in the test chamber must vary exponentially with the distance corresponding to altitude in the atmosphere. The more general implication is, of course, that the test chamber must duplicate variations of ρ/ρ_0 in the atmosphere, whatever they may be, although the absolute magnitudes of ρ and ρ_0 may be quite different from those in the atmosphere. The static temperature of the air in the test chamber is, as in the case of the atmosphere, presumed to be small by comparison to missile recovery temperature (see ref. 2 in connection with this point as it relates to the derivation of eqs. (2) through (5)).

It will be stipulated now that model and missile be geometrically similar in structure and configuration, and made of the same material. Furthermore, the condition is imposed that the model enter the test chamber at the same speed and temperature as the missile enters the atmosphere. Finally, it is required that model and missile have the same Reynolds numbers (based on local conditions outside the boundary layer) at corresponding points $\beta y'$ in their trajectories. By corresponding points it is meant where the product $\beta y'$ is the same for model and missile. It should be recognized, of course, that, in general, β and y' will individually be grossly different for model and missile.

It follows from these requirements and equation (2) that the heat transfer per unit mass Q/m to model and missile will be the same at corresponding points $\beta y'$ provided V is the same, since C_f' and $C_f'S/C_DA$ are the same. But from equation (3) the velocity V will be the same at corresponding $\beta y'$ only if $C_D\rho_0 A/\beta m\sin\theta_e$ is the same. If the subscript mo refers to model and mi to missile, then the last provision may be written.

$$\frac{(\rho_0 D)_{mi}}{(\rho_0 D)_{mo}}=\left(\frac{D_{mi}}{D_{mo}}\right)^2\frac{(y'/\sin\theta_e)_{mo}}{(y'/\sin\theta_e)_{mi}} \tag{6}$$

But model and missile Reynolds numbers, velocities, and disturbed air temperatures [5] are the same, hence

$$(\rho_0 D)_{mi}=(\rho_0 D)_{mo} \tag{7}$$

and equation (6) may be written

$$\left(\frac{y_e'}{\sin\theta_e}\right)_{mo}=L=\left(\frac{y_e'}{\sin\theta_e}\right)_{mi}\left(\frac{D_{mo}}{D_{mi}}\right)^2 \tag{8}$$

This expression fixes the length L of the test chamber in terms of the portion of the atmosphere to be simulated therein and the ratio of model to missile size.[6] If equation (8) and the previously set forth requirements are satisfied, then model and missile should experience equal heat transfer per unit mass, and hence equal average temperature rise at corresponding points in their trajectories. These quantities are significant, of course, because they tend to determine whether a missile will melt or perhaps burn during flight.

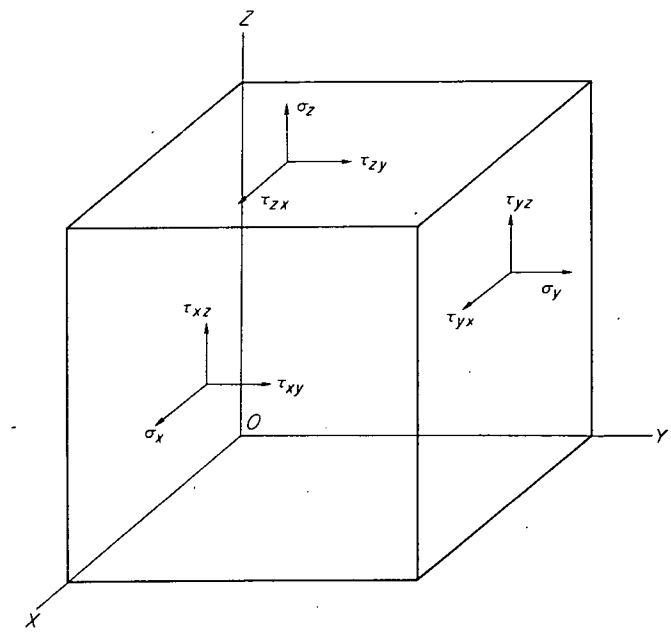
The next question is how do the heat-transfer rates compare in the case of model and missile? It is easily deduced from equations (4) and (5) and the conditions for equal heat transfer per unit mass that

$$\left(\frac{dH_{av}}{dt}\right)_{mo}=\frac{D_{mi}}{D_{mo}}\left(\frac{dH_{av}}{dt}\right)_{mi} \tag{9}$$

and

$$\left(\frac{dH_s}{dt}\right)_{mo}=\frac{D_{mi}}{D_{mo}}\left(\frac{dH_s}{dt}\right)_{mi} \tag{10}$$

at corresponding points $\beta y'$. That is to say, the average and stagnation point heat-transfer rates are higher for the model in proportion to the ratio of missile to model size. But perhaps the foremost importance of heat-transfer rates is, as discussed earlier, in how they influence thermal stresses in the missile structure and, for example, lead to ablation of surface material. Evidently, then, it would be most desirable if equations (9) and (10) implied equal thermal stresses in model and missile. This possibility is easily checked using modified equilibrium thermal-stress equations for an unrestrained isotropic elastic body (see ref. (4) and sketch).



[5] This observation with regard to disturbed air temperatures is easily verified by considering flow near the surface of a missile with a stagnation point. Assuming for simplicity that air in the disturbed flow behaves ideally, we have at the stagnation point $T_s\approx V^2/2C_p$ since $M^2>>1$. Then the temperature of the air just outside the boundary layer is given by the expression $T_l=\frac{V^2}{2C_p}\left(1+\frac{\gamma-1}{2}M_l^2\right)^{-1}$. Hence if V and M_l are the same for model and missile, then T_l and V_l are the same, independent of ambient air temperature. We are assured of equal M_l's by the freeze principle (see footnote 4).

[6] Since model and missile velocities are the same at corresponding points in their trajectories, it follows from equation (8) that the time of flight in the test chamber is reduced below that of atmospheric entry by the ratio $(D_{mo}/D_{mi})^2$.

Thus

$$\left.\begin{aligned}\frac{\partial\sigma_x}{\partial\bar{x}}+\frac{\partial\tau_{xy}}{\partial\bar{y}}+\frac{\partial\tau_{xz}}{\partial\bar{z}}-\frac{\alpha E}{1-2\nu}\frac{\partial T}{\partial\bar{x}}=0\\ \frac{\partial\sigma_y}{\partial\bar{y}}+\frac{\partial\tau_{xy}}{\partial\bar{x}}+\frac{\partial\tau_{yz}}{\partial\bar{z}}-\frac{\alpha E}{1-2\nu}\frac{\partial T}{\partial\bar{y}}=0\\ \frac{\partial\sigma_z}{\partial\bar{z}}+\frac{\partial\tau_{xz}}{\partial\bar{x}}+\frac{\partial\tau_{yz}}{\partial\bar{y}}-\frac{\alpha E}{1-2\nu}\frac{\partial T}{\partial\bar{z}}=0\end{aligned}\right\} \tag{11}$$

where the stresses are not true thermal stresses, but rather they are the stresses produced by the "body forces," $\frac{-\alpha E}{1-2\nu}\frac{\partial T}{\partial\bar{x}}$, etc.

The corresponding compatibility conditions are

$$\left.\begin{aligned}\nabla^2\sigma_x+\frac{1}{1+\nu}\frac{\partial^2\psi}{\partial\bar{x}^2}=\frac{\alpha E}{1-2\nu}\left(\frac{\nu}{1-\nu}\nabla^2T+2\frac{\partial^2T}{\partial\bar{x}^2}\right)\\ \nabla^2\sigma_y+\frac{1}{1+\nu}\frac{\partial^2\psi}{\partial\bar{y}^2}=\frac{\alpha E}{1-2\nu}\left(\frac{\nu}{1-\nu}\nabla^2T+2\frac{\partial^2T}{\partial\bar{y}^2}\right)\\ \nabla^2\sigma_z+\frac{1}{1+\nu}\frac{\partial^2\psi}{\partial\bar{z}^2}=\frac{\alpha E}{1-2\nu}\left(\frac{\nu}{1-\nu}\nabla^2T+2\frac{\partial^2T}{\partial\bar{z}^2}\right)\\ \nabla^2\tau_{yz}+\frac{1}{1+\nu}\frac{\partial^2\psi}{\partial\bar{y}\partial\bar{z}}=2\frac{\alpha E}{1-2\nu}\frac{\partial^2T}{\partial\bar{y}\partial\bar{z}}\\ \nabla^2\tau_{xz}+\frac{1}{1+\nu}\frac{\partial^2\psi}{\partial\bar{x}\partial\bar{z}}=2\frac{\alpha E}{1-2\nu}\frac{\partial^2T}{\partial\bar{x}\partial\bar{z}}\\ \nabla^2\tau_{xy}+\frac{1}{1+\nu}\frac{\partial^2\psi}{\partial\bar{x}\partial\bar{y}}=2\frac{\alpha E}{1-2\nu}\frac{\partial^2T}{\partial\bar{x}\partial\bar{y}}\end{aligned}\right\} \tag{12a}$$

where

$$\nabla^2=\frac{\partial^2}{\partial\bar{x}^2}+\frac{\partial^2}{\partial\bar{y}^2}+\frac{\partial^2}{\partial\bar{z}^2}$$

$$\psi=\sigma_x+\sigma_y+\sigma_z$$

and the boundary conditions are

$$\left.\begin{aligned}\sigma_x\xi+\tau_{xy}\eta+\tau_{xz}\zeta=\frac{\alpha ET}{1-2\nu}\xi\\ \sigma_y\eta+\tau_{yz}\zeta+\tau_{xy}\xi=\frac{\alpha ET}{1-2\nu}\eta\\ \sigma_z\zeta+\tau_{xz}\xi+\tau_{yz}\eta=\frac{\alpha ET}{1-2\nu}\zeta\end{aligned}\right\} \tag{12b}$$

The heat-flow equation is (see ref. (5))

$$\nabla^2T=\frac{\partial^2T}{\partial\bar{x}^2}+\frac{\partial^2T}{\partial\bar{y}^2}+\frac{\partial^2T}{\partial\bar{z}^2}=\frac{1}{K}\frac{\partial T}{\partial\bar{t}} \tag{13}$$

with boundary conditions

$$\left.\begin{aligned}(T_{wall})_{initial}=\text{known}\\ k\frac{\partial T}{\partial\bar{n}}\bigg|_{\substack{outer\\surface}}=D\frac{dH}{dt}\\ \text{and (probably)}\\ k\frac{\partial T}{\partial\bar{n}}\bigg|_{\substack{inner\\surface}}=0\end{aligned}\right\} \tag{14}$$

Now the thermal stresses are given by superposing the "hydrostatic" pressure $\alpha ET/1-2\nu$ on solutions to equations (11) consistent with the compatibility and boundary conditions (eqs. (12)) and the solution to the heat-flow equation (13) along with its boundary conditions (eqs. (14)). But if equations (9) and (10) along with the requirements necessary for their development are satisfied, then equations (11) through (14) (and the "hydrostatic" pressure) are mathematically identical for model and missile. Hence, the thermal stresses must be the same in model and missile at corresponding $\beta y'$ in their trajectories.

Necessary conditions for simulating aerodynamic heating and resulting thermal stresses in a ballistic missile are then, according to this analysis, as follows. First, model and missile must be geometrically similar and made of the same material. In addition, they must have the same flight speeds and Reynolds numbers (based on local conditions outside the boundary layer) at corresponding points in their trajectories. Finally, in order to meet these conditions and to insure equal heating of model and missile, the test chamber must contain air at relatively low temperature and with variations in ρ/ρ_0 along the model flight path equal to those in the atmosphere along the missile flight path.

With this knowledge we are in a position to consider the practical problems of simulating atmospheric entry.

A PRACTICAL ATMOSPHERE ENTRY SIMULATOR

It is appropriate to determine first how to provide a model with the correct initial hypervelocity required for simulation. For this purpose it is suggested that a hypervelocity gun can be employed. Several such guns have been developed (see e. g., ref. 6) to launch small models at speeds above 15,000 feet per second. These speeds correspond to those of ballistic missiles (see ref. 1) with ranges of the order of 2,000 miles and greater. Both speed and range fall, then, into the categories of interest in this paper.

The next question is how to provide a model test chamber which simulates the lower portion of the earth's atmosphere. For this purpose it is suggested that a special supersonic nozzle can be used to advantage. To illustrate, it was found in reference 2 (see fig. 4 therein) that the major part of the aerodynamic heating of a ballistic missile entering the atmosphere occurs over a range of about 100,000 feet in altitude. In this altitude range ρ/ρ_0 varies by a factor of about 10^{-2}. A corresponding variation in density can be obtained between the settling chamber and exit section of a Mach number 5 supersonic nozzle (see ref. 7). Imagine, then, a hypervelocity gun positioned to launch a model upstream along the axis of such a nozzle. The nozzle is designed to provide an essentially exponential variation in density along its axis, the density decreasing from a very high value in the settling chamber to a very low value at the exit. Accordingly, a model proceeding upstream through the nozzle encounters an increasingly dense atmosphere like that presented by the earth to a descending ballistic missile. Now, to be sure, unlike atmospheric air, the air in the nozzle is in motion. However, the air velocity is small by comparison to the hypervelocity of the model, and therefore this difference between nozzle air and atmospheric air should mar

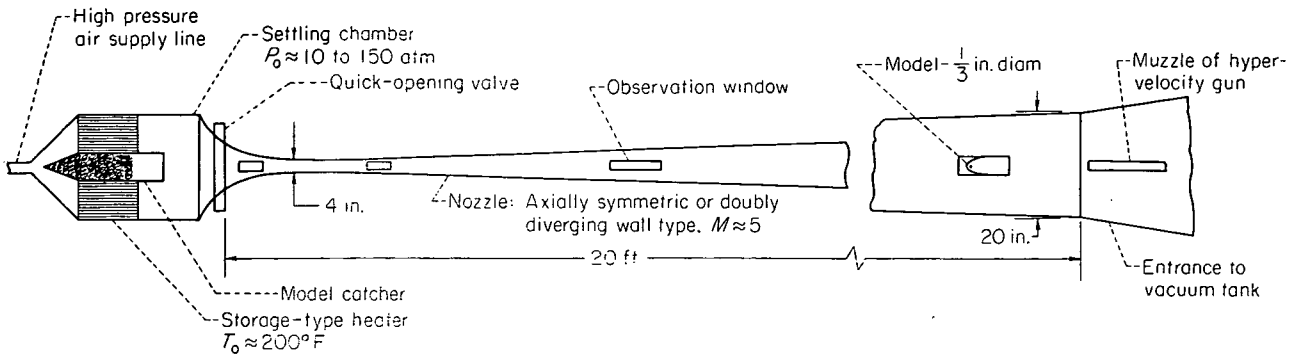


FIGURE 1.—Example atmosphere entry simulator.

only slightly the function of the nozzle as a test chamber.[7]

The combination of hypervelocity gun and supersonic nozzle merits attention, then, as an atmosphere entry simulator. An example simulator of this type will therefore be considered next.

EXAMPLE SIMULATOR

Consistent with the previous discussion, a Mach number 5 nozzle is chosen to simulate the earth's atmosphere over 100,000 feet of altitude. Now let us assume that ballistic missiles with up to 4,000 miles range are to be studied with this simulator. The corresponding range of atmospheric entrance angles θ_e is from 45° down to about 30° (see ref. 1). The length of the nozzle is fixed according to equation (8) by the maximum values of $(y_e'/\sin\theta_e)_{mi}$ and D_{mo}/D_{mi}. This value of $(y_e'/\sin\theta_e)_{mi}$ is, from the above specifications, $\frac{100{,}000}{\sin 30°} =$ 200,000 feet. The maximum value of D_{mo}/D_{mi} will be dictated by the size of the largest model which can be launched by the special gun available and by the size of the smallest missile to be simulated. For the purpose of this discussion it suffices to observe that the model size will probably be of the order of a fraction of an inch, while the missile size will probably be of the order of several feet. It follows that the maximum value of D_{mo}/D_{mi} should be of the order of 10^{-2}. In this event we have from equation (8) that the length of the nozzle is of the order of 20 feet, and from equation (7) the nozzle stagnation density is of the order of 100 times sea level air density. A missile 3 feet in diameter and weighing 5,000 pounds would thus be simulated by a model 0.36 inch in diameter and weighing 0.005 pound.

On the basis of these considerations our example simulator might appear something like the one shown in figure 1. The required nozzle stagnation densities are obtained for running times of the order of a second by using a settling chamber charged with high pressure air. A wide range of settling-chamber pressures and, hence, densities makes it possible to vary the range of altitudes simulated. The storage heater in the settling chamber maintains the air temperatures above those for which liquefaction can occur in the nozzle. The nozzle contour will tend to have very small slopes in the streamwise direction. Hence it is anticipated that flow in the nozzle will not depart radically from the one-dimensional type. Air from the nozzle passes into a vacuum tank which is of sufficient size to maintain the nozzle compression ratios required for supersonic flow during the course of a test. Observation windows are located at short intervals along the nozzle side walls to permit photographing models in flight and determining effects of aerodynamic heating. In this regard it would quite likely prove desirable to employ a spectrometer to identify the sources of radiation energy emitted in the vicinity of models. The simulator would be instrumented for measuring settling-chamber pressure and temperature and, of course, the time-distance history of models. Models would be launched from a hypervelocity gun located at or near the end of the nozzle, and they would be arrested in a catcher located in the settling chamber. The damage to models in the catcher should be negligible for low impacting velocities, thereby permitting the study of recovered models to determine changes which occurred during atmospheric entry.

We have, then, some idea of how the proposed simulator might be employed in practice. It is important, however, to be aware of the points of difficulty which may limit the performance of the device as a simulator.

PERFORMANCE LIMITATIONS

First, it should be noted that pressure-induced stresses in the model will be higher than those in the missile by the ratio D_{mi}/D_{mo}. This point may prove troublesome, although not unduly so if these stresses are very low (as they tend to be) in the missile. It should be remembered too that by proper model design (e. g., the use of internal pressurization or other bracing) this problem can be minimized. Careful attention must, of course, be given to both model and sabot design from the standpoint of minimizing stresses in the model during launching.

Another point of difficulty may be encountered if material properties (e. g., yield point) are a significant function of time under rapid heating conditions. There is some indication (see ref. 8 and papers cited therein) that at the very high heating rates of long-range ballistic missiles (corresponding to temperature-rise rates of the order of 100° F/sec and more), the importance of time is small. It is indicated too that this remains true, and, more important, that material properties remain essentially the same at the much

[7] It is interesting to note that the supersonic nozzle when used in the proposed manner has compensating features; namely, as model velocity decreases, the air velocity decreases and, as model recovery temperature decreases, the air static temperature rises up toward atmospheric air temperature. These features are, of course, favorable to simulating atmospheric entry in that they tend to preserve the required similarity between atmospheric air and nozzle air. In this manner, too, the possibility of correcting for small differences between these media is enhanced.

higher heating rates produced in the simulator.[8] Far more information is needed, however, before the significance of time in the sense of this discussion can be fully assessed.

A further question which should be raised is whether or not a body can distort fast enough with changes in temperature to remain in stress-strain equilibrium (i. e., acceleration terms negligible) as was assumed in deriving equations (11) and (12). This situation would be more serious in the case of the model than in the case of the missile. A crude check on the matter is easily obtained for a body which behaves elastically. To illustrate, the time required for the model to make small adjustments in stress-strain equilibrium should be of the same order as the time required for an elastic wave to travel the length of the model. For a typical steel model ($D=\frac{1}{3}$ in.) in the simulator, this latter time would be about 10^{-6} seconds. If we assume that the model experiences a total temperature rise of 1500° F while traveling through the simulator, then 10^{-6} seconds is also the time required for only about 1° temperature change in the model material. Accordingly, only small adjustments in stress-strain equilibrium are evidently required in this time, and hence equilibrium should tend to be realized in model as well as missile. If time-dependent plastic deformation should become significant, then this statement obviously no longer holds.[9] Thus, for example, the simulator may not (in view of its foreshortened time scale) duplicate more than qualitatively a fracture process (see ref. 9) although it should tend to duplicate thermal deformation up to and including the beginning of fracture. If fracture occurs on a molecular scale, like ablation by sublimation, then the phenomenon will tend to be properly reproduced in the simulator provided the sublimation rate is proportional to heat-transfer rate.

There is, too, the possibility of a missile being aerodynamically heated to temperatures where it will burn during descent through the earth's atmosphere. The simulator should tend to duplicate conditions leading up to this phenomenon; however, there is a question as to how well burning would be duplicated. The complexity and lack of complete understanding of metal burning (see, e. g., ref. 10) preclude the possibility of obtaining a quantitative answer to this question at the present time. From the qualitative viewpoint it is reasonable to expect that the effects of increased partial pressure of oxygen (acting to increase burning rate) and the reduced model size (acting to decrease the amount of material to be burned) should combine in the simulator to compensate for its foreshortened time scale, thereby more nearly providing simulation of missile burning. Burning should be accurately simulated for cases where burning rate is directly proportional to the partial pressure of oxygen.

As a final point, it is appropriate to consider the matter of dissociation and association of the oxygen and nitrogen in air. The simulator produces essentially the same disturbed air temperatures as the missile entering the atmosphere. Accordingly, the potential for dissociation and association is duplicated by the simulator. At the present time, however, it is felt that these two phenomena obey different rate laws (see Appendix). In this event, neither the phenomena nor their effects on heating of a ballistic missile can be duplicated except by 1 to 1 simulation (i. e., the equivalent of flight tests with the full-scale missile). An indication of the possible error that this situation may introduce in tests with the proposed simulator can be obtained from the calculations of reference 11 which suggest that the net effect of equilibrium dissociation and association in free flight may be to increase the rate of heat transfer to a stagnation point by only about 50 percent.[10] This increase should be well within the design safety factor of a missile.

CONCLUDING REMARKS

It has been found that an atmosphere entry simulator consisting of a hypervelocity gun combined with a special supersonic nozzle may be used to study the conditions of extreme heat transfer and thermal stress which introduce such serious problems in the flight of a long-range ballistic missile. The effects of aerodynamic heating on the model can be observed with relative ease, and further, the tests can be conducted at a cost which is negligible by comparison to that of flight tests. Indeed, in the simplest test, the simulator could provide with one photograph of a model rather substantial evidence as to whether or not the corresponding missile would remain essentially intact while traversing the atmosphere.

AMES AERONAUTICAL LABORATORY
NATIONAL ADVISORY COMMITTEE FOR AERONAUTICS
MOFFETT FIELD, CALIF., *Sept. 15, 1955*

[8] This discussion should not be construed to mean that material properties are the same under conditions of high rates of heating as they are under steady state conditions (see ref. 8).

[9] Thus with a slow process, like creep, model deformation would not simulate missile deformation (see, e. g., ref. 9), but rather, it would be less by the ratio of $(D_{m_0}/D_{m_i})^2$ due to the foreshortened time scale in the simulator. Even in the case of the missile, however, the entry time may be so short (of the order of seconds) that creep plays a minor role in deforming the vehicle.

[10] Dissociation and association may have especially marked effects on stagnation point heat transfer since these phenomena can strongly affect both the inviscid and viscous flows in this region.

APPENDIX A

DISSOCIATION AND ASSOCIATION RATES

The dissociation of O_2 and N_2 is thought (see, e. g., refs. 12 and 13) to obey the linear law

$$\frac{dN}{dt}=C_1(T)N \tag{A1}$$

where N is the concentration (or density in particles per unit volume) and $C_1(T)$ is the rate constant which usually depends only upon temperature. On the other hand, the corresponding association process (e. g., $O+O\rightarrow O_2$) is thought to obey the second-order law[1]

$$\frac{dN}{dt}=C_2(T)N^2 \tag{A2}$$

Now disturbed air velocities are the same in the case of model and missile, while disturbed air densities are higher in the case of the model by the ratio of D_{mi}/D_{mo}. It follows then that the simulator will tend to duplicate a rate process in which the percentage rate of change of concentration of a given type of particle is proportional to the concentration of that particle, namely,

$$\frac{1}{N}\frac{dN}{dt}=C(T)N \tag{A3}$$

But the simulator tends to duplicate temperature and type of particle; hence, it should duplicate the "association" rate process given by equation (A2) since $C(T)=C_2(T)$. It will apparently not, however, duplicate the "dissociation" rate process given by equation (A1).

[1] Actually there is some question as to the correctness of either equation (A1) or (A2) (see e. g,, ref. (14)) for pure media and there is the further complication of impurities which could lead, for example, to a third-order rate process.

REFERENCES

1. Eggers, A. J., Jr., Allen, H. Julian, and Neice, Stanford E.: A Comparative Analysis of the Performance of Long-Range Hypervelocity Vehicles. NACA TN 4046, 1957 (Supersedes NACA RM A54L10).
2. Allen, H. Julian, and Eggers, A. J., Jr.: A Study of the Motion and Aerodynamic Heating of Missiles Entering the Earth's Atmosphere at High Supersonic Speeds. NACA TN 4047, 1957 (Supersedes NACA RM A53D28).
3. Oswatitsch, Klaus: Similarity Laws for Hypersonic Flow. KTH Aero. TN 16, Royal Inst. of Tech., Division of Aeronautics, Stockholm, Sweden, 1950.
4. Timoshenko, S., and Goodier, J. N.: Theory of Elasticity. McGraw-Hill Book Co., 1951, pp. 423–424.
5. Carslaw, H. S., and Jaeger, J. C.: Conduction of Heat in Solids. Oxford Univ. Press, 1948, p. 8.
6. Charters, A. C., Denardo, B. Pat, and Rossow, Vernon J.: Development of a Piston-Compressor Type Light-Gas Gun for the Launching of Free-Flight Models at High Velocity. NACA TN 4143, 1957 (Supersedes NACA RM A55G11).
7. Ames Research Staff: Equations, Tables, and Charts for Compressible Flow. NACA Rep. 1135, 1953.
8. Heimerl, George J., and Inge, John E.: Tensile Properties of Some Sheet Materials Under Rapid-Heating Conditions. NACA RM L55E12b, 1955.
9. Nadai, A.: Theory of Flow and Fracture of Solids. McGraw-Hill Book Co., 1950, pp. 395–397.
10. Coffin, Kenneth P.: Burning Times of Magnesium Ribbons in Various Atmospheres. NACA TN 3332, 1954.
11. Eggers, A. J., Jr., Hansen, C. Frederick, and Cunningham, Bernard E.: Theoretical and Experimental Investigation of the Effect of Yaw on Heat Transfer to Cylinders in Hypersonic Flow. NACA TN 4229, 1958.
12. Bethe, H. E., and Teller, E.: Deviations from Thermal Equilibrium in Shock Waves. BRL Rep. X–117, Aberdeen Proving Grounds, 1945.
13. Krieger, F. J., and White, W. B.: The Composition and Thermodynamic Properties of Air at Temperatures from 500 to 8000° K and Pressures from 0.00001 to 100 Atmospheres. RAND Rep. R–149, 1949.
14. Prutton, Carl F., and Maron, Samuel H.: Fundamental Principles of Physical Chemistry. The Macmillan Co., 1944, pp. 610–611.

REPORT 1379

TABLE OF CONTENTS

	Page
SUMMARY	1017
INTRODUCTION	1017
GENERAL EQUATIONS	1018
Boundary-Layer Equations	1018
Stewartson's Transformation	1018
Similar Solutions	1019
Independence Principle	1020
Stagnation-Line Flow	1020
PROPERTIES OF SOLUTIONS	1021
Velocity and Enthalpy Profiles	1021
Skin Friction	1026
Secondary Flow	1027
Heat Transfer and Adiabatic Wall Temperature	1028
Reynolds Analogy	1029
Boundary-Layer Thickness	1029
ENGINEERING HEAT-TRANSFER RELATIONS FOR STAGNATION-LINE FLOW	1029
Fluid Properties at the Wall	1029
Chordwise Velocity Gradient	1029
Heat-Transfer Parameter	1030
Effect of Yaw Angle and Mach Number on Heat-Transfer Coefficient at the Stagnation Line	1030
SUMMARY OF RESULTS	1031
APPENDIXES	
A—SYMBOLS	1033
B—SOLUTION OF ORDINARY DIFFERENTIAL EQUATIONS	1034
C—ASYMPTOTIC SOLUTION	1036
D—STAGNATION-LINE RECOVERY FACTOR FOR YAWED CYLINDER	1038
REFERENCES	1038

REPORT 1379

COMPRESSIBLE LAMINAR BOUNDARY LAYER OVER A YAWED INFINITE CYLINDER WITH HEAT TRANSFER AND ARBITRARY PRANDTL NUMBER [1,2]

By Eli Reshotko and Ivan E. Beckwith

SUMMARY

The equations are presented for the development of the compressible laminar boundary layer over a yawed infinite cylinder. For compressible flow with a pressure gradient the chordwise and spanwise flows are not independent. Using the Stewartson transformation and a linear viscosity-temperature relation yields a set of three simultaneous ordinary differential equations in a form yielding similar solutions. These equations are solved for stagnation-line flow for surface temperatures from zero to twice the free-stream stagnation temperature and for a wide range of yaw angle and free-stream Mach number.

The results indicate that the effect of yaw on the heat-transfer coefficient at the stagnation line depends markedly on the free-stream Mach number. For subsonic Mach numbers the decrease in heat-transfer coefficient with yaw angle Λ *is about* $\sqrt{\cos \Lambda}$, *which is the decrease for incompressible flow. However, for free-stream Mach numbers greater than approximately 2, the variation in heat-transfer coefficient with yaw angle is somewhat less than* $\cos \Lambda$ *except when the normal component of the stream Mach number is subsonic; then the variation tends to approach* $\sqrt{\cos \Lambda}$. *This decrease in heat-transfer coefficient with yaw angle is practically independent of wall temperature and Prandtl number for the values of these parameters used in the present calculations. The recovery factor, defined in terms of the local external temperature, can be approximated as the square root of the Prandtl number for the range of yaw angle, Mach number, and Prandtl number, included in the calculations.*

An unusual result of the solutions is that for large yaw angles and stream Mach numbers the chordwise velocity within the boundary layer exceeds the local external chordwise velocity, even for a highly cooled wall.

INTRODUCTION

As flight speeds are increased, the problem of aerodynamic heating becomes more serious, and the temperatures of critical areas such as the nose of an aircraft or the wing leading edge may exceed the design specifications. An accurate knowledge of the laminar-boundary-layer characteristics then becomes desirable, not only for predicting heat-transfer rates, but also for calculating the stability of the boundary-layer flow. The yawed infinite cylinder approximately simulates the leading edge of a sweptback wing or of a body of high fineness ratio at angle of attack and also allows a basic simplification of the boundary-layer theory.

Almost simultaneously, Prandtl (ref. 2), Struminsky (ref. 3), Jones (ref. 4), and Sears (ref. 5) observed that for incompressible flow over a yawed infinite cylinder the boundary-layer development in the chordwise direction (normal to the cylinder axis) is independent of the spanwise flow. For compressible flow, however, this "independence principle" does not apply, because the density variation must depend on the velocities in both the chordwise direction and the spanwise direction (refs. 3 and 6).

Where the independence principle applies, the solutions for boundary-layer development in the chordwise plane are those that have been obtained for incompressible two-dimensional flow. A number of investigators have integrated the spanwise momentum equation for the various solutions to this problem. Sears (ref. 5) has obtained the spanwise solution corresponding to the series-type solution about a cylinder. Wild (ref. 7), by an integral technique, has obtained the spanwise solution for Howarth's elliptic cylinder, and Cooke (ref. 8) has tabulated the spanwise solutions corresponding to Hartree's solutions (ref. 9) to the equations of Falkner and Skan. Further, Goland (ref. 10) has shown that the heat-transfer coefficient of a yawed cylinder varies as the square root of the Reynolds number based on the normal component of the stream velocity. Thus, for a given stream velocity, the heat-transfer coefficient decreases as the square root of the cosine of the yaw angle. This decrease in heat-transfer coefficient is associated with the increase in boundary-layer thickness due to yaw.

For compressible flow where the independence principle does not apply, the momentum equations for both the chordwise flow and the spanwise flow must be solved simultaneously. Solutions to the compressible-flow problem with zero heat transfer and a Prandtl number of 1 have been given by Crabtree (ref. 11) and Tinkler (ref. 12). Both of these solutions are for flows where the spanwise Mach number at the stagnation line of the cylinder is 1 or less. Consequently, for high stream Mach numbers these solutions apply only to cases where the yaw angle is small. From the

[1] Supersedes NACA Technical Note 3986, by Eli Reshotko and Ivan E. Beckwith, 1957.

[2] This report combines the results of two independent investigations, one at the Lewis Flight Propulsion Laboratory and the other at the Langley Aeronautical Laboratory. The principal results of the investigation at the Lewis laboratory were presented by the senior author before the 1956 Heat Transfer and Fluid Mechanics Institute at Stanford University on June 22, 1956. A brief written version of that talk appears in the proceedings of the institute (ref. 1).

observation that for a Prandtl number of 1 the energy equation and the spanwise momentum equations are similar (ref. 6), Moore (ref. 13) has indicated the form that Crabtree's equations take for a noninsulated surface.

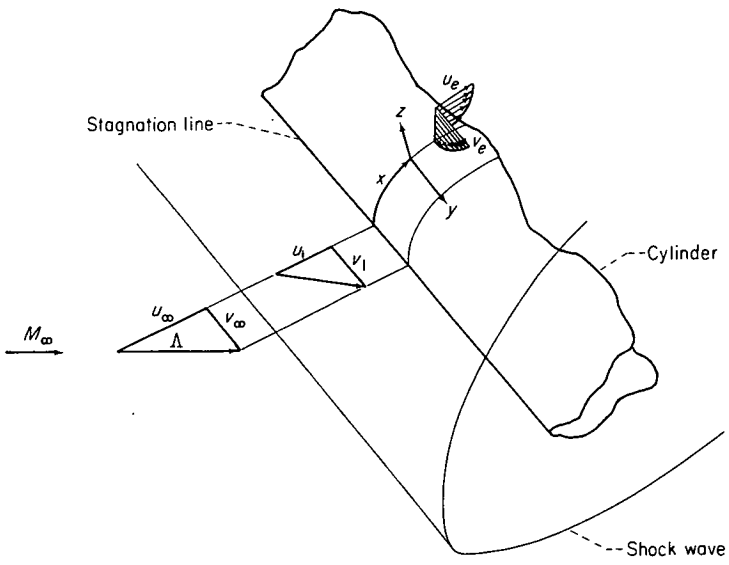
The present report extends the work of Crabtree, Tinkler, and Moore to the more general case of arbitrary Prandtl number and an isothermal wall at arbitrary temperature in flows where both Mach number and yaw angle may be large. The boundary-layer equations are first simplified by the assumption of a linear viscosity-temperature relation and by the application of Stewartson's transformation (ref. 14). The resulting system of partial differential equations is simplified further by assuming an external chordwise velocity distribution of the Falkner-Skan type in the transformed coordinate system. The conditions required to reduce the system to ordinary differential equations are discussed. Numerical solutions for stagnation-line flow with Prandtl numbers of 1 and 0.7 are presented. Expressions are given for shear, heat transfer, and the variation of heat-transfer coefficient with yaw angle.

GENERAL EQUATIONS

BOUNDARY-LAYER EQUATIONS

The compressible-boundary-layer equations for a three-dimensional flow are obtained by application of the Prandtl boundary-layer assumptions to the general equations governing the motion of a compressible, viscous, heat-conducting gas (see, e. g., refs. 6 and 13). One of these assumptions which may be emphasized for the present application is that the boundary-layer thickness is small compared with the local radius of curvature of the surface. Consequently, the pressure gradient normal to the surface may be neglected, and the boundary-layer equations are expected to be valid in the region of the stagnation line on a yawed cylinder.

The boundary-layer equations for a yawed infinite cylinder are obtained from the three-dimensional boundary-layer equations by noting that all spanwise derivatives are identically zero. The coordinate system used is defined by the following sketch:



where the x-coordinate is the distance along the cylinder surface measured in the chordwise direction from the leading-edge stagnation line, y is the spanwise coordinate, and z is the coordinate normal to the cylinder surface. (All symbols are defined in appendix A.)

The equations of motion of the steady compressible laminar boundary layer over a yawed infinite cylinder are therefore:
Continuity:

$$\frac{\partial(\rho u)}{\partial x}+\frac{\partial(\rho w)}{\partial z}=0 \tag{1}$$

Momentum:

$$\rho u\frac{\partial u}{\partial x}+\rho w\frac{\partial u}{\partial z}=-\frac{\partial p}{\partial x}+\frac{\partial}{\partial z}\left(\mu\frac{\partial u}{\partial z}\right) \tag{2a}$$

$$\rho u\frac{\partial v}{\partial x}+\rho w\frac{\partial v}{\partial z}=\frac{\partial}{\partial z}\left(\mu\frac{\partial v}{\partial z}\right) \tag{2b}$$

$$\frac{\partial p}{\partial z}=0 \tag{2c}$$

Energy:

$$\rho u\frac{\partial H}{\partial x}+\rho w\frac{\partial H}{\partial z}=\frac{\partial}{\partial z}\left(\frac{\mu}{Pr}\frac{\partial H}{\partial z}\right)-\frac{\partial}{\partial z}\left[\mu\left(\frac{1}{Pr}-1\right)\frac{\partial}{\partial z}\left(\frac{u^2+v^2}{2}\right)\right] \tag{3}$$

where H is the total or stagnation enthalpy.
State:

$$p=\rho Rt$$

The boundary conditions for equations (1) to (4) are:
At $z=0$

$$u=v=w=0 \text{ and } H=H_w \text{ or } \frac{\partial H}{\partial z}=0$$

At $z\to\infty$

$$u=u_e,\ v=v_e, \text{ and } H=H_e$$

The viscosity is assumed to be a linear function of the temperature according to the relation

$$\mu=\frac{\mu_w}{t_w}t$$

where t_w is a known function of x, and μ_w may be taken as any desired function of t_w, such as the Sutherland viscosity-temperature equation. The chordwise velocity outside the boundary layer satisfies the following form of Bernoulli's equation:

$$\rho_e u_e\frac{\mathrm{d}u_e}{\mathrm{d}x}=-\frac{\mathrm{d}p_e}{\mathrm{d}x}=-\frac{\partial p}{\partial x} \tag{5}$$

since from equation (2c) the pressure is constant in the direction normal to the surface.

STEWARTSON'S TRANSFORMATION

The velocities in the equations of motion (eqs. (1) to (3)) can be replaced through the definition of a stream function:

$$\left.\begin{aligned}\psi_z&\equiv\frac{\rho u}{\rho_0}\\ \psi_x&\equiv-\frac{\rho w}{\rho_0}\end{aligned}\right\} \tag{6}$$

so that the continuity equation (eq. (1)) is automatically satisfied.

Stewartson's transformation (ref. 14) is now introduced, and in a slightly modified form may be written

$$X=\int_0^x\left(\frac{\mu_w}{\mu_0}\frac{t_0}{t_w}\right)\frac{a_e}{a_0}\frac{p_e}{p_0}\,dx \tag{7}$$

$$Z=\frac{a_e}{a_0}\int_0^z\frac{\rho}{\rho_0}\,dz \tag{8}$$

The quantity $\left(\frac{\mu_w}{\mu_0}\frac{t_0}{t_w}\right)$ of equation (7) is exactly the quantity λ of reference 15. The transformed coordinates are now represented by uppercase letters (X, Z), and the subscript e refers to local conditions at the outer edge of the boundary layer (external). The subscript 0 refers to free-stream stagnation values.

With the assumptions of constant Prandtl number, constant specific heat, and an isothermal surface and by use of the adiabatic energy equation for the external flow

$$a_0^2=a_e^2+\frac{\gamma-1}{2}(u_e^2+v_e^2) \tag{9}$$

equations (2a), (2b), and (3) become

$$\psi_z\psi_{xz}-\psi_x\psi_{zz}=U_eU_{e_X}\left[1+\left(\frac{t_0}{t_{N_0}}-1\right)(1-g^2)+\left(\frac{t_w}{t_0}-1\right)\left(\frac{t_0}{t_{N_0}}\right)(1-\theta)\right]+\nu_0\psi_{zzz} \tag{10}$$

$$\psi_zg_x-\psi_xg_z=\nu_0g_{zz} \tag{11}$$

$$\psi_z\theta_x-\psi_x\theta_z=-\frac{\nu_0}{Pr}\frac{(1-Pr)(\gamma-1)}{2a_0^2\left(1-\frac{t_w}{t_0}\right)}\left[\left(\frac{a_e}{a_0}\right)^2(\psi_z^2)_{zz}+v_e^2(g^2)_{zz}\right]+\frac{\nu_0}{Pr}\theta_{zz} \tag{12}$$

where

$$g=\frac{v}{v_e} \tag{13}$$

$$\theta=\frac{H-H_w}{H_e-H_w} \tag{14}$$

and

$$\frac{t_0}{t_{N_0}}=\frac{1+\frac{\gamma-1}{2}M_\infty^2}{1+\frac{\gamma-1}{2}M_\infty^2\cos^2\Lambda} \tag{15}$$

The ratio t_0/t_{N_0} combines the effect of both yaw angle and Mach number in a single parameter. The physical interpretation of this parameter is simply the ratio of the total or stagnation temperature of the stream to the stagnation temperature of the normal component of the stream. The variation of the parameter with yaw angle for various Mach numbers is shown in figure 1. It is seen that $t_0/t_{N_0}\leq\sec^2\Lambda$ and becomes large only for large yaw angles combined with high Mach numbers.

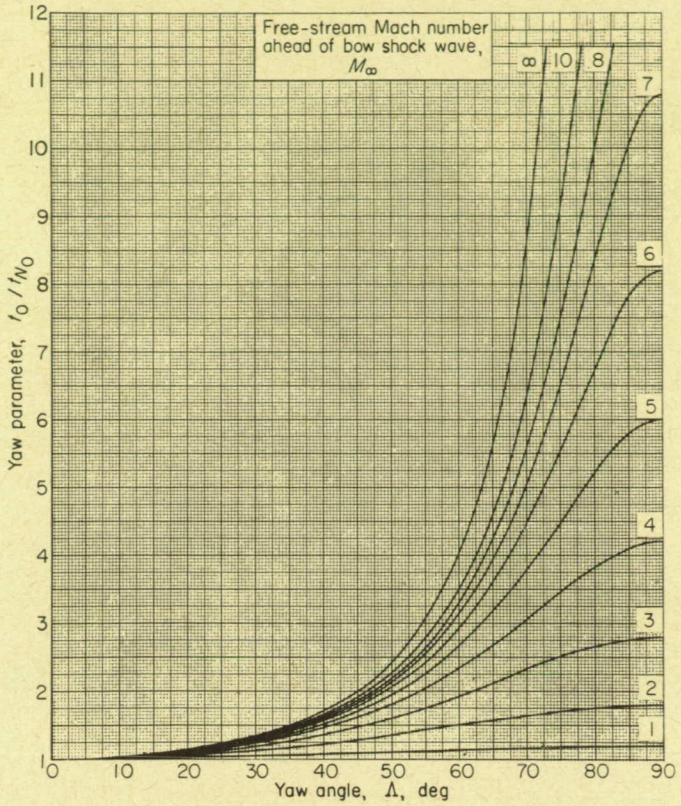


FIGURE 1.—Effect of yaw angle on yaw parameter. Ratio of specific heats, 1.4.

For a Prandtl number of 1, $g=\theta$, since equations (11) and (12) are similar and since the functions g and θ satisfy the same boundary conditions.

In terms of the transformed velocities, which are defined

$$\left.\begin{aligned}U&\equiv\psi_z\\W&\equiv-\psi_x\end{aligned}\right\} \tag{16}$$

equations (10) to (12) can be written

$$UU_x+WU_z=U_eU_{e_X}\left[1+\left(\frac{t_0}{t_{N_0}}-1\right)(1-g^2)+\left(\frac{t_w}{t_0}-1\right)\frac{t_0}{t_{N_0}}(1-\theta)\right]+\nu_0U_{zz} \tag{17}$$

$$Ug_X+Wg_z=\nu_0g_{zz} \tag{18}$$

$$U\theta_X+W\theta_z=\frac{\nu_0}{Pr}\left\{\theta_{zz}-\left(\frac{\gamma-1}{2a_0^2}\right)\left(\frac{1-Pr}{1-\frac{t_w}{t_0}}\right)\left[\left(\frac{a_e}{a_0}\right)^2(U^2)_{zz}+v_e^2(g^2)_{zz}\right]\right\} \tag{19}$$

These equations should be useful in formulating integral methods for calculation of laminar boundary layers over yawed cylinders.

SIMILAR SOLUTIONS

In order to obtain similar solutions, an external flow of the Falkner-Skan type

$$U_e=CX^m \tag{20}$$

is assumed, which together with the transformation

$$\left.\begin{aligned}\psi&=f(\eta)\sqrt{\frac{2\nu_0 U_e X}{m+1}}\\ g&=g(\eta)\\ \theta&=\theta(\eta)\\ \eta&=Z\sqrt{\frac{m+1}{2}\frac{U_e}{\nu_0 X}}\end{aligned}\right\} \tag{21}$$

yields the system of differential equations

$$f'''+ff''=\beta\left[f'^2-1-\left(\frac{t_0}{t_{N_0}}-1\right)(1-g^2)-\frac{t_0}{t_{N_0}}\left(\frac{t_w}{t_0}-1\right)(1-\theta)\right] \tag{22a}$$

$$g''+fg'=0 \tag{22b}$$

$$\theta''+Prf\theta'=\frac{1-Pr}{\left(1-\frac{t_w}{t_0}\right)}\left[\frac{\gamma-1}{2}\left(\frac{u_e}{a_0}\right)^2(f'^2)''+\left(1-\frac{t_{N_0}}{t_0}\right)(g^2)''\right] \tag{22c}$$

where

$$\beta=\frac{2m}{m+1} \tag{23}$$

The boundary conditions for the system of equations (22) are:

At $\eta=0$

$$\text{At } \eta\to\infty \quad \left.\begin{aligned}f=f'=g=\theta=0\\ f'=g=\theta=1\end{aligned}\right\} \tag{24}$$

Since u_e may in general depend on x, the right member of the energy equation (eq. (22c)) is not yet functionally consistent with the left member for arbitrary u_e and Pr. The right member of the equation must be zero or a function of η to be consistent with the left member. This may be achieved in the following ways: (1) The external chordwise velocity may be a constant other than zero, (2) the external chordwise velocity may be zero, (3) the Prandtl number may equal 1, (4) the factor $\left[\frac{\gamma-1}{2}\left(\frac{u_e}{a_0}\right)^2\right]$ may approach the constant $t_{N0}/t_0=\cos^2\Lambda$ corresponding to hypersonic flow, or (5) the ratio of specific heats γ may equal 1.

INDEPENDENCE PRINCIPLE

The independence principle can be demonstrated from the general stystem of equations (22). The chordwise momentum equation (eq. (22a)) is independent of the spanwise momentum and energy equations under the following conditions:

(1) Flat-plate flows ($m=\beta=0$) for all Mach numbers, Prandtl numbers, and heat transfers

(2) The conditions $t_0=t_{N0}$, $t_w=t_0$, which correspond to incompressible flow

Independence does not exist for compressible flow with pressure gradient, even for zero heat transfer.

STAGNATION-LINE FLOW

All solutions presented in this report are for stagnation-line flow where $m=\beta=1$. Two of the previously described requirements for similarity are separately considered in these solutions. The first requirement is that of Prandtl number equal to 1. The system of equations (22) for this case is reduced to the following two differential equations, since equations (22b) and (22c) become identical:

$$f'''+ff''=f'^2-1-\left(\frac{t_0}{t_{N_0}}-1\right)(1-\theta^2)-\frac{t_0}{t_{N_0}}\left(\frac{t_w}{t_0}-1\right)(1-\theta) \tag{25a}$$

$$\theta''+f\theta'=0 \tag{25b}$$

with the boundary conditions:

At $\eta=0$

$$\text{At } \eta\to\infty \quad \left.\begin{aligned}f=f'=\theta=0\\ f'=\theta=1\end{aligned}\right\} \tag{26}$$

For the case of zero yaw, equations (25) reduce to those presented in reference 15, while for the insulated surface $\left(\frac{t_w}{t_0}=1 \text{ for } Pr=1\right)$ they reduce to those of Crabtree (ref. 11).

The second requirement considered is that of zero external chordwise velocity, which allows arbitrary Prandtl number. For this case equations (22) become

$$f'''+ff''=f'^2-1-\left(\frac{t_0}{t_{N_0}}-1\right)(1-g^2)-\frac{t_0}{t_{N_0}}\left(\frac{t_w}{t_0}-1\right)(1-\theta) \tag{27a}$$

$$g''+fg'=0 \tag{27b}$$

$$\theta''+Prf\theta'=(1-Pr)\frac{1-\frac{t_{N_0}}{t_0}}{1-\frac{t_w}{t_0}}(g^2)'' \tag{27c}$$

With heat transfer, the boundary conditions of equations (27) are equations (24).

For the case of the insulated wall an additional boundary condition is necessary, since the wall temperature is no longer arbitrary. The heat-transfer rate to the wall may be expressed as

$$q_w=k_w\left(\frac{\partial t}{\partial z}\right)_w \tag{28}$$

which for stagnation-line flow becomes, with use of expressions (8), (14), and (21),

$$q_w=\frac{\rho_w}{\rho_0}\frac{a_e}{a_0}\sqrt{\frac{C}{\nu_0}}k_w(t_0-t_w)\theta'_w \tag{29}$$

For the insulated surface, $q_w=0$; and since with arbitrary Prandtl number the surface temperature is generally not equal to the stagnation temperature, the additional boundary condition from equation (29) is

$$\theta'_w=0 \tag{30}$$

Thus, for the insulated surface with arbitrary Prandtl number, equations (27) are solved subject to the conditions of equations (24) and (30). For convenience in computing, the temperature ratio t_w/t_0 was replaced by the following expression involving the local recovery factor ζ_w:

$$\frac{t_w}{t_0}=\frac{t_{aw}}{t_0}=\zeta_w\left(1-\frac{t_{N_0}}{t_0}\right)+\frac{t_{N_0}}{t_0} \tag{31}$$

Values of ζ_w then resulted from the solutions.

Equations (25) and (27) were solved numerically for both insulated and noninsulated surfaces. The techniques used at the two laboratories were different. These techniques are discussed in appendix B. It is interesting and gratifying to note that the different techniques yielded numerical results that were in excellent agreement.

PROPERTIES OF SOLUTIONS

In the following sections the solutions obtained in this study are presented and their properties discussed. All solutions are presented in tabular form. Table I shows the values of f, f', f'', θ, and θ' tabulated against η for a Prandtl number of 1. Table II presents $f, f', f'', g, g', \theta$, and θ' against η for a Prandtl number of 0.7. Table III presents a summary of the values of f''_w (related to wall shear), g'_w (related to spanwise shear), and θ'_w (related to heat transfer) for the cases of tables I and II.[3] The solutions for $Pr=1.0$ apply whenever the external chordwise velocity satisfies equation (20) with $m=1$; whereas, the solutions for $Pr\neq 1.0$ apply rigorously only at the stagnation line where $u_e=0$. For practical purposes, however, the solutions for $Pr\neq 1.0$ are expected to apply also in the vicinity of the stagnation line where $u_e<<a_0$.

VELOCITY AND ENTHALPY PROFILES

The chordwise and spanwise velocity and enthalpy profiles obtained from the tabulated solutions are presented as functions of η in figures 2 and 3.

The chordwise velocity ratio can be expressed

$$\frac{u}{u_e}=f' \tag{32}$$

from the definitions of ψ, z, and η. It should be remembered that for the $Pr=1$ solutions the normalized temperature and spanwise velocity profiles are identical. For $Pr=0.7$ (fig. 3) the spanwise velocity and enthalpy profiles are separately plotted. The distance z normal to the surface at a given station x in the physical plane is related to the similarity variable η through relations (8) and (21) and may be expressed as

$$z=\frac{a_0}{a_e}\frac{p_0}{p_e}\sqrt{\frac{\nu_0 X}{U_e}\left(\frac{2}{m+1}\right)}\int_0^\eta \frac{t}{t_0}\,d\eta \tag{33}$$

where

$$\frac{t}{t_0}=1+\left(\frac{t_w}{t_0}-1\right)(1-\theta)-\frac{\gamma-1}{2}\left(\frac{u_e}{a_0}\right)^2 f'^2-\left(1-\frac{t_{N_0}}{t_0}\right)g^2 \tag{34}$$

At the stagnation line, equations (33) and (34) become

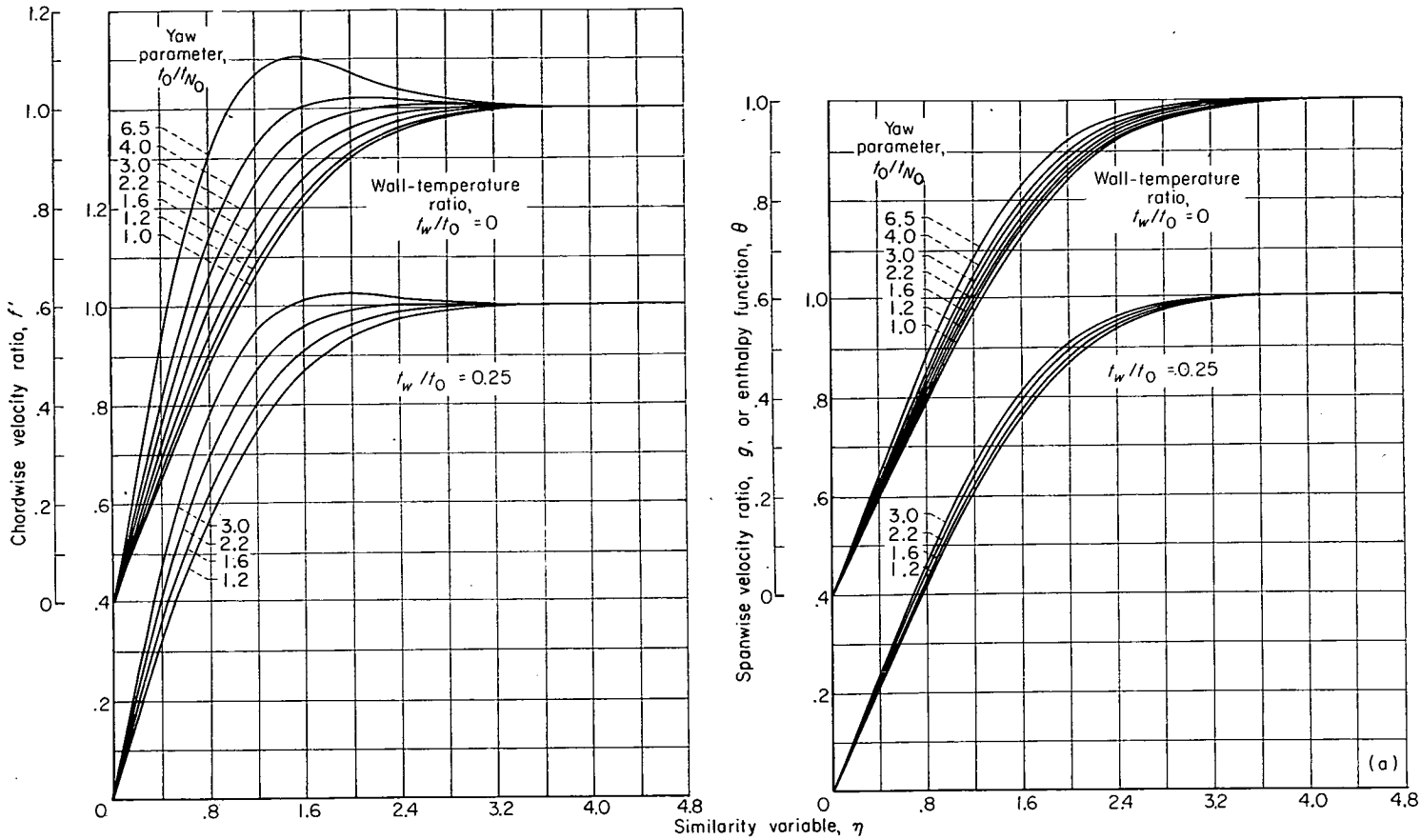
$$z=\frac{t_0}{t_w}\sqrt{\frac{\nu_w}{\left(\frac{du_e}{dx}\right)}}\int_0^\eta\left[1+\left(\frac{t_w}{t_0}-1\right)(1-\theta)-\left(1-\frac{t_{N_0}}{t_0}\right)g^2\right]d\eta \tag{35}$$

The differences in the profiles for different values of the yaw-angle parameter t_0/t_{N_0} and the wall-temperature parameter t_w/t_0 (fig. 2) can be attributed to the effect of compressibility, since for incompressible flow the chordwise velocity profiles and the temperature profiles are independent of the spanwise flow. The chordwise velocity ratios are especially affected by compressibility; for large values of t_0/t_{N_0} these ratios are greater than 1 within the boundary layer, even for cases where the wall is highly cooled. This same phenomenon has been observed in solutions of the two-dimensional compressible boundary layer (e.g., refs. 15 and 16) for cases of a heated wall and favorable pressure gradient, and in reference 15 was termed "velocity overshoot." According to reference 15, the physical explanation for this effect is: When the wall is heated, the density in the outer part of the boundary layer is reduced sufficiently so that the local flow is accelerated more than the external flow. The same basic explanation appears plausible in the present solutions, except that the additional heat required to reduce the local density is generated by the shear of the spanwise boundary layer, and, hence, the phenomenon can occur even when the wall temperature is less than the recovery temperature. The solutions given by Moore for the compressible-boundary-layer equations for a cone at large angle of attack (ref. 17) also show similar results; that is, the circumferential velocity ratios are greater than unity within the boundary layer. Furthermore, this effect becomes larger as the angle of attack of the cone is reduced.[4] In the present solutions this is analogous to increasing the yaw angle, which also has the effect of increasing the excess of the local velocities over the external velocity. Note also that this excess chordwise velocity is reduced by reducing the wall temperature, as might be expected from the preceding discussion.

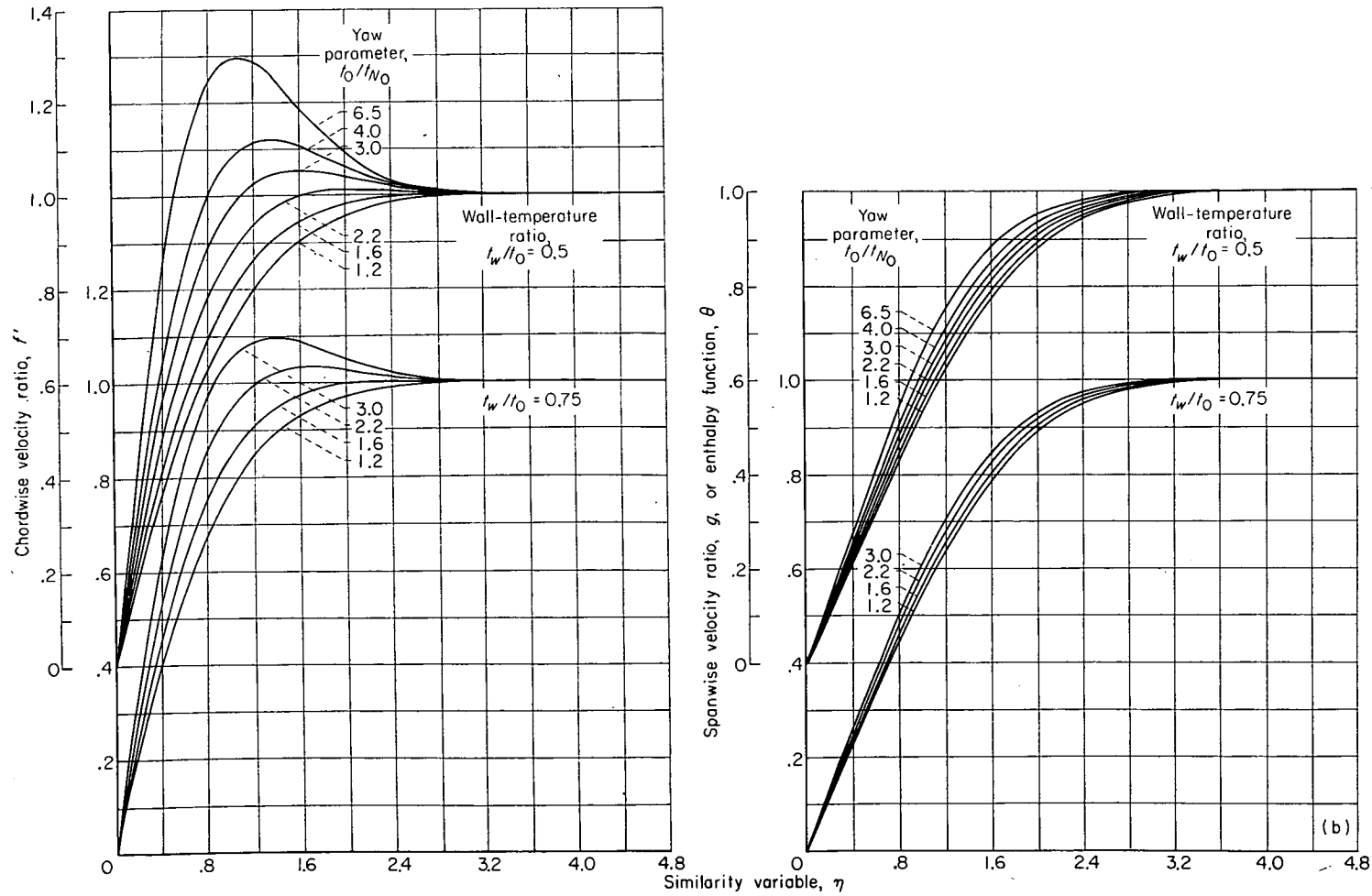
Twelve solutions were computed with $Pr=0.7$; four of these are for zero heat transfer and give a recovery factor, and eight are for cooled-wall conditions with $t_w/t_0=0$ and 0.5. The velocity and enthalpy profiles for these solutions are shown in figure 3, and the numerical values of the functions are given in tables II and III. For corresponding values of t_0/t_{N_0} and for $t_w/t_0=0$ or 0.5, the f', g, and θ profiles are almost the same as those for $Pr=1$. For $t_w=t_{aw}$, the f' and g profiles are also similar to those for $Pr=1$ with $t_w=t_0$; however, the θ profiles for $Pr=0.7$ and $t_w=t_{aw}$ (fig. 3(a)) are considerably different from the corresponding profiles for $Pr=1$. The fact that $\theta>1$ for this case indicates that the local stagnation enthalpy within the boundary layer exceeds the stagnation enthalpy outside the boundary layer. This excess of local stagnation enthalpy over the external value

[3] Comparison of the results of reference 11 with the solution given here for $Pr=1$, $t_w/t_0=1$, $t_0/t_{N_0}=1.2$ shows that the present values for f' and θ (corresponding to $f_1'+\omega f_2'$ and $g_1+\omega g_2$ in the notation of ref. 11) are considerably larger than the values given in reference 11 at the same η. According to private communication with Dr. Crabtree, the original numerical results of reference 11 were in error. The corrected results obtained from Dr. Crabtree, also by private communication, are in substantial agreement with the present solution.

[4] The angle of yaw as defined herein is the complement of the cone angle of attack.

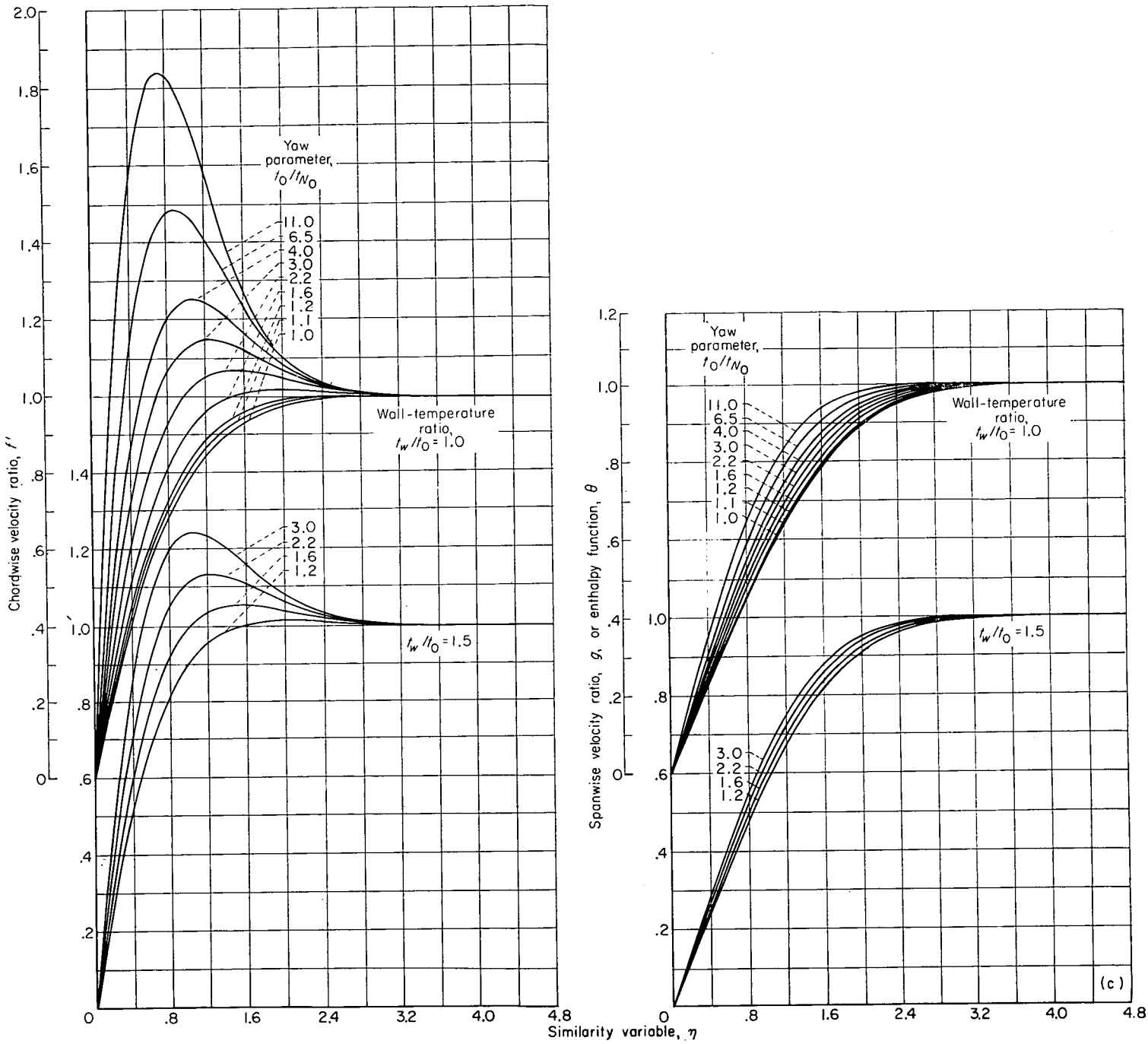


(a) Wall-temperature ratio, 0 and 0.25.



(b) Wall-temperature ratio. 0.50 and 0.75.

FIGURE 2.—Velocity and enthalpy profiles for Prandtl number of 1.



(c) Wall-temperature ratio, 1.0 and 1.5.

FIGURE 2.—Continued. Velocity and enthalpy profiles for Prandtl number of 1.

for zero heat transfer (and also to a lesser extent for a cooled wall) is apparently caused by the relative increase in the quantity of heat conducted away from the wall into the outer layers of the boundary layer when $Pr<1$. For $Pr=1$ and zero heat transfer ($t_w=t_0$) the relative effects of viscosity and conductivity are balanced and $H/H_e=1$ throughout the boundary layer. These same effects have been previously noted in solutions of the flat-plate boundary layer (e. g., ref. 18).

The domains of velocity and temperature overshoot can be identified with the aid of the asymptotic solution to equations (27) (appendix C). For simplicity, the discussion that follows is restricted to a Prandtl number of 1. A more general treatment is given in appendix C.

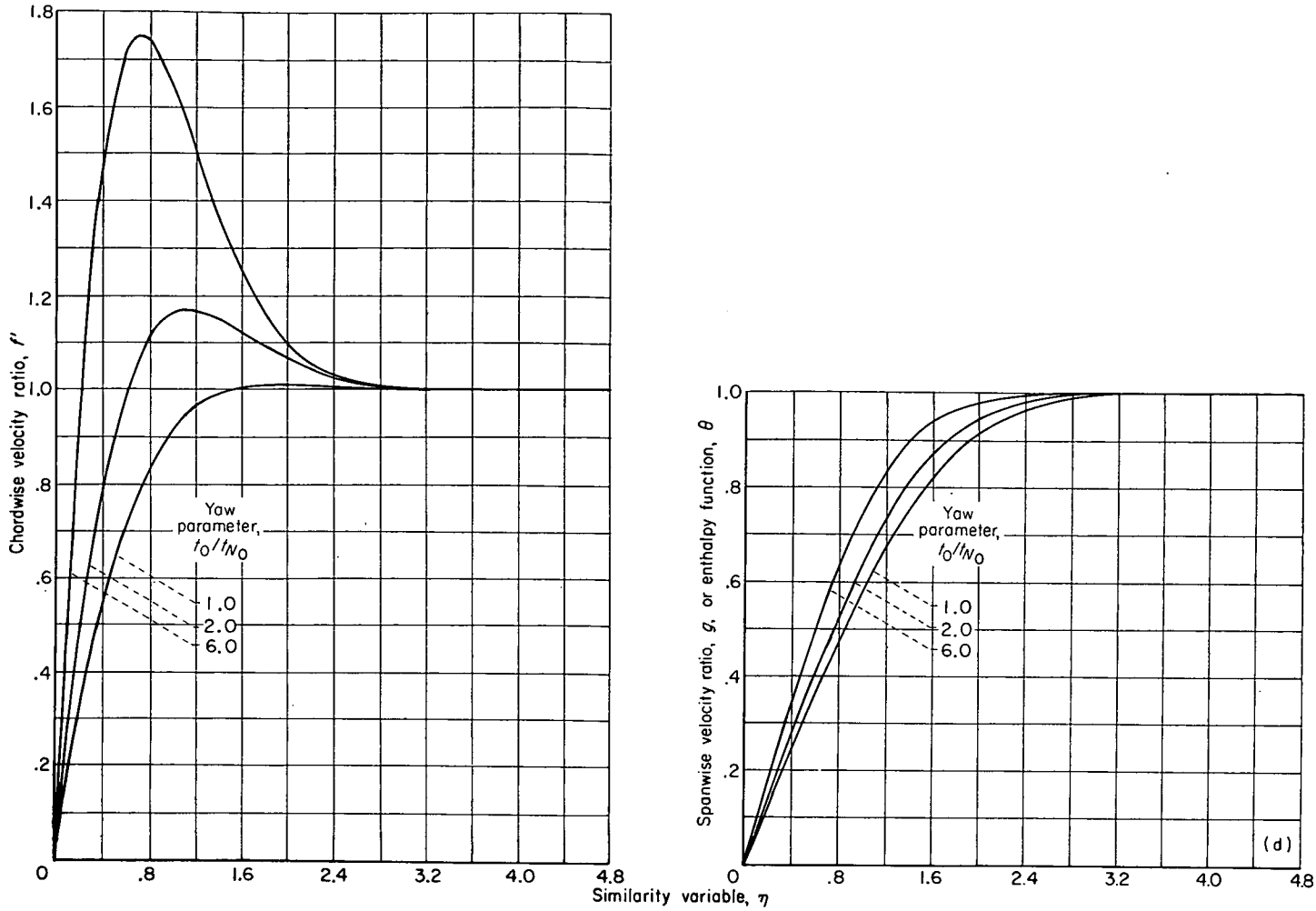
The asymptotic expressions for chordwise and spanwise velocity functions for a Prandtl number of 1 from appendix C are, respectively,

$$\tilde{f}'=1+\frac{A_1}{4}\left[2\left(\frac{t_0}{t_{N_0}}-1\right)+\frac{t_0}{t_{N_0}}\left(\frac{t_w}{t_0}-1\right)\right](\eta-\kappa)^{-1}\,exp\left[-\frac{(\eta-\kappa)^2}{2}\right]+A_3(\eta-\kappa)^{-3}\,exp\left[-\frac{(\eta-\kappa)^2}{2}\right] \quad (36)$$

and

$$\tilde{g}=1-\frac{A_1}{2}(\eta-\kappa)^{-1}\,exp\left[-\frac{(\eta-\kappa)^2}{2}\right] \quad (37)$$

Examination of equation (36) shows that for large η the term involving A_1 is dominant, and thus $(f'-1)$ will have the



(d) Wall-temperature ratio, 2.0.

FIGURE 2.—Concluded. Velocity and enthalpy profiles for Prandtl number of 1.

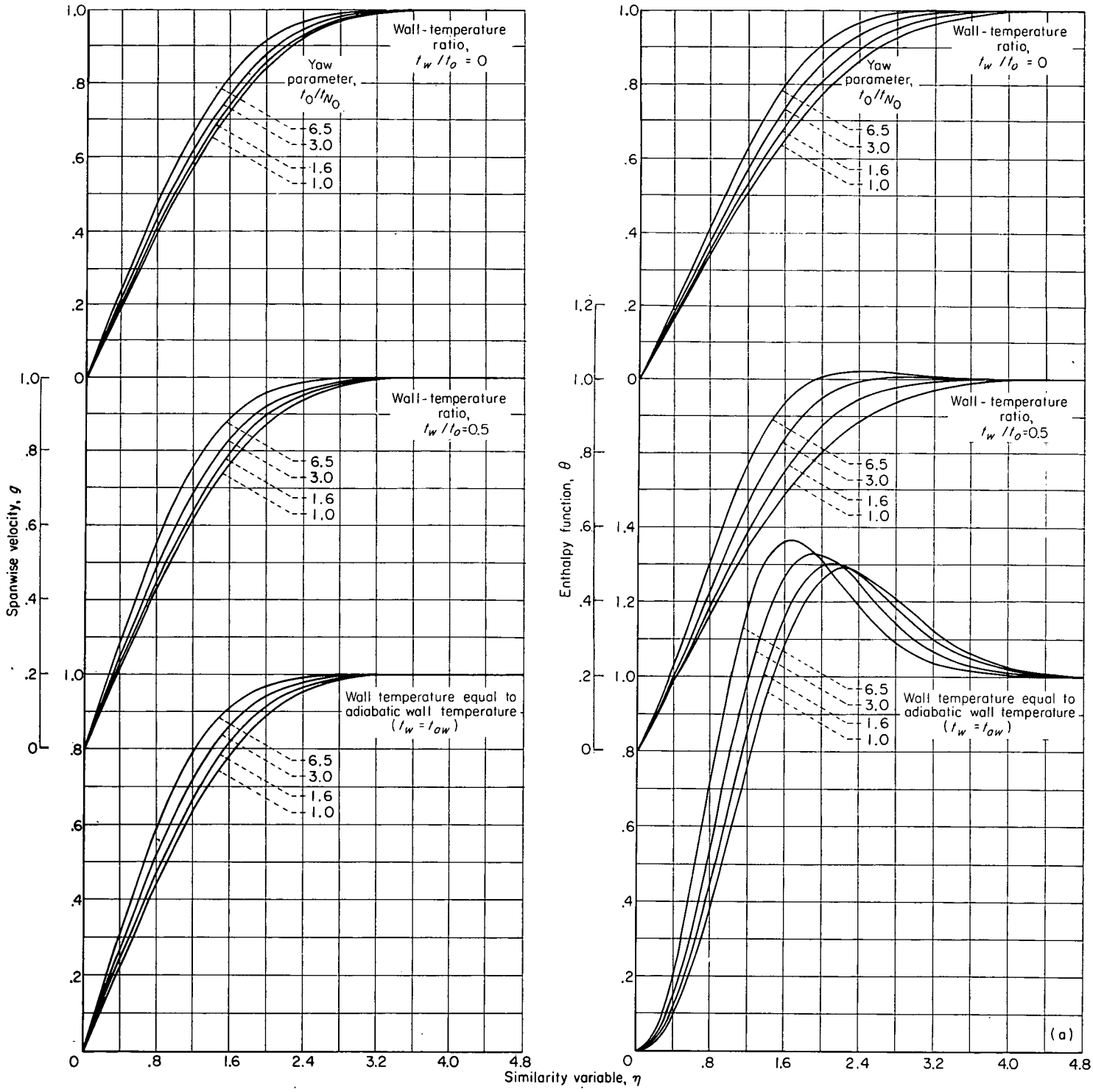
same sign as A_1. Since the g function for a Prandtl number of 1 (fig. 2) always approaches its boundary condition from below, A_1 is always positive, and, consequently, the existence of chordwise velocity overshoot depends directly on whether the quantity $\left[2\left(\frac{t_0}{t_{N_0}}-1\right)+\frac{t_0}{t_{N_0}}\left(\frac{t_w}{t_0}-1\right)\right]$ is positive. This quantity is positive when $t_w+t_0>2t_{N_0}$. The domain of chordwise velocity overshoot is shown in figure 4. It may be seen that for cold surfaces there is only a small range of t_0/t_{N_0} in which no overshoot occurs.

For Prandtl numbers other than 1, the behavior of the stagnation-temperature profile must be considered separately from the spanwise velocity profile. From appendix C the asymptotic variation of θ is

$$\tilde{\theta}=1+A_1\frac{\left(1-\frac{t_{N_0}}{t_0}\right)}{\left(\frac{t_w}{t_0}-1\right)}(\eta-\kappa)^{-1}\,exp\left[-\frac{(\eta-\kappa)^2}{2}\right]-$$

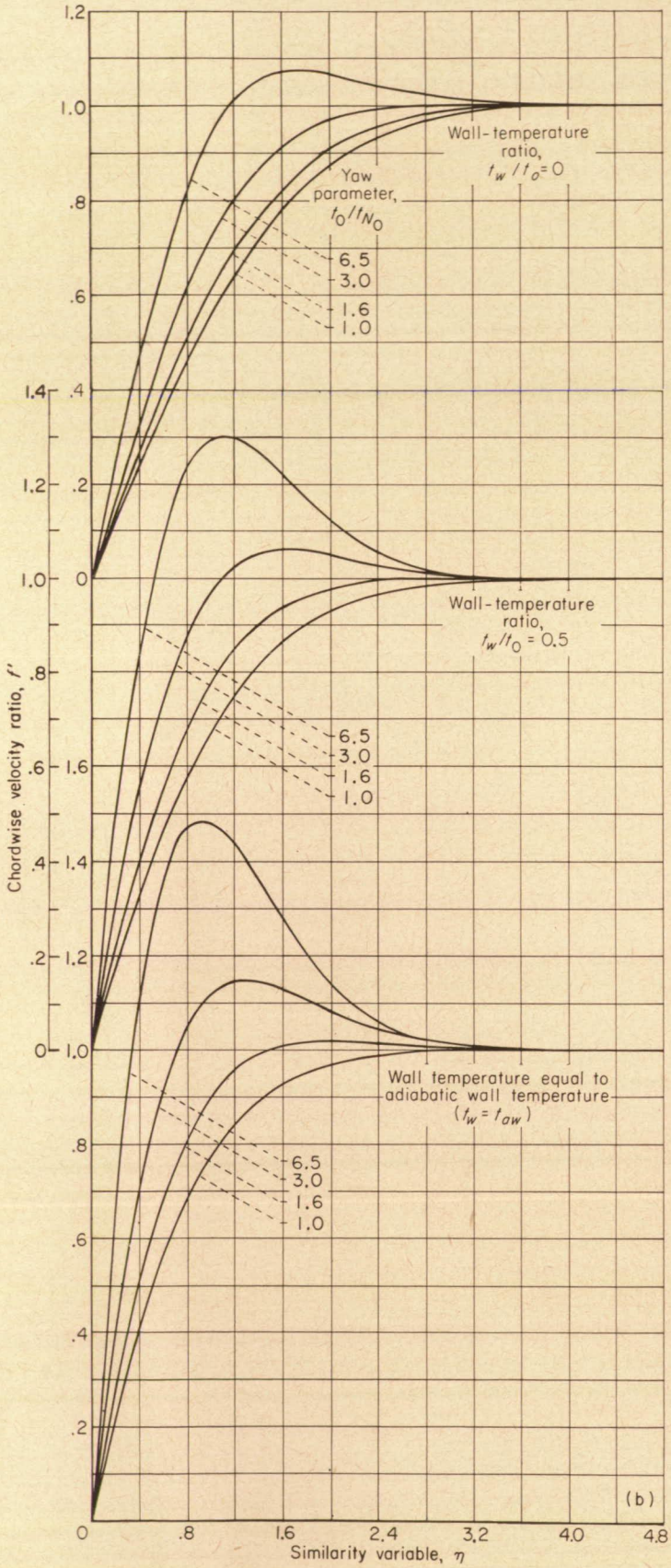
$$\frac{A_1}{2}\left[\frac{2\left(1-\frac{t_{N_0}}{t_0}\right)+\frac{t_w}{t_0}-1}{\frac{t_w}{t_0}-1}\right](\eta-\kappa)^{-1}\,exp\left[-\frac{Pr(\eta-\kappa)^2}{2}\right] \quad (38)$$

Figure 3 indicates that even for a Prandtl number of 0.7 the obtained spanwise velocity profiles approach the boundary condition from below; hence, A_1 is positive from equation (37). For Prandtl numbers less than 1 the dominant term in equation (38) is the last one; thus the existence of temperature overshoot is dependent on whether the quantity $\left[\frac{2\left(1-\frac{t_{N_0}}{t_0}\right)+\frac{t_w}{t_0}-1}{\frac{t_w}{t_0}-1}\right]$ is negative. The quantity is negative when the numerator is positive with $t_w/t_0<1$. It must, of course, be realized that for $t_w/t_0>1$ the stagnation temperatures in the boundary layer are always higher than the stream stagnation temperature. In appendix C it is shown



(a) Spanwise velocity and enthalpy function.

FIGURE 3.—Velocity and enthalpy profiles for Prandtl number of 0.7.



(b) Chordwise velocity.

FIGURE 3.—Concluded. Velocity and enthalpy profiles for Prandtl number of 0.7.

that the chordwise velocity overshoot domain for a Prandtl number of 0.7 is the same as for a Prandtl number of 1. Thus for a cold wall with $Pr=0.7$, velocity overshoot and enthalpy overshoot occur simultaneously. The various regions of overshoot are summarized in figure 4.

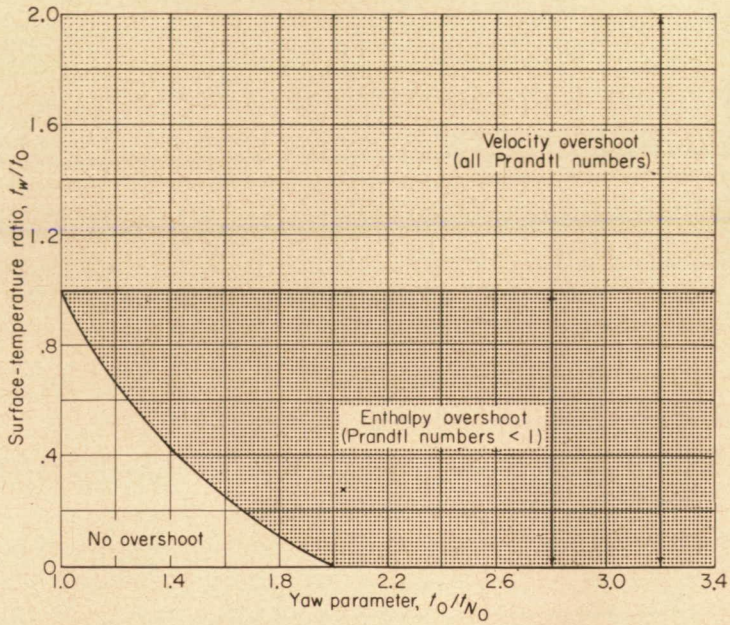


FIGURE 4.—Domains of velocity and enthalpy overshoot for stagnation-line flow over yawed cylinder.

SKIN FRICTION

The chordwise and spanwise components of shear stress at the wall are defined, respectively, as

$$\tau_c \equiv \mu_w \left(\frac{\partial u}{\partial z}\right)_w = \mu_w u_e f_w'' \sqrt{\frac{U_e}{\nu_0 X}\frac{m+1}{2}}\frac{\rho_w}{\rho_0}\frac{a_e}{a_0} \tag{39}$$

$$\tau_s \equiv \mu_w \left(\frac{\partial v}{\partial x}\right)_w = \mu_w v_e g_w' \sqrt{\frac{U_e}{\nu_0 X}\frac{m+1}{2}}\frac{\rho_w}{\rho_0}\frac{a_e}{a_0} \tag{40}$$

These can be represented in dimensionless form by local skin-friction coefficients:

$$\frac{\tau_c}{\frac{1}{2}\rho_w u_e^2}\sqrt{\frac{u_e x}{\nu_w}} = 2f_w''\sqrt{\frac{m+1}{2}\frac{\mathrm{d}\ln X}{\mathrm{d}\ln x}} \tag{41}$$

$$\frac{\tau_s}{\frac{1}{2}\rho_w v_e^2}\sqrt{\frac{v_e x}{\nu_w}} = 2\sqrt{\frac{u_e}{v_e}}\,g_w'\sqrt{\frac{m+1}{2}\frac{\mathrm{d}\ln X}{\mathrm{d}\ln x}} \tag{42}$$

For the specific case of stagnation-line flow $U_e=CX$ the quantity C is related to the physical chordwise velocity gradient as follows:

$$C=\frac{U_e}{X}=\frac{\mathrm{d}U_e}{\mathrm{d}X}=\left[\frac{1+\frac{\gamma-1}{2}\left(\frac{u_e}{a_e}\right)^2}{\frac{\mu_w}{\mu_0}\frac{t_0}{t_w}\left(\frac{a_e}{a_0}\right)\frac{p_e}{p_0}}\right]\frac{\mathrm{d}u_e}{\mathrm{d}x} \tag{43}$$

By use of equation (43), equations (39) and (40) can then be written in the form of skin-friction coefficients based on free-stream conditions, which for stagnation-line flow are

$$c_{f,c}=\frac{\tau_c}{\frac{1}{2}\rho_\infty(u_\infty^2+v_\infty^2)}$$

$$=2f_w''\frac{\rho_w}{\rho_\infty}\frac{u_e}{u_\infty^2}\cos^2\Lambda\left\{\left[1+\frac{\gamma-1}{2}\left(\frac{u_e}{a_e}\right)^2\right]\nu_w\frac{du_e}{dx}\right\}^{\frac{1}{2}} \quad (44)$$

$$c_{f,s}=\frac{\tau_s}{\frac{1}{2}\rho_\infty(u_\infty^2+v_\infty^2)}=g_w'\frac{\rho_w}{\rho_\infty}\frac{\sin 2\Lambda}{u_\infty}\left\{\left[1+\frac{\gamma-1}{2}\left(\frac{u_e}{a_e}\right)^2\right]\nu_w\frac{du_e}{dx}\right\}^{\frac{1}{2}} \quad (45)$$

At the stagnation line itself, the chordwise velocity in the boundary layer is identically zero; hence, there is zero chordwise viscous shearing stress. The dimensionless wall-shear function f_w'' is nevertheless of interest, since it can be used in calculating $c_{f,c}$ from equation (44) in the region close to the stagnation line. For the presented solutions, values of f_w'' are summarized in table III and plotted in figure 5. Significant increases in the wall-shear function occur with increases in the yaw parameter t_0/t_{N_0}. This is an indication of the effect of lack of independence between the spanwise and chordwise flows.

In the evaluation of the spanwise skin-friction coefficient for a Prandtl number of 1, the function g_w' is exactly θ_w', as indicated in table III and in figure 6. For a Prandtl number of 0.7, the values of g_w' for the obtained solutions are listed in table III. It may be readily seen from the table that for corresponding values of surface temperature and yaw parameter t_0/t_{N_0} there is very little effect of Prandtl number on the spanwise shear parameter g_w'.

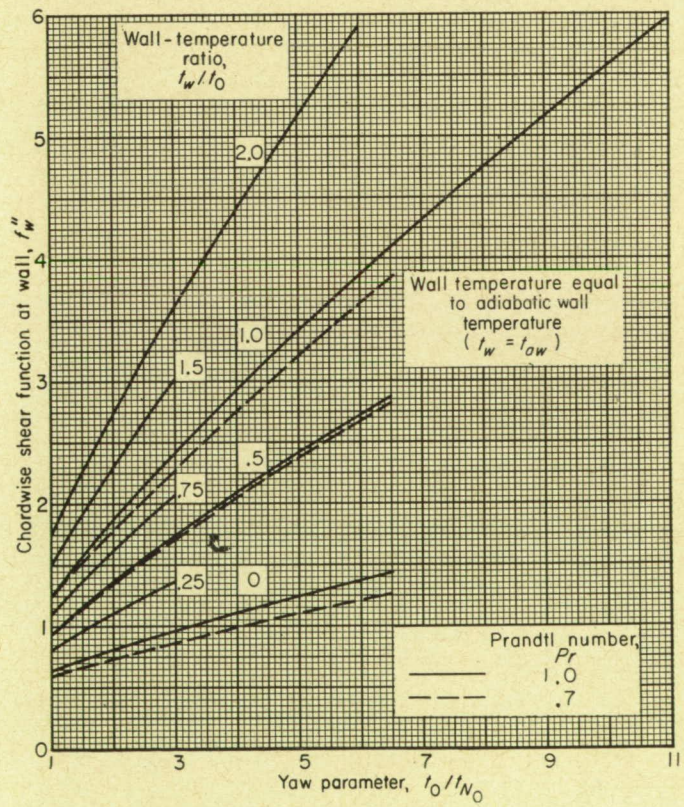


FIGURE 5.—Effect of yaw on wall-shear function for stagnation-line flow.

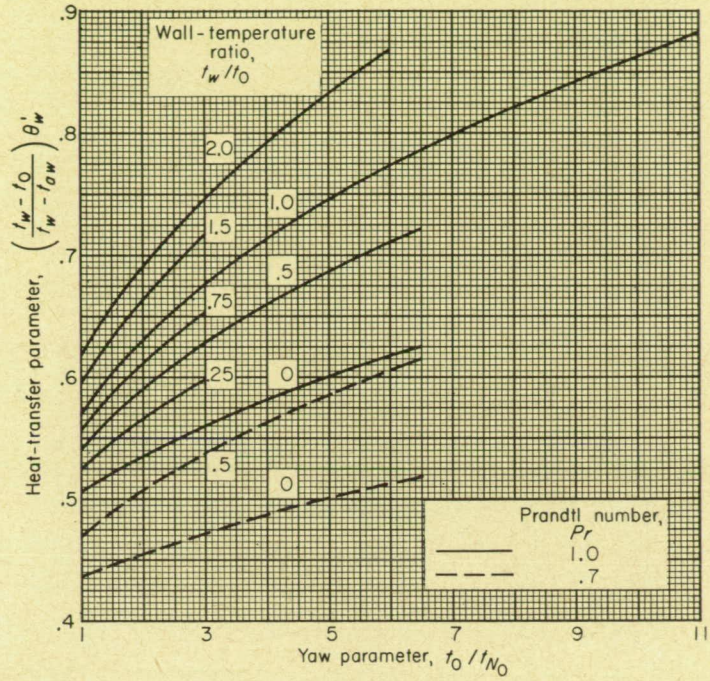


FIGURE 6.—Effect of yaw on heat-transfer parameter for stagnation-line flow. (For Prandtl number of 1, spanwise shear parameter g_w' is equal to heat-transfer parameter θ_w'.)

SECONDARY FLOW

Secondary flows are generally present in boundary layers whenever the direction of the pressure gradient impressed by the free-stream flow is different from the external flow direction. A comparison of the directions of the surface streamline and a corresponding streamline in the external flow provides a measure of the degree of secondary flow in the boundary layer.

The direction α of the streamline in the vicinity of the surface is given by the expression

$$\tan\alpha_w=\frac{\left(\frac{\partial u}{\partial z}\right)_w}{\left(\frac{\partial v}{\partial z}\right)_w}=\frac{\tau_c}{\tau_s}=\frac{u_e f_w''}{v_e g_w'} \quad (46)$$

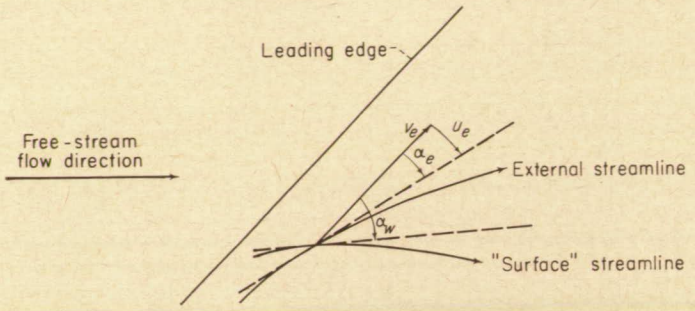
and the direction of the external streamline is

$$\tan\alpha_e=\frac{u_e}{v_e} \quad (47)$$

The ratio

$$\frac{\tan\alpha_w}{\tan\alpha_e}=\frac{f_w''}{g_w'} \quad (48)$$

is then indicative of the degree of secondary flow in the boundary layer. The angles α_e and α_w are defined in the following sketch:



Values of the ratio f''_w/g'_w for the obtained solutions are given in table III and are also plotted in figure 7. As the yaw parameter is increased, large relative increases in the secondary flow are obtained.

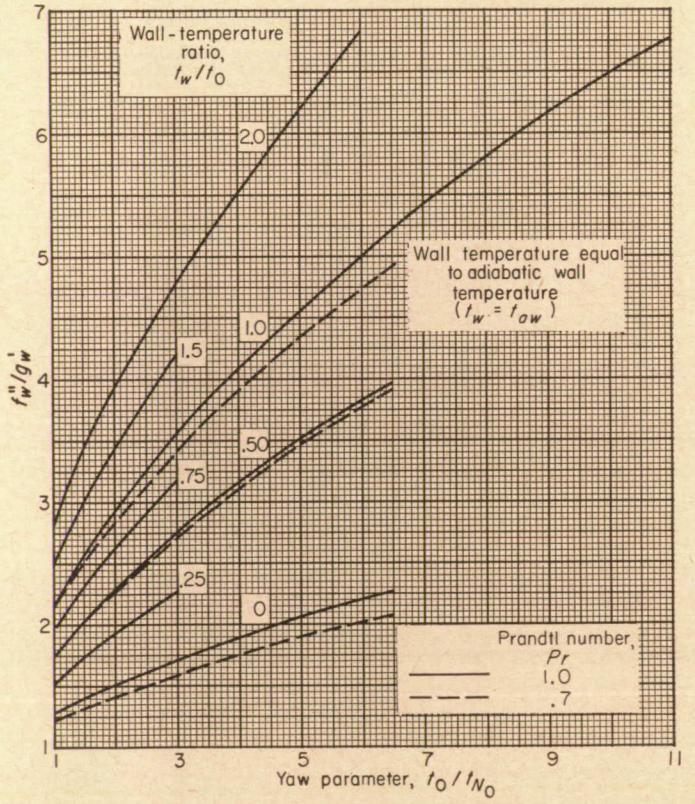


FIGURE 7.—Ratio of chordwise to spanwise surface-shear parameters for stagnation-line flow. $\left(\text{For Prandtl number of 1, } \frac{f''_w}{g'_w}=\frac{f''_w}{\theta'_w}.\right)$

HEAT TRANSFER AND ADIABATIC WALL TEMPERATURE

The heat-transfer coefficient is defined as $h=\frac{q_w}{t_{aw}-t_w}$, and by use of equations (7), (8), (21), and (28) may be written in the dimensionless form

$$\frac{Nu}{\sqrt{Re_w}}\equiv\frac{hx}{k_w}\sqrt{\frac{\nu_w}{u_e x}}=\left(\frac{t_0-t_w}{t_{aw}-t_w}\right)\theta'_w\sqrt{\frac{m+1}{2}\frac{\mathrm{d}\ln X}{\mathrm{d}\ln x}} \tag{49}$$

In terms of physical quantities, the heat-transfer coefficient for stagnation-line flow may be expressed as

$$h=\left[\left(\frac{t_0-t_w}{t_{aw}-t_w}\right)\theta'_w\right]\frac{k_w}{\sqrt{\nu_w}}\sqrt{\frac{\mathrm{d}u_e}{\mathrm{d}x}\left[1+\frac{\gamma-1}{2}\left(\frac{u_e}{a_e}\right)^2\right]} \tag{50}$$

The pertinent parameter from the exact solution is the quantity $\left(\frac{t_0-t_w}{t_{aw}-t_w}\right)\theta'_w$. For a Prandtl number of 1, where $t_{aw}=t_0$, this quantity reduces to just θ'_w. However, for Prandtl numbers other than 1, the complete expression is necessary, and the adiabatic wall temperature is required. The quantity $\left(\frac{t_0-t_w}{t_{aw}-t_w}\right)\theta'_w$ for stagnation-line flow is plotted in figure 6 for the present solutions. Figures 5 and 6 show that, while yaw tends to increase both the wall-shear and the heat-transfer functions, the magnitude of the effect on heat transfer is much smaller than the corresponding effect on wall shear. For example, for $t_0/t_{N_0}\leq 2$ and $\Lambda\leq 45°$, which from figure 1 includes all free-stream Mach numbers, the heat-transfer parameter is increased less than 13 percent over the value for $t_0/t_{N_0}=1$. This indicates that, for many practical problems, the effects of lack of independence on heat transfer may not be of great significance.

A comparison of the solutions for $Pr=0.7$ and $Pr=1$ at $t_w/t_0=0$ and 0.5 indicates that the effect of Prandtl number, on the heat-transfer parameter is essentially independent of the yaw parameter and can be approximately accounted for by the expression

$$\left[\left(\frac{t_0-t_w}{t_{aw}-t_w}\right)\theta'_w\right]_{Pr}=Pr^{0.46}(\theta'_w)_{Pr=1} \tag{51}$$

The factor $Pr^{0.46}$ in equation (51) represents an approximate average of the effect of Prandtl number on heat transfer based on the presented exact solutions. This factor differs slightly from the expression $Pr^{0.4}$ proposed by Squire (ref. 19) for the unyawed stagnation-point flow.

The adiabatic wall or recovery temperature at the stagnation line can be calculated from equation (31), where the quantity ζ_w is the local recovery factor defined by

$$\zeta_w=\frac{t_{aw}-t_{N_0}}{t_0-t_{N_0}} \tag{52}$$

Values of ζ_w have been calculated and are presented in table IV. The values for incompressible flow ($t_0/t_{N_0}=1$) have been calculated by the method described in appendix D, while those for $t_0/t_{N_0}>1$ and $Pr=0.7$ were obtained by solving equations (27) subject to the boundary conditions of equations (24) and (30), as described in the section Similar Solutions.

The results for $t_0/t_{N_0}=1$ may be closely represented by $Pr^{0.46}$, and for $t_0/t_{N_0}>1$ there is only a slight rise in recovery factor from the incompressible value. It is thus felt that the use of the conventional laminar recovery factor $Pr^{1/2}$ would be adequate for most purposes.

The local recovery factor may be converted to a recovery factor $\mathscr{R}$ based on free-stream temperature through the expression

$$\mathscr{R}\equiv\frac{t_{aw}-t_\infty}{t_0-t_\infty}=1-(1-\zeta_w)\sin^2\Lambda \tag{53}$$

REYNOLDS ANALOGY

From equations (41) and (49) a Reynolds analogy parameter between heat transfer and chordwise shear may be written

$$\frac{\left(\frac{\tau_c}{\frac{1}{2}\rho_w u_e^2}\right)\left(\frac{u_e x}{\nu_w}\right)}{\frac{hx}{k_w}}=\frac{2f_w''}{\left(\frac{t_0-t_w}{t_{aw}-t_w}\right)\theta_w'} \tag{54}$$

For a Prandtl number of 1, this equation reduces to $2f_w''/\theta_w'$, which is just twice the secondary-flow parameter listed in table III and plotted in figure 7.

A more interesting and perhaps more useful Reynolds analogy can be written in terms of the spanwise shear. From equations (42), (49), and (51),

$$\frac{\left(\frac{\tau_s}{\frac{1}{2}\rho_w v_e^2}\right)\left(\frac{v_e x}{\nu_w}\right)}{\frac{hx}{k_w}}=\frac{2g_w'}{\left(\frac{t_0-t_w}{t_{aw}-t_w}\right)\theta_w'}=\frac{2}{Pr^{0.46}} \tag{55}$$

This latter approximate relation applies to all the present solutions, since for a Prandtl number of 1, $g_w'=\theta_w'$; and the results shown in table III indicate that $(g_w')_{Pr=1}$ is approximately equal to $(g_w')_{Pr=0.7}$. The resemblance of equation (55) to the conventional flat-plate Reynolds analogy is due to the zero pressure gradient in the spanwise direction.

BOUNDARY-LAYER THICKNESS

The boundary-layer thickness in the physical plane can be computed from equation (35). By definition of the boundary-layer thickness δ as the value of z at which $\theta=0.9990$ (i. e., $\eta=\eta_\delta$), the expression for boundary-layer thickness for a Prandtl number of 1 becomes (from eq. (35))

$$\delta\sqrt{\frac{u_\infty}{\nu_w D}\left(\frac{D}{u_\infty}\frac{du_e}{dx}\right)}\frac{t_w}{t_0}=\int_0^{\eta_\delta}\left[\left(1-\frac{t_w}{t_0}\right)\theta-\left(1-\frac{t_{N_0}}{t_0}\right)\theta^2+\frac{t_w}{t_0}\right]d\eta \tag{56}$$

This expression has been evaluated for a range of values of t_w/t_0, and the results are shown in figure 8. The actual boundary-layer thickness may then be computed easily for any given combination of flow variables and wall temperature.

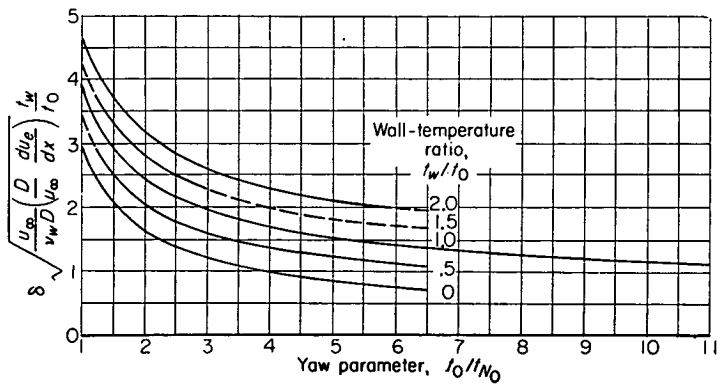


FIGURE 8.—Boundary-layer thickness at stagnation line of yawed cylinder. Prandtl number, 1.

ENGINEERING HEAT-TRANSFER RELATIONS FOR STAGNATION-LINE FLOW

The local rate of heat transfer to the wall per unit wall area is calculated from the relation

$$q_w=h(t_{aw}-t_w) \tag{57}$$

which requires a knowledge of the heat-transfer coefficient h and the adiabatic wall temperature t_{aw}.

The adiabatic wall temperature at the stagnation line is obtained from equation (52) with the recovery factor evaluated from table IV.

The expression for heat-transfer coefficient is

$$h=\frac{k_w}{\sqrt{\nu_w}}\left[\left(\frac{t_0-t_w}{t_{aw}-t_w}\right)\theta_w'\right]\sqrt{\frac{du_e}{dx}\left[1+\frac{\gamma-1}{2}\left(\frac{u_e}{a_e}\right)^2\right]} \tag{50}$$

To evaluate the heat-transfer coefficient h in the stagnation-line region of a given yawed cylinder, it is necessary to evaluate the fluid properties at the wall, the chordwise velocity gradient du_e/dx and the heat-transfer parameter $\left(\frac{t_0-t_w}{t_{aw}-t_w}\right)\theta_w'$. The evaluation of these items with consideration of the effects of yaw is discussed in the following paragraphs.

FLUID PROPERTIES AT THE WALL

The thermal conductivity and absolute viscosity can be considered as functions of temperature alone, but the density varies also with the pressure according to the equation of state. The static pressure is determined from the inviscid flow. When the chordwise component of the free-stream velocity is supersonic, the wall pressure at the stagnation line is that which would be sensed by a Pitot tube placed normal to the shock. This pressure is related to the free-stream static pressure by the expression

$$\frac{p_{w_{sl}}}{p_\infty}=\left(\frac{\gamma+1}{2}M_{N_\infty}^2\right)^{\frac{\gamma}{\gamma-1}}\left[\frac{\gamma+1}{2\gamma M_{N_\infty}^2-(\gamma-1)}\right]^{\frac{1}{\gamma-1}} \tag{58}$$

(where $M_{N_\infty}=M_\infty\cos\Lambda$). For subsonic chordwise flow

$$\frac{p_{w_{sl}}}{p_\infty}=\left(1+\frac{\gamma-1}{2}M_{N_\infty}^2\right)^{\frac{\gamma}{\gamma-1}} \tag{59}$$

CHORDWISE VELOCITY GRADIENT

Based on the observation (refs. 20 and 21) that for normal circular cylinders at free-stream Mach numbers greater than 2 the pressure coefficient varies about the cylinder as

$$\frac{C_p}{C_{p,max}}\approx\cos^2\left(\frac{2x}{D}\right) \tag{60}$$

an expression for the velocity gradient at the stagnation line du_e/dx was derived. This relation in dimensionless form is

$$\frac{D}{u_\infty}\left(\frac{du_e}{dx}\right)=\frac{2a_0}{M_\infty a_\infty}\sqrt{\frac{2}{\gamma}\left(1-\frac{p_\infty}{p_{w_{sl,\Lambda=0}}}\right)} \tag{61}$$

Penland (ref. 20) further observed that equation (60) reasonably represents the chordwise pressure distribution over a yawed cylinder. Therefore, equation (61) for a yawed cylinder becomes just a function of the normal Mach number. With a normal Mach number greater than about 2 and upon introduction of the proper stagnation-line fluid properties, equation (61) becomes

$$\frac{D}{u_\infty}\frac{du_e}{dx}=\frac{2a_{N_0}}{a_\infty M_{N_\infty}}\sqrt{\frac{2}{\gamma}\left(1-\frac{p_\infty}{p_{w_{sl,\Lambda}}}\right)} \tag{62}$$

It must be remembered that in equation (62) u_∞ is the chordwise component of the free-stream velocity.

For subsonic chordwise flow (according to ref. 22),

$$\frac{D}{u_\infty}\frac{du_e}{dx}=4(1-0.416M_{N_\infty}^2-0.164M_{N_\infty}^4) \tag{63}$$

Relations (62) and (63) are plotted in figure 9 along with available data on the chordwise velocity gradient from references 20 and 23 to 25. It is to be noted that for subsonic normal Mach numbers the experimental values of $\frac{D}{u_\infty}\frac{du_e}{dx}$ differ somewhat from the values of equation (63). It is therefore recommended that these experimental values be used in place of the equation. The broken line in figure 9 in the region $0.8<M_\infty \cos\Lambda<1.5$ was drawn as an estimate of the velocity-gradient variation, since neither equation (62) nor equation (63) is strictly applicable and there are no experimental data available for that range.

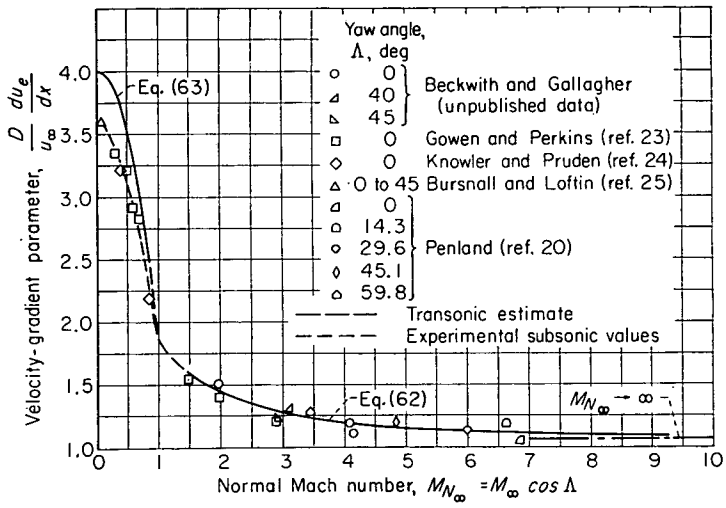


FIGURE 9.—Chordwise-velocity-gradient parameter as function of normal Mach number component for flow at stagnation line of yawed circular cylinder.

HEAT-TRANSFER PARAMETER

For the general case of arbitrary Prandtl number and surface temperature, it is reasonable to assume from equation (51) that

$$\left[\left(\frac{t_0-t_w}{t_{aw}-t_w}\right)\theta_w'\right]_{Pr}=(\theta_w')_{Pr=1}Pr^{0.46} \tag{64}$$

Values of $(\theta_w')_{Pr=1}$ may be obtained from either table III or figure 6.

When equations (58) to (64) are combined as required, equation (50) becomes, for the stagnation line of a yawed cylinder,

$$h_\Lambda=k_w(\theta_w')_{Pr=1}Pr^{0.46}\sqrt{\frac{u_\infty}{\mu_w D}\frac{p_\infty}{Rt_w}\left(\frac{p_{w_{sl,\Lambda}}}{p_\infty}\right)\left(\frac{D}{u_\infty}\frac{du_e}{dx}\right)} \tag{65}$$

EFFECT OF YAW ANGLE AND MACH NUMBER ON HEAT-TRANSFER COEFFICENT AT THE STAGNATION LINE

The ratio of yawed to normal heat-transfer coefficient for a given cylinder with the same conditions of free-stream and surface temperatures is, from equation (65),

$$\frac{h_\Lambda}{h_{\Lambda=0}}=\left(\frac{\theta'_{w_\Lambda}}{\theta'_{w_{\Lambda=0}}}\right)_{Pr=1}\sqrt{\cos\Lambda\,\frac{\left(\frac{p_{w_{sl,\Lambda}}}{p_\infty}\right)}{\left(\frac{p_{w_{sl,\Lambda=0}}}{p_\infty}\right)}\,\frac{\left(\frac{D}{u_\infty}\frac{du_e}{dx}\right)_{M_{N_\infty}}}{\left(\frac{D}{u_\infty}\frac{du_e}{dx}\right)_{M_\infty}}} \tag{66}$$

This relation is plotted in figure 10 as a function of yaw angle and Mach number for an essentially insulated surface $\left(\frac{t_w}{t_0}\approx 1\right)$. The value of $\frac{D}{u_\infty}\frac{du_e}{dx}$ for these calculations was taken as the modified Newtonian value for $M_\infty \cos\Lambda>1.5$ (eq. (62)) and from the dotted line of figure 9 for $M_\infty \cos\Lambda<1.5$.

For incompressible flow $\left(\frac{t_0}{t_{N_0}}=1\right)$ the ratio of yawed to normal heat-transfer coefficient becomes

$$\left(\frac{h_\Lambda}{h_{\Lambda=0}}\right)_{M_\infty=0}=(\cos\Lambda)^{\frac{1}{2}} \tag{67}$$

which is exactly that indicated experimentally for hot wires by Schubauer and Klebanoff (ref. 26). For subsonic speeds the yaw effect is very close to that for incompressible flow. The curve for $M_\infty=1$ is in some doubt because of the lack of suitable experimental information on the chordwise velocity gradient. The effect of yaw for supersonic flow depends on the normal component of the stream Mach number. In the region where the normal component of the stream Mach number is supersonic, the curves of the ratio of yawed to normal heat-transfer coefficient are all very close to each other and somewhat below $\cos\Lambda$ (fig. 10). As the normal Mach number becomes transonic, the ratio exceeds $\cos\Lambda$, and at large yaw angles where the normal Mach number is subsonic, the curves tend to approach a $(\cos\Lambda)^{\frac{1}{2}}$ variation.

The influence of the exact solutions reported herein can be seen by comparing the curve for $M_\infty=7$ with that for the same Mach number but for θ_w' assumed constant at the zero-yaw value. For a Mach number of infinity the ratio of yawed to normal heat-transfer coefficient (not shown in fig. 10) is only slightly below that for $M_\infty=7$ and from equations (58) and (66) is given by the relation

$$\left(\frac{h_\Lambda}{h_{\Lambda=0}}\right)_{M_\infty\to\infty}=\frac{(\theta_w')_{t_0/t_{N_0}=\sec^2\Lambda}}{(\theta_w')_{\Lambda=0}}(\cos\Lambda)^{\frac{1}{2}} \tag{68}$$

The application of the results of this investigation must be terminated before the case of the parallel cylinder ($\Lambda=90°$), since the initial hypothesis that spanwise derivatives are identically zero does not apply.

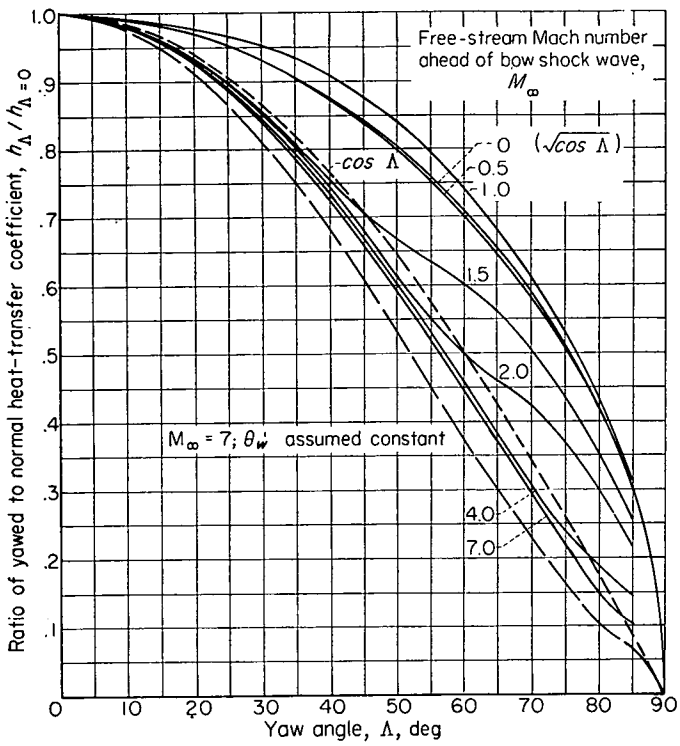


FIGURE 10.—Effect of yaw on heat-transfer coefficient at stagnation line of circular cylinder with nearly insulated surface. Wall-temperature ratio, t_w/t_0, 1.0; Prandtl number, 1.

The effect of heating or cooling on the ratio of yawed to normal heat-transfer coefficient is shown in figure 11 for a Prandtl number of 1 in terms of a modification factor to the nearly insulated result. The factor is

$$\frac{\left(\frac{h_\Lambda}{h_{\Lambda=0}}\right)_{t_w/t_0}}{\left(\frac{h_\Lambda}{h_{\Lambda=0}}\right)_{t_w/t_0=1}} = \frac{\left(\frac{\theta'_{w\Lambda}}{\theta'_{w\Lambda=0}}\right)_{t_w/t_0}}{\left(\frac{\theta'_{w\Lambda}}{\theta'_{w\Lambda=0}}\right)_{t_w/t_0=1}} \tag{69}$$

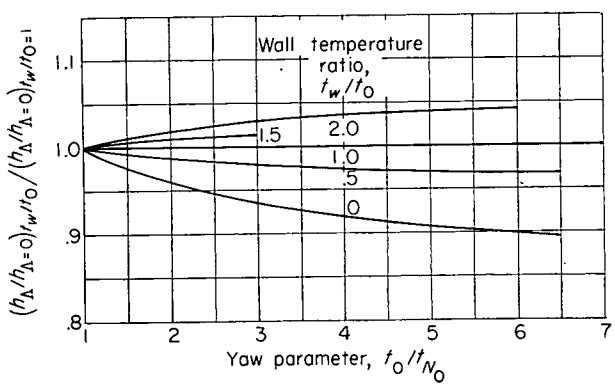


FIGURE 11.—Effect of surface-temperature level on heat-transfer-coefficient ratio. Prandtl number, 1.

The effect of surface-temperature level from absolute zero to twice free-stream stagnation temperature on the ratio of heat-transfer coefficients is shown in figure 11 to be within ± 10 percent of the insulated heat-transfer-coefficient ratio for $t_0/t_{N_0} < 6.5$.

The curves of figures 10 and 11 are essentially independent of Prandtl number, since the effect of Prandtl number on heat transfer has been approximately included through a modification to the $Pr=1$ solutions. The effect of Prandtl number is accounted for exactly through the expression

$$\frac{\left(\frac{h_\Lambda}{h_{\Lambda=0}}\right)_{Pr=0.7}}{\left(\frac{h_\Lambda}{h_{\Lambda=0}}\right)_{Pr=1}} = \frac{\left[\frac{\left(\frac{t_0-t_w}{t_{aw}-t_w}\right)\theta'_{w\Lambda}}{\left(\frac{t_0-t_w}{t_{aw}-t_w}\right)\theta'_{w\Lambda=0}}\right]_{Pr=0.7}}{\left(\frac{\theta'_{w\Lambda}}{\theta'_{w\Lambda=0}}\right)_{Pr=1}} \tag{70}$$

which is shown in figure 12 for $t_w/t_0=0$ and 0.5. For a Prandtl number of 0.7 there is a maximum effect of approximately 4 percent, which occurs for large values of the yaw parameter and a highly cooled wall.

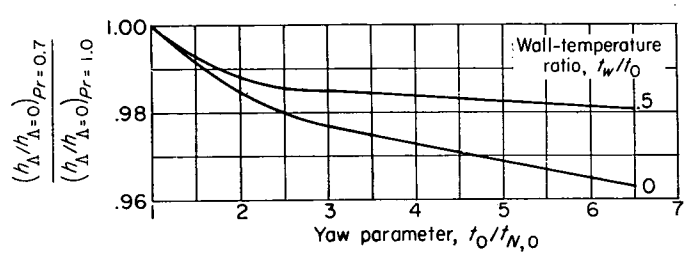


FIGURE 12.—Effect of Prandtl number on heat-transfer-coefficient ratio.

SUMMARY OF RESULTS

The equations for compressible-boundary-layer development over a yawed infinite cylinder with heat transfer have been presented and solutions obtained for stagnation-line flow. The following are among the results obtained:

1. The ratio of yawed to normal heat-transfer coefficient for the stagnation line of a given cylinder varies with yaw angle Λ as $(\cos\Lambda)^{\frac{1}{2}}$ for incompressible flow and shows nearly that variation for much of the subsonic range. Where the velocity normal to the cylinder is supersonic, this ratio is again almost a unique function of yaw angle, the ratio being in this case somewhat lower than cos Λ. Most of this decrease in heat-transfer coefficient with yaw angle can be accounted for by the change in local flow quantities outside the boundary layer that occurs as the normal Mach number and strength of the bow shock change with yaw angle.

2. The effect of large amounts of heating or cooling on the ratio of yawed to normal heat-transfer coefficient is less than 10 percent for values of the yaw parameter t_0/t_{N_0} less than 6 for surface-temperature levels from absolute zero to twice free-stream stagnation temperature. Changing the Prandtl number Pr from 1 to 0.7 had at most a 4-percent effect on the ratio of yawed to normal heat-transfer coefficient.

3. The local recovery factor at the stagnation line of yawed cylinders is closely represented by $Pr^{0.46}$. For most purposes this may be approximated by the square root of the Prandtl number.

4. Where the independence principle does not apply, the effects of yaw on chordwise wall shear are much larger on a percentage basis than the corresponding effects on spanwise

shear or heat transfer. For yaw angles up to 45° and for all Mach numbers, values of a local heat-transfer parameter $Nu/\sqrt{Re_w}$ (where Nu is Nusselt number and Re_w is the Reynolds number at the wall) for stagnation-line flow are less than 13 percent above the zero-yaw value.

5. For favorable pressure gradient, a chordwise velocity overshoot is obtained where the sum of the surface temperature and the free-stream stagnation temperature is greater than twice the external temperature ($t_w+t_0>2t_{N_0}$). While in the unyawed case velocity overshoot is obtained only for heated surfaces, with yaw it is obtained also for cooled surfaces. Another unusual effect noted was that for Prandtl numbers less than unity, when velocity overshoot was obtained for an insulated or cooled surface, the local stagnation enthalpy within the boundary layer exceeded the stream stagnation enthalpy.

6. The degree of secondary flow, as evidenced by the deflection of the "wall" streamline compared with the external streamline, increased with wall temperature and yaw-angle parameter.

LEWIS FLIGHT PROPULSION LABORATORY
NATIONAL ADVISORY COMMITTEE FOR AERONAUTICS
CLEVELAND, OHIO, *April 4, 1957*

APPENDIX A

SYMBOLS

$A_2, \ldots$	constants in asymptotic solution
a	sonic velocity
C	stagnation-line chordwise velocity gradient, $C=\frac{U_e}{X}=\frac{dU_e}{dX}$
C_p	pressure coefficient, $\frac{p-p_\infty}{\frac{1}{2}\rho_\infty u_\infty^2}$
C_f	local skin-friction coefficient
c_p	specific heat at constant pressure
D	diameter of cylinder at stagnation line
f	function related to stream function, $\psi\sqrt{\frac{m+1}{2\nu_0 U_e X}}$
g	spanwise velocity variable
H	total enthalpy, $c_p t+\frac{u^2+v^2}{2}$
h	heat-transfer coefficient
k	thermal conductivity
k_{Su}	Sutherland's constant
M	Mach number
m	exponent from $U_e=CX^m$
Nu	Nusselt number, hx/k_w
Pr	Prandtl number
p	pressure
q_w	heat-transfer rate to wall per unit area
R	gas constant
r	free-stream recovery factor, $\frac{t_{aw}-t_\infty}{t_0-t_\infty}$
Re_w	Reynolds number at the wall, $\frac{\rho_w u_e x}{\mu_w}$
t	static temperature
u	transformed chordwise velocity component
v	chordwise velocity component
w	spanwise velocity component
V	transformed normal velocity component
v_N	normal velocity component
X	transformed chordwise coordinate
x	chordwise coordinate
y	spanwise coordinate
Z	transformed normal coordinate
z	normal coordinate
α	streamline inclination
β	pressure-gradient parameter, $\frac{2m}{m+1}$
γ	ratio of specific heats
δ	boundary-layer thickness
ζ	spanwise temperature-difference parameter
ζ_w	local recovery factor
η	similarity variable, $Z\sqrt{\frac{m+1}{2}}\frac{U_e}{\nu_0 X}$
θ	normalized enthalpy function, $\frac{H-H_w}{H_e-H_w}$
κ	constant in asymptotic solution
Λ	yaw angle
λ	$\lambda=\frac{\mu/\mu_0}{t/t_0}=\left(\frac{t_0+k_{Su}}{t_w+k_{Su}}\right)\sqrt{\frac{t_w}{t_0}}$
μ	absolute viscosity
ν	kinematic viscosity
ρ	density
τ	wall shear stress
ψ	stream function

Subscripts:

aw	adiabatic wall
c	chordwise
e	local flow outside boundary layer (external)
max	maximum
N	component normal to cylinder axis
s	spanwise
sl	stagnation line
w	wall or surface value
∞	free-stream quantity ahead of bow shock wave
0	free-stream stagnation value
Λ	quantity pertaining to yawed cylinder
$\Lambda=0$	quantity pertaining to normal cylinder

Superscripts:

$'$	differentiation with respect to η
$\sim$	asymptotic quantity

APPENDIX B

SOLUTION OF ORDINARY DIFFERENTIAL EQUATIONS

Solutions to equations (25) were obtained independently at both the NACA Lewis and Langley laboratories. The solutions to equations (27) were obtained at the Langley laboratory. The procedure used at the Lewis laboratory was the forward integration technique described in appendix B of reference 27, and is based on five-point integration formulas. This is the same procedure as that used in obtaining some of the solutions presented in reference 15. An IBM card-programmed electronic calculator was used.

At the Langley laboratory the step-by-step integration procedure described in reference 28 was used. This procedure seems somewhat superior to the five-point technique and some of the results will therefore be described in detail. This particular procedure is a modification of the Runge-Kutta method and was developed primarily for automatic digital computing machines. The Bell Telephone Laboratories X–66744 relay computer at Langley is one of this type and was used for the present solutions. A step size of 0.2 was used for all the solutions, although a few solutions were also calculated with a step size of 0.1 for the purpose of evaluating the error due to step size. The calculations were carried out to $\eta=6.0$, since the results showed that the stream boundary conditions could always be satisfied to the desired degree of accuracy for $\eta \leq 6.0$.

CONVERGENCE TO BOUNDARY CONDITIONS

The integration of the present equations constitutes a "two-point boundary-value problem" in which the correct initial values at $\eta=0$ (such that the boundary conditions for large η are satisfied) of the functions or their derivatives are usually found by a trial-and-error or interpolation method.

The procedure used to obtain convergence for the present solutions involved an adaptation of Newton's method to three variables and the idea that for large η the value of the functions depends on the assumed initial values at $\eta=0$. Applying this procedure to equations (27) with boundary conditions of equations (24) results in the following general functional forms:

$$\left.\begin{aligned} f'_\infty &= f'_\infty(f''_w, \theta'_w, g'_w) \\ \theta_\infty &= \theta_\infty(f''_w, \theta'_w, g'_w) \\ g_\infty &= g_\infty(f''_w, \theta'_w, g'_w) \end{aligned}\right\} \tag{B1}$$

where the subscripts ∞ and w denote the computed values of the function at large η and at $\eta=0$, respectively. The error in the functions at large η is then given by

$$\left.\begin{aligned} \mathrm{d}f'_\infty &= \frac{\partial f'_\infty}{\partial f''_w}\mathrm{d}f''_w + \frac{\partial f'_\infty}{\partial \theta'_w}\mathrm{d}\theta'_w + \frac{\partial f'_\infty}{\partial g'_w}\mathrm{d}g'_w \\ \mathrm{d}\theta_\infty &= \frac{\partial \theta_\infty}{\partial f''_w}\mathrm{d}f''_w + \frac{\partial \theta_\infty}{\partial \theta'_w}\mathrm{d}\theta'_w + \frac{\partial \theta_\infty}{\partial g'_w}\mathrm{d}g'_w \\ \mathrm{d}g_\infty &= \frac{\partial g_\infty}{\partial f''_w}\mathrm{d}f''_w + \frac{\partial g_\infty}{\partial \theta'_w}\mathrm{d}\theta'_w + \frac{\partial g_\infty}{\partial g'_w}\mathrm{d}g'_w \end{aligned}\right\} \tag{B}$$

The various partial derivatives in equations (B2) may evaluated approximately from four trial solutions accordi to the following table:

Trial solution	Initial values			Partial derivative
	f''_w	θ'_w	g'_w	
1	f''_{w_1}	θ'_{w_1}	g'_{w_1}	$\partial/\partial f''_w$
2	f''_{w_2}	θ'_{w_1}	g'_{w_1}	$\partial/\partial f''_w$
3	f''_{w_2}	θ'_{w_2}	g'_{w_1}	$\partial/\partial g'_w$
4	f''_{w_2}	θ'_{w_2}	g'_{w_2}	$\partial/\partial g'_w$

$\partial/\partial\theta'_w$

The best solution of these four, for example solution i, is th used to obtain the errors, which from equations (24) are

$$\left.\begin{aligned} \mathrm{d}f'_\infty &= f'(\infty) - f'_{\infty_i} = 1 - f'_{\infty_i} \\ \mathrm{d}\theta_\infty &= \theta(\infty) - \theta_{\infty_i} = 1 - \theta_{\infty_i} \\ \mathrm{d}g_\infty &= g(\infty) - g_{\infty_i} = 1 - g_{\infty_i} \end{aligned}\right\} \tag{I}$$

where f'_{∞_i}, θ_{∞_i}, and g_{∞_i} are the computed values at larg from the best solution.

Equations (B2) are then solved simultaneously $\mathrm{d}f''_w$, $\mathrm{d}\theta'_w$, and $\mathrm{d}g'_w$. The corrected initial values are

$$\left.\begin{aligned} f''_{w_3} &= f''_{w_i} + \mathrm{d}f''_w \\ \theta'_{w_3} &= \theta'_{w_i} + \mathrm{d}\theta'_w \\ g'_{w_3} &= g'_{w_i} + \mathrm{d}g'_w \end{aligned}\right\} \tag{I}$$

which may be used for repeating the whole procedure u convergence is attained. In the present problem, howe

atisfactory convergence was attained by computing a trial olution with the corrected initial values and then using he results of this new solution to reevaluate df'_∞, $d\theta_\infty$, nd dg_∞ from equations (B3); equations (B2) were then olved for df''_w, $d\theta'_w$, and dg'_w by using the partial derivatives lready obtained. A new set of initial values is computed rom equation (B4) and the results of the new solution, nd the procedure is repeated until the boundary conditions re satisfied to the desired degree of accuracy. In most ases four or five more trial solutions were required for this urpose, which made a total of about nine trial solutions or any one case. Note, however, that in accordance with Newton's method the preceding procedure cannot be expected o give satisfactory convergence unless the errors df'_∞, θ_∞, and dg_∞ from the original four solutions are reasonably mall. In the present problem these errors were limited o about 0.4 before the partial derivatives were evaluated.

ACCURACY OF SOLUTION

The inherent error in the Runge-Kutta method is of the rder of the step size to the fifth power. A discussion of the rrors in the integration procedure used here is given in eference 28.

An example of the errors due to step size and initial values or one of the present solutions is given in the following able for the case $t_w/t_0=1.5$, $t_0/t_{N_0}=1.2$, and $Pr=1$:

Step size	Initial values		Boundary conditions at $\eta=6.0$	
	f''_w	θ'_w	$f'(6.0)$	$\theta(6.0)$
0.2	1.664076	0.610859	0.999684	0.999998
.2	1.664085	.610863	.999987	.999999
.1	1.664085	.610863	.999328	1.000027

Inspection of the table indicates that the value of f' at large η s relatively sensitive to both the initial values and the step ize. This is in accordance with the values of the partial erivatives, which for this case were

$$\frac{\partial f'_\infty}{\partial f''_w}=28.4 \qquad \frac{\partial f'_\infty}{\partial \theta'_w}=15.4$$

$$\frac{\partial \theta_\infty}{\partial f''_w}=0.51 \qquad \frac{\partial \theta_\infty}{\partial \theta'_w}=1.56$$

In general, all the solutions were repeated until the maximum error in the boundary conditions was at most 0.0001 in f' and 0.00001 in θ or g at $\eta=6.0$ with a step size of 0.2. Reducing the step size to 0.1 gives a more accurate solution, which can be used to evaluate the errors in the initial values f''_w and θ'_w for the 0.2 step size. Thus, the sample solutions given in the table indicate that reducing the step size to 0.1, but using the same initial values, increases the errors in the outer boundary conditions by 0.00066 for $f'(6.0)$ and by 0.00003 for $\theta(6.0)$. Adding these changes to the maximum allowable computing errors of 0.0001 in $f'(6.0)$ and 0.00001 in $\theta(6.0)$ results in an improved evaluation of the actual errors, which would be approximately 0.0007 in $f'(6.0)$ and 0.00004 in $\theta(6.0)$. From these errors in f' and θ and the values of the partial derivatives just given, the *maximum* errors in the initial values as obtained from equations (B2) (modified for the case of $Pr=1$) are

$$df''_w=\pm 0.00001$$
$$d\theta'_w=\pm 0.00003$$

Thus, the initial values are accurate to at least the fourth decimal place, assuming that a further decrease in step size would not have much additional effect on the solutions. The functions f' and θ are evidently accurate to the third and fourth decimal places, respectively, for large values of η.

COMPARISON OF THE TWO TECHNIQUES

Among the cases calculated, three for $t_w/t_0=1$ were done independently by both techniques. Comparisons of values of f''_w and θ'_w as well as values of f, f', f'', θ and θ' at $\eta=4$ are given in the following tables:

t_0/t_{N_0}	f''_w		θ_w	
	Five-point	Runge-Kutta	Five-point	Runge-Kutta
1.1	1.29887	1.29886	0.57760	0.57763
1.2	1.36401	1.36400	.58446	.58447
3.0	2.40863	2.40857	.67698	.67699

t_0/t_{N_0}	f (4)		f' (4)		f'' (4)		θ (4)		θ' (4)	
	Five-point	Runge-Kutta	Five-point	Runge-Kutta	Five-point	Runge-Kutta	Five-point	Runge-Kutta	Five-point	Runge-Kutta
1.1	3.3902	3.3901	1.0000	1.0000	0.0001	0	0.9996	0.9996	0.0016	0.0016
1.2	3.4265	3.4263	1.0002	1.0000	0	−.0001	.9997	.9996	.0015	.0015
3.0	3.8946	3.8947	1.0002	1.0001	−.0006	−.0007	.9999	.9999	.0004	.0004

There is a difference of not more than 0.0001 in the initial values and not more than 0.0002 in the functions near the outer edge of the boundary layer. An examination of other values of the functions shows them to differ by 0.0002 or less for all values of η. It is felt therefore that all tabulated values in tables I, II, and III are certainly correct to three decimal places and that most of the tabulations are probably correct to ± 0.0005.

APPENDIX C

ASYMPTOTIC SOLUTION

In examining the behavior of the presented solutions near the outer edge of the boundary layer, it is useful to find a solution of the system

$$f'''+ff''=f'^2-1-\left(\frac{t_0}{t_{N_0}}-1\right)(1-g^2)-\frac{t_0}{t_{N_0}}\left(\frac{t_w}{t_0}-1\right)(1-\theta) \tag{27a}$$

$$g''+fg'=0 \tag{27b}$$

$$\theta''+Prf\theta'=(1-Pr)\frac{1-\frac{t_{N_0}}{t_0}}{1-\frac{t_w}{t_0}}(g^2)'' \tag{27c}$$

for large η.

The asymptotic form for f (designated $\tilde{f}$) is assumed to consist of a sum of terms, each smaller than the preceding. Only the first two terms are considered herein. The corresponding solutions for the spanwise velocity function $\tilde{g}$ and the stagnation enthalpy function $\tilde{\theta}$ are also obtained.

Let

$$\tilde{f}=\tilde{f}_1+\tilde{f}_2 \tag{C1}$$

where

$$\tilde{f}_2\ll\tilde{f}_1$$

$$\tilde{f}_2'\ll\tilde{f}_1'$$

Since $\lim_{N\to\infty}f'=1$, let

$$\tilde{f}_1=\eta-\kappa \tag{C2}$$

where κ is an undetermined constant. If $\tilde{f}_1$ is inserted into equation (27), the corresponding spanwise velocity function $\tilde{g}_1$ and enthalpy function $\tilde{\theta}_1$ must both be 1. Inserting equations (C1) and (C2) into equations (27) and dropping higher order terms result in

$$\tilde{f}_2'''+(\eta-\kappa)\tilde{f}_2''=2\tilde{f}_2'+2\left(\frac{t_0}{t_{N_0}}-1\right)\tilde{g}_2+\frac{t_0}{t_{N_0}}\left(\frac{t_w}{t_0}-1\right)\tilde{\theta}_2 \tag{C3}$$

$$\tilde{g}_2''+(\eta-\kappa)\tilde{g}_2'=0 \tag{C4}$$

$$\tilde{\theta}_2''+Pr(\eta-\kappa)\tilde{\theta}_2'=-\frac{2(1-Pr)}{\frac{t_w}{t_0}-1}\left(1-\frac{t_{N_0}}{t_0}\right)\tilde{g}_2'' \tag{C5}$$

Equations (C3), (C4), and (C5) are very similar to equations (B3) of reference 15. For $Pr=1$ and $t_0/t_{N_0}=1$, they are identical. The procedure for obtaining the asymptotic solution is similar to that in appendix B of reference 1 Equation (C4) can be integrated directly to give

$$\tilde{g}_2'=A_1\,exp-\frac{(\eta-\kappa)^2}{2} \tag{C}$$

which integrates once again to the complementary err function

$$\tilde{g}_2=-A_1\int_\eta^\infty exp-\frac{(\eta-\kappa)^2}{2}\,d\eta$$

or

$$\tilde{g}_2=-\frac{A_1}{\sqrt{2}}\frac{\sqrt{\pi}}{2}\,cerf\left[\frac{(\eta-\kappa)}{\sqrt{2}}\right] \tag{C}$$

By use of equations (C4) and (C6), equation (C5) can no be written

$$\tilde{\theta}_2''+Pr(\eta-\kappa)\tilde{\theta}_2'=\frac{2(1-Pr)}{\frac{t_w}{t_o}-1}\left(1-\frac{t_{N_0}}{t_0}\right)(\eta-\kappa)A_1\,exp-\frac{(\eta-\kappa)^2}{2} \tag{C8}$$

Which has as its complete solution

$$\tilde{\theta}_2=\frac{A_1}{\sqrt{2}}\frac{2}{\left(\frac{t_w}{t_0}-1\right)}\left(1-\frac{t_{N_0}}{t_0}\right)\frac{\sqrt{\pi}}{2}\,cerf\left[\frac{(\eta-\kappa)}{\sqrt{2}}\right]-$$

$$A_2\sqrt{\frac{Pr}{2}}\frac{\sqrt{\pi}}{2}\,cerf\left[(\eta-\kappa)\sqrt{\frac{Pr}{2}}\right] \tag{C9}$$

where the coefficient A_2 may be evaluated by recognizin that the asymptotic forms $\tilde{g}_2$ and $\tilde{\theta}_2$ are identical for a Prand number of 1. From equations (C7) and (C9) with $Pr=$

$$A_2=A_1\left[\frac{2\left(1-\frac{t_{N_0}}{t_0}\right)+\left(\frac{t_w}{t_0}-1\right)}{\frac{t_w}{t_0}-1}\right] \tag{C10}$$

Assume that this expression holds for $Pr\neq1$. Equatio (C9) then becomes

$$\tilde{\theta}_2=\frac{A_1}{\sqrt{2}}\left\{\frac{2\left(1-\frac{t_{N_0}}{t_0}\right)}{\frac{t_w}{t_0}-1}\frac{\sqrt{\pi}}{2}\,cerf\left[\frac{(\eta-\kappa)}{\sqrt{2}}\right]-\right.$$

$$\left.\sqrt{Pr}\left[\frac{2\left(1-\frac{t_{N_0}}{t_0}\right)+\left(\frac{t_w}{t_0}-1\right)}{\frac{t_w}{t_0}-1}\right]\frac{\sqrt{\pi}}{2}\,cerf\left[(\eta-\kappa)\sqrt{\frac{Pr}{2}}\right]\right\} \tag{C11}$$

The expressions (C7) and (C11) for $\tilde{\eta}_2$ and $\tilde{\theta}_2$, respectively, may now be substituted into the differential equation (C3) for $\tilde{f}_2'$:

$$\tilde{f}_2'''+(\eta-\kappa)\tilde{f}_2''-2\tilde{f}_2'=-A_1\sqrt{\frac{Pr}{2}}\left[2\left(\frac{t_0}{t_{N_0}}-1\right)+\frac{t_0}{t_{N_0}}\left(\frac{t_w}{t_0}-1\right)\right]\frac{\sqrt{\pi}}{2}\,cerf\left[(\eta-\kappa)\sqrt{\frac{Pr}{2}}\right] \quad \text{(C12)}$$

For large η the right side of equation (C12) can be rewritten using the leading term of the following expansion of the complementary error function

$$\frac{\sqrt{\pi}}{2}\,cerf\,x=\frac{e^{-x^2}}{2x}\left(1-\frac{1}{2x^2}+\cdots\right) \quad \text{(C13)}$$

Equation (C12) then becomes

$$\tilde{f}_2'''+(\eta-\kappa)\tilde{f}_2''-2\tilde{f}_2'=-\frac{A_1}{2}\left[2\left(\frac{t_0}{t_{N_0}}-1\right)+\frac{t_0}{t_{N_0}}\left(\frac{t_w}{t_0}-1\right)\right](\eta-\kappa)^{-1}\,exp\left[-\frac{Pr}{2}(\eta-\kappa)^2\right] \quad \text{(C14)}$$

A particular solution to equation (C14) is sought wherein the leading term is of the form

$$\tilde{f}_2'=B(\eta-\kappa)^N\,exp\left[-\frac{Pr}{2}(\eta-\kappa)^2\right] \quad \text{(C15)}$$

Substituting equation (C15) into equation (C14) and examining the results separately for $Pr\neq 1$ and for $Pr=1$ result in the following particular solutions:
For $Pr\neq 1$

$$\tilde{f}_{2p}'=-\frac{A_1}{2Pr(Pr-1)}\left[2\left(\frac{t_0}{t_{N_0}}-1\right)+\frac{t_0}{t_{N_0}}\left(\frac{t_w}{t_0}-1\right)\right](\eta-\kappa)^{-3}\,exp\left[-\frac{Pr}{2}(\eta-\kappa)^2\right] \quad \text{(C16)}$$

and for $Pr=1$

$$\tilde{f}_{2p}'=\frac{A_1}{4}\left[2\left(\frac{t_0}{t_{N_0}}-1\right)+\frac{t_0}{t_{N_0}}\left(\frac{t_w}{t_0}-1\right)\right](\eta-\kappa)^{-1}\,exp\left[-\frac{(\eta-\kappa)^2}{2}\right] \quad \text{(C17)}$$

It is to be noted that for $Pr<1$, equations (C16) and (C17) have the same qualitative behavior; that is, they are both positive or negative depending on whether the quantity $\left[2\left(\frac{t_0}{t_{N_0}}-1\right)+\frac{t_0}{t_{N_0}}\left(\frac{t_w}{t_0}-1\right)\right]$ is positive or negative.

The complementary function for $\tilde{f}_2'$ can be found by noting that the homogeneous part of equation (C12) is Weber's equation. Hartree (ref. 9) gives the general solution for large values of the argument $\eta-\kappa$, which can be written

$$\tilde{f}_2'=A_3(\eta-\kappa)^{-3}\,exp\left[-\frac{(\eta-\kappa)^2}{2}\right]+A_4(\eta-\kappa)^2 \quad \text{(C18)}$$

In order to satisfy the boundary condition $\lim_{\eta\to\infty}\tilde{f}_2'=0$, it is necessary to take $A_4=0$ in equation (C18).

The asymptotic variations of velocity and enthalpy functions are, from equations (C7), (C11), (C13), (C16), (C17), and (C18)

$$(\tilde{f}')_{Pr\neq 1}=1+\frac{A_1}{2Pr(1-Pr)}\left[2\left(\frac{t_0}{t_{N_0}}-1\right)+\frac{t_0}{t_{N_0}}\left(\frac{t_w}{t_0}-1\right)\right](\eta-\kappa)^{-3}\,exp\left[-\frac{Pr}{2}(\eta-\kappa)^2\right]+A_3(\eta-\kappa)^{-3}\,exp\left[-\frac{(\eta-\kappa)^2}{2}\right] \quad \text{(C19)}$$

$$(\tilde{f}')_{Pr=1}=1+\frac{A_1}{4}\left[2\left(\frac{t_0}{t_{N_0}}-1\right)+\frac{t_0}{t_{N_0}}\left(\frac{t_w}{t_0}-1\right)\right](\eta-\kappa)^{-1}\,exp\left[-\frac{(\eta-\kappa)^2}{2}\right]+A_3(\eta-\kappa)^{-3}\,exp\left[-\frac{(\eta-\kappa)^2}{2}\right] \quad \text{(36)}$$

$$\tilde{g}=1-\frac{A_1}{2}(\eta-\kappa)^{-1}\,exp\left[-\frac{(\eta-\kappa)^2}{2}\right] \quad \text{(37)}$$

$$\tilde{\theta}=1+A_1\frac{\left(1-\frac{t_{N_0}}{t_0}\right)}{\left(\frac{t_w}{t_0}-1\right)}(\eta-\kappa)^{-1}\,exp\left[-\frac{(\eta-\kappa)^2}{2}\right]-\frac{A_1}{2}\left[\frac{2\left(1-\frac{t_{N_0}}{t_0}\right)+\left(\frac{t_w}{t_0}-1\right)}{\left(\frac{t_w}{t_0}-1\right)}\right](\eta-\kappa)^{-1}\,exp\left[-\frac{Pr}{2}(\eta-\kappa)^2\right] \quad \text{(38)}$$

An examination of equations (C18) for $Pr<1$ and equation (36) for $Pr=1$ shows that the velocity functions in these cases have the same qualitative asymptotic behavior, since the A_1 terms in both cases dominate over the A_3 terms.

APPENDIX D

STAGNATION-LINE RECOVERY FACTOR FOR YAWED CYLINDER

The evaluation of the recovery factor for the stagnation line of a yawed cylinder in essentially incompressible flow is accomplished by rewriting equations (27) with the quantity t_{N_0}/t_0 replaced by the equivalent expression $1-\frac{v_e^2}{2c_p t_0}$, where $\frac{v_e^2}{2c_p t_0} << 1$ and with $\left(1-\frac{t_w}{t_0}\right) << 1$. The resulting equations are

$$f'''+ff''=f'^2-1 \tag{D1}$$

$$g''+fg'=0 \tag{D2}$$

$$\theta''+Pr\,f\theta'=(1-Pr)\frac{\frac{v_e^2}{2c_p t_0}}{\left(1-\frac{t_w}{t_0}\right)}(g^2)'' \tag{D3}$$

The first two of these equations are recognized as the momentum equations for chordwise and spanwise incompressible stagnation-line flow over a yawed cylinder. The energy equation (eq. (D3)) must be further reduced by writing θ in terms of the temperature-difference parameter

$$\zeta=\frac{t-t_e}{\frac{v_e^2}{2c_p}} \tag{D4}$$

The expression for θ in terms of ζ becomes from equations (14) and (D4)

$$\theta=1+\frac{(g^2+\zeta-1)\frac{v_e^2}{2c_p}}{t_0-t_w} \tag{D5}$$

Substitution of relations (D5) and (D2) into equation (D3) yields for finite $\frac{v_e^2}{2c_p t_0}$

$$\zeta''+Pr\,f\zeta'+2Pr\,g'^2=0 \tag{D6}$$

Equation (D6) is identical to that of Schuh (ref. 29). With the boundary conditions:

At $\eta=0$

$$\zeta'=0$$

At $\eta\to\infty$

$$\zeta=0$$

the value of ζ at the wall becomes the recovery factor and from equations (D1), (D2), and (D6) can be written

$$\zeta_w=-2Pr\,g_w'^2\int_\eta^\infty e^{-\int_0^\eta Pr\,f\,d\eta}\int_0^\eta e^{-(Pr-2)\int_0^\eta f\,d\eta}\,d\eta\,d\eta \tag{D7}$$

where

$$g_w'=\frac{1}{\int_0^\infty e^{-\int_0^\eta f\,d\eta}\,d\eta} \tag{D8}$$

For the present paper, values of ζ_w were obtained for $Pr=0.7$, 0.8, 0.9, and 1 and are shown in table IV. The value indicated for $Pr=0.7$ agrees with that of Schuh.

A recovery factor for the stagnation line defined in terms of free-stream static temperature is related to ζ_w as follows:

$$\mathscr{R}\equiv\frac{t_{aw}-t_\infty}{t_0-t_\infty}=1-(1-\zeta_w)\sin^2\Lambda \tag{D8}$$

REFERENCES

1. Reshotko, Eli: Heat Transfer to a Yawed Infinite Cylinder in Compressible Flow. Proc. 1956 Heat Transfer and Fluid Mech. Inst., Stanford Univ. Press, June 1956, pp. 205–220.
2. Prandtl, L.: On Boundary Layers in Three-Dimensional Flow. Rep. and Trans. No. 64, British MAP, May 1, 1946.
3. Struminsky, V. V.: Sideslip in a Viscous Compressible Gas. NACA TM 1276, 1951.
4. Jones, Robert T.: Effects of Sweepback on Boundary Layer and Separation. NACA Rep. 884, 1947. (Supersedes NACA TN 1402.)
5. Sears, W. R.: The Boundary Layer of Yawed Cylinders. Jour. Aero. Sci., vol. 15, no. 1, Jan. 1948, pp. 49–52.
6. Moore, Franklin K.: Three-Dimensional Compressible Laminar Boundary-Layer Flow. NACA TN 2279, 1951.
7. Wild, J. M.: The Boundary Layer of Yawed Infinite Wings. Jour. Aero. Sci., vol. 16, no. 1, Jan. 1949, pp. 41–45.
8. Cooke, J. C.: The Boundary Layer of a Class of Infinite Yawed Cylinders. Proc. Cambridge Phil. Soc., pt. 4, vol. 46, Oct. 1950, pp. 645–648.
9. Hartree, D. R.: On an Equation Occurring in Falkner and Skan's Approximate Treatment of the Equations of the Boundary Laver. Proc. Cambridge Phil. Soc., pt. 2, vol. 33, Apr. 1937, pp. 223–239.
10. Goland, Leonard: A Theoretical Investigation of Heat Transfer in the Laminar Flow Regions of Airfoils. Jour. Aero. Sci., vol. 17, no. 7, July 1950, pp. 436–440.
11. Crabtree, L. F.: The Compressible Laminar Boundary Layer on a Yawed Infinite Wing. Aero. Quarterly, vol. 5, May-Nov. 1954, pp. 85–100.
12. Tinkler, J.: Effect of Yaw on the Compressible Laminar Boundary Layer. R. & M. No. 3005, British ARC, 1955.
13. Moore, Frarklin K.: Three-Dimensional Boundary Layer Theory. Vol. IV of Advances in Appl. Mech., Academic Press, Inc., 1956, pp. 159–228.
14. Stewartson, K.: Correlated Incompressible and Compressible Boundary Layers. Proc. Roy. Soc. (London), ser. A, vol. 200, no. A1060, Dec. 22, 1949, pp. 84–100.

15. Cohen, Clarence B., and Reshotko, Eli: Similar Solutions for the Compressible Laminar Boundary Layer with Heat Transfer and Pressure Gradient. NACA Rep. 1293, 1956. (Supersedes NACA TN 3325.)

16. Brown, W. Byron, and Donoughe, Patrick L.: Tables of Exact Laminar-Boundary-Layer Solutions When the Wall is Porous and Fluid Properties are Variable. NACA TN 2479, 1951.

17. Moore, Franklin K.: Laminar Boundary Layer on Cone in Supersonic Flow at Large Angle of Attack. NACA Rep. 1132, 1953. (Supersedes NACA TN 2844.)

18. Van Driest, E. R.: Investigation of Laminar Boundary Layer in Compressible Fluids Using the Crocco Method. NACA TN 2597, 1952.

19. Goldstein, Sydney, ed.: Modern Developments in Fluid Dynamics. Vol. 2. Clarendon Press (Oxford), 1938, pp. 631–632.

20. Penland, Jim A.: Aerodynamic Characteristics of a Circular Cylinder at Mach Number 6.86 and Angles of Attack up to 90°. NACA TN 3861, 1956. (Supersedes NACA RM L54A14.)

21. Lees, Lester: Hypersonic Flow. Preprint No. 554, Inst. Aero. Sci., June 1955.

22. Reshotko, Eli, and Cohen, Clarence B.: Heat Transfer at the Forward Stagnation Point of Blunt Bodies. NACA TN 3513, 1955.

23. Gowen, Forrest E., and Perkins, Edward W.: Drag of Circular Cylinders for a Wide Range of Reynolds Numbers and Mach Numbers. NACA TN 2960, 1953. (Supersedes NACA RM A52C20.)

24. Knowler, A. E., and Pruden, F. W.: On the Drag of Circular Cylinders at High Speeds. R. & M. No. 1933, British ARC, Feb. 18, 1944.

25. Bursnall, William J., and Loftin, Laurence K., Jr.: Experimental Investigation of the Pressure Distribution About a Yawed Circular Cylinder in the Critical Reynolds Number Range. NACA TN 2463, 1951.

26. Schubauer, G. B., and Klebanoff, P. S.: Theory and Application of Hot-Wire Instruments in the Investigation of Turbulent Boundary Layers. NACA WR W–86, 1946. (Supersedes NACA ACR 5K27.)

27. Ostrach, Simon: An Analysis of Laminar Free-Convection Flow and Heat Transfer About a Flat Plate Parallel to the Direction of the Generating Body Force. NACA Rep. 1111, 1953. (Supersedes NACA TN 2635.)

28. Gill, S.: A Process for the Step-by-Step Integration of Differential Equations in an Automatic Digital Computing Machine. Proc. Cambridge Phil. Soc., pt. 1, vol. 47, Jan. 1951, pp. 96–108.

29. Schuh, H.: Aerodynamic Heating on Yawed Infinite Wings and on Bodies of Arbitrary Shape. KTH AERO TN 35, Div. Aero., Royal Inst. Tech., Stockholm, July 5, 1955.

TABLE I.—STAGNATION-LINE FLOW SOLUTIONS FOR YAWED INFINITE CYLINDER WITH PRANDTL NUMBER OF 1

$\frac{t_w}{t_0}=0$; $\frac{t_0}{t_{N_0}}=1.0$

η	f	f'	f''	θ	θ'
0	0. 0000	0. 0000	0. 6489	0. 0000	0. 5067
. 2	. 0129	. 1291	. 6393	. 1013	. 5062
. 4	. 0514	. 2546	. 6128	. 2023	. 5032
. 6	. 1143	. 3734	. 5728	. 3023	. 4951
. 8	. 2001	. 4830	. 5226	. 3999	. 4800
1. 0	. 3068	. 5819	. 4654	. 4937	. 4564
1. 2	. 4321	. 6690	. 4045	. 5819	. 4240
1. 4	. 5736	. 7437	. 3427	. 6627	. 3835
1. 6	. 7288	. 8062	. 2828	. 7349	. 3368
1. 8	. 8953	. 8571	. 2270	. 7972	. 2863
2. 0	1. 0709	. 8973	. 1769	. 8494	. 2353
2. 2	1. 2536	. 9283	. 1338	. 8915	. 1865
2. 4	1. 4417	. 9513	. 0980	. 9243	. 1424
2. 6	1. 6337	. 9680	. 0694	. 9489	. 1047
2. 8	1. 8285	. 9795	. 0476	. 9666	. 0741
3. 0	2. 0253	. 9874	. 0315	. 9790	. 0504
3. 2	2. 2233	. 9924	. 0201	. 9872	. 0330
3. 4	2. 4221	. 9956	. 0124	. 9925	. 0207
3. 6	2. 6214	. 9976	. 0073	. 9958	. 0125
3. 8	2. 8211	. 9987	. 0042	. 9977	. 0073
4. 0	3. 0209	. 9993	. 0023	. 9988	. 0040
4. 2	3. 2208	. 9997	. 0012	. 9994	. 0022
4. 4	3. 4208	. 9999	. 0006	. 9997	. 0011
4. 6	3. 6207	. 9999	. 0003	. 9999	. 0006
4. 8	3. 8207	1. 0000	. 0001	1. 0000	. 0003

$\frac{t_w}{t_0}=0$; $\frac{t_0}{t_{N_0}}=1.2$

η	f	f'	f''	θ	θ'
0	0. 0000	0. 0000	0. 6823	0. 0000	0. 5130
. 2	. 0136	. 1357	. 6708	. 1026	. 5125
. 4	. 0540	. 2670	. 6392	. 2048	. 5093
. 6	. 1199	. 3903	. 5920	. 3059	. 5007
. 8	. 2094	. 5031	. 5338	. 4046	. 4847
1. 0	. 3203	. 6034	. 4688	. 4992	. 4598
1. 2	. 4499	. 6904	. 4010	. 5879	. 4259
1. 4	. 5955	. 7638	. 3339	. 6690	. 3837
1. 6	. 7545	. 8242	. 2704	. 7410	. 3353
1. 8	. 9244	. 8724	. 2128	. 8029	. 2835
2. 0	1. 1028	. 9098	. 1627	. 8544	. 2315
2. 2	1. 2877	. 9380	. 1206	. 8957	. 1823
2. 4	1. 4775	. 9586	. 0866	. 9277	. 1383
2. 6	1. 6707	. 9731	. 0603	. 9515	. 1009
2. 8	1. 8664	. 9831	. 0406	. 9685	. 0709
3. 0	2. 0638	. 9897	. 0264	. 9803	. 0479
3. 2	2. 2622	. 9940	. 0166	. 9881	. 0311
3. 4	2. 4612	. 9966	. 0101	. 9931	. 0194
3. 6	2. 6607	. 9981	. 0059	. 9961	. 0116
3. 8	2. 8605	. 9990	. 0033	. 9979	. 0067
4. 0	3. 0603	. 9995	. 0018	. 9989	. 0037
4. 2	3. 2603	. 9998	. 0010	. 9994	. 0020
4. 4	3. 4602	1. 0000	. 0005	. 9997	. 0010
4. 6	3. 6602	1. 0000	. 0003	. 9999	. 0005
4. 8	3. 8603	1. 0001	. 0002	. 9999	. 0002
5. 0	4. 0603	1. 0001	. 0001	1. 0000	. 0001
5. 2	4. 2603	1. 0001	. 0001	1. 0000	. 0000
5. 4	4. 4603	1. 0001	. 0001	1. 0000	. 0000
5. 6	4. 6603	1. 0001	. 0001	1. 0000	. 0000
5. 8	4. 8604	1. 0002	. 0001	1. 0000	. 0000
6. 0	5. 0604	1. 0002	. 0001	1. 0000	. 0000

526597—60——68

TABLE I.—Continued. STAGNATION-LINE FLOW SOLUTIONS FOR YAWED INFINITE CYLINDER WITH PRANDTL NUMBER OF 1

$\frac{t_w}{t_0}=0$; $\frac{t_0}{t_{N_0}}=1.6$

η	f	f'	f''	θ	θ'
0	0. 0000	0. 0000	0. 7475	0. 0000	0. 5249
. 2	. 0149	. 1484	. 7319	. 1049	. 5243
. 4	. 0590	. 2910	. 6898	. 2095	. 5207
. 6	. 1306	. 4230	. 6282	. 3128	. 5112
. 8	. 2273	. 5414	. 5540	. 4134	. 4934
1. 0	. 3461	. 6442	. 4735	. 5095	. 4661
1. 2	. 4839	. 7308	. 3924	. 5992	. 4291
1. 4	. 6374	. 8015	. 3153	. 6806	. 3836
1. 6	. 8035	. 8574	. 2455	. 7523	. 3322
1. 8	. 9795	. 9003	. 1853	. 8133	. 2780
2. 0	1. 1629	. 9322	. 1355	. 8635	. 2244
2. 2	1. 3518	. 9552	. 0960	. 9033	. 1745
2. 4	1. 5445	. 9712	. 0659	. 9337	. 1307
2. 6	1. 7399	. 9820	. 0438	. 9561	. 0941
2. 8	1. 9371	. 9891	. 0281	. 9719	. 0651
3. 0	2. 1354	. 9936	. 0175	. 9826	. 0434
3. 2	2. 3344	. 9964	. 0106	. 9896	. 0277
3. 4	2. 5338	. 9980	. 0061	. 9940	. 0171
3. 6	2. 7335	. 9989	. 0035	. 9967	. 0101
3. 8	2. 9334	. 9995	. 0019	. 9982	. 0057
4. 0	3. 1333	. 9997	. 0010	. 9991	. 0031
4. 2	3. 3333	. 9999	. 0005	. 9995	. 0016
4. 4	3. 5333	. 9999	. 0002	. 9998	. 0008
4. 6	3. 7333	1. 0000	. 0001	. 9999	. 0004
4. 8	3. 9332	1. 0000	. 0001	1. 0000	. 0002
5. 0	4. 1333	1. 0000	. 0000	1. 0000	. 0001
5. 2	4. 3333	1. 0000	. 0000	1. 0000	. 0000
5. 4	4. 5333	1. 0000	. 0000	1. 0000	. 0000
5. 6	4. 7333	1. 0000	. 0000	1. 0000	. 0000
5. 8	4. 9333	1. 0000	. 0000	1. 0000	. 0000
6. 0	5. 1333	1. 0000	. 0000	1. 0000	. 0000

$\frac{t_w}{t_0}=0$; $\frac{t_0}{t_{N_0}}=2.0$

η	f	f'	f''	θ	θ'
0	0. 0000	0. 0000	0. 8105	0. 0000	0. 5358
. 2	. 0161	. 1608	. 7907	. 1071	. 5353
. 4	. 0638	. 3141	. 7379	. 2139	. 5313
. 6	. 1409	. 4544	. 6617	. 3192	. 5207
. 8	. 2444	. 5778	. 5716	. 4216	. 5013
1. 0	. 3708	. 6826	. 4759	. 5190	. 4715
1. 2	. 5162	. 7683	. 3821	. 6095	. 4316
1. 4	. 6769	. 8359	. 2957	. 6911	. 3832
1. 6	. 8495	. 8874	. 2206	. 7624	. 3290
1. 8	1. 0309	. 9251	. 1586	. 8226	. 2726
2. 0	1. 2188	. 9517	. 1099	. 8715	. 2177
2. 2	1. 4111	. 9699	. 0734	. 9100	. 1674
2. 4	1. 6063	. 9818	. 0473	. 9389	. 1238
2. 6	1. 8035	. 9893	. 0294	. 9600	. 0880
2. 8	2. 0018	. 9939	. 0176	. 9747	. 0602
3. 0	2. 2009	. 9966	. 0102	. 9845	. 0395
3. 2	2. 4004	. 9981	. 0057	. 9909	. 0249
3. 4	2. 6002	. 9990	. 0030	. 9948	. 0151
3. 6	2. 8000	. 9994	. 0015	. 9972	. 0088
3. 8	2. 9999	. 9997	. 0007	. 9985	. 0049
4. 0	3. 1999	. 9998	. 0003	. 9993	. 0027
4. 2	3. 3998	. 9998	. 0001	. 9997	. 0014
4. 4	3. 5998	. 9998	. 0000	. 9998	. 0007
4. 6	3. 7998	. 9998	. 0000	. 9999	. 0003

TABLE I.—Continued. STAGNATION-LINE FLOW SOLUTIONS FOR YAWED INFINITE CYLINDER WITH PRANDTL NUMBER OF 1

$\frac{t_w}{t_0}=0$; $\frac{t_0}{t_N}=2.2$					
η	f	f'	f''	θ	θ'
0	0. 0000	0. 0000	0. 8413	0. 0000	0. 5410
. 2	. 0168	. 1668	. 8194	. 1082	. 5404
. 4	. 0662	. 3253	. 7611	. 2159	. 5362
. 6	. 1459	. 4695	. 6776	. 3222	. 5252
. 8	. 2528	. 5954	. 5795	. 4254	. 5049
1. 0	. 3828	. 7010	. 4763	. 5235	. 4740
1. 2	. 5318	. 7862	. 3764	. 6143	. 4327
1. 4	. 6959	. 8522	. 2857	. 6960	. 3828
1. 6	. 8716	. 9013	. 2083	. 7671	. 3273
1. 8	1. 0555	. 9365	. 1457	. 8268	. 2700
2. 0	1. 2454	. 9606	. 0978	. 8752	. 2145
2. 2	1. 4392	. 9765	. 0629	. 9129	. 1640
2. 4	1. 6356	. 9865	. 0388	. 9412	. 1206
2. 6	1. 8336	. 9925	. 0230	. 9617	. 0853
2. 8	2. 0325	. 9960	. 0130	. 9759	. 0579
3. 0	2. 2319	. 9980	. 0070	. 9853	. 0378
3. 2	2. 4316	. 9990	. 0036	. 9914	. 0237
3. 4	2. 6315	. 9996	. 0018	. 9951	. 0143
3. 6	2. 8314	. 9999	. 0009	. 9973	. 0083
3. 8	3. 0314	. 9999	. 0004	. 9986	. 0046
4. 0	3. 2314	1. 0000	. 0002	. 9993	. 0025
4. 2	3. 4314	1. 0000	. 0001	. 9996	. 0013
4. 4	3. 6314	1. 0000	. 0000	. 9998	. 0006
4. 6	3. 8314	1. 0000	. 0000	. 9999	. 0003
4. 8	4. 0314	1. 0000	. 0000	1. 0000	. 0001
5. 0	4. 2314	1. 0000	. 0000	1. 0000	. 0001
5. 2	4. 4314	1. 0000	. 0000	1. 0000	. 0000
5. 4	4. 6314	1. 0000	. 0000	1. 0000	. 0000
5. 6	4. 8314	1. 0000	. 0000	1. 0000	. 0000
5. 8	5. 0314	1. 0000	. 0000	1. 0000	. 0000
6. 0	5. 2314	1. 0000	. 0000	1. 0000	. 0000

$\frac{t_w}{t_0}=0$; $\frac{t_0}{t_{N_0}}=3.0$					
η	f	f'	f''	θ	θ'
0	0. 0000	0. 0000	0. 9607	0. 0000	0. 5603
. 2	. 0191	. 1900	. 9300	. 1120	. 5595
. 4	. 0753	. 3687	. 8494	. 2235	. 5546
. 6	. 1653	. 5276	. 7361	. 3333	. 5417
. 8	. 2847	. 6620	. 6061	. 4395	. 5181
1. 0	. 4283	. 7699	. 4738	. 5398	. 4826
1. 2	. 5909	. 8521	. 3507	. 6318	. 4360
1. 4	. 7676	. 9113	. 2446	. 7136	. 3807
1. 6	. 9542	. 9514	. 1596	. 7838	. 3205
1. 8	1. 1472	. 9766	. 0963	. 8418	. 2598
2. 0	1. 3441	. 9912	. 0527	. 8879	. 2025
2. 2	1. 5432	. 9987	. 0249	. 9232	. 1517
2. 4	1. 7433	1. 0019	. 0089	. 9492	. 1092
2. 6	1. 9438	1. 0028	. 0008	. 9675	. 0756
2. 8	2. 1444	1. 0026	—. 0025	. 9799	. 0502
3. 0	2. 3449	1. 0020	—. 0032	. 9880	. 0321
3. 2	2. 5452	1. 0014	—. 0028	. 9931	. 0197
3. 4	2. 7454	1. 0009	—. 0021	. 9962	. 0116
3. 6	2. 9456	1. 0005	—. 0014	. 9980	. 0066
3. 8	3. 1456	1. 0003	—. 0009	. 9989	. 0036
4. 0	3. 3457	1. 0002	—. 0005	. 9995	. 0019
4. 2	3. 5457	1. 0001	—. 0003	. 9997	. 0009
4. 4	3. 7457	1. 0000	—. 0001	. 9999	. 0004
4. 6	3. 9457	1. 0000	—. 0001	. 9999	. 0002
4. 8	4. 1457	1. 0000	. 0000	1. 0000	. 0001
5. 0	4. 3457	1. 0000	. 0000	1. 0000	. 0000
5. 2	4. 5457	1. 0000	. 0000	1. 0000	. 0000
5. 4	4. 7457	1. 0000	. 0000	1. 0000	. 0000
5. 6	4. 9457	1. 0000	. 0000	1. 0000	. 0000
5. 8	5. 1457	1. 0000	. 0000	1. 0000	. 0000
6. 0	5. 3457	1. 0000	. 0000	1. 0000	. 0000

TABLE I.—Continued. STAGNATION-LINE FLOW SOLUTIONS FOR YAWED INFINITE CYLINDER WITH PRANDTL NUMBER OF 1

$\frac{t_w}{t_0}=0$; $\frac{t_0}{t_{N_0}}=4.0$

η	f	f'	f''	θ	θ'
0	0. 0000	0. 0000	1. 1025	0. 0000	0. 5815
. 2	. 0219	. 2176	1. 0603	. 1163	. 5806
. 4	. 0860	. 4196	. 9509	. 2319	. 5748
. 6	. 1880	. 5952	. 7997	. 3455	. 5596
. 8	. 3219	. 7383	. 6304	. 4549	. 5320
1. 0	. 4811	. 8475	. 4632	. 5574	. 4911
1. 2	. 6588	. 9248	. 3138	. 6506	. 4383
1. 4	. 8492	. 9748	. 1918	. 7322	. 3770
1. 6	1. 0474	1. 0036	. 1009	. 8011	. 3119
1. 8	1. 2496	1. 0172	. 0397	. 8571	. 2479
2. 0	1. 4536	1. 0211	. 0032	. 9007	. 1892
2. 2	1. 6577	1. 0197	−. 0149	. 9333	. 1386
2. 4	1. 8613	1. 0159	−. 0210	. 9567	. 0975
2. 6	2. 0641	1. 0117	−. 0203	. 9729	. 0659
2. 8	2. 2660	1. 0080	−. 0165	. 9836	. 0427
3. 0	2. 4673	1. 0051	−. 0121	. 9905	. 0266
3. 2	2. 6682	1. 0031	−. 0082	. 9946	. 0159
3. 4	2. 8686	1. 0018	−. 0052	. 9971	. 0092
3. 6	3. 0689	1. 0010	−. 0031	. 9985	. 0051
3. 8	3. 2691	1. 0005	−. 0017	. 9992	. 0027
4. 0	3. 4691	1. 0003	−. 0009	. 9996	. 0014
4. 2	3. 6692	1. 0001	−. 0005	. 9998	. 0007
4. 4	3. 8692	1. 0001	−. 0002	. 9999	. 0003
4. 6	4. 0692	1. 0000	−. 0001	1. 0000	. 0001
4. 8	4. 2692	1. 0000	−. 0001	1. 0000	. 0001
5. 0	4. 4692	1. 0000	. 0000	1. 0000	. 0000
5. 2	4. 6692	1. 0000	. 0000	1. 0000	. 0000
5. 4	4. 8692	1. 0000	. 0000	1. 0000	. 0000
5. 6	5. 0692	1. 0000	. 0000	1. 0000	. 0000
5. 8	5. 2692	1. 0000	. 0000	1. 0000	. 0000
6. 0	5. 4692	1. 0000	. 0000	1. 0000	. 0000

$\frac{t_w}{t_0}=0$; $\frac{t_0}{t_{N_0}}=6.0$

η	f	f'	f''	θ	θ'
0	0. 0000	0. 0000	1. 3679	0. 0000	0. 6174
. 2	. 0271	. 2690	1. 3014	. 1234	. 6163
. 4	. 1060	. 5137	1. 1320	. 2461	. 6086
. 6	. 2299	. 7179	. 9038	. 3661	. 5889
. 8	. 3899	. 8740	. 6570	. 4806	. 5538
1. 0	. 5763	. 9817	. 4249	. 5865	. 5030
1. 2	. 7797	1. 0465	. 2307	. 6810	. 4393
1. 4	. 9926	1. 0773	. 0861	. 7618	. 3680
1. 6	1. 2091	1. 0843	−. 0082	. 8281	. 2953
1. 8	1. 4254	1. 0770	−. 0590	. 8802	. 2269
2. 0	1. 6394	1. 0629	−. 0776	. 9194	. 1670
2. 2	1. 8504	1. 0473	−. 0759	. 9477	. 1178
2. 4	2. 0584	1. 0332	−. 0638	. 9673	. 0797
2. 6	2. 2639	1. 0220	−. 0484	. 9802	. 0517
2. 8	2. 4674	1. 0138	−. 0340	. 9885	. 0322
3. 0	2. 6696	1. 0082	−. 0223	. 9936	. 0193
3. 2	2. 8709	1. 0046	−. 0137	. 9965	. 0111
3. 4	3. 0715	1. 0025	−. 0080	. 9982	. 0061
3. 6	3. 2719	1. 0013	−. 0044	. 9991	. 0032
3. 8	3. 4721	1. 0006	−. 0021	. 9996	. 0017
4. 0	3. 6722	1. 0002	−. 0005	. 9998	. 0008
4. 2	3. 8722	1. 0001	. 0013	. 9999	. 0004

TABLE I.—Continued. STAGNATION-LINE FLOW SOLUTIONS FOR YAWED INFINITE CYLINDER WITH PRANDTL NUMBER OF 1

$\frac{t_w}{t_0}=0$; $\frac{t_0}{t_{N_0}}=6.5$

η	f	f'	f''	θ	θ'
0	0. 0000	0. 0000	1. 4313	0. 0000	0. 6254
. 2	. 0284	. 2813	1. 3584	. 1250	. 6242
. 4	. 1107	. 5359	1. 1736	. 2492	. 6161
. 6	. 2398	. 7465	. 9259	. 3706	. 5953
. 8	. 4059	. 9051	. 6601	. 4862	. 5584
1. 0	. 5984	1. 0118	. 4128	. 5928	. 5052
1. 2	. 8076	1. 0731	. 2089	. 6874	. 4390
1. 4	1. 0253	1. 0990	. 0602	. 7680	. 3655
1. 6	1. 2456	1. 1008	−. 0334	. 8336	. 2913
1. 8	1. 4648	1. 0887	−. 0807	. 8848	. 2221
2. 0	1. 6808	1. 0707	−. 0946	. 9231	. 1622
2. 2	1. 8930	1. 0522	−. 0880	. 9504	. 1134
2. 4	2. 1018	1. 0361	−. 0718	. 9692	. 0761
2. 6	2. 3077	1. 0236	−. 0533	. 9815	. 0490
2. 8	2. 5115	1. 0146	−. 0368	. 9893	. 0302
3. 0	2. 7138	1. 0086	−. 0238	. 9941	. 0179
3. 2	2. 9151	1. 0049	−. 0145	. 9968	. 0102
3. 4	3. 1158	1. 0026	−. 0084	. 9983	. 0056
3. 6	3. 3162	1. 0014	−. 0046	. 9992	. 0029
3. 8	3. 5164	1. 0007	−. 0024	. 9996	. 0015
4. 0	3. 7165	1. 0003	−. 0012	. 9998	. 0007
4. 2	3. 9166	1. 0002	−. 0006	. 9999	. 0003
4. 4	4. 1166	1. 0001	−. 0003	1. 0000	. 0001
4. 6	4. 3166	1. 0000	−. 0001	1. 0000	. 0001
4. 8	4. 5166	1. 0000	. 0000	1. 0000	. 0000
5. 0	4. 7166	1. 0000	. 0000	1. 0000	. 0000
5. 2	4. 9166	1. 0000	. 0000	1. 0000	. 0000
5. 4	5. 1166	1. 0000	. 0000	1. 0000	. 0000
5. 6	5. 3166	1. 0000	. 0000	1. 0000	. 0000
5. 8	5. 5166	1. 0000	. 0000	1. 0000	. 0000
6. 0	5. 7166	1. 0000	. 0000	1. 0000	. 0000

$\frac{t_w}{t_0}=0.25$; $\frac{t_0}{t_{N_0}}=1.2$

η	f	f'	f''	θ	θ'
0	0. 0000	0. 0000	0. 8673	0. 0000	0. 5344
. 2	. 0169	. 1669	. 7988	. 1068	. 5338
. 4	. 0657	. 3187	. 7175	. 2133	. 5297
. 6	. 1432	. 4534	. 6292	. 3183	. 5189
. 8	. 2459	. 5702	. 5387	. 4203	. 4993
1. 0	. 3701	. 6690	. 4503	. 5173	. 4697
1. 2	. 5124	. 7506	. 3672	. 6075	. 4301
1. 4	. 6693	. 8164	. 2919	. 6888	. 3822
1. 6	. 8380	. 8680	. 2261	. 7600	. 3288
1. 8	1. 0157	. 9075	. 1703	. 8202	. 2732
2. 0	1. 2003	. 9368	. 1247	. 8694	. 2189
2. 2	1. 3899	. 9580	. 0887	. 9081	. 1690
2. 4	1. 5831	. 9729	. 0612	. 9374	. 1255
2. 6	1. 7788	. 9830	. 0410	. 9588	. 0897
2. 8	1. 9761	. 9897	. 0265	. 9738	. 0616
3. 0	2. 1745	. 9939	. 0166	. 9839	. 0407
3. 2	2. 3736	. 9965	. 0101	. 9905	. 0258
3. 4	2. 5730	. 9981	. 0059	. 9945	. 0158
3. 6	2. 7728	. 9990	. 0034	. 9970	. 0092
3. 8	2. 9726	. 9995	. 0019	. 9984	. 0052
4. 0	3. 1725	. 9998	. 0010	. 9992	. 0028
4. 2	3. 3725	. 9999	. 0005	. 9996	. 0015
4. 4	3. 5725	1. 0000	. 0003	. 9998	. 0007
4. 6	3. 7725	1. 0001	. 0002	. 9999	. 0004
4. 8	3. 9725	1. 0001	. 0001	1. 0000	. 0002
5. 0	4. 1726	1. 0001	. 0001	1. 0000	. 0001
5. 2	4. 3726	1. 0001	. 0001	1. 0000	. 0000
5. 4	4. 5726	1. 0001	. 0001	1. 0000	. 0000
5. 6	4. 7726	1. 0001	. 0001	1. 0000	. 0000
5. 8	4. 9727	1. 0002	. 0001	1. 0000	. 0000
6. 0	5. 1727	1. 0002	. 0001	1. 0000	. 0000

TABLE I.—Continued. STAGNATION-LINE FLOW SOLUTIONS FOR YAWED INFINITE CYLINDER WITH PRANDTL NUMBER OF 1

$\frac{t_w}{t_0}=0.25$; $\frac{t_0}{t_{N_0}}=1.6$

η	f	f'	f''	θ	θ'
0	0. 0000	0. 0000	0. 9850	0. 0000	0. 5507
. 2	. 0191	. 1882	. 8935	. 1101	. 5500
. 4	. 0739	. 3563	. 7856	. 2197	. 5452
. 6	. 1602	. 5019	. 6699	. 3277	. 5329
. 8	. 2732	. 6243	. 5542	. 4322	. 5105
1. 0	. 4084	. 7240	. 4445	. 5312	. 4770
1. 2	. 5614	. 8028	. 3453	. 6223	. 4330
1. 4	. 7283	. 8630	. 2597	. 7038	. 3807
1. 6	. 9056	. 9076	. 1889	. 7743	. 3234
1. 8	1. 0905	. 9395	. 1328	. 8331	. 2649
2. 0	1. 2807	. 9616	. 0902	. 8004	. 2090
2. 2	1. 4746	. 9764	. 0592	. 9171	. 1587
2. 4	1. 6709	. 9859	. 0375	. 9444	. 1159
2. 6	1. 8688	. 9919	. 0230	. 9640	. 0813
2. 8	2. 0675	. 9954	. 0136	. 9774	. 0549
3. 0	2. 2669	. 9975	. 0078	. 9864	. 0356
3. 2	2. 4665	. 9987	. 0043	. 9921	. 0222
3. 4	2. 6663	. 9994	. 0023	. 9955	. 0133
3. 6	2. 8662	. 9997	. 0012	. 9976	. 0076
3. 8	3. 0662	. 9999	. 0006	. 9987	. 0042
4. 0	3. 2662	. 9999	. 0003	. 9994	. 0022
4. 2	3. 4661	1. 0000	. 0001	. 9997	. 0011
4. 4	3. 6661	1. 0000	. 0001	. 9999	. 0006
4. 6	3. 8661	1. 0000	. 0000	. 9999	. 0003
4. 8	4. 0661	1. 0000	. 0000	1. 0000	. 0001
5. 0	4. 2662	1. 0000	. 0000	1. 0000	. 0001
5. 2	4. 4662	1. 0000	. 0000	1. 0000	. 0000
5. 4	4. 6662	1. 0000	. 0000	1. 0000	. 0000
5. 6	4. 8662	1. 0000	. 0000	1. 0000	. 0000
5. 8	5. 0662	1. 0000	. 0000	1. 0000	. 0000
6. 0	5. 2662	1. 0000	. 0000	1. 0000	. 0000

$\frac{t_w}{t_0}=0.25$; $\frac{t_0}{t_{N_0}}=2.2$

η	f	f'	f''	θ	θ'
0	0. 0000	0. 0000	1. 1530	0. 0000	0. 5724
. 2	. 0223	. 2185	1. 0268	. 1144	. 5716
. 4	. 0856	. 4093	. 8787	. 2283	. 5658
. 6	. 1839	. 5694	. 7224	. 3402	. 5511
. 8	. 3113	. 6985	. 5698	. 4479	. 5247
1. 0	. 4614	. 7982	. 4299	. 5492	. 4858
1. 2	. 6288	. 8717	. 3092	. 6415	. 4358
1. 4	. 8086	. 9233	. 2109	. 7229	. 3775
1. 6	. 9970	. 9576	. 1355	. 7922	. 3152
1. 8	1. 1908	. 9789	. 0812	. 8490	. 2532
2. 0	1. 3880	. 9912	. 0446	. 8939	. 1957
2. 2	1. 5869	. 9977	. 0217	. 9278	. 1453
2. 4	1. 7868	1. 0005	. 0086	. 9525	. 1037
2. 6	1. 9870	1. 0015	. 0019	. 9699	. 0711
2. 8	2. 1873	1. 0015	—. 0010	. 9815	. 0469
3. 0	2. 3876	1. 0012	—. 0018	. 9891	. 0297
3. 2	2. 5878	1. 0009	—. 0017	. 9938	. 0180
3. 4	2. 7880	1. 0006	—. 0013	. 9966	. 0105
3. 6	2. 9881	1. 0003	—. 0009	. 9982	. 0059
3. 8	3. 1881	1. 0002	—. 0005	. 9991	. 0032
4. 0	3. 3881	1. 0001	—. 0003	. 9995	. 0017
4. 2	3. 5882	1. 0001	—. 0002	. 9998	. 0008
4. 4	3. 7882	1. 0000	—. 0001	. 9999	. 0004
4. 6	3. 9882	1. 0000	. 0000	1. 0000	. 0002
4. 8	4. 1882	1. 0000	. 0000	1. 0000	. 0001
5. 0	4. 3882	1. 0000	. 0000	1. 0000	. 0000
5. 2	4. 5882	1. 0000	. 0000	1. 0000	. 0000
5. 4	4. 7882	1. 0000	. 0000	1. 0000	. 0000
5. 6	4. 9882	1. 0000	. 0000	1. 0000	. 0000
5. 8	5. 1882	1. 0000	. 0000	1. 0000	. 0000
6. 0	5. 3882	1. 0000	. 0000	1. 0000	. 0000

TABLE I.—Continued. STAGNATION-LINE FLOW SOLUTIONS FOR YAWED INFINITE CYLINDER WITH PRANDTL NUMBER OF 1

$\frac{t_w}{t_0}=0.25$; $\frac{t_0}{t_{N_0}}=3.0$					
η	f	f'	f''	θ	θ'
0	0. 0000	0. 0000	1. 3644	0. 0000	0. 5976
. 2	. 0262	. 2563	1. 1918	. 1195	. 5965
. 4	. 1000	. 4748	. 9898	. 2382	. 5895
. 6	. 2134	. 6517	. 7799	. 3545	. 5716
. 8	. 3580	. 7874	. 5799	. 4659	. 5401
1. 0	. 5258	. 8852	. 4029	. 5696	. 4946
1. 2	. 7099	. 9905	. 2574	. 6630	. 4372
1. 4	. 9044	1. 0115	. 1466	. 7440	. 3721
1. 6	1. 1049	1. 0200	. 0690	. 8116	. 3044
1. 8	1. 3082	1. 0210	. 0200	. 8659	. 2391
2. 0	1. 5124	1. 0182	−. 0070	. 9077	. 1803
2. 2	1. 7163	1. 0141	−. 0187	. 9386	. 1306
2. 4	1. 9195	1. 0100	−. 0211	. 9606	. 0908
2. 6	2. 1219	1. 0067	−. 0187	. 9756	. 0606
2. 8	2. 3236	1. 0042	−. 0145	. 9854	. 0389
3. 0	2. 5247	1. 0025	−. 0103	. 9916	. 0239
3. 2	2. 7253	1. 0014	−. 0068	. 9953	. 0142
3. 4	2. 9257	1. 0008	−. 0042	. 9975	. 0081
3. 6	3. 1259	1. 0004	−. 0024	. 9987	. 0044
3. 8	3. 3260	1. 0002	−. 0013	. 9994	. 0023
4. 0	3. 5261	1. 0001	−. 0007	. 9997	. 0012
4. 2	3. 7261	1. 0001	−. 0004	. 9999	. 0006
4. 4	3. 9261	1. 0000	−. 0002	. 9999	. 0003
4. 6	4. 1262	1. 0000	. 0000	1. 0000	. 0001
4. 8	4. 3262	1. 0000	. 0000	1. 0000	. 0001
5. 0	4. 5262	1. 0000	. 0000	1. 0000	. 0000
5. 2	4. 7262	1. 0000	. 0000	1. 0000	. 0000
5. 4	4. 9262	1. 0000	. 0000	1. 0000	. 0000
5. 6	5. 1262	1. 00 0	. 0000	1. 0000	. 0000
5. 8	5. 3262	1. 0000	. 0000	1. 0000	. 0000
6. 0	5. 5262	1. 0000	. 0000	1. 0000	. 0000

$\frac{t_w}{t_0}=0.5$; $\frac{t_0}{t_{N_0}}=1.2$					
η	f	f'	f''	θ	θ'
0	0. 0000	0. 0000	1. 0409	0. 0000	0. 5530
. 2	. 0200	. 1958	. 9158	. 1106	. 5522
. 4	. 0766	. 3660	. 7859	. 2206	. 5472
. 6	. 1647	. 5103	. 6582	. 3289	. 5344
. 8	. 2791	. 6298	. 5379	. 4337	. 5114
1. 0	. 4151	. 7262	. 4288	. 5328	. 4773
1. 2	. 5682	. 8022	. 3331	. 6239	. 4327
1. 4	. 7348	. 8605	. 2521	. 7053	. 3799
1. 6	. 9114	. 9040	. 1856	. 7756	. 3223
1. 8	1. 0956	. 9356	. 1329	. 8341	. 2637
2. 0	1. 2851	. 9579	. 0925	. 8812	. 2079
2. 2	1. 4783	. 9733	. 0625	. 9177	. 1577
2. 4	1. 6740	. 9835	. 0410	. 9448	. 1151
2. 6	1. 8714	. 9901	. 0260	. 9642	. 0807
2. 8	2. 0699	. 9942	. 0160	. 9776	. 0544
3. 0	2. 2690	. 9967	. 0096	. 9865	. 0353
3. 2	2. 4685	. 9982	. 0055	. 9921	. 0220
3. 4	2. 6683	. 9990	. 0031	. 9956	. 0131
3. 6	2. 8681	. 9995	. 0017	. 9976	. 0076
3. 8	3. 0680	. 9997	. 0009	. 9987	. 0042
4. 0	3. 2680	. 9999	. 0004	. 9994	. 0022
4. 2	3. 4680	. 9999	. 0002	. 9997	. 0011
4. 4	3. 6680	. 9999	. 0001	. 9999	. 0006
4. 6	3. 8680	1. 0000	. 0000	. 9999	. 0003
4. 8	4. 0680	1. 0000	. 0000	1. 0000	. 0001
5. 0	4. 2680	1. 0000	. 0000	1. 0000	. 0000
5. 2	4. 4680	1. 0000	. 0000	1. 0000	. 0000
5. 4	4. 6680	1. 0000	. 0000	1. 0000	. 0000
5. 6	4. 8679	1. 0000	. 0000	1. 0000	. 0000
5. 8	5. 0679	1. 0000	. 0000	1. 0000	. 0000
6. 0	5. 2679	1. 0000	. 0000	1. 0000	. 0000

TABLE I.—Continued. STAGNATION-LINE FLOW SOLUTIONS FOR YAWED INFINITE CYLINDER WITH PRANDTL NUMBER OF 1

$\frac{t_w}{t_0}=0.5$; $\frac{t_0}{t_{N_0}}=1.6$					
η	f	f'	f''	θ	θ'
0	0. 0000	0. 0000	1. 2062	0. 0000	0. 5728
. 2	. 0230	. 2247	1. 0394	. 1145	. 5719
. 4	. 0876	. 4154	. 8973	. 2284	. 5659
. 6	. 1869	. 5720	. 7005	. 3403	. 5509
. 8	. 3143	. 6965	. 5469	. 4480	. 5242
1. 0	. 4636	. 7920	. 4120	. 5491	. 4851
1. 2	. 6295	. 8627	. 2988	. 6413	. 4350
1. 4	. 8073	. 9130	. 2080	. 7226	. 3768
1. 6	. 9936	. 9473	. 1385	. 7918	. 3148
1. 8	1. 1855	. 9697	. 0880	. 8485	. 2532
2. 0	1. 3809	. 9836	. 0531	. 8933	. 1959
2. 2	1. 5786	. 9917	. 0302	. 9273	. 1460
2. 4	1. 7774	. 9962	. 0160	. 9522	. 1042
2. 6	1. 9769	. 9985	. 0078	. 9696	. 0716
2. 8	2. 1767	. 9996	. 0034	. 9813	. 0472
3. 0	2. 3767	1. 0000	. 0012	. 9889	. 0300
3. 2	2. 5767	1. 0001	. 0003	. 9937	. 0183
3. 4	2. 7767	1. 0002	−. 0001	. 9965	. 0107
3. 6	2. 9768	1. 0001	−. 0001	. 9982	. 0060
3. 8	3. 1768	1. 0001	−. 0001	. 9991	. 0033
4. 0	3. 3768	1. 0001	−. 0001	. 9995	. 0017
4. 2	3. 5768	1. 0001	. 0000	. 9998	. 0008
4. 4	3. 7768	1. 0001	. 0000	. 9999	. 0004
4. 6	3. 9769	1. 0001	. 0000	1. 0000	. 0002
4. 8	4. 1769	1. 0001	. 0000	1. 0000	. 0001
5. 0	4. 3769	1. 0001	. 0000	1. 0000	. 0000
5. 2	4. 5769	1. 0001	. 0000	1. 0000	. 0000
5. 4	4. 7769	1. 0001	. 0000	1. 0000	. 0000
5. 6	4. 9769	1. 0001	. 0000	1. 0000	. 0000
5. 8	5. 1770	1. 0001	. 0000	1. 0000	. 0000
6. 0	5. 3770	1. 0001	. 0000	1. 0000	. 0000

$\frac{t_w}{t_0}=0.5$; $\frac{t_0}{t_{N_0}}=2.2$					
η	f	f'	f''	θ	θ'
0	0. 0000	0. 0000	1. 4406	0. 0000	0. 5986
. 2	. 0273	. 2654	1. 2111	. 1197	. 5975
. 4	. 1031	. 4841	. 9760	. 2386	. 5902
. 6	. 2179	. 6565	. 7518	. 3550	. 5719
. 8	. 3628	. 7863	. 5506	. 4664	. 5398
1. 0	. 5299	. 8788	. 3803	. 5700	. 4939
1. 2	. 7123	. 9407	. 2446	. 6632	. 4363
1. 4	. 9047	. 9790	. 1433	. 7440	. 3712
1. 6	1. 1028	1. 0001	. 0730	. 8115	. 3037
1. 8	1. 3040	1. 0098	. 0283	. 8657	. 2387
2. 0	1. 5063	1. 0127	. 0029	. 9074	. 1803
2. 2	1. 7088	1. 0119	−. 0091	. 9384	. 1307
2. 4	1. 9110	1. 0096	−. 0129	. 9604	. 0910
2. 6	2. 1126	1. 0070	−. 0124	. 9754	. 0609
2. 8	2. 3138	1. 0047	−. 0100	. 9853	. 0391
3. 0	2. 5146	1. 0030	−. 0072	. 9915	. 0241
3. 2	2. 7150	1. 0018	−. 0048	. 9953	. 0143
3. 4	2. 9153	1. 0010	−. 0030	. 9974	. 0082
3. 6	3. 1155	1. 0006	−. 0018	. 9987	. 0045
3. 8	3. 3155	1. 0003	−. 0010	. 9993	. 0023
4. 0	3. 5156	1. 0001	−. 0005	. 9997	. 0012
4. 2	3. 7156	1. 0001	−. 0003	. 9998	. 0006
4. 4	3. 9156	1. 0000	−. 0001	. 9999	. 0003
4. 6	4. 1156	1. 0000	. 0000	1. 0000	. 0001
4. 8	4. 3156	1. 0000	. 0000	1. 0000	. 0000
5. 0	4. 5156	1. 0000	. 0000	1. 0000	. 0000
5. 2	4. 7156	1. 0000	. 0000	1. 0000	. 0000
5. 4	4. 9156	1. 0000	. 0000	1. 0000	. 0000
5. 6	5. 1157	1. 0000	. 0000	1. 0000	. 0000
5. 8	5. 3157	1. 0000	. 0000	1. 0000	. 0000
6. 0	5. 5157	1. 0000	. 0000	1. 0000	. 0000

TABLE I.—Continued. STAGNATION-LINE FLOW SOLUTIONS FOR YAWED INFINITE CYLINDER WITH PRANDTL NUMBER OF 1

$\frac{t_w}{t_0}=0.5$; $\frac{t_0}{t_{N_0}}=3.0$

η	f	f'	f''	θ	θ'
0	0. 0000	0. 0000	1. 7341	0. 0000	0. 6280
. 2	. 0326	. 3158	1. 4210	. 1255	. 6266
. 4	. 1221	. 5680	1. 1024	. 2501	. 6175
. 6	. 2557	. 7581	. 8035	. 3716	. 5950
. 8	. 4216	. 8919	. 5425	. 4870	. 5563
1. 0	. 6094	. 9784	. 3303	. 5931	. 5020
1. 2	. 8105	1. 0276	. 1706	. 6870	. 4356
1. 4	1. 0186	1. 0499	. 0610	. 7669	. 3628
1. 6	1. 2293	1. 0548	−. 0058	. 8321	. 2898
1. 8	1. 4399	1. 0498	−. 0398	. 8832	. 2219
2. 0	1. 6490	1. 0403	−. 0513	. 9215	. 1629
2. 2	1. 8560	1. 0301	−. 0493	. 9490	. 1148
2. 4	2. 0611	1. 0210	−. 0409	. 9681	. 0776
2. 6	2. 2646	1. 0138	−. 0308	. 9807	. 0503
2. 8	2. 4668	1. 0086	−. 0214	. 9887	. 0314
3. 0	2. 6681	1. 0051	−. 0140	. 9937	. 0188
3. 2	2. 8689	1. 0029	−. 0086	. 9966	. 0108
3. 4	3. 0694	1. 0016	−. 0050	. 9982	. 0060
3. 6	3. 2696	1. 0008	−. 0028	. 9991	. 0032
3. 8	3. 4697	1. 0004	−. 0015	. 9996	. 0016
4. 0	3. 6698	1. 0002	−. 0008	. 9998	. 0008
4. 2	3. 8698	1. 0001	−. 0004	. 9999	. 0004
4. 4	4. 0698	1. 0000	−. 0002	1. 0000	. 0001
4. 6	4. 2698	1. 0000	−. 0001	1. 0000	. 0001
4. 8	4. 4698	1. 0000	. 0000	1. 0000	. 0000
5. 0	4. 6698	1. 0000	. 0000	1. 0000	. 0000
5. 2	4. 8698	1. 0000	. 0000	1. 0000	. 0000
5. 4	5. 0698	1. 0000	. 0000	1. 0000	. 0000
5. 6	5. 2698	1. 0000	. 0000	1. 0000	. 0000
5. 8	5. 4698	1. 0000	. 0000	1. 0000	. 0000
6. 0	5. 6698	1. 0000	. 0000	1. 0000	. 0000

$\frac{t_w}{t_0}=0.5$; $\frac{t_0}{t_{N_0}}=4.0$

η	f	f'	f''	θ	θ'
0	0. 0000	0. 0000	2. 0785	0. 0000	0. 6593
. 2	. 0389	. 3744	1. 6608	. 1318	. 6576
. 4	. 1441	. 6640	1. 2386	. 2624	. 6463
. 6	. 2990	. 8720	. 8491	. 3892	. 6187
. 8	. 4881	1. 0076	. 5184	. 5086	. 5721
1. 0	. 6982	1. 0842	. 2604	. 9168	. 5083
1. 2	. 9189	1. 1168	. 0783	. 7111	. 4324
1. 4	1. 1430	1. 1200	−. 0350	. 7895	. 3519
1. 6	1. 3658	1. 1065	−. 0926	. 8520	. 2738
1. 8	1. 5851	1. 0856	−. 1105	. 8995	. 2038
2. 0	1. 8000	1. 0638	−. 1043	. 9342	. 1453
2. 2	2. 0108	1. 0446	−. 0862	. 9585	. 0992
2. 4	2. 2182	1. 0295	−. 0649	. 9747	. 0650
2. 6	2. 4229	1. 0185	−. 0454	. 9852	. 0409
2. 8	2. 6258	1. 0111	−. 0298	. 9916	. 0247
3. 0	2. 8275	1. 0063	−. 0185	. 9954	. 0143
3. 2	3. 0284	1. 0035	−. 0109	. 9976	. 0080
3. 4	3. 2290	1. 0018	−. 0061	. 9988	. 0043
3. 6	3. 4293	1. 0009	−. 0032	. 9994	. 0022
3. 8	3. 6294	1. 0004	−. 0017	. 9997	. 0010
4. 0	3. 8294	1. 0001	−. 0008	. 9999	. 0005
4. 2	4. 0295	1. 0001	−. 0004	1. 0000	. 0002
4. 4	4. 2295	1. 0000	−. 0002	1. 0000	. 0001
4. 6	4. 4295	1. 0000	−. 0001	1. 0000	. 0000
4. 8	4. 6295	1. 0000	. 0000	1. 0000	. 0000
5. 0	4. 8295	1. 0000	. 0000	1. 0000	. 0000
5. 2	5. 0295	1. 0000	. 0000	1. 0000	. 0000
5. 4	5. 2295	1. 0000	. 0000	1. 0000	. 0000
5. 6	5. 4295	1. 0000	. 0000	1. 0000	. 0000
5. 8	5. 6295	1. 0000	. 0000	1. 0000	. 0000
6. 0	5. 8295	1. 0000	. 0000	1. 0000	. 0000

TABLE I.—Continued. STAGNATION-LINE FLOW SOLUTIONS FOR YAWED INFINITE CYLINDER WITH PRANDTL NUMBER OF 1

$\frac{t_w}{t_0}=0.5$; $\frac{t_0}{t_{N_0}}=6.5$

η	f	f'	f''	θ	θ'
0	0. 0000	0. 0000	2. 8663	0. 0000	0. 7213
. 2	. 0529	. 5060	2. 1868	. 1441	. 7187
. 4	. 1933	. 8749	1. 5090	. 2865	. 7021
. 6	. 3943	1. 1145	. 9042	. 4234	. 6626
. 8	. 6318	1. 2445	. 4183	. 5498	. 5982
1. 0	. 8866	1. 2910	. 0709	. 6613	. 5140
1. 2	1. 1446	1. 2817	—. 1423	. 7548	. 4195
1. 4	1. 3973	1. 2414	—. 2440	. 8292	. 3253
1. 6	1. 6404	1. 1893	—. 2657	. 8855	. 2401
1. 8	1. 8731	1. 1382	—. 2396	. 9261	. 1689
2. 0	2. 0963	1. 0948	—. 1921	. 9541	. 1136
2. 2	2. 3117	1. 0615	—. 1411	. 9725	. 0731
2. 4	2. 5215	1. 0379	—. 0964	. 9842	. 0451
2. 6	2. 7274	1. 0223	—. 0619	. 9912	. 0267
2. 8	2. 9308	1. 0125	—. 0375	. 9953	. 0152
3. 0	3. 1327	1. 0067	—. 0216	. 9976	. 0083
3. 2	3. 3337	1. 0034	—. 0119	. 9988	. 0043
3. 4	3. 5342	1. 0017	—. 0062	. 9994	. 0022
3. 6	3. 7344	1. 0008	—. 0031	. 9997	. 0011
3. 8	3. 9345	1. 0003	—. 0015	. 9999	. 0005
4. 0	4. 1346	1. 0001	—. 0007	. 9999	. 0002
4. 2	4. 3346	1. 0000	—. 0003	1. 0000	. 0001
4. 4	4. 5346	1. 0000	—. 0001	1. 0000	. 0000
4. 6	4. 7346	1. 0000	—. 0001	1. 0000	. 0000
4. 8	4. 9346	1. 0000	. 0000	1. 0000	. 0000
5. 0	5. 1346	1. 0000	. 0000	1. 0000	. 0000
5. 2	5. 3346	1. 0000	. 0000	1. 0000	. 0000
5. 4	5. 5346	1. 0000	. 0000	1. 0000	. 0000
5. 6	5. 7346	1. 0000	. 0000	1. 0000	. 0000
5. 8	5. 9346	1. 0000	. 0000	1. 0000	. 0000
6. 0	6. 1346	1. 0000	. 0000	1. 0000	. 0000

$\frac{t_w}{t_0}=0.75$; $\frac{t_0}{t_{N_0}}=1.2$

η	f	f'	f''	θ	θ'
0	0. 0000	0. 0000	1. 2059	0. 0000	0. 5995
. 2	. 0229	. 2230	1. 0244	. 1139	. 5686
. 4	. 0868	. 4100	. 8469	. 2271	. 5628
. 6	. 1846	. 5626	. 6814	. 3384	. 5480
. 8	. 3098	. 6837	. 5332	. 4455	. 5218
1. 0	. 4563	. 7772	. 4054	. 5463	. 4834
1. 2	. 6191	. 8473	. 2993	. 6382	. 4342
1. 4	. 7940	. 8983	. 2142	. 7194	. 3771
1. 6	. 9775	. 9343	. 1484	. 7887	. 3159
1. 8	1. 1669	. 9588	. 0995	. 8458	. 2550
2. 0	1. 3604	. 9750	. 0645	. 8910	. 1980
2. 2	1. 5566	. 9853	. 0403	. 9255	. 1479
2. 4	1. 7543	. 9917	. 0243	. 9507	. 1062
2. 6	1. 9531	. 9954	. 0142	. 9685	. 0733
2. 8	2. 1524	. 9976	. 0079	. 9806	. 0487
3. 0	2. 3520	. 9988	. 0043	. 9885	. 0310
3. 2	2. 5518	. 9994	. 0022	. 9934	. 0190
3. 4	2. 7518	. 9997	. 0011	. 9963	. 0112
3. 6	2. 9517	. 9999	. 0005	. 9980	. 0063
3. 8	3. 1517	. 9999	. 0002	. 9990	. 0034
4. 0	3. 3517	1. 0000	. 0001	. 9995	. 0018
4. 2	3. 5517	1. 0000	. 0000	. 9998	. 0009
4. 4	3. 7517	1. 0000	. 0000	. 9999	. 0004
4. 6	3. 9517	1. 0000	. 0000	1. 0000	. 0002
4. 8	4. 1517	1. 0000	. 0000	1. 0000	. 0001
5. 0	4. 3517	1. 0000	. 0000	1. 0000	. 0000
5. 2	4. 5517	1. 0000	. 0000	1. 0000	. 0000
5. 4	4. 7517	1. 0000	. 0000	1. 0000	. 0000
5. 6	4. 9517	1. 0000	. 0000	1. 0000	. 0000
5. 8	5. 1516	1. 0000	. 0000	1. 0000	. 0000
6. 0	5. 3516	1. 0000	. 0000	1. 0000	. 0000

TABLE I.—Continued. STAGNATION-LINE FLOW SOLUTIONS FOR YAWED INFINITE CYLINDER WITH PRANDTL NUMBER OF 1

$\frac{t_w}{t_0}=0.75$; $\frac{t_0}{t_{N_0}}=1.6$

η	f	f'	f''	θ	θ'
0	0. 0000	0. 0000	1. 4153	0. 0000	0. 5921
. 2	. 0267	. 2589	1. 1735	. 1184	. 5910
. 4	. 1004	. 4699	. 9388	. 2360	. 5840
. 6	. 2117	. 6357	. 7231	. 3512	. 5663
. 8	. 3520	. 7610	. 5347	. 4617	. 5355
1. 0	. 5137	. 8516	. 3777	. 5645	. 4913
1. 2	. 6908	. 9142	. 2532	. 6574	. 4356
1. 4	. 8780	. 9550	. 1597	. 7383	. 3724
1. 6	1. 0717	. 9798	. 0932	. 8062	. 3065
1. 8	1. 2692	. 9937	. 0490	. 8610	. 2425
2. 0	1. 4687	1. 0006	. 0218	. 9036	. 1844
2. 2	1. 6692	1. 0032	. 0065	. 9353	. 1348
2. 4	1. 8699	1. 0037	−. 0009	. 9581	. 0946
2. 6	2. 0706	1. 0032	−. 0037	. 9738	. 0638
2. 8	2. 2711	1. 0024	−. 0041	. 9842	. 0413
3. 0	2. 4715	1. 0016	−. 0034	. 9908	. 0257
3. 2	2. 6718	1. 0010	−. 0025	. 9948	. 0154
3. 4	2. 8720	1. 0006	−. 0016	. 9972	. 0088
3. 6	3. 0720	1. 0004	−. 0010	. 9984	. 0049
3. 8	3. 2721	1. 0002	−. 0006	. 9993	. 0026
4. 0	3. 4721	1. 0001	−. 0003	. 9996	. 0013
4. 2	3. 6721	1. 0001	−. 0002	. 9998	. 0007
4. 4	3. 8722	1. 0000	−. 0001	. 9999	. 0003
4. 6	4. 0722	1. 0000	. 0000	1. 0000	. 0001
4. 8	4. 2722	1. 0000	. 0000	1. 0000	. 0001
5. 0	4. 4722	1. 0000	. 0000	1. 0000	. 0000
5. 2	4. 6722	1. 0000	. 0000	1. 0000	. 0000
5. 4	4. 8722	1. 0000	. 0000	1. 0000	. 0000
5. 6	5. 0722	1. 0000	. 0000	1. 0000	. 0000
5. 8	5. 2722	1. 0000	. 0000	1. 0000	. 0000
6. 0	5. 4722	1. 0000	. 0000	1. 0000	. 0000

$\frac{t_w}{t_0}=0.75$; $\frac{t_0}{t_{N_0}}=2.2$

η	f	f'	f''	θ	θ'
0	0. 0000	0. 0000	1. 7110	0. 0000	0. 6212
. 2	. 0320	. 3090	1. 3790	. 1242	. 6199
. 4	. 1192	. 5524	1. 0592	. 2474	. 6111
. 6	. 2489	. 7347	. 7706	. 3677	. 5894
. 8	. 4096	. 8636	. 5254	. 4821	. 5520
1. 0	. 5914	. 9482	. 3294	. 5875	. 4996
1. 2	. 7866	. 9986	. 1829	. 6812	. 4354
1. 4	. 9892	1. 0243	. 0816	. 7612	. 3646
1. 6	1. 1953	1. 0337	. 0182	. 8270	. 2930
1. 8	1. 4021	1. 0335	−. 0163	. 8787	. 2260
2. 0	1. 6084	1. 0285	−. 0308	. 9179	. 1673
2. 2	1. 8134	1. 0220	−. 0331	. 9463	. 1188
2. 4	2. 0172	1. 0157	−. 0290	. 9661	. 0810
2. 6	2. 2198	1. 0105	−. 0225	. 9794	. 0530
2. 8	2. 4215	1. 0067	−. 0161	. 9879	. 0333
3. 0	2. 6226	1. 0040	−. 0107	. 9931	. 0201
3. 2	2. 8232	1. 0023	−. 0067	. 9963	. 0117
3. 4	3. 0235	1. 0013	−. 0040	. 9980	. 0065
3. 6	3. 2237	1. 0007	−. 0022	. 9990	. 0035
3. 8	3. 4238	1. 0003	−. 0012	. 9995	. 0018
4. 0	3. 6239	1. 0002	−. 0006	. 9998	. 0009
4. 2	3. 8239	1. 0001	−. 0003	. 9999	. 0004
4. 4	4. 0239	1. 0000	−. 0001	1. 0000	. 0002
4. 6	4. 2239	1. 0000	−. 0001	1. 0000	. 0001
4. 8	4. 4239	1. 0000	. 0000	1. 0000	. 0000
5. 0	4. 6239	1. 0000	. 0000	1. 0000	. 0000
5. 2	4. 8239	1. 0000	. 0000	1. 0000	. 0000
5. 4	5. 0239	1. 0000	. 0000	1. 0000	. 0000
5. 6	5. 2239	1. 0000	. 0000	1. 0000	. 0000
5. 8	5. 4239	1. 0000	. 0000	1. 0000	. 0000
6. 0	5. 6239	1. 0000	. 0000	1. 0000	. 0000

TABLE I.—Continued. STAGNATION-LINE FLOW SOLUTIONS FOR YAWED INFINITE CYLINDER WITH PRANDTL NUMBER OF 1

$\frac{t_w}{t_0}=0.75$; $\frac{t_0}{t_{N_0}}=3.0$

η	f	f'	f''	θ	θ'
0	0. 0000	0. 0000	2. 0802	0. 0000	0. 6541
. 2	. 0386	. 3708	1. 6278	. 1307	. 6524
. 4	. 1424	. 6525	1. 1961	. 2603	. 6413
. 6	. 2942	. 8525	. 8139	. 3862	. 6143
. 8	. 4788	. 9825	. 4987	. 5048	. 5688
1. 0	. 6835	1. 0569	. 2579	. 6126	. 5066
1. 2	. 8988	1. 0905	. 0896	. 7066	. 4325
1. 4	1. 1179	1. 0969	−. 0150	. 7852	. 3535
1. 6	1. 3366	1. 0878	−. 0694	. 8481	. 2766
1. 8	1. 5526	1. 0715	−. 0884	. 8963	. 2072
2. 0	1. 7651	1. 0538	−. 0855	. 9317	. 1487
2. 2	1. 9743	1. 0380	−. 0718	. 9566	. 1023
2. 4	2. 1805	1. 0253	−. 0547	. 9734	. 0675
2. 6	2. 3846	1. 0160	−. 0386	. 9843	. 0428
2. 8	2. 5871	1. 0097	−. 0255	. 9910	. 0260
3. 0	2. 7886	1. 0056	−. 0159	. 9951	. 0152
3. 2	2. 9895	1. 0031	−. 0094	. 9974	. 0085
3. 4	3. 1899	1. 0016	−. 0053	. 9987	. 0046
3. 6	3. 3902	1. 0008	−. 0029	. 9993	. 0024
3. 8	3. 5903	1. 0004	−. 0015	. 9997	. 0012
4. 0	3. 7904	1. 0002	−. 0007	. 9999	. 0006
4. 2	3. 9904	1. 0001	−. 0003	. 9999	. 0003
4. 4	4. 1904	1. 0001	−. 0001	1. 0000	. 0001
4. 6	4. 3904	1. 0001	. 0000	1. 0000	. 0001
4. 8	4. 5904	1. 0001	. 0000	1. 0000	. 0000
5. 0	4. 7905	1. 0001	. 0000	1. 0000	. 0000
5. 2	4. 9905	1. 0001	. 0000	1. 0000	. 0000
5. 4	5. 1905	1. 0001	. 0000	1. 0000	. 0000
5. 6	5. 3905	1. 0001	. 0000	1. 0000	. 0000
5. 8	5. 5905	1. 0001	. 0000	1. 0000	. 0000
6. 0	5. 7905	1. 0001	. 0000	1. 0000	. 0000

$\frac{t_w}{t_0}=1.0$; $\frac{t_0}{t_{N_0}}=1.1$

η	f	f'	f''	θ	θ'
0	0. 0000	0. 0000	1. 2989	0. 0000	0. 5776
. 2	. 0245	. 2379	1. 0810	. 1155	. 5767
. 4	. 0923	. 4332	. 8747	. 2303	. 5703
. 6	. 1952	. 5891	. 6880	. 3430	. 5545
. 8	. 3256	. 7100	. 5256	. 4513	. 5265
1. 0	. 4772	. 8011	. 3896	. 5527	. 4861
1. 2	. 6444	. 8676	. 2798	. 6450	. 4346
1. 4	. 8229	. 9146	. 1944	. 7261	. 3753
1. 6	1. 0093	. 9468	. 1305	. 7949	. 3125
1. 8	1. 2009	. 9680	. 0844	. 8511	. 2506
2. 0	1. 3960	. 9815	. 0525	. 8954	. 1933
2. 2	1. 5932	. 9897	. 0314	. 9289	. 1434
2. 4	1. 7916	. 9945	. 0180	. 9533	. 1022
2. 6	1. 9909	. 9972	. 0098	. 9704	. 0700
2. 8	2. 1905	. 9987	. 0051	. 9819	. 0461
3. 0	2. 3903	. 9994	. 0025	. 9893	. 0292
3. 2	2. 5902	. 9997	. 0012	. 9939	. 0177
3. 4	2. 7902	. 9999	. 0005	. 9967	. 0104
3. 6	2. 9901	1. 0000	. 0002	. 9982	. 0058
3. 8	3. 1901	1. 0000	. 0001	. 9991	. 0031
4. 0	3. 3901	1. 0000	. 0000	. 9996	. 0016
4. 2	3. 5901	1. 0000	. 0000	. 9998	. 0008
4. 4	3. 7901	1. 0000	. 0000	. 9999	. 0004
4. 6	3. 9901	1. 0000	. 0000	1. 0000	. 0002
4. 8	4. 1901	1. 0000	. 0000	1. 0000	. 0001
5. 0	4. 3901	1. 0000	. 0000	1. 0000	. 0000
5. 2	4. 5901	1. 0000	. 0000	1. 0000	. 0000
5. 4	4. 7901	1. 0000	. 0000	1. 0000	. 0000
5. 6	4. 9901	1. 0000	. 0000	1. 0000	. 0000
5. 8	5. 1901	1. 0000	. 0000	1. 0000	. 0000
6. 0	5. 3901	1. 0000	. 0000	1. 0000	. 0000

TABLE I.—Continued. STAGNATION-LINE FLOW SOLUTIONS FOR YAWED INFINITE CYLINDER WITH PRANDTL NUMBER OF 1

$\frac{t_w}{t_0}=1.0$; $\frac{t_0}{t_{N_0}}=1.2$

η	f	f'	f''	θ	θ'
0	0. 0000	0. 0000	1. 3640	0. 0000	0. 5845
. 2	. 0257	. 2489	1. 1265	. 1168	. 5834
. 4	. 0965	. 4515	. 9020	. 2330	. 5768
. 6	. 2034	. 6112	. 6999	. 3469	. 5600
. 8	. 3385	. 7333	. 5254	. 4561	. 5307
1. 0	. 4946	. 8234	. 3808	. 5583	. 4884
1. 2	. 6661	. 8875	. 2658	. 6508	. 4350
1. 4	. 8483	. 9315	. 1780	. 7317	. 3739
1. 6	1. 0377	. 9603	. 1140	. 8001	. 3097
1. 8	1. 2317	. 9784	. 0694	. 8557	. 2468
2. 0	1. 4286	. 9891	. 0399	. 8992	. 1892
2. 2	1. 6271	. 9950	. 0214	. 9319	. 1394
2. 4	1. 8264	. 9981	. 0105	. 9555	. 0987
2. 6	2. 0262	. 9995	. 0045	. 9720	. 0671
2. 8	2. 2262	1. 0001	. 0015	. 9829	. 0439
3. 0	2. 4262	1. 0002	. 0002	. 9900	. 0276
3. 2	2. 6263	1. 0002	−. 0003	. 9943	. 0166
3. 4	2. 8263	1. 0002	−. 0003	. 9969	. 0096
3. 6	3. 0263	1. 0001	−. 0003	. 9984	. 0054
3. 8	3. 2263	1. 0001	−. 0002	. 9992	. 0029
4. 0	3. 4263	1. 0000	−. 0001	. 9996	. 0015
4. 2	3. 6264	1. 0000	−. 0001	. 9998	. 0007
4. 4	3. 8264	1. 0000	. 0000	. 9999	. 0003
4. 6	4. 0264	1. 0000	. 0000	1. 0000	. 0002
4. 8	4. 2264	1. 0000	. 0000	1. 0000	. 0001
5. 0	4. 4263	1. 0000	. 0000	1. 0000	. 0000
5. 2	4. 6263	1. 0000	. 0000	1. 0000	. 0000
5. 4	4. 8263	1. 0000	. 0000	1. 0000	. 0000
5. 6	5. 0263	1. 0000	. 0000	1. 0000	. 0000
5. 8	5. 2263	1. 0000	. 0000	1. 0000	. 0000
6. 0	5. 4263	1. 0000	. 0000	1. 0000	. 0000

$\frac{t_w}{t_0}=1.0$; $\frac{t_0}{t_{N_0}}=1.5$

η	f	f'	f''	θ	θ'
0	0. 0000	0. 0000	1. 5535	0. 0000	0. 6035
. 2	. 0291	. 2809	1. 2569	. 1206	. 6023
. 4	. 1085	. 5040	. 9785	. 2405	. 5945
. 6	. 2272	. 6743	. 7309	. 3577	. 5752
. 8	. 3752	. 7989	. 5152	. 4696	. 5418
1. 0	. 5442	. 8855	. 3523	. 5735	. 4944
1. 2	. 7274	. 9424	. 2231	. 6666	. 4354
1. 4	. 9197	. 9772	. 1299	. 7472	. 3694
1. 6	1. 1173	. 9964	. 0668	. 8142	. 3013
1. 8	1. 3176	1. 0055	. 0275	. 8679	. 2362
2. 0	1. 5191	1. 0085	. 0053	. 9091	. 1779
2. 2	1. 7208	1. 0084	−. 0053	. 9396	. 1286
2. 4	1. 9223	1. 0069	−. 0090	. 9613	. 0894
2. 6	2. 1235	1. 0050	−. 0090	. 9760	. 0596
2. 8	2. 3244	1. 0034	−. 0073	. 9857	. 0382
3. 0	2. 5249	1. 0021	−. 0054	. 9917	. 0235
3. 2	2. 7252	1. 0012	−. 0036	. 9954	. 0139
3. 4	2. 9254	1. 0007	−. 0023	. 9975	. 0079
3. 6	3. 1255	1. 0003	−. 0014	. 9987	. 0043
3. 8	3. 3255	1. 0001	−. 0008	. 9994	. 0023
4. 0	3. 5255	1. 0000	−. 0005	. 9997	. 0011
4. 2	3. 7255	. 9999	−. 0003	. 9999	. 0006

TABLE I.—Continued. STAGNATION-LINE FLOW SOLUTIONS FOR YAWED INFINITE CYLINDER WITH PRANDTL NUMBER OF 1

$\frac{t_w}{t_0}=1.0; \frac{t_0}{t_{N_0}}=1.6$					
η	f	f'	f''	θ	θ'
0	0. 0000	0. 0000	1. 6149	0. 0000	0. 6094
. 2	. 0302	. 2912	1. 2987	. 1218	. 6082
. 4	. 1124	. 5208	1. 0024	. 2428	. 6000
. 6	. 2348	. 6944	. 7398	. 3610	. 5799
. 8	. 3869	. 8195	. 5188	. 4738	. 5452
1. 0	. 5599	. 9049	. 3423	. 5781	. 4961
1. 2	. 7468	. 9593	. 2089	. 6714	. 4354
1. 4	. 9422	. 9910	. 1143	. 7518	. 3678
1. 6	1. 1422	1. 0071	. 0520	. 8184	. 2986
1. 8	1. 3444	1. 0134	. 0146	. 8714	. 2329
2. 0	1. 5472	1. 0141	−. 0050	. 9120	. 1744
2. 2	1. 7499	1. 0127	−. 0131	. 9418	. 1254
2. 4	1. 9520	1. 0093	−. 0145	. 9629	. 0866
2. 6	2. 1536	1. 0066	−. 0126	. 9771	. 0575
2. 8	2. 3547	1. 0043	−. 0097	. 9864	. 0366
3. 0	2. 5554	1. 0027	−. 0068	. 9922	. 0224
3. 2	2. 7558	1. 0016	−. 0044	. 9957	. 0132
3. 4	2. 9560	1. 0009	−. 0027	. 9977	. 0075
3. 6	3. 1562	1. 0005	−. 0016	. 9988	. 0041
3. 8	3. 3562	1. 0002	−. 0009	. 9994	. 0021
4. 0	3. 5563	1. 0001	−. 0005	. 9997	. 0011
4. 2	3. 7563	1. 0000	−. 0002	. 9999	. 0005
4. 4	3. 9563	1. 0000	−. 0001	1. 0000	. 0002
4. 6	4. 1563	1. 0000	−. 0001	1. 0000	. 0001
4. 8	4. 3563	1. 0000	. 0000	1. 0000	. 0000
5. 0	4. 5563	1. 0000	. 0000	1. 0000	. 0000
5. 2	4. 7563	1. 0000	. 0000	1. 0000	. 0000
5. 4	4. 9563	1. 0000	. 0000	1. 0000	. 0000
5. 6	5. 1563	1. 0000	. 0000	1. 0000	. 0000
5. 8	5. 3563	1. 0000	. 0000	1. 0000	. 0000
6. 0	5. 5563	1. 0000	. 0000	1. 0000	. 0000

$\frac{t_w}{t_0}=1.0; \frac{t_0}{t_{N_0}}=2.0$					
η	f	f'	f''	θ	θ'
0	0. 0000	0. 0000	1. 8532	0. 0000	0. 6313
. 2	. 0344	. 3309	1. 4583	. 1262	. 6298
. 4	. 1272	. 5852	1. 0910	. 2514	. 6202
. 6	. 2639	. 7704	. 7698	. 3733	. 5968
. 8	. 4315	. 8969	. 5051	. 4890	. 5569
1. 0	. 6195	. 9764	. 3000	. 5951	. 5015
1. 2	. 8197	1. 0207	. 1520	. 6888	. 4344
1. 4	1. 0261	1. 0405	. 0538	. 7684	. 3612
1. 6	1. 2349	1. 0449	−. 0044	. 8333	. 2881
1. 8	1. 4435	1. 0407	−. 0331	. 8840	. 2204
2. 0	1. 6509	1. 0329	−. 0425	. 9221	. 1617
2. 2	1. 8567	1. 0245	−. 0406	. 9494	. 1139
2. 4	2. 0608	1. 0170	−. 0335	. 9683	. 0770
2. 6	2. 2636	1. 0112	−. 0251	. 9809	. 0499
2. 8	2. 4654	1. 0069	−. 0174	. 9889	. 0311
3. 0	2. 6664	1. 0041	−. 0114	. 9937	. 0186
3. 2	2. 8671	1. 0023	−. 0070	. 9966	. 0107
3. 4	3. 0674	1. 0012	−. 0041	. 9982	. 0059
3. 6	3. 2676	1. 0006	−. 0023	. 9991	. 0031
3. 8	3. 4676	1. 0002	−. 0012	. 9996	. 0016
4. 0	3. 6677	1. 0000	−. 0007	. 9998	. 0008
4. 2	3. 8677	. 9999	−. 0004	. 9999	. 0004
4. 4	4. 0676	. 9999	−. 0002	1. 0000	. 0002

TABLE I.—Continued. STAGNATION-LINE FLOW SOLUTIONS FOR YAWED INFINITE CYLINDER WITH PRANDTL NUMBER OF 1

$\frac{t_w}{t_0}=1.0$; $\frac{t_0}{t_{N_0}}=2.2$

η	f	f'	f''	θ	θ'
0	0. 0000	0. 0000	1. 9684	0. 0000	0. 6413
. 2	. 0365	. 3500	1. 5343	. 1282	. 6397
. 4	. 1344	. 6158	1. 1317	. 2553	. 6295
. 6	. 2778	. 8062	. 7819	. 3790	. 6044
. 8	. 4526	. 9328	. 4962	. 4959	. 5621
1. 0	. 6476	1. 0092	. 2781	. 6027	. 5037
1. 2	. 8539	1. 0483	. 1239	. 6966	. 4335
1. 4	1. 0653	1. 0623	. 0249	. 7757	. 3578
1. 6	1. 2778	1. 0611	—. 0305	. 8398	. 2831
1. 8	1. 4892	1. 0522	—. 0546	. 8894	. 2146
2. 0	1. 6985	1. 0406	—. 0588	. 9263	. 1561
2. 2	1. 9055	1. 0294	—. 0522	. 9526	. 1088
2. 4	2. 1104	1. 0200	—. 0412	. 9706	. 0728
2. 6	2. 3137	1. 0129	—. 0299	. 9824	. 0468
2. 8	2. 5157	1. 0079	—. 0203	. 9898	. 0289
3. 0	2. 7170	1. 0046	—. 0129	. 9943	. 0171
3. 2	2. 9177	1. 0026	—. 0078	. 9970	. 0098
3. 4	3. 1181	1. 0014	—. 0045	. 9984	. 0053
3. 6	3. 3183	1. 0007	—. 0025	. 9992	. 0028
3. 8	3. 5184	1. 0003	—. 0013	. 9996	. 0014
4. 0	3. 7184	1. 0002	—. 0006	. 9998	. 0007
4. 2	3. 9184	1. 0001	—. 0003	. 9999	. 0003
4. 4	4. 1184	1. 0000	—. 0001	1. 0000	. 0001
4. 6	4. 3184	1. 0000	—. 0001	1. 0000	. 0001
4. 8	4. 5184	1. 0000	. 0000	1. 0000	. 0000
5. 0	4. 7184	1. 0000	. 0000	1. 0000	. 0000
5. 2	4. 9184	1. 0000	. 0000	1. 0000	. 0000
5. 4	5. 1184	1. 0000	. 0000	1. 0000	. 0000
5. 6	5. 3184	1. 0000	. 0000	1. 0000	. 0000
5. 8	5. 5184	1. 0000	. 0000	1. 0000	. 0000
6. 0	5. 7184	1. 0000	. 0000	1. 0000	. 0000

$\frac{t_w}{t_0}=1.0$; $\frac{t_0}{t_{N_0}}=3.0$

η	f	f'	f''	θ	θ'
0	0. 0000	0. 0000	2. 4086	0. 0000	0. 6770
. 2	. 0442	. 4222	1. 8178	. 1353	. 6750
. 4	. 1613	. 7304	1. 2760	. 2692	. 6619
. 6	. 3297	. 9380	. 8149	. 3988	. 6306
. 8	. 5310	1. 0628	. 4508	. 5201	. 5789
1. 0	. 7507	1. 1249	. 1865	. 6292	. 5093
1. 2	. 9781	1. 1435	. 0136	. 7231	. 4285
1. 4	1. 2063	1. 1353	—. 0836	. 8003	. 3444
1. 6	1. 4314	1. 1137	—. 1246	. 8611	. 2645
1. 8	1. 6516	1. 0879	—. 1288	. 9068	. 1943
2. 0	1. 8667	1. 0635	—. 1129	. 9397	. 1367
2. 2	2. 0773	1. 0433	—. 0889	. 9624	. 0921
2. 4	2. 2843	1. 0279	—. 0645	. 9774	. 0596
2. 6	2. 4888	1. 0172	—. 0438	. 9869	. 0370
2. 8	2. 6914	1. 0101	—. 0280	. 9926	. 0220
3. 0	2. 8930	1. 0059	—. 0170	. 9960	. 0126
3. 2	3. 0938	1. 0030	—. 0980	. 9979	. 0069
3. 4	3. 2943	1. 0016	—. 0054	. 9990	. 0037
3. 6	3. 4945	1. 0008	—. 0028	. 9995	. 0019
3. 8	3. 6946	1. 0004	—. 0014	. 9998	. 0009
4. 0	3. 8947	1. 0001	—. 0007	. 9999	. 0004
4. 2	4. 0947	1. 0001	—. 0003	. 9999	. 0002
4. 4	4. 2947	1. 0000	—. 0001	1. 0000	. 0001
4. 6	4. 4947	1. 0000	—. 0001	1. 0000	. 0000
4. 8	4. 6947	1. 0000	. 0000	1. 0000	. 0000
5. 0	4. 8947	1. 0000	. 0000	1. 0000	. 0000
5. 2	5. 0947	1. 0000	. 0000	1. 0000	. 0000
5. 4	5. 2947	1. 0000	. 0000	1. 0000	. 0000
5. 6	5. 4947	1. 0000	. 0000	1. 0000	. 0000
5. 8	5. 6947	1. 0000	. 0000	1. 0000	. 0000
6. 0	5. 8947	1. 0000	. 0000	1. 0000	. 0000

TABLE I.—Continued. STAGNATION-LINE FLOW SOLUTIONS FOR YAWED INFINITE CYLINDER WITH PRANDTL NUMBER OF 1

$\frac{t_w}{t_0}=1.0$; $\frac{t_0}{t_{N_0}}=4.0$

η	f	f'	f''	θ	θ'
0	0. 0000	0. 0000	2. 9230	0. 0000	0. 7143
. 2	. 0532	. 5053	2. 1371	. 1427	. 7117
. 4	. 1921	. 8597	1. 4243	. 2837	. 6953
. 6	. 3884	1. 0830	. 8312	. 4193	. 6566
. 8	. 6184	1. 2016	. 3790	. 5448	. 5940
1. 0	. 8640	1. 2440	. 0684	. 6556	. 5122
1. 2	1. 1128	1. 2372	−. 1170	. 7490	. 4203
1. 4	1. 3572	1. 2037	−. 2038	. 8238	. 3283
1. 6	1. 5936	1. 1601	−. 2224	. 8808	. 2444
1. 8	1. 8213	1. 1173	−. 2010	. 9224	. 1737
2. 0	2. 0410	1. 0808	−. 1617	. 9513	. 1180
2. 2	2. 2542	1. 0528	−. 1193	. 9706	. 0768
2. 4	2. 4627	1. 0328	−. 0820	. 9828	. 0479
2. 6	2. 6678	1. 0194	−. 0531	. 9904	. 0287
2. 8	2. 8707	1. 0110	−. 0325	. 9948	. 0165
3. 0	3. 0724	1. 0059	−. 0189	. 9973	. 0091
3. 2	3. 2733	1. 0031	−. 0104	. 9986	. 0048
3. 4	3. 4737	1. 0015	−. 0055	. 9993	. 0025
3. 6	3. 6739	1. 0007	−. 0028	. 9997	. 0012
3. 8	3. 8740	1. 0003	−. 0014	. 9999	. 0006
4. 0	4. 0741	1. 0001	−. 0006	. 9999	. 0003
4. 2	4. 2741	1. 0001	−. 0002	1. 0000	. 0001
4. 4	4. 4741	1. 0000	−. 0001	1. 0000	. 0000
4. 6	4. 6741	1. 0000	−. 0001	1. 0000	. 0000
4. 8	4. 8741	1. 0000	. 0000	1. 0000	. 0000
5. 0	5. 0741	1. 0000	. 0000	1. 0000	. 0000
5. 2	5. 2741	1. 0000	. 0000	1. 0000	. 0000
5. 4	5. 4741	1. 0000	. 0000	1. 0000	. 0000
5. 6	5. 6741	1. 0000	. 0000	1. 0000	. 0000
5. 8	5. 8741	1. 0000	. 0000	1. 0000	. 0000
6. 0	6. 0741	1. 0000	. 0000	1. 0000	. 0000

$\frac{t_w}{t_0}=1.0$; $\frac{t_0}{t_{N_0}}=6.0$

η	f	f'	f''	θ	θ'
0	0. 0000	0. 0000	3. 8711	0. 0000	0. 7742
. 2	. 0695	. 6555	2. 6962	. 1546	. 7705
. 4	. 2472	1. 0872	1. 6505	. 3069	. 7476
. 6	. 4917	1. 3296	. 8114	. 4517	. 6949
. 8	. 7694	1. 4276	. 2088	. 5829	. 6127
1. 0	1. 0563	1. 4283	−. 1669	. 6954	. 5105
1. 2	1. 3371	1. 3735	−. 3537	. 7866	. 4018
1. 4	1. 6042	1. 2959	−. 4042	. 8565	. 2993
1. 6	1. 8554	1. 2173	−. 3719	. 9073	. 2117
1. 8	2. 0919	1. 1497	−. 3012	. 9425	. 1426
2. 0	2. 3163	1. 0974	−. 2224	. 9656	. 0917
2. 2	2. 5318	1. 0601	−. 1524	. 9802	. 0565
2. 4	2. 7412	1. 0354	−. 0979	. 9890	. 0333
2. 6	2. 9466	1. 0199	−. 0594	. 9941	. 0189
2. 8	3. 1496	1. 0107	−. 0342	. 9969	. 0103
3. 0	3. 3511	1. 0055	−. 0188	. 9985	. 0053
3. 2	3. 5519	1. 0028	−. 0098	. 9992	. 0027
3. 4	3. 7523	1. 0013	−. 0050	. 9996	. 0012
3. 6	3. 9525	1. 0006	−. 0025	. 9998	. 0004
3. 8	4. 1526	1. 0003	−. 0014	. 9999	. 0003
4. 0	4. 3527	1. 0001	−. 0001	. 9999	. 0002

TABLE I.—Continued. STAGNATION-LINE FLOW SOLUTIONS FOR YAWED INFINITE CYLINDER WITH PRANDTL NUMBER OF 1

$\frac{t_w}{t_0}=1.0$; $\frac{t_0}{t_{N_0}}=6.5$

η	f	f'	f''	θ	θ'
0	0. 0000	0. 0000	4. 0951	0. 0000	0. 7871
. 2	. 0734	. 6904	2. 8234	. 1572	. 7832
. 4	. 2602	1. 1390	1. 6963	. 3118	. 7586
. 6	. 5155	1. 3843	. 7992	. 4585	. 7026
. 8	. 8038	1. 4761	. 1635	. 5908	. 6160
1. 0	1. 0993	1. 4661	−. 2239	. 7035	. 5092
1. 2	1. 3866	1. 3999	−. 4073	. 7941	. 3971
1. 4	1. 6580	1. 3125	−. 4468	. 8629	. 2928
1. 6	1. 9118	1. 2266	−. 4016	. 9123	. 2048
1. 8	2. 1496	1. 1542	−. 3195	. 9461	. 1364
2. 0	2. 3747	1. 0991	−. 2323	. 9681	. 0868
2. 2	2. 5904	1. 0604	−. 1569	. 9819	. 0528
2. 4	2. 7997	1. 0351	−. 0995	. 9901	. 0308
2. 6	3. 0050	1. 0194	−. 0596	. 9947	. 0173
2. 8	3. 2079	1. 0103	−. 0339	. 9973	. 0093
3. 0	3. 4094	1. 0052	−. 0183	. 9987	. 0048
3. 2	3. 6101	1. 0025	−. 0095	. 9994	. 0024
3. 4	3. 8105	1. 0012	−. 0047	. 9997	. 0011
3. 6	4. 0106	1. 0005	−. 0022	. 9999	. 0005
3. 8	4. 2107	1. 0002	−. 0010	. 9999	. 0002
4. 0	4. 4107	1. 0001	−. 0005	1. 0000	. 0001
4. 2	4. 6107	1. 0000	−. 0002	1. 0000	. 0000
4. 4	4. 8107	1. 0000	−. 0001	1. 0000	. 0000
4. 6	5. 0107	1. 0000	. 0000	1. 0000	. 0000
4. 8	5. 2107	1. 0000	. 0000	1. 0000	. 0000
5. 0	5. 4107	1. 0000	. 0000	1. 0000	. 0000
5. 2	5. 6107	1. 0000	. 0000	1. 0000	. 0000
5. 4	5. 8107	1. 0000	. 0000	1. 0000	. 0000
5. 6	6. 0107	1. 0000	. 0000	1. 0000	. 0000
5. 8	6. 2107	1. 0000	. 0000	1. 0000	. 0000
6. 0	6. 4106	1. 0000	. 0000	1. 0000	. 0000

$\frac{t_w}{t_0}=1.0$; $\frac{t_0}{t_{N_0}}=11.0$

η	f	f'	f''	θ	θ'
0	0. 0000	0. 0000	5. 9629	0. 0000	0. 8808
. 2	. 1047	. 9757	3. 8229	. 1758	. 8744
. 4	. 3634	1. 5496	1. 9846	. 3476	. 8360
. 6	. 7030	1. 8006	. 6093	. 5072	. 7521
. 8	1. 0687	1. 8268	−. 2673	. 6458	. 6300
1. 0	1. 4251	1. 7230	−. 7058	. 7580	. 4908
1. 2	1. 7544	1. 5659	−. 8231	. 8425	. 3569
1. 4	2. 0514	1. 4065	−. 7489	. 9022	. 2437
1. 6	2. 3187	1. 2718	−. 5914	. 9418	. 1573
1. 8	2. 5623	1. 1706	−. 4223	. 9668	. 0956
2. 0	2. 7890	1. 1011	−. 2784	. 9818	. 0565
2. 2	3. 0045	1. 0567	−. 1715	. 9905	. 0317
2. 4	3. 2129	1. 0302	−. 0995	. 9952	. 0170
2. 6	3. 4173	1. 0151	−. 0545	. 9977	. 0087
2. 8	3. 6194	1. 0071	−. 0282	. 9990	. 0042
3. 0	3. 8204	1. 0029	−. 0135	. 9996	. 0017
3. 2	4. 0207	1. 0009	−. 0051	. 9999	. 0000

TABLE I.—Continued. STAGNATION-LINE FLOW SOLUTIONS FOR YAWED INFINITE CYLINDER WITH PRANDTL NUMBER OF 1

$\frac{t_w}{t_0}=1.5$; $\frac{t_0}{t_{N_0}}=1.2$

η	f	f'	f''	θ	θ'
0	0. 0000	0. 0000	1. 6641	0. 0000	0. 6109
. 2	. 0309	. 2975	1. 3149	. 1221	. 6096
. 4	. 1146	. 5282	. 9987	. 2434	. 6012
. 6	. 2383	. 6999	. 7266	. 3618	. 5807
. 8	. 3912	. 8221	. 5035	. 4747	. 5455
1. 0	. 5645	. 9045	. 3294	. 5990	. 4959
1. 2	. 7511	. 9568	. 2005	. 6723	. 4349
1. 4	. 9458	. 9873	. 1105	. 7525	. 3671
1. 6	1. 1450	1. 0031	. 0519	. 8190	. 2978
1. 8	1. 3464	1. 0096	. 0169	. 8719	. 2322
2. 0	1. 5485	1. 0109	−. 0016	. 9123	. 1738
2. 2	1. 7506	1. 0097	−. 0095	. 9420	. 1250
2. 4	1. 9523	1. 0075	−. 0113	. 9630	. 0863
2. 6	2. 1536	1. 0053	−. 0101	. 9772	. 0572
2. 8	2. 3545	1. 0035	−. 0078	. 9864	. 0365
3. 0	2. 5551	1. 0022	−. 0055	. 9922	. 0223
3. 2	2. 7554	1. 0013	−. 0036	. 9957	. 0131
3. 4	2. 9556	1. 0007	−. 0022	. 9977	. 0074
3. 6	3. 1557	1. 0004	−. 0013	. 9988	. 0040
3. 8	3. 3558	1. 0002	−. 0007	. 9994	. 0021
4. 0	3. 5556	1. 0001	−. 0003	. 9997	. 0011
4. 2	3. 7558	1. 0000	−. 0002	. 9999	. 0005
4. 4	3. 9558	1. 0000	−. 0001	. 9999	. 0002
4. 6	4. 1558	1. 0000	. 0000	1. 0000	. 0001
4. 8	4. 3558	1. 0000	. 0000	1. 0000	. 0000
5. 0	4. 5558	1. 0000	. 0000	1. 0000	. 0000
5. 2	4. 7558	1. 0000	. 0000	1. 0000	. 0000
5. 4	4. 9558	1. 0000	. 0000	1. 0000	. 0000
5. 6	5. 1558	1. 0000	. 0000	1. 0000	. 0000
5. 8	5. 3558	1. 0000	. 0000	1. 0000	. 0000
6. 0	5. 5558	1. 0000	. 0000	1. 0000	. 0000

$\frac{t_w}{t_0}=1.5$; $\frac{t_0}{t_{N_0}}=1.6$

η	f	f'	f''	θ	θ'
0	0. 0000	0. 0000	1. 9924	0. 0000	0. 6397
. 2	. 0367	. 3514	1. 5280	. 1278	. 6381
. 4	. 1347	. 6144	1. 1117	. 2546	. 6278
. 6	. 2774	. 8004	. 7600	. 3780	. 6028
. 8	. 4507	. 9232	. 4798	. 4946	. 5607
1. 0	. 6434	. 9970	. 2701	. 6012	. 5027
1. 2	. 8472	1. 0354	. 1241	. 6949	. 4332
1. 4	1. 0560	1. 0502	. 0313	. 7741	. 3582
1. 6	1. 2663	1. 0506	−. 0206	. 8382	. 2839
1. 8	1. 4758	1. 0438	−. 0437	. 8880	. 2158
2. 0	1. 6836	1. 0343	−. 0486	. 9252	. 1574
2. 2	1. 8896	1. 2498	−. 0438	. 9517	. 1101
2. 4	2. 0937	1, 0171	−. 0349	. 9699	. 0739
2. 6	2. 2965	1. 0111	−. 0254	. 9819	. 0747
2. 8	2. 4983	1. 0068	−. 0173	. 9895	. 0295
3. 0	2. 6994	1. 0040	−. 0111	. 9942	. 0176
3. 2	2. 9000	1. 0022	−. 0067	. 9969	. 0100
3. 4	3. 1003	1. 0012	−. 0039	. 9984	. 0055
3. 6	3. 3005	1. 0006	−. 0021	. 9992	. 0029
3. 8	3. 5006	1. 0003	−. 0011	. 9996	. 0015
4. 0	3. 7006	1. 0002	−. 0006	. 9998	. 0007
4. 2	3. 9006	1. 0001	−. 0002	. 9999	. 0003
4. 4	4. 1007	1. 0000	−. 0001	1. 0000	. 0001
4. 6	4. 3007	1. 0000	. 0000	1. 0000	. 0001
4. 8	4. 5007	1. 0000	. 0000	1. 0000	. 0000
5. 0	4. 7007	1. 0000	. 0000	1. 0000	. 0000
5. 2	4. 9007	1. 0000	. 0000	1. 0000	. 0000
5. 4	5. 1007	1. 0000	. 0000	1. 0000	. 0000
5. 6	5. 3007	1. 0000	. 0000	1. 0000	. 0000
5. 8	5. 5007	1. 0000	. 0000	1. 0000	. 0000
6. 0	5. 7007	1. 0000	. 0000	1. 0000	. 0000

TABLE I.—Continued. STAGNATION-LINE FLOW SOLUTIONS FOR YAWED INFINITE CYLINDER WITH PRANDTL NUMBER OF 1

$\frac{t_w}{t_0}=1.5$; $\frac{t_0}{t_{N_0}}=2.2$

η	f	f'	f''	θ	θ'
0	0. 0000	0. 0000	2. 4534	0. 0000	0. 6761
. 2	. 0448	. 4261	1. 8168	. 1351	. 6740
. 4	. 1624	. 7316	1. 2532	. 2688	. 6609
. 6	. 3306	. 9339	. 7880	. 3982	. 6295
. 8	. 5306	1. 0539	. 4301	. 5193	. 5778
1. 0	. 7481	1. 1129	. 1762	. 6281	. 5085
1. 2	. 9730	1. 1304	. 0134	. 7219	. 4282
1. 4	1. 1187	1. 1230	−. 0766	. 7992	. 3446
1. 6	1. 4214	1. 1033	−. 1138	. 8600	. 2651
1. 8	1. 6397	1. 0797	−. 1172	. 9059	. 1952
2. 0	1. 8534	1. 0575	−. 1024	. 9389	. 1377
2. 2	2. 0630	1. 0392	−. 0805	. 9618	. 0931
2. 4	2. 2694	1. 0253	−. 0584	. 9770	. 0603
2. 6	2. 4734	1. 0156	−. 0397	. 9866	. 0376
2. 8	2. 6759	1. 0092	−. 0254	. 9925	. 0225
3. 0	2. 8773	1. 0051	−. 0154	. 9959	. 0129
3. 2	3. 0780	1. 0028	−. 0089	. 9979	. 0071
3. 4	3. 2784	1. 0014	−. 0049	. 9989	. 0038
3. 6	3. 4786	1. 0007	−. 0026	. 9995	. 0019
3. 8	3. 6787	1. 0003	−. 0013	. 9998	. 0009
4. 0	3. 8788	1. 0001	−. 0006	. 9999	. 0004
4. 2	4. 0788	1. 0001	−. 0002	1. 0000	. 0002
4. 4	4. 2788	1. 0000	−. 0001	1. 0000	. 0001
4. 6	4. 4788	1. 0000	−. 0001	1. 0000	. 0000
4. 8	4. 6788	1. 0000	. 0000	1. 0000	. 0000
5. 0	4. 8788	1. 0000	. 0000	1. 0000	. 0000
5. 2	5. 0788	1. 0000	. 0000	1. 0000	. 0000
5. 4	5. 2788	1. 0000	. 0000	1. 0000	. 0000
5. 6	5. 4788	1. 0000	. 0000	1. 0000	. 0000
5. 8	5. 6788	1. 0000	. 0000	1. 0000	. 0000
6. 0	5. 8788	1. 0000	. 0000	1. 0000	. 0000

$\frac{t_w}{t_0}=1.5$; $\frac{t_0}{t_{N_0}}=3.0$

η	f	f'	f''	θ	θ'
0	0. 0000	0. 0000	3. 0259	0. 0000	0. 7163
. 2	. 0547	. 5173	2. 1607	. 1431	. 7136
. 4	. 1961	. 8716	1. 4056	. 2845	. 6968
. 6	. 3943	1. 0893	. 7977	. 4203	. 6573
. 8	. 6249	1. 2012	. 3482	. 5458	. 5939
1. 0	. 8699	1. 2385	. 0481	. 6566	. 5115
1. 2	1. 1172	1. 2289	−. 1253	. 7497	. 4193
1. 4	1. 3598	1. 1947	−. 2028	. 8243	. 3273
1. 6	1. 5946	1. 1520	−. 2159	. 8812	. 2435
1. 8	1. 8208	1. 1107	−. 1924	. 9226	. 1731
2. 0	2. 0393	1. 0760	−. 1534	. 9514	. 1176
2. 2	2. 2517	1. 0414	−. 1125	. 9706	. 0769
2. 4	2. 4596	1. 0306	−. 0770	. 9829	. 0478
2. 6	2. 6644	1. 0181	−. 0496	. 9904	. 0287
2. 8	2. 8671	1. 0102	−. 0303	. 9948	. 0165
3. 0	3. 0687	1. 0055	−. 0176	. 9973	. 0091
3. 2	3. 2695	1. 0029	−. 0097	. 9986	. 0048
3. 4	3. 4699	1. 0014	−. 0051	. 9993	. 0025
3. 6	3. 6701	1. 0007	−. 0026	. 9997	. 0012
3. 8	3. 8702	1. 0003	−. 0012	. 9999	. 0006
4. 0	4. 0703	1. 0001	−. 0006	. 9999	. 0003
4. 2	4. 2703	1. 0001	−. 0002	1. 0000	. 0001
4. 4	4. 4703	1. 0001	−. 0001	1. 0000	. 0000
4. 6	4. 6703	1. 0000	. 0000	1. 0000	. 0000
4. 8	4. 8703	1. 0000	. 0000	1. 0000	. 0000
5. 0	5. 0703	1. 0000	. 0000	1. 0000	. 0000
5. 2	5. 2703	1. 0000	. 0000	1. 0000	. 0000
5. 4	5. 4703	1. 0000	. 0000	1. 0000	. 0000
5. 6	5. 6703	1. 0000	. 0000	1. 0000	. 0000
5. 8	5. 8703	1. 0000	. 0000	1. 0000	. 0000
6. 0	6. 0704	1. 0000	. 0000	1. 0000	. 0000

TABLE I.—Continued. STAGNATION-LINE FLOW SOLUTIONS FOR YAWED INFINITE CYLINDER WITH PRANDTL NUMBER OF 1

$\frac{t_w}{t_0}=2.0$; $\frac{t_0}{t_{N_0}}=1.0$

η	f	f'	f''	θ	θ'
0	0. 0000	0. 0000	1. 7638	0. 0000	0. 6154
. 2	. 0321	. 3084	1. 3526	. 1230	. 6140
. 4	. 1185	. 5439	1. 0114	. 2451	. 6053
. 6	. 2455	. 7165	. 7232	. 3643	. 5840
. 8	. 4016	. 8370	. 4915	. 4777	. 5476
1. 0	. 5776	. 9167	. 3142	. 5824	. 4967
1. 2	. 7663	. 9659	. 1857	. 6757	. 4343
1. 4	. 9625	. 9936	. 0979	. 7556	. 3654
1. 6	1. 1628	1. 0073	. 0422	. 8217	. 2954
1. 8	1. 3648	1. 0122	. 0101	. 8741	. 2294
2. 0	1. 5673	1. 0123	−. 0061	. 9140	. 1711
2. 2	1. 7696	1. 0104	−. 0123	. 9432	. 1226
2. 4	1. 9714	1. 0078	−. 0130	. 9637	. 0843
2. 6	2. 1728	1. 0053	−. 0111	. 9776	. 0557
2. 8	2. 3736	1. 0034	−. 0085	. 9866	. 0354
3. 0	2. 5741	1. 0020	−. 0059	. 9922	. 0216
3. 2	2. 7744	1. 0010	−. 0040	. 9955	. 0126
3. 4	2. 9746	1. 0003	−. 0026	. 9974	. 0071
3. 6	3. 1746	. 9999	−. 0016	. 9985	. 0038

$\frac{t_w}{t_0}=2.0$; $\frac{t_0}{t_{N_0}}=2.0$

η	f	f'	f''	θ	θ'
0	0. 0000	0. 0000	2. 7262	0. 0000	0. 6931
. 2	. 0493	. 4676	1. 9638	. 1385	. 6908
. 4	. 1775	. 7925	1. 3058	. 2755	. 6760
. 6	. 3584	. 9986	. 7777	. 4076	. 6412
. 8	. 5708	1. 1127	. 3846	. 5305	. 5845
1. 0	. 7991	1. 1609	. 1168	. 6401	. 5098
1. 2	1. 0323	1. 1665	−. 0453	. 7337	. 4245
1. 4	1. 2641	1. 1481	−. 1265	. 8098	. 3373
1. 6	1. 4909	1. 1196	−. 1520	. 8690	. 2561
1. 8	1. 7118	1. 0896	−. 1439	. 9130	. 1859
2. 0	1. 9270	1. 0631	−. 1196	. 9443	. 1292
2. 2	2. 1374	1. 0420	−. 0906	. 9656	. 0860
2. 4	2. 3442	1. 0267	−. 0639	. 9795	. 0549
2. 6	2. 5483	1. 0161	−. 0423	. 9882	. 0337
2. 8	2. 7509	1. 0093	−. 0265	. 9934	. 0198
3. 0	2. 9523	1. 0052	−. 0158	. 9965	. 0112
3. 2	3. 1531	1. 0028	−. 0090	. 9982	. 0061
3. 4	3. 3535	1. 0014	−. 0049	. 9991	. 0032
3. 6	3. 5537	1. 0007	−. 0025	. 9995	. 0016
3. 8	3. 7538	1. 0003	−. 0013	. 9997	. 0008
4. 0	3. 9538	1. 0002	−. 0007	. 9998	. 0003
4. 2	4. 1539	1. 0001	−. 0004	. 9999	. 0000

TABLE I.—Concluded. STAGNATION-LINE FLOW SOLUTIONS FOR YAWED INFINITE CYLINDER WITH PRANDTL NUMBER OF 1

$\frac{t_w}{t_0}=2.0$; $\frac{t_0}{t_{N_0}}=6.0$

η	f	f'	f''	θ	θ'
0	0. 0000	0. 0000	5. 9032	0. 0000	0. 8666
. 2	. 1025	. 9500	3. 6549	. 1730	. 8605
. 4	. 3527	1. 4913	1. 8409	. 3421	. 8236
. 6	. 6783	1. 7214	. 5479	. 4995	. 7435
. 8	1. 0274	1. 7438	−. 2461	. 6370	. 6270
1. 0	1. 3681	1. 6502	−. 6321	. 7492	. 4933
1. 2	1. 6845	1. 5100	−. 7325	. 8346	. 3633
1. 4	1. 9721	1. 3682	−. 6667	. 8957	. 2519
1. 6	2. 2332	1. 2480	−. 5290	. 9370	. 1653
1. 8	2. 4732	1. 1572	−. 3809	. 9635	. 1032
2. 0	2. 6980	1. 0943	−. 2537	. 9797	. 0615
2. 2	2. 9124	1. 0536	−. 1583	. 9891	. 0351
2. 4	3. 1205	1. 0289	−. 0931	. 9944	. 0192
2. 6	3. 3247	1. 0148	−. 0519	. 9973	. 0101
2. 8	3. 5268	1. 0071	−. 0275	. 9987	. 0050
3. 0	3. 7278	1. 0031	−. 0140	. 9995	. 0023
3. 2	3. 9282	1. 0011	−. 0071	. 9998	. 0007

TABLE II.—STAGNATION-LINE SOLUTIONS FOR YAWED INFINITE CYLINDER WITH PRANDTL NUMBER OF 0.7

$\frac{t_w}{t_0}=0$; $\frac{t_0}{t_{N_0}}=1.0$

η	f	f'	f''	g	g'	θ	θ'
0	0. 0000	0. 0000	0. 6071	0. 0000	0. 4970	0. 0000	0. 4362
. 2	. 0121	. 1209	. 5989	. 0994	. 4966	. 0872	. 4360
. 4	. 0481	. 2386	. 5762	. 1985	. 4938	. 1743	. 4343
. 6	. 1072	. 3506	. 5418	. 2966	. 4864	. 2608	. 4297
. 8	. 1878	. 4547	. 4987	. 3926	. 4724	. 3459	. 4210
1. 0	. 2884	. 4596	. 4496	. 4850	. 4506	. 4288	. 4073
1. 2	. 4070	. 6343	. 3970	. 5723	. 4204	. 5085	. 3880
1. 4	. 5415	. 7084	. 3433	. 6527	. 3825	. 5837	. 3632
1. 6	. 6897	. 7717	. 2905	. 7249	. 3382	. 6534	. 3332
1. 8	. 8495	. 8247	. 2405	. 7877	. 2900	. 7167	. 2992
2. 0	1. 0189	. 8682	. 1946	. 8408	. 2407	. 7729	. 2626
2. 2	1. 1962	. 9029	. 1538	. 8841	. 1929	. 8217	. 2249
2. 4	1. 3796	. 9301	. 1186	. 9182	. 1491	. 8629	. 1878
2. 6	1. 5678	. 9507	. 0892	. 9441	. 1110	. 8969	. 1528
2. 8	1. 7595	. 9661	. 0654	. 9631	. 0796	. 9242	. 1210
3. 0	1. 9539	. 9772	. 0467	. 9764	. 0549	. 9456	. 0933
3. 2	2. 1502	. 9851	. 0324	. 9854	. 0364	. 9619	. 0700
3. 4	2. 3478	. 9905	. 0219	. 9913	. 0232	. 9739	. 0511
3. 6	2. 5463	. 9940	. 0144	. 9950	. 0143	. 9826	. 0363
3. 8	2. 7453	. 9964	. 0092	. 9972	. 0084	. 9887	. 0251
4. 0	2. 9448	. 9979	. 0058	. 9985	. 0048	. 9928	. 0168
4. 2	3. 1444	. 9988	. 0035	. 9992	. 0026	. 9955	. 0110
4. 4	3. 3443	. 9993	. 0021	. 9996	. 0014	. 9973	. 0070
4. 6	3. 5441	. 9996	. 0012	. 9998	. 0007	. 9984	. 0043
4. 8	3. 7441	. 9998	. 0007	. 9999	. 0003	. 9991	. 0026
5. 0	3. 9441	. 9999	. 0004	1. 0000	. 0001	. 9995	. 0015
5. 2	4. 1440	. 9999	. 0002	1. 0000	. 0001	. 9997	. 0009
5. 4	4. 3440	1. 0000	. 0001	1. 0000	. 0000	. 9999	. 0005
5. 6	4. 5440	1. 0000	. 0000	1. 0000	. 0000	. 9999	. 0003
5. 8	4. 7440	1. 0000	. 0000	1. 0000	. 0000	1. 0000	. 0001
6. 0	4. 9440	1. 0000	. 0000	1. 0000	. 0000	1. 0000	. 0001

$\frac{t_w}{t_0}=0$; $\frac{t_0}{t_{N_0}}=1.6$

η	f	f'	f''	g	g'	θ	θ'
0	0. 0000	0. 0000	0. 6870	0. 0000	0. 5129	0. 0000	0. 4226
. 2	. 0137	. 1365	. 6744	. 1025	. 5124	. 0857	. 4342
. 4	. 0543	. 2683	. 6403	. 2048	. 5091	. 1735	. 4438
. 6	. 1205	. 3916	. 5901	. 3058	. 5005	. 2630	. 4495
. 8	. 2102	. 5036	. 5290	. 4045	. 4844	. 3529	. 4488
1. 0	. 3211	. 6028	. 4620	. 4990	. 4595	4419	. 4399
1. 2	. 4504	. 6883	. 3933	. 5877	. 4255	. 5282	. 4214
1. 4	. 5955	. 7602	. 3265	. 6687	. 3834	. 6098	. 3930
1. 6	. 7536	. 8192	. 2645	. 7406	. 3350	. 6849	. 3559
1. 8	. 9224	. 8665	. 2091	. 8025	. 2834	. 7518	. 3121
2. 0	1. 0995	. 9034	. 1613	. 8540	. 2315	. 8095	. 2647
2. 2	1. 2832	. 9315	. 1215	. 8953	. 1825	. 8576	. 2170
2. 4	1. 4717	. 9525	. 0894	. 9273	. 1385	. 8964	. 1718
2. 6	1. 6638	. 9677	. 0642	. 9511	. 1013	. 9267	. 1315
2. 8	1. 8585	. 9786	. 0450	. 9683	. 0712	. 9494	. 0973
3. 0	2. 0550	. 9861	. 0308	. 9801	. 0481	. 9660	. 0698
3. 2	2. 2527	. 9911	. 0206	. 9879	. 0313	. 9778	. 0485
3. 4	2. 4513	. 9945	. 0134	. 9930	. 0196	. 9858	. 0327
3. 6	2. 6505	. 9967	. 0085	. 9960	. 0117	. 9911	. 0214
3. 8	2. 8499	. 9980	. 0053	. 9978	. 0068	. 9946	. 0137
4. 0	3. 0496	. 9989	. 0032	. 9989	. 0038	. 9968	. 0085
4. 2	3. 2495	. 9994	. 0019	. 9994	. 0020	. 9981	. 0052
4. 4	3. 4494	. 9996	. 0011	. 9997	. 0010	. 9989	. 0031
4. 6	3. 6493	. 9998	. 0006	. 9999	. 0005	. 9994	. 0018
4. 8	3. 8493	. 9999	. 0003	. 9999	. 0002	. 9997	. 0010
5. 0	4. 0493	. 9999	. 0002	1. 0000	. 0001	. 9998	. 0006
5. 2	4. 2493	1. 0000	. 0001	1. 0000	. 0000	. 9999	. 0003
5. 4	4. 4493	1. 0000	. 0000	1. 0000	. 0000	1. 0000	. 0002
5. 6	4. 6493	1. 0000	. 0000	1. 0000	. 0000	1. 0000	. 0001
5. 8	4. 8493	1. 0000	. 0000	1. 0000	. 0000	1. 0000	. 0000
6. 0	5. 0493	1. 0000	. 0000	1. 0000	. 0000	1. 0000	. 0000

TABLE II.—Continued. STAGNATION-LINE SOLUTIONS FOR YAWED INFINITE CYLINDER WITH PRANDTL NUMBER OF 0.7

$\frac{t_w}{t_0}=0$; $\frac{t_0}{t_{N_0}}=3.0$

η	f	f'	f''	g	g'	θ	θ'
0	0. 0000	0. 0000	0. 8617	0. 0000	0. 5444	0. 0000	0. 4262
. 2	. 0172	. 1707	. 8382	. 1088	. 5438	. 0876	. 4495
. 4	. 0677	. 3327	. 7761	. 2173	. 5395	. 1796	. 4702
. 6	. 1492	. 4794	. 6876	. 3242	. 5282	. 2753	. 4847
. 8	. 2582	. 6068	. 5844	. 4279	. 5073	. 3728	. 4892
1. 0	. 3905	. 7129	. 4768	. 5264	. 4756	. 4701	. 4806
1. 2	. 5419	. 7978	. 3733	. 6174	. 4334	. 5641	. 4570
1. 4	. 7083	. 8629	. 2803	. 6992	. 3825	. 6519	. 4186
1. 6	. 8860	. 9108	. 2015	. 7701	. 3262	. 7307	. 3683
1. 8	1. 0717	. 9445	. 1385	. 8295	. 2682	. 7987	. 3104
2. 0	1. 2630	. 9672	. 0907	. 8775	. 2124	. 8547	. 2503
2. 2	1. 4581	. 9817	. 0565	. 9148	. 1618	. 8990	. 1929
2. 4	1. 6554	. 9905	. 0332	. 9427	. 1185	. 9323	. 1422
2. 6	1. 8540	. 9956	. 0183	. 9628	. 0835	. 9564	. 1001
2. 8	2. 0534	. 9982	. 0093	. 9767	. 0565	. 9730	. 0674
3. 0	2. 2532	. 9995	. 0042	. 9859	. 0367	. 9840	. 0434
3. 2	2. 4532	1. 0001	. 0015	. 9917	. 0229	. 9909	. 0267
3. 4	2. 6533	1. 0002	. 0003	. 9953	. 0138	. 9950	. 0157
3. 6	2. 8533	1. 0003	−. 0002	. 9975	. 0079	. 9974	. 0088
3. 8	3. 0534	1. 0002	−. 0003	. 9987	. 0044	. 9987	. 0047
4. 0	3. 2534	1. 0001	−. 0003	. 9993	. 0023	. 9994	. 0024
4. 2	3. 4534	1. 0001	−. 0002	. 9997	. 0012	. 9997	. 0011
4. 4	3. 6534	1. 0000	−. 0001	. 9998	. 0006	. 9999	. 0005
4. 6	3. 8534	1. 0000	−. 0001	. 9999	. 0003	1. 0000	. 0002
4. 8	4. 0534	1. 0000	. 0000	1. 0000	. 0001	1. 0000	. 0001
5. 0	4. 2534	1. 0000	. 0000	1. 0000	. 0001	1. 0000	. 0000
5. 2	4. 4534	1. 0000	. 0000	1. 0000	. 0000	1. 0000	. 0000
5. 4	4. 6534	1. 0000	. 0000	1. 0000	. 0000	1. 0000	. 0000
5. 6	4. 8534	1. 0000	. 0000	1. 0000	. 0000	1. 0000	. 0000
5. 8	5. 0534	1. 0000	. 0000	1. 0000	. 0000	1. 0000	. 0000
6. 0	5. 2534	1. 0000	. 0000	1. 0000	. 0000	1. 0000	. 0000

$\frac{t_w}{t_0}=0$; $\frac{t_0}{t_{N_0}}=6.5$

η	f	f'	f''	g	g'	θ	θ'
0	0. 0000	0. 0000	1. 2526	0. 0000	0. 6041	0. 0000	0. 4582
. 2	. 0249	. 2468	1. 1988	. 1208	. 6031	. 0953	. 4946
. 4	. 0974	. 4739	1. 0608	. 2408	. 5962	. 1975	. 5264
. 6	. 2122	. 6678	. 8723	. 3585	. 5784	. 3052	. 5473
. 8	. 3619	. 8215	. 6642	. 4713	. 5464	. 4153	. 5509
1. 0	. 5381	. 9339	. 4625	. 5761	. 4996	. 5240	. 5322
1. 2	. 7329	1. 0082	. 2864	. 6702	. 4401	. 6266	. 4903
1. 4	. 9393	1. 0508	. 1467	. 7516	. 3724	. 7188	. 4289
1. 6	1. 1517	1. 0695	. 0468	. 8190	. 3021	. 7974	. 3552
1. 8	1. 3661	1. 0720	−. 0164	. 8726	. 2349	. 8607	. 2780
2. 0	1. 5799	1. 0649	−. 0497	. 9135	. 1749	. 9089	. 2056
2. 2	1. 7918	1. 0535	−. 0615	. 9433	. 1249	. 9436	. 1434
2. 4	2. 0012	1. 0412	−. 0599	. 9641	. 0855	. 9671	. 0943
2. 6	2. 2083	1. 0300	−. 0513	. 9781	. 0561	. 9822	. 0583
2. 8	2. 4133	1. 0208	−. 0403	. 9871	. 0353	. 9912	. 0336
3. 0	2. 6168	1. 0138	−. 0296	. 9927	. 0214	. 9962	. 0179
3. 2	2. 8190	1. 0088	−. 0206	. 9960	. 0124	. 9988	. 0085
3. 4	3. 0204	1. 0054	−. 0136	. 9979	. 0069	. 9999	. 0035
3. 6	3. 2212	1. 0032	−. 0087	. 9989	. 0037	1. 0003	. 0009
3. 8	3. 4217	1. 0019	−. 0053	. 9995	. 0019	1. 0004	−. 0001
4. 0	3. 6220	1. 0010	−. 0031	. 9997	. 0009	1. 0003	−. 0004
4. 2	3. 8222	1. 0006	−. 0018	. 9999	. 0004	1. 0002	−. 0004
4. 4	4. 0223	1. 0003	−. 0010	. 9999	. 0002	1. 0001	−. 0003
4. 6	4. 2223	1. 0001	−. 0005	1. 0000	. 0001	1. 0001	−. 0002
4. 8	4. 4223	1. 0001	−. 0003	1. 0000	. 0000	1. 0000	−. 0001
5. 0	4. 6223	1. 0000	−. 0001	1. 0000	. 0000	1. 0000	−. 0001
5. 2	4. 8223	1. 0000	−. 0001	1. 0000	. 0000	1. 0000	. 0000
5. 4	5. 0223	1. 0000	. 0000	1. 0000	. 0000	1. 0000	. 0000
5. 6	5. 2224	1. 0000	. 0000	1. 0000	. 0000	1. 0000	. 0000
5. 8	5. 4224	1. 0000	. 0000	1. 0000	. 0000	1. 0000	. 0000
6. 0	5. 6224	1. 0000	. 0000	1. 0000	. 0000	1. 0000	. 0000

TABLE II.—Continued. STAGNATION-LINE SOLUTIONS FOR YAWED INFINITE CYLINDER WITH PRANDTL NUMBER OF 0.7

$\frac{t_w}{t_0}=0.5$; $\frac{t_0}{t_{N_0}}=1.0$

η	f	f'	f''	g	g'	θ	θ'
0	0. 0000	0. 0000	0. 9362	0. 0000	0. 5382	0. 0000	0. 4696
. 2	. 0180	. 1770	. 8326	. 1076	. 5375	. 0939	. 4692
. 4	. 0694	. 3328	. 7258	. 2148	. 5331	. 1875	. 4665
. 6	. 1498	. 4674	. 6207	. 3204	. 5218	. 2802	. 4596
. 8	. 2550	. 5815	. 5210	. 4229	. 5013	. 3710	. 4468
1. 0	. 3811	. 6763	. 4293	. 5202	. 4705	. 4585	. 4275
1. 2	. 5244	. 7538	. 3472	. 6104	. 4299	. 5415	. 4013
1. 4	. 6816	. 8159	. 2756	. 6916	. 3812	. 6186	. 3689
1. 6	. 8499	. 8648	. 2146	. 7625	. 3271	. 6887	. 3314
1. 8	1. 0268	. 9025	. 1639	. 8223	. 2712	. 7510	. 2906
2. 0	1. 2102	. 9310	. 1226	. 8711	. 2168	. 8049	. 2485
2. 2	1. 3987	. 9521	. 0899	. 9094	. 1670	. 8504	. 2071
2. 4	1. 5907	. 9674	. 0645	. 9384	. 1239	. 8879	. 1680
2. 6	1. 7853	. 9783	. 0452	. 9595	. 0884	. 9179	. 1326
2. 8	1. 9818	. 9858	. 0310	. 9742	. 0607	. 9412	. 1019
3. 0	2. 1795	. 9909	. 0208	. 9842	. 0400	. 9589	. 0761
3. 2	2. 3780	. 9943	. 0136	. 9906	. 0254	. 9720	. 0553
3. 4	2. 5772	. 9965	. 0087	. 9946	. 0155	. 9814	. 0391
3. 6	2. 7766	. 9979	. 0054	. 9970	. 0091	. 9879	. 0269
3. 8	2. 9763	. 9988	. 0033	. 9984	. 0051	. 9924	. 0180
4. 0	3. 1761	. 9993	. 0020	. 9992	. 0028	. 9953	. 0117
4. 2	3. 3760	. 9996	. 0011	. 9996	. 0014	. 9972	. 0074
4. 4	3. 5760	. 9998	. 0006	. 9998	. 0007	. 9983	. 0045
4. 6	3. 7759	. 9999	. 0003	. 9999	. 0003	. 9991	. 0027
4. 8	3. 9759	. 9999	. 0002	1. 0000	. 0002	. 9995	. 0016
5. 0	4. 1759	1. 0000	. 0001	1. 0000	. 0001	. 9997	. 0009
5. 2	4. 3759	1. 0000	. 0000	1. 0000	. 0000	. 9999	. 0005
5. 4	4. 5759	1. 0000	. 0000	1. 0000	. 0000	. 9999	. 0003
5. 6	4. 7759	1. 0000	. 0000	1. 0000	. 0000	1. 0000	. 0001
5. 8	4. 9759	1. 0000	. 0000	1. 0000	. 0000	1. 0000	. 0001
6. 0	5. 1759	1. 0000	. 0000	1. 0000	. 0000	1. 0000	. 0000

$\frac{t_w}{t_0}=0.5$; $\frac{t_0}{t_{N_0}}=1.6$

η	f	f'	f''	g	g'	θ	θ'
0	0. 0000	0. 0000	1. 1824	0. 0000	0. 5692	0. 0000	0. 4386
. 2	. 0226	. 2201	1. 0175	. 1138	. 5683	. 0906	. 4672
. 4	. 0858	. 4068	. 8502	. 2270	. 5625	. 1866	. 4922
. 6	. 1831	. 5606	. 6898	. 3382	. 5479	. 2869	. 5088
. 8	. 3080	. 6836	. 5429	. 4454	. 5218	. 3893	. 5125
1. 0	. 4547	. 7790	. 4140	. 5461	. 4837	. 4908	. 4999
1. 2	. 6181	. 8506	. 3053	. 6381	. 4346	. 5881	. 4694
1. 4	. 7937	. 9025	. 2173	. 7194	. 3774	. 6775	. 4228
1. 6	. 9780	. 9388	. 1490	. 7888	. 3162	. 7564	. 3641
1. 8	1. 1684	. 9632	. 0981	. 8459	. 2551	. 8227	. 2993
2. 0	1. 3628	. 9790	. 0618	. 8911	. 1981	. 8761	. 2345
2. 2	1. 5596	. 9887	. 0371	. 9256	. 1479	. 9169	. 1750
2. 4	1. 7580	. 9944	. 0210	. 9509	. 1061	. 9467	. 1244
2. 6	1. 9572	. 9975	. 0111	. 9686	. 0732	. 9673	. 0841
2. 8	2. 1569	. 9991	. 0054	. 9807	. 0485	. 9810	. 0540
3. 0	2. 3568	. 9999	. 0023	. 9885	. 0309	. 9895	. 0329
3. 2	2. 5568	1. 0001	. 0007	. 9934	. 0189	. 9946	. 0189
3. 4	2. 7569	1. 0002	. 0000	. 9964	. 0111	. 9975	. 0102
3. 6	2. 9569	1. 0002	−. 0002	. 9981	. 0063	. 9989	. 0051
3. 8	3. 1569	1. 0002	−. 0002	. 9990	. 0034	. 9996	. 0023
4. 0	3. 3570	1. 0001	−. 0002	. 9995	. 0018	. 9999	. 0009
4. 2	3. 5570	1. 0001	−. 0001	. 9998	. 0009	1. 0000	. 0002
4. 4	3. 7570	1. 0001	−. 0001	. 9999	. 0004	1. 0001	. 0000
4. 6	3. 9570	1. 0001	. 0000	. 9999	. 0002	1. 0001	−. 0001
4. 8	4. 1570	1. 0001	. 0000	1. 0000	. 0001	1. 0000	−. 0001
5. 0	4. 3570	1. 0001	. 0000	1. 0000	. 0000	1. 0000	−. 0001
5. 2	4. 5571	1. 0001	. 0000	1. 0000	. 0000	1. 0000	. 0000
5. 4	4. 7571	1. 0001	. 0000	1. 0000	. 0000	1. 0000	. 0000
5. 6	4. 9571	1. 0001	. 0000	1. 0000	. 0000	1. 0000	. 0000
5. 8	5. 1571	1. 0001	. 0000	1. 0000	. 0000	1. 0000	. 0000
6. 0	5. 3571	1. 0001	. 0000	1. 0000	. 0000	1. 0000	. 0000

TABLE II.—Continued. STAGNATION-LINE SOLUTIONS FOR YAWED INFINITE CYLINDER WITH PRANDTL NUMBER OF 0.7

$\frac{t_w}{t_0}=0.5$; $\frac{t_0}{t_{N_0}}=3.0$

η	f	f'	f''	g	g'	θ	θ'
0	0. 0000	0. 0000	1. 7009	0. 0000	0. 6252	0. 0000	0. 4350
. 2	. 0320	. 3096	1. 3928	. 1250	. 6238	. 0932	. 4966
. 4	. 1197	. 5572	1. 0861	. 2490	. 6150	. 1982	. 5515
. 6	. 2509	. 7455	. 8016	. 3701	. 5930	. 3127	. 5898
. 8	. 4144	. 8803	. 5537	. 4851	. 5550	. 4324	. 6020
1. 0	. 6001	. 9699	. 3505	. 5901	. 5017	. 5513	. 5817
1. 2	. 8000	1. 0236	. 1946	. 6850	. 4362	. 6629	. 5291
1. 4	1. 0078	1. 0507	. 0836	. 7651	. 3641	. 7612	. 4509
1. 6	1. 2191	1. 0597	. 0117	. 8306	. 2914	. 8423	. 3587
1. 8	1. 4309	1. 0575	−. 0292	. 8820	. 2236	. 9046	. 2653
2. 0	1. 6417	1. 0495	−. 0475	. 9206	. 1644	. 9490	. 1811
2. 2	1. 8506	1. 0394	−. 0511	. 9484	. 1160	. 9781	. 1126
2. 4	2. 0575	1. 0295	−. 0465	. 9677	. 0785	. 9953	. 0620
2. 6	2. 2625	1. 0210	−. 0381	. 9805	. 0509	1. 0040	. 0281
2. 8	2. 4660	1. 0143	−. 0290	. 9886	. 0318	1. 0074	. 0077
3. 0	2. 6684	1. 0094	−. 0208	. 9936	. 0190	1. 0077	−. 0029
3. 2	2. 8699	1. 0059	−. 0142	. 9965	. 0109	1. 0066	−. 0072
3. 4	3. 0708	1. 0036	−. 0092	. 9982	. 0060	1. 0051	−. 0078
3. 6	3. 2714	1. 0021	−. 0058	. 9991	. 0032	1. 0036	−. 0068
3. 8	3. 4717	1. 0012	−. 0035	. 9996	. 0016	1. 0024	−. 0052
4. 0	3. 6719	1. 0007	−. 0020	. 9998	. 0008	1. 0015	−. 0037
4. 2	3. 8720	1. 0004	−. 0011	. 9999	. 0004	1. 0009	−. 0024
4. 4	4. 0720	1. 0002	−. 0006	1. 0000	. 0002	1. 0005	−. 0015
4. 6	4. 2721	1. 0001	−. 0003	1. 0000	. 0001	1. 0003	−. 0009
4. 8	4. 4721	1. 0001	−. 0002	1. 0000	. 0000	1. 0002	−. 0005
5. 0	4. 6721	1. 0000	−. 0001	1. 0000	. 0000	1. 0001	−. 0003
5. 2	4. 8721	1. 0000	. 0000	1. 0000	. 0000	1. 0000	−. 0001
5. 4	5. 0721	1. 0000	. 0000	1. 0000	. 0000	1. 0000	−. 0001
5. 6	5. 2721	1. 0000	. 0000	1. 0000	. 0000	1. 0000	. 0000
5. 8	5. 4721	1. 0000	. 0000	1. 0000	. 0000	1. 0000	. 0000
6. 0	5. 6721	1. 0000	. 0000	1. 0000	. 0000	1. 0000	. 0000

$\frac{t_w}{t_0}=0.5$; $\frac{t_0}{t_{N_0}}=6.5$

η	f	f'	f''	g	g'	θ	θ'
0	0. 0000	0. 0000	2. 8164	0. 0000	0. 7200	0. 0000	0. 4717
. 2	. 0520	. 4970	2. 1505	. 1439	. 7175	. 1048	. 5752
. 4	. 1900	. 8615	1. 5030	. 2860	. 7012	. 2291	. 6639
. 6	. 3884	1. 1032	. 9307	. 4228	. 6623	. 3679	. 7167
. 8	. 6244	1. 2410	. 4683	. 5493	. 5988	. 5121	. 7155
1. 0	. 8796	1. 2987	. 1294	. 6610	. 5153	. 6501	. 6550
1. 2	1. 1403	1. 3006	−. 0904	. 7547	. 4210	. 7709	. 5468
1. 4	1. 3977	1. 2691	−. 2091	. 8294	. 3266	. 8672	. 4140
1. 6	1. 6469	1. 2220	−. 2519	. 8859	. 2409	. 9366	. 2820
1. 8	1. 8863	1. 1716	−. 2449	. 9267	. 1692	. 9813	. 1695
2. 0	2. 1159	1. 1257	−. 2110	. 9546	. 1134	1. 0063	. 0855
2. 2	2. 3371	1. 0878	−. 1671	. 9730	. 0726	1. 0174	. 0302
2. 4	2. 5516	1. 0588	−. 1239	. 9845	. 0446	1. 0199	−. 0013
2. 6	2. 7612	1. 0378	−. 0869	. 9914	. 0262	1. 0180	−. 0158
2. 8	2. 9672	1. 0235	−. 0581	. 9954	. 0148	1. 0143	−. 0198
3. 0	3. 1709	1. 0141	−. 0372	. 9977	. 0080	1. 0104	−. 0183
3. 2	3. 3731	1. 0082	−. 0229	. 9988	. 0042	1. 0071	−. 0146
3. 4	3. 5743	1. 0046	−. 0136	. 9994	. 0021	1. 0046	−. 0106
3. 6	3. 7750	1. 0025	−. 0078	. 9997	. 0010	1. 0028	−. 0072
3. 8	3. 9754	1. 0013	−. 0043	. 9999	. 0005	1. 0017	−. 0046
4. 0	4. 1756	1. 0007	−. 0023	. 9999	. 0002	1. 0009	−. 0028
4. 2	4. 3757	1. 0004	−. 0012	1. 0000	. 0001	1. 0005	−. 0016
4. 4	4. 5757	1. 0002	−. 0006	1. 0000	. 0000	1. 0003	−. 0009
4. 6	4. 7757	1. 0001	−. 0003	1. 0000	. 0000	1. 0001	−. 0005
4. 8	4. 9758	1. 0000	−. 0001	1. 0000	. 0000	1. 0001	−. 0002
5. 0	5. 1758	1. 0000	−. 0001	1. 0000	. 0000	1. 0000	−. 0001
5. 2	5. 3758	1. 0000	. 0000	1. 0000	. 0000	1. 0000	−. 0001
5. 4	5. 5758	1. 0000	. 0000	1. 0000	. 0000	1. 0000	. 0000
5. 6	5. 7758	1. 0000	. 0000	1. 0000	. 0000	1. 0000	. 0000
5. 8	5. 9758	1. 0000	. 0000	1. 0000	. 0000	1. 0000	. 0000
6. 0	6. 1758	1. 0000	. 0000	1. 0000	. 0000	1. 0000	. 0000

TABLE II.—Continued. STAGNATION-LINE SOLUTIONS FOR YAWED INFINITE CYLINDER WITH PRANDTL NUMBER OF 0.7

Insulated surface; $\frac{t_{aw}}{t_0}=1.0$, $\frac{t_0}{t_{N_0}}=1.0$, $\zeta_w=0.8485$

η	f	f'	f''	g	g'	θ	θ'
0	0. 0000	0. 0000	1. 2326	0. 0000	0. 5705	0. 0000	0. 0000
. 2	. 0233	. 2266	1. 0344	. 1140	. 5696	. 0258	. 2571
. 4	. 0881	. 4144	. 8463	. 2275	. 5636	. 1022	. 5046
. 6	. 1867	. 5663	. 6752	. 3389	. 5486	. 2256	. 7213
. 8	. 3124	. 6859	. 5251	. 4462	. 5221	. 3869	. 8794
1. 0	. 4592	. 7778	. 3980	. 5469	. 4835	. 5718	. 9542
1. 2	. 6220	. 8466	. 2938	. 6388	. 4340	. 7621	. 9333
1. 4	. 7967	. 8968	. 2110	. 7200	. 3767	. 9390	. 8218
1. 6	. 9798	. 9323	. 1474	. 7892	. 3154	1. 0863	. 6424
1. 8	1. 1689	. 9568	. 1000	. 8462	. 2545	1. 1937	. 4290
2. 0	1. 3260	. 9732	. 0659	. 8913	. 1976	1. 2580	. 2172
2. 2	1. 5578	. 9838	. 0421	. 9257	. 1475	1. 2826	. 0359
2. 4	1. 7553	. 9905	. 0260	. 9509	. 1059	1. 2755	−. 0975
2. 6	1. 9538	. 9946	. 0156	. 9686	. 0731	1. 2470	−. 1788
2. 8	2. 1530	. 9970	. 0091	. 9807	. 0485	1. 2071	−. 2135
3. 0	2. 3526	. 9984	. 0051	. 9885	. 0309	1. 1640	−. 2128
3. 2	2. 5523	. 9992	. 0028	. 9934	. 0189	1. 1234	−. 1897
3. 4	2. 7522	. 9996	. 0014	. 9963	. 0111	1. 0887	−. 1559
3. 6	2. 9522	. 9998	. 0007	. 9980	. 0063	1. 0611	−. 1200
3. 8	3. 1521	. 9999	. 0004	. 9990	. 0034	1. 0405	−. 0873
4. 0	3. 3521	1. 0000	. 0002	. 9995	. 0018	1. 0258	−. 0604
4. 2	3. 5521	1. 0000	. 0001	. 9998	. 0009	1. 0159	−. 0400
4. 4	3. 7521	1. 0000	. 0000	. 9999	. 0004	1. 0094	−. 0254
4. 6	3. 9521	1. 0000	. 0000	. 9999	. 0002	1. 0054	−. 0155
4. 8	4. 1521	1. 0000	. 0000	1. 0000	. 0001	1. 0030	−. 0091
5. 0	4. 3521	1. 0000	. 0000	1. 0000	. 0000	1. 0016	−. 0052
5. 2	4. 5521	1. 0000	. 0000	1. 0000	. 0000	1. 0008	−. 0028
5. 4	4. 7521	1. 0000	. 0000	1. 0000	. 0000	1. 0004	−. 0015
5. 6	4. 9521	1. 0000	. 0000	1. 0000	. 0000	1. 0002	−. 0008
5. 8	5. 1521	1. 0000	. 0000	1. 0000	. 0000	1. 0001	−. 0004
6. 0	5. 3521	1. 0000	. 0000	1. 0000	. 0000	1. 0000	−. 0002

Insulated surface; $\frac{t_{aw}}{t_0}=0.9444$; $\frac{t_0}{t_{N_0}}=1.6$; $\zeta_w=0.8518$

η	f	f'	f''	g	g'	θ	θ'
0	0. 0000	0. 0000	1. 5724	0. 0000	0. 6067	0. 0000	0. 0000
. 2	. 0294	. 2844	1. 2736	. 1213	. 6055	. 0298	. 2971
. 4	. 1099	. 5107	. 9930	. 2418	. 5976	. 1180	. 5804
. 6	. 2302	. 6836	. 7429	. 3595	. 5780	. 2591	. 8200
. 8	. 3803	. 8103	. 5305	. 4720	. 5440	. 4406	. 9794
1. 0	. 5518	. 8985	. 3585	. 5762	. 4957	. 6435	1. 0302
1. 2	. 7377	. 9563	. 2259	. 6695	. 4358	. 8448	. 9646
1. 4	. 9328	. 9913	. 1292	. 7500	. 3688	1. 0227	. 7997
1. 6	1. 1331	1. 0100	. 0630	. 8169	. 3000	1. 1606	. 5728
1. 8	1. 3361	1. 0181	. 0211	. 8702	. 2344	1. 2506	. 3290
2. 0	1. 5400	1. 0197	−. 0027	. 9111	. 1758	1. 2938	. 1089
2. 2	1. 7438	1. 0178	−. 0142	. 9412	. 1266	1. 2975	−. 0612
2. 4	1. 9470	1. 0145	−. 0178	. 9624	. 0875	1. 2733	−. 1709
2. 6	2. 1496	1. 0110	−. 0170	. 9768	. 0581	1. 2329	−. 2241
2. 8	2. 3514	1. 0078	−. 0142	. 9862	. 0371	1. 1866	−. 2329
3. 0	2. 5527	1. 0053	−. 0109	. 9921	. 0227	1. 1416	−. 2126
3. 2	2. 7536	1. 0035	−. 0078	. 9956	. 0134	1. 1024	−. 1773
3. 4	2. 9542	1. 0022	−. 0053	. 9977	. 0076	1. 0709	−. 1377
3. 6	3. 1545	1. 0013	−. 0034	. 9988	. 0041	1. 0471	−. 1009
3. 8	3. 3547	1. 0008	−. 0021	. 9994	. 0021	1. 0301	−. 0702
4. 0	3. 5548	1. 0004	−. 0013	. 9997	. 0011	1. 0186	−. 0466
4. 2	3. 7549	1. 0002	−. 0007	. 9999	. 0005	1. 0111	−. 0296
4. 4	3. 9549	1. 0001	−. 0004	. 9999	. 0002	1. 0064	−. 0181
4. 6	4. 1550	1. 0001	−. 0002	1. 0000	. 0001	1. 0035	−. 0107
4. 8	4. 3550	1. 0000	−. 0001	1. 0000	. 0000	1. 0019	−. 0061
5. 0	4. 5550	1. 0000	. 0000	1. 0000	. 0000	1. 0010	−. 0033
5. 2	4. 7550	1. 0000	. 0000	1. 0000	. 0000	1. 0005	−. 0018
5. 4	4. 9550	1. 0000	. 0000	1. 0000	. 0000	1. 0002	−. 0009
5. 6	5. 1550	1. 0000	. 0000	1. 0000	. 0000	1. 0001	−. 0005
5. 8	5. 3550	1. 0000	. 0000	1. 0000	. 0000	1. 0000	−. 0002
6. 0	5. 5550	1. 0000	. 0000	1. 0000	. 0000	1. 0000	−. 0001

TABLE II.—Concluded. STAGNATION-LINE SOLUTIONS FOR YAWED INFINITE CYLINDER WITH PRANDTL NUMBER OF 0.7

Insulated surface; $\frac{t_{aw}}{t_0}=0.9045$; $\frac{t_0}{t_{N_0}}=3.0$; $\zeta_w=0.8567$

η	f	f'	f''	g	g'	θ	θ'
0	0. 0000	0. 0000	2. 2902	0. 0000	0. 6716	0. 0000	0. 0000
. 2	. 0422	. 4042	1. 7554	. 1342	. 6696	. 0377	. 3758
. 4	. 1548	. 7049	1. 2622	. 2671	. 6572	. 1488	. 7269
. 6	. 3181	. 9136	. 8375	. 3959	. 6273	. 3235	1. 0028
. 8	. 5152	1. 0454	. 4952	. 5167	. 5774	. 5411	1. 1487
1. 0	. 7323	1. 1174	. 2384	. 6257	. 5098	. 7721	1. 1345
1. 2	. 9593	1. 1460	. 0612	. 7199	. 4305	. 9849	. 9710
1. 4	1. 1889	1. 1463	−. 0479	. 7976	. 3473	1. 1538	. 7070
1. 6	1. 4168	1. 1304	−. 1041	. 8590	. 2676	1. 2654	. 4087
1. 8	1. 6406	1. 1071	−. 1228	. 9053	. 1971	1. 3190	. 1365
2. 0	1. 8596	1. 0827	−. 1182	. 9387	. 1389	1. 3243	−. 0707
2. 2	2. 0738	1. 0607	−. 1013	. 9617	. 0937	1. 2960	−. 1998
2. 4	2. 2841	1. 0425	−. 0801	. 9770	. 0606	1. 2491	−. 2576
2. 6	2. 4911	1. 0285	−. 0595	. 9867	. 0376	1. 1964	−. 2620
2. 8	2. 6958	1. 0185	−. 0419	. 9925	. 0224	1. 1464	−. 2336
3. 0	2. 8987	1. 0115	−. 0281	. 9960	. 0128	1. 1038	−. 1901
3. 2	3. 1005	1. 0070	−. 0181	. 9979	. 0070	1. 0704	−. 1441
3. 4	3. 3016	1. 0041	−. 0112	. 9990	. 0037	1. 0458	−. 1029
3. 6	3. 5022	1. 0023	−. 0067	. 9995	. 0019	1. 0287	−. 0698
3. 8	3. 7026	1. 0013	−. 0039	. 9998	. 0009	1. 0173	−. 0453
4. 0	3. 9028	1. 0007	−. 0021	. 9999	. 0004	1. 0101	−. 0281
4. 2	4. 1029	1. 0004	−. 0012	. 9999	. 0002	1. 0057	−. 0168
4. 4	4. 3030	1. 0002	−. 0006	1. 0000	. 0001	1. 0031	−. 0097
4. 6	4. 5030	1. 0001	−. 0003	1. 0000	. 0000	1. 0016	−. 0054
4. 8	4. 7030	1. 0001	−. 0001	1. 0000	. 0000	1. 0008	−. 0029
5. 0	4. 9030	1. 0001	−. 0001	1. 0000	. 0000	1. 0004	−. 0015
5. 2	5. 1030	1. 0001	. 0000	1. 0000	. 0000	1. 0002	−. 0007
5. 4	5. 3030	1. 0001	. 0000	1. 0000	. 0000	1. 0001	−. 0004
5. 6	5. 5031	1. 0001	. 0000	1. 0000	. 0000	1. 0000	−. 0002
5. 8	5. 7031	1. 0001	. 0000	1. 0000	. 0000	1. 0000	−. 0001
6. 0	5. 9031	1. 0001	. 0000	1. 0000	. 0000	1. 0000	. 0000

Insulated surface; $\frac{t_{aw}}{t_0}=0.8838$; $\frac{t_0}{t_{N_0}}=6.5$; $\zeta_w=0.8627$

η	f	f'	f''	g	g'	θ	θ'
0	0. 0000	0. 0000	3. 8392	0. 0000	0. 7797	0. 0000	0. 0000
. 2	. 0692	. 6541	2. 7135	. 1557	. 7760	. 0530	. 5270
. 4	. 2474	1. 0934	1. 7066	. 3091	. 7530	. 2073	. 9987
. 6	. 4945	1. 3493	. 8885	. 4549	. 6998	. 4419	1. 3117
. 8	. 7778	1. 4631	. 2863	. 5869	. 6164	. 7154	1. 3802
1. 0	1. 0732	1. 4776	−. 1068	. 7000	. 5123	. 9769	1. 1976
1. 2	1. 3649	1. 4320	−. 3220	. 7914	. 4014	1. 1829	. 8438
1. 4	1. 6442	1. 3576	−. 4032	. 8610	. 2970	1. 3111	. 4394
1. 6	1. 9076	1. 2764	−. 3968	. 9112	. 2082	1. 3623	. 0882
1. 8	2. 1553	1. 2019	−. 3428	. 9456	. 1386	1. 3536	−. 1548
2. 0	2. 3893	1. 1404	−. 2709	. 9679	. 0880	1. 3080	−. 2825
2. 2	2. 6124	1. 0934	−. 1999	. 9818	. 0534	1. 2466	−. 3181
2. 4	2. 8275	1. 0597	−. 1393	. 9901	. 0310	1. 1845	−. 2949
2. 6	3. 0370	1. 0367	−. 0924	. 9948	. 0173	1. 1304	−. 2430
2. 8	3. 2428	1. 0218	−. 0587	. 9974	. 0092	1. 0877	−. 1840
3. 0	3. 4461	1. 0126	−. 0358	. 9987	. 0047	1. 0564	−. 1304
3. 2	3. 6480	1. 0070	−. 0210	. 9994	. 0023	1. 0348	−. 0873
3. 4	3. 8491	1. 0038	−. 0119	. 9997	. 0011	1. 0207	−. 0557
3. 6	4. 0496	1. 0020	−. 0065	. 9999	. 0005	1. 0118	−. 0340
3. 8	4. 2499	1. 0010	−. 0035	. 9999	. 0002	1. 0065	−. 0199
4. 0	4. 4501	1. 0005	−. 0018	1. 0000	. 0001	1. 0035	−. 0112
4. 2	4. 6501	1. 0003	−. 0009	1. 0000	. 0000	1. 0018	−. 0061
4. 4	4. 8502	1. 0001	−. 0004	1. 0000	. 0000	1. 0009	−. 0032
4. 6	5. 0502	1. 0001	−. 0002	1. 0000	. 0000	1. 0004	−. 0016
4. 8	5. 2502	1. 0000	−. 0001	1. 0000	. 0000	1. 0002	−. 0008
5. 0	5. 4502	1. 0000	. 0000	1. 0000	. 0000	1. 0001	−. 0004
5. 2	5. 6502	1. 0000	. 0000	1. 0000	. 0000	1. 0000	−. 0002
5. 4	5. 8502	1. 0000	. 0000	1. 0000	. 0000	1. 0000	−. 0001
5. 6	6. 0502	1. 0000	. 0000	1. 0000	. 0000	1. 0000	. 0000
5. 8	6. 2502	1. 0000	. 0000	1. 0000	. 0000	1. 0000	. 0000
6. 0	6. 4502	1. 0000	. 0000	1. 0000	. 0000	1. 0000	. 0000

TABLE III.—SUMMARY OF HEAT-TRANSFER AND SKIN-FRICTION PARAMETERS FOR YAWED STAGNATION LINE

(a) Prandtl number, 1

$\frac{t_w}{t_0}$	$\frac{t_0}{t_{N_0}}$	f''_w	θ'_w or g'_w	$\frac{f''_w}{\theta'_w}$
0	1.0	0.6489	0.5067	1.2807
	1.2	.6823	.5130	1.3300
	1.6	.7475	.5249	1.4241
	2.0	.8105	.5358	1.5127
	2.2	.8413	.5410	1.5551
	3.0	.9607	.5603	1.7146
	4.0	1.1025	.5815	1.8960
	6.0	1.3679	.6174	2.2156
	6.5	1.4313	.6254	2.2886
0.25	1.2	0.8673	0.5344	1.6229
	1.6	.9850	.5507	1.7886
	2.2	1.1530	.5724	2.0143
	3.0	1.3644	.5976	2.2831
0.50	1.2	1.0409	0.5530	1.8823
	1.6	1.2062	.5728	2.1058
	2.2	1.4406	.5986	2.4066
	3.0	1.7341	.6280	2.7613
	4.0	2.0785	.6593	3.1526
	6.5	2.8663	.7213	3.9738
0.75	1.2	1.2059	0.5695	2.1175
	1.6	1.4153	.5921	2.3903
	2.2	1.7110	.6212	2.7543
	3.0	2.0802	.6541	3.1802
1.00	1.0	1.2326	0.5704	2.1610
	1.1	1.2989	.5776	2.2488
	1.2	1.3640	.5845	2.3336
	1.5	1.5535	.6035	2.5742
	1.6	1.6149	.6094	2.6500
	2.0	1.8532	.6313	2.9355
	2.2	1.9684	.6413	3.0694
	3.0	2.4086	.6770	3.5578
	4.0	2.9230	.7143	4.0921
	6.0	3.8711	.7742	5.0001
	6.5	4.0951	.7871	5.2028
	11.0	5.9630	.8808	6.7700
1.50	1.2	1.6641	0.6109	2.7240
	1.6	1.9924	.6397	3.1146
	2.2	2.4534	.6761	3.6288
	3.0	3.0259	.7163	4.2243
2.00	1.0	1.7368	0.6154	2.8223
	2.0	2.7262	.6931	3.9334
	6.0	5.9032	.8666	6.8119

TABLE III.—Continued. SUMMARY OF HEAT-TRANSFER AND SKIN-FRICTION PARAMETERS FOR YAWED STAGNATION LINE

(b) Prandtl number, 0.7

$\frac{t_w}{t_0}$	$\frac{t_0}{t_{N_0}}$	f''_w	g'_w	θ'_w	$\frac{f''_w}{g'_w}$	$\left(\frac{t_w-t_0}{t_w-t_{aw}}\right)\theta'_w$
0.0000	1.0	0.6071	0.4970	0.4362	1.2216	0.4362
	1.6	.6870	.5129	.4226	1.3395	.4475
	3.0	.8617	.5444	.4262	1.5827	.4712
	6.5	1.2526	.6041	.4582	2.0734	.5184
0.5	1.0	0.9362	0.5382	0.4696	1.7395	0.4696
	1.6	1.1824	.5692	.4386	2.0773	.4935
	3.0	1.7009	.6252	.4350	2.7206	.5377
	6.5	2.8164	.7200	.4717	3.9117	.6145
1.0	1.0	1.2326	0.5705	0.0000	2.1606	
.9444	1.6	1.5724	.6067	.0000	2.5917	
.9045	3.0	2.2902	.6716	.0000	3.4101	
.8838	6.5	3.8392	.7797	.0000	4.9239	

TABLE IV.—LOCAL RECOVERY FACTORS FOR YAWED STAGNATION LINE

Yaw parameter, $\frac{t_0}{t_{N_0}}$	Local recovery factor, ξ_w			
	Prandtl number			
	0.7	0.8	0.9	1.0
1.0	0.8485	0.903	0.953	1.000
1.6	.8518	------	------	1.000
3.0	.8567	------	------	1.000
6.5	.8627	------	------	1.000

REPORT 1380

AN ANALYSIS OF PRESSURE STUDIES AND EXPERIMENTAL AND THEORETICAL DOWNWASH AND SIDEWASH BEHIND FIVE POINTED-TIP WINGS AT SUPERSONIC SPEEDS [1]

By William B. Boatright

SUMMARY

Flow-angle and pressure surveys behind five, thin, pointed-tip wings of varying plan form have been made at Mach numbers 1.62 and 2.41. Schlieren studies at a Mach number 1.93 for the same five plan-form wings were made to illustrate the behavior of the vortex sheet. The surveys were conducted at 1.5, 3, and 4 root chords behind three triangular wings of 50°, 63°, and 72° leading-edge sweep angle, and behind the 50° triangular wing reversed. The flow behind a pointed-tip wing having a sweptback leading edge and a sweptforward trailing edge (both 50°) was also surveyed.

In the analysis of the data, especial attention was focused on the validity of the various theoretical methods for predicting the flow at wing angles of attack sufficiently high for the behavior of the vortex sheet to become important.

For the low-aspect-ratio triangular wings (where the Mach number component normal to the leading edge is subsonic), the vortex sheet rolls up rapidly into a single concentrated region of vorticity and the theoretical model of the flow was assumed as a single bent line vortex for comparing the theoretical prediction with experiment at moderately high angles of attack (9° to 17°). An adjustment to the method for determining the vertical location at stations behind the wing is suggested.

For the high-aspect-ratio triangular wings (where the Mach number component normal to the leading edge is supersonic), the more complex nature of the vortex sheet is illustrated, and for the triangular wing with 50° leading-edge sweep angle, various theoretical methods for predicting the flow field are compared with experiment.

Experiment and one of the theoretical methods are compared for the reversed triangular wing and the pointed-tip wing with the 50° sweptback leading edge and sweptforward trailing edge.

INTRODUCTION

A knowledge of the flow fields behind wings at supersonic speeds is important in assessing the stability characteristics of aircraft and missiles. A general study of the complex nature of the problem and the relative significance of wing lift coefficient, aspect ratio, and distance behind the wing, on the nonlinearities involved in estimating the flow field characteristics, is treated theoretically in reference 1. Point measurements of the flow angle are reported in references 2 to 10 for wings of rectangular, triangular, trapezoidal, and sweptback plan forms at various supersonic Mach numbers, and studies of the flow fields behind wing-body combinations for both airplane and missile configurations are reported in references 11 to 14. It can be seen that these references include some downwash measurements at transonic and low supersonic speeds. Various theoretical estimates are being used to approximate the flow behind different wings, but as yet sufficient systematic tests are not available to assess completely their validity at various locations behind the wing or throughout the variations in plan form and lift coefficient that might exist. Data are being accumulated, however, particularly in the high-aspect-ratio case.

Although the scope of the present investigation includes only wing-alone tests, the flow field for this case becomes very complex at moderate and high angles of attack for different variations in plan form; and theoretical predictions of the flow field have met with little success, particularly for downstream locations inboard of the wing tips.

Most of the theoretical work on predicting the flow fields behind wings has been developed by using linear theory and assuming that the wing and vortex sheet behind the wing remain in one horizontal plane throughout the angle-of-attack range. (When such an assumption is used, agreement between theory and experiment can be expected only at low angles of attack.) Examples of theoretical methods of this type include the conical-flow technique of references 15 to 17, vortex and lifting-line methods of references 18 and 19, doublet method of reference 20, and a line-source method in reference 21. (This latter method uses a line source to build up solutions that are applied to a particular plan form in the same fashion as are those of the conical-flow technique.) When applying any of these methods to configurations at higher angle of attack, some success has been obtained by correcting for the deflection of the vortex sheet at successive spanwise stations to determine the actual location of a particular field point with respect to this vortex sheet (refs. 2 and 4). However, for those cases where the rolling up of the vortex sheet becomes more important (higher angles of attack, lower aspect ratio, or larger distances behind the wing), other theoretical treatments would appear to be better for predicting the downwash or

[1] Supersedes recently declassified NACA Research Memorandum L54B10 by William B. Boatright, 1954.

Preceding Page Blank

sidewash. Such theoretical methods assume either that the vortex sheet is completely rolled up and can be represented by a single line vortex, or else that the vortex sheet can be represented with a number of two-dimensional line vortices which are allowed to float and deform as is done in references 22 and 23.

The purpose of the present investigation is to supplement available experimental data on flow fields behind wings, as well as to furnish more quantitative information on the choice of the theoretical method for a given configuration and the accuracy to be expected when such a method is used. The experimental phase of the investigation consisted of downwash, sidewash, and total pressure measurements in planes normal to the free-stream direction at stations 1.5, 3, and 4 root chords behind the wing trailing edge. Three thin, triangular-plan-form wings, having leading edges swept back 50°, 63°, and 72°, were surveyed at free-stream Mach numbers 1.62 and 2.41. In addition surveys were conducted at a Mach number of 1.62 for the same stations behind the 50° sweptback triangular wing reversed (i.e., apex downstream), and a straight, 0-taper-ratio (diamond plan form) wing with 50° swept leading and trailing edges.

SYMBOLS

A	aspect ratio
$a=\tan \Lambda$	(appendix A)
b	variable denoting ratio of tangent of conical ray from apex of triangular wing to tangent of Mach angle (appendix A)
b'	wing semispan
C_L	lift coefficient
$c_{l,m}$	wing section lift coefficient at wing midspan
c_r	wing root chord
$E(t')$	complete elliptic integral of second kind of modulus t', where $t'=\sqrt{1-\beta^2 \cot^2 \Lambda}$
k	distance from origin to apex of two intersecting line vortices (appendix C)
M	free-stream Mach number
m	tangent of Mach angle (appendix A) or slope of line vortex (appendix C)
p_t	tunnel stagnation pressure
p_t'	measured total pressure
$p_{t,\infty}$	free-stream total pressure
p_w	pressure on wedge surface
R	Reynolds number (based on c_r)
r	radius of conical ray in polar coordinate system (appendix A), $\frac{\beta\sqrt{y^2+z^2}}{x}$; also, in appendix D, radius from line vortex
u	perturbation velocity in x-direction
u'	perturbation velocity in x-direction on triangular wing at plane of symmetry (appendix A)
u_0	perturbation velocity in x-direction on supersonic leading-edge triangular wing for region between leading edge and Mach line from apex (appendix A)
V	free-stream velocity
v	perturbation velocity in y-direction
w	perturbation velocity in z-direction
x	longitudinal coordinate parallel to free-stream direction, measured from wing trailing edge
x'	longitudinal coordinate measured from wing apex
y	horizontal coordinate, normal to free-stream direction
y_0	one-half of distance apart of streamwise legs of bent-line vortex model of flow (appendix C)
z	vertical coordinate, normal to free-stream direction
α	angle of attack, deg
β	$\sqrt{M^2-1}$
Γ	circulation
Γ_m	wing circulation at plane of symmetry
ϵ	downwash angle, deg
$\theta=\tan^{-1}\frac{z}{y}$	(appendix A)
Λ	sweepback of wing leading edge, deg
Λ_{TE}	sweep of wing trailing edge
σ	sidewash angle, deg
ϕ	angle in vertical plane between line vortex and free-stream direction, deg
Subscripts:	
B	body
W	wing
T	tail
TE	trailing edge
∞	free stream

APPARATUS

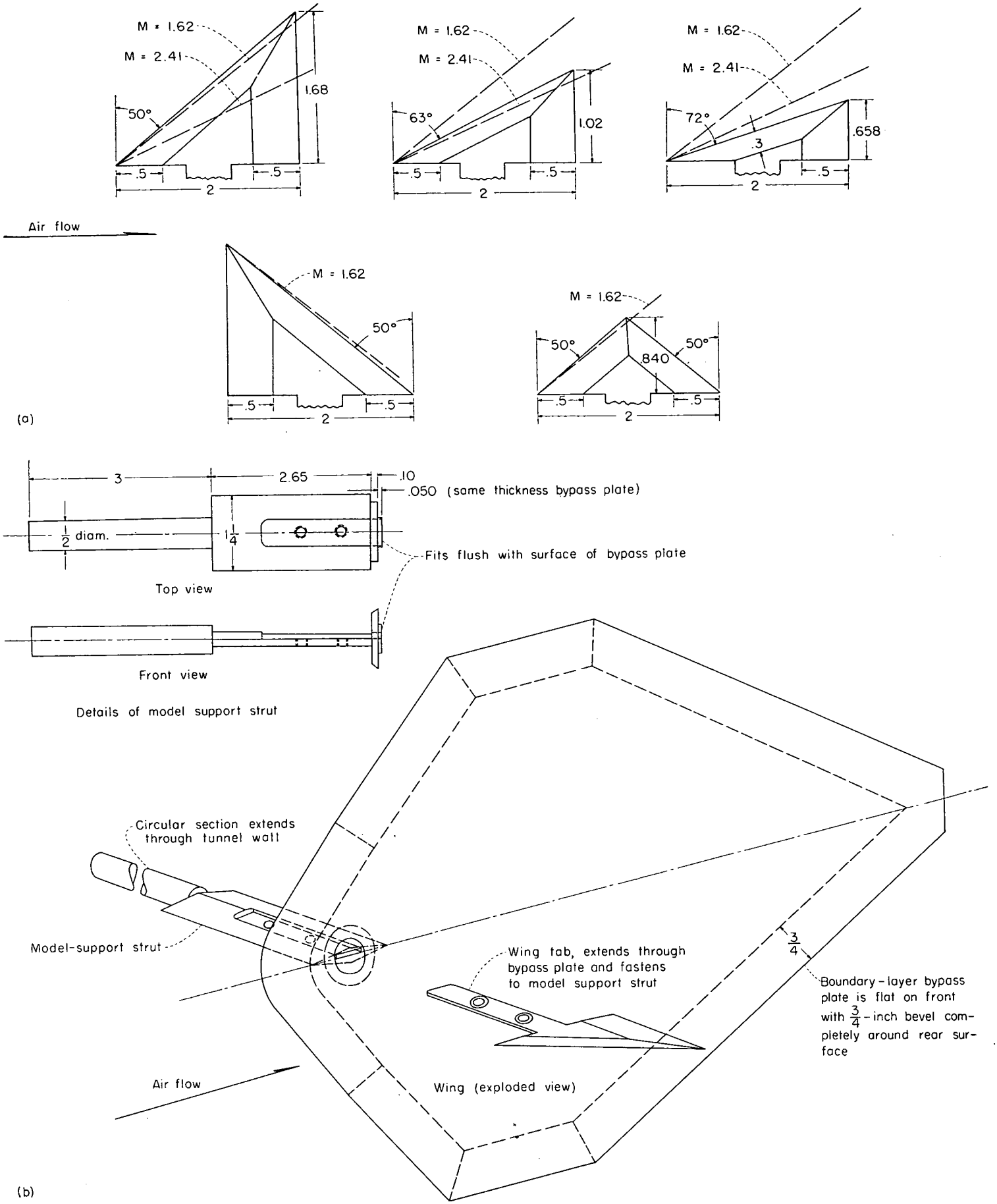
WIND TUNNEL

All tests were made in the Langley 9-inch supersonic tunnel, which is a continuously operating, closed-circuit wind tunnel in which the temperature, pressure, and humidity can be controlled. The test Mach number is varied by interchangeable nozzles which form a test section about 9 inches square.

MODELS AND MODEL-SUPPORT APPARATUS

The five semispan wings tested are shown in figure 1 (a). The wings were solid steel flat plates with beveled leading and trailing edges. All wings had the same root chord, and the maximum thickness of the root chord was 2.5 percent.

The wings were mounted from a boundary-layer bypass plate so that the wing angle of attack could be changed with the bypass plate remaining stationary. With the model-support design illustrated in figure 1 (b), there was no appreciable leakage of air through the bypass plate at the wing-plate juncture or from the bottom wing surface to the top. The plan form of the plate was conservatively designed so that a disturbance from behind the plate could not bleed around the leading edge and influence the flow field in the region of the surveys. The photograph of figure 2 (a), viewed obliquely downstream, illustrates the bypass plate and a wing model, as well as the survey apparatus, mounted in a mockup using dummy sidewalls to represent the tunnel.



(a) Wing models illustrating Mach cone leading-edge configuration. All wings 2.5 percent thick (root chord).
(b) Method of model support.

FIGURE 1.—Models and model-support apparatus. All dimensions in inches.

SURVEY APPARATUS

Measurements of total pressure and downwash and sidewash angle were made in the flow fields behind the wing. The photograph in figure 2 (b) illustrates the total pressure rake, which consisted of eleven 0.040-inch-outside-diameter tubes mounted 3/16 inch apart in a vertical row. A 2-inch-outside-diameter tube (0.050-in. wall thickness) with its leading edge cut oblique to its longitudinal axis and beveled on the outside was the supporting strut. The complete rake could be traversed both spanwise and vertically with the tunnel in operation. The spanwise motion was accomplished by a lead screw directly coupled to a counter which indicated the spanwise position of the rake in the tunnel (1 count=0.0025 in.), and the vertical motion was accomplished by a gear and rack at the rear end of the supporting strut. The vertical location was determined by sighting directly on a reference wedge with a cathetometer. It was necessary to stop the tunnel to change the longitudinal location.

The downwash and sidewash angles were obtained by means of a rake of small wedges such as is illustrated in the photograph of figure 2 (c). Details of the construction of the individual wedges are illustrated in the sketches of figures 2 (d) and 2 (e). Because the smaller size wedges used during the tests at $M=2.41$ responded too slowly to pressure changes, a larger version of the wedges was used for the tests at $M=1.62$. With the larger wedges, it was necessary to increase the spacing of the wedges on the rake from 1/4 to 3/8 inch in order to prevent any interference effects between the wedges. The wedges were mounted on the rake alternately horizontally and vertically, so that they would measure downwash and sidewash, respectively. Also mounted on the rake was a small 1/16-inch-diameter mirror (fig. 2 (c)), which was used in conjunction with an external light source and a calibrated scale, for referencing the horizontal angle of the rake in the tunnel. The small 1-inch-long bar at the top of the rake was used for referencing the vertical angle of the rake in the tunnel, as it afforded a convenient surface on which to sight a cathetometer.

TESTS AND METHODS

TEST CONDITIONS

The surveys were conducted at free-stream Mach numbers of 1.62 and 2.41. At each Mach number the tunnel stagnation pressure was adjusted to obtain data at two Reynolds numbers of 0.71×10^6 and 1.42×10^6 (based on the wing root chord which was the same for all models).

The tunnel stagnation temperatures were around 95° F for the low-pressure tests and 105° F for the high-pressure tests.

The moisture content of the tunnel air was sufficiently low for all the tests to ensure that any effects of condensation in the test section were negligible.

TEST PROCEDURE

Schlieren studies.—Prior to the detailed surveys, schlieren studies were undertaken of wings of the same plan form as used in the detailed surveys in order to obtain a general picture of the flow fields (fig. 3). These tests were made at $M=1.93$. For all the schlieren tests, the knife edge was horizontal in order to illustrate the density gradients in the vertical direction and thus show the trails of the vortices. The angles of attack of the tests were approximately the same as the maximum angles of attack of the wings used for the surveys.

Side views and plan views of the flow patterns were photographed. In the side views, the body was painted in a checkerboard fashion to show up the location of the wing trailing edge. Two tiny wires were stretched across the tunnel window to define the free-stream direction. These can be seen in the plan view of figure 3 (a) at about 1.5 semispans from the body center line. The silhouettes in the lower left-hand corner of all the side views of figure 3 merely serve to identify the plan form of the wing being tested. (In fig. 3 (b), this silhouette is rotated 90° from its position in the other figures.)

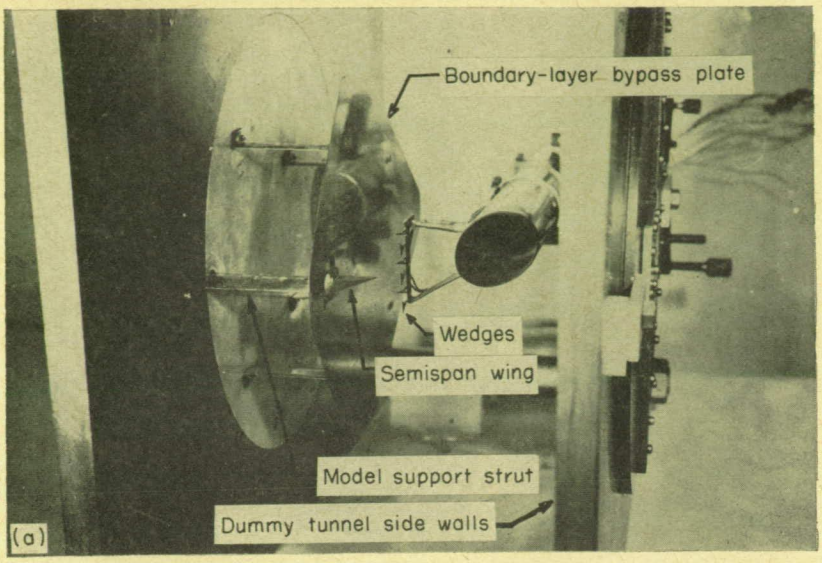
Figure 4 shows the locations of the paths of high vorticity, such as were sketched from enlargements of figure 3, and is presented to aid in the interpretation of the schlieren photographs.

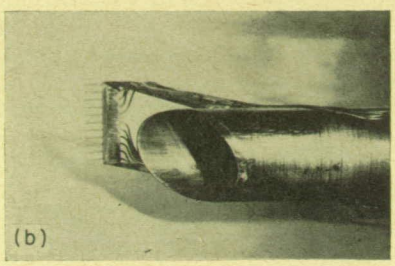
Total-pressure measurements.—Total-pressure tubes are not sensitive to small differences in alinement between the tube axis and the direction of the flow. For example, at $M=1.62$, calibrations have shown that a misalinement of 5° is not discernible in the pressure reading. For 10° misalinement, the error in p_t'/p_t amounts to about 1.3 percent. For this reason no provision or correction for the misalinement of the total-pressure tubes with the local flow angle was made in the present investigation.

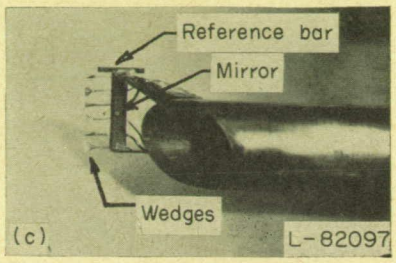
The flow field was surveyed with the boundary-layer bypass plate installed, both with and without the wing. The longitudinal location of the crossflow planes that were surveyed were 1.5, 3, and 4 root chords behind the wing trailing edge.

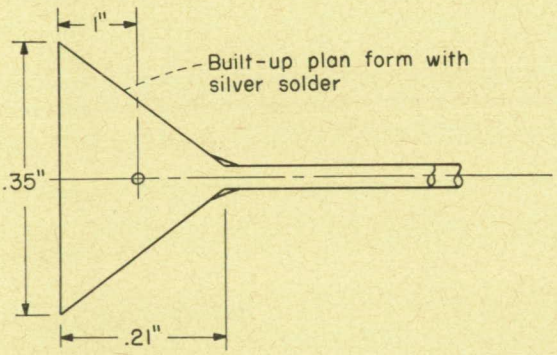
With the wing installed, the wing angle of attack was held constant while the pressure survey was conducted throughout each plane perpendicular to the free-stream direction. It was necessary to stop the tunnel in order to change the longitudinal location. During each survey at a longitudinal station, the wing angle of attack was changed without stopping the tunnel, and the survey in the same crossflow plane was repeated. The wing angles of attack used were —3°, 0°, and 3° for all the wings, as well as two higher angles of attack. The highest angles of attack of the tests were about 17° for the 72° sweptback triangular wing, about 14° for the 63° sweptback triangular wing, and about 12° for the other wings.

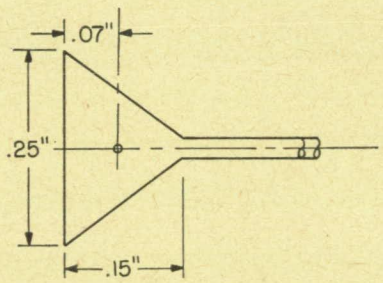
In the survey of a crossflow plane at an assigned value of wing angle of attack and longitudinal location, the following procedure was used: The rake was set at a desired spanwise location, then moved vertically until one of its tubes registered the peak of minimum pressure in the viscous wake or vortex. The pressure and location data were then recorded. With the rake at the same spanwise station, the vertical location was then changed by about one-half the distance between the tubes (3/32 in.), and the new data were taken. This was the usual procedure; however, in some cases where double peaks were observed in the wake profile,

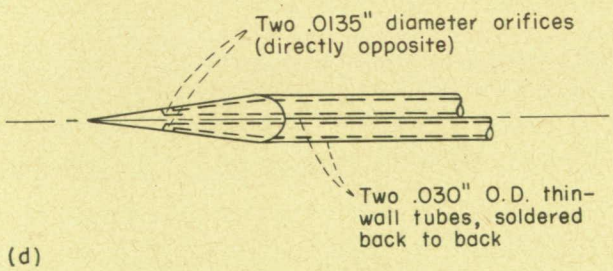


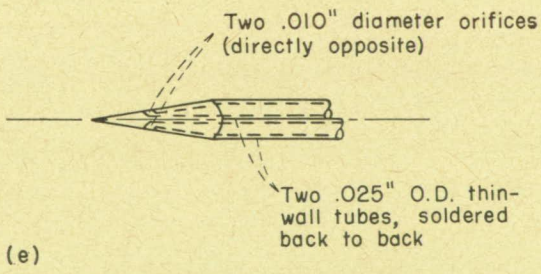












(a) Arrangement of model, bypass plate, and survey apparatus.

(b) Pitot rake.

(c) Wedge rake.

(d) Typical wedge used in tests at $M=1.62$.

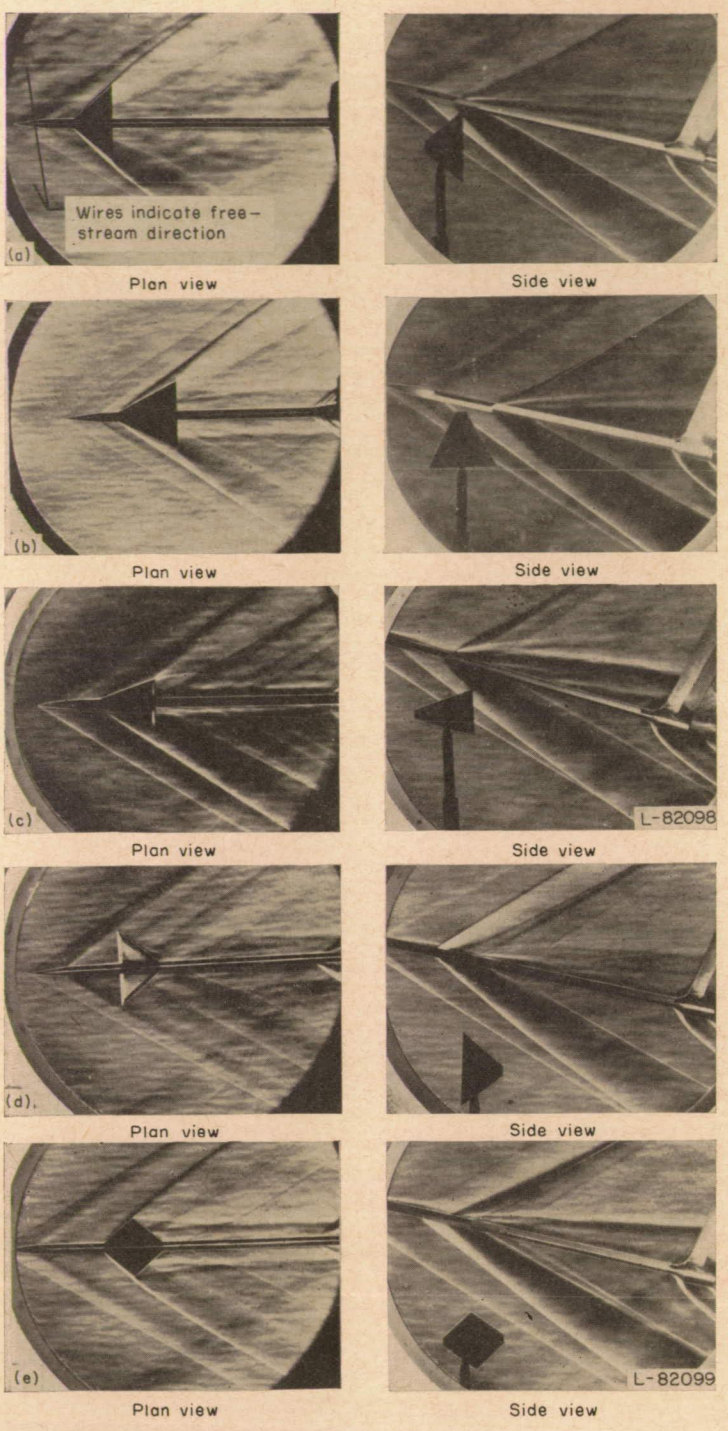
(e) Typical wedge used in tests at $M=2.41$.

FIGURE 2.—Test apparatus.

more than two vertical locations of the rake were used in order to define the wake profile more accurately. The spanwise stations selected for obtaining wake profiles were the same as those for which flow-angle measurements were made.

Flow-angle measurements.—The flow angle was determined by using the pressures, as measured on opposite sides of the previously described wedges, and the value of the total pressure at the same point. The sidewash and downwash were measured at the same point by taking measurements at two vertical locations of the rake. (The equal spacing of the six wedges on the rake in a vertical row alternately horizontally and vertically permitted this.) The tests were conducted in the same manner as for the total-pressure measurements except that selected values of vertical location were used instead of any peak value, as was the case with the total-pressure measurements. Prior to observing and recording the vertical and horizontal location of the rake, the alinement of the rake in the tunnel both in the horizontal and vertical plane was checked by

526597—60——70

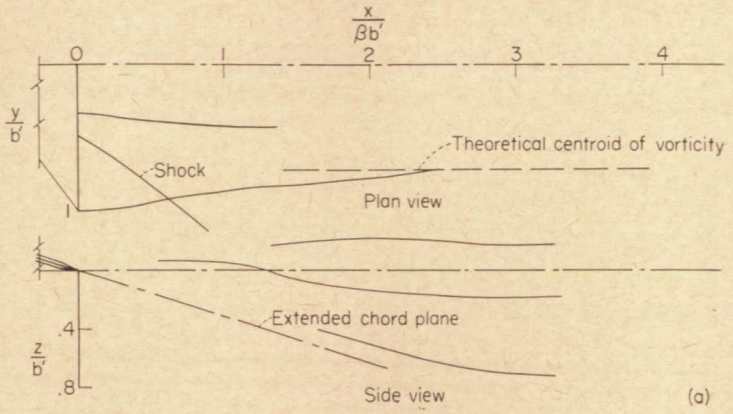


(a) Triangular wing; $\Lambda=50°$; $\alpha=12°$.
(b) Triangular wing; $\Lambda=63°$; $\alpha=12°$.
(c) Triangular wing; $\Lambda=72°$; $\alpha=18°$.
(d) Triangular wing reversed; $\Lambda=0°$; $\Lambda_{TE}=-50°$; $\alpha=12°$.
(e) Diamond plan form; $\alpha=12°$.

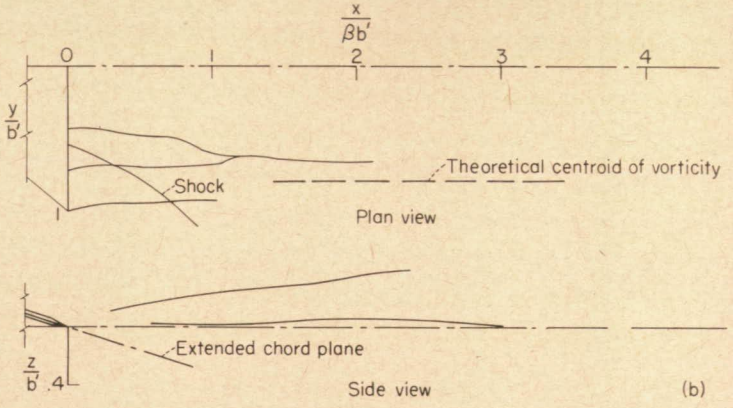
FIGURE 3.—Schlieren photographs illustrating the flow behind various wings. $M=1.93$.

the referencing system described under "Apparatus."

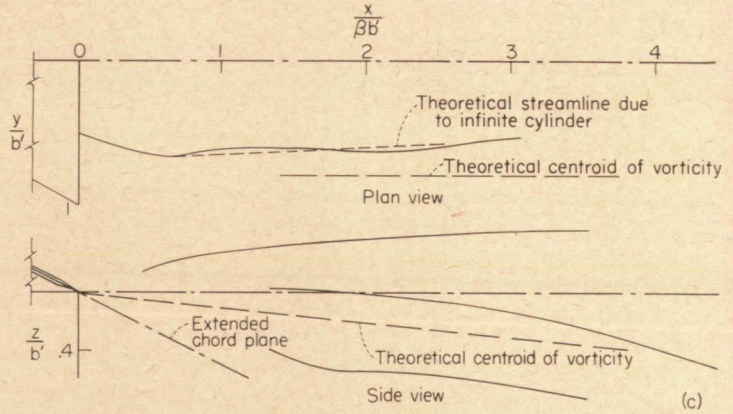
All flow-angle measurements were made at the desired locations, first with only the boundary bypass plate in the tunnel and no wing, then with both the bypass plate and the wing in the tunnel. When the flow-angle values determined from the no-wing tests were subtracted from those with the wing present, the flow angle caused by the wing was obtained independent of any small variations in stream



(a) Triangular wing; $\Lambda=50°$; $\alpha=12°$; $M=1.93$; $R=0.323\times10^6$.



(b) Triangular wing; $\Lambda=63°$; $\alpha=12°$; $M=1.93$; $R=0.485\times10^6$.



(c) Triangular wing; $\Lambda=72°$; $\alpha=18°$; $M=1.93$; $R=0.485\times10^6$.

FIGURE 4.—Sketches illustrating the locations of the paths of high vorticity behind triangular wings.

angle. Also, since the wedges were in the same position with respect to the rake for both the wing-on and the wing-off tests, the use of differences avoided the question of how accurately the angle of the small wedges with respect to the rake could be determined.

DATA REDUCTION

The data were mechanically reduced and printed in the form of the ratio of the measured pressure to the tunnel stagnation pressure. All total-pressure data are presented in this form; however, further reduction was necessary in

order to obtain the downwash and sidewash. Figure 5 illustrates the type of chart that was used to obtain the downwash and sidewash. The dashed lines of this chart indicate the Mach number and flow angle with respect to the wedge axis for given pressure ratios such as two-dimensional wedge theory predicts. The ordinate p_w/p_t' (upper or outboard, depending on whether a downwash or sidewash wedge is used) is the ratio of the pressure on the wedge to the measured total pressure (uncorrected for the normal shock at the nose of the tube). Similarly, the abscissa is this same pressure ratio for the opposite surface of the wedge. With these pressure ratios and the wedge angle known, the angle of the flow with respect to the wedge and the local Mach number can be determined. When the chart of figure 5 is used for the determination of flow angle, the parameters are very insensitive to changes in wedge angle. The maximum discrepancy between the chart of figure 5, which was constructed for an 8° half-wedge angle, and a chart which was constructed for a 7° half-wedge angle was less than 0.2° with regard to predicting the flow angle. However, with regard to predicting the Mach number, the parameters of the chart are very sensitive to wedge angle and since the wedges used for the tests of this report were so small that the wedge angle could not be accurately determined, no Mach number data are presented for the flow surveys.

Superimposed on the theoretical curves of figure 5 are the experimental points obtained when a typical wedge is varied through an angle-of-attack range at three different Mach

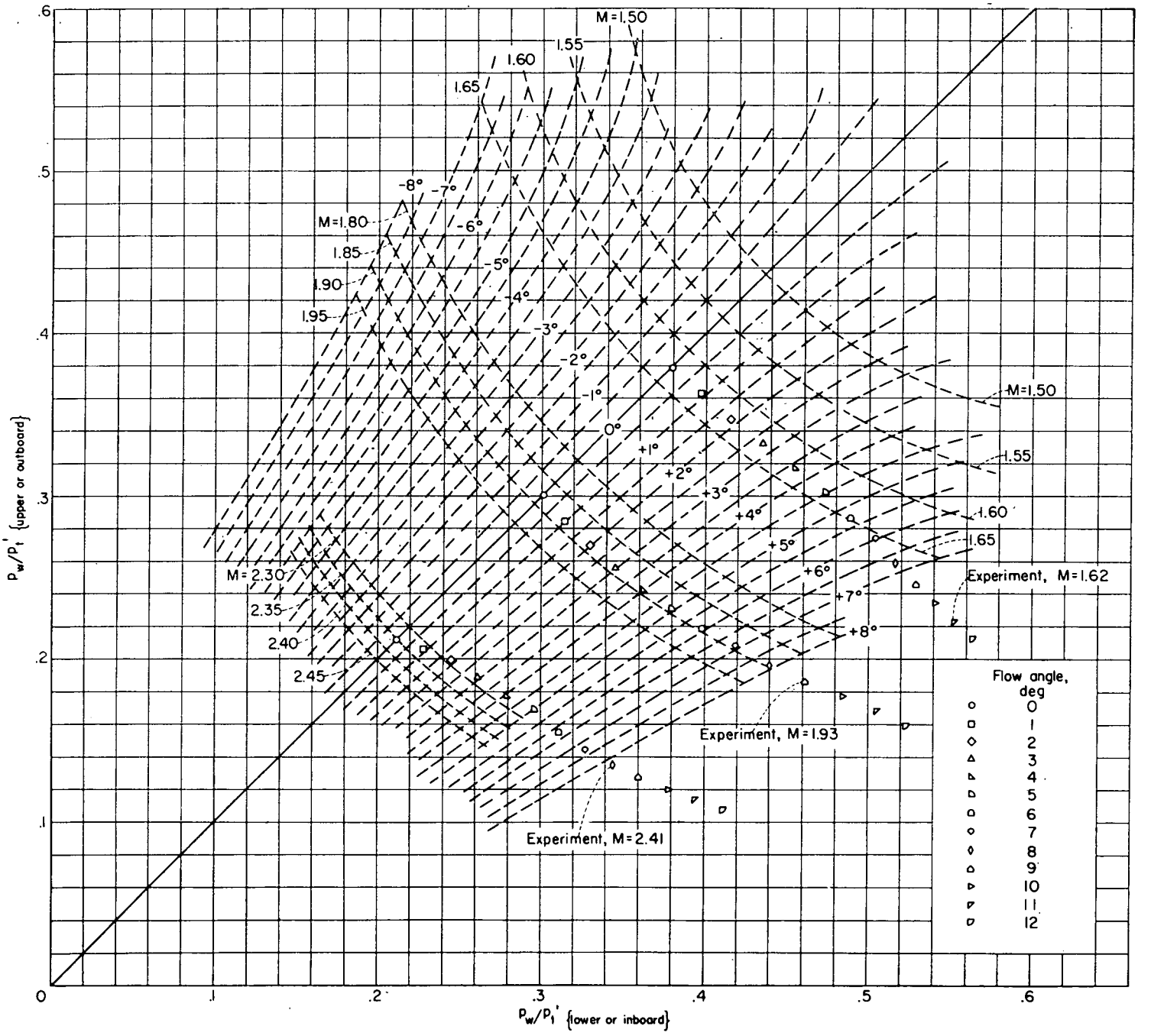


FIGURE 5.—Chart illustrating wedge pressure readings as a function of angle of flow with respect to wedge and the local Mach number (8° half-angle wedge).

numbers. The good agreement of the calibration with the theoretical lines of the chart at $M=2.41$, with regard to predicting the flow angle, is shown. Consequently, the chart was used directly for reducing the flow-angle data at $M=2.41$. At $M=1.62$, the discrepancy between experiment and theory is larger than at $M=2.41$. These discrepancies are probably due to a side-edge effect, although theoretically these effects should not start appearing until the angle of attack of the wedge is about 4° or 5°. Because of these discrepancies, it was necessary to calibrate the wedge rake for the tests at $M=1.62$. This calibration was made at both tunnel stagnation pressures for which the tests were conducted, and the correction was applied to each individual wedge reading throughout the tests.

As previously stated, no Mach number data are presented. A comparison of the experimental points with theory in figure 5 indicates that even if the wedge angle were known exactly, the Mach number as indicated by the wedge theory would still be unreliable, since, in general, the experimental points indicate that the lines of constant Mach number on the chart are of a different shape than predicted by theory.

PRECISION

The estimated accuracies of the controlled conditions during a test are as follows:

M	±0.01
α, deg	±0.1
x, in.	1/64
y, in.	±0.005
z, in.	±0.005

Checks between the values of the pressures as read directly, and the pressure ratios which were reduced mechanically, established a precision of ±0.003 for the p_t'/p_t values. The precision of ϵ and σ, when estimated from the largest possible combination of inaccuracies in the pressures, with and without the wing present, reduce to ±0.4°. In the case of the flow-angle measurements, it should be further pointed out that for the tests at Mach number 1.62, an unknown source of error existed because of the fact that the calibration tests were conducted at Mach number 1.62, instead of at the particular local Mach number at which each wedge was operating. Throughout most of the flow field this error is probably negligible. A further source of an unknown effect on the precision of the flow-angle measurements depends upon how well the finite wedge sizes approximate a point measurement. Although the wedges were made as small as was practicable, the results in a large pressure gradient might be subject to considerable inaccuracy due to this source. This effect would be especially significant for the tests at Mach number 1.62 of the 72° sweptback delta wing, where the wedge span is approximately ½ the wing span.

RESULTS AND DISCUSSION

BASIC DATA

Preliminary schlieren studies at $M=1.93$.—The schlieren observations, such as are shown in figure 3, were made at $M=1.93$ in order to aid in planning the test program. In this figure, the regions of primary interest are regions where large changes occur in density in the vertical direction, such as accompany regions of concentrated vorticity. Although the free-stream Mach number is between the two Mach numbers for which the detailed surveys were made, the schlieren photographs serve to illustrate qualitatively what can be expected with regard to the locations of the concentrated regions of vorticity behind the wings.

Although the wings utilized for the schlieren studies are of the same plan form as the semispan wings for which the detailed surveys were made, they are smaller and are mounted on a slender body. The angles of attack of the various wings were near the same theoretical lift coefficient in order to illustrate the variations in the flow patterns due primarily to aspect ratio. The flow patterns for the triangular wing plan forms of figures 3 (a), 3 (b), and 3 (c) show that the region of vorticity for the lower-aspect-ratio wings is more distinct and concentrated.

The paths of the main vortices behind the various triangular wings are shown in figure 4. This figure was sketched from enlargements of the schlieren photographs. For figures 4 (a) and 4 (b), where a wing shock was discernible, the location of this shock is shown as a solid line.

Since theoretical estimates of the flow angularity behind triangular wing configurations often approximate the flow fields obtained by using a line vortex which is located along the theoretical centroid of vorticity, the path of this streamline has been superposed in figure 4 for each wing. The discrepancy inherent in this assumption is apparent. The term "centroid of vorticity" is used to indicate the resultant weighted center of all the vorticity in a given region. It is analogous to the center of gravity of a similar system of point masses.

Pressure contours.—The contours of pressure ratio p_t'/p_t are presented in figures 6 to 32. The dashed lines of figures 6 to 32, which were constructed from the total pressure measurements, represent lines of constant pressure in the crossflow planes for the various configurations tested. Since the values of pressure were not corrected for the shock at the nose of the tube, the numbers given in the plots are not the true total pressure loss. Nevertheless, the contours do give a good pictorial representation as to the nature of the flow field behind each wing. The z/b' location (y/b' axis) for all the figures is referenced to the wing trailing edge.

It can be seen that at approximately 0° angle of attack for all the wings tested, there is a relatively flat sheet of low dynamic pressure approximately straight behind the wing trailing edge. For the range covered by the tests (1.5 to 4 chords behind the wing trailing edge), the variation, both in shape and intensity, of the viscous wake with distance downstream is slight if any (e.g., figs. 6 (b) and 8 (b)).

As the angle of attack of a wing is increased, the line of maximum pressure deficiency deflects downward for inboard spanwise locations and upward for the outboard locations (e.g., figs. 6 (c), 6 (d), 6 (e), 7 (a), 7 (b), 8 (c), and 8 (d)). Also, at various spanwise locations along this line, concentrations of lower dynamic pressure form. These are probably concentrated regions of high vorticity which occur as the vorticity in the vortex sheet redistributes itself. The formation of these regions makes it more difficult to trace the actual sheet of vorticity (or of minimum total pressure) throughout its breadth at high angles of attack than at low angles of

attack. Actually, the interpretation of the vorticity existing as a sheet becomes doubtful, since practically all the vorticity will be contained in these concentrated regions. At the same angle of attack, it is much easier to identify the existence of the vortex sheet as a sheet for the wings of higher aspect ratio (lower sweep) than for wings of lower aspect ratio. (For example, the sheet is much more readily discernible in figure 6 (d), or even 6 (e), than it is in the subsonic leading-edge configuration of figure 12 (d), where the vorticity is more concentrated. Similarly, at $M=1.62$, the existence of the vortex sheet as a sheet is more apparent in figure 15 (d) than in figure 21 (d).)

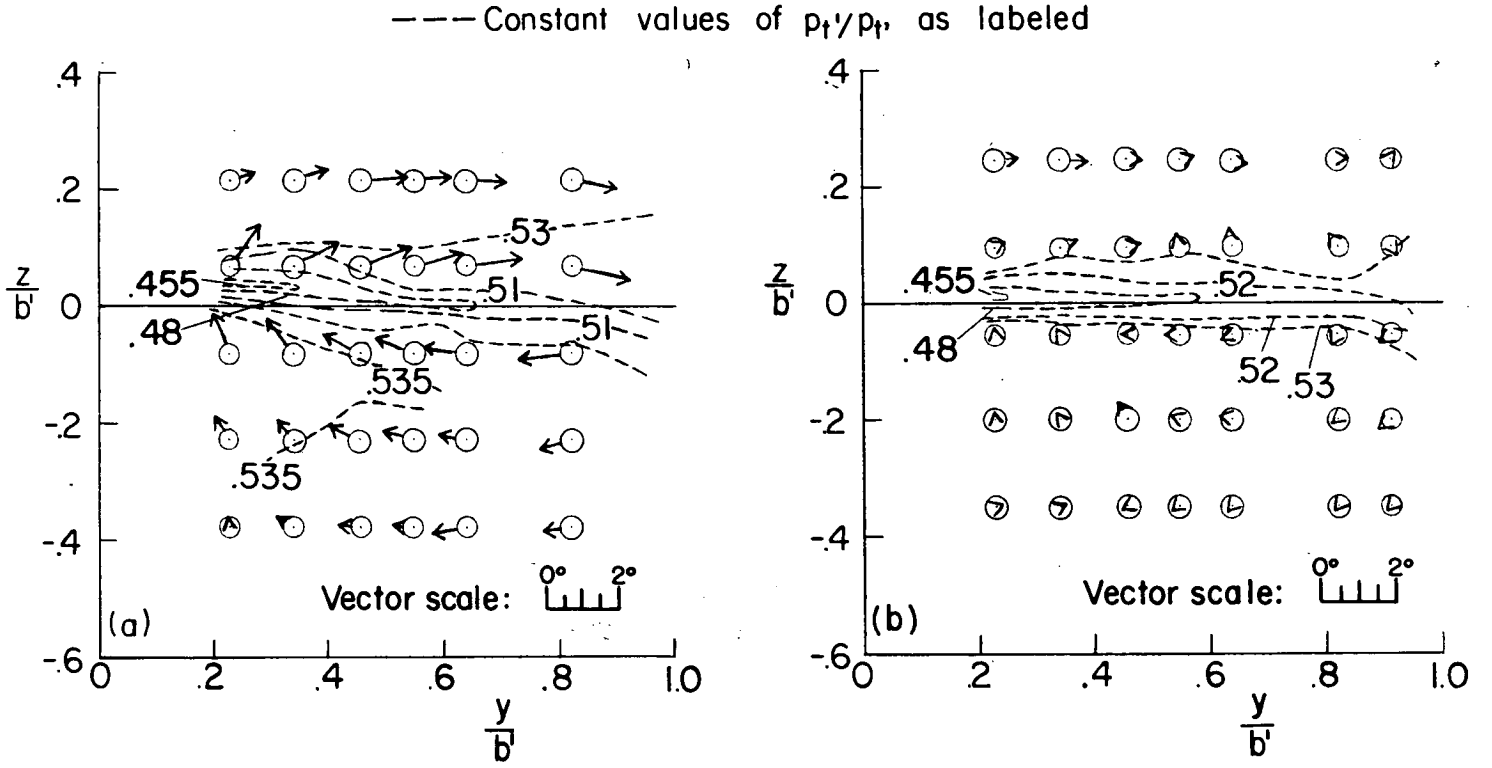
Downwash and sidewash.—In addition to the pressure contours, figures 6 to 32 present a vector presentation of the flow angles existing in crossflow planes behind the various wings. The projection of a vector on a vertical line is the downwash or upwash, and its projection on a horizontal line is the sidewash. The length of each vector is referenced from the center of each small circle, which is plotted at the location for which the measurement was made. The magnitude of a 1° reference vector indicates a perturbation velocity sufficient to deflect the local stream angles by 1° in the indicated direction. In some of the figures, flow-angle data at the lower Reynolds number are shown as dashed vectors. For those figures which show flow-angle data at both $R=1.42\times10^6$ and 0.71×10^6, the pressure contours are for the higher Reynolds number. Otherwise, the pressure contours are for the same Reynolds number as the flow-angle data.

Although a more detailed and quantitative analysis will appear in succeeding figures, the vector diagrams afford a good pictorial representation of the flow angles behind the wings, and illustrate some of the following features of the flow.

At wing angles of attack of approximately zero degrees, the values of the flow angle which were measured are small. This result indicates that the thickness effect is small for the thin wings of these tests.

At the same angle of attack, the largest vectors (largest flow angles) occur behind the wings of lower aspect ratio (higher sweep). Also, there is a tendency for the intersection of the normals of the vectors for the lower-aspect-ratio wings to define a smaller region such as would be predicted by a theoretical model of the flow using a single line vortex behind each wing panel. For example, at $M=2.41$, the flow behind the 50° sweptback triangular wing tends to circulate about the whole sheet of low pressure as defined by the pressure contours (fig. 8 (e)), whereas the flow behind the 72° sweptback triangular wing tends to circulate about the small circular region of lowest pressure, which is defined by the pressure contours (fig. 14 (d) or 14 (e)). For all cases where this small low-pressure region exists, it is the vectors nearest this region that are largest and whose normals come closest to intersecting in this region. Those vectors which are farther away indicate that the path of the fluid is more distorted from a true circle.

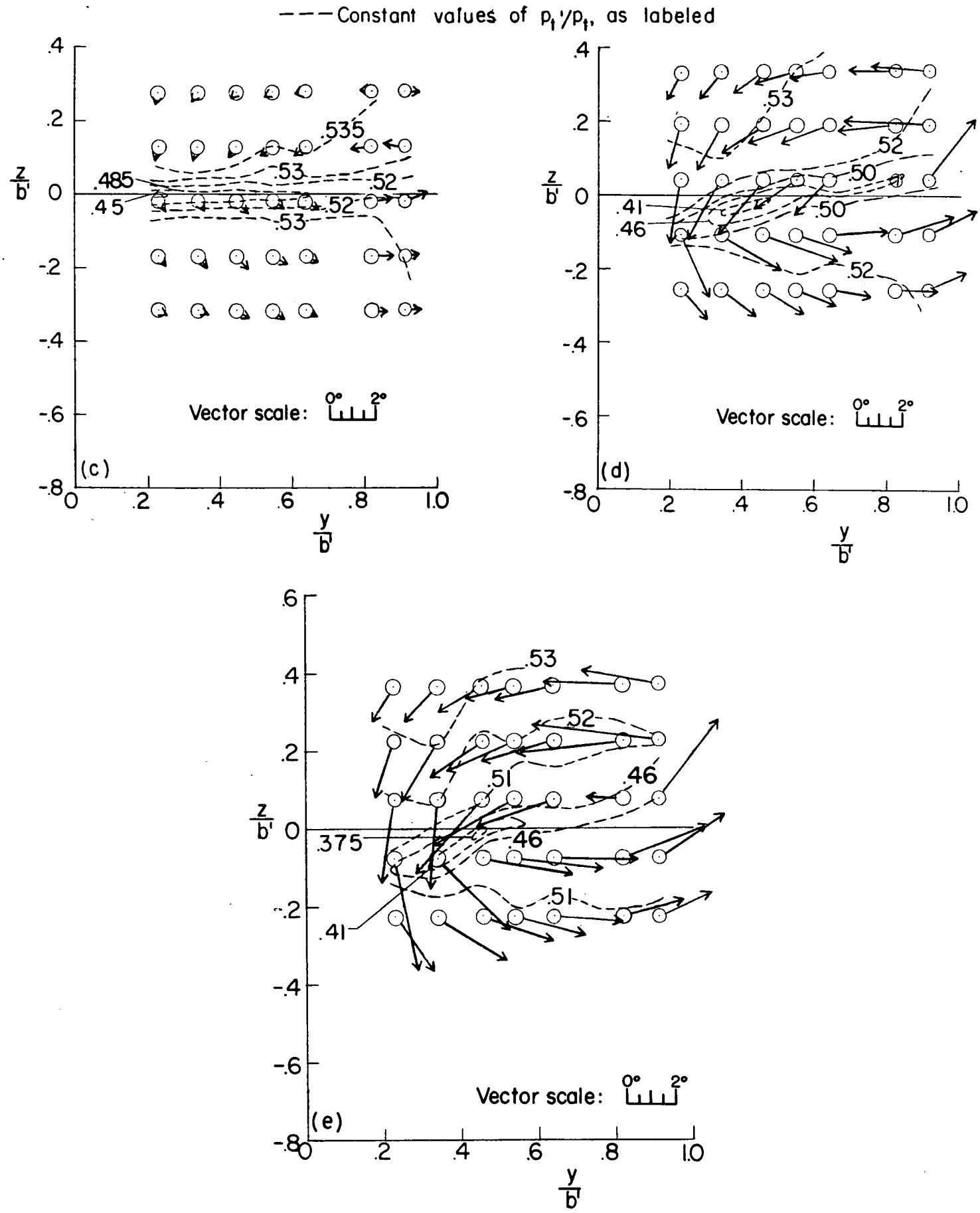
No systematic variations due to Reynolds number were observed for the range tested. Minor differences in the high and low Reynolds number data (as for example, fig. 15 (d), or figs. 23 (a) and 23 (b) as compared with figs. 24 (a) and 24 (b)) can be observed, but the vectors are very similar in size and direction so that the effects of the Reynolds number are apparently of a secondary nature.



(a) $\alpha=-3.50°$.

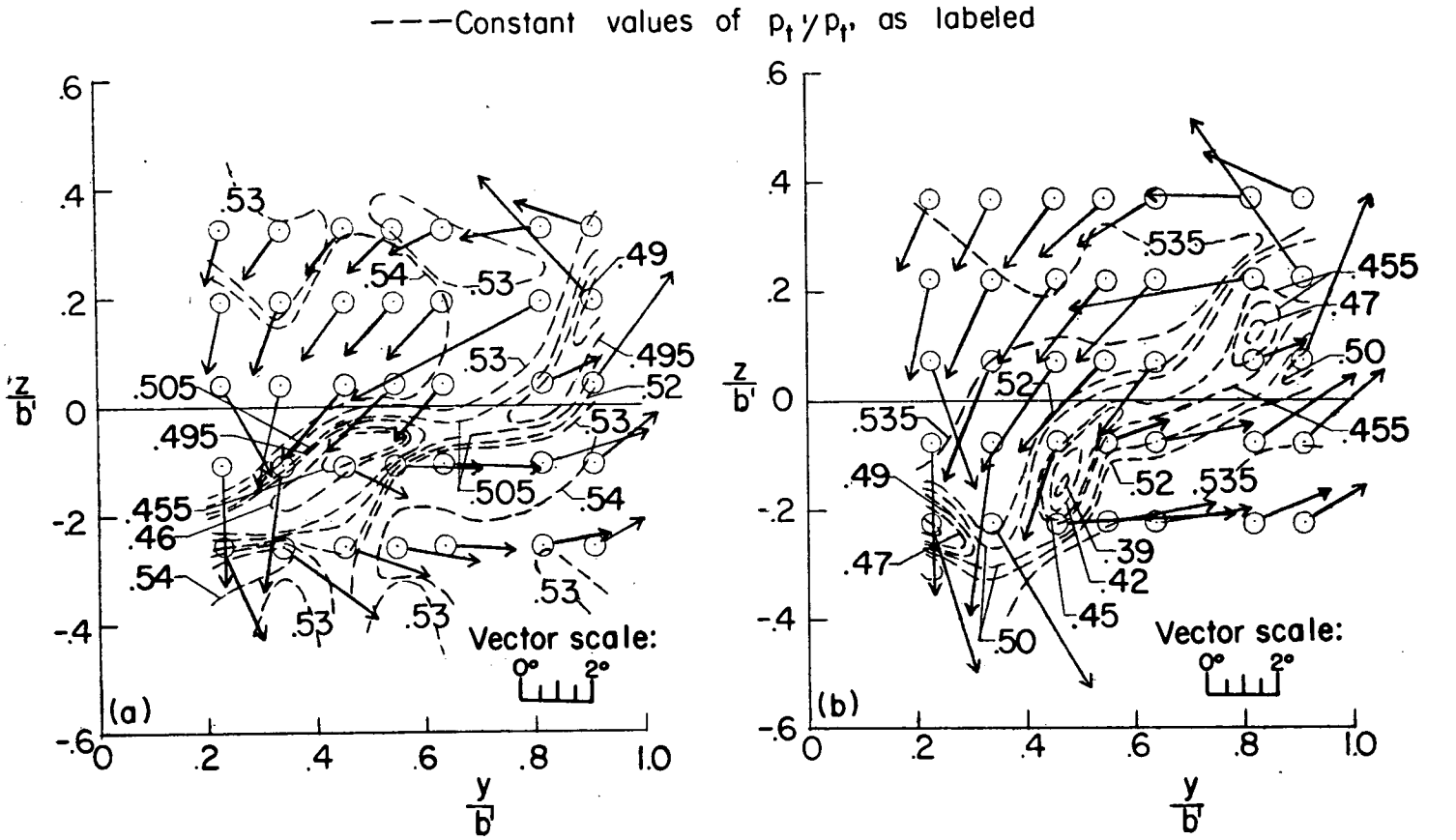
(b) $\alpha=-0.50°$.

FIGURE 6.—Pressure contours and vector representation of the flow behind a triangular wing. $\Lambda=50°$; $M=2.41$; $x=1.5c_r$; $R=1.42\times10^6$; $\frac{p_{t,\infty}}{p_t}=0.536$.



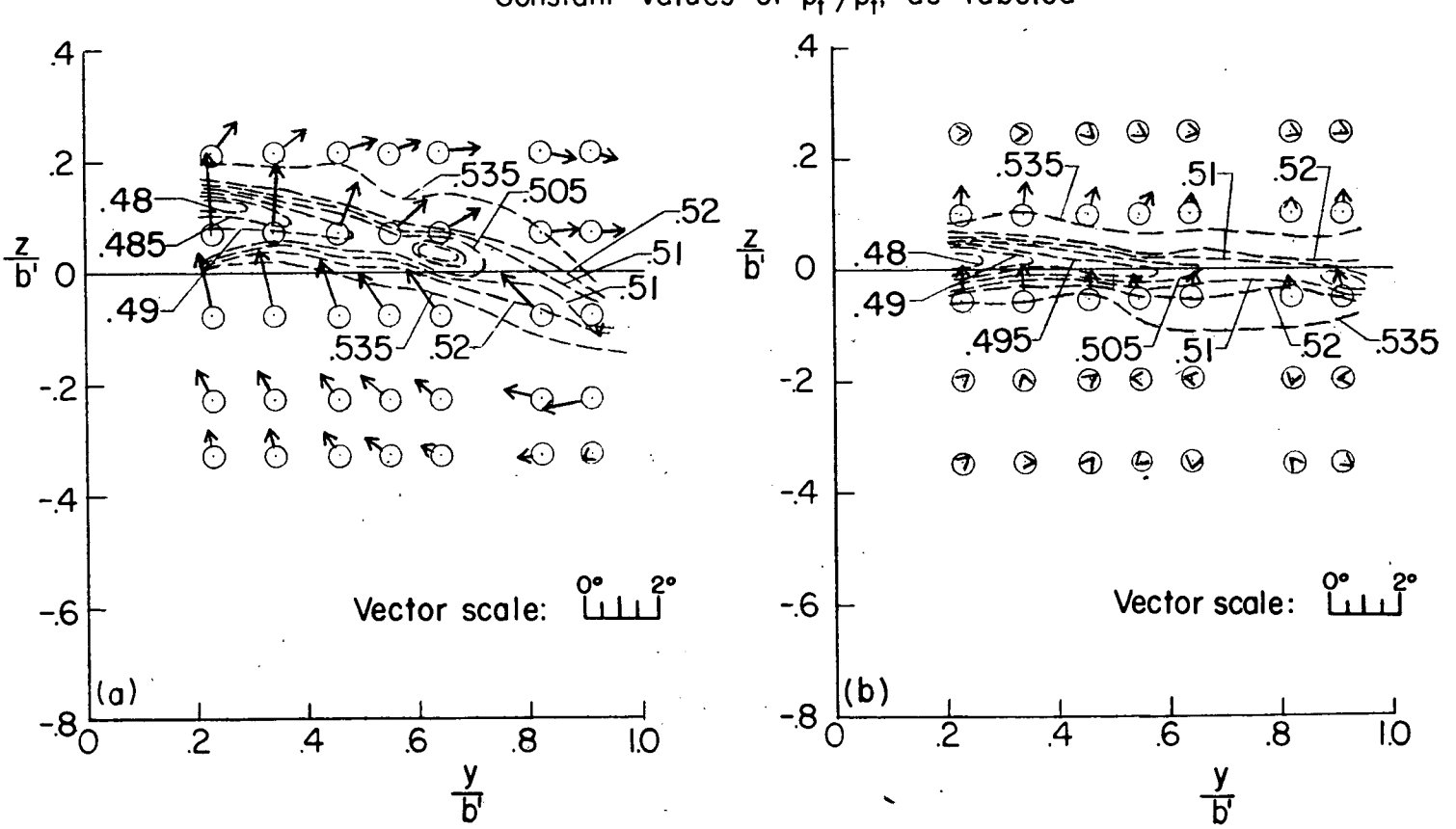
(c) $\alpha = 2.50°$. (d) $\alpha = 8.50°$.
(e) $\alpha = 11.50°$.

FIGURE 6.—Concluded.



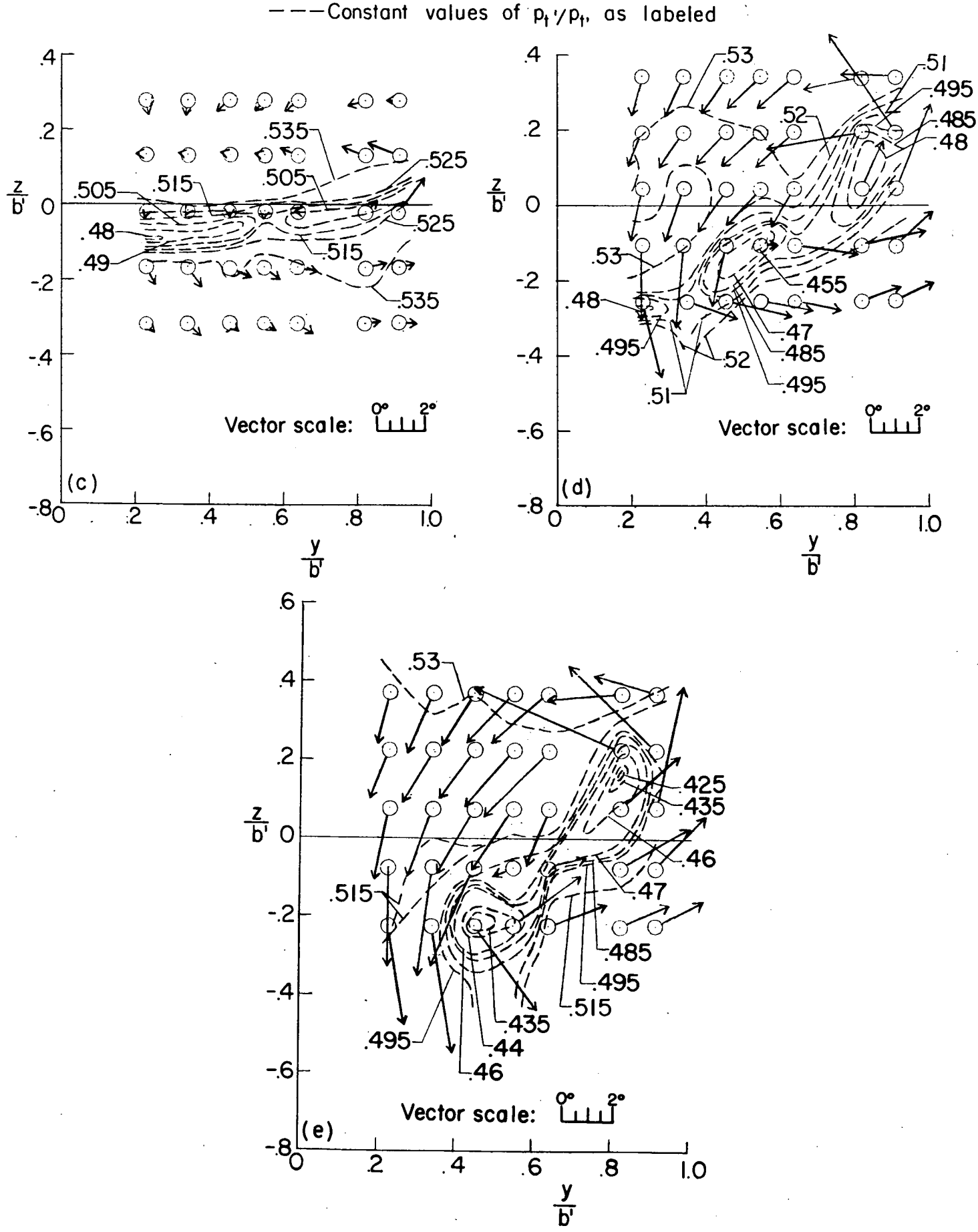
(a) $\alpha=8.50°$. (b) $\alpha=11.50°$.

FIGURE 7.—Pressure contours and vector representation of the flow behind a triangular wing. $\Lambda=50°$; $M=2.41$; $x=3c_r$; $R=1.42\times10^6$; $\frac{p_{t,\infty}}{p_t}=0.536$.



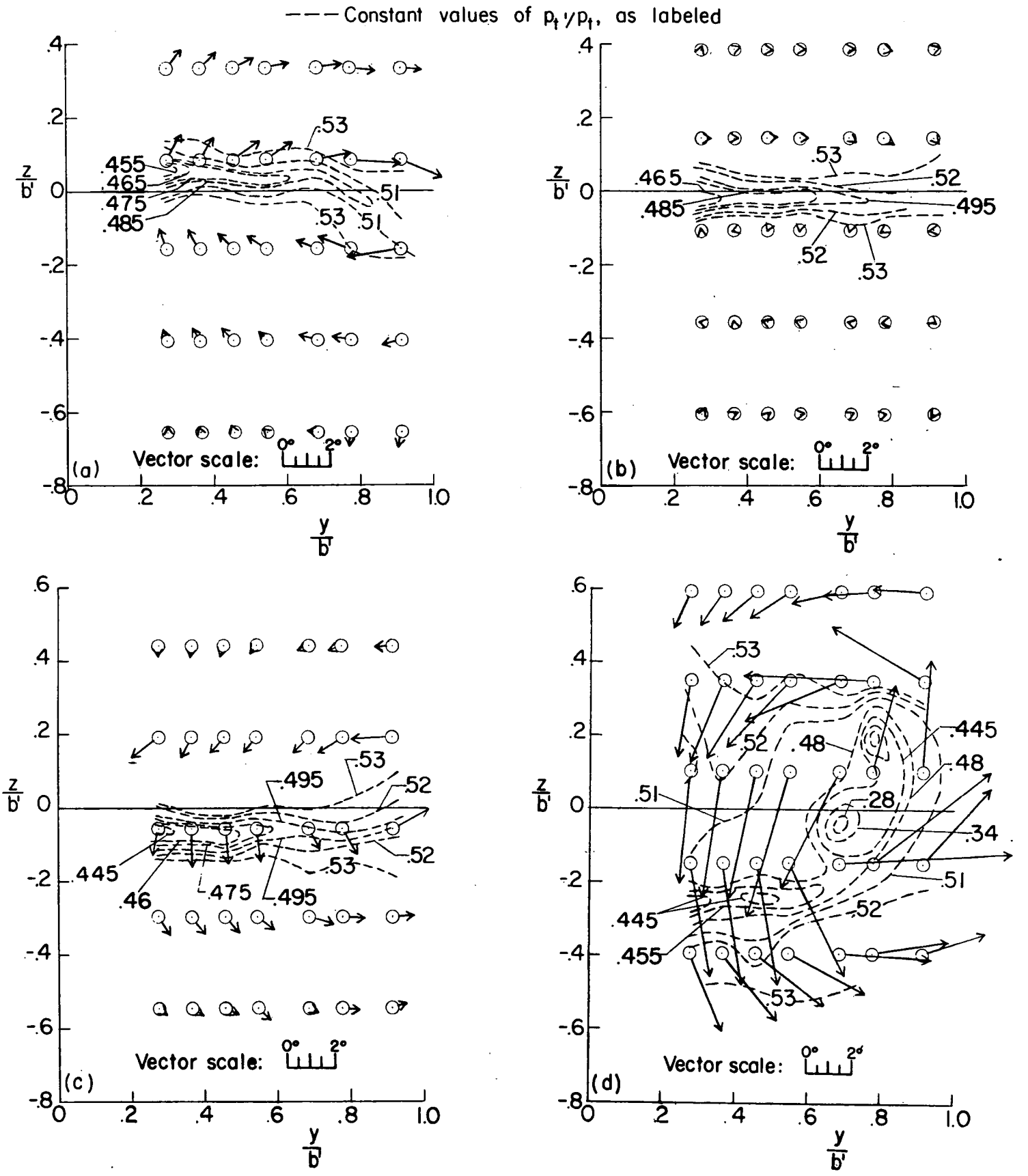
(a) $\alpha=-3.50°$. (b) $\alpha=-0.50°$.

FIGURE 8.—Pressure contours and vector representation of the flow behind a triangular wing. $\Lambda=50°$; $M=2.41$; $x=4c_r$; $R=1.42\times10^6$; $\frac{p_{t,\infty}}{p_t}=0.536$.



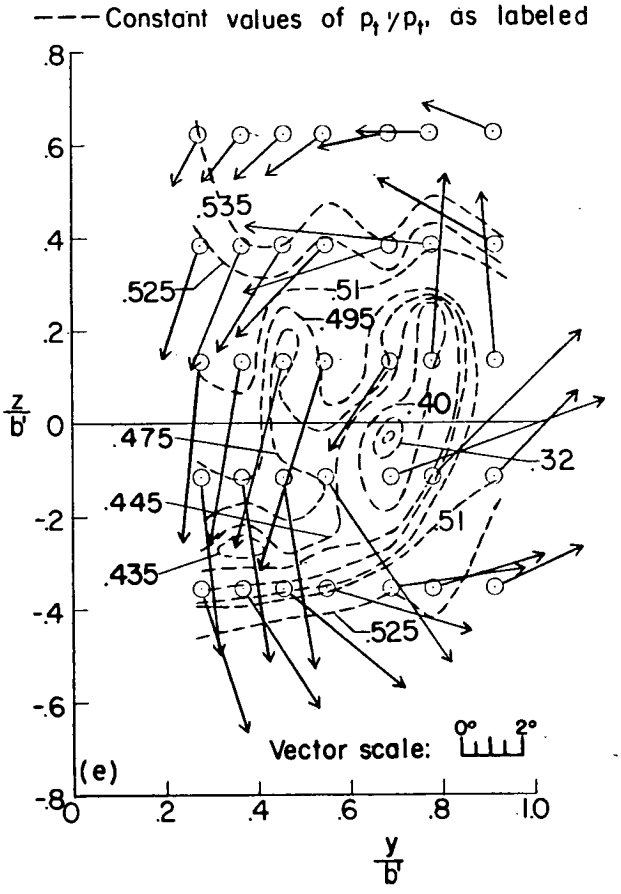
(c) $\alpha=2.50°$. (d) $\alpha=8.50°$.
(e) $\alpha=11.50°$.

FIGURE 8.—Concluded.



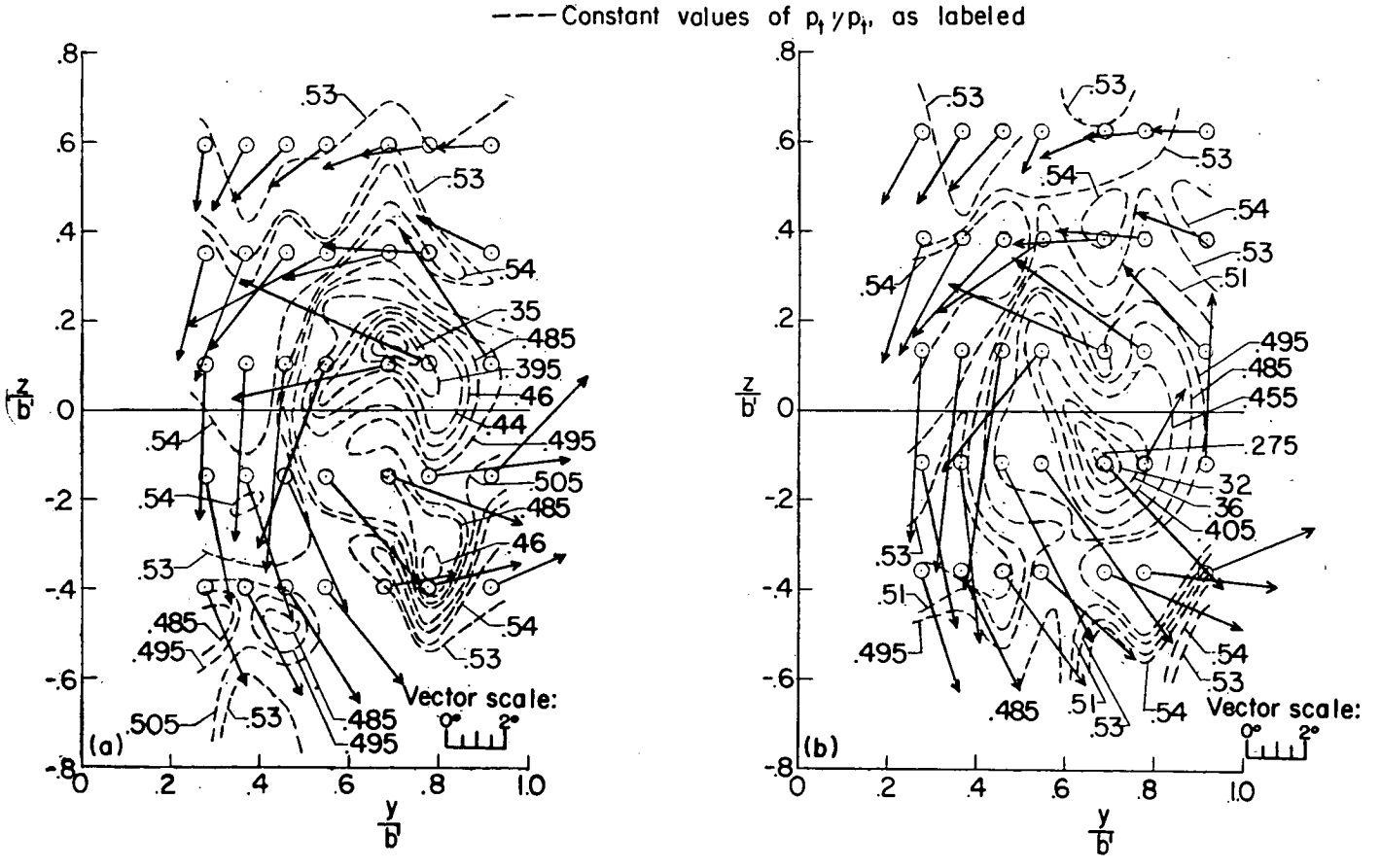
(a) $\alpha = -3.00°$.
(b) $\alpha = -0.10°$.
(c) $\alpha = 3.00°$.
(d) $\alpha = 11.95°$.

FIGURE 9.—Pressure contours and vector representation of the flow behind a triangular wing. $\Lambda = 63°$; $M = 2.41$; $x = 1.5c_r$; $R = 1.42 \times 10^6$; $\frac{p_{t,\infty}}{p_t} = 0.536$.



(e) $\alpha = 13.95°$.

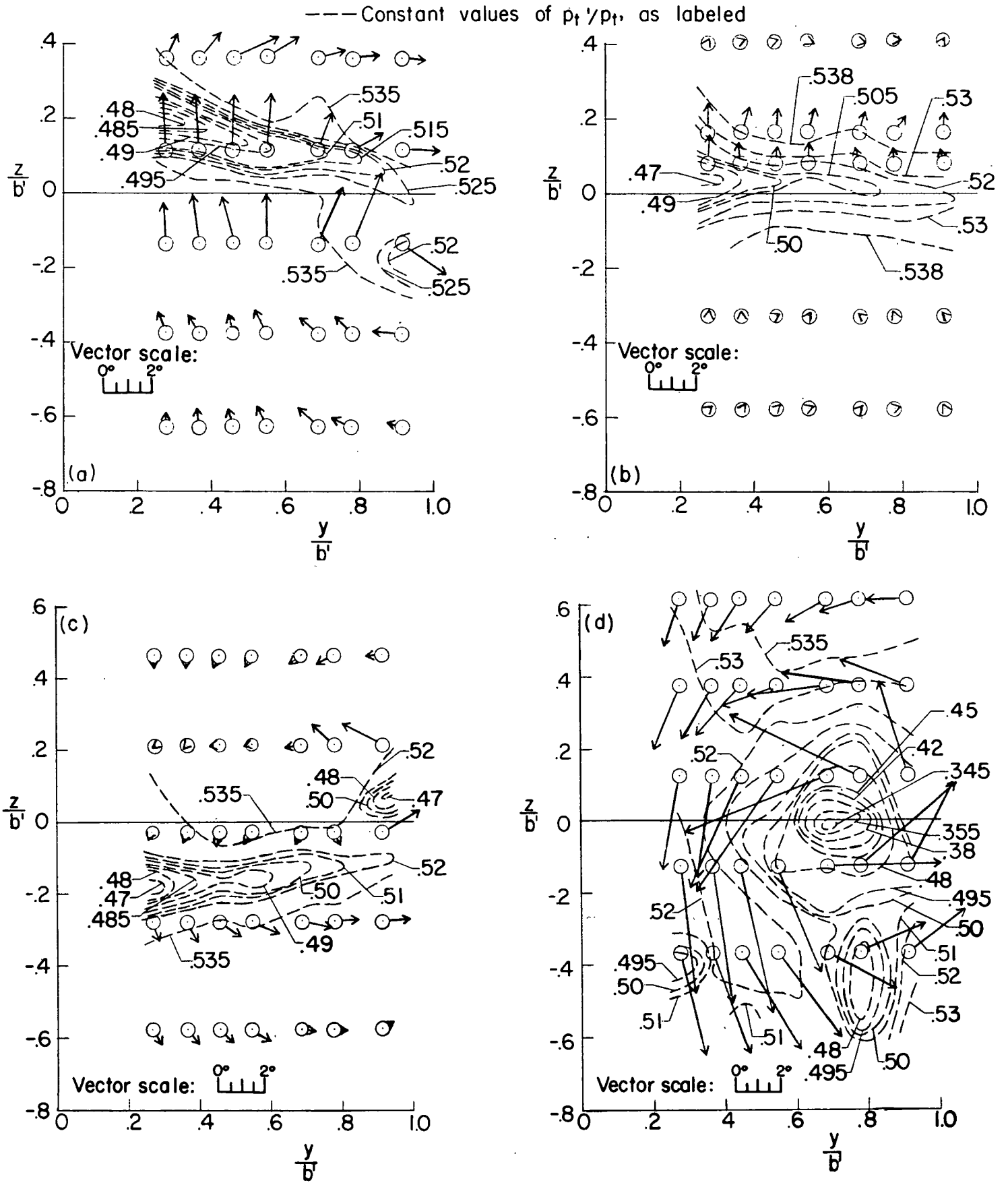
FIGURE 9.—Concluded.



(a) $\alpha = 11.95°$.

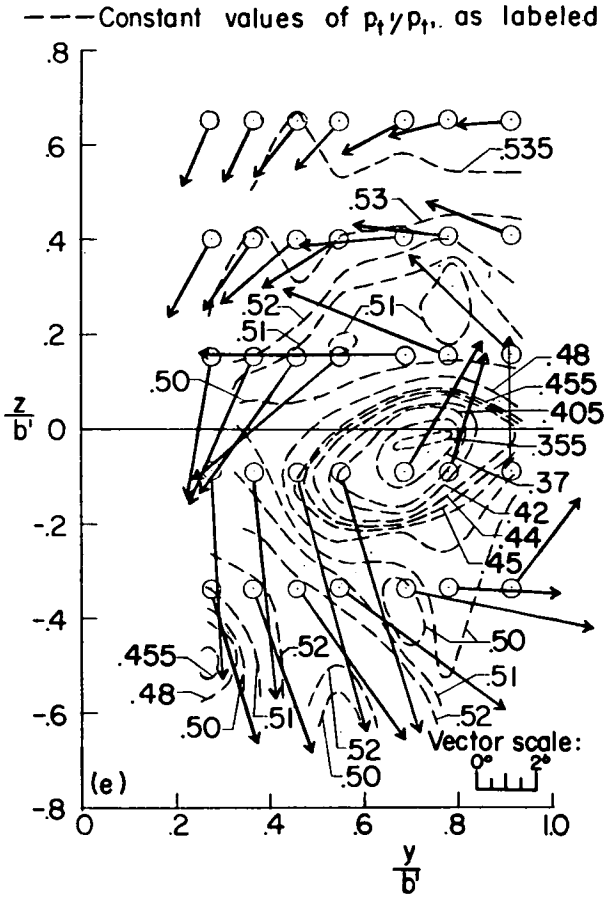
(b) $\alpha = 13.95°$.

FIGURE 10.—Pressure contours and vector representation of the flow behind a triangular wing. $\Lambda = 63°$; $M = 2.41$; $x = 3c_r$; $R = 1.42 \times 10^6$; $\frac{p_{t,\infty}}{p_t} = 0.536$.



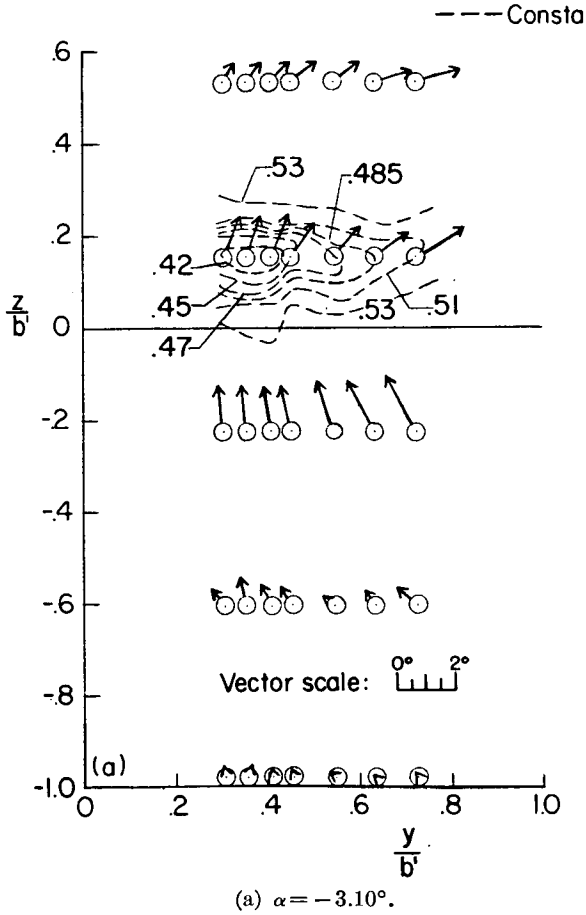
(a) $\alpha = -3.00°$.
(b) $\alpha = -0.10°$.
(c) $\alpha = 3.00°$.
(d) $\alpha = 11.95°$.

FIGURE 11.—Pressure contours and vector representation of the flow behind a triangular wing. $\Lambda = 63°$; $M = 2.41$; $x = 4c_r$; $R = 1\ 42 \times 10^6$; $\frac{p_{t,\infty}}{p_t} = 0.536$.

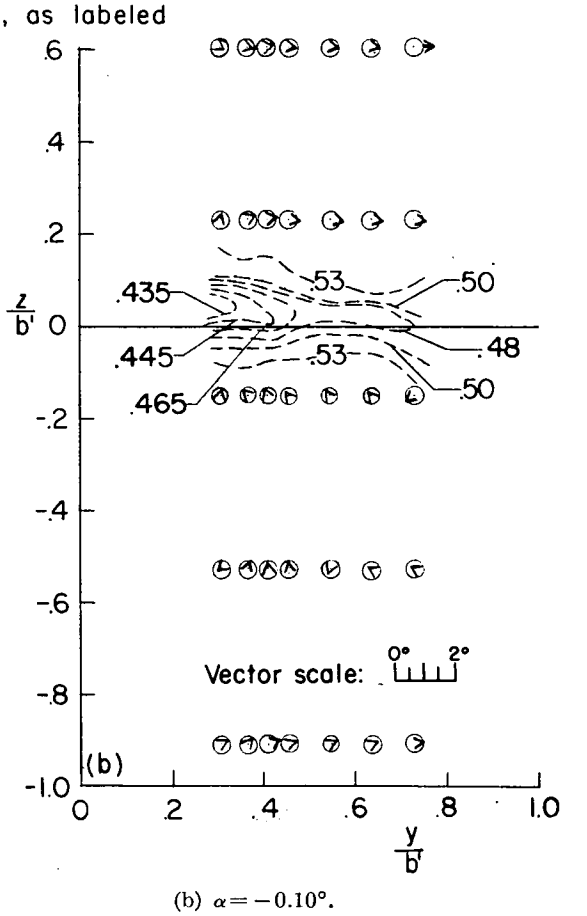


(e) $\alpha = 13.95°$.

FIGURE 11.—Concluded.

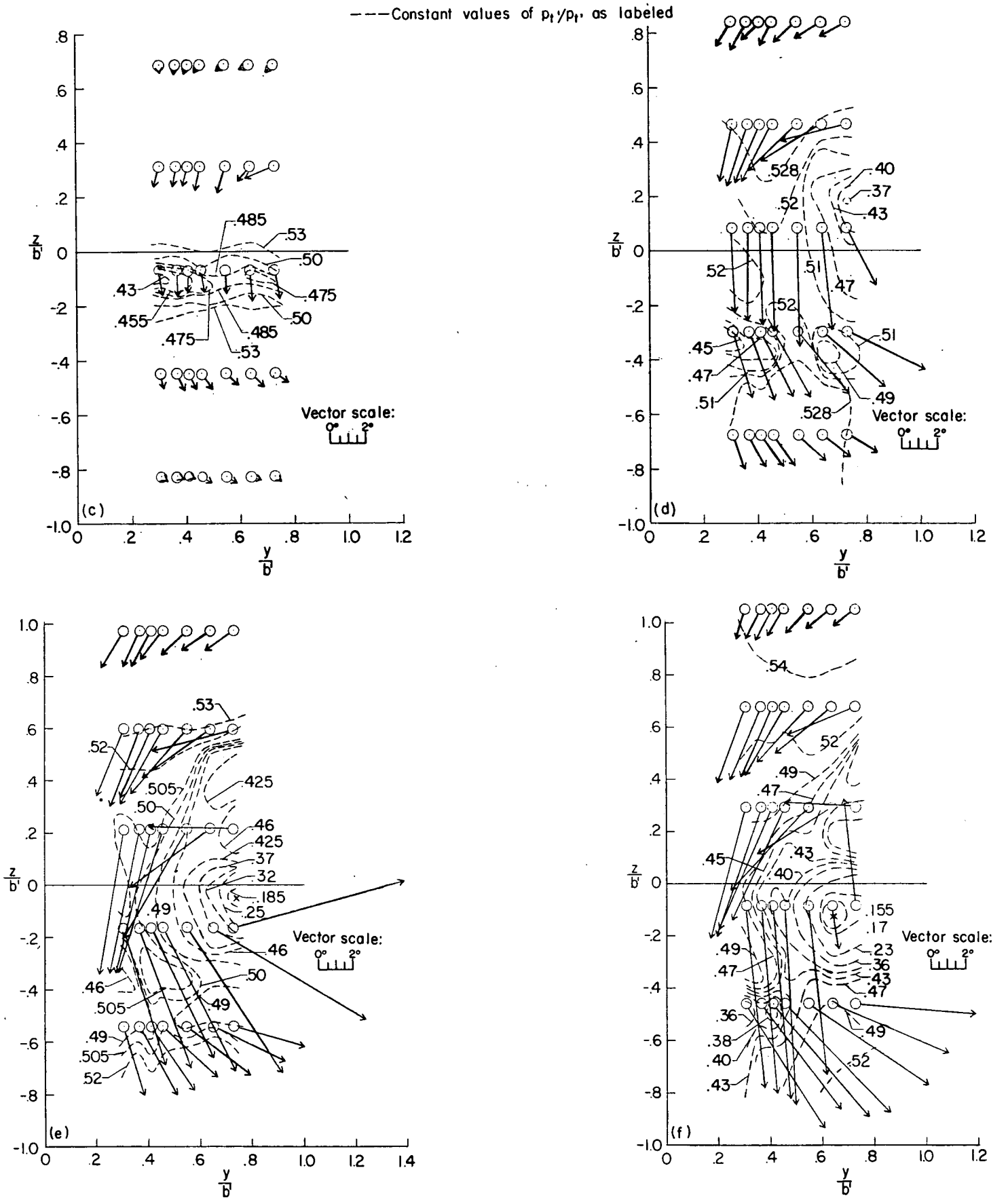


(a) $\alpha = -3.10°$.



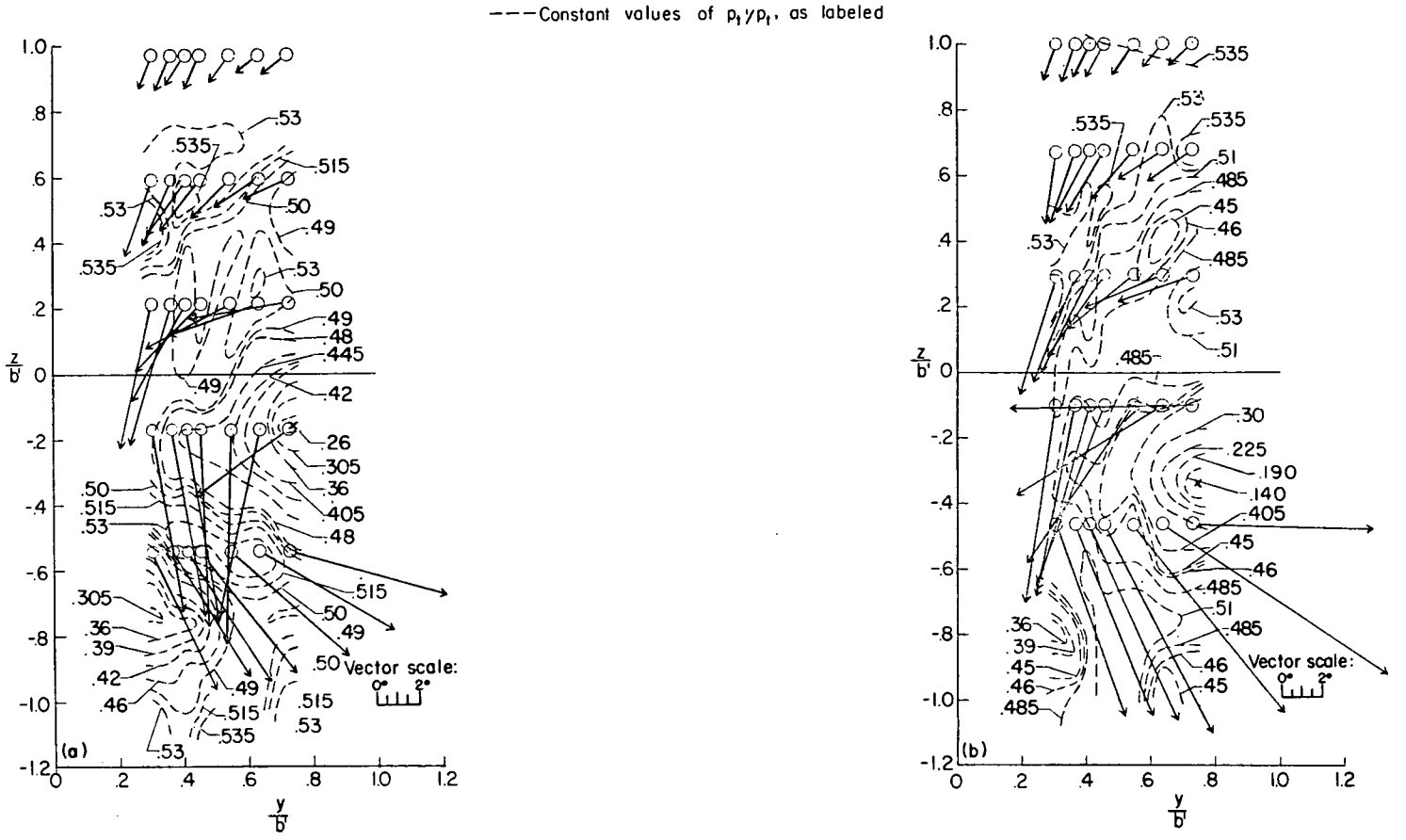
(b) $\alpha = -0.10°$.

FIGURE 12.—Pressure contours and vector representation of the flow behind a triangular wing. $\Lambda = 72°$; $M = 2.41$; $x = 1.5c_r$; $R = 1.42 \times 10^6$; $\frac{p_{t,\infty}}{p_t} = 0.536$.



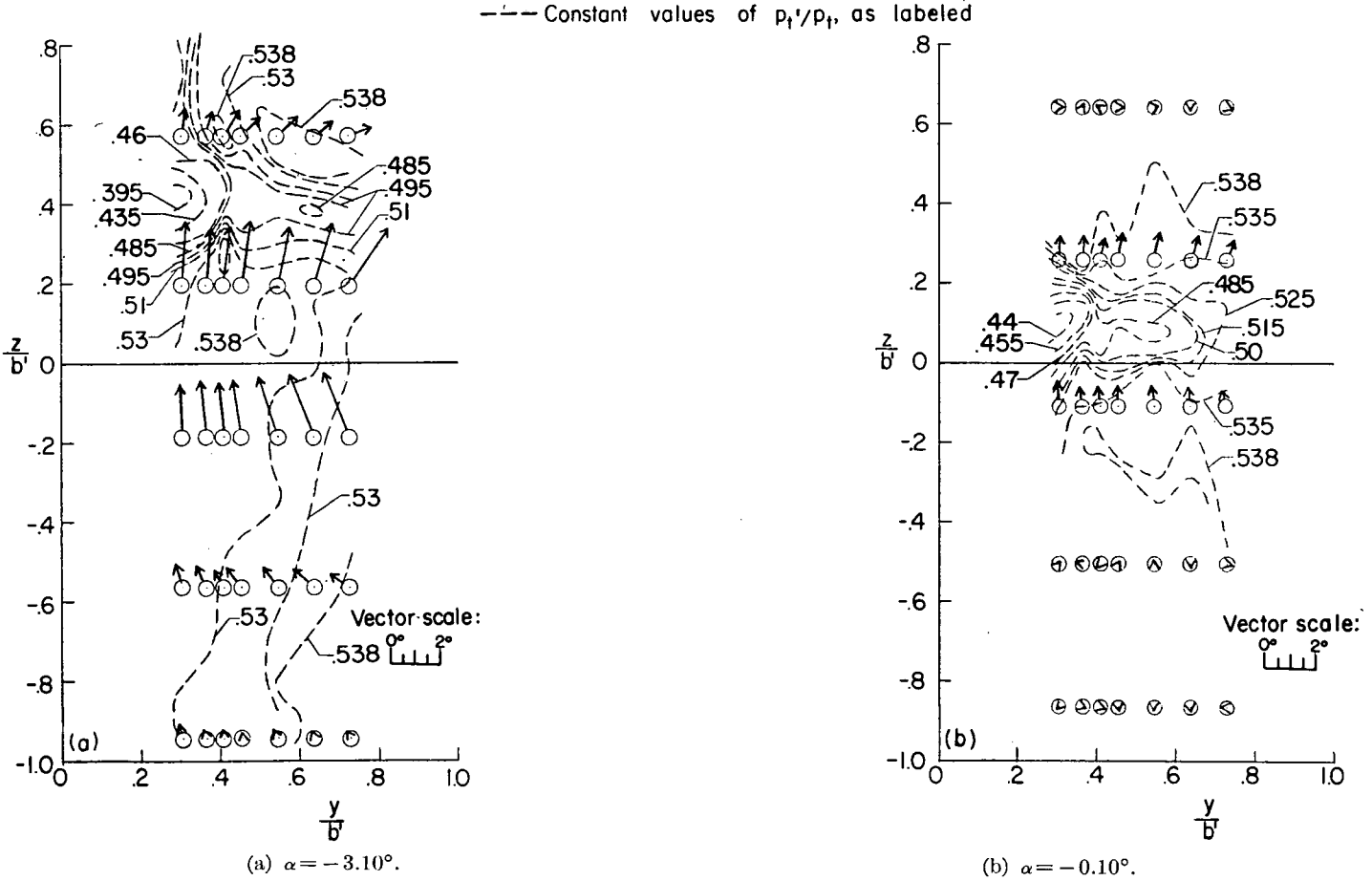
(c) $\alpha = 3.00°$. (d) $\alpha = 8.95°$.
(e) $\alpha = 14.00°$. (f) $\alpha = 16.90°$.

FIGURE 12.—Concluded.



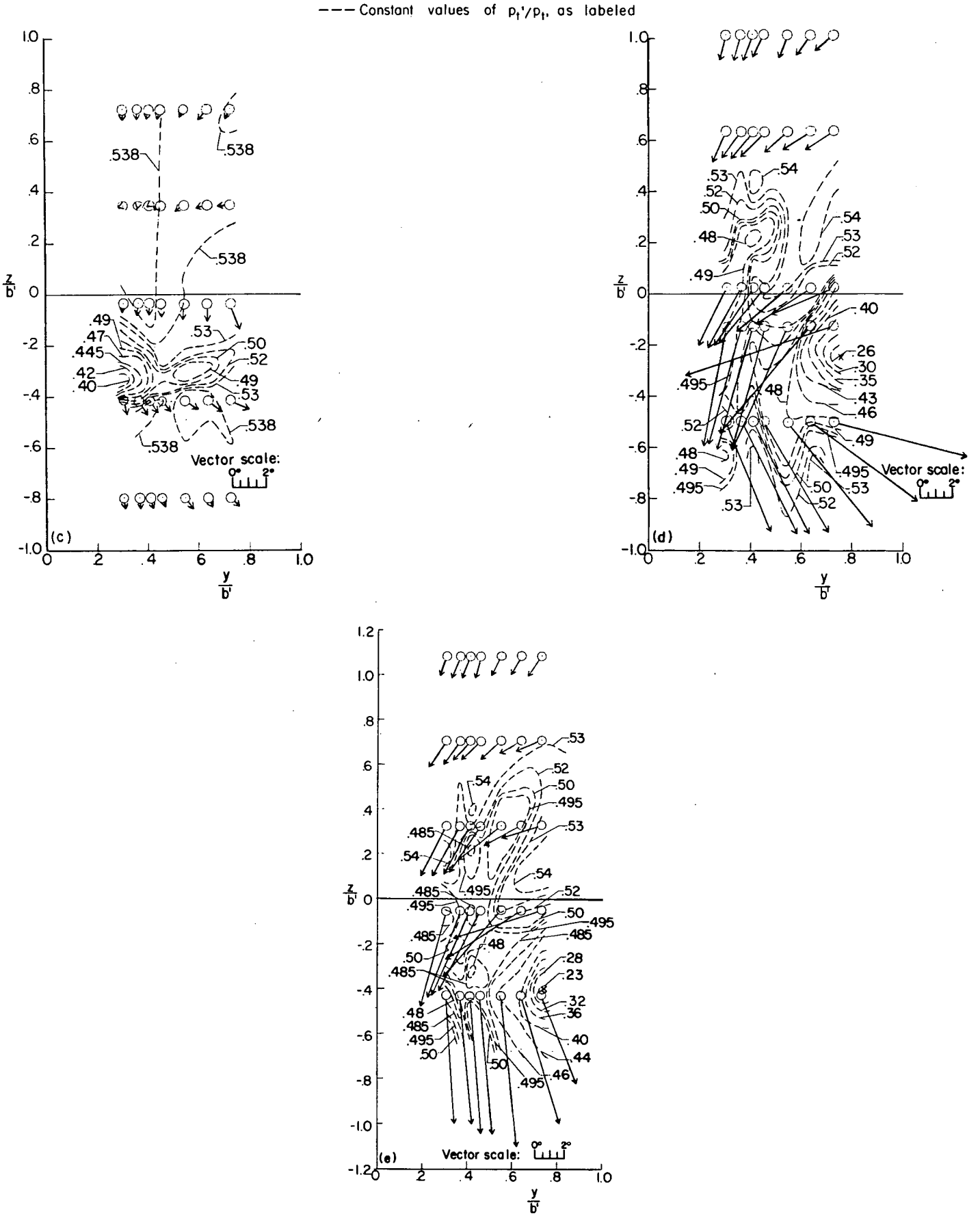
(a) $\alpha = 14.00°$. (b) $\alpha = 16.90°$.

FIGURE 13.—Pressure contours and vector representation of the flow behind a triangular wing. $\Lambda = 72°$; $M = 2.41$; $x = 3c_r$; $R = 1.42 \times 10^6$; $\frac{p_{t,\infty}}{p_t} = 0.536$.



(a) $\alpha = -3.10°$. (b) $\alpha = -0.10°$.

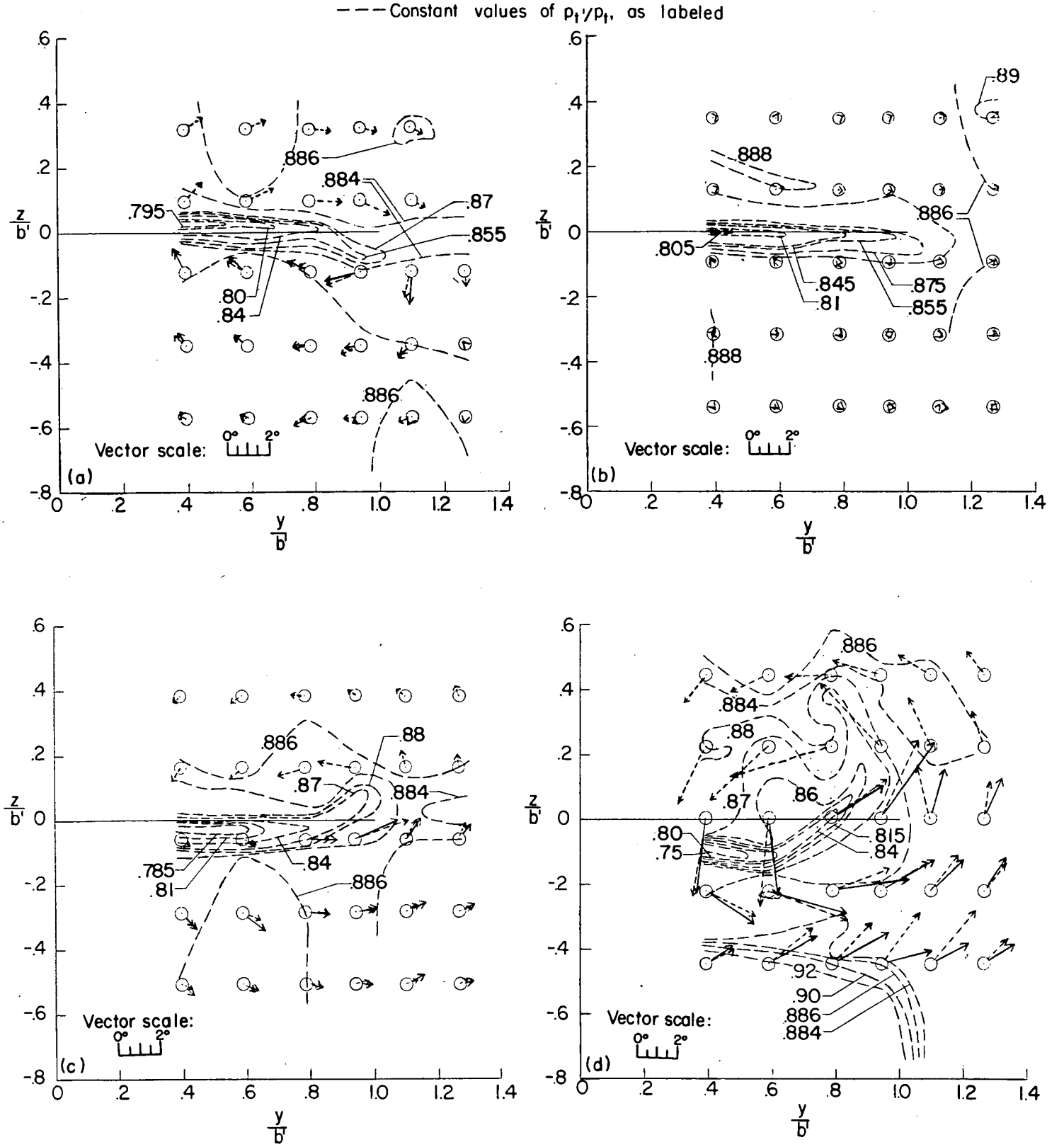
FIGURE 14.—Pressure contours and vector representation of the flow behind a triangular wing $\Lambda = 72°$; $M = 2.41$; $x = 4c_r$; $R = 1.42 \times 10^6$; $\frac{p_{t,\infty}}{p_t} = 0.536$.



(c) $\alpha = 3.00°$. (d) $\alpha = 14.00°$.

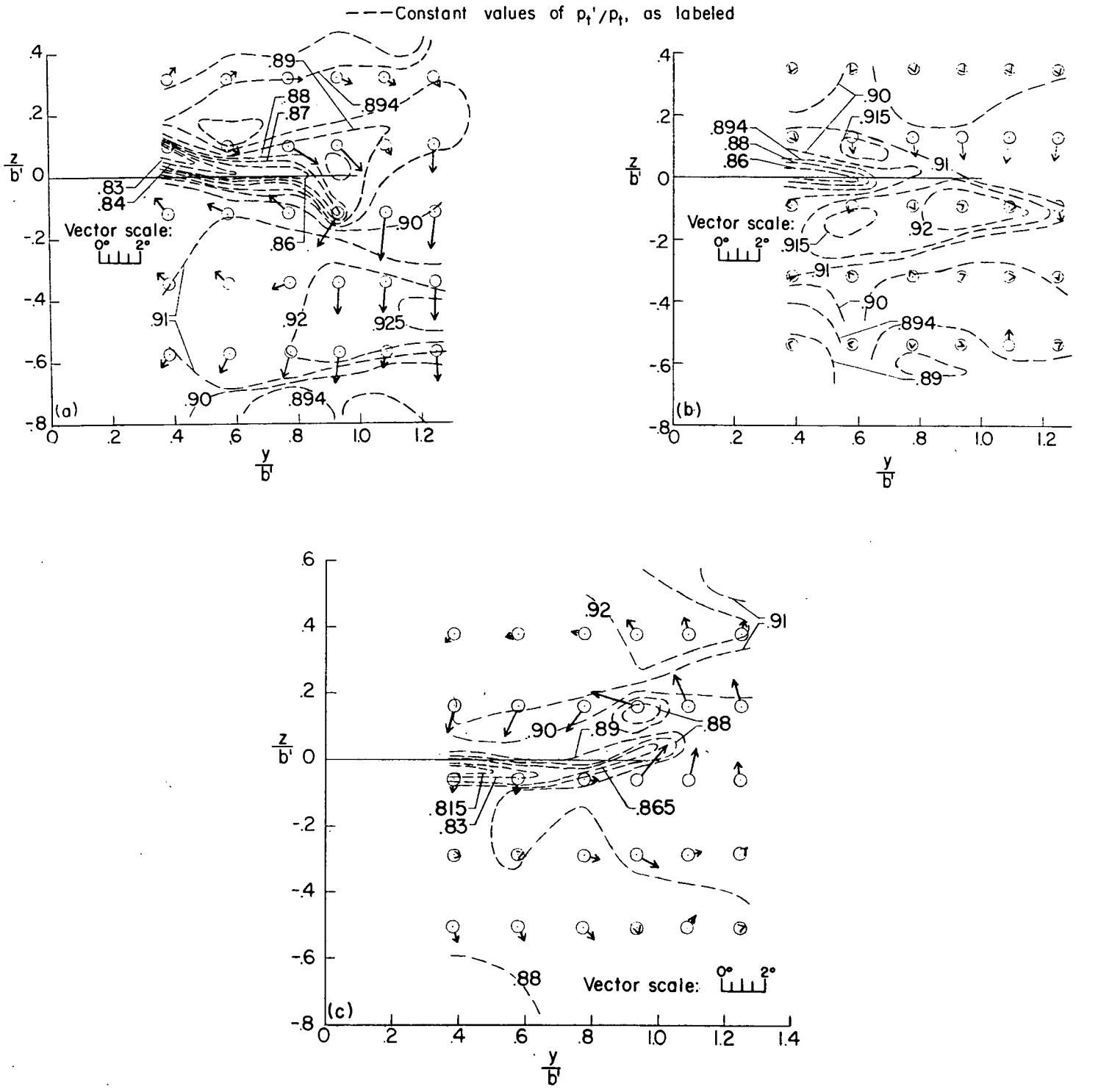
(e) $\alpha = 16.90°$.

FIGURE 14.—Concluded.



(a) $\alpha = -3.40°$.
(b) $\alpha = -0.45°$.
(c) $\alpha = 2.70°$.
(d) $\alpha = 8.60°$.

FIGURE 15.—Pressure contours and vector representation of the flow behind a triangular wing. $\Lambda = 50°$; $M = 1.62$; $x = 1.5c_r$; $R = 0.71 \times 10^6$ and 1.42×10^6; $\frac{p_{t,\infty}}{p_t} = 0.888$.

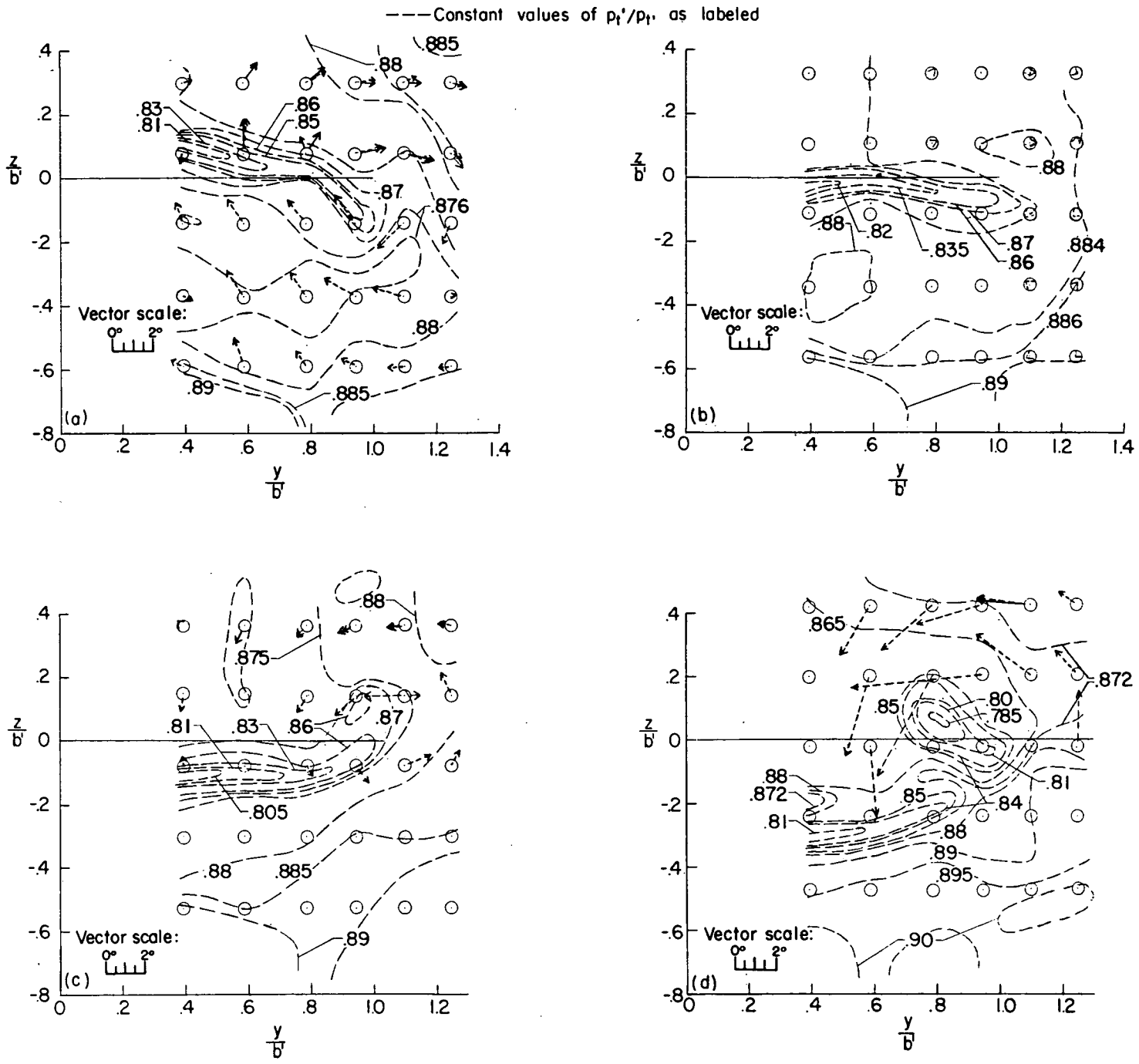


(a) $\alpha = -3.40°$.

(b) $\alpha = -0.50°$.

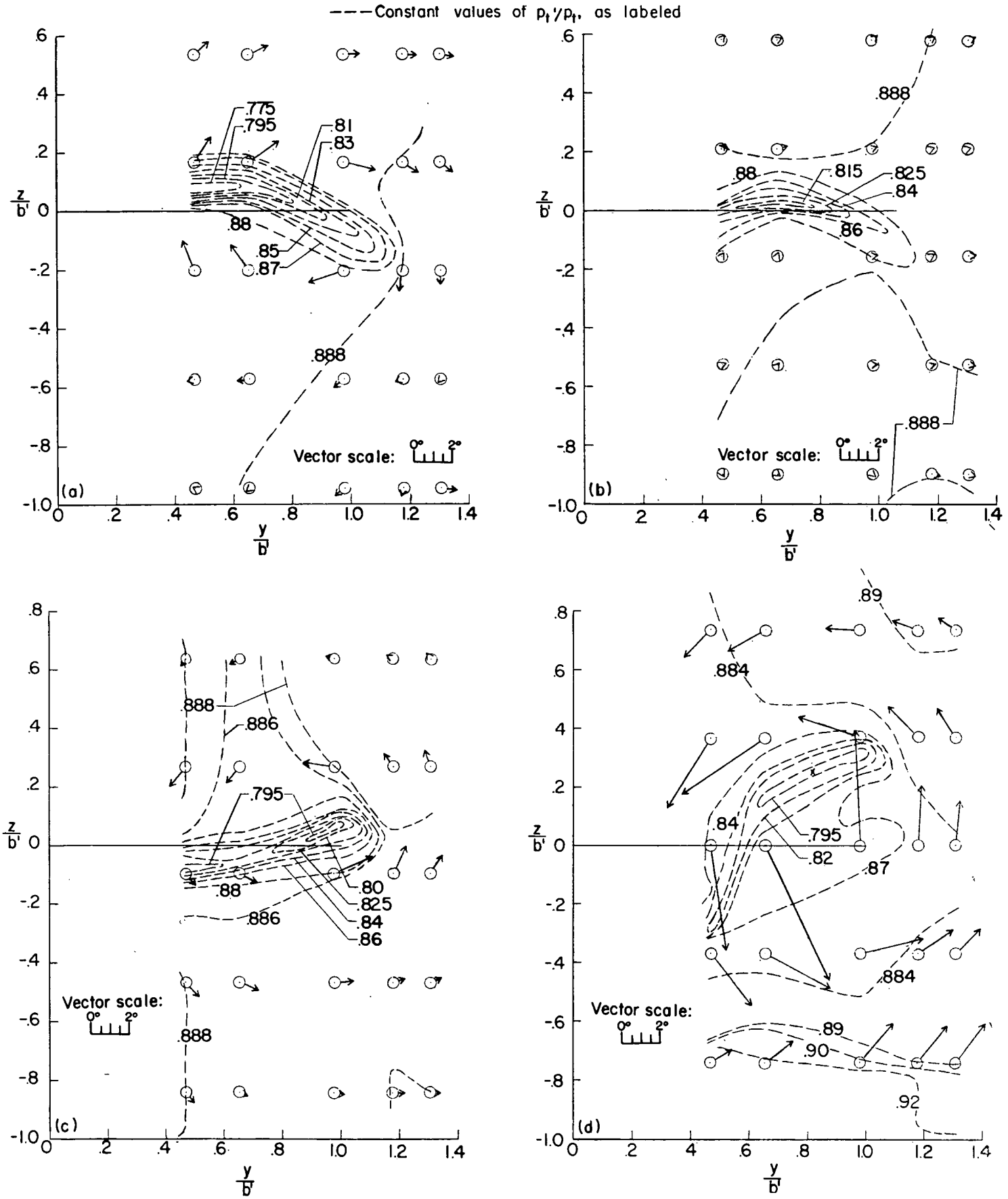
(c) $\alpha = 2.65°$.

FIGURE 16.—Pressure contours and vector representation of the flow behind a triangular wing. $\Lambda = 50°$; $M = 1.62$; $x = 3c_r$; $R = 1.42 \times 10^6$; $\frac{p_{t,\infty}}{p_t} = 0.888$.



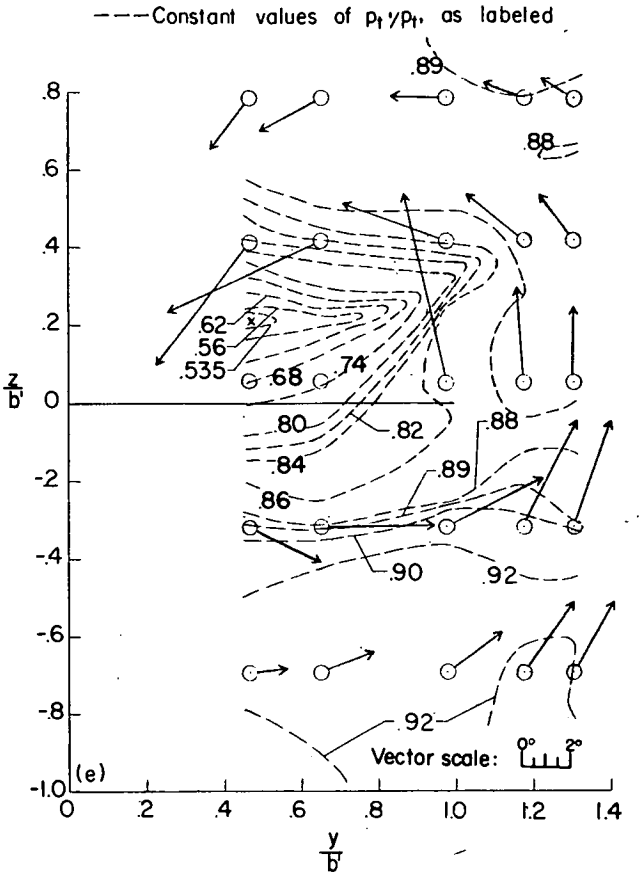
(a) $\alpha = -3.40°$.
(b) $\alpha = -0.50°$.
(c) $\alpha = 2.60°$.
(d) $\alpha = 8.50°$.

FIGURE 17.—Pressure contours and vector representation of the flow behind a triangular wing. $\Lambda = 50°$; $M = 1.62$; $x = 4c_r$; $R = 0.71 \times 10^6$ and 1.42×10^6; $\frac{p_{t,\infty}}{p_t} = 0.888$.



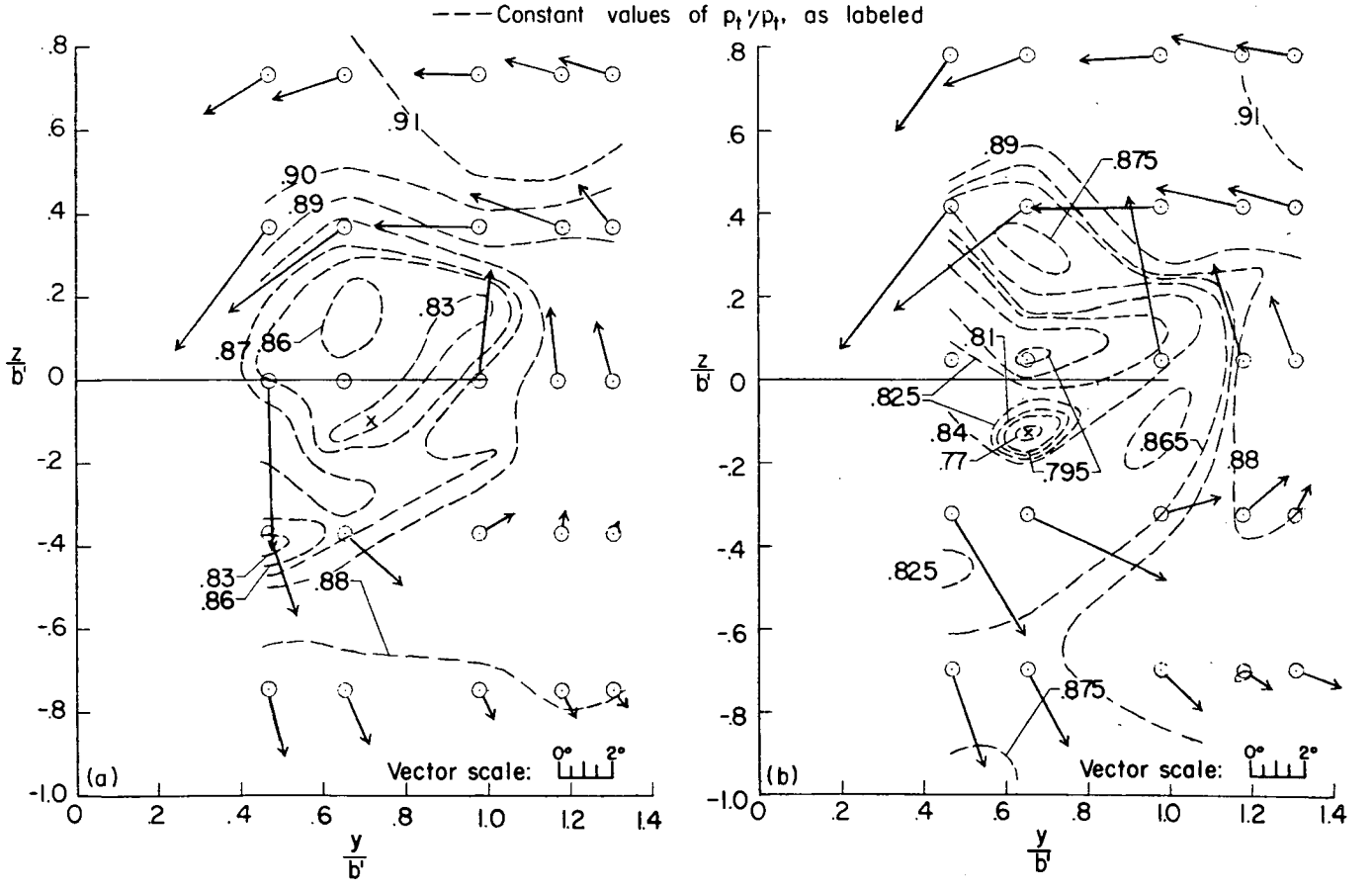
(a) $\alpha = -3.05°$.
(b) $\alpha = -0.15°$.
(c) $\alpha = 3.00°$.
(d) $\alpha = 8.95°$.

FIGURE 18.—Pressure contours and vector representation of the flow behind a triangular wing. $\Lambda = 63°$; $M = 1.62$; $x = 1.5c_r$; $R = 1.42 \times 10^6$; $\frac{p_{t,\infty}}{p_t} = 0.888$.



(e) $\alpha = 11.90°$.

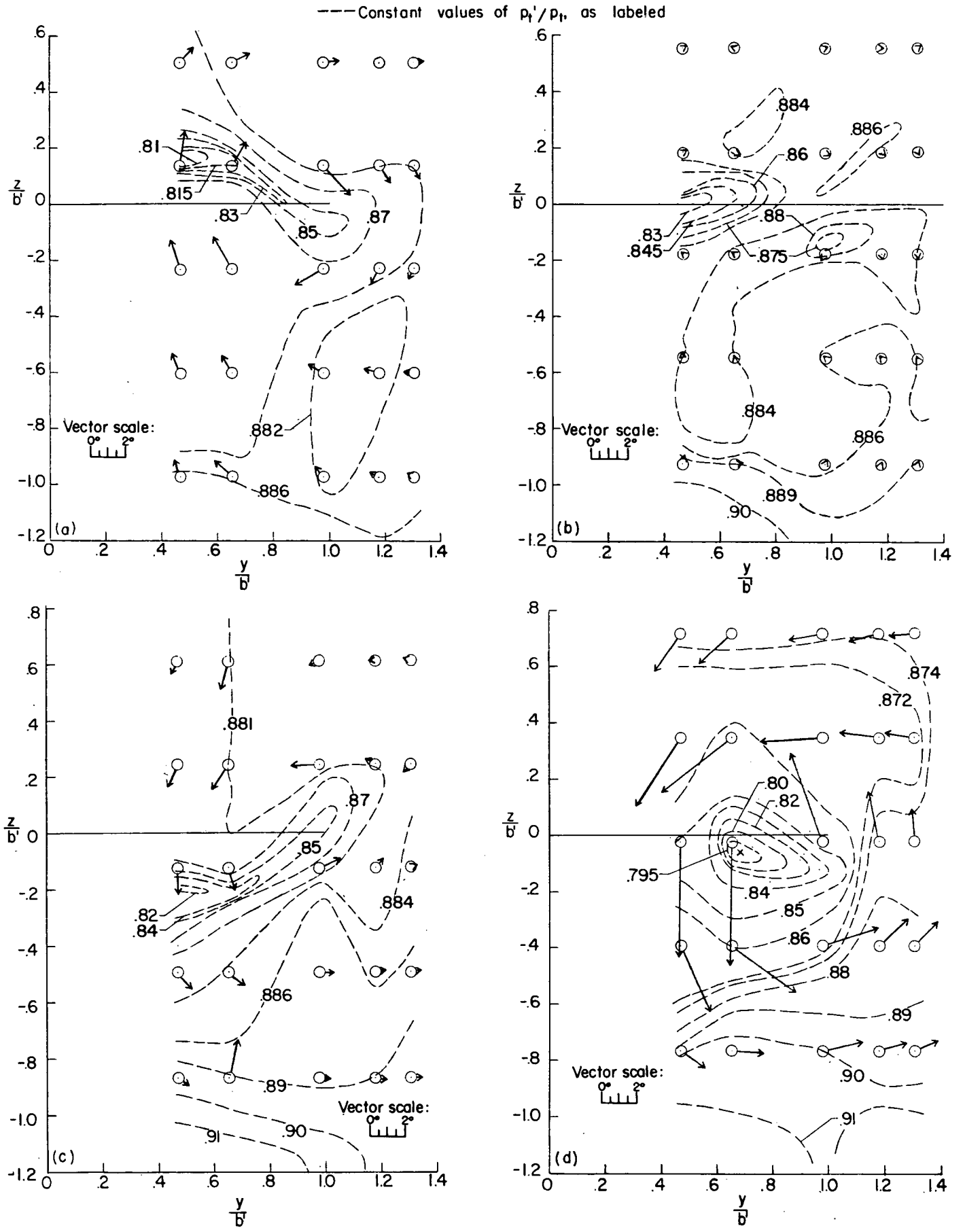
FIGURE 18.—Concluded.



(a) $\alpha = 8.55°$.

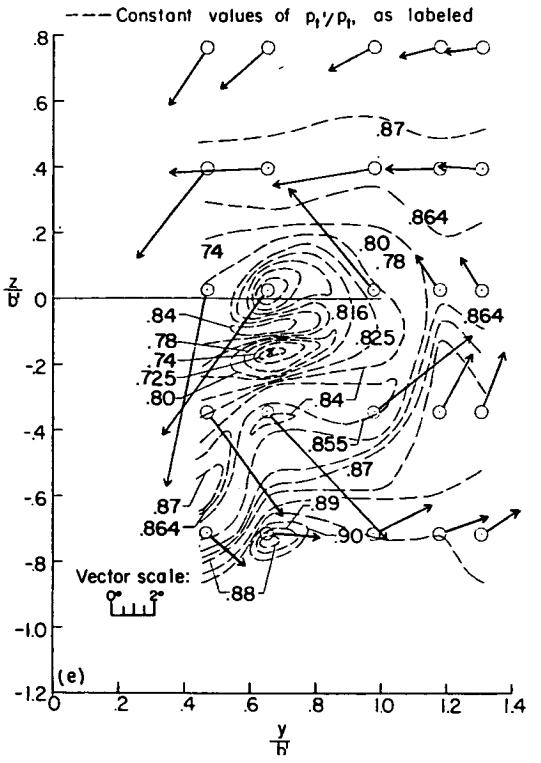
(b) $\alpha = 11.65°$.

FIGURE 19.—Pressure contours and vector representation of the flow behind a triangular wing. $\Lambda = 63°$; $M = 1.62$; $x = 3c_r$; $R = 1.42 \times 10^6$; $\frac{p_{t,\infty}}{p_t} = 0.888$.



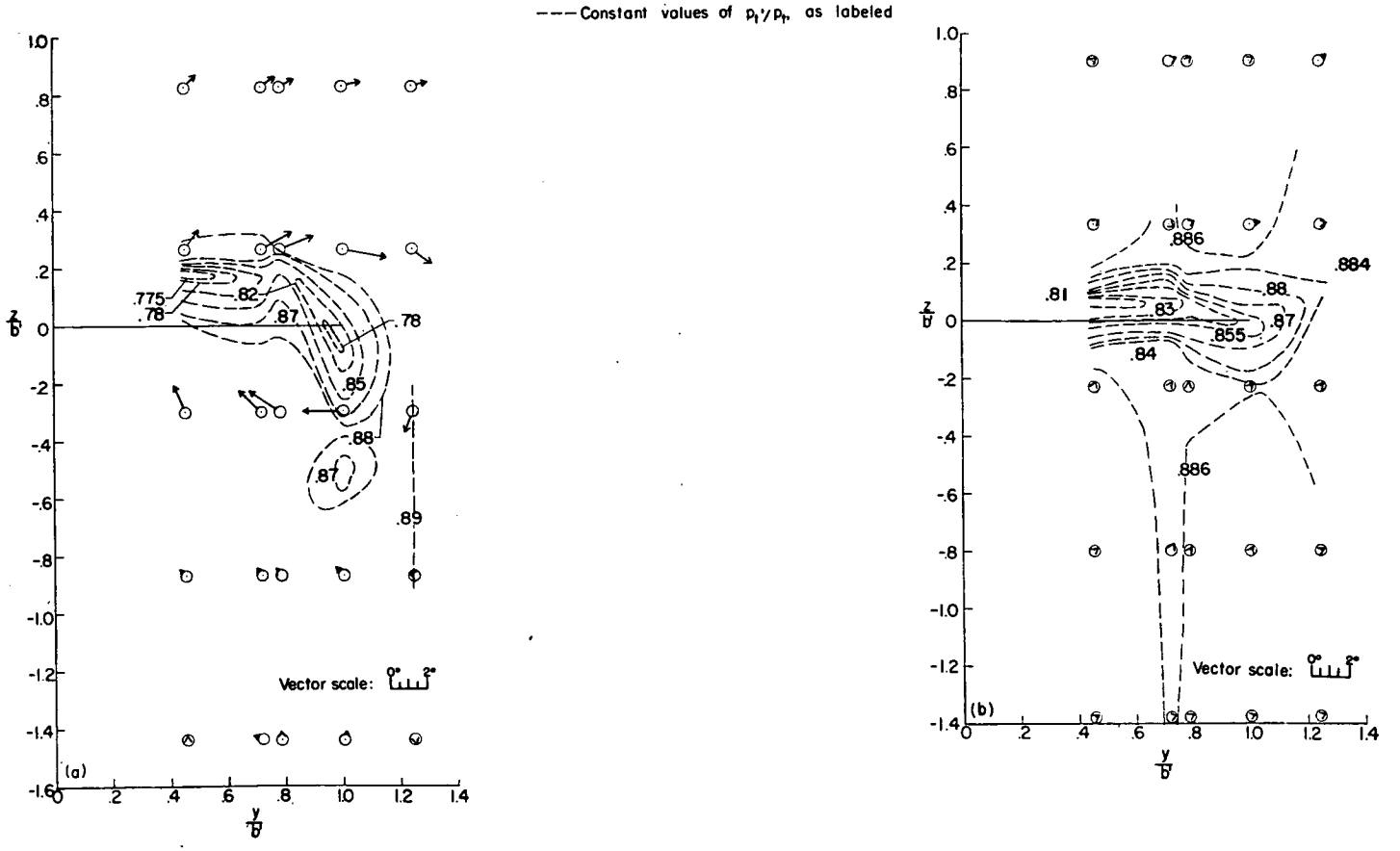
(a) $\alpha = -3.30°$.
(b) $\alpha = -0.35°$.
(c) $\alpha = 2.85°$.
(d) $\alpha = 8.90°$.

FIGURE 20.—Pressure contours and vector representation of the flow behind a triangular wing. $\Lambda = 63°$; $M = 1.62$; $x = 4c_r$; $R = 1.42 \times 10^6$; $\frac{p_{t,\infty}}{p_t} = 0.888$.



(e) $\alpha=11.65°$.

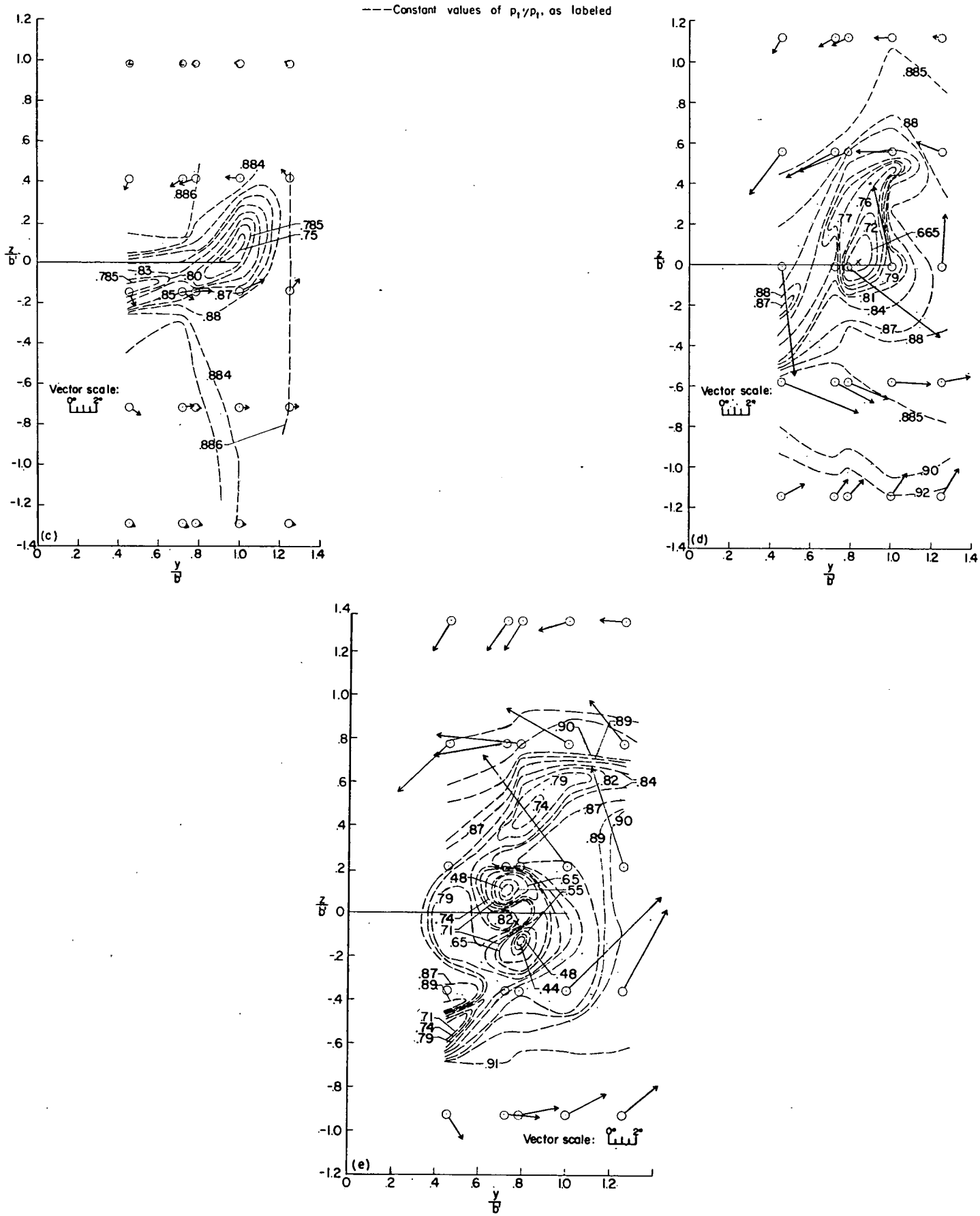
FIGURE 20.—Concluded.



(a) $\alpha=-3.00°$.

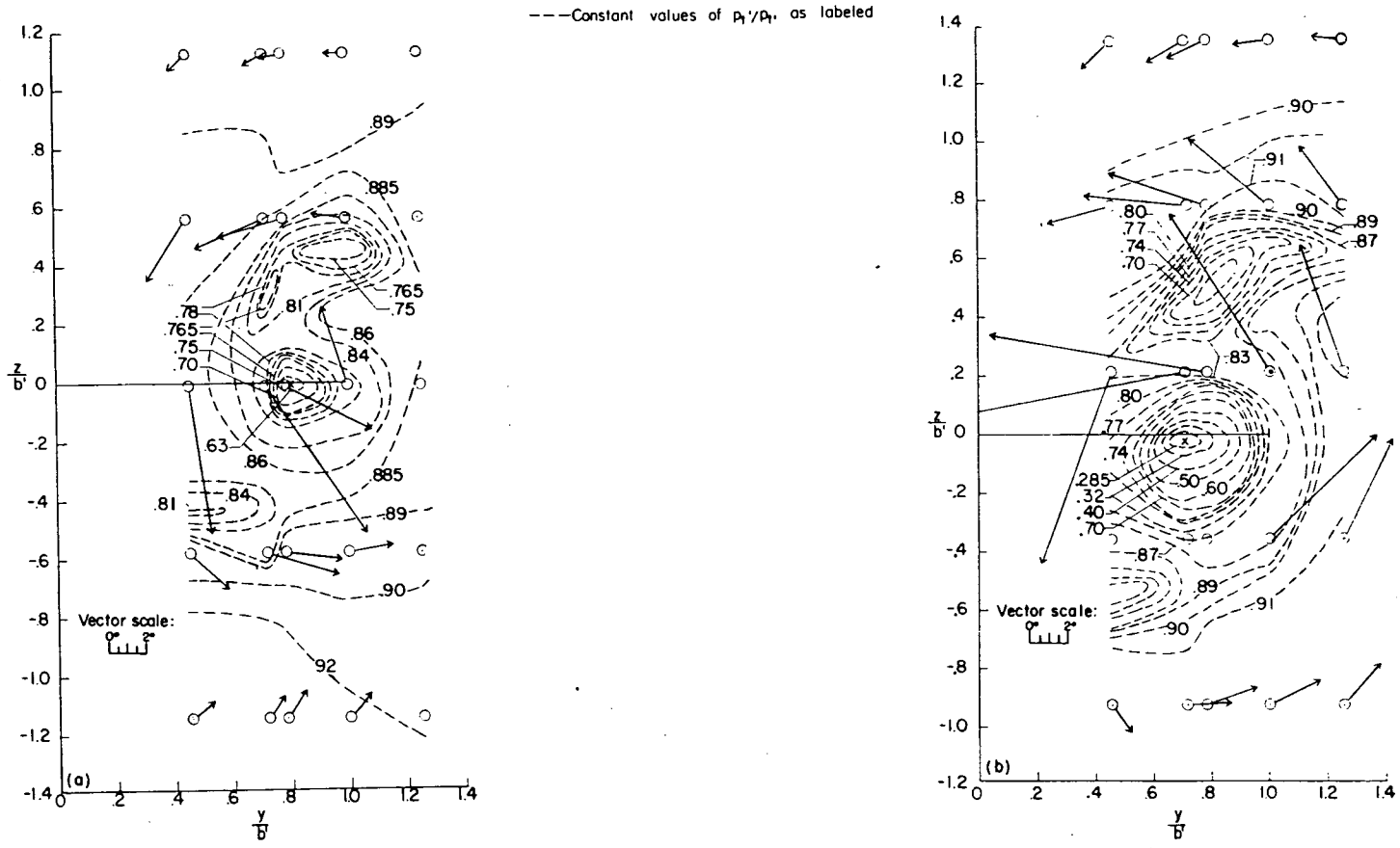
(b) $\alpha=0.05°$.

FIGURE 21.—Pressure contours and vector representation of the flow behind a triangular wing. $\Lambda=72°$; $M=1.62$; $x=1.5c_r$; $R=1.42\times10^6$; $\frac{p_{t,\infty}}{p_t}=0.088$.



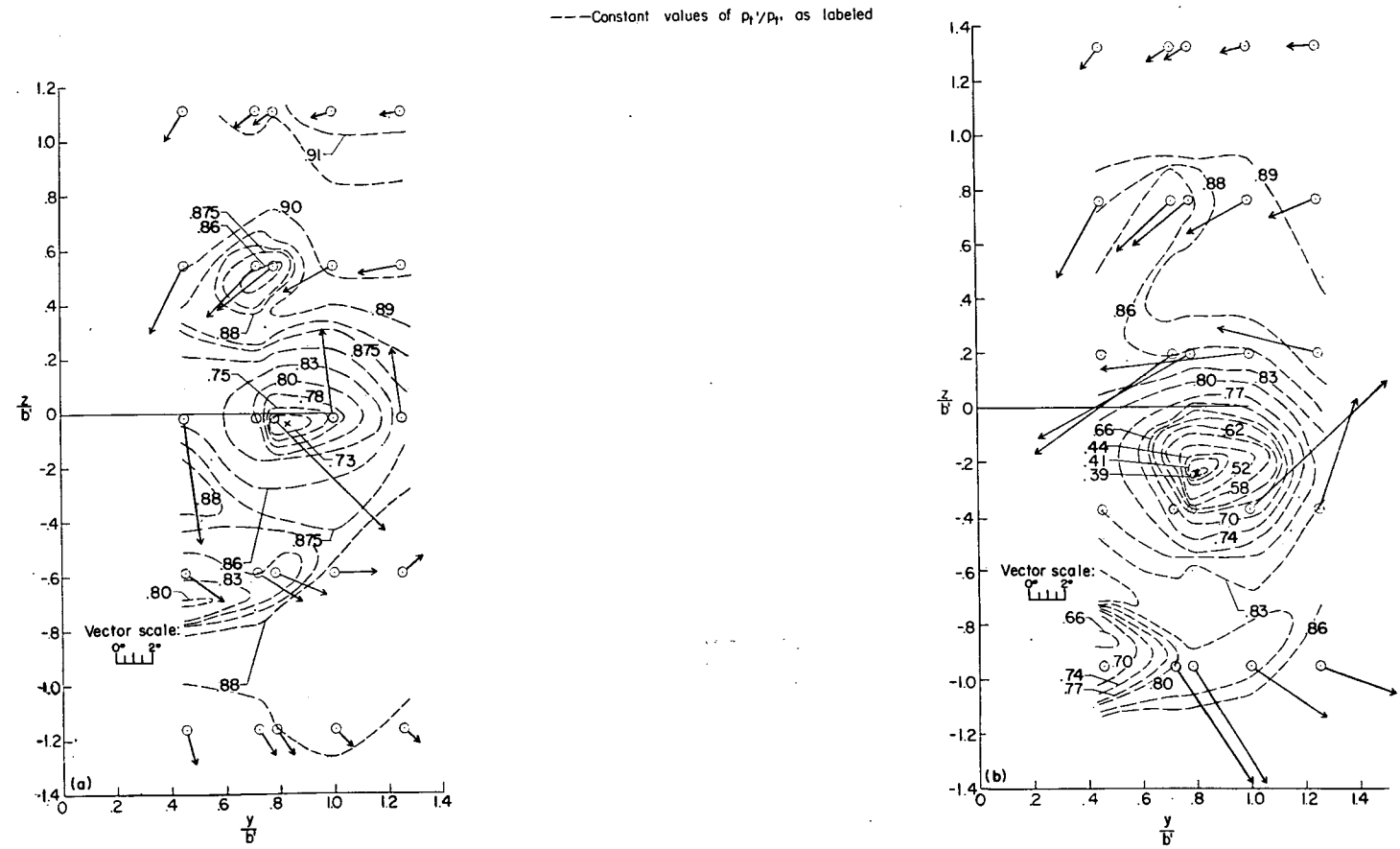
(c) $\alpha = 3.15°$. (d) $\alpha = 8.95°$.
(e) $\alpha = 16.85°$.

FIGURE 21.—Concluded.



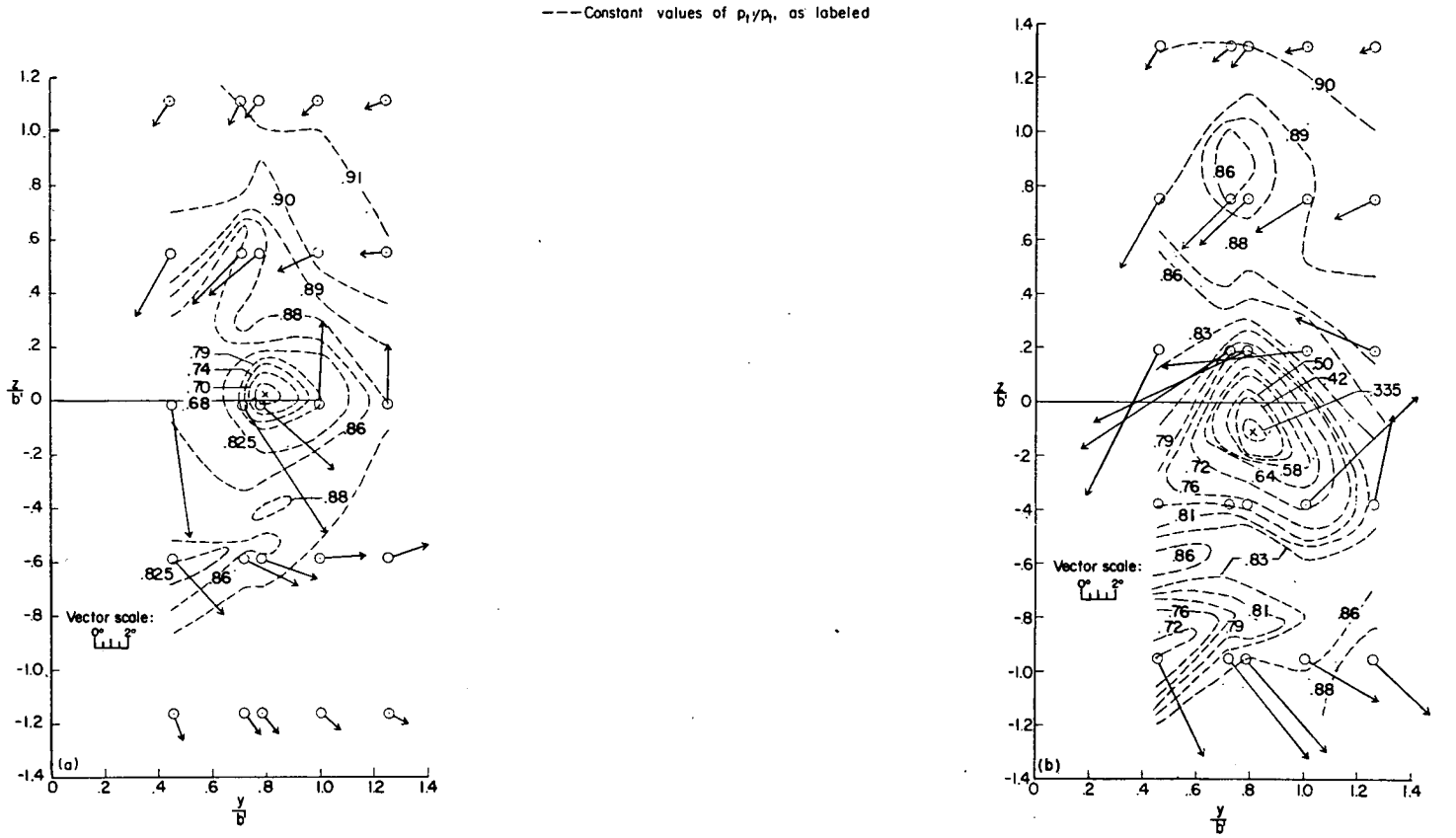
(a) $\alpha=8.95°$. (b) $\alpha=16.85°$.

FIGURE 22.—Pressure contours and vector representation of the flow behind a triangular wing. $\Lambda=72°$; $M=1.62$; $x=1.5c_r$; $R=0.71\times10^6$; $\frac{p_{t,\infty}}{p_t}=0.888$.



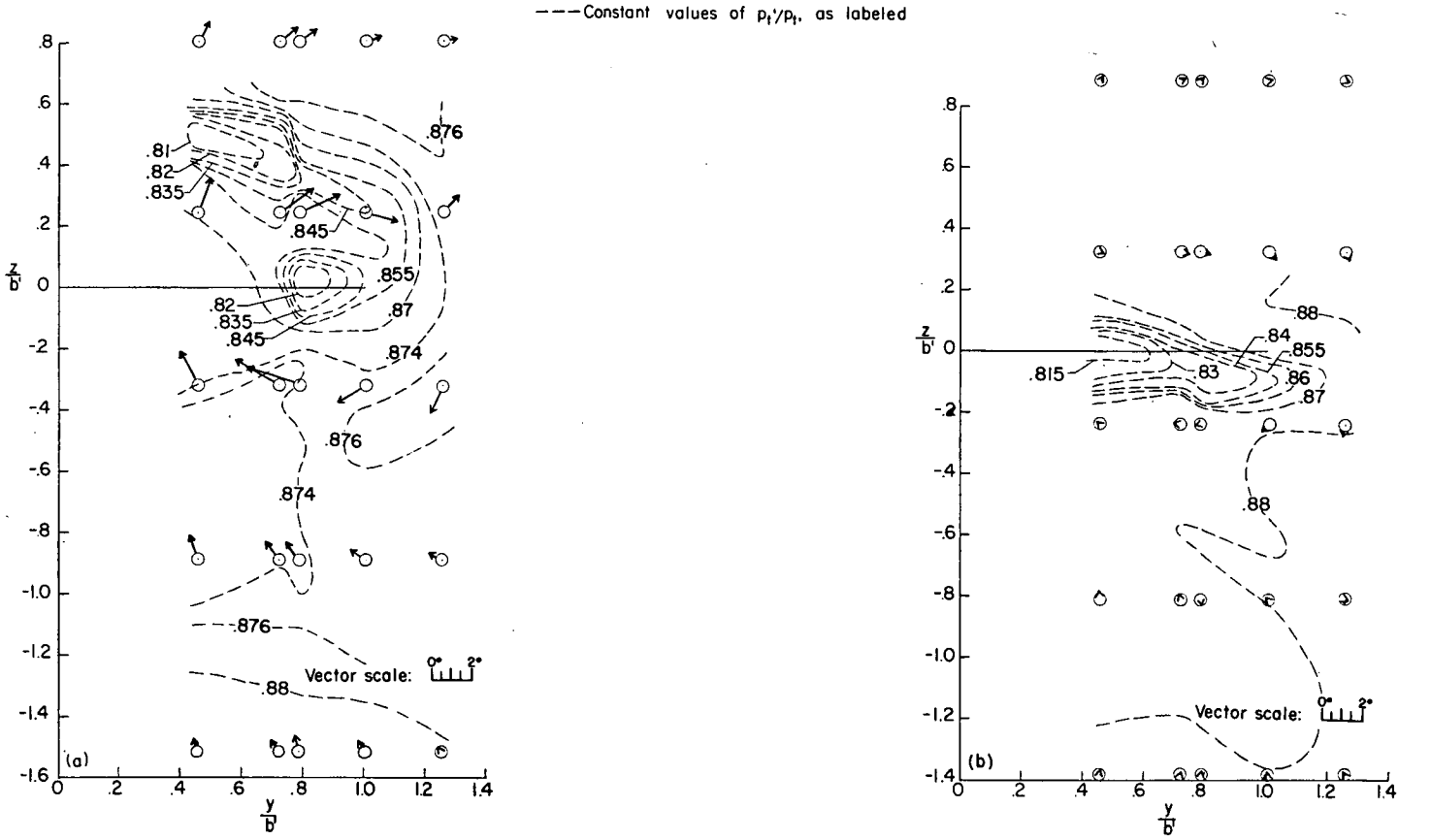
(a) $\alpha=8.90°$. (b) $\alpha=16.80°$.

FIGURE 23.—Pressure contours and vector representation of the flow behind a triangular wing. $\Lambda=72°$; $M=1.62$; $x=3c_r$; $R=1.42\times10^6$; $\frac{p_{t,\infty}}{p_t}=0.888$.



(a) $\alpha=8.90°$. (b) $\alpha=16.80°$.

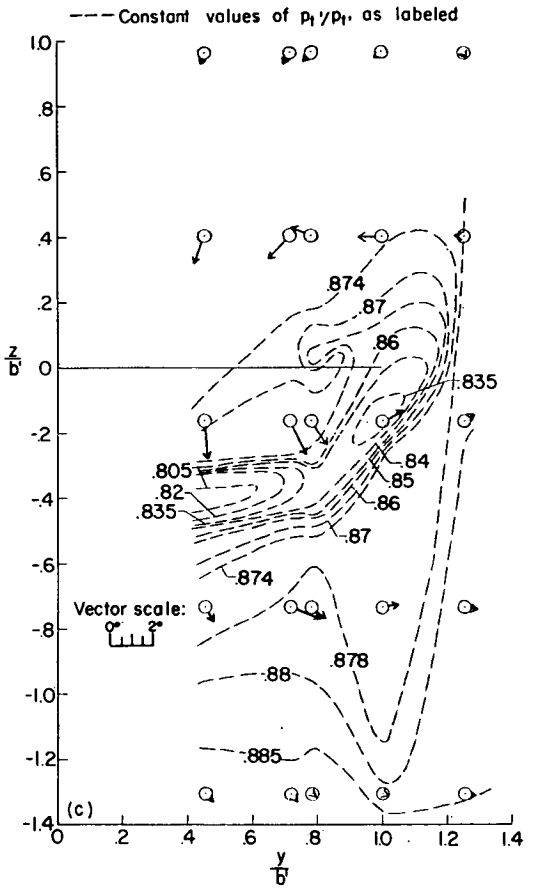
FIGURE 24.—Pressure contours and vector representation of the flow behind a triangular wing. $\Lambda=72°$; $M=1.62$; $x=3c_r$; $R=0.71\times10^6$; $\frac{p_{t,\infty}}{p_t}=0.888$.



(a) $\alpha=-2.90°$. (b) $\alpha=-0.30°$.

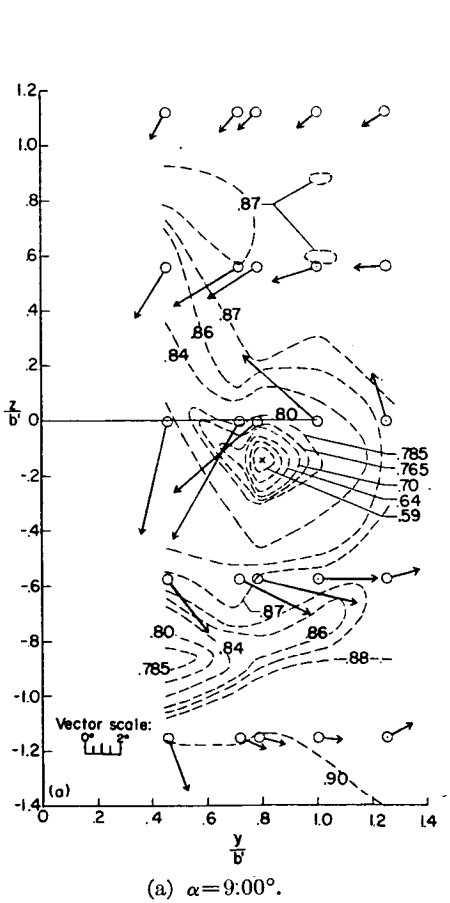
FIGURE 25.—Pressure contours and vector representation of the flow behind a triangular wing. $\Lambda=72°$; $M=1.62$; $x=4c_r$; $R=1.42\times10^6$; $\frac{p_{t,\infty}}{p_t}=0.888$.

526597—60——71

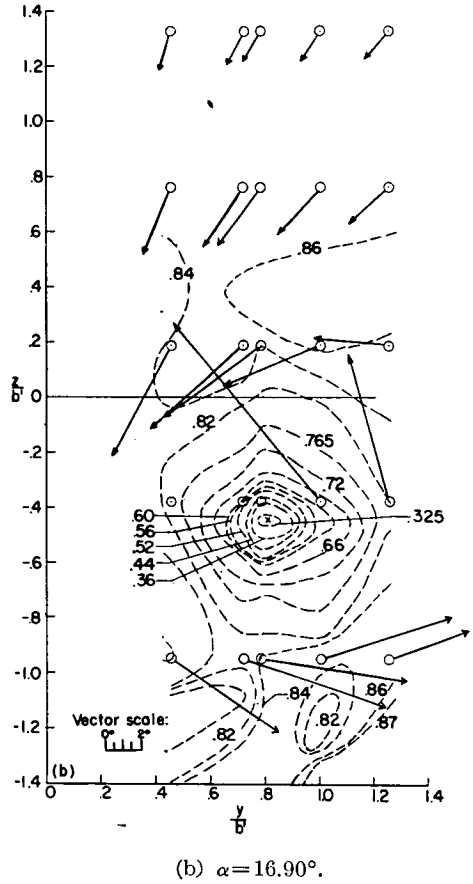


(c) $\alpha=3.10°$.

FIGURE 25.—Concluded.

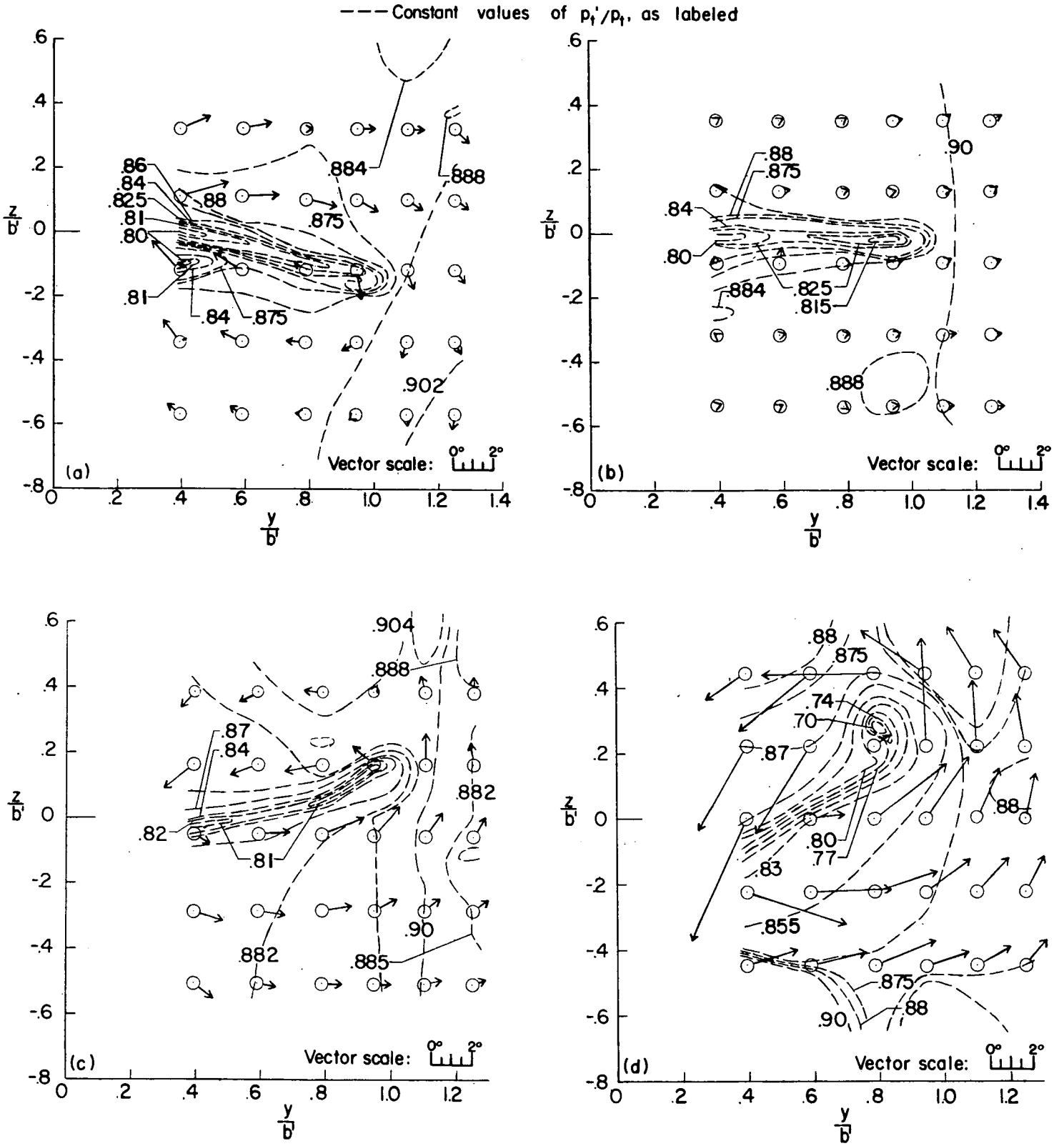


(a) $\alpha=9.00°$.



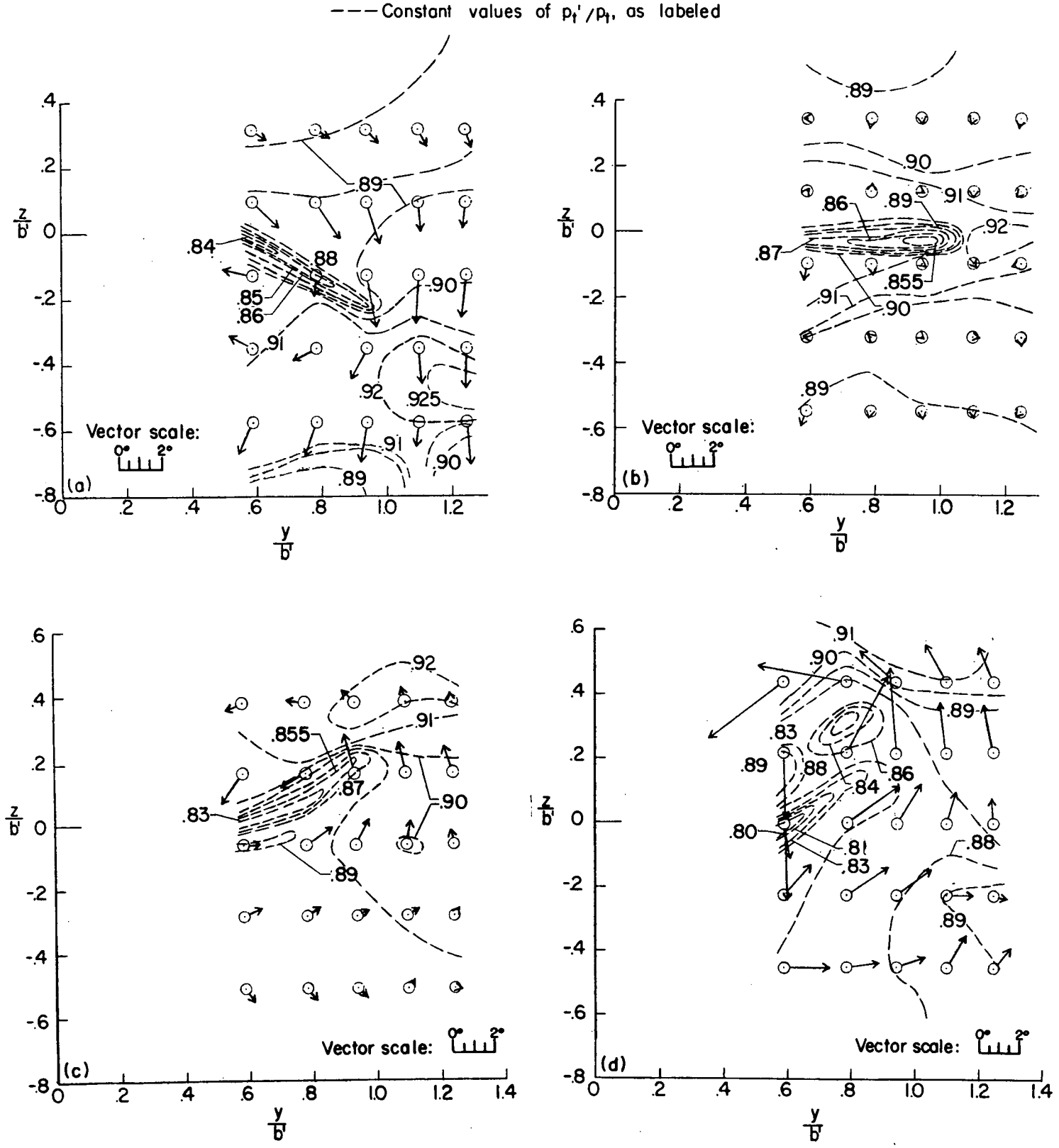
(b) $\alpha=16.90°$.

FIGURE 26.—Pressure contours and vector representation of the flow behind a triangular wing. $\Lambda=72°$; $M=1.62$; $x=4c_r$; $R=0.71\times10^6$; $\frac{p_{t,\infty}}{p_t}=0.888$.



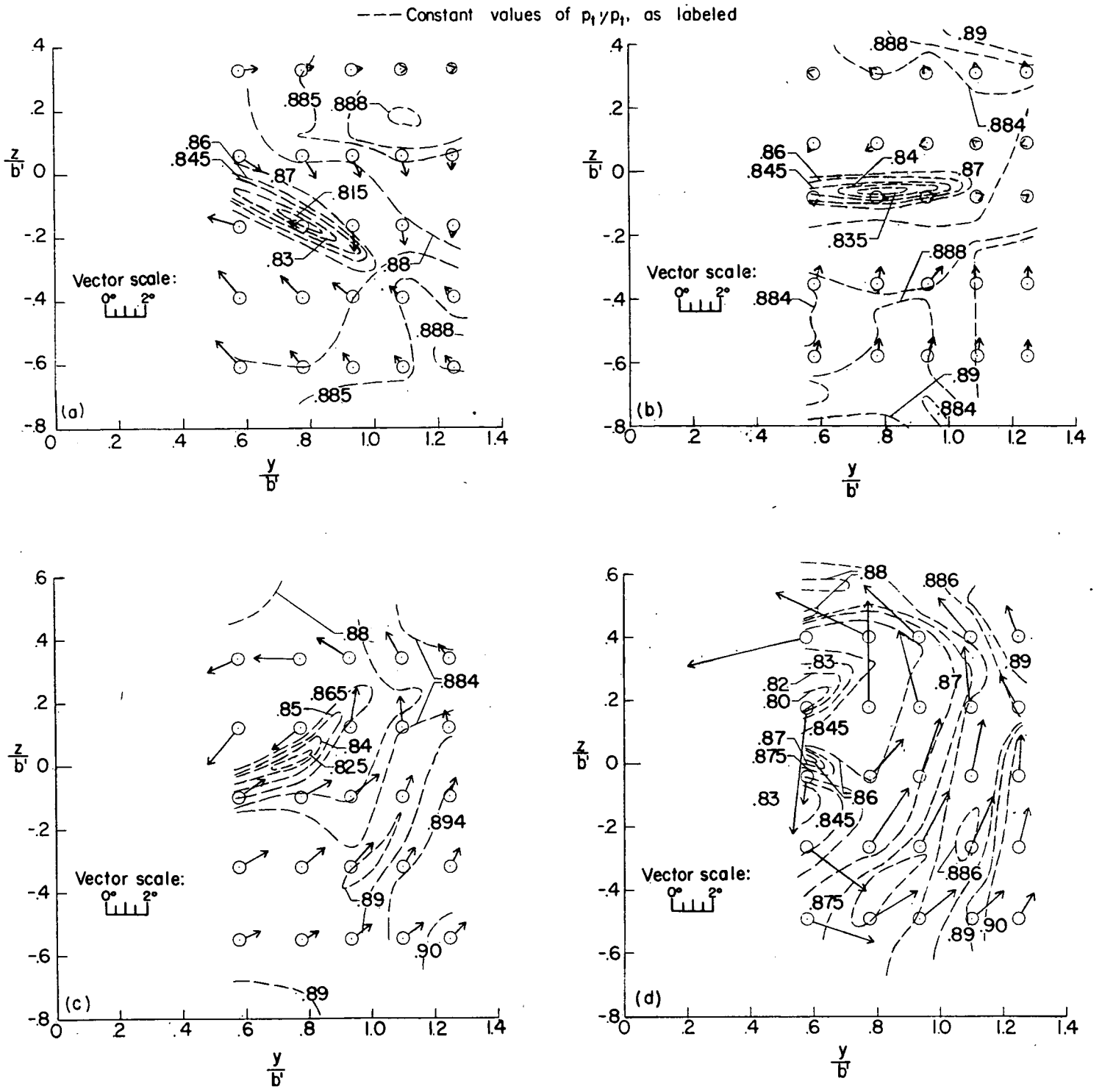
(a) $\alpha = -3.30°$.
(b) $\alpha = -0.45°$.
(c) $\alpha = 2.70°$.
(d) $\alpha = 8.60°$.

FIGURE 27.—Pressure contours and vector representation of the flow behind a reversed triangular wing. $\Lambda_{TE} = -50°$; $M = 1.62$; $x = 1.5c_r$; $R = 1.42 \times 10^6$; $\frac{p_{t,\infty}}{p_t} = 0.888$.



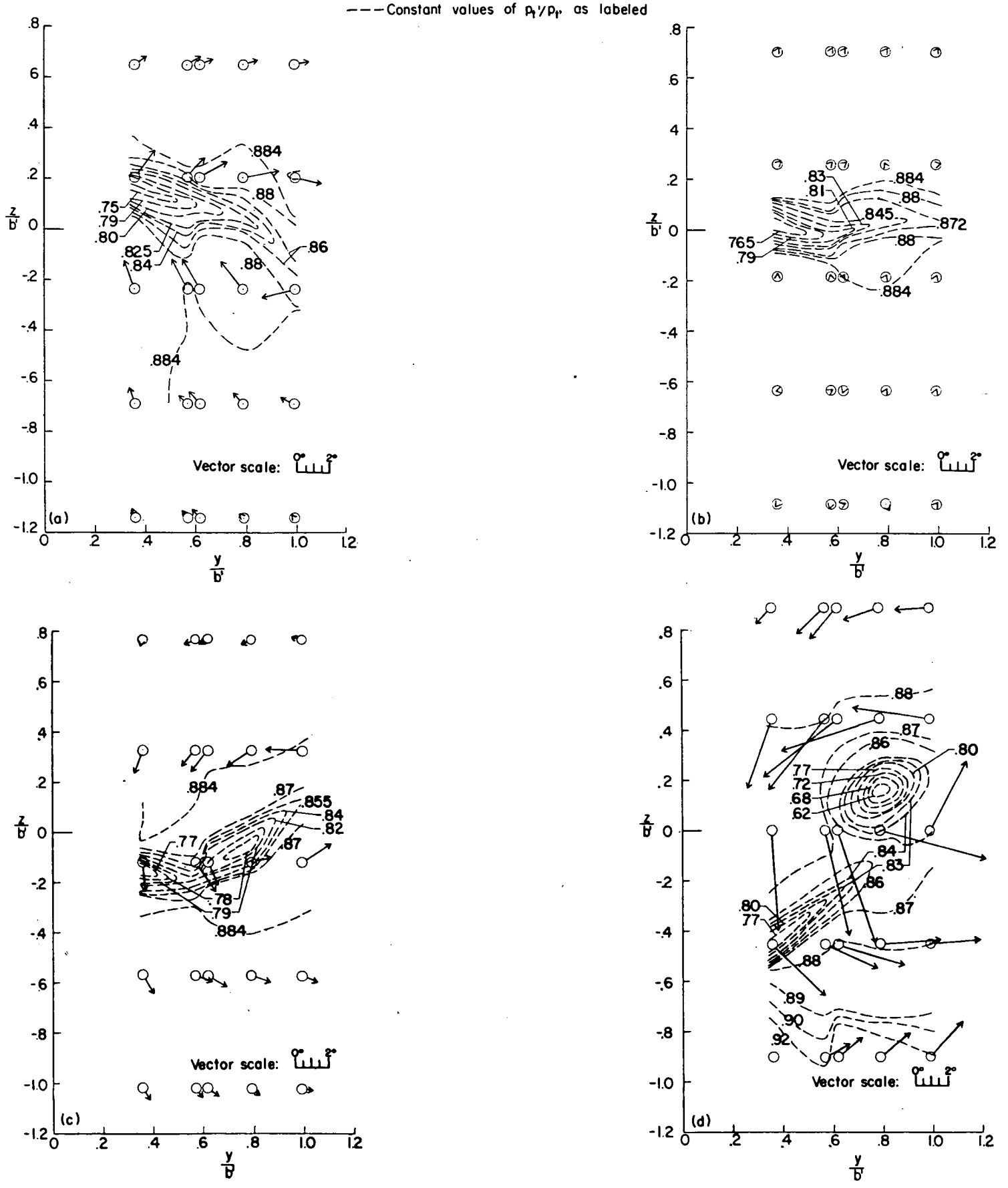
(a) $\alpha = -3.50°$.
(b) $\alpha = -0.45°$.
(c) $\alpha = 2.70°$.
(d) $\alpha = 8.55°$.

FIGURE 28.—Pressure contours and vector representation of the flow behind a reversed triangular wing. $\Lambda_{TE} = -50°$; $M = 1.62$; $x = 3c_r$; $R = 1.42 \times 10^6$; $\frac{p_{t,\infty}}{p_t} = 0.888$.



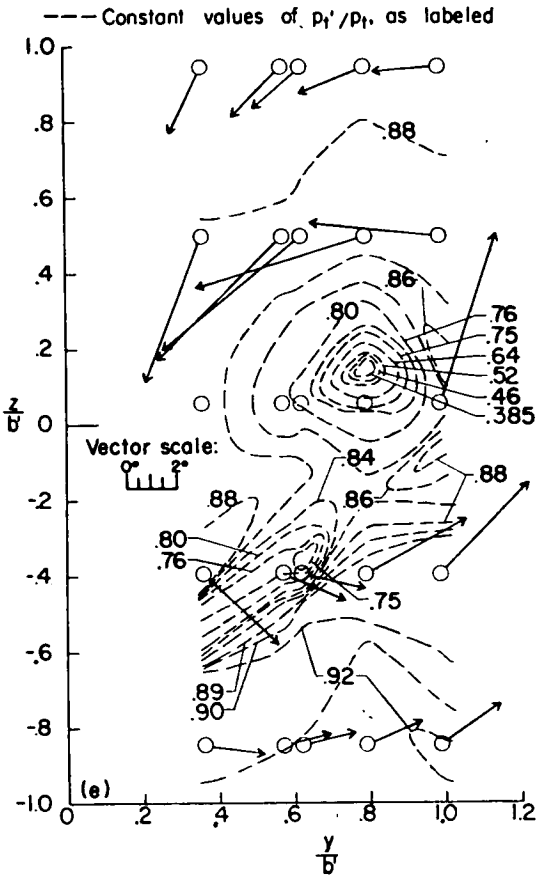
(a) $\alpha = -3.35°$.
(b) $\alpha = -0.15°$.
(c) $\alpha = 2.90°$.
(d) $\alpha = 8.60°$.

FIGURE 29.—Pressure contours and vector representation of the flow behind a reversed triangular wing. $\Lambda_{TE} = -50°$; $M = 1.62$; $x = 4c_r$; $R = 1.42 \times 10^6$; $\frac{p_{t,\infty}}{p_t} = 0.888$.



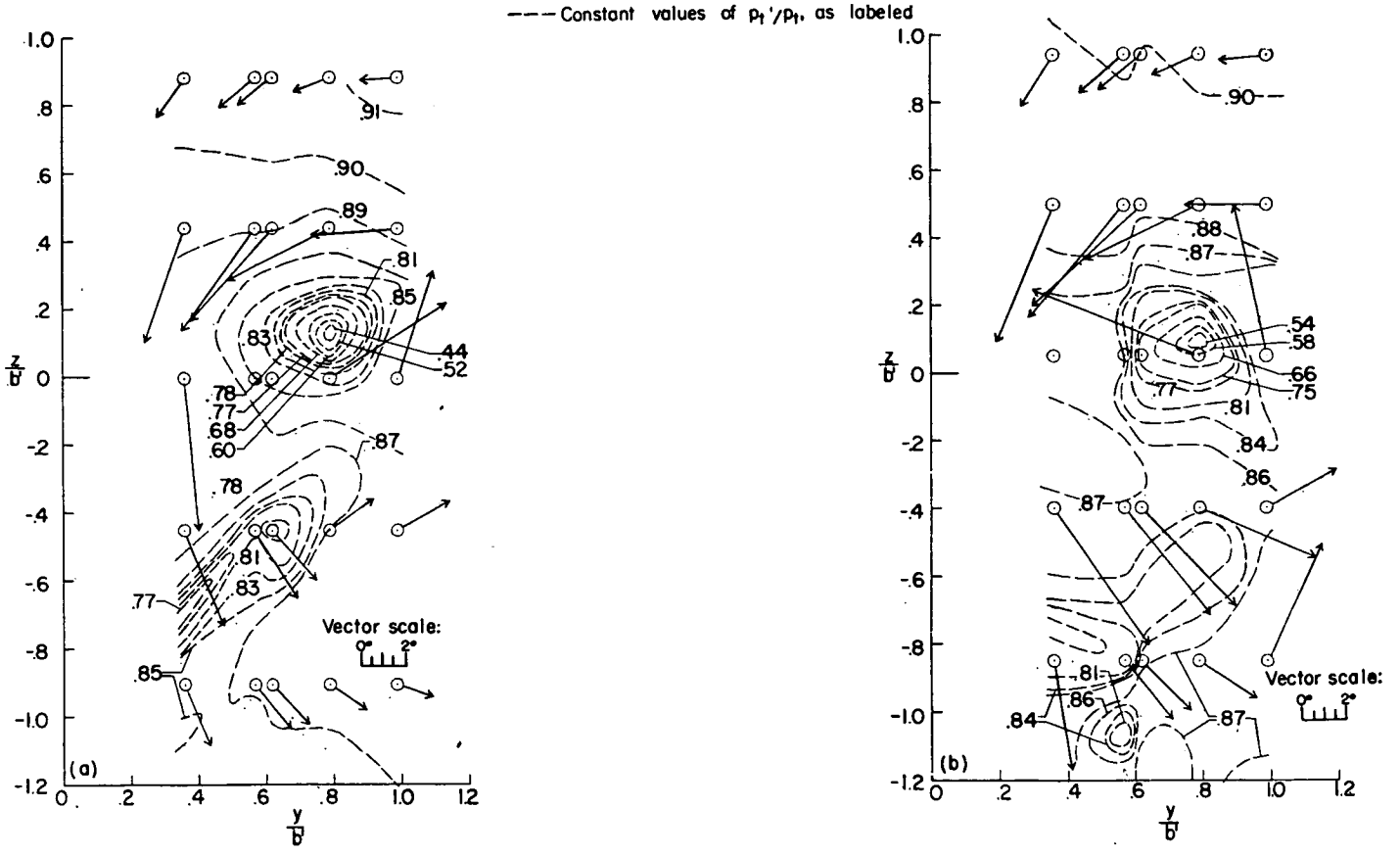
(a) $\alpha = -3.00°$.
(b) $\alpha = 0°$.
(c) $\alpha = 3.00°$.
(d) $\alpha = 8.90°$.

FIGURE 30.—Pressure contours and vector representation of the flow behind a diamond-plan-form wing. $\Lambda = -\Lambda_{TE} = 50°$; $M = 1.62$; $x = 1.5c_r$; $R = 1.42 \times 10^6$; $\frac{p_{t,\infty}}{p_t} = 0.888$.



(e) $\alpha=11.90°$.

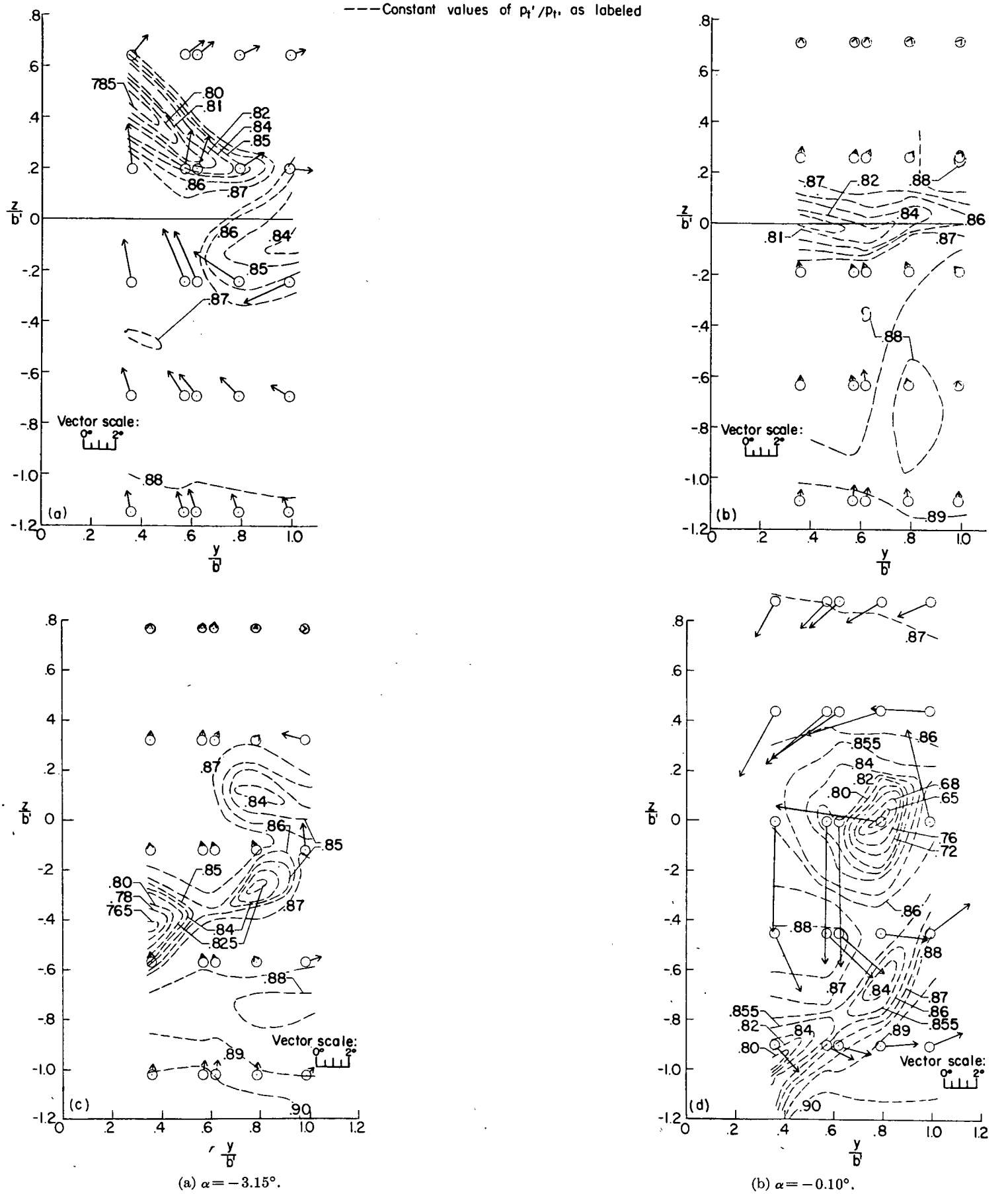
FIGURE 30.—Concluded.



(a) $\alpha=8.60°$.

(b) $\alpha=11.90°$.

FIGURE 31.—Pressure contours and vector representation of the flow behind a diamond-plan-form wing. $\Lambda=-\Lambda_{TE}=50°$; $M=1.62$; $x=3c_r$; $R=1.42\times10^6$; $\frac{p_{t,\infty}}{p_t}=0.888$.



(a) $\alpha = -3.15°$.
(b) $\alpha = -0.10°$.
(c) $\alpha = 2.90°$.
(d) $\alpha = 8.75°$.

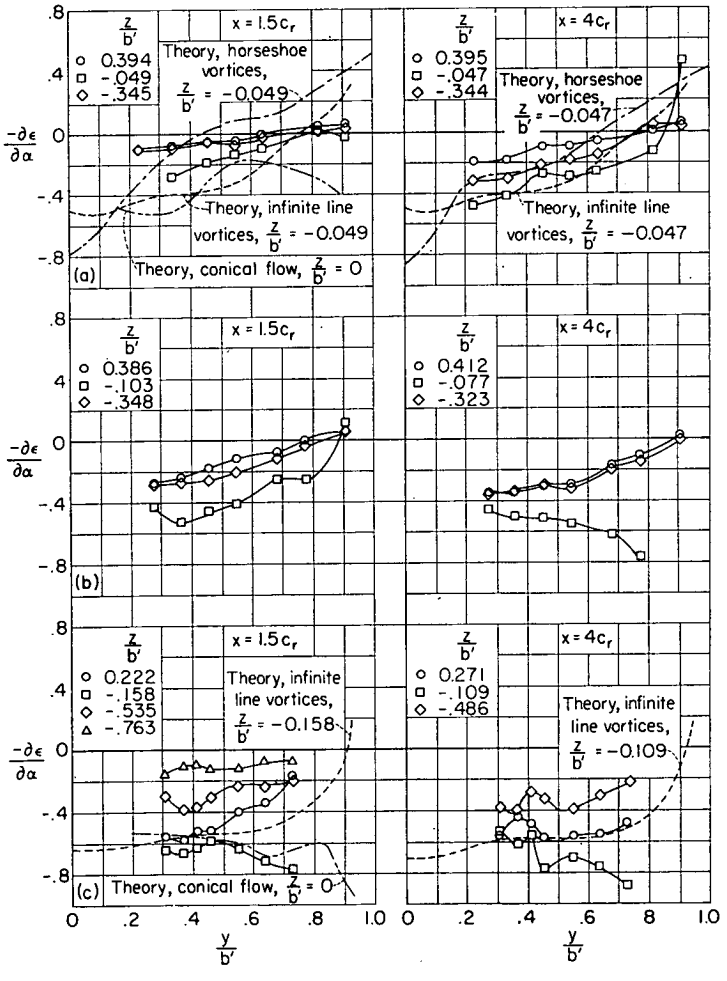
FIGURE 32.—Pressure contours and vector representation of the flow behind a diamond-plan-form wing. $\Lambda = -\Lambda_{TE} = 50°$; $M = 1.62$; $x = 4c_r$; $R = 1.42 \times 10^6$; $\frac{p_{t,\infty}}{p_t} = 0.888$.

ANALYSIS

All wings at low angles of attack.—The flow data for low angles of attack are summarized in figures 33 to 35. In these plots, values of $-\partial\epsilon/\partial\alpha$ below the zero axis are downwash, and values above are upwash. Each experimental point represents the slope of a curve of ϵ against α, which was drawn through the measured values of ϵ at wing angles of attack of approximately $-3°$, $0°$, and $3°$. Thus, the values are not necessarily the true values of $-\partial\epsilon/\partial\alpha$ near $\alpha=0°$, such as should be compared with the theoretical curves, but represent the average slope over a finite angle-of-attack range ($\pm3°$). The z/b' values quoted in these figures refer to the distance above and below the wing trailing edge at the root chord.

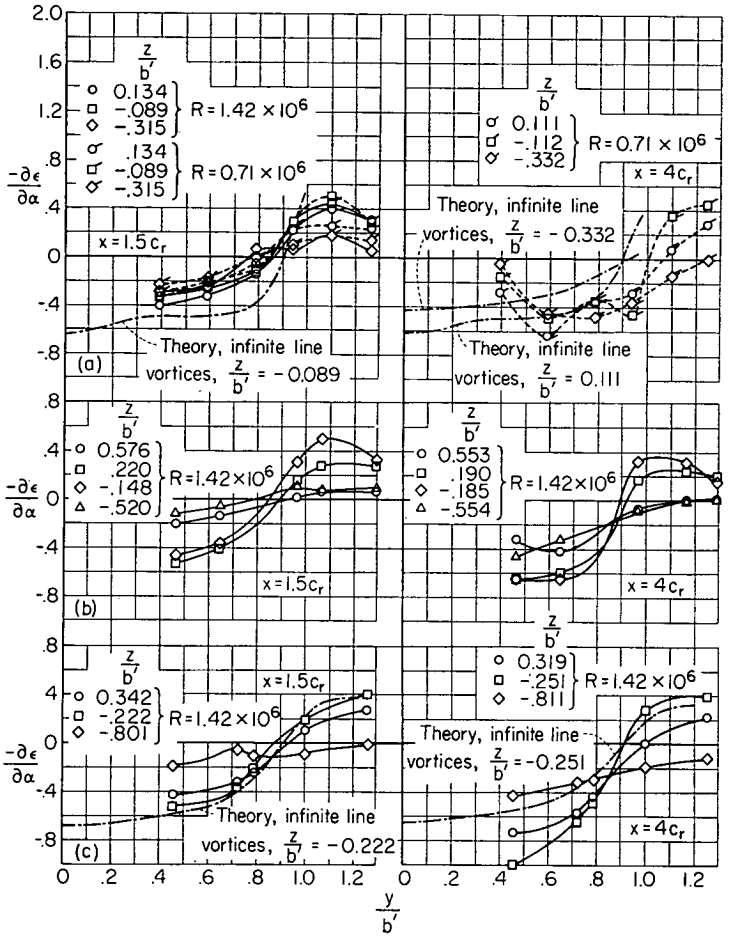
Because the point at which the downwash was being measured remained fixed, while the wing angle of attack was varied, the experimental values correspond, physically, to the case of the downwash at the tail behind a variable-incidence wing, rather than to the usual case where the measuring point is fixed with reference to the wing chord plane extended.

In figures 33 to 35, various theoretical calculations are presented. In these calculations the vortex sheet was assumed flat, undistorted, and located in the $z/b'=0$ plane. Details of these theoretical methods are presented in appendixes A to D.



(a) Triangular wing, $\Lambda=50°$.
(b) Triangular wing, $\Lambda=63°$.
(c) Triangular wing, $\Lambda=72°$.

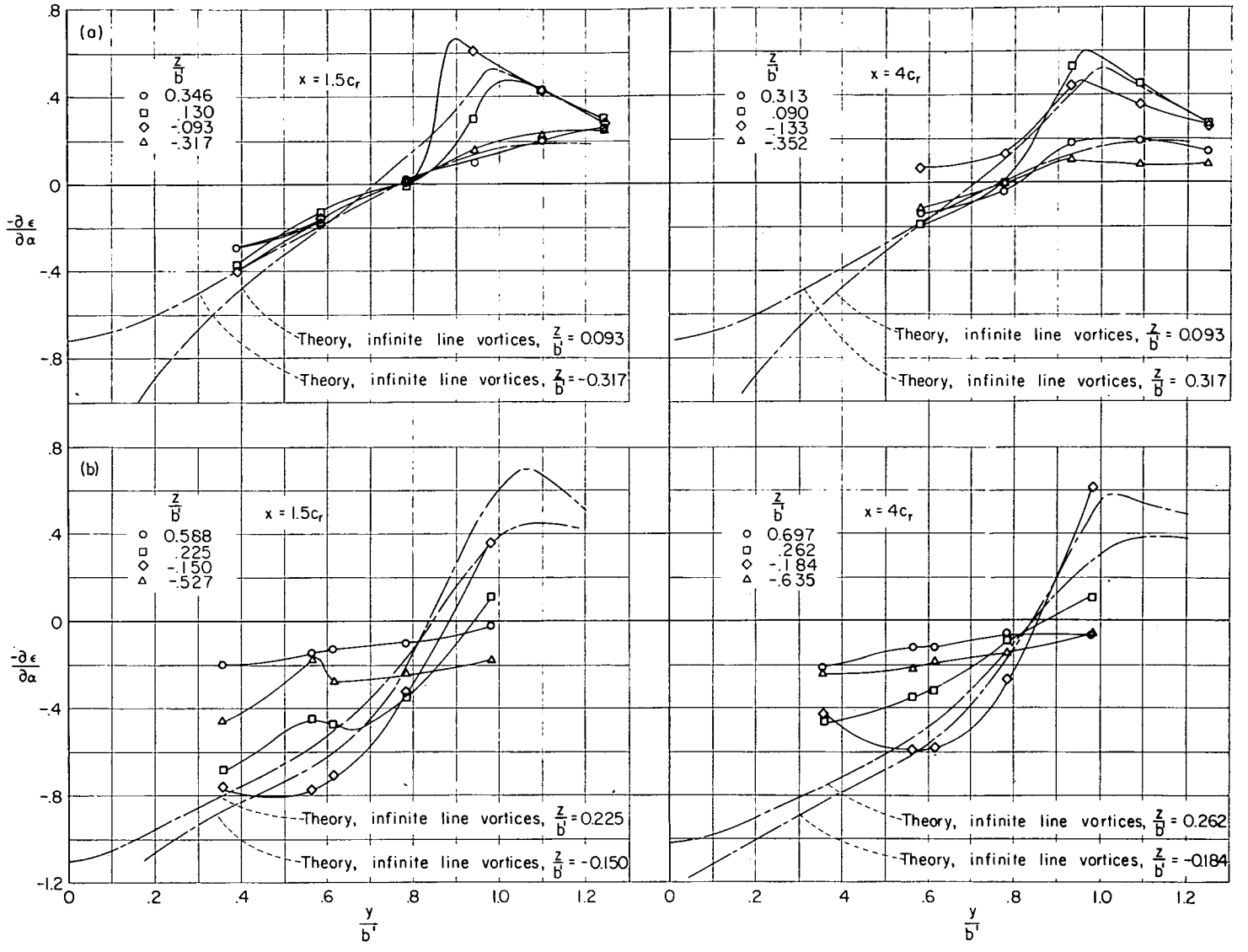
FIGURE 33.—Spanwise variation in $\frac{-\partial\epsilon}{\partial\alpha}$ near $\alpha=0°$ ($\pm3°$) for three triangular wings. $M=2.41$; $R=1.42\times10^6$.



(a) Triangular wing, $\Lambda=50°$.
(b) Triangular wing, $\Lambda=63°$.
(c) Triangular wing, $\Lambda=72°$.

FIGURE 34.—Spanwise variation in $\frac{-\partial\epsilon}{\partial\alpha}$ near $\alpha=0°$ ($\pm3°$) for three triangular wings. $M=1.62$; $R=1.42\times10^6$.

Three theoretical estimates are presented in the plot on the left of figure 33 (a) to compare with the experimental spanwise $-\partial\epsilon/\partial\alpha$ variation for a z/b' location of -0.049. This comparison is for the triangular wing whose leading edge is most supersonic and for the longitudinal location which is closest behind the trailing edge ($x=1.5c_r$). Because the experimental z/b' value was so near 0, the theoretical conical-flow calculations were made at $z/b'=0$ to facilitate computations. The agreement was poor and the conical-flow method does not appear to give any better agreement than the less rigorous vortex methods. Further downstream, as in the plot on the right of figure 33 (a), the infinite-line-vortex method gives closer agreement with experiment. This result might be expected since any effect of chordwise loading becomes less important with distance downstream, and the assumption of infinite line vortices becomes more realistic. The theoretical estimate made by the horseshoe-vortex method shows this same trend of better agreement between theory and experiment with distance downstream.



(a) Reversed triangular wing, $\Lambda_{TE}=-50°$.
(b) Diamond-plan-form wing, $\Lambda=-\Lambda_{TE}=50°$.

FIGURE 35.—Spanwise variation in $\frac{-\partial\epsilon}{\partial\alpha}$ near $\alpha=0°$ ($\pm 3°$) for two reversed triangular and diamond-plan-form wings. $M=1.62$; $R=1.42\times10^6$.

As the wing aspect ratio is progressively decreased (sweepback increased) at a constant Mach number, the values of $-\partial\epsilon/\partial\alpha$ become more negative. (Compare figs. 33 (a), 33 (b), and 33 (c).)

At a Mach number of 1.62, similar comparisons between experiment and theory are made in figure 34. The experimental curves at $x=1.5c_r$ (left side of fig. 34 (a)) show that the Reynolds number effect is small. The wing of this figure has a supersonic leading edge, although the leading-edge shock is detached. The agreement between infinite-line-vortex theory and experiment is not too good, nor does it improve much with distance downstream, as can be seen from the curves at the right of figure 34 (a). Figures 34 (b) and 34 (c) are for wings whose leading edges are subsonic.

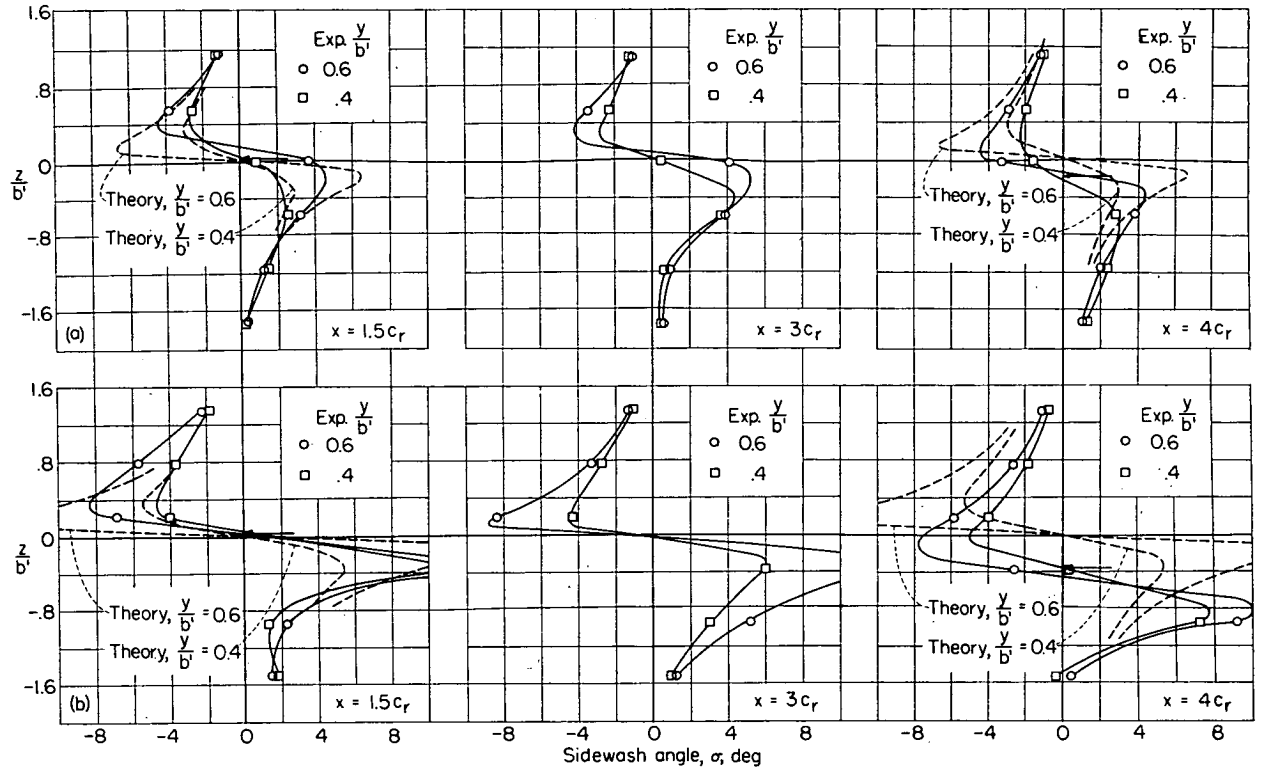
For the subsonic leading-edge wing of figure 34 (c), theory and experiment are in good agreement close behind the wing ($x=1.5c_r$). However, for the midspan portion of the wing, more negative experimental $-\partial\epsilon/\partial\alpha$ values are encountered than theory predicts, at the farther downstream station ($x=4c_r$).

Figure 35 (a) presents the spanwise variation of $-\partial\epsilon/\partial\alpha$ for the reversed triangular wing. The theoretical loading for the wing is triangular and the equally spaced infinite line vortices give good agreement between theory and experiment at both longitudinal stations.

Figure 35 (b) presents the spanwise $-\partial\epsilon/\partial\alpha$ variation for the diamond plan-form wing. For this wing, the spanwise $-\partial\epsilon/\partial\alpha$ variation resembles the variation as obtained for the triangular wings.

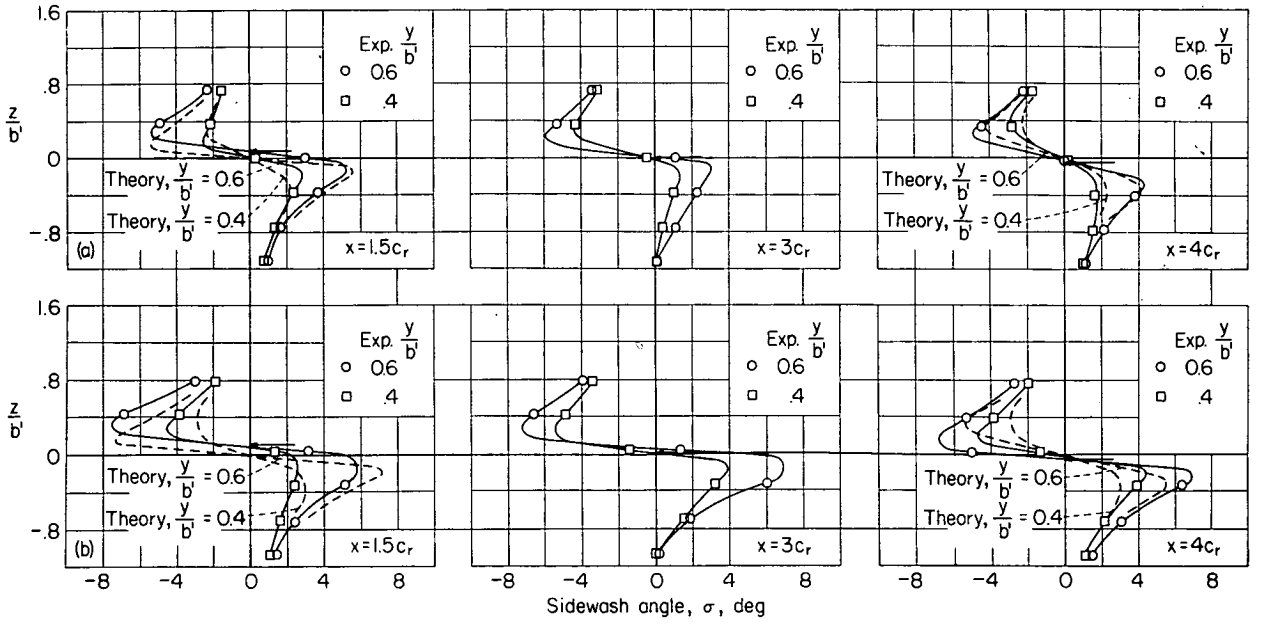
Subsonic leading-edge triangular wings at higher angles of attack.—Because of the tendency for the vortex sheet behind the subsonic leading-edge triangular wings to roll up rapidly into a single strong region of vorticity (see vector plots), the use of a single bent-line vortex (appendix C) seemed justifiable to represent the flow field behind the wing.

The proper location of this bent-line vortex, however, should be examined. In order to study the vertical locations of the vortex sheet, plots are presented in figures 36 to 38 to show the vertical variation of the sidewash for the three subsonic leading-edge triangular-wing configurations. The



(a) $\alpha=9°$.
(b) $\alpha=17°$.

FIGURE 36.—Vertical variation of the sidewash at stations behind 72° sweptback triangular wing. $M=1.62$; $R=0.71\times10^6$.

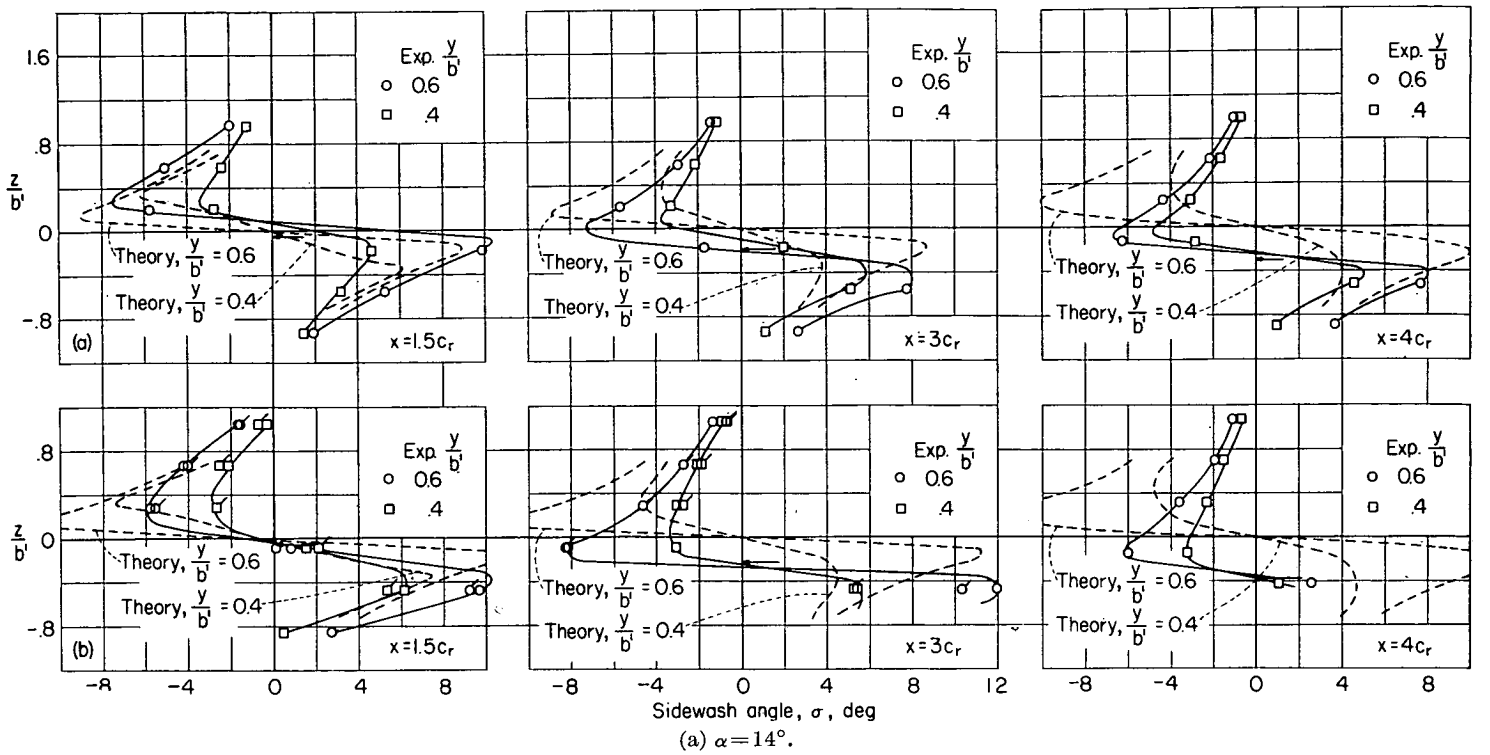


(a) $\alpha=9°$.
(b) $\alpha=12°$.

FIGURE 37.—Vertical variation of the sidewash at stations behind 63° sweptback triangular wing. $M=1.62$; $R=1.42\times10^6$.

experimental points were cross-plotted from curves of σ against span for the various z/b' locations. Curves are shown in each of the plots of these figures for two values of y/b' inboard of the theoretical centroid of vorticity (which is located at about $0.8b'$). The missing points near the peaks in figure 38 (b), behind the lower side of the wing, are not shown because the values were beyond the calibration curves of the wedges, and although not presented, they are known to be greater than 10°.

The experimental curves of figures 36 to 38 are compared with theory and in this case were computed by assuming a single bent-line vortex to represent the flow field. The bound portion of this line vortex was placed along the wing center-of-pressure location, and the spanwise distance



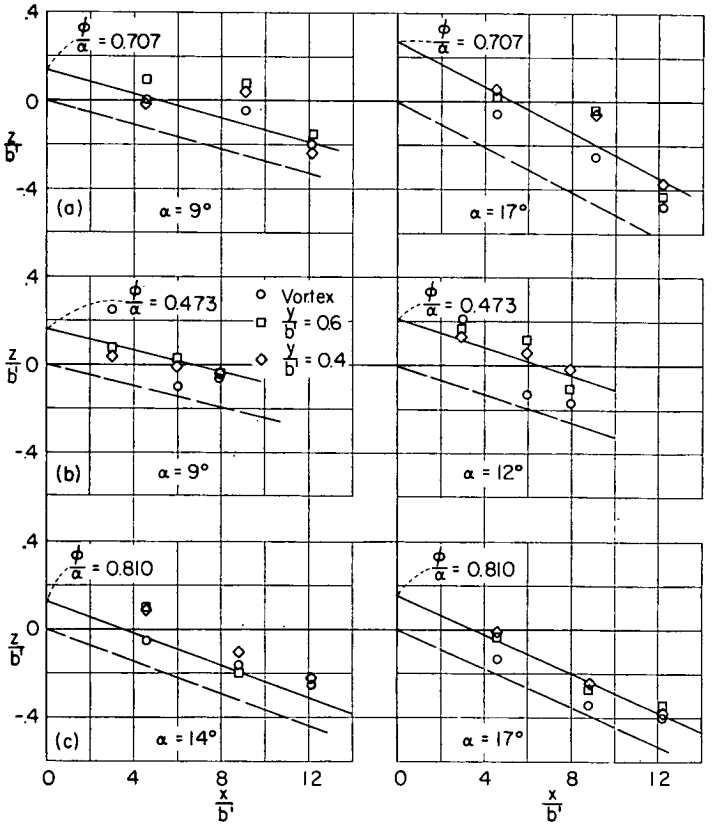
(a) $\alpha=14°$.
(b) $\alpha=17°$.

FIGURE 38.—Vertical variation of the sidewash at stations behind 72° sweptback triangular wing. $M=2.41$; $R=1.42\times10^6$. (Flagged symbols denote $R=0.71\times10^6$.)

between the semi-infinite legs of the vortex and the strength of the vortex was determined from the theoretical span load curve. The expression for the potential in the field of this bent-line vortex was taken from reference 19 and differentiated with respect to y to obtain the sidewash. (See appendix C.) The theoretical curves shown in figures 36 to 38 were all constructed on the assumption that the vortex remained in the free-stream direction downstream of the wing. The horizontal arrow on each plot denotes the z/b' location of the zero-sidewash point to which the theoretical curves may be shifted according to an over-all empirical correlation based on the present set of data. This point will be discussed subsequently. Comparison of the theoretical and experimental curves of these figures without performing this shift corresponds to the assumption that the vortex follows the free stream from the wing trailing edge. The improved agreement when the shift is made can be visualized in these figures. Furthermore, it can be seen that if the shift is made, the single bent-line vortex predicts the sidewash reasonably well.

The z/b' locations where the sidewash changes direction are plotted against the distance behind the wing trailing edge in figure 39. The square and diamond symbols on these curves came from figures 36 to 38. The circular symbols are for the z/b' location of the vortex as obtained from the pressure contours.

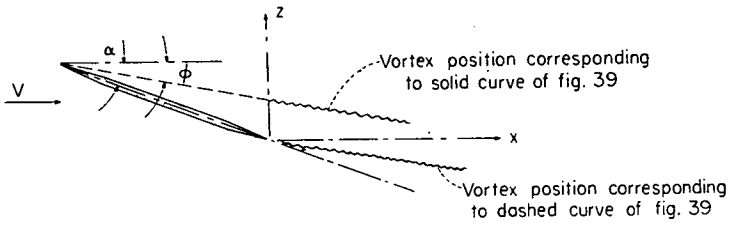
The dashed curves in the plots of figure 39 are a side view of the paths of the vortices behind the wing, obtained by assuming that the vortices left the wing trailing edge and moved at an angle with the free-stream direction because of the induced velocity from the vortex of the opposite panel.



(a) Triangular wing; $\Lambda=72°$; $M=1.62$; β cot $\Lambda=0.414$.
(b) Triangular wing; $\Lambda=63°$; $M=1.62$; β cot $\Lambda=0.650$.
(c) Triangular wing; $\Lambda=72°$; $M=2.41$; β cot $\Lambda=0.712$.

FIGURE 39.—Side view of the effective vortex-sheet locations for the three subsonic leading-edge, triangular-wing configurations.

The angles ϕ and α referred to in figure 39 (also fig. 40) are illustrated in sketch 1. The solid-line curve of figure 39



Sketch 1.

is a line faired through an approximate average of the experimental points parallel to the dashed curve and having the same ϕ/α values at both angles of attack. The fact that this solid-line curve is above the wing trailing edge at $x/b'=0$ might be expected, since previous experiments (for example, refs. 24 and 25) have established that for a subsonic leading-edge triangular wing, a leading-edge vortex is formed above the upper wing surface. It would necessarily follow that the centroid of vorticity at a longitudinal station corresponding to the wing trailing edge is above the trailing edge. Such a conclusion is definitely indicated in figure 39 in spite of the scatter of test points. It is from the solid-line curve of figure 39 that the locations of the previously mentioned horizontal arrows of figures 36 to 38 were taken.

Since the slope of the solid-line curve of figure 39 can be predicted by theory, it would be possible to obtain a more accurate prediction of the flow field if the height of the starting point of this curve above the trailing edge could be predicted by theory. At the present time, a theoretical method for the prediction of the location of the leading-edge vortex above the wing surface is not available. Various attempts were made to correlate the ϕ/α values as given by figure 39 with β cot Λ, and the parameter selected as the ordinate in figure 40 plotted against β cot Λ appeared to give a reasonable variation. The complete elliptic integral of the second kind ($E(t')$), occurring in this parameter comes from the expression for the lift coefficient of a subsonic leading-edge triangular wing. Although each experimental point of figure 40 represents two angle-of-attack conditions, there are in reality still too few points to generalize on this empirical relation. The chart of figure 40 is presented, however, as a preliminary approach to the problem since the data cover a fairly wide range of β cot Λ suitable for current missile design and since any correction for the height of the centroid of vorticity above the trailing edge will probably greatly improve estimates of the location of the line vortex at distances behind the wing.

The lack of any correction for the height of the centroid of vorticity above the wing trailing edge was very noticeable in the plots of sidewash against span such as figures 41 and 42. Without the correction, theory and experiment were often of opposite sign. The theoretical curves that are shown in figures 41 and 42 were calculated by using the correction for the height of the centroid of vorticity above the trailing edge as obtained from the solid line of figure 39.

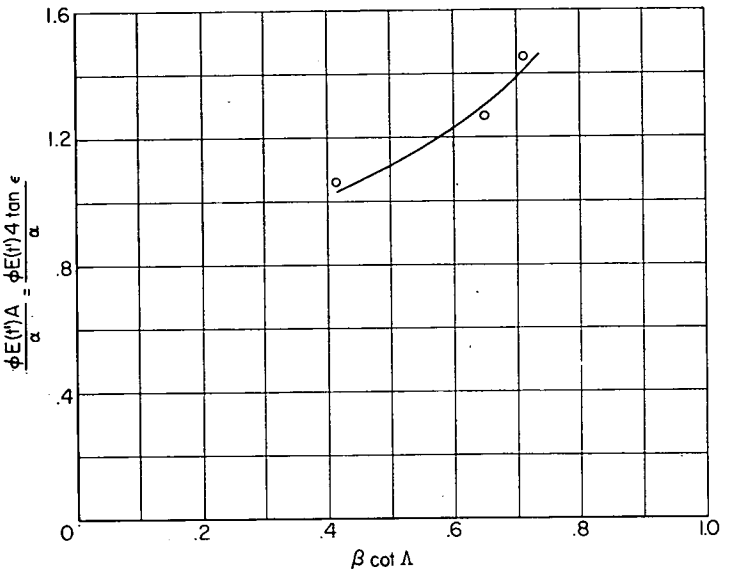
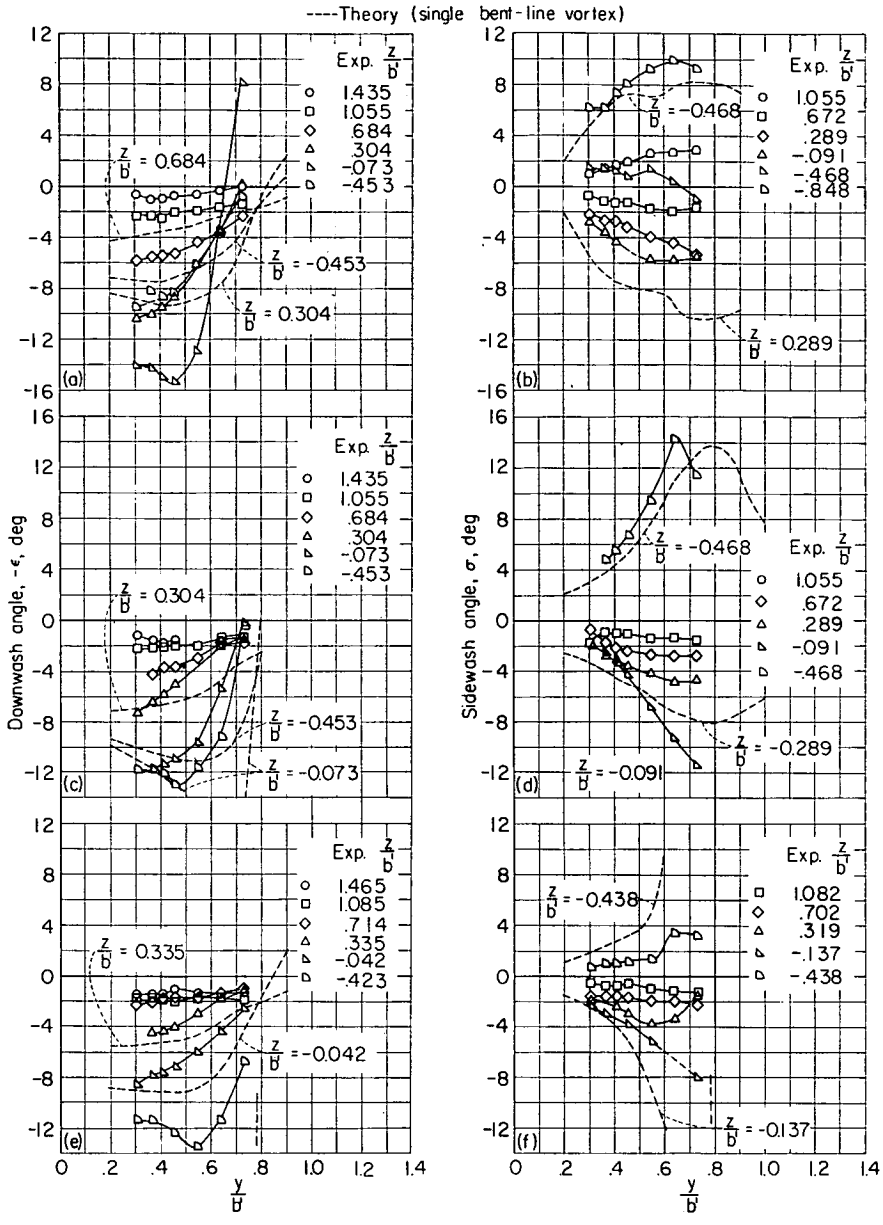


FIGURE 40.—Chart illustrating height of centroid of vorticity above the trailing edges of triangular wings with subsonic leading edges.

In order to check the accuracy and the importance of making the correction for the vertical location of the line vortex as it leaves the wing trailing edge in the theoretical model of the flow, calculations of the tail efficiency for model $BW_{5F}{}^{o}T_4$ of reference 12 were made by using the height of the vortex above the wing trailing edge as taken from figure 40. The calculations were made for a fixed wing-tail missile of this type but are not presented since the correction was negligible. This might be expected since, at higher angles of attack where the correction becomes sizeable, the location of the tail is too far from the line vortex to experience much difference in the downwash estimate acting on it. With a shorter tail arm the correction could become significant. Also, for the case of a missile with a variable-incidence wing, the correction might prove important.

Some lift data for a variable-incidence wing configuration are illustrated in figure 43. The data shown are for a delta wing and body configuration at Mach number 1.50 and were taken from reference 26. The data shown in figure 43 are for a wing incidence of 8° relative to the body.

Figure 43 illustrates the relative importance of the components that enter into an accurate prediction of the stability characteristics of such a missile. The dashed theoretical curve represents the lift curve that would be predicted by a theory derived by Warren A. Tucker at the Langley Laboratory. This theory considers all the interference lifts between the wing, body, and tail exclusive of the wing downwash effects. This theoretical curve should be compared with the experimental $C_{L_{(BT-B)+BW}}$ curve, which is the experimental lift of the missile exclusive of downwash effects. The two dot-dashed curves are the resulting lift curves when the downwash, as determined with and without the vertical displacement correction of the vortex, is applied. For a given downwash estimate, the reverse-flow theorem was used to obtain the incremental tail lift, which was in turn applied



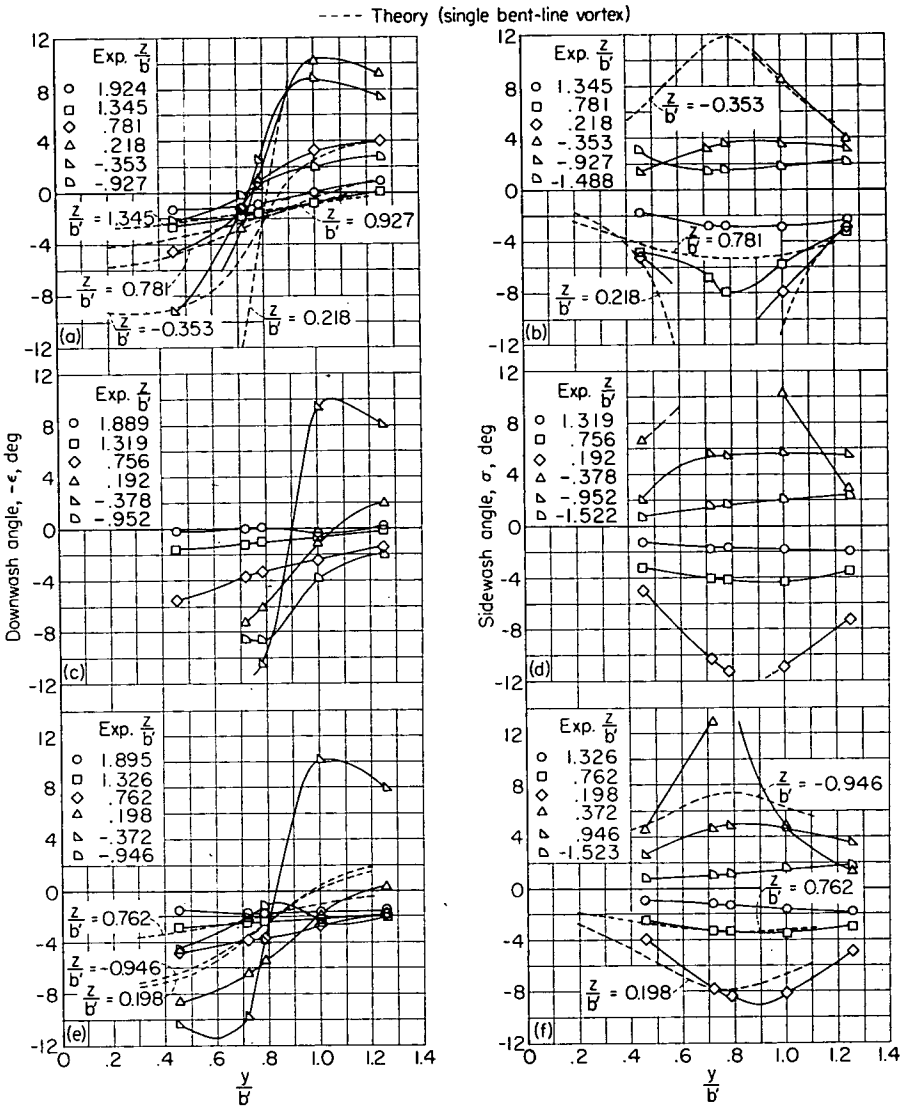
(a) Downwash; $x=1.5c_r$.
(b) Sidewash; $x=1.5c_r$.
(c) Downwash; $x=3c_r$.
(d) Sidewash; $x=3c_r$.
(e) Downwash; $x=4c_r$.
(f) Sidewash; $x=4c_r$.

FIGURE 41.—Spanwise variation of downwash and sidewash for 72° sweptback triangular wing. $M=2.41$; $R=1.42\times10^6$; $\alpha=17°$.

to the theoretical lift curve predicted by Tucker's theory. These two theoretical dot-dashed curves should be compared to the $C_{L_{BWT}}$ curve.

In the estimate of the downwash, the line vortex from each wing panel was allowed to deflect with distance downstream as in reference 27 (i.e., with an induced velocity as determined by the vortex from the opposite panel, and the image vortices in the body, as well as the induced velocity from the body crossflow). The only difference in the two curves is that one included the vertical displacement correction at the wing trailing edge and the other did not.

It is interesting to note that if Tucker's theory predicted the lift correctly, then near a body of angle of attack of 0°, which is where the wing-alone data of this report are most applicable, the theory using the displacement correction for the vertical location of the vortex and the experimental $C_{L_{BWT}}$ curve would almost coincide. At higher angles of attack, the use of the vertical displacement correction to the theoretical downwash estimate gives poorer agreement. If the theory underpredicted the downwash at large distances from the vortex (i.e., the vorticity is more diffused and not concentrated in a single line as assumed by the theory), then this poorer agreement might be expected since the vertical displacement correction is predicting that the vortex is farther from the tail with the correction than without. Indications in figures 41 and 42 are that, at large distances from the vortex, theory tends to underpredict the downwash.



(a) Downwash; $x=1.5c_r$.
(b) Sidewash; $x=1.5c_r$.
(c) Downwash; $x=3c_r$.
(d) Sidewash; $x=3c_r$.
(e) Downwash; $x=4c_r$.
(f) Sidewash; $x=4c_r$.

FIGURE 42.—Spanwise variation of downwash and sidewash for 72° sweptback triangular wing. $M=1.62$; $R=1.42\times10^6$; $\alpha=17°$.

Supersonic leading-edge triangular wings at higher angles of attack.—Although no abrupt transition is apparent in the character of the flow fields when the leading edge of a triangular wing undergoes a change from a subsonic to a supersonic configuration, there is a difference in the types of flow in that, for comparable angles of attack (or even comparable lift coefficients), the vorticity behind a wing having a supersonic leading edge appears as more than one region of strong vorticity or possibly still retains its identity as a sheet. The 50° sweptback triangular wing at a Mach number of 2.41 (the wing whose leading edge is most supersonic) was selected for comparison with the various theoretical techniques of predicting the flow angles behind the wing, inasmuch as the other configurations with supersonic leading edges will be bracketed by this wing and the wings with subsonic leading edges. The comparison of figure 44 should best illustrate the advantages or disadvantages of the various theoretical methods. In this figure, the location of the experimental wake center line as determined from the pressure profiles is plotted as the circular symbols. Comparing the location of the vortex sheet as determined by the various theories with the experimental location of the wake center line should give a good over-all indication of the merits of the various theoretical methods.

The location of the vortex sheet for the conical-flow theory was computed by calculating the downwash in the $z=0$ plane at stations 0, 0.25, 0.50, 0.75, 1.0, 1.25, and 1.5 chords behind the wing trailing edge. Since $z=\int_0^x \frac{w}{V}\,dx \approx \int_0^x \epsilon\,dx$, plots of ϵ against x for given spanwise stations, when mechanically integrated, determined the vertical locations of the vortex sheet that are shown in figure 44.

The location of the vortex sheet for the horseshoe-vortex theory was computed in the same manner as for the conical-flow theory except that, in the evaluation of the downwash

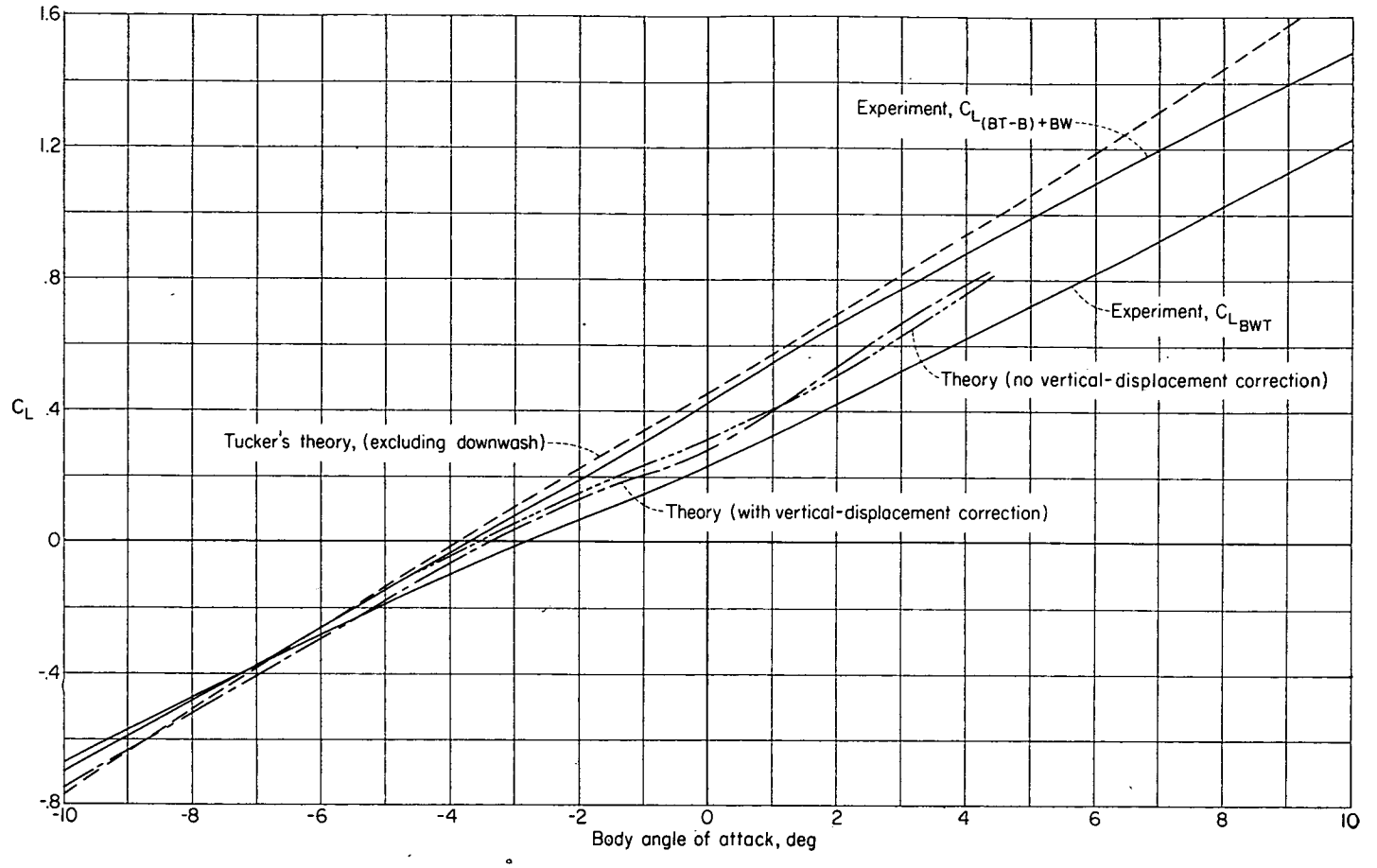
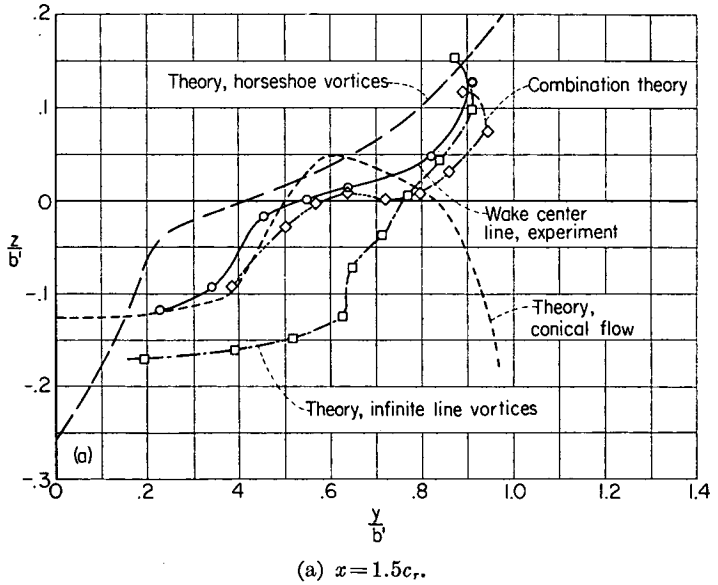
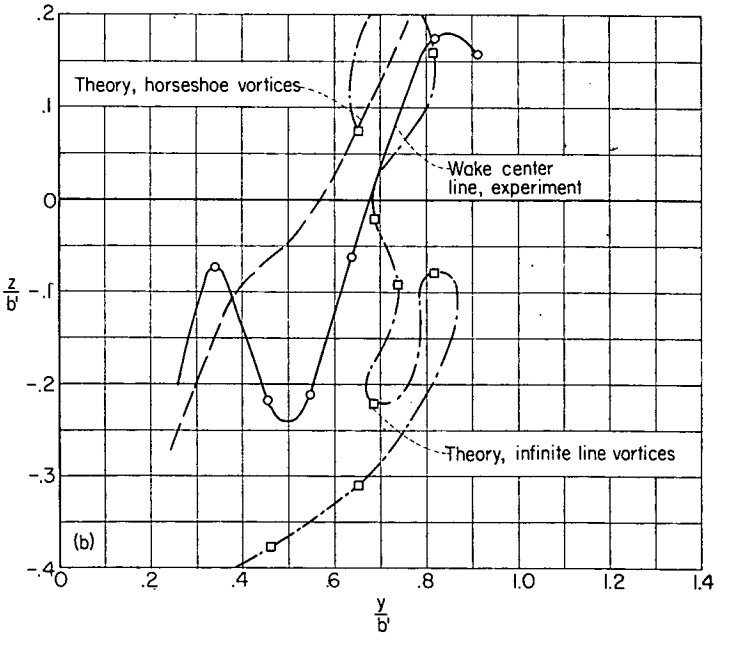


FIGURE 43.—Comparison of theoretical and experimental lift for a missile having a triangular wing and tail with the wing at 8° incidence, using theoretical downwash estimates. (Experimental data from ref. 26 at $M=1.50$.)



(a) $x=1.5c_r$.

FIGURE 44.—Wake center-line location and comparison with various theories for the 50° sweptback triangular wing. $M=2.41$.



(b) $x=4c_r$.

FIGURE 44.—Concluded.

at the various longitudinal locations, the horseshoe-vortex theory was used.

The square symbols of figure 44 show the locations of ten equal-strength infinite-line vortices, whose resulting location was determined on the assumption that they left the wing trailing edge with a lateral spacing in accordance with the theoretical wing span load distribution and followed a path calculated in a step-by-step process (such as ref. 22), where each vortex moved vertically and laterally in accordance with the velocities induced by the other nineteen line vortices (considering both wing panels).

It can be seen in figure 44 (a) that, at $x=1.5c_r$, the two vortex-line methods bracket the experimental wake center-line location just as they did in the plots of $-\partial\epsilon/\partial\alpha$ in figure

33. Behind the tip region, the infinite line vortices approximate very closely the experimental wake center-line location. On the other hand, conical-flow theory is in excellent agreement with experiment behind the inboard portion of the wing.

The agreement of the infinite-line-vortex theory with experiment behind the tip region and the agreement of the conical-flow theory behind the inboard portion of the wing (fig. 44 (a)) suggests that a theoretical method employing a combination of the two methods might predict the actual flow field closely. For this combination theory, the vertical location of the vortex sheet was determined at points along Mach lines from the tip using conical-flow theory. With these locations as the starting points of the infinite line vortices, the method using infinite line vortices was employed for distances farther downstream. Details of this method of calculation are given in appendix E.

It can be seen in figure 44 that this combination theory produces excellent agreement with experiment at the longitudinal station ($x=1.5c_r$) close to the intersection of the two Mach lines from the tip. Since the rolling-up process of the vortex sheet starts behind the tip (ref. 1), where the effects of chordwise loading are small, the good agreement of the combination theory with experiment is not surprising. It uses the best features of both conical-flow and infinite-line-vortex theory. Actually any of the rigorous theories, which are exact within the linearizing approximations, such as the doublet theory of reference 20, could have been used instead of conical-flow theory with the same results.

Because of the tediousness of using the combination theory, the infinite-line-vortex method has received the most emphasis in the comparisons between theory and experiment in this analysis. The advantage of using this seemingly more approximate method as compared to the planar methods is that the simple relation for the induced velocity in the field, from an infinite line vortex, permits the angle-of-attack effects (that is, the distortion of a vortex sheet) to be better approximated. However, wing chord loading effects, as well as variations of Mach number in the wake itself with distance downstream, are overlooked completely by the theory. Also, in supersonic flow, the pressures or velocities experienced by a point in the field are influenced only by those disturbances in the Mach forecone from the point. The method used, which considered the induced velocities in successive crossflow planes has some justification, however, in that those line vortices closest to the point most strongly affect the velocities at the point.

It is realized that although the wing-alone tests of this investigation permitted theoretical calculations based on ten infinite line vortices from each wing panel, such calculations for the practical case of a wing and body would be too lengthy. However, the calculations were carried out, since the large number of line vortices permitted a study of the way they grouped themselves, and possibly would permit assigning strengths and locations to a fewer number of line vortices to obtain a better theoretical model of the flow, if agreement using the ten infinite line vortices could be obtained.

The theoretical paths of these infinite line vortices are shown in figure 45 by the dashed lines. The shapes of the vortex sheet at the various longitudinal stations are the solid curves. A theoretical study presented in reference 23 and vapor-screen studies of the vortex sheet made at the NACA Ames Laboratory have established the fact that for supersonic leading-edge delta wings the vortex sheet rolls up in a conventional manner behind the inboard section of the wing, and forms an "S" shaped pattern behind the triangular loaded tip region. In figure 45, vortices a, b, and c illustrate the conventional rolling up, and the rest of the vortices illustrate the formation of the "S" shaped pattern. In this figure, the "S" shaped pattern becomes distorted downstream of about $x/c_r=2$. This distortion is probably due to inaccuracies in graphically selecting the initial locations of the line vortices and to the use of an insufficient number of streamwise increments in the computations. However, when the paths for this particular wing were recomputed by using more accurately selected initial locations and smaller streamwise increments for the entire range of calculations, the deformation of the "S" shaped structure of the vortex sheet was still observed. This result suggests that there is a limit to how practical the method is, since at higher angles of attack, and at larger distances behind the wing, smaller streamwise increments would be required. In this connection, the patterns such as are shown in figure 45 should be considered as rough approximations at large downstream distances. However, because of the practical limit to the method for determining the shape of the vortex sheet, the accuracy with which the flow angle can be predicted by the approximate patterns such as those shown in figure 45 may be of interest.

In figures 46 (a) and 46 (b), the experimental and theoretical downwash and sidewash for this same wing at the same Mach number are compared by using the locations of the infinite line vortices as shown in figure 44, both for the infinite-line-vortex theory and the combination theory. Near the vortex sheet ($z/b'=-0.075$), the combination theory gives the better agreement with the experimental spanwise downwash distribution in comparison with the theory of infinite line vortices; however, there is still considerable discrepancy. This discrepancy between theory and experiment is also present at a z/b' location farther from the vortex sheet ($z/b'=0.223$). The same statements apply to the sidewash in figure 46(b), except that, for the spanwise range covered, the agreement between the combination theory and experiment at $z/b'=0.223$ is excellent. Farther downstream (figs. 46(e) and 46(f)) the line vortices have grouped themselves so close together in many instances that, although the spanwise locations were selected midway between line vortices for evaluating the downwash and sidewash, there are unreal variations in the theoretical curves, because of the proximity of a vortex to the field point being calculated. All the theoretical curves shown in figures 46(e) and 46(f) were based on the infinite-line-vortex theory, and there is considerable discrepancy between theory and experiment.

Reversed triangular wing at higher angles of attack.—One purpose of using the ten infinite line vortices for the theoretical calculations of all the supersonic leading-edge wings, analyzed in this report, was to study their behavior as they moved downstream. This possibly would permit a better

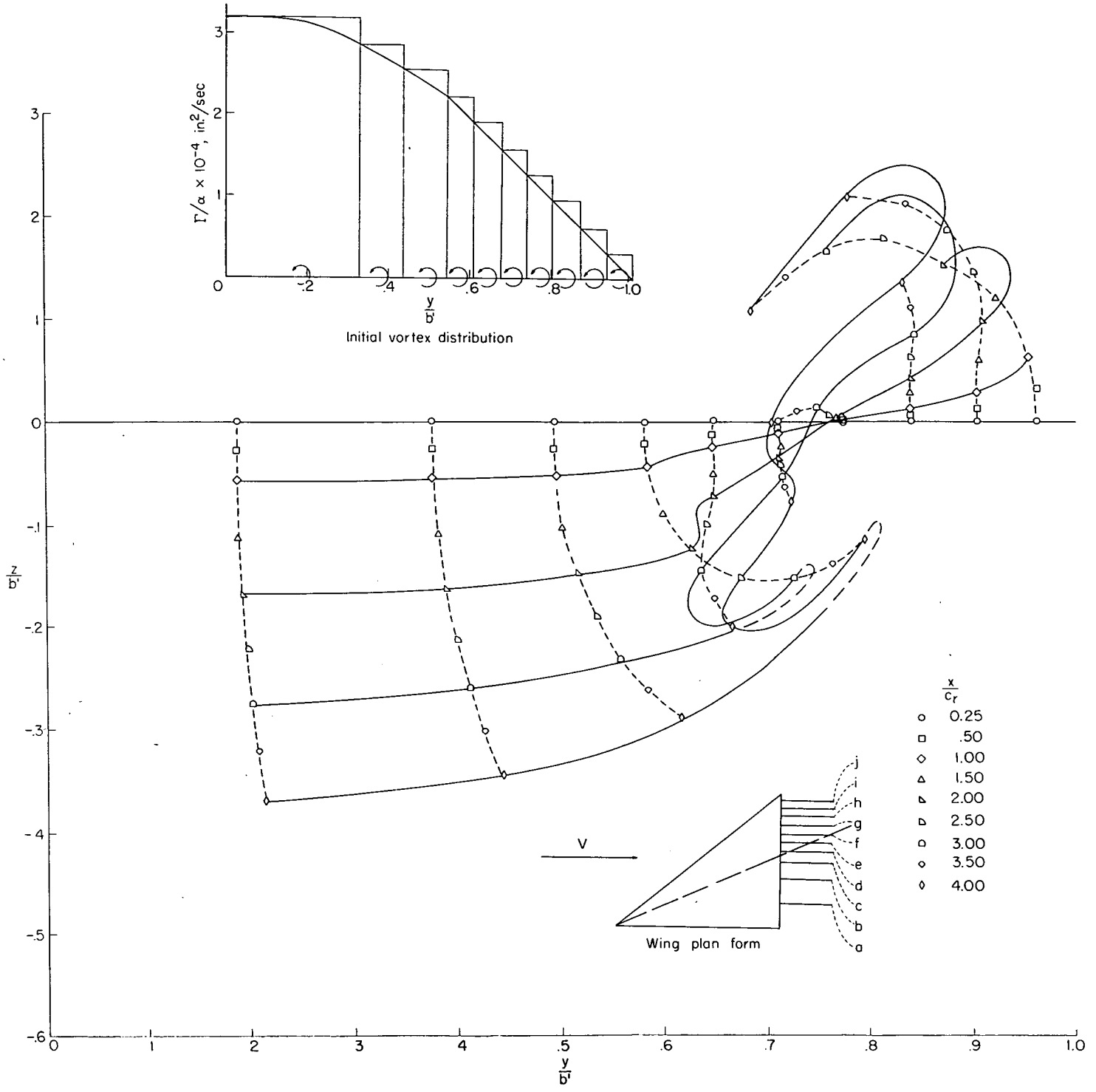
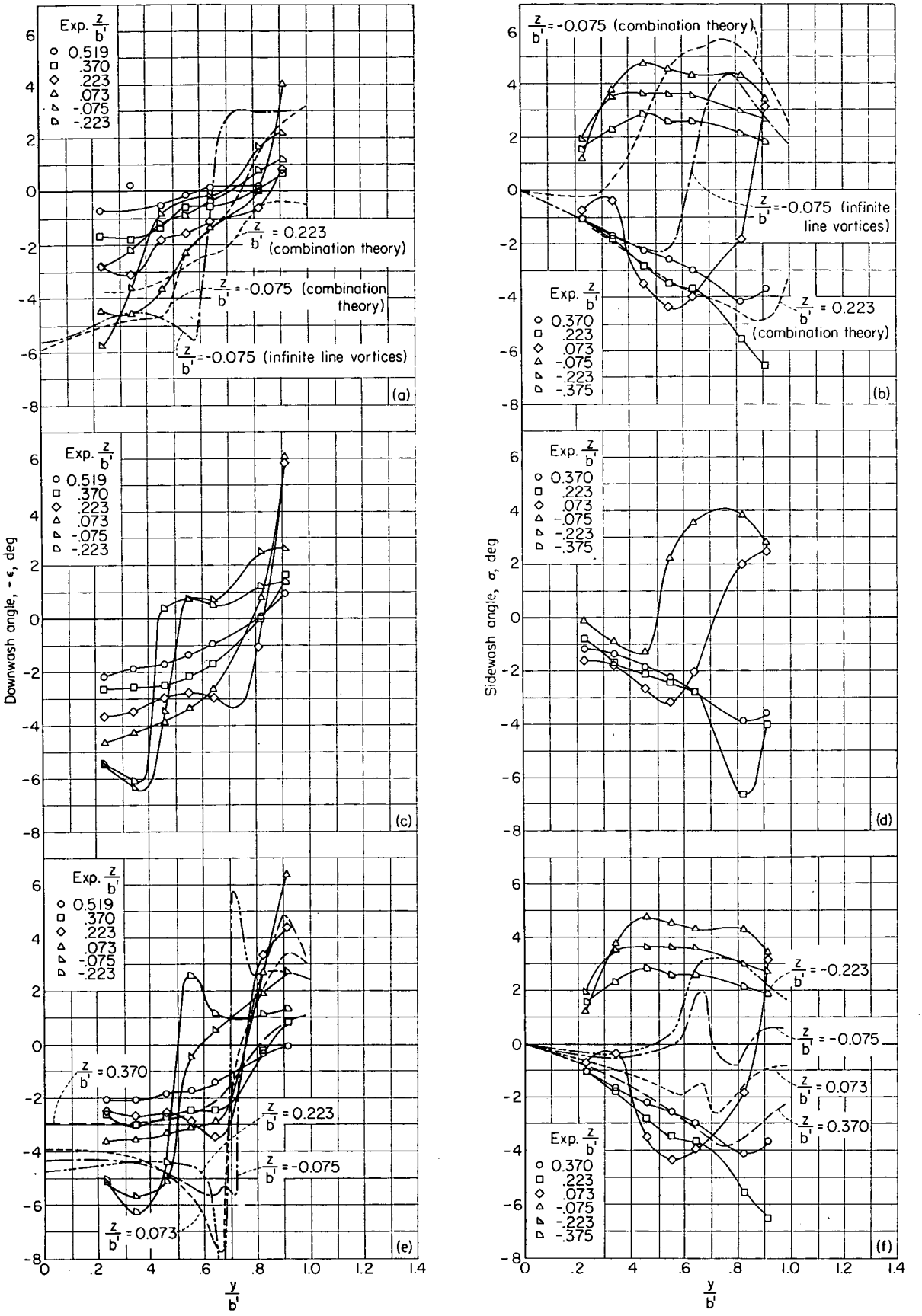


FIGURE 45.—Theoretical paths of ten infinite line vortices behind the 50° sweptback triangular wing. $M=2.41$; $\alpha=12°$.

assignment of strength and locations to a fewer number of line vortices to be applied to the wing-body problem. For the reversed triangular wing the span loading is triangular and the ten equal-strength vortices are also equally spaced. The tendency for the vortices to divide into two separate groups was particularly evident. (See fig. 47.) Whether such a result would take place if many more streamwise increments had been used in the computations is not certain. Since the experimental pressure contours (figs. 28 (d) and 29 (d)) exhibit a tendency for the sheet to form concentrated regions of vorticity, the arrangement of the vorticity shown in figure 47 probably represents a good approximation of the arrangement of the vortex sheet. The separation of the sheet into these two regions suggests that a model of the flow with two vortices from each wing panel would be a simpler representation of the flow. The outboard vortex should have a strength $0.6\Gamma_m$ (six line vortices are in the outer group) and the inner vortex would have a strength of $0.4\Gamma_m$. This model of the flow (though probably considerably better than a single vortex) was not further investigated since it would be a cruder model of the flow than one represented by the theoretical method using ten line vortices.

The theoretical prediction of the downwash and sidewash obtained by using ten line vortices are compared in figure 48.



(a) Downwash; $x=1.5c_r$.
(b) Sidewash; $x=1.5c_r$.
(c) Downwash; $x=3c_r$.
(d) Sidewash; $x=3c_r$.
(e) Downwash; $x=4c_r$.
(f) Sidewash; $x=4c_r$.

FIGURE 46.—Spanwise variation of downwash and sidewash for the 50° sweptback triangular wing. $M=2.41$; $R=1.42\times10^6$; $\alpha=11.50°$.

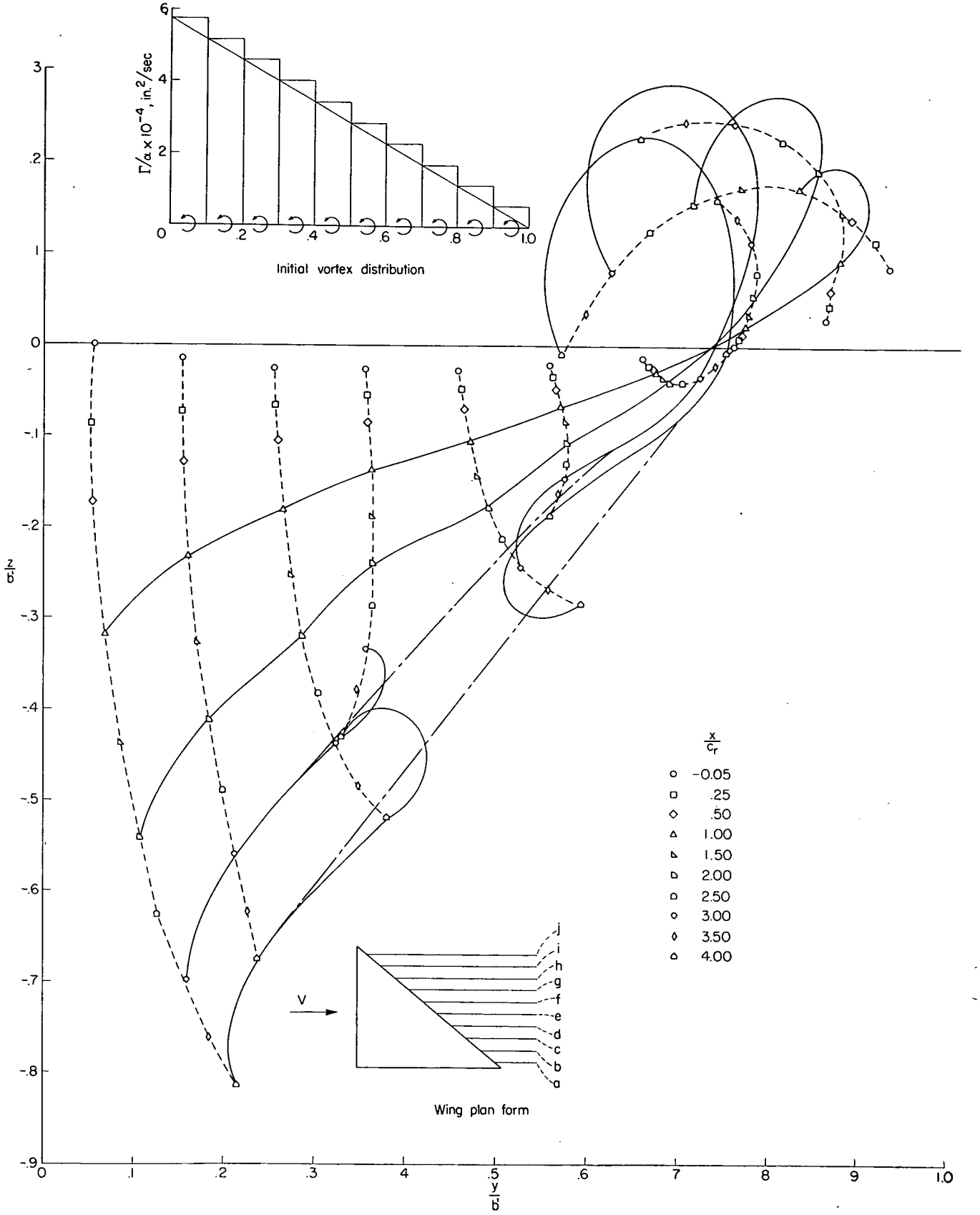
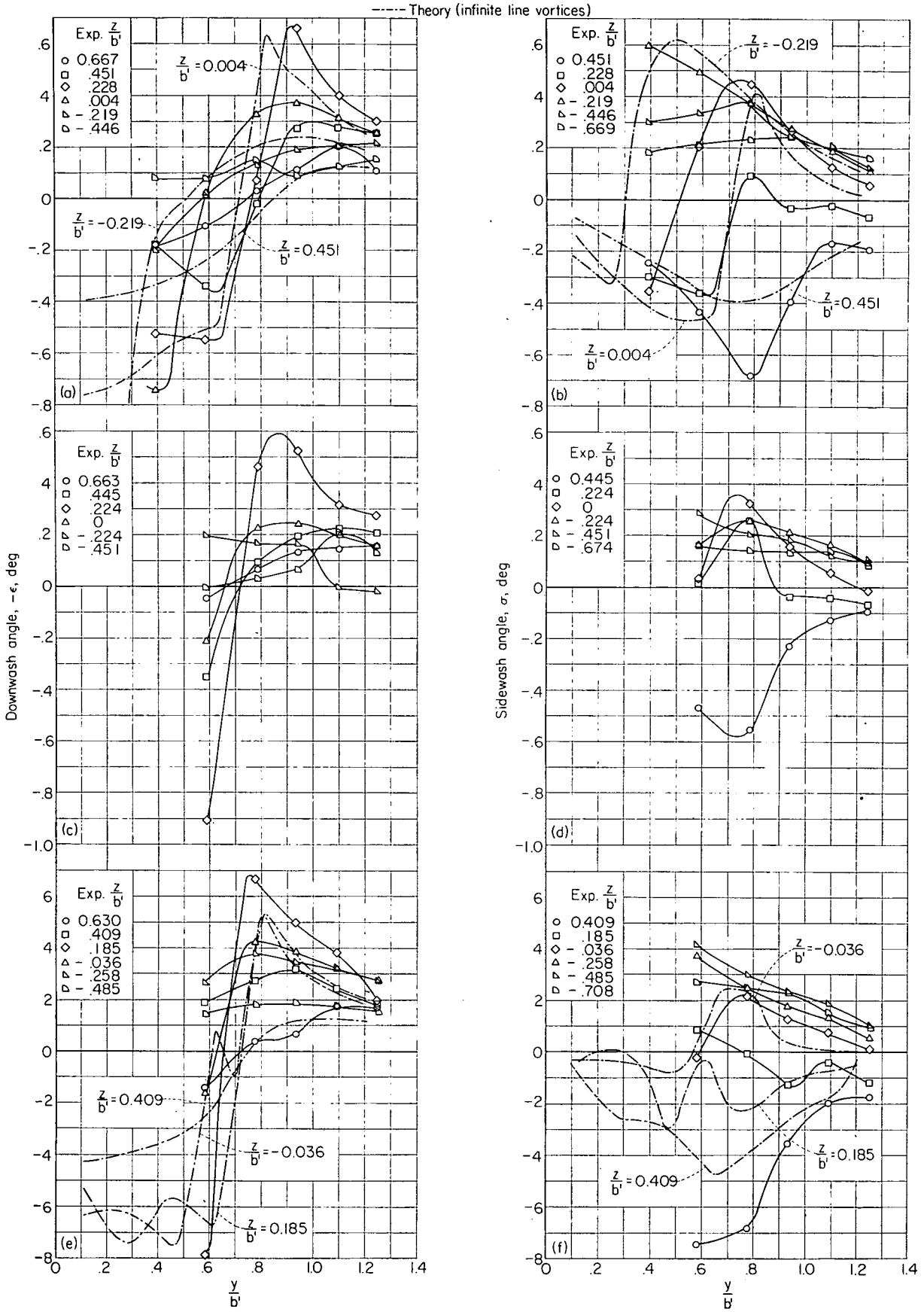


FIGURE 47.—Theoretical paths of ten infinite line vortices behind the reversed triangular wing. $M=1.62$; $\alpha=9°$. Values of x/c_r are referenced from trailing-edge root-chord juncture.



(a) Downwash; $x=1.5c_r$.
(b) Sidewash; $x=1.5c_r$.
(c) Downwash; $x=3c_r$.
(d) Sidewash; $x=3c_r$.
(e) Downwash; $x=4c_r$.
(f) Sidewash; $x=4c_r$.

FIGURE 48.—Spanwise variation of the downwash and sidewash for the reversed triangular wing ($\Lambda_{TE}=-50°$). $M=1.62$; $R=1.42\times10^6$; $\alpha=9°$.

For this case, although the same shapes of the curves are evident in both experiment and theory, the agreement is not too good. It is obvious in figure 48, however, that the method used, predicts the downwash better than would a single line vortex from each wing panel, since with a single line vortex the downwash would change sign at $y/b'=0.5$. Both experiment and the theoretical method using ten line vortices show that the spanwise location where the downwash changes sign is outboard of $y/b'=0.5$.

Diamond-plan-form wing ($\Lambda=-\Lambda_{TE}=50°$) at higher angles of attack.—The theoretical paths of the ten infinite line vortices behind a diamond-plan-form wing are shown in figure 49. The vortex sheet appears to roll up in the conventional manner. The leading edge of the wing is slightly supersonic at this Mach number but the shock is detached even at $\alpha=0°$. The pressure contours (fig. 32 (d)) show three regions of apparently higher vorticity along the vortex sheet, but the two inboard regions are so much weaker than the one which remains straight behind the point on the wing at $0.8b'$, that the flow picture can be assumed to be the conventional rolling-up pattern indicated by the theoretical calculations of figure 49.

The spanwise downwash and sidewash distributions for the diamond-plan-form wing are shown in figure 50. Also shown are the theoretical curves to be compared with the appropriate experimental curve. The theoretical curves were computed using the locations of the infinite line vortices such as shown in figure 49 for the appropriate streamwise location. The agreement between experiment and theory is poor.

CONCLUSIONS

Schlieren studies, total-pressure profiles, and flow-angle surveys were made behind five thin, pointed-tip wings. The flow behind three triangular wings of 50°, 63°, and 72° leading-edge sweep was surveyed at Mach numbers 1.62 and 2.41. The flow behind a reversed triangular wing (−50° trailing-edge sweep angle) and a diamond-plan-form wing ($\Lambda=-\Lambda_{TE}=50°$) was surveyed at Mach number 1.62. The analysis of the data and comparison of the results with theoretical predictions indicated the following conclusions:

1. The vortex sheet behind triangular wings with subsonic leading edges tends to form rapidly into one distinct region of high vorticity behind the wing as it moves downstream, as in the case for triangular wings in subsonic flow. For subsonic leading-edge triangular wings at moderate and high angles of attack, the use of a single bent-line vortex to represent the flow field agrees with the physical picture and predicts the downwash and sidewash reasonably well if its location can be estimated with sufficient accuracy. A proposed empirical adjustment of the method for determining vertical location of this line vortex at stations behind the wing gives a good representation of the flow field (particularly the sidewash).

2. For triangular wings with supersonic leading edges, the flow tends to rotate more about a sheet of vorticity, which still retains its identity as a sheet at lift coefficients and downstream distances comparable to those for subsonic leading-edge wings. The vortex sheet itself appeared to have more than one region of high vorticity along any semispan of its width. At moderate angles of attack (12°), a lifting-surface theory such as conical-flow theory best predicts the location of the vortex sheet near the plane of symmetry, whereas use of infinite line vortices and a step-by-step process best predicts the location of the vortex sheet behind the tip region. Using a combination of the two methods gave an accurate representation of the vortex sheet at a longitudinal station 1.5 chords behind the trailing edge (near the location where the Mach lines from the tip intersect) and improved the agreement of the theoretical and experimental downwash and sidewash. The method was not evaluated at stations farther behind the wing, since the number of line vortices and the smallness of the streamwise increments would probably cause the method to become too cumbersome for a practical wing-body problem.

3. For the reversed triangular wing both experiment and the theory using ten infinite line vortices exhibited a tendency for the vortex sheet to concentrate into two regions, with the outboard region containing the most vorticity. The actual prediction of the flow angles was poor at moderately high angles of attack, although the curves of the experimental and theoretical spanwise downwash and sidewash distributions appeared to have the same shape.

4. For the diamond-plan-form wing with a leading edge that was only slightly supersonic, the vortex sheet rolled up in a manner typical of subsonic configurations in the theoretical calculations and, except for a couple of weak inboard concentrations of vorticity, the same pattern was evident in the experimental flow. However, the prediction of the flow angle was poor.

LANGLEY AERONAUTICAL LABORATORY,
NATIONAL ADVISORY COMMITTEE FOR AERONAUTICS,
LANGLEY FIELD, VA., *January 22, 1954.*

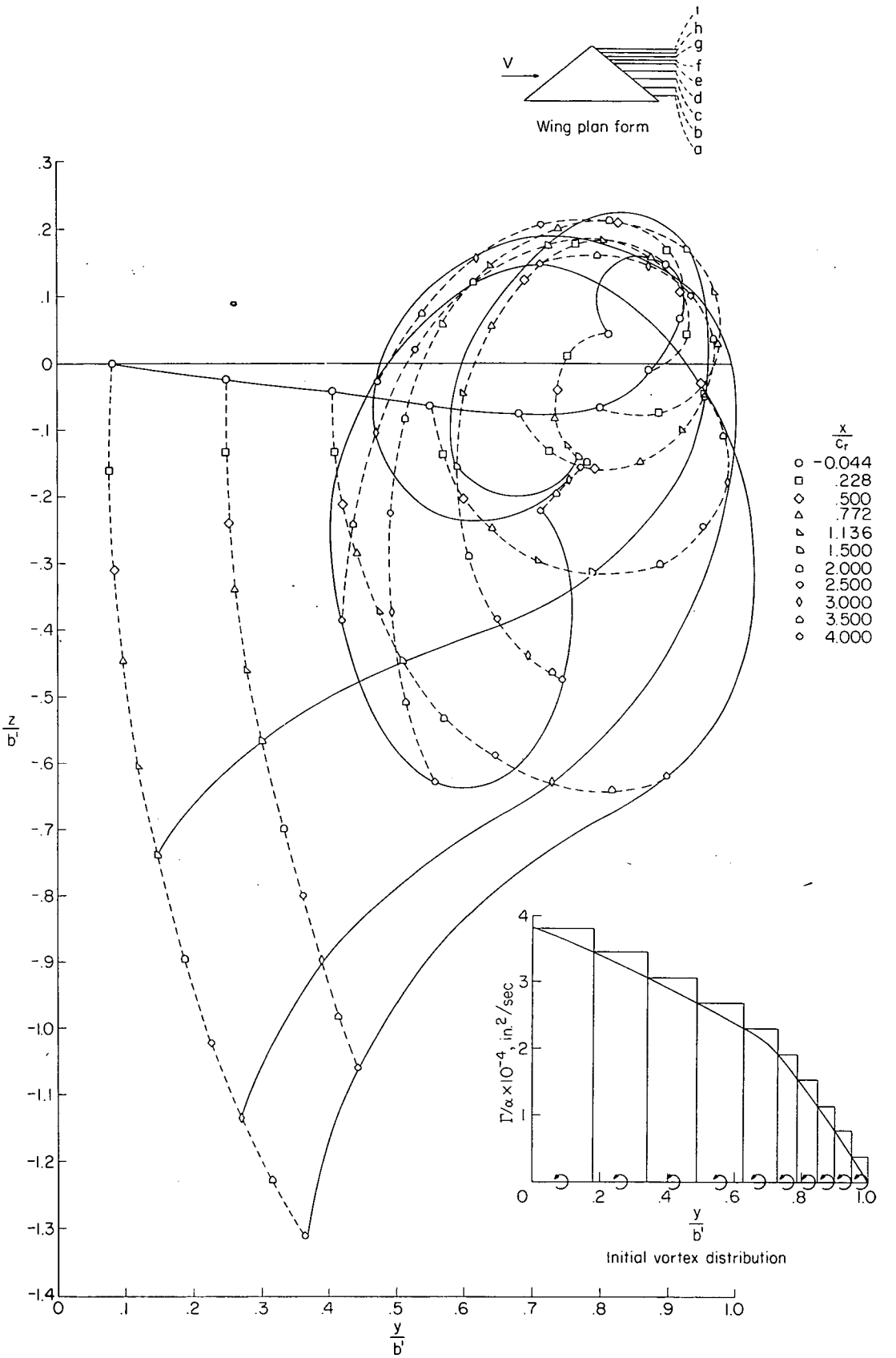
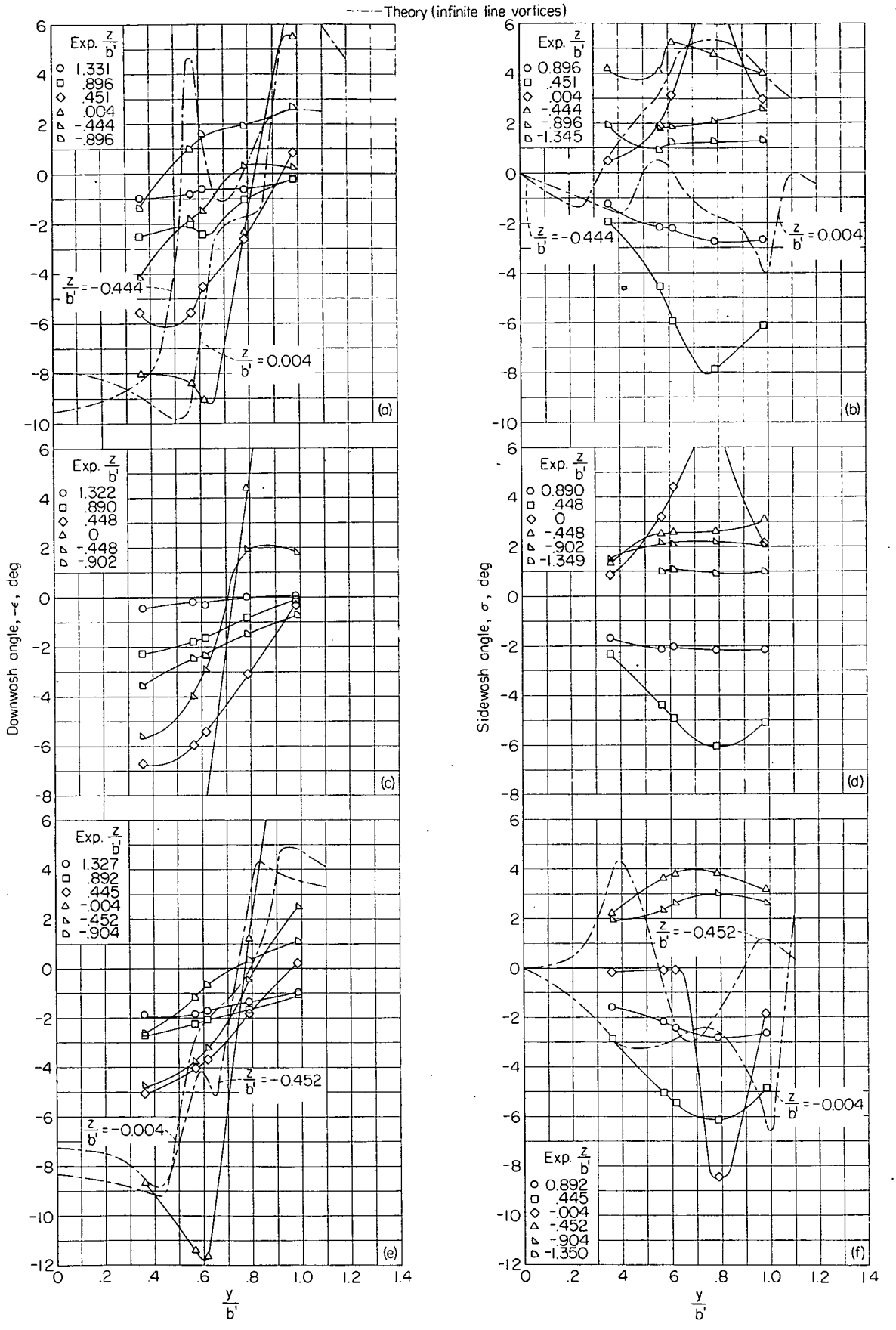


FIGURE 49.—Theoretical paths of ten infinite line vortices behind the diamond-plan-form wing ($\Lambda = -\Lambda_{TE} = 50°$). $M = 1.62$; $R = 1.42 \times 10^6$; $\alpha = 9°$. Values of x/c_r are referenced from trailing-edge root-chord juncture.



(a) Downwash; $x=1.5c_r$.
(b) Sidewash; $x=1.5c_r$.
(c) Downwash; $x=3c_r$.
(d) Sidewash; $x=3c_r$.
(e) Downwash; $x=4c_r$.
(f) Sidewash; $x=4c_r$.

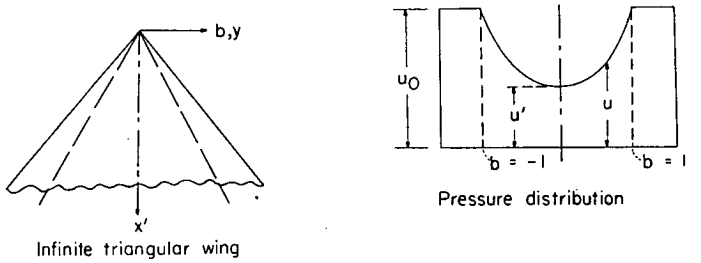
FIGURE 50.—Spanwise variation of the downwash and sidewash behind the diamond-plan-form wing ($\Lambda=-\Lambda_{TE}=50°$). $M=1.62$; $R=1.42\times10^6$; $\alpha=9°$.

APPENDIX A

DETAILS OF CONICAL-FLOW METHOD

The calculation of downwash and sidewash behind a wing at supersonic speeds by using conical flows has been presented in references 15 to 17. The principle of the method depends on the fact that when the downwash or sidewash is known for certain specified plan forms, other plan forms can be formed by the superposition of these known plan forms. The resulting downwash or sidewash is then the combined effect of the known solutions. An example follows for the supersonic leading-edge triangular wing.

The upwash at any point in the field (x',y,z) due to an infinite triangular wing can be found from the charts of reference 28. (For $z=0$, $-\partial\epsilon/\partial\alpha=w/\alpha V=-1$). The sketches shown in this appendix illustrate the steps that are required in order to cancel the lifting pressures of an infinite triangular wing, at a desired x' location, which is to be the trailing edge of the wing. For each plan form, the corresponding pressure distribution, for the particular step involved, is also shown by the solid lines. The dashed lines indicate the canceling pressure which is being applied. All pressures are for the upper surface only. The expressions for u and u_0 shown in sketch 2 can be obtained from reference 29.



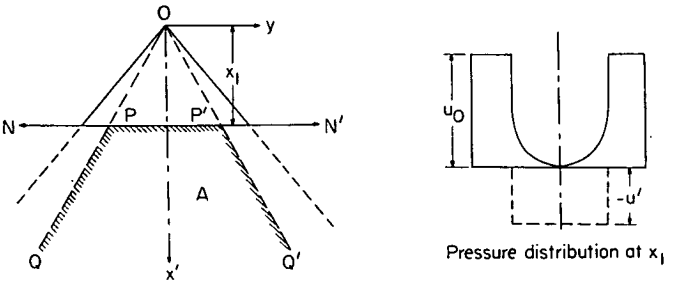
Sketch 2.

These equations are:

$$u_0=\frac{\alpha V}{\beta\sqrt{1-\frac{a^2}{\beta^2}}} \tag{A1}$$

$$\frac{u}{u_0}=\frac{1}{\pi}\cos^{-1}\left[1+\frac{2\left(\frac{a^2}{\beta^2}-1\right)}{1-a^2\left(\frac{b}{x'}\right)^2}\right] \tag{A2}$$

Sketch 3 illustrates the addition of wing A which is at constant pressure u' and cancels the pressures as shown in the following sketch. Wing A is formed by subtracting two

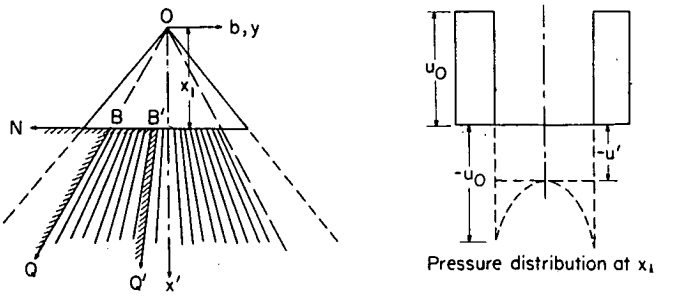


Sketch 3.

conical wings, N,P,Q and N′,P′,Q′, from a two-dimensional wing. In the sketch, N,Q,Q′, and N′ are at infinity in the designated direction. If the expressions for the $G(-1,r,\theta)$ and $G(1,r,\theta)$ functions that are given in reference 15 are used, the resulting upwash in the $z=0$ plane due to wing A is

$$\frac{w}{V_\alpha}=-1-\left[G(-1,r,\theta)\frac{u'}{m}+G(1,r,\theta)\frac{u'}{m}\right] \tag{A3}$$

Sketch 4 illustrates the process whereby conical wings each of a different constant pressure are used to cancel the pressure between the two Mach lines from the apex. The upwash due to a typical conical wing Q,B,B′,Q′ is formed



Sketch 4.

by subtracting the upwash due to two conical wings at the same pressure u; that is, wing N,B′,Q′ minus wing N,B,Q. The resulting expression for the upwash due to the canceling wings in sketch 4 is

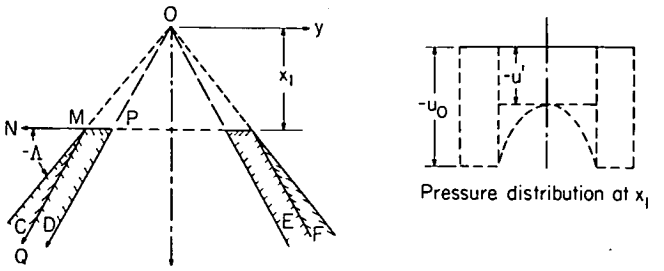
$$\frac{w}{\alpha V}=-\beta\left\{\int_0^{-1}[G(-b,r,\theta)-G(-1,r,\theta)]\frac{du}{db}\right\}db+$$
$$\beta\left\{\int_0^{1}[G(b,r,\theta)-G(1,r,\theta)]\frac{du}{db}\right\}db \tag{A4}$$

The expressions for the $G(b,r,\theta)$ functions are given in reference 15 and

$$\frac{du}{db}=\frac{2\alpha Vab}{\pi\beta^2\left(1-\frac{a^2}{\beta^2}b^2\right)\sqrt{1-b^2}} \tag{A5}$$

The integration was performed mechanically by using ten wings for each half of the conical field between the Mach lines.

Sketch 5 illustrates the final step in canceling the pressures (u values) everywhere downstream of the wing trailing edge.



Sketch 5.

Wings C + D and E + F are at constant pressure u_0. The expression for the downwash due to wings C and F may be obtained from reference 16. The expression, as is given in reference 16, is for $M=\sqrt{2}$. When the Mach number terms are reinstalled, the expression as applied to wing C is

$$G''(-1,r,\theta)=\frac{w}{\alpha V}$$

$$=\frac{1}{\pi}\left[\cot\beta+\frac{\tan(-\Lambda)}{\beta}\right]\log R'-$$

$$\sqrt{1-\frac{\tan^2(-\Lambda)}{\beta^2}}\left\{\tan^{-1}\frac{2\sqrt{1-\frac{\tan^2(-\Lambda)}{\beta^2}}\left[R'\cos\theta+\frac{\tan(-\Lambda)}{\beta}\right]}{R^2-1+\frac{2\tan^2(-\Lambda)}{\beta^2}+\frac{2R'}{\beta}\cos\theta\tan(-\Lambda)}-\tan^{-1}\frac{\sqrt{1-\frac{\tan^2(-\Lambda)}{\beta^2}}}{\frac{\tan(-\Lambda)}{\beta}}\right\} \tag{A6}$$

The symbols are defined in reference 16 or reference 15, where, for $z=0$,

$$R'=\frac{1-\sqrt{\frac{x^2}{\beta^2}-y^2}}{y}$$

and $\theta=0°$ or 180°.

In applying formula (A6) to the calculation of upwash due to wings C and F of sketch 5, the axis must be shifted to M and N (that is, define the field points x', y, and z with respect to M and N instead of with respect to 0). The upwash due to wings D and E of sketch 5 was also determined by a scheme which employed a shift in the y coordinates of the field points for which the upwash was being calculated by the distance MP. For wing D, the upwash was that of the conical wing N,P,Q′ minus the conical wing N,M,Q, where the wing N,M,Q was determined from the $G'(-1,r,\theta)$ function based on the shifted y coordinates of the field points; that is (due to wings D and E),

$$\frac{w}{V_\alpha}=\beta u_0\left[G(-1,r,\theta)-G'(-1,r,\theta)\right]+\beta u_0\left[G(1,r,\theta)-G'(1,r,\theta)\right] \tag{A7}$$

After the evaluation of all of the above component contributions to the upwash, the final value for the upwash as obtained at any field point was merely the algebraic sum. Charts constructed for all the G functions greatly expedited the calculations. The case of the supersonic leading-edge wing, which is illustrated, is the most tedious. For subsonic leading-edge wings, it is necessary to carry the calculations only through the steps illustrated in sketches 2, 3, and 4.

APPENDIX B

DETAILS OF HORSESHOE-VORTEX METHOD

The estimation of the downwash and sidewash behind triangular wings by the horseshoe-vortex theory is one of the methods described in reference 19. The theoretical model of the flow suggested in reference 19, which places the corners of the horseshoe vortices along a line representing the center of pressure of the triangular wing, was tried. Also, a different theoretical representation which placed the corners of the horseshoe vortices in equal x' increments (although they might lie outside the wing plan form) was tried. The difference in the downwash, as calculated by the two methods, was very slight. All the theoretical curves presented herein for the horseshoe vortex method were calculated by the latter method.

APPENDIX C

DETAILS OF SINGLE-BENT-LINE-VORTEX METHOD

For the low-aspect-ratio triangular wings, a single bent-line vortex physically approximates the flow field. The expression for the upwash, which is given explicitly in reference 1, was used for those theoretical calculations where the theoretical model of the flow was a single bent-line vortex. In order to obtain the expression for the sidewash due to a single bent-line vortex, the expression for the potential as given in reference 19 was differentiated with respect to y.

The resulting equation is

$$\frac{2\pi v}{\Gamma}=z\left\{\frac{\left[(y-y_0)\left(x'-\frac{y+k}{m}\right)-\frac{z^2}{m}\right]\left[\frac{-\beta^2(y^2-y_0^2)}{\sqrt{\left(x'-\frac{y_0+k}{m}\right)^2-\beta^2(y-y_0)^2-\beta^2z^2}}\right]}{\left[(y-y_0)\left(x'-\frac{y+k}{m}\right)-\frac{z^2}{m}\right]^2+z^2\left[\left(x'-\frac{y_0+k}{m}\right)^2-\beta^2(y-y_0)^2-\beta^2z^2\right]}-\right.$$

$$\left.\frac{\sqrt{\left(x'-\frac{y_0+k}{m}\right)^2-\beta^2(y-y_0)^2-\beta^2z^2}\left[x'-\left(\frac{2y+k-y_0}{m}\right)\right]}{\left[(y-y_0)\left(x'-\frac{y+k}{m}\right)-\frac{z^2}{m}\right]^2+z^2\left[\left(x'-\frac{y_0+k}{m}\right)^2-\beta^2(y-y_0)^2-\beta^2z^2\right]}\right\}-$$

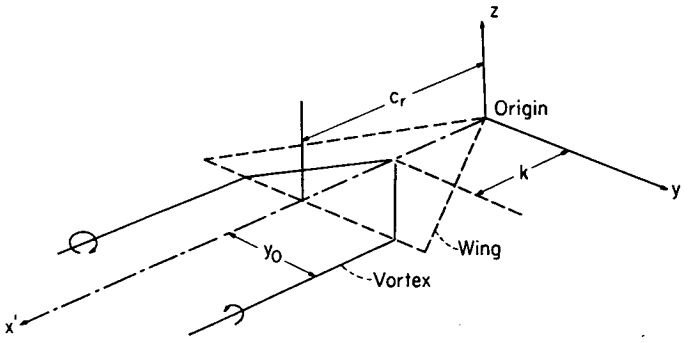
$$z\left\{\frac{\left[(y-y_0)\left(x'+\frac{y-k}{m}\right)+\frac{z^2}{m}\right]\left[\frac{-\beta^2(y+y_0)}{\sqrt{\left(x'-\frac{y_0+k}{m}\right)^2-\beta^2(y+y_0)^2-\beta^2z^2}}\right]}{\left[(y+y_0)\left(x'+\frac{y-k}{m}\right)+\frac{z^2}{m}\right]^2+z^2\left[\left(x'-\frac{y_0+k}{m}\right)^2-\beta^2(y+y_0)^2-\beta^2z^2\right]}-\right.$$

$$\left.\frac{\sqrt{\left(x'-\frac{y_0+k}{m}\right)^2-\beta^2(y+y_0)^2-\beta^2z^2}\,(mx'+2y-k+y_0)}{\left[(y+y_0)\left(x'+\frac{y-k}{m}\right)+\frac{z^2}{m}\right]^2+z^2\left[\left(x'-\frac{y_0+k}{m}\right)^2-\beta^2(y+y_0)^2-\beta^2z^2\right]}\right\}+$$

$$\frac{mz\left[\frac{y(mx'+y-k)+z^2(-\beta^2y)}{\sqrt{\left(x'-\frac{k}{m}\right)^2-\beta^2(y^2+z^2)}}-(mx'+2y-k)\sqrt{\left(x'-\frac{k}{m}\right)^2-\beta^2(y^2+z^2)}\right]}{[y(mx'+y-k)+z^2]^2+m^2z^2\left[\left(x'-\frac{k}{m}\right)^2-\beta^2(y^2+z^2)\right]}-$$

$$\frac{mz\left[\frac{[y(mx'-y-k)-z^2](-\beta^2y)}{\sqrt{\left(x'-\frac{k}{m}\right)^2-\beta^2(y^2+z^2)}}-(mx'-2y-k)\sqrt{\left(x'-\frac{k}{m}\right)^2-\beta^2(y^2+z^2)}\right]}{[y(mx'-y-k)-z^2]^2+m^2z^2\left[\left(x'-\frac{k}{m}\right)^2-\beta^2(y^2+z^2)\right]}$$

where x', y, z, k, c_r, and y_0 are defined in sketch 6.



Sketch 6.

APPENDIX D

DETAILS OF INFINITE-LINE-VORTEX METHOD

At angles of attack where the deflection and the distortion of the vortex sheet behind a wing become important, yet where the wing aspect ratio is too high, or the distance behind the wing too short to represent the vorticity behind the wing with a single bent-line vortex, a method such as was used in references 22 and 23 was employed to estimate the shape of the vortex sheet and to approximate the resulting downwash and sidewash. The equivalence of the supersonic and the incompressible line vortex, when both have zero slope, was pointed out in reference 18. The simple relation for the induced tangential velocity at points in the field of an infinite line vortex is

$$v_T=\frac{\Gamma}{2\pi r} \tag{D1}$$

or, as used in this paper,

$$\left.\begin{aligned}\frac{wb'}{\Gamma}&=\frac{\frac{y}{b'}}{\sqrt{\left(\frac{y}{b'}\right)^2+\left(\frac{z}{b'}\right)^2}}\\ \frac{vb'}{\Gamma}&=\frac{\frac{z}{b'}}{\sqrt{\left(\frac{y}{b'}\right)^2+\left(\frac{z}{b'}\right)^2}}\end{aligned}\right\} \tag{D2}$$

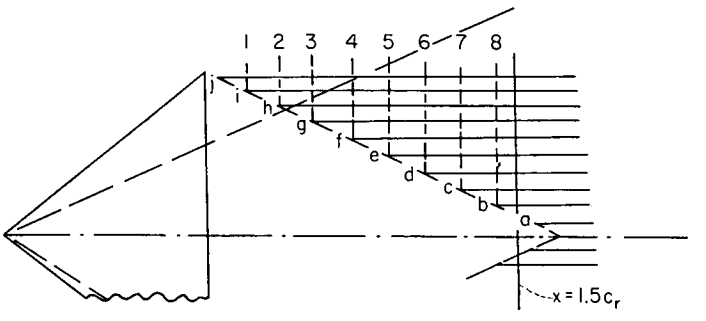
The simplicity of these expressions permitted the use of an iteration procedure, such as that used in reference 22, to approximate the location and shape of the vortex sheet.

APPENDIX E

DETAILS OF THE METHOD FOR THE COMBINATION OF THE CONICAL-FLOW AND THE INFINITE-LINE-VORTEX THEORIES

The region between the two Mach lines from the tips was taken as an arbitrary range of applicability of conical-flow theory. The deflection of the vortex sheet above or below the reference streamwise plane was computed at various spanwise stations by using conical-flow theory. These locations correspond to points a through j in sketch 7. The spanwise location of points a through j were determined from the wing span load distribution in the same manner as was used for setting up the infinite-line-vortex calculations.

With the location of points a through j as the starting points of the infinite line vortices, the induced velocities and corresponding paths of each vortex were computed in the same step-by-step manner (from station 1, to 2, to 3, etc.) as was used for the calculations made by using infinite line vortices alone. However, only those vortices which were



Sketch 7.

actually present at any longitudinal station were considered to have any effect on the adjacent line vortices. (For example, at station 5, the total induced velocity on g was the sum of the induced velocities from e, f, h, i, and j.)

REFERENCES

1. Sprieter, John R., and Sacks, Alvin H.: The Rolling Up of the Trailing Vortex Sheet and Its Effect on the Downwash Behind Wings. Jour. Aero. Sci., vol. 18, no. 1, Jan. 1951, pp. 21–32, 72.
2. Perkins, Edward W., and Canning, Thomas N.: Investigation of Downwash and Wake Characteristics at a Mach Number of 1.53. I—Rectangular Wing. NACA RM A8L16, 1949.
3. Perkins, Edward W., and Canning, Thomas N.: Investigation of Downwash and Wake Characteristics at a Mach Number of 1.53. II—Triangular Wing. NACA RM A9D20, 1949.
4. Adamson, D., and Boatright, William B.: Investigation of Downwash, Sidewash, and Mach Number Distribution Behind a Rectangular Wing at a Mach Number of 2.41. NACA Rep. 1340, 1957. (Supersedes NACA RM L50G12.)
5. Cummings, John L., and Haefeli, Rudolph C.: Downwash in Vortex Region Behind Rectangular Half-Wing at Mach Number 1.91. NACA RM E50H10, 1950.
6. Davis, Theodore: Experimental Investigation of Downwash and Sidewash Behind a Rectangular Wing at a Mach Number of 1.60. Meteor Rep. UAC-45, United Aircraft Corp., Jan. 1950.
7. Walker, Harold J., Stivers, Louis S., Jr., and Beard, Luther, Jr.: Experimental Downwash and Wake Characteristics at Subsonic and Supersonic Mach Numbers Behind an Unswept Tapered Wing of Aspect Ratio 2.67 With Leading- and Trailing-Edge Flaps. NACA RM A51B16, 1951.
8. Cummings, J. L., Mirels, H., Baughman, L. E.: Downwash in Vortex Region Behind Trapezoidal-Wing Tip at Mach Number 1.91. NACA RM E9H15, 1949.
9. Perkins, Edward W., and Canning, Thomas N.: Investigation of Downwash and Wake Characteristics at a Mach Number of 1.53. III—Swept Wings. NACA RM A9K02, 1950.
10. Walker, Harold J., and Stivers, Louis S., Jr.: Investigation of the Downwash and Wake Behind a Triangular Wing of Aspect Ratio 4 at Subsonic and Supersonic Mach Numbers. NACA RM A50I14a, 1950.
11. Boatright, William B.: Total-Pressure and Schlieren Studies of the Wakes of Various Canard Control Surfaces Mounted on a Missile Body at Mach Number of 1.93. NACA RM L52I29, 1952.
12. Grigsby, Carl E.: The Use of the Rolled-Up Vortex Concept for Predicting Wing-Tail Interference and Comparison With Experiment at Mach Number of 1.62 for a Series of Missile Configurations Having Tandem Cruciform Lifting Surfaces. NACA RM L52H05, 1952.
13. Fradenburgh, Evan A., Obery, Leonard J., and Mello, John F.: Influence of Fuselage and Canard-Type Control Surface on the Flow Field Adjacent to a Rearward Fuselage Station at a Mach Number of 2.0. Data Presentation. NACA RM E51K05, 1952.
14. Weil, Joseph, Campbell, George S., and Diederich, Margaret S.: An Analysis of Estimated and Experimental Transonic Downwash Characteristics as Affected by Plan Form and Thickness for Wing and Wing-Fuselage Configurations. NACA TN 3628, 1956. (Supersedes NACA RM L52I22.)
15. Lagerstrom, P. A., Graham, Martha E., and Grosslight, G.: Downwash and Sidewash Induced by Three-Dimensional Lifting Wings in Supersonic Flow. Rep. No. SM–13007, Douglas Aircraft Co., Inc., Apr. 14, 1947.
16. Lagerstrom, P. A.: Linearized Supersonic Theory of Conical Wings (Corrected copy). NACA TN 1685, 1950.
17. Busemann, Adolf: Infinitesimal Conical Supersonic Flow. NACA TM 1100, 1947.
18. Mirels, Harold, and Haefeli, Rudolph C.: Line-Vortex Theory for Calculation of Supersonic Downwash. NACA Rep. 983, 1950.
19. Martin, John C.: The Calculation of Downwash Behind Wings of Arbitrary Plan Form at Supersonic Speeds. NACA TN 2135, 1950.
20. Heaslet, Max A., and Lomax, Harvard: The Calculation of Downwash Behind Supersonic Wings With Application to Triangular Plan Forms. NACA TN 1620, 1948.
21. Harmon, Sidney M.: Method for Calculating Downwash Field Due to Lifting Surfaces at Subsonic and Supersonic Speeds. NACA TN 2344, 1951.
22. Westwater, F. L.: Rolling Up of the Surface of Discontinuity Behind an Aerofoil of Finite Span. R. & M. No. 1692, British A.R.C., 1935.
23. Rogers, Arthur Wm.: Application of Two-Dimensional Vortex Theory to the Prediction of Flow Fields Behind Wings of Wing-Body Combinations at Subsonic and Supersonic Speeds. NACA TN 3227, 1954.
24. Boyd, John W., and Phelps, E. Ray: A Comparison of the Experimental and Theoretical Loading Over Triangular Wings at Supersonic Speeds. NACA RM A50J17, 1951.
25. Hatch, John E., Jr., and Hargrave, L. Keith: Effects of Reynolds Number on Aerodynamic Characteristics of a Delta Wing at a Mach Number of 2.41. NACA RM L51H06, 1951.
26. Beal, R. R.: Analysis of Force and Moment Characteristics From Supersonic Wind-Tunnel Tests of a 13.5-Percent-Scale Model of the Sparrow 14–B at Mach Number=1.50 Including the Effects of Systematic Variations of Wing Planform. Rep. No. SM–20175, Douglas Aircraft Co., Inc., Aug. 31, 1951.
27. Lagerstrom, P. A., and Graham, M. E.: Aerodynamic Interference in Supersonic Missiles. Rep. No. SM–13743, Douglas Aircraft Co., Inc., July 1950.
28. Nielson, Jack N., and Perkins, Edward W.: Charts for the Conical Part of the Downwash Field of Swept Wings at Supersonic Speeds. NACA TN 1780, 1948.
29. Lagerstrom, P. A., Wall, D., and Graham, M. E.: Formulas in Three-Dimensional Wing Theory. Rep. No. SM–11901, Douglas Aircraft Co., Inc., July 8, 1946.

REPORT 1381

A STUDY OF THE MOTION AND AERODYNAMIC HEATING OF BALLISTIC MISSILES ENTERING THE EARTH'S ATMOSPHERE AT HIGH SUPERSONIC SPEEDS [1]

By H. JULIAN ALLEN and A. J. EGGERS, Jr.

SUMMARY

A simplified analysis is made of the velocity and deceleration history of ballistic missiles entering the earth's atmosphere at high supersonic speeds. It is found that, in general, the gravity force is negligible compared to the aerodynamic drag force and, hence, that the trajectory is essentially a straight line. A constant drag coefficient and an exponential variation of density with altitude are assumed and generalized curves for the variation of missile speed and deceleration with altitude are obtained. A curious finding is that the maximum deceleration is independent of physical characteristics of a missile (e. g., mass, size, and drag coefficient) and is determined only by entry speed and flight-path angle, provided this deceleration occurs before impact.

The results of the motion analysis are employed to determine means available to the designer for minimizing aerodynamic heating. Emphasis is placed upon the convective-heating problem including not only the total heat transfer but also the maximum average and local rates of heat transfer per unit area. It is found that if a missile is so heavy as to be retarded only slightly by aerodynamic drag, irrespective of the magnitude of the drag force, then convective heating is minimized by minimizing the total shear force acting on the body. This condition is achieved by employing shapes with a low pressure drag. On the other hand, if a missile is so light as to be decelerated to relatively low speeds, even if acted upon by low drag forces, then convective heating is minimized by employing shapes with a high pressure drag, thereby maximizing the amount of heat delivered to the atmosphere and minimizing the amount delivered to the body in the deceleration process. Blunt shapes appear superior to slender shapes from the standpoint of having lower maximum convective heat-transfer rates in the region of the nose. The maximum average heat-transfer rate per unit area can be reduced by employing either slender or blunt shapes rather than shapes of intermediate slenderness. Generally, the blunt shape with high pressure drag would appear to offer considerable promise of minimizing the heat transfer to missiles of the sizes, weights, and speeds of usual interest.

INTRODUCTION

For long-range ballistic trajectories one of the most difficult phases of flight the designer must cope with is the reentry into the earth's atmosphere, wherein the aerodynamic heating associated with the high flight speeds is intense. The air temperature in the boundary layer may reach values in the tens of thousands of degrees Fahrenheit which, combined with the high surface shear, promotes very great convective heat transfer to the surface. Heat-absorbent material must therefore be provided to prevent destruction of the essential elements of the missile. It is characteristic of long-range rockets that for every pound of material which is carried to "burn-out," many pounds of fuel are required in the booster to obtain the flight range. It is clear, therefore, that the amount of material added for protection from excessive aerodynamic heating must be minimized in order to keep the take-off weight to a practicable value. The importance of reducing the heat transferred to the missile to the least amount is thus evident.

For missiles designed to absorb the heat within the solid surface of the missile shell, a factor which may be important, in addition to the total amount of heat transferred, is the rate at which it is transferred since there is a maximum rate at which the surface material can safely conduct the heat within itself. An excessively high time rate of heat input may promote such large temperature differences as to cause spalling of the surface, and thus result in loss of valuable heat-absorbent material, or even structural failure as a result of stresses induced by the temperature gradients.

For missiles designed to absorb the heat with liquid coolants (e. g., by transpiration cooling where the surface heat-transfer rate is high, or by circulating liquid coolants within the shell where the surface heat-transfer rate is lower), the time rate of heat transfer is similarly of interest since it determines the required liquid pumping rate.

These heating problems, of course, have been given considerable study in connection with the design of particular missiles, but these studies are very detailed in scope. There has been need for a generalized heating analysis intended to show in the broad sense the means available for minimizing the heating problems. Wagner, reference 1, made a step toward satisfying this need by developing a laudably simple motion analysis. This analysis was not generalized, however, since it was his purpose to study the motion and heating of a particular missile.

It is the purpose of this report to simplify and generalize the analysis of the heating problem in order that the salient features of this problem will be made clear so that successful solutions of the problem will suggest themselves.

A motion analysis, having the basic character of Wagner's approach, precedes the heating analysis. The generalized results of this analysis are of considerable interest in themselves and, accordingly, are treated in detail.

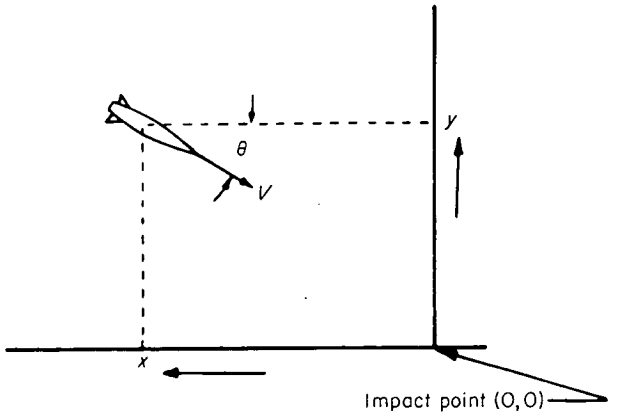
[1] Supersedes NACA Technical Note 4047 by H. Julian Allen and A. J. Eggers, Jr., 1957.

Preceding Page Blank

ANALYSIS

MOTION OF THE BODY

Consider a body of mass m entering the atmosphere from great height. If, at any altitude y, the speed is V and the angle of approach is θ to the horizontal (see sketch), the



parametric equations of motion can be written [2]

$$\left.\begin{aligned}\frac{d^2y}{dt^2}&=-g+\frac{C_D\rho V^2A}{2m}\sin\theta\\ \frac{d^2x}{dt^2}&=\frac{C_D\rho V^2A}{2m}\cos\theta\end{aligned}\right\} \tag{1}$$

where

C_D drag coefficient, dimensionless
V speed, ft/sec
A reference area for drag evaluation, sq ft
m mass of the body, slugs
ρ mass density of the air, slugs/ft^3
g acceleration of gravity, ft/sec^2
x,y horizontal and vertical distance from the point of impact with the earth, ft
θ angle between the flight path and the horizontal, deg

(See Appendix A for complete list of symbols.)

In general, the drag coefficient varies with Mach number and Reynolds number, while the density and, to a very minor extent, the acceleration of gravity vary with altitude. Hence it is clear that exact solution of these equations is formidable. Let us first, then, consider the following simplified case:

1. The body descends vertically.
2. The drag coefficient is constant.[3]
3. The acceleration of gravity is constant.[4]
4. The density as a function of altitude is given by the relation

$$\rho=\rho_o e^{-\beta y} \tag{2}$$

where ρ_o and β are constants. This relation is consistent with the assumption of an isothermal atmosphere.

[2] Properly, the analysis should consider those effects resulting from the fact that the earth is a rotating sphere, but since the altitude range for which drag effects are important is less than 1 percent of the radius of the earth, the rectilinear treatment given in this analysis is permissible.

[3] As is well known, this assumption is generally of good accuracy at the high Mach numbers under consideration, at least as long as the total drag is largely pressure drag.

[4] The acceleration of gravity decreases by only 1 percent for every 100,000-foot increase in altitude.

Equations (1) then reduce to the single equation

$$\frac{d^2y}{dt^2}=-\frac{dV}{dt}=-g+\frac{C_D\rho_oA}{2m}e^{-\beta y}V^2 \tag{3}$$

Noting that

$$\frac{dV}{dt}=-V\frac{dV}{dy}$$

we let

$$Z=V^2$$

and equation (3) becomes the linear differential equation

$$\frac{dZ}{dy}-\frac{C_D\rho_oA}{m}e^{-\beta y}Z+2g=0 \tag{4}$$

which has the well-known solution

$$Z=e^{\int\frac{C_D\rho_oA}{m}e^{-\beta y}dy}\left(-2g\int e^{-\int\frac{C_D\rho_oA}{m}e^{-\beta y}dy}dy+const.\right)$$

Performing the integrations, we obtain as the solution of this relation

$$Z=V^2=e^{-\frac{C_D\rho_oA}{\beta m}e^{-\beta y}}\left[\frac{2g}{\beta}\sum_{n=1}^{\infty}\frac{\left(\frac{C_D\rho_oA}{\beta m}e^{-\beta y}\right)^n}{n\underline{|n}}-2gy+const.\right] \tag{5}$$

so that the deceleration becomes, in terms of gravity acceleration,

$$-\frac{\frac{dV}{dt}}{g}=\frac{C_D\rho_oA}{2mg}e^{-\beta y}e^{-\frac{C_D\rho_oA}{\beta m}e^{-\beta y}}\left[\frac{2g}{\beta}\sum_{n=1}^{\infty}\frac{\left(\frac{C_D\rho_oA}{\beta m}e^{-\beta y}\right)^n}{n\underline{|n}}-2gy+const.\right]-1 \tag{6}$$

As an example, consider the vertical descent of a solid iron sphere having a diameter of 1 foot. For a sphere the drag coefficient may be taken as unity, based on the frontal area for all Mach numbers greater than about 1.4. In equation (2), which describes the variation of density with altitude, the constants should clearly be so chosen as to give accurate values of the density over the range of altitudes for which the deceleration is large. It is seen in figure 1 that for

$$\rho_o=0.0034 \text{ slugs/ft}^3$$

and

$$\beta=\frac{1}{22{,}000}\text{ ft}^{-1}$$

which yields

$$\rho=0.0034\,e^{-\frac{y}{22{,}000}} \tag{7}$$

the calculated density is in good agreement with the NACA standard atmosphere values obtained from references 2 and 3 for the altitude range from 20,000 to 180,000 feet. These relations have been used in calculating the velocity and deceleration of the sphere for various altitudes, assuming

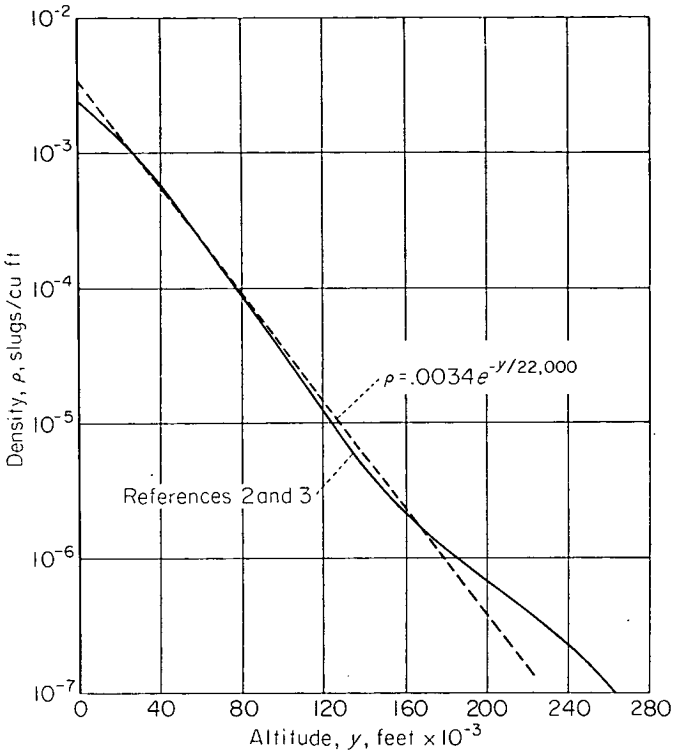


FIGURE 1.—Variation of density with altitude.

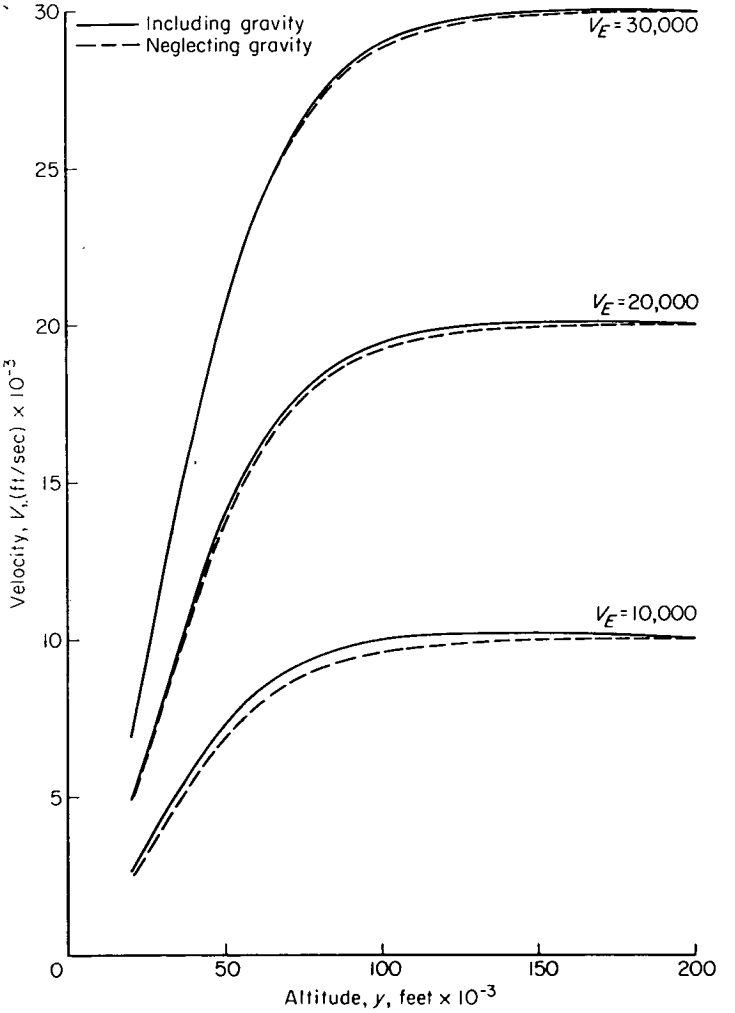


FIGURE 2.—Variations of velocity with altitude for a 1-foot diameter, solid iron sphere entering the earth's atmosphere vertically at velocities of 10,000, 20,000, and 30,000 ft/sec.

vertical entrance velocities of 10,000, 20,000, and 30,000 feet per second at 40 miles altitude which, for these cases, may be considered the "outer reach" of the atmosphere. The results of these calculations are presented as the solid curves in figures 2 and 3.

It is seen in figure 3 that for the high entrance speeds considered, the decelerations reach large values compared to the acceleration of gravity. This suggests that the gravity term in equation (3) may be neglected without seriously affecting the results.[5] When this term is neglected the equation of motion becomes

$$-\frac{dV}{dt}=V\frac{dV}{dy}=\frac{C_D\rho_o A}{2m}e^{-\beta y}V^2 \tag{8}$$

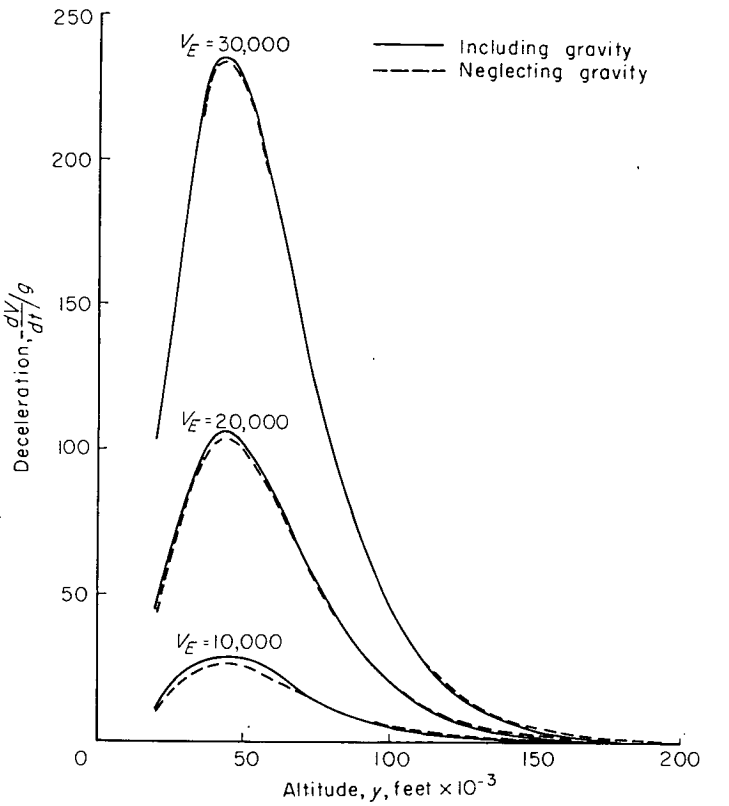


FIGURE 3.—Variations of deceleration with altitude for a 1-foot diameter, solid iron sphere entering the earth's atmosphere vertically at velocities of 10,000, 20,000, and 30,000 ft/sec.

Integration gives

$$ln\ V=-\frac{C_D\rho_o A}{2\beta m}e^{-\beta y}+const.$$

or

$$V=const.\times e^{-\frac{C_D\rho_o A}{2\beta m}e^{-\beta y}}$$

At the altitude of 40 miles it can readily be shown that the term

$$e^{-\frac{C_D\rho_o A}{2\beta m}e^{-\beta y}}$$

is very nearly unity so that the velocity may be written

$$V=V_E e^{-\frac{C_D\rho_o A}{2\beta m}e^{-\beta y}} \tag{9}$$

[5] It is usual to neglect the gravity acceleration a priori (see e. g., refs. 1 and 4.)

and

$$-\frac{\frac{dV}{dt}}{g}=\frac{C_D\rho_o A V_E^2}{2mg}e^{-\beta y}e^{-\frac{C_D\rho_o A}{\beta m}e^{-\beta y}} \tag{10}$$

where V_E is the entrance speed.

By use of equations (9) and (10) the vertical-descent speeds and decelerations for the 1-foot-diameter sphere previously considered have been calculated for the same entrance speeds. The results are shown as the dashed curves in figures 2 and 3. It is seen that these approximate calculations agree very well with those based on the more complete equation of motion (eq. (3)).

The above finding is important, for it indicates that in the general case, wherein the body enters the atmosphere at high speed at angle θ_E to the horizontal, the gravity term, provided θ_E is not too small, may be neglected in equation (1) to yield

$$\left.\begin{aligned}\frac{d^2y}{dt^2}&=\frac{C_D\rho V^2 A\sin\theta_E}{2m}\\ \frac{d^2x}{dt^2}&=\frac{C_D\rho V^2 A\cos\theta_E}{2m}\end{aligned}\right\} \tag{11}$$

so that the flight path is essentially a straight line (i. e., $\theta=\theta_E$), and the resultant deceleration equation becomes

$$-\frac{dV}{dt}=\frac{C_D\rho A V^2}{2m} \tag{12}$$

Now, again, if the density relation given by equation (2) is used and it is noted that

$$V=\frac{-\frac{dy}{dt}}{\sin\theta_E}\text{ or }-\frac{dV}{dt}=V\sin\theta_E\frac{dV}{dy}$$

equation (12) becomes

$$\frac{dV}{V}=\frac{C_D\rho_o A}{2m\sin\theta_E}e^{-\beta y}dy$$

which can be integrated to yield

$$V=V_E e^{-\frac{C_D\rho_o A}{2\beta m\sin\theta_E}e^{-\beta y}} \tag{13}$$

and the deceleration is then

$$-\frac{\frac{dV}{dt}}{g}=\frac{C_D\rho_o A V_E^2}{2mg}e^{-\beta y}e^{-\frac{C_D\rho_o A}{\beta m\sin\theta_E}e^{-\beta y}} \tag{14}$$

The altitude y_1 at which the maximum deceleration occurs is found from this relation to be

$$y_1=\frac{1}{\beta}\ln\frac{C_D\rho_o A}{\beta m\sin\theta_E} \tag{15}$$

If y_1 is positive the velocity V_1 (from eqs. (13) and (15)) at which the maximum deceleration occurs becomes

$$V_1=V_E e^{-\frac{1}{2}}\cong 0.61V_E \tag{16}$$

and the value of the maximum deceleration is

$$-\left(\frac{\frac{dV}{dt}}{g}\right)_{max}=-\left(\frac{\frac{dV}{dt}}{g}\right)_1=\frac{\beta V_E^2\sin\theta_E}{2ge} \tag{17}$$

If equations (13) and (14) are rewritten to make the altitude reference point y_1 rather than zero, then

$$V=V_E e^{-\frac{C_D\rho_o A}{2\beta m\sin\theta_E}e^{-\beta(y_1+\Delta y)}}$$

and

$$-\frac{\frac{dV}{dt}}{g}=\frac{C_D\rho_o A V_E^2}{2mg}e^{-\beta(y_1+\Delta y)}e^{-\frac{C_D\rho_o A}{\beta m\sin\theta_E}e^{-\beta(y_1+\Delta y)}}$$

respectively, where Δy is the change in altitude from y_1. Substitution of equation (15) into these expressions can readily be shown to give

$$\frac{V_{\Delta y}}{V_E}=e^{-\frac{1}{2}e^{-\beta\Delta y}}=F'(\beta\Delta y) \tag{18}$$

and

$$\frac{\left(\frac{dV/dt}{g}\right)_{\Delta y}}{\left(\frac{dV/dt}{g}\right)_1}=e^{-\beta\Delta y}e^{(1-e^{-\beta\Delta y})}=F''(\beta\Delta y) \tag{19}$$

Equations (18) and (19) are generalized expressions for velocity and deceleration for bodies of constant drag coefficient and, together with equations (15) and (17), can be used to determine the variation of these quantities with altitude for specific cases. The dependence of $F'(\beta\Delta y)$ and $F''(\beta\Delta y)$ on $\beta\Delta y$ is shown in figure 4.

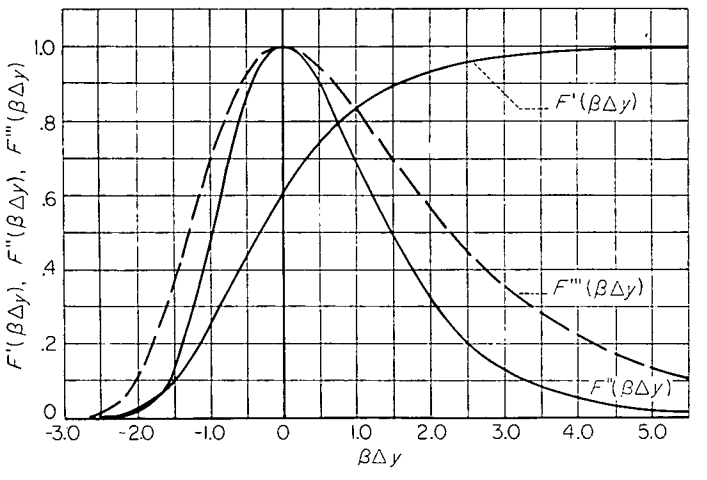


FIGURE 4.—Variations of $F'(\beta\Delta y)$, $F''(\beta\Delta y)$, and $F'''(\beta\Delta y)$ with $\beta\Delta y$.

The maximum deceleration and the velocity for maximum deceleration as given by equations (17) and (16) apply only if the altitude y_1, given by equation (15), is positive. Otherwise the maximum deceleration in flight occurs at sea level with the velocity (see eq. (13))

$$V=V_o=V_E e^{-\frac{C_D\rho_o A}{2\beta m\sin\theta_E}} \tag{20}$$

and has the value

$$-\left(\frac{\frac{dV}{dt}}{g}\right)_{max}=-\left(\frac{\frac{dV}{dt}}{g}\right)_0=\frac{C_D\rho_0AV_E^2}{2mg}\,e^{-\frac{C_D\rho_0A}{\beta m\sin\theta_E}} \qquad (21)$$

HEATING OF THE BODY

It was noted previously that for practicable rocket missiles, it is vital that the weight of the missile be kept to a minimum. The total heat transferred to a missile from the air must be absorbed by some "coolant" material. Since this material has a maximum allowable temperature, it follows that it can accept only a given amount of heat per unit weight. Hence, the total heat input to the missile must be kept at a minimum for minimum missile weight.

Often the coolant material is simply the shell of the missile and as such must provide the structural strength and rigidity for the missile as well. The strength of the structure is dictated, in part, by the stresses induced by temperature gradients within the shell. Since these temperature gradients are proportional to the time rate of heat input, the maximum time rate of heat input is important in missile design. The heating, of course, varies along the surface but, since the shell transmits heat along as well as through itself, the strength of the structure as a whole may be determined by the maximum value of the average heat-transfer rate over the surface. This is simply the maximum value of the time rate of heat input per unit area. On the other hand, the structural strength at local points on the surface may be determined primarily by the local rate of heat input. Hence, the maximum time rate of heat input per unit area at the surface element where the heat transfer is greatest may also be of importance in design.

If liquid cooling is employed, the maximum surface heat-transfer rates retain their significance but, now, in the sense that they dictate such requirements as maximum coolant pumping rate, or perhaps shell porosity as well in the case of transpiration cooling. Whichever the case, in the analysis to follow, these elements of the heating problem will be treated:

1. The total heat input.
2. The maximum time rate of average heat input per unit area.
3. The maximum time rate of local heat input per unit area.

Since it is the primary function of this report to study means available to the missile designer to minimize the heating problem, the analysis is simplified to facilitate comparison of the relative heating of one missile with respect to another—accurate determination of the absolute heating of individual missiles is not attempted. With this point in mind, the following assumptions, discussed in Appendix B, are made:

1. Convective heat transfer predominates (i. e., radiation effects are negligible).
2. Effects of gaseous imperfections may be neglected.
3. Shock-wave boundary-layer interaction may be neglected.
4. Reynolds' analogy is applicable.
5. The Prandtl number is unity.

Total heat input.—The time rate of convective heat transfer from the air to any element of surface of the body may be expressed by the well-known relation

$$\frac{dH}{dt}=h_l(T_r-T_w)_l \qquad (22)$$

where

H heat transferred per unit area, ft-lb/ft^2

h convective heat-transfer coefficient, $\frac{\text{ft-lb}}{\text{ft}^2\ \text{sec}^\circ\text{R}}$

T_r recovery temperature, °R

T_w temperature of the wall, °R

t time, sec

and the subscript l denotes local conditions at any element of the surface dS.

It is convenient in part of this analysis to determine the heating as a function of altitude. To this end, noting that

$$dt=\frac{-dy}{V\sin\theta_E}$$

we see that equation (22) may be written

$$\frac{dH}{dy}=-\frac{h_l(T_r-T_w)_l}{V\sin\theta_E} \qquad (23)$$

With the assumption that the Prandtl number is unity, the recovery temperature is

$$T_r=T_l\left(1+\frac{\gamma-1}{2}M_l^2\right)=T\left(1+\frac{\gamma-1}{2}M^2\right)$$

where

M Mach number at the altitude y, dimensionless

γ the ratio of specific heat at constant pressure to that at constant volume, C_p/C_v, dimensionless

T static temperature at the altitude y, °R

so that

$$(T_r-T_w)_l=T-T_{w_l}+\frac{\gamma-1}{2}M^2T$$

It is seen that for large values of the Mach number, which is the case of principal interest, the third term is large compared to reasonably allowable values of $T-T_w$. It will therefore be assumed that $T-T_w$ is negligible [6] so that

$$(T_r-T_w)_l=\frac{\gamma-1}{2}M^2T \qquad (24)$$

Moreover, since

$$M^2T=\frac{V^2}{(\gamma-1)C_p}$$

equation (24) may be written

$$(T_r-T_w)_l=\frac{V^2}{2C_p} \qquad (25)$$

[6] It should be noted that without this assumption, the heat-input determination would be greatly complicated since the changing wall temperature with altitude would have to be considered to obtain the heat input (see e. g., ref. 1). For high-speed missiles which maintain high speed during descent, the assumption is obviously permissible. Even for high-speed missiles which finally decelerate to low speeds, the assumption is generally still adequate since the total heat input is largely determined by the heat transfer during the high-speed portion of flight.

Now the local heat-transfer coefficient h_l is, by Reynolds' analogy, for the assumed Prandtl number of unity

$$h_l=\frac{1}{2}C_{f_l}C_{p_l}\rho_l V_l \tag{26}$$

where C_{f_l} is the local skin-friction coefficient based on conditions ρ_l, V_l, etc., just outside the boundary layer. Thus, since (T_r-T_w) is essentially constant over the entire surface S, the rate of total heat transfer with altitude becomes from equations (23) through (26)

$$\frac{dQ}{dy}=\int_S \frac{dH}{dy}\,dS=-\frac{V}{4C_p\sin\theta_E}\int_S C_{f_l}C_{p_l}\rho_l V_l\,dS$$

where Q is the heat transferred to the whole surface S. This equation may be written

$$\frac{dQ}{dy}=-\frac{C_f'\rho V^2 S}{4\sin\theta_E} \tag{27}$$

wherein C_{p_l} is set equal to C_p and

$$C_f'=\frac{1}{S}\int_S C_{f_l}\left(\frac{\rho_l}{\rho}\right)\left(\frac{V_l}{V}\right)dS \tag{28}$$

The parameter C_f' is termed "the equivalent friction coefficient," and will be assumed constant,[7] independent of altitude, again on the premise that relative rather than absolute heating is of interest. With equations (2) and (13), then, equation (27) is written

$$\frac{dQ}{dy}=-\frac{C_f'S\rho_o V_E^2}{4\sin\theta_E}e^{-\beta y}e^{-\frac{C_D\rho_o A}{\beta m\sin\theta_E}e^{-\beta y}} \tag{29}$$

Comparison of equation (29) with equation (14) shows that the altitude rate of heat transfer is directly proportional to the deceleration, so that

$$\frac{dQ/dy}{\left(\frac{dV/dt}{g}\right)}=\frac{mg}{2\sin\theta_E}\left(\frac{C_f'S}{C_DA}\right) \tag{30}$$

and therefore the maximum altitude rate of heat transfer occurs at the altitude y_1 (see eq. (15)) and is given by

$$\left(\frac{dQ}{dy}\right)_{max}=\left(\frac{dQ}{dy}\right)_1=-\frac{\beta m V_E^2}{4e}\left(\frac{C_f'S}{C_DA}\right) \tag{31}$$

It follows, of course, that the altitude rate of heat transfer varies with incremental change in altitude from y_1 in the same manner as deceleration, and thus (see eq. (19))

$$\frac{(dQ/dy)_{\Delta y}}{(dQ/dy)_1}=F''(\beta\Delta y) \tag{32}$$

[7] This assumption would appear poor at first glance since the Mach number and Reynolds number variations are so large. Analysis has indicated, however, that the effects of Mach number and Reynolds number variation are nearly compensating. The variation in C_f' for typical conical missiles was found to be, at most, about 50 percent from the maximum C_f' in the altitude range in which 80 percent of the heat is transferred.

The total heat input to the body at impact follows from equation (29) (integrating over the limits $0\leq y\leq\infty$) and is

$$Q=\frac{1}{4}\left(\frac{C_f'S}{C_DA}\right)mV_E^2\left(1-e^{-\frac{C_D\rho_o A}{\beta m\sin\theta_E}}\right) \tag{33}$$

The impact velocity, V_o (the velocity of body at $y=0$), is

$$V_o=V_E e^{-\frac{C_D\rho_o A}{2\beta m\sin\theta_E}}$$

so that equation (33) may be written in the alternative form

$$Q=\frac{m}{4}\left(\frac{C_f'S}{C_DA}\right)(V_E^2-V_o^2) \tag{34}$$

Maximum time rate of average heat input per unit area.—To determine the time rate of average heat transfer per unit area, equations (25), (26), and (28) with equation (22) may be shown to give

$$\frac{dH_{av}}{dt}=\tfrac{1}{4}C_f'\rho V^3 \tag{35}$$

which, together with equations (2) and (13), becomes at altitude y

$$\frac{dH_{av}}{dt}=\frac{C_f'\rho_o V_E^3}{4}e^{-\beta y}e^{-\frac{3C_D\rho_o A}{2\beta m\sin\theta_E}e^{-\beta y}} \tag{36}$$

The maximum time rate of average heat transfer per unit area is found from this expression to be

$$\left(\frac{dH_{av}}{dt}\right)_{max}=\left(\frac{dH_{av}}{dt}\right)_2=\frac{\beta}{6e}\left(\frac{C_f'}{C_DA}\right)mV_E^3\sin\theta_E \tag{37}$$

and it occurs at the altitude

$$y_2=\frac{1}{\beta}\ln\left(\frac{3C_D\rho_o A}{2\beta m\sin\theta_E}\right) \tag{38}$$

where the velocity is

$$V_2=V_E e^{-\frac{1}{2}}\cong 0.72\,V_E \tag{39}$$

As with altitude rate of heat transfer, it can be shown that

$$\frac{(dH_{av}/dt)_{\Delta y}}{(dH_{av}/dt)_2}=F''(\beta\Delta y) \tag{40}$$

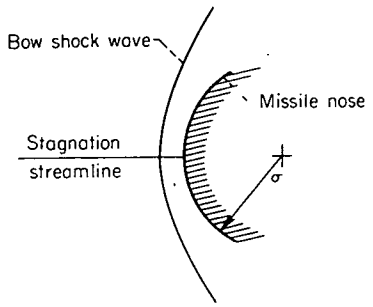
Equations (37), (38), and (39) apply if the altitude for maximum time rate of average heat transfer per unit area occurs above sea level. If y_2, by equation (38), is negative, then this rate occurs at sea level and is, from equation (36),

$$\left(\frac{dH_{av}}{dt}\right)_{max}=\left(\frac{dH_{av}}{dt}\right)_o=\frac{C_f'\rho_o V_E^3}{4}e^{-\frac{3C_D\rho_o A}{2\beta m\sin\theta_E}} \tag{41}$$

Maximum time rate of local heat input per unit area.—The elemental surface which is subject to the greatest heat transfer per unit area is, except in unusual cases, the tip of the missile nose which first meets the air. It seems unlikely that a pointed nose will be of practical interest for high-speed missiles since not only is the local heat-transfer rate exceedingly large in this case, but the capacity for heat retention is small. Thus a truly pointed nose would burn away.

Body shapes of interest for high-speed missiles would more probably, then, be those with nose shapes having nearly hemispherical tips. The following analysis applies at such tips.

It is well known that for any truly blunt body, the bow shock wave is detached and there exists a stagnation point at the nose. Consider conditions at this point and assume that the local radius of curvature of the body is σ (see sketch).



The bow shock wave is normal to the stagnation streamline and converts the supersonic flow ahead of the shock to a low subsonic speed flow at high static temperature downstream of the shock. Thus, it is suggested that conditions near the stagnation point may be investigated by treating the nose section as if it were a segment of a sphere in a subsonic flow field.

The heat-transfer rate per unit area at the stagnation point is given by the relation

$$\frac{dH_s}{dt}=-\frac{Nu_r k_r (T_w-T_r)}{\sigma}$$

where k_r is the thermal conductivity of the gas at the recovery temperature (i. e., total temperature) T_r, and Nu_r is the Nusselt number of the flow. If the flow is assumed to be laminar and incompressible,[8] Nu_r is given, according to reference 5, by the relationship

$$Nu_r=0.934 Re_\sigma^{1/2} Pr^{2/5}$$

We retain the assumption that the Prandtl number is unity, note that $Re_\sigma=\rho V\sigma/\mu_r$, and substitute equation (25) into equation (42) to obtain

$$\frac{dH_s}{dt}=0.47\sqrt{\frac{\rho V\mu_r}{\sigma}}\,V^2 \tag{43}$$

Now it is well known that at the high temperatures of interest here, the coefficient of viscosity μ_r varies nearly as the square root of the absolute temperature and is given by the relation

$$\mu_r=2.31\times10^{-8}T_r^{1/2}$$

If this expression is combined with equation (25) (neglecting T_w), equation (43) may then be written [9]

$$\frac{dH_s}{dt}=6.8\times10^{-6}\sqrt{\frac{\rho}{\sigma}}\,V^3 \tag{44}$$

which, when combined with equations (2) and (13), becomes

$$\frac{dH_s}{dt}=6.8\times10^{-6}\sqrt{\frac{\rho_o}{\sigma}}\,V_E^3 e^{-\frac{\beta y}{2}} e^{-\frac{3C_D\rho_o A}{2\beta m\sin\theta_E}e^{-\beta y}} \tag{45}$$

The maximum value of dH_s/dt can readily be shown to be

$$\left(\frac{dH_s}{dt}\right)_{max}=\left(\frac{dH_s}{dt}\right)_3=6.8\times10^{-6}\sqrt{\frac{\beta m\sin\theta_E}{3eC_D\sigma A}}\,V_E^3 \tag{46}$$

which occurs at the altitude

$$y_3=\frac{1}{\beta}\ln\left(\frac{3C_D\rho_o A}{\beta m\sin\theta_E}\right) \tag{47}$$

corresponding to the velocity

$$V_3=V_E e^{-\frac{1}{6}}\cong0.85V_E \tag{48}$$

The manner in which the heat-transfer rate per unit area at the stagnation point varies with incremental change in altitude from y_3 can be shown to be

$$\frac{(dH_s/dt)_{\Delta y}}{(dH_s/dt)_3}=e^{-\frac{\beta\Delta y}{2}} e^{\frac{1}{2}(1-e^{-\beta\Delta y})}=F'''(\beta\Delta y) \tag{49}$$

The dependence of $F'''(\beta\Delta y)$ on $\beta\Delta y$ is shown in figure 4.

Equation (46) applies only if y_3 is above sea level. If y_3, from equation (47), is negative, then the maximum heat-transfer rate per unit area at the stagnation point occurs at sea level and is

$$\left(\frac{dH_s}{dt}\right)_{max}=\left(\frac{dH_s}{dt}\right)_0=6.8\times10^{-6}\sqrt{\frac{\rho_o}{\sigma}}\,V_E^3 e^{-\frac{3C_D\rho_o A}{2\beta m\sin\theta_E}} \tag{50}$$

DISCUSSION

MOTION

The motion study shows some important features about the high-speed descent of missiles through the atmosphere. The major assumptions of this analysis were that the drag coefficient was constant and the density varied exponentially with altitude. It was found that the deceleration due to drag was generally large compared to the acceleration of gravity and, consequently, that the acceleration of gravity could be neglected in the differential equations of motion. The flight path was then seen to be a straight line, the missile maintaining the flight-path angle it had at entry to the atmosphere.

For most missiles, the maximum deceleration will occur at altitude. One of the most interesting features of the flight of such a missile is that the maximum deceleration is independent of physical characteristics (such as mass, size, and drag coefficient of the missile), being dependent only on the entry speed and flight-path angle (see eq. (17)). The missile speed at maximum deceleration (eq. (16)) bears a fixed relation to the entrance speed (61 percent of entrance speed), while the corresponding altitude (eq. (15)) depends on the physical characteristics and the flight-path angle but not on the entrance speed. It is also notable that for a given incremental change in altitude from the altitude for

[8] The assumption of constant density certainly may invalidate this analysis for any quantitative study of the relatively "cold-wall" flows of interest here. For the purpose of studying relative heat transfer it should, however, prove adequate.

[9] The constant in equation (44) is obtained with the assumption of incompressible flow in the stagnation region. The effects of compressibility and dissociation of the molecules of air in the region tend to increase the value of the constant by as much as a factor 2 in the speed range of interest in this report. For the comparative purpose of this report it is unnecessary to take these effects into account.

maximum deceleration, the deceleration and speed bear fixed ratios to the maximum deceleration and the entry speed, respectively (see fig. 4 and eqs. (19) and (18)), hence, the deceleration and speed variation with altitude can readily be determined.

If the missile is very heavy, the calculated altitude for maximum deceleration (eq. (15)) may be fictitious (i. e., this altitude is negative) so the maximum deceleration in flight, which occurs just before impact at sea level, is less than that calculated by equation (17) and is dependent on the body characteristics as well as the entry speed and flight-path angle (see eq. (21)). However, the variation of speed and deceleration with altitude from the fictitious altitude given by equation (15) can still be obtained from figure 4.

HEATING

Total heat input.—In the heating analysis, a number of simplifying assumptions were made which should limit its applicability to the determination of relative values of heating at hypersonic speeds. It is in this relative sense that the following discussion pertains.

In considering the total heat transferred by convection to a missile, it is evident from equation (33) that the course the designer should take to obtain the least heating is affected by the value of the factor

$$\frac{C_D\rho_o A}{\beta m \sin\theta_E}=B \tag{51}$$

To illustrate, first consider the case of a "relatively heavy" missile for which this factor is small compared to unity (the term "relatively heavy" is used to denote that the denominator involving the mass is very large as compared to the numerator involving the drag per unit dynamic pressure, C_DA). Then

$$1-e^{-\frac{C_D\rho_o A}{\beta m \sin\theta_E}}$$

is small compared to 1. If this function is expanded in series and only the leading term retained, equation (33) becomes

$$Q\cong\frac{C_f'S\rho_o V_E^2}{4\beta\sin\theta_E} \tag{52}$$

For the relatively heavy missile, then, the least heat will be transferred when $C_f'S$ is a minimum—that is to say, when the total shear force acting on the body is a minimum. This result is as would be expected, if one notes that requiring $B<<1$ is tantamount to requiring the missile to be so heavy that it is retarded only slightly by aerodynamic drag in its motion through the atmosphere. Hence, the heat input to the missile is simply proportional to the shear force.

Now let us consider the case when $B>>1$, or, in other words, when this missile is "relatively light." In this event,

$$1-e^{-\frac{C_D\rho_o A}{\beta m \sin\theta_E}}\cong 1$$

and equation (31) can be approximated

$$Q\cong\frac{1}{4}mV_E^2\left(\frac{C_f'S}{C_DA}\right)$$

For the relatively light missile, then, the least convective heating is obtained when $C_f'S/C_DA$ is a minimum. This is at first glance a rather surprising result, for it indicates that the heating is reduced by increasing the total drag, provided the equivalent frictional drag is not increased proportionately as fast. Physically, this anomaly is resolved if the problem is viewed in the following way: The missile entering the atmosphere has the kinetic energy $\frac{1}{2}mV_E^2$ but, if

$$e^{-\frac{C_D\rho_o A}{\beta m \sin\theta_E}}=\left(\frac{V_o}{V_E}\right)^2$$

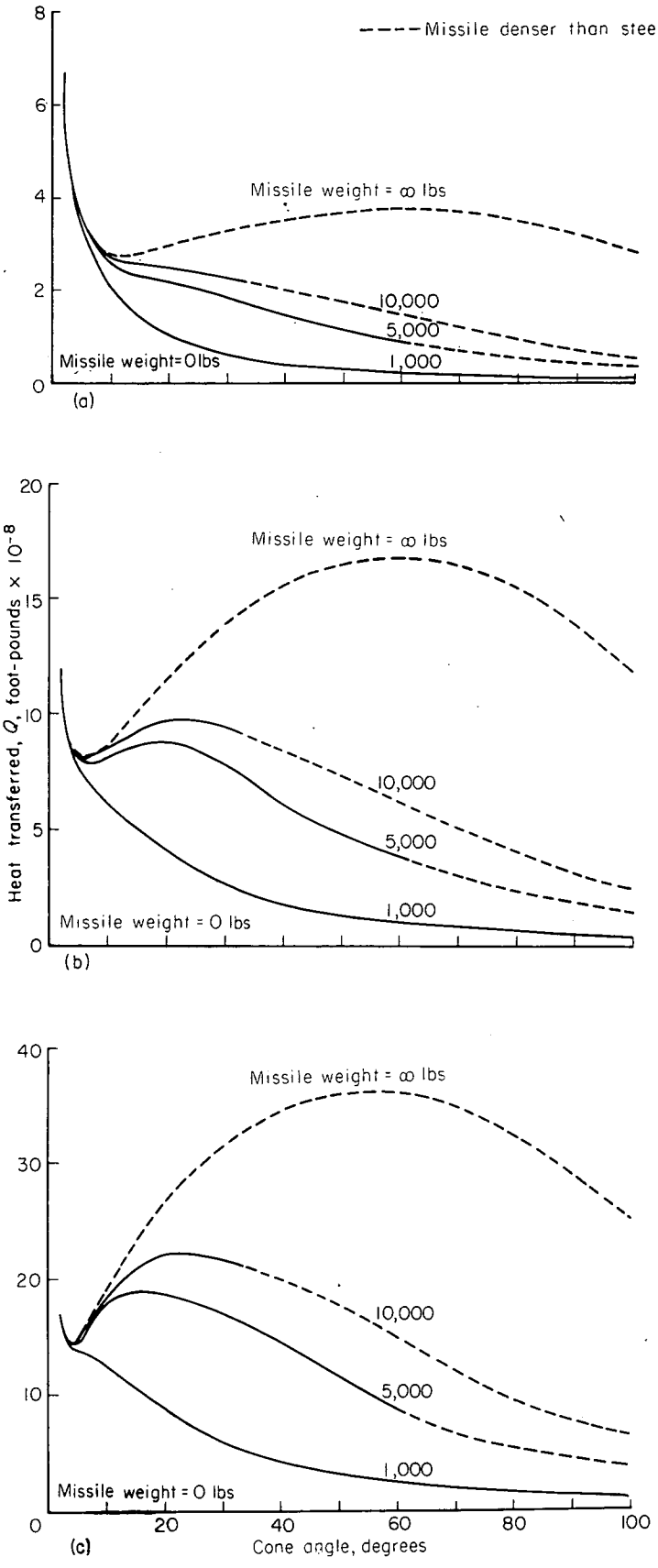
is small, then nearly all its entrance kinetic energy is lost, due to the action of aerodynamic forces, and must appear as heating of both the atmosphere and the missile. The fraction of the total heat which is given to the missile is,[10] from equation (33),

$$\frac{1}{2}\left(\frac{C_f'S}{C_DA}\right)$$

Thus, by keeping this ratio a minimum, as much as possible of the energy is given to the atmosphere and the missile heating is therefore least.

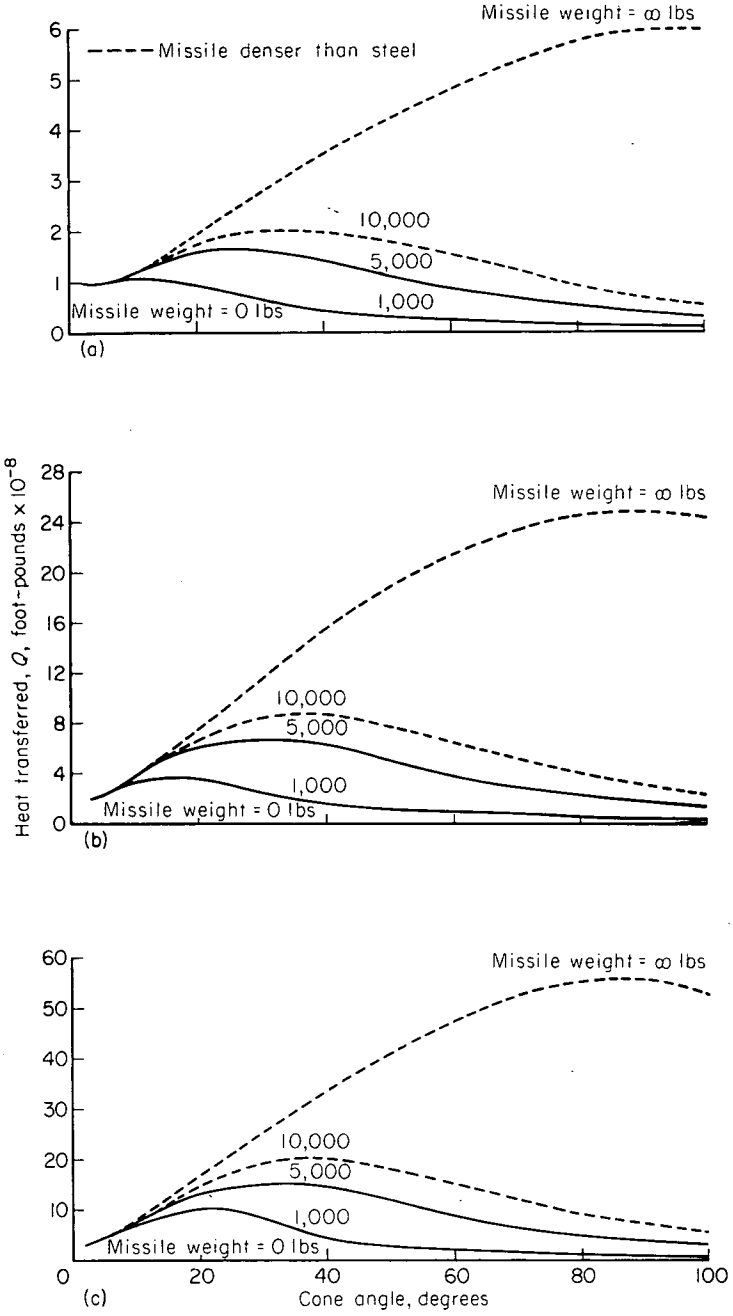
In order to illustrate these considerations in greater detail, calculations have been made using the previously developed equations to determine the heat transferred by convection to a series of conical missiles. Two classes of missiles have been considered. Missiles in the first class were required to have a base area of 10 square feet. Missiles in the second class were required to have a volume of 16 cubic feet. Gross weights of 0, 1,000, 5,000, 10,000, and ∞ pounds have been assumed, and the entrance angle, θ_E, has been taken as 30° of arc in all cases. Missile heating, up to the time of impact, has been calculated as a function of cone angle for entrance speeds of 10,000, 20,000, and 30,000 feet per second. In these calculations the pressure drag coefficient was taken as constant for a particular cone at the value corresponding to the entrance Mach number (a value of $T_E=500°$ R was assumed throughout). These coefficients were determined from reference 6 for cone angles of 10° and greater. For cone angles less than 10°, reference 7 was employed to determine these coefficients (base drag was neglected in all cases). The total drag coefficient was taken as the sum of the pressure drag coefficient plus the skin-friction coefficient, the latter coefficient being taken at its value for maximum total heat-input rate with altitude. The boundary layer was assumed to be wholly turbulent since the Reynolds number, based on length of run along the surface of a cone and local conditions just outside the boundary layer, was always greater than about 6×10^6 and, in fact, was of the order of billions for the more slender cones. Turbulent-boundary-layer data were obtained from references 8 and 9, and Sutherland's law for the variation of viscosity with temperature was used in obtaining "equivalent flat-plate" heat-transfer coefficients.

[10] Note that even that if all drag is frictional drag, only half the heat is transferred to the body. The other half is contained in the boundary layer and is left in the air in the body wake.



(a) V_E=10,000 ft/sec
(b) V_E=20,000 ft/sec
(c) V_E=30,000 ft/sec

FIGURE 5.—Convective heat transferred at impact to conical missiles of same area entering the earth's atmosphere at an angle of 30° to the horizontal and velocities of 10,000, 20,000, and 30,000 ft/sec (base area=10 sq ft).



(a) V_E=10,000 ft/sec
(b) V_E=20,000 ft/sec
(c) V_E=30,000 ft/sec

FIGURE 6.—Convective heat transferred at impact to conical missiles of same volume entering the earth's atmosphere at an angle of 30° to the horizontal and velocities of 10,000, 20,000, and 30,000 ft/sec (volume=16.34 cu ft).

Missile heating calculated in this manner for the fixed-base-area and fixed-volume cones is presented in figures 5 and 6, respectively. Curves for missiles having densities greater than steel are considered improbable and are shown as dashed lines. It is clear that for both classes of bodies, when the missile is relatively heavy, the optimum solution is obtained by making $C_f'S$ as small as possible (small cone angle case) and this optimum is accentuated with increase in speed. On the other hand, when the missile is relatively light, reduced heating is obtained by making $C_f'S/C_DA$ as small as possible (the large cone angle case). It is noted

also that, in general, the advantage of reduced heating of the relatively light, blunt cones is more pronounced in the fixed-base-area case than in the fixed-volume case.

Maximum time rate of average heat input per unit area.—It was previously noted that the maximum time rate of average heat input per unit area may be of serious importance in determining the structural integrity of missiles entering the atmosphere at high speeds.[11] In order to illustrate this fact, consider the case of a missile having a shell made of solid material and assume that the rate of heat transfer per unit area does not vary rapidly from one surface element to the next. Then the rate of transfer of heat along the shell will be small compared with the rate of transfer through the shell. The shell stress due to heat transfer is that resulting from the tendency toward differential expansion through the shell and it is proportional to $dT_\eta/d\eta$ where T_η is the temperature at any point η within the shell and η is measured perpendicular from the shell surface. We define k_η as the thermal conductivity of the shell material; then the rate at which heat transfers through the shell per unit area is $k_\eta(dT_\eta/d\eta)$ and this must, at $\eta=0$, equal the rate of heat input per unit surface area. For the missile considered as a whole, the maximum value of the average thermal stress in the shell is a measure of the over-all structural integrity and the maximum value of this stress will occur at the surface when

$$\frac{dH_{av}}{dt}=\frac{1}{S}\left(\frac{dQ}{dt}\right)$$

is a maximum.

The course the designer should take to minimize the thermal stress for the missile as a whole is dependent, as for the case of total heat input, upon whether the missile is relatively heavy or light. For the relatively heavy missile the value of B, given by equation (51), is small compared to unity. The maximum value of the average thermal stress in this case is proportional to (see eq. (41))

$$\left(\frac{dH_{av}}{dt}\right)_o=\frac{C_f'\rho_o V_E^3}{4} \tag{54}$$

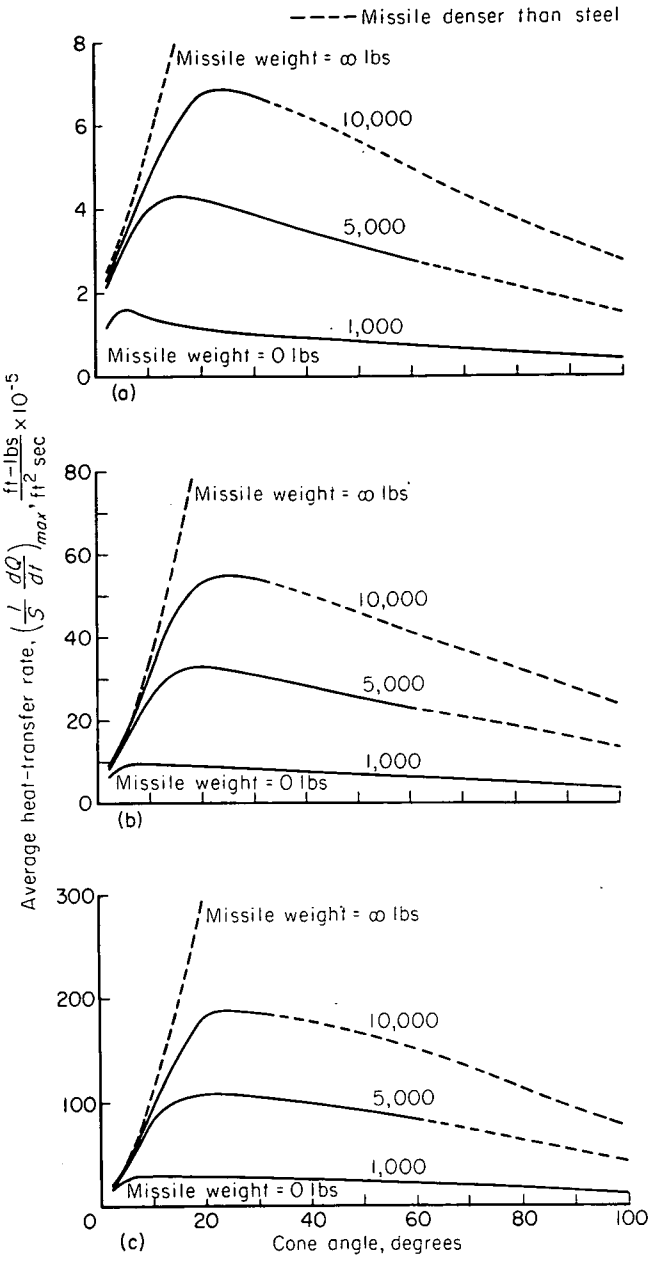
and, hence, the least average thermal stress is obtained by making C_f' a minimum. On the other hand, for the relatively light missile the maximum value of the average thermal stress is proportional to (see eq. (37))

$$\left(\frac{dH_{av}}{dt}\right)_2=\left(\frac{C_f'}{C_DA}\right)\frac{\beta m V_E^3 \sin\theta_E}{6e} \tag{55}$$

and, hence, the least average thermal stress occurs when C_f'/C_DA is a minimum.

In order to illustrate these considerations in greater detail, the maximum values of the time rate of average heat input per unit area have been calculated for the constant-base-area and the constant-volume cones previously discussed in the section on total heat input. These values were determined in much the same manner as those of total heat input, with the exception that C_f' was evaluated at y_2 (rather than y_1), given by equation (38) when it applies, and otherwise at $y_0=0$. The results are shown in figures 7 and 8. It is seen that the

[11] This is the common case when the shell material acts as structural support and must also transport or absorb the heat.



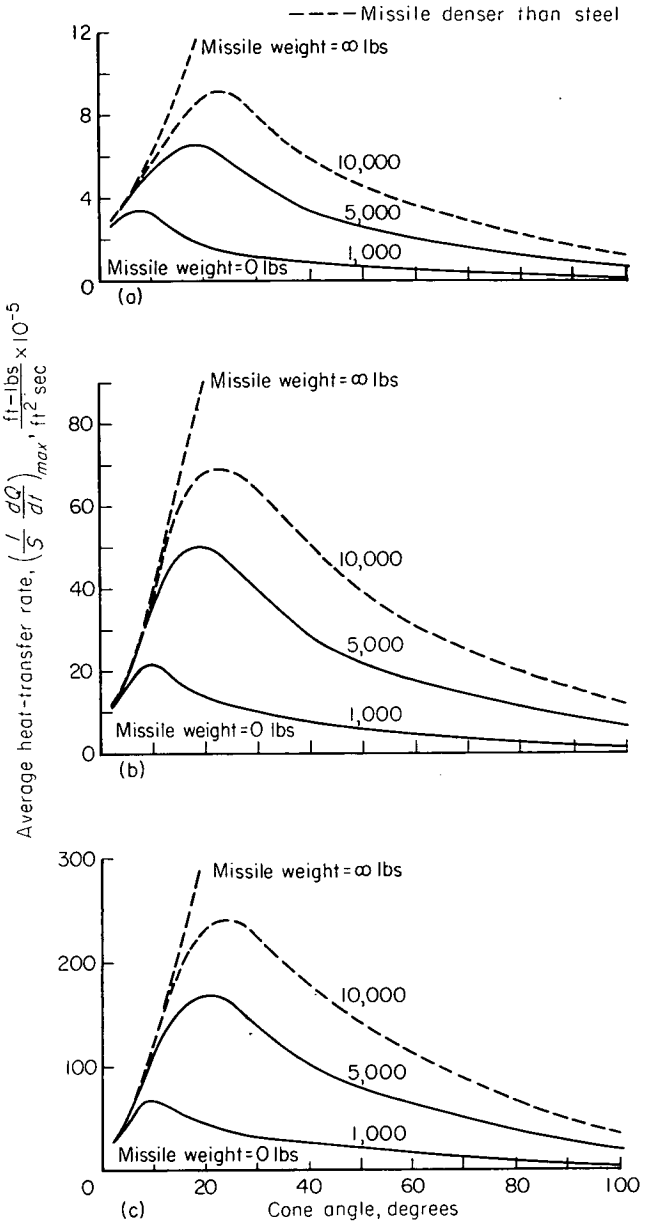
(a) V_E=10,000 ft/sec
(b) V_E=20,000 ft/sec
(c) V_E=30,000 ft/sec

FIGURE 7.—Maximum average rate of convective heat transfer to conical missiles of the same base area entering the earth's atmosphere at an angle of 30° to the horizontal and velocities of 10,000, 20,000, and 30,000 ft/sec (base area=10 sq ft).

maximum values of average thermal stress are reduced for both the slender cones and blunt cones as compared to the relatively large values of this stress experienced by cones of intermediate slenderness.

Maximum time rate of local heat input per unit area.—Perhaps even more important than the maximum value of the average shell stress is the maximum stress that occurs in the shell at the surface element of the missile nose,[12] where the local heat-transfer rate is probably the greatest, for, in general, this latter stress is many times larger. In fact, this rate of local heat input can be so large as to promote

[12] In this report we are concerned only with bodies. If wings or stabilizers are used, their leading edges are similarly surface elements which experience intense heat transfer.



(a) V_E=10,000 ft/sec
(b) V_E=20,000 ft/sec
(c) V_E=30,000 ft/sec

FIGURE 8.—Maximum average rate of convective heat transfer to conical missiles of the same volume entering the earth's atmosphere at an angle of 30° to the horizontal and velocities of 10,000, 20,000, and 30,000 ft/sec (volume=16.34 cu ft).

temperature gradients through the shell that are intolerable even with the most highly conductive materials (copper, silver, etc.).[13] Thus some additional means of cooling, such as transpiration cooling, may, in any case, be required in this region.

It was stated previously that pointed-nose bodies are undesirable due, in part, to the fact that the local heat-transfer rate per unit area at the tip is excessive. The validity of this statement is demonstrated by the results of the analysis. It is clear (see eq. (44)) that since the local transfer rate varies inversely with the square root of the tip radius, not only should pointed bodies be avoided, but the rounded nose should have as large a radius as possible. The question then arises; if the nose radius is arbitrarily fixed, what course is available to the missile designer to minimize the problem of local heating at the stagnation point? From both equations (46) and (50), it is seen that for an arbitrary nose radius, if the mass, entry speed, and flight-path angle are fixed, then the only way to reduce the stagnation rate of heat input per unit area is to increase the product C_DA. In fact, a relative stagnation-point heat-transfer rate per unit area, ψ may be expressed in terms of B (see eq. (51)), if it is defined as the ratio of the maximum stagnation-point heat-transfer rate per unit area for a given missile to the maximum rate the same missile would experience if it were infinitely heavy. For the infinitely heavy missile, the maximum rate occurs at sea level and is (see eq. (50))

$$6.8\times10^{-6}\sqrt{\frac{\rho_o}{\sigma}}\,V_E^3$$

so that from equation (50)

$$\psi=e^{-\frac{3C_D\rho_oA}{2\beta m\sin\theta_E}}=e^{-\frac{3}{2}B} \tag{56}$$

if the given missile also attains its maximum rate at sea level (i. e., $y_3=0$; eq. (47)); whereas

$$\psi=\sqrt{\frac{\beta m\sin\theta_E}{3eC_D\rho_oA}}=\frac{1}{\sqrt{3eB}} \tag{57}$$

if the given missile attains its maximum rate above sea level (eq. (46), y_3 positive). The variation of ψ with $1/B$ is shown in figure 9. Clearly, the high pressure drag shape has the advantage over the slender shape in this respect.

In order to illustrate these considerations in greater detail, again consider the constant-base-area and constant-volume cones discussed earlier. Assume the pointed tips of all the

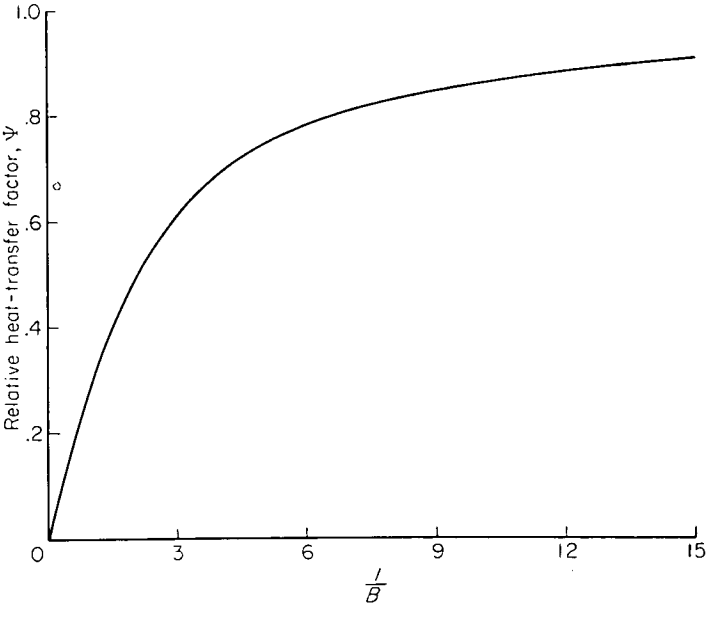


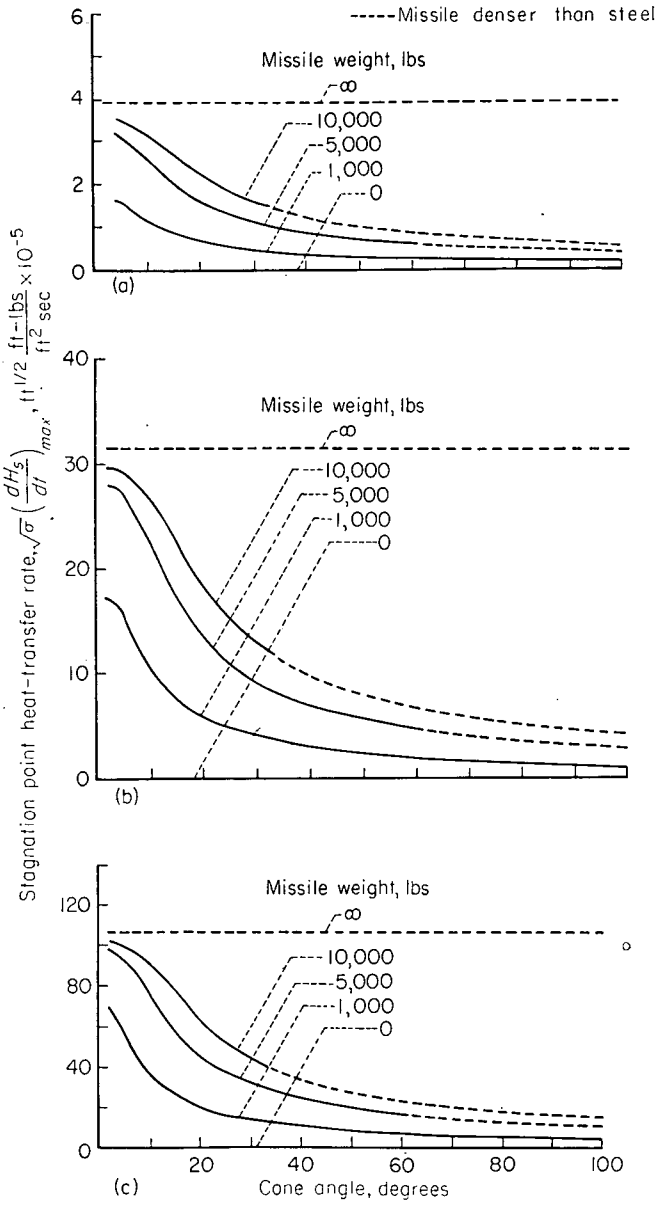
FIGURE 9.—Variation of relative heat-transfer factor ψ with $\frac{1}{B}$.

[13] See reference 1 for further discussion.

cones are replaced by spherical tips of the same radius σ. The relative effect of varying the cone angle on the stagnation-point heating can than be assessed by determining the variation of the product

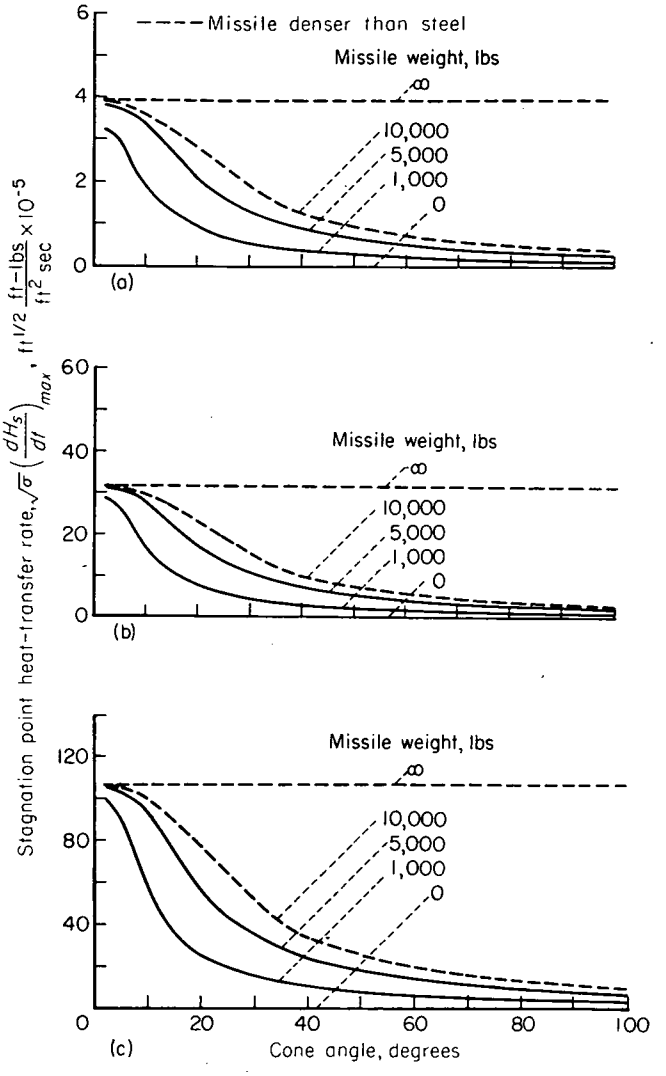
$$\sqrt{\sigma}\left(\frac{dH_s}{dt}\right)_{max}$$

This product has been calculated for the various cones, assuming C_D to be unaffected by the addition of the hemispherical tip (the tip radius may be arbitrarily small), and the results are shown in figures 10 and 11. It is seen again that the missiles having large cone angle (high drag coefficient) are considerably superior.



(a) V_E=10,000 ft/sec
(b) V_E=20,000 ft/sec
(c) V_E=30,000 ft/sec

FIGURE 10.—Maximum rate of convective heat transfer to the stagnation point of spherically tipped cones of the same base area entering the earth's atmosphere at an angle of 30° to the horizontal and velocities of 10,000, 20,000, and 30,000 ft/sec (base area=10 sq ft).



(a) V_E=10,000 ft/sec
(b) V_E=20,000 ft/sec
(c) V_E=30,000 ft/sec

FIGURE 11.—Maximum rate of convective heat transfer to the stagnation point of spherically tipped cones of the same volume entering the earth's atmosphere at an angle of 30° to the horizontal and velocities of 10,000, 20,000, and 30,000 ft/sec (volume=16.34 cu ft).

DESIGN CONSIDERATIONS AND CONCLUDING REMARKS

In the foregoing analysis and discussion, two aspects of the heating problem for missiles entering the atmosphere were treated. The first concerned the total heat absorbed by the missile and was related to the coolant required to prevent its disintegration. It was found that if a missile were relatively light, the least required weight of coolant (and hence of missile) is obtained with a shape having a high pressure drag coefficient, that is to say, a blunt shape. On the other hand, it was found that if the missile were relatively heavy the least required weight of coolant, and hence of missile, is obtained with a shape having a low skin-friction drag coefficient, that is to say, a long slender shape.

The second aspect of the heating problem treated was concerned with the rate of heat input, particularly with regard to thermal shell stresses resulting therefrom. It was seen that the maximum average heat-input rate and, hence, maximum average thermal stress could be decreased by

using either a blunt or a slender missile, while missiles of intermediate slenderness were definitely to be avoided in this connection. The region of highest local heat-transfer rate and, hence, probably greatest thermal stress was reasoned to be located at the forward tip of the missile in most cases. This was assumed to be the case and it was found that the magnitude of this stress was reduced by employing a shape having the largest permissible tip radius and over-all drag coefficient; that is to say, the blunt, high drag shape always appears to have the advantage in this respect.

These results provide us with rather crude, but useful, bases for determining shapes of missiles entering the atmosphere which have minimized heat-transfer problems. If the over-all design considerations of payload, booster, et al, dictate that the re-entry missile be relatively heavy in the sense of this report, then it may be most desirable to make this missile long and slender, especially if the entry speed is very high (say 20,000 ft/sec or greater). Perhaps the slender conical shape is appropriate for such a missile. It seems clear, too, that the tip of this missile should be given the largest practicable nose radius in order to minimize the maximum local heat-transfer rate and hence maximum local shell stress problem. Even then it may be necessary to employ additional means to minimize the heat-transfer rate and, hence, thermal stress encountered in this region (e. g., by transpiration cooling).

Let us now consider the case where the over-all design conditions dictate that the re-entry missile be relatively light in the sense of this report. This case will be the more usual one and, therefore, will be treated at greater length.

A shape which should warrant attention for such missile application is the sphere, for it has the following advantages:

1. It is a high drag shape and the frictional drag is only a few percent of the total drag.
2. It has the maximum volume for a given surface area.
3. The continuously curved surface is inherently stiff and strong.
4. The large stagnation-point radius significantly assists in reducing the maximum thermal stress in the shell.
5. Aerodynamic forces are not sensitive to attitude and, hence, a sphere may need no stabilizing surfaces.
6. Because of this insensitivity to attitude, a sphere may purposely be rotated slowly, and perhaps even randomly[14] during flight, in order to subject all surface elements to about the same amount of heating and thereby approach uniform shell heating.

On the other hand, the sphere, in common with other very high drag shapes may be unacceptable if:

1. The low terminal speed cannot be permitted (e. g., because of excessive wind drift).
2. The magnitude of the maximum deceleration is greater than can be allowed.

The first of these disadvantages of the sphere might be minimized by protruding a flow-separation-inducing spike from the front of the sphere to reduce the drag coefficient to roughly half (see ref. 11). Stabilization would now be required but only to the extent required to counterbalance the moment produced by the spike. Special provision would have to be made for cooling the spike.

Both of the disadvantages of very high drag shapes may however be alleviated by using variable geometry arrangements. For example, an arrangement which suggests itself is a round-nosed shape with conical afterbody of low apex angle employing an extensible skirt at the base. With the skirt flared, the advantages of high drag are obtained during the entry phase of flight where the aerodynamic heating is intense. Later, the skirt flare may be decreased to vary the drag so as to produce the desired deceleration and speed history. If the deceleration is specified in the equation of motion (see motion analysis), the required variation of drag coefficient with altitude can be calculated.

The examples considered, of course, are included only to demonstrate some of the means the designer has at hand to control and diminish the aerodynamic heating problem. For simplicity, this problem has been treated, for the most part, in a relative rather than absolute fashion. In any final design, there is, clearly, no substitute for step-by-step or other more accurate calculation of both the motion and aerodynamic heating of a missile.

Even from a qualitative point of view, a further word of caution must be given concerning the analysis of this paper. In particular, throughout, we have neglected effects of gaseous imperfections (such as dissociation) and shock-wave boundary-layer interaction on convective heat transfer to a missile, and of radiative heat transfer to or from the missile. One would not anticipate that these phenomena would significantly alter the conclusions reached on the relative merits of slender and blunt shapes from the standpoint of heat transfer at entrance speeds at least up to about 10,000 feet per second. It cannot tacitly be assumed, however, that this will be the case at higher entrance speeds (see Appendix B). Accurate conclusions regarding the dependence of heat transfer on shape for missiles entering the atmosphere at extremely high supersonic speeds must await the availability of more reliable data on the static and dynamic properties of air at the high temperatures and pressures that will be encountered.

AMES AERONAUTICAL LABORATORY
NATIONAL ADVISORY COMMITTEE FOR AERONAUTICS
MOFFETT FIELD, CALIF., *Apr. 28, 1953*

[14] Note that if rotation is permitted, slow, random motion may be required in order to prevent Magnus forces from causing deviation of the flight path from the target. It should also be noted that at subsonic and low supersonic speeds gun-fired spheres, presumably not rotating, have shown rather large lateral motions in flight (see ref. 10). It is not known whether such behavior occurs at high supersonic speeds.

APPENDIX A

SYMBOLS

A	reference area for drag evaluation, ft^2
B	body factor, dimensionless (See eq. (51).)
C_D	drag coefficient, dimensionless
C_f	skin-friction coefficient based on conditions just outside the boundary layer, dimensionless
C_f'	equivalent skin-friction coefficient, dimensionless (See eq. (28).)
C_p	specific heat at constant pressure, $\frac{\text{ft-lb}}{\text{slug } °R}$
C_v	specific heat at constant volume, $\frac{\text{ft-lb}}{\text{slug } °R}$
F',F'',F'''	functions of $\beta\Delta y$, dimensionless (See eqs. (18), (19), and (49).)
g	acceleration due to force of gravity $\left(\text{taken as } 32.2 \frac{\text{ft}}{\text{sec}^2}\right)$
h	convective heat-transfer coefficient, $\frac{\text{ft-lb}}{\text{ft}^2 \text{ sec } °R}$
H	heat transferred per unit area, $\frac{\text{ft-lb}}{\text{ft}^2}$
k	thermal conductivity, $\frac{\text{ft-lb}}{\text{sec ft}^2 (°R/\text{ft})}$
m	mass, slugs
M	Mach number, dimensionless
Nu	Nusselt number, dimensionless
Pr	Prandtl number, dimensionless
Q	total heat transferred, ft-lb
Re	Reynolds number, dimensionless
S	surface area, ft^2
T	temperature (ambient temperature of air at altitude y unless otherwise specified), °R
t	time, sec
V	velocity, $\frac{\text{ft}}{\text{sec}}$
x,y	horizontal and vertical distance from impact point, ft
Z	variable of integration, $\frac{\text{ft}^2}{\text{sec}^2}$
β	constant in density—altitude relation, ft^{-1} (See eq. (2).)
γ	ratio of specific heat at constant pressure to specific heat at constant volume, C_p/C_v dimensionless
Δ	increment
η	distance within the shell measured normal to shell surface, ft
θ	angle of flight path with respect to horizontal, deg
μ	coefficient of absolute viscosity, $\frac{\text{slugs}}{\text{ft sec}}$
ρ	air density, $\frac{\text{slug}}{\text{ft}^3}$
σ	radius, ft
ψ	relative heat-transfer factor, dimensionless (See eqs. (56) and (57).)

SUBSCRIPTS

0	conditions at sea level ($y=0$)
1	conditions at altitude y_1 (eq. (15))
2	conditions at altitude y_2 (eq. (38))
3	conditions at altitude y_3 (eq. (47))
E	conditions at entrance to earth's atmosphere
l	local conditions
r	recovery conditions
s	stagnation conditions
w	wall conditions
η	conditions within the shell of the missile

APPENDIX B

SIMPLIFYING ASSUMPTIONS IN THE CALCULATION OF AERODYNAMIC HEATING

As noted in the main body of the report, the heating analysis is simplified by making the following assumptions:

1. Convective heat transfer is of foremost importance; that is, radiative effects may be neglected.
2. Effects of gaseous imperfections, in particular dissociation, may be neglected.
3. Effects of shock-wave boundary-layer interaction may be neglected.
4. Reynolds' analogy is applicable.
5. Prandtl number is unity.

The restrictions imposed by these assumptions will now be considered in some detail.

In assumption 1, two simplifications are involved; namely, (1) radiation from the surface of the body is neglected, and (2) radiation to the body from the high-temperature disturbed air between the shock wave and the surface is neglected. The first simplification may be justified on the premise that the maximum allowable surface temperature will be about the same for one body as compared with another, irrespective of shape, and, consequently, radiation away from the surface will be approximately the same. Hence, neglecting this form of heat transfer should not appreciably change the relative heating which is of principal interest in this paper.

The second simplification of ignoring radiative heat transfer from the disturbed air to the body is not so easily treated. At ordinary flight speeds this form of heat transfer is negligible since it is well established that at temperatures not too different from ambient temperature, air is both a poor radiator and a poor absorber. At the flight speeds of interest, temperatures in the tens of thousands of degrees Fahrenheit may be easily obtained in the disburbed air flow, especially about the heavier blunt bodies. At these temperatures it does not follow, a priori, that air is a poor radiator. Data on the properties of air at these temperatures are indeed meager. Hence, it is clear that calculations of radiative heat transfer from air under these conditions must, at best, be qualitative. Nevertheless, several such calculations have been made, assuming for lack of better information that air behaves as a grey body radiator and that Wein's law may be used to relate the wave length at which the maximum amount of radiation is emitted to the temperature of the air (this assumption, in effect, enables low-temperature data on the emissivity of air to be used in calculating radiation at high temperatures). In these calculations effects of dissociation in reducing the temperature of the disturbed air have also been neglected and hence from this standpoint, at least, conservative (i. e., too high) estimates of radiative heat transfer should evolve. The results of these calculations indicate the following: (1) Radiative heat transfer from the disturbed air to the body is of negligible importance compared to convective heat transfer at entrance speeds in the neighborhood of, or less than, 10,000 feet per second; (2) Radiative heat transfer, in the case of relatively massive blunt bodies, may have to be considered in heat-transfer calculations at entrance speeds in the neighborhood of 20,000 feet per second; (3) Radiative heat transfer, in the case of relatively massive blunt bodies, may be of comparable importance to convective heat transfer at entrance speeds in the neighborhood of 30,000 feet per second. From these results, we conclude, then, that the neglect of radiative heat transfer from the disturbed air to the body is probably permissible for all except, perhaps, very blunt and heavy shapes at entrance speeds up to 20,000 feet per second. However, this simplification may not be permissible, especially in the case of heavy blunt bodies entering the atmosphere at speeds in the neighborhood of, or greater than, 30,000 feet per second.

In assumption 2, the neglect of effects of gaseous imperfections, particularly dissociation, on convective heat transfer would appear to be permissible at entrance speeds up to and in the neighborhood of 10,000 feet per second, since at such speeds the temperatures of the disturbed air are not high enough for these imperfections to become significantly manifest. On the other hand, as the entrance speeds approach 20,000 feet per second, temperatures of the disturbed air may easily exceed 10,000° Rankine, in which case appreciable dissociation may be anticipated, inside the boundary layer for all bodies, and inside and outside the boundary layer in the case of blunt bodies. The magnitude of these effects is at present in some doubt (see, e. g., the results of refs. 12 and 13.) Hence, for the present, the neglect of effects of gaseous imperfections on convective heat transfer is not demonstrably permissible at entrance speeds in the neighborhood of 20,000 feet per second or greater.

In assumption 3, it has been shown by Lees and Probstein (ref. 14), and more recently by Li and Nagamatsu (ref. 15), that shock-wave boundary-layer interaction may significantly increase laminar skin-friction coefficients on a flat plate at zero incidence and Mach numbers in excess of about 10. Lees and Probstein found somewhat the opposite effect on heat-transfer rate in the case of weak interaction. It is not now known how this phenomenon depends upon body shape or type of boundary layer. However, it is reasonable to anticipate that there will be some effect, and certainly if the skin-friction coefficient is increased in order of magnitude at Mach numbers approaching 20, as indicated by the results of Li and Nagamatsu for strong interaction, then the phenomenon cannot be presumed negligible. Hence, we conclude that from this standpoint, also, the convective

heat-transfer calculations of this report may be in error at entrance speeds of the order of 20,000 feet per second or greater.

The assumption that Reynolds' analogy may be used to relate skin-friction and heat-transfer coefficient does not, especially in the light of recent work by Rubesin (ref. 16), seem out of line with the purposes of this paper, at least at entrance speeds up to and in the neighborhood of 10,000 feet per second. However, it does not follow, a priori, that this assumption remains valid at substantially higher entrance speeds, especially in view of the imperfect gas and shock-wave boundary-layer-interaction effects already discussed.

The assumption of Prandtl number equal to unity would also appear permissible for the analysis of relative heating of missiles at the lower entrance speeds considered here. However, in view of the questionable effect (see again refs. 12 and 13) of dissociation on Prandtl number, it is not clear that this assumption is strictly valid at the intermediate and higher entrance speeds treated in this report.

From these considerations it is concluded that the simplifying assumptions made in the main heat-transfer analysis of this paper will not significantly influence the results at entrance speeds in the neighborhood of or less than 10,000 feet per second. However, at entrance speeds in the neighborhood of and greater than 20,000 feet per second, these results must be viewed with skepticism. More accurate calculations of heat transfer at these speeds must, among other things, await more accurate determinations of both the static and dynamic properties of air under these circumstances.

REFERENCES

1. Wagner, Carl: Skin Temperature of Missiles Entering The Atmosphere at Hypersonic Speed. Tech. Rep. No. 60, Ord Res. & Dev. Division, Dept. of Army, Oct. 1949.
2. Diehl, Walter S.: Standard Atmosphere—Tables and Data. NACA Rep. No. 218, 1925.
3. Warfield, Calvin N.: Tentative Tables for the Properties of the Upper Atmosphere. NACA TN 1200, 1947.
4. Grimminger, G.: Probability that a Meteorite Will Hit or Penetrate a Body Situated in the Vicinity of the Earth. Jour. Appl. Phys., vol. 19, no. 10, Oct. 1948, pp. 947–956.
5. Sibulkin, M.: Heat Transfer Near the Forward Stagnation Point of a Body of Revolution. Jour. Aero. Sci., vol. 19, no. 8, Aug. 1952, pp. 570–571.
6. Mass. Inst. of Tech. Dept. of Elec. Engr., Center of Analysis: Tables of Supersonic Flow Around Cones, by the Staff of the Computing Section, Center of Analysis, under direction of Zdenek Kopal: Tech. Rep. No. 1, Cambridge, 1947.
7. Eggers, A. J. Jr., and Savin, Raymond C.: Approximate Methods for Calculating the Flow About Nonlifting Bodies of Revolution at High Supersonic Airspeeds. NACA TN 2579, 1951.
8. Van Driest, E. R.: Turbulent Boundary Layer in Compressible Fluids. Jour. Aero. Sci., vol. 18, no. 3, Mar. 1951, pp. 145–146.
9. Van Driest, E. R.: Turbulent Boundary Layer on a Cone in a Supersonic Flow at Zero Angle of Attack. Jour. Aero. Sci., vol. 19, no. 1, Jan. 1952, pp. 55–57.
10. Richards, Elizabeth: Compar ative Dispersion and Drag of Spheres and Right Cylinders. Aberdeen Proving Ground, Md., Ballistic Research Laboratories, Rep. 717, 1950.
11. Moeckel, W. E.: Flow Separation Ahead of a Blunt Axially Symmetric Body at Mach Numbers 1.76 to 2.10. NACA RM E51I25, 1951.
12. Moore, L. L.: A solution of the Laminar Boundary-Layer Equations for a Compressible Fluid with Variable Properties, Including Dissociation. Jour. Aero. Sci., vol. 19, no. 8, Aug. 1952, pp. 505–518.
13. Crown, J. Conrad: The Laminar Boundary Layer at Hypersonic Speeds. NAVORD Rep. 2299, Apr. 15, 1952.
14. Lees, Lester, and Probstein, Ronald F.: Hypersonic Viscous Flow Over a Flat Plate. Princeton University Aeronautical Engineering Laboratory Rep. 195, Apr. 20, 1952.
15. Li, Ting-Yi, and Nagamatsu, Henry T.: Shock Wave Effects on the Laminar Skin Friction of an Insulated Flat Plate at Hypersonic Speeds. GALCIT Memorandum No. 9, July 1, 1952.
16. Rubesin, Morris W.: A Modified Reynolds Analogy for the Compressible Turbulent Boundary Layer on a Flat Plate. NACA TN 2917, 1953

REPORT 1382

A COMPARATIVE ANALYSIS OF THE PERFORMANCE OF LONG-RANGE HYPERVELOCITY VEHICLES [1]

By Alfred J. Eggers, Jr., H. Julian Allen, and Stanford E. Neice

SUMMARY

Long-range hypervelocity vehicles are studied in terms of their motion in powered flight, and their motion and aerodynamic heating in unpowered flight. Powered flight is analyzed for an idealized propulsion system which approximates rocket motors. Unpowered flight is characterized by a return to earth along a ballistic, skip, or glide trajectory. Only those trajectories are treated which yield the maximum range for a given velocity at the end of powered flight. Aerodynamic heating is treated in a manner similar to that employed previously by the senior authors in studying ballistic missiles (NACA Rep. 1381), with the exception that radiant as well as convective heat transfer is considered in connection with glide and skip vehicles.

The ballistic vehicle is found to be the least efficient of the several types studied in the sense that it generally requires the highest velocity at the end of powered flight in order to attain a given range. This disadvantage may be offset, however, by reducing convective heat transfer to the re-entry body through the artifice of increasing pressure drag in relation to friction drag—that is, by using a blunt body. Thus the kinetic energy required by the vehicle at the end of powered flight may be reduced by minimizing the mass of coolant material involved.

The glide vehicle developing lift-drag ratios in the neighborhood of and greater than 4 is far superior to the ballistic vehicle in ability to convert velocity into range. It has the disadvantage of having far more heat convected to it; however, it has the compensating advantage that this heat can in the main be radiated back to the atmosphere. Consequently, the mass of coolant material may be kept relatively low.

The skip vehicle developing lift-drag ratios from about 1 to 4 is found to be superior to comparable ballistic and glide vehicles in converting velocity into range. At lift-drag ratios below 1 it is found to be about equal to comparable ballistic vehicles while at lift-drag ratios above 4 it is about equal to comparable glide vehicles. The skip vehicle experiences extremely large loads, however, and it encounters most severe aerodynamic heating.

As a final performance consideration, it is shown that on the basis of equal ratios of mass at take-off to mass at the end of powered flight, the hypervelocity vehicle compares favorably with the supersonic airplane for ranges in the neighborhood of and greater than one half the circumference of the earth. In the light of this and previous findings, it is concluded that the ballistic and glide vehicles have, in addition to the advantages usually ascribed to great speed, the attractive possibility of providing relatively efficient long-range flight.

Design aspects of manned hypervelocity vehicles are touched on briefly. It is indicated that if such a vehicle is to develop relatively high lift-drag ratios, the wing and tail surfaces should have highly swept, rounded leading edges in order to alleviate the local heating problem with minimum drag penalty. The nose of the body should also be rounded somewhat to reduce local heating rates in this region. If a manned vehicle is designed for global range flight, the large majority of lift is obtained from centrifugal force, and aerodynamic lift-drag ratio becomes of secondary importance while aerodynamic heating becomes of primary importance. In this case a glide vehicle which enters the atmosphere at high angles of attack, and hence high lift, becomes especially attractive with a more or less rounded bottom to minimize heating over the entire lower surface. The blunt ballistic vehicle is characterized by especially low heating, and it too may be a practical manned vehicle for ranges in excess of semiglobal if great care is taken in supporting the occupant to withstand the order of 10 g's maximum deceleration encountered during atmospheric entry.

INTRODUCTION

It is generally recognized that hypervelocity vehicles are especially suited for military application because of the great difficulty of defending against them. It is also possible that for long-range operation, hypervelocity vehicles may not be overly extravagant in cost. A satellite vehicle, for example, can attain arbitrarily long range with a finite speed and hence finite energy input. E. Sanger was among the first to recognize this favorable connection between speed and range (ref. 1) and was, with Bredt, perhaps the first to exploit the speed factor in designing a long-range bomber (ref. 2). This design envisioned a rocket-boost vehicle attaining hypervelocities at burnout and returning to earth along a combined skip-glide trajectory. Considerable attention was given to the propulsion and motion analysis; however, little attention was given to what is now considered to be a principal problem associated with any type of hypersonic aircraft, namely that of aerodynamic heating. In addition, the category of expendable vehicles, perhaps best characterized by the ballistic missile, was not treated.

Since the work of Sanger and Bredt there have been, of course, many treatments of long-range hypervelocity vehi-

[1] Supersedes NACA Technical Note 4046 by Alfred J. Eggers, Jr., H. Julian Allen, and Stanford E. Neice, 1957.

cles in which the propulsion, motion, and heating problems have been studied in considerable detail. However, these analyses have been devoted in the main to particular designs and are not intended to reveal, for example, the relative advantages and disadvantages of ballistic-, skip-, and glide-type vehicles. Furthermore, it appears that the extent to which these vehicles can compete on a simple efficiency basis with lower speed aircraft of either the expendable or nonexpendable type has not been well established.

It has therefore been undertaken in the present report to make a comparative analysis of the performance of hypervelocity vehicles having ballistic, skip, and glide trajectories. An idealized propulsion system, whose performance approximates that of rocket motors, is assumed. The motion analysis is simplified by treating, for the most part, only optimum trajectories yielding the maximum range for given initial kinetic energy per unit mass in the unpowered portion of flight. Aerodynamic heating is treated in a manner analogous to that employed by the senior authors in studying ballistic missiles (ref. 3) with the exception that radiant heat transfer, as well as convective heat transfer, is considered in the treatment of glide and skip vehicles. The efficiencies of these vehicles are compared with supersonic aircraft with typical air-breathing power plants.

NOTATION

A	reference area for lift and drag evaluation, sq ft
c	specific heat of vehicle material, ft-lb/slug °R
C_D	drag coefficient
C_L	lift coefficient
C_F	skin-friction coefficient
C_F'	equivalent skin-friction coefficient (see eq. (40))
C_p	specific heat of air at constant pressure, ft-lb/slug °R
C_v	specific heat of air at constant volume, ft-lb/slug °R
D	drag, lb
e	Naperian logarithm base
E	performance efficiency factor (see eq. (85))
f	general functional designation
F_a, F_b	functions of ΔJ, (see eqs. (74) and (80))
G	ratio of maximum deceleration to gravity acceleration (32.2 ft/sec^2)
g	acceleration due to force of gravity, ft/sec^2
h	convective heat-transfer coefficient, ft-lb/ft^2 sec °R
H	convective heat transferred per unit area (unless otherwise designated), ft-lb/ft^2
I	specific impulse, sec
J	range parameter for glide vehicle (see eq. (68))
k	Stefan-Boltzmann constant for black body radiation (3.7×10^{-10} ft-lb/ft^2 sec °R^4)
K	constant in stagnation point heat-transfer equation, slug $^{1/2}$/ft (see eq. (44))
L	lift, lb
m	mass, slugs
M	Mach number
Q	convective heat transferred (unless otherwise designated), ft-lb
r	distance from center of the earth, ft
r_c	radius of curvature of flight path, ft
r_o	radius of earth, ft
R	range, ft
s	distance along flight path, ft
S	surface area, sq ft
t	time, sec
T	temperature (ambient air temperature unless otherwise specified), °R
V	velocity, ft/sec
$\overline{V}$	ratio of velocity to satellite velocity
V_S	velocity of satellite at earth's surface (taken as 25,930 ft/sec)
W	weight, lb
y	vertical distance from surface of earth, ft
α	angle of attack, radians unless otherwise specified
β	constant in density-altitude relation, (22,000 ft^{-1}; see eq. (15))
γ	ratio of specific heats, C_p/C_v
δ	semivertex angle of cones, radians unless otherwise specified
Δ	increment
η	lift-drag efficiency factor, (see eq. (B27))
θ	angle of flight path to horizontal, radians unless otherwise specified
Λ	leading edge sweep angle, deg
ρ	air density, slugs/cu ft ($\rho_o=0.0034$)
σ	nose or leading-edge radius of body or wing, ft
φ	partial range, radians
Φ	total range, radians
ψ	remaining range ($\Phi-\varphi$), radians

Subscripts

o	conditions at zero angle of attack
1, 2, 3, . . .	conditions at end of particular rocket stages
a	conditions at point of maximum average heat-transfer rate
av	average values
b	conditions at point of maximum local heat-transfer rate
C	convection
e	effective values
en	conditions at entrance to earth's atmosphere
ex	conditions at exit from earth's atmosphere
f	conditions at end of powered flight
i	initial conditions
l	local conditions
n	ballistic phases of skip vehicles
N	total number of rocket stages
p	pressure effects
P	pay load
r	recovery conditions
R	radiation
s	stagnation conditions
T	total values
w	wall conditions

ANALYSIS

GENERAL CONSIDERATIONS

In the following analysis of long-range hypervelocity vehicles, only flight in planes containing the great circle arc between take-off and landing is considered. The flight is thought of in two phases: (a) the powered phase in which sufficient kinetic energy, as well as control, is imparted to the vehicle to bring it to a prescribed velocity, orientation, and position in space; and (b) the unpowered phase, in which the vehicle travels to its destination under the influence of gravity and aerodynamic forces.

The analyses of motion and aerodynamic heating during unpowered flight will, of necessity, differ widely for the several types of vehicles under consideration. On the other hand, motion in the powered phase is conveniently treated by a method common to all vehicles. The study of powered flight and its relation to range is therefore taken as a starting point in the analysis.

POWERED FLIGHT AND THE BREGUET RANGE EQUATION

In this part of the study, the following simplifying assumptions are made: (a) aerodynamic heating can be neglected on the premise that high flight speeds are not attained until the vehicle is in the rarefied upper atmosphere;[2] (b) sufficient stability and control is available to provide proper orientation and positioning of the vehicle in space; (c) the distance traveled while under power is negligible by comparison to the overall range; and finally, (d) the thrust is very large compared to the retarding aerodynamic and gravity forces. In terms of present-day power plants, the last assumption is tantamount to assuming a rocket drive for the vehicle.

The velocity at burnout of the first stage of a multistage rocket (or the final velocity of a single-stage rocket) can then be expressed as (see, e. g., ref. 4):

$$\overline{V}_{f_1}=\frac{gI}{V_S}\ln\left(\frac{m_i}{m_{f_1}}\right) \tag{1}$$

where the initial velocity is taken as zero. In this expression, m_i and m_{f_1} represent the mass of the vehicle at the beginning and ending of first-stage flight, and $\overline{V}_{f_1}=V_{f_1}/V_S$ where $V_S=\sqrt{gr_o}=25{,}930$ feet per second is the satellite velocity at the surface of the earth. The coefficient g is the acceleration due to gravity and is, along with the specific impulse I, considered constant in this phase of the analysis. The final velocity of the vehicle at the end of the N stages of powered flight can be expressed as

$$\overline{V}_f=\overline{V}_N=\frac{gI}{V_S}\ln\left[\left(\frac{m_i}{m_{f_1}}\right)\left(\frac{m_{i_2}}{m_{f_2}}\right)\cdots\left(\frac{m_{i_N}}{m_f}\right)\right] \tag{2}$$

where the initial mass of any given stage differs from the final mass of the previous stage by the amount of structure, etc., jettisoned.

Now let us define an equivalent single-stage rocket having the same initial and final mass as the N-stage rocket and the same initial and final velocity. There is, then, an effective specific impulse defined by

$$I_e=I\frac{\ln\left[\left(\frac{m_i}{m_{f_1}}\right)\left(\frac{m_{i_2}}{m_{f_2}}\right)\cdots\left(\frac{m_{i_N}}{m_f}\right)\right]}{\ln\left(\frac{m_i}{m_f}\right)} \tag{3}$$

whereby equation (2) can be written as

$$\overline{V}_f=\frac{gI_e}{V_S}\ln\left(\frac{m_i}{m_f}\right) \tag{4}$$

The effective specific impulse I_e is always somewhat less than the actual specific impulse, but for an efficient design they are not too different. Throughout the remainder of the analysis the effective impulse I_e will be used.

Equation (4) might be termed the "ideal power plant" equation for accelerated flight because, when considered in combination with the assumptions underlying its development, attention is naturally focused on the salient factors leading to maximum increase in velocity for given expenditure of propellant. Thus the thrust acts only in overcoming inertia forces, and the increase in vehicle velocity is directly proportional to the exhaust velocity (gI) of the propellant.

Now we recognize that an essential feature of the hypervelocity vehicles under study here is that they use their velocity (or kinetic energy per unit mass) to obtain range. For this reason, equation (4) also constitutes a basic performance equation for these vehicles because it provides a connecting link between range requirements and powerplant requirements.

In addition to comparing various types of hypervelocity vehicles, our attention will also be focused upon comparison of these vehicles with lower speed, more conventional types of aircraft. For this purpose it is useful to develop an alternate form of equation (4). We observe that the kinetic energy imparted to the vehicle is

$$\tfrac{1}{2}m_fV_f^2$$

This energy is equated to an effective work done, defined as the product of the range traveled and a constant retarding force. (Note that the useful kinetic energy at the end of powered flight is zero.) This force is termed the "effective drag" D_e. Thus

$$D_eR=\tfrac{1}{2}m_fV_f^2 \tag{5}$$

where R is flight range measured along the surface of the earth. Similarly, we may define an "effective lift" L_e, equal to the final weight of the vehicle

$$L_e=W_f=m_fg$$

from which it follows that equation (5) may be written as

$$R=\left(\frac{L}{D}\right)_e\frac{V_f^2}{2g} \tag{6}$$

where $(L/D)_e$ is termed the "effective lift-drag ratio." Combining equations (4) and (6), we obtain

$$R=\left(\frac{L}{D}\right)_e I_eV_e\ln\left(\frac{m_i}{m_f}\right) \tag{7}$$

[2] This assumption is in the main permissible. A possible exception occurs, however, with the glide vehicle for which heat-transfer rates near the end of powered flight can be comparable to those experienced in unpowered gliding flight.

where

$$V_e=\frac{V_f}{2} \tag{8}$$

and represents an "effective" flight velocity of the vehicle. Equation (7) will prove useful in comparing hypersonic vehicles with conventional aircraft because of its analogy to the Breguet range equation,

$$R=\frac{L}{D} IV \ln\left(\frac{m_i}{m_f}\right) \tag{9}$$

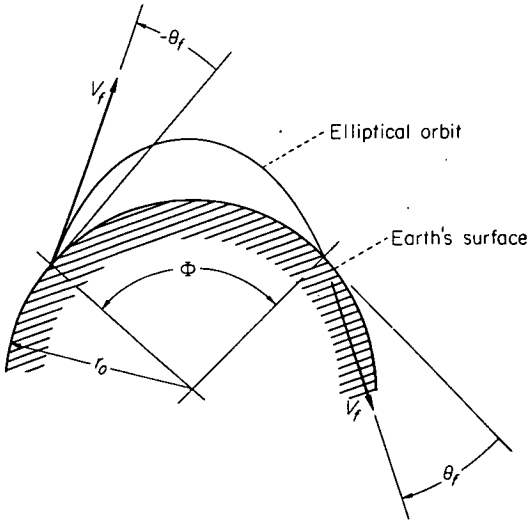
It will also prove useful to have equation (7) in the dimensionless form obtained by dividing through with r_o, the radius of the earth. In this case we have

$$\Phi=\frac{R}{r_o}=\left(\frac{L}{D}\right)_e \overline{V}_e \left(\frac{gI_e}{V_S}\right) \ln\left(\frac{m_i}{m_f}\right) \tag{10}$$

where Φ is the range in radians of arc traversed along the surface of the earth.

MOTION IN UNPOWERED FLIGHT

Ballistic trajectory.—In studying the motion of long-range vehicles in this trajectory, advantage is taken of the fact that the traverse through the earth's atmosphere generally forms only a small part of the total trajectory. Therefore, the deflection and deceleration encountered in the re-entry phase (discussed in detail in ref. 3) are neglected in the computation of the total range and rotation of the earth is neglected in this and all other phases of the analysis. With the added simplification that the contribution to range of the powered phase of flight is negligible, the ballistic trajectory becomes one of Kepler's planetary ellipses, the major axis of which bisects the total angle of arc Φ traveled around the earth. For the trajectories of interest here ($\overline{V}_f \leq 1$), the far focus of the ellipse is at the mass center of the earth. For purposes of range computation, then, the ballistic vehicle leaves and returns to the earth's surface at the same absolute magnitude of velocity and incidence (see sketch).



The expression for range follows easily from the equation of the ellipse (see, e. g., ref. 5) and can be written

$$\Phi=\frac{R}{r_0}=2\tan^{-1}\left(\frac{\sin\theta_f\cos\theta_f}{\frac{1}{\overline{V}_f^2}-\cos^2\theta_f}\right) \tag{11}$$

where the angle of incidence θ_f is considered positive. In order to determine the optimum trajectory giving maximum range for a given velocity V_f, equation (11) is differentiated with respect to θ_f and equated to 0, yielding

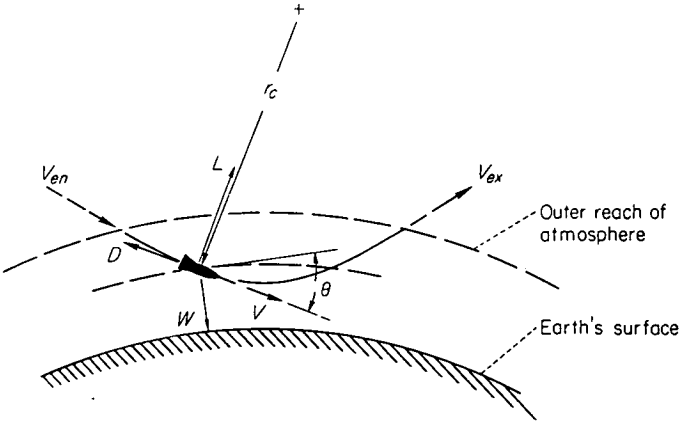
$$\left.\begin{aligned}\overline{V}_f^2=\frac{V_f^2}{V_S^2}=1-\tan^2\theta_f\\ \Phi=\frac{R}{r_0}=\pi-4\theta_f\end{aligned}\right\} \tag{12}$$

Equations (11) and (12) have been employed to determine velocity as a function of incidence for various values of range and the results are presented in figure 1. The "minimum velocity line" of figure 1 corresponds to the optimum trajectories (eqs. (12)).

The effective lift-drag ratios can easily be calculated for optimum ballistic vehicles using equation (6) in combination with the information of figure 1. The required values of $(L/D)_e$ as a function of range are presented in figure 2.

Skip trajectory.—This trajectory can be thought of as a succession of ballistic trajectories, each connected to the next by a "skipping phase" during which the vehicle enters the atmosphere, negotiates a turn, and is then ejected from the atmosphere. The motion analysis for the ballistic missile can, of course, be applied to the ballistic phases of the skip trajectory. It remains, then, to analyze the skipping phases and to combine this analysis with the ballistic analysis to determine over-all range.

To this end, consider a vehicle in the process of executing a skip from the atmosphere (see sketch).



The parametric equations of motion in directions perpendicular and parallel to the flight path s are, respectively,

$$\left.\begin{aligned}C_L\frac{\rho V^2}{2}A-mg\cos\theta=\frac{mV^2}{r_c}\\ -C_{D'}\frac{\rho V^2}{2}A+mg\sin\theta=m\frac{dV}{dt}\end{aligned}\right\} \tag{13}$$

where r_c is the local radius of curvature of the flight path, θ is the local inclination to the horizontal (positive downward), ρ is the local air density, and C_L and C_D are the lift and drag

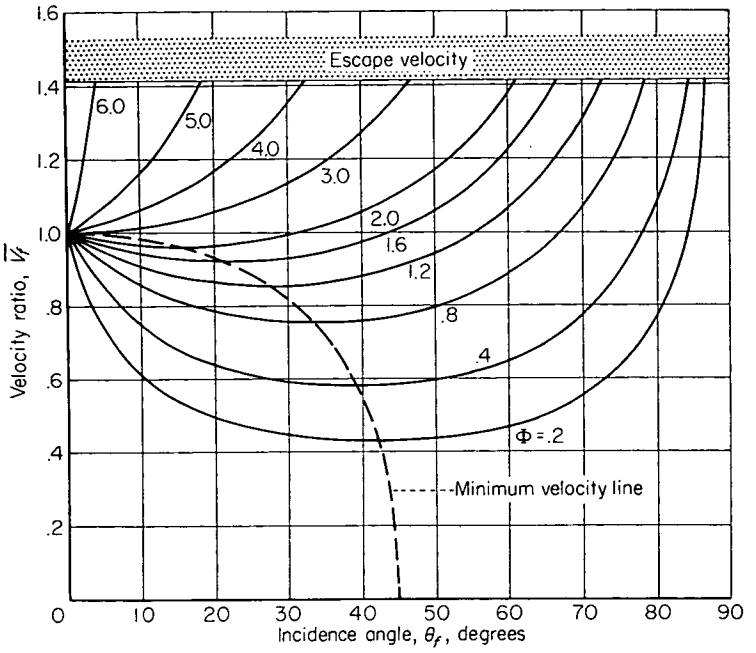


FIGURE 1.— Variation of velocity with incidence angle for various values of range of ballistic vehicle.

coefficients, respectively, based on the reference area, A, of the aircraft.

In the turning process, aerodynamic lift must obviously predominate over the gravity component, $mg \cos \theta$. By analogy to the atmospheric re-entry of ballistic missiles (see ref. 3), aerodynamic drag generally predominates over the gravity component, $mg \sin \theta$. Moreover, the integrated contribution to velocity of this gravity component during descent in a skip is largely balanced by an opposite contribution during ascent.

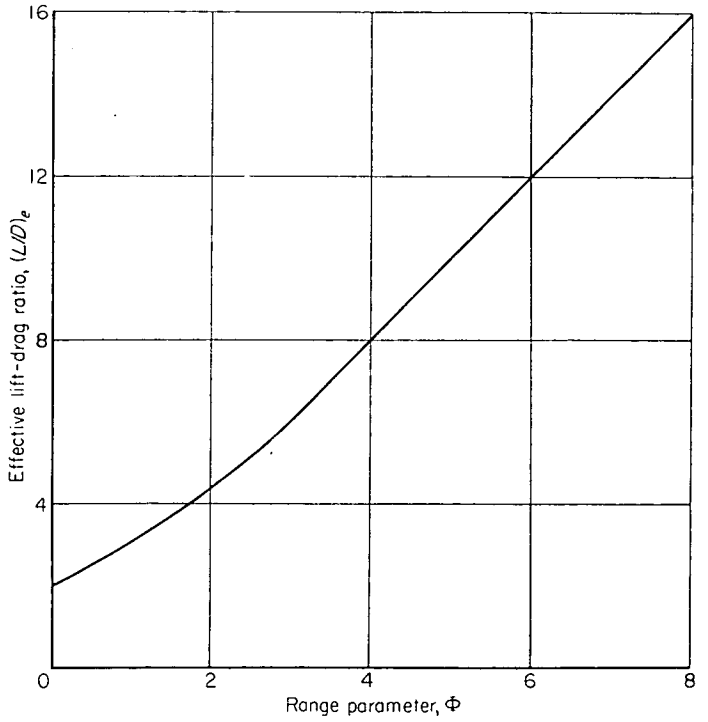


FIGURE 2.—Variation of effective lift-drag ratio with range for optimum ballistic vehicle.

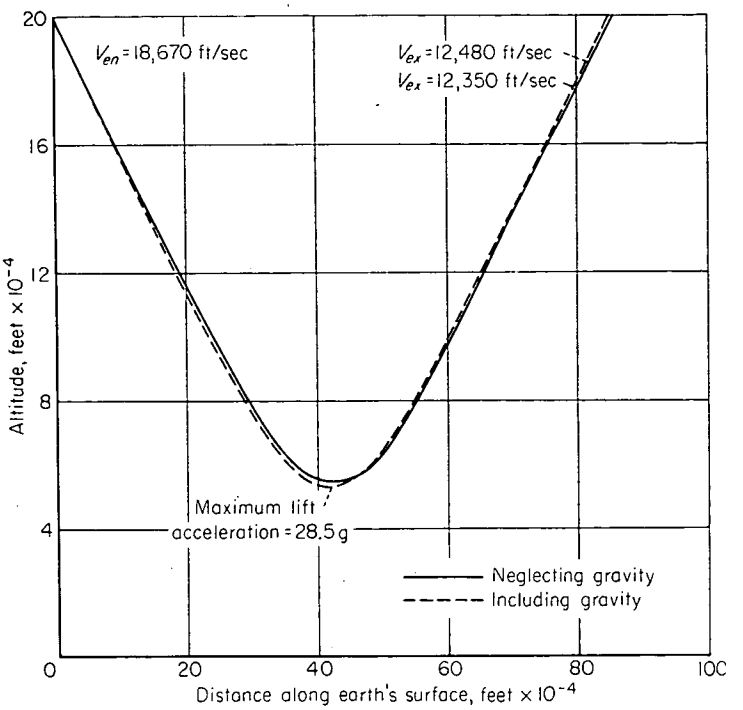


FIGURE 3.—Trajectory of the first skipping phase for a skip vehicle with a lift-drag ratio of 2 and a total range of 3440 nautical miles ($\Phi=1$).

For these reasons we will idealize the analysis by neglecting gravity entirely. This approach is analogous to the classical treatment of impact problems in which all forces exclusive of impact forces (aerodynamic forces in this case) are neglected as being of secondary importance. Gravity is shown to be of secondary importance in figure 3 where the trajectory results obtainable from equations (13) and (14) are presented for the first skipping phase of an $L/D=2$, $\Phi=1$ skip missile.

With gravity terms neglected, equations (13) reduce to

$$\left.\begin{aligned} \frac{1}{2} C_L \rho V^2 A &= -m V^2 \frac{d\theta}{ds} \\ -\frac{1}{2} C_D \rho V^2 A &= m \frac{dV}{dt} \end{aligned}\right\} \tag{14}$$

where $d\theta/ds = -\frac{1}{r_c}$ to the accuracy of this analysis.

Now we assume an isothermal atmosphere, in which case

$$\rho = \rho_o e^{-\beta y} \tag{15}$$

where ρ_o and β are constants, and $y=(r-r_o)$ is the altitude from sea level (see ref. 3 for discussion of accuracy of this assumption). Noting that $dy/ds = -\sin \theta$, we combine the first of equations (14) with equation (15) to yield

$$\frac{C_L \rho_o A}{2m} e^{-\beta y} dy = \sin \theta \, d\theta \tag{16}$$

This expression can be integrated to give

$$\frac{C_L \rho_o A}{2\beta m} e^{-\beta y} = \cos \theta - \cos \theta_{en} \tag{17}$$

where ρ is taken as zero at the altitude corresponding to the effective "outer reach" of the atmosphere. Equation (17) points out an important feature of the skip path; namely,

$\cos\theta$ is a single-valued function of altitude. Since θ proceeds from positive to negative values, it is evident that

$$\theta_{en_{n-1}}=-\theta_{ex_n} \tag{18}$$

where the subscripts *en* and *ex* refer to atmospheric entrance and exit conditions, respectively, and the numbers $n-1$ and n refer to successive ballistic phases of the trajectory. Now since

$$\frac{dV}{dt}=V\frac{dV}{ds}=\frac{1}{2}\frac{dV^2}{ds}$$

equations (14) may be combined to obtain

$$\frac{1}{2}\frac{dV^2}{ds}=\frac{V^2}{L/D}\frac{d\theta}{ds} \tag{19}$$

which, for constant L/D, can be integrated to yield

$$\frac{V_{ex_n}}{V_{en_{n-1}}}=e^{\frac{\theta_{ex_n}-\theta_{en_{n-1}}}{L/D}} \tag{20}$$

With the aid of equation (18), this expression may be written

$$\frac{V_{ex_n}}{V_{en_{n-1}}}=e^{-\frac{2\theta_{en_{n-1}}}{L/D}} \tag{21}$$

which relates the velocities at the beginning and end of a skip to the lift-drag ratio and the entrance angle of the vehicle to the earth's atmosphere. From equation (18) it follows further that the entrance angle for each skip in the trajectory is the same, so that

$$\theta_{en_n}=\theta_{en_{n-1}}=\cdots=\theta_f$$

and hence equation (21) becomes

$$\frac{V_{ex_n}}{V_{en_{n-1}}}=e^{-\frac{2\theta_f}{L/D}} \tag{22}$$

We now combine this result of the skip analysis with that of the ballistic analysis to obtain the total flight range. From equation (11) the range of the nth ballistic segment of the trajectory is

$$\varphi_n=2\tan^{-1}\left[\frac{\sin\theta_f\cos\theta_f}{\left(\frac{V_s}{V_{ex_n}}\right)^2-\cos^2\theta_f}\right] \tag{23}$$

Consistent with the idealization of the skipping process as an impact problem, we neglect the contribution to range of each skipping phase so that the total range is simply the sum of the ballistic contributions. From equations (22) and (23) this range is then

$$\Phi=\frac{R}{r_o}=\sum_{n=1}^{\infty}\varphi_n=2\sum_{n=1}^{\infty}\tan^{-1}\left[\frac{\sin\theta_f\cos\theta_f}{\frac{1}{\overline{V}_f^2}e^{\frac{4(n-1)\theta_f}{L/D}}-\cos^2\theta_f}\right] \tag{24}$$

From this expression we see that for any given velocity at the end of powered flight there is a definite skipping angle which maximizes the range of an aircraft developing a particular lift-drag ratio. These skipping angles have been obtained with the aid of an IBM CPC, and the corresponding values of $\overline{V}_f$ as a function of range for various L/D are presented in figure 4. Corresponding values of $(L/D)_e$ have been obtained using equation (6) and the results are shown in figure 5.

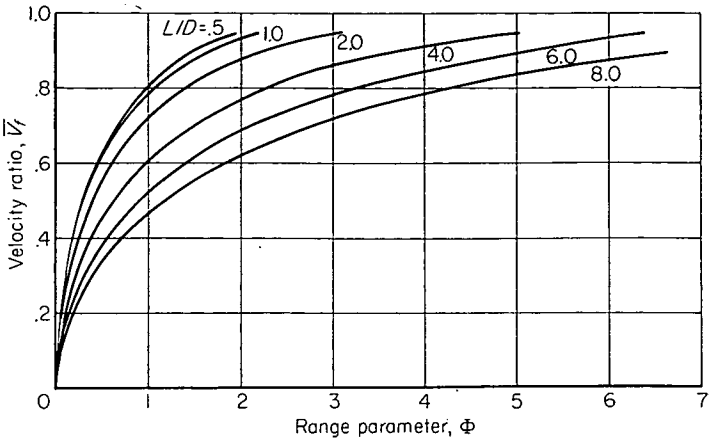
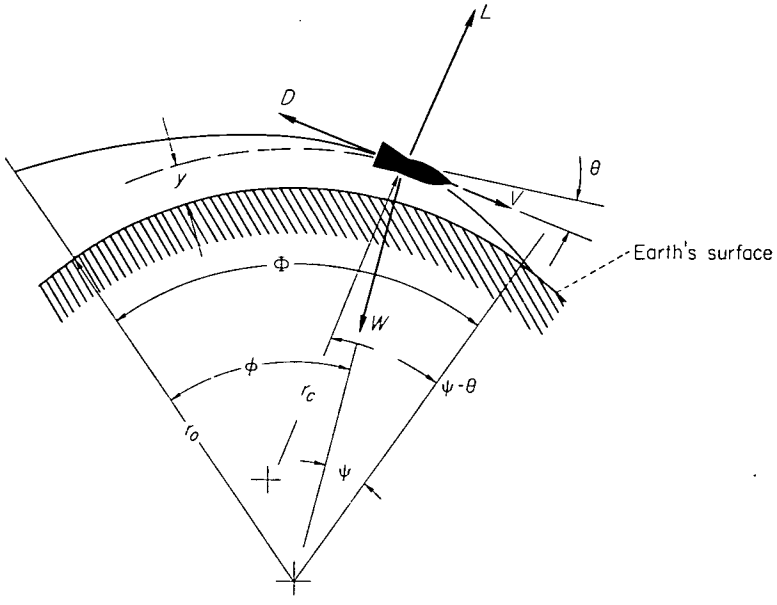


FIGURE 4.—Variation of velocity with range for various values of lift-drag ratio for skip vehicle.

Glide trajectory.—The trajectory of the glide vehicle is illustrated in the accompanying sketch. As in the previous analyses, the distance covered in the powered phase will be neglected in the determination of total range.



The parametric equations of motion normal and parallel to the direction of flight are the relations of equations (13) rewritten in the form

$$\left.\begin{aligned}L-mg\cos\theta&=-\frac{mV^2}{r_c}\\-D+mg\sin\theta&=m\frac{dV}{dt}\end{aligned}\right\} \tag{25}$$

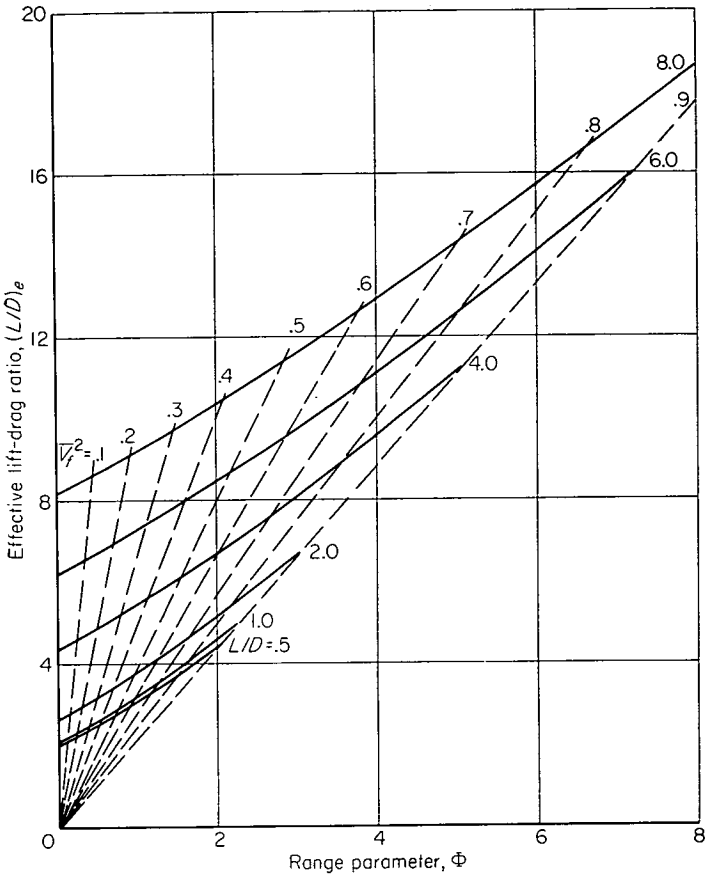


FIGURE 5.—Variation of effective lift-drag ratio with range for various values of aerodynamic lift-drag ratio of skip vehicle.

Under the assumption of small inclination angle θ to the horizontal (thus $\cos\theta \approx 1$, $\sin\theta \approx \theta$), constant gravity acceleration $\left(\text{i. e., } \frac{r}{r_o} \approx 1\right)$, and noting the following relations

$$\left.\begin{aligned} \frac{dV}{dt} &= V\frac{dV}{ds} = \frac{1}{2}\frac{dV^2}{ds} \\ -\frac{1}{r_c} &= \frac{d(\psi-\theta)}{ds} \\ -\frac{d\psi}{ds} &= \frac{\cos\theta}{r} \approx \frac{1}{r_o} \end{aligned}\right\} \tag{26}$$

equations (25) can be written in the forms

$$\left.\begin{aligned} L &= -mV^2\frac{d\theta}{ds} + mg - \frac{mV^2}{r_o} \\ D &= -\frac{1}{2}m\frac{dV^2}{ds} + mg\theta \end{aligned}\right\} \tag{27}$$

Dividing the first of equations (27) by the second yields the following differential equation

$$g\left(1-\frac{L}{D}\theta\right) + \left(\frac{1}{2}\frac{L}{D}\frac{dV^2}{ds} - V^2\frac{d\theta}{ds}\right) - \frac{V^2}{r_o} = 0 \tag{28}$$

But, as is demonstrated in Appendix A, the terms $\frac{L}{D}g\theta$ and $V^2\frac{d\theta}{ds}$ may be neglected so that equation (28) reduces to

$$\frac{dV^2}{ds} - \frac{2}{r_o(L/D)}V^2 + \frac{2g}{L/D} = 0 \tag{29}$$

Since

$$V_s^2 = gr_o$$

equation (29) can be integrated for constant $\frac{L}{D}$ to give the velocity in nondimensional form as

$$\overline{V}^2 = 1 - (1-\overline{V}_f^2)e^{\frac{2\varphi}{L/D}} \tag{30}$$

This expression gives velocity as a function of range for what Sanger (ref. 2) has termed the equilibrium trajectory—that is, the trajectory for which the gravity force is essentially balanced by the aerodynamic lift and centrifugal force, or

$$\frac{L}{W} \approx 1 - \overline{V}^2 \tag{31}$$

It follows from equation (31) that velocity can be expressed in the form

$$\overline{V}^2 = \frac{1}{1+\frac{C_L A V_s^2 \rho}{2mg}} \tag{32}$$

Now it is intuitively obvious that as the maximum range is approached, $L/W \to 1$ and hence $\overline{V}^2$ becomes small compared to one (see eq. (31)). In this event it follows from equation (30) that the maximum range for the glide vehicle is given by

$$\Phi = \frac{R}{r_o} = \frac{1}{2}\left(\frac{L}{D}\right)\ln\left(\frac{1}{1-\overline{V}_f^2}\right) \tag{33}$$

The relation between velocity and range has been determined with equation (33) for various values of L/D and the results are presented in figure 6. Corresponding values of $(L/D)_e$ have been obtained using equation (6) and are presented in figure 7.

These considerations complete the motion analysis and attention is now turned to the aerodynamic heating of the several types of vehicles under consideration.

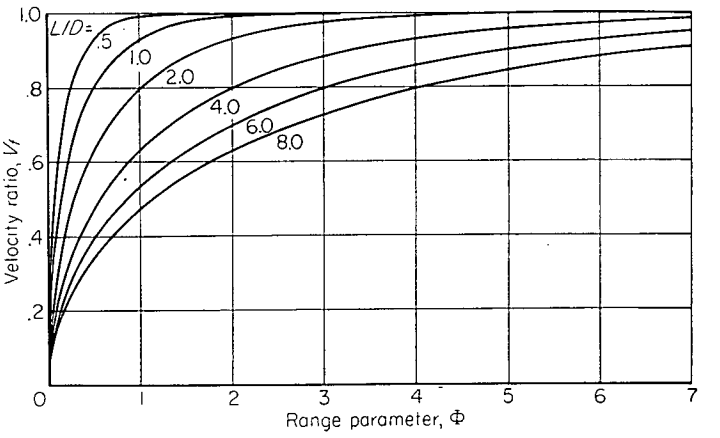


FIGURE 6.—Variation of velocity with range for various values of lift-drag ratio of glide vehicle.

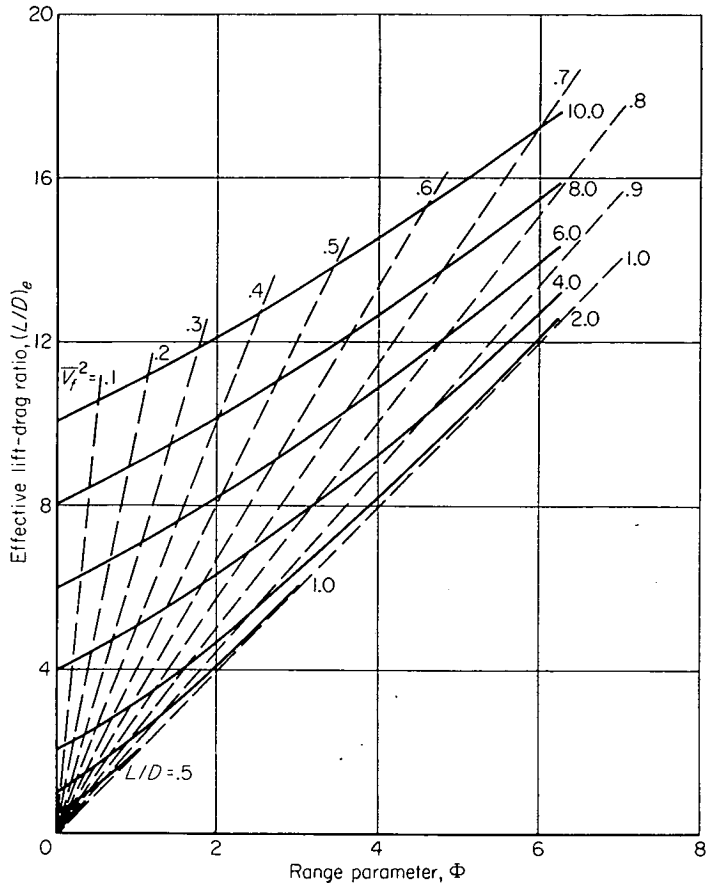


FIGURE 7.—Variation of effective lift-drag ratio with range for various values of aerodynamic lift-drag ratio of glide vehicle.

HEATING IN UNPOWERED FLIGHT

General considerations.—Three aspects of the aerodynamic heating of hypervelocity vehicles will be treated here; namely,

1. The total heat input
2. The maximum time rate of average heat input per unit area
3. The maximum time rate of local heat input per unit area

Total heat input is, of course, an important factor in determining over-all coolant weight, whether the coolant be solid (e. g., the structure), liquid, or gas, or a combination thereof. The maximum time rate of average heat input per unit area can determine peak average flow rates in the case of fluid coolants and may dictate over-all structural strength in the event that thermal stresses predominate.

Excessive local heating is, of course, a serious problem with hypervelocity vehicles. This problem may vary depending upon the type of the vehicle. Thus, for the ballistic vehicle, an important local "hot spot" is the stagnation region of the nose, while for the skip or glide vehicle attention may also be focused on the leading edges of planar surfaces used for developing lift and obtaining stable and controlled flight. In this analysis attention is, for the purpose of simplicity, restricted to the "hot spot" at the nose. In particular, we consider the maximum time rate of local heat input per unit area because of its bearing on local coolant flow rates and local structural strength.

It is undertaken to treat only convective heat transfer at this stage of the study. As will be demonstrated, radiant heat transfer from the surface should not appreciably influence convective heat transfer to a vehicle. Therefore, alleviating effects of radiation are reserved for attention in the discussion of particular vehicles later in the paper. This analysis is further simplified by making the assumptions that

1. Effects of gaseous imperfections may be neglected
2. Shock-wave boundary-layer interaction may be neglected
3. Prandtl number is unity
4. Reynolds analogy is applicable

These assumptions are obviously not permissible for an accurate quantitative study of a specific vehicle. Nevertheless they should not invalidate this comparative analysis which is only intended to yield information of a general nature regarding the relative merits and problems of different types of vehicle (see ref. 3 for a more complete discussion of these assumptions in connection with ballistic vehicles).

In calculating convective heat transfer to hypervelocity vehicles, the theoretical approach taken in reference 3 for ballistic vehicles is, up to a point, quite general and can be employed here. Thus, on the basis of the foregoing assumptions, it follows that for large Mach numbers, the difference between the local recovery temperature and wall temperature can be expressed as

$$(T_r - T_w)_l = \frac{V^2}{2C_p} \tag{34}$$

It is clear, however, that the walls of a vehicle should be maintained sufficiently cool to insure structural integrity. It follows in this case that the recovery temperature at hypervelocities will be large by comparison to the wall temperature and equation (34) may be simplified to read

$$T_{r_l} = \frac{V^2}{2C_p} \tag{35}$$

To the accuracy of this analysis, then, the convective heat transfer is independent of wall temperature. Therefore, as previously asserted, radiant heat transfer should not appreciably influence convective heat transfer and the one can be studied independently of the other.

Now, according to Reynolds analogy, the local heat-transfer coefficient h_l is, for a Prandtl number of unity, given by the expression

$$h_l = \tfrac{1}{2} C_{F_l} C_{p_l} \rho_l V_l \tag{36}$$

where C_{F_l} is the local skin-friction coefficient based on conditions just outside the boundary layer. With the aid of equations (35) and (36) the time rate of local heat transfer per unit area,

$$\frac{dH}{dt} = h_l (T_r - T_w)_l \tag{37}$$

can be written as

$$\frac{dH}{dt} = \frac{V^2}{4C_p} (C_{F_l} C_{p_l} \rho_l V_l) \tag{38}$$

Equation (38) can be integrated over the surface of a body to yield the time rate of total heat input as follows

$$\frac{dQ}{dt}=\int_S \frac{dH}{dt}\,dS=\frac{1}{4}\rho V^3 C_F' S \tag{39}$$

wherein C_{F_l} is set equal to C_F and

$$C_F'=\frac{1}{S}\int_S C_{F_l}\frac{\rho_l}{\rho}\frac{V_l}{V}\,dS \tag{40}$$

The parameter C_F' is termed the "equivalent skin-friction coefficient" and will be assumed constant at a mean value for a particular vehicle. From equation (39) we can obtain two alternate forms which will prove useful; namely, the altitude rate of total heat input defined by (note that dy is negative for dt positive)

$$-\frac{dQ}{dy}=\frac{1}{V\sin\theta}\frac{dQ}{dt}=\frac{\rho V^2 C_F' S}{4\sin\theta} \tag{41}$$

and the range rate of total heat input defined as

$$\frac{dQ}{d(r_o\varphi)}=\frac{1}{V\cos\theta}\frac{dQ}{dt}=\frac{\rho V^2 C_F' S}{4\cos\theta} \tag{42}$$

The total heat input may be obtained by integration of equations (39), (41) or (42), depending upon the particular variable used.

The time rate of average heat input per unit area may be obtained from equation (39) as

$$\frac{dH_{av}}{dt}=\frac{1}{S}\frac{dQ}{dt}=\frac{1}{4}\rho V^3 C_F' \tag{43}$$

Consider next the local convective heat transfer in the region of the nose. The time rate of local heat input per unit area was determined in reference 3 under the assumptions that viscosity coefficient varies as the square root of the absolute temperature, and that flow between the bow shock wave and the stagnation point is incompressible. In this case it was found that

$$\frac{dH_s}{dt}=K\sqrt{\frac{\rho}{\sigma}}\,V^3 \tag{44}$$

where $K=6.8\times10^{-6}$. A more detailed study of stagnation region flow, including effects of compressibility and dissociation of air molecules (ref. 6), shows that the constant, K, should have a value more like twice the above value at the hypervelocities of interest here.

With these relations we are now in a position to study the heating of the several types of vehicles of interest.

Ballistic vehicle.—The heating for this case has already been analyzed in reference 3. Only the results will be given here.

The ratio of the total heat input to the initial kinetic energy was found to be

$$\frac{Q}{\frac{1}{2}mV_f^2}=\frac{1}{2}\frac{C_F' S}{C_D A}\left(1-e^{-\frac{C_D\rho_o A}{\beta m\sin\theta_f}}\right) \tag{45}$$

For the "relatively light missile," which is of principal interest here,

$$e^{-\frac{C_D\rho_o A}{\beta m\sin\theta_f}}<<1 \tag{46}$$

and equation (45) reduces to

$$\frac{Q}{\frac{1}{2}mV_f^2}=\frac{1}{2}\frac{C_F' S}{C_D A} \tag{47}$$

The time rate of average heat input per unit area was found to be

$$\frac{dH_{av}}{dt}=\frac{1}{S}\frac{dQ}{dt}=\frac{C_F'\rho_o V_f^3}{4}e^{-\beta y}e^{-\frac{3C_D\rho_o A}{2\beta m\sin\theta_f}e^{-\beta y}} \tag{48}$$

which has the maximum value

$$\left(\frac{dH_{av}}{dt}\right)_{max}=\left(\frac{dH_{av}}{dt}\right)_{y_a}=\frac{\beta}{6e}\frac{C_F'}{C_D A}\,mV_f^3\sin\theta_f \tag{49}$$

at the altitude

$$y_a=\frac{1}{\beta}\ln\left(\frac{3C_D\rho_o A}{2\beta m\sin\theta_f}\right) \tag{50}$$

Equation (49) applies, of course, only if the altitude, y_a, is above ground level. If the value of y_a is negative then the maximum average heating rate will, of course, occur at sea level.

The time rate of local heat input per unit area to the stagnation region of the nose was found to be

$$\frac{dH_s}{dt}=K\sqrt{\frac{\rho_o}{\sigma}}\,V_f^3 e^{-\frac{\beta y}{2}}e^{-\frac{3C_D\rho_o A}{2\beta m\sin\theta_f}e^{-\beta y}} \tag{51}$$

having a maximum value of

$$\left(\frac{dH_s}{dt}\right)_{max}=\left(\frac{dH_s}{dt}\right)_{y_b}=K\sqrt{\frac{\beta m\sin\theta_f}{3eC_D\sigma A}}\,V_f^3 \tag{52}$$

occurring at the altitude

$$y_b=\frac{1}{\beta}\ln\left(\frac{3C_D\rho_o A}{\beta m\sin\theta_f}\right) \tag{53}$$

If the value of y_b is negative, then the maximum value occurs at ground level.

Skip vehicle.—With the aid of equation (17), the density at any point in a given skipping phase is found to be

$$\rho=\rho_o e^{-\beta y}=\frac{2\beta m}{C_L A}(\cos\theta-\cos\theta_f) \tag{54}$$

where it is to be recalled that $\theta_{en}=\theta_f$. The corresponding velocity for constant L/D is, from equation (19),

$$V=V_{en}e^{-\frac{\theta_f-\theta}{L/D}} \tag{55}$$

By substitution of equations (54) and (55) into equation (39), the time rate of total heat input at any point in a skipping phase can be expressed as follows:

$$\frac{dQ}{dt}=\frac{1}{2}\frac{C_F'S}{C_DA}\frac{\beta m}{L/D}V_{en}^3(\cos\theta-\cos\theta_f)e^{-\frac{3(\theta_f-\theta)}{L/D}} \tag{56}$$

Now, recalling that $ds/dt=V$, the first of equations (14) may be combined with equation (17) to yield

$$\frac{d\theta}{dt}=-\beta V(\cos\theta-\cos\theta_f) \tag{57}$$

and we note further from equation (22) that

$$\frac{(V_{en})_n}{(V_{en})_{n=1}}=\frac{(V_{en})_n}{V_f}=e^{-(n-1)\frac{2\theta_f}{L/D}} \tag{58}$$

With the aid of equations (57) and (58), equation (56) can be integrated to give the total heat input for a given skipping phase, thus we obtain

$$\frac{Q_n}{\frac{1}{2}mV_f^2}=\frac{1}{2}\frac{C_F'S}{C_DA}\left(1-e^{-\frac{4\theta_f}{L/D}}\right)e^{-(n-1)\frac{4\theta_f}{L/D}} \tag{59}$$

The total heat input for the entire trajectory can be obtained by summing up the heat inputs for each separate skipping phase. Performing this operation yields

$$\frac{Q}{\frac{1}{2}mV_f^2}=\sum_{n=1}^{\infty}\frac{Q_n}{\frac{1}{2}mV_f^2}=\frac{1}{2}\frac{C_F'S}{C_DA}\left(1-e^{-\frac{4\theta_f}{L/D}}\right)\sum_{n=1}^{\infty}e^{-(n-1)\frac{4\theta_f}{L/D}} \tag{60}$$

or

$$\frac{Q}{\frac{1}{2}mV_f^2}=\frac{1}{2}\frac{C_F'S}{C_DA} \tag{61}$$

which is identical to the result obtained for the light ballistic missile (eq. (47)). This result applies, in fact, to all hypervelocity vehicles which lose the large majority of their kinetic energy during atmospheric entry.

The time rate of average heat input per unit area is obtained by dividing equation (56) with the surface area, thus yielding

$$\frac{dH_{av}}{dt}=\frac{1}{2}\frac{C_F'}{C_DA}\frac{\beta m}{L/D}V_{en}^3(\cos\theta-\cos\theta_f)e^{-\frac{3(\theta_f-\theta)}{L/D}} \tag{62}$$

It can be shown that this expression has a peak value at a point in the skip, θ_a, given by

$$(\cos\theta_a-\cos\theta_f)=\frac{L/D}{3}\sin\theta_a$$

or

$$\theta_a=\tan^{-1}\frac{3}{L/D}-\sin^{-1}\frac{\cos\theta_f}{\sqrt{1+\left(\frac{L/D}{3}\right)^2}} \tag{63}$$

From equation (22) it can be concluded that the maximum heat-transfer rate will occur in the first skip where $V_{en}=V_f$; consequently,

$$\left(\frac{dH_{av}}{dt}\right)_{max}=\frac{\beta m}{6}\frac{C_F'}{C_DA}V_f^3\sin\theta_a e^{-\frac{3(\theta_f-\theta_a)}{L/D}} \tag{64}$$

The time rate of local heat input per unit area in the stagnation region of the nose is obtained by introducing equations (54) and (55) into equation (44) with the following result:

$$\frac{dH_s}{dt}=K\left(\frac{2\beta m}{C_LA\sigma}\right)^{\frac{1}{2}}(\cos\theta-\cos\theta_f)^{\frac{1}{2}}V_{en}^3e^{-\frac{3(\theta_f-\theta)}{L/D}} \tag{65}$$

Equation (65) has a peak value at a point θ_b in a skip given by

$$(\cos\theta_b-\cos\theta_f)=\frac{L/D}{6}\sin\theta_b$$

or

$$\theta_b=\tan^{-1}\frac{6}{L/D}-\sin^{-1}\frac{\cos\theta_f}{\sqrt{1+\left(\frac{L/D}{6}\right)^2}} \tag{66}$$

It is clear in this case also that the heat-transfer rate will have its maximum value in the first skipping phase where the velocities are highest. Since $V_{en}=V_f$ in the first skip, equation (65) becomes

$$\left(\frac{dH_s}{dt}\right)_{max}=K\left[\frac{\beta m(L/D)\sin\theta_b}{3C_LA\sigma}\right]^{\frac{1}{2}}V_f^3e^{-\frac{3(\theta_f-\theta_b)}{L/D}} \tag{67}$$

Glide vehicle.—From equations (30) and (32), the density at a point in the glide trajectory is found to be

$$\rho=\frac{2mg}{C_LAV_S^2}\frac{(1-\overline{V}_f^2)e^J}{1-(1-\overline{V}_f^2)e^J} \tag{68}$$

where

$$J=\frac{2\varphi}{L/D}$$

By substitution of equations (30) and (68) into equation (39), the time rate of total heat input can be expressed as

$$\frac{dQ}{dt}=\frac{1}{2}\frac{C_F'S}{C_DA}\frac{mgV_S}{L/D}(1-\overline{V}_f^2)e^J[1-(1-\overline{V}_f^2)e^J]^{\frac{1}{2}} \tag{69}$$

If equations (30) and (33) are combined with this expression, we again obtain

$$\frac{Q}{\frac{1}{2}mV_f^2}=\frac{1}{2}\frac{C_F'S}{C_DA} \tag{70}$$

for the heat transfer to a hypervelocity vehicle during atmospheric entry.

Now the time rate of average heat input per unit area of a glide vehicle is found by dividing equation (69) with the surface area, thus yielding

$$\frac{dH_{av}}{dt}=\frac{1}{2}\frac{C_F'}{C_DA}\frac{mgV_S}{L/D}(1-\overline{V}_f^2)e^J[1-(1-\overline{V}_f^2)e^J]^{\frac{1}{2}} \tag{71}$$

It follows from this expression that the maximum time rate of average heat input per unit area is

$$\left(\frac{dH_{av}}{dt}\right)_{max}=\left(\frac{dH_{av}}{dt}\right)_{J_a}=\frac{1}{3\sqrt{3}}\frac{C_F'}{C_DA}\frac{mgV_S}{L/D} \tag{72}$$

at a value J_a given by

$$J_a=-\ln\tfrac{3}{2}(1-\overline{V}_f^2) \tag{73}$$

If J_a is taken as a reference value, and equations (71) and (72) expressed in terms of J_a and incremental changes $\Delta J = J - J_a$, it can easily be shown that

$$\frac{dH_{av}/dt}{(dH_{av}/dt)_{max}} = e^{\Delta J}(3-2e^{\Delta J})^{1/2} = F_a(\Delta J) \tag{74}$$

The dependence of $F_a(\Delta J)$ on ΔJ is shown in figure 8.

The velocity at which the maximum average heat input rate occurs can be obtained by substituting equation (73) into equation (30) yielding

$$\overline{V} = \frac{1}{\sqrt{3}} \tag{75}$$

Equations (72), (73), and (74) apply, of course, only when $\overline{V}_f \geq (1/\sqrt{3})$.

For cases when $\overline{V}_f \leq (1/\sqrt{3})$, the maximum time rate of average heat input per unit area will occur at the start of unpowered flight and is given by

$$\left(\frac{dH_{av}}{dt}\right)_{max} = \left(\frac{dH_{av}}{dt}\right)_{J_a=0} = \frac{1}{2}\frac{C_F'}{C_D A}\frac{mgV_s}{L/D}(1-\overline{V}_f^2)\overline{V}_f \tag{76}$$

The maximum time rate of local heat input per unit area in the stagnation region of the nose is found by first substituting equations (30) and (68) into equation (44) to obtain

$$\frac{dH_s}{dt} = K\sqrt{\frac{2mg}{C_L A\sigma}}\, V_S^2[1-(1-\overline{V}_f^2)e^J][(1-\overline{V}_f^2)e^J]^{1/2} \tag{77}$$

The maximum time rate is then

$$\left(\frac{dH_s}{dt}\right)_{max} = \left(\frac{dH_s}{dt}\right)_{J_b} = \frac{2}{3\sqrt{3}} K\sqrt{\frac{2mg}{C_L A\sigma}}\, V_S^2 \tag{78}$$

occurring at a value of J_b given by

$$J_b = -\ln 3(1-\overline{V}_f^2) \tag{79}$$

With J_b as a reference, it can easily be shown that

$$\frac{dH_s/dt}{(dH_s/dt)_{max}} = \frac{1}{2}e^{\frac{\Delta J}{2}}(3-e^{\Delta J}) = F_b(\Delta J) \tag{80}$$

where

$$\Delta J = J - J_b$$

The dependence of $F_b(\Delta J)$ on ΔJ is shown in figure 8.

With reference to equations (30) and (74) it can be seen that the maximum time rate of local heat transfer in the stagnation region occurs when

$$\overline{V} = \sqrt{\frac{2}{3}} \tag{81}$$

It is apparent then that equations (77), (78), and (79) apply only when $\overline{V}_f \geq \sqrt{2/3}$. For cases where $\overline{V}_f \leq \sqrt{2/3}$, the maximum time rate of local heat input per unit area will occur at the start of unpowered flight and is given by

$$\left(\frac{dH_s}{dt}\right)_{max} = \left(\frac{dH_s}{dt}\right)_{J_b=0} = K\sqrt{\frac{2mg}{C_L A\sigma}}\, V_S^2 \overline{V}_f^2(1-\overline{V}_f^2)^{1/2} \tag{82}$$

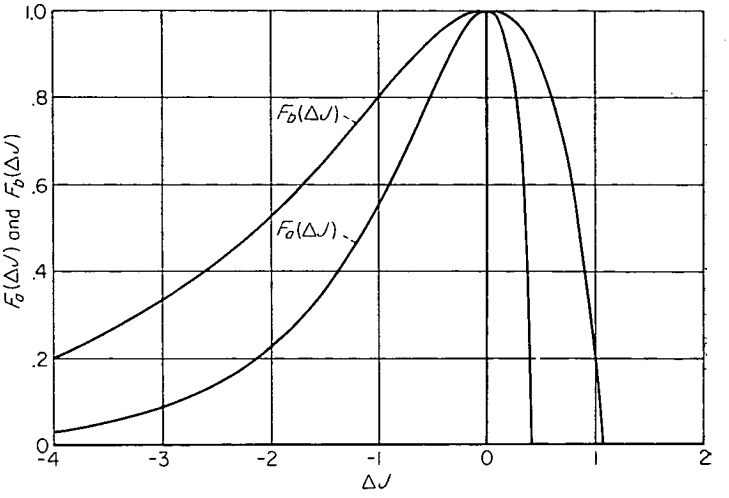


FIGURE 8.—Variations of $F_a(\Delta J)$ and $F_b(\Delta J)$ with ΔJ.

DISCUSSION

PERFORMANCE OF HYPERVELOCITY VEHICLES

In this study the point of view is taken that the performance of long-range hypervelocity vehicles is measured by their efficiency of flight. Thus, for example, it is presumed that the advantages (military and otherwise) of short time of flight accrue equally to all vehicles.

The efficiency of flight is perhaps best measured by the cost of delivering a given pay load a given range—the higher the cost, the lower the efficiency. Quite obviously it is far beyond the scope of the present paper to actually compute this cost. Rather, then, we adopt a more accessible parameter of hypervelocity flight, namely, the initial mass of the vehicle, as a measure of cost. In effect, then, the assumption is made that the higher the initial mass of a vehicle the higher the cost and the lower the efficiency. With these thoughts in mind, it is constructive to reconsider the basic performance equation (eq. (4)) written in the form

$$m_i = m_f e^{V_f/gI_e} \tag{83}$$

This expression clearly demonstrates the roles played by the three factors which influence the initial mass of a vehicle required to travel a given range. For one thing there is the power plant, and as we would expect, increasing the effective specific impulse increases the over-all efficiency of flight in the sense that it tends to reduce the initial mass. The velocity at burnout influences initial mass by dictating the amount of fuel required, and it is not surprising that decreasing the required burnout velocity (e. g., by increasing the L/D of a skip or glide vehicle) tends to decrease the initial mass. Finally, we see that the initial mass is proportional to the final mass which consists of the pay load, structure (and associated equipment), and coolant. If we presume the mass of the pay load to be some fixed quantity, then the initial mass will vary in accordance with this mass of structure and coolant.

Now we assume for comparative purposes that the power plant for one vehicle is equally as good as the power plant for another vehicle—that is to say I_e is a more or less fixed quantity. In this event it is permissible to restrict our attention to two main performance considerations; namely.

the prescribed motion as it influences the required burnout velocity, and the resulting aerodynamic heating as it influences structure and coolant. We therefore proceed to discuss the comparative performance of long-range hypervelocity vehicles in terms of these considerations.

Motion.—The dependence of burnout velocity V_f on range was determined in the analysis of motion in unpowered flight and the results obtained for the several types of hypervelocity vehicles under study were presented in figures 1, 4, and 6. Using these results in combination with the basic performance equation we have calculated the corresponding initial to final mass ratios m_i/m_f as a function of range. For these and subsequent calculations it has been assumed that the rocket power plant develops an effective specific impulse of 300 seconds. The results of these calculations are presented in figure 9 and we observe that, in general, the mass ratios are highest for the ballistic vehicle. The glide and skip vehicles have comparable and relatively low mass ratios at lift-drag ratios in the neighborhood of 4 and greater. The skip vehicle is superior, however, to the glide vehicle at lift-drag ratios in the neighborhood of 2. From considerations of motion alone, then, we conclude that the skip vehicle and the glide vehicle developing lift-drag ratios greater than 2 are superior efficiencywise, in the sense of this report, to the ballistic vehicle. Let us now determine how these observations are modified by considerations of aerodynamic heating.

Aerodynamic heating.—The analysis has revealed one particularly salient factor in regard to the heat transferred by convection to hypervelocity vehicles that expend the majority of their kinetic energy of flight in traveling through the earth's atmosphere. This factor is that the amount of kinetic energy which appears in the body in the form of heat is proportional to the ratio of friction force to total drag force acting on the body (see eqs. (47), (61), and (70)). With the possible exception of the relatively heavy ballistic vehicle (see ref. 3) all of the hypervelocity vehicles treated here do expend the major part of their kinetic energy in flight. It is, in fact, only by virtue of this expenditure of energy that the skip and glide vehicles achieve long range. From the standpoint, then, of reducing the total heat transferred by convection, the problem is to determine how the ratio of friction force to total drag force can be reduced. This matter was discussed in detail in reference 3 in connection with ballistic vehicles and it was demonstrated that the ratio could be reduced by employing high-pressure-drag (i. e., blunt) shapes. It would be most fortunate if this avenue of solution were open also to the skip and glide vehicles; however, it is readily apparent that such is not the case. This conclusion follows simply from the fact that the skip and glide vehicles must develop reasonably high lift-drag ratios to achieve long range. But, as is well known, high lift-drag ratios and high pressure drag are incompatible aerodynamic properties. Evidently, then, the skip and glide vehicles will be relatively slender and they will, by comparison to blunt ballistic vehicles, be required to absorb large amounts of their kinetic energy of flight in the form of heat. On the basis of the calculations of reference 3, it does not seem feasible for slender hypervelocity vehicles to absorb and retain so much heat (of the order of one-tenth the kinetic energy of flight). We are led, therefore, to consider the possibility of radiating part or all of this heat back to the atmosphere.

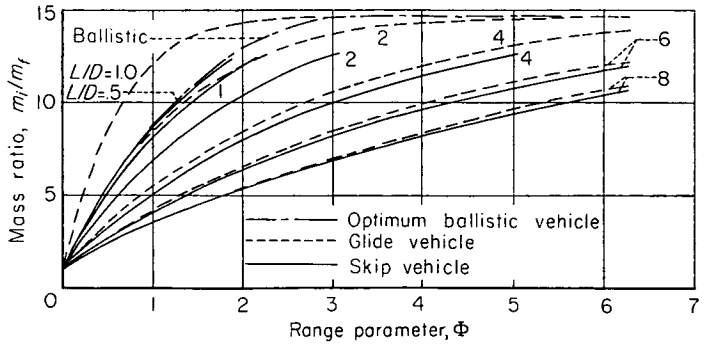


FIGURE 9.—Variation of mass ratio with range for various lift-drag ratios of hypervelocity vehicles.

Let us first consider radiation heat transfer from the surface of a glide vehicle. For purposes of simplicity we presume a vehicle conical in shape. The base diameter is taken as 3 feet and the weight as 5,000 pounds. We consider two slender cones which, according to hypersonic theory including friction drag, can develop maximum lift-drag ratios of 4 and 6 (see Appendix B). We find (see Appendix C) that the $L/D=4$ glide vehicle can radiate heat like a black body at a rate equal to the maximum average convective heat-transfer rate if the surface temperature is allowed to rise to about 1500° F. If the vehicle develops a lift-drag ratio of 6, then the allowable surface temperature must be increased to about 1800° F. These surface temperatures are high; nevertheless they are within the range of useful strengths of available alloys (see, e. g., ref. 7). Furthermore, they can, if necessary, be reduced somewhat by designing a less dense vehicle (or, more specifically, a vehicle of lower wing loading, W/S; see Appendix C).

It is indicated, then, that the glide vehicle has the attractive possibility of radiating back to the atmosphere a large fraction of the heat transferred to it by convection. As a result the mass of coolant required to protect the vehicle may be greatly reduced. Just as with the ballistic vehicle, however (see ref. 3), it is evident that additional means, such as transpiration cooling, may be necessary to protect local hot spots on the surface, like the stagnation region of the nose. It is also well to note that the alleviating effects of radiative cooling are not limited to the glide vehicle alone, but would apply to any hypervelocity vehicle in level flight.

We inquire now if the skip vehicle is capable of radiating heat at a rate comparable to the maximum convective heat-transfer rate. For this purpose it suffices to confine our attention to the first skip wherein the maximum convective heat-transfer rates are encountered (see eq. (64)). Calculations of maximum average rates using equations (63) and (64), for long-range skip vehicles developing lift-drag ratios of 4 and 6, indicate that these rates are an order of magnitude higher than those for comparable glide vehicles. The corresponding equilibrium surface temperatures of the skip vehicles are the order of two or more times as high as those of the glide vehicle. Accordingly they may be far in excess of

3000° F. We conclude, therefore, that long range, high L/D skip vehicles cannot radiate heat at a rate equivalent to the maximum convective rate because the surface temperatures required for radiation to offset convection would exceed the temperatures at which known structural materials retain appreciable strength (see ref. 7).

Now the skip vehicle operating at lift-drag ratios in the neighborhood of 2 will absorb less heat than skip vehicles developing higher lift-drag ratios. However, as shown in Appendix C, the former vehicle still absorbs more heat than a comparable high-pressure-drag ballistic vehicle and it accrues no appreciable advantage by radiation. From the standpoint of heat transfer, then, it is indicated that the skip vehicle is inferior to both the ballistic and glide vehicles. That is to say, proportionately more coolant of one form or another would be required to protect the skip vehicle than would be required to protect ballistic or glide vehicles of the same range. The skip vehicle has other disadvantages as well. Certainly one of the most serious of these is the very high lateral loads (see fig. 3) that the vehicle would be required to withstand during a skip from the earth's atmosphere. These loads, coupled with simultaneous high thermal stresses (due to high convective rates), would require the structure to be stronger and, consequently, heavier than that of a comparable glide vehicle.[3] For these and other reasons concerned with problems of stability, control, and guidance, the skip vehicle is thought to be the least promising of the three types of hypervelocity vehicle considered here.

In essence, then, the preceding study has indicated that the ballistic vehicle exhibits the possibility of being relatively efficient for hypervelocity flight by virtue of the fact that aerodynamic heating can be markedly reduced through the artifice of using blunt, high-pressure-drag re-entry shapes. The disadvantage of using the relatively inefficient ballistic trajectory is counterbalanced by this advantage which tends to keep initial mass down by reducing coolant mass. The glide vehicle appears promising for hypervelocity flight because it has, coupled with the relatively high efficiency of the glide trajectory, the possibility of radiating a large fraction of the heat absorbed by convection.

Up to this point we have considered the performance efficiency of the several types of hypervelocity vehicle by comparison with each other. It is of interest now to compare, insofar as is possible, the efficiency of flight of these vehicles with that of lower speed, more conventional type aircraft.

COMPARISON OF HYPERVELOCITY VEHICLES WITH THE SUPERSONIC AIRPLANE

In the analysis of powered flight it was found that the basic performance equation for hypervelocity vehicles could be written in a form analogous to the Breguet range equation. Thus, according to equations (7) and (9), we have for both hypervelocity and lower speed vehicles that

$$R=\left(\frac{L}{D}\right)_e I_e V_e \ln\left(\frac{m_i}{m_f}\right) \tag{84}$$

where it is understood that the effective quantities are the same as the actual quantities in the case of the lower speed, more conventional aircraft. Now let us consider the product $(L/D)_e I_e V_e$. Taking first the supersonic airplane we assume flight at a maximum lift-drag ratio of 6. The product $I_e V_e$ for a ram-jet or turbojet can reasonably be expected to have a value of about 4.4×10^6 feet.[4] The product $(L/D)_e I_e V_e$ is then 26.4×10^6 feet for the airplane. Now let us compare these quantities with the corresponding quantities for a ballistic vehicle and let us presume that the range will be half the circumference of the earth. In this event, the effective lift-drag ratio for the ballistic vehicle is 2π (see fig. 2) which is slightly greater than that for the airplane, while the effective velocity is just half the satellite velocity, or 13,000 feet per second. Let us again assume that the effective specific impulse is 300 seconds. In this case, the product of $I_e V_e$ is 3.9×10^6 feet and the product $(L/D)_e I_e V_e$ is about 24.5×10^6 feet which is only slightly less than that for the supersonic airplane. Thus we have our first suggestion that the hypervelocity vehicle is not necessarily an inefficient type vehicle for long-range flight.

In order to pursue this point further, a performance efficiency factor (see eq. (10)) defined as

$$E=\left(\frac{L}{D}\right)_e \overline{V}_e \frac{gI_e}{V_S}=\frac{\Phi}{\ln\left(\frac{m_i}{m_f}\right)} \tag{85}$$

has been calculated for ballistic and glide vehicles for $I_e=300$ seconds, and ranges up to the circumference of the earth. The corresponding quantity E has been calculated for the supersonic airplane ($I_e V_e=4.4\times10^6$ feet) for several lift-drag ratios. The results of these calculations are presented in figure 10 and we observe, as our example calculation suggested, that both the ballistic and glide vehicles compare favorably with the supersonic airplane for ranges in the neighborhood of and greater than half the circumference of the earth. The glide vehicle is again superior to the ballistic vehicle at lift-drag ratios in excess of 2 and, as a result, it compares favorably with the airplane at shorter ranges than the ballistic vehicle.

It should be kept in mind, of course, that m_f may be substantially greater than m_P, the mass of the pay load. This point is significant because it reminds us that m_i/m_P, and not m_i/m_f, is considered the better measure of cost. Thus, noting that $m_i/m_P=(m_i/m_f)(m_f/m_P)$, and recognizing that m_f/m_P is probably lowest for the ballistic vehicle, we anticipate that the ballistic vehicle would appear to better advantage than shown in figure 10.

CONCLUDING REMARKS AND SOME DESIGN CONSIDERATIONS FOR MANNED HYPERVELOCITY VEHICLES

During the course of this study it has been indicated that ballistic and glide vehicles can be operated at hypervelocities with the reasonable assurance that problems of aerodynamic

[3] Added weight means, of course, added coolant (see, again, eq. (61)) and one can easily demonstrate that ultimately the coolant is being added to cool coolant. This situation must obviously be avoided.

[4] This value should hold approximately for any air-breathing engine—note that the maximum value of $I_e V_e$ is simply the product of the thermal efficiency (taken as 0.3—see, e. g., ref. 8) and the specific heat content of the fuel (taken as 14.6×10^6 feet for gasoline-type fuels).

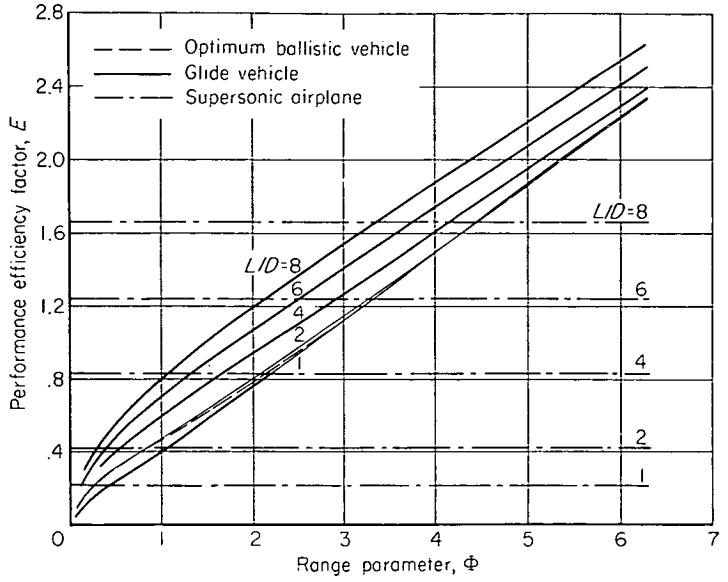


FIGURE 10.—Variation of performance efficiency factor with total range for ballistic and glide vehicles and the supersonic airplane.

heating can be largely alleviated by proper design. Skip vehicles appeared substantially less promising in this as well as other respects. It was further demonstrated that on the basis of equal ratios of initial to final mass, the long-range hypervelocity vehicle compares favorably with the supersonic airplane. These considerations suggest that the ballistic and glide vehicles have, in addition to the advantages usually ascribed to great speed, the attractive possibility of providing relatively efficient long-range flight.

In view of these findings, it seems appropriate as a final point to consider what appear to be favorable design features of manned hypervelocity vehicles. It is fair to assume that the glide vehicle has the man-carrying capability if suitable living quarters are provided inside the vehicle, particularly as regards composition and temperature of the interior atmosphere. However, whether or not the ballistic vehicle has this capability is not obvious and requires some clarification. The principle question in this regard is the magnitude of the decelerations experienced by the vehicle and its occupants during atmospheric entry. Some light is shed on this matter by figure 11 where the maximum deceleration in g's of a ballistic vehicle is shown as a function of range.

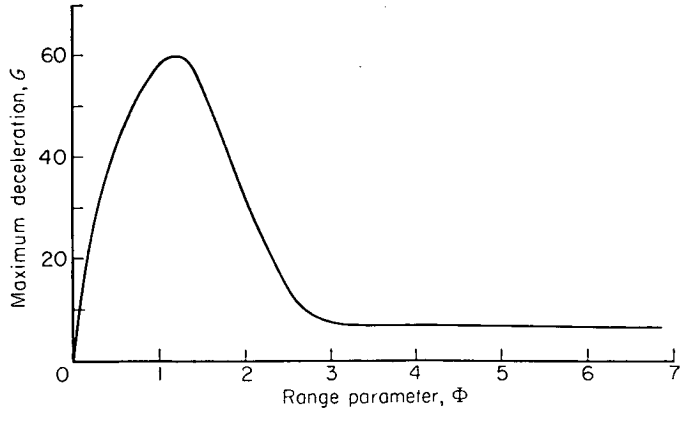


FIGURE 11.—Maximum deceleration of ballistic vehicles during atmospheric entry.

These decelerations were calculated by the method of reference 3 for large entry angles, and with equations (13), ($C_L=0$) for entry angles near zero, using the velocities and entry angles as a function of range given by equations (12). It seems reasonable to conclude from the results shown in figure 11 that the decelerations are in excess of those humanly tolerable except for very short range flight and for very long range flight. The latter case is of principal interest to us, and it is noted specifically that maximum decelerations can probably be kept to the order of 10 g's or slightly less for ranges of the order of semiglobal and greater. It may be remarked further that decelerations exceed 5g's for less than a minute, and they exceed 1 g for not more than about 3 minutes. In this respect, then, (see ref. 9) the ballistic vehicle appears to be a practical man-carrying machine, provided extreme care is exercised in supporting the man during atmospheric entry. From the aerodynamic heating point of view the ballistic vehicle can, of course, be made especially attractive by employing the blunt body concepts of reference 3.

The glide vehicle experiences maximum decelerations in g's equal to approximately D/L (see eq. (31) and note $D/W \to D/L$ as $V^2 \to 0$), and so with any significant lift-drag ratio it is far superior to the ballistic vehicle in this respect. In addition, the glider has the important advantage of maneuverability during atmospheric entry. These factors and its potential for relatively high performance efficiency make the glider generally attractive as a man-carrying machine.

It will be assumed that if the glider is to develop reasonably high lift-drag ratios it should be slender in shape. But the nose of the body and the leading edges of the wing (and tail surfaces) should be blunt to alleviate the local heating problem. Blunting the nose of the body may not, if properly done, increase the drag of the vehicle (see refs. 10 and 11). Blunting the leading edge of the wing will, however, incur a drag penalty and thereby reduce the lift-drag ratio. This difficulty may be largely circumvented by sweeping the leading edge of the wing. The contribution to total drag of the drag at the leading edge is, according to Newtonian theory, reduced in this manner by the square of the cosine of the angle of sweep for constant span. The question which arises is how does sweep influence heat-transfer rate. The nature of this influence (ref. 6) is shown in figure 12 and it is observed that sweep decreases heat-transfer rate very substantially, although not to the extent that it decreases drag. We are led then to the conclusion that the wing on a hypervelocity glide vehicle which develops reasonably high lift-drag ratio should have highly swept leading edges. This observation coupled with the fact that wing weight should be minimized suggests for our consideration the low-aspect-ratio delta wing. In addition to the wing it is anticipated that a vertical tail will be needed to provide directional stability and control, and so we are led to imagine as one possibility a hypervelocity glider of the type shown in figure 13.

The potential of the glider to have relatively high performance efficiency hinges strongly on the finding that the large majority of the heat convected to it may be radiated

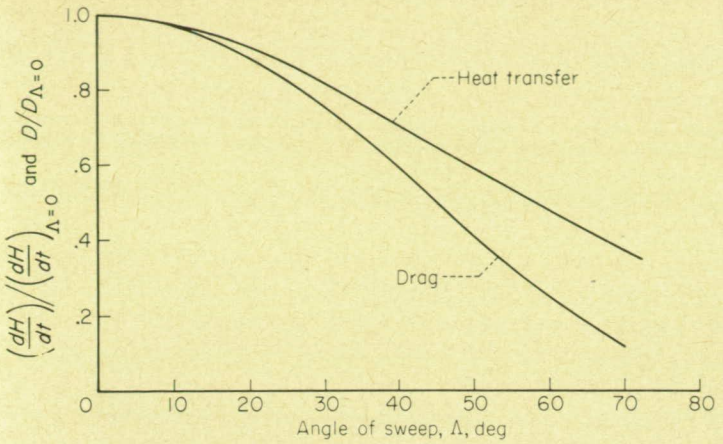


FIGURE 12.—Effect of sweep on drag and heat transfer to circular cylinders.

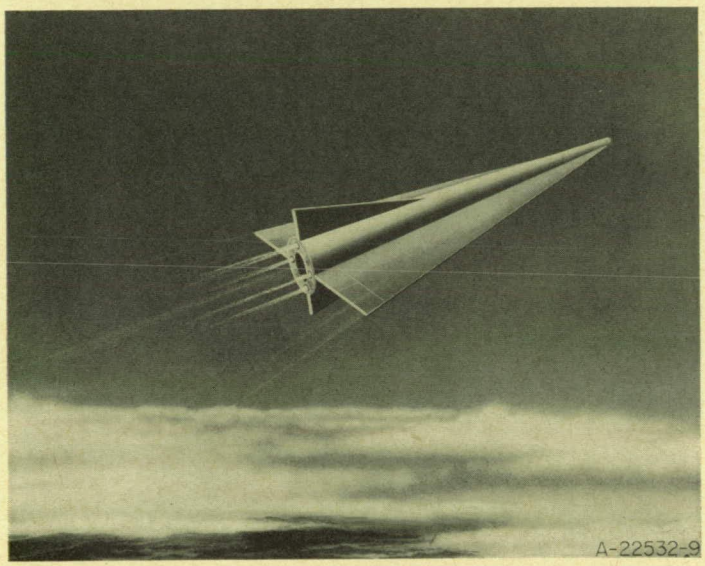


FIGURE 13.—Example high lift-drag ratio glider.

away at reasonably low surface temperatures. But it is never possible to build a perfect radiation shield. There is always a certain amount of heat which leaks through the shield to the internal structure. As the duration of flight increases this heat leakage problem may assume major proportions if substantially more structure (or coolant) is required to absorb the heat. If, at the same time, the action of aerodynamic forces has, at best, a minor influence on range then the high lift-drag-ratio glider may cease to be an attractive machine. For flights approaching global range these two factors tend to come into play. That is, flight time becomes relatively long (of the order of an hour and a half or more) with the attendant increase in seriousness of the heat leakage problem, while lift-drag ratio assumes a

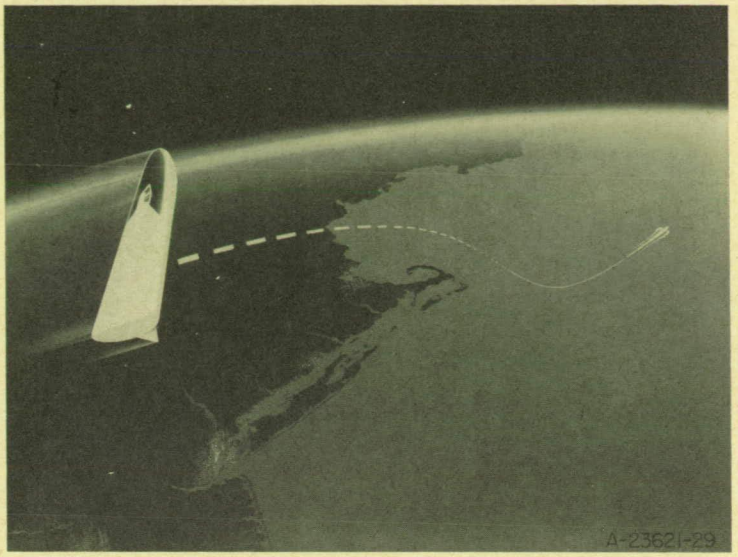


FIGURE 14.—Example high lift glider.

relatively minor role in terms of performance efficiency (see fig. 10). Accordingly, it may be attractive to launch a global glider into a low altitude satellite orbit which it follows over the large majority of its range and from which it enters the atmosphere in the terminal phase of flight to glide the short remaining distance to its landing point. Under these circumstances, the vehicle may be designed to minimize aerodynamic heating during atmospheric entry and for this purpose we are attracted to the use of high lift [5] as well as low wing loading (see eqs. (76) and (77)) to reduce heating rates and surface temperatures. Accordingly, the vehicle may glide into the atmosphere at a high angle of attack for high lift coefficient, maintaining this attitude until speed has been reduced to a supersonic value where heating has become a relatively minor problem. The angle of attack may then be reduced to increase L/D, thereby extending the glide and increasing maneuverability to achieve the desired landing point. For this type of application the vehicle might have more of the appearance shown in figure 14, again being of the delta-wing plan form but having a more or less rounded bottom and sides to minimize heating rates over the leading edge as well as the entire lower surface during re-entry. Such a configuration bears a resemblance to a motorboat and it may in fact be suited for landing on water as shown.

AMES AERONAUTICAL LABORATORY
NATIONAL ADVISORY COMMITTEE FOR AERONAUTICS
MOFFETT FIELD, CALIF., *Dec. 10, 1954*

[5] High lift tends, of course, to mean increased decelerations because of reduced L/D during atmospheric entry; however, even for L/D's of the order of unity these decelerations remain modest and they should not, therefore, constitute a serious piloting problem.

APPENDIX A

SIMPLIFYING ASSUMPTIONS IN THE ANALYSIS OF THE GLIDE TRAJECTORY

The assumption of small deflection angle ($\theta << 1$) was used throughout the study of the glide trajectory. In addition, equation (28) was simplified on the assumptions that

$$(L/D)\theta << 1 \tag{A1}$$

and

$$V^2 \frac{d\theta}{ds} << \frac{L/D}{2} \frac{dV^2}{ds} \tag{A2}$$

The extent to which these assumptions are permissible can be checked by deriving an expression for $(L/D)\theta$ and examining its variation over a range of trajectory parameters.

From equations (15), (30), and (31) the altitude of any point in a glide trajectory is found to be

$$y = \frac{1}{\beta}\left\{\ln\left[\frac{1-(1-\overline{V}_f^2)e^J}{(1-\overline{V}_f^2)e^J}\right] + \ln\left[\frac{1-\overline{V}^2_{r=r_o}}{\overline{V}^2_{r=r_o}}\right]\right\} \tag{A3}$$

By retaining the assumption of small inclination angle, whereby $\theta \approx -dy/ds$, and recalling that $J=(2s/r_o)/(L/D)$, we find the inclination angle by differentiating equation (A3). Performing this operation and making use of equation (30) reduces the expression for $(L/D)\theta$ to

$$\frac{L}{D}\theta = \frac{2}{\beta r_o}\left[\frac{1}{1-(1-\overline{V}_f^2)e^J}\right] = \frac{2.105\times 10^{-3}}{\overline{V}^2} \tag{A4}$$

Since $\overline{V}^2$ becomes very small toward the end of the trajectory, it is apparent from equation (A4) that the assumption of small $(L/D)\theta$ cannot be justified in this portion of flight. The problem then is to determine the conditions under which $(L/D)\theta$ remains negligibly small over the major part of the trajectory.

With the aid of equations (30) and (33), equation (A4) can be modified to the following form

$$\frac{\varphi}{\Phi} = 1 - \frac{L/D}{2\Phi}\ln\left\{\frac{1}{1-\left[\frac{2/\beta r_o}{(L/D)\theta}\right]}\right\} \tag{A5}$$

For given values of L/D and total range Φ, equation (A5) determines the fractional part of the total range which corresponds to a given value of $(L/D)\theta$. Since the deflection angle is always increasing, we can therefore determine the portion of the total range through which $(L/D)\theta$ remains equal to or less than a given value. A computation of this nature was performed for a value of $(L/D)\theta \leq 0.05$, and the results are presented in figure 15. From this figure we can see that except for short ranges and large lift-drag ratios, $(L/D)\theta$ (as well as θ) remains at a value less than 0.05 for better than 90 percent of the total range.

The second assumption, equation (A2), can also be verified from the results of the analysis. By differentiation of equation (A–4) we find that

$$V^2 \frac{d\theta}{ds} = \frac{4V_s^2}{\beta r_o^2 (L/D)^2}\left[\frac{(1-\overline{V}_f^2)e^J}{\overline{V}^2}\right] \tag{A6}$$

while differentiation of equation (30) yields

$$\frac{1}{2}(L/D)\frac{dV^2}{ds} = -\frac{V_s^2(1-\overline{V}_f^2)e^J}{r_o} \tag{A7}$$

Dividing equation (A6) by equation (A7), and making use of equation (A4), we find that

$$\frac{V^2\frac{d\theta}{ds}}{\frac{1}{2}(L/D)\frac{dV^2}{ds}} = \frac{2\theta}{(L/D)} = \frac{2}{(L/D)^2}[(L/D)\theta] \tag{A8}$$

By comparing equation (A8) with the previous results obtained for $(L/D)\theta$ (fig. 15), we can readily see that the assumption of equation (A2) is actually less stringent than that of equation (A1) for values of L/D of the order of 1 and greater.

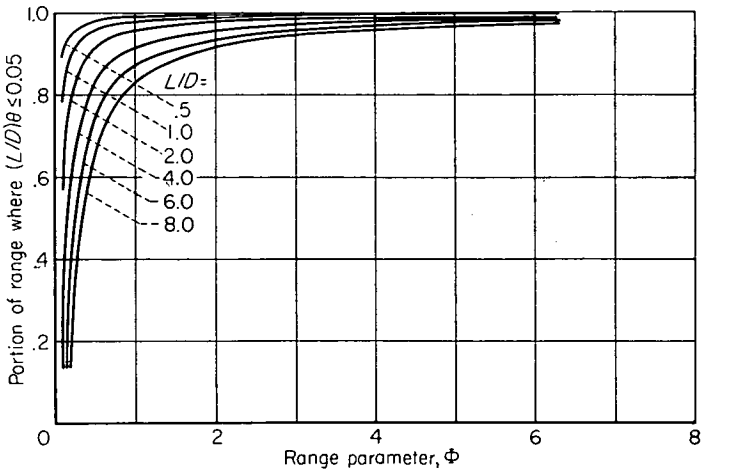


FIGURE 15.—Portion of range where $(L/D)\theta \leq 0.05$ as a function of range for various values of lift-drag ratio.

APPENDIX B

THE RELATION BETWEEN $\frac{C_F'S}{C_DA}$ AND $\left(\frac{L}{D}\right)_{max}$ FOR CONICAL MISSILES

The lift and drag coefficients for slender cones at small angles of attack can be expressed in the following manner:

$$C_L=2\alpha \tag{B1}$$

$$C_D=C_{D_o}+\alpha C_L \tag{B2}$$

from which it follows that the lift-drag ratio is

$$\frac{L}{D}=\frac{C_L}{C_{D_o}+\alpha C_L}=\frac{C_L}{C_{D_o}+C_L^2/2} \tag{B3}$$

It can be shown that equation (B3) has a maximum value when

$$C_{D_o}=C_L^2/2 \tag{B4}$$

whereby

$$(C_D)_{(L/D)_{max}}=2C_{D_o} \tag{B5}$$

Using equations (B1) through (B5), one can express the maximum value of the lift-drag ratio in the following ways:

$$\left(\frac{L}{D}\right)_{max}=\frac{1}{2\alpha}=\frac{1}{C_L}=\frac{1}{\sqrt{2C_{D_o}}} \tag{B6}$$

The drag coefficient at zero angle of attack appearing in equation (B2) can be broken down into its component parts to yield

$$C_{D_o}=(C_{D_o})_p+C_{F_o}S/A \tag{B7}$$

where $(C_{D_o})_p$ is the zero-lift pressure drag coefficient and C_{F_o} is the zero-lift skin-friction coefficient based on wetted area. The skin-friction coefficient C_{F_o} in equation (B7) can be related to the equivalent skin-friction coefficient C_F' (see eq. (43)) by considering average conditions over the surface of the cone. Equating the friction drags as determined from free-stream and local average conditions, it is found that

$$C_{F_o}=(C_{F_l})_{av}\frac{(\rho_l)_{av}(V_l)_{av}^2}{\rho V^2} \tag{B8}$$

By referring to local average conditions on the body surface, the expression for C_F', equation (40), can be written as

$$C_F'=(C_{F_l})_{av}\frac{(\rho_l)_{av}(V_l)_{av}}{\rho V} \tag{B9}$$

Comparing equations (B8) and (B9) it is apparent that

$$C_{F_o}=C_F'\frac{(V_l)_{av}}{V} \tag{B10}$$

For slender shapes at hypersonic speeds, the local velocity does not differ appreciably from the free-stream value. Also, for small angles of attack, the skin-friction coefficient should remain fairly constant. Consequently, equation (B10) can be written as

$$C_{F_o}=C_F=C_F'=\text{constant} \tag{B11}$$

and equation (B7) then becomes

$$C_{D_o}=(C_{D_o})_p+\frac{C_F'S}{A} \tag{B12}$$

From equations (B5) and (B12) it can then be shown that

$$\left(\frac{C_F'S}{C_DA}\right)_{(L/D)_{max}}=\frac{1}{2}\left[1-\frac{(C_{D_o})_p}{C_{D_o}}\right] \tag{B13}$$

From the Newtonian impact theory, the zero-lift pressure drag coefficient for slender cones at hypersonic speeds can be expressed as

$$(C_{D_o})_p=2\delta^2 \tag{B14}$$

where δ is the semivertex angle of the cone. By further noting that for slender cones

$$\frac{S}{A}=\frac{1}{\delta} \tag{B15}$$

equation (B12) then becomes

$$C_{D_o}=2\delta^2+\frac{C_F'}{\delta} \tag{B16}$$

For a given value of C_F' it can be shown that equation (B16) has minimum value when [6]

$$\delta=\delta_{opt}=\left(\frac{C_F'}{4}\right)^{1/3} \tag{B17}$$

whereby, at $\delta=\delta_{opt}$

$$(C_{D_o})_{min}=6\delta_{opt}^2=3(C_{D_o})_p \tag{B18}$$

Obviously, then, the highest value of maximum lift-drag ratio (eq. (B6)) will be attained by the cone with the semivertex angle given by equation (B17). By substitution from equation (B18) into equation (B6), the optimum value of maximum lift-drag ratio is found to be

$$\left(\frac{L}{D}\right)_{max}=\frac{1}{2\sqrt{3}}\left(\frac{4}{C_F'}\right)^{1/3}=\frac{1}{2\sqrt{3}\delta_{opt}} \tag{B19}$$

By further substituting the expression for minimum zero-lift drag coefficient, equation (B18), into equation

[6] The remaining analysis assumes C_F' constant. Although this is certainly not the situation in practice, the analysis provides an "order of magnitude" estimate of pertinent parameters.

(B13), the following relation, corresponding to the condition of optimum maximum lift-drag ratio, is obtained:

$$\left(\frac{C_F'S}{C_DA}\right)_{(L/D)_{max}}=\frac{1}{3} \tag{B20}$$

With the aid of equations (B14) and (B16), equation (B13) can also be expressed in the following form, corresponding to any maximum lift-drag ratio including the optimum value:

$$\left(\frac{C_F'S}{C_DA}\right)_{(L/D)_{max}}=\frac{1}{2}\left(1-\frac{1}{1+\frac{C_F'}{2\delta^3}}\right) \tag{B21}$$

From equations (B20) and (B21) it can readily be seen that in the case of the optimum $(L/D)_{max}$

$$\frac{C_F'}{2\delta_{opt}{}^3}=2 \tag{B22}$$

from which it follows directly that

$$\frac{C_F'}{2\delta^3}=2\left(\frac{\delta_{opt}}{\delta}\right)^3 \tag{B23}$$

so that equation (B21) may be written as

$$\left(\frac{C_F'S}{C_DA}\right)_{(L/D)_{max}}=\frac{1}{2+\left(\frac{\delta}{\delta_{opt}}\right)^3} \tag{B24}$$

With the aid of equations (B16) and (B23), the expression for any $(L/D)_{max}$ (eq. (B6)) can be shown to be

$$\left(\frac{L}{D}\right)_{max}=\frac{1}{2\delta\left[1+2\left(\frac{\delta_{opt}}{\delta}\right)^3\right]^{1/2}} \tag{B25}$$

and it follows directly from equation (B19) that the ratio η of $(L/D)_{max}$ for any cone to that for the optimum cone is

$$\eta=\frac{\delta_{opt}}{\delta}\left[\frac{3}{1+2\left(\frac{\delta_{opt}}{\delta}\right)^3}\right]^{1/2} \tag{B26}$$

where η is defined as the "lift-drag efficiency factor." By substitution from equation (B24), the ratio of $(L/D)_{max}$ to the optimum value can then be expressed in terms of $(C_F'S/C_DA)$ as follows:

$$\eta=\sqrt{3}\left(\frac{C_F'S}{C_DA}\right)^{1/3}\left(1-2\frac{C_F'S}{C_DA}\right)^{1/6} \tag{B27}$$

The dependence of η on $C_F'S/C_DA$ is shown in figure 16. It should be noted, however, that for small values of η the assumption of slender cones will be violated, although the results as shown will be qualitatively correct in that $C_F'S/C_DA$ will become exceedingly small for low values of $(L/D)_{max}$, regardless of body shape.

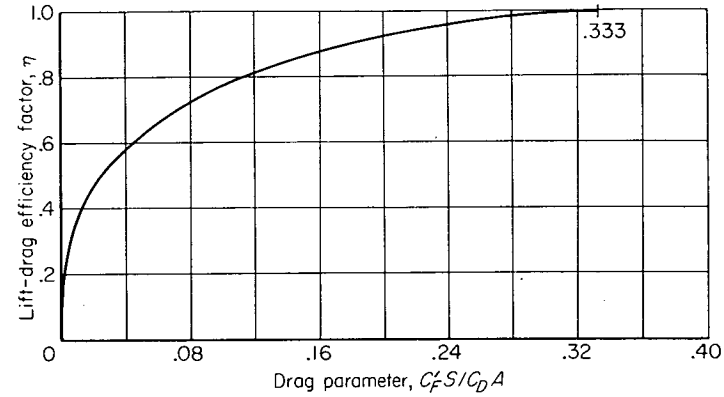


FIGURE 16.—Variation of lift-drag efficiency factor with drag parameter for cones.

APPENDIX C

COMPUTATION OF HEATING ASSOCIATED WITH ROCKET VEHICLES

RADIATION OF HEAT FROM GLIDE VEHICLES

From equation (72), the maximum time rate of total heat input to the glide vehicle can be expressed as

$$\left(\frac{dQ}{dt}\right)_{max}=S\left(\frac{dH_{av}}{dt}\right)_{max}=\frac{mgV_S}{3\sqrt{3}(L/D)}\left(\frac{C_F'S}{C_DA}\right) \tag{C1}$$

The rate of heat radiation from the vehicle is given by the relation

$$S\frac{dH_R}{dt}=kT_R{}^4S \tag{C2}$$

Using equations (C1) and (C2), the requirement for continuous radiation of all convective heat input to a surface at a temperature 2000° R can be expressed as

$$\frac{mg}{S(L/D)}\frac{C_F'S}{C_DA}\leq 1.20 \tag{C3}$$

If a value of $(L/D)_{\substack{max\\opt}}=6$ is assumed, values of the parameter $C_F'S/C_DA$ and cone angle, δ, can be determined as a function of $(L/D)_{max}$ from the analysis given in Appendix B. A vehicle weight of 5000 pounds with a maximum diameter of 3 feet is assumed whereby equation (C3) can be evaluated for various (L/D) giving the results in the following table:

L/D	$C_F'S/C_DA$	δ, deg	S, sq ft	$\frac{mg}{S(L/D)}\frac{C_F'S}{C_DA}$
6	0.333	2.75	147	1.89
4	.0600	6.73	60.2	1.24
2	.00710	14.3	28.6	.619
1	.000890	29.6	14.3	.312
½	.000115	55.8	8.55	.135

We see, therefore, that at surface temperatures of 2000° R and for an L/D of 4, this glide-type vehicle can radiate heat at a rate equal to or greater than the maximum convective heat rate.

RADIATIVE AND CONVECTIVE HEAT TRANSFER ASSOCIATED WITH SKIP VEHICLES

In this section the problem is to determine the extent to which heat absorbed by a skip vehicle in the first skipping

phase can be reradiated during the subsequent ballistic phase. The quantity of heat absorbed in the first skipping phase has already been obtained in the heating analysis, (eq. (59) for $n=1$)

$$\frac{Q_1}{\frac{1}{2}mV_f^2}=\frac{1}{2}\frac{C_F'S}{C_DA}\left(1-e^{-\frac{4\theta_f}{L/D}}\right) \tag{C4}$$

where the total heat absorbed throughout the entire trajectory is

$$\frac{Q_T}{\frac{1}{2}mV_f^2}=\frac{1}{2}\frac{C_F'S}{C_DA} \tag{C5}$$

In order to determine the heat radiated, three quantities must be determined:

1. Temperature of the vehicle at the start of the second ballistic phase
2. Temperature of the vehicle at the end of the second ballistic phase
3. The time duration of the second ballistic phase

To determine the first of the above quantities, we employ the relation for heat absorbed

$$Q_1=cW_e\Delta T \tag{C6}$$

where c is the specific heat of the material, W_e is the effective weight of material absorbing heat, and ΔT is the temperature rise during the first skip. If it is assumed that 1/3 of the missile weight will absorb heat, equation (C6) becomes

$$\Delta T=\frac{3}{gc}\left(\frac{Q_1}{m}\right) \tag{C7}$$

where m is the total mass of the vehicle. It is assumed that the material has a specific heat of 0.11 Btu/lb °R. If it is also assumed that the temperature at the start of the first skip is 500° R, equation (C7) becomes

$$T_{ex_2}=500+1.1\times10^{-3}\left(\frac{Q_1}{m}\right) \tag{C8}$$

which defines the temperature at the beginning of the second ballastic phase.

To find the temperature at the end of the second ballistic phase, we equate the radiant heat-transfer rate from the body to the rate of heat loss in terms of the temperature drop of the body

$$-kT^4S\,dt=cW_e\,dT \tag{C9}$$

This expression can be integrated to yield

$$T_{en_2}^{\ 3}=\frac{1}{(7.95\times10^{-15})St+\frac{1}{T_{ex_2}^{\ 3}}} \tag{C10}$$

for a vehicle weight of 5000 pounds (effective absorbing weight of 1667 pounds) where T_{en_2} is the temperature at the end of the second ballistic phase and t is the total flight time of the second ballistic phase. The total heat lost by radiation can now be expressed in terms of the temperature drop as

$$Q_{R_2}=(T_{ex_2}-T_{en_2})W_ec$$

or

$$Q_{R_2}=1.41\times10^5(T_{ex_2}-T_{en_2}) \tag{C11}$$

The time of flight in any ballistic trajectory can be shown to be

$$t=\frac{2r_o}{V_s}\frac{\left(1-\cos\frac{\Phi}{2}\right)^{3/2}}{(1-i^2)}\left[\tan\theta_f+\frac{2}{\sqrt{1-i^2}}\tan^{-1}\left(\sqrt{\frac{1+i}{1-i}}\tan\frac{\Phi}{4}\right)\right] \tag{C12}$$

where

$$i=\frac{\tan\theta_f}{\sin\frac{\Phi}{2}+\tan\theta_f\cos\frac{\Phi}{2}}$$

$$\frac{\Phi}{2}=\tan^{-1}\left(\frac{\sin\theta_f\cos\theta_f}{\frac{1}{\overline{V}^2}-\cos^2\theta_f}\right)$$

The foregoing relations were applied to a computation of the radiative cooling of a missile weighing 5000 pounds and traversing a total range of 3440 nautical miles ($\Phi=1.0$). Values of θ_f were obtained in the motion analysis, and values of $C_F'S/C_DA$ and S obtained in the previous calculation with regard to the glide missile will apply to this case also. The computations are summarized in the following table. Note that the case of $L/D=½$ is essentially the ballistic vehicle (see fig. 9).

L/D	θ_f, deg	$\overline{V}_f^2$	$Q_1\times10^{-5}$	Q_1/Q_T	t, sec	T_{ex_2}, °R	T_{en_2}, °R	$Q_{R_2}\times10^{-5}$	Q_{R_2}/Q_1
6	12.5	0 275	3115	0.135	213	2710	1490	1725	0.554
4	17.0	.315	1470	.258	335	1542	1323	316	.211
2	24.0	.525	549	.575	395	889	885	27	.049
1	27.5	.620	122	.853	247	587	585	3	.023
½	30.0	.650	19	.985	80.4	514	514	0	0

We see, therefore, that the quantity of heat which must be absorbed by this skip vehicle decreases rapidly with decreasing lift-drag ratio. The quantity of heat which must be absorbed by a ballistic vehicle ($L/D\cong1/2$) is almost negligible compared with the quantities associated with vehicles with an $L/D=2$ or greater. Comparison of the heat absorbed in the first skipping phase with the heat radiated in the second ballistic phase indicates no appreciable advantage is obtained due to radiation for values of $L/D=2$ and lower. To be sure, this situation could be substantially altered (near $L/D=2$) by allowing the surface temperatures to reach higher values during the skip; however, it seems unlikely that the net heat absorbed by the skip vehicle could ever be reduced to the low value of the ballistic vehicle for any reasonable surface temperature.

REFERENCES

1. Sanger, Eugen: Rakenten-flugtechnik. R. Oldenbourg (Berlin), 1933.
2. Sanger, Eugen, and Bredt, J.: A Rocket Drive for Long Range Bombers. Tech. Information Branch, Navy Department, Trans. CGD-32, 1944.
3. Allen, H. Julian, and Eggers, A. J., Jr.: A Study of the Motion and Aerodynamic Heating of Missiles Entering the Earth's Atmosphere at High Supersonic Speeds. NACA Rep. 1381, 1958. (Supersedes NACA TN 4047)
4. Malina, Frank J., and Summerfield, Martin: The Problem of Escape from the Earth by Rocket. Jour. Aero. Sci., vol. 14, no. 8, Aug. 1947, pp. 471–480.

526597—60——75

5. Timoshenko, S., and Young, D. H.: Advanced Dynamics. McGraw-Hill Book Co., Inc., 1948.
6. Eggers, A. J., Jr., Hansen, C. Frederick, and Cunningham, Bernard E.: Stagnation-Point Heat Transfer to Blunt Shapes in Hypersonic Flight, Including Effects of Yaw. NACA TN 4229, 1958.
7. Batdorf, Samuel B.: Structural Problems in Hypersonic Flight. Jet Propulsion, vol. 27, no. 11, Nov. 1957, pp. 1157–1161.
8. Rutowski, Edward S.: Energy Approach to the General Aircraft Performance Problem. Jour. Aero. Sci., vol. 21, no. 3, March 1954.
9. Beckman, E. L., Ziegler, J. E., Duane, T. D., and Hunter, H. N.: Some Observations on Human Tolerance to Accelerative Stress. Phase II: Preliminary Studies on Primates Subjected to Maximum Simple Accelerative Loads. Jour. Aviation Medicine, vol. 24, no. 5, Oct. 1953, pp. 377–392.
10. Eggers, A. J., Jr., Dennis, David H., and Resnikoff, Meyer M.: Bodies of Revolution for Minimum Drag at High Supersonic Airspeeds. NACA RM A51K27, 1952.
11. Sommer, Simon C., and Stark, James A.: The Effect of Bluntness on the Drag of Spherical Tipped Truncated Cones of Fineness Ratio 3 at Mach Numbers 1.2 to 7.4. NACA RM A52B13, 1952.

REPORT 1383

SURVEY OF HYDROGEN COMBUSTION PROPERTIES[1]

By Isadore L. Drell and Frank E. Belles

SUMMARY

The literature on the combustion properties of hydrogen-air mixtures is surveyed to provide a single source of information useful in research and development work in which hydrogen is burned. Data are presented on flame temperature, burning velocity, quenching distance, flammability composition limits, minimum spark ignition energy, flashback and blow off limits, detonation properties, explosion limits, spontaneous ignition, and the chemistry of hydrogen oxidation. The survey is not meant to be historically complete or exhaustive but to cover the basic material of importance for flight-propulsion applications.

The validity of experimental methods is discussed, and the data are assessed wherever possible. Recommended values for the combustion properties of hydrogen-air mixtures are presented. Some original material is also included. Relations among various combustion properties of hydrogen are discussed. Calculated adiabatic flame temperatures are presented for a pressure range from 0.01 to 100 atmospheres and an initial-temperature range from 0° to 1400° K for all possible hydrogen-air mixtures; and the variation of spontaneous-ignition lag with temperature, pressure, and composition based on the reaction kinetics of hydrogen oxidation is treated theoretically.

INTRODUCTION

The use of hydrogen as a possible fuel for aircraft and missiles has been considered for a number of years (ref. 1). Among the many problems associated with the use of this material are those of efficient burning under a variety of conditions. In the research and development effort that will be necessary before these problems can be fully solved, it would be useful to have a single source of information on the many aspects of hydrogen combustion. Therefore, as a part of the fundamental combustion work at the NACA Lewis laboratory, the literature was surveyed and the present knowledge on hydrogen-air flames was collected and digested.

A great deal of literature exists because hydrogen has often been used as a fuel in combustion research from the earliest studies up to the present. One reason for this has been the ready availability of hydrogen in a fairly pure state. Furthermore, its high burning velocity, wide flammability range, high heating value per unit weight, and great flame stability are of much scientific interest. Of the common fuel-oxidant systems, the hydrogen-oxygen (or hydrogen-air) system is probably the simplest, the one about which much of the chemistry is known, and thus the one about which there is the greatest likelihood of learning more.

The survey is not meant to be historically complete or exhaustive, but to cover the important basic material. It is mainly concerned with hydrogen-air combustion properties, but some data are included for hydrogen-oxygen and hydrogen-oxygen-nitrogen systems. The combustion data presented include observations on (1) flame temperature, (2) burning velocity, (3) quenching distance, (4) flammability limits, (5) spark ignition energy, (6) flame stability, (7) detonation properties, and (8) explosion limits, spontaneous ignition, and the chemistry of hydrogen oxidation. Values of the combustion properties are given under stated conditions of temperature, pressure, and composition (and vessel size and other specifications of the apparatus when significant). The variation of each property with temperature, pressure, and composition is then discussed if information is available.

Experimental methods and data are interpreted and evaluated, and recommended values are given. Relations among various combustion properties of hydrogen are discussed. Other original material includes calculated adiabatic flame temperatures over the entire hydrogen-air composition range for pressures of 0.01 to 100 atmospheres and initial temperatures of 0° to 1400° K, and a theoretical treatment of the effects of temperature, pressure, and composition on spontaneous-ignition lag based on the reaction kinetics of hydrogen oxidation.

SYMBOLS

c_p	specific heat at constant pressure
c_1,c_3	proportionality constants
$c_2(T)$	temperature-dependent proportionality constant
D	width of flameholder
d	diameter of burner tube
d_q	quenching distance
E	activation energy, cal/mole
F	Fanning friction factor
g	boundary velocity gradient, (cm/sec)/cm
I	spark ignition energy, millijoules
i	rate of initiation (rate of formation of OH radicals per unit time and volume)

[1] Supersedes recently declassified NACA Research Memorandum E57D24, by Isadore L. Drell and Frank E. Belles, 1957.

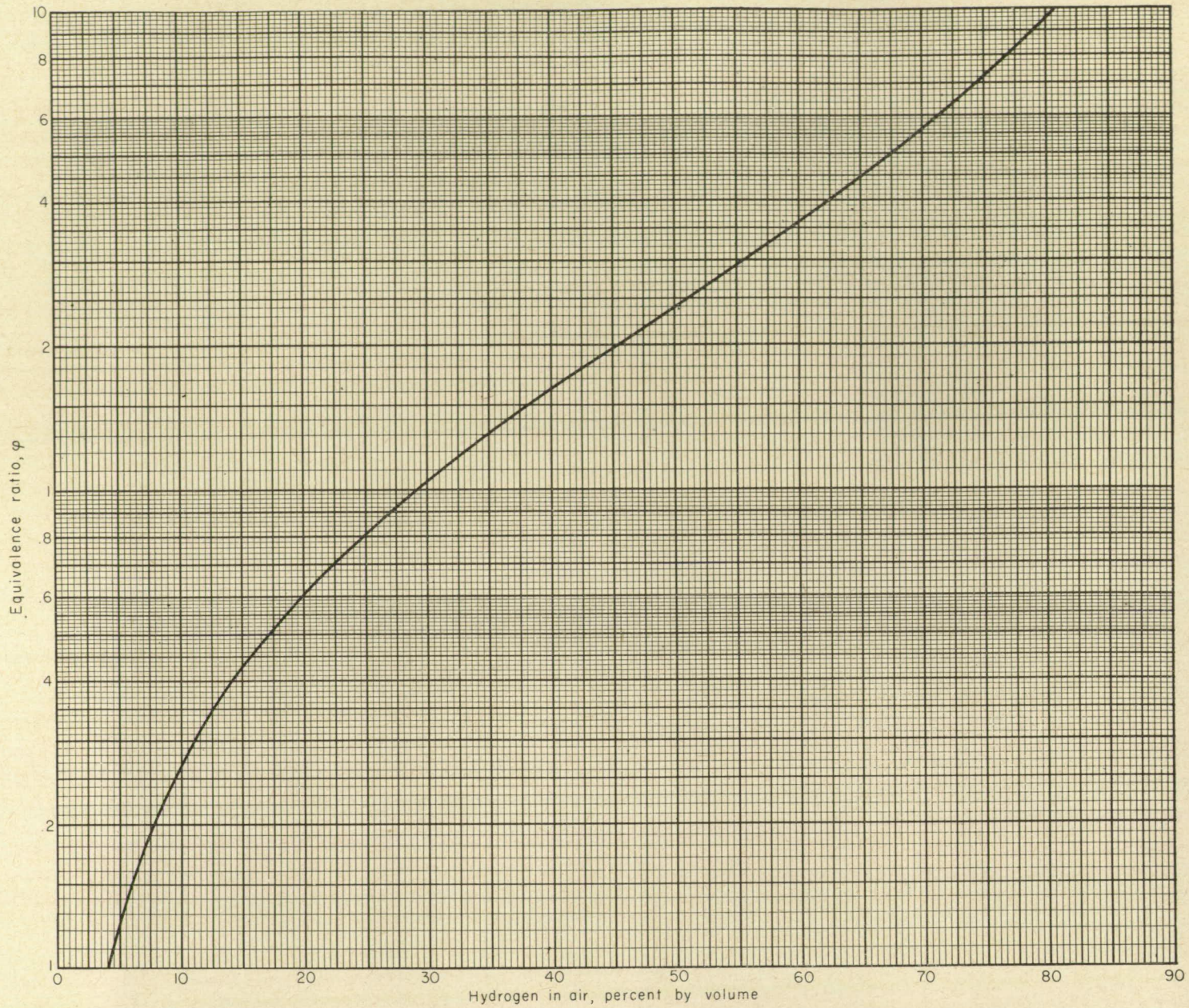


FIGURE 1.—Relation between equivalence ratio and volume-percent hydrogen for hydrogen-air mixtures.

K_1, K_2	constants
$k_1, k_2 \ldots$	rate constants for chemical reactions
L	length of recirculation zone behind flameholder
$[M]$	molar concentration of all molecules other than free radicals
N_o	fuel concentration in unburned mixture, molecules/cm^3
n_o	mole fraction of fuel in unburned mixture
P	pressure, atm
R	gas constant, cal/(mole)(°K)
Re	Reynolds number
T	temperature, °K
T_F	equilibrium adiabatic flame temperature, °K
T_o	initial mixture temperature, °K
t	ignition time available behind flameholder, sec
t^*	characteristic ignition time of mixture, sec
U	average flow velocity
U_L	laminar burning velocity, cm/sec
x, y, z	empirical exponents
τ	ignition lag, sec
φ	equivalence ratio, fuel-oxidant ratio divided by stoichiometric fuel-oxidant ratio (mixture compositions in this paper are given as mole-percent by volume or as equivalence ratio; the relation between these units for hydrogen-air mixtures is shown in fig. 1)
ω	reaction rate
$\bar{\omega}_F$	average reaction rate in flame
Subscripts:	
a	condition a
b	condition b
bo	blowoff
fb	flashback
L	laminar
max	maximum
T	turbulent
300	300° K initial mixture temperature

FLAME TEMPERATURE

One of the most important factors that characterize and influence combustion behavior in any fuel-oxidant system is the flame temperature. Flame temperature, as used here, refers to flames burning at constant pressure with no appreciable external heat losses or gains. Table I and figure 2 give measured and calculated flame temperatures for hydrogen-air mixtures reported since 1930; earlier data are not considered reliable. The data are for a pressure of 1 atmosphere and an initial mixture temperature of 25° C.

The criterion of negligible heat loss makes any experimental measurement very difficult. The values of Passauer (ref. 2, pp. 314 to 316 and 319) are thought to be low because they were obtained with rather large thermocouples. For temperatures above 2223° K, he used a thermocouple made of 0.48-millimeter wire. The hot junction was placed 1 millimeter above the cone tip of a flame on a 4-millimeter cylindrical burner, both with and without a split-flame tube (Smithells separator) that enclosed the primary zone and isolated it from surrounding air.

The sodium-D-line-reversal measurements of Morgan and Kane (ref. 3) were of an approximate nature; furthermore, they were made at a position 4 millimeters above the tip of a flame on a 4.8-millimeter-nozzle burner, which admittedly may not be the locus of maximum temperature. The earlier line-reversal measurements of Jones, Lewis, and Seaman (ref. 4) probably furnish the best experimental values. They

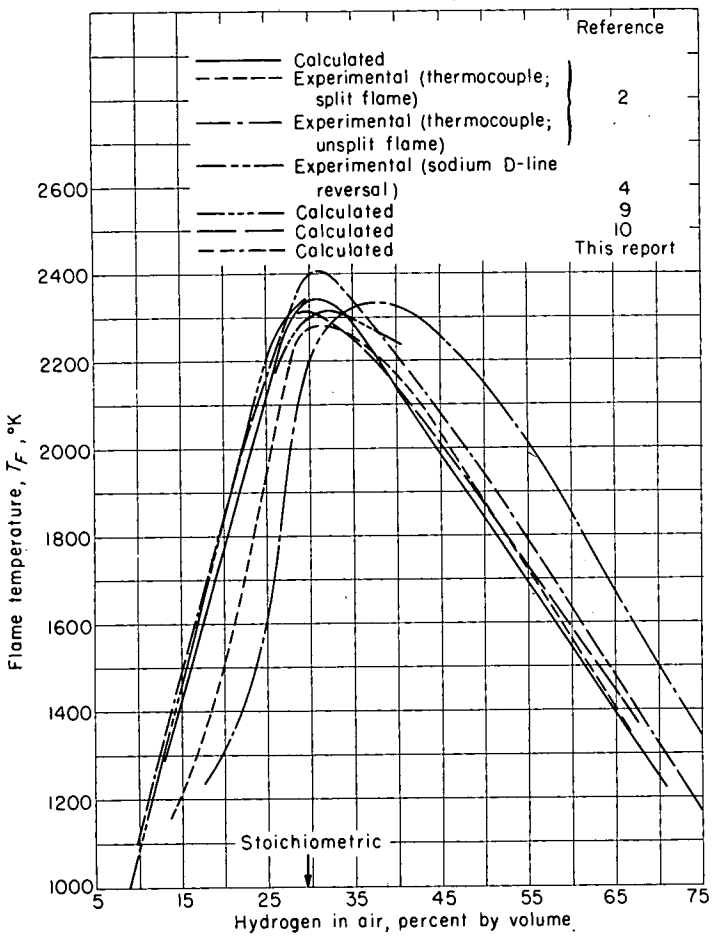


FIGURE 2.—Calculated and measured flame temperatures for hydrogen-air mixtures. Pressure, 1 atmosphere; initial temperature, 25° C.

obtained flame temperatures of 2293° K for the stoichiometric mixture (29.5 percent hydrogen) and 2318° K for the maximum-temperature mixture (31.6 percent hydrogen). Even these values may be somewhat low because of heat transfer to the Meker burner that was used and because of the inherent averaging effect of the line-reversal technique

Calculated flame temperatures, accounting for dissociation, are obtained with the assumptions of an adiabatic system and of chemical equilibrium among all species present in the burned gas. The calculated values are in error if these assumptions are not justified or if the thermodynamic data used are inaccurate. Good agreement between calculated and measured flame temperatures has been obtained by a refined thermocouple method (ref. 5) for very lean propane-air flames. This tends to support the validity of the calculated temperatures. However, various sources of error exist in any method of measuring flame temperature, and it is not always clear just how corrections should be applied. In reference 5 the errors were minimized, and after the raw data were corrected as carefully as possible, a measured temperature of 1530° K was obtained, compared with a calculated value of 1560° K. Equally good agreement cannot be expected in every case, especially in richer mixtures with hotter flames. In short, it is not possible at present to confirm the general validity of calculated flame temperature by experiment. Therefore, the attitude of this report is that the calculated temperatures are valid, particularly for premixed laminar flames large enough so that quenching effects are not significant. Premixed flames on small burners where there is appreciable heat loss, diffusion flames, and turbulent flames will normally fail to reach the full theoretical temperature (ref. 6).

The theoretical hydrogen-air flame temperatures from the recent literature (refs. 3 and 6 to 10) vary considerably. In fact, the difference between high and low values for stoichiometric mixtures is 65° K (table I), which is almost as great as the range of experimental temperatures. This spread is probably due to differences in thermodynamic data and air composition assumed by various workers. The theoretical values computed for this report are 2387° K for the stoichiometric mixture and 2403° K for the maximum-temperature mixture.

For hydrogen-oxygen flames under the same initial conditions the theoretical flame temperature for the stoichiometric mixture (66.7 percent hydrogen in oxygen) is about 3080° K (ref. 6, p. 280, and refs. 8, 11, and 12); the maximum is practically the same. Line-reversal measurements by Pothmann (quoted in ref. 13) agree fairly well with theoretical values. These measurements gave a maximum of 3123° K at 66 percent hydrogen; surprisingly, this is higher than the theoretical value. Lurie and Sherman (ref. 13) reported a lower temperature, 2933° K, by the same method. Their reported maximum-temperature mixture of 78 percent hydrogen in oxygen is widely different from the calculated result and from Pothmann's measurement.

Effect of mixture composition.—Figure 2 shows that the maximum flame temperature is obtained with a slightly rich mixture. Most of the curves presented, including the most recent one calculated for this report, show the maximum at

approximately 31 percent hydrogen in air (φ=1.07). The curves drop off regularly on both sides of the maximum. Flame temperatures below 1300° K are obtained as the flammability limits are approached.

The two experimental curves of Passauer, obtained for open flames and for flames on a Smithells burner with the primary zone enclosed, show an interesting effect: The split-flame burner gave lower flame temperatures than the ordinary open burner for rich mixtures (above 32 percent hydrogen), while below that concentration the reverse was found. Thus, the two kinds of flames may not have comparable temperatures except near 32 percent hydrogen. The differences were thought to be due to diffusion or induced mixing of secondary air from the surrounding atmosphere into the open flame; these effects would tend to raise temperatures for rich mixtures and to lower them for lean mixtures.

According to Byrne (ref. 14), secondary oxygen does not penetrate to the inner cone of a rich flame; however, it does enter the outer mantle, where it reacts with excess fuel in certain rich Bunsen flames (such as methane- or propane-air flames) and raises the temperature. Heat transfer then raises the temperature of the mixture burning in the inner cone and increases the burning velocity. However, Byrne observed little effect of secondary oxygen on the size and shape (and consequently on the burning velocity) of a rich hydrogen-air flame. He concluded that in this case hydrogen molecules and atoms diffuse away from the flame faster than oxygen travels inward (whereas in most hydrocarbon flames the reverse is true); thus secondary burning occurs far from the inner cone and can have little effect upon it. This seeming discrepancy with the results of Passauer may be due to the fact that the burning velocity of hydrogen is not as dependent on temperature as is the burning velocity of hydrocarbons. In other words, the temperature did presumably rise, but not enough to affect the burning velocity perceptibly. Consequently, the conclusion of Passauer (ref. 2) that rich hydrogen flames in the open air have higher flame temperatures than enclosed flames because of admixing of air may be valid.

Effect of initial mixture temperature.—Theoretical adiabatic equilibrium flame temperatures were calculated for various hydrogen-air mixtures over a range of initial temperatures from 0° to 1400° K. The results are shown in figure 3. Rich mixtures are shown by solid lines and lean-to-stoichiometric mixtures by dashed lines. Except for mixtures near stoichiometric, the flame temperature increases almost linearly with initial temperature. In very rich or lean mixtures, where flame temperatures are low and there is little dissociation, flame temperature increases degree for degree with mixture temperature. As the composition approaches stoichiometric, however, dissociation becomes more important and flame temperature becomes less dependent on initial mixture temperature.

Passauer (ref. 2), using the older thermochemical data, calculated a curve for the stoichiometric mixture that is quite similar to the one in figure 3. He obtained approximately the same flame temperature for an initial temperature of 300° K as that from the present calculation, but his curve has greater slope.

Effect of pressure.—Dissociation of the burned gas is favored by reduced pressures, so that flame temperature decreases as pressure is decreased. However, the size of the effect depends strongly on the general level of flame temperatures produced by a given mixture. Figure 4 shows calculated flame temperatures as a function of pressure for hydrogen-air mixtures at initial temperatures of 298°, 600°, and 1000° K. Near-stoichiometric mixtures show a strong dependence of flame temperature on pressure, while lean and rich mixtures have little or no dependence. Mixtures that are quite lean or rich have flame temperatures too low to cause much dissociation, thus, pressure has little effect.

Edse (ref. 12, p. 39) presented a plot similar to figure 4 for a stoichiometric hydrogen-oxygen mixture. The calculations covered pressures from 1 to 100 atmospheres.

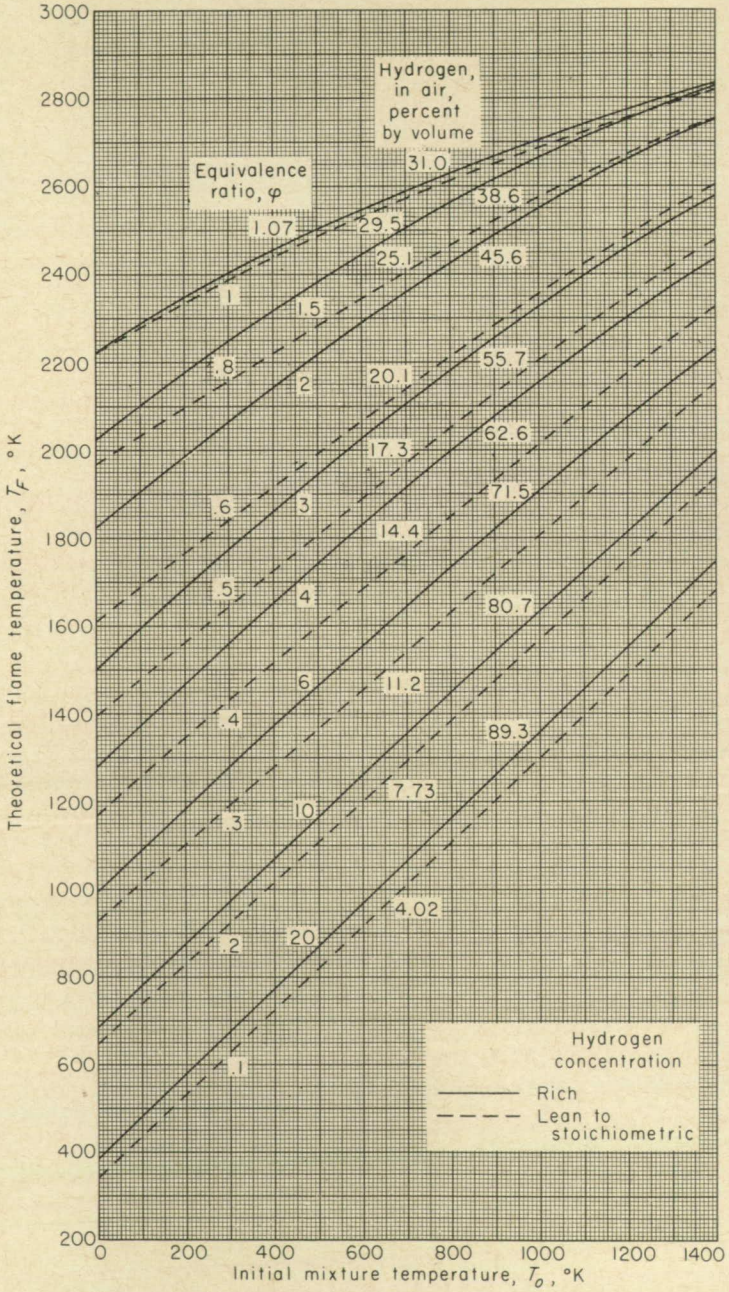


FIGURE 3.—Effect of initial mixture temperature on calculated flame temperature of hydrogen-air mixtures. Pressure, 1 atmosphere.

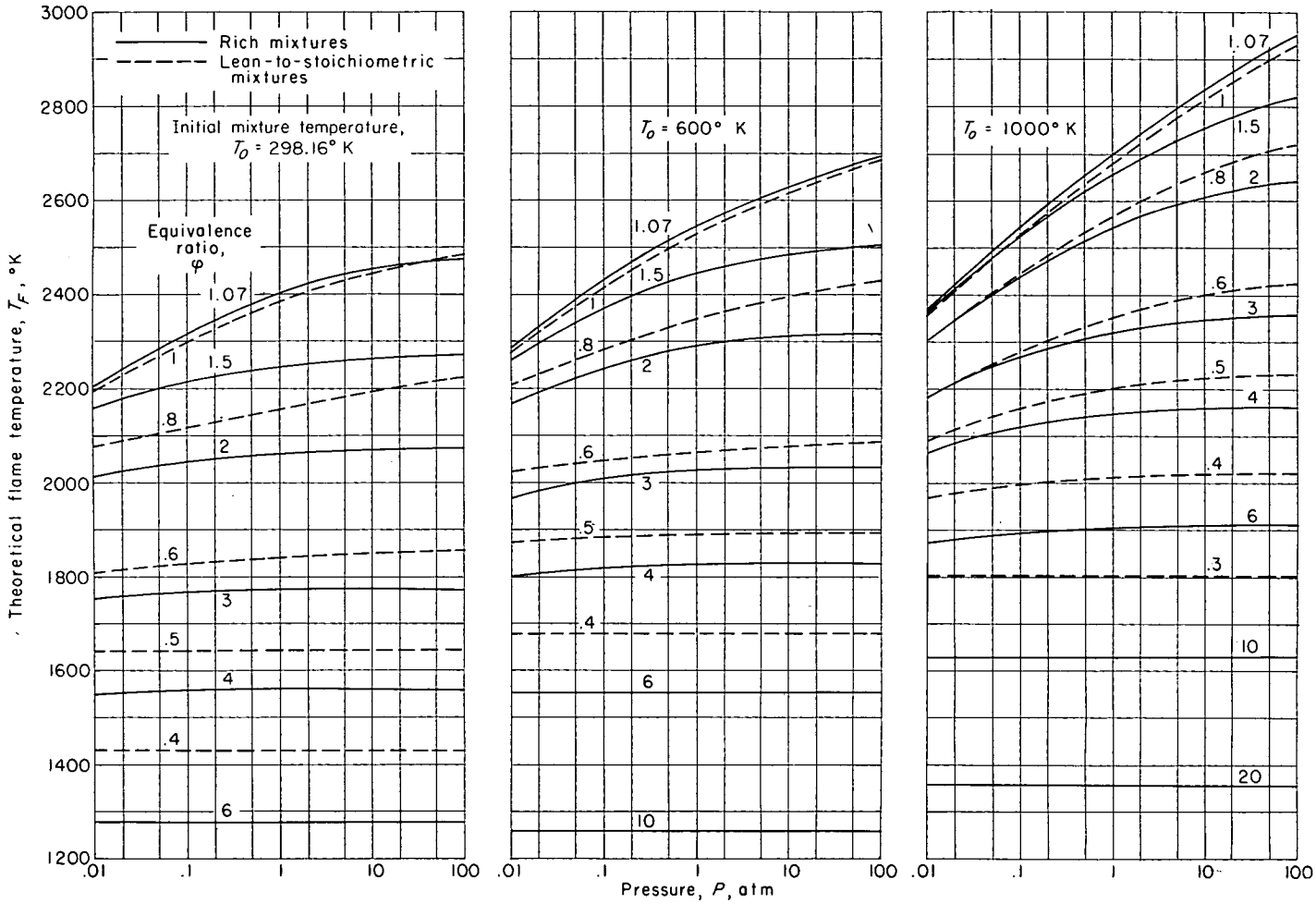


FIGURE 4.—Effect of pressure on calculated flame temperatures of hydrogen-air mixtures.

Recommended flame temperatures.—In view of the experimental difficulties in measuring flame temperatures, as well as the limited range of conditions over which measurements have been made, it is recommended that the calculated values of this report be used. These data are summarized in figure 5, where flame temperature is plotted against hydrogen concentration over the complete range of composition. There are atmospheric-pressure curves for initial temperatures of 0°, 298.16°, 600°, 1000°, and 1400° K. In addition, curves for 0.01 and 100 atmospheres were computed for initial temperatures of 298.16°, 600°, and 1000° K. The calculations for extremely fuel-rich mixtures and for high initial temperatures are included for use in the consideration of novel engine cycles and of flight conditions where inlet temperatures are high.

Burned-gas composition.—The calculations of equilibrium adiabatic flame temperatures for this report also provided data on the composition of the burned gas. The data are listed in table II. Mole fractions at various pressures, initial temperatures, and mixture compositions are given for the following atoms and molecules: H, O, N, OH, NO, N_2, O_2, H_2, and H_2O. Figure 6 is a plot of these data as a function of equivalence ratio for a pressure of 1 atmosphere and an initial temperature of 298.16° K. This figure is presented mainly to show the typical orders of magnitude of the amounts of various constituents in the burned gas. The mole fractions range from about 10^{-6} to values approaching 1. Figure 6 also illustrates how dissociation depends on flame temperature; the mole fractions of the main dissociation products, H, O, and OH, peak not far from the equivalence ratio for maximum flame temperature. The equivalence ratios for these four maximums do not coincide, however, because the dissociation equilibria depend on concentration as well as on temperature.

BURNING VELOCITY

LAMINAR BURNING VELOCITY

The laminar burning velocity is defined as the velocity at which unburned gas of given composition, pressure, and temperature flows into a flame in a direction normal to the flame surface. The normal direction is specified in order to make burning velocity independent of the actual shape of the flame. The aim in measuring laminar burning velocity is always to obtain a physical constant for the mixture that is free of any effects of geometry, external heat sources or sinks, and nature of the flow. The burning velocity should be distinguished from the spatial flame speed, which is simply the gross speed of a flame traveling through a mixture.

Table III gives burning velocities for the hydrogen-air stoichiometric mixture and the mixture of maximum burning velocity at atmospheric pressure and room temperature. Results of 18 investigations covering the years between 1889 and 1956 are reported (refs. 2, 3, 8, 10, and 15 to 27). About

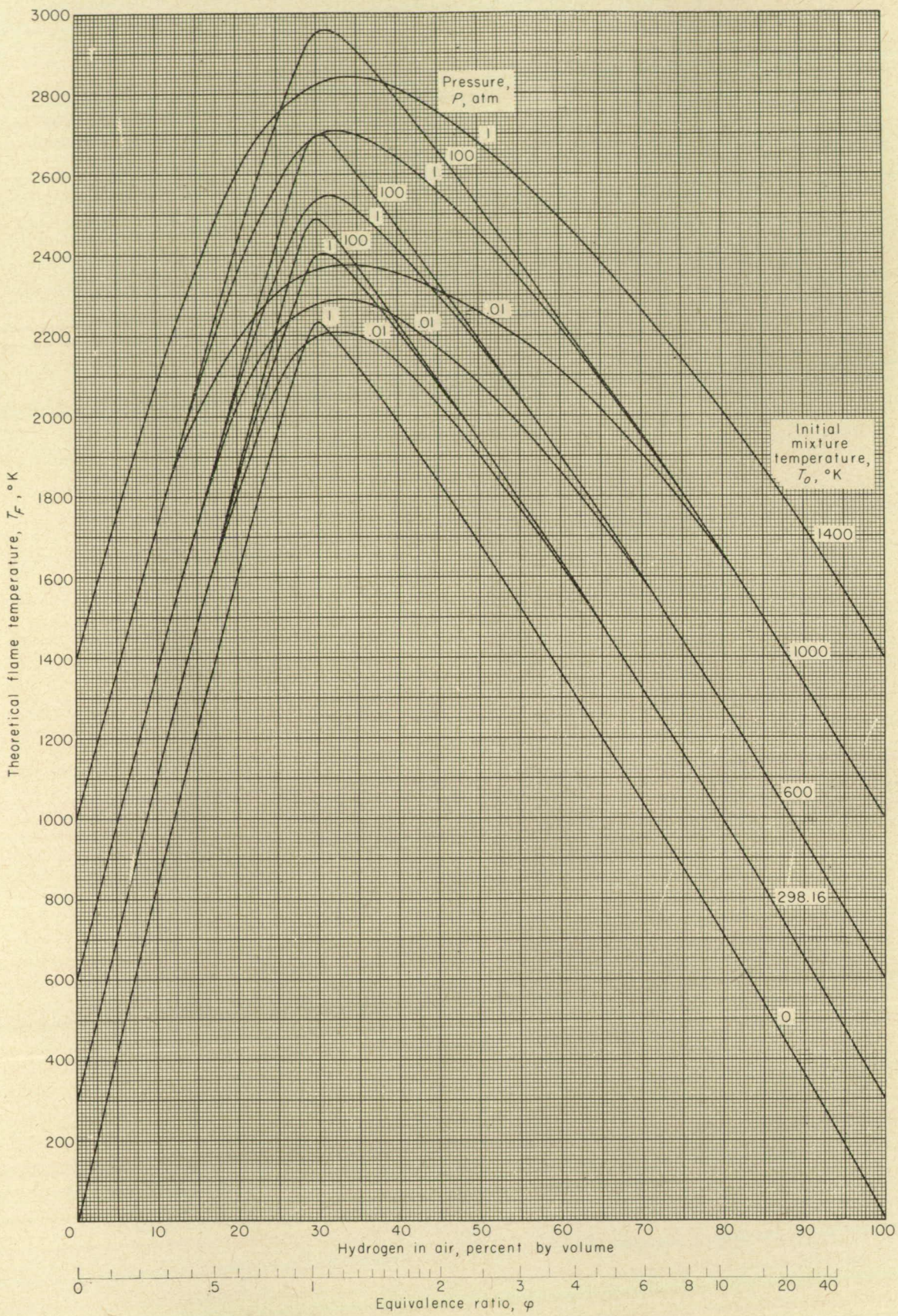


FIGURE 5.—Summary of effects of initial temperature, pressure, and composition on calculated flame temperatures of hydrogen-air mixtures.

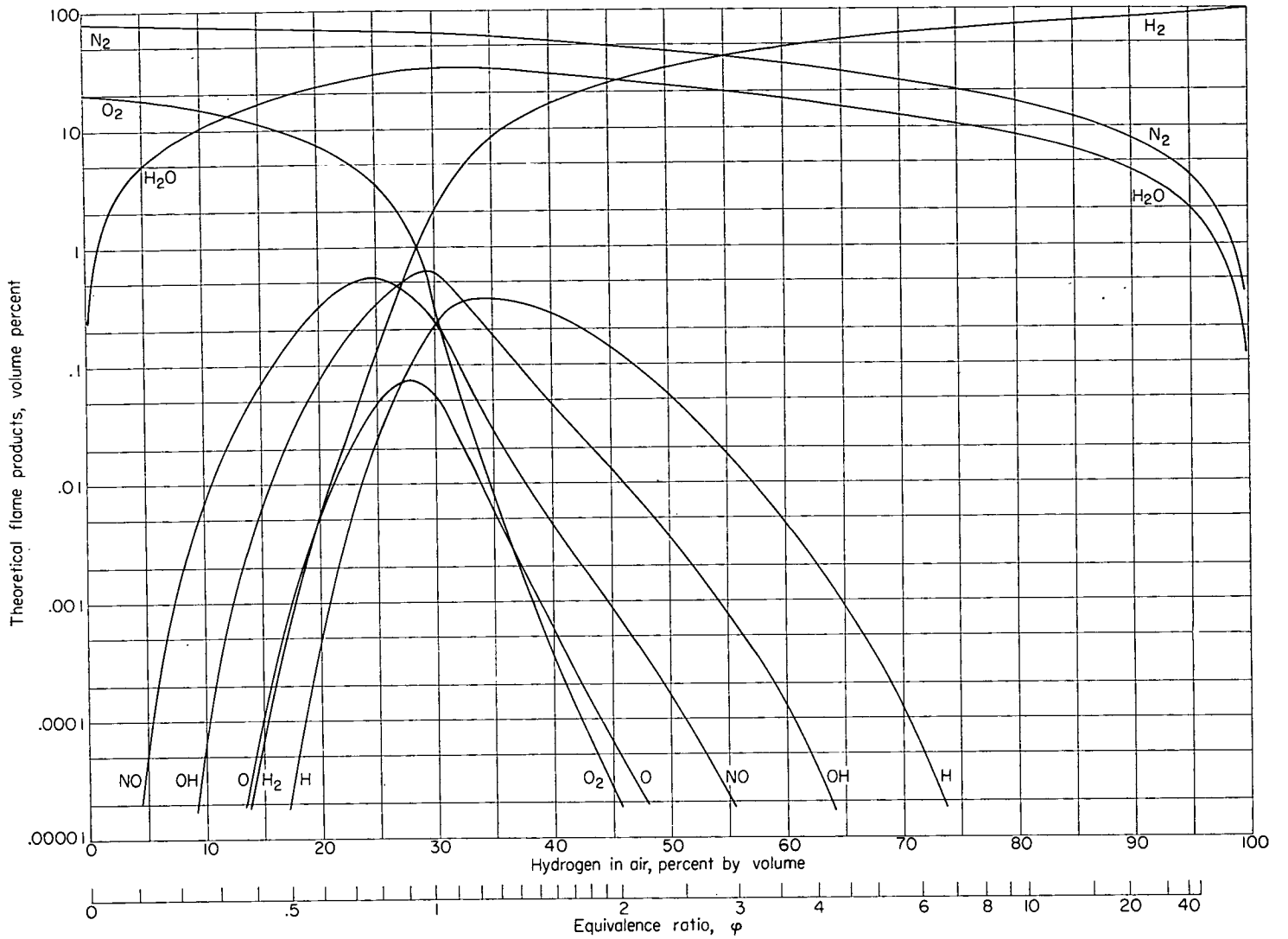


FIGURE 6.—Theoretical adiabatic flame composition for hydrogen-air mixtures. Pressure, 1 atmosphere; initial mixture temperature, 298.16° K.

six spatial flame speeds, starting with the work of Mallard and Le Chatelier in 1881 (ref. 28), have been omitted.

The values in table III have a large spread for a quantity that is defined so as to be a physical constant. The burning velocities range from 153 to 232 centimeters per second for the stoichiometric mixture and from 200 to 320 centimeters per second for the mixture of maximum burning velocity. Furthermore, the reported hydrogen concentrations for the maximum burning velocity vary from 40 to 46 percent. Of course, not all the work was done under strictly comparable conditions, since the ambient pressure and temperature and the degree of saturation with water vapor differed. However, the effects of these variables are thought to be less important than the effects of the experimental method.

An experimental measurement of burning velocity on a Bunsen or nozzle burner in essence requires recording an optical image of some surface in the flame zone and then measuring the area of the surface or its inclination to the flow. All the workers cited in table III used some form of this general method, except Manton and Milliken (ref. 26), who used a spherical constant-volume bomb. Both steps in the burner method are subject to error. At present it is believed that schlieren observation is best, since it gives a flame surface with a temperature close to that of the unburned gas (ref. 29). The best method of measuring the area of the surface is not so clearly defined.

In the bomb method used by Manton and Milliken (ref. 26) the radius of a spherically expanding flame was recorded as a function of time by schlieren photography. Simultaneously, the pressure in the bomb was recorded. From various well-founded thermodynamic assumptions, burning velocities may be calculated from both types of data, and the agreement provides an internal check of the assumptions. In the bomb method there are no heat losses such as occur near the base of a burner flame, and flame curvature effects are minimized by making measurements on flames of large radius.

It is believed that the data of references 3, 10, 23, 24, 26, 27, and 30 represent the best values of burning velocity for hydrogen-air mixtures. These are recent data, and they were obtained by satisfactory experimental techniques. It is not possible at present to choose any single investigation as the best. Therefore, the recommended burning velocities for hydrogen-air mixtures at 1 atmosphere and about 300° K initial temperatures are averages of the values from these seven sources. The recommended maximum burning veloc-

526597—60——76

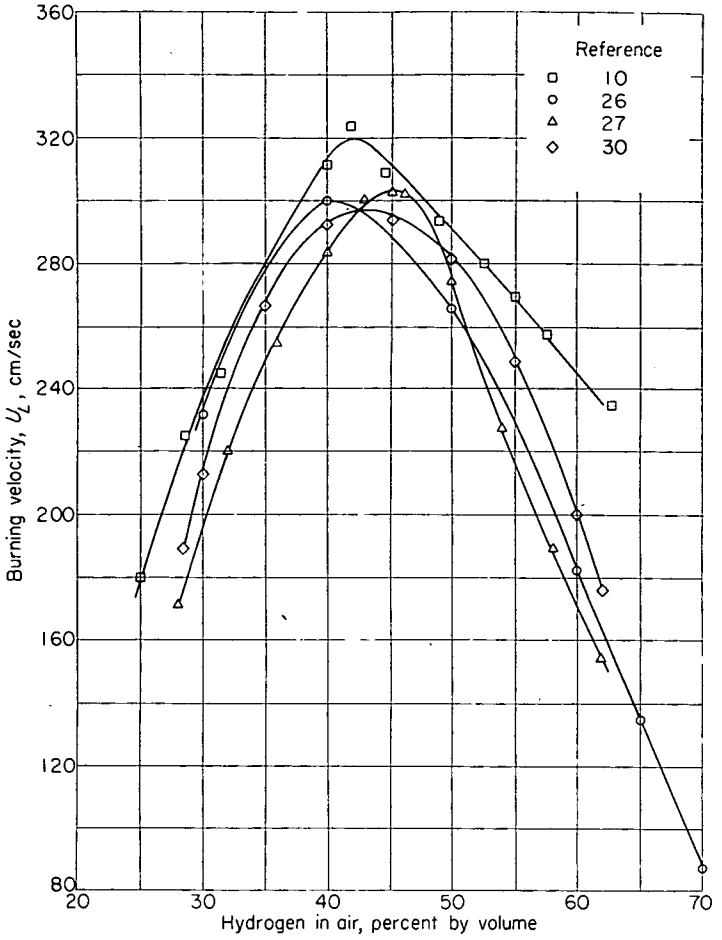


FIGURE 7.—Effect of hydrogen concentration on burning velocities of hydrogen-air mixtures. Pressure, 1 atmosphere; initial temperature, 300° K.

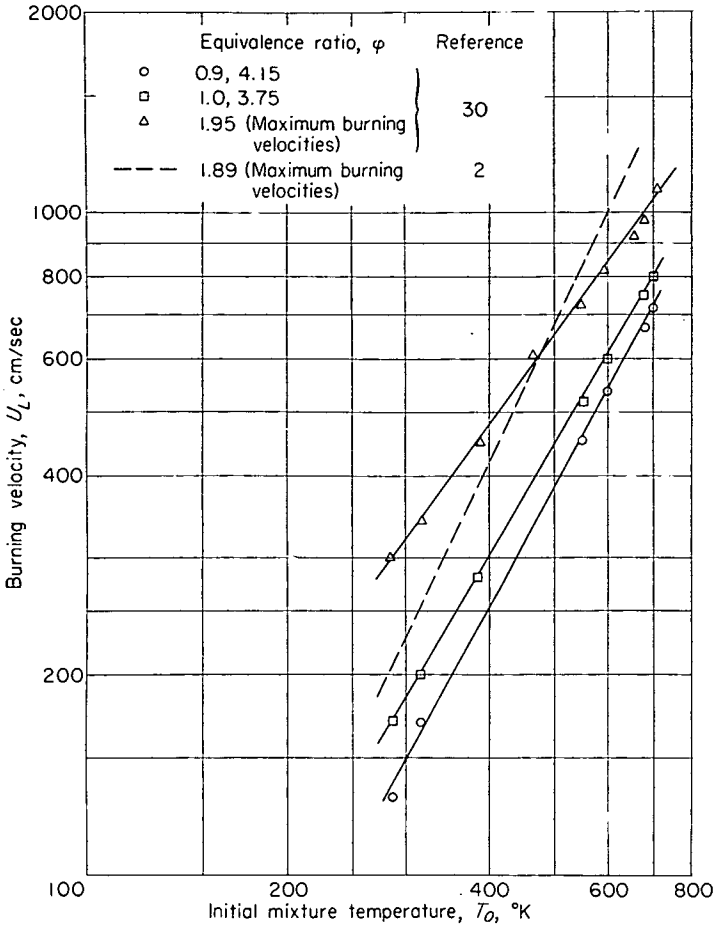


FIGURE 8.—Effect of initial temperature on burning velocities of hydrogen-air mixtures. Pressure, 1 atmosphere.

ity is 310 centimeters per second at about 43 percent hydrogen (φ=1.8). The stoichiometric burning velocities show a larger spread than the maximum burning velocities from the same sources and range from 193 to 232 centimeters per second, with an average of 215 centimeters per second. Since burning velocity changes very rapidly with hydrogen concentration near stoichiometric, the wide range of values is to be expected.

Effect of mixture composition.—Figure 7 shows typical plots of burning velocity against hydrogen concentration taken from four recent investigations (refs. 10, 26, 27, and 30). As already stated, the maximum occurs near a 43-percent hydrogen concentration; the curves fall off smoothly on either side. It should be noted that the maximum burning velocity occurs in a mixture richer than either the stoichiometric mixture or the maximum-flame-temperature mixture. Discrepancies among results of various workers become quite large on a percentage basis, especially for mixtures rich of the maximum-burning-velocity mixture. It does not seem possible to account for these differences at present.

Burning-velocity measurements cannot be extended too far to the lean side of stoichiometric. Because of preferential diffusion effects, the tip of a burner flame may open up in mixtures leaner than 17 percent hydrogen (ref. 31), and a stream of mixture may escape the flame zone without being burned.

Effect of initial mixture temperature.—Figure 8 is a logarithmic plot of burning velocity against initial temperature for several mixtures. The solid lines with symbols are data from reference 30. The dashed line represents the maximum burning velocities of Passauer (ref. 2), which are considered less reliable than the more recent data. It appears from figure 8 that the mixture of maximum burning velocity is least sensitive to changes in initial temperature. The following equation expresses the relation between initial temperature and maximum burning velocity over the range of temperatures given:

$$U_{L.max}=0.09908\ T_o^{1.413} \tag{1}$$

The exponent on T_o is considerably less for hydrogen-air mixtures than for hydrocarbon-air mixtures. For example, expressing some of the data of reference 32 in the form of equation (1) gives temperature dependencies of $U_{L.max}$ of about $T_o^{1.64}$ and $T_o^{1.85}$ for n-heptane and isooctane, respectively.

Effect of pressure.—Measurements of burning velocity at pressures other than atmospheric are difficult; this is especially true for reduced pressures. The experimental difficulties are reflected in large discrepancies in the data of the few workers who have studied hydrogen-air mixtures. Reference 17 reports nearly constant burning velocity at total pressures from 1 to 4 atmospheres. Reference 33 gives burning-velocity values of 164 centimeters per second at

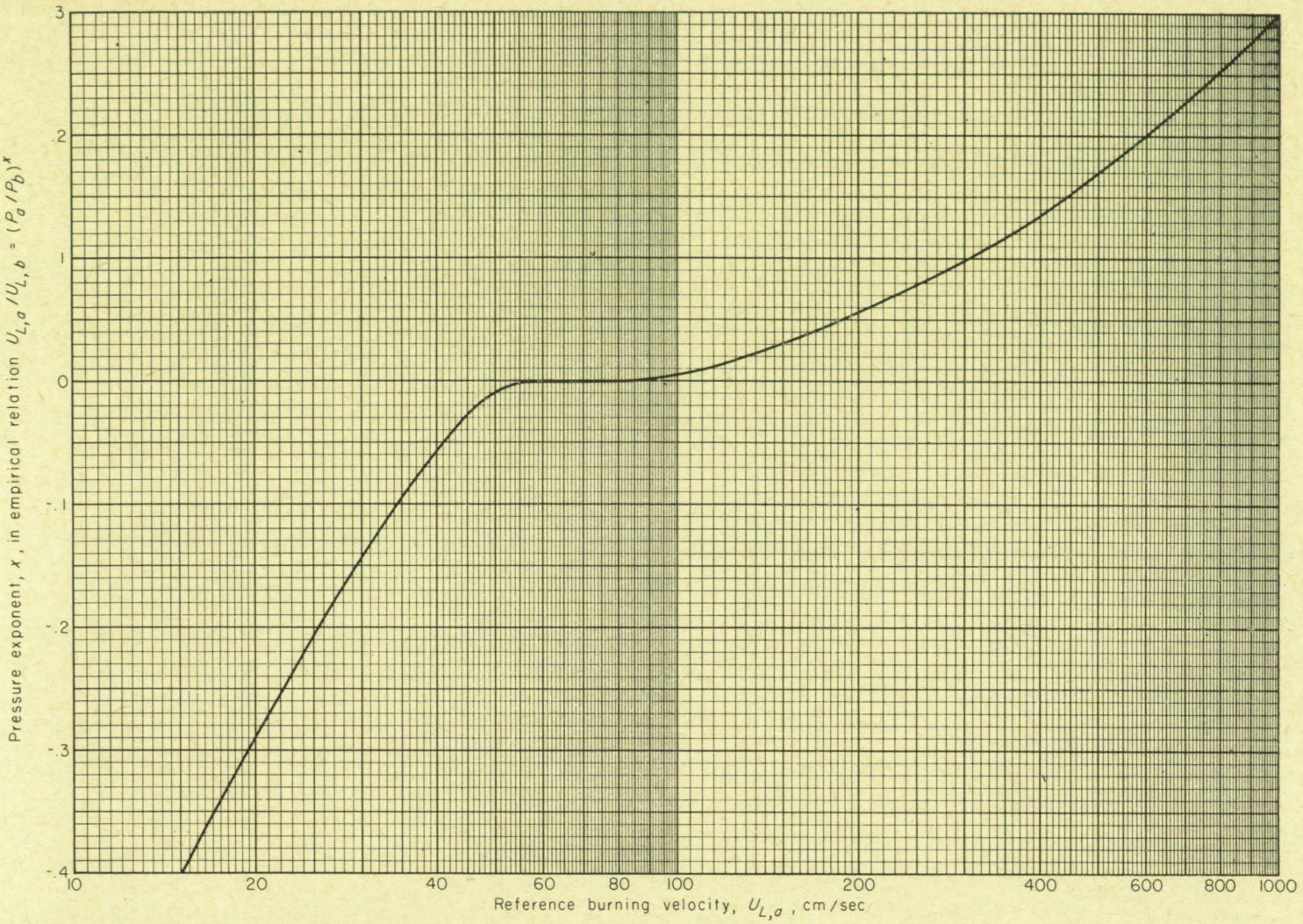


FIGURE 9.—Variation of pressure dependence of burning velocity with reference burning velocity (ref. 26).

0.393 atmosphere and 140 centimeters per second at 1 atmosphere for a mixture with $\varphi=4.78$. Reference 26 reports that the burning velocity of a mixture with $\varphi=3.58$ increased when the pressure was raised from 0.25 to 1.0 atmosphere, and reference 27 gives data showing the same trend between φ of 1.10 and 1.90.

The data of reference 26 are probably most nearly right, because the spherical-bomb technique is not subject to some of the important sources of error that affect results obtained by other methods. Moreover, a previously unsuspected effect was discovered that may explain some of the discrepancies in pressure dependence reported in the literature. It is generally agreed that burning velocity is proportional to the pressure raised to some power. The disagreements concern the value and sign of the exponent. Manton and Milliken (ref. 26) studied many fuel—oxygen—inert-gas mixtures with atmospheric burning velocities from 8 to 1000 centimeters per second and determined x for each mixture from the empirical relation

$$\frac{U_{L,a}}{U_{L,b}}=\left(\frac{P_a}{P_b}\right)^x \tag{2}$$

When these values of x were plotted against the reference burning velocity $U_{L,a}$ (the value at atmospheric pressure), data for all mixtures defined a single curve. The curve, which is reproduced from reference 26 in figure 9, shows that the pressure dependence of burning velocity is variable and depends on the reference burning velocity. Thus, slow-burning mixtures ($U_L<50$ cm/sec) have a negative pressure exponent, and hence U_L increases as pressure decreases; whereas for fast-burning mixtures ($U_L>100$ cm/sec) the reverse is true. In the intermediate range (50 cm/sec$<U_L<$100 cm/sec) there is no effect of pressure. Figure 7 shows that both zero and positive pressure exponents may be expected for hydrogen-air mixtures, depending on the fuel concentration; negative exponents should appear for very rich or very lean mixtures only. In any case, the exponent should be small.

The work of reference 27 agrees qualitatively with that of reference 26 but shows pressure dependence to be much larger. Figure 10 shows burning velocities from references 26 and 27 plotted logarithmically against pressure for four rich equivalence ratios. The data from reference 27 were obtained by a Bunsen burner total-area method, and care was taken to avoid quenching effects from too-small burner tubes. The straight lines obtained support the assumption of reference 26 that the data follow a relation like equation (2); however, the slope x varies randomly between 0.208

and 0.256 for equivalence ratios from 1.10 to 1.90, the average value being 0.23 (ref. 27), whereas figure 9 would predict a slope of less than 0.1.

The cause of the discrepancy between references 26 and 27 is not known. Reference 27 tries to resolve the question with the aid of certain theoretical relations among combustion properties, but the result is inconclusive. One relation favors the small pressure dependence of reference 26, while the other favors the larger dependence of reference 27. In any event, recent work agrees that burning velocity of hydrogen-air flames increases with increasing pressure. Pending further evidence, it is suggested that a pressure exponent of 0.16 may be used to estimate the pressure effect for mixtures near the maximum buring velocity without causing too great an error. The suggested value is the average of those reported in references 26 and 27.

TURBULENT BURNING VELOCITY

A flame in turbulent flow differs considerably in appearance from a laminar flame. Both views with the naked eye and time-exposed photographs show the luminous zone as a brush-like region, thin near the burner port, thicker toward the top of the flame, and of more or less indefinite extent.

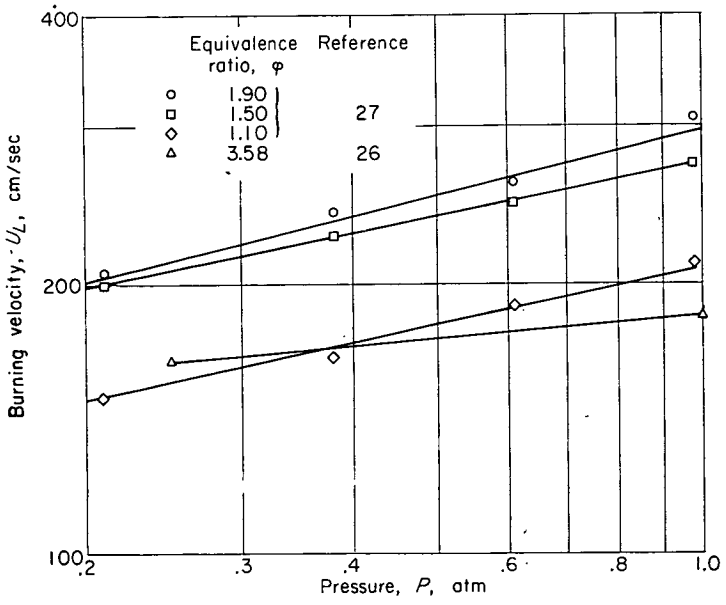


FIGURE 10.—Effect of pressure on burning velocity of hydrogen-air flames.

It is not yet known whether the flame brush represents a thickened reaction zone or a laminar flame that has been wrinkled, distorted, and caused to fluctuate by the turbulence. As a result, there is no flame surface on which burning-velocity measurements should obviously be based, and it is necessary to choose some arbitrary surface.

The only turbulent burning velocities that have been measured for hydrogen-air flames are given in reference 34. A mean flame surface was chosen in images of visible flames, and its area was measured. All measurements were made on a 1.02-centimeter-diameter burner at a Reynolds number of 3500, over a range of pressures from 0.30 to 0.75 atmosphere, and at an equivalence ratio of 1.80. The data are shown in figure 11; the laminar-burning-velocity curve (ref. 27) is included for comparison. As is generally observed, the turbulent burning velocities are higher than the laminar under the same conditions of temperature, pressure, and composition. The turbulent burning velocities appear to depend on pressure a little more than do the laminar, and as a result the extrapolated turbulent line crosses the experimental laminar line. It is very difficult to understand why this should be true; one suspects that turbulent burning velocities based on a mean flame surface may have little meaning at low pressures. Much work needs to be done on the nature of turbulent flames before turbulent burning velocity can have real meaning. At present it is only possible to make the following qualitative statement: For the most part, turbulent flames consume mixture more rapidly than laminar flames; that is, the maximum flow velocity at which the mixture can be completely burned is larger for turbulent flames than for laminar flames.

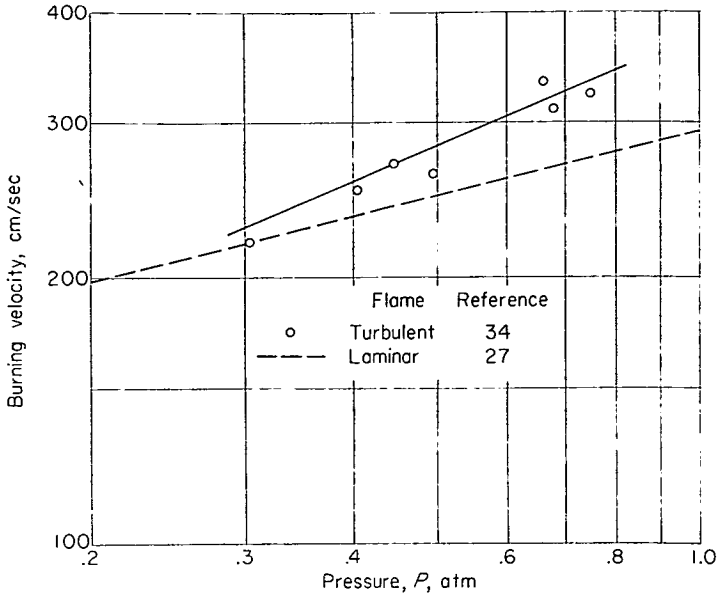


FIGURE 11.—Comparison of turbulent and laminar burning velocities for hydrogen-air mixtures as function of pressure. Equivalence ratio, 1.80.

QUENCHING DISTANCE

Flames are quenched by excessive loss of heat or active particles or both, to adjacent walls. Experiments have shown that flames in a mixture of given temperature, pressure, and composition cannot pass through openings smaller than some minimum size. This size is the quenching distance. Its actual magnitude depends on the geometry; for instance, the minimum diameter for a cylinder is greater than the minimum separation distance of parallel plates. The geometrical relations among quenching distances for ducts of various shapes have been worked out theoretically and agree quite well with experiment (refs. 35 and 36).

Effect of mixture composition.—In figure 12 quenching distances (minimum separation of parallel plates) from reference 37 (pp. 408 to 412) are plotted against fuel concentration. The data were obtained in connection with measurements of ignition energy. The curves show minimum quenching distances at or near stoichiometric composition. The minimum quenching distance at 1 atmosphere and am-

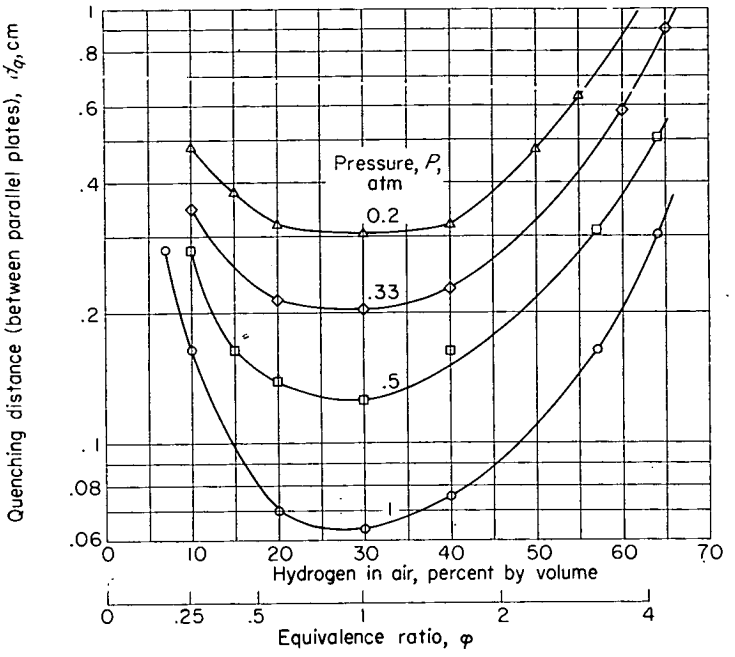


FIGURE 12.—Effect of hydrogen concentration on quenching distance of hydrogen-air mixtures (data from ref. 37).

bient temperature is 0.063 centimeter. From data given by Friedman (ref. 8), a value of 0.057 centimeter may be interpolated for a stoichiometric hydrogen-air mixture. This number, obtained in an entirely different way (by the flash-back technique), agrees fairly well with the value given by reference 37.

For a stoichiometric hydrogen-oxygen mixture, Friedman's data indicate a quenching distance of 0.019 centimeter (ref. 8). It is not known how close this would be to the minimum of the curve.

Effect of pressure.—Figure 13 is a logarithmic plot of quenching distance for parallel plates against pressure. There

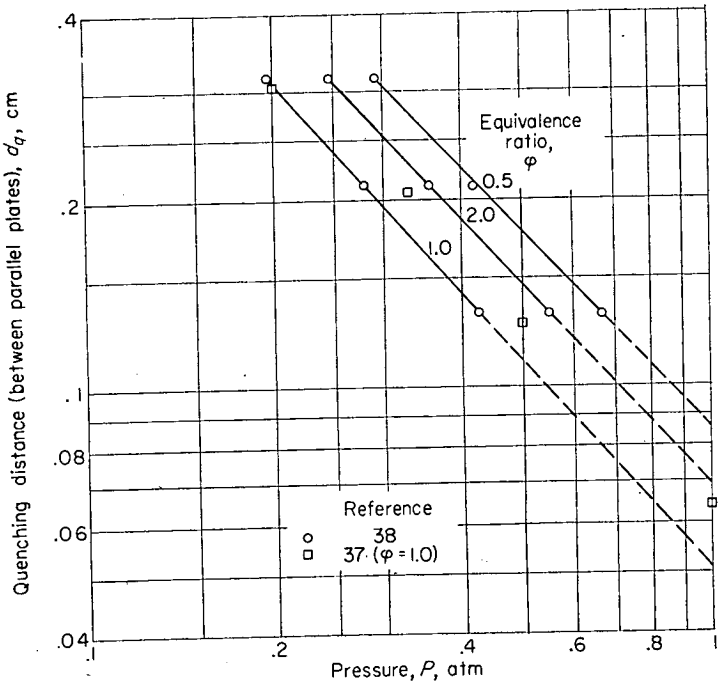


FIGURE 13.—Effect of pressure on quenching distance of hydrogen-air mixtures.

are data for three equivalence ratios from reference 38. Four points from work by Lewis and von Elbe (ref. 37) for an equivalence ratio of 1.0 are also included. It is believed that the data of reference 38 are more nearly correct because of the method used (described in ref. 39).

The straight lines in figure 13 show that

$$d_q \propto P^{-x} \tag{3}$$

The pressure exponent x varies with hydrogen concentration. The data of reference 38 give the following pressure dependencies: For $\varphi=0.5$, $x=1.051$; for $\varphi=1.0$, $x=1.138$; and for $\varphi=2.0, x=1.097$.

Effect of temperature.—No data are available on the temperature dependence of quenching distance for hydrogen-air mixtures. However, it may be assumed that the quenching distance decreases as the temperature of the mixture (and of the surface) is raised; in other words, the flames will be able to pass through smaller openings. This statement is based both on theory (ref. 40) and on the behavior observed for propane-air flames (ref. 41).

Effect of nature of quenching surface.—No appreciable effect of the nature of the surface on quenching distance has ever been found. In an attempt to observe a change for hydrogen flames, Friedman (ref. 8) lined his apparatus with platinum, which is an efficient catalyst for hydrogen atom recombination. No effect was found for the hydrogen-oxygen-nitrogen mixture used.

Flame traps.—In the quenching-distance experiments just discussed, there was no large pressure gradient driving the flame and hot gas, and the flame had to propagate on its own through the constricted space. In practical operations the situation is often quite different. For example, a flame traveling through a long duct filled with combustible mixture may build up a large pressure, and the flame may be driven through a gap narrower than the quenching distance. Flame traps are commonly used to protect such systems. For hydrocarbon-air mixtures fine-mesh screens are often used; hydrogen flames are more difficult to quench, however, and other methods are necessary.

The value of sintered metals as flame traps was studied in the work of reference 42. These traps were able to stop flames in stoichiometric hydrogen-oxygen mixtures, and thus would be even more effective with hydrogen-air flames. Also important is the fact that the sintered-metal traps cause surprisingly small pressure drops.

The results of reference 42 are reported in terms of the limiting safe pressures below which the trap will always stop the flame. A sintered bronze disk 0.235 inch thick, with a statistical particle size of 0.01575 inch and a porosity of 29.6 percent, gave a limiting safe pressure of more than 1 atmosphere for stoichiometric hydrogen-oxygen flames. Little correlation was found between flame-trap effectiveness and porosity, but there was a gain in effectiveness as the disks were made thicker. Sintered bronze was more effective than sintered stainless steel.

The work of reference 42 was of a preliminary nature, and it is not clear how specific the results may have been to the particular apparatus used. It appears at present that the

only sure way to design a flame trap for a given hydrogen-air system is by means of tests on a full-scale model. A word of caution: These sintered disks are *flame* stoppers, and they may not be effective against detonations. (Detonation waves and the transition of flames to detonations are discussed in a later section.)

FLAMMABILITY LIMITS

The rich and lean flammability limits are the fuel concentrations that bound the flammable range at a given temperature and pressure. Mixtures containing more fuel than the rich limit or less than the lean limit will not sustain a flame. No extensive survey of flammability limits was made for the present work, since this had already been done by Coward and Jones (ref. 43).

Flammability limits should be physicochemical constants of a fuel-oxidant combination and should be free of apparatus effects. However, wall-quenching may have an effect on flammability limits. It was therefore desired to delay consideration of the subject until flame quenching had been discussed.

In the usual method of measuring flammability limits (ref. 43), mixtures are ignited at one end of a tube that is wide enough to preclude quenching by an ignition source strong enough to ensure that it is not the limiting factor. The tube is quite long (about 4 ft) so that the observer can be sure the flame does indeed propagate on its own and is not driven by excess ignition energy. If the flame travels the full length of the tube, the mixture is considered flammable. Various mixtures are tested until the flammability limits are defined.

Effect of direction of propagation.—The flammability limits for most fuels vary, depending on whether they are measured for upward- or downward-propagating flames, because convection assists flames traveling upward. For instance, the lean and rich limits of methane are: upward, 5.3 and 13.9 percent by volume in air; downward, 5.8 and 13.6 percent by volume in air (ref. 43). For hydrogen the behavior is different. The rich limit of hydrogen is the same for both directions of flame travel, 74 percent by volume in air (ref. 43). The lean limit is affected, but not in the usual way. It is 9.0 percent for downward propagation (ref. 43), whereas for upward propagation there are two lean limits. One of them is called the limit of coherent flames; it is 9.0 percent (ref. 44) and is the leanest mixture that burns completely. Leaner mixtures down to the noncoherent limit of 4.0 percent hydrogen are still flammable (ref. 44), but the flame is made up of separated globules that slowly ascend the tube. Although these globules do not consume all the fuel, they have to be reckoned with for safety. The noncoherent flames occur because of the high diffusivity of hydrogen; it appears that the flamelets actually consume a mixture richer in hydrogen than the original mixture (refs. 37 and 43).

Flammable range.—The flammable range (i. e., the difference between the rich- and lean-limit concentrations) is exceptionally wide for hydrogen. Coherent flames can propagate in lean hydrogen-air mixtures down to 9.0 mole percent fuel, as already stated. This is an equivalence ratio of about 0.24, as compared with a lean flammability limit of about $\varphi=0.5$ for most hydrocarbon fuels. The very high rich limit, 74 percent or $\varphi=6.8$, is also outstandingly different from those for most ordinary fuels. From figure 2, it may be seen that the lean- and rich-limit flame temperatures are about 1000° and 1200° K, respectively, which are values much lower than those for hydrocarbons (ref. 44). Egerton suggests that these effects peculiar to hydrogen are due to the high concentration of active particles and their high mobility (ref. 44).

Recommended limits at atmospheric temperature and pressure.—As shown by the data collected in reference 43, the various workers who have used the accepted method agree with one another quite well. It is therefore unnecessary to make any further assessment of the data. The following table gives recommended flammability limits for hydrogen in air at atmospheric pressure and about 3000° K:

	Flammability limits, volume percent hydrogen in air	
	Lean	Rich
Upward propagation		
Coherent flame	[a] 9.0	[b] 74
Noncoherent flame	[a] 4.0	
Downward propagation	[b] 9.0	[b] 74

[a] Ref. 44, [b] Ref. 43.

For hydrogen burning in pure oxygen the lean limits are about the same and behave in the same way as those for hydrogen in air. The rich limit for upward propagation is 93.9 percent (ref. 43).

Effect of mixture temperature.—The flammable range is widened by heating the unburned mixtures. That is, the lean limit occurs at lower concentrations and the rich limit at higher concentrations as the mixture temperature is increased. The data of White (ref. 45), which are considered most reliable by Coward and Jones, are plotted in figure 14. These are limits for downward propagation, so that the lean limits refer to coherent flames. There is a linear change in the limits with mixture temperature, and the rich limit is somewhat more strongly affected than the lean. From figure 14 and the flame temperatures of figure 5, it can be seen that the rich limit for all mixture temperatures occurs for mixtures having a nearly constant flame temperature of about 1300° K. The lean-limit flame temperature is lower but more variable; for $T_o=300°$ K, it is 1060° K; and for $T_o=600°$ K, it is 1140° K.

Effect of inert diluents.—By addition of enough inert gas to a flammable hydrogen-air mixture, the mixture can be diluted to nonflammability. Figure 15 shows the limits as a function of the amount of carbon dioxide or of added nitrogen in air (ref. 43). The rich limit is sharply decreased as inert gas is added, whereas the lean limit is scarcely changed. From the coordinates of the "nose" of the curve it may be calculated that no mixture of hydrogen, air, and nitrogen can propagate flame at atmospheric temperature and pressure if it contains less than 4.9 percent oxygen;

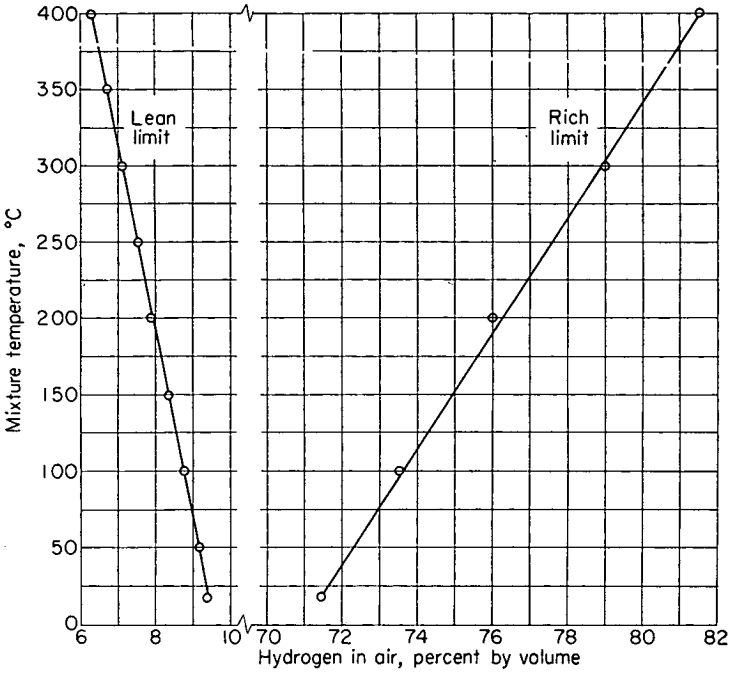


FIGURE 14.—Effect of temperature on flammability limits of hydrogen in air for downward propagation (ref. 45).

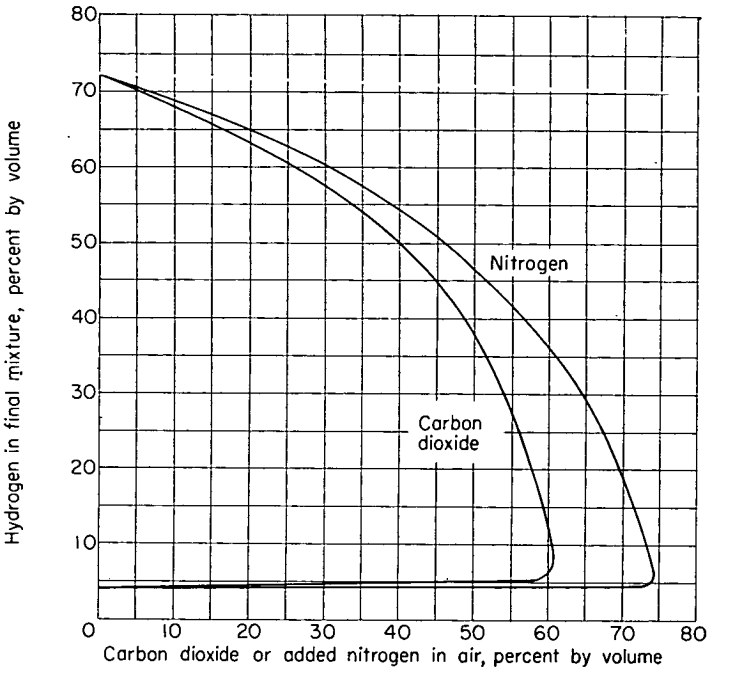


FIGURE 15.—Flammability limits of hydrogen in air diluted with nitrogen or carbon dioxide (ref. 43).

similarly, no mixture of hydrogen, air, and carbon dioxide can propagate flame if it contains less than 7.5 percent oxygen. It thus takes more nitrogen than carbon dioxide to prevent flame propagation, presumably because of the greater heat capacity of the latter. Water vapor behaves approximately like carbon dioxide, even though it is a product of combustion; the oxygen limit in this case is about 7.5 percent at 86° C (ref. 43).

Other diluents are much more effective than nitrogen or carbon dioxide in reducing flammability. "Air" containing 14.8 percent methylbromide or 39 percent dichlorodifluoromethane cannot form flammable mixtures with hydrogen (ref. 46). Such compounds may interfere chemically with combustion reactions and should not be considered merely inert diluents. Reference 43 warns that the result obtained with methylbromide may not apply in practice, because some mixtures of methylbromide and air are themselves flammable with a sufficiently strong ignition source.

Effect of pressures below 1 atmosphere.—Coward and Jones (ref. 43) summarized the literature on effects of reduced pressure on flammability limits. They observed that the flammable range narrowed as the pressure was reduced, gradually at first, and more rapidly below 200 or 300 millimeters of mercury. A minimum pressure was reached, below which no mixture propagated a flame. It is now known that such results are due to wall-quenching. As shown in the section on quenching distance, the walls exert a larger effect at low pressures. It has been found that a plot of "flammability limit" against pressure is merely a curve showing the concentrations and pressures for which the quenching distance is equal to the diameter of the flame tube (ref. 47).

In other words, it appears that the flammability limits are unchanged at reduced pressures and that flame can propagate down to extremely low pressures if the flame tube is large enough. For example, Garner and Pugh (ref. 48) found a

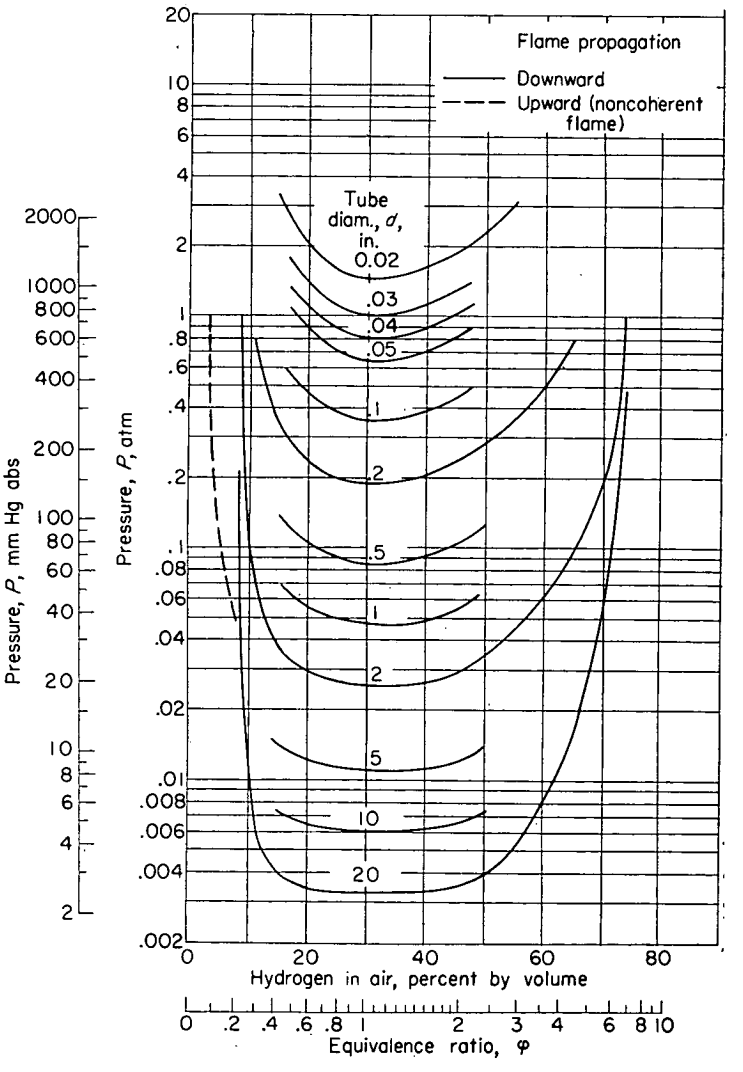


FIGURE 16.—Estimated pressure limits of flame propagation for hydrogen-air mixtures with various tube diameters. Based on extrapolations of quenching data of reference 38.

limit of 4 millimeters of mercury for hydrogen-oxygen flames in a 10-centimeter tube. Presumably this trend would continue to still lower pressures with larger tubes.

The pressure-concentration boundary for flame propagation imposed by quenching in a particular tube is often useful for practical applications. Although such data have not been measured for hydrogen-air flames, they may be estimated from quenching distances. Figure 16 shows estimated curves for downward flame propagation in cylindrical tubes from 0.02 to 20 inches in diameter. The curves were constructed from the quenching distances of reference 38 (measured with parallel plates) multiplied by a geometrical factor of 1.53 (ref. 36) to convert them to quenching distances for cylindrical tubes. Flames are expected to propagate at pressures as low as 2 to 3 millimeters of mercury in a 20-inch-diameter tube (fig. 16). Some of the curves are extended to rich and lean mixtures to illustrate the probable behavior as the rich and lean flammability limits are approached. An estimated curve is also included for upward propagation of noncoherent flames in lean mixtures in a 2-inch-diameter tube. Although figure 16 represents the best estimates that can be made, it is emphasized that the curves for the larger tube diameters were obtained from long extrapolations of the data of reference 38.

Effect of pressures above 1 atmosphere.—The effects of high pressure on flammability limits are not well established. The data surveyed in reference 43 indicate that the flammable range is narrowed by the first increases in pressure, perhaps up to 5 atmospheres; thereafter, the range is gradually widened. In any event, the effects appear to be small. At pressures as high as 100 atmospheres, the limits are not much different from the atmospheric values.

SPARK IGNITION ENERGY

The modern method of measuring spark ignition energy was designed mainly by Lewis and von Elbe and is discussed fully in reference 37. A measured amount of electrical energy in the form of a short-duration capacitance spark is introduced very rapidly into a mixture of given pressure, temperature, and composition and with a given electrode separation. The smallest energy that will ignite the mixture is found, and the process is repeated for other electrode spacings to find the gap for which the energy is least. The data are more reproducible if the electrodes are flanged at the tips with a dielectric material. Then the spacing for minimum ignition is equal to the quenching distance. Lewis and von Elbe were the first to recognize the importance of the quenching effect in such measurements.

The ignition-energy data to be discussed were all obtained by the general method just described. However, they represent ideal conditions that are not met outside the laboratory; therefore, one should not expect the small energies found under these conditions to be sufficient for practical ignition systems. For instance, the gap of a sparkplug is fixed so that it may be less than the quenching distance under some conditions (although ignition is still sometimes possible if enough energy is expended to heat the electrodes and to increase the volume of the discharge). Furthermore, the laboratory measurements are made in quiescent mixtures, whereas in practical cases the gas is usually moving and may be turbulent. Finally, the spark duration may affect the energy needed for ignition. No work is known to have been done on the effects of flow velocity, turbulence level, and spark duration on ignition energies of hydrogen-air mixtures. Studies with propane-air mixtures show that ignition energy increases with velocity and turbulence intensity (ref. 49), and the same trends would no doubt appear with hydrogen-air mixtures. As to the effect of spark duration, for hydrocarbon fuels, sparks lasting 100 to 1000 microseconds give lower ignition energies than slower or faster sparks (refs. 49 and 50).

The remaining variables—composition, pressure, and temperature—have been studied and are discussed in the next paragraphs. It is again pointed out that the small energies cited may not suffice for practical cases, but the trends should apply.

Effect of mixture composition.—Figure 17 is a plot of ignition energy in millijoules against fuel concentration for mixtures at atmospheric temperature and several pressures (ref. 37). The 1-atmosphere curve indicates a minimum energy of 0.019 millijoule at about the stoichiometric mixture and rises steeply toward the lean and rich flammability limits. By way of contrast, the ignition energy of a 70-

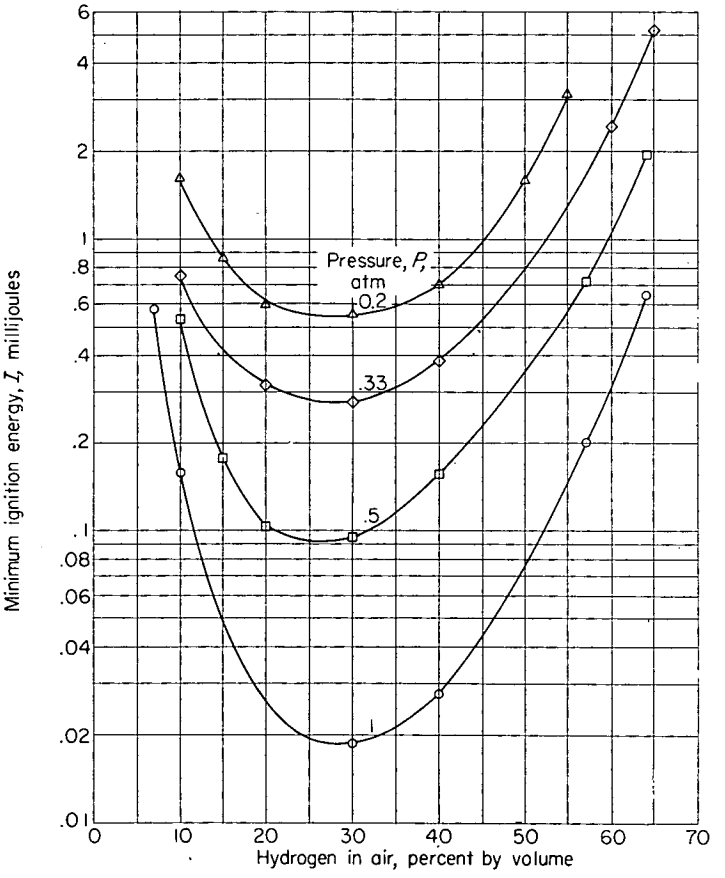


FIGURE 17.—Spark ignition energies for hydrogen-air mixtures at various pressures (ref. 37).

percent mixture of hydrogen in oxygen is 0.007 millijoule (ref. 37), and this is apparently not the minimum of the ignition-energy—concentration curve.

Effect of pressure.—As the pressure is lowered, the ignition energy increases rapidly, as shown by figure 17. Although there are too few points to define the curves closely, it appears that the minimum occurs near stoichiometric regardless of the pressure. The minimum ignition energies change by more than an order of magnitude over the pressure range studied.

Figure 18 is a logarithmic cross plot of data from figure 17 for three equivalence ratios. Although curves might have been faired through the data more closely, a linear relation was assumed in order to show the average effect of pressure. This effect is, approximately,

$$I \propto P^{-x} \tag{4}$$

Data from reference 9 for stoichiometric mixtures are also included; the points are higher than those from reference 37 and also show a greater pressure dependence. There is too much scatter in both sets of data to define the slopes of the lines very well, but in general the exponent x in equation (4) has a value of about 2.

Minimum ignition pressures are sometimes reported for various fuels. These pressures are obtained with fixed electrode spacings and occur either because of quenching effects or because of the limited spark energy available. In other words, it has not yet been shown that there is an absolute low-pressure limit below which ignition can never occur. However, minimum ignition pressures are of practical value. For example, it is possible to ignite the most favorable hydrogen-air mixture down to 0.015 atmosphere by use of a gap 0.28 centimeter wide and 8.64 joules of energy (ref. 51). This is one of the cases mentioned previously, in which the quenching effect may be overpowered by sufficient energy, because the gap is less than the quenching distance at pressures less than about 0.2 atmosphere (fig. 13).

Effect of temperature.—Reference 52 contains the only work found on the effect of mixture temperature on spark ignition energy. The authors state that the following relation holds, except perhaps at temperatures less than 243° K:

$$\log I \propto 1/T_o \tag{5}$$

The position of the minimum in curves of ignition energy against fuel concentration shifted to leaner mixtures as the temperature was increased. The following table gives the data of reference 52 for stoichiometric hydrogen-air mixtures at a pressure of 1 atmosphere:

Mixture temperature, °K	Spark ignition energy, millijoules
273	0.0315
298	.028
373	.018

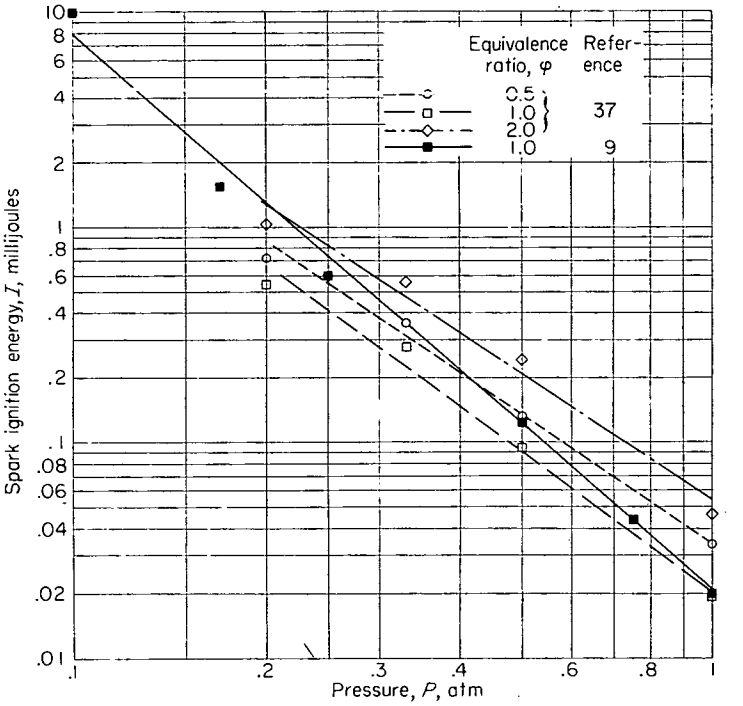


FIGURE 18.—Effect of pressure on spark ignition energy.

FLAME STABILITY

Flames are stable because of interactions among the flame, the flow, and nearby solid surfaces. If a condition of a stable flame seated on a burner port or flameholder is changed (e. g., flow velocity), the flame may not remain seated. With burner flames, flashback or blowoff may occur; with flames on flameholders in ducts, only blowoff is usually encountered, not flashback. The mechanisms of stabilization for the two kinds of flames are different; therefore the data are discussed separately.

FLASHBACK AND BLOWOFF OF BURNER FLAMES

The flashback and blowoff of burner flames are governed by the gradient of flow velocity near the burner wall, as pointed out by Lewis and von Elbe (ref. 37). Burner stability data are, therefore, usually correlated by plotting the critical boundary velocity gradient calculated for the conditions at flashback g_{fb} or at blowoff g_{bo} against fuel concentration. The gradients are given by the following expression (ref. 53):

$$g_{fb,\,bo}=\frac{FU\,Re}{2d} \tag{6}$$

Reference 53 contains friction factors to be used for various regimes of laminar and turbulent flow. For laminar flow in long cylindrical tubes, $F=16/Re$; hence,

$$(g_{fb,\,bo})_L=8U/d \tag{7}$$

Flashback.—Figure 19 shows the only data found for flashback of laminar hydrogen-air burner flames at atmospheric temperature and pressure (ref. 54). Critical boundary velocity gradients are plotted against fuel concentration. The solid curve represents flashback completely into the burner tube. The dashed curves refer to cases in which the flames tilted and partly entered the tube before finally flashing back. In these cases the burner wall was presumably well heated, and thus quenching was reduced and the flames were more prone to flash back; consequently, for a given mixture and burner diameter a higher flow velocity was required to prevent flashback, and $g_{fb,L}$ was accordingly greater.

The effects of reduced pressure on flashback of laminar hydrogen-air flames have recently been studied (ref. 27). In that work tilted flames were considered to have flashed back, even though they only partially entered the burner. Since tilted flames existed over a pressure range of only a few millimeters of mercury, little error was incurred. Figure 20 shows curves of $g_{fb,L}$ against fuel concentration for two reduced pressures; the atmospheric curve from figure 19 is repeated for comparison. The maximum occurs near 38 percent hydrogen regardless of the pressure. The pressure dependence of $g_{fb,L}$ for equivalence ratios from 0.95 to 2.25 can be expressed as follows (ref. 27):

$$g_{fb,L} \propto P^{1.35} \tag{8}$$

All the data discussed were obtained with a water-cooled burner. If the burner is not cooled, the results are not reproducible and depend on the burner size and the

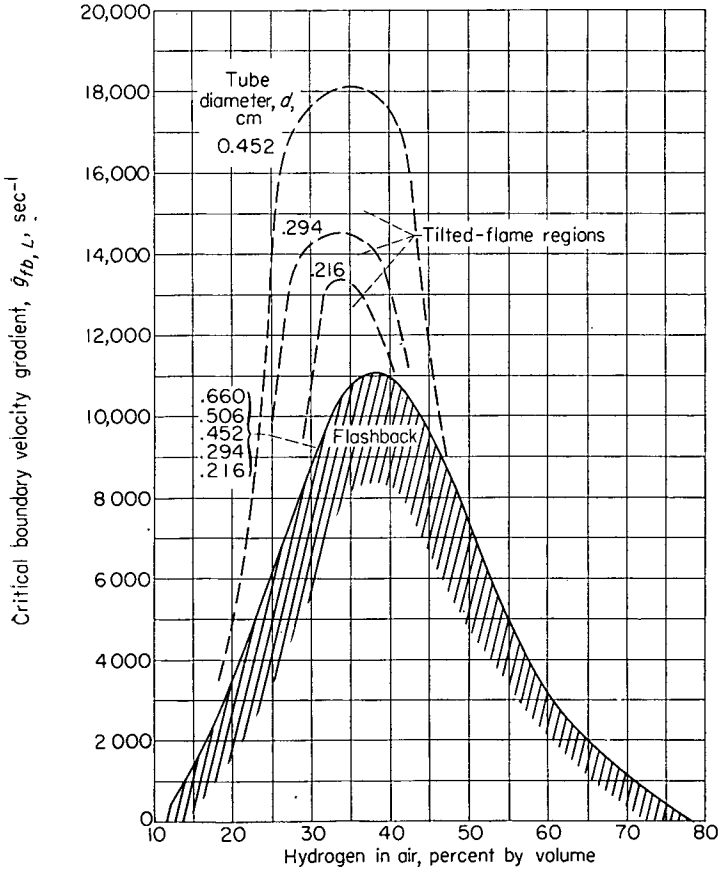


FIGURE 19.—Flashback of laminar hydrogen-air flames at atmospheric pressure (ref. 54).

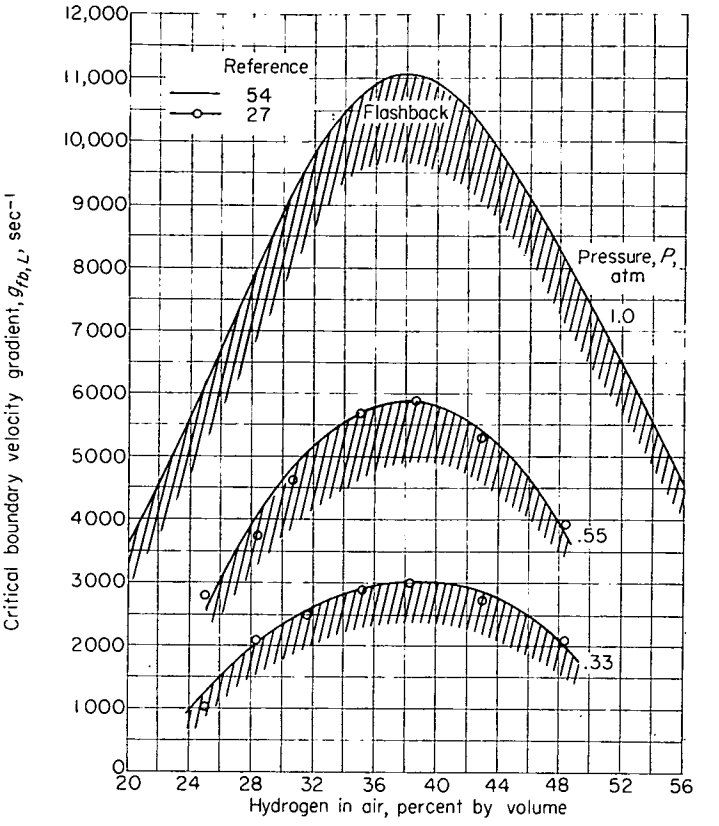


FIGURE 20.—Effect of pressure on critical boundary velocity gradient for flashback of laminar hydrogen-air flames.

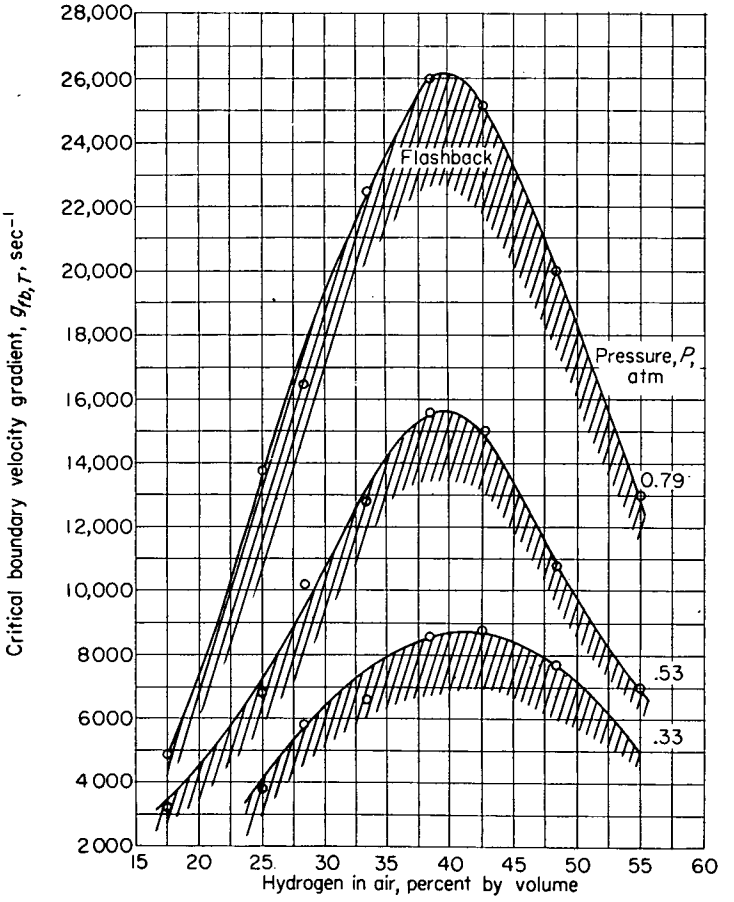


FIGURE 21.—Effect of pressure on critical boundary velocity gradient for flashback of turbulent hydrogen-air flames (ref. 34).

thickness and material of the burner wall. Such effects were studied by Bollinger and Edse for hydrogen-oxygen mixtures (ref. 55).

Reference 34 extends the study of flashback at reduced pressures to turbulent flow. The critical boundary velocity gradients for flashback $g_{fb,T}$ were calculated by means of equation (6) by use of the appropriate friction factor. In figure 21 data from reference 34 for three pressures are plotted against mole percent of hydrogen in air. Comparison of figure 21 with figure 20 shows that the values of $g_{fb,T}$ are much larger than those of $g_{fb,L}$ but that the peaks of the curves occur at about the same concentration. Reference 34 reports the following pressure dependence of $g_{fb,T}$:

$$g_{fb,T} \propto P^{1.31} \tag{9}$$

Within experimental error the exponent is the same as that for laminar flames (eq. (8)). Therefore, the following relation holds, regardless of pressure, burner diameter, and composition:

$$\frac{g_{fb,T}}{g_{fb,L}} = 2.8 \tag{10}$$

It is hard to explain why $g_{fb,T}$ should be almost three times as large as $g_{fb,L}$. Turbulent burning velocities are not enough greater than laminar burning velocities to account for equation (10). Reference 34 tentatively concludes that the explanation lies in the penetration of the flame into the laminar sublayer at the burner wall and that the flame approaches the wall more closely in turbulent then in laminar flow.

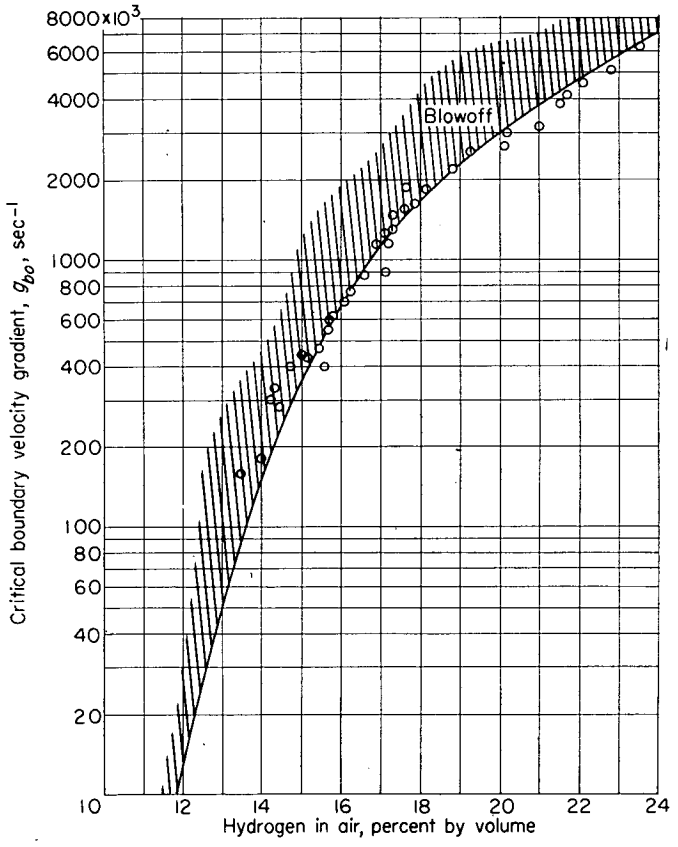


FIGURE 22.—Blowoff of hydrogen-air Bunsen-burner flames at atmospheric pressure (refs. 54 and 56).

Blowoff.—In figure 22 the known data for blowoff of hydrogen-air burner flames at atmospheric pressure are shown as g_{bo} plotted against fuel concentration. The work was done by von Elbe and Mentser (ref. 54), who correlated their data in terms of g_{bo} as calculated by equation (7), the simple equation for laminar flow. However, the points they took in the turbulent flow regime fell off the curve. It was later shown by Wohl, Kapp, and Gazley (ref. 56) that all the data would fall nicely on a single curve if g_{bo} were calculated by the correct expression, equation (6). It is the latter curve that is reproduced in figure 22. For laminar flow, equation (7) was used; while for turbulent flow, the gradient was calculated from equation (6) in the following form:

$$g_{bo,T} = \frac{0.023\, Re^{0.8} U}{d} \tag{11}$$

The data cover only a limited range of hydrogen concentrations (those lean to stoichiometric). However, on the basis of work with other fuels, the blowoff curve for open burner flames is expected to level off with increasing equivalence ratio; at some rich equivalence ratio blowoff would stop and would be replaced by flame lifting (ref. 56). This would occur because of dilution of rich mixtures by ambient air. If ambient air is excluded, as in a Smithells burner, the blowoff curve peaks at a concentration near that for maximum burning velocity, just as does the flashback curve (see figs. 19 to 21).

Further burner blowoff data, obtained at reduced pressures in both laminar and turbulent flow, are reported in reference 34. These data do not fit into a simple correlation with boundary velocity gradient, such as the one shown in figure 22. Blowoff of hydrogen-air flames from burners is not fully understood, and the theoretical model (ref. 37), which leads to the concept of a critical boundary velocity gradient, may have to be modified (ref. 34).

BLOWOFF OF CONFINED FLAMES FROM FLAMEHOLDERS

Flames held on bluff bodies in ducts owe their stability to the recirculation zone behind the flameholder. This zone may be thought of as a pilot that keeps the main flame established as long as it is able to ignite the mixture flowing past. Blowoff occurs if the main stream flows so fast that sustained ignition cannot be achieved. The flow velocity at which this condition arises depends on the size and shape of the flameholder as well as on the temperature, pressure, and composition of the incoming mixture.

Most flameholder blowoff data are correlated on a single curve by plotting fuel concentration against a parameter of the form

$$\frac{U_{bo}}{D^x P^y T_o^z} = f(\varphi) \tag{12}$$

where x, y, and z are empirical exponents, all positive in sign (ref. 53).

DeZubay reports the following correlation parameter for blowoff of hydrogen flames from disk-type flameholders in reference 57:

$$\frac{U_{bo}}{D^{0.74} P^{0.61}} = f(\varphi) \tag{13}$$

(The data are not given in ref. 57, however.) The work on which this parameter is based was done at reduced pressures. The effects of mixture temperature were not studied. DeZubay points out that the maximum value obtained for the parameter is 11 times as great as the corresponding maximum value for propane-air flames, an effect that reflects the much greater stability of hydrogen flames.

Reference 58, which deals with the effects of the diameter of water-cooled cylindrical-rod flameholders, found that there are the following two separate regimes of flameholder stability:

(1) Laminar-flame regime. The composition of the mixture burning in the recirculation zone behind the flameholder is affected by molecular diffusion. Since hydrogen diffuses more readily than oxygen, in contrast to almost all ordinary fuels, small flameholders actually stabilize hydrogen flames to higher flow velocities than do larger flameholders at a given lean equivalence ratio.

(2) Turbulent-flame regime. At a Reynolds number near 10^4 the recirculation-zone shear region becomes turbulent. The stability behavior of lean hydrogen flames reverses, and larger flameholders become more effective. Zukoski (ref. 58) concludes from an examination of the literature that for mixtures near stoichiometric the blowoff velocity for any fuel varies approximately as the square root of the flameholder diameter in the turbulent-flame regime. His data are not complete enough to support this conclusion for the specific case of hydrogen-air flames; however, DeZubay's statement that $U_{bo} \propto D^{0.74}$ for hydrogen flames supported on disks (ref. 59) is in general agreement with Zukoski's conclusion.

These points are perhaps clarified by figure 23, which shows data adapted from reference 58. It appeared that the blowoff velocities and rod diameters corresponding to low Reynolds numbers could be correlated roughly by the parameter $U_{bo}/D^{-0.384}$. (Note the negative diameter exponent, which agrees with the discussion just given of the laminar-flame regime.) This parameter was accordingly plotted against equivalence ratio. Solid data points correspond to flow velocities and rod diameters such that $Re > 10^4$, and open data points correspond to those such that $Re < 10^4$. It is clear from figure 23 that two blowoff curves are obtained. One is defined by points for which $Re > 10^4$, and the other by points for which $Re < 10^4$.

The fact that flames were stabilized at very lean equivalence ratios (fig. 23) provides added proof that the recirculation zone is enriched by diffusion. The mixtures were homogeneous and would not ordinarily be expected to support combustion below the flammability limit for coherent flames (i. e., below $\varphi \approx 0.24$).

Figure 23 also makes it clear that much work remains to be done on the flameholder stability of hydrogen-air flames; the data are confined to lean mixtures and small flameholders. The difficulty is that the flames are extremely stable, and large air-handling facilities are needed to provide flows high enough to cause blowoff.

DETONATION PROPERTIES

Under certain conditions an ordinary flame traveling through a vessel filled with combustible mixture can transform into a detonation. The detonation wave then advances at several times the speed of sound in the unburned mixture.

Whereas in ordinary flames there is a small pressure drop from the unburned to the burned gas, in a detonation there is a very considerable pressure rise. The calculated ratio of pressure behind the wave, in the burned gas, to that ahead of the wave is 18 for a stoichiometric hydrogen-oxygen mixture and about 15 for a stoichiometric hydrogen-air mixture (ref. 37, p. 607). Moreover, there is a strong convective flow of burned gas following the wave. When such a pressure wave meets an obstacle, the momentum of the burned gas is added to the pressure effect, and very large forces may be exerted.

The reasons for the transformation from ordinary burning to detonation are not fully understood. In the usual laboratory experiments the strength of the ignition source and the diameter and surface roughness of the tube affect the runup distance (the distance from the igniter at which detonation occurs). These variables are, therefore, carefully controlled. The flame, ignited with a minimal ignition source, must travel a considerable distance in a smooth tube before

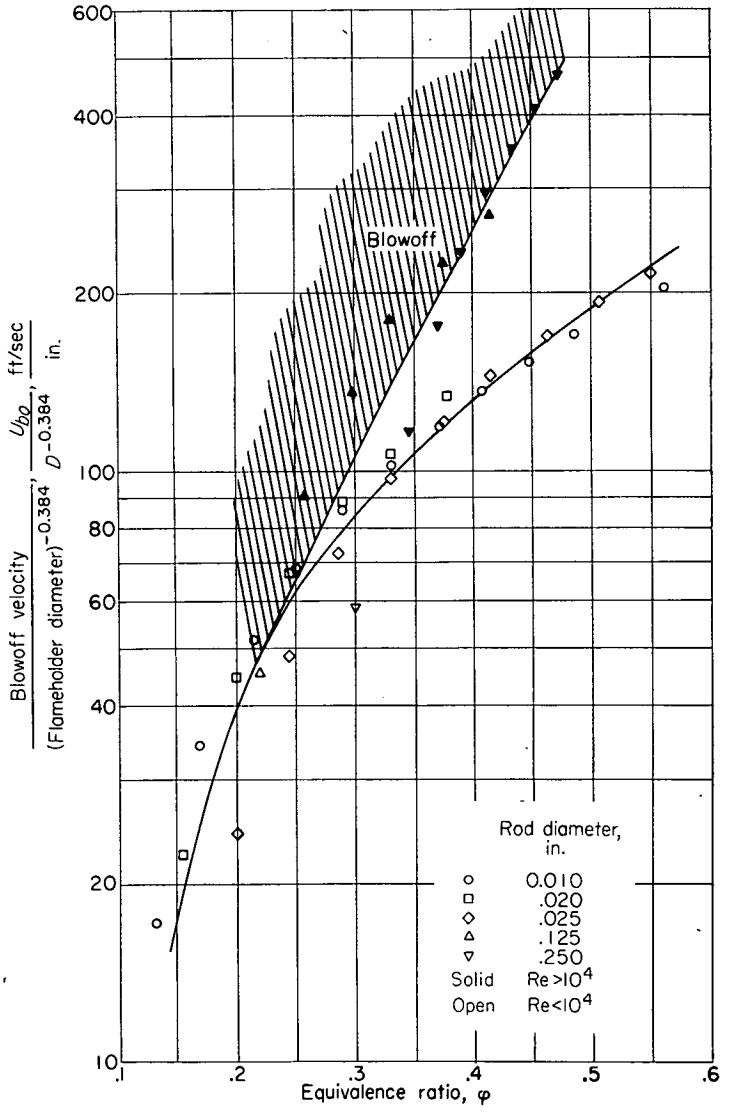


FIGURE 23.—Blowoff of lean hydrogen-air flames at atmospheric pressure from water-cooled cylindrical rods (ref. 58).

detonation occurs. For a stoichiometric hydrogen-oxygen mixture, for example, the flame must travel 70 centimeters in a 25-millimeter tube at an initial pressure of 1 atmosphere (ref. 37, p. 588). The runup distance decreases with increasing pressure.

In practical cases, however, these distances probably do not apply. Excess ignition energy may tend to drive the flame, and rough walls may cause the gas flowing ahead of it to become turbulent. Both factors would tend to shorten the distance for runup to detonation. Thus, one should not count on a definite runup distance; it is safer to assume that the possibility of detonation always exists if the mixture is within the limits of detonability. However, the onset of detonation could be delayed by making the tube walls of an acoustically attenuating material, such as porous sintered bronze (ref. 60). The runup distance could be increased by as much as a factor of 2. Another safety device is a sudden enlargement in a duct. Reference 61 shows that detonation waves traveling through stoichiometric hydrogen-oxygen mixtures in a 7-millimeter tube were transformed to slow-moving flames on passing an abrupt transition to a larger tube. However, if the larger tube were long enough, a new transition to detonation would subsequently occur.

Figure 24 shows detonation velocities in hydrogen-air and hydrogen-oxygen mixtures plotted against fuel concentration (ref. 37, pp. 585 and 586). The limits of detonability are also shown. For hydrogen-air mixtures these are 18.3 and 59.0 percent, and for hydrogen-oxygen mixtures, 15 and 90 percent. Since these concentrations are within the flammability limits, not all flammable mixtures are detonable. It is interesting to note that the detonation velocity does not have a pronounced peak at some favored equivalence ratio, as burning velocity does.

It is also noteworthy that detonation velocity depends much less on temperature and pressure than does burning velocity. This can be seen from the data in table IV (ref. 37, p. 583). A temperature increase from 283° to 373° K at constant pressure actually causes a slight drop in detonation velocity, perhaps because the density decreases. At constant temperature the velocity apparently increases slowly with pressure. The same conclusion is reached in reference 62, which extends the study of hydrogen-oxygen mixtures to a pressure of 10 atmospheres. The changes, although consistent in direction, are not far outside the expected error of the measurement.

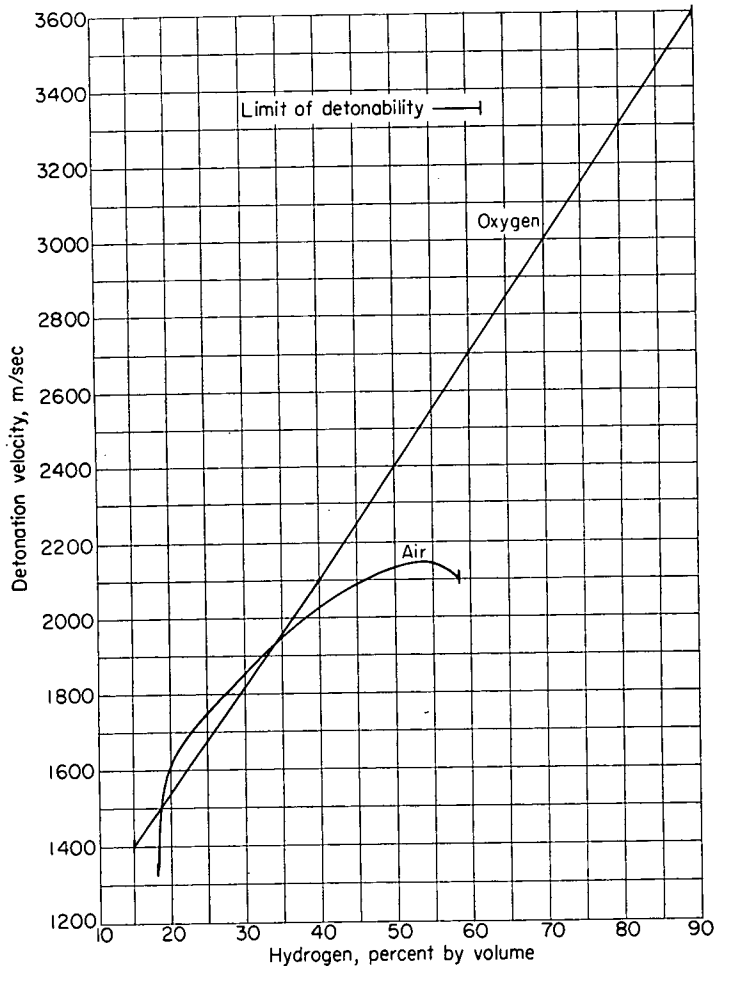


FIGURE 24.—Detonation velocities of hydrogen-air and hydrogen-oxygen mixtures (ref. 37).

EXPLOSION LIMITS, SPONTANEOUS IGNITION, AND THE CHEMISTRY OF HYDROGEN OXIDATION

EXPLOSION LIMITS

Description of phenomenon.—When heated to a high enough temperature, a mixture of hydrogen and oxidant may spontaneously ignite after the lapse of some time called

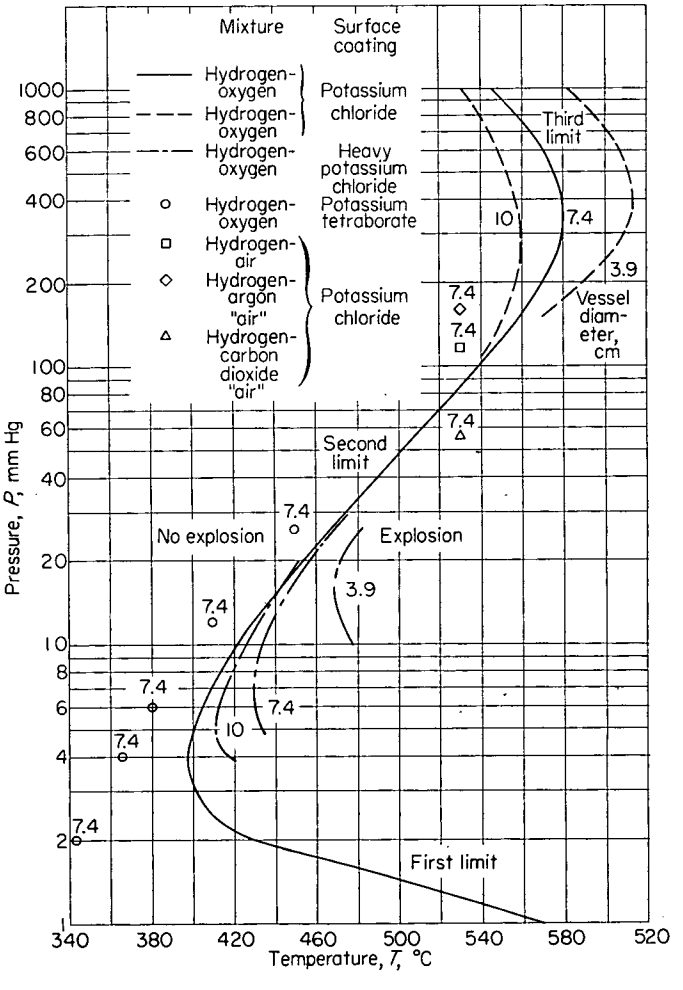


FIGURE 25.—Explosion limits of stoichiometric hydrogen mixtures (ref. 37).

the ignition lag. But with certain combinations of pressure and vessel size, the mixture may fail to ignite at a temperature that would cause ignition under other conditions; this is the phenomenon of explosion limits. It is not in the province of this report to give a thorough review of explosion limits; this has been done elsewhere (e. g., ref. 37). In the present report the phenomenon is described, some data are shown, and some of the important conclusions as to the chemistry of hydrogen oxidation are presented.

Explosion limits are measured in closed vessels at relatively low temperatures (usually 600° C or less). The ignition lags are reasonably long at such temperatures; in fact, as is pointed out later, ignition lags are effectively infinite.

Figure 25 is a collection of curves of explosion limits as a function of temperature and pressure (ref. 37). Consider the solid curve, which is for a stoichiometric hydrogen-oxygen mixture in a spherical vessel 7.4 centimeters in diameter lightly coated with potassium chloride. Along a vertical line of constant temperature there is at first no explosion. Then at some low pressure the first explosion limit is reached, and the mixture remains explosive with increasing pressure until the second limit is reached. Above the pressure of the second limit (which increases with increasing temperature) the mixture is nonexplosive and only undergoes slow reaction up to the pressure of the third limit. At all higher pressures the mixture remains explosive.

This curve represents limits in the following sense: If data were taken at a series of temperatures and constant pressure, as along the 1000-millimeter-of-mercury isobar of figure 25, the ignition lags would increase more and more rapidly as the temperature was decreased toward 542° C. These lags refer to the time from the instant at which mixture is introduced into the hot vessel until the explosion occurs. Near the temperature of the limit the lags would go up very rapidly from a finite value at a temperature just over 542° C to effectively an infinite value at a temperature just under 542° C. Since the system is closed, what really happens is that below a critical temperature the reactants are used up and diluted with product (water), and these effects overpower those due to acceleration of the reaction by self-heating and chain-branching.

Effects of variables on explosion limits.—Explosion limits depend on the size of the vessel and the nature of the walls. This is indicated by the dashed curves in figure 25. The larger the vessel, the lower the pressure of the third limit. The junction of the first and second limits is displaced to higher temperatures as the vessel is made smaller. Along the second-limit curve, vessel size has little effect if the diameter is large (7.4 to 10 cm for the data shown), but the pressure is decreased considerably for small vessels.

The effects of surface coating with various salts are very pronounced, especially near the junction of the first and second limits. For example, this junction occurs for a 7.4-centimeter flask at about 340° C if the walls are coated with potassium tetraborate and at 400° C if they are lightly coated with potassium chloride.

If nitrogen is added to the stoichiometric hydrogen-oxygen mixture so as to make the mixture stoichiometric hydrogen in air, the second limit in a 7.4-centimeter vessel (with sodium chloride coating) at 530° C is raised from 85 to 117 millimeters of mercury. The mole fraction of nitrogen in such a mixture is 0.558. Other inert gases in the same amount have quite different effects. In argon "air" under the same conditions the limit is raised to about 160 millimeters of mercury. In carbon dioxide "air" the effect is reversed, and the second limit is lowered to 56 millimeters of mercury. The specific effects of these inert gases are clearer if the partial pressures of hydrogen and oxygen in the mixtures are compared, rather than the total pressures. On this basis, argon has no specific effect, because the partial pressures of hydrogen and oxygen total 85 millimeters of mercury. Nitrogen and carbon dioxide both reduce the partial pressure at the second limit, nitrogen, from 85 to 65 millimeters of mercury, and carbon dioxide, from 85 to 31 millimeters of mercury.

In view of the very complicated behavior of explosion limits and their sensitivity to surface effects, it is difficult to answer questions on safety. For example, the question whether it is safe to heat a static mixture to a given temperature should be accompanied by a statement of the pressure, vessel diameter, and surface nature. Even then, it is unlikely that any experimental data will be found to answer practical questions dealing with metal containers and with the precise mixture under consideration. The data in figure 25 do no more than set very approximate bounds.

CHEMISTRY OF HYDROGEN OXIDATION

The complex behavior of explosion limits has been used to establish the details of the oxidation of hydrogen. The full story is not given here, but may be found in references 37 and 63. The basic fact is that the oxidation reaction proceeds by a chain mechanism, with the hydrogen and oxygen atoms (H and O) and the hydroxyl free radical (OH) as chain carriers:

$$OH + H_2 \xrightarrow{k_1} H_2O + H \qquad (I)$$

$$H + O_2 \xrightarrow{k_2} OH + O \qquad (II)$$

$$O + H_2 \xrightarrow{k_3} OH + H \qquad (III)$$

The OH radicals that start the sequence are assumed to arise by a reaction between O_2 and H_2, the details of which are not specified (ref. 37). The radicals lead directly to the final product, water, and in so doing produce a hydrogen atom. This starts chain branching (reactions (II) and (III)) in which two chain carriers are produced for each one used up. If left unchecked, chain branching will lead to an explosion through an exponential growth in chain-carrier concentration, and hence in reaction rate. Actually, reaction (II) is strongly endothermic and occurs very rarely until a sufficiently high temperature is reached. It is for

this reason that hydrogen-oxygen mixtures are stable at room temperature.

Chain-breaking imposes another check on the exponential increase in chain carriers. H, O, and OH may be destroyed if they meet a wall. This is the reason for the existence of the first explosion limit. It occurs at pressures so low that, on the average, a chain carrier strikes the wall before it has a fruitful collision in the gas phase. However, if the wall reflects rather than destroys the chain carrier, the limit is shifted; this explains the dependence on surface nature.

Chain carriers are also destroyed in the gas phase. The mechanism is probably as follows:

$$H+O_2+M \xrightarrow{k_4} HO_2+M \qquad \text{(IV)}$$

where M is any molecule other than a chain carrier. HO_2, while reactive, still can survive long enough to reach the wall, where it may be destroyed. The frequency of these three-body reactions increases with increasing pressure, until at some critical pressure they overcome the chain branching and thereby produce the second explosion limit. Since the second limit is caused by gas-phase events, it is relatively insensitive to vessel factors; but there are some effects when the wall is reflective toward HO_2 and returns it to the reaction zone.

The mixture again becomes explosive at the third limit, where the pressure is so high that HO_2 cannot get to the wall before reacting. It is likely that the reaction of HO_2 in the gas phase is

$$HO_2+H_2 \xrightarrow{k_5} H_2O_2+H \qquad \text{(V)}$$

(ref. 37). This reaction restores the chain carrier lost in reaction (IV), and chain breaking can no longer overcome chain branching.

This brief discussion explains qualitatively the existence of explosion limits, but is not complete enough to explain all the details of the observed effects, particularly of surface effects. The arguments may be summarized by stating that explosion limits arise because of competition in the gas and at the wall between reactions that inactivate the chain carriers H, O, and OH and those that perpetuate the carriers and increase their number.

SPONTANEOUS IGNITION

Relation between spontaneous ignition and explosion limits.—In the discussion of explosion limits, it is pointed out that the limit could be obtained from the variation of ignition lag with temperature at constant pressure. This would be a spontaneous-ignition experiment. In other words, spontaneous-ignition temperatures lie in the region to the right of an explosion-limit curve such as shown in figure 25.

In general, modern work on spontaneous-ignition temperatures (to which this review is limited) has dealt with conditions that give short ignition lags. Therefore, it has been necessary to use flow systems rather than the static closed systems used in the study of explosion limits, in which the time needed to admit mixture to the hot vessel becomes long compared with the ignition lag. For every spontaneous-ignition apparatus there should be a particular explosion-limit curve for a given hydrogen mixture, fixed by the size, shape, and material of construction. The curves are seldom determined in practice, so spontaneous-ignition data are taken at conditions removed an unknown distance from the limit curve. Thus, the contributions of the various gas-phase and surface reactions to the spontaneous-ignition process are hard to estimate, even though the chemistry is no doubt the same as it is at the explosion limits.

In summary, explosion limits are determined by the balance between chain-breaking and -branching and are independent of time. Spontaneous ignition, on the other hand, is a rate process that may be affected to a greater or lesser degree by chain breaking or chain branching, depending on the apparatus, the pressure, and the temperature.

Theoretical considerations.—The complexity of the chemistry of spontaneous ignition has led to attempts to simplify the concepts. The general procedure is to consider the process as a whole and to ignore the individual steps of the reaction mechanism; this type of approach has recently been reviewed in reference 64. For the hydrogen-oxygen reaction one might hope that the reaction rate could be expressed in the following Arrhenius form:

$$\omega=[H_2]^x[0_2]^y exp\left(-\frac{E}{RT}\right) \qquad (14)$$

(Chemical symbols in brackets denote molar concentrations.) The reasonable assumption is then made that the ignition lag is inversely proportional to the reaction rate:

$$\tau \propto 1/\omega \qquad (15)$$

From equations (14) and (15) the following relation may be obtained:

$$\ln \tau=\frac{E}{RT}-x \ln [H_2]-y \ln [0_2]+\text{Constant} \qquad (16)$$

If the concentrations are converted to molecules per unit volume by means of the gas law, the expected pressure dependence may be found:

$$\ln \tau=\frac{E}{RT}-(x+y) \ln P+(x+y) \ln T+\text{Constant} \qquad (17)$$

Equation (17) holds for a given mixture.

Equations (16) and (17) are really little more than guides for handling spontaneous-ignition data; they show how to plot the results with a reasonable expectation of getting straight lines. Furthermore, if a plot of $\ln \tau$ against $1/T$ is linear, its slope has the value E/R; hence, the slope yields an over-all activation energy, but this value cannot be related to the real chemistry of the process without further consideration.

The procedure just described is about all one can do on theoretical grounds with most fuels, because the combustion chemistry is poorly understood. But hydrogen is one of

the few fuels for which the chemistry is known; therefore the theory of spontaneous ignition can be elaborated. This is done in the following paragraphs, which give new interpretations of the effects of temperature, pressure, and concentration on spontaneous-ignition lags of hydrogen.

Reactions (I) to (IV) represent only a part of the total mechanism operative at the explosion limits. The surface chemistry is left out altogether. But for a homogeneous reaction under conditions where the walls are unimportant (i. e., at reasonably high pressures), these equations may be sufficient to describe the reaction.

The over-all reaction rate ω is the rate of formation of water:

$$\omega=\mathrm{d}[H_2O]/\mathrm{d}t \tag{18}$$

From reaction (I),

$$\mathrm{d}[H_2O]/\mathrm{d}t=k_1[H_2][OH] \tag{19}$$

After a short induction period, the rate of water formation attains a steady state, and OH concentration becomes (ref. 37, p. 10)

$$[OH]=\frac{i}{k_1[H_2]\left(1-\frac{2k_2}{k_4[M]}\right)} \tag{20}$$

Combining equations (19) and (20) gives

$$\frac{\mathrm{d}[H_2O]}{\mathrm{d}t}=\frac{i}{1-\frac{2k_2}{k_4[M]}} \tag{21}$$

It is next assumed, as before, that the ignition lag is inversely proportional to the over-all rate (eq. (18)). The following relation is obtained:

$$\tau=c_1\left(\frac{1-\frac{2k_2}{k_4[M]}}{i}\right) \tag{22}$$

The nature of the initiation reactions, which are lumped together in the term i, is fairly well understood (ref. 37, p. 42). If they are introduced explicitly into the simple scheme of reactions (I) to (IV), the calculations become very complicated. For the present purpose it is sufficient to use the pressure dependence of the rate of initiation, and this is known from explosion-limit work to be at least as great as second order (ref. 37, p. 37). Therefore, it is assumed that

$$\left.\begin{array}{l} i\propto P^2 \\ \text{or} \quad i=c_2(T)P^2 \end{array}\right\} \tag{23}$$

where $c_2(T)$ is a proportionality constant dependent on temperature. The concentration $[M]$, which refers to any of the molecules of the mixture, is directly proportional to the pressure and inversely proportional to the temperature:

$$[M]=c_3\frac{P}{T} \tag{24}$$

When equations (23) and (24) are combined with equation (22), the following expression is obtained:

$$\tau=\frac{c_1}{c_2(T)P^2}\left(1-\frac{2k_2}{k_4c_3}\frac{T}{P}\right) \tag{25}$$

In this equation the terms $c_2(T)$, k_2, and k_4 are all functions of temperature. If the temperature is held constant, the variation of ignition lag with pressure may be investigated. Equation (25), in that case, takes the following form:

$$\tau=\frac{K_1}{P^2}-\frac{K_2}{P^3} \tag{26}$$

Differentiation of equation (26) with respect to pressure shows that the curve of τ against P has either a maximum or a minimum at the place where

$$P=\frac{3K_2}{2K_1} \tag{27}$$

Differentiation a second time shows that at this value of P the second derivative is negative. Therefore, the curve of τ against P at constant temperature should have a maximum. Of course, the pressure at which the maximum occurs could not be calculated unless the values of the constants were known.

Some remarks may also be made about the variation of ignition lag with temperature at constant pressure. Equation (17), derived from the simplified concepts discussed first, predicts a linear plot of ln τ against $1/T$ with a slope E/R. (Data are usually taken over too small a temperature range to show any effect of the other temperature-dependent term in equation (17).) Later in this report it is shown that spontaneous-ignition data do conform to this simple relation. Examination of equation (25) shows that, in order that the linear relation hold, the second term inside the parentheses should be relatively independent of temperature. Then,

$$\tau\propto\frac{1}{c_2(T)} \tag{28}$$

Since the factor $c_2(T)$ expresses a chemical rate, it may be expected to vary as $exp(-E/RT)$. The observed relation then follows. The advantage of this treatment is that it focuses attention on the reaction whose activation energy is actually obtained from the plot of ln τ against $1/T$; that is, on the chain-initiation reaction, not on the propagation or chain-breaking reaction. Physically, it is logical that this should be so in a spontaneous-ignition process.

Finally, the expected dependence of ignition lag on hydrogen concentration may be discussed. The approximate relation (eq. (28)) is used. Since $c_2(T)$ is related to the chemical rate expression for the chain-initiation process, $c_2(T)$ depends not only on temperature but also on concentration. Once again, the dependence cannot be stated explicitly because the complete chemical mechanism has not been used. However, explosion-limit studies show that the rate of initiation increases strongly with increasing hydrogen concentration and depends hardly at all on oxygen concentration (ref. 37, p. 40). In fact, oxygen seems to be simply an inert diluent as far as chain initiation is concerned. Therefore, ignition lag should decrease sharply with increasing hydrogen concentration.

The main conclusions of the extended treatment of spontaneous ignition of hydrogen based on real reaction kinetics may be summarized as follows:

(1) The curve of ignition lag against pressure at constant temperature should show a maximum.

(2) The observed linear dependence of ln τ on $1/T$ shows that the chain-initiation process is dominant in spontaneous-ignition experiments. Activation energies derived from such plots apply to the initiation process.

(3) Ignition lags should decrease sharply with increasing hydrogen concentration and should show little, if any, dependence on oxygen concentration.

Sources of spontaneous-ignition data.—The subject of the spontaneous ignition of hydrogen is a very old one, but much of the earlier work is only qualitative. The following paragraphs consider the more recent work contained in references 65 to 68. Despite the extensive work on spontaneous ignition, even the data from recent sources are strongly dependent on apparatus. Therefore, data for a particular application are best chosen from work done in a manner that resembles the practical situation in question. For this reason the general features of the experiments reported in references 65 to 68 are described here.

References 65 and 66 report studies at lower temperature and long ignition lags (0.1 to 10 sec). The delays were therefore measured directly and refer to the time from the instant of mixing of hot streams of hydrogen and oxidant to the instant at which flame appeared. References 67 and 68 cover spontaneous-ignition temperatures high enough to give ignition delays in the millisecond range. In these cases stable flame fronts were formed in the ducts, and the lags were calculated from the known average flow velocity and the distance from a zero-reaction point to the flame. The high spontaneous-ignition temperatures are probably not the only cause of the short lags reported in references 67 and 68; the presence of the flame may also have had an effect.

Other sources of discrepancy are the degree of mixing and the method of heating. In the work of reference 67 the hydrogen was injected into an airs treamheated (and vitiated) by preburning upstream. In the work of reference 65 the fuel and air were heated separately, and no special effort was made to produce rapid mixing. In reference 66 the gases were heated separately and rapidly mixed. And in the work of reference 68 a premixed stream was heated to a static temperature below the spontaneous-ignition temperature and then passed into a diffuser, where the increase in static temperature and pressure caused reaction to start. The zero-reaction point in this case was arbitrarily chosen as the diffuser exit.

Effect of temperature.—It has already been pointed out that simple theory anticipates a linear relation between the logarithm of the ignition lag and the reciprocal of the spontaneous-ignition temperature. Figure 26 (taken from ref. 64) shows that this relation does hold for data of two investigators, and it is assumed to hold for the data of reference 66 as well. This linear relation also reemphasizes the large discrepancies among the various methods, differences of as much as two orders of magnitude.

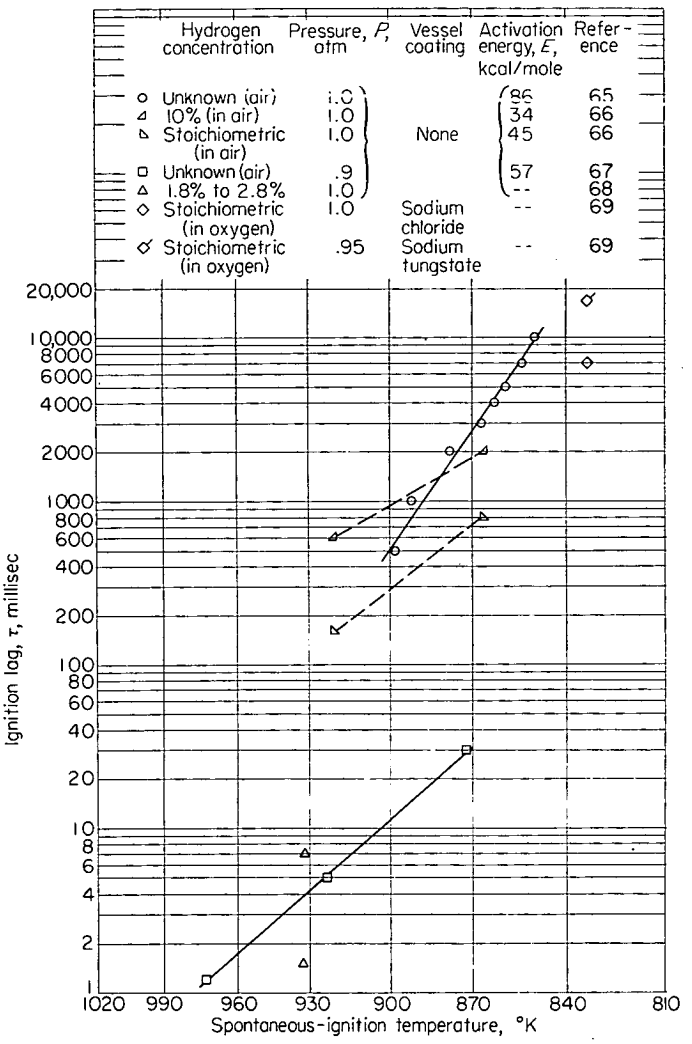


FIGURE 26.—Effect of spontaneous-ignition temperature on ignition lag.

According to equation (16) or (17), over-all activation energies may be computed from the slopes of these lines. Values are listed on figure 26; they range from 34 to 86 kilocalories per mole. The extended theory points out that the activation energies are over-all values for the chain-initiation process. The wide spread probably means that unrecognized experimental variables affected the results. For example, two points are included in figure 26 from work of von Elbe and Lewis on explosion limits (ref. 69). At pressures near atmospheric such data lie in the same range as those from some of the experiments in flowing systems. However, the presence of a surface effect in this work (salt or sodium tungstate coating) shows that such effects may very well be present in the other data. Chain initiation is indirectly tied in with surface effects through the following reactions (ref. 37, pp. 42 to 43):

$$2HO_2 \xrightarrow{\text{wall}} H_2O_2+O_2 \qquad \text{(VI)}$$

$$H_2O_2 \xrightarrow{\text{wall}} H_2O+\tfrac{1}{2}O_2 \qquad \text{(VII)}$$

$$H_2+O_2 \xrightarrow{\text{wall}} H_2O_2 \qquad \text{(VIII)}$$

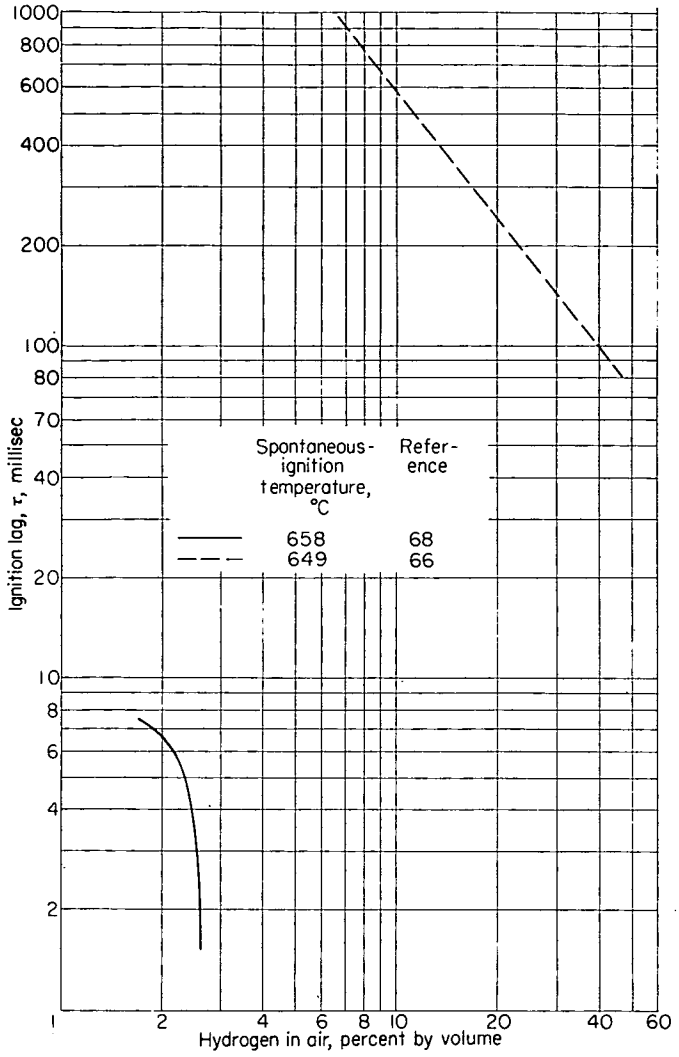


FIGURE 27.—Effect of hydrogen concentration on ignition lag at atmospheric pressure.

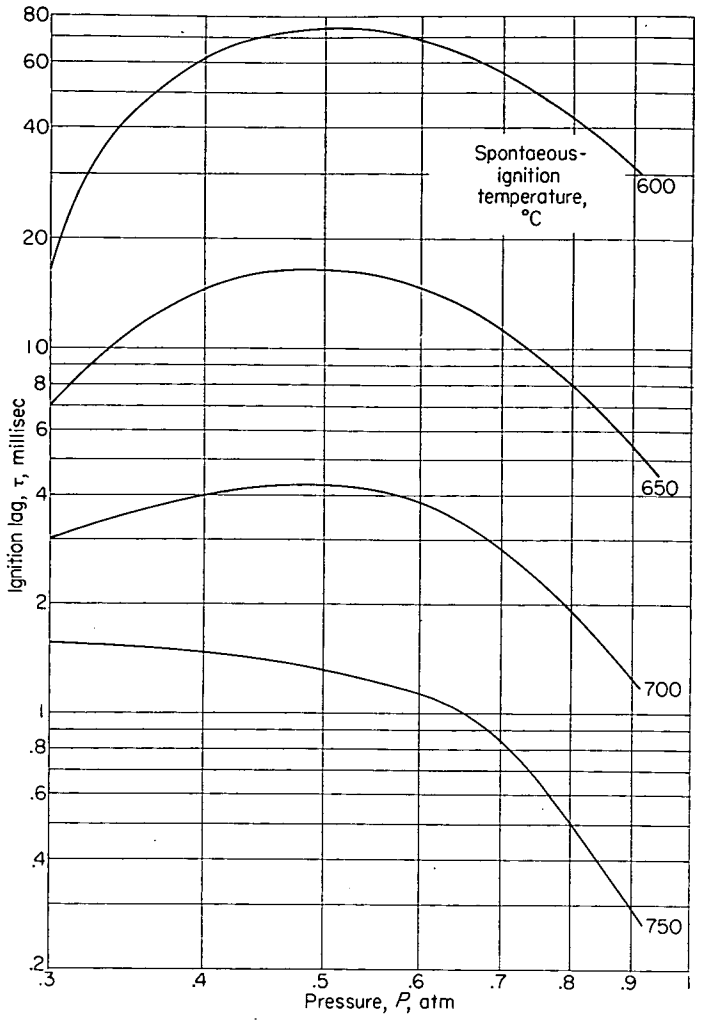


FIGURE 28.—Effect of pressure on ignition lag of hydrogen-air mixtures (ref. 67).

Therefore, wall effects may affect the observed activation energy if they act to inhibit one or more of the preceding reactions. This is a subject that has not been dealt with in spontaneous-ignition work.

Effect of fuel concentration.—It was concluded from the theoretical considerations that ignition lag should decrease with increasing hydrogen concentration but should be quite independent of oxygen concentration. Mullins found no variation with over-all fuel-air ratio for carbon monoxide or methane and implicitly assumed that this result holds for very lean mixtures of any fuel (ref. 67). But in the two experiments in which hydrogen concentration was actually known and was varied, a strong hydrogen-concentration dependence was found. Data of references 66 and 68 are shown in figure 27. Both experiments showed that the ignition lag decreases with increasing hydrogen concentration over the range covered. However, both the form of the dependence and the orders of magnitude of the lags are entirely different in the two cases, even though the spontaneous-ignition temperatures are nearly the same.

There have been no studies in which the oxygen concentration of homogeneous mixtures was systematically varied; however, the data of reference 66 (fig. 27) represent changes in oxygen content from about 13 to 20 percent because of the wide range of hydrogen concentrations covered. The data would be expected to deviate from a straight line if there were a very strong effect of oxygen concentration. Other evidence comes from Dixon's experiments (ref. 65), in which hydrogen was injected into both air and oxygen and the differences in the spontaneous-ignition temperature were only 3° to 6° C for a 0.5-second ignition lag. Both sets of data therefore confirm the prediction that ignition lag should be independent of oxygen concentration.

Effect of pressure.—Both Dixon (ref. 65) and Mullins (ref. 67) studied the effect of pressure on spontaneous ignition. Mullins' data are plotted in figure 28; the curves of ignition lag against pressure at constant spontaneous-ignition temperature have maximums. This agrees with the prediction of the extended theory of spontaneous ignition. As pressure is decreased below 1 atmosphere, ignition lags increase until a pressure near 0.5 atmosphere is reached; further decreases in pressure cause the lags to decrease. Dixon noted similar behavior for constant 0.5-second ignition lag, that is, as pressure was decreased from about 1.5 atmospheres, the curve of spontaneous-ignition temperature against pressure went through a maximum near 1 atmosphere (ref. 65). Thus, there is a difference of about 0.5 atmosphere in the pressure at which these two authors found

the promoting effect of reduced pressure to begin. Furthermore, the spontaneous-ignition temperatures at which Dixon found 0.5-second lags were in the range where Mullins found lags of a few milliseconds, so again there was the kind of discrepancy noted in figure 27.

SAFETY CONSIDERATIONS

In view of the many factors that affect ignition lags and spontaneous-ignition temperatures and the wide discrepancies in the results obtained, it is not possible to state absolutely safe limits of temperature and soaking time for hydrogen mixtures. However, it seems significant that the really large differences are found when one compares experiments with and without a stabilized flame. In both figures 26 and 27 the lags found by Mullins and by Fouré with a flame present throughout the test (refs. 67 and 68, respectively) are in the millisecond range; those of all other workers were obtained from systems in which a flame was not initially present and are about two orders of magnitude greater. Considering all the data, it is likely that, in the absence of a flame, hydrogen-air mixtures at 1 atmosphere, either flowing or static, may be held at temperatures up to 550° C for at least 1 second.

In recent work at the Bureau of Mines, minimum spontaneous-ignition temperatures were measured for hydrogen-air mixtures diluted with water vapor (ref. 70). The minimum spontaneous-ignition temperature is the lowest temperature at which a mixture will ignite in a closed apparatus, even if allowed to soak for a very long time, and is therefore the same as an explosion-limit temperature. Reference 70 reports minimum spontaneous-ignition temperatures from 515° C (no water vapor) to 580° C (30 percent water vapor) at a pressure of 7.8 atmospheres. Other tests showed that pressure has little effect in the interval from 1 to 10 atmospheres. On the basis of these and other data, reference 70 recommends that any temperature above 500° C be considered a potential spontaneous-ignition hazard for long soaking times at pressures near atmospheric. At low pressures, with certain surfaces, ignition can occur at temperatures as low as 340° C (fig. 25).

RELATIONS AMONG COMBUSTION PROPERTIES

The combustion properties of hydrogen have been discussed more or less individually, and the data are valuable in themselves. However, there are also interrelations among several of the properties that should be pointed out. The importance of these relations is twofold. First, they may be used to estimate voids in the data on one property from available data on another. Second, there are relations between burning velocity and quenching distance from which chemical rates in flames may be estimated. The rates are significant in establishing the volumetric requirements for combustion.

FLAME REACTION RATES

Combustion properties in general depend both on chemical rates and on transport processes. Certain combustion properties can, however, be combined to give quantities that depend only on one or the other. This can be done only for flames of a given chemical family, such as hydrogen-oxygen-nitrogen flames. In reference 71, a thermal quenching equation

$$\text{Quenching distance} \propto \sqrt{\frac{\text{Transport property}}{\text{Reaction rate}}} \tag{29}$$

is combined with a thermal burning-velocity equation

$$\text{Burning velocity} \propto \sqrt{(\text{Reaction rate})(\text{Transport property})} \tag{30}$$

to give

$$\frac{\text{Burning velocity}}{\text{Quenching distance}} \propto \text{Reaction rate} \tag{31}$$

From this approach, it was calculated (ref. 71) that the average reaction rate in a stoichiometric hydrogen-air flame is 169 moles per liter per second. The average rates for hydrocarbon fuels are very much lower. The values reported in reference 71 for propane-air and isooctane-air mixtures are 1.04 and 0.24 moles per liter per second, respectively.

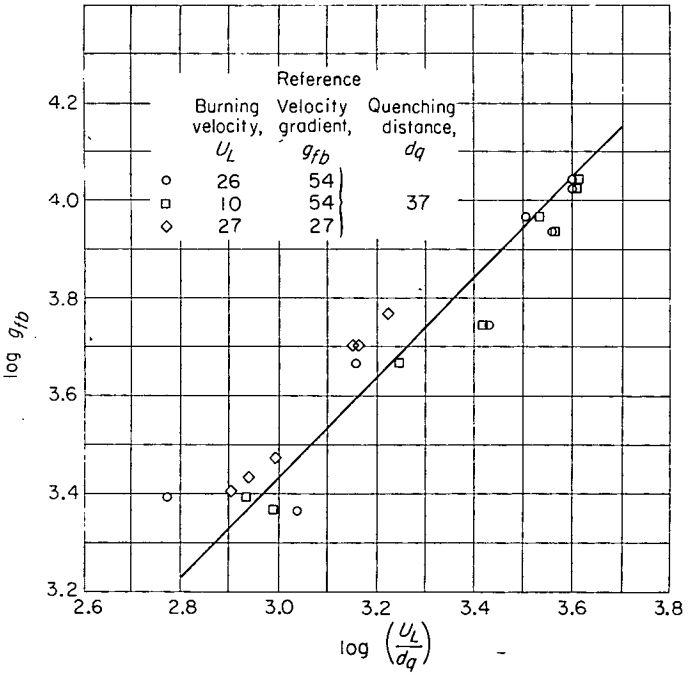


FIGURE 29.—Relation between reaction-rate parameters for hydrogen-air mixtures.

The very high reaction rate is the basic reason for the outstanding vigor of hydrogen flames compared with flames of hydrocarbon fuels. Flame temperatures are not much different, so flame temperature is not the driving force of the hydrogen reaction. Hydrogen is oxidized by a free-radical chain mechanism, and the same is probably true for hydrocarbons at or near flame temperatures. It is quite possible that the activation energies of the individual steps of the reaction mechanism are comparable in both cases. However, absolute rate theory shows that reactions of atoms and other small free radicals with the polyatomic hydrocarbon molecules will be as much as 10^{-4} slower than the corresponding reactions with the simple diatomic hydrogen molecule, even if activation energies are similar for the two cases. One might speculate, therefore, that hydrogen burns so vigorously because it is a very simple molecule.

RELATIONS USEFUL FOR ESTIMATING DATA

Flashback velocity gradient, burning velocity, and quenching distance.—Reference 56 states that the boundary velocity gradient for flashback is directly proportional to the reaction

rate. Reference 72 extends this concept and shows that the reaction rate in question is not complicated by the effects of transport processes and that the following relation holds for flames of a given chemical family:

$$g_{fb}^{0.857} \propto \frac{\bar{\omega}_F}{N_o} \tag{32}$$

It had previously been shown (ref. 71) that burning velocity, quenching distance, and reaction rate are related as follows, as implied by equation (31):

$$\frac{U_L}{d_q} \propto \frac{\bar{\omega}_F}{N_o} \tag{33}$$

When equations (32) and (33) are combined, the following is obtained:

$$g_{fb} \propto \left(\frac{U_L}{d_q}\right)^{1.168} \tag{34}$$

Figure 29 is a logarithmic plot based on equation (34) for data on hydrogen-air mixtures at 25° C and various pressures. Two sets of recent atmospheric-pressure burning-velocity data (refs. 10 and 26) were used to show the spread that may be expected (in spite of which the correlation is definite). The line as drawn has a slope of 1.03 rather than 1.168 as predicted by equation (34).

Figure 29 may be used to estimate data on one of the properties involved if the other two properties are known. Aside from this practical purpose, the plot is valuable because it shows that the theoretical ideas leading to equation (34) are probably correct; the same basic chemistry is involved in flashback, flame propagation, and flame quenching. The consistency shown when the results of various workers are plotted in the form of figure 29 indicates that the data are basically correct, even though there is some spread from the usual experimental errors. Results that depart widely from the correlation should be suspected; such a departure might result, for example, if burning velocity were measured at low pressure without proper care to prevent quenching effects.

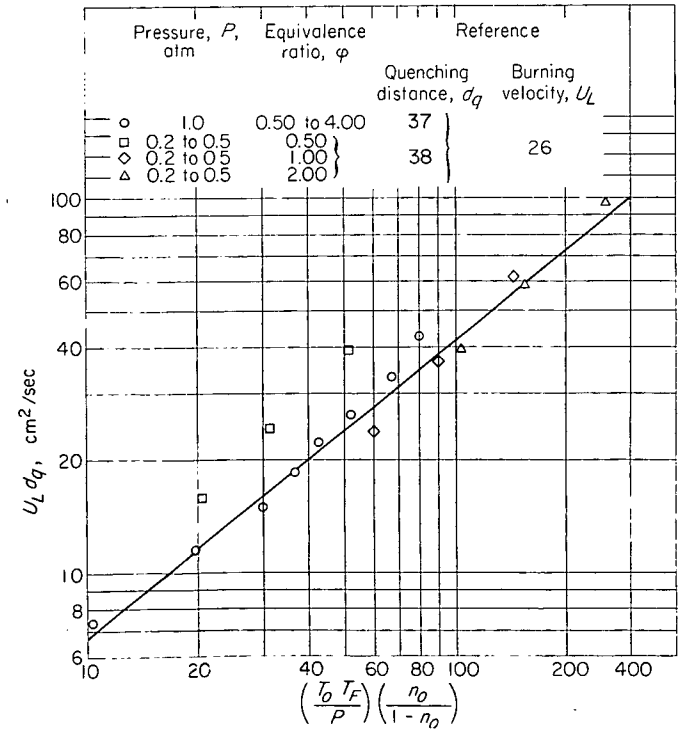


FIGURE 30.—Relation between product of quenching distance and burning velocity and transport parameters of hydrogen-air mixtures.

Burning velocity and quenching distance.—Reference 71 points out that the product of burning velocity and quenching distance should be proportional to a transport property, namely the apparent thermal conductivity (see eqs. (29) and (30)), for chemically similar systems such as various hydrocarbon-oxygen-nitrogen mixtures. From the definition of apparent thermal conductivity given in reference 71 it was predicted that the following relation should hold for such systems:

$$U_L d_q \propto \frac{T_o T_F}{P} \tag{35}$$

It was found that equation (35) holds very well for hydrocarbon-oxygen-nitrogen flames. But attempts to apply the relation to hydrogen-air flames fail, because no account is taken of the very large effects of hydrogen concentration on the transport process. It was found empirically that the following modified relation fits the data fairly well:

$$U_L d_q \propto \left[\left(\frac{T_o T_F}{P}\right)\left(\frac{n_o}{1-n_o}\right)\right]^x \tag{36}$$

No attempt is made here to justify equation (36) on theoretical grounds. Figure 30 is a logarithmic plot made according

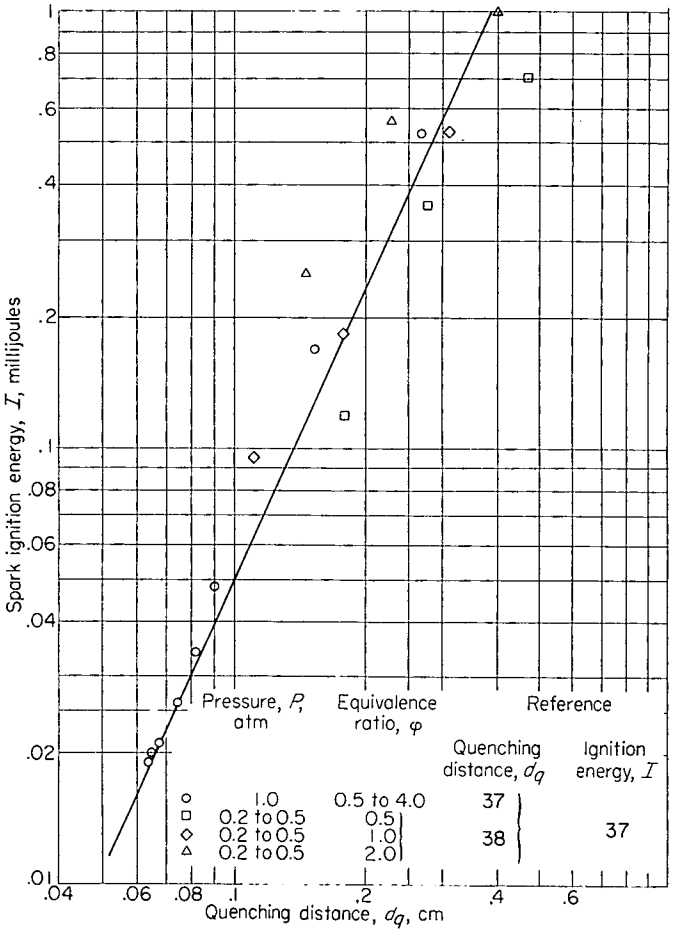


FIGURE 31.—Relation between spark ignition energy and quenching distance (between parallel plates) for hydrogen-air mixtures.

to equation (36) for various hydrogen-air mixtures at reduced and atmospheric pressures. Except for three points at an equivalence ratio of 0.5 and pressures from 0.2 to 0.5 atmosphere, there is little scatter. The chief use of figure 30 is in finding the effect of initial mixture temperature on quenching distance. This effect can be found by use of available data that show the effect of temperature on burning velocity.

Spark ignition energy and quenching distance.—Lewis and von Elbe first pointed out that spark ignition energy and quenching distance yield a correlation line when plotted logarithmically (ref. 37, p. 415). Figure 31 shows such a plot for hydrogen-air mixtures at reduced and atmospheric pressures. The line shown is a segment of a general correlation that fits data on many fuel-oxidant combinations over a range of four orders of magnitude in ignition energy. The theoretical basis for the correlation is not well understood.

Flashback velocity gradient and blowoff from flameholders.—Studies by Zukoski and Marble (refs. 73 and 74) strongly indicate that the mechanism of flameholding on bluff bodies depends on ignition time, provided that the shear region between the free stream and the flameholder wake is fully turbulent. The length of the wake is essentially independent of stream velocity; for cylindrical-rod flameholders, the data of reference 74 indicate that the following relation holds for a wide range of flow velocities:

$$\frac{L}{\sqrt{D}}=\text{Constant}=5.5 \tag{37}$$

where L and D are in inches. The ignition time available to the gases flowing along the shear region is

$$t=L/U \tag{38}$$

where U is in inches per second. If t is equal to or less than a characteristic value for the given mixture, blowoff will occur because the gas cannot ignite and form a propagating flame; then, equation (38) becomes:

$$t^*=L/U_{bo} \tag{39}$$

Combining equations (37) and (39) yields, for cylindrical-rod flameholders,

$$U_{bo}=5.5\frac{\sqrt{D}}{t^*} \tag{40}$$

Ignition along the flameholder wake is known to occur at a temperature close to flame temperature (ref. 74). Therefore, it is reasonable to suppose that the process is one of spontaneous ignition at high temperature. It is assumed in the earlier discussion of spontaneous ignition that the ignition time is inversely proportional to the reaction rate, and in view of the high temperature at which ignition occurs, the rate in question may be taken as the average rate of reaction in a flame. It has already been pointed out that flashback velocity gradient depends on average flame reaction rate in the manner shown by equation (32). Thus, it follows that

$$t^*\propto\left(\frac{1}{N_o g_{fb}}\right)^{0.857} \tag{41}$$

Data on the blowoff of hydrogen-air flames from cylindrical-rod flameholders at atmospheric pressure have been obtained only for lean mixtures and at low and intermediate Reynolds numbers (ref. 58). However, a complete flashback curve is available. With the aid of the relations just developed, it is therefore possible to estimate a complete blowoff curve. It should be noted that the curve will apply only when Reynolds number is high enough to give a fully turbulent shear layer between the wake and the free stream ($Re>10^4$).

Since the proportionality constant in equation (41) is unknown, the following procedure is used:

(1) From equation (40), a characteristic time $t_a{}^*$ is computed for a given mixture for which the blowoff velocity from a rod of a particular diameter has been measured.

(2) From equation (41), the following relation may then be expected to hold for other mixtures:

$$t^*=\frac{(t^* N_o g_{fb}^{0.857})_a}{N_o g_{fb}^{0.857}} \tag{42}$$

Equations (40) and (42) are combined to give the following result:

$$\frac{U_{bo}}{\sqrt{D}}=\frac{5.5\,N_o g_{fb}^{0.857}}{(t^* N_o g_{fb}^{0.857})_a}=f(\varphi) \tag{43}$$

For hydrogen-air flames at 1 atmosphere, the normalization point for computing t_a^* was chosen at $\varphi=0.5$, D=0.254 inch, and U_{bo}=900 feet per second (ref. 58). The flashback data are from reference 54 (see fig. 19). The estimated blowoff curve is shown in figure 32. For comparison, the same procedure was followed for methane-air flames, using flashback data from reference 75 and blowoff data from reference 73.

Figure 32 shows that the maximum predicted value of $U_{bo}/\sqrt{D}$ for hydrogen-air flames is more than an order of magnitude greater than that for methane-air flames. This is similar to the result of DeZubay, who found that the maximum value of the correlating parameter for blowoff of hydrogen-air flames at reduced pressure was 11 times greater than that for propane-air flames (ref. 57). Stability is expected to remain high even in very rich mixtures. The few data points available agree with the calculated curves as well as could be expected, in view of the many approximations involved. Moreover, some of the points actually

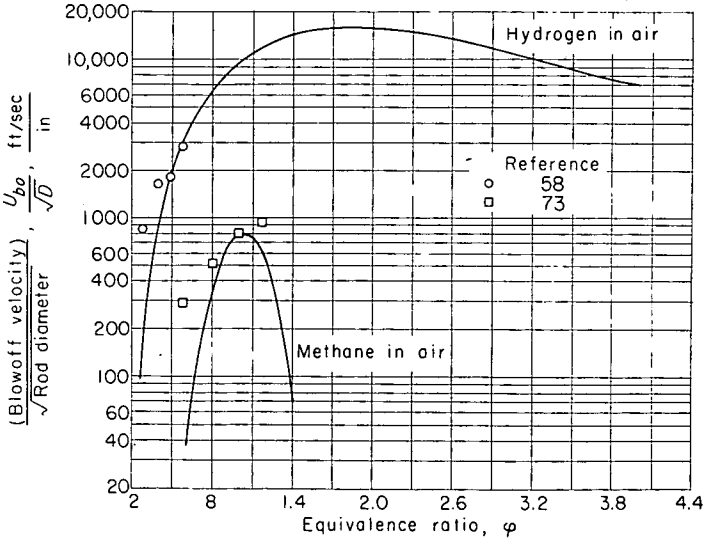


FIGURE 32.—Comparison of experimental data with blowoff curves calculated from flashback data of references 54 and 75. Cylindrical flameholders.

apply to conditions where the shear layer may not be fully turbulent, and these points of course would not be expected to lie on the curve.

According to equations (32) and (33), the blowoff curve could have been calculated equally well by use of U_L/d_q in place of $g_{fb}^{0.857}$. The choice of g_{fb} was arbitrary.

The effects of pressure on blowoff could be estimated, if, in addition to present knowledge, the variation of wake length with pressure were known. Work is needed to establish the effects of pressure on the flameholder wake.

A final comment about the calculated blowoff curve: The effects of compressibility are not really known. From the work of reference 74, equation (37) appears to hold up to free-stream Mach numbers of about 0.7. However, the peak value of $U_{bo}/\sqrt{D}$ in figure 32 implies that the blowoff velocity would be sonic (1640 ft/sec) for a flameholder only about 0.01 inch in diameter. It is not clear how the present analysis might be modified under such conditions.

SUMMARY OF RECOMMENDED VALUES OF COMBUSTION PROPERTIES

Table V presents a summary of recommended values of the various combustion properties of hydrogen-air mixtures. The values listed are for standard conditions, a pressure of 1 atmosphere, and an initial temperature of about 25° C. Wherever possible, data are given for both the stoichiometric mixture and the mixture showing the maximum (or minimum) value. The form of the pressure and temperature dependence is stated, if known. Since some of the numbers are averages or involve the judgment of the authors, references are omitted from table V.

LEWIS FLIGHT PROPULSION LABORATORY
NATIONAL ADVISORY COMMITTEE FOR AERONAUTICS
CLEVELAND, OHIO, *April 26, 1957*

REFERENCES

1. Olson, Walter T., and Gibbons, Louis C.: Status of Combustion Research on High-Energy Fuels for Ram Jets. NACA RM E51D23, 1951.
2. Passauer, H. Eisenstein: Verbrennungsgeschwindigkeit und Verbrennungstemperatur bei Vorwärmung von Gas und Luft. Das Gas—und Masserfach, Jahrg. 73, Heft 17, Apr. 26, 1930, pp. 313-319; 343-348; 369-372; and 392-397.
3. Morgan, Gerry H., and Kane, Walter R.: Some Effects of Inert Diluents on Flame Speeds and Temperatures. Fourth Symposium (International) on Combustion, The Williams & Wilkins Co. (Baltimore), 1953, pp. 313-320.
4. Jones, G. W., Lewis, Bernard, and Seaman, Henry: The Flame Temperatures of Mixtures of Methane-Oxygen, Methane-Hydrogen, and Methane-Acetylene with Air. Jour. Am. Chem. Soc., vol. 53, no. 11, Nov. 1931, pp. 3992-4001.
5. Friedman, Raymond: Measurement of the Temperature Profile in a Laminar Flame. Fourth Symposium (International) on Combustion, The Williams & Wilkins Co. (Baltimore), 1953, pp. 259–263.
6. Gaydon, A. G., and Wolfhard, H. G.: Flames—Their Structure, Radiation, and Temperature. Chapman & Hall (London), 1953.
7. Lewis, Bernard, and von Elbe, Guenther: Remarks on the Experimental Determination and Theoretical Calculation of Flame Temperatures and Explosion Pressures. Phil. Magazine, ser. 7, vol. 20, July 1935, pp. 44–65.
8. Friedman, Raymond: The Quenching of Laminar Oxyhydrogen Flames by Solid Surfaces. Third Symposium on Combustion and Flame and Explosion Phenomena, The Williams & Wilkins Co. (Baltimore), 1949, pp. 110–120.
9. Fenn, John B.: Lean Inflammability Limit and Minimum Spark Ignition Energy. Ind. and Eng. Chem., vol. 43, no. 12, Dec. 1951, pp. 2865–2868.
10. Burwasser, Herman, and Pease, Robert N.: Burning Velocities of Hydrogen-Air Flames. Jour. Am. Chem. Soc., vol. 77, no. 22, Nov. 20, 1955, pp. 5806–5808.
11. Bartholomé, E.: Die Flammengeschwindigkeit in stationär brennenden Flammen. Die Naturwissenschaften, Jahrg. 23, Heft 6, 1949, pp. 171–175; 206–213.
12. Edse, Rudolf: Studies on Burner Flames of Hydrogen-Oxygen Mixtures at High Pressures. Tech. Rep. 52–59, Flight Res. Lab., WADC, Apr. 1952.
13. Lurie, H. H., and Sherman, G. W.: Flame Temperatures of Combustible Gas-Oxygen Mixtures. Ind. and Eng. Chem., vol. 25, no. 4, Apr. 1933, pp. 404–409.
14. Byrne, John F.: The Influence of Atmospheric Oxygen on Bunsen Flames. Fourth Symposium (International) on Combustion, The Williams & Wilkins Co. (Baltimore), 1953, pp. 345–348.
15. Michelson, W.: Ueber die normale Entzündungsgeschwindigkeit explosiver Gasgemische. Ann. der Phys. und Chem., Bd. 37, 1889, pp. 1–24.
16. Ubbelohde, L., und Hofsass, M.: Über die Entzündungsgeschwindigkeit im Innenkegel der Bunsenflamme. Jour. Gasbel., Jahrg. 56, Nr. 51, Dec. 20, 1913, pp. 1225–1232; 1253–1262.
17. Ubbelohde, L., und Koelliker, E.: Zur Kenntnis des Innenkegels der Bunsenflamme. Jour. Gasbel., Jahrg. 59, 1916, pp. 49–57; 65–69; 82–86; 98–104.
18. Bunte, K., und Steding, A.: Über den Einfluss der Wärmeeinstrahlung auf die Entzündungsgeschwindigkeit der Gase. Gas u. Wasserfach, Bd. 71, 1928, pp. 673–677; 701–705; 731–734.
19. Bunte, K., und Litterscheidt, Walter: Die Entzündungsgeschwindigkeit von Gasgemischen. Gas u. Wasserfach, Bd. 73, 1930, pp. 837–842; 871–878; 890–896.
20. Corsiglia, John: New Method for Determining Ignition Velocity of Air and Gas Mixtures. Am. Gas Assoc. Monthly, vol. XIII, no. 10, Oct. 1931, pp. 437–442.
21. Jahn, Georg: Der Zündvorgang in Gasgemischen. Verlag R. Olenbourg, München and Berlin, 1934.
22. Smith, Francis A., and Pickering, S. F.: Measurements of Flame Velocity by a Modified Burner Method. Jour. Res. Nat. Bur. Standards, vol. 17, no. 1, July 1936, pp. 7–43.
23. Bartholomé, E.: Zur Methoden der Messung von Flammengeschwindigkeiten. Zs. Elektrochem., Bd. 53, Nr. 4, Aug. 1949, pp. 191–196.
24. Calcote, Hartwell F., Barnett, Charles M., and Irby, Moreland R.: The Burning Velocity of Various Compounds by the Bunsen Burner Method. Abstracts of Papers, 116th Meeting Am. Chem. Soc., 1949, p. 38P.
25. Fenn, John B., and Calcote, Hartwell F.: Activation Energies in High Temperature Combustion. Fourth Symposium (International) on Combustion, The Williams & Wilkins Co. (Baltimore), 1953, pp. 231–239.
26. Manton, John, and Milliken, B. B.: Study of Pressure Dependence of Burning Velocity by the Spherical Vessel Method. Proc. Gas Dynamics Symposium (Aerothermochem.), Northwestern Univ., 1956, pp. 151–157.
27. Fine, Burton: Stability Limits and Burning Velocities of Laminar Hydrogen-Air Flames at Reduced Pressures. NACA TN 3833, 1956.
28. Bone, W. A., and Townend, Donald T. A.: Flame and Combustion in Gases. Longmans, Green & Co., Ltd. (London), 1927, p. 505.
29. Linnett, J. W.: Methods of Measuring Burning Velocity. Fourth Symposium (International) on Combustion, The Williams & Wilkins Co. (Baltimore), 1953, pp. 20–35.

30. Heimel, Sheldon: Effect of Initial Mixture-Temperature on Burning Velocity of Hydrogen-Air Mixtures with Preheating and Simulated Preburning. NACA TN 4156, 1957.
31. Garside, J. E., and Jackson, B.: The Formation and Some Properties of Polyhedral Burner Flames. Fourth Symposium (International) on Combustion, The Williams & Wilkins Co. (Baltimore), 1953, pp. 545–552.
32. Heimel, Sheldon, and Weast, Robert C.: Effect of Initial Mixture Temperature on the Burning Velocity of Benzene-Air, *n*-Heptane-Air, and Isooctane-Air Mixtures. Sixth Symposium (International) on Combustion, Reinhold Pub. Corp., 1957, pp. 296–302.
33. Dixon-Lewis, G.: Temperature Distribution in Flame Reaction Zones. Fourth Symposium (International) on Combustion, The Williams & Wilkins Co. (Baltimore), 1953, pp. 263–267.
34. Fine, Burton: Further Experiments on the Stability of Laminar and Turbulent Hydrogen-Air Flames at Reduced Pressures. NACA TN 3977, 1957.
35. Simon, Dorothy M., Belles, Frank E., and Spakowski, Adolph E.: Investigation and Interpretation of the Flammability Region for Some Lean Hydrocarbon-Air Mixtures. Fourth Symposium (International) on Combustion, The Williams & Wilkins Co. (Baltimore), 1953, pp. 126–138.
36. Berlad, A. L., and Potter, A. E.: Prediction of the Quenching Effect of Various Surface Geometries. Fifth Symposium (International) on Combustion, The Reinhold Pub. Corp., 1955, pp. 728–735.
37. Lewis, Bernard, and von Elbe, Guenther: Combustion, Flames and Explosions of Gases. Academic Press, Inc., 1951.
38. Potter, A. E., Jr., and Berlad, A. L.: The Effect of Fuel Type and Pressure on Flame Quenching. Sixth Symposium (International) on Combustion, Reinhold Pub. Corp., 1957, pp. 27–36.
39. Berlad, Abraham L.: Flame Quenching by a Variable-Width Rectangular-Slot Burner as a Function of Pressure for Various Propane-Oxygen-Nitrogen Mixtures. NACA RM E53K30, 1954. (See also Jour. Phys. Chem., vol. 58, no. 11, Nov. 1954, pp. 1023–1026.)
40. Belles, Frank E., and Berlad, A. L.: Chain Breaking and Branching in the Active-Particle Diffusion Concept of Quenching. NACA TN 3409, 1955.
41. Friedman, Raymond, and Johnston, W. C.: The Wall-Quenching of Laminar Flames as a Function of Pressure, Temperature, and Air-Fuel Ratio. Jour. Appl. Phys., vol. 21, no. 8, Aug. 1950, pp. 791–795.
42. Egerton, A. C., Everett, A. J., and Moore, N. P. W.: Sintered Metals as Flame Traps. Fourth Symposium (International) on Combustion, The Williams & Wilkins Co. (Baltimore), 1953, pp. 689–695.
43. Coward, H. F., and Jones, G. W.: Limits of Flammability of Gases and Vapors. Bull. 503, Bur. Mines, 1952.
44. Egerton, Alfred C.: Limits of Inflammability. Fourth Symposium (International) on Combustion, The Williams & Wilkins Co. (Baltimore), 1953, pp. 4–13.
45. White, Albert Greville: Limits for the Propagation of Flame in Inflammable Gas-Air Mixtures. III—The Effect of Temperature on the Limits. Jour. Chem. Soc. Trans. (London), vol. CXXVII, pt. I, 1925, pp. 672–684.
46. Burgoyne, J. H., and Williams-Leir, G.: The Influence of Incombustible Vapours on the Limits of Inflammability of Gases and Vapours in Air. Proc. Roy. Soc. (London), ser. A, vol. 193, July 21, 1948, pp. 525–539.
47. Belles, Frank E., Simon, Dorothy M., and Weast, Robert C.: Pressure Limits of Flame Propagation of Propane-Air Mixtures—Influence of Wall Quenching. Ind. and Eng. Chem., vol. 46, no. 5, May 1954, pp. 1010–1013.
48. Garner, W. E., and Pugh, A.: The Propagation of Flame in Hydrogen-Oxygen Mixtures. Trans. Faraday Soc., vol. 35, Jan. 1939, pp. 283–295.
49. Swett, Clyde C., Jr.: Spark Ignition of Flowing Gases. NACA Rep. 1287, 1956.
50. Jones, G. W., et al.: Research on the Flammability Characteristics of Aircraft Fuels. Tech. Rep. 52–35, Feb. 19, 1950–Feb. 19, 1952, WADC, June 1952. (Contract AF 33(038) 50–1293E.)
51. Lakin, W. P., Thwaites, H. L., Skarstrom, C. W., and Baum, A. W.: Fourth Annual Report on Fundamental Studies of Combustion. Rep. No. RL–5M–48(69), Esso Labs., Res. Div. (Standard Oil Dev. Co.), Nov. 30, 1948.(Contract N6–ori–109.)
52. King, I. R., and Calcote, H. F.: Effect of Initial Temperature on Minimum Spark-Ignition Energy. Jour. Chem. Phys., vol. 23, no. 12, Dec. 1955, pp. 2444–2445.
53. Belles, Frank E.: Flame Propagation in Premixed Gases. Literature on the Combustion of Petroleum, Monograph No. 20, Advances in Chem. Ser., 1958, pp. 166–186.
54. von Elbe, Guenther, and Mentser, Morris: Further Studies of the Structure and Stability of Burner Flames. Jour. Chem. Phys., vol. 13, no. 2, Feb. 1945, pp. 89–100.
55. Bollinger, Loren E., and Edse, Rudolph: Effect of Burner-Tip Temperature on Flashback of Hydrogen-Oxygen Flames. Tech. Rep. 53–325, WADC, Oct. 1953. (Contract AF–33(616)–44.)
56. Wohl, Kurt, Kapp, Numer M., and Gazley, Carl: The Stability of Open Flames. Third Symposium on Combustion and Flame and Explosion Phenomena, The Williams & Wilkins Co. (Baltimore), 1949, pp. 3–21.
57. Friedman, J., Bennet, W. J., and Zwick, E. B.: The Engineering Application of Combustion Research to Ramjet Engines. Fourth Symposium (International) on Combustion, The Williams & Wilkins Co. (Baltimore), 1953, pp. 756–764; discussion by E. A. DeZubay, p. 764.
58. Zukoski, Edward Edom: Flame Stabilization on Bluff Bodies at Low and Intermediate Reynolds Numbers. Rep. 20–75, Jet Prop. Lab., C. I. T., June 30, 1954. (Contract DA–04–495–ORD–18.)
59. Longwell, J. P.: Flame Stabilization by Bluff Bodies and Turbulent Flames in Ducts. Fourth Symposium (International) on Combustion, The Williams & Wilkins Co. (Baltimore), 1953, pp. 90–97; discussion by E. A. DeZubay, p. 97.
60. Evans, Marjorie W., Given, Frank I., and Richeson, William E., Jr.: Effects of Attenuating Materials on Detonation Induction Distances. Jour. Appl. Phys., vol. 26, no. 9, Sept. 1955, pp. 1111–1113.
61. Laffitte, M. P.: Sur la propagation de l'onde explosive. Comptes Rendus, Dec. 15, 1924, pp. 1394–1396.
62. Hoelzer, C. A., and Stobaugh, W. K.: Influence of Initial Pressure on Detonation Parameters in Combustible Gases. GAE 54–11, Air Force Inst. Tech., Mar. 1954.
63. Hinshelwood, C. N., and Williamson, A. T.: The Reaction Between Hydrogen and Oxygen. Clarendon Press (Oxford), 1934.
64. Brokaw, R. S.: Thermal Ignition, with Particular Reference to High Temperatures. Selected Combustion Problems. Vol. II. Butterworths Sci. Pub. (London), 1956, pp. 115–138.
65. Coward, H. F.: Ignition Temperatures of Gases. "Concentric Tube" Experiments of (the late) Harold Bailey Dixon. Jour. Chem. Soc. (London), pt. II, July–Dec. 1934, pp. 1382–1406.
66. Anagnostou, E., Brokaw, R. S., and Butler, J. N.: Effect of Concentration on Ignition Delays for Various Fuel-Oxygen-Nitrogen Mixtures at Elevated Temperatures. NACA TN 3887, 1956.
67. Mullins, B. P.: Studies of the Spontaneous Ignition of Fuel Injected into a Hot Air Stream. IV—Ignition Delay Measurements on Some Gaseous Fuels at Atmospheric and Reduced Static Pressures. Fuel, vol. XXXII, no. 3, July 1953, pp. 343–362.
68. Fouré, C.: Stationary Flames in Cylindrical Flow of Homogeneous Air-Hydrogen Mixtures. Fifth Symposium (International) on Combustion, Reinhold Pub. Corp., 1955, pp. 736–741.
69. von Elbe, G., and Lewis, B.: Mechanism of the Thermal Reaction between Hydrogen and Oxygen. Jour. Chem. Phys., vol. 10, no. 6, June 1942, pp. 366–393.

70. Zabetakis, Michael G.: Research on the Combustion and Explosion Hazards of Hydrogen-Water Vapor-Air Mixtures. AECU–3327, Tech. Information Service Extension, U. S. Atomic Energy Comm., Sept. 4, 1956.
71. Potter, A. E., Jr., and Berlad, A. L.: A Relation Between Burning Velocity and Quenching Distance. NACA TN 3882, 1956.
72. Berlad, A. L., and Potter, A. E., Jr.: Relation of Boundary Velocity Gradient for Flash-back to Burning Velocity and Quenching Distance. Combustion and Flame, vol. 1, no. 1, Mar. 1957, pp. 127–128.
73. Zukoski, Edward E., and Marble, Frank E.: The Role of Wake Transition in the Process of Flame Stabilization on Bluff Bodies. Combustion Researches and Reviews, Butterworths Sci. Pub., 1955, pp. 167–180.
74. Zukoski, Edward E., and Marble, Frank E.: Experiments Concerning the Mechanism of Flame Blowoff from Bluff Bodies. Proc. Gas Dynamics Symposium (Aerothermochem.), Northwestern Univ., 1956, pp. 205–210.
75. Harris, Margaret E., Grumer, Joseph, von Elbe, Guenther, and Lewis, Bernard: Burning Velocities, Quenching, and Stability Data on Nonturbulent Flames of Methane and Propane with Oxygen and Nitrogen. Third Symposium on Combustion and Flame and Explosion Phenomena, The Williams & Wilkins Co. (Baltimore), 1949, pp. 80–89.
76. Huff, Vearl N., Gordon, Sanford, and Morrell, Virginia E.: General Method and Thermodynamic Tables for Computation of Equilibrium Composition and Temperature of Chemical Reactions. NACA Rep. 1037, 1951. (Supersedes NACA TN's 2113 and 2161.)
77. Glatt, Leonard, Adams, Joan H. and Johnston, Herrick L.: Thermodynamic Properties of the H_2O Molecule from Spectroscopic Data. Tech. Rep. 316–8, Cryogenic Lab., Dept. Chem., Ohio State Univ., June 1, 1953. (Navy Contract N6onr–225.)

TABLE I.—HYDROGEN-AIR FLAME TEMPERATURES

[Pressure, 1 atm; initial temperature, 25° C.]

Source and date	Reference	Stoichiometric mixture temperature, °K	Maximum temperature, ° K	Hydrogen in maximum-temperature mixture, volume percent
Experimental				
Passauer, 1930 (split flame)	2	2263	2283	31
Jones, Lewis, and Seaman, 1931	4	2293	2318	31. 6
Morgan and Kane, 1953	3 (fig. 7)	2220	----	------
Theoretical				
Lewis and von Elbe, 1935	7	----	2320	31. 6
Friedman, 1949	8	2375	----	------
Fenn, 1951	9	2345	----	------
Morgan and Kane, 1953	3 (fig. 7)	2380	----	------
Gaydon and Wolfhard, 1953	6	2373	----	------
Burwasser and Pease, 1955	10	2315	----	------
This report	----	2387	2403	30. 9

TABLE II.—COMPUTED EQUILIBRIUM ADIABATIC FLAME TEMPERATURES, THERMODYNAMIC PROPERTIES, AND BURNED-GAS COMPOSITIONS FOR HYDROGEN-AIR MIXTURES [a]

Initial temperature, T_o, °K	Pressure, P, atm	Equivalence ratio, φ	Flame temperature, T_F, °K	Molecular weight, g/mole	Specific heat, c_v, cal (g) (°K)	Ratio of specific heats	Burned-gas composition, volume fraction								
							H_2	H_2O	N_2	OH	O_2	NO	H	O	N
0	1.00	0.50	1393.1	26.493	0.3347	1.289	0.000000	0.190201	0.714432	0.000026	0.094860	0.000482	0.000000	0.000000	0.000000
		1.00	2220.2	24.410	.5375	1.200	.008303	.335483	.648369	.002891	.002763	.001443	.000573	.00175	.000000
		2.00	1822.5	18.732	.4992	1.271	.257692	.257782	.484294	.000013	.000000	.000001	.000219	.000000	.000000
		10.00	683.9	7.475	.9680	1.379	.757665	.084185	.158150	.000000	.000000	.000000	.000000	.000000	.000000
298.16	0.01	0.10	630.3	28.342	0.2610	1.367	0.000000	0.041176	0.773532	0.000000	0.185291	0.000000	0.000000	0.000000	0.000000
		.50	1639.8	26.486	.3581	1.267	.000065	.189753	.713721	.000693	.094127	.001556	.000007	.000079	.000000
		1.00	2193.4	23.893	1.1218	1.130	.030211	.297739	.633952	.011089	.011769	.002774	.009408	.003057	.000000
		2.00	2013.2	18.642	.7075	1.204	.252586	.255679	.481949	.000786	.000010	.000046	.008918	.000026	.000000
		10.00	971.7	7.475	1.0038	1.360	.757665	.084185	.158150	.000000	.000000	.000000	.000000	.000000	.000000
	1.00	0.10	630.3	28.342	0.2610	1.367	0.000000	0.041176	0.773532	0.000000	0.185291	0.000000	0.000000	0.000000	0.000000
		.50	1642.7	26.491	.3494	1.274	.000007	.190084	.713844	.000224	.094257	.001575	.000000	.000008	.000000
		1.00	2387.2	24.272	.6497	1.177	.015519	.324028	.644061	.006178	.005006	.002729	.001859	.003618	.000000
		2.00	2063.3	18.721	.5314	1.255	.257090	.257518	.484013	.000120	.000000	.000008	.001251	.000001	.000000
		10.00	971.7	7.475	1.0039	1.360	.757665	.084185	.158150	.000000	.000000	.000000	.000000	.000000	.000000
	100	0.10	630.3	28.342	0.2610	1.367	0.000000	0.041176	0.773533	0.000000	0.185292	0.000000	0.000000	0.000000	0.000000
		.50	1643.5	26.492	.3474	1.276	.000001	.190175	.713874	.000071	.094298	.001580	.000000	.000001	.000000
		1.00	2486.2	24.461	.4778	1.218	.005277	.339886	.649619	.001997	.001314	.001683	.000171	.000053	.000000
		2.00	2070.6	18.733	.5072	1.265	.257748	.257793	.484315	.000013	.000000	.000001	.000131	.000000	.000000
		10.00	971.7	7.475	1.0039	1.360	.757665	.084185	.158150	.000000	.000000	.000000	.000000	.000000	.000000
600	0.01	0.10	916.4	28.342	0.2779	1.337	0.000000	0.041176	0.773526	0.000000	0.185286	0.000012	0.000000	0.000000	0.000000
		.50	1871.2	26.451	.4167	1.231	.000630	.187662	.711787	.003081	.092399	.003501	.000159	.000781	.000000
		1.00	2273.7	23.574	1.4339	1.119	.039989	.277393	.624995	.015803	.015497	.003766	.016820	.005737	.000000
		2.00	2165.9	18.487	1.0079	1.164	.244933	.251144	.477866	.002681	.000090	.000197	.022866	.000224	.000000
		10.00	1258.8	7.475	1.0486	1.340	.757660	.084185	.158150	.000000	.000000	.000000	.000000	000000	.000000
	1.00	0.10	916.4	28.342	0.2779	1.337	0.000000	0.041176	0.773526	0.000000	0.185285	0.000012	0.000000	0.000000	0.000000
		.50	1888.8	26.483	.3700	1.257	.000074	.189528	.712567	.001083	.092940	.003710	.000006	.000091	.000000
		1.00	2529.4	24.075	.7930	1.160	.024431	.308757	.638019	.010732	.007685	.004347	.004454	.001574	.000000
		2.00	2291.2	18.684	.6026	1.230	.255199	.256405	.483017	.000651	.000005	.000055	.004659	.000010	.000000
		10.00	1258.8	7.475	1.0481	1.340	.757664	.084185	.158150	.000000	.000000	.000000	.000000	.000000	.000000
	100	0.10	916.4	28.342	0.2779	1.337	0.000000	0.041176	0.773526	0.000000	0.185285	0.000012	0.000000	0.000000	0.000000
		.50	1892.9	26.490	.3611	1.263	.000008	.190013	.712728	.000351	.093129	.003761	.000000	.000009	.000000
		1.00	2689.6	24.384	.5276	1.204	.009791	.333003	.646851	.004184	.002336	.003117	.000539	.000178	.000000
		2.00	2319.4	18.728	.5235	1.256	.257520	.257658	.484195	.000078	.000000	.000007	.000541	.000000	.000000
		10.00	1258.8	7.475	1.0481	1.340	.757665	.084185	.158150	.000000	.000000	.000000	.000000	.000000	.000000

See footnote at end of table.

526597—60——77

TABLE II.—COMPUTED EQUILIBRIUM ADIABATIC FLAME TEMPERATURES, THERMODYNAMIC PROPERTIES, AND BURNED-GAS COMPOSITIONS FOR HYDROGEN-AIR MIXTURES [a]—Continued

Initial temperature, T_o, °K	Pressure, P, atm	Equivalence ratio, φ	Flame temperature, T_F, °K	Molecular weight, g/mole	Specific heat, c_p, cal (g) (°K)	Ratio of specific heats	Burned-gas composition, volume fraction								
							H_2	H_2O	N_2	OH	O_2	NO	H	O	N
1000	0. 01	0. 10	1297. 1	28. 342	0. 2967	1. 310	0. 000000	0. 041168	0. 773333	0. 000015	0. 185090	0. 000392	0. 000000	0. 000001	0. 000000
		1. 00	2360. 3	23. 094	1. 8861	1. 111	. 051719	. 249278	. 611572	. 022011	. 019949	. 005039	. 029770	. 010660	. 000001
		2. 00	2306. 8	18. 177	1. 5852	1. 133	. 232489	. 240180	. 469637	. 007084	. 000505	. 000631	. 048219	. 001257	. 000000
		10. 00	1627. 5	7. 473	1. 1496	1. 305	. 757113	. 084156	. 158100	. 000002	. 000000	. 000000	. 000629	. 000000	. 000000
	1. 00	0. 10	1297. 2	28. 342	0. 2965	1. 310	0. 000000	0. 041173	0. 773335	0. 000005	0. 185094	0. 000392	0. 000000	0. 000000	0. 000000
		. 50	2204. 8	26. 436	. 4272	1. 225	. 000737	. 186575	. 708992	. 004832	. 089500	. 008301	. 000157	. 000906	. 000000
		1. 00	2688. 0	23. 730	1. 0207	1. 145	. 037467	. 284133	. 627622	. 018113	. 011467	. 006787	. 010481	. 003928	. 000001
		2. 00	2550. 5	18. 552	. 7990	1. 192	. 249685	. 251637	. 479477	. 003069	. 000060	. 000344	. 015575	. 000153	. 000000
		10. 00	1631. 2	7. 475	1. 1082	1. 316	. 757607	. 084182	. 158145	. 000000	. 000000	. 000000	. 000065	. 000000	. 000000
	100	0. 10	1297. 2	28. 342	0. 2964	1. 310	0. 000000	0. 041175	0. 773336	0. 000002	0. 185095	0. 000393	0. 000000	0. 000000	0. 000000
		1. 00	2940. 9	24. 220	. 6142	1. 187	. 018460	. 319026	. 641119	. 008922	. 004193	. 005869	. 001777	. 000633	. 000001
		2. 00	2648. 6	18. 707	. 5617	1. 242	. 256594	. 256861	. 483607	. 000515	. 000001	. 000063	. 002355	. 000004	. 000000
		10. 00	1631. 5	7. 475	1. 1038	1. 317	. 757659	. 084185	. 158150	. 000000	. 000000	. 000000	. 000007	. 000000	. 000000
1400	1. 00	0. 10	1680. 2	28. 341	0. 3149	1. 287	0. 000002	0. 041092	0. 772167	0. 000161	0. 183907	0. 002654	0. 000000	0. 000017	0. 000000
		. 50	2480. 8	26. 283	. 5517	1. 188	. 003367	. 178316	. 702080	. 012715	. 084201	. 013875	. 001336	. 004110	. 000000
		1. 00	2820. 8	23. 307	1. 2763	1. 136	. 050357	. 256652	. 615111	. 026116	. 015065	. 009313	. 019683	. 007698	. 000003
		2. 00	2750. 1	18. 311	1. 1223	1. 163	. 241908	. 241251	. 472862	. 008130	. 000331	. 001096	. 033558	. 000863	. 000002
		10. 00	1996. 4	7. 470	1. 2180	1. 286	. 756456	. 084113	. 158040	. 000013	. 000000	. 000000	. 001377	. 000000	. 000000

[a] The method and thermochemical data for these computations were taken from ref. 76, with the following exceptions: Data for water were taken from ref. 77, and the equilibrium constants for the dissociation of N_2 were revised to conform with the recently accepted value of its dissociation energy, 9.756 electron volts. For simplicity, air was assumed to consist of oxygen and nitrogen only, in the molar ratio 1:3.7572, or 21.02 percent oxygen. The enthalpy change of this fictitious "air" between 300° and 2400° K is the same as that of standard air, which contains 20.95 percent oxygen plus nitrogen, argon, and other gases.

TABLE III.—HYDROGEN-AIR BURNING VELOCITIES

[Atmospheric pressure; room temperature.]

Source and date	Reference	Apparatus	Flame surface	Measurement	Stoichiometric burning velocity, cm/sec	Maximum burning velocity, cm/sec	Hydrogen in maximum-burning-velocity mixture, volume-percent
Michelson, 1889	15	Cylindrical burner	Visible	Total area	230	277	40
Ubbelohde and Hofsass, 1913	16	Cylindrical burner	Visible	Cone height	153	200	45
Ubbelohde and Koelliker, 1916	17	Cylindrical burner	Visible	Cone height	155	200	46
Bunte and Steding, 1928	18	Cylindrical burner, cooled	Visible	Cone height	190	258	40
Bunte and Litterscheidt, 1930	19	Cylindrical burner	Visible	Cone height	185	266	42
Passauer, 1930	2	Cylindrical burner, cooled, enclosed	Visible	Cone height	167	210	44
Corsiglia, 1931	20	Cylindrical burner, cooled	Visible	Approximate area	200	285	42
Jahn, 1934	21	Cylindrical burner, cooled	Visible	Cone height	187	267	43
Smith and Pickering, 1936	22	Cylindrical burner	Visible	Angle	170	252	42
Friedman, 1949	8	Cylindrical burner, cooled		Cone height (corrected)	177	------	------
Bartholomé, 1949	23	Nozzle burner	Visible	Angle	------	320	42
Calcote, Barnett, and Irby, 1949	24	Cylindrical burner	Shadowgraph	Frustum area	213	317	42
Fenn and Calcote, 1953	25	Cylindrical burner			170	------	------
Morgan and Kane, 1953	3	Nozzle burner, cooled	Schlieren	Area	215	------	------
Burwasser and Pease, 1955	10	Cylindrical burner, cooled, enclosed	Shadowgraph	Angle	230	320	42
Manton and Milliken, 1956	26	Spherical bomb	Schlieren	Flame diameter and pressure	232	300	41
Fine, 1956	27	Cylindrical burner, cooled	Schlieren	Total area	193	304	45
Heimel, 1956	30	Cylindrical burner, cooled	Schlieren	Total area	206	297	43

TABLE IV.—DETONATION VELOCITIES OF STOICHIOMETRIC HYDROGEN-OXYGEN MIXTURES

[Data from ref. 37, p. 583.]

Temperature, T, °K	Pressure, P, atm	Detonation velocity, m/sec
283	0.263	2627
	.395	2705
	.658	2775
	1.000	2821
	1.448	2856
	1.975	2872
373	0.513	2697
	.658	2738
	1.000	2790
	1.316	2828
	1.908	2842

TABLE V.—RECOMMENDED STANDARD VALUES OF HYDROGEN-AIR COMBUSTION PROPERTIES

Property	Value at equivalence ratio of 1.00 (stoichiometric)	Maximum or minimum value	Equivalence ratio for maximum or minimum of property	Pressure dependence	Temperature dependence	Remarks
Flame temperature, T_F	2387° K	2403° K	1.06	See fig. 4	$T_F \cong T_{F,300} + 0.5(T_o - 300)$ (near maximum). $T_F \cong T_{F,300} + (T_o - 300)$ (rich and lean mixtures).	
Laminar burning velocity, U_L.	215 cm/sec	310 cm/sec	1.80	$U_L \propto P^{0.16}$	$U_{L,max} = 0.09908\ T_o^{1.413}$	
Turbulent burning velocity, U_T.						Meaning of turbulent burning velocity measurements is not clear at present.
Quenching distance, d_q	0.057 cm		1.00	$d_q \propto P^{-1.051}(\varphi = 0.5)$ $d_q \propto P^{-1.138}(\varphi = 1.0)$ $d_q \propto P^{-1.097}(\varphi = 2.0)$	Unknown	
Spark ignition energy, I	0.019 millijoules		1.00	$I \propto P^{-2}$	$\log I \propto \frac{1}{T_o}$	
Detonation velocity	1850 m/sec	2150 m/sec	2.75	Small	Small	Limits of detonability: 18.3 to 59.0 percent by volume.
Explosion limits and spontaneous-ignition temperature.						Consider mixtures at temperatures over 500° C as potential explosion hazards; at low pressures, explosions may occur at temperatures as low as 340° C.
Flammability limits				None for reduced pressures; slight for high pressures.	See fig. 14	Upward propagation: Lean limit, 4.0 percent hydrogen. Rich limit, 74 percent hydrogen. Downward propagation: Lean limit, 9.0 percent hydrogen. Rich limit, 74 percent hydrogen.

REPORT 1384

A SUMMARY OF PRELIMINARY INVESTIGATIONS INTO THE CHARACTERISTICS OF COMBUSTION SCREECH IN DUCTED BURNERS [1]

By Lewis Laboratory Staff

SUMMARY

Increasing demands for higher afterburner performance have required operation at progressively higher fuel-air ratios, which has increased the occurrence and intensity of screeching combustion. The onset of screech may be followed by rapid destruction of the combustor shell and other combustor parts. Because of its destructive characteristics, considerable effort has been expended to understand and eliminate screech. NACA work on the screeching combustion problem prior to 1954 is summarized herein. These studies showed that resonant acoustic oscillations are a primary component of the screech mechanism in the burners thus far investigated. Detailed studies of frequency, amplitude, and phase relations were made in burners 6 to 37 inches in diameter; these oscillations were identified as a transverse mode. In various full-scale afterburners the observed frequencies were those to be expected from a transverse oscillation. The effects of design and operational variables on screech intensity have been investigated. Attempts to eliminate screech by reducing the driving potential of the gas stream were generally unsuccessful, but the use of an acoustic damper completely eliminated screech in all burner configurations in which it was used.

INTRODUCTION

The increasing demand for higher performance from turbojet engine afterburners and ramjet engine combustors has required operation of these combustors at the high temperatures obtainable only near stoichiometric fuel-air ratios. Combustor operation at high fuel-air ratios has often led to the phenomenon known throughout the aircraft industry as screech. The high combustion pressures and temperatures accompanying low-altitude high-speed flight are also conducive to screech. This phenomenon derives its name from the shrill scream or screech accompanying it. Other manifestations of screech are high-frequency pressure oscillations in the combustion zone, increased rate of flame propagation, usually improved afterburner combustion efficiency, higher operating temperatures of the combustor parts and shell, and, under moderate to severe screeching conditions, rapid deterioration or failure of combustor shell, flameholder, and other combustor parts. An example of an afterburner failure produced by screeching combustion is shown in figure 1. Because of the severe deterioration of the combustor under screeching operating conditions, it has been essential that an understanding of the screech phenomenon be gained and that a method of controlling or eliminating screech be devised.

Many investigators have studied the screech problem (e. g., refs. 1 to 6). From these investigations and others, several theories have been evolved in an attempt to describe the screech phenomenon. These theories have been based either on some phase of combustion kinetics, aerodynamics, or self-exciting acoustic resonance or on a combination of these. Under combustion kinetics, consideration has been given to phenomena similar to knock in reciprocating engines, such as detonation and flashback, and to properties of the fuel such as flame speed. Among the aerodynamic factors considered have been vortex strength, vortex interaction from flameholders, boundary-layer effects, and flow separation. Theories based on acoustical resonance have included longitudinal or organ-pipe vibrations, radial modes of vibration, and transverse modes of vibration.

The NACA Lewis laboratory has investigated most of these possibilities. The evidence collected, although it

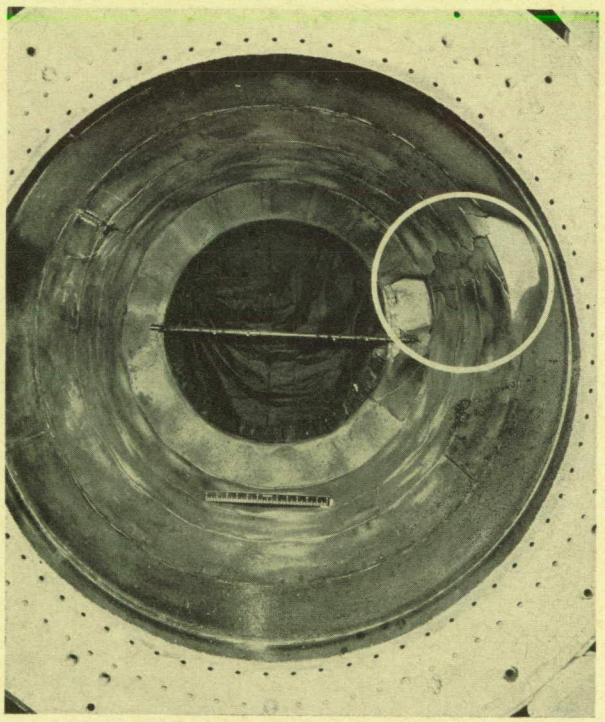


Figure 1.—Example of screech-produced afterburner shell failure.

[1] Supersedes recently declassified NACA Research Memorandum E54B02 by the Lewis Laboratory Staff, 1954.

does not completely describe screech, has strongly indicated some of the predominant characteristics of screech. The present paper summarizes the more important phases of the analytical work, small and large duct experiments, and full-scale engine investigations conducted at the NACA Lewis laboratory prior to 1954. These results are compared with the works of other experimenters to correlate the predominant characteristics of screech. A mechanism for control or elimination of screech is described.

SYMBOLS

The following symbols are used in this report:

a	speed of sound
B	constant of integration (eq. (1))
d	gutter radius
f	frequency, cps
h	function defined by eqs. (1) and (2)
J_n,N_n	Bessel functions of the first and second kind, respectively
n,m	mode numbers such that n and $m+1$ are the number of nodal diameters and nodal circles, respectively
P'	pressure fluctuation
p/p_o	ratio of local to free-stream static pressure
R,R_i	center-wall and innerbody radii, respectively
t	time
x,r,θ	cylindrical coordinates
α,α_{nm}	reduced frequency determined by solving eq. (5) or (7)
β	amplification numbers (eq. (8))

ANALYSIS

Preliminary experimental investigations at the Lewis laboratory, as well as information available from work done elsewhere, led to the belief that acoustic oscillations were present during screeching combustion. Hence, coincident with the continuing experimental studies, a theoretical analysis has been made of the possibilities of sonic resonance in a combustor. Once it is assumed that acoustic resonance may be present in a screeching combustor, the problem becomes one of finding what forms these oscillations may take and which modes are most likely to occur. To this end, as a model, there may be considered a circular cylindrical duct having, in the steady state, a relatively slow uniform through flow and an axial steady temperature variation (and hence axial variation in the speed of sound a). The hardware in the combustor may reasonably be assumed irrelevant provided the chamber is relatively clean downstream of the flameholder. Within these assumptions, the unsteady pressure fluctuation P' must satisfy

$$a^2\left(P'_{rr}+\frac{P'_r}{r}+\frac{P'_{\theta\theta}}{r^2}\right)+(a^2P'_x)_x=P'_{tt}$$

(The subscripts denote differentiation.) Solutions of this equation may be written

$$P'=e^{i(2\pi ft\pm n\theta)}[J_n(\alpha_{nm}\pi r/R)+BN_n(\alpha_{nm}\pi r/R)]\,h(x) \qquad (1)$$

where α_{nm} (hereinafter written simply α) is chosen such that there is no flow across the chamber wall ($r=R$), where $h(x)$ is such that

$$(a^2h_x)_x+\pi^2\left[4f^2-\left(\frac{a\alpha}{R}\right)^2\right]h=0 \qquad (2)$$

and J_n and N_n are the Bessel functions of the first and second kinds, respectively. If a more complex model had been assumed, say, one in which the steady-state pressure and axial velocity were assumed to vary with x, then equation (1) would still apply but equation (2) would be more involved. This remark would also apply if a uniform axial through flow of large magnitude were included, or if a longitudinally varying heat release were considered.

The integers n and m may be related to the number of pressure nodes in the oscillation. Thus, n is the number of nodal lines (which lie along diameters) and $m+1$ is the number of nodal circles.

MODES OF ACOUSTIC RESONANCE

Equation (1) embraces all the possible resonant oscillations in a circular cylinder. These are well known (cf. ref. 7) but are briefly described herein. The solution involving N_n is rejected because it is singular at the pipe axis and hence is inadmissible when there is no centerbody. For simplicity of description, the speed of sound is assumed constant. The modes are:

(1) **Purely longitudinal (organ-pipe).**—If a is constant, equation (2) has the solution

$$h=e^{i\pi\sqrt{\frac{4f^2}{a^2}-\frac{\alpha^2}{R^2}}\,x} \qquad (3)$$

If n and α are chosen to be zero,

$$P'=e^{2\pi if\,(t\pm x/a)} \qquad (4a)$$

(2) **Radial and transverse.**—If $2fR/a=\alpha$, a permissible solution of equation (2) is $h=1$. In that case

$$P'=e^{i\left[\left(\frac{\pi\alpha a}{R}\right)t\pm n\theta\right]}J_n(\pi\alpha_{nm}r/R) \qquad (4b)$$

It may be noted that for $n=0$ there are obtained the radial modes, while for $n\neq 0$ there are found what will be called the transverse modes. In figure 2, there are sketched the particle paths and pressure amplitude contours (mutually orthogonal) for the (1,0) transverse mode. The notation (1,0) means $n=1$, $m=0$. Pressure amplitude contours are shown in figures 3 and 4. The radial $(0,m)$ modes have a pressure maximum at the center of the duct while all the other (transverse) modes show zero pressure amplitude at that point. In figure 3 the wall would be at stations a, b, c, and so forth, depending on whether the first, second, third, or a higher radial mode occurred. It may also be observed that the $(n,1)$ modes (fig. 4(b)) contain the pattern for the $(n,0)$ modes (fig. 4(a)) as a core inside the dashed circle.

(3) **Combined lateral-longitudinal.**—If a is a constant, the combined modes may be written

$$P'=e^{i\left(2\pi ft\pm n\theta\pm\pi\sqrt{\frac{4f^2}{a^2}-\frac{\alpha^2}{R^2}}\,x\right)}J_n\left(\alpha\pi\frac{r}{R}\right) \qquad (4c)$$

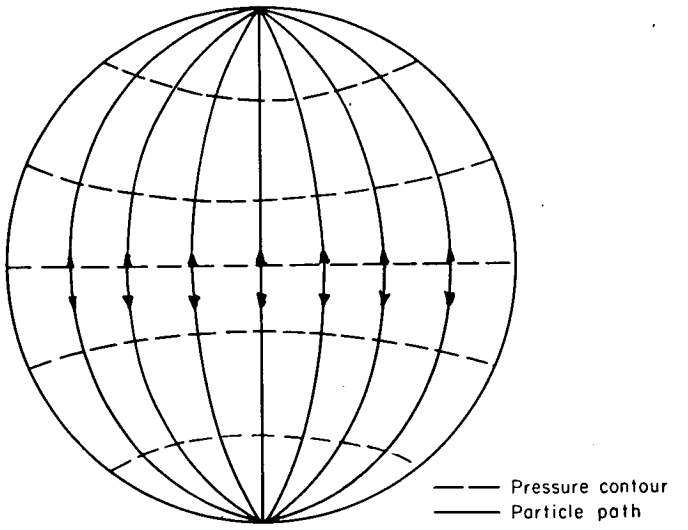


FIGURE 2.—Loci of particle paths and pressures for first transverse mode (1,0).

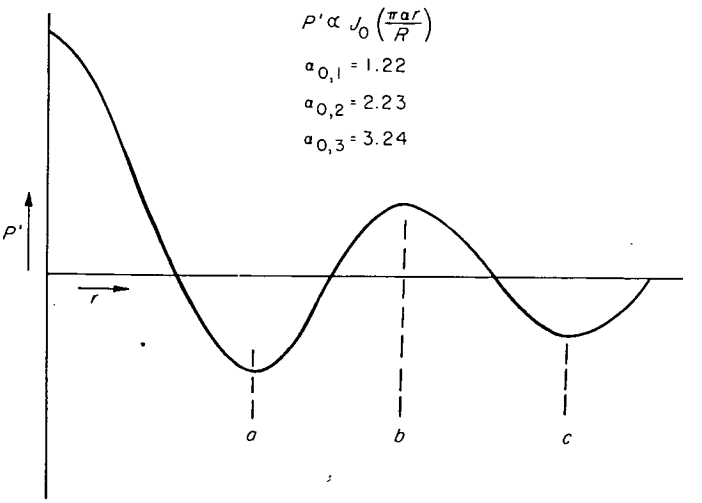
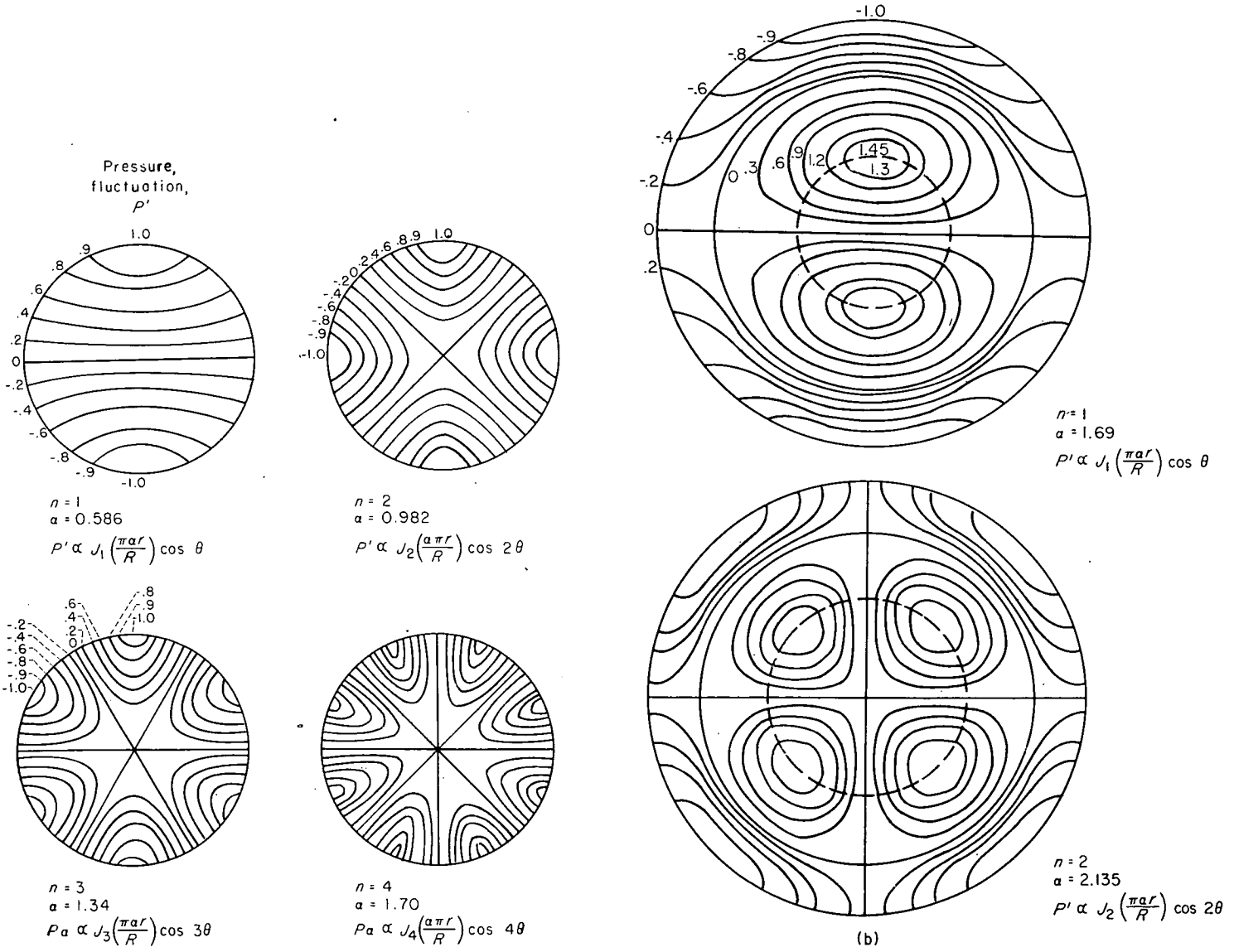


FIGURE 3.—Variation of pressure with radius for radial mode.



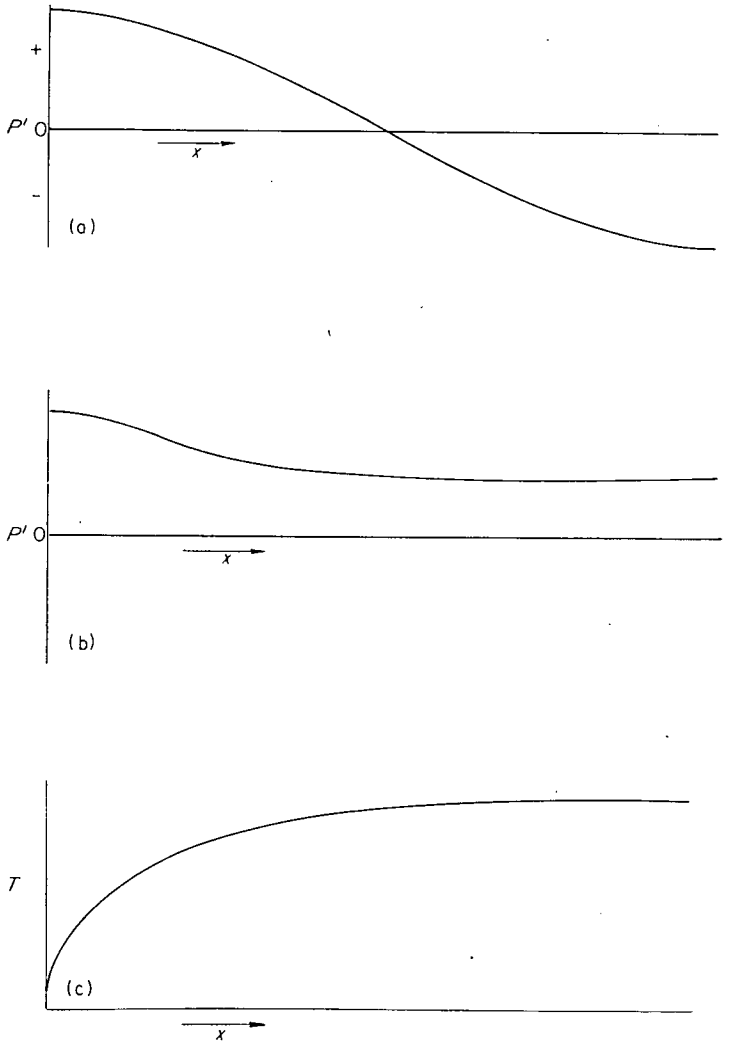
(a) $m=0$. (b) $m=1$.

FIGURE 4.—Pressure contours for various transverse modes.

If, in the three cases described, the speed of sound had been assumed variable, results similar to those given would be obtained except that the longitudinal factor $h(x)$ in the wave would be more complex and not, in general, easily represented.

It may be important for the purpose of experimental identification to distinguish between the effect produced by a longitudinal (organ-pipe) mode and the effect which may be produced by temperature. The organ-pipe mode (fig. 5(a)) is such that in a given wave length there is symmetry about the midpoint and, at a given time, the spatial average of the pressure fluctuation P' is zero. The effect of temperature may be something quite different. Figure 5(b) shows the pressure amplitude profile found when equation (2) was integrated numerically for the temperature profile of figure 5(c). In this case the effect of temperature was simply to modify an otherwise constant pressure amplitude. This latter effect (of modifying the longitudinal pressure profile) must be present when the chamber temperature (and hence the speed of sound) varies.

In a practical combustor the manner in which the oscillation is driven will modify the motion. If the motion is driven in one region of the burner by, say, a combustion oscillation, it may be that the oscillation in another region will exhibit a phase lag relative to the region where the driving occurs. This is simply because the motion is formed of waves originating at the driving station, and these will take an appreciable time (relative to the period of oscillation) to reach another portion of the chamber.



(a) Pressure amplitude for pure longitudinal wave.
(b) Pressure variation due to temperature variation of figure 5(c).
(c) Typical temperature distribution.

FIGURE 5.—Two types of longitudinal pressure variation.

RESONANCE FREQUENCIES

The constant α_{nm} is the value of the argument of J_n such that

$$\frac{\mathrm{d}}{\mathrm{d}r}[J_n(\pi\alpha r/R)]_{r=R}=0 \tag{5}$$

and equals the reduced frequency $2fR/a$ for purely radial or transverse oscillations. Since J_n is an oscillating function of its argument, it follows that, for any n, an infinite sequence of values (m) of α exists for which $\frac{\mathrm{d}}{\mathrm{d}r}\left[J_n\left(\frac{\pi\alpha r}{R}\right)\right]_{r=R}=0$. This sequence of m's and n's yields a doubly infinite set of possible reduced frequencies. If a longitudinal oscillation is included (eq. (4c)), the frequency of the mode is altered and a third infinity of possible frequencies is introduced. In general, the frequency is found from equation (4c) and is given by

$$f=\frac{a}{2}\sqrt{\left(\frac{\alpha}{R}\right)^2+\left(\frac{n_x}{l}\right)^2} \tag{6}$$

where n_x/l is the half wave length of the longitudinal mode. For example, if the first (1,0) transverse mode occurs, the frequency in a 6-inch duct would be about 3000 cycles per second with usual burner temperatures. If this mode appears in conjunction with the first longitudinal mode (assuming that the ratio of diameter to length is 1/3), the transverse frequency will be raised about 100 cycles per second.

At this point, it is appropriate to note that the wave systems discussed are for standing waves, that is, for waves having fixed nodal diameters. It is also possible to have transverse traveling waves, such that the amplitude of the wave pattern is fixed but the whole pattern rotates. The discussion of frequencies given previously applies equally to standing and traveling waves.

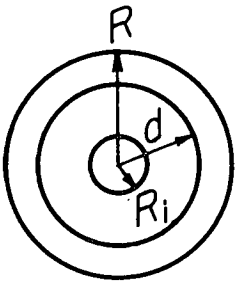
Centerbody.—In order to take into account a central body, the solution must include both Bessel functions (eq. (1)). In such a case, the reduced frequency α is determined by solving the equation

$$\left[\frac{\frac{\mathrm{d}}{\mathrm{d}r}J_n\left(\frac{\alpha\pi r}{R}\right)}{\frac{\mathrm{d}}{\mathrm{d}r}N_n\left(\frac{\alpha\pi r}{R}\right)}\right]_{r=R}=\left[\frac{\frac{\mathrm{d}}{\mathrm{d}r}J_n\left(\frac{\alpha\pi r}{R}\right)}{\frac{\mathrm{d}}{\mathrm{d}r}N_n\left(\frac{\alpha\pi r}{R}\right)}\right]_{r=R_i} \tag{7}$$

where R_i and R are the wall radii. This expression is found from the condition that the radial velocity and hence $\partial P'/\partial r$ vanish at the walls. In general, it follows from the solution of this equation that for the first radial mode (0,1) the presence of a centerbody increases the frequency, while for a transverse mode of the form $(n,0)$ the frequency will be decreased. For other modes the frequency will be either

increased, decreased, or unaltered, depending on the ratio of centerbody to outer-wall diameter. Although the theory assumes that the centerbody extends to the ends of the chamber, the results are probably valid if it extends a substantial distance downstream of the flameholder.

Heat addition.—It appears that, when screech occurs, there is a violent disturbance of the flame behind the gutters. This occurrence should be accompanied by a variation in the local heat release. If the local pressure or temperature rises, the heat release should increase in this region of unsteady burning. The heat release in this disturbed region (assumed here to be annular) will act on the remaining fluid somewhat in the manner of a mass source; thus, the energy addition will cause an incremental flow away from the annulus, which for a thin annulus may be represented by a radial velocity discontinuity at that station (d in the following sketch). The temperature fluctuations are related to the



pressure changes. It is assumed for simplicity that there are no time lags involved. With this model of the effect of annular heat addition, two solutions, similar to equation (1) and applying on either side of $r=d$, are found. However, in this case the frequency $\alpha a/2R$ is complex, and the following expression may be written:

$$P'=e^{\beta t}\cos\left(\frac{\pi\alpha a t}{R}\right)(\text{function of } r,\theta) \qquad (8)$$

where β is always positive and real and $\alpha a/2R$ is the frequency found from equation (7), which applies in the absence of this added disturbance.

The relative amplification is plotted for various cases in figures 6 and 7. The factor plotted is β divided by a constant depending on the pressure and temperature sensitivity of the flame. From figure 6, it appears that the radial mode is most likely for burning near the axis; otherwise, a transverse mode should occur. Further, the driving is strongest for the transverse modes if the heat is added near the outer wall. The main trend to be observed in figure 7 is that the driving (of the first transverse mode) increases with gutter diameter regardless of the centerbody diameter. If, as may be the case, the driving of the oscillation is associated with unsteady burning in the high-shear region near the wall, this analysis would indicate a stronger preference for a transverse mode. It should be emphasized here that the total heat release has been assumed the same for all gutter positions. This assumption represents a highly idealized picture, particularly for locations near the wall and near the center of the duct.

Although it appears that for burning near the outer wall the higher (n) modes are driven most strongly, other factors

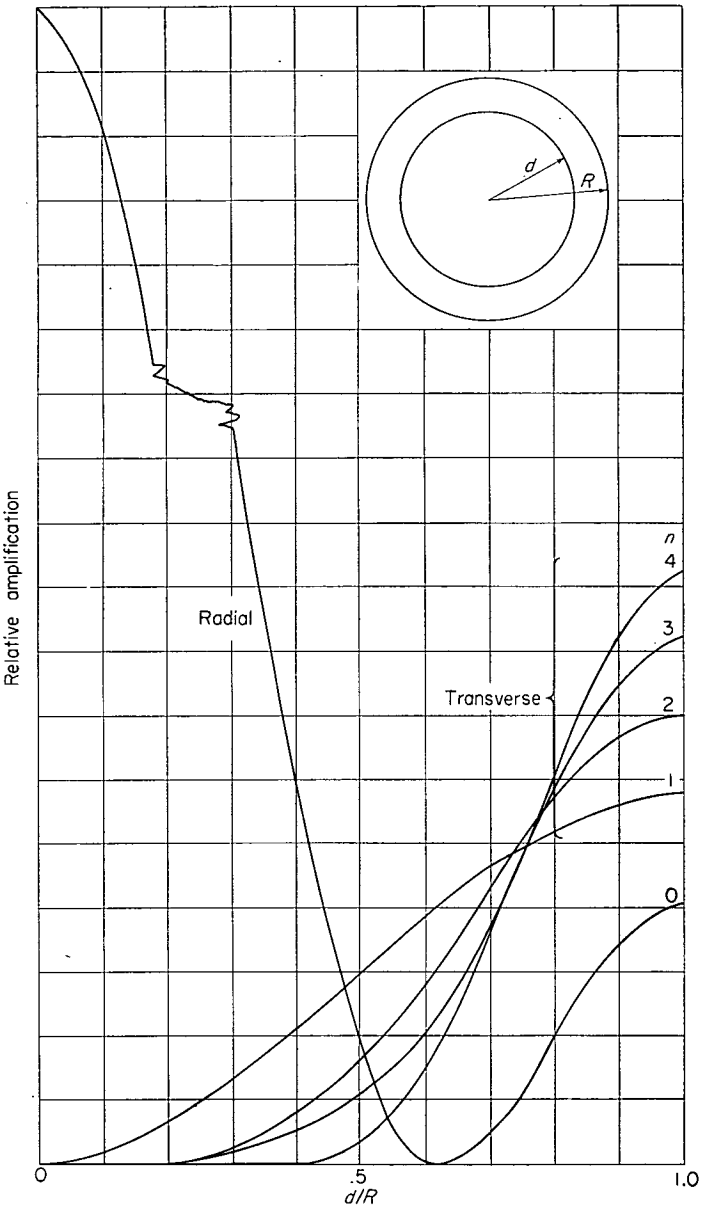


FIGURE 6.—Relative amplification for several modes (no centerbody).

tend to counteract this. It has been shown (see, e. g., ref. 8) that, as might be expected, viscous damping of a transverse wave at the wall increases with frequency. Hence, it is reasonable to expect that for a flameholder near the axis the radial mode is most likely, while for a configuration wherein the gutter is far from the axis one of the lower frequency transverse modes is most probable.

If this model had included the effect of an induction time lag, which is a function of the inlet conditions, flameholder, fuel, and the like, the triply infinite set of possible frequencies of oscillation would become a virtually continuous spectrum, especially for the higher modes. Hence, identification of a mode by means of phase relations, rather than by frequency, is likely to be more fruitful. The lowest possible frequency (excluding longitudinal modes) remains that of the first transverse mode (1,0).

Further, it should be remembered that the analysis described here is a linear one based on small disturbances. In the actual screeching combustor, the oscillations are very large and phenomenon is certainly nonlinear. In such

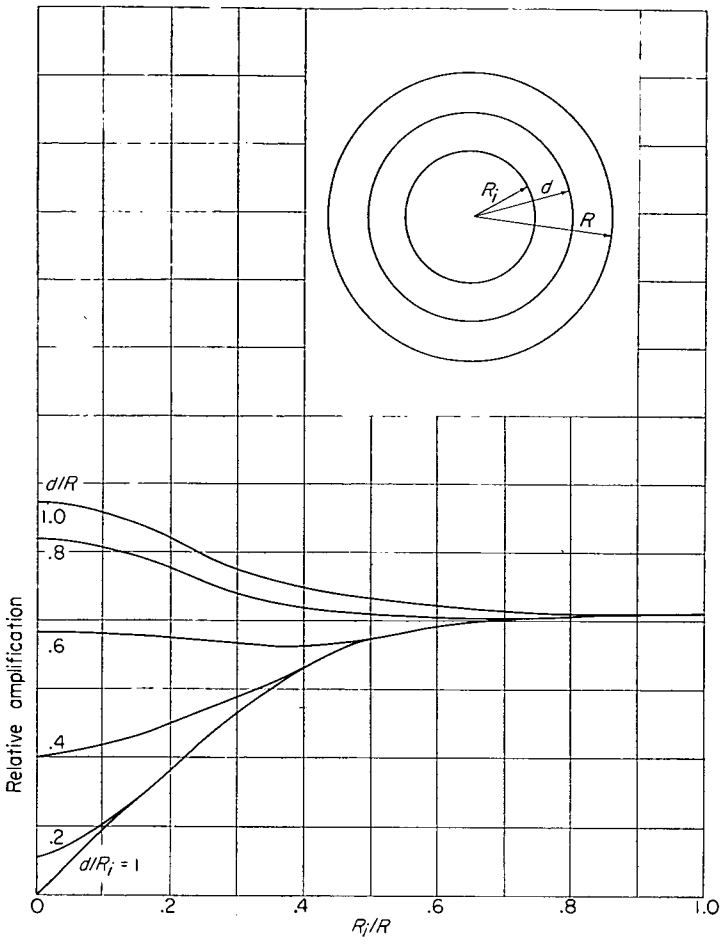


FIGURE 7.—Relative amplification versus centerbody diameter for first transverse mode (1,0).

a case it may be expected that such things as phase relations may be somewhat modified, although the results indicated by the present analysis should be reasonably accurate. When there is a high average through-flow velocity, the wave system may deviate sufficiently from the simplified picture given here to give appreciable changes in frequency. This point is discussed further in reference 2.

SUMMARY OF THEORETICAL PREDICTIONS

(1) The extreme "density" of possible resonant-pipe oscillations suggests that experimental identification of acoustic mode not be attempted on the basis of frequency alone. Rather, phase relations should be found. Because of variations of fuel, gutter geometry, inlet conditions, and the like, the coupling of unsteady heat release with pressure oscillation will probably cause appreciable variations in the frequency of acoustic oscillations. Also, the theoretical frequencies depend upon some average chamber temperature, a quantity which may be very difficult to determine accurately.

(2) If energy is added to the oscillation at an annulus near the center of the duct, radial oscillations appear most probable; if near the outer shell, transverse modes are more probable.

(3) The presence of a centerbody will not necessarily increase the frequency of lateral oscillation; in fact, if a transverse oscillation of the type $(n, 0)$ occurs, the frequency must be reduced.

EXPERIMENTAL DETERMINATION OF SCREECH MECHANISM

Three modes of acoustical resonance were discussed in the preceding section as possible elements of the screech mechanism. Concurrently with the analytical work, the screech mechanism was experimentally investigated in ducted burners having diameters of 6, 8, 14, 20, and 26 inches. These studies included amplitude, frequency, and phase measurements during screeching combustion.

AMPLITUDE DISTRIBUTION

The relative pressure amplitude during screech at various positions across the diameter of the 6-inch combustor of reference 1 is shown in figure 8 for a survey made ¾ inch downstream of the flameholder. The amplitude exhibits a pronounced dip near the center of the duct. This is the amplitude pattern to be expected with a transverse mode of oscillation; such a pattern could not result from radial or longitudinal oscillations.

Figure 9 shows values of pressure amplitude at the wall of the 6-inch burner at various positions along the length of

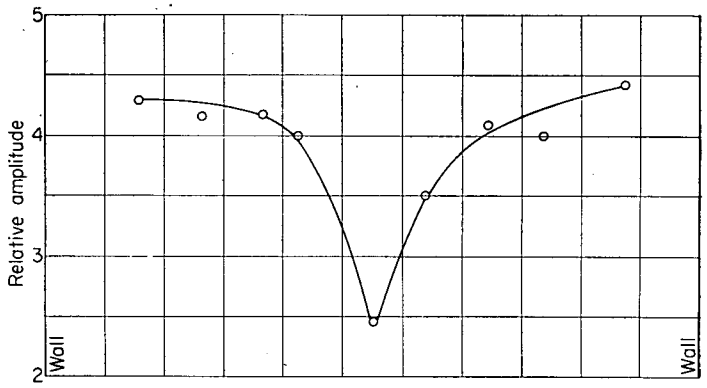


FIGURE 8.—Amplitude profile across 6-inch burner.

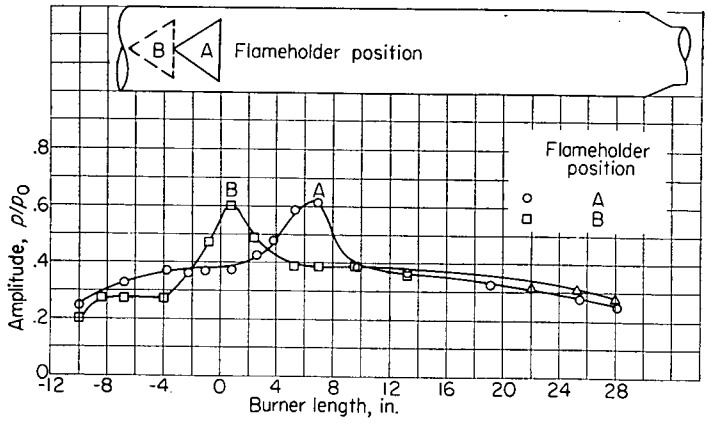


FIGURE 9.—Amplitude distribution for two flameholder positions in 6-inch burner.

the burner. A peak exists in the pressure amplitude 4 to 6 inches downstream of the flameholder. The pattern of amplitude against burner length shown in figure 9 does not indicate the presence of a standing longitudinal wave. The region of maximum amplitude just downstream of the flameholder lies where the maximum heat-release rate might be expected. If there existed a combined transverse and longitudinal oscillation, and if the longitudinal component is

to appreciably affect the indicated frequencies, the half wave length would have to be on the order of a diameter (eq. (6)). With a half wave length of this magnitude, multiple pressure nodes would occur in the 38-inch length surveyed in figure 9. Since multiple nodes are not evidenced in figure 9, there exist no longitudinal components which can appreciably affect the frequency. The screech frequency can therefore be expressed by the relation

$$f=\frac{\alpha a}{2R}$$

FREQUENCY

An observed screech frequency in the 6-inch burner of approximately 3300 cycles per second was obtained at an over-all equivalence ratio of 0.94 and an inlet temperature of 800° F. This frequency can be produced by the first transverse mode (1,0) of oscillation ($\alpha=0.586$) if the speed of sound is 2920 feet per second, or by the second transverse mode (2,0) ($\alpha=0.972$) if the speed of sound is 1710 feet per second. These values for the speed of sound correspond to average temperatures of 3560° and 800° F, respectively. The higher of these temperatures approaches the theoretical flame temperature; the lower is the temperature of the inlet gas. Considerations of screech frequency therefore indicate that the oscillation could consist of the first transverse mode in the hot gas or the second transverse mode in the inlet stream. For transverse modes of oscillation, the pressure will be out of phase on opposite sides of the combustor for odd values of n and in phase on opposite sides of the combustor for even values of n, along any diameter except an antinodal diameter. Phase measurements should therefore make it possible to determine whether the first (1,0) or the second (2,0) transverse mode occurs in the 6-inch burner.

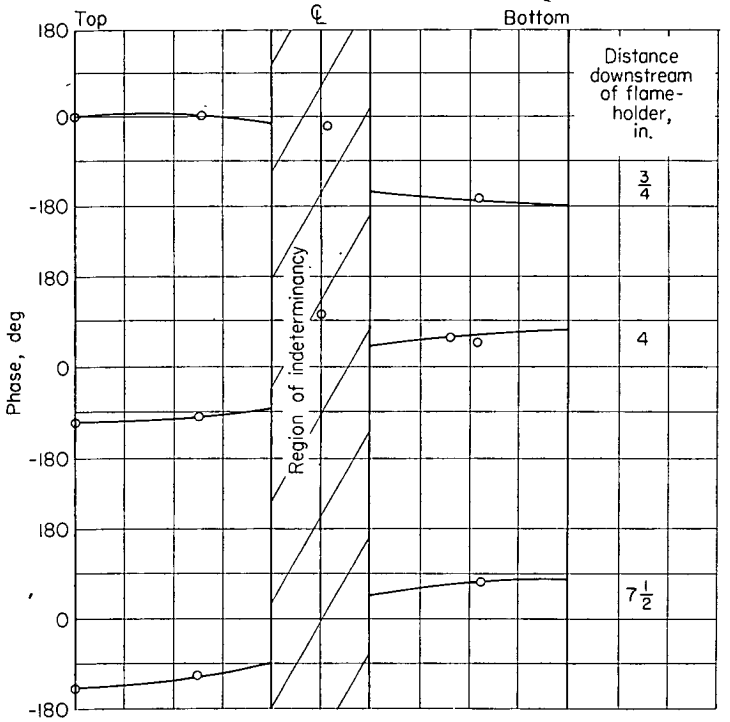


FIGURE 10.—Phase of pressure signal relative to signal at top of burner ¾ inch downstream of flameholder for three flameholder positions.

PHASE MEASUREMENTS

By means of the special microphones for studying phase relations described in reference 1, vertical diametric surveys of pressure amplitude were made at three distances downstream of the flameholder in the 6-inch burner. The phase of the pressure signal relative to the signal obtained at a point near the flameholder is shown in figure 10. The 180° phase shift across a diameter indicates that the first transverse mode of oscillation persisted in the burner. The data of figure 10 also indicate a shift along the length of the burner. This is further shown by the data in figure 11, which presents the relative phase of the pressure signal at various positions along the length of the burner. A pronounced phase shift in the vicinity of the flameholder indicates that in this region the waves have appreciable longitudinal components. The absence of a phase shift in the hot gases farther downstream of the flameholder indicates the presence of pure transverse oscillation in this region.

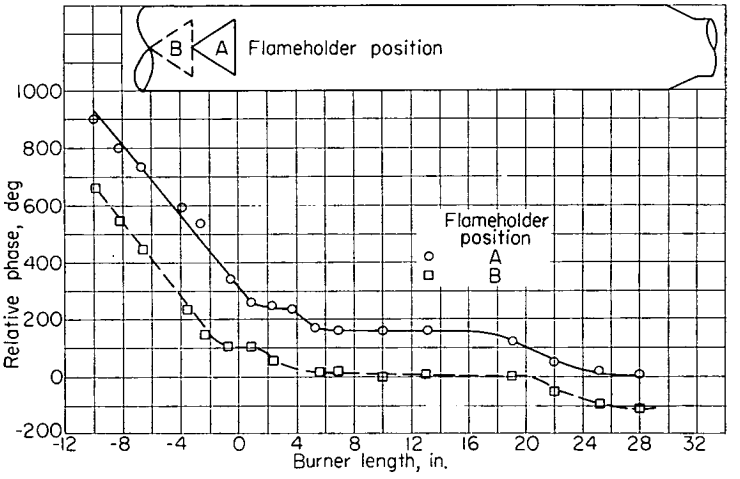
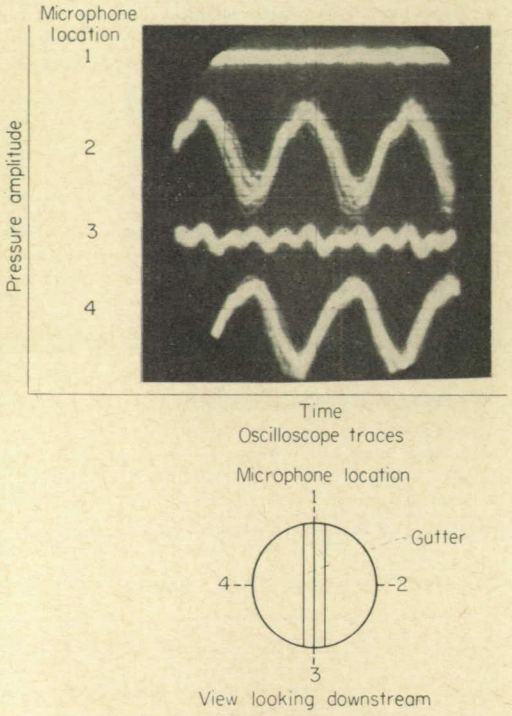


FIGURE 11.—Phase distribution for two flameholder positions in 6-inch burner.

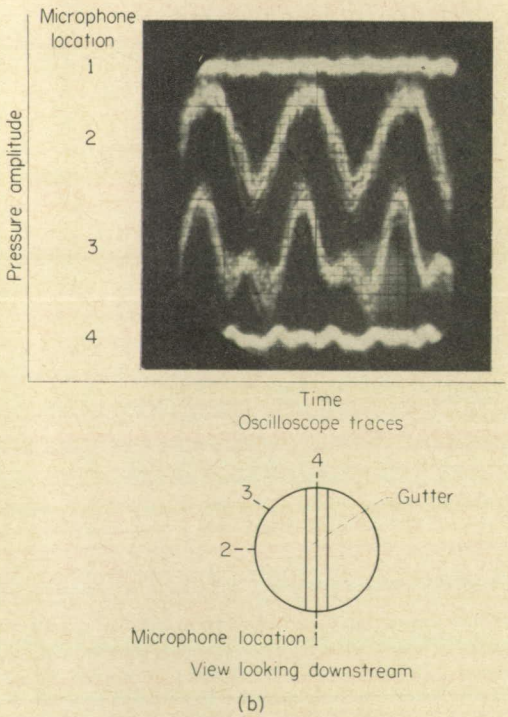
Phase measurements in the 26-inch ducted burner are shown in figure 12. Figure 12(a) shows oscilloscope traces with four microphone pressure pickups equally spaced on the outer wall of the burner. Pickups 1 and 3 were located at opposite ends of the diametric V-gutter flameholder and showed little variation in the burner pressure. Pickups 2 and 4 were located at opposite walls of the burner on an axis at right angles to the flameholder, and these pickups indicated marked variations in pressure which were approximately 180° out of phase between the two pickups. Figure 12(b) shows additional oscilloscope traces obtained with unequally spaced microphone pickups as indicated. Pickups 1 and 4, which were alined with the main axis of the flameholder, indicated little variation in pressure. Pickup 2, which was midway between pickups 1 and 4, showed a marked variation in pressure. Pickup 3, which was located between pickups 2 and 4, showed a variation in pressure in phase with that indicated by pickup 2, but having smaller magnitude. The oscilloscope traces of figures 12(a) and (b) are what would be expected with the first standing transverse mode (1,0) of oscillation in the burner and with an antinodal line coincident with the axis of the flameholder.

Similar pressure records obtained with a different flameholder (5 in. wide) are shown in figure 12(c). Pressure pickups 1 and 4, which were located on an axis normal to the flameholder, showed very little variation in pressure. Pickup



(a)

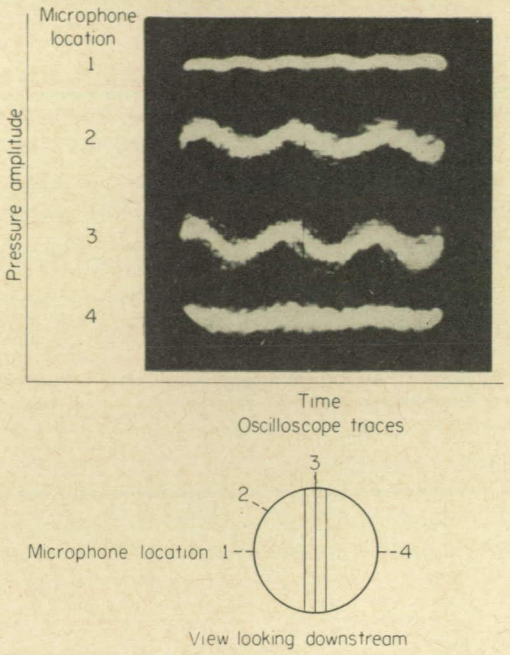
(a) Microphones equally spaced; location of microphone taps, 1.0 inch downstream of flameholder; flameholder width, 8 inches; screech frequency, 650 cycles per second.



(b)

(b) Microphones unequally spaced; location of microphone taps, 1.0 inch downstream of flameholder; flameholder width, 8 inches; screech frequency, 650 cycles per second.

FIGURE 12.—Phase relations of screech oscillations in 26-inch-diameter burner with diametrical V-gutter flameholder.



(c)

(c) Microphones unequally spaced; location of microphone taps, 5.2 inches downstream of flameholder; flameholder width, 5 inches; screech frequency, 550 cycles per second.

FIGURE 12.—Concluded. Phase relations of screech oscillations in 26-inch-diameter burner with diametrical V-gutter flameholder.

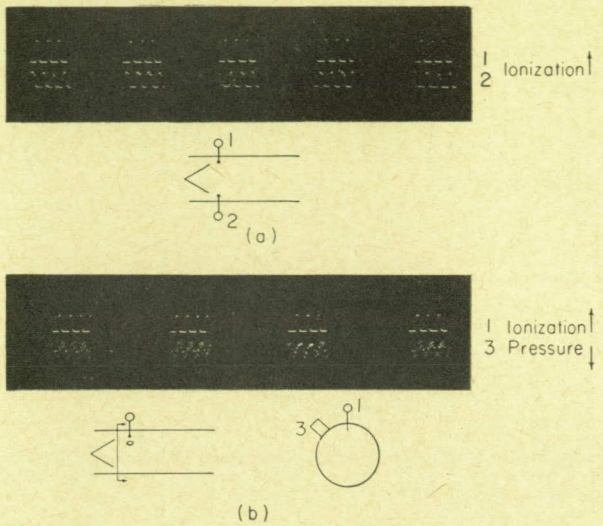
3 (located on the flameholder axis) and pickup 2 (located between pickups 1 and 3) indicated marked variations in pressure which were in phase between these two pickups. These data indicate the existence of the standing (1,0) mode of oscillation with an antinodal line normal to the axis of the flameholder.

The data of figure 12 indicate the existence of the standing transverse mode of oscillation. In the 6-inch burner with a central single-cone flameholder, however, stroboscopic motion pictures indicate the existence of a traveling (spinning) transverse oscillation. Apparently either the standing or the traveling oscillations can occur; the spinning oscillation may be favored when the flameholder is symmetric.

PHASE RELATIONS BETWEEN FLAME PRESSURE PULSES

With two ionization gaps located 180° apart, ¾ inch downstream of the flameholder, and extending ¾ inch from the burner walls, the signals shown in figure 13 were obtained in the 6-inch burner. The flame striking the ionization gaps was 180° out of phase on opposite sides of the burner. Simultaneous measurement of pressure and flame-produced ionization near the flameholder showed that the outward flame-front motion was nearly in phase with the pressure at this station. The small phase difference between the pressure and ionization traces in figure 13(b) is just that found between pressure measurements at the two stations. On the basis of these phase measurements and measurements similar to those shown in figure 11, a time sequence of events in the screech cycle can be constructed as shown in figure 14. The relation between the pressure and the flame-front displacement is that expected with a transverse oscillation. Also, it is of interest that the region of maximum amplitude

separates the downstream region having a uniform transverse oscillation from a region in which waves appear to be propagated upstream at approximately the speed of sound relative to the moving gas.



(a) Ionization traces at top and bottom of burner ¾ inch from wall.
(b) Ionization and pressure traces at top and 60° from top, respectively.

FIGURE 13.—Ionization and pressure traces ¾ inch downstream of flameholder in 6-inch burner.

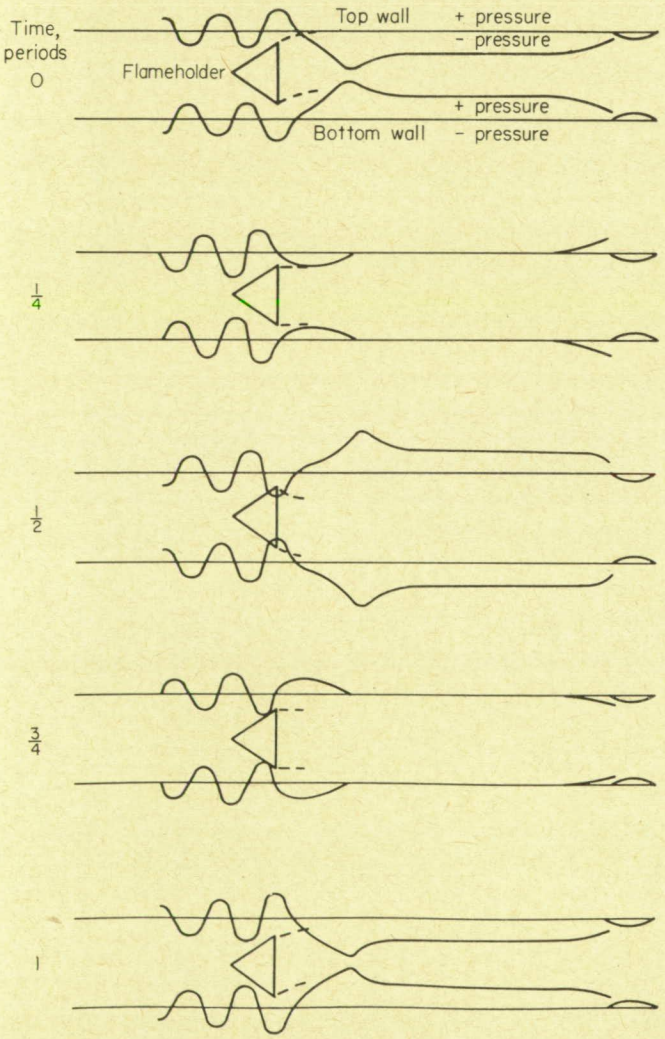


FIGURE 14.—Reconstruction of pressure and flame displacement sequence.

SPECULATION REGARDING SCREECH MECHANISM

The data thus far indicate that the gas in those burners investigated does, in fact, execute a transverse oscillation during screech. It yet remains to find the cause and origin of screech. Obviously, some source of energy or driving potential is required to maintain the resonant oscillations. If this source of energy can be found, screech can be prevented by reducing or removing the energy source. Two sources of energy are available in the burner: (1) the kinetic energy in the flowing gas stream, and (2) the chemical energy released during the combustion process. Of these two sources, the chemical energy is far greater. In order for this energy to be made available to overcome damping and maintain the oscillations at a high amplitude, it is necessary for it to be involved in some time-varying work cycle. The criterion proposed by Rayleigh (ref. 9) is that, if the heat input occurs at locations where the pressure varies and at a time when the pressure is near its maximum, the driving is a maximum. For the case where the oscillations are driven by the kinetic energy of the flowing stream, the heat release plays a part in intermittently storing and releasing this kinetic energy in such a manner that the oscillation is maintained (ref. 10). In either event, it is obvious that the oscillation may be driven only when the heat release undergoes a variation with time. This may be brought about in many ways.

A coupling between the chemical reaction and the acoustic oscillations could result from the effect of pressure and temperature on the chemical kinetics. The rate of energy release per unit volume in high-speed combustion equipment has been shown to increase with increase in pressure and temperature (refs. 11 and 12). The increase in pressure and temperature accompanying the arrival of each pressure pulse at the flame zone could therefore be expected to increase the heat-release rate. This coupling is described in the analysis section in the discussion leading to equation (8). For small oscillations, the effect is possibly negligible, but for large waves the increased heat-release rate could be very important in maintaining screech.

Increases in flame-front area resulting from pressure pulses could also account for the necessary coupling. That flame-front disturbances do exist is evident from the data of figures 13 and 14 as well as from the schlieren photographs shown in reference 3. If the rate of heat release is proportional to the product of the normal laminar flame speed and the flame-front area, wrinkling of the flame due to the action of pressure pulses could result in the necessary coupling. There is a strong possibility that a flame-front extension is caused by the scattering of waves at the flameholder and hence will depend on flameholder size. This mechanism might amplify small oscillations and thus be important at the onset of screech.

Additional coupling between the chemical reaction and the acoustic oscillations may occur because of the phenomenon of detonation. However, no definite evidence of its presence has been found in afterburners.

The energy in the oscillation is lost in at least three ways. Energy is radiated upstream in an amount proportional to the gas density and the cross-sectional area of the duct;

energy is conveyed out of the exhaust nozzle in an amount proportional to the mass rate of flow; and energy is imparted to the wall of the burner itself through friction and flection. All these rates of energy loss will depend on the square of the pressure amplitude.

The energy supplied to the oscillation by the mechanisms already discussed varies with pressure amplitude in different fashions. At the onset of screech the flame distortion due to scattering of waves at the flameholder may be the most important driving factor. As the amplitude builds up, this driving mechanism might be superseded by the effect of increased heat release due to adiabatic compression.

There are certain beneficial aspects of screech which make it worthwhile to consider whether or not a controlled screech might be desirable. Often, an increased combustion efficiency accompanies screech. Another advantage is the possible gain in over-all cycle efficiency for a given thermal efficiency. A gain in cycle efficiency might occur because more of the heat is released at a higher pressure level during screech. It is not known how much, if any, of such energy is available beyond that required to drive the oscillation.

EFFECT OF OPERATIONAL VARIABLES ON SCREECH LIMITS AND INTENSITY

PRESSURE

The effect of pressure on screech amplitude in the 6-inch burner is shown in figure 15. The peak-to-peak pressure amplitude showed a general increase with increase in burner pressure. The airflow rate is noted for each data point of figure 15. At an airflow of 1.5 pounds per second, the pressure limit for screech was 20 inches of mercury; below this pressure, screech was not encountered. At the screech

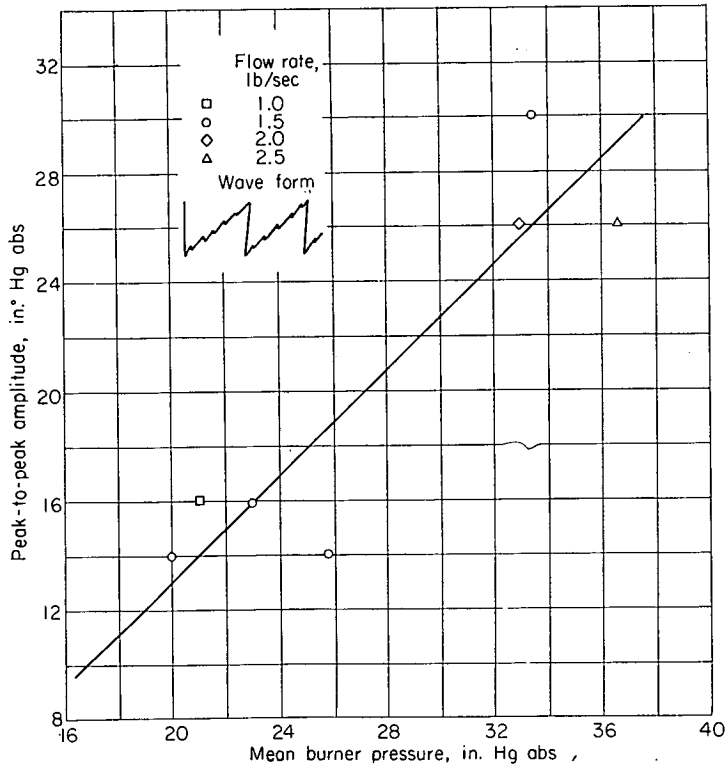


FIGURE 15.—Peak-to-peak screech amplitudes measured 5¼ inches upstream of flameholder for four different flow rates.

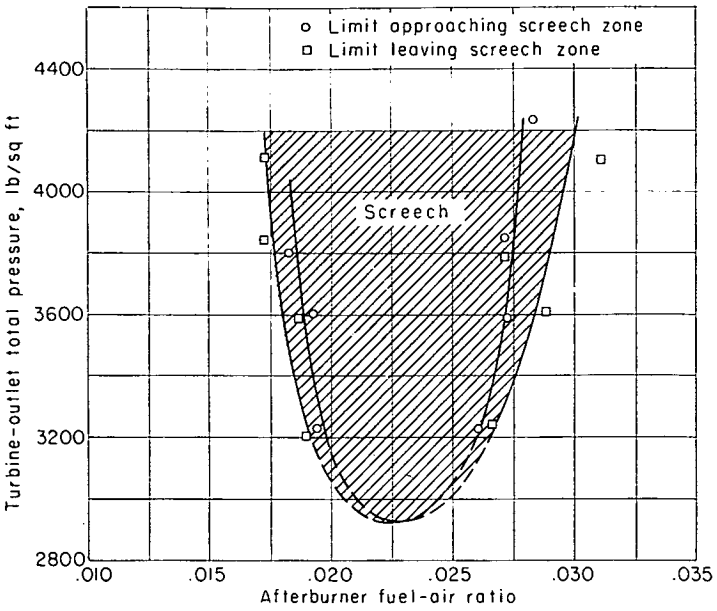


FIGURE 16.—Variation of screech limits with afterburner-inlet total pressure for 36-inch-diameter afterburner. Afterburner-inlet temperature, 1685° R.

limit the combustor screeched intermittently; the short burst of screech at this limit had peak-to-peak amplitudes of 14 inches of mercury, as indicated in figure 15.

The effect of pressure on the range of fuel-air ratios over which screech was encountered in a 36-inch-diameter afterburner is shown in figure 16. The afterburner construction details are shown in figure 17. The range of fuel-air ratios bracketing the screech zone increased progressively as the combustor pressure was increased. This is in agreement with the expectation that screech will be more prevalent when there is more energy available for driving.

No detailed measurements have been made of variations in frequency with pressure; sufficient observations have been made, however, to ascertain that only small changes in frequency occur as pressure is varied.

FLOW RATE

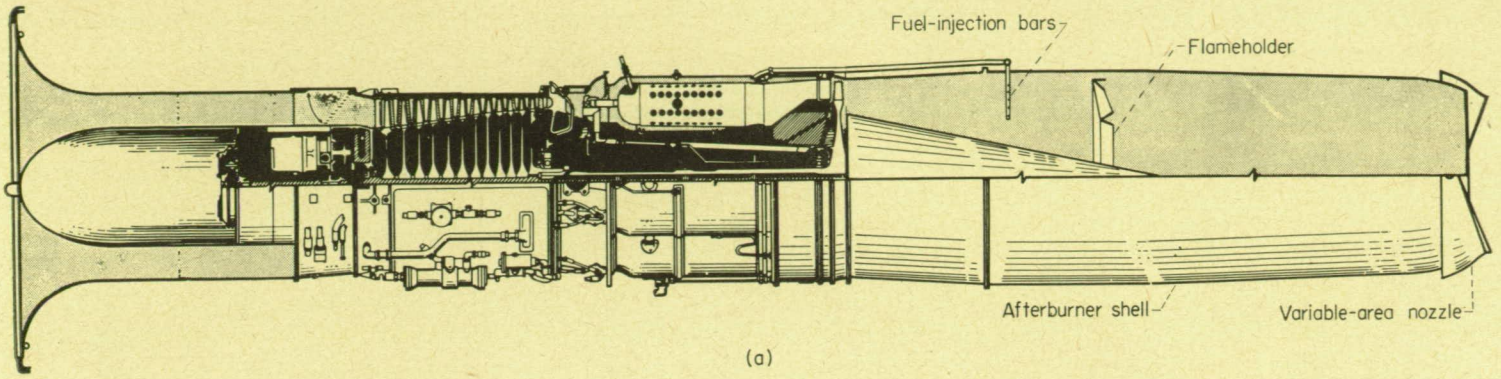
The 6-inch burner screeched throughout most of its operating range, as shown in figure 18. Screech was encountered at progressively lower pressure as gas-flow rate was decreased. During screech the combustion efficiency was 90 to 100 percent; the efficiency dropped abruptly by approximately 35 percent and the pressure by 17 percent when screech ceased. This abrupt change is indicated by the "jump" band in which stable operation was impossible.

No effect of flow rate on screech frequency was observed in the 6-inch burner.

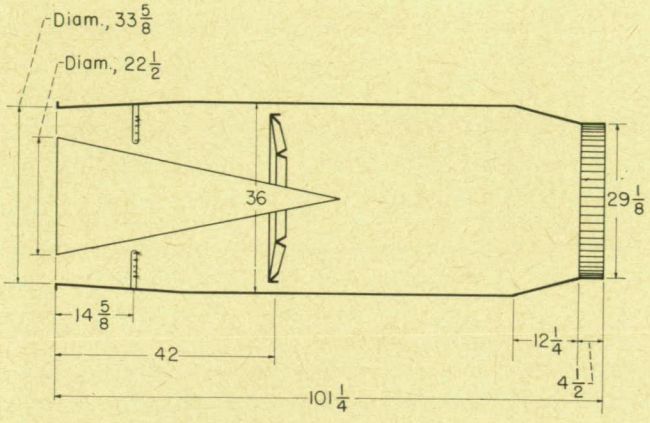
FUEL-AIR RATIO

The effect of fuel-air ratio on screech limits for the 36-inch-diameter afterburner is shown in figure 16. For each pressure the afterburner screeched over a range of fuel-air ratios corresponding to the highest combustor-outlet temperatures.

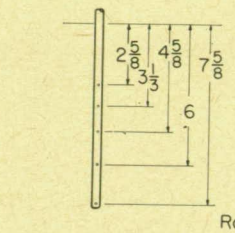
The effect of fuel-air ratio on screech frequency in the 6-inch burner was as follows: A maximum frequency of 3500 cycles per second was obtained at a fuel-air ratio of 0.076. Screech frequency decreased as fuel-air ratio was



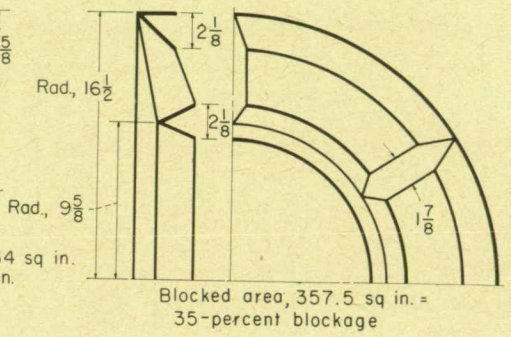
(a) Afterburner mounted on turbojet engine showing primary components.



(b) Location of afterburner components.



(c) Fuel-injection bars.



(d) Flameholder.

FIGURE 17.—Construction details of afterburner configuration A. (All dimensions are in inches.)

decreased below this value. The frequency was 3350 cycles per second at a fuel-air ratio of 0.063 and 2800 cycles per second near the lean blowout limit. These results are in agreement with the expectation that the screech frequency would increase with increase in sound speed or temperature of the combustion gases.

BURNER LENGTH AND DIAMETER

The length of the 6-inch burner could be varied from 34 to 45 inches by altering the position of the flameholder upstream of the exhaust nozzle. No appreciable change in screech frequency accompanied changes in flameholder position. At one position of the flameholder, a longitudinal mode of oscillation appeared. This longitudinal oscillation did not replace the screech but merely accompanied and modulated it.

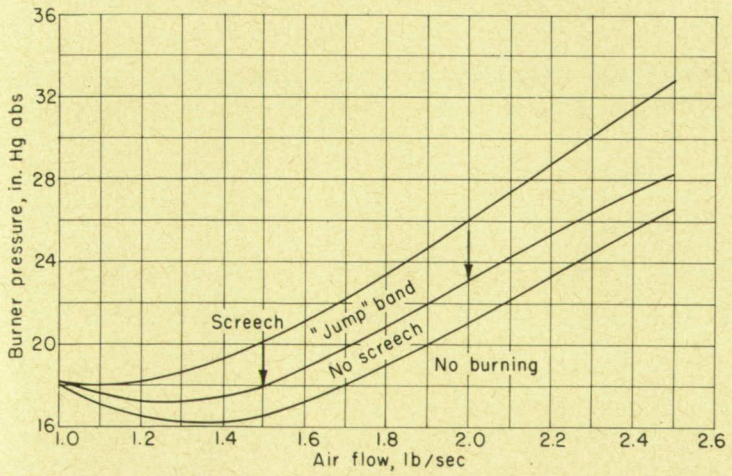


FIGURE 18.—Lower pressure limits for screech and burning at four mass flows. Equivalence ratio, 1.

The chief result of changing the burner diameter was a change in the screech frequency, the screech frequency varying inversely with burner diameter for most cases. Screech frequencies reported in the literature (refs. 3 to 6) for various full-scale afterburners can be explained by assuming transverse oscillation in the combustors. Figure 19 shows a plot of screech frequency as a function of combustor diameter. The theoretical screech frequencies for various modes of transverse oscillation in the hot gases are indicated by bands in the figure. Bands rather than discrete lines allow for variations in gas temperatures. The experimental points lie within the range of frequencies theoretically possible with transverse oscillations. The oscillations in the 6- to 20-inch combustors (refs. 1 and 2) correspond to the first transverse mode in the hot gases. For the larger combustors, higher modes have been experienced. In all cases in which phase measurements were made, the mode indicated by such observations was the same as that indicated on a frequency basis. The only data falling outside the theoretical range in figure 19 are some of the data for the 8-inch burner in which very high through velocities were used. Under these circumstances, as suggested in the analysis section and discussed further in reference 2, it is reasonable to expect the measured fre-

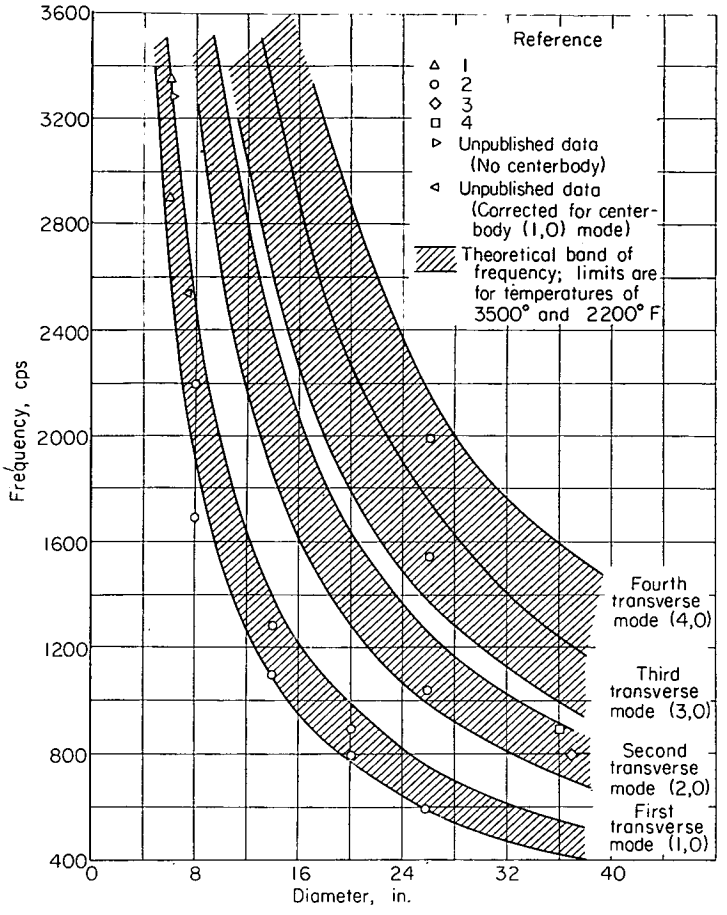


Figure 19.—Variation of frequency with burner diameter.

quencies to deviate from the theoretical ones. This low frequency may be partly due to the reduced combustion efficiency caused by the high through velocity but cannot be entirely explained by this phenomenon.

In another investigation (unpublished data) an increase in frequency occurred when a centerbody downstream of the flameholder was removed. A transverse mode would allow such an effect, whereas a radial mode would not. The theoretical frequency with the centerbody used in that study and the observed frequencies are also given in figure 19.

SCREECH PREVENTION

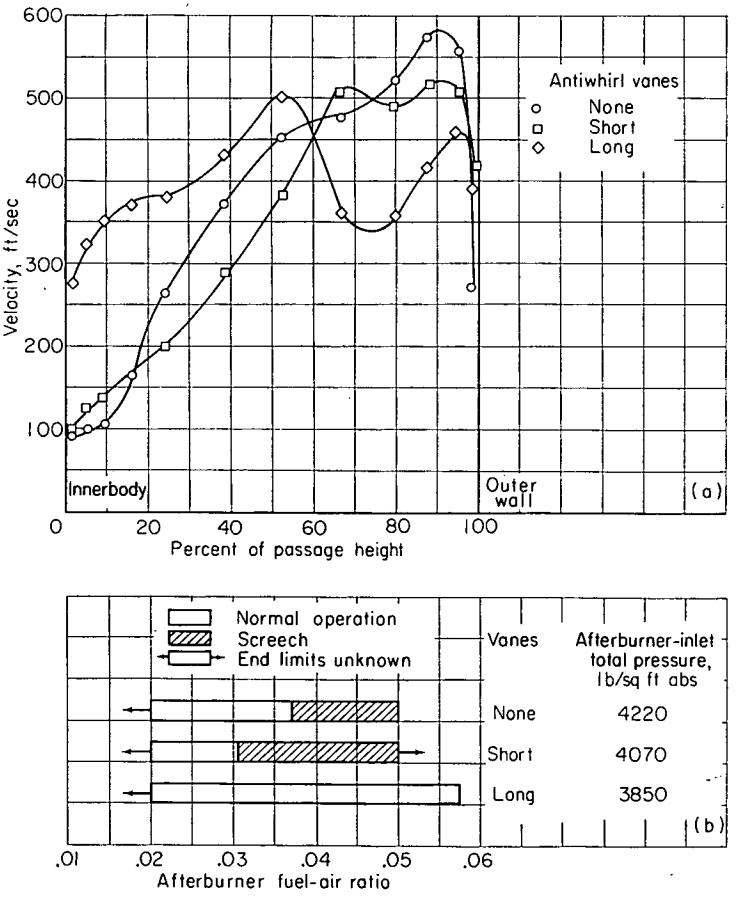
The tendency of a combustor to screech can be reduced in two ways: (1) by reducing the driving potential, and (2) by increasing the damping potential of the combustor. Various afterburner configuration changes which might affect the driving potential are discussed in the following section, while the adaptations based on damping are treated in a later section.

REDUCTION OF DRIVING POTENTIAL

In general, the driving potential can be reduced by designing the combustor so that the principal combustion zones do not coincide with regions of maximum pressure amplitude, for example, areas near the walls for transverse modes. The driving potential might also be reduced by altering the chemical composition of the reacting mixture so that the reaction rate will be relatively insensitive to changes in pressure and temperature, or so that an appreciable time lag will precede any marked change in the reaction rate. Sufficient understanding of the screech driving mechanism and of the kinetics of the chemical reaction is not available to indicate practical schemes for tailoring the combustor and the fuel to take advantage of these principles. Consequently, attempts to reduce the driving potential must, at this time, be based on trial-and-error procedures in which those design features which might affect the driving potential are varied.

Many of the combustor design modifications described in this section of the report were made prior to the identification of the nature of combustion screech. Some of the design factors discussed in this section might induce changes in the damping potential of the combustor; however, their primary effect is believed to be on the driving mechanism. These design changes represent various exploratory researches into the aerodynamic and chemical characteristics of a combustor to try to find what factor might be the source or cause of screech. For example, the velocity distribution described in the following paragraphs involves, of course, aerodynamic considerations.

Velocity distribution.—The use of turbine-outlet antiwhirl vanes to improve the afterburner-inlet gas velocity profile removed the tendency to screech for the configuration of figure 17. Whirl in this engine had been as high as 30° counter to turbine rotation. The improvement in velocity profile with the addition of the antiwhirl vanes is shown in figure 20(a), and the accompanying change from screeching



(a) Diffuser-exit velocity profile.
(b) Screech limits.

FIGURE 20.—Effect of antiwhirl vanes on performance of afterburner configuration A.

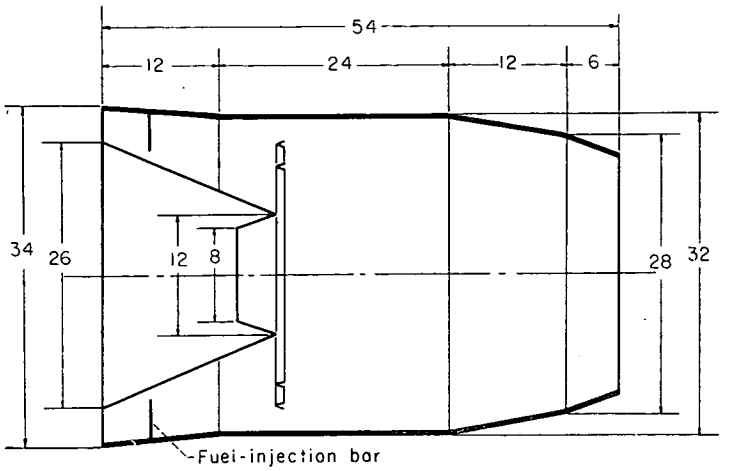


FIGURE 21.—Construction details of short afterburner, configuration B. (All dimensions are in inches.)

to nonscreeching combustion is shown by the bar graphs of figure 20(b). Although improving the velocity profile at the afterburner inlet eliminated the screech in the configuration of figure 17, screech could not be eliminated in the afterburner of figure 21 by the use of antiwhirl vanes, vortex generators, or improved diffusers to improve the velocity profile.

Experience with several afterburners, including that of figure 21, has shown that burners having a strong tendency to screech are not greatly helped by improving velocity profiles. Further evidence that good velocity profile will not assure screech-free combustion is provided by the fact that screech is readily obtained in the 6- and 26-inch-diameter ducts discussed earlier, even though there were no diffuser inner cones and the velocity profiles were quite flat.

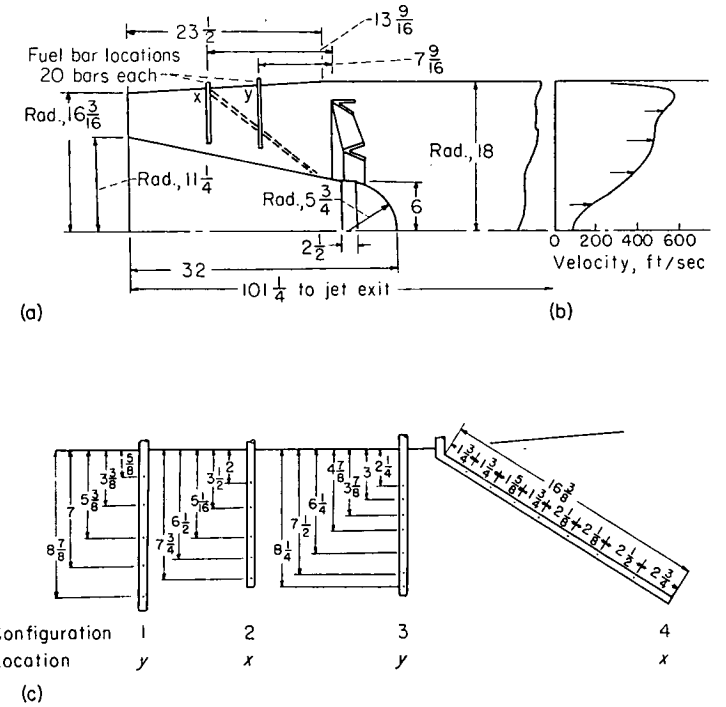
The investigation reported in reference 3 associated screech with combustion in low-velocity regions such as separated regions or vortex sheets in the wake of struts in the fuel mixing zone. In these experiments combustion was observed on the surface of the diffuser innerbody. (Other investigations have also shown combustion to exist in some burner installations on the lee side of support struts or along the outer wall of the diffuser.) The velocity near the diffuser inner-cone wall was less than 90 feet per second as compared to a peak gas velocity of nearly 600 feet per second.

Several afterburner configurations were investigated to determine the validity of the impression that screech was primarily associated with combustion in the low-velocity regions in the fuel mixing zone. In several of these configurations fuel injectors were moved radially outward to remove any fuel from the low-velocity region along the inner cone and thus preclude combustion in this region. One example (configuration A, fig. 21) had the fuel-injection bars mounted 15¼ inches upstream of the flameholder. The fuel-injection bars used for this phase of the investigation had the innermost fuel-injection orifice 5⅛ inches from the innerbody. Screeching combustion was encountered with this configuration at a burner-inlet pressure of about 4000 pounds per square foot. Visual observation through a quartz window verified that there was no burning along the innerbody at any time.

These observations are typical of those made with several other configurations investigated. In addition, the 26-inch-duct burner without an innerbody and with fuel injection maintained several inches from the outer wall, so that combustion could not occur in the vicinity of any wall, also screeched. It was concluded, therefore, that screeching combustion was not necessarily associated with burning along the diffuser innerbody or in other low-velocity regions in the fuel-mixing zone. The possibility of such combustion driving screech in some combustors, however, should not be ignored, since data of reference 3 and other evidence indicated that flames may occur in a separated flow region adjacent to shell and innerbody walls concurrently with screech.

Fuel distribution.—Several investigations of screech have been conducted such as that of reference 4, in which the effects on screech of large variations in fuel distribution were studied. In general, screeching combustion could not be eliminated by changes in fuel distribution. This insensitivity of screeching combustion to fuel distribution was particularly true with a reasonably uniform diffuser-outlet velocity profile.

Exceptions to the absence of a fuel distribution effect were encountered only with a severe diffuser-outlet velocity gradient such as that of configuration C (fig. 22). In this afterburner, fuel-injection bar configurations 1 and 2 provided fuel injection across the entire diffuser passage to within about ½ inch of the innerbody wall, whereas configurations 3 and 4 injected fuel to within approximately 1½ inches of the innerbody. Shifting the fuel concentration radially outward away from the innerbody (fuel-injection bar configurations 3 and 4) eliminated the screech previously encountered (configurations 1 and 2) at an afterburner-inlet



(a) Afterburner details.
(b) Typical velocity profile immediately upstream of flameholder.
(c) Fuel-injection bar configurations.

FIGURE 22.—Construction details of afterburner configuration C. (All dimensions are in inches.)

total pressure of 4200 pounds per square foot. This exception indicates that, when the afterburner-inlet velocity gradient is severe, alterations in radial fuel distribution may be effective in eliminating screech. (The possibility of unsteady combustion upstream of the flameholder was considered in this case, but no flame could be observed upstream through observation windows in the afterburner shell.)

It has also been observed that even with good velocity profiles a reduction in fuel-mixing length (distance fuel-injection bars are located upstream of flameholder) will reduce the tendency for screech. However, this is not always effective in eliminating screech; in addition, as a result of reduced mixing of fuel and air and reduced vaporization in the mixing zone, the combustion efficiency is generally impaired. The observed reduction in screech tendency may be due entirely to the increased time lag accompanying energy release in the chamber.

Fuel characteristics.—A limited number of fuel variations have been investigated with regard to screech tendencies of the afterburner. Fuels purchased under specifications MIL–F–5624A, grades JP–3 (Reid vapor pressure, 5.5 lb/sq in.) and JP–4 (Reid vapor pressure, 2.6 lb/sq in.) showed no difference in screech limits in a 37-inch-diameter afterburner. If, however, the fuel system had been located close to the flameholder, an increased fuel volatility might have increased the heat release (driving potential) in the primary combustion zone. In addition, since it has been suggested that screech could be driven by a detonation type of disturbance, aviation tetraethyl lead was added to the JP–3 fuel (5.3 ml/gal) as a detonation suppressor. The addition of the lead had no effect on the screech limits of the afterburner.

Flameholder geometry.—Of the almost infinite number of possible variations in flameholder geometry, it has been feasible to correlate only a few with tendency to screech. No consistent trend has been found with such variables as position of flameholders with respect to the burner wall, flameholder configuration (diametrical, circumferential, and radial flameholders), number of flameholders, or gutter shape. However, a very definite trend has been found in both the large-scale and small-scale duct work and in full-scale afterburners with gutter width or size. An example of the effect of flameholder width and flameholder blockage on screech limits in the 36-inch-diameter afterburners is shown in figure 23. With gutter widths of approximately 2½ inches,

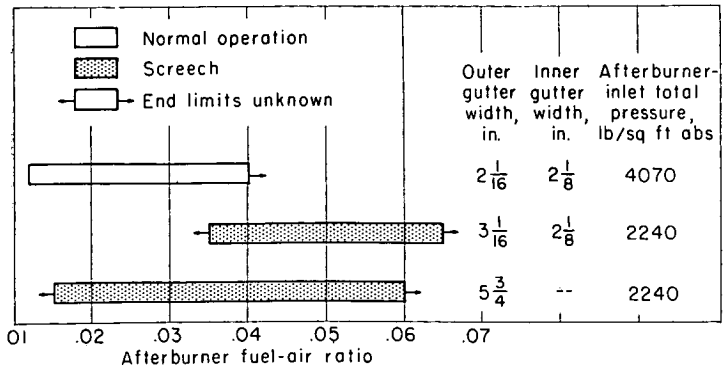


FIGURE 23.—Effect of flameholder gutter width on screech limits for afterburner configuration A.

screech was not encountered at burner-inlet total pressures up to 4070 pounds per square foot. With the outer gutter width increased to 3 1/16 inches, screech was encountered at a burner-inlet pressure of 2240 pounds per square foot at fuel-air ratios above 0.04. The 5¾-inch-wide gutter screeched over the entire range investigated at 2240 pounds per square foot. Observations such as the foregoing indicate that flameholder gutter width and blockage are factors in controlling screech.

Additional evidence of the effect of gutter width on screech is found in a statistical summary that has been made of the flameholder configurations operated in the investigation of the burner shell of figure 17. This summary is shown in figure 24, where the vertical scale indicates the number of different configurations in which a flameholder of a given width was incorporated. From this summary, which in-

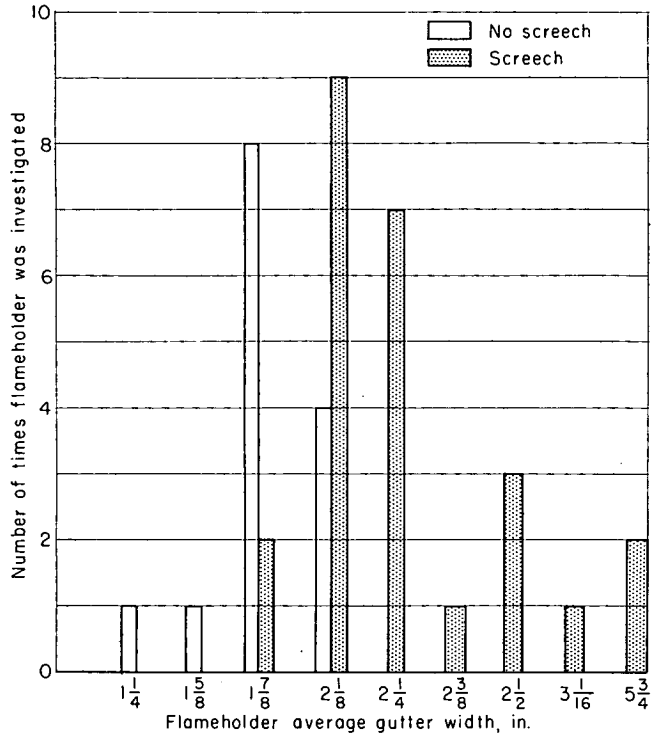


FIGURE 24.—Variation of flameholder tendency to screech with gutter width at afterburner-inlet total pressures from 3850 to 4220 pounds per square foot absolute. Flameholder blockage, 32 to 40 percent of flow area. Afterburner configuration A.

cludes gutter widths from 1¼ to 5¾ inches, it is evident that increasing the gutter width increased the tendency for screech. Although no screech was encountered in this investigation with flameholders having gutter widths of 1½ inches or less, the 1½-inch width does not have general significance because screech has been encountered in the short afterburner of figure 21 with gutter widths as small as ¾ inch. However, even in the latter afterburner the screech was much less severe than with the wider gutter flameholders. Although flameholder blockage varied from 32 to 40 percent of the flow area in this investigation, flameholder width and not blockage was the controlling variable, because several of the nonscreeching flameholders had blockage as high as 39 percent. It is therefore concluded that flameholder gutter width is an important variable in controlling screech.

INCREASE OF DAMPING POTENTIAL

The damping potential of a combustor can be increased by increasing the sound absorption in the combustor and by increasing the interference of pressure waves reflected from various surfaces within the combustor. These techniques, if carried to the ultimate, will produce an anechoic chamber. Practical design techniques for increasing damping are obvious, and several of these are discussed in the following paragraphs.

Longitudinal fins.—One of several systems designed to increase damping consisted of 24 two-inch-wide fins attached to the inner surface of the 32-inch-diameter afterburner shell as shown in figure 25. It was postulated that the longitudinal fins would interfere with the particle motion corresponding to the oscillation modes and thereby possibly eliminate the screech. The use of these fins changed the screech limit and frequency as follows:

	Screech limit, minimum fuel-air ratio	Screech frequency, cps
Operation without longitudinal fins	0.042	1560
Operation with longitudinal fins	.054	1760

Although the acoustic fins materially decreased the screech tendency, screech was not eliminated. Extension of the fins farther downstream, as shown by the dashed lines in figure 25, had no further effect on screech limits.

The change in frequency (from 1560 to 1760 cps) is essentially that which would have been predicted if the duct diameter had been reduced to 28 inches, the diameter of the space within the longitudinal fins.

Another type of longitudinal fin examined consisted of a single plate anchored at the vertex of the cone flameholder and extending downstream of the flameholder. Three modifications were studied in the 26-inch-diameter afterburner. First a single-ring 2-inch-wide gutter flameholder was tested with and without a cylindrical fin extending 9 inches downstream of the flameholder lip.

The results, shown in figure 26, indicate that the fin was partly successful in eliminating screech. One possible reason for this partial success was thought to be the action of the fin in inhibiting possible vortex interaction in the wake of

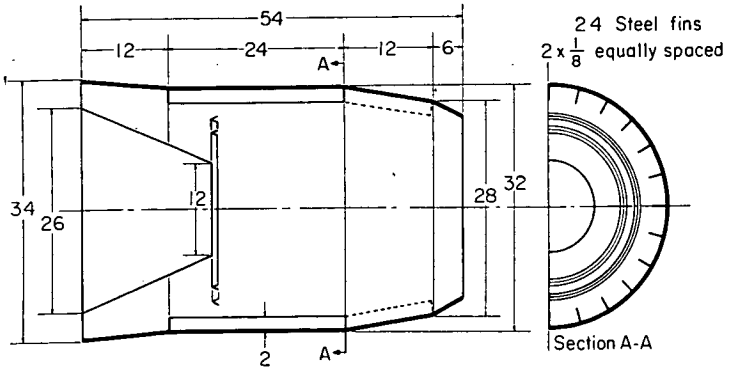
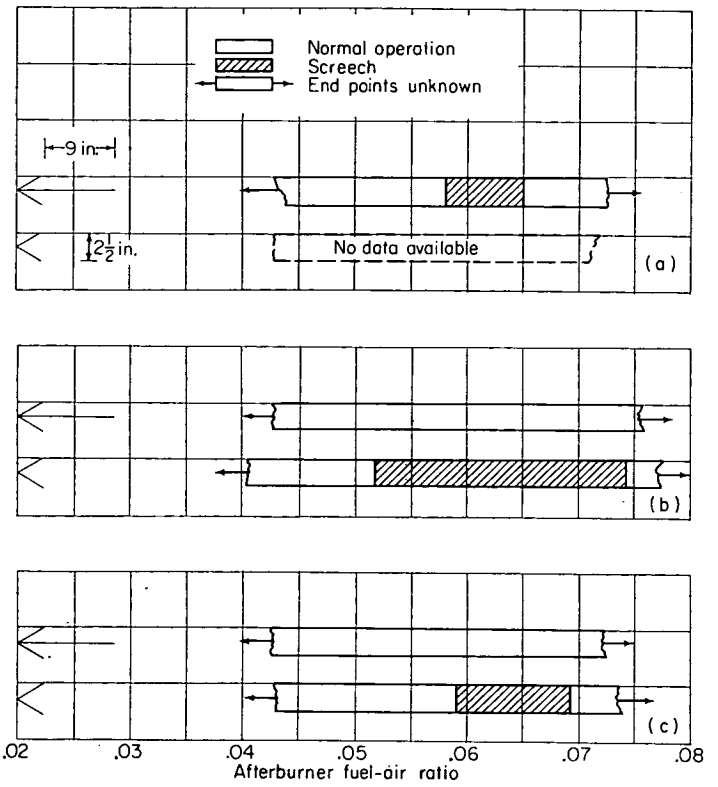


FIGURE 25.—Longitudinal fins installed in short afterburner, configuration D. (All dimensions are in inches.)



(a) Airflow, 30 pounds per second; burner-inlet pressure, 1080 pounds per square foot.
(b) Airflow, 20 pounds per second; burner-inlet pressure, 990 pounds per square foot.
(c) Airflow, 17.5 pounds per second; burner-inlet pressure, 870 pounds per square foot.

FIGURE 26.—Effect of splitter on screech limits of 26-inch-diameter burner.

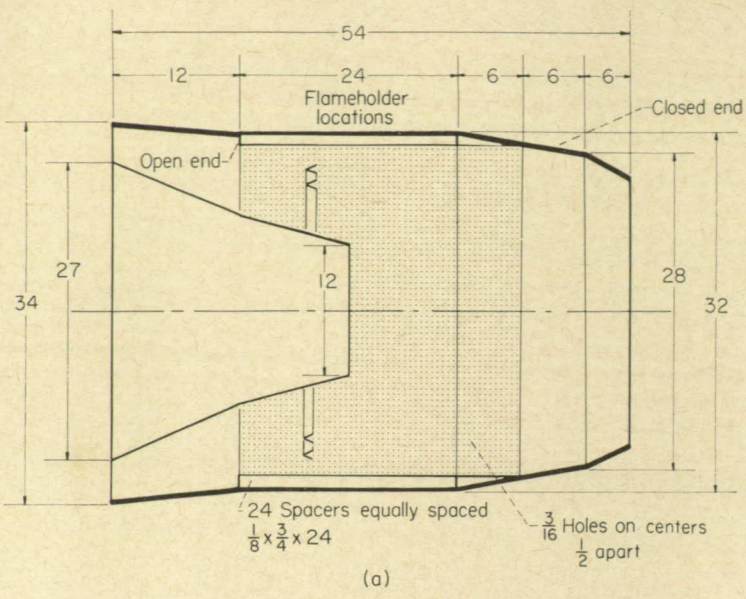
the flameholder. To examine this possibility the next two modifications were tested.

First a splitter extending 6 inches downstream of a 7-inch-diameter flameholder lip and alined with the flameholder was tested in the 26-inch-diameter afterburner. The screech tendency was observed to be only slightly less with this splitter than without.

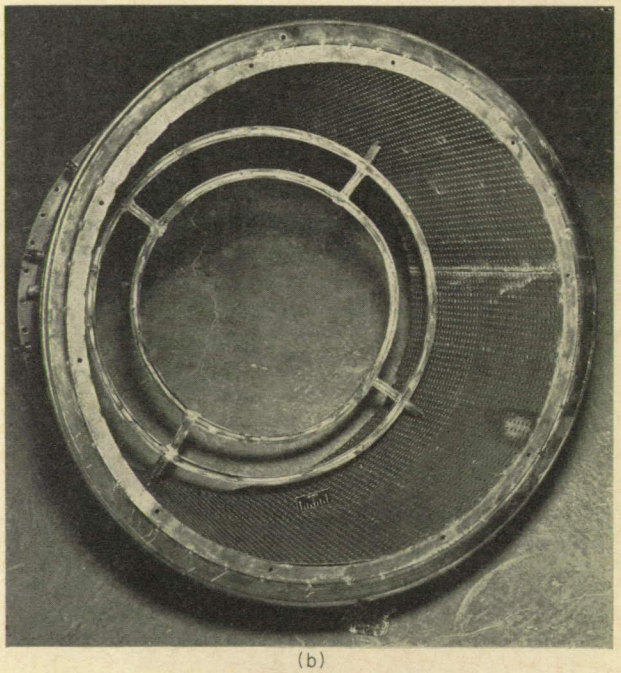
To this configuration was added a second splitter perpendicular to the first, oriented along the combustor centerline, and extending 9 inches downstream of the flameholder. This change caused a marked reduction in screech tendency.

It was concluded from these tests that such fins alter the screech tendency by acoustic interference.

Tapered burner.—It was felt that a tapered burner might eliminate screech, since it was not apparent that a simple resonance, such as has been described for cylinders, could exist in such a configuration. Consequently, a burner 45 inches long was constructed with the diameter tapering from 26 inches at the inlet to 18.6 inches at the exit. This was the maximum taper believed practical. When the burner was tested in the 26-inch-duct rig, no difference in screech tendency was observed over that of a straight-walled burner. These results are not too surprising, since a straight-walled burner will screech well even though the natural frequency at the inlet is different from that at the exit because of the temperature rise through the burner.



(a) Afterburner details showing perforated liner with ¾-inch-wide two-V-gutter flameholder having blocked area of 36 percent. (All dimensions are in inches.)



(b) Photograph of perforated liner installation.

FIGURE 27.—Perforated liner installed in 32-inch-diameter afterburner, configuration E.

Perforated liner.—A perforated liner was designed for maximum acoustic damping and was installed in the same afterburner (fig. 25) used to investigate the longitudinal fins. The construction details of the perforated liner are shown in figure 27(a), and a photograph of the liner installed in the afterburner is shown in figure 27(b). The use of this liner completely eliminated screech with the two-ring ¾-inch-wide V-gutter flameholder. Inasmuch as larger gutter widths were shown to increase the tendency to screech, a single-ring 1½-inch-wide gutter flameholder and a single-ring 3-inch-wide V-gutter flameholder were investigated in turn with the perforated liner. Screech could not be obtained at any fuel-air ratio with either of the larger flameholders. Further attempts to force screech with the perforated liner included the introduction of large variations in both radial and circumferential fuel distribution. Screech could not be produced with the perforated liner. This result was felt to be particularly significant, since the screech tendencies of this afterburner were very strong.

Additional investigations were then conducted with a 19-inch length of perforated liner in the 26-inch-duct burner (fig. 28). The results of this investigation are shown in figure 29. Without the perforated liner the burner screeched at all conditions investigated. Using the 19-inch-long perforated liner eliminated screech at a burner-inlet pressure

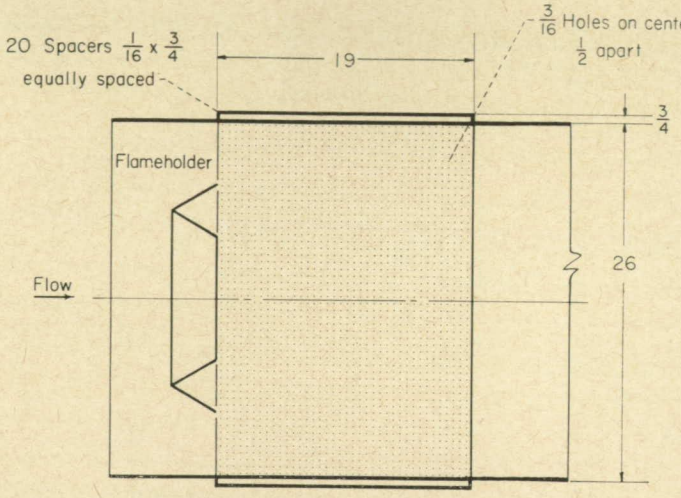
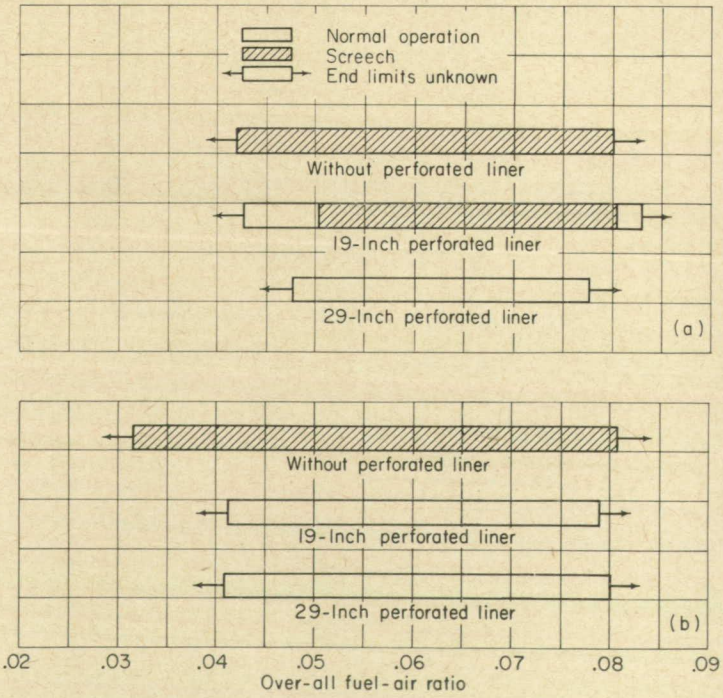


FIGURE 28.—Construction details of perforated liner installed in 26-inch-diameter combustor with 4½-inch-wide V-gutter flameholder having blocked area of 36 percent. (All dimensions are in inches.)



(a) Burner-inlet total pressure, 1750 pounds per square foot.
(b) Burner-inlet total pressure, 1400 pounds per square foot.

FIGURE 29.—Effect of perforated liner on screech limits in 26-inch-diameter duct, configuration E.

of 1400 pounds per square foot, and although screech was encountered at fuel-air ratios from 0.05 to 0.08, it was not severe. The addition of another 10 inches of liner (29-in. length) completely eliminated the screech at a burner-inlet pressure of 1750 pounds per square foot. In addition, the burner operated at about 2200 pounds per square foot without screech at any fuel-air ratio.

The use of the perforated liner to increase the damping potential of the burner has been by far the most effective mechanism for control of screech that has been investigated at the Lewis laboratory. The length of liner required will undoubtedly vary with peak gas velocity and combustion rate in the burner. The liner should enclose the region of maximum heat release, as this is the region of greatest driving potential.

The perforated liner of figure 27 also served as a cooling liner with the relatively cool turbine-discharge gases flowing between the liner and the afterburner shell. The liner was quite effective in eliminating hot spots on the afterburner shell. The perforated liner from the cooled installation was essentially free of buckling and warping, whereas the liner of figure 28, which was not cooled, was badly buckled after a relatively few hours of operation.

Two perforated or louvered cooling liners (figs. 30 and 31) which have also served as acoustic dampers have recently been investigated. These liners were installed in a 32-inch-diameter afterburner and were operated over a range of burner-inlet total pressures from 670 to 3100 pounds per square foot and fuel-air ratios as high as 0.062 without encountering screech at any of the conditions investigated. A large number of flameholder and fuel-injection system variables were included in these operations (refs. 13 to 15).

OTHER COMBUSTION INSTABILITY PHENOMENA

Although the present paper is intended to summarize some of the aspects of screech, a brief mention of other

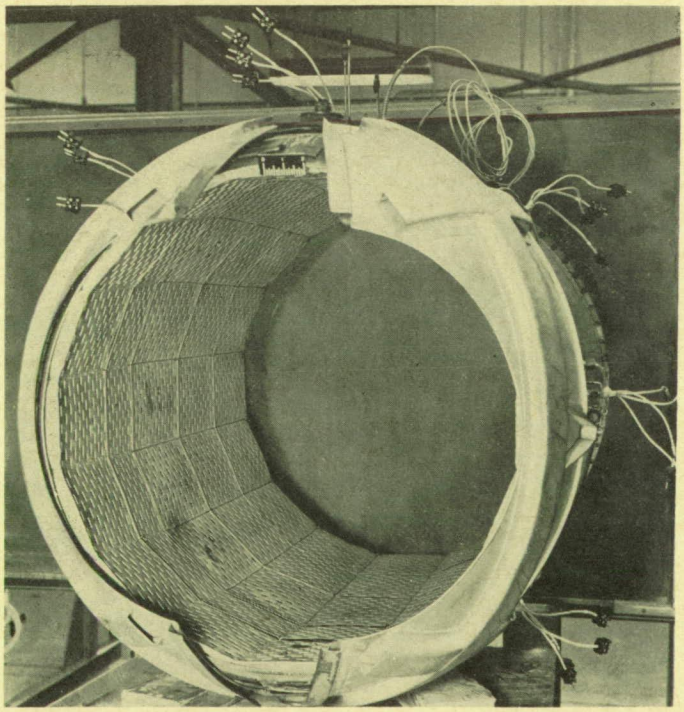


FIGURE 30.—Louvered cooling liner.

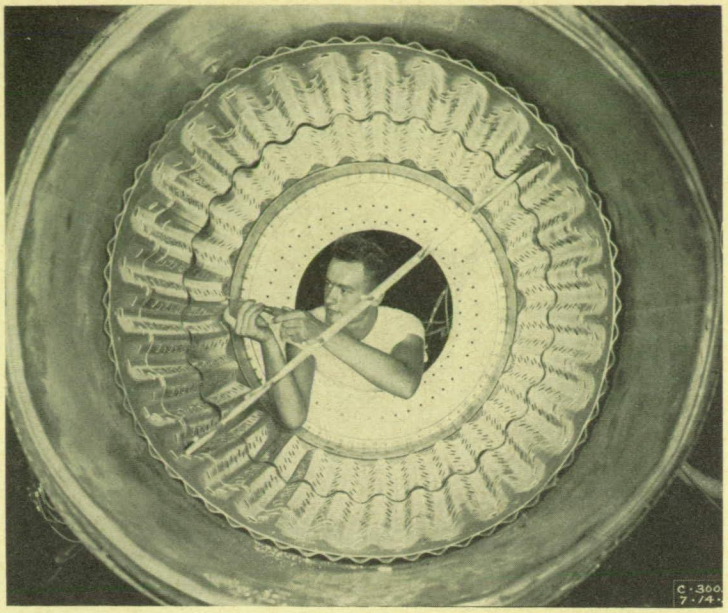


FIGURE 31.—Corrugated louvered cooling liner.

combustion instability problems is in order. In afterburners and ramjet combustors, other forms of combustion instability encountered have been referred to as "rumble" and "buzz."

RUMBLE

The type of combustion instability referred to as rumble is usually caused by explosions of large pockets of combustible mixture. This violent instability usually occurs at frequencies of 1 to 4 cycles per second, and generally occurs only for a few cycles at ignition of the burner or near either rich or lean blowout. During starts, observations through windows in the burner shell indicated that the rumble is due to flashback into the fuel-mixing zone upstream of the flameholder; near the blowout limits it is probably caused by the blowout and reignition of local pockets of fuel-air mixture at or downstream of the flameholder that momentarily exceed the combustible limits of fuel-air ratio (see ref. 6).

BUZZING

Buzzing is a term used to denote combustion which produces pressure pulsations of intermediate frequency of the order of 10 to 50 cycles per second. High-speed schlieren motion pictures of a two-dimensional ramjet model with transparent walls have provided an explanation of this type of instability as follows:

(1) Upon ignition, a flame front fans out from each flame stabilizer and intersects either a wall or the flame front from the adjacent flame stabilizer at a point some distance downstream.

(2) A curved flame front starts at the point of intersection and travels upstream with increasing velocity through the wedge-shaped pocket of combustibles bounded by the intersecting flame fronts.

(3) The curved flame front progresses to a point somewhat upstream of the flameholder, whereupon combustion ceases as the flame front reaches an unconditioned fuel-air mixture. The pressure pulse produced by this curved flame front

momentarily stops or reverses the direction of flow of the gas column.

(4) Following dissipation of the pressure pulse, the flow is reestablished and a fresh charge of combustible mixture displaces the burner charge, whereupon ignition occurs and the cycle repeats.

Rumble, buzz, and screech are each different phenomena and are characterized by low-, low-to-intermediate-, and high-frequency oscillations. Each can be severe enough to cause engine damage, but the very high energy dissipation from the high-frequency oscillations has been the greatest offender in combustion studies at the NACA Lewis laboratory.

Combustion instability has also been experienced in rocket engines. Rocket engine combustion instabilities have been attributed to either "chugging" or "screaming" (refs. 8, 16, and 17).

CHUGGING

Chugging is a hydrodynamic coupling between combustion-chamber pressure and feed-line flow and produces a pulsing operation. Chugging is characterized by relatively low frequencies, 20 to 200 cycles per second.

SCREAMING

Screaming is characterized by relatively high frequencies, up to 10,000 cycles per second, and is similar in its other characteristics to screech. Research on rocket screaming at the Lewis laboratory has identified transverse oscillations in a rocket motor which exist concurrently and independently of the longitudinal mode of vibration. Rocket screaming frequencies, however, have generally been correlated with the closed-closed pipe organ or longitudinal mode of oscillation. With the small rockets in use in many investigations, the frequency of a transverse mode of oscillation would be too high to measure with the instrumentation usually employed. However, the presence of transverse oscillation in rocket engines is described in reference 18, and these oscillations have also been identified during studies of screaming rockets at the Lewis laboratory. These oscillations are observed to spin, as did those discussed in reference 18.

CONCLUDING REMARKS

The present studies have shown that screech is characterized by resonant acoustic oscillation in a transverse mode in afterburners so far investigated. The energy for driving this oscillation is probably derived from the combustion process, although the possibility that some energy may be supplied by the kinetic energy of the stream cannot be ignored. Various schemes for eliminating or controlling screech by reducing the driving potential have proved marginal, their utility varying from one configuration to the next. On the other hand, a perforated liner in the combustion chamber eliminated screech entirely in all the configurations tested, including burners which screeched very severely without the liner. These studies strongly indicate that such a liner will serve as a satisfactory screech-control device in any burner.

Since the amount of damping can be varied by varying the length of the perforated liner downstream of the flameholder, it might be possible to establish a screech of controlled amplitude in the combustion chamber. A thorough quantitative investigation of this control technique is required to determine the extent to which possible beneficial effects of screech, such as increased combustion efficiency, can be utilized without producing destructive oscillations.

LEWIS FLIGHT PROPULSION LABORATORY
NATIONAL ADVISORY COMMITTEE FOR AERONAUTICS
CLEVELAND, OHIO, *February 8, 1954*

REFERENCES

1. Blackshear, Perry L., Rayle, Warren D., and Tower, Leonard K.: Experimental Determination of Gas Motions Accompanying Screeching Combustion in a 6-Inch Simulated Afterburner. NACA RM E53I28, 1953.
2. Harp, James L., Jr., Velie, Wallace W., and Bryant, Lively: Investigation of Combustion Screech and a Method of Its Control. NACA RM E53L24b, 1953.
3. Conrad, E. William, Schulze, Frederick W., and Usow, Karl H.: Effect of Diffuser Design, Diffuser-Exit Velocity Profile, and Fuel Distribution on Altitude Performance of Several Afterburner Configurations. NACA RM E53A30, 1953.
4. Usow, Karl H., Meyer, Carl L., and Schulze, Frederick W.: Experimental Investigation of Screeching Combustion in Full-Scale Afterburner. NACA RM E53I01, 1953.
5. Conrad, E. William, and Campbell, Carl E.: Altitude Investigation of Several Afterburner Configurations for the J40–WE–8 Turbojet Engine. NACA RM E52L10, 1953.
6. Conrad, E. William, and Campbell, Carl E.: Altitude Wind Tunnel Investigation of High-Temperature Afterburners. NACA RM E51L07, 1952.
7. Morse, Philip M.: Vibration and Sound. Second ed., McGraw-Hill Book Co., Inc., 1948.
8. Beatty, Ralph E., Jr.: Boundary Layer Attenuation of Higher Order Modes in Rectangular and Circular Tubes. Jour. Acoustic Soc. Am., vol. 22, no. 6, Nov. 1950, pp. 850–854.
9. Rayleigh: The Theory of Sound. Vol. II. Dover Pub., 1945.
10. Blackshear, Perry L.: Driving Standing Waves by Heat Addition. NACA TN 2772, 1952.
11. Childs, J. Howard, McCafferty, Richard J., and Surine, Oakley W.: Effect of Combustor-Inlet Conditions on Performance of an Annular Turbojet Combustor. NACA Rep. 881, 1947. (Supersedes NACA TN 1357.)
12. Childs, J. Howard: Preliminary Correlation of Efficiency of Aircraft Gas-Turbine Combustors for Different Operating Conditions. NACA RM E50F15, 1950.
13. Jansen, Emmert T., Velie, Wallace W., and Wilsted, H. Dean: Experimental Investigation of the Effect of Fuel-Injection-System Design Variables on Afterburner Performance. NACA RM E53K16, 1953.
14. Renas, Paul E., and Jansen, Emmert T.: Effect of Flame-Holder Design on Altitude Performance of Louvered-Liner Afterburner. NACA RM E53H15, 1953.
15. Braithwaite, Willis M., Walker, Curtis L., and Sivo, Joseph N.: Altitude Evaluation of Several Afterburner Design Variables on a J47–GE–17 Turbojet Engine. NACA RM E53F10, 1953.
16. Tischler, Adelbert O., Massa, Rudolph V., and Mantler, Raymond L.: An Investigation of High-Frequency Combustion Oscillations in Liquid-Propellant Rocket Engines. NACA RM E53B27, 1953.
17. Ellis, Herbert, et al.: Experimental Investigation of Combustion Instability on Rocket Motors. Fourth Symposium (International) on Combustion, The Williams & Wilkins Co., 1953, pp. 880–885.
18. Smith, R. P., and Sprenger, D. F.: Combustion Instability in Solid-Propellant Rockets. Fourth Symposium (International) on Combustion, The Williams & Wilkins Co., 1953, pp. 893–906.

REPORT 1385

DRAG MINIMIZATION FOR WINGS AND BODIES IN SUPERSONIC FLOW [1]

By Max. A. Heaslet and Franklyn B. Fuller

SUMMARY

The minimization of inviscid fluid drag is studied for aerodynamic shapes satisfying the conditions of linearized theory, and subject to imposed constraints on lift, pitching moment, base area, or volume. The problem is transformed to one of determining two-dimensional potential flows satisfying either Laplace's or Poisson's equations with boundary values fixed by the imposed conditions. A general method for determining integral relations between perturbation velocity components is developed. This analysis is not restricted in application to optimum cases; it may be used for any supersonic wing problem.

For given base area, general formulas are found that cover as special cases quasi-cylindrical bodies of revolution, wings having plan forms with fore-and-aft symmetry, slender bodies, and certain classes of yawed wings. The drag can in fact be determined from a unidimensional flow analysis in a duct of known shape. For given volume, minimum wave drag of a ducted body of revolution of arbitrary radius is expressed in closed analytic form. The elliptic wing is treated, and a possible source of difficulty connected with unreal shapes in given volume problems is found. In the case of ducted bodies of revolution, the singularity distribution corresponding to the minimum drag is determined.

Particularly simple results are found for a family of wings with curved leading edges with lift specified and center of pressure fixed at the 60-percent-chord position. General relations for integrated loading along oblique lines are derived for this family of wings.

INTRODUCTION

To seek conditions under which the wave and vortex drag of a given wing or body is minimized is to seek conditions for economical supersonic flight. It is also a common experience, in the study of such problems, to find that a gratuitous economy appears to affect the analysis itself. Almost invariably, simplicity characterizes the final forms of the results in comparison with predictions carried out for wings and bodies chosen with less discrimination. In the present paper, the minimization of wave and vortex drag for various aerodynamic shapes is studied. Some side conditions, such as given lift, given volume, etc., must be specified in order to set a meaningful variational problem for the shape at hand. The side condition of given base area is noteworthy as leading to results with the simplicity mentioned above, for, as will be shown, the general expression for minimum drag assumes the most elementary form possible while at the same time retaining the relevant parameters and being dimensionally correct.

The starting point of the present work was the expression for drag given by G. N. Ward (ref. 1) in his study of thin lifting bodies, that is, wings and bodies for which linearized supersonic flow theory applies. Work of this type was first reported by Nicolsky in reference 2, and detailed results (refs. 3 and 4) have since become available. The body shape is assumed to be enclosed by a characteristic surface generated as the envelope of both the downstream-facing Mach cones, with vertices on the forward edge of the body, and the upstream-facing Mach cones, with vertices on the trailing edge of the body. The drag (wave plus vortex) is then given by a surface integral of the induced velocities over the downstream portion of the Mach envelope, and other forces, moments, and geometrical properties are similarly determined. This particular control surface has analytical advantages similar to those exploited by R. T. Jones (refs. 5 and 6) in the use of combined flow fields. Jones adopts a perturbation potential equal to the sum of the potentials in forward and reverse flow. He then shows, for example, that for a plan form of given base area the necessary condition for minimum wave drag is that the pressure in the combined flow field be a constant over the plan form. It follows that locally the combined flow potential is a two-dimensional harmonic function. The direct use of combined flow fields has been further extended and applied by Graham (ref. 7), and is used in combination with the control surface mentioned above by Germain (refs. 8 and 9). Along the Mach envelope used by Ward the perturbation potential in forward flow is equal to its value in the combined flow field. Drag minimization then determines conditions on the control surface, and the potential on this surface differs from a two-dimensional harmonic function by a known amount. The conventional perturbation potential is retained, but the determination of the body shape is still not direct. Mathematically, one needs to invert an integral equation, and questions as to existence and uniqueness of the solution arise. In the case of ducted bodies of revolution of given base area or volume, the integral equation will be solved explicity in a later section.

When the expressions for the forces and moments and geometrical quantities in terms of integrals over the same control surface are known, it is possible to combine the drag with one or more of the others, as constraints, and set up an optimization problem. Variational methods then yield the result that, in general, the potential in the control surface must satisfy a Poisson equation in the lateral coordinates. Inspection leads to a number of cases in which solution by

[1] Supersedes NACA Technical Note 3289 by Max. A. Heaslet, 1957, and NACA Technical Note 4227 by Max. A. Heaslet and Franklyn B. Fuller, 1958.

analytical methods is possible, and recourse to numerical techniques is not required, though it is of course available for more difficult problems.

Finally, a method for generating integral relations among perturbation velocity components is outlined. By these, it is possible to gain knowledge of aerodynamic loading on the wing integrated along oblique lines. So long as the obliquity of the lines is such that the component of stream velocity normal to them is supersonic, the variation of the integrated loading in the stream direction is obtainable. The so-called chord loading is a special case of these results. The span loading is a by-product of the solution of the variational problem, for this involves determination of the perturbation potential in the rear Mach surface springing from the trailing edge. Then, when the perturbation potential on the trailing edge is known, the span loading is found directly.

IMPORTANT SYMBOLS

A	base area of wing or body
C_D	drag coefficient
C_L	lift coefficient
C_1, C_2	curves bounding a region in an x=const. plane (see fig. 2)
D	drag of wing or body in a supersonic flow
$f(y,z)$	function defining (by $x=f(y,z)$) a characteristic surface springing from a trailing edge
l	streamwise extent of wing or body
L	lift
$\frac{L(x_0,\theta)}{q_\infty}$	integral of local loading $\left(\frac{\Delta p}{q_\infty}\right)$ along oblique line (see eq. (66))
m	tangent of angle of sweep or yaw
M_∞	Mach number in the free stream
$\mathbf{M}$	pitching moment, positive for a nose-up moment, taken about the line $x=x_m$, $y=z=0$
n	inner normal to a plane curve
N	inner normal to a surface
p	pressure
$\frac{\Delta p}{q_\infty}$	load coefficient (upper-surface pressure minus lower-surface pressure divided by free-stream dynamic pressure)
q	local velocity
q_∞	free-stream dynamic pressure, $\frac{1}{2}\rho_\infty U_\infty^2$
r	radial coordinate in axially-symmetric problems
s	arc length
S	region in an x=const. plane (see fig. 2)
u,v,w	perturbation velocity components in x,y,z directions
U_∞	speed of free stream along x axis
V	volume of a wing or body
x,y,z	Cartesian coordinates
β^2	M_∞^2-1
Γ_1	space curve (defined in fig. 1)
λ,μ,σ,τ	Lagrange multipliers (see eq. (11))
ν	conormal (see eq. (18a))
ρ_∞	density in the free stream
$\Sigma_0,\Sigma_1,\Sigma_2$	surfaces
φ	perturbation velocity potential
χ	perturbation potential on surface $x=f(y,z)$; $\chi=\varphi[f(y,z),y,z]$
∇^2	two-dimensional Laplace operator, $\frac{\partial^2}{\partial x^2}+\frac{\partial^2}{\partial y^2}$

ANALYSIS

The following analysis is divided into several sections. First, the geometrical quantities, base area and volume, are expressed in terms of integrals over a given control surface. Then relations for the lift, drag, and pitching moment are given. These results can be combined in various ways to set up variational problems where drag is minimized while one or more of the remaining quantities is held fixed. Finally, a method by which integral relations among the perturbation components can be derived is outlined.

In all this work, it is assumed that supersonic small-disturbance theory applies. There is then a perturbation potential function $\varphi(x,y,z)$ satisfying the equation

$$\beta^2\varphi_{xx}-\varphi_{yy}-\varphi_{zz}=0 \tag{1}$$

where

$$\beta^2=M_\infty^2-1$$

The velocity components in the coordinate directions are $U_\infty+\varphi_x,\varphi_y,\varphi_z$. It will be assumed that the given body can be represented by a planar or cylindrical reference surface, the latter having directrices parallel to $0x$, the free-stream direction. Boundary conditions are to be satisfied on the reference surface. In order to avoid difficulties concerning gaps or holes in the body surface, it will be assumed that unique leading and trailing edges exist, and that the thickness distribution function does not vanish between these extremities.

RELATIONS FOR BASE AREA AND VOLUME

Consider a cylindrical reference surface as mentioned above, and draw in the enclosing characteristic surfaces as shown in figure 1. The reference surface itself is denoted Σ_0. The envelope of Mach cones springing from the leading edge is Σ_1, and the envelope of Mach cones from the trailing edge is Σ_2. These surfaces, Σ_1 and Σ_2, intersect along a space curve Γ_1, as shown in figure 1. The relations

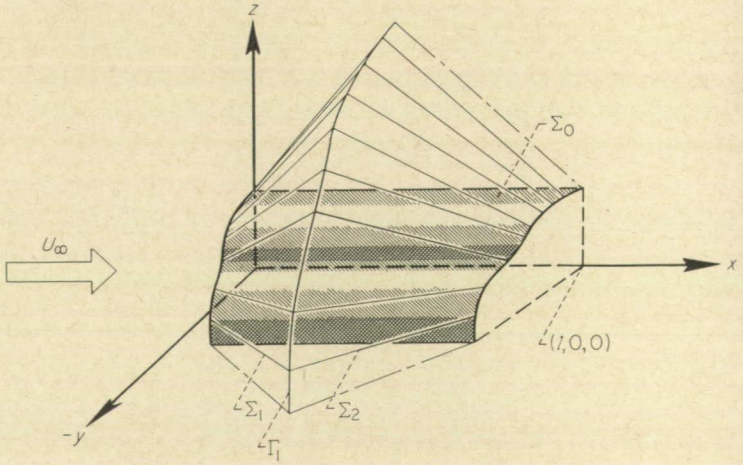


FIGURE 1.—Reference surface and characteristic enveloping surfaces.

for base area and volume of the body represented by the reference surface Σ_0 will be derived by applying Green's theorem to the volume bounded by the surfaces Σ_0, Σ_1, and Σ_2.

The following form of Green's theorem will be used:

$$\iiint_\tau F(\overrightarrow{\nabla U})\cdot(\overrightarrow{\nabla V})\,d\tau=-\iint_{\Sigma_0+\Sigma_1+\Sigma_2} FV\frac{\partial U}{\partial N}d\Sigma-\iiint_\tau F[\nabla\cdot(F\overrightarrow{\nabla U})]\,d\tau$$

where

τ	volume bounded by $\Sigma_0+\Sigma_1+\Sigma_2$
F, U, V	arbitrary scalar functions of position
N	interior normal to a surface
∇	vector differential operator, grad

Now set

$$F=\rho=\rho_\infty\left(1-M_\infty{}^2\frac{\varphi_x}{U_\infty}\right)\text{ to first order}$$

$$U=\Phi=U_\infty x+\varphi(x,y,z)=\text{total potential}$$

$$V=x^k$$

The integral relation becomes

$$\iiint_\tau \rho(U_\infty+\varphi_x)kx^{k-1}\,d\tau=-\iint_{\Sigma_0+\Sigma_1+\Sigma_2}\rho x^k\frac{\partial\Phi}{\partial N}d\Sigma-\iiint_\tau x^k[\nabla\cdot(\rho\overrightarrow{\nabla\Phi})]\,d\tau$$

and the last integral on the right vanishes by virtue of the continuity equation for steady flow. The remaining quantities are

$$\iiint_\tau kx^{k-1}\rho(U_\infty+\varphi_x)\,d\tau=-\iint_{\Sigma_0+\Sigma_1+\Sigma_2}\rho x^k\frac{\partial\Phi}{\partial N}\,d\Sigma \tag{2a}$$

Take first the case $k=0$. The left side of equation (2a) vanishes and one has

$$\iint_{\Sigma_0}\rho\frac{\partial\Phi}{\partial N}d\Sigma+\iint_{\Sigma_1}\rho\frac{\partial\Phi}{\partial N}d\Sigma+\iint_{\Sigma_2}\rho\frac{\partial\Phi}{\partial N}d\Sigma=0 \tag{2b}$$

The integral over Σ_0 is, to first order,

$$\iint_{\Sigma_0}\rho\frac{\partial\Phi}{\partial N}d\Sigma=\rho_\infty U_\infty\iint_{\Sigma_0}\frac{\varphi_z}{U_\infty}dy\,dx=\rho_\infty U_\infty\iint_{\Sigma_0}\frac{\partial Z}{\partial x}dx\,dy$$

where $Z=Z(x,y)$ is the equation of the surface of the wing or body. The integral therefore gives the increment in frontal area of the wing or body between the leading and trailing edges, symbolized here as A;

$$A=\iint_{\Sigma_0}\frac{\partial Z}{\partial x}dx\,dy$$

Next, consider the integrals over Σ_1 and Σ_2. Let the surface Σ_2 be defined by the equation

$$x=f(y,z) \tag{3}$$

The normal N to Σ_2 has direction cosines

$$N_1:N_2:N_3=-\frac{1}{M_\infty}:\frac{f_y}{M_\infty}:\frac{f_z}{M_\infty}$$

and the normal to Σ_1 has clearly $N_1=1/M_\infty$. Thus equation (2b) becomes (since $\varphi=0$ on Σ_1)

$$\rho_\infty U_\infty A=\rho_\infty\iint_{\Sigma_2}(-\beta^2\varphi_x-f_y\varphi_y-f_z\varphi_z)dy\,dz$$

An essential simplification of this formula results if one introduces the function $\chi(y,z)$ where

$$\chi=\varphi[f(y,z),y,z]$$

and $x=f(y,z)$ is the equation of the rear characteristic surface Σ_2. Then, since

$$\chi_y=\varphi_x f_y+\varphi_y;\quad \chi_z=\varphi_x f_z+\varphi_z$$

and $f_y{}^2+f_z{}^2=\beta^2$, the relation for base area becomes

$$A=-\frac{1}{U_\infty}\iint_S(f_y\chi_y+f_z\chi_z)dy\,dz \tag{4a}$$

In equation (4a), S is the projection, shown in figure 2, of the surface Σ_2 on an $x=$const. plane. As shown also, C_1 is

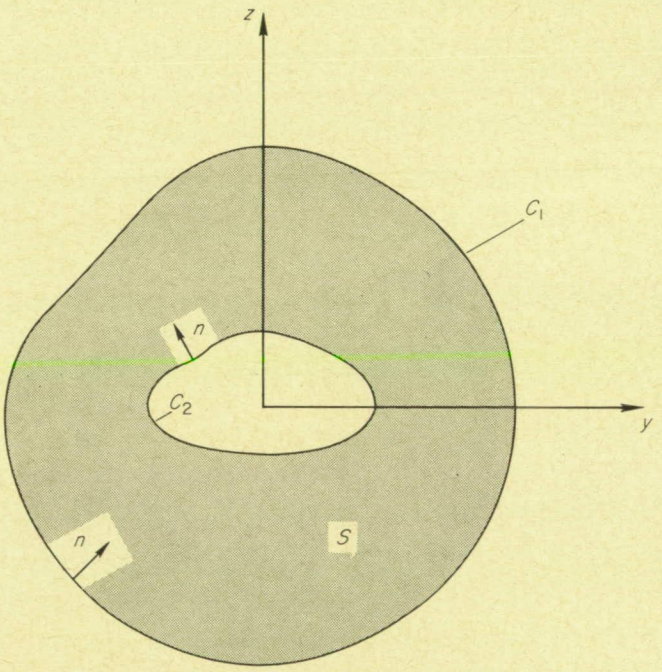


FIGURE 2.—Projection of rear characteristic surface Σ_2 in an $x=$const. plane.

its outer boundary, or the projection of the space curve Γ_1 shown in figure 1, and C_2 is the projection of the reference surface of the wing or body. By application of Green's theorem, and the knowledge that $\chi=0$ on Γ_1, hence on C_1, equation (4a) can be rewritten in the forms

$$A=\frac{1}{U_\infty}\iint_S\chi\nabla^2 f\,dy\,dz+\frac{1}{U_\infty}\int_{C_2}\chi\frac{\partial f}{\partial n}ds \tag{4b}$$

$$=\frac{1}{U_\infty}\iint_S f\nabla^2\chi\,dy\,dz+\frac{1}{U_\infty}\int_{C_1+C}f\frac{\partial\chi}{\partial n}ds \tag{4c}$$

where

n interior normal to curve in x=const. plane

s arc length in x=const. plane

The formula relating the volume of a wing or body to integrals of the function χ follows by taking $k=1$ in equation (2a); one has

$$V=\int_{C_2} fh(f,s)ds-\frac{1}{2U_\infty}\iint_S \chi(\nabla^2 f^2+2\beta^2)dy\,dz-\frac{1}{2U_\infty}\int_{C_2}\chi\frac{\partial f^2}{\partial n}ds \tag{5}$$

where

V incremental volume of wing or body

$h(f,s)$ deviation of body from control surface at trailing edge

Equation (5) gives the volume of bodies that are either open or closed at the base. The first integral on the right of equation (5) may vanish for several reasons aside from the obvious case of zero base area; in these cases the volume is expressed as

$$V=-\frac{1}{2U_\infty}\iint_S \chi(2\beta^2+\nabla^2 f^2)dy\,dz-\frac{1}{2U_\infty}\int_{C_2}\chi\frac{\partial f^2}{\partial n}ds \tag{6a}$$

$$=-\frac{1}{2U_\infty}\iint_S f^2\nabla^2\chi\,dy\,dz-\frac{\beta^2}{U_\infty}\iint_S \chi\,dy\,dz-\frac{1}{2U_\infty}\int_{C_1+C_2} f^2\frac{\partial\chi}{\partial n}ds \tag{6b}$$

It is worth noting that since neither base area nor volume can be influenced by position of the center of coordinates, it is possible sometimes to effect certain economies in algebraic manipulation by a judicious choice of origin.

FORCE AND MOMENT RELATIONS

Expressions for lift and drag forces are obtained by application of the law of conservation of momentum in the volume bounded by Σ_0, Σ_1, and Σ_2 (see fig. 1). The vector force relation is

$$\vec{F}=-\iint_{\Sigma_1+\Sigma_2} p\vec{N}\,d\Sigma-\iint_{\Sigma_1+\Sigma_2}\rho\vec{q}(\vec{q}\cdot\vec{N})d\Sigma$$

where

$\vec{F}$ vector force on body

$\vec{q}$ local velocity vector

$\vec{N}$ unit inner normal to surface

p local pressure

ρ local density

The force can be resolved into lift and drag components, and the results consistent with linearized theory are (as given in ref. 1)

$$L=-\rho_\infty U_\infty\iint_S \chi_z\,dy\,dz \tag{7a}$$

$$=\rho_\infty U_\infty\int_{C_2}\chi\cos(z,n)\,ds \tag{7b}$$

$$D=-\frac{\rho_\infty}{2}\iint_S \chi\nabla^2\chi dy\,dz-\frac{\rho_\infty}{2}\int_{C_2}\chi\frac{\partial\chi}{\partial n}ds \tag{8a}$$

$$=\frac{\rho_\infty}{2}\iint_S(\chi_y^2+\chi_z^2)dy\,dz \tag{8b}$$

The pitching moment is next found. The vector moment relation is

$$\vec{\mathbf{M}}=-\iint_{\Sigma_1+\Sigma_2}\rho(\vec{q}\cdot\vec{N})(\vec{r}_m\times\vec{q})d\Sigma-\iint_{\Sigma_1+\Sigma_2}p(\vec{r}_m\times\vec{N})d\Sigma$$

where $\vec{r}_m$ is the vector distance between the moment center and an integration element on the control surface. If only the pitching moment is considered, with nose-up pitching moment taken as positive, and moment center at $(x_m, 0, 0)$, the linearized result is

$$\mathbf{M}=-\rho_\infty U_\infty\iint_S \chi\nabla^2(zf)dy\,dz-\rho_\infty U_\infty\int_{C_2}\chi\left[\frac{\partial(zf)}{\partial n}-x_m\cos(z,n)\right]ds \tag{9}$$

If lift $L=0$ or $x_m=0$ so that pitching moment is calculated about the origin, one finds

$$\mathbf{M}=-\rho_\infty U_\infty\iint_S \chi\nabla^2(zf)dy\,dz-\rho_\infty U_\infty\int_{C_2}\chi\frac{\partial(zf)}{\partial n}ds \tag{10a}$$

$$=-\rho_\infty U_\infty\iint_S zf\nabla^2\chi dy\,dz-\rho_\infty U_\infty\int_{C_1+C_2} zf\frac{\partial\chi}{\partial n}ds \tag{10b}$$

VARIATIONAL PROBLEMS

The problem of minimizing drag under the constraint of given base area, or volume, or lift, or pitching moment can be set up with the aid of equations (4), (6), (7), (8), and (10). It is only necessary to apply standard variational procedure to any of the expressions

$$\left.\begin{aligned} I_1&=D-\lambda A\\ I_2&=D+\mu V\\ I_3&=D-\sigma L\\ I_4&=D-\tau\mathbf{M}\end{aligned}\right\} \tag{11}$$

where λ, μ, σ, τ are Lagrange multipliers. In the language of combined flow fields (refs. 5 and 6) the Lagrange multipliers yielding minimum drag can be identified with constant values of the longitudinal and vertical velocity components or their gradients. In this way, for example, λ and μ are, respectively, constant pressure and pressure gradient in the combined

field. Less general interpretations may possibly be given the Lagrange multipliers in specific classes of problems. One such interpretation is given in the discussion following equation (40) of this report.

It is possible to combine the variational problems with each other. For example, if it be required to find minimum drag with given base area and lift, the quantity to be minimized would be $D-\lambda A-\sigma L$ and so forth. The results found by applying the variational procedure to equations (11) will be given next. Each is a two-dimensional flow problem in the lateral variables y,z.

Given base area:

$$\left.\begin{aligned} \nabla^2\left(\chi+\frac{\lambda}{\rho_\infty U_\infty} f\right)&=0 \qquad \text{in } S \\ \frac{\partial}{\partial n}\left(\chi+\frac{\lambda}{\rho_\infty U_\infty} f\right)&=0 \qquad \text{on } C_2 \\ \chi&=0 \qquad \text{on } C_1 \end{aligned}\right\} \tag{12a}$$

$$D=\frac{\lambda}{2} A \tag{12b}$$

Given volume (zero base area):

$$\left.\begin{aligned} \nabla^2\left[\chi+\frac{\mu}{2\rho_\infty U_\infty}(f^2+kf)\right]&=-\beta^2\frac{\mu}{\rho_\infty U_\infty} \text{ in } S \\ \frac{\partial}{\partial n}\left[\chi+\frac{\mu}{2\rho_\infty U_\infty}(f^2+kf)\right]&=0 \qquad \text{on } C_2 \\ \chi&=0 \qquad \text{on } C_1 \end{aligned}\right\} \tag{13a}$$

$$D=-\frac{\mu}{2} V \tag{13b}$$

where k is a constant to be determined by application of the zero base area condition.

Given lift:

$$\left.\begin{aligned} \nabla^2\chi&=0 \quad \text{in} \quad S \\ \frac{\partial}{\partial n}(\chi+U_\infty\sigma z)&=0 \quad \text{on} \quad C_2 \\ \chi&=0 \quad \text{on} \quad C_1 \end{aligned}\right\} \tag{14a}$$

$$D=\frac{\sigma}{2} L \tag{14b}$$

Given pitching moment (zero lift):

$$\left.\begin{aligned} \nabla^2(\chi+U_\infty\tau z f)&=0 \qquad \text{in } S \\ \frac{\partial}{\partial n}(\chi+U_\infty\tau z f)&=k\frac{\partial z}{\partial n} \text{ on } C_2 \\ \chi&=0 \qquad \text{on } C_1 \end{aligned}\right\} \tag{15a}$$

$$D=-\frac{\tau}{2}\mathbf{M} \tag{15b}$$

where k is a constant to be determined by the condition of zero lift.

In each of the problems listed in equations (12) through (15), the possibility of obtaining a solution depends largely upon the boundary curve C_1. Several cases where exact solutions are obtainable will be treated in later sections. However, recourse to approximate methods is usually indicated. One approximation in which the wing is distorted slightly in order to obtain a boundary curve C_1 for which the two-dimensional problem is solvable is discussed in reference 10. Germain (ref. 8) has used development in series.

INTEGRAL RELATIONS BETWEEN PERTURBATION VELOCITY COMPONENTS

Some useful and interesting relations between integrals of the potential function φ taken across the reference surface Σ_0 to integrals of χ in Σ_2 (see fig. 1) will now be derived. These results are not specialized to minimum-drag solutions, but apply to any case. Consider a planar, supersonic-edged wing, and choose a line in the wing plane ($z=0$) that cuts the x axis in $(x_0,0,0)$ and which makes an angle μ_0 with the y axis;

$$x-y\tan\mu_0=x_0 \tag{16}$$

Further, let the angle μ_0 be such that $\tan\mu_0\leq\beta$, making the normal component of free-stream velocity always supersonic. This line will always lie in the supersonic "zone of silence" corresponding to the point $(x_0, 0, 0)$. Under this condition, a plane, Σ_3, tangent to the Mach cone springing from $(x_0, 0, 0)$ can be made to pass through the line given by equation (16). This plane is (in a notation introduced by Hayes, ref. 11)

$$x-\beta\cos\theta y+\beta\sin\theta z=x_0 \tag{17}$$

where $\beta\cos\theta=\tan\mu_0$. The resulting situation is shown in figure 3 for the case of a sonic-edged wing.

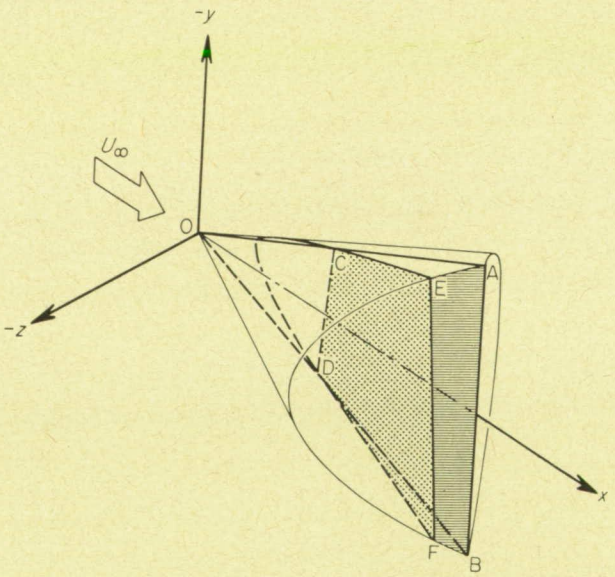


FIGURE 3.—Characteristic plane cutting wing and enveloping surfaces.

If Green's theorem for equation (1) is applied to an arbitrary region enclosed by a continuous surface Σ, the fundamental integral relation

$$\iint_\Sigma \Lambda\frac{\partial\varphi}{\partial\nu}\,d\Sigma=0 \tag{18a}$$

results. The derivative $\partial\varphi/\partial\nu$ is the gradient of potential along the conormal ν with direction cosines ν_1, ν_2, ν_3 that are related to the direction cosines n_1, n_2, n_3 of the inner normal to the surface Σ by the equations

$$-\beta^2 n_1=\Lambda\nu_1,\ n_2=\Lambda\nu_2,\ n_3=\Lambda\nu_3$$

Consider now the region bounded by Σ_0, Σ_1, and Σ_3, and in which $z>0$ (in fig. 3, Σ_0, Σ_1, Σ_2, are defined as in fig. 1; Σ_3 is the plane of equation (17)). On Σ_1 and Σ_3, it is easily found that $\Lambda=\beta$, and on Σ_0, $\Lambda=1$ For this region, equation (18a) becomes

$$\frac{1}{\beta}\iint_{\Sigma_0}\frac{\partial\varphi}{\partial\nu}d\Sigma+\iint_{\Sigma_1}\frac{\partial\varphi}{\partial\nu}d\Sigma+\iint_{\Sigma_3}\frac{\partial\varphi}{\partial\nu}d\Sigma=0 \tag{18b}$$

Since the conormal ν lies in the surface Σ_1, (and also in Σ_3), the integral over Σ_1 will vanish because φ is zero thereon. Further, on Σ_0, $\partial/\partial\nu=\partial/\partial z$ and $d\Sigma=dx\,dy$. Equation (18b) now becomes

$$\frac{1}{\beta}\iint_{\Sigma_0}\varphi_z dx\,dy+\iint_{\Sigma_3}\frac{\partial\varphi}{\partial\nu}d\Sigma=0 \tag{19a}$$

The integral over Σ_3 in equation (19a) will be greatly simplified if one takes $d\Sigma=d\nu\,ds$, where ds is an element of length normal to $d\nu$, and lying in the plane Σ_3. It can be shown that under these conditions, ds always lies in an $x=$const. plane. Equation (19a) now becomes

$$\frac{1}{\beta}\iint_{\Sigma_0}\varphi_z dx\,dy=-\int_C^D\varphi\,ds \tag{19b}$$

where the line CD is the intersection of the plane given by equation (17) with the wing plan form.

Next, one can repeat this analysis for the region ahead of Σ_3, within Σ_1 and Σ_2, and below the wing plane. This time, the surface Σ_2 will form a portion of the bounding surface, and a line integral across Σ_2 will result. One can then combine the relations obtained for the two regions and relate an integral of potential across the wing surface to one across the surface Σ_2. A detailed application will be made in a later section.

APPLICATIONS

The analysis discussed in the previous sections will now be applied to some particular problems. These will include a number of cases in which the configuration of the wing or body permits simple analytic solution of one or more of the variational problems listed as equations (12) through (15). Quasi-cylindrical bodies of revolution were mentioned in the Introduction as constituting a class of shapes for which a full solution to the minimum-drag problem is available. The simulating axial source distribution, from which surface shape can be calculated, is derived herein, leading, incidentally, to an interesting identity involving integrals of elliptic integrals. Finally, the results pertaining to integrals of wing loading along oblique lines across the wing are applied to a particular family of minimum-drag wings.

WINGS AND BODIES WITH GIVEN BASE AREA

By combining equations (8a) and (12a) and using Green's formula, one gets for the drag of an optimum wing or body with the given base area

$$D=\frac{\lambda^2}{4q_\infty}\iint_S(f_y^2+f_z^2)dy\,dz+\frac{\lambda}{2U_\infty}\int_{C_1}f\left(\frac{\partial\chi}{\partial n}+\frac{\lambda}{\rho_\infty U_\infty}\frac{\partial f}{\partial n}\right)ds$$
$$=\frac{\beta^2\lambda^2}{4q_\infty}S+\frac{\lambda}{2U_\infty}\int_{C_1}f\left(\frac{\partial\chi}{\partial n}+\frac{\lambda}{\rho_\infty U_\infty}\frac{\partial f}{\partial n}\right)ds \tag{20}$$

where q_∞ is the free-stream dynamic pressure, $(1/2)\rho_\infty U_\infty^2$. Further evaluation of the drag by equation (20) requires explicit knowledge of the function χ, obtained by solving the potential problem of equations (12a). A large and particularly interesting class of wings and bodies for which the solution is immediate is characterized by the condition that $f=$const. on C_1. This implies that the outer rim Γ_1, the intersection of the characteristic envelopes in figure 1, lies in a plane normal to the free-stream direction. For example, all wings with plan forms having fore-and-aft symmetry satisfy this requirement as do also all pointed configurations with subsonic edges so long as the nose and tail vertices determine a line parallel to the free-stream direction.

In such cases, the solution of equations (12a) is

$$\chi=0$$

and equation (20) gives for the drag

$$D=\frac{\beta^2\lambda^2}{4q_\infty}S \tag{21}$$

By combining this with equation (12b) and eliminating λ, one gets

$$\frac{D}{q_\infty}=\frac{A^2}{\beta^2 S} \tag{22}$$

The simplicity of equation (22) is remarkable, and examples of its diverse applicability are given below. Before proceeding to these applications however, it should be noted that a similar result applies to all planar wings whose enveloping surfaces Σ_1 and Σ_2 intersect in any plane parallel to the z axis. In this case,

$$x=f=m(y+b_0)$$

on the curve C_1, where $m(<\beta)$ is the slope of the plane of Γ_1 relative to the stream direction. The solution of equations (12a) once more gives $\chi=0$, and then, for the drag from equation (20),

$$D=\frac{\beta^2\lambda^2 S}{4q_\infty}+\frac{\lambda^2}{4q_\infty}\int_{C1}f\frac{\partial f}{\partial n}ds=\frac{\beta^2\lambda^2 S}{4q_\infty}-\frac{\lambda^2 m^2 S}{4q_\infty} \tag{23}$$

Again eliminating λ with the aid of equation (12b), one has

$$\frac{D}{q_\infty}=\frac{A^2}{(\beta^2-m^2)S} \tag{24}$$

Ducted body of revolution with prescribed end diameters.—This problem has been considered by Parker in reference 12, and by Nicolsky (see ref. 2). As shown in figure 4,

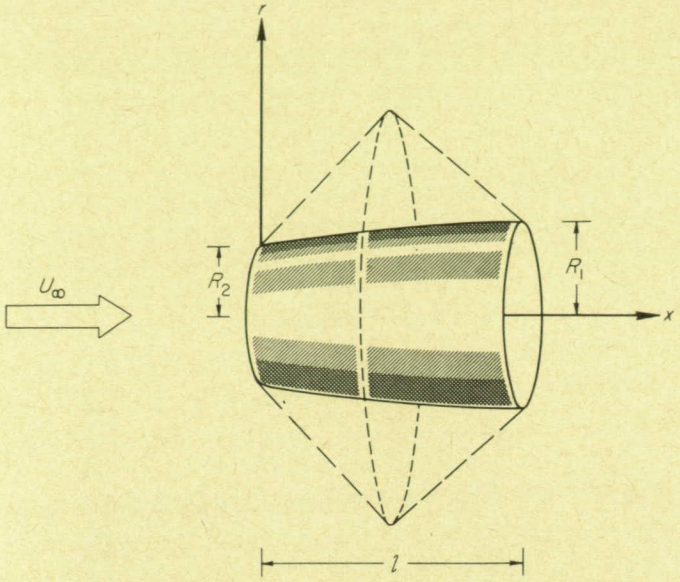


FIGURE 4.—Optimum body with prescribed end radii.

a shape with minimum external wave drag is constructed so as to have an initial radius R_2 and a final radius R_1. In order that the previous linear theory should apply, the restriction is made that the ratio $\beta|R_1-R_2|/l$ should be a small quantity. If the origin of axes is in the front face of the body, the fore-and-aft Mach surfaces are

$$x=\beta(r-R_2), \qquad x-l=-\beta(r-R_1)$$

and the curve C_1 is a circle of radius R_0 where

$$R_0=(l+\beta R_1+\beta R_2)/2\beta$$

From equation (22) drag is

$$\frac{D}{q_\infty}=\frac{4(R_1^2-R_2^2)^2\pi}{(l+\beta R_1+\beta R_2)^2-4\beta^2R_1^2} \tag{25a}$$

Equation (25a) is of particular interest since it represents a whole spectrum of results that extends from slender-body theory, for $\beta R_1/l$ and $\beta R_2/l$ small, to two-dimensional theory, for $\beta R_1/l$ and $\beta R_2/l$ large. The slender-body result leads directly to the familiar Kármán ogive formula (ref. 13),

$$\frac{D_K}{q_\infty}=\frac{4A^2}{\pi l^2} \tag{25b}$$

The two-dimensional result applies to the upper half of an optimum wing (a flat plate), and is found to be

$$C_D=\frac{D}{2\pi Rlq_\infty}\simeq\frac{2\alpha^2}{\beta} \tag{25c}$$

where R is mean radius and $\alpha=(R_1-R_2)/l$.

Elliptic plan form with afterbody.—The problem of given base area along the rear edge of an elliptic wing was considered first by R. T. Jones (ref. 6). The figure is a semi-infinite body with a cylindrical shape drawn downstream of the rear edge of an ellipse, see figure 5. The equation of the plan form outline is assumed to be

$$\frac{x^2}{a^2}+\frac{y^2}{b^2}=1$$

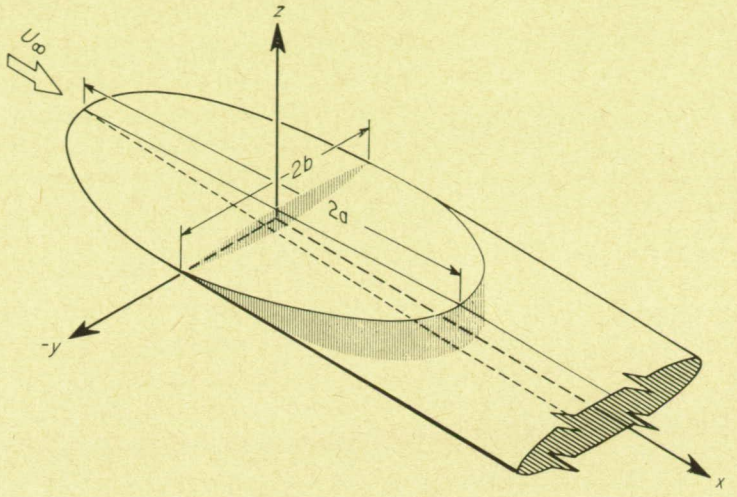


FIGURE 5.—Elliptic wing of given base area.

and the enveloping Mach surfaces are determined completely by the fore-and-aft Mach cones with vertices along the supersonic-edged portion of the plan form $\left(\text{where } \beta\frac{dy}{dx}>1\right)$, that is, the abscissas of the vertices lie within the region

$$|x|<a^2/(a^2+b^2\beta^2)^{1/2}$$

The curve C_1 has the equation

$$\frac{y^2}{[(a^2+b^2\beta^2)^{1/2}/\beta]^2}+\frac{z^2}{(a/\beta)^2}=1$$

and is an ellipse with foci at $(\pm b,0)$. Equation (22) then yields

$$\frac{D}{q_\infty}=\frac{A^2}{\pi a(a^2+b^2\beta^2)^{1/2}} \tag{26a}$$

If drag coefficient C_D is based on plan-form area, equation (26a) can be re-expressed as

$$C_D=\left(\frac{A}{4b^2}\right)^2\frac{\mathcal{AR}^2}{[\beta^2+(4/\pi\mathcal{AR})^2]^{1/2}} \tag{26b}$$

since the aspect ratio of the wing is $\mathcal{AR}=(4b)/(\pi a)$. Perhaps the most convenient formula for comparison follows from equations (25b) and (26a) if the drag of the wing is expressed in terms of the drag of a Kármán ogive with the same length and base area. The ratio is given by

$$\frac{D}{D_K}=\frac{a}{(a^2+b^2\beta^2)^{1/2}}=\frac{1}{[1+(\pi\beta\mathcal{AR}/4)^2]^{1/2}} \tag{27}$$

The wave drag of the elliptic wing with cylindrical afterbody, in the limit as aspect ratio approaches zero, is equal to the drag of the Kármán ogive and afterbody. For finite values of aspect ratio, the wave drag of the flat wing is smaller than that of the body of revolution, the initial deviation of the ratio from unity being proportional to $(\beta\mathcal{AR})^2$.

Tapered plan form with afterbody.—As a third example, consider a plan form of arbitrary taper ratio with base area along its trailing edge fixed. When the trailing edge is of subsonic type a cylindrical afterbody is assumed added.

As shown in figure 6, root chord is equal to $2a$ and span equal to $2b$. The tip chord is $2d$ so that taper ratio λ_0 and aspect ratio $\mathcal{AR}$ may be introduced in the form

$$\lambda_0=d/a$$

$$\mathcal{AR}=2b/[a(1+\lambda_0)]$$

So long as the leading edge of the wing is supersonic the characteristic trace C_1 is as shown in figure 7 and is composed of arcs of circles and straight lines, the radii of the inner and outer circles being a/β and d/β, respectively. The distance between the centers of the two outer circles is $2b$. Once the leading edge of the plan form is subsonic, the central circle of figure 7 blankets the other parts of the figure and C_1 is the circle of radius a/β.

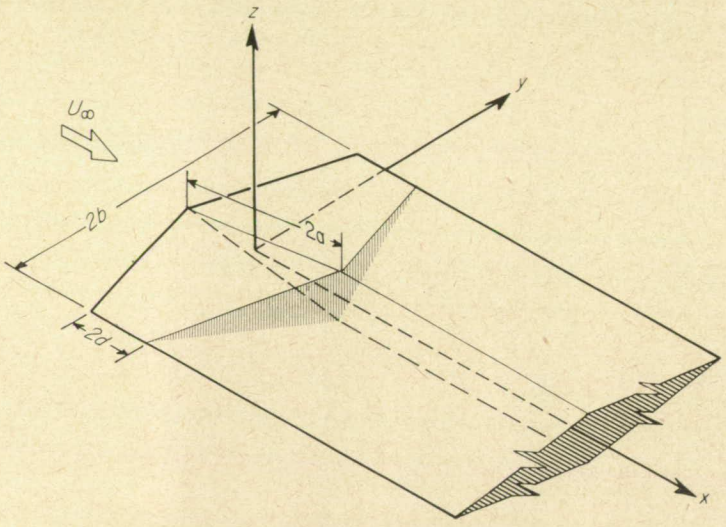


FIGURE 6.—Tapered plan form with given base area.

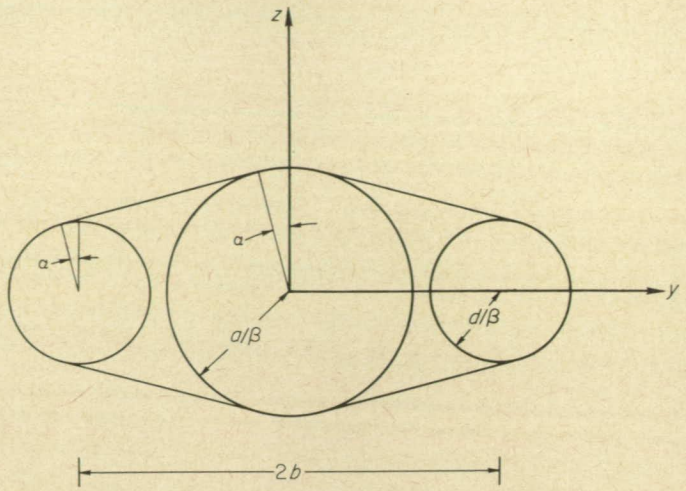


FIGURE 7.—Characteristic trace for wing with tapered plan form.

The area S is the sum of elementary geometric areas and is given by

$$S=\frac{2a^2}{\beta^2}\left[\frac{\pi}{2}\lambda_0^2+\frac{(1+\lambda_0)^2}{2}\beta\mathcal{AR}\cos\alpha+\alpha(1-\lambda_0^2)\right]$$

where α, shown in figure 7, is given by

$$\alpha=\begin{cases}\text{arc sin}\dfrac{2(1-\lambda_0)}{\beta\mathcal{AR}(1+\lambda_0)}, & 2(1-\lambda_0)\leqq\beta\mathcal{AR}(1+\lambda_0)\\[2ex] \dfrac{\pi}{2}, & 2(1-\lambda_0)\geqq\beta\mathcal{AR}(1+\lambda_0)\end{cases}$$

From equations (22) and 25b), the minimum drag of the tapered wing relative to the drag of the Kármán ogive of equal length and base area is

$$\left.\begin{aligned}\frac{D}{D_K}&=\frac{\pi}{\pi+(1+\lambda_0)[(1+\lambda_0)^2\beta^2\mathcal{AR}^2-4(1-\lambda_0)^2]^{1/2}-2(1-\lambda_0^2)\arccos\left[\dfrac{2(1-\lambda_0)}{\beta\mathcal{AR}(1+\lambda_0)}\right]}\\ &\text{when}\quad 2(1-\lambda_0)\leqq\beta\mathcal{AR}(1+\lambda_0)\\ \frac{D}{D_K}&=1\\ &\text{when}\quad 2(1-\lambda_0)\geqq\beta\mathcal{AR}(1+\lambda_0)\end{aligned}\right\}\tag{28}$$

Special cases of interest are:

Rectangular wing ($\lambda_0=1$)

$$\frac{D}{D_K}=\frac{1}{1+(4\beta\mathcal{AR})/\pi}\tag{29}$$

Diamond wing ($\lambda_0=0$)

$$\left.\begin{aligned}\frac{D}{D_K}&=\frac{1}{1+\dfrac{1}{\pi}[(\beta\mathcal{AR})^2-4]^{1/2}-\dfrac{2}{\pi}\arccos\left(\dfrac{2}{\beta\mathcal{AR}}\right)}, \quad 2\leqq\beta\mathcal{AR}\\ &=1, \qquad \beta\mathcal{AR}\leqq 2\end{aligned}\right\}\tag{30}$$

Figure 8 shows a plot of D/D_K against $\beta\mathcal{AR}$ for the elliptic, rectangular, tapered, and diamond plan forms. Base area and length of the wings are equal to these parameters for the Kármán ogive. For large values of $\beta\mathcal{AR}$ the relative drag decreases as $1/\beta\mathcal{AR}$. As the wing plan forms become slender, drag of the elliptic and rectangular wings approaches in the limit of vanishing $\beta\mathcal{AR}$ the drag of the ogive. The tapered wing, on the other hand, has a value of drag equal to that of the ogive for all values of taper ratio and aspect ratio satisfying the inequality $2(1-\lambda_0)\geqq\beta\mathcal{AR}(1+\lambda_0)$. This relation is satisfied so long as the edges of the wing are subsonic. Changes in sweep angle of the leading and trailing edges produce no further change in the minimum drag of the configuration so long as the base area is held fixed. The value D_K is the minimum drag for all such configurations lying within the fore-and-aft Mach cones from the nose and tail of the wing. Except in the case of the rectangular

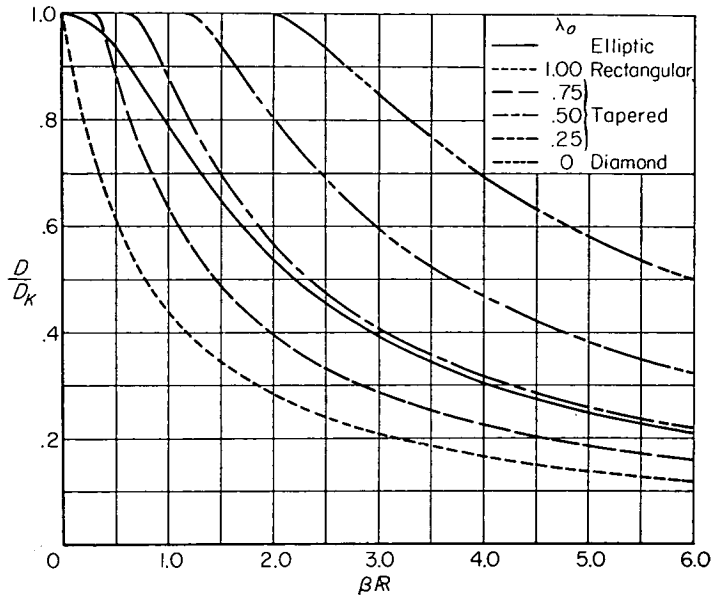


FIGURE 8.—Optimum drag for various plan forms, given base areas.

plan form, the curves of D/D_K have zero slope at their peak values.

Yawed elliptic plan form with afterbody.—For given base area, the drag of an elliptic plan form at angle of yaw ψ can be calculated from equation (24). In order to justify this statement it is sufficient to show that the characteristic curve Γ_1 lies in the plane $x=f=m(y+b_0)$. The trace of Γ_1 in a yz plane is, in fact, another ellipse and the dimensional relationships between the plan form and the trace are as shown in figure 9. It is convenient in the derivation of these results to proceed inversely and to determine the plan form as an envelope of curves given by the intersections in the xy plane of fore-and-aft facing cones with vertices on Γ_1. Since the streamwise position of the origin is of no direct significance, the space curve Γ_1 may be assumed given by

$$\left.\begin{aligned} \frac{y^2}{B^2}+\frac{z^2}{C^2}&=1, \qquad B\geq C \\ x&=my, \qquad m<\beta \end{aligned}\right\} \tag{31}$$

The Mach cones with vertices at the point (x_1, y_1, z_1) on Γ_1 are

$$(x-x_1)^2=\beta^2[(y-y_1)^2+(z-z_1)^2] \tag{32}$$

where

$$x_1=my_1, \qquad z_1^2=\frac{C^2}{B^2}(B^2-y_1^2)$$

The parametric equation of the envelope in the yz plane is found from equation (32) with $z=0$ and the y_1 derivative of the same expression, that is, by elimination of y_1 from the relations

$$B^2[(x-my_1)^2-\beta^2(y-y_1)^2]=\beta^2C^2(B^2-y_1^2)$$

$$[B^2m^2-\beta^2(B^2-C^2)]y_1=(mx-\beta^2y)B^2$$

The envelope is, therefore,

$$(B^2-C^2)x^2-2mB^2xy+(m^2B^2+\beta^2C^2)y^2=C^2[\beta^2(B^2-C^2)-m^2B^2] \tag{33}$$

Equation (33) represents an ellipse so long as the initially chosen m satisfies the inequality

$$m^2<\beta^2(B^2-C^2)/B^2 \tag{34}$$

The elliptical plan form is fixed by its major and minor axes and angle of yaw. The relationship between the plan form and trace curve is more conveniently carried out, however, in terms of the three quantities l, b, δ where l is streamwise length of the plan form, $2b$ its width, and $x=\delta y$ is the line passing through the points on the plan form where $y=\pm b$.

Elementary calculations performed with equation (33) yield the following relations

$$l/2=(B^2m^2+\beta^2C^2)^{1/2} \tag{35a}$$

$$b=(B^2-C^2)^{1/2} \tag{35b}$$

$$\delta=\frac{mB^2}{B^2-C^2} \tag{35c}$$

$$\tan 2\psi=\frac{-2mB^2}{(B^2-C^2)-(m^2B^2+\beta^2C^2)} \tag{35d}$$

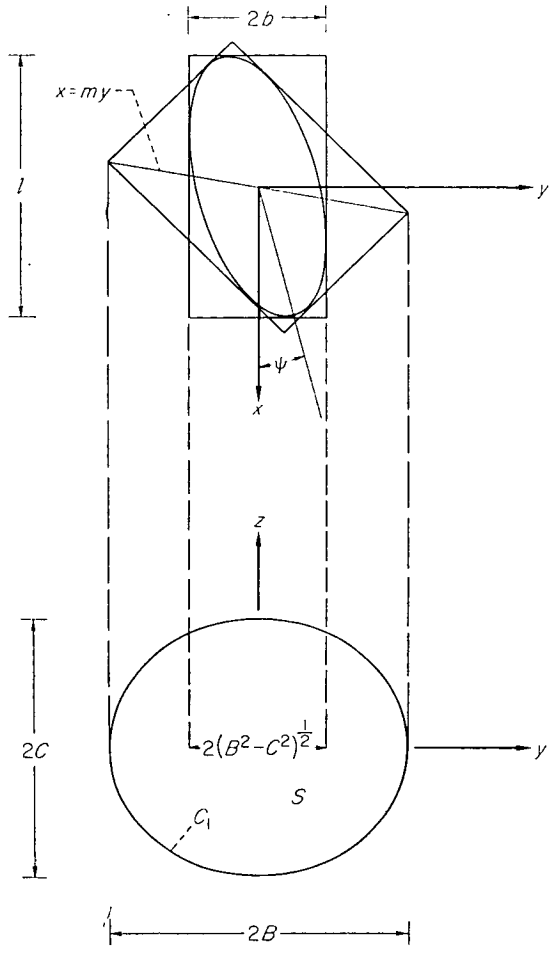


FIGURE 9.—Yawed elliptic wing and characteristic trace.

In figure 9 the plan form is also circumscribed by a parallelogram with sides inclined at the Mach angle. The equations of these lines are

$$x=\beta y\pm(\beta-m)B, \qquad x=-\beta y\pm(\beta+m)B$$

from which it follows that their outermost intersection points are at $y=\pm B$ and the line connecting the intersection points is $x=my$.

The above results thus show that the Mach lines circumscribing the plan form can be used to determine the span of the trace of Γ_1 and the angle of inclination of the plane of Γ_1. The span of the plan form is, moreover, equal to the distance between the foci of the elliptic trace.

From equations (24) and (25b) the drag of the wing and afterbody relative to the drag of the Kármán ogive of equal length and base area is given by

$$\frac{D}{D_K}=\frac{l^2}{4BC(\beta^2-m^2)}=\frac{B^2m^2+\beta^2C^2}{BC(\beta^2-m^2)} \tag{36}$$

The results can be summarized as follows

$$\frac{D}{D_K}=\left\{\frac{1+\beta^2\xi^2+[(1+\beta^2\xi^2)^2-4\beta^2\delta^2\xi^4]^{1/2}}{1-\beta^2\xi^2+[(1+\beta^2\xi^2)^2-4\beta^2\delta^2\xi^4]^{1/2}}\right\}^{1/2}\frac{1}{[(1+\beta^2\xi^2)^2-4\beta^2\delta^2\xi^4]^{1/2}} \tag{37}$$

$$\mathcal{AR}=\frac{4\xi}{\pi(1-\delta^2\xi^2)^{1/2}},\ \xi=2b/l \tag{38}$$

$$\tan 2\psi=\frac{2\delta\xi^2}{1-\xi^2} \tag{39}$$

Figure 10 is a plot of D/D_K against angle of yaw for $M=\sqrt{2}$ and $\mathcal{AR}=4/\pi$, 4, 8. The smallest of these values of aspect ratio corresponds to a circular plan form and obviously must be independent of ψ; the drag ratio is $D/D_K=\sqrt{2}/2$ and this is in agreement with equation (27) for the special case of the circular wing. Several limiting forms of equation (37) are of interest in showing the variation of drag. For example, when $\delta=0$, the plan form is unyawed, $\mathcal{AR}=4\xi/\pi$ and

$$\frac{D}{D_K}=\frac{1}{(1+\beta^2\xi^2)^{1/2}}=\frac{1}{[1+(\pi\beta\mathcal{AR}/4)^2]^{1/2}}$$

as given in equation (27). This relation furnishes the values of D/D_K in figure 10 at $\psi=90°$. If $\delta\xi=1$ and $\xi\neq0$ one has $\mathcal{AR}=\infty$, $\psi=\arctan\xi$ and

$$\frac{D}{D_K}=\frac{1}{(1-\beta^2\tan^2\psi)^{3/2}}$$

This is the general drag relation for the yawed wing when aspect ratio becomes infinite. It is to be noted that drag remains finite except when the angle of yaw is equal to the free-stream Mach angle. In figure 10 the drag curve for infinite aspect ratio must therefore have a singularity at $\psi=45°$. If $\delta\xi\to 1$ and $\xi\to0$ so that aspect ratio remains finite, it follows that $\psi\to0$ and $D/D_K=1$.

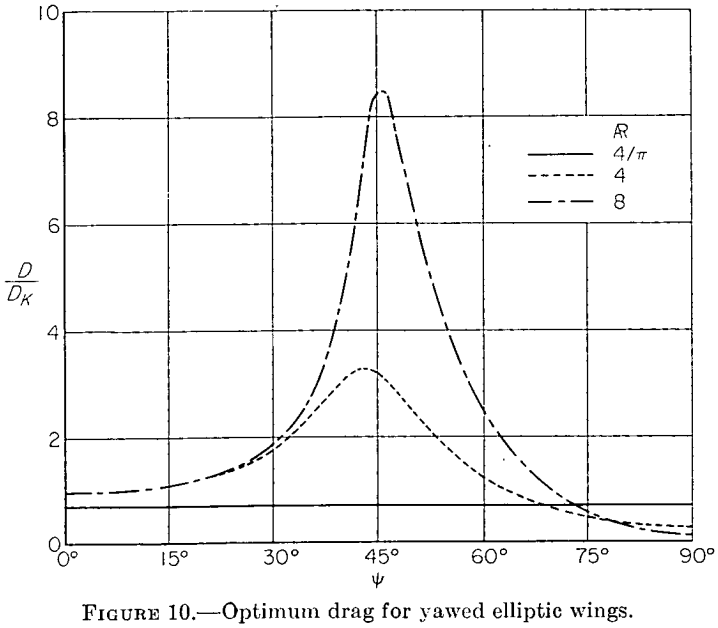


FIGURE 10.—Optimum drag for yawed elliptic wings.

General results in connection with minimum drag with fixed base area.—The connection between the Lagrange multipliers of the variational problems (see eqs. (12) through (15)) and certain quantities in the combined flow field has been mentioned. Another interesting interpretation for the parameter λ can be found. In the case when $f=$const. on C_1, λ can be evaluated explicitly in terms of the geometry in the plane of Γ_1; from equations (12b) and (22)

$$\frac{\lambda}{q_\infty}\equiv 2\frac{A}{\beta^2 S} \tag{40}$$

Equation (40) states that $-\lambda/q_\infty$ is equal to the pressure coefficient predicted on the linearized theory for the unidimensional duct flow bounded internally and externally by the characteristic traces, that is, by the curves C_1 and C_2, as in figure 2. By the other interpretation, λ/q_∞ is also the pressure coefficient in the combined flow field. This result can also be generalized to the case where $x=f=my+b_0$ by sweeping back the entrance to the duct by the same amount as the plane of Γ_1.

Another point that should be made in regard to the optimum configurations for which $f=0$ on Γ_1 follows from equation (22). That is, the Kármán ogive has the greatest value of minimum drag for given length, base area, and Mach number. This follows directly from equation (22) by noting that the area S is a minimum when the trace C_1 is the circle connected with the Kármán ogive of the prescribed length and base area. The curves in figure 8 show this result clearly.

The final result of a general nature to be noted here is found by comparing equations (12a) and (14a), the minimizing conditions for given base area and for given lift, respectively. If differences of over-all sign (because of the quadratic dependence of drag upon χ) are disregarded, the two problems will lead to the same χ, hence the same drag, if

$$\left.\begin{aligned}\nabla^2 f&=0 && \text{in } S\\ 2q_\infty\sigma&=\lim_{z\to0}(\lambda f_z) && \text{on } C_2\end{aligned}\right\} \tag{41}$$

It is found that a supersonic-edged wing with a straight supersonic trailing edge, parallel to $x=ky$, leads to a function f which satisfies equations (41). If the trailing edge is

$$x-ky=a \quad (k<\beta)$$

then the surface Σ_2 (see fig. 1) is an inclined plane:

$$x=f(y,z)=ky-(\beta^2-k^2)^{1/2}z+a \quad (z\geq 0)$$

so that

$$f_z=-(\beta^2-k^2)^{1/2}$$

$$\nabla^2 f=0$$

From the second of equations (41),

$$2q_\infty\sigma=-(\beta^2-k^2)^{1/2}\lambda$$

The drags of the two cases are equal, giving, by equations (14b) and (12b),

$$A=-\frac{(\beta^2-k^2)^{1/2}}{2}\frac{L}{q_\infty}$$

Thus one has the result that if the minimum drag due to lift of a supersonic-edged wing with a straight supersonic trailing edge parallel to $x=ky$ is known, then a nonlifting wing of the same plan form and with base area given by

$$A=\frac{(\beta^2-k^2)^{1/2}}{2}\frac{L}{q_\infty}$$

will have the same optimum drag.

WINGS AND BODIES WITH GIVEN VOLUME

The variational problem in terms of χ for the case of prescribed volume with zero base area (eqs. (13)) contains an arbitrary constant k whose magnitude is to be determined by application of the zero base-area condition to the solution of the boundary-value problem. Thus set

$$\chi+\frac{\mu}{2\rho_\infty U_\infty}\left[f^2+kf+\frac{\beta^2}{2}(y^2+z^2)\right]=\Omega(y,z)$$

The problem in terms of Ω is then, by equations (13),

$$\left.\begin{aligned}
&\nabla^2\Omega=0 && \text{in } S\\
&\frac{\partial\Omega}{\partial n}=\frac{\mu\beta^2}{4\rho_\infty U_\infty}\frac{\partial r^2}{\partial n} && \text{on } C_2\\
&\Omega=\frac{\mu}{2\rho_\infty U_\infty}\left(f^2+kf+\frac{\beta^2 r^2}{2}\right) && \text{on } C_1
\end{aligned}\right\} \tag{42}$$

The closure condition can be expressed as

$$\iint_S (f_y\chi_y+f_z\chi_z)\,dy\,dz=0$$

which becomes, after an application of Green's theorem,

$$\frac{\beta^2\mu}{2\rho_\infty U_\infty}kS=-\int_{C_1} f\frac{\partial}{\partial n}\left(\Omega-\frac{\beta^2\mu}{4\rho_\infty U_\infty}r^2\right)ds \tag{43}$$

Clearly now, if $f=0$ on C_1, also $k=0$. Again, as in the given base-area case, proper positioning of the origin can simplify the analysis.

526597—60——79

Quasi-cylindrical body of given volume.—The body and notation are shown in figure 11. The external wave drag is to be minimized under the conditions that volume is fixed and base area is zero.

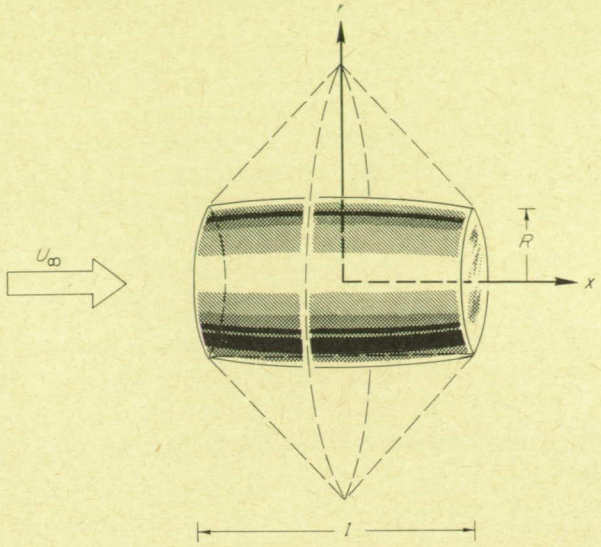


FIGURE 11.—Optimum body of revolution with given volume.

In this case, Σ_2 is the surface of the conical frustum, whose equation is

$$x=f(r)=\beta(h+R-r);\ h=l/2\beta$$

Since $f=0$ on C_1 in this case, the remarks on k, just above, apply, and the boundary-value problem is

$$\left.\begin{aligned}
&\nabla^2\left(\chi+\frac{\mu}{2\rho_\infty U_\infty}f^2\right)=-\frac{\beta^2\mu}{\rho_\infty U_\infty} && \text{in } S\\
&\frac{\partial}{\partial n}\left(\chi+\frac{\mu}{2\rho_\infty U_\infty}f^2\right)=0 && \text{on } C_2\\
&\chi=0 && \text{on } C_1
\end{aligned}\right\} \tag{44a}$$

Since C_1 and C_2 are circles, and the problem is independent of the peripheral variable θ, the solution of equations (44a) can be written in the form

$$\chi+\frac{\mu f^2}{2\rho_\infty U_\infty}=\frac{\mu\beta^2}{\rho_\infty U_\infty}\left(ar^2+b+c\ln\frac{R+h}{r}\right) \tag{44b}$$

where a, b, c are to be determined from the boundary conditions. One easily finds that

$$a=-\frac{1}{4};\quad b=\frac{1}{4}(R+h)^2;\quad c=-\frac{1}{2}R^2$$

The drag is then determined as

$$D=\frac{\rho_\infty}{2}\iint_S(\chi_y^2+\chi_z^2)dy\,dz=\pi\rho_\infty\int_R^{R+h}r\chi_r^2 dr$$

$$=\frac{\pi\beta^4\mu^2}{8q_\infty}\left\{\frac{h(h+2R)}{4}[(R+h)^2-3R^2]+R^4\ln\frac{R+h}{R}\right\}$$

From equation (13b), the parameter μ can be replaced by $2D/V$, giving finally

$$\frac{D}{q_\infty}=\frac{2V^2}{\pi\beta^4}\left\{\frac{h(h+2R)}{4}[(R+h)^2-3R^2]+R^4 ln\frac{R+h}{R}\right\}^{-1}$$
$$=\frac{V^2}{l^4}\frac{1}{C(\sigma)} \tag{45}$$

where $\sigma=\beta R/l$, and

$$C(\sigma)=\frac{\pi}{128}\left\{(1+4\sigma)[(1+2\sigma)^2-12\sigma^2]+64\sigma^4 ln\frac{1+2\sigma}{2\sigma}\right\} \tag{46}$$

The result of equation (45), as in the case of given base area, covers the entire spectrum of fineness ratios and yields, in its limiting forms, the results of two-dimensional airfoil theory (biconvex section) and slender-body theory. The latter case, which is the Sears-Haack slender body with drag D_{S-H} (refs. 14 and 15), corresponds to $\sigma=0$. Equation (45) then becomes

$$\frac{D_{S-H}}{q_\infty}=\frac{128V^2}{\pi l^4}$$

The above problem was considered previously by Heaslet and Fuller (ref. 16) without recourse to the present techniques but, rather, by minimizing after expressing drag in terms of the source distribution that could be assumed to generate the external shape of the body. In this approach, it becomes necessary to find first the source-distribution function, under minimizing conditions, and to calculate drag and volume subsequently. The details of the calculation are thus less direct since the desired quantities are expressed as integrals involving the hyperbolic influence function of the supersonic source. In reference 16, the function $C(\sigma)$ of equation (46) appeared in the form (in a modified notation)

$$C(\sigma)=\frac{1}{3}\int_0^1[(\eta+2\sigma)(1-\eta+2\sigma)]^{1/2}[\eta(1-\eta)E-$$
$$\sigma(1-4\sigma)(K-E)]d\eta$$

where K and E are elliptic integrals of first and second kind, respectively, of modulus

$$k=\left[\frac{\eta(1-\eta)}{(\eta+2\sigma)(1-\eta+2\sigma)}\right]^{1/2}$$

The immediate advantage of equation (46) is, of course, the natural one provided by any analytic representation with its precise determination of magnitude and rate of change. From a disparate point of view, the equivalence of the two results gives not only a new fundamental identity in the theory of elliptic functions, but also indicates a method whereby further identities may be generated. From the standpoint of direct application, however, the results of reference 16 remain unmodified. The calculations that were used to plot the variation of $C(\sigma)$ were found to check to at least four significant figures with the present formula, and thus provided a satisfying confirmation of the numerical techniques used in the original evaluation.

Elliptic wings of given volume.—As noted previously, a wing of elliptic plan form leads to a boundary curve C_1 that is also an ellipse. Figure 12 shows the wing, the boundary curves C_1 and C_2, and the region S. Let C_1 be given by

$$\frac{y^2}{B^2}+\frac{z^2}{C^2}=1$$

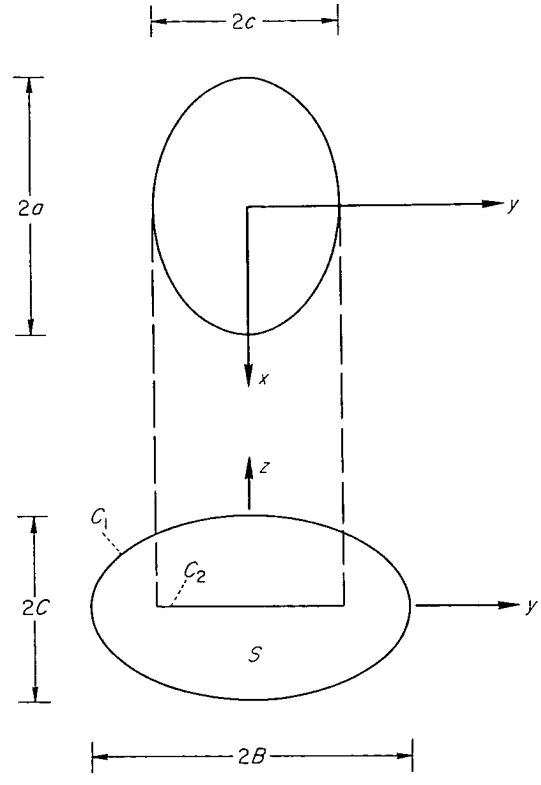


FIGURE 12.—Elliptic wing and characteristic trace.

The curve C_2 is now merely a segment of the y axis. The solution of the problem where minimum drag is sought, for given volume and zero base area, is eased by the fact that by manipulation of equation (6b), using the extremum conditions of equations (13) (with $k=0$), the expression for the volume can be put in the form

$$V=-\frac{\beta^2}{U_\infty}\iint_S\left(\chi+\frac{\mu}{2\rho_\infty U_\infty}f^2\right)dy\,dz \tag{47}$$

Thus, explicit determination of χ from equations (13a) is avoided, and the complicated expression for f need not be exhibited; only the fact that it vanishes on the outer boundary curve C_1 is required. It is found that

$$\chi+\frac{\mu}{2\rho_\infty U_\infty}f^2=-\frac{\mu}{2\rho_\infty U_\infty}\frac{\beta^2B^2C^2}{B^2+C^2}\left(\frac{y^2}{B^2}+\frac{z^2}{C^2}-1\right) \tag{48}$$

satisfies equations (13a) (with $k=0$). Substitution of equation (48) in equation (47) yields

$$V=-\frac{\mu}{8q_\infty}\beta^4\frac{B^2C^2S}{B^2+C^2}$$

where S $(=\pi BC)$ is the area enclosed by C_1. Now, from equation (13b), the drag can be evaluated as

$$\frac{D}{q_\infty}=\frac{4V^2}{\beta^4S}\left(\frac{1}{B^2}+\frac{1}{C^2}\right) \tag{49a}$$

Finally, in terms of the original wing parameters (see fig. 12),

$$B^2=a^2+\beta^{-2}c^2$$

$$C^2=\beta^{-2}c^2$$

$$\frac{D}{q_\infty}=\frac{4V^2}{(\pi ac)c^2}\frac{\beta^2+2\frac{c^2}{a^2}}{(\beta^2+c^2/a^2)^{3/2}} \tag{49b}$$

which agrees with the result of Jones in reference 6. (A typographical error in the reference has been corrected in equation (49b).)

It might be supposed that, once again, a simple extension of the above results would lead to the minimum-drag result for a yawed elliptic wing of given volume. This, unfortunately, is not the case. The drag found by the present method is much lower than the known value, being correct only in the limiting case of zero yaw, as above. The reason is, presumably, that strict closure along the trailing edge has not been enforced, only the condition that base area vanish. An unreal wing has therefore been evolved in the yawed case, with patches of negative base area where upper and lower surfaces have crossed. It does not seem feasible to enforce pointwise closure of the trailing edge in conjunction with the present method for drag calculation. Thus, caution is necessary when using this method for given volume problems. Of course, this difficulty does not arise when treating lifting surfaces, for in that case, a negative ordinate for the upper surface is of no concern.

CASES OF GIVEN LIFT AND MOMENT

A family of wings with supersonic edges.—Consider the family of wings whose plan forms are all portions of the hyperbola asymptotic to Mach lines through the point $(-d,0,0)$. The equation of the leading edge is

$$\beta^2y^2=2dx+x^2$$

and the trailing edge is

$$x=l$$

where the quantities d and l are shown in figure 13. The root chord of the resulting wing is l. If $d\to 0$, the wing becomes a triangle with sonic edges, and if $d/l>>1$, the wing has very large span compared with its chord.

The surface Σ_2 (fig. 1) is composed of a pair of inclined planes

$$x=f(y,z)=l-\beta|z| \tag{50a}$$

and the boundary curve C_1 (fig. 13) is made up of two parabolas

$$\beta^2y^2=(2d+l)(l-2\beta|z|) \tag{50b}$$

If minimum drag for fixed lift and center of pressure is sought for the wings of this family, the variation leads to the problem

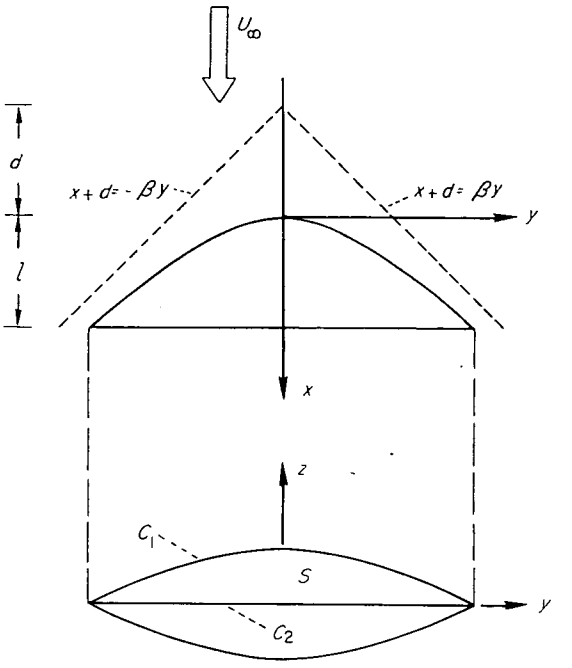


FIGURE 13.—Hyperbolic-edged wing and characteristic trace.

$$\left.\begin{aligned} \nabla^2(\chi+U_\infty\tau zf)&=0 \quad \text{in } S\\ \frac{\partial}{\partial n}\left[\chi+U_\infty(\sigma-x_m\tau)z+U_\infty\tau zf\right]&=0 \quad \text{on } C_2\\ \chi&=0 \quad \text{on } C_1 \end{aligned}\right\} \tag{51}$$

where x_m is the coordinate of the center of pressure. A simple, exact solution of equations (51) follows directly if

$$x_m=d+\tfrac{3}{5}l$$

in which case

$$\chi=-\frac{3}{16q_\infty}\frac{U_\infty\beta L}{[l(2d+l)]^{3/2}}\frac{z}{|z|}\left[\beta^2y^2+(2d+l)(2\beta|z|-l)\right] \tag{52}$$

In this event, the drag is given by

$$\frac{D}{q_\infty}=\frac{3}{4}\beta^2\left(\frac{L}{q_\infty}\right)^2\frac{d+\frac{3}{5}l}{[l(2d+l)]^{3/2}} \tag{53}$$

where L is the given lift. Since the wing area is

$$\frac{1}{\beta}\left[(d+l)\sqrt{l(2d+l)}-d^2\cosh^{-1}\frac{d+l}{d}\right]$$

the drag parameter is, written in terms of $\zeta=d/l$

$$\frac{C_D}{\beta C_L^2}=\frac{9}{40}\frac{1+\frac{5}{3}\zeta}{(1+2\zeta)^{3/2}}\left[(1+\zeta)\sqrt{1+2\zeta}-\zeta^2\cosh^{-1}(1+\zeta)\right] \tag{54}$$

Figure 14 shows the variation of the drag with ζ. This latter parameter is, in geometrical terms, $\beta^2\rho_0/l$, where ρ_0 is the radius of curvature of the leading edge at the apex, and l is root chord. As ζ varies from 0 to ∞, the plan form ranges from a sonic-edged triangle to a wing that has nearly a parabolic leading edge.

In the limit $\zeta \to 0$, when a sonic-edged triangular wing results, the value of the drag parameter given by equation (54) is

$$\frac{C_D}{\beta C_L^2}=0.225 \tag{55}$$

This value is in agreement with the result of reference 8 for center of pressure at 60 percent of root chord. Also, the approximate result for given lift alone from reference 10 is quite close to that of equation (55), being 0.223. This would indicate that the center of pressure is near the 60-percent-chord position for given lift. In fact, from the results of reference 8, it is found that the center of pressure for given lift alone lies at 63 percent of the chord.

At the other extreme, $\zeta \to \infty$, the wing plan form is very nearly a parabolic segment. The center of area of such a parabolic segment lies at 60 percent of the chord, which indicates that the loading is uniform over the wing. This is the correct result for minimum drag with given lift in two-dimensional flow, and the wing is indeed becoming nearly a two-dimensional case at $\zeta \to \infty$.

DETERMINATION OF SURFACE SHAPE OF OPTIMUM BODIES OF REVOLUTION

Generally speaking, the information gained by solving a minimum-drag problem according to the method used in this report includes knowledge of the function χ, which is of course the perturbation potential φ evaluated in the rear enveloping characteristic surface Σ_2 of figure 1. It would be useful if this information could be used then to determine the singularity distribution, and ultimately the surface shape, that gives rise to the flow field having the optimal properties in question. In general, however, no such method at present exists,[2] although various approaches involving some degree of approximation have been indicated (ref. 8). In one case, where the singularities lie on a single line, a complete analytical solution is possible, and will be considered next.

Ducted body of revolution with prescribed base area.—The potential due to a line distribution of sources is given by

$$\varphi(x,r)=-\frac{1}{2\pi}\int_{-\beta R}^{x-\beta r}\frac{B(x_1)dx_1}{[(x-x_1)^2-\beta^2 r^2]^{1/2}}$$

where $B(x)$ is the source strength per unit length, and the lower limit, $x=-\beta R$, indicates the starting point for the distribution; $B(x)=0$ for $x\leq -\beta R$. In this, R is the radius of the control cylinder on which the boundary conditions are satisfied; the initial point of the body is $x=0$ when the sources start at $x=-\beta R$.

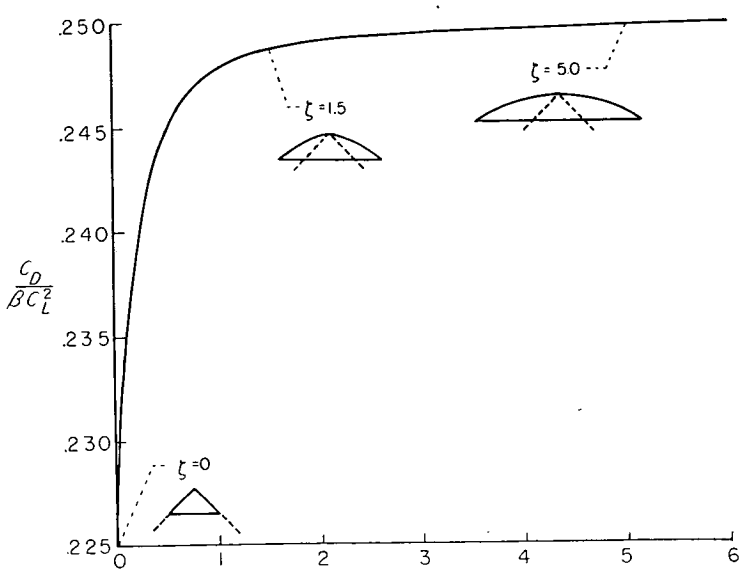


FIGURE 14.—Variation of optimum drag for hyperbolic-edged wings.

In this coordinate system, the surface Σ_2 is the conical frustum given by

$$x=f(r)=l+\beta R-\beta r=\beta(2h+R-r);\quad 2\beta h=l$$

The function χ is found by inserting this value for x in the above potential relation;

$$\chi(r)=-\frac{1}{2\pi}\int_{-\beta R}^{\beta(2h+R-2r)}\frac{B(x_1)dx_1}{[\beta(2h+R)-x_1]^{1/2}\,[\beta(2h+R-2r)-x_1]^{1/2}} \tag{56a}$$

Now set

$$\left.\begin{aligned} B(x_1)&=[\beta(2h+R)-x_1]^{1/2}\,\mathbf{B}(x_1)\\ \beta(2h+R)-2\beta r&=t;\quad r=\frac{\beta(2h+R)-t}{\beta}\end{aligned}\right\} \tag{56b}$$

and equation (56a) becomes

$$\chi(r)=-\frac{1}{2\pi}\int_{-\beta R}^{t}\frac{\mathbf{B}(x_1)dx_1}{(t-x_1)^{1/2}}=-\frac{1}{2\pi}\int_0^{\tau}\frac{\mathbf{B}(x_2)dx_2}{(\tau-x_2)^{1/2}}$$

where $\tau=t+\beta R$ and $x_2=x_1+\beta R$. Further, since $\frac{d}{dr}=-2\beta\frac{d}{d\tau}$, the last equation can be written

$$\chi_r=\frac{\beta}{\pi}\frac{d}{d\tau}\int_0^{\tau}\frac{\mathbf{B}(x_2)dx_2}{(\tau-x_2)^{1/2}} \tag{57}$$

Equation (57) is recognized as the dual relation to the Abel integral equation, namely

$$\mathbf{B}(\tau)=\frac{1}{\beta}\int_0^{\tau}\frac{\chi_r(x_2)\,dx_2}{(\tau-x_2)^{1/2}} \tag{58}$$

[2] Since the completion of the work of this report, the authors have seen a paper by E. W. Graham, "A Geometrical Problem Related to the Optimum Distribution of Lift on a Planar Wing in Supersonic Flow," Rep. SM-23020, Douglas Aircraft Co., Nov. 1957. In this paper, a solution is given to the problem of determining lift distribution on a wing when oblique line integrals of the loading taken across the wing are known. Now the lines along which such integrals are known all lie in the supersonic "zone of silence" associated with a given point, and Graham makes a continuation of the function representing the integrated loading as a function of the angle of the oblique line so that the integrated loading can be considered known for all lines through a given point. The integral equation expressing the integrated loading in terms of local loading is then inverted. Presumably, an analogous procedure will hold for the thickness case. For bodies of revolution, however, all oblique lines cut the singularity distribution in a point, no dependence on the angle of obliquity exists, and the inverse problem of finding the singularity distribution can be solved without difficulty.

Thus, when χ_r is known, the evaluation of $\mathbf{B}(x)$, hence of $B(x)$, is immediate.

In order to determine χ and hence χ_r, one has, from equations (12a)

$$\nabla^2\left(\chi+\frac{\lambda}{2\rho_\infty U_\infty}f\right)=0 \qquad \text{in } R<r<R+h$$

$$\frac{\partial}{\partial r}\left(\chi+\frac{\lambda}{2\rho_\infty U_\infty}f\right)=0 \qquad \text{at } r=R$$

$$\chi=0 \qquad \text{at } r=R+h$$

Thus, the solution for χ is readily seen to be

$$\chi=\frac{\lambda\beta}{2\rho_\infty U_\infty}(r-R-h)$$

and so

$$\chi_r=\frac{\lambda\beta}{2\rho_\infty U_\infty}$$

The solution for the source-distribution function can now be found by using equation (58);

$$\mathbf{B}(\tau)=\frac{\lambda}{\rho_\infty U_\infty}\sqrt{\tau}=\frac{\lambda}{\rho_\infty U_\infty}\sqrt{t+\beta R}$$

Then

$$B(x)=\frac{\lambda}{\rho_\infty U_\infty}[(x+\beta R)(l+\beta R-x)]^{1/2}$$

which checks with the result of reference 12, since, by equations (12b) and (21), it is found that

$$\lambda=\frac{\rho_\infty U_\infty{}^2 A}{\beta^2 S}$$

and so

$$B(x)=\frac{U_\infty A}{\beta^2 S}[(x+\beta R)(l+\beta R-x)]^{1/2} \tag{59}$$

The surface shape of the body is now readily found, and this has been done in reference 16.

Ducted body of revolution of given volume.—For this case, it is convenient to place the origin at the center of the body, since χ is already known from equation (44b). The same solution, as given by equation (58) with appropriate changes, can be used, and the resulting source-distribution function is

$$B(x)=-\frac{\mu}{2\rho_\infty U_\infty}\left\{(l-2x)[(x+\beta R)(l+\beta R-x)]^{1/2}-2\beta^2R^2\cos^{-1}\frac{l-2x}{l+2\beta R}\right\}$$

where for this expression the source distribution starts at $x=-\beta R$ as in the last example. From equations (13b) and (45), one finds that

$$-\frac{\mu}{2\rho_\infty U_\infty}=\frac{U_\infty V}{2l^4 C(\sigma)}$$

where $C(\sigma)$ is defined in equation (46). The source strength is then

$$B(x)=\frac{U_\infty V}{2l^4 C(\sigma)}\left\{(l-2x)[(x+\beta R)(l+\beta R-x)]^{1/2}-2\beta^2R^2\cos^{-1}\frac{l-2x}{l+2\beta R}\right\} \tag{60}$$

Again, determination of the shape is made in reference 16.

DETERMINATION OF OBLIQUE INTEGRATED LOADINGS

A procedure has been outlined for relating integrals of the perturbation potential φ taken across various lines in the surface of a wing and in the rear characteristic surface Σ_2 (see, e. g., eq. (19b)). The analysis will now be carried out in detail for the family of hyperbolic-edged wings treated above. For the special case of the sonic-edged member of the family, some of the geometrical relationships are shown in figure 3. The auxiliary plane Σ_3 (given by eq. (17)) is seen to cut the wing plane Σ_0 in the line CD, and to cut the lower part of the Σ_2 surface in the line EF. Clearly, as the inclination of CD, or the chordwise position of x_0, is changed, the line will eventually cease cutting the right leading edge of the wing and intersect the wing trailing edge. These regimes are distinguished by dividing the range of x_0 into Region I and Region II (as shown in fig. 15), whose bounds are functions of the angle θ;

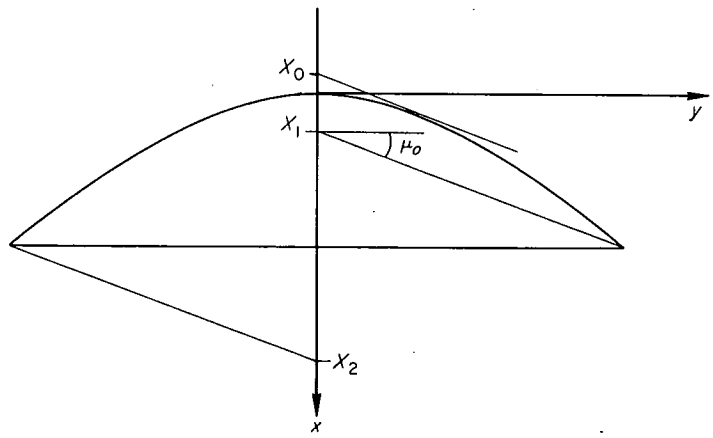


FIGURE 15.—Dividing points distinguishing regions I and II.

$$\left.\begin{aligned}&\text{Region I: } X_0=-d(1-\sin\theta)\le x_0\le X_1=l-\sqrt{l^2+2dl}\cos\theta\\&\text{Region II: } X_1\le x_0\le X_2=l+\sqrt{l^2+2dl}\cos\theta\end{aligned}\right\} \tag{61}$$

where d and l are defined as in figure 13, and $\cos\theta=\beta\tan\mu_0$. The regions will be considered in order.

Region I.—The integral relation that results from application of Green's theorem to the region bounded by Σ_1, Σ_3 and Σ_0 (see fig 3) and for which $z>0$ has been given as equation (19b). If Green's theorem (eq. (18a)) is applied to the lower portion, the following relation results:

$$-\frac{1}{\beta}\iint_{\Sigma_0}\varphi_z\,dx\,dy+\iint_{\Sigma_3}\frac{\partial\varphi}{\partial\nu}d\Sigma+\iint_{\Sigma_2}\frac{\partial\varphi}{\partial\nu}d\Sigma=0$$

Using again the coordinates ν, s in the separate planes, one finds

$$-\frac{1}{\beta}\iint_{\Sigma_0}\varphi_z dx\,dy+\left[\int_E^F\varphi(\Sigma_2\Sigma_3)ds-\int_C^D\varphi(\Sigma_0\Sigma_3)ds\right]+\int_E^F\varphi(\Sigma_2\Sigma_3)ds=0 \tag{62}$$

The notation $\varphi\ (\Sigma_2\Sigma_3)$, etc., means that φ is to be evaluated along the intersection of the surfaces Σ_2 and Σ_3.

In order to express the element ds in terms of, say, dy along the various lines, one can set up the coordinate transformation to express the N,ν,s system as a rigid rotation of the x,y,z system. It is thereby found that along CD, $ds=dy$ sin θ, and along EF, $ds=dy$. The relations (19b) and (62) then become

$$\frac{1}{\beta}\iint_{\Sigma_0}\varphi_z dx\,dy+\sin\theta\int_C^D\varphi(\Sigma_0\Sigma_3)dy=0\quad(z>0) \tag{63a}$$

$$-\frac{1}{\beta}\iint_{\Sigma_0}\varphi_z dx\,dy+2\int_E^F\varphi(\Sigma_2\Sigma_3)dy-\sin\theta\int_C^D\varphi(\Sigma_0\Sigma_3)dy=0\quad(z<0) \tag{63b}$$

where the $z>0$, $z<0$ are necessary because φ is discontinuous at the $z=0$ plane.

If the limits of integration for the surface integral over Σ_0 are inserted and the equations differentiated with respect to x_0 (recall that $\varphi=0$ on the surface Σ_1), equations (63) become

$$\int_C^D\varphi_z(x_0+\beta\cos\theta y,y)dy=-\beta\sin\theta\int_C^D\varphi_x(x_0+\beta\cos\theta y,y)dy \tag{64a}$$

$$\int_C^D\varphi_z(x_0+\beta\cos\theta y,y)dy=-\beta\sin\theta\int_C^D\varphi_x(x_0+\beta\cos\theta y,y)dy+2\beta\int_E^F\frac{\partial}{\partial x_0}[\varphi(\Sigma_2\Sigma_3)dy] \tag{64b}$$

where once again the results apply respectively to the cases where z approaches zero from above and from below.

Equation (64a) is seen to be a relation between integrals of perturbation components taken along the same oblique line across a supersonic-edged wing. If the integrated loading

$$\frac{L(x_0,\theta)}{q_\infty}=\frac{4}{U_\infty}\int_C^D\varphi_x dy \tag{65}$$

is introduced, equation (64a) becomes [3]

$$\frac{L(x_0,\theta)}{q_\infty}=-\frac{4}{U_\infty\beta\sin\theta}\int_C^D w(x_0+\beta\cos\theta y,y)dy \tag{66}$$

where w is the vertical perturbation component. Thus, the integrated loading is proportional to the averaged wing slope, both taken along the same line across the wing; the line in question lying somewhere in the "zone of silence" corresponding to the point $(x_0,0,0)$. Once again, these results are not confined to the case of optimum wings.

Now return to equations (64). It is necessary to determine the argument of φ in the last integral on the right in equation (64b), and this is done by solving for x and z in terms of y from the equations of Σ_2 and Σ_3;

$$\Sigma_2\colon x=l+\beta z$$

$$\Sigma_3\colon x=x_0+\beta\cos\theta y-\beta\sin\theta z$$

One finds that

$$\varphi(\Sigma_2\Sigma_3)=\varphi\left[\frac{l\sin\theta+x_0+\beta\cos\theta y}{1+\sin\theta},y,\frac{-l+x_0+\beta\cos\theta y}{\beta(1+\sin\theta)}\right]$$

If the differentiation with respect to x_0 is now performed in equation (64b), and the result subtracted from equation (64a), one gets the relation

$$\int_C^D\varphi_x(x_0+\beta\cos\theta y,y)dy=-\frac{1}{\beta\sin\theta(1+\sin\theta)}\int_E^F(\beta u+w)dy=\frac{-\int_E^F\chi_z dy}{\beta\sin\theta(1+\sin\theta)} \tag{67}$$

Making use of the definition of integrated loading given in equation (65), one has finally

$$\frac{L(x_0,\theta)}{q_\infty}=-\frac{4}{U_\infty\beta\sin\theta(1+\sin\theta)}\int_E^F\chi_z dy \tag{68}$$

which relates the integrated loading for a point in region I to an integral of the function χ_z across the rear enveloping surface Σ_2. This form of the result is well adapted to the case of optimum wings since, in general, surface values of the slope are not known, whereas, in the present method of optimizing, the function χ is known.

Region II.—The plane Σ_3 now intersects the trailing edge of the wing, and the boundary of the region of integration will include a portion of the rear enveloping surface Σ_2 for both $z>0$ and $z<0$. Figure 16 shows a trace in an $x=$const.

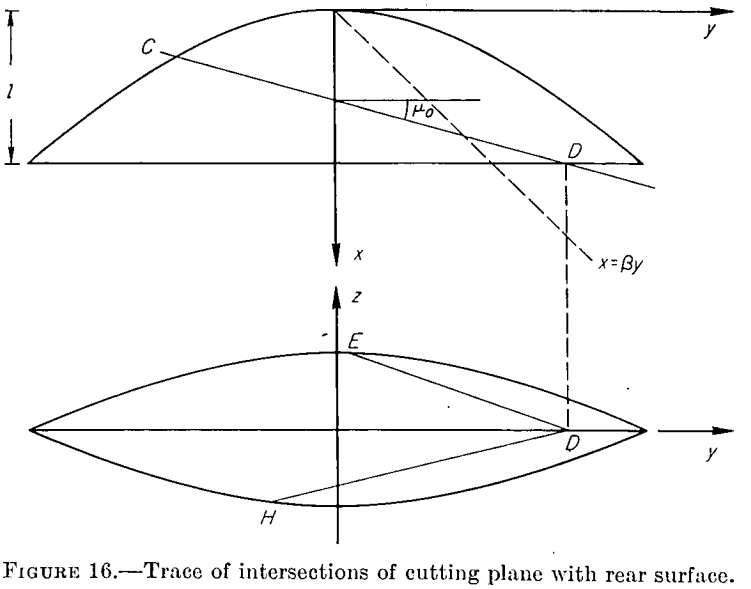


FIGURE 16.—Trace of intersections of cutting plane with rear surface.

[3] The authors are indebted to Professor P. A. Lagerstrom and Dr. M. E. Graham for pointing out an error in the definition of the line element ds which introduced an incorrect dependence on θ in the versions of the present formulas (66), (68), and (70) given in the original NACA Technical Note 4227 (see footnote 1).

plane of the lines of intersection of the cutting plane Σ_3 with both upper and lower portions of Σ_2. The oblique line across the wing intersecting the trailing edge is also shown, and the figure serves to define the notation used in this section.

The formulas resulting from application of equation (18a) to both upper and lower portions of the volume bounded by the forward Mach surface, the rear enveloping surface, and the plane Σ_3 are as follows:

$$\frac{1}{\beta}\iint_{\Sigma_0}\varphi_z dx\,dy+2\int_E^D\varphi(\Sigma_2\Sigma_3)ds+\int_C^D\varphi(\Sigma_0\Sigma_3)ds+\int_D^*\varphi(\Sigma_0\Sigma_2)ds=0 \qquad (z>0) \quad (69a)$$

$$-\frac{1}{\beta}\iint_{\Sigma_0}\varphi_z dx\,dy+2\int_H^D\varphi(\Sigma_2\Sigma_3)ds-\int_C^D\varphi(\Sigma_0\Sigma_3)ds+\int_D^*\varphi(\Sigma_0\Sigma_2)ds=0 \qquad (z<0) \quad (69b)$$

In these equations, the limit indicated by an asterisk is the intersection of leading and trailing edges of the wing. Once again the equations are differentiated with respect to x_0 and the results combined. Thus one finds for a point x_0 in region II (see eqs. (61))

$$\frac{L(x_0,\theta)}{q_\infty}=\frac{4}{U_\infty\beta\cos\theta}\chi\left(\frac{l-x_0}{\beta\cos\theta},0\right)+\frac{4}{U_\infty\beta\sin\theta}\left(\frac{\int_H^D\chi_z dy}{1-\sin\theta}-\frac{\int_E^D\chi_z dy}{1+\sin\theta}\right) \quad (70)$$

For the case of interest here, χ_z is a constant, as is seen from equation (52). After substituting the values for χ and χ_z in equations (68) and (70), and using the dimensionless variables

$$\xi_0=\frac{x_0}{l},\quad \eta=\frac{\beta y}{l},\quad \zeta=\frac{d}{l}$$

one gets the following results for the integrated loading:

Region I:

$$\frac{lL(\xi_0,\theta)}{L}=\frac{3}{2\sqrt{1+2\zeta}}\frac{\eta_F-\eta_E}{\sin\theta(1+\sin\theta)} \quad (71a)$$

Region II:

$$\frac{lL(\xi_0,\theta)}{L}=\frac{3}{4(1+2\zeta)^{3/2}}\frac{(1+2\zeta)-\eta_D^2}{\cos\theta}+\frac{3}{2\sqrt{1+2\zeta}}\frac{\frac{\eta_H-\eta_D}{1-\sin\theta}+\frac{\eta_D-\eta_E}{1+\sin\theta}}{\sin\theta} \quad (71b)$$

where

$$\eta_F=(1+\sin\theta)^{-1}\{(1+2\zeta)\cos\theta+\sqrt{2(1+2\zeta)(1+\sin\theta)[\xi_0+\zeta(1-\sin\theta)]}\}$$

$$\eta_E=(1+\sin\theta)^{-1}\{(1+2\zeta)\cos\theta-\sqrt{2(1+2\zeta)(1+\sin\theta)[\xi_0+\zeta(1-\sin\theta)]}\}$$

$$\eta_H=(1-\sin\theta)^{-1}\{(1+2\zeta)\cos\theta-\sqrt{2(1+2\zeta)(1-\sin\theta)[\xi_0+\zeta(1+\sin\theta)]}\}$$

$$\eta_D=(1-\xi_0)/\cos\theta$$

In figure 17 these integrated loadings are drawn for the three members of the family corresponding to $\zeta=d/l=0$, 1.5, 5, with $\beta=1$ and $\mu_0=0°$, 15°, 30°, 45° in each case. The dimensionless quantity plotted is

$$P(\xi_0,\theta)=lL(\xi_0,\theta)/L$$

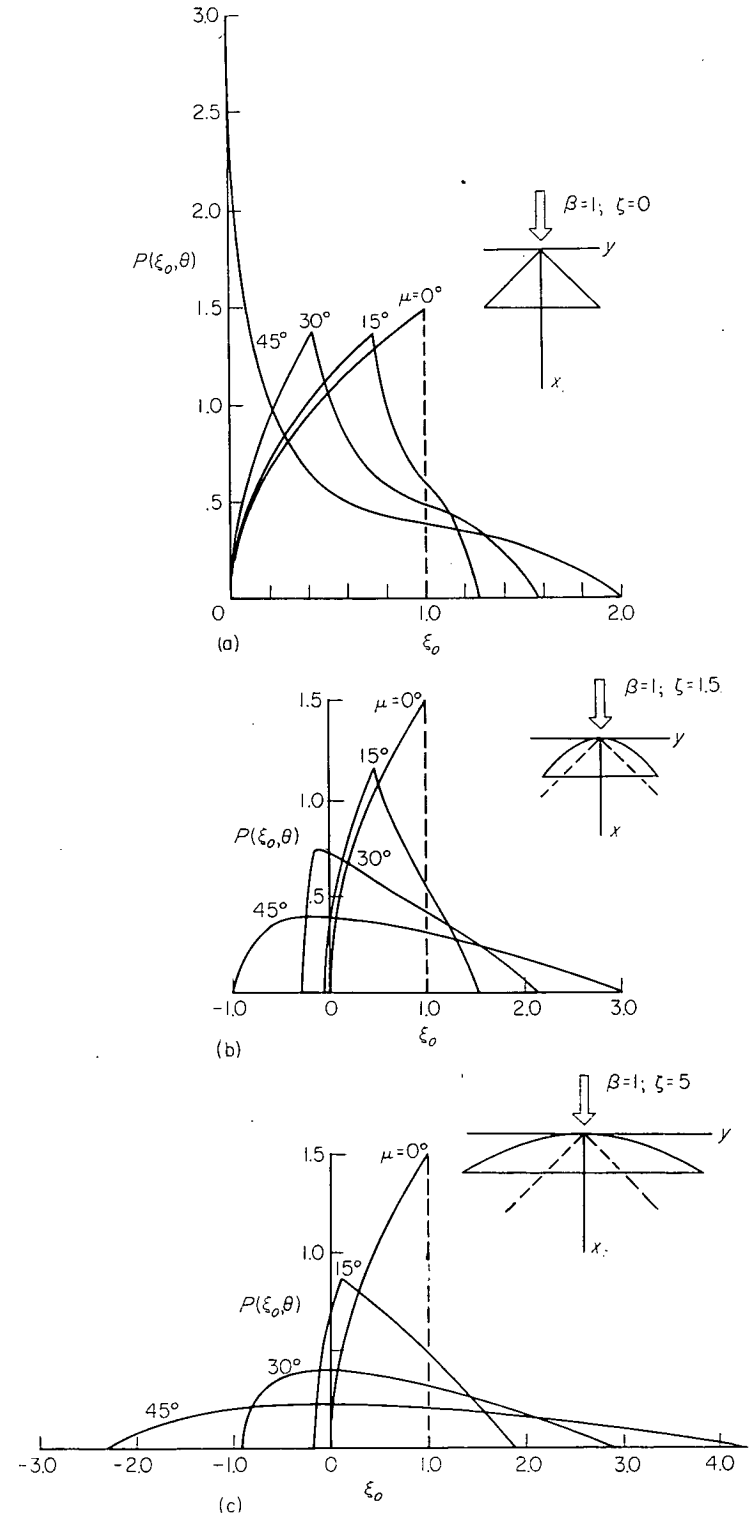


FIGURE 17.—Integrated loadings for family of wings with hyperbolic edges.

It is to be observed that when $\mu=0°$, $\theta=\pi/2$ and region II ceases to exist. In this case, the integrated loading is precisely the chord loading of the wing. One then gets

$$\frac{lL(\xi_0,\theta)'}{L}=\frac{3}{2}\sqrt{\xi_0} \tag{72}$$

independent of the shape parameter ζ.

AMES AERONAUTICAL LABORATORY
NATIONAL ADVISORY COMMITTEE FOR AERONAUTICS
MOFFETT FIELD, CALIF., *Nov. 29, 1957*

REFERENCES

1. Ward, G. N.: On the Minimum Drag of Thin Lifting Bodies in Steady Supersonic Flows. British A. R. C. Rep. 18,711, FM 2459, Oct. 1, 1956.
2. Nicolsky, A. A.: On the Theory of Axially Symmetric Supersonic Flows and Flows With Axisymmetric Hodographs. IX Int. Cong. Appl. Mech., Brussels, Sept. 1956.
3. Kogan, M. N.: On Bodies of Minimum Drag in a Supersonic Gas Stream. Prikladnaia Matematika y Mechanika, vol. XXI, no. 2, 1957, pp. 207–212.
4. Zhilin, Yu. L.: Wings of Minimum Drag. Prikladnaia Matematika y Mechanika, vol. XXI, no. 2, 1957, pp. 213–220.
5. Jones, Robert T.: The Minimum Drag of Thin Wings in Frictionless Flow. Jour. Aero. Sci., vol. 18, no. 2, Feb. 1951, pp. 75–81.
6. Jones, Robert T.: Theoretical Determination of the Minimum Drag of Airfoils at Supersonic Speeds. Jour. Aero. Sci., vol. 19, no. 12, Dec. 1952, pp. 812–822.
7. Graham, E. W.: The Calculation of Minimum Supersonic Drag by Solution of an Equivalent Two-Dimensional Potential Problem. Rep. No. SM–22666, Douglas Aircraft Co., Dec. 1956.
8. Germain, Paul: Sur le minimum de traînée d'une aile de forme en plan donnée. Comptes Rendus de l'Académie des Sciences, tome 244, no. 9, 25 Fevrier, 1957, pp. 1135–1138.
9. Germain, Paul: Aile symétrique à portance nulle et de volume donné realisant le minimum de traînée en écoulement supersonique. Comptes Rendus de l'Académie des Sciences, tome 244, no. 22, 27 Mai 1957, pp. 2691–2693.
10. Graham, M. E.: Examples of Calculation of Minimum Supersonic Drag Due to Lift by Solution of Two-Dimensional Potential Problem: Elliptical-Planform Wings and an Approximate Delta-Planform Wing. Rep. No. SM-22754, Douglas Aircraft Co., Mar. 1957.
11. Hayes, Wallace D.: Linearized Supersonic Flow. Rep. No. AL–222, North American Aviation, Inc., June 18, 1947.
12. Parker, Hermon M.: Minimum-Drag Ducted and Pointed Bodies of Revolution Based on Linearized Supersonic Theory. NACA Rep. 1213, 1955. (Supersedes NACA TN 3189).
13. von Karman, Th.: The Problem of Resistance in Compressible Fluids. Proc. Fifth Volta Congress, Rome, Sept. 30–Oct. 6, 1935. (Also available as GALCIT Pub. 75).
14. Sears, William R.: On Projectiles of Minimum Wave Drag. Quart. Appl. Math., vol. IV, no. 4, Jan. 1947, pp. 361–366.
15. Haack, W.: Geschossformen kleinsten Wellen-widerstandes. Lilienthal-Gesellschaft für Luftfahrtforschung, Bericht 139, Teil 1 Oct. 9–10, 1941, pp. 14–28.
16. Heaslet, Max. A., and Fuller, Franklyn B.: Axially Symmetric Shapes With Minimum Wave Drag. NACA Rep. 1256, 1956. (Supersedes NACA TN 3389).

REPORT 1386

INVESTIGATION OF THE DRAG OF VARIOUS AXIALLY SYMMETRIC NOSE SHAPES OF FINENESS RATIO 3 FOR MACH NUMBERS FROM 1.24 TO 7.4 [1]

By Edward W. Perkins, Leland H. Jorgensen, and Simon C. Sommer

SUMMARY

Drag measurements have been made at zero angle of attack for a series of fineness ratio 3 nose shapes. The models included various theoretically derived minimum drag shapes, hemispherically blunted cones, and other more common profiles. Pressure-distribution measurements for a series of hemispherically blunted cones were also obtained. The Mach number and Reynolds number ranges of the test were 1.24 to 7.4 and 1.0×10^6 to 7.5×10^6 (based on model length), respectively.

Of the models tested, the paraboloid of revolution had the least foredrag below a Mach number of 1.5, and the theoretically minimum drag shape for a given length and diameter based upon Newton's impact theory had the least foredrag above a Mach number of 1.5. The theoretical shapes for minimum pressure drag for the auxiliary conditions of given length and diameter or given diameter and volume derived by von Kármán and by Haack do not have less drag than all other possible shapes having identical values of the same parameters. No model had the least foredrag for the complete Mach number range. Wherever possible, theoretical values of the foredrag based upon the sum of the theoretical skin-friction drag and the theoretical wave drag were calculated for comparison with the experimental results.

The results for the series of hemispherically blunted cones have important practical significance since it was found that the diameter of the hemispherical tip may be fairly large without markedly increasing the foredrag over that of a sharp pointed cone of the same fineness ratio. In fact, for a fixed fineness ratio of 3, the foredrag is reduced somewhat by a small degree of blunting, although for a fixed cone angle blunting always increased the drag. An empirical expression, applicable for free-stream Mach numbers greater than 2, is developed for calculating the wave drag of the series of hemispherically blunted cones.

INTRODUCTION

The allied problems of predicting the drag of bodies of revolution and of minimizing the drag by proper shaping of the body have been the objects of numerous theoretical investigations. With regard to the problem of predicting the drag, that part of the drag which has thus far proved most amenable to theoretical calculation is the wave drag. For pointed bodies of revolution at Mach numbers sufficiently high for shock-wave attachment, the wave drag may be calculated by either perturbation theory or by the method of characteristics. For highly blunted nose shapes there is no simple theoretical method for predicting the pressure distribution and drag. Therefore experimental results have been relied upon for this information.

The first part of the present investigation is a study of the pressure distribution and drag of a series of hemispherically blunted cones. Although it might seem that the use of such a blunt nose would result in a high drag penalty, preliminary estimates [2] have indicated that the drag of a nose shape consisting of a hemispherical surface faired into an expanding conical surface can be less than that of a sharp cone of the same length-to-diameter ratio. The results of preliminary estimates of the variation of drag with the ratio of hemispherical tip diameter to base diameter for fineness ratio 3 have indicated that a small reduction in drag can be realized at all supersonic Mach numbers. Perhaps more important than the reduction in drag is the indication that a relatively large hemispherical tip can be used without incurring any drag increase above that of a sharp-nosed cone of the same fineness ratio. In order to verify these predictions and to provide quantitative drag data the present investigation was undertaken.

The second phase of the investigation is a study of minimum drag nose shapes. Most theoretical approaches have been directed toward the mimimization of the wave drag only. Von Kármán (ref. 1) developed an integral equation for the wave drag of slender bodies of revolution at moderate Mach numbers. Using this equation, he derived a minimum drag nose shape (commonly referred to as the Kármán ogive) for a given length and diameter. Subsequently, Haack (ref. 2) and others (refs. 3 and 4) have used the Kármán integral equation in developing minimum drag shapes for other auxiliary conditions, such as given length and volume or given volume and diameter. Through the use of the Kármán

[2] These preliminary estimates were made by summing the experimentally determined wave drag of the hemispherical nose and the theoretical pressure drag of the conical afterbody, assuming that the pressure on the surface of the conical afterbody was the same as that for a sharp cone of the same slope.

[1] Supersedes NACA Research Memorandum A52H28 by Edward W. Perkins and Leland H. Jorgensen, 1952, and NACA Research Memorandum A52B13 by Simon C. Sommer and James A. Stark, 1952.

526597—60——80

integral equation as the basis for these derivations, the apparently unnecessary yet simplifying assumption of zero slope of the meridian at the base has been imposed. This restriction is pointed out by Ward in reference 5, wherein he shows that his more general expression for wave drag reduces to that obtained by von Kármán for the special case of a body having zero slope at the base. In a later paper (ref. 6) Ferrari developed a minimum drag nose shape for a given length and diameter which has a finite slope of the meridian at the base. For the high supersonic Mach number range, minimum drag shapes based upon Newton's law of resistance have been derived by Eggers, Resnikoff, and Dennis (ref. 7). These shapes differ appreciably from comparable optimum shapes for low supersonic Mach numbers, although the theoretical optimum shapes in both instances have blunt noses when the length is fixed and sharp noses when the length is allowed to vary.

Due to the basic assumptions in the derivation of the Kármán integral equation, it may be expected that the shapes resulting from the use of this equation are theoretically optimum from a minimum drag standpoint only for large fineness ratios and low supersonic Mach numbers. In contrast, the shapes resulting from the Newtonian theory may be expected to be optimum only at high supersonic Mach numbers. However, for low fineness ratio shapes at moderate Mach numbers, it is impossible to say a priori which of the theoretically optimum shapes will have the lesser wave drag, or in fact if either of the theories is capable of predicting the least-drag profile. One of the purposes of the present investigation is, therefore, to compare the experimental drags of these theoretically optimum shapes and of other more common profiles for an intermediate fineness ratio over a wide Mach number range. To this end a series of fineness ratio 3 models of these theoretically optimum shapes have been tested in the Mach number range from 1.24 to 3.67.

SYMBOLS

A model base area, sq in.

C_D total drag coefficient, $\frac{\text{total drag}}{qA}$

C_{D_F} foredrag coefficient based on base area, $\frac{\text{total drag—base drag}}{qA}$

C'_{D_F} foredrag coefficient based on volume to the $\frac{2}{3}$ power, $\frac{\text{total drag—base drag}}{qV^{2/3}}$

C_{D_W} wave drag coefficient, $\frac{\text{wave drag}}{qA}$

d hemisphere diameter, in.

D model base diameter, in.

K similarity parameter, $\frac{M}{L/D}$

L model length, in.

M free-stream Mach number

P pressure coefficient, $\frac{p_l-p}{q}$

P_t pitot-pressure coefficient, $\frac{p_t-p}{q}$

P_ω cone pressure coefficient, $\frac{p_\omega-p}{q}$

p_l local static pressure, lb/sq in.

p free-stream static pressure, lb/sq in.

p_t pitot total-head pressure, lb/sq in.

p_ω cone static pressure, lb/sq in.

q free-stream dynamic pressure, $\frac{\gamma}{2}pM^2$, lb/sq in.

r model local radius, in.

R model base radius, in.

Re free-stream Reynolds number based on body length

V model volume, cu in.

X axial distance from the nose, in.

α angle of attack, deg

γ ratio of specific heats of air, taken as 1.40

θ circumferential angle of hemisphere measured from the upstream stagnation point, deg

ω cone half angle, deg

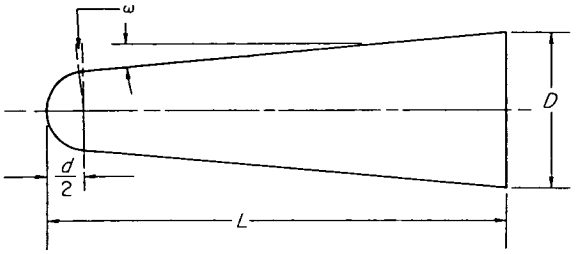
APPARATUS AND TESTS

The experimental investigation was conducted in three facilities, the Ames 1- by 3-foot supersonic wind tunnels No. 1 and No. 2, and the Ames supersonic free-flight wind tunnel. The two 1- by 3-foot wind tunnels are conventional tunnels which are equipped with flexible top and bottom plates for varying the test section Mach number.

For the tests in the supersonic free-flight tunnel the models were launched from a smooth-bore 20mm gun, and were supported in the gun by plastic sabots. Separation of the model from the sabot was achieved by a muzzle constriction which retarded the sabot and allowed the model to proceed in free flight through the test section of the wind tunnel. A more detailed description of this facility is given in reference 8.

MODELS

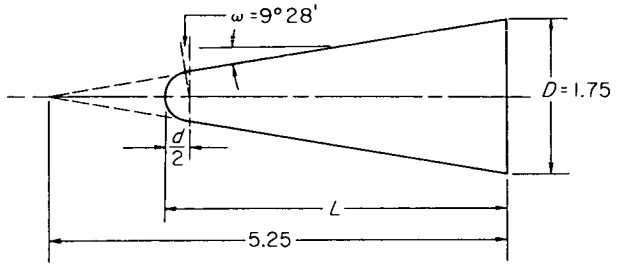
Sketches of the models tested, including dimensions, specified parameters, and defining equations, are presented in figure 1. For the series of hemispherically blunted cones shown in figure 1(a) the length-to-diameter ratio of 3 is constant, and the cone angle is decreased as the bluntness (ratio of hemisphere diameter to base diameter) is increased. For the series in figure 1(b) the base diameter and cone angle are constant, and the length decreases with increase in bluntness.



Model no	$\frac{d}{D}$	ω	D
1	0	9° 28'	1.75
1f	0	9° 28'	0.45
2	.075	8° 52'	1.75
2f	.075	8° 52'	0.45
3	.150	8° 15'	1.75
3f	.150	8° 15'	0.45
4	.300	6° 59'	1.75
4f	.300	6° 59'	0.45
4p	.300	6° 59'	2.00
5	.500	5° 10'	1.75
5f	.500	5° 10'	0.45
5p	.500	5° 10'	2.00
6p	1.000	0	4.00

Note: 4p, 5p, and 6p are pressure distribution models.
Models 1f through 5f, are free-flight models.

(a)



Model no	$\frac{d}{D}$	$\frac{L}{D}$
1	0	3.00
7	.075	2.81
8	.150	2.62
9	.300	2.24

(b)

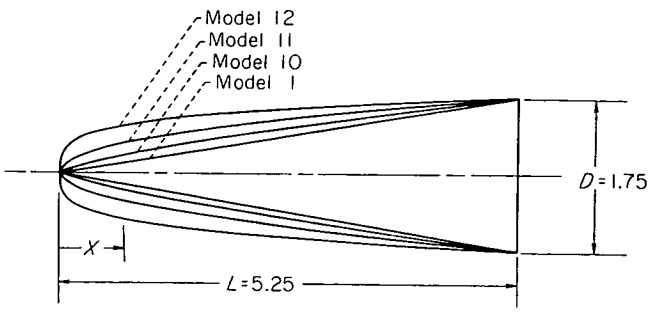
(a) Hemisphere-cone series for constant $\frac{L}{D}=3$.

(b) Hemisphere-cone series for constant cone angle.

FIGURE 1.—Model profiles. (Dimensions are in inches.)

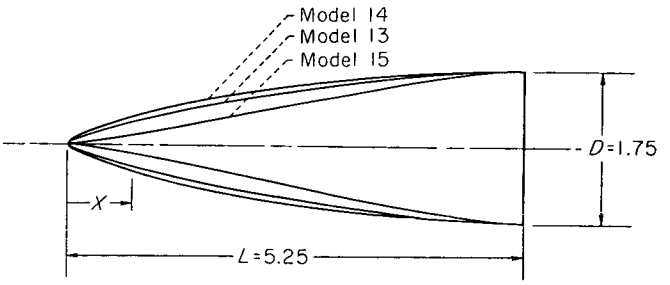
The family of fineness ratio 3 models defined by the equation $r=R(X/L)^n$ is shown in figure 1(c). For length and base diameter specified, the profiles of the hypersonic optimum (Newtonian) nose and the nose developed by Ferrari (ref. 6) can both be very closely approximated by the above equation for n=¾. (See fig. 2.) Since the ¾-power nose is a reasonable approximation to these theoretically derived optimum shapes, it alone has been tested and is referred to throughout the report as the hypersonic optimum nose.

Fineness ratio 3 models of the minimum drag shapes based upon the work of von Kármán and subsequently Haack are shown in figure 1(d). For any two specified parameters such as length and diameter, length and volume, or diameter and volume, these are the theoretical optimum nose shapes and for convenience have been designated as the *L-D*, *L-V*, and *D-V* Haack noses. A similar designation has been used for the circular-arc tangent ogive and cone shown in figure 1(e). The *L-V* ogive has the same length and volume as the *L-V* Haack model, and the *D-V* cone has the same diameter and volume as the *D-V* Haack model. Also shown in figure 1(e) is a fineness-ratio-3 ellipsoid.



Model no	Designation	n
1	Cone	1
10	Hypersonic opt.	3/4
11	Paraboloid	1/2
12	1/4 Power	1/4

(c)



Model no	Designation	Specified parameters	c
13	L-D Haack	Length, dia.	0
14	L-V Haack	Length, vol.	1/3
15	D-V Haack	Dia, vol.	-2/3

(d)

(c) Profile defined by $r=R\left(\frac{X}{L}\right)^n$

(d) Haack minimum drag noses defined by $r=\frac{R}{\sqrt{\pi}}\sqrt{\varphi-\frac{1}{2}\sin 2\varphi+c\sin^3\varphi}$,

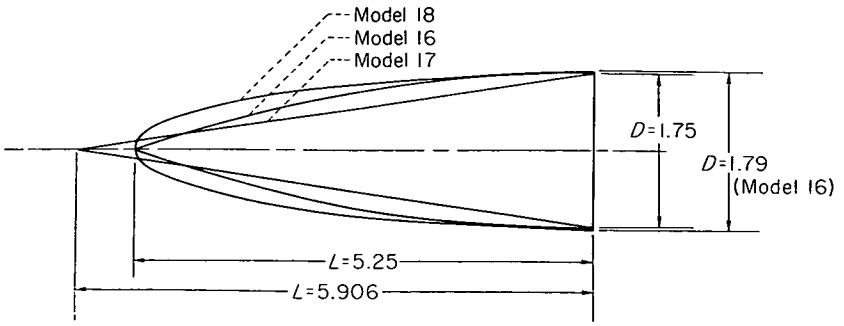
$$\varphi=\arccos\left(1-\frac{2X}{L}\right).$$

FIGURE 1.—Continued.

Except for the pressure-distribution models, all the nose shapes were constructed of duralumin. The 30- and 50-percent hemispherically blunted cone pressure-distribution models (models 4p and 5p) were cast of tin and bismuth, and the hemisphere-cylinder pressure-distribution model (model 6p) was constructed of steel.

TESTS

Wind tunnels No. 1 and No. 2.—The total drag was measured by means of a strain-gage balance located in the model support housing. The base pressure was determined through the use of a liquid manometer connected to two holes in the supporting sting at the base of the model. Experimental values of foredrag were then taken as the difference between



Model no	Designation	$\frac{L}{D}$
16	L-V Ogive	2.93
17	D-V Cone	3.38
18	Ellipsoid	3

(e)

(e) Other profiles.

FIGURE 1.—Concluded.

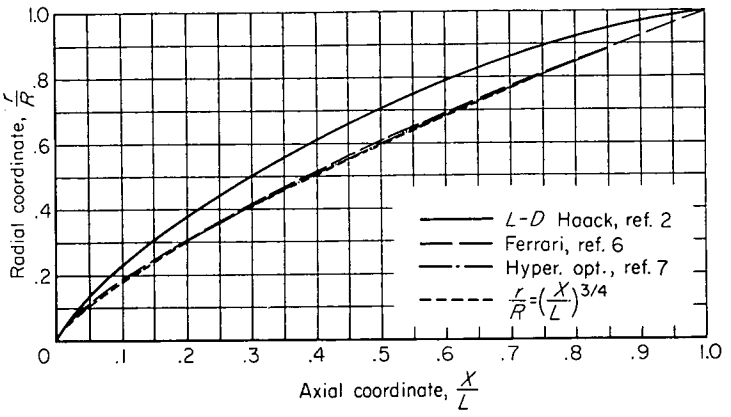


FIGURE 2.—Comparison of profiles of minimum drag noses for given length and base diameter.

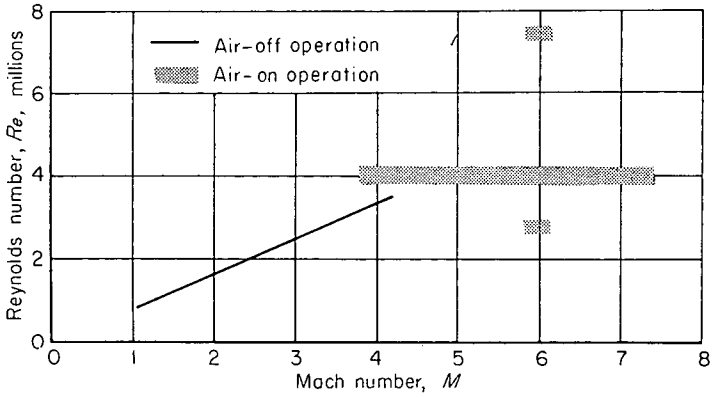


FIGURE 3.—Range of Mach numbers and Reynolds numbers of tests in the Ames supersonic free flight wind tunnel.

the measured total drag and base pressure drag. Because of the operating characteristics of the tunnels, it was not possible to maintain a constant Reynolds number throughout the Mach number range of 1.24 to 3.67; however, an attempt was made to keep the Reynolds number constant for all models at each Mach number. In the following table the average Reynolds number (based on model length) and its limit of variation for all models tested at each Mach number are listed:

M	$Re\times10^{-6}$	Tunnel No.
1.24	2.42±0.14	1
1.44	1.17±0.01	1
	3.14±0.20	
1.54	4.10±0.10	2
1.96	4.14±0.12	2
1.99	2.01±0.01	1
2.86	4.00±0.10	2
3.06	4.00±0.19	2
3.67	3.45±0.07	2

The pressure-distribution tests were all made in tunnel No. 2 at Mach numbers of 1.5, 2, 3, and 3.7 and at an average Reynolds number of about 4×10^6. Pressure distributions for the hemisphere-cone pressure models (models 4p, 5p, and 6p) were determined through the use of a liquid manometer system connected to two rows of orifices along the models and spaced 180° apart. The models were rotated and a longitudinal pressure distribution at each 30° increment in circumferential angle was obtained. The resulting pressure coefficients at each longitudinal station were averaged to obtain the values presented.

Free-flight wind tunnel.—With no air flow through the wind tunnel, Mach numbers varied from 1.2 to 4.2, depending on the model launching velocity. This condition is referred to as "air off." Reynolds number varied linearly with Mach number from 1.0×10^6 to 3.3×10^6, as shown in figure 3. With air flow established in the wind tunnel, referred to as "air on," the combined velocities of the model and Mach number 2 air stream, with the reduced speed of sound in the test section, provided test Mach numbers from 3.8 to 7.4. In this region of testing, Reynolds number was held approximately at 4×10^6 by controlling test-section static pressure. In addition, some models were tested at approximate Reynolds numbers of 3×10^6 at Mach number 6.

Drag coefficient was obtained by recording the time-distance history of the flight of the model with the aid of a chronograph and four shadowgraph stations at 5-foot intervals along the test section. From these data, deceleration was computed and converted to drag coefficient. This report includes only the data from models which had maximum observed angles of attack of less than 3°, since larger angles measurably increased the drag.

ANALYSIS OF DATA

REDUCTION OF DATA

All the experimental data have been reduced to coefficient form and the data from wind tunnels Nos. 1 and 2 have been corrected for the effects of the small nonuniformities in the wind-tunnel flow. The free-stream static-pressure variations in the model-free tunnel have been applied as corrections to the drag and pressure-distribution data by simple linear superposition. Corrections due to the effects of stream-angle variation were well within the limits of accuracy of the data and have therefore been neglected. No corrections were necessary for the data obtained in the free-flight tunnel.

PRECISION

The uncertainty of the experimental data from tunnels No. 1 and No. 2 was calculated by considering the possible errors in the individual measurements which entered into the determination of the stream characteristics, pressure distributions, and drag. The final uncertainty in a quantity was taken as the square root of the sum of the squares of the possible errors in the individual measurements. The resulting uncertainties in the final quantities are as follows:

Quantity	Uncertainty
P	± 0.004
C_{D_F}	± 0.004
α	$\pm 0.15°$

The variation of the free-stream Mach number over the length of each model tested was less than ± 0.01 for all test Mach numbers. The uncertainty in the Mach number at a given point in the stream is ± 0.003.

The magnitude of the calculated uncertainty in the drag coefficient appears rather large relative to the observed scatter of the data. Drag coefficients for repeated tests generally agreed within ± 0.002. It is therefore believed that the drags of models relative to one another are sufficiently accurate for comparative purposes, although the absolute magnitudes of the drag coefficients for the models at a particular Mach number may be in error by the magnitude of the uncertainty.

Since there are no known systematic errors in the data from the free-flight tunnel, the accuracy of the results is indicated by the repeatability of the data. Examination of these data shows that repeat firings of similar models under almost identical conditions of Reynolds number and Mach number yielded results for which the average deviation from the faired curve was 1 percent and the maximum deviation was 4 percent.

THEORETICAL CONSIDERATIONS

WAVE DRAG

With the exception of some of the very bluntest models (models 11, 12, and 18) the wave drag of each model was either calculated by theoretical methods or was estimated from existing experimental results. Values for the wave drag of the cone and the tangent ogive were obtained from the exact Taylor-Maccoll theory (refs. 9 and 10) and the method of characteristics (ref. 11), respectively. For the theoretical optimum nose shapes the second-order theory of Van Dyke was used. The exact procedure employed in using the second-order theory was that given in reference 12, in which the approximate boundary conditions at the body surface are used in the calculation of the perturbation velocities, and the exact pressure relation is used to evaluate the pressure coefficients.[3] The method presented therein is strictly applicable to sharp-nosed bodies of revolution at Mach numbers less than that at which the Mach cone becomes tangent to the model vertex. Since the theoretical optimum nose shapes for which the length is fixed (models 10, 13, and 14) have infinite slopes at their vertices (yet may be considered sharp for most practical purposes), an approximation to the shape at the vertex was made to enable use of the theory. The blunt tip was replaced by a short conical section tangent to the original contour. The cone angle, and hence the point of tangency, was selected so that the cone half-angle did not exceed 94 percent of the Mach angle. In the subsequent integrations for the wave drag from the resulting pressure distributions, the data were plotted as rP versus r so that the curves could be smoothly faired through the origin.

A simple method of estimating the wave drag of the hemispherically blunted conical noses has been suggested. It has been proposed that the wave drag of the hemispherical tip, which could be obtained from existing experimental data, be added to the pressure drag of the conical portion of the nose, based upon the assumption that the pressure on the conical surface would be the same as on a pointed cone of the same slope. Hence, the pressure drag of the conical portion of the nose could be obtained by exact theory.

The following empirical expression, based upon certain of the experimental results, is suggested for calculating the wave drag of the hemispherical tip for Mach numbers of 2 and greater:

$$C_{D_W}=\frac{2P_t-1}{3} \tag{1}$$

where P_t is the pitot-pressure coefficient at the tip of the hemisphere which may be calculated with the aid of Rayleigh's equation. This expression was obtained from the results of the pressure-distribution tests, and its derivation is discussed in more detail in the section of the report which is concerned with the pressure-distribution tests. When this expression is used for the wave drag coefficient of the hemispherical portion, the expression for the wave drag coefficient of the complete model for Mach numbers of 2 and greater becomes

$$C_{D_W}=\left(\frac{d}{D}\right)^2\left(\frac{2P_t-1}{3}-P_\omega\right)+P_\omega \tag{2}$$

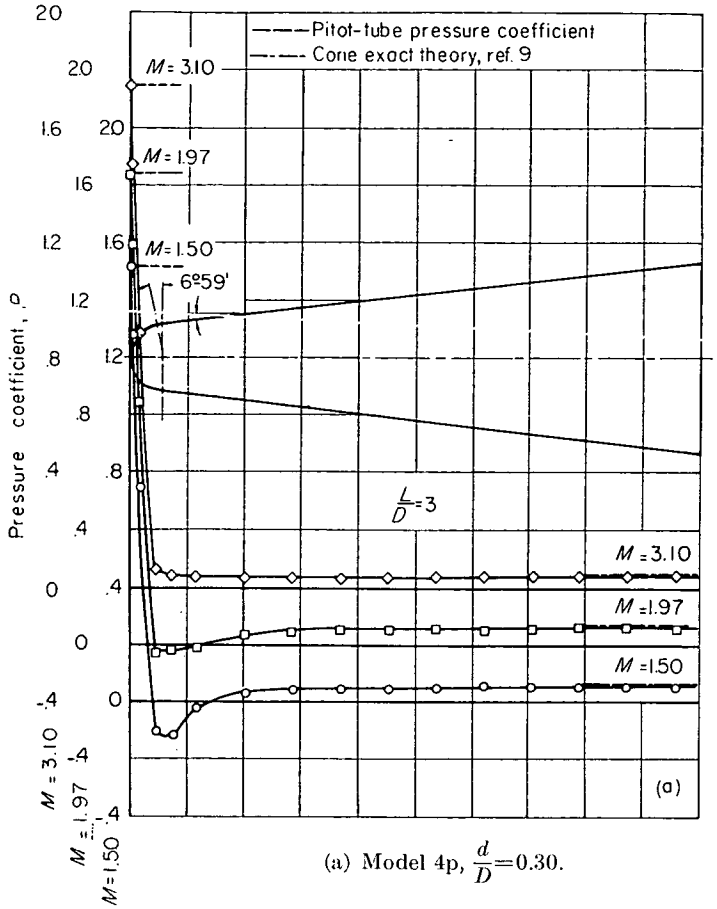
where P_ω is the surface pressure coefficient or pressure drag coefficient (refs. 9 or 10) for a cone of half apex angle ω at the free-stream Mach number. An approximate expression for ω which is sufficiently accurate for the drag estimates is

$$\omega \cong \tan^{-1}\left[\frac{1-(d/D)}{2(L/D)-(d/D)}\right] \tag{3}$$

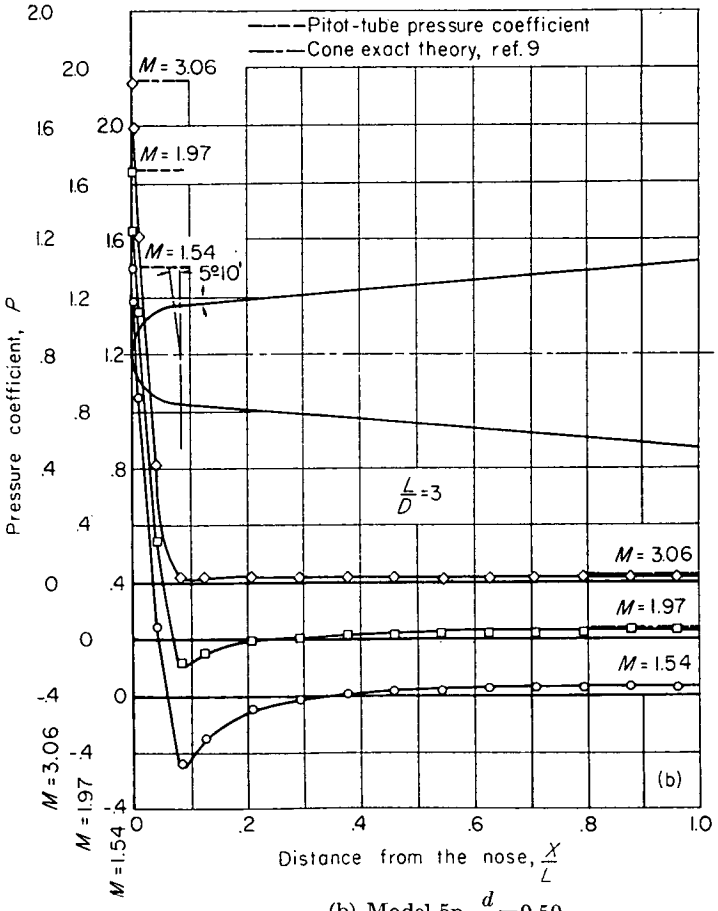
FOREDRAG

Values of the foredrag have been calculated by the addition of the estimated or theoretical wave drag and the theoretical

[3] In the application of this method a first-order solution is necessarily obtained.

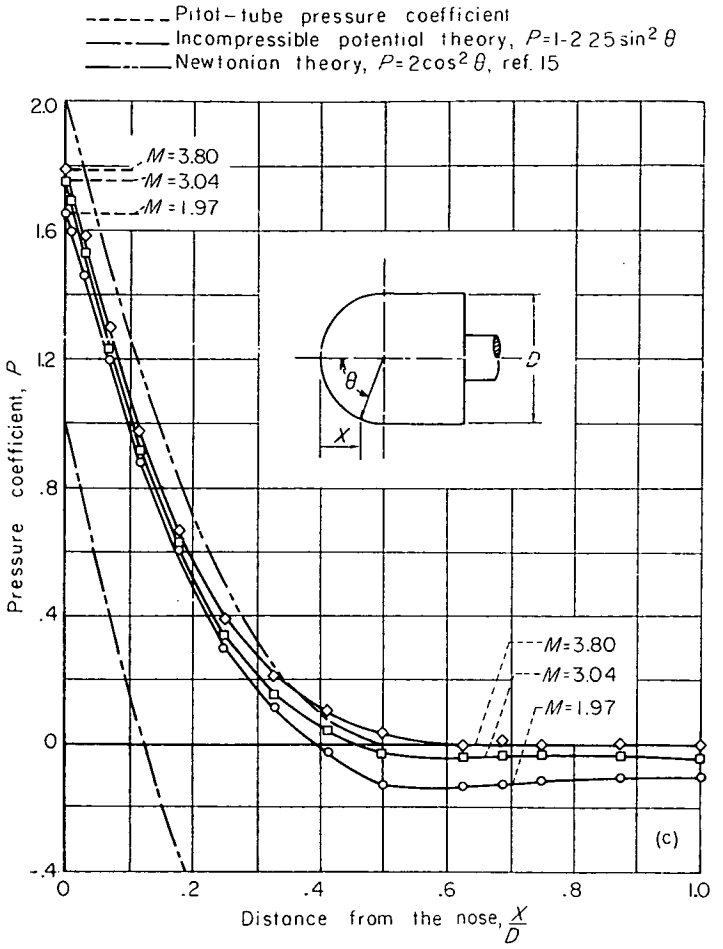


(a) Model 4p, $\frac{d}{D}$=0.30.



(b) Model 5p, $\frac{d}{D}$=0.50.

FIGURE 4.—Longitudinal distribution of pressure coefficient for hemisphere-cones at 0° angle of attack.



(c) Model 6p, $\frac{d}{D}$=1.00

FIGURE 4.—Concluded.

skin-friction drag. Since the skin-friction drag for laminar-boundary-layer flow contributes so little to the foredrag, the inclusion of the small effects of body shape and compressibility on the skin-friction drag was not considered justified. Therefore, the laminar-skin-friction drag coefficients were calculated by the Blasius formula for flat-plate incompressible boundary-layer flow (ref. 13). For the estimates of the skin-friction drag for turbulent-boundary-layer flow, the body shape effects were neglected, but the effect of compressibility was evaluated by means of the interpolation formula of reference 14 which is based upon an extended Frankl and Voishel analysis.

RESULTS AND DISCUSSION

HEMISPHERICALLY BLUNTED CONES

Pressure distributions.—The pressure-distribution data obtained for models 4p, 5p, and 6p at Mach numbers between 1.5 and 3.8 are shown in figure 4. The data are referred to the free-stream Mach number ahead of the normal shock wave at the nose of each model. Although these Mach numbers were approximately the same for each model, they differed slightly because of the differences in positions of the models within the test section. For each of the models, the pressure coefficient at the nose agrees with the pitot-pressure coefficient calculated by Rayleigh's

equation and shown for comparison by the dashed lines. For models 4p and 5p at Mach numbers 1.97 and 1.5 (figs. 4 (a) and 4(b)) the rapid expansion of the flow over the hemispherical tip is followed by a recompression over the forward part of the conical portion of the nose. The pressure on the conical surface recovers to, or almost to, the theoretical value of the pressure coefficient for a sharp-nosed cone of the same slope. For a Mach number of 3.1, the expanding flow on the hemisphere does not reach a lower pressure than the theoretical surface pressure for a cone of the same slope as the conical afterbody, and it is found that the pressure is constant over most of the conical portion of the nose. From these data it appears that the assumption made in the drag estimates, namely, that the pressure over the conical portion of the nose is constant and equal to the theoretical value for a sharp-nosed cone of the same slope, is essentially correct for free-stream Mach numbers of 3 and greater. For Mach numbers less than 3 the average pressure over the conical section is less than that assumed in the estimates, and hence the estimated drag contribution from this part of the nose will be too high.

A more detailed study of the pressure distribution over the hemispherical portion of this type body is available from the data of figure 4(c). For comparison with these experimental data, the theoretical incompressible distribution (only part of which is shown for simplicity) and the distribution predicted by Newtonian theory (ref. 15) are shown. It is apparent that as the Mach number is increased the pressure distribution approaches that predicted by Newtonian theory. In spite of this trend, it is evident that the distribution would never agree exactly with the Newtonian because the peak pressure coefficient at the nose would be somewhat less than the Newtonian value of 2. An additional factor which has been neglected in the Newtonian theory is the effect of centrifugal forces which, although negligible for the lower Mach numbers, would tend to reduce the theoretical pressure coefficients over the hemisphere in the high Mach number range.

The study of the comparisons of the experimental pressure distributions for the hemisphere with that predicted by Newtonian theory (fig. 4(c)) indicates that an empirical expression for the pressure distribution, which yields reasonably accurate values of the wave drag, may be written. The development of the expression is based upon two experimental results: First, the pressure at the tip of the hemisphere is the stagnation pressure and may be calculated exactly from the Rayleigh equation. Second, at the high Mach numbers the subsequent expansion of the flow is similar to that predicted by Newtonian theory, and the local pressure differs from the Newtonian value by an amount which varies approximately as the cosine of the angle θ. Based upon these observations the following empirical expression for the pressure distribution on a hemisphere may be written:

$$P=2\cos^2\theta-(2-P_t)\cos\theta \tag{4}$$

where P_t is the pitot-pressure coefficient at the stagnation point on the hemisphere. The expression predicts a pressure coefficient that is exact at $\theta=0$ and agrees with the Newtonian value of $P=0$ at $\theta=90°$. It is apparent from the data of figure 4(c) that, although the resulting pressure distribution will closely approximate the experimental distribution at high Mach numbers, the predicted pressures near $\theta=90°$ will be considerably in error for lower Mach numbers. However, this should not result in a serious error in the pressure drag, since the surface slope is small in this region, and thus the resulting drag contribution is also small. A simple expression for the wave drag coefficient of the hemisphere results from this empirical equation for the pressure distribution. Thus, based upon the maximum cross-section area,

$$C_{D_W}=\frac{2P_t-1}{3} \tag{1}$$

Values computed from this equation are compared in figure 5 with estimates of the wave drag from total drag measure-

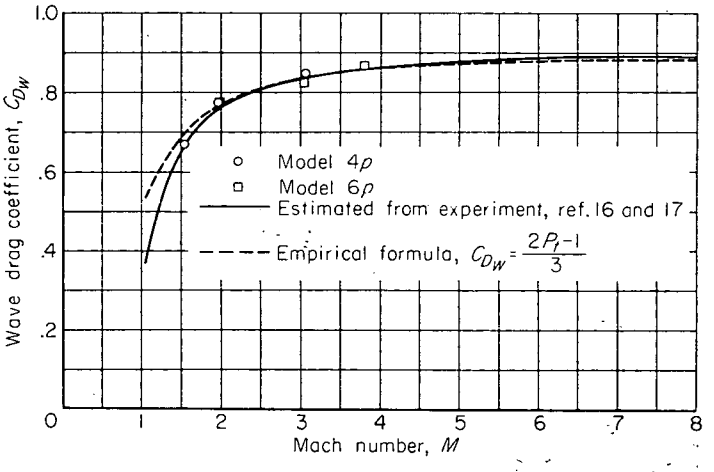
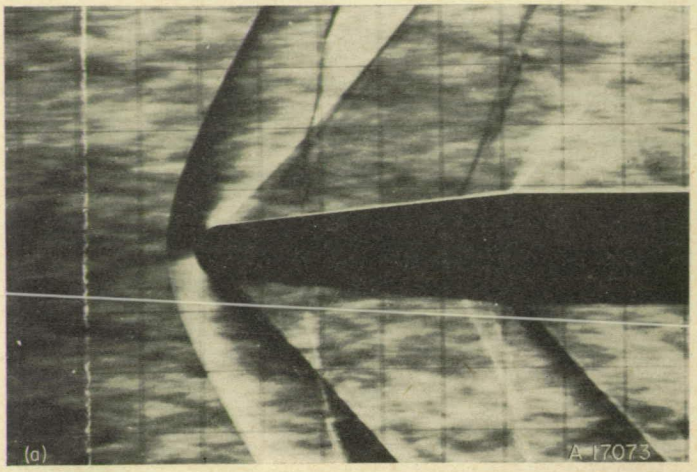


FIGURE 5.—Variation of wave drag coefficient with Mach number for a hemisphere.

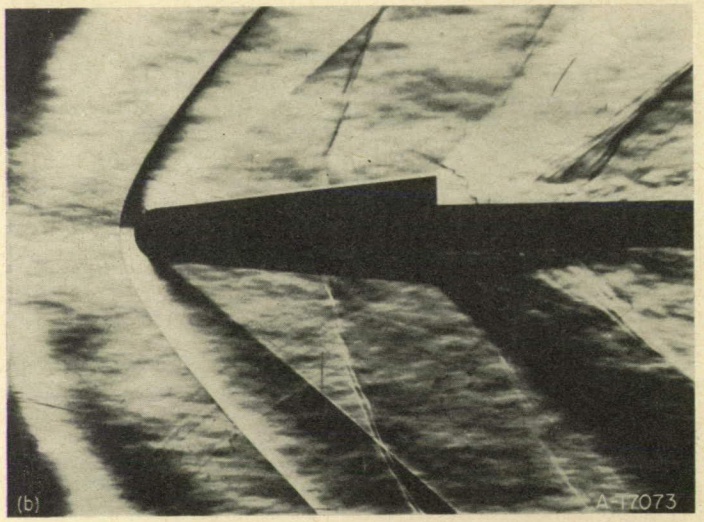
ments (refs. 16 and 17) and with the experimental pressure drag determined from the pressure distributions of figure 4. For Mach numbers between 2 and 8 the agreement is excellent. As would be expected from the pressure-distribution results, the values from the empirical expression are too large in the lower Mach number range.

From these data it appears that for the estimates of the wave drag of the hemispherically blunted cones, the contribution of the hemispherical tip to the total wave drag at Mach numbers of 2 and greater may be calculated accurately with the proposed empirical expression.

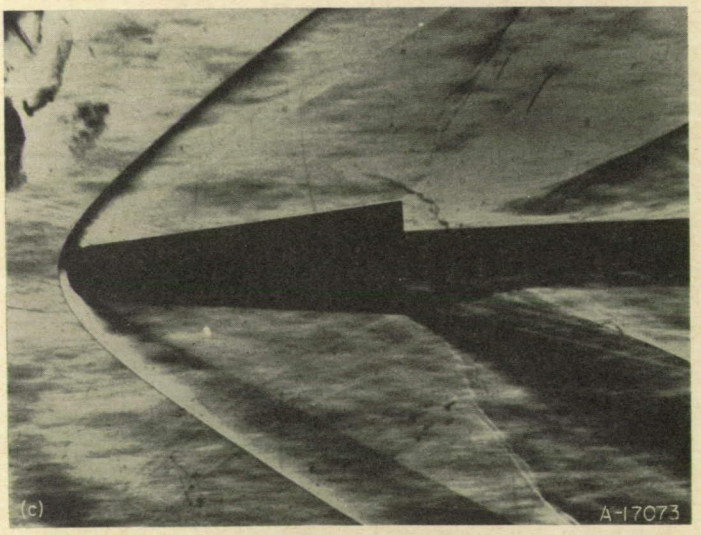
Flow field.—The recompression of the flow over the upstream portion of the conical afterbody, which was noted previously in the discussion of the pressure distributions, is associated with the appearance, a short distance downstream from the bow wave, of an approximately conical shock wave in the flow field. The schlieren pictures for model 5 (fig. 6) are typical for all the hemispherically blunted cones (models 1 through 5) throughout the Mach number range These pictures show that the intensity of the wave decreases with increasing Mach number. At Mach number 3.06 the wave is no longer evident within the bounds of the schlieren field. The decrease in intensity of the wave is in accord with the changes found in the pressure distribution data.



(a) $M=1.24$

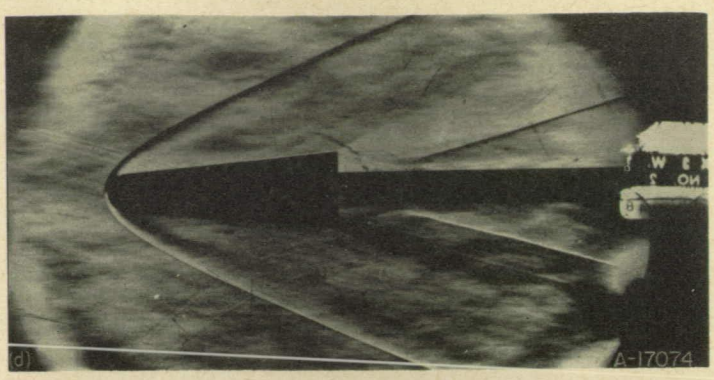


(b) $M=1.54$

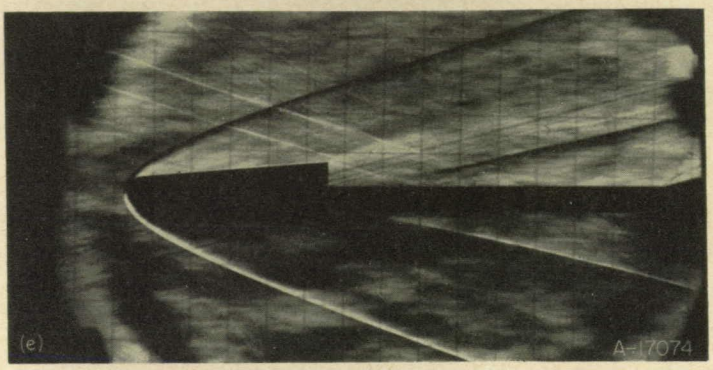


(c) $M=1.96$

FIGURE 6.—Schlieren pictures for 50-percent hemispherically blunted cone, model 5, at various Mach numbers.



(d) $M=3.06$



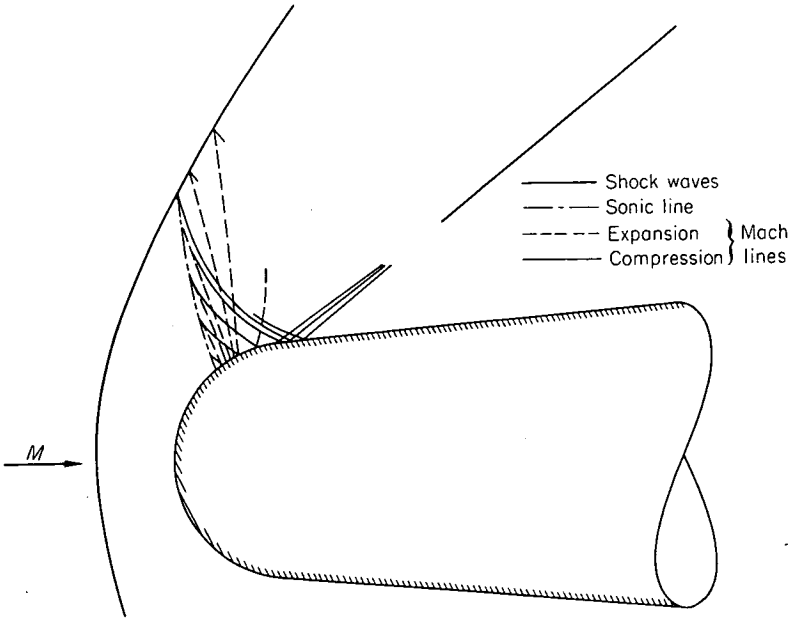
(e) $M=3.67$

Figure 6.—Concluded.

(See fig. 4.) At first glance it might appear that this wave could be associated with a region of separated flow on the hemispherical tip, with subsequent reattachment accompanied by a shock wave. However, the schlieren pictures show no evidence of flow separation. Additionally, it is apparent from the schlieren pictures that this shock wave does not extend from the outer flow down to the body surface but appears to be diffused near the surface. These observations lead to the speculation that the origin of the wave must be associated with the transonic or mixed type of flow which occurs in the vicinity of the nose of the body.

The mechanism by which the compression wave is formed may be much the same as that discussed in reference 18 for the two-dimensional flow around a sharp-nosed double-wedge airfoil section with detached bow wave. It is believed that the wave results from a coalescence of weak compression waves reflected from the body surface. (The existence of the compression region is confirmed by the pressure-distribution data.) These waves apparently originate as expansion waves from the body surface downstream from the sonic point. As indicated in the sketch, these expansion waves which travel along characteristic lines are reflected from the sonic line and the bow wave as compression waves which are in turn reflected from the body surface. The reflection of these wavelets from the body surface occurs in such a manner that they coalesce to form a shock wave.

The dependence of this phenomenon on both the free-stream Mach number and the inclination of the body surface just downstream of the point of tangency of the hemisphere



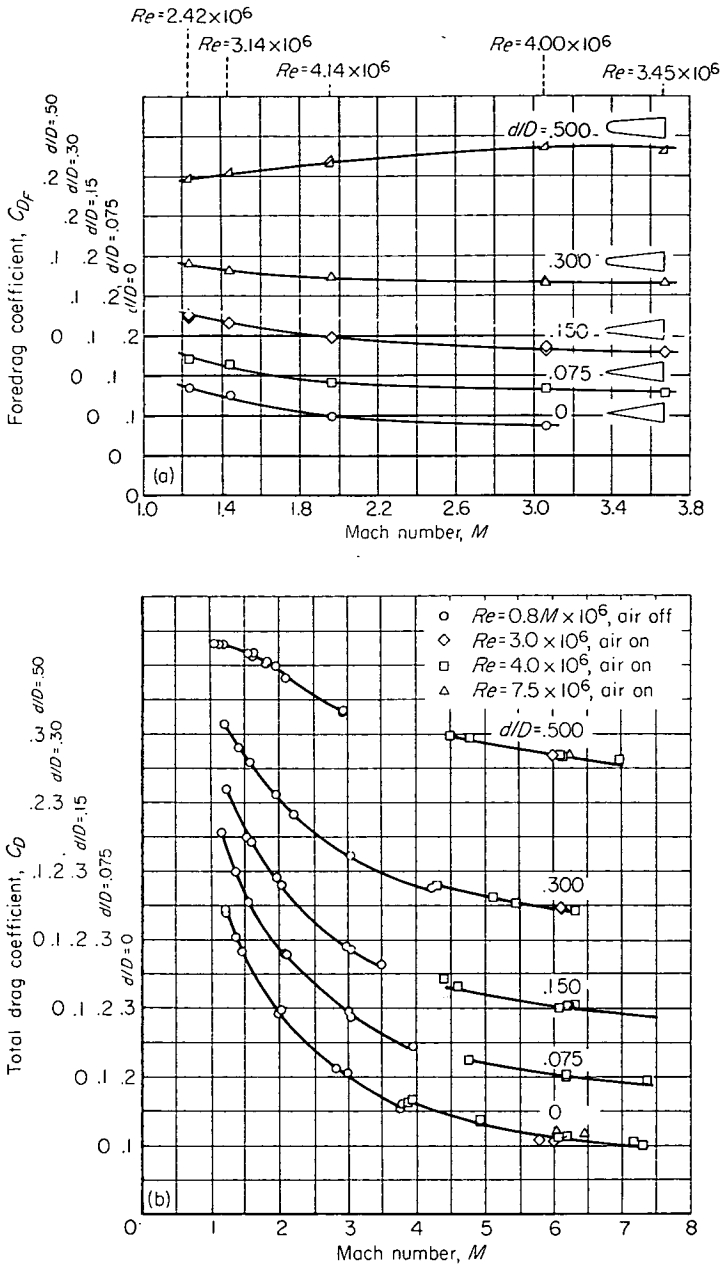
with the afterbody is demonstrated by the following observations. For the hemispherically blunted cones, neither the shock wave nor the region of recompression on the body surface was found for Mach numbers above 3.06. The disappearance of this shock wave and region of compression results from the combination of the movement of the bow wave closer to the body surface and the small upstream movement of the sonic point with increasing Mach number. These changes reduce the extent of the mixed flow region so that for Mach numbers above approximately 3 most of the compression wavelets reflected from the sonic line and bow wave are incident upon the body surface in the expansion region between the sonic point and the point of tangency of the hemisphere with the afterbody and hence are canceled. The importance of the inclination of the body surface in the region of the reflections is indicated by the fact that, although the pressure-distribution data for model 6p (fig. 4(c)) show that at the lowest test Mach number there exists a region of recompression just downstream from the juncture of the hemisphere and cylindrical afterbody, the magnitude of the recompression is very small and does not result in a secondary shock wave that can be detected in the schlieren pictures.

Drag.—The variation of drag coefficient with Mach number for the hemispherically blunted cones of fineness ratio 3 (models 1 through 5) are presented in figure 7. Because of the differences in test technique, the data from the wind tunnels and from the free-flight facility are presented separately. Since the models vary progressively from the sharp-nosed cone to the very blunt model with the large hemispherical tip ($d/D=0.5$), the variation of the foredrag coefficient with Mach number (fig. 7(a)) changes progressively from the familiar variation for a cone (foredrag coefficient decreases with increasing Mach number) to the variation characteristic of a hemisphere (fig. 5). Variation with Mach number of the total drag coefficient (fig. 7(b))[4] is similar for all models in that the drag coefficient continually decreased with increasing Mach number.

The data from figure 7(a) are replotted in figure 8 to show the variation of foredrag with nose bluntness at constant Mach numbers and provide comparisons with the estimated foredrag characteristics. For this series of fineness ratio 3 noses, a small saving in foredrag may be achieved through the use of a hemispherically blunted cone in place of a sharp cone of the same fineness ratio. Perhaps more important is the fact that a relatively large increase in volume over that of a sharp-nosed cone may be realized without incurring any increase in foredrag. An additional factor to be considered is that the hemispherical nose provides an ideal housing for search radar gear. These data show that with increasing Mach number there is a decrease in both the degree of blunting which results in minimum foredrag as well as the maximum blunting allowable such that the foredrag is not greater than that of the sharp-nosed cone. These results are in essential agreement with the preliminary foredrag estimates.

Although the results (fig. 8) show that for this fineness ratio 3 series of models there is some drag reduction with increase in bluntness, the magnitude of the possible drag reduction which is obtainable by this method of blunting decreases rapidly with increasing fineness ratio. In fact, there appears to be an upper limit to the fineness ratio for which this type of blunting will yield any drag reduction. Some indications of the magnitude of this limiting fineness ratio which varies with Mach number have been obtained by comparing the variation with fineness ratio of the estimated wave drag of the $d/D=0.075$ model with that of a cone of the same fineness ratio at Mach numbers of 2 and 3. These results (fig. 9) indicate that the wave drag of the cone is less than that of this moderately blunt model for length-to-diameter ratios in excess of approximately 5.4 and 5.0 at Mach numbers of 2 and 3, respectively. These results also show that the range of nose fineness ratios for which

[4] No attempt has been made to join the air-off data and air-on data because of the differences in Reynolds number, recovery temperature, and stream turbulence,



(a) Wind tunnel results.
(b) Free-flight results.

FIGURE 7.—Variation of drag coefficient with Mach number for hemisphere-cone series, constant $\frac{L}{D}=3$.

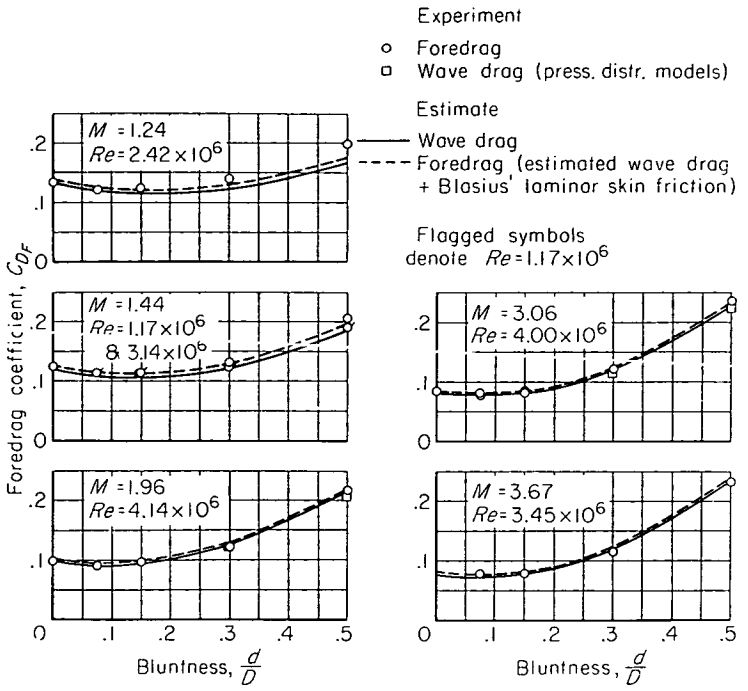


FIGURE 8.—Variation of foredrag coefficient with bluntness for hemisphere-cone series, constant $\frac{L}{D}=3$.

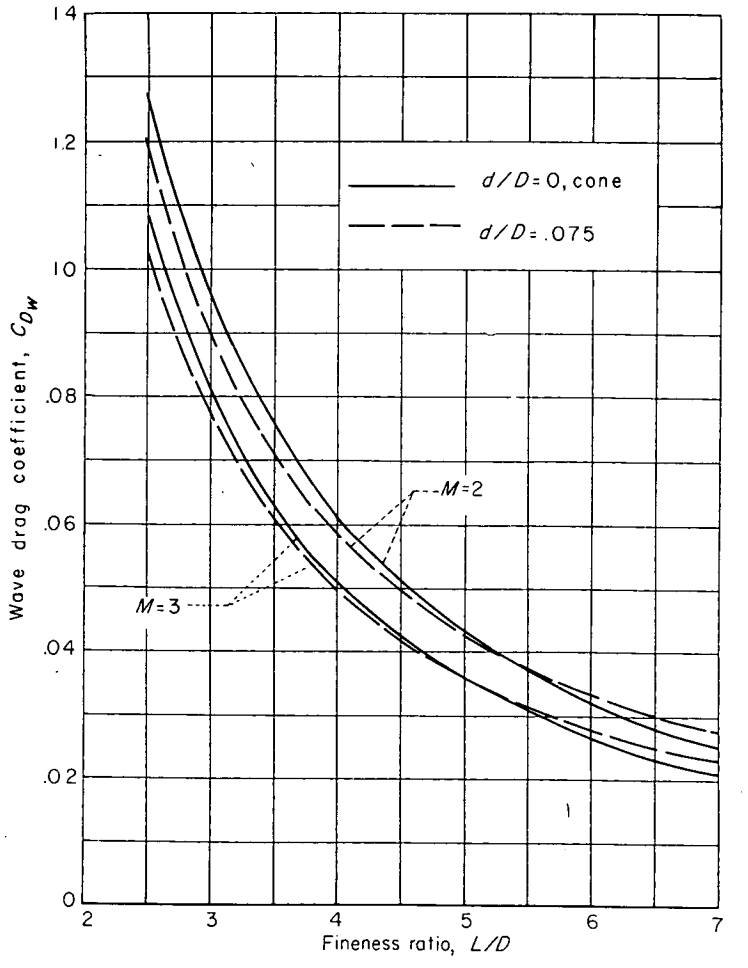


FIGURE 9.—Comparison of the estimated wave drag variation with fineness ratio for a sharp-pointed cone and a 7.5-percent hemispherically blunted cone at Mach numbers 2 and 3.

this type of blunting would be advantageous decreases with increasing Mach numbers.

It should also be pointed out that the drag penalty associated with the use of excessive blunting increases rapidly with increasing fineness ratio. At a Mach number of about 3.1 the data of the present report (fig. 8) indicate that the foredrag coefficient of a 20-percent blunt cone is about 0.01 greater than that of the sharp-nosed cone of the same fineness ratio. This increment represents approximately a 12-percent increase in foredrag and may be compared with the data of reference 19, wherein it is shown that the same degree of blunting for a fineness ratio 8 body results in an increment in wave drag coefficient of 0.053, corresponding to an increase in pressure drag of more than 300 percent.

The estimated wave drag coefficients for the $d/D=0.30$

and 0.50 models at Mach numbers of 3.06 and 1.96 are in very good agreement with the wave drag determined from the pressure distribution models (see fig. 8). Similarly the agreement between the experimental foredrag and the estimated foredrag based upon the estimated wave drag plus laminar incompressible skin-friction drag is very good for Mach numbers 1.96, 3.06, and 3.67. For the tests at these Mach numbers the schlieren pictures taken during the tests indicated that the boundary layer was completely laminar over each of the models. An interesting effect of body shape upon boundary-layer transition is indicated by the results of the tests at $M=1.44$ and 1.24. From the schlieren pictures and the foredrag data it was evident that turbulent boundary-layer flow existed on part of the conical afterbodies of the $d/D=0.30$ and $d/D=0.50$ bodies for the higher Reynolds number at $M=1.44$ and 1.24. In contrast, the boundary-layer flow was laminar over the entire surface of the cone for the identical test conditions. It is believed that the difference between the results for the cone and the blunt bodies results largely from the effects of the differences in body pressure distributions. For the cone the pressure is constant along the surface and therefore neutral insofar as its effect on the boundary-layer flow is concerned. For both the blunt bodies at the low Mach numbers, the pressure gradient in the streamwise direction is positive just downstream from the point of tangency of the nose with the conical section (see fig. 4) and hence tends to thicken the boundary layer and promote transition. Both the schlieren pictures and the force measurements indicate that for the high Reynolds numbers the boundary layer is turbulent over a much greater portion of the surface of the blunter of the two bodies. This result is in agreement with what might be expected on the basis of the differences in the pressure distributions for the two models. Although the adverse gradients for both the $d/D=0.30$ and $d/D=0.50$ models start at essentially the same longitudinal station along the models, and initially are of approximately equal magnitude, the adverse gradient for the blunter model, $d/D=0.50$, extends over most of the conical section of the model; whereas the gradient for the $d/D=0.30$ model is neutral over most of the conical section. Hence, it appears reasonable to expect a lower Reynolds number of transition for the blunter of the two models.

For the $d/D=0.30$ and $d/D=0.50$ models at Mach numbers of 1.24 and 1.44, equation (2) yields values of the wave drag alone which are even greater than the measured foredrags at the lower Reynolds numbers. This discrepancy is attributed to the fact that at these Mach numbers the empirical expression includes too large a value for the wave drag of the hemispherical portion of these models. (See fig. 5.) Hence, for the foredrag estimates shown in figure 8 for Mach numbers 1.24 and 1.44, the lower values of the wave drag of the hemispherical portion of the models obtained from experiment (fig. 5) were used. For all other Mach numbers the empirical expression (eq. (2)) was used. The estimated foredrag results obtained are in fair agreement with the experimental data.

As previously discussed, preliminary estimates and experiment have both shown that a small saving in foredrag may be achieved through the use of a hemispherically blunted cone in place of a sharp cone of the same fineness ratio. Although this type of blunting can be beneficial, preliminary estimates have also indicated that no drag reduction can be achieved by simply replacing the sharp nose of a given cone with a hemispherical tip. In this case the cone angle is not reduced, since the length of the model is reduced instead. In order to verify these results, tests have been made at Mach numbers 1.44 and 1.99 for a series of hemispherically blunted cones, formed by progressively blunting an $L/D=3$ cone. Both the experimental foredrag results and the estimated values of foredrag are plotted in figure 10. It is evident from the figure that there is good agreement between experiment and theory, and that, as expected, there is no drag reduction due to mere blunting of the parent cone.

THEORETICAL MINIMUM DRAG NOSE SHAPES

Comparison of experimental and theoretical foredrag.—Comparisons of the experimental and theoretical foredrag variations with Mach number for the theoretical minimum drag noses, the $L/D=3$ cone and the L-V ogive, are shown in figure 11. The theoretical drag calculations have been

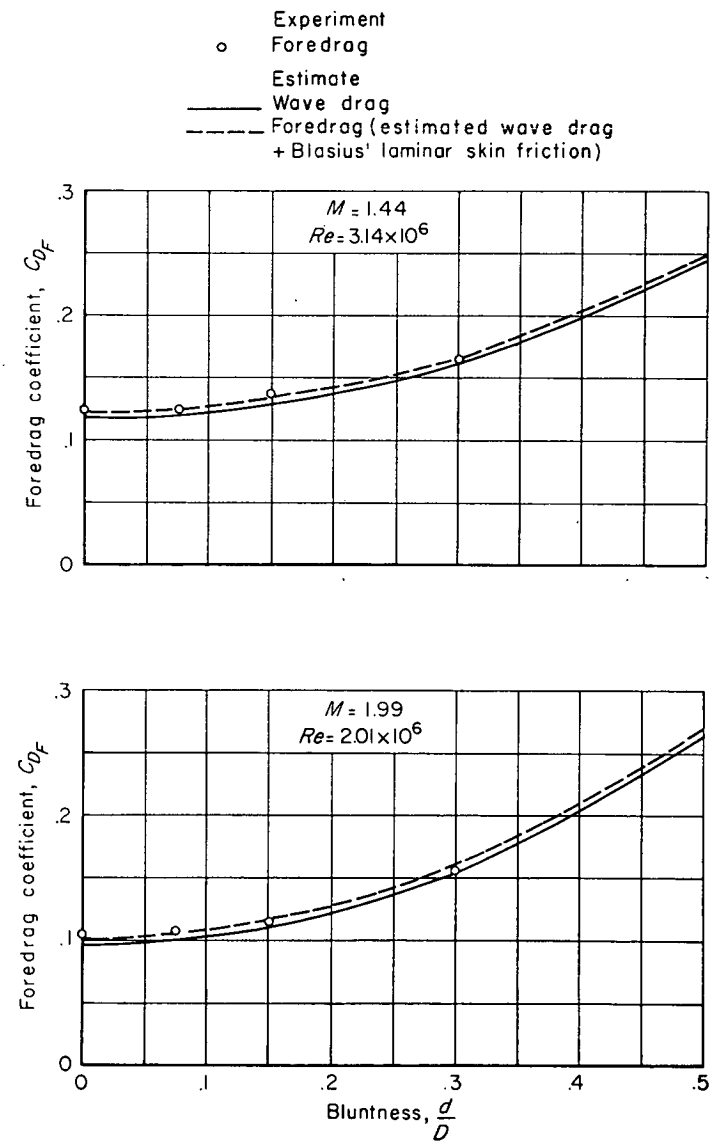
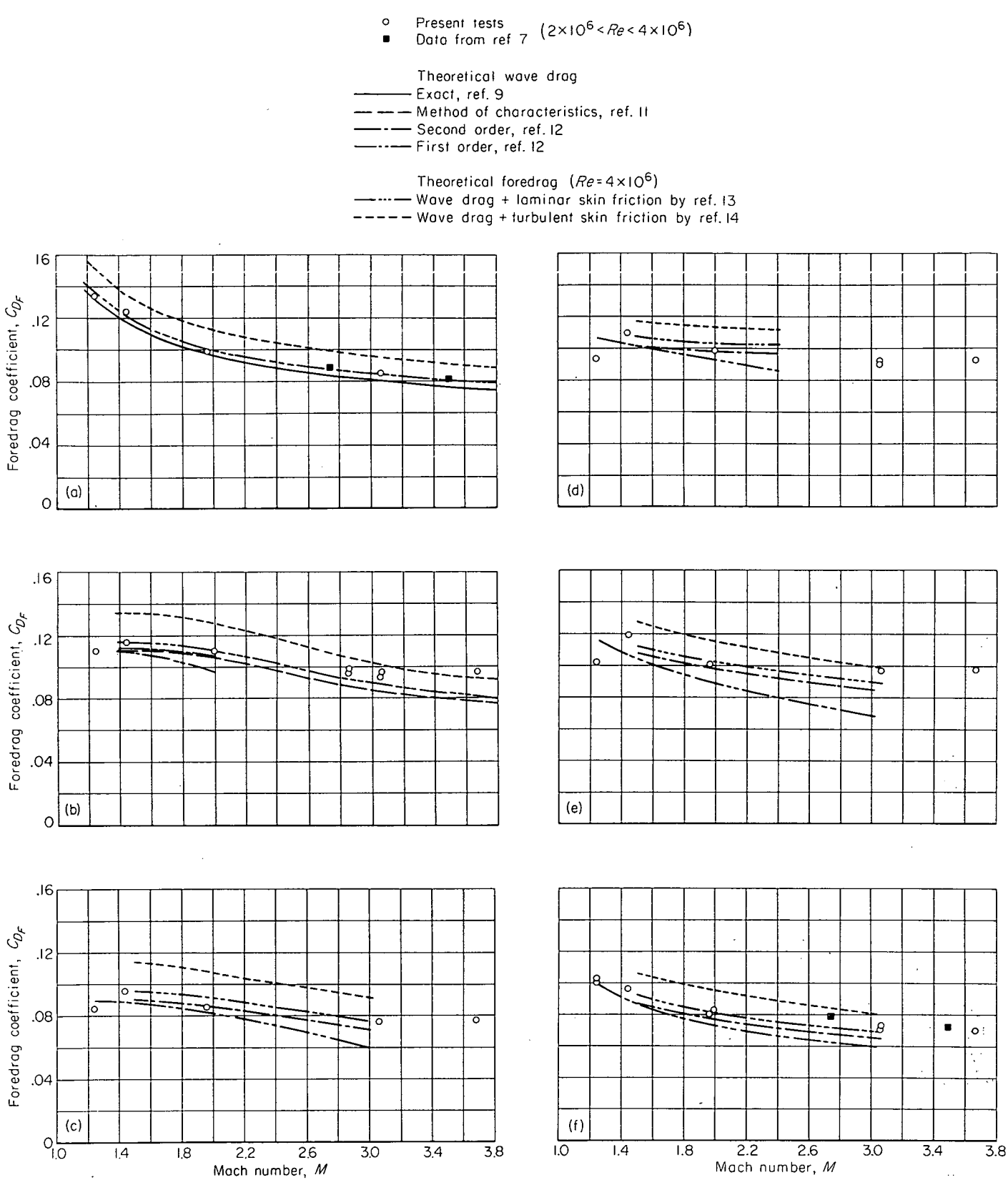


FIGURE 10.—Variation of foredrag coefficient with bluntness for hemisphere-cone series, constant cone angle=18°56′.



(a) Model No. 1, cone, $\frac{L}{D}=3$.

(b) Model No. 16, L–V Ogive, $\frac{L}{D}=2.93$.

(c) Model No. 13, L–D Haack, $\frac{L}{D}=3$.

(d) Model No. 14, L–V Haack, $\frac{L}{D}=3$.

(e) Model No. 15, D–V Haack, $\frac{L}{D}=3$.

(f) Model No. 10, Hypersonic Opt., $\frac{L}{D}=3$.

FIGURE 11.—Comparison of experimental and theoretical foredrag for various models.

limited in most cases to a smaller Mach number range than that for which experimental results are available. For Mach numbers less than 1.4 or greater than about 3, the conical tip approximations to the true body shapes which would have been necessary for application of the perturbation theory to the minimum drag shapes were considered unreasonably large; hence, the second-order theoretical results were limited to Mach numbers between 1.4 and 3. In fact, for the *L-V* Haack nose the theoretical calculations were limited to Mach number 2.4, as an excessive amount of conical tip modification would be necessary for the theory to be applicable at higher Mach numbers. Theoretical estimates of the foredrag have been made by the addition of flat-plate skin-friction values to the computed wave drag, the skin friction being calculated for a Reynolds number of 4×10^6. Although some of the experimental data were taken at lower Reynolds numbers (between 2×10^6 and 4×10^6), the error introduced by calculation of the skin friction at one Reynolds number is small and certainly well within the accuracy of the experimental results. Either completely laminar (ref. 13) or completely turbulent (ref. 14) skin-friction drag has been assumed, although the schlieren pictures indicated that for the tests at Mach numbers of 3.06 and 3.67 boundary-layer transition occurred on some of the models.

A comparison of the experimental and theoretical foredrag for the $L/D=3$ cone has been included in figure 11, since such a comparison indicates how well the skin-friction drag may be calculated and also provides an indication of the accuracy of the other experimental results. For the Reynolds numbers of this investigation, schlieren observations indicated laminar-boundary-layer flow on the cone at all Mach numbers. The foredrag of the cone was closely estimated by the addition of the exact Taylor-Maccoll wave drag and Blasius' incompressible laminar skin friction.[5]

In general, good agreement between the experimental and theoretical foredrag for laminar-boundary-layer flow was obtained for most of the models at Mach numbers of 1.4 and 2.0. Nevertheless, at Mach number 2 the foredrag of the *L-D* and *L-V* Haack shapes are overestimated by about the magnitude of the theoretical laminar-skin-friction drag. For a Mach number of 3 the foredrag of the cone and the foredrag of the *L-D* Haack shape are in good agreement with the theory for laminar-boundary-layer flow. However, the comparisons indicate that the boundary-layer flow for the *L-V* ogive, the *D-V* Haack shape, and the hypersonic optimum shape were at least partially turbulent at this Mach number. At the maximum Mach number ($M=3.67$) the experimental foredrag of the *L-V* ogive exceeds even the theoretical value for completely turbulent boundary-layer flow. This same result is also inferred from the comparison for the *D-V* model. It is not clear which part of the theoretical foredrag is at fault, that is, the wave drag or the skin-friction drag. However, it appears most likely that the theoretical-skin-friction drag is too small, since considerable confidence may be placed in the wave drag value, particularly for the *L-V* ogive.[6]

The data also show that for these particular body shapes, the first-order theory yields acceptable values of wave drag for Mach numbers close to 1.4 only. At the higher Mach numbers, the first-order theory yields results which are too low.

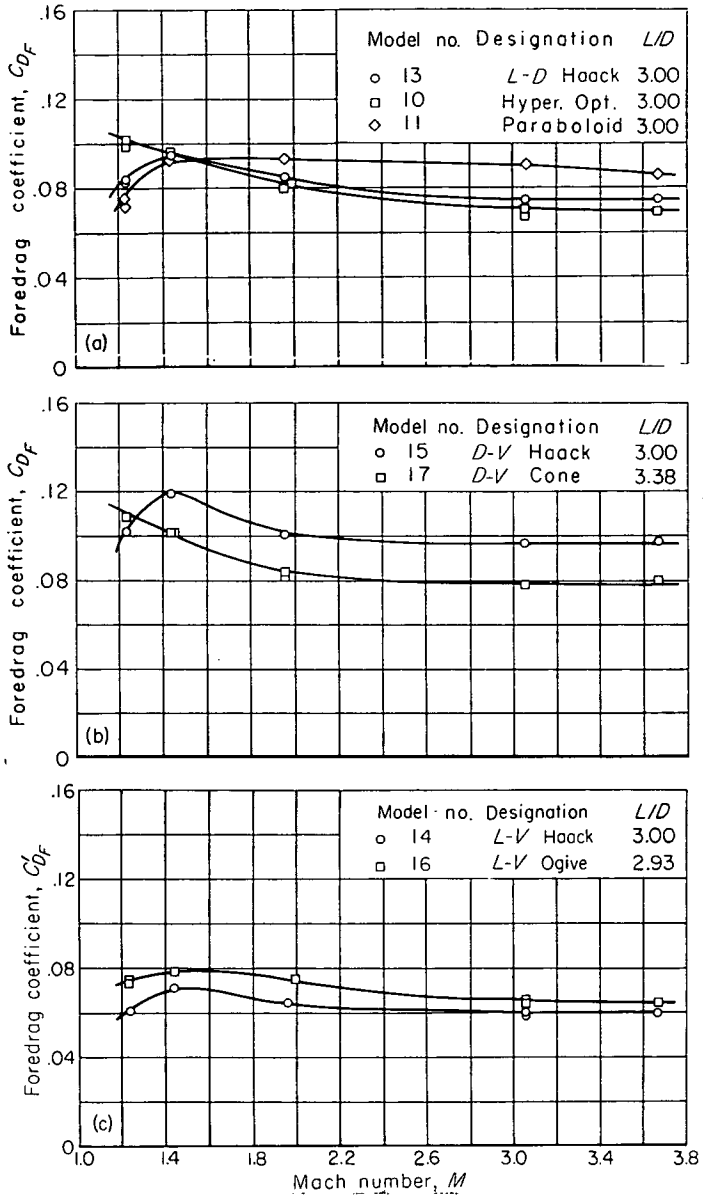
Although slender-body theory has sometimes been used to calculate the wave drag of shapes with fineness ratios as low as these, the wave drag coefficients of 1/9, 1/8, and 1/6 for the *L-D*, *L-V*, and *D-V* Haack shapes (ref. 2), respectively, are too large at all Mach numbers as compared with the results in figures 11(c), 11(d), and 11(e).

Comparison of foredrag of theoretical minimum drag nose shapes with foredrag of other nose shapes.—In order to assess the theoretical minimum drag shapes for the three auxiliary conditions of given length and diameter, given length and volume, or given diameter and volume, other common shapes with identical values of these parameters have been tested and comparisons of the results are shown in figure 12. Although the Reynolds number was not constant throughout the Mach number range, it was unchanged for all the tests at each Mach number. Hence, differences in foredrag between models compared at a given Mach number may not be attributed to differences in Reynolds number.

The foredrag coefficients of the theoretical minimum drag shapes for a given length and diameter, the *L-D* Haack nose (or Kármán ogive), and the hypersonic optimum nose (¾ power and Ferrari shape, see fig. 2) are compared with the foredrag coefficients of the parabolic nose in figure 12(a). It is noteworthy that the *L-D* Haack nose is not the least-drag shape for any Mach number within the range of the tests. For the major portion of the Mach number range (above Mach number 1.5), the hypersonic optimum shape has the least foredrag. It is somewhat surprising that an optimum shape based upon Newtonian impact theory should have less drag than the *L-D* Haack nose at these relatively low supersonic Mach numbers. It is not clear whether this anomaly results from the restriction of zero slope at the base which was evidently assumed in the derivation of the *L-D* Haack nose, or whether this is a result of the low fineness ratio of the models. To investigate this latter point, the wave drag coefficients of both the *L-D* Haack and the hypersonic optimum shapes were calculated by second-order theory for fineness ratios of 3, 5, and 7 at a Mach number of 3. These results (fig. 13) show that the wave drag coefficient of the "Haack" shape is the larger for fineness ratios of 3 and 5. For fineness ratio 7 any difference in wave drag between the *L-D* Haack and the hypersonic optimum shapes is so small as to be within the limits of uncertainty of the calculations. To provide a better indication of the combinations of Mach number and fineness ratio for which the hypersonic optimum nose has less wave

[5] The Handtzche and Wendt transformation of laminar-boundary-layer skin-friction drag of a flat plate to that of a cone was neglected since its inclusion would have increased the foredrag by only 1 percent.

[6] The foredrag values reported herein for the *L-V* ogive ($L/D=2.93$) are about 10 percent lower than those reported in reference 7 for an $L/D=3$ ogive, although the foredrag results for the cone and hypersonic optimum shapes (figs. 11 (a) and 11 (f)) are in agreement. Even though the tests have been rerun and the data have been carefully checked, no satisfactory explanation has, as yet, been found for this difference.



(a) Length and diameter given.
(b) Diameter and volume given.
(c) Length and volume given.

FIGURE 12.—Comparison of foredrag of Haack models with other models having the same two specified parameters.

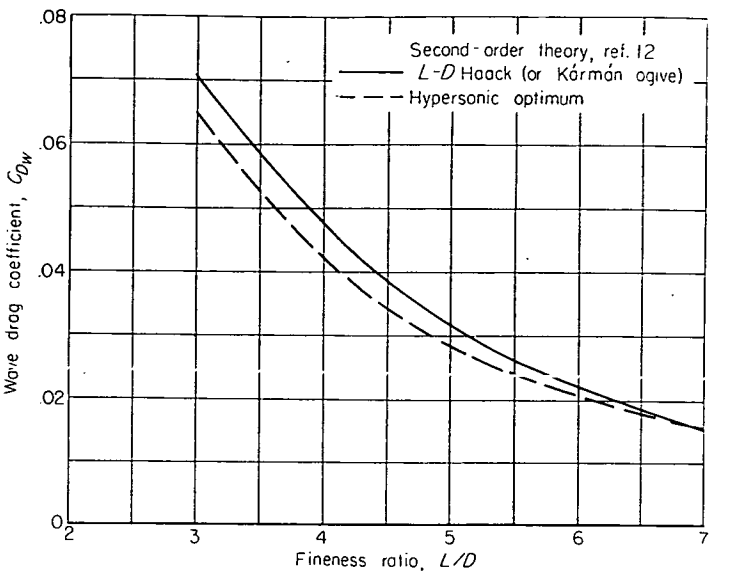


FIGURE 13.—Variation of wave drag coefficient with fineness ratio for the theoretical minimum drag nose shapes of specified length and diameter at Mach number 3.

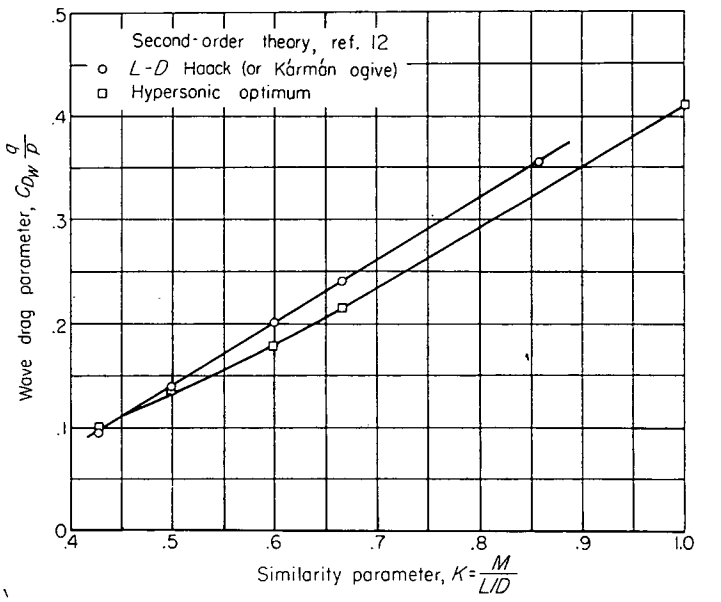


FIGURE 14.—Variation of wave drag parameter, $C_{D_W}\frac{q}{p}$, with the similarity parameter for the theoretical minimum drag nose shapes of specified length and diameter.

drag than the *L-D* Haack nose, the results of all of the available second-order solutions for these shapes have been plotted in figure 14. The plot is made in terms of the hypersonic similarity parameter, $K=M/(L/D)$, and indicates that for values of K in excess of about 0.4 or 0.5 the hypersonic optimum shape has the lower wave drag.

The foredrag of the theoretical minimum drag shape for a given diameter and volume (*D-V* Haack, model 15) is compared in figure 12(b) with the foredrag of a cone (*D-V* cone, model 17) having identical values of diameter and volume. Except for Mach numbers below about 1.4, the foredrag of the cone is of the order of 20 percent lower than that of the theoretical optimum shape. Again, this result may be due either to the low fineness ratio of the bodies tested or the failure of the slender-body theory to predict the correct minimum drag shape for all possible shapes rather than the correct minimum drag shape for bodies with zero slope at the base. In any event, it could be expected that the drag difference would be much less for higher fineness ratio noses.

The foredrag of the theoretical minimum drag shape for a given length and volume (*L-V* Haack, model 14) is compared in figure 12(c) with the foredrag of a circular-arc ogive (*L-V* ogive, model 16) having identical values of length and volume. Since the base areas of these noses differ, the foredrag coefficients are based on $(\text{volume})^{2/3}$ instead of base area in order that a direct comparison of the foredrags may be conveniently made. Over the complete Mach number range the foredrag coefficient of the *L-V* Haack model is between 8 and 16 percent lower than the foredrag coefficient of the *L-V* ogive. For both models the variation of foredrag coefficient with Mach number is similar.

Foredrag of nose shapes defined by $r=R(X/L)^n$.—In reference 7 foredrag results of fineness ratio 3 models for $n=1$, ¾, ½, and ¼ are presented for the Mach number range of 2.73 to 5.00 and for length Reynolds numbers between 2×10^6 and 3×10^6. In the present investigation similar models have been tested at Mach numbers from 1.24 to 3.67 and Reynolds numbers between 2×10^6 and 4×10^6 in order to extend the Mach number range of available drag data. The foredrag results of this investigation are presented in figure 15 and are compared with part of the results of reference 7, replotted for the overlapping Mach number

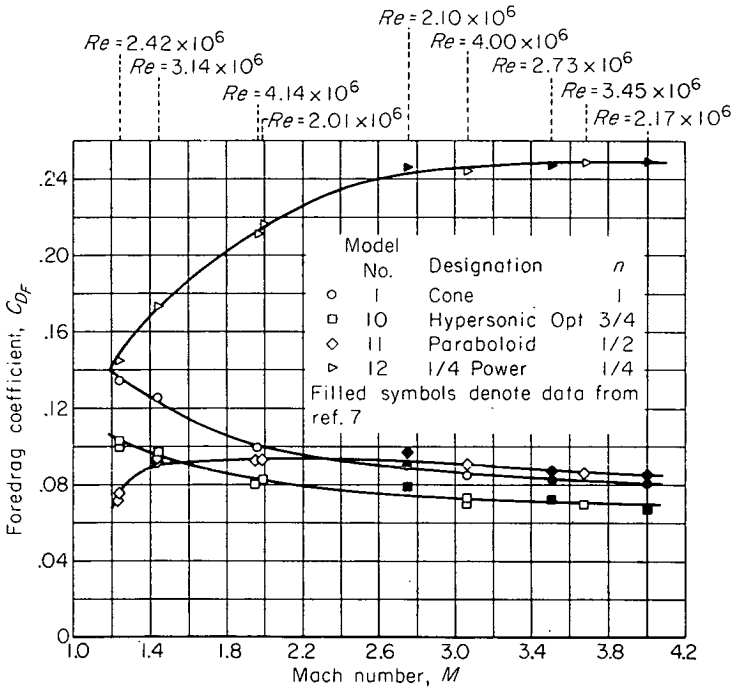


FIGURE 15.—Variation of foredrag coefficient with Mach number for the family of $\frac{L}{D}=3$ nose shapes defined by $r=R\left(\frac{X}{L}\right)^n$.

range of both investigations. In general, there is good agreement between the data from both sources, although there are small differences which may be attributed to variations in Reynolds number. Both the hypersonic optimum nose ($n=¾$) and the conical nose ($n=1$) show a similar decrease in foredrag coefficient with increase in Mach number over the complete Mach number range. The hypersonic optimum nose, however, has much the lower foredrag (about 24 percent lower at Mach number 1.24 and 15 percent lower at Mach number 3.67). In contrast with the decrease in the foredrag coefficient with increasing Mach number for the hypersonic optimum and conical noses, the foredrag coefficients for the parabolic and ¼-power noses increase with increasing Mach number in the lower part of the Mach number range.

COMPARISON OF FOREDRAG OF ALL THE FORCE MODELS

In figure 16 a comparison of the variation of foredrag coefficient with Mach number for all the force models tested is shown. In general, it is seen that for the more blunt noses (models 5, 12, and 18) the foredrag coefficient increases with increase in Mach number, while for the other noses the foredrag coefficient decreases with increase in Mach number over most of the range. It is of interest to note that the ellipsoid (model 18), although showing a large increase in foredrag coefficient with increase in Mach number to Mach number 2, has constant foredrag coefficient for Mach numbers above 2. There is no minimum drag nose for the complete Mach number range, although the hypersonic optimum nose (model 10) has the least drag for Mach numbers above 1.5. Below Mach number 1.5 the paraboloid (model 11) has the lowest drag, slightly less than the drag of the *L–D* Haack nose (model 13). Of special note is the observation that many of the nose shapes have less drag than the cone (model 1), particularly at the lower Mach numbers.

CONCLUSIONS

Drag measurements at zero angle of attack have been made for various hemispherically blunted cones, theoretical minimum drag nose shapes, and other more common profiles of fineness ratio 3. An analysis of the results for a Mach number range of 1.24 to 7.4 and for Reynolds numbers between 1.0×10^6 and 7.5×10^6 has led to the following conclusions:

1. No model had the least foredrag for the complete Mach number range.
2. Of the models tested the paraboloid of revolution had the least foredrag below a Mach number of 1.5, and the hypersonic optimum shape had the least foredrag above a Mach number of 1.5.
3. The theoretical shapes for minimum pressure drag derived by von Kármán and by Haack for given length and diameter or given diameter and volume do not have less drag than all other possible shapes having identical values of the same parameters.
4. For the hemispherically blunted cones of low fineness ratios (of the order of 3):
   a. Small reductions in foredrag may be achieved by hemispherical blunting (hemisphere diameter approximately 15 percent of base diameter) if the fineness ratio is held constant and, hence, the cone angle reduced with increased blunting. If the cone angle is held constant and the fineness ratio reduced, hemispherical blunting results in increased foredrag.
   b. A relatively large hemispherical tip diameter (as large as 30 percent of the base diameter at Mach numbers of 1.24 and 1.44) may be used without increasing the drag above that of a sharp-nosed cone of the same fineness ratio.
   c. For large spherical bluntnesses (nose diameters of the order of 50 percent of the base diameter) drag penalties were moderate at Mach numbers less than 1.5 but became severe with increasing Mach number.
   d. For Mach numbers of 2 and greater the wave drag may be accurately estimated by the addition of the wave drag of the hemispherical tip calculated from an empirical expression and the wave drag of the conical portion from Taylor-Maccoll theory.

AMES AERONAUTICAL LABORATORY,
NATIONAL ADVISORY COMMITTEE FOR AERONAUTICS,
MOFFETT FIELD, CALIF., *Aug. 28, 1952.*

Model	No	Designation	d/D	L/D
○	1	Hemisphere-Cone,	0.000	3.00
□	2	Hemisphere-Cone,	.075	3.00
◇	3	Hemisphere-Cone,	150	3.00
▷	4	Hemisphere-Cone,	300	3.00
▽	5	Hemisphere-Cone,	.500	3.00
▽	7	Hemisphere-Cone,	.075	2.81
▷	8	Hemisphere-Cone,	150	2.62
○	9	Hemisphere-Cone	300	2.24

Model	No	Designation	L/D
◇	10	Hyper. Opt	3.00
▷	11	Paraboloid	3.00
◐	12	1/4 Power	3.00
◧	13	L-D Haack	3.00
◆	14	L-V Haack	3.00
▶	15	D-V Haack	3.00
▼	16	L-V Ogive	2.93
◨	17	D-V Cone	3.38
◗	18	Ellipsoid	3.00

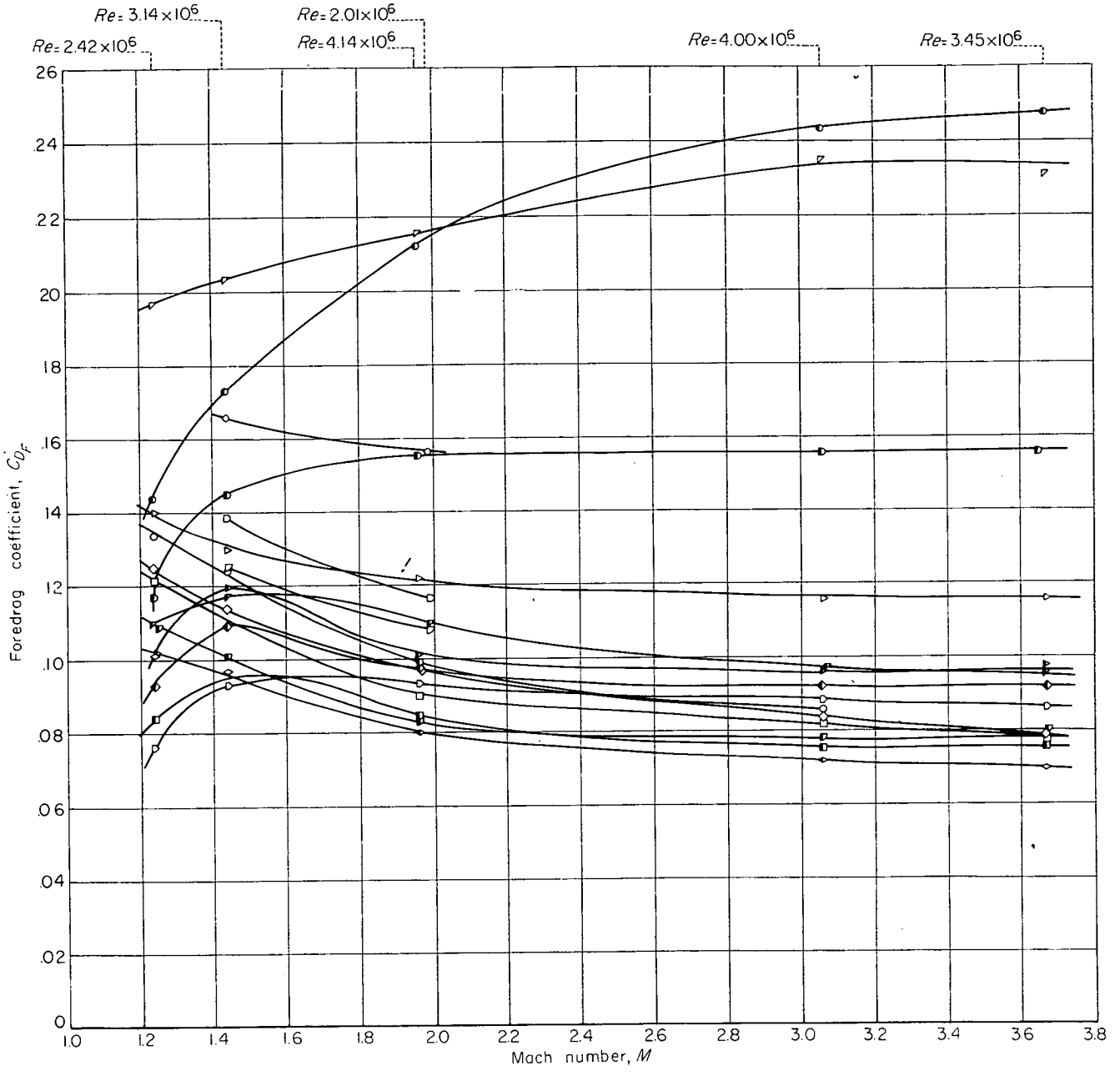


FIGURE 16.—Variation of foredrag coefficient with Mach number for all the force models tested.

REFERENCES

1. von Kármán, Th.: The Problems of Resistance in Compressible Fluids. R. Accad. d' Italia, Cl. Sci. Frs. Mat. e Nat., vol XIV, 1936, pp. 222–276. (Fifth Volta Congress held in Rome, Sept. 30–Oct. 6, 1935).
2. Haack, W.: Projectile Forms of Minimum Wave Resistance. (Translation) Douglas Aircraft Company, Inc., Rep. 288, 1946.
3. Lighthill, M. J.: Supersonic Flow Past Bodies of Revolution. R. & M. No. 2003, British A. R. C., 1945.
4. Sears, William R.: On Projectiles of Minimum Wave Drag. Quart. Appl. Math., vol. IV, no. 4, Jan. 1947, pp. 361–366.
5. Ward, G. N.: Supersonic Flow Past Slender Pointed Bodies. Quart. Jour. Mech. and Appl. Math., vol. II, pt. 1, March 1949, pp. 75–99.
6. Ferrari, Carlo: The Body and Ogival Contour Giving Minimum Wave Drag. Atti dell Accademia delle Scienze di Torino, vol. 84, no. 1, pp. 3–18, 1949–50. (Translated by R. H. Cramer, Cornell Aero. Lab., Inc., Buffalo, New York, presented at session of Reale Accademia delle Scienze di Torino, Nov. 23, 1949.
7. Eggers, A. J., Jr., Resnikoff, Meyer M., and Dennis, David H.: Bodies of Revolution for Minimum Drag at High Supersonic Airspeeds. NACA Rep. 1306, 1957 (Supersedes NACA TN 3666).
8. Seiff, Alvin: A Free-Flight Wind Tunnel For Aerodynamic Testing at Hypersonic Speeds. NACA Rep. 1222, 1955 (Supersedes NACA RM A52A24).
9. Mass. Inst. of Tech., Dept. of Elect. Engr., Center of Analysis. Tables of Supersonic Flow Around Cones, by the Staff of the Computing Section, Center of Analysis, under the direction of Zdenek Kopal. Tech. Rep. No. 3, Cambridge, 1949.
10. Stewart, H. J.: The Theoretical Lift and Drag of Cones at Supersonic Speeds. Jet Propulsion Lab., GALCIT Memo. No. 4–14, Nov. 18, 1946.
11. Ehret, Dorris M., Rossow, Vernon J., and Stevens, Victor I.: An Analysis of the Applicability of the Hypersonic Similarity Law to the Study of Flow About Bodies of Revolution at Zero Angle of Attack. NACA TN 2250, 1950.
12. Van Dyke, Milton D.: Practical Calculation of Second-Order Supersonic Flow Past Nonlifting Bodies of Revolution. NACA TN 2744, 1952.
13. Blasius, H.: Grenzschichten un Fliissigkeiten mit kleiner Rubung. Zx. Math. un. Phys. Bd 56, p. 1 (1908).
14. Rubesin, Morris W., Maydew, Randall C., and Varga, Steven A.: An Analytical and Experimental Investigation of the Skin Friction of the Turbulent Boundary Layer on a Flat Plate at Supersonic Speeds. NACA TN 2305, 1951.
15. Grimminger, G., William, E. P., and Young, G. B. W.: Lift on Inclined Bodies of Revolution in Hypersonic Flow. Jour. Aero. Sci., vol. 17, no. 1, November 1950, pp. 675–690.
16. Hodges, A. J.: The Drag Coefficient of Very High Velocity Spheres. Jour. Aero. Sci., vol. 24, no. 10, Oct. 1957, pp. 755–758.
17. Hart, Roger G.: Flight Investigation of the Drag of Round-Nosed Bodies of Revolution at Mach Numbers From 0.6 to 1.5 Using Rocket Propelled Test Vehicles. NACA RM L51E24, 1951.
18. Vincenti, Walter G., and Wagoner, Cleo B.: Transonic Flow Past a Wedge Profile with Detached Bow Wave. NACA TN 2339, 1951. NACA Rep. 1095, 1953 (Supersedes NACA TN's 2339 and 2588).
19. Jack, John R., and Gould, Lawrence I.: Aerodynamics of Slender Bodies at Mach Number of 3.12 and Reynolds Numbers from 2×10^6 to 15×10^6. II-Aerodynamic Load Distributions of Series of Five Bodies Having Conical Noses and Cylindrical Afterbodies. NACA RM E52C10, 1952.

REPORT 1387

FULL-SCALE INVESTIGATION OF SEVERAL JET-ENGINE NOISE-REDUCTION NOZZLES[1]

By Willard D. Coles and Edmund E. Callaghan

SUMMARY

A number of noise-suppression nozzles were tested on full-scale engines. In general, these nozzles achieved noise reduction by the mixing interference of adjacent jets; that is, by using multiple-slot nozzles. Several of the nozzles achieved reductions in sound power of approximately 5 decibels (nearly 70 percent) with small thrust losses (approx. 1 percent).

The maximum sound-pressure level was reduced by as much as 18 decibels in particular frequency bands. Some of the nozzles showed considerable spatial asymmetry; that is, the sound field was not rotationally symmetrical.

A method of calculating the limiting frequency effected by such nozzles is presented. Furthermore, data are shown that appear to indicate that further reductions in sound power will not be easily achieved from nozzles using mixing interference as a means of noise suppression.

INTRODUCTION

The normal development of the jet engine has produced sizable increases in thrust and also, unfortunately, in jet-engine noise. In fact, current jet engines are truly awesome noise producers. There are several approaches to reducing this jet-engine noise: The takeoff and climb-out pattern of the aircraft (ref. 1) can be adjusted to cause the least annoyance, or the engine itself can be made quieter.

It is well established that the principal source of jet-engine noise is the turbulent mixing of the jet with the surrounding atmosphere (ref. 2). The noise generated by this process is a function of the product of the eighth power of the jet velocity and the jet area (refs. 2 and 3). Consequently, reductions in jet velocity will greatly reduce noise. To accomplish this, however, there must be a change in the engine cycle (e. g., the bypass engine) or a completely new engine design concept (such as the low-temperature engine (ref. 4)). In any case, such a development program requires considerable time before a reliable and tested product can be installed on new aircraft. Therefore, the present problem is to quiet existing engines.

Since the noise generation results from the turbulent mixing of the jet, a change in this process should result in a change in noise. Most of the noise-reduction devices tested during the past several years have been based on this principle. A great many different devices have been tried (refs. 5 to 7), but, in general, all seek to alter the mixing process either by odd-shaped nozzles or by the interference of multiple jets.

A theory relating jet turbulence to noise generation is discussed in reference 8. The most significant result of this work relates the eddy size and the turbulent intensity to noise generation. As a result of this analysis, it appears that reduction of noise generation can be accomplished in one of the following ways: (1) Eddy size is decreased at constant turbulent intensity, (2) turbulent intensity is decreased at constant eddy size, or (3), most desirable, both eddy size and intensity are decreased. The fact that it is known how noise reduction may be accomplished helps somewhat, but it is certainly not readily apparent what physical devices will result in any of the three suggested means of noise reduction.

The devices discussed herein follow the general principles outlined for accomplishing noise reduction. Some of these devices have been tried elsewhere and are presented as confirmation of previous work. The investigation was conducted at the NACA Lewis laboratory as part of a long-range study of jet noise and means for its suppression.

SYMBOLS

A	exit area of nozzle, sq ft
a_0	ambient speed of sound, ft/sec
D	nozzle diameter, ft
F	engine thrust, lb
$\frac{F/\delta}{(F/\delta)_{std}}$	corrected-thrust ratio
f	frequency, cps
f_x	frequency corresponding to x distance, cps
h	jet height (see fig. 6 (b)), ft
N	engine speed, percent of rated rpm
n	number of spaces between nozzle segments
P	sound power of suppressor nozzle, w
P_{std}	sound power of standard nozzle, w
s	jet spacing (see fig. 6 (b)), ft
T	exhaust-gas temperature, °R
V	jet velocity, ft/sec
w	jet width (see fig. 6 (b)), ft
x	distance from nozzle exit to point at which adjacent jets impinge, ft
δ	ratio of engine-inlet total pressure to NACA standard sea-level pressure of 2,116 lb/sq ft
θ	ratio of engine-inlet total temperature to NACA standard sea-level temperature of 518.7° R
ρ_0	atmospheric air density, slugs/cu ft

[1] Supersedes NACA Technical Note 3974 by Willard D. Coles and Edmund E. Callaghan, 1957.

Preceding Page Blank

APPARATUS AND PROCEDURE

TURBOJET ENGINES

Two axial-flow turbojet engines, with rated sea-level thrusts of approximately 5,000 and 10,000 pounds, were used in this investigation. At rated conditions, the total- to static-pressure ratio across the exit nozzle was approximately 1.7 for the low-thrust engine and 2.3 for the high-thrust engine. The jet velocities were approximately 1,730 and 1,900 feet per second, respectively. These engines were mounted in an engine thrust stand, shown in figure 1 with the 5,000-pound-thrust engine installed. The centerline of the engine is located 8 feet above the ground plane. The engines were equipped with large inlet bellmouth sections and were provided with screens at the bellmouth entrance to prevent ingestion of foreign material.

Engine thrust was measured by means of temperature-compensated strain-gage thrust links of appropriate range, which gave measurements accurate to ½ percent. Engine airflow was measured by means of static-pressure rakes and wall taps to within an accuracy of ½ percent. Additional instrumentation was provided for measuring fuel flow, exhaust-nozzle total pressure, and jet temperature.

Three different engine exhaust cones (two larger than standard) were used with the 5,000-pound-thrust engine. The larger cones were used in conjunction with the noise-suppressor nozzles. The standard cone was used only with the standard conical convergent nozzle.

ACOUSTIC MEASUREMENTS

The thrust stand (fig. 1) is located in an area that is unobstructed rearward and to the sides for over ½ mile. The nearest reflecting surface, other than a small control room, was located approximately 400 feet in front of the thrust stand. The reflective effects from the control room should be extremely small at all the measuring stations shown in figure 2, because no measuring stations are close to the building and because of the small size of the building and the angle at which it is located. Measurements of the over-all sound-pressure level [2] were made approximately 8 feet above ground level at 15° intervals from the jet axis and at a 200-foot radius from the jet exit for all the positions shown in figure 2. Sound-pressure level was measured with a commercial sound-level meter set to a flat response from 20 to 10,000 cycles per second. Spectrum data were obtained with an automatic audiofrequency analyzer and recorder. The frequency range of this system is from 35 to 18,000 cycles per second and is divided into 27 ⅓-octave bands. The spectrum recorder and related equipment were mounted in a specially adapted, insulated panel truck. Before each test, both the sound-level meter and the frequency-recording

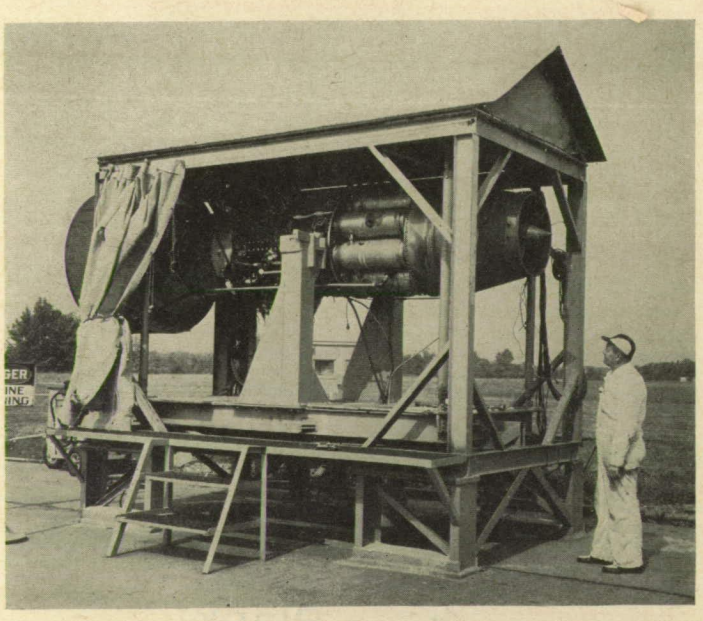


FIGURE 1.—Thrust stand with 5,000-pound-thrust engine.

TABLE I.—NOISE-SUPPRESSION NOZZLES

Letter designation	Rated thrust of test engine, lb	Description of nozzle	Details in figure 3
A	5, 000	Six-corrugation or Greatrex type (ref. 6) nozzle.	(a)
B	5, 000	Three-segment nozzle	(b)
C	10, 000	Twelve-segment nozzle with centerbody.	(c)
D	5, 000	Nine-section rectangular (3 in. wide by 12 in. high) slotted nozzle.	(d)
E	5, 000	Nine-section rectangular (2 in. wide by 18 in. high) slotted nozzle.	(e)
F	5, 000	Seven-section rectangular (2⅜ in. wide by 18 in. high) slotted nozzle (modification of nozzle E).	(f)
G	5, 000	Six-section rectangular (6 in. wide by 9 in. high) slotted nozzle.	(g)
H	5, 000	Six-section rectangular (9 in. wide by 6 in. high) slotted nozzle.	(h)
I	5, 000	Six-section rectangular (9 in. wide by 6 in. high) offset (different exit planes) slotted nozzle.	(i)
J	5, 000	Eighteen-section rectangular (2.7 in. wide by 6 in. high) slotted nozzle.	(j)
K	5, 000	Twelve-section rectangular (4 in. wide by 6 in. high) slotted nozzle (modification of nozzle J).	(k)

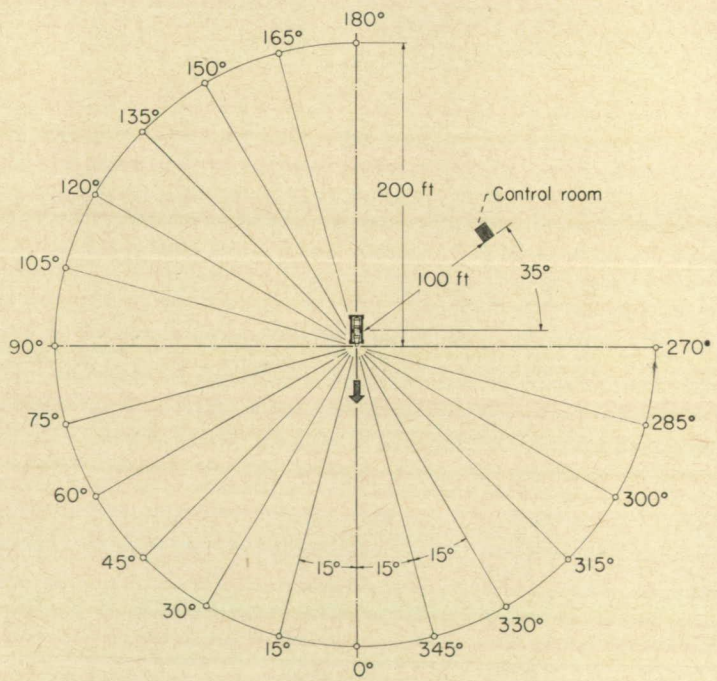


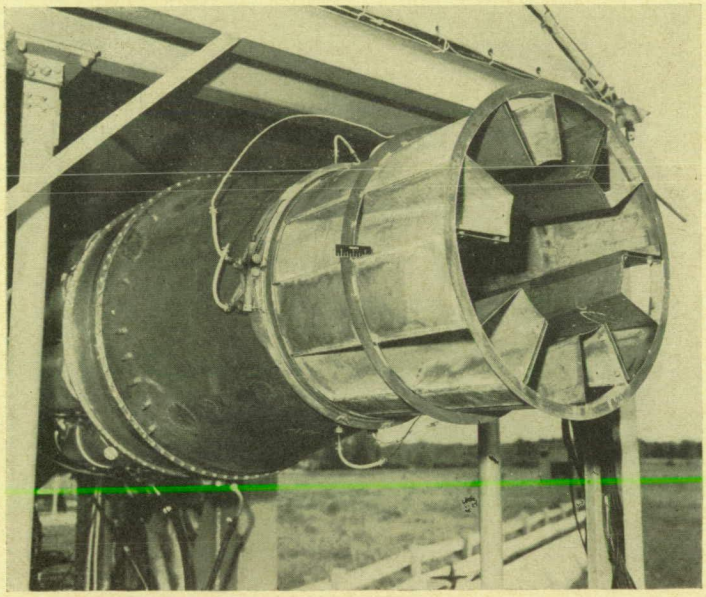
FIGURE 2.—Location of survey stations in sound field around engine thrust stand.

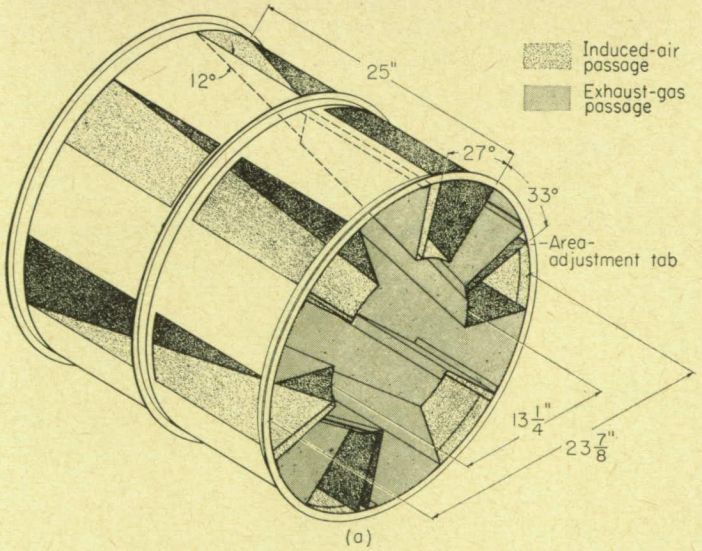
[2] The nomenclature of acoustic terms (sound pressure, sound-pressure level, sound power, and spectrum level) used in this report is that of reference 9.

system were calibrated with a small loud-speaker-type calibrator driven by a transistor oscillator.

Although extreme care was taken to calibrate the sound-measuring equipment, other sources of error affected the results. The wind has an appreciable effect on jet direction and hence distorts the sound field. No tests were made at wind velocities greater than 14 miles per hour, but some errors do occur because of wind gusts. Tests made on different days with the same nozzle showed that local sound-pressure-level variations might be as high as ± 3 decibels because of displacement of the jet. However, the sound-power levels always varied less than ± 1 decibel. The sound-power data should be expected to be less in error since they result from an integration over the whole sound field, and errors in local values tend to average out.

Normally, acoustic measurements were made at engine rotational speeds of 100, 97.5, 92.5, and 87.5 percent of rated speed. At each engine speed, spectrum measurements required about 20 minutes. In most cases, no spectrum measurements were made at 100-percent speed.



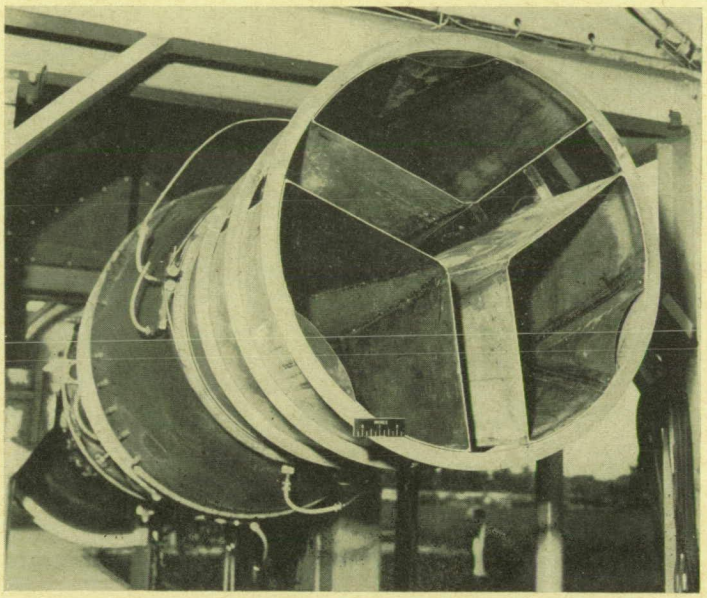


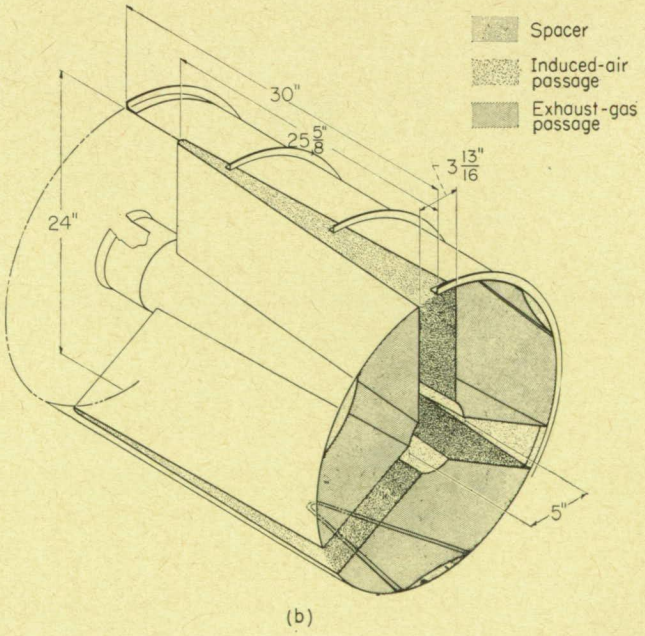
(a) Nozzle A: Six-corrugation or Greatrex type (ref. 6).

NOISE-SUPPRESSION NOZZLES

The noise-suppression nozzles used in this investigation are listed in table I. For convenience, each nozzle has been assigned a letter designation (given in table I), such as "nozzle A," and so forth, and will be referred to in this manner in the succeeding discussion. Pertinent details of the nozzles are shown in figure 3.

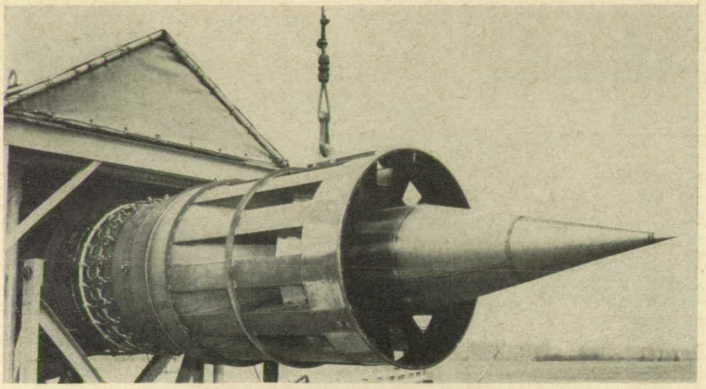
It should be noted that area-adjustment tabs have been provided at the exits of all the nozzles (e. g., fig. 3 (a)). These tabs are used to trim the exhaust area to obtain the correct relation between engine speed and exhaust-gas temperature (i. e., rated exhaust-gas temperature at rated engine speed).

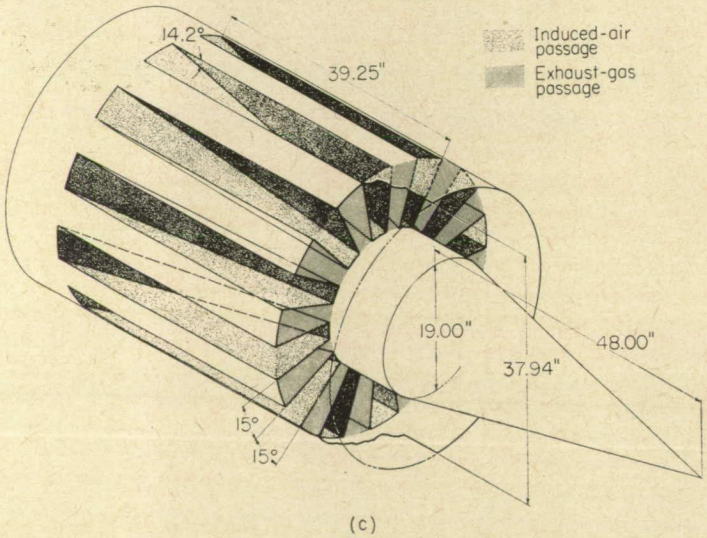




(b) Nozzle B: Three-segment nozzle.

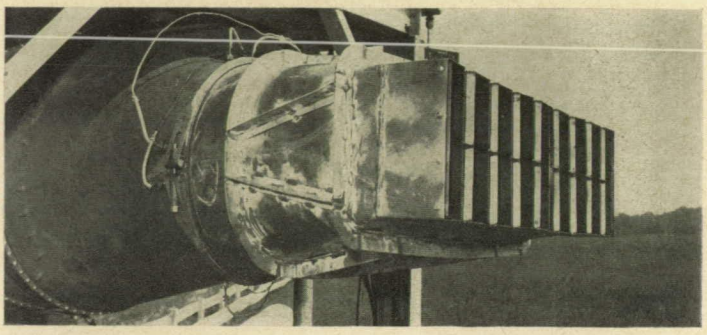
FIGURE 3.—Noise-suppression nozzles investigated.

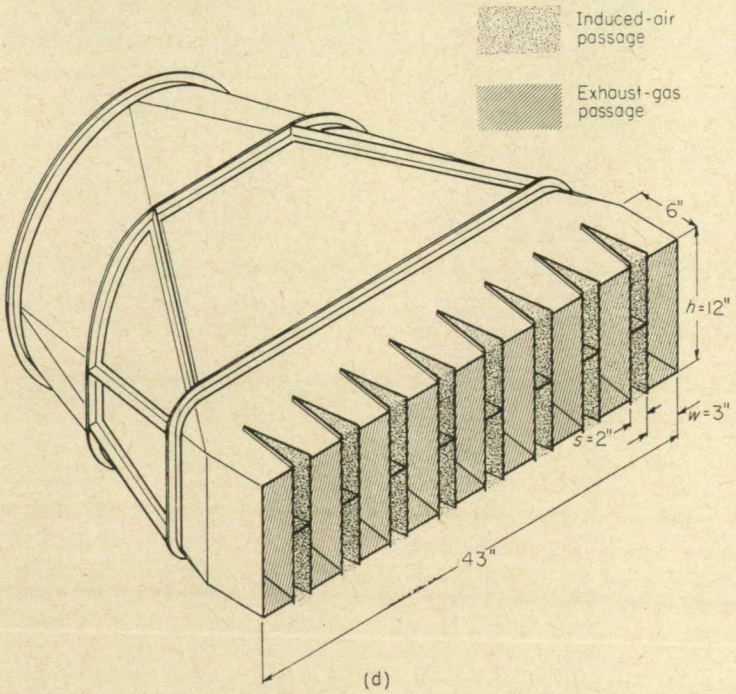




(c)

(c) Nozzle C: Twelve-segment nozzle with centerbody.

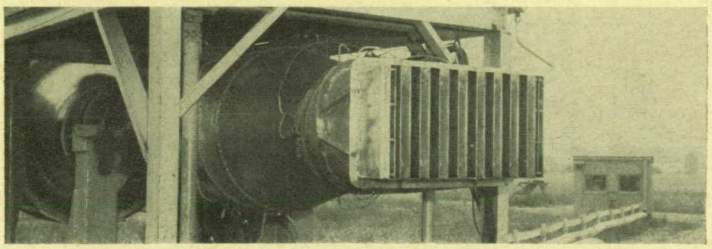


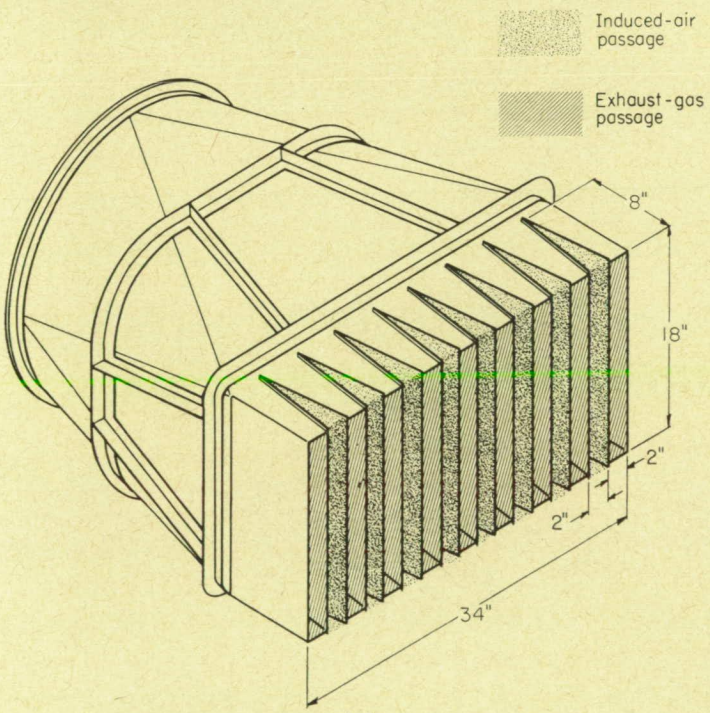


(d)

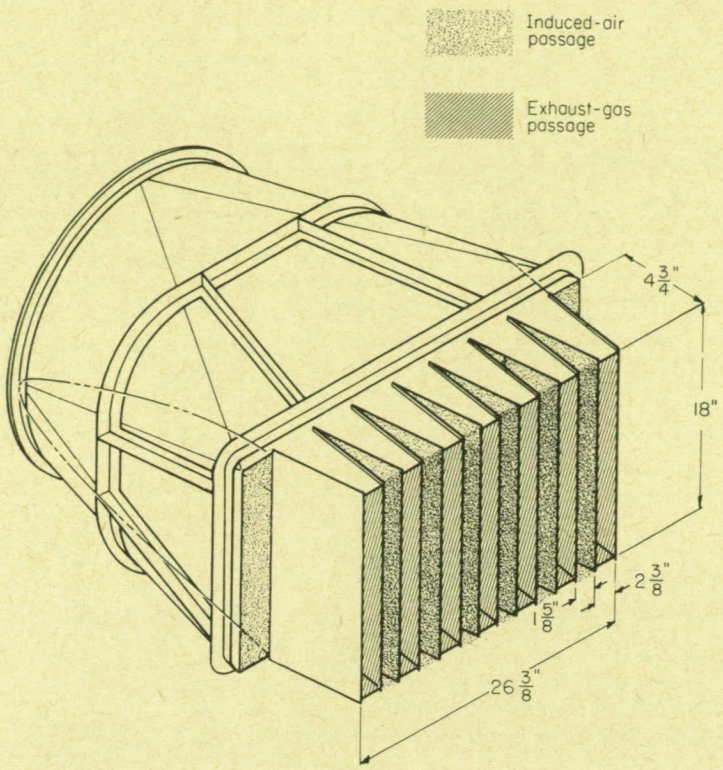
(d) Nozzle D: Nine-section rectangular (3 in. wide by 12 in. high) slotted nozzle.

FIGURE 3.—Continued. Noise-suppression nozzles investigated.

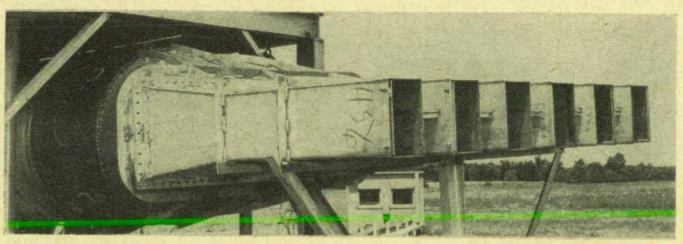


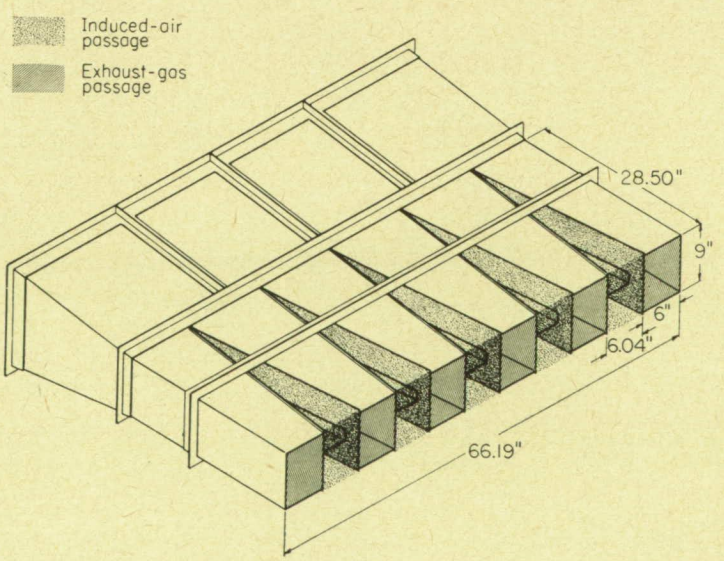


(e) Nozzle E: Nine-section rectangular (2 in. wide by 18 in. high) slotted nozzle.



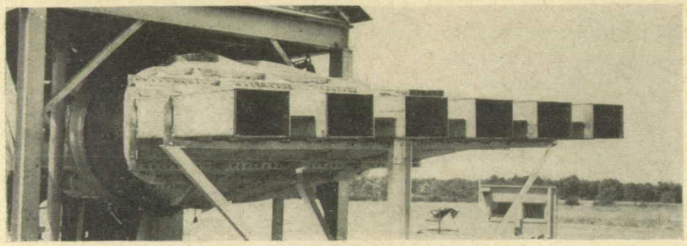
(f) Nozzle F: Seven-section rectangular (2⅜ in. wide by 18 in. high) slotted nozzle.

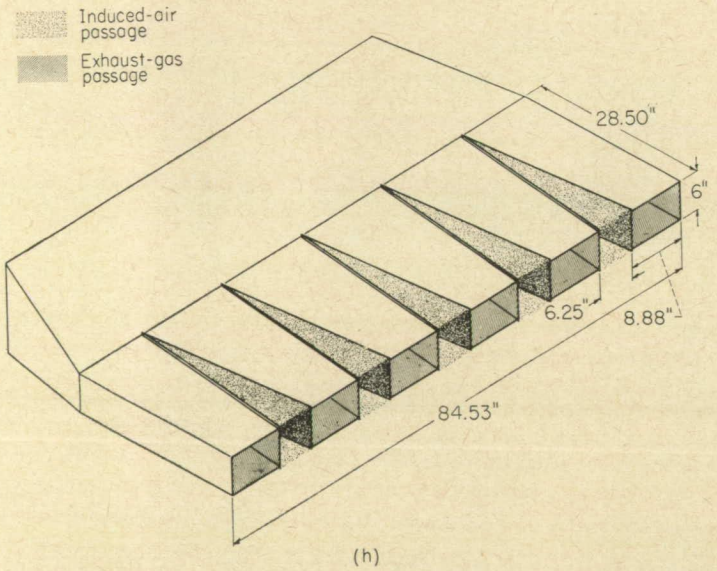




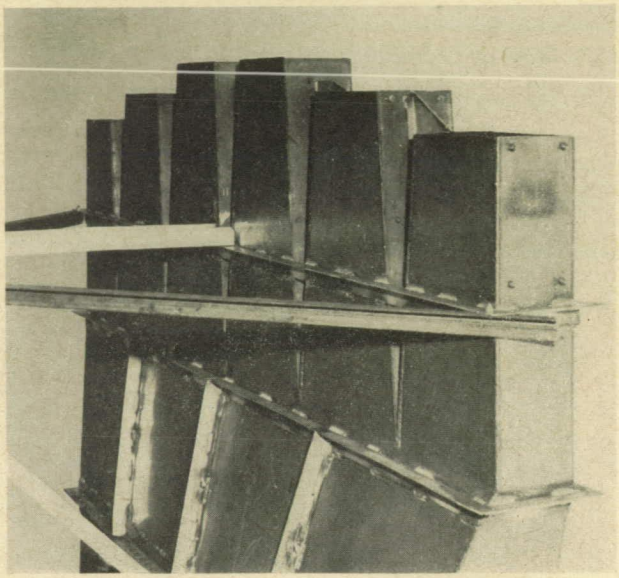
(g) Nozzle G: Six-section rectangular (6 in. wide by 9 in. high) slotted nozzle.

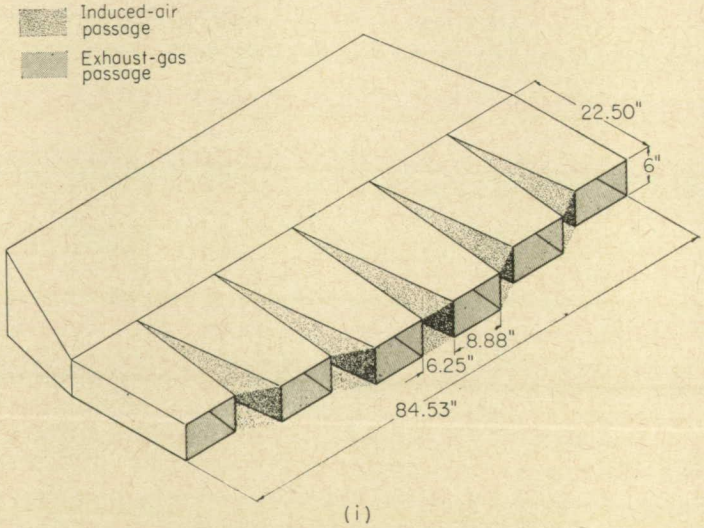
FIGURE 3.—Continued. Noise-suppression nozzles investigated.





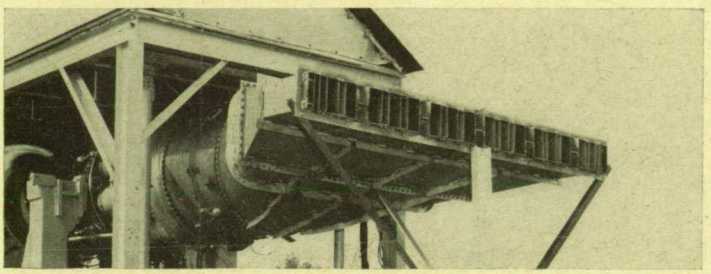
(h) Nozzle H: Six-section rectangular (9 in. wide by 6 in. high) slotted nozzle

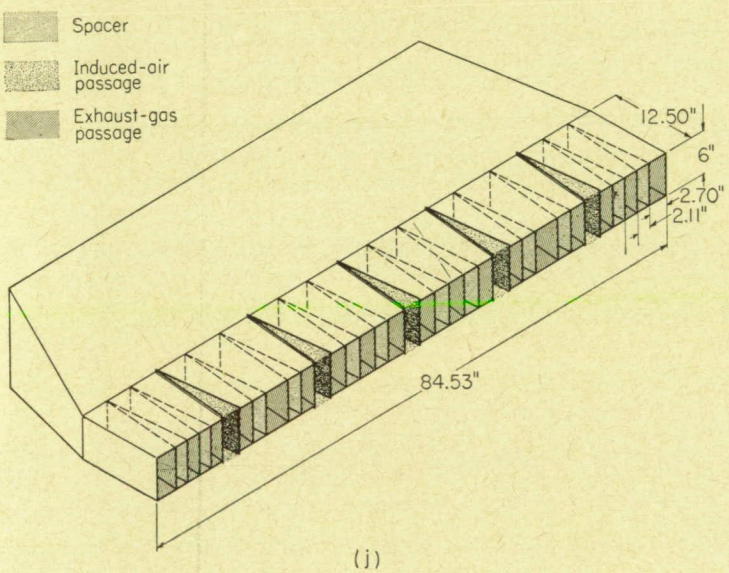




(i) Nozzle I: Six-section rectangular (9 in. wide by 6 in. high) offset slotted nozzle.

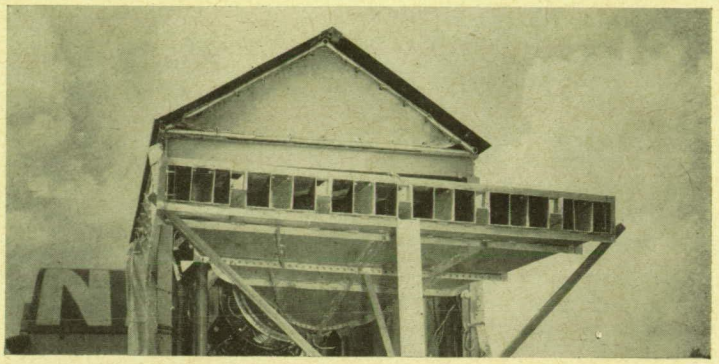
FIGURE 3.—Continued. Noise-suppression nozzles investigated.

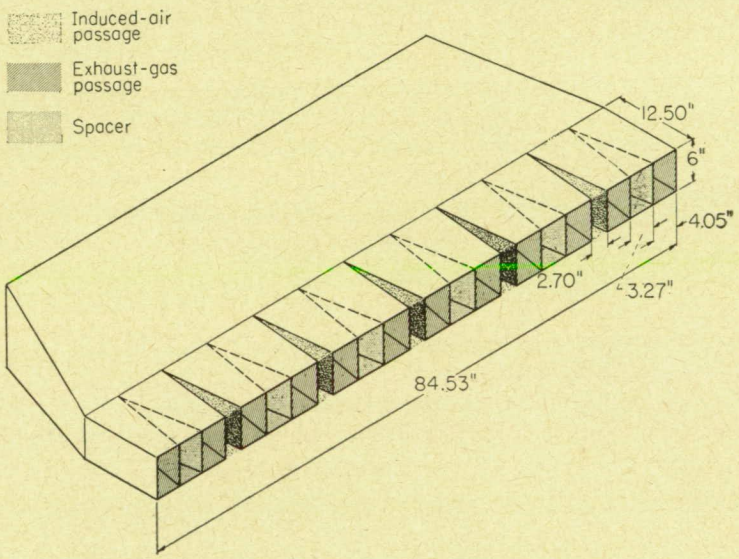




(j)

(j) Nozzle J: Eighteen-section rectangular (2.7 in. wide by 6 in. high) slotted nozzle.





(k) Nozzle K: Twelve-section rectangular (4 in. wide by 6 in. high) slotted nozzle.

FIGURE 3.—Concluded. Noise-suppression nozzles investigated.

526597—60——81

RESULTS

The effectiveness of the noise-suppression devices is demonstrated by comparison with the original noise source. Initially, comparisons are made of the total sound power radiated, the spectrum level (sound-pressure level per cycle), and the directionality pattern for the various suppressor devices and a standard conical convergent nozzle.

Such comparisons are useful for showing trends but cannot be used as absolute measures of effectiveness, since ambient conditions affect both the engine operation and the sound generation. Data are presented for a fixed engine speed of either 97.5 or 100 percent of rated engine speed. The over-all sound-pressure levels generally are presented for 100 percent and the spectrum level for 97.5 percent of rated engine speed for the reasons discussed in APPARATUS AND PROCEDURE section. With regard to both acoustics and engine operation, final comparisons of the various nozzles are made using normalized parameters that eliminate daily temperature and pressure variations. Furthermore, comparisons between different engines equipped with suppressor nozzles are only possible with normalized parameters.

NOZZLE A, SIX-CORRUGATION NOZZLE

Figure 4 (a) shows the directional distribution of the sound for a six-corrugation nozzle (nozzle A, fig. 3 (a)) and a standard nozzle. In this and subsequent similar figures, only half the total sound field is shown. The values of sound-pressure level presented are averages of the values on opposite sides of the jet axis. This has been done in order to minimize the wind effects discussed previously.

It is evident that this particular suppressor nozzle shows very little effect on the directional pattern and level of the sound. In fact, the total sound power radiated for this nozzle was 164.3 decibels compared with 166.1 decibels for the standard nozzle. These results, in general, confirm the work of Greatrex on a similar nozzle (ref. 6). Greatrex has shown that deeper corrugations will provide greater reductions in the area of maximum sound-pressure level (30° to 60° azimuths). Several frequency distributions of sound pressure obtained with this nozzle are shown in figure 4 (b). The spectrum levels at azimuths of 90° and 150° are practically the same as for the standard nozzle. At a 30° azimuth, there is a decrease in energy between frequencies of 150 and 600 cycles per second, with slight increases on either side of this frequency range. It is not surprising, therefore, that the power-level distribution with frequency is practically unchanged from that of the standard nozzle (fig. 4 (c)).

NOZZLE B, THREE-SEGMENT NOZZLE

Nozzle B (three-segment nozzle) reflects the trend toward deeper corrugations mentioned previously (ref. 6). Figure 5 (a) shows a polar plot of the over-all sound-pressure level for the three-segment nozzle (fig. 3 (b)) and the standard nozzle. It is evident from the figure that this suppressor had little effect on either directionality or sound-pressure level. Consequently, the total power radiated was reduced only slightly from that of the standard nozzle; that is, less than 1.0 decibel.

The spectrum levels (fig. 5 (b)) at the 90° and 150° azimuths are quite similar to those of the standard nozzle, and only the spectrum level at the 30° azimuth shows any significant changes. Here there is a decrease in energy between frequencies of 150 and 750 cycles per second with increased values on either side of the frequency range. As might be expected, the frequency distribution of the sound was only slightly different from that of the standard nozzle (fig. 5 (c)).

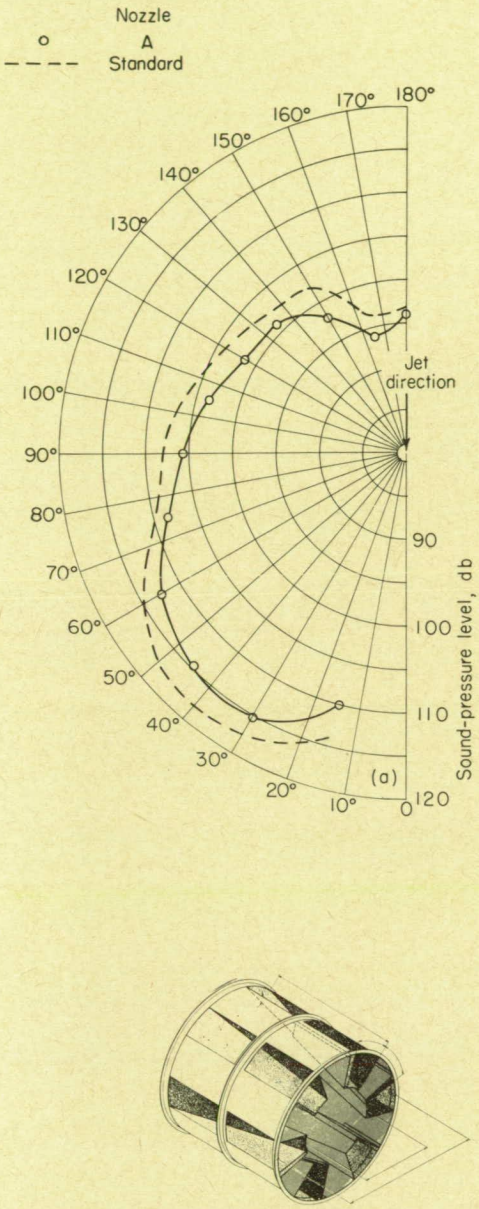
NOZZLE C, TWELVE-SEGMENT NOZZLE WITH CENTERBODY

Nozzle C was the only one investigated on the high-thrust engine; and, as pointed out previously, the results should only be compared with other suppressor nozzles on the basis of normalized parameters. This nozzle utilizes the idea of deep corrugations but has 12 separate segments through which the gas issues (fig. 3 (c)).

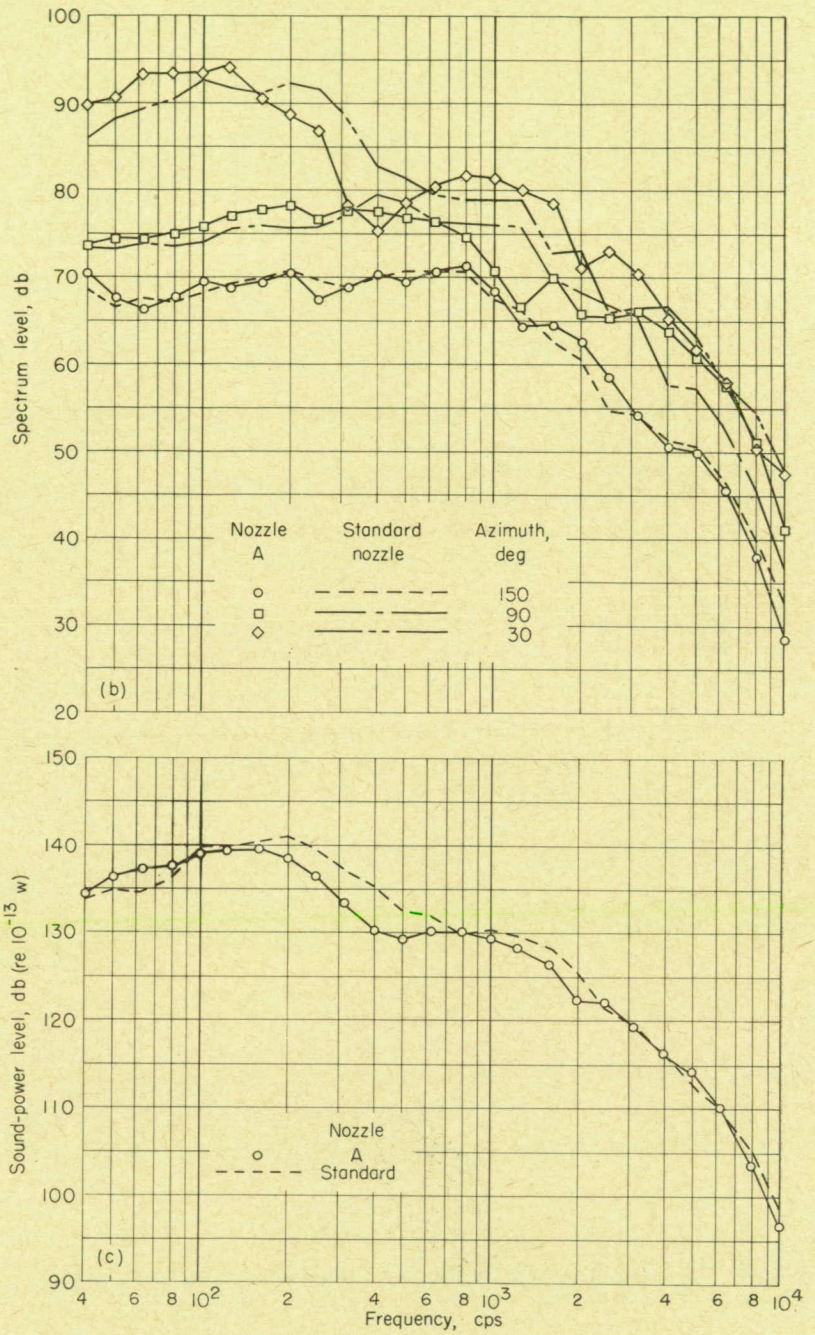
The sound polar plot of the over-all sound-pressure level for suppressor nozzle C and a standard nozzle is shown in figure 6 (a). These data show a marked reduction in sound-pressure level both rearward and to the sides of the engine. In fact, the peak sound-pressure level (at the 30° azimuth) has been reduced by 11 decibels. The over-all effect has resulted in a sound-power reduction of 8.5 decibels. Most of this reduction in sound power occurred in the frequency range from 40 to 1,000 cycles per second, as shown in figure 6 (c). In fact, the reduction at a frequency of 200 cycles per second is about 15 decibels. Furthermore, the spectrum levels at various azimuth angles (fig. 6 (b)) show rather interesting characteristics. At a 30° azimuth, the spectrum level is decreased in the frequency range between 40 and 100 cycles per second; at a 90° azimuth, the spectrum level is decreased in the frequency range between 40 and 300 cycles per second; and at a 150° azimuth, the spectrum level is reduced in the frequency range between 40 and 2,000 cycles per second.

NOZZLE D, NINE-SECTION RECTANGULAR (3 IN. WIDE BY 12 IN. HIGH) SLOTTED NOZZLE

The effectiveness of nozzle D (nine-section rectangular slotted nozzle) as a noise suppressor is shown by the polar diagram of over-all sound-pressure level (fig. 7 (a)). Data are presented for the nozzle mounted both horizontally (fig. 3 (d)) and vertically. It is evident that measurements made in a horizontal plane show a different pattern, depending on nozzle orientation; hence, the usual assumption of spatial symmetry does not hold. This effect was expected, however, since the results of reference 2 for single nozzles with elongated cross sections (ellipses) show this tendency. It was expected that this effect might be amplified by the use of multiple slots. The effect of nozzle orientation (fig. 7 (a)) shows that the over-all sound-pressure levels increased somewhat from the 45° to the 90° azimuth and decreased from the 15° to the 30° azimuth when the nozzle was mounted vertically.

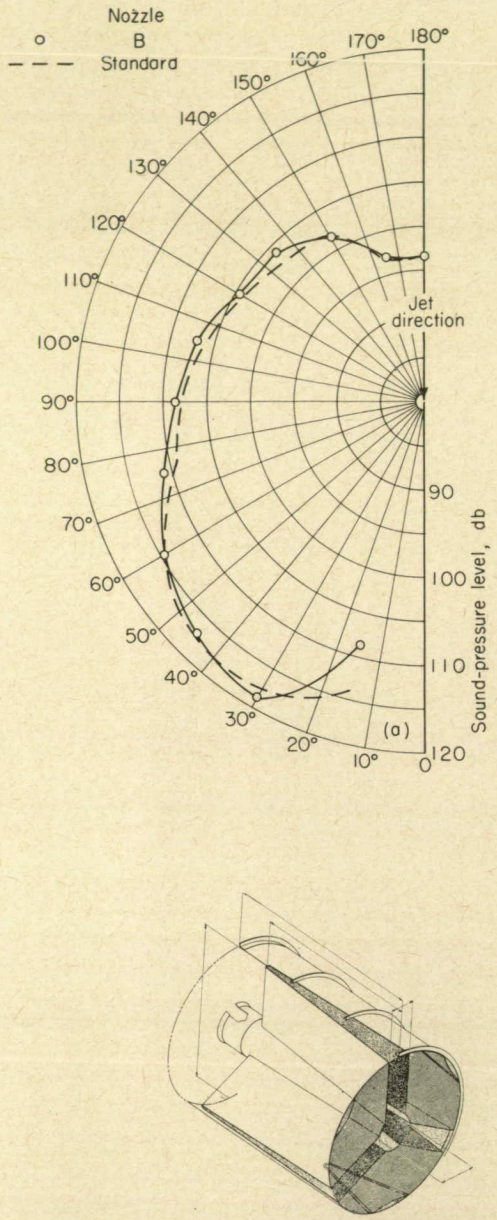


(a) Directionality pattern.

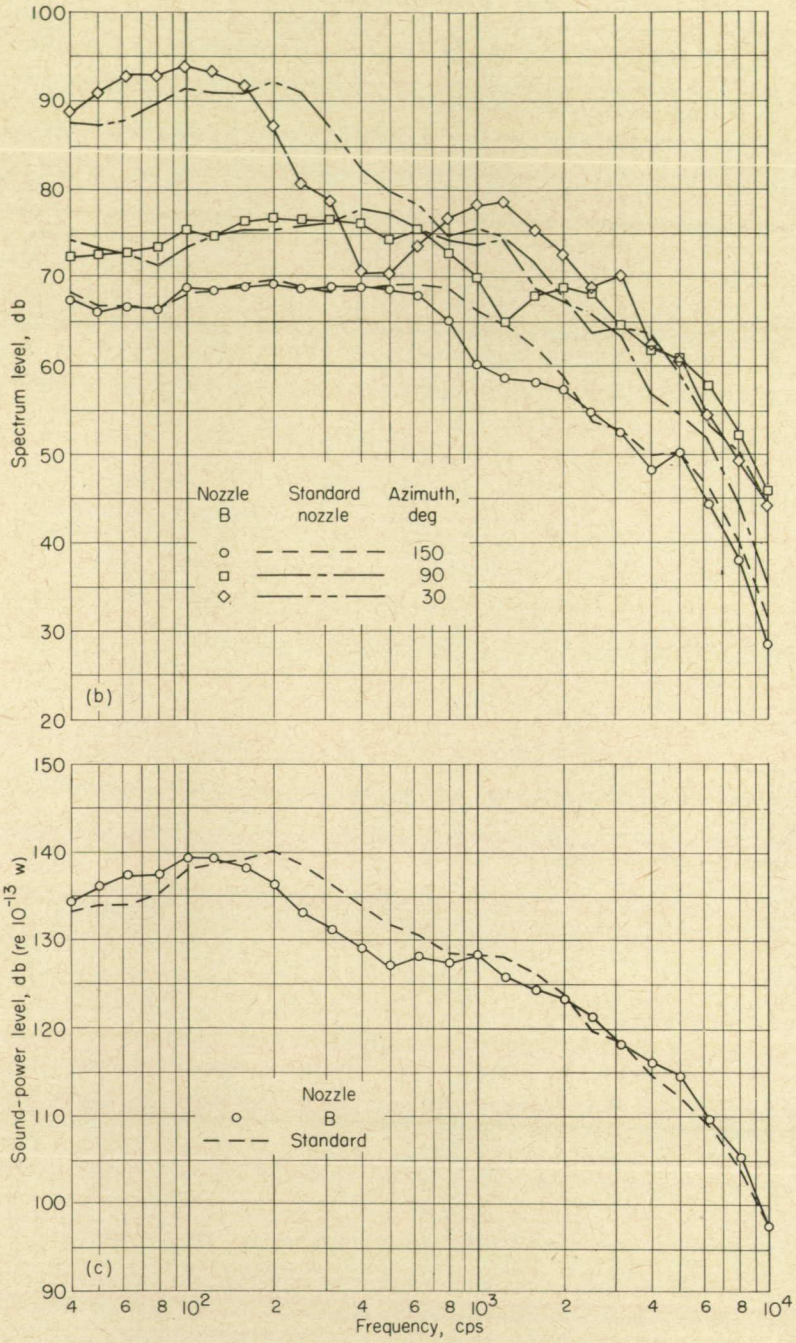


(b) Spectrum levels at three azimuths.
(c) Frequency distribution of sound power.

FIGURE 4.—Sound-field characteristics of nozzle A.

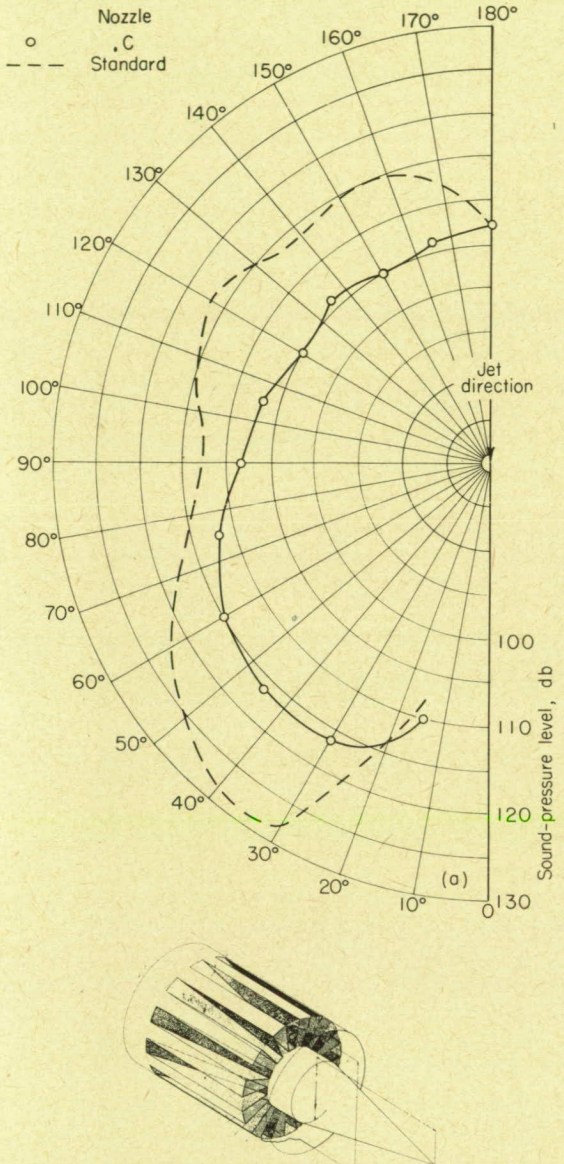


(a) Directionality pattern.

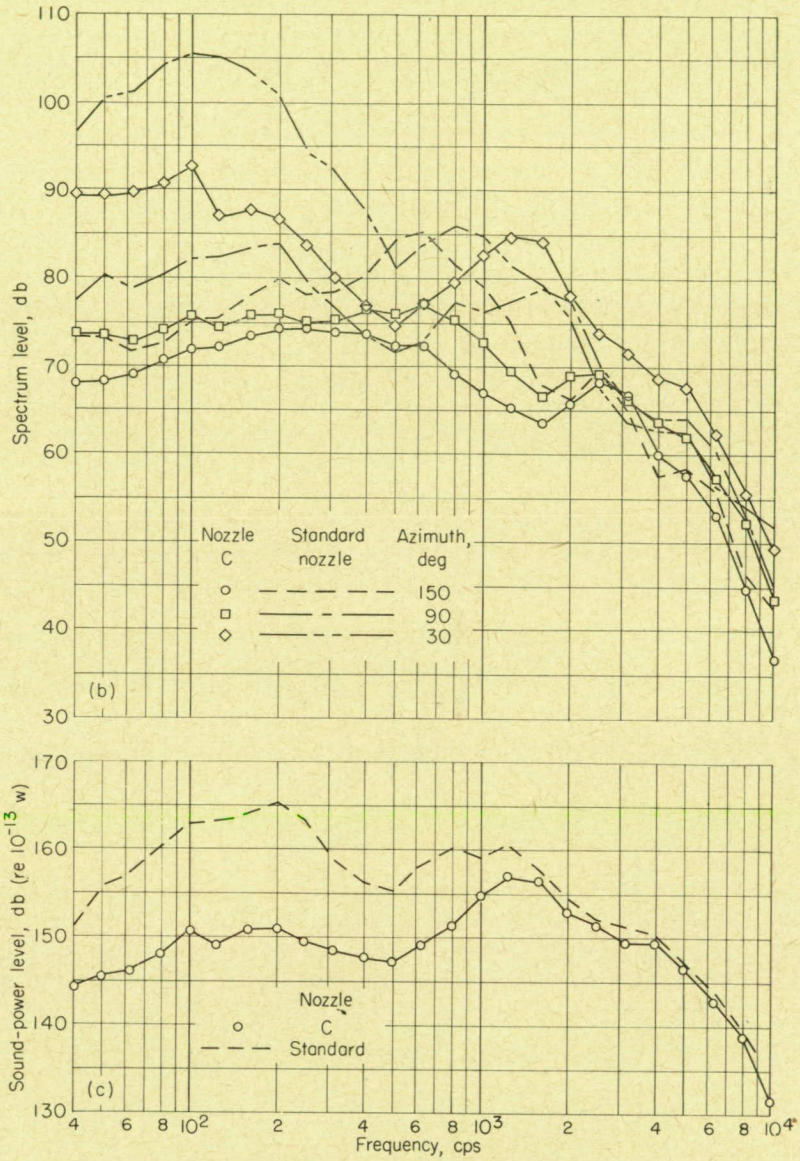


(b) Spectrum levels at three azimuths.
(c) Frequency distribution of sound power.

FIGURE 5.—Sound-field characteristics of nozzle B.

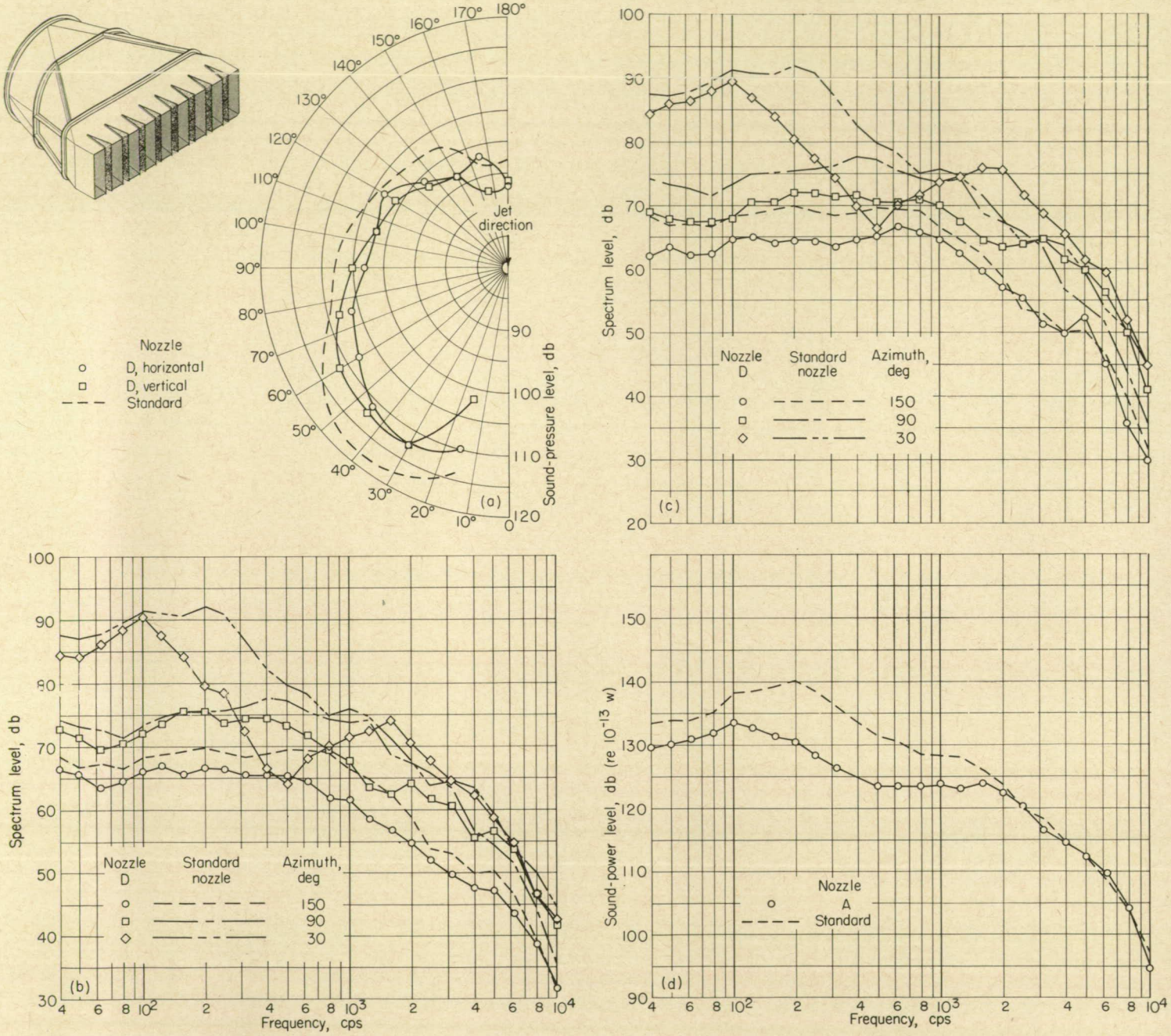


(a) Directionality pattern.



(b) Spectrum level at three azimuths.
(c) Frequency distribution of sound power.

FIGURE 6.—Sound-field characteristics of nozzle C.



(a) Directionality pattern.
(b) Spectrum level at three azimuths, nozzle horizontal.
(c) Spectrum level at three azimuths, nozzle vertical.
(d) Frequency distribution of sound power.

FIGURE 7.—Sound-field characteristics of nozzle D.

The distribution of sound pressure with frequency does not appear to differ greatly with nozzle orientation, as shown by the spectrum levels (figs. 7 (b) and (c)). Aside from slight shifts in sound-pressure levels, which reflect the results shown in figure 7 (a), there are small differences in the shapes, which indicate an energy shift toward higher frequencies for the nozzle mounted vertically. In essence, this means that, for a nozzle mounted horizontally, the sound pressures in the vertical plane (vertical to ground and containing the jet axis) are somewhat greater and have more high-frequency energy than those in the horizontal plane (parallel to ground and containing the jet axis).

The fact that the sound field is not rotationally symmetrical about the jet axis means that the sound-power radiation (over-all or in frequency bands) should be calculated using average values. From the results shown in figure 7 (a), it is evident that a simple arithmetic average of the intensities is sufficient to give good accuracy for either total sound power or power levels in frequency bands.

The distribution of sound power with frequency is shown in figure 7 (d). It is evident that considerable decreases have been obtained at frequencies from 100 to 2,000 cycles per second when compared with the performance of a standard nozzle. The total power radiated is 161.4 decibels as compared with 166.1 decibels for a standard nozzle.

NOZZLE F, NINE-SECTION RECTANGULAR (2 IN. WIDE BY 18 IN. HIGH) SLOTTED NOZZLE

Figure 8 (a) shows the sound polar diagram for nozzle E (nine-section rectangular nozzle) mounted in both the horizontal (fig. 3 (e)) and vertical positions. It is evident that the use of long narrow slots (2 by 18 in.) has resulted in considerable sound emanation at approximately right angles to the jet (90° azimuth), as evidenced by the data for the vertical position. It would appear that, in general, nozzle E produces greater sound pressures than nozzle D and hence is a less effective noise suppressor. The total sound power radiated by nozzle E is 163.9 decibels, which is 2.5 decibels more than for nozzle D but somewhat less than for the standard nozzle (166.1 db).

The distribution of sound power with frequency for nozzle E is compared with that for a standard nozzle in figure 8 (d). It is evident that some low-frequency energy (100 to 1,500 cps) has been shifted to higher frequencies, leaving the total power radiated approximately the same in both cases. It is evident from the spectrum-level curves of figures 8 (b) (nozzle horizontal) and 8 (c) (nozzle vertical) that the shift in total power spectrum results chiefly from the shift in energy in the region of maximum sound radiation (30° azimuth) and from the increased energy at higher frequencies for the 90° azimuth.

NOZZLE F, SEVEN-SECTION RECTANGULAR (2⅜ IN. WIDE BY 18 IN. HIGH) SLOTTED NOZZLE

Nozzle F (seven-section rectangular slotted nozzle, fig. 3 (f)) is a modification of nozzle E discussed in the preceding section. The original nozzle (nozzle E) was cut back and the two outer slots blocked off by an internal fairing. Both nozzle F and the original nozzle show somewhat the same characteristics. The polar diagram of over-all sound-pressure levels (fig. 9 (a)) shows considerable radiation at nearly right angle to the jet axis, as does that for the original nozzle. There is one very important difference, however. Nozzle F shows practically no effect of nozzle orientation on over-all sound-pressure level, whereas the original nozzle shows appreciable effects. It is evident from a comparison of figures 8 (a) and 9 (a) that nozzle F is not appreciably different from the original nozzle, E. The sound power radiated is 163.5 decibels for the modified nozzle and 163.9 decibels for the original nozzle, compared with 166.1 decibels for the standard nozzle.

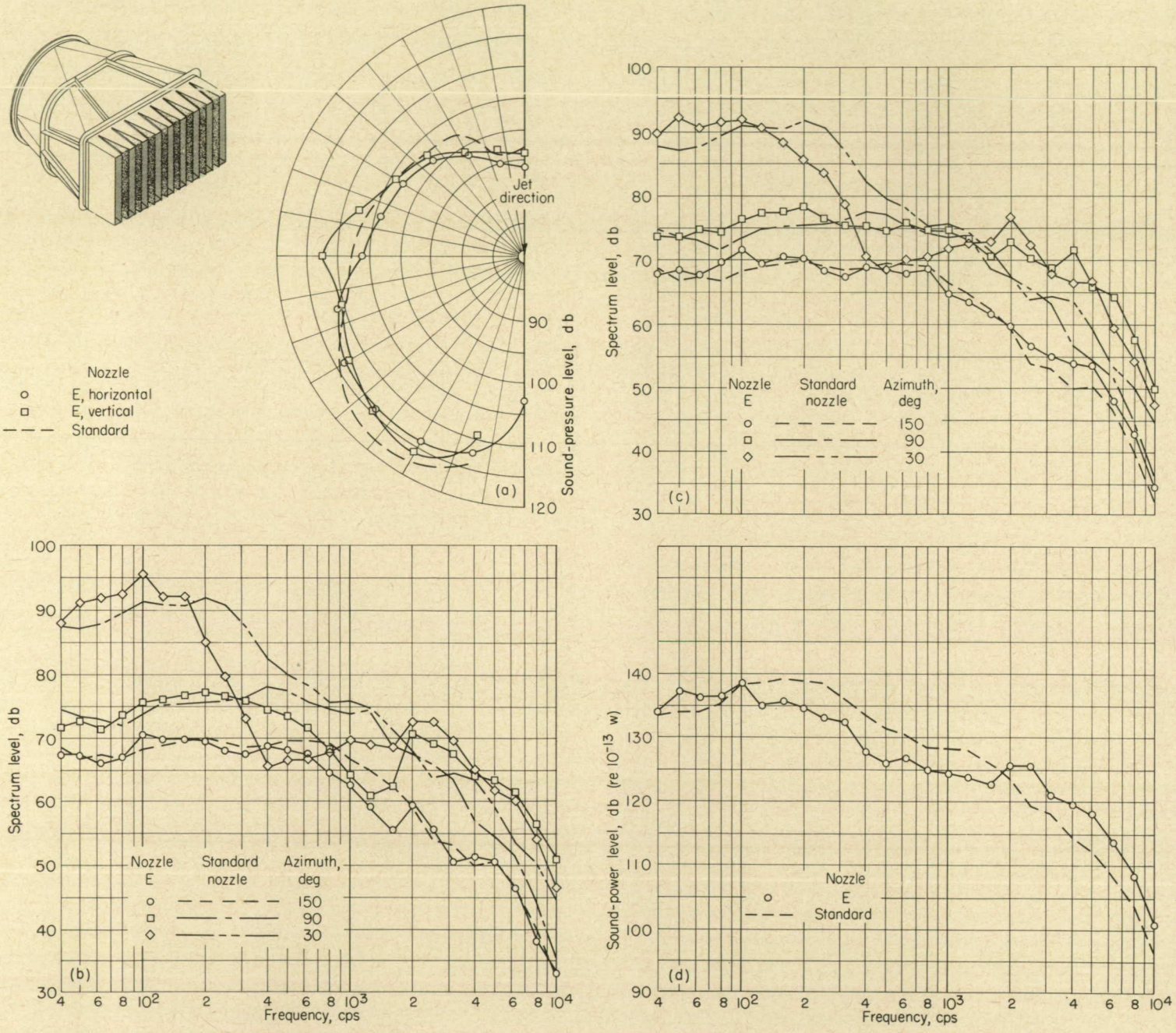
The distribution of sound power for this nozzle (fig. 9 (d)) shows only small differences from the original nozzle. Furthermore, the spectra at the three azimuth positions (figs. 9 (b) and (c)) are quite similar to those obtained with nozzle E. At the 30° azimuth, the spectrum dip is greater for nozzle E than for nozzle F (both mounted horizontally). With vertical nozzle orientation, the reverse is true. A comparison of the spectra vertically and horizontally for nozzle F shows that, while there is spatial symmetry of the over-all sound pressure (fig. 9 (a)), there is not symmetry for the individual frequency bands.

In fact, at frequencies near 1,000 cycles per second (for the 30° azimuth), data for the nozzle mounted vertically (fig. 9 (c)) show reductions in spectrum level (from that of the standard nozzle) of as much as 25 decibels. For the nozzle mounted horizontally (fig. 9 (b)), data for the same azimuth and frequency show negligible reduction. The net effect on sound power is therefore quite small (fig. 9 (d)).

NOZZLE G, SIX-SECTION RECTANGULAR (6 IN. WIDE BY 9 IN. HIGH) SLOTTED NOZZLE

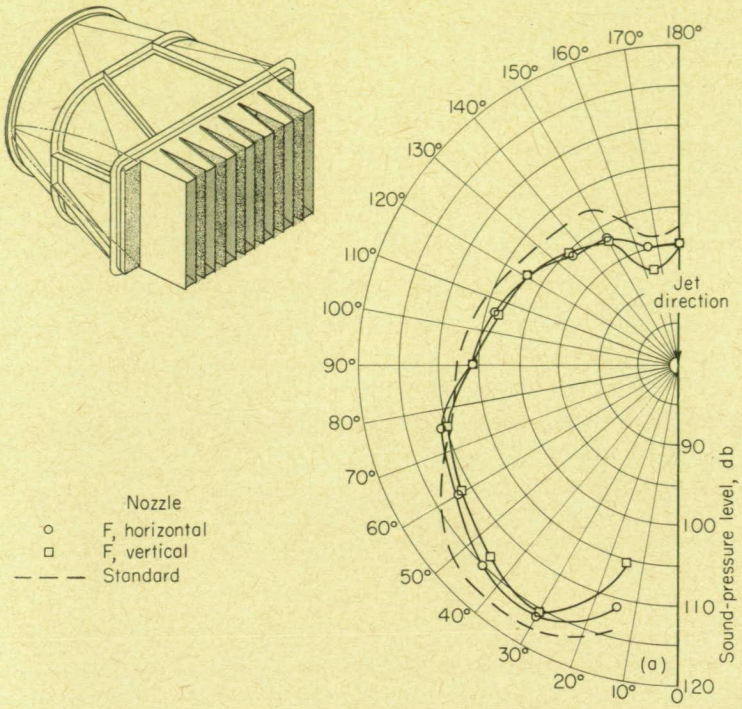
The sound polar diagrams for nozzle G (mounted horizontally, fig. 3 (g)) and the standard nozzle are shown in figure 10 (a). There is a reduction in sound pressure for nozzle G (six-section rectangular slotted nozzle) in all directions. A check of this nozzle mounted vertically showed no appreciable changes in the sound-pressure level. The distribution of the sound power (assuming spatial symmetry) is shown in figure 10 (c). Comparison of the distribution with that of the standard nozzle shows that the reduction of total power from 166.1 to 162.6 decibels results from a reduction in sound power at the frequencies below 600 cycles per second.

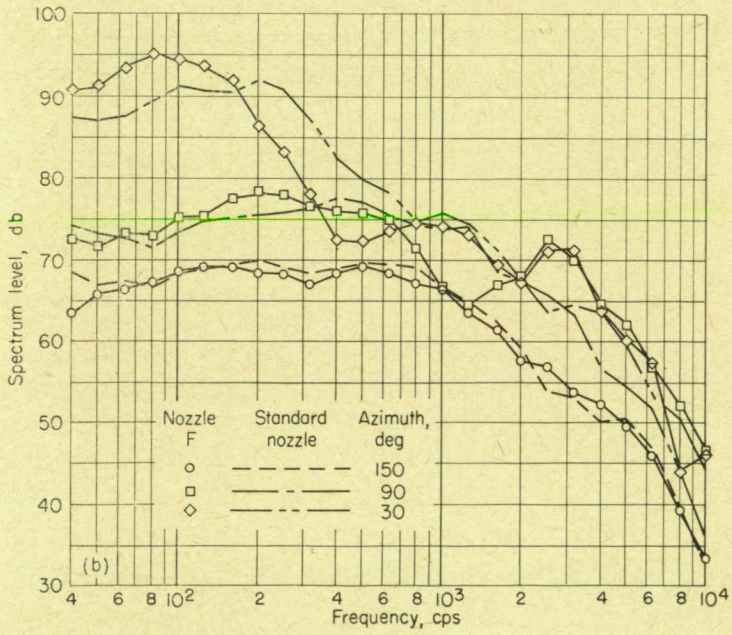
The spectrum-level curves (fig. 10 (b)) show rather interesting characteristics when compared with those of a standard nozzle. At the 30° azimuth, there is considerable decrease in energy below frequencies of 500 cycles per second and considerable increase above frequencies of 700 cycles per second. At the 90° azimuth, the data show little effect at low frequencies but a dip in energy at frequencies between 700 and 3,200 cycles per second. The results at the 150° azimuth are quite similar for both this nozzle and the standard nozzle. It is interesting that the shift in energy upward in frequency on the 30° azimuth is mostly offset by the decrease in energy above a frequency of 700 cycles per second radiated at the 90° azimuth. The resultant effect (fig. 10 (c)) shows little change in the total energy above a frequency of 700 cycles per second when compared with the standard nozzle.



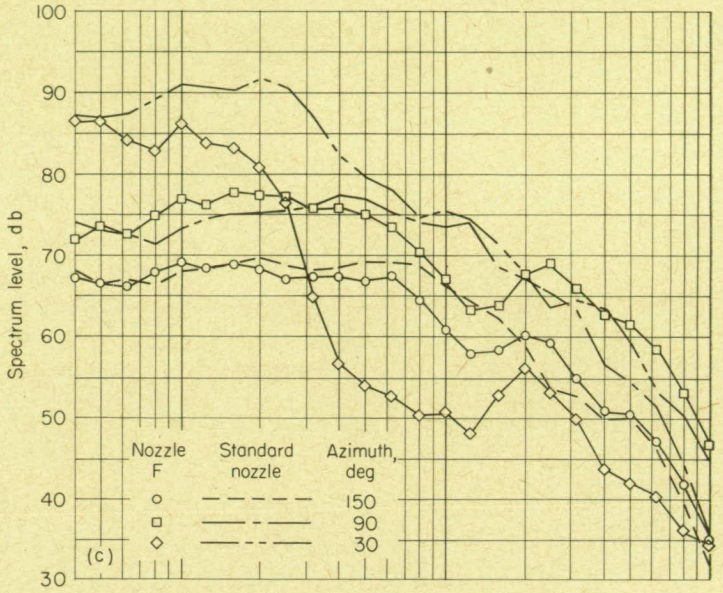
(a) Directionality pattern.
(b) Spectrum level at three azimuths, nozzle horizontal.
(c) Spectrum level at three azimuths, nozzle vertical.
(d) Frequency distribution of sound power.

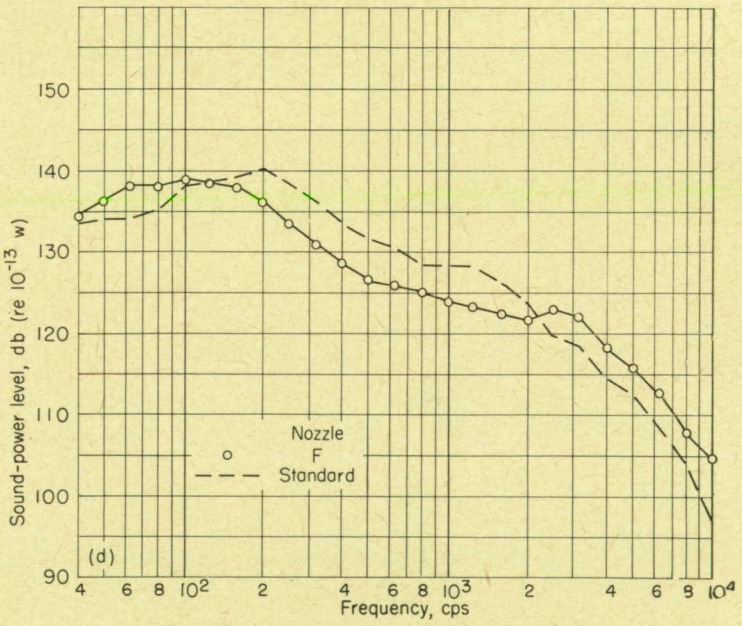
FIGURE 8.—Sound-field characteristics of nozzle E.





(a) Directionality pattern.
(b) Spectrum level at three azimuths, nozzle horizontal.

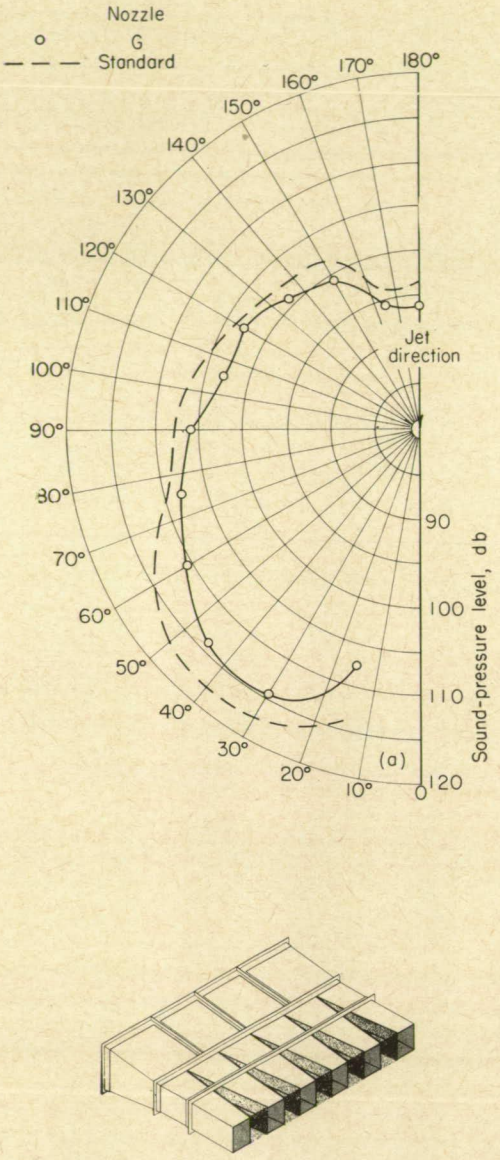




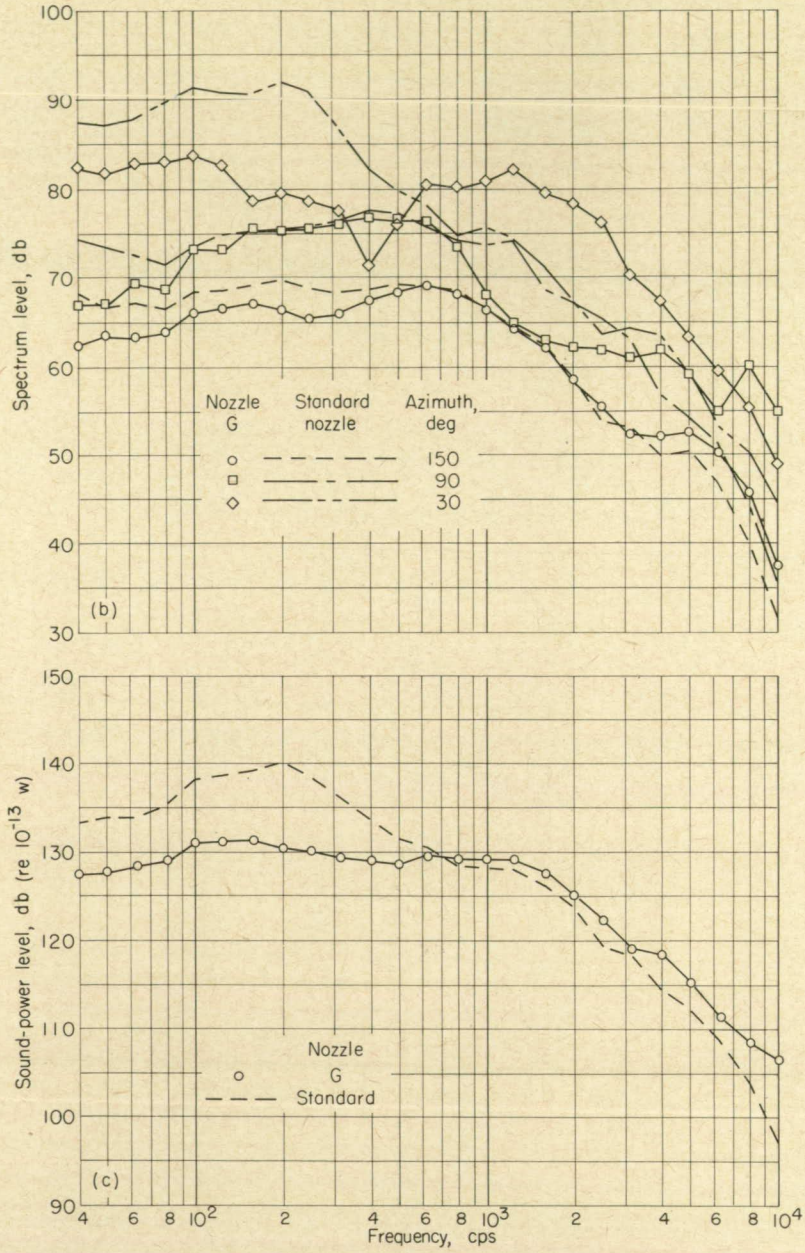
(c) Spectrum level at three azimuths, nozzle vertical.
(d) Frequency distribution of sound power.

FIGURE 9.—Sound-field characteristics of nozzle F.

526597—60——82



(a) Directionality pattern.



(b) Spectrum level at three azimuths.
(c) Frequency distribution of sound power.

FIGURE 10.—Sound-field characteristics of nozzle G.

NOZZLE H, SIX-SECTION RECTANGULAR (9 IN. WIDE BY 6 IN. HIGH) SLOTTED NOZZLE

The characteristics of nozzle H (six-section rectangular slotted nozzle, fig. 3 (h)) are very similar to the characteristics of nozzle G. The total power radiated was somewhat less, 161.3 decibels compared with 162.6 decibels, and the over-all sound pressures were slightly reduced (fig. 11 (a)); but, in general, the discussion given in the preceding section applies equally well for both nozzles.

NOZZLE I, SIX-SECTION RECTANGULAR (9 IN. WIDE BY 6 IN. HIGH) OFFSET SLOTTED NOZZLE

Nozzle I (six-section rectangular offset slotted nozzle) is a modification of nozzle H. The outer slots were cut back 6 inches, and the next inner pair 3 inches (fig. 3 (i)). Internal trimmers were used to obtain the same slot width. As might be expected, the polar diagram of sound-pressure level (fig. 12 (a)), the sound power (161.4 db), and the distribution of sound power frequency (fig. 12 (c)) are nearly the same for both the modified nozzle I and the original nozzle H.

The spectrum-level curves (fig. 12 (b)) show some variation from those of nozzle H, but the general trends remain the same. There is a slight shift and increase in the dip of the frequency-distribution curves at a frequency of about 400 cycles per second for the 30° azimuth data. At a 90° azimuth, there is a peak in energy at a frequency of 2,500 cycles per second instead of the dip obtained with the original nozzle. The total effects of these changes, are not large, and it would appear that the slightly noncoplanar slotted nozzle is not significantly different acoustically from the coplanar nozzle.

NOZZLE J, EIGHTEEN-SECTION RECTANGULAR (2.7 IN. WIDE BY 6 IN. HIGH) SLOTTED NOZZLE

Sound polar diagrams for nozzle J (eighteen-section slotted nozzle) mounted both horizontally (fig. 3 (j)) and vertically are shown in figure 13 (a). It is evident that considerably higher sound-pressure levels were obtained with the nozzle mounted in the vertical position; that is, the sound field is not rotationally symmetrical. Spectrum-level curves (figs. 13 (b) and (c)) for the nozzle mounted in both the horizontal and vertical positions show a considerable decrease in the low-frequency energy with some increase of high-frequency energy. This is clearly evident at the 30° azimuth for both nozzle orientations. The trend to less low-frequency noise is evident at both the 90° and 150° azimuths. The over-all effect, shown in figure 13 (d), indicates a 10-decibel decrease in sound pressure at a frequency of 200 cycles per second with a slight increase in the energy above a frequency of 2,000 cycles per second. The total power radiated by nozzle J was 5.0 decibels less than that of the standard nozzle.

NOZZLE K, TWELVE-SECTION RECTANGULAR (4 IN. WIDE BY 6 IN. HIGH) SLOTTED NOZZLE

Nozzle K (twelve-section rectangular slotted nozzle, fig. 3 (k)) is a modification of nozzle J. The sound-pressure field obtained with this nozzle mounted horizontally is shown by the polar diagram of figure 14 (a). The spectrum-level curves at three positions are shown in figure 14 (b). A comparison of these results with the results for the previous nozzle does not show any significant changes, and in fact the twelve-section nozzle appears to be a less effective suppressor. This results largely from the spectrum changes at the 30° azimuth in the frequency range between 300 and 1,000 cycles per second (fig. 14 (b)). Because this nozzle was not particularly different and not as good a suppressor as the eighteen-section slotted nozzle, it was not tested in the vertical position. Hence, no power levels are available, since the sound field cannot be assumed rotationally symmetrical for such a configuration.

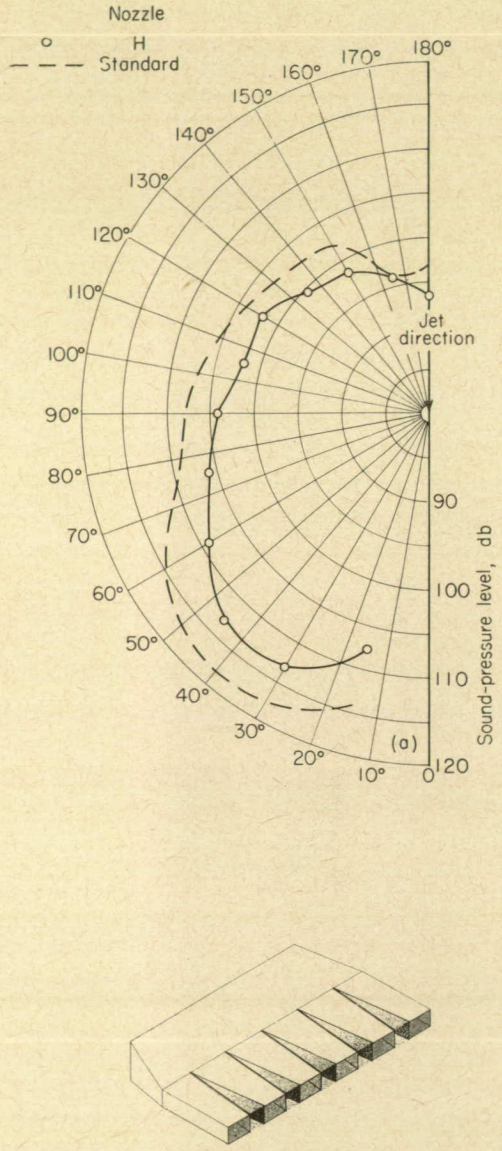
COMPARISON OF SOUND-POWER RADIATION BY MEANS OF LIGHTHILL'S PARAMETER

In order to provide a valid comparison of the sound power radiated with the various nozzles with regard to both acoustics and engine operation, the data must be normalized so that effects of daily temperature and pressure variations are insignificant. For the engine this is accomplished by properly trimming the exhaust-nozzle area so that the engine always operates with the proper relation between corrected exhaust-gas temperature T/θ and corrected engine speed $N/\sqrt{\theta}$. It is well established (refs. 2 and 10) that the sound power radiated from a jet issuing from a circular convergent nozzle can be correlated with the Lighthill parameter $\rho_0 A V^8/a_0^5$. Reference 2 shows that both small air-jet and full-scale engines are well correlated by a single relation if the velocity V used for the engine is defined as the ratio of engine thrust to mass flow. The linear relation of sound power and Lighthill's parameter, both in watts, was found to apply even though the nozzle pressure ratio slightly exceeded the choking value (ref. 2). Thrust losses show up as a decrease in velocity and a consequent decrease in Lighthill's parameter. This is an extremely important point, since any device that reduces thrust and hence Lighthill's parameter must show greater noise reductions than those that could be obtained by throttling back the engine (with a standard nozzle) to an equal thrust value.

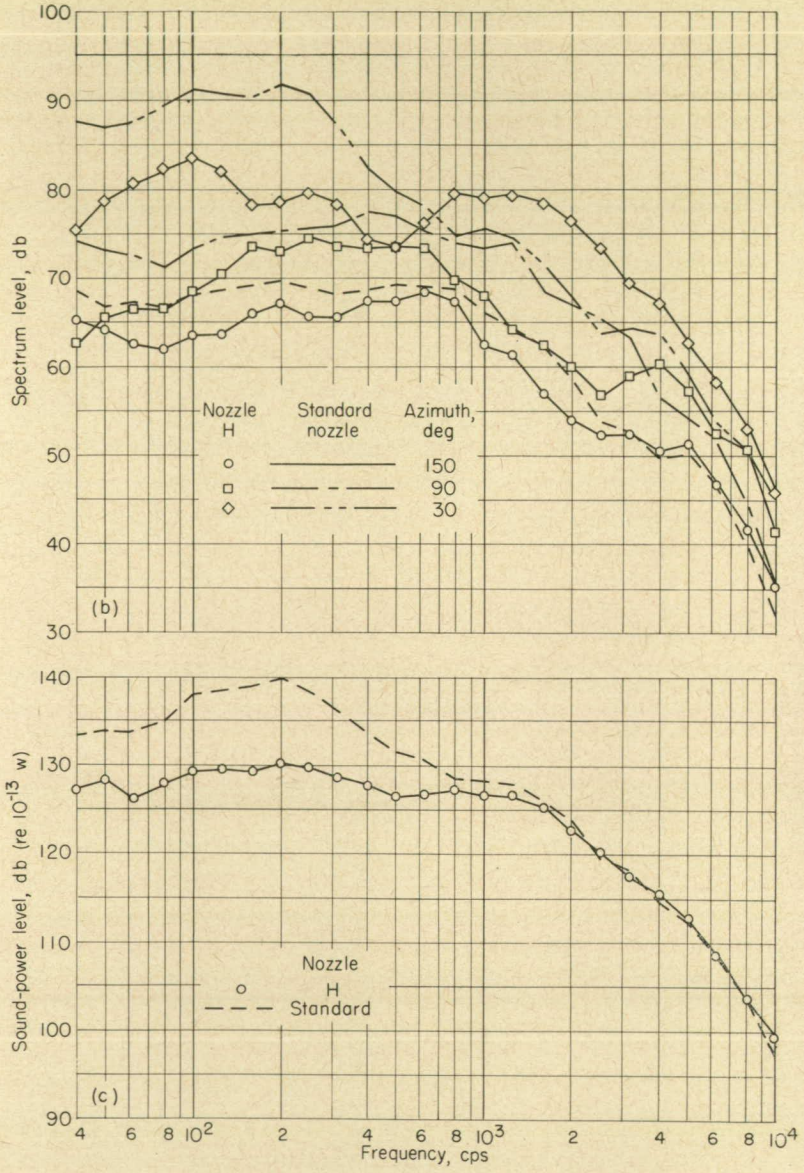
Figure 15 shows the sound-power ratio (ratio of suppressor-nozzle sound power to standard-nozzle sound power) for all the nozzles plotted against Lighthill's parameter. Nozzles C, D, G, H, I, and J all give substantial reductions and, in fact, reduce the sound power by 50 to 75 percent (3 to 6 db) at rated engine power.

THRUST LOSS OF SUPPRESSOR NOZZLES

As mentioned previously, conditions at the jet exit of an engine are dependent on the ambient conditions. It is well established (ref. 11) that engine thrust can be normalized by plotting corrected thrust F/δ against corrected engine speed $N/\sqrt{\theta}$. Figure 16 shows the corrected-thrust ratio (ratio of suppressor-nozzle corrected thrust to standard-

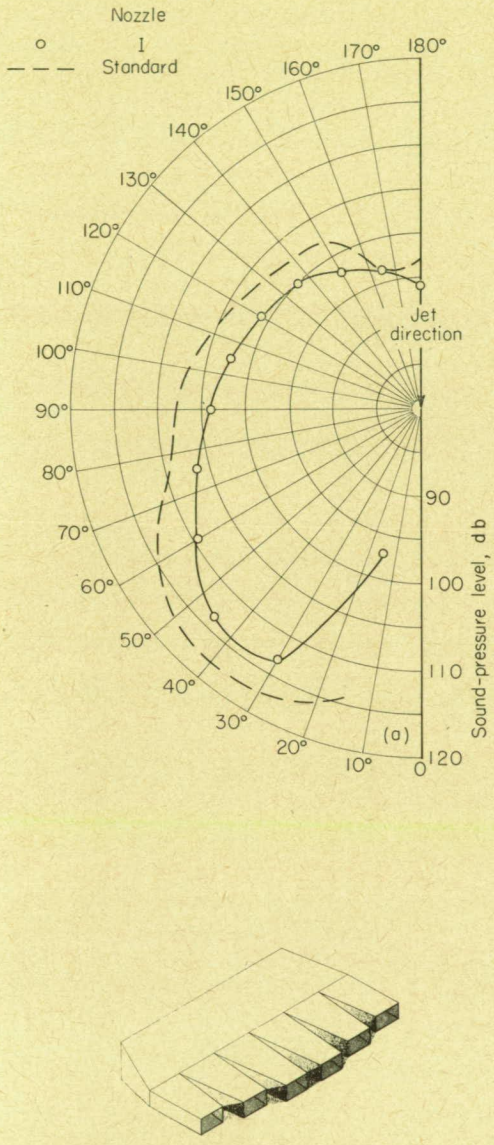


(a) Directionality pattern.

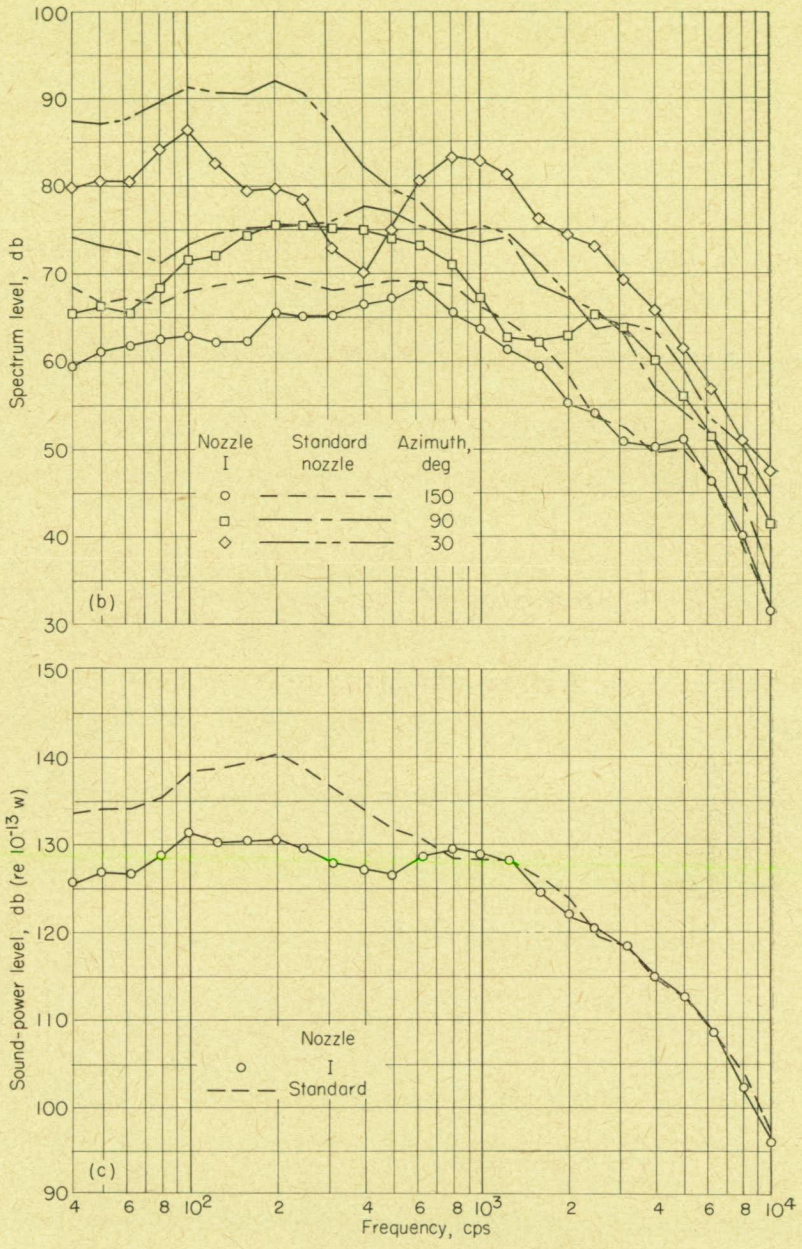


(b) Spectrum level at three azimuths.
(c) Frequency distribution of sound power.

FIGURE 11.—Sound-field characteristics of nozzle H.

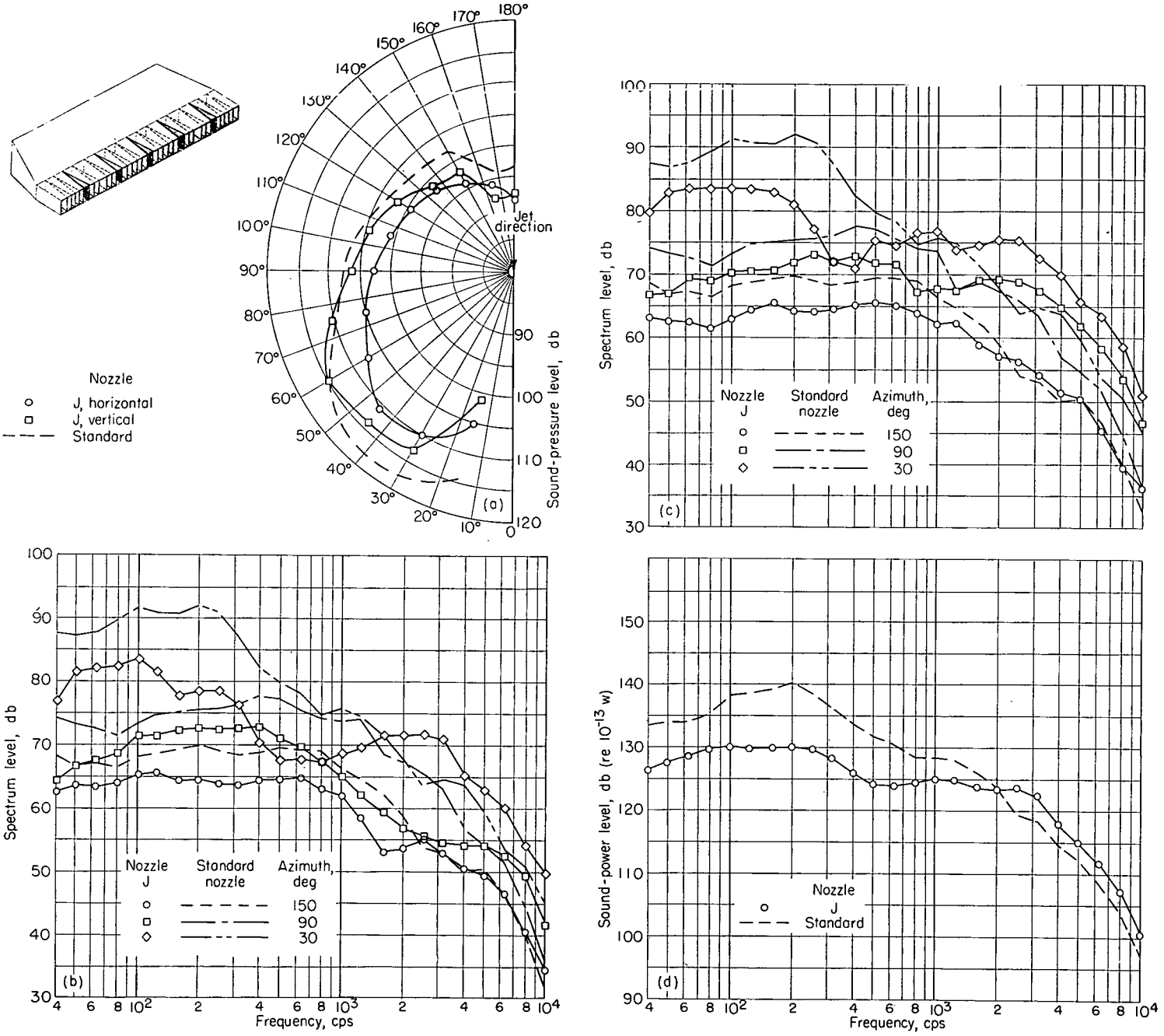


(a) Directionality pattern.



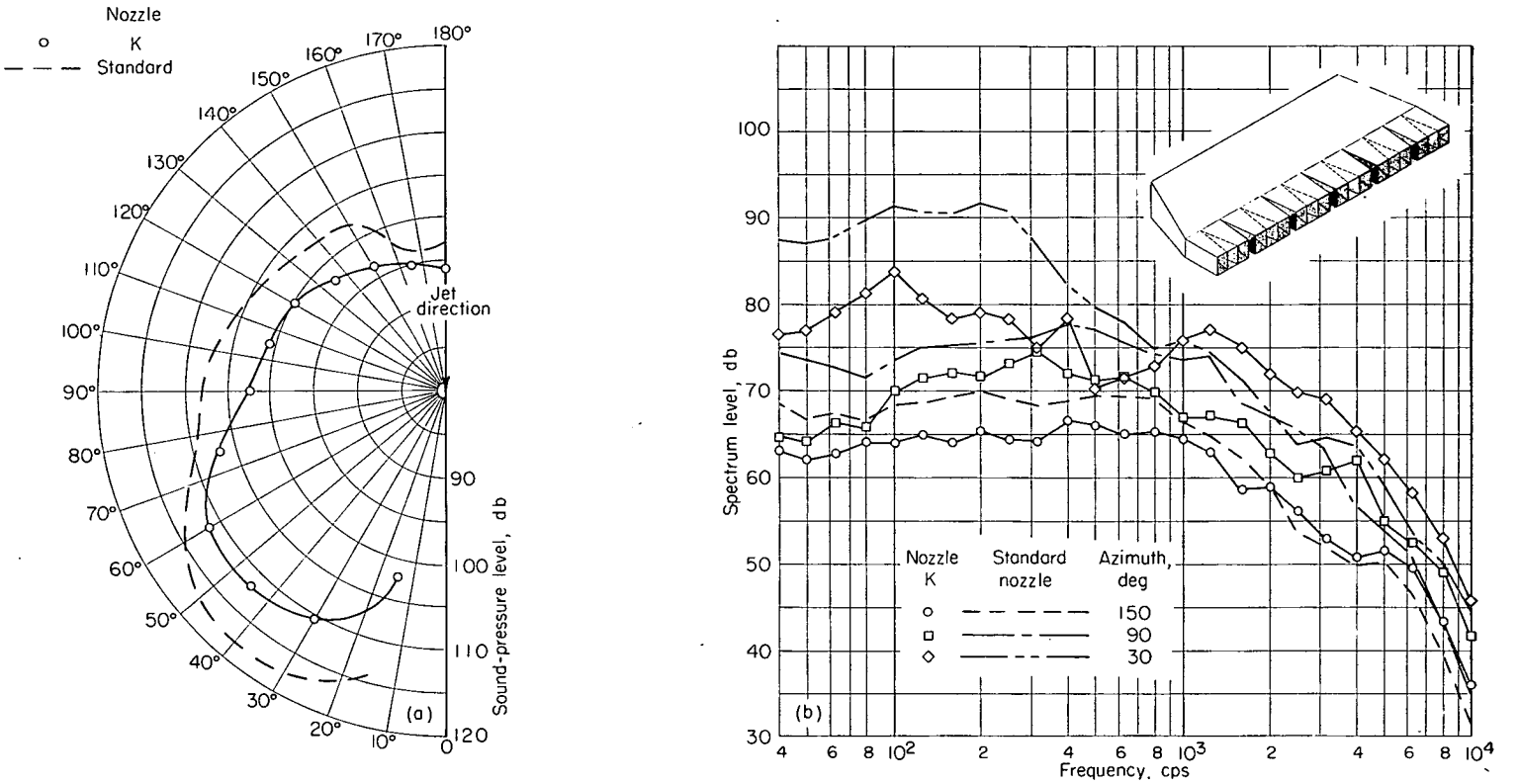
(b) Spectrum level at three azimuths.
(c) Frequency distribution of sound power.

FIGURE 12.—Sound-field characteristics of nozzle I.



(a) Directionality pattern.
(b) Spectrum level at three azimuths, nozzle horizontal.
(c) Spectrum level at three azimuths, nozzle vertical.
(d) Frequency distribution of sound power.

FIGURE 13.—Sound-field characteristics of nozzle J.



(a) Directionality pattern.

(b) Spectrum level at three azimuths.

FIGURE 14.—Sound-field characteristics of nozzle K (nozzle horizontal).

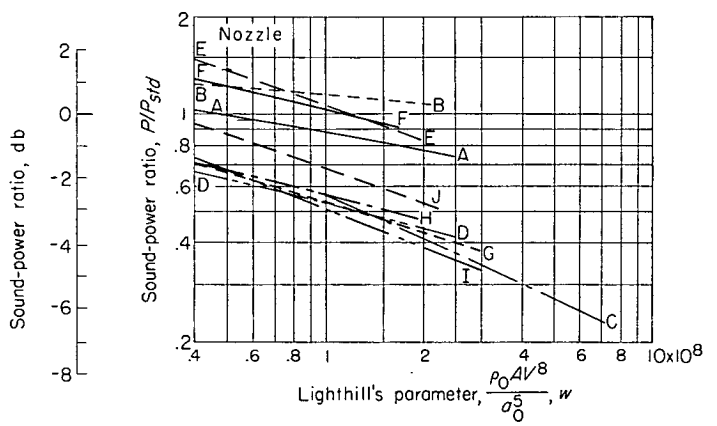


FIGURE 15.—Sound-power ratio as function of Lighthill's parameter.

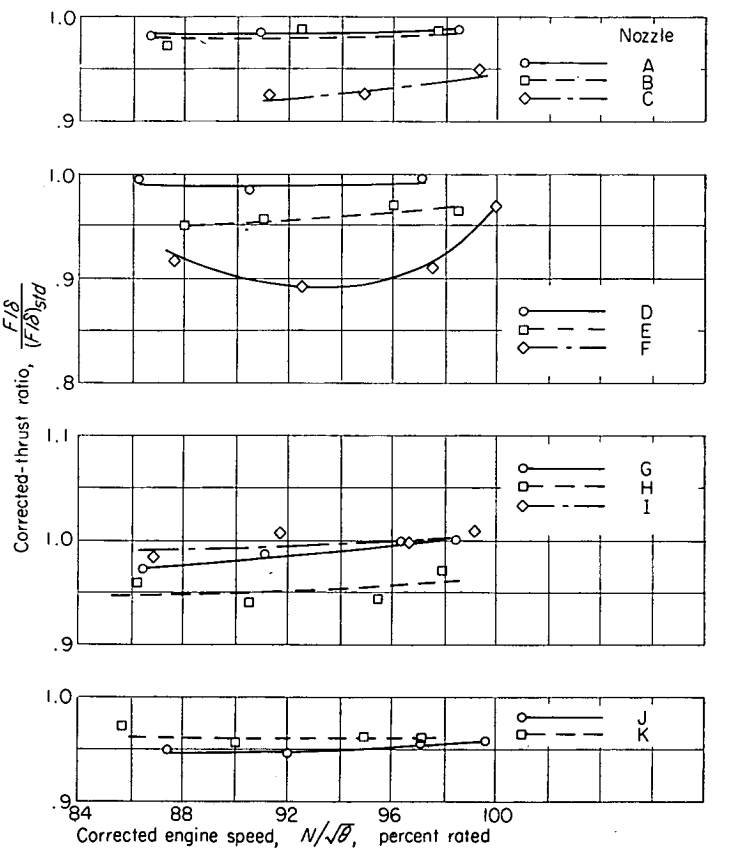


FIGURE 16.—Thrust ratio as function of corrected engine speed.

nozzle corrected thrust) plotted as a function of corrected engine speed. It is evident there is a notable range of thrust losses. The extremely large thrust loss of nozzle F (seven-segment, 2⅜ by 18 in., rectangular nozzle) was probably caused by low pressures acting on the surfaces between the segments. Such low pressures result from the relatively high induced velocities of the mixing air in traversing the long narrow slots between adjacent jets.

The large thrust losses of nozzle C with the large centerbody also probably result from low pressures. In this case, the hot gases separate from the cone and low pressures result. As might be expected, the thrust loss decreases at rated speed since the nozzle pressure ratio is high (2.3) and hence the flow will expand and flow farther along the cone. It is quite possible that some of this loss might be decreased by using better aerodynamic design.

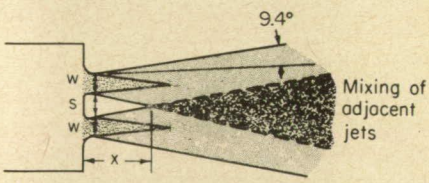
It is interesting to note that nozzles G, I, and D were among the best devices tested for noise reduction, and all have quite small thrust losses. Several of the data points for nozzle I are slightly greater than unity. This results from decreased pressure losses associated with the larger-than-standard exhaust cone used with this nozzle.

DISCUSSION OF RESULTS

SPECTRUM OF NOISE

In all cases where significant noise reduction was achieved (nozzles C, D, G, H, I, and J), the effect occurred at low frequencies. At high frequencies, the noise was either unaltered or slightly increased. For example (fig. 7 (d)), nozzle D shows reduction only at frequencies less than 2,400 cycles per second, while at the higher frequencies the sound-power level was virtually unchanged. The reasons for this can be explained in the following manner.

When two adjacent jets, as shown in the following sketch,



emerge from the nozzle, they mix with the surrounding air and spread. At some point downstream, the mixing zones intersect. The noise generated by each of the jets between the nozzle exit and the point of intersection should remain virtually unchanged, whereas the noise generated downstream of this point would be altered. This does not necessarily mean that the high-frequency noise (generated near the jet exit) measured in the far field would be unaltered. It would be expected that the mixing of the two jets would result in decreased eddy sizes and a consequent decrease in the low-frequency noise generated downstream with an increase in the high-frequency generation. If the turbulent intensity in the mixing region of the adjacent jets is reduced (ref. 12), then an increase in high-frequency radiation may not be too significant in terms of total sound power. This decrease in both eddy size and turbulent intensity would fulfill the requirements for noise reduction stated in reference 8.

TABLE II.—FREQUENCY f_x AT DISTANCE x DOWNSTREAM WHERE ADJACENT JETS IMPINGE

Nozzle	f_x, cps	
	Calculated	Measured
B	1,223	1,000 (fig. 5 (c))
C	1,365	1,600 (fig. 6 (c))
D	2,600	2,400 (fig. 7 (d))
E	1,815	1,800 (fig. 8 (d))
F	3,170	2,200 (fig. 9 (d))
G	914	720 (fig. 10 (c))
H	850	800 (fig. 11 (c))
J	2,270	2,100 (fig. 13 (d))

If the adjacent jets are considered to expand uniformly at a half-angle of 9.4° (ref. 13), then it is possible to calculate the distance downstream x at which the two jets impinge. It would be expected that, in general, the frequencies most affected would be those generated principally downstream of point x.

In reference 13 a curve is given of the apparent positions of the acoustic sources in a jet as a function of the axial downstream distance, the high frequencies being generated near the jet exit and the lower frequencies downstream. These data are presented in terms of the dimensionless parameter, Strouhal number fD/V, against downstream distance in exit diameters (fig. 16 of ref. 13). Unpublished NACA data show that the relation given holds over a wide range of nozzle diameters and jet velocities. If it is assumed that rectangular slots generate sound in the same manner and that the important dimension is the jet width, then it is possible to calculate the highest frequency affected by mixing interference f_x. This has been done, and the results are given in table II. These calculations were made for the conditions at a nominal engine speed of 97.5 percent of rated speed. Estimates of f_x have been made for both nozzles B and C using an effective width and spacing. The effective width and spacing were calculated by assuming that, since the gas passages are roughly trapezoidal, the effective width is approximately two-thirds the distance between the outer and inner shells and, of course, nearer the outer shell. No estimates were attempted for nozzle I, which has non-coplanar exits.

A comparison of the calculations with the frequencies estimated from the appropriate power-level distribution curves shows that, in general, the agreement is quite good. The notable exception is nozzle F. Since this nozzle was a very ineffective suppressor, the difference probably results from the dissimilarity between the actual flow conditions as compared with the simplified calculations.

SOUND-POWER GENERATION

Further study of the preceding sketch would indicate that the ratio of the volume in which mixing interference occurs to the total volume of the adjacent jets is proportional to s/w. Furthermore, the volume ratio depends on the total number of jets for which mixing interference occurs. Since it might be expected that the outside halves of the end jets would be relatively unaffected, then the total volume ratio would be approximately the product of s/w and the number of jets less one (i. e., the number of spaces between nozzle segments n). The noise suppression of the slotted nozzles would therefore be expected to be a function of ns/w.

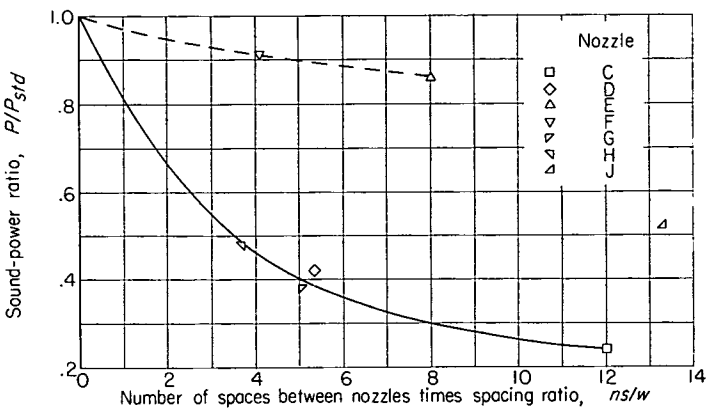


FIGURE 17.—Sound-power ratio at rated engine conditions as function of ns/w.

A simple measure of the suppression of the slotted nozzles is shown by the ratio of the sound power generated by the suppressor nozzle to that of the standard nozzle (fig. 15). Figure 17 shows this sound-power ratio (at rated engine conditions) as a function of ns/w. Also shown on this curve are the data for nozzle C, which has no end effects. The general result would appear to be that all the data except those for nozzles E, F, and J can be represented by a single curve. Undoubtedly the slot height has some effect. It would appear that this effect is small for all the nozzles except E and F. As long as there is sufficient room between adjacent jets for the mixing air to freely traverse down the slots, then the solid curve applies. If this is not the case, then the curve is shifted upward, as shown in figure 17. This upward shift probably occurs abruptly, as is usual with phenomena related to jet attachment to surfaces. Such phenomena usually occur because of a pressure differential, and the jet will try to maintain its normal pattern and then suddenly shift as a certain pressure differential is reached. From an examination of the geometry of the configurations, it would appear that this shift occurred somewhere between a spacing-to-height ratio s/h of 0.167 and 0.111.

The results for nozzle J might well be high, since this nozzle showed marked differences in the sound field dependent on the nozzle orientation. A single average of the sound powers (vertical and horizontal nozzle orientation) may not be sufficient for this particular nozzle.

It might be expected that the solid curve representing the better noise suppressors would hold generally for all suppressors of this type. In fact, unpublished data using model jets show good agreement with this curve for comparable values of jet pressure ratio. Since this is the case, then figure 17 indicates that the most noise reduction that could be expected from such suppressors occurs near ns/w of 12. It appears that further increases in ns/w will not result in substantial noise decreases. Certainly increases in s/w will tend to increase noise levels, since jets spaced far apart should be relatively unaffected by mixing interference. In fact, at large values of s/w the levels should return to that for the standard nozzle.

CONCLUDING REMARKS

It is evident from the results presented herein that it is possible to greatly alleviate the noise problems of current jet engines. It is not possible, however, to recommend any specific nozzle as appreciably better than all the others. Nozzles C, D, G, H, I, and J all appear to be reasonably good suppressors and reduce sound power by 50 to 75 percent (3 to 6 db). The reductions in the power in various frequency bands is as much as 15 decibels. The sound-pressure levels at particular positions showed reductions of 5 to 12 decibels with as much as 18 decibels in various frequency bands. In some cases the sound fields (nozzles D and J) are not rotationally symmetrical and hence will cause special problems. Nozzles C, H, and J had considerable thrust loss (about 4 to 7 percent), whereas nozzles D, G, and I had quite small thrust losses.

Apparently it is not possible to achieve a great deal more sound reduction from the types of nozzles presented herein. The conversion of the test nozzles to flying hardware represents a considerable development effort. Furthermore, a great many practical problems with regard to nozzle weight and drag in flight remain to be answered. Certainly all the nozzles tested will require further study to minimize these effects.

LEWIS FLIGHT PROPULSION LABORATORY
NATIONAL ADVISORY COMMITTEE FOR AERONAUTICS
CLEVELAND, OHIO, *January 22, 1957*

REFERENCES

1. North, Warren J.: Effect of Climb Technique on Jet-Transport Noise. NACA TN 3582, 1956.
2. Callaghan, Edmund E., and Coles, Willard D.: Far Noise Field of Jets and Jet Engines. NACA Rep. 1329, 1957. (Supersedes NACA TN's 3590 and 3591.)
3. Lighthill, M. J.: On Sound Generated Aerodynamically. I—General Theory. Proc. Roy. Soc. (London), ser. A., vol. 211, no. 1107, Mar. 20, 1952, pp. 564–587.
4. Silverstein, Abe, and Sanders, Newell D.: Concepts on Turbojet Engines for Transport Application. Preprint No. 727, SAE, 1956.
5. Tyler, John, and Towle, George: A Jet Exhaust Silencer. Preprint No. 508, SAE, 1955.
6. Greatrex, F. B.: Jet Noise. Preprint No. 559, Inst. Aero. Sci., June 1955.
7. Withington, Holden W.: Silencing the Jet Aircraft. Aero Eng. Rev., vol. 15, no. 4, Apr. 1956, pp. 56–63; con't. p. 84.
8. Sanders, Newell D., and Laurence, James C.: Fundamental Investigation of Noise Generation by Turbulent Jets. Preprint No. 744, SAE, 1956.
9. Bolt, R. H., Lukasik, S. J., Nolle, A. W., and Frost, A. D., eds.: Handbook of Acoustic Noise Control. Vol. 1. Physical Acoustics. Tech. Rep. 52–204, Aero. Medical Lab., WADC, Dec. 1952. (Contract AF 33(038)–20572.)
10. Tyler, John M., and Perry, Edward C.: Jet Noise. Preprint No. 287, SAE, 1954.
11. Sanders, Newell D.: Performance Parameters for Jet-Propulsion Engines. NACA TN 1106, 1946.
12. Laurence, James C., and Benninghoff, Jean M.: Turbulence Measurements in Multiple Interfering Air Jets. NACA TN 4029, 1957.
13. Howes, Walton L., Callaghan, Edmund E., Coles, Willard D., and Mull, Harold R.: Near Noise Field of a Jet-Engine Exhaust. NACA Rep. 1338, 1957. (Supersedes NACA TN's 3763 and 3764.)

REPORT 1388

NACA RESEARCH ON SLURRY FUELS

By M. L. Pinns, W. T. Olson, H. C. Barnett, and R. Breitwieser

SUMMARY

An extensive program was conducted to investigate the use of concentrated slurries of boron and magnesium in liquid hydrocarbon as fuels for afterburners and ramjet engines. Analytical calculations indicated that magnesium fuel would give greater thrust and that boron fuel would give greater range than are obtainable from jet hydrocarbon fuel alone. It was hoped that the use of these solid elements in slurry form would permit the improvement to be obtained without requiring unconventional fuel systems or combustors.

Slurries consisting of 50 percent or more magnesium or boron in JP fuels were prepared, although it was difficult to obtain successive batches with uniform properties. A vaporization process was devised for the preparation of very finely divided magnesium. The storage stability, spray characteristics, and non-Newtonian flow behavior of the slurries varied with the particle size of the metal and the type and concentration of the additives incorporated. The storage stability was limited to 6 months or less, but some types of magnesium slurries could readily be reconstituted by mixing. Slurry fuels formed coarser sprays than jet hydrocarbon fuel did.

Tests in pipe-connected combustors of various designs showed that slurried magnesium burned very readily even under conditions where jet hydrocarbon fuel itself would not burn, and the expected improvement in thrust was obtained. Data from tests on afterburners indicated that coolant injection would accentuate the improvement. However, some modification of conventional fuel systems and combustors was required to compensate for the difference in flow properties between jet hydrocarbon and slurry fuels.

Small ramjet vehicles fueled with magnesium slurry were flown successfully, but the test flights indicated that further improvement of combustors and fuel systems was needed.

In contrast to the favorable results with magnesium slurries, the boron slurries that were prepared were more difficult to burn than conventional jet fuel and formed objectionable deposits in the combustor.

INTRODUCTION

This report summarizes the NACA research program on slurry fuels that was conducted from 1947 to 1957. Since it encompasses about forty NACA Research Memorandums (see reference list), which represent the work of many individuals, this report presents only the highlights of those memorandums.

The slurry fuels considered herein are suspensions of metals in hydrocarbons. For flight propulsion, certain metals as fuels offer the possibilities of more flight range or more thrust than can be obtained with conventional hydrocarbons. They may also provide combustion under operating conditions where hydrocarbons alone will not burn. A discussion of metals and their compounds as fuels and a review of experimental work on them by the NACA and others up to 1951 are presented in reference 1, and more recent reviews are presented in references 2 and 3. References 1 and 3 also consider the selection of particular fuels for the research effort. The reasons for interest in certain metals as fuels are reviewed here with the aid of four figures:

Figure 1 presents the heating values of a few selected fuels relative to JP–4 jet fuel as 1. Boron and a typical boron hydride, pentaborane, have more heating value on a weight basis than JP–4. Magnesium, aluminum, boron, and pentaborane all have greater heating values than JP–4 fuel on a volume basis. These fuels also have greater heating values per pound of air burned in stoichiometric mixtures.

Higher heating values on a weight and volume basis make longer flight range possible (ref. 4). Heating value per pound of air burned is indicative of the amount of thrust that can be obtained from an engine of a given size. However, because much of the heat of combustion may be used to volatilize and dissociate the combustion products, the heating value per pound of air cannot be used directly. The cross-hatched parts of the bars in figure 1 therefore indicate the relative net thrust that theoretically can be achieved after making appropriate corrections for these effects.

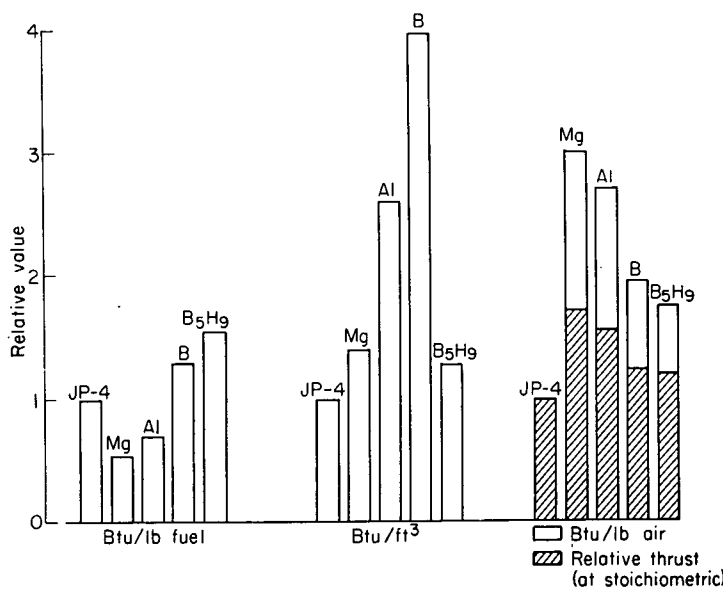


FIGURE 1.—Relative heating values (ref. 2).

Preceding Page Blank

Figure 2 is a plot of fuel-weight specific impulse against air specific impulse for a number of fuels (see also refs. 5 to 7). Air specific impulse, which is an index of thrust, is the number of pounds of total stream thrust per pound of airflow per second. Fuel-weight specific impulse, an index of fuel economy on a weight basis, is air specific impulse divided by fuel-air ratio. Because aluminum, boron, and magnesium burn at higher temperatures and at higher over-all fuel-air ratios, they can give higher thrust per pound of air than is possible with hydrocarbon jet fuel. Up to an air specific impulse of 152 seconds, hydrogen, boron hydrides, and boron all require less fuel flow to maintain a given thrust than would jet fuel (represented in fig. 2 by octene-1) and hence would give increased flight range.

Figure 3 shows the relative flight range calculated for a ramjet-powered missile at 60,000 feet and Mach 3.2 following

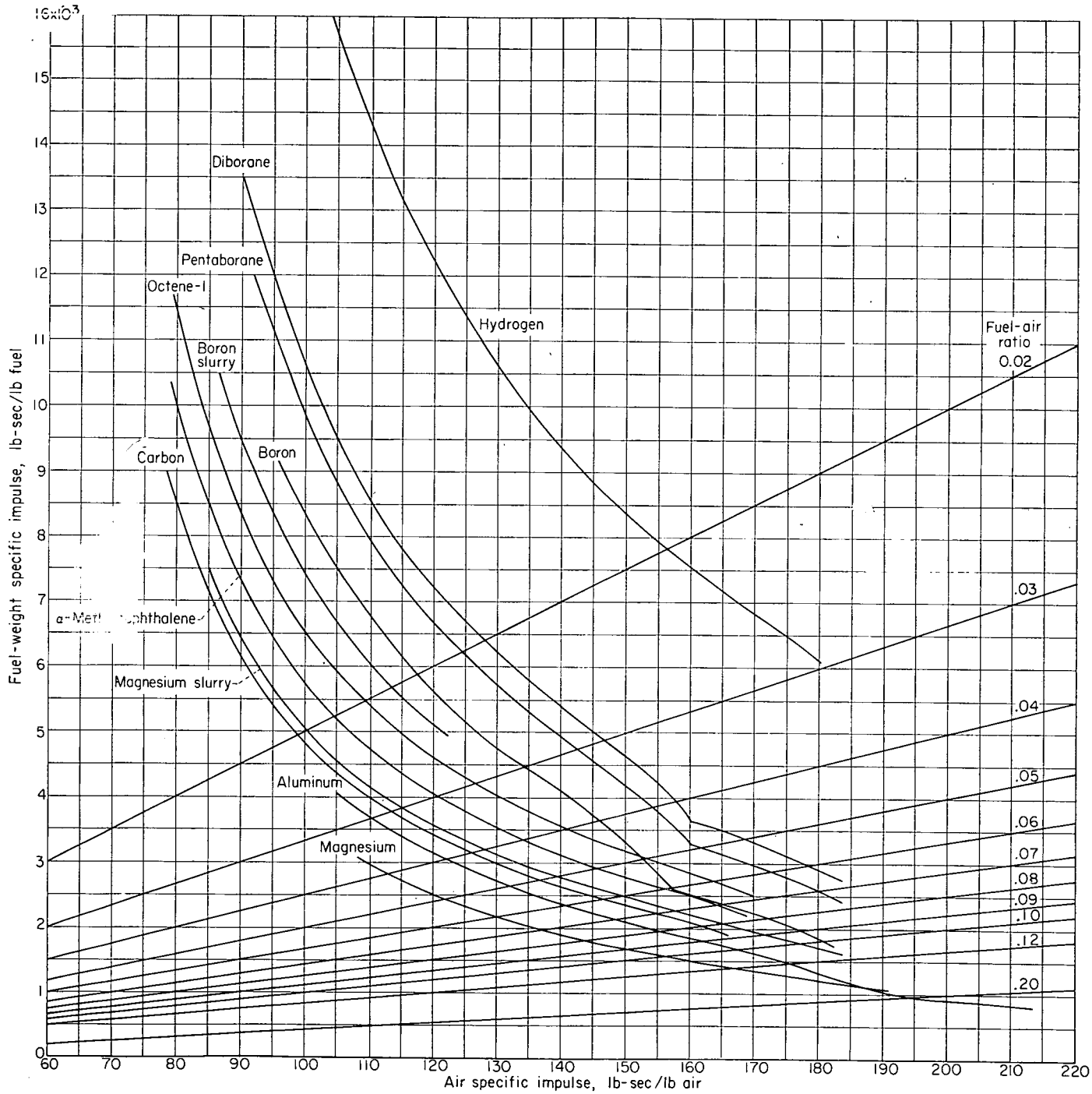


FIGURE 2.—Theoretical combustion performance of representative high-energy fuels. Slurry fuels, 50 percent metal by weight in octene-1. Combustor-inlet air temperature, 100° F; inlet air pressure, 2 atmospheres (ref. 7).

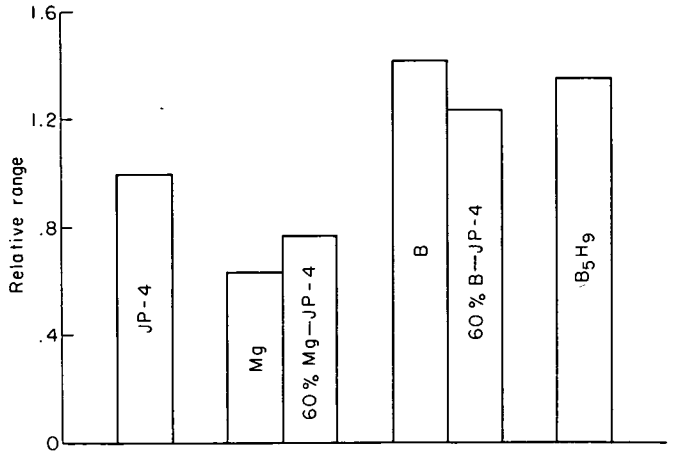


FIGURE 3.—Relative range of ramjet missile. Initial altitude, 60,000 feet; free-stream Mach number, 3.2; Breguet flight path (ref. 2).

a Breguet flight path (ref. 4). The reason for interest in boron is evident from this figure.

Figure 4 illustrates the advantages to be obtained from the high thrust possible with magnesium. A typical bomber was selected for illustrative purposes. With no thrust augmentation, the bomber did not take off even with many thousands of feet of runway. With 43-percent thrust augmentation from JP–4 fuel, the bomber takes off at 13,500 feet over a 10-foot obstacle. This distance is shortened to 10,700 feet at 67-percent thrust augmentation with a magnesium slurry. With 100-percent thrust augmentation with magnesium slurry and water injection combined, the takeoff distance over a 10-foot obstacle is about 8000 feet.

These, then, were the reasons for interest in metals as aircraft fuels. Long flight range is theoretically achievable with boron, while high thrust for afterburners or for ramjet engines might be obtained from aluminum, boron, or magnesium.

Since little or nothing was known regarding methods of combustion of metals in jet engines, it was first necessary to learn how to use these metals as aircraft fuels. The earliest NACA studies were based on the combustion of aluminum as wire or powder (ref. 8). The efforts of other organizations along analogous lines have been reviewed in reference 1.

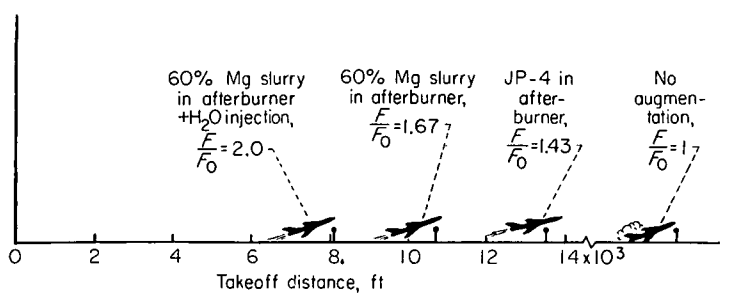


FIGURE 4.—Takeoff characteristics of turbojet bomber over 10-foot obstacle (ref. 2). (F, augmented thrust; F_0, unaugmented thrust.)

Aluminum was very early dropped from the program in favor of magnesium, because the sticky, molten aluminum oxide caused a very serious deposit problem in the combustor. Magnesium oxide does not melt appreciably at the flame temperature normally encountered and does not stick to the combustor walls as aluminum oxide does.

Handling difficulties indicated that slurries of metal powder in liquid hydrocarbon might be more satisfactory than the pure metal because they could probably be used without radical departure from conventional fuel systems and combustors. It then became necessary to learn how to prepare boron and magnesium slurries that would perform satisfactorily. The preparation of slurries, the study of their physical and combustion properties, and the development of combustors to burn slurries were conducted concurrently at the NACA Lewis laboratory.

SLURRY PROPERTIES DESIRED AND METHODS OF MEASUREMENT

OBJECTIVES

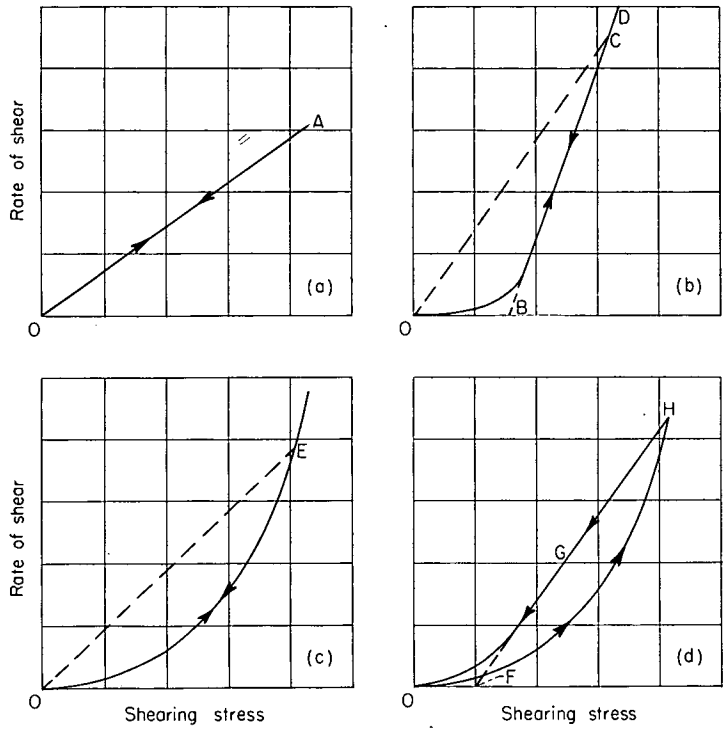
The objective in slurry preparation was to achieve a metal concentration of 50 percent or more (by weight) in JP–3, JP–4, or JP–5 (all three described in specification MIL–F–5624C) jet-engine hydrocarbon fuel in order to obtain a worthwhile increase in performance. It was necessary to achieve sufficient fluidity to permit flow and injection into more or less conventional jet-engine combustors and still maintain the slurry consistency at a sufficiently high level to prevent the suspended particles from settling too rapidly. Furthermore, as will be discussed later, it was desirable to use the most finely divided boron and magnesium available in order to obtain the best combustion characteristics. When the particles were relatively coarse, the suspension was relatively fluid, and it was necessary to thicken the hydrocarbon medium. When the particles were very fine, the mixture was a stiff mud unless a surface-active additive was used to promote wetting of the particles by the hydrocarbon. The quantity of metal that could be suspended and the properties of the suspension were functions of the particle shape and size distribution, the composition of the hydrocarbon medium, and the type and concentration of additives.

MEASUREMENT OF CHARACTERISTICS

Slurry fuels, like other concentrated suspensions, have non-Newtonian flow properties; that is, the rate at which they flow is not directly proportional to the force applied. The variable relation is conveniently measured with viscometers, several of which were used at various stages in the program. A modified Stormer viscometer (described in ref. 9) was used at rates of shear up to 1800 seconds^{-1}, and an automatic recording viscometer (described in ref. 10) was used over a wide range of rates of shear to obtain plots of rate of shear or rate of rotation of spindle against shearing stress or driving force.

Schematic diagrams of such plots shown in figure 5 represent various types of flow behavior. Figures 5 (b), (c), and (d) are idealized plots that only approximate the actual behavior of slurries. The arrows in the figures indicate that the curves were obtained by first continuously increasing the shearing stress (up-curve) and then continuously decreasing it (down-curve). The rate of shear of Newtonian materials varies linearly with the shearing stress, and the viscosity is proportional to the reciprocal of the slope of the plot (fig. 5 (a)). For plastic materials, a finite shearing stress must be applied before the rate of shear becomes a linear function of shearing stress (fig. 5 (b)). The plastic viscosity is measured by the reciprocal of the slope of the linear portion of the plot. The yield value is defined as the intercept of the extrapolated linear portion with the shearing stress axis (fig. 5 (b)). The rate of shear of pseudoplastic materials increases nonlinearly with shearing stress (fig. 5 (c)). When the shearing stress required to effect a given rate of shear decreases upon prolonged application of the stress, the material is thixotropic, and the up- and down-curves do not coincide (fig. 5 (d)). The apparent viscosity at any selected point on the flow curve is proportional to the reciprocal of the slope of a straight line drawn from that point to the origin, as in figures 5 (b) and (c).

Low plastic or apparent viscosity and low yield value facilitate the pumping of a slurry; while high levels of viscosity, yield value, and thixotropy retard the settling of the suspended particles.



(a) Newtonian material: Viscosity=(Instrument constant)/(Slope of OA).

(b) Plastic material: Plastic viscosity=(Instrument constant)/(Slope of BCD); Yield value=Length OB along axis; Apparent viscosity=(Instrument constant)/(Slope of OC).

(c) Pseudoplastic material: Apparent viscosity=(Instrument constant)/(Slope of OE).

(d) Thixotropic material: Plastic viscosity=(Instrument constant)/(Slope of FGH); Yield value=Length of OF along axis.

FIGURE 5.—Schematic plots of rate of shear against shearing stress. Arrows indicate path of increasing rate of shear followed by decreasing rate of shear.

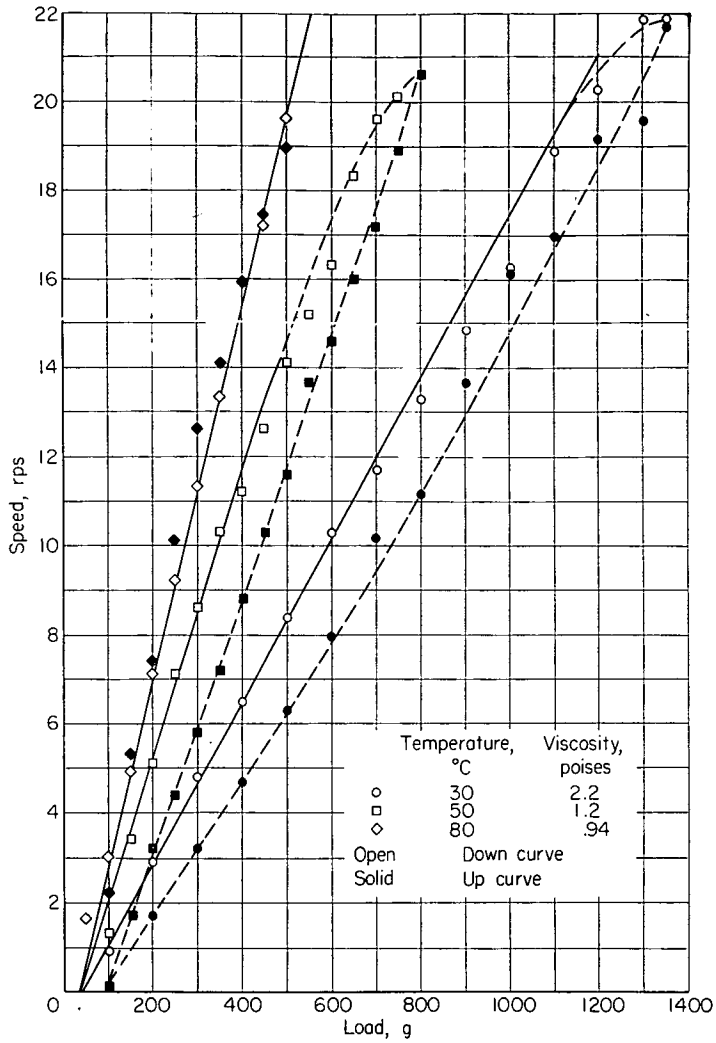


FIGURE 6.—Effect of temperature on curves obtained with Stormer viscometer one day after preparation of slurry containing 50 percent boron, 48.1 percent JP–5, 1.6 percent glyceryl sorbitan laurate, and 0.3 percent aluminum octoate (ref. 17).

Other viscometers used were the Severs Extrusion Rheometer at about 1000 to 24,000 seconds^{-1} and a Brookfield viscometer at about 0.5 and 10 seconds^{-1}. They are described in reference 11. The Brookfield instrument gave apparent viscosities that were very convenient comparative measurements. Unless otherwise indicated, all viscosity measurements were made at about 86° F.

Stability toward settling was commonly measured by observing sedimentation of the slurry in 50-milliliter graduated cylinders immersed in a water bath at 86° F. The extent of settling was then expressed as the settling ratio, defined as the ratio of depth of the sediment layer to the initial depth of slurry in the cylinder. Qualitative observations were also made of settling in larger containers.

The relative ease with which a settled slurry could be redispersed was estimated for some slurries by shaking under controlled conditions (described in ref. 11) the 50-milliliter cylinder of slurry used in the settling test. The "percent redispersible" was the percent of sediment layer that could be poured out after shaking.

Dielectric properties of boron and magnesium suspended in mineral oil were studied in order to learn about sedimentation, particle shapes, and particle agglomeration, and to form the basis for an instrumental method of estimating the concentration of metal in a suspension (refs. 12 to 14).

PREPARATION AND PROPERTIES OF BORON SLURRIES

BORON

The boron powder used in most of the work was a commercial product prepared by the thermal reduction of boric oxide with magnesium. Analysis of a large number of samples of this grade of boron showed that the purity ranged from 87 to 91 percent free boron. Among the known impurities were magnesium, boron oxide, moisture, and traces of acid. Average particle sizes ranged from approximately 0.6 to 1.4 microns, as determined by the air permeability method with a Fisher Sub-Sieve Sizer. Electron micrographs showed the particles to be irregularly shaped (ref. 15).

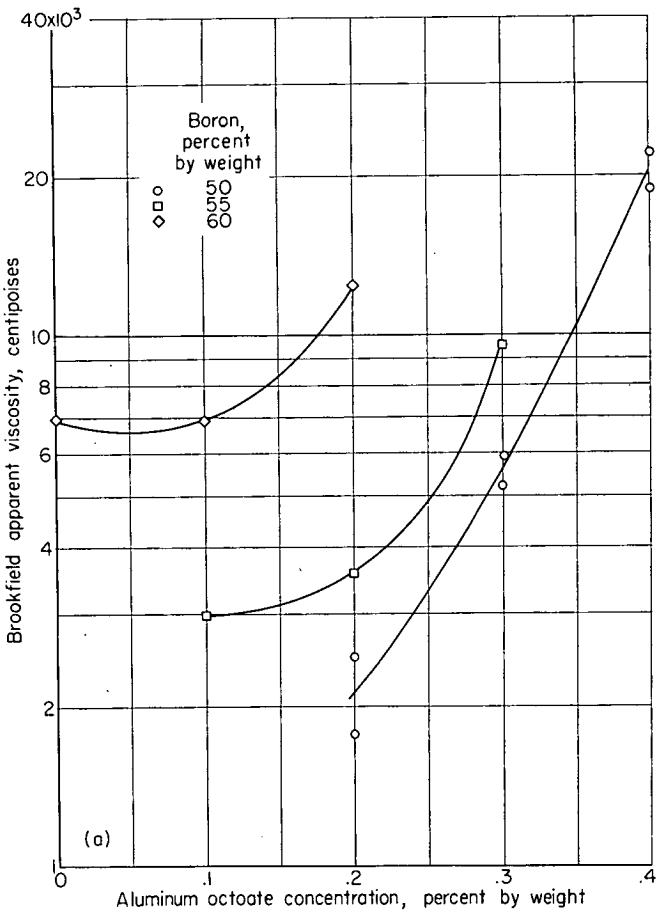
Another grade of boron, prepared by an electrochemical process, contained about 97 percent elemental boron and had an average particle diameter less than 1 micron.

METHOD OF PREPARATION OF BORON SLURRIES

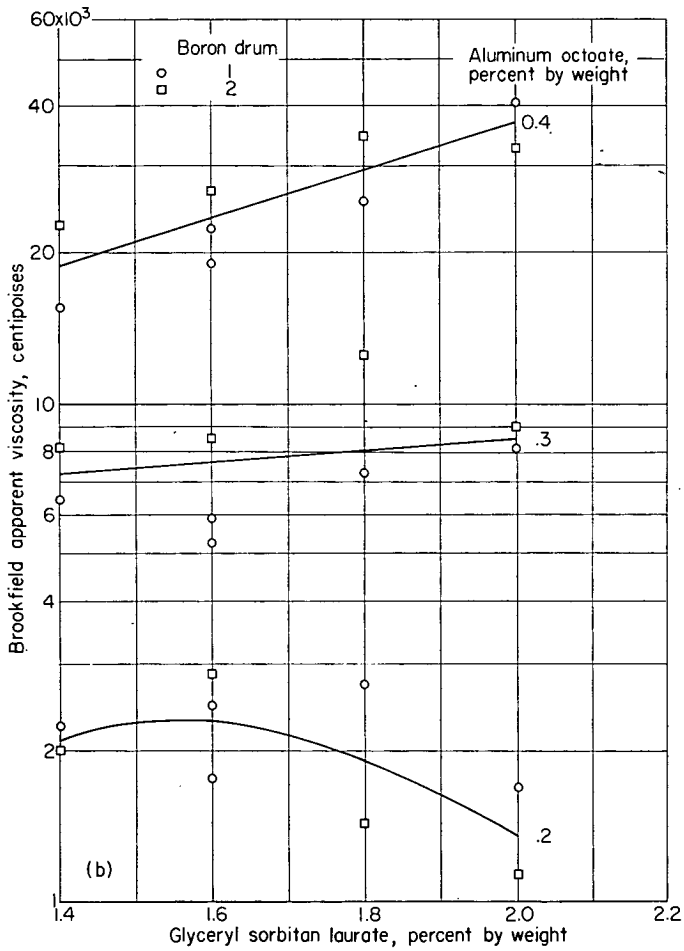
The addition of the surface-active additive glyceryl sorbitan laurate and the gelling additive aluminum octoate was desirable in order to obtain satisfactory flow properties (ref. 15). Later experience suggests that other surface-active additives could have been used equally well. Of the various grades of aluminum octoate available, the one used was prepared by reacting aluminum chloride with 2-ethylhexoic acid. Limited data indicated that acetylene black, silica aerogel, and certain processed bentonites might be substituted for the aluminum octoate (ref. 16). The slurries were prepared at room temperature. The additives were thoroughly dispersed in the hydrocarbon, and the boron powder was then added in small portions. Intensive mixing was applied during the entire preparation procedure by use of a high-speed mixer that is illustrated in reference 15.

FLOW PROPERTIES OF BORON SLURRIES

The more satisfactory slurries were thixotropic at room temperature but tended to lose this characteristic when the temperature was raised to 80° C, as shown in figure 6. This behavior is discussed in references 15 and 17. A wide range of initial Brookfield apparent viscosities, from about 1500 to over 100,000 centipoises, was obtained by varying the concentrations of boron from 50 to 60 percent, of gelling additive from 0 to 0.4 percent, and of glyceryl sorbitan laurate from 0.5 to 4.0 percent (all proportions by weight). The variation of initial Brookfield apparent viscosity with additive concentration is shown in figure 7. The Brookfield viscosity increased so rapidly with boron concentration that it was impractical to use more than about 60 percent boron (ref. 15).



(a) Glyceryl sorbitan laurate concentration, 1.6 percent (ref. 15).



(b) Boron concentration, 50 percent (adapted from ref. 15).

FIGURE 7.—Effect of additive concentration on Brookfield apparent viscosities of boron slurries in JP–5 fuel.

STORAGE LIFE OF BORON SLURRIES

The gel structure of the boron slurries deteriorated during storage. After a time the boron settled to form a gummy cake that could not readily be redispersed, a condition representing the end of useful life of the slurry. This effect was sometimes accompanied by a decrease in Brookfield apparent viscosity, as shown in figure 8. This figure also indicates that at a given concentration of surface-active additive a higher concentration of aluminum octoate increased the useful life. However, the use of as much as 0.4 percent aluminum octoate was feasible only when the boron concentration did not exceed 50 percent. One factor that influenced the useful life was the acidity of the boron, as reflected by the *p*H of a water extract of the powder. Another factor was the moisture content, as measured by the percent weight loss of the powder at 105° C. When the *p*H was as high as 5.2 and the weight loss was as low as 0.4 percent, the initial viscosity was increased and useful life of laboratory samples extended beyond 6 months (ref. 15).

PREPARATION AND PROPERTIES OF MAGNESIUM SLURRIES

PREPARATION OF MAGNESIUM

Much of the experimental work on magnesium slurries was conducted with comparatively coarse, commercially available, 13- to 24-micron magnesium powder, prepared by atomization of the molten metal. This powder contained 94 percent or more elemental magnesium, the remainder being mainly oxide. The particles were predominantly spherical. Average particle diameters and particle size distributions were variously determined with sieves, microscope, Fisher Sub-Sieve Sizer, and Roller Analyzer (ref. 11).

After combustion studies indicated the desirability of using more finely divided magnesium, sources of such material were sought. Very limited quantities of 0.6- to 5-micron magnesium were obtained as byproducts of the commercial atomization process. The particles of this powder were irregularly shaped, but not appreciably flat or elongated. Attempts to grind magnesium gave flattened, elongated particles that yielded slurries with very poor flow properties.

The development of a process for making suitable, finely divided magnesium was undertaken because of the very limited commercial availability of such material. The result was a vapor process, based on the shock-chilling of magnesium vapor with jet-engine hydrocarbon fuel (refs. 18 and 19). Figure 9 is a diagram of a laboratory-size plant in which magnesium metal was vaporized at 2000° F in a 4-inch-diameter steel crucible heated with an induction coil. The helium atmosphere in the furnace chamber was kept at a pressure of 11 pounds per square inch gage, and a constant stream of helium carried the magnesium vapor through a heated orifice into a series of hydrocarbon sprays. Solidified magnesium that was deposited at the inlet to the condensing chamber tended to block the orifice, but the difficulty was alleviated by using a cylindrical chamber with thermal insulation on the inner face of the wall at the inlet. The best design permitted clog-free operation for about 6 hours. The dilute hydrocarbon suspension of magnesium was permitted to settle, and the sediment was centrifuged to produce a concentrate containing about 60 percent solids. The solids consisted of about 90 percent elemental magnesium. Electron micrographs indicated that the particles were irregularly shaped and that about 90 percent of them were 0.2 micron

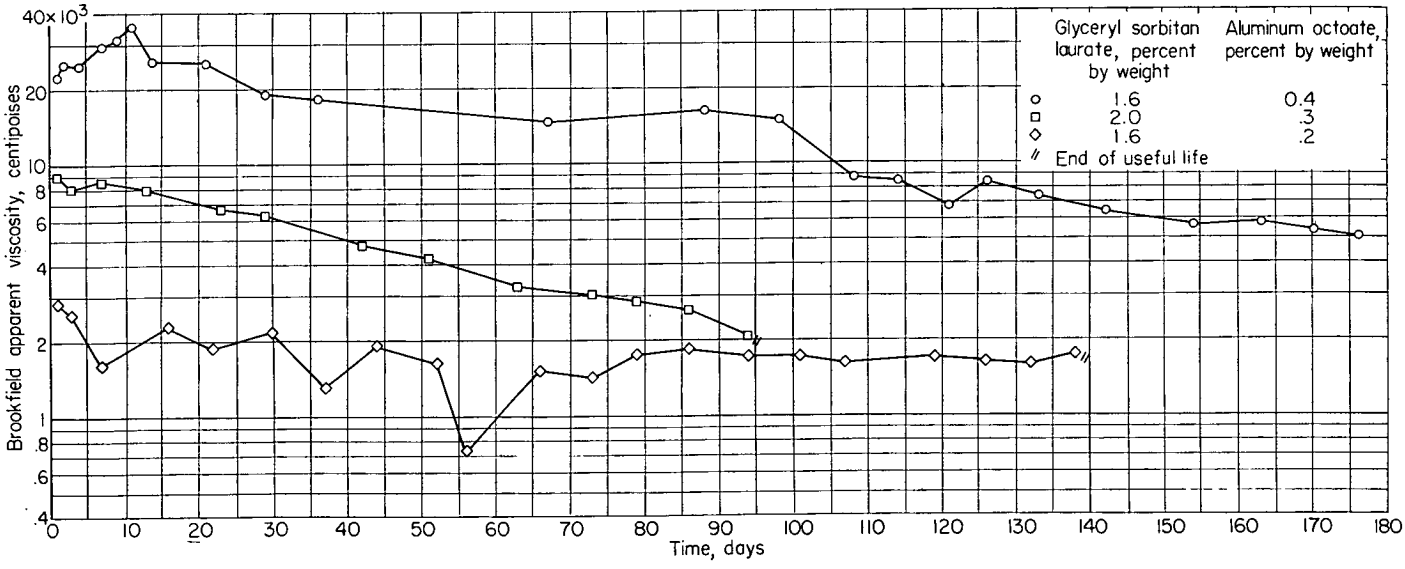


FIGURE 8.—Change of Brookfield apparent viscosity with age of boron slurries made with JP–5 fuel. Boron concentration, 50 percent (ref. 15).

or less in the longest dimension. Calculations based on minima in plots of yield value and Brookfield apparent viscosity against concentration of cetyl alcohol added to the slurry indicated the average equivalent spherical diameter to be 0.2 to 0.4 micron (ref. 20).

MAGNESIUM SLURRIES FLUIDIZED WITH SURFACE-ACTIVE ADDITIVES

Preparation.—The 60 percent solids concentrate of vapor-process magnesium was a pasty mass that had poor flow properties even when diluted to 50 percent solids with jet-engine hydrocarbon fuel. A 50 percent concentration of atomized magnesium with an average particle diameter less than about 2 microns also formed a paste. In order to obtain a smooth fluid suspension of either type of magnesium, it was necessary to stir in a surface-active additive and then run the suspension through a colloid mill.

A study of assorted surface-active additives showed that oil-dispersible compounds whose molecular structure included a hydroxyl group together with an ester, metal salt, or polyoxyethylene group were the most effective (refs. 9 and 21). Examples of such compounds are polyoxyethylene sorbitol tetraoleate and glyceryl sorbitan laurate. It is believed that these combinations of functional groups were so effective because they provided a maximum of interaction between the molecules of additive and the oxide, hydrated oxide, sorbed moisture, or metal at the surfaces of the magnesium particles. In the case of oxide or hydrated surfaces, the interaction may have occurred through coordination and hydrogen bonding. In the case of metal surfaces, dipole interaction may have been involved (ref. 22).

Flow properties.—Slurries containing 50 percent of vapor-process magnesium or 1.5-micron atomized magnesium and no surface-active additive were thixotropic and behaved like pseudoplastic materials. When successively greater percentages of surface-active additive were incorporated, the flow behavior became more like that of a plastic material and the thixotropy disappeared (refs. 9 and 21). Figure 10 (also ref. 21) shows how the yield value, plastic viscosity, and Brookfield apparent viscosity of slurries of vapor-process magnesium decreased from their high values at 0 or 0.5 percent additive to their low values at 3 to 5 percent additive. Data in reference 9 indicate that slurries con-

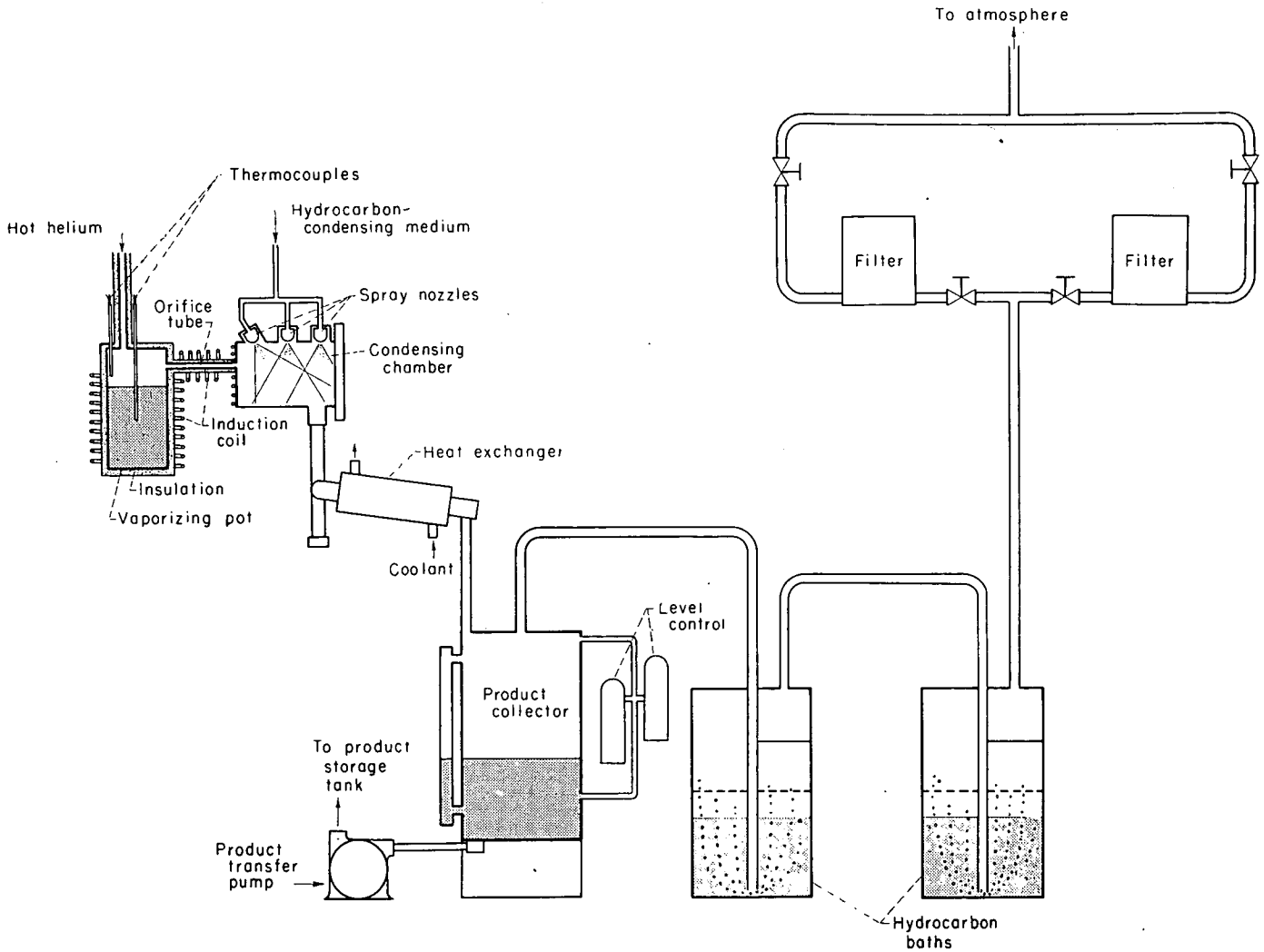


FIGURE 9.—Schematic diagram of magnesium vaporization unit (ref. 19).

taining 50 percent of 1.5-micron magnesium and only 1 percent surface-active additive were very fluid (plastic viscosity, 7 centipoises; yield value, 9 dynes/cm^2; Brookfield apparent viscosity, 200 centipoises). Acceptable slurries containing 55 or 60 percent of 1.5-micron magnesium could readily be prepared. Data in reference 17 show that the viscosities and yield values were often decreased by two-thirds or more when the temperature was increased to 212° F. The effect of increasing the temperature was most pronounced for the thicker slurries. The slurries also tended to become more fluid during aging for about 1 month after they were first prepared. Good uniformity of successive mixes of slurry was readily obtained as long as the same batches of ingredients were used, but the effect of changing batches of magnesium was particularly noticeable (ref. 9).

Relation of flow properties to piping, spraying, and storage.—The flow properties of magnesium slurries were studied not only in viscometers, but also in a piping system consisting of nominal ⅜-inch- and 1-inch-diameter straight pipe and standard pipe fittings (ref. 23). The results indicated that published Newtonian pressure-loss coefficients can be satisfactorily used in the design of aircraft fuel systems for non-Newtonian slurries if account is taken of the flow properties of the slurries as determined with a suitable viscometer. The spray characteristics of slurries of vapor-process magnesium were relatively independent of plastic viscosity in the range of 220 to 510 centipoises and of yield value in the range of 150 to 810 dynes per square centimeter (ref. 24). This fact indicates that considerable leeway is permissible in the specification of the flow properties of these slurries insofar as they affect the injection of slurry into a jet-engine combustor.

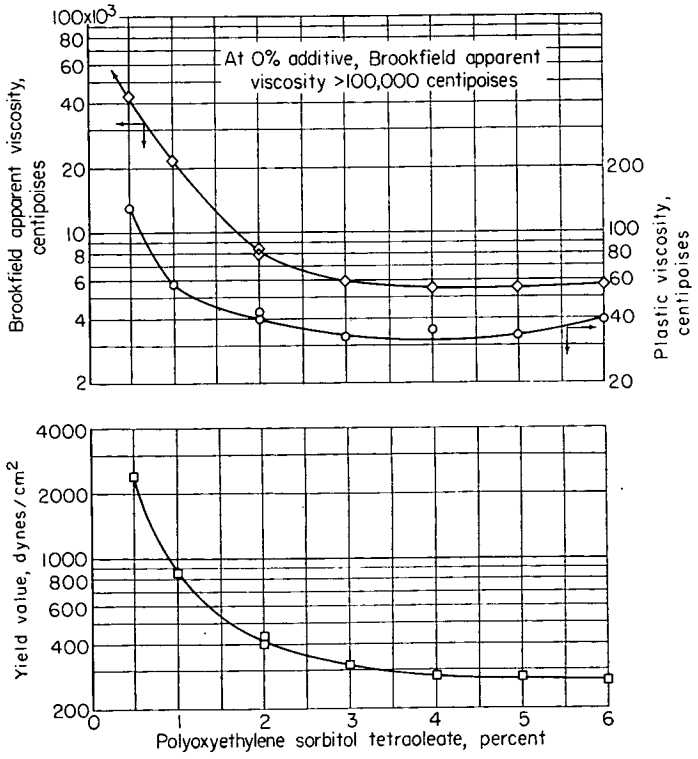


FIGURE 10.—Effect of concentration of additive on Brookfield apparent viscosity, plastic viscosity, and yield value of slurry containing 50 percent vapor-process magnesium. Additive, polyoxyethylene sorbitol tetraoleate (ref. 21).

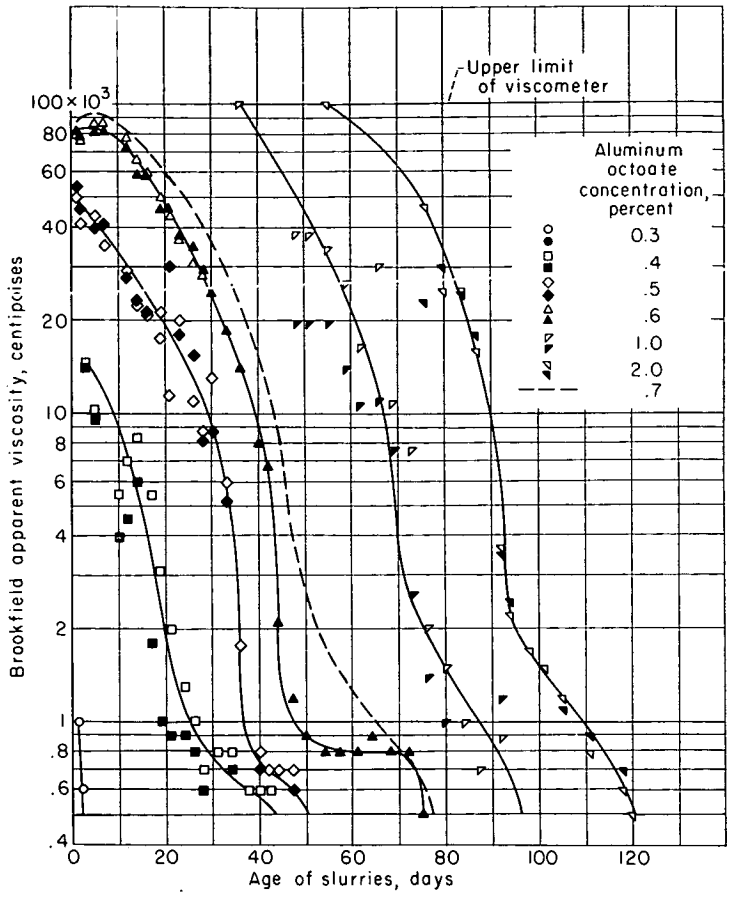
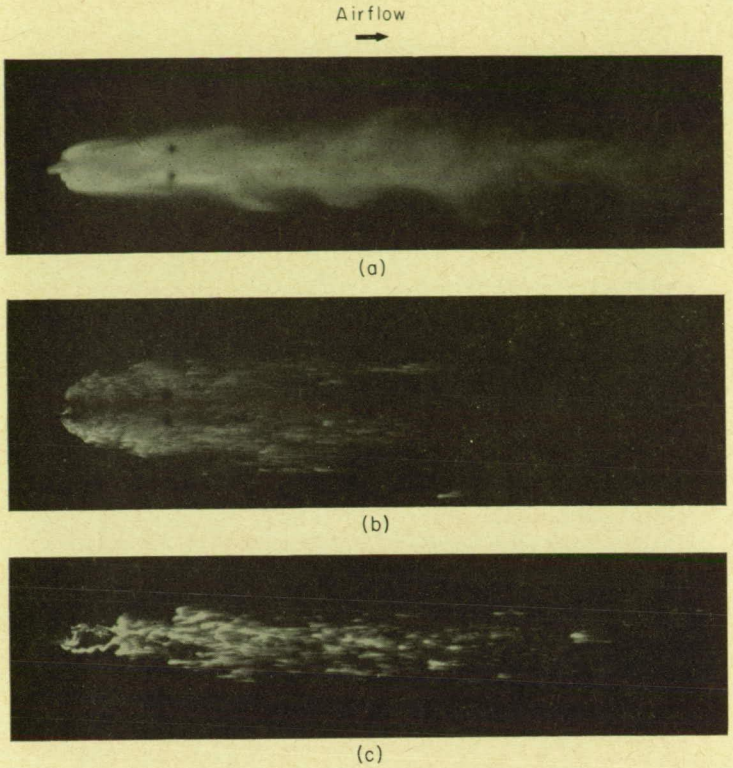


FIGURE 11.—Change of Brookfield apparent viscosity with age of slurries containing 50 percent 13-micron magnesium. Slurry gelled at approximately 110° F (ref. 26).

The settling and storage properties of slurries fluidized with surface-active additives were closely correlated with the flow properties (refs. 9 and 21). When the Brookfield apparent viscosity of slurries containing 50 percent 1.5-micron magnesium was 2500 to 4000 centipoises, only a small quantity of supernatant liquid formed during four weeks storage in 50-milliliter graduated cylinders. These slurries could readily be reconstituted by mixing. When these slurries were made progressively more fluid by the use of larger concentrations of surface-active additive, the quantity of supernatant liquid increased correspondingly until, at a Brookfield viscosity of about 200 centipoises, the magnesium settled into a hard cake that was difficult to redisperse in the abundant supernatant liquid. Even the most fluid slurries containing 50 percent vapor-process magnesium had a Brookfield viscosity of about 3500 centipoises, and they settled as little, and were as easily reconstituted, as the slurries of 1.5-micron magnesium of the same Brookfield viscosity.

MAGNESIUM SLURRIES THICKENED WITH GELLING AGENTS

Preparation.—As previously indicated, slurries of coarser, atomized magnesium were also examined. When the average particle size was about 4 microns or more it was necessary to thicken the hydrocarbon medium to retard settling. One method was to gel the hydrocarbon. The best gelling additive consisted of aluminum octoate, which was principally aluminum di(2-ethylhexoate) and was similar to the gelling additive used for boron slurries. Up to 1.2 percent of other grades of aluminum octoate in combination with other addi-



(a) JP–3 fuel; viscosity, 4 centipoises; no magnesium.
(b) 30-percent slurry of magnesium containing gelling additive; apparent viscosity, 300 to 400 centipoises.
(c) 30-percent slurry of magnesium containing gelling additive; apparent viscosity, 800 to 1600 centipoises.

FIGURE 12.—Photographs showing effect of gelling additive and magnesium on spray formation. Inlet air velocity, 400 feet per second; fuel jet velocity, approximately 26 feet per second; inlet air temperature, 80° F; inlet air density, 0.048 pound per cubic foot (ref. 27).

tives was used in earlier work (ref. 25). Various mixing procedures were used, but for batches weighing up to 200 pounds the combined ingredients were generally rolled in cans or drums on a roller enclosed in a box that could be heated. When 0.6 percent of aluminum octoate was used, a 100-pound batch of slurry containing 50 percent of 15-micron magnesium was gelled in about 4 hours at 90° F (ref. 26). Under closely controlled conditions, successive batches with very similar flow properties could be obtained from a single drum of magnesium; but, as in the case of the boron slurries, the gel structure was very sensitive to impurities and to small variations in the gelling additive or processing conditions.

Flow properties and storage behavior.—The flow properties of gelled magnesium slurries were similar to those of the gelled boron slurries. Although no studies were made over a range of rates of shear, the slurries were observed to be thixotropic. Also like the boron slurries, they deteriorated during storage, as shown by plots of Brookfield apparent viscosity against time in figure 11 (also ref. 26). This figure also indicates the effect of the concentration of gelling additive on the consistency of the slurry. The use of more than 0.7 percent gelling additive gave a very thick slurry initially and extended the length of time the gel structure was retained; but, even when 2.0 percent was used, the gel structure disappeared to such an extent in about 110 days that the slurry was no longer considered usable. However, these measurements were made on small samples, two of which, containing 0.6 percent aluminum octoate, were taken from larger batches. It was later discovered that the remainders, which had been kept sealed in their original containers, were still of usable quality even after 5½ months of storage. It therefore appears that the storage life of gelled slurries may be subject to more variables than have been investigated and may be longer than is indicated in figure 11.

The relation of apparent viscosity to spray characteristics of gelled magnesium slurry is shown in high-speed photographs in figure 12 (taken from ref. 27). At an apparent viscosity of 800 to 1600 centipoises, the spray was coarser than at 300 to 400 centipoises, and both these sprays were much coarser than a spray of JP–3 fuel. This behavior appears to be in contrast with the previously mentioned lack of correlation between spray characteristics and flow properties of slurries of vapor-process magnesium. The difference may be at least partially attributable to the absence of gel structure in the latter slurries.

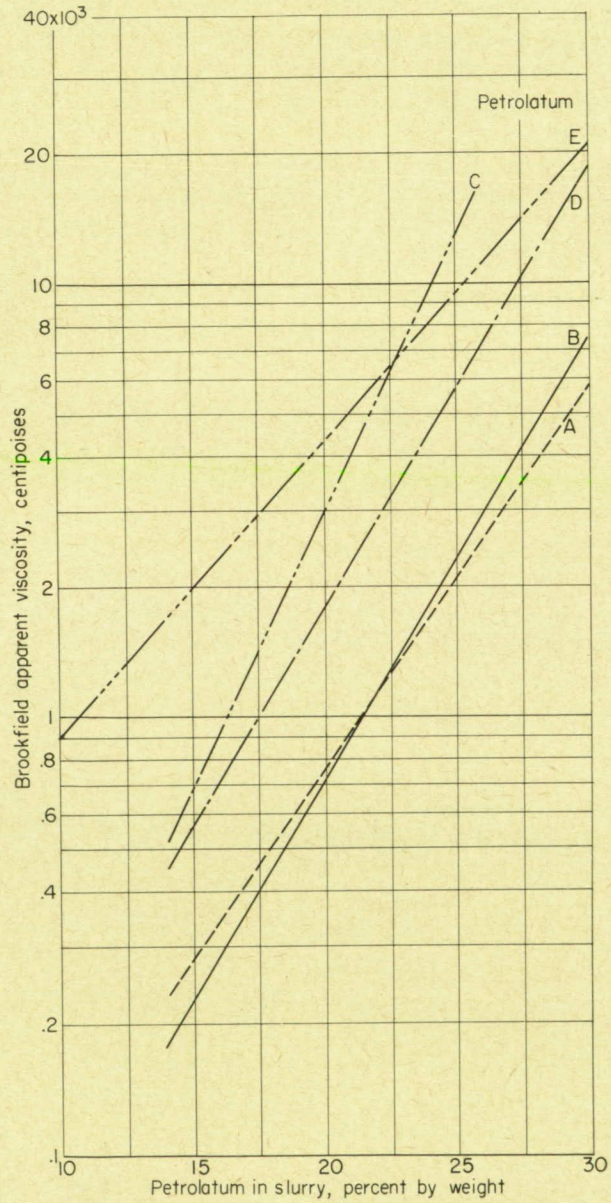


FIGURE 13.—Effect of concentration of various grades of petrolatum on Brookfield apparent viscosity of slurries containing JP–4 fuel and 50 percent 18-micron magnesium (ref. 11).

MAGNESIUM SLURRIES THICKENED WITH PETROLATUM

Preparation.—Another method used to stabilize slurries of coarser magnesium was to replace part of the jet fuel with petrolatum. When petrolatum with an ASTM melting point of 161° F and an ASTM penetration of 80 (petrolatum E in fig. 13) was used, the incorporation of 18 to 22 percent petrolatum in a slurry containing 50 percent 18-micron atomized magnesium gave the most satisfactory results (ref. 11). The magnesium concentration could also be increased to 65 percent by decreasing the petrolatum to 10 percent. The best preparative procedure was to mix the petrolatum with part of the jet fuel at 175° to 195° F, add the remainder of the jet fuel, add the magnesium powder and mix it in at 140° to 160° F, and then cool the mixture. Uniformity of successive mixes was readily obtained as long as the petrolatum came from the same batch, but the petrolatum concentration had to be adjusted for different batches of petrolatum.

Flow properties and storage behavior.—Limited data obtained for slurries containing 50 percent 18-micron magnesium and 18 to 26 percent petrolatum indicated that the slurries were plastic or slightly pseudoplastic mixtures (ref. 11). The Brookfield apparent viscosity was readily adjustable over a wide range (from about 160 centipoises, like thin paint, to about 16,000 centipoises, like apple butter) merely by selecting a suitable grade of petrolatum and varying the petrolatum concentration from 10 to 30 percent of the weight of slurry (fig. 13). Other factors controlling the viscosity were particle size and concentration of the magnesium (ref. 28). By choosing an appropriate concentration of petrolatum and keeping the average diameter of the spherical magnesium particles above about 7 microns, a satisfactory degree of fluidity could be maintained even when the magnesium concentration was raised to 60 or 65 percent.

The extent of settling that occurred during 28 days could be correlated quite closely with the Brookfield viscosity of the slurry. Some supernatant liquid always formed during this period, but when the Brookfield viscosity was about 4000 centipoises, the extent of settling was small and the slurry could readily be restored to its original condition by mixing. The extent of settling was minimized when the 4000-centipoise viscosity was attained by raising the magnesium concentration above 50 percent (ref. 11).

Photographs in reference 29 suggest that petrolatum-thickened slurry gave a more stringy spray than gelled slurry gave.

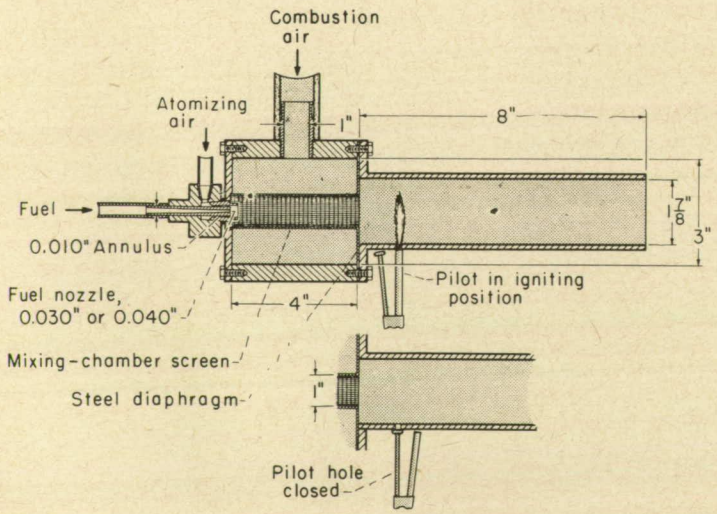


FIGURE 14.—Slurry burner for measurement of blowout velocities (ref. 30).

SUMMARY OF SLURRY PREPARATION AND PROPERTIES

Slurries can be made with high concentrations of finely divided boron or magnesium. Their shortcomings are (1) some nonuniformity of successive batches, particularly of boron slurries, (2) limited storage life, and (3) limited availability of the high purity, finely divided metals.

Exact slurry formulations cannot be recommended because of the difficulty of obtaining uniform batches of components and preparing uniform batches of product. However, when the components used are very similar to those that have been described, slurries comparable to the most satisfactory ones that were made can be prepared by using the following approximate formulations:

Boron slurry.—50 Percent boron (prepared by the magnesium reduction process), 0.2 to 0.4 percent aluminum octoate, 1.3 to 2.0 percent glyceryl sorbitan laurate, and 47.6 to 48.5 percent JP fuel.

Vapor-process magnesium slurry.—50 Percent vapor-process magnesium (in the form of a concentrate containing liquid hydrocarbon), 2.0 to 4.0 percent glyceryl sorbitan laurate, and 46 to 48 percent total hydrocarbon.

Gelled magnesium slurry.—50 Percent atomized magnesium (13 to 18 microns average particle diameter), 0.4 to 0.6 percent aluminum octoate, and 49.4 to 49.6 percent JP fuel.

Petrolatum-stabilized magnesium slurry.—50 Percent atomized magnesium (13 to 18 microns average particle diameter), 18 to 22 percent petrolatum, and 28 to 32 percent JP fuel.

COMBUSTION OF BORON SLURRIES

EXPLORATORY STUDIES

Exploratory studies were made of two combustion properties: blowout velocity (velocity of combustion air required to extinguish the flame), and combustion efficiency (percent conversion of each fuel component to oxidized products). Blowout velocities were measured in the burner shown in

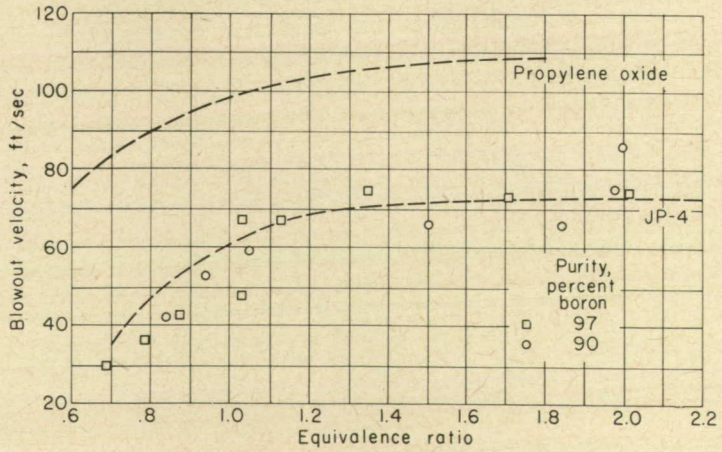


FIGURE 15.—Blowout velocities of propylene oxide, JP–4, and two 50 percent-boron slurries in 1⅞-inch-diameter burner. Slurries made with JP–4 fuel (ref. 2).

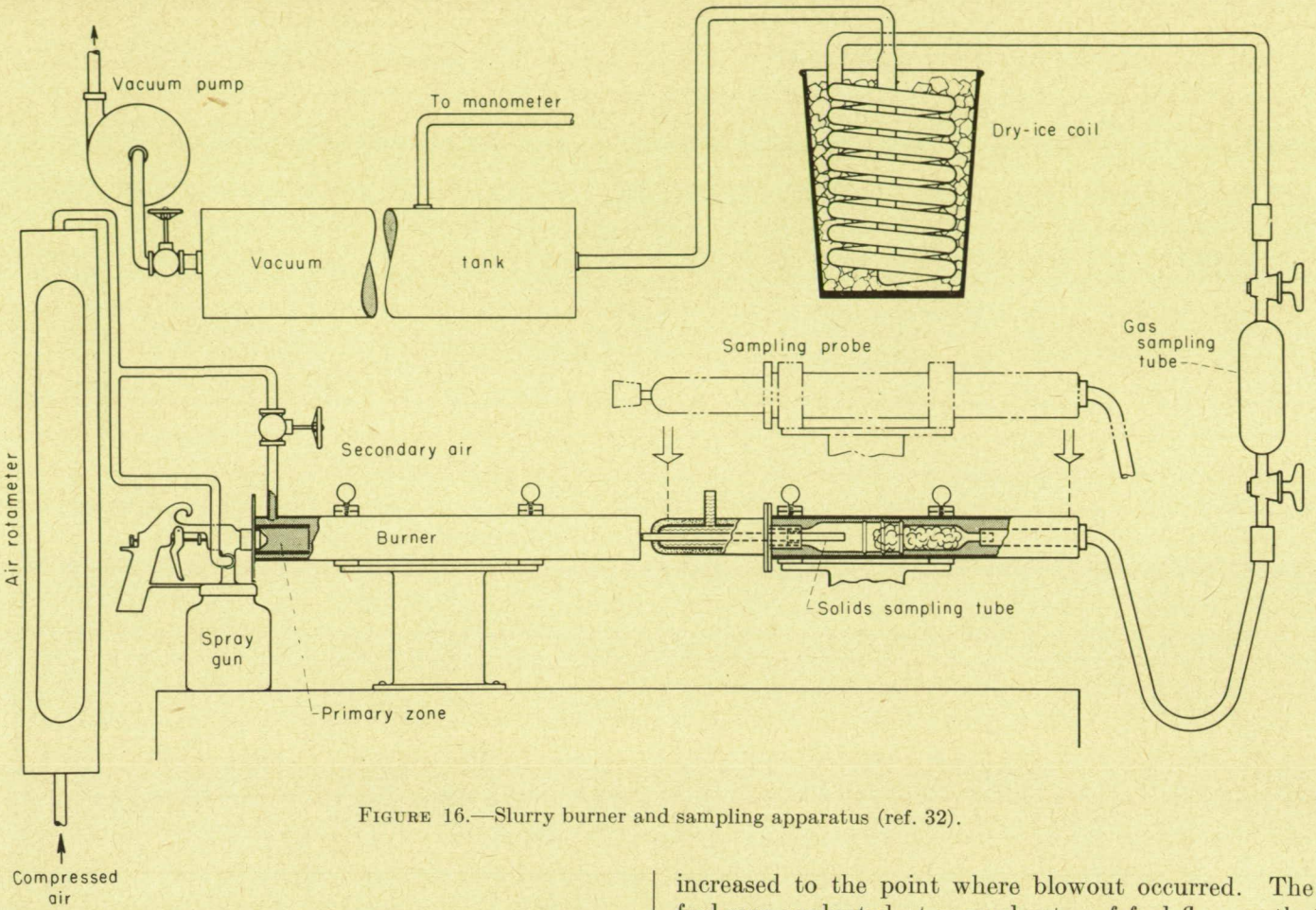


FIGURE 16.—Slurry burner and sampling apparatus (ref. 32).

figure 14 and in reference 30. The fuel was introduced through a small orifice and atomized with air. The atomized fuel entered a mixture preparation zone in which additional combustion air was added. The additional combustion air was introduced through a wall made of wire cloth that prevented the accumulation of solid particles on the wall of the preparation zone. The flame was seated in the recirculation zone established by the sudden expansion to the 1⅞-inch-inside-diameter tube. The mixture was ignited by a pilot flame that extended through a hole that was closed after ignition. The flow of combustion air was increased to the point where blowout occurred. The test fuel was evaluated at several rates of fuel flow so that the blowout velocity could be determined for various fuel-air ratios.

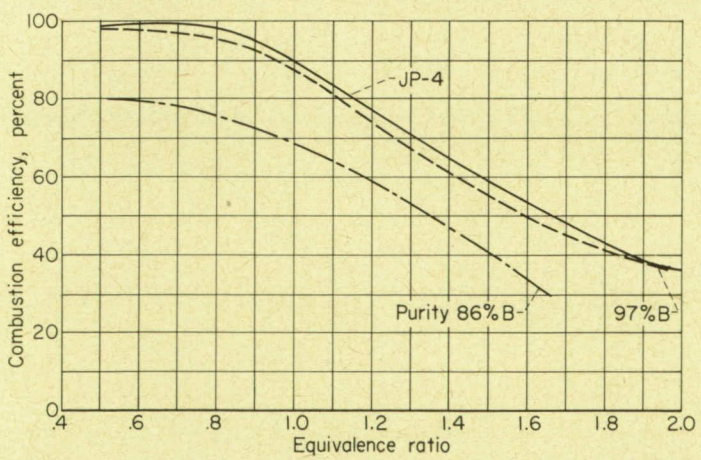


FIGURE 17.—Combustion efficiency of JP–4 and two 30-percent-boron slurries made with JP–4 fuel (ref. 2). Apparatus shown in figure 16.

Boron-slurry blowout velocities are reported in references 30 and 31. Figure 15 compares plots of blowout velocity against equivalence ratio (actual fuel-air ratio divided by stoichiometric fuel-air ratio) up to 2.0 for JP–4, propylene oxide, and two slurries containing 50 percent boron. Propylene oxide is a convenient comparison fuel, since it has roughly twice the laminar flame speed of hydrocarbons of the type found in JP–4. Although the two boron slurries differed somewhat in composition (90 percent boron purity, 1.0-micron average particle size, 1.6 percent surface-active agent, no gelling additive, against 97 percent, 0.7 micron, 1.3 percent, and 0.5 percent gelling additive), their blowout velocities were similar. As shown in figure 15, the boron slurries and the JP–4 fuel had substantially the same blowout velocities.

A similar exploration of combustion efficiency was conducted by analyzing combustion products. The apparatus shown in figure 16 was used. Boron slurry was injected with a modified paint spray gun, and the addition of secondary air formed a combustible mixture. The combustion products issuing from the combustor outlet passed through glass wool, which trapped the solid products, and the filtered gaseous products were collected in sampling tubes.

Figure 17 (based on data from ref. 32) shows combustion-efficiency data over the range of equivalence ratios of interest for JP–4 fuel and two slurries containing 30 percent boron but no additives. The combustion efficiency of the slurry

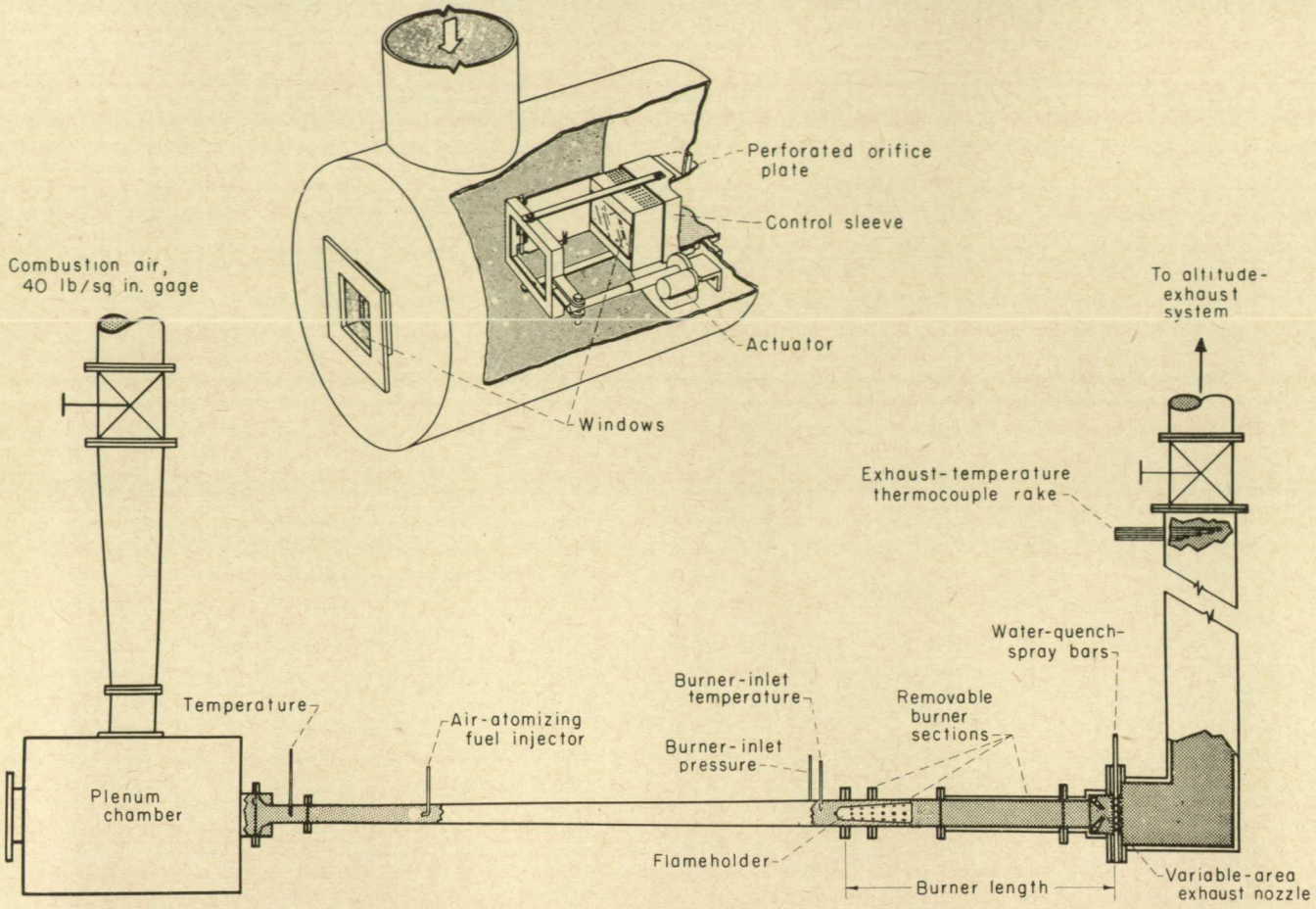


FIGURE 18.—Schematic diagram of 5-inch-diameter ramjet burner (ref. 33).

of 97-percent-pure boron was only a little lower than that of JP–4 over the entire range of equivalence ratios, while that of the slurry of 86-percent pure boron was 15 to 20 percentage points poorer.

LARGER-SCALE STUDIES

Since the exploratory data indicated that slurried boron could be made to burn almost as vigorously and efficiently as JP–4 fuel, it was next burned in the 5-inch-diameter simulated ramjet burner sketched in figure 18, taken from reference 33. Preheated air at pressures up to 40 pounds per square inch gage was supplied through a choked diffuser into the combustion zone. The combustion chamber length was varied between 40 and 52 inches; the combustor terminated in a variable-area exhaust nozzle. A water spray

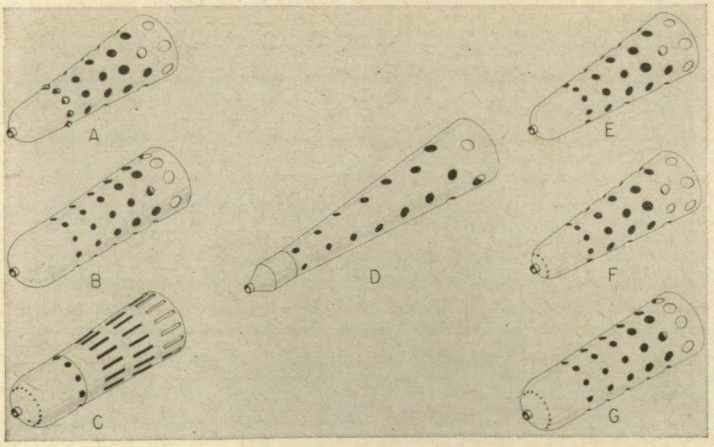


FIGURE 19.—Boron-slurry flameholders (ref. 2).

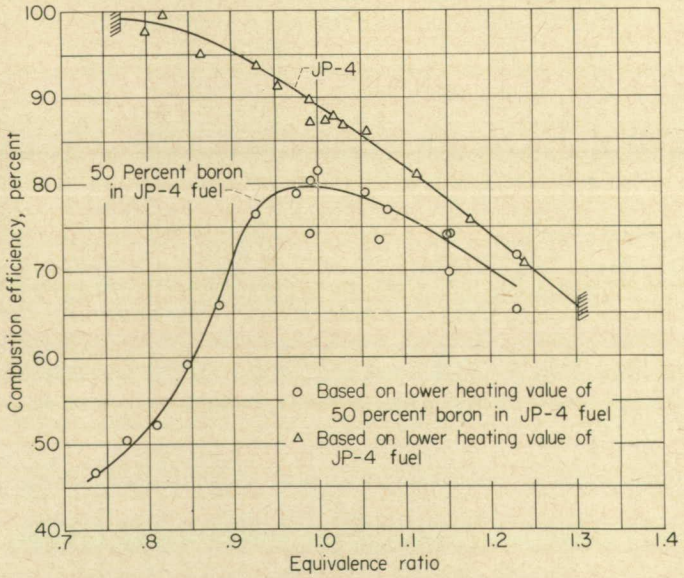


FIGURE 20.—Combustion efficiency of JP–4 fuel and boron slurry in 5-inch-diameter ramjet burner. Flameholder A shown in figure 19; burner length, 40 and 52 inches; inlet mixture temperature, 171° to 235° F; inlet pressure, 1692 to 2478 pounds per square foot absolute; inlet velocity, 123 to 181 feet per second; boron purity, 87 to 91 percent (ref. 33).

quenched the exhaust gases immediately downstream of the exhaust nozzle. The temperature of the quenched gases was measured by thermocouples downstream. Combustion efficiency was calculated from a heat balance across the system.

The can-type flameholders used in this program are shown in figure 19. The V-gutter types of flameholders originally used were discontinued because of poor combustion performance. The modifications in the can-type flameholders included the usual combustor design variables, such as blocked area, airflow distribution, and combustion-chamber length. Flameholder A in figure 19 gave the best performance. It was felt that the fuel-collecting scoops or shrouds around the first band of holes encouraged the recirculation of the boron into the upstream region of this flameholder.

The data from the 5-inch-diameter burner are summarized in figure 20 (taken from ref. 33), in which combustion efficiency is plotted against equivalence ratio. Gelled boron slurries consisting of 50 percent boron powder, 1.6 percent glyceryl sorbitan laurate, 0.4 percent aluminum octoate, and 48 percent JP–4 were evaluated and compared with JP–4 fuel alone. The boron powder was 87 to 91 percent pure, since the 97-percent-pure boron, which gave the more favorable results in the 1⅞-inch burner, was not available in sufficient quantity. The highest combustion efficiency obtained from the slurries was approximately 80 percent, considerably lower than that of JP–4, particularly at low equivalence ratios. The performance was about the same as that obtained with the corresponding grade of boron in the 1⅞-inch burner (fig. 17).

The principal observations that were made as a result of these and other data in the program were as follows: Heat outputs higher than the theoretical for JP–4 fuel were attained with boron fuels at high fuel-air ratios. A very high flame temperature was necessary for efficient combustion, as indicated by the high efficiencies only at near-stoichiometric fuel-air ratio. Scoops to encourage the recirculation of boron in the primary zone increased the efficiency. Combustion-chamber-length variations between 40 and 52 inches had little influence on combustion efficiency. Small variations in fuel composition had little influence on combustion performance.

Since the primary application for boron slurries would be in long-range, ramjet-powered vehicles where it is desirable to operate at low temperature ratios and hence low over-all fuel-air ratios, it seemed that some type of flow stratification to produce a rich fuel mixture in the combustion chamber was necessary to achieve high combustion efficiencies.

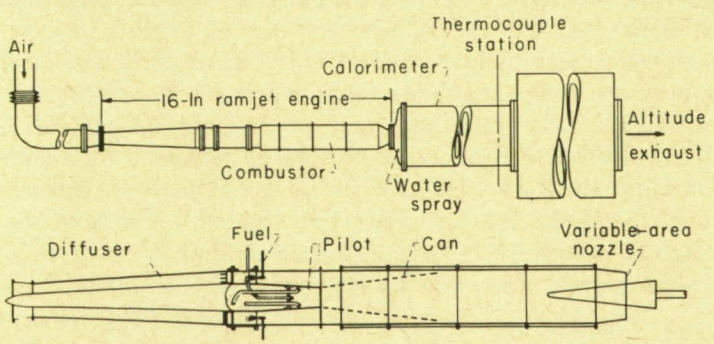


FIGURE 21.—16-Inch-diameter ramjet engine used for boron fuels (ref. 2).

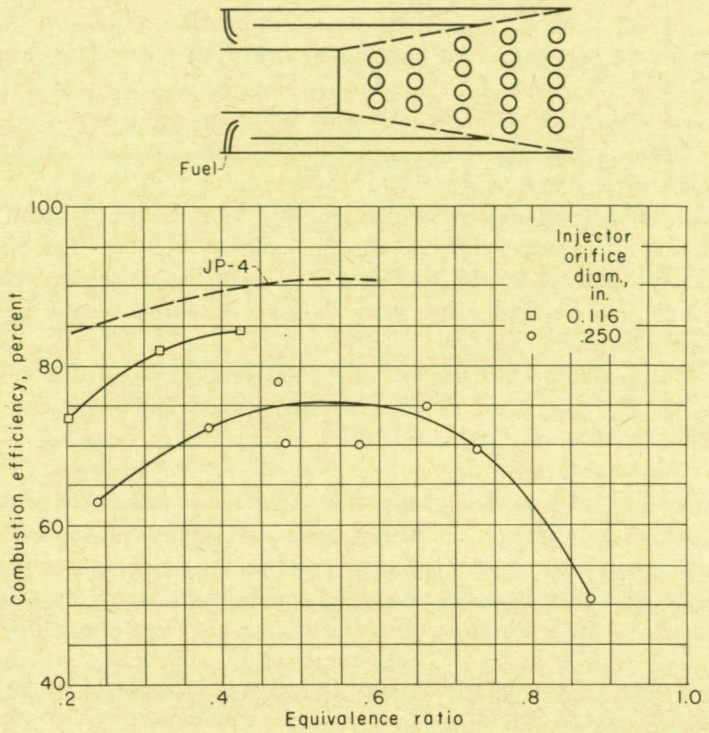


FIGURE 22.—Combustion efficiency of JP–4 fuel and boron slurry in 16-inch-diameter ramjet combustor. Pressure, 1 atmosphere; velocity, 260 feet per second; temperature, 560° F (ref. 2).

The 16-inch-diameter ramjet engine shown in figure 21 (ref. 2) was used to facilitate construction of combustors with a bypass or stratified combustion zone. The fuel was fed from air-atomizing injectors. The fuel was kept inside a cylindrical sleeve that ensured fuel-air ratios near stoichiometric in the primary zone of the combustor even at over-all fuel-air ratios that were lean. The remainder of the air was bypassed around the fuel-control sleeve and was mixed downstream of the primary zone. The details of the 16-inch-diameter engine resemble actual design layouts used in ramjet engines. Combustion efficiency was measured by heat balance across the system.

One set of data that was obtained in this equipment is shown in figure 22 (data from ref. 34). Combustion efficiency is plotted against equivalence ratio for two injector systems. The maximum combustion efficiency with the injectors with 0.250-inch fuel orifices was 75 percent at an equivalence ratio of 0.5. The use of smaller injectors

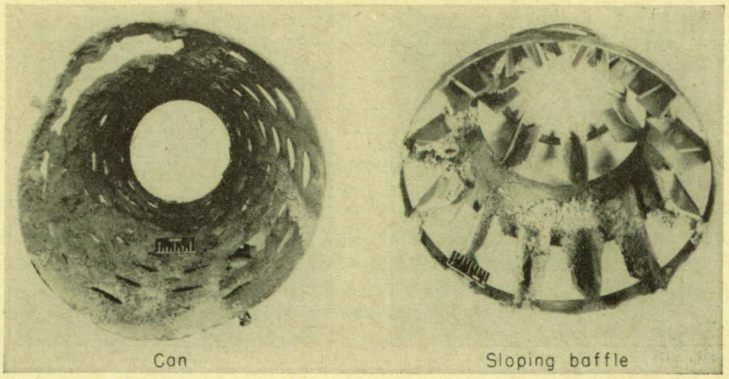


FIGURE 23.—Combustors after boron slurry was burned in them (ref. 2).

At high water-air ratios, the temperature at the end of the afterburner decreased with both JP–3 fuel and with the 60 percent magnesium slurry because of the high dilution with water. Further analysis of the data, however, shows that the combustion efficiency of the JP–3 fuel was much reduced at water-air ratios above 0.04, while the combustion efficiency of 60 percent magnesium slurry was essentially unaffected. Unlike hydrocarbons, magnesium slurry burned quite vigorously and at high combustion efficiencies in the small afterburner even at high water-flow rates.

Thrust-augmentation data are summarized in figure 29. Curve A shows thrust augmentation obtained experimentally in a full-scale turbojet engine with coolant (75 percent water and 25 percent alcohol, by weight) injection, but without an afterburner. About 27-percent augmentation was achieved at a liquid ratio of about 7; that is, seven times the normal fuel-flow rate of the engine with no thrust augmentation. About 52-percent thrust augmentation was obtained experimentally by afterburning without coolant injection, as indicated by the circle; a liquid ratio of 4 was required. When experimental runs were made using coolant injection combined with stoichiometric combustion of JP–3 fuel in an afterburner, curve B was obtained. The maximum augmentation achieved in these runs was about 70 percent; higher coolant-flow rates caused unstable operation (ref. 2).

If slurry fuel containing 60 percent magnesium were burned stoichiometrically in a full-scale afterburner, and no coolant injection were used, the estimated augmentation would be as shown by the square in figure 29. This estimate is based on the combustion efficiency of the slurry in the small-scale afterburner of figure 28. When the latter combustion efficiency is combined with coolant injection, the estimated augmentation is that indicated by curve C, which predicts 100-percent thrust increase at a liquid ratio of 13.5. This prediction assumes that coolant injection would give the same combustion efficiency as water injection (indicated in ref. 39).

One very short-duration run with 60 percent magnesium slurry has been made. Combustion was stoichiometric and no water injection was used. The experimental thrust augmentation, indicated in figure 29 by the diamond, agreed quite closely with the predicted performance, indicated by the square.

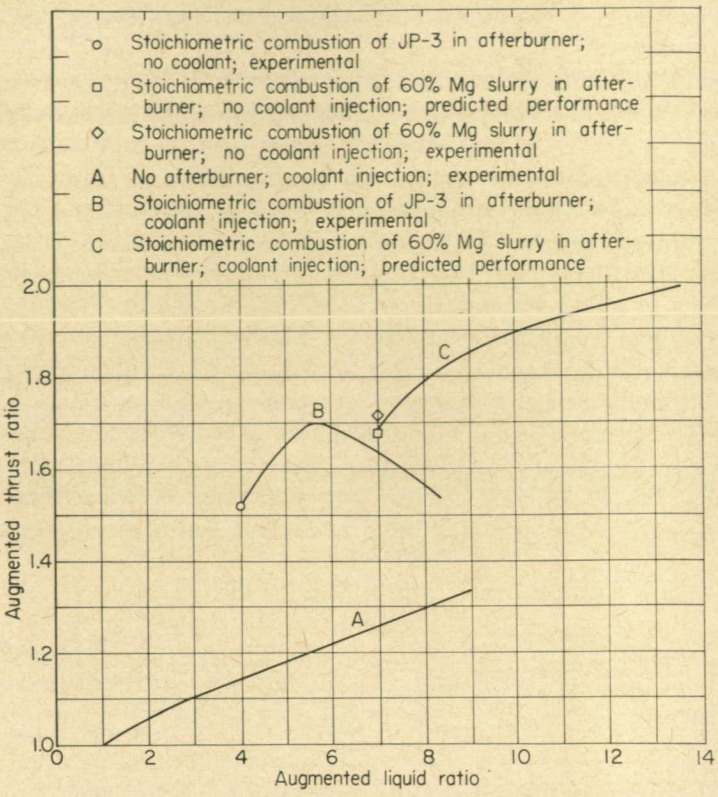
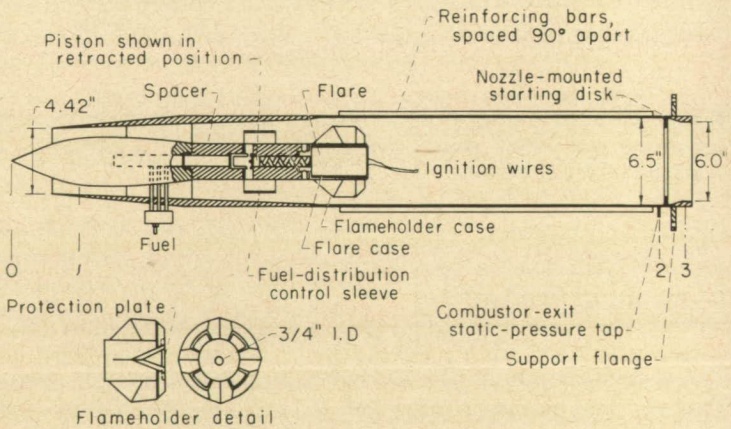


FIGURE 29.—Static sea-level thrust augmentation of turbojet engine combining afterburning with water or coolant injection. Coolant, 75 percent water plus 25 percent alcohol. (Adapted from ref. 38 with data added from ref. 2.)

COMBUSTION IN RAMJET MOUNTED IN CONNECTED-PIPE FACILITY

Magnesium slurry was also considered as a fuel for ramjet engines. Its high chemical reactivity, high air specific-impulse potential, and high fuel-volume specific impulse indicated magnesium slurry should be suitable for short-range ramjet vehicles. A joint program with the NACA Langley laboratory was undertaken to develop a ground-launched, rocket-boosted vehicle. It was expected that extension of the magnesium-slurry fuel research to a flight application would uncover difficulties that might otherwise have been missed. The Langley laboratory had an ethylene-fueled, aerodynamic test vehicle (ref. 40) that could be adapted to burn magnesium slurry. Ethylene had originally been selected, despite its low density, because its high flame speed made it suitable for use in a short combustor.

The engine used in connected-pipe tests for developing a slurry fuel is shown in figure 30. Its design was the result of an extensive study for fuel-injection devices, flameholders, starting disks, and other features that are discussed in references 41 and 42. Slurry fuel was introduced through a spring-loaded, variable-port-area injector with four longitudinal slots spaced 90° apart. Ignition was achieved with an electrically ignited flare, as shown in the figure. The



Station	Distance from reference (0), in.	Open area, sq ft
1	4.5	0.065
2	42.5	231
3	46.6	196

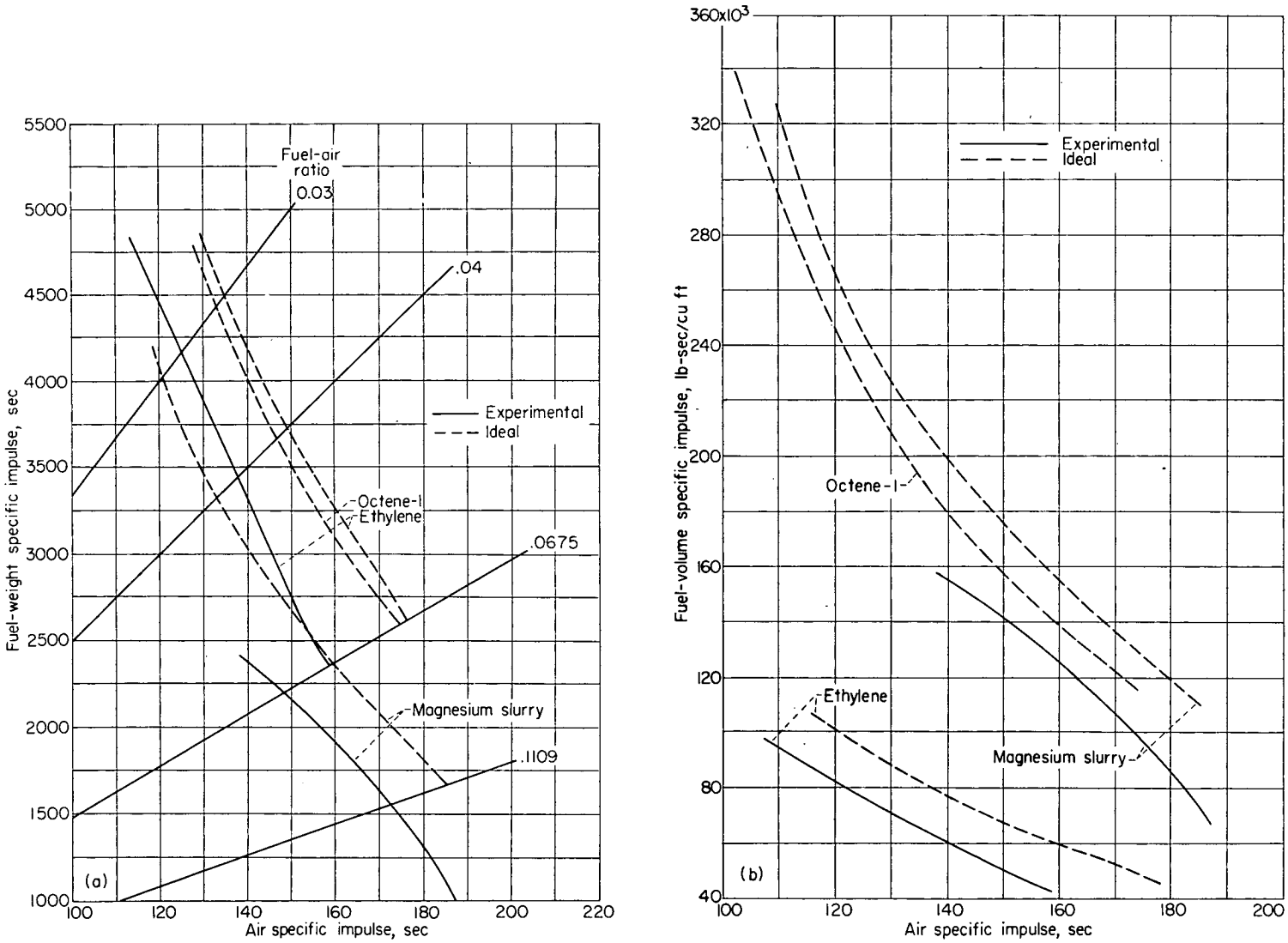
FIGURE 30.—Ramjet engine for development of combustor for flight tests (ref. 42).

combustion chamber was 19 inches long, and the gutter-funnel-type flameholder blocked 46 percent of the combustor cross-sectional area. Starting was facilitated by mounting an aluminum disk upstream of the exit nozzle to block part of the nozzle area (ref. 42). After ignition occurred, the disk mountings burned away rapidly and permitted the disk to be expelled through the nozzle.

This engine was connected to a pipe facility that fed air at 30 to 60 pounds per square inch absolute and 63° to 367° F into the inlet. The combustion products were discharged into a barrel-type thrust target mounted in a plenum chamber and were eventually discharged to the atmosphere.

The performance of magnesium-slurry fuel consisting of 50 percent of 93-percent-pure atomized magnesium of 1.5-micron average particle diameter, 50 percent JP–4, and no additives has been compared with the performance of ethylene in a similar engine (ref. 42). Fuel-weight specific impulse is plotted against air specific impulse for slurry and ethylene fuels in figure 31 (a). The ideal performance data for the slurry and octene-1 fuels were obtained from reference 7, and for ethylene from reference 43. Over the range of air specific impulse obtained with ethylene, the fuel-weight specific impulse of ethylene was greater than that of the slurry. At an air specific impulse of 159 seconds, which was the maximum obtained with ethylene, the fuel-weight specific impulses of the ethylene and the slurry were 2350 and 1950 seconds, respectively. The slurry fuel permitted operation up to an air specific impulse of 187 seconds at a maximum combustor efficiency of about 82 percent (ref. 42).

Fuel-volume specific impulse, an index of fuel economy on a volume basis obtained by multiplying air specific impulse by fuel density and dividing by fuel-air ratio, is presented in figure 31 (b) as a function of air specific impulse. A density of 18.3 pounds per cubic foot was used for the ethylene volume impulse computation. This density was obtained when the flight fuel tank was pressurized to 1200 pounds per square inch. The fuel-volume specific impulse of the slurry was 2.6 and 2.9 times that of ethylene at air specific impulses of 140 and 159 seconds, respectively. At air specific impulses of 150 to 170, the experimental fuel-volume impulse of the slurry was about 10 percent lower than the ideal volume impulse for octene-1.



(a) Fuel-weight specific impulse as function of air specific impulse.

(b) Fuel-volume specific impulse as function of air specific impulse.

FIGURE 31.—Comparison of impulse data for three fuels. Slurry, 50 percent 1.5-micron magnesium, 50 percent JP–4, and no additives; combustor-inlet stagnation temperature, 350° F; sonic discharge of exhaust products (ref. 42).

The fuel-volume specific impulse is a significant parameter when applied to vehicles that have a small ratio of fuel weight to gross vehicle weight. For example, the Langley flight vehicle had an ethylene fuel- to gross-weight ratio of 0.1. Hence, a large increase in volume specific fuel consumption can make possible a correspondingly large increase in fuel load with only a small increase in vehicle gross weight. It was therefore concluded that the replacement of ethylene by magnesium slurry in the NACA Langley flight-test vehicle should result in improved performance.

PERFORMANCE OF MAGNESIUM SLURRY IN FLIGHT TESTS

Three flight tests of small rocket-launched ramjet test vehicles fueled with magnesium slurry were conducted at the Langley Pilotless Aircraft Research Station. The engines of these vehicles were similar to the 6.5-inch ramjet combustor that has been discussed. The first and third tests, conducted with single-engine vehicles, were considered successful, since good flame stability and reasonably good over-all performance of fuel and mechanical components were achieved (refs. 44 and 45). The second test, using a twin-engine vehicle, was less satisfactory because an abrupt decrease in thrust occurred during flight (ref. 46). The difficulty was attributed to the clogging of a fuel line by a lump of magnesium paste.

Some of the data from these tests are listed in table I, which shows that, as expected, the fuel-weight specific impulse of magnesium slurry was lower and the fuel-volume specific impulse was greater than obtainable with ethylene in similar vehicles.

TABLE I.—PERFORMANCE OF RAMJET TEST VEHICLES FUELED WITH MAGNESIUM SLURRY AND ETHYLENE

	First test, single engine (ref. 44) [a]	Second test, twin engine (ref. 46) [b]	Third test, single engine (ref. 45) [c]	Ethylene fuel in twin engine (refs. 40 and 48)
Fuel-weight specific impulse, sec[d]	549	---	770	961; 1059
Fuel-volume specific impulse, lb-sec/cu ft[d]	[e] 37, 000	---	[e] 51, 800	[f] 17, 500; 19, 300
Maximum air specific impulse, sec	151	---	150	------
Acceleration, g	4. 6	---	6. 1	4. 13; 3. 6
Maximum gross-thrust coefficient	0. 658	0. 664	0. 760	0. 885

[a] Slurry consisted of 50 percent 1.5-micron magnesium, 50 percent JP–4. Brookfield apparent viscosity, 6800 centipoises.

[b] Slurry consisted of 50.7 percent 0.6-micron magnesium, 49.3 percent JP–4. Brookfield apparent viscosity, approx. 8000 centipoises.

[c] Slurry consisted of 52.4 percent 1-micron (max.) magnesium, 47.1 percent JP–4, and 0.5 percent surface-active additive.

[d] Fuel specific impulses are based on gross thrust and hence are not directly comparable with those shown in figure 31.

[e] Calculated from fuel-weight specific impulse and density of slurry. Density of slurry calculated from specific gravity 1.08 given in ref. 44.

[f] Calculated from fuel-weight specific impulse and density of compressed ethylene. Density of ethylene calculated from data in ref. 48.

FUEL SYSTEMS FOR EXPERIMENTAL COMBUSTION OF SLURRY FUELS

The unique physical properties of slurries have created many problems that must be considered by designers of handling devices such as pumps, meters, valves, or injectors (ref. 47). The following are several problems faced in the design of slurry-fuel systems:

(1) Metal particles tend to clog passageways and orifices even though the openings may be considerably larger than the maximum particle size. Slurries of milled magnesium powder are more prone to clog constrictions in fuel lines than are slurries of atomized metal powder. Flow restriction caused by this kind of clogging is often progressive and does not always result in complete flow blockage. The effect may be intermittent so that the flow rate and pressure will vary unpredictably.

(2) Metal particles will adhere to valve seats unless one of the surfaces is of rubber or the mating surfaces are wiped clean before contact as in tight-fitting plug valves.

(3) Metal particles tend to enter clearance space between sliding and rotating surfaces. As the parts move, the particles become wedged in and weld to the surface until the mechanism jams.

(4) If the ambient temperature reaches the boiling point of the carrier fluid, a hard, impermeable cake of dry powder can form. This type of clogging, which is most likely to occur when the fuel flow is interrupted for a period of time, is due to fuel drying and is found most frequently in injection nozzles or adjacent piping. These parts are exposed to radiation from the flame zone or are often in a stream of preheated combustion air. The attachment of nozzles and piping to duct walls and combustors results in additional heating by conduction.

In order to overcome these difficulties, it has been necessary to evaluate certain types of equipment to determine whether the fuel systems are satisfactory for use with slurry fuels. In some cases, existing commercial equipment has been adapted for this purpose, and in other cases custom-built equipment has been utilized. The following sections describe some of the experiences encountered in the use of this equipment.

PUMPS

Initial attempts to use gear pumps for aluminum slurries or screw-type, positive displacement, all-steel pumps for magnesium slurry failed because the all-metal parts seized immediately. Later, pumps that could handle magnesium slurry for limited periods were obtained.

A 0.26-gpm/100-rpm screw-type pump could be operated for more than 5 hours when constructed with a tool-steel rotor and a rubber stator. It pumped magnesium slurry at 700 to 800 rpm and a discharge pressure of 200 to 250 pounds per square inch in the recirculating-fuel system described in reference 27. The slurry was made with JP–3 fuel containing only 10 percent aromatics in order to minimize swelling of the rubber. A more solvent-resistant rubber stator could probably have been used.

An air-turbine-driven centrifugal fuel booster pump with an aluminum impeller delivered 180 pounds of magnesium slurry per minute at 300 pounds per square inch before slurry began to leak past the seal and into the bearings. The bearings seized after 17 hours of total running time. Excessively thick slurries that cavitated at the inlet and permitted the pump to overspeed also caused bearing failure. There was no evidence of abrasion of the impeller.

A vertical centrifugal pump of NACA design (fig. 32) also suffered bearing failure (ref. 47). The 6-inch-diameter impeller developed an outlet pressure of 70 pounds per square inch when driven at 3600 rpm by a geared 2.5-horsepower air motor. Even though the slurry level was kept well below the seal, slurry invariably penetrated the seal and damaged the bearings. It appears that centrifugal pumps might continue to operate for long periods if pressurized lubricant were used to prevent seepage of slurry past the seal.

DISPLACEMENT SYSTEMS

Diagrams of three systems for pumping slurries by displacement with a hydraulic fluid are shown in figure 33. Jet fuel was used as the pumping medium and to flush the slurry system after a test run.

In small-diameter systems with tight-fitting pistons (figs. 33 (a) and (b)), if leakage occurred around the pistons during pumping of very viscous slurries, the jet fuel channeled through the slurry and flowed directly to the discharge, mixing only slightly with the slurry. The cylinders in figure 33 (a) (also ref. 30) had an inside diameter of 5 inches. On the piston were two ¼-inch-thick O-rings of 5⅛-inch outside diameter. The jet fuel caused the O-rings to swell. Excessive swelling over a period of time will cause piston seizure.

Experience showed that in large-diameter (approx. 36-in.) systems with loosely fitting pistons, channelling of the jet fuel through the slurry was not a problem. Figure 33 (c) illustrates such a piston, which is actually a wooden disk of such density that it floated between the slurry and the jet fuel. The displacement systems were not suitable for unstable slurries, since none of them provided for recirculation or agitation of the slurry.

Preliminary work has been done on a displacement system in which Cordite is used as a source of high-pressure gas to propel the piston. This system was used in the flight tests of ramjet vehicles. Design and performance data on such a system are given in reference 44.

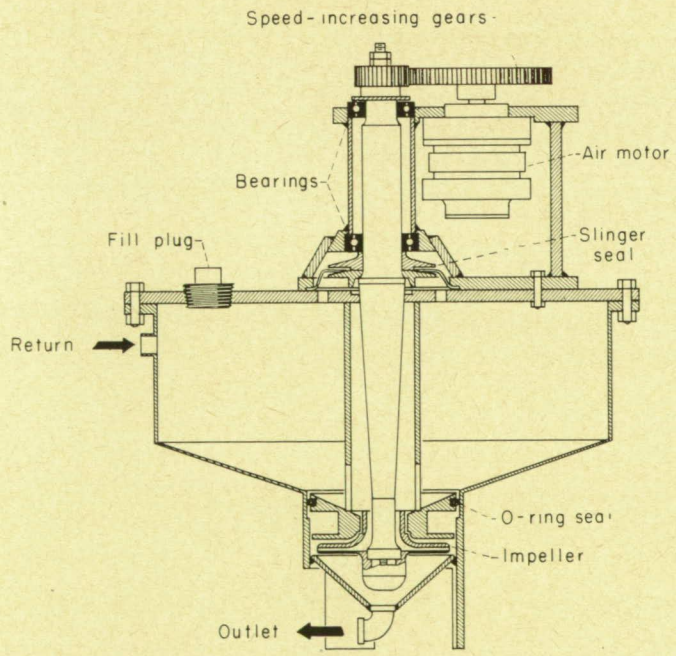
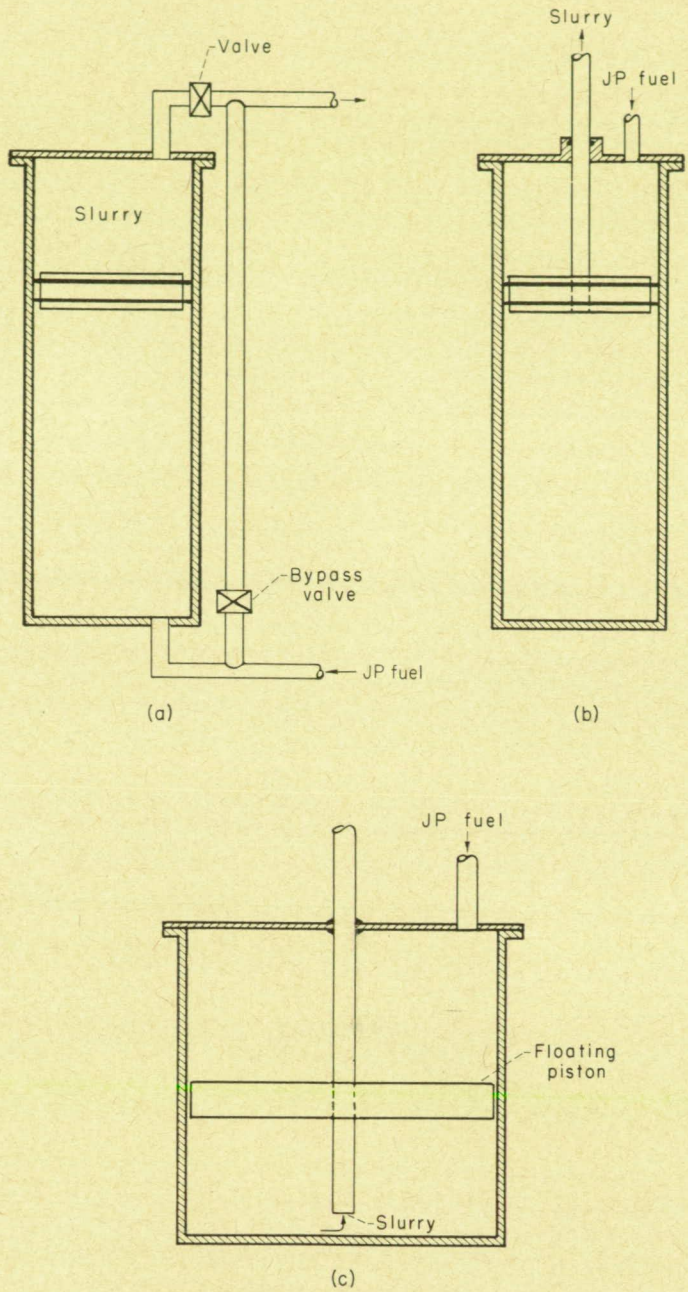


FIGURE 32.—Vertical centrifugal slurry pump (ref. 47).



(a) Free piston (b) Discharge through piston.
(c) Floating piston.

FIGURE 33.—Slurry displacement systems (ref. 47).

VALVES FOR SLURRY SYSTEMS

The problem of finding suitable valves for slurries was not so imposing as the development of suitable pumping equipment. Spring-loaded plug valves with manual or mechanically linked shutoff have been used successfully. These valves, which may be obtained with two-, three-, or four-way bodies, did not leak at a pressure of 125 pounds per square inch and were not damaged by magnesium particles. Unfortunately, however, such valves do not permit fine regulation of flow.

For flow regulation, commercially available valves with rubber membranes that can be moved to vary the flow-passage opening were used. Positive shutoff is reliable because the rubber can close tightly over the metal particles that are trapped on the closure or valve-seating surfaces.

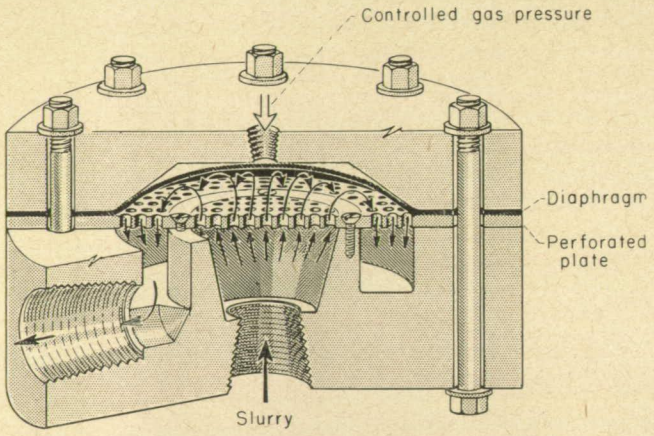


FIGURE 34.—Pressure-relief valve (ref. 47).

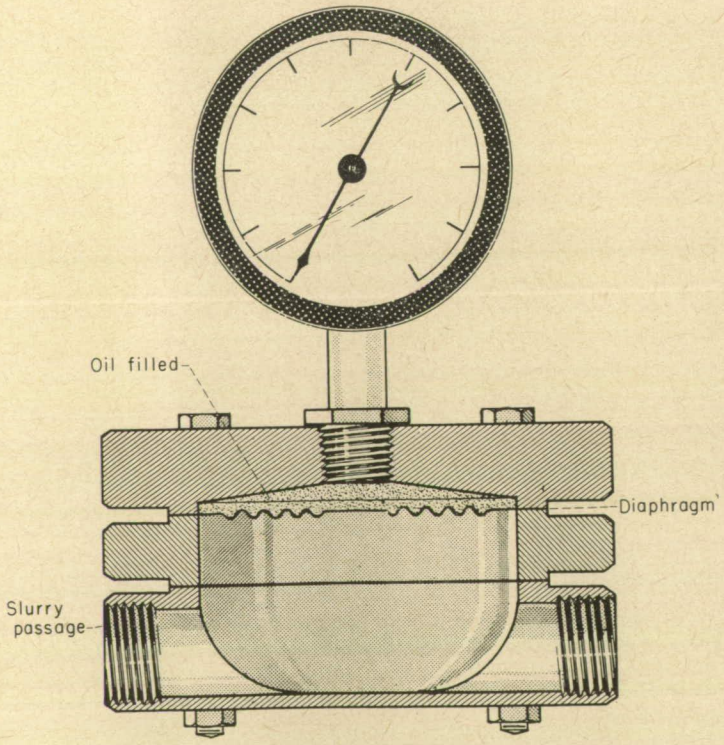


FIGURE 35.—Diaphragm-sealed pressure gage (ref. 47).

Also, the membrane seals the sliding metal valve parts from contact with the slurry.

The pressure-relief valve shown in figure 34 was used in the recirculating-fuel system described in reference 27. Operation with this valve was entirely satisfactory.

FLOW AND PRESSURE MEASUREMENT

The physical and hydraulic properties of slurries that affect flow and pressure measurement are discussed in appendix B of reference 47. Sharp-edged orifices and Venturi tubes can be used to meter slurries, but the success of such devices depends on the development of pressure gages that will not be affected by solid particles. Ordinary gages have Bourdon tubes, bellows, or diaphragm chambers that contain stagnant zones in which slurries may settle. The resulting sediment impedes the motion of the indicating linkage and is extremely difficult to remove.

In order to avoid these difficulties, several methods have been used to provide for an indirect measurement of slurry flow. For the displacement pumping systems described previously (fig. 33), the jet fuel is metered and the slurry flow rate is determined from the ratio of the densities of the slurry and jet fuel.

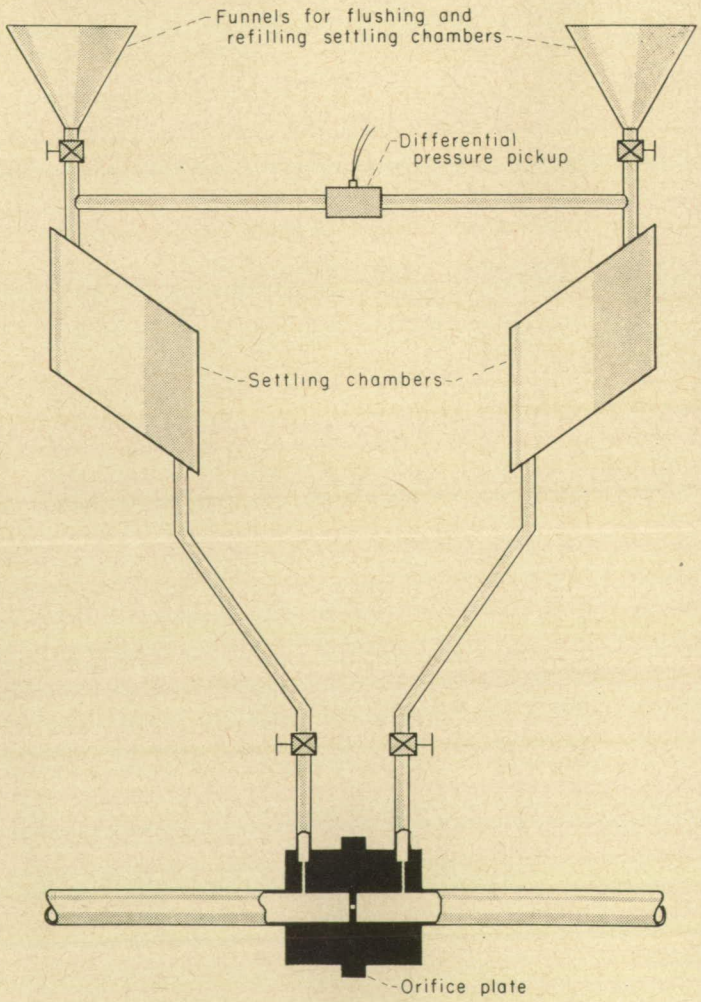
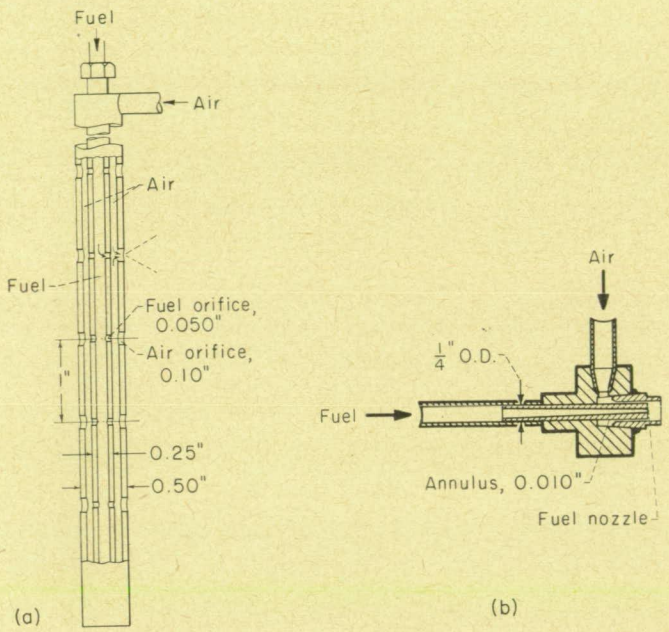


FIGURE 36.—Settling chambers for differential pressure gage (ref. 47).

The slurry fuel system described in reference 41 had a fuel tank suspended from a strain gage connected to a strip-chart recorder that plotted fuel weight as a function of time. This type of setup is suitable for tests run at nearly constant fuel-flow rates.

A rotating-vane flowmeter was used in the investigation reported in reference 42. A permanent magnet in the rotor generated an alternating potential having a frequency proportional to the flow. The meter was modified by the manufacturer to incorporate additional clearance in the bearings and bleed holes for continuously flushing the bearings. The slurry passed through this meter at a rate of 0.275 to 0.8 pound per second. The inside diameter of the meter was $\frac{3}{8}$ inch. A smaller-size meter clogged with a 50 percent magnesium slurry.



(a) Aspirating spray bar. (b) Air-atomizing nozzle.

FIGURE 37.—Air-atomizing devices for slurry fuels (refs. 27 and 30).

Pressures in slurry fuel-flow systems have been measured by means of diaphragm-sealed pressure gages. As indicated in figure 35, the slurry is not in contact with the pressure-measuring instrument. The pressure of the slurry acting on the diaphragm is transmitted to the gage.

Differential pressures across the orifices or Venturi flowmeters are usually measured by remote-indicating diaphragm-actuated pressure pickups, such as the arrangement described in reference 27. The pickup is protected by a series of settling chambers (fig. 36) filled with jet fuel, which has a lower density than the slurry. Flushing the chambers between tests prevented the slurry from entering the pressure pickup.

SLURRY FUEL INJECTORS

The creation of a homogeneous fuel-air mixture at the entrance to a combustor flame-seating zone is one of the requirements of good combustor design. In turbojet afterburners the duct length available for fuel-air mixing before the flameholders is severely limited by weight and size considerations.

In the case of slurry fuels, the problem of obtaining a homogeneous mixture at the flame seat is further complicated by the extremely viscous nature of the slurry, which tends to promote coarse atomization and uneven fuel-spray distribution. High-speed photographs of slurry sprays (fig. 12 and refs. 27 and 29) illustrate the magnitude of the droplet-size difference between conventional and slurry fuels and indicate that spray patterns and distribution of gelled magnesium slurry are influenced by slurry viscosity. Other

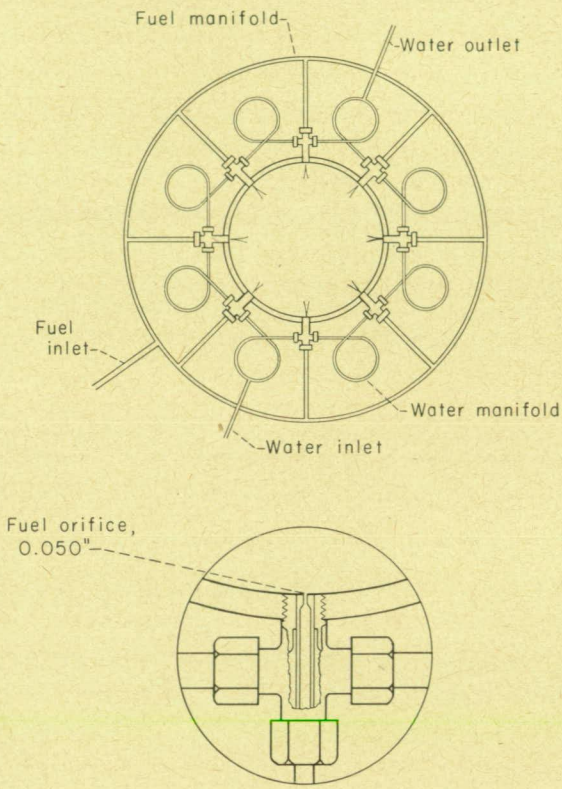


FIGURE 38.—Water-jacketed fuel injector (ref. 27).

tests (ref. 27) indicated that air could be used to promote better atomization. Details of air-atomizing nozzles that have been used successfully are shown in figure 37 (also refs. 27 and 30).

With nozzles of the air-atomizing type, the airstream shields the slurry from the high temperatures of the combustion zone and atomizes the fuel. If the atomizing-air supply is shut off after the slurry flow is interrupted and before the combustor has cooled, the jet-fuel carrier in the slurry quickly boils off and leaves a hard plug of dried powder clogging the injector. When fuel is injected without air atomization, it is often necessary to provide a means of cooling the fuel injector. A water-jacketed slurry injector is illustrated in figure 38 (also ref. 27). Water-cooling may be unnecessary, however, if the slurry injection is preceded by jet-fuel injection. The jet fuel cools the injector; and, if slurry is introduced at a high flow rate, the injector remains cool. Slurry injection may be followed by jet-fuel flow to flush the injector.

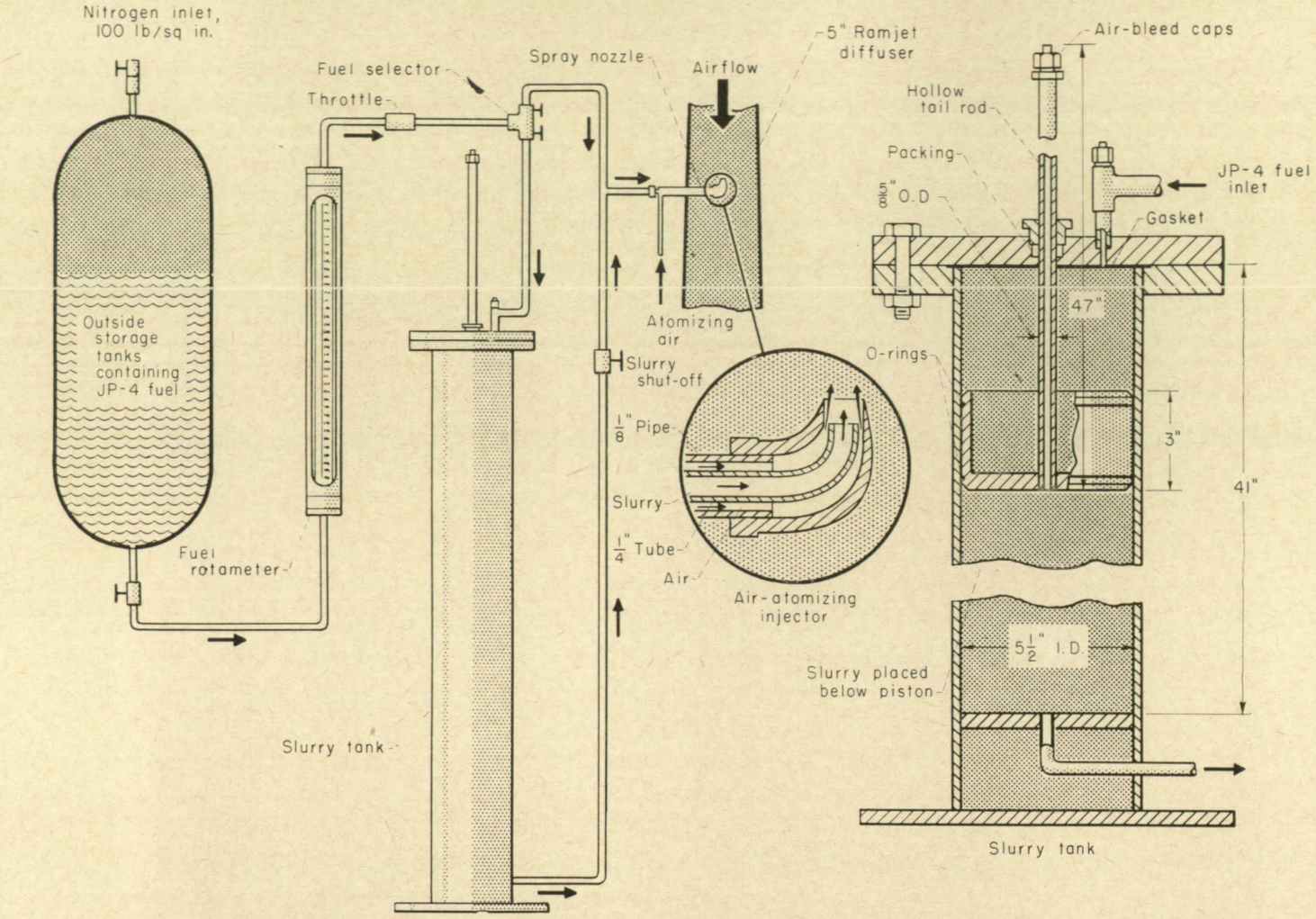


FIGURE 39.—Diagram of fuel system used in conjunction with 5-inch-diameter ramjet burner for tests on boron slurry (ref. 33).

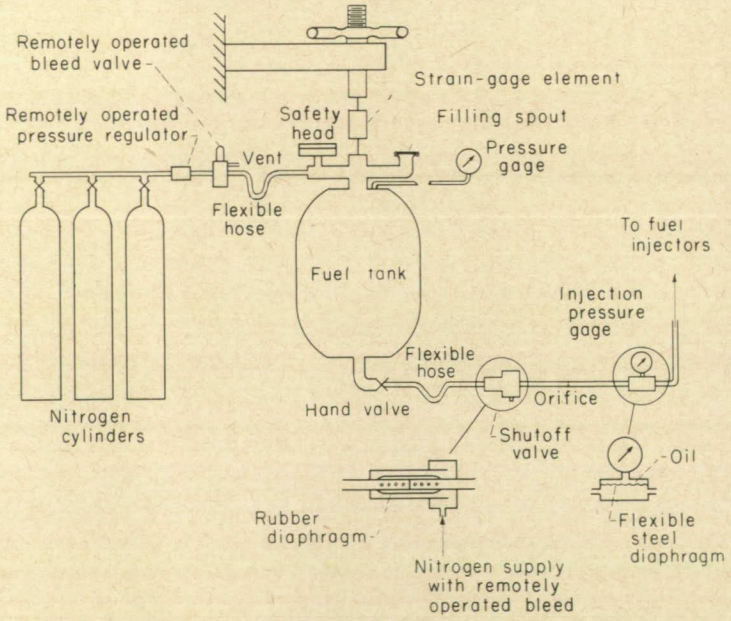


FIGURE 40.—Diagram of fuel system used in conjunction with 6.5-inch-diameter ramjet engine for tests on magnesium slurry (ref. 41).

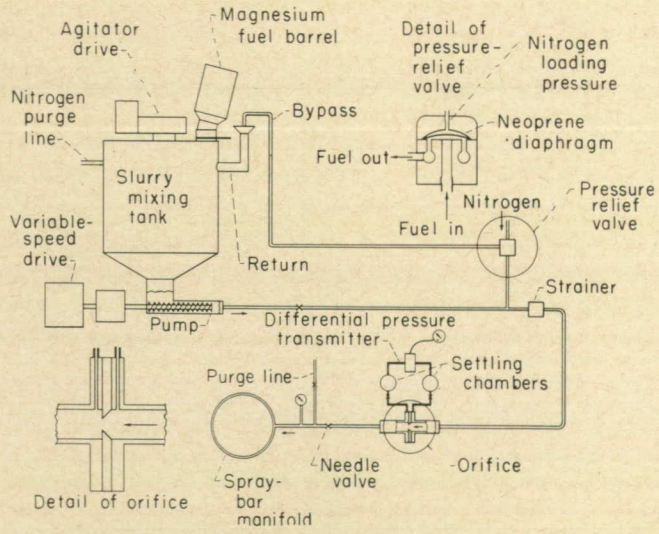


FIGURE 41.—Diagram of afterburner fuel system used for tests of magnesium slurry (ref. 27).

Slurries have been atomized by being impinged on a splash plate or sleeve mounted in the airstream (ref. 41).

Examples of ways the various elements of fuel systems have been combined are shown in figures 39 to 41 and are discussed in some detail in references 27, 41, 42, and 45. Figures 39 and 40 illustrate the transfer of slurries to ramjet engines by displacement with pressurized JP–4 and nitrogen, respectively. Figure 41 shows the use of a pump to force slurry into an afterburner. All these systems, having been designed to operate on the ground and to yield a maximum of operational data, were too heavy and bulky to be usable in aircraft, but probably could be modified for this purpose. The gas-generator pressurized systems used in the Pilotless Aircraft Research Station tests are examples of displacement systems designed for small flight vehicles. Considerably more work would be required to design slurry fuel systems for large flight vehicles.

CONCLUDING REMARKS

The results of the research program indicate that boron-slurry fuels were not satisfactory for use in afterburners and ramjet engines because of the poor combustion efficiency of the boron. Magnesium-slurry fuels performed successfully but can only provide greater thrust than conventional hydrocarbon fuels, not increased range. The flow and combustion characteristics of magnesium slurry necessitated some modifications in conventional fuel systems and combustors. Toward the end of the slurry-fuel program, attention was turned to liquid nonhydrocarbon fuels that were under study and that offered more satisfactory handling characteristics than did magnesium slurry, as well as greater thrust and range than obtainable from hydrocarbons. Consequently, the slurry-fuel program was terminated.

The information obtained on the preparation, flow properties, and stability of concentrated suspensions of boron and magnesium in hydrocarbon may be applicable to the use of suspensions for other purposes.

LEWIS FLIGHT PROPULSION LABORATORY
NATIONAL ADVISORY COMMITTEE FOR AERONAUTICS
CLEVELAND, OHIO, *August 15, 1958*

REFERENCES

1. Olson, Walter T., and Gibbons, Louis C.: Status of Combustion Research on High-Energy Fuels for Ram Jets. NACA RM E51D23, 1951.
2. Olson, Walter T., and Breitwieser, Roland: NACA Research on Slurry Fuels Through 1954. NACA RM E55B14, 1955.
3. Olson, Walter T.: Possibilities and Problems of Some High Energy Fuels for Aircraft. Paper 41B, SAE Nat. Aero. Meeting (NY), April 1958.
4. Henneberry, Hugh M.: Effect of Fuel Density and Heating Value on Ram-Jet Airplane Range. NACA RM E51L21, 1952.
5. Tower, Leonard K.: Analytic Evaluation of Effect of Inlet-Air Temperature and Combustion Pressure on Combustion Performance of Boron Slurries and Blends of Pentaborane in Octene-1. NACA RM E55A31, 1955.
6. Tower, Leonard K.: Analytic Evaluation of Effect of Inlet-Air Temperature and Combustion Pressure on Combustion Performance of Boron Slurries and Blends of Pentaborane in Octene-1. Supplement I—Influence of New Boric-Oxide Vapor-Pressure Data on Calculated Performance of Pentaborane. NACA RM E56D02, 1956.
7. Tower, Leonard K., Breitwieser, Roland, and Gammon, Benson E.: Theoretical Combustion Performance of Several High-Energy Fuels for Ramjet Engines. NACA Rep. 1362, 1958. (Supersedes NACA RM's E51C12, E51C23, E51D25, E51F05, E52L08, and E53G14.)
8. Branstetter, J. Robert, Lord, Albert M., and Gerstein, Melvin: Combustion Properties of Aluminum as Ram-Jet Fuel. NACA RM E51B02, 1951.
9. Pinns, Murray L.: Effect of Surface-Active Additives on the Physical Behavior of 50-Percent Slurries of 1.5-Micron Magnesium in *n*-Decane. NACA RM E54K22a, 1955.
10. Weltmann, Ruth N., and Kuhns, Perry W.: An Automatic Viscometer for Non-Newtonian Materials. NACA TN 3510, 1955.
11. Pinns, Murray L., and Goodman, Irving A.: Study of the Physical Properties of Petrolatum-Stabilized Magnesium-Hydrocarbon Slurry Fuels. NACA RM E53J16, 1954.
12. Altshuller, Aubrey P.: Some Dielectric Properties of Suspensions of Boron Powders in Mineral Oil. NACA RM E55F02, 1955.
13. Altshuller, Aubrey P.: The Shapes of Particles from Dielectric Constant Studies of Suspensions. Jour. Phys. Chem., vol. 58, no. 7, July 1954, pp. 544–547.
14. Altshuller, Aubrey P.: Study of Some Dielectric Properties of Suspensions of Magnesium Particles in Mineral Oil. NACA RM E53L09, 1954.
15. Goodman, Irving A., and Fenn, Virginia O.: Preparation and Properties of Concentrated Boron-Hydrocarbon Slurry Fuels. NACA RM E54F18a, 1954.
16. Goodman, Irving A., and Fenn, Virginia O.: Preparation of 50 Percent Boron-Hydrocarbon Slurries Using Combinations of Glycerol Sorbitan Laurate with Various Thickeners. NACA RM E55E17, 1955.
17. Hipsher, Harold F.: Effect of Temperature on Viscosity of Slurries of Boron and Magnesium in JP–5 Fuel. NACA RM E55E19, 1955.
18. Witzke, Walter R., Prok, George M., and Walsh, Thomas J.: A Preliminary Study of the Preparation of Slurry Fuels from Vaporized Magnesium. NACA RM E53K23, 1954.
19. Witzke, Walter R., Prok, George M., and Keller, Thomas A.: Design Considerations of a Condensing System for Vaporized Magnesium. NACA RM E55I20, 1955.
20. Pinns, Murray L.: Estimation of Specific Surface of Finely Divided Magnesium. NACA RM E56D10a, 1956.
21. Pinns, Murray L.: Effect of Surface-Active Additives on Physical Properties of Slurries of Vapor-Process Magnesium. NACA RM E55H26, 1955.
22. Pinns, Murray L.: The Effect of Surface-Active Additives on the Behavior of Magnesium-Decane Slurries. M. S. Thesis, Case Inst. Tech., 1954.
23. Weltmann, Ruth N., and Keller, Thomas A.: Pressure Losses of Titania and Magnesium Slurries in Pipes and Pipeline Transitions. NACA TN 3889, 1957.
24. Prok, George M.: Effect of Plastic Viscosity and Yield Value on Spray Characteristics of Magnesium-Slurry Fuel. NACA RM E56J19a, 1957.
25. Gibbs, James B., and Cook, Preston N., Jr.: Preparation and Physical Properties of Metal Slurry Fuels. NACA RM E52A23, 1952.
26. Caves, Robert M.: Stabilization of 50-Percent Magnesium—JP–4 Slurries with Some Aluminum Soaps of C_8 Acids. NACA RM E54C10, 1954.
27. Tower, Leonard K., and Branstetter, J. Robert: Combustion Performance Evaluation of Magnesium-Hydrocarbon Slurry Blends in a Simulated Tail-Pipe Burner. NACA RM E51C26, 1951.

526597—60——84

28. Lamberti, Joseph M.: The Effect of Magnesium Particles of Various Equivalent Diameters on Some Physical Properties of Petrolatum-Stabilized Magnesium-Hydrocarbon Slurries. NACA RM E54A22, 1954.
29. Cook, Preston N., Jr., Evans, Vernida E., and Lezberg, Erwin A.: Experimental Investigation of Physical and Combustion Properties of Several Residual Fuel Oil sand Magnesium—Fuel-Oil Slurries in a Ram-Jet-Type Combustor. NACA RM E53D30, 1953.
30. Cook, Preston N., Jr., Lord, Albert M., and Kaye, Samuel: Blow-Out Velocities of Various Petroleum, Slurry, and Hydride Fuels in a 1⅞-Inch-Diameter Combustor. NACA RM E54A28, 1954.
31. Morris, James F., Caves, Robert M., and Lord, Albert M.: Blow-Out Velocities of Several Slurry and Liquid Fuels in a 1⅞-Inch-Diameter Combustor. NACA RM E54L27a, 1955.
32. Lord, Albert M.: An Experimental Investigation of the Combustion Properties of a Hydrocarbon Fuel and Several Magnesium and Boron Slurries. NACA RM E52B01, 1952.
33. Reynolds, Thaine W., and Haas, Donald P.: Performance of Slurries of 50 Percent Boron in JP–4 Fuel in 5-Inch Ram-Jet Burner. NACA RM E54D07, 1954.
34. Kerslake, William R., Dangle, E. E., and Cervenka, A. J.: Experimental Evaluation of Boron-Hydrocarbon Slurry in a 16-Inch Ram-Jet Combustor. NACA RM E55C07, 1955.
35. Rabinovich, B. V.: Viscosity of Borax and Boric Anhydride in Interval of Softening. Jour. Phys. Chem (U. S. S. R.), vol. 16, 1942, pp. 23–26.
36. Lord, Albert M., and Evans, Vernida E.: Effect of Particle Size and Stabilizing Additives on the Combustion Properties of Magnesium Slurry. NACA RM E52K12, 1953.
37. Coffin, Kenneth P.: Burning Times of Magnesium Ribbons in Various Atmospheres. NACA TN 3332, 1954.
38. Tower, Leonard K.: Effect of Water Vapor on Combustion of Magnesium-Hydrocarbon Slurry Fuels in Small-Scale Afterburner. NACA RM E52H25, 1952.
39. Povolny, John H., Useller, James W., and Chelko, Louis J.: Experimental Investigation of Thrust Augmentation of 4000-Pound-Thrust Axial-Flow-Type Turbojet Engine by Interstage Injection of Water-Alcohol Mixtures in Compressor. NACA RM E9K30, 1950.
40. Dettwyler, H. Rudolph, and Bond, Aleck C.: Flight Performance of a Twin-Engine Supersonic Ram Jet from 2,300 to 67,200 Feet Altitude. NACA RM L50L27, 1951.
41. Branstetter, J. Robert, Gibbs, James B., and Kaufman, Warner B.: Magnesium-Slurry Combustion Performance in 6.5-Inch-Diameter Ram-Jet Engine Mounted in Connected-Pipe Facility. NACA RM E53E27, 1953.
42. Gibbs, James B.: Starting Characteristics and Combustion Performance of Magnesium Slurry in 6.5-Inch-Diameter Ram-Jet Engine Mounted in Connected-Pipe Facility. NACA RM E53K05, 1954.
43. Simon, Dorothy M., and Wong, Edgar L.: Flame Velocities over a Wide Composition Range for Pentane-Air, Ethylene-Air, and Propyne-Air Flames. NACA RM E51H09, 1951.
44. Bartlett, Walter A., Jr., and Hagginbothom, William K., Jr.: Flight and Preflight Tests of a Ram Jet Burning Magnesium Slurry Fuel and Utilizing a Solid-Propellant Gas Generator for Fuel Expulsion. NACA RM L55A24, 1955.
45. Bartlett, Walter A., Jr., and Merlet, Charles F.: Flight Investigation of a Ram Jet Burning Magnesium Slurry Fuel and Having a Conical Shock Inlet Designed for a Mach Number of 4.1. NACA RM L56I24a, 1957.
46. Trout, Otto F., Jr., and Kennedy, Thomas L.: Preflight and Flight-Test Investigation of a 50-Percent-Magnesium 50-Percent JP–4 Slurry Fuel in a Twin-Engine Ram-Jet Vehicle. NACA RM L56C06, 1956.
47. Barnett, Henry C., Lord, A. M., and Wise, P. H.: Preparation and Handling of Magnesium-Hydrocarbon Slurries for Jet-Engine Applications. NACA RM E55D01, 1955.
48. Faget, Maxime A., and Dettwyler, H. Rudolph: Initial Flight Investigation of a Twin-Engine Supersonic Ram Jet. NACA RM L50H10, 1950.

REPORT 1389

CHARACTERISTICS OF THE LANGLEY 8-FOOT TRANSONIC TUNNEL WITH SLOTTED TEST SECTION [1]

By Ray H. Wright, Virgil S. Ritchie, and Albin O. Pearson

SUMMARY

A large wind tunnel, approximately 8 feet in diameter, has been converted to transonic operation by means of slots in the boundary extending in the direction of flow. The usefulness of such a slotted wind tunnel, already known with respect to the reduction of the subsonic blockage interference and the production of continuously variable supersonic flows, has been augmented by devising a slot shape with which a supersonic test region with excellent flow quality could be produced. The flow in this ⅛-open slotted test section was surveyed extensively and calibrated at Mach numbers up to about 1.14. The uniformity and angularity characteristics of the flow were entirely satisfactory for testing purposes. The uniform Mach number in the test region was infinitely variable up to supersonic Mach numbers without change of tunnel geometry. The power required for operation of the slotted tunnel was considerably in excess of that for the closed tunnel but could be somewhat reduced. The flow principles involved in the operation of such a wind tunnel are discussed in some detail.

The reliability of pressure-distribution measurements for a fineness-ratio-12 nonlifting body of revolution in the slotted test section was established by comparisons with body pressure distributions obtained from theory, from free-fall tests, and from other wind-tunnel tests. The effects of boundary interference on the body pressure distributions measured in the slotted test section were shown to be negligible at subsonic Mach numbers and at the higher supersonic Mach numbers obtained. At low supersonic Mach numbers, however, portions of the body pressure distributions were influenced by boundary-reflected disturbances which increased in intensity and moved downstream with increase in Mach number. The effect of the disturbances on body pressures was ascertained and their effect on body drag was shown to be small, particularly when the body was located off the test-section center line to reduce focusing of the reflected disturbance waves.

Experimental locations of detached shock waves ahead of axially symmetric bodies at low supersonic speeds in the slotted test section agreed satisfactorily with predictions obtained by use of existing approximate methods.

INTRODUCTION

In reference 1, a type of wind tunnel having a slotted test section is described in which the tunnel boundary interference due to solid blockage can be greatly decreased or reduced to zero and in which tunnel choking does not exist. The stream Mach number in the slotted test section can be varied continuously up to and through a value of 1.0 and the Mach number in the supersonic range is, moreover, continuously variable.

In order to take advantage of these favorable characteristics the Langley 8-foot high-speed tunnel, which was operated with an axisymmetrical fixed nozzle to produce subsonic Mach numbers up to 0.99 and a supersonic Mach number of 1.2 (see ref. 2), was converted to slotted-tunnel operation early in 1950 and henceforth will be designated as the Langley 8-foot transonic tunnel. The present paper describes this modification and the subsequent changes necessary to produce a test section with uniform Mach number. In addition, an investigation was made (1) to survey and calibrate the flow in the slotted test section and (2) to ascertain the reliability of pressure-distribution measurements for a typical nonlifting transonic model in the slotted test section. The latter part of the investigation included extensive pressure measurements and schlieren observations needed to evaluate the nature and approximate magnitude of test-section boundary effects on the model pressures.

SYMBOLS

a	speed of sound in air
C_D	body drag coefficient based on body frontal area
L_M	axial distance required for free-stream Mach line, starting at model nose, to traverse the supersonic flow to test-section boundary and reflect back to surface of model near test-section center line
L_S	axial distance required for model nose shock to traverse the supersonic flow to test-section boundary and reflect back to surface of model near test-section center line
l	basic length of body-of-revolution model
M	Mach number, V/a
M_{TC}	Mach number corresponding to ratio of stream total pressure to pressure in test chamber surrounding the slotted section
M_o	average Mach number in test section; stream Mach number; Mach number ahead of shock
M_1	Mach number behind shock
P	pressure coefficient, $\frac{p_1-p_o}{q_o}$

[1] Supersedes NACA Research Memorandum L51H10 by Ray H. Wright and Virgil S. Ritchie, 1951, and NACA Research Memorandum L51K14 by Virgil S. Ritchie and Albin O. Pearson, 1952.

$(\Delta P)_{max}$ maximum change in pressure coefficient at model surface due to effect of boundary-reflected distrubances at supersonic speeds

P_{sonic} pressure coefficient corresponding to the speed of sound

p_l local static pressure

p_o stream static pressure

q_o stream dynamic pressure, $\frac{1}{2}\rho V^2$

V airspeed

x axial distance downstream of slot origin; distance downstream of model nose

x_{SB} axial distance from sonic point on body to location of detached shock ahead of body nose

y radial distance from tunnel center line

y_{SB} radial distance from body center line to sonic point on body surface

α angle of attack of model

β acute angle between weak shock wave and the flow direction

θ_v mean flow inclination to the horizontal (measured in vertical plane through center line of tunnel), positive for upflow, deg

ρ mass density of air

APPARATUS AND METHODS

DESIGN OF TEST SECTION

The modification of the Langley 8-foot high-speed tunnel was limited by the desire to preserve intact the original reinforced concrete structure. The length available for the test section was therefore restricted to the 15-foot-long region between the downstream end of the entrance cone and the upstream end of the diffuser; the maximum transverse dimension could not exceed the approximately 96-inch minimum diameter of the entrance cone and diffuser. Moreover, because of the necessity of taking into the diffuser the low-speed air from the mixing region at the slots and because of the expansion required for supersonic flow, the cross-sectional area at the throat had to be reduced to a value less than that at the diffuser entrance—about 20 percent less as suggested by the experiments of reference 1.

In order to accomplish this reduction of area at the throat, a liner was inserted into the original tunnel. The liner and test section were made polygonal in cross section to facilitate construction and to provide plane surfaces for windows. The twelve-sided regular polygon was chosen, as it provided a sufficiently near approach to the circular cross section of the entrance and diffuser to make enough space available for the supporting structure at all points between the original entrance cone and the liner and to allow the fairing into the circular diffuser entrance to be relatively easy. The sides were sufficiently wide to accommodate windows approximately 12 inches square. A cutaway view of the installation is shown in figure 1.

The shape of the entrance liner, given in figure 2, was based on that of the plaster nozzle described in reference 2. This entrance shape, which near its downstream end diverged to an angle of 5 minutes with the center line of the tunnel, was designed to produce a very gradual expansion, so that the Mach number at tunnel station 0 (origin for tapered slots) is nearly uniform and, for all supersonic test-section Mach numbers, is equal to unity all over the cross section. The boundary-layer development is responsible (see ref. 2) for the fact that the effective minimum section (cross section at which the Mach number is unity) exists at or near the slot origin rather than 32 inches upstream at the geometric minimum section. With this liner the maximum possible ratio of diffuser-entrance cross-sectional area to throat cross-sectional area is about 1.18.

The test section was made of steel panels reinforced on the back and supported at the ends. Between the panels, at the corners of the polygon, slot spaces were left sufficiently wide to permit the attachment of strips forming rounded slot edges. By changing these slot edges, constructed of wood to facilitate their modification, various slot shapes (plan forms) could be tested. The spaces between the panels were made sufficiently wide to permit slot widths considerably in excess of the width corresponding to a total opening of one-ninth of the periphery, which is the ratio of open to total jet boundary judged from reference 1 to be required (with 12 equally spaced slots) for zero solid blockage.

In the original design, windows were placed in three panels on each side of the test section, but in assembly, in order to facilitate model observation, one of these glazed panels was interchanged with the top panel (fig. 1, section C-C).

The panels were originally installed with a divergence angle of 45 minutes relative to the center line of the tunnel. To reach this divergence from the 5-minute divergence at the downstream end of the approach section, the upstream end of every panel was gradually curved over the first 18 inches. The shape of this curved region is shown in figure 3 (a).

The stream-side surfaces of the panels and of the downstream 10 feet of the entrance cone were carefully machined, and precautions were taken to assure the smoothness and continuity of the surface. In particular, considerable care was exercised to minimize any differences in surface level at the juncture between the panels and the entrance cone. Inaccuracies in window installation caused disturbances which were removed by fairing the edges or by reinstallation.

At 125.6 inches from their upstream ends the panels joined with a transition section (fig. 3 (a)) which led into the circular diffuser entrance at the 180-inch station. This transition section was made up of curved elements and flat triangular parts as shown in figure 1. The triangular flats made an angle of approximately 2°30′ with the center line of the tunnel so that a discontinuity in slope existed at the 125.6-inch station. The transition section was slotted but the slots could be filled and thus stopped at any position between the 125.6- and 180-inch stations. Because the panels were of essentially constant width, the slot width in this divergent region increased from 2.6 inches to about 3.5 inches.

As indicated in figure 1, section C-C, the structure of the panels was such that open channels existed under the slots. Because of the turbulent mixing at the slots and the expansion to supersonic flow, the jet must expand into the channels. Continuity then requires, since the chamber surrounding the slots is sealed, that air which came out through the slots

must reenter and pass into the diffuser. In order to guide this air into the diffuser entrance, noses were placed in the channels at the downstream ends of the slots as shown in figure 3. Several different nose shapes were tried, the first of which is indicated in figure 1. The nose shape used for most of the test discussed in this report is shown in figure 4 (a). This nose could be moved upstream or downstream to match the position of the downstream end of the slot. A later modification (fig. 4 (b)), including side plates which restricted the downstream channel width, was designed to reduce the power consumption. (See ref. 3.) The flap (fig. 4 (b)), which was open for subsonic operation and closed for supersonic operation, was designed to relieve a subsonic negative Mach number gradient introduced into the test region by this nose shape.

The original dome-shaped test chamber was used as the sealed tank surrounding the slots. (See fig. 1.) This chamber was adequately large, having a maximum diameter of 40 feet. It nowhere approached the slotted test section closer than 6 feet. Glass observation ports were provided in the top, at one side, and in the chamber door.

SLOT SHAPES

The slot shapes tested are shown in figure 5. For the rectangular shape (number 10) originally designed, the edges were made of steel, and two of these edges contained rows of pressure orifices. Figure 6 shows the location of these and other orifice rows. The other slot shapes tested were constructed with wood edges to facilitate their modification.

FLOW-SURVEY INSTRUMENTATION AND METHODS

The characteristics of the flow in the slotted test section were investigated by means of pressure measurements and schlieren observations near the center line and by means of pressure measurements at the wall.

Pressure and temperature measurements.—Static-pressure measurements were obtained from 0.031-inch-diameter orifices located in the surfaces along the center lines of diametrically opposed wall panels 5 and 11, and in the surface of a 2-inch-diameter cylindrical survey tube (fig. 1). The wall orifices were located approximately 2 inches apart axially in the slotted section and as far as 60 inches upstream of the slot origin. The cylindrical-tube orifices were arranged in four axial rows spaced 90° apart. A single row contained orifices located 6 inches apart in a 60-inch-long region immediately upstream of the slot origin, 2 inches apart in a 24-inch-long region just downstream of the slot origin, 6 inches apart in the 24- to 60-inch downstream region, and 2 inches apart in the region extending from 60 to 160 inches downstream of the slot origin. The three other rows contained orifices spaced 2 inches apart in the region from about 72 to 112 inches downstream of the slot origin; in this region the orifice locations in the four rows were staggered so that static-pressure measurements could be obtained at ½-inch intervals. The surface of the cylindrical tube was kept free of irregularities in the vicinity of pressure orifices.

The cylindrical survey tube was alined approximately parallel to the geometric center line of the slotted test section. The nose of the tube was located about 9 feet upstream of the slot origin and was held in position by means of three 0.060-inch-diameter stay wires spaced 120° apart angularly; the downstream end was located in the tunnel diffuser and was supported by means of the model-support system shown in figure 1. A small amount of sag existed along the unsupported length of the tube but this did not affect the pressure measurements. The tube was capable of axial movement to permit measurements at intervals as close as desired. Interchangeable offset adapters were used to locate the tube 6 inches and 15 inches off the center line at any desired angular position.

Local static-pressure measurements obtained by means of the orifices in the wall panel and in the cylindrical-tube surfaces were assumed to be equal to those outside the boundary layer except in the vicinity of a shock where the pressure changes would occur over an axial distance greater at the surface than outside the boundary layer.

Stream total-pressure measurements were obtained in the subsonic flow region upstream of the slot origin by means of several total-pressure tubes, one located in the ellipsoidal nose of the cylindrical survey tube (fig. 1) and the others in the low-speed section upstream of the contraction cone. Measurements also were obtained near the center line of the slotted test section by using a total-pressure rake consisting of eight 0.050-inch-diameter tubes, 3 inches long, mounted ahead of a 1° included-angle wedge.

Pressures were measured by use of multiple-tube manometers containing tetrabromoethane and by use of U-tubes containing kerosene. All manometer tubes were photographed simultaneously.

The temperature of the flow mixture in the tunnel was controlled in order to reduce possible humidity effects on the flow in the test section. Temperature measurements were obtained at a number of stations between the tunnel center line and wall in the low-speed section upstream of the contraction cone by use of thermocouples in conjunction with a recording potentiometer.

Schlieren optical system.—In order to supplement the pressure measurements, schlieren observations of flow phenomena were made by use of the temporary single-pass system shown in figure 7. This system utilized 1-foot-diameter parabolic mirrors and was mounted on large movable support structures which permitted observations at any desired test-section windows in the horizontal plane or in a plane 30° from the horizontal. A spark source was used for photographic recording. The entire system was located within the test chamber and was operated by remote control.

Determination of Mach number.—The flow Mach number, the parameter used for presenting most of the results of the present surveys, was obtained by relating simultaneously measured values of the stream total pressure and local static pressures. Indications of the flow Mach number were also obtained from measured values of the angularity of weak shock waves produced by small two-dimensional surface irregularities on opposite wall panels. Conical shock waves produced by a 10° included-angle cone of 1-inch maximum diameter were used not only for indicating the value of the stream Mach number but also for indicating the degree of flow uniformity in the slotted test section.

Flow angularity measurements.—The mean angularity of the flow with respect to a horizontal plane near the center line of the slotted test section was measured by use of the null-pressure-type instrument shown in figure 8. This instrument, a 3° included-angle cone, contained 0.010-inch-diameter static-pressure orifices located symmetrically in opposite surfaces. The sensitivity of this instrument to angle-of-attack changes, expressed in terms of the pressure differential between orifices in opposite surfaces and in the plane of angle change, was about 0.6 percent of the stream dynamic pressure per degree change of angle in the transonic speed range. This sensitivity, though not great, was within the possible error in instrument-attitude measurements. Such measurements, obtained by careful use of a cathetometer during actual testing, were estimated to include possible inaccuracies not exceeding 0.1°. The procedure for measuring the flow inclination consisted of, first, orienting the instrument so that pressure orifices in opposite surfaces were situated in the vertical plane of measurement, and second, varying the instrument attitude by means of a remotely controlled angle-changing mechanism in the support system until the pressures at the opposite surfaces were equal. The instrument attitude was determined carefully by means of cathetometer readings for this indicated null-pressure condition, and the procedure was repeated with the instrument inverted. The arithmetical average of instrument-attitude measurements made with the instrument erect and inverted was assumed to compensate for possible asymmetry of the instrument and to indicate the mean direction of the flow.

Rapid variations of the flow angularity with time were indicated by means of pressure-fluctuation measurements in the slotted test section. For these measurements a 3° included-angle cone was equipped with a small electrical pressure cell (mounted inside the cone) which connected directly with static-pressure orifices located 180° apart in the cone surface. Periodic differences in pressure between the orifices in opposite surfaces of the cone were measured by means of a recording oscillograph. The indicated pressure differences were expressed in terms of flow-angularity changes by use of a steady-state calibration of the pressure differential between orifices in opposite surfaces of the cone with respect to cone-attitude changes in the plane of the orifices. This pressure differential in the transonic range was about 5 pounds per square foot per degree change in cone attitude with respect to the flow, whereas the sensitivity of the pressure cell was approximately 0.25 pound per square foot. The accuracy of the pressure cell was maintained over a frequency range from 0 to 300 cycles per second.

Jet-boundary interference effects.—In order to ascertain the value of the slotted test section for testing purposes a high-fineness-ratio body of revolution was tested at zero angle of attack through the Mach number range from about 0.60 to 1.14 and the measured body-surface pressure distributions were compared with essentially interference-free distributions from other sources. The particular body shape used in this investigation, a fineness-ratio-12 body for which coordinates are given in reference 4, was selected because of the availability of theoretical and experimental pressure distributions. The wind-tunnel model consisted of the forward 83.7 percent (33.5 inches) of a 40-inch-long basic body; a 3.25° semiangle support sting joined the body at the 83.7-percent station (see fig. 9). This model contained static-pressure orifices (0.020 inch in diameter) spaced 2 inches apart axially along the length of the body and arranged in rows at various angular locations (ref. 5) but only the pressure measurements at the upper and lower surfaces were used for the comparisons shown in this report. Small surface discontinuities existed at model-component junctures, at an embedded mirror in the upper surface, and at faired surfaces over filled bolt holes.

The reflection of disturbances from the slotted-test-section boundary and the effect of such reflections on model pressure distributions were examined by testing both the body of revolution (fig. 9) and a wing-body combination (fig. 10) at supersonic speeds and correlating the measured pressures at model and wall surfaces with schlieren pictures of the flow field near the model surface. The wing-body combination consisted of the previously described body of revolution (fig. 9 (c)) fitted with a 45° sweptback airfoil of NACA 65A006 section, 12-inch semispan, and 1-square-foot planform area. Static-pressure orifices (0.020 inch in diameter) were located in the upper and lower surfaces of the airfoil at five semispan stations (see ref. 5) but for the present surveys pressures were measured mainly at the 60-percent and 80-percent semispan stations where the airfoil chords were about 5.70 and 5.05 inches, respectively. Pressure orifices at these wing stations were located at chordwise intervals no greater than 10 percent of the chord. Static-pressure orifices (0.018 inch in diameter) also were located at axial intervals of about 0.75 inch along the length of the model-support sting in order to measure pressures in the compression region at the base of the model and to aid in locating wall-reflected disturbances. Transition was fixed at 10-percent-chord and 12-percent-body-length stations for the wing and body of revolution, respectively.

The control of model attitude during tests in the slotted test section was effected by means of cathetometer observations and a remotely controlled angle-changing mechanism in the model-support system.

PRECISION OF DATA

The maximum random error in the indicated Mach number, as obtained from pressure measurements throughout the transonic range covered by these surveys, was estimated to be no greater than 0.003 in shock-free flow. For measurements behind shocks an additional error in the indicated Mach number was possible because of failure to correct for changes of the stream total pressure through the shocks; this error, however, was negligible at the lower supersonic Mach numbers and did not exceed 0.002 for normal shocks at a Mach number of 1.14.

Probable errors in Mach numbers indicated by angularity measurements of weak shocks in supersonic flow were about 0.002. This error corresponds to an estimated inaccuracy of 0.2° in the measurement of the angularity of two-dimensional shocks from the test section walls. The angularity of

sharply defined conical shocks could be measured with an inaccuracy of only about 0.1°.

The differences between Mach numbers determined from pressure measurements and those from shock-angularity measurements at supersonic speeds corresponded closely to the estimated probable errors in determining the Mach number. (See fig. 11.)

Estimated possible errors in the model-surface pressure coefficients obtained from tests in the slotted test section were generally about 0.005 and did not exceed about 0.010.

The sensitivity of the schlieren optical system, when properly adjusted, was sufficient to permit the detection of a conical shock whose strength corresponded to a Mach number change of about 0.003.

The maximum possible error in measuring the flow angularity was estimated to be about 0.1°. A like error in measuring the model angularity introduced the possibility of errors as great as 0.2° in model alinement with respect to the flow direction.

RESULTS AND DISCUSSION

PRELIMINARY INVESTIGATIONS

Inasmuch as the 8-foot transonic tunnel was the first large slotted tunnel constructed at the Langley Laboratory, the first task was to study its general characteristics. Such a study was facilitated by the large size of the test chamber, which permitted direct observation during tunnel operation from positions near the slots. Such observation was limited, however, by the noise, which became painful at Mach numbers greater than about 0.6, and by the danger of a sudden large pressure increase due to power failure at large Mach number, which might result in physical injury to the observer. The test chamber was also uncomfortably hot because of the necessity of operating the tunnel with high stagnation temperature, up to 180° F, in order to prevent condensation difficulties.

In an investigation of the noise, the natural fundamental frequency of the system of test chamber and slots was roughly estimated at about 3 cycles per second. Measurements of the frequency and intensity of the sound in the test chamber indicated a vibration with about this frequency, but the greater part of the energy was rather widely distributed in general noise. This noise, which arose from the tunnel fan, from the vorticity and general turbulence in the slots, and from the general diffuser flow, reached an intensity in excess of 130 decibels at Mach numbers near unity. In addition, sections of the test-chamber floor vibrated, apparently with their natural frequencies, but these vibrations were not excessive. To minimize noise and vibration, blunt diffuser entrance noses are believed to be desirable, because sharp noses might be expected to produce oscillations when struck by the vortices proceeding downstream just outside the slots.

In addition to the vibration, a general circulatory movement of the air in the test chamber was observed. The scrubbing action at the slots entrains air from the test chamber and carries it along toward the diffuser entrance, where it is separated from the tunnel flow at the diffuser entrance noses, deflected out into the surrounding chamber, and circulated back toward the upstream ends of the slots.

The first tests were made with the rectangular slot shape and with a panel divergence of 45 minutes. The indicated Mach number distributions at the various orifice rows are shown in figure 6. In this figure M_{TC} is the Mach number corresponding to test chamber pressure. The total pressure for these and all other Mach number distributions presented in this report is that near the center of the tunnel stream.

The Mach number distribution shown in figure 6 is evidently unsatisfactory for model testing. As pointed out in reference 2, the flow disturbances in a circular tunnel are concentrated at the center; as might be expected, the 12-sided tunnel with regular polygonal cross section behaves in a similar manner, that is, the Mach number oscillations shown in figure 6 are considerably greater near the center of the tunnel than at the center of a panel. Special care is therefore required to obtain a model test region with uniform Mach number. The solution to this problem was deduced from tests with various slot widths and shapes, from additional tests which had previously been carried out in the apparatus of reference 1, and from a fundamental conception of the part to be played by the slots in producing the supersonic flow. Previous tests had already led to the belief that one of the most important causes of the Mach number oscillations was the overexpansion in the upstream part of the slotted section, similar to that which occurs when a supersonic jet debouches into a region having a pressure less than that at the jet exit. The function of the slot shape is conceived to be the control of this expansion in such a way that the Mach number will gradually approach its final test-section value without exceeding this value at any section. With the 45-minute divergence of the panels such control was found to be impossible, although a number of different slot shapes were tried, because the flow expansion produced by the curvature and divergence of the panels already exceeded that required.

The possibility existed of removing most of this divergence by turning end-for-end the part of the panels between stations 0 and 125.6 inches. This modification as accomplished is shown in figure 3 (b). The panels are straight for the first 107 inches with a 5-minute slope continuous with that of the entrance cone. The curved part of the plates now lies between the 107- and 125.6-inch stations, and curved liners have been added between the 125.6- and 141.6-inch stations in order to relieve the discontinuity in slope at that station and thus to prevent large flow disturbances with attendant shocks in this region.

The efficacy of changing the panel divergence from 45 to 5 minutes is shown in figure 12. A considerable reduction in the Mach number oscillations has been obtained, particularly near the center of the tunnel. The slot is now fulfilling its function of controlling the development of the supersonic flow, and changes in slot shape might therefore be utilized to improve the Mach number distribution at the center of the tunnel.

INVESTIGATION OF SLOT SHAPES

The establishment of supersonic flow suitably uniform for model testing in the slotted region of the Langley 8-foot transonic tunnel was the primary purpose of the investigation of slot shapes, since the production of satisfactorily

uniform flow at speeds up to and slightly exceeding the speed of sound was easily achieved simply by the installation of rectangular-plan-form slots. (See fig. 13.) The performance of rectangular slots, reported in reference 1 for the case of a 12-inch-diameter throat, was verified experimentally in the 88-inch effective-diameter throat of the Langley 8-foot transonic tunnel. A characteristic feature of supersonic flow in a throat equipped with rectangular slots is a rapid initial expansion and a subsequent compression of the flow immediately downstream of the slot origin. At Mach numbers greater than about 1.02 disturbances associated with the initial expansion-compression appear in the slotted-test-section flow, and the magnitude of the disturbances increases with Mach number. This performance is illustrated in figure 13, which presents the results of flow surveys in the 8-foot tunnel with rectangular slots and with the throat geometry of figure 3 (b). The disturbances shown in figure 13 are sufficiently severe to preclude the use of rectangular-plan-form slots at supersonic speeds in this test section.

The use of tapered slots to reduce the rapidity of the initial flow expansion and the severity of the accompanying disturbances, which was originally reported in reference 6, was followed in investigating suitable slot shapes for the Langley 8-foot transonic tunnel. For this investigation the tunnel throat geometry of figure 3 (b) was maintained. For some of these tests, the curved liner shown in figure 3 was replaced by a "boat-tail" as indicated at the top of figure 14, but this change did not significantly affect the flow in the test section. The first slot shape investigated was a straight-taper design, somewhat similar to one for which fairly good flow characteristics were reported in reference 6. This slot shape is identified in figure 5 as shape 1. The slot originated as a point at the effective minimum section of the tunnel (station 0) and opened with an angle of 0.77° between the edge and center line of the slot. The tapered portion extended 96 inches (1.09 jet diameters) downstream, after which the slot width remained constant. In this region of constant slot width, the open portion of the boundary comprised approximately one-ninth of the total periphery of the tunnel wall. The flow characteristics of the slotted section equipped with slot shape 1 (see fig. 14) corresponded approximately to those for the tapered slot reported in reference 6 for a 12-inch-diameter tunnel throat. The supersonic flow in both tunnels attained approximately the same maximum and minimum Mach numbers at equivalent distances (jet diameters) downstream of the slot origin. The existence of the compression region following the initial expansion was sufficient, however, to justify investigating the control of slotted-section flow characteristics by means of slot-shape modifications.

Other tapered slots were then investigated in an attempt to reduce the initial flow overexpansion and the compression that followed. The flow characteristics for slot shapes 4 and 9, which opened with only about half the angle of slot shape 1 over the first 48 inches downstream of the slot origin (see fig. 5), are shown in figures 15 and 16, respectively. Comparison of these data with those for slot shape 1 indicated that the reduction in the initial rate of opening of the tapered slot produced a corresponding reduction in the rate of flow expansion; also, the slight overexpansion and following compression of the supersonic flow produced by slot shape 1 was practically eliminated by use of shape 9. The flow expansions produced by slots 4 and 9 were almost identical in spite of the fact that slot shape 4 opens more abruptly downstream of the 48-inch station. In the test section the degree of flow uniformity was slightly less for shape 4 than for shape 9, and it is therefore surmised that small flow-uniformity gains may be expected by changing the slot shape gradually over the downstream portion of its taper.

Slot shapes 6 and 7 (see fig. 5) utilized over their first 12 inches of length essentially the same initial taper angles as were employed for shapes 9 and 1, respectively; but following this 12-inch straight-taper region slots 6 and 7 opened with greater angles of divergence than did shapes 9 and 1 and attained their full-open widths at 76 and 74 inches downstream of the slot origin. The results of flow surveys for these slot shapes, presented in figures 17 and 18, revealed that the supersonic flow downstream of the initial straight-taper region expanded more rapidly and compressed more severely than did the flow for slot shapes 9 and 1. The data for slot shapes 1, 9, 6, and 7 indicated that, for tapered slots whose initial opening angles are no greater than the 0.77-degree half-angle taper used for shape 1, the important factor in controlling the flow expansion and compression is the proper shaping of the slot over the long region in which most of the opening to full slot width takes place.

Slot shape 8, which opened in a straight taper of 1.18° half angle over its first 48 inches from the slot origin (see fig. 5), produced the Mach number distributions shown in figure 19. The supersonic-flow expansion occurred more rapidly for slot shape 8 than for any of the other tapered shapes investigated, as might be expected from the greater angle at which it opened. At the higher Mach numbers the distribution became saddle-shaped.

From the center-line Mach number distributions corresponding to slot shapes 1, 4, 6, 7, 8, and 9, the possibility now existed of relating slot-shape changes to the corresponding Mach number changes and thereby effecting modifications designed to improve the distribution. For the direction and a qualitative indication of the magnitude of the slot-width changes required, the conception of the function of the slots in producing the supersonic flow served as a guide. Thus, for instance, if at some point along the center line the flow has expanded to a Mach number in excess of that indicated by the test-chamber pressure, this overexpansion can be traced back along a Mach line to a region on the tunnel boundary; if in this region the pressure on the panels is greater than that in the test chamber, a decrease in slot width is indicated in order to reduce the flow expansion at that section.

In selecting a slot shape to serve as a basis for the new design, shape 9 was chosen because it already produced a supersonic flow of considerable uniformity. In addition to the changes intended to improve the flow uniformity, which were accomplished by interpolating among the slot shapes previously tested and by applying the ideas discussed in the previous paragraph, a further modification was made in order to decrease the length required for establishment of

the uniform flow. For this purpose the angle of taper at the upstream end was increased to a value approaching that for shape 8. This increase in taper angle at the upstream end was consistent with a decrease between the 55- and 75-inch stations, where such a decrease was believed to be desirable in order to decrease the Mach number oscillations in the test region. The final slot shape is shown as number 11 in figure 5.

The results of the flow surveys with slot shape 11, which are presented in figure 20, show a slight improvement in flow uniformity at Mach numbers greater than 1.1. The overexpansion with subsequent compression is practically eliminated, and, moreover, this uniform flow is reached in a shorter distance than with slot shape 9. The length of the essentially gradient-free region available for testing purposes varies from about 80 inches at a stream Mach number of 1.07 to approximately 40 inches at a stream Mach number of about 1.13. Extensive surveys, including static-pressure measurements at axial intervals as close as ¼ inch, in the slotted section equipped with tapered slot shape 11 indicated Mach number deviations no greater than those shown in figure 20. In a typical model-testing region approximately 36 inches long and 30 inches in diameter, the Mach number deviations increased with Mach number to values not exceeding ± 0.006 at a stream Mach number of 1.13. This degree of flow uniformity was considered satisfactory for model-testing purposes, and slot shape 11 was therefore chosen for the final test-section configuration.

The coordinates for slot shape 11 are given in figure 21. Also included in this figure is the approximate shape of the slot edge, which was slightly over 0.5-inch thick and which remained essentially the same for all the slot shapes investigated. Immediately outside the slot edges, the channel between the edges and the test chamber opened abruptly as indicated in section C-C of figure 1. If the thickness of the slot edges and the size of the channel immediately outside the slot opening had been greatly different, the characteristics of the flow through the slots might have been influenced sufficiently to have resulted in a final slot shape somewhat different from shape 11. The large size of the channels results in the maintenance of the pressure just outside the slots at a value very close to that in the test chamber; and the thinness of the slot edges tends to reduce the inertia effects due to flow in the slots, which might aggravate the oscillation in the test region. The rounding of the slot edges may not be necessary, but was taken as a precaution against disturbances that might arise from flow separation at sharp corners.

TEST-SECTION CALIBRATION

Flow uniformity.—The results of extensive pressure surveys in the slotted test section using slot shape 11 are presented in figures 22 and 23 in terms of the local Mach number. The stream total pressure used, in conjunction with local static pressures, to determine the Mach number distributions of figures 22 and 23 was found to be essentially constant throughout the survey region near the test-section center line and was in close agreement with values measured in low-speed regions upstream of the slotted section. The Mach number distributions shown in figure 22 are associated with the flow characteristics soon after installation of the slotted throat and with a diffuser-entrance nose located 142.5 inches downstream of the slot origin (nose A). Figure 23 presents wall and center-line Mach number distributions obtained from surveys conducted at a later date and with a longer diffuser-entrance nose (nose B, ref. 3) located 114.6 inches downstream of the slot origin.

The Mach number distributions in the slotted test section with diffuser-entrance nose A (fig. 22) indicated that (1) the flow in the slotted test section was essentially free of gradients (except in the Mach number range from about 0.90 to 1.08 where a slight positive Mach number gradient existed), (2) the length of the uniform-flow region available for model-testing purposes decreased with Mach number but was approximately 60 inches long at a Mach number of 1.13, (3) the Mach numbers measured near the center line of the uniform-flow region agreed reasonably well with those at the wall, and (4) the quality of the flow in the slotted test section with slot shape 11 was fully equal to that in the most carefully designed two-dimensional solid nozzles. This result is the more remarkable when it is realized that the slot shape was reached without the benefit of any such theory as is available for the solid nozzle design and that, moreover, this uniform-flow test region was attained in a tunnel of approximately circular cross section, for which the solid nozzle design is particularly critical. It seems reasonable, therefore, to conclude that the design is much less critical for the slotted nozzle than for the solid nozzle. This easing of the design requirements is perhaps due to the fact that the slots in conjunction with the panels produce an effective integrated damped elastic pressure boundary in contrast to the unyielding solid boundary of the solid nozzle. This pressure boundary is incapable of supporting the large pressure gradients that can exist at a completely solid boundary and, therefore, all disturbances at the boundary tend to be spread out into shallow oscillations instead of being concentrated into shocks as may occur in a solid nozzle.

In other respects the flow in the slotted nozzle is similar to that in a solid nozzle. Thus, just as in a solid nozzle, irregularities on the solid surfaces produce disturbances extending into the interior of the flow. Disturbances produced by strings 0.010 inch in diameter on the top and bottom panels at a Mach number of 1.074 are shown by the schlieren photograph inset in figure 24. These disturbances are propagated along lines at angles very close to the Mach angle. This behavior corresponds with the assumption, involved in the derivation of the slot shapes, that the only part of a slot effective at a point of the flow is that upstream of the intersection of that slot with the upstream Mach cone through the point.

The results of surveys in the slotted test section after a long period of model testing and with diffuser-entrance nose B (fig. 23) indicate that the Mach number attainable at maximum tunnel power was increased slightly but the test section was shortened at its downstream end by use of the new diffuser-entrance-nose arrangement. The Mach number distributions of figure 23 also indicate a decrease in the uniformity of the test-section flow since the time of the

initial surveys; over a 36-inch-long region the maximum deviations from the average stream Mach numbers indicated in figure 23 were as much as 0.010 as compared with deviations of as much as 0.006 in figure 22. This deterioration of the flow was assumed to be due to the effect of discontinuities appearing in the wall-panel surfaces, as near window edges, during prolonged periods of tunnel operation when insufficient attention was given to maintenance of wall-panel smoothness.

The degree of test-section flow uniformity indicated by Mach number distributions was verified over a portion of the test region at supersonic speeds by examining schlieren pictures for the presence of stream disturbances equal to or stronger than a shock of known strength introduced into the flow. The results of the flow-uniformity check are illustrated in figure 25. A 10° included-angle cone was alined approximately parallel to the flow near the test-section center line, and schlieren pictures were made of the flow field about and ahead of the cone at stream Mach numbers of 1.035 and 1.075. The schlieren pictures were obtained for only the horizontal plane (light path through windows in panels 3 and 9) since the largest wall-surface discontinuities were known to exist on wall panel 12, and disturbances from this panel were most readily detected from horizontal schlieren surveys. The attached conical shocks were the only disturbances visible in the schlieren pictures (fig. 25) and, since these shocks were three dimensional and therefore more difficult to detect than two-dimensional disturbances, it was concluded that no abrupt disturbances of greater strength than that of the conical shock existed in the flow. (Because the conical shocks shown in figure 25 were weak, they are not very distinct in the schlieren pictures; dots have therefore been superimposed on the shock lines to emphasize their location.) The strength of the attached conical shock, expressed in terms of the Mach number decrement through the shock, is no greater than 0.004 and 0.003 at stream Mach numbers of 1.035 and 1.075, respectively (fig. 25). Mach number decrements calculated from conical-flow theory (ref. 7) are in close agreement with the two experimental points. In determining these experimental points the Mach number decrements across the cone shocks were obtained by use of oblique-shock theory (ref. 8) with shock angles measured directly from the schlieren pictures. For the stream Mach numbers and the test-section region concerned, the experimental schlieren-survey data of figure 25 appear to be consistent with the pressure-survey data in indicating the presence of no abrupt steady-flow disturbances of significant strength.

The measured angularity of conical shocks (fig. 25) offered indications of the value of the supersonic Mach number which were consistent with those indicated by pressure measurements (figs. 22 and 23) and by the angularity of weak two-dimensional disturbances from wall panels (fig. 11).

Flow calibration.—The stream flow in the slotted test section was calibrated with respect to the pressure in the chamber surrounding the slotted section, a procedure employed for smaller slotted tunnels in the investigations reported in references 1 and 6.

A typical calibration curve with the model removed from the tunnel shows the variation with test-chamber Mach number of the average Mach number over a region 30 inches in diameter and 36 inches long near the test-section center line (fig. 26). The data for this calibration were taken from the distributions of figure 22. An average value of the stream Mach number over the 30-inch-diameter region was obtained by fairing through the test points from the ten different positions of the survey tube. This faired value for the average stream Mach number varied almost linearly with, but was always smaller than, the indicated test-chamber Mach number. The Mach numbers measured at the ten survey locations did not differ from the average stream Mach number by more than 0.004 and 0.006 up to Mach numbers of 1.00 and 1.13, respectively.

In figure 27 a comparison is made of flow calibrations at the test-section center line for a region 36 inches long (from 68 to 104 inches downstream of the slot origin) with the model removed from the tunnel. The data of the comparison are taken from figure 22 (early surveys with diffuser-entrance nose A) and from figure 23 (later surveys with diffuser-entrance nose B). The agreement between the two surveys is shown to be very good for the particular flow region calibrated.

The effect of a model on the Mach number of the incoming flow upstream of the model test region was examined. The use of pressure measurements at the wall to verify the trend of the stream flow ahead of the model was considered applicable, particularly at supersonic speeds where disturbances are propagated approximately along Mach lines. This supposition was checked experimentally by comparing Mach number distributions along the slotted-section wall upstream of a wing-fuselage model (fig. 10) with wall distributions for the model-removed case. The results of this comparison for small lifting attitudes of the model (fig. 28) indicated close agreement between model-in and model-removed Mach number distributions upstream of the model location. The only discrepancy in the data of figure 28 appears immediately upstream of the model nose at a test-chamber Mach number of 1.025, where the bow wave ahead of the nose influences the model-in Mach number slightly. The evidence of figure 28 was supported by additional measurements with the same model at higher angles of attack (fig. 29). The latter data are presented to show the variation with test-chamber Mach number of the model-in and model-removed Mach numbers at the test-section wall approximately 10 inches upstream of the model-nose location. The data shown in figure 29 were obtained over a long period of time and included measurements with the wing-fuselage model at angles of attack as great as 20° and with diffuser-entrance noses A and B; the data from the many separate runs were in relatively close agreement. The combined data of figures 28 and 29 reveal generally that, for this ratio of model size to tunnel size, the pressures on the test-section wall ahead of the model were not greatly influenced (and therefore the validity of the model-removed calibration was not much affected) by the presence of the model at different lifting attitudes.

Although no quantitative comparisons are presented, it is believed from past experience in the calibration of high-speed

wind tunnels that the overall precision of calibration of a slotted test section, when the test-chamber pressure is used as a calibration reference, is superior to that of a conventional closed test section for subsonic speeds. In particular, the use of the pressure in the sealed chamber surrounding the slots as a reference pressure in calibrating the stream flow is believed to avoid the inconsistencies which may arise from the use of the static pressure indicated by a wall orifice located upstream of the minimum section.

Flow angularity.—The mean angularity of the flow in the slotted test section was measured at a center-line station 85 inches downstream of the slot origin. The measurements were limited to the vertical plane and employed the null-pressure-type instrument of figure 8 and the methods outlined earlier. A 2° included-angle wedge was first used for the flow-inclination measurements but it proved inadequate because of excessive bending near the leading edge and damage to the leading edge caused by the impact of foreign particles in the airstream. The 3° included-angle cone was less sensitive than the wedge but was superior in its relative freedom from tip bending and damage. The flow-inclination results (fig. 30), obtained from average measurements with the cone erect and inverted, indicated a mean upflow angle of approximately 0.1° which did not appear to change appreciably with Mach number. The scatter in measurements ranged up to about $\pm 0.1°$ from the mean indicated angularity. Careful measurements of the angularity of wall panels 6 and 12 revealed that the geometric center line between these two panels differed from the horizontal by approximately 0.05° in the direction of the indicated upflow.

Fluctuations of the stream angularity with time were measured by means of an electrical pressure pickup in the 3° included-angle cone. The results of these measurements indicated rapid variations of about 0.4° from the mean flow angle shown in figure 30. The fluctuations were greatest at frequencies from approximately 10 to 85 cycles per second throughout the transonic speed range.

MODEL TESTING AND BOUNDARY INTERFERENCE

A preliminary investigation of boundary interference effects on pressure-distribution and drag measurements for a nonlifting body of revolution (fig. 9) in the slotted test section was conducted in order to ascertain the reliability of typical model test data obtained from the slotted test section of the Langley 8-foot transonic tunnel. This investigation involved the comparison of experimental body data from the slotted test section with essentially interference-free data from other sources and the examination of the slotted-test-section data for the presence of solid blockage and boundary-reflection effects. Experimental data from the investigation were also used in examining several flow phenomena of concern with regard to transonic testing in the slotted test section. The stream Mach numbers at which body data were obtained in the slotted test section ranged from about 0.6 to 1.136. The test Reynolds number, based on model length, ranged from approximately 9.5×10^6 to 11.0×10^6.

Flow phenomena, including shock reflections, with nonlifting body of revolution and wing-body combination at center line of slotted test section.—Some flow phenomena of interest in connection with the transonic testing of models in the slotted test section are illustrated in figures 31 and 32. These data were obtained from tests of the nonlifting body of revolution (fig. 9 (c)) and the wing-body combination (fig. 10) at the center line of the slotted test section.

At very high subsonic speeds (figs. 31 (a) to 31 (c)) the supersonic-flow expansions around the maximum-thickness region of the body of revolution (and the local shock formations associated with model-surface discontinuities and with the compression region near the base of the body) did not extend to the test-section boundary. The failure of the model-field expansions to affect significantly the Mach number distributions at the test-section wall at a stream Mach number of 0.990 (fig. 31 (c)) offered evidence as to the essential absence of boundary interference for the model size used and also indicated an alleviation of choking in the slotted test section (tests of the body in a closed test section of the same size would have resulted in choking at a stream Mach number of about 0.985).

At low supersonic speeds (figs. 31 (d) to 31 (*l*) and 32 (a) to 32 (d)) the model-field shocks and expansions are shown to impinge upon the test-section boundary at axial locations which permit the reflection of disturbances back to the surface of the model. The model nose shock (bow wave) and the expansions over the upstream portion of the model are the disturbances of concern with regard to the production of boundary interference effects on model measurements. The shock-wave reflections are illustrated (figs. 31 (d) to 31 (n) and fig. 32) by means of both schlieren pictures and model-surface and wall Mach number distributions. In these figures the lines drawn to connect the schlieren-field shocks with shock locations (maximum compression regions) at the wall do not necessarily represent accurately the actual shock curvature in either the stream or the boundary layer.

Effect of boundary interference on pressure-distribution and drag measurements for nonlifting body of revolution at center line of slotted test section.—The comparisons of figures 33 to 35 were employed to ascertain the reliability of body pressure-distribution measurements in the slotted test section and, in particular, to obtain approximate effects of boundary interference on the body pressures at supersonic speeds. The interference-free model-surface pressure distributions given in figure 33 include those obtained from theory for the basic shape of the body (fig. 9 (a)), from free-fall tests for a 120-inch-long model (fig. 9 (b)), and from tests of the wind-tunnel model (fig. 9 (c)) in the 92-inch-diameter axisymmetrical closed test section of reference 2. The closed-test-section data, which were obtained at high subsonic speeds, were corrected for blockage effects by means of relations described in reference 9. The free-fall and theoretical distributions shown in figure 33 were obtained from reference 4, which utilized linearized theory and Prandtl-Glauert adjustments for the theoretical distributions at subsonic stream Mach numbers up to 0.95 and methods of reference 10 for the distributions at Mach numbers of and larger than about 1.05. The essentially interference-free pressure distributions shown in figures 34 and 35 were obtained from tests of the wind-tunnel model in the slotted test section of the Langley 16-foot transonic tunnel.

The wind-tunnel pressure coefficients used in figures 33 to 35 were averaged from coefficients for upper and lower surfaces in order to reduce possible deviations due to model alinement errors and surface irregularities; coefficients from the Langley 8-foot transonic tunnel were also average values from a number of different runs which repeated the model pressure measurements closely.

At subcritical speeds ($M_o \leqq 0.95$) no significant effects of boundary interference on body pressures were expected, since reference 1 reported essentially zero interference for a nonlifting body in a slotted test section with a ratio of body cross-sectional area to tunnel cross-sectional area of 0.123, and the ratio was only about 0.0014 for the body and test section used in the present investigation. The close agreement expected between the pressure distributions from the slotted test section of the Langley 8-foot transonic tunnel and the various interference-free distributions was realized (figs. 33 (a), 34 (a), 34 (b), and 35), except for discrepancies in the comparisons with free-fall data in the maximum-thickness region of the body (fig. 33 (a)). These descrepancies cannot be readily explained unless the free-fall body, which was three times the size of the wind-tunnel model, differed slightly in shape from the wind-tunnel model and the basic shape in this region. Apparent discrepancies in the comparison with free-fall and theoretical pressure distributions near the base of the body (fig. 33 (a)) are to be expected since the shapes of both the basic body and the free-fall body differed from that of the wind-tunnel model in this region.

At supercritical stream Mach numbers from about 0.95 to 1.00 the agreement of the pressure-distribution measurements from the slotted test section of the Langley 8-foot transonic tunnel with those from the Langley 16-foot transonic tunnel (fig. 34 (b)) and from free-fall tests (fig. 33 (a)) was consistent with the agreement at lower speeds; this agreement attested the essential absence of boundary-interference effects on pressure measurements for the model (cross-sectional area of model only 0.14 percent of tunnel cross-sectional area) in the ⅛-open slotted test section at stream Mach numbers up to 1.00.

At very low supersonic Mach numbers ($M_o \leqq 1.025$) no appreciable effects of boundary-reflected compression waves on model-surface pressures could be detected (figs. 31 (e), 33 (b), 34 (c), and 35) but significant effects of reflected overexpansions were indicated (figs. 34 (c), 35 (b), and 35 (c)). Pressure distributions from the Langley 16-foot transonic tunnel, used as a basis for reference in figures 34 and 35, were not available at Mach number intervals close enough to define completely the variation of the interference-free pressure distribution with Mach number, nor did the data appear to be entirely free of interference effects at a Mach number of 1.019 where overexpansions (apparently due to reflected boundary disturbances similar to those described for the Langley 8-foot transonic tunnel) were indicated (figs. 34 (c) and 35 (f)). The data were sufficient, however, to provide approximate indications of boundary effects on pressure-distribution measurements for the body in the slotted test section of the Langley 8-foot transonic tunnel.

At supersonic Mach numbers slightly greater than 1.025, the effects of reflected compression shocks on model-surface pressures became significant and increased with Mach number. At Mach numbers of and greater than about 1.040, the reflected shocks were visible in schlieren pictures (figs. 31 (g) to 31 (n)) and influenced the model-surface pressures strongly (figs. 33(b), 34(c), and 35(b) to 35(f)). The model-surface pressures downstream of the region affected by the reflected compression wave were influenced by overexpansions and those upstream of the compression region were free of boundary interference. At $M \geqq 1.120$ the reflected compression was downstream of the model base (fig. 31 (n)) and no boundary interference was apparent (fig. 33 (b)). The agreement at Mach number 1.2 of interference-free pressure distributions from tests of the model in the 92-inch-diameter axisymmetrical closed test section of reference 2 with theoretical and free-fall distributions from reference 4 is consistent with that of the interference-free slotted-test-section data at lower supersonic Mach numbers (fig. 33 (b)). The close agreement of interference-free body-surface distributions from the slotted and closed test sections of the Langley 8-foot transonic tunnel with theoretical distributions (fig. 33 (b)) constitutes an experimental verification of the methods of reference 10 for computing pressure distributions on a slender body of revolution at supersonic speeds.

The maximum effects of boundary-reflected disturbances on surface pressures for the fineness-ratio-12 body of revolution in the Langley 8-foot transonic tunnel at supersonic speeds (fig. 36) were determined from maximum differences between experimental pressure coefficients from the Langley 8-foot and 16-foot transonic tunnels as shown in figure 35. The expansion components of boundary-reflected disturbances for the body tested in the ⅛-open slotted test section of the Langley 8-foot transonic tunnel were shown to affect body-surface pressures more strongly than did the compression components at stream Mach numbers less than 1.035, whereas the reverse was indicated at Mach numbers greater than 1.035. The indications of figure 36 are only approximate, however, because of the limited amount of data available from the Langley 16-foot transonic tunnel.

The effects of boundary-reflected disturbances on pressure distributions for the nonlifting body of revolution at the center line of the slotted test section of the Langley 8-foot transonic tunnel (figs. 33 to 36) were interpreted in terms of effects on body drag coefficients. In ascertaining these effects, the body drag coefficients obtained from pressure-distribution and force tests in the slotted test section of the Langley 8-foot transonic tunnel were compared with essentially interference-free data from free-fall tests (ref. 4) and from pressure-distribution tests in the Langley 16-foot transonic tunnel (slight interference effects present in the latter data measured at $M_o = 1.019$ were removed, approximately, before determining the pressure drag). (See fig. 37.) The drag coefficients from pressure-distribution tests were obtained by integrating measured model-surface pressures and included skin-friction drag estimates from reference 11. The force-test body drag coefficients shown in figure 37 were obtained from unpublished experimental data for the model described in reference 12 and were corrected for sting-support tares. Estimated maximum inaccuracies of

the body drag coefficients (based on body frontal area) shown in figure 37 were approximately ± 0.016 for the data obtained from force tests in the Langley 8-foot transonic tunnel and within ± 0.010 for those obtained from free-fall tests.

Approximate boundary-interference effects on body drag measurements for the nonlifting body of revolution at the center line of the Langley 8-foot transonic tunnel slotted test section were taken as the differences between these drag measurements and the interference-free measurements (fig. 37). Correlation of these drag differences (fig. 37) with corresponding body-surface pressure distributions (figs. 33 to 35) revealed the close interrelation of the pressure-distribution and drag measurements and the dependence of the drag-coefficient changes on the effects of boundary-reflected disturbances. The indicated body drag decrements (fig. 37) at Mach numbers from 1.00 to 1.02 were apparently due to the effect of reflected overexpansions slightly upstream of the maximum-thickness region of the body, whereas drag increments at Mach numbers from 1.02 to 1.07 and drag decrements at Mach numbers from 1.07 to about 1.12 were due to the passage over the rear portion of the body of reflected overexpansions and compressions, respectively. At Mach numbers greater than about 1.12 the slight discrepancy between the free-fall data and those from force and pressure-distribution tests in the Langley 8-foot transonic tunnel could be attributed to differences in body shape or to possible inadequacies in sting-support tare corrections, but the magnitude of the indicated discrepancy is within estimated possible inaccuracies in the experimental data. The maximum effects of boundary reflections on body drag coefficients with the body at the slotted-test-section center line did not exceed about 0.04 when coefficients were based on body frontal area. Although these maximum boundary-reflection effects were not much greater than the errors of measurement normally present when the internal balance system is used for measuring model forces, they were considered sufficient to justify a brief experimental investigation of a possible means of reducing the effects.

Reduction of interference effects at supersonic speeds by testing model off center line of slotted test section.—An attempt to reduce the intensity of boundary-reflected disturbances at the model was made by testing the nonlifting body of revolution (fig. 9 (c)) at a distance of about 10.3 inches off the geometric center line of the slotted test section. Body drag coefficients obtained from pressure-distribution measurements with the body located off the test-section center line were affected less by boundary interference than were those obtained from tests of the body at the center line (see fig. 37). This reduction in interference effects on body drag can be attributed to a slight reduction in intensity (and to distribution over a greater axial distance) of boundary-reflected disturbances at the body surface, as shown by the comparison (fig. 38) of center-line and off-center body-surface Mach number distributions at a stream Mach number of 1.050 (this Mach number was used for the comparisons in order that effects of both compression and expansion components of boundary-reflected disturbances might be illustrated). The off-center location of the model appears advantageous with regard to the reduction in intensity of boundary-reflected disturbances, especially the expansion components of such disturbances, and the attendant reduction in interference effects on model drag and pressure-distribution measurements. A disadvantage of the off-center location, however, lies in the significant reduction in length of the region available for strictly interference-free supersonic testing.

Model lengths for interference-free supersonic testing at center line of slotted test section.—It has been shown that at supersonic Mach numbers the model-surface pressures upstream of the region affected by the boundary-reflected compression are free of boundary-interference effects (figs. 33 to 35) and that for a given Mach number the length of the interference-free region is greatest when the model is located at the center line of the test section (fig. 38). The axial distance L_S required for the bow wave ahead of the model to reflect from the test-section boundary and strike the surface of the model at the test-section center line is shown in figure 39. This distance, obtained from schlieren pictures and pressure measurements at stream Mach numbers from 1.04 to 1.126 and from pressure measurements at Mach numbers as low as 1.025, is expressed in terms of the distance L_M required for the reflection of Mach lines from the tunnel wall. The ratio L_S/L_M increased from a value of about 0.35 at a stream Mach number of 1.025 to about 0.81 at a Mach number of about 1.10, after which the ratio remained approximately constant except near a Mach number of 1.109 where it tended to increase slightly and then decrease as the reflected shock approached and moved downstream of the base of the model. This influence of the model tail shock on the progress of the reflected shock past the base of the model is illustrated in figures 31 (*l*) and 31 (m). An L_S/L_M value of 0.815 obtained from tests of a somewhat similar body at a stream Mach number of 1.2 in the closed nozzle of reference 2 was consistent with the ratios shown in figure 39 for Mach numbers greater than about 1.10. At the low supersonic Mach numbers of this investigation, the L_S/L_M ratio was approximately the same for both the axisymmetrical fuselage and the sweptback wing attached to the fuselage.

The distance ratios given in figure 39 neglect the effect of the model boundary layer, which permits the compression due to the incident shock to be transmitted several inches upstream of the shock location, and are therefore not strictly representative of axial distances available for interference-free supersonic testing. If the compression region is assumed to extend about 3 inches upstream of the shock location, the axial distances available for interference-free supersonic testing with the model at the center line of the slotted test section would range from about 4 inches at a Mach number of 1.025 to approximately 36 inches at a Mach number of 1.14 (fig. 40) and would not exceed 75 percent of the axial distance required for the reflection of Mach lines. At the very low supersonic Mach numbers the length of the interference-free test region is influenced to some extent by the location of the detached shock wave ahead of the model.

Location of detached shocks ahead of axisymmetrical nonlifting bodies.—Schlieren and pressure data for the body

of revolution (see fig. 31) and schlieren pictures of shocks ahead of blunt-nose (90° angle) total-pressure tubes (fig. 41) tested in the slotted section of the Langley 8-foot transonic tunnel provided experimental information concerning the location of detached shock waves ahead of axisymmetrical bodies at low-supersonic speeds. The experimental data from the Langley 8-foot transonic tunnel are compared with experimental data from other sources (refs. 4 and 13 to 15) and with approximate theory (ref. 13) in figure 42. The data used in these comparisons are expressed in terms of the ratio of shock distance ahead of the body sonic point to the body radius at the sonic point, x_{SB}/y_{SB}, a parameter used in reference 13. The sonic point for the body of revolution tested in the Langley 8-foot transonic tunnel was obtained from body-surface pressure measurements (average values from a large number of runs) at each test Mach number; the sonic point for the 90° body (total-pressure tube) tested in the Langley 8-foot transonic tunnel was assumed to occur at the shoulder of the body for all Mach numbers.

The experimental locations of the bow waves ahead of the body of revolution in the slotted test section of the Langley 8-foot transonic tunnel agreed closely with experimental data from references 4 and 13 to 15; those for the 90° body in the Langley 8-foot transonic tunnel agreed closely except at stream Mach numbers of 1.015 and 1.036 (fig. 42). The apparent discrepancies offered by these two experimental points are not due to errors in measurement; they are believed to be due to the two-dimensional nature of the bow wave ahead of the row of total-pressure tubes. (Ref. 13 shows that the ratio x_{SB}/y_{SB} is much larger for the two-dimensional case than for the axisymmetrical case.) The single bow wave existing ahead of the row of eight total-pressure tubes at the low-supersonic Mach numbers of 1.015 and 1.036 changes to individual bow waves ahead of each tube at higher Mach numbers (fig. 41).

The general agreement of the experimental data with theoretical approximations (geometric and continuity methods) from reference 13 is considered satisfactory. The experimental data appear to agree more closely with the geometric-method approximations at very low supersonic Mach numbers and with the continuity-method approximations at stream Mach numbers greater than approximately 1.10.

Applicability of boundary-reflection information from present investigation to tests of other models in slotted test section.—Although each wind-tunnel test model offers a different problem with regard to the effects of boundary-reflected disturbances, the results of the body-of-revolution tests reported earlier in this paper should prove useful in predicting disturbance phenomena and evaluating experimental data for other models.

For strictly interference-free supersonic testing the model length is dependent on the axial distance required for model disturbances to reflect from the test-section boundary back to the model surface; this distance varies with Mach number and is greatest when the model is located at the test-section center line. The shock-reflection distances shown in figure 39 and the interference-free model lengths given in figure 40 are applicable only for center-line testing of models of approximately the size and shape of the body of revolution used in this investigation; larger models of this shape or bluff bodies of the same maximum diameter will produce bow waves located farther upstream and thereby reduce the reflection distances and model lengths shown in figures 39 and 40, respectively. The approximate interference-free model length for a given axially symmetric shape can be estimated by use of figures 39 and 42, together with knowledge of the sonic-point location and the model radius at the sonic point. At very low supersonic Mach numbers the use of figure 42 to ascertain detached shock locations ahead of axially symmetric bodies is limited to single bodies; several adjacent axially symmetric bodies located in the same plane of measurement may produce detached shocks located considerably upstream of the shock for a single body (see figs. 41 and 42).

For supersonic testing of models whose lengths permit the impingement of boundary-reflected disturbances, the effects of boundary interference on the free-air characteristics of the models are dependent on the model configurations and the model locations with respect to the test-section center line (interference effects are less for model off center line than for one on center line). The effects of boundary reflections on pressure and drag measurements for the fineness-ratio-12 body of revolution used in the present investigation are applicable only for models of approximately the same size and shape, but the described flow phenomena with the body of revolution in the slotted test section should be useful in interpreting the direction of boundary-reflection effects on test data for other models. The influence of model-attitude changes on indicated boundary-reflection effects for the body of revolution was not included in the present investigation, but approximate influences may be inferred from experimental results given in reference 16. Reference 16 also indicates that flow disturbances capable of introducing drag-coefficient changes of approximately 0.002 (drag coefficient based on wing plan-form area) may not greatly affect the lift and pitching-moment characteristics of a complete airplane model. Additional studies are needed to verify and supplement these preliminary indications of boundary-reflection effects on models at lifting attitudes in the slotted test section.

GENERAL DISCUSSION

The theory of the subsonic operation of the slotted test section has been presented in reference 1. It is of interest to consider in a qualitative manner some features of the supersonic operation. As pointed out in reference 17, the supersonic flow in a tunnel with porous walls is established by expansion through the walls. In a slotted tunnel a similar expansion must occur through the slots, but this expansion must be influenced by the boundary layer on the panels. In fact, a general knowledge of the behavior of boundary layers indicates that in the expansion the boundary layer tends to run off the panels into the slots. The effects of the slots must thus be extended over the whole periphery of the tunnel. It therefore seems that the slotted tunnel would behave more like a porous-wall tunnel than might at first be supposed. The role of the slots in controlling the expansion has already been noted.

The development of the supersonic flow in the slotted test section will now be considered in detail. At subsonic

speeds the pressure in the test chamber evidently must take a value which is some weighted average of the pressures at the slots. Moreover, in accordance with the equation of motion, as the pressures in the diffuser (including that at the diffuser entrance) are decreased, the speed in the tunnel must increase until a Mach number of 1.0 is reached at the effective minimum section, section B-B in figure 1. Consider first the case of a wall divergence of 45 minutes. With the first attainment of a Mach number of 1.0 at the minimum section, the Mach number in the slotted test section has been found to be also essentially 1.0, as is shown for a different divergence angle in figure 13; but on the curved surfaces of the panels (fig. 3 (a)) supersonic regions terminated by shocks resulting from the higher pressures in the slots must already have appeared in conformance with general flow theory. The flow within the slotted test section is thus not absolutely uniform, but consists of slightly supersonic regions terminated by shocks, which are in turn followed by slightly subsonic regions. This flow pattern can be repeated several times because in any subsonic region the pressure may be greater than that in the chamber surrounding the slots. Equalization of the pressure through the slots thus accelerates the flow, and if the panel is curved in that region or if a change in shape occurs, the flow may again become supersonic.

When the pressure at the diffuser entrance is decreased (by increasing the rotational speed of the tunnel fan) below that just necessary to produce a Mach number of 1.0 at the throat, the pressure decrease cannot be transmitted upstream through the supersonic regions in the slotted test section. This pressure decrease is, however, transmitted out through the slots in the region just upstream of the diffuser entrance. The pressure in the surrounding chamber is thus decreased and, as a result of the reaction through the upstream part of the slots, the flow in the subsonic regions is further accelerated, the shocks are moved downstream, and the supersonic regions are expanded.

This movement of the shocks downstream has been noted in schlieren observations. If the curvature and divergence of the panels are small, only a small decrease of pressure below that required for the establishment of a Mach number of 1.0 at the throat is sufficient to sweep the shocks out of the test section. In such a case one shock only may exist. With the configuration of figure 3 (a), this shock is located slightly downstream from the discontinuity in slope at the 125.6-inch station. It is evidenced in figure 6 by a rather sudden decrease in Mach number to values less than 1.0, which occurs between the 130- and 140-inch stations. At this position the shock extends across the whole central part of the flow. In all of the upstream slotted test section the stream Mach number is then greater than 1.0. At the upstream end the boundary layer flows out, so that the stream is allowed to expand, as it must do if the Mach number is to increase from the value of unity at the throat to some greater value somewhat downstream. This outward flow must evidently be balanced by an equivalent rate of mass flow into the slots near their downstream ends. Perhaps because of induced velocities due to flow through the slots, the pressures (indicated by Mach numbers in fig. 6) near the slot edges are less than those near the center of a panel, and the test chamber pressure lies generally between these two extremes.

Except for the improvement in control of the expansions obtainable by means of the slots, which has already been mentioned, the manner of operation of the slotted test section with 5-minute divergence is similar to that with 45-minute divergence. However, because with the 5-minute divergence the curved region of the panels is located at the downstream end, the shocks must first form at that end, leaving the upstream end essentially shock free, even at Mach numbers near unity. An indication of this freedom from shock disturbances was afforded by limited schlieren observations and is indicated in the Mach number distributions (figs. 13 to 20). With the 5-minute divergence of the panels the shock-disturbed Mach number range near unity is thus eliminated, and uniform test section Mach numbers continuously variable through 1.0 are possible.

The conditions at the downstream end of the slotted section will now be considered. In this region, for the configurations discussed in this report, the air flow which has been extruded from the upstream part of the slots must be taken back into the tunnel stream. Because of the turbulent mixing with the air in the chamber surrounding the slots, this extruded air has lost most of its kinetic energy; but once this air has reentered the slots, it is again accelerated by mixing with the main stream. This mixing process is believed to be accelerated by vorticity generated by inflow over the slot edges.

The mixing is known to be an inefficient process and must in any case entail a power loss; but even greater power losses may occur if, because of the intake of this low-energy air, the diffuser flow is spoiled. Conditions are necessarily particularly critical near the diffuser entrance, both because of the inflow of the low-energy air and because in this region the kinetic energy of the main stream is large. Because of the mixing (ejector principle) some diffusion would occur in this region even if the expansion angle of the diffuser were zero. Indeed, the mixing is so strong that, as may be seen from figures 13 to 20, the diffusion starts even slightly upstream of the diffuser entrance noses.

Because of space limitations the original expansion angle at the upstream end of the diffuser was made greater than was considered desirable, and when the panels were reversed this angle was increased still more, to 3°45′, as shown in figure 3 (b). In the region of the diffuser entrance noses the effective expansion is somewhat less than this value because the upper surfaces of the noses fall outside the panel surfaces (fig. 3). At some sacrifice of test-section length, nose shape B (fig. 4 (b)), which extended farther upstream, furnished a short region of essentially constant effective cross-sectional area at the beginning of the diffuser. Such a length of essentially constant or only slightly varying diffuser area is believed to be desirable in order to provide a mixing region without too great diffusion, but no investigations have been conducted to determine the proper length or divergence of such a region for minimum power.

The need for a length of diffuser with small or zero expansion near the diffuser entrance is accentuated by the presence of the shock. In reference 2 it was shown that in

such a region the boundary layer behind a shock terminating the test region at a Mach number of 1.2 recovered rapidly without separation. In a diverging channel, on the other hand, such a shock might easily lead to separation. The shocks indicated at the diffuser entrance in figures 13 to 20 appear to be oblique rather than normal shocks, since the greater disturbance occurs at the center and that at the wall is spread out and does not decrease the indicated Mach number below unity. The use of a region of zero expansion at the diffuser entrance should spread these disturbances still farther and may very well effect their practical elimination.

The shock at the diffuser entrance is similar to one which might exist ahead of a nose inlet. Because the high-speed flow is limited to a jet, however, it should be possible to draw the shock down into the diffuser, but in this case the power required would almost certainly be greater than if the shock were close to the diffuser entrance. The most favorable configuration, for minimum power, is believed to be that for which the shock stands just inside an essentially zero-divergence region at the diffuser entrance or has been practically eliminated in the mixing region.

The minimum diffuser entrance cross-sectional area constitutes, in effect, a second throat. If this second throat is too small the flow will be choked and the Mach number attainable will be limited. Because of the thick boundary layer formed by the inflow through the slots, the required area of the second throat is greater than would be necessary for a closed nozzle with the same size of first minimum. With increase in supersonic Mach number the required area of the second throat increases on account of both the increase in entropy through the shocks and the increasing flow through the slots. With the configuration of figure 3 (b), a diffuser minimum area 13 percent greater than the first throat area was sufficient to permit the attainment of a Mach number of 1.14. With the reduction in slot area and the provision of an essentially constant-area mixing region provided by nose B, the required area at the second minimum was reduced to a value 9 percent greater than that at the first. Because of the thick boundary layer, choking is not sharp at the second minimum; but after a Mach number of 1.0 has been reached in the main stream, the volume flow can still be increased by acceleration of the boundary layer, though the cost in power rapidly becomes excessive.

Because of the larger minimum diffuser area required for the supersonic flow, the diffuser entrance area is greater than that required for the subsonic flow. Since the flow attaches to the diffuser entrance noses, diffusion, and consequently negative Mach number gradient, occurs upstream from the noses. This effect was sufficiently severe in the case of nose shape B to require the provision of flaps which, when open, permitted the entrained flow to pass over the noses and thus prevented attachment of the main flow. Moreover, inasmuch as the diffuser entrance area affects the diffusion, physical considerations would suggest that the power required is also affected. Tests carried out in the Langley 24-inch tunnel have shown this to be the case. An increase of the diffuser minimum cross section appreciably beyond the size necessary for the required Mach number results in an increase in the power required. An increase in noise and vibration is also believed to be likely. It is suggested that, in any future slotted tunnel installation similar to that discussed herein, the effective diffuser entrance area be made adjustable by means of radially adjustable diffuser entrance noses.

It was thought that the heavy boundary layer due to the inflow into the slots might spoil the diffuser, but an extensive investigation by means of tufts failed to reveal any separation, though separation may have existed on the diffuser entrance noses. Because of the large amount of kinetic energy in that region, the possibility of significant power loss is greater near the diffuser entrance than farther downstream.

An examination of power data for varying slot area showed that, as might be expected, the power required for a given Mach number decreases as the slot area decreases. Power consumption is therefore also less if the diffuser entrance nose is as far upstream as possible. This effect may be expected to become relatively less important as the Mach number is increased, because the increasing required outflow through the upstream part of the slots and the corresponding inflow at the downstream ends is only weakly dependent on the slot area. It also appears likely that with increasing inflow of this low-energy air the essentially constant-area mixing region required for its acceleration might have to be increased in order to avoid spoiling the diffuser flow. Economy of power might indeed, at higher Mach numbers, require that this low-energy air be pumped to approximately stream total pressure by means of a separate compressor rather than by means of turbulent mixing in the diffuser. The use of a separate compressor, however, might affect the use of the tank pressure as a reference pressure for determining Mach number.

The power absorption per square foot of throat area in the Langley 8-foot transonic tunnel is shown in figure 43. These data were taken from a number of different runs, as indicated in the figure. The power data have been adjusted to the same stagnation pressure and temperatures through the assumption that, for constant geometry and Mach number, power is proportional to $p_t\sqrt{T_t}$, where p_t is the stagnation pressure and T_t is the absolute value of the stagnation temperature. The power for the slotted tunnel is compared with that for the Langley 8-foot transonic tunnel with slots closed, that for the plaster nozzle of reference 2, and that for a closed-tunnel estimate based on reference 18. The reduction in power due to the installation of diffuser entrance nose B (fig. 4 (b)) is seen from a comparison of the power for this nose with that for nose A (fig. 4 (a)). A more detailed investigation of the power losses is given in reference 3.

CONCLUDING REMARKS

The Langley 8-foot high-speed tunnel was converted to transonic operation and the characteristics of the transonic flow in the slotted test section were investigated. The results of flow surveys with various slot shapes, and with and without a typical model in the slotted test section, warrant the following conclusions:

1. As a result of the investigation of the flow characteristics of the tunnel with various slot shapes, a configuration

which produced nearly uniform supersonic flow has been devised.

2. With this configuration the Mach number was continuously variable up to the greatest value, approximately 1.14, permitted by the power available; the quality of the flow was entirely satisfactory for testing purposes and compared favorably with that in the best two-dimensional solid supersonic nozzles. Deviations from the average stream Mach number in a model test region 36 inches long and 30 inches in diameter generally increased with Mach number but did not exceed approximately 0.006 at stream Mach numbers up to 1.13, provided the tunnel wall surfaces were kept sufficiently smooth.

3. The Mach number distribution was found to be affected by the detailed slot shape if the divergence angle between the panels and the center line of the test section was sufficiently small.

4. The power required at a given Mach number was considerably in excess of that necessary for a closed tunnel at the same Mach number.

5. The ratio of the test-chamber pressure to the stream total pressure provided a reliable index of the test-section Mach number independent of model configuration or attitude.

6. The direction of the airstream agreed within the limits of experimental error (0.1°) with the geometric center line of the test section.

7. The use of slots to reduce choking limitations at stream Mach numbers near 1.0, reported earlier for small tunnels, was substantiated by tests of a 3.33-inch-diameter body of revolution in the approximately 88-inch-diameter slotted test section.

8. Interference effects due to boundary-reflected disturbances were present in pressure-distribution and drag measurements for a 33.5-inch-long nonlifting body of revolution with a fineness ratio of 12 in the slotted test section at low supersonic speeds; the effects were reduced by testing the body off the test-section center line in order to avoid focusing of the reflected disturbance waves. No boundary interference was present at the higher supersonic speeds attained.

9. The model length for interference-free supersonic testing increased with Mach number but did not exceed about 75 percent of the axial distance required for reflection of Mach lines.

10. Experimental locations of bow waves ahead of axially symmetric bodies were in satisfactory agreement with theoretical locations predicted by the approximate methods of NACA TN 1921.

11. An experimental verification of the method of NACA TN 1768 for predicting pressure distributions over slender bodies of revolution at supersonic speeds is afforded by the close agreement of theoretical pressure distributions for a fineness-ratio-12 body of revolution with interference-free distributions measured in the Langley 8-foot transonic tunnel.

LANGLEY AERONAUTICAL LABORATORY,
NATIONAL ADVISORY COMMITTEE FOR AERONAUTICS,
LANGLEY FIELD, VA., *July 3, 1958.*

REFERENCES

1. Wright, Ray H., and Ward, Vernon G.: NACA Transonic Wind-Tunnel Test Sections. NACA Rep. 1231, 1955. (Supersedes NACA RM L8J06.)
2. Ritchie, Virgil S., Wright, Ray H., and Tulin, Marshall P.: An 8-Foot Axisymmetrical Fixed Nozzle for Subsonic Mach Numbers up to 0.99 and for a Supersonic Mach Number of 1.2. NACA RM L50A03a, 1950.
3. Whitcomb, Richard T., Carmel, Melvin M., and Morgan, Francis G., Jr.: An Investigation of the Stream-Tube Power Losses and an Improvement of the Diffuser-Entrance Nose in the Langley 8-Foot Transonic Tunnel. NACA RM L52E20, 1952.
4. Thompson, Jim Rogers: Measurements of the Drag and Pressure Distribution on a Body of Revolution Throughout Transition From Subsonic to Supersonic Speeds. NACA RM L9J27, 1950.
5. Loving, Donald L., and Estabrooks, Bruce B.: Transonic-Wing Investigation in the Langley 8-Foot High-Speed Tunnel at High Subsonic Mach Numbers and at a Mach Number of 1.2—Analysis of Pressure Distribution of Wing-Fuselage Configuration Having a Wing of 45° Sweepback, Aspect Ratio 4, Taper Ratio 0.6, and NACA 65A006 Airfoil Section. NACA RM L51F07, 1951.
6. Ward, Vernon G., Whitcomb, Charles F., and Pearson, Merwin D.: An NACA Transonic Test Section With Tapered Slots Tested at Mach Numbers to 1.26. NACA RM L50B14, 1950.
7. Staff of the Computing Section, Center of Analysis (Under Direction of Zdeněk Kopal): Tables of Supersonic Flow Around Cones. Tech. Rep. No. 1 (NOrd Contract No. 9169), M.I.T., 1947.
8. Neice, Mary M.: Tables and Charts of Flow Parameters Across Oblique Shocks. NACA TN 1673, 1948.
9. Herriot, John G.: Blockage Corrections for Three-Dimensional-Flow Closed-Throat Wind Tunnels, With Consideration of the Effect of Compressibility. NACA Rep. 995, 1950. (Supersedes NACA RM A7B28.)
10. Thompson, Jim Rogers: A Rapid Graphical Method for Computing the Pressure Distribution at Supersonic Speeds on a Slender Arbitrary Body of Revolution. NACA TN 1768, 1949.
11. Young, A. D.: The Calculation of the Total and Skin Friction Drags of Bodies of Revolution at Zero Incidence. R. & M. No. 1874, British A.R.C., 1939.
12. Osborne, Robert S.: A Transonic-Wing Investigation in the Langley 8-Foot High-Speed Tunnel at High Subsonic Mach Numbers and at a Mach Number of 1.2—Wing-Fuselage Configuration Having a Wing of 45° Sweepback, Aspect Ratio 4, Taper Ratio 0.6, and NACA 65A006 Airfoil Section. NACA RM L50H08, 1950.
13. Moeckel, W. E.: Approximate Method for Predicting Form and Location of Detached Shock Waves Ahead of Plane or Axially Symmetric Bodies. NACA TN 1921, 1949.
14. Heberle, Juergen W., Wood, George P., and Gooderum, Paul B.: Data on Shape and Location of Detached Shock Waves on Cones and Spheres. NACA TN 2000, 1950.
15. Laitone, Edmund V., and Pardee, Otway O'M.: Location of Detached Shock Wave in Front of a Body Moving at Supersonic Speeds. NACA RM A7B10, 1947.
16. Ritchie, Virgil S.: Effects of Certain Flow Nonuniformities on Lift, Drag, and Pitching Moment for a Transonic-Airplane Model Investigated at a Mach Number of 1.2 in a Nozzle of Circular Cross Section. NACA RM L9E20a, 1949.
17. Nelson, William J., and Klevatt, Paul L.: Preliminary Investigation of Constant-Geometry, Variable Mach Number, Supersonic Tunnel With Porous Walls. NACA RM L50B01, 1950.
18. Goethert, Bernhard: Power Requirements and Maximum Reynolds Number in Transonic Wind Tunnels Having a Maximum Mach Number of 2.0. AAF TR No. 5564, Air Materiel Command, Army Air Forces, Mar. 25, 1947.

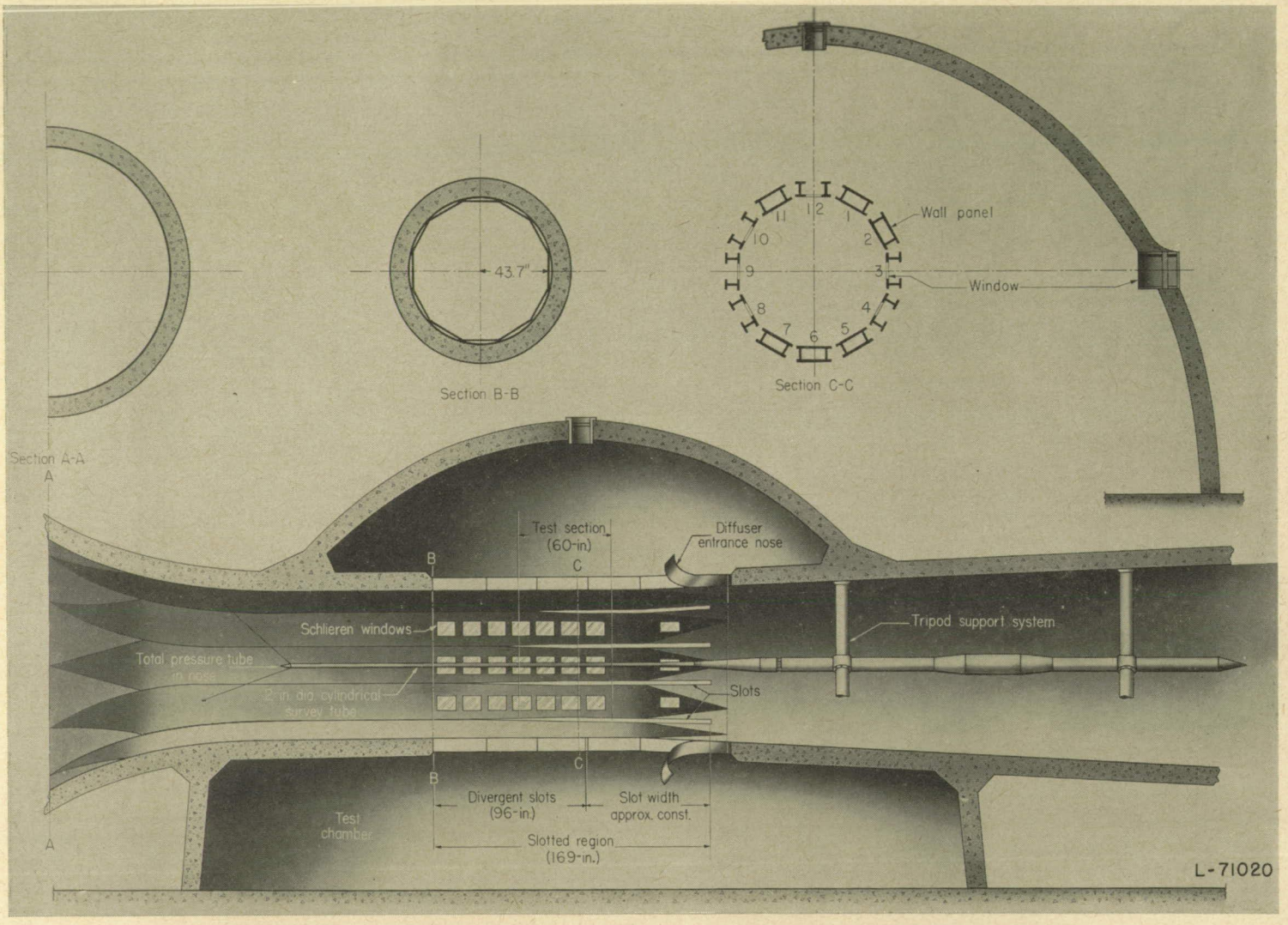
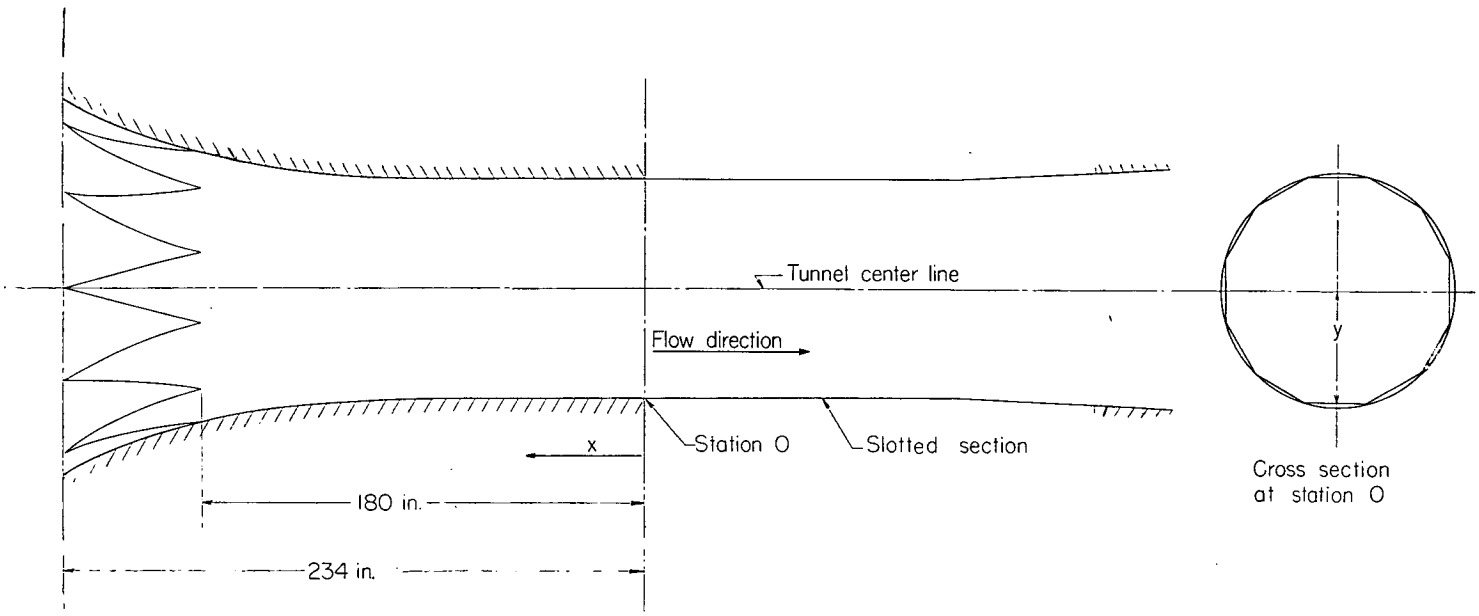


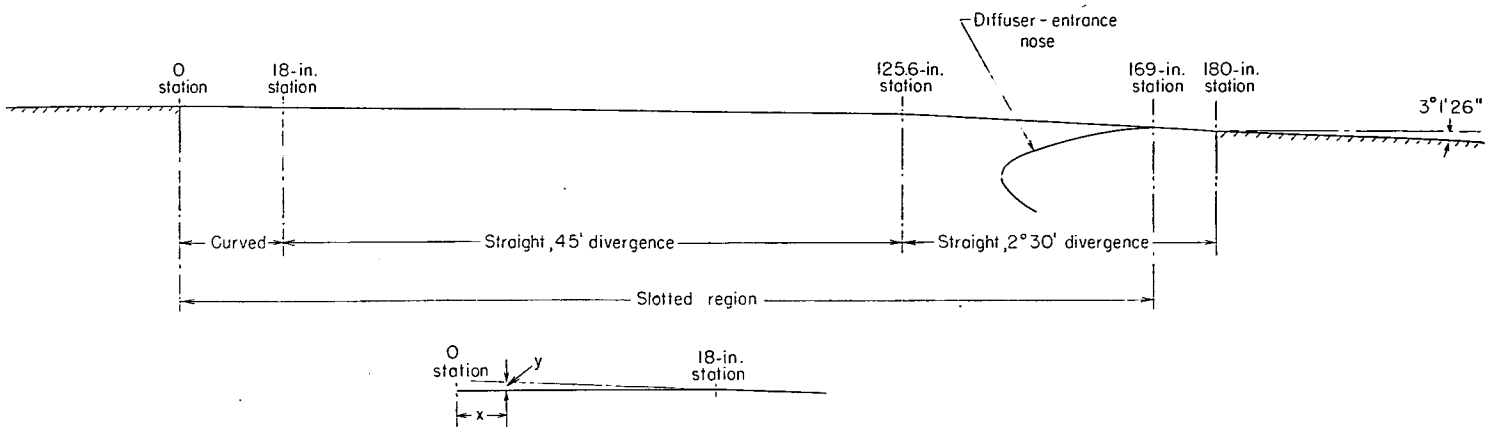
FIGURE 1.—Views of throat region of Langley 8-foot transonic tunnel showing slotted test section, cylindrical survey tube, and support system.



x (in.)	y (in.)	x (in.)	y (in.)	x (in.)	y (in.)	x (in.)	y (in.)
0	43.700	24	43.668	48	43.685	140	47.593
2	43.697	26	43.666	50	43.692	150	48.882
4	43.694	28	43.665	55	43.715	160	50.459
6	43.691	30	43.664	60	43.748	170	52.365
8	43.688	32	43.663	65	43.793	180	54.641
10	43.685	34	43.663	70	43.851	190	57.333
12	43.682	36	43.664	80	44.018	200	60.488
14	43.679	38	43.665	90	44.266	210	64.480
16	43.677	40	43.667	100	44.618	220	69.200
18	43.674	42	43.670	110	45.099	228	73.680
20	43.672	44	43.674	120	45.735	230	74.860
22	43.670	46	43.679	130	46.555	234	77.188

x=Distance upstream of station 0
y=Distance from tunnel center line to center of panel

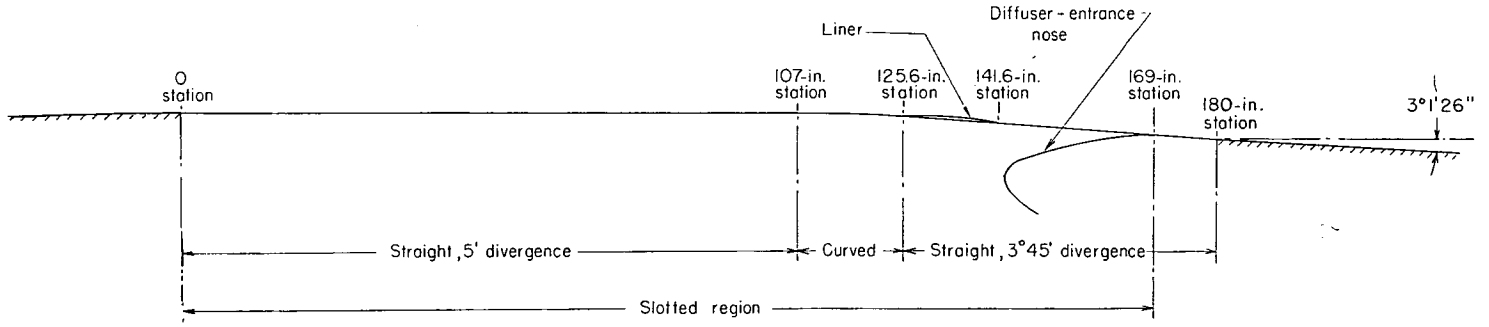
FIGURE 2.—Coordinates of approach to slotted region of tunnel throat.

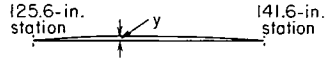


Coordinates of curved region

x (in.)	y (in.)
0	0.105
2	.083
4	.064
6	.047
8	.033
10	.020
12	.012
14	.006
16	.001
18	0

(a)





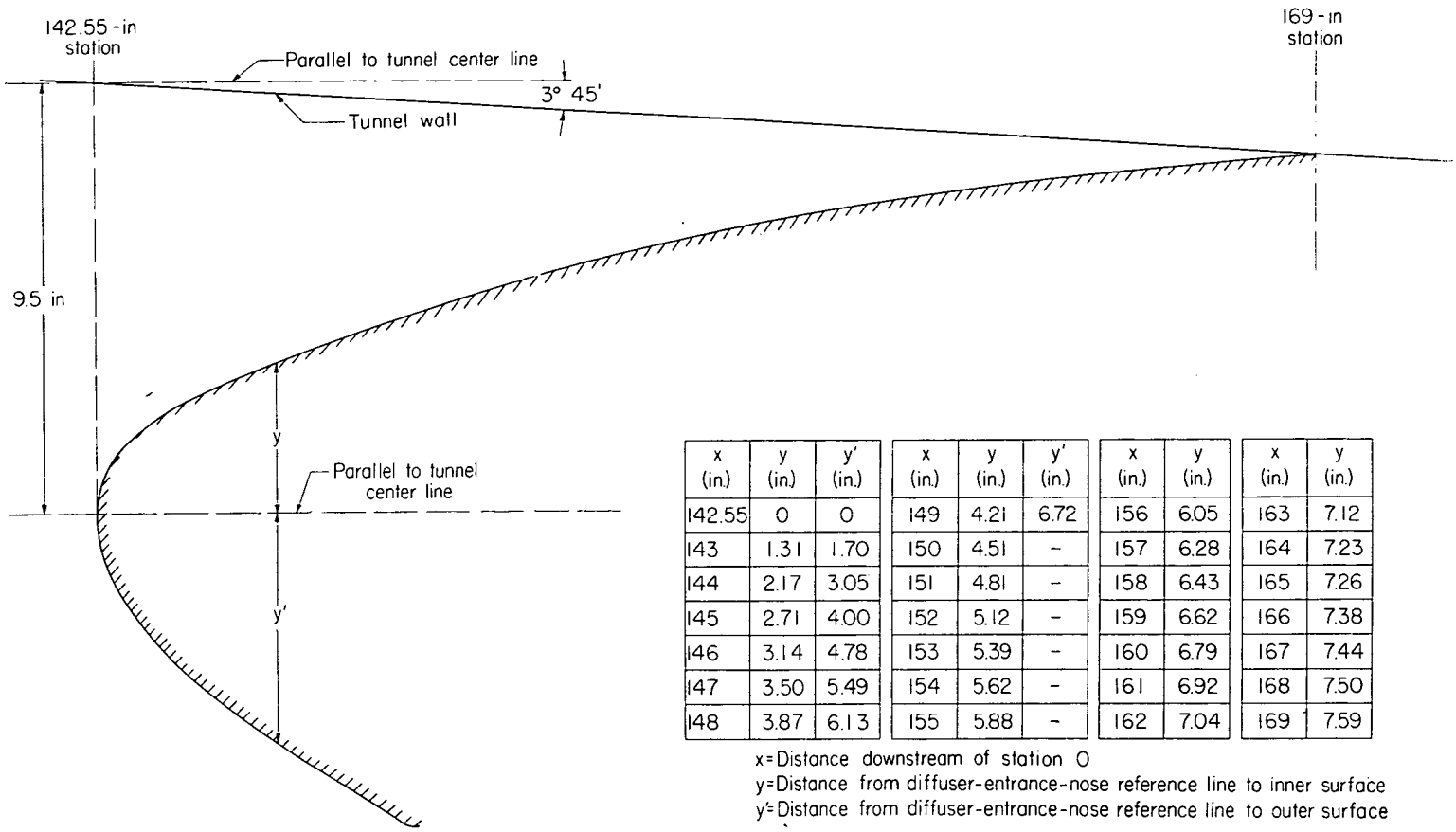
Coordinates for liner

x (in.)	y (in.)
125.6	0
128.0	0.132
130.0	.204
132.0	.242
134.0	.250
136.0	.240
138.0	.200
141.6	.030

(b)

(a) Original wall-panel arrangement with 45-minute divergence in test section.
(b) Reversed wall panels with 5-minute divergence in test section.

FIGURE 3.—Tunnel throat geometry including diffuser-entrance nose shape and wall divergence

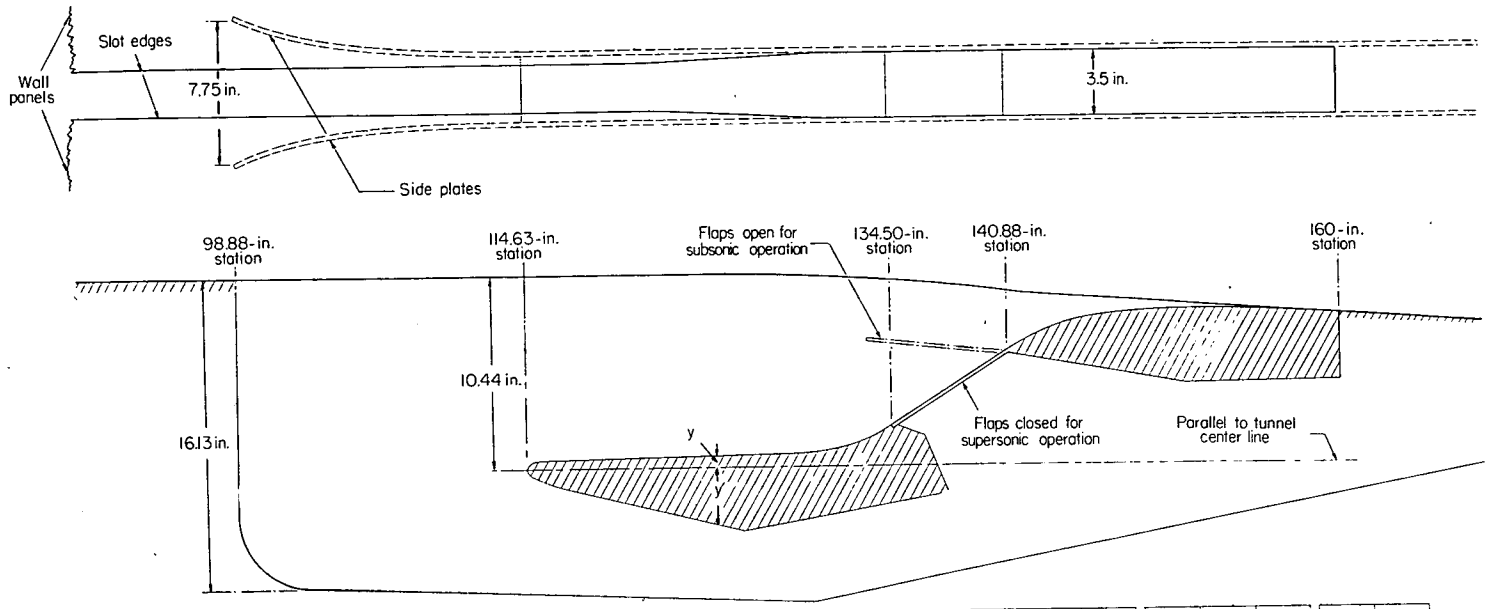


x (in.)	y (in.)	y' (in.)	x (in.)	y (in.)	y' (in.)	x (in.)	y (in.)	x (in.)	y (in.)
142.55	0	0	149	4.21	6.72	156	6.05	163	7.12
143	1.31	1.70	150	4.51	-	157	6.28	164	7.23
144	2.17	3.05	151	4.81	-	158	6.43	165	7.26
145	2.71	4.00	152	5.12	-	159	6.62	166	7.38
146	3.14	4.78	153	5.39	-	160	6.79	167	7.44
147	3.50	5.49	154	5.62	-	161	6.92	168	7.50
148	3.87	6.13	155	5.88	-	162	7.04	169	7.59

x=Distance downstream of station 0
y=Distance from diffuser-entrance-nose reference line to inner surface
y'=Distance from diffuser-entrance-nose reference line to outer surface

(a) Shape A.

FIGURE 4.—Coordinates of diffuser-entrance nose shapes.



x (in.)	y (in.)	y' (in.)	x (in.)	y (in.)	y' (in.)	x (in.)	y (in.)
114.63	0	0	126	.65	3.33	146	8.00
115	.42	.47	128	.71	3.82	148	8.20
115.50	.47	.67	130	.82	–	150	8.29
116	.48	.85	132	1.07	–	152	8.31
118	.52	1.36	134.50	2.12	–	154	8.30
120	.55	1.86	140.88	6.30	–	156	8.28
122	.59	2.33	142	6.66	–	158	8.15
124	.62	2.83	144	7.58	–	160	8.03

x = Distance downstream of station 0
y = Distance from diffuser-entrance-nose reference line to inner surface
y' = Distance from diffuser-entrance-nose reference line to outer surface

(b) Shape B.

FIGURE 4.—Concluded.

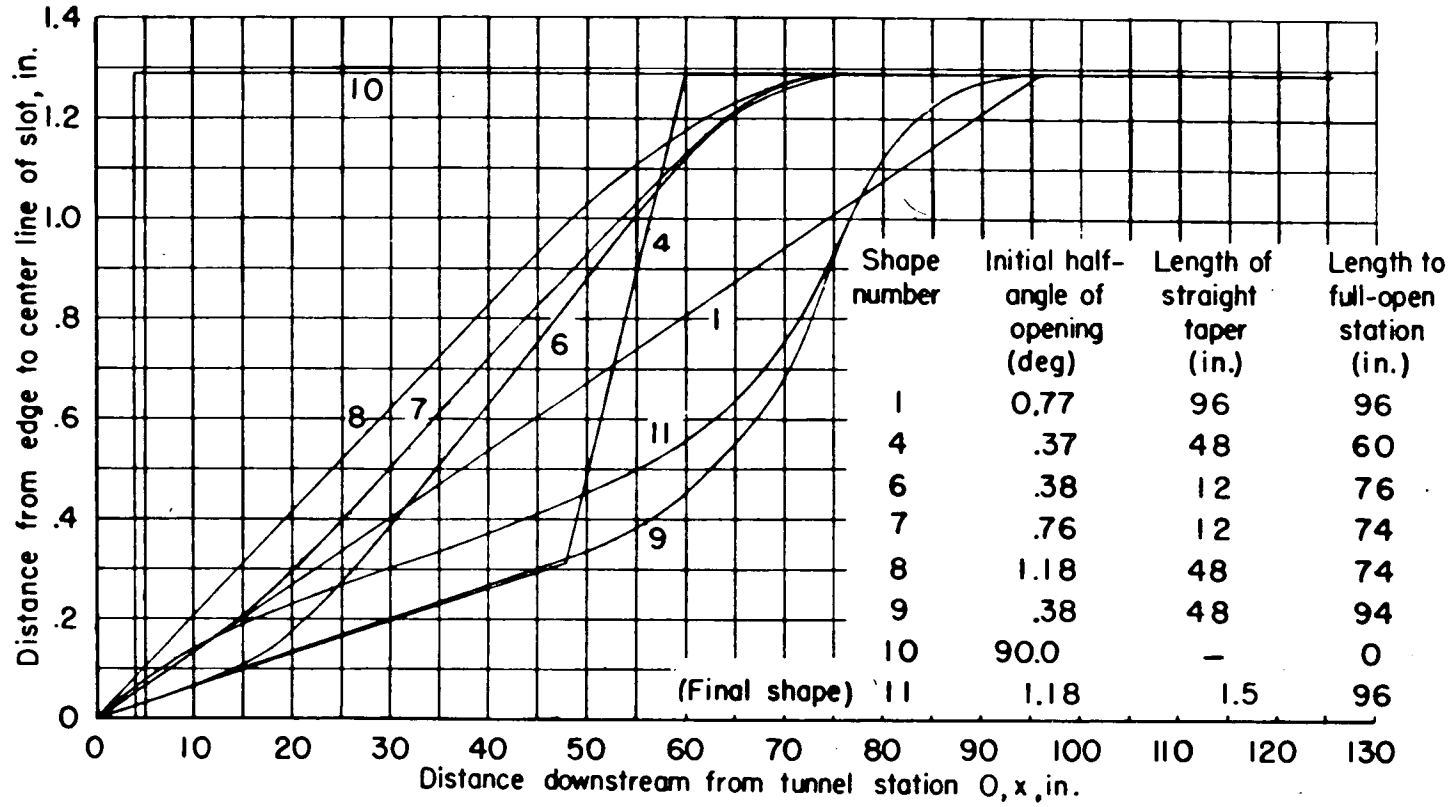


FIGURE 5.—Various slot shapes investigated in the Langley 8-foot high-speed tunnel with 5-minute wall-panel divergence in test section.

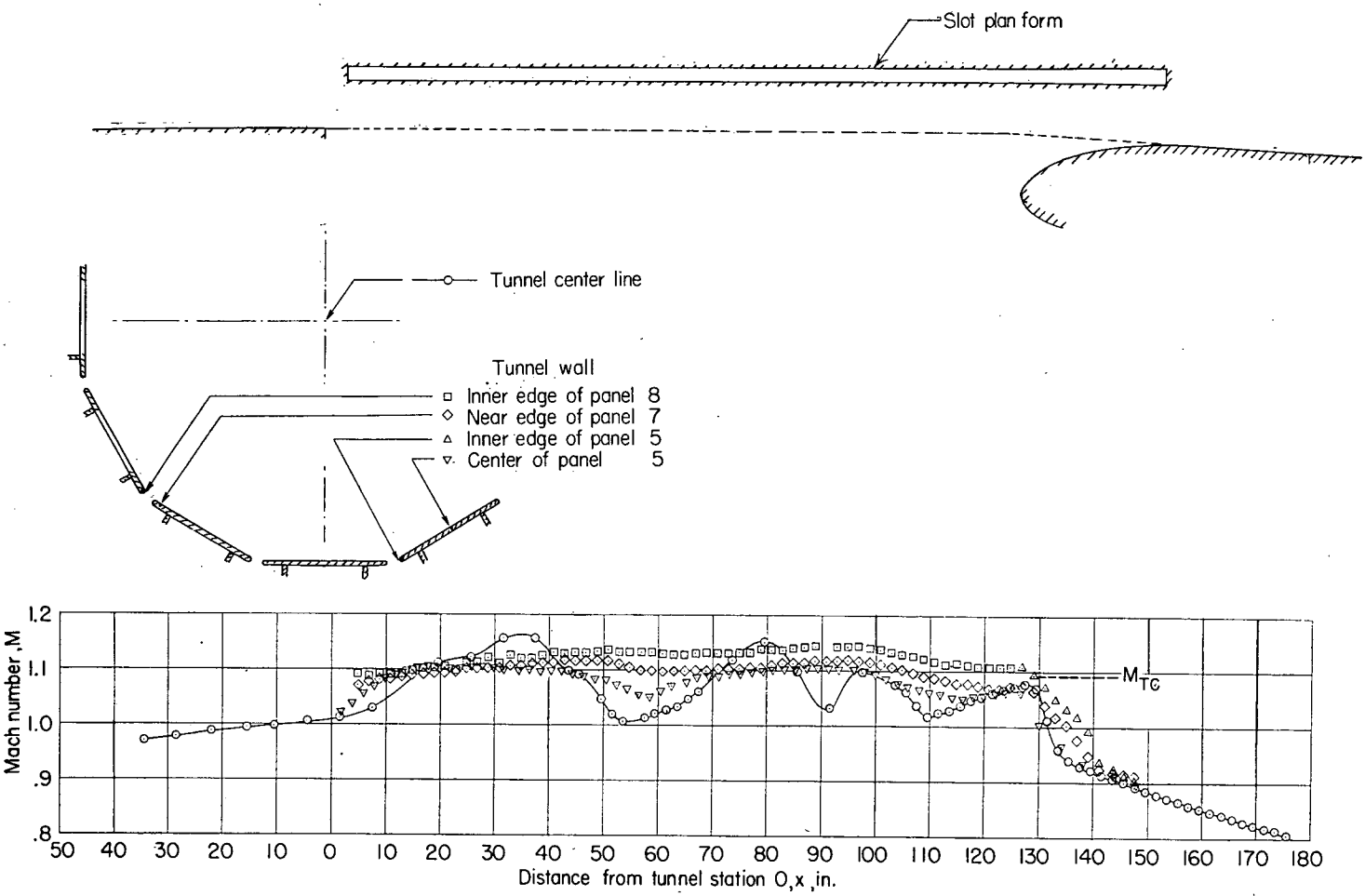


FIGURE 6.—Comparison of Mach number distributions measured axially along tunnel center line with those measured along center and edges of wall panels. Nose A; slot shape 10 (rectangular); 45-minute divergence of wall panels in test section; $M_{TC}=1.092$.

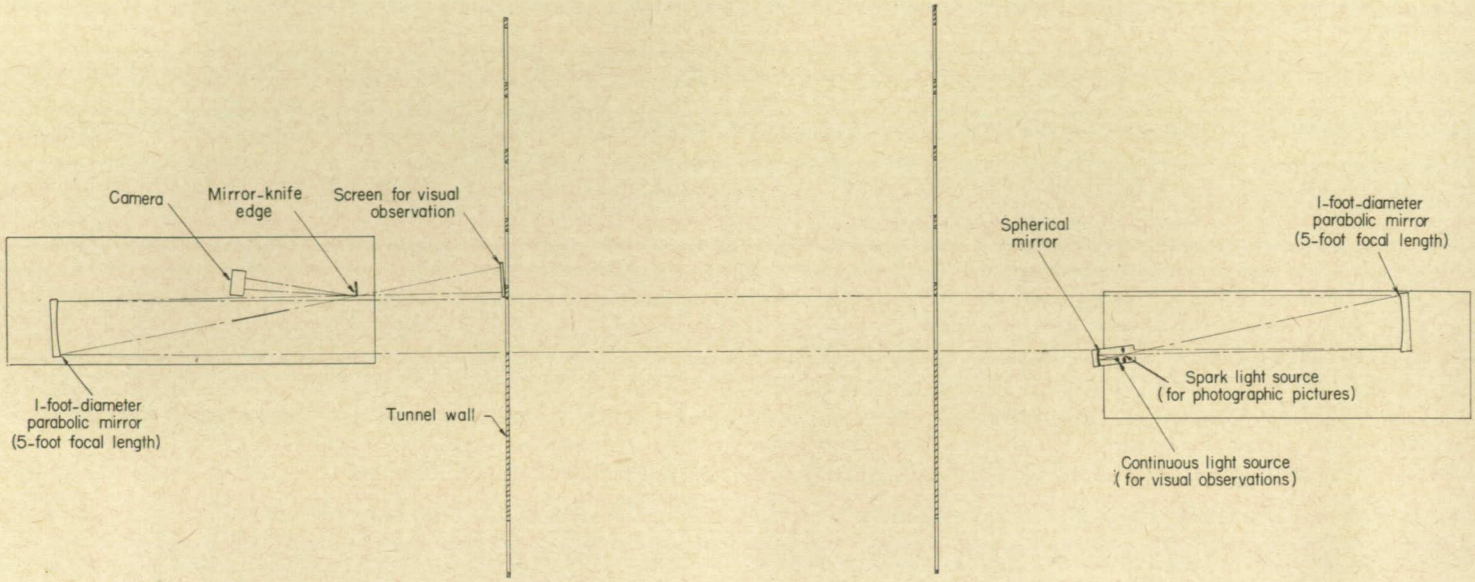


FIGURE 7.—Temporary schlieren system used in connection with slotted-test-section flow surveys.

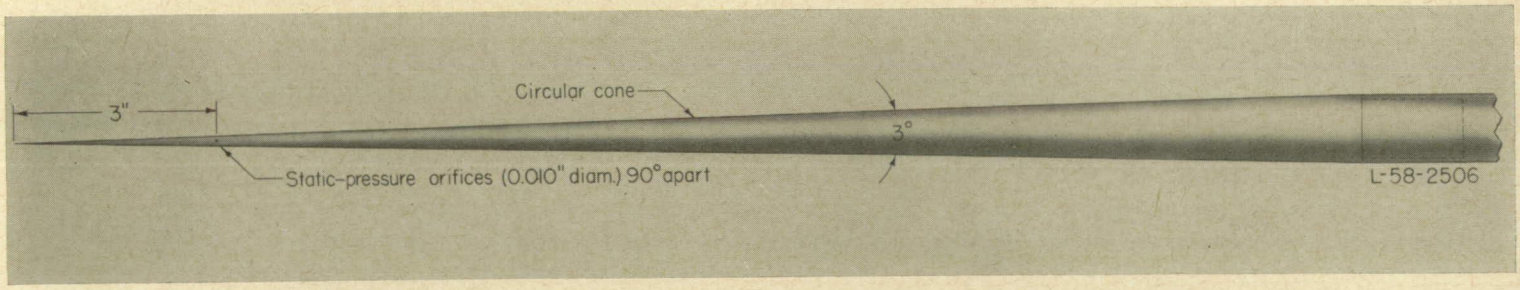
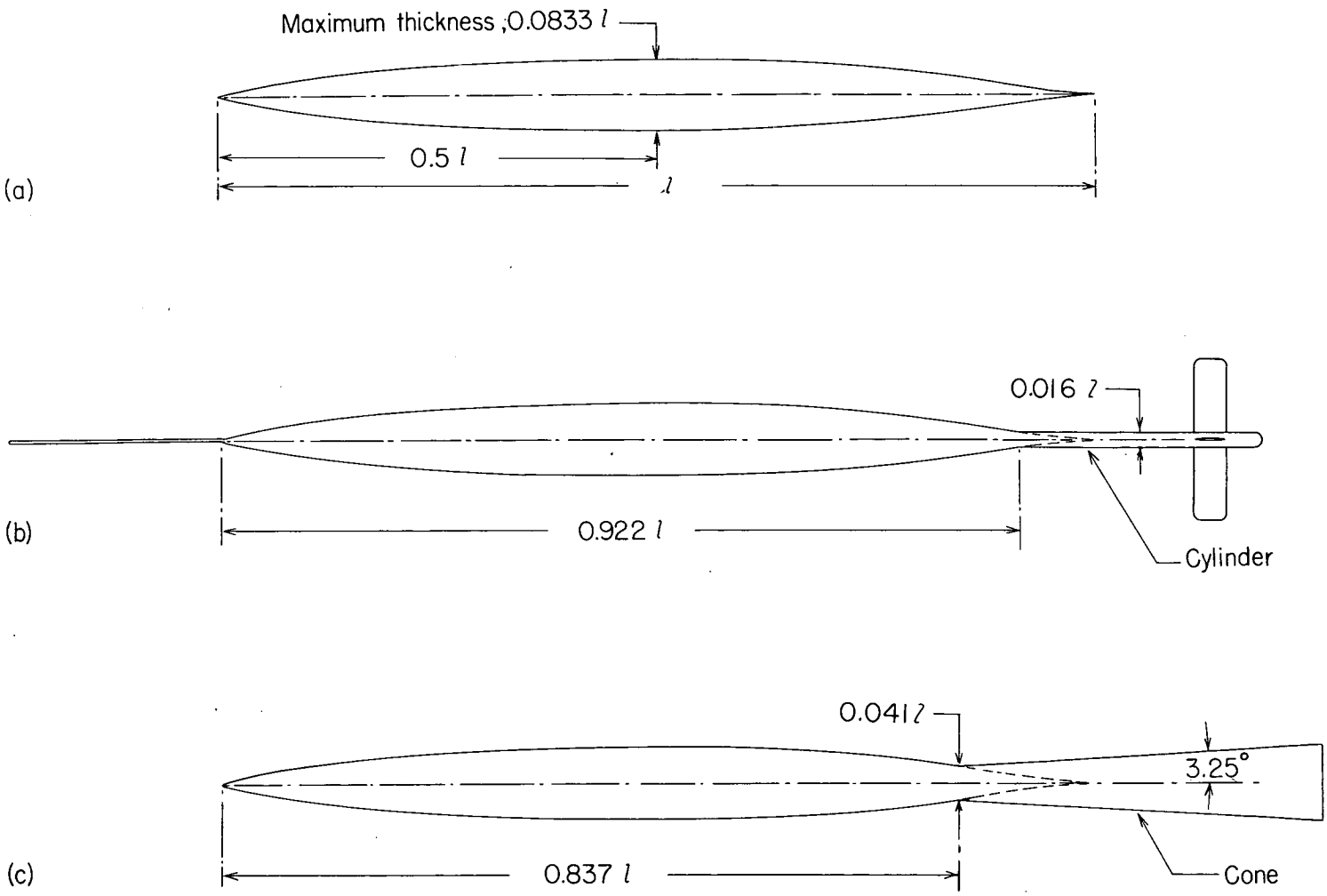


FIGURE 8.—Null-pressure-type instrument (3° cone) used for measuring angularity of flow in slotted test section.



(a) Basic body shape.
(b) Free-fall body.
(c) Wind-tunnel model.

FIGURE 9.—Body of revolution used for comparison of body-surface pressure distributions obtained from wind-tunnel tests with those from free-fall tests and theory.

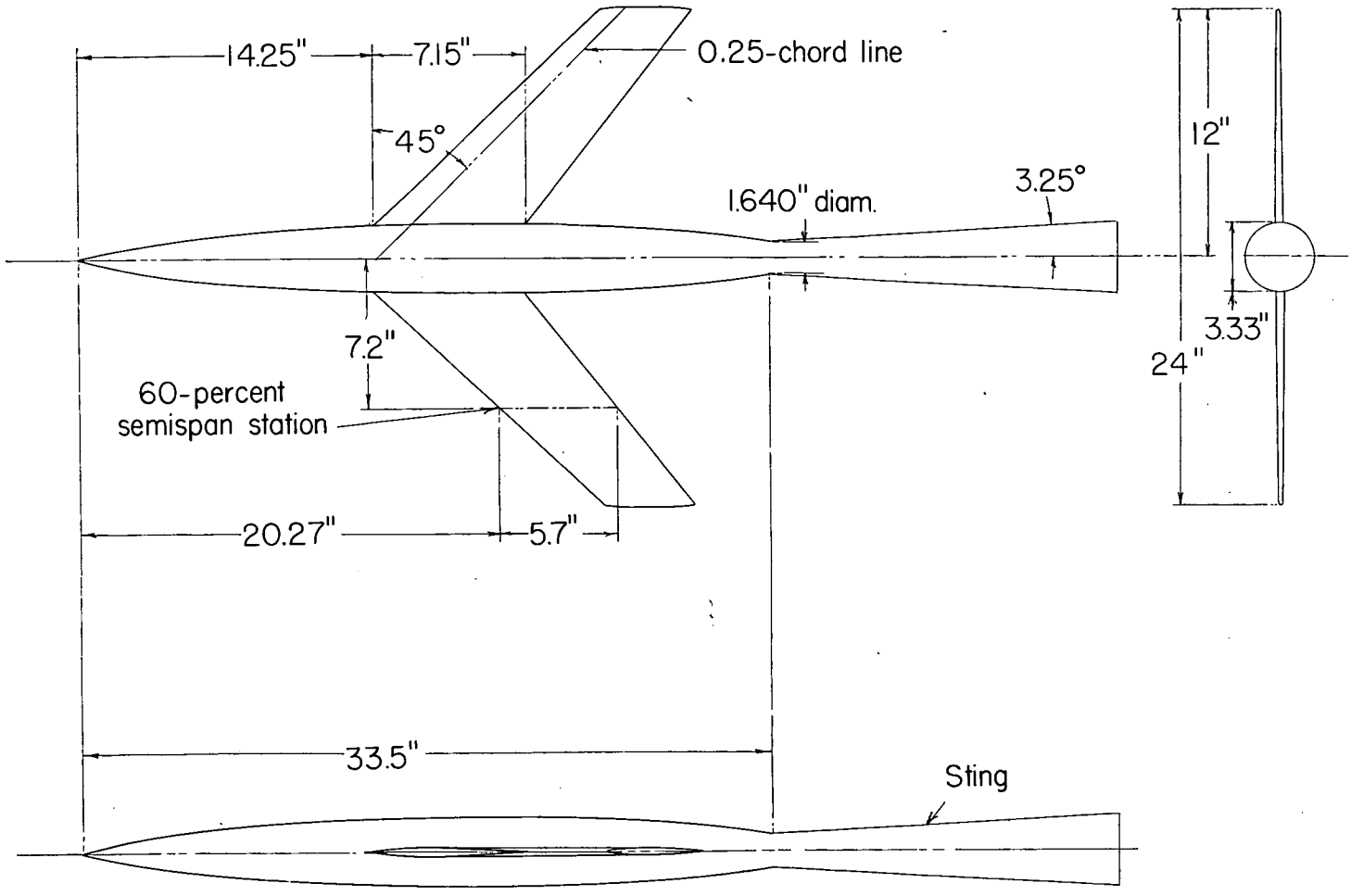


FIGURE 10.—Transonic-airplane model investigated in connection with flow surveys in slotted test section.

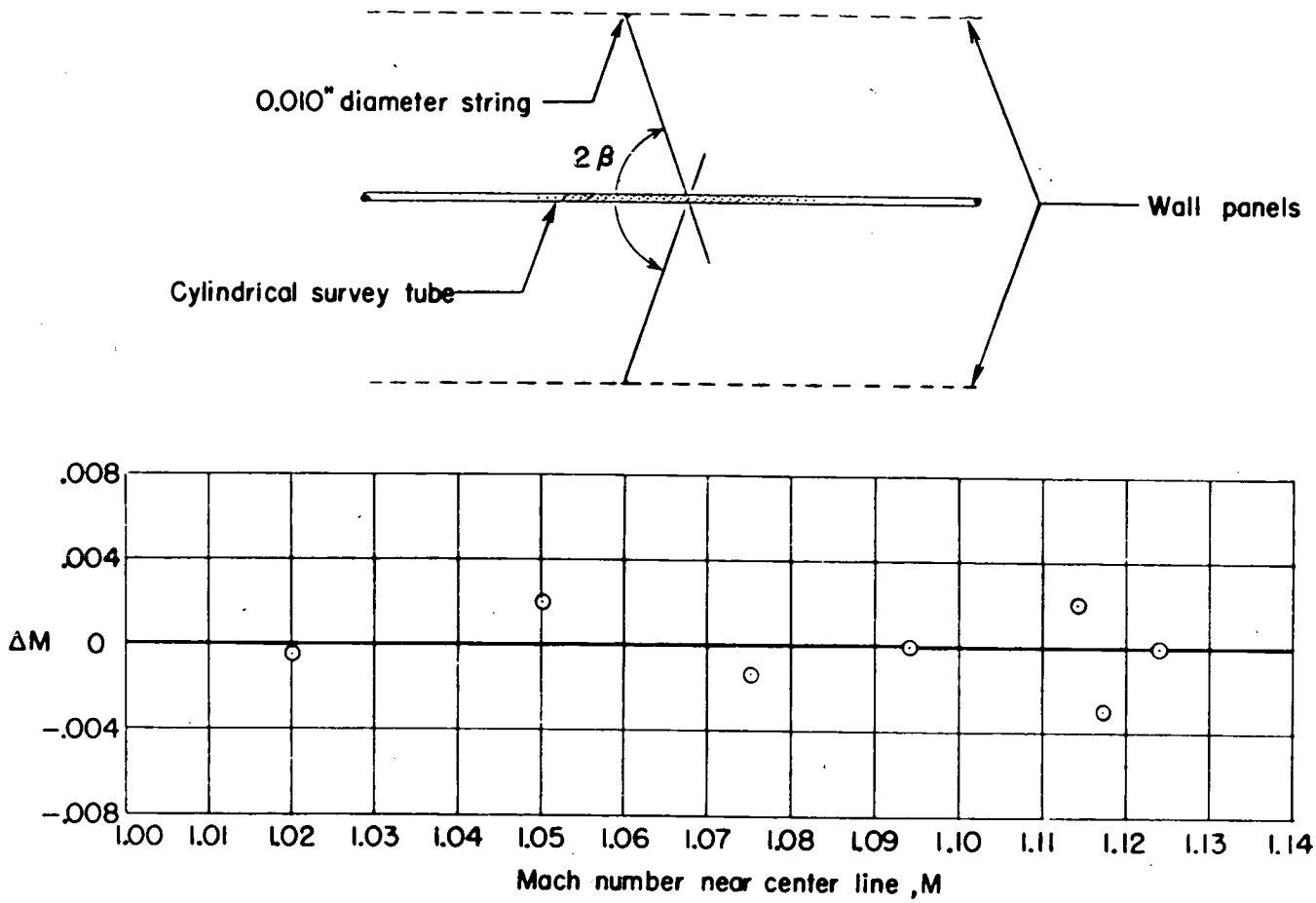


FIGURE 11.—Agreement of flow Mach numbers obtained from pressure measurements at test-section center line with those indicated by measured angularity of weak shocks produced by 0.010-inch-diameter strings fastened to wall panels. ΔM is the Mach number from pressure measurements minus the Mach number indicated by shock angles.

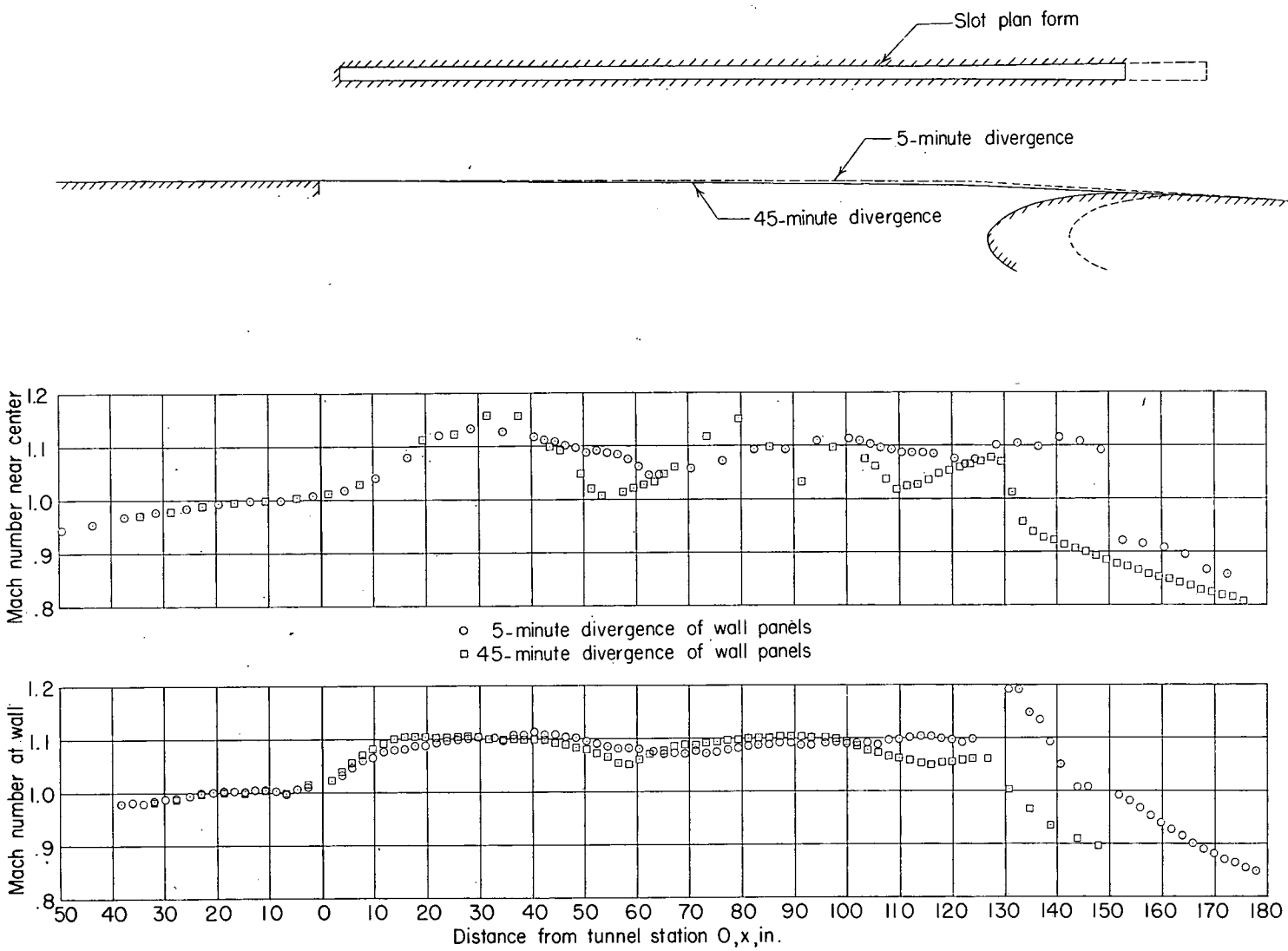


FIGURE 12.—Comparison of Mach number distributions axially along center line and wall of the slotted throat with 5-minute and 45-minute divergence of test-section wall panels. Slot shape 10; $M_{TC}=1.093$.

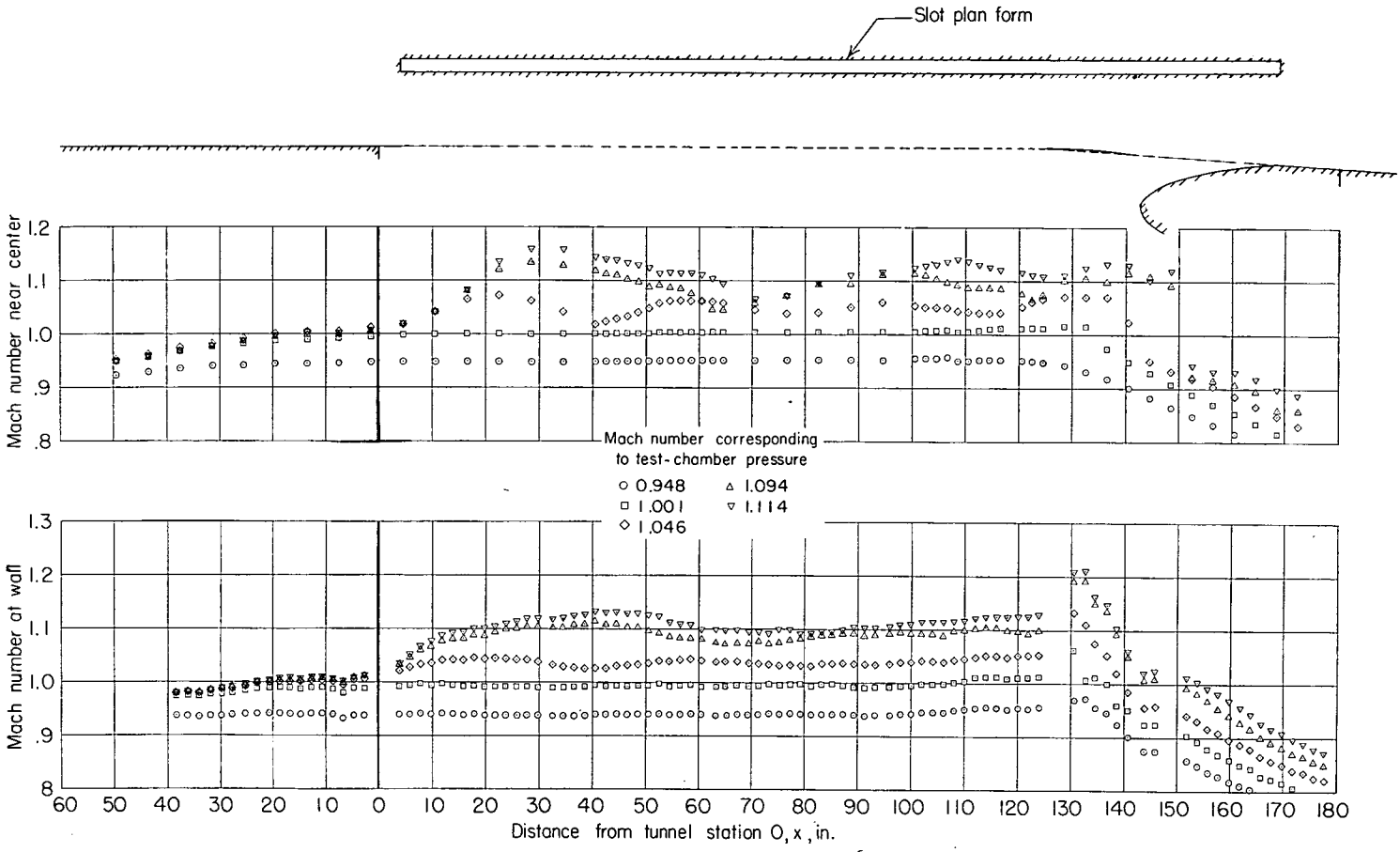


FIGURE 13.—Mach number distributions axially along center line and wall of the slotted throat with 5-minute divergence of test-section wall panels. Slot shape 10.

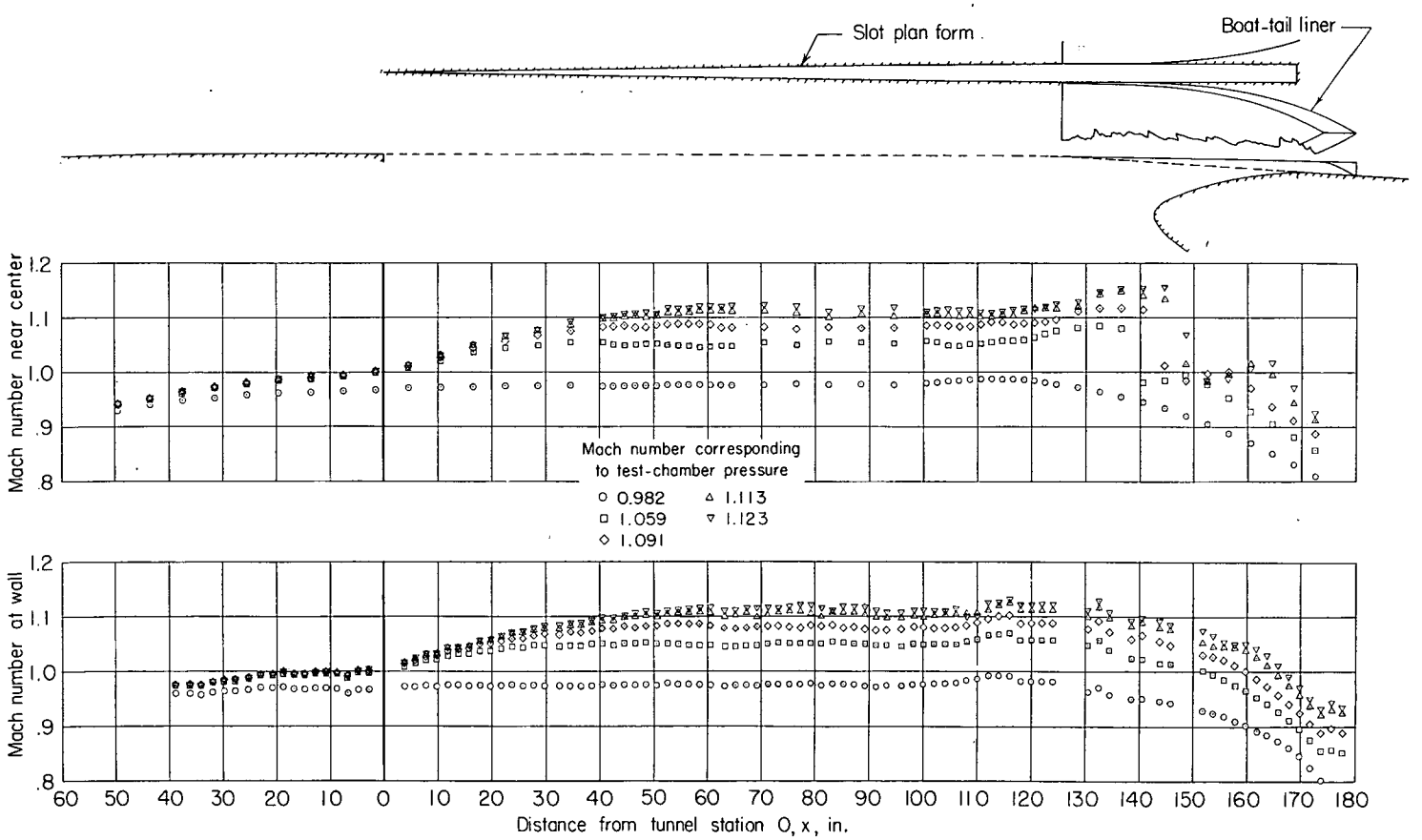


FIGURE 14.—Mach number distributions axially along center line and wall of the slotted throat with 5-minute divergence of test-section wall panels. Slot shape 1.

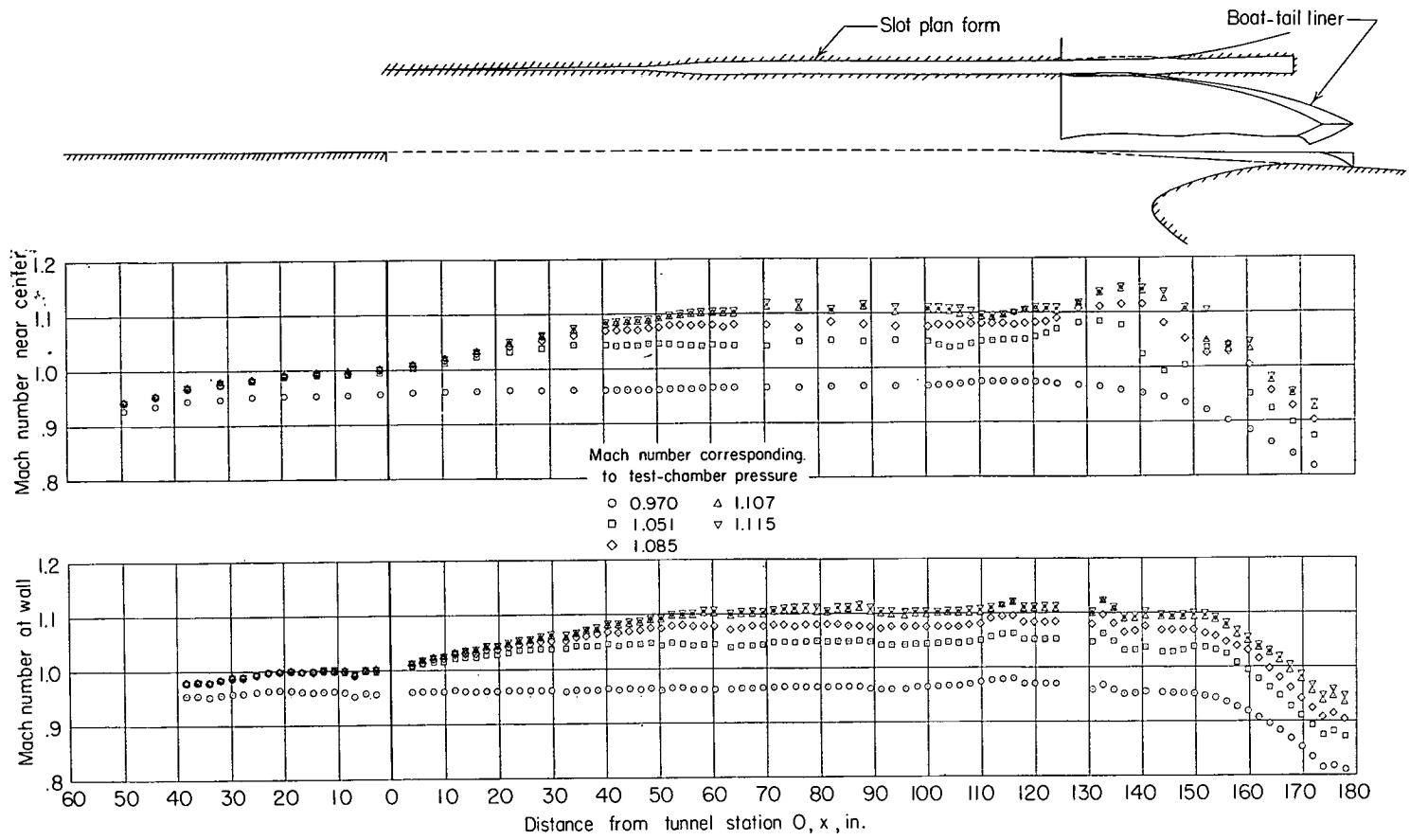


FIGURE 15.—Mach number distributions axially along center line and wall of the slotted throat with 5-minute divergence of test-section wall panels. Slot shape 4.

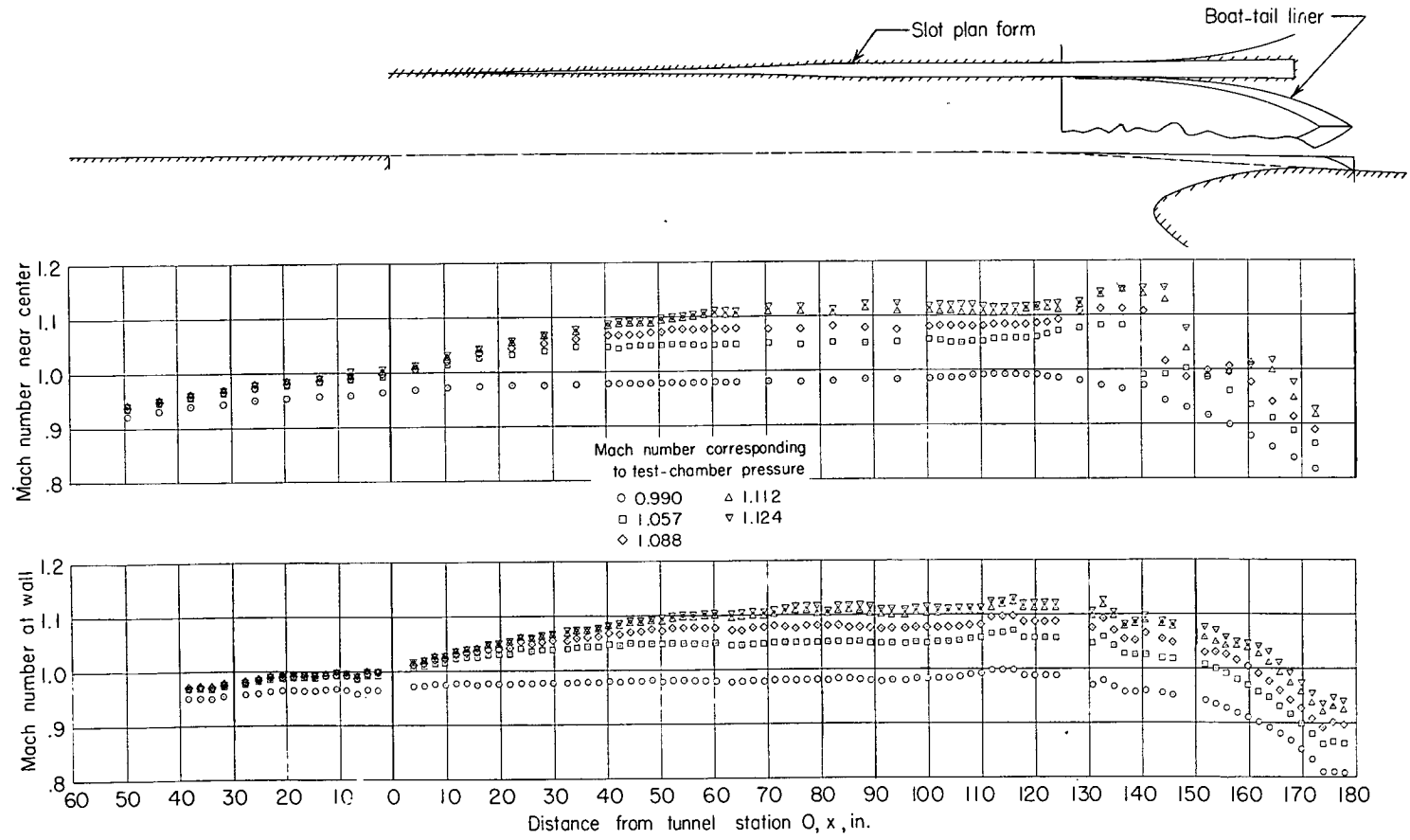


FIGURE 16.—Mach number distributions axially along center line and wall of the slotted throat with 5-minute divergence of test-section wall panels. Slot shape 9.

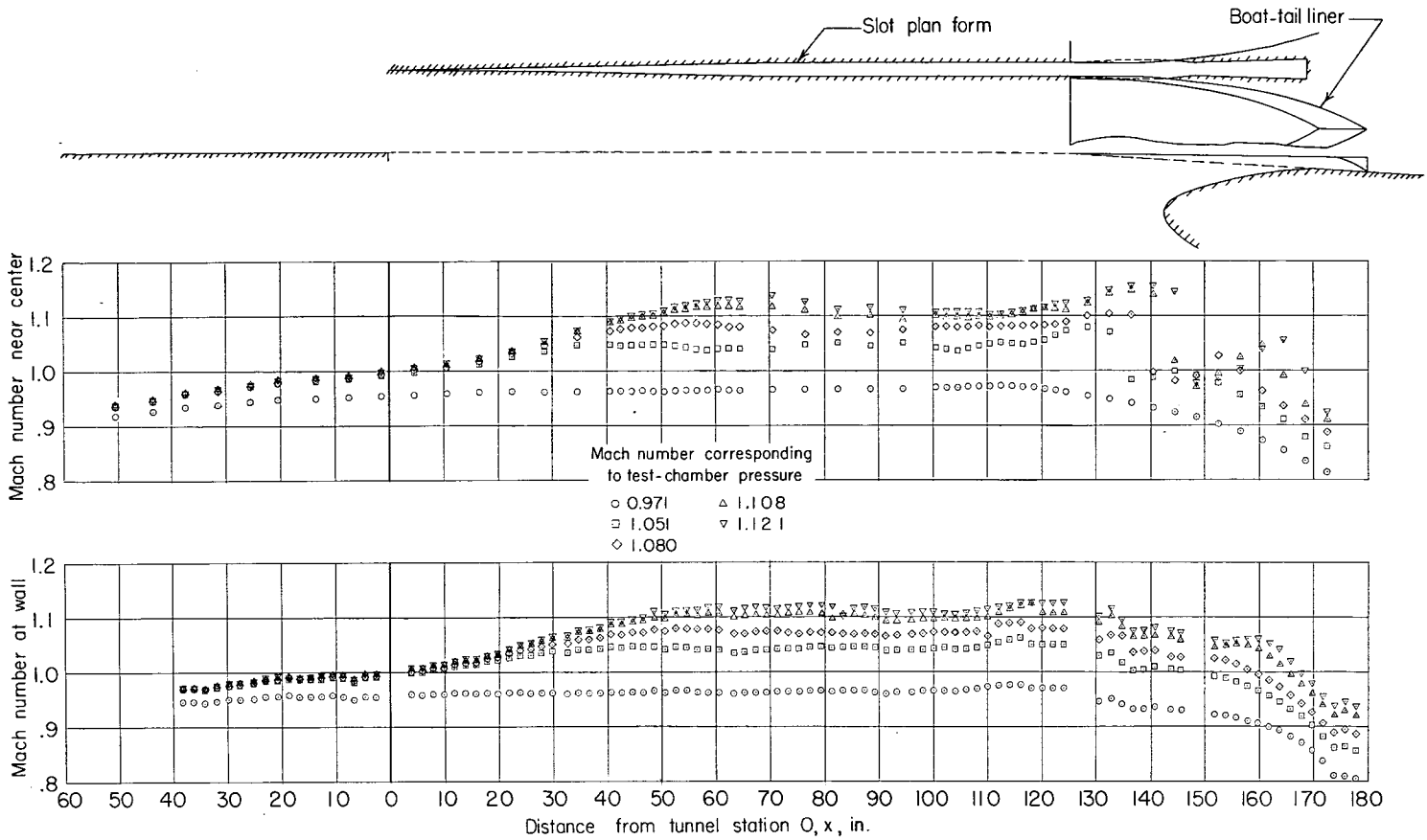


FIGURE 17.—Mach number distributions axially along center line and wall of the slotted throat with 5-minute divergence of test-section wall panels. Slot shape 6.

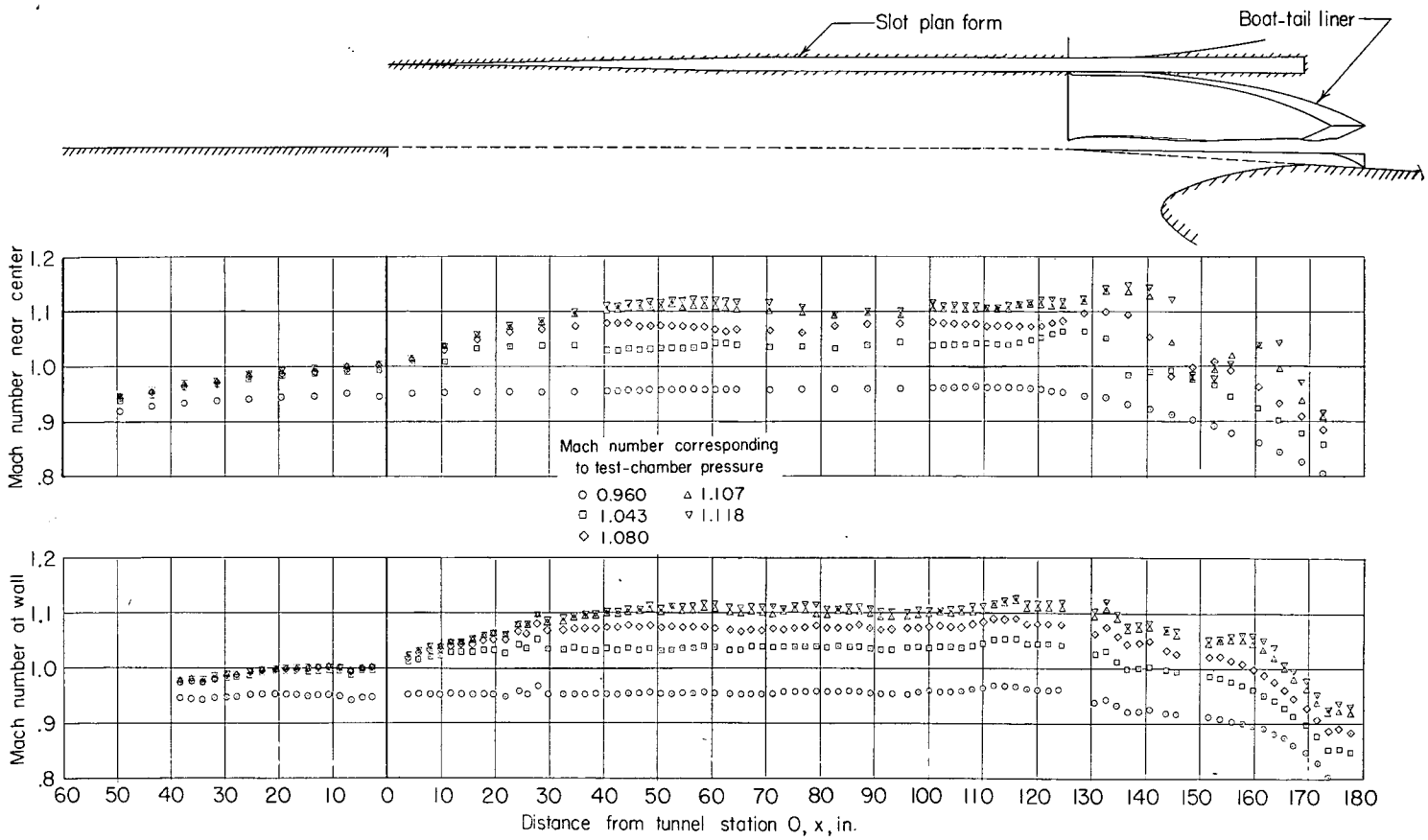


FIGURE 18.—Mach number distributions axially along center line and wall of the slotted throat with 5-minute divergence of test-section wall panels. Slot shape 7.

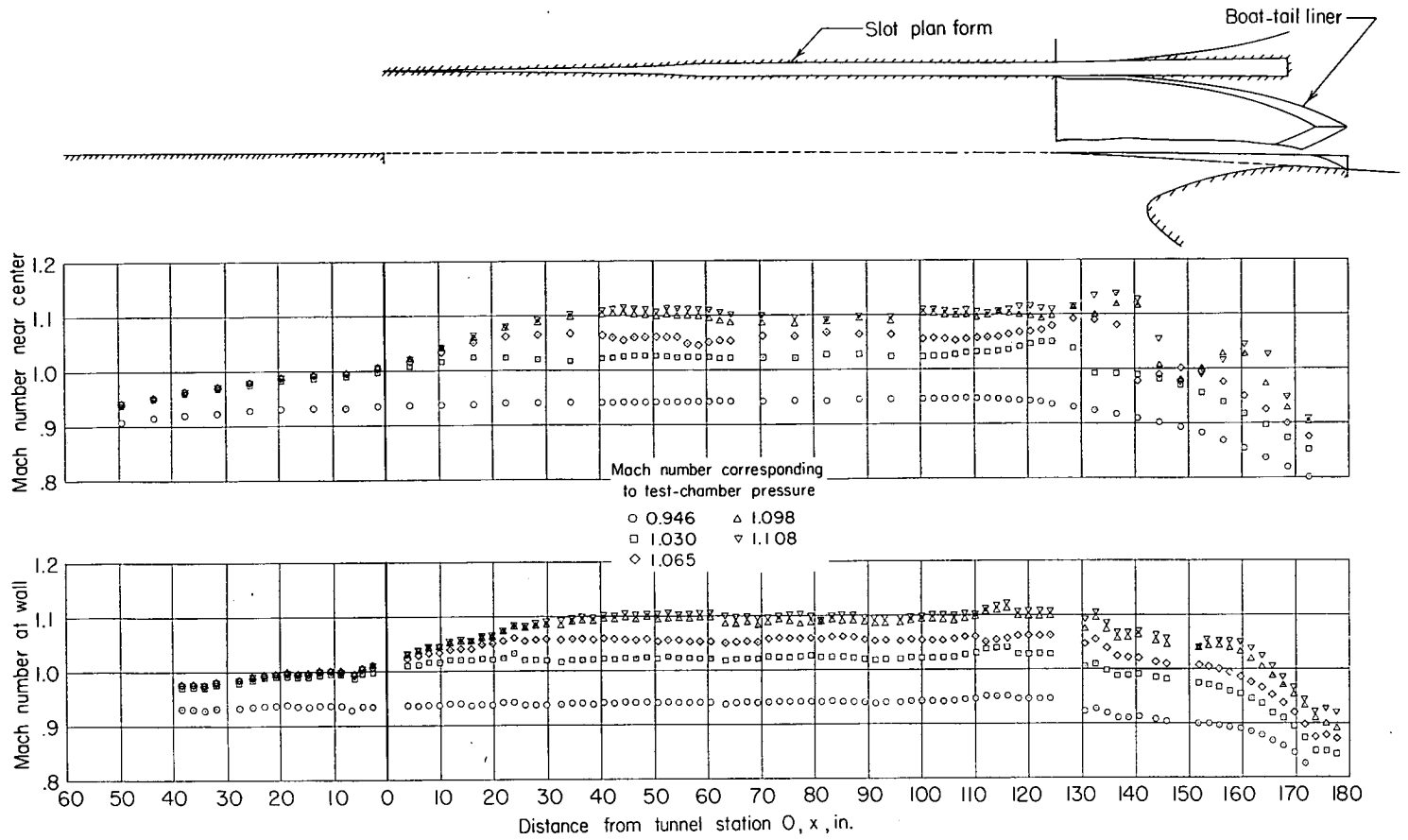


FIGURE 19.—Mach number distributions axially along center line and wall of the slotted throat with 5-minute divergence of test-section wall panels. Slot shape 8.

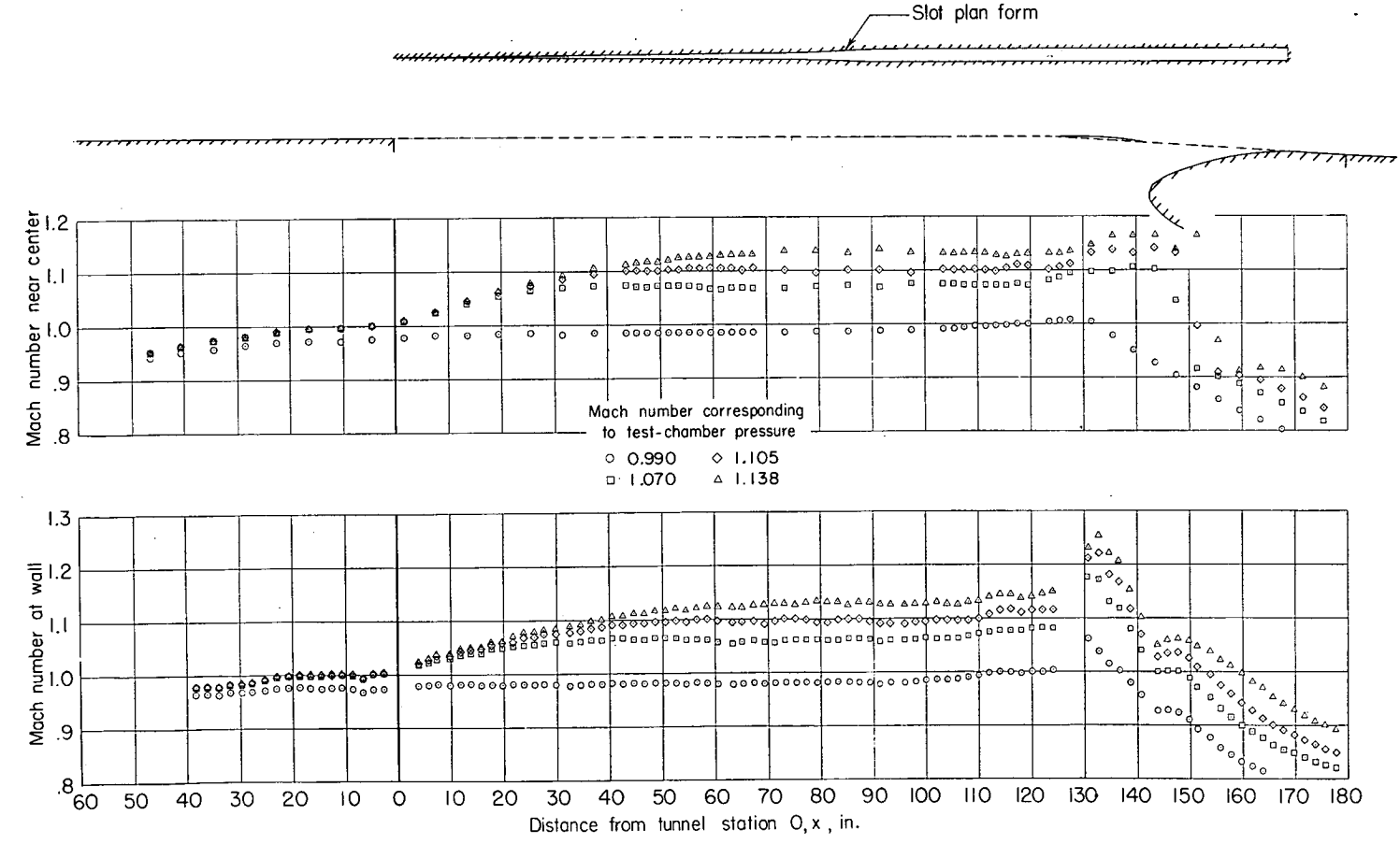
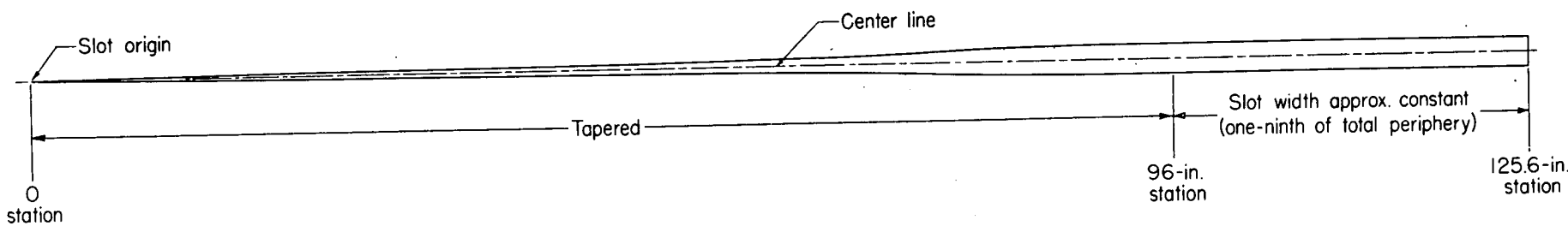


FIGURE 20.—Mach number distributions axially along center line and wall of the slotted throat with 5-minute divergence of test-section wall panels. Slot shape 11.

526597—60——86



x (in.)	y (in.)	x (in.)	y (in.)	x (in.)	y (in.)	x (in.)	y (in.)	x (in.)	y (in.)
0	0	20	.233	40	.371	60	.556	80	1.120
2	.037	22	.250	42	.386	62	.585	82	1.170
4	.068	24	.263	44	.403	64	.618	84	1.210
6	.098	26	.278	46	.418	66	.656	86	1.240
8	.122	28	.290	48	.433	68	.700	88	1.260
10	.144	30	.303	50	.451	70	.751	90	1.273
12	.165	32	.316	52	.469	72	.812	92	1.281
14	.185	34	.329	54	.486	74	.882	94	1.288
16	.202	36	.343	56	.508	76	.969	96	1.290
18	.219	38	.356	58	.530	78	1.060	125.6	1.291

x = Distance downstream of slot origin
y = Distance from slot edge to center line

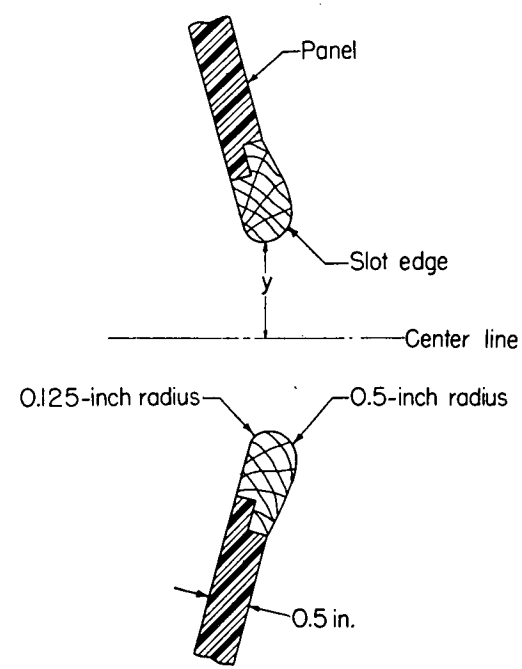
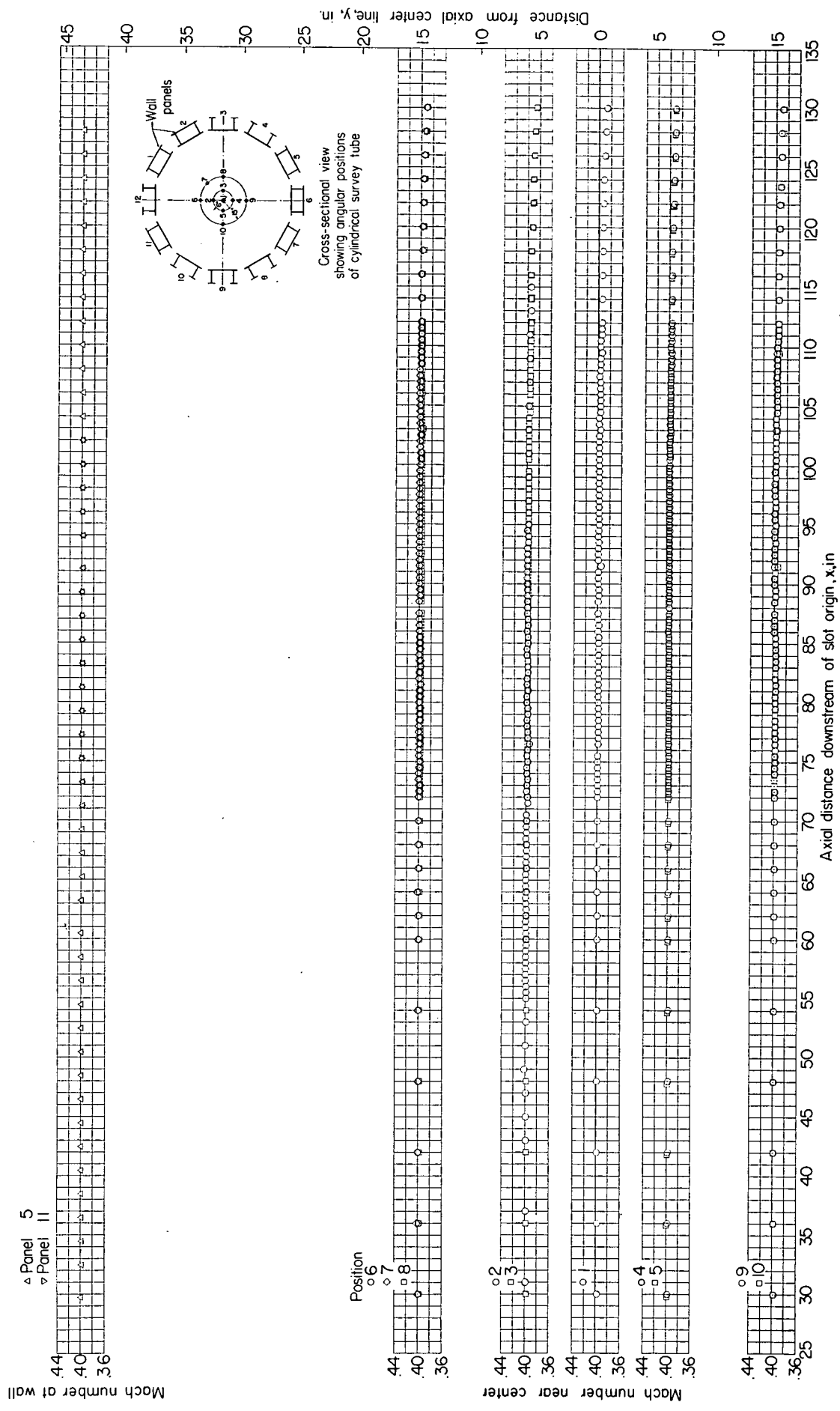
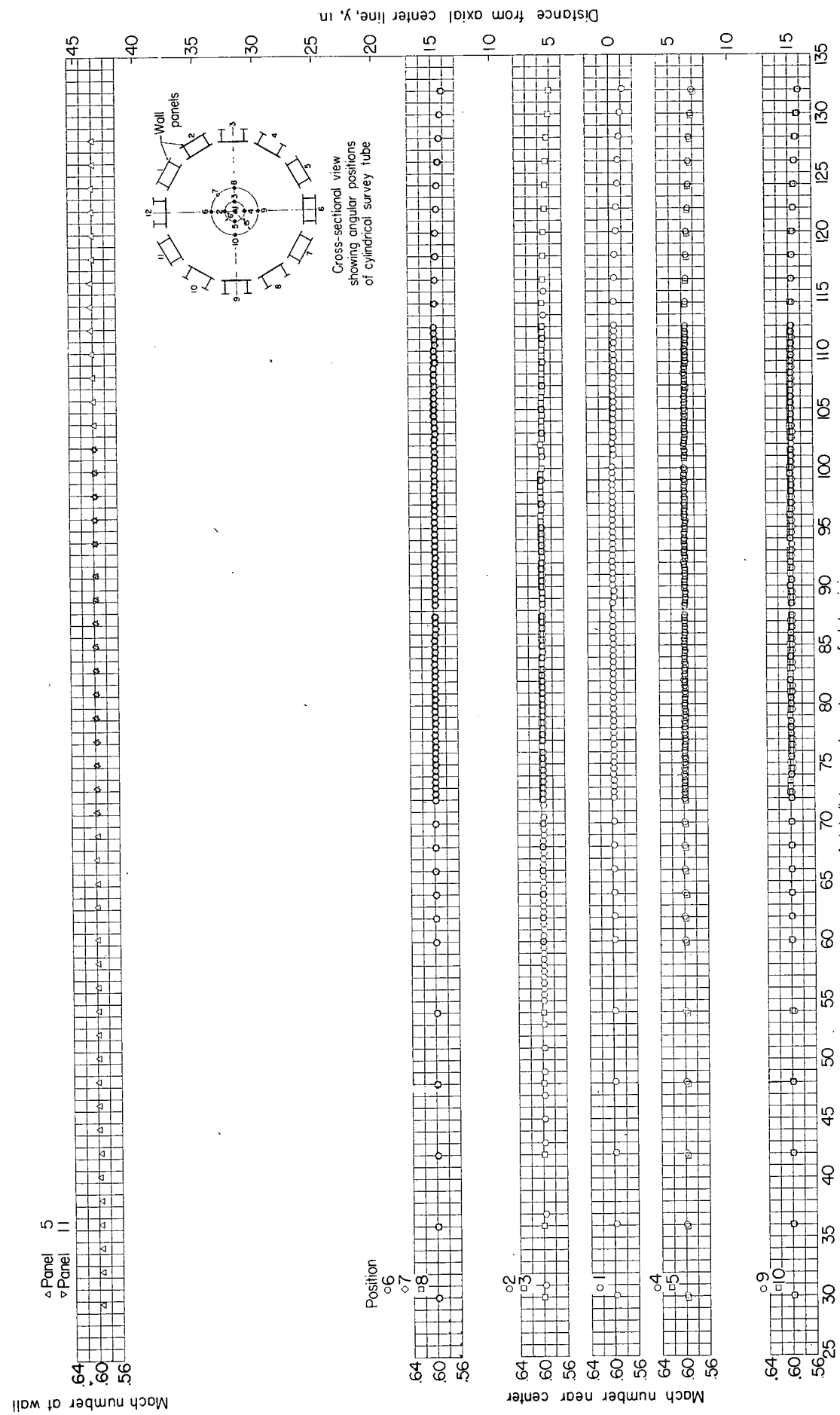


FIGURE 21.—Coordinates of final slot shape developed for use in the Langley 8-foot transonic tunnel.



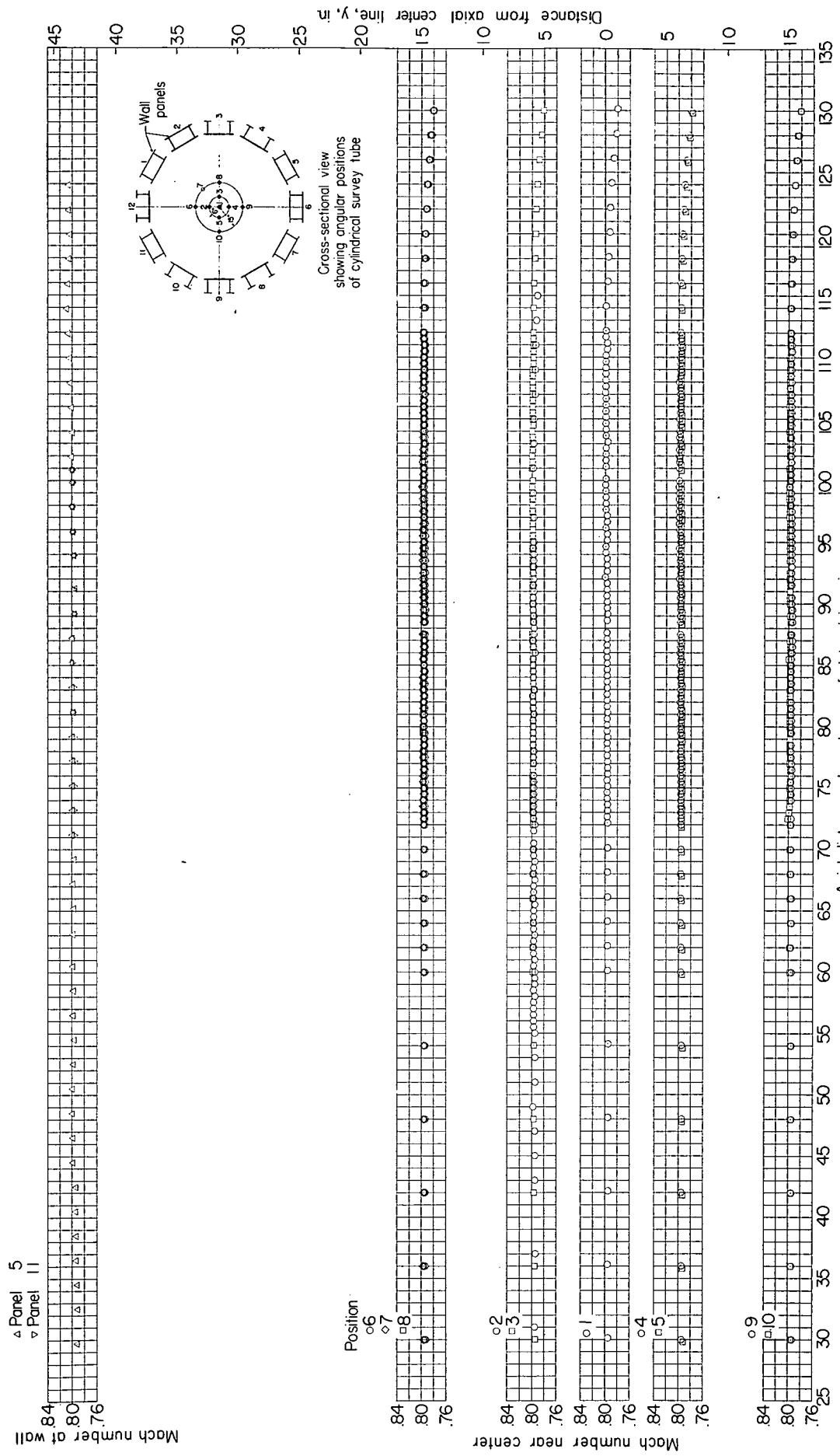
(a) $M_{TC}=0.40$.

FIGURE 22.—Basic flow-survey charts showing Mach number distributions axially along wall and near center line of slotted test section with model removed. Diffuser-entrance nose A. Slot shape 11.



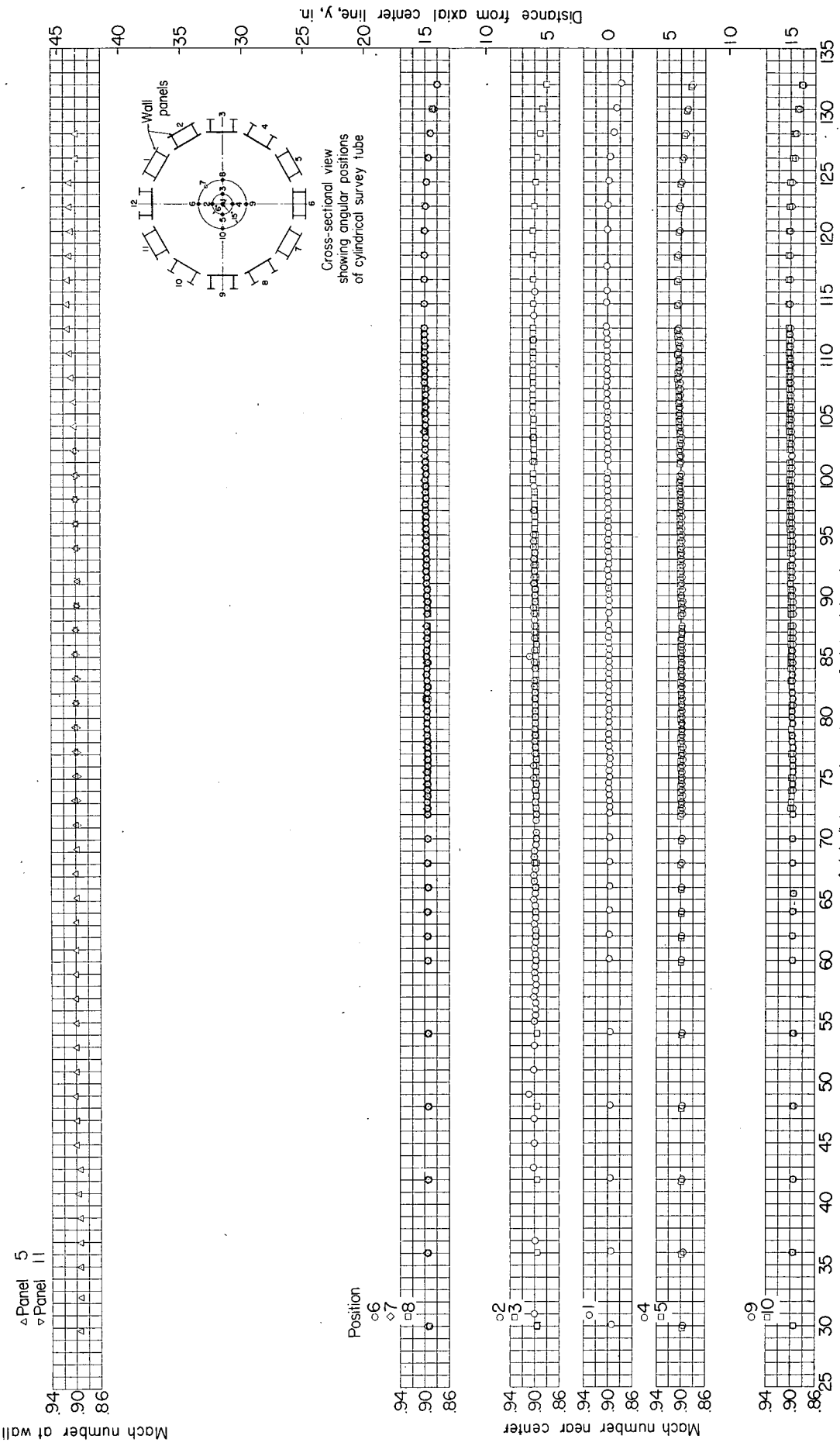
(b) $M_{rc}=0.60$.

FIGURE 22.—Continued.



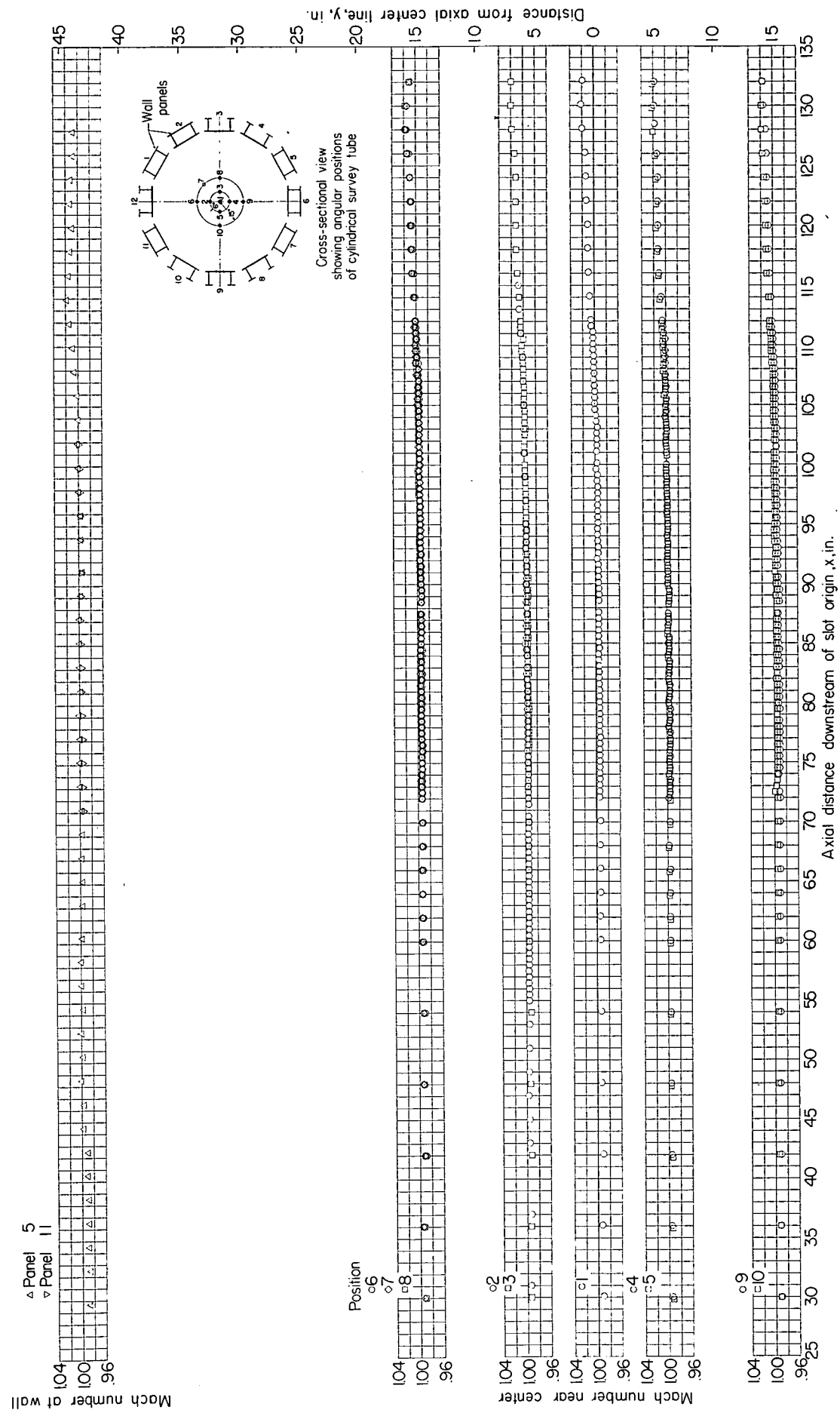
(c) $M_{TC}=0.80$.

FIGURE 22.—Continued.



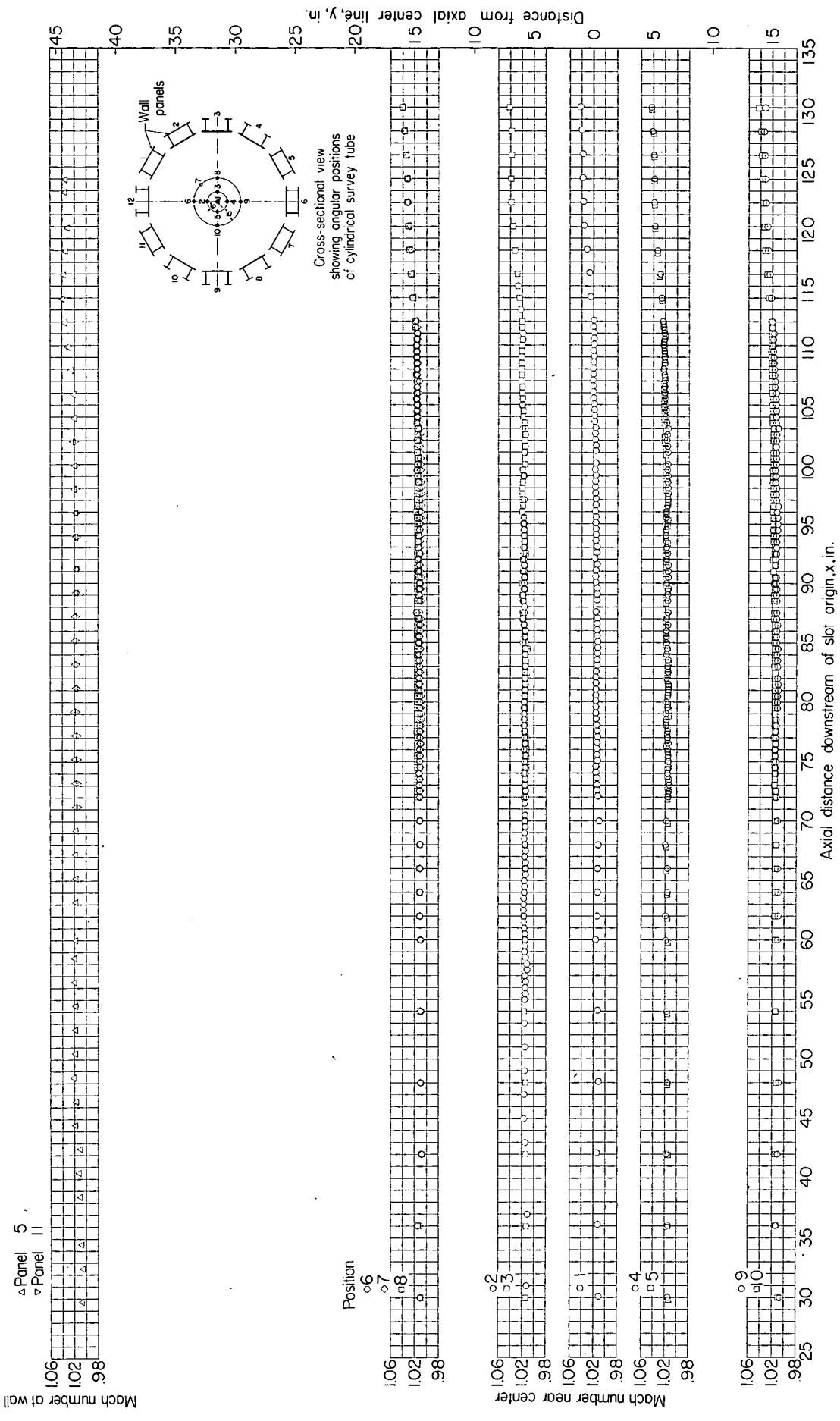
(d) $M_{TC}=0.90$.

FIGURE 22.—Continued.



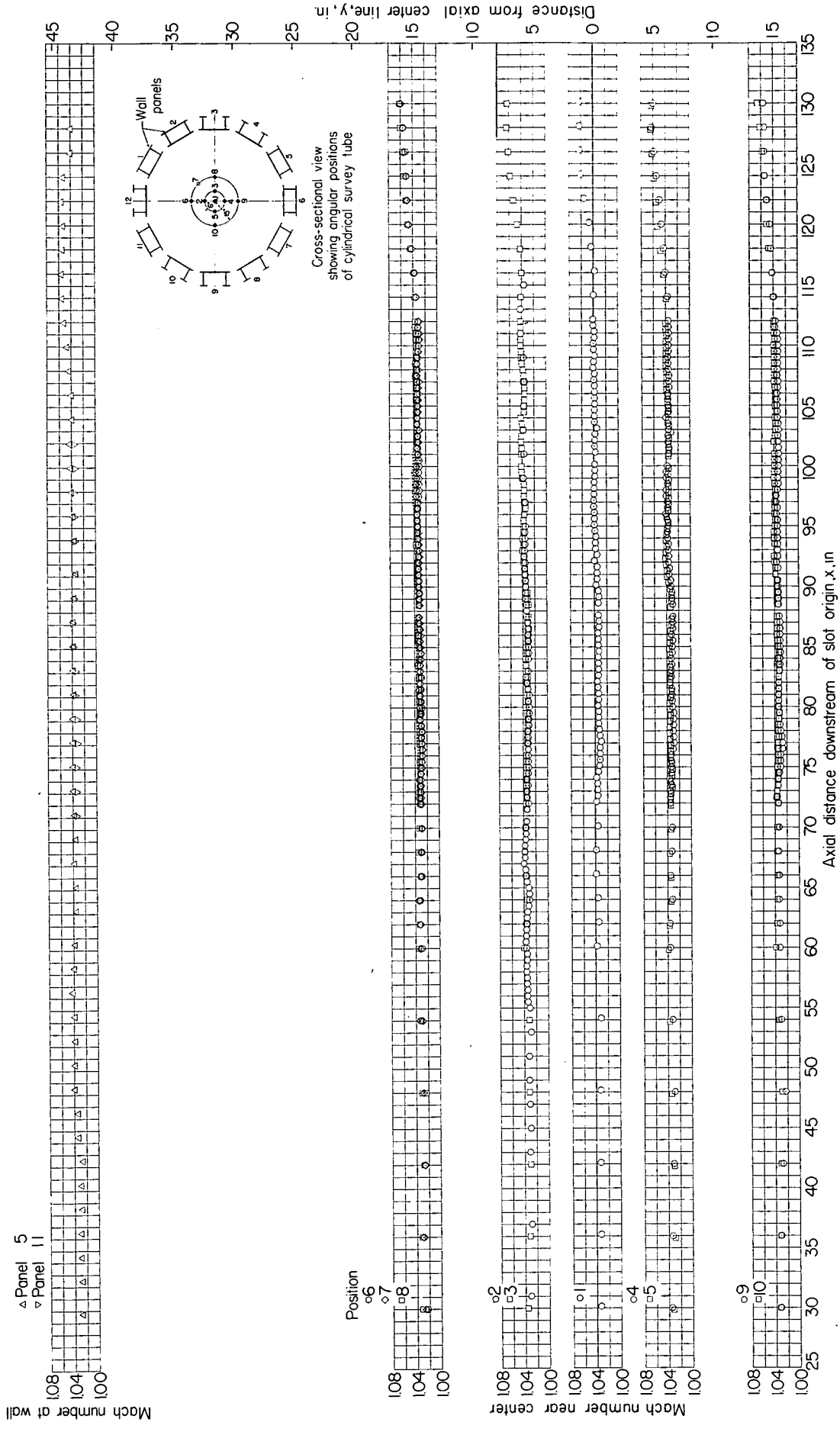
(e) $M_{\infty}=1.00$.

FIGURE 22.—Continued.



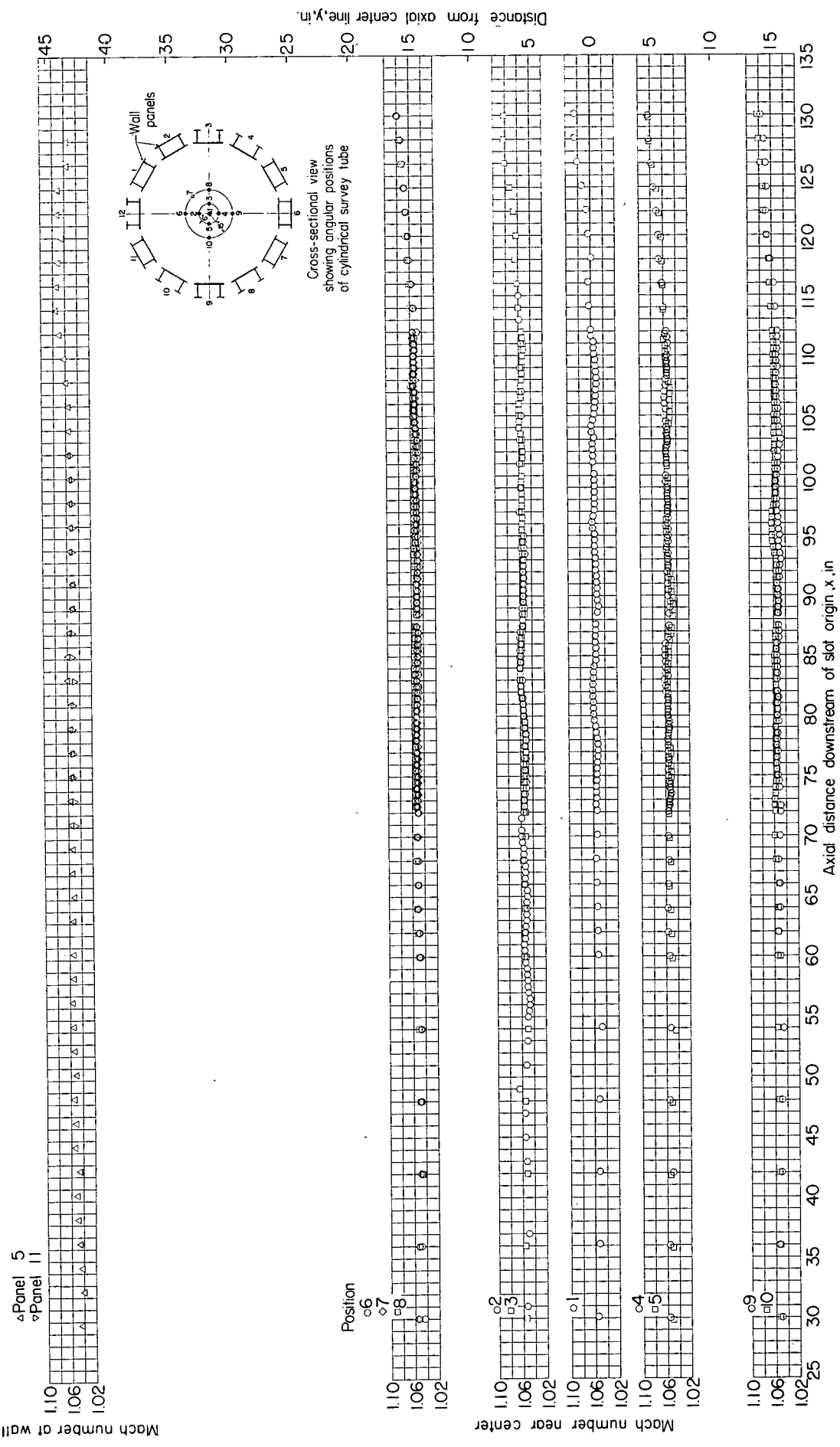
(f) $M_{TC}=1.02$.

FIGURE 22.—Continued.



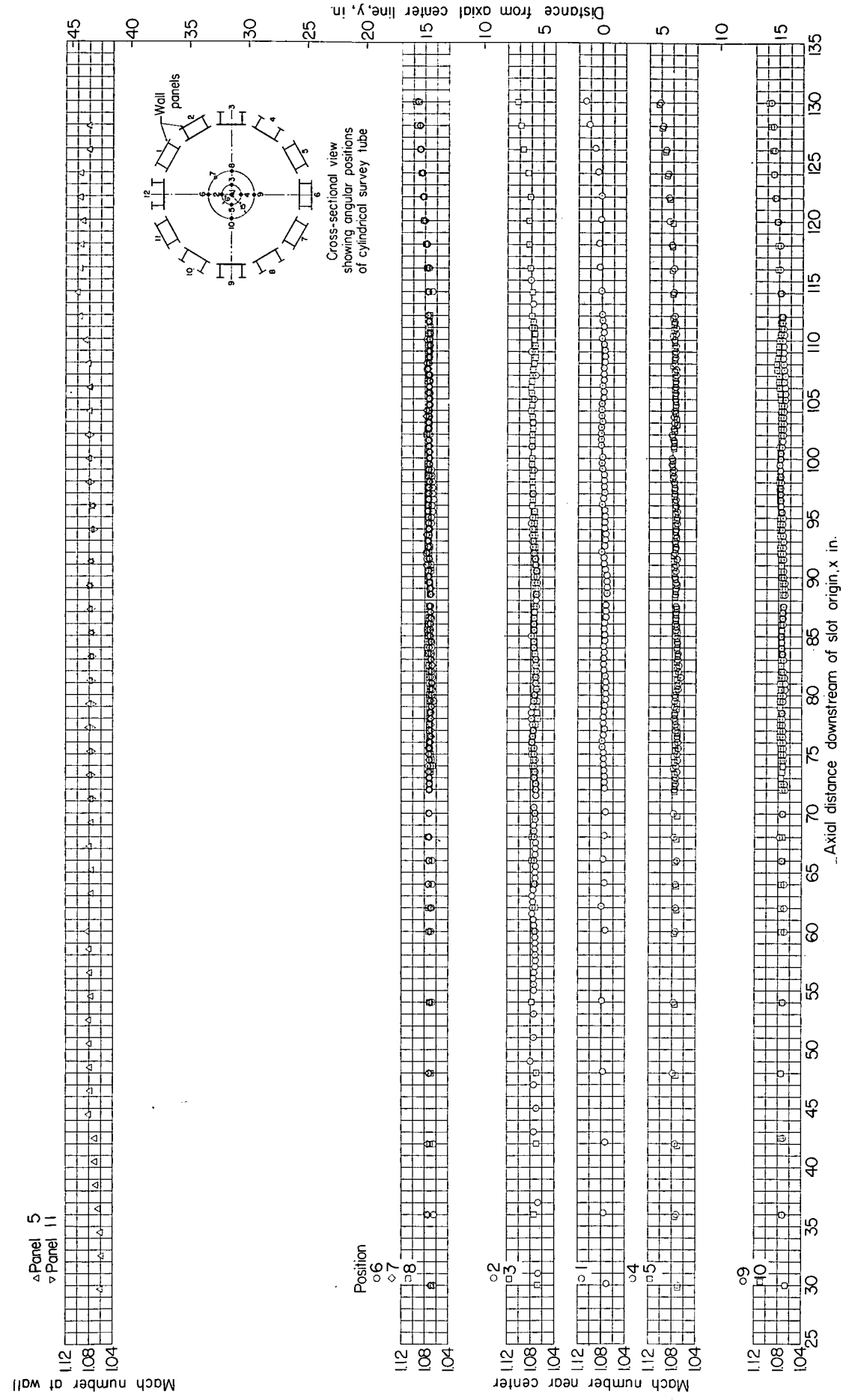
(g) $M_{TC} = 1.04$.

FIGURE 22.—Continued.



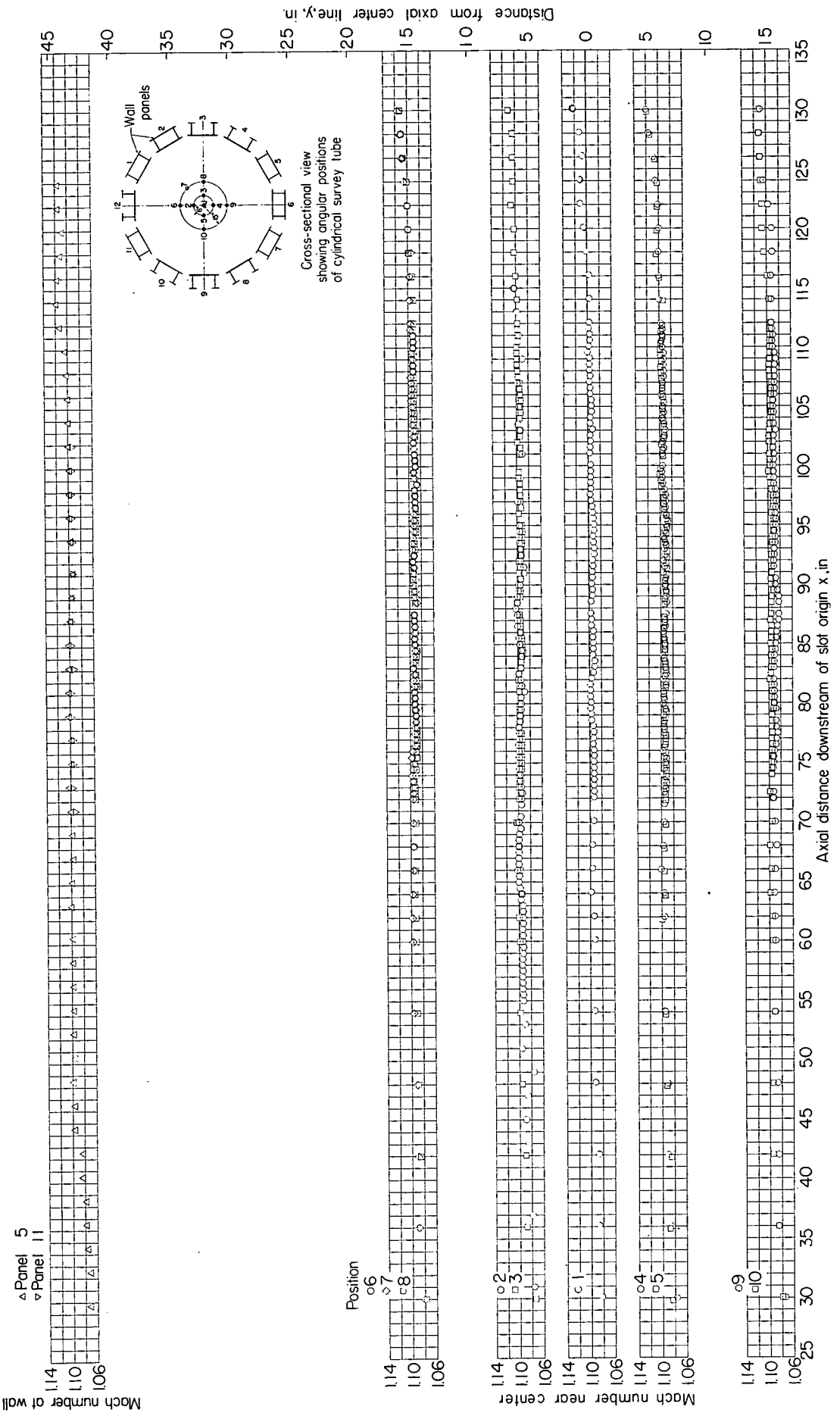
(h) $M_{TC}=1.06$.

FIGURE 22.—Continued.



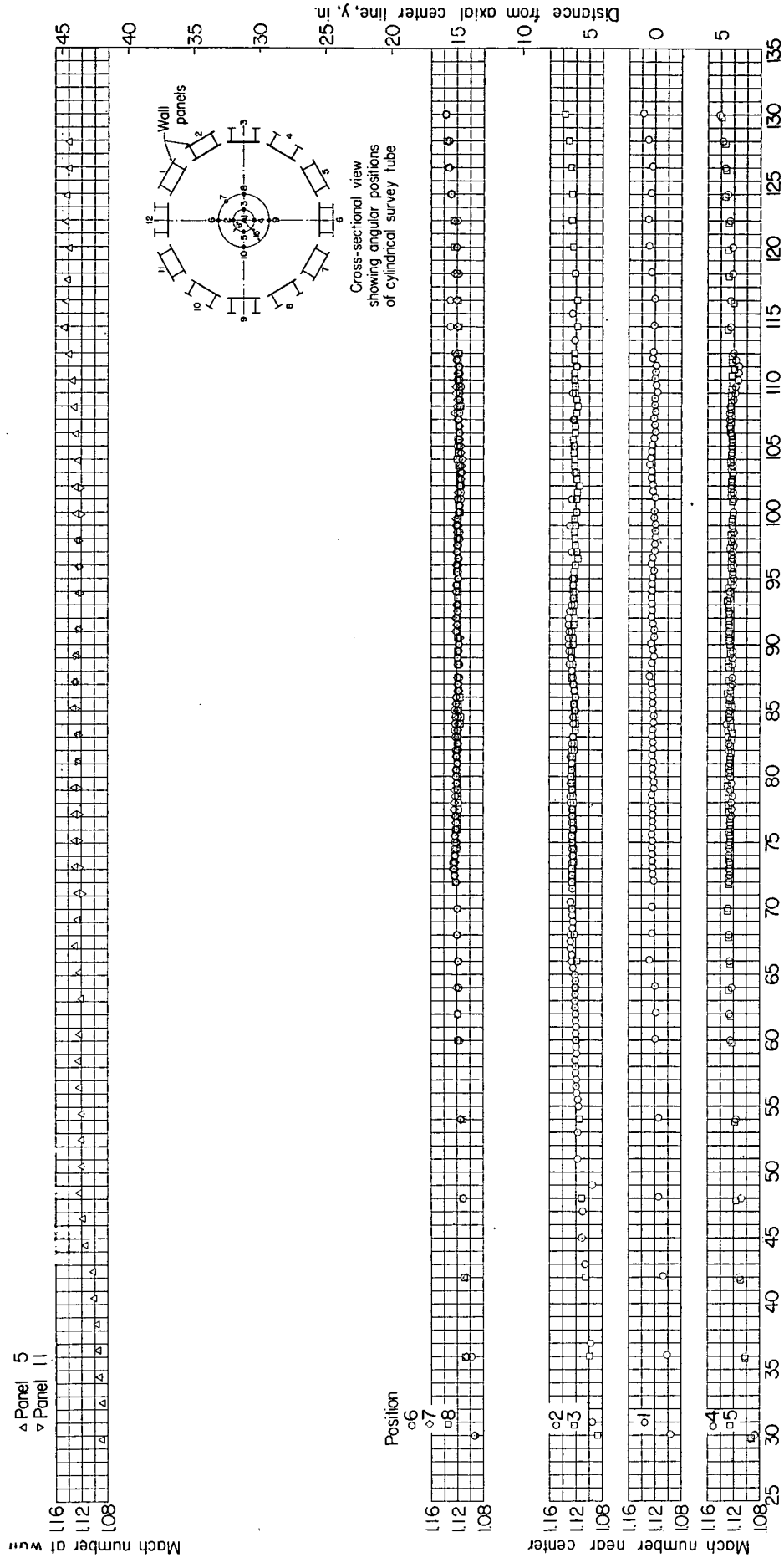
(i) $M_{TC}=1.08$.

FIGURE 22.—Continued.



(j) $M_{rc}=1.10$.

FIGURE 22.—Continued.



(k) $M_{TC}=1.13$.

FIGURE 22.—Concluded.

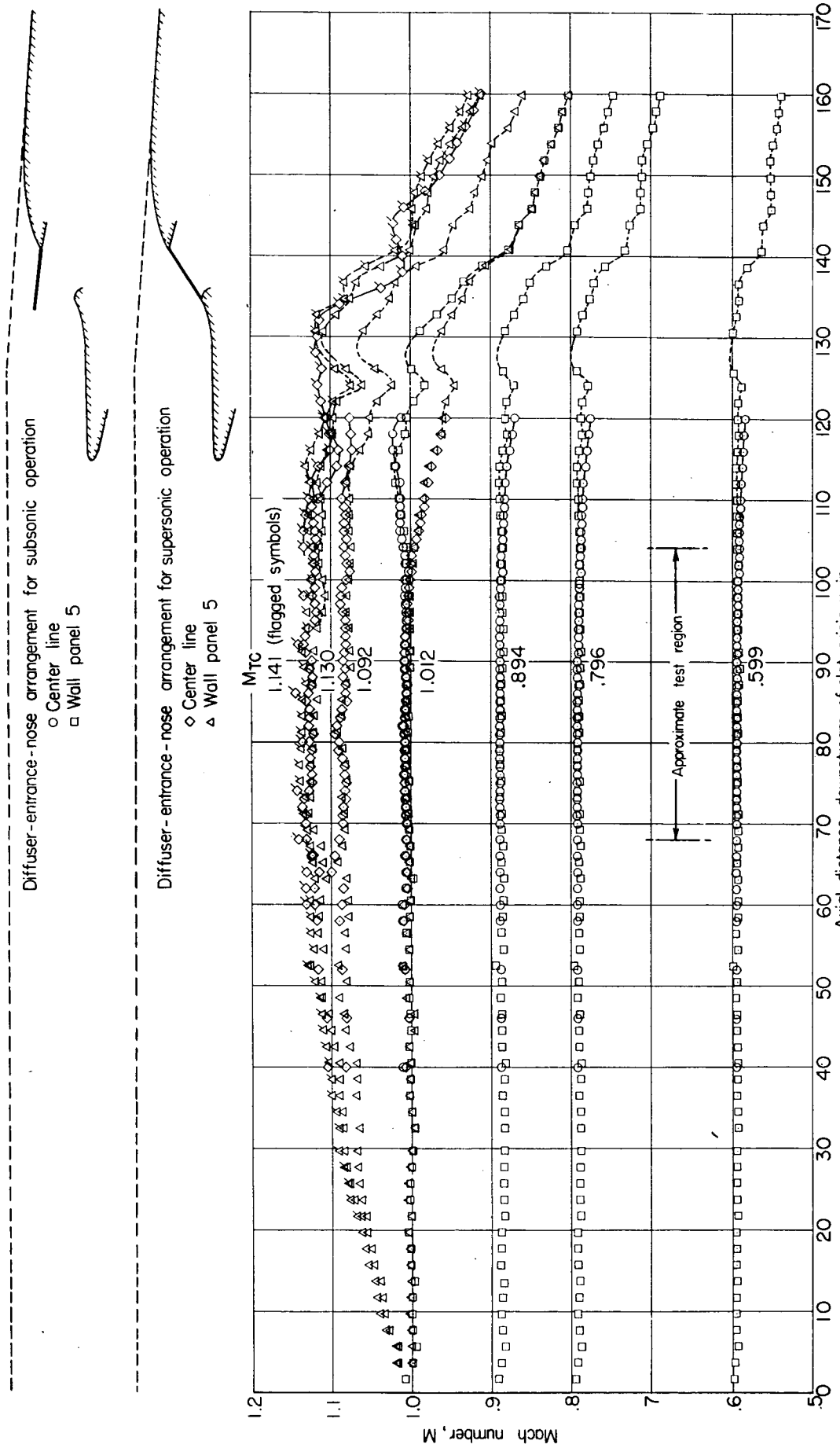


FIGURE 23.—Mach number distributions measured axially along center line and wall of slotted test section with a diffuser-entrance nose arrangement for reduction of tunnel power requirements and attainment of higher Mach number. Model removed; diffuser-entrance nose B; slot shape 11.

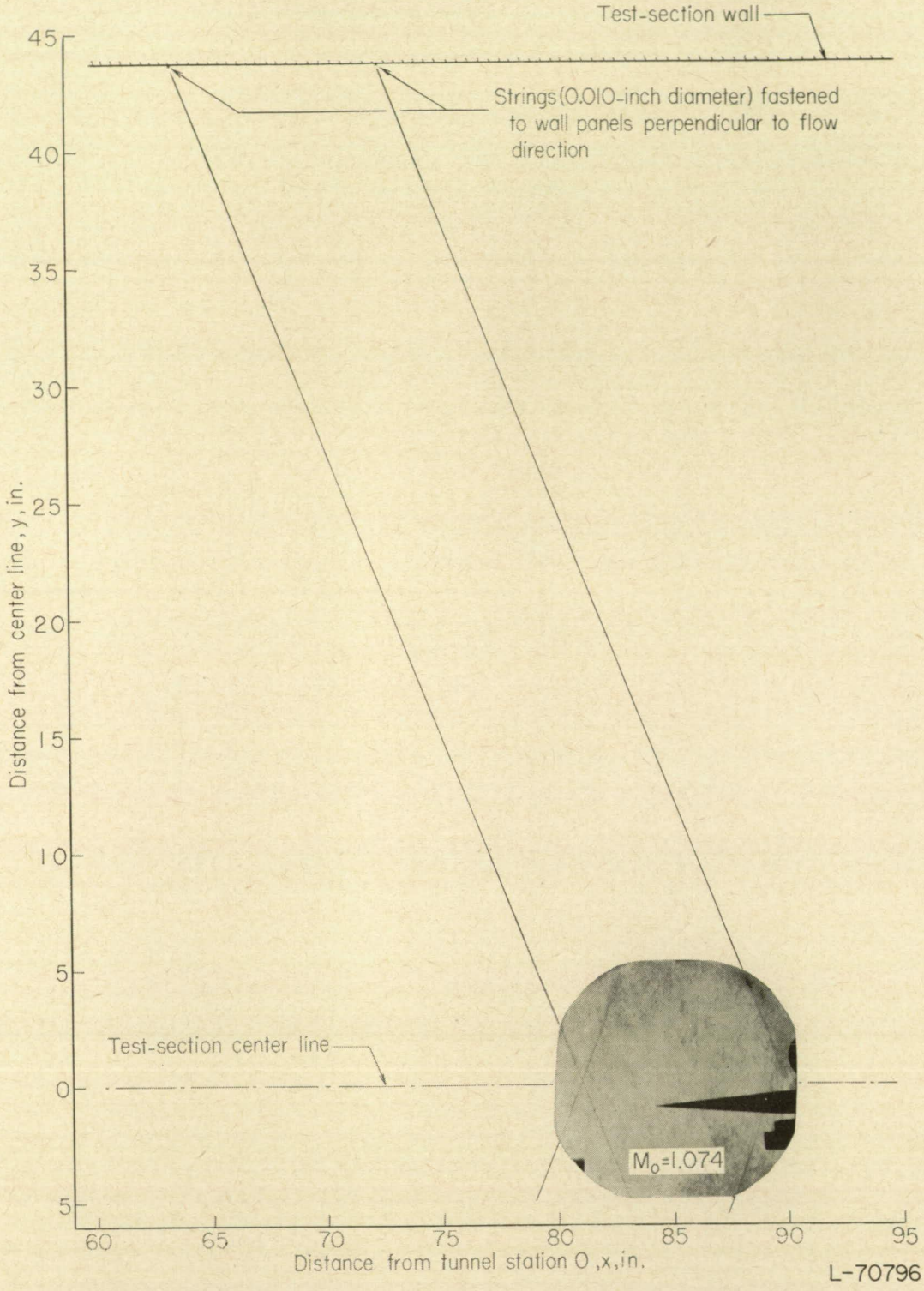
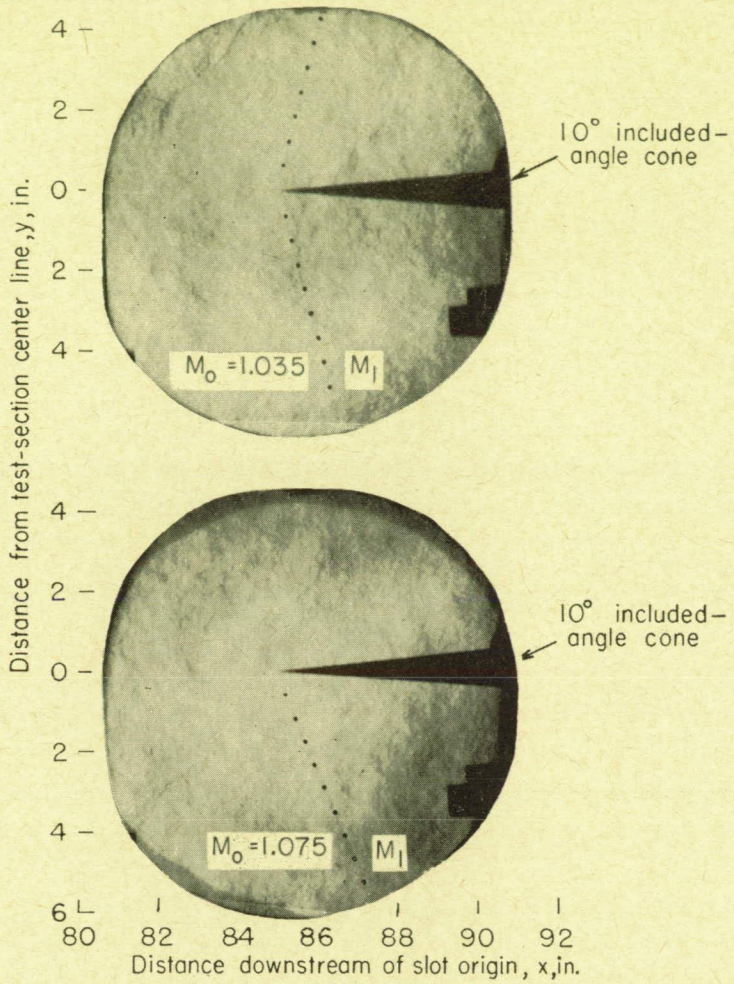


FIGURE 24.—Schlieren picture illustrating the propagation of weak disturbances in supersonic flow in the slotted test section. M_o=1.074.



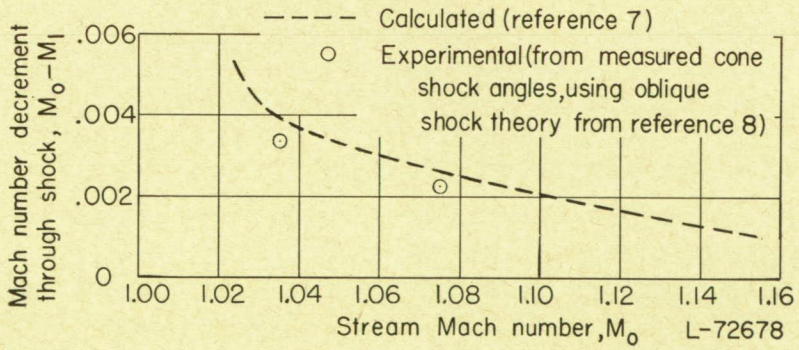


FIGURE 25.—An illustration of the degree of flow uniformity in a region of the slotted test section. Shock waves of known strength (produced by a 10° included-angle cone at zero angle) are used as the flow-uniformity criterion. Diffuser-entrance nose A.

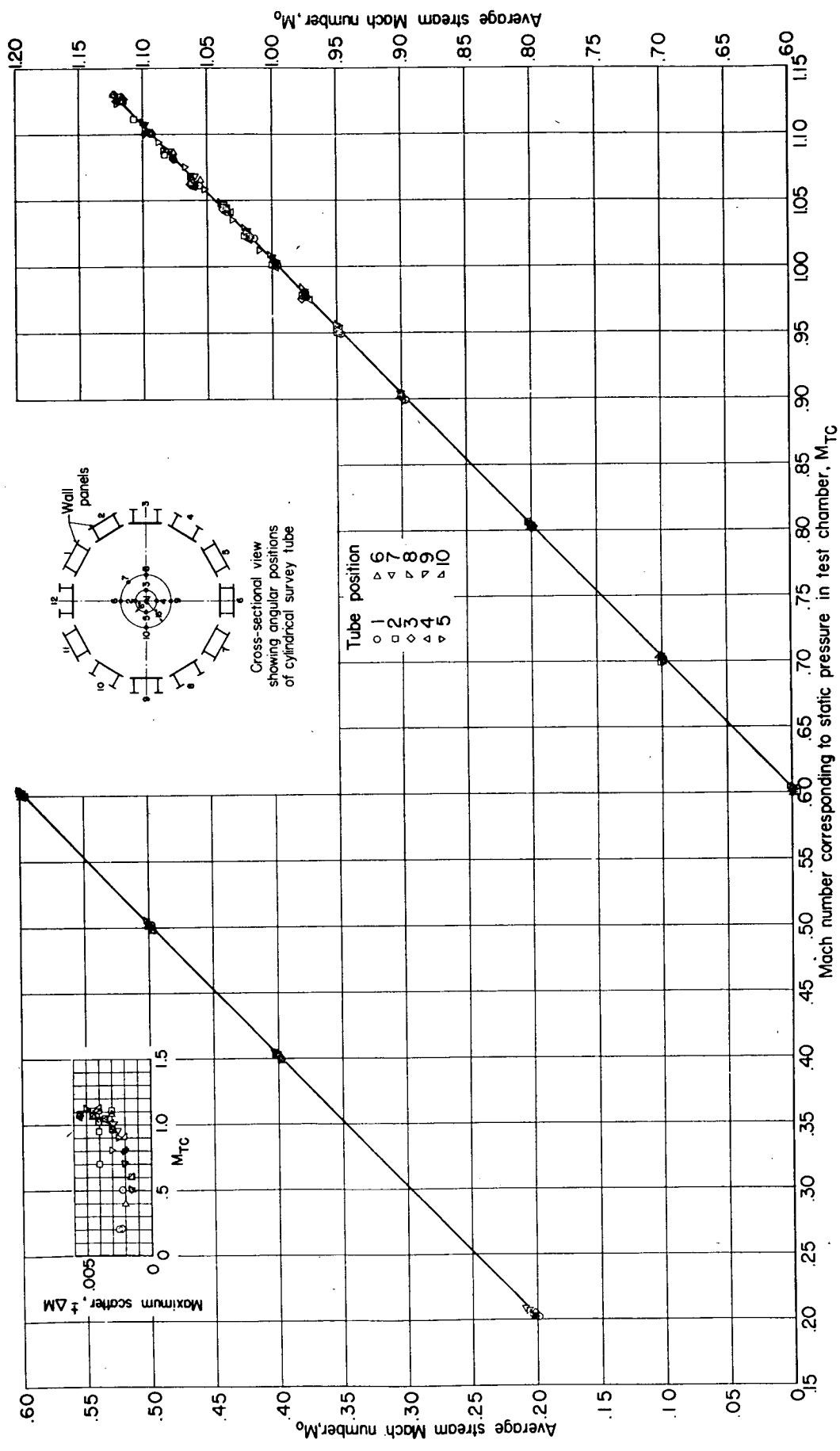


FIGURE 26.—Typical calibration curve showing the variation with test-chamber Mach number of the average Mach number over a test region 36 inches long and 30 inches in diameter near the center line of the slotted test section with diffuser-entrance nose A. Model removed; slot shape 11.

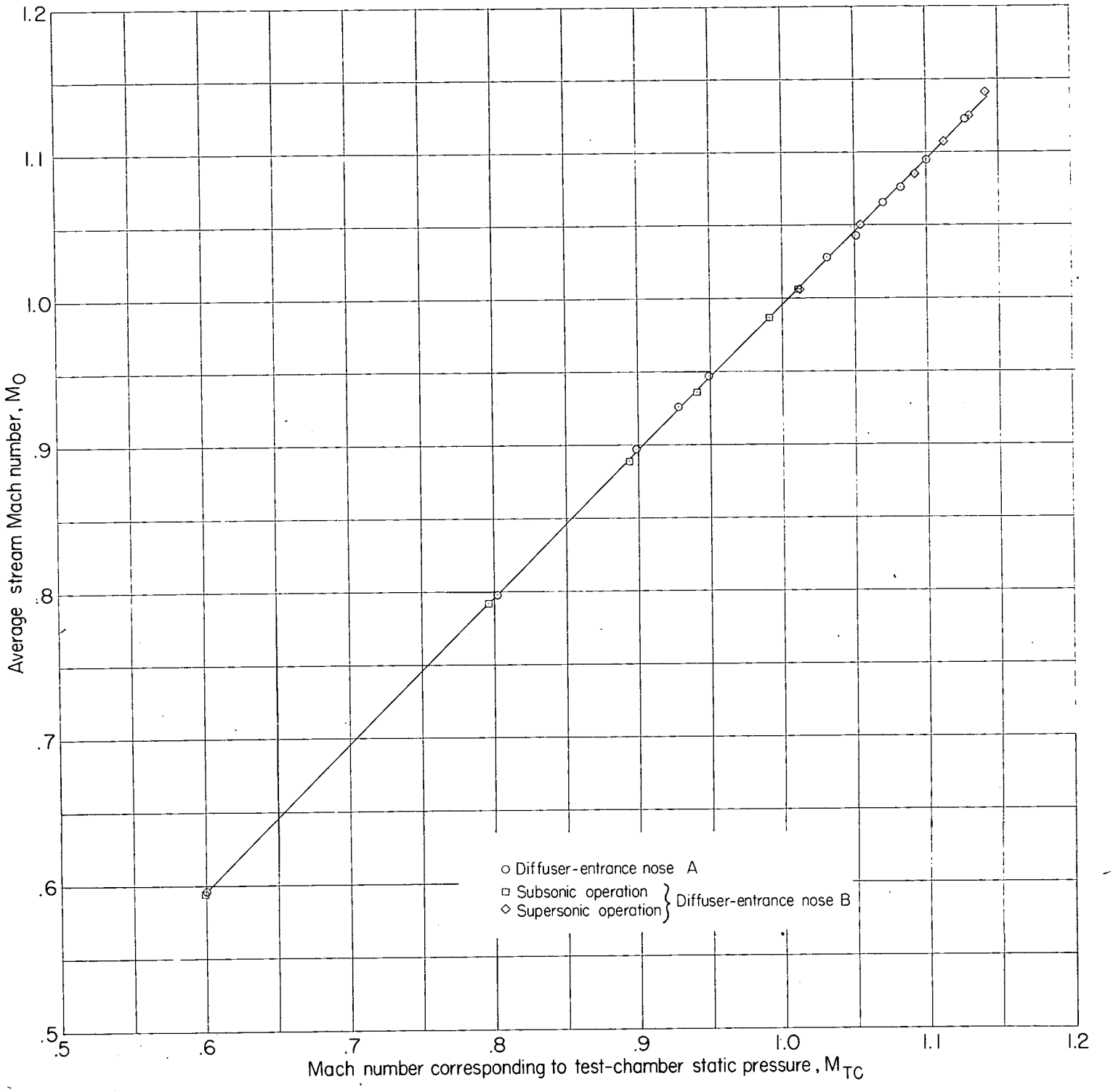


FIGURE 27.—Agreement of calibrations of the average Mach number over a 36-inch-long region at the center line of the slotted test section with diffuser-entrance noses A and B. Model removed; slot shape 11. Maximum deviations in Mach number for surveys with nose A and nose B are within 0.006 and 0.010, respectively.

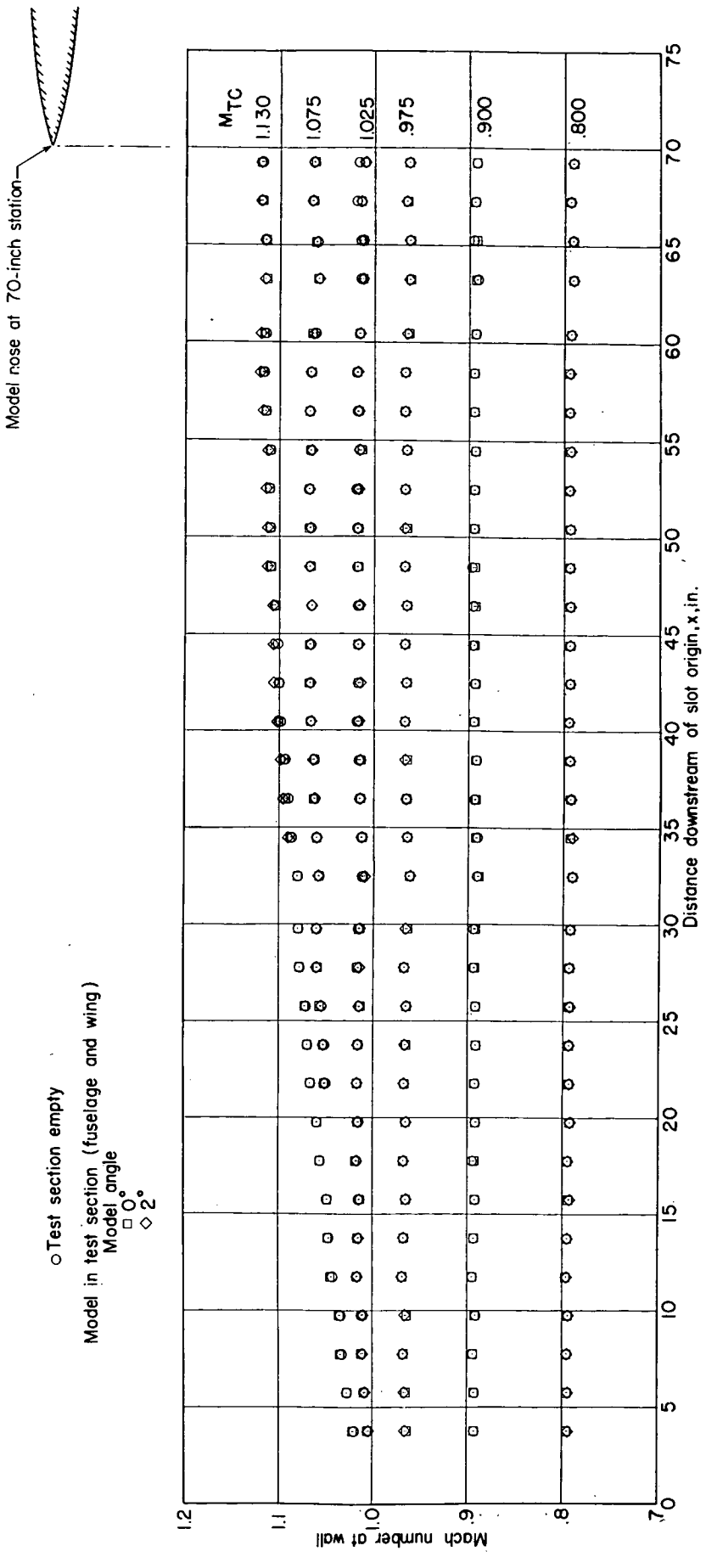


FIGURE 28.—Agreement of Mach number distributions axially along wall of slotted test section upstream of model location with model in and model removed. Diffuser-entrance nose A; slot shape 11.

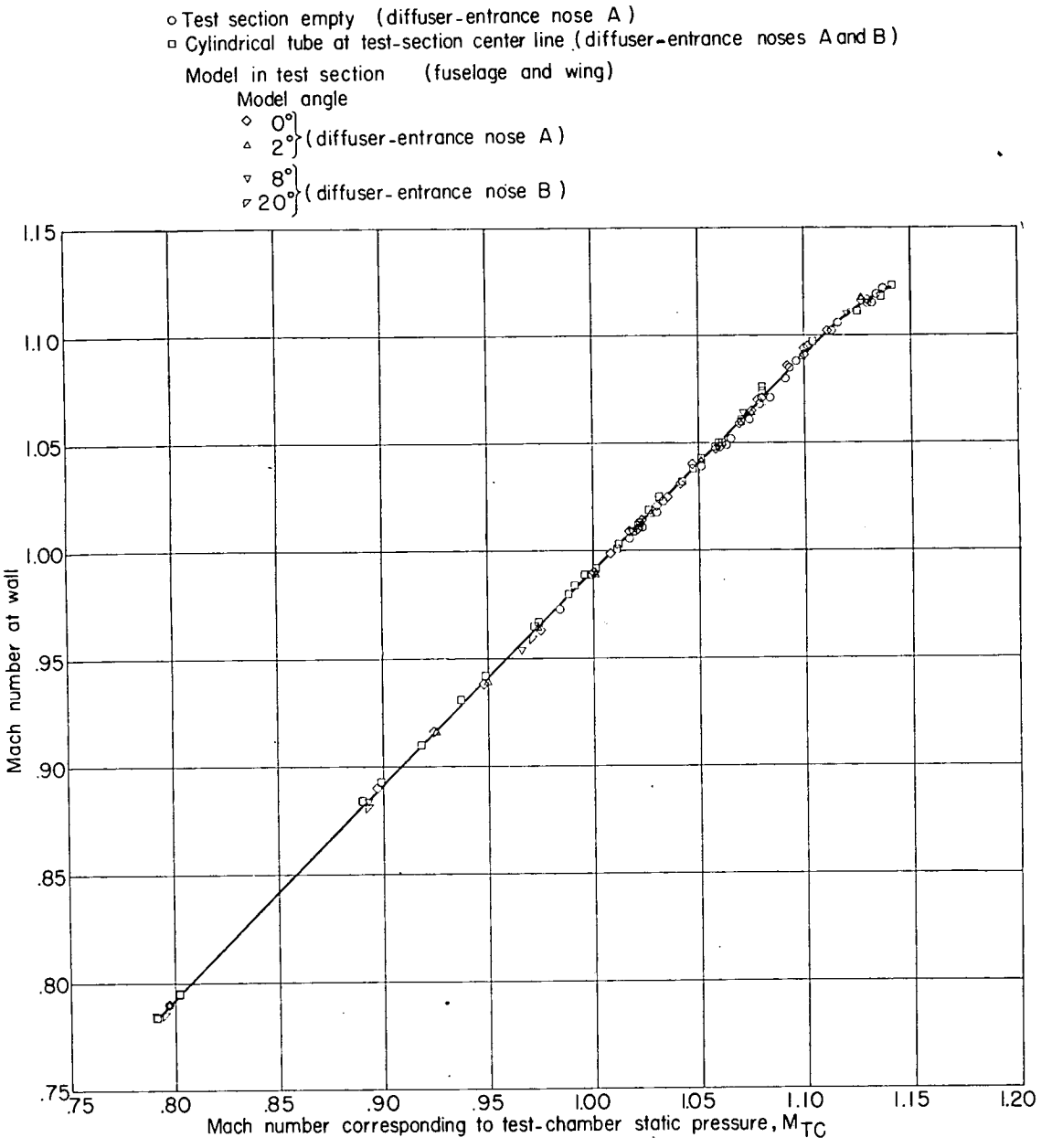


FIGURE 29.—Variation with test-chamber Mach number of Mach numbers measured on tunnel wall approximately 10 inches upstream of model nose (model at different angles of attack) and Mach numbers measured at the same axial station with model removed. Slot shape 11.

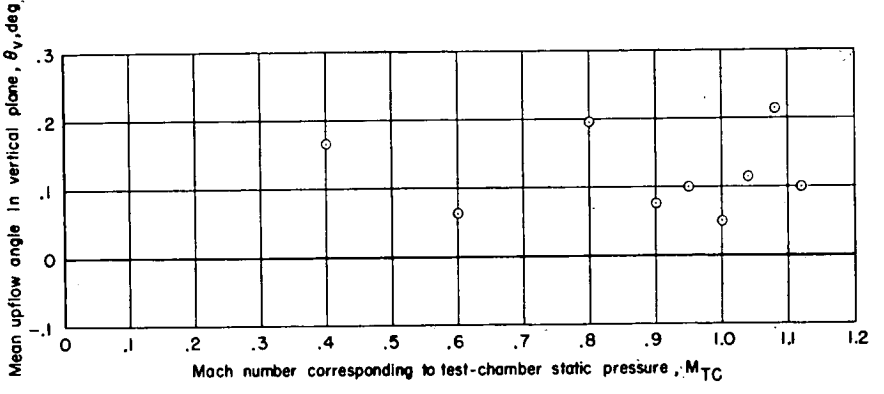
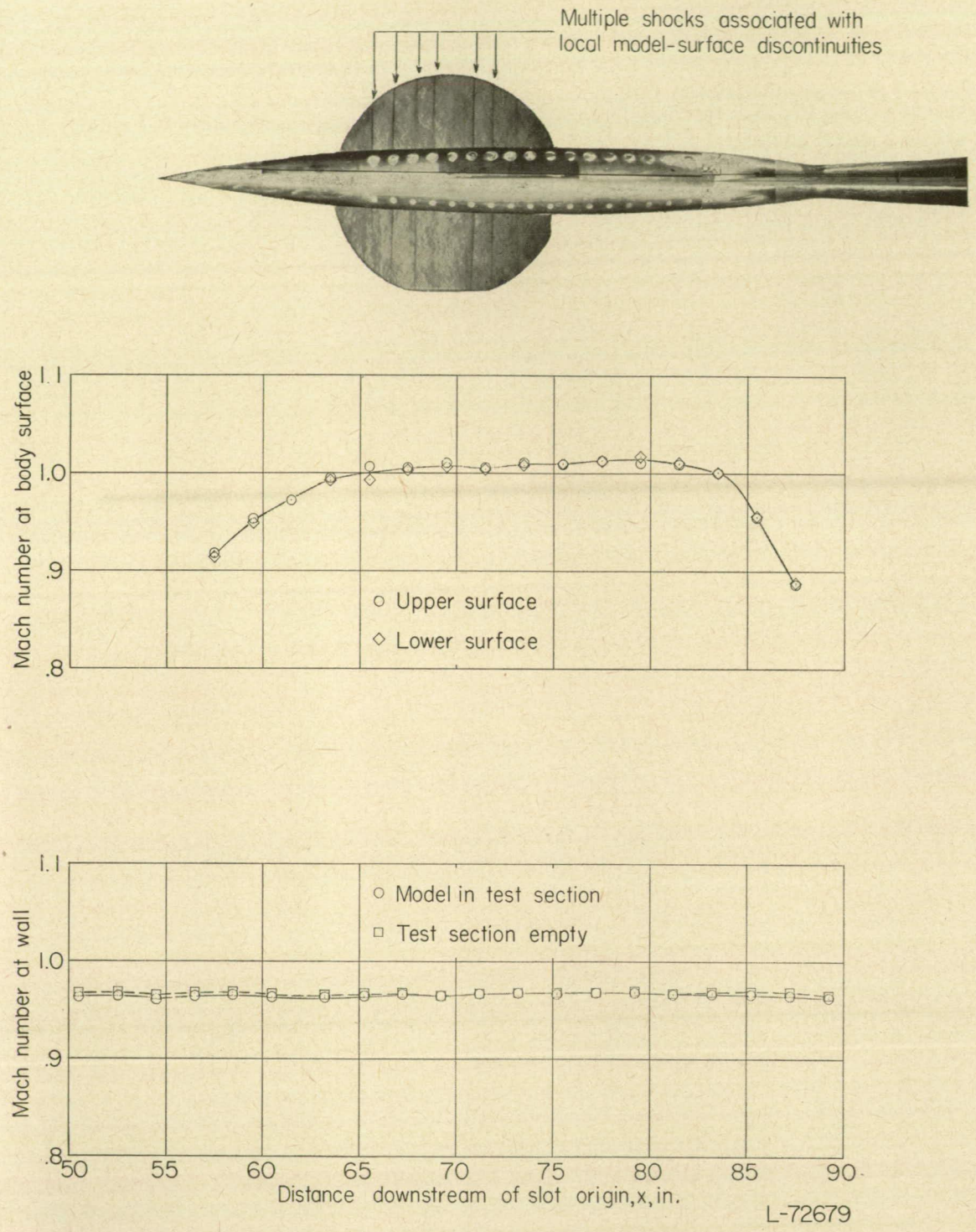
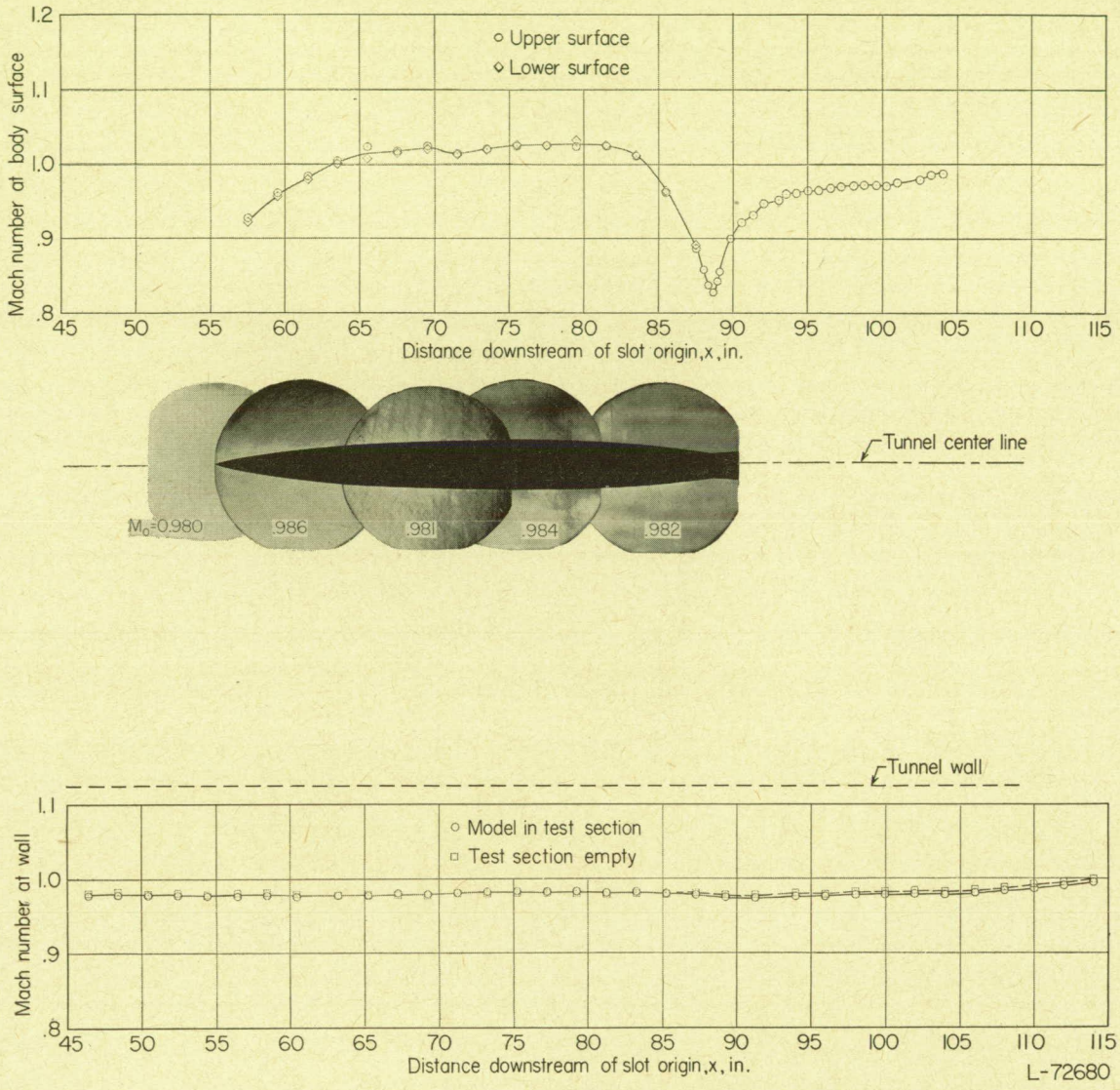


FIGURE 30.—Flow angularity in vertical plane, indicated by null-pressure cone-surface measurements at test-section center line 85 inches downstream of slot origin. Slot shape 11.



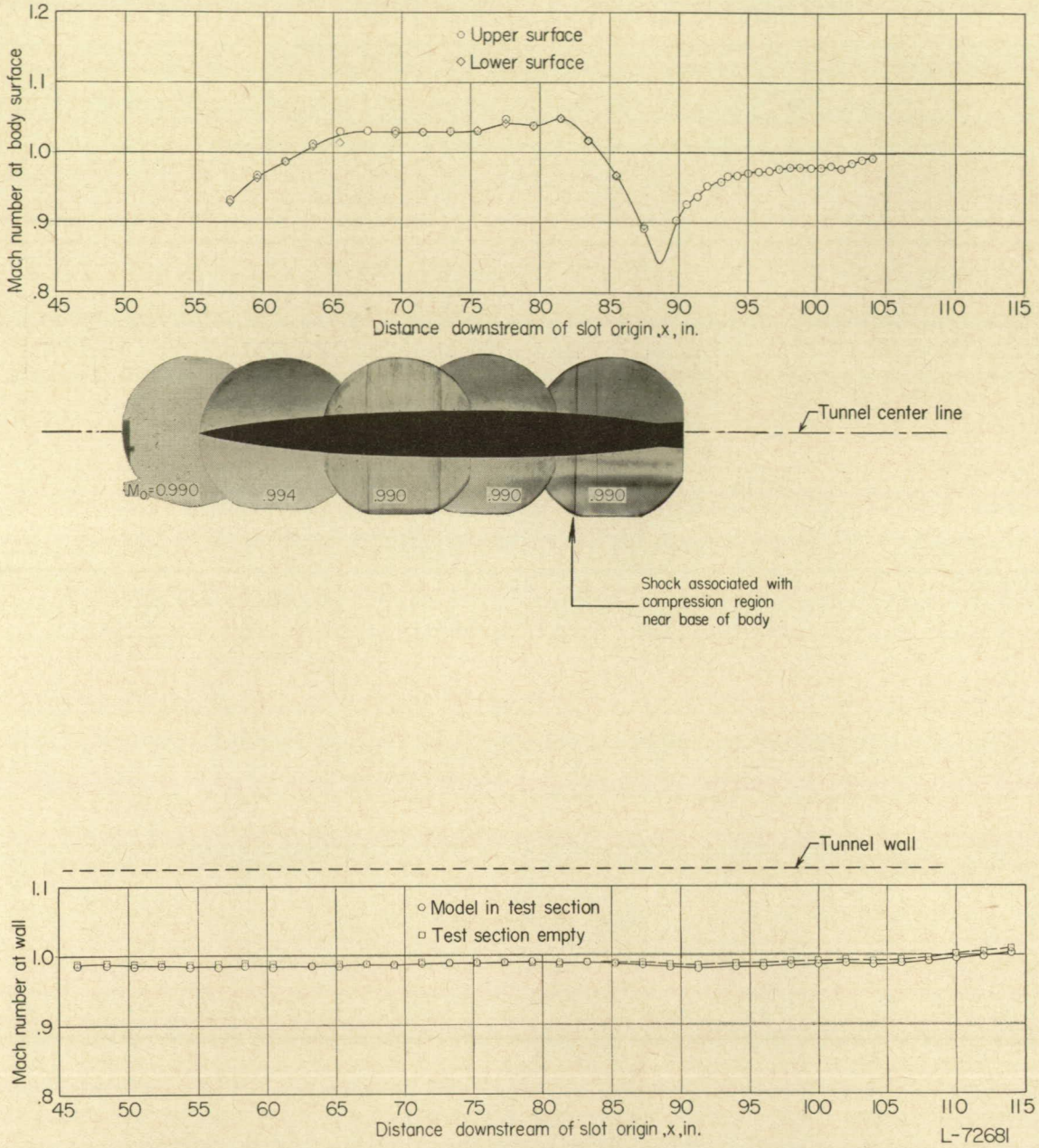
(a) $M_o = 0.970$.

FIGURE 31.—Shock formations and reflections at transonic speeds with body-of-revolution model at center line of slotted test section. $\alpha = 0°$; diffuser-entrance nose A; slot shape 11.



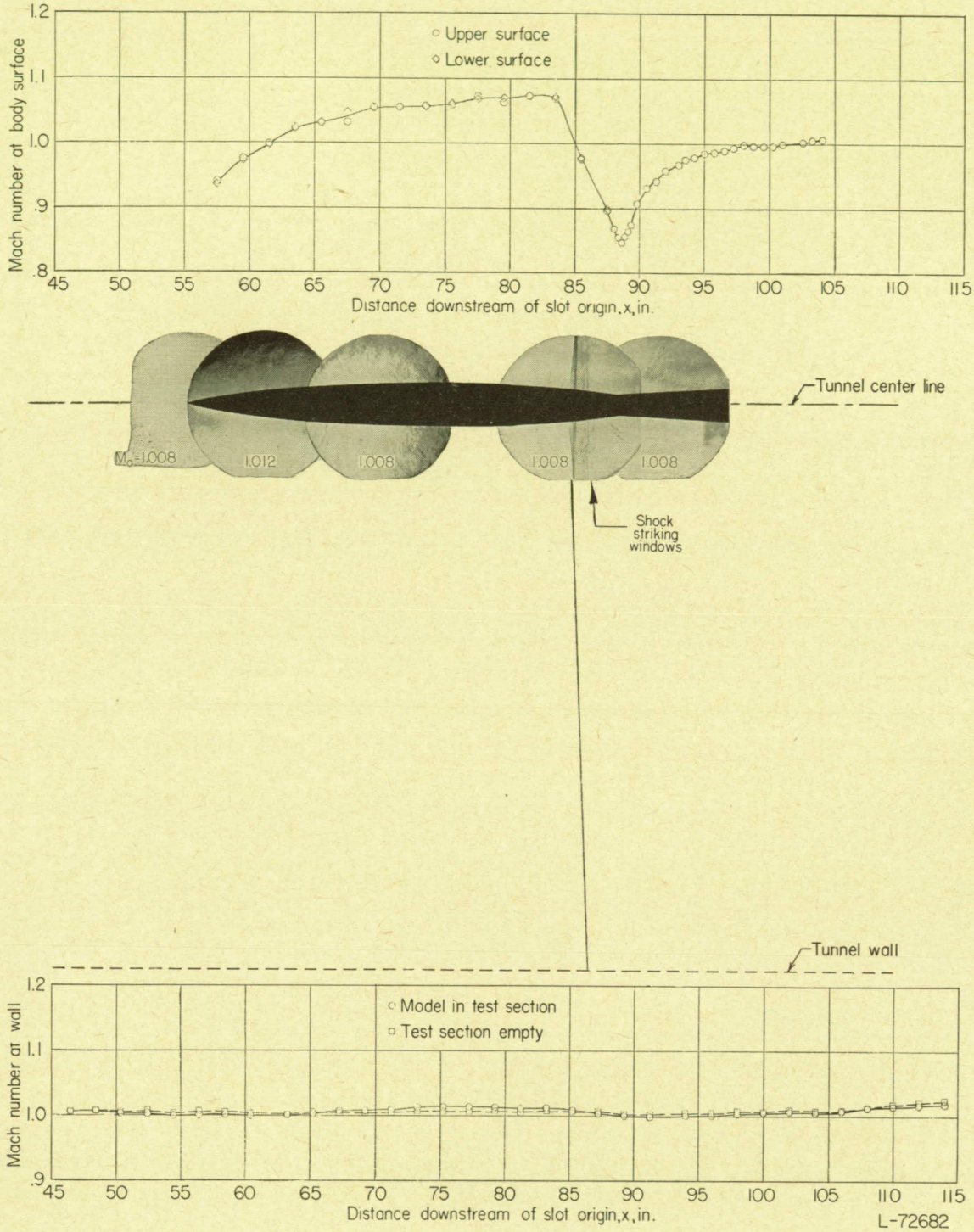
(b) $M_o = 0.980$.

FIGURE 31.—Continued.



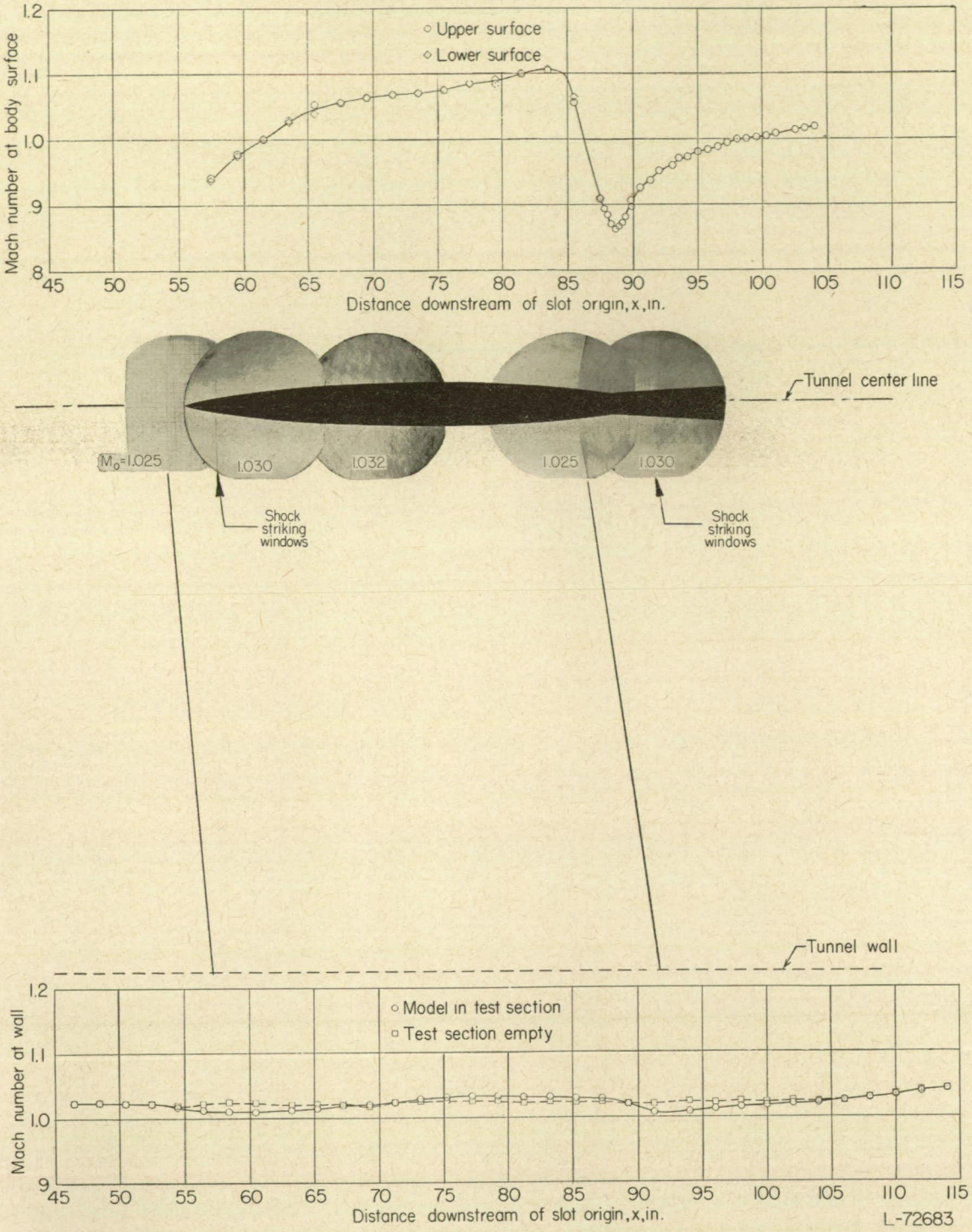
(c) $M_o=0.990$.

FIGURE 31.—Continued.



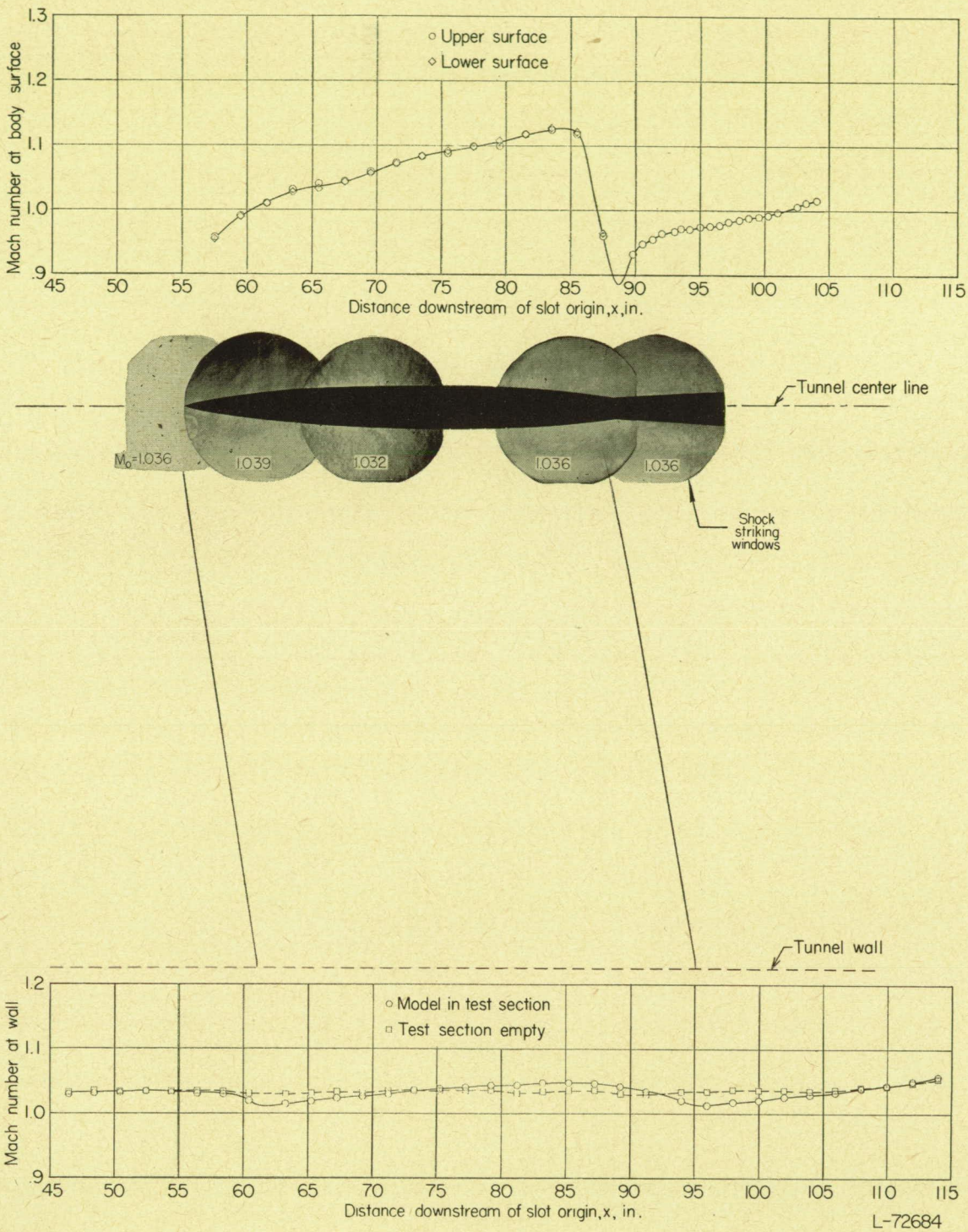
(d) M_o=1.008.

FIGURE 31.—Continued.



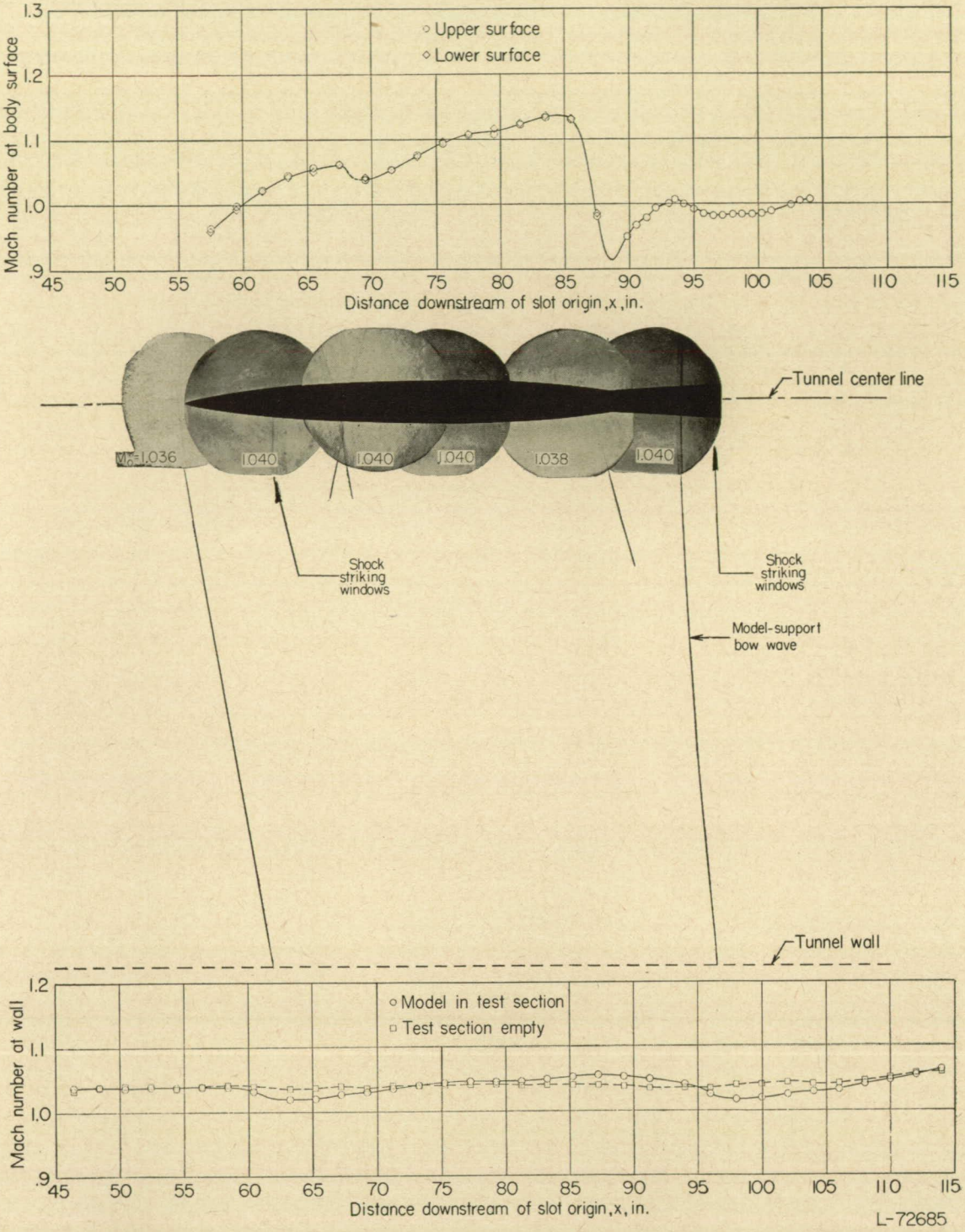
(e) M_o=1.025.

FIGURE 31.—Continued.



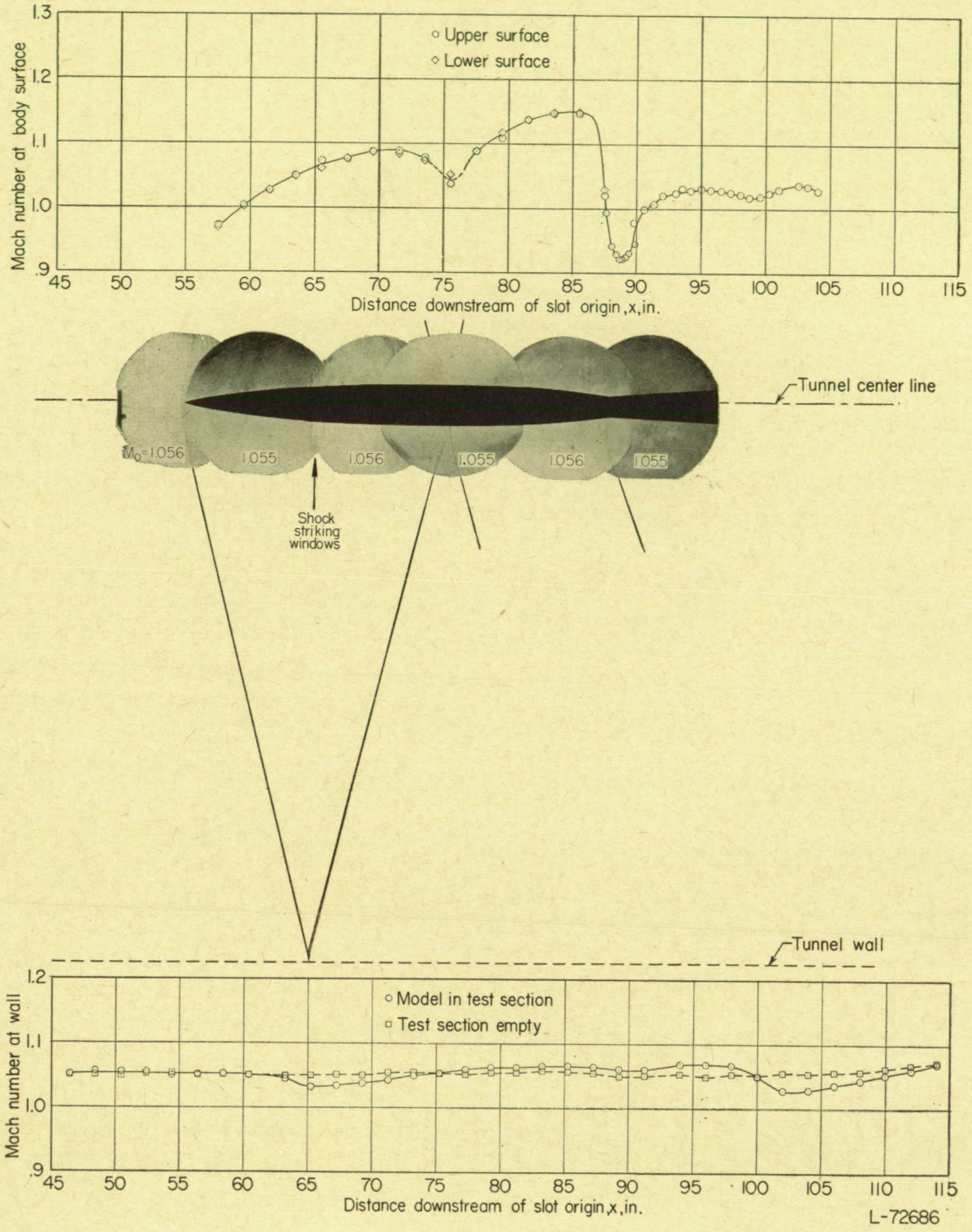
(f) $M_o = 1.036$.

FIGURE 31.—Continued.



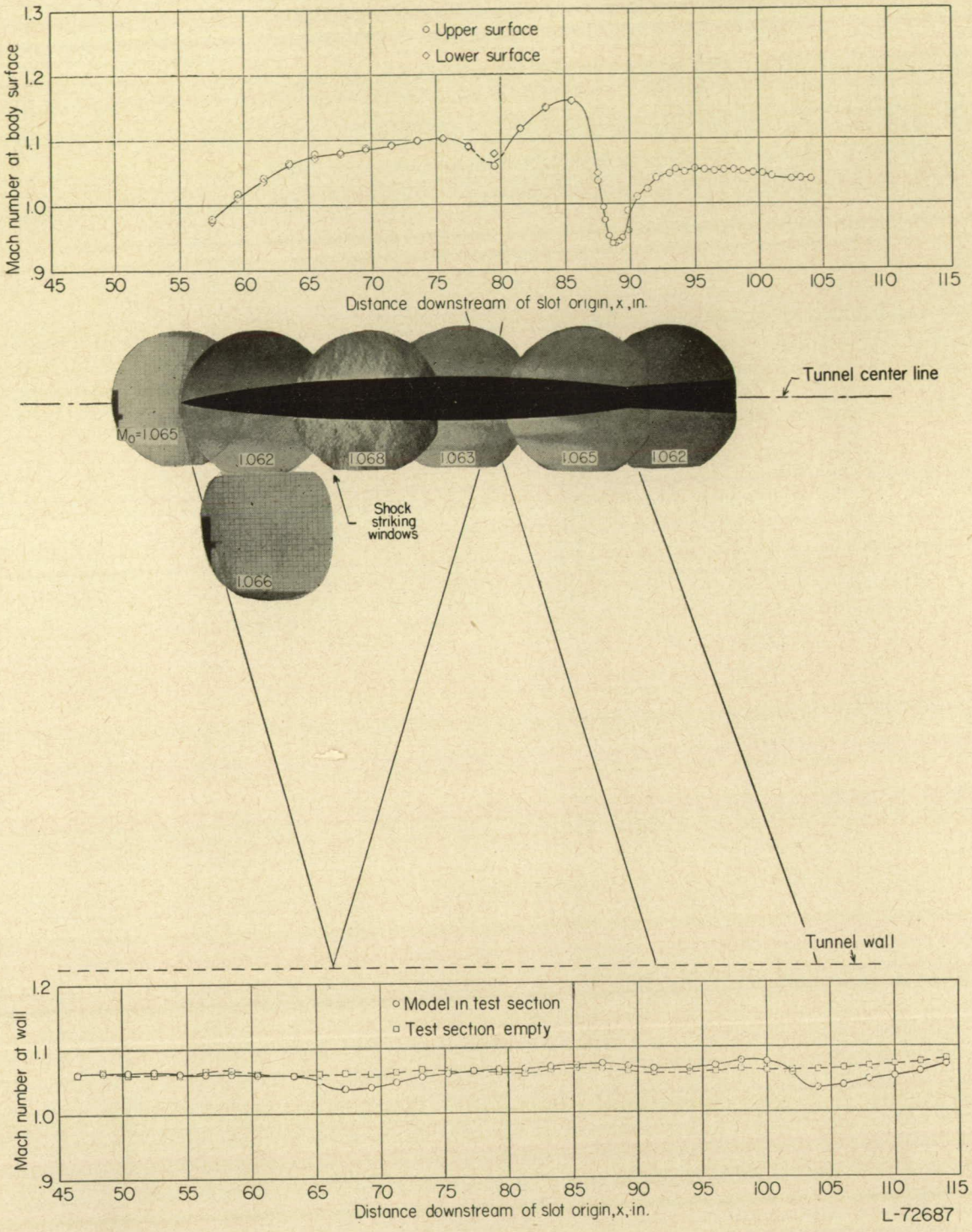
(g) $M_o = 1.042$.

FIGURE 31.—Continued.



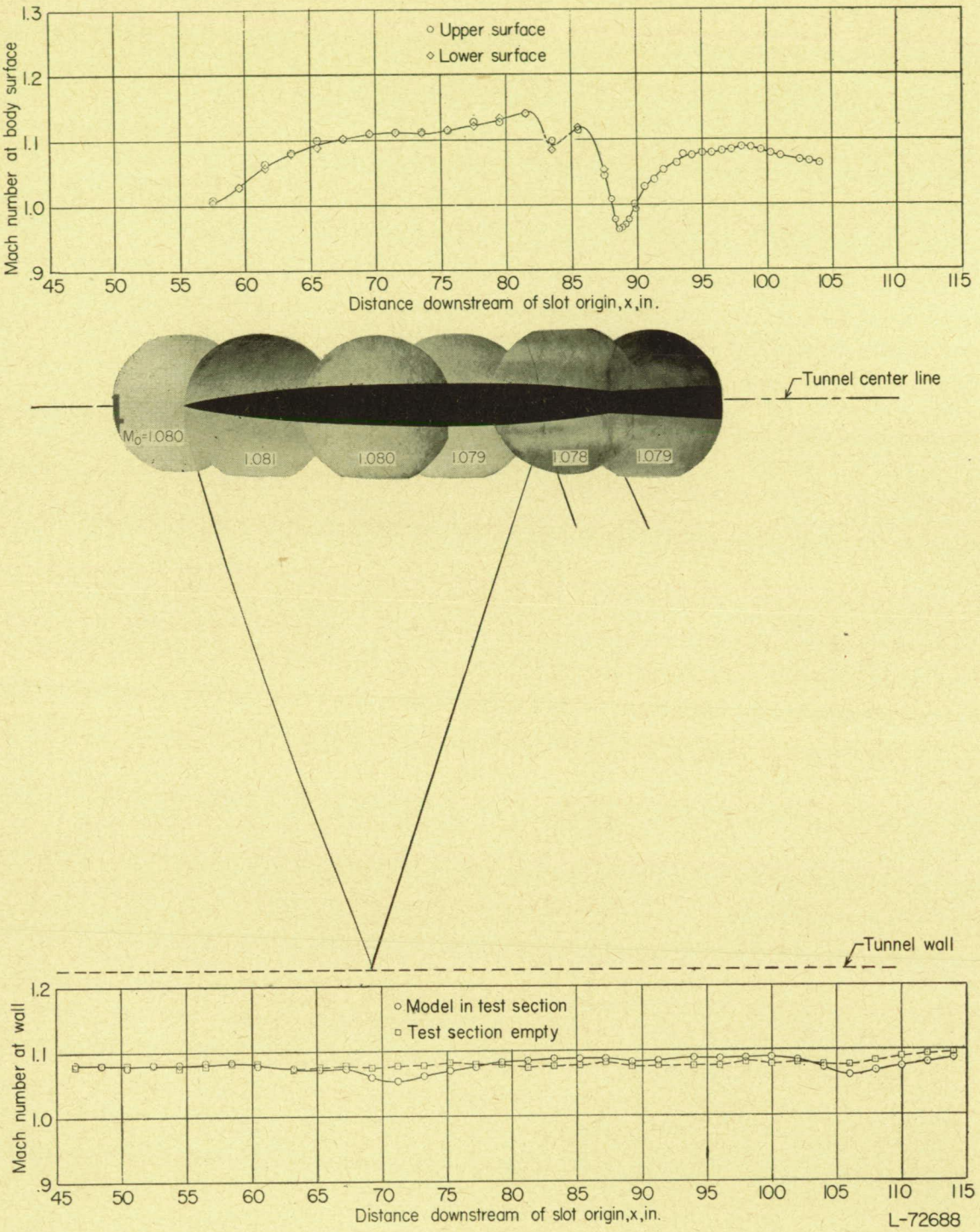
(h) $M_o = 1.056$.

FIGURE 31.—Continued.



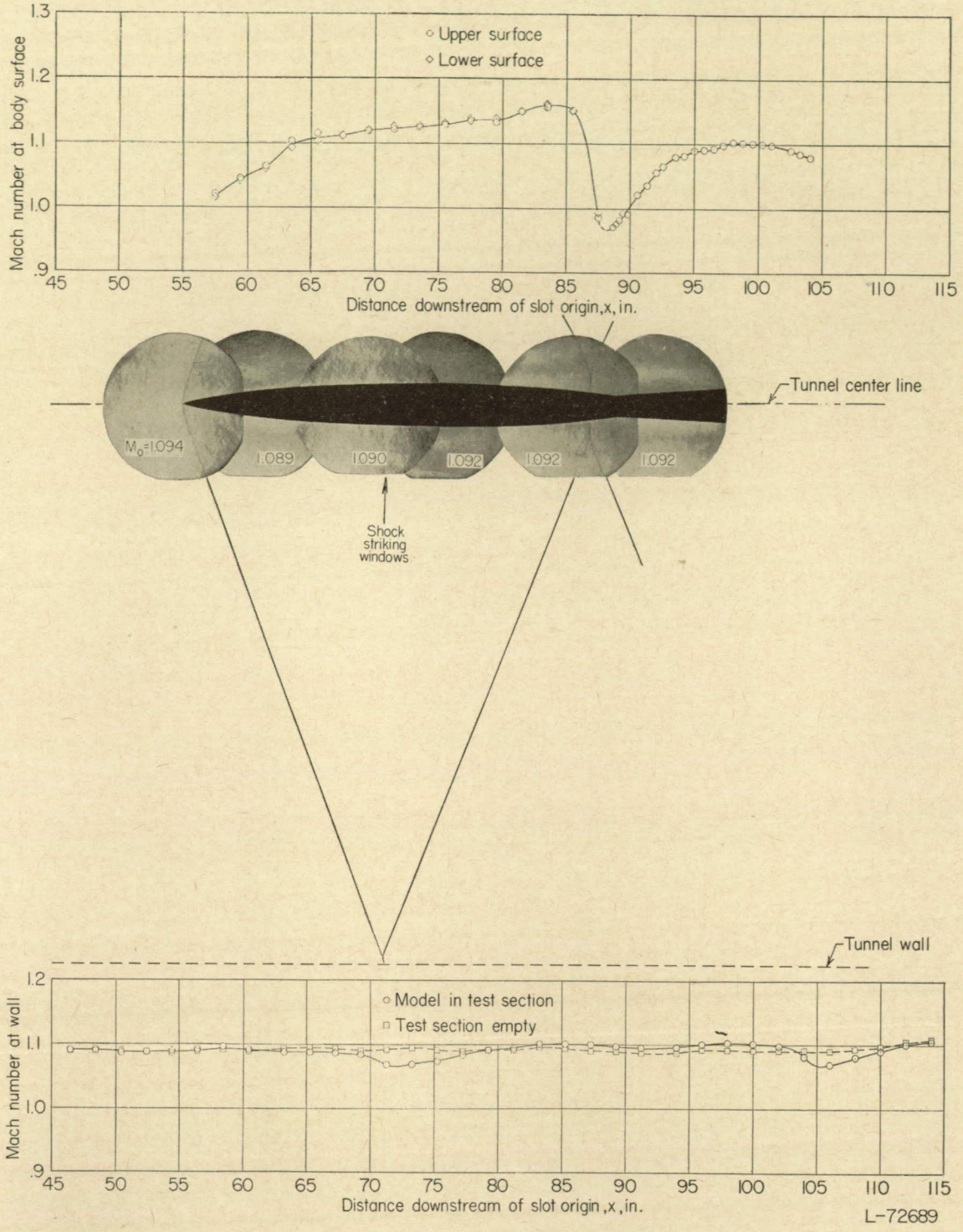
(i) $M_o=1.065$.

FIGURE 31.—Continued.



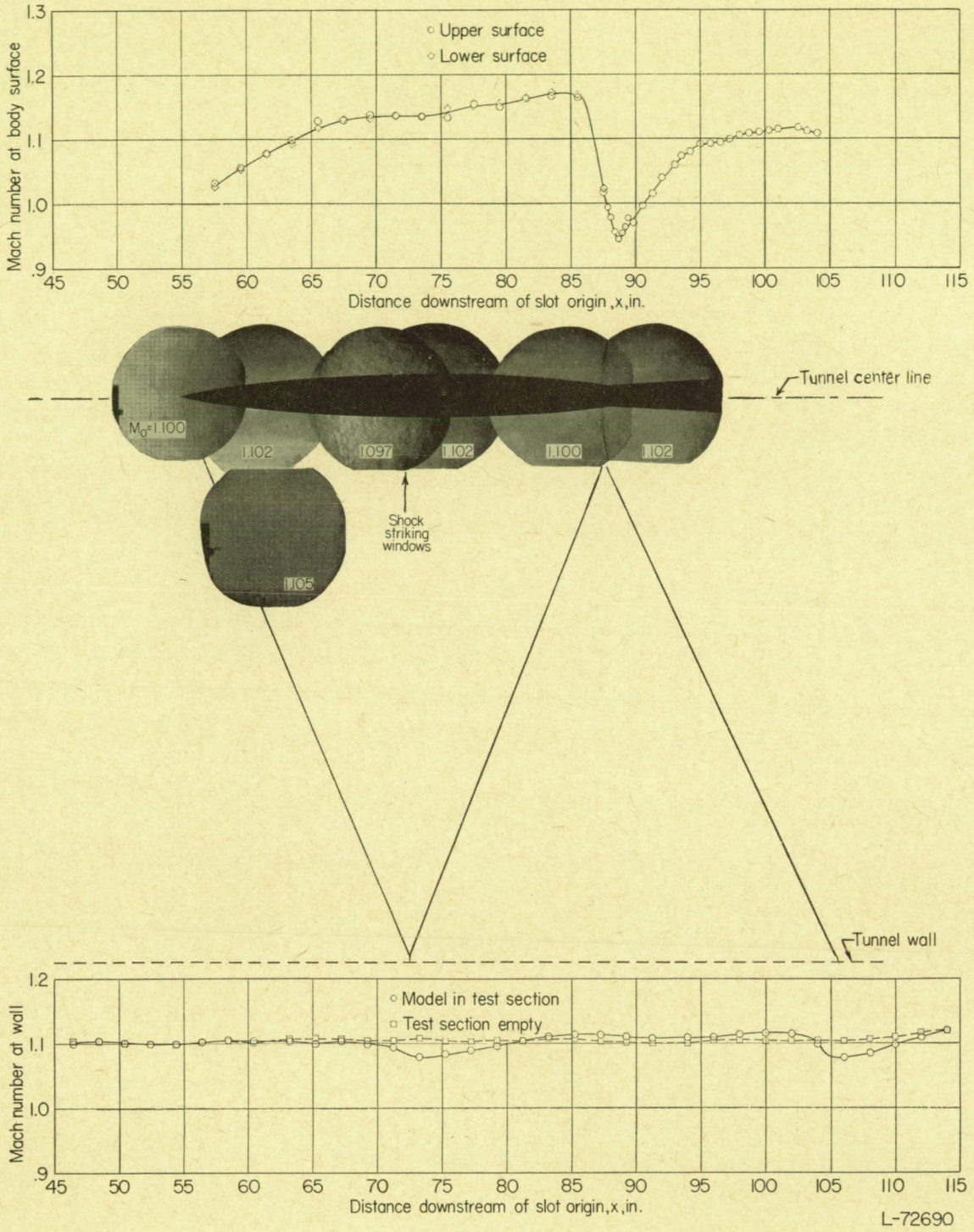
(j) M_o=1.080.

FIGURE 31.—Continued.



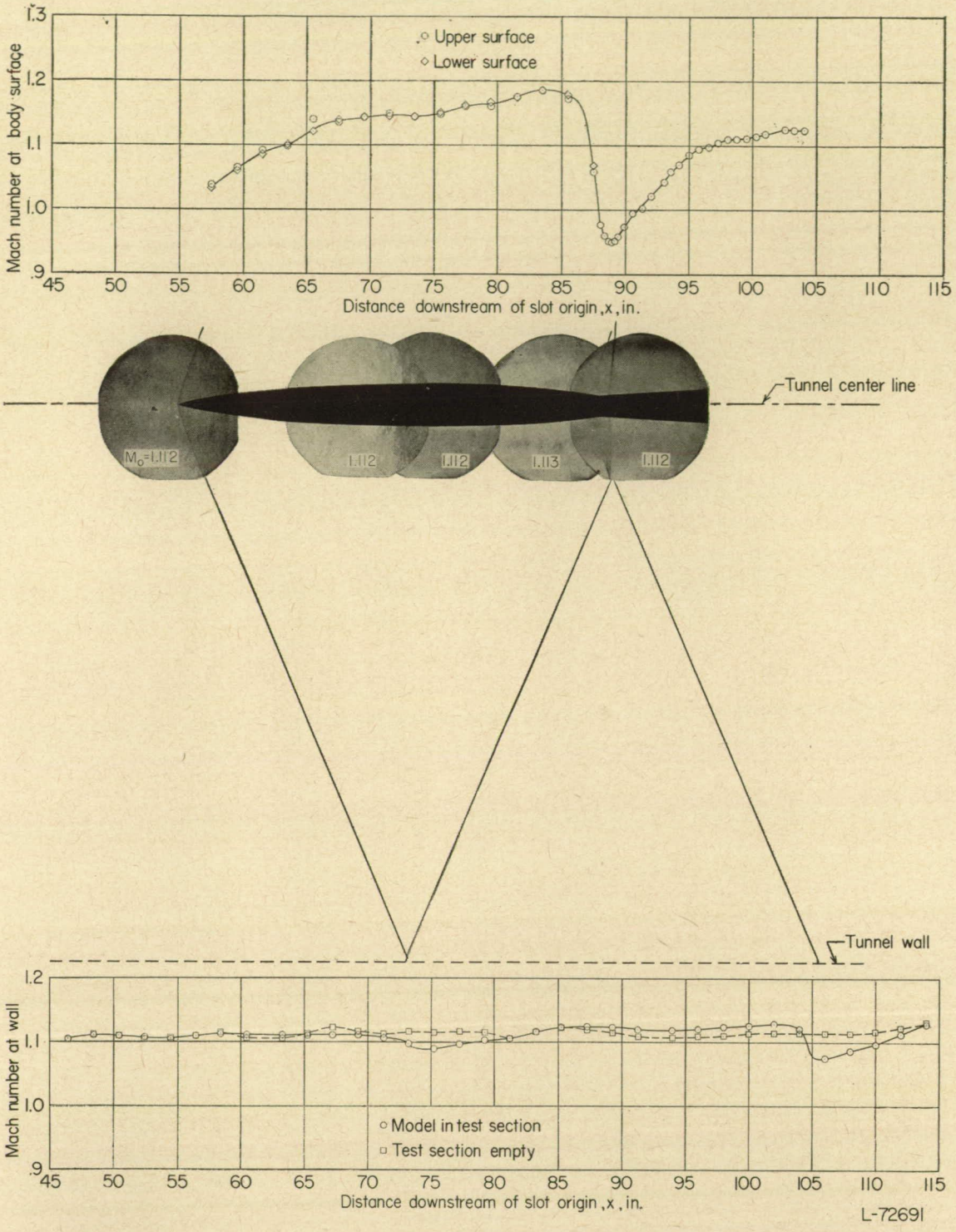
(k) $M_o=1.092$.

FIGURE 31.—Continued.



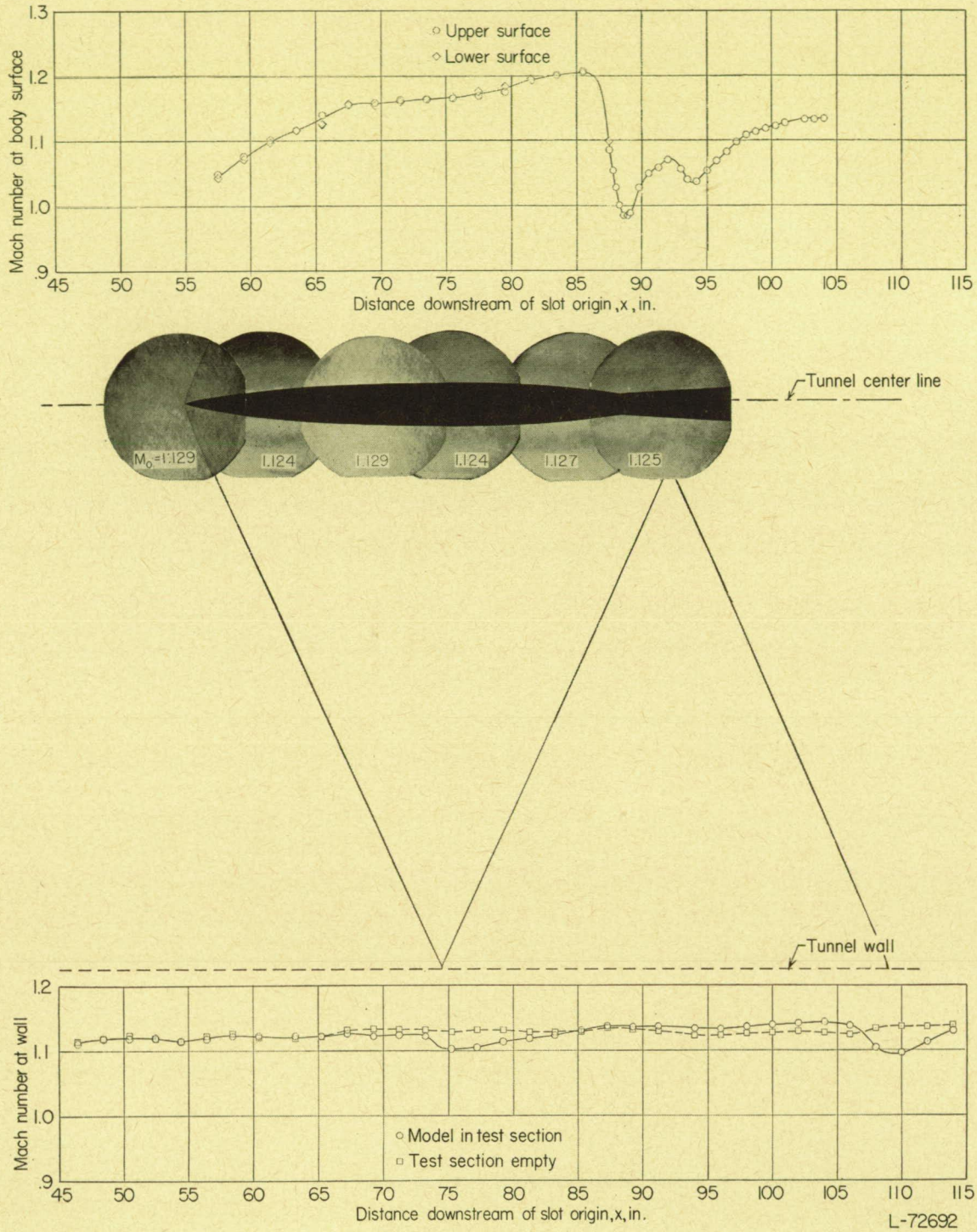
(*l*) $M_o = 1.105$.

FIGURE 31.—Continued.



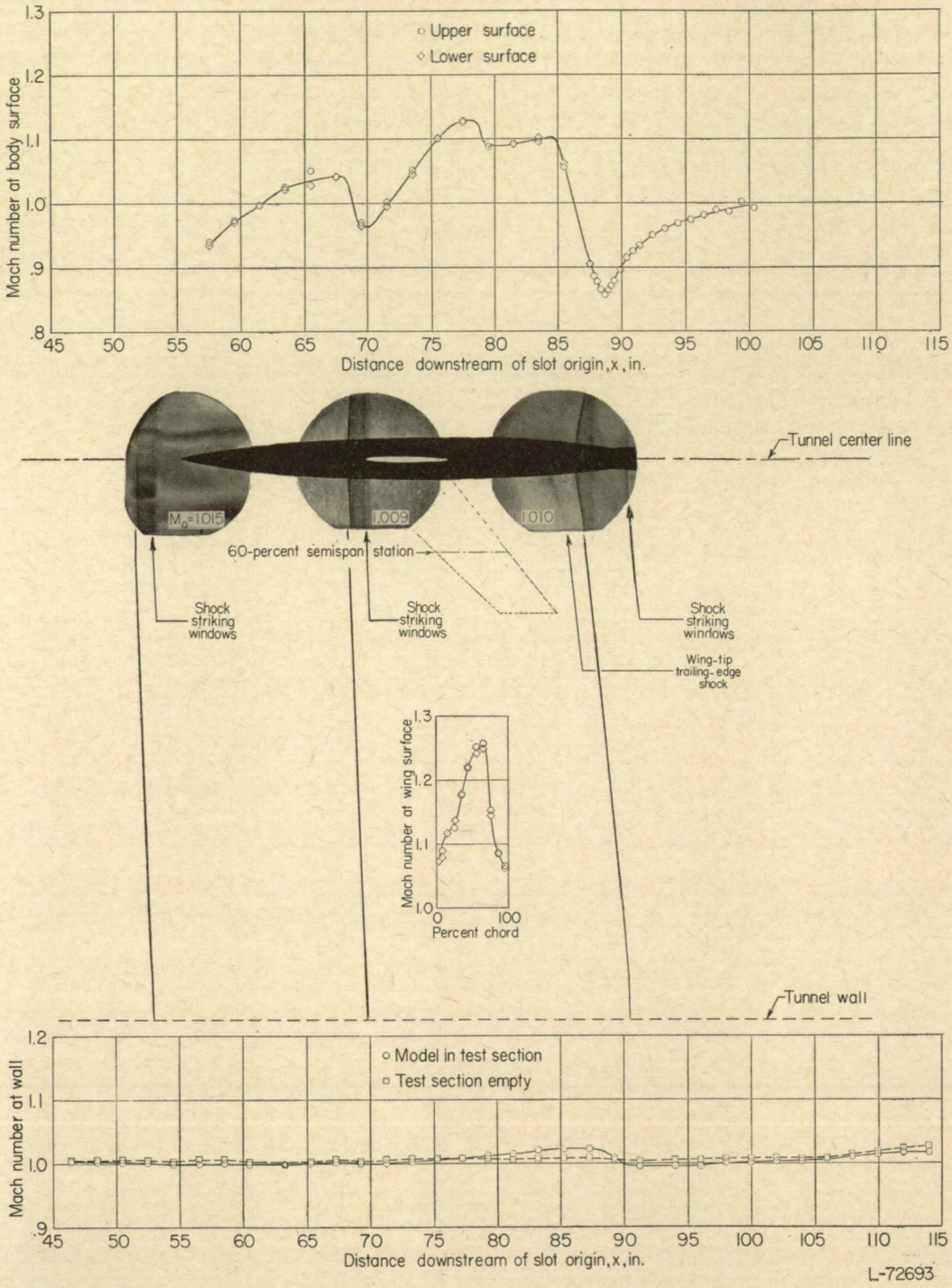
(m) $M_o = 1.113$.

FIGURE 31.—Continued.



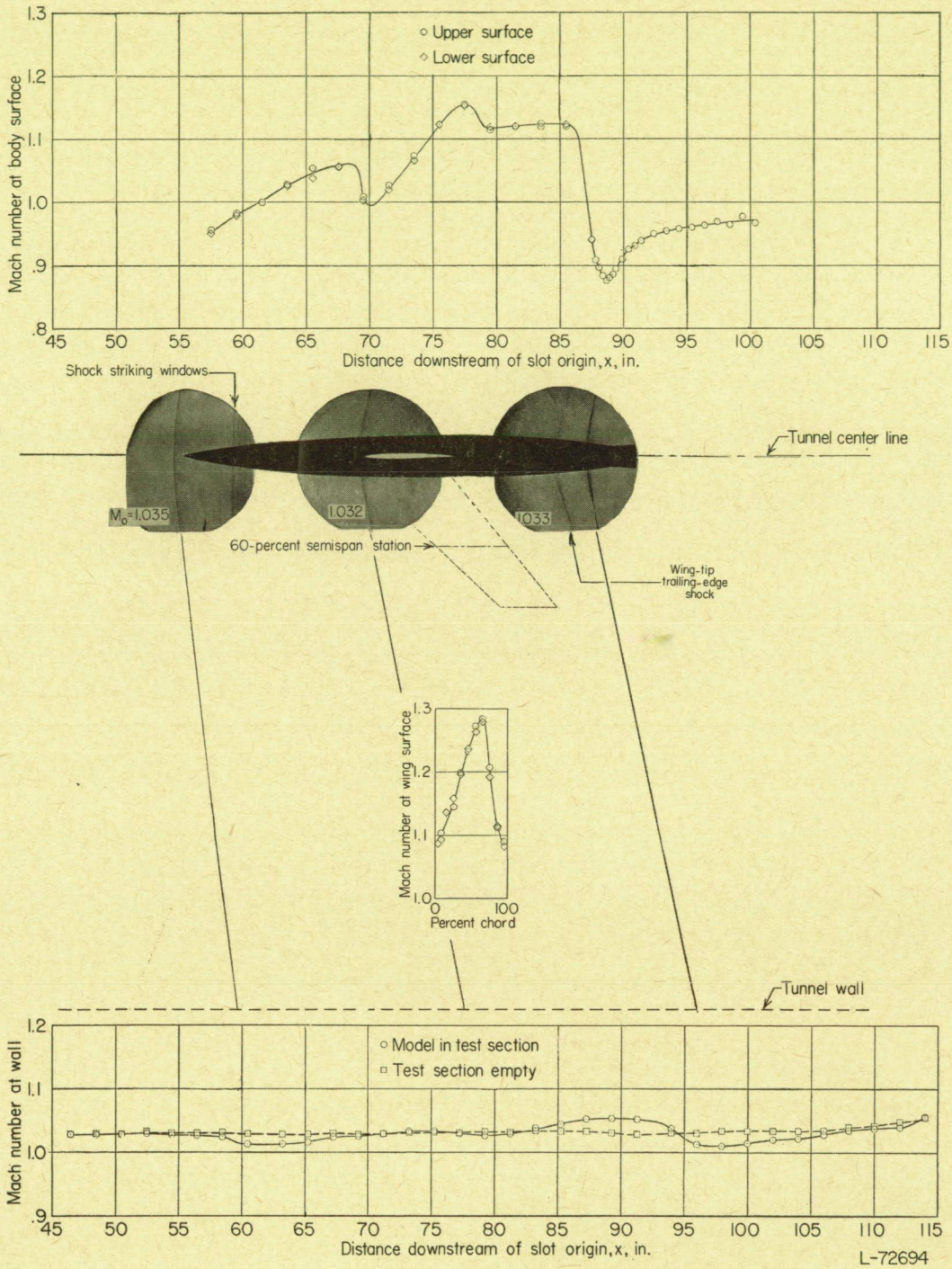
(n) M_o=1.129.

FIGURE 31.—Concluded.



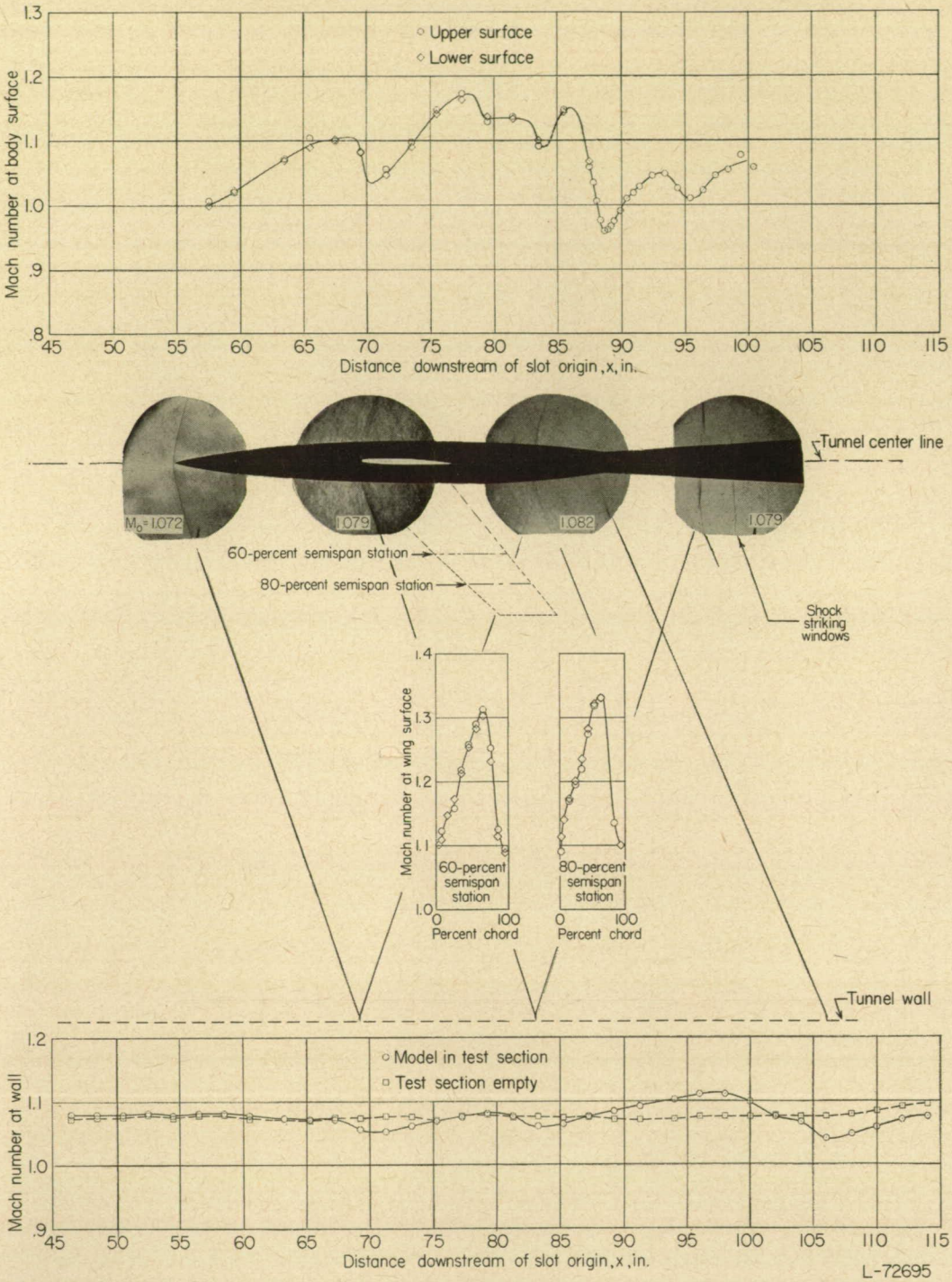
(a) $M_o = 1.009$.

FIGURE 32.—Shock formations and reflections at low-supersonic speeds with wing-body model at center line of slotted test section. $\alpha = 0°$; diffuser-entrance nose A; slot shape 11.



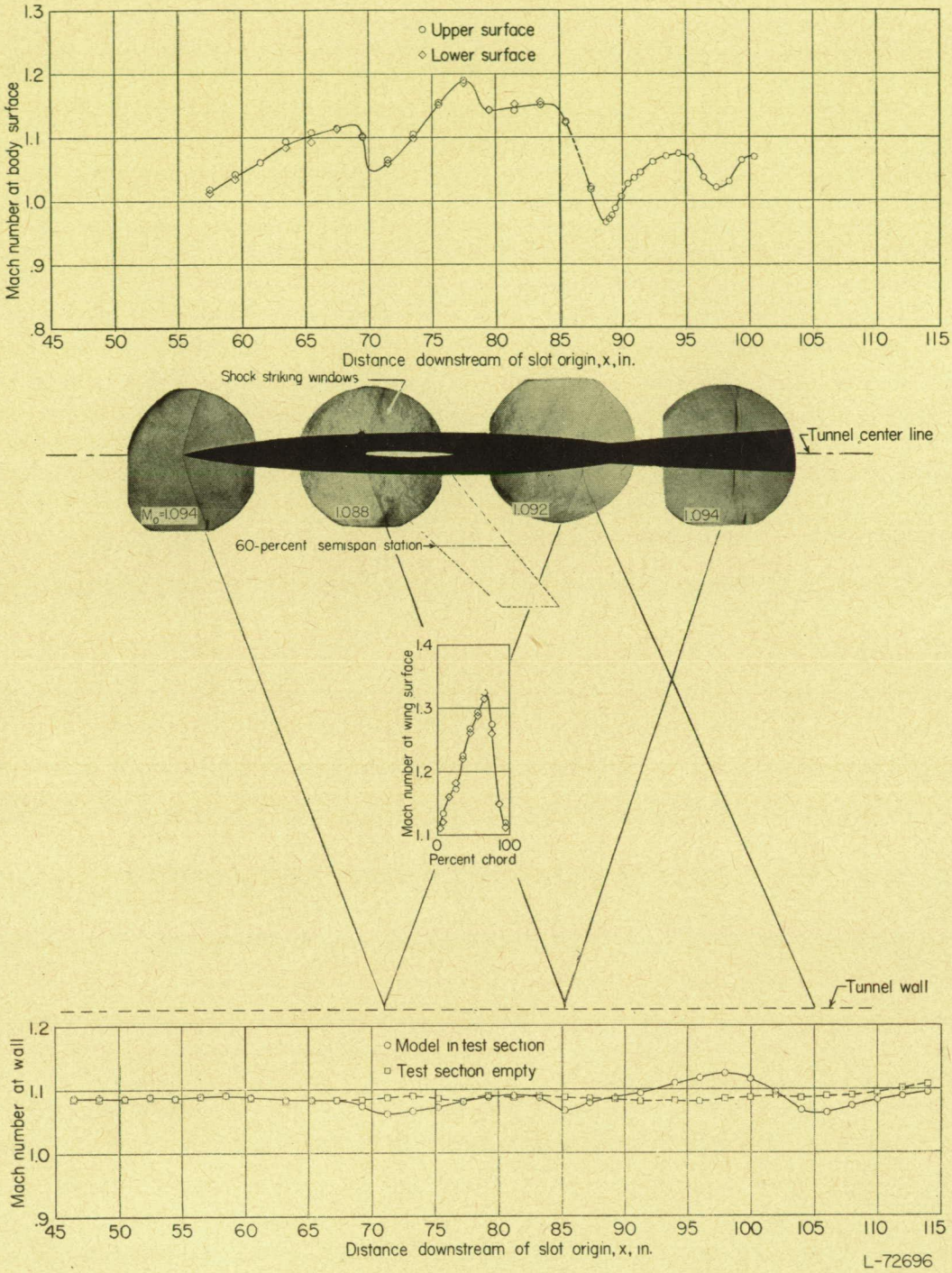
(b) $M_o = 1.034$.

FIGURE 32.—Continued.



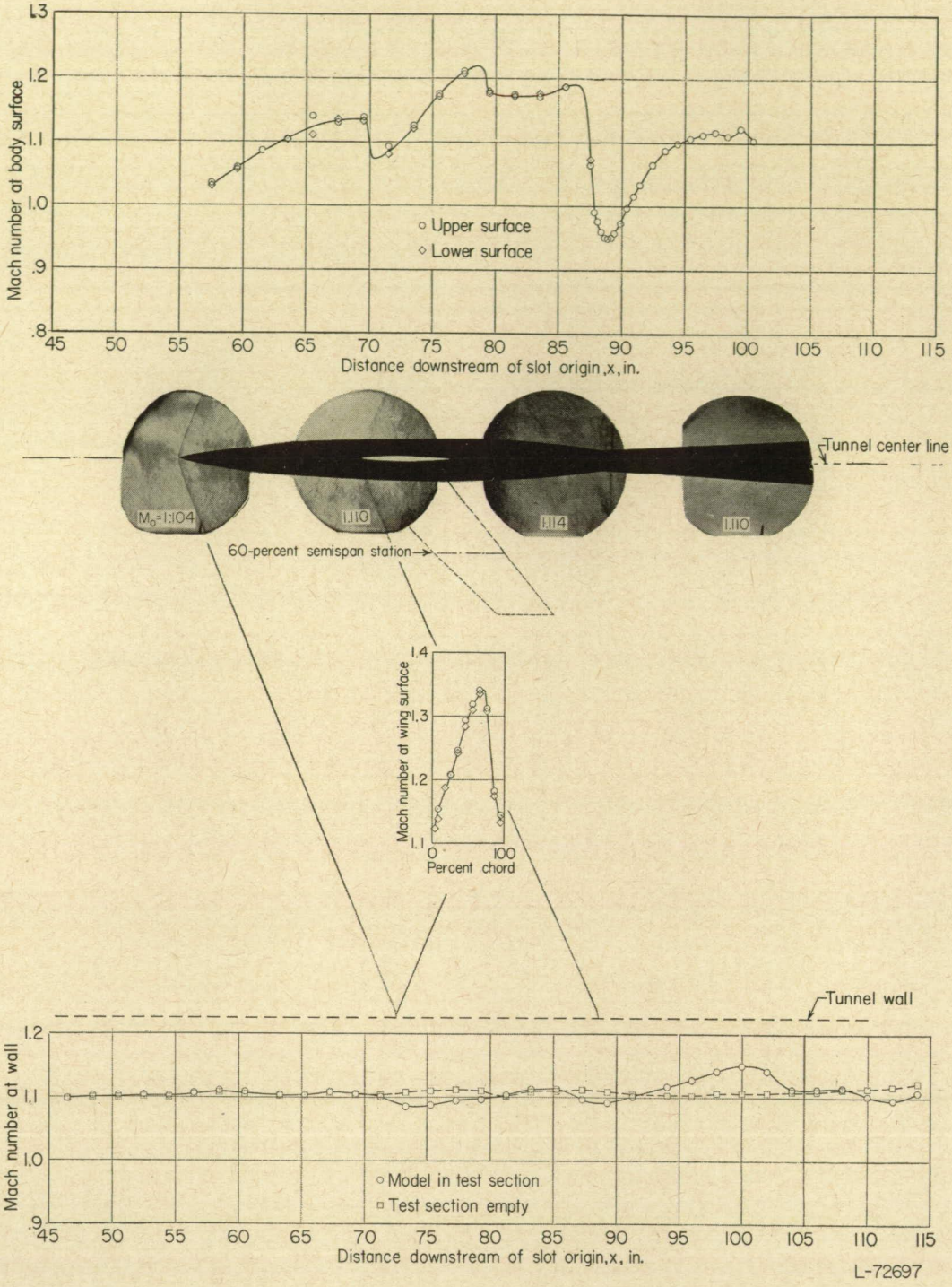
(c) M_o=1.079.

FIGURE 32.—Continued.



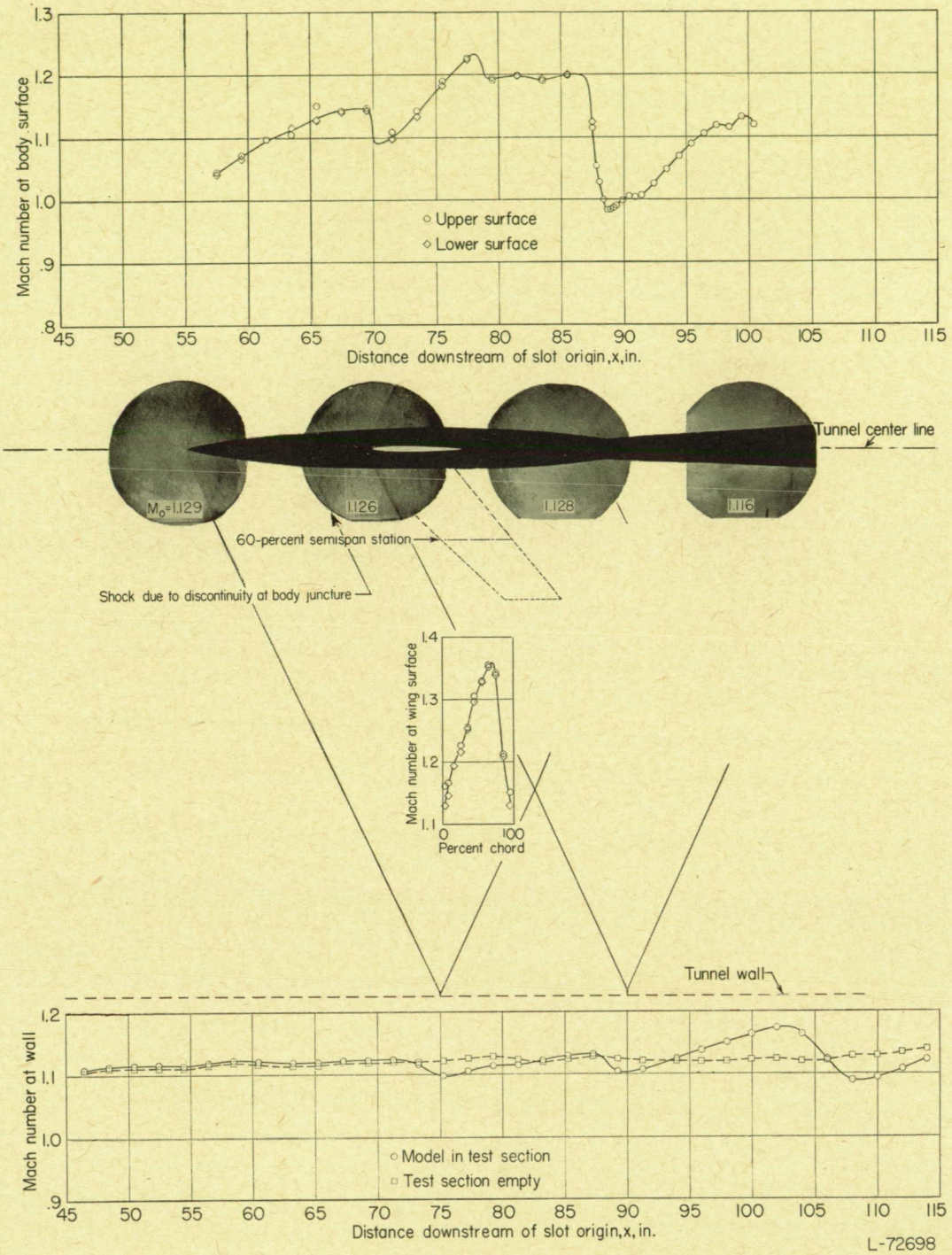
(d) $M_o = 1.088$.

FIGURE 32.—Continued.



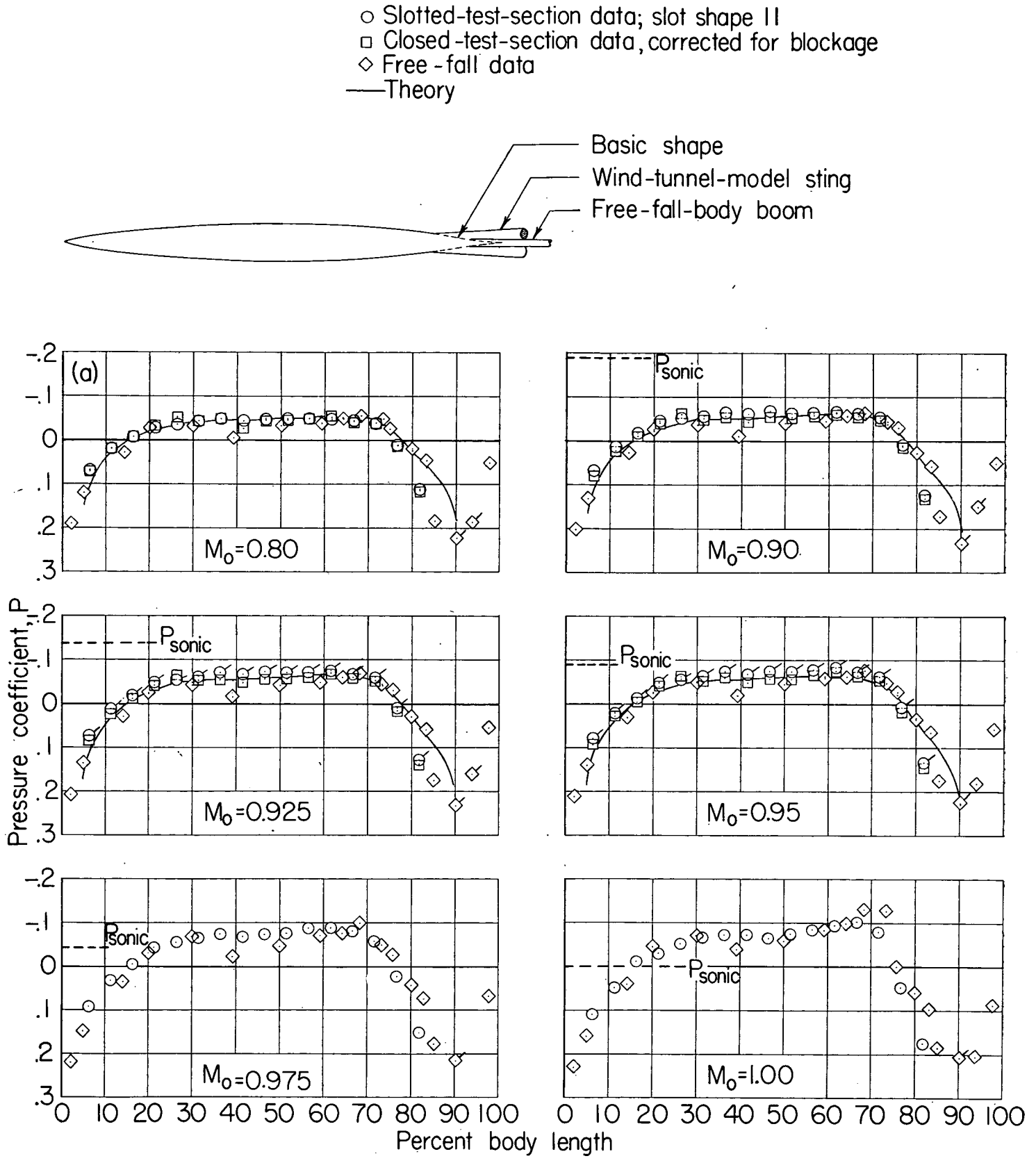
(e) $M_o = 1.110$.

FIGURE 32.—Continued.



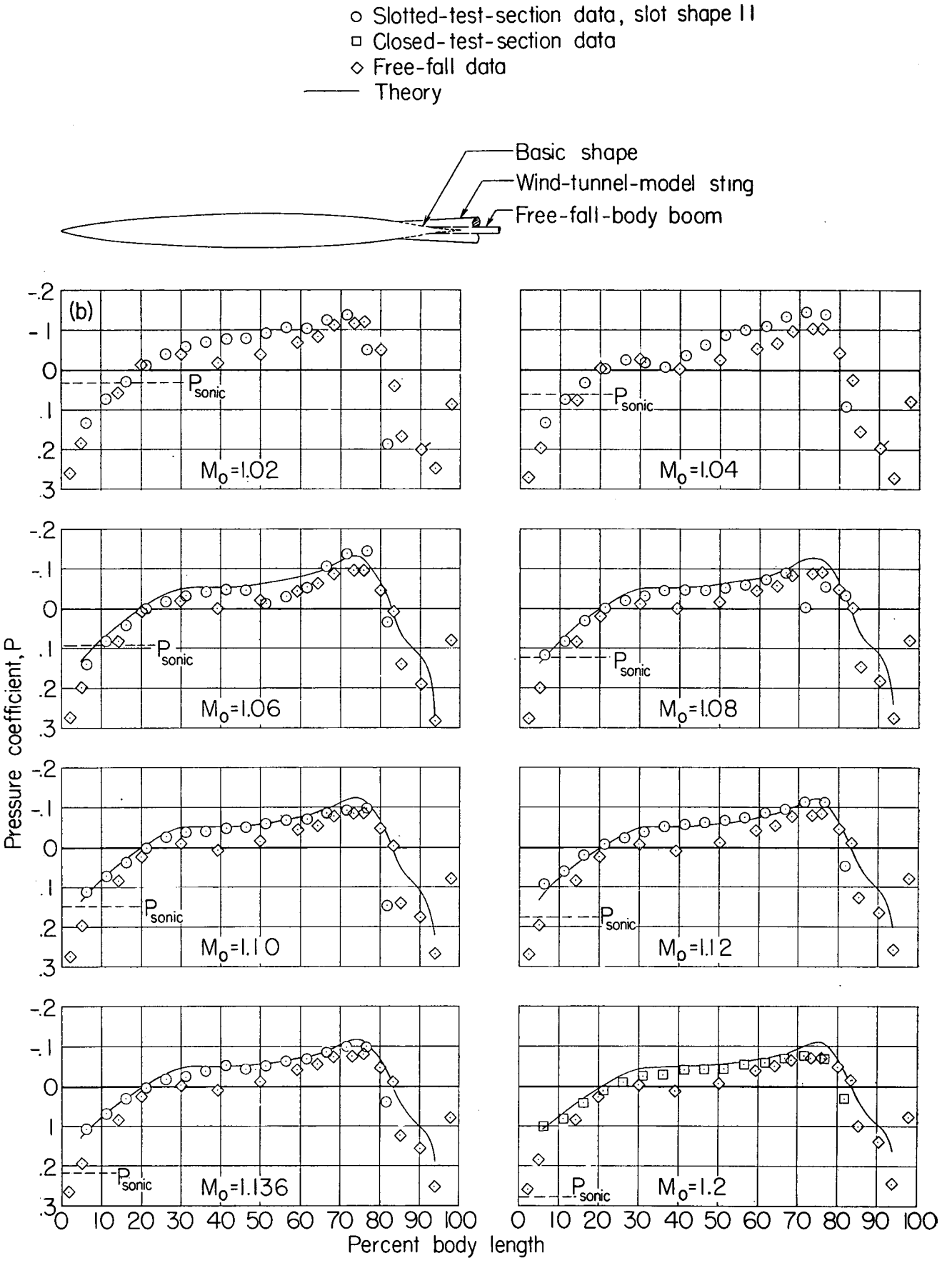
(f) $M_o = 1.126$.

FIGURE 32.—Concluded.



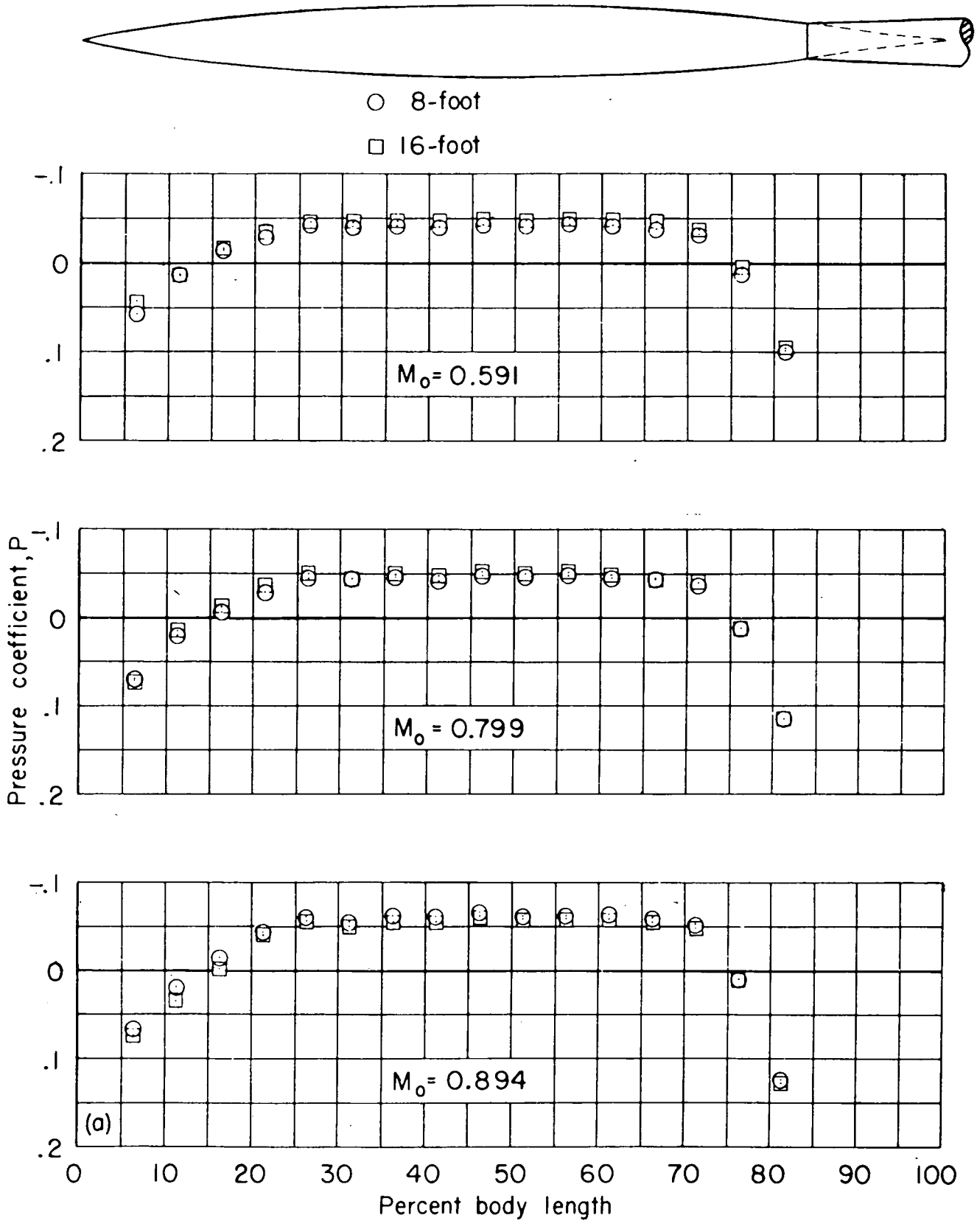
(a) Subsonic and sonic speeds.

FIGURE 33.—Comparison of body-surface pressure distributions obtained from tests of a body of revolution in the slotted test section with those from closed-test-section tests, free-fall tests, and theory. Flagged symbols indicate data obtained from faired curves.



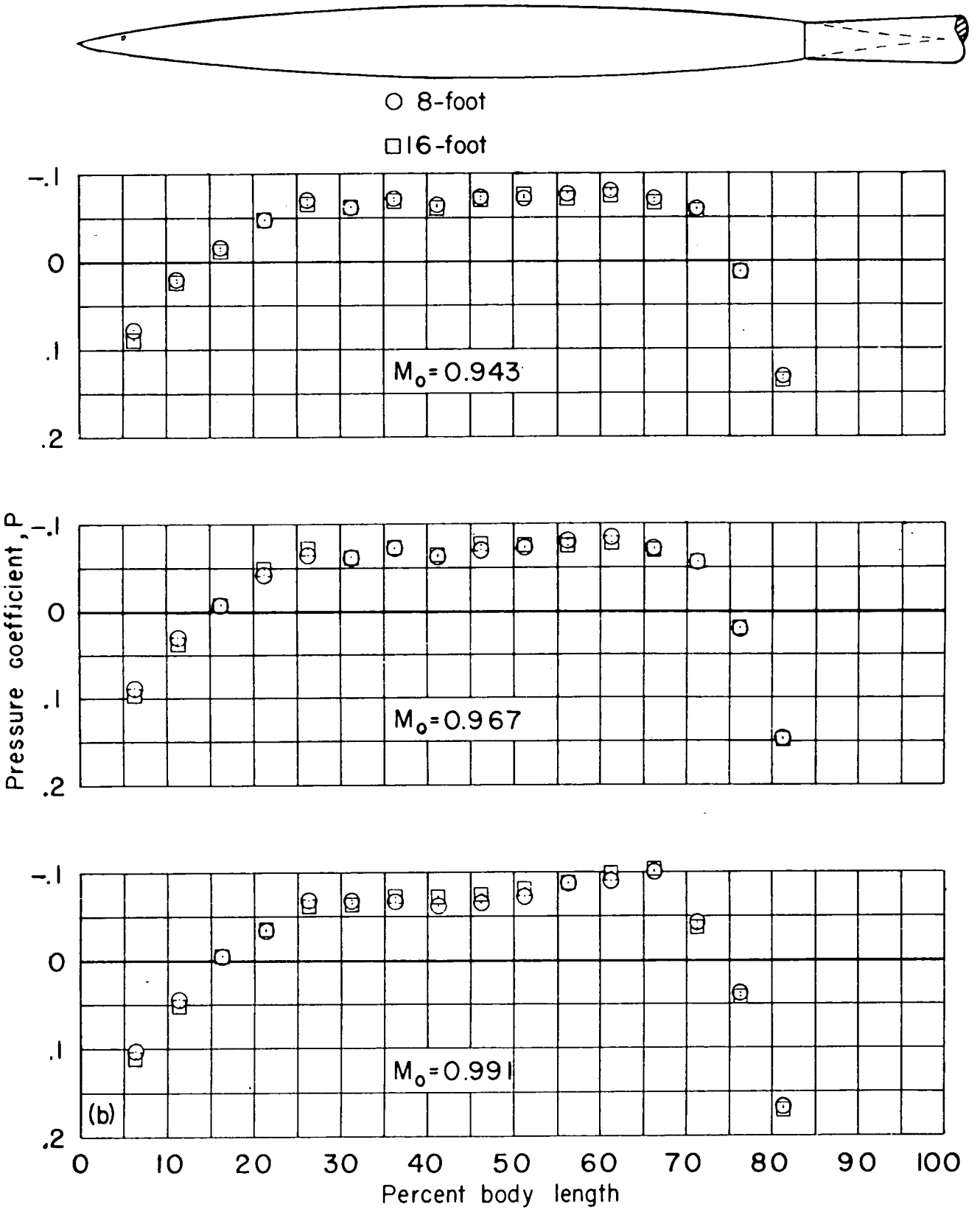
(b) Supersonic speeds.

FIGURE 33.—Concluded.



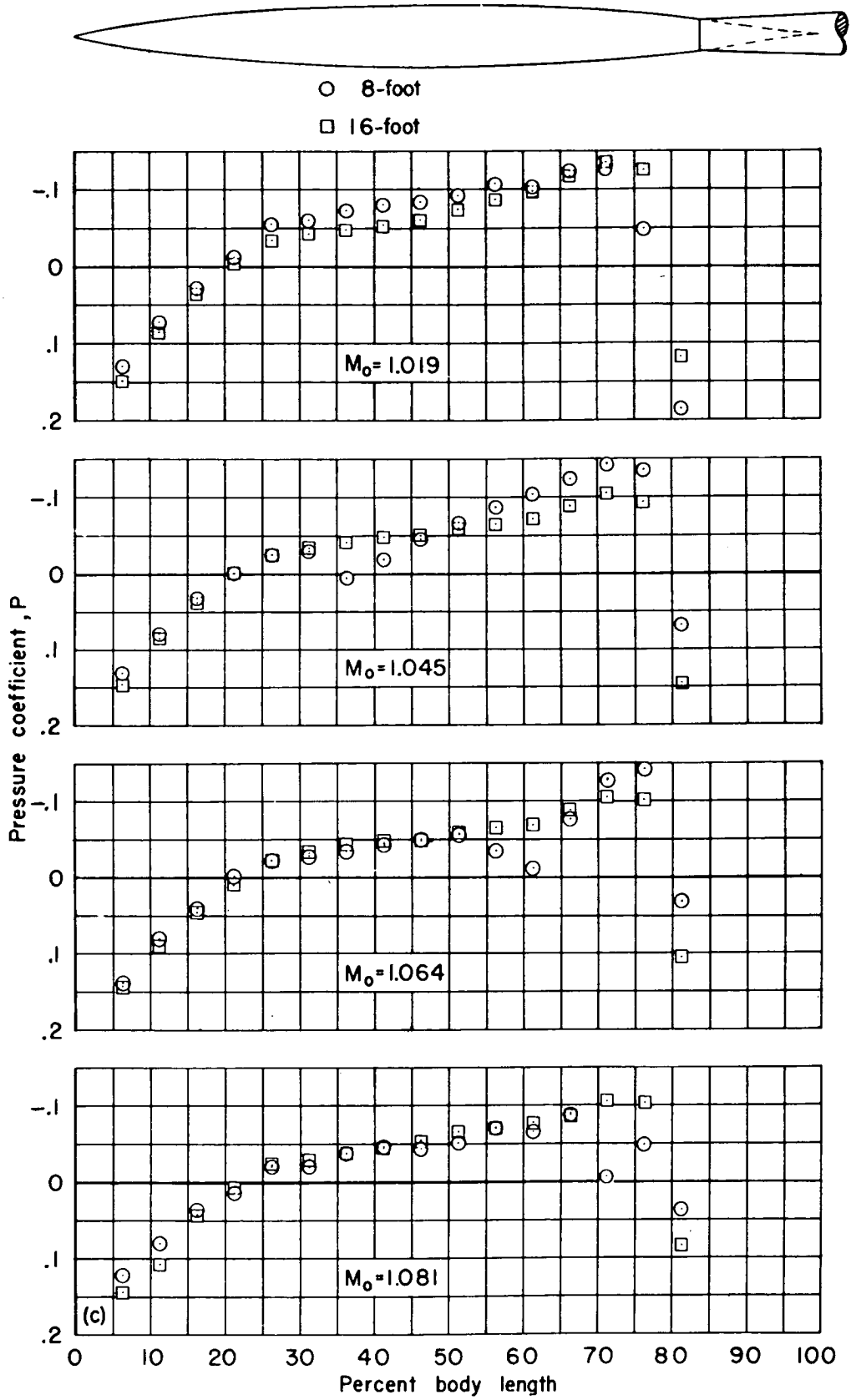
(a) Subsonic speeds (M_o from 0.591 to 0.894).

FIGURE 34.—Comparison of body-surface pressure distributions obtained from tests of a body of revolution at zero angle of attack in the slotted test sections of the Langley 8-foot and 16-foot transonic tunnels.



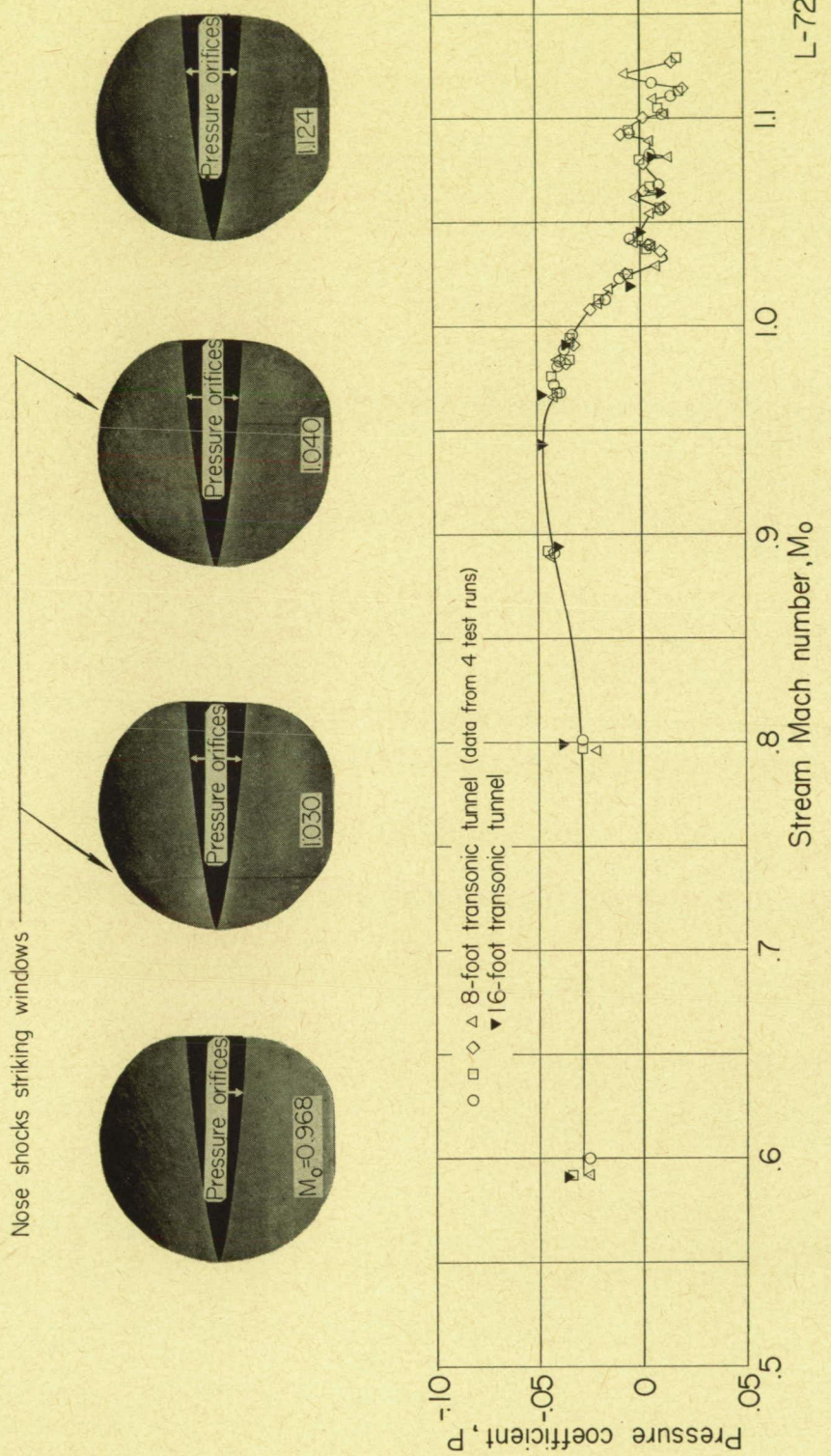
(b) Subsonic speeds (M_o from 0.943 to 0.991).

FIGURE 34.—Continued.



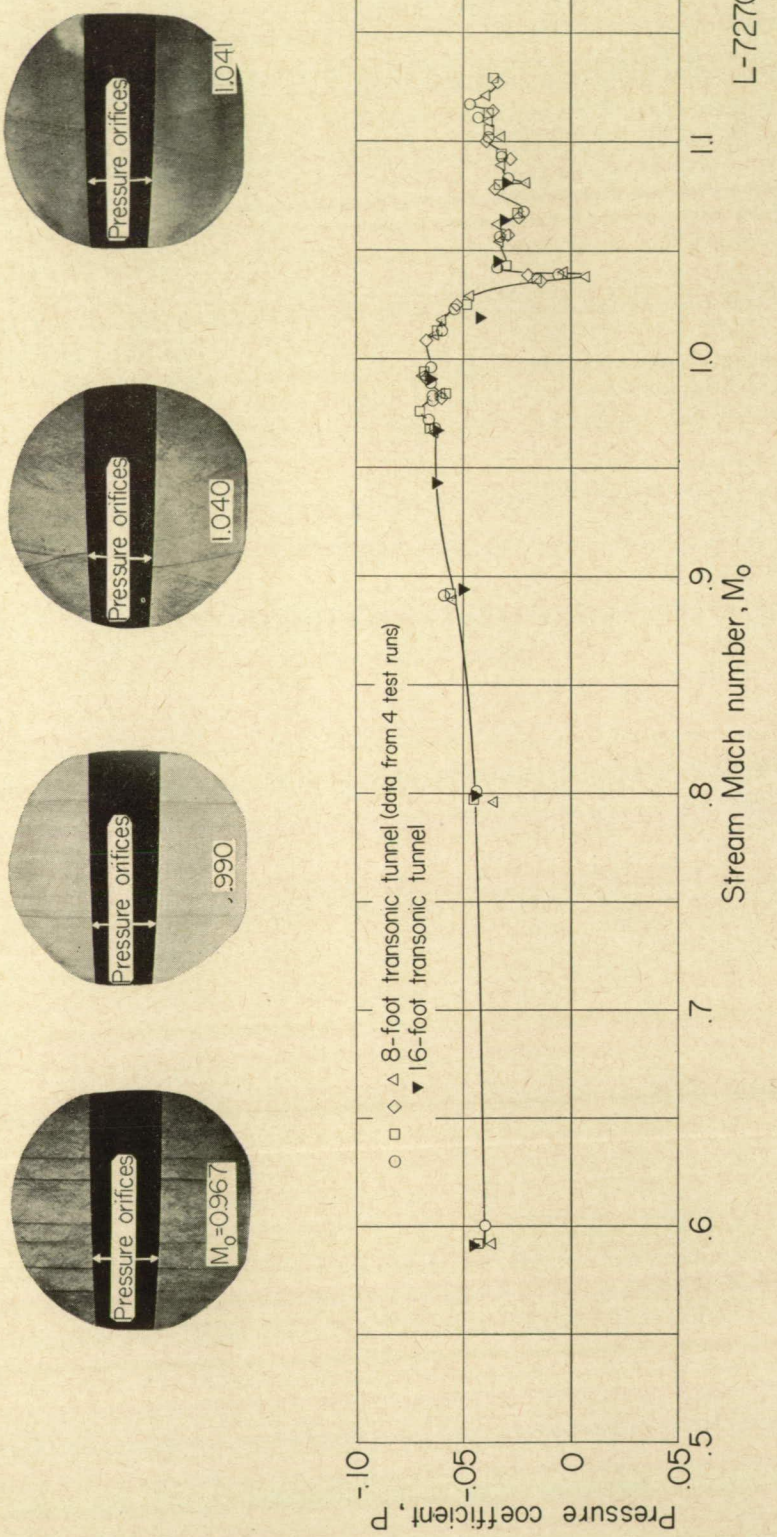
(c) Supersonic speeds (M_o from 1.019 to 1.081).

FIGURE 34.—Concluded.



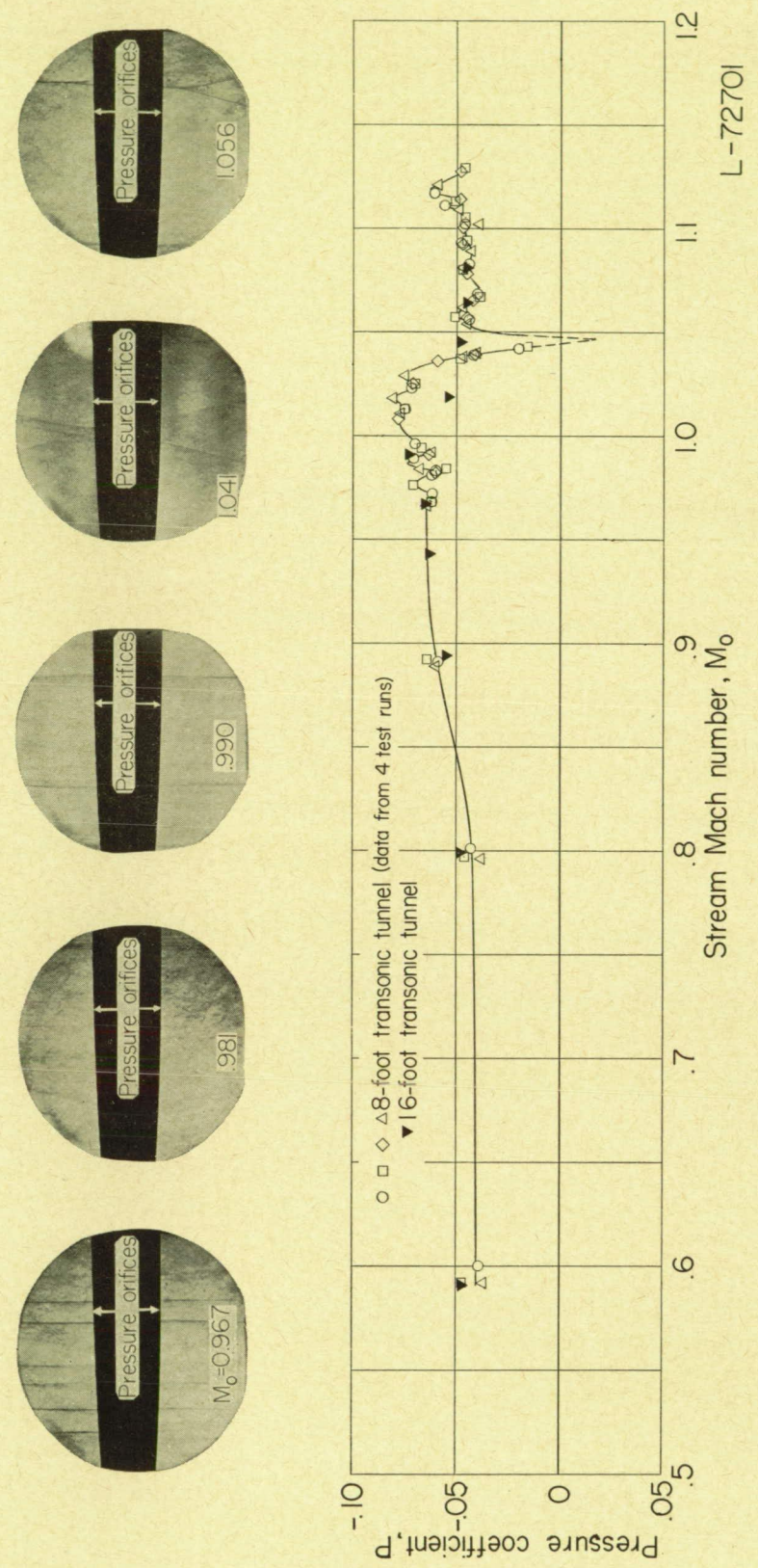
(a) $\frac{x}{l}$=0.2125.

FIGURE 35.—Variation with stream Mach number of the pressure coefficients at six axial stations on the body of revolution in the slotted test sections of the Langley 8-foot and 16-foot transonic tunnels.



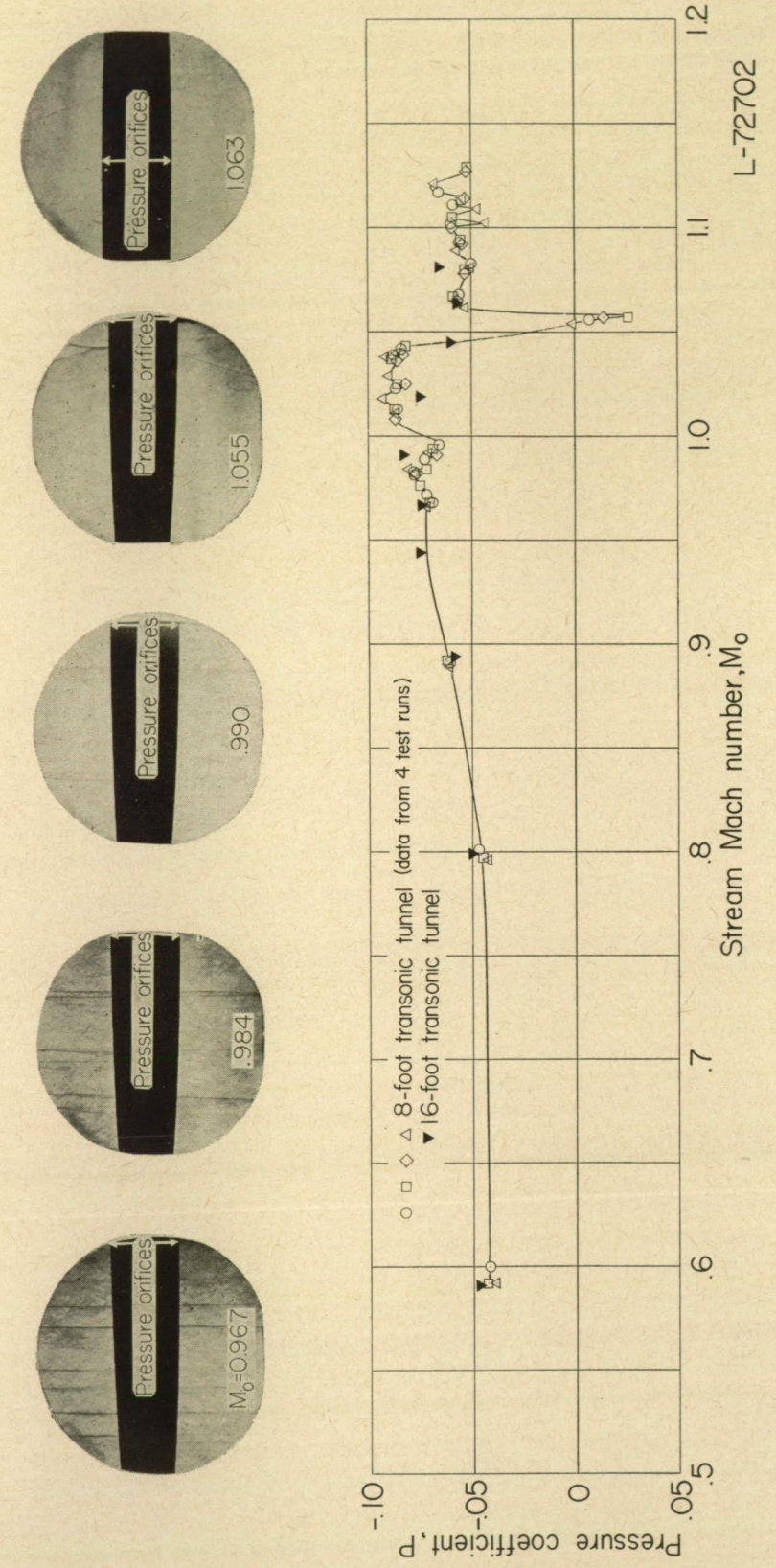
(b) $\frac{x}{l}$=0.3125.

FIGURE 35.—Continued.



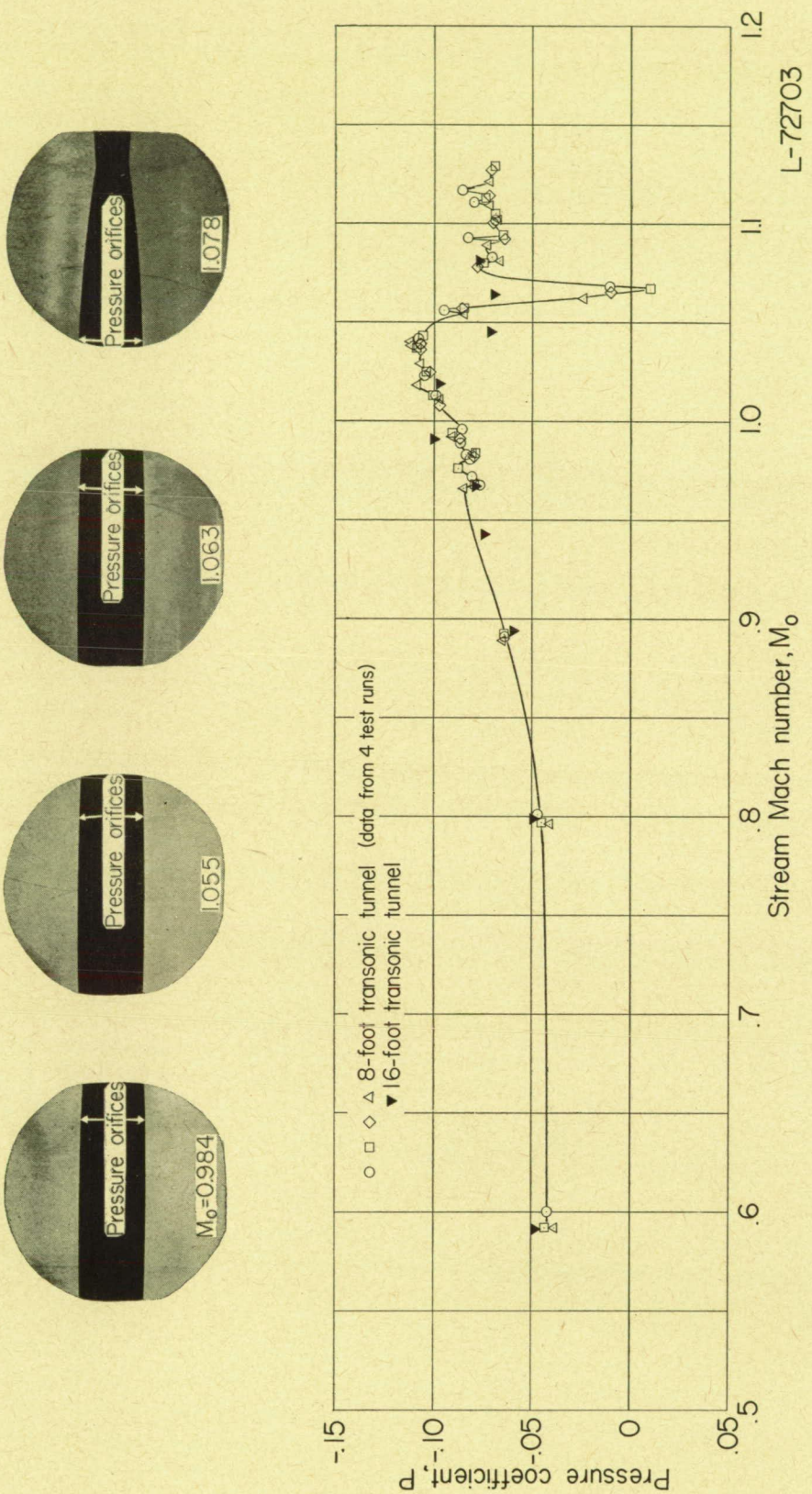
(c) $\frac{x}{l}=0.4125$.

FIGURE 35.—Continued.



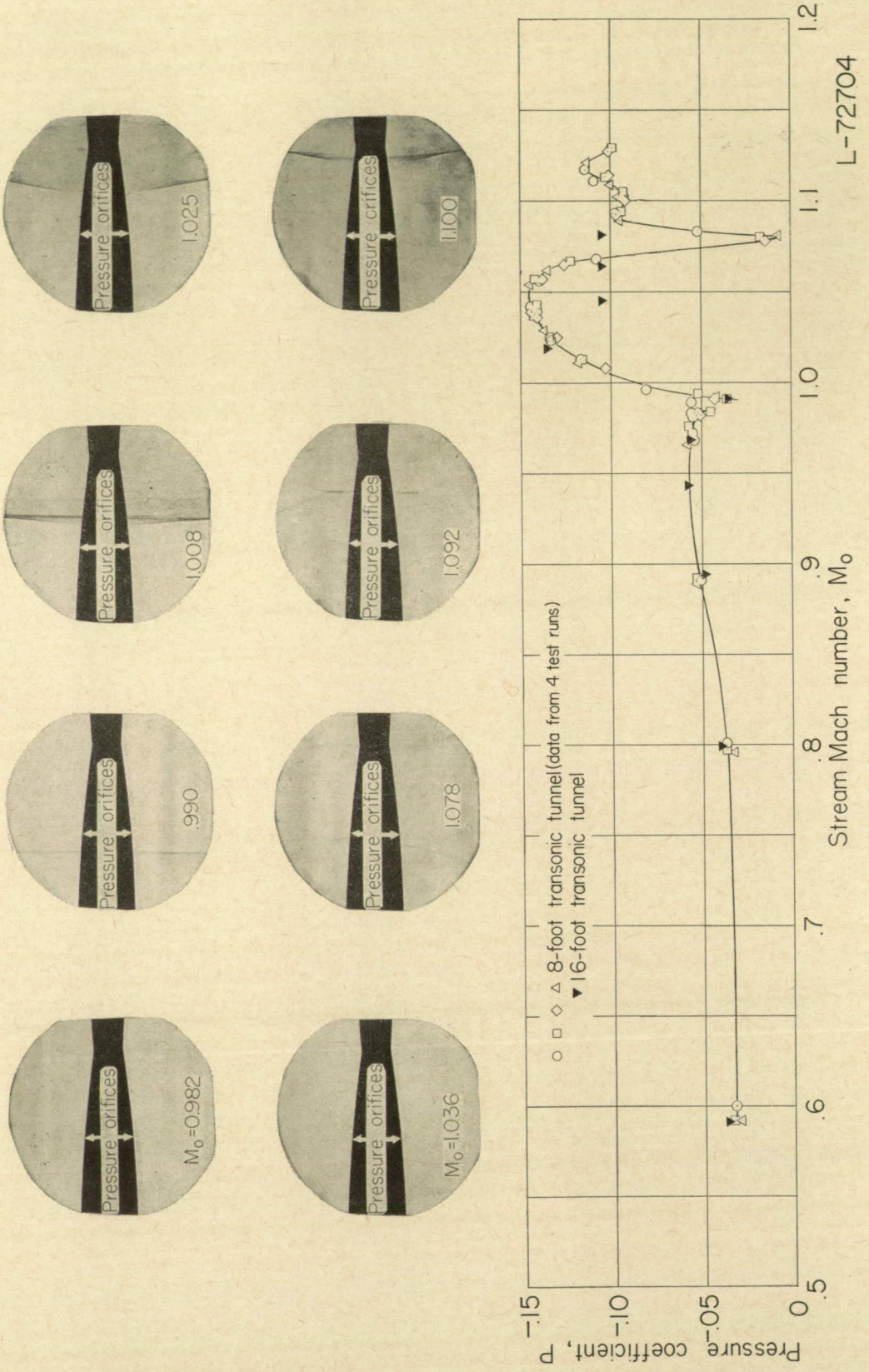
(d) $\frac{x}{l}$=0.5125.

FIGURE 35.—Continued.



(e) $\frac{x}{l}$=0.6125.

FIGURE 35.—Continued.



(f) $\frac{x}{l}=0.7125$.

FIGURE 35.—Concluded.

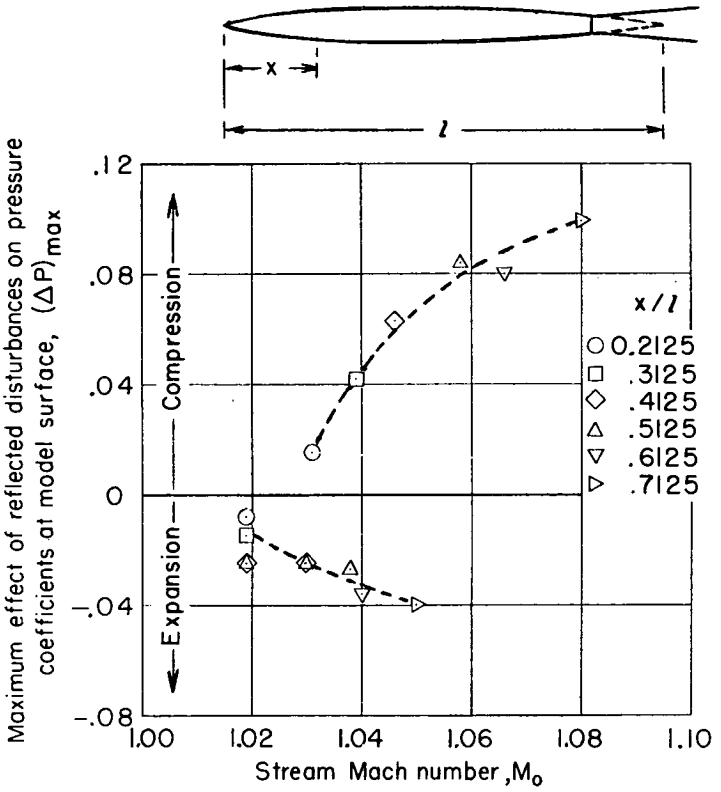


FIGURE 36.—Maximum effect of reflected compressions and expansions on pressure coefficients at model surface, as indicated by differences between measurements in the Langley 8-foot and 16-foot transonic tunnels.

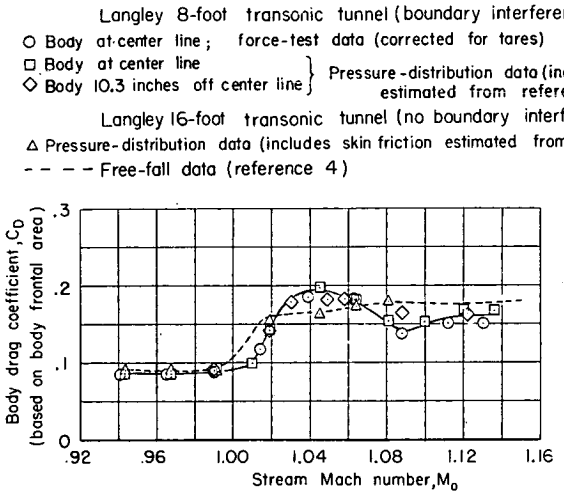


FIGURE 37.—Effect of boundary-reflected disturbances on body drag coefficients for a 33.5-inch-long nonlifting body of revolution in the slotted test section.

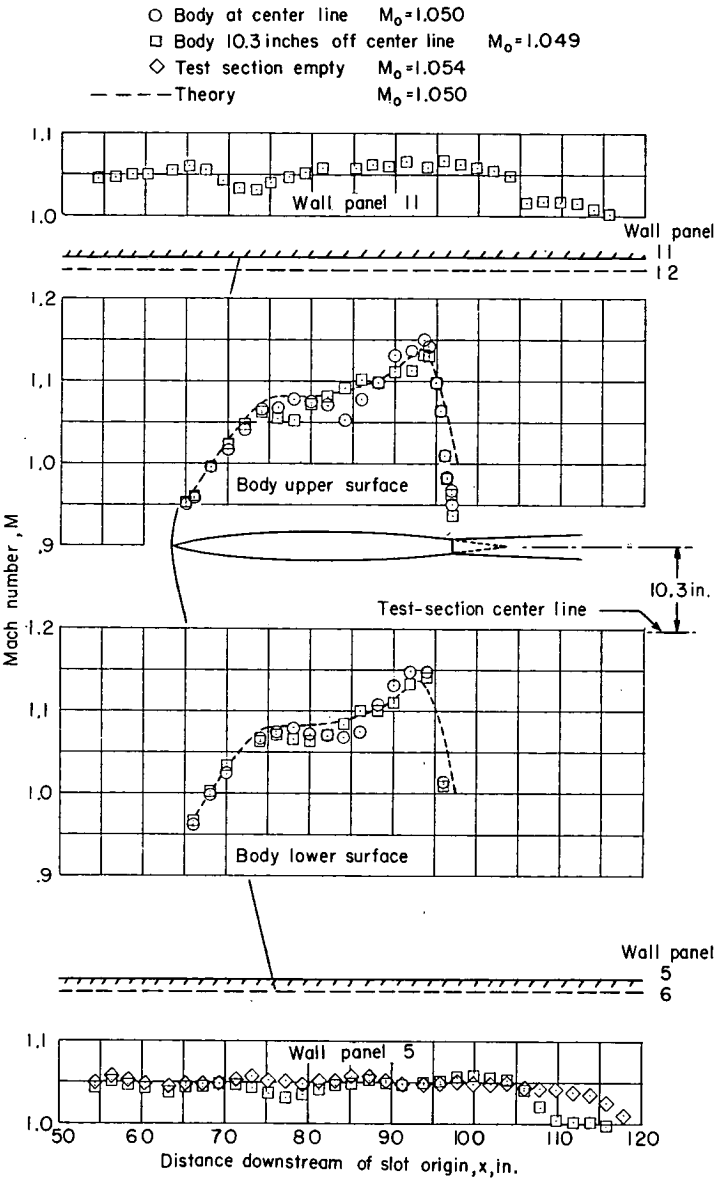


FIGURE 38.—Comparison of body-surface Mach number distributions obtained from tests of a body of revolution at the center line and approximately 10.3 inches off the center line of the slotted test section. $\alpha=0°$; $M_o=1.050$ (approximately).

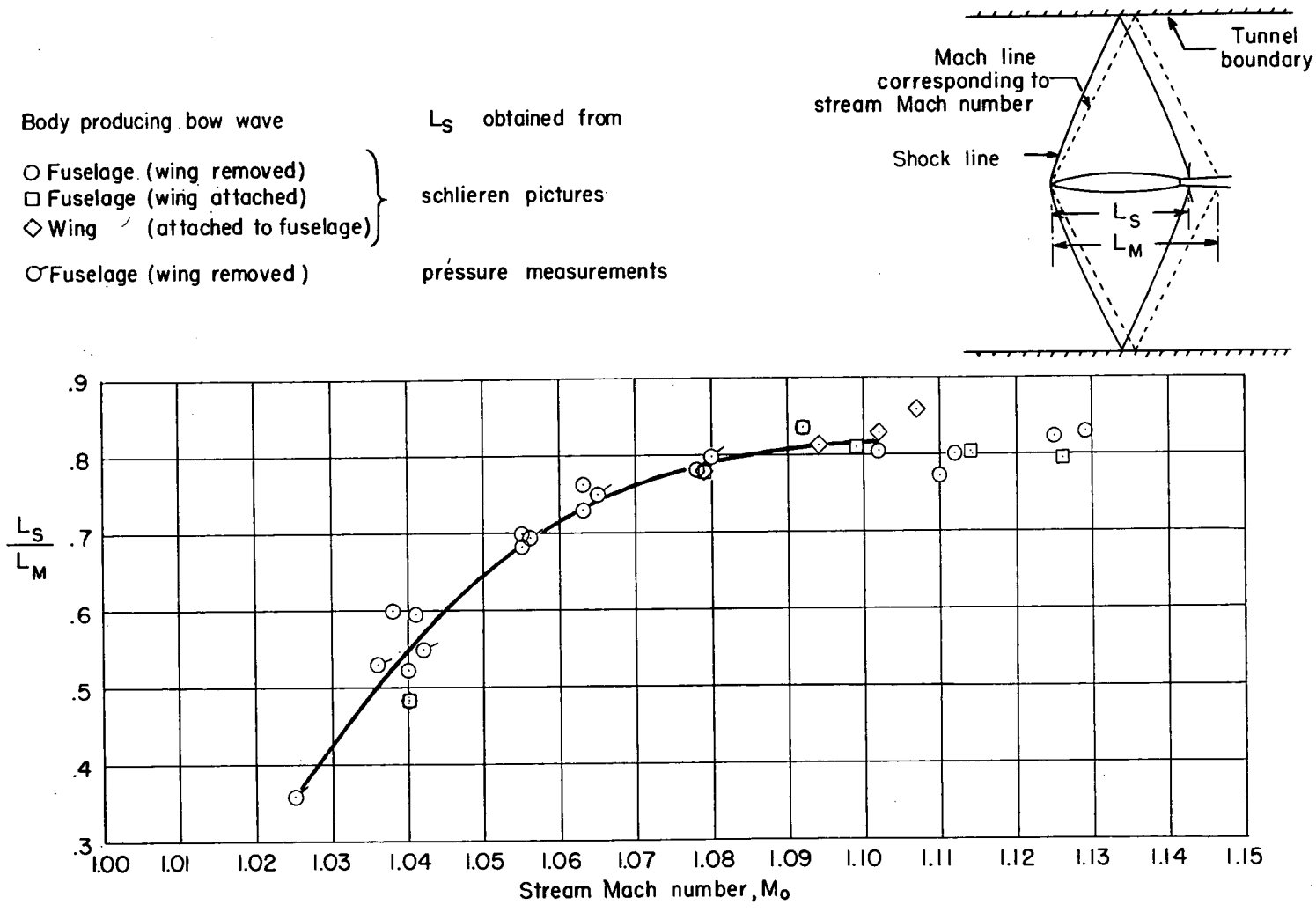


FIGURE 39.—Axial distance required for model bow wave to reflect from test-section wall and strike surface of model near center line. $\alpha=0°$

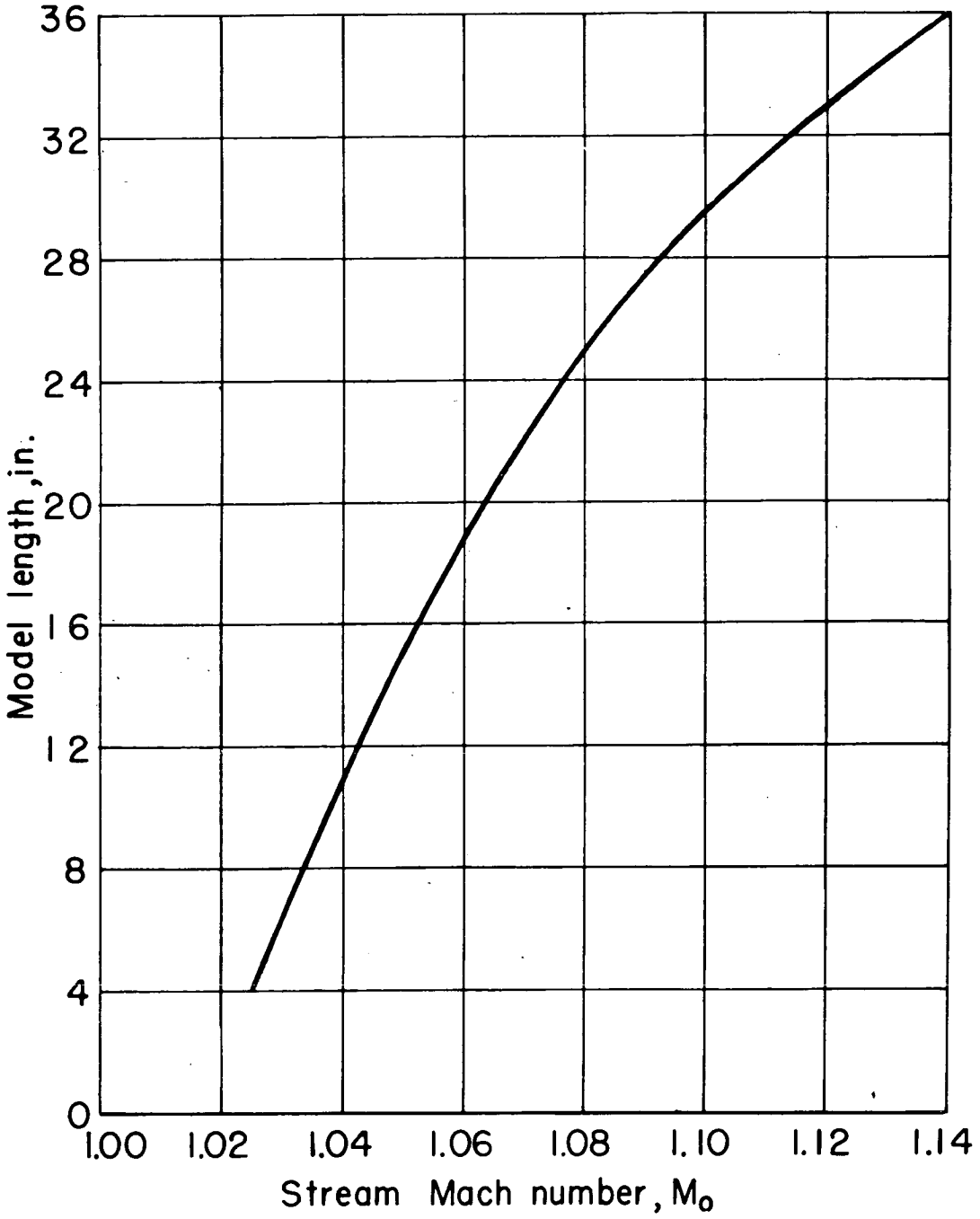


FIGURE 40.—Approximate model lengths for interference-free supersonic testing at center line of slotted test section measuring approximately 43.8 inches from center line to wall.

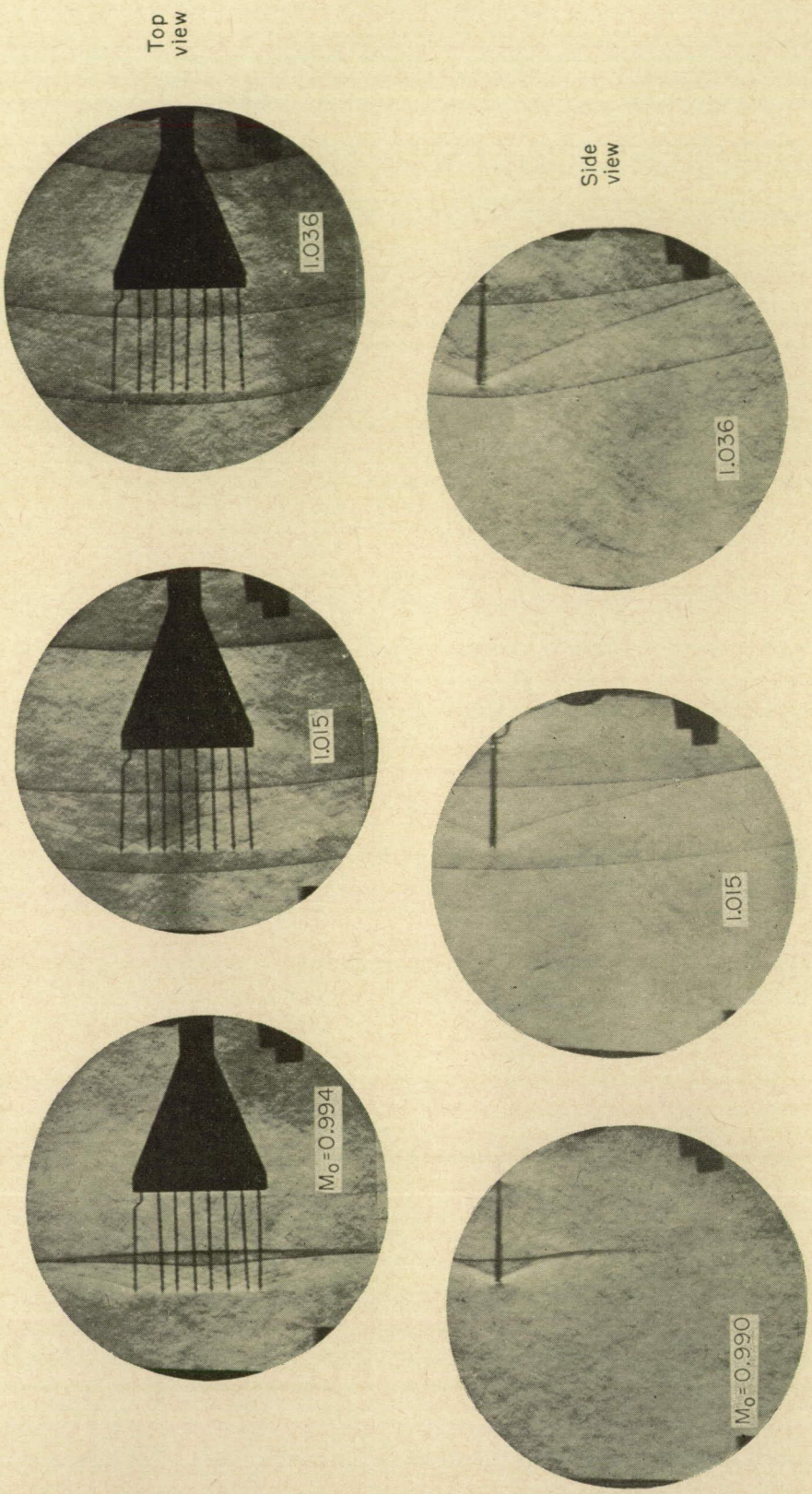


FIGURE 41.—Shock formations at transonic speeds with total-pressure rake (0.050-inch-diameter tubes projecting 3 inches ahead of 1° included-angle wedge) near center line of slotted test section.

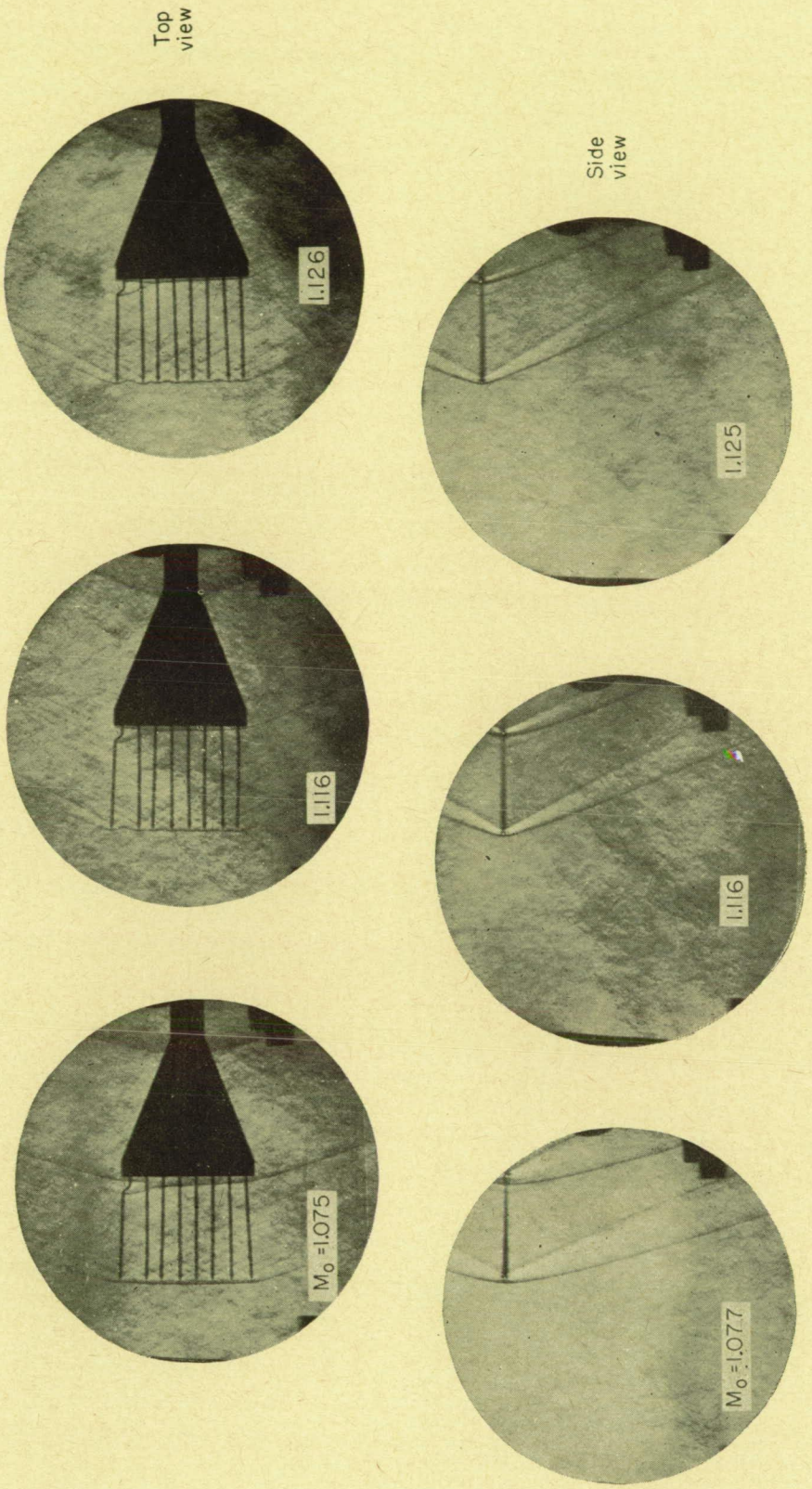
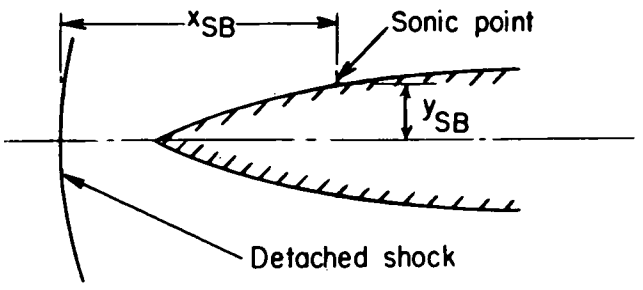


FIGURE 41.—Concluded.



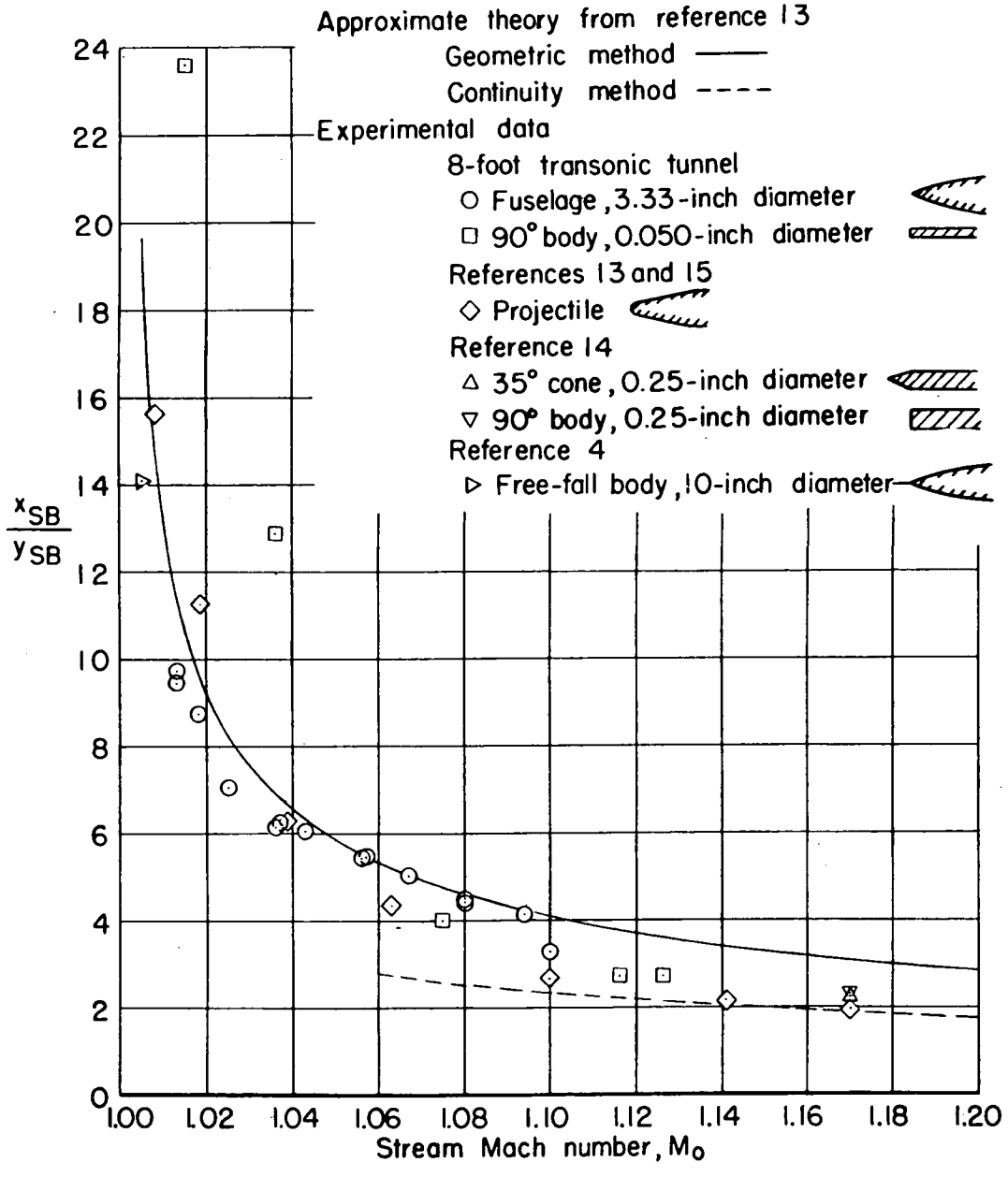
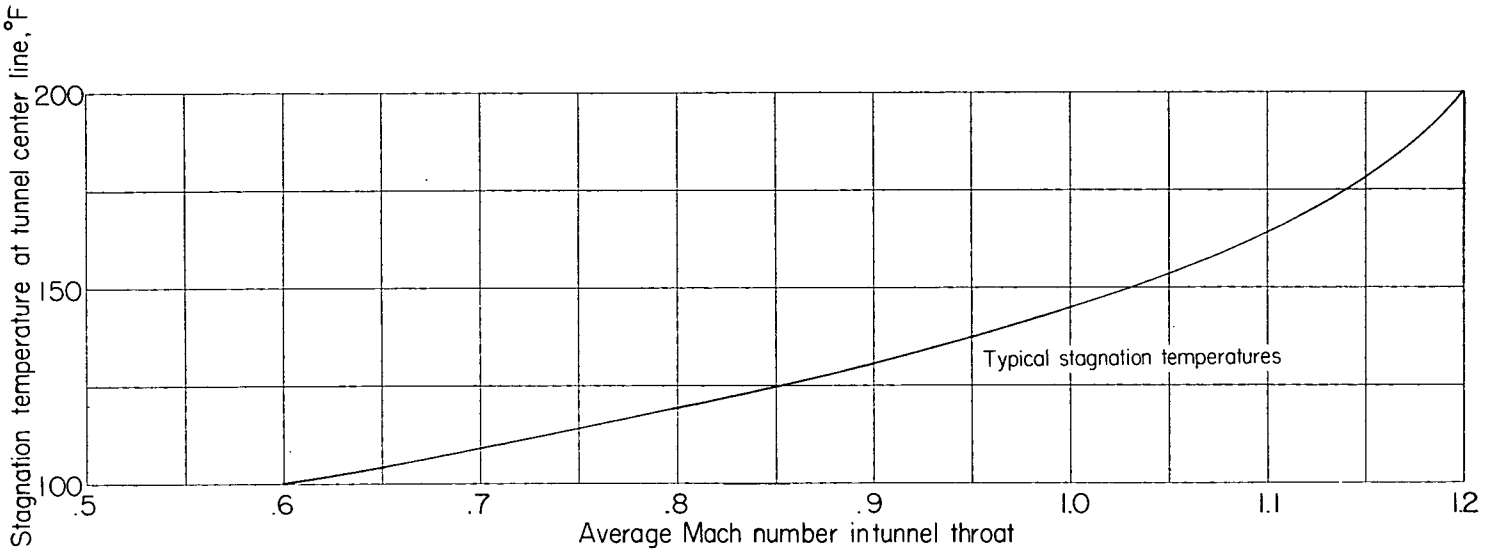


FIGURE 42.—Location of detached shock waves ahead of various axially symmetric bodies at low-supersonic speeds. $\alpha=0°$.



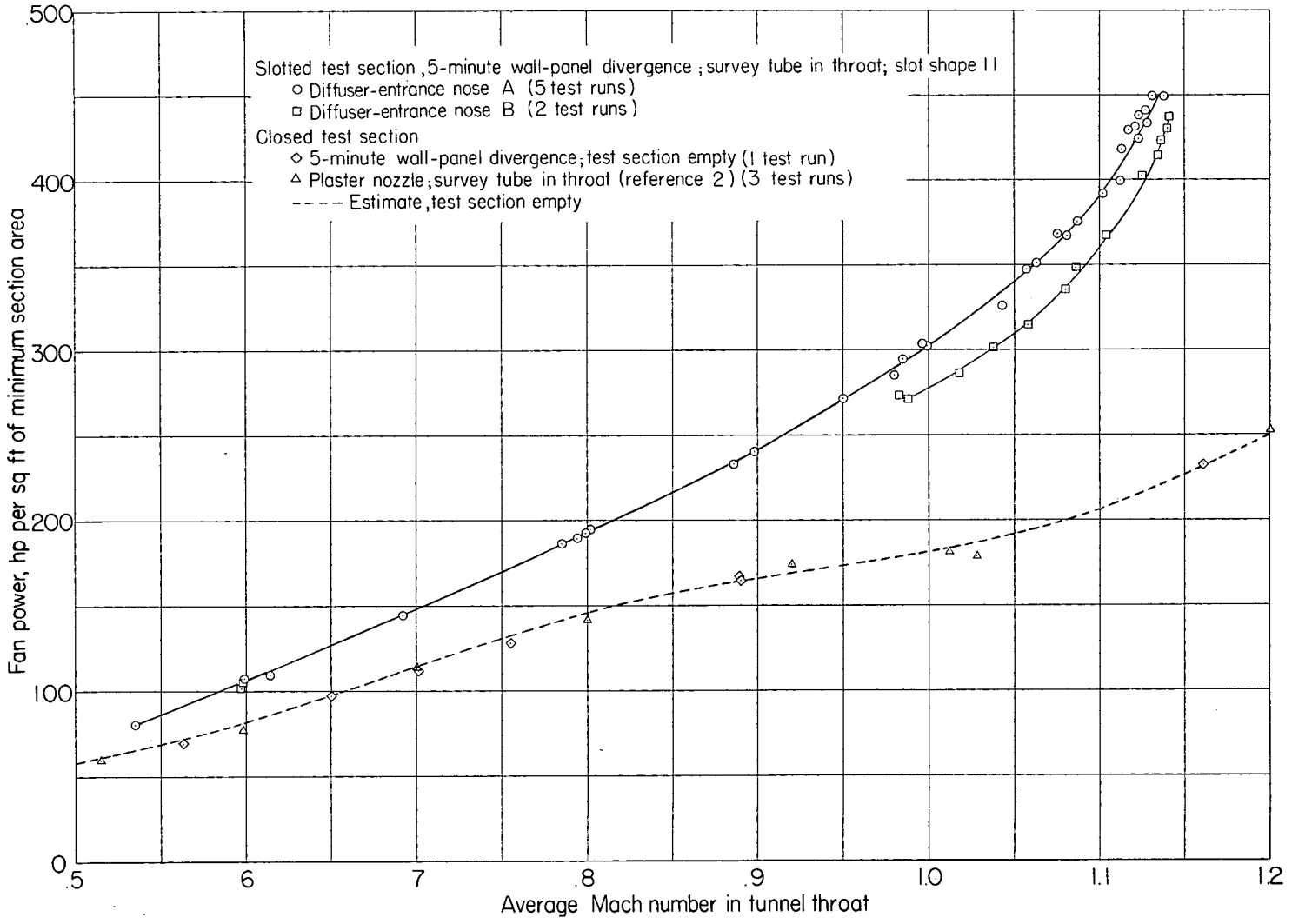


FIGURE 43.—Power requirements for transonic operation of 8-foot tunnel with closed and slotted test sections. All power data reduced to typical stagnation temperatures shown and to stagnation pressure of 2,120 pounds per square foot.

526597—60——89

REPORT 1390

INCOMPRESSIBLE FLUTTER CHARACTERISTICS OF REPRESENTATIVE AIRCRAFT WINGS [1]

By C. H. WILTS

SUMMARY

The present report gives the results of a detailed study of the flutter characteristics of four representative aircraft wings. This study was made using the electric-analog computer at the California Institute of Technology. During the course of this investigation eight important parameters of each wing were varied and, in addition, the effects of mass, inertia, pitching spring, and location of a concentrated mass were investigated for all four wings and at several sweepback angles.

The introduction of this report discusses in general terms the flutter characteristics of airplanes. The second section contains a discussion of the electric-analog principles that made a study of this magnitude feasible. The third section contains a discussion of the aerodynamic and structural approximations made for simplifying the flutter analysis of a wing. The fourth section gives information relating to the errors introduced by the finite-difference approximations to continuous aeroelastic systems. In addition, data are given pertaining to the flutter characteristics of a swept-wing wind-tunnel model, and the results of computations based on two assumptions regarding aerodynamic forces on a swept wing are also given. The fifth section lists the physical characteristics of the four representative aircraft wings and the sixth section contains the computed flutter characteristics of the four wings.

INTRODUCTION

Flutter is a phenomenon which is observed in the transient or unforced response of an aerodynamic system. Mathematically speaking, it is observed in the solution of the homogeneous differential equation describing the behavior of an airplane in flight through still nonturbulent air. An airplane wing which is considered to be a continuous beamlike or platelike structure has an infinite number of degrees of freedom, and the characteristic equation which describes the transient response has an infinite number of roots. Experience has shown that only the roots of lower magnitude (frequency) exhibit the problem of instability or flutter. It is this fact which makes it possible to predict flutter using an analog computer, which represents only the lower frequency modes of the structure, or using a few normal modes in either digital or analog computation.

The exponents in the transient response of a linear system are the roots of the characteristic equation. Since the characteristic equation involves real parameters, the roots are real or occur as complex conjugate pairs. The latter roots are the ones of interest here. The real part of a conjugate pair is the reciprocal of the time constant in the transient response and the (positive) imaginary part is the frequency of oscillation. This is illustrated in figure 1. Mathematical description of the transient term is

$$y=A_1e^{(\sigma+i\omega)t}+A_2e^{(\sigma-i\omega)t}$$

or in terms of real functions

$$y=Ae^{\sigma t}\cos(\omega t+\phi)$$

If the real part of the pair of roots σ is negative the "transient" dies out and the root is said to be stable. If the real part is positive the transient grows exponentially until limited by nonlinearities or destruction, and the root is said to flutter. The terminology is not strictly correct, but it is common practice to refer to the exponents of the transient response as flutter roots since they are numerically equal to the roots of the characteristic equation. Throughout this report such terminology will be used.

Damping of flutter roots may be measured by two dimensionless numbers ζ and g, which differ from each other by a factor of 2. The former is generally used by control-system engineers; the latter, by flutter analysts. They can be defined by the equation for the particular term in the transient response given earlier

$$y=Ae^{\sigma t}\cos(\omega t+\phi)=Ae^{-\zeta\omega_n t}\cos\left[\sqrt{(1-\zeta^2)}\omega_n t+\phi\right]$$

$$=Ae^{-\frac{g\omega_n t}{2}}\cos\left\{\sqrt{[1-(g^2/4)]}\,\omega_n t+\phi\right\}$$

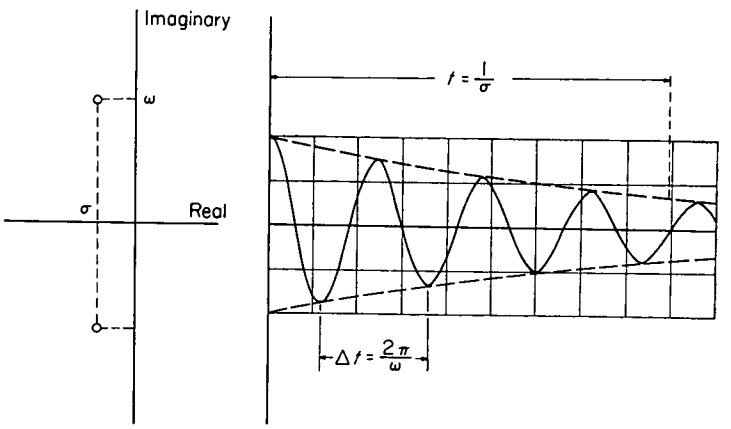


FIGURE 1.—Transient response corresponding to roots of characteristic equation.

[1] Supersedes NACA TN 3780, "Incompressible Flutter Characteristics of Representative Aircraft Wings" by C. H. Wilts, 1957.

Preceding Page Blank

Flutter computations are usually centered around regions where the value of g lies in the range $-0.2<g<0.2$. In such cases the factor $\sqrt{1-\zeta^2}$ differs from unity by less than 0.5 percent. For this reason it is customary to omit this factor in the trigonometric term giving the following approximation:

$$y=Ae^{-\frac{g\omega_n t}{2}}\cos(\omega_n t+\phi)$$

This practice will be followed in this report. For damping which is small, an approximate rule of thumb is that the damping factor g is nearly equal to the per unit decrement per cycle divided by π. If percent decrement per cycle δ is used, there results the convenient approximation

$$g\approx\frac{\delta}{100\pi}$$

The flutter roots of an airplane are complex functions of all geometrical, structural, and inertial properties of the airframe as well as of the airspeed and air density. With all other properties held constant, the lowest airspeed at which the flutter root exhibits neutral stability is called the flutter speed. If g is plotted as a function of velocity, the abscissa (speed) at which the curve first crosses the axis $g=0$ is the flutter speed. In this study such curves were used to determine the flutter speed, but such curves are used in this report only to illustrate the behavior of some unusual flutter roots. A tabulation of flutter speeds does not always give a good picture of the flutter characteristics. An example is shown in figure 2, where the damping of two roots is shown. One root becomes unstable at a speed of about 300 miles per hour and the other, at a speed of about 600 miles per hour. If a parameter variation increases the damping g of both roots by 0.03, one flutter speed is raised to 350 miles per hour, a 17-percent increase; the other is raised to 603 miles per hour, a 0.5-percent increase. A further increase in g of 0.02 will raise the second flutter speed 0.4 percent to 605 miles per hour, while the first root will now exhibit no flutter. It should be emphasized that even though a design speed of, say, 500 miles per hour has been surpassed, the system may still be regarded as unsatisfactory. A system so close to flutter at a speed of 360 miles per hour might actually flutter because of weight (fuel) variations or minor differences in stiffness resulting from variations within the manufacturing tolerances. From the standpoint of this report all three of the sets of roots discussed above will be regarded as having essentially the same flutter characteristics even though they exhibit radically different theoretical flutter speeds. Emphasis is given to this point because remarks to be made later in this report may be misunderstood without a clear conception of this viewpoint.

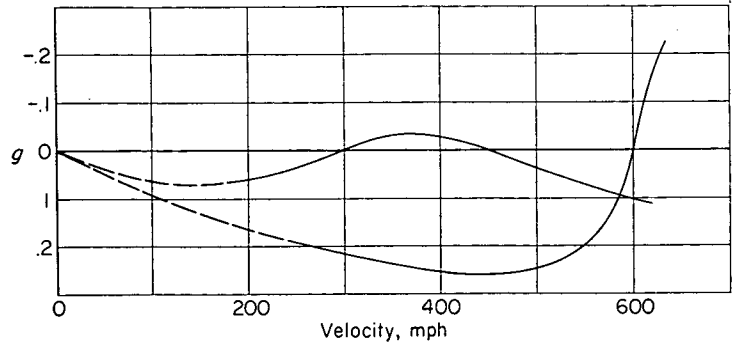


FIGURE 2.—Variation of g with velocity for typical flutter roots.

This investigation was conducted at the California Institute of Technology under the sponsorship and with the financial assistance of the National Advisory Committee for Aeronautics.

SYMBOLS

A, A_1, A_2	constants
b	half chord
b_r	half chord at root
b_x	half chord at tip
$C\left(\frac{bp}{v_n}\right)$	symbolic representation of circulatory component of lift force due to angle of attack
C_{L_α}	lift coefficient
d	wing station from root, in.
E	Young's modulus of elasticity
EI	equivalent beam flexural rigidity, (lb) (sq in.)
e	experimental; used as subscript
f_f	flutter frequency, cps
f_n	normal mode frequency of cantilevered engine and nacelle, cps
f_∞	flutter frequency for continuous structure
G	shear modulus
GJ	equivalent beam torsional rigidity, (lb) (sq in.)
g	damping factor of a damped sinusoid, $e^{-\frac{g\omega_n t}{2}}\cos\omega t$
h	vertical deflection, positive down, in.
I	moment of inertia per unit length, lb sec^2
J	torsional stiffness
j	increase in stiffness, percent
k	radius of gyration, in.
l	semispan of wing
M, M_1, M_2, M_3, M_4, M_5	twisting moment about elastic axis per unit length of wing, positive nose up, lb
m	mass per unit length, lb sec^2/sq in.
m_c	mass of concentrated mass
m_f	fuselage mass
m_w	total wing mass, lb sec^2/in.
m_{w_f}	total wing mass outside of fuselage
$\overline{m}$	lumped mass
P, P_1, P_2, P_3, P_4	lift force per unit length of wing, positive nose down, lb/in.
p	Laplace transformation variable
q_n	dynamic pressure based on normal component of velocity, (1/2) ρv_n^2, lb/sq in.
t	time, sec
v	airstream velocity, in./sec
v_b	flutter velocity of airplane with bare wing
v_f	airstream velocity at which flutter occurs, in./sec
v_n	component of airstream velocity perpendicular to elastic axis, $v\cos\Lambda$, in./sec
v_o	reference velocity, in./sec
v_∞	flutter velocity for continuous wing
w	distance measured along wing
x_o	distance from midchord aft to elastic axis, in.

x_1 distance from quarter chord aft to elastic axis, $x_o+(b/2)$, in.
x_2 distance from three-fourths chord forward to elastic axis, $b-x_1$, in.
x_3 distance from elastic axis aft to center of mass, in.
y general variable
Δy cell size for finite-difference structure
α absolute pitch angle about elastic axis, positive nose up, radians
δ percent decrement per cycle
ζ per unit critical damping
θ slope of elastic axis or roll about horizontal axis normal to elastic axis, positive tip down, radians
Λ sweepback angle of elastic axis, deg
ρ air density, lb-sec^2/in.^{4}
τ wing twisting gradient, $\partial\alpha/\partial w$
σ real part of pair of roots
ω angular frequency, radians/sec
ω_n undamped natural frequency, radians/sec
$(\dot{}), (\ddot{})$ derivatives with respect to time

ELECTRIC-ANALOG METHODS OF FLUTTER ANALYSIS

The use of electrical analogs for the solution of aeroelastic problems has been discussed in detail in reference 1. The purpose of the present section is to summarize the principles briefly. For purposes of flutter analysis the structural system is assumed to be linear, and a linear electrical network is constructed whose electrical behavior approximates the dynamic behavior of the linearized structure. For this purpose, capacitors are ordinarily used to represent concentrated or lumped inertia properties, inductors are used to represent lumped flexibility properties, and transformers are used to represent the geometrical properties of the structure (refs. 1 and 2). In such electrical analogs voltages throughout the network represent velocities in the structure and currents represent forces. Electronic equipment is used to produce currents which depend on voltages in the electrical system in the same manner in which aerodynamic forces depend upon the velocities of the airfoil.

The composite electrical structure can be regarded as an electrical model of the aircraft in the same manner that a wind-tunnel model would be regarded as a structural model. The advantage of this approach lies in the relative ease with which one can alter the properties of the model, thus performing flutter computations with great rapidity. It should be emphasized that the normal modes of the structure are not used as tools or elements in the analysis. The analysis consists, in fact, in observing the behavior of an electrical model of an aircraft in flight.

That behavior which is most readily observed is the transient response to a sudden disturbance. This method is therefore similar to the testing technique which is ordinarily used for wind-tunnel models. An advantage of the electrical method is that tuned pulses may be used so that separation of two or more nearly unstable or slightly unstable modes of oscillation is more readily accomplished. Basic recorded data consist of the logarithmic decrement of the response and the frequency of oscillation. Flutter speed and frequency for any configuration are ordinarily found by computing the damping g and frequency f for specific values of velocity and interpolating to find the frequency and speed at which g is zero.

APPROXIMATIONS FOR SIMPLIFYING FLUTTER ANALYSIS

STRUCTURAL REPRESENTATION

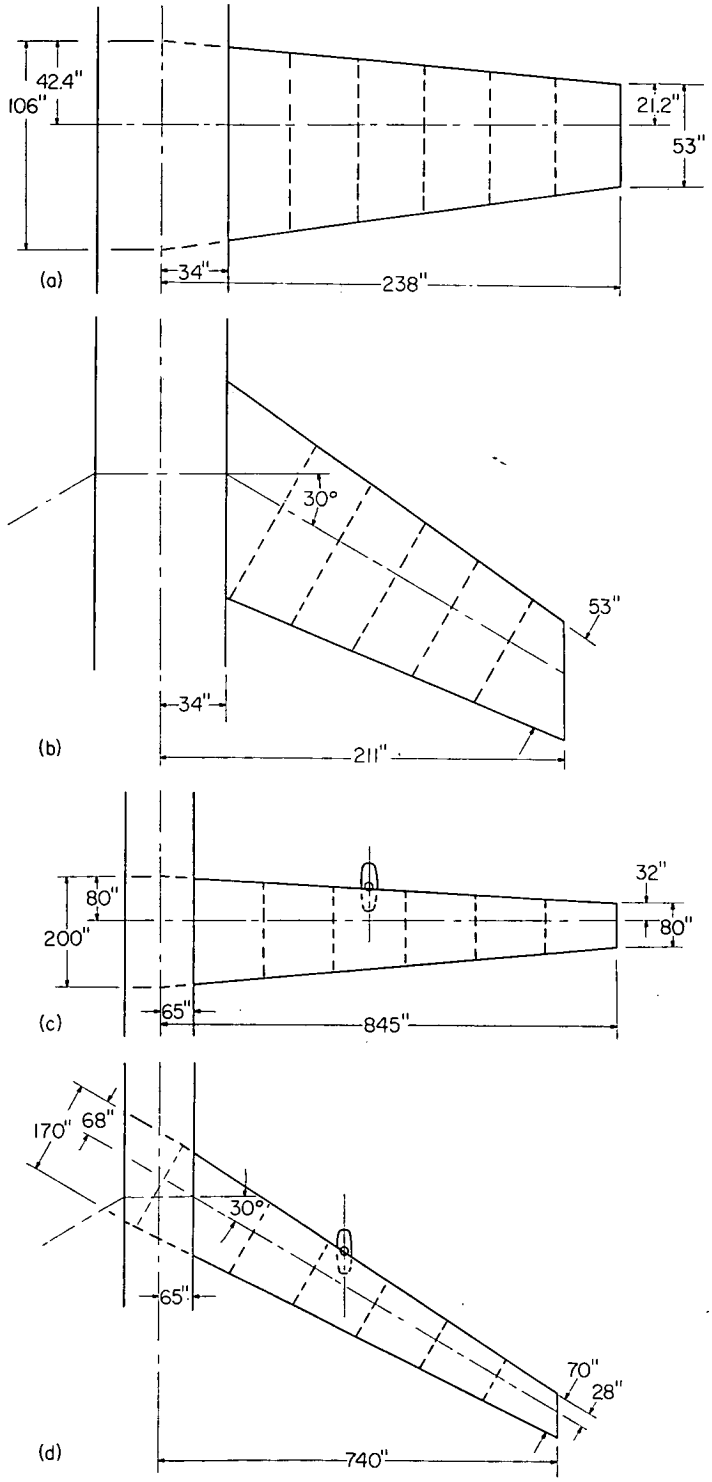
For dynamic analysis of airplane wings of large aspect ratio, it is customary to treat the wing as a beamlike structure in both vertical bending and torsion. It is usually assumed for simplicity that an elastic axis exists. For an unswept wing this is a straight line which undergoes no vertical displacement when the wing is subjected to a pure torque parallel to this axis and along which no twisting gradient exists when vertical loads are applied anywhere along this line. For an unswept wing of conventional construction this simplification is usually quite accurate. For a swept wing an elastic axis may be defined as a straight line which assumes a constant slope over its entire length when a twisting moment is applied parallel to this line and which has no twisting gradient when vertical loads are applied anywhere along this line. For aspect ratios greater than 5 or 6 and for conventional wing construction, a line can be found on the structure which satisfies this definition reasonably well except near the root. It is not uncommon to find an equivalent elastic axis at about the 35- or 40-percent chord, a line located aft of the leading edge a distance equal to 35 or 40 percent of the local chord.

The assumption of an elastic axis involves the tacit assumption that chordwise bending of the wing is negligible. It follows, then, that the motion of the wing at any spanwise coordinate can be described by two coordinates, the vertical displacement of some point on the chord, and the angle of twist of the chord. If wing motion is described in terms of vertical motion of the elastic axis and twisting motion about this line, then these motions are not coupled through the action of elastic forces in the wing except in the root region for a swept wing.

The root region of a swept wing is necessarily a relatively complicated structure. However, for aeroelastic problems an equivalent simple structure can be found which is completely satisfactory for wings of large aspect ratio. This can be demonstrated by the following reasoning. The outer sections of a wing exhibit definite beamlike properties, but in the region of the root considerable warping of the wing surface must take place. The aerodynamic forces near the root of the wing are therefore not adequately described by strip theory (see discussion of strip theory under "Aerodynamic Forces"). In addition, the inertia effects of this section are not readily computed. However, the effects of the aerodynamic forces on the root section are insignificant for ordinary flutter computations. This has been demonstrated many times with the analog computer by removing the aerodynamic forces on the inboard cell of the finite-difference structure. The inertia forces are also insignificant compared with the elastic forces transmitted by the root section, and it is therefore possible to replace this section for purposes of analysis by a set of "influence coefficients" relating transmitted forces to displacement of an outer sec-

tion of the wing relative to the fuselage. It has been found that in some cases these influence coefficients resemble coefficients for a simple beam extending straight into the fuselage and attaching there in some simple way. The wing structural axis then consists of a short section which may be perpendicular to the fuselage center line and which is simply attached to a swept back elastic axis which extends to the wing tip.

Methods for determining the equivalent structure are outside the scope of this report. Since this structure varies greatly with the particular wing construction used, it was necessary to choose a simple though typical root structure for this study. The structure chosen is illustrated in figure 3 where the elastic axes are shown by broken lines. The break in the elastic axis is assumed to be at the edge of the fuselage, and the axis inside the fuselage is assumed to be straight and perpendicular to the airplane center line. The wing is assumed to be pinned at the side of the fuselage. Consequently, all twisting moment is removed at this point and it is not necessary to make any assumptions regarding twisting rigidity inside the fuselage. Bending rigidity inside the fuselage is, however, important for symmetric motion. During the past 6 years extensive flutter computations have been made with the electric-analog computer for commercial and military aircraft as well as for wind-tunnel models including those described in references 3 and 4. In all cases investigated, it has been found that relatively large variations in root conditions have a negligible effect on the flutter characteristics (in the sense described in the Introduction). Observed changes in damping were usually in the range $0<|\Delta g|<0.05$, which has very small effect on flutter speed unless the curve of g against velocity is very flat, near zero values of g. Needless to say, both symmetric and antisymmetric motion of the airplane must be permitted since the flutter characteristics for the two types of motion may be quite different.



(a) Fighter A. (b) Fighter B. (c) Bomber A. (d) Bomber B.

FIGURE 3.—Plan forms and cell division of basic airplane.

Fuselage stiffness and inertia properties usually have values such that an assumption of a rigid fuselage for symmetric motion alters the flutter characteristics little. For fighter planes the error introduced is negligible. For large bombers the change in flutter speed may be appreciable, but it does not alter the trends to be observed upon variation of wing properties. It has therefore been assumed in this study that the airplane fuselage is rigid. Tail-surface flexibility does not significantly affect wing flutter problems. A rigid tail surface with sufficient area to provide satisfactory static stability has therefore been assumed.

AERODYNAMIC FORCES

For all the flutter computations given in this report, the aerodynamic forces have been simplified by two important assumptions:

(1) The air flow is incompressible.

(2) If the airfoil is divided into strips perpendicular to the elastic axis, then the forces on each strip can be computed as a function of the normal component of the airstream velocity and the motion of that strip can be computed independently of the motion of adjacent strips.

The first assumption is not required by analog methods in general, but its use greatly increases the rapidity with which data can be obtained. Since the purpose of the study is not to obtain specific accurate flutter speeds but to study trends in flutter characteristics, this assumption does not seem unreasonable. With regard to the use of strip theory two assumptions are often found in the literature. In using the "airstream method" the wind is divided into strips parallel to the airstream, and the forces and moments on each strip are computed as though the wing were not swept and the air flow about the section were a two-dimensional incompressible flow. The aerodynamic coefficients may be taken

to be the same as those for an unswept wing or may be modified by a factor cos Λ. In applying the "normal-component method," the wing is divided into strips perpendicular to the elastic axis. The aerodynamic forces and moments are computed as though the effective air velocity were the normal component v cos Λ, and the forces depend only on the motion of the individual strip and not upon the motion of adjacent strips (except that some small terms may be included which are proportional to the twisting gradient and therefore dependent upon the motion of the nearest strips). A critical discussion of the two alternatives is given in reference 5. This reference recommends use of the normal-component method.

Before adopting the second assumption, an effort was made to find some correlation with experimental results. Reference 3 contains experimental flutter speeds for a wind-tunnel model wing with sweepback angle equal to about 35°. This angle is sufficient to give an appreciable difference in results obtained with the various assumptions mentioned above. The section entitled "Finite-Difference Errors" in the present report contains the results of computations which show that the normal-component method gives results which are as satisfactory as those given by any other method used.

Equations for determining the aerodynamic forces by this method are given in reference 5. In the equations given there, several terms are found whose theoretical justification is not well established. These terms (grouped in special brackets on p. 16 of ref. 5) were found to have negligible effect on sample flutter computations. It seems reasonable, therefore, to omit these terms from computations involved in the present trend study. With these omissions and with obvious changes to conform to the symbols and notation used in the present report, the equations are:

$$P=P_1+P_2+P_3$$

$$M_\alpha=M_1+M_2+M_3+M_4$$

$$P_1=-2\pi(q_n)(2b)C\left(\frac{bp}{v_n}\right)\left[\frac{\dot{h}}{v_n}+(\alpha+\theta\tan\Lambda)+\frac{x_2}{v_n}(\dot{\alpha}+\dot{\theta}\tan\Lambda)\right]$$

$$P_2=-2\pi(q_n)\left(\frac{b^2}{v_n}\right)(\dot{\alpha})$$

$$P_3=-\pi\rho b^2(\ddot{h}-x_o\alpha)$$

$$P_4=-2\pi(q_n)(2b)\left[C\left(\frac{bp}{v_n}\right)\left(-\frac{x_2}{v_n}\dot{\theta}+x_2\tau\right)+\frac{b}{v_n}(\dot{\theta}-x_o\dot{\tau})\right]\tan\Lambda$$

$$M_1=-x_1P_1$$

$$M_2=-x_1P_2$$

$$M_3=-2\pi(q_n)\left(\frac{b^3}{v_n}\right)(\dot{\alpha})$$

$$M_4=-\pi\rho b^2\left[\left(\frac{b^2}{8}+x_o^2\right)\alpha-x_o\ddot{h}\right]$$

$$M_5=2\pi(q_n)(b^2)\left[2\left(\frac{x_1}{b}\right)C\left(\frac{bp}{v_n}\right)\left(-\frac{x_2}{v_n}\dot{\theta}+x_2\tau\right)+\frac{b}{2}\tau+\frac{x_o}{v_n}\dot{\theta}-\left(\frac{b^2}{8}+x_o^2\right)\frac{\dot{\tau}}{v_n}\right]\tan\Lambda$$

The terms are grouped in the order shown for convenience in establishing analog circuits. The last term in P_1 is not found in the corresponding equation of reference 5. This term is removed (mathematically) by insertion of an equal but opposite term in P_4 and a similar term in M_5.

It is added to P_1 here because the circuits which generate the term $\alpha+\theta$ tan Λ also provide the term $(x_2/v_n)(\dot{\alpha}+\dot{\theta}$ tan Λ), the last part of which is not found in reference 5. As is pointed out below, this term has a negligible effect so that its inclusion is of no importance, but it is indicated in the expression for P_1 for the sake of completeness. It should be emphasized that the dynamic pressure q_n is based on v_n, where v_n is the velocity component normal to the elastic axis. The coordinates α and θ are both measured in elastic-axis coordinates. The symbolism $C(bp/v_n)$ is used to represent the Theodorsen or Wagner function. A short discussion of the interpretation of this symbolic representation can be found in reference 6.

All terms found above can be represented by simple analog circuits with the exception of P_4 and M_5. Examination of equations 6 and 7 of reference 5 shows that each term in P_4 and M_5 is similar to (if not equal to) a term found in the special brackets. Since the latter terms have been omitted, there seems to be no logical reason for retaining P_4 and M_5. Inasmuch as their inclusion greatly complicates the analog circuits, these terms were also omitted.

In addition to the finite-difference approximations and those contained in the assumptions of incompressible flow and strip theory, three other aerodynamic approximations should be mentioned. The first of these is the failure to modify aerodynamic forces at the wing tip. The delay in the growth of lift forces, as described by the Wagner or Theodorsen functions for two-dimensional flow, cannot apply near the tip. Indeed, both the delay in lift and the magnitude of the lift must go to zero at the tip. The extent of the error introduced depends upon the importance of tip forces in flutter computations. Insofar as their location is concerned, these forces are quite important, but, because of wing taper, the magnitude of the total force per unit length diminishes near the tip. Since wings of considerable taper are involved in this investigation, it is to be expected that the error will be relatively small. The second approximation is failure to compute aerodynamic forces properly at the root of a swept wing. As stated earlier, the error introduced by this approximation is negligible since the aerodynamic force for a large section of the wing root can be omitted entirely without an appreciable change in flutter speed. The third approximation is introduced by the necessity of computing the Wagner function (or the Theodorsen function) electrically. This function is computed using networks shown in reference 1 with an error no greater than 2 percent over the frequency range or time interval of interest.

FINITE-DIFFERENCE ERRORS

It is the purpose of this section to summarize work which was carried out at the Analysis Laboratory of the California Institute of Technology to determine finite-difference errors in flutter computations for several specific structures.

FINITE-DIFFERENCE STRUCTURES

No practical methods have been devised for representing general continuous structures with continuous electrical systems. The electric-analog computer utilizes lumped elec-

trical elements which can, in principle, be used only to construct analogs for lumped mechanical systems. However, as pointed out in references 1 and 2, it is possible to represent the dynamic characteristics of beamlike structures by a lumped structure based upon finite-difference approximations to partial differential equations. It is convenient to call this lumped system a finite-difference structure, whether it is a mechanical model or an electrical analog. These references outline the process by which inertia and stiffness properties and aerodynamic forces are averaged or replaced by single concentrated inertias, springs, or forces in the finite-difference structure.

It should be remarked, at this point, that the assumption of a finite-difference structure insures a finite number of flutter roots or exponential functions in the transient response, whereas the continuous structure has, in principle, an infinite number. Since the higher frequency roots have high damping, only the lower frequency roots are of interest. Two or three of these may, however, show essentially zero damping simultaneously at a given velocity, and it is sometimes necessary to determine the characteristics of several flutter roots. There is obviously a lower limit to the number of cells that must be used to obtain satisfactory accuracy, since each cell adds roughly two roots to the system.

There is little information in the literature which pertains to the accuracy with which such structures represent the continuous system. Reference 7 gives data for static-deflection and normal-mode characteristics of certain finite-difference structures but no information about accuracy of flutter computations.

Using equations for aerodynamic forces based on two-dimensional strip theory and linear incompressible fluid flow, several "exact solutions" have been obtained for flutter problems. Some of these are found in references 8 and 9. These solutions are exact in the sense that no further physical or mathematical simplifications are involved and the only errors are introduced by round-off errors in evaluating transcendental functions and infinite series. Solution of these same problems by use of finite-difference approximations to partial differential equations provides the most practical way of estimating finite-difference errors for other configurations for which exact solutions are not obtainable. It is true that, in all cases mentioned above, the airfoil has been assumed to have uniform spanwise properties and that in most practical cases the airfoil has a significant taper. On the other hand, reference 7 contains a study of the finite-difference errors in the deflection characteristics and normal-mode properties of both uniform and tapered beams. This study showed no unusual differences in these properties, and so it is assumed that the results obtained for flutter of uniform airfoils are typical of results that would be obtained for flutter of tapered airfoils.

UNIFORM AIRFOIL WITH PINNED ENDS

A uniform beam with pinned ends will support only sinusoidal modes in both bending and torsion. Flutter modes are also of sinusoidal shape and it is therefore possible to reduce the flutter problem to an eigenvalue problem which can be solved with a high degree of numerical accuracy. The finite-difference analogs for a pinned-pinned beam likewise will support only sinusoidal modes. It is possible therefore to get exact solutions for the finite-difference approximations to the continuous airfoil.

TABLE I.—PHYSICAL CHARACTERISTICS OF A PINNED-PINNED AIRFOIL

Length, in.	288
Half chord, b, in.	48
Mass per unit length, m, lb sec^2/sq in.	0.01035
Inertia per unit length, I, lb sec^2	5.176
Bending rigidity, EI, lb in.^{2}	1.412×10^9
Torsional rigidity, GJ, lb in.^{2}	6.87×10^8
x_1, in.	9.6
x_3, in.	−9.6
Air density, ρ, lb sec^2/in.^{4}	0.0845×10^{-6}

The airfoil chosen for this analysis is described in table I. For the continuous wing, the flutter speed and frequency were found to be $v_f=692$ miles per hour and $f_f=12.72$ cycles per second, respectively. Analysis of the finite-difference structure was carried out using eight-, four-, and two-cell divisions between the pinned ends. Results are given in table II and figure 4. For this particular case it is necessary to use more than four cells if flutter speed is to be obtained with less than 2-percent error. By use of symmetry conditions at the center of the beam it is necessary to use only half this number of cells with an electric-analog computer. Thus, use of two analog cells gives a theoretical error of about 2.2 percent, and use of four analog cells gives an error of only 0.6 percent.

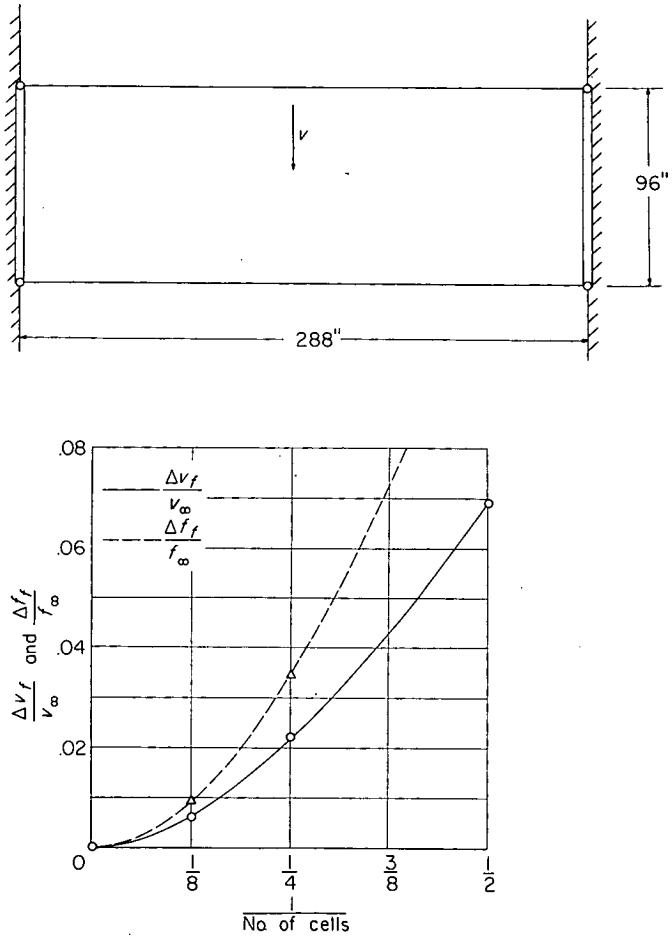


FIGURE 4.—Finite-difference flutter-speed errors of pinned-pinned beam.

TABLE II.—COMPUTED FLUTTER SPEED AND FREQUENCY OF FINITE-DIFFERENCE PINNED-PINNED AIRFOIL

Number of cells	v_f, mph	$\Delta v_f/v_\infty$	f_f, cps	$\Delta f_f/f_\infty$
∞	692	0	12. 7	0
8	688	. 006	12. 6	. 008
4	677	. 022	12. 3	. 032
2	644	. 069	11. 0	. 134

UNIFORM CANTILEVER WING WITH CONCENTRATED MASS

Analytical determination of the flutter speed of a cantilever wing is much more difficult than that for a beam with pinned ends. However, other investigators have obtained accurate numerical solutions for a few configurations. The most important of these is described in reference 9. This case is of importance for two reasons: It involves several spanwise positions of a large eccentric concentrated mass which greatly affects the flutter speed; and for some positions at least two completely different flutter roots can be found.

Table III presents the physical characteristics of the airfoil analyzed in reference 9. In this reference, the flutter speed and flutter frequency were computed for seven mass locations, data for which are reproduced in table IV. Since the location of a concentrated mass may be important in flutter analysis, and since all points on a finite-difference beam are not equally suitable as an attachment point for a concentrated mass, it was believed that a comparison of the above data with finite-difference solutions was quite important. Unfortunately, similar accurate solutions for a finite-difference structure are not readily obtained, so it was necessary to use the electric-analog computer to obtain these solutions. The resulting comparison therefore contains both finite-difference and analog-computer errors. Previous work has indicated that the latter are probably not greater than 1 percent if the Theodorsen function is represented accurately.

TABLE III.—PHYSICAL CHARACTERISTICS OF UNIFORM CANTILEVER WING

Half chord, b, in.	4
Span, l, in.	48
Mass per unit length, m, lb sec^2/sq in.	1.877×10^{-4}
Pitching inertia per unit length, lb sec^2	8.00×10^{-4}
Flexural rigidity, EI, (lb) (sq in.)	1.407×10^{5}
Torsional rigidity, GJ, (lb) (sq in.)	0.692×10^{5}
Elastic-axis position, x_o, in.	−0. 504
Center-of-mass position, x_3, in.	0. 156
Mass of concentrated mass, m_c, lb sec^2/in.	8.23×10^{-3}
Pitch inertia of concentrated mass, lb sec^2/in.	0. 1636
Center of mass of concentrated mass, $(x_3)_c$, in.	−3. 274
Air density, ρ, lb sec^2/in.^{4}	1.155×10^{-7}

In this analysis two slightly different beam analogs were used. In both, the beamlike properties were represented by a system of levers (transformers), but in one group the lumped forces were applied at the junctions of the levers and in the second group the forces were applied at the midpoints of the levers. The analog of the second group was once thought to give a better approximation since it resembles the Russell beam analog discussed in reference 7. Recent investigation has shown that this belief is without foundation, and the second analog is now preferred only as a matter of convenience for sweptback wings since it provides the wing slope directly at the force stations where it is needed for computation of aerodynamic forces. In both cases the cantilever condition at the root was provided by a half cell at the root, and the forces nearest the tip were applied one-half cell from the tip. Thus the first group involved an integral number of cells, and the second group involved a half integral (integer plus one-half) number of cells. Five cases were investigated; 2, 2½, 4, 5½, and 6 cells. Since it was shown in the previous section that less than 4 cells was of no interest for present purposes, only the results of 4, 5½, and 6 cells are presented in this report.

TABLE IV.—THEORETICAL AND EXPERIMENTAL FLUTTER CHARACTERISTICS OF CANTILEVER WING WITH CONCENTRATED MASS

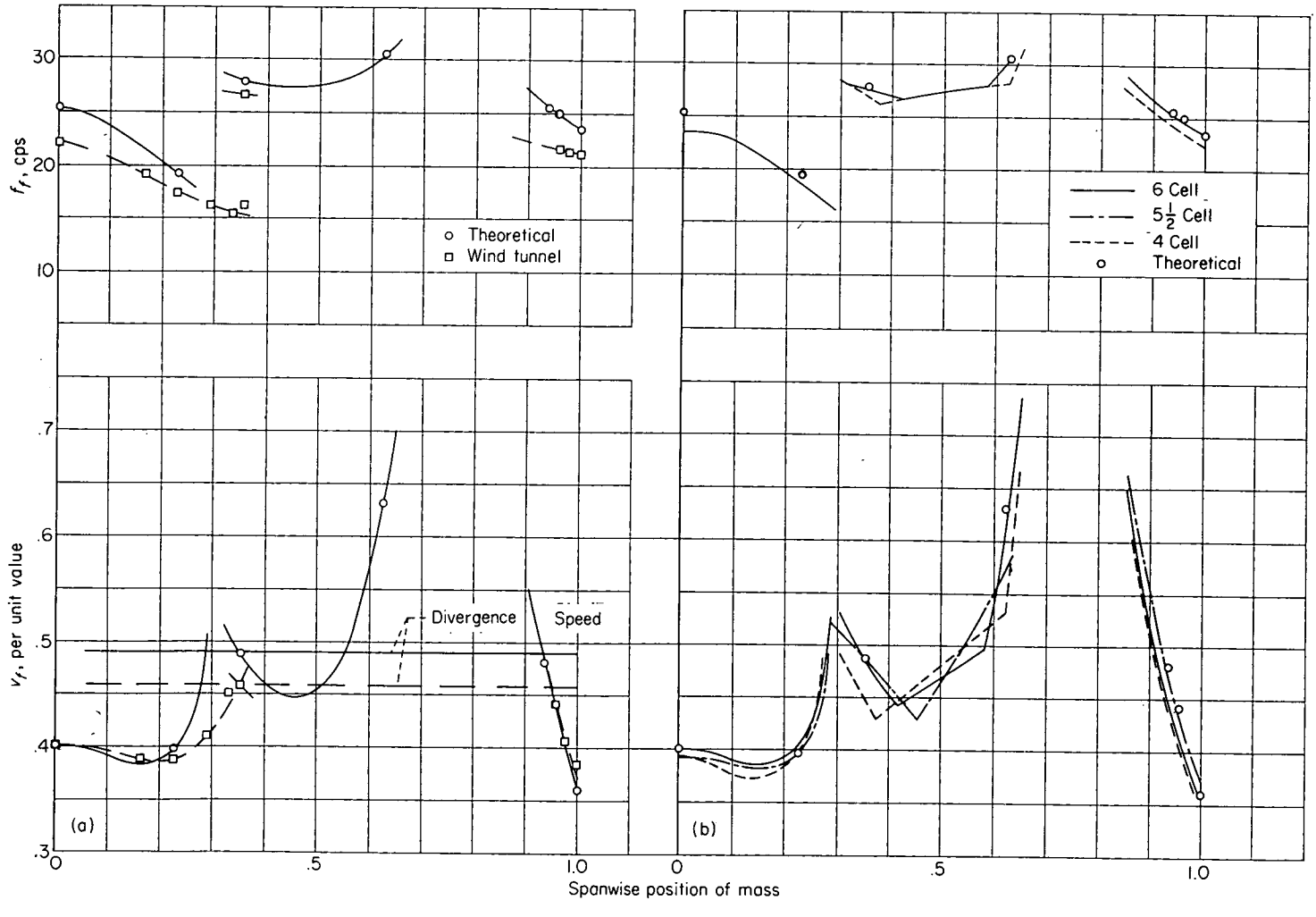
[Data taken from references 9 and 11]

Mass location, per unit span	Calculated			Experimental		
	v_f, mph	v_f, per unit [a]	f_f, cps	v_f, mph	v_f, per unit, [a]	f_f, cps
0	227	0. 400	25. 27	228	0. 401	22. 1
. 167	------	------	------	221	. 388	19. 1
. 229	226	. 397	19. 23	221	. 388	17. 4
. 292	------	------	------	233	. 410	16. 3
. 333	------	------	------	256	. 451	15. 5
. 354	277	. 488	28. 04	260	. 458	[b] 16. 3-26. 8
. 625	[c] 359	. 631	30. 68	-----	------	[d]
. 938	273	. 481	25. 67	261	. 459	[d]
. 959	251	. 442	24. 87	251	. 442	21. 8
. 979	------	------	------	231	. 407	21. 6
1. 000	205	. 360	23. 60	218	. 384	21. 4

[a] 1.0 per unit velocity is 10^4 in./sec or 568 mph.
[b] This experimental record seems to show nearly simultaneous divergence and flutter at two frequencies.
[c] Calculated divergence speed is about 279 mph. However, a flutter speed can still be calculated mathematically.
[d] Divergence was observed experimentally.

In view of the simplicity of the flutter curves shown in reference 9, it was expected that data would be taken at only a few spanwise mass locations. However, it was soon found that the flutter characteristics were much more complicated than anticipated, and data were taken at 24 mass locations in the 6-cell case. The flutter characteristics of the wing with variable location of the concentrated mass are sketched in figure 5 (a). As the concentrated mass is moved outward from the root, the flutter speed drops slightly. At a distance about 16 percent of the total span from the root a minimum is reached, and beyond the 25-percent position the flutter speed rises very rapidly. At the 30-percent position the flutter speed for this root has become equal to the flutter speed of a completely different root. The flutter speed for this second root drops with increasing spanwise position of the mass making it impossible to determine with the analog computer the speed for the original root beyond the 30-percent position. The flutter speed for the second root reaches a minimum with the mass at the 45-percent position, then rises to a very high value as the mass is moved toward the 75-percent position. A flutter root which is probably the second is observed for mass positions near the tip, the lowest flutter speed occurring with mass at the tip. It was also observed that divergence of the wing occurred whenever the flutter speed exceeded about 5,000 inches per second. Because of divergence, it was not possible to measure with accuracy flutter speeds which exceeded divergence speed by more than about 50 percent. As a result, flutter speeds with mass near the 75-percent span could not be measured.

The flutter characteristics for the 4-, $5\frac{1}{2}$-, and 6-cell structures are shown in table V and figure 5 (b). Data for the seven positions analyzed in reference 9 are also plotted in the figure. Inspection of these curves shows that many more accurate numerical solutions are required to determine the finite-difference errors for all mass positions. In spite of the inadequate numerical data, an attempt was made to draw a smooth curve through the known points taken from reference 9. In doing this the $5\frac{1}{2}$- and 6-cell analog data were used as a guide in determining the shape of the curve. This curve, shown in figure 5(a), has already been discussed. It is realized that a significant error of as much as 2 or 3 percent may exist in this curve for some mass positions, but there was no other method for obtaining estimated errors for the finite-difference structures. With the understanding that the comparison data may be in error in some regions, figure 6



(a) Theoretical and wind-tunnel flutter characteristics.
(b) Flutter characteristics of finite-difference analog.

FIGURE 5.—Flutter characteristics of uniform cantilever wing with concentrated mass.

TABLE V.—FLUTTER CHARACTERISTICS OF FINITE-DIFFERENCE ANALOG OF UNIFORM CANTILEVER WING

Mass position [a]	v_f, mph	v_f, per unit [b]	f_f, cps
4 cell			
0	224	0. 394	23. 9
. 125	212	. 373	----
. 150	213	. 374	----
. 225	225	. 396	18. 9
. 250	241	. 424	18. 1
. 275	275	. 484	----
. 325	269	. 473	27. 7
. 350	258	. 454	27. 2
. 375	245	. 431	26. 3
. 500	273	. 480	27. 6
. 600	297	. 522	28. 2
. 625	303	. 533	28. 4
. 650	376	. 661	31. 4
. 875	327	. 576	26. 7
. 950	237	. 417	24. 0
1. 000	197	. 346	22. 4
5½ cell			
0	223	0. 392	23. 8
. 182	218	. 383	20. 3
. 236	227	. 399	18. 6
. 254	236	. 415	17. 8
. 273	249	. 439	17. 3
. 291	295	. 520	28. 5
. 309	289	. 508	28. 0
. 328	284	. 500	28. 3
. 364	274	. 482	27. 9
. 454	244	. 430	27. 2
. 546	284	. 500	28. 3
. 600	313	. 550	29. 7
. 636	333	. 586	30. 7
. 855	377	. 664	29. 4
. 909	305	. 537	27. 0
. 946	258	. 454	25. 5
1. 000	212	. 373	23. 9
6 cell			
0	228	0. 401	23. 7
. 083	223	. 393	23. 3
. 167	219	. 386	20. 8
. 217	226	. 398	18. 7
. 250	239	. 420	18. 0
. 267	255	. 448	17. 1
. 284	286	. 504	16. 7
. 317	296	. 521	28. 2
. 367	270	. 476	27. 5
. 417	252	. 443	26. 8
. 450	258	. 454	27. 2
. 500	266	. 468	27. 6
. 550	277	. 487	27. 8
. 583	282	. 496	28. 2
. 600	306	. 539	28. 9
. 616	334	. 588	30. 1
. 667	≈477	≈. 840	----
. 868	349	. 614	28. 4
. 883	319	. 562	27. 4
. 917	276	. 486	26. 3
. 950	242	. 426	25. 1
. 965	226	. 398	24. 6
. 984	213	. 375	24. 2
1. 000	201	. 353	23. 6

[a] Mass position is per unit span measured from root.
[b] 1.0 per unit velocity=568 mph.

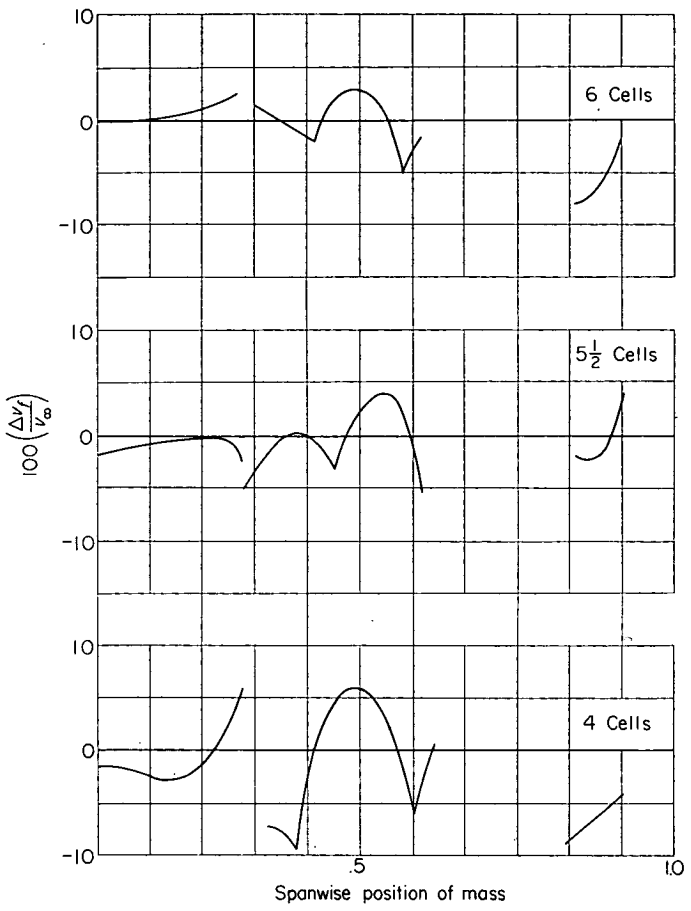


FIGURE 6.—Flutter-speed errors of finite-difference analog of uniform cantilever wing with concentrated mass.

was prepared showing the percentage error in flutter speed for the various analogs as functions of the mass location. For 5½- and 6-cell structures the average errors are about 2 percent. It can be readily seen that, although a 4-cell analog gives very satisfactory results for the bare wing (mass position 0), it is necessary to use more than 4 cells if errors less than 5 percent are required at other mass locations. A further discussion of this investigation will be found in reference 10.

As a result of this analysis, it was decided that all flutter computations made in this trend study would be made using 6½ cells to represent one-half of the airplane wing.

EXPERIMENTAL CORRELATION

Wind-tunnel tests have been made of many model structures. It is difficult, however, to find unclassified data in which the structure is completely and accurately described. In the course of this investigation, two cases were found in which a correlation between experimental and computed characteristics could be attempted. The first of these is the uniform unswept cantilever wing discussed in the preceding section. The flutter speed and frequency observed in a wind tunnel are reported in reference 9 and a companion report, reference 11. These data are summarized in table IV, which also contains the computed values of reference 9. A better understanding of the correlation is obtained if the experimental data are plotted with the assumed analytic solution. Figure 5 (a) shows such a comparison. The correlation for this case seems unusually good.

FLUTTER SPEED OF A SWEPT-WING MODEL

The second case for which correlation with experiment is possible is found in reference 3. This reference gives results of wind-tunnel tests to determine the flutter speed of a model wing with sweepback angle equal to 34.5°. This wing had two concentrated masses attached at approximately the 30- and 80-percent span positions. In an effort to compare the airstream and normal-component aerodynamics for flutter computations, an electrical analog was constructed for this wing. For any sweepback angle it is to be expected that the two methods will give flutter speeds differing by a factor of approximately $(\cos \Lambda)^{1/2}$, unless the aerodynamic coefficients are modified by the factor cos Λ in the airstream method, in which case the two methods should give similar results. The principal difficulty encountered was determination of the properties of the concentrated masses on the wing, since reference 3 does not give complete information about these masses and their geometrical location. The best data that could be deduced from this report are given in table VI. Since the masses are alined with the airstream but are represented in elastic-axis coordinates, a product of inertia between roll and pitch exists. Since no such information was available, the product of inertia was omitted from computations, and the rolling inertia about a chord line was assumed to be one-half as large as the pitching inertia about the elastic axis. It is believed that these approximations and simplifications will affect the results by less than 1 percent.

A comparison of observed and computed characteristics is given in table VII. The first three normal-mode frequencies show satisfactory agreement, with differences of 1, 5, and 3 percent, respectively. The flutter speed computed with either representation of aerodynamic forces is lower than the wind-tunnel value. In the case of the airstream method, the discrepancy is 19 percent, or, if the aerodynamic coefficients are modified, 11 percent. Using the normal-component method, the discrepancy is 12 percent. Flutter frequency is in error about 20 percent in all cases. Although the observed differences are relatively large in all cases, it is concluded that the normal-component method recommended in reference 5 is satisfactory for this model.

CHARACTERISTICS OF FOUR REPRESENTATIVE AIRCRAFT

Plan forms and stiffness and inertia data were chosen after surveying the various fighter, bomber, and transport planes developed in recent years. Four representative airplanes were chosen, two fighters and two large bombers. Smaller attack bombers and transports were not included because of lack of time. The airplanes chosen are not similar in all respects to any particular set of four airplanes, but they do have stiffness and inertia properties which resemble four specific aircraft. Plan form, sweepback angle, elastic-axis location, and concentrated-mass locations were, however, chosen more arbitrarily so that this report could remain unclassified. The four basic plan forms are shown in figure 3. The basic fighter A has a bare unswept wing with span of about 500 inches, taper ratio of 2.0, and aspect ratio 6. The basic fighter B has a wing sweepback angle of 30°, a span of about 400 inches, and a taper ratio of 2.0. The two basic wings have the same length measured along the elastic axis and the same chords measured perpendicular to the elastic axis.

TABLE VI.—PHYSICAL CHARACTERISTICS OF SWEPTBACK WING WITH CONCENTRATED MASS

[Data taken from reference 3; more detailed information will be found in this reference. Mass of wing is for portion outboard of root restraint. Data for concentrated masses are not given explicitly in reference 3 and must be regarded as only approximate.]

Wing characteristics:		
[a] Span, in.		48. 3
[b] Root half chord, b_r, in.		5. 2
[b] Tip half chord, b_x, in.		2. 36
Wing total mass, m_w, lb sec²/in.		0. 00784
Tunnel fluid density, ρ, lb sec²/in.⁴		3.40×10^{-7}
Sweepback angle, Λ, deg		34. 5
Concentrated-mass characteristics:	Inboard	Outboard
Mass, m_c, lb sec²/in.	0. 00806	0. 00452
Pitch inertia about elastic axis, lb sec²/in.	0. 0712	0. 0192
Per unit spanwise position (from root)	0. 30	0. 78
Center-of-mass position, $(x_3)_c$, in.	−1. 74	0. 50

[a] Measured along elastic axis.
[b] Measured perpendicular to elastic axis.

TABLE VII.—EXPERIMENTAL AND COMPUTED FLUTTER CHARACTERISTICS OF SWEPTBACK WING WITH CONCENTRATED MASS

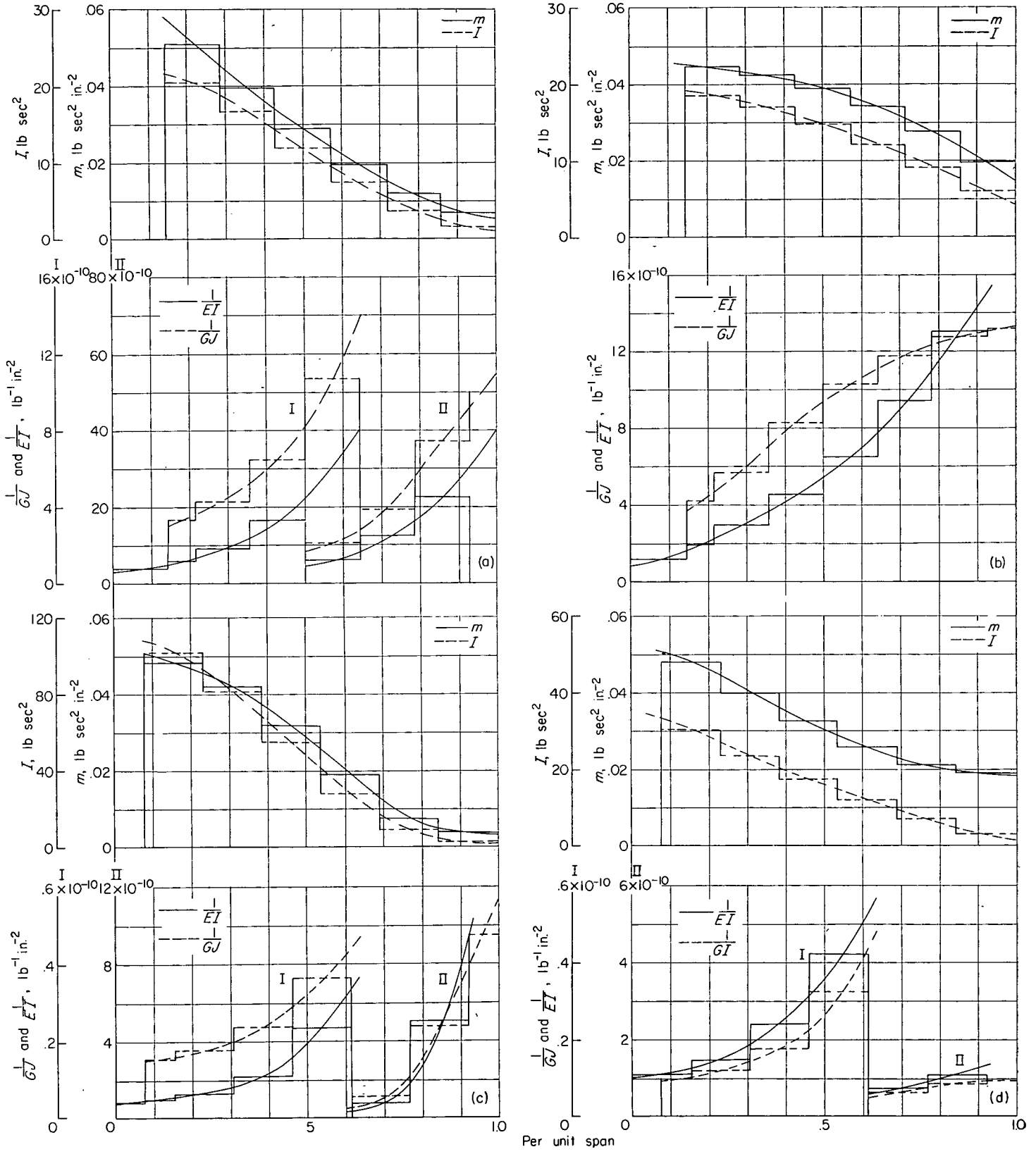
Type of frequency	Normal mode frequencies, cps, at—		
	Mode 1	Mode 2	Mode 3
Experimental model frequency	6. 97	30. 9	37. 9
Measured analog frequency	6. 91	32. 6	39. 1

Type of result	Flutter characteristics		
	v_f, mph	$\Delta v_f/v_{f_e}$	f_f, cps
Wind-tunnel results, v_{f_e}	193	0	20. 1
Analog results, normal-component method	170	−. 12	24. 2
Analog results, airstream method [a]	157	−. 19	24. 0
Analog results, airstream method [b]	173	−. 11	24. 0

[a] Lift coefficient $C_{L_\alpha}=2\pi$.
[b] Lift coefficient $C_{L_\alpha}=2\pi \cos \Lambda$.

The basic bomber A has an unswept wing with span of about 1,700 inches, taper ratio of 2.5, and aspect ratio 12. It has a concentrated mass representing an engine nacelle at the 0.46-span position with center of mass about one-half chord forward of the elastic axis. The basic bomber B has a wing sweepback angle of 30°, a span of about 1,500 inches, and a taper ratio of 2.4. It also has a concentrated mass representing an engine nacelle at the same relative position as for bomber A. The two basic wings have the same length measured along the elastic axis and approximately equal chords when measured parallel to the airstream.

Mass per unit length, pitch inertia per unit length, bending rigidity, and torsional rigidity were drawn as smooth curves approximating the characteristics of some typical modern aircraft. As described in reference 2, these data must be collected or lumped over distances corresponding to the cell length of the analog finite-difference structure. The assumed curves and the lumped values are shown in figure 7.



(a) Basic fighter A.
(b) Basic fighter B.
(c) Basic bomber A.
(d) Basic bomber B.

FIGURE 7.—Inertia and stiffness properties of wing.

The lumped values are also listed in tables VIII to XI, which give all pertinent characteristics of the basic airplanes.

Eight important parameters of the basic airplane wings were varied in an effort to find similar features in the flutter characteristics of the various wings. The quantities varied and the extent of their variation are summarized as follows:

Quantity varied	Minimum value	Maximum value
Wing mass density, per unit basic	0. 5	2. 0
Wing pitch inertia, per unit basic	0. 5	2. 0
Bending rigidity, per unit basic	0. 67	1. 5
Torsional rigidity, per unit basic	0. 67	1. 5
Center-of-mass location, percent chord	25	60
Elastic-axis location, percent chord	30	50
Chord, per unit basic	0. 67	1. 5
Sweepback angle, deg	0	45

With the exception of sweepback angle, these quantities were varied one at a time from their basic value. However, for all four basic airplanes, some or all of the parameters were varied for two or three values of sweepback angle. It is realized that the above variations do not constitute a comprehensive survey. However, to a considerable extent the changes in flutter speed due to several variations are additive if the variations are small and are made simultaneously. Another limitation is that the flutter characteristics are affected by the spanwise variation in the first seven

TABLE VIII.—CHARACTERISTICS OF BASIC FIGHTER A

(a) Physical characteristics

Sweepback angle, Λ, deg	0
Semispan of wing,[a] l, in.	238
Cell size for finite-difference structure, Δy, in.	34
Root chord,[b] b_r, in.	106
Tip chord,[b] b_x, in.	53
Taper ratio	2. 00
Aspect ratio	6
Wing elastic axis, percent chord	40
Wing center of mass, percent chord	40
Total wing mass external of fuselage, m_{w_f}, lb sec^2/in.	10. 7
Fuselage mass, m_f, lb sec^2/in.	21
Fuselage radius of gyration, pitch,[c] in.	100
Fuselage radius of gyration, roll, in.	25
Fuselage center of mass aft of elastic axis, in.	0
Tail center of pressure aft of elastic axis, in.	230
Tail area, sq in.	3, 000
Air density, ρ, lb sec^2/in.^{4}	1. 146$\times 10^{-7}$

(b) Inertia and stiffness values lumped for finite-difference structure

Station	1	2	3	4	5	6
Per unit span [a]	0. 214	0. 357	0. 500	0. 643	0. 786	0. 928
Half chord,[b] b, in.	47. 3	43. 5	39. 8	36. 0	32. 2	28. 4
Lumped mass, $\overline{m}$, lb sec^2/in.	1. 73	1. 34	0. 98	0. 66	0. 40	0. 23
Lumped pitch inertia	695	568	405	253	126	53
[d] $10^{10}\int(dy/EI)$	19. 8	61. 3	112	205	415	773
[d] $10^{10}\int(dy/GJ)$	56. 3	145	219	365	667	1, 260	850

[a] Measured along elastic axis.
[b] Measured perpendicular to elastic axis.
[c] About elastic axis.
[d] Stiffness values are lumped between mass stations.

TABLE IX.—CHARACTERISTICS OF BASIC FIGHTER B

(a) Physical characteristics

Sweepback angle, Λ, deg	30
Semispan of wing,[a] l, in.	238
Cell size for finite-difference structure, Δy, in.	34
Root chord,[b] b_r, in.	106
Tip chord,[b] b_x, in.	53
Taper ratio	2. 00
Wing elastic axis, percent chord	40
Wing center of mass, percent chord	40
Total wing mass external of fuselage, m_{w_f}, lb sec^2/in.	14. 06
Fuselage mass, m_f, lb sec^2/in.	21
Fuselage radius of gyration, pitch,[c] in.	100
Fuselage radius of gyration, roll, in.	25
Fuselage center of mass aft of elastic axis, in.	0
Tail center of pressure aft of elastic axis, in.	230
Tail area, sq in.	3, 000
Air density, ρ, lb sec^2/in.^{4}	1. 146$\times 10^{-7}$

(b) Inertia and stiffness values lumped for finite-difference structure

Station	1	2	3	4	5	6
Per unit span [a]	0. 214	0. 357	0. 500	0. 643	0. 786	0. 928
Half chord,[b] b, in.	47. 3	43. 5	39. 8	36. 0	32. 2	28. 4
Lumped mass, $\overline{m}$, lb sec^2/in.	1. 52	1. 43	1. 32	1. 16	0. 94	0. 66
Lumped pitch inertia	628	577	503	411	310	204
[d] $10^{10}\int(dy/EI)$	33. 0	100	156	221	321	447
[d] $10^{10}\int(dy/GJ)$	71. 4	193	283	551	400	436	224

[a] Measured along elastic axis.
[b] Measured perpendicular to elastic axis.
[c] About elastic axis.
[d] Stiffness values are lumped between mass stations.

quantities listed. The four basic cases, two fighter and two bomber airplanes, can be regarded as four cases in which spanwise variations have been made. However, since five or six of the quantities are varied in going from one case to another, it is not possible to determine the effect of spanwise variation of only one of the parameters. Other quantities which were thought to have second-order effects were not considered. Among these are altitude (represented by ratio of air density to wing mass), fuselage mass and pitching inertia, and tail configuration. This does not imply that flutter velocity is independent of altitude, but with very minor variations the flutter velocity varies inversely as the square root of the air density. Sea-level air density was used throughout this study.

It is improbable that bombers of the plan form and size studied will be flown without engines on the wing. Consequently, the basic cases of interest are those in which a concentrated mass is located there. On the other hand, it is of some interest to compare the characteristics of the bare wing as well as those of a wing with concentrated mass. Both bombers A and B were studied with bare wing as well as with concentrated mass in the basic position on the wing.

For purpose of reference it is necessary to assign a number to designate each particular case. The group discussed above comprises 175 cases. The assignment of case numbers is shown in table XII. This table shows most rapidly the various cases that were studied.

TABLE X.—CHARACTERISTICS OF BASIC BOMBER A

(a) Physical characteristics

Sweepback angle, Λ, deg	0
Semispan of wing,[a] l, in.	845
Cell size for finite-difference structure, Δy, in.	130
Root chord,[b] b_r, in.	200
Tip chord,[b] b_x, in.	80
Taper ratio	2. 50
Aspect ratio	12
Wing elastic axis, percent chord	40
Wing center of mass, percent chord	40
Total wing mass external of fuselage, m_{wf}, lb sec²/in.	39. 7
Fuselage mass, m_f, lb sec²/in.	120
Fuselage radius of gyration—pitch,[c] in.	240
Fuselage radius of gyration—roll, in.	50
Fuselage center of mass aft of elastic axis, in.	0
Tail center of pressure aft of elastic axis, in.	700
Tail area, sq in.	20, 000
Air density, ρ, lb sec²/in.⁴	1.146×10^{-7}

(b) Inertia and stiffness values lumped for finite-difference structure

Station	1	2	3	4	5	6	
Per unit span,[a]	0. 154	0. 308	0. 461	0. 615	0. 769	0. 923	
Half chord,[b] b, in.	90. 8	81. 5	72. 3	63. 1	53. 9	44. 6	
Lumped mass, $\overline{m}$, lb sec²/in.	6. 28	5. 46	4. 16	2. 47	0. 98	0. 50	
Lumped pitch intertia	13, 300	10, 600	7, 150	3, 640	1, 170	360	
[d] $10^{10}\int(dy/EI)$	3. 3	8. 4	14. 3	30. 5	101	650	----
[d] $10^{10}\int(dy/GJ)$	10. 0	23. 1	30. 9	47. 5	143	618	618

[a] Measured along elastic axis.
[b] Measured perpendicular to elastic axis.
[c] About elastic axis.
[d] Stiffness values are lumped between mass stations.

Concentrated masses on fighter wings usually consist of fuel tanks, bombs, or similar stores. It is impossible, therefore, to select a single value for mass and inertia which can be regarded as typical. For certain positions many values for mass and inertia were chosen, although in most of the cases studied the number of values was restricted by the time available for computations. For reference purposes, the basic mass for fighter planes was arbitrarily chosen to be one-quarter of the mass of the entire wing (half of the mass of one side), the pitching radius of gyration was set equal to 30 inches, and the roll radius of gyration was assumed to be 15 inches or less. Specific data for the two fighters are listed in table XIII.

Concentrated masses for bomber airplanes are usually engine nacelles, with a mass which can be predicted within a factor of 2. Nevertheless, it is of some interest to study the effect of various mass values in these cases also. Basic mass value for both bombers was assumed to be 15 pounds-seconds squared per inch, which corresponds to a weight of nearly 6,000 pounds. Pitching radius of gyration was assumed to be 35 inches. Basic mass position was assumed to be at the 0.46-span position and 60 inches in front of the elastic axis. These data are also tabulated in table XIII.

The concentrated-mass characteristics varied in this study are:

(1) Mass
(2) Pitching inertia about center of mass
(3) Spanwise location
(4) Chordwise location
(5) Pitching flexibility

The assignment of case numbers is more difficult for this phase of the study. Although specific spanwise positions were chosen, it was not possible to choose chordwise positions beforehand. The chordwise positions were chosen as the data were obtained. In some cases more than 20 positions were used for a given spanwise location. Consequently, one case number was assigned to all chordwise variations at a given spanwise location. A summary of all variations with the corresponding case numbers is given in table XIV.

Pitching flexibility of the concentrated mass was varied in six cases involving both bombers. In all cases, the chordwise location of the center of mass was basic (table XIII). In three cases the mass was in basic spanwise position and in three cases the mass was at the tip. Case numbers are given in table XIV.

TABLE XI.—CHARACTERISTICS OF BASIC BOMBER B

(a) Physical characteristics

Sweepback angle, Λ, deg	30
Semispan of wing,[a] l, in.	845
Cell size for finite-difference structure, Δy, in.	130
Root chord,[b] b_r, in.	170
Tip chord, [b] b_x, in.	70
Taper ratio	2. 43
Wing elastic axis, percent chord	40
Wing center of mass, percent chord	40
Total wing mass external of fuselage, m_{wf}, lb sec²/in.	48. 7
Fuselage mass, m_f, lb sec²/in.	120
Fuselage radius of gyration, pitch,[c] in.	240
Fuselage radius of gyration, roll, in.	50
Fuselage center of mass aft of elastic axis, in.	150
Tail center of pressure aft of elastic axis, in.	700
Tail area, sq in.	20, 000
Air density, ρ, lb sec²/in.⁴	1.146×10^{-7}

(b) Inertia and stiffness values lumped for finite difference structure

Station	1	2	3	4	5	6	
Per unit span[a]	0. 154	0. 308	0. 461	0. 615	0. 769	0. 923	
Half chord,[b] b, in.	77. 3	69. 6	61. 9	54. 2	46. 5	38. 8	
Lumped mass, $\overline{m}$, lb sec²/in.	6. 28	5. 23	4. 26	3. 35	2. 74	2. 47	
Lumped pitch inertia	3, 940	3, 080	2, 200	1, 560	910	390	
[d] $10^{10}\int(dy/EI)$	7. 12	18. 8	31. 0	54. 9	91. 6	141. 0	----
[d] $10^{10}\int(dy/GJ)$	6. 31	15. 5	22. 6	42. 2	77. 8	110. 0	60

[a] Measured along elastic axis.
[b] Measured perpendicular to elastic axis.
[c] About elastic axis.
[d] Stiffness values are lumped between mass stations.

TRENDS IN FLUTTER CHARACTERISTICS

REFERENCE QUANTITIES AND GRAPHICAL PRESENTATION

Results of the study of trends in flutter characteristics which are listed in table XV are given in miles per hour

TABLE XII.—ASSIGNMENT OF CASE NUMBERS

Variable factor	Value or type	Case number of—												
		Fighter A; $\Lambda=0°$	Fighter A; $\Lambda=45°$	Fighter B; $\Lambda=0°$	Fighter B; $\Lambda=45°$	Bomber A; $\Lambda=0°$ [a]M	Bomber A; $\Lambda=30°$; [a]M	Bomber A; $\Lambda=0°$; [a]B	Bomber B; $\Lambda=30°$; [a]M	Bomber B; $\Lambda=0°$; [a]M	Bomber B; $\Lambda=45°$; [a]M	Bomber B; $\Lambda=30°$; [a]B	Bomber B; $\Lambda=0°$; [a]B	Bomber B; $\Lambda=45°$; [a]B
Basic		1	----	23	42	58	72	84	98	113	114	137	152	153
Mass factor	2	2	----	24	43	59	74	85	99	115	126	138	154	165
	1/2	3	----	25	44	60	75	86	100	116	127	139	155	166
Pitch inertia factor	2	4	----	26	45	61	76	87	101	117	128	140	156	167
	1/2	5	----	27	46	62	77	88	102	118	129	141	157	168
Bending rigidity factor	3/2	6	----	28	47	63	78	89	103	119	130	142	158	169
	2/3	7	----	29	48	64	79	90	104	120	131	143	159	170
Torsional rigidity factor	3/2	8	----	30	49	65	80	91	105	121	132	144	160	171
	2/3	9	----	31	50	66	81	92	106	122	133	145	161	172
Local stiffness variation		10	----	32	----	67	----	93	----	----	----	----	----	----
[b] Center of mass, percent	25	----	----	----	51	----	----	----	----	----	----	----	----	----
	32.5	----	20	----	52	----	----	----	----	----	----	----	----	----
	40	1	19	23	42	58	72	84	98	113	114	137	152	153
	45	11	----	33	53	68	----	94	107	123	134	146	162	173
	50	12	21	34	54	69	82	95	108	124	135	147	163	174
	60	13	22	35	55	70	83	96	109	125	136	148	164	175
[b] Elastic axis, percent	30	----	----	----	56	----	----	----	----	----	----	----	----	----
	35	----	----	36	----	----	----	----	----	----	----	----	----	----
	40	1	----	23	42	58	----	84	98	----	----	137	----	----
	50	14	----	37	57	71	----	97	110	----	----	149	----	----
Chord factor	3/2	15	----	38	----	----	----	----	111	----	----	150	----	----
	2/3	16	----	39	----	----	----	----	112	----	----	151	----	----
Sweepback angle, deg	0	1	----	23	23	58	58	----	113	113	113	152	152	152
	15	17	----	40	40	----	----	----	----	----	----	----	----	----
	30	18	----	41	41	72	72	----	98	98	98	137	137	137
	45	19	----	42	42	73	73	----	114	114	114	153	153	153
Nacelle pitch flexibility	Mass at station 3	----	----	----	----	176	----	----	178	177	----	----	----	----
	Mass at tip	----	----	----	----	179	----	----	181	180	----	----	----	----

[a] M, concentrated mass on wing; B, bare wing.

[b] Center of mass and elastic axis measured in percent chord from leading edge.

TABLE XIII.—CONCENTRATED-MASS CHARACTERISTICS AND LOCATIONS

(a) Characteristics

	Fighter	Bomber
Basic mass, lb sec²/in.	2. 68	15. 0
Pitch radius of gyration,[a] in.	30	35
	15	17. 5
	6	7
Roll radius of gyration, in.	15	------
	0	------
Basic spanwise position,[b] in.	------	390
Basic chordwise position,[c] in.	------	60

[a] About elastic axis; airstream coordinates.
[b] Outboard from center line measured along elastic axis.
[c] Forward of elastic axis, parallel to airstream.

(b) Location

Airplane	Locations of concentrated mass, per unit span,[a] at station—								
	1	2	3	4	4.5	5	5.5	6	Tip
Fighter	0. 214	0. 358	0. 500	0. 643	---	0. 786	---	0. 929	1. 00
Bomber	. 154	. 308	. 461	. 615	0. 692	. 769	0. 846	. 923	1. 00

[a] Distances are measured in per unit span along elastic axis.

and in per unit values of a reference speed. The reference velocity chosen is

$$v_o = 10^4 \text{ in./sec} = 568 \text{ mph}$$

Obviously a flutter speed of 1.5 would not represent a realistic value since this would correspond to supersonic speed with a Mach number of about 1.1. However, such a number still has useful significance for two reasons: (1) A major purpose of this study is to establish trends and to determine what configurations tend to be more or less stable than others, and (2) a change in stiffness is equivalent to a change in velocity, so that a structure with one-half the stiffness of another, but otherwise unchanged, would exhibit a flutter speed $1/\sqrt{2}$ times as great as that of the other, a value equal to 1.06 or 600 miles per hour in the case given above.

All geometrical, structural, and inertia quantities are given in per unit values. For example, distances are measured in units of the airplane semispan, and masses in terms of a basic value. Specific numerical values can be obtained using figure 3 which gives linear dimensions of the airplanes, figure 7 which gives inertia per unit length and rigidity values, and tables VIII to XI which list all other pertinent characteristics of the four basic airplanes. The density of air at sea level was used throughout these computations. The value chosen is:

$$\rho = 1.146 \times 10^{-7} \text{ lb sec}^2 \text{ in.}^{-4}$$

In presenting results graphically, flutter speeds have, in general, been reduced to dimensionless values by using the flutter speed of the basic configuration as the velocity unit. For example, when plotting antisymmetric flutter speed as a function of wing mass density for a particular wing such as that of fighter B with $\Lambda = 45°$, the flutter speeds have been divided by the antisymmetric flutter speed of fighter B, $\Lambda = 45°$, with basic wing mass. Symmetric and antisymmetric results are both presented, rather than choosing the one which gives lowest flutter speed. Where such results are presented in the same figure, symmetric results are generally indicated by solid lines, and antisymmetric results, by dotted lines. Specific numerical values for the flutter speeds and flutter frequencies are found in table XV.

MASS AND INERTIA VARIATIONS

In most practical configurations the normal mode of vibration with lowest frequency is predominantly a bending mode and is usually called the first wing bending mode. In the absence of a large concentrated mass on the wing, a predominant torsional motion is usually observed in the third or fourth mode. Simple flutter can often be predicted with engineering accuracy using only these two modes as the normal coordinates of the structure. When a large concentrated mass is involved, the situation is much more complex. Two or more torsion modes as well as two or more bending modes become important in flutter computations, and several flutter roots may be observed which predominantly involve various ones of these modes. For eccentric masses it becomes, in fact, impossible to speak of bending and torsion modes since many modes will involve both large bending and torsion displacements.

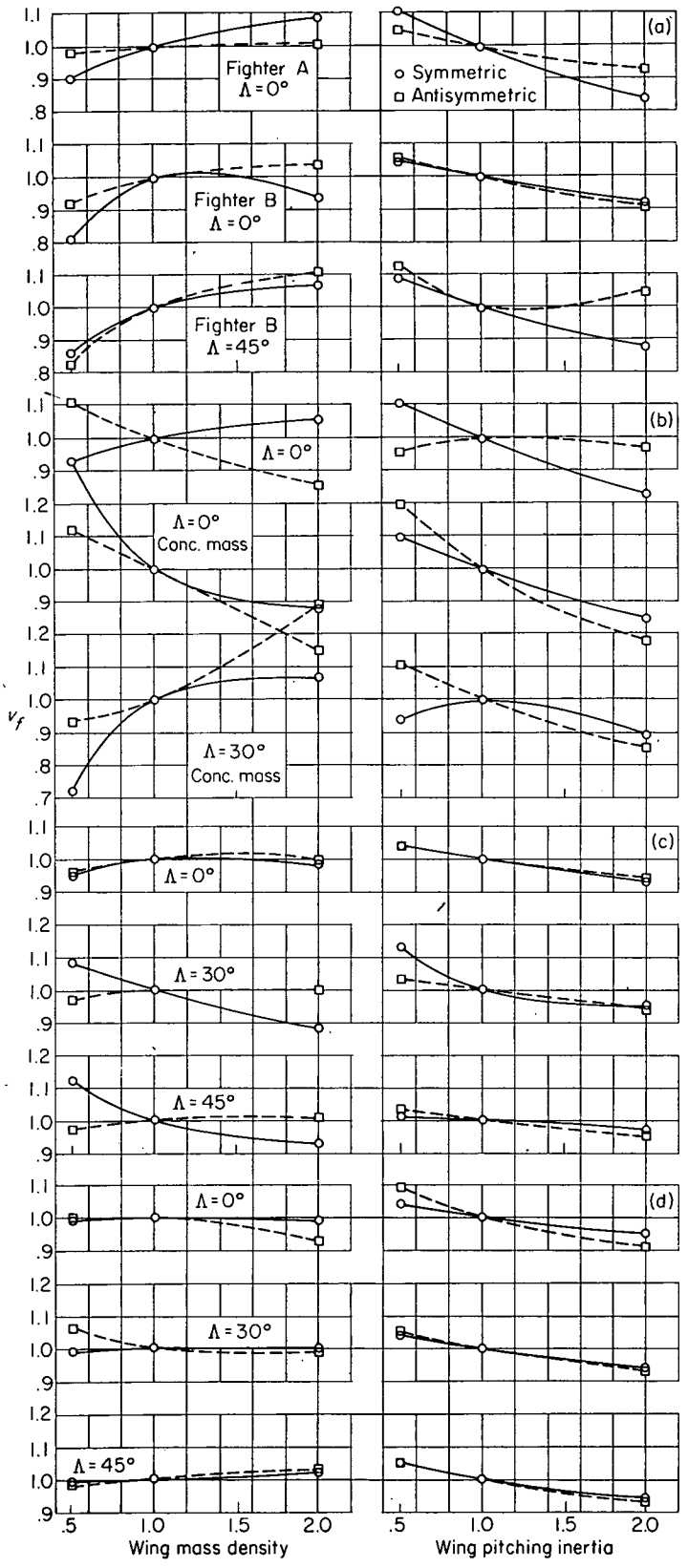
In those cases in which flutter involves a bending mode and a higher frequency torsion mode, it can be said that a structural change which separates the frequencies of these modes ordinarily raises the flutter speed, and a change which makes the frequencies more nearly equal lowers the flutter speed. This generalization is not always valid. A change in mass density without change in pitching inertia has greatest effect on first bending frequency even in cases with large sweepback. Consequently, increase in wing mass density would be expected to give an increase in flutter speed, and a decrease in mass density, a decrease in flutter speed. Changes in pitching inertia would normally be expected to have an opposite effect. Such variations were made for three fighter configurations, four bare-wing bomber configurations, and five bomber configurations with concentrated mass. The mass density and pitching inertia were separately changed by factors of 2.0 and 0.5, making a total of 48 configurations in addition to the 12 basic cases. Reference case numbers are given in table XII.

Tabulation of flutter speed and frequency for each case will be found in table XV. The results are also shown in figure 8. As mentioned earlier, the flutter speeds have been reduced to dimensionless values by using as the velocity unit the flutter speed of the basic wing for each basic configuration. The trends predicted above are found in most cases. In the

TABLE XIV.—CASE NUMBERS FOR CONCENTRATED-MASS VARIATIONS

m/m_{basic}	Station	Fighter A, $\Lambda=0°$, with radius of gyration, in., of—			Fighter A, $\Lambda=45°$, with radius of gyration, in., of—			Bomber A, $\Lambda=0°$, with radius of gyration, in., of—	Bomber B, $\Lambda=0°$, with radius of gyration, in., of—	Bomber B, $\Lambda=0°$, with radius of gyration, in., of—
		6	15	30	6	15	30	35	35	35
1	Root	------	------	------	------	------	------	248	----------	----------
	1	------	------	------	------	------	------	----------	----------	276
	2	------	182	183	218	219	220	249	264	277
	3	------	184	185	221	222	223	250	265	278
	4	------	------	------	224	225	226	251	266	279
	4. 5	------	------	------	------	------	------	252	----------	----------
	5	186	187	188	227	228	229	253	267	280
	5. 5	------	------	------	------	------	------	254	----------	----------
	6	189	190	191	230	231	232	255	268	281
	Tip	192	193	194	233	234	235	256	269	282
0. 50	1	------	------	------	------	------	------	----------	----------	283
	2	------	------	------	------	------	------	257	270	284
	3	------	------	------	------	------	------	258	271	285
	4	------	------	------	------	------	------	259	272	286
	5	------	------	------	------	------	------	260	273	287
	5. 5	------	------	------	------	------	------	261	----------	----------
	6	------	------	------	------	------	------	262	274	288
	Tip	------	------	------	------	------	------	263	275	289
2	Tip	195	196	197	------	------	------	----------	----------	----------
1		192	193	194	233	234	235	----------	----------	----------
. 50		198	199	200	236	237	238	----------	----------	----------
. 16		201	202	203	------	------	------	----------	----------	----------
. 08		204	205	206	------	------	------	----------	----------	----------
. 037		207	208	209	------	------	------	----------	----------	----------
. 015		210	------	------	------	------	------	----------	----------	----------
. 008		211	------	------	------	------	------	----------	----------	----------
1	5	186	187	188	227	228	229	----------	----------	----------
. 50		------	------	------	239	240	241	----------	----------	----------
. 16		212	213	214	------	------	------	----------	----------	----------
. 037		215	216	217	------	------	------	----------	----------	----------
1	Tip	[a] 242	[a] 243	[a] 244	[a] 245	[a] 246	[a] 247	----------	----------	----------

[a] Case number for fighter B.



(a) Fighters A and B.
(b) Bomber A.
(c) Bomber B.
(d) Bomber B; concentrated mass on wing.

FIGURE 8.—Effect of wing mass and inertia variations.

case of bare-wing fighters the effect is very systematic. The average of all cases is given as follows:

Mass value	Pitch inertia value	Average change in v_f, percent
0.5	1.0	−12
2.0	1.0	6
1.0	.5	8
1.0	2.0	−9

The effect, though uniform, is quite small.

The results for bombers show much less consistency. For cases both with and without concentrated masses, the effect of wing-mass density variation is unpredictable. Nearly half of the cases show trends which are opposite to that predicted above. The addition of a concentrated mass at the 0.46-span position reversed the trend in several cases. On the other hand, change in wing pitching inertia did show a systematic trend for all bomber cases. On the average a change in pitching inertia by a factor of 2 changed the flutter speed about 7 percent.

The following conclusions can be drawn:

(1) A change of wing pitching inertia shows a systematic trend for all wings although the effect is small.
(2) A change of wing mass shows a definite trend for typical fighters although the effect is small.
(3) Change of wing mass for typical large bombers with or without concentrated masses shows no systematic trend.

STIFFNESS VARIATIONS

It has been pointed out (e. g., ref. 1, p. 783) that when incompressible fluid flow is assumed, a change of stiffness is equivalent to a change of velocity insofar as transient response of an airfoil is concerned. Consequently, it can be said that a uniform increase in stiffness will raise the flutter speed by the square root of the factor by which stiffness is increased. In most airplanes it is found that the increase in torsional rigidity is primarily responsible for the increase in flutter speed and that, in general, a change in bending rigidity over rather wide limits does not change the flutter speed significantly.

As shown in table XII, 12 configurations were studied to support this conclusion. Since both bending rigidity and torsional rigidity were separately changed by factors of 0.67 and 1.50, there are a total of 48 case numbers assigned to this group. The results of this study are listed in table XV and presented graphically in figure 9. For ease of comparison flutter speeds are converted to dimensionless values, and flutter characteristics for changes in bending and torsional rigidity are plotted side by side. In general, it was found that change in torsional rigidity by a factor of ½ or ⅔ increased or decreased the flutter speed by 20 percent and that a similar change in bending rigidity had a negligible effect upon the flutter speed. Among the 12 configurations studied, the following exceptions to this trend were noted:

(1) Bomber A, Λ=0°: In the antisymmetric case both bending and torsional rigidity had roughly equal effect, flutter speed changing ±10 percent for a rigidity change of ½ or ⅔.

TABLE XV.—FLUTTER SPEED AND FREQUENCY

Case	Airplane	Symmetric			Antisymmetric		
		v_f, mph	v_f, per unit	f_f, cps	v_f, mph	v_f, per unit	f_f, cps
1	Fighter A	989	1. 74	14. 2	1, 091	1. 92	8. 7
2		1, 080	1. 90	10. 4	1, 102	1. 94	6. 13
3		892	1. 57	16. 8	1, 068	1. 88	11. 3
4		835	1. 47	12. 4	1, 011	1. 78	8. 1
5		1, 102	1. 94	15. 0	1, 142	2. 01	8. 7
6		972	1. 71	14. 8	1, 085	1. 91	9. 1
7		1, 000	1. 76	13. 7	1, 119	1. 97	8. 3
8		1, 222	2. 15	16. 8	1, 369	2. 41	10. 2
9		795	1. 40	12. 0	886	1. 56	7. 4
11		813	1. 43	14. 0	989	1. 74	8. 6
12		710	1. 25	13. 9	636	1. 12	16. 6
					892	1. 57	8. 5
13		619	1. 09	12. 9	545	. 96	16. 0
					778	1. 37	7. 9
14		773	1. 36	14. 1	858	1. 51	8. 2
15		795	1. 4	12. 0	790	1. 39	7. 1
16		1, 295	2. 28	15. 7	------	------	------
17		938	1. 65	14. 4	733	1. 29	17. 2
18		949	1. 67	15. 0	750	1. 32	17. 7
19		1, 028	1. 81	15. 7	881	1. 55	17. 5
20		1, 415	2. 49	14. 5	1, 267	2. 23	16. 1
21		847	1. 49	14. 9	784	1. 38	17. 0
22		790	1. 39	14. 6	795	1. 40	15. 9
23	Fighter B	1, 074	1. 89	7. 4	1, 017	1. 79	6. 9
24		1, 006	1. 77	5. 3	1, 057	1. 86	4. 8
25		875	1. 54	10. 8	938	1. 65	9. 2
26		989	1. 74	6. 6	926	1. 63	6. 1
27		1, 131	1. 99	8. 0	1, 074	1. 89	7. 4
28		1, 023	1. 80	8. 2	1, 017	1. 79	7. 2
29		1, 040	1. 83	6. 8	1, 017	1. 79	6. 8
30		1, 273	2. 24	8. 4	1, 244	2. 19	8. 3
31		835	1. 47	6. 7	830	1. 46	5. 9
33		881	1. 55	8. 0	898	1. 58	6. 5
34		767	1. 35	8. 1	824	1. 45	6. 1
35		653	1. 15	7. 3	710	1. 25	------
36		1, 244	2. 19	7. 8	1, 227	2. 16	7. 3
37		852	1. 50	7. 4	813	1. 43	6. 5
38		784	1. 38	7. 1	727	1. 28	5. 5
39		1, 358	2. 39	8. 5	1, 392	2. 45	8. 3
40		943	1. 66	8. 1	750	1. 32	11. 2
41		932	1. 64	9. 0	801	1. 41	11. 4
42		983	1. 73	9. 2	1, 023	1. 80	11. 5
43		1, 051	1. 85	6. 7	1, 131	1. 99	9. 2
44		847	1. 49	11. 8	847	1. 49	13. 9
45		864	1. 52	8. 0	1, 080	1. 90	10. 0
46		1, 074	1. 89	9. 8	1, 159	2. 04	12. 6
47		983	1. 73	10. 2	983	1. 73	12. 9
48		960	1. 69	8. 7	1, 074	1. 89	11. 2
49		1, 176	2. 07	11. 7	1, 313	2. 31	13. 8
50		801	1. 41	8. 3	801	1. 41	10. 6
51		2, 171	3. 82	11. 5	2, 057	3. 62	13. 8
52		1, 188	2. 09	8. 8	1, 142	2. 01	12. 0
53		898	1. 58	9. 3	1, 017	1. 79	11. 2
54		835	1. 47	8. 9	1, 307	2. 30	7. 9
55		756	1. 33	8. 4	989	1. 74	6. 4
56		1, 347	2. 37	10. 2	1, 250	2. 20	12. 4
57		784	1. 38	8. 0	949	1. 67	11. 4

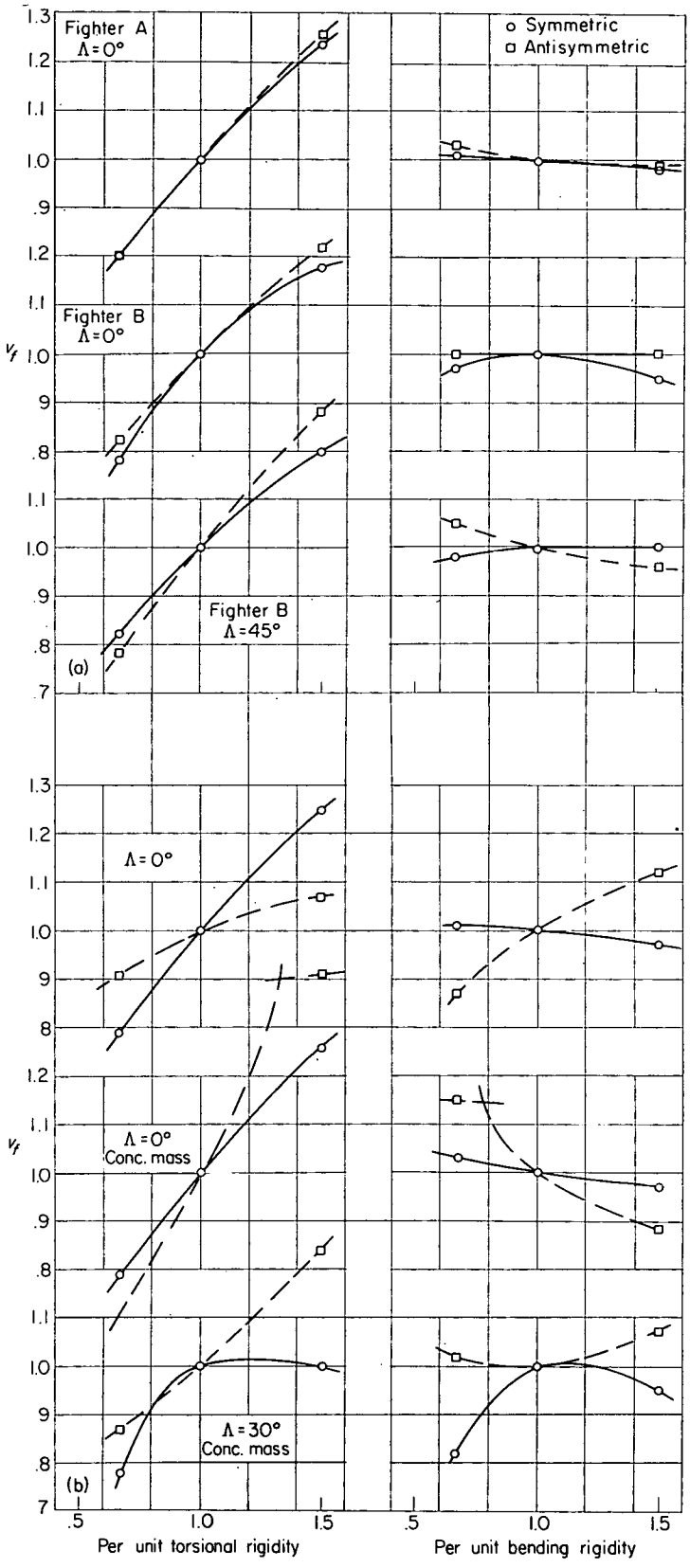
TABLE XV.—FLUTTER SPEED AND FREQUENCY—Continued

Case	Airplane	Symmetric			Antisymmetric		
		v_f, mph	v_f, per unit	f_f, cps	v_f, mph	v_f, per unit	f_f, cps
58	Bomber A	710	1. 25	9. 4	869	1. 53	8. 8
59		625	1. 10	7. 5	648	1. 14	7. 0
60		943	1. 66	12. 2	972	1. 71	16. 8
61		602	1. 06	8. 2	682	1. 20	7. 5
62		784	1. 38	10. 2	1, 040	1. 83	9. 9
63		688	1. 21	9. 7	761	1. 34	8. 6
64		733	1. 29	9. 3	1, 000	1. 76	12. 6
65		898	1. 58	11. 4	1, 227	2. 16	------
66		563	. 99	7. 9	619	1. 09	7. 0
68		625	1. 10	8. 8	676	1. 19	8. 0
69		585	1. 03	8. 4	563	. 99	7. 4
70		540	. 95	7. 8	455	. 80	6. 7
71		534	. 94	8. 6	528	. 93	7. 7
72		1, 085	1. 91	17. 9	699	1. 23	9. 6
					835	1. 47	(a)
73		1, 193	2. 10	17. 7	886	1. 56	10. 6
					1, 011	1. 78	18. 9
74		784	1. 38	8. 6	653	1. 15	7. 5
75		1, 165	2. 05	20. 9	903	1. 59	20. 1
76		966	1. 70	14. 5	597	1. 05	8. 2
					705	1. 24	15. 4
77		1, 017	1. 79	21. 8	778	1. 37	9. 9
78		1, 034	1. 82	17. 4	744	1. 31	9. 7
79		886	1. 56	19. 3	710	1. 25	9. 0
80		1, 085	1. 91	23. 7	869	1. 53	11. 0
81		847	1. 49	14. 2	608	1. 07	7. 9
82		750	1. 32	18. 3	642	1. 13	8. 7
					676	1. 19	(a)
83		580	1. 02	17. 5	563	. 99	17. 4
					608	1. 07	8. 0
84		818	1. 44	9. 4	886	1. 56	9. 9
85		864	1. 52	7. 8	767	1. 35	8. 7
86		761	1. 34	11. 4	983	1. 73	9. 6
87		676	1. 19	8. 0	864	1. 52	7. 1
88		909	1. 60	10. 8	852	1. 50	12. 0
89		790	1. 39	9. 6	989	1. 74	8. 1
90		830	1. 46	9. 6	773	1. 36	10. 1
91		1, 017	1. 79	11. 8	949	1. 67	12. 5
92		648	1. 14	7. 8	807	1. 42	6. 6
94		705	1. 24	9. 5	648	1. 14	9. 8
95		636	1. 12	8. 9	563	. 99	10. 5
96		540	. 95	8. 1	466	. 82	10. 5
97		614	1. 08	9. 8	563	. 99	10. 7
98	Bomber B	1, 295	2. 28	10. 7	1, 261	2. 22	9. 8
99		1, 290	2. 27	7. 3	1, 250	2. 20	7. 0
100		1, 278	2. 25	14. 1	1, 341	2. 36	14. 3
101		1, 216	2. 14	9. 9	1, 176	2. 07	9. 5
102		1, 341	2. 36	11. 1	1, 318	2. 32	10. 3
103		1, 307	2. 30	10. 9	1, 244	2. 19	10. 2
104		1, 273	2. 24	10. 5	1, 278	2. 25	10. 6
105		1, 563	2. 75	12. 9	1, 568	2. 76	13. 0
106		1, 068	1. 88	8. 9	1, 017	1. 79	8. 3
107		1, 148	2. 02	10. 1	1, 108	1. 95	9. 4
108		1, 040	1. 83	9. 2	1, 011	1. 78	8. 9
109		898	1. 58	8. 1	875	1. 54	8. 0
110		1, 023	1. 80	9. 3	1, 000	1. 76	9. 1
111		966	1. 70	8. 8	909	1. 60	8. 2
112		1, 699	2. 99	12. 5	1, 750	3. 08	12. 6
113		1, 295	2. 28	10. 2	1, 352	2. 38	8. 8
114		1, 489	2. 62	11. 7	1, 432	2. 52	11. 3
115		1, 284	2. 26	7. 1	1, 261	2. 22	6. 6

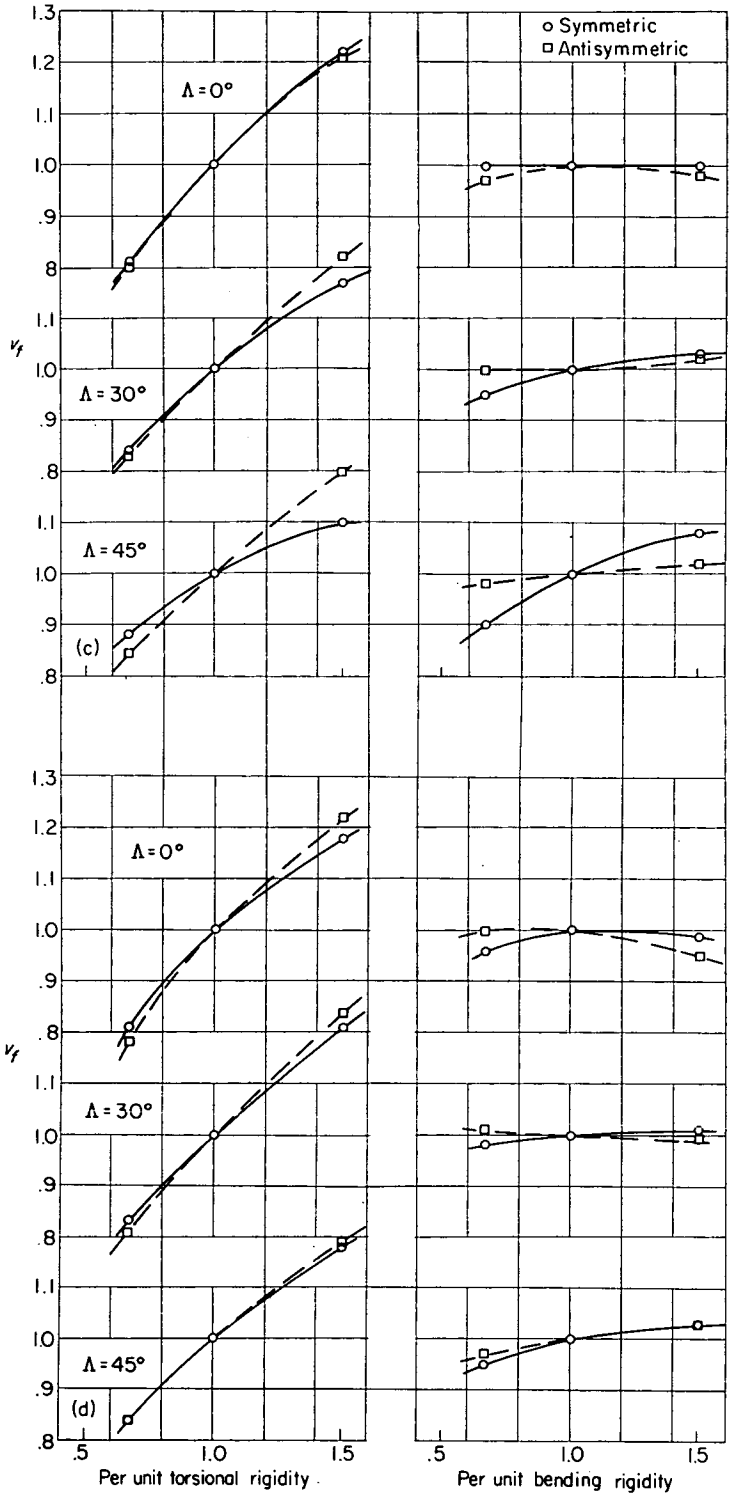
[a] High frequency.

TABLE XV.—FLUTTER SPEED AND FREQUENCY—Concluded

Case	Airplane	Symmetric			Antisymmetric		
		v_f, mph	v_f, per unit	f_f, cps	v_f, mph	v_f, per unit	f_f, cps
116	Bomber B	1, 284	2. 26	13. 7	1, 347	2. 37	15. 3
117		1, 227	2. 16	9. 4	1, 239	2. 18	8. 4
118		1, 341	2. 36	10. 8	1, 477	2. 60	9. 6 11. 4
119		1, 284	2. 26	10. 2	1, 284	2. 26	9. 3
120		1, 250	2. 20	10. 6	1, 347	2. 37	11. 3
121		1, 534	2. 70	13. 0	1, 653	2. 91	13. 8
122		1, 051	1. 85	8. 3	1, 051	1. 85	7. 6
123		1, 108	1. 95	9. 2	1, 074	1. 89	8. 3
124		983	1. 73	8. 6	955	1. 68	7. 8
125		813	1. 43	7. 4	773	1. 36	7. 0
126		1, 523	2. 68	8. 8	1, 477	2. 60	7. 8
127		1, 472	2. 59	15. 5	1, 409	2. 48	14. 8
128		1, 392	2. 45	10. 4	1, 335	2. 35	10. 5
129		1, 557	2. 74	12. 2	1, 500	2. 64	12. 0
130		1, 528	2. 69	11. 5	1, 477	2. 60	11. 0
131		1, 420	2. 50	11. 3	1, 386	2. 44	10. 7
132		1, 738	3. 06	12. 6	1, 699	2. 99	13. 1
133		1, 250	2. 20	9. 4	1, 205	2. 12	9. 0
134		1, 364	2. 40	11. 0	1, 284	2. 26	11. 0
135		1, 261	2. 22	10. 2	1, 188	2. 09	10. 6
136		1, 119	1. 97	8. 7	1, 080	1. 90	10. 2
137		1, 165	2. 05	7. 1	1, 244	2. 19	10. 3
138		1, 023	1. 80	4. 5	1, 239	2. 18	7. 0
139		1, 261	2. 22	13. 7	1, 205	2. 12	14. 2
140		1, 108	1. 95	7. 0	1, 170	2. 06	9. 8
141		1, 182	2. 08	7. 3	1, 284	2. 26	10. 4
142		1, 205	2. 12	8. 1	1, 267	2. 23	10. 7
143		1, 108	1. 95	6. 1	1, 239	2. 18	9. 6
144		1, 358	2. 39	7. 5	1, 517	2. 67	11. 8
145		983	1. 73	6. 6	1, 034	1. 82	8. 7
146		1, 074	1. 89	7. 3	1, 131	1. 99	10. 2
147		1, 023	1. 80	7. 7	1, 034	1. 82	9. 6
148		898	1. 58	8. 3	898	1. 58	8. 6
149		972	1. 71	6. 7	1, 023	1. 80	9. 7
150		881	1. 55	7. 2	909	1. 60	8. 5
151		1, 483	2. 61	7. 3	1, 665	2. 93	10. 8
152		1, 216	2. 14	10. 1	1, 216	2. 14	10. 4
153		1, 114	1. 96	6. 6	1, 421	2. 50	10. 4
154		1, 193	2. 10	6. 5	1, 216	2. 14	6. 7
155		1, 159	2. 04	13. 8	1, 170	2. 06	13. 9
156		1, 136	2. 00	9. 4	1, 142	2. 01	9. 2
157		1, 261	2. 22	10. 5	1, 261	2. 22	10. 4
158		1, 199	2. 11	10. 0	1, 193	2. 10	9. 9
159		1, 199	2. 11	9. 9	1, 182	2. 08	10. 1
160		1, 466	2. 58	12. 1	1, 449	2. 55	12. 4
161		977	1. 72	8. 1	977	1. 72	8. 1
162		1, 057	1. 86	9. 9	1, 057	1. 86	9. 8
163		949	1. 67	9. 4	960	1. 69	9. 6
164		818	1. 44	8. 7	818	1. 44	8. 6
165		1, 040	1. 83	4. 3	1, 438	2. 53	7. 16
166		1, 244	2. 19	10. 2	1, 375	2. 42	14. 0
167		1, 080	1. 90	6. 4	1, 347	2. 37	10. 0
168		1, 125	1. 98	6. 6	1, 460	2. 57	10. 5
169		1, 205	2. 12	7. 4	1, 455	2. 56	11. 2
170		1, 000	1. 76	5. 5	1, 386	2. 44	9. 7
171		1, 227	2. 16	6. 7	1, 699	2. 99	11. 9
172		983	1. 73	6. 0	1, 188	2. 09	9. 1
173		1, 040	1. 83	6. 5	1, 313	2. 31	10. 9
174		1, 000	1. 76	6. 5	1, 216	2. 14	11. 0
175		920	1. 62	6. 5	1, 085	1. 91	10. 5



(a) Fighters A and B.
(b) Bomber A; bare wing and concentrated mass on wing.



(c) Bomber B; bare wing.
(d) Bomber B; concentrated mass on wing.

FIGURE 9.—Flutter speed as a function of wing rigidity.

(2) Bomber B, $\Lambda=45°$: Symmetric case same as case (1) above.

(3) Bomber A, concentrated mass at 0.46 span, $\Lambda=0°$: In the antisymmetric case torsional rigidity had a 50 percent greater effect ($\pm$30-percent change in flutter speed) and bending rigidity had a negative effect ($\mp$10-percent change in flutter speed).

(4) Bomber A, concentrated mass, $\Lambda=30°$: In the symmetric case, the trend was normal only for decrease in torsional rigidity and increase in bending rigidity.

These exceptions do not constitute a major deviation, and the trend is considered well established.

LOCAL STIFFNESS VARIATIONS

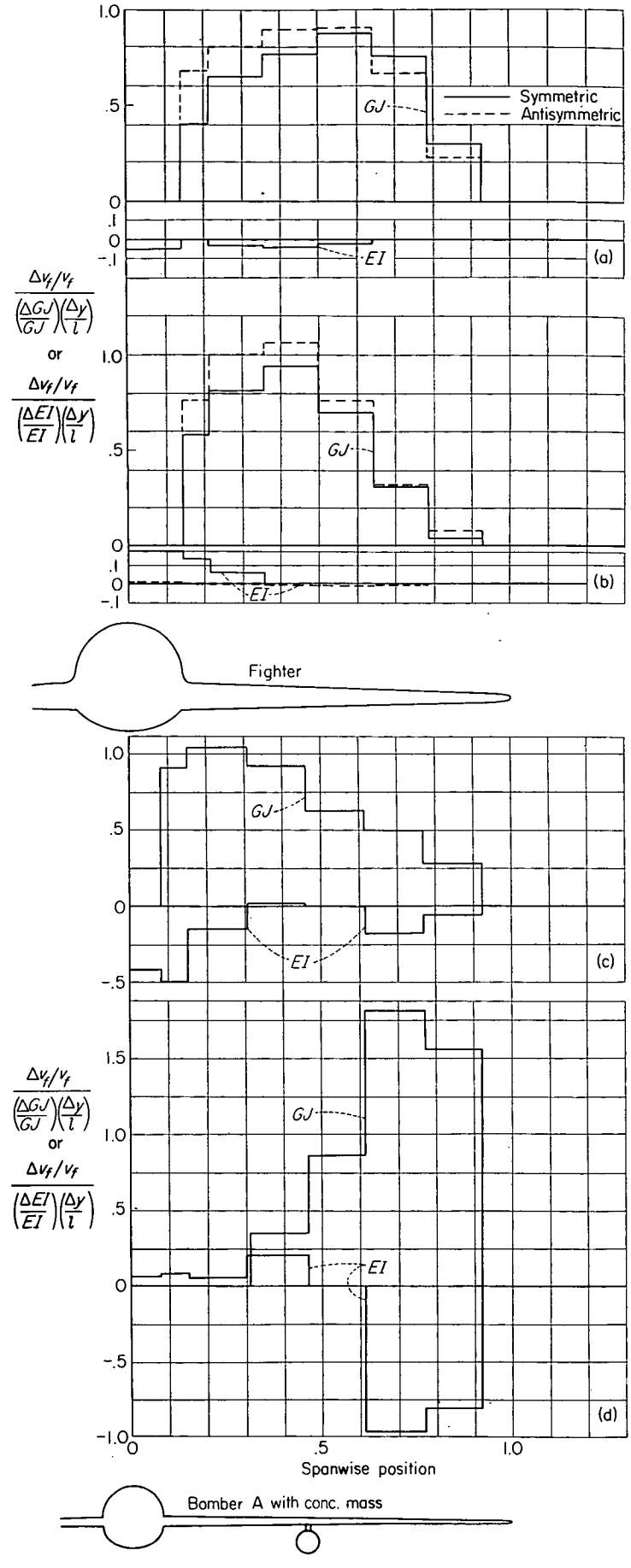
It is not to be expected that the effect discussed in the preceding section will be observed if torsional rigidity is changed at various stations along the wing. In the absence of a concentrated tip mass, any effect on flutter speed must vanish for stations near the tip, and presumably the largest effect will be observed for stations near the fuselage. Because of the great ease with which these data could be obtained, the effect of local stiffness variation was obtained for several configurations.

The analog computer requires lumping or averaging of inertia and stiffness properties. Consequently, it is possible to determine readily only the effect of a stiffness variation which must be assumed to extend over the entire length of a cell in the finite-difference structure. The basic data consist therefore of step curves. To obtain an approximate value for the per unit change in flutter speed per unit change in stiffness per unit length at any point along the wing, it is necessary to draw a smooth curve passing through the step curve such that the areas under the two curves are approximately equal. It is believed more suitable to present the step curve and let the reader do any smoothing his application requires. The configurations studied are listed below:

(1) Fighter A, $\Lambda=0°$, symmetric and antisymmetric, case 10
(2) Fighter B, $\Lambda=0°$, symmetric and antisymmetric, case 32
(3) Bomber A, $\Lambda=0°$, bare wing, symmetric, case 93
(4) Bomber A, $\Lambda=0°$, concentrated mass at 0.46 span, symmetric, case 67

Results of this study are presented in figure 10. The abscissa of a curve is the spanwise station at which the bending or torsional rigidity variation is made. The ordinate is the per unit change in flutter speed per unit change in stiffness per unit length along the wing. If, for example, the stiffness is increased j percent over a distance w along a wing of semispan l between the stations $d-(w/2)$ and $d+(w/2)$, then the ordinate of the smoothed curve at the abscissa d/l when multiplied by $j(w/l)$ will give the approximate percent change in flutter speed.

Data for the two fighters show great similarity both for symmetric and antisymmetric conditions. The greatest effect is obtained by changing torsional rigidity near the midspan position, slightly outboard for fighter A and slightly inboard for fighter B. The effect of a bending-rigidity change was found to be small at all stations. In most cases



(a) Fighter A.
(b) Fighter B.
(c) Bomber A; bare wing.
(d) Bomber A; concentrated mass at 0.46 span.

FIGURE 10.—Effect of local stiffness variation on flutter speed.

a small negative effect was observed, the flutter speed dropping slightly as the bending rigidity was increased.

Bomber A without concentrated mass showed a similar trend with the following exceptions:

(1) Maximum improvement was obtained by changing torsional rigidity near the root of the wing (0.25-span position).

(2) Increase in bending rigidity was observed to decrease the flutter speed by an amount which was 5 to 10 times greater than that for fighter A.

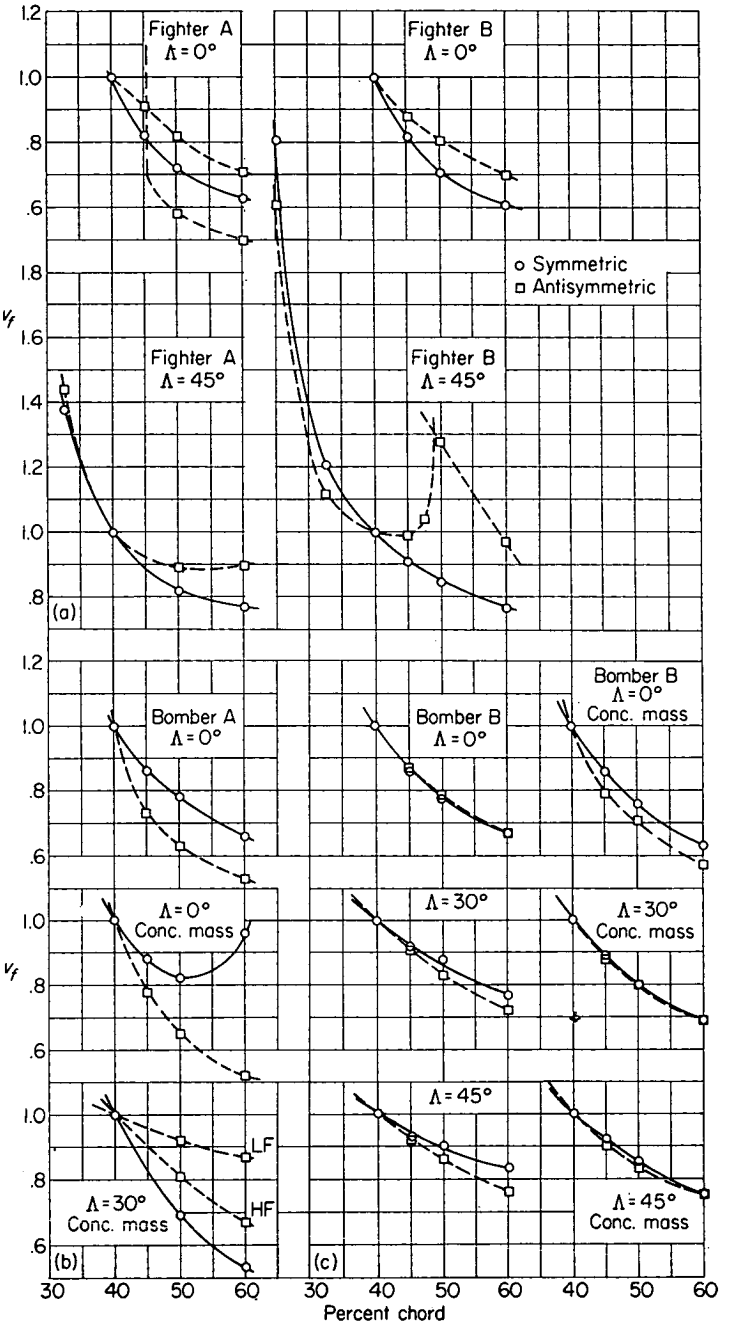
Addition of a concentrated mass at spanwise station 0.46 has a great effect on this characteristic. The mass chosen is typical for an airplane engine and is sufficiently large so that the wing is, to a certain extent, pinned at this point for the particular flutter root involved. Consequently, stiffness changes inboard of the engine have a negligible effect, and changes outboard have an effect very similar to that observed for a bare wing of reduced length.

It should be remarked at this point that the result discussed above is not to be regarded as a trend for all configurations. When the flutter is primarily an outer-wing bending-torsion flutter, this result is to be expected. Experience has shown, however, that occasionally an inner-panel torsion mode is involved in flutter, and change in torsional rigidity outboard of the nacelle has no significant effect. It is unfortunate that such a configuration was not investigated for this report.

CENTER-OF-MASS LOCATION

The location of the wing center of mass has a great effect upon flutter speed of an airplane wing. The general trend is that flutter speed increases as the center of mass moves forward. It is not generally true that it is at a constant chord location at all spanwise stations. However, for purposes of studying the trends, it is necessary to assume some basic position for the center of mass. Past experience has shown that a center-of-mass location near the elastic axis (usually slightly aft) is both realistic and typical. For this reason the basic position of the center of mass was assumed to be the elastic axis or 40 percent chord. Variation in center-of-mass location was between the 25- and 60-percent-chord points. Thirteen configurations were studied, the various center-of-mass locations comprising 53 cases listed in table XII.

The results are listed in table XV and are shown graphically in dimensionless form in figure 11. The general trend is that the flutter speed increases as the center of mass moves forward and decreases as the center of mass moves aft, except for center-of-mass locations far behind the elastic axis. For positions near the elastic axis the flutter speed changes about 3 percent for a shift in center of mass equal to 1 percent of the chord. For the extreme aft positions (60 percent chord) most of the curves become quite flat, and in about four cases the flutter speed has started to rise slightly as the center of mass is moved farther aft. On the other hand, the curves become very steep for center-of-mass locations forward of the elastic axis. In most cases the increase in flutter speed was so great that data could not be obtained for the 25- and 32.5-percent-chord locations because the flutter speed greatly exceeded the divergence



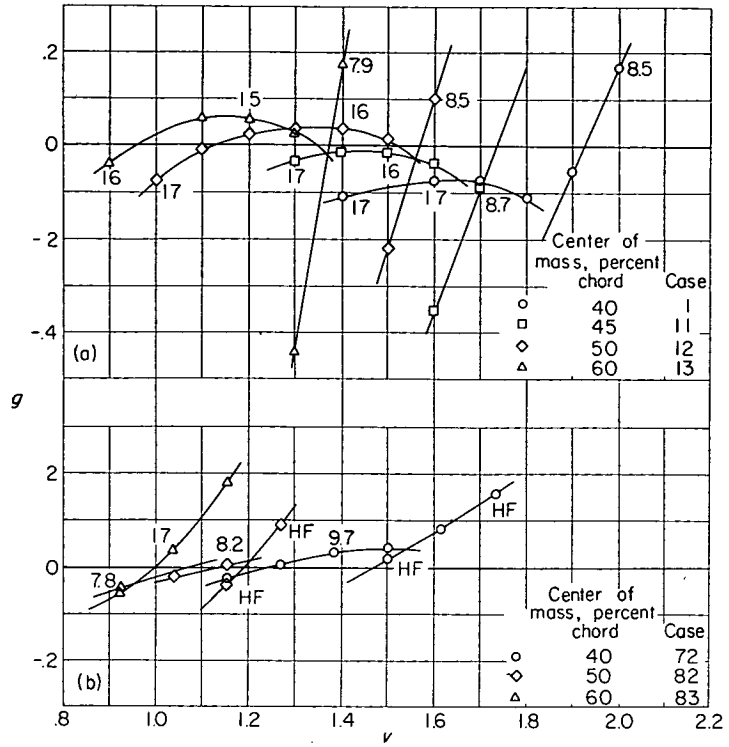
(a) Fighters A and B. (b) Bombers A and B.

FIGURE 11.—Flutter speed as function of center-of-mass position in percent chord.

speed. The average percentage change in flutter speed for a shift in center of mass equal to 1 percent of the chord depends upon location of the center of mass as indicated below:

Center-of-mass location, percent chord	40	50	60
Change in flutter speed, percent	3.1	1.7	0.8

One unusual case was noted. The results for fighter B, Λ=45°, in figure 11 (a) show an unusual behavior for aft center-of-mass location in the antisymmetric case. A study of the frequency of oscillation for each position tends to support the conclusion that two different flutter roots are involved. In any case the results are anomalous and could bear further investigation.



(a) Fighter A; $\Lambda=0°$; antisymmetric.
(b) Bomber A; $\Lambda=30°$; concentrated mass on wing; antisymmetric.
HF, high frequency.

FIGURE 12.—Plot of damping factor g against velocity for some unusual flutter roots.

Fighter A, $\Lambda=0°$, shows another unusual characteristic in the antisymmetric case. One flutter root disappears as the center of mass is moved forward of the 46-percent-chord location. This result, shown in figure 11 (a), is more easily understood by referring to figure 12 where the curves of g against v are plotted for this configuration. A similar case shown in figure 11 (b) has two readily observable flutter roots, one with low and the other with high flutter frequency. Data for both cases are given in figure 11 (b). It is true that only the one with the lower flutter speed is of practical interest, but for purposes of studying trends both are equally important. A plot of g against v for this case is also shown in figure 12.

ELASTIC-AXIS LOCATION

A main component of the aerodynamic pressures on an airfoil is equivalent to a force applied at the quarter chord. Consequently, the elastic-axis location relative to the quarter chord determines the nature of the coupling between aerodynamic forces and the structure. If elastic-axis location alone were changed, both center of pressure and center of mass would change with respect to the assumed structural axis. In order to separate the effects due to these two changes, the center of mass was moved with the elastic axis in the configurations discussed here. Aerodynamic coupling in which the center of pressure (quarter chord) is forward of the elastic axis may have a destabilizing influence while a center of pressure aft of the elastic axis generally has a stabilizing effect.

Elastic-axis locations between the 30 and 50 percent chord were used in the 16 cases listed in table XII. Results are

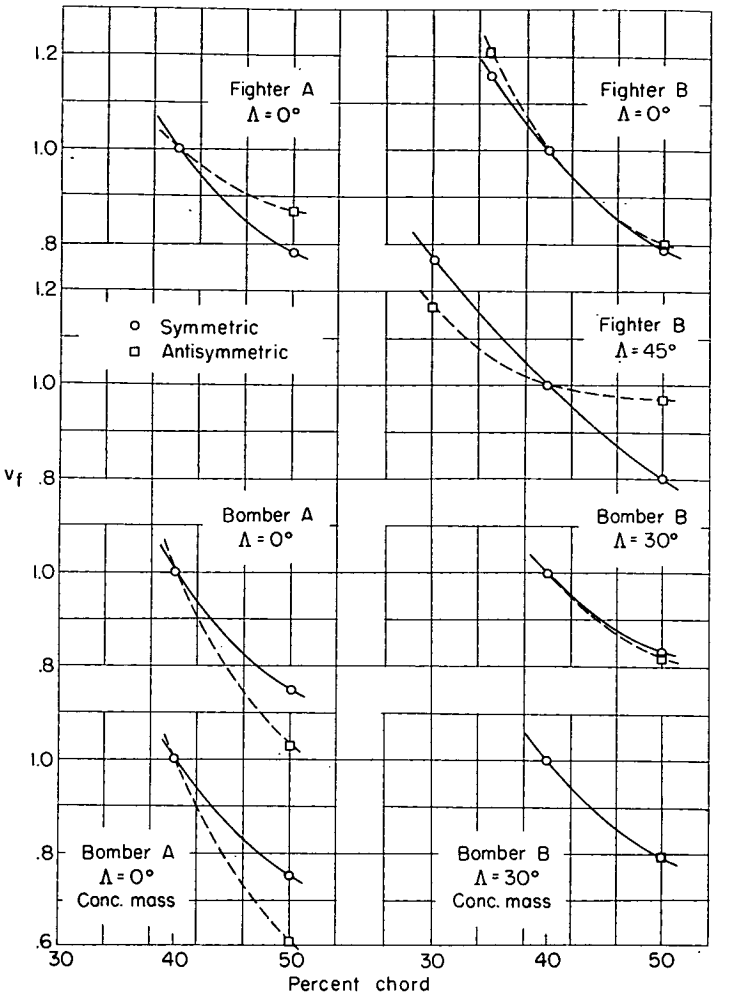


FIGURE 13.—Flutter speed as a function of elastic-axis position in percent chord.

given in table XV and figure 13. In all cases the expected trend was observed. For an elastic axis near the 40 percent chord, the flutter speed changed 3.2 percent on the average for a shift in elastic axis equal to 1 percent of the chord. This effect is not linear over a wide range; however, the flutter speed increases more rapidly as the quarter chord is approached and decreases more slowly as the elastic axis is moved aft. For an elastic axis at the 50 percent chord, the corresponding change in flutter speed was only 1.8 percent.

CHORD VARIATIONS

A change in chord of a wing is usually accompanied by significant changes in mass, inertia, and stiffness as well as changes in other characteristics. In an effort to assess the effect of aerodynamic pressures alone, variations were made in which mass, inertia, and stiffness were held constant while the chord length was changed. Location of the elastic axis was maintained at a constant per unit chord station so that the distance between quarter chord and elastic axis changed in proportion to the change in the chord length. Since the magnitude of the aerodynamic force increases with chord length and since the predominantly destabilizing lag of the Theodorsen function increases with chord length, it is to be expected that the flutter speed will decrease as the chord length is increased.

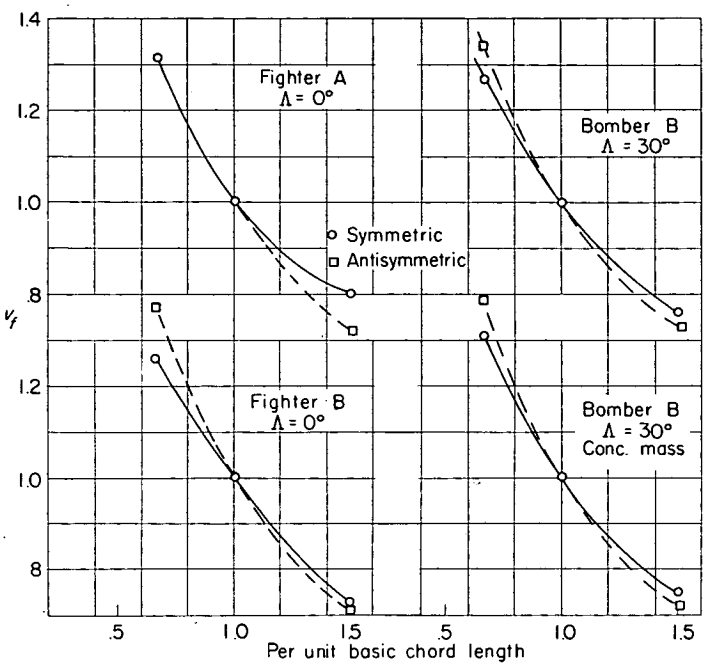


FIGURE 14.—Flutter speed as function of chord length.

Four configurations were studied in which the chord length was changed by factors of 0.67 and 1.50. The eight cases and the configurations are listed in table XII. Flutter characteristics are given in table XV and figure 14. The results are remarkably uniform. On the average, a 7-percent change in flutter speed results from a 10-percent change in chord, smaller chords giving a higher flutter speed.

SWEEPBACK

The effect of sweepback upon flutter speed depends upon many factors. In conventional wing design, the root structure varies greatly with sweepback angle, and the equivalent elastic axis may show considerable variation in position. For wings of large sweepback angle and low aspect ratio, the concept of an elastic axis may not be useful in describing structural properties. From another point of view the problem is even more perplexing since there is not general agreement about the nature of the aerodynamic forces on a swept wing. In the section of this report entitled "Finite-Difference Errors" the results of three methods of computation were compared with results of wind-tunnel tests of a model wing which was sweptback 34.5°. Two methods were found to give similar results, which were significantly better than those of the third. Although the agreement was not entirely satisfactory, it was decided to use the aerodynamic forces recommended in reference 5. For the present investigation, the following assumptions were therefore made:

(1) Aerodynamic forces are as discussed in the section entitled "Finite-Difference Errors."

(2) To achieve a sweepback angle, the wing is rotated about a vertical axis through the intersection of the unswept elastic axis and the side of the fuselage. The tip is, however, terminated parallel to the airstream so that only the span measured along the elastic axis is unchanged in length.

(3) Structural properties of the wing are unchanged by sweepback.

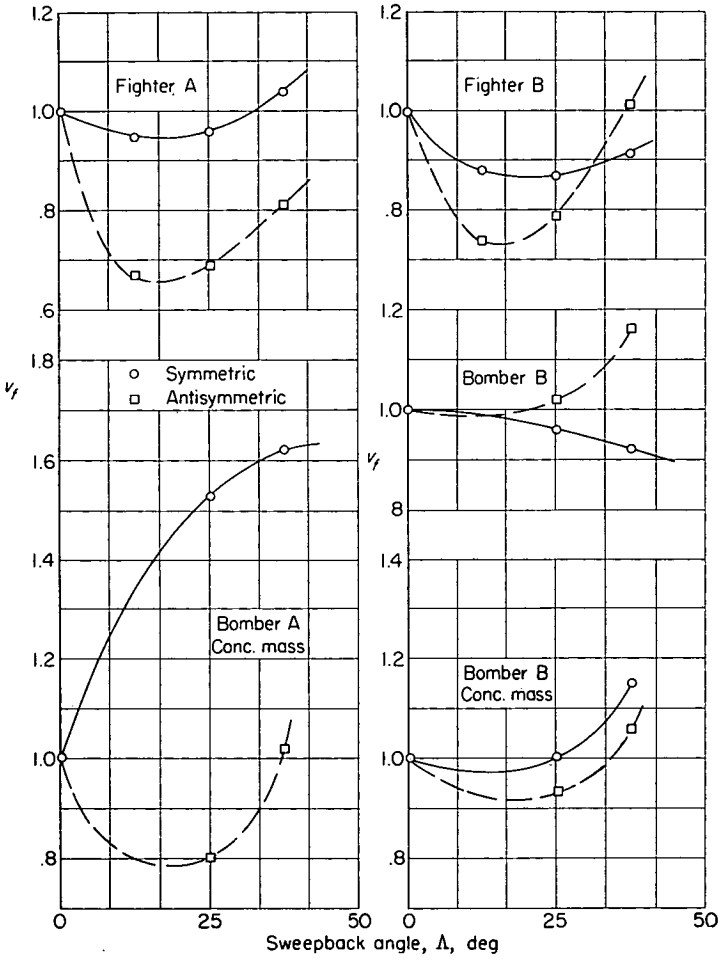


FIGURE 15.—Flutter speed as function of sweepback angle

(4) The center of mass of the fuselage is moved aft as the sweepback angle is increased so that it coincides roughly with the center of pressure of the wing.

(5) No modifications were made for aerodynamic forces at the tip.

The five basic configurations are shown in table XII, which gives reference numbers for the 17 cases. The results are given in table XV and figure 15. Flutter characteristics of the two fighters show a reasonable correlation, and, in general, a decrease in flutter speed for sweepback angles other than zero. However, the bombers do not show a correlation with the fighters or with each other. It is significant that a substantial change in flutter speed with sweepback angle was observed. In one case, flutter speed increased more than 60 percent for a 45° sweepback, while other cases showed a 30-percent decrease for sweepback angle of about 25°.

In addition to the cases above it is possible to crossplot the variation of flutter speed with sweepback angle for the following parameter variations of bomber B: Wing mass density, wing pitching inertia, bending rigidity, torsional rigidity, and center-of-mass location. Most of these are plotted in figure 16. It is interesting to note that the general trend for bomber B is to a great extent independent of these variations.

CONCENTRATED-MASS PITCHING FLEXIBILITY

The engines on present-day bombers are sometimes mounted in nacelles on pylons some distance below the wing.

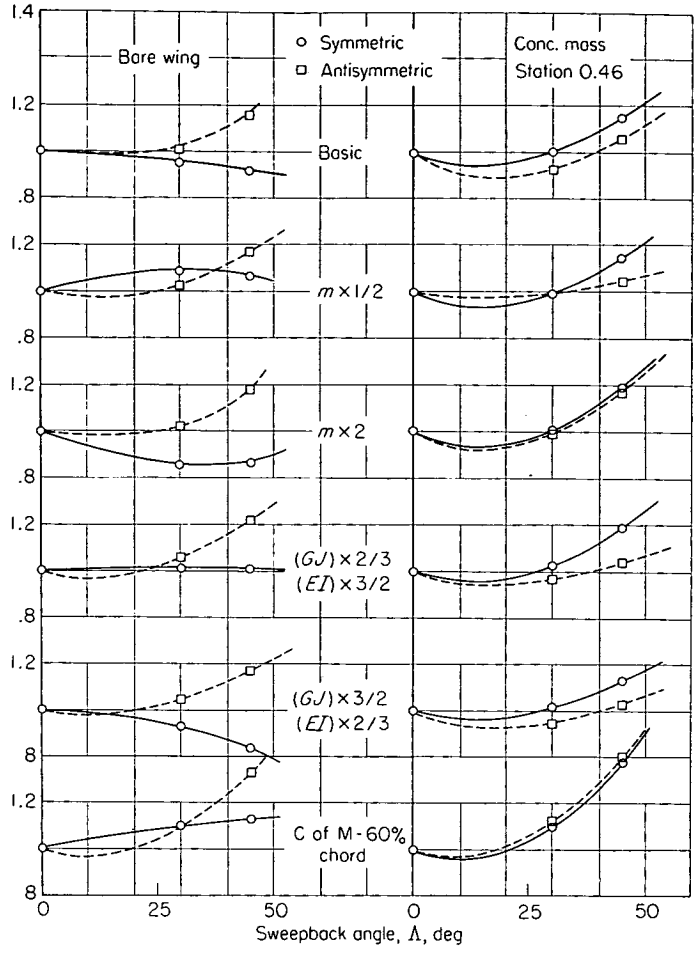


FIGURE 16.—Effect of sweepback on various modifications of bomber B

Because of the inherent flexibility in such a structure and its fastening to the wing, the dynamic characteristics of the engine are altered. Because of the symmetry of the structure, it is possible to write two sets of equations for the nacelle, one involving pitching, vertical, and fore and aft motion and the other involving lateral, rolling, and yawing motion. These sets are uncoupled except through interactions with the wing. The characteristics represented by the equations involving pitch have a greater effect on flutter characteristics, or, stated in another way, the assumption of a rigid pylon for lateral motion has not ordinarily been observed to introduce great differences in flutter characteristics. This assumption becomes less valid for wings with large sweepback. On the other hand, a significant variation may be observed as the pitching flexibilities are varied. For pitching motion it is usually quite accurate to assume an effective center of rotation at some point in front of and below the elastic axis. Unless a specific case is to be considered, however, it is just as satisfactory to assume this center of rotation at the elastic axis, since variation in the location of this point has only a second-order effect. Consequently, in this study the center of rotation for pitching motion was established at the elastic axis and the pylon was assumed rigid for lateral motion.

Six cases shown in table XII were investigated:

(1) Bomber A, $\Lambda=0°$, mass at 0.46 span, case 176
(2) Bomber A, $\Lambda=0°$, mass at tip, case 179
(3) Bomber B, $\Lambda=0°$, mass at 0.46 span, case 177
(4) Bomber B, $\Lambda=0°$, mass at tip, case 180
(5) Bomber B, $\Lambda=30°$, mass at 0.46 span, case 178
(6) Bomber B, $\Lambda=30°$, mass at tip, case 181

In all of these cases the chordwise position of the mass was basic, 60 inches forward of the elastic axis.

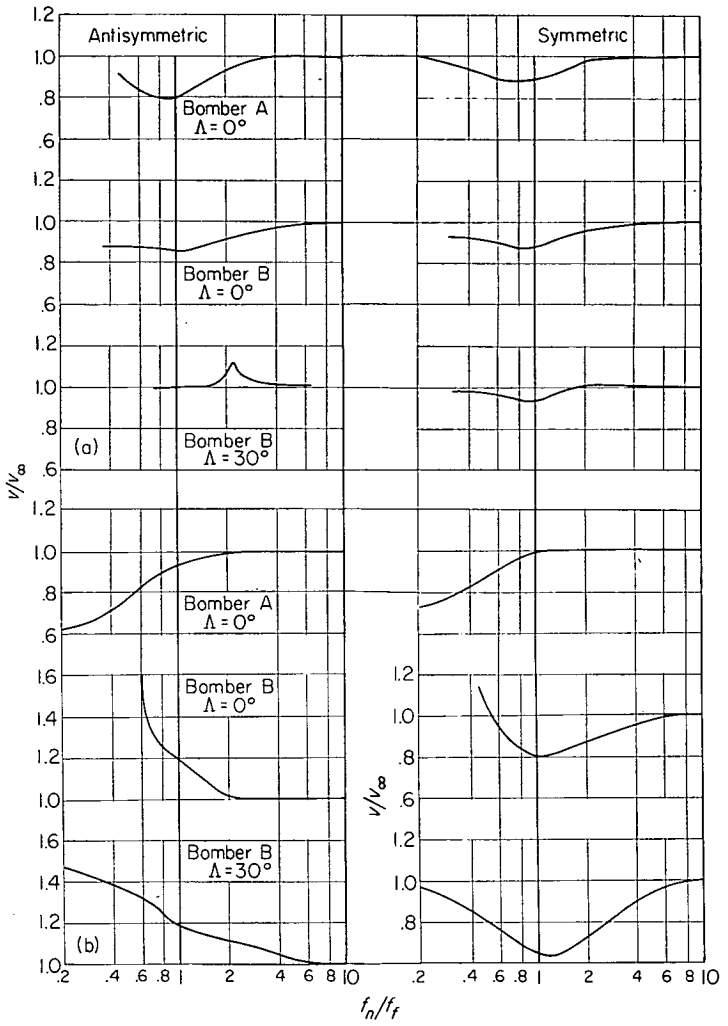
In presenting the results an effort has been made to put the data in dimensionless form. Thus, the flutter speed is given as a per unit value of the flutter speed with rigid connection. This basic flutter speed can be found in table XIV. The flexibility is conveniently measured by the normal-mode vibration frequency of the nacelle with the wing held rigid in pitch. However, instead of using the value of frequency in cycles per second, this frequency is measured in per unit value of the flutter frequency with rigid connection. Values for the flutter frequency with rigid connection can also be found in table XIV. There are two frequencies of the nacelle which might be regarded as significant. One of these is the cantilever frequency in which the wing is held rigid in both pitch and plunge. However, for large bombers, the wing has such great flexibility in vertical bending that greater significance might be attached to the frequency when pitching motion is constrained and vertical motion is completely unrestrained. Because of the location chosen for the basic mass, the difference in these frequencies is a factor of 2, the frequency with vertical motion unrestrained being higher. For presentation of data this higher value of frequency was chosen, because in those cases where a "tuning" effect was observed the maximum effect occurred when this frequency was equal to the flutter frequency for the basic rigid mass. One exception to this is observed in the discussion below.

Results are plotted in figure 17. Nine of the twelve cases show a predominant decrease in flutter speed as the rigidity is reduced from an infinite value. Seven of these cases show a minimum flutter speed when the nacelle frequency is nearly equal to the rigid flutter frequency. This decrease varies between 7 and 37 percent with an average value of 18 percent. Two cases show a decrease in flutter speed but no tuning effect. The maximum rate of decrease occurs, in fact, when the nacelle frequency is far below the rigid flutter frequency. In both cases the flutter speed drops to an asymptotic value about six-tenths of the basic value.

Three of the twelve cases show an increase in flutter speed as the rigidity is reduced from an infinite value. In two cases increase takes place in the region where nacelle frequency is roughly equal to the flutter frequency, and in both cases the flutter speed increases more than 50 percent. The last anomalous case shows a resonance or tuning effect. It is anomalous for two reasons: (1) The flutter speed rises to a sharp peak about 10 percent above basic value, and (2) this occurs when nacelle frequency is twice as great as the flutter frequency. It should be pointed out that, for this rigidity, the flutter frequency is equal to the nacelle frequency with wing attachment constrained in bending as well as pitch.

EFFECT OF A CONCENTRATED MASS

Many aircraft structures have engines, stores, or external fuel tanks attached to the wing in such a way that they act dynamically as concentrated masses. It has long been



(a) Mass at 0.46 span.
(b) Mass at tip.

FIGURE 17.—Flutter speed as a function of concentrated-mass pitching frequency.

known that the location of such a mass has a significant effect on flutter. Unfortunately, other aerodynamic and some structural problems do not permit location of such a mass so that maximum flutter speed is obtained. On the other hand, within the restrictions imposed by other considerations, it is often possible to improve flutter characteristics significantly by proper choice of mass locations.

This investigation has included a detailed examination of the effect of a concentrated mass on the flutter characteristics of several configurations of the four basic airplane wings. Preliminary study of this effect showed such interesting and unusual effects that the scope of the investigation was expanded beyond that originally proposed. The resulting data are so voluminous that it is difficult to present them effectively. In particular, it is impractical to construct a table which gives all of the data obtained, and so graphical presentation is required. Two methods have been adopted in this report. For a given spanwise location of the mass, the flutter speed can be plotted as a function of the chordwise location. This has been done for all cases investigated. Since the concentrated mass is alined with the airstream, it is most convenient in cases with sweepback to move the mass parallel to the airstream rather than perpendicular to the elastic axis. Where sufficient data are available, these curves can be summarized in a single diagram in which lines of constant flutter speed are shown on a drawing of the wing plan form. For the concentrated mass located anywhere on such a contour line, the flutter speed will be the same. The result is essentially a topographic map of the flutter-speed surface, where each point on the plan form represents a possible location for the concentrated mass.

Several difficulties arise with both methods of presentation. The main source of difficulty lies in the fact that several important flutter roots exist for a wing with concentrated mass. For certain locations of the mass, one root will show lowest flutter speed, while for other locations another root will have the lowest flutter speed. Since the analog computer is essentially an electrical model, it is usually impossible to find one of these flutter speeds if another root has a flutter speed far below the first. It is possible, therefore, to find with certainty only those portions of a given flutter-root surface which lie beneath all other flutter-root surfaces. For one configuration studied, four such distinct surfaces were positively identified and it was not possible to establish that surfaces appearing at widely separated regions were or were not related. In most cases the roots were differentiated by obtaining essentially marginal stability for two distinct roots along the line where the two surfaces intersect. It can be readily appreciated that many points are required to establish the flutter-speed contours, particularly where several intersecting surfaces are involved. It was, in fact, impossible in the time available to obtain sufficient data to establish all interesting features about these contours. However, it is believed that all important features are shown correctly in the figures presented here.

The curves which show flutter speed as a function of chordwise position at a fixed span frequently show intersections between different flutter roots. In identifying these roots, it is useful to know the flutter frequency associated with each root. The simplest way to present these data is to show the value of frequency at a few selected points along each curve. Where roots intersect and both frequencies were measured, both values are shown. In some cases where actual frequencies were not measured, low, medium, or high frequency is indicated.

For convenience the concentrated mass was placed at the center of a finite-difference cell except in three cases where additional information was obtained by placing it halfway between cells. It is convenient to identify these locations by the cell number as has been done in table XIV, which assigns a case number to each configuration. It must be remembered, however, that the cell divisions are slightly different for bomber and fighter airplanes, and therefore the spanwise station for a given cell number will be different. The location of these stations in terms of unit span is given in table XIII. In the figures, the spanwise position is correctly given as a fraction or per unit value of the wing semispan.

The size of the concentrated mass and its pitching and rolling inertia also affect the flutter speed. Since past experience has shown that rolling inertia has a small effect, a few

cases were chosen for further investigation of the magnitude of this effect. For a concentrated mass located in the wing it is reasonable to assume a radius of gyration which is a small fraction of the average half chord. For a mass suspended below the wing it is unlikely that the distance will exceed half of the average half chord. Two radii of gyration equal to 0.1 and 0.5 times the average chord for the fighter planes were chosen. In all cases considered there was no significant difference in flutter characteristics when the rolling inertia was varied from zero to the maximum value. The variation was, in fact, so insignificant that none of the data is presented in this report. In what follows it may be assumed that the rolling inertia of the concentrated mass has any value between the above limits. Since the mass of the concentrated mass and its pitching inertia have a greater effect, it is necessary to consider variations in these quantities in several typical cases. The basic values for mass and pitching inertia (or radius of gyration k) have been discussed in the section entitled "Characteristics of Four Representative Aircraft" and are given in table XIII. The variations of these values are summarized in table XIV.

The most logical way to give the results is to present first the flutter characteristics for the basic mass on each particular airplane. Five airplanes were chosen:

(1) Fighter A, $\Lambda=0°$
(2) Fighter A, $\Lambda=45°$
(3) Bomber A, $\Lambda=0°$
(4) Bomber B, $\Lambda=0°$
(5) Bomber B, $\Lambda=30°$

It was difficult to choose a typical radius of gyration for a mass on a fighter plane. The values used, 6, 15, and 30 inches, are shown in table XIV. Figures 18 (a) and 18 (b) show the effect of chordwise location of the mass at five spanwise positions for fighter A with $\Lambda=0°$. Results for all three radii of gyration in pitch are plotted on the same sheet using different symbols for each value. Circles are used for the smallest value, $k=6$ inches; triangles are used for $k=30$ inches; a solid line with no symbols is used for the intermediate value. Abscissas for all curves are chordwise distance from the elastic axis measured as per unit value of the wing semispan. Similar data for fighter A, $\Lambda=45°$, are shown in figures 18 (c) and 18 (d); six spanwise stations were used in this case. One surprising feature can be noted in all of these figures: The characteristics are relatively independent of the pitching inertia, even though this inertia is varied from a very large value ($k=30$ inches) to nearly zero ($k=6$ inches). This does not mean that at any particular point the flutter speeds are identical, but the overall shapes of the curves are remarkably similar.

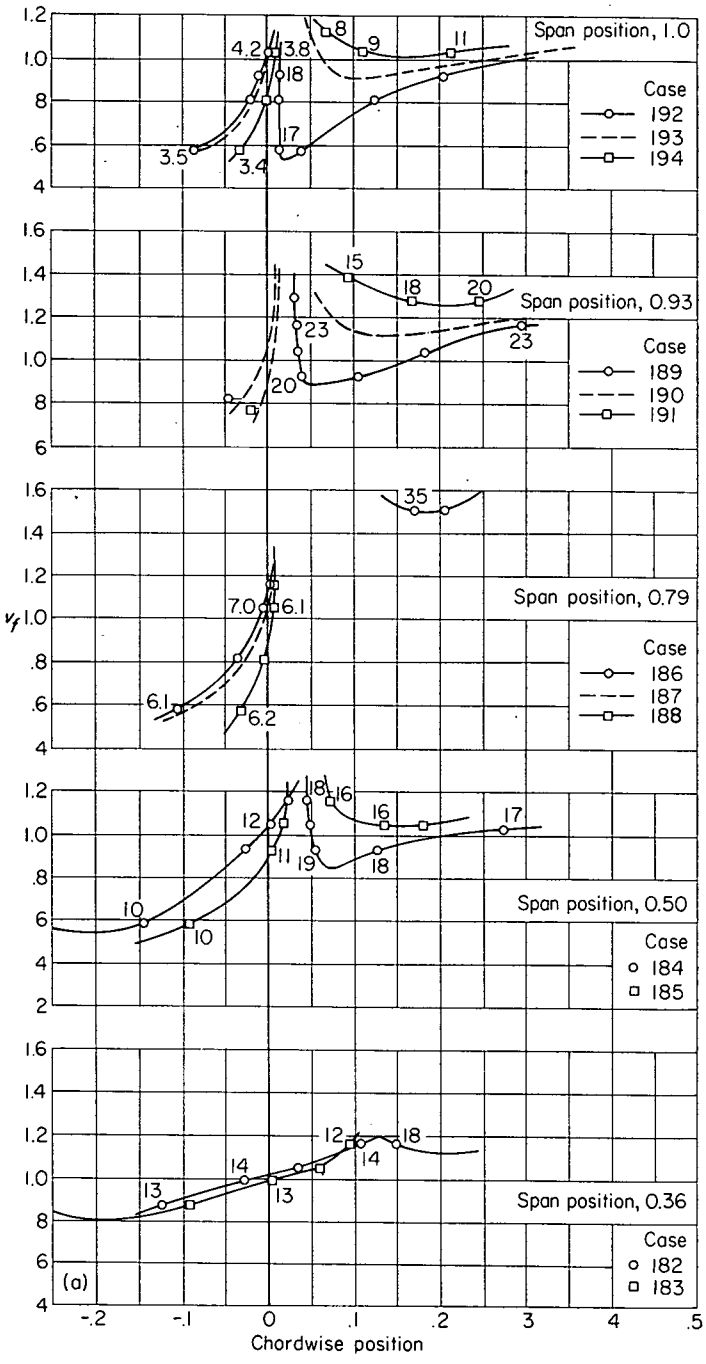
Although these figures (figs. 18 (a) to 18 (k)) give a good picture of the flutter characteristics, it is easier to interpret the results if all data are combined to construct flutter contours as discussed earlier. Such contours for the minimum and maximum values of k are shown in figures 19 (a) to 19 (h). These figures support the following conclusions:

(1) A chordwise position aft of the elastic axis is almost always undesirable.

(2) The 30- to 50-percent-span position and the tip location are generally undesirable.

(3) A position forward of the elastic axis and near the 70- to 80-percent-span position will, in general, greatly increase the flutter speed.

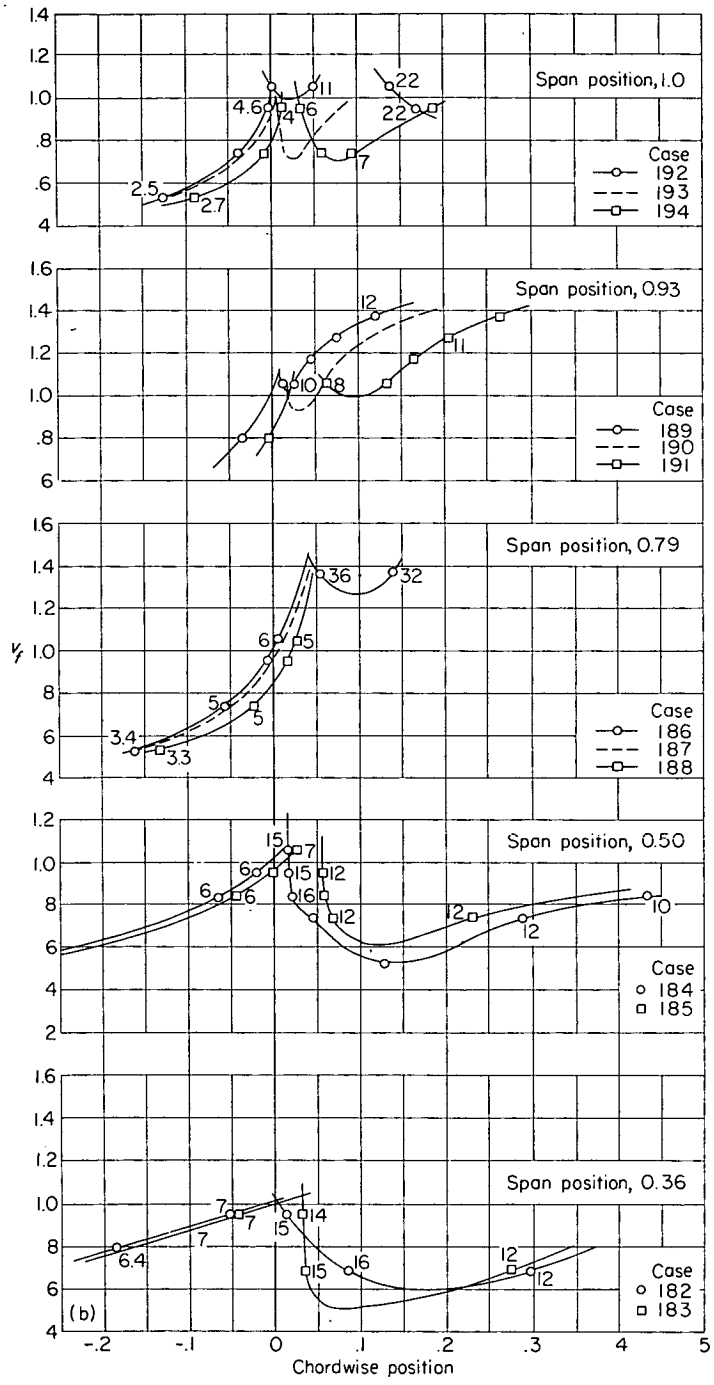
Since time did not permit a complete study of the characteristics for fighter B, data were obtained only for the cases of 0° and 45° sweepback with mass at the tip. Comparison of the results shown in figure 18 (e) with the corresponding data for fighter A in figures 18 (a), 18 (b), 18 (c), and 18 (d) shows that for this location there does not seem to be any significant difference in characteristics. Whether it is safe to extrapolate this result to other mass locations cannot be said at this time.



(a) Fighter A; $\Lambda=0°$; symmetric.

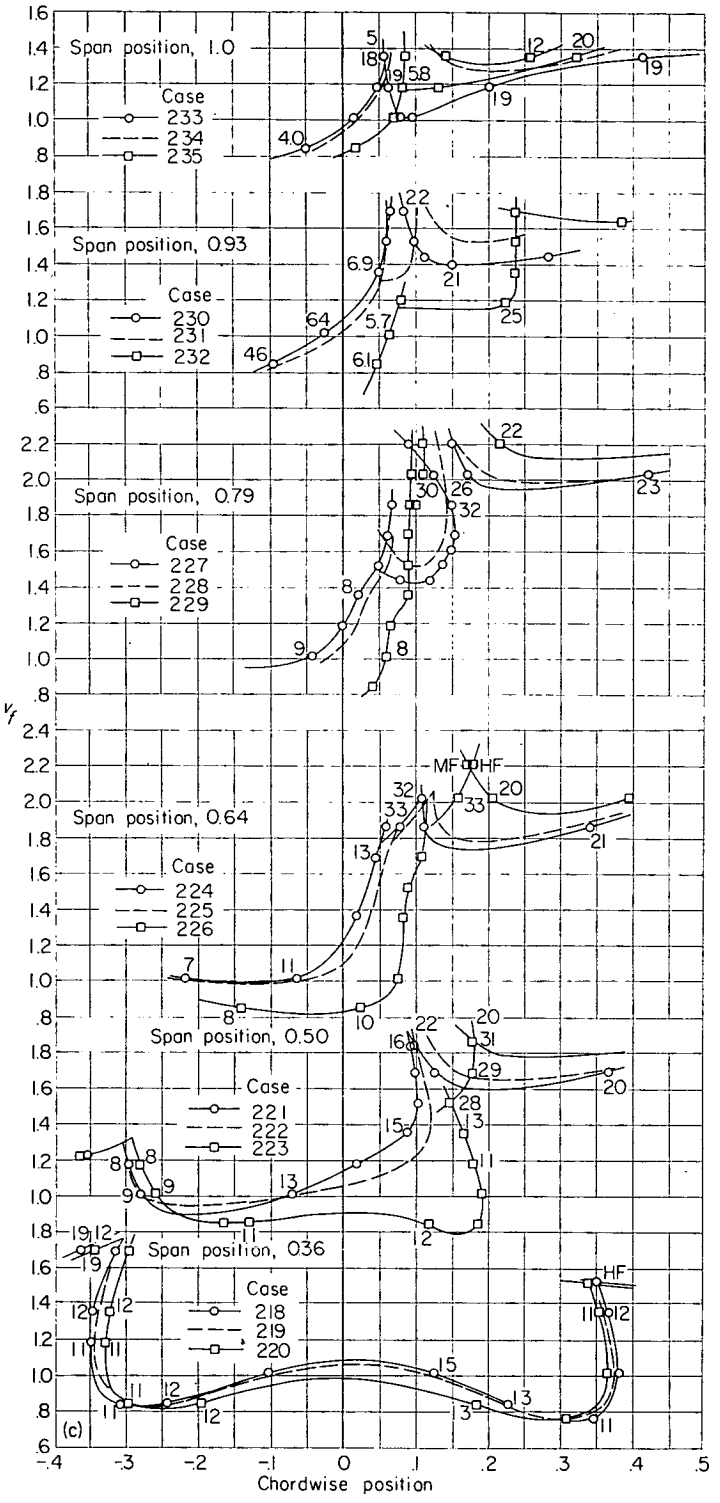
FIGURE 18.—Flutter characteristics against chordwise position of concentrated mass. HF, high frequency; MF, medium frequency; LF, low frequency.

Since the study of fighter A showed that the pitch radius of gyration had a small effect and since the pitch radius of gyration of a bomber engine is relatively well defined, it was decided to use only one value in the study of bomber airplanes. However, the practice of using one engine or two engines on a single pylon, as well as the different sizes of engines, gives a possible variation in mass which might well exceed a factor of 2. All bomber data were therefore obtained with both basic mass and half basic mass. For ease of comparison, the two sets of data are plotted side by side in the figures. Data for bomber A, $\Lambda=0°$, are contained in figures 18 (f) and 18 (g). Results for bomber B, $\Lambda=0°$,



(b) Fighter A; $\Lambda=0°$; antisymmetric.

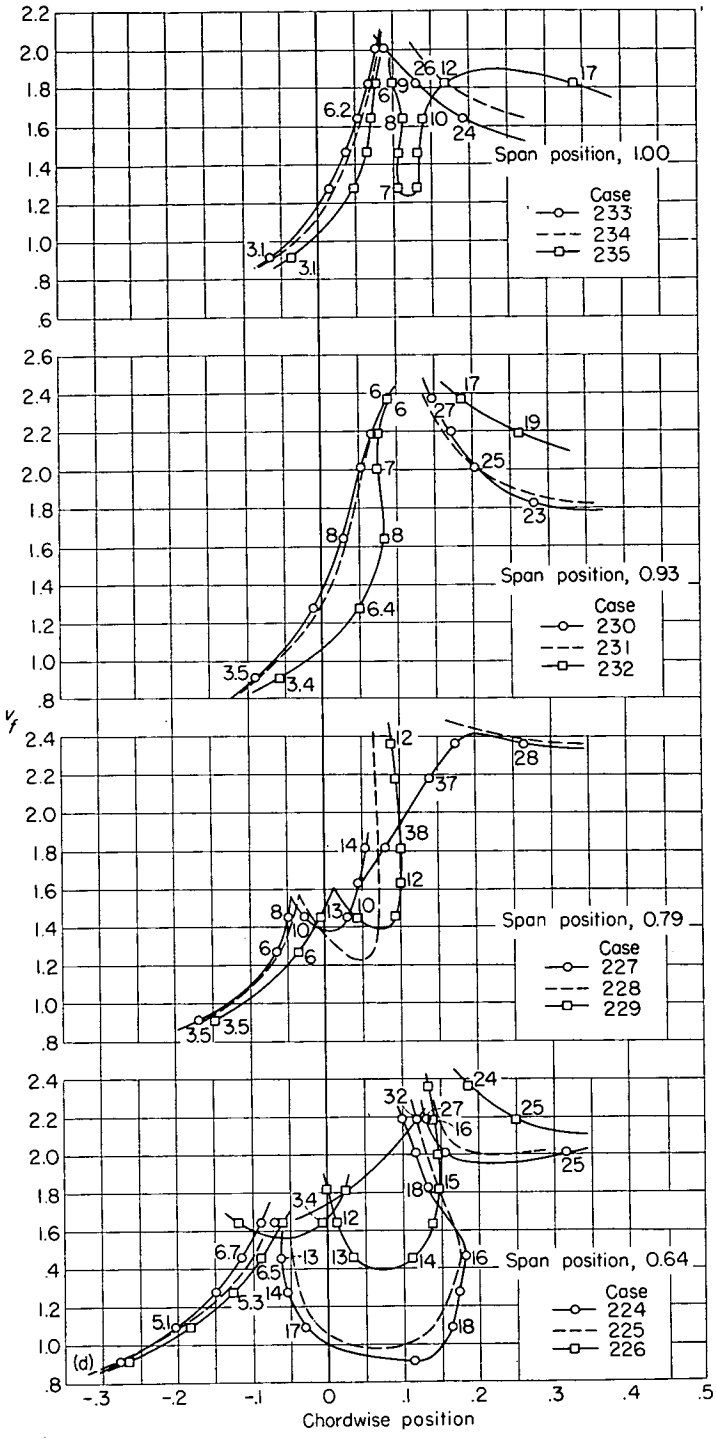
FIGURE 18.—Continued.



(c) Fighter A; $\Lambda=45°$; symmetric.

FIGURE 18.—Continued.

are given in figures 18 (h) and 18 (i), and the case of bomber B, $\Lambda=30°$, is summarized in figures 18 (j) and 18 (k). Again it is possible to simplify interpretation of these figures by combining the results into flutter-speed contours. However, it can be seen that data for basic mass and half basic mass are very similar, and such contours have been prepared only for the cases with basic mass. The flutter-speed contours are shown in figures 19 (i) to 19 (n). A study of these



(d) Fighter A; $\Lambda=45°$; antisymmetric.

FIGURE 18.—Continued.

figures shows some deviations from the results for fighter airplanes. The following conclusions can be drawn:

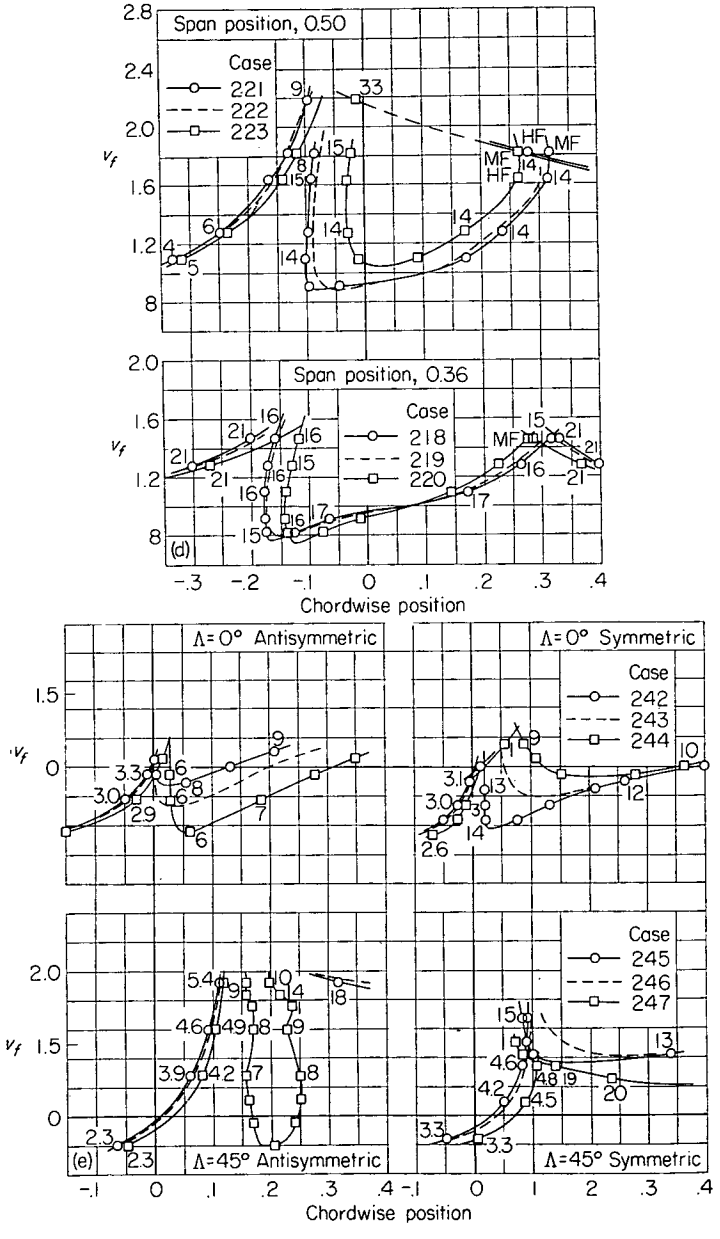
(1) A position aft of the elastic axis is almost always undesirable.

(2) The tip region is generally undesirable as a location for the mass.

(3) With few exceptions, any position forward of the elastic axis and between the root and the 90-percent-span position will give flutter speed equal to or greater than the bare-wing flutter speed.

(4) There are, in most cases, no practical locations which give any significant improvement in flutter characteristics. Two cases will be noted in which the speed might be increased 40 percent. The others are restricted to a 10- or 20-percent improvement.

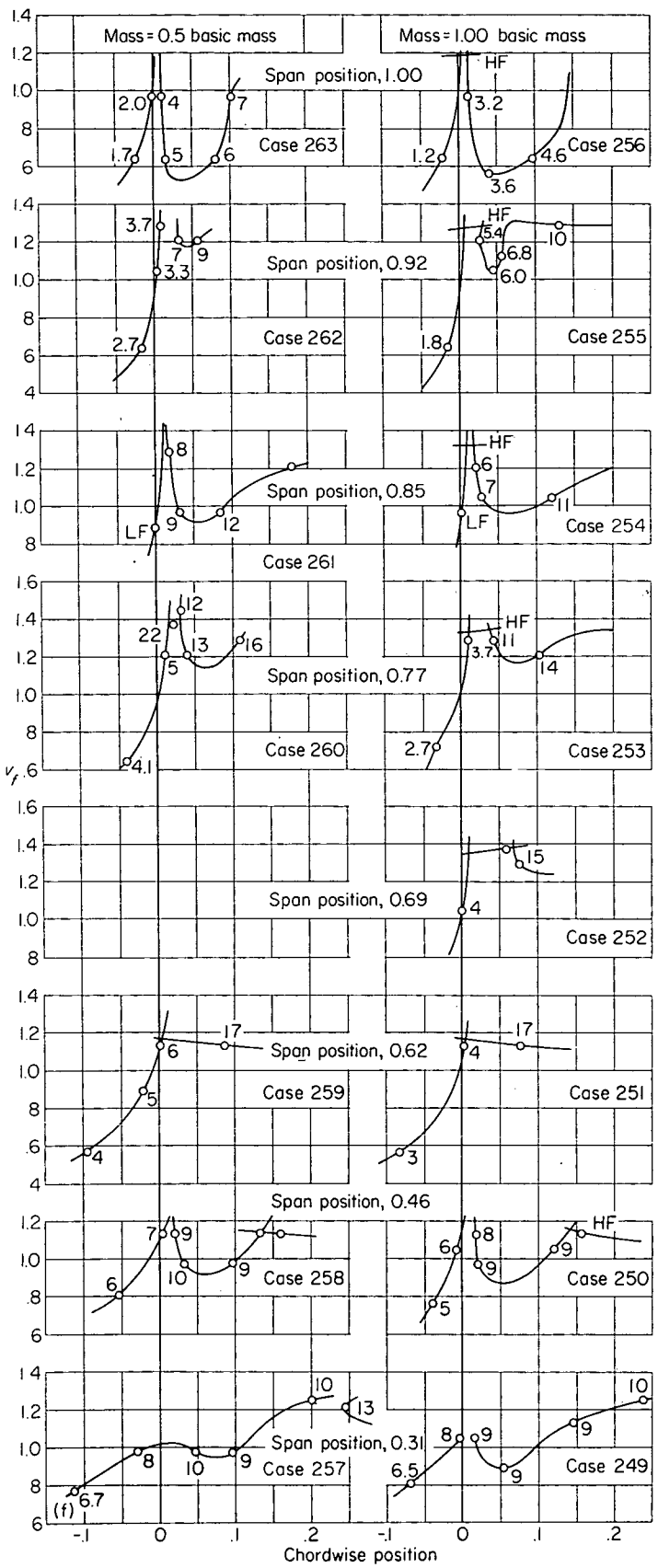
Since fighter planes showed remarkable variation in flutter characteristics with mass position, it was believed to be necessary to examine the effect of changes in the size (mass) of the concentrated mass. This was first studied at two spanwise positions for fighter A, $\Lambda=0°$. The positions are the tip and station 5 (0.79 span). Flutter characteristics as functions of chordwise position were measured for several values of mass. The three values of radius of gyration given in table XIII were used for all mass values, except that for very small values of mass only the 6-inch value was



(d) Continued.

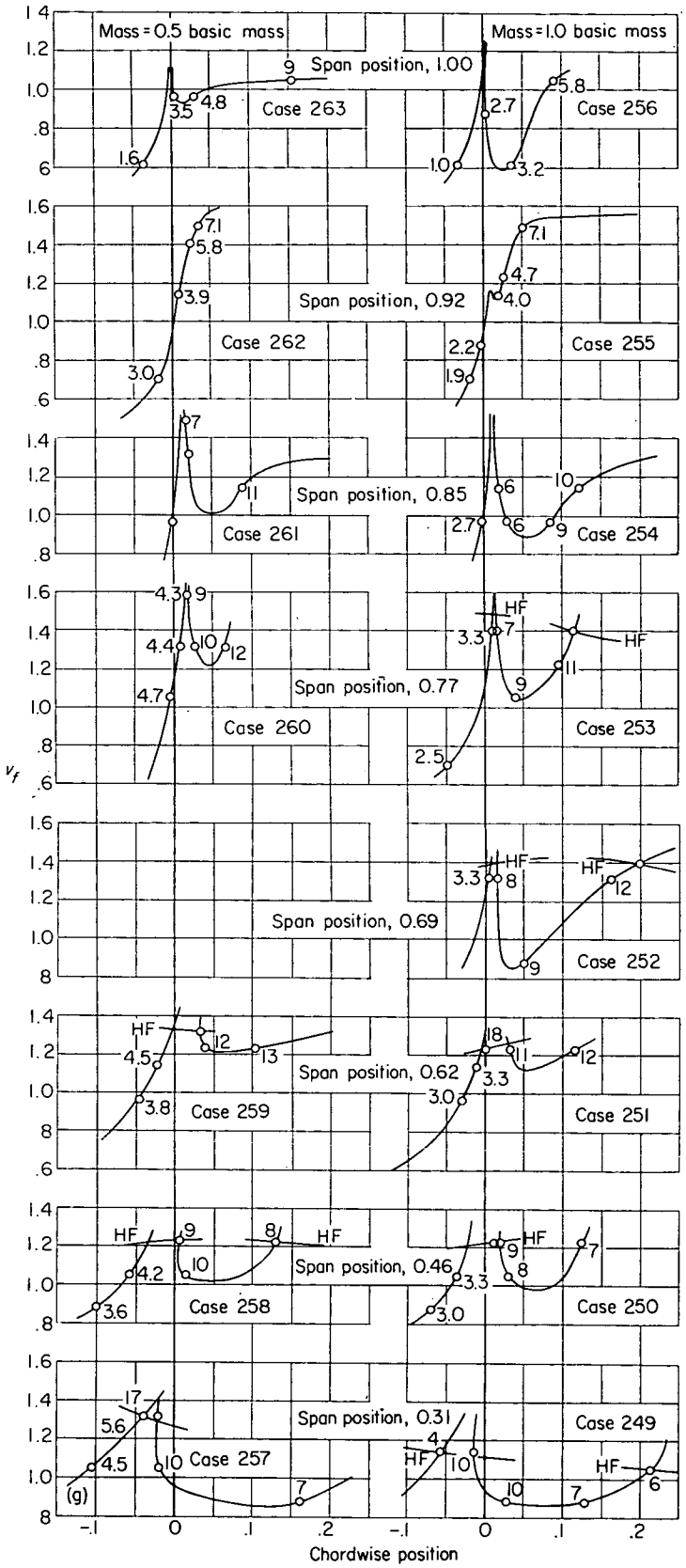
(e) Fighter B; data taken at tip.

FIGURE 18.—Continued.



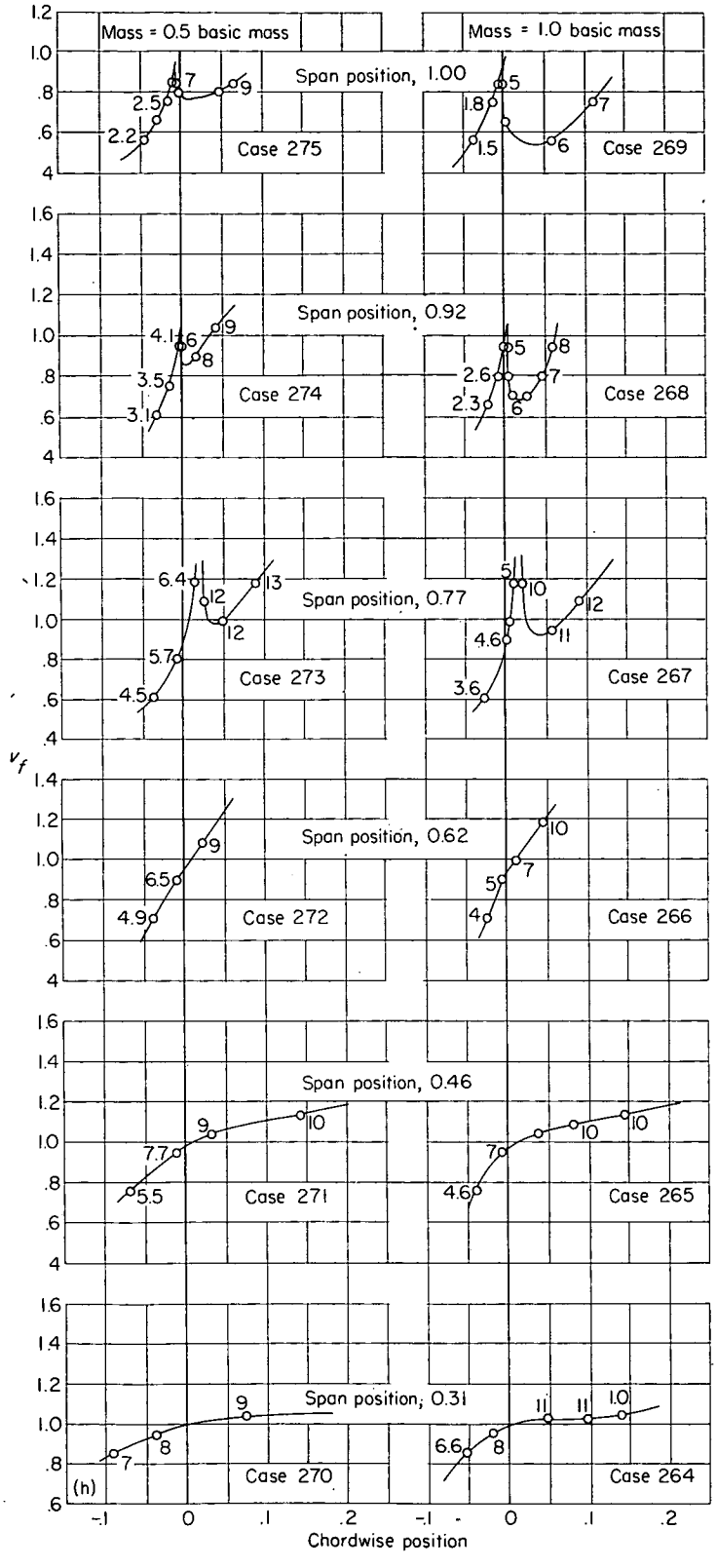
(f) Bomber A; $\Lambda = 0°$; symmetric.

FIGURE 18.—Continued.



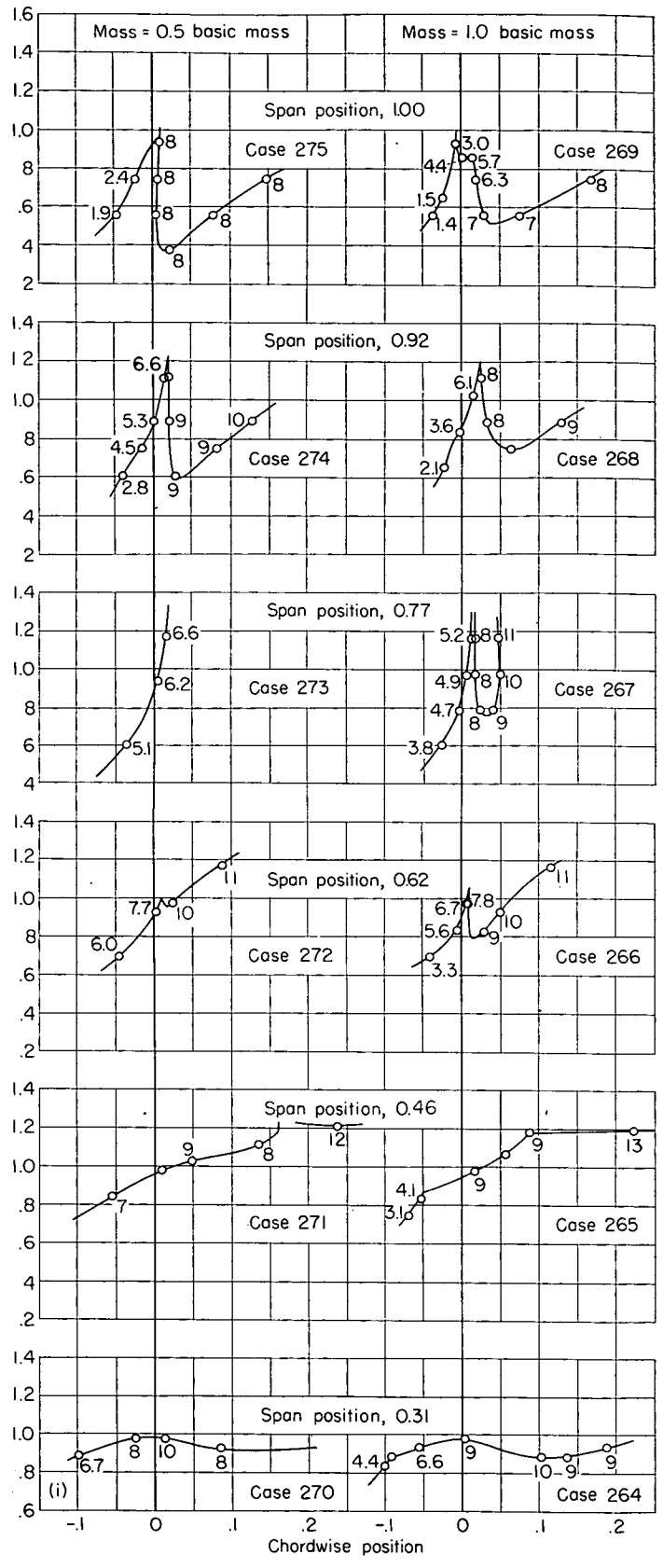
(g) Bomber A; $\Lambda = 0°$; antisymmetric.

FIGURE 18.—Continued.



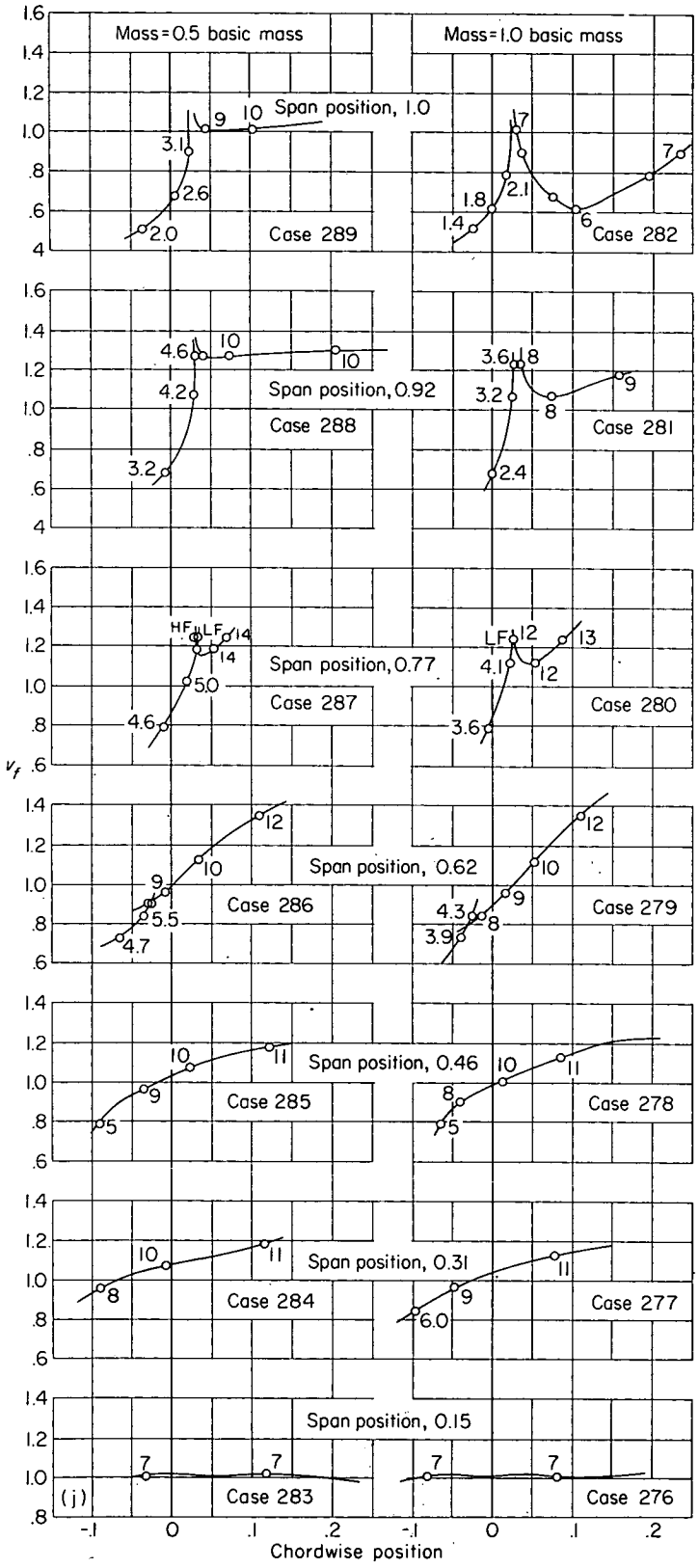
(h) Bomber B; $\Lambda=0°$; symmetric.

FIGURE 18.—Continued.



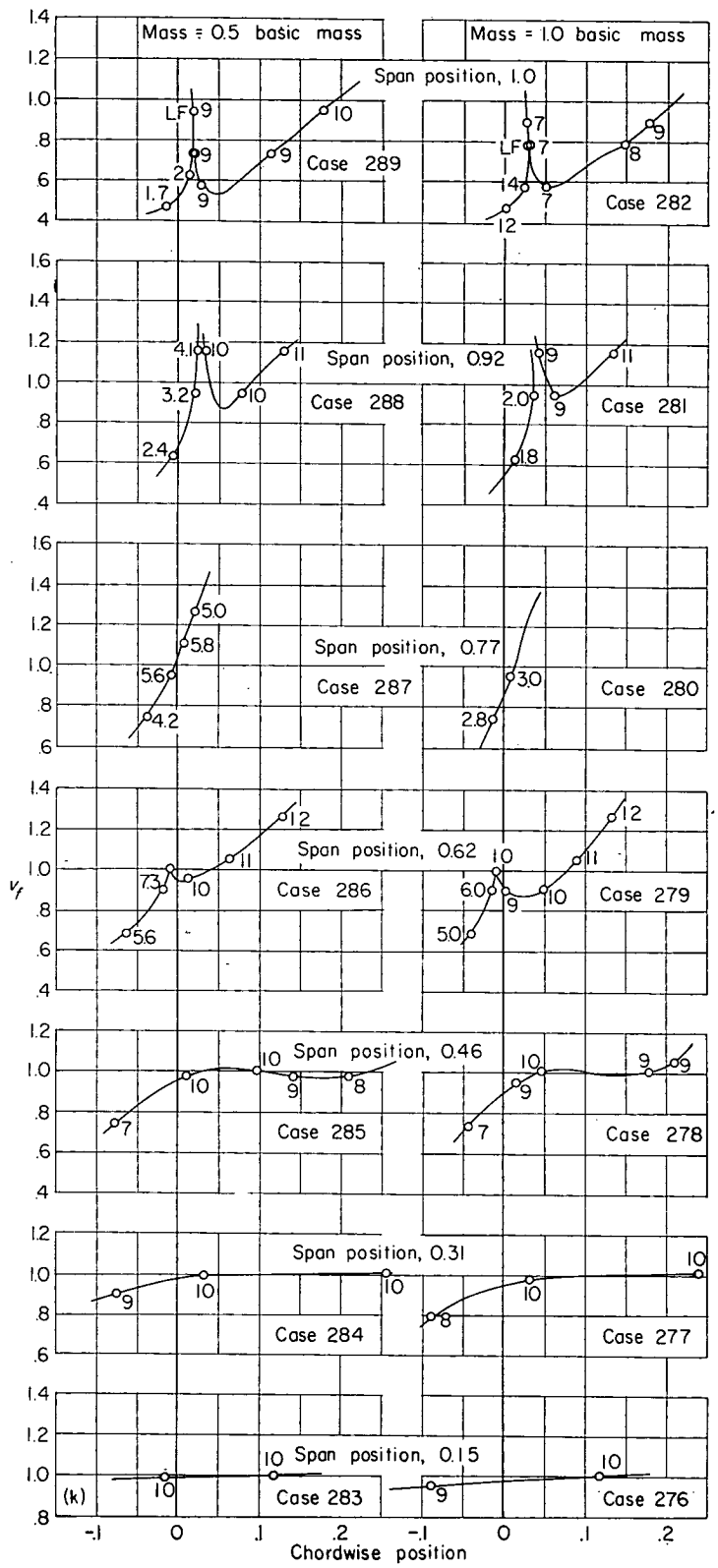
(i) Bomber B; $\Lambda=0°$; antisymmetric.

FIGURE 18.—Continued.



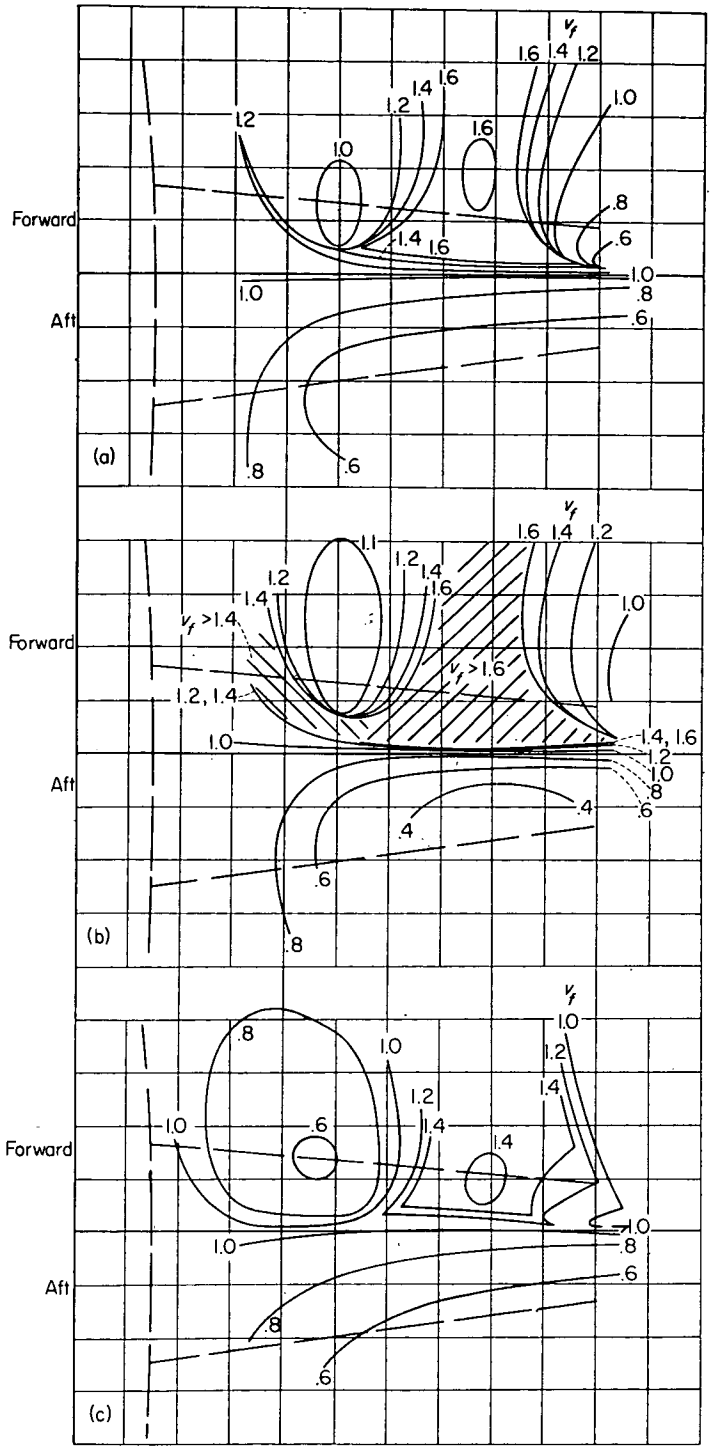
(j) Bomber B; Λ=30°; symmetric.

FIGURE 18.—Continued.



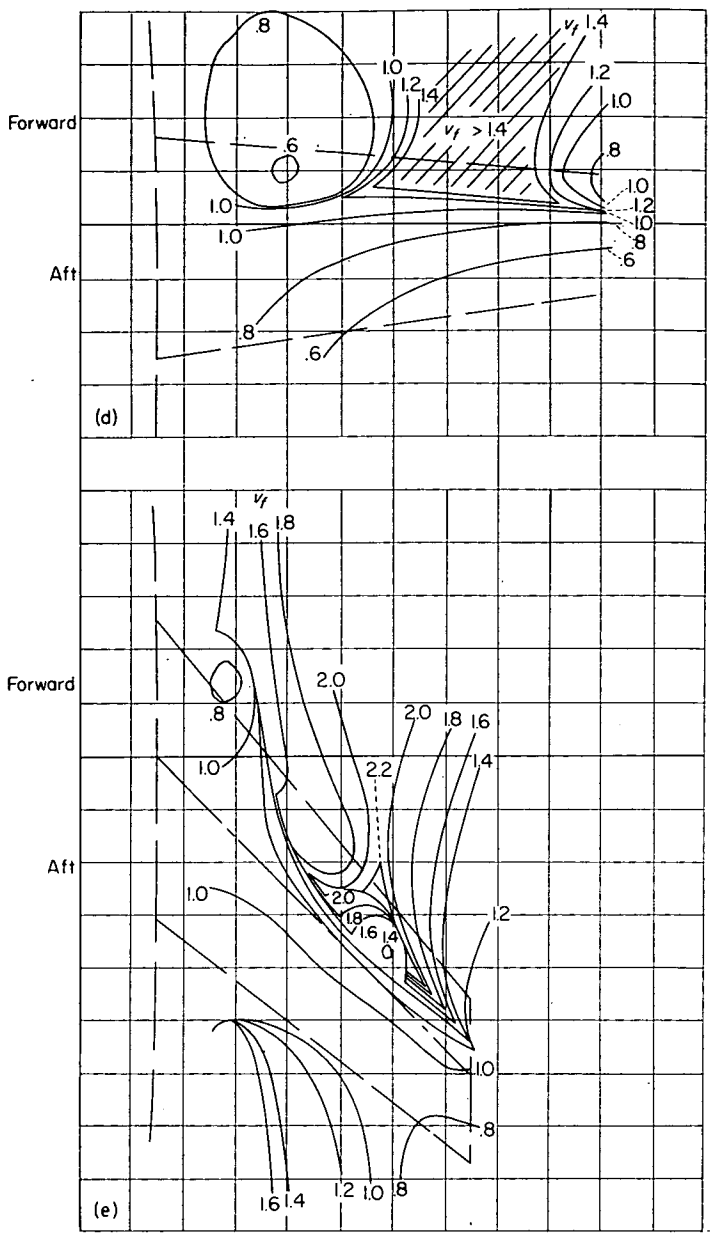
(k) Bomber B; Λ=30°; antisymmetric.

FIGURE 18.—Concluded.



(a) Fighter A; $\Lambda=0°$; symmetric; radius of gyration, 6 inches; $1.0v_f=989$ miles per hour.
(b) Fighter A; $\Lambda=0°$; symmetric; radius of gyration, 30 inches; $1.0v_f=989$ miles per hour.
(c) Fighter A; $\Lambda=0°$; antisymmetric; radius of gyration, 6 inches; $1.0v_f=1{,}091$ miles per hour.

FIGURE 19.—Contours of constant flutter speed with concentrated mass.

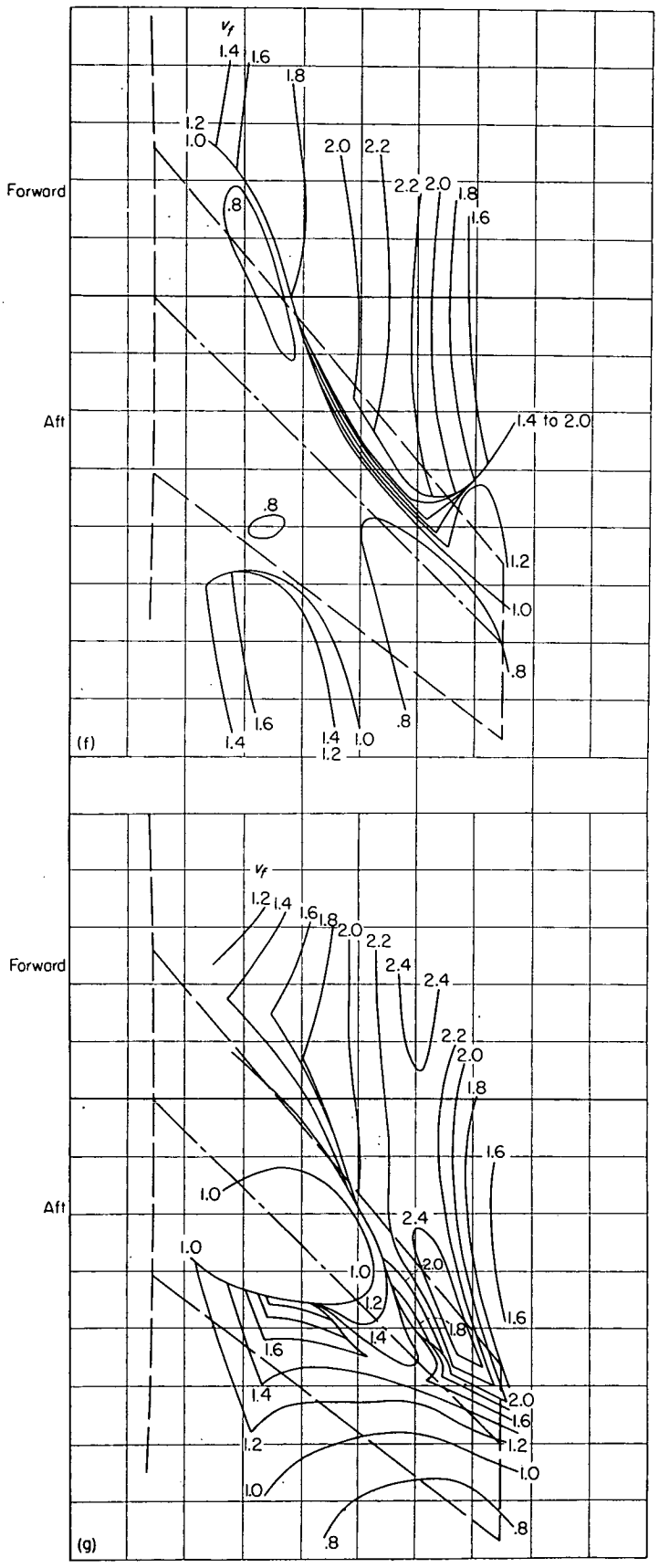


(d) Fighter A; $\Lambda=0°$; antisymmetric; radius of gyration, 30 inches; $1.0v_f=1{,}091$ miles per hour.
(e) Fighter A; $\Lambda=45°$; symmetric; radius of gyration, 6 inches; $1.0v_f=1{,}028$ miles per hour.

FIGURE 19.—Continued.

used. However, because of the similarity of results, data are presented only for the maximum value ($k=30$ inches) and minimum value ($k=6$ inches). Case numbers are listed in table XIV.

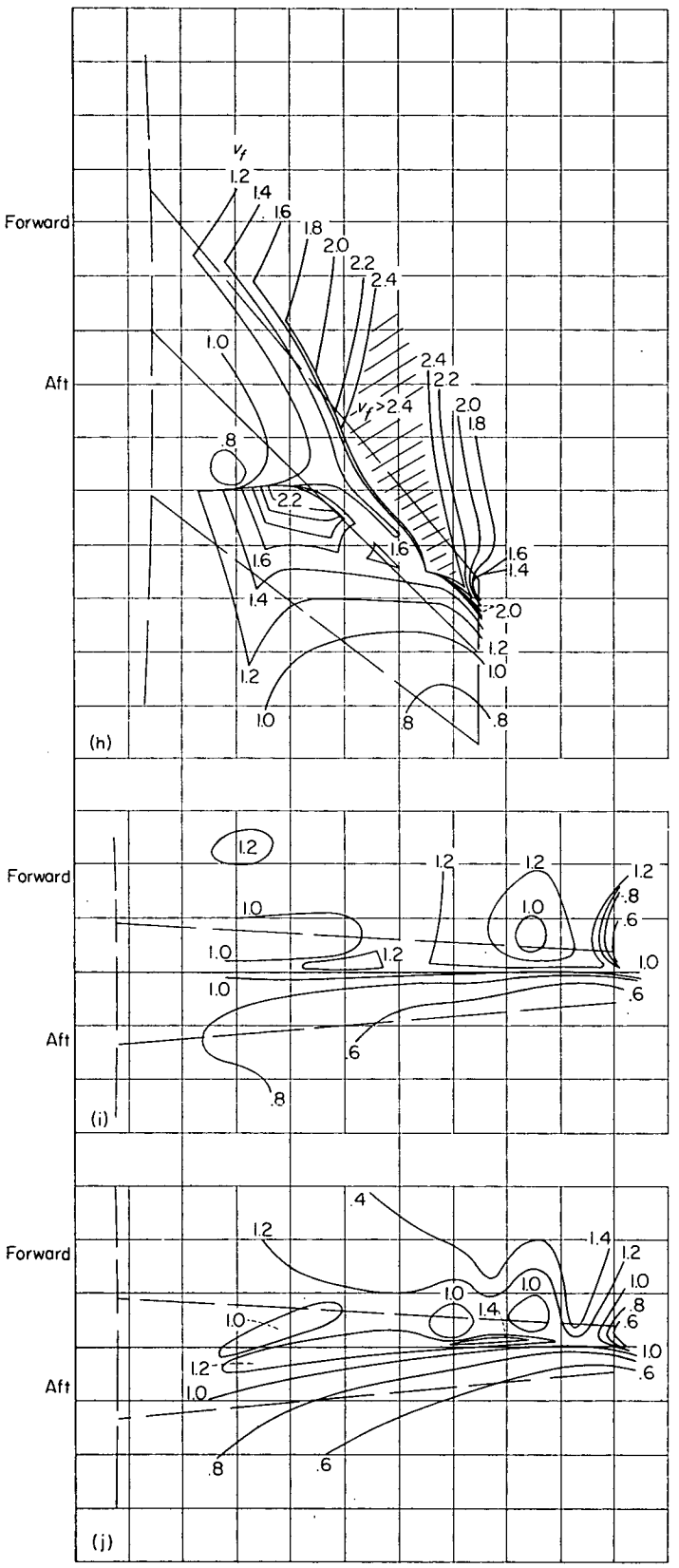
The results for tip location shown in figure 20 (a) show a very interesting progression in characteristics as the mass is reduced to zero. Most striking is the fact that no significant change takes place when the mass is varied from twice basic value to half basic value. Even with mass reduced to 8 percent of basic value, the three flutter roots for antisymmetric motion and the two flutter roots for symmetric motion can still be identified though their characteristics are by this time somewhat altered. Similar data for the mass at 0.79 span are presented in figure 20 (b). Figure 20 (a) also illustrates graphically the danger in extrapolating results. For a mass at the 0.10 chordwise position and symmetric motion, a mass equal to 0.008 basic mass increases flutter speed to 1.07. Doubling the mass increases it to 1.16. Again doubling it will increase the speed to some unknown value greater than 1.40. However, if the mass is again



(f) Fighter A; $\Lambda=45°$; symmetric; radius of gyration, 30 inches; $1.0v_f=1{,}028$ miles per hour.

(g) Fighter A; $\Lambda=45°$; antisymmetric; radius of gyration, 6 inches; $1.0v_f=881$ miles per hour.

FIGURE 19.—Continued.

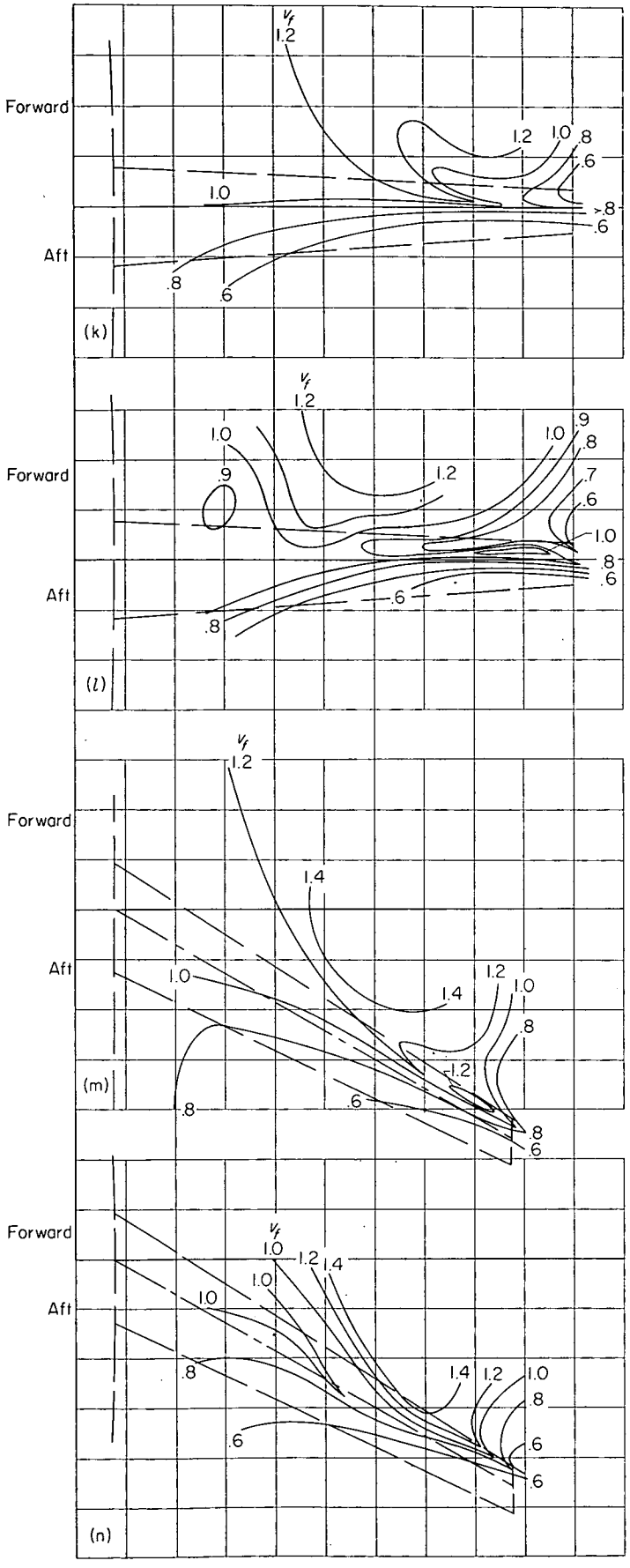


(h) Fighter A; $\Lambda=45°$; antisymmetric; radius of gyration, 30 inches; $1.0v_f=881$ miles per hour.

(i) Bomber A; symmetric; $1.0v_f=818$ miles per hour.

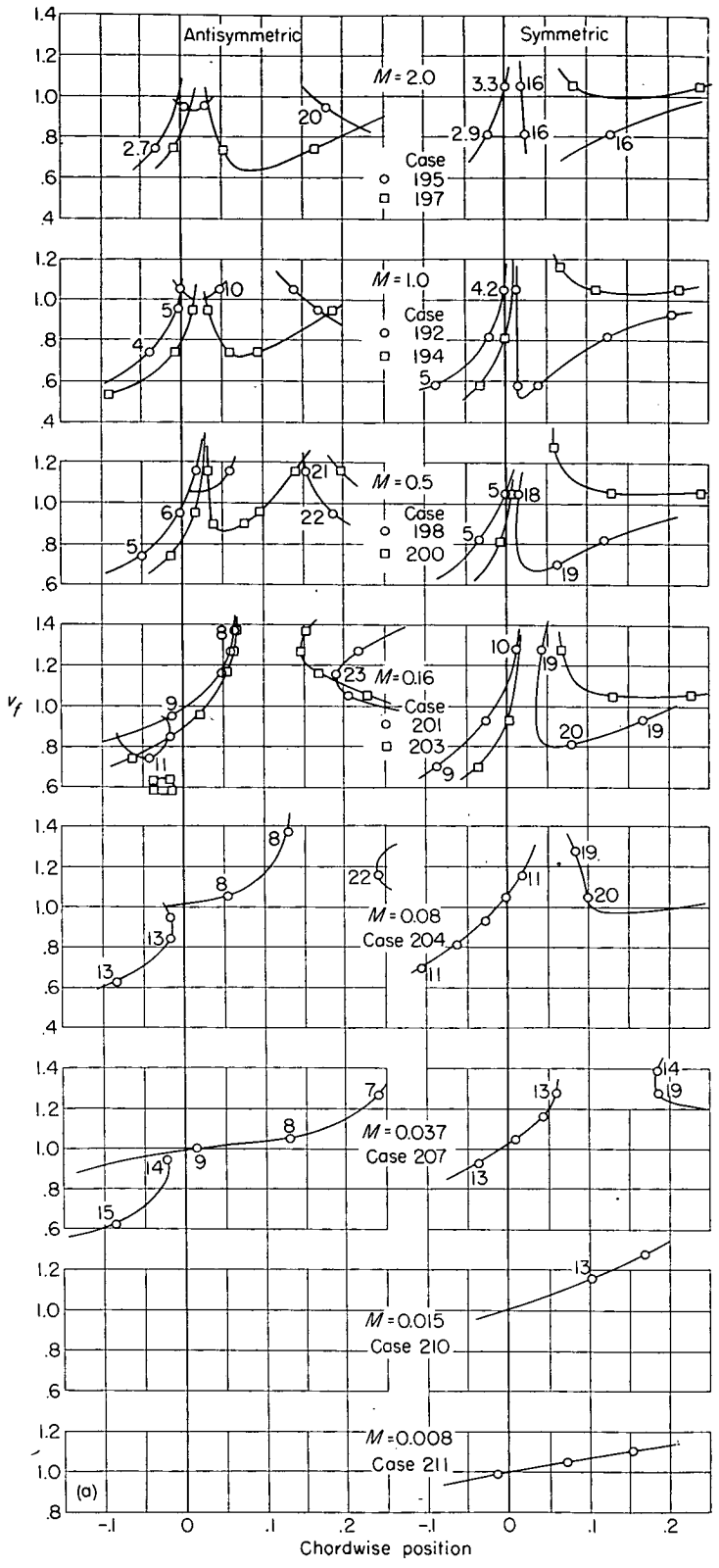
(j) Bomber A; antisymmetric; $1.0v_f=886$ miles per hour.

FIGURE 19.—Continued.



(k) Bomber B; symmetric; $1.0v_f=1{,}216$ miles per hour.
(l) Bomber B; antisymmetric; $1.0v_f=1{,}216$ miles per hour.
(m) Bomber B; symmetric; $1.0v_f=1{,}165$ miles per hour.
(n) Bomber B; antisymmetric; $1.0v_f=1{,}244$ miles per hour.

FIGURE 19.—Concluded.

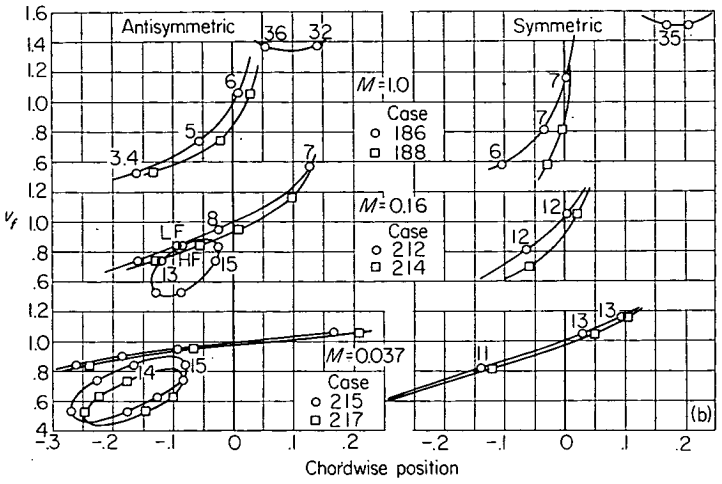


(a) Concentrated mass at tip.

FIGURE 20.—Effect of size of concentrated mass on flutter characteristics. Fighter A; $\Lambda=0°$.

increased by a factor of about 2.8, the flutter speed (of another root) will have dropped to 1.00 again.

Flutter characteristics were also measured for basic and half basic mass at the wing tip with sweepback angle of 45°. This case was chosen because the antisymmetric characteristic for a 30-inch radius of gyration (fig. 18 (d)) showed a



(b) Concentrated mass at 0.79-span position.

FIGURE 20.—Concluded.

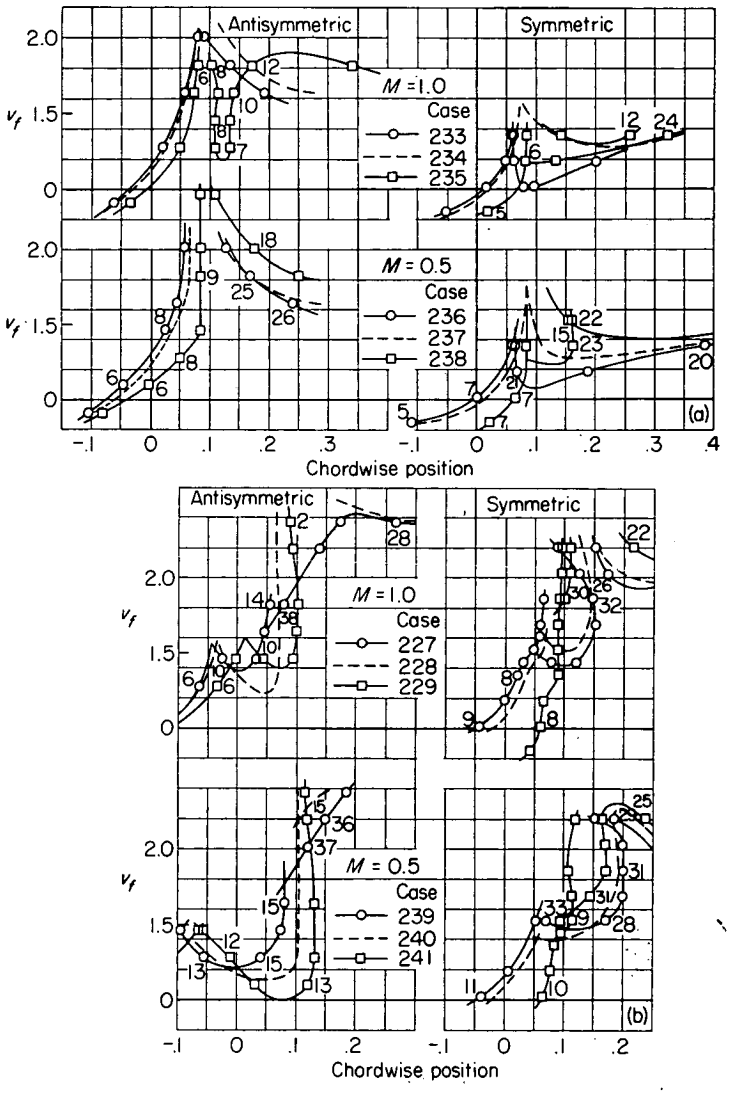
very unusual characteristic. Figure 21 (a) shows that reduction of the mass by a factor of 2 eliminates the anomalous behavior, but in all other respects gives results which are essentially the same as the basic mass. Figure 21 (b) gives similar data for the mass at the 0.79 span position with $\Lambda = 45°$. Again the results for basic mass and half basic mass are not significantly different. It is perhaps unwise to attempt any general statement, but there is every indication that the essential features shown in the flutter-speed contours of figure 19 would not be profoundly altered if either mass or pitching inertia were increased or decreased by a factor as large as 2.0.

ACCURACY AND PROBABLE ERRORS

It is believed that a discussion of the expected accuracy of the results will be more meaningful now that the reader has observed the nature and scope of the data obtained. The analog computer is not composed of perfect electrical elements. For example, the inductors used in this study have loss characteristics corresponding to a damping factor of about $g=0.01$. Transformers also have significant losses. The electrical analog of the airplanes studied in this report had an electrical damping corresponding to a structural damping between $g=0.02$ and $g=0.03$. This is not greatly different from the damping to be found in conventional aircraft construction, so no corrections were made for this internal damping.

No general statement can be made about the effect of random computer errors. Some give rise primarily to an error in the damping factor of the roots, in which the $(g-v)$ curve is shifted vertically. Other errors give rise basically to an error in velocity, in which the curve is primarily shifted horizontally. Since the slope of the curve of g against v is by no means constant, it becomes impossible to give a specific figure for accuracy of flutter speed. In unusual cases, where roots are of the type shown in figure 12, flutter may be predicted when in fact it will not occur for these roots at all. This distinction, which must be made mathematically, is of no importance in practical cases. An airplane which shows a flutter damping of $g=0.01$ and is therefore theoretically stable is not to be regarded as any more satisfactory or useful than one which shows a damping $g=-0.01$ and would therefore theoretically fly apart. Manufacturing tolerances and the safety factors required in aircraft will not permit use of an aircraft unless it is moderately stable for a significant variation in all structural parameters. It is believed that, exclusive of errors introduced by the finite-difference structure and approximations in the aerodynamic theory, the results obtained in this study have a probable error in damping factor of about $g=\pm 0.02$ or a probable error in flutter speed of about 2 percent, whichever is applicable in the light of the above discussion. However, trends obtained by variation of structural parameters are considerably more accurate than this would imply, since any error would persist with roughly the same value in all cases involving such parameter variations.

For cases 1 to 181, it is possible to construct curves of g against v although they have not been made a part of this report. These curves serve to show the steepness with which the roots pass through flutter and give some indication of the accuracy of the flutter speed. This situation does not exist for cases 181 to 289. For concentrated-mass variations,



(a) Basic mass and 0.5 basic mass at tip.
(b) Basic mass and 0.5 basic mass at 0.79-span position.

FIGURE 21.—Comparison of characteristics for basic mass and 0.5 basic mass. Fighter A; $\Lambda = 45°$.

computations were carried out in such a way that only flutter speeds and frequency were obtained. Consequently, it is not possible to delineate areas which are "safe" from the standpoint of flutter. It is known, for example, that where a long pendant lobe is observed, as for case 235 in figure 18 (d), the system is barely unstable everywhere within this lobe. There are similar regions where the system is barely unstable within an elliptical-shaped boundary, for example, case 212 (fig. 20 (b)). Similarly, case 214 is barely stable in this region and yet no flutter root is even shown since the system does not become actually unstable at any point.

These remarks are not made to show the flutter curves to be valueless, but to caution the reader against making inferences not contained in the report and not legitimately supported by the data presented here.

SUMMARY OF RESULTS

Certain trends in flutter characteristics for typical modern aircraft seem to be indicated by this study of the incompressible flutter characteristics of aircraft wings. In some cases a few deviations are found. It is probable that if more extreme aircraft designs were considered even more would be observed. Nevertheless, this summary may serve as a useful guide.

(1) In the following table are listed the average changes in flutter speed for a 1-percent change in each parameter, the change being made from the basic value except for center-of-mass and elastic-axis location, in which cases several locations are assumed.

Change in parameter	Average change in flutter speed, percent
Increase wing mass 1 percent	0
Increase wing pitching inertia 1 percent	—. 1
Increase bending rigidity 1 percent	0
Increase torsional rigidity 1 percent	. 5
Increase wing chord 1 percent	—. 7
Center of mass forward 1 percent of chord from—	
40-percent location	3. 0
50-percent location	1. 7
60-percent location	. 8
Elastic axis forward 1 percent of chord from—	
40-percent location	3. 2
50-percent location	1. 8

(2) Localized change in torsional rigidity is most effective in changing flutter speed of a bare-wing airplane if the change is made between midspan and root. For bombers with large concentrated mass on the wing, torsional rigidity either inboard or outboard of the mass will usually govern flutter speed, depending on the type of flutter existing. Sweepback was not observed to have a systematic effect. Pitching flexibility of the concentrated-mass support has a definite influence on flutter speed. In many cases a tuning effect was observed, with a 10- to 40-percent decrease in flutter speed. This effect was not always observed; in some cases, the flutter speed was significantly increased.

(3) Perhaps the most interesting results will be found in the effects of a concentrated-mass location. For a wide range of mass and radius-of-gyration values the results were very systematic. For fighter-type planes it was found that:

(a) Aft chordwise positions are usually undesirable.
(b) The 30- to 50-percent-span and tip locations are generally undesirable.
(c) A forward location near the 70- to 80-percent-span position will, in general, greatly increase flutter speed.

For bomber-type planes these results are somewhat modified:

(a) Aft chordwise positions are usually undesirable.
(b) The tip location is generally undesirable.
(c) With few exceptions any location forward of the elastic axis and between root and 0.90-span position is satisfactory, although flutter speed is rarely greater than bare-wing flutter speed by any significant amount.

There is perhaps no need to remark that these results can be altered by introduction of a flexibility in the concentrated-mass support.

CALIFORNIA INSTITUTE OF TECHNOLOGY,
PASADENA, CALIF., *June 6, 1955.*

REFERENCES

1. MacNeal, R. H., McCann, G. D., and Wilts, C. H.: The Solution of Aeroelastic Problems by Means of Electrical Analogies. Jour. Aero. Sci., vol. 18, no. 12, Dec. 1951, pp. 777–789.
2. Benscoter, Stanley U., and MacNeal, Richard H.: Introduction to Electrical-Circuit Analogies for Beam Analysis. NACA TN 2785, 1952.
3. Sewall, John L.: Experimental and Analytical Investigation of Flutter of a Nonuniform Sweptback Cantilever Wing With Two Concentrated Weights. NACA RM L51H09a, 1951.
4. Nelson, Herbert C., and Tomassoni, John E.: Experimental Investigation of the Effects of Sweepback on the Flutter of a Uniform Cantilever Wing With a Variably Located Concentrated Mass. NACA RM L9F24, 1949.
5. Barmby, J. G., Cunningham, H. J., and Garrick, I. E.: Study of Effects of Sweep on the Flutter of Cantilever Wings. NACA Rep. 1014, 1951. (Supersedes NACA TN 2121.)
6. Scanlan, Robert H., and Rosenbaum, Robert: Introduction to the Study of Aircraft Vibration and Flutter. The Macmillan Co., 1951.
7. McCann, G. D., and Braham, H. S.: A Study of the Accuracy of Lumped Parameter and Analog Computer Representations of Cantilevered Beams Under Conditions of Static Stress and Dynamic Vibrations. Rep. No. 3, Contract AF 18(600)-669, Office of Sci. Res. and C. I. T., 1955.
8. Goland, Martin, and Luke, Y. L.: The Flutter of a Uniform Wing With Tip Weights. Jour. Appl. Mech., vol. 15, no. 1, Mar. 1948, pp. 13–20.
9. Runyan, Harry L., and Watkins, Charles E.: Flutter of a Uniform Wing With an Arbitrarily Placed Mass According to a Differential-Equation Analysis and a Comparison With Experiment. NACA Rep. 966, 1950. (Supersedes NACA TN 1848.)
10. Wilts, C. H.: Finite Difference Errors in the Flutter Speed of a Uniform Wing With an Arbitrarily Placed Mass. Analysis Lab. Rep., C. I. T., June 1954.
11. Runyan, Harry L., and Sewall, John L.: Experimental Investigation of the Effects of Concentrated Weights on Flutter Characteristics of a Straight Cantilever Wing. NACA TN 1594, 1948.

REPORT 1391

INVESTIGATION OF A NONLINEAR CONTROL SYSTEM [1]

By I. Flügge-Lotz, C. F. Taylor, and H. E. Lindberg

SUMMARY

Nonlinear elements are sometimes added to linear control systems in order to improve the response of the system to an arbitrary input. This can be done in different ways, one of them being the variation of the coefficients of the differential equation describing the system before the nonlinear elements are added. This variation of the coefficients may be done in a continuous or in a discontinuous way. In the present paper a discontinuous variation of the coefficients is studied in detail and investigated for practical use.

The nonlinear feedback is applied to a second-order system. From former analytical considerations the process of control is visualized as establishing an ensemble of linear second-order differential equations (some with stable and some with unstable homogeneous solutions) and switching from one equation to another so as to maintain small instantaneous error for relatively arbitrary inputs. Physically, this control process is realized with a linear second-order control system to which have been added possible discrete combinations of proportional and derivative feedback. The particular combination of feedback employed at any instant is determined by a feedback switching circuit which is in turn operated by sensed binary information obtained from the output, output derivative, error, and error derivative (namely, the signs of these variables). Techniques that are common to the digital computer field are used to implement this switching circuit.

Once physical realization is completed, simulation techniques are used to study and evaluate the performance of the nonlinear control system and to compare it with a linear system for a wide variety of inputs. A detailed quantitative study of the influence of relay delays and of a transport delay is also given. In addition, the effects of physical imperfections that are likely to be encountered in any application of the control theory are considered (e. g., velocity and acceleration limits).

An analysis of the experimental results shows that this type of nonlinear control system performs better than a linear control system having a natural frequency 15 times greater. For this comparison, performance is evaluated in terms of the average value of the magnitude of the instantaneous error for band-limited inputs. Further, in contrast with the linear system, the nonlinear system performance is virtually independent of variation in the damping factor of the system.

A preliminary extension of this type of nonlinear control concept to higher order systems is presented. Experimental results are given for a third-order system. These results show that just as in the second-order case the nonlinear system performance is better than that of a comparable linear system.

INTRODUCTION

With the demand for more exacting performance, more emphasis has been placed on nonlinear aspects of control systems. The term "control systems" can be interpreted to include active networks and feedback amplifiers as well as servomechanisms. From the standpoint of analysis, unintentional nonlinearities have to be taken into account to explain performance. From the standpoint of synthesis, intentional nonlinearities have been introduced to improve performance. However, up to this date only in special cases have advancements been obtained in the field of nonlinear control systems.

The designs of nonlinear control systems have inherent advantages. One advantage is that the response of a nonlinear system at a certain time can be made less dependent upon past response than can a linear system of comparable power-handling capability.[2] This means that the nonlinear system can be made to follow more arbitrary classes of inputs with less dynamic error than the comparable linear system. Another advantage is that the mathematical difficulties encountered may actually be conducive to consideration of more realistic criteria of performance. In the nonlinear realm it is essentially as easy to invoke a criterion such as the minimization of instantaneous error for nonstationary random inputs as it is to invoke the largest possible flat amplitude response for sinusoidal inputs.

In the present paper a control system of second order, which was first suggested by Flügge-Lotz and Wunch on the basis of analytical studies (ref. 1), is investigated. The physical realization of this system and its performance are studied in great detail by Dr. I. Flügge-Lotz and Dr. C. F. Taylor. A detailed quantitative study of the influence of relay delays and of a transport delay was made by Dr. H. E. Lindberg and is given in appendix A.

This investigation was conducted at Stanford University under the sponsorship and with the financial assistance of the National Advisory Committee for Aeronautics. The authors wish to thank Dr. A. M. Peterson of the Electrical Engineering Department of Stanford University for his continued interest and his most helpful advice on the

[1] Supersedes NACA TN 3826, "Investigation of a Nonlinear Control System" by I. Flügge-Lotz and C. F. Taylor, 1957.

[2] In linear theory, the impulse response or the autocorrelation function of the system gives an indication of how past response is weighed.

electronic problems which were encountered during this investigation. They also wish to thank Dr. G. S. Bahrs for his useful suggestions for a special transistor switching circuit.

SYMBOLS

A	peak-to-peak amplitude of input
a,b,c	parameters defining a system
a^+,b^+,c^+	constants used in appendix B
$\bar{a},\bar{b},\bar{c},$	parameters in differential equation for control servo
B	viscous damping of motor and reflected load referred to motor shaft
D	linear damping factor
$E=y-x=-e$	
e	instantaneous error, $x-y$
f	function
g_i,g_o	input and output of Padé circuit, respectively
$H(p)$	transfer function, $1/(\alpha p+1)$
I	inertia of motor rotor, gears, and reflected load
$i=\sqrt{-1}$	
K_1,K_2	gain constants
k_m	constant of proportionality between output velocity and back electromotive force
M	constant depending on initial conditions
p	operator, indicating differentiation with respect to independent variable; that is, d/dt if real time variable is used and $d/d\tau$ if nondimensional time variable is used
T	repetition rate or period
t	time
t_d	switching delay
t_{md}	maximum allowable switching delay
V	input voltage
x	input into system
y	output from system
$\bar{y}$	approximation of output
α	symbol used to denote different constants
$\beta_m=-{}_1\beta \operatorname{sgn}(y'e)-{}_2\beta \operatorname{sgn}(y'e')$	
$(\beta_m,\gamma_n)_{min}$	smallest values of parameters giving good nonlinear system performance
${}_1\beta,{}_2\beta,{}_1\gamma,{}_2\gamma$	positive constants
$\gamma_n=-{}_1\gamma \operatorname{sgn}(ye)-{}_2\gamma \operatorname{sgn}(ye')$	
δ	positive constant
ϵ	small positive quantity
μ,ν	coordinates introduced in appendix E
ρ	radius of curvature
σ	real part of complex frequency variable $\sigma+i\omega$
τ	nondimensional time variable normalized with respect to ω_ν, $\omega_\nu t$
Ω	nondimensional frequency, ω/ω_ν
ω	frequency
ω_ν	natural frequency of undamped linear system
$\operatorname{sgn}(f)=f/\lvert f\rvert$	
$\overline{(\ )}$	time average
$(\ )'$	$d(\ )/d\tau$
$(\ )''$	$d^2(\ )/d\tau^2$
$\overset{o}{=}$	equality sign in equations which describe operations (see eqs. (2) and (3))

Subscripts:

as	at an actual switch point
d	ideal or desirable
e	error
i	initial or input
im	image
L	limit
lin	linear
$m,n=0,1,2,3$	
max	maximum or upper bound
min	minimum or lower bound
$nonlin$	nonlinear
o	optimum, output

REVIEW OF LINEAR CONTROL THEORY

It is desirable to obtain from linear control theory some useful concepts that can be generalized to the nonlinear case. These concepts are:

(1) Operational notation
  (a) Transfer functions
  (b) Block-diagram representations
(2) Control criteria
(3) Control through parameters

At the onset second-order systems are considered. However, there is no difficulty in extending these concepts to higher order systems.

OPERATIONAL NOTATION, TRANSFER FUNCTIONS, AND BLOCK DIAGRAMS

Consider a physical process or situation in which the output is described in terms of the input as

$$a\frac{d^2y}{dt^2}+b\frac{dy}{dt}+cy=x(t) \tag{1}$$

where a, b, and c are constants, $y=y(t)$ is the output, and $x=x(t)$ is the input.

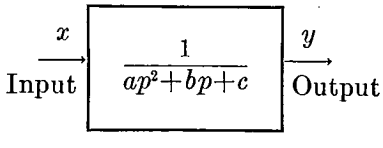
Utilizing the operator $p=d/dt$, equation (1) may be written

$$(ap^2+bp+c)y\overset{o}{=}x \tag{2}$$

(Eq. (2) reads "(ap^2+bp+c) operating on y equals operationally x.") Formal solution of equation (2) for the ratio of output over input yields by definition the operational transfer function for the system. Thus

$$\frac{y}{x}\overset{o}{=}\frac{1}{ap^2+bp+c} \tag{3}$$

The operational block diagram for the system is obtained by placing inside a box the transfer function, equation (3). Coming into the box is the input; going out of the box is the output (see sketch a).



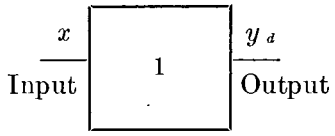
Sketch a

Here transfer functions and block diagrams are utilized merely as shorthand operational notations for differential equations. This is opposed to the Laplace transformation

viewpoint where transfer functions (and thus block diagrams) have the properties of functions of the complex frequency variable, $p=\sigma+i\omega$. The reason for stressing this interpretation is that shorthand (operational) notation has proven useful in the transition to nonlinear control whereas the Laplace transformation viewpoint (e. g., synthesis in the complex frequency plane in terms of poles and zeros) has not.

CONTROL CRITERIA

To gage the performance of an actual system an ideal or desirable system is usually established as a straight through connection (i. e., $y_d=x$ as denoted in sketch b, a block diagram of an ideal system).



Sketch b

Comparison between the desired output y_d and actual output y is accomplished by utilizing the instantaneous error:

$$e=(y_d-y)=(x-y)$$

A control criterion or criterion of performance is defined as the minimization of some property of the instantaneous error e for a given class of inputs. The minimizing process can be exact (i. e., resulting from a variational formulation of the problem) or approximate.

CONTROL THROUGH PARAMETERS

In linear systems the process of control is usually physically obtained by applying feedback and/or compensation to the system that is to be controlled. A control criterion is realized (as closely as possible) by adjustment of these applied quantities. The concept of control through parameters is an interpretation of this control process in terms of the differential equation describing the process. A simple example illustrates this concept.

Consider the position control servo shown in figure 1. The uncontrolled (open-loop) system consists of an amplifier, armature-controlled motor, gear train, and load. Closed-loop operation is obtained by utilizing proportional and derivative feedback. The gain constants K_1 and K_2 are adjustable. Armature inductance has been neglected.

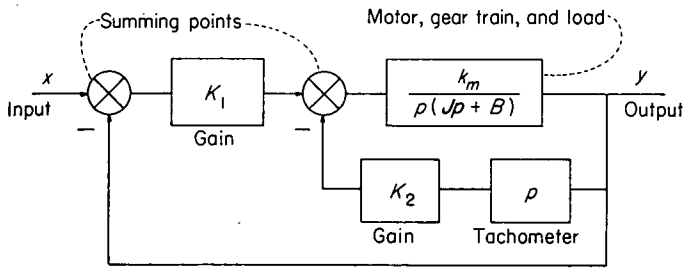


FIGURE 1.—Block diagram of simple positional servo. J, inertia of motor rotor, gears, and reflected load; B, viscous damping of motor and reflected load referred to motor shaft; k_m, constant of proportionality between output velocity and back electromotive force (it includes armature resistance and gear ratio from motor shaft to load).

From the block diagram the differential equation for the open-loop system may be written:

$$\left(\frac{I}{K_1k_m}\right)\frac{d^2y}{dt^2}+\left(\frac{B}{K_1k_m}\right)\frac{dy}{dt}=x(t) \tag{4}$$

Similarly, the closed-loop differential equation is

$$\left(\frac{I}{K_1k_m}\right)\frac{d^2y}{dt^2}+\left(\frac{B+K_2k_m}{K_1k_m}\right)\frac{dy}{dt}+(1)y=x(t) \tag{5}$$

In either case the differential equation is of the form

$$\bar{a}\,\frac{d^2y}{dt^2}+\bar{b}\,\frac{dy}{dt}+\bar{c}y=x(t) \tag{6}$$

where a set of three parameters $\bar{a}$, $\bar{b}$, and $\bar{c}$ completely characterizes the system. It is possible, then, to view the process of control in terms of these parameters. One starts with a parameter set (a,b,c) defining the uncontrolled system. A control criterion yields an optimum parameter set $(a,b,c)_o$. Control (feedback and/or compensation) is introduced ideally making it possible to adjust (a,b,c) to $(a,b,c)_o$. In the above example the gain constants K_1 and K_2 afford this adjustment.

This adjustment of the coefficients may be done in a continuous or a discontinuous way. In reference 2 Schmidt and Triplett have described an interesting and efficient way to vary the coefficients of a basically linear system continuously.

NONLINEAR CONTROL

TRANSITION TO NONLINEAR CONTROL

In the preceding section it has been mentioned that the process of linear control of second-order systems may be visualized as the adjustment of the parameter set (a,b,c) to the set $(a,b,c)_o$. The term optimum was used in the sense that some criterion of performance was approached as closely as possible.

It still seems logical in the transition to nonlinear control to hypothesize control through parameters. The transition is obtained by allowing the parameters to become functions of the output $y(t)$ and the input $x(t)$; that is,

$$a\rightarrow a(x,y)$$
$$b\rightarrow b(x,y)$$
$$c\rightarrow c(x,y)$$

The mathematical description of the system is now

$$a(x,y)\,\frac{d^2y}{dt^2}+b(x,y)\,\frac{dy}{dt}+c(x,y)y=x(t) \tag{7}$$

Without knowing the specific nature of the functions $a(x,y)$, $b(x,y)$, and $c(x,y)$ it may be seen that equation (7) is a nonlinear, inhomogeneous, and/or nonautonomous differential equation. Mathematically, little in general can be said about the solution of equation (7) given the function set $a(x,y)$, $b(x,y)$, and $c(x,y)$. It seems, then, even more hopeless to attempt a synthesis problem which involves both finding the function set $[a(x,y), b(x,y), c(x,y)]_o$ for a specified control criterion and then physically realizing the system described mathematically.

NONLINEAR CONTROL THEORY

One analytical attack on the nonlinear control-system-synthesis problem has been made by Flügge-Lotz and Wunch (refs. 1 and 3 to 5). They suggested varying the coefficients a, b, and c, not continuously, but discontinuously. That means that for $t_1<t<t_2$ there is one set of coefficients, for $t_2<t<t_3$ there is another set of coefficients, and so on. The different sets of coefficients are chosen in advance, but the times t_i for change from one set to another are determined by the value and the decrease or increase of the deviation $(x\text{-}y)$. In other words, the system is linear in any interval $t_i<t<t_{i+1}$, but is nonlinear in the whole. The transition at any switching time t_i occurs with continuous values of $y(t)$ and dy/dt, but discontinuous values of (d^2y/dt^2).

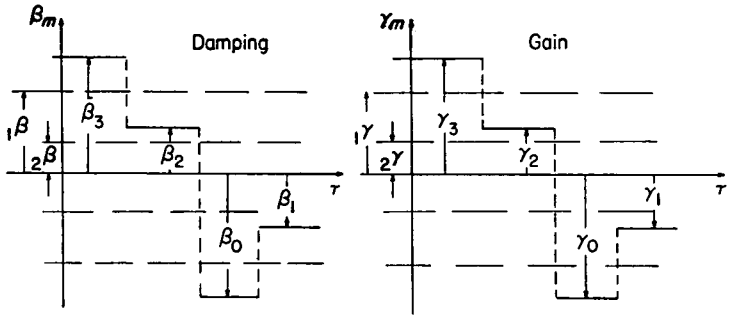


FIGURE 2.—Illustration of stepwise nature of parameters β_m and γ_n.

Phase-plane techniques were used for studying appropriate sets of coefficients and the appropriate dependence of the switching times on the deviations.[3] The authors of references 1 and 3 to 5 succeeded in finding a switching rule which assures good performance in a multitude of cases. Their control system is mathematically described in the following way:

$$\frac{d^2y}{d\tau^2}+2D(1+\beta_m)\frac{dy}{d\tau}+(1+\gamma_n)y=x(\tau) \tag{8}$$

where

$x(\tau)$ input

$y(\tau)$ output

D linear damping factor (when $\beta_m=\gamma_n=0$)

τ nondimensional time variable normalized with respect to ω_ν; that is, $\tau=\omega_\nu t$

ω_ν natural frequency of undamped linear system, $D=\beta_m=\gamma_n=0$

$\beta_m=-{}_1\beta \operatorname{sgn}(y'e)-{}_2\beta \operatorname{sgn}(y'e')$

$m=0, 1, 2, 3$

$\gamma_n=-{}_1\gamma \operatorname{sgn}(ye)-{}_2\gamma \operatorname{sgn}(ye')$

$n=0, 1, 2, 3,$

$_1\beta,{}_2\beta,{}_1\gamma,{}_2\gamma$ positive constants

$$\operatorname{sgn}(f)=\frac{f}{|f|}=\begin{cases}+1 \text{ for } f>0\\ -1 \text{ for } f<0\end{cases}$$

[3] For details the reader is referred to references 1 and 3 to 5. Reference 1 contains the ideas but is so condensed that the inquisitive reader will find it useful to read references 3 to 5, of which reference 5 is probably the most accessible. Figure 3, p. 12, and figure 30, p. 70, of reference 5 will help in getting acquainted with the phase-plane trajectory of an output. Some of the original studies are described again later in the present paper when the performance of the system is discussed.

e instantaneous error, $e=(y_d-y)=(x-y)$

$(\ )'=d(\ )/d\tau$

Actually, equation (8) is a normalized form of the control equation derived by Flügge-Lotz and Wunch. However, the notation has been somewhat changed. See appendix B for a comparison of notations and the normalization involved.

The subscript convention is

$$\left.\begin{aligned}
\beta_3&={}_1\beta+{}_2\beta & \gamma_3&={}_1\gamma+{}_2\gamma\\
\beta_2&={}_1\beta-{}_2\beta & \gamma_2&={}_1\gamma-{}_2\gamma\\
\beta_1&=-{}_1\beta+{}_2\beta=-\beta_2 & \gamma_1&=-{}_1\gamma+{}_2\gamma=-\gamma_2\\
\beta_0&=-{}_1\beta-{}_2\beta=-\beta_3 & \gamma_0&=-{}_1\gamma-{}_2\gamma=-\gamma_3
\end{aligned}\right\} \tag{9}$$

PROPERTIES OF EQUATION (8)

The following properties of equation (8) are noteworthy:

(1) Equation (8) is a piecewise linear but overall nonlinear differential equation.

(2) The parameters β_m and γ_n are stepwise switching functions of time (their implicit variable). This property is illustrated in figure 2.

(3) The time of switching and the particular combination of the parameters β_m and γ_n employed at any instant are explicit functions of the output y and the input x. Specifically, they are determined by quantized information derived from the output, output derivative, error, and error derivative, namely, the sign of the products sgn $(y'e)$, sgn $(y'e')$, sgn (ye), and sgn (ye').

(4) There are basically 16 m,n subscript combinations and thus 16 β_m,γ_n parameter combinations. However, a detailed study of property (3) shows that only 8 are allowed. The allowed combinations may be

$$m=n=0, 1, 2, 3$$

or

$$m\neq n$$

$$m+n=3$$

The reason for the "exclusion principle" on coefficient combinations stems from a desire to obtain mirrored-image outputs for mirrored-image inputs; that is,

$$y_{im}(\tau)=-y(\tau)$$

is desired when

$$x_{im}(\tau)=-x(\tau)$$

(5) The control criterion that was employed in obtaining the functional dependence of β_m and γ_n was

$$|y_d-y|=|x-y|=|e|<\epsilon$$

where ϵ is a small positive quantity. This criterion of maintenance of small instantaneous error between desired output and actual output enabled reduction of equation (8) to the approximate autonomous differential equation (see refs. 1 and 3 to 5)

$$y''+2D(1+\beta_m)y'+\gamma_n y=(x-y)$$
$$\approx 0 \tag{10}$$

Thus phase-plane techniques could be employed to find the functional dependence of β_m and γ_n.

(6) Once the linear damping factor D is fixed the process of control is obtained by switching parameters β_m and γ_n. Equation (8) consists of an ensemble of eight (see property (4)) linear differential equations with constant coefficients. The process of control may be visualized as the switching from one member of the ensemble to another. This switching is determined by quantized information derived from the input and output (see property (3)). From another point of view (consistent with the approximation described in property (5)), the output y is to be forced to satisfy two conditions simultaneously, that is, both sides of equation (10). This is approximately possible by switching to various β_m and γ_n parameter combinations and can be visualized as the process of switching to various phase trajectories of equation (10) in the phase plane of y' against y.

DISCUSSION OF NONLINEAR CONTROL

In the section entitled "Transition to Nonlinear Control" a logical transition to nonlinear control systems utilizing the concept of control through parameters is suggested. However, mathematical difficulty hampers the development of this approach. In the next two sections a particular nonlinear control theory is presented. This theory constitutes the first step in the synthesis of a nonlinear control system which obtains control through parameters. Since the functional dependence of the parameters has been established, the problem is reduced to finding a set of five (constant) parameters $(D,_1\beta,_2\beta,_1\gamma,_2\gamma)_o$. It should be appreciated, however, that even the optimization of this five-parameter set cannot in general be accomplished analytically because of the overall nonlinear nature of the problem.

Aside from questions on the analytical optimization of parameters in equation (8), there are equally important practical questions such as:

(1) Can a useful control system that is described by the nonlinear differential equation (eq. (8)) be realized?

(2) If the system is realizable, what is its physical nature?

(3) If the system is realizable, how does it compare in performance and complexity with a "good" second-order linear control system?

There are then mathematical difficulties on the one hand and physical difficulties on the other. The mathematical difficulties could be handled by numerical methods of integration of the differential equation (e. g., utilizing a digital computer). However, this would give little insight into the nature of a system that is controlled through discontinuous variation of the parameters β_m and γ_n. It has been found advantageous to investigate the physical questions first and then to utilize simulation techniques (analog computer) to investigate the analytical properties of this type of control.

PHYSICAL REALIZATION

PHYSICAL MODEL

It is desirable to study the nature of a physical control system that is described by an ensemble of eight linear differential equations with control being accomplished by switching from one member of the ensemble to another. To do this, equation (8) is rearranged as shown below:

$$\frac{d^2y}{d\tau^2}+2D\frac{dy}{d\tau}+y=x(\tau)-\left(2D\beta_m\frac{dy}{d\tau}+\gamma_n y\right) \tag{11}$$

or in operational notation

$$(p^2+2Dp+1)y\overset{o}{=}x-(2D\beta_m p+\gamma_n)y \tag{12}$$

Forgetting for the time being that the parameters β_m and γ_n are actually functions, one interpretation of this operational equation and thus of equation (8) is shown in figure 3.

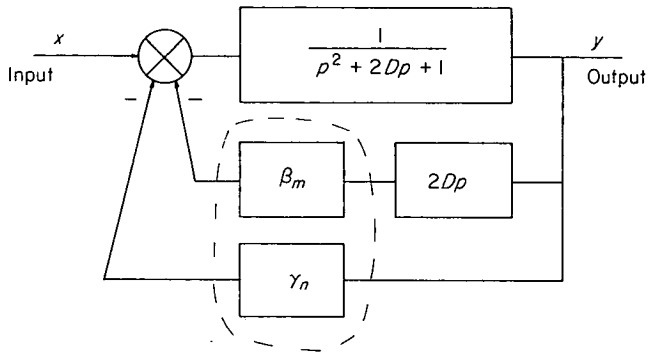


FIGURE 3.—Block diagram of equation (8) assuming that β_m and γ_n are constant (denoted by encircling dotted line).

Figure 3 can be modified to take into account the fact that β_m and γ_n are stepwise switching functions of time, their implicit variable (i. e., β_m and γ_n can each take on four discrete values). This is shown symbolically in figure 4. The explicit functional dependence of the parameters β_m and γ_n has not yet been given and is thus indicated as a switching logic of undefined character.

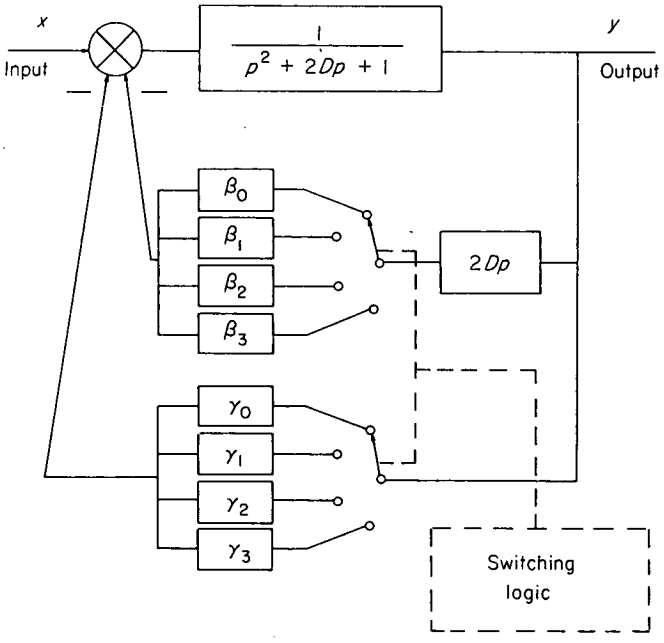


FIGURE 4.—Block diagram of equation (8) taking into account stepwise switching nature of β_m and γ_n.

Utilizing the block diagram of figure 4, the physical interpretation of the nonlinear control system described by equation (8) is quite straightforward. This system consists of:

(1) A linear feedforward portion. This portion could be a linear control system in itself (e. g., the simple position control servo of figure 1 and equation (5)).

(2) A feedback switching circuit comprised of:

(a) Four discrete values of proportional feedback γ_n (two positive and two negative as shown in fig. 2)

(b) Four discrete values of derivative feedback $2D\beta_m$ (two positive and two negative as shown in fig. 2)

(c) A switching logic which at any instant determines the particular combination of derivative and proportional feedback $2D\beta_m,\gamma_n$ employed.

SWITCHING LOGIC

In this section it is shown that digital-computer techniques can be utilized to establish the switching logic for the feedback switching circuit mentioned in the previous section.

Recall that the parameters β_m and γ_n have been defined as functions; that is,

$$\left.\begin{aligned} \beta_m &= -{}_1\beta \operatorname{sgn}(y'e) - {}_2\beta \operatorname{sgn}(y'e') \\ & m=0,1,2,3 \\ \gamma_n &= -{}_1\gamma \operatorname{sgn}(ye) - {}_2\gamma \operatorname{sgn}(ye') \\ & n=0,1,2,3 \end{aligned}\right\} \tag{13}$$

where the subscript convention has been given by equations (9). Equations (13) determine the switching logic. Thus, for example, β_3 is chosen when $(y'e)<0$ and $(y'e')<0$ and γ_0 is chosen when $(ye)>0$ and $(ye')>0$, so that the combination $\beta_3\gamma_0$ is chosen when $(y'e)<0$, $(y'e')<0$, $(ye)>0$, and $(ye')>0$. At this point it appears necessary to form the products ye, ye', $y'e$, and $y'e'$ and then to find the sign of these products in order to establish the switching logic. Physically, however, the process of multiplication is to be avoided if possible. That there is a possibility of avoiding multiplication may be gleaned by realizing that

$$\operatorname{sgn}(ab)=\operatorname{sgn}(a)\operatorname{sgn}(b)$$

since

$$\frac{ab}{|ab|}=\frac{a}{|a|}\frac{b}{|b|}$$

Thus equations (13) may be rewritten as

$$\left.\begin{aligned} \beta_m &= -\operatorname{sgn}(y')[{}_1\beta \operatorname{sgn}(e) + {}_2\beta \operatorname{sgn}(e')] \\ & m=0,1,2,3 \\ \gamma_n &= -\operatorname{sgn}(y)[{}_1\gamma \operatorname{sgn}(e) + {}_2\gamma \operatorname{sgn})e')] \\ & n=0,1,2,3 \end{aligned}\right\} \tag{14}$$

Again the subscript convention is defined by equations (9).

Thus, utilizing equations (13), for example, β_3 is chosen when

$$y'>0,\ e<0,\ e'<0$$

or when

$$y'<0,\ e>0,\ e'>0$$

γ_0 is chosen when

$$y>0,\ e>0,\ e'>0$$

or when

$$y<0,\ e<0,\ e'<0$$

so that the combination (β_3,γ_0) is chosen when

$$y>0,\ y'<0,\ e>0,\ e'>0$$

or when

$$y<0,\ y'>0,\ e<0,\ e'<0$$

From this example it can be seen that it is not necessary to find the signs of products but rather that it is sufficient to find separately the signs of y, y', e, and e'.

Since the sign of a variable is quantized binary information of the variable, it is convenient to utilize digital-computer techniques to further the switching logic. This may be done as follows:

Let the convention be adopted that $y>0$ be represented by 0 (binary zero), $y<0$ be represented by 1 (binary one), and similarly for y', e, and e'. If the ordered sequence is now established as

$$(y,\ y',\ e,\ e')$$

four-digit binary logic may be employed to encode equation (14). In particular, a binary coded decimal may be used (see table 1).

It was mentioned in property (4) of the section "Properties of Equation (8)" that not all of the 16 possible β_m,γ_n parameter combinations were allowed under their definition. This was termed an exclusion principle on the allowed coefficient combinations. One of the advantages of the suggested binary coding scheme of table 1 is that this exclusion principle is built into the code. To understand this, consider the example of the combination $\beta_3\gamma_0$ given previously. In the code language $\beta_3\gamma_0$ is chosen when the binary number 0100 or 1011 occurs. What is implied by this example is that a binary number and its complement must be identical (i. e., 0000=1111, 0111=1000) as far as the switching logic is concerned. Thus out of the 16 possible four-digit binary numbers only the first 8 are unique. That is, in counting from 0 to 7 in a binary coded decimal, if complements are included then so are the other 8 possibilities, 8 to 15 (see table 1).

The allowed β_m,γ_n parameter combinations along with the encoded logic of table 1 are summarized in matrix form in table 2. Examples are given to illustrate the meaning of the table. In general the allowed subscript combinations are

$$m=n=0,\ 1,\ 2,\ 3$$

or

$$m\neq n$$

$$m+n=3$$

REALIZATION COMPLETED

Now that equation (14) has been successfully interpreted (encoded) in binary-logic form (table 2), the realization of a feedback switching circuit utilizing this encoded logic is a typical digital-computer switching-circuit problem. As is characteristic of any synthesis process there will, in general, be many ways to design this feedback switching circuit.

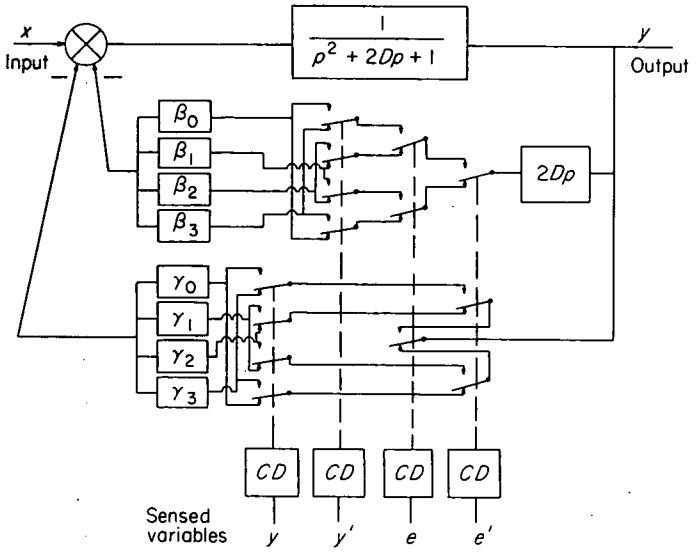


FIGURE 5.—Block diagram showing complete physical interpretation of equation (8). *CD*, zero-coincidence detectors.

The block diagram of figure 5 shows one design that completes the physical interpretation of equation (8) along the lines started in figures 3 and 4.

In figure 5 the feedback switching circuit consists of:

(1) The four discrete values of both derivative and proportional feedback $2D\beta_m,\gamma_n$

(2) A relay switching circuit that connects the proper feedback combination

(3) Zero-coincidence detectors *CD* that drive the banks of relays to one position or the other depending upon the signs of the sensed variables

It should be noted that, depending upon the application, other forms of sign-sensing devices and other switching devices such as diodes, transistors, electronic switches, and/or magnetic amplifiers could be employed to obtain other realizations of equation (8). In any case the following properties are basic to any realization:

(1) The signs of the four variables y, y', e, and e' are sensed. This may be thought of as the process of "reading in" the four-digit binary logic of table 1.

(2) On the basis of the 2^4 possible binary decisions the required feedback combinations $2D\beta_m,\gamma_n$ as defined in table 2 are connected around a linear second-order member.

It is important to stress that the only types of nonlinear operations required in the realization of this nonlinear control system are switching-type operations. In addition, all the switching is to be performed in feedback paths, which means that the switching can be done at low electronic power levels. These practical features are definite design advantages. Thus, in summary, it can be said that this type of nonlinear control system is not only physically realizable but also practical from an instrumentation standpoint.

EXPERIMENTAL VERIFICATION OF NONLINEAR CONTROL THEORY

DISCUSSION OF SIMULATION TECHNIQUES

Simulation techniques were chosen as an experimental mode of investigation of performance of the nonlinear control system realized from equation (8). These techniques offer the following advantages:

(1) Proximity to the actual control system. This means that the same practical features with regard to instrumentation (see the section entitled "Realization Completed") are exploited to fullest advantage. Thus, just as in the actual system, the only nonlinear device required for the simulated model is a binary logic feedback switching circuit (see appendix C for details). The linear portion of the system is simulated on an analog computer. Here the only operations required are summations, two integrations, and one differentiation. These are all operations which an analog computer does well. It can be said then that the accuracy to which the simulated model simulates equation (8) depends primarily upon the realized feedback switching circuit. The most essential type of imperfection to be expected in this switching circuit is time delay in switching. Exactly the same type of imperfection will be met in the physical control system. Thus there will be more nearly a one-to-one correspondence between the simulated model and the actual system than between either and equation (8).

(2) Convenience in experimental investigation. In order to characterize the output y of the nonlinear system completely, a set of five parameters

$$(D,\ {}_1\beta,\ {}_2\beta,\ {}_1\gamma,\ {}_2\gamma)$$

and the input x must be specified. In the performance evaluation of the system it is necessary to be able to vary these characterizing quantities conveniently. Simulation techniques allow this.

PRESENTATION OF EXPERIMENTAL RESULTS

Figures 6 to 17 present experimental results obtained from the simulation studies of equation (8). Briefly, the results are presented as follows:

Figures 6 to 12 compare the responses (output y and error e) of the nonlinear system with that of a linear system for various classes of inputs x. (In comparing the linear and nonlinear responses it will be noted that there is not exact synchronism of events because, with the available experimental facilities, it was necessary to obtain the two responses separately.) The linear system utilized is that which constitutes the feedforward member of the nonlinear system corresponding to the case where $\beta_m=\gamma_n=0$. The nonlinear system for figures 6 to 15 is

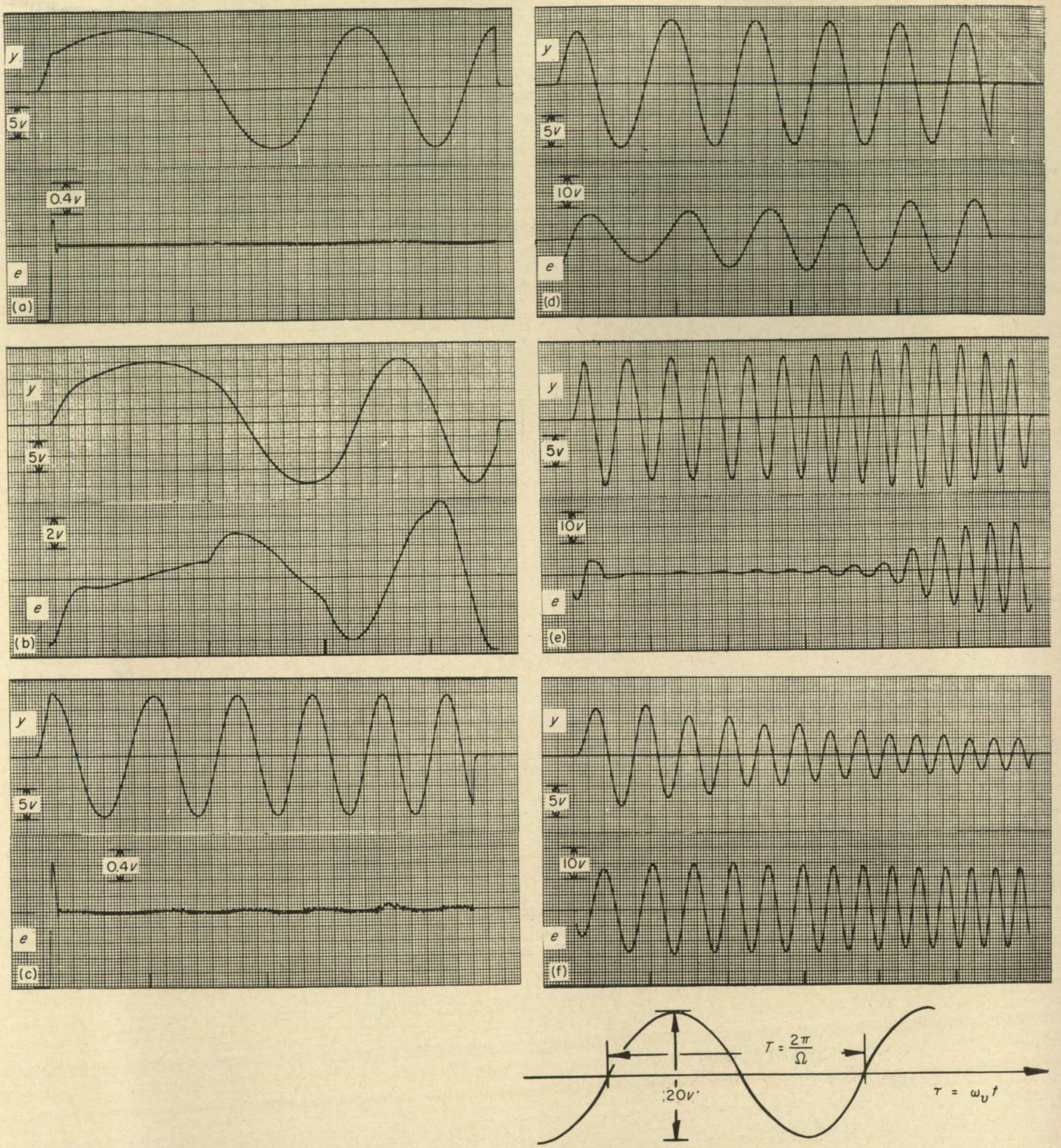
$$\beta_3=-\beta_0=2$$

$$\beta_2=-\beta_1=0.5$$

$$\gamma_3=-\gamma_0=2$$

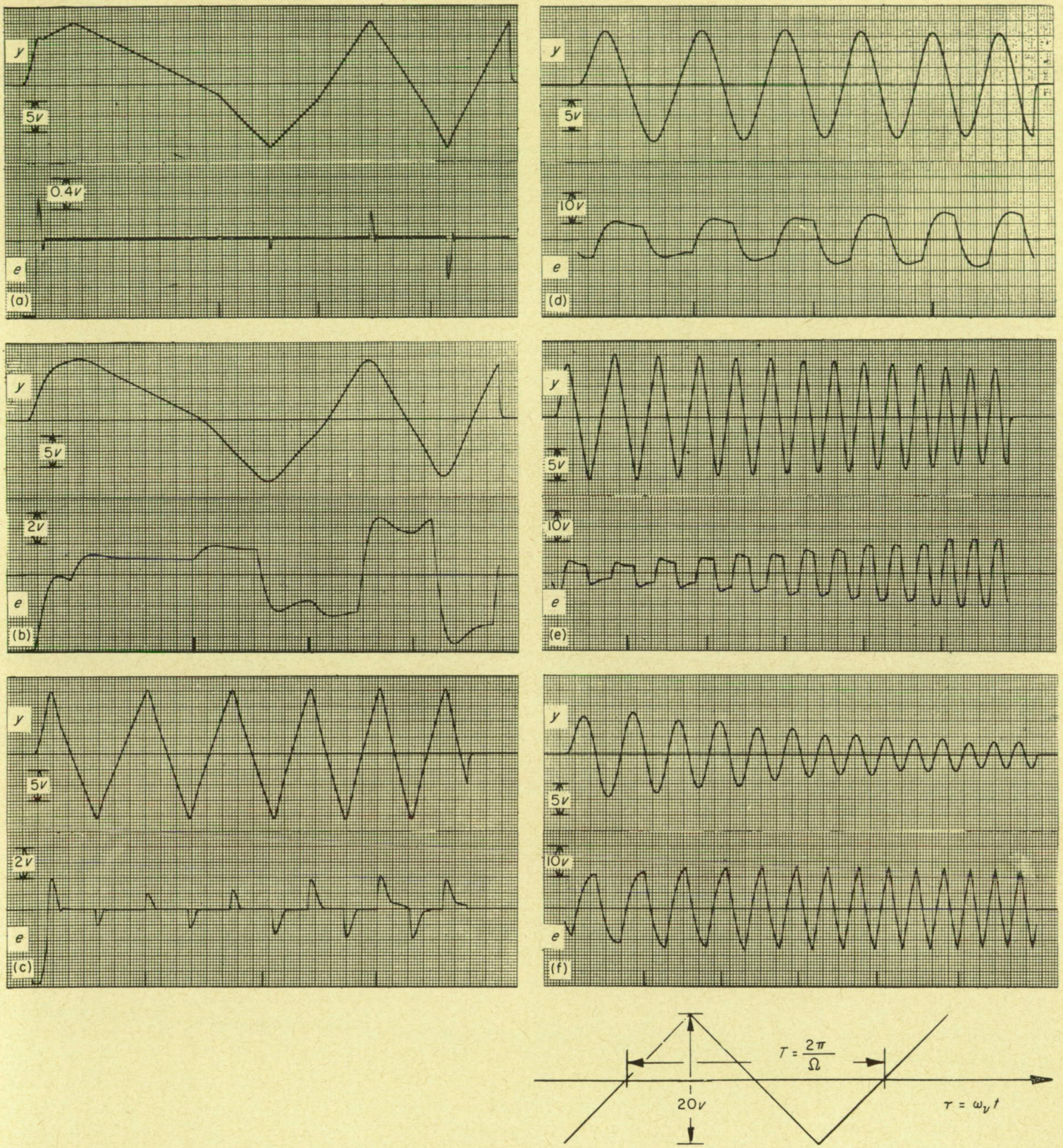
$$\gamma_2=-\gamma_1=0.5$$

Figure 6 compares the system responses to sinusoidal inputs and figure 7 shows the responses to triangular-wave inputs. A partially integrated square wave $x(\tau)$ is defined as the output of a first-order linear system characterized by the transfer function $H(p)=1/(\alpha p+1)$, when the input $x_1(\tau)$ is a square wave. The responses of linear and nonlinear systems to this type of input are given in figure 8.



(a) Nonlinear system; $\Omega=\omega/\omega_v=0.1$ to 0.4 in 0.1 steps.
(b) Linear system; $\Omega=\omega/\omega_v=0.1$ to 0.4 in 0.1 steps.
(c) Nonlinear system; $\Omega=\omega/\omega_v=0.5$ to 0.8 in 0.1 steps.
(d) Linear system; $\Omega=\omega/\omega_v=0.5$ to 0.8 in 0.1 steps.
(e) Nonlinear system; $\Omega=\omega/\omega_v=1.0$ to 2.0 in 0.2 steps.
(f) Linear system; $\Omega=\omega/\omega_v=1.0$ to 2.0 in 0.2 steps.

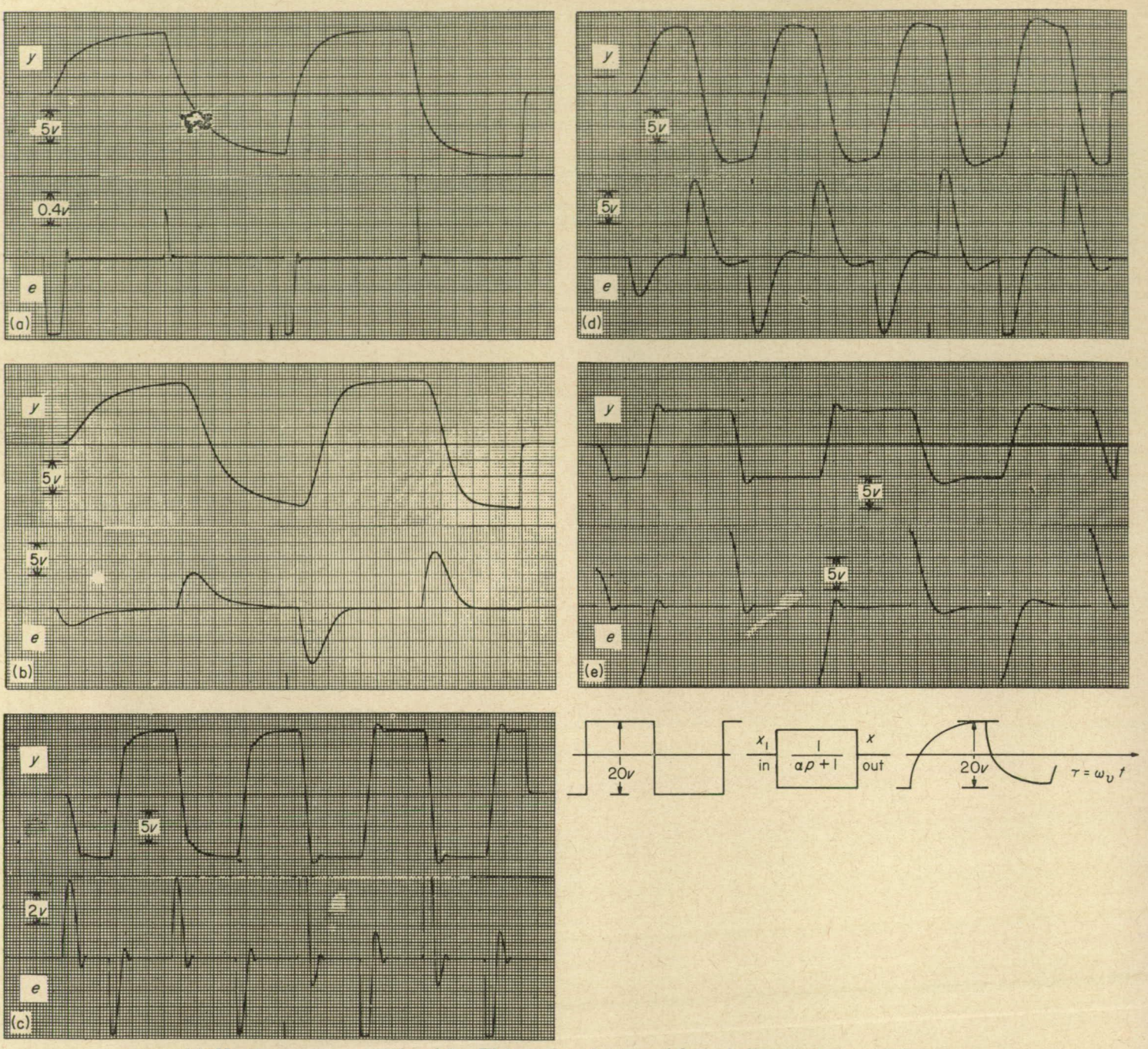
FIGURE 6.—Linear and nonlinear system responses for 20-volt peak-to-peak sinusoidal inputs with frequency Ω varied. $D=0.6$; 2.5 small divisions on time scale=1 normalized time unit; tick marks at bottom of figures indicate when frequency was varied.



(a) Nonlinear system; $\Omega = 2\pi/T = 0.1$ to 0.4 in 0.1 steps.
(b) Linear system; $\Omega = 2\pi/T = 0.1$ to 0.4 in 0.1 steps.
(c) Nonlinear system; $\Omega = 2\pi/T = 0.5$ to 0.8 in 0.1 steps.
(d) Linear system; $\Omega = 2\pi/T = 0.5$ to 0.8 in 0.1 steps.
(e) Nonlinear system; $\Omega = 2\pi/T = 1.0$ to 2.0 in 0.2 steps.
(f) Linear system; $\Omega = 2\pi/T = 1.0$ to 2.0 in 0.2 steps.

FIGURE 7.—Linear and nonlinear system responses to 20-volt peak-to-peak triangular-wave inputs with period T varied. $D = 0.6$; 2.5 small divisions on time scale = 1 normalized time unit; tick marks at bottom of figures indicate when periods were varied.

526597—60——92



(a) Nonlinear system; $\alpha=4$ and 2. Tick mark at bottom of figure indicates when α was varied.
(b) Linear system; $\alpha=4$ and 2. Tick mark at bottom of figure indicates when α was varied.
(c) Nonlinear system; $\alpha=1$ and 0.5. Tick mark at bottom of figure indicates when α was varied.
(d) Linear system; $\alpha=1$ and 0.5. Tick mark at bottom of figure indicates when α was varied.
(e) Nonlinear and linear systems; $\alpha=0$. Tick mark at bottom of figure indicates demarcation between nonlinear and linear systems.

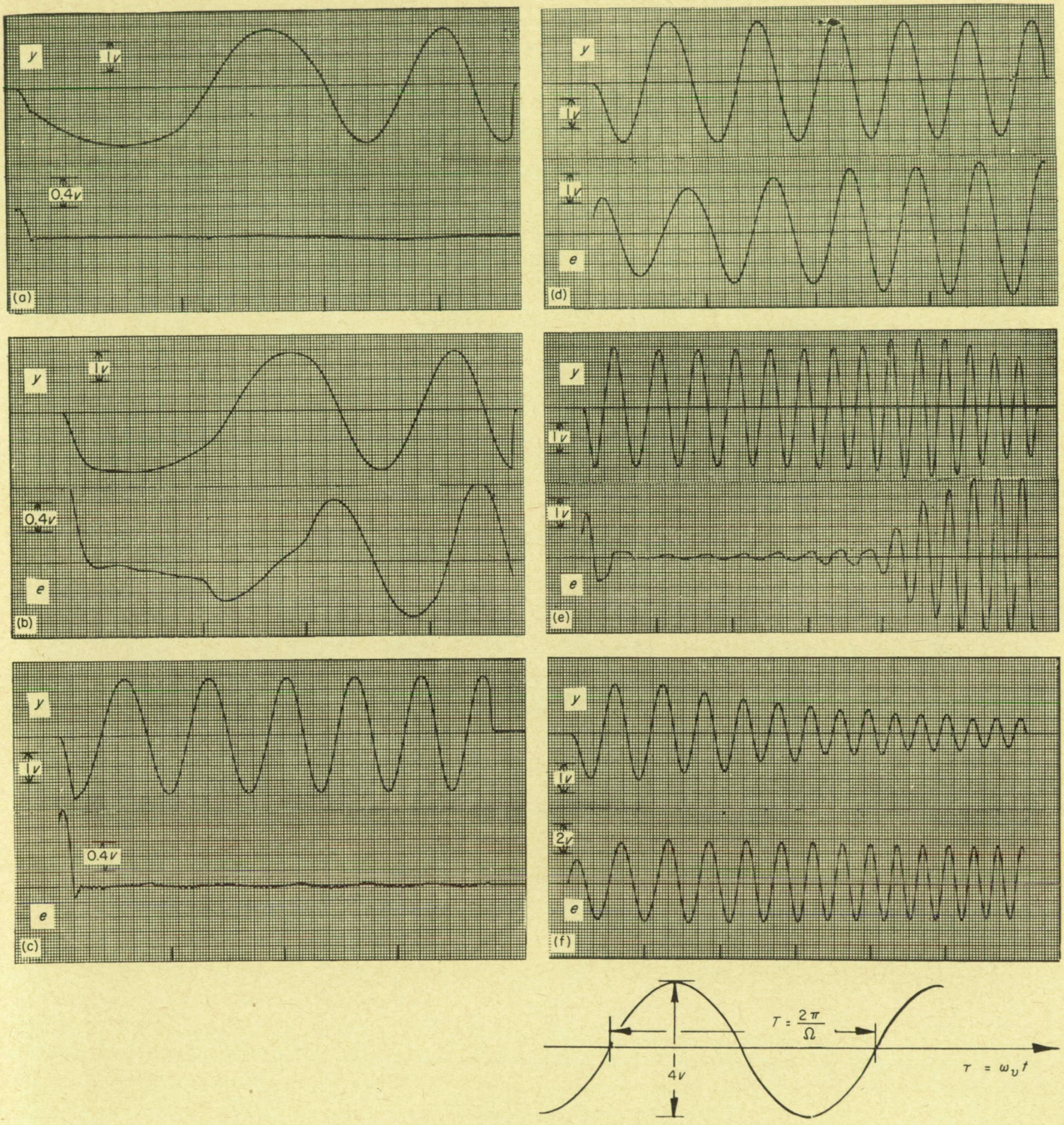
FIGURE 8.—Linear and nonlinear system responses to 20-volt peak-to-peak partially integrated square-wave input. $D=0.6$; 2.5 small divisions on time scale = 1 normalized time unit.

The responses of the systems to small sinusoidal inputs are given in figure 9. Figure 10 gives the responses to clipped sinusoidal inputs. Figure 11 shows the response of the nonlinear system to sinusoidal inputs that have been displaced with a direct-current component. Figure 12 shows the responses of linear and nonlinear systems to a triangular-wave input whose periods and amplitudes are randomly modulated.

Figures 13 to 15 deal with the effects of imperfections that are likely to be encountered in the actual control system. Figure 13(a) gives the results and data of an experimental investigation on the effects of switching delays due to threshold in sensing the sign of the error, sgn (e) for a triangular-wave input. The experimental results for a constant 9-volt input (see fig. 13(b)) are given below:

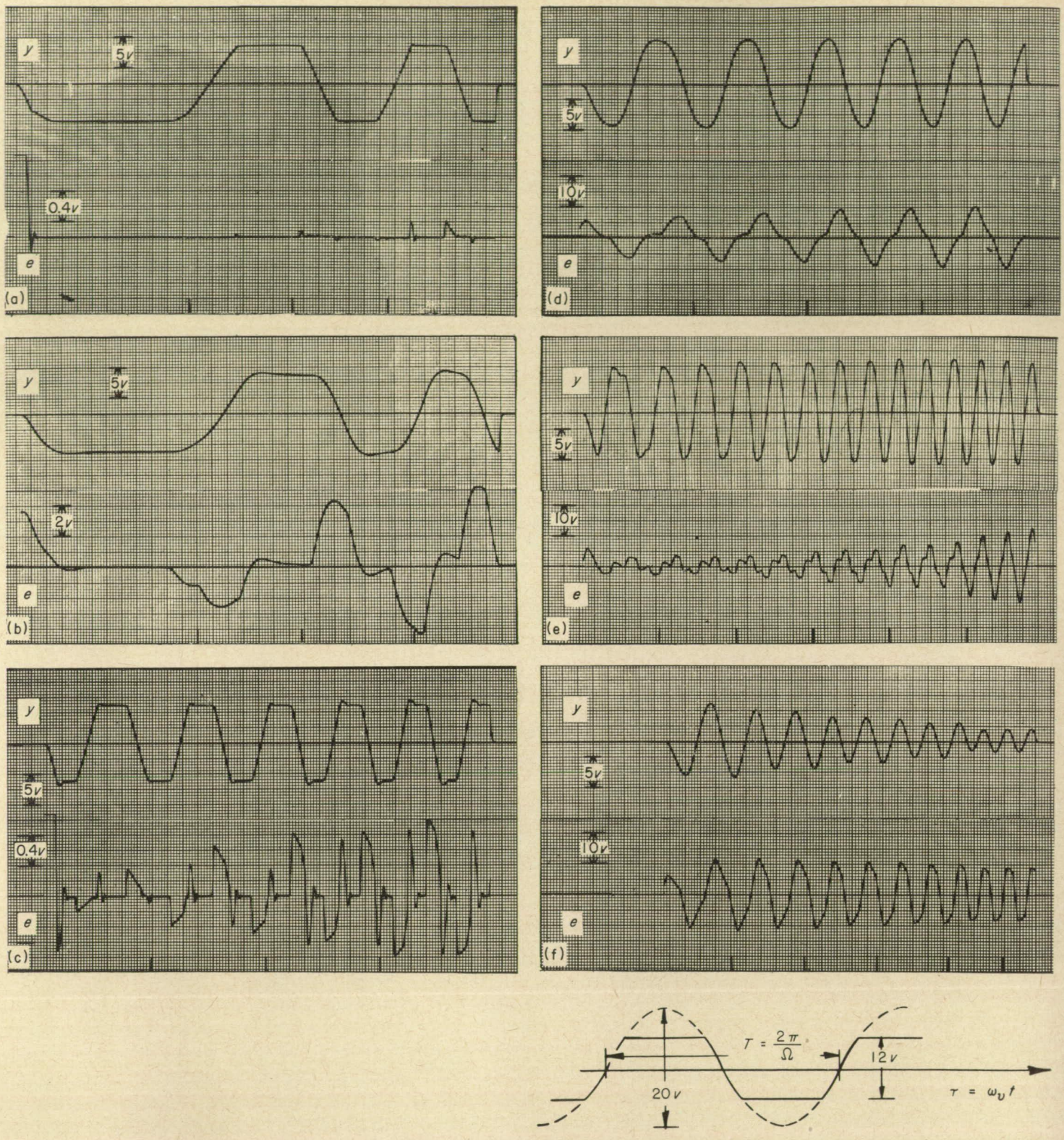
Threshold, mv	14	26	36	44
Peak-to-peak error, mv	44	124	220	290

Figure 14 shows the effects of placing progressively smaller limits on the acceleration of the nonlinear control system. For each value of y'' limit considered, the output, output derivative, output acceleration, and instantaneous error are shown. The effects of a velocity limit on performance of the nonlinear and linear systems are compared in figure 15.



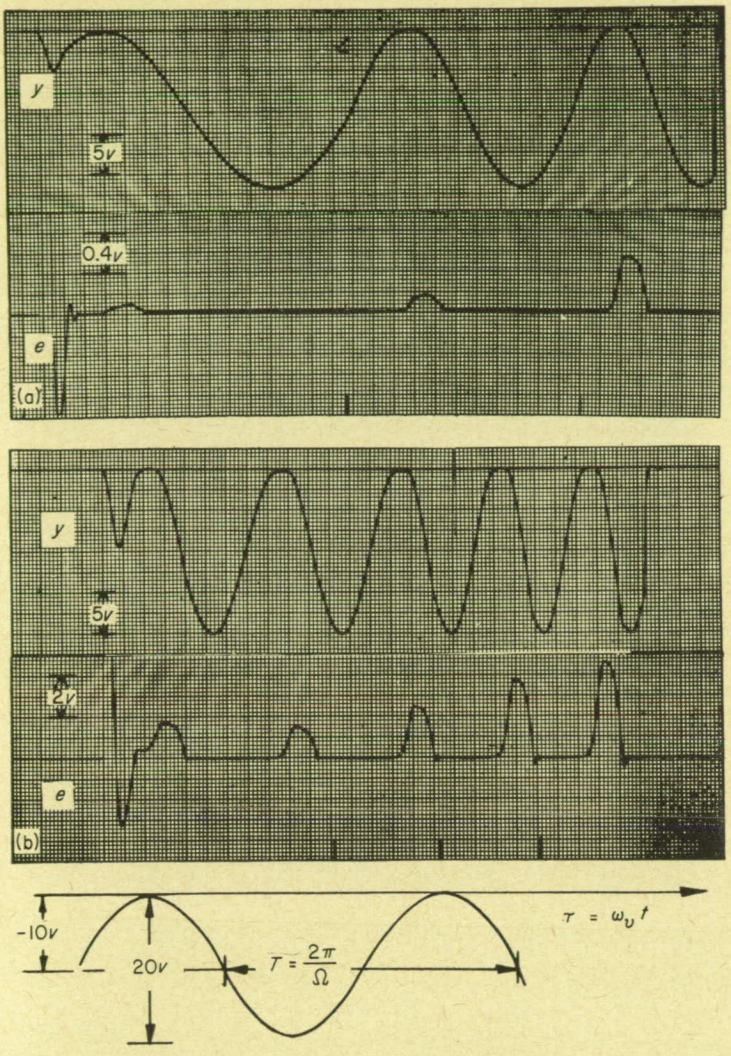
(a) Nonlinear system; $\Omega = \omega/\omega_v = 0.1$ to 0.4 in 0.1 steps.
(b) Linear system; $\Omega = \omega/\omega_v = 0.1$ to 0.4 in 0.1 steps.
(c) Nonlinear system; $\Omega = \omega/\omega_v = 0.5$ to 0.8 in 0.1 steps.
(d) Linear system; $\Omega = \omega/\omega_v = 0.5$ to 0.8 in 0.1 steps.
(e) Nonlinear system; $\Omega = \omega/\omega_v = 1.0$ to 2.0 in 0.2 steps.
(f) Linear system; $\Omega = \omega/\omega_v = 1.0$ to 2.0 in 0.2 steps.

FIGURE 9.—Linear and nonlinear system responses to 4-volt peak-to-peak sinusoidal inputs with frequency Ω varied. $D = 0.6$; 2.5 small division on time scale = 1 normalized time unit; tick marks at bottom of figures indicate when frequency was varied.



(a) Nonlinear system; $\Omega=\omega/\omega_v=0.1$ to 0.4 in 0.1 steps.
(b) Linear system; $\Omega=\omega/\omega_v=0.1$ to 0.4 in 0.1 steps.
(c) Nonlinear system; $\Omega=\omega/\omega_v=0.5$ to 0.8 in 0.1 steps.
(d) Linear system; $\Omega=\omega/\omega_v=0.5$ to 0.8 in 0.1 steps.
(e) Nonlinear system; $\Omega=\omega/\omega_v=1.0$ to 2.0 in 0.2 steps.
(f) Linear system; $\Omega=\omega/\omega_v=1.0$ to 2.0 in 0.2 steps.

FIGURE 10.—Linear and nonlinear system responses to 20-volt peak-to-peak sinusoidal inputs with frequency Ω varied that are clipped symmetrically at ± 6 volts. $D=0.6$; 2.5 small divisions on time scale = 1 normalized time unit; tick marks at bottom of figures indicate when frequency was varied.



(a) $\Omega = \omega/\omega_v = 0.1$ to 0.4 in 0.1 steps.
(b) $\Omega = \omega/\omega_v = 0.5$ to 0.8 in 0.1 steps.

FIGURE 11.—Nonlinear system responses of 20-volt peak-to-peak sinusoidal input with frequency Ω varied that has been displaced by -10 volts (direct-current component) for obtaining osculation. $D = 0.6$; 2.5 small divisions on time scale = 1 normalized time unit; tick marks at bottom of figures indicate when frequency was varied.

Figure 16 presents the responses of some special cases of the nonlinear system (special with respect to the choice of the β_m and γ_n parameter values). In this figure the system responses to a triangular-wave input are given for four different parameter sets. The parameters pertinent to these results are listed in table 3 for easy reference.

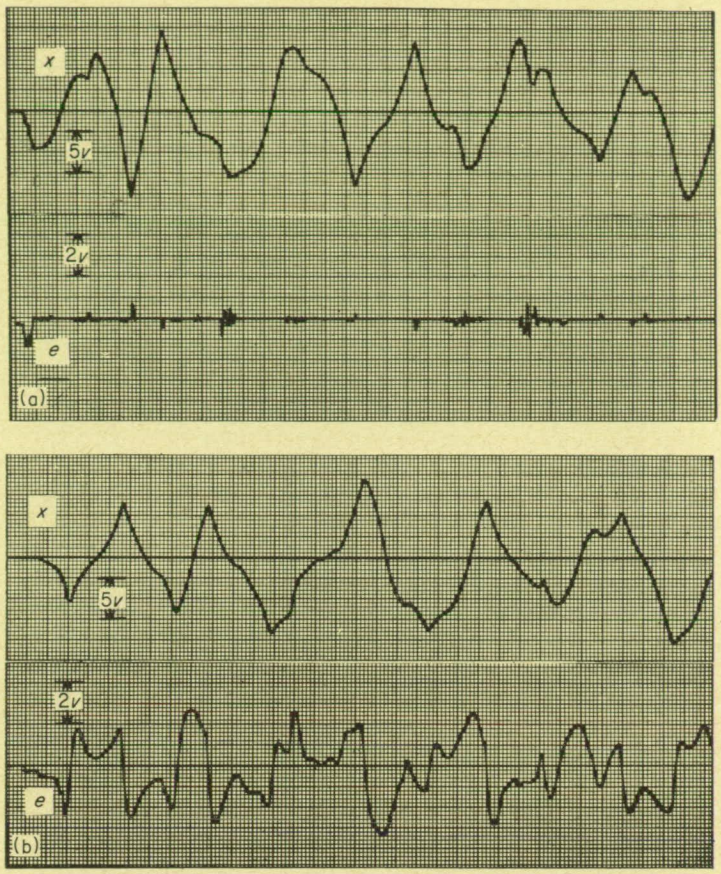
Figure 17 gives the response of the nonlinear system possessing a low linear damping factor $D = 0.1$. The responses are for a triangular-wave input whose frequency was varied in the same manner as that of figures 7(a) and 7(c).

Detailed discussions of these results are given in the section entitled "Discussion of Results."

DISCUSSION OF RESULTS

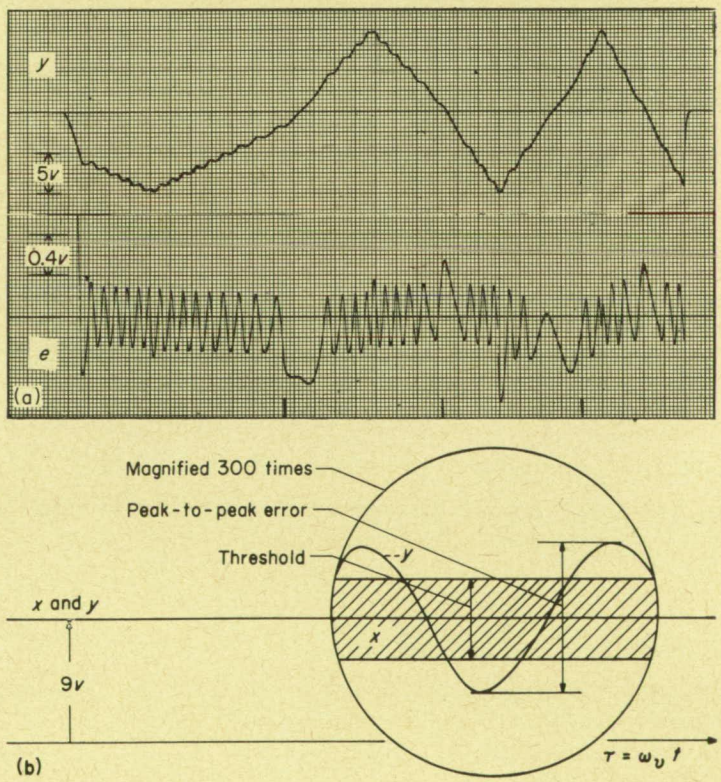
PERFORMANCE EVALUATION OF SINUSOIDAL INPUTS

To complete the synthesis of the nonlinear control system that has been derived from equation (8), it is necessary to choose the magnitudes of the parameters that characterize the system, that is, $(D,_1\beta,_2\beta,_1\gamma,_2\gamma)$ or $(D,\beta_3,\beta_2,\gamma_3,\gamma_2)$. It is expected that the performance of the system depends on



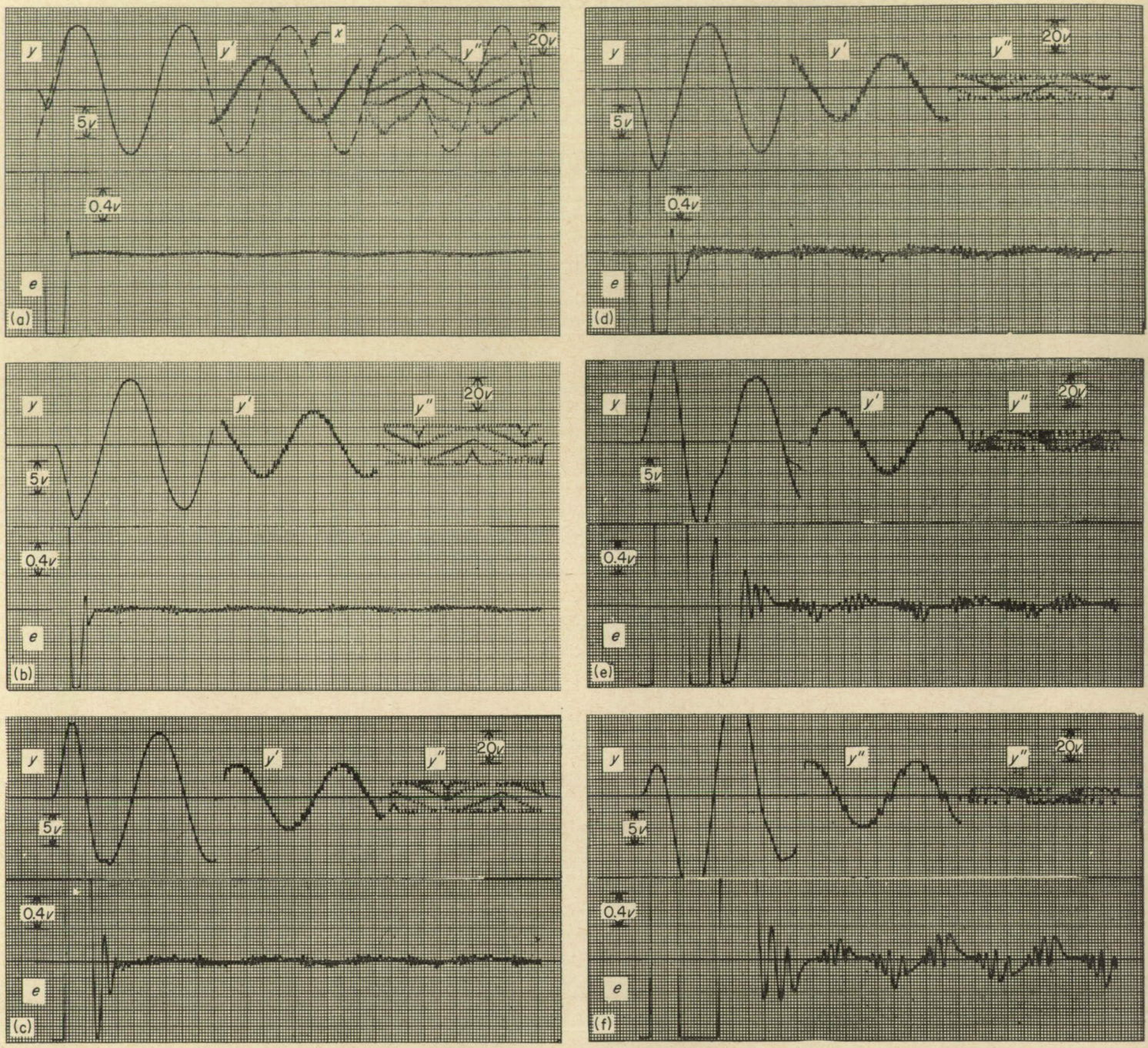
(a) Nonlinear system. (b) Linear system.

FIGURE 12.—Linear and nonlinear system responses for triangular-wave input whose period and amplitude are randomly modulated. $D = 0.6$; 1 small division on time scale = 1 normalized time unit.



(a) Nonlinear system response to triangular-wave input with period varied as in figure 7 (a). $D = 0.6$; tick marks at bottom of figure indicate when period was varied. Threshold in sensing sgn e was 44 millivolts.
(b) Constant input $x(\tau)$ was 9 volts.

FIGURE 13.—Effects of switching delays due to threshold in sensing sgn e.



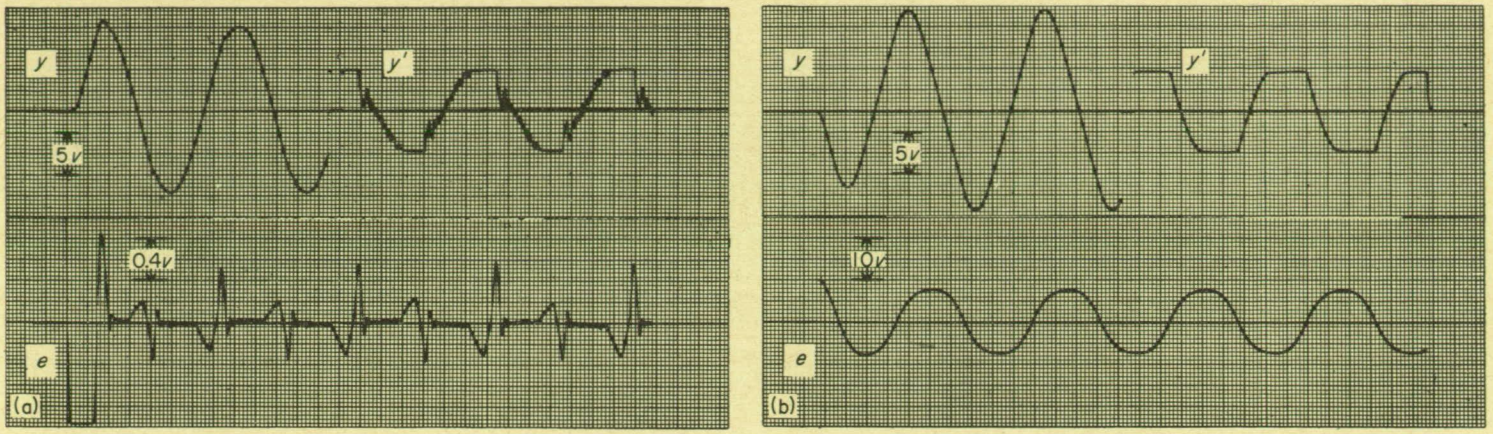
(a) Nonlinear system; no y'' limit.
(b) Nonlinear system; ± 12-volt y'' limit.
(c) Nonlinear system; ± 9-volt y'' limit.
(d) Nonlinear system; $\pm 7\frac{1}{2}$-volt y'' limit.
(e) Nonlinear system; ± 6-volt y'' limit.
(f) Nonlinear system; $\pm 4\frac{1}{2}$-volt y'' limit.

FIGURE 14.—Nonlinear system responses to 20-volt peak-to-peak sinusoidal input with varying acceleration limits. $D=0.6$; $\Omega=\omega/\omega_r=0.5$; 2.5 small divisions on time scale = 1 normalized time unit.

the choice of these parameters. For studying their influence, simulation techniques proved to be very convenient. Experimental results were given in figures 6 to 12 where the response (output y and error e) of the nonlinear system was compared with the response of a linear system for a variety of inputs. This gives the possibility of establishing the properties of the nonlinear system not only by itself but also with respect to a linear standard. The linear system employed for this purpose was that which constitutes the feedforward member of the nonlinear system (i.e., $\beta_m=\gamma_v=0$).

These experiments allow parameter values for good performance of the nonlinear system to be found. Analytical and practical considerations that aid in the optimization are treated later in the section entitled "Choice of Parameter Values."

The sinusoidal responses of the nonlinear and linear systems are compared in figure 6. Here, the frequency range considered was $0.1 \leqq \Omega=\omega/\omega_r \leqq 2$. The peak-to-peak input amplitude was 20 volts. These results show that the nonlinear system reproduced the sinusoidal inputs up to the frequency



(a) Nonlinear system.
(b) Linear system.

FIGURE 15.—Linear and nonlinear system responses to 20-volt peak-to-peak sinusoidal input with $\pm 4\frac{1}{2}$-volt velocity limit. $D=0.6$; $\Omega=2\pi/T=0.5$; 2.5 small divisions on time scale = 1 normalized time unit.

$\Omega=1.4$ with virtually no instantaneous error when compared with that of the linear system. For higher frequencies the error for the nonlinear system increased rapidly to the same order of magnitude as that of the linear system.

Substantially the same comparative performance was displayed by the two systems when the input was a smaller (4-volt peak-to-peak) sinusoid as is shown in figure 9.

Figure 11 gives the response of the nonlinear system to a 20-volt peak-to-peak osculating sinusoid over the frequency range $0.1 \leqq \Omega \leqq 0.8$. This is a severe type of input for the nonlinear system since both x and x' simultaneously go to zero. This implies that y and y' are also small so that in equation (8) the discontinuous variations of the parameters β_m, γ_n cannot be so effective in determining the acceleration y'', since

$$y''=x-[2D(1+\beta_m)y'+(1+\gamma_n)y] \tag{15}$$

From the figures it is seen that the nonlinear system did have some difficulties near the osculating regions; further, the peak error increased as the frequency was increased (see appendix D). As might be expected from equation (15) this error for small values of y and y' can be reduced by increasing the magnitudes of the parameters (this will be discussed in more detail in the section entitled "Choice of Parameters"). At any rate, by comparison, the error for the present system is always less than that of the linear system of figure 6. (In the linear realm, error is independent of a shift in the direct-current level of the input.)

Taken collectively, the 20-volt, the 4-volt, and the osculating 20-volt sinusoidal inputs tend to form a more realistic appraisal of the nonlinear system performance than does a single input amplitude. There is still much that can be learned from a detailed study of these three responses, but first it is desirable to obtain some sort of a quantitative comparison between the nonlinear and the linear system performance. One such comparison can be made as follows:

(1) Assume that the input to both systems $x(\tau)$ is, and has been for a long time, a 4-volt peak-to-peak sinusoid of frequency

$$\Omega=\omega/\omega_\nu=0.1$$

so that as far as the linear system is concerned this is a steady-state alternating-current input.

(2) Determine how much the band width or the natural frequency ω_ν of the linear system must be increased in order that the time average of the magnitude of the instantaneous error

$$\overline{|e|}=\frac{\Omega}{2\pi}\int_0^{2\pi/\Omega}|e|d\tau$$

for the linear system be reduced to that value given by the nonlinear system.

Here it is easy to show that for the low-frequency steady-state alternating-current case

$$\overline{|e|}_{lin}\approx\frac{4D}{\pi}\,\Omega|x|_{max} \tag{16}$$

For an input $x=|x|_{max}e^{i\Omega\tau}$ the steady-state error is given by

$$e\triangleq x-y=|x|_{max}\left(1-\frac{1}{1+i\Omega 2D-\Omega^2}\right)e^{i\Omega\tau}$$

For small values of Ω this equation yields

$$e\approx|x|_{max}[1-(1-i\Omega 2D+\ \ldots)]e^{i\Omega\tau}$$
$$\approx|x|_{max}(i\Omega 2D)e^{i\Omega\tau}$$

or

$$|e|_{max}\approx 2D\Omega|x|_{max}$$

but

$$\overline{|e|}_{lin}=\frac{1}{\pi}\int_0^{\pi}|e|_{max}\sin\Omega\tau\,d\Omega\tau=\frac{2}{\pi}|e|_{max}$$

therefore

$$\overline{|e|}_{lin}\approx\frac{4D}{\pi}\,\Omega|x|_{max} \tag{17}$$

For the given system and input

$$\overline{|e|}_{lin}\approx 0.15$$

For the nonlinear system and the same input (approximate calculation from the much larger and clearer original of fig. 9 (a))

$$\overline{|e|}_{nonlin}\approx 0.01$$

Thus,

$$\overline{|e|}_{nonlin}\approx\frac{1}{15}\,\overline{|e|}_{lin}$$

Now from equation (17), since $\Omega=\omega/\omega_\nu$, it is seen that in order to reduce $\overline{|e|}_{lin}$ by this factor of 15, ω_ν must be increased by the same factor.

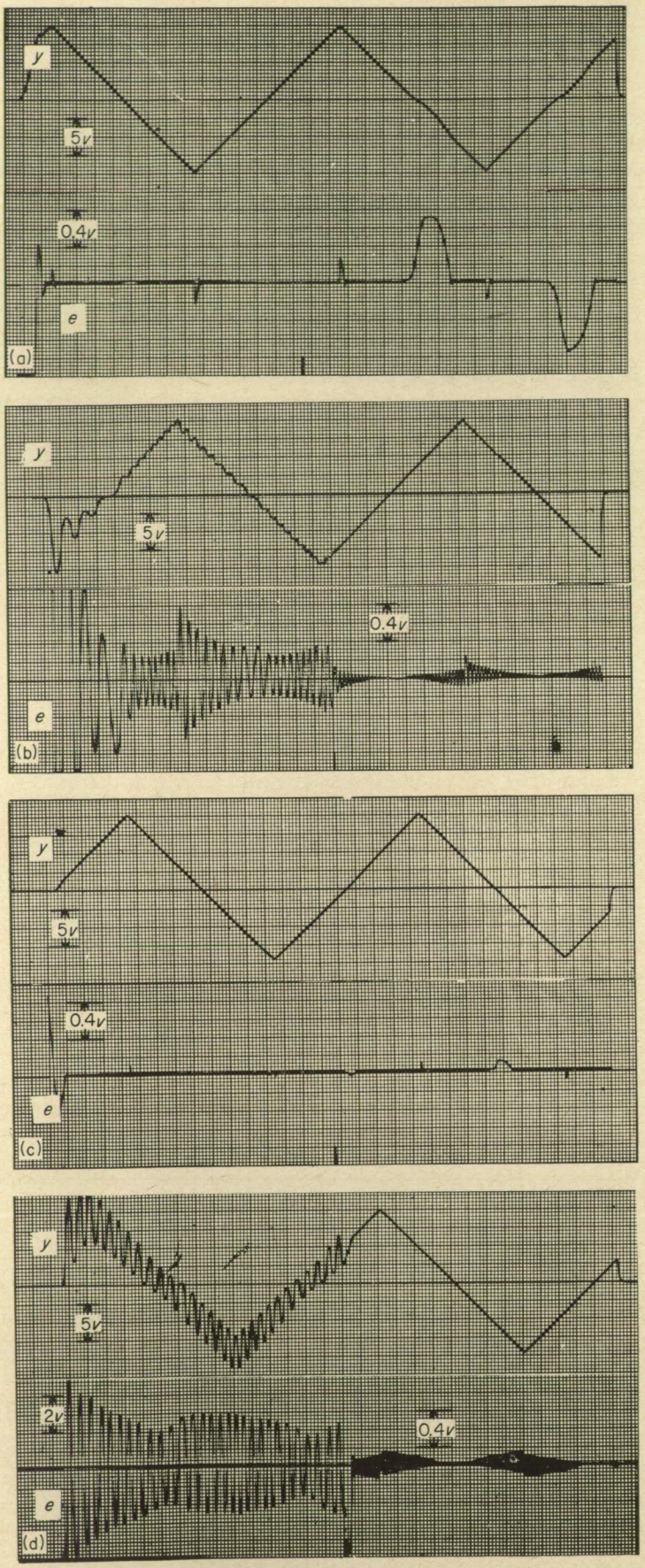


FIGURE 16.—Responses of nonlinear system with four different parameter sets to a 20-volt peak-to-peak triangular-wave input with fixed period $T=10\pi$. $D=0.6$; 2.5 small divisions on time scale=1 normalized time unit; tick marks at bottom of figures indicate demarcation between systems. For systems' numbering see table 3

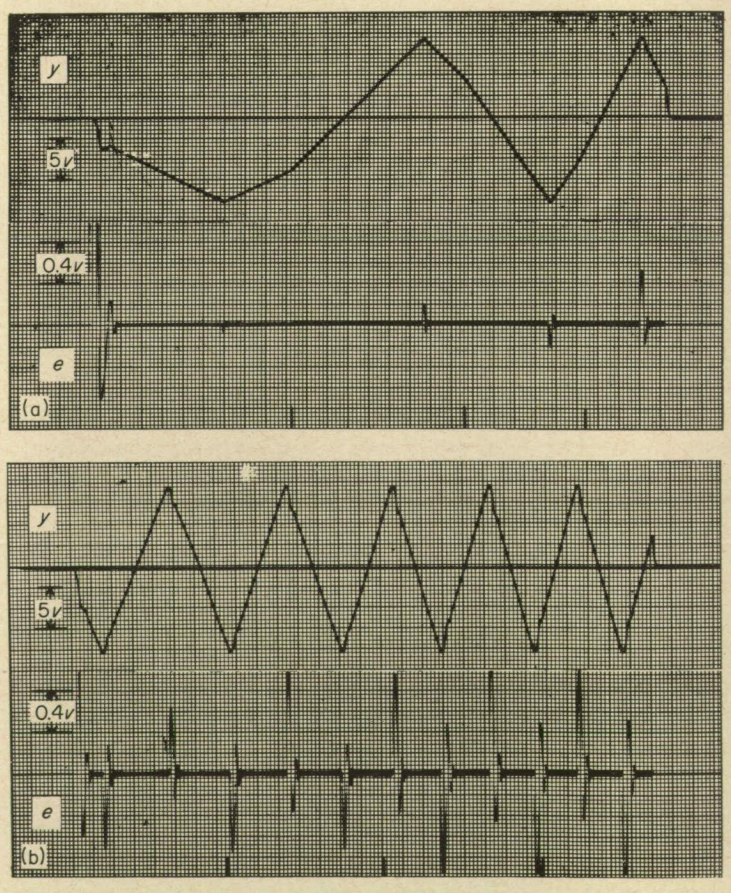
(a) Complete system 1 and system with no derivative feedback 2.
System 1: $\beta_3=-\beta_0=2$; $\beta_2=-\beta_1=0.5$; $\gamma_3=-\gamma_0=2$; $\gamma_2=-\gamma_1=0.5$.
System 2: $\beta_3=-\beta_0=0$; $\beta_2=-\beta_1=0$; $\gamma_3=-\gamma_0=2$; $\gamma_2=-\gamma_1=0.5$.
(b) System with no e' sensing 3 and system with no e sensing in derivative feedback loop and no e' sensing in proportional feedback loop 4.
System 3; $\beta_3=-\beta_0=2$; $\beta_2=-\beta_1=2$; $\gamma_3=-\gamma_0=2$; $\gamma_2=-\gamma_1=2$.
System 4: $\beta_3=-\beta_0=2$; $\beta_2=-\beta_1=-2$; $\gamma_3=-\gamma_0=2$; $\gamma_2=-\gamma_1=2$.
(c) Complete system 5 and system with no derivative feedback 6.
System 5: $\beta_3=-\beta_0=10$; $\beta_2=-\beta_1=1$; $\gamma_3=-\gamma_0=10$; $\gamma_2=-\gamma_1=1$.
System 6: $\beta_3=-\beta_0=0$; $\beta_2=-\beta_1=0$; $\gamma_3=-\gamma_0=10$; $\gamma_2=-\gamma_1=1$.
(d) System with no e' sensing 7 and system with no e sensing in derivative feedback loop and no e' sensing in proportional feedback loop 8.
System 7: $\beta_3=-\beta_0=10$; $\beta_2=-\beta_1=10$; $\gamma_3=-\gamma_0=10$; $\gamma_2=-\gamma_1=10$.
System 8: $\beta_3=-\beta_0=10$; $\beta_2=-\beta_1=-10$; $\gamma_3=-\gamma_0=10$; $\gamma_2=-\gamma_1=10$.

FIGURE 16.—Continued.

In the example of the linear control system of figure 1 and equation (5) this increase in ω_ν by a factor of 15 would mean that the gain K_1 must be increased by the order of magnitude of $(15)^2$ since

$$\frac{K_1 k_m}{I}=(\omega_\nu)^2$$

The gain K_2 must be increased by an order of magnitude of 15 if the value of D shall not change. Such an increase in the loop gains is frequently not at all physically possible.



(a) $\Omega=2\pi/T=0.1$ to 0.4 in 0.1 steps.
(b) $\Omega=2\pi/T=0.5$ to 0.8 in 0.1 steps.

FIGURE 17.—Nonlinear system responses to 20-volt peak-to-peak triangular-wave input with period T varied. $D=0.1$; $\beta_3=-\beta_0=12$; $\beta_2=-\beta_1=3$; $\gamma_3=-\gamma_0=2$; $\gamma_2=-\gamma_1=0.5$; 2.5 small divisions on time scale=1 normalized time unit; tick marks at bottom of figures indicate when period was varied

Up to this point little attention has been given to the detailed nature of the nonlinear system response. Closer inspection of, for example, figures 6 (a) and 6 (c) shows that the output y is a function that links serpentine fashion (oscillates) at a very high rate about the input x, but still the magnitude of the error is small. In fact, it is necessary to inspect the error at a scale 20 times larger than that of the output even to notice this phenomenon. Mathematically this means that the functions x and y approach one another closely but that their derivatives differ appreciably. Physically, however, this is not at all undesirable as long as the magnitude of the error is small. (Actually for mechanical systems this property would be useful in preventing static friction.) This fine-grained oscillating character of y is the very essence of the nonlinear control theory. Every time the error or error derivative goes through zero the parameter set β_m,γ_n of equation (8) changes discretely as defined in equations (13) or by the binary logic of table 2. The discrete changes in the parameters cause discontinuities in the second derivative y'', which when integrated twice give y its serpentine character. To illustrate this point, the sketch of figure 18 shows samples of the superposed input and output of the nonlinear system. The input in this case could be that of figure 6 (a) or 9 (a).

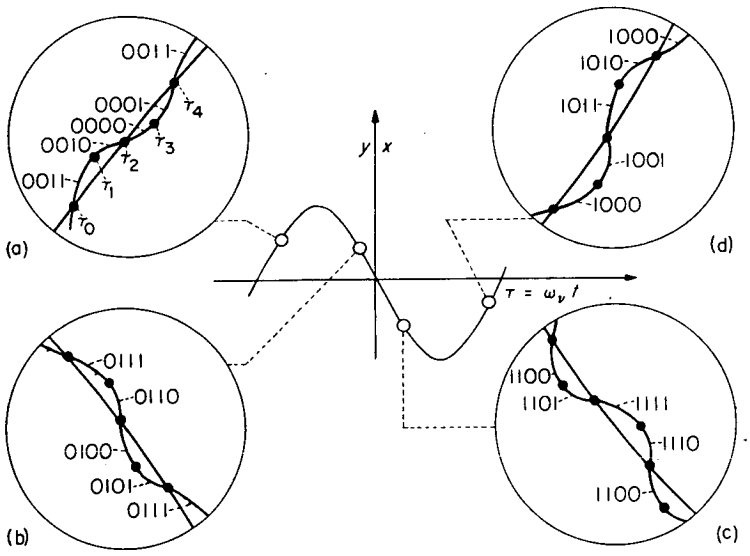


FIGURE 18.—Sketch showing portions of superposed input and output of nonlinear system magnified approximately 100 times.

Circle (a) in figure 18 is a typical cycle of the oscillating character of the output y. Commencing at τ_0, the error changes sign at τ_0, the binary number 0011 is "read into" the feedback switching circuit of figure 5, and using the notation of table 2 the parameter combination $\beta_3\gamma_3$ is switched into the circuit. This causes an immediate reversal in the sign of the output acceleration y'', so that at time τ_1 the error derivative changes sign, the binary number 0010 is read in, and the parameter combination $\beta_2\gamma_2$ is switched into the circuit; acceleration is still in the same direction but weaker. At time τ_2 the error again changes sign, the binary number 0000 occurs, and the combination $\beta_0\gamma_0$ is switched into the circuit; acceleration is in the opposite direction. At time τ_3 the error derivative changes sign, the binary number 0001 occurs, and $\beta_1\gamma_1$ is switched in; this reduces the acceleration until at time τ_4 the error again changes sign, 0011 occurs, $\beta_3\gamma_3$ is again switched in; the cycle is complete. Although it was not mentioned at the time, figure 2 shows this sequence of β_m,γ_n combinations. The nature of the acceleration resulting from the switching can be seen in figure 14 (a).

The comparable switching cycle for $y>0$ and $y'<0$ as shown in circle (b) of figure 18 is:

Logic	Parameters
0111	$\beta_0\gamma_3$
0110	$\beta_1\gamma_2$
0100	$\beta_3\gamma_0$
0101	$\beta_2\gamma_1$
0111	$\beta_0\gamma_3$

Similarly, for $y<0$ and $y'<0$ as shown in circle (c) of figure 18:

Logic	Parameters
1100	$\beta_3\gamma_3$
1101	$\beta_2\gamma_2$
1111	$\beta_0\gamma_0$
1110	$\beta_1\gamma_1$
1100	$\beta_3\gamma_3$

This is the mirror-image switching cycle for circle (a) (see property (4) in the section "Properties of Equation (8)" and also the discussion in the section "Switching Logic").

Finally, for $y<0$ and $y'>0$ as in circle (d) of figure 18:

Logic	Parameters
1000	$\beta_0\gamma_3$
1001	$\beta_1\gamma_2$
1011	$\beta_3\gamma_0$
1010	$\beta_2\gamma_1$
1000	$\beta_0\gamma_3$

This is the mirror-image switching cycle for circle (b).

With this insight into the detailed behavior of the nonlinear system more information can be obtained from the experimental sinusoidal responses of figures 6, 9, and 11 that have up until now been treated from a macroscopic rather than microscopic viewpoint. Along these lines, the following experimentally observed facts are noteworthy:

(1) In comparing the errors for the 4-volt and the 20-volt peak-to-peak sinusoidal inputs in the frequency range of good reproduction $0.1 \leqq \Omega \leqq 0.8$, it is seen that:

(a) The magnitudes of the errors are nearly the same (see figs. 6 (a) and 6 (c) and 9 (a) and 9 (c)).

(b) The period of the error is generally smaller in the larger amplitude case. This is even more pronounced if the 4-volt peak-to-peak case is compared with figure 11 for y in the region of -20 volts.

(2) Good reproduction is characterized by many e and e' switchings (see fig. 18) per cycle of the input. As input frequency is increased and the upper limit of small error is reached (fig. 6 (e) and 9 (e)) the e and e' switchings become more infrequent until there are finally only two of each per cycle of the input.

The fact that the period of the error is smaller for larger inputs can be gleaned from equation (8) when it is rearranged as

$$y''=-[2D(1+\beta_m)y'+\gamma_n y]+(x-y)$$

or roughly

$$y''\approx-[2D(1+\beta_m)x'+\gamma_n x] \tag{18}$$

For a system with specified β_m,γ_n parameter values, the larger input and input derivatives will give stronger discontinuities in y'' as the β_m,γ_n combinations change. This implies that β_m,γ_n will change more often making the period of the error smaller. See figure 14 (a) for the justification of the approximations in equation (18) since y, y', y'', and x are shown in this figure. (The input x was sketched in by hand.)

In the frequency range of good reproduction the reason that the magnitude of the error is virtually independent of the input amplitude cannot be explained from equation (8) since this fact is intimately tied in with the imperfections in the feedback switching circuit (see section entitled "Effects of Switching Imperfections" for details). As measured from the experimental sinusoidal responses, $|e|_{max}$ is of the order of 15 to 20 millivolts. It might be noted that earlier in this section the smaller 4-volt peak-to-peak input sinusoid was employed in the comparison when it was determined that ω_p should be increased by a factor of 15 in order to obtain the same $\overline{\overline{|e|}}_{lin}$. This choice of the smaller input was decidedly in favor of the linear system since the linear error increases linearly with input amplitude. Thus, if the 20-volt peak-to-peak input were used, an increase in ω_p by a factor of $5\times15=75$ would be required to obtain the same $\overline{\overline{|e|}}_{lin}$.

The fact that there is a correlation between good reproduction (small error) and the existence of many error and error-derivative switchings is very important since it is the key to understanding the upper limits of good performance of the nonlinear system. One approximate way to investigate this matter is to establish a deficiency between the output acceleration required for good reproduction (many switchings) and the available output acceleration. Equation (18) gives an approximation to the output acceleration when the system is functioning well. As an example of this approach consider the input x to be a sinusoid of frequency Ω (fig. 6 or 9). Since

$$|x''|_{max}=\Omega^2|x|_{max}$$

it is to be expected that the nonlinear system will have the greatest difficulty in the vicinity of $|x|_{max}$ where, from equation (18),

$$|y''|_{max}\approx|\gamma_n x|_{max}$$

Thus, if in this region the output y is going to interweave the input x (as is characteristic of good reproduction), then

$$|y''|_{max}>|x''|_{max}$$

This inequality then places an upper limit on good performance of the system in response to sinusoids

$$\Omega<\sqrt{|\gamma_n|_{max}} \tag{19}$$

or the system used in obtaining the experimental results of figures 6 and 9, $|\gamma_n|_{max}=2$; therefore,

$$\Omega<\sqrt{2}$$

Inspection of both figures 6 (e) and 9 (e) tends to substantiate the above result. For example, in figure 9 (e) it is seen for $\Omega=1.2$ (after the transient caused by turning on the input has been absorbed) that as the input goes through its maximum, frequent e and e' switchings stop and do not occur again as the frequency is increased.

PERFORMANCE EVALUATION OF INPUTS OTHER THAN SINUSOIDAL

In the preceding section only the sinusoidal response of the nonlinear control system was discussed in studying performance. However, it is easy to see that the nonlinear system will cope with any input in the same manner as it does with sinusoids. Thus, as long as the magnitude of input acceleration does not continuously exceed the available magnitude of the output acceleration the switching process will commence and excellent reproduction will result. This type includes inputs with discontinuous derivatives and discontinuous inputs. The experimental sinusoidal responses of figures 6, 9, and 11 themselves give some indication of these facts. For example, in figure 6 (a) there was an initial discontinuity in the input and there were discontinuities in the input derivative when the frequency was changed. The results in figures 7, 8, 10, and 12 prove further that the nonlinear system response is not dependent upon any specific type of input. Given in these figures are triangular-wave, partially integrated square-wave (including square-wave), clipped sinusoidal, and random[4] inputs, respectively.

It should be noted that in the literature (refs. 1 and 3 to 5) a marginal-type input that would present a case of indecision to the switching circuit of the nonlinear system is discussed. This case has never been encountered experimentally even when the attempt was to produce this case. Thus, the marginal-type input is not considered practically important.

USE OF PHASE-PLANE METHODS TO STUDY PERFORMANCE

The phase-plane methods that were used in the original analytical development of equation (8) (refs. 1 and 3 to 5) can also be gainfully employed in studying the performance of the nonlinear control system derived from equation (8) once the β_m and γ_n parameter values have been specified. (In this section it is important to distinguish between β_m and γ_n parameter values, i. e., $\beta_3=2$, $\beta_2=1$, etc., and $\beta_m\gamma_n$ parameter combinations, i. e., $\beta_3\gamma_0$, etc.)

---

[4] In the strict statistical sense the probability that the inputs shown in figures 12 (a) and 12 (b) are not samples of random stationary time series is admittedly high because of existing experimental facilities. These inputs were obtained by random manual modulation (both frequency and amplitude) of a triangular-wave input of peak-to-peak amplitude A and period T where

$$0\leqq A\leqq20 \text{ volts}$$

$$0.1\leqq\Omega=2\pi/T\leqq0.8$$

Random manual modulation means that the operator varied by hand both the frequency and amplitude controls of the input generator as randomly as possible. In the present investigation the comparative results of the linear and nonlinear responses to what appear to be band-limited random inputs are felt to be more important than the exact statistical properties of the inputs.

If in equation (8) the error $e=(x-y)$ is assumed small, then the output y can be approximated by portions of curves that satisfy the autonomous differential equation

$$\frac{d^2\bar{y}}{d\tau^2}+2D(1+\beta_m)\frac{d\bar{y}}{d\tau}+\gamma_n\bar{y}=0 \qquad (20)$$

where D, β_m, and γ_n are defined in the section "Nonlinear Control Theory." Further, if $d\bar{y}/d\tau=\bar{y}'$, these approximating curves are defined in the $\bar{y}'\bar{y}$ phase plane by

$$(\bar{y}\lambda_2-\bar{y}')^{\lambda_2}=M(\bar{y}\lambda_1-\bar{y}')^{\lambda_1} \qquad (21)$$

where M is a constant depending on initial conditions and

$$\lambda_{1,2}=-D(1+\beta_m)\pm\sqrt{D^2(1+\beta_m)^2-\gamma_n}$$

Equation (21) comes from integration of the first-order differential equation

$$\frac{d\bar{y}'}{d\bar{y}}=\frac{-2D(1+\beta_m)\bar{y}'-\gamma_n\bar{y}}{\bar{y}'_1}$$

$$=-2D(1+\beta_m)-\gamma_n\frac{\bar{y}}{\bar{y}'} \qquad (22)$$

Since the particular β_m, γ_n combination employed in each point of the phase plane depends upon $\bar{y}$, $\bar{y}'$, e, and e', four approximating curves go through each point (see appendix E). The tangents to these curves (eq. (22)) indicate four directions which lie in an angular sector (see fig. 19). This angular sector is defined by the two extreme directions which apply if e and e' have the same sign. The two inner direction values apply if e and e' have opposite signs. By superposing the input $x'x$ phase plane on this $\bar{y}'\bar{y}$ plane it can be stated that at any point the tangent to the input phase curve must be included within the shaded angular sector (discussed above) if small error is to be obtained. Thus, equation (22) can be used to study performance. The width of the angular sector changes with the ratio $\bar{y}/\bar{y}'$ for given β_m and γ_n parameter values. It is largest (180°) for $\bar{y}'_1\to 0$ and smallest for $\bar{y}=0$ if $(1+\beta_m)$ and γ_n have the same sign. However, the width for $\bar{y}'\to 0$ is not significant since all phase curves (including the input) have infinite slope there. Thus, along the line $\bar{y}'=0$ the curvature of the input phase curve must be used to determine limits on good performance. The radius of curvature of the input must be smaller than that of the flattest approximating curve.

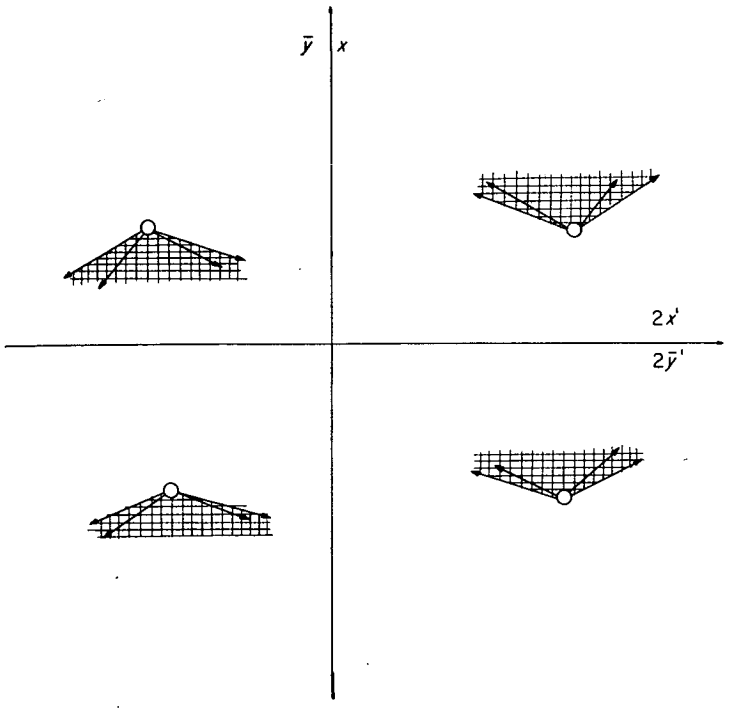


FIGURE 19.—Phase-plane angular sectors defined by equation (22) for the given parameter values. ${}_1\beta=1.5$; ${}_2\beta=0.5$; ${}_1\gamma=0.45$; ${}_2\gamma=0.05$; $2D=0.25$; $\omega_r=2$.

In order to illustrate the use of these phase-plane methods in predicting limits of good performance consider the example of a sinusoidal input $x=\sin\Omega\tau$. In this case the input is represented by an ellipse in the phase plane and

$$\frac{d(x')}{dx}=-\Omega^2\cdot\frac{x}{x'}$$

In the superposed xx' and $\bar{y}\bar{y}'$ phase planes of figure 20 are shown three sinusoidal-input phase curves (i. e., three different frequencies) and the families of phase trajectories of equation (22) for the β_m, γ_n combinations where e and e' have the same sign. (In order to avoid extensive computations the parameter values indicated in fig. 20 are those of an earlier investigation (see ref. 1).) Thus, the tangents to two intersecting phase curves define the angular sector at that point, as has been discussed. By tracing the inputs with different values of Ω it can be understood that good performance for the presented system can be obtained only for $\Omega<\Omega_o$ where Ω_o is the parameter belonging to that ellipse which has the same radius of curvature as the curve through $(\bar{y},\bar{y}')=(1,0)$. (Note that the radius of curvature of the approximating curves jumps at $\bar{y}'=0$ and is smaller for $\bar{y}'<0$.) In the first quadrant (i. e., approaching $\bar{y}'=0$ from $\bar{y}'>0$) this radius of curvature is given by

$$\rho_{max}=|\rho|_{\bar{y}'=+0}=\gamma_n\bar{y}$$

Since at this point the ellipse radius of curvature is $\Omega^2/1$.

$$\Omega^2<\gamma_n\bar{y}$$

Therefore, for the first quadrant

$$\Omega<\sqrt{\gamma_3} \qquad (23)$$

Here it should be noted that this is the same result as that obtained in the section entitled "Performance Evaluation of Sinusoidal Inputs" even though the parameter values are different. For the system of figure 20, $\gamma_3=0.5$; thus $\Omega<\sqrt{0.5}$.

Another example is given by the input $x=1-e^{-\alpha\tau}$ with $d(x')/dx=-\alpha$. Since the smallest angular sector is at $\bar{y}=0$, $\alpha=2D(1+\beta_{max})$ determines the limits on performance. This means that for the system represented in figure 20 good control can be expected for a value of α slightly smaller than 0.75.

A step input is represented by $x=1-e^{-\alpha\tau}$ with $\alpha\to\infty$. The picture in the phase plane is $x=1-(1/\alpha)x'$ with $\alpha\to\infty$. For very large values of α this is a straight line which forms a

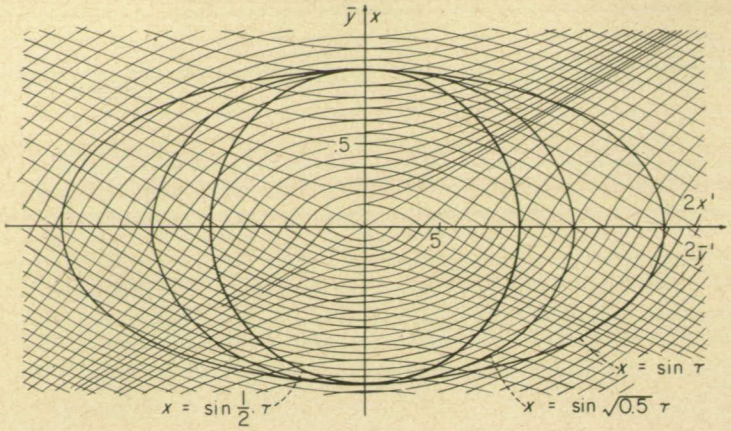


FIGURE 20.—Superposed input and output phase planes showing available angular sectors for sinusoidal inputs. ${}_1\beta=1.5$; ${}_1\gamma=0.45$; ${}_2\beta=0.5$; ${}_2\gamma=0.05$; $2D=0.25$; $\omega_\nu=2$; $|\beta|_{max}=2$; $|\gamma|_{max}=0.5$; $|\beta|_{min}=1$; $|\gamma|_{min}=0.4$.

small angle with $x'=0$. For $\alpha\to\infty$ the curve degenerates to a point ($x=1, x'=0$). There is no doubt that a perfect followup of a step is not possible because for practical reasons the line for large values of α does not lie in the allowed angular sector at any point it is passing through.

Related to the step input is the square-wave input. A portion of the output phase trajectory for a square-wave input to the system of figure 8 (e) is shown in figure 21. Figure 21 is computed with the help of the differential equation

$$\frac{dy}{dy'_1}=-\frac{y'_1}{2D(1+\beta_m)y'_1+(1+\gamma_n)y-x}$$

This equation is obtained from equation (8) by replacing $d^2y/d\tau^2$ by $y'^1(dy'_1/dy)$. In this example one cannot immediately use approximating curves for designing the output because the error is too big at the start of the motion. The computed diagram is in good agreement with the test run shown in figure 8 (e).

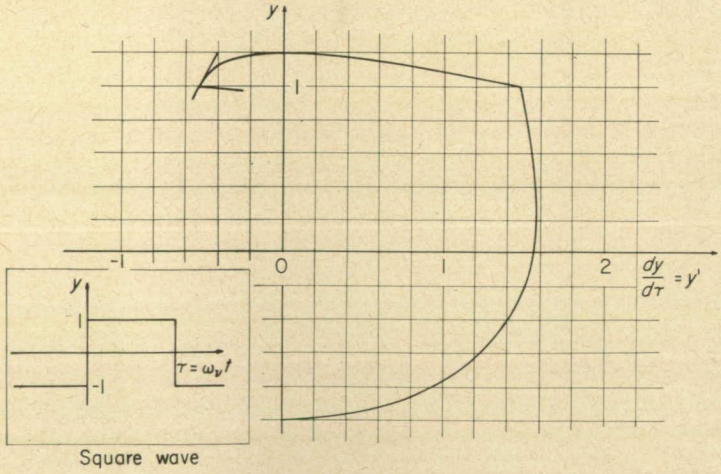


FIGURE 21.—Portion of output phase diagram for square-wave input. $\beta_3=-\beta_0=2$; $\beta_2=-\beta_1=0.5$; $\gamma_3=-\gamma_0=2$; $\gamma_2=-\gamma_1=0.5$; $D=0.6$; $\omega_\nu=1$.

EFFECTS OF SWITCHING IMPERFECTIONS

In equation (8) it is assumed that the parameters β_m and γ_n change upon exact zero coincidence of any one or more of the variables y, y', e, and e' as defined in equation (13) or by the logic of table 2. Physical imperfections, however, preclude this possibility. Thus, in the simulated model of equation (8), exact zero coincidence cannot be detected because of threshold effects, and relays are subject to time lag (both mechanical and electrical), dead zone, and chatter.

In the present section an attempt is made to evaluate the effects that these switching imperfections had on the experimental result in order to obtain some practical design criteria for specifying switching requirements for good performance in other applications of this method of nonlinear control.

The experimental results of figures 6, 9, and 11 can be used to demonstrate that relay imperfections were not important in the simulated model. Comparison of the sinusoidal responses in these figures has shown that the period of the error became smaller as the magnitude of the input amplitude was increased. (This was discussed in the section "Performance Evaluation of Sinusoidal Inputs.") From figure 11 (a) in the region of $|y|\approx 20$ volts (the largest magnitude considered in all the experimental studies) the period of the error T_e is measured as

$$T_e=\omega_\nu t_e\approx 0.2$$

There are four parameter switchings per error cycle (see fig. 18). Assuming these to be approximately uniformly spaced, the minimum time between parameter switchings is approximately $T_e/4$. Now assuming that the relays must be capable of closure in at least one-fifth of this time, the maximum allowable (real time) switching delay t_{md} is

$$\omega_\nu t_{md}\approx T_e/20=10^{-2} \qquad (24)$$

In this simulated model $\omega_\nu=1$ radian per second. Therefore,

$$t_{md}\approx 10 \text{ millisec}$$

As given in table 4, the relays employed were capable of closure in 3 milliseconds or less so that they were entirely adequate for the experimental studies.

(After the investigation reported here in the main text was finished, Dr. H. E. Lindberg performed a number of experiments to study quantitatively the influence of time delays on the performance of this control system (see appendix A). He investigated the influence of switching delays in the individual relays and additionally that of a delay in the output line of all relays (represented by an analog-computer approximation of $e^{-t_d p}$). The results indicate that for sinusoidal inputs with frequencies up to 0.8 of the natural frequency of the undamped linear member ω_ν, for example, the maximum error can be held within 5 percent of the maximum value of the input with relay delays as large as $47/\omega_\nu$ milliseconds. For a natural frequency of 10 cps this would be a delay of 0.75 millisecond. After this relay delay is selected, the maximum error per input cycle is considerably less for lower input frequencies. For instance, at $\omega=0.1\omega_\nu$ the maximum error per input cycle would be slightly more than 1 percent. Also, the average error would be less than this (see fig. 31).)

The ability to disregard the relays in the evaluation of the effects of switching imperfection on performance leaves only threshold effect in sensing the sign of the variables y, y', e, and e' to be considered. As has been observed and discussed in the section "Performance Evaluation of Sinusoidal Inputs" the amplitude of the error for the nonlinear system was relatively independent of the magnitude of the input (i. e., when the system is operating in the rapid e to e' switching sequence

so that this is the minimum-error case). This constancy of the lower limit on the error magnitude is caused by switching imperfections and thus threshold in sensing the signs of variables. Since under a normal switching sequence there are many more e and e' switchings than y or y' switchings and since the error is of an order of magnitude less than the error derivative, the primary cause of the lower limit on error is localized as threshold in sensing the sign of the error. Figure 13 shows the results of an investigation of this threshold effect. In all system-response figures except figure 13 the peak-to-peak threshold was approximately 14 millivolts. In figure 13 (a) the peak-to-peak threshold was 44 millivolts so that figures 7 (a) and 13 give a good comparison of the effects of these two threshold values.

CHOICE OF PARAMETER VALUES

The performance of a completely specified nonlinear system has been discussed. The parameter values for this system, that is,

$$D=0.6$$
$$\beta_3=-\beta_0=2$$
$$\beta_2=-\beta_1=0.5$$
$$\gamma_3=-\gamma_0=2$$
$$\gamma_2=-\gamma_1=0.5$$

were initially chosen in the following manner: D was first selected to give good linear system performance; then the smallest values of the β_m and γ_n parameters giving good nonlinear system performance were chosen experimentally from a systematic variation of parameters utilizing the simulated system. This particular set of β_m and γ_n parameter values can thus be denoted as $(\beta_m,\gamma_n)_{min}$ since they establish the lower bound on parameter values for good nonlinear system performance. The physical significance of $(\beta_m,\gamma_n)_{min}$ is that loop gains and acceleration requirements of the linear member are minimized since β_m and γ_n are feedback gain constants.

From the discussion in the section "Performance Evaluation of Sinusoidal Inputs" centering about equation (18) or from the phase-plane methods of the preceding section it is to be expected that a general increase in the parameter values over $(\beta_m,\gamma_n)_{min}$ will result in improved nonlinear system performance by increasing the available acceleration of the system or increasing the angular sectors in the phase plane. Inspection of figures 16 (a), system 1, and 16 (c), system 5, shows this to be true. In figure 16 (a) the parameter values were $(\beta_m,\gamma_n)_{min}$ as given above, and in figure 16 (c), system 5, they were

$$\beta_3=-\beta_0=10'$$
$$\beta_2=-\beta_1=1$$
$$\gamma_3=-\gamma_0=10$$
$$\gamma_2=-\gamma_1=1$$

On comparing the performance of these two systems it is noted that the corners of the input triangular wave are reproduced with less error by the system of figure 16 (c). Thus far then it would seem that there is no upper bound on the parameter values; that is

$$(\beta_m,\gamma_n)_{max}\to\infty$$

Invariably, however, there will be upper bounds on the values of the parameters because of acceleration limits in the physical system. Figure 14 shows the effects of placing progressively smaller acceleration limits on the system. Here it is seen that for $|y''|_L>0.3|y''|_{max}$ performance is not appreciably affected but for values less than this good performance is no longer obtained so that acceleration limits definitely tend to determine $(\beta_m,\gamma_n)_{max}$. In general, then, there will be a whole range of values of β_m and γ_n; that is,

$$(\beta_m,\gamma_n)_{max}>(\beta_m,\gamma_n)>(\beta_m,\gamma_n)_{min}$$

for which good nonlinear system performance results. The final choice must depend upon the particular application and can easily be found experimentally.

There are certain special cases of the β_m and γ_n parameter values that lead to simplified feedback switching circuits and thus lead to nonlinear systems that are simpler to realize. In table 3 three of these are denoted as case (1) no derivative feedback, case (2) no e' sensing, and case (3) no e sensing in derivative feedback loop and no e' sensing in proportional feedback loop.

By making inoperative the appropriate relays in figure 5 the simplified switching circuits for these cases are easily obtained. It is desirable then to inspect the performance of these special cases (in comparison with that of the complete system) to ascertain whether or not as good performance can be obtained with less complexity. Figure 16 shows the response of these cases in comparison with that of the complete system. Figures 16 (a) and 16 (b) differ from figures 16 (c) and 16 (d) in that the general magnitude of the parameters was increased in figures 16 (c) and 16 (d).

These results show that case (2) is not worthy of much consideration since the magnitude of the oscillating error is large. Cases (1) and (3), however, should be considered for certain applications. For example, if it were known that the amplitude distribution of the input was relatively void near zero, then case (1) would serve as well as the case of the complete system. Case (3) shows nearly constant percentage error so that it could be useful in cases where accuracy was not so important as economy in components.

To this point the parameter D has received little attention mainly because its value (within limits) is not particularly important. It has been observed experimentally that D may be anywhere in the range $0\leqq D\leqq 1$ even for $(\beta_m,\gamma_n)_{min}$ and performance of the nonlinear system is not affected. Inspection of the block diagram of the nonlinear system (fig. 4 or 5) shows that the physical significance of the variation of D for given values of β_m,γ_n is that the damping factor of the linear member and the derivative feedback around the linear member change simultaneously. A case of more practical importance such as might arise in aerodynamic applications of this type of control system is the variation of D for given values of $D\beta_m,\gamma_n$. That is, the damping factor of the linear member alone varies while the

feedback values around this member remain unaffected. Even in this case it has been found that the nonlinear system performs well. For example, figure 17 shows the response of the nonlinear system

$$D=0.1$$
$$\beta_3=-\beta_0=12$$
$$\beta_2=-\beta_1=3$$
$$\gamma_3=-\gamma_0=12$$
$$\gamma_2=-\gamma_0=0.5$$

to triangular-wave inputs, while figure 7 shows the response of the system

$$D=0.6$$
$$\beta_3=-\beta_0=2$$
$$\beta_2=-\beta_1=0.5$$
$$\gamma_3=-\gamma_1=2$$
$$\gamma_3=-\gamma_0=0.5$$

to the same inputs. Comparing these results it is seen that performance is nearly the same for both systems.

PRELIMINARY EXTENSION TO HIGHER ORDER SYSTEMS

From a practical standpoint, limitations in the applicability of the nonlinear control system described by equation (8) do not stem from the inability to realize the feedback switching circuit but rather from assuming the linear member to be of second order. In many cases a more realistic approach is to consider the linear member to be of higher order but still predominantly second order. Figure 22 shows the block diagram of a third-order system of this nature. The linear feedforward member could be, for example, the servo of figure 1 including the effects of armature inductance. The same second-order feedback switching circuit was still employed. However, it could not be

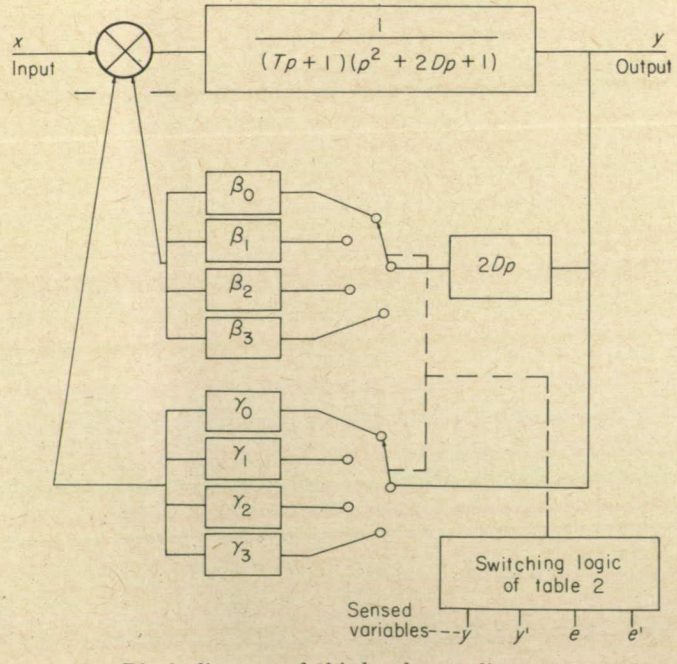
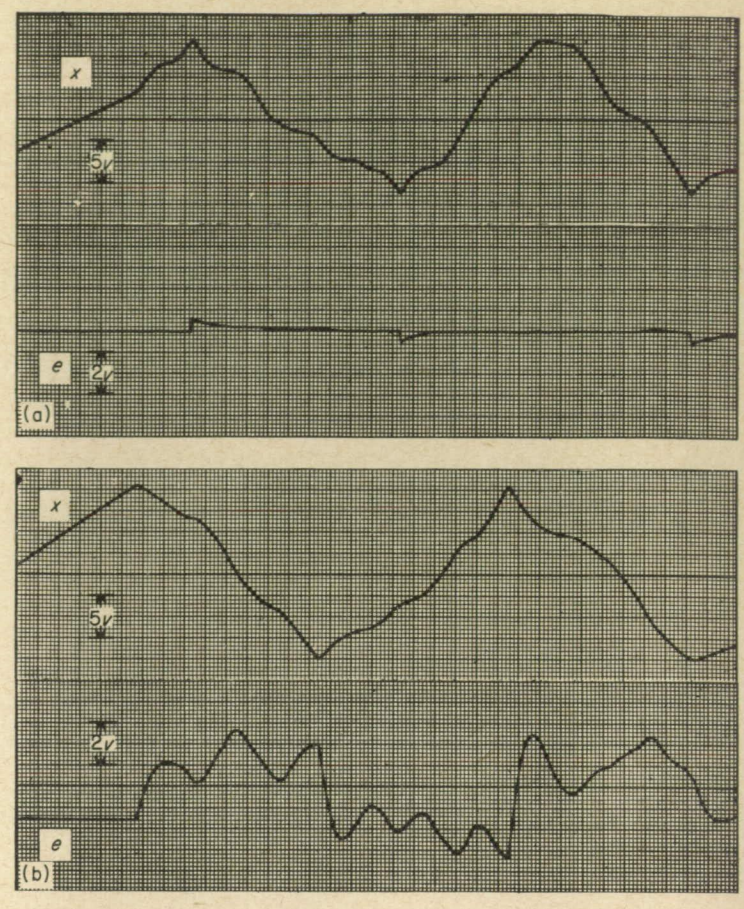


FIGURE 22.—Block diagram of third-order nonlinear control system.



(a) Nonlinear system. $\beta_3=-\beta_0=2$; $\beta_2=-\beta_1=0.1$; $\gamma_3=-\gamma_0=2$; $\gamma_2=-\gamma_1=-0.5$.
(b) Linear system.

FIGURE 23.—Linear and nonlinear third-order system responses to random input. $T=0.1$; $D=0.6$; 2.5 small divisions on time scale = 1 normalized time unit.

expected that the β_m,γ_n parameter values remain the same. Figure 23 compares the response of a third-order linear and nonlinear system. Here it is seen that the nonlinear system still responded with much less error than the linear system.

On the basis of the comparative performance of these two systems it seems important to further studies toward control of general higher order systems using techniques similar to those developed in this investigation.

CONCLUDING REMARKS

From control equation (8) a second-order nonlinear control system that tends to maintain small instantaneous error for relatively arbitrary inputs has been synthesized using digital-computer techniques. The only type of nonlinear operations required in the realization are switching-type operations (zero-coincidence detection and parameter switching). The switching requirements are severe from the aspect of detector sensitivity and switching time delay but not impractical since all the switching is done in feedback paths at low power levels and may thus be performed electronically.

The system demands sensing of error and error rate of change. Since general noise in a system of this type has to be expected, both error and error rate are smoothed. The influence of time delay in the relays and of a general transport delay on the performance of the system has been investigated

and diagrams have been developed which allow one to estimate the maximum error due to imperfections.

It is a difficult task to compare the performance of a nonlinear system with that of a linear system because no general criterion for comparison is available. Since for nonlinear systems the law of superposition does not hold, it is not adequate to choose the response to a certain input (e. g., the step input) as a criterion for performance comparisons. A number of different inputs therefore have been chosen for exhibiting the qualities of the nonlinear system.

Experimental results indicate that this type of nonlinear control system performs better than a linear control system having a normalized frequency 15 times greater. Performance is evaluated in terms of the average value of the magnitude of the instantaneous error for band-limited inputs. Further, the nonlinear system performance is virtually independent of variations in the damping factor of the system.

STANFORD UNIVERSITY,
STANFORD, CALIF., *October 18, 1957.*

APPENDIX A

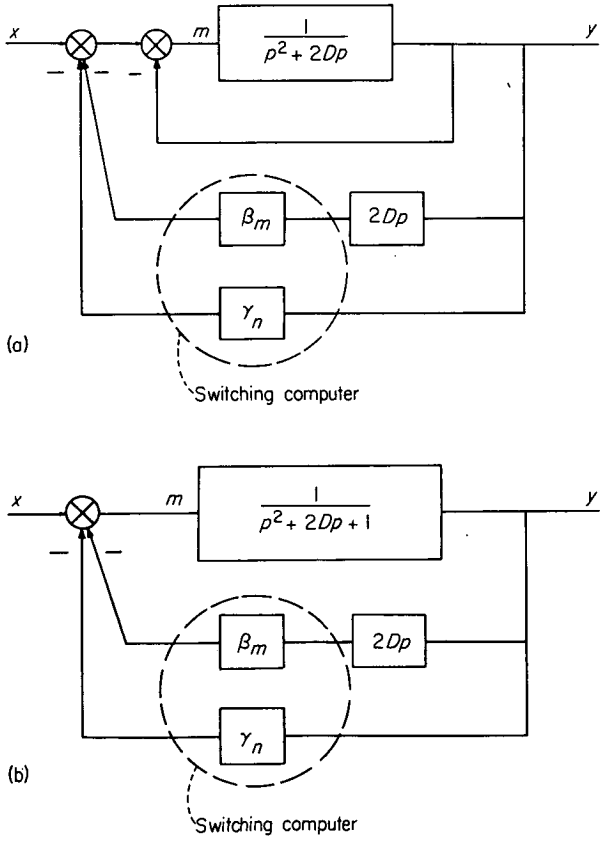
INFLUENCE OF TIME DELAYS

By H. E. Lindberg

In the experiments reported in the main text of this report, the relays were carefully selected in order to keep the bad effects of finite closure time to a minimum and no really quantitative study of such closure delays was made at that time. Later, studies of this particular system were continued and quantitative information about the influence of imperfections on the performance of the control system is presented here.

One numerical and two experimental methods of finding response with relay delays are used. Plots of maximum error incurred per input cycle are given for sinusoidal inputs of various frequencies and for various relay delays. Effects of a transport time delay are also discussed.

Influence zones and types of delays.—The system described by equation (8) can be interpreted as describing either of the systems shown in figure 24 if there are no imperfections to be considered. However, there are certainly relay imperfections and there may be transport delays. Relay imperfections would affect directly those parts of the systems that are encircled by dotted lines in figure 24, that is, only the discontinuous feedback paths. If no further imperfections are considered, the results of such a study apply equally well to both configurations shown in figure 24 because the switching computer sees the same linear member in either case. Other studies, however, can conceivably be made on these systems where the difference between the two configurations becomes significant. A study of transport delays introduced at points m, for instance, would certainly give different results for figures 24 (a) and 24 (b) because in figure 24 (a) the output y is fed directly through this point while in figure 24 (b) no such feedback is present because the equivalent of such a feedback is built into the differential equation of the mechanism being controlled (equivalent, i. e., when there are no imperfections).



(a) Motor-load system.
(b) Simplified airframe system.

FIGURE 24.—Block diagrams of two physical systems giving same differential equation providing no imperfections exist. m, point transport delay is introduced into circuit.

One of the most serious imperfections to be considered in the design of a relay servomechanism is the time lag between the application of a signal to the relay and the actual closing or opening of the relay. Associated very closely with this imperfection are other phenomena, such as signal threshold, relay dead time (the period of time in which the relay arm is in contact with neither terminal), and contact bounce. The only imperfection studied here is relay time lag, because in most relays dead time is very small as compared with the relay lag time. Contact bounce is also a secondary effect and is better studied in an actual installation. By appropriate interpretation, the results of this time-lag study can be extended to include the effect of signal threshold which is, of course, a variable time delay.

Rather than increasing the natural frequency of the system being studied until the effect of inherent relay lag became noticeable, an artificial lag was introduced while the system was allowed to operate in a conveniently low frequency range. Two techniques were used to provide the time lag. The first was a direct delay of each relay signal, effected by providing an additional relay in series with each original relay and a resistance-capacitance delay circuit in between (this will be referred to as the electromechanical simulation). The second method consisted of inserting an analog-computer approximation of $e^{-t_d p}$ in the total output line of all of the relays. The two methods gave consistent results.

Electromechanical simulation of time delay.—The armature of each logic relay in the control system with no intentional delays was energized by the plate current of a zero-coincidence detector circuit. In the delayed system, the plate current is made to flow through an added relay. This relay energizes an adjustable resistance-capacitance time-delay circuit which in turn feeds the armature of the logic relay. Two of the four circuits are shown in figure 25.

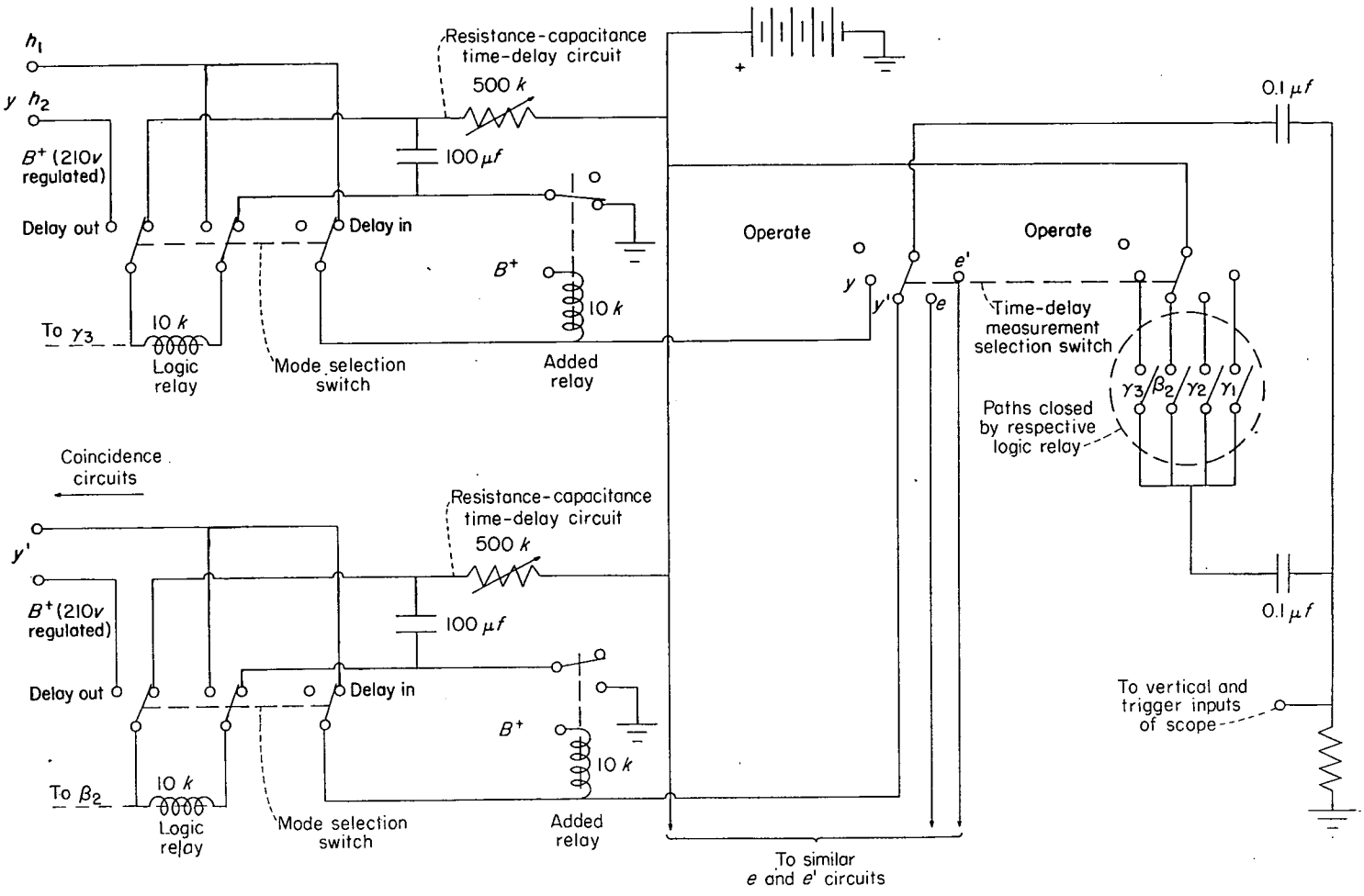


FIGURE 25.—Schematic diagram of electromechanical switching-delay simulation.

The amount of delay between activation of the zero-coincidence circuit and the closing or opening of the logic relay was measured by observing the coincidence pulse and the logic-relay contact pulse with a long-persistence oscilloscope whose beam traversed the scope at a known rate and was triggered by the coincidence pulse. The voltage supply in the time-delay circuit was adjusted so that the closing and opening delays were roughly equal. It is estimated that the accuracy of time-delay measurement was of the order of 10 percent. Delays of less than 25 milliseconds ($t=\tau$ with the analog-computer wiring used) were difficult to measure by this method, and, more important, could not be easily simulated by this particular circuit because of high contact current in the added relay which caused the contacts to weld.

The delayed system was operated using sinusoidal inputs of 20-volt peak-to-peak amplitude at frequencies from 1/10 the natural frequency of the undamped linear system to the full value of the natural frequency. Nondimensional time delays of $\omega_n t_d=0.05, 0.075, 0.100$, and 0.150 were used. Knowing that the error caused by these delays should vary linearly with the applied voltage (see the section "Response to sinusoidal inputs" which follows), runs were also made at 10- and 40-volt peak-to-peak amplitudes as a check of the self-consistency of the data.

Analog-computer simulation of time delay.—An analog-computer approximation of $e^{-t_d p}$ was wired using a circuit suggested by Morrill (ref. 6). The circuit is based on the Padé second-order approximation of $e^{-t_d p}$

$$\frac{12-6t_dp+t_d^2p^2}{12+6t_dp+t_d^2p^2}=1-t_dp+\frac{t_d^2p^2}{2}-\frac{t_d^3p^3}{6}+\frac{t_d^4p^4}{24}-\frac{t_d^5p^5}{144}+0t_d^6p^6-\frac{t_d^7p^7}{1,728}+\ldots \quad \text{(A1a)}$$

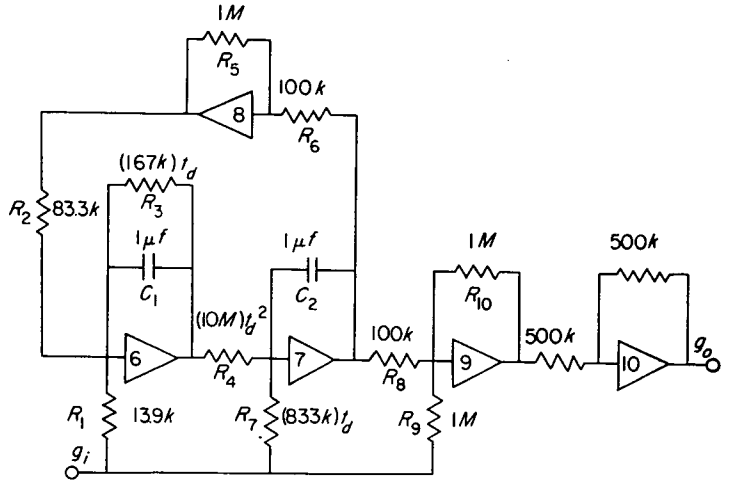
which is roughly equivalent to the first six terms of the Taylor expansion of $e^{-t_d p}$ about $t_dp=0$:

$$e^{-t_dp}=1-t_dp+\frac{t_d^2p^2}{2}-\frac{t_d^3p^3}{6}+\frac{t_d^4p^4}{24}-\frac{t_d^5p^5}{120}+\frac{t_d^6p^6}{720}-\ldots+\ldots \quad \text{(A1b)}$$

The circuit is shown in figure 26. The element values were found by comparing the transfer functions of the circuit with the desired Padé polynomial fraction and equating coefficients of powers of p. The transfer function of the circuit in a nondimensional form is:

$$\frac{g_o}{g_i}=\frac{R_{10}'}{R_9}-\frac{\dfrac{R_{10}}{R_1}-\dfrac{R_4R_{10}}{R_3R_7}-\dfrac{R_4R_{10}C_1}{R_7}p}{\dfrac{R_8R_5}{R_2R_6}+\dfrac{R_4R_8C_2}{R_3}p+(R_4R_8C_1C_2)p^2} \quad \text{(A2)}$$

where the resistances R_n are as shown in figure 26.



$$\frac{g_o}{g_i}=\frac{12-6t_dp+t_d^2p^2}{12+6t_dp+t_d^2p^2}\approx e^{-t_dp}$$

FIGURE 26.—Analog-computer circuit for Padé second-order approximation for e^{-t_dp}.

Comparing this with the Padé approximation written

$$e^{-t_dp}\approx 1-\frac{12t_dp}{12+6t_dp+t_d^2p^2} \tag{A3}$$

6 equations for the 10 resistors and 2 capacitors can be written in terms of the time delay t_d. The resulting six degrees of freedom on the circuit parameters were used to select the convenient values shown. Figure 27 shows the location of this delay circuit in the overall simulation of the relay control system.

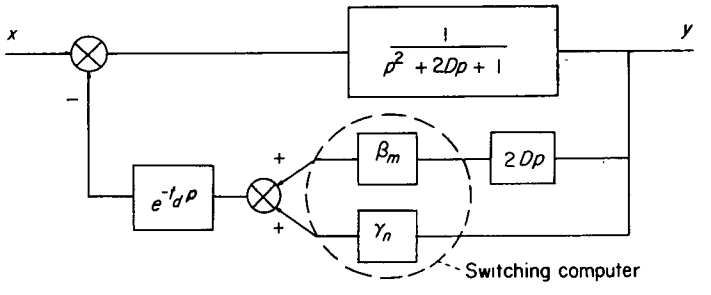


FIGURE 27.—Insertion of time-delay circuit of figure 26 into control-system analog.

Since this method was used only as a check on the electromechanical method, the only input studied was a constant of 10 volts at delays of $t_d=0.025, 0.050, 0.075$, and 0.100 second.

Simulation of a time delay by this method allowed greater flexibility of the location of the time delay. The delay was inserted as shown in figure 28 to simulate the effect of a transport time delay in the system. The output for this configuration was essentially the same as that found for relay delays. This result was to be expected because the essential difference between a transport delay and relay delay in this system is that relay delays affect only the feedback terms which go through the relays while transport delays affect the input x as well. But for the great majority of operation, x changes very slowly as compared with the changes in the feedback terms and hence, it makes very little difference in the response whether the input x is delayed.

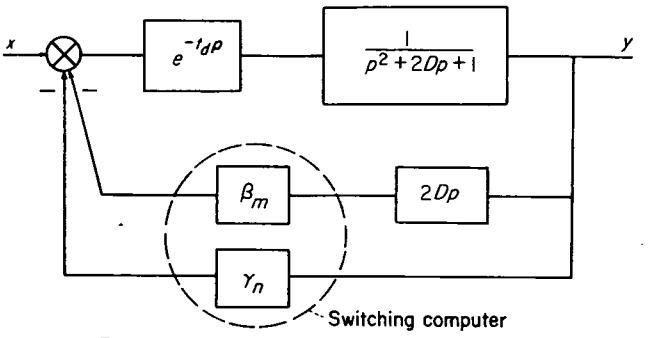


FIGURE 28.—Insertion of time-delay circuit for study of transport delays.

The responses of the two configurations become more nearly identical as the magnitude of the time delay decreases. If the basic controlled element is a motor load as shown in figure 24 (a) and if a transport delay were introduced at point m, the resulting output would differ somewhat more from a relay-delayed output because then both x and the direct y path as well as the discontinuous relay signals would be delayed. No tests were run with this configuration.

Computational study of relay delay.—Response of the system with relay lag was computed using the differential equations directly. To simplify the amount of calculations, only response to constant inputs were computed. Calculations were based on approximating the output with a series of parabolic arcs. This is equivalent to assuming that y'' is constant during each computation interval, a reasonable assumption except for large time delays. The input studied was $x=10$ and calculations were made until the limit cycles on a plot of E against $\frac{dE}{d\tau}$ were approached within the accuracy of computation. Computations were made such that the limit cycles were approached from the inside in some cases and from the outside in others. Limit cycles for various time delays are shown in figure 29. Computation intervals were such that two parabolic arcs were used in each quadrant.

The computation details are as follows: With the assumption that the output is a series of parabolic arcs, the equation for the error during the nth interval between switch points is:

$$E_n=E_{ni}+E_{ni}'\tau_n+\tfrac{1}{2}E_{ni}''\tau_n^2 \tag{A4}$$

where $\tau_n=0$ at the start of any interval and E_{ni}, E_{ni}', and E_{ni}'' are the initial error, error velocity, and error acceleration, respectively, for the nth interval. Upon differentiating, the velocity during any interval becomes:

$$E_n'=E_{ni}'+E_{ni}''\tau_n \tag{A5}$$

Eliminating the time τ_n between these two equations, the equation of the phase-plane trajectories becomes:

$$E_n-\left[E_{ni}-\frac{1}{2}\frac{(E_{ni}')^2}{E_{ni}''}\right]=\frac{1}{2E_{ni}''}(E_n')^2 \tag{A6}$$

Equations (A4) and (A5) are used to find E_{as} and E_{as}' at an actual switch point by letting $\tau_n=\omega_v t_d$ (the delay time) and using as initial conditions E at $E'=0$ or E' at $E=0$ (the conditions at a theoretical switch point). When this point is found, equation (A6) is used with $E_{ni}=E_{as}$ and $E_{ni}'=E_{as}'$ and the next theoretical switch point is computed

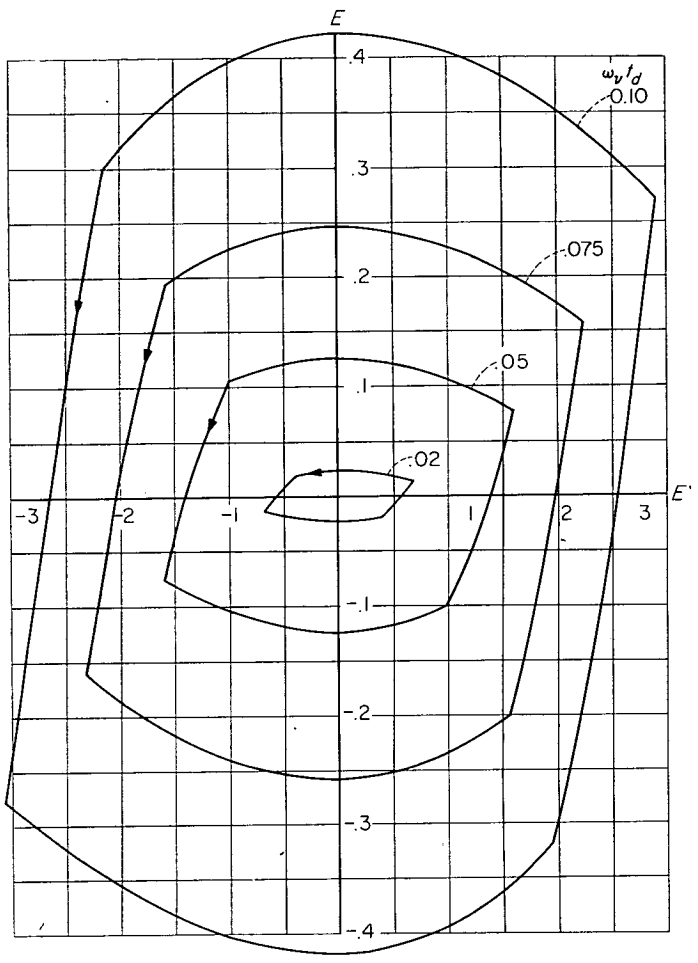


FIGURE 29.—Error limit cycles due to switching delays for a constant input of $x=10$ volts.

by setting either $E_n=0$ or $E_n'=0$ depending on which type of switch point is being approached. In all cases the acceleration E_{ni}'' is found from the differential equation of the control system, equation (8). For the special case where $x=10$, equation (8) can be rewritten using $y=E+x$ as:

$$E''+2D(1+\beta_m)E'+(1+\gamma_n)E=-10\gamma_n \qquad \text{(A7)}$$

An effort was made to determine some general method for predicting the limit cycles as an analytic function of t_d, D, β_m, and γ_n but, even with this very simple input, the limit cycles are approached in such a complicated way that finding such a function would be a formidable task at best. However, a systematic series of calculations as shown here could be made and charts plotted to indicate the effect of these various parameters.

Comparison of the three methods for constant inputs.—For a constant input of $x=10$ a good comparison of results from the three methods of studying relay delay was made by constructing a logarithmic plot of error versus time delay. Data from the two experimental methods had to be modified slightly to account for actual relays delays and thresholds of zero coincidence. The modification consisted of measuring the system error with no intentional delay, finding the delay required to produce this error from the calculated plot of error versus delay, and adding this delay to each of the experimental points. (The effective unintentional relay delay was found to be 20 milliseconds. This is considerably greater than the 3-millisecond delay specified by the relay manufacturer. The additional effective delay is due to the inherent thresholds in the switching circuit which can be considered as a variable time delay. Also, the actual delay of the relays may have exceeded 3 milliseconds.)

After this modification, the analog-computer data were indistinguishable from the calculated data. Data from the electromechanical method also agreed quite well but differed from the computed results by as much as 10 percent at a time delay of 0.12. (See fig. 30.)

Response to sinusoidal inputs.—As mentioned before, the error resulting from relay lags varies linearly with the magnitude of the input x. That this is true is easily seen by examining equation (8). If x is replaced by Kx and y by Ky where K is a constant, the differential equation remains unchanged and the error $e=x-y$ is now $e^*=Kx-Ky=Ke$.

The reader should be warned that although this is a well known property of linear differential equations, this system remains essentially nonlinear. Using the definitions of β_m and γ_n given in the text following it, equation (8) can be written:

$$y''+2D(\operatorname{sgn} y'-{}_1\beta \operatorname{sgn} e-{}_2\beta \operatorname{sgn} e')|y'|+ (\operatorname{sgn} y-{}_1\gamma \operatorname{sgn} e-{}_2\gamma \operatorname{sgn} e')|y|=x \qquad \text{(A8)}$$

With the equation in this form, the reader can easily verify that if y_1 and y_2 are solutions to equation (A8) in its homogeneous form ($x=0$) then y_1+y_2 is not necessarily a solution

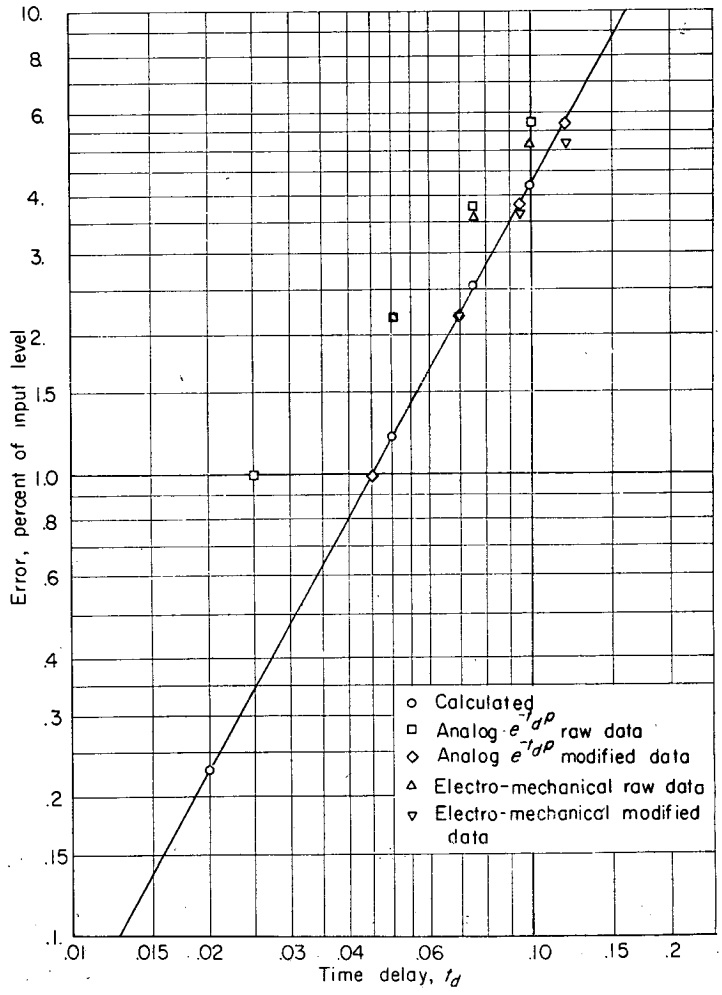
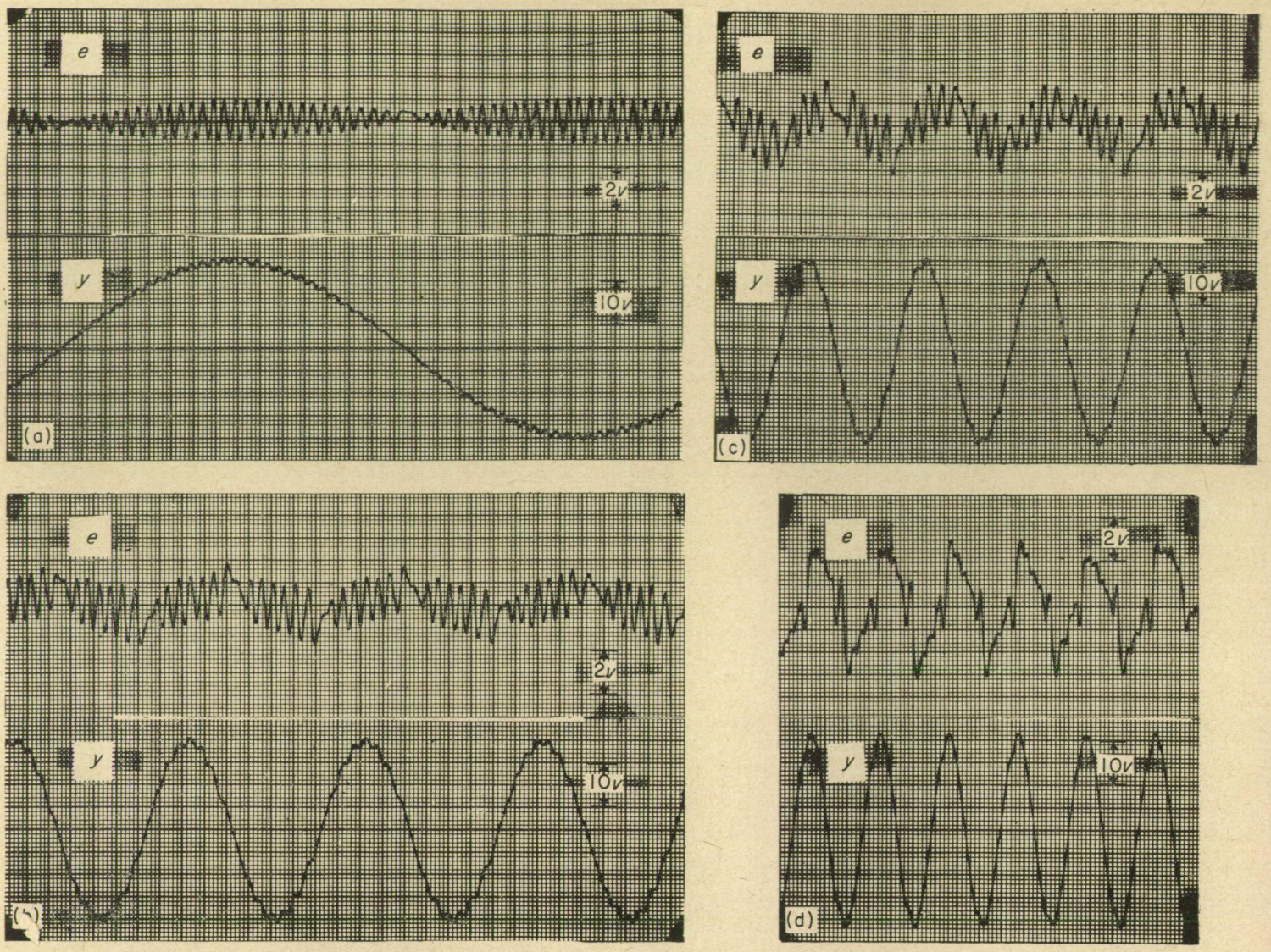


FIGURE 30.—Comparison of methods of switching-delay study with a constant input of $x=10$ volts.



(a) $\omega=0.1\omega_v$.
(b) $\omega=0.4\omega_v$.
(c) $\omega=0.6\omega_v$.
(d) $\omega=\omega_v$.

FIGURE 31.—Responses for inputs of various frequencies with relay delays of $\omega_v t_d=0.10$.

because of the nonlinear character of the absolute value and signum functions.

However, it can be concluded from the linear property that if the error encountered for any constant input is obtained, the error for any other constant input can be found by a simple scale change. For very low frequency sinusoidal inputs where x' and x'' are relatively small it was found that the error was governed almost entirely by this consideration. This is demonstrated by figure 31 (a) for a 40-volt peak-to-peak input with $\omega=0.1\omega_v$ and a delay of $\omega_v t_d=0.100$. Notice that the envelope of the error is very nearly a sine wave with its peak value occurring at the peak value of the input.

As the input frequency is increased, the point of greatest error shifts away from the peak of the input. In figure 31 (b) for $\omega=0.4\omega_v$ the greatest error occurs almost ¼ cycle after the input reaches its peak in either direction. This is because the $(1+\beta_m)y'$ term becomes sizable in this frequency range during the acceleration period (i. e., as $|x'|$ increases) and reaches a maximum at ¼ cycle past the input peak. This large feedback term is applied in an undesired direction for 0.10 unit of nondimensional time and causes the large lag error.

At still higher frequencies the y'' term coupled with the $(1+\gamma_n)y$ term both reach their maximum at the peak value of the input and the greatest error again occurs near this time. An example of this is given in figure 31 (d) for an input frequency of $\omega=1.0\omega_v$. For intermediate frequencies the peak shifts around depending on initial conditions as shown for $\omega=0.6\omega_v$ in figure 31 (c).

From an overall standpoint a plot of the greatest error versus frequency showed an approximately linear increase of error with frequency (see fig. 32). Similarly, a plot of greatest error versus time delay is linear up to about $\omega_v t_d=0.10$ for frequencies up to $\omega=0.8\omega_v$ (see fig. 33). An interesting comparison of these results and the results found for the system with no intentional delays is shown in figure 34. Also plotted in this figure is the maximum error for the linear system alone $(y''+2Dy'+y=x)$.

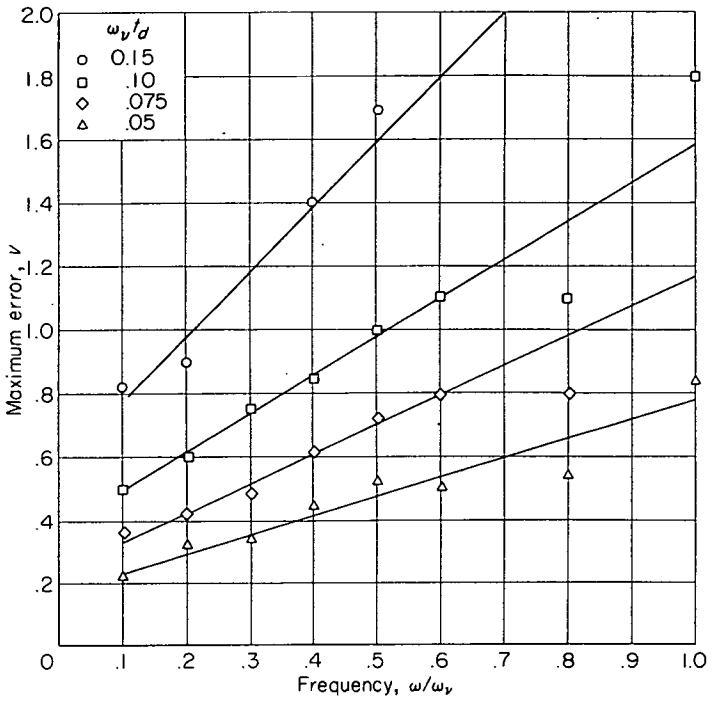


FIGURE 32.—Maximum error occurring during each input cycle plotted against input frequency with switching delay as a parameter.

$$x=10 \sin \omega t=10 \sin\left(\frac{\omega}{\omega_\nu}\right)\tau \text{ volts; } \beta_3=-\beta_0=2;$$

$$\beta_2=-\beta_1=0.5;\ \gamma_3=-\gamma_2=2;$$

$$\gamma_2=-\gamma_1=0.5;\ D=0.6;\ \omega_\nu=1.0.$$

Specification of time-delay tolerances.—If an actual system were to be set up such as that described by equation (8), figure 32 would provide an indication to the designer of how to specify relay-delay tolerances. Take, for example, a system which has an undamped natural frequency $f_\nu=10$ cps. If the error of this system is to remain below 5 percent of the maximum value of the input for frequencies up to $\omega=0.8\omega_\nu$, then the relay delays must be held below 0.75 millisecond. This result is found by first finding that value of $\omega_\nu t_d$ on the $\omega=0.8\omega_\nu$ curve of figure 33 at which the maximum error is 5 percent. This value of $\omega_\nu t_d$ is 0.047. The actual time delay t_d is:

$$t_d=\frac{0.047}{\omega_\nu}=\frac{0.047}{2\pi f_\nu}=\frac{0.047}{20\pi}=0.00075 \text{ sec} \qquad \text{(A9)}$$

This value of time delay will not necessarily assure that the error will always remain within 5 percent of the input for other types of inputs which are band-limited to $0.8\omega_\nu$ because of the nonlinear nature of the system. However, it is known from the special type of inputs studied that if the error is to be as specified the time delay can be at most 0.75 millisecond.

For sinusoidal inputs with $\omega<0.8\omega_\nu$ the maximum error will be less than 5 percent of the maximum value of the input. For example, at $\omega=0.1\omega_\nu$ the maximum error will be slightly more than 1 percent.

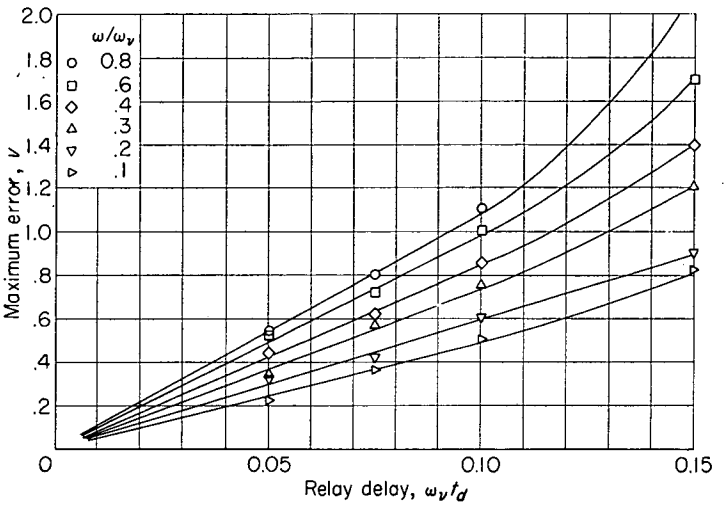


FIGURE 33.—Maximum error occurring during each input cycle plotted against switching delay with input frequency as a parameter (same data as for fig. 32).

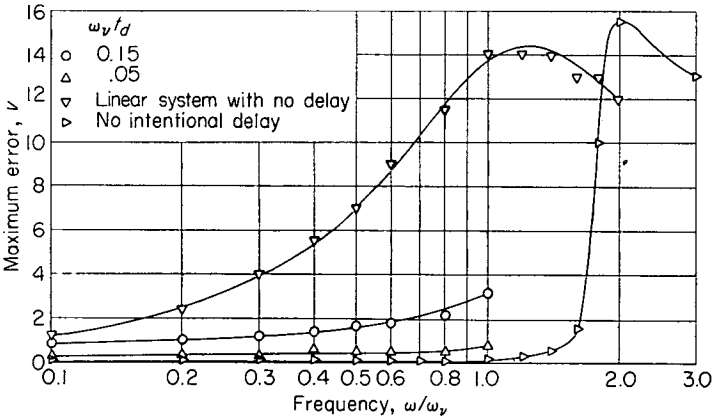


FIGURE 34.—Maximum error plotted against input frequency for several time delays and for linear member only.

APPENDIX B

COMPARISON OF EQUATION (8) AND NONLINEAR CONTROL EQUATION OF REFERENCES 1 AND 3 TO 5

COMPARISON OF NOTATIONS

In original notation the nonlinear control equation was given as (refs. 1 and 3 to 5)

$$a^+\frac{d^2y_o}{dt^2}+b\frac{dy_o}{dt}+cy_o=y_i(t) \qquad \text{(B1)}$$

where

$y_o(t)$	output
$y_i(t)$	input

$$b=b^+\left[1+\frac{\Delta b_1}{b^+}\operatorname{sgn}(y_o'E)+\frac{\Delta b_2}{b^+}\operatorname{sgn}(y_o'E')\right]$$

$$c=c^+\left[1+\frac{\Delta c_1}{c^+}\operatorname{sgn}(y_oE)+\frac{\Delta c_2}{c^+}\operatorname{sgn}(y_oE')\right]$$

$E=(y_o-y_i)$.

$(\ )'=d(\ )/dt$

$\Delta b_1,\Delta b_2,\Delta c_1,\Delta c_2$	constants, $\Delta b_1>\Delta b_2,\Delta c_1>\Delta c_2$
a^+,b^+,c^+	constants

In terms of the notation of equation (8) the above equation is written

$$a^+\frac{d^2y}{dt^2}+b^+(1+\beta_m)\frac{dy}{dt}+c^+(1+\gamma_n)y=x(t) \qquad \text{(B2)}$$

where

$\beta_m=-{}_1\beta \operatorname{sgn}(y'e)-{}_2\beta \operatorname{sgn}(y'e')$; $m=0, 1, 2, 3$

$\gamma_n=-{}_1\gamma \operatorname{sgn}(ye)-{}_2\gamma \operatorname{sgn}(ye')$; $n=0, 1, 2, 3$

$e=(x-y)$

${}_1\beta, {}_2\beta, {}_1\gamma, {}_2\gamma$ constants, ${}_1\beta > {}_2\beta$, ${}_1\gamma > {}_2\gamma$

a^+, b^+, c^+ constants

The subscript convention is

$$\beta_3={}_1\beta+{}_2\beta \qquad \gamma_3={}_1\gamma+{}_2\gamma$$

$$\beta_2={}_1\beta-{}_2\beta \qquad \gamma_2={}_1\gamma-{}_2\gamma$$

$$\beta_1=-\beta_2 \qquad \gamma_1=-\gamma_2$$

$$\beta_0=-\beta_3 \qquad \gamma_0=-\gamma_3$$

Evidently, the correlation between equations (B1) and (B2) is then

$$y=y_o$$

$$x=y_i$$

$${}_1\beta=\frac{\Delta b_1}{b^+},\ {}_2\beta=\frac{\Delta b_2}{b^+},\ {}_1\gamma=\frac{\Delta c_1}{c^+},\ {}_2\gamma=\frac{\Delta c_2}{c^+}$$

$$e=-E$$

and a^+, b^+, and c^+ are the same.

In either notation a set of seven (constant) parameters is needed to characterize the system. For example, in equation (B2) the set $(a^+, b^+, c^+, {}_1\beta, {}_2\beta, {}_1\gamma, {}_2\gamma)$ is sufficient.

NORMALIZATION OF NONLINEAR CONTROL EQUATION

When considering control systems it is possible to reduce the number of parameters necessary to specify the nonlinear system. To do this a form of normalization familiar to linear theory is utilized. First, it should be realized that if error is to be defined as $e=(x-y)$ then $c^+=1$. Thus, assuming $c^+=1$ equation (B2) may be written

$$\frac{1}{\omega_\nu^2}\frac{d^2y}{dt^2}+\frac{2D}{\omega_\nu}(1+\beta_m)\frac{dy}{dt}+(1+\gamma_n)y=x(t) \qquad \text{(B3)}$$

where

$$\omega_\nu^2=\frac{1}{a^+}$$

$$\frac{2D}{\omega_\nu}=b^+$$

Introducing normalized time $\tau=\omega_\nu t$, equation (B3) becomes

$$\frac{d^2y}{d\tau^2}+2D(1+\beta_m)\frac{dy}{d\tau}+(1+\gamma_n)y=x(\tau) \qquad \text{(B4)}$$

Thus, knowing the natural frequency of the undamped linear system, ω_ν, the number of parameters necessary to specify performance in the nonlinear case is five, that is,

$$(D, {}_1\beta, {}_2\beta, {}_1\gamma, {}_2\gamma)$$

or alternatively

$$(D, \beta_3, \beta_2, \gamma_3, \gamma_2)$$

APPENDIX C

SIMULATION OF SECOND-ORDER NONLINEAR CONTROL SYSTEM

EQUIPMENT

Experimental studies were carried out with the following equipment:

(1) General equipment:
- (a) Analog computer, Beckman Ease
- (b) Low-frequency function generator, hp 202 A (input device)
- (c) Pen recorder, Sanborn Twin-Viso (output device)
- (d) Vacuum-tube voltmeter, RCA WV–97A
- (e) Oscilloscope, Dumont 304–A

(2) Special equipment:
- (a) Binary-logic switching circuit employed in conjunction with (a), described in detail in section "Binary-Logic Relay Switching Circuit."

COMPUTER SETUP

The computer diagram for the differential equation

$$\frac{d^2y}{d\tau^2}+2D(1+\beta_m)\frac{dy}{d\tau}+(1+\gamma_n)y=x(\tau) \qquad \text{(C1)}$$

is given in figure 35. The correspondence between this simulated system and the block diagram of figure 4 or 5 is straightforward (see ref. 7). Operational amplifiers 1 to 6 are used in simulating the linear member of the physical nonlinear system. Resistor R_1 provides adjustment of the linear damping factor D. The input to this simulated linear member is $x-(2D\beta_m y'+\gamma_n y)$ where x is obtained from the input device, while the values of feedback $2D\beta_m y'$ and $\gamma_n y$ are obtained with resistors R_2 through R_9 (see table 5) connected to y' and y through a binary-logic relay switching circuit derived in the following section. Amplifiers 7 to 10 are sign changers. The four variables y, y', e, and e' whose signs are to be sensed are made available as shown in the lower right of figure 35.

BINARY-LOGIC RELAY SWITCHING CIRCUIT

To complete the simulation of equation (8) it is necessary to implement the binary logic of table 2. Figure 5 shows a relay switching circuit (designed on an "and/or" basis) that realizes the necessary logic.

In order to preclude the possibility of time delay in switching, "fast" relays have been employed. The average properties of the 14 double-pole single-throw relays comprising the switching circuit are given in table 4.

The necessary synchronism in relays connected by dashed lines (fig. 5) is obtained by series connection of field coils.

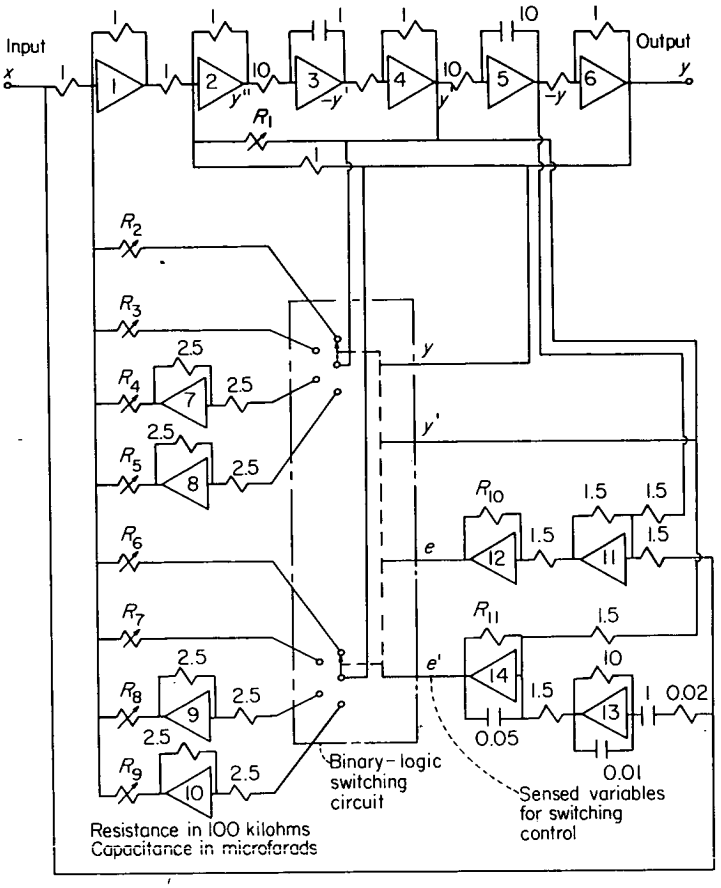


FIGURE 35.—Computer diagram for simulation of equation (8).

Into the four channels of field coils thus formed is read the four-digit binary logic of table 2 where now

$$0 = \text{Function} > 0 = \text{No coil current}$$

$$1 = \text{Function} < 0 = \text{Coil current}$$

This process of reading in the binary logic may be done by monitoring the variable (y, y', e, e') with four separate zero-coincidence detectors or amplitude selectors (denoted *CD* in fig. 5 and described in detail in the following section). The output of these coincidence detectors then drives the respective channels of relay coils.

SENSITIVE TRANSISTORIZED ZERO-COINCIDENCE DETECTOR

One of the four identical amplitude selectors designed for use with the switching circuit of figure 5 is shown in figure 36. This circuit basically consists of a grounded emitter PNP transistor stage T_1 driving a pentode pulse amplifier T_2. (It should be possible to utilize a transistor in place of the pentode if desired.) Four relay coils connected in series form the plate load of T_2. Positive feedback R_3 has been incorporated for regenerative switching.

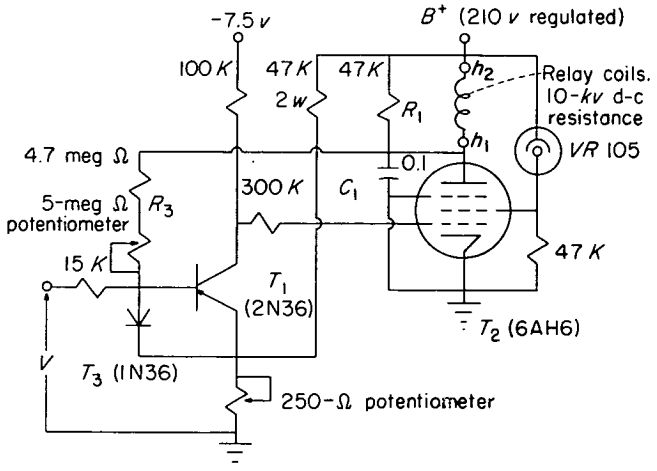


FIGURE 36.—Transistorized zero-coincidence detector.

The operation of this circuit is as follows: When the input voltage V becomes more negative than −50 millivolts, current starts to flow in the base-emitter region of T_1. This initiates collector-emitter current which effectively grounds the collector and thus the grid of T_2. Plate current flows in T_2 so that the relays which form this plate load are switched to the up position (fig. 5). Positive feedback R_3 has been incorporated to make the switching regenerative. Stages T_1 and T_2 will continue to conduct until V goes positive by 50 millivolts, at which time current is cut off in T_1 and thus T_2; the relays return to the normally closed positions (down in fig. 5).

Refinements that have been included in this circuit are:

(1) Adjustable positive feedback R_3. This feedback gives control over the zero-sensing threshold of the detector. The greater the positive feedback the greater the threshold. This adjustment is desirable for studying the effects of threshold in sensing discussed in the section "Effects of Switching Imperfections." The measured peak-to-peak threshold values obtainable with this arrangement were a maximum of 400 millivolts and a minimum of 60 millivolts. (In the computer setup it was necessary to amplify error e that formed the input to one of these detectors five times in order to bring the switching threshold down to 15 millivolts, peak to peak.)

(2) Adjustable bias for emitter of T_1. This is necessary to compensate for the slight positive bias (approximately equal to 100 millivolts) given to the base of T_1 by the positive feedback R_3.

(3) A clamping or clipping diode T_3 to protect the transistor T_1 from excessive base-emitter inverse voltages. Thus it can be seen that the input impedance of this coincidence detector is 15 kilohms since the base of T_1 is effectively always grounded.

APPENDIX D

BEHAVIOR OF OUTPUT IF INPUT AND INPUT DERIVATIVE ARE SIMULTANEOUSLY SMALL

Assume that the input is a curve which may be approximated by

$$x=\alpha\tau^2$$

for values $\tau<\delta$. Since $x'=2\alpha\tau$, both input and input derivative vanish with $\tau\to 0$. The input phase curve is

$$x=\frac{1}{4\alpha}(x')^2$$

The output depends on the initial conditions:

(1) For $y(0)=0$ and $y'(0)=0$

$$y=\alpha\left[\frac{\tau^4}{12}+\frac{D(1+\beta_m)}{30}\tau^5+\ldots\right]$$

(2) For $y(0)=0$ and $y'(0)=\epsilon_1$

$$y=\epsilon_1[\tau-D(1+\beta_m)\tau^2+\ldots]$$

(3) For $y(0)=\epsilon_2$ and $y'(0)=0$

$$y=\epsilon_2\left[1+\left(\frac{1+\gamma_n}{2}\right)\tau^2+\ldots\right]$$

In all cases reproduction of the input is not perfect very close to $\tau=0$; however, in cases (2) and (3) switch points may occur for rather small values of τ. In case (1) no switch point close to $\tau=0$ can be expected. This case will rarely occur; in most cases neither $y(0)$ nor $y'(0)$ will be zero. Then the output is a superposition of cases (2) and (3). In this event the error $e=x-y$ is given by

$$e=-\epsilon_2-\epsilon_1\tau+\left[\alpha+\epsilon_1 D(1+\beta_m)-\epsilon_2\left(\frac{1+\gamma_n}{2}\right)+\ldots\right]\tau^2$$

It is evident that for small values of ϵ_1 and ϵ_2 the error grows with α. This can easily be seen in the results of figure 11. The input was $x=A(1-\sin\Omega\tau)$; that means, near $x=0$, the input may be approximated by a parabola with $\alpha=1/2(\Omega^2)A$ or the errors near $x=0$ grow with Ω^2.

APPENDIX E

APPROXIMATING CURVES

The approximating curves which can be used to trace the output for a given input form a network in the phase plane. It has proved practical to present the network for e and e' with the same sign in one sheet (e. g., see fig. 20) and the network for e and e' with opposite signs on another sheet. Superposition of both sheets allows establishing of the four approximating curves through each point of the phase plane.

The approximating phase curves are determined by equation (21). Since the values λ_1 and λ_2 change from quadrant to quadrant the curves are composed of portions of different analytical curves which are patched at $y'=0$ and $y=0$.

The roots λ_1 and λ_2 depend on D, β_m, and γ_n; they may be complex or real. If the roots are complex, the approximating curves are curves of the spiral type which wind around the origin of the phase plane. In the case of real roots the curves have a quite different character. This can easily be understood by transforming the equation of the approximating curves (see refs. 1 and 3 to 5 and ch. V of ref. 8). For real roots the new coordinates μ and ν are introduced:

$$\bar{y}\lambda_1-\bar{y}'=\mu$$
$$\bar{y}\lambda_2-\bar{y}'=\nu$$

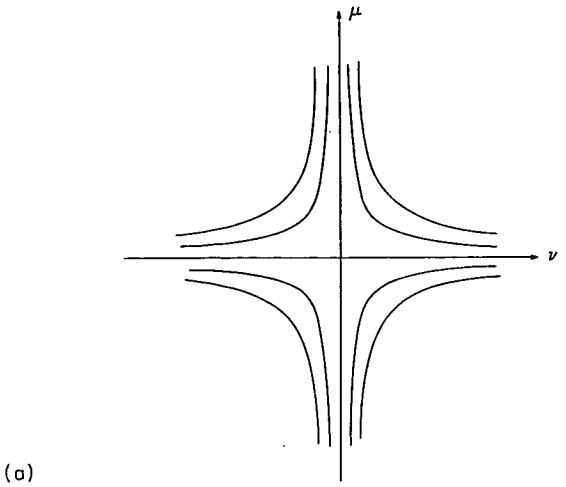
Then equation (21) yields

$$\nu^{\lambda_2}=M\mu^{\lambda_1}$$

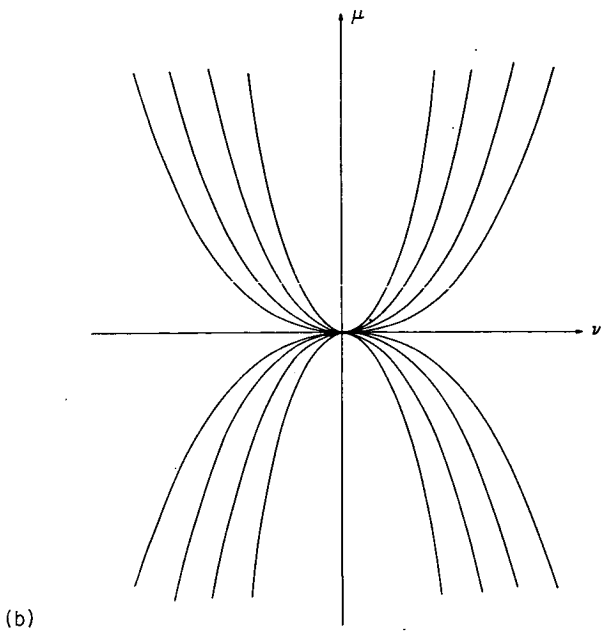
If λ_1 and λ_2 are real and of opposite sign, the curves in the $\mu\nu$ plane have a hyperbolic character with $(\mu,\nu)=(0,0)$ as saddle point (see fig. 37 (a)). If λ_1 and λ_2 are of equal sign, the curves have a nodal point (see figs. 37 (b) and 37 (c)). In figures 38 and 39 phase curves with saddle point and stable and unstable node are shown in the original $\bar{y}\,\bar{y}'$ plane.

The approximating curves are composed of portions of these different types (see fig. 40).

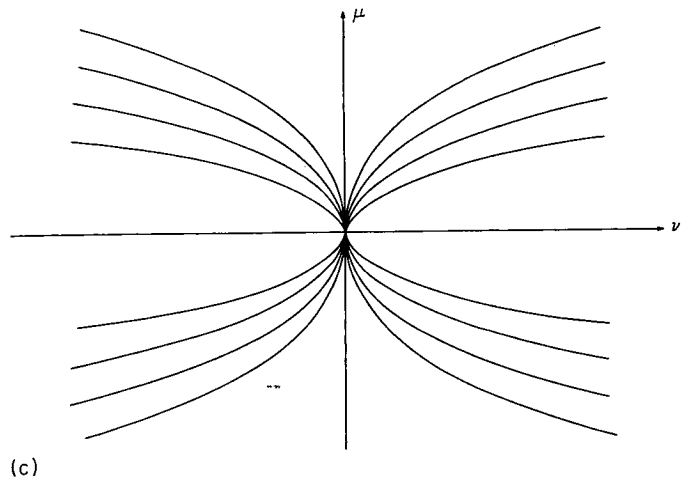
There is no need of avoiding β_m,γ_n combinations which lead to node-type approximating curves because only portions of these curves are used. In the earlier publications it appeared as if (in either one of the networks of approximating curves) one set of curves had to be formed by curves of spiral character (complex roots λ). However, this has proved to be an unnecessary restriction. There might be some trouble with node-type curves if large delays in switching should occur (e. g., delays in $y'=0$ switching in fig. 40).



(a)



(b)



(c)

(a) $\frac{\lambda_2}{\lambda_1} < 0$.

(b) $\frac{\lambda_2}{\lambda_1} > 1$.

(c) $0 < \frac{\lambda_2}{\lambda_1} < 1$.

FIGURE 37.—Curves in $\mu\nu$ plane.

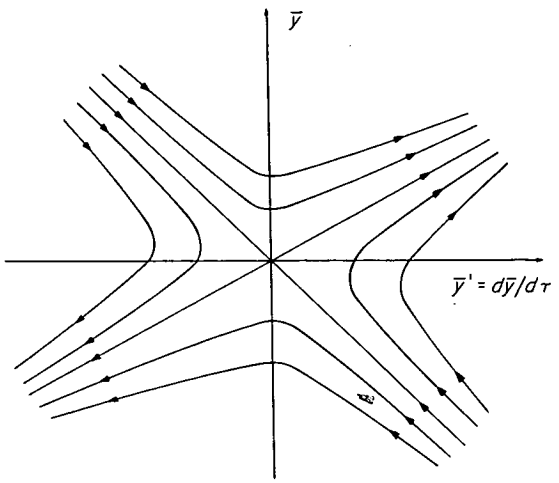
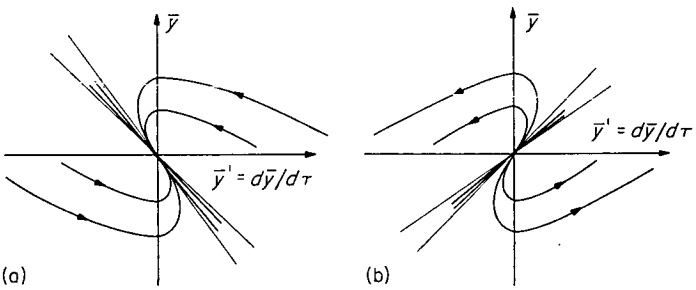


FIGURE 38.—Phase curves with saddle point.



(a) Stable node.
(b) Unstable node.

FIGURE 39.—Phase curves with nodal point.

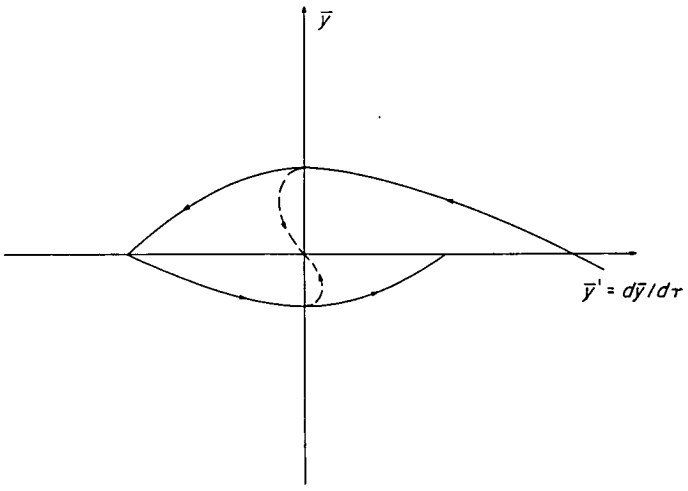


FIGURE 40.—Composition of an approximating curve.

REFERENCES

1. Flügge-Lotz, I., and Wunch, W. S.: On a Nonlinear Transfer System. Jour. Appl. Phys., vol. 26, no. 4, Apr. 1955, pp. 484–488.
2. Schmidt, Stanley F., and Triplett, William C.: Use of Nonlinearities to Compensate for the Effects of a Rate-Limited Servo on the Response of an Automatically Controlled Aircraft. NACA TN 3387, 1955.
3. Flügge-Lotz, Irmgard, and Wunch, W. S.: Mechanical Reproduction of an Arbitrary Function of Time. TR-No. 19 (Pt. I), Contract N6-onr-251, Task Order 2, Office of Nav. Res. and Div. Eng. Mech., Stanford Univ., Mar. 1, 1952.
4. Flügge-Lotz, Irmgard, and Wunch, W. S.: The Reproduction of an Arbitrary Function of Time (Reducing Transfer Function Dynamic Errors by Nonlinear Components). TR-No. 19 (Pt. II), Contract N6-onr-251, Task Order 2, Office of Nav. Res. and Div. Eng. Mech., Stanford Univ., Sept. 15, 1952.
5. Wunch, W. S.: The Reproduction of an Arbitrary Function of Time by Discontinuous Control. Ph. D. Thesis, Stanford Univ., May 1953.
6. Morrill, C. D.: A Sub-Audio Time Delay Circuit. Trans. Inst. Radio Eng., PGEC, vol. EC-3, no. 2, June 1954, pp. 45–49.
7. Korn, Granino A., and Korn, Theresa M.: Analog Computers. First ed., McGraw-Hill Book Co., Inc., 1952.
8. Andronow, A. A., and Chaikin, C. E.: Theory of Oscillations. Princeton Univ. Press, 1949.

TABLE 1.—CODING SCHEME FOR SWITCHING LOGIC FROM EQUATION (14)

[0, function>0; 1, function<0]

Binary coded decimal				Decimal
y	y'	e	e'	0
0	0	0	0	0
0	0	0	1	1
0	0	1	0	2
0	0	1	1	3
0	1	0	0	4
0	1	0	1	5
0	1	1	0	6
0	1	1	1	7
1	0	0	0	8
1	0	0	1	9
1	0	1	0	10
1	0	1	1	11
1	1	0	0	12
1	1	0	1	13
1	1	1	0	14
1	1	1	1	15

TABLE 2.—MATRIX OF ALLOWED β_m, γ_n COMBINATIONS AS DETERMINED BY ENCODED SWITCHING LOGIC OBTAINED FROM EQUATION (14)[a]

	β_0	β_1	β_2	β_3
γ_0	0000 1111			0100 1011
γ_1		0001 1110	0101 1010	
γ_2		0110 1001	0010 1101	
γ_3	0111 1000			0011 1100

[a] Examples:
(1) $\beta_3\gamma_0$ is chosen when 0100 occurs, i. e., ($y>0$, $y'<0$, $e>0$, $e'>0$), or when 1011 occurs, i. e., ($y<0$, $y'>0$, $e<0$, $e'<0$);
(2) $\beta_2\gamma_1$ is chosen when 0101 occurs, i. e., ($y>0$, $y'<0$, $e>0$, $e'<0$), or when 1010 occurs, i. e., ($y<0$, $y'>0$, $e<0$, $e'>0$);
(3) $\beta_1\gamma_3$ is not possible.

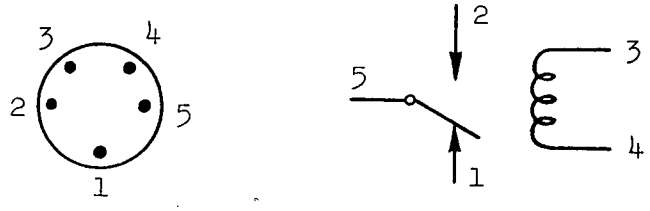
TABLE 3.—PARAMETERS FOR FIGURE 16

Figs. 16(a) and 16(b)	Figs. 16(c) and 16(d)
Complete system	
System 1: $\beta_3=-\beta_0=2$ $\gamma_3=-\gamma_0=2$; $\beta_2=-\beta_1=0.5$ $\gamma_2=-\gamma_1=0.5$	System 5: $\beta_3=-\beta_0=10$ $\gamma_3=-\gamma_0=10$; $\beta_2=-\beta_1=1$ $\gamma_2=-\gamma_1=1$
Case (1) No derivative feedback	
System 2: $\beta_3=-\beta_0=0$ $\gamma_3=-\gamma_0=2$; $\beta_2=-\beta_1=0$ $\gamma_2=-\gamma_1=0.5$	System 6: $\beta_3=-\beta_0=0$ $\gamma_3=-\gamma_0=10$; $\beta_2=-\beta_1=0$ $\gamma_2=-\gamma_1=1$
Case (2) No e' sensing	
System 3: $\beta_3=-\beta_0=2$ $\gamma_3=-\gamma_0=2$; $\beta_2=-\beta_1=2$ $\gamma_2=-\gamma_1=2$	System 7: $\beta_3=-\beta_0=10$ $\gamma_3=-\gamma_0=10$; $\beta_2=-\beta_1=10$ $\gamma_2=-\gamma_1=10$
Case (3) No e sensing in derivative feedback loop and no e' sensing in proportional feedback loop	
System 4: $\beta_3=-\beta_0=2$ $\gamma_3=-\gamma_0=2$; $\beta_2=-\beta_1=-2$ $\gamma_2=-\gamma_1=2$	System 8: $\beta_3=-\beta_0=10$ $\gamma_3=-\gamma_0=10$; $\beta_2=-\beta_1=-10$ $\gamma_2=-\gamma_1=10$

TABLE 4.—AVERAGE PROPERTIES OF RELAYS FOR SWITCHING CIRCUIT OF FIGURE 5

Description: General Electric CR-2791 double-pole single-throw relay mounted on 5-prong Amphenol base with permanent aluminum dust cover

Connections:



Electrical Properties	Values
Coil resistance	2.5 kilohms
Coil current for positive action	5 to 10 ma
Pull-in time	2 millisec
Drop-out time	3 millisec

TABLE 5.—CORRESPONDENCE BETWEEN ADJUSTABLE COMPUTER ELEMENTS AND PARAMETERS OF EQUATION (8)

Element	Corresponds to	Units, kilohms
R_1	$(2D)^{-1}$	100
R_2	$(2D\beta_0)^{-1}$	100
R_3	$(2D\beta_1)^{-1}$	100
R_4	$(2D\beta_2)^{-1}$	100
R_5	$(2D\beta_3)^{-1}$	100
R_6	$(\gamma_0)^{-1}$	100
R_7	$(\gamma_1)^{-1}$	100
R_8	$(\gamma_2)^{-1}$	100
R_9	$(\gamma_3)^{-1}$	100

REPORT 1392

BORON AND ZIRCONIUM FROM CRUCIBLE REFRACTORIES IN A COMPLEX HEAT-RESISTANT ALLOY [1]

By R. F. Decker, John P. Rowe, and J. W. Freeman

SUMMARY

In a laboratory study of the factors involved in the influence of induction vacuum melting on a 55Ni-20Cr-15Co-4Mo-3Ti-3Al heat-resistant alloy, it was found that the major factor was the type of ceramic used as the crucible. Creep-rupture properties at 1,600° F and hot-workability of the ingots were improved in proportion to the increase in trace amounts of zirconium derived from reaction of the melt with zirconia crucibles. Boron derived from the usual contamination of magnesia with boron compounds was even more effective for heats melted in magnesia crucibles. Material melted in alumina crucibles with no introduction of boron or zirconium had very low strength and ductility in rupture tests and was very prone to crack during hot-working. These findings indicate that variable amounts of boron or zirconium introduced into alloys of the type considered through reaction with crucible ceramics or unknowingly in the charge have been a major cause of variability in commercial production. Moreover, it indicates that there must be minimum amounts of one or both of these elements to obtain a practical alloy. When both boron and zirconium are present in optimum amounts, better properties apparently result than can be obtained from either element alone. Too much zirconium plus boron reduces creep-rupture properties and results in poor hot-workability. Excessive boron alone also reduces hot-workability. Good metallurgical practice, therefore, requires the addition of the optimum amounts.

A microstructural investigation was conducted to establish the mechanism of the pronounced benefits of boron and zirconium. Materials with varying boron and zirconium content were exposed to creep at 1,600° F and the microstructures were analyzed by optical and electron microscopy, electron diffraction, microfractography, and hardness measurements.

The improvement in creep-rupture properties was found to result from a pronounced stabilizing effect of boron and zirconium on the grain boundaries of the alloy. The alloy with low boron and zirconium was subject to rapid agglomeration of $M_{23}C_6$ and γ' in the grain boundaries, followed by depletion of γ' and intergranular microcracking at the grain boundaries transverse to applied stress. Brittle fracture then occurred by linking of microcracks. Additions of zirconium, boron, and boron plus zirconium decreased this tendency in that order. In the absence of these elements extensive microcracking was found late in first-stage creep at relatively short time periods and fracture occurred prematurely with very little deformation. Proper amounts of boron plus zirconium delayed microcracking until after third-stage creep had started so that creep-rupture life was greatly prolonged and ductility to fracture markedly increased.

INTRODUCTION

Although melting practice has long been known to influence the properties of heat-resistant alloys, the factors involved have not been understood. Part of the lack of understanding has been due to variable and often unpredictable differences in properties with a supposedly constant melting practice.

The major reason for initiating the present investigation was to help clarify the role of vacuum melting in the production of blade alloys for the gas turbines of jet engines. Vacuum melting with resultant improved properties had been adopted quite widely for the production of such alloys, although erratic results were being obtained by producers. Neither the causes for the erratic properties nor those resulting in the improvement in properties attributed to vacuum melting were known.

During the course of investigating the role of melting practice on the high-temperature properties of a 55Ni-20Cr-15Co-4Mo-3Ti-3Al alloy, the present authors discovered that trace amounts of boron or zirconium derived from reaction of the melt with the crucible refractories improved creep-rupture properties at 1,600° F. Boron was most effective and in addition markedly improved hot-workability.

The work of Koffler, Pennington, and Richmond (ref. 1) showed benefits to both creep-rupture life and ductility of M252, Udimet 500, Inconel 700, Nimonic 90, and Waspaloy alloys from additions of boron and zirconium. The literature cites numerous cases where beneficial effects were obtained by minute additions of certain alloying elements (ref. 2). Deoxidation with certain elements, including boron and zirconium, has been reported to improve hot-workability and properties at high temperatures for nickel-base alloys (refs. 3, 4, and 5). Confirmation of effects of boron on commercial nickel-base alloys was presented by Darmara (ref. 6) and Jones (ref. 7). The effects, however, are not restricted to nickel-base alloys. Similar benefication of

[1] Supersedes NACA Technical Note 4049, "Influence of Crucible Materials on High-Temperature Properties of Vacuum-Melted Nickel-Chromium-Cobalt Alloy," by R. F. Decker, John P. Rowe, and J. W. Freeman, 1957, and NACA Technical Note 4286, "Mechanism of Beneficial Effects of Boron and Zirconium on Creep-Rupture Properties of a Complex Heat-Resistant Alloy," by R. F. Decker and J. W. Freeman, 1958.

creep-rupture properties of numerous other alloys had been established in the past. Variations in properties of alloys at high temperatures from variations in melting and deoxidation practice has long been known.

Because vacuum melting excludes exposure to air during melting and reduces oxygen and nitrogen in alloys to lower values than are typical of air melting, the investigation originally was intended to study the influence of oxygen and nitrogen as a function of the melting technique. It soon became evident that the creep-rupture properties were mainly governed by some factor other than oxygen and nitrogen. Creep-rupture properties of the experimental heats, regardless of the oxygen and nitrogen level or other melting technique variables, were markedly inferior to those considered typical of the comercially produced alloy. Because it was known that additions of boron and zirconium had the ability to improve properties, it was demonstrated that such additions to the laboratory heats did result in properties equivalent to the alloy as commercially produced. Commercial producers, however, insisted that the alloy could be made with high properties without such additions and that there must be some other factor in vacuum melting which had been overlooked in the research. Continued modifications of the melting technique, however, failed to improve the alloy to the expected level.

The Utica Drop Forge and Tool Co. (now the Utica Drop Forge and Tool Division of Kelsey-Hayes Co.) had developed adequate methods of analysis for zirconium, and their cooperation in analyzing the experimental heats disclosed that the variations which existed in properties correlated with variations in trace amounts of zirconium. The properties increased regularly with increases in the amounts of zirconium. Because zirconium was not added to the heat and was not present in the melting stock, it must have been the product of reaction between the melt and the crucible refractory. The highest strength heat, however, was no better than those on the low side of the range of values for commercially produced material.

The fact that zirconium derived from zirconia crucibles during melting explained the variations in properties prompted the decision to investigate heats made in other refractories. When heats were melted in magnesia, the refractory generally used commercially, a marked but variable improvement in properties was found, with one heat being comparable to the best commercially produced material. Heats melted in alumina had uniformly very poor properties. Moreover the hot-workability of the material melted in alumina was very poor while it was markedly better for the high-strength heats melted in magnesia.

The first thought was that magnesium derived from reaction between the melt and the magnesia was responsible for the improved properties. Neither chemical analyses nor attempts to add magnesium to heats supported this possibility. The Universal-Cyclops Steel Corp. had presented a report (ref. 1) which showed marked improvement in properties from boron and zirconium additions for a number of nickel-base titanium and aluminum heat-resistant alloys. Accordingly their assistance in analyzing for boron was obtained. Practically no boron was found in heats melted in alumina or zirconia. However, very small but significant amounts of boron were found in the heats melted in magnesia, with those heats containing the largest amounts of boron having the best properties and hot-workability. Boron compounds normally present in commercial magnesia as an impurity were the source of the boron. The responsibility of boron or zirconium derived from reaction with crucible refractories for the change in properties was verified by adding these elements to heats melted in alumina crucibles with resultant properties equivalent to the heats melted in magnesia or zirconia. A few heats were also made with simultaneous additions of both boron and zirconium.

Because of the previous difficulties producers immediately checked the first indication that trace amounts of boron derived from magnesia were responsible for improved properties. A large number of heats in which boron or zirconium were not knowingly added were quickly determined by the producers to have properties correlating with boron and/or zirconium content either derived from reaction with crucible refractories or unknowingly added in the melting stock. Accordingly it seemed to be useless to make more heats in the experimental furnace and this report is based on the relatively few heats from which the original discovery was made.

The investigation was then broadened to study microstructures to obtain information on the mechanism by which trace amounts of boron and zirconium improved creep-rupture properties and it seemed logical to study their effects on the structural characteristics which had previously been shown to control properties. It would increase knowledge of the theory of alloying and give a more basic understanding of alloy design to resist creep and rupture. In addition, it might also reveal the nature and cause of rupture in these materials.

Since it had been established that the source of the boron and/or zirconium was not important, the mechanism study was not limited to heats in which these elements had been derived from the crucible refractory. Rather, heats were chosen which contained what appeared to be optimum amounts of each element.

It is generally accepted that the favorable high-temperature properties of the nickel-base alloys hardened with titanium plus aluminum result from the precipitation of the intermetallic γ' phase within the matrix of the alloy. The γ' phase has been shown to have a face-centered cubic structure similar to that of the Ni_3Al phase of the nickel-aluminum system with a lattice parameter closely matched to that of the matrix of the alloys (refs. 8 and 9). Compositionally, the phase has been shown to dissolve titanium and is frequently referred to as $Ni_3(Al,Ti)$.

Although the creep resistance of these alloys has been attributed to the presence of γ' in fine dispersion within the matrix (refs. 8 and 10), attempts to relate the distribution of the γ' particles with the metallurgical properties have been only moderately successful to date. Frey, Freeman, and White (ref. 11) and subsequently Brockway and Bigelow (ref. 12) found that dispersion of the γ' particles in Inconel-X alloy correlated with creep-rupture properties at 1,200° F, which was low in the aging range for this alloy; however, no correlation was obtained for rupture tests at 1,500° F, which was high in the aging range. Betteridge and Smith (ref. 13) studied the relations between structure and creep properties

of several Nimonic alloys when tested high in the aging range. Highest creep-rupture properties were obtained with the greatest volume percent of γ'. Baillie (ref. 14) found that best creep resistance in Ni-Cr-Al-Ti alloys was obtained with the highest density of γ' particles.

Carbide reactions occur in the titanium- and aluminum-hardened nickel-base alloys and have been related to properties. Among the carbides identified are $M_{23}C_6$ (refs. 12, 15, and 16), M_6C (refs. 15 and 16), Cr_7C_3 (ref. 17), and TiC (refs. 15 and 16). The occurrence of a type of carbide is dependent both on the alloy content and the temperature of treatment. In general, the carbide reactions in these alloys are poorly understood. Their probable importance in controlling properties was indicated by Betteridge and Franklin (ref. 17) who established the benefits on rupture life of obtaining a high-temperature precipitate of Cr_7C_3 before creep exposure of Nimonic alloys.

This investigation was conducted at the University of Michigan Research Institute under the sponsorship and with the financial assistance of the National Advisory Committee for Aeronautics. The chemical analyses were supplied gratis by the Utica Drop Forge and Tool Division of Kelsey-Hayes Co. and the Universal-Cyclops Steel Corp. Particular credit is due Dr. W. C. Bigelow and Mr. J. A. Amy for the phase identifications, which were part of a program of research in identification of minor phases in heat-resistant alloys sponsored by Metallurgy Research Branch, Aeronautical Research Laboratory, Wright Air Development Center.

EXPERIMENTAL PROCEDURES

MELTING

The experimental heats were induction-melted in the University of Michigan vacuum-melting unit shown in figure 1. Pressures before meltdown and after pouring were less than 5 microns as measured by both Stokes and thermocouple gages. No gases were purposely added to the chamber during the melting cycle. Melt temperatures were meaured with an immersion thermocouple with one platinum and one platinum and rhodium wire. Melting cycles for all the heats are detailed in table I and figure 2.

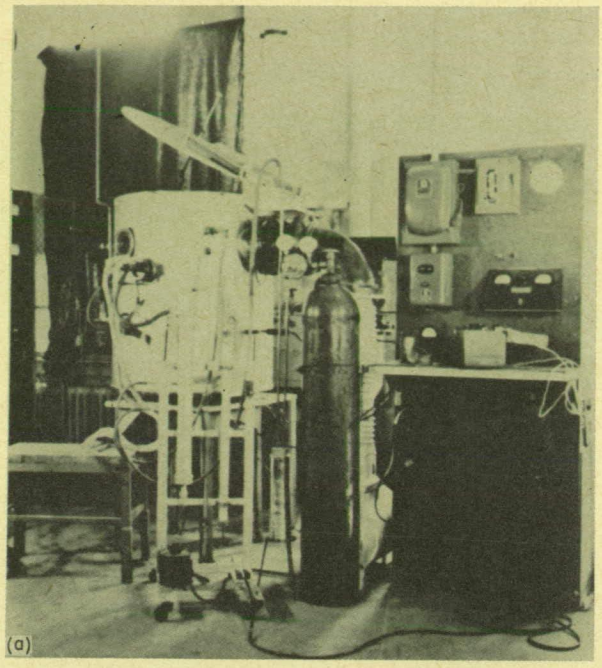
The aim of the analysis for the basic alloy, in weight percent, for all heats was as follows:

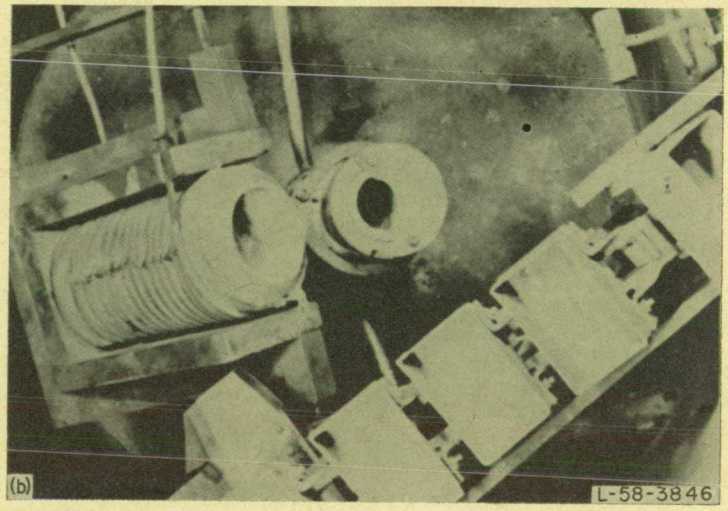
Chromium	Cobalt	Molybdenum	Titanium	Aluminum	Manganese	Silicon	Carbon	Nickel
20.0	15.0	4.0	3.1	3.1	0.12	0.12	0.08 to 0.15	Balance

Varied amounts of boron and zirconium were added to certain heats for the purposes of the investigation.

Laboratory-grade electrolytic nickel, chromium, cobalt, and manganese melting stocks were used. The other elements were added in the form of low-carbon arc-melted molybdenum, Ti–55A bar titanium, 99.99-percent-pure ingot aluminum, 99.9-percent-pure silicon powder, sponge zirconium, nickel-boron master alloy, and powdered or chuck graphite.

The crucible refractories were alumina, zirconia, and magnesia. Pertinent data on these materials are listed in





(a) External view.
(b) Internal view showing crucible, charge buckets, and ingot mold.

FIGURE 1.—University of Michigan vacuum-melting furnace.

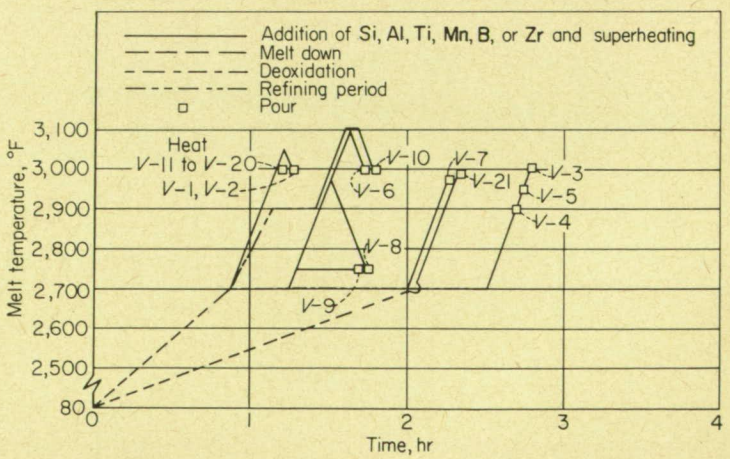
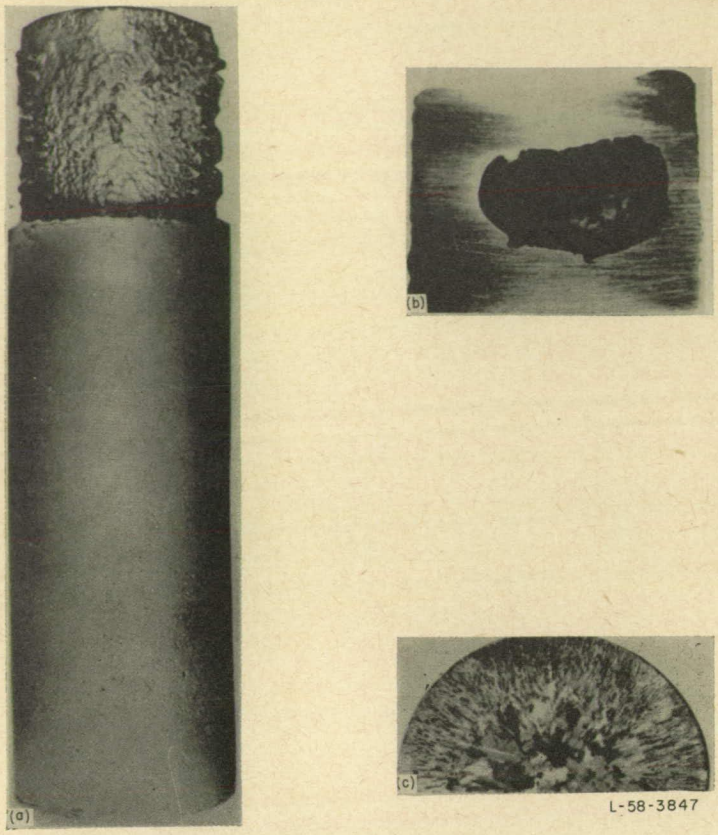


FIGURE 2.—Melting cycles used in study of effect of melting variables on high-temperature properties of experimental alloy.



(a) As-cast ingot 9 inches long with 2.5-inch diameter; weight, 10 pounds.
(b) Section of hot top showing isolation of pipe to hot top.
(c) Macrostructure of ingot section.

FIGURE 3.—Typical as-cast ingot from experimental heats.

table II with chemical compositions obtained from the suppliers.

Ten-pound heats were poured into an open-bottomed copper mold which rested on a massive copper block. An insulating refractory ring mounted in the top of the copper mold served as the hot top. An as-cast ingot, a hot-top section, and the ingot structure are shown in figure 3.

HOT-WORKING AND HEAT TREATMENT

Most of the 10-pound ingots were processed as follows:

(1) Homogenized 1 hour at 2,300° F, air-cooled.
(2) Surface-ground.
(3) Rolled at 2,150° F to ⅞-inch bar stock using 22 passes with 21 reheats of 10 minutes between passes. The last pass was a 7-percent reduction followed by air-cooling.

Heats V–20, V–21, and V–24 were not homogenized or ground, and heats V–18 and V–19 were rolled at 2,000° F to ⅞-inch bar stock using 36 passes with 35 reheats.

All of the stock was solution-treated at 2,150° F for 2 hours and then air-cooled. The rupture tests were conducted on the material in this condition. In conducting the tests the specimens were preheated for 4 hours at 1,600° F before the stress was applied. The 2-hour treatment at 2,150° F also was applied prior to aging experiments.

The evaluation of hot-workability was limited to visual observations of the type and degree of cracking during rolling and to comparison of the limitations during working necessary to obtain usable bar stock.

CHEMICAL ANALYSIS

Samples for chemical analysis were cut from the midpoint of the as-rolled bar stock. This metal was originally in the center of the ingot. Titanium, aluminum, molybdenum, chromium, cobalt, manganese, magnesium, copper, iron, and zirconium were determined spectographically through the courtesy of the Utica Drop Forge and Tool Corp. Carbon, sulfur, and phosphorus were determined by chemical analysis of machined chips. Residual calcium, iron, copper, and magnesium were checked spectrographically on heats V–13, V–20, and V–21. The difficult and time-consuming analyses for boron, provided gratis by the Universal-Cyclops Steel Corp., were made by a wet-chemical method.

SPECIMENS FOR DETERMINING PROPERTIES AT HIGH TEMPERATURES

Specimens having a 0.250-inch diameter by 1-inch long gage section were machined from the heat-treated bar stock. The original ⅞-inch stock was quartered lengthwise to provide specimen blanks from each quarter. The high-temperature properties of the experimental heats were evaluated by rupture tests on these specimens at 1,600° F and 25,000 psi. In part of the tests creep data were taken on the specimens using an optical extensometer having a sensitivity of 0.000005 inch per inch for strain measurements.

MECHANISM STUDIES

The mechanism studies were concentrated on the four heats with the largest differences in properties from the trace-element effects. Heat V–15 (see table III) was selected as representative of material with very low boron and zirconium. A relatively high zirconium content for the series of heats available was represented by heat V–6. Heat V–12 was representative of a fairly high boron content and heat V–14 had significant amounts of both boron and zirconium.

Samples from these heats were subjected to extensive microstructural studies using both optical and electron microscopic techniques. Phase identifications were carried out using electron diffraction on extraction replicas. To define the influence of boron and zirconium it was found necessary to age samples with and without stress. The samples aged under stress were obtained by interrupting creep-rupture tests. Several features of the microstructure had to be evaluated by counting techniques. The details of the procedures are presented in the following sections.

Procedures with aged specimens.—Small samples were heated in a muffle furnace for time periods up to 500 hours at 1,600° F to provide specimens with structural changes characteristic of those produced in the absence of stress. These samples were subjected to hardness tests as well as to microstructural examination. Diamond pyramid hardness (DPH) was measured with a 50-kilogram load. Three impressions were made on each sample. Analysis of testing variability established that in the range of 200 to 340 DPH a difference of 7 DPH was significant while in the range of 340 to 400 DPH a difference of 9 DPH was required to be significant.

Specimens aged under stress were obtained by starting tests at 1,600° F in the same manner as for rupture tests. The objective was to obtain specimens showing the microstructural changes occurring during the course of the creep-

rupture tests. When the required time had elapsed, the load was released and the specimen was immediately removed from the furnace to cool in air. Creep data were taken during these aging treatments so that the structural changes could be expressed as a function of deformation as well as of time. Fractured rupture specimens were also examined. In one series, the stresses were adjusted to give approximately equal creep rates in all four heats.

All specimens were sectioned lengthwise to present surfaces for examination which were parallel to both the direction of rolling and the direction of the stress for specimens subjected to creep.

Light microscopy.—Metallographic samples were mechanically polished through wet papers to 600 grit and then the majority were polished on wet cloths with Linde A and Linde B powders. A few, as noted in the figures, were electropolished after 600 grit paper in a solution of 10 parts of 70-percent perchloric acid and 90 parts of glacial acetic acid at 50 volts with a current density of 2 amperes per square inch. Cyclic polishing of 5 seconds on and 5 seconds off was employed for a total period of electrolysis of 30 seconds.

The procedure and etchant developed by Bigelow, Amy, and Brockway (ref. 18) was used to reveal best the precipitating phases at 100, 1,000 and 2,000 diameters. This involved etching electrolytically at 6 volts and a current density of 0.8 ampere per square inch for periods of 5 to 7 seconds, depending upon the sample condition. The etchant composition was 12 parts of 85-percent phosphoric acid, 47 parts of 96-percent sulfuric acid, and 41 parts of 70-percent nitric acid.

Electron microscopy.—Metallographic samples were mechanically polished through wet papers to 600 grit. This polishing was followed by electropolishing using the procedure described in the previous section on light microscopy.

Etching for examination with the electron microscope was accomplished with the etchant described under light microscopy with the etching time reduced to periods of 1 second to 5 seconds.

After etching, collodion replicas of the metallic surface were made. These were shadowed with palladium to increase contrast and reveal surface contours. Polystyrene latex spheres approximately 3,400 angstrom units in diameter were placed on the replicas prior to shadowing to indicate the angle and direction of shadowing and to provide an internal standard for measurement of magnification. The micrographs reproduced in this report are copies of direct prints from the original negatives; consequently, the polystyrene spheres appear black and the "shadows" formed by the palladium appear white.

Quantitative structural evaluations and techniques.—During the course of the structural studies it became evident that certain features were related to properties. The most significant were microcracks formed in the grain boundaries, depletion of the γ' phase from the matrix adjacent to the grain boundaries, "nodules" of precipitates which formed within the grains, the dispersion of γ' particles in the matrix, and cracks originating at the surface.

In order to make the trends and comparisons quantitative, counts were made of the number of depleted grain boundaries, microcracks, and nodules in an 0.008-square-inch area using a magnification of X1,000 on mechanically polished and etched specimens. An area of 0.008 square inch was surveyed as eight strips, each 0.2 by 0.005 inch. In the case of interrupted creep tests, the strips were longitudinal to the specimen axis at the center of the specimen and at the minimum cross section. In ruptured samples, the strips were again longitudinal, starting in the grains at the fracture surface and progressing away from the fracture.

A depleted grain boundary was counted when a clear, white strip of matrix free of γ' particles was clearly seen along a grain boundary.

Microcracks were easily distinguishable by their blackness which was in complete contrast with all other intragranular and intergranular features of the samples. Early doubts about the identity of microcracks were eliminated when electropolishing enlarged and accentuated these black voids and when fins on electron-microscope replicas were found where these had filled the microcracks. Each distinct microcrack was counted. A crack had to be 1 micron in length to be counted because shorter microcracks were not distinguishable from carbide-matrix interfaces. Counting of nodules was arbitrarily limited to those more than 5 microns in diameter.

Intergranular surface cracks were counted on mechanically polished specimens by traversing longitudinal section surfaces at 500 diameters. This cracking was found to be quite uniform over the reduced section of the specimens. In the case of interrupted creep specimens the cracks were counted over the center 0.75 inch, while in ruptured samples counts were made for 0.50 inch starting at the fracture. Intergranular cracks penetrating less than 0.003-inch deep were not counted.

A rough measure of γ' dispersion was obtained by the surface density of γ' particles in electron micrographs. An area large enough to contain at least 100 particles was surveyed at 12,000 diameters.

The above techniques allow quantitative comparison of the tendency of the four heats to undergo structural changes. It is recognized that percent of grain-boundary area cracked, percent of grain-boundary area depleted, volume percent of nodules, and volume percent and interparticle distance of γ' would be fundamentally more sound quantities for correlation. However, these more refined and time-consuming techniques would not alter the conclusions of this paper and, therefore, were not considered necessary.

Phase identification.—The extraction-replica technique of Fisher (ref. 19) was used to identify precipitated phases by electron diffraction. In this procedure a replica is placed on the surface of the sample and the metal surface then selectively etched so that the precipitate of interest is left adhering to the surface of the replica.

For extraction of intragranular γ', the initial specimen preparation was identical to the electropolishing and etching used for electron metallography. The specimen preparation for extraction of intragranular precipitates consisted of electropolishing and then electrolytically etching for 15 minutes in 1 part 85-percent phosphoric acid to 4 parts water in order to remove the γ' particles.

For extraction of intergranular particles, the microfractographic techniques of Plateau, Henry, and Crussard (ref. 20)

proved adequate. Specimens were cooled in liquid nitrogen and then fractured using a hammer and chisel, the fracture being intercrystalline. The fracture surface was then etched with the same procedure described above for electron microscopy.

Carbon replica films were deposited on the prepared surfaces by the method of Bradley (ref. 21) and were backed by thicker supporting films of collodion. The surfaces were then etched electrolytically in a solution of 1 part 85-percent phosphoric acid to 4 parts water until the compound replica films separated from the surface. The films were transferred to the surface of clean distilled water and allowed to wash by diffusion, picked up on nickel screens, washed again, and the collodion backing films dissolved from the carbon films with amyl acetate by the method of Fullam (ref. 22). The replicas were then shadowed with aluminum to provide an internal standard for interplanar distances. Electron-diffraction patterns were obtained from the particles by selected area electron-diffraction techniques on the microscope. Electron micrographs were obtained from the replicas in an electron microscope to show the phases subjected to electron diffraction.

RESULTS

The data obtained gave two main results: (1) The establishment of the marked improvement of creep-rupture properties and hot-workability from zirconium or boron derived from reaction between the melt and crucible refractories; and (2) the delineation of the mechanisms by which boron and/or zirconium improved the creep-rupture properties.

INFLUENCE OF CRUCIBLE REFRACTORY

The poorest hot-workability and the lowest rupture life and ductility were found for heats melted in alumina crucibles. Better properties were found for heats melted in zirconia and still better for those melted in magnesia. In presenting the results, the chemical composition of the melted heats will be discussed first because the cause for the observed property effects was found through the chemical analyses. The hot-workability of the heats will be presented second and the creep-rupture properties third.

Chemical composition.—The composition variables of primary interest in this investigation proved to be boron and zirconium. The levels investigated varied depending on the type of crucible employed for the melting and whether deliberate trace-element additions were made to the heats. The results of chemical analyses on heats melted with no deliberate additions of boron or zirconium (see table III) indicate the following ranges of analysis for these elements:

Type of crucible	Range in analysis, weight percent	
	B	Zr
Alumina	0.0002 to 0.0003	<0.01
Zirconia	.0004 to 0.0005	<0.03 to 0.19
Magnesia	.0004 to 0.0017	<0.01

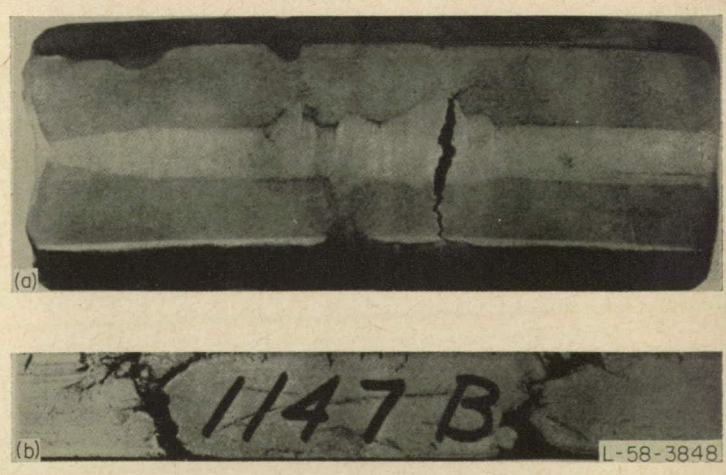
In order to verify that the boron and/or zirconium were the controlling variables independent of their source and to extend the study to higher levels than were obtainable by reaction with the crucibles, additional heats were made in all three types of crucibles with deliberate additions of boron and/or zirconium during melting. This increased the range of boron up to 0.0089 percent and gave heats melted in alumina for which essentially none of the boron and/or zirconium was derived from reaction with the crucible.

The lower limit of sensitivity for zirconium during the analysis of heats V–1 through V–10 was 0.03 percent. The sensitivity had improved to 0.01 percent for heats V–11 through V–24.

Although the majority of the heats had carbon contents in the range of 0.05 to 0.12 percent, several heats contained carbon levels above this range. Titanium and aluminum also varied because of the wide range of melting techniques used. In addition, the degree of reliability of analyses for magnesium, calcium, and copper is uncertain. The results obtained, however, did not disclose significant variations for these elements.

Hot-workability.—Working conditions for the alloy were found to be limited in temperature range, amount of reduction per pass, and the reheat time between passes because of the tendency for cracking to occur. The most successful practice found for the heats with less than 0.01 percent zirconium and less than 0.001 percent boron was to roll from 2,150° F using approximately 7-percent reductions per pass with a 10-minute reheat at 2,150° F between passes. Therefore, this practice was adopted for all rolling except for heats V–18 and V–19, which were rolled from 2,000° F with smaller reductions to avoid the hot-shortness at temperatures above 2,000° F which was related to combined content of boron and zirconium.

Observation of hot-working revealed that two distinctly different types of cracking occurred. The first type was a severe internal rupturing of the stock. The appearance of one of these ruptures is shown in figure 4. The second



(a) Ingot after three passes at 2,150° F.
(b) ⅞-inch bar stock rolled from cracked section of ingot shown in (a). Large cracks could not be ground out.

FIGURE 4.—Internal rupture in heat V–14 with 0.0088 percent boron and 0.01 percent zirconium and resultant bar stock after continued hot-rolling.



(a) Heat V–13 with 0.0003 percent boron and less than 0.01 percent zirconium.
(b) Heat V–1 with 0.09 percent zirconium with no boron addition.
(c) Heat V–6 with 0.19 percent zirconium and 0.0004 percent boron.
(d) Heat V–11 with 0.0017 percent boron and less than 0.01 percent zirconium.
(e) Heat V–12 with 0.0089 percent boron and less than 0.01 percent zirconium.

FIGURE 5.—Effect of boron or zirconium content on corner cracking of experimental heats when rolled to ⅞-inch-square bars at 2,150° F.

type was corner cracking (fig. 5) which occurred after the round ingot had been broken down to square bar stock in the rolling mill. It was found that both types of cracking were related to trace element content.

The 2,300° F treatment included in the standard rolling practices was first adopted using heats with no boron in the belief that it would minimize corner-cracking problems during rolling by homogenizing the as-cast ingot. It is possible that this treatment magnified the internal-rupture problem in heats to which boron was added. The introduction of the 2,300° F treatment was based on experience with one of the higher zirconium heats and it is now considered that the zirconium and not the heat treatment was responsible for the improved hot-workability.

The cracking characteristics are presented in terms of the boron and/or zirconium contents alone. The relationship of these elements to crucible refractories will be discussed in detail in the subsequent section on rupture properties.

Internal cracking during rolling: The relationships governing internal rupturing during ingot breakdown were:

(1) The base alloy as melted in alumina was not subject to internal rupturing.

(2) Zirconium content of the heats melted in zirconia or alumina without boron additions apparently did not introduce internal rupturing. The relation held up to a zirconium content of 0.19 percent (heat V–6).

(3) Increasing boron content in the presence of less than 0.01 percent zirconium did introduce internal rupturing. This was first noticed in the finished bar stock of heat V–12 (0.0089 percent B) which exhibited some small voids along the center line resulting from internal rupture during ingot breakdown.

(4) The presence of both boron and zirconium in the amounts investigated markedly increased internal rupturing during ingot breakdown. Figure 4 illustrates the severity of this in heat V–14 which contained 0.0088 percent boron and 0.01 percent zirconium. Thus, the small increase in zirconium content from less than 0.01 percent (the lower limit of analysis) in heat V–12 to a definite 0.01 percent in heat V–14 in the presence of a boron content of near 0.009 percent was enough to intensify internal rupturing. In general, the severity of the internal rupturing in the heats containing 0.0069 to 0.0090 percent of boron (heats V–12, V–14, V–17, V–18, and V–19) increased with zirconium content in the range from less than 0.01 to 0.09 percent of zirconium. Heats V–18 (0.0069 percent B and 0.09 percent Zr) and V–19 (0.0090 percent B and 0.04 percent Zr) were very hot-short during the first passes in the standard rolling schedule.

(5) The time of internal rupturing in the rolling cycle was a function of the boron and zirconium levels. In heat V-14 (0.0088 percent B and 0.01 percent Zr), internal rupturing was limited to the first three passes at 2,150° F where it occurred along the as-cast grain boundaries. Once the original as-cast structure was recrystallized, internal rupturing ceased and the stock was reduced to ⅞-inch bar stock successfully with the standard rolling procedure. However, in heat V-18 (0.0069 percent B and 0.09 percent Zr) and heat V-19 (0.0090 percent B and 0.04 percent Zr), internal rupturing persisted after recrystallization of the as-cast grains. In order to minimize this rupturing throughout the rolling cycle, the rolling temperature was lowered to 2,000° F and the reductions per pass to 3 percent. With this procedure it was possible to obtain some useful stock for rupture-testing.

Corner cracking during rolling: After the round ingots had been broken down to 1 3/16-inch squares in the rolling mill, shallow corner cracking occurred in some of the experimental heats. These cracks could be ground out between passes rather easily but reoccurred during subsequent passes. The severity of this cracking was variable; some of the heats were very malleable with no corner cracking while others underwent cracking with each pass.

As seen in figure 5, the relationships governing corner cracking during rolling of the bar stock were:

(1) In heats melted in alumina or zirconia crucibles with no boron additions, cracking decreased with increasing zirconium content (figs. 5(a) and 5(b)).

(2) In heats with less than 0.01 percent zironium (melted in alumina or magnesia crucibles), cracking decreased with increasing boron content (figs. 5(d) and 5(e)).

(3) Corner cracking was not a problem in the heats containing moderate amounts of both boron and zirconium (fig. 5(c)).

Stress-rupture properties.—The evaluation of the influence of boron and/or zirconium was based on creep-rupture tests at 1,600° F and 25,000 psi. (See table IV and figs. 6 through 12.) The data obtained showed that rupture time and ductility increased with zirconium content and

526597—60——94

that boron was more effective than zirconium. The presence of certain amounts of both boron and zirconium gave even higher strength, although the properties fell off when zirconium increased above 0.01 percent in the presence of 0.0069 to 0.0090 percent of boron. A major result of the experiments was the demonstration that properties correlated with boron and zirconium contents whether these were derived from reaction with the crucible refractory or deliberately added to the heats.

Zirconium from zirconia crucibles: The rupture properties of heats V-1 to V-10 correlated with the amount of zirconium in the heats (figs. 6 and 7), and the rupture life increased regularly with increased zirconium up to 0.19 percent. The rupture life, however, seemed to be dependent on the amount of titanium plus aluminum in the heats, as is indicated in figure 6 by the arbitrary grouping of the data for heats with less than or more than 6.5 percent of titanium plus aluminum. Elongation and reduction-of-area values increased when the heat contained up to about 0.10 percent zirconium independent of the titanium-plus-aluminum content, except in the cases of the high values for the high-carbon heats V-8, V-9, and V-10 where the high carbon contents appear to increase ductility of the alloy in rupture tests.

Heats V-1 through V-10 were all melted in zirconia crucible with no zirconium added. The zirconium contents represented the variable amounts introduced into the heats as a result of reaction between the melts and the crucible refractories. The variable amounts of zirconium presumably were due to the wide ranges in refining practice, deoxidation practice, superheat temperature, pouring temperature, and time of melting used in making the heats. These variables represented widely varying conditions for reaction between the melt and the zirconia. The amount of zirconium derived from the crucible was, however, a more complicated factor than these melting variables inasmuch as no relations to the melting technique could be discerned in the data.

The important result of these tests was the determination that the zirconium content was the overwhelming variable and wide variations in melting technique had, at most, minor effects. The heats melted in alumina had still lower properties than the poorest heat melted in zirconia. Analytical procedures were not sufficiently sensitive to detect

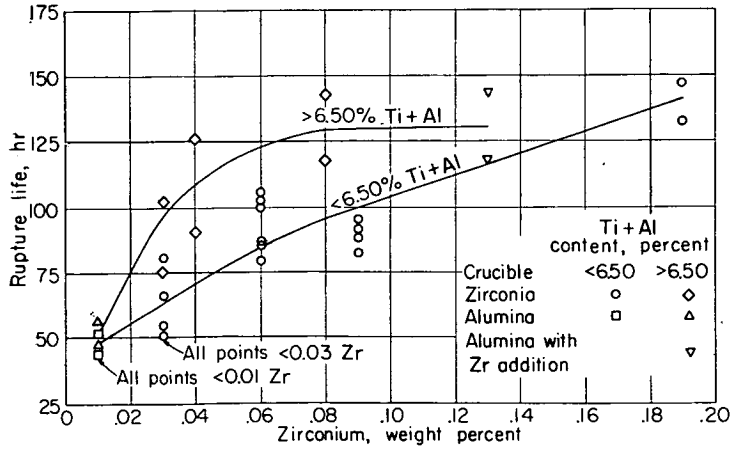


FIGURE 6.—Effect of zirconium content on rupture life at 1,600° F and 25,000 psi of experimental heats melted in zirconia or alumina with very low boron.

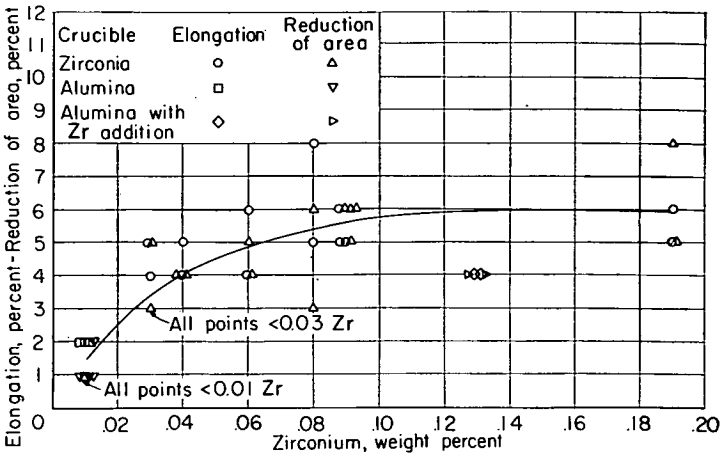


FIGURE 7.—Effect of zirconium content on ductility in rupture tests at 1,600° F and 25,000 psi of experimental heats melted in zirconia or alumina with very low boron.

the difference in zirconium contents of the heats melted in alumina and the lowest zirconium heats melted in zirconia. Presumably there were slight benefits from zirconium for amounts less than 0.03 percent, the lower limit of analytical sensitivity when heats V–1 through V–10 were analyzed. Confirmation of the controlling effect of zirconium independent of the other variables was obtained with heat V–16 by adding zirconium to a heat melted in alumina. The rupture times and ductilities (figs. 6 and 7) agreed with those expected on the basis of zirconium content within the limits of the experimental variables.

Boron from magnesia crucibles: The determination that zirconium derived from the zirconia crucibles was the controlling factor in the creep-rupture properties suggested that other refractories should be investigated as crucible materials. Accordingly, heats V–11, V–20, and V–21 were melted in magnesia crucibles. Heats V–11 and V–20 had rupture times of about 200 hours (fig. 8) in comparison with heat V–21 at about 100 hours. The ductility of all three heats (fig. 9) was in the range of 3 to 5 percent. The 100 hours for rupture for heat V–21 was equivalent to that for material with up to 0.10 percent zirconium based on the results for heats melted in zirconia (fig. 6). Heats V–11 and V–20 had

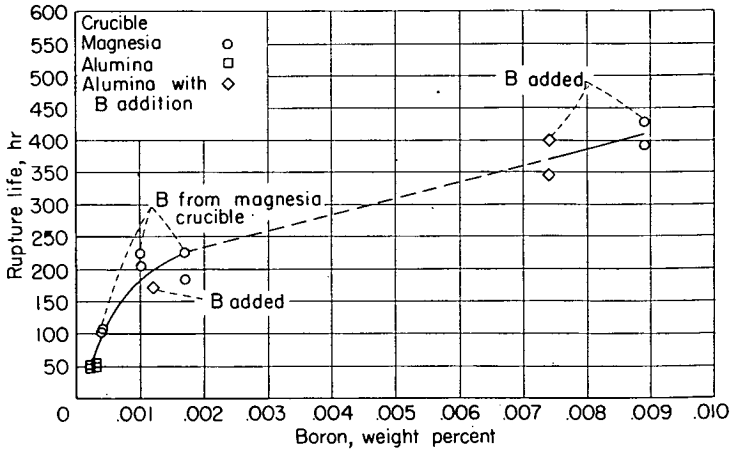


FIGURE 8.—Effect of boron content on rupture life at 1,600° F and 25,000 psi of experimental healts melted in alumina or magnesia with less than 0.01 percent zirconium.

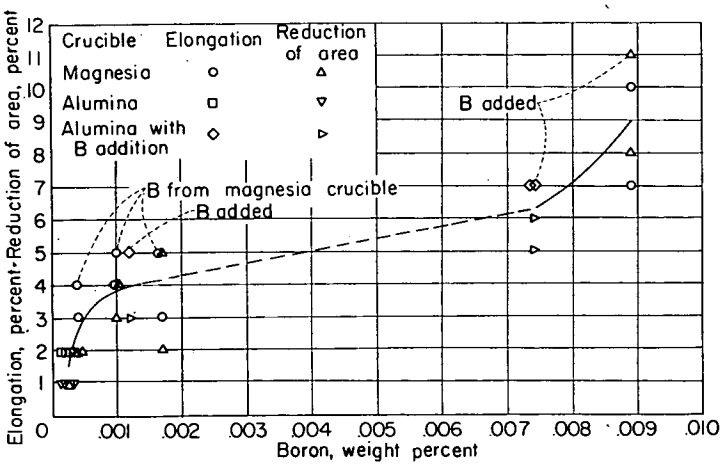


FIGURE 9.—Effect of boron content on ductility in rupture tests at 1,600° F and 25,000 psi of experimental heats melted in alumina or magnesia crucibles with less than 0.01 percent zirconium.

higher rupture strength than any of the heats melted in zirconia.

Analysis of the heats indicated that the boron contents of heats melted in magnesia were 0.0004 percent in heat V–21, 0.0010 percent in heat V–20, and 0.0017 percent in heat V–11. In view of the known powerful improving effect of boron on the properties of the alloy, this suggested that the boron was the controlling factor. This was confirmed by adding boron to heat V–24 melted in alumina (see figs. 8 and 9). Heat V–17, also melted in alumina, contained considerably more boron than was derived from crucible reaction in other heats as a result of a boron addition. This confirmed the marked improvement from boron for heats melted in alumina. Furthermore, it seemed to correlate with the expected effect of boron based on the results from heat V–12 in which boron had been added while melting in magnesia.

The boron in the heats melted in magnesia apparently came from the boron compounds which were present in the crucible. When the presence of boron in the heats melted in magnesia was first established, a check of the literature indicated that commercial magnesia is normally contaminated with boron compounds. The producer of the crucibles furnished the analysis shown in table II. The highest boron heat was the first one made in a fresh crucible. The amount of boron derived from the crucible decreased with succeeding heats. (Compare heats V–20 and V–21.)

The general agreement in properties for heats melted in alumina with those for heats melted in magnesia for the same boron content indicated that magnesia was contributing very little to improved characteristics other than by adding boron. It was first thought that magnesium might be involved since this element is often used as a deoxidizer with beneficial effects; however, there was practically no indication that magnesium was having much effect in the heats. Attempts to add magnesium during vacuum-melting proved inconclusive because of the very rapid evolution of magnesium as a vapor.

Alumina crucibles: Alumina crucibles were introduced into the program to check further the role of refractories. Any increase in aluminum content as a result of reaction between the crucible and the melt would be negligible in view of the large aluminum content of the heats. Two of the heats melted in alumina (V–13 and V–15) had the lowest strengths and ductilities of all the heats melted as was to be expected from the very low amounts or absence of zirconium and boron. For this reason the properties of heats V–13 and V–15 have been used in figures 6 through 9 to show the effects of very low amounts of these trace elements. As previously discussed, adding zirconium or boron to heats melted in alumina resulted in properties to be expected from the zirconium or boron contents.

So far as is known the alumina crucible did not contain sufficient boron or zirconium (table II) to expect a measurable addition of these elements to the heats. This seems verified by the analyzed compositions of the heats. The silicon dioxide in the alumina may have resulted in a very slight increase in silicon content of the heats.

Boron-plus-zirconium effects: In view of the pronounced improvement in properties obtained from boron derived from magnesia crucibles or by addition of boron to heats melted in magnesia, boron was added to a heat melted in zirconia (heat V–14). This heat had the highest rupture strength (646 hours) and ductility (14-percent elongation) of any of the heats made. However, heats V–18 and V–19, made in alumina with boron and zirconium additions, did not have as high properties as did heat V–14. The analyzed borons for the three heats ranged from 0.0069 to 0.0090 percent. The zirconium content of heat V–14 was only 0.01 percent while it was 0.04 and 0.09 percent for heats V–19 and V–18. When the rupture times and ductilities were plotted as a function of zirconium content for heats with boron contents of 0.0069 to 0.0090 percent (fig. 10), an apparent optimum amount of zirconium of approximately 0.01 percent is indicated.

It should be noted, as was remarked earlier, that heats V–18 and V–19 had to be rolled from 2,000° F rather than from 2,150° F because of hot-shortness. In addition, it is possible that use of the 2,300° F homogenizing treatment before rolling had an adverse effect when the boron and zirconium level was comparatively high. Therefore, any conclusions drawn from figure 10 should be qualified by recognizing that the differences in hot-working temperatures and the use of the 2,300° F treatment could have influenced the properties.

Comparison with commercial material: The basic alloy studied for the investigation was based on the commercial alloy Udimet 500 developed by the Utica Drop Forge and Tool Corp. Figure 11 shows a band which would encompass the curves of stress against rupture time at 1,600° F as reported for the alloy by the manufacturer. The rupture time for heat V–13 is shown in figure 11 to indicate the low strength of the experimental heats made in alumina crucibles with resultant very low zirconium and boron. The best heat made in zirconia (heat V–6 with 0.19 percent zirconium) had strength near the lower side of the band for commercial heats. Heat V–11, the highest boron heat melted in magnesia, was just within the band. When boron was added to a heat melted in magnesia (heat V–12) to bring the boron up to 0.0089 percent, properties near the upper side of the band were obtained. The strongest heat

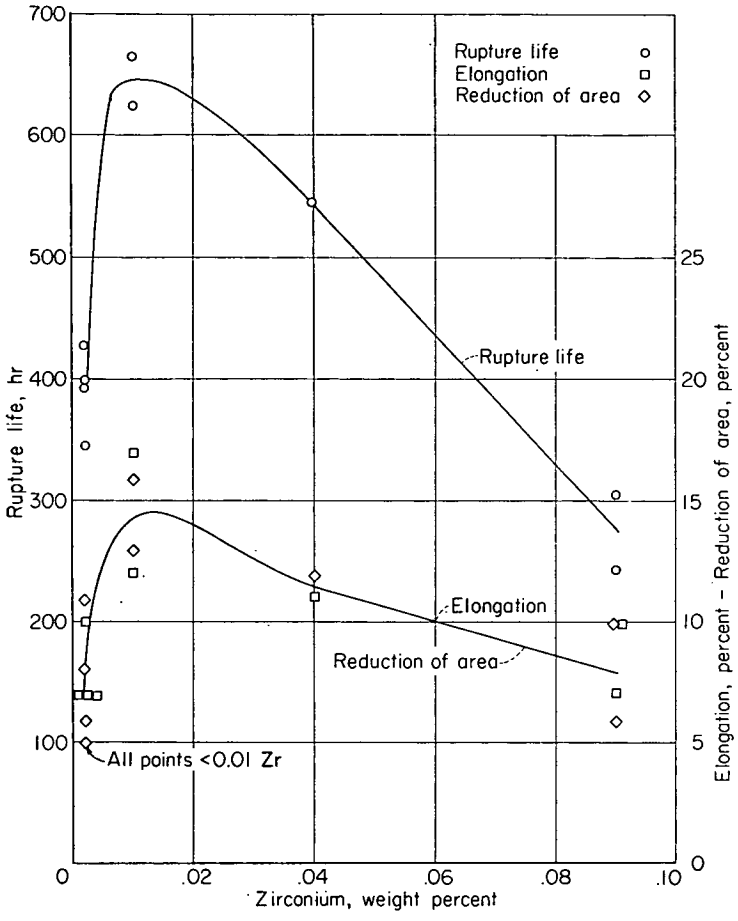


FIGURE 10.—Effect of zirconium content on rupture life and ductility at 1,600° F and 25,000 psi in presence of boron contents of 0.0069 to 0.0090 percent.

made (heat V–14) with 0.0088 percent boron and 0.01 percent zirconium was slightly stronger than the commercial material.

In connection with the mechanism studies a few rupture tests were conducted at stresses other than 25,000 psi. The data obtained are given in table V and the points are shown graphically in figure 11. While the data are too sparse to permit drawing curves of stress against rupture time, there

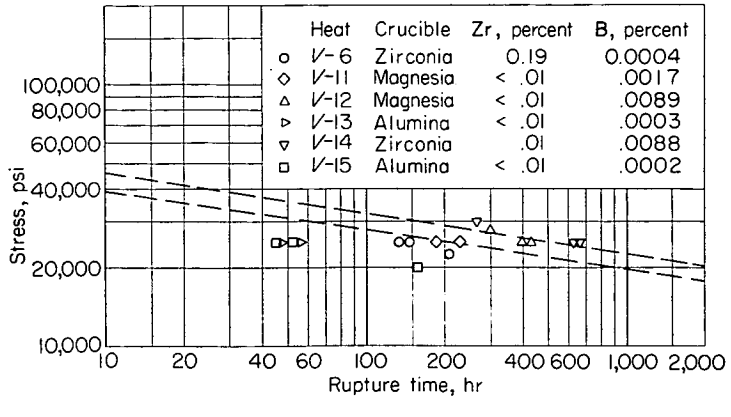


FIGURE 11.—Effect of stress on rupture life at 1,600° F. Data plotted as dashed rupture band were from two heats of commercial Udimet 500 alloy as reported by Utica Drop Forge and Tool Div. of Kelsey-Hayes Co. Heat treatment for commercial alloy was 2 hours at 2,150° F, air-cooled, plus 4 hours at 1,975° F, air-cooled, plus 24 hours at 1,550° F, air-cooled plus 16 hours at 1,400° F, air-cooled.

is a suggestion of steeper curves in two cases than is typical for the curves for Udimet 500.

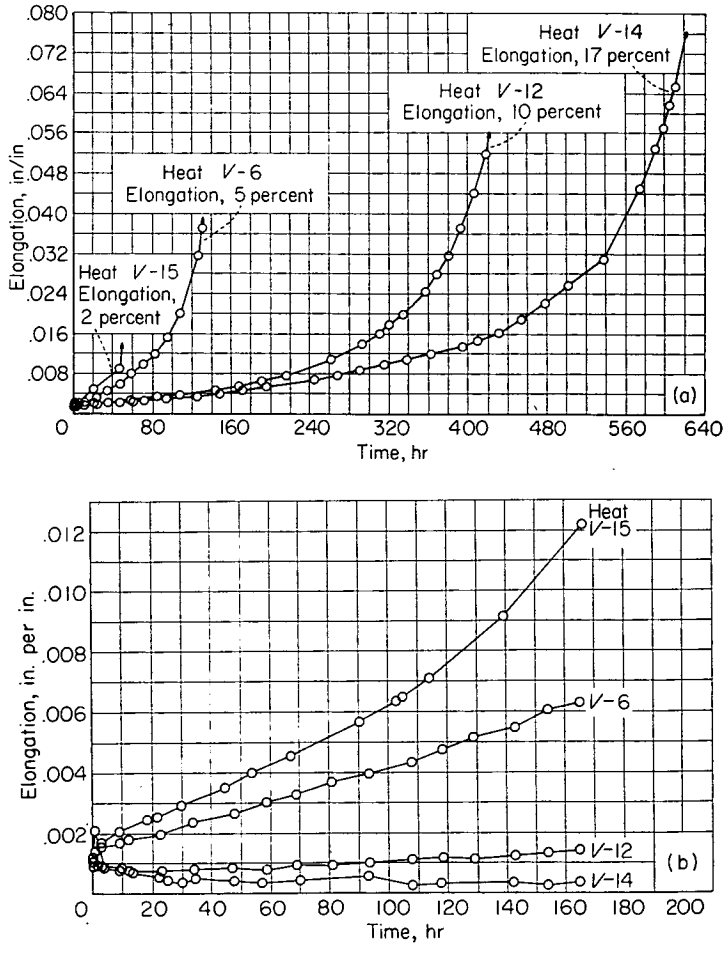
Creep characteristics: Typical creep curves from the rupture tests at 1,600° F at stresses of 25,000 and 20,000 psi are shown in figure 12. These curves are limited to material melted in alumina (heat V–15) with low boron and zirconium, heat V–6 with 0.19 percent zirconium resulting from reaction with the zirconia crucible, heat V–12 with 0.0089 percent boron, and heat V–14 with 0.0088 percent boron and 0.01 percent zirconium. Other heats had intermediate curves in accordance with their rupture strengths.

The effect of boron and zirconium on creep characteristics for the conditions considered can be summarized as follows:

(1) Neither boron nor zirconium had much effect on primary creep.

(2) Secondary creep rates decreased (i. e., creep strength increased) with zirconium. Boron reduced creep rates still more and boron plus zirconium in the amounts in heat V–14 resulted in the lowest second-stage creep rates (see fig. 13). In fact, the boron heat and the boron-plus-zirconium heat decreased in length during tests at 20,000 psi (fig. 12 (b)). Boron also prolonged second-stage creep (fig. 12 (a)).

(3) Both zirconium and boron prolonged third-stage creep and increased the amount of third-stage creep before fracture occurred (fig. 12 (a)). The amount of boron plus zirconium in heat V–14 was most effective in this respect.



(a) Stress, 25,000 psi.
(b) Stress, 20,000 psi.

FIGURE 12.—Comparative creep curves at 1,600° F.

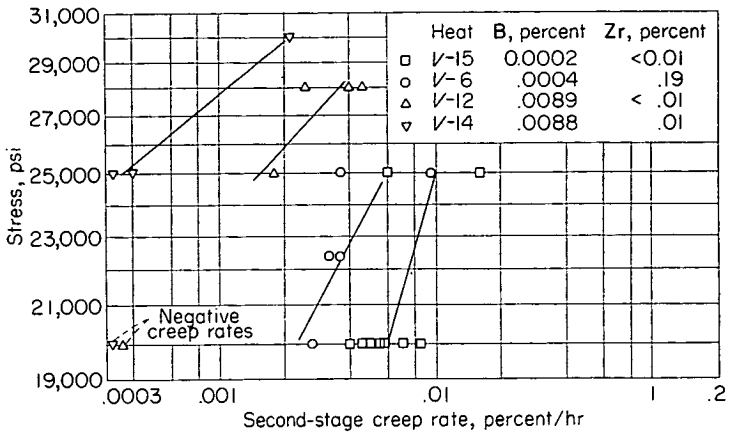


FIGURE 13.—Influence of stress on second-stage creep rate at 1,600° F.

Discussion.—The properties of the experimental alloy were influenced to a marked extent by the type of ceramic used for induction melting in vacuum. The chemical analyses indicate that, if boron or zirconium were not introduced into the melt by reaction with the crucible, rather inferior properties resulted. There seems to be little doubt that the effects of the reaction with crucibles can be a major factor in the variation in strength and ductility at high temperatures and in hot-workability of vacuum-melted heat-resistant alloys containing titanium and aluminum.

Most commercial induction vacuum melting uses magnesia or high-magnesia-content refractories for crucibles. Variation in the amount of reaction with the crucible could be, and probably is, a source of variable properties. Less effect in the second than in the first heat from a magnesia crucible suggests that the effect varies between successive heats from one crucible. The use of patching between heats and other possibilities of erratically providing fresh ceramic surfaces with increased reactivity to melts could be involved. Consideration of the possibility of other sources of boron compounds, such as ceramic binders, should be recognized.

Boron compounds are usually associated with magnesia as a contaminant; therefore, the derivation of boron from the crucible appears to be readily explainable. However, it is probable that recoveries of boron vary with a number of factors including the temperature and time of contact of the melt with the crucible, the ratio of crucible surface to melt volume, the number of heats, the variation in boron content of the magnesia crucible, and probably the compositional variations of the alloy.

The stability of the crucible materials may differ with melting atmosphere and pressure. Although considerable melt-crucible reaction occurred in vacuum melting, such crucible reactions may be limited in air melting by the higher pressure and the presence of slag and skull on the crucible walls.

The results also serve to suggest that the inadvertent introduction of even minute amounts of boron with the charge could be responsible for considerable variation in properties. The chances are that this occurs frequently, even though it may be unrecognized.

The data indicate that there are optimum amounts of boron when other trace elements, such as zirconium, are present. It seems probable that this has operated to give confusing results when elements such as boron and zirconium were knowingly or unknowingly added to heats simultaneously. There is a good chance that alloying elements other than boron and zirconium which are not yet recognized could exert a profound effect.

The relationship of the analyzed boron and zirconium contents to properties should not be accepted as complete establishment of compositional effects without further proof. There may be efficiency effects depending on their reaction with other elements not present in the heats studied so that total boron or zirconium content may not be directly related to properties. Furthermore, there is a possibility that heat and ingot size along with hot-working conditions were influencing results. It is also important to realize that analysis methods for boron and zirconium are subject to variation and that different laboratories might differ in the amounts reported.

The rupture tests were carried out on material heat-treated at 2,150° F and air-cooled. This differs from the usual heat treatment of 4 hours at 1,975° F plus 24 hours at 1,550° F plus 16 hours at 1,400° F. Other research in progress indicates that the treatment at 2,150° F minimizes variation in properties due to the influence of hot-working conditions. In particular, it appears to prevent abnormally low strength sometimes encountered when a 1,975° F treatment is applied to as-hot-worked material. A subsequent treatment at 1,975° F after a 2,150° F treatment usually gives the same properties as a single treatment at 2,150° F. Very little difference in rupture strength and ductility has been observed for inclusion or omission of the aging treatments. Possibly the 4 hours used to equalize temperatures before testing cause the inclusion or omission of prior aging to have little influence. All experiences to date indicate the test results reported for a simple solution treatment at 2,150° F to be generally characteristic of the alloy when treated at 1,975° F except for the elimination of occasional low strength values.

Carbon content of the alloys varied more than was desired. The major reason for the variability of carbon content was the wide range of melting conditions employed with the consequent difficulty of controlling carbon recovery. This may be an additional factor in the variation of properties.

The data on the influence of titanium and aluminum content are not so complete as would be desirable. More variation than was intended occurred in the heats. As noted previously, there apparently was longer rupture life with a given zirconium content when titanium-plus-aluminum content was high. This probably resulted from the higher titanium-plus-aluminum level providing a larger percent by volume of $Ni_3(Al,Ti)$ during stress-rupture testing.

The relationships between crucible ceramics and properties were developed for induction vacuum melting. The amount of such effects under other conditions of melting is not clear at this point. It is interesting to note that the ductility in rupture tests was low when the alloy was made in alumina crucibles. Low-zirconium heats made in zirconia crucibles and a low boron heat made in magnesia also had low ductility. This suggests that a part of the usual increase in ductility attributed to vacuum melting may be due to the opportunity

offered by vacuum melting to introduce effective trace elements from crucibles. Also, addition of trace elements other than boron and zirconium by other melting procedures may alter the effectiveness of a given boron and zirconium level.

The crucible-reaction effects were discovered as a result of inability to define the effects of variable-melting practices and the role of oxygen and nitrogen, the original objectives of the investigation. The crucible reactions must be controlled before the influence of the melting variables can be defined. Because of the sensitivity of properties to reactions with magnesia along with interrelated effects from such factors as hot-workability, very careful research will be necessary to define the effects clearly. While the data of this report suggest that many melting variables are secondary to the introduction of boron or zirconium from the crucibles, there may be extenuating circumstances which mask the effects. The subject is of sufficient complexity that probably the only way it can be cleared is by clarification of the mechanism by which as little as 15 parts per million of boron can increase rupture life 5 times.

In spite of the limitations on the generality of the results it is believed that the data reported reflect production experience quite well. Many of the variations in properties in the experimental investigation and in commercially produced alloys of the type investigated seem to be explainable in terms of the results of the investigation.

MECHANISM OF BENEFICIAL EFFECTS OF BORON AND ZIRCONIUM

Marked differences in microstructures after exposure to creep at 1,600° F were found in the four heats which showed extremes in properties as a function of boron and zirconium. In terms of properties, the most significant effects were found at those grain boundaries approximately normal to the applied stress during creep. In the low-boron-and-zirconium heat V–15, a process of agglomeration of $M_{23}C_6$ type carbide was accompanied by depletion of the γ' precipitate from the adjacent matrix and finally microcracking leading to early brittle fracture. This process was found to be retarded by the zirconium in heat V–6. Boron in heat V–12 retarded the process even more while the boron plus zirconium in heat V–14 was most effective. This increasingly effective retardation of eventual microcracking appeared to be mainly responsible for improved properties. Other less effective structural differences were observed between the heats.

Few, if any, significant differences in microstructure as a function of composition were present in specimens aged at 1,600° F without stress. Specimens which were fractured in rupture tests also showed few significant differences. The structures of specimens after varying amounts of creep provided the most useful information. The exposure conditions for the specimens of the four heats studied are summarized in table V. The conditions of exposure were selected to show structures after rupture under 25,000 psi and after varying amounts of creep under 20,000 psi. Stresses were also adjusted so that a series of specimens representative of all four heats could be examined after undergoing approximately the same amount of creep in the same time periods.

The microstructural features were found to be best expressed on a "quantitative" basis. Accordingly, the observations for the samples aged under stress are summarized in table VI and for those aged without stress, in table VII. The significant features are discussed in the following sections.

Microstructures in initial condition.—After the initial homogenizing treatment of 2 hours at 2,150° F and air-cooling the experimental heats were similar in grain size, inclusion count, and distribution (figs. 14 (a) to 14 (d)), and in grain-boundary precipitate (figs. 14 and 15). During the air-cooling after the 2,150° F treatment γ' precipitated. Some slight differences in dispersion of intragranular γ' existed but these were not found to be significant (as discussed later). Hardnesses (figs. 14 (a) to 14 (d)) did not differ significantly in this condition.

Agglomeration in grain boundaries.—A network of carbides enveloped by γ' accumulated in the grain boundaries of all samples during exposure at 1,600° F. In heat V–15 the rate of accumulation was comparatively rapid, the carbide phase being extensive and blocky and the γ' layer thick after 165-hour exposure with 1.2-percent creep deformation (figs. 16 and 17). The amount of agglomeration under these conditions was somewhat lower in the presence of zirconium (heat V–6) and much lower when boron (heat V–12) or boron plus zirconium (heat V–14) were present (figs. 16 (e) to 16 (h) and 17).

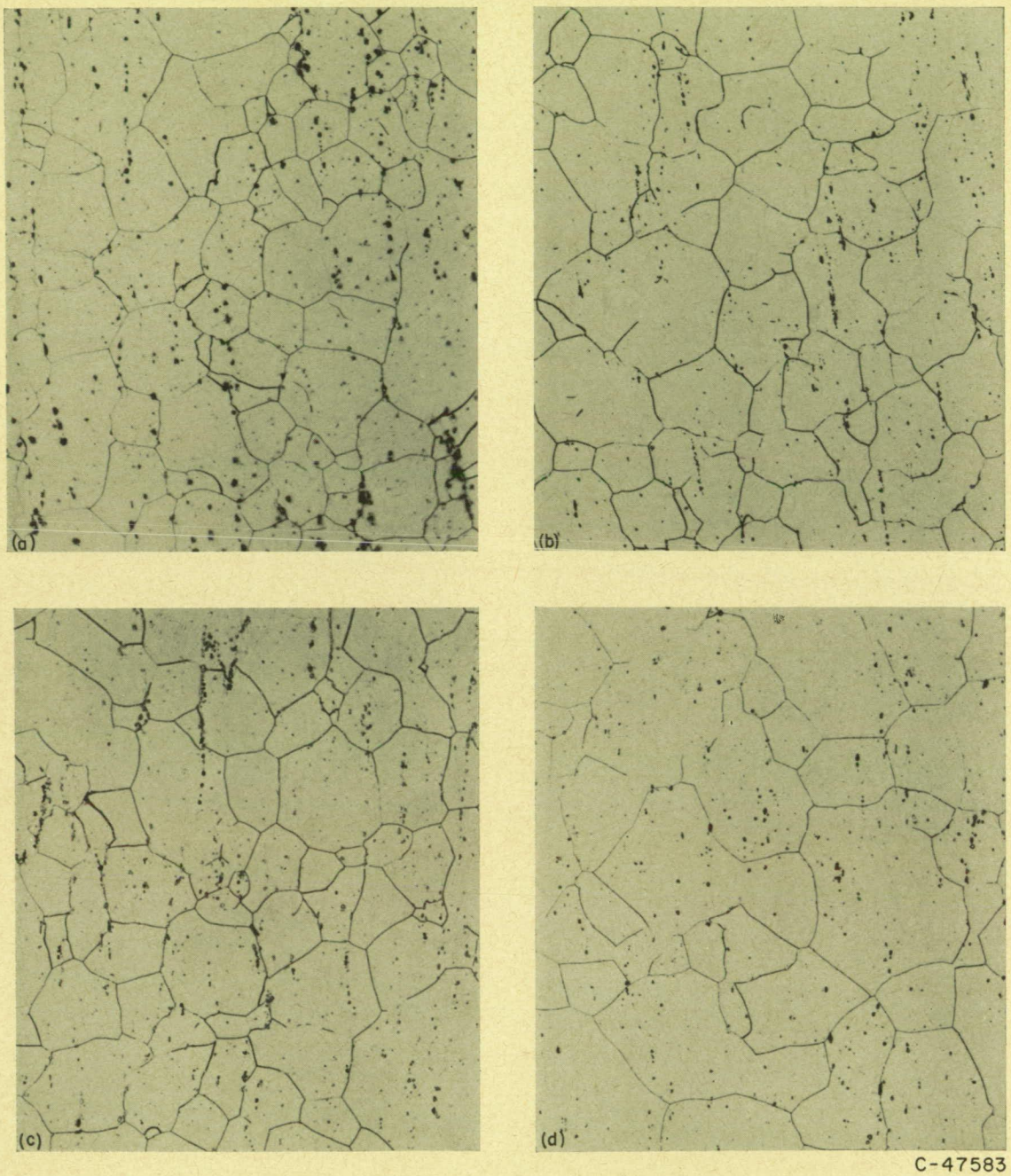
The agglomerated γ' was easily identified by etching characteristics. The agglomerate reacted to etching in the same manner as did the intragranular γ' in all the experimental work carried out. It always was in the same relief and had the same appearance as did the intragranular γ'.

Microfractographic techniques were used to identify the carbide phase and obtain more information on its form. Samples from heats V–15 and V–12 after 1.2-percent creep deformation at 1,600° F in 165 to 188 hours were cooled in liquid nitrogen and then fractured. Extraction replication from the fractured surface removed the grain-boundary carbide and retained it in the replica. Electron micrographs showing the size and distribution of carbides in the grain boundaries are shown in figure 18. The extracted particles from the heat free from boron or zirconium (V–15) were larger, more extensive and thicker than those from the heat with boron (V–12). The electron diffraction spots obtained on the replicas of the two samples indexed for $M_{23}C_6$.

Depletion of γ' at grain boundary.—Subsequent to the agglomeration of $M_{23}C_6$ in the grain boundaries, strips of matrix were depleted of γ' particles along transverse grain boundaries of the specimens aged under stress (fig. 19). This occurred most often adjacent to $M_{23}C_6$ particles. This was in contrast with samples aged without stress, where the

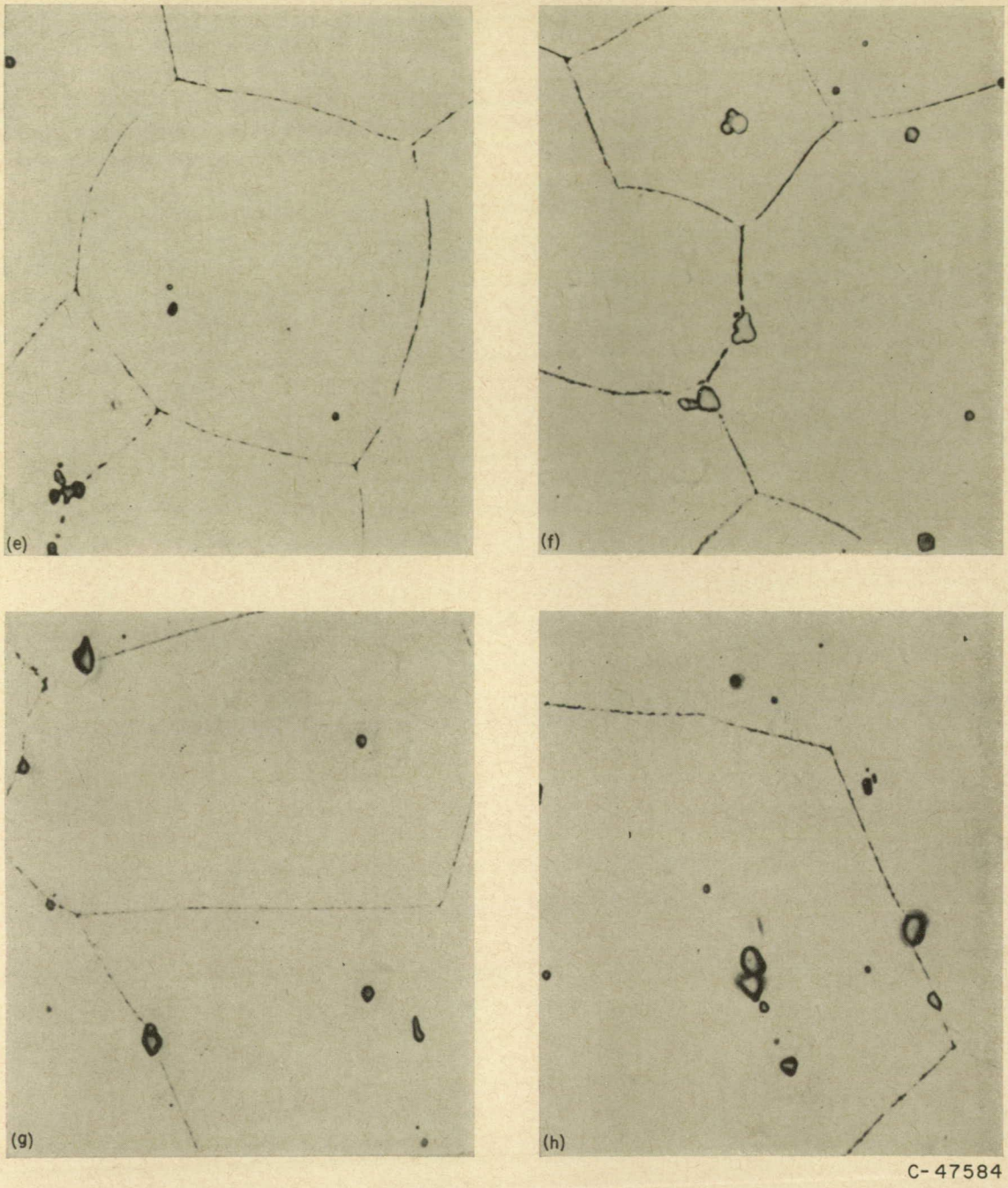
intergranular $M_{23}C_6$ was always enveloped by γ' and where the fine γ' particles extended up to the grain boundary (figs. 20 and 21).

In figure 19 the amount of this depletion is related to creep deformation for the experimental heats exposed to give equal strain at equal time at 1,600° F. It is evident that boron and zirconium are effective in reducing the amount of this depletion with a given strain at 1,600° F. Since the samples were stressed to give comparable strain rates, it follows that depletion in a given time at 1,600° F was reduced. Despite this retarding influence, however, the amounts of depletion at fracture became comparable in



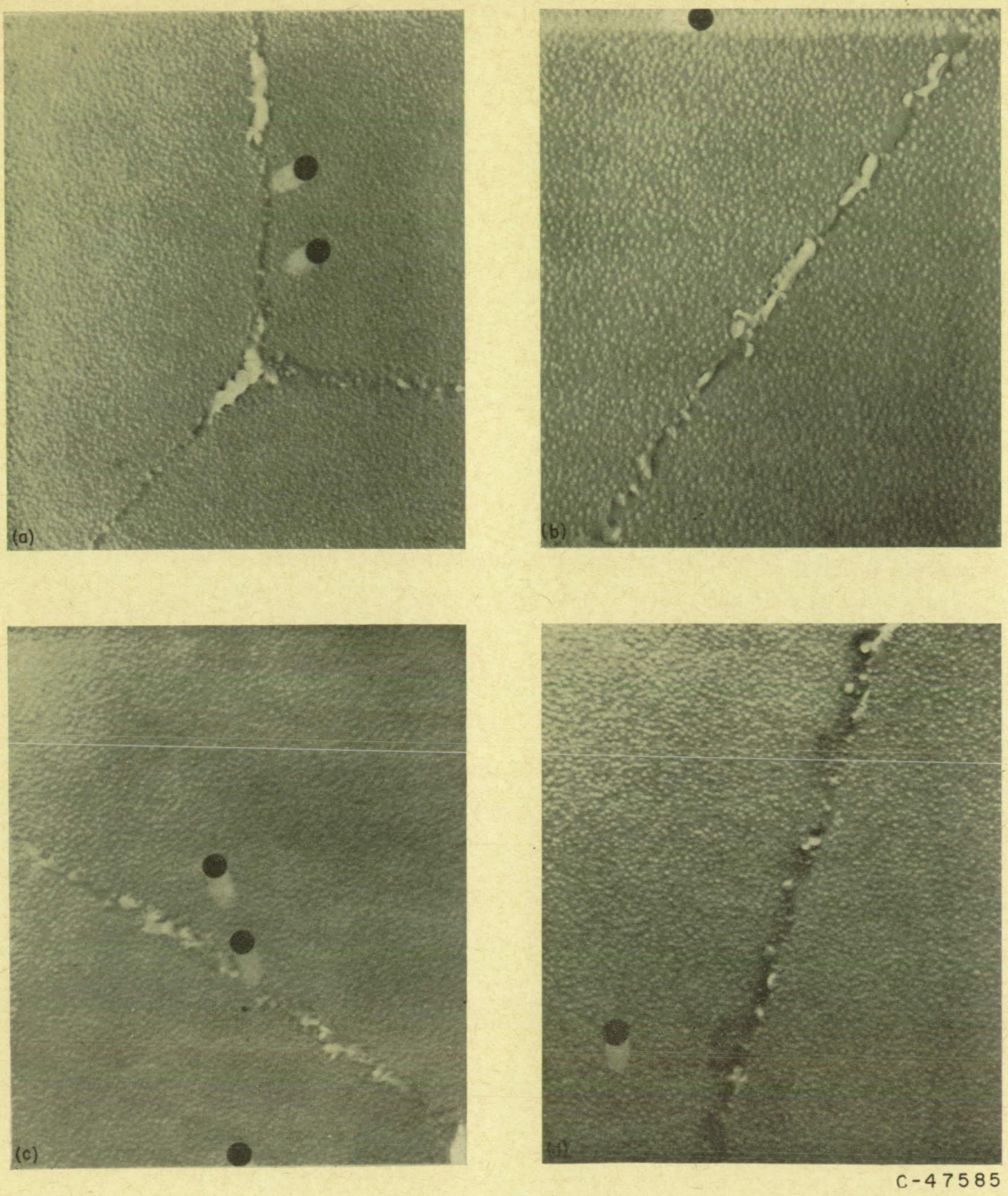
(a) Heat V–15; diamond pyramid hardness, 354; X100.
(b) Heat V–6; diamond pyramid hardness, 353; X100.
(c) Heat V–12; diamond pyramid hardness, 345; X100.
(d) Heat V–14; diamond pyramid hardness, 348; X100.

FIGURE 14.—Microstructures of specimens treated 2 hours at 2,150° F, then air-cooled. Optical micrographs; X100 and X1,000.



(e) Heat V–15; X1,000.
(f) Heat V–6; X1,000.
(g) Heat V–12; X1,000.
(h) Heat V–14; X1,000.

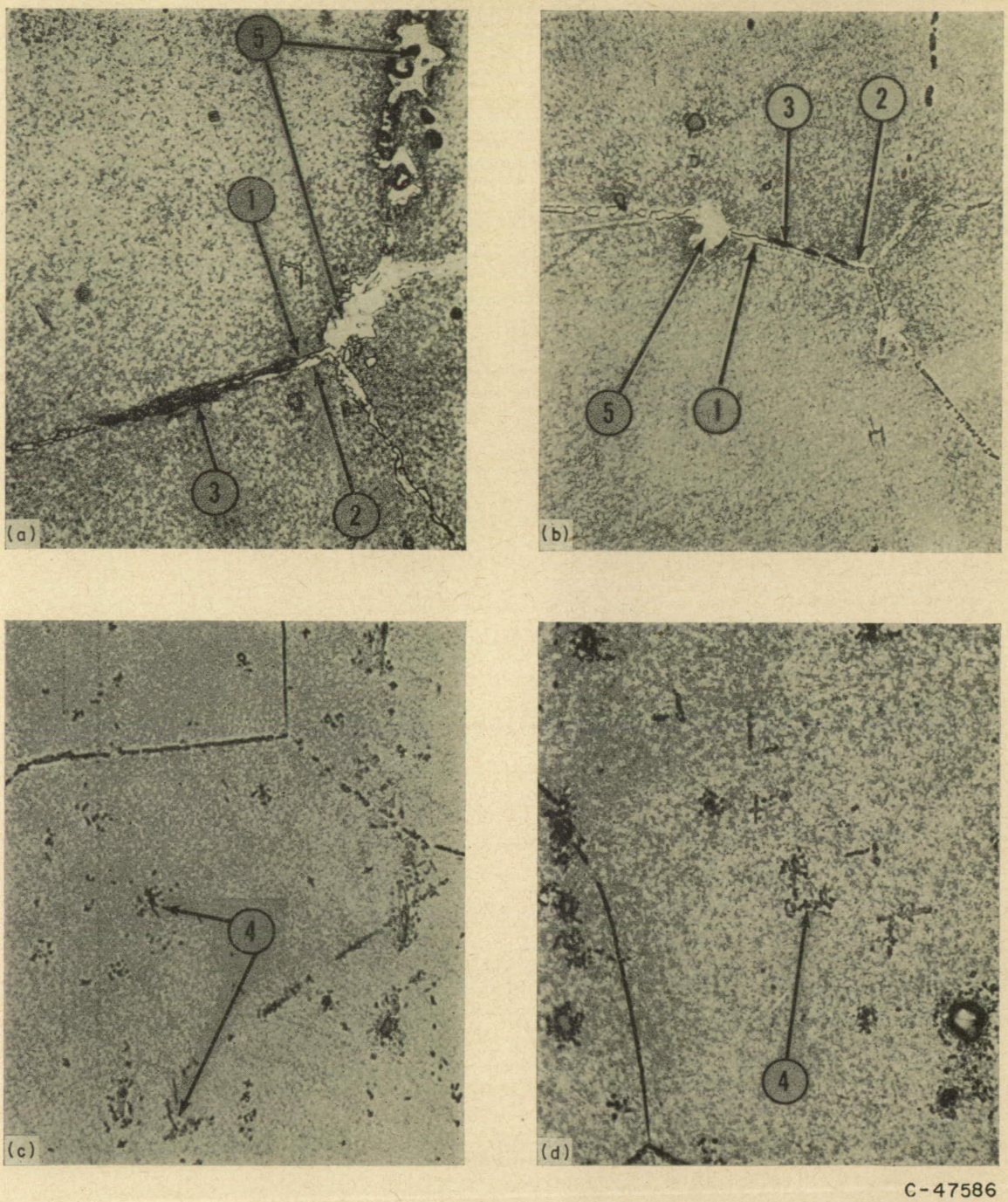
FIGURE 14.—Concluded.



(a) Heat V–15.
(b) Heat V–6.
(c) Heat V–12.
(d) Heat V–14.

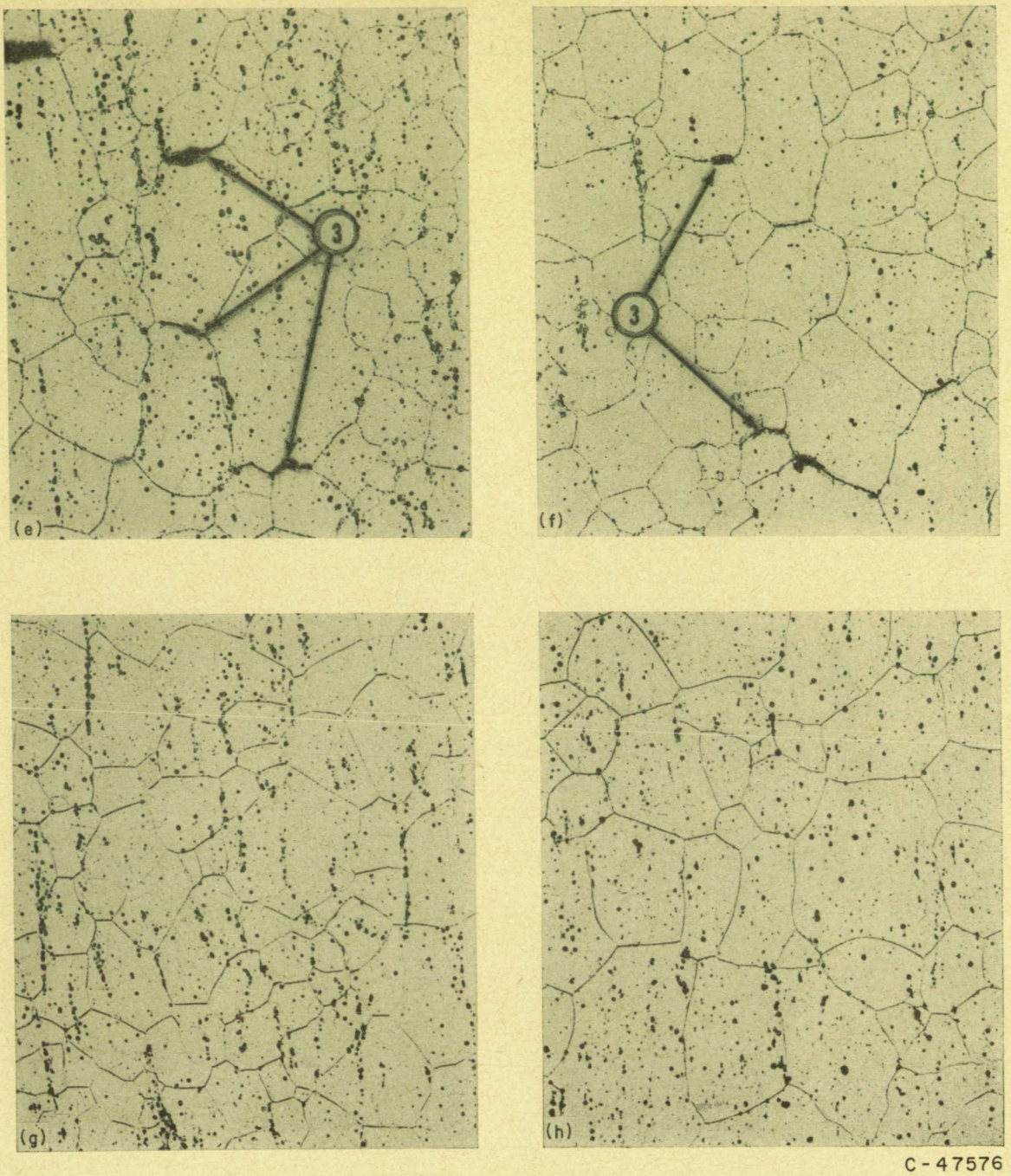
FIGURE 15.—Microstructures of specimens treated 2 hours at 2,150° F, then air-cooled. Electron micrographs; X12,000.

526597—60—— 93



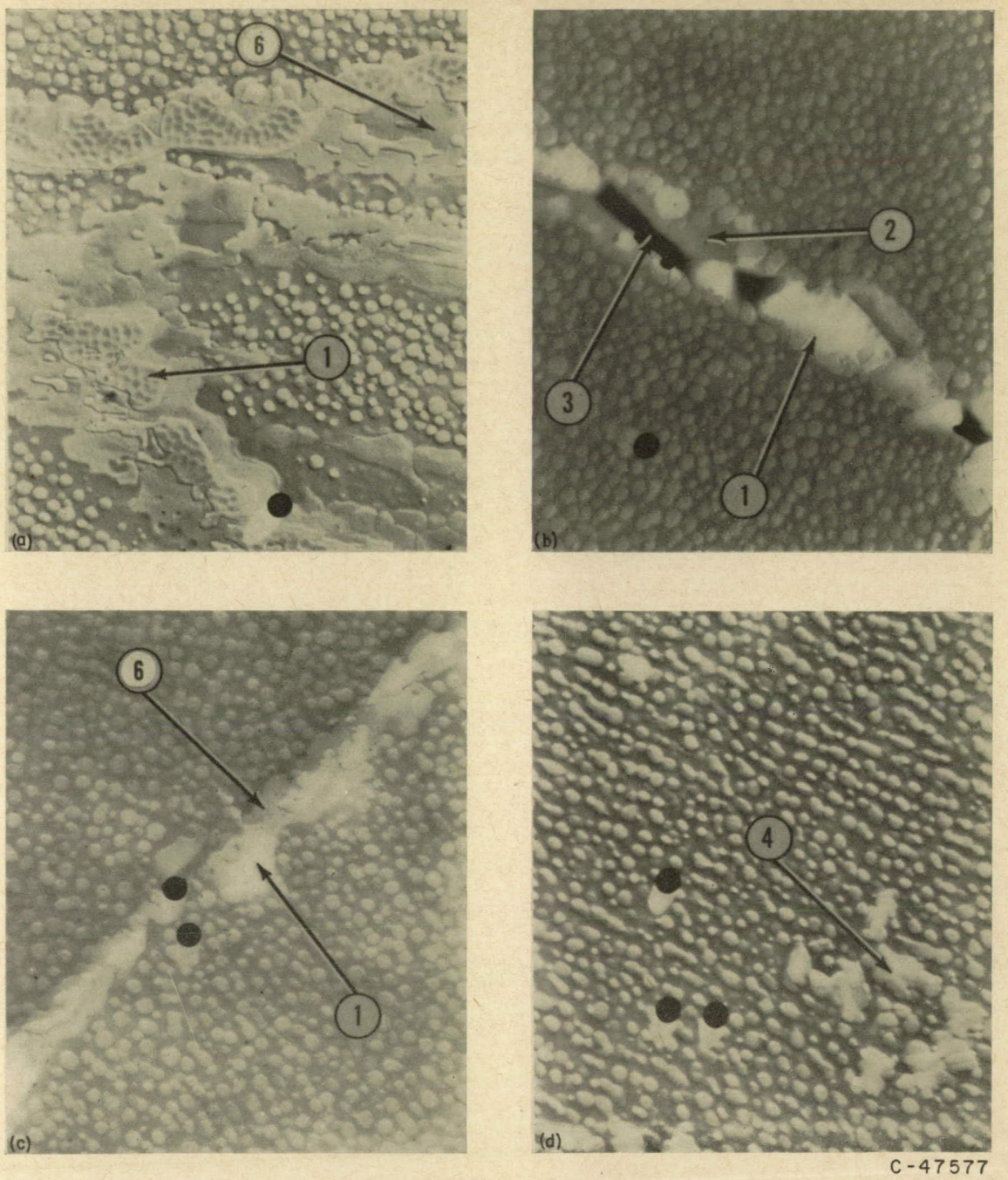
(a) Heat V–15; X1,000.
(b) Heat V–6; X1,000.
(c) Heat V–12; X1,000.
(d) Heat V–14; X1,000.

FIGURE 16.—Microstructures of specimens after 1.2-percent deformation by creep at 1,600° F in 165 to 214 hours. Optical micrographs; X100 and X1,000. 1, intergranular $M_{23}C_6$; 2, depleted grain boundary; 3, microcrack; 4, intragranular carbide; 5, nodule.



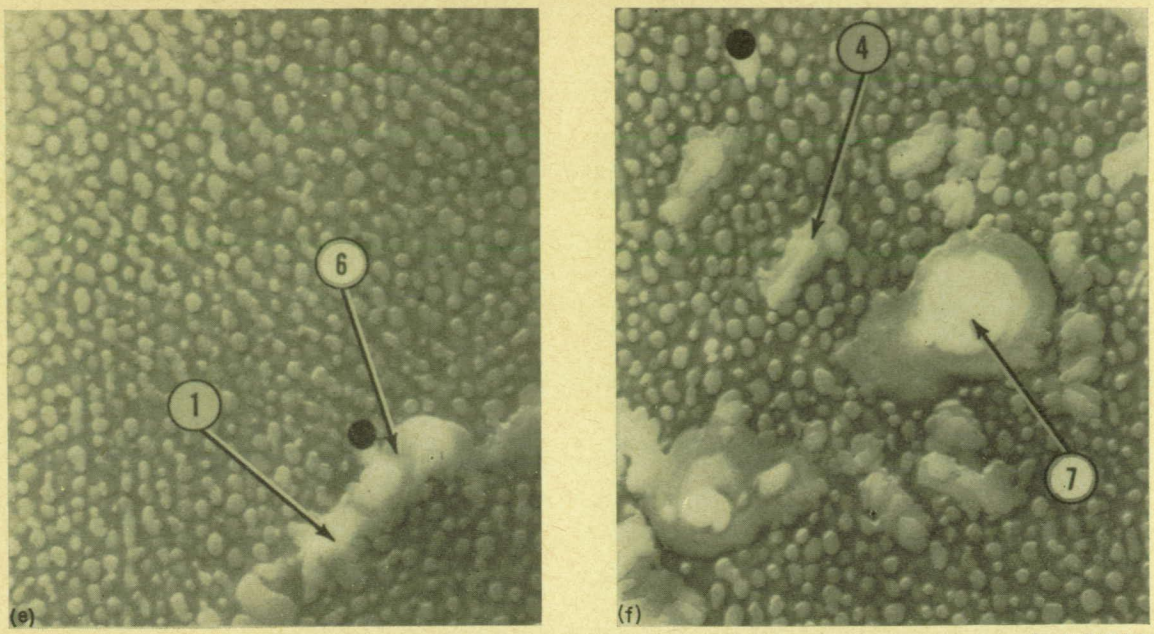
(e) Heat V–15; electropolished; X100.
(f) Heat V–6; electropolished; X100.
(g) Heat V–12; electropolished; X100.
(h) Heat V–14; electropolished; X100.

FIGURE 16.—Concluded.



(a) Heat V–15; typical grain boundaries.
(b) Heat V–6; depleted and cracked grain boundary at typical $M_{23}C_6$ precipitate.
(c) Heat V–12; typical grain boundary.
(d) Heat V–12; intragranular carbides and alinement of γ'.

FIGURE 17.—Microstructures of specimens after 1.2-percent deformation by creep at 1,600° F in 165 to 214 hours. Electron micrographs; X12,000. 1, intergranular $M_{23}C_6$; 2, depleted grain boundary; 3, microcrack; 4, intragranular carbide; 6, γ'; 7, Ti(C,N).



(e) Heat V–14; typical grain boundary and alinement of γ'.
(f) Heat V–14; intragranular carbides surrounding Ti(C,N).

FIGURE 17.—Concluded.

the heats with zirconium, boron, or boron plus zirconium. Presumably the increased strain to fracture was responsible.

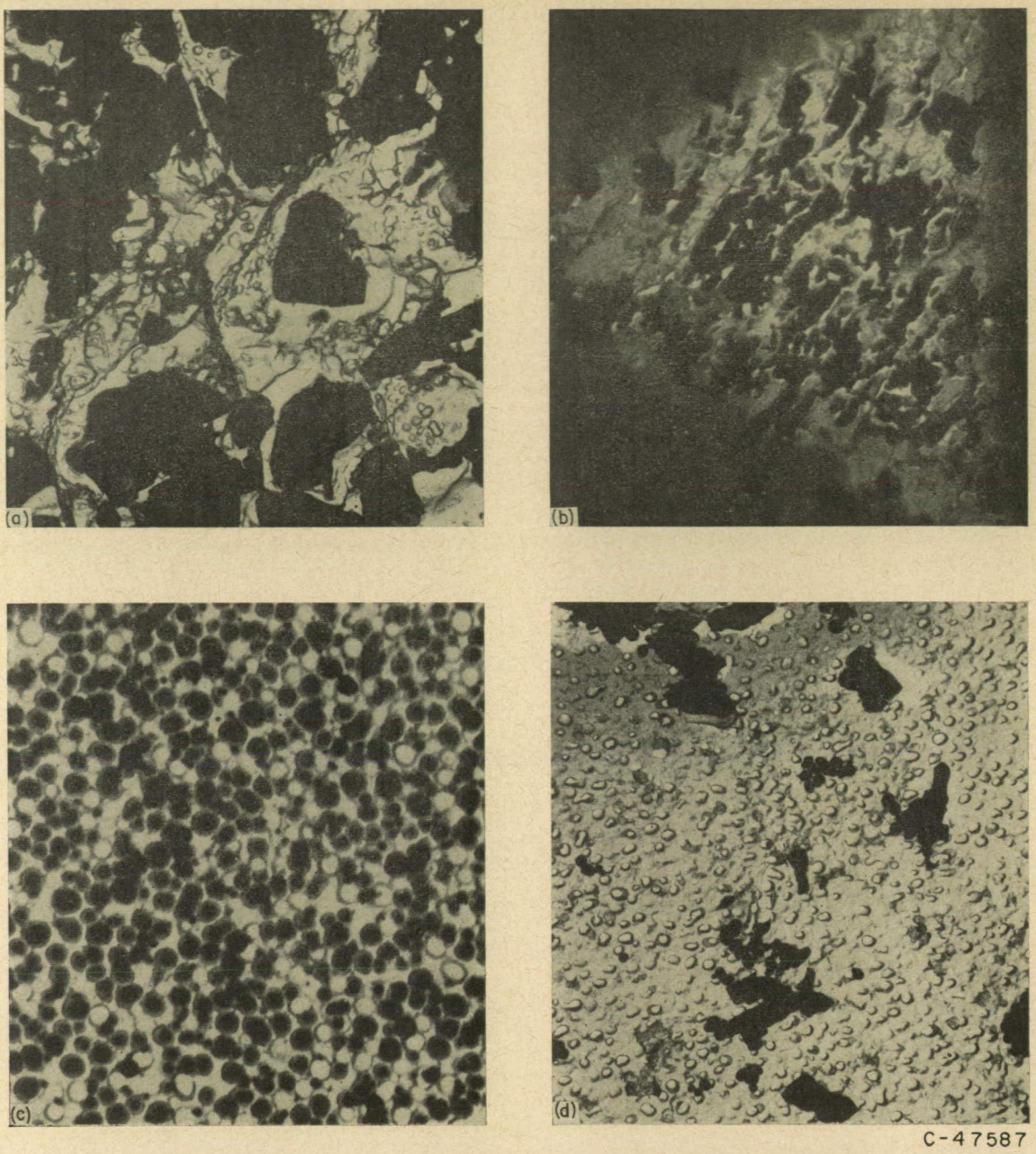
In samples ruptured at 1,600° F and 25,000 psi (fig. 22) the depletion was extensive. Often, layers of precipitate-free matrix as thick as 5 to 10 microns were found. In this case comparison of retardation was limited by the unequal exposure times and strains, although the effectiveness of zirconium, boron, and boron plus zirconium was very evident.

After 165 hours at 1,600° F at an equal stress of 20,000 psi, the retarding effect of boron and zirconium was even more evident. While 264 depleted boundaries were found in heat V–15, only 72 were found in the heat V–6 with zirconium, 16 in heat V–12 with boron, and none in heat V–14 with boron plus zirconium (table VI).

Microcracks.—Following agglomeration of $M_{23}C_6$ and depletion of γ' in the grain boundaries, microcracks appeared. These appeared as dark areas in mechanically polished samples (figs. 16(a) to 16(d)). Confirming evidence of cracks was found in electron microscopy where the replicas contained fins where the collodion had filled microcracks and then had been extracted during stripping of the replica from the metal surface. The fins appeared black in the electron micrographs (fig. 17) with white shadows from palladium.

The microcracks were associated with $M_{23}C_6$ particles in the grain boundaries transverse or nearly transverse to the applied stress, usually being at an $M_{23}C_6$ matrix interface or between tips of $M_{23}C_6$ particles, in both cases where depletion of γ' had occurred. Often, several separate microcracks were detected in one grain boundary with no preference being shown for triple points. These separate cracks seemed to link together with further creep exposure, constituting the mode of fracture in heat V–15 (no boron or zirconium).

Figure 23 relates microcracking to creep deformation for exposure to equal strain in equal time at 1,600° F. The number of cracks for a given creep strain or exposure time diminished with zirconium (heat V–6), boron (heat V–12), and boron plus zirconium content (heat V–14) in that order from the boron-and-zirconium-free material (heat V–15). Five microcracks were detected in heat V–15 at the end of first-stage creep when only 15 percent of the rupture life was expended. When boron plus zirconium was present (heat V–14), only 2 microcracks were found at 80 percent of the rupture life when tertiary creep had already commenced. The amount of microcracking at fracture also diminished in the heats in the following order: heat V–15, heat V–6, heat



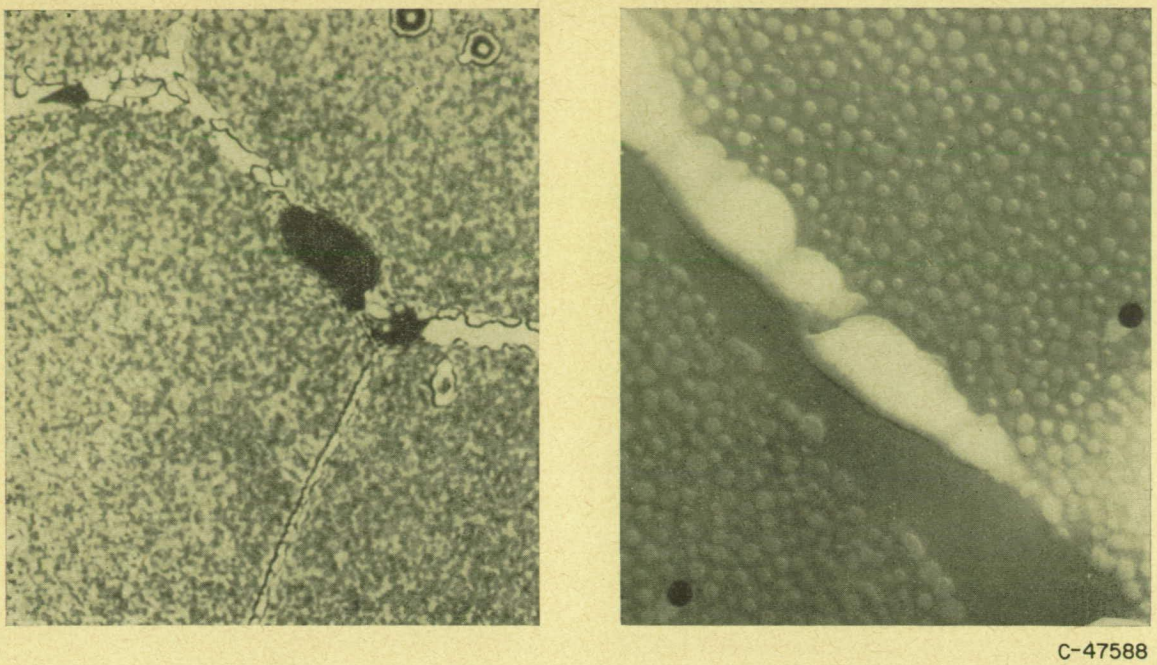
(a) Extraction replica of carbide from intergranular fracture surface of heat V–15 after 1.2-percent creep deformation in 165 hours at 1,600° F. All selected-area electron-diffraction spots indexed as $M_{23}C_6$. X8,000.

(b) Extraction replica of carbide from intergranular fracture surface of heat V–12 after 1.2-percent creep deformation in 188 hours at 1,600° F. All selected-area electron-diffraction spots indexed as $M_{23}C_6$. X8,000.

(c) Extraction replica of intragranular γ' from heat V–6 after aging 10 hours at 1,600° F. All selected-area electron-diffraction spots indexed as γ'. X36,000.

(d) Extraction replica of intragranular carbide from heat V–12 after 1.2-percent creep deformation in 188 hours at 1,600° F. Most selected-area electron-diffraction spots indexed as M_6C; a few, as $M_{23}C_6$. X8,000.

FIGURE 18.—Electron micrographs of phases produced by extraction replica technique. Extracted particles of phases appear black.



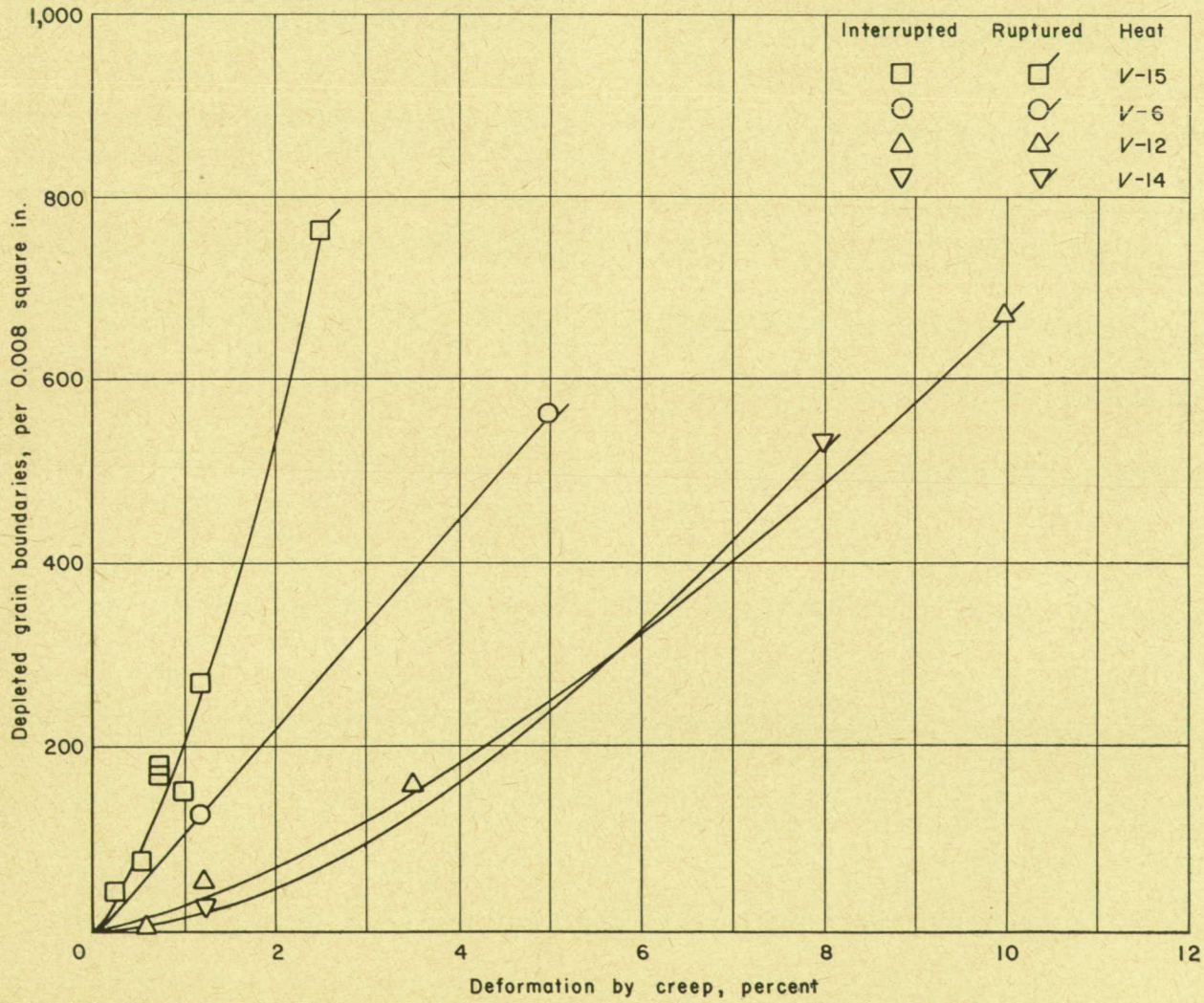
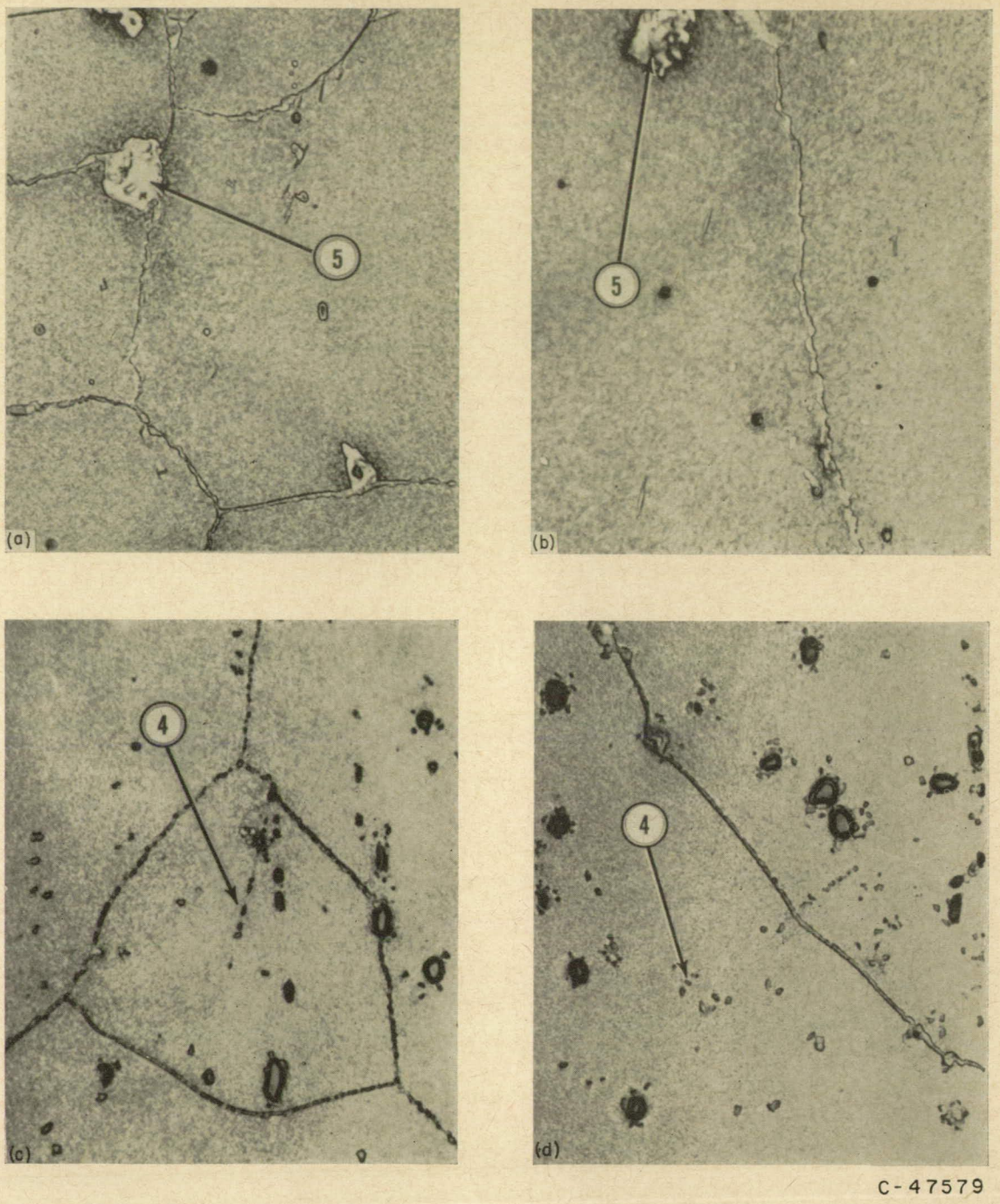
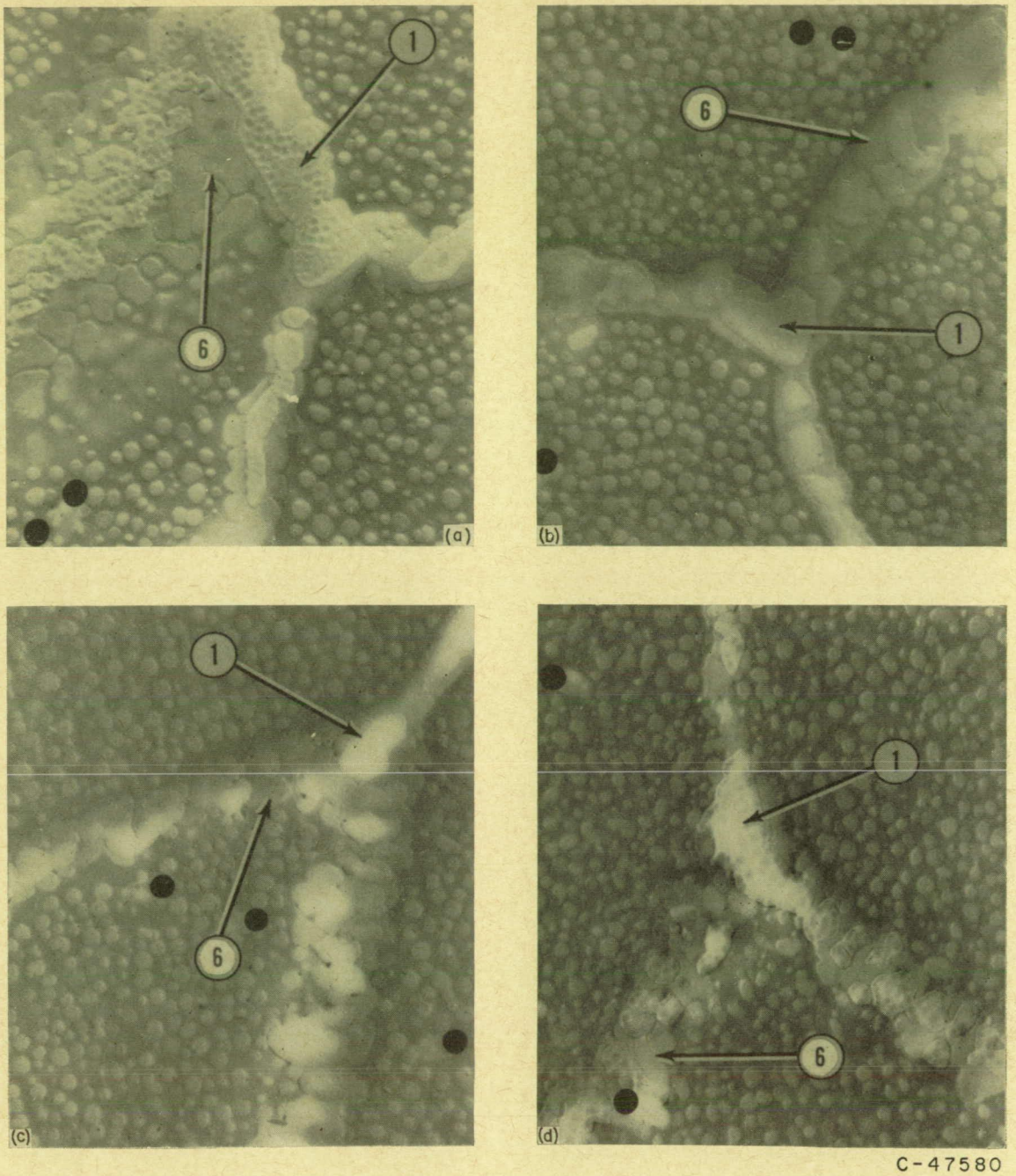


FIGURE 19.—Effect of creep deformation at 1,600° F on depletion of γ' adjacent to grain boundaries. Specimens were stressed to give comparable strain rates. Micrographs of typical depleted grain boundaries are shown for electropolished specimen.



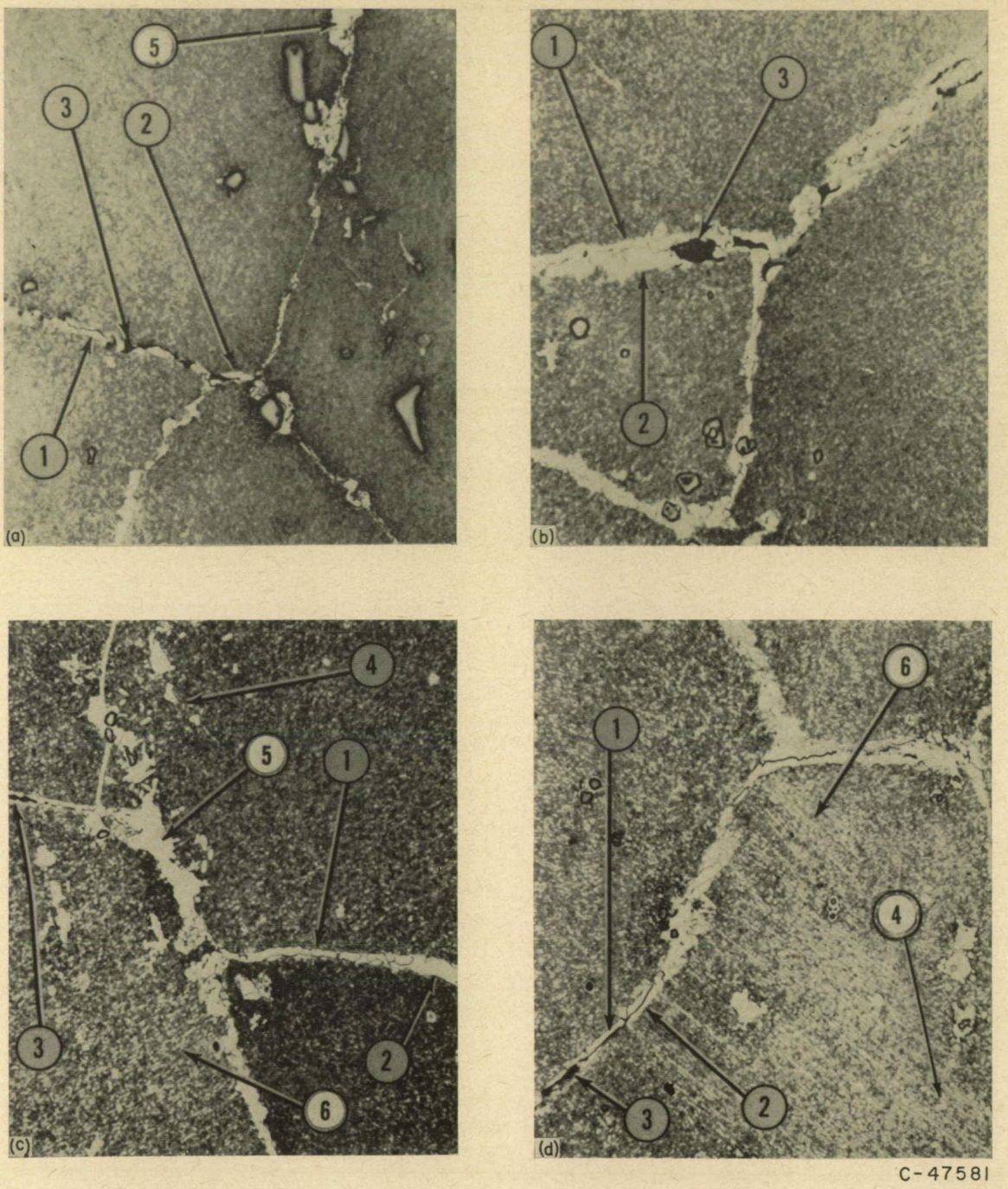
(a) Heat V–15. Diamond pyramid hardness, 338.
(b) Heat V–6. Diamond pyramid hardness, 342.
(c) Heat V–12. Diamond pyramid hardness, 340.
(d) Heat V–14. Diamond pyramid hardness, 353.

FIGURE 20.—Microstructures of specimens after aging without stress for 188 hours at 1,600° F. Optical micrographs; X1,000. 4, intragranular carbide; 5, nodule.



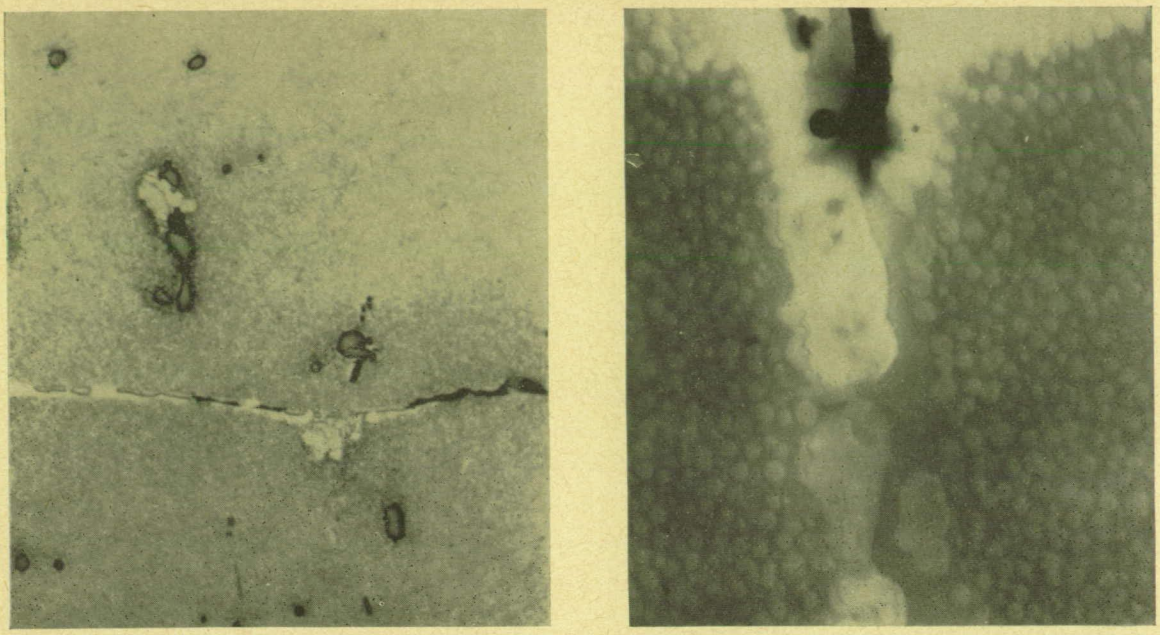
(a) Heat V–15.
(b) Heat V–6.
(c) Heat V–12.
(d) Heat V–14.

FIGURE 21.—Microstructures of specimens after aging without stress for 188 hours at 1,600° F. Electron micrographs; X12,000. 1, intergranular $M_{23}C_6$; 6, γ'.



(a) Heat V–15.
(b) Heat V–6.
(c) Heat V–12.
(d) Heat V–14.

FIGURE 22.—Microstructures of specimens after rupture at 1,600° F and 25,000 psi. Optical micrographs; X1,000. 1, intergranular $M_{23}C_6$; 2, depleted grain boundary; 3, microcrack; 4, intragranular carbide; 5, nodule; 6, alinement of γ'.



C-47589

X1,000
Light micrograph

X12,000
Electron micrograph

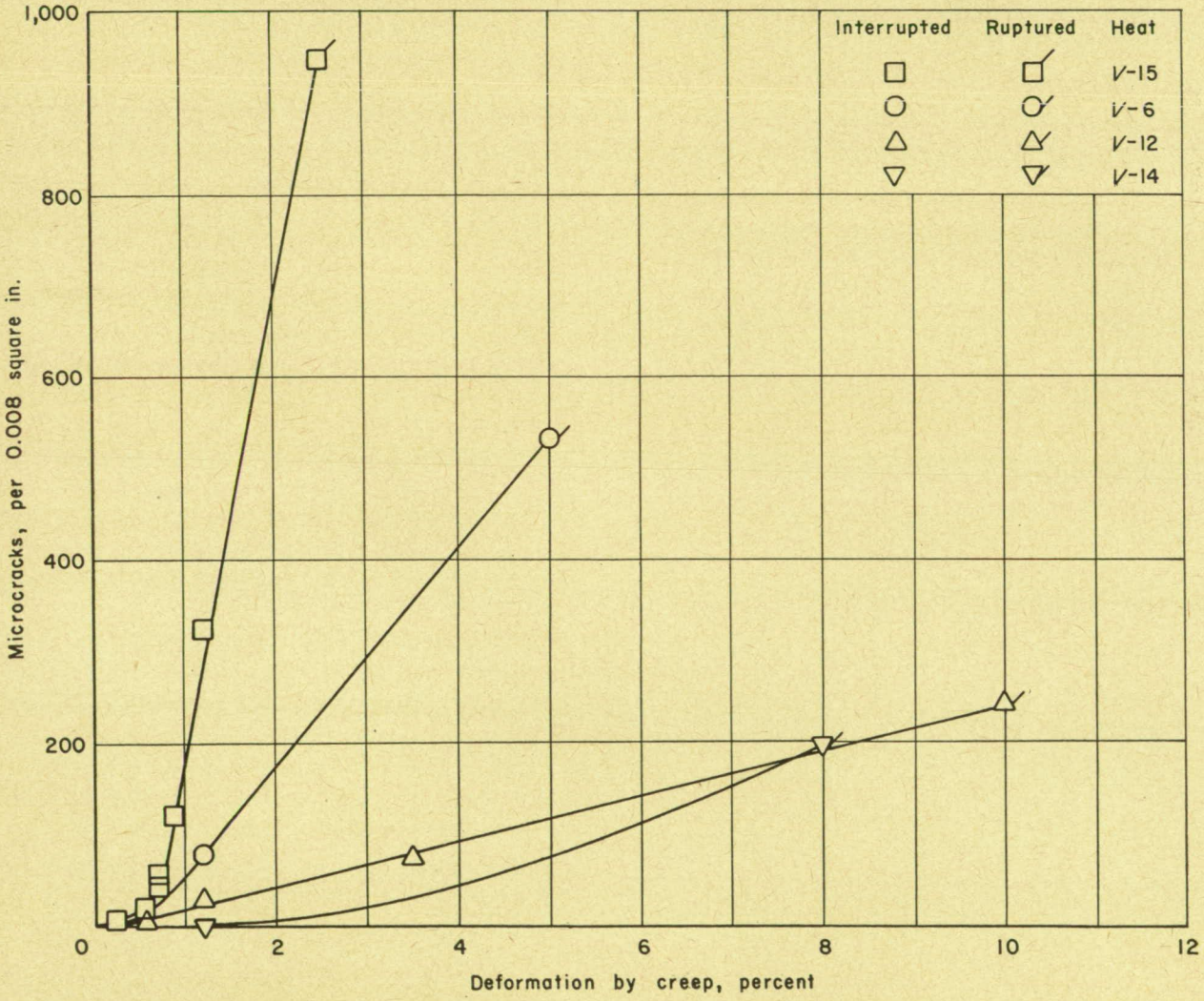
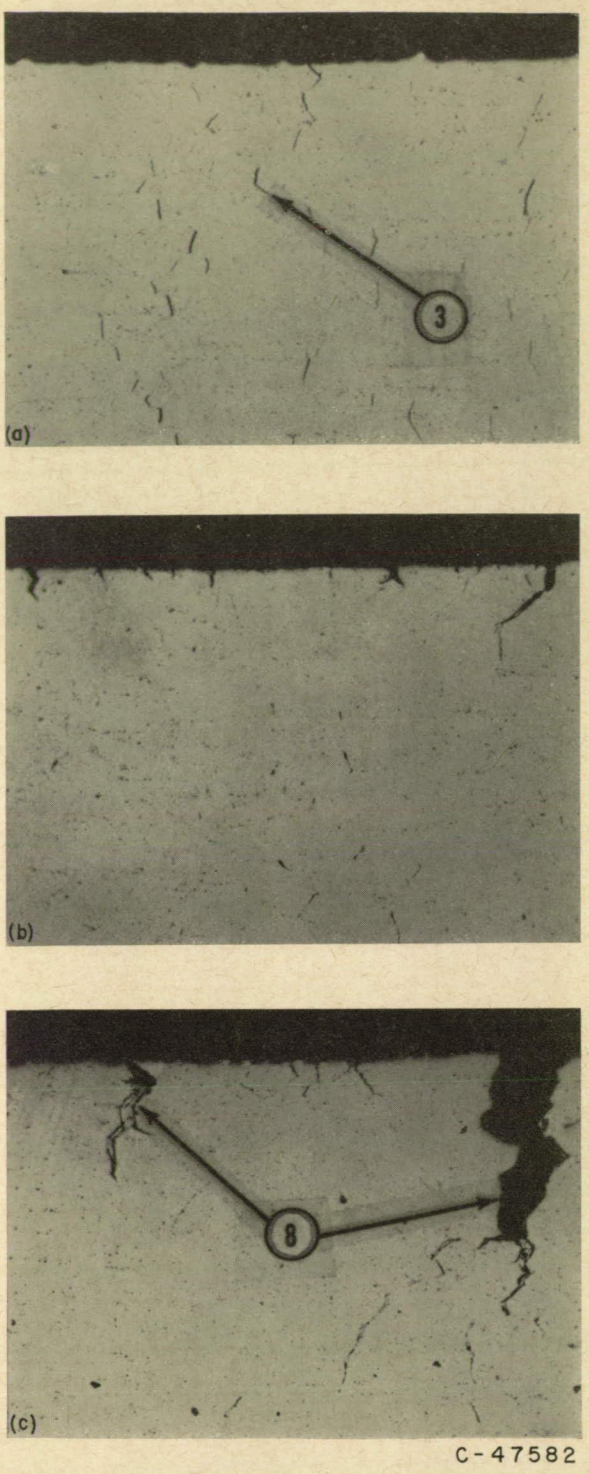


FIGURE 23.—Effect of creep deformation at 1,600° F on microcracking of specimens stressed to give comparable strain rates. Micrographs of of typical microcracks are shown. Tension axis was horizontal to electron micrograph.



(a) Heat V–15; ruptured in 52 hours at 1,600° F and 25,000 psi; 13 surface cracks and 376 microcracks.
(b) Heat V–12; ruptured in 296 hours at 1,600° F and 28,000 psi; 160 surface cracks and 243 microcracks.
(c) Heat V–14; ruptured in 266 hours at 1,600° F and 30,000 psi; 300 surface cracks and 198 microcracks.

FIGURE 24.—Change in mode of cracking. Surface cracks are number penetrating more than 0.003 inch per inch of specimen. Microcracks are number in 0.008 square inch. X32; 3, microcrack; 8, surface cracks.

V–12, and heat V–14. When the four heats were exposed 165 hours at 1,600° F and 20,000 psi, the difference in microcracking was even more pronounced. The counts showed 314 microcracks in the boron-and-zirconium-free heat V–15 while only 9 were present in the zirconium-bearing heat V–6 and none in the heats with boron or boron plus zirconium.

It was evident from the specimens tested at 1,600° F and 25,000 psi that, although the microcracking was retarded, it was not prevented by boron and zirconium (table VI).

Intergranular surface cracks.—In addition to microcracks within the specimens, the heats were subject to intergranular cracking from the specimen surface during creep-rupture tests. Initiation of these cracks was definitely from the specimen surface with a gradual increase in number and depth during creep exposure. Some of these cracks are illustrated in figure 24 which has quantitative data on amounts listed. This figure demonstrates that the specimen from the boron-and-zirconium-free heat V–15 tested at 1,600° F and 25,000 psi showed negligible surface cracking at the time of rupture, 52 hours. The mode of fracture by linking of the interior microcracks is also shown in this figure. However, in the boron-bearing heat V–12 tested at 1,600° F and 28,000 psi, the amount of microcracking was diminished but surface cracking had occurred. The importance of these surface cracks in fracture is indicated by the sample from the heat with boron plus zirconium (V–14) tested at 1,600° F and 30,000 psi, where some of the surface cracks penetrated more than ¼ of the specimen radius.

The quantitative data for surface cracks seem to indicate that the trace-element additions modified the mode of fracture. Surface cracking increasingly competed with microcracking as a source of fracture when the tendency for microcracking was reduced by zirconium and/or boron.

Intragranular precipitation of carbide.—In addition to a decreased tendency for the precipitation of intergranular $M_{23}C_6$-type carbides, boron caused carbides to precipitate intragranularly during exposure at 1,600° F (fig. 17).

The form of this phase was stress dependent. Short platelike carbides formed in samples aged without stress. In the samples aged under stress these were more elongated in form (cf. figs. 16 and 20) and had a tendency to precipitate on preferred matrix planes. As shown in figure 18 when these precipitates were extracted from the boron heat (V–12) after 1.2-percent creep strain in 188 hours at 1,600° F, the majority of spots in the electron-diffraction pattern indexed for M_6C with some spots corresponding to $M_{23}C_6$. Therefore, it seemed that some of the intragranular carbide phase, if not all, was M_6C rather than $M_{23}C_6$.

The intragranular carbide was distributed fairly uniformly throughout the grains in the heats with boron (V–12 and V–14) with some concentration near the Ti(C,N) particles.

There was some evidence that intragranular carbides diminished and carbides in the grain boundaries increased during long time exposure, which indicates that carbon was diffusing to the grain boundaries.

Intragranular γ'.—The intragranular precipitates of γ' grew and agglomerated during aging at 1,600° F. As measured by the surface density of γ' particles in electron micrographs there was no significant effect of boron, zirconium, or stress on this reaction (fig. 25). Therefore, the differences in surface density of γ' existing after the original heat treatment of air-cooling from 2,150° F were not lasting and appeared to be unimportant.

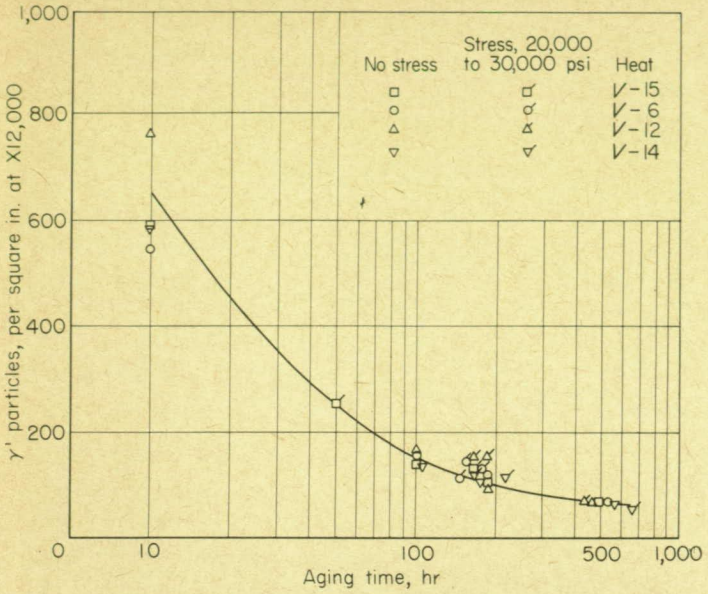


FIGURE 25.—Effect of aging time at 1,600° F with or without stress on γ' particle density.

As a further means of evaluating effects of trace elements on aging of γ' at 1,600° F, the change of hardness with aging time at 1,600° F was measured (fig. 26 and table VII). The hardness changes for the four experimental heats were very similar except that the heat with boron plus zirconium (V–14) aged to a higher hardness up to 500 hours. All heats reached maximum hardness at 1,600° F at about 1 hour and then overaged at longer times. Electron micrographs typical of the alloy showing γ' density are included in figure 26.

Although creep strain did not affect the density of γ' particles, it did modify the distribution of particles. Creep strains within the grains resulted in some preferential agglomeration of γ' on the slip planes, as evidenced by an alinement of γ'. This was especially noticeable after high creep strain (fig. 22).

Nodular precipitate.—All the heats exhibited nodules of a precipitate to some extent after aging at 1,600° F (fig. 27 and tables VI and VII). The nodules, which often were seen to envelop or abut on carbon-rich Ti(C,N) particles, appeared to be of mixed carbide and γ'. Their occurrence was definitely accelerated by strain, especially in the heat free from boron or zirconium (V–15). Likewise, they were trace-element controlled in that their formation was retarded by boron and zirconium.

Check of boron content after creep exposure.—A specimen from the heat with boron (V–12) was analyzed for boron content after rupture in 428 hours at 1,600° F and 25,000 psi. The cross section of the specimen showed 0.0090 percent boron. A surface layer of approximately 0.010-inch thickness contained 0.0079 percent boron. These analyses compared well with the analysis of 0.0089 percent boron obtained in the as-rolled bar stock.

Discussion.—The microstructural studies revealed the role of boron and zirconium in increasing creep-rupture life and ductility of the 55Ni-20Cr-15Co-4Mo-3Ti-3Al alloy.

In the absence of boron and zirconium, $M_{23}C_6$ and γ' particles rapidly formed a network in the grain boundaries of the alloy during creep at 1,600° F. This was followed by depletion of γ' precipitates in the metal adjacent to the transverse grain boundaries and early intergranular microcracking at the $M_{23}C_6$-depleted zone interfaces. The microcracks grew, linked, and initiated early fracture in a brittle manner. Boron and zirconium retarded this grain boundary process, thereby allowing longer creep exposure and higher creep deformation before the fracture mechanism operated.

Additional experimental support for the mechanism is obtained by relating creep-rupture life and ductility (fig. 28) at 1,600° F and 25,000 psi to the tendency of the experimental heats to undergo depletion of grain boundaries and microcracking during 1.2-percent creep deformation in 165 to 214 hours at 1,600° F.

It is evident from the data that the increase in creep-rupture life and ductility from the trace-element addition results from retardation, but not prevention, of the grain-boundary mechanism of carbide formation, grain-boundary depletion, and microcracking. The specimens from all the experimental heats were similar in these respects after rupture at 1,600° F and 25,000 psi. However, both the time and deformation at which the grain-boundary effects occurred and initiated fracture were increased by boron and zirconium.

The finding that boron and zirconium retards the microcracking process does not imply that their beneficial effects are only temporary in nickel-base alloys. All available data indicate that the heats containing boron and zirconium are superior to those free of boron and zirconium even at low stresses and long time exposure.

The chemical analyses on heat V–12 after rupture-testing indicated that loss of boron from the sample during testing did not occur except possibly at the surface. Deboronization does not appear to be the cause of the eventual appearance of the grain-boundary changes in boron-bearing materials.

Interpretation of other microstructural changes: Apparently the occurrence of intragranular carbide in the heats with boron was related to retardation of $M_{23}C_6$ agglomeration in the grain boundaries. In a sense, a redistribution of carbide was effected by boron. While zirconium addition suppressed the grain-boundary agglomeration, it did not cause formation of intragranular carbides.

The intragranular carbide in the boron heats may have had a direct effect on properties in addition to tying up carbon to retard $M_{23}C_6$ agglomeration in grain boundaries. The form of the precipitate after creep indicates that it is strain-induced and may lower creep rate in a manner proposed by Cottrell (ref. 23). According to Cottrell, resistance to creep is obtained by nucleation and growth of precipitates in dislocations, which prevent further movement of the dislocations through the lattice. The reaction would resemble strain-aging, although the resulting precipitate would be more advanced in growth than that usually associated with strain-aging.

The negative creep and slight serrated effect in the creep curves of the boron heats at 1,600° F and 20,000 psi appear to be additional evidence of strain-induced precipitation. These phenomena have been observed in unpublished work

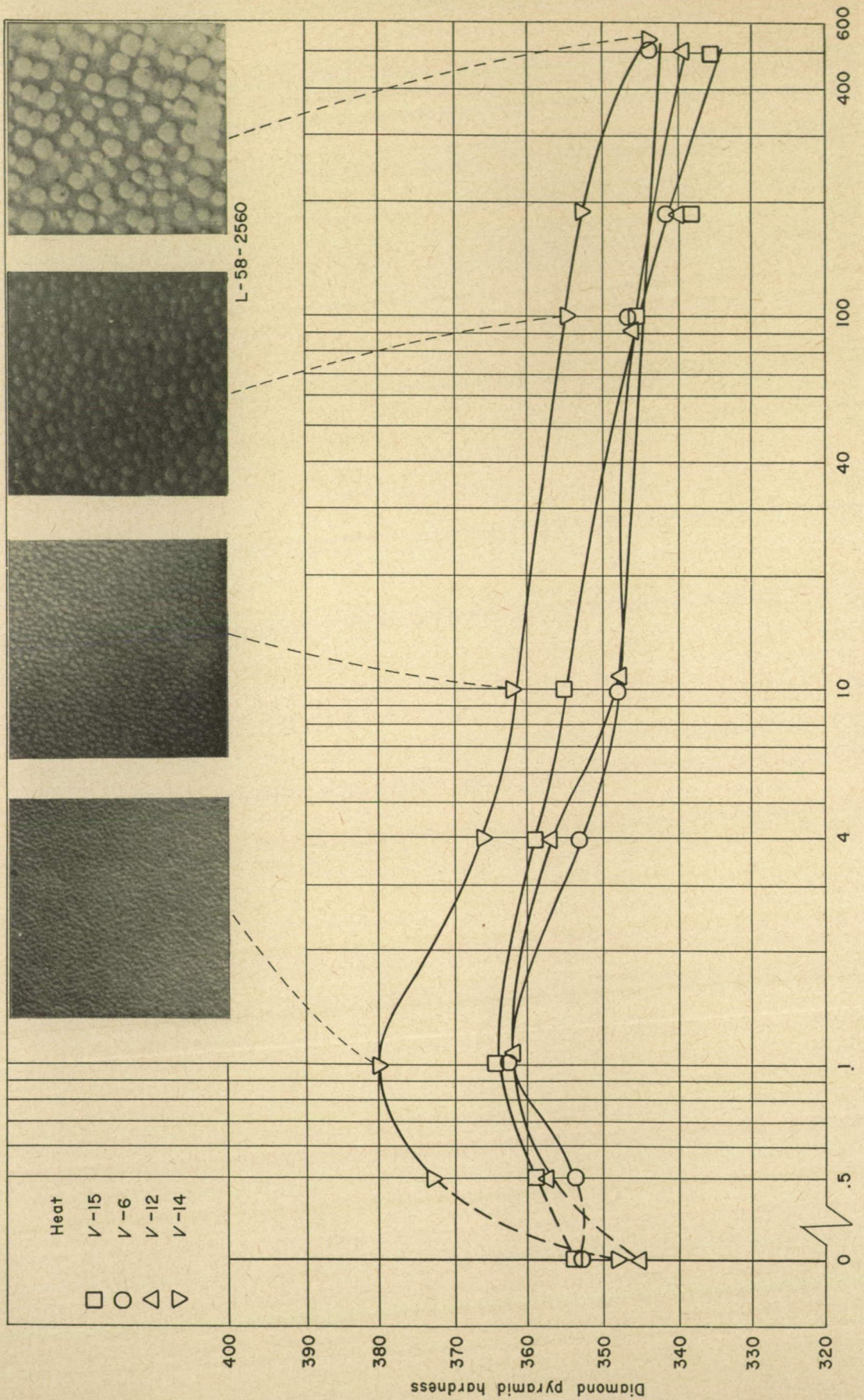
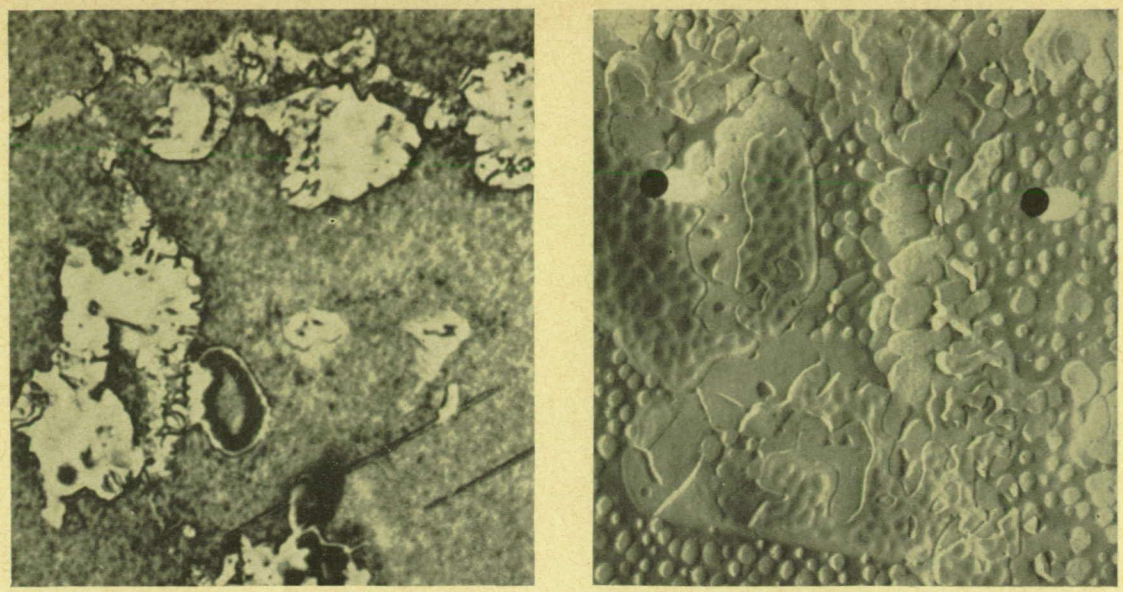


FIGURE 26.—Effect of aging at 1,600° F without stress on hardness and γ' dispersion. Typical electron micrographs at X12,000 show γ' dispersion.



C-47591

X2,000
Light micrograph

X12,000
Electron micrograph

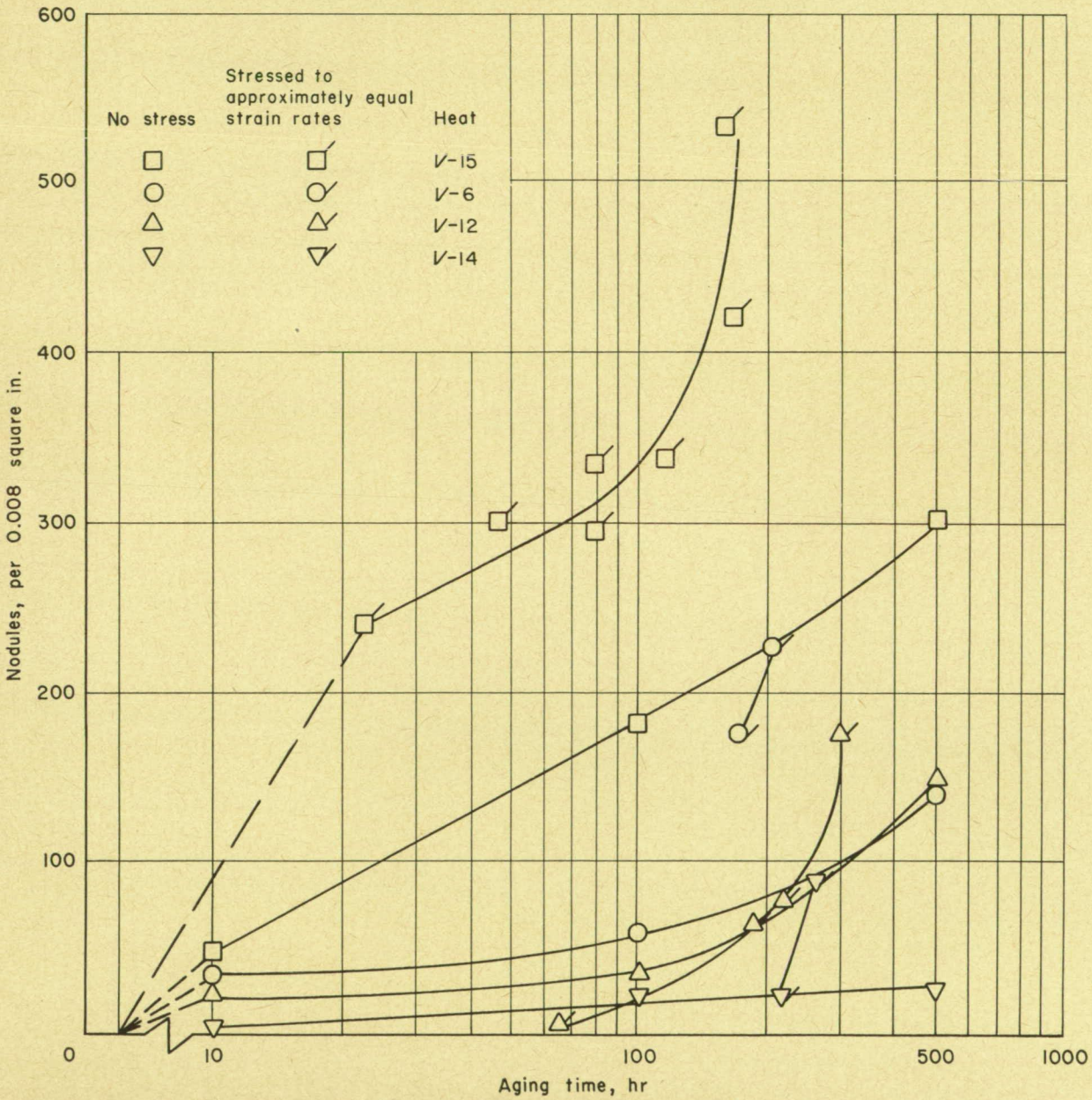
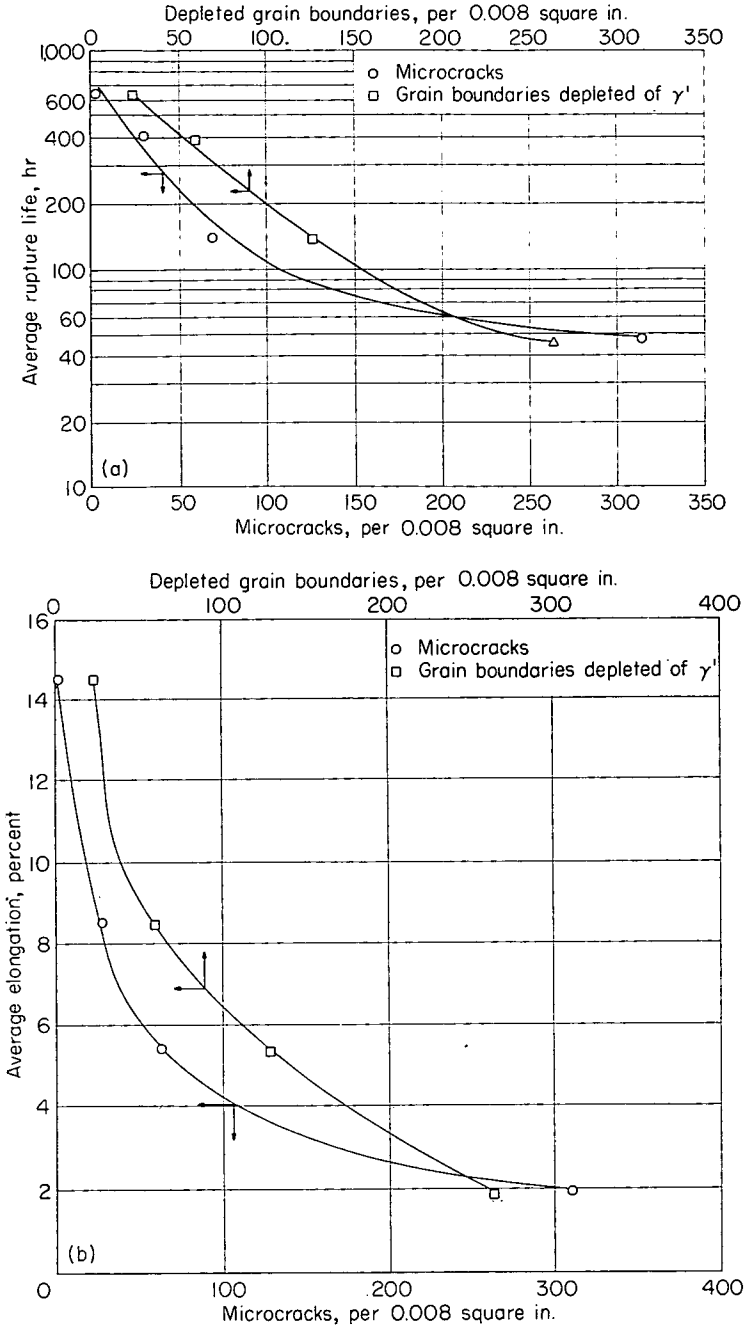


FIGURE 27.—Effect of aging time at 1,600° F on nodule density. Micrographs of typical nodules are shown.



(a) Rupture life.
(b) Elongation.

FIGURE 28.—Relation of rupture life and elongation at 1,600° F and 25,000 psi to microcracking and γ' depletion tendencies at grain boundaries measured after 1.2-percent deformation in 165 to 214 hours.

in this laboratory in other nickel-base alloys containing boron. The presence of strain-aging-type reactions in nickel-base alloys is not totally unexpected in that Waché (ref. 24) has detected serrated stress-strain curves for 80Ni–20Cr alloys at temperatures up to 1,292° F. Although the above evidence indicates that a strain-induced carbide precipitate might have lowered creep rate, the proof was not considered positive.

The depletion of γ' definitely required stress. No evidence of its occurrence was observed in any case of exposure to 1,600° F without stress. In addition, depletion was more prevalent in the transverse grain boundaries. The absence of γ' depletion when the alloy was aged at 1,600° F without stress indicates that the reaction was not due to simple depletion of elements forming γ' from the adjoining matrix by the grain-boundary precipitates. It seems probable that localized strain concentration at the grain boundaries during creep induced γ' agglomeration.

The information obtained on surface cracking was not sufficiently extensive for one to be sure of its role. The indications were that when boron or zirconium retarded microcracking to allow longer creep exposures or more highly stressed creep exposures, fracture was at least in part initiated by surface cracks.

It was initially thought that boron and zirconium might operate through some influence on the size, distribution, or stability of the intragranular γ' reaction. Since Baillie (ref. 14) succeeded in correlating creep-rupture properties with the surface density of γ' particles as measured in electron micrographs, surface density was used to detect possible effects of boron and zirconium on the γ' which would increase rupture life. No significant effect was found. In fact, these elements had so little effect on any aspect of γ' (other than in suppressing agglomeration and depletion of γ' at grain boundaries) that it seems certain that the boron-zirconium effect did not operate in this manner.

In the absence of any observable effect of boron or zirconium on the γ' precipitates the reason for the higher hardness of the heat with boron plus zirconium (V–14) is uncertain. It was noted that the hardness values were in the same order as the total titanium plus aluminum in the heats. The slightly higher titanium-plus-aluminum content may account for the higher hardness of heat V–14.

The distribution of the γ' after creep exposure was found to be a good indicator of the mode and location of creep deformation. Alinement of γ' seemed to indicate that creep deformation had been accommodated within the grains as coarse slip. This alinement had previously been shown by Bueckle and Poulignier (ref. 25) to indicate the mode of deformation in nickel-base alloys.

The role of the nodules of mixed carbide and γ' was not clear. No evidence was found to indicate that cracking was initiated by their presence. It is possible that the nodules contributed to the depletion of γ' from the matrix adjacent to the grain boundaries by acting as a final location for the γ'. This hypothesis is somewhat supported by the accelerating effect of stress on nodule formation at 1,600° F, particularly when γ' depletion occurred.

Relation of mechanism to published information: The accumulation of $M_{23}C_6$ carbide in grain boundaries has striking parallels to sensitization of stainless steels. Simpkinson (ref. 26) and Bungardt and Lennartz (ref. 27) have identified $Cr_{23}C_6$ as the grain-boundary phase leading to stress corrosion of 18–8 stainless steels. In addition, Plateau, Henry, and Crussard (ref. 20) found the size, shape, and distribution of $Cr_{23}C_6$ in 18–8 stainless steels to be similar to that of $M_{23}C_6$ found in this study.

The agglomeration at grain boundaries during creep of nickel-base alloys hardened with titanium and aluminum has been noted by Baillie and Poulignier (ref. 28) and Mathieu

(ref. 29). Mathieu hypothesized that the precipitate was γ' and chromium compounds. Although it was stated that this agglomeration was probably important in determining rupture life, further details on the mechanism were not given.

In accordance with the theories of Chang and Grant (ref. 30), depletion of precipitates in layers of matrix adjacent to grain boundaries would promote microcracking and fracture by concentrating deformation at these weak grain boundaries. It is possible that this mechanism operates in many high-temperature alloys to give brittle fractures when the creep resistance of the material remains high. Such an explanation was offered by Wever and Schrader (ref. 31) for brittle fracture of Cr-Ni-Mo steels in long-time service at 500° C. They found that localized precipitation of Mo_2C from the matrix adjacent to the grain boundaries left a condition of strong grains and depleted grain boundaries. Further confirmation is obtained from work on the effect of cellular precipitation (refs. 32 and 33) where this resulted in depleted regions in the grain boundaries and led to premature and brittle rupture by creep.

The location of microcracks at the $M_{23}C_6$ precipitate matrix interface was interesting in light of the work of Resnick and Seigle (ref. 34), who established that zinc oxide particles were heterogeneous nuclei for microcracks in α-brass. As shown by Machlin (ref. 35), particle-matrix bonding is important in nucleation of microcracks. In general, the presence of second-phase particles makes nucleation more probable, especially when bonding is poor. Considering these effects, it seems probable that the $M_{23}C_6$ particles acted as nuclei for microcracks, possibly because of poor bonding.

The mechanism of nucleation and growth of microcracks is not clear. Several authors (refs. 34, 35, 36, 37, and 38) have proposed condensation of vacancies formed during creep by dislocation movements; others (refs. 30, 39, and 40) emphasized local stress concentrations as the cause. Grain-boundary sliding is usually considered to set up the local stress concentrations at the transverse boundaries to cause loss of cohesion. Chang and Grant (ref. 30) hypothesize that the rate of growth of microcracks in grain boundaries depends upon the stress pattern at the boundaries. Propagation of microcracking is caused primarily by the normal stress at the grain boundary and the inability of the material to relieve this stress. The overall rate of growth depends upon the ability of the grains to accommodate the normal stresses by deformation within the grain. From this it can be inferred that microcracking increases as the severity of localization of deformation at grain boundaries increases. Therefore, change of the mode of deformation from intragranular slip to grain-boundary creep can be expected to increase grain-boundary microcracking by redistribution of stresses. In fact, in α-brass the occurrence of microcracking is coincident with the change from coarse slip to grain-boundary sliding (ref. 36). The evidence of increased intragranular slip and decreased microcracking in the heats with boron and zirconium is in full agreement with the above theories. It appears feasible that the elements have changed the mode of deformation by maintaining the grain-boundary strength.

The discrepancies in the literature on the time of microcrack nucleation are not surprising, considering the effect of trace elements in this study. While several instances have been found of microcracking early in second-stage creep (refs. 37, 41, and 42), other cases exist where none was found until tertiary creep (refs. 36, 43, and 44). In the present study, the case exists where, on one alloy, nucleation of microcracks was delayed from late in first-stage creep to third-stage creep by trace elements.

Regarding the effect of microcracks on properties, the Russian theorists (refs. 38, 42, and 45) attribute tertiary creep and rupture to a gradual destruction of the metal by microcracking. This implies that microcracking raises creep rate and lowers life and ductility. In addition, the normal break in the stress-rupture curve of commercial alloys associated with a change from transgranular to intergranular fracture is an important consideration. This change in fracture mechanism, which is essentially an increase in intergranular microcracking, results in lower life and ductility than predicted from higher stress data where microcracking was less predominant.

Causes of effect of boron and zirconium on grain-boundary stability: The experimental evidence established that trace amounts of boron and zirconium retard agglomeration at grain boundaries and thereby retard the microcracking mechanism. Several causes of this retardation of agglomeration might be proposed.

A possibility would be that the trace elements promote stabilization of carbon indirectly by promoting the nucleation and growth of one carbide at the expense of another. This might result from solid solution of boron or zirconium in the complex carbides of the M_6C or $M_{23}C_6$ type. Indeed the detection of intragranular carbides, apparently of the M_6C type, when boron was present is compatible with this hypothesis. However, lack of promotion of additional carbides by zirconium additions does not support this hypothesis.

An alternative reason might be found in equilibrium segregation. Cahn (ref. 46) has reviewed the relationships of grain boundaries to impurity distribution. When elements of odd atomic size exist in alloys, they are subject to inhomogeneous distribution. Because they do not fit well in the crystal lattice where high regularity exists, the odd-sized atoms segregate to regions of lower regularity where larger vacancies exist. Grain boundaries are a prime region of concentration because of their inherent irregularity. Experimental confirmation for this was obtained by Thomas and Chalmers (ref. 47) who found that polonium segregates to grain boundaries in lead-bismuth alloys.

The segregating tendencies of two competing odd-sized elements can be related to their degree of misfit in that the most odd-sized atoms will seek the grain boundary most rapidly. Thus, small amounts of one very odd-sized element can be utilized to heal the grain boundary, thereby retarding the segregation of a less odd-sized element by decreasing the available flaws in the grain boundary. The possibility exists that boron and zirconium are retarding carbon segregation by this mechanism.

Study of the atomic diameters of carbon, boron, and zirconium might reveal the feasibility of this. Speiser, Spretnak, and Taylor (ref. 48) have shown that the effective diameter of carbon γ-Fe is 1.36 angstrom units, while they postulate that boron has an effective diameter equivalent to or greater than 1.85 to 1.90 angstrom units. Goldschmidt's

metallic diameter (for coordination number of 12) for zirconium is 3.20 angstrom units. The available lattice spaces in the 55Ni–20Cr–15Co–4Mo–3Ti–3Al alloy can be calculated from the lattice parameter of 3.58 angstrom units established in unpublished work at this laboratory. The vacant interstitial space in solid solution is 1.05 angstrom units in diameter. Using the data on atomic diameters, the carbon atom is 30 percent larger, boron is 78 percent larger, and zirconium is 200 percent larger than the available space. In the case of substitutional solution, the boron atom is approximately 26 percent smaller, and zirconium 26 percent larger than the substitutional space with a 2.53-angstrom-unit diameter. Therefore, it appears that carbon fits moderately well interstitially but that boron and zirconium fit poorly both as interstitials and in substitution. Then it seems feasible that boron and zirconium are segregating preferentially to grain boundaries, healing them and retarding carbon segregation.

Other aspects of the data lend support to the theory of equilibrium segregation. Decreased tendency for γ' agglomeration at the grain boundaries in the boron and zirconium heats could result from the boron and zirconium healing the grain boundaries. The promotion of intragranular carbide by boron might be the indirect result of this. The decreased segregation would leave a higher carbon content within the grains, making precipitation of intragranular carbides more probable.

Additional support for the theory of equilibrium segregation is in the literature. Brown (ref. 49) proposed that boron additions beneficiated iron-base alloys by this mechanism. Strauss (ref. 2) emphasized that marked beneficiation of properties by trace-element additions usually occurs with elements with characteristics which would lead to segregation to grain boundaries.

Role of carbon: The apparent harmful effect of $M_{23}C_6$ in the grain boundaries of the alloy and the possible helpful effect of the intragranular carbide promoted by boron make the role of carbon in nickel-base alloys of great interest.

One might conclude from the results that a relatively carbon-free alloy would be free of the grain-boundary carbide agglomeration and, therefore, have properties equivalent to the heat with boron plus zirconium (V–14). This, however, is not the case. It has been shown in unpublished work at this laboratory that both rupture life and ductility increase as carbon is increased from less than 0.01 to 0.04 percent in the boron- and zirconium-free alloy. Therefore, it seems that carbon can also have a beneficial role in the alloy. The reason for this effect is not at all clear at this time but it could be one of several mechanisms including improved degassing, solid-solution strengthening, or prevention of other embrittling grain-boundary reactions.

Generality of results: The beneficial effects of boron and zirconium in nickel-base titanium-plus-aluminum refractory alloys is common knowledge. Therefore, it follows that properties of such alloys in the absence of these elements will generally be inferior to their properties when the proper amounts are present. The particular alloy used to study the boron-zirconium mechanism is certainly not unusual in this respect. The results presented do in fact increase the confidence which can be placed in the alloy studied through clarification of the mechanism involved.

It is confidently expected that the basic mechanism established for the influence of trace amounts of boron and zirconium will be generally applicable. However, there will be variants in individual alloys and within a specific alloy depending on prior history, heat treatment, and testing conditions. With this in mind, the limitations of the present results should be clearly recognized. Only one alloy with one heat treatment was studied. The test conditions were limited to 1,600° F on material made in a small vacuum furnace and hot-worked under idealized laboratory conditions.

In the type of alloy considered it is expected that boron and zirconium will generally be found to suppress the formation of noncoherent phases in grain boundaries and the weakening of the adjacent matrix material through depletion of γ'. Both the details of the mechanism and the effectiveness can be expected to vary depending on the major alloying elements in specific alloys and the variations of other elements in trace amounts. Because such factors as grain size, carbide composition and distribution, and cold-work are prior-history sensitive, the effectiveness of the boron and zirconium can be expected to vary with the basic microstructure of the alloy. It should be recognized that the boron and zirconium must be present in an effective form. For instance, they must be added under conditions in which their effectiveness is not nullified by reaction with oxygen or nitrogen.

The mechanism of creep can be expected to vary with test temperatures and stress. Conditions which favor creep within the grains (temperatures on the low side of the creep range and high stresses) apparently would reduce the effectiveness of boron and zirconium under the mechanism observed. Variations in the conditions of formation of γ' or in the amounts through variation in titanium and aluminum would also be involved. It is becoming evident through the research efforts of others that the type of carbide formed can be temperature and time dependent. Again this would alter the effectiveness of the boron-zirconium reaction.

It was shown by figure 10 that there can be sharp optimums in the properties depending on the amounts of boron plus zirconium. This aspect of the mechanism has not yet been established although it is expected that it will arise from some modification of the observed mechanism. It was also shown that boron and zirconium up to limiting amounts were very effective in reducing cracking during hot-working. This demonstrates that they are effective at temperatures much higher than 1,600° F. It is not certain if the same mechanism as that observed at 1,600° F is involved.

Boron, at least, is effective in raising creep-rupture properties of alloys other than the nickel-base alloys containing titanium plus aluminum. The results of this investigation suggest that it may operate in these cases through modification of carbide reactions. The further possibility also exists that boron, by itself or through modification of carbon-nitrogen reactions, introduces strain-aging-type reactions.

CONCLUSIONS

The following conclusions can be drawn from the present investigation of the effects of trace elements in a complex heat-resistant alloy:

1. The type of ceramic crucible used was an important variable in induction vacuum melting of a 55Ni-20Cr-15Co-4Mo-3Ti-3Al heat-resistant alloy. Properties at high temperature and hot-workability were found to be markedly improved when 10 to 20 parts per million of boron were introduced into the heats as a result of reaction between the melt and magnesia crucibles due to the usual contamination of magnesia with boron compounds. Zirconium derived from reaction with zirconia also improved properties but to a lesser extent than boron. Heats melted in alumina had poor properties and hot-workability because neither boron nor zirconium were introduced into the heats.

2. The finding that trace amounts of boron or zirconium derived from reaction between the melt and crucible refractories were so influential on properties appears to explain many of the variabilities encountered in producing alloys by induction vacuum melting. The experience in the laboratory indicates that the amounts introduced by reaction with refractories can vary from practically none to amounts improving properties to a substantial degree. The conditions of melting which control the pickup of boron and zirconium are not understood.

3. Apparently trace amounts of boron or zirconium are necessary for usable properties and hot-workability. Boron and/or zirconium have had to be present in the alloy studied to attain the properties considered characteristic of the alloy. When good properties were obtained without knowingly adding these elements, they were introduced unknowingly by crucible reaction or in the charge. Therefore, good metallurgical practice appears to require that the optimum amounts be specifically added.

4. Deliberate simultaneous additions of boron and zirconium indicate that there are interaction effects leading to optimum amounts for best properties and hot-workability. Better properties were obtained by simultaneous additions of certain amounts of the two elements than by adding either singly. Excessive amounts led to poor hot-workability and reduced properties.

5. The improvement in creep-rupture properties was found to be due to the ability of zirconium, boron, and optimum amounts of boron plus zirconium, in that order of effectiveness, to retard structural deterioration at the grain boundaries. In the absence of boron or zirconium, creep at 1,600° F caused agglomeration of $M_{23}C_6$ type carbides at the grain boundaries normal to the applied stress. The adjacent matrix became depleted of the γ' precipitate which provides the basic strength of the alloy. Microcracks formed at the interface of the $M_{23}C_6$ particles and the matrix weakened by the depletion of γ' grew and linked together to cause early brittle fracture.

6. Zirconium retarded this process. Boron was more effective and the optimum amount of boron plus zirconium was most effective. The rupture life was improved through decreased rate and increased duration of secondary creep, as well as by a marked increase in the amout of tertiary creep before fracture. The appearance of microcracks was shifted from late in primary creep for material without boron or zirconium until well into tertiary-stage creep for material with optimum boron plus zirconium. Boron appeared to be most effective because it shifted the initial carbide precipitation from the grain boundaries to within the grains in the form of M_6C rather than $M_{23}C_6$ compounds.

UNIVERSITY OF MICHIGAN,
ANN ARBOR, MICH., *August 5, 1958.*

REFERENCES

1. Koffler, R. W., Pennington, W. J., and Richmond, F. M.: The Effect of Small Amounts of Boron and Zirconium on the High Temperature Properties of Vacuum-Melted Super Alloys. Rep. 48, Res. and Dev. Dept., Universal-Cyclops Steel Corp., June 11, 1956.
2. Strauss, J.: Micrometallurgy—The Metallurgy of Minute Additions. Proc. ASTM, vol. 53, 1953, pp. 577–595.
3. Mudge, W. A.: The Melting of Nickel. Nonferrous Melting Practice. Inst. Met. Div. Symposium Ser., AIME (New York), 1946, pp. 74–78.
4. Martin, L. H., and Bieber, L. O.: Methods of Evaluating Hot Malleability of Nickel and High-Nickel Alloys. Vol. II, Nonferrous Rolling Practice. Inst. Met. Div. Symposium Ser., AIME (New York), 1948, pp. 15–31.
5. Bieber, C.: The Melting and Hot Rolling of Nickel and Nickel Alloys. Metals Handbook, ASM (Cleveland), 1948, pp. 1028–1029.
6. Darmara, F. N.: Quality Control Achieved by Vacuum Melting and Effects on High Temperature Properties. Paper presented at Regional High-Temperature Materials Conf., Cleveland Sec. of AIME, Apr. 17, 1957.
7. Jones, W. E.: Vacuum Induction Melting-Process Considerations. Metal Prog., vol. 72, no. 4, Oct. 1957, pp. 133–138, 220–222.
8. Nordheim, R., and Grant, N. J.: Aging Characteristics of Nickel-Chromium Alloys Hardened with Titanium and Aluminum. Jour. Metals, vol. 6, no. 2, sec. 2 (Trans.), Feb. 1954, pp. 211–218.
9. Taylor, A.: Constitution of Nickel-Rich Quaternary Alloys of the Ni-Cr-Ti-Al System. Jour. Metals, vol. 9, no. 1, sec. 2 (Trans.), Jan. 1957, pp. 71–75.
10. Betteridge, W., and Franklin, A. W.: Les Progrès des alliages à base de nickel-chrome en service à haute température. Rev. mètallurgie, t. 53, pt. 4, Apr. 1956, pp. 271–284.
11. Frey, D. N., Freeman, J. W., and White, A. E.: Fundamental Aging Effects Influencing High-Temperature Properties of Solution-Treated Inconel X. NACA TN 2385, 1951.
12. Brockway, L. O., and Bigelow, W. C.: The Investigation of the Minor Phases of Heat-Resistant Alloys by Electron Diffraction and Electron Microscopy, WADC TR 54–589, Contract AF–33(616)–23, WADC and Univ. of Mich., May 1955.
13. Betteridge, W., and Smith, R. A.: Effect of Heat Treatment and Structure Upon Creep Properties of Nimonic Alloys Between 750° and 950° C. Symposium on Metallic Materials for Service at Temperatures Above 1,600° F. Special Tech. Pub. No. 174, ASTM, 1956, p. 29.
14. Baillie, Y.: Quelques résultats de l'étude au microscope électronique des alliages Ni-Cr-Al-Ti employés dans les turbines aeronautiques. Revue Univ. des Mines, t. 12, no. 10, ser. 9, Oct. 1956, pp. 507–512.
15. Beattie, H. J., and VerSnyder, F. L.: The Influence of Molybdenum on the Phase Relationships of a High Temperature Alloy. Trans. ASM, vol. 49, 1957, pp. 883–895.
16. Wilde, Robert F., and Grant, Nicholas J.: Aging in Complex Commercial Ni-Cr Alloys Hardened with Titanium and Aluminum. Jour. Metals, vol. 9, no. 7, sec. 2 (Trans.), July 1957, pp. 865–872.

17. Betteridge, W., and Franklin, A. W.: The Effect of Heat-Treatment and Structure on the Creep and Stress-Rupture Properties of Nimonic 80A. Jour. Inst. Metals, vol. 85, pt. II, 1957, pp. 473–479.
18. Bigelow, W. C., Amy, J. A., and Brockway, L. O.: Electron Microscopic Identification of the γ' Phase of Nickel-Base Alloys. Proc. ASTM, vol. 56, 1956, pp. 945–953.
19. Fisher, R. M.: Electron Microstructure of Steels by Extraction Replica Technique. Symposium on Techniques for Electron Metallography. Special Tech. Pub. No. 155, ASTM, 1953, pp. 49–63.
20. Plateau, J., Henry, G., and Crussard, C.: Quelques nouvelles applications de la microfractographie. Rev. mètallurgie, t. 54, pt. 3, Mar. 1957, pp. 200–216.
21. Bradley, D. E.: Evaporated Carbon Films for Use in Electron Microscopy. Brit. Jour. Appl. Phys., vol. 5, Feb. 1954, pp. 65–66.
22. Fullam, Ernest F.: Replica Washing Methods. Symposium on Techniques for Electron Metallography. Special Tech. Pub. No. 155, ASTM, 1953, pp. 101–108.
23. Cottrell, A. H.: Creep and Ageing Effects in Solid Solutions. Symposium on Creep and Fracture of Metals at High Temperatures (May 31–June 2, 1954), Nat. Phys. Lab. (London), 1956, pp. 141–152.
24. Waché, Xavier: Allongement discontinu des austénites soumises à l'essai de traction ordinaire à hautes températures. Comp. rend., Acad. Sci. (Paris), t. 240, May 1955, pp. 1892–1896.
25. Bueckle, C., and Poulignier, J.: Étude métallographique de l'écrouissage dans les alliages du type nickel-chrome, 80/20 tenaces à chord. Rev. métallurgie, t. 53, pt. 3, Mar. 1956, pp. 179–188.
26. Simpkinson, T. V.: Metallography of Titanium-Stabilized 18–8 Stainless Steels. Trans. ASM, vol. 49, 1957, pp. 721–746.
27. Bungardt, Karl, and Lennartz, Gustav: Ausscheidungsvorgänge in einem mit Titan stabilisierten austenitischen Chrom-Nickel-Stahl und ihre Beziehung zur interkristallinen Korrosion. Archiv Eisenhuttenwesen, Jahrg. 27, Heft 2, Feb. 1956, pp. 127–133.
28. Baillie, Y., and Poulignier, J.: Etude de la précipitation submicroscopique dans les alliages refractaires nickel-chrome. Rev. métallurgie, t. 51, pt. 3, Mar. 1954, pp. 179–191.
29. Mathieu, M.: Contribution à la connaissance des alliages Ni-Cr 80/20 modifies resistant à chaud. La Recherche Aero., no. 51, May-June 1956, pp. 43–51.
30. Chang, H. C., and Grant, Nicholas J.: Mechanism of Intercrystalline Fracture. Jour. Metals, vol. 8, no. 5, sec. 2 (Trans.), May 1956, pp. 544–551.
31. Wever, Franz, and Schrader, Angelica: Elektronenmikroskopische Untersuchung der Gefügeveränderungen eines Chrom-Nickel-Molybdän-Stahles unter langzeitiger Zugbeanspruchung bei 500°. Archiv Eisenhuttenwesen, Jahrg. 26, Heft 8, Aug. 1955, pp. 475–481.
32. Roberts, C. S.: Interaction of Precipitation and Creep in MG–Al Alloys. Jour. Metals, vol. 8, no. 2, sec. 2 (Trans.), Feb. 1956, pp. 146–148.
33. Sully, A. H.: Discussion of Papers by C. H. M. Jenkins and W. Betteridge. Symposium on Creep and Fracture of Metals at High Temperatures (May 31–June 2, 1954), Nat. Phys. Lab. (London), 1956, p. 308.
34. Resnick, R., and Seigle, L.: Nucleation of Voids in Metals During Diffusion and Creep. Jour. Metals, vol. 9, no. 1, sec. 2 (Trans.), Jan. 1957, pp. 87–93.
35. Machlin, E. S.: Creep-Rupture by Vacancy Condensation. Jour. Metals, vol. 8, no. 2, sec. 2 (Trans.), Feb. 1956, pp. 106–111.
36. Greenwood, J. N., Miller, D. R., and Suiter, J. W.: Intergranular Cavitation in Stressed Metals. Acta Metallurgica, vol. 2, no. 2, Mar. 1954, pp. 250–258.
37. Crussard, C., and Friedel, J.: Theory of Accelerated Creep and Rupture. Symposium on Creep and Fracture of Metals at High Temperatures (May 31–June 2, 1954), Nat. Phys. Lab. (London), 1956, pp. 243–262.
38. Guy, A. G.: Russian Theory for Creep Fracture. Metal Prog., vol. 69, no. 3, Mar. 1956, pp. 158–160.
39. McLean, D.: A Note on the Metallography of Cracking During Creep. Jour. Inst. Metals, vol. 85, pt. II, July 1957, pp. 468–471.
40. Nield, B. J., and Quarrell, A. G.: Intercrystalline Cracking in Creep in Some Aluminum Alloys. Jour. Inst. Metals, vol. 85, pt. II, July 1957, pp. 480–485.
41. Nield, B. J.: Discussion of Papers by C. H. M. Jenkins and W. Betteridge. Symposium on Creep and Fracture of Metals at High Temperatures (May 31–June 2, 1954), Nat. Phys. Lab. (London), 1956, pp. 308–311.
42. Kishkin, S. T.: Mechanism of Weakening and Fracture of Crystalline Bodies as a Function of Time at High Temperature. Doklady Akad. Nauk SSSR, vol. 95, 1954, pp. 789–791.
43. McAdam, D. J., Jr., Giel, G. W., and Woodard, D. H.: Influence of Strain Rate and Temperature on the Mechanical Properties of Monel Metal and Copper. Proc. ASTM, vol. 46, 1946, pp. 902–950.
44. Kirkby, H. W.: Discussion of "Grain Boundary Participation in Creep Deformation and Fracture," by N. J. Grant. Symposium on Creep and Fracture of Metals at High Temperatures (May 31–June 2, 1954), Nat. Phys. Lab. (London), 1956, p. 331.
45. Dekhtiar, I. I., and Osipov, K. A.: Fracture of Metals at High Temperatures. Doklady Akad. Nauk SSSR, vol. 104, no. 2, 1955, pp. 229–232.
46. Cahn, R. W.: Grain Boundaries, Substructures and Impurities. ASM Seminar on Impurities and Imperfections, Thirty-sixth Nat. Metal Congress and Exposition (Chicago), Oct. 30–Nov. 5, 1955, pp. 41–83.
47. Thomas, W. R., and Chalmers, B.: The Segregation of Impurities to Grain Boundaries. Acta Metallurgica, vol. 3, no. 1, Jan. 1955, pp. 17–21.
48. Speiser, Rudolph, Spretnak, J. W., and Taylor, W. J.: Effective Diameter of Solute Atoms in Interstitial Solid Solution. Trans. ASM, vol. 46, 1954, pp. 1168–1175.
49. Brown, J. T., and Bulina, J.: W–545—A New High Temperature Turbine Disc Alloy. Paper presented at Regional High-Temperature Materials Conf., Cleveland Sec. of AIME, Apr. 16, 1957.

TABLE I

MELTING PRACTICE FOR EXPERIMENTAL HEATS

Heat	Crucible	Heat in crucible	Refining time, min	Refining temperature, °F	Deoxidant	Superheat temperature, °F	Pouring temperature, °F	Addition, percent
V-1	Zirconia	1	0	-----	C in charge	3,050	3,000	----------
V-2	Zirconia	2	0	-----	C in charge	3,050	3,000	----------
V-3	Zirconia	1	20	2,700	C in charge plus chunk C	3,000	3,000	----------
V-4	Zirconia	1	20	2,700	Chunk C	2,900	2,900	----------
[a] V-5	Zirconia	2	20	2,700	Chunk C	2,950	2,950	----------
V-6	Zirconia	3	20	2,700	Al	3,100	3,000	----------
V-7	Zirconia	4	20	2,700	Si	2,975	2,975	----------
V-8	Zirconia	1	20	2,700	Al	2,975	2,750	----------
V-9	Zirconia	2	20	2,700	Al	2,750	2,750	----------
V-10	Zirconia	3	20	2,900	Al	3,100	3,000	----------
V-11	Magnesia	1	0	-----	C in charge	3,000	3,000	----------
V-12	Magnesia	2	0	-----	C in charge	3,000	3,000	0.01B
V-13	Alumina	1	0	-----	C in charge	3,000	3,000	----------
V-14	Zirconia	1	0	-----	C in charge	3,000	3,000	.01B
V-15	Alumina	1	0	-----	C in charge	3,000	3,000	----------
V-16	Alumina	2	0	-----	C in charge	3,000	3,000	.15Zr
V-17	Alumina	3	0	-----	C in charge	3,000	3,000	.01B
V-18	Alumina	4	0	-----	C in charge	3,000	3,000	.01B, 0.10Zr
V-19	Alumina	5	0	-----	C in charge	3,000	3,000	.01B, 0.10Zr
V-20	Magnesia	1	0	-----	C in charge	3,000	3,000	----------
[b] V-21	Magnesia	2	0	-----	C in charge	3,000	3,000	----------
V-24	Alumina	6	0	-----	C in charge	3,000	3,000	.0025B

[a] Cast in tapered mold (other heats cast in straight mold).
[b] Melt-down time, 2 hr (other heats, 1 hr).

TABLE II

CRUCIBLE MATERIALS

Material	Brand name	Supplier	Chemical composition, weight percent								
			Al_2O_3	ZrO_2	MgO	SiO_2	CaO	Fe_2O_3	TiO_2	B_2O_3	Alkalies
Alumina	Taycor	The Charles Taylor's Sons Co.	87.6	----	0.04	11.4	0.03	0.21	0.07	Not detected	0.41
Zirconia	Stabilized zirconia	Titanium Alloy Mfg. Div., National Lead Co.	.02	93.8	.05	.5	4.9	.02	.63	Not detected	<.01
Magnesia	Magnorite	Norton Co	----	----	97.0	1.5 to 2.0	1.3 to 1.5	0.1 to 0.2	----	0.1 to 0.2	----

TABLE III

RESULTS OF CHEMICAL ANALYSIS OF HEATS

[Balance is nickel]

Heat	Crucible	Elements present, weight percent															
		Cr	Co	Mo	Ti	Al	Si	Mn	C	S	P	Zr	B	Ca	Mg	Fe	Cu
V-1	Zirconia	21.2	14.9	4.00	2.82	3.30	0.12	0.13	0.05	----	0.003	0.09	-----	-----	<0.01	<0.20	<0.10
V-2	Zirconia	21.7	14.6	4.00	3.17	3.45	.14	<.10	.04	----	.004	.08	-----	-----	<.01	<.20	<.10
V-3	Zirconia	20.7	14.8	4.00	3.22	3.35	.11	.16	.06	----	.005	.04	0.0004	-----	<.01	<.20	<.10
V-4	Zirconia	18.1	15.2	4.10	2.98	3.10	.10	.10	.05	----	.006	.06	.0005	-----	<.01	<.30	<.10
V-5	Zirconia	18.2	15.1	4.20	3.18	3.15	.10	.10	.09	----	.008	.09	-----	-----	<.01	<.30	<.10
V-6	Zirconia	18.8	15.1	4.15	3.14	3.14	.10	<.10	.08	0.008	.003	.19	.0004	-----	-----	<.30	-----
V-7	Zirconia	19.4	15.0	4.10	3.30	3.35	.14	.15	.08	----	.006	<.03	-----	-----	-----	<.30	-----
V-8	Zirconia	19.2	14.5	4.20	2.98	3.00	.22	.15	.20	-----	.007	<.03	-----	-----	<.01	-----	<.10
V-8	Zirconia	19.8	14.5	4.10	2.98	2.85	.23	.13	.19	----	.004	<.03	.0004	-----	<.01	-----	<.10
V-10	Zirconia	19.8	15.2	4.10	3.05	3.15	.12	.10	.13	----	.005	.06	-----	-----	<.01	<.30	<.10
V-11	Magnesia	20.0	16.2	4.20	3.25	3.58	.18	.10	.05	----	.004	<.01	.0017	-----	<.01	<.30	<.10
V-12	Magnesia	20.9	14.8	4.20	3.15	3.25	.20	<.10	.10	----	.004	<.01	.0089	-----	<.01	<.30	<.10
V-13	Alumina	20.4	14.8	4.20	3.25	3.37	.25	.12	.05	----	.007	<.01	.0003	<0.01	<.001	<.01	<.01
V-14	Zirconia	20.8	14.8	4.20	3.20	3.30	.19	.11	.09	----	.007	.01	.0088	-----	<.01	<.30	<.10
V-15	Alumina	19.7	15.0	3.90	3.08	3.35	.17	.13	.08	.007	.006	<.01	.0002	-----	<.01	<.30	<.10
V-16	Alumina	20.0	16.0	3.90	3.12	3.39	.17	.10	.06	----	.006	.13	.0009	-----	<.01	<.30	<.10
V-17	Alumina	19.4	16.5	3.75	3.02	3.26	.16	.12	.07	----	.008	<.01	.0074	-----	<.01	<.30	<.10
V-18	Alumina	19.8	15.7	3.70	3.10	3.26	.12	.13	.07	----	.006	.09	.0069	-----	<.01	<.30	<.10
V-19	Alumina	20.8	16.0	3.90	3.17	3.38	.13	.12	.08	----	.006	.04	.0090	-----	<.01	<.30	<.10
V-20	Magnesia	----	----	----	----	----	---	----	.12	----	.007	----	.0010	<.01	<.001	<.01	<.01
V-21	Magnesia	----	----	----	----	----	---	----	.15	----	.007	----	.0004	<.01	<.001	<.01	<.01
V-24	Alumina	19.8	15.9	4.05	2.92	3.06	.16	<.10	.13	----	----	<.01	.0012	<.10	<.01	<.30	-----

TABLE IV

STRESS RUPTURE DATA AT 1,600° F AND 25,000 PSI

[As-rolled bar stock was heat-treated 2 hours at 2,150° F and air-cooled unless otherwise noted; specimens were preheated 4 hours at test temperature before loading]

Heat	Crucible material	Rupture time, hr	Elongation, percent	Reduction of area, percent	Compositional variable, percent			
					C	Zr	B	Ti+Al
V–1	Zirconia	[a]82. 3	------	5	0. 05	0. 09	------	6. 12
		96. 6	5	6				
V–2	Zirconia	117. 7	8	3	. 04	. 08	------	6. 62
		143. 5	5	6				
V–3	Zirconia	90. 7	4	4	. 06	. 04	0. 0004	6. 57
		126. 0	5	4				
V–4	Zirconia	[a]99. 5	6	4	. 05	. 06	. 0005	6. 08
		106. 3	4	5				
V–5	Zirconia	[a]87. 1	6	6	. 09	. 09	------	6. 33
		91. 2	5	6				
V–6	Zirconia	147. 4	5	5	. 08	. 19	. 0004	6. 28
		133. 7	6	8				
V–7	Zirconia	75. 5	4	3	. 08	<. 03	------	6. 65
		103. 1	5	5				
V–8	Zirconia	81. 2	8	12	. 20	<. 03	------	5. 98
		66. 3	11	9				
V–9	Zirconia	50. 8	8	12	. 19	<. 03	. 0004	5. 78
		54. 6	6	8				
V–10	Zirconia	85. 5	9	9	. 13	. 06	------	6. 20
		86. 5	8	10				
		79. 9	6	6				
		102. 8	8	9				
V–11	Magnesia	185. 2	3	2	. 05	<. 01	. 0017	6. 83
		229. 9	5	5				
V–12	Magnesia	428. 8	10	11	. 10	<. 01	. 0089	6. 40
		393. 5	7	8				
V–13	Alumina	56. 9	2	2	. 05	<. 01	. 0003	6. 62
		47. 5	1	1				
V–14	Zirconia	666. 3	17	16	. 09	. 01	. 0088	6. 50
		626. 8	12	13				
V–15	Alumina	44. 6	2	1	. 08	<. 01	. 0002	6. 43
		52. 0	2	1				
V–16	Alumina	144. 0	4	4	. 06	. 13	. 0009	6. 51
		118. 9	4	4				
V–17	Alumina	400. 4	7	6	. 07	<. 01	. 0074	6. 28
		346. 0	7	5				
V–18	Alumina	243. 8	7	6	. 07	. 09	. 0069	6. 36
		304. 5	10	10				
V–19	Alumina	546. 6	11	12	. 08	. 04	. 0090	6. 55
V–20	Magnesia, first heat	225. 2	5	4	. 12	<. 01	. 0010	------
		206. 9	4	3				
V–21	Magnesia, second heat	103. 4	4	2	. 15	<. 01	. 0004	------
		106. 0	3	2				
V–24	Alumina	170. 0	5	3	------	<. 01	. 0012	5. 98

[a] Heat-treated 1 hr at 2,150° F, air-cooled.

TABLE V

CREEP-RUPTURE DATA AT 1,600° F

[Initial condition: 2 hr at 2,150° F, air-cooled, plus 4-hr preheat at 1,600° F before loading]

Heat	Stress, psi	Minimum second-stage creep rate, percent/hr	Rupture			Interruption	
			Time, hr	Elongation, percent	Reduction of area, percent	Time, hr	Total deformation, percent
V–15	25, 000	0. 0160	45	2	1	----------	----------
		. 0060	52	2	1	----------	----------
	20, 000	0. 0070	158	3	2	----------	----------
		. 0040	--------	--------	--------	165	1. 23
		. 0058	--------	--------	--------	117	1. 00
		. 0046	--------	--------	--------	85	. 76
		. 0052	--------	--------	--------	85	. 76
		. 0084	--------	--------	--------	47	. 55
		. 0058	--------	--------	--------	23	. 29
V–6	25, 000	0. 0036	147	5	5	--------	--------
		. 0095	134	6	8	--------	--------
	22, 500	0. 0032	208	5	4	--------	--------
		. 0036	--------	--------	--------	172	1. 25
	20, 000	0. 0027	--------	--------	--------	165	0. 63
V–12	28, 000	0. 0025	296	10	14	--------	--------
		. 0040	--------	--------	--------	214	3. 45
		----------	--------	--------	--------	188	1. 21
		. 0046	--------	--------	--------	68	. 56
	25, 000	0. 0018	429	10	11	--------	--------
		----------	394	7	8	--------	--------
	20, 000	Negative	--------	--------	--------	165	0. 15
V–14	30, 000	0. 0021	266	8	9	--------	--------
		----------	--------	--------	--------	214	1. 18
	25, 000	0. 0004	666	17	16	--------	--------
		. 0003	627	12	13	--------	--------
	20, 000	Negative	--------	--------	--------	165	0. 04

TABLE VI

MICROSTRUCTURAL FEATURES OF SPECIMENS AFTER AGING UNDER STRESS AT 1,600° F

Condition	Heat V-15				Heat V-6				Heat V-12				Heat V-14			
	Nodules (a)	γ' density (b)	Depleted grain boundaries (c)	Microcracks (d)	Nodules (a)	γ' density (b)	Depleted grain boundaries (c)	Microcracks (d)	Nodules (a)	γ' density (b)	Depleted grain boundaries (c)	Microcracks (d)	Nodules (a)	γ' density (b)	Depleted grain boundaries (c)	Microcracks (d)
Approximately equal-strain-rate study																
0.3 percent creep deformation	239	---	49	5	---	---	---	---	---	---	---	---	---	---	---	---
0.6 percent creep deformation	301	---	76	17	---	---	---	---	5	---	2	2	---	---	---	---
0.8 percent creep deformation	332	---	184	34	---	---	---	---	---	---	---	---	---	---	---	---
1.0 percent creep deformation	288	---	173	31	---	---	---	---	---	---	---	---	---	---	---	---
1.2 percent creep deformation	334	---	151	118	---	---	---	---	---	---	---	---	---	---	---	---
3.5 percent creep deformation	418	134	264	314	175	137	127	78	63	157	60	30	20	117	23	2
Ruptured	---	---	---	---	---	---	---	---	79	---	165	77	---	---	---	---
	532	---	764	958	228	---	568	532	176	---	676	243	86	---	538	198
Equal-stress study																
165 hr at 20,000 psi	418	134	264	314	129	151	72	9	25	158	16	None detected	0	125	None detected	None detected
Ruptured at 25,000 psi	225	256	192	374	254	109	916	145	145	67	442	166	86	51	661	402
	218	---	211	378	---	---	---	---	---	---	---	---	90	---	530	330

[a] Mixed carbide and γ' nodule with greater than 5-micron diam., number in 0.008 sq in.
[b] Number of γ' particles per sq in. at 12,000 diam.
[c] Grain boundaries where depletion was detected at 1,000 diam., number in 0.008 sq in.
[d] Microcracks detected at 1,000 diam., number in 0.008 sq in.

TABLE VII

MICROSTRUCTURAL FEATURES OF SPECIMENS AGED WITHOUT STRESS AT 1,600° F

Aging time, hr	Heat V-15			Heat V-6			Heat V-12			Heat V-14		
	DPH	Nodules (a)	γ' density (b)	DPH	Nodules (a)	γ' density (b)	DPH	Nodules (a)	γ' density (b)	DPH	Nodules (a)	γ' density (b)
0.5	359	---	---	354	---	---	357	---	---	373	---	---
1	364	---	---	362	---	---	362	---	---	380	---	---
4	359	---	---	353	---	---	357	---	---	366	---	---
10	355	45	588	348	32	544	348	16	768	362	0	584
100	345	180	134	346	57	147	346	33	168	355	19	137
188	338	---	107	342	---	116	340	---	101	353	---	103
500	335	300	65	344	139	67	339	149	68	344	25	64

[a] Nodules with greater than 5-micron diam., number in 0.008 sq in.
[b] Number of γ' particles per sq in. at 12,000 diam.

U.S. GOVERNMENT PRINTING OFFICE: 1960